# Systems & Control Transactions

## Volume 4

Proceedings of the 35th

**European Symposium on Computer Aided Process Engineering**

**ESCAPE 35**



PSE PRESS

**Jan F.M. Van Impe**
**Grégoire Léonard**
**Satyajeet S. Bhonsale**
**Monika E. Polańska**
**Filip Logist**

# Systems & Control Transactions

## Vol 4

Proceedings of the 35th European Symposium on Computer Aided Process Engineering

**ESCAPE 35**

July 6–9, 2025
Ghent, Belgium

PSE PRESS

PSEcommunity.org

PSE Press • Hamilton • Notre Dame

Systems & Control Transactions, Volume 4
PSE Press
Hamilton, Ontario, Canada

Individual articles copyright © 2025 by the authors and licensed to PSEcommunity.org and PSE Press.
Remaining text © 2025 by the PSE Press. All rights reserved.
Cover photo credit: Photo 119650316 © Scanrail | Dreamstime.com

This book and all individual articles are released under the Creative Commons CC-BY-SA 4.0 License
Credit must be given to creator and adaptations must be shared under the same terms.
See https://creativecommons.org/licenses/by-sa/4.0/ for license details.




**Living Archive for Process Systems Engineering (LAPSE) Archive ID**: LAPSE:2025.0150
**Digital Object Identifier (DOI):** 10.69997/sct.173479

**Library and Archives Canada Catalogue**
A catalogue record and copy of this book is available from Library and Archives Canada

**Archival Permissions**
This book as well as individual articles may be deposited in digital research archives, personal archives, or institutional archives.

Electronic Book
ISBN (Volume 4) 978-1-7779403-3-1
ISSN (Series): 2818-4734

10 9 8 7 6 5 4 3 2 1

The information presented in this book was provided by individual contributors in the form of new scientific research contributions, data, and findings that were believed to be reliable and provided in good faith. Some, but not all, content has undergone peer review as marked. Neither the PSE Press, PSEcommunity.org, KU Leuven, the EFCE CAPE Working Party, the CACHE Foundation, Inc., the editors, nor authors guarantee the accuracy or completeness of any information provided, nor shall they be responsible for errors, omissions, incomplete information, or damages arising from its use. The information within does not consist of engineering or professional services.

Typeset in Inter

*Suggested Citation for Individual Articles*
Student MC, Supervisor QR. Title of the article. *Systems & Control Transactions* **4**:*startpage-endpage* (2025). https://doi.org/10.69997/sct.restofarticledoi

*Suggested Citation for Entire Proceedings*
Van Impe JFM, Léonard G, Bhonsale SS, Polańska ME, and Logist F (eds). Proceedings of the 35th European Symposium on Computer Aided Process Engineering, Ghent, Belgium, July 6-9 (2025). ISBN: 978-1-7779403-3-1

*Scientific Editors*
Jan Van Impe (*KU Leuven*), Grégoire Léonard (*ULiège*), Satyajeet Sheetal Bhonsale (*KU Leuven*), Monika Polanska (*KU Leuven*), and Filip Logist (*BASF Antwerp, KU Leuven*)

*Production Editors*
Thomas A. Adams II (*NTNU*), Daniel R. Lewin (*Technion*)

# Table of Contents

## PREFACE

**Introduction** ..... **xxviii**
Jan Van Impe, Grégoire Léonard, Satyajeet Sheetal Bhonsale, Monika Polanska, and Filip Logist

**Peer Review Policy** ..... **xxix**

**International Scientific Committee** ..... **xxxi**

## PEER REVIEWED CONFERENCE PROCEEDINGS

### Section 1: Modelling and Simulation

**Computational Intelligence Applied to the Mathematical Modeling of the Esterification of Fatty Acids with Sugars** ..... **2**
Lorenzo G. Tonetti, Ruy de Sousa Jr.

**Numerical Analysis of the Hydrodynamics of Proximity Impellers using the SPH Method** ..... **8**
Maria Soledad Hernández-Rivera, Karen Guadalupe Medina-Elizarraraz, Jazmín Cortez-González, Rodolfo Murrieta-Dueñas, Carlos E. Alvarado-Rodríguez, José de Jesús Ramírez-Minguela, Juan Gabriel Segovia Hernández

**Surrogate Modeling of Twin-Screw Extruders Using a Recurrent Deep Embedding Network** ..... **14**
Po-Hsun Huang, David Shan-Hill Wong, Yen-Ming Chen, Chih-Yu Chen, Meng-Hsin Chen, Yuan Yao

**Dimple Shape Design to Enhance Heat Transfer in Plate Heat Exchangers** ..... **20**
Mitchell J. Stolycia, Lande Liu

**Data-Driven Modelling of Biogas Production Using Multi-Task Gaussian Processes** ..... **26**
Benaissa Dekhici, Michael Short

**Synthesis of Liquid Mixture Separation Networks Using Multi-Material Membranes** ..... **33**
Harshit Verma, Christos T. Maravelias

**Transferring Graph Neural Networks for Soft Sensor Modeling using Process Topologies** ..... **40**
M.F. Theisen, G.M.H. Meesters, A.M. Schweidtmann

**Techno – Economic Evaluation of Incineration, Gasification, and Pyrolysis of Refuse Derived Fuel** ..... **46**
Matej Koritár, Maroš Križan, Juma Haydary

**Dynamic Operability Analysis of modular heterogeneous electrolyzer plants using system co-simulation** ..... **53**
Michael Große, Isabell Viedt, Hannes Lange, Leon Urbas

**High-pressure Membrane Reactor for Ammonia Decomposition: Modeling, Simulation and Scale-up using a Python-Aspen Custom Modeler Interface.** ..... **60**
Leonardo A. C. Avilez, Antonio E. Bresciani, Claudio A. O. Nascimento, Rita M. B. Alves

**A 2D Axisymmetric Transient State CFD Modelling of a Fixed-bed Reactor for Ammonia Synthesis** ..... **67**
Leonardo Bravo, Camilo Rengifo, Martha Cobo, Manuel Figueredo

**Kernel-based estimation of wind farm power probability density considering wind speed and wake effects due to wind direction** ..... **73**
Samuel Martínez-Gutiérrez, Daniel Sarabia, Alejandro Merino

**Thermo-Hydraulic Performance of Pillow-Plate Heat Exchangers with Streamlined Secondary Structures: A Numerical Analysis** ..... **79**
Reza Afsahnoudeh, Julia Riese, Eugeny Y. Kenig

**Optimisation of Biomass-Energy-Water-Food Nexus under Uncertainty** ..... **86**
Md Shamsul Alam, I. David L. Bogle, Vivek Dua

**A Century of Data: Thermodynamics and Kinetics for Ammonia Synthesis on Various Commercial Iron-based Catalysts** ..... **92**
Hilbert Keestra, Yordi Slotboom, Kevin H.R. Rouwenhorst, Derk W.F. Brilman

**Reaction Pathway Optimization Using Reinforcement Learning in Steam Methane Reforming and Associated Parallel Reactions** ..... **98**
Martín Rodríguez-Fragoso, Octavio Elizalde-Solis, Edgar Ramírez-Jiménez

**Integration of Yield Gradient Information in Numerical Modeling of the Fluid Catalytic Cracking Process** ..... **104**
Wenle Xu, Baohua Chen, Tong Qiu

**Hybrid Modelling for Reaction Network Simulation in Syngas Methanol Production** ..... **111**
Harry Kay, Fernando Vega-Ramon, Dongda Zhang

**Data-Driven Chance-Constrained Mixed Integer Nonlinear Bi-level Optimisation Via Copulas: Application To Integrated Planning And Scheduling Problems** ..... **117**
Syu-Ning Johnn, Hasan Nikkhah, Meng-Lin Tsai, Styliani Avraamidou, Burcu Beykal, Vassilis M. Charitopoulos

**Diagnosing Faults in Wastewater Systems: A Data-Driven Approach to Handle Imbalanced Big Data** ..... **123**
M. Zadkarami, K.V. Gernaey, A.A. Safavi, P. Ramin

**Modelling of a Heat Recovery System (HRS) Integrated with Steam Turbine Combined Heat and Power (CHP) Unit in a Petrochemical Plant** ..... **129**
Daniel Sousa, Miguel Castro Oliveira, Maria Cristina Fernandes

**Integrating Thermodynamic Simulation and Surrogate Modeling to Find Optimal Drive Cycle Strategies for Hydrogen-Powered Trucks** ..... **135**
Laura Stops, Alexander Stary, Johannes Hamacher, Daniel Siebe, Thomas Funke, Sebastian Rehfeldt, Harald Klein

**Wind Turbines Power Coefficient Estimation Using Manufacturer's Information and Real Data** ..... **141**
Carlos Gutiérrez Ortega, Daniel Sarabia Ortiz, Alejandro Merino Gómez

**Leveraging Pilot-Scale Data for Real-Time Analysis of Ion Exchange Chromatography** ..... **147**
Søren Villumsen, Jesper Frandsen, Jakob Kjøbsted Huusom, Xiaodong Liang, Jens Abildskov

**Model Based Flowsheet Studies on Cement Clinker Production Processes** ..... **153**
George Melitos, Bart de Groot, Fabrizio Bezzo

**Techno-economic analysis of a novel small-scale blue H2 and N2 production system** ..... **159**
Adrian R. Irhamna, George M. Bollas

**A Comparative Evaluation of Complexity in Mechanistic and Surrogate Modeling Approaches for Digital Twins** ..... **166**
Shreyas Parbat, Isabell Viedt, Leon Urbas

**Co-gasification of Crude Glycerol and Plastic Waste using Air/Steam Mixtures: A Modelling Approach ..... 173**
Bahizire Martin Mukeru, Bilal Patel

**Automated Identification of Kinetic Models for Nucleophilic Aromatic Substitution Reaction via DoE-SINDy .... 179**
Wenyao Lyu, Federico Galvanin

**System analysis and optimization of replacing surplus refinery fuel gas by coprocessing with HTL bio-crude off-gas in oil refineries. ..... 186**
Erik Lopez-Basto, Eliana Lozano Sanchez, Samantha Eleanor Tanzer, Andrea Ramirez Ramirez

**Surrogate Model-Based Optimization of Pressure-Swing Distillation Sequences with Variable Feed Composition ..... 192**
Laszlo Hegely, Peter Lang

**Economic Evaluation of Solvay Processes for Sodium Bicarbonate Production with Brine and Carbon Tax considerations ..... 198**
Dina Ewis, Zeyad M. Ghazi, Sabla Y. Alnouri, Muftah H. El-Naas

**Application of K-means for Identification of Multiphase Flows Based on Computational Fluid Dynamics ..... 203**
Patrick S. Lima, Leonardo S. Souza, Leizer Schnitman, Idelfonso B. R. Nogueira

**A New Method to Assess Performance Loss due to Catalyst Deactivation in Fixed- and Fluidized-bed Reactors ..... 209**
M. Andrea Pappagallo, Tilman J. Schildhauer, Oliver Kröcher, Emanuele Moioli

**Enhancing hydrodynamics simulations in Distillation Columns Using Smoothed Particle Hydrodynamics (SPH) ..... 216**
Rodolfo Murrieta-Dueñas, Jazmín Cortez-González, Roberto Gutiérrez-Guerra, Juan Gabriel Segovia Hernández, Carlos E. Alvarado-Rodríguez

**Kinetic Modelling and Optimisation of Co2 Capture and Utilisation to Methane on Dual Function Material..... 222**
Meshkat Dolat, Andrew D. Wright, Mohammadamin Zarei, Melis S. Duyar, Michael Short

**Data-Driven Dynamic Process Modeling Using Temporal RNN Incorporating Output Variable Autocorrelation and Stacked Autoencoder..... 229**
Yujie Hu, Lingyu Zhu, Han Gong, Xi Chen

**Real-time carbon accounting and forecasting for reduced emissions in grid-connected processes..... 235**
Rafael Castro-Amoedo, Alessio Santecchia, Henrique A. Matos, François Maréchal

**Twin Roll Press Washer Blockage Prediction: A Pulp and Paper Plant Case Study ..... 241**
Bryan Li, Isaac Severinsen, Wei Yu, Timothy Walmsley, Brent Young

**A Novel Bayesian Framework for Inverse Problems in Precision Agriculture ..... 246**
Zeyuan Song, Zheyu Jiang

**Role of process integration and green technologies utilization for the decarbonization of the watchmaking sector. ..... 252**
Pullah Bhatnagar, Daniel Florez-Orrego, Vibhu Baibhav, Manuele Margni, Francois Marechal

**Liquid Organic Hydrogen Carriers: comparing alternatives through H2 equivalent analysis ..... 258**
Elvira Spatolisano, Federica Restelli, Laura A. Pellegrini

**Towards the Decarbonization of a Conventional Ammonia Plant by the Gradual Incorporation of Green Hydrogen..... 264**
João Fortunato, Pedro M. Castro, Diogo A. C. Narciso, Henrique A. Matos

**Simulation and Experimental Validation of Biomass Gasification in a Spouted Bed Reactor: Troubleshooting Using DWSIM ..... 271**
C. Moliner, V. Carozzo, M. Curti, E. Arato

**Identification of Suitable Operational Conditions and Dimensions for Supersonic Water Separation in Exhaust Gases from Offshore Turbines: A Case Study ..... 276**
Jonatas de O. S. Cavalcante, Marcelo da C. Amaral, Ewerton E. da S. Calixto, Fernando L. P. Pessoa

**On Optimal Hydrogen Pathway Selection Using the SECA Multi-Criteria Decision-Making Method ..... 282**
Caroline Kaitano, Thokozani Majozi

**Energy Integration of an Intensified Biorefinery Scheme from Waste Cooking Oil to Produce Sustainable Aviation Fuel ..... 288**
Ma. Teresa Carrasco-Suárez, Araceli Guadalupe Romero-Izquierdo

**A Computational Framework for Cyclic Steady-State Simulation of Dynamic Catalysis Systems: Application to Ammonia Synthesis..... 294**
Carolina Colombo Tedesco, John R. Kitchin, Carl D. Laird

**Comparative Analysis of Conventional and Novel Low-Temperature and Hybrid Technologies for Carbon Dioxide Removal from Natural Gas ..... 301**
Federica Restelli, Giorgia De Guido

**Development of a virtual CFD model for regulating temperature in a liquid tank ..... 307**
Jinxin Wang, Feng Xu, Yuka Sakai, Hisashi Takahashi, Ruizi Zhang, Hiroaki Kanayama, Daisuke Satou, Yasuki Kansha

**Accelerated Process Modelling for Light-Mediated Controlled Radical Polymerization ..... 313**
Rui Liu, Xi Chen, Antonios Armaou

**Plantwide Control of a Green Formic Acid Production Process..... 320**
Mohammad Mahdi Ghasemi Aliabadi, Alexandros Anagnostou, Francia Gallardo Gonzalez, Shivam Pandey, Farzad Mousazadeh, Anton Kiss

**Energy Water Nexus Resilience Analysis Using Integrated Resource Allocation Approach ..... 327**
Hesan Elfaki, Mohammad Lameh, Dhabia M. Al-Mohannadi

**Technoeconomic Analysis of a Novel Amine-Free Direct Air Capture System Integrated with HVAC ..... 333**
Yasser M. Abdullatif, Ikhlas Ghiat, Riham Surkatti, Yusuf Bicer, Tareq Al-Ansarl, Abdulkarem I. Amhamed

**Exploiting Operator Training Systems in chemical plants: learnings from industrial practice at BASF ..... 339**
Frederic Cuypers, Tom Boelen, Filip Logist

**Comparative Assessment of Aspen Plus Modeling Strategies for Biomass Steam Co-gasification..... 346**
Usman Khan Jadoon, Ismael Díaz, Manuel Rodríguez

**Enhancing the Technical and Economic Performance of Proton Exchange Membrane Fuel Cells Through Three Critical Advancements ..... 352**
Željko Penga, Jure Penga, Yuanjing Zhao, Lei Xing

**Cell culture process dynamics and metabolic flux distributions using hybrid models ..... 358**
Rajiv Kailasanathan, Abhishek Sivaram, Seyed Soheil Mansouri

**Development and Integration of a Co-Current Hollow Fiber Membrane Unit for Gas Separation in Process Simulators Using CAPE-OPEN Standards ..... 364**
Loretta Salano, Ilaria Dagna, Mattia Vallerio, Flavio Manenti

**A Comparative Study of Aspen Plus and Machine Learning Models for Syngas Prediction in Biomass-Plastic Waste Co-gasification** ..... **370**
Usman Khan Jadoon, Ismael Díaz, Manuel Rodríguez

**Multiscale Modeling of Internal Reforming in Solid Oxide Fuel Cells: A Study of Electrode Morphology and Gradient Microstructures** ..... **376**
Hamid Reza Abbasi, Masoud Babaei, Constantinos Theodoropoulos

**Process simulation and thermodynamic analysis of newly synthesized pre-combustion $CO_2$ capture system using novel Ionic liquids for $H_2$ production** ..... **382**
Sadah Mohammed, Fadwa Eljack

**Mechanistic and Data-Driven Models for Predicting Biogas Production in Anaerobic Digestion Processes** ..... **388**
Rohit Murali, Benaissa Dekhici, Tao Chen, Dongda Zhang, Michael Short

**Dynamic analysis for prediction of flow patterns in an oscillatory baffled reactor using machine learning** ..... **394**
Hideyuki Matsumoto, Yuma Kambayashi, Shiro Yoshikawa, Shinichi Ookawara

**Comparative Analysis of PharmHGT, GCN, and GAT Models for Predicting LogCMC in Surfactants.** ..... **399**
Gabriela C. Theis Marchan, Teslim Olayiwola, Jose Romagnoli

**Short-Cut Correlations for CO2 Capture Technologies in Small-Scale Applications** ..... **406**
So-mang Kim, Joanne Kalbusch, Grégoire Léonard

**Numerical Modelling of Carbon Dioxide Adsorption in Dual Function Materials: An CFD approach** ..... **412**
Andrés F. Soto-Cañón, Rodinson R. Arrieta-Peréz, Camilo Rengifo, Martha Cobo, Manuel Figueredo

**Design Considerations for Hardware Based Acceleration of Molecular Dynamics** ..... **418**
Joseph Middleton, Joan Cordiner

**An Automated $CO_2$ Capture Pilot Plant at ULiège: A Platform for the Validation of Process Models and Advanced Control** ..... **423**
Cristhian Molina-Fernández, Patrick Kreit, Brieuc Beguin, Sofiane Bekhti, Cédric Calberg, Joanne Kalbusch, Grégoire Léonard

**New Directions and Software Tools Within the Process Systems Engineering Ecosystem** ..... **430**
S. Burroughs, B. Lincoln, A. Adeel, I. Severinsen, A. Lee, O. Amusat, D. Gunter, B. Nicholson, M. Apperley, B. Young, J. Siirola, T. G. Walmsle

## Section 2: Sustainable Product Development and Process Design

**Steady-State Digital Twin Development for Heat and Shaft-Work Integration in a Dual-Stage Pressure Nitric Acid Plant Retrofit** ..... **438**
Stanislav Boldyryev, Goran Krajacic

**Simulation of Decarbonization of Natural Gas to Methanol Conversion Process Using Microwave-Assisted Dry Reforming with Integrated Chemical Looping for Hydrogen Production** ..... **444**
Omar Almaraz, Srinivas Palanki, Jianli Hu

**Modeling and Simulation of a Novel Process that Converts Low Density Polyethylene to Ethylene** ..... **450**
Xiaoyan Wang, Omar Almaraz, Jianli Hu, Srinivas Palanki

**A global sensitivity analysis for a bipolar membrane electrodialysis capturing carbon dioxide from the air** ..... **456**
Grazia Leonzio, Alexia Thill, Nilay Shah

**Intensified Alternative for Sustainable Gamma-Valerolactone Production from Levulinic Acid ..... 462**
Brenda Huerta-Rosas, Melanie Coronel-Muñoz, Juan José Quiroz-Ramírez, Carlos Rodrigo Caceres-Barrera, Gabriel Contreras-Zarazua, Juan Gabriel Segovia-Hernández, Eduardo Sánchez-Ramírez

**Environmental assessment of the catalytic arabinose oxidation ..... 468**
Mouad Hachhach, Dmitry Yu. Murzin, Tapio Salmi

**Green Industrial-Scale Plant Design for Syngas Fermentation to Isopropyl Alcohol and Acetone: Economic and Environmental Sustainability Assessment..... 473**
Gijs J.A. Brouwer, Tamara Jankovic, Adrie J.J. Straathof, Anton A. Kiss, John A. Posada

**Energy Efficient Process Designs for Acrylonitrile Production by Propylene Ammoxidation..... 479**
Qing Li, Alexandre C. Dimian, Anton A. Kiss

**Optimizing the Selection of Solvents for the Dissolution and Precipitation of Polyethylene..... 485**
Riccardo Standish, Jian Yin, Mirjana Minceva, Jakob Burger, Amparo Galindo, George Jackson, Claire S. Adjiman

**Sustainable Downstream Process Design for HMF Conversion to Value-Added Chemicals.....491**
Norbert B. Mihály, Miruna Prodan, Vasile M. Cristea, Anton A. Kiss

**Solar Desalination and Porphyrin Mediated Visible-Light Photocatalysis in Decolouration of Dyes as Biological Analogues Applied in Advanced Water Treatment ..... 497**
Evans M. N. Chirwa, Bezza F. Andualem, Osemeikhain Ogbeifun, Shepherd M. Tichapondwa, Wesley Lawrence, Bonhle Manoto

**Technical Assessment of direct air capture using piperazine in an advanced solvent-based absorption process..... 503**
Shengyuan Huang, Olajide Otitoju, Yao Zhang, Meihong Wang

**Valorization of refinery fuel gas and biogenic gases from thermochemical conversion into low-carbon methanol ..... 509**
Eliana Lozano Sanchez, Erik Lopez-Basto, Andrea Ramirez Ramirez

**System scale design and mesoscale modeling for natural gas dehydration process .....515**
Zhehao Jin, Zhongde Dai, Yiyang Dai

**Digital Twin supported Model-based Design of Experiments and Quality by Design.....521**
Amy Koch, Jessica Ebert, Isabell Viedt, Andreas Bamberg, Leon Urbas

**Sustainable Development Goals Assessment of Alternative Acetic Acid Synthesis Routes..... 528**
Juan D. Medrano-García, Sachin Jog, Abhinandan Nabera, Gonzalo Guillén-Gosálbez

**Synergies Between the Distillation of First- and Second-Generation Sugarcane Ethanol for Sustainable Biofuel Production ..... 534**
Luiz M. Costa, Abhay Athaley, Zach Losordo, Adriano P. Mariano, John Posada, Lee R. Lynd

**Superstructure as a Communication Tool in Pre-Emptive Life Cycle Design Engaging Society: Findings from Case Studies on Battery Chemicals, Plastics, and Regional Resources..... 540**
Yasunori Kikuchi, Ayumi Yamaki, Aya Heiho, Jun Nakatani, Shoma Fujii, Ichiro Daigo, Chiharu Tokoro, Shinsuke Murakami, Satoshi Ohara

**Integration of renewable energy and reversible solid oxide cells to decarbonize secondary aluminium production and urban systems ..... 546**
Daniel Flórez-Orrego, Dareen Dardor, Meire Ellen Ribeiro Domingos, Reginald Germanier, Francois Marechal

**Assessing the economic viability of green methanol production: The critical role of CO2 purity in green methanol production ..... 553**
Franc González-Cazorla, Jordi Pujol, Oriol Martínez, Lluis Soler, Moisès Graells

**Gate-to-Gate Life Cycle Assessment of CO2 Utilisation in Enhanced Oil Recovery: Sustainability and Environmental Impacts in Dukhan Field, Qatar ..... 559**
Razan Sawaly, Ahmad S. Abushaikha, Tareq Al-Ansari

**Sustainable Two-Column Design for the Separation of Ethyl Acetate, Methanol, and Water ..... 565**
Prakhar Srivastava, Nitin Kaistha

**Robust Flowsheet Synthesis for Ethyl Acetate, Methanol and Water Separation ..... 571**
Aayush Gupta, Kartavya Maurya, Nitin Kaistha

**Environmental Impacts of Trichlorosilane: Process Optimization, Life Cycle Assessment, and the Importance of Processing History ..... 577**
Ethan Errington, Deniz Etit, Tom Vinestock, Jaewook Lee, Jerry Heng, Miao Guo

**Sodium bicarbonate production from CO2 captured in Waste-to-Energy plants: an Italian case-study..... 583**
Elvira Spatolisano, Giorgia De Guido, Laura A. Pellegrini, Elena Riva Redolfi, Mauro Corradi, Davide Alberti, Adriano Carrara

**Modelling of the Co-precipitation of Ni-Mn-Co Hydroxides. ..... 589**
Erik G. Resendiz-Mora, Solomon F. Brown

**A System-Dynamics Based Approach for Modeling Circular Economy Networks: Application to the Polyethylene Terephthalate (PET) Supply Chain..... 595**
Daniel Pert, Ana Inés Torres

**Sustainable production of L-lactic acid from lignocellulosic biomass using an alternative buffer system: Process development and techno-economic and environmental analysis.....601**
Donggeun Kang, Donghyeon Kim, Dongin Jung, Siuk Roh, Jiyong Kim

**Potential of chemical looping for green hydrogen production from biogas: process design and techno-economic-environmental analysis ..... 607**
Donghyeon Kim, Minseong Park, Donggeun Kang, Dongin Jung, Siuk Roh, Jiyong Kim

**Decarbonized Hydrogen Production: Integrating Renewable Energy into Electrified SMR Process with $CO_2$ Capture .....613**
Joohwa Lee, Haryn Park, Bogdan Dorneanu, Jin-Kuk Kim, Arellano-Garcia Harvey

**Assessing the Synergies of Thermochemical Energy Storage with Concentrated Solar Power and Carbon Capture .....619**
Nitin Dhanenjey R, Ishan Bajaj

**Modelling of Wood Biomass Gasification for Process Optimization..... 625**
Yu Hui Kok, Yasuki Kansha

**Optimal Design and Analysis of Thermochemical Storage and Release of Hydrogen via the Reversible Redox of Iron Oxide/Iron.....631**
Richard Yentumi, Constantin Jurischka, Bogdan Dorneanu, Harvey Arellano-Garcia

**Robust pharmaceutical tableting process through combined probabilistic design space and flexibility analysis ..... 637**
Ashish Yewale, Xuming Yuan, Brahim Benyahia

**Separation Sequencing in Batch Distillation: An Extension of Marginal Vapor Rate Method..... 644**
Prachi Sharma, Sujit S. Jogwar

**Steel Plant Electrification: A Pathway to Sustainable Production and Carbon Reduction .....651**
Rachid Klaimi, Sabla Y. Alnouri, Vladimir Stijepovic, Aleksa Miladinovic, Mirko Stijepovic

**Conceptual design of energy storage systems for continuous operations in renewable-powered chemical processes** ..... **656**
Andrea Isella, Alfonso Pascarella, Angelo Matichecchia, Raffaele Ostuni, Davide Manca

**Olefins production through sustainable pathways: techno-economic and environmental assessment** ..... **662**
Oktay Boztas, Meire E. G. R. Domingos, Daniel A. Flórez-Orrego, François Maréchal

**Integrating Chemical Recycling into Brownfield Processes: Waste Polyethylene Pyrolysis and Naphtha Steam Cracking** ..... **668**
Marc Caballero, Thanyanart Sroisamut, Anton A. Kiss, Ana Somoza-Tornos

**Integrated LCA and Eco-design Process for Hydrogen Technologies: Case Study of the Solid Oxide Electrolyser** ..... **674**
Gabriel Magnaval, Tristan Debonnet, Manuele Margni

**Assessing Distillation Processes through Sustainability Indicators Aligned with the Sustainable Development Goals** ..... **681**
Ömer Faruk Karaman, Peter Lang, Laszlo Hegely

**Integrating Direct Air Capture and HVAC Systems: An Economic Perspective on Cost Savings** ..... **687**
Ikhlas Ghiat, Yasser M. Abdullatif, Yusuf Bicer, Abdulkarem I. Amhamed, Tareq Al-Ansari

**Insights on $CO_2$ Utilization through Reverse Water Gas Shift Reaction in Membrane Reactors: A Multi-scale Mathematical Modeling Approach** ..... **692**
Zhaofeng Li, Anan Uziri, Zahir Aghayev, Burcu Beykal, Michael Patrascu

**Optimized integration strategies for the PMR-based $H_2$ production with $CO_2$ capture process** ..... **698**
Donghoi Kim, Zhongxuan Liu, Rahul Anantharaman, Thijs A. Peters, Truls Gundersen

**Design and Cost Analysis of a Reactive Distillation Column to Produce Ethyl Levulinate Using Excess Levulinic Acid** ..... **704**
Igor F. Fioravante, Riann de Q. Nóbrega, Rubens Maciel Filho, Jean F. Leal Silva

## Section 3: Large Scale Design and Planning/Scheduling

**Analysis for CFD of the Claus Reaction Furnace with Operating Conditions: Temperature and Excess Air for Sulfur Recovery** ..... **711**
Pablo Vizguerra Morales, Miguel Ángel Morales Cabrera, Fabian S. Mederos Nieto

**A Transparent Techno-Enviro-Economic Assessment of a Coal-Fired Power Plant: Integrating Biomass Co-Firing and $CO_2$ Sequestration Technology in a Carbon-Priced Environment** ..... **717**
N. F. E. Nor Fadzil, N. Abdul Manaf, N. Shah

**Genetic Algorithm-Driven Design of CCUS and Hydrogen Pipeline Networks: Decentralised Expansion with Complex Geographical Constraints** ..... **723**
Joseph Hammond, Solomon Brown

**A Forest Biomass-to-Hydrogen Supply Chain Mathematical Model for Optimizing Carbon Emissions and Economic Metrics** ..... **729**
Frank Piedra-Jimenez, Rishabh Mehta, Valeria Larnaudie, Maria Analia Rodriguez, Ana Inés Torres

**A Novel Detailed Representation of Batch Processes for Production Scheduling** ..... **735**
Alexandros Koulouris, Georgios P. Georgiadis

**Enhancing Large-Scale Production Scheduling Using Machine-Learning Techniques** ..... **741**
Maria E. Samouilidou, Nikolaos Passalis, Georgios P. Georgiadis, Michael C. Georgiadis

**Multiscale analysis through the use of biomass residues and $CO_2$ towards energetic security at country scale via methane production** ..... **747**
Guillermo Galán, Manuel Taifouris, Mariano Martín, Ignacio E. Grossmann

**Integrating Time-Varying Environmental Indicators into an Energy Systems Modeling and Optimization Framework for Enhanced Sustainability** ..... **753**
Marco P. De Sousa, Rahul Kakodkar, Betsie M. Flores, Saatvi Suresh, Harsh B. Shah, Dustin Kenefake, Iosif Pappas, Xiao Fu, Doga C. Demirhan, Brianna Ruggiero, Mete Mutlu, Efstratios N. Pistikopoulos

**Modular and Heterogeneous Electrolysis Systems: a System Flexibility Comparison** ..... **759**
Hannes Lange, Michael Große, Isabell Viedt, Leon Urbas

**Methods for Efficient Solutions of Spatially Explicit Biofuels Supply Chain Models** ..... **765**
Phuc M. Tran, Eric G. O'Neill, Christos T. Maravelias

**Integrating Carbon Value Vectors in the Energy and Materials Transition Nexus: A Case Study on Mobility Optimization** ..... **771**
Betsie S. M. Montano Flores, Rahul Kakodkar, Marco P. De Sousa, Shayan S. Niknezhad, Efstratios N. Pistikopoulos

**Assessing Operational Resilience Within the Natural Gas Monetisation Network for Enhanced Production Risk Management: Qatar as a Case Study** ..... **778**
Noor Yusuf, Ahmed AlNouss, Roberto Baldacci, Tareq Al-Ansari

**Minimization of Hydrogen Consumption via Optimization of Power Allocation Between the Stacks of a Dual-Stack Fuel Cell System** ..... **785**
Beril Tümer, Deniz Sanli Yildiz, Yaman Arkun

**A Novel Global Sequence-based Mathematical Formulation for Energy-efficient Flexible Job Shop Scheduling Problem** ..... **791**
D. Li, T.C. Zheng, J. Li

**Materials-Related Challenges of Energy Transition** ..... **798**
Fatemeh Rostami, Piera Patrizio, Laureano Jimenez, Carlos Pozo, Niall Mac Dowell

**A Modern Portfolio Theory Approach for Chemical Production with Supply Chain Considerations for Efficient Investment Planning** ..... **805**
Mohamad Almoussaoui, Dhabia M. Al-Mohannadi

**Optimization models and algorithms for the Unit Commitment problem** ..... **812**
Javal Vyas, Carl Laird, Ignacio E. Grossmann, Ricardo M. Lima, Iiro Harjunkoski, Jan Poland

**Development of a hybrid, semi-parametric Simulation Model of an AEM Electrolysis Stack Unit for large-scale System Simulations** ..... **818**
Isabell Viedt, Michel Große (né Mock), Leon Urbas

**Energy system modelling for studying flexibility on industrial sites** ..... **824**
Jon Vegard Venås, Lucas Ferreira Bernardino, Kasper Emil Thorvaldsen, Sigrid Aunsmo, Sigmund Eggen Holm, Halvor Aarnes Krog, Ove Wolfgang, Ingeborg Treu Røe

**An MIQCP Reformulation for the Optimal Synthesis of Thermally Coupled Distillation Networks** ..... **831**
Kevin Pfau, Arsh Bhatia, Carl D. Laird, George Ostace, Goutham Kotamreddy

**Multi-objective Optimization of Steam Cracking Microgrid for Clean Olefins Production** ..... **837**
Saba Ghasemi Naraghi, Tylee Kareck, Zheyu Jiang

**Pareto optimal solutions for decarbonization of oil refineries under different electricity grid decarbonization scenarios** ..... **844**
Keerthana Karthikeyan, Sampriti Chattopadhyay, Rahul Gandhi, Ignacio E Grossmann, Ana I Torres

**Green Hydrogen Transport across the Mediterranean Sea: A Comparative Study of Liquefied Hydrogen and Ammonia as Carriers** ..... **850**
Federica Restelli, Elvira Spatolisano, Laura A. Pellegrini

**Integrating offshore wind energy into the optimal deployment of a hydrogen supply chain: a case study in Occitanie** ..... **856**
Melissa Cherrouk, Catherine Azzaro-Pantel, Florian Dupriez Robin, Marie Robert

**Optimisation Under Uncertain Meteorology: Stochastic Modelling of Hydrogen Export Systems** ..... **863**
Cameron Aldren, Nilay Shah, Adam Hawkes

**Process integration and waste valorization for sustainable biodiesel production toward a transportation sector energy transition** ..... **869**
Vibhu Baibhav, Daniel Florez Orrego, Pullah Bhatnagar, Francois Maréchal

**Optimization-based planning of carbon-neutral strategy: Economic priority between CCU vs CCS** ..... **876**
Siuk Roh, Chanhee You, Woochang Jeong, Donggeun Kang, Dongin Jung, Donghyun Kim, Jiyong Kim

**Joint Optimization of Fair Facility Allocation and Robust Inventory Management for Perishable Consumer Products** ..... **882**
Saba Ghasemi Naraghi, Zheyu Jiang

**A two-level model to assess the economic feasibility of renewable urea production from agricultural waste** ... **888**
Diego C. Lopes, Moisés Teles dos Santos

**Evolutionary Algorithm Based Real-time Scheduling via Simulation-Optimization for Multiproduct Batch Plants** ..... **894**
Engelbert Pasieka, Sebastian Engell

**Pipeline Network Growth Optimisation for CCUS: A Case Study on the North Sea Port Cluster** ..... **900**
Victoria Brown, Joseph Hammond, Diarmid Roberts, Solomon Brown

**Flow Simulation of Plastic Life Cycle Considering Carbon Renewability and Environmental Impact** ..... **906**
Kota Chida, Heng Yi Teah, Yuichiro Kanematsu, Yasunori Kikuchi

**A Digital Scheduling Hub for Natural Gas Processing: a Petrobras Case-Study Using Rigorous Process Simulation** ..... **912**
Tayná E. G. Souza, Letícia C. dos Santos, Caio R. Soares

**Temporal Decomposition Scheme for Designing Large-Scale $CO_2$ Supply Chains Using a Neural Network-Based Model for Forecasting $CO_2$ Emissions** ..... **918**
José A. Álvarez-Menchero, Rubén Ruiz-Femenia, Raquel Salcedo-Diaz, Isabela Fons Moreno-Palancas, José A. Caballero

**Agent-Based Simulation of Integrated Process and Energy Supply Chains: A Case Study on Biofuel Production** ..... **924**
Farshid Babaei, David B. Robins, Robert Milton, Solomon F. Brown

**Comparison of optimization methods for studying the energy mix of infrastructures. Application to an infrastructure in Oise, France** ..... **930**
Julien JEAN VICTOR, Zakaria A. SOULEYMANE, Augustin MPANDA, Philippe TRUBERT, Laurent FONTANELLI, Sébastien POTEL, Arnaud DUJANY

**Integration of MILP and Discrete-Event Simulation for Flowshop Scheduling Using Benders Decomposition ... 936**
Roderich Wallrath, Edwin Zondervan, Meik B. Franke

**A Blockchain-Supported Framework for Transparent Resource Trading and Emission Management in Eco-Industrial Parks (EIPs) ... 942**
Manar Y. Oqbi, Dhabia M. Al-Mohannadi

## Section 4: Model Based Optimisation and Advanced Control

**Implementation and assessment of fractional controllers for an extractive distillation system ... 950**
Luis R. Flores-Gómez, Fernando I. Gómez-Castro, Francisco López-Villarreal, Vicente Rico-Ramírez

**Refinery Optimal Transitions by Iterative Linear Programming ... 956**
Michael Mulholland

**Optimization Of Heat Exchangers Through an Enhanced Metaheuristic Strategy: The Success-Based Optimization Algorithm ... 962**
Oscar D. Lara-Montaño, Fernando I. Gómez-Castro, Claudia Gutiérrez-Antonio, Elena N. Dragoi

**Production scheduling based on Real-time Optimization and Zone Control Nonlinear Model Predictive Controller ... 968**
José Matias, Alvaro Acevedo

**A simple model for control and optimisation of a produced water re-injection facility ... 974**
Rafael D. De Oliveira, Edmary Altamiranda, Gjermund Mathisen, Johannes Jäschke

**Design of Process Systems for Flexibility and Resilience Using Multi-Parametric Programming ... 980**
Natasha J. Chrisandina, Eleftherios Iakovou, Efstratios N. Pistikopoulos, Mahmoud M. El-Halwagi

**Learning-based Control Approach for Nanobody-scorpion Antivenom Optimization ... 986**
Juan Camilo Acosta-Pavas, David Camilo Corrales, Susana María Alonso Villela, Balkiss Bouhaouala-Zahar, Georgios Georgakilas, Konstantinos Mexis, Stefanos Xenios, Theodore Dalamagas, Antonis Kokossis, Michael O'donohue, Luc Fillaudeau, César Arturo Aceves-Lara

**Safe Bayesian Optimization in Process System Engineering ... 993**
Donggyu Lee, Ehecatl Antonio del Rio Chanona

**Multi-Model Predictive Control of a Distillation Column ... 999**
Mehmet Arici, Wachira Daosud, Jozef Vargan, Miroslav Fikar

**Optimal Design of Extraction-Distillation Hybrid Processes by Combining Equilibrium and Rate-Based Modeling ... 1005**
Kai F. Kruber, Anjali Kabra, Lukas Polte, Andreas Jupke, Mirko Skiborowski

**Advanced Regulatory Control Structure for Proton Exchange Membrane Water Electrolysis Systems ... 1011**
Marius Fredriksen, Johannes Jäschke

**Design of Microfluidic Mixers using Bayesian Shape Optimization ... 1017**
Rui Fonseca, Fernando Bernardo

**Probabilistic Model Predictive Control for Mineral Flotation using Gaussian Processes ... 1023**
Victor Dehon, Paulina Quintanilla, Antonio Del Rio Chanona

**A Bayesian optimization approach for data-driven Petlyuk distillation column ... 1029**
Alexander Panales-Pérez, Antonio Flores-Tlacuahuac, Luis Fabián Fuentes-Cortés, Miguel Angel Gutierrez-Limon, Mauricio Sales-Cruz

**Accelerating Solvent Design Optimisation with Group-Contribution Machine Learning Surrogate Classifiers** ..... **1035**
Lifeng Zhang, Benoît Chachuat, Claire S. Adjiman

**Machine Learning-Aided Robust Optimisation for Identifying Optimal Operational Spaces under Uncertainty** ..... **1041**
Sam Kay, Mengjia Zhu, Amanda Lane, Jane Shaw, Philip Martin, Dongda Zhang

**Enhancing Energy Efficiency of Industrial Brackish Water Reverse Osmosis Desalination Process using Waste Heat** ..... **1047**
Alanood A. Alsarayreh, Mudhar A. Al-Obaidi, Iqbal M. Mujtaba

**Optimization of Heat Transfer Area for Multiple Effects Desalination (MED) Process** ..... **1053**
Salih M. Alsadaie, Sana I. Abukanisha, Amhamed A. Omar, Iqbal M. Mujtaba

**Physics-based and data-driven hybrid modelling and dynamic adaptive multi-objective optimization of chemical reactors for $CO_2$ capture via enhanced weathering** ..... **1059**
Yalun Zhao, Jin Xuan, Lei Xing

**Integrating Dynamic Risk Assessment with Explicit Model Predictive Control via Chance-Constrained Programming** ..... **1065**
Sahithi Srijana Akundi, Yuanxing Liu, Austin Braniff, Beatriz Dantas, Shayan S Niknezhad, Faisal Khan, Yuhe Tian, Efstratios N Pistikopoulos

**Analysis of Control Properties as a Sustainability Indicator in Intensified Processes for Levulinic Acid Purification** ..... **1071**
Tadeo E. Velázquez-Sámano, Heriberto Alcocer-García, Eduardo Sánchez-Ramírez, Carlos R. Caceres-Barrera, Juan G. Segovia-Hernández

**Systematic design of structured packings based on shape optimization** ..... **1077**
Alina Dobschall, Elvis Michaelis, Mirko Skiborowski

**Enhancing Consumer Engagement in Plastic Waste Reduction: A Stackelberg Game** ..... **1083**
Chunyan Si, Yee Van Fan, Monika Dokl, Lidija Cucek, Zdravko Kravanja, Petar Sabev Varbanov

**Utilizing ML Surrogates in CAPD: Case Study of an Amine-based Carbon-Capture Process** ..... **1089**
Florian Baakes, Gustavo Chaparro, Thomas Bernet, George Jackson, Amparo Galindo, Claire S. Adjiman

**Evaluation of the Controllability of Distillation with Multiple Reactive Stages** ..... **1095**
Josué J. Herrera Velázquez, J. Rafael Alcántara Avila, Salvador Hernández, Julián Cabrera Ruiz

**Revenue Optimization for Dynamic Operation of a Hybrid Solar Thermal Power Plant** ..... **1101**
Dibyajyoti Baidya, Mani Bhushan, Sharad Bhartiya

**Control of the WWTP Water Line Using Traditional and Model Predictive Approaches** ..... **1108**
Gheorghe A. Bodescu, Romina G. Daraban, Norbert B. Mihály, Castelia E. Cristea, Elisabeta C. Timiș, Anton A. Kiss, Vasile M. Cristea

**Optimization of the Power Conversion System for a Pulsed Fusion Power Plant with Multiple Heat Sources using a Dynamic Process Model** ..... **1114**
Oliver M. G. Ward, Federico Galvanin, Nelia Jurado, Daniel Blackburn, Robert J. Warren, Eric S. Fraga

**Optimization of steam power systems in industrial parks considering the distributed heat supply and auxiliary steam turbines** ..... **1120**
Lingwei Zhang, Yufei Wang

**Optimisation of a Haber-Bosch Synthesis Loop for PtA** ..... **1126**
Joachim W. Rosbo, Anker D. Jensen, John B. Jørgensen, Sigurd Skogestad, Jakob. K. Huusom

**Data-Driven Reinforcement Learning for Greenhouse Temperature Control ..... 1133**
Farhat Mahmood, Sarah Namany, Rajesh Govindan

**Aotearoa-New Zealand's Energy Future: A Model for Industrial Electrification through Renewable Integration ..... 1139**
Daniel J S Chong, Timothy G Walmsley, Martin J Atkins, Botond Bertok, Michael RW Walmsley

**Non-Linear Model Predictive Control for Oil Production in Wells Using Electric Submersible Pumps ..... 1145**
Carine Menezes Rebello, Erbet Almeida Costa, Marcos Pellegrini Ribeiro, Marcio Fontana, Leizer Schnitman, Idelfonso Bessa dos Reis Nogueira

**MORL4PC: Multi-Objective Reinforcement Learning for Process Control ..... 1151**
Niki Kotecha, Max Bloor, Calvin Tsay, Antonio del Rio Chanona

**Extremum seeking control applied to operation of dividing wall column – DWC ..... 1157**
Ivar J. Halvorsen, Leontine I.M. Aarnoudse, Mark A.M. Haring, Sigurd Skogestad

**Modeling, Simulation and Optimization of a Carbon Capture Process Through a TSA Column ..... 1163**
Eduardo S. Funcia, Yuri S. Beleli, Enrique V. Garcia, Marcelo M. Seckler, José L. Paiva, Galo A. C. Le Roux

**Safe Reinforcement Learning with Lyapunov-Based Constraints for Control of an Unstable Reactor ..... 1169**
José R. Torraca Neto, Bruno D. O. Capron, Argimiro R. Secchi, Antonio d.R. Chanona

**Cost-effective Process Design and Optimization for Decarbonized Utility Systems Integrated with Renewable Energy and Carbon Capture Systems ..... 1175**
Haryn Park, Joohwa Lee, Bogdan Dorneanu, Havey Arellano-Garcia, Jin-Kuk Kim

**A Subset Selection Strategy for Gaussian Process Q-Learning of Process Optimization and Control ..... 1181**
Maximilian Bloor, Tom Savage, Calvin Tsay, Ehecatl Antonio Del Rio Chanona, Max Mowbray

**Optimal Operation of Middle Vessel Batch Distillation using Model Predictive Control ..... 1187**
Surendra Beniwal, Sujit S. Jogwar

**Perturbation Methods for Modifier Adaptation with Quadratic Approximation ..... 1194**
Mohamed Aboelnour, Sebastian Engell

**Optimal Energy Scheduling for Battery and Hydrogen Storage Systems Using Reinforcement Learning ..... 1201**
Moritz Zebenholzer, Lukas Kasper, Alexander Schirrer, René Hofmann

**Recurrent Deep Learning Models for Multi-step Ahead Prediction: Comparison and Evaluation for Real Electrical Submersible Pump (ESP) System. ..... 1208**
Vinicius V. Santana, Carine M. Rebello, Erbet A. Costa, Odilon S. L. Abreu, Galdir Reges, Téofilo P. G. Mendes, Leizer Schnitman, Marcos P. Ribeiro, Márcio Fontana, Idelfonso Nogueira

**Enhanced Computational Approach for Simulation and Optimisation of Vacuum (Pressure) Swing Adsorption ..... 1214**
Yangyanbing Liao, Andrew Wright, Jie Li

**NLP Deterministic Optimization of Shell and Tube Heat Exchangers with Twisted Tape Turbulence Promoters ..... 1221**
Jamel Eduardo Rumbo-Arias, Fabián Pino, Martin Picón-Nuñez, Fernando Israel Gómez-Castro, Jorge Luis García-Castillo

**Optimizing Methane Conversion in a Flow Reactor System Using Bayesian Optimization and Model-Based Design of Experiments Approaches: A Comparative Study ..... 1228**
Michael Aku, Solomon Gajere Bawa, Arun Pankajakshan, Lauren Ye Seol Lee, Federico Galvanin

**A Decomposition Approach to Feasibility for Decentralized Operation of Multi-stage Processes ..... 1237**
Ekundayo Olorunshe, Nilay Shah, Benoît Chachuat, Max Mowbray

**Simulation and Optimisation of Cryogenic Distillation and Isotopic Equilibrator Cascades for Hydrogen Isotope Separation Processes in the Fusion Fuel Cycle ..... 1244**
Emma A. Barrow, Iryna Bennett, Franjo Cecelja, Eduardo Garciadiego-Ortega, Megan Thompson, Dimitrios Tsaoulidis

**Efficient approximation of the Koopman operator for large-scale nonlinear systems ..... 1251**
Gajanand Verma, William Heath, Constantinos Theodoropoulos

**Optimal Control of PSA Units Based on Extremum Seeking ..... 1257**
Beatriz C. da Silva, Ana M. Ribeiro, Alexandre F.P. Ferreira, Diogo Rodrigues, Idelfonso B.R. Nogueira

**Machine Learning-Based Soft Sensor for Hydrogen Sulfide Monitoring in the Gas Treatment Section of an Industrial-Scale Oil Regeneration Plant ..... 1263**
Luis F. Sánchez, Eva C. Coelho, Francesco Negri, Francesco Gallo, Mattia Vallerio, Henrique A. Matos, Flavio Manenti

**Principles and Applications of Model-free Extremum Seeking – A Tutorial Review ..... 1269**
Laurent Dewasme, Alain Vande Wouwer

**Updated-Absolute Expected Value Solution Approach for multistage stochastic programming problems ..... 1275**
Yasuhiro Shoji, Selen Cremaschi

## Section 5: Concepts, Methods and Tools

**A Python/Numpy-based package to support model discrimination and identification ..... 1282**
Seyed Zuhair Bolourchian Tabrizi, Elena Barbera, Wilson Ricardo Leal da Silva, Fabrizio Bezzo

**The Paradigm of Water and Energy Integration Systems (WEIS): Methodology and Performance Indicators ... 1288**
Miguel Castro Oliveira, Rita Castro Oliveira, Pedro M. Castro, Henrique A. Matos

**Comparison of Multi-Fidelity Modelling Methods for Bayesian Optimization ..... 1294**
Stefan Tönnis, Luise F. Kaven, Eike Cramer

**AutoJSA: A Knowledge-Enhanced Large Language Model Framework for Improving Job Safety Analysis ..... 1300**
Shuo Xu, Jinsong Zhao

**Refrigerant Selection and Cycle Design for Industrial Heat Pump Applications exemplified for Distillation Processes ..... 1306**
Jonas Schnurr, Momme Adami, Mirko Skiborowski

**Companies' Operation and Trading Strategies under the Triple Trading and Gaming of Electricity, Carbon Quota and Commodities: A Game Theory Optimization Modeling ..... 1312**
Chenxi Li, Nilay Shah, Zheng Li, Pei Liu

**Design of Experiments Algorithm for Comprehensive Exploration and Rapid Optimization in Chemical Space ..... 1318**
Kazuhiro Takeda, Masaru Kondo, Muthu Karuppasamy, Mohamed S. H. Salem, Shinobu Takizawa

**Multi-Objective Optimization and Analytical Hierarchical Process for Sustainable Power Generation Alternatives in the High Mountain Region of Santurbán: case of Pamplona, Colombia ..... 1324**
Nicolas Cabrera, A.M Rosso-Cerón, Viatcheslav Kafarov

**A Comparison of Robust Modeling Approaches to Cope with Uncertainty in Independent Terms, considering the Forest Supply Chain Case Study** ..... **1330**
Frank Piedra-Jimenez, Ana Inés Torres, Maria Analia Rodriguez

**Introducing Competition in a Multi-Agent System for Hybrid Optimization** ..... **1336**
Veerawat Udomvorakulchai, Miguel Pineda, Eric S. Fraga

**A Component Property Modeling Framework Utilizing Molecular Similarity for Accurate Predictions and Uncertainty Quantification** ..... **1342**
Youquan Xu, Zhijiang Shao, Anjan K. Tula

**Phenomena-Based Graph Representations and Applications to Chemical Process Simulation** ..... **1348**
Yoel R. Corte´s-Pen, Victor M. Zava

**A Benchmark Simulation Model of Ammonia Production: Enabling Safe Innovation in the Emerging Renewable Hydrogen Economy** ..... **1354**
Niklas Groll, Gürkan Sin

**Bayesian uncertainty quantification of graph neural networks using stochastic gradient Hamiltonian Monte Carlo** ..... **1360**
Qinghe Gao, Daniel C. Miedema, Yidong Zhao, Jana M. Weber, Qian Tao, Artur M. Schweidtmann

**pyDEXPI: A Python framework for piping and instrumentation diagrams (P&IDs) using the DEXPI information model** ..... **1365**
Dominik P. Goldstein, Lukas Schulze Balhorn, Achmad Anggawirya Alimin, Artur M. Schweidtmann

**Kolmogorov Arnold Networks (KANs) as surrogate models for global process optimization** ..... **1371**
Tanuj Karia, Giacomo Lastrucci, Artur M. Schweidtmann

**Redefining Stage Efficiency in Liquid-Liquid Extraction: Development and Application of a Modified Murphree Efficiency** ..... **1377**
Mahdi Mousavi, Ville Alopaeus

**A Stochastic Techno-Economic Assessment of Emerging Artificial Photosynthetic Bio-Electrochemical Systems for CO2 Conversion** ..... **1383**
Haris Saeed, Aidong Yang, Wei Huang

**Soft-Sensor-Enhanced Monitoring of an Alkylation Unit via Multi-Fidelity Model Correction** ..... **1389**
Rastislav Fáber, Marco Vaccari, Riccardo Bacci di Capaci, Karol Lubušký, Gabriele Pannocchia, Radoslav Paulen

**Differentiation between Process and Equipment Drifts in Chemical Plants** ..... **1396**
Linda Eydam, Lukas Furtner, Julius Lorenz, Leon Urbas

**Enhanced Reinforcement Learning-driven Process Design via Quantum Machine Learning** ..... **1403**
Austin Braniff, Fengqi You, Yuhe Tian

**Comparative and Statistical Study on Aspen Plus Interfaces Used for Stochastic Optimization** ..... **1409**
Josué J. Herrera Velázquez, Erik L. Piñón Hernández, Luis A. Vega Vega, Dana E. Carrillo Espinoza, J. Rafael Alcántara Avila, Julián Cabrera Ruiz

**Handling discrete decisions in bilevel optimization via neural network embeddings** ..... **1415**
Isabela Fons Moreno-Palancas, Raquel Salcedo Díaz, Rubén Ruiz Femenia, José A. Caballero

**Linear and non-linear convolutional approaches and XAI for spectral data: classification of waste lubricant oils** ..... **1421**
Ruben Gariso, João P. L. Coutinho, Tiago J. Rato, Marco S. Reis

**Unveiling Probability Histograms from Random Signals using a Variable-Order Quadrature Method of Moments** ..... **1427**
Menwer Attarakih, Mark W. Hlawitschka, Linda Al-Hmoud, and Hans-Jörg Bart

**Sensitivity Analysis of Key Parameters in LES-DEM Simulations of Fluidized Bed Systems Using Generalized Polynomial Chaos** ..... **1433**
Radouan Boukharfane, Nabil El Moçayd

**An Efficient Convex Training Algorithm for Artificial Neural Networks by Utilizing Piecewise Linear Approximations and Semi-Continuous Formulations** ..... **1438**
Ece S. Köksal, Erdal Aydin, Metin Türkay

**A combined approach to optimization of soft sensor architecture and physical sensor configuration** ..... **1445**
Lukas Furtner, Isabell Viedt, Leon Urbas

**Flexibility Assessment via Affine Bounds Evaluation** ..... **1450**
Diogo A. C. Narciso, Steven Sachio, Maria M. Papathanasiou

**A Novel Objective Reduction Algorithm for Nonlinear Many-Objective Optimization Problems** ..... **1456**
Hongxuan Wang, Andrew Allman

**Applying Quality by Design to Digital Twin Supported Scale-Up of Methyl Acetate Synthesis** ..... **1462**
Jessica Ebert, Amy Koch, Isabell Viedt, Leon Urbas

**Tune Decomposition Schemes for Large-Scale Mixed-Integer Programs by Bayesian Optimization** ..... **1468**
Guido Sand, Sophie Hildebrandt, Sina Nunes, Chung-On Yip, Meik Franke

**A Superstructure Approach for Optimization of Simulated Moving Bed (SMB) Chromatography** ..... **1474**
Eva Sorensen, Dian Ning Chia, Fanyi Duanmu

**Development of anomaly detection models independent of noise and missing values using graph Laplacian regularization** ..... **1480**
Yuna Tahashi, Koichi Fujiwara

**A Modelling and Simulation Software for Polymerization with Microscopic Resolution** ..... **1486**
Shenhua Jiao, Xiaowen Lin, Rui Liu, Xi Chen

**Interval Hessian-based Optimization Algorithm for Unconstrained Non-convex Problems** ..... **1492**
Ashutosh Sharma, Gauransh Dingwani, Ishan Bajaj

**Design Space Exploration via Gaussian Process Regression and Alpha Shape Visualization** ..... **1498**
Elizaveta Marich, Andrea Galeazzi, Steven Sachio, Foteini Michalopoulou, Maria M. Papathanasiou

**Langmuir.jl: An Efficient and composable Julia Package for Adsorption Thermodynamics** ..... **1505**
Vinicius Santana, Andrés Riedemann, Pierre J. Walker, Idelfonso Nogueira

**Systematic comparison between Graph Neural Networks and UNIFAC-IL for solvent pre-selection in liquid-liquid extraction** ..... **1512**
Edgar Ivan Sanchez Medina, Ann-Joelle Minor, Kai Sundmacher

**Knowledge Discovery in Large-Scale Batch Processes through Explainable Boosted Models and Uncertainty Quantification: Application to Rubber Mixing** ..... **1518**
Louis Berthier, Ahmed Shokry, Eric Moulines, Guillaume Ramelet, Sylvain Desroziers

**Electricity Bidding with Variable Loads** ..... **1524**
Iiro Harjunkoski

**Nonmyopic Bayesian process optimization with a finite budget** ..... **1530**
José L. Pitarch, Leopoldo Armesto, Antonio Sala

**Life-Cycle Assessment of Chemical Sugar Synthesis Based on Process Design for Biomanufacturing** .....**1536**
Hiro Tabata, Satoshi Ohara, Yuichiro Kanematsu, Heng Yi Teah, Yasunori Kikuchi

**Decision Support Tool for Sustainable Small to Medium-Volume Natural Gas Utilization** .....**1542**
Patience B. Shamaki, Pedro H. Callil-Soares, Galo A. C. Le Roux

**Enhancing Batch Chemical Manufacturing via Development of Deep Learning based Predictive Monitoring with Transfer Learning** .....**1548**
Hong Yee Hung, Zhao Jinsong

**Prospective Life Cycle Design Enhanced by Computer Aided Process Modeling: A Case Study of Air Conditioners** .....**1555**
Shoma Fujii, Yuko Oshita, Ayumi Yamaki, Yasunori Kikuchi

**Solving Complex Combinatorial Optimization Problems Using Quantum Annealing Approaches** ..... **1561**
Vasileios K. Mappas, Bogdan Dorneanu, Harvey Arellano-Garcia

**A Propagated Uncertainty Active Learning Method for Bayesian Classification Problems** .....**1567**
Arun Pankajakshan, Sayan Pal, Maximilian O. Besenhard, Asterios Gavriilidis, Luca Mazzei, Federico Galvanin

**Optimizing Individual-based Modelling: A Grid-based Approach to Computationally Efficient Microbial Simulations** .....**1573**
Ihab Hashem, Jian Wang, Jan F.M. Van Impe

**A data-driven hybrid multi-objective optimization framework for pressure swing adsorption systems** .....**1579**
Siyang Ma, Jie Li

**Multi-Objective Optimization for Sustainable Design of Power-to-Ammonia Plants**.....**1586**
Andrea Isella, Davide Manca

**Global Robust Optimisation for Non-Convex Quadratic Programs: Application to Pooling Problems**.....**1592**
Asimina Marousi, Vassilis M. Charitopoulos

**GRAPSE: Graph-Based Retrieval Augmentation for Process Systems Engineering**.....**1598**
Daniel Ovalle, Arpan Seth, John R. Kitchin, Carl D. Laird, Ignacio E. Grossmann

**A Fault Detection Method Based on Key Variable Forecasting**..... **1605**
Borui Yang, Jinsong Zhao

**Optimizing Industrial Heat Electrification: Balancing Cost and Emissions**..... **1612**
Soha Mousa, Dhabia Al-Mohannadi

**Assessing Triviality in Random Mixed-Integer Bilevel Optimization Problems to Improve Problem Generators and Libraries**..... **1618**
Meng-Lin Tsai, Styliani Avraamidou

**Integration of Graph Theory and Machine Learning for Enhanced Process Synthesis and Design of Wastewater Transportation Networks**.....**1625**
Andres Castellar-Freile, Jean Pimentel, Alec Guerra, Pratap Kodate, Kirti M. Yenkie

**A Framework Utilizing a Seamless Integration of Python with AspenPlus® for a Multi-Criteria Process E valuation**..... **1631**
Simon Maier, Julia Weyand, Ginif Kaur, Oliver Erdmann, Ralph-Uwe Dietrich

Section 6: Digitalization and AI

**Optimal Design of Process Equipment Through Hybrid Mechanistic-ANN Models: Effect of Hybridization ..... 1638**
Zaira Jelena Mosqueda-Huerta, Oscar Daniel Lara-Montaño, Fernando Israel Gómez-Castro, Manuel Toledano-Ayala

**Modelling of a Propylene Glycol Production Process With Artificial Neural Networks: Optimization of the Architecture ..... 1644**
Emilio Alba-Robles, Oscar Daniel Lara-Montaño, Fernando Israel Gómez-Castro, Jahaziel Alberto Sánchez-Gómez, Manuel Toledano-Ayala

**Developing a Digital Twin System Based on a Physics-informed Neural Network for Pipeline Leakage Detection ..... 1650**
Wei-Shiang Lin, Yi-Hsiang Cheng, Zhen-Yu Hung, Yuan Yao

**Rule-Based Autocorrection of Piping and Instrumentation Diagrams (P&IDs) on Graphs ..... 1656**
Lukas Schulze Balhorn, Niels Seijsener, Kevin Dao, Minji Kim, Dominik P. Goldstein, Ge H. M. Driessen, Artur M. Schweidtmann

**Thermodynamics-informed Graph Neural Networks for Phase Transition Enthalpies ..... 1662**
Roel Leenhouts, Sebastien Jankelevitch, Roel Raike, Simon Müller, Florence Vermeire

**Automated Interpretation of Chemical Engineering Diagrams Using Computer Vision ..... 1670**
Maged Eid, Giancarlo Dalle Ave

**Talking like Piping and Instrumentation Diagrams (P&IDs) ..... 1676**
Achmad Anggawirya Alimin, Dominik P. Goldstein, Lukas Schulze Balhorn, Artur M. Schweidtmann

**Hybrid machine-learning for dynamic plant-wide biomanufacturing ..... 1682**
Shabnam Shahhoseyni, Arijit Chakraborty, Mohammad Reza Boskabadi, Venkat Venkatasubramanian, Seyed Soheil Mansouri

**Leveraging Machine Learning for Real-Time Performance Prediction of Near Infrared Separators in Waste Sorting Plant ..... 1688**
Imam M. Iqbal, Xinyu Wang, Isabell Viedt, Leonhard Urbas

**Exploring Industrial Text Data for Monitoring Chemical Manufacturing Processes ..... 1694**
Eugeniu Strelet, Ivan Castillo, You Peng, Swee-Teng Chin, Anna Zink, Ricardo Rendall, Marco S. Reis

**Optimal Design and Control of Chemical Reactors using PINN-based frameworks ..... 1700**
Isabela Fons Moreno-Palancas, Raquel Salcedo Díaz, Rubén Ruiz Femenia, José A. Caballero

**Text2Model: Generating dynamic chemical reactor models using large language models (LLMs) ..... 1706**
Sophia Rupprecht, Yassine Hounat, Monisha Kumar, Giacomo Lastrucci, Artur M. Schweidtmann

**Enhancing Fault diagnosis for Chemical Processes via MSCNN with Hyperparameters Optimization ..... 1712**
Jingkang Liang, GürkanSin

**Picard-KKT-hPINN: Enforcing Nonlinear Enthalpy Balances for Physically Consistent Neural Networks ..... 1718**
Giacomo Lastrucci, Tanuj Karia, Zoë Gromotka, Artur M. Schweidtmann

**AI-Driven Automatic Mechanistic Model Transfer Learning for Accelerating Process Development ..... 1724**
Alexander W. Rogers, Amanda Lane, Philip Martin, Dongda Zhang

**Industrial Time Series Forecasting for Fluid Catalytic Cracking Process ..... 1730**
Qiming Zhao, Yaning Zhang, Tong Qiu

**A White-Box AI Framework for Interpretable Global Warming Potential Prediction ..... 1737**
Jaewook Lee, Ethan Errington, Miao Guo

**Computational Assessment of Molecular Synthetic Accessibility using Economic Indicators ..... 1744**
Friedrich Hastedt, Klaus Hellgardt, Sophia Yaliraki, Antonio del Rio Chanona, Dongda Zhang

**A Physics-Informed Approach to Dynamic Modeling and Parameter Estimation in Biotechnology ..... 1750**
Konstantinos Mexis, Stefanos Xenios, Nikolaos Trokanas, Antonis Kokossis

**Physics-Informed Automated Discovery of Kinetic Models ..... 1756**
Miguel Ángel de Carvalho Servia, Ilya Orson Sandoval, King Kuok (Mimi) Hii, Klaus Hellgardt, Dongda Zhang, Ehecatl Antonio del Rio Chanona

**Empowering LLMs for Mathematical Reasoning and Optimization: A Multi-Agent Symbolic Regression System ..... 1762**
Shaurya Vats, Sai Phani Chatti, Aravind Devanand, Sandeep Krishnan, Rohit Karanth Kota

**Application of Artificial Intelligence in process simulation tool ..... 1769**
Nikhil Rajeev, Suresh Jayaraman, Prajnan Das, Srividya Varada

**Hybrid Models Identification and Training through Evolutionary Algorithms ..... 1775**
Ulderico Di Caprio, M. Enis Leblebici

**Physics-Informed Graph Neural Networks for Modeling Spatially Distributed Dynamically Operated Processes ..... 1781**
Md Meraj Khalid, Luisa Peterson, Edgar Ivan Sanchez Medina, Kai Sundmacher

**Network Theoretical Analysis of the Reaction Space in Biorefineries ..... 1787**
Jakub Kontak, Jana M. Weber

**Structural Optimization of Translucent Monolith Reactors through Multi-objective Bayesian Optimization ..... 1794**
Onur C. Boy, Ulderico Di Caprio, Idelfonso B.R. Nogueira, M. Enis Leblebici

**A Novel Symbol Recognition Framework for Digitization of Piping and Instrumentation Diagrams ..... 1800**
Zhiyuan Li, Jinsong Zhao, Huahui Zhou, Xiaoxin Hu

**Enhancing Predictive Maintenance in Used Oil Re-Refining: a Hybrid Machine Learning Approach ..... 1806**
Francesco Negri, Andrea Galeazzi, Francesco Gallo, Flavio Manenti

**An Integrated Machine Learning Framework for Predicting HPNA Formation in Hydrocracking Units Using Forecasted Operational Parameters ..... 1812**
Pelin Dologlu, Ibrahim Bayar

**Optimization of Shell and Tube Heat Exchangers Using Reinforcement Learning ..... 1818**
Luana P. Queiroz, Olve R. Bruaset, Ana M. Ribeiro, Idelfonso B. R. Nogueira

**Multi-Agent LLMs for Automating Sustainable Operational Decision-Making ..... 1824**
Emma Pajak, Abdullah Bahamdan, Klaus Hellgardt, Antonio del Río-Chanona

**On the role of artificial intelligence in feature oriented multi-criteria decision analysis ..... 1830**
Heyuan Liu, Yi Zhao, Francois Maréchal

**Selection of Fitness Criteria for Learning Interpretable PDE Solutions via Symbolic Regression ..... 1837**
Benjamin G. Cohen, Burcu Beykal, George M. Bollas

**Towards Self-Tuning PID Controllers: A Data-Driven, Reinforcement Learning Approach for Industrial Automation ..... 1843**
Kyle Territo, Peter Vallet, Jose Romagnoli

**CompArt: Next-Generation Compartmental Models for Complex Systems Powered by Artificial Intelligence ..... 1849**
Antonello Raponi, Zoltan Nagy

**ML-based adsorption isotherm prediction of metal-organic frameworks for carbon dioxide and methane separation adsorbent screening.....1854**
Dongin Jung, Hyeon Yang, Donggeun Kang, Donghyeon Kim, Siuk Roh, Jiyong Kim

**Data-Driven Soft Sensors for Process Industries: Case Study on a Delayed Coker Unit ..... 1860**
Wei Sun, James G. Brigman, Cheng Ji, Pratap Nair, Fangyuan Ma, Jingde Wang

**Streamlining Catalyst Development through Machine Learning: Insights from Heterogeneous Catalysis and Photocatalysis .....1866**
Parisa Shafiee, Mitra Jafari, Julia Schowarte, Bogdan Dorneanu, Harvey Arellano-Garcia

**A Novel Approach to Gradient Evaluation and Efficient Deep Learning: A Hybrid Method .....1872**
Bogdan Dorneanu, Vasileios K. Mappas, Harvey Arellano-Garcia

**A Comparative Analysis of Industrial MLOps prototype for ML Application Deployment at the edge devices ..1878**
Fatima Rani, Fenin Jose, Lucas Vogt, Leonhard Urbas

**The Smart HPLC Robot: Fully Autonomous Method Development Guided by A Mechanistic Model Framework1884**
Dian Ning Chia, Fanyi Duanmu, Luca Mazzei, Eva Sorensen, Maximilian O. Besenhard

**Predicting Surface Tension of Organic Molecules using COSMO-RS Theory and Machine Learning ..... 1890**
Flora Esposito, Ulderico Di Caprio, Bruno Rodrigues, Florence H. Vermeire, Idelfonso B.R. Nogueira, M.Enis Leblebici

**Hybrid model development for Succinic Acid fermentation: relevance of ensemble learning for enhancing model prediction.....1896**
Juan Federico Herrera-Ruiz, Javier Fontalvo, Oscar Andrés Prado-Rubio

**Reinforcement learning for distillation process synthesis using transformer blocks.....1902**
N. Slager, M.B. Franke

**Physics-informed Data-driven control of Electrochemical Separation Processes ..... 1908**
Teslim Olayiwola, Kyle Territo, Jose Romagnoli

**A Novel AI-Driven Approach for Parameter Estimation in Gas-Phase Fixed-Bed Experiments..... 1915**
Rui D. G. Matias, Alexandre F.P. Ferreira, Idelfonso B.R. Nogueira, Ana M. Ribeiro

## Section 7: CAPEing with Societal Challenges (Green Deal, Energy Transition)

**Engineering the Final Frontier: The Role of Chemical and Process Systems Engineering in Space Exploration .....1922**
Edwin Zondervan

**Green Solvent Alternative for Extractive Distillation of 1,3-Butadiene .....1928**
João P. Gomes, Rodrigo Silva, Clemente Nunes, Domingos Barbosa

**Modelling and Analysis of CO2 Electrolyzers Integrated with Downstream Separation Processes via Heat Pumps..... 1934**
Riccardo Dal Mas, Andrea Carta, Ana Somoza-Tornos, Anton A. Kiss

**Optimization of Sustainable Fuel Station Retrofitting: A Set-Covering Approach considering Environmental and Economic Objectives..... 1940**
Daniel Vázquez, Raul Calvo-Serrano

**Optimizing Heat Recovery: Advanced Design of Integrated Heat Exchanger Networks with ORCs and Heat Pumps..... 1946**
Zinet Mekidiche, Juan A. Labarta, José A. Caballero

**CO2 recycling plant for decarbonizing hard-to-abate industries: Empirical modelling and Process design of a CCU plant- A case study. ..... 1951**
Jose Antonio Abarca, Stephanie Arias-Lugo, Lucia Gomez-Coma, Guillermo Diaz-Sainz, Angel Irabien

**Techno-economic Assessment of Sustainable Aviation Fuel Production via H2/CO2-Based Methanol Pathway.....1957**
Pierre Guilloteau, Hugo Silva, Anders Andreasen, Niklas Groll, Anker Degn Jensen, Gürkan Sin

**Assessing the Environmental Impact of Global Hydrogen Supply through the Lens of Planetary Boundaries...1963**
Jesmyl-Elisa Cordova-Cordova, Carlos Pozo

**Integration of Direct Air Capture with $CO_2$ Utilization Technologies powered by Renewable Energy Sources to deliver Negative Carbon Emissions .....1969**
Calin-Cristian Cormos, Arthur-Maximilian Báthori, Angéla-Mária Kasza, Maria Mihet, Letitia Petrescu, Ana-Maria Cormos

**Towards Sustainable Processing Of Municipal Household Organic Waste: The Role Of Energy Mix Grids.....1975**
Christian Ottini, Gwenola Yannou-Le Bris, Sandra Domenek, Felipe Buendia

**Repurposing Existing Combined Cycle Power Plants with Methane Production for Renewable Energy Storage..... 1981**
Diego Santamaría, Antonio Sánchez, Mariano Martín

**On the Economic Uncertainty and Crisis Resiliency of Decarbonization Solutions for the Aluminium Industry 1987**
Dareen Dardor, Daniel Flórez-Orrego, Reginald Germanier, Manuele Margni, François Maréchal

**A Data-Driven Conceptual Approach to Heat Pump Sizing in Chemical Processes with Fluctuating Heat Supply and Demand..... 1994**
Thorben Hochhaus, Johannes Wloch, Marcus Grünewald, Julia Riese

**Optimization of prospective circular economy in sewage sludge to biofuel production pathways via hydrothermal liquefaction using P-graph .....2000**
Safdar Abbas, Paraskevi Karka, Stavros Papadokonstantakis

**Model-based Operability and Safety Optimization for PEM Water Electrolysis ..... 2007**
Beatriz Dantas, Sahithi S. Akundi, Yuanxing Liu, Austin Braniff, Shayan S. Niknezhad

**Multi-Stakeholder Optimization for Identification of Relevant Life Cycle Assessment Endpoint Indicators.....2013**
Dat Huynh, Oluwadare Badejo, Borja Hernández, Marianthi Ierapetritou

**Lignocellulosic Waste Supply Chain Network Design for Sustainable Aviation Fuels Production through Solar Pyrolysis .....2019**
Stavroula Zervopoulou, Stavros Papadokonstantakis, Mika Järvinen, Muddasser Inayat

**Resource and Pathways Analysis for Decarbonizing the Pulp and Paper Sector in Quebec ..... 2026**
Marie-Hélène Talbot, Mélissa Lemire

**Methanol and Ammonia as Green Fuels and Hydrogen Carriers: A Comparative Analysis for Fuel Cell Power Generation ..... 2032**
Antonio Sánchez, Elena C. Blanco, Mariano Martín

**The Green Hydrogen Supply Chain in The Brazilian State of Bahia: A Deterministic Approach ..... 2038**
Leonardo O. S. de Santana, Gustavo S. dos Santos, Fernando L. P. Pessoa, Ana P. Barbosa-Póvoa

**Design of a policy framework in support of the Transformation of the Dutch Industry ..... 2044**
Jan van Schijndel, Rutger de Mare, Nort Thijssen, Jim van der Valk Bouman

**Green Hydrogen Supply Chains Design in Portugal: Economic Efficiency vs Water Sustainability ..... 2051**
Tânia Pinto-Varela, João Imaginário, Nelson Chibeles-Martins

**Life Cycle Assessment of Synthetic Methanol Production: Integrating Alkaline Electrolysis and Direct Air Capture Across Regional Grid Scenarios..... 2057**
Ankur Singhal, Pratham Arora

**Waste-heat upgrading from alkaline and PEM electrolyzers using heat pumps ..... 2063**
Aldwin-Lois Galvan-Cara, Dominik Bongartz

**A Techno-Economic Optimization Approach to an Integrated Biomethane and Hydrogen Supply Chain ..... 2069**
Sandra Cecilia Cerda Flores, Catherine Azzaro-Pantel, Fabricio Nápoles Rivera

**On Optimisation of Operating Conditions for Maximum Hydrogen Storage in Metal Hydrides ..... 2075**
Chizembi Sakulanda, Thokozani Majozi

**Integrating Renewable Energy and $CO_2$ Utilization for Sustainable Chemical Production: A Superstructure Optimization Approach ..... 2081**
Tianen Lim, Yuxuan Xu, Zhihong Yuan

**An Integrated Approach for the Sustainable Water Resources Optimization..... 2088**
Michaela C. Zaroula, Emilia M. Kondili, John K. Kaldellis

**Optimization of hydrogen system deployment via environmental and economic life cycle assessment ..... 2094**
Alessandro Poles, Catherine Azzaro-Pantel, Henri Schneider, Renato Luise

**Taking into account social aspects for the development of industrial ecology on a territory..... 2101**
Maud Verneuil, Sydney Thomas, Marianne Boix

**Life cycle assessment of a post-combustion $CO_2$ capture unit through chemical absorption ..... 2108**
Agathe Gabrion, Sydney Thomas, Marianne Boix, Stéphane Negny

**Dynamic Simulation and Life Cycle Assessment of Energy Storage Systems Connecting Variable Renewable Sources with Regional Energy Demand ..... 2114**
Ayumi Yamaki, Shoma Fujii, Yuichiro Kanematsu, Yasunori Kikuchi

**Optimisation of Carbon Capture Utilisation and Storage Supply Chains Under Carbon Trading and Taxation.. 2121**
Hourissa Soleymani Babadi, Lazaros G. Papageorgiou

**Evaluation of Energy Transition Pathways for Industries with Low-Temperature Heat Demand: The Case of Laundry and Syrup Sectors..... 2127**
Juliette M. Limpach, Muhammad Salman, Daniel Florez-Orrego, François Maréchal, Grégoire Léonard

**Impact of energy sources on Global Warming Potential of hydrogen production: Case study of Uruguay ..... 2133**
V. Olave, J. Pineda, V. Larnaudie, M. Corengia

**An Optimization-Based Law of Mass Action Precipitation/Dissolution Model ..... 2140**
Chris A. Laliwala, Oluwamayowa O. Amusat, Ana I. Torres

**Sustainable Aviation Fuels Production via Biogas Reforming and Fischer-Tropsch Integrated with Solid Oxide Electrolysis..... 2146**
Muhammad Nizami, Konstantinos Anastasakis

**Socioeconomic Impacts and Land Use Change of Integrating Biofuel Production with Livestock Farming in Brazil: A Computable General Equilibrium (CGE) Approach** ..... **2152**
Igor L. R. Dias, Matheus S. Lacerda, Geraldo B. Martha Jr, Terezinha F. Cardoso, Ana C. M. Jimenez, Tassia L. Junqueira, Flávia Barbosa, Adriano P. Mariano, Antonio Bonomi, Marcelo P. Cunha

**Optimal Hydrogen Flux in a Catalytic Membrane Water Gas Shift Reactor** ..... **2158**
Nabeel S. Abo-Ghander, Filip Logist

**Solar-Driven Hydrogen Economy Potential in the Greater Middle East: Geographic, Economic, and Environmental Perspectives** ..... **2165**
Abiha Abbas, Muhammad Mustafa Tahir, Jay Liu, Rofice Dickson

## Section 8: CAPE Education and Knowledge Transfer

**Food for thought: Delicious problems for Process System Engineering (PSE) courses** ..... **2172**
Daniel R. Lewin

**The flipped classroom: The good, the bad, and the surprising** ..... **2178**
Daniel R. Lewin, Nilay Shah, Abigail Barzilai

**Digital Shadow of a Pilot Scale Packed Batch Distillation Column for Real-Time Operator Training- and Support** ..... **2185**
Mads Stevnsborg, Krist V. Gernaey, Jakob K. Huusom

**Teaching Automatic Control for Chemical Engineers** ..... **2191**
Miroslav Fikar, Lenka Galcíková

**Teaching Computational Tools in Chemical Engineering Curriculum in Preparation for the Capstone Design Project** ..... **2197**
D. Kamel, A. Tsatse, S. Badmos

**Closing the loop: customized coding courses and chatbots embedded in a virtual lab to teach bioprocesses** ..... **2203**
Fiammetta Caccavale, Carina L. Gargalo, Krist V. Gernaey, Ulrich Krühne

**Beyond ChatGMP: Improving LLM generation through user preferences** ..... **2209**
Fiammetta Caccavale, Carina L. Gargalo, Krist V. Gernaey, Ulrich Krühne, Alessandra Russo

**Teaching Digital Twins in Process Control Using the Temperature Control Lab** ..... **2215**
Alexander W. Dowling, Molly Dougher, Madelynn J. Watson, Hailey G. Lynch, Zhicheng Lu, Daniel J. Laky

**An integrated VR/MR and flipped classroom concept for enhanced chemical and biochemical engineering education** ..... **2222**
Marcos Fallanza, Antonio Dominguez-Ramos, Seyed Soheil Mansouri

**From Sugar to Bioethanol – Simulation, Optimization, and Process Technology in One Module** ..... **2228**
Jan Schöneberger, Burcu Aker

**Exergy Examples for the Chemical Engineering Classroom** ..... **2234**
Thomas A. Adams II

**Teaching of Process Design Courses – The CMU experience, trends and challenges** ..... **2242**
Ana I. Torres, Ignacio E. Grossmann

**Integrated Project in the Master of Chemical Engineering and Materials Science at the University of Liège** ..... **2247**
Marie-Noëlle Dumont, Marc Philippart de Foy, Grégoire Léonard

**Computer-based Chemical Engineering Education for Green and Digital Transformation ..... 2253**
Zorka Novak Pintaric, Miloš Bogataj, Zdravko Kravanja

**Novel PSE applications and knowledge transfer in joint industry - university energy-related postgraduate education ..... 2259**
A. S. Stefanakis, D.Kolokotsa, E. Kapartzianis, J. Bonis, J.K. Kaldellis

**Sociotechnical Transition: An Exploratory Study on the Social Appropriability of Users of Smart Meters in Wallonia..... 2265**
Boissézon Elisa

**Smart Manufacturing Course: Proposed and Executed Curriculum Integrating Modern Digital Tools into Chemical Engineering Education ..... 2271**
Montgomery D. Laky, Gintaras V. Reklaitis, Zoltan K. Nagy, Joseph F. Pekny

## Section 9: PSE4Food and Biochemical

**Valorization of suspended solids from wine effluents through hydrothermal liquefaction: a sustainable solution for residual sludge management..... 2278**
Carlos E. Guzmán Martínez, Sergio I. Martínez Guido, Valeria Caltzontzin Rabell, Salvador Hernández, Claudia Gutiérrez Antonio

**Adaptable dividing-wall column design for intensified purification of butanediols after fermentation..... 2284**
Tamara Jankovic, Siddhant Sharma, Anton A. Kiss

**Optimization-based operational space design for effective bioprocess performance under uncertainty.....2291**
Mengjia Zhu, Oliver Pennington, Sam Kay, Amin Zarei, Michael Short, Dongda Zhang

**Fed-batch bioprocess prediction and dynamic optimization from hybrid modelling and transfer learning ..... 2297**
Oliver Pennington, Youping Xie, Keju Jing, Dongda Zhang

**Plant-wide Modelling of a Biorefinery: Microalgae for the Valorization of Digestate in Biomethane plants .....2303**
Davide Carecci, Elena Ficara, Ignazio Geraci, Alberto Leva, Gianni Ferretti

**Modelling of agro-zootechnical anaerobic co-digestion for full-scale applications.....2310**
Davide Carecci, Giulia Quarta, Arianna Catenacci, Gianni Ferretti, Elena Ficara

**Multi-Omics biological embeddings for ML-models.....2316**
Lennart B. Otte, Christer Hogstrand, Adil Mardinoglu, Miao Guo

**Process design for a novel fungal biomass valorisation approach..... 2322**
Theresa Rücker, Matteo Gilardi, Thomas Brück, Bernd Wittgens

**Metabolic optimization of Vibrio natriegens based on metaheuristic algorithms and the genome-scale metabolic model..... 2328**
Yixin Wei, Tong Qiu, Zhen Chen

**Machine learning-enhanced Sensitivity Analysis for Complex Pharmaceutical Systems ..... 2334**
Daniele Pessina, Roberto Andrea Abbiati, Davide Manca, Maria M. Papathanasiou

**Incorporating Process Knowledge into Latent Variable Models: An Application to Root Cause Analysis in Bioprocesses .....2341**
Tobias Overgaard, Maria-Ona Bertran, John B. Jørgensen, Bo F. Nielsen

**Exploring Design Space and Optimization of nutrient factors for maximizing lipid production in Metchnikowia pulcherrima with Design of Experiments ..... 2348**
Nichakorn Fungprasertkul, James Winterburn, Peter Martin

**Computer-Aided Design and Optimization of Lycopene Production Process from Tomato Waste ..... 2355**
Nereyda Vanessa Hernández-Camacho, Fernando Israel Gómez-Castro, Mariano Martín, Ehecatl Antonio del Rio-Chanona, Oscar Daniel Lara-Montaño

**Optimizing Crop Schedules and Environmental Impact in Climate-Controlled Greenhouses: A Hydroponic vs. Soil-Based Case Study .....2361**
Sarah Namany, Farhat Mahmoud, Tareq Al-Ansari

**Computer-Aided Design of a Local Biorefinery Scheme from Water lily (Eichhornia Crassipes) to Produce Power and Bioproducts ..... 2367**
Maria de Lourdes Cinco-Izquierdo, Araceli Guadalupe Romero-Izquierdo, Ricardo Musule-Lagunes, Marco Antonio Martínez-Cinco

**Future Forecasting of Dissolved Oxygen Concentration in Wastewater Treatment Plants using Deep Learning Techniques ..... 2373**
Sena Kurban, Asli Yasmal, Oktay Samur, Ocan Sahin, Gizem Kusoglu Kaya, Kutay Atlar, Gözde Akkoç

**Modelling the in vitro FooD Digestion SIMulator FooDSIM ..... 2379**
Stylianos Floros, Satyajeet S. Bhonsale, Sotiria Gaspari, Simen Akkermans, Jan F.M. Van Impe

**Machine Learning Models for Predicting the Amount of Nutrients Required in a Microalgae Cultivation System ..... 2385**
Geovani R. Freitas, Sara M. Badenes, Rui Oliveira, Fernando G. Martins

**A Physics-based, Data-driven Numerical Framework for Anomalous Diffusion of Water in Soil .....2391**
Zeyuan Song, Zheyu Jiang

**CFD Simulations of Mixing Dynamics and Photobioreaction Kinetics in Miniature Bioreactors under Transitional Flow Regimes. ..... 2398**
Bovinille Anye Cho, George Mbella Teke, Godfrey K. Gakingo, Robert W.M. Pott, Dongda Zhang

**Parameter Estimation and Model Comparison for Mixed Substrate Biomass Fermentation..... 2405**
Tom Vinestock, Miao Guo

**Integrated hybrid modelling of lignin bioconversion ..... 2411**
Sidharth Laxminarayan, Lily Cheung, Fani Boukouvala

**Metabolic network reduction based on Extreme Pathway sets..... 2417**
Wannes Mores, Satyajeet S. Bhonsale, Filip Logist, Jan F.M. Van Impe

**Real-time dynamic optimisation for sustainable biogas production through anaerobic co-digestion with hybrid models ..... 2423**
Mohammadamin Zarei, Meshkat Dolat, Rohit Murali, Mengjia Zhu, Oliver Pennington, Dongda Zhang, Michael Short

**Computer-Aided Molecular Design for Bio-Based Solvent Selection from Citrus and Coffee Wastes for Furfural Extraction..... 2429**
Giovana C. A. Netto, Moisés Teles dos Santos, Vincent Gerbaud

**An MILP model to identify optimal strategies to convert soybean straw into value-added products..... 2435**
Ivaldir J. Tamagno Junior, Bruno F. Santoro, Omar Guerra, Moisés Teles dos Santos

**A Generalized Optimization Approach for the Characterization of Non-Conventional Streams..... 2441**
Michaela Vasilaki, Effie Marcoulaki, Antonis Kokossis

**A Comprehensive study on PHB biosynthesis and biodegradation through kinetic modelling ..... 2447**
Ariyan Amirifar, Constantinos Theodoropoulos

**Machine Learning Applications in Dairy Production** ..... **2454**
Alexandra Petrokolou, Satyajeet Sheetal Bhonsale, Jan FM Van Impe, Efstathia Tsakali

**Multi-Dimensional Singular Value Decomposition of Scale-Varying CFD Data: Analyzing Scale-Up Effects in Fermentation Processes** ..... **2460**
Pedro M. Pereira, Bruno S. Ferreira, Fernando P. Bernardo

**Application of pqEDMD to Modeling and Control of Bioprocesses** ..... **2466**
Camilo Garcia-Tenorio, Guilherme A. Pimentel, Laurent Dewasme, Alain Vande Wouwer

**Deacidification of Used Cooking Oil: Modeling and Validation of Ethanolic Extraction in a Liquid-Liquid Film Contactor** ..... **2472**
Sergio A. Rojas, Álvaro Orjuela, Paulo C. Narváez

## Section 10: PSE4BioMedical and (Bio)Pharma

**Predicting Final Properties in Ibuprofen Production with Variable Batch Durations** ..... **2480**
Kuan-Che Huang, David Shan-Hill Wong, Yuan Yao

**Model Predictive Control to Avoid Oxygen Limitations in Microbial Cultivations - A Comparative Simulation Study** ..... **2486**
Philipp Pably, Jakob K. Huusom, Julian Kager

**A hybrid-modeling approach to monoclonal antibody production process design using automated bioreactor equipment** ..... **2492**
Kosuke Nemoto, Sara Badr, Yusuke Hayashi, Yuki Yoshiyama, Kozue Okamura, Mizuki Morisasa, Junshin Iwabuchi, Hirokazu Sugiyama

**Kinetic modeling of drug substance synthesis considering slug flow characteristics in a liquid-liquid reaction** ..... **2498**
Shunsei Yayabe, Junu Kim, Yusuke Hayashi, Kazuya Okamoto, Keisuke Shibukawa, Hayao Nakanishi, Hirokazu Sugiyama

**Model-based approach to template-induced macromolecule crystallisation** ..... **2504**
Daniele Pessina, Jorge Calderon de Anda, Claire Heffernan, Tony Tian, Oliver Watson, Jerry Y. Heng, Maria M. Papathanasiou

**Cost-optimal Solvent Selection for Batch Cooling Crystallisation of Flurbiprofen** ..... **2510**
Matthew Blair, Dimitrios I. Gerogiorgis

**Active Pharmaceutical Ingredients from Unused Solid Drugs** ..... **2516**
Shrivatsa Korde, Aishwarya Menon, Gintaras V. Reklaitis, Zoltan K. Nagy

**Integrating process and demand uncertainty in capacity planning for next-generation pharmaceutical supply chains** ..... **2522**
Miriam Sarkis, Nilay Shah, Maria M. Papathanasiou

**Dynamic Life Cycle Assessment in Continuous Biomanufacturing** ..... **2530**
Ada Robinson Medici, Mohammad Reza Boskabadi, Pedram Ramin, Seyed Soheil Mansouri, Stavros Papadokonstantakis

**Reactive Crystallization Modeling for Process Integration Simulation** ..... **2537**
Zachary M. Hillman, Gintaras V. Reklaitis, Zoltan K. Nagy

**Data-driven Modeling of a Continuous Direct Compression Tableting Process using SINDy** ..... **2542**
Pau Lapiedra Carrasquer, Satyajeet S. Bhonsale, Carlos André Muñoz López, Kristof Dockx, Jan F.M. Van Impe

**Balancing modelling complexity and experimental effort for conducting QbD on lipid nanoparticles (LNPs) systems** ..... **2548**
Daniel V. Batista, Marco S. Reis

**Bayesian Optimization for Enhancing Spherical Crystallization Derived from Emulsions: A Case Study on Ibuprofen** ..... **2554**
Xinyu Cao, Yifan Song, Jiayuan Wang, Linyu Zhu, Xi Chen

**Probabilistic Design Space Identification for Upstream Bioprocesses under Limited Data Availability** ..... **2561**
Ranjith Chiplunkar, Syazana Mohamad Pauzi, Steven Sachio, Maria M Papathanasiou, Cleo Kontoravdi

**Robust Techno-economic Analysis, Life Cycle Assessment, and Quality and Sustainability by Digital Design of Three Alternative Continuous Pharmaceutical Tablet Manufacturing Processes** ..... **2568**
Shang Gao, Brahim Benyahia

**Systematic Model Builder, Model-Based Design of Experiments, and Design Space Identification for A Multistep Pharmaceutical Process – Toward Quality by Digital Design** ..... **2574**
Xuming Yuan, Ashish Yewale, Brahim Benyahia

**Eco-Designing Pharmaceutical Supply Chains: A Process Engineering Approach to Life Cycle Inventory Generation** ..... **2580**
Indra CASTRO VIVAR, Catherine AZZARO-PANTEL, Alberto A. AGUILAR LASSERRE, Fernando MORALES-MENDOZA

**Closed-Loop Data-Driven Model Predictive Control For A Wet Granulation Process Of Continuous Pharmaceutical Tablet Production** ..... **2586**
Consuelo Del Pilar Vega Zambrano, Nikolaos A. Diangelakis, Vassilis M. Charitopoulos

**Development of a Hybrid Model for the Paracetamol Batch Dissolution in Ethanol Using Universal Differential Equations** ..... **2592**
Fernando Arrais R. D. Lima, Amyr Crissaff Silva, Marcellus G. F. de Moraes, Amaro G. Barreto Jr., Argimiro R. Secchi, Idelfonso Nogueira, Maurício B. de Souza Jr.

**From Experiment Design to Data-Driven Modeling of Powder Compaction Process** ..... **2598**
René Brands, Vikas Kumar Mishra, Jens Bartsch, Mohammad Al Khatib, Markus Thommes, Naim Bajcinca

**Data-driven Digital Design of Pharmaceutical Crystallization Processes** ..... **2604**
Yash Barhate, Yung Shun Kang, Neda Nazemifard, Ben Renner, Yihui Yang, Charles Papageorgiou, Zoltan K. Nagy

**Process analysis of end-to-end continuous pharmaceutical manufacturing using PharmaPy** ..... **2610**
Mohammad Shahab, Kensaku Matsunami, Zoltan Nagy, Gintaras Reklaitis

**Modeling the Impact of Non-Ideal Mixing on Continuous Crystallization: A Non-Dimensional Approach** ..... **2616**
Jan Trnka, František Štepánek

**Process Design of an Industrial Crystallization Based on Degree of Agglomeration** ..... **2622**
Yung Shun Kang, Hemalatha Kilari, Neda Nazemifard, Ben Renner, Yihui Yang, Charles Papageorgiou, Zoltan K. Nagy

## INDEX

**Author Index** ..... **2629**

**Keyword Index** ..... **2368**

# Introduction

**Jan Van Impe, Grégoire Léonard, Satyajeet Sheetal Bhonsale, Monika Polanska, and Filip Logist (eds)**

The 35th European Symposium on Computer Aided Process Engineering (ESCAPE|35) was held at KU Leu-ven/Campus Gent, Belgium, July 6–9, 2025. Continuing a tradition that began in 1991 under the auspices of the EFCE Working Party on Computer Aided Process Engineering CAPE), the ESCAPE series stands as a premier annual event for the global Process Systems Engineering (PSE) community. ESCAPE returned to Belgium for the second time - following the 1998 edition in Bruges - and took place as part of KU Leuven's 600th anniversary celebrations. The 35th edition was organised jointly by KU Leuven/BioTeC+ and University of Liège/PEP.

The 2025 conference embraced the theme "Closing the Loop 2.0", underscoring the evolving role of PSE in ena-bling a circular economy. The program highlighted both core process engineering disciplines – such as modeling, con-trol, design, and optimization - and cutting-edge approaches involving artificial intelligence, machine learning, and quantum computing, applied across diverse sectors including energy, chemicals, biotechnology, and advanced mate-rials.

ESCAPE|35 received 673 abstract submissions, of which 563 were invited for a 5-to-8-page full paper or a 2- page short paper after a first review round. Upon rigorous re-review of all papers submitted, 423 full paper contribu-tions have been published in full open access (and LAPSE and DOI indexed) by PSE Press as a separate volume of the *Systems & Control Transactions* series. Another 140 contributions have been made available as two pages short pa-pers published by EUROSIS-ETI.

The scientific contributions were organized into thematic sessions, poster presentations, workshops, and demon-strations, within ten thematic tracks:

- T01: Modelling and Simulation
- T02: Sustainable Product Development and Process Design
- T03: Large Scale Design and Planning/Scheduling
- T04: Model-Based Optimisation and Advanced Control
- T05: Concepts, Methods and Tools
- T06: Digitalization and AI
- T07: CAPEing with Societal Challenges (Green Deal, Energy Transition, …)
- T08: CAPE Education and Knowledge Transfer
- T09: PSE4Food and Biochemical (*new in 2025*)
- T10: PSE4BioMedical and (Bio)Pharma (*new in 2025*)

Tracks T09 and T10 were introduced in this year's edition to broaden the application scope of PSE methods in food, biochemical, (bio)pharma and biomedical systems - fields of increasing relevance to the community.

We extend our sincere thanks to all authors, reviewers, topic coordinators, plenary and keynote speakers, and members of the Scientific and Organizing Committees. We gratefully acknowledge KU Leuven and University of Liège for their support and express our heartfelt appreciation to our numerous sponsors. This edition also marks the inaugural collaboration with PSE Press as the official publisher of the ESCAPE proceedings (full papers volume) - a milestone in promoting high-quality, open access dissemination of PSE research. Many thanks to EUROSIS-ETI as well for publish-ing the short papers volume, ISBN indexed.

We hope these volumes capture the scientific excellence, collaborative spirit, and forward-looking vision that defined ESCAPE|35 and continue to serve as a valuable reference for researchers and practitioners in the years ahead.

**ESCAPE|35 - European Symposium on Computer Aided Process Engineering**
Ghent, Belgium. 6-9 July 2025

# Peer Review Policy

## TERMINOLOGY

- **Conference Paper:** This is a peer-reviewed research paper describing an **original** research contribution and published in the conference proceedings.

## APPLICATION

- All conference papers are subject to peer review.

## PUBLICATIONS

- All conference papers which have passed peer review and have been accepted by the conference chairs will be published in the conference proceedings.

## PEER REVIEW PROCESS

### Initial Screening

The conference chairs will screen the initial submissions (one-page abstracts) of contributed papers. At their option, chairs may choose to reject these submissions for any reason, but the primary reasons for rejection at this stage are (a) subject does not match conference themes and topics; (b) in appropriate, unprofessional, unethical, or dishonest material; (c) duplicate submissions; (d) abandoned submissions; (e) multiple submissions from same presenter; (f) obvious poor quality; (g) reasonable suspicion of machine-generated text; (h) need to limit acceptances because of conference space constraints. Chairs may also transfer papers between sessions at this stage.

Conference chairs will then invite authors of the one-page abstracts that have passed the initial screening to submit a conference paper for peer review.

### Conference Paper Peer Review

Conference chairs act as editors. They will assign peer reviewers to assess the quality of the conference papers and manage the peer review process for each paper. Peer reviewers are generally selected from the International Scientific Committee who are scientists, engineers, or researchers with technical expertise in the conference topic. Peer reviewers must be considered technical experts in their field, hold a PhD, and have published peer reviewed scientific works previously. Each work must be reviewed by a minimum of two peer-reviewers.

A “single-blind” peer review system is used, in which the peer reviewers have access to the identities of the authors, but the authors are never given the identities of the peer reviewers. This is consistent with most journal peer-review procedures in our field.

Peer reviewers will be given a set of quality criteria that may include scientific and technical quality, quality of writing, originality and novelty, appropriateness for the conference topic and theme, interest to the community, and other factors of merit. Peer reviewers are expected to be rigorous and critical in their technical assessments and adhere to the highest standards in the field in order to ensure high quality. Peer reviewers are asked to comment on their assigned conference papers and issue a recommendation to the conference chairs based on this quality criteria. Reviewers may recommend one of the following:

- **Accept Paper.** No technical changes are necessary before publication. Only typographical, spelling, grammar, or other minor changes are necessary which do not require technical review.
- **Accept Paper with Minor Revisions.** Some minor technical issues need to be addressed either through technical changes to the manuscript or through rebuttal to reviewer comments. The reviewer does not believe the issues are significant enough to require additional technical review by the reviewers. The reviewer has provided enough commentary such that the editor can decide if the minor issues have been addressed in a future revision.
- **Revise Paper with Re-Review.** Major technical issues need to be addressed either through technical changes

to the manuscript or through rebuttal to reviewer comments. The reviewer believes the issues are significant enough to require that the revised manuscript receive additional review by the reviewers.

- **Reject Without Reconsideration.** The technical issues are so significant that it is unlikely that an acceptable manuscript could be produced by the deadline; or, the manuscript is out of scope, inappropriate, or computer-generated.

Peer reviewers may be asked to provide numerical scores or rankings, as well as provide written comments intended for the chairs and/or the authors. Peer reviewers are encouraged to provide specific and constructive feedback that will aid the authors in improving the work and provide advice to the chairs.

The conference chairs are responsible for making the final decision on each paper and may require several rounds of author changes if necessary to meet quality standards. Conference chairs are not required to follow the recommendations of the peer reviewers in making these decisions. It is possible that conference chairs will choose to not accept some papers that still pass through rigorous technical peer review, especially when limited by available space or when papers do not sufficiently promote conference objectives. Conference chairs may also transfer papers between sessions as desired.

## CONFLICTS OF INTEREST AND ETHICAL GUIDELINES

The chairs and peer reviewers must ensure they do not have a conflict of interest that may bias their decisions, such as ensuring that authors are at “arm’s length” and have no financial conflicts of interest. Peer reviewers and chairs must disclose if they have such a conflict of interest with a specific submission, and if so, a different chair and/or peer reviewer should be assigned to handle that submission.

To help determine conflicts of interest, and for all other ethical guidelines, we use the Systems and Control Transactions ethical guidelines described at: https://psecommunity.org/contributor-guidelines

# International Scientific Committee

| | |
|---|---|
| **Abderrazak Latifi** | U. of Lorraine, Lab. Réactions et Génie des Procédés, CNRS – ENSIC |
| **Achim Kienle** | Otto von Guericke University Magdeburg |
| **Adel Mhamdi** | RWTH Aachen University |
| **Ahmad Naquash** | Argonne National Laboratory |
| **Alain Vande Wouwer** | University of Mons |
| **Alessandro Di Pretoro** | Institut National Polytechnique de Toulouse |
| **Alexander Mitsos** | RWTH Aachen University, AVT – Aachener Verfahrenstechnik, PSE |
| **Alexander W Dowling** | University of Notre Dame |
| **Alexandros Koulouris** | International Hellenic University |
| **Ana Barbosa Povoa** | Instituto Superior Tecnico, Dept. Engenharia e Gestao |
| **Ana Somoza-Tornos** | Delft University of Technology |
| **André Bardow** | ETH Zurich |
| **Andrzej Kraslawski** | Lappeenranta University of Technology, Depart. Chemical Technology |
| **Angélique Léonard** | ULiège |
| **Antoine Rouxhet** | University of Liège |
| **Antonio Dominguez-Ramos** | University of Cantabria |
| **Antonio Espuña** | U. Politecnica de Catalunya, Centre d'Eng. de Proc. i Medi Ambient |
| **Antonios Armaou** | University of Patras |
| **Antonis Kokossis** | National Technical University of Athens |
| **Argimiro R. Secchi** | Universidade Federal do Rio de Janeiro – UFRJ |
| **Arnaud Dujany** | UniLaSalle |
| **Artur Schweidtmann** | Delft University of Technology |
| **Attila Egedy** | University of Pannonia |
| **Bilal Patel** | University of South Africa |
| **Boram Gu** | Chonnam National University |
| **Boris Houska** | ShanghaiTech University |
| **Brahim Benyahia** | Loughborough University |
| **Brent Richmond Young** | The University of Auckland |
| **Brook Tesfamichael Teferra** | Addis Ababa University |
| **Cameron Brown** | University of Strathclyde |
| **Carl Laird** | Carnegie Mellon University |
| **Carlos A. M. Riascos** | Universidad Nacional de Colombia |
| **Catherine Azzaropantel** | Toulouse INP |
| **Chengtian Cui** | Delft University of Technology |
| **Christos Maravelias** | Princeton University |
| **Claire Adjiman** | Imperial College London |
| **Cornelius Masuku** | Purdue University |
| **Cristhian Almeida-Rivera** | Organisation for the Prohibition of Chemical Weapons |
| **Cristhian Molina Fernández** | University of Liège |
| **Cristina Peretti** | AVEVA |
| **Daniel Florez-Orrego** | Ecole Polytechnique Federale de Lausanne |
| **Daniel Lewin** | Technion |
| **David Bogle** | University College London, Department of Chemical Engineering |
| **David Danaci** | Imperial College London |
| **Davide Manca** | Politecnico di Milano |
| **Dhabia Al-Mohannadi** | Hamad Bin Khalifa University |

| | |
|---|---|
| **Dhurjati Prasad Chakrabarti** | The University of the West Indies |
| **Dimitrios I. Gerogiorgis** | University of Edinburgh |
| **Diogo Narciso** | Instituto Superior Técnico |
| **Dominik Bongartz** | KU Leuven |
| **Dongda Zhang** | University of Manchester |
| **Edgar Ramirez** | Instituto Politecnico Nacional |
| **Eduardo Sanchez-Ramirez** | University of Guanajuato |
| **Edwin Zondervan** | University of Twente |
| **Effie Marcoulaki** | National Centre for Scientific Research “Demokritos” |
| **Efstathia Tsakali** | University of West Attica |
| **Eike Cramer** | RWTH Aachen University |
| **Eirini Velliou** | University College London |
| **Erik Esche** | Bundesanstalt für Materialforschung und -prüfung |
| **Eva Sorensen** | University College London |
| **Fabrizio Bezzo** | University of Padova |
| **Fatima Rani** | Technische Universität Dresden |
| **Fengqi You** | Cornell University |
| **Fernando G. Martins** | UP-FEUP |
| **Filip Logist** | BASF Antwerpen N.V. |
| **Filippo Bisotti** | SINTEF AS |
| **Flavio Manenti** | Politecnico di Milano, Dipartimento CMIC “Giulio Natta”, SuPER |
| **Francisca Pizarro Galleguillos** | KU Leuven |
| **František Štepánek** | University of Chemistry and Technology, Prague |
| **Galo A. C. Le Roux** | University of Sao Paulo |
| **Gintaras Reklaitis** | Purdue University, Davidson School of Chemical Engineering |
| **Goerge M. Bollas** | University of Connecticut |
| **Gonzalo Guillén-Gosálbez** | ETH Zurich |
| **Grégory François** | University of Applied Sciences and Arts, HES-SO Valais Wallis |
| **Guido Sand** | Pforzheim University of Applied Science |
| **Gürkan Sin** | Tech. University of Denmark, Depart. Chem. Biochem. Eng. PROSYS |
| **Harvey Arellano-Garcia** | Brandenburg University of Technology |
| **Hector Octavio Rubiera Landa** | Vrije Universiteit Brussel |
| **Heiko Briesen** | TU München |
| **Heinz A Preisig** | Norvegian University of Science and Technology, NTNU |
| **Henrique Matos** | CERENA – Instituto Superior Técnico, Universidade de Lisboa |
| **Heyen Georges** | University of Liège |
| **Hideyuki Matsumoto** | Institute of Science Tokyo |
| **Hirokazu Sugiyama** | The University of Tokyo |
| **Huabin Luo** | KU Leuven |
| **Ignacio E Grossmann** | Carnegie Mellon University |
| **Igor Plazl** | University of Ljubljana, Dept. of Chemical Engineering |
| **Ihab Hashem** | KU Leuven |
| **Iiro Harjunkoski** | Aalto University |
| **Il Moon** | Yonsei University |
| **Ilias Mitrai** | The University of Texas at Austin |
| **Iosif Pappas** | Shell Global Solutions International B.V. |
| **Iqbal M Mujtaba** | University of Bradford |
| **Jacques Gilbert de Cauwer** | University of Liège |
| **Jakob Kjøbsted Huusom** | Technical University of Denmark |
| **Jan Van Impe** | KU Leuven |

| | |
|---|---|
| **Jan van Schijndel** | QuoMare |
| **Javier Fontalvo** | Universidad Nacional de Colombia, Sede Manizales |
| **Jean Felipe Leal Silva** | University of Campinas |
| **Jean-Marc Commenge** | Université de Lorraine, CNRS, LRGP |
| **Jean-Pierre Corriou** | Université de Lorraine |
| **Jesus Pico** | Universitat Politècnica de Valencia |
| **Jin-Kuk Kim** | Hanyang University |
| **Jinsong Zhao** | Tsinghua University |
| **Jochen Steimel** | Aveva Deutschland GmbH |
| **Joel Paulson** | The Ohio State University |
| **Johannes Jaschke** | Norwegian University of Science and Technology, NTNU |
| **John Siirola** | Sandia National Laboratories |
| **Jose Alberto Romagnoli** | Louisiana State University |
| **Jose Antonio Abarca** | University of Cantabria |
| **Jose Antonio Luceño Sanchez** | University of Salamanca |
| **Jose María Ponce-Ortega** | Universidad Michoacana de San Nicolás de Hidalgo |
| **Joshua Pulsipher** | University of Waterloo |
| **Juan Segovia-Hernandez** | Universidad De Guanajuato |
| **Justin Barras** | University of Liège |
| **Kai Sundmacher** | Max Planck Institute for Dynamics of Complex Technical Systems |
| **Karen Pontes** | UFBA |
| **Keigo Matsuda** | Nagoya University |
| **Kondili Emilia** | University of West Attica |
| **Konstantinos Anastasakis** | Aarhus University |
| **Krist Gernaey** | Technical University of Denmark |
| **Lande Liu** | University of Huddersfield |
| **Laurent Dewasme** | University of Mons |
| **Lazaros Papageorgiou** | University College London |
| **Léonard Grégoire** | ULiège |
| **Leonhard Urbas** | Technische Universität Dresden |
| **Leyla Ozkan** | Eindhoven University of Technology |
| **Lidija Cucek** | University of Maribor |
| **Loris Baggio** | ULiège |
| **Ludovic Montastruc** | University of Toulouse, INP Toulouse |
| **Lydia Katsini** | KU Leuven |
| **Manabu Kano** | Kyoto University |
| **Manuel Rodriguez** | Technical University of Madrid |
| **Mar Perez-Fortes** | Delft University of Technology |
| **Marcellus de Moraes** | State University of Rio de Janeiro |
| **Marco Seabra Reis** | University of Coimbra |
| **Margherita Pettinato** | University of Genoa |
| **Maria Papathanasiou** | Imperial College London |
| **Marianne Boix** | Laboratoire de Génie Chimique |
| **Mariano Martin** | Universidad de Salamanca |
| **Marija Tasic** | University of Nis, Faculty of Technology |
| **Martin Pedemonte** | Facultad de Ingeniería, Universidad de la República |
| **Mattia Vallerio** | Politecnico di Milano |
| **Meik Franke** | University of Twente |
| **Menwer Attarakih** | The University of Jordan |
| **Metin Turkay** | Koc University |

| | |
|---|---|
| **Michael Fairweather** | University of Leeds |
| **Michael Georgiadis** | Aristotle University of Thessaloniki, Department of Chem. Engineering |
| **Michael Mangold** | Bingen University of Applied Sciences |
| **Michael Short** | University of Surrey |
| **Mirko Skiborowski** | Hamburg University of Technology |
| **Mirko Stijepovic** | Faculty of Technology and Metallurgy, University of Belgrade |
| **Miroslav Fikar** | STU in Bratislava |
| **Moisès Graells** | Universitat Politècnica de Catalunya |
| **Muhammad Salman** | Université de Liège |
| **Muhammad Shahbaz** | Teesside University |
| **Mumin Enis Leblebici** | KU Leuven |
| **Nabeel Aboghander** | King Fahd University of Petroleum & Minerals |
| **Nelly Olivier-Maget** | Laboratoire de Génie Chimique Toulouse INP ENSIACET |
| **Olga Arsenyeva** | O.M. Beketov National University of Urban Economy in Kharkiv |
| **Pascal Floquet** | Université de Toulouse |
| **Pascual Eduardo Murillo-Alvarado** | Universidad de La Ciénega del Estado de Michoacán de Ocampo |
| **Pau Lapiedra Carrasquer** | KU Leuven |
| **Pedro Mendes** | Instituto Superior Técnico |
| **Peter Mizsey** | University of Miskolc |
| **Prashant Mhaskar** | McMaster University |
| **Pratham Arora** | IIT Roorkee |
| **Rachid Ouaret** | Laboratoire de Génie Chimique, U de Toulouse, CNRS, INPT, UPS |
| **Radoslav Paulen** | Slovak University of Technology in Bratislava |
| **Rafiqul Gani** | PSE4Speed |
| **Rajagopalan Srinivasan** | Indian Institute of Technology Madras |
| **Rofice Dickson** | Aalto University |
| **Ryan Muir** | AVEVA |
| **Sabla Alnouri** | Qatar University |
| **Sebastian Engell** | TU Dortmund |
| **Sergio Lucia** | TU Dortmund University |
| **Sergio Medina-Gonzalez** | Tecnológico de Monterrey |
| **Seyed Soheil Mansouri** | Technical University of Denmark, Chemical and Biochem. Engineering |
| **Sigurd Skogestad** | Norwegian University of Science and Technology |
| **Simen Akkermans** | KU Leuven |
| **Solomon Brown** | University of Sheffield |
| **So-mang Kim** | University of Liège |
| **Srinivas Palanki** | West Virginia University |
| **Stavros Papadokonstantakis** | TU Wien |
| **Stefan Radl** | TU Graz |
| **Stéphane Negny** | Laboratoire de Génie Chimique |
| **Stratos Pistikopoulos** | Texas A&M |
| **Sujit Jogwar** | Indian Institute of Technology Bombay |
| **Sungho Shin** | MIT |
| **Tapio Salmi** | Åbo Akademi |
| **Teresa Lopez-Arenas** | Universidad Autónoma Metropolitana – Cuajimalpa |
| **Thomas Alan Adams II** | Norwegian University of Science and Technology, NTNU |
| **Timothy Gordon Walmsley** | University of Waikato |
| **Ulderico Di Caprio** | KU Leuven |
| **Valentin Plesu** | University of Science and Technology POLITEHNICA of Bucharest |
| **Vasile Mircea Cristea** | Babes-Bolyai University of Cluj-Napoca |

| | |
|---|---|
| **Ville Alopeus** | Aalto University |
| **Vincenzo Russo** | University of Naples Federico II |
| **Vivek Dua** | University College London |
| **Wannes Mores** | KU Leuven |
| **Yoshiaki Kawajiri** | Nagoya University |
| **Yuhe Tian** | West Virginia University |
| **Yusuke Hayashi** | The University of Tokyo |
| **Zdravko Kravanja** | University of Maribor, Faculty of Chemistry and Chemical Engineering |
| **Zedong Peng** | MIT |
| **Zhihong Yuan** | Tsinghua University |
| **Zoltan Nagy** | Purdue University |
| **Zorka Novak-Pintaric** | University of Maribor |

# Section 1

## Modelling and Simulation

Systems & Control Transactions

**Research Article - Peer Reviewed Conference Proceeding**
ESCAPE 35 - European Symposium on Computer Aided Process Engineering
Ghent, Belgium. 6-9 July 2025
Jan F.M. Van Impe, Grégoire Léonard, Satyajeet S. Bhonsale,
Monika E. Polańska, Filip Logist (Eds.)

PSE PRESS

# Computational Intelligence Applied to the Mathematical Modeling of the Esterification of Fatty Acids with Sugars

**Lorenzo G. Tonetti[a], Ruy de Sousa Jr.[a*]**

[a] Federal University of São Carlos, Department of Chemical Engineering, São Carlos-SP, Brazil
* Corresponding Author: ruy@ufscar.br.

## ABSTRACT

The mathematical modeling of enzymatic reactors for esterification of fatty acids with sugars in the production of biosurfactants has been a useful tool for studying and optimizing the process. In particular, artificial neural networks and fuzzy systems emerge as promising methods for developing models for those processes. In this work, regarding artificial neural networks application, coupling of networks to reactor mass balances was considered in hybrid models to infer reactant concentrations over time. Computationally, an algorithm was constructed incorporating material balances, neural reaction rates, and step-by-step numerical integration (employing the classical Runge-Kutta method). Besides, based on an available set of experimental data, fuzzy logic was applied for modeling and optimization of the conversion of esterification as a function of operational process parameters (such as time, temperature and molar ratio of substrates). All computational development was carried out using the Matlab software. The neural networks were able to predict the kinetic behavior of xylose esterification process by applying them to reactor mass balances, obtaining $R^2$ values above 0.94, indicating a good predictive capacity. The trained fuzzy models were able to simulate the relationships between input variables and the output variable, enabling the construction of surfaces and estimating the optimal operational condition at 60 h of reaction, 55°C, molar ratio of substrates of 5:1 and enzyme loading of 37.5 U/g. The same condition was obtained when applying the particle swarm optimization algorithm. Thus, this work presented a complete tool based on computational intelligence for modeling, simulation, and optimization of biosurfactant synthesis.

**Keywords**: Biosurfactants, Artificial neural networks, Fuzzy modeling.

## INTRODUCTION

Given the need for more sustainable alternatives to products available in the market, biosurfactants emerge as a promising option to synthetic surfactants [1]. Like as to synthetic surfactants, biosurfactants can form micelles and reduce surface and interfacial tensions, making them suitable for commercial applications [2]. Biosurfactants stand out to synthetic surfactants due to their biodegradability, low toxicity, use of substrates from renewable sources and waste from various production processes, which can reduce manufacturing costs, making them more attractive to industries [3,4]. Furthermore, biosurfactants are more efficient as they further reduce surface tension compared to chemical surfactants, requiring a lower concentration for maximum surface tension reduction, in a way that can be used in commercial products of the food, beverage, and cosmetics industries [5,6].

The esterification of fatty acids with carbohydrates has a significant commercial interest [7], because it yields sugar fatty acid esters, which find extensive applications in the food, pharmaceutical, cosmetic, and petrochemical industries [8]. This reaction can be carried out through either chemical or enzymatic routes, with the chemical route requiring high temperatures and an alkaline catalyst, potentially leading to the formation of toxic by-products [9]. In contrast, the enzymatic route offers mild reaction conditions, along with high selectivity, low toxicity, and high product quality and purity [10]. The mathematical modeling of enzymatic reactors for the esterification of fatty acids with sugars in the production of

biosurfactants can be a useful tool for studying and optimizing the process. Particularly, artificial neural networks and fuzzy systems emerge as promising methods for developing models for the mentioned process.

Artificial Neural Networks (ANNs) are a powerful technique for problem-solving in chemical engineering, capable of modeling nonlinear systems with a relatively simple neural network structure [11,12]. The use of ANNs in the mathematical modeling of enzymatic esterification reactors has been extensively studied by various authors, aiming to optimize the production of biodiesel, esters of aromatic carboxylic acids, and biosurfactants [13-15]. ANNs also may be used to enhance productivity, quality, and consistency, having applications in medical chemistry, hydrology, engineering, and pharmaceutical research [16,17].

The Adaptive Neuro-Fuzzy Inference System (ANFIS) is a technique that combines the power of neural networks and fuzzy inference systems, providing a method for the fuzzy modeling procedure to learn information on a data set [18,19]. ANFIS has been presented as a powerful tool for optimizing the reaction parameters of enzymatic reactors to produce biosurfactants and biodiesel, and other applications [20-22].

The production of biosurfactants through the esterification of fatty acids (oleic and lauric) and carbohydrates (fructose, lactose and xylose) in the presence of solvents such as tert-butanol and 2-methyl-2-butanol, using the commercial immobilized lipase B from *Candida antarctica* and with silica magnetic microparticles (SMMPs) as biocatalysts, has been experimentally evaluated by Lima et al. [23,24]. Torres [14], in turn, performed the kinetic modeling of this process through three distinct approaches: semi-mechanistic phenomenological modeling, the use of a model based on the Ping Pong Bi Bi mechanism; by using artificial neural networks in an empirical kinetic modeling; and the initial development of a fuzzy model.

In this context, the present work aims to contribute to the mathematical modeling of biosurfactant production by developing a hybrid-neural model capable of calculating xylose concentration values over time. This involves using neural networks to directly infer reaction rates. More specifically, hybrid-neural models for inferring the concentrations of reactants over time were developed, employing neural networks to directly provide reaction rates, being the kinetics coupled with reactor mass balances. Additionally, to complement the fuzzy model developed by Torres et al. [25] (also described in Torres [14]), data was incorporated from the factorial design by Lima et al. [23], allowing a more comprehensive understanding of the effect of input variables on the system output. This way, fuzzy logic was employed to create a model aimed at predicting optimal operational process conditions (such as time, temperature, molar ratio of substrates, etc.), to maximize product conversion.

# MATERIAL AND METHODS

## Application of Neural Networks to Infer Reaction Rates

For the development of artificial neural networks, data provided by Lima et al. [23] were employed, pertaining to the kinetics of xylose ester synthesis obtained through the esterification of oleic or lauric acid in tert-butyl alcohol medium. The experimental conditions included 300 rpm agitation, 1g of molecular sieve, a fatty acid/xylose molar ratio (SMR) of 5:1 (or 1:0.2), an enzyme activity load of 37.5 U/g of acid, and an initial xylose concentration of 20mM. Kinetic data were collected from the beginning of the reaction up till 72 hours, conducting experiments with both fatty acids at temperatures of 46ºC and 55ºC. The biocatalysts employed were commercial lipase B from *Candida antarctica* immobilized (CALB-IM-T2-350) and derivatives of CALB immobilized on silica magnetic microparticles (SMMPs) with octyl groups (CALB-SMMP-octyl) or with octyl and glutaraldehyde groups (CALB-SMMP-octyl-GLU).

To construct the neural network for the hybrid-neural model application, concentrations of xylose (mM) and reaction temperature were used. The neural networks were grouped based on the type of fatty acid and biocatalyst. The target response variable used in training the networks was the sugar consumption rate ($mmol.L^{-1}.h^{-1}$), calculated using the numerical derivative method from experimental data on concentration and time. Table 1 presents the sets of neural networks trained with experimental data for both temperatures, 46ºC and 55ºC.

**Table 1:** Specification of each trained ANN set.

| Network | Biocatalyst | Fatty Acid |
|---|---|---|
| ANN1-3 | CALB-IM-T2-350 | Oleic |
| ANN2-1 | CALB-IM-T2-350 | Lauric |
| ANN3-1 | CALB-SMMP-octyl | Lauric |
| ANN4-2 | CALB-SMMP-octyl-GLU | Oleic |
| ANN5-2 | CALB-SMMP-octyl-GLU | Lauric |

To develop the hybrid-neural model, the coupling of neural networks to reactor mass balances was performed, aiming to infer concentrations of reactants over time. As the experiments were conducted in a batch reactor, Equation 1 represents the mass balance for this reactor type.

$$\frac{dX}{dt} = -\Gamma_X \quad (1)$$

Where $\Gamma_X$ is the xylose consumption rate, $X$ is the xylose concentration, and $t$ is the reaction time. In the implementation of the hybrid-neural model, $\Gamma_X$ is the output

of the neural network; therefore, is possible to obtain xylose concentration values over time by solving the differential equation. For this purpose, the classical Runge-Kutta method can be used for integration. The integration method was applied using the "ode15s" subroutine in the software Matlab.

The construction and training of neural networks were performed using the "feedforwardnet" function in the software Matlab. This function also allows data splitting for training, validation, and testing, with a distribution of 50%, 25%, and 25%, respectively, ensuring at least three data points for each training stage.

In this work, feed-forward neural networks with an input layer, a hidden layer, and one neuron in the output layer were employed. The training was conducted using the "trainlm" function, which implements the Levenberg-Marquardt method. The model's performance criteria included evaluating the determination coefficients for both the network training stage and the final response of the hybrid-neural model.

## Development of Fuzzy Systems Modeling

For the development of the ANFIS modeling, kinetic data provided by Lima et al. [23] were employed for the xylose esterification with fatty acids (oleic or lauric) in tert-butyl alcohol medium. The experimental conditions included 300 rpm agitation, 1g of molecular sieve, a fatty acid/sugar molar ratio of 1:0.2, 20mM of xylose, and an enzyme load of 37.5 U/g of acid. Data collection spanned from the beginning of the reaction until 72 hours, conducting the experiment at temperatures of 46ºC and 55ºC for each type of biocatalyst used, namely CALB-IM-T2-350, CALB-SMMP-octyl, and CALB-SMMP-octyl-GLU.

In addition to the kinetic data provided by Lima et al. [23], data from an experimental design procedure were also utilized in this stage. The operational conditions are outlined in Table 2, with a reaction time of 48 hours. These data were used in conjunction with the kinetic data for constructing the fuzzy models.

**Table 2:** Operational Conditions of the factorial design [23].

| Fatty acid | Oleic | Lauric | |
|---|---|---|---|
| Temperature(ºC) | 40.6 | 46.0 | 51.30 |
| Acid/sugar ratio (SMR) | 0.60 | 1.00 | 1.39 |
| Enzymatic Load (U/g) | 30.10 | 37.50 | 44.90 |

The Neuro Fuzzy Designer tool in the software Matlab was employed for model construction, enabling the creation of the ANFIS model through graphical user interfaces. The datasets were separated based on the catalyst type used, resulting in three distinct models: ANFIS1 for CALB-IM-T2-350, ANFIS2 for CALB-SMMP-octyl, and ANFIS3 for CALB-SMMP-octyl-GLU. To enhance the fitting quality, additional data points were incorporated through interpolation in the kinetic data at the 36-hour mark.

The input data for ANFIS were organized in a file, with columns representing the values for fatty acid, temperature, SMR (substrate molar ratio), enzyme load, time, and xylose conversion, respectively. Each row represented one of the experimental data points. These data were loaded into the software, and in conjunction with the Neuro Fuzzy Designer tool, linguistic values of the model and the membership function were defined.

## Optimization of reaction parameters through PSO

From the trained ANFIS networks, the particle swarm optimization (PSO) algorithm was employed to assess the optimized operational condition for the xylose esterification reaction in each network and for each fatty acid. The software Matlab, utilizing the PSO routine, can be utilized for this purpose, enabling the application of the PSO algorithm in the fuzzy network. Due to the routine's nature of seeking the global minimum, the ANFIS network output was defined as negative to pursue the global maximum of the network [26]. Import to say that other optimization methods could also be considered, such as genetic algorithms or simulated annealing. All are classical robust algorithms often used to solve global optimization problems.

# RESULTS

## Development of Modeling by Artificial Neural Networks

The neural networks were trained with the aim to inferring xylose consumption rate in the esterification reaction during biosurfactant synthesis, using concentration and temperature information as input for the network. During training, the network utilized experimental data to learn data behaviors, while validation was conducted to assess the network's generalization ability using some data, and testing was performed to evaluate the neural model's performance. The adopted criterion was the coefficient of determination ($R^2$), obtained by comparing the network output value with the experimental value of the output variable. For the network to be considered promising, the final $R^2$ values need to exceed 0.95.

The number of neurons in the hidden layer was determined following the same training criterion, evaluating the final behavior of the network in the hybrid model. There is a possibility that the network is promising with two different quantities of neurons, or they differ only due to the randomness of the training initialization. For these reasons, it is possible to obtain more than one network for each dataset. The neural networks ANN1-3, ANN3-1, ANN4-2 and ANN5-2 have three neurons in the

hidden layer, while the neural network ANN2-1 has two neurons. Overall, all networks have $R^2$ values above 0.98, due to the criterion adopted during training, with some exceeding 0.99.

The developed neural networks were coupled to reactor mass balances in a hybrid model to infer the concentrations of reactants over time, using the Runge-Kutta method for numerical integration. To achieve this, Equation 1 is applied in conjunction with these networks, and the differential equations are solved using the "ode15s" subroutine. Figure 1 illustrates the resulting curves of the hybrid modeling for the ANN2-1 neural network, where the determination coefficients of the model with the experimental data at temperatures of 46°C and 55°C are, respectively, 0.9741 and 0.9935. Overall, the results obtained from the hybrid modeling with direct neural kinetics fully satisfy the conditions imposed as performance criterion, where the value of $R^2$ should be greater than 0.95 (except for the RNA4-2, which presented a slightly lower but also good value of 0.9249 at 46°C). Thus, the application of mass balance together with neural networks has successfully constructed kinetic curves capable of inferring the concentration of xylose throughout the esterification reaction.

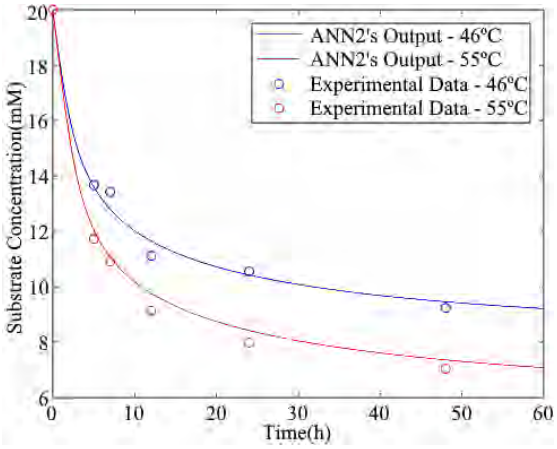



**Figure 1:** Response curves for the hybrid-neural model at temperatures of 46°C and 55°C, using the neural network ANN2-1.

## Development of Fuzzy System Modeling

The application of fuzzy logic in the mathematical modeling of biosurfactant production through esterification was carried out using a dataset derived from a factorial design and another set of kinetic data. These datasets were classified based on the catalyst used, generating fuzzy networks for each distinct catalyst. With the trained ANFIS models, the ability to simulate experimental data was tested. For this purpose, a regression of the model-derived data with experimental data was performed. Coefficient of determination values close to or greater than 0.98 were obtained, indicating that the training was effective in preparing the network to accurately infer the experimental data. Figure 2 illustrates the kinetics resulting from the fuzzy model prediction at temperatures of 46°C and 55°C, with the lauric acid experimental data.

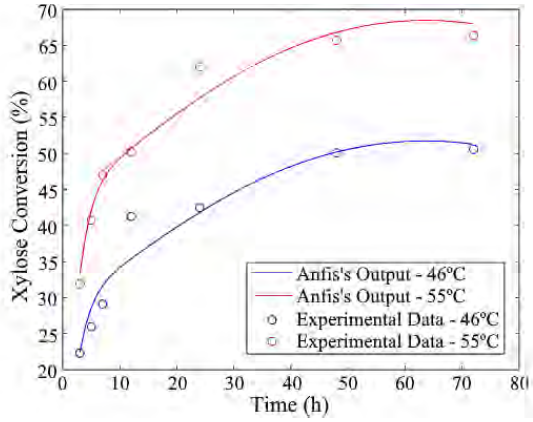



**Figure 2:** ANFIS modeling at temperatures of 46°C and 55°C from ANFIS3-1 network, for lauric acid.

Fuzzy modeling has a high ability to infer the output variable based on an input value within its domain. In this context, surface plots were developed from combinations of input variables, evaluating batch temperature (constant during each batch) combined with time (to terminate the batch), fatty acid/sugar ratio combined with enzyme load, and temperature combined with fatty acid/sugar ratio. Figure 3 illustrates these surfaces, allowing a comprehensive visualization of the fuzzy modeling. The problem had a pattern input of a fatty acid/sugar ratio of 5.0, temperature of 55°C, enzyme load of 37.50 UE/g, and a reaction time of 48 hours, when kept invariable (i.e., when some not being one of the variables whose effects are being analysed). The obtained results show the region with global maximum conversion under the following conditions: above 48 hours, temperature of 55°C, acid/sugar ratio of 1:0.2, and enzymatic load of 37.5 U/g, even with variations in linguistic values and the biocatalyst used. This is consistent with the results obtained by Torres [14]. Additionally, the local maximum appearing in regions of SMR values below 1:0.2 represent the optimal condition for the data obtained in the factorial design by Lima et al. [23]. One impact of including data from the experimental design is the possibility of also identifying this local maximum.

### Application of particle swarm optimization in the ANFIS model

The particle swarm optimization algorithm was applied to the constructed fuzzy models with the aim of optimizing operational conditions for biosurfactant synthe-

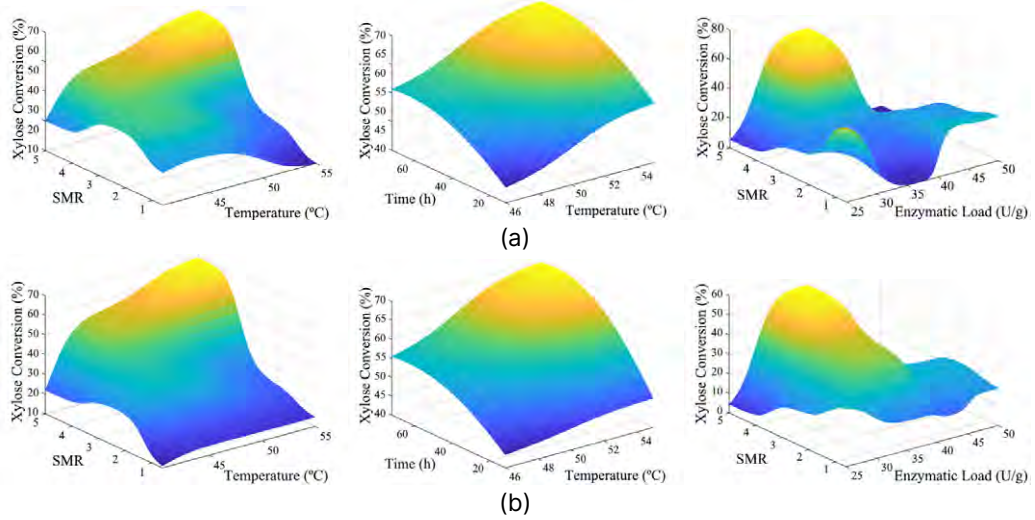



**Figure 3:** Surfaces developed by the ANFIS model for lauric acid (a) and oleic acid (b) from the ANFIS3-1.

sis. The optimization was carried out using the "particleswarm" command in software Matlab. Table 3 presents the optimized conditions obtained by the optimization algorithm for each of the developed models (the respective optimal temperature and SMR values for all networks are 55ºC and 5).

**Table 3:** Optimized conditions obtained by PSO.

| Network | FA | Load (U/g) | t (h) | (%) |
|---|---|---|---|---|
| ANFIS1-2 | Lauric | 37.48785 | 64.931 | 69.19 |
| ANFIS1-2 | Oleic | 37.48769 | 63.714 | 70.16 |
| ANFIS2-1 | Lauric | 40.41127 | 65.509 | 74.12 |
| ANFIS2-1 | Oleic | 40.41144 | 65.508 | 68.65 |
| ANFIS3-1 | Lauric | 36.90347 | 63.572 | 68.58 |
| ANFIS3-1 | Oleic | 36.90348 | 63.573 | 70.33 |

The global optimal conditions found by the particle swarm optimization algorithm show values close to the point with the highest conversion (temperature of 55ºC, SMR of 5, enzyme load of 37.5 U/g, and 72 hours of reaction).

## CONCLUSION

The training of neural networks was effective in producing neural networks capable of inferring experimental data. When applying the hybrid-neural model, the neural networks were able to predict the kinetic behavior of the xylose esterification process in biosurfactant synthesis, applied to reactor mass balances.

The fuzzy models were able to simulate the relationships between input variables (temperature, time, SMR, and enzyme load) and the output variable (xylose conversion), allowing the construction of various response combinations. The application of the particle swarm optimization to fuzzy models demonstrated the ability of this optimization technique to estimate the optimized operational condition.

## ACKNOWLEDGEMENTS

This study was financed in part by the Coordenação de Aperfeiçoamento de Pessoal de Nível Superior – Brasil (CAPES) – Finance Code 001. Besides, this work was carried out with the support of the National Council for Scientific and Technological Development, CNPq.

## REFERENCES

1. Nitschke M, Pastore GM. Biosurfactants: properties and applications. *Quím Nova*. 25:772–6 (2002)
2. Drakontis, CE. Amin, S. Biosurfactants: Formulations, properties, and applications. *COCIS* 48:77-90 (2020)
3. Kreling NE, Zaparoli M, Margarites AC, Zampieri D, Colla LM. Biosurfactant production: intracellular manoproteins and extracellular sophorolipids by *Saccharomyces cerevisiae*. *ABES* 24:1209-19 (2019)
4. Santos ECL, Miranda DAR, Silva ALS, López AMQ. Biosurfactant Production by Bacillus strains isolated from sugar cane mill wastewaters. *Braz arch biol technol* 67 (2024). https://doi.org/10.1590/1678-4324-2019170630
5. Cameotra SS, Makkar RS. Recent applications of biosurfactants as biological and immunological molecules. *COMICR 7*:262–6 (2004)
6. Oliveira EM, Sales VHG, Dias EDC, Andrade MS, Araújo RS, Borges WL, et al. . Biosurfactant by *Serratia* sp. BR13816: Fermentation Optimization and Nanoemulsion Formation. *Braz arch biol technol* 67 (2024). https://doi.org/10.1590/1678-4324-2024220225.

7. Vescovi V, Santos JBC, Tardioli, PW. Porcine pancreatic lipase hydrophobically adsorbed on octyl-silica: A robust biocatalyst for syntheses of xylose fatty acid esters. *Biocatal Biotrans* 35:298–305 (2016)
8. Torres ACL, Lima LN, Tardioli PW, Júnior RS. Mathematical modeling of enzymatic syntheses of biosurfactants catalyzed by immobilized lipases. *Reac Kinet Mech Cat* 130:699–712 (2020)
9. Yan Y, Bornscheuer, UT, Stadler, G. Lutz-Wahl S, Reuss M, Schmid, RD. Production of sugar fatty acid esters by enzymatic esterification in a stirred-tank membrane reactor: Optimization of parameters by response surface methodology. *J Amer Oil Chem Soc* 78:147–53 (2001)
10. An D, Zhang X, Liang F, Xian M, Feng D, Ye Z. Synthesis, surface properties of glucosyl esters from renewable materials for use as biosurfactants. *Colloids Surfaces A* 577:257–64 (2019)
11. Beigi M, Torki-Harchegani M, Mahmoodi-Eshkaftaki M. Prediction of paddy drying kinetics: A comparative study between mathematical and artificial neural network modelling. *Chem Ind & Chem Eng Q* 23:251–8 (2017). https://doi.org/10.2298/CICEQ160524039B
12. Eyng E, Silva FV, Palú F, Fileti AMF. Neural network based control of an absorption column in the process of bioethanol production. *Braz arch biol technol* 52:961–72 (2009). https://doi.org/10.1590/S1516-91320090004000020
13. Manohar B, Divakar S. An artificial neural network analysis of porcine pancreas lipase catalysed esterification of anthranilic acid with methanol. *Process Biochem* 403372–6 (2005)
14. Torres ACL. Modelagem matemática para sínteses enzimáticas de biossurfactantes catalisadas por lipases imobilizadas. São Carlos: Universidade Federal de São Carlos (2021)
15. Soltani S, Shojaei TR, Khanian N, Choong TSY, Asim N, Zhao Y. Artificial neural network method modeling of microwave-assisted esterification of PFAD over mesoporous TiO2—ZnO catalyst. *J Renew Energy* 87:760–73 (2022)
16. Singh I, Kaur J, Kaur S, Barik BR, Pahwa R. Artificial Neural Networks and Neuro-Fuzzy Models: Applications in Pharmaceutical Product Development. *Braz arch biol technol* 66 (2023). https://doi.org/10.1590/1678-4324-2023210769
17. Souza GR, Bello IP, Corrêa FV, Oliveira LFC. Artificial Neural Networks for Filling Missing Streamflow Data in Rio do Carmo Basin, Minas Gerais, Brazil. *Braz arch biol technol* 63 (2020). https://doi.org/10.1590/1678-4324-2020180522
18. Betiku E, Odude VO, Ishola NB, Bamimore A, Osunleke AS, Okeleye AA. Predictive capability evaluation of RSM, ANFIS and ANN: A case of reduction of high free fatty acid of palm kernel oil via esterification process. *Energy Convers Manag* 124:219–30 (2016)
19. Bressan GM, Azevedo BCF de, Souza RM de. A Fuzzy Approach for Diabetes Mellitus Type 2 Classification. *Braz arch biol technol* 63 (2020). https://doi.org/10.1590/1678-4324-2020180742
20. Santos B, Ponezi A, Fileti A. Development of Artificial Intelligence Models to Monitor Biosurfactant Concentration in Real-Time using Waste as Substrate in Bioreactor Through Fermentation by *Bacillus subtilis*. *Chem Eng Trans* 57:1009-14 (2017)
21. Ighose BO, Adeleke IA, Damos M, Junaid HA, Okpalaeke KE, Betiku E. Optimization of biodiesel production from Thevetia peruviana seed oil by adaptive neuro-fuzzy inference system coupled with genetic algorithm and response surface methodology. *Energy Convers Manag* 132:231–40 (2017)
22. Sadi M, Ahari SJ, Zarrinpashne S. Application of adaptive neuro fuzzy inference system to modeling oxidative coupling of methane reaction at elevated pressure. *J Pet Technol* 4: 43-55 (2014)
23. Lima LN, Vieira GNA, Kopp W, Tardioli PW, Giordano RLC. Mono- and heterofunctionalized silica magnetic microparticles (SMMPs) as new carriers for immobilization of lipases. *J Mol Catal B Enzym* 133:S491–99 (2016)
24. Lima LN, Mendes AA, Fernandez-Lafuente R, Tardioli PW, Giordano RLC. Performance of Different Immobilized Lipases in the Syntheses of Short- and Long-Chain Carboxylic Acid Esters by Esterification Reactions in Organic Media. *Molecules* 23:766 (2018)
25. Torres ACL, Akisue RA, Lima LN, Tardioli PW, Júnior RS. Computational intelligence applied to the mathematical modeling of enzymatic syntheses of biosurfactants. *Comput Aided Chem* Eng 51;139-44 (2022)
26. Kennedy J, Eberhart R. Particle swarm optimization. *Proceedings of ICNN'95 - International Conference on Neural Networks* 4:1942–48 (1995)

© 2025 by the authors. Licensed to PSEcommunity.org and PSE Press. This is an open access article under the creative commons CC-BY-SA licensing terms. Credit must be given to creator and adaptations must be shared under the same terms. See https://creativecommons.org/licenses/by-sa/4.0/



Systems & Control Transactions

**Research Article - Peer Reviewed Conference Proceeding**
ESCAPE 35 - European Symposium on Computer Aided Process Engineering
Ghent, Belgium. 6-9 July 2025
Jan F.M. Van Impe, Grégoire Léonard, Satyajeet S. Bhonsale,
Monika E. Polańska, Filip Logist (Eds.)

PSE PRESS

# Numerical Analysis of the Hydrodynamics of Proximity Impellers using the SPH Method

**Maria Soledad Hernández-Rivera[a], Karen Guadalupe Medina-Elizarraraz[a], Jazmín Cortez-González[a,*], Rodolfo Murrieta-Dueñas[a], Carlos E. Alvarado-Rodríguez[b,c], José de Jesús Ramírez-Minguela[b], Juan Gabriel Segovia Hernández[b]**

[a] Tecnológico Nacional de México / Campus Irapuato, Departamento de Ingeniería Química, Irapuato, Guanajuato, México
[b] Universidad de Guanajuato, Departamento de Ingeniería Química, Guanajuato, Guanajuato, México.
[c] Secretaria de Ciencias, Humanidades, Tecnología e Innovación, Ciudad de México, México
* Corresponding Author: jazmin.cg@irapuato.tecnm.mx

## ABSTRACT

Mixing is a critical operation in numerous industrial processes, traditionally performed in agitated tanks to ensure homogenization. Despite its importance, the design of tanks and impellers is often neglected during agitation system selection, resulting in excessive energy consumption and inefficient mixing. To mitigate these challenges, Computational Fluid Dynamics (CFD) serves as a powerful tool for analyzing tank hydrodynamics and quantifying mixing times. CFD employs mathematical models to simulate mass, heat, and momentum transport phenomena within fluid systems. Among the latest advancements in modeling stirred tank hydrodynamics is Smoothed Particle Hydrodynamics (SPH), a mesh-free Lagrangian approach that tracks individual particles characterized by properties such as mass, position, velocity, and pressure. SPH provides significant advantages over traditional mesh-based methods by accurately capturing fluid behavior through particle interactions. In this study, the performance of three impellers—double ribbon, paravisc, and hybrid—was evaluated based on hydrodynamics and mixing times during the homogenization of water and ethanol in a 0.5 L stirred tank. The tank and impellers were meticulously designed, operating at 70% capacity, with the fluids exhibiting the following rheological properties: $\rho_1$ = 1000 kg/m$^3$, $\rho_2$ = 789 kg/m$^3$, $\mu_1$ = 1E-6 m$^2$/s, and $\mu_2$ = 1.52E-6 m$^2$/s. The simulations were conducted under turbulent flow conditions (Reynolds number of 10,000) for a duration of 2 minutes using the DualSPHysics software. The stirring speed was set at 34 rpm, and the initial particle spacing was configured to 1 mm, generating 270,232 fluid particles and 187,512 boundary particles representing the tank and agitator. The analysis included velocity profiles, flow patterns, vorticity, divergence, and density fields to assess mixing performance. The Q-criterion was employed to discern the dominance of rotational or deformational motion and to identify stagnation zones. The results revealed that the double ribbon impeller exhibited superior performance, achieving 88.28% mixing within approximately 100 seconds, while the paravisc and hybrid impellers reached mixing efficiencies of 12.36% and 11.8%, respectively. These findings underscore the potential of SPH as a robust computational approach for linking hydrodynamic behavior with mixing efficiency and identifying key parameters to optimize mixing processes.

**Keywords**: CFD, hydrodynamics, Proximity impellers, SPH, homogenization

## 1. INTRODUCTION

The numerical analysis of fluid distribution in stirred tanks is an essential tool for evaluating impeller performance. It enables the characterization of axial and radial flow patterns, velocity profiles, mixing times, stagnation zones, and vortex formation. These analyses are typically conducted using Computational Fluid Dynamics (CFD), which provides detailed insights that are often unattainable through experimental methods. However, CFD

simulations demand significant computational resources (Gelves et al., 2013). Analyzing mixing times numerically is particularly valuable for understanding the distribution of species within chemical or biological reactors. This parameter is critical for assessing the overall effectiveness of stirred tanks. Previous studies have extensively investigated the influence of stirrer geometry on hydrodynamics and mixing times in such reactors. Many of these efforts have focused on optimizing conventional impellers, such as the Rushton turbine, to enhance their performance. Despite these advances, there has been limited investigation into proximity impellers—specialized designs that operate at a short distance from the tank walls. These impellers are commonly employed for mixing non-Newtonian fluids and are characterized by lower operational speeds compared to conventional designs. In this work, the mixing process for achieving a homogeneous 50% water-ethanol solution is simulated using the Smoothed Particle Hydrodynamics (SPH) method. The primary objective is to develop a robust methodology for analyzing the hydrodynamics of mixing processes in stirred tanks equipped with different impeller designs. The performance of the impellers is subsequently compared to identify the most effective option for the fluids under investigation.

## 2. METHODOLOGY

### 2.1 CAD design of the impellers

In this work, three proximity impellers: double ribbon, paravisc and hybrid, were used to simulate the mixing process of the ethanol-water solution. Figure 1 shows the proximity impellers analyzed. The double Ribbon agitator consists of two opposite helical ribbons fitted on an axis, one of these ribbons has the job of moving the materials to be mixed in a single direction and the other does the same as the previous one, however, it does it in an opposite direction, as a consequence of these movements the materials to be mixed acquire a single direction, making this system ideal to be used as a continuous mixer (Londoño, 2019). This impeller is generally used in industries to be able to combine powdered, granulated and viscous materials. The effectiveness of the mixing process will depend on factors, such as the rotation speed, the design of the belts, the mixing time and the physical properties of the materials (Flores & Cuevas, 2008).

Paravisc is a proximity impeller that works efficiently with high viscosity mixtures, however, it can be coupled to different stages of the process with the possibility of accomplishing an efficient homogenization. This type of impeller, like the previous one, works inside a mixing tank with circular geometry, in which there is a minimum separation with the internal wall of the tank and also the space between the blades and the bottom surface, which means that the mechanical operation of this impeller is made circular through the action of the axial pumping. This type of impeller can work without problem with internal baffles to improve power, heat transfer and to obtain an adequate mixing incorporating all the solids of the more viscous medium. The hybrid agitator is a novel design reported by Alvarado-Rodriguez et al. (2023). It is a proximity stirrer that combines the characteristics of the anchor stirrer with the double ribbon stirrer. Its efficiency lies in favoring mixing in both axial and radial directions.



a) Double Ribbon b) Paravisc c) Hybrid

**Figure 1**. CAD design of the selected proximity impellers.

### 2.2 SPH method

Computational Fluid Dynamics (CFD) simulation has proven to be a powerful tool to study and optimize mixing processes, contributing to the development of more efficient processes (Yin, et al., 2022). CFD numerical analysis allows a better comprehension of the momentum, mass and energy transport phenomena of different systems. In stirring systems, emulsification, homogenization and mixing mechanisms are analyzed numerically to describe the behavior of fluids inside the tank (Zawawi, et al., 2018).

Recently, within computational fluid dynamics, the method of smoothed particle hydrodynamics has been implemented to analyze the behavior of fluids. SPH is a method for meshless Lagrangian and dissipative particle dynamics transporting physical properties such as mass, position, velocity and pressure. It is able to follow the trajectory of these particles, can analyze highly complex flows and where there are deformations or phenomena at macro or meso scale. It is able to handle complex geometries and boundary conditions. SPH tracks individual fluid particles by calculating their interactions to simulate the fluid behavior. Equations 1 to 3 present the equations describing the hydrodynamics of stirred tanks.

$$\frac{d\rho}{dt} = -\rho\nabla \cdot \mathbf{v}, \tag{1}$$

$$\frac{d\mathbf{v}}{dt} = -\frac{\nabla P}{\rho} + \frac{\mu}{\rho}\nabla^2\mathbf{v} + \boldsymbol{g}, \tag{2}$$

$$\frac{dC}{dt} = D\nabla^2 C - \nabla \cdot (C\mathbf{v}) + \mathbf{v} \cdot \nabla C, \quad (3)$$

where: $\rho$ is the density, $t$ is time, $\mathbf{v}$ is velocity, $P$ is pressure, $\mu$ is viscosity, $\boldsymbol{g}$ is gravity, $C$ is concentration and $D$ is the mass diffusion coefficient.

Equations 1 to 3 are shown in the SPH formalism in equations 4 to 6 which are closed by the Tait´s equation of state shown in the equation 7

$$\frac{d\rho_a}{dt} = -\rho_a \sum_b^n m_b \frac{\mathbf{v}_b}{\rho_b} \cdot \nabla W_{ab} \quad (4)$$

$$\frac{d\mathbf{v_a}}{dt} = -\sum_b^n m_b \left(\frac{p_a + p_b}{\rho_a \rho_b}\right) \nabla_a W_{ab} + 2\nu \sum_b^n m_b \frac{\mathbf{v}_{ab}\, r_{ab} \cdot \nabla W_{ab}}{\bar{\rho}_{ab} {r_{ab}}^2 + \varepsilon^2} + \boldsymbol{g} \quad (5)$$

$$\frac{dC_a}{dt} = \sum_b^n \frac{m_b}{\rho_b} \frac{C_{ab} D \cdot \nabla W_{ab}}{{r_{ab}}^2 + \varepsilon^2} - \sum_b^n m_b \frac{C_b}{\rho_b} (\mathbf{v}_a \cdot \nabla_a W_{ab}) \quad (6)$$

$$p = B\left[\left(\frac{\rho}{\tilde{\rho}}\right)^{\gamma} - 1\right] \quad (7)$$

where the subscripts *a*, *b* are referent to the mean particle *a* or neighbor particles *b*, *W* is the kernel function, *m* is the mass of the particle, $r_{ab} = r_a - r_a$, where *r* is the position vector, *v* is the kinematic viscosity, $\bar{\rho}_{ab} = \frac{\rho_a + \rho_b}{2}$, *D* is the diffusion coefficient, $C_{ab} = C_a - C_b$, $\varepsilon$ is a small regularization term to prevent singularities, $B = c^2\rho/\gamma$, $\gamma = 7$ for liquids, $\tilde{\rho}$ is a reference density and *c* is a numerical speed of sound which must be at least 10 times higher than the maximum velocity of the fluid in the system to ensure a maximum density fluctuation of 1% satisfying the compressibility condition.

Finally, the properties of the particles as de density, position, velocity and concentration are advanced from time $t^{n+1} = t^n + \Delta t$ using the Verlet algorithm according to equations 8 to 11.

$${\rho_a}^{n+1} = {\rho_a}^{n-1} + 2\Delta t \left(\frac{d\rho_a}{dt}\right)^n, \quad (8)$$

$${\boldsymbol{r}_a}^{n+1} = {r_a}^n + \Delta t \mathbf{v}_a^n + 0.5\Delta t^2 \left(\frac{d\boldsymbol{x}_a}{dt}\right)^n, \quad (9)$$

$${\mathbf{v}_a}^{n+1} = {\mathbf{v}_a}^{n-1} + 2\Delta t \left(\frac{d\mathbf{v}_a}{dt}\right)^n, \quad (10)$$

$${C_a}^{n+1} = {C_a}^{n-1} + 2\Delta t \left(\frac{dC_a}{dt}\right)^n, \quad (11)$$

Where n is the value of step and $\Delta t$ is the time step calculated with the equation 12.

$$\Delta t = min\left[\left(\frac{h}{{d\mathbf{v}_a}/{dt}}\right)^{1/2}, \frac{h}{(c + \Delta t_{v,a})}, \frac{h^2}{2D}\right] \quad (12)$$

Where h is the smoothing length of the kernel function and $\Delta t_{v,a} = max_b |h r_{ab} \cdot \mathbf{v}_{ab} / (r_{ab} \cdot r_{ba} + \varepsilon^2)|$.

Using the Verlet algorithm, numerical coupling of the discrete SPH equations is ensured during the evolution by alternating the step $t^{n-1}$ in in the first term of the right side in equations 8, 10 and 11 every N≈40 steps by the step $t^n$.

### 2.3 Numerical simulation

Numerical simulations were performed using the DualSPHysics software (Domínguez et al., 2022) which is based on the SPH method. The tank and impellers geometries generated in CAD were imported into the DualSPHysics software to generate the fixed and moving boundary conditions in the simulation. The tank was filled to 70% volume, being 35% water at the bottom and 35% ethanol at the top of the liquid. An isothermal mixing process at 25°C was considered. The initial distance between particles is 1 mm generating a total of 270232 fluid particles and 187512 contour particles (tank plus stirrer). The initial velocity of the liquids is zero and a no-slip boundary condition is established on the tank surface. The stirring speed for the three stirrers is 33.9 rpm setting a Reynolds number of 10000. The initial stirrer speed is zero and is accelerated at 16.95 rpm for 1 second until the constant stirring speed is reached. Two minutes of mixing time was simulated and the percentage of mixing over time was evaluated, as well as the average velocity after 1.5 minutes of stirring. The fluid parameters used in the simulation are shown in Table 1.

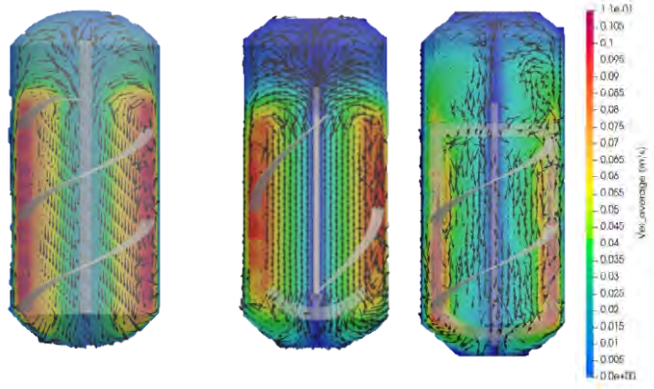
**Table 1.** Properties of water, ethanol and the mixture.

| | Water | Ethanol | Mixture |
|---|---|---|---|
| Density (kg/m³) | 1000 | 789 | 894.5 |
| Kinematic Viscosity (m²/s) | 1 E-06 | 1.52 E -06 | 1.17 E-06 |

## 4. RESULTS

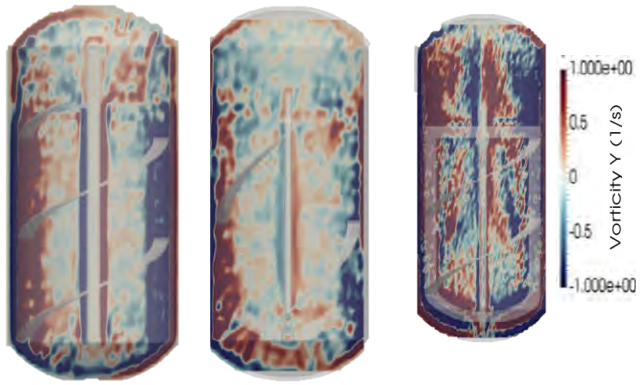
The numerical simulations provided detailed insights into the mixing performance and hydrodynamic behavior within the stirred tank. Key parameters such as the mixing percentage over the simulated time, average velocity, velocity gradient, divergence, and vorticity of the flow were quantified. Additionally, the Q-criterion was employed to further analyze the hydrodynamic characteristics of the fluid within the tank. Density and density gradient fields within the tank were also visualized to identify regions of high mixing efficiency and to evaluate the relationship between the mixing performance and the flow patterns generated by each impeller. The primary

goal was to determine which impeller achieved the highest mixing percentage within 2 minutes and to correlate this performance with the hydrodynamic features induced by the impeller design. Figure 2 illustrates the average velocity profiles for the different impellers. For all configurations, the highest velocity was observed near the tank walls. Furthermore, vortices were consistently present in the regions of highest velocity for each impeller. These vortices facilitated fluid circulation, directing the flow upward along the tank walls and creating a downward flow in the central region of the tank. This circulation pattern played a crucial role in promoting effective mixing within the tank.



a) Double Ribbon b) Paravisc c) Hybrid

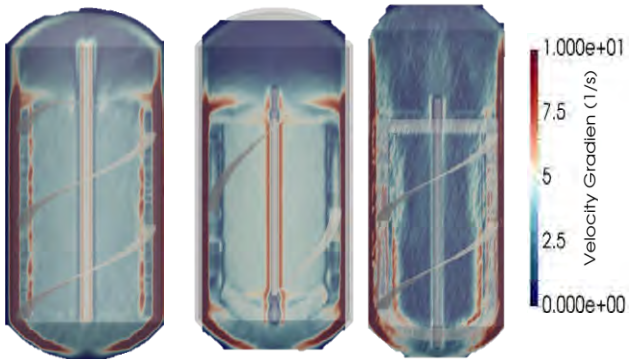
**Figure 2**. Average velocity generated by the impellers inside the tank.




a) Double Ribbon b) Paravisc c) Hybrid

**Figure 3**. Vorticity calculated from the average velocity.

Figure 3 shows the behavior of the vorticity generated by the fluid inside the tank in each impeller. The red color represents regions of high vorticity, indicating strong twists and rotations of the fluid in those areas. These regions usually form near the proximity stirrer blades due to the force imposed on the fluid. Conversely, low vorticity zones (blue color), indicate areas of more stable and less disturbed flow, suggesting a limited mixing pattern in this region. The intermediate colors show a more efficient and homogeneous mixing.Figure 4 shows the velocity gradient of the fluid inside the tank. This value indicates the change of direction of the fluid with respect to the movement of the impeller. According to Figure 4, the gradient is higher near the wall. However, the zone with the lowest gradient, which is the center, represents only half of this gradient.




a) Double Ribbon b) Paravisc c) Hybrid

**Figure 4**. Velocity gradient inside the tank.




a) Double Ribbon b) Paravisc c) Hybrid

**Figure 5**. Criterion Q obtained inside the tank.

Figure 5 is presenting the Q Criterion in our system which gives us a trend for zones where rotation is dominant over deformation. For positive values of Q the rotation is dominant and for negative values of Q the deformation is dominant. According to the results obtained, in the paravisc and hybrid proximity impellers shakers the fluid deformation predominates over vorticity, that is, the divergence value is much higher than the vorticity value mainly in the proximity of the impeller, this suggests that this type of impellers is recommended for viscous fluids or non-Newtonian fluids. Figure 6 shows the density field with the different impellers over time from 0 to 60

seconds, which is related to the mixing inside the tank. Initially, water is at the bottom and ethanol at the top. The volume fraction of both components corresponds to 50%. With the double ribbon impeller, a density field with values close to the density of the mixture is generated after 36 seconds and increases considerably after 60 seconds. For the paravisc impeller, the evolution of the density change is obtained in a representative manner up to 60 seconds of mixing. Using the paravisc impeller, it is observed that the mixing is obtained mainly in the center of the tank. Finally, the Hybrid impeller presents an intermediate homogenization between the paravisc impeller and the double ribbon impeller.

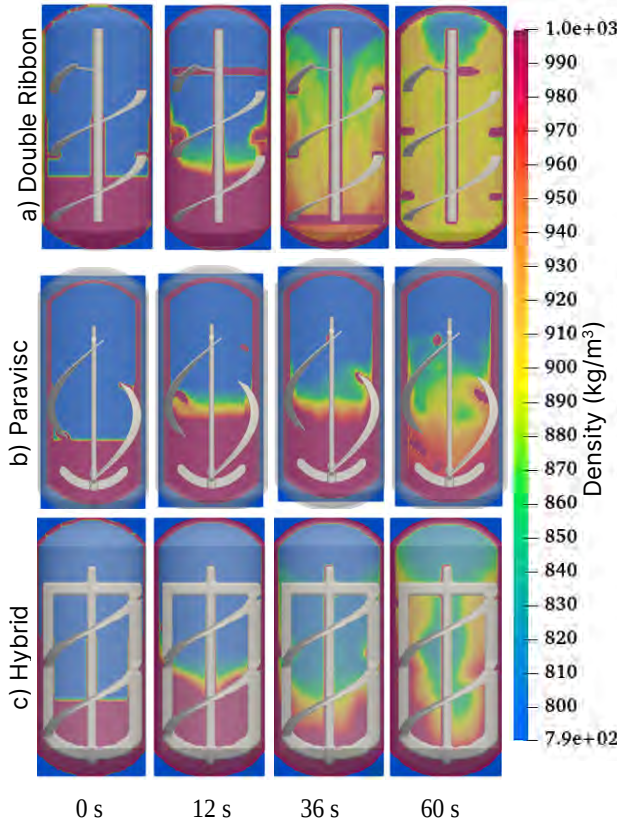



**Figure 6.** Density field at different times obtained in all cases.

## 5. CONCLUSIONS

This study presents a numerical analysis of the hydrodynamics of different impellers to evaluate their performance based on velocity profiles, vorticity, divergence, and the Q-criterion, which correlates fluid deformation with rotational motion within a stirred tank. The results demonstrate that the Double Ribbon impeller exhibited significantly superior performance compared to the Paravisc and hybrid impellers, achieving a mixing efficiency of 88.28% within approximately 100 seconds. The exceptional performance of the Double Ribbon impeller can be attributed to its unique design, featuring two intertwined ribbons that promote a more uniform and turbulent flow within the tank. This design enhances mixing efficiency and ensures effective homogenization of the fluid mixture. The findings underscore the critical role of impeller design in optimizing mixing performance and highlight the Double Ribbon impeller as a highly effective solution for applications requiring efficient and rapid homogenization.

## ACKNOWLEDGEMENTS

We are in agreement with the National Technological Institute of Mexico for the support provided for this research. C.E.A.R thanks SECIHTI for the support provided through project 368 within the program Investigadoras e Invetsigadores por México.

## REFERENCES

1. Chambergo, J.C., Valverde, Q., Pachas, A. A., & Yepez, H. (2017). Estudio del Comportamiento Fluido-Dinámico de un Agitador a Escala Reducida Mediante Simulación Numérica. Información tecnológica, vol. 28(3), 37-46.
2. Flores, C. J., & Cuevas, C. N. (2008). Diseño de una mezcladora dosificadora de cremas cosméticas. [Tesis de licenciatura, Escuela Politécnica Nacional]. Repositorio Digital - EPN.
3. Gil, I. D., Guevara, J. R., García, J. L., Leguizamón, A., & Rodríguez, G. (2016). Process Analysis and Simulation in Chemical Engineering. Springer International Publishing.
4. Londoño, J. (2019). Propuesta de mejora en la línea de vegetales para la empresa PANAMERICANA DE ALIMENTOS SAS, mediante un sistema automático de transporte dosificación y mezcla de granos. [Tesis de licenciatura, INSTITUTO TECNOLÓGICO METROPOLITANO]. Repositorio Institucional ITM.
5. Miño Valdés, J. E., Benítez Cortés, I., & Pérez Martínez, A. (2020). Simulación de procesos químicos y aplicaciones del simulador SuperPro Designer. Universidad Nacional de Misiones.
6. Monaghan, J. J. (1992), Smoothed Particle Hydrodynamics, Annual Review of Astronomy and Astrophysics, Volume 30, 543-574,
7. Rodríguez, J.C., Luviano, J.L. & Vargas, J.C. (2018). Análisis de la hidrodinámica de fluidos en tanques agitados. JOVENES DE LA CIENCIA Revista de Divulgación Científica, Vol. 4 (no. 1), 5(2), 3036.
8. Uribe, A. R., Rivera, R., Aguilera, A., y Murrieta, E. (2012). AGITACION Y MEZCLADO. Departamento de Ingeniería Química, División de Ciencias

Naturales y Exactas, Universidad de Guanajuato. Repositorio Institucional de la Universidad de Guanajuato. http://repositorio.ugto.mx/bitstream/20.500.12059/6256/1/3_Agitaci%c3%b3n %20y%20mezclado.pdf
9. Ye, T., Pan, D., Huang, C., & Liu, M. (2019). Smoothed particle hydrodynamics (SPH) for complex fluid flows: Recent developments in methodology and applications. Physics of Fluids, 31(1).
10. Yin, C., Zheng, K., He, J., Xiong, Y., Tian, Z., Lin, Y., & Long, D. (2022). Turbulent CFD Simulation of Two Rotor-Stator Agitators for High Homogeneity and Liquid Level Stability in Stirred Tank. Materials, 15(23), 8563. https://doi.org/10.3390/ma15238563 Zawawi, M. H., Saleha, A., Salwa, A., Hassan, N. H., Zahari, N. M., Ramli, M. Z., & Muda, Z. C. (2018). A review: Fundamentals of computational fluid dynamics (CFD). In AIP conference proceedings, vol. 2030, No. 1.

© 2025 by the authors. Licensed to PSEcommunity.org and PSE Press. This is an open access article under the creative commons CC-BY-SA licensing terms. Credit must be given to creator and adaptations must be shared under the same terms. See https://creativecommons.org/licenses/by-sa/4.0/



Systems & Control Transactions

**Research Article - Peer Reviewed Conference Proceeding**
ESCAPE 35 - European Symposium on Computer Aided Process Engineering
Ghent, Belgium. 6-9 July 2025
Jan F.M. Van Impe, Grégoire Léonard, Satyajeet S. Bhonsale,
Monika E. Polańska, Filip Logist (Eds.)

PSE PRESS

# Surrogate Modeling of Twin-Screw Extruders Using a Recurrent Deep Embedding Network

**Po-Hsun Huang[a], David Shan-Hill Wong[a], Yen-Ming Chen[b], Chih-Yu Chen[b], Meng-Hsin Chen[b], and Yuan Yao[a]***

[a] Department of Chemical Engineering, National Tsing Hua University, Hsinchu 30013, Taiwan
[b] Industrial Technology Research Institute Material and Chemical Research Laboratories, Hsinchu 30013, Taiwan
* Corresponding Author: yyao@mx.nthu.edu.tw.

## ABSTRACT

Optimizing twin-screw extruder (TSE) performance is critical in the plastics industry but is often resource-intensive. This study introduces a novel surrogate modeling approach using a Recurrent Deep Embedding Network (RDEN) that integrates deep autoencoders with recurrent neural networks to capture sequential dependencies and physical relationships in TSE processes. Leveraging Progressive Latin Hypercube Sampling (PLHS), the RDEN achieves robust predictions of key process variable, like mean residence time. Results demonstrate the model's accuracy, generalization capabilities, and potential for automated screw design optimization.

**Keywords**: twin-screw extruder, deep learning, surrogate modeling

## INTRODUCTION

Twin-screw extruders (TSEs) are extensively used in the plastics processing industry, with their performance highly dependent on operating conditions and screw configurations. However, optimizing these parameters through experimental trials is often time-consuming and resource-intensive. Although some neural network models have been proposed to tackle the screw arrangement problem [1], they didn't account for the physical and positional information of the screw elements. To overcome this challenge, we propose a recurrent deep embedding network (RDEN) that leverages a deep autoencoder with a recurrent neural network (RNN) structure to develop a surrogate model based on numerical simulation data [2, 3].

The details are as follows [4]. An autoencoder is a neural network architecture designed to learn latent representations of input data. In this study, we integrate the autoencoder with an RNN to capture the complex physical relationships between the operating conditions, screw configurations of TSEs, and their corresponding performance metrics. A schematic of TSEs simulation system is depicted in **Figure 1**. To further enhance the model's ability to represent screw positions, we incorporate an RNN layer and this addition allows the model to more effectively capture the spatial relationships between the screw elements.

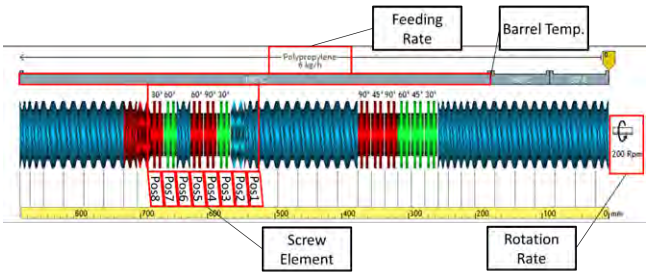



**Figure 1.** Schematic of TSEs simulation from Ludovic

## METHODOLOGY

In this section, we would introduce the methods used for data collection and RDEN model building.

### Progressive Latin Hypercube Sampling (PLHS)

Space filling is essential for sampling methods when working with small datasets, as it ensures optimal coverage of the parameter space while maintaining relatively few sample points. To address the problem, we apply Progressive Latin Hypercube Sampling (PLHS) [5].

PLHS is an extension of Latin Hypercube Sampling

(LHS), designed to enhance sampling efficiency in environmental modeling. Unlike LHS, which generates the entire sample set at once, PLHS progressively creates a series of smaller subsets while striving to maintain LHS characteristics in each subset. This approach is particularly advantageous for large and complex environmental models, offering improved stratification and more accurate representation of the input space.

To understand PLHS, we first describe the LHS method. For LHS, let $S(n,p)$ be a sample matrix containing $(n \times p)$ elements $x_{i,j} \in [0,1]$, where $i = 1,\dots,n$ and $j = 1,\dots,p$. The factor space $[0,1]^p$ is divided into $n$ non-overlapping intervals $([0,1/n),[1/n,2/n),\dots,[(n-1)/n,1])$, with each interval indexed by $q$ along each dimension, where $q = 1,\dots,n$. To represent the relationship between sampling points and intervals, we define an auxiliary binary variable $y_{q,j}$ as follows:

$$y_{q,j} = \begin{cases} 1 & \begin{matrix} if\ there\ exists\ any\ i \\ such\ that\ x_{i,j}\ lies\ within\ interval\ q \end{matrix} \\ 0 & otherwise \end{cases} \quad (1)$$

The sample matrix $S(n,p)$ is considered a Latin hypercube when the following condition is met:

$$\frac{1}{n \cdot p} \sum_{j=1}^{p} \sum_{q=1}^{n} y_{i,j} = 1 \quad (2)$$

This condition ensures that each interval is sampled exactly once in each dimension, maintaining the Latin hypercube property.

For PLHS, we extend this formulation by defining an auxiliary binary variable $y_{q,j}^t$ corresponding to the sample matrix $L^t = \cup_{k=1}^{t} S_k(n_k,p)$, where $t = 1,2,\dots,T$ represents the slice number. The number of sample points is $n_t = \sum_{k=1}^{t} n_k$, and the factor space $[0,1]^p$ is divided into $n_t$ non-overlapping intervals. The necessary and sufficient condition for the sample to be a progressive Latin hypercube is:

$$\frac{1}{n_t \cdot p} \sum_{t=1}^{T} \sum_{j=1}^{p} \sum_{q=1}^{n_t} y_{q,j^t} = T \quad (3)$$

The left side of the equation represents the sum of Latin hypercube properties across all $T$ slices. Thus, generating a PLHS can be expressed as an optimization problem:

$$\max\left( \sum_{t=1}^{T} \frac{1}{n_t \cdot p} \sum_{j=1}^{p} \sum_{q=1}^{n_t} y_{q,j}^t \right) \quad (4)$$

subject to the Latin hypercube constraints:

$$\begin{aligned} &\sum_{i=1}^{n_t} x_{i,j} = 1 \qquad \forall t, \forall j \\ &y_{q,j}^t \in 0,1 \quad \forall t, \forall q, \forall j \end{aligned} \quad (5)$$

where $x_{i,j}$ are decision variables representing sample point regions, and $y_{q,j}^t$ are auxiliary variables ensuring the Latin hypercube property.

The PLHS method offers several advantages for data collection. It allows for incremental addition of sample points, adapting to different computational budgets and analysis needs. By generating samples progressively, PLHS can better cover the input space with fewer points, avoiding repeated sampling in the same regions and reducing computational costs, and the workflow is shown in **Figure 2**.

In the workflow, PLHS enables progressive construction of RDEN dataset while allowing for additional constraints, ensuring desired stratification properties in each subset and combined set in further practical process applications.

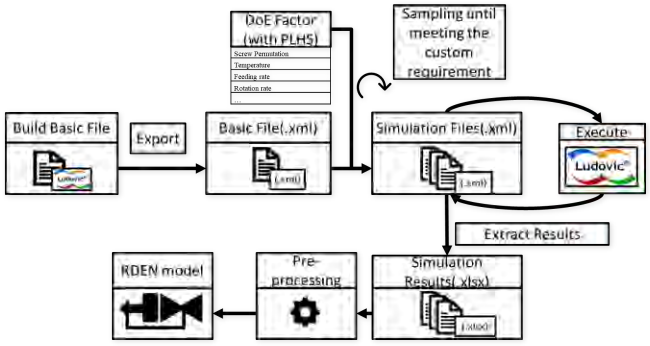



**Figure 2.** Workflow of dataset and model

## DEN with RNN Structure

The DEN has emerged as a powerful technique in TSE modeling, demonstrating the ability to extract latent physical information. However, the original model faces challenges of capturing sequential dependencies which are inherent in extruder element arrangements.

To address this limitation, we propose integrating the DEN with an RNN structure. Specifically, the input to the autoencoder structure consists of a series of screw elements, denoted as $z$, with each element represented in one-hot encoded format. The autoencoder reduces the dimensionality of the coding of each screw element while reconstructing it as $\hat{z}$. To ensure the latent variables extracted from different screw positions remain physically consistent, the autoencoder is designed to share the same parameters across all screw inputs.

For the prediction task, we employ Gated Recurrent Unit (GRU) cells to process the sequential arrangement of extruder elements and their associated process con-

ditions. The GRU utilizes the latent variables from the autoencoder, denoted as $h$, alongside the process conditions, represented by $c$. This integrated input allows the model to effectively capture sequential trends, enabling the transfer of information from earlier extruder elements to subsequent GRU cells.

The combined RDEN structure offers enhanced flexibility and scalability, making it well-suited for various extrusion process configurations. The model structure and pseudo code are depicted in **Figure 3** and the following section separately.

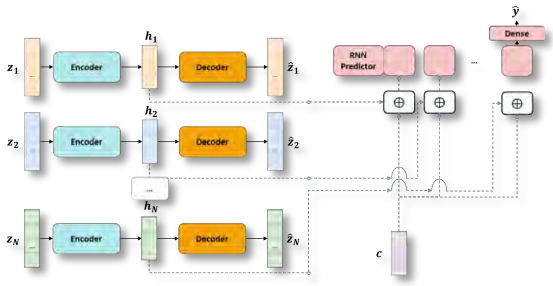



**Figure 3.** RDEN model structure

```
START ALGORITHM
FOR iter = 1 TO max_training_iter DO
    batch ← SAMPLE_BATCH(training_data)
    FOR EACH ((z1, …, zN), c, y) IN batch DO
        // AutoEncoder and reconstruct
        FOR j = 1 TO Pos DO
            h_j ← ENCODER(z_j)
            z_j_recon ← DECODER(h_j)
            L_recon ← L_recon + |z_j,
z_j_recon|²
        END FOR
        // Predict output
        y_pred ← PREDICTOR(h1, …, hN, c)
        L_pred ← L_pred +|y, y_pred|²
    END FOR
    // Update parameters
    L_total ← L_recon + L_pred
    UPDATE_PARAMETERS(ENCODER, DECODER, PRE-
DICTOR)
END FOR
END ALGORITHM
```

The model outputs include predictions of materials' final physical properties, capturing the dynamic nature of the extrusion process, as well as the autoencoder reconstruction. For data normalization, the dataset is reshaped into three dimensions: samples, position series, and process variables; then, we apply the min-max scaling to inputs and the z-score to output, along the variables' direction. Such normalization ensures that the model preserves output trends without necessitating extensive hyperparameter tuning. The model's loss functions, incorporating both reconstruction and prediction errors, are mathematically represented in (6) and calculated using the mean squared error.

$$L_1 = E\left(\sum_{i=1}^{n}(z_i - \hat{z_i})^T(z_i - \hat{z_i})\right)$$
$$L_2 = E((y_i - \hat{y_i})^T(y_i - \hat{y_i})) \quad (6)$$

## RESULTS AND DISCUSSIONS

We successfully established the settings for the Ludovic simulation system and generated data based on the experimental design (DoE) table, presented in **Table 1**. The Ludovic system simulates a twin-screw extruder that models material flow, temperature, pressure, and residence time across the screw configuration. By incorporating detailed screw configurations and process conditions, the Ludovic simulation provides a detailed representation of the twin-screw extruder (TSE) process, modeling material flow, temperature distribution, pressure variations, and residence time across different screw configurations.

**Table 1:** DoE Table

| Factor | | Unit | Design Range |
|---|---|---|---|
| Screw Element | Position: [525, 545] | - | "20-20-L2", "20-20-R2", "KB-20-5-30a-L2", "KB-20-5-30a-R2", "KB-20-5-45a-L2", "KB-20-5-45a-R2", "KB-20-5-60a-L2", "KB-20-5-60a-R2", "KB-20-5-90a-L2", "KB-20-5-90a-R2", "SME-20-20-R2", "ZME-20-20-L2" |
| | Position: [545, 565] | - | |
| | Position: [565, 585] | - | |
| | Position: [585, 605] | - | |
| | Position: [605, 625] | - | |
| | Position: [625, 645] | - | |
| | Position: [645, 665] | - | |
| | Position: [665, 685] | - | |
| Temp | Position: [525, 685] | ˚C | [180, 220] |
| Rotation rate | Position: [525, 685] | rpm | [200, 300] |
| Feeding rate | Position: [525, 685] | kg/hr | [15, 25] |

This study focuses on a system with eight adjustable screw element positions, as illustrated in Figure 1,

where key design factors—the 8-position screw arrangement, feeding rate, barrel temperature, and rotation rate—are highlighted with red boxes. The arrangement is varied using a set of candidate screw elements, shown in **Figure 4**, including conveying elements (20-20-L2, 20-20-R2), kneading blocks with various staggering angles (KB-20-5-30a, KB-20-5-45a, KB-20-5-60a, KB-20-5-90a), and specialized mixing elements (SME-20-20-R2, ZME-20-20-L2). Building on this foundation, we systematically explored various element arrangements and analyzed their impacts on the process variables.

Detailed investigations into mean residence time were conducted, offering insights into their interdependencies and contributions to overall process efficiency. Furthermore, the incorporation of progressive Latin hypercube sampling provided a robust framework to optimize the sampling process, enabling comprehensive exploration of the factor space with proper sampling size.

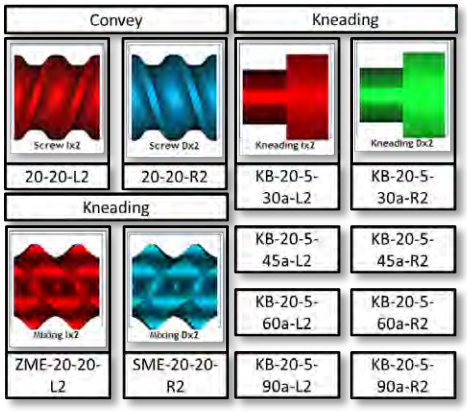



**Figure 4.** Schematic of Ludovic Screw Element

The objective of this study is to predict a critical process variable, the mean residence time, across the entire screw configuration system. Specifically, the model is designed to analyze an eight-position screw assembly, with each position containing a number of candidate screw elements.

To ensure the robustness and generalization of our model, the dataset was meticulously divided into training, validation, and testing sets, adhering to proportions as detailed in **Table 2**.

**Table 2.** Dataset Deviation

| | Sample Size | Percentage |
|---|---|---|
| Training set | 14386 | 0.85 |
| Validation set | 1690 | 0.10 |
| Test set | 844 | 0.05 |

For model training, we employ the RDEN framework described in the previous section to process the training set, guided with a carefully designed loss function. The parameters of both the autoencoder and the predictor are trained simultaneously on the training data. Additionally, the validation set is employed to fine-tune the model and mitigate the risk of overfitting.

The training process is managed using several callback functions to enhance model performance and ensure proper training. Specifically, we use early stopping to halt training when the model's performance on the validation set stops improving. Model checkpoints are used to save the model weights at each epoch, ensuring that the best performing model is retained. Furthermore, the best performing epoch is identified and recorded, helping to capture the model's peak performance.

The results demonstrate that the model performs exceptionally well across all three datasets, with $R^2$ scores over 0.99 and RMSE values below 1, which is within the commonly accepted tolerance for mean residence time. These findings highlight the model's accuracy. The final prediction results are presented below.

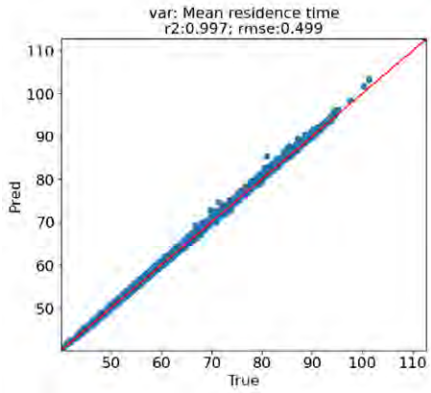



**Figure 5.** Parity plot of the training dataset for mean residence time

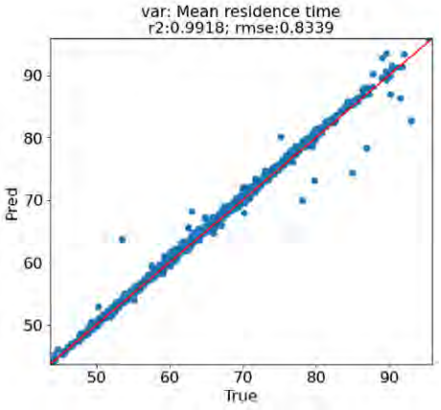



**Figure 6.** Parity plot of the validation dataset for mean residence time

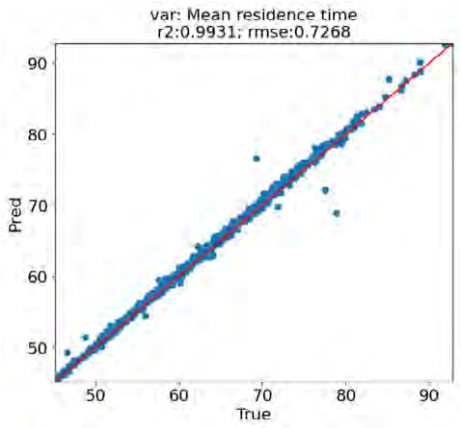



**Figure 7.** Parity plot of the test dataset for mean residence time

In TSE systems, screw elements are typically categorized according to their functionality. Conveying elements, such as 20-20-L2 and 20-20-R2, are primarily responsible for material transportation. Kneading elements, including KB-20-5-30a-L2, KB-20-5-45a-L2, KB-20-5-60a-L2, KB-20-5-90a-L2, KB-20-5-30a-R2, KB-20-5-45a-R2, KB-20-5-60a-R2, and KB-20-5-90a-R2, are designed to apply shearing forces to the material for better dispersion and distribution. Mixing elements, represented by SME-20-20-R2 and ZME-20-20-L2, enhance material blending through intensive mechanical mixing.

The latent space visualization in **Figure 8**. demonstrates distinct clustering patterns, revealing the model's ability to capture inherent physical characteristics of screw elements. For instance, a clear spatial separation was observed between left- and right-rotating elements. Additionally, the demarcation between kneading and conveying elements indicates that the learned representations align with the mechanical principles governing the extrusion process. These systematic clustering patterns across different screw configurations validate the model's capability to encode physical phenomena and provide insights into the functional relationships between various screw elements in the system. By analyzing these patterns, we gain a deeper understanding of the interrelations between the variables, emphasizing the model's capability to elucidate the intricate mechanisms governing the process.

## CONCLUSIONS

In this paper, we introduced a novel model, RDEN, which synergizes the strengths of Deep Embedding Networks and Recurrent Neural Networks. This hybrid architecture exhibits two key capabilities. First is physical information Extraction. The DEN component effectively captures latent physical information from the extrusion process data. Second is sequential prediction. The RNN structure accurately predicts sequential variables inherent in the arrangement of extruder elements. This is achieved through a three-dimensional data structure that significantly reduces redundancy in the dataset and training process, thereby enhancing computational efficiency without compromising performance.

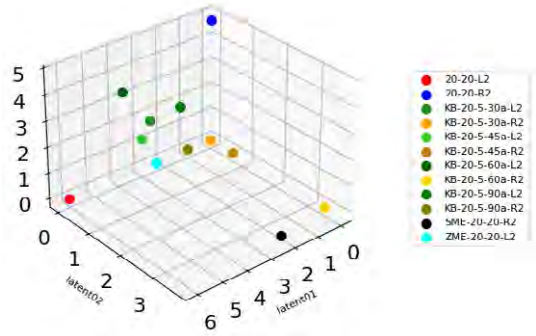



**Figure 8.** Scatter plot of latent variables

The predictive results for process variables demonstrate the model's reliability as a surrogate for extruder systems. Additionally, the latent screw representations learned by the model reveal meaningful patterns in the extrusion process, highlighting its potential for generating valuable process insights.

While our current work establishes RDEN as an effective modeling approach, the development of an optimization framework that leverages this model to recommend optimal screw arrangements remains a promising direction for future research, rather than a validated finding of this study. Our ongoing efforts will focus on exploring this potential application to further establish RDEN as a versatile and powerful tool for advanced process modeling and optimization in polymer extrusion and related fields.

## REFERENCES

1. Kowalski, R.J., E. Pietrysiak, and G.M. Ganjyal, Optimizing screw profiles for twin-screw food extrusion processing through genetic algorithms and neural networks. *J. Food. Eng.*, 303. (2021) https://doi.org/10.1016/j.jfoodeng.2021.110589
2. Yi L, Glatt M, Ehmsen S, Duan W, Aurich JC., Process monitoring of economic and environmental performance of a material extrusion printer using an augmented reality-based digital twin. *Addit. Manuf.*, 48. (2021) https://doi.org/10.1016/j.addma.2021.102388
3. Corradini, F. and M. Silvestri, Design and testing of a digital twin for monitoring and quality assessment of material extrusion process. *Addit. Manuf.*, 51. (2022)

https://doi.org/10.1016/j.addma.2022.102633
4. Wu H, Lo YH, Zhou L, Yao Y., Process modeling by integrating quantitative and qualitative information using a deep embedding network and its application to an extrusion process. *J. Process Control,* 115: p. 48-57. (2022) https://doi.org/10.1016/j.jprocont.2022.04.018
5. Sheikholeslami, R. and S. Razavi, Progressive Latin Hypercube Sampling: An efficient approach for robust sampling-based analysis of environmental models. *Environ. Model Softw.*, 93: p. 109-126. (2017) https://doi.org/10.1016/j.envsoft.2017.03.010

© 2025 by the authors. Licensed to PSEcommunity.org and PSE Press. This is an open access article under the creative commons CC-BY-SA licensing terms. Credit must be given to creator and adaptations must be shared under the same terms. See https://creativecommons.org/licenses/by-sa/4.0/



Systems & Control Transactions

**Research Article - Peer Reviewed Conference Proceeding**
ESCAPE 35 - European Symposium on Computer Aided Process Engineering
Ghent, Belgium. 6-9 July 2025
Jan F.M. Van Impe, Grégoire Léonard, Satyajeet S. Bhonsale,
Monika E. Polańska, Filip Logist (Eds.)

PSE PRESS

# Dimple Shape Design to Enhance Heat Transfer in Plate Heat Exchangers

**Mitchell J. Stolycia[a], and Lande Liu***

[a] School of Applied Sciences, University of Huddersfield, Huddersfield, HD1 3DH, UK
* Corresponding Author: l.liu@hud.ac.uk.

## ABSTRACT

This article studies four dimple shapes: spherical, smoothed-spherical, normal distribution, and error distribution and how they enhance heat transfer on a plate within a plate heat exchanger using computational fluid dynamics. The dimple that showed the greatest efficiency of heat transfer was the normal distribution dimple, giving a temperature increase of 7.5 times of the smoothed-spherical and 15% more than the error distribution dimple shape. This was primarily due to the large increase in the turbulent kinetic energy caused by the eddies created upon the flow over the normal distribution shape. With the normal distribution shape being found to be the most effective in enhancing heat transfer, a layout of multiple normal distribution dimples based on the stage of flow development was also studied. It was found that a fully developed flow resulted in 9.5% more efficiency than half developed flow and 31% more efficient than placing dimples directly next to each other.

**Keywords**: Ansys Fluent, CFD, Dimple, Heat transfer enhancement, Plate Heat Exchangers

## INTRODUCTION

Heat exchangers play an important role in both everyday life and large-scale production. Heat exchangers can be found in many places, from some of the world's largest companies to the radiators in your very home. There are many kinds of heat exchangers, such as the ones in a refrigerator which use a coolant fluid to absorb heat [1], or a plate heat exchanger (PHE) of which was studied in this paper. The main function of a heat exchanger is to transfer heat from one source to another and they are generally used to heat or cool a required element via conduction [1, 2]. In an industrial setting, heat exchangers are often found between multiple reactors in order to increase or decrease the temperature of a fluid after one reaction, before entering the following reactor [3]. This is often done to reduce costs as less fluid material will be required and/or to reduce waste by recycling the stream. For these reasons, the efficiency of a heat exchanger is very important.

Plates within PHEs, are produced as a large sheet of metal with many indentations. These indentations are known as "dimples" and serve to increase the surface area of the plate and encourage turbulent flow [4]. When the surface area available for heat transfer as well as the Reynolds number increases, the temperature change should also increase. This makes the PHE more efficient than it would be otherwise.

In this paper, the plates within a plate heat exchanger were assessed and computationally experimented upon in order to provide an extensive coverage of how to improve the efficiency of a PHE by solely changing the shape of the dimples upon the plates within it. This was done via a computational fluid dynamics (CFD) program known as Ansys Fluent.

Computational fluid dynamics (CFD) is defined as "the method of mathematically modelling a physical phenomenon involving fluid flow and solving it numerically using analytical prowess" [5]. The primary benefit to using CFD in an industrial setting is that it is faster than and comparable to a physical experiment. This allows companies to run simulations in order to gain a realistic idea of what the final process of their production will be.

This paper aimed to simulate realistic fluid flow and dynamics over four different dimple shapes: spherical, smoothed-spherical, normal distribution and error distribution. This was done to obtain values for the Reynolds number, pressure and temperature change across a set

time and distance. A fair comparison of dimple shapes was to be achieved to effectively display which shapes and configurations were more efficient for the transfer of heat in a PHE.

## METHODOLOGY

This study was performed with 2D models and simulations due to the symmetrical structure of the dimple shape and flow channels in radial direction. Nonetheless, 2D models were deemed appropriate to realistically simulate what would occur in an industrial setting, as the results can still be used to compare the heat exchange between different dimple shapes. 2D models also accurately replicate a side-on view of a 3D model without the necessity of a third dimension, i.e. the temperature and velocity profiles would be similar between a 2D and a 3D simulation if viewed from the perspective where the z axis is equal to zero.

For the simulations whereby dimple shape was compared, a pipe was set up with a length of 1 m and a diameter of 0.1 m with the pipe walls being aluminium. The inlet pressure was set to 101325 Pa (1 atm) for all simulations.

For the method, two key areas were explored: simulations over different dimple shapes; and simulating over multiple dimples. The first of which was to find the most efficient dimple shape, and the latter to find the best layout for these dimples over a single plate in a PHE.

## SIMULATING OVER DIFFERENT DIMPLE SHAPES

### Set-up

A 0.5 m/s flowrate was selected, giving a Reynolds number of 48,500, and thus a very turbulent flow. The inlet streams were all set to 300 K, with the walls at a constant 350 K. Dimples were added separately to their respective simulations. Figure 1 demonstrates a sketch of a single spherical dimple.

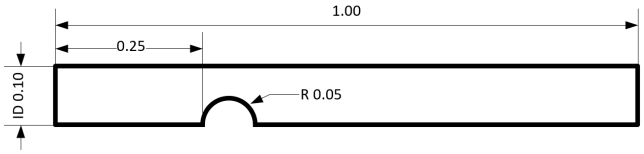



**Figure 1.** A sketch of a 2D pipe with a single spherical dimple, with dimensions in metres.

The cross-sectional area (CSA) of this dimple was then calculated to be $3.927 \times 10^{-3}$ m$^2$. This CSA was to be used across all dimple sizes in order to maintain a fair test, as well as all dimples having a peak height of 0.05 m, while being 0.3 m from the pipe inlet. Figure 2 shows the sketch for the smoothed-spherical dimple, while Figure 3 shows a diagram of the finalised normal and error distribution shapes respectively.

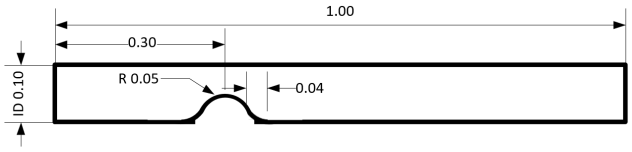



**Figure 2.** A sketch of a 2D pipe with a single spherical dimple, with dimensions in metres.



**Figure 3.** A diagram of the final pipe containing the normal and error distribution curves, respectively.

### Results

Of the different dimple shapes tested: spherical, smoothed-spherical (SS), normal distribution (ND), and error distribution (ED), the ND dimple demonstrated the greatest heat exchange rate, with the average water temperature increasing by 0.53 K in 1.5 s. This is displayed clearly in Figure 4.

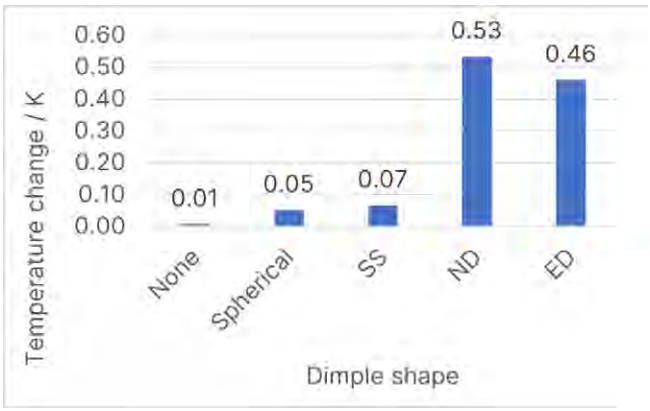



**Figure 4.** Average temperature change of water across different dimple shapes.

It was found that the primary driver for the temperature increase over the ND and ED dimples compared to the rest was the intensity of the eddies created. This was measured by comparing the average values for post-dimple turbulence kinetic energy (TKE), which represent "the mean kinetic energy per unit mass associated with eddies in turbulent flow" [6]. The values for post-dimple TKE are shown in Figure 5.

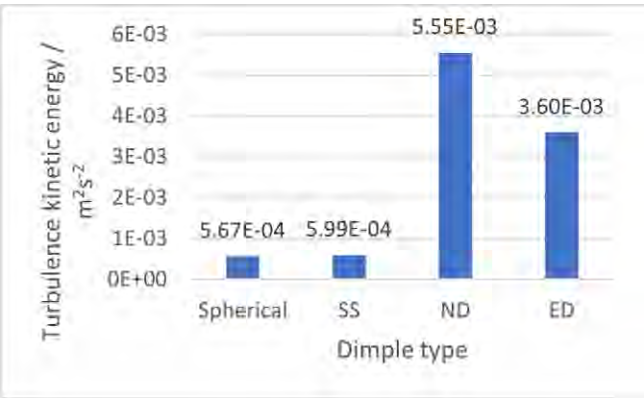



**Figure 5.** Post-dimple TKE for different dimple shapes.

Figure 5 demonstrates the effect eddies have on heat transfer as the values are proportional to the temperature values in Figure 4. Therefore, as the TKE and thus eddy intensity increases across the fluid flow, the heat transfer also increases.

Regarding the other variables that were measured – Reynolds number, pressure, and velocity – the normal distribution (ND) dimple showed surprisingly little change in most of these areas in comparison to the other dimple shapes. This is shown in Table 1.

**Table 1.** A comparison after 1.5 s between the simulation of a pipe with different dimple shapes while the fluid is heated by the pipe walls.

| **Dimple type** | ***Re* change** | ***P* change / Pa** | ***T* change / K** | ***u* change / m s$^{-1}$** |
|---|---|---|---|---|
| None | 0 | -0.3 | 0.01 | 0.00 |
| Spherical | 13536 | -82.7 | 0.05 | 0.14 |
| SS | 12597 | -78.9 | 0.07 | 0.13 |
| ND | 8480 | -142.6 | 0.53 | 0.09 |
| ED | 13354 | -141.8 | 0.46 | 0.14 |

Compared to the spherical and smoothed-spherical dimples, the ND dimple provides, at the least, 7.5 times more efficiency in terms of heat exchange with a pressure change that is less than doubled. Notably, the ND had the smallest velocity change, of the dimpled pipes, meaning the fluid had more time to heat up. The Reynolds number also had the lowest change of the dimpled pipes. However, since the fluid flow was very turbulent to begin with, and remained very turbulent throughout the pipe in all cases, a difference less than 4000 in the *Re* between the ND dimple and the spherical is negligible. Finally, while the ND dimple does prove to have the greatest pressure drop, the great increase in efficiency outweighs this minor drawback. Taking these factors into account, the ND dimple was clearly the most efficient overall and is the recommended shape, of these four, for a dimpled plate in a PHE despite the pressure drop.

## SIMULATING OVER MULTIPLE DIMPLES

### Set-up

Once the most efficient dimple shape for heat transfer was found to be the ND dimple, it was implemented multiple times into a 5 m long pipe. The distances between the dimples were varied in relation to the hydrodynamic entrance length for turbulent flow [7]:

$$\frac{L_e}{D} = 1.36Re^{\frac{1}{4}} \quad (1)$$

where $L_e$ is the entrance distance, $D$ is the inner diameter of the pipe and $Re$ is the Reynolds number. The $Re$ at the peak of the normal distribution dimple was found to be approximately 96000, giving a $L_e$ of 2.39 m. However, Çengel and Cimbala [8] write "in many pipe flows of practical engineering interest, the entrance effects become insignificant beyond a pipe length of 10 diameters" before showing that

$$L_e \approx 10D \quad (2)$$

In this case, the result obtained for the hydrodynamic entrance length was 1.0 m, thus the pipe was to be extended to 5 m for the resultant simulations. When comparing different dimple shapes, this did mean that fully developed flow had not recovered by the end of the 1 m pipe in Figure 1 and Figure 3. This made little difference to the previous single dimple shape comparison results however, as the difference in heat transfer values from one dimple shape to another will have been equally impacted.

Both $L_e$ distances were compared and gave average velocities approximately 4% from the average outlet velocity 5 m along the pipe, by which time the fluid had certainly fully developed. As both regions gave the same accuracy, the shorter 1.0 m distance was used. In industry, the shorter hydrodynamic entrance length will be favoured as more dimples can be used over a set area. This is because the fluid flow will be able to fully develop more often, and thus be disrupted more often, resulting in an increased rate of heat transfer.

Once the hydrodynamic entrance length of 1.0 m was established, simulations were run over a 5 m long pipe consisting of three ND dimples. For this setup, the following three simulations were run:

- Three ND dimples directly next to each other to simulate flow which was not at all developed. This meant that their peaks were 0.2 m from one another as the radius of the dimples was 0.1 m.
- Three ND dimples with their peaks 0.5 m apart from one another to simulate half developed (or developing) flow.

- Three ND dimples with their peaks 1.0 m apart from one another to simulate fully developed flow.

For all three of these simulations, the initial dimple was setup as before, with its peak 0.3 m into the pipe. An example of the half developed flow setup is shown below.

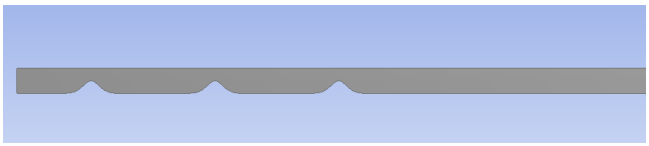


**Figure 6.** The first half of the final model for half developed flow over three ND dimples. The remainder of the pipe contains no dimples.

### Results

For multiple ND dimples, the temperature change across the entire pipe was 3.79 K, 4.54 K, and 4.97 K for a none developed flow, a half-developed flow, and a fully developed flow respectively. From this it is clear that the more developed the fluid flow is before being disrupted, the more heat is exchanged from the pipe walls to the fluid.

This is useful because it can be applied to design plates for PHEs in industry. Knowing that fully developed flow provides the best heat transfer between the plates and fluids within a PHE, companies that require specialist PHEs designed for their process should purchase plates that are distanced such to ensure fully developed flow between dimples. In this case for example, each dimple should be imprinted upon a plate 1 m apart in order to maximise heat transfer. Additionally, as the dimples are more spread out when compared to a less developed flow, firms could reduce their cost per plate as they will require a lower surface area, meaning less material is being used. Depending on the specific material required, the number of plates, and the size of the plates, the cost savings could differ significantly.

## REPEATING DIMPLES

In order to more accurately translate these results into industrial heat exchangers, ND dimples were also repeated as much as possible over a 5 m pipe, as opposed to using only three dimples. For these simulations, the dimples were repeated at distances of 0.2 m (directly next to one another), 0.4 m, 0.6 m, and 1.0 m (fully developed velocity profile).

In order from the least to most temperature change, these repeated dimples for the layouts of no dimples, 1 m between dimple peaks, 0.6 m between dimple peaks, 0.4 m between dimple peaks, and 0.2 m between dimple peaks (without the final dimple), showed average outlet temperatures of 306.4 K, 308.3 K, 309.5 K, 310.8 K, and 311.5 K respectively.

Contrary to the previous results, which showed fully developed flow to have the greatest temperature increase, these results argue in favour of the dimples being directly next to one-another, as is currently common practice in industry. However, each of these pipes, unlike in the previous simulations, have drastically different lengths – which is comparable to the surface area of a 3D model. The length of the pipe containing the dimples with their peaks 0.2 m apart had now increased by 13.9% from the original 5 m length of pipe, and a 6.2% increase in length from the pipe with dimples with 0.4 m between their peaks. As these simulations contain 0.3 m of pipe before a dimple peak is present, in an industrial setting these percentages would be even greater.

What this means is that while maintaining none-developed flow between dimples still shows promise in an industrial setting, this temperature change is offset somewhat by the increase in material required. Instead, a good alternative would be to remove every other dimple – which in this case is represented by the dimple peaks being 0.4 m apart – as it is still one of the most temperature-efficient models. This layout only has a decrease of 0.2% temperature change compared to completely none-developed flow, while saving half of the material used in the imprinting of dimples upon a plate.

## A MAJOR DRAWBACK OF 2D MODELLING

3D models are clearly the next step to further develop and analyse the results of this work.

3D models have been attempted over the course of this project. The models were created such that the different dimples to compare were the same as in the 2D models. This was done by revolving the dimple shapes around the y-axis. For these experiments, only the ND and spherical dimples were compared.

Simulations were performed over a square based pipe, and a circular based pipe. The circular based pipe however suffered from having the dimples clip through the wall, thus causing inequal losses in both volume and surface area between the different dimple shapes. This is demonstrated in Figure 7.

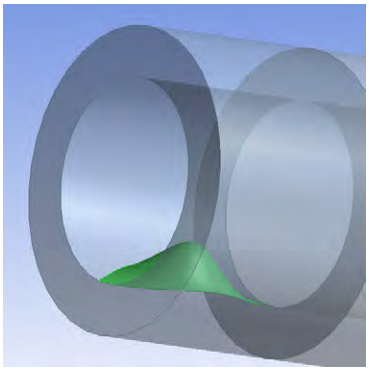


**Figure 7.** The ND dimple being cut due from the wall of a spherical pipe.

Due to this, for the following results, only the square based pipe results are presented.

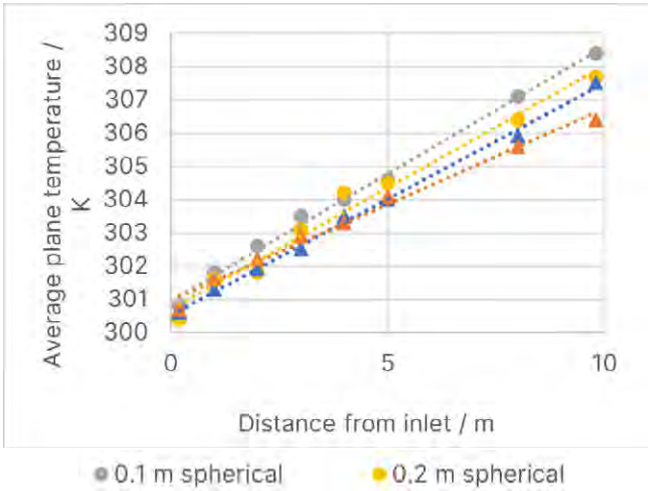



**Figure 8.** Average temperature of the fluid at different distances, both for the two dimple shapes and differing distances between dimples.

The heat transfer results shown in Figure 8 do not line up with the results achieved from the 2D simulations. This is clear as the spherical dimples outperform the ND dimples regardless of distance between dimple peaks – whether it be 0.1 m or 0.2 m for the spherical dimples, or 0.2 m and 0.4 m in the case of the ND dimples. The reason for this was that the control variable carried forward from the 2D simulations to 3D regarding dimple shape was the cross-sectional area (CSA) of the dimple. This worked well for a 2D simulation, but not when a third dimension was added.

When scaling the CSA of a 2D model up into a 3D model, the resultant measurements correlate to the volume of the dimple. These 3D simulations therefore unfairly compared the two dimple types, as they had different surface areas. This is important because the surface area should be a control variable, in order to maintain the same amount of surface in which the water could be heated over.

For future work, 3D simulations should be run with the surface areas of the dimples equal, as opposed to the cross-sectional area, which was carried over directly from its 2D counterpart.

## CONCLUSIONS & RECOMMENDATIONS FOR FUTURE WORK

The normal distribution (ND) dimple shape provided the greatest heat transfer showing an increase in temper-ature 7.5× the smoothed-spherical, with a 15% uplift from the error distribution (ED) shape. Despite having the greatest pressure drop of 142.6 Pa, the large increase in temperature far outweighed this downside.

Eddy intensity was the primary cause for this efficiency of heat exchange. The ND dimple demonstrated a 54% increase in turbulent kinetic energy over the next greatest – the ED dimple. This meant that the intensity and number of eddies produced proved more meaningful for heat transfer than the surface area of the plates.

Fully developed flow was more susceptible to being disrupted than other flow states, being 9.5% more heat transfer efficient than disrupting half developed flow, and 31% more efficient than none developed flow. However, when repeated over a larger scale, it is not wholly viable to have repeated dimples up to 1 m apart. Instead, a compromise should be made where dimples are separated by one-dimple length. In practice, this would mean removing every other dimple from the current plate-printing process. This would still ensure a high temperature change (a 0.2% decrease from none developed flow), while saving half the material used to imprint dimples.

The primary recommendation for future work is to develop and simulate 3D models for a more realistic approach and more easily applicable results to industry. This would be more demonstrative of how dimple shapes and flow development can affect heat exchange, due to its real-world nature. In contrast with the initial 3D models presented, future simulations would have dimple surface area as a control variable, in order to achieve fair an reliable results.

## ACKNOWLEDGEMENT

Funding from the Engineering and Physical Science Research Council of UK is gratefully acknowledged.

## REFERENCES

1. B. Zohuri, "Chapter 12 - Heat Exchangers," *Physics of Cryogenics*, B. Zohuri, ed., pp. 299-330: Elsevier, 2018.
2. E. F. Curd, J. Railio, J. A. N. Gustavsson, J. Hogeling, M. E. H. Assad, J. A. N. Emilsen, S.

Mazzacane, and R. Wiksten, "9 - AIR-HANDLING PROCESSES," *Industrial Ventilation Design Guidebook*, H. Goodfellow and E. Tähti, eds., pp. 677-806, San Diego: Academic Press, 2001.
3. E. Edreis, and A. Petrov, “Types of heat exchangers in industry, their advantages and disadvantages, and the study of their parameters,” *IOP Conference Series: Materials Science and Engineering,* vol. 963, no. 1, pp. 012027, 2020/11/01, 2020.
4. S. Rashidi, F. Hormozi, B. Sundén, and O. Mahian, “Energy saving in thermal energy systems using dimpled surface technology – A review on mechanisms and applications,” *Applied Energy,* vol. 250, pp. 1491-1547, 2019/09/15/, 2019.
5. S. Pullela, “Editorial on Computational Fluid Dynamics,” *Journal of Civil & Environmental Engineering,* vol. 11, no. 3, 2021.
6. R. S. Dondapati, and V. V. Rao, “Influence of mass flow rate on Turbulent Kinetic Energy (TKE) distribution in Cable-in-Conduit Conductors (CICCs) used for fusion grade magnets,” *Fusion Engineering and Design,* vol. 88, no. 5, pp. 341-349, 2013/06/01/, 2013.
7. C. Kleinstreuer, *Modern Fluid Dynamics: Basic Theory and Selected Applications in Macro- and Micro-Fluidics*, p.^pp. 195-198: Springer Netherlands, 2010.
8. Y. Çengel, and J. Cimbala, *Fluid Mechanics Fundamentals and Applications: Third Edition*: MCGRAW-HILL US HIGHER ED, 2013.

© 2025 by the authors. Licensed to PSEcommunity.org and PSE Press. This is an open access article under the creative commons CC-BY-SA licensing terms. Credit must be given to creator and adaptations must be shared under the same terms. See https://creativecommons.org/licenses/by-sa/4.0/



Systems & Control Transactions

**Research Article - Peer Reviewed Conference Proceeding**
ESCAPE 35 - European Symposium on Computer Aided Process Engineering
Ghent, Belgium. 6-9 July 2025
Jan F.M. Van Impe, Grégoire Léonard, Satyajeet S. Bhonsale,
Monika E. Polańska, Filip Logist (Eds.)

PSE PRESS

# Data-Driven Modelling of Biogas Production Using Multi-Task Gaussian Processes

**Benaissa Dekhici[a,b] and Michael Short[a,b]***

[a] School of Chemistry and Chemical Engineering, University of Surrey, Guildford, Surrey, GU2 7XH, United Kingdom.
[b] Supergen Bioenergy Impact Hub, Energy and Bioproducts Research Institute, UK.
* Corresponding Author: m.short@surrey.ac.uk.

## ABSTRACT

This study introduces the novel application of a Multi-Task Gaussian Process (MTGP) model to predict biogas production and critical anaerobic digestion (AD) performance indicators (soluble COD, volatile fatty acids (VFAs)), addressing feedstock variability and dynamic process behavior. We compare the MTGP against the widely used mechanistic AM2 model to evaluate its accuracy and applicability for probabilistic modeling in AD systems. The MTGP framework leverages multi-output correlations and uncertainty quantification, trained on experimental data, achieving superior predictive performance over AM2in this study, with lower RMSE (SCOD: 0.32 g/L; VFAs: 0.87 mmol/L; biogas: 0.15 L/day) and higher $R^2$ values (SCOD:0.91, VFAs:0.94, biogas :0.88) under the conditions tested. While AM2 provides biochemical insights, its reliance on unvalidated assumptions may limits robustness. The flexibility of MTGP and precision suggest its potential for real-world applications such as Bayesian Optimization and Design of Experiments, enabling data-driven process enhancement without mechanistic constraints. This work establishes MTGP as a pioneering tool for AD optimization, bridging data-driven efficiency with practical bioenergy challenges.

**Keywords**: Anaerobic Digestion, Biogas Production, Multi-Task Gaussian Process, Data-driven Modelling, Mechanistic Modeling, Predictive Analytics.

## INTRODUCTION

Modelling and optimising anaerobic digestion (AD) processes is critical for designing wastewater treatment and biogas plants, evaluating system performance, and assessing the feasibility of diverse substrates under varying conditions [8]. AD models are broadly categorized as mechanistic models, which rely on biological, physical, and chemical principles, or empirical machine learning models, which leverage observed process data to establish relationships between inputs and outputs [8]. Mechanistic models describe AD processes through differential equations that capture bacterial growth, inhibition, and physico-chemical interactions. These models range in complexity: simpler ones address single-step processes, intermediate models like AM2 [6] incorporate multiple microbial populations and interactions, and advanced models such as ADM1 [5] offer comprehensive system descriptions but demand extensive parameter estimation. The AM2 model, in particular, balances simplicity and accuracy, making it suitable for monitoring and controlling AD processes rather than detailed simulations [9]. Machine learning techniques such as k-nearest neighbors (KNN), support vector machines (SVM), random forests (RF), artificial neural networks (ANN), Dynamic Mode Decomposition (DMD), and the Koopman operator theory [8,3,12] have all been applied to model the complex, nonlinear interactions in AD processes. In this work, we use Gaussian Process (GP) a non-parametric, Bayesian approach to regression that models the underlying distribution of data as a continuous stochastic process [4]. A GP based approach is utilised because of its capacity to manage intricate and uncertain systems. While GPs have been applied in various fields, their use in predicting biogas production from AD has not yet been tested. This problem is critical given the need for reliable models to optimise biogas production from highly variable waste materials. The GP model is used to predict biogas production and other key performance indicators in a continuous anaerobic digester fed with hydrothermal carbonization (HTC) products [1]. The feedstock consists of hydrochar and HTC liquor derived from sewage sludge

and agro-industrial waste, which exhibit significant variability in composition and degradation profiles, complicating predictive modelling. The remainder of this paper is structured as follows. Section 2 outlines the experimental procedures and data collection process, followed by the development of a mechanistic model for anaerobic digestion and a data-driven modeling approach based on Multi-Task Gaussian Processes (MTGP). Section 3 explores the structure of the dataset, presents the outcomes of parameter estimation for the mechanistic model, and evaluates the performance of the MTGP framework. A comparative analysis is provided to assess the relative strengths and limitations of the mechanistic and MTGP approaches. The paper concludes with a summary of key findings and recommendations for future work.

# METHODS

## Experimental Setup and Data Generation

The dataset used in this study stems from a 164-day AD experiment with HTC biomass as the substrate, previously detailed by the authors in [9]. The experiments investigated the effects of HTC process conditions and operational parameters, such as dilution rate (D), influent soluble chemical oxygen demand ($SCOD_{in}$), organic loading rate (OLR), and pH, on AD performance metrics, including biogas yield, effluent SCOD, and volatile fatty acids (VFA) concentrations. Conducted in laboratory-scale reactors under controlled conditions (**Figure 1**), these experiments aimed to enhance the biodegradability of organic feedstocks for improved biogas production [1]. The mechanistic AM2 model [6] was applied to describe the AD system dynamics. The same parameter estimation and simulation procedures were applied from the original study [9], ensuring consistency and facilitating direct comparisons with the MTGP approach.

## Mechanistic Model Development

In this study, the AM2 model developed within the framework of the Europe Research Project called AMOCO [6] is used due to its simplicity and accuracy in similar studies. The AM2 model represents AD in just two stages (Acidogenesis-Methanogenesis) and it is deduced from the mass balance law as in [9]:

$$\begin{aligned} \dot{S_1} &= D(S_{1in} - S_1) - k_1\mu_1(S_1)X_1 \\ \dot{X_1} &= (\mu_1(S_1) - k_{d1} - \alpha D)X_1 \\ \dot{S_2} &= D(S_{2in} - S_2) + k_2\mu_1(S_1)X_1 - k_3\mu_2(S_2)X_2 \\ \dot{X_2} &= (\mu_2(S_2) - k_{d2} - \alpha D)X_2 \end{aligned} \quad (1)$$

With

$$\mu_1(S_1) = \mu_{1max}\frac{S_1}{S_1+K_1}, \quad (2)$$

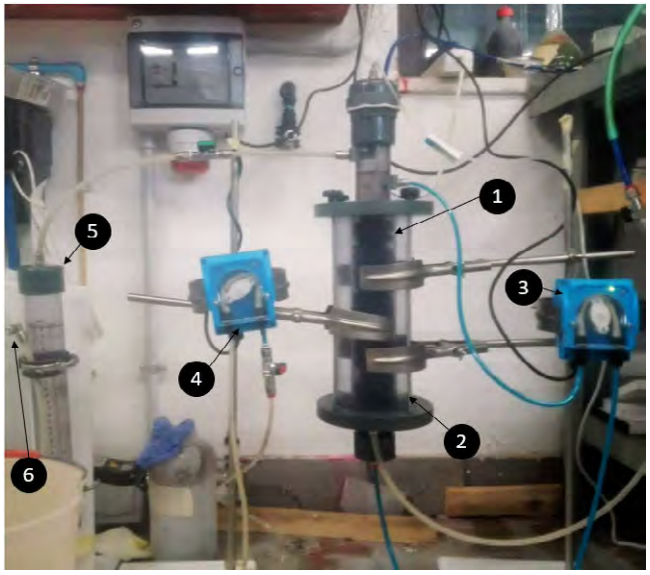



**Figure 1.** Laboratory picture of the anaerobic filter, in which: 1- Anaerobic filter, 2- Heating Jacket, 3- Recycle Pump, 4- Inlet Pump, 5- Biogas Measurement Device, 6- Outlet [1,9].

$$\mu_2(S_2) = \mu_{2max}\frac{S_2}{\frac{S_2^2}{K_i}+S_2+K_2}\left\{1 - \exp\left[-3\left(\frac{pH-pH_H}{pH_H-pH_L}\right)^2\right]\right\} \quad (3)$$

Where $X_1$ and $X_2$ represent the concentrations of acidogenic and methanogenic bacteria (g/L) respectively, while $S_1$ and $S_2$ denote the SCOD (g/L) and VFA (mmol/L) concentrations. $k_i$ are the stoichiometric coefficients associated with the two reactions. $D = \frac{F}{V}$ and $D$ is the dilution rate (F is the flow rate and V is the volume of the vessel), $S_{1in}$ and $S_{2in}$ are respectively the input concentrations of the substrates $S_1$ and $S_2$, and α is the fraction of the bacteria in the liquid phase. Death rates for $X_1$ and $X_2$ are $k_{d1}$, $k_{d2}$, respectively. The specific growth rate $\mu_1(S_1)$ and $\mu_2(S_2)$ are governed by Monod kinetics in (2) and Haldane kinetics in (3), with $\mu_{1max}$ and $\mu_{2max}$ as the maximum growth rates, $K_1$ and $K_2$ are the half-saturation constants, and $K_i$ are the inhibition constant for $S_2$. Additionally, $pH_L$ and $pH_H$ define the lower and upper pH bounds, with inhibition effects on $\mu_2(S_2)$ . The biogas flow rate ($CH_4$ plus $CO_2$) can be expressed as a function of the state variables given by:

$$Q_{biogas} = k_{gas}\mu_2(S_2)X_2 \quad (4)$$

Where $k_{gas}$ is the yield for biogas production. To identify the model that best fits the experimental data, an appropriate criterion must be selected for optimising the model's parameter vector. Various cost functions are commonly used for parameter estimation in AD models, typically based on output-error criteria that quantify the discrepancy between model outputs and actual system outputs. [9]. The sum of least squares is a widely used and effective cost function in optimisation procedures,

especially when measurement error variances fluctuate over time.

$$J(\theta) = \min \sum_{t=1}^{N} \left( \frac{Y_{Measured}(t) - Y_{Model}(t,\theta)}{Y_{Measured}(t)} \right)^2 \quad (5)$$

Where $J$ is the objective function to be minimised, $Y_{Measured}$ is the collected measurements vector, $Y_{Model}$ is the model-predicted outputs vector with respect to model parameters $\theta$ to be determined and *N* is the number of measurements point. The measurements vector $Y$ is defined by:

$$Y = \begin{bmatrix} S_1 & S_2 & Q_{biogas} \end{bmatrix}^T \quad (6)$$

The vector parameters $\theta$ is defined by:

$$\theta = \left[ \mu_{1Max}, K_1, \mu_{2Max}, K_i, K_2, k_1, k_2, k_3, k_{gas} \right]^T \quad (7)$$

The other parameters α, $k_{d1}$ and $k_{d2}$ have been fixed with analogy to [9].

## Multi-Task Gaussian Processes (MTGP)

### Gaussian Process overview

A Gaussian Process (GP) is a non-parametric, Bayesian approach to regression that models the underlying distribution of data as a continuous stochastic process [4]. GPs are well-suited for complex, nonlinear systems, as they do not require explicit formulation of system dynamics. Instead, they operate by defining a prior distribution over functions that is updated as data is observed, making them a powerful tool in predicting outputs with uncertainty quantification. A GP is commonly viewed as a prior over functions $f: \mathbb{R}^P \to \mathbb{R}$ where P denotes the dimensionality of the input space. Consider a set of P-dimensional input points $\boldsymbol{X} \in \mathbb{R}^{P \times N}$ and corresponding scalar outputs $\boldsymbol{y} \in \mathbb{R}^N$. A GP is defined by a mean function, often assumed to be zero without loss of generality, and a kernel function $k: \mathbb{R}^P \times \mathbb{R}^P \to \mathbb{R}$, which measures the similarity between input points. The GP regression model with noisy observations is expressed as:

$$\boldsymbol{y_i} = f(\boldsymbol{x}_i) + \epsilon, \quad f \sim \mathcal{GP}\left(0, k(x_i, x_i')\right), \quad (8)$$

Where $\epsilon \sim \mathcal{N}(0, \sigma^2)$ represents Gaussian noise. Alternatively, this can be written as a multivariate normal distribution:

$$\boldsymbol{y} \sim \mathcal{N}(0, \boldsymbol{K}_{XX} + \sigma^2 \boldsymbol{I}_N), \quad (9)$$

where $\boldsymbol{K}_{XX} \in \mathbb{R}^{N \times N}$ is the kernel matrix formed by evaluating $k(x_i, x_j)$ for all pairs of input points, and $\boldsymbol{I}_N$ is the identity matrix. Given a new set of inputs $\boldsymbol{X}_* \in \mathbb{R}^{P \times M}$, the conditional distribution of the corresponding outputs $\mathbf{f}_* \in \mathbb{R}^M$ is:

$$\mathbf{f}_* | \, \boldsymbol{y}, \boldsymbol{X}, \boldsymbol{X}_* \sim \mathcal{N}(\mu, \Sigma), \quad (10)$$

Where:

$$\mu = \boldsymbol{K}_{\boldsymbol{X}_* \boldsymbol{X}} \boldsymbol{K}_{\boldsymbol{XX}}^{-1} \boldsymbol{y}, \quad (11)$$

$$\Sigma = \boldsymbol{K}_{\boldsymbol{X}_* \boldsymbol{X}_*} - \boldsymbol{K}_{\boldsymbol{X}_* \boldsymbol{X}} \boldsymbol{K}_{\boldsymbol{XX}}^{-1} \boldsymbol{K}_{\boldsymbol{X} \boldsymbol{X}_*}. \quad (12)$$

The presented traditional GPs are limited to producing a single scalar output, but in many cases, it is essential to explore the relationship between inputs and multiple outputs.

### Multi-Output gaussian processes:

Standard GPs accommodate only a single scalar output. In practical applications, however, multiple outputs are often desired, such that $f: \mathbb{R}^P \to \mathbb{R}^Q$, where $Q$ denotes the number of outputs. A naïve solution involves employing $Q$ independent GPs, each modeling one output dimension [7]. However, this neglects correlations between outputs. To address this, advanced approaches like the Linear Model of Coregionalization (LMC) [10] have been developed. The LMC assumes L shared latent Gaussian processes $\{f_\ell\}_{\ell=1}^L$. The observed outputs for sample *i* are modeled as:

$$\boldsymbol{y_i} = \boldsymbol{W} \mathbf{f_i} + \boldsymbol{\epsilon}, \quad (13)$$

where $\mathbf{f_i} = [\mathrm{f_1(x_i)}, \ldots, \mathrm{f_L(x_i)}]^\top$, $\boldsymbol{W} \in \mathbb{R}^{\mathrm{Q} \times \mathrm{L}}$ is a matrix of loadings that maps latent functions to outputs, and $\boldsymbol{\epsilon} \sim \mathcal{N}(\boldsymbol{0}, \boldsymbol{\sigma^2 I}_Q)$, Each latent function $f_\ell$ is drawn from a GP:

$$f_\ell \sim \mathcal{GP}(\boldsymbol{0}, \boldsymbol{K_\ell}) \quad (14)$$

where $\boldsymbol{K_\ell}$ is the kernel function for the $\boldsymbol{\ell}$-th latent GP. The covariance between outputs $y_{iq}$ and $y_{jq'}$ is given by:

$$Cov(y_{iq}, y_{jq'}) = \sum_{\ell=1}^{L} k_\ell(\boldsymbol{x}_i, \boldsymbol{x}_j) w_{q\ell} w_{q'\ell}, \quad (15)$$

where $w_{q\ell}$ is the element of $\boldsymbol{W}$ at row q and column $\boldsymbol{\ell}$. The joint distribution of all outputs $\boldsymbol{Y}$ is multivariate normal:

$$vec(\boldsymbol{Y}) \sim \mathcal{N}(\boldsymbol{0}, \Sigma + \boldsymbol{\sigma^2 I}_{NQ}), \quad (16)$$

Where:

$$\Sigma = \sum_{\ell=1}^{L} \boldsymbol{K}_\ell \otimes \boldsymbol{w}_\ell \boldsymbol{w}_\ell^\top, \quad (17)$$

with $\otimes$ denoting the Kronecker product and $vec\,(\cdot)$ the vectorization operator. If all latent GPs share the same kernel function, the covariance simplifies to:

$$\Sigma = \boldsymbol{K} \otimes \boldsymbol{W} \boldsymbol{W}^\top, \quad (18)$$

This model captures output correlations through $\boldsymbol{W}$, allowing flexible multi-output modelling while preserving non-linearities from the latent GPs. For this study, the MTGP framework jointly models three key AD outputs: biogas production $Q_{biogas}$, SCOD, and VFA concentrations.

Each task is modelled by a shared latent function structure, leveraging the correlations between outputs to improve overall prediction accuracy. We adopt the LMC with a Radial Basis Function kernel for latent functions:

$$k(x, x') = \sum_{\ell=1}^{L} B_\ell \exp\left(-\frac{||x-x'||^2}{2l_\ell^2}\right), \quad (19)$$

where $B_\ell$ is a coregionalisation matrix for latent function $\ell$, $l_\ell$ is the length scale, and L is the number of latent functions. The MTGP prior for task outputs $\mathbf{f} = [\mathbf{f}_1, \ldots, \mathbf{f}_D]$ follows:

$$\mathbf{f} \sim \mathcal{N}(0, \boldsymbol{K_f}), \quad (20)$$

where $\boldsymbol{K_f} = \sum_{\ell=1}^{L} \boldsymbol{B}_\ell \otimes \boldsymbol{K}_\ell(\boldsymbol{X}, \boldsymbol{X})$ capturing within-task and cross-task covariances. The MTGP model, trained over AD data across various conditions, maximises marginal likelihood using an Adam optimiser [11]. The likelihood is:

$$\log p(\boldsymbol{Y}|\boldsymbol{\theta}) = -\frac{1}{2}\boldsymbol{Y}^\top \boldsymbol{K_f^{-1}} \boldsymbol{Y} - \frac{1}{2}\log|\boldsymbol{K_f}| - \frac{nD}{2}\log(2\pi), \quad (21)$$

where $\boldsymbol{\theta}$ comprises hyperparameters. For new input $\boldsymbol{X}_*$ the predictive mean and variance are:

$$\boldsymbol{\mu}_* = \mathbf{K}(\mathbf{X}_*, \mathbf{X})\mathbf{K_f^{-1}}\mathbf{Y}, \quad (22)$$

$$\boldsymbol{\Sigma}_* = \boldsymbol{K}(\boldsymbol{X}_*, \boldsymbol{X}_*) - \boldsymbol{K}(\boldsymbol{X}_*, \boldsymbol{X})\boldsymbol{K_f^{-1}}\boldsymbol{K}(\boldsymbol{X}, \boldsymbol{X}_*). \quad (23)$$

These equations provide predictions along with uncertainty estimates, which are essential for assessing the reliability of all output's forecasts.

# RESULTS AND DISSCUSION

## Data Structure and Preprocessing

The dataset includes time-series input parameters (time, D, $SCOD_{in}$, OLR, and pH) and outputs (SCOD, VFA, and biogas production). Pre-processing steps included: i) Interpolation of missing or irregular data using cubic splines for consistent time scales; ii) Log transformation of outputs (with a small constant added) to stabilize variance and enhance model performance; and iii) Data splitting into training (one-third of the data) and testing subsets (half of the data) to ensure balanced coverage of operational variability for model development and validation. To assess the accuracy of the models, statistical metrics were calculated for each output, such as Root Mean Squared Error (RMSE) given by:

$$RMSE = \sqrt{\frac{1}{n}\sum_{i=1}^{n}\left(Y_{Model,i} - Y_{Measuredi}\right)^2} \quad (24)$$

and the coefficient of determination ($R^2$) given by:

$$R^2 = 1 - \frac{\sum_{i=1}^{n}\left(Y_{Measured,i} - Y_{Model,i}\right)^2}{\sum_{i=1}^{n}\left(Y_{Measured,i} - \overline{Y}_{Measured}\right)^2} \quad (25)$$

Where $\overline{Y}_{Measured}$: Mean of the observed values

## Parameter Estimation for the AM2 Model

The AM2 model was employed to describe the dynamics of the AD process under investigation. Parameter estimation was conducted using the Pyomo optimisation framework with the IPOPT solver, offering an efficient and robust alternative to the MATLAB approach used in [9]. This procedure calibrated key kinetic and stoichiometric parameters based on a 164-day experimental dataset. Initial conditions and parameter guesses were derived from [9], and the optimisation problem was formulated as a nonlinear program. **Figure 2** compares model predictions for SCOD ($S_1$), VFA ($S_2$), and biogas production ($Q_{biogas}$) with experimental data, showing agreement. **Table 1** presents the estimated parameters, reflecting the kinetic and stoichiometric characteristics of the AD process. These parameters reflect the influence of HTC-treated substrates on microbial kinetics and reactor performance. The results confirm the utility of the AM2 model as a mechanistic tool for understanding and predicting the behavior of AD systems. The calibrated parameters provide valuable insights into substrate degradation and methane production dynamic, however there are clear areas of poor predictive performance.

**Table 1:** Estimated model parameter values

| Parameter | Value | Unit |
|---|---|---|
| $\mu_{1_{max}}$ | 0.04 | 1/day |
| $K_1$ | 31.01 | g/L |
| $\mu_{2_{max}}$ | 0.08 | 1/day |
| $K_i$ | 19.93 | mmol/L |
| $K_2$ | 125.42 | mmol/L |
| $k_1$ | 2374.50 | -- |
| $k_2$ | 2975.26 | mmol/L |
| $k_3$ | 11558.51 | mmol/L |
| $k_{gas}$ | 593 | mmol/L |

## Multi-Task Gaussian Processes for Biogas Production Modeling

In this section, a data-driven approach was employed to predict AD outputs. The method leverages a MTGP framework, exploiting correlations among these multiple outputs to enhance predictive accuracy while providing uncertainty quantification. A dataset of $N$= 164 samples (where $N$ corresponds to the total number of time points in the experiment) was compiled to include five operational parameters: time, dilution rate D, influent SCOD, OLR, and pH as inputs to the GP. These were stacked into a matrix $\mathbf{X} \in \mathbb{R}^{164\times5}$. Three outputs: SCOD, VFA, and biogas production, were similarly arranged into a matrix $\mathbf{Y} \in \mathbb{R}^{164\times3}$. The MTGP model leverages a variational inference strategy, enabling simultaneous

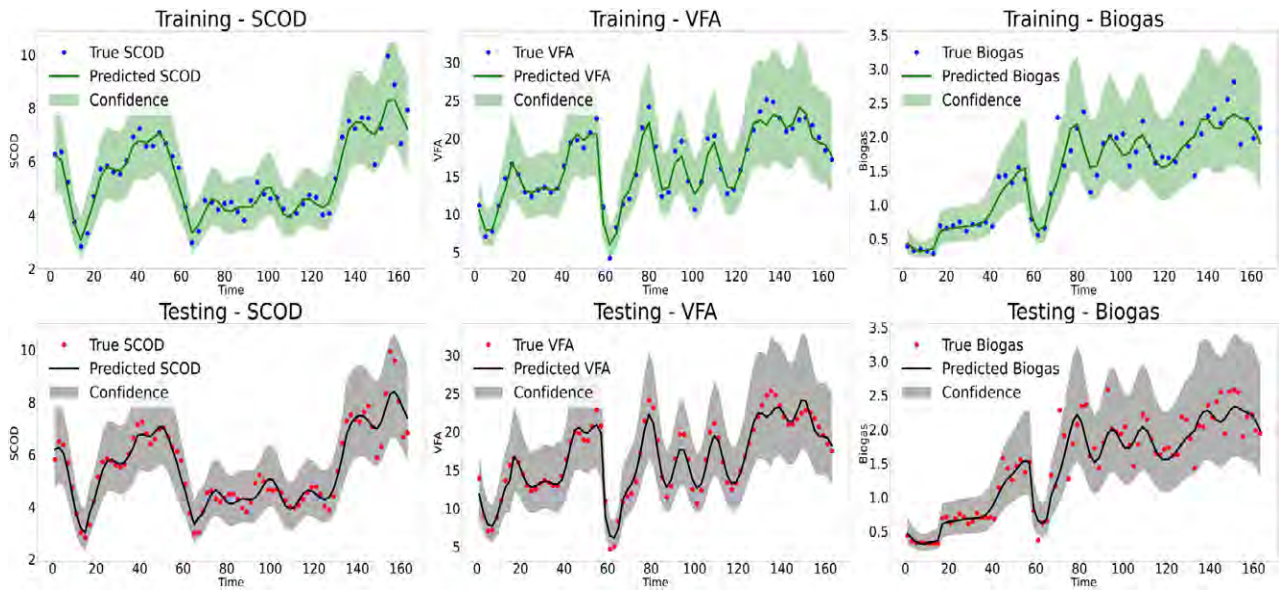



**Figure 3:** Comparison of MTGP model predictions with measured data for SCOD, VFA, and biogas production: training predictions and testing predictions, illustrating the model's performance in capturing AD outputs.

modelling of multiple outputs. Using the LMC with three latent functions, the model effectively shared information across tasks. With a training set of 55 data points, all served as inducing points, optimising computational efficiency for multi-output modelling. Confidence intervals provided insights into time points or operational regimes with greater uncertainty, crucial for real-world applications where factors like pH and substrate variability affect biogas yields. **Figure 3** illustrates the model's strong performance in tracking SCOD, VFA, and biogas production for both training and testing data, with confidence intervals conveying predictive accuracy and uncertainty. The MTGP framework demonstrated robust capabilities in capturing interdependencies among outputs, with inter-task learning enhancing predictive accuracy.

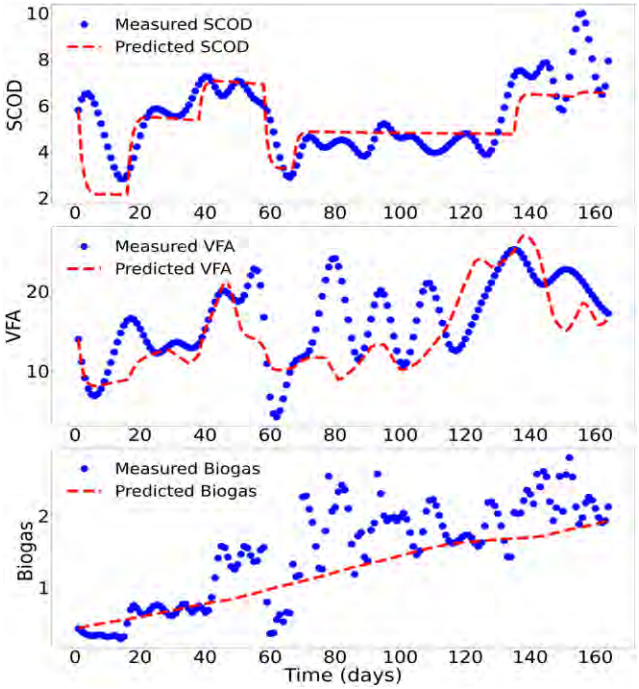



**Figure 2.** AM2 Model fit with experimental data using the set of optimal parameters obtained

## Model Performance Comparison

The evaluation metrics presented in **Table 2** and **Table 3** highlight a performance difference between the AM2 mechanistic model and the MTGP model. For SCOD predictions, the MTGP model achieved a lower RMSE (0.32 g/L) and a higher $R^2$ value (0.91) compared to the AM2 model (RMSE: 1.37 g/L, $R^2$: 0.15) in this dataset.

Similarly, for VFA predictions, the MTGP model showed improved accuracy for the conditions tested, with an RMSE of 0.87 mmol/L and $R^2$of 0.94, appearing to outperform the AM2 model, which had an RMSE of 4.62 mmol/L and $R^2$ of 0.11. For biogas production, the MTGP model also showed better predictive performance with an RMSE of 0.15 L/day and $R^2$ of 0.88, as compared to the AM2 model's RMSE of 0.47 L/day and $R^2$ of 0.52. These results suggest that the MTGP model can leverage multi-task learning and inter-output correlations to potentially yield more accurate and reliable predictions across all key outputs in this study. The comparison between the AM2 mechanistic model and the MTGP model highlights complementary strengths in their approaches to modeling AD processes. While the MTGP model exhibits superior predictive accuracy, with significantly lower RMSE and higher $R^2$ values across all outputs (**Table 3**), the AM2 model's interpretability and biochemical grounding remain critical assets. The AM2 model captures the intricate biochemical and microbial dynamics of AD, which are essential for understanding the underlying system behavior. The AM2 model incorporates acidogenic/methanogenic biomass states, enhancing biological interpretability, but its reliance on unmeasured microbial groups and assumed kinetics (e.g., growth rates) introduces predictive uncertainty without experimental validation. In contrast, the MTGP avoids microbial complexity, simplifying calibration at the cost of mechanistic detail.

**Table 2:** The RMSE and $R^2$ for the AM2 model

| Measurements | RMSE | $R^2$ | Unit |
|---|---|---|---|
| SCOD($S_1$) | 1.37 | 0.15 | g/L |
| VFA($S_2$) | 4.62 | 0.11 | Mmol/L |
| Biogas ($Q_{biogas}$) | 0.47 | 0.52 | L/day |

**Table 3:** The RMSE and $R^2$ for the MTGP model

| Measurements | RMSE | $R^2$ | Unit |
|---|---|---|---|
| SCOD | 0.32 | 0.91 | g/L |
| VFA | 0.87 | 0.94 | Mmol/L |
| Biogas | 0.15 | 0.88 | L/day |

## CONCLUSION

This work demonstrates the application of Multi-Task Gaussian Processes as a powerful data-driven framework for modelling and predicting the performance of AD systems. By leveraging input-output correlations and employing the linear model of coregionalisation, the MTGP model demonstrated improved predictive accuracy compared to the AM2 mechanistic model. While MTGP showed strong predictive accuracy and adaptability in this context, the AM2 model provided essential interpretability and biochemical insights, underscoring the complementary strengths of these two approaches.

Future research should explore the integration of these two approaches into hybrid models that combine the interpretability of mechanistic frameworks with the predictive power of data-driven techniques.

## ACKNOWLEDGEMENTS

The first author thanks Prof. Luca Fiori and Prof. Gianni Andreottola for their support at the University of Trento and the experimental data central to this study. The authors also acknowledge the financial support provided by the Supergen Bioenergy Impact Hub, which made this research possible.

## REFERENCES

1. Ahmed M, Sartori F, Merzari F, Fiori L, Elagroudy S, Negm MS, Andreottola G. Anaerobic degradation of digestate-based hydrothermal carbonization products in a continuous hybrid fixed bed anaerobic filter. Bioresour Technol 330:124971 (2021) https://doi.org/10.1016/j.biortech.2021.124971
2. Alvi M, Batstone D, Mbamba CK, Keymer P, French T, Ward A, Dwyer J, Cardell-Oliver R. Deep learning in wastewater treatment: a critical review. Water Res 245:120518 (2023) https://doi.org/10.1016/j.watres.2023.120518
3. Bynum, Michael L., Gabriel A. Hackebeil, William E. Hart, Carl D. Laird, Bethany L. Nicholson, John D. Siirola, Jean-Paul Watson, and David L. Woodruff. Pyomo - Optimization Modeling in Python. Third Edition Vol. 67. Springer, 2021.
4. Rasmussen CE, Williams CKI. Gaussian Processes for Machine Learning. The MIT Press (2005) https://doi.org/10.7551/mitpress/3206.001.0001
5. Batstone D, Keller J, Angelidaki I, Kalyuzhnyi S, Pavlostathis S, Rozzi A, Sanders W, Siegrist H, Vavilin V. The IWA Anaerobic Digestion Model No 1 (ADM1). Water Sci Technol 45:65–73 (2002) https://doi.org/10.2166/wst.2002.0292
6. Bernard O, Hadj-Sadok Z, Dochain D, Genovesi A, Steyer J-P. Dynamical model development and parameter identification for an anaerobic wastewater treatment process. Biotechnol Bioeng 75:424–438 (2001)
7. Bonilla EV, Chai K, Williams C. Multi-task Gaussian process prediction. In: Platt J, Koller D, Singer Y, Roweis S (Eds.) Advances in Neural Information Processing Systems, Vol. 20. Curran Associates, Inc. (2007)
8. Dekhici B. Data-driven modeling, order reduction and control of anaerobic digestion processes. Ph.D. thesis, University of Tlemcen (2024)
9. Dekhici B, Benyahia B, Cherki B, Fiori L, Andreottola

G. Modeling of biogas production from hydrothermal carbonization products in a continuous anaerobic digester. ACM Trans Model Comput Simul 34: (2024) https://doi.org/10.1145/3680281
10. Goulard M, Voltz M. Linear coregionalization model: Tools for estimation and choice of cross-variogram matrix. Math Geol 24:269–286 (1992)
11. Kingma DP, Ba J. Adam: A method for stochastic optimization. arXiv:1412.6980 (2017) https://arxiv.org/abs/1412.6980
12. Dekhici B, Benyahia B and Cherki B, Data-driven control of the chemostat using the Koopman operator theory, U.P.B. Sci. Bull., Series C, Vol. 85, Issu. 2, pp 137-150, 2023.

© 2025 by the authors. Licensed to PSEcommunity.org and PSE Press. This is an open access article under the creative commons CC-BY-SA licensing terms. Credit must be given to creator and adaptations must be shared under the same terms. See https://creativecommons.org/licenses/by-sa/4.0/



Systems & Control Transactions

**Research Article - Peer Reviewed Conference Proceeding**
ESCAPE 35 - European Symposium on Computer Aided Process Engineering
Ghent, Belgium. 6-9 July 2025
Jan F.M. Van Impe, Grégoire Léonard, Satyajeet S. Bhonsale,
Monika E. Polańska, Filip Logist (Eds.)

PSE PRESS

# Synthesis of Liquid Mixture Separation Networks Using Multi-Material Membranes

**Harshit Verma[a], Christos T. Maravelias[a,b,*]**

[a] Princeton University, Department of Chemical and Biological Engineering, Princeton, New Jersey, USA
[b] Andlinger Center for the Energy and Environment, Princeton University, Princeton, New Jersey, USA
* Corresponding Author: maravelias@princeton.edu.

## ABSTRACT

The synthesis of membrane networks to recover components from liquid mixture is challenging due to an extensive array of feasible network configurations and the added complexity of modeling membrane permeators caused by nonidealities in liquid mixtures. We present a mixed-integer nonlinear programming (MINLP) framework for synthesizing membrane networks to recover multiple components from liquid mixtures. First, we develop a physics-based nonlinear surrogate model to accurately describe crossflow membrane permeation. Second, we propose a richly connected superstructure to represent numerous potential network configurations. Third, the two aforementioned elements are integrated into an MINLP model to determine the optimal network configuration. Finally, the effectiveness of the proposed approach is demonstrated through a range of applications.

**Keywords**: Liquid Mixture Separations, Membrane Network Synthesis, Superstructure-based Optimization, Mixed-Integer Nonlinear Programming.

## INTRODUCTION

Membranes for liquid separation are recognized as a promising technology, offering several advantages including low energy requirements and chemical-free operation [1]. Polymeric membranes, in particular, have emerged as a preferred choice due to their scalability. The two key properties of polymeric membranes are permeability and selectivity. High permeability facilitates enhanced recovery, while high selectivity ensures high purity. However, polymeric membranes inherently exhibit a trade-off between selectivity and permeability [2]. Therefore, utilizing a single-stage membrane unit to achieve both high recovery and purity simultaneously is often impractical or incurs high operating and capital costs. To address this limitation, a multi-stage membrane network must be synthesized.

Multiple configurations of membrane networks, differentiated by the number of membrane stages and stream connections, can be synthesized for a given separation task. However, the energy consumptions and capital costs of these configurations can vary significantly depending on the total utilized membrane area and the operating conditions. The two primary methods for synthesizing membrane networks are simulation-based and optimization-based methods. In the former, a network is chosen from various potential network configurations and the operating conditions are subsequently determined [3]. However, with an increase in the number of membrane stages, this method becomes increasingly cumbersome due to the significant increase in the number of potential network configurations, so only a limited number of network configurations can be evaluated, potentially leading to suboptimal designs. In optimization-based methods, the network configuration and operating conditions are determined simultaneously by solving an optimization model [4]. In general, a superstructure is constructed to include all potential network configurations. Then, a mixed-integer nonlinear programming (MINLP) model is formulated based on the superstructure, with binary and continuous variables used to represent the configurational and operational decisions, respectively. However, the accuracy of unit models is limited due to the approximations required to formulate a computationally tractable optimization model. This work

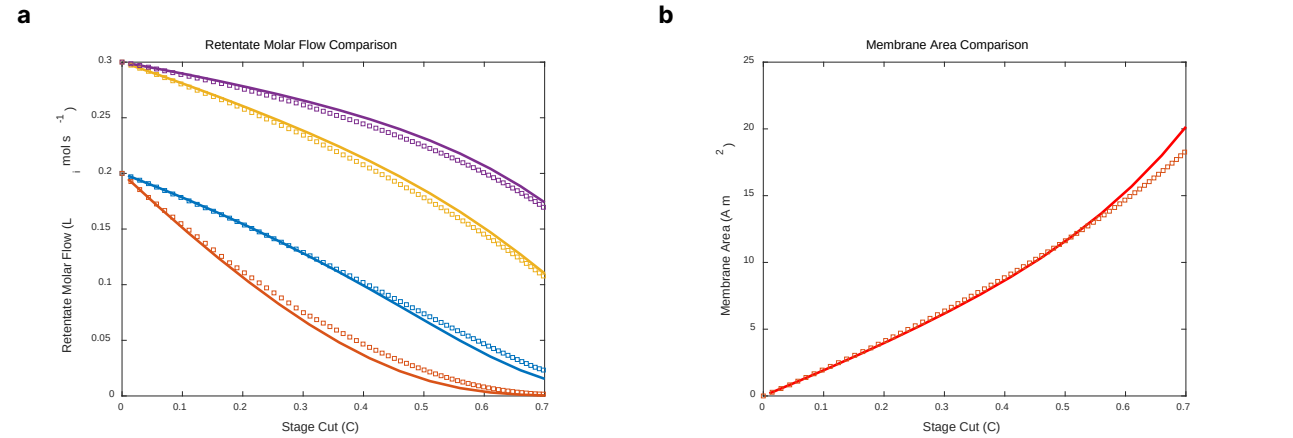



**Figure 1:** Comparison between the NLAE (solid lines) and the DAE (square markers) unit model. **a,** Retentate flow rate comparison: Blue, orange, yellow, and violet colors represent the flow rate of methyl acetate, ethyl acetate, isopropanol, and 1-butanol, respectively. **b**, membrane area comparison.

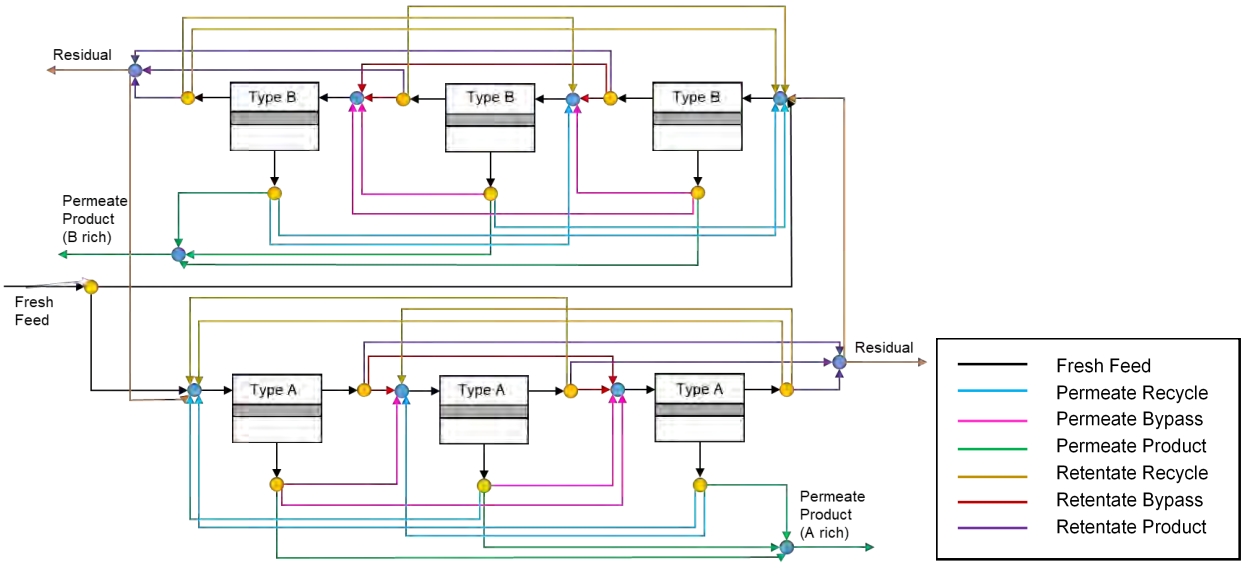



**Figure 2:** Schematic of a superstructure with two sub-network, each with three stages, with distinct membrane types. Yellow and blue disks represent splitters and mixers, respectively.

addresses this limitation by using an accurate membrane unit model.

Various membrane unit models for gas separation have been proposed. Marriott and Sørensen incorporated mass, momentum, and energy balances, employing partial differential-algebraic equations (PDAE), to model membrane separation [5]. The crossflow models proposed by Weller and Steiner [6] and Shindo et al. [7], formulated as differential-algebraic equations (DAE), have been commonly utilized to model the separation of gas and liquid mixture. However, integrating PDAE/DAE systems in an optimization model to achieve a globally optimal solution presents significant challenges [8]. Thus, various discretization techniques are employed to reformulate the PDAE/DAE systems into a system of algebraic equations. However, discretization schemes involve a trade-off between model complexity and solution accuracy. While finer discretization provides high accuracy, it also increases the number of nonlinear equations, making it computationally challenging to attain global optimality. Additionally, building on the work of Weller and Steiner [6] and Shindo et al. [8], Chen et al. [9] and Taifan and Maravelias [10] developed a unit model for the separation of multicomponent gas mixtures. Moreover, Chavez Velasco et al. [11] developed a unit model specifically for the separation of binary liquid mixtures. As a result, current unit models are limited to the separation of either binary liquid mixtures or multicomponent gas mixtures. Thus, there is a critical gap in the development of membrane unit models for the separation of multicomponent liquid mixtures.

Numerous computational methods have been proposed for the synthesis of membrane networks. Pathare and Agrawal [12] devised a method that

systematically enumerates all networks and solves a nonlinear program (NLP) for each. However, this approach becomes increasingly computationally intensive as the number of potential networks increases. Other existing optimization models for synthesizing membrane networks typically rely on local optimization or meta-heuristic methods [13–15]. The studies aiming to obtain global optimality generally focus on the separation of binary mixtures [11,14]. Moreover, the optimization models developed by Chen et al. [9] and Taifan and Maravelias [10] specifically target multicomponent gas mixtures and impose restrictions on the stream connections within the membrane network superstructure. This limitation excludes some feasible network configurations, potentially leading to suboptimal solutions.

In this work, we present a novel approach for synthesizing optimal membrane networks for multicomponent liquid mixture separation [16]. We propose a generalized optimization model that incorporates three elements. First, we develop a physics-based nonlinear surrogate unit model to describe crossflow membrane permeation for multicomponent liquid mixtures. Second, we propose a highly interconnected superstructure to represent an extensive array of potential network configurations. Third, we formulate an optimization model to determine the configuration and operating conditions that minimize the total required membrane area. Finally, we present multiple applications to showcase the effectiveness of our approach.

## MEMBRANE UNIT MODEL

First, we adapt the DAE-based crossflow membrane unit model from Shindo et al. [7] for multicomponent liquid mixtures. Next, the DAE unit model is reformulated to a nonlinear algebraic unit model (NLAE). Finally, we assess accuracy by comparing the NLAE unit model with the original DAE model.

### DAE Unit Model

In an idealized crossflow membrane unit, the liquid mixture on the feed-side exhibits plug flow with no longitudinal mixing. The permeating components selectively pass through the membrane and enter the permeate-side without mixing with the permeate bulk flow. The DAE unit model is based on the following assumptions: (1) component permeabilities are independent of pressure and composition, (2) material transport follows Fick's law of diffusion, (3) negligible concentration polarization, (4) only transmembrane pressure drop is observed, (5) isothermal operation, (6) negligible mass transfer resistance, and (7) uniform membrane thickness. In the DAE model, material transport across polymeric membranes is described by the solution-diffusion theory, which has been widely employed and extensively validated against experimental data from physical systems [17]. The DAE unit model for the pervaporation process is given by the following equations [7]:

$$\frac{dF_i^{\mathrm{F}}}{dA} = -\pi_i\left(G_i\hat{X}_i - \tau_i\hat{Y}_i\right) \qquad \forall\, i \in \mathbf{I} \qquad (1)$$

$$\hat{Y}_i = \frac{\pi_i(G_i\hat{X}_i - \tau_i\hat{Y}_i)}{\sum_{i'\in\mathbf{I}}\pi_{i'}(G_{i'}\hat{X}_{i'} - \tau_{i'}\hat{Y}_{i'})} \qquad \forall\, i \in \mathbf{I} \qquad (2)$$

$$\dot{F}^{\mathrm{F}}\hat{X}_i = F_i \qquad \forall\, i \in \mathbf{I} \qquad (3)$$

$$F_i^{\mathrm{F}}\big|_{\dot{F}^{\mathrm{F}}=\dot{F}} = F_i \qquad \forall\, i \in \mathbf{I} \qquad (4)$$

where $\hat{X}_i/\hat{Y}_i$ represent the molar fraction of component $i$ on the feed-side/permeate-side, while $F_i^{\mathrm{F}}/F_i$ and $\dot{F}^{\mathrm{F}}/\dot{F}$ denote the molar flow rate of component $i$ in the feed-side/fresh feed and the total molar flow rate in the feed-side/fresh feed, respectively; $G_i, \tau_i,$ and $\pi_i$ represent the activity coefficient, normalized permeate pressure, and permeance of component $i$, respectively. Finally, given the initial conditions and the desired separation specifications, composition profiles and the required membrane area can be determined.

### NLAE Unit Model

Discretization schemes are primarily employed to convert DAE systems into algebraic equations. However, this approach increases computational complexity, making it difficult for optimization solvers to achieve global optimality. We utilize a different approach, based on the assumption of a uniform collective driving force, $B$, and activity coefficients, $G_i$, across the membrane surface. The DAE model can be reformulated into differential equations, which can be integrated to obtain the following set of nonlinear algebraic equations:

$$\ln\left(\frac{L_i}{F_i}\right) = \left(\frac{\pi_i G_i}{B+\pi_i\tau_i}\right)\ln(1-C) \qquad \forall\, i \in \mathbf{I} \qquad (5)$$

$$\sum_{i\in\mathbf{I}} L_i = (1-C)\sum_{i\in\mathbf{I}} F_i \qquad (6)$$

$$A = \frac{1}{B}\left(\dot{F} - \dot{L}\right) \qquad (7)$$

where $F_i/L_i$ and $\dot{F}/\dot{L}$ are the molar flow rates of component $i$ and the total molar flow rate in the feed/retentate stream, while $C$ and $A$ represents the stage cut and the required area, respectively. Detailed reformulation steps are provided in the Supplementary Material. Further, the accuracy of the NLAE unit model is essential for its integration in the optimization model. Thus, we validate the developed NLAE unit model by comparing it with the DAE unit model using simulations in MATLAB, focusing on two key variables: the retentate flow rate and the membrane area, under varying final stage cut, $C$, for both models. Data for the simulation is provided in the Supplementary Material. For the DAE unit model, the retentate flow rate and the membrane area are determined by solving Eq. $(1), (2), (3),$ and $(4)$, while

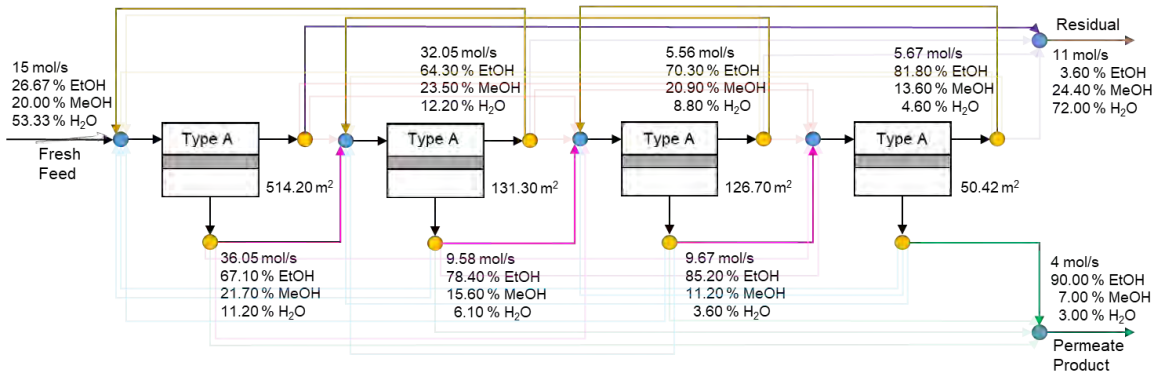



**Figure 3:** Single component separation: global optimal network to recover EtOH at the desired recovery and purity of 90%.

for the NLAE unit model, they are calculated using Eq. $(5), (6), \text{and } (7)$. Consequently, the comparison between the two unit models, shown in Figure 1, demonstrates good agreement.

## SUPERSTRUCTURE REPRESENTATION

We present a superstructure with rich interconnections designed to recover multiple target components from a liquid mixture. The superstructure can employ distinct membrane materials, each specifically selective for different target components. Moreover, it incorporates multiple sub-networks that are interconnected to achieve the required separation task. Within each sub-network, the superstructure employs a unique membrane material and allows for: (1) a retentate/permeate to be sent to any of the previous stages as a retentate/permeate recycle, (2) a retentate/permeate to be sent to any of the subsequent stages as a retentate/permeate bypass, and (3) a retentate/permeate to be collected from any stage as a retentate/permeate product. The permeate final product from a sub-network contains a recovered target component, while the retentate final product is fed into other sub-networks for further separation of remaining target components. Additionally, each sub-network utilizes one mixer for each feed entering a stage, two mixers for retentate and permeate products, two splitters for each retentate and permeate leaving a stage, and one splitter for the fresh feed stream. Finally, to minimize the number of symmetrical solutions, the fresh feed is allowed to enter only the first stage of each sub-network. For illustration, Figure 2 shows a schematic of a superstructure with two sub-networks, each with three stages employing Type A and Type B membranes, to recover target components A and B from a liquid mixture, respectively.

In the mathematical formulation, binary variables are utilized to denote the activation of membrane stages for specific membrane types. Thus, the binary variable $Z_{n,m}$ is introduced to denote whether stage $n$ of membrane type $m$ is active. Additionally, the location of the fresh feed inlet to one of the sub-networks plays a critical role. Therefore, the binary variable $Y_m$ is used to denote if the fresh feed enters the sub-network with membrane type $m$. Further, material balances are introduced around all the mixers, splitters, and around each stage of the sub-network. A detailed mathematical formulation is provided in the Supplementary Material. In practical applications, condensers and pumps are utilized to condense permeate vapors and adjust the pressure of the permeate stream for further recycling, bypassing, or collection of the permeate. However, the objective of the proposed model is to minimize the overall membrane area. Thus, calculations for condenser and vacuum pump units are excluded.

## APPLICATIONS

First, we study the behaviour of a membrane network that utilizes a single sub-network with a unique material for the separation of one target component from an alcohol/water mixture. Second, we show the effectiveness of the proposed method using an example with three components for the simultaneous separation of two target components. All optimization models are written in GAMS 46.4.1 and are solved using BARON 24.3.10 on a Windows machine with a 1.60 GHz CPU and 32 GB RAM.

### Single Component Separation

We analyze a membrane network system that processes a fresh feed, pressurized at 1 atm with a flow rate of 15 mol/s, of an alcohol/water mixture. The mixture consists of 26.67% ethanol (EtOH), 20% methanol (MeOH) and 53.33% water ($H_2O$) on a molar basis. The feed-side pressure in a membrane unit is set to match the pressure of the fresh feed, while the permeate-side

pressure is maintained at 0.01 atm to facilitate pervaporation. Isothermal operation is assumed at 323.15 K. The permeance values for EtOH, MeOH, and $H_2O$ for an ethanol-selective membrane are 0.088, 0.051, 0.018 (mol/m$^2$/s), and for a methanol-selective membrane type are 0.025, 0.18, 0.018 (mol/m$^2$/s) respectively, which fall in the range of Nafion membranes.

The proposed model is employed with a single membrane type, thus we construct a four-stage superstructure with an ethanol-selective membrane type (Type A), as shown in Figure S1. First, we determine the optimal network for the separation of ethanol from the liquid mixture at the desired purity and recovery of 90%. The model contains 309 equations and 247 variables (4 binaries) and is solved to global optimality within 60 s. The global optimal network configuration, shown in Figure 3, requires four membrane stages with a total area of 204.87 m$^2$. In the optimal network, EtOH permeates through the active stages of Type A membrane and is bypassed to the subsequent stages, facilitating effective separation by concentrating the EtOH rich permeate. Accordingly, the final permeate product is collected from the last stage meeting the higher recovery and purity specifications, while the residual mixture is collected as the retentate final product.

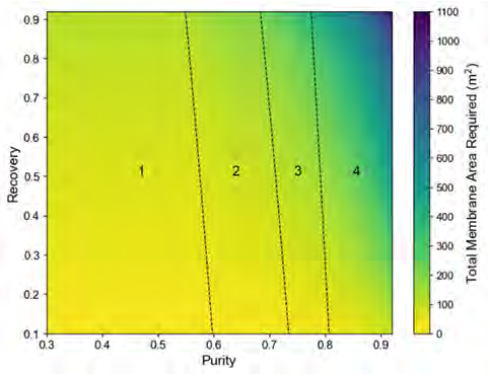



**Figure 4:** Total membrane area and number of required stages under varying recovery and purity specifications.

Next, we study the impact of purity and recovery specifications for EtOH on the network's configuration and operation by solving the model under varying purity and recovery specifications. Figure 4 illustrates the variation in the total required area and the number of stages needed as the desired recovery and purity increase. Accordingly, the purity specification significantly influences the network design, including the number of required stages and the total required area, compared to the specified recovery. However, the purity threshold for installing an additional stage is lower at higher recovery, suggesting a modest impact of specified recovery on network performance.

## Two Component Separation

The separation and recovery of iso-butanol (i-BuOH) and ethanol (EtOH) are of significant importance in biological systems, particularly in the context of biofuel production and sustainable energy solutions. However, their separation presents challenges due to their similar boiling points and azeotropic behaviours. Therefore, membrane-based separation technology can be employed to effectively recover both i-BuOH and EtOH. In this example, we study the simultaneous separation and recovery of i-BuOH and EtOH from an aqueous mixture using a multi-material membrane network system. We consider a fresh feed pressurized at 1 atm with a flow rate of 15 mol/s, consisting of an aqueous i-BuOH/EtOH mixture. This mixture comprises 26.67% i-BuOH, 20% EtOH and 53.33% water ($H_2O$) on a molar basis. The feed-side pressure in a membrane unit is set to match the pressure of the fresh feed, while the permeate-side pressure is maintained at 0.01 atm to facilitate pervaporation. Isothermal operation at 323.15 K is assumed. Permeance values for i-BuOH, EtOH, and $H_2O$ for an iso-butanol-selective membrane are 0.057, 0.023, 0.017 (mol/m$^2$/s), and for an ethanol-selective membrane type are 0.004, 0.138, 0.017 (mol/m$^2$/s), respectively.

We employ an iso-butanol-selective membrane type (Type A) and an ethanol-selective membrane type (Type B) across two interconnected sub-networks (see Figure 2). Additionally, we allow each sub-network to include four stages to facilitate separation at higher purity and recovery specifications. The proposed model is solved at the desired purity and recovery specification of 90% for both i-BuOH and EtOH, respectively. The model consists of 506 equations and 495 variables (10 binaries) and is solved to global optimality within 240 s. The globally optimal network configuration is shown in Figure 5.

The optimal network incorporates three stages of Type B membrane and utilizes all four available stages of Type A membrane, requiring a total area of 1158.3 m$^2$. The higher permeance of EtOH in Type B membrane, compared to the permeance of i-BuOH in Type A membrane, facilitates the separation of EtOH as the initial step. Therefore, the fresh feed is fed to the sub-network with Type B membranes. As a result, EtOH is first separated and gets collected in the final permeate product in the sub-network with Type B membranes. In contrast, the final retentate product from the sub-network with Type B membranes, mainly comprising i-BuOH and $H_2O$, is subsequently fed to the sub-network with Type A membranes for the further separation of i-BuOH from the remaining aqueous mixture. Finally, i-BuOH is separated and collected as the final permeate product from the sub-network with Type A membranes, while the remaining aqueous mixture, predominantly

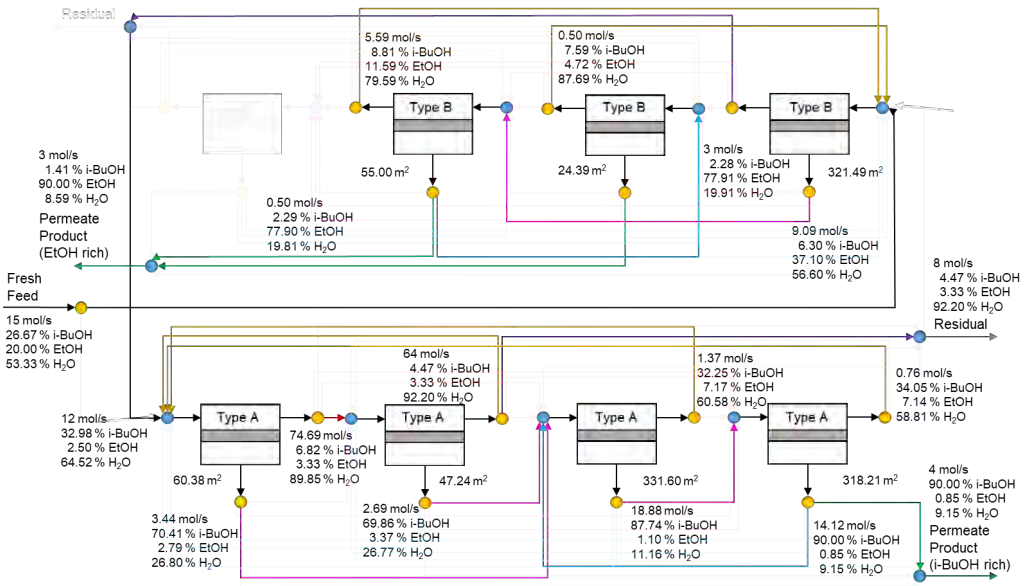



**Figure 5:** Two component separation: global optimal network to recover i-BuOH and EtOH at the desired recovery

containing $H_2O$, is collected as the residual.

## CONCLUSIONS

In this study, we proposed an optimization model for membrane network synthesis tailored for the separation of multiple components from liquid mixtures. First, we developed a physics-based nonlinear surrogate model to describe pervaporation-based crossflow membrane permeation for liquid mixtures. Second, we proposed a comprehensive superstructure, incorporating multiple sub-networks, each with distinct membrane types, featuring multiple stages with rich stream interconnections. Third, we formulated a mixed-integer nonlinear programming model, integrating the two aforementioned elements, to determine the network configuration and operating conditions that minimize the overall network area. The proposed optimization model effectively identifies the global optimal network, as illustrated by the applications presented.

## DIGITAL SUPPLEMENTARY MATERIAL

DAE unit model reformulation, simulation data, figures, and the mathematical formulation for the optimization model is presented in the Supplementary Material (LAPSE:2025.0008).

## ACKNOWLEDGEMENT

This effort was funded by the U.S. Department of Energy, Office of Energy Efficiency and Renewable Energy under Award Number DE-EE0009494 and the Great Lakes Bioenergy Research Center, U.S. Department of Energy, Office of Science, Office of Biological and Environmental Research under Award Number DE-SC0018409.

## REFERENCES

1. H. Strathmann, Membrane separation processes, Journal of Membrane Science 9 (1981) 121–189. https://doi.org/10.1016/S0376-7388(00)85121-2.
2. L.M. Robeson, The upper bound revisited, Journal of Membrane Science 320 (2008) 390–400. https://doi.org/10.1016/j.memsci.2008.04.030.
3. P.F. Zito, A. Brunetti, G. Barbieri, Multi-step membrane process for biogas upgrading, Journal of Membrane Science 652 (2022) 120454. https://doi.org/10.1016/j.memsci.2022.120454.
4. I.E. Grossmann, Mixed-Integer Optimization Techniques for Algorithmic Process Synthesis, in: J.L. Anderson (Ed.), Advances in Chemical Engineering, Academic Press, 1996: pp. 171–246. https://doi.org/10.1016/S0065-2377(08)60203-3.
5. J. Marriott, E. Sørensen, A general approach to modelling membrane modules, Chemical Engineering Science 58 (2003) 4975–4990. https://doi.org/10.1016/j.ces.2003.07.005.
6. S. Weller, W.A. Steiner, Separation of Gases by Fractional Permeation through Membranes, Journal of Applied Physics 21 (1950) 279–283. https://doi.org/10.1063/1.1699653.
7. Y. Shindo, T. Hakuta, H. Yoshitome, H. Inoue, Calculation Methods for Multicomponent Gas Separation by Permeation, Separation Science and Technology 20 (1985) 445–459. https://doi.org/10.1080/01496398508060692.

8. J.K. Scott, P.I. Barton, Reachability Analysis and Deterministic Global Optimization of DAE Models, in: A. Ilchmann, T. Reis (Eds.), Surveys in Differential-Algebraic Equations III, Springer International Publishing, Cham, 2015: pp. 61–116. https://doi.org/10.1007/978-3-319-22428-2_2.
9. Z. Chen, M. Tawarmalani, R. Agrawal, Global minimization of power consumptions for multicomponent gas membrane cascades, Computers & Chemical Engineering 180 (2024) 108464. https://doi.org/10.1016/j.compchemeng.2023.108464.
10. G.S.P. Taifan, C.T. Maravelias, Generalized optimization-based synthesis of membrane systems for multicomponent gas mixture separation, Chemical Engineering Science 252 (2022) 117482. https://doi.org/10.1016/j.ces.2022.117482.
11. J.A. Chavez Velasco, R. Tumbalam Gooty, M. Tawarmalani, R. Agrawal, Optimal design of membrane cascades for gaseous and liquid mixtures via MINLP, Journal of Membrane Science 636 (2021) 119514. https://doi.org/10.1016/j.memsci.2021.119514.
12. R. Pathare, R. Agrawal, Design of membrane cascades for gas separation, Journal of Membrane Science 364 (2010) 263–277. https://doi.org/10.1016/j.memsci.2010.08.029.
13. R. Qi, M.A. Henson, Membrane system design for multicomponent gas mixtures via mixed-integer nonlinear programming, Computers & Chemical Engineering 24 (2000) 2719–2737. https://doi.org/10.1016/S0098-1354(00)00625-6.
14. A. Aliaga-Vicente, J.A. Caballero, M.J. Fernández-Torres, Synthesis and optimization of membrane cascade for gas separation via mixed-integer nonlinear programming, AIChE Journal 63 (2017) 1989–2006. https://doi.org/10.1002/aic.15631.
15. V.S.K. Adi, M. Cook, L.G. Peeva, A.G. Livingston, B. Chachuat, Optimization of OSN Membrane Cascades for Separating Organic Mixtures, in: Z. Kravanja, M. Bogataj (Eds.), Computer Aided Chemical Engineering, Elsevier, 2016: pp. 379–384. https://doi.org/10.1016/B978-0-444-63428-3.50068-0.
16. H. Verma, D. Jassby, C.T. Maravelias, Superstructure-based Optimization of Membrane Network Systems for Multicomponent Liquid Mixture Separation, Journal of Membrane Science (2024) 123574. https://doi.org/10.1016/j.memsci.2024.123574.
17. J.G. Wijmans, R.W. Baker, The solution-diffusion model: a review, Journal of Membrane Science 107 (1995) 1-21. https://doi.org/10.1016/0376-7388(95)00102-I

© 2025 by the authors. Licensed to PSEcommunity.org and PSE Press. This is an open access article under the creative commons CC-BY-SA licensing terms. Credit must be given to creator and adaptations must be shared under the same terms. See https://creativecommons.org/licenses/by-sa/4.0/



Systems & Control Transactions

**Research Article - Peer Reviewed Conference Proceeding**
ESCAPE 35 - European Symposium on Computer Aided Process Engineering
Ghent, Belgium. 6-9 July 2025
Jan F.M. Van Impe, Grégoire Léonard, Satyajeet S. Bhonsale,
Monika E. Polańska, Filip Logist (Eds.)

PSE PRESS

# Transferring Graph Neural Networks for Soft Sensor Modeling using Process Topologies

**M.F. Theisen[a], G.M.H. Meesters[b], A.M. Schweidtmann[a*]**

[a] Process Intelligence Research Group, Department of Chemical Engineering, Delft University of Technology, Van der Maasweg 9, Delft 2629 HZ, The Netherlands
[b] Product and Process Engineering, Department of Chemical Engineering, Delft University of Technology, Van der Maasweg 9, Delft 2629 HZ, The Netherlands
* Corresponding Author: a.schweidtmann@tudelft.nl

## ABSTRACT

Data-driven soft sensors help in process operations by providing real-time estimates of otherwise hard to measure process quantities, e.g., viscosities or product concentrations. Currently, soft sensors need to be developed individually per plant. Using transfer learning, machine learning based soft sensors could be re-used and fine-tuned across plants and applications. However, transferring data-driven soft sensor models is in practice often not possible, because the fixed input structure of standard soft sensor models prohibits transfer if, e.g., the sensor information is not identical in all plants. We propose a topology-aware graph neural network approach for transfer learning of soft sensor models across multiple plants. In our method, plants are modeled as graphs: Unit operations are nodes, streams are edges, and sensors are embedded as attributes. Our approach brings two advantages for transfer learning: First, we not only include sensor data but also crucial information on the plant topology. Second, the graph neural network algorithm is flexible with respect to its sensor inputs. This allows us to model data from different plants with different sensor networks. We test the transfer learning capabilities of our modeling approach on ammonia synthesis loops with different process topologies [1]. We build a soft sensor predicting the ammonia concentration in the product. After training on data from one process, we successfully transfer our soft sensor model to a previously unseen process with a different topology. Our approach promises to extend the data-driven soft sensors to cases to leverage data from multiple plants.

**Keywords**: Digital twins, Transfer learning, Data-driven modeling

## INTRODUCTION

Data-driven soft sensors promise to increase operating efficiency in chemical plants by providing real time estimates of hard to measure quantities. Previous works have shown the merit of soft sensors in many applications, e.g., estimating viscosity or product concentrations [2,3]. However, data scarcity remains a major hinderance in developing machine learning based solutions such as soft sensors in industry [4].

Transfer learning offers an opportunity to decrease data requirements for soft sensor modeling but is often not possible for processes with different topologies. In transfer learning, a machine learning model pretrained on one domain is transferred to another domain. Transfer learning for soft sensors has shown several advantages, such as reduced data requirements, zero-shot capabilities and improved performance [5]. In previous literature, transfer learning has been explored in multiple situations for reducing data requirements in soft sensor development. For domain adaptation, the model transfers knowledge between different operating points [2]. Similarly, transfer learning has been leveraged to transfer between batch runs [6]. It has even been applied to transfer between identical process lines [7,8]. While different types of models have been used in these works (multilayer perceptrons (MLPs), extreme learning machines,

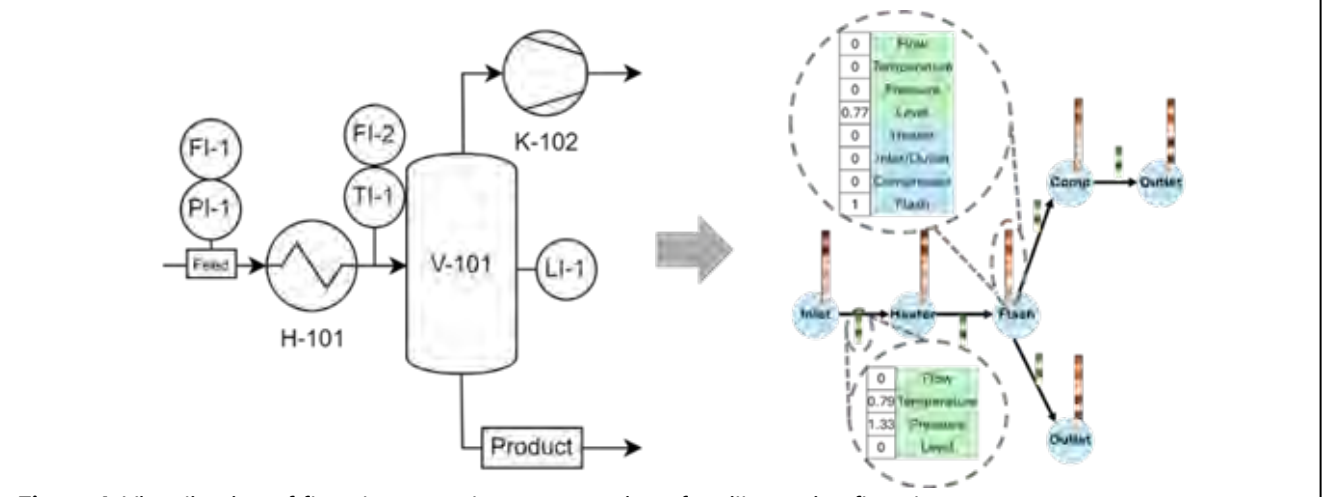



**Figure 1:** Visualization of flowsheet graph representation of an illustrative flowsheet.

recurrent neural networks), it is not possible to transfer these soft sensor models between plants with different topologies, e.g., with respect with to sensor locations or equipment types, due to the fixed input structure of the models.

We propose a new soft sensor architecture that uses spatio-temporal graph neural networks (GNNs) on the process topology and sensor data. This enables transfer learning between different processes due to its flexible input structure and topology-awareness. We model chemical processes as graphs, with unit operations as nodes, streams as edges and sensor data embedded as attributes. Our approach allows to incorporate information about the process topology along with the sensor measurements. We argue that this approach has two advantages for transfer learning: First, this data representation provides context of the process to the model. This enables the model to learn about the process and thus transfer information to related processes. Second, our graph-based model does not have a fixed input size, meaning that it can be transferred between processes with different sensor networks. We demonstrate our modeling approach on two ammonia synthesis loops. The processes are similar, but topologically different, making them challenging for standard transfer learning approaches.

# METHODS

## Spatio-temporal modeling of soft sensors with graphs

To enable transfer learning between processes, we utilize a graph-based representation of the process topology and the soft sensor data to enable topology-awareness together with a model that accounts for both spatial and temporal dependencies in the data.

We represent the underlying Process as a directed graph, representing the topology of the process, see Figure 1. We model unit operations as nodes. To model different types of units, we one-hot encode the unit type into the node attribute vector. We further represent streams as directed edges. The direction of the edge follows the direction of the material. Finally, we encode sensor measurements according to their location in the process into the attribute vectors of nodes and edges.

A complete overview of the modeling framework can be found in Figure 2. We model the spatial relationships between the graph-encoded data and the soft sensor target using GNNs for each timestep. We deploy a message passing GNN [9], allowing us to utilize both node and edge information. The output is an individual flowsheet embedding for each timestep, see Figure 2.

To model the temporal relationship and thus dynamics of the process, we use a transformer. The transformer encoder inputs the graph-encoded flowsheet embeddings. In its final layer, the encoder averages over the latent space along the number of timesteps, resulting in single output vector. A three layer MLP then predicts sensor target $\hat{y}_t$ for the current time step $y$.

## Transfer learning

The transfer learning process in this work is conducted in two stages. First, the model undergoes initial training on the source domain. Subsequently, a partial retraining is performed on the target domain. We also test the case of no retraining on the target domain, which is referred to as zero-shot transfer learning.

To further stabilize the training, we scale our input data by applying a log-scale. Since each process has a different topology and set of embedded sensor measurements due to different sensor information, different streams etc., we cannot uniformly apply per-feature normalization across them. We however found that with learning rates sufficiently small, the training is still stable.

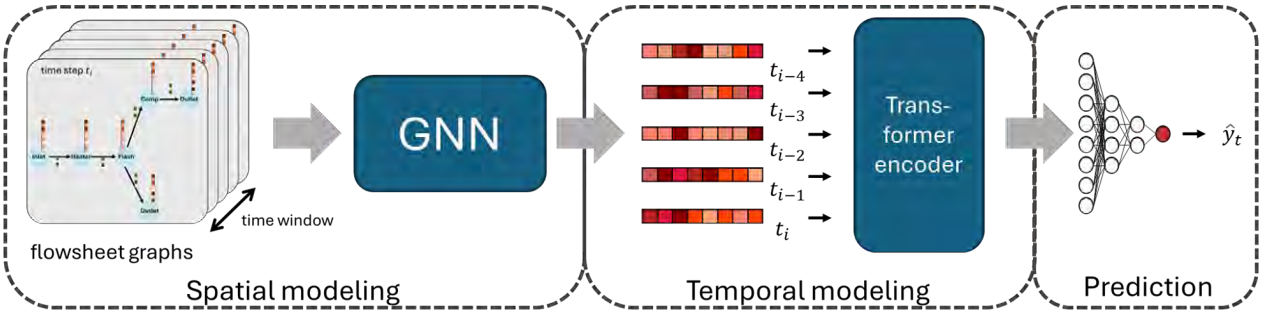



**Figure 2:** Illustration of the model used for spatio-temporal modeling, here with a look back window of 5 time steps.

We do normalize our soft sensor target to zero mean and unit standard deviation.

We evaluate the model prediction $\hat{y}$ against the ground truth $y$ on our test set $N_{\text{test}}$ for all time steps t using the root mean squared error (RMSE) on the normalized data:

$$RMSE = \sqrt{\frac{1}{N_{\text{test}}} \sum_{t=1}^{N_{\text{test}}} (y_t - \hat{y}_t)^2} \quad (1)$$

## CASE STUDY: AMMONIA SYNTHESIS LOOPS

We consider two ammonia synthesis loops as illustrative case studies with the same equipment sizing and feed flows but different topologies. In both processes, ammonia is produced from N2 and H2 under high pressure. The soft sensor target is the concentration of ammonia in the respective product streams. Both processes consist of four types of processing steps: (1) Compressions, (2) Separation via flashing, (3) Heating/Cooling, and (4) Reaction with three reactor beds. The combination of those major units however differs between the two processes, reflecting different topologies found in industry [1].

In Process A (see Figure 3, left), the feed is first compressed in compressor K-101 and mixed with the recycle. The mixture is then further compressed in compressor K-102 and heated before entering the reactor R-101. The effluent leaving the reactor is flashed in the flash V-101. The liquid phase leaving V-101 is the product stream while the vapor phase of flash V-101 is purged and mixed with the inlet gas.

In Process B (see Figure 3, right), the feed is first compressed in compressor K-101 and mixed with the reactor R-101 outlet. The mixture of the reactor effluent and the fresh feed is then cooled and flashed in V-101, removing the ammonia as a liquid. The liquid ammonia then leaves the process as its product. The vapor phase leaving the flash V-101 is further compressed in compressor K-102 and heated and after that sent into the reactor R-101. The reactor outlet is purged before being mixed with the inlet stream.

Both processes are controlled using PID control. The control scheme follows the “Mode I” as detailed by [10]. Both the feed and the purge stream are controlled with a flow controller (FC-1 and FC-2, respectively). The level in the flash vessels is controlled with a level controller (LC-1). The reactor inlet temperature is controlled with the temperature controller (TC-1).

We simulate dynamic operating datasets from the processes using the dynamic simulation software Aspen Plus Dynamics V12. As a design basis, we use the simulation files by Araújo and Skogestad [10]. To generate a dataset of dynamic operation, we randomly vary the set points of controllers in a range of 1-20% deviation from the original, running the simulation until steady state is reached on the new setpoint. Then, we revert the setpoint back to the original. This way, we simulate 80 hours of operation. We sample sensor data every 36 seconds. This results in approximately 8000 datapoints for both datasets. We split the dataset 80/20/20 between for training, validation and testing in a chronological split.

## RESULTS AND DISCUSSION

We carry out the transfer learning with our topology-aware GNN in a two-step process: (1) We first train our model on the dataset of Process A until we reach convergence on our validation set. (2) We then test the transfer capabilities of the GNN model on Process B.

To apply the transfer learning framework, we fine-tune the pretrained model on fractions of Process B, specifically on up to 51 points. This low number of training points reflects the often limited number of soft sensor target measurements available in industrial settings. For comparison, we also train a model on the data from Process B from scratch. We additionally test the zero-shot capability of the model pretrained on Process A. We train each model nine times using different seeds to mitigate the effects of training noise, and plot both the mean and standard deviation of the nine models combined. For

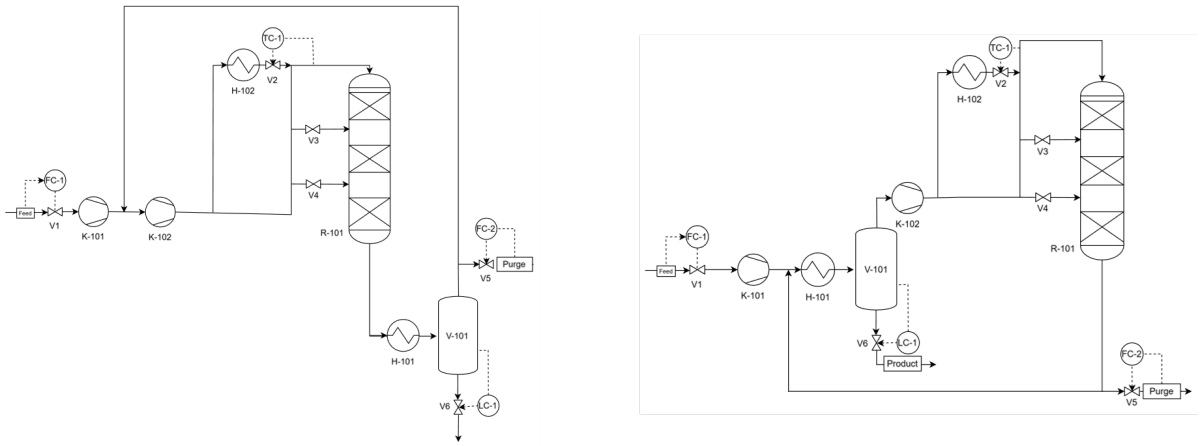



**Figure 3:** Two ammonia synthesis loops are used in this work. In Process A (left) the feed is first sent to the reactor and then flashed. In Process B (right), the feed is first mixed with the reactor outlet, then flashed and sent to the reactor.

training, we used a NVIDIA GeFORCE RTX 3090. The training times varied between 30 minutes for the full training dataset and less than 5 minutes for a fraction of the dataset.

The results are shown in Figure 4. We plot the fraction of the data from Process B used for training vs. RMSE on the test set of Process B. We also illustrate the zero-shot capabilities of the pretrained model by adding a data point for 0 datapoints used for training.

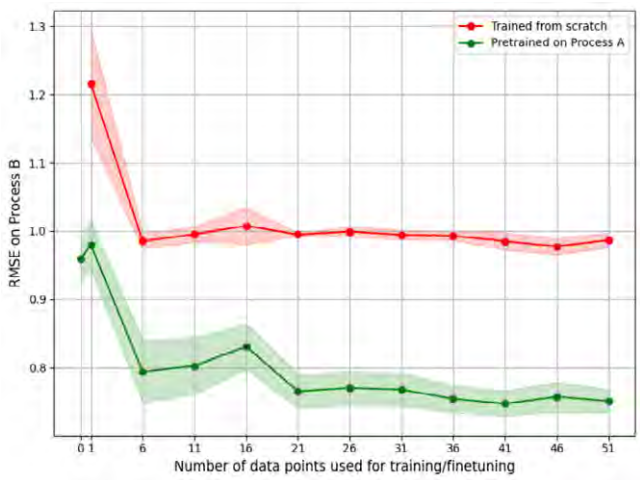



**Figure 4**: Pretrained vs training from scratch for varying number of datapoints. The shaded area shows the standard deviation due to different weight initializations.

By analyzing the results shown in Figure 4, we observe three notable trends: (1) The zero-shot performance of the pretrained model is significant, achieving an RMSE of 0.9753 on Process B without any training data from Process B. In contrast, the model trained from scratch requires 46 datapoints to reach a similar performance level. We attribute this to the pretrained model's ability to transfer learned dynamics from Process A to the previously unseen Process B. (2) Both models improve their RMSE scores on Process B when trained on more data. The pretrained model achieves an RMSE of 0.7633 when trained on 51 datapoints, while the model trained from scratch also shows improvement, reaching an RMSE of 0.9776. However, the pretrained model consistently outperforms the model trained from scratch across different training data sizes. (3) The performance of the pretrained model deteriorates when fine-tuned on a single datapoint from Process B, performing worse than its zero-shot performance. We hypothesize that this might be due to the lack of sufficient information in a single data point, which could lead to overfitting or misrepresentation of the underlying process dynamics of Process B.

**Table 1:** Average percentage RMSE reduction when using the pretrained soft sensor model compared to the model trained from scratch on Process B.

| Number of data points | RMSE reduction |
|---|---|
| 1 | 19.38% |
| 11 | 19.36% |
| 21 | 23.08% |
| 31 | 22.80% |
| 41 | 24.15% |
| 51 | 23.87% |

The relative reduction in RMSE when using the soft sensor model pretrained on Process A compared to the soft sensor model trained from scratch is further calculated in Table 1, showing up to 24.15% in reduction. It is notable that the relative reduction in RMSE increases with more training data from Process B. We thus hypothesize that the model pretrained on Process A may benefit more from additional training data of process B than the model trained from scratch in this limited data regime.

We further visualize the effect of finetuning in Figure 5. We visualize the ground truth alongside the zero-shot predictions from the pretrained model and the predictions from the finetuned model over time on the Process B test set. The zero-shot model under-predicts the ammonia concentration consistently. This is even the case during steady state, e.g., between minute 500 and 800. This can be explained by the fact that the ammonia concentration in Process A and Process B are not identical, and thus the model still predicts an ammonia concentration as it would occur in Process A. With fine tuning, this offset is reduced, as shown by the prediction of the finetuned model between minutes 500 and 800. Nevertheless, some of the dynamics, e.g., between minute 0 and 350, are still not well captured by the finetuned model.

## CONCLUSION

We propose a spatio-temporal soft sensor modeling framework using GNNs to enable transfer learning across topologically different processes. We utilize two similar but topologically different ammonia synthesis loops as our case study. We show that the topology-aware GNN is transferred from one process to the other. We further demonstrate how transfer learning reduces data requirement through good performance without any data on the target domain and even better performance on very little additional data. We show that using the pretrained model, we can reduce the RMSE by up to 24.15% when trained on 46 datapoints compared to the model trained from scratch.

This work presents a flexible framework that can be extended to various chemical process systems. Future work could focus on adapting this transfer learning framework to multi-process environments generalizing beyond one-process pretraining. Further, the approach is yet to be verified on industrial data, which often poses additional challenges.

## REFERENCES


1. Moulijn JA. Chemical Process Technology. Ed: Makkee M, Diepen A. John Wiley & Sons Inc (2013)
2. Liu Y, Yang C, Liu K, Chen B, Yao Y. Domain adaptation transfer learning soft sensor for product quality prediction. Chemom Intell Lab Syst 192:103813 (2019) https://doi.org/10.1016/j.chemolab.2019.103813
3. Bispo VD, Scheid CM, Calçada LA, Meleiro LA. Development of an ANN-based soft-sensor to estimate the apparent viscosity of water-based drilling fluids. J Pet Sci Eng 150:69-73 (2017) https://doi.org/10.1016/j.petrol.2016.11.030
4. Bortz M, Dadhe K, Engell S, Gepert V, Kockmann N, Müller-Pfefferkorn R, Urbas L. AI in process industries – current status and future prospects. Chemie Ingenieur Technik 95:975-988 (2023) https://doi.org/10.1002/cite.202200247
5. Curreri F, Patanè L, Xibilia MG. Soft sensor transferability: a survey. Appl Sci 11:7710 (2021) https://doi.org/10.3390/app11167710
6. Kay S, Kay H, Mowbray M, Lane A, Mendoza C, Martin P, Zhang D. Integrating transfer learning within data-driven soft sensor design to accelerate product quality control. Dig Chem Eng 10:100142 (2024) https://doi.org/10.1016/j.dche.2024.100142
7. Curreri F, Patanè L, Xibilia MG. RNN- and LSTM-based soft sensors transferability for an industrial process. Sensors 21:823 (2021) https://doi.org/10.3390/s21030823
8. Farahani HS, Fatehi A, Nadali A, Shoorehdeli MA.

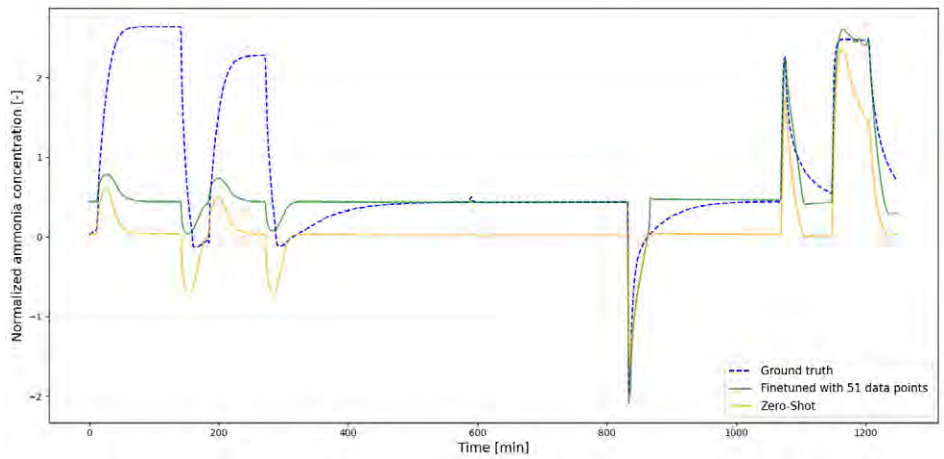




**Figure 5:** Visualization of test set (blue) vs finetuned model (orange, green). We visualize both the zero-shot performance (orange) and the model finetuned on 51 datapoints.

Domain adversarial neural network regression to design transferable soft sensor in a power plant. Comput Ind 132:103489 (2021) https://doi.org/10.1016/j.compind.2021.103489
9. Gilmer J, Schoenholz SS, Riley PF, Vinyals O, Dahl GE. Neural message passing for quantum chemistry. arXiv preprint arXiv:1704.01212 (2017)
10. Araújo A, Skogestad S. Control structure design for the ammonia synthesis process. Comput Chem Eng 32:2920-2932 (2008) https://doi.org/10.1016/j.compchemeng.2008.03.001

© 2025 by the authors. Licensed to PSEcommunity.org and PSE Press. This is an open access article under the creative commons CC-BY-SA licensing terms. Credit must be given to creator and adaptations must be shared under the same terms. See https://creativecommons.org/licenses/by-sa/4.0/



Systems & Control Transactions

**Research Article - Peer Reviewed Conference Proceeding**
ESCAPE 35 - European Symposium on Computer Aided Process Engineering
Ghent, Belgium. 6-9 July 2025
Jan F.M. Van Impe, Grégoire Léonard, Satyajeet S. Bhonsale,
Monika E. Polańska, Filip Logist (Eds.)

PSE PRESS

# Techno – Economic Evaluation of Incineration, Gasification, and Pyrolysis of Refuse Derived Fuel

**Matej Koritár[a], Maroš Križan[a], and Juma Haydary[a]***

[a] Slovak University of Technology, Department of Chemical and Biochemical Engineering, Bratislava, Slovakia
* Corresponding Author: juma.haydary@stuba.sk.

## ABSTRACT

New ways of reducing environmental impact of solid waste are constantly developed. Thermochemical conversion with focus on material or energy recovery is one of the viable options. To make the feedstock properties more suitable for such a process, refuse derived fuel (RDF) is created. Although several studies have focused on thermochemical conversion in recent years, only few have comprehensively compared the main aspects of incineration, gasification, and pyrolysis processes from multiple aspects. This study focuses on mathematical modeling of these three processes in the Aspen Plus environment. Comparison from economic, safety, and environmental viewpoints was performed. As a base for the calculations, 10 t/h of RDF was selected. All three processes demonstrated the suitability to be used for energy recovery. Pyrolysis showed the greatest potential for material recovery. Payback period was used as a parameter of economic comparison with pyrolysis being the most profitable process. Based on the calculated Dow Fire and Explosion Index (F&EI) and Chemical Exposure Index (CEI) gasification was identified as the most hazardous process. In summary, based on this extensive techno-economic analysis, the ranking of processes from an economic standpoint is as follows: pyrolysis, incineration, gasification. From an environmental perspective, the ranking is: gasification, pyrolysis, incineration. In terms of safety, the order is: incineration, pyrolysis, gasification.

**Keywords**: refuse derived fuel, incineration, gasification, pyrolysis

## INTRODUCTION

Waste generation presents environmental challenges that require direct attention. Within the European Union, generation of waste remains a significant problem with the amount of municipal solid waste increasing each year. Landfilling emerges as the primary environmental consequence of MSW [1]. However, shifts in legislative require the decrease of landfill disposal. Sustainable solutions are being explored, emphasizing the optimization of recyclable material and energy recovery. Solid waste not suitable for material recycling still contains high calorific value and can serve as a partial replacement of fossil fuels. This waste can be transformed into refuse derived fuel (RDF), which has more suitable properties for thermochemical conversion. Heating value of MSW is around 8-12 MJ/kg [2], which is significantly lower than that of RDF reaching as high as 27 MJ/kg [3]. The most common method of energy recovery from MSW is incineration. Alternative processes of thermochemical conversion are gasification and pyrolysis, which provide higher efficiency of energy and material recovery compared to incineration. The main drawback of waste feedstock processing is that it contains contaminants. Common contaminants in MSW and RDF include sulfur and chlorine containing compounds and heavy metals, these are carried into the products of the treatment process, where they cause damage to the equipment. Moreover, they are environmental pollutants. Therefore, it is necessary to minimize their production and decrease their concentration in the products to acceptable levels by purification. This work aims to compare three processes of thermochemical conversion of RDF: incineration, gasification, and pyrolysis. Due to their complex nature, studies comprehensively comparing the techno-economic aspects of the processes using mathematical models are quite rare.

## SIMULATION

Aspen Plus simulation software was used to create mathematical models of all three processes. As a base for the calculations, 10 000 kg/h of non-pretreated RDF was chosen. Peng-Robinson equation of state was used as the main thermodynamic model in all calculations. Equilibrium thermodynamic model, minimizing free Gibbs energy of the entire system, was employed to simulate thermochemical conversion of feedstock with the following assumptions [4]:

- Steady state flow in the reactor.
- No temperature or concentration gradients.
- Infinite residence time, chemical equilibrium is reached.
- Only chosen compounds are evaluated.

Equilibrium model is not suitable for processes where the deviation from the chemical equilibrium is too large, e.g. pyrolysis. Therefore, a mathematical model applying experimentally determined yields of the main products and composition of gaseous and solid products was used. To calculate the exact composition of liquid pyrolysis product, elemental balance of representative compounds was applied.

### Feedstock properties

Proximate and ultimate composition of RDF pellets was determined in previous experimental work [5] and is shown in **Table 1**. Lower heating value (LHV) of the RDF sample was determined to be 23.89 MJ/kg [5].

**Table 1:** Proximate and ultimate composition of RDF [% mass]

| | | | |
|---|---|---|---|
| C | 55.6 | Moisture | 0.73 |
| H | 7.83 | Volatile matter | 77.10 |
| N | 0.63 | Fixed carbon | 7.78 |
| S | 0.35 | Ash | 15.12 |
| Cl | 0.88 | | |
| O | 19.58 | | |

### Incineration

Incineration was the least complicated of the three processes studied. Incineration generates heat, part of which is turned into electricity. Material outlet steams are

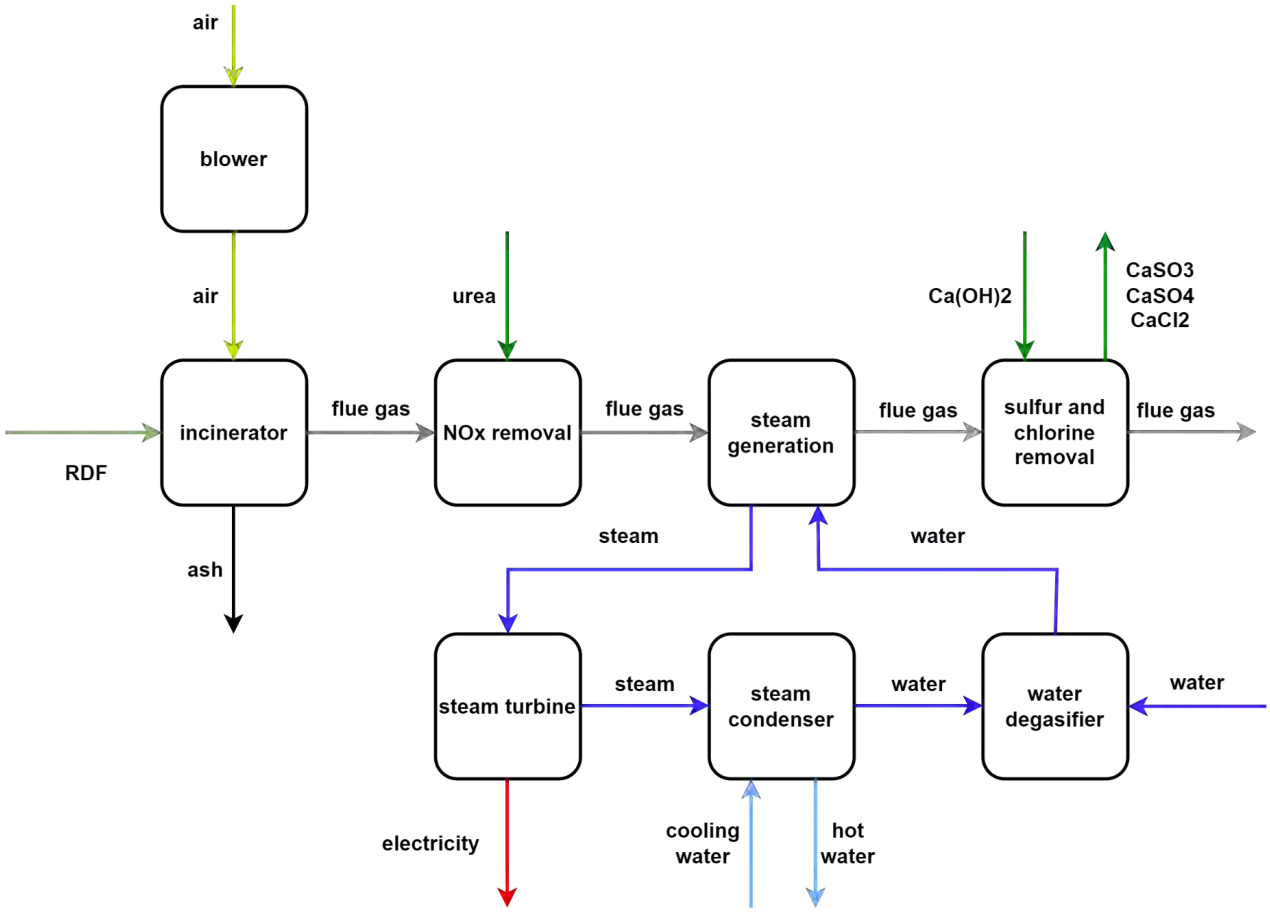



**Figure 1:** Simplified incineration flowsheet

flue gas and ash. Flue gas contained contaminants, such as $NO_x$, $SO_2$, $SO_3$, $Cl_2$ and HCl, and thus its purification was necessary. In **Figure 1**, a simplified flowsheet of this process is shown. Raw RDF enters the incinerator, where it burns in an excess of oxygen. Hot flue gas exiting the incinerator is purified to remove $NO_x$ contaminants by selective non-catalytic reduction (SNCR). $NO_x$ is reduced to $N_2$ via the reaction with urea in water solution. The still hot flue gas is then used for the generation of steam, which generates electricity in the steam turbine. From the cooled flue gas, sulfur, and chlorine contaminants are removed by adsorption using $Ca(OH)_2$.

The amount of incineration air was controlled to maintain 11% of oxygen in the flue gas [6]. Temperature of the exiting flue gas was 1 057°C and it was regulated by the temperature of the combustion air, which was preheated to 135°C. The amount of dry air required was 133 706 $Nm^3/h$. The process generated 1 361 kg/h of ash and 140 190 $Nm^3/h$ of flue gas.

Composition of flue gas exiting the incinerator is shown in **Table 2**. To purify it from $NO_x$ components, 758 kg/h of 9% urea aqueous solution was required. When the flue gas was cooled to 130°C, it was purified from $SO_2$ and HCl by the wet process using 140 kg/h of $Ca(OH)_2$. Flue gas purification processes were simulated using a stoichiometric reactor model with defined conversion [8]. Concentrations of contaminants in the purified syngas in **Table 2** were below the required values for the waste incineration, which are 200, 250, 250 and 10 $mg/Nm^3$ for $SO_2$, $NO_x$, CO, and HCl, respectively, for incinerators with nominal power below 100 MW [7].

**Table 2:** Composition of flue gas and contaminants concentrations in [$mg/Nm^3$] at 6% reference of $O_2$

| | Vol. fraction | Concentration in raw syngas | Concentration in purified syngas |
|---|---|---|---|
| $H_2O$ | 0.065 | - | - |
| $O_2$ | 0.114 | - | - |
| $N_2$ | 0.754 | - | - |
| $CO_2$ | 0.067 | - | - |
| CO | $5.35x10^{-4}$ | 0.51 | 0.51 |
| NO | $3.77x10^{-4}$ | 3 870.60 | 193.78 |
| $NO_2$ | $2.57x10^{-6}$ | 40.50 | 40.50 |
| $SO_2$ | $1.52x10^{-4}$ | 3 333.80 | 50.25 |
| $SO_3$ | $5.08x10^{-6}$ | 139.26 | 139.26 |
| HCl | $3.57x10^{-4}$ | 4 458.03 | 8.96 |
| $Cl_2$ | $3.84x10^{-8}$ | 0.93 | 0.93 |

Superheated steam (600°C, 9 MPa) was generated by flue gas cooling. This steam expanded to 0.25 MPa in the isentropic steam turbine with isentropic efficiency of 0.8, generating 9.5 MW of electric energy. Part of which was spent by the equipment in the process, mainly the air blower, which required 880 kW. To condense the steam exiting the turbine, water for district heating was generated with the heat content of 29.2 MW.

## Gasification

Simulation of RDF gasification was significantly more complicated than that of incineration due to the nature of the process. **Figure 2** shows a simplified

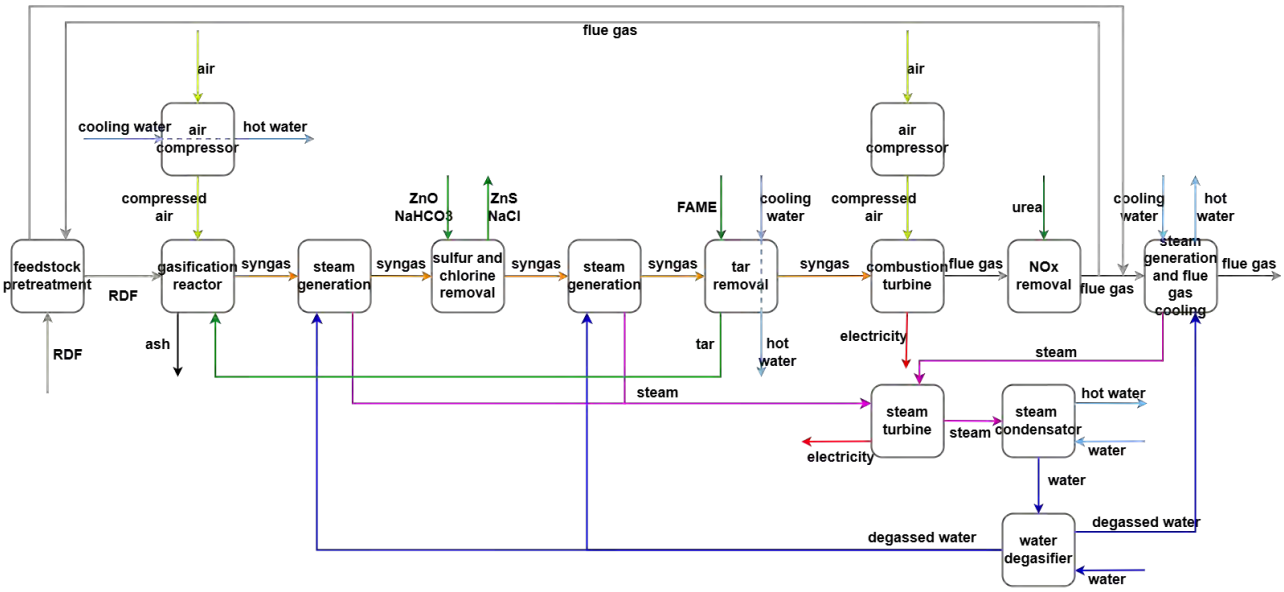



**Figure 2**: Simplified gasification flowsheet

gasification flowsheet. Before entering the gasification reactor, RDF was pretreated by drying using hot flue gas. Air, as the gasification medium, was compressed by a three-stage compressor with intercooling. Tar removed from syngas was recycled back into the reactor. Hot syngas exiting the reactor was purified from $H_2S$, HCl, and tar, while its energetic content was used for steam generation. Purified syngas was led into the combustion turbine to generate electricity. Hot flue gas from the turbine was purified only from $NO_x$ contaminants and used for steam generation.

To simulate the gasification reactor, an equilibrium model including tar generation was used. Concentration of tar in syngas was 3.15 g/Nm$^3$ [2], and tar was represented by naphthalene. Air entered the gasification reactor at 36 bars and 227°C. Such high pressure ensures that no additional syngas compression is required before the combustion turbine. Sub-stoichiometric amount of air was used in the process, which is 25 148 Nm$^3$/h. Gasification conditions were controlled by the amount of air led into the reactor so that 100% carbon conversion was achieved and LHV of syngas was maximized. The amount of syngas exiting the reactor was 37 690 Nm$^3$/h, with LHV of 4.38 MJ/Nm$^3$ and temperature of 902°C.

**Table 3:** Syngas composition and contaminants concentrations in [mg/Nm$^3$]

| | Vol. fraction | Concentration in raw syngas | Concentration in purified syngas |
|---|---|---|---|
| $H_2O$ | 0.049 | - | - |
| $H_2$ | 0.163 | - | - |
| $O_2$ | 0.000 | - | - |
| $N_2$ | 0.531 | - | - |
| NO | $1.35x10^{-13}$ | $1.81x10^{-7}$ | $1.81x10^{-7}$ |
| $SO_2$ | $3.60x10^{-11}$ | $1.03x10^{-4}$ | $1.03x10^{-4}$ |
| $Cl_2$ | $1.03x10^{-14}$ | $3.23x10^{-8}$ | $3.23x10^{-8}$ |
| HCl | $1.34x10^{-3}$ | 2 139.32 | 1.06 |
| CO | 0.206 | - | - |
| $CO_2$ | 0.048 | - | - |
| $H_2S$ | $5.88x10^{-4}$ | 879.34 | 4.34 |
| $NH_3$ | $3.70x10^{-4}$ | 275.06 | 275.06 |
| tar | $5.51x10^{-4}$ | 3 098.00 | 3.45 |

In **Table 3** syngas composition and contaminants' concentrations are shown. Dry method of purification was used to remove $H_2S$ and HCl from syngas by high temperature adsorption to 80 kg/h of ZnO and 191 kg/h of $NaHCO_3$ mixed with 2 707 kg/h of water. The process was simulated by the same method as in RDF incineration. Tar was removed by absorption into 124 kg/h of fatty acid methyl esters (FAME); methyl oleate was selected as a representative absorbent. Concentrations in the purified syngas met the requirements for combustion turbine fuel, which are 30, 20, and 1.5 mg/Nm$^3$ for tar, $H_2S$, and HCl, respectively [9].

**Table 4:** Concentrations of contaminants in purified flue gas

| | Concentration [mg/Nm$^3$] |
|---|---|
| NO | 213.58 |
| $NO_2$ | 17.95 |
| $SO_2$ | 3.43 |
| $SO_3$ | 0.03 |
| HCl | 0.45 |
| $Cl_2$ | $2.31x10^{-6}$ |
| CO | 73.30 |

Purified syngas, along with 44 938 Nm$^3$/h of air (36 bars, 697°C), entered the combustion turbine. Its amount was regulated so that 3% of $O_2$ was present in the flue gas exiting the turbine at 768°C. Turboexpander generated 30.5 MW of power, a portion of which was spent to power air compressors in the system. Hot flue gas was purified from $NO_x$ contaminants by the same process as in RDF incineration using 2580 kg/h of 9% aqueous urea solution. After purification (**Table 4**), flue gas met the purity requirements. In summary, 20.7 MW of electric energy was generated in the process and 24.3 MW of heat in form of hot water for district heating was generated using heat from steam condensation and cooling process streams.

## Pyrolysis

RDF pyrolysis was focused on recovery of material products, such as pyrolysis oil or activated carbon (AC) adsorbent, while the excess heat was used for district heating. **Figure 3** shows a process flowsheet of pyrolysis. Raw RDF was pretreated in the same way as in RDF gasification. Two streams exit the pyrolysis reactor: gas together with oil, and char. Char is upgraded to AC by steam gasification while pyrolysis oil is separated from the gas and upgraded by distillation into three fractions (**Table 6**). Gases from the pyrolysis and steam gasification reactors are mixed and combusted to generate heat required for the process. Flue gas is purified from the contaminants.

**Table 5:** Pyrolysis product yields [12]

| Product | Yield [%] | Mass flow [kg/h] |
|---|---|---|
| Char | 25 | 2 267.6 |
| Oil + water | 43 | 3 898.5 |
| Gas | 32 | 2 901.2 |

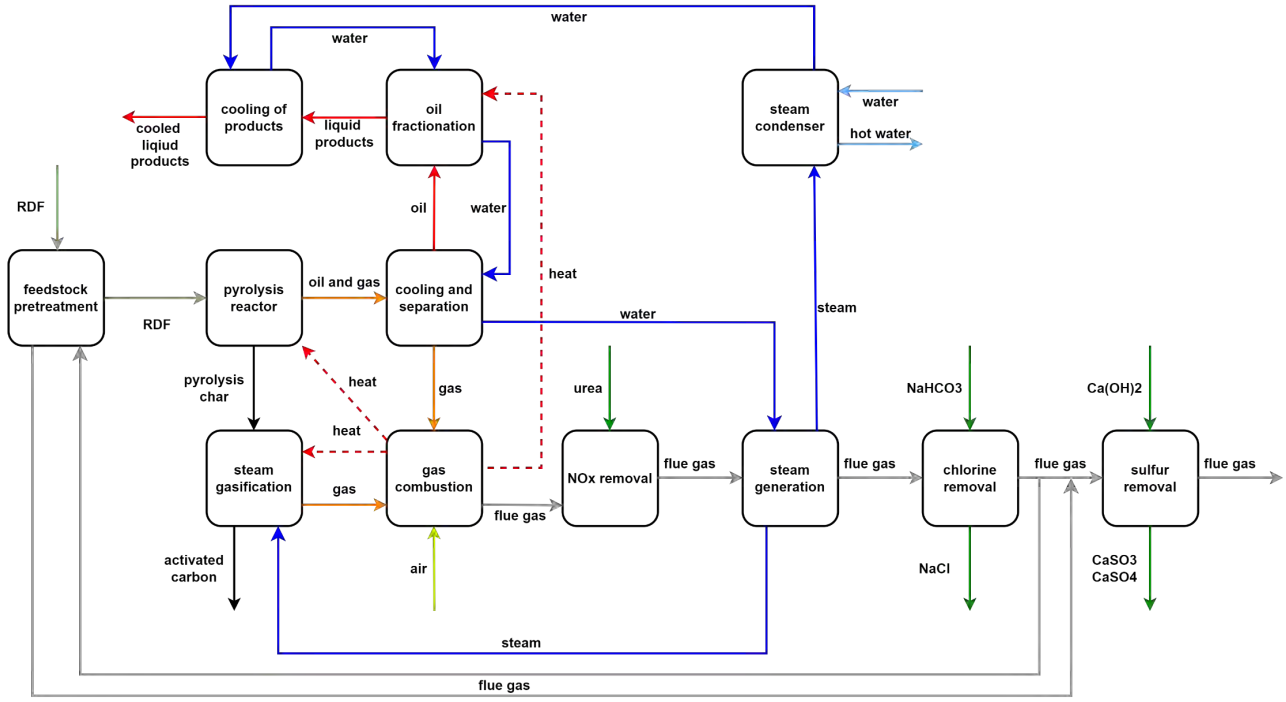



**Figure 3:** Simplified pyrolysis flowsheet

**Table 6:** Separated pyrolysis oil fractions

| Fraction | Mass flow [kg/h] | BP range [°C] |
|---|---|---|
| Light | 841 | 100 – 218 |
| Medium | 952 | 218 – 340 |
| Heavy | 1 781 | 340 – 438 |

Pyrolysis took place at 600°C. For these conditions, yields of the products (**Table 5**), composition of the gas phase and char [10], and representative molecules for the liquid phase [5], [11] were chosen. No oxidation medium was used in this process. The exact composition of pyrolysis oil was calculated from the elemental balance. For the pyrolysis process, 9.3 MW of heat was required. Steam gasification of char took place at 6 bars and 900°C, with the supply of 1140 kg/h of steam (1 MPa, 250°C) to the reactor at the rate of 0.0279 mol/g/h [13]. The reactor required an additional 3.2 MW of heat to produce 1 655 kg/h of AC. Following assumptions were made when calculating the yield and composition of AC:

- All volatile matter is converted into gas
- All ash stays in the AC
- Yield of AC is 73% [13]

Then, 4 980 kg/h of gas created in the process was combusted in the presence of 28 380 $Nm^3/h$ of air. This process was regulated to maintain 5% of $O_2$ in purified flue gas (**Table 7**). The same purification processes were employed as in RDF incineration and gasification. To achieve the desired purity, 134 kg/h of urea, 172 kg/h of $NaHCO_3$, 66 kg/h of $Ca(OH)_2$, and 8 330 kg/h of water were required and 10.5 MW of heat in form of hot water for district heating was exported from the process.

**Table 7:** Concentrations of contaminants in raw and purified flue gas in [$mg/Nm^3$]

| | Concentration in raw syngas | Concentration in purified syngas |
|---|---|---|
| CO | 47.96 | 47.96 |
| NO | 4 335.6 | 207.0 |
| $NO_2$ | 5.84 | 5.57 |
| $SO_2$ | 1 967.4 | 187.8 |
| $SO_3$ | 3.65 | 3.49 |
| HCl | 2553.6 | 9.75 |
| $Cl_2$ | 0.12 | 0.12 |

## Economic and safety analysis

Complex economic analysis was performed for all three processes of thermochemical conversion; results are provided in **Table 8**. Payback period (PBP) was used to compare economic feasibility of processes. The shortest PBP was in case of pyrolysis due to low EC and relatively high sales. However, this assumes that there is demand for the material products at the set price. Gasification was not economically feasible due to the high cost of equipment and operational costs. Incineration seemed less feasible than pyrolysis, however there will be always demand for electricity.

To compare the safety of the processes, Dow fire and explosion index (F&EI) as well as chemical exposure index (CEI) were used (**Table 9**). Equipment with the highest values was chosen as representative. Gasification had the highest risk of fire due to the high pressure in the process and handling of large amounts of flammable oils (FAME). The results for incineration and pyrolysis were similar.

**Table 8:** Economic parameters: equipment cost (EC) [$]; total capital investment (TCI) [$]; annual sales (AS) [$], and payback period (PBP) [years]

| | Incineration | Gasification | Pyrolysis |
|---|---|---|---|
| EC | $1.07x10^7$ | $4.93x10^7$ | $8.24x10^6$ |
| TCI | $5.66x10^7$ | $2.25x10^8$ | $4.86x10^7$ |
| AS | $1.32x10^7$ | $2.07x10^7$ | $1.79x10^7$ |
| PBP | 11.4 | 43.5 | 5.3 |

**Table 9:** Results of safety analysis

| | Incineration | Gasification | Pyrolysis |
|---|---|---|---|
| F&EI | 67.64 | 159.32 | 81.00 |
| Risk | Moderate | Severe | Moderate |
| CEI | 12.45 | 17.10 | 15.15 |
| Risk | Severe | Severe | Severe |

## CONCLUSION

In this work, RDF incineration, gasification and pyrolysis were compared considering technical, economic, safety, and environmental aspects. A mathematical model of each process was created in the Aspen Plus environment. Incineration is the simplest process focusing on energy recovery. In this process, 8.6 MW of electric energy and 29.2 MW of heat for district heating is generated. Gasification is more complicated from the technical point of view, providing 20.7 MW of electric energy and 24.3 MW of heat. Pyrolysis is focused mainly on material recovery, producing three fractions of pyrolysis oil with different boiling point ranges and 1 655 kg/h of activated carbon adsorbent, as well as 10.5 MW of excess heat exported as hot water for district heating. From the economic aspect, pyrolysis is the most feasible process, with a payback period of 5.3 years, assuming that there is a demand for its material products. From the safety aspect, incineration is the safest, followed by pyrolysis, and gasification. From the process and environmental point of view, requirements for the contaminants' concentration in syngas and flue gas were satisfied in all three processes. However, pyrolysis produces the most byproducts of gas purification and wastewater, followed by incineration, and gasification.

## ACKNOWLEDGEMENT

This work was supported by the Slovak Research and Development Agency under the contract No. APVV-19-0170 and by the program for supporting young researchers funded by the Slovak University of Technology.

## REFERENCES

1. G. Gałko, I. Mazur, M. Rejdak, B. Jagustyn, J. Hrabak, M. Ouadi, H. Jahangiri, M. Sajdak, Evaluation of alternative refuse-derived fuel use as a valuable resource in various valorised applications, Energy 263 (2023). https://doi.org/10.1016/j.energy.2022.125920
2. M. Alfè, V. Gargiulo, M. Porto, R. Migliaccio, A. Le Pera, M. Sellaro, C. Pellegrino, A.A. Abe, M. Urciuolo, P. Caputo, P. Calandra, V. Loise, C.O. Rossi, G. Ruoppolo, Pyrolysis and Gasification of a Real Refuse-Derived Fuel (RDF): The Potential Use of the Products under a Circular Economy Vision, Molecules 27 (2022). https://doi.org/10.3390/molecules27238114
3. O.A. Osibote, A. Hlaba, A. Rabiu, A. Otolorin, O. 2+, Refuse Derived Fuel Pellets as a Renewable Energy Source, (2017). https://doi.org/10.7763/IPCBEE
4. J. Haydary, Gasification of Refuse-Derived Fuel (RDF), GeoScience Engineering 62 (2016) 37–44. https://doi.org/10.1515/gse-2016-0007
5. M. Polakovič, Purification of synthesis gas produced by thermo-catalytic gasification of mixed waste, Master Thesis, STU Bratislava, 2023
6. A. Sitka, W. Jodkowski, P. Szulc, D. Smykowski, B. Szumiło, Study of the properties and particulate matter content of the gas from the innovative pilot-scale gasification installation with integrated ceramic filter, Energies (Basel) 14 (2021). https://doi.org/10.3390/en14227476
7. Slov – Lex, Špecifické požiadavky na spaľovacie zariadenia. available January 28, 2025
8. E. Jannelli, M. Minutillo, Simulation of the flue gas cleaning system of an RDF incineration power plant, Waste Management 27 (2007)
9. V. Marcantonio, E. Bocci, J.P. Ouweltjes, L. Del Zotto, D. Monarca, Evaluation of sorbents for high temperature removal of tars, hydrogen sulphide, hydrogen chloride and ammonia from biomass-derived syngas by using Aspen Plus, Int J Hydrogen Energy 45 (2020) 6651–6662. https://doi.org/10.1016/j.ijhydene.2019.12.142
10. M. Zajemska, A. Magdziarz, J. Iwaszko, M. Skrzyniarz, A. Poskart, Numerical and experimental analysis of pyrolysis process of RDF containing a high percentage of plastic waste, Fuel 320 (2022). https://doi.org/10.1016/j.fuel.2022.123981

11. I.H. Hwang, J. Kobayashi, K. Kawamoto, Characterization of products obtained from pyrolysis and steam gasification of wood waste, RDF, and RPF, Waste Management 34 (2014) 402–410. https://doi.org/10.1016/j.wasman.2013.10.009
12. V. Cozzanij, C. Nicolella, L. Petarcaj, M. Rovatti, L. Togno, A Fundamental Study on Conventional Pyrolysis of a Refuse-Derived Fuel, 2006
13. W.K. Buah, P.T. Williams, Activated carbons prepared from refuse derived fuel and their gold adsorption characteristics, Environ Technol 31 (2010) 125–137. https://doi.org/10.1080/09593330903386741

© 2025 by the authors. Licensed to PSEcommunity.org and PSE Press. This is an open access article under the creative commons CC-BY-SA licensing terms. Credit must be given to creator and adaptations must be shared under the same terms. See https://creativecommons.org/licenses/by-sa/4.0/



Systems & Control Transactions

**Research Article - Peer Reviewed Conference Proceeding**
ESCAPE 35 - European Symposium on Computer Aided Process Engineering
Ghent, Belgium. 6-9 July 2025
Jan F.M. Van Impe, Grégoire Léonard, Satyajeet S. Bhonsale,
Monika E. Polańska, Filip Logist (Eds.)

PSE PRESS

# Dynamic Operability Analysis of modular heterogeneous electrolyzer plants using system co-simulation

**Michael Große[a,c]*, Isabell Viedt[b,c], Hannes Lange[b,c] and Leon Urbas[a,b,c]**

[a] Technische Universität Dresden, Process-to-Order Group, Chair of Process Control Systems
[b] Technische Universität Dresden, Process-to-Order Group, Process Systems Engineering Group
[c] Technische Universität Dresden, Process-to-Order Group, P2O Lab Learning Factory
* Corresponding Author: michael.grosse@tu-dresden.de

## ABSTRACT

In the upcoming decades, the scale-up of hydrogen production will play a crucial role for the integration of renewable energy into energy system. One scale-up strategy is the numbering-up of standardized electrolysis units in modular plant concepts. The use of modular plants can support the integration of different technologies into heterogeneous electrolyzer plants to leverage technology-specific advantages and counteract disadvantages. This work focuses on the analysis of technical operability of large-scale modular electrolyzer plants in heterogeneous plant layouts using co-simulation. Developed process models of low-temperature electrolysis components are combined in Simulink as shared environment. Strategies to control process parameters, like temperatures, pressures and flowrates in the subsystems and the overall plant, are developed and presented. An operability analysis is carried out to verify the functionality of the presented plant layout and control strategies. The dynamic progression of all parameters is presented for different operative states, like start-up, continuous operation, load change and hot-standby behavior. It is observed that the exemplary plant is operational, as all relevant process parameter can be held within the allowed operating range during all operative states. Some limitations, regarding the possible operating range of individual technologies, are introduced and solution approaches are conceptualized. Additionally, relevant metrics for efficiency, such as the specific energy consumption and flexibility are calculated to prove the feasibility and show the advantages of heterogeneous electrolyzer plant layouts, such as a heightened operational flexibility without mayor reductions in efficiency.

**Keywords**: Hydrogen, Modelling & Simulations, Process Control, Process Operations, MATLAB, Co-Simulation

## INTRODUCTION & BACKGROUND

The rising demand for hydrogen and the necessary integration of fluctuating energy sources into chemical value chains remains a mayor challenge for the transition to renewable energy and a more sustainable chemical industry [1]. The numbering-up of standardized electrolysis units in a modular plant has been conceptualized as a reliable way to scale-up hydrogen production quickly [2]. Furthermore, the use of the modular plant concept allows for a more individualized and flexible scale-up by enabling the combination of modules from different providers. That way electrolysis plants can be designed to include different electrolysis technologies more easily to leverage technology-specific advantages and counteract disadvantages [2], [3]. The necessary components within such modular electrolysis plants of different technologies have been outlined in [4] and can be used as a reference for scale-up scenarios. An exemplary modular, electrolysis system is depicted in Figure 1. Before such plant layouts of pre-engineered and generic Process Equipment Assemblies (PEAs), can be connected and operated, the functionality and operability of such a heterogeneous plant layout of different technologies and varying PEA providers must be verified to ensure safe and efficient operation.

This paper aims to support this verification of heterogeneous modular electrolysis plants investigating the different steps of a dynamic operability analysis with a simple but exemplary use case as depicted in Figure 1.

The study aims to identify prerequisites and efforts as well as potential and limitations to prove safe and efficient operation of a such systems by assessing their ability to hold parameters within a Desired Output Set (DOS) [5]. In the context of modular plants and the integration of renewable energy sources in Power-to-X value chains, the dynamics of the plant must be taken into account to assess the plant operation during load or state changes [6]. This necessitates the calculation of specific metrics for dynamic operability evaluation of processes, as described in [7], on top of the steady-state operability. The necessary metrics shall be specified for the utilized use-case in the following chapter.

The depicted plant, consisting of individual modules from potentially varying suppliers, must therefore be simulated in an overall dynamic system simulation. As the internal knowledge of the modules is protected, the dynamic models are provided as black box models with their respective input-output behavior [8]. The black box models, potentially developed in different tools and with their individual solvers, are combined as Functional Mock-Up Units (FMUs) in a system co-simulation, as the Functional Mock-Up Interface (FMI) "enables an unprecedented level of integration of models (as black boxes) provided by different and even competing suppliers." [9]

# METHODOLOGY

## Definitions & Assumptions

Goal of the dynamic operability analysis is to provide proof, that a developed modular electrolysis system is operable. An operable process is defined as:

> "A process is operable if the available set of inputs is capable of satisfying the desired steady-state and dynamic performance requirements defined at the design stage, in the presence of the set of anticipated disturbances, without violating any process constraints." [7]

This necessitates the definition of varying aspects, that must be included in the operability analysis of modular electrolysis plants, such as the DOS, the dynamic Available Input Space (dAIS), the dynamic Desired Operating Space (dDOpS) and the Expected Disturbance Space (EDS) [5, 8]. The assumption of a modular plant design makes the variation of design input variables of the PEAs unsuitable, which is why the focus is on the operational variables of the PEAs. The ability to operate the combined heterogeneous modular electrolysis system out of predefined PEAs is to be evaluated.

A list of the included variables, their description and allowed ranges can be found in Tables 1-3 for the aspects of the operability analysis and their respective PEA. As each PEA encapsulates their individual behaviour and requirements, the presented method is applicable independently of the chosen plant layout. Due to limitations in the model capabilities, identified optima, simplifications or limited available data, the setpoints for some potential operating variables, such as the lye mass fraction or load change rates, are kept constant.

The dAIS entails the remaining setpoints, including the temperature, pressure and flow rate setpoints of the circulation and the production rate setpoint of the Stack-Unit. Additionally, the chosen lye mass fraction setpoint and load change rates over time are included in Table 1.

**Table 1:** Operating input variables in the dAIS and ranges taken from [2] or mapped to showcase from [10]

| Operational input variable | Value/Range |
|---|---|
| Circulation: Outlet temperature setpoint [°C] | 50-80 |
| Circulation: Outlet flowrate setpoint [kg/s] | AEL: 30-90<br>PEMEL: 4.75-14 |
| Circulation: Gas outlet pressure setpoint [bar] | 3-16 |
| Circulation: Lye mass fraction setpoint [m%] | 30 |
| Stack-Unit: Load setpoint [%] | 20–100 |
| Stack-Unit: Upramp load change rate [%/s] | AEL: 30<br>PEMEL: 50 |
| Stack-Unit: Downramp load change rate [%/s] | AEL: 10<br>PEMEL: 40,6 |

The DOS includes the constraints, that apply for the PEAs, such as the allowed operating ranges for temperature, pressure, flowrate and component mass fractions in the entire system of PEAs. These constraints are extended by the dDOpS with the allowed change rates over time of the relevant parameters during nominal operation or in case of operational disturbances. The EDS includes the disturbances in the input variables that are assumed to enter the process, such as variations in the water inlet temperature or short outages of the cooling cycle.

**Table 2:** Output variables and dynamics in the DOS and dDOpS and allowed ranges assumed or adjusted from [2] and [10]

| Output variable | Value/Range |
|---|---|
| Maximum allowed temperature in the Stack-Unit [°C] | AEL: 100<br>PEM: 90 |
| Maximum temperature change rate in the Stack-Unit [K/min] | AEL: 1,5<br>PEMEL: 1 |
| Maximum fluid velocity [m/s] | 1 |
| Maximum "H2 in O2" or "O2 in H2" values [mol%] | 2 |
| AEL: Maximum pressure difference between stack-sides [bar] | 0.1 |

**Table 3:** Disturbances in the input variables and considered ranges

| Input variable disturbances | Value/Range |
|---|---|
| Fresh water inlet / cooling water inlet / ambient temperature [°C] | 15–30 |
| Cooling cycle restart time [min] | 5 |

These collected variables serve as the inputs and variations in the operability analysis of the heterogeneous modular electrolysis plant considered in this paper.

## Calculated metrics

The calculated metrics within the operability analysis in this paper include the Achievable Output Set (AOS), the dynamic Achievable Operating Space (dAOpS), the Desired Input Space (DIS) and the dynamic operability.

The AOS is the "set of controlled variables that the system can achieve for the considered AIS and EDS." [5] In this case study, it includes the behaviour of the controlled variables in the system, such as temperature, pressure, flowrate and mass fractions, at steady state.

The extension of the AOS is the dAOpS as the "operating space representing the dynamic performance that can be achieved by the system for a given choice of the dAIS, DOS, and EDS." [7] That way the dynamic behaviour of the plant can be considered and violations of the maximum change rates or short-term deviations from the permitted working range can be identified.

The DIS is the "set of input values required for the system to reach all outputs in the DOS" [5], [7] and shall be identified by comparing the dAOpS and the DOS. The resulting edge cases, at which the dAOpS deviates from the DOS restrict the allowed operating range in the AIS and EDS, that are suited for compliance with the DOS.

In addition to the operability evaluations, the specific energy consumption and the "Lange-Große-Coefficient for hydrogen demand" ($LGC_{H2}$) of the system can be calculated from the simulated data for each operating point to determine optimal operating points within the allowed operating range. The specific energy consumption of the overall plant serves as a metric to determine an optimal operation scheme at least qualitatively. It is calculated as:

$$e_{spec}\left[\frac{kWh}{kg_{H_2}}\right] = \frac{P_{sys,cons}}{\dot{m}_{H_2,sys}} \quad (1)$$

With $P_{sys,cons}$ as the power consumption of the entire modular plant in *kW* and $\dot{m}_{H_2,stacks}$ as the combined produced hydrogen in all Stack-Unit PEAs in *kg/h*. For the scope of this paper, the efficiency evaluation is limited to the overall system efficiency at 100 % load.

The $LGC_{H2}$ value shall serve as an initial measurement to assess the inertia and consequently the flexibility to output hydrogen for different system configurations or operating points. It can be calculated for each load step or for a production scenario according to:

$$LGC_{H2}\,[-] = \int_{t_{scenario,start}}^{t_{scenario,end}} \frac{abs(\dot{m}_{H_2,sys}(t) - \dot{m}_{H_2,sys,stat}(t))}{\dot{m}_{H_2,sys,stat}(t)}\,dt \quad (2)$$

With $\dot{m}_{H_2,sys}(t)$ as the current hydrogen production at time step $t$ and $\dot{m}_{H_2,sys,stat}(t)$ as the stationary hydrogen production of the load setpoint at time step $t$, both in kg/h. The result is the part of the hydrogen production in %, that could not be met by the system and operating point under consideration for a production scenario.

## Model capabilities & Implementation

The analysis is carried out as a co-simulation scenario of FMUs, that simulate the dynamic behavior of chosen PEAs identified in [4], namely the water supply, Stack-Unit and circulation PEAs, as depicted in Figure 2. Although the hydrogen purification PEA is neglected in the simulation the presented methodology is still applicable within the scope of this paper. The system simulation is set up in MATLAB Simulink as a co-simulation environment with the developed FMUs. In the context of protection of the PEAs internal knowledge a detailed description of the FMUs is not necessary for the presented method and beyond the scope of this paper. A basic description of the model, including capabilities, interfaces and setpoints shall suffice. A detailed model description and structure of the electrolyzer stack-units, the balance of plant components and control strategies shall be specified elsewhere [11].

The FMUs provide the dynamic input-output behaviour of the mass, components and energy in the individual PEAs to changes in their respective setpoints and inlets. The FMU interfaces follow the interface description in [12], providing ports for material streams, energy and information, such as setpoints for the controlled variables. Necessary system parameters of the individual technologies for the chosen scenario are taken from [13] for the AEL subsystem, are scaled from values in [14] for the PEMEL subsystem and are collected in Table 4.

Both subsystems are assumed to connect multiple Stack-Unit PEAs to one circulation PEA. Additionally, the circulation PEAs of each electrolyzer technology are both connected to the water supply PEA. For the scope of this paper, the only information exchange between the PEAs shall be the necessary supply of deionized water from the water supply PEA to the circulation PEA to hold the liquid level in the gas separation tanks constant. This necessary supply is used as the flowrate setpoint for the water supply PEAs internal flowrate control. The production load setpoint is used as input in the Stack-Unit PEA to control the hydrogen production rate. The operating variables temperature, pressure and flowrate in the Stack-Units and the rest of the system are controlled as setpoints in the circulation PEA. Restarting the cooling cycle is also controlled in the circulation PEA. Controlling these variables should suffice for the basic operation of the presented heterogeneous modular electrolyzer system.

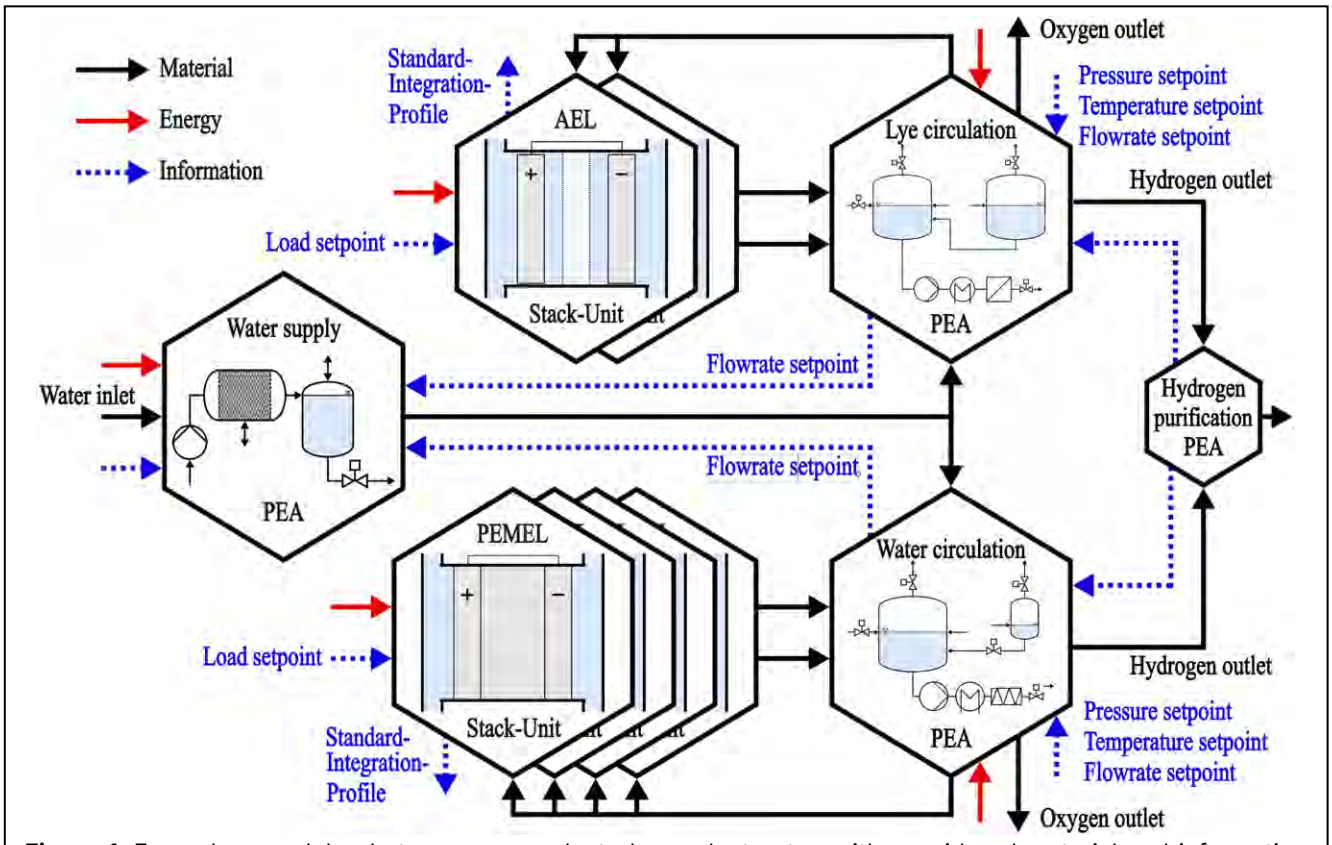



**Figure 1:** Exemplary modular, heterogeneous electrolyzer plant setup with considered material and information inlets and outlets in the dAIS and EDS

**Table 4:** Necessary system parameters of the individual subsystems taken or adjusted from [13] and [14]

| System parameter | Value PEMEL | Value AEL |
|---|---|---|
| Number of Stack-Units per system [-] | 4 | 2 |
| Number of cells per Stack-Unit [-] | 150 | 326 |
| Active area of an electrolysis cell [$m^2$] | 87.5e-3 | 2.66 |
| Nominal power of a Stack-Unit [MW] | 0.25 | 3 |
| Free volume of an electrolysis cell [$m^3$] | 8.75e-4 | 0.027 |
| Separation tank volume [$m^3$] | 1.06 | 14.14 |
| Maximum operating pressure [bar] | 55 | 16 |

## OPERABILITY ANALYSIS RESULTS

The operability analysis was successful as the modular, heterogeneous electrolysis system is operable in most of the operating states and ranges. However, at a few boundary conditions of the operating range and in the hot-standby state the DOS was exceeded, as shown for an exemplary inoperable operating point in Figure 2.

It can be seen, that at high temperatures, high pressures and low flowrates in the system, multiple criteria in the DOS are exceeded during nominal operation. The Stack-Unit outlet temperatures rise above the limit of 90 °C (upper left). Additionally, the $H_2$ in $O_2$ contamination in the AEL system exceeds the allowed threshold of 2 mol% at the 20 % Stack-Unit load setpoint (lower left). The temperature change rate during the cooling cycle shutdown rises above 1 K/min in the circulation however, in the Stack-Unit the temperature change rate stays below the threshold (upper right). The hot-standby state is not operable with the chosen PEAs and control strategies, as the difference pressure and the contaminations in the system rise above the set threshold in the dDOpS (lower left and right). Consequently, the current PEA selection and control strategies are not sufficient for the hot-standby state and complete operability is not given under the specified conditions. Further evaluations of specific energy consumption and $LGC_{H2}$ shall therefore be done for the nominal operation state without consideration of the hot-standby state. The DIS for the nominal operation state can be seen in Figure 3 as the filled circles in the evaluation of specific energy consumption and $LGC_{H2}$. The unfilled circles represent the operating points, that are not operable in the nominal operation state with the chosen PEAs and control strategies.

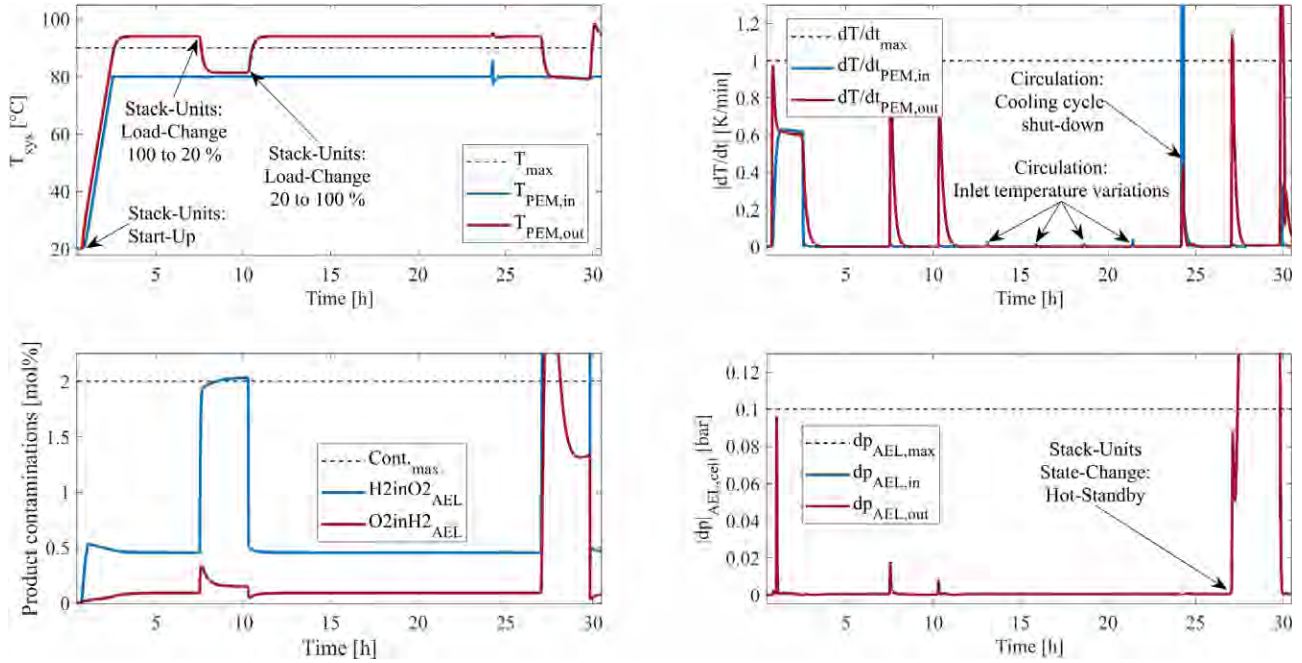



**Figure 2:** Examplary progression of relevant variables in the dAOpS with marked state changes for the dAIS setpoints: $T_{Set}$ = 80 °C, $p_{Set}$ = 16 bar, $f_{AEL,Set}$ = 30,6 kg/s & $f_{PEM,Set}$ = 4,76 kg/s

## System efficiency and LHCH2

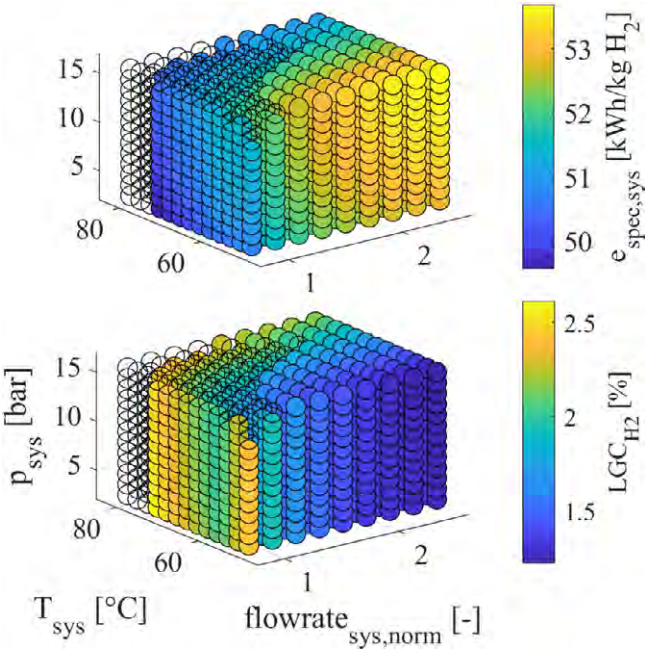



**Figure 3:** System efficiency and $LGC_{H2}$ evaluation

The relevant system efficiency and $LGC_{H2}$ are evaluated for all setpoints in the operable range of temperature, pressure and flowrate. Other system variables stay at their mean values in Tables 1-3. The results are depicted in Figure 3, with an optimal system efficiency of 49,57 kWh/kg H2, at the lowest pressure of 3 bar, the highest operable temperature of 72.5 °C and the lowest normalized flowrate of 0.85.

## Limitations & Solution approaches

As the plant layout and control strategies have been simplified for the scope of this paper, some limitations to the significance and validity of the presented results must be made. The first aspect that must be considered for a more reliable operability analysis is the extension of the plant structure to include the purification and post-processing of produced hydrogen. The current results for system efficiency and $LGC_{H2}$ are limited to the hydrogen generation and first separation stage leading to the assessment of high efficiency at lower pressures and high temperatures while neglecting potential losses due to necessary compression or drying of hydrogen in the post-processing. The inclusion of these steps in the operability analysis and system efficiency evaluation is necessary to provide a more meaningful understanding of electrolysis and their optimal operating conditions.

Secondly the hot-standby state can not be operated with the included control strategies due to a lack of inertization or strategies to deal with the gas crossover within the provided FMUs. Especially at high gas pressures, the difference in partial pressures between the hydrogen and oxygen side lead to a steady cross-over of gases in the hot-standby state. Without inerting or stopping the fluid circulation the contaminations and pressure differences between the gas sides rise.

## CONCLUSION & OUTLOOK

In conclusion the operability of a modular, heterogeneous electrolysis system was verified with restrictions.

The possible operating ranges and variations in the operating regiment have been collected and introduced to a dynamic operability analysis. Extensive simulation studies using co-simulation of FMUs show the operability of the presented plant in most of the outlined operating range. Possible disturbances to the system inputs can be dealt with in the required time. Operating points for optimal system efficiency and flexibility of the plant have been identified, although the applicability to a more complex electrolysis system with downstream equipment is limited. For future work the presented solution approaches and additions to the system layout and control strategies with additional information exchange between PEAs, such as states and safety relevant variables, can provide a more comprehensive understanding of the operability and optimal performance of modular, heterogeneous electrolysis plants.

## Digital supplementary material

The P2O Lab Learning Factory provides a Github-group repository which contains the individual model repositories of the developed simulation models. It is currently only available upon individual request at https://github.com/orgs/p2o-lab/teams/ap2_external/repositories. The repositories will be openly accessible starting from October 2025.

## ACKNOWLEDGEMENTS

We would like to thank the German Federal Ministry of Education and Research and the project management organization Jülich for their financial support within the framework of the eModule research project (FKZ 03 HY 116 A) of the H2Giga lead platform.

## REFERENCES

1. U. Remme, “Global Hydrogen Review 2024,” 2024.
2. H. Lange, A. Klose, W. Lippmann, and L. Urbas, “Technical evaluation of the flexibility of water electrolysis systems to increase energy flexibility: A review,” *Int. J. Hydrog. Energy*, vol. 48, no. 42, pp. 15771–15783, May 2023, doi: 10.1016/j.ijhydene.2023.01.044.
3. M. Mock, I. Viedt, H. Lange, and L. Urbas, “Heterogenous electrolysis plants as enabler of efficient and flexible Power-to-X value chains,” in *Computer Aided Chemical Engineering*, vol. 53, Elsevier, 2024, pp. 1885–1890. doi: 10.1016/B978-0-443-28824-1.50315-X.
4. H. Lange, A. Klose, L. Beisswenger, D. Erdmann, and L. Urbas, “Modularization approach for large-scale electrolysis systems: a review,” *Sustain. Energy Fuels*, vol. 8, no. 6, pp. 1208–1224, 2024, doi: 10.1039/D3SE01588B.
5. V. Gazzaneo, J. C. Carrasco, D. R. Vinson, and F. V. Lima, “Process Operability Algorithms: Past, Present, and Future Developments,” *Ind. Eng. Chem. Res.*, vol. 59, no. 6, pp. 2457–2470, Feb. 2020, doi: 10.1021/acs.iecr.9b05181.
6. P. Rentschler, C. Klahn, and R. Dittmeyer, “The Need for Dynamic Process Simulation: A Review of Offshore Power-to-X Systems,” *Chem. Ing. Tech.*, vol. 96, no. 1–2, pp. 114–125, Jan. 2024, doi: 10.1002/cite.202300156.
7. D. Uztürk and C. Georgakis, “Inherent Dynamic Operability of Processes: General Definitions and Analysis of SISO Cases,” *Ind. Eng. Chem. Res.*, vol. 41, no. 3, pp. 421–432, Feb. 2002, doi: 10.1021/ie0101792.
8. J. Mädler, I. Viedt, J. Lorenz, and L. Urbas, “Requirements to a digital twin-centered concept for smart manufacturing in modular plants considering distributed knowledge,” in *Computer Aided Chemical Engineering*, vol. 49, Y. Yamashita and M. Kano, Eds., in 14 International Symposium on Process Systems Engineering, vol. 49. , Elsevier, 2022, pp. 1507–1512. doi: 10.1016/B978-0-323-85159-6.50251-7.
9. T. Ören, B. P. Zeigler, and A. Tolk, Eds., *Body of Knowledge for Modeling and Simulation: A Handbook by the Society for Modeling and Simulation International*. in Simulation Foundations, Methods and Applications. Cham: Springer International Publishing, 2023. doi: 10.1007/978-3-031-11085-6.
10. G. Tsotridis and A. Pilenga, *EU harmonized protocols for testing of low temperature water electrolysis*. Luxembourg: Publications Office of the European Union, 2021.
11. M. Grosse, I. Viedt, H. Lange, and L. Urbas, “Low-temperature electrolysis stack modeling for dynamic system co-simulation of modular hydrogen plants,” *Int. J. Hydrog. Energy*, 2025.
12. M. Mock, I. Viedt, and L. Urbas, “Towards Usability of Process Models for Co-Simulation-Based Operability Analysis of Modular Electrolysis Plants,” in *2024 IEEE 29th International Conference on Emerging Technologies and Factory Automation (ETFA)*, Padova, Italy: IEEE, Sep. 2024, pp. 1–4. doi: 10.1109/ETFA61755.2024.10711068.
13. [13] G. Sakas, A. Ibáñez-Rioja, V. Ruuskanen, A. Kosonen, J. Ahola, and O. Bergmann, “Dynamic energy and mass balance model for an industrial alkaline water electrolyzer plant process,” *Int. J. Hydrog.*

*Energy*, vol. 47, no. 7, pp. 4328–4345, Jan. 2022, doi: 10.1016/j.ijhydene.2021.11.126.
14. G. Sakas *et al.*, “Dynamic Mass and Energy Balance Model of a 50 Kw Proton Exchange Membrane Electrolyzer System,” 2024. doi: 10.2139/ssrn.4799709.

© 2025 by the authors. Licensed to PSEcommunity.org and PSE Press. This is an open access article under the creative commons CC-BY-SA licensing terms. Credit must be given to creator and adaptations must be shared under the same terms. See https://creativecommons.org/licenses/by-sa/4.0/



Systems & Control Transactions

**Research Article - Peer Reviewed Conference Proceeding**
ESCAPE 35 - European Symposium on Computer Aided Process Engineering
Ghent, Belgium. 6-9 July 2025
Jan F.M. Van Impe, Grégoire Léonard, Satyajeet S. Bhonsale,
Monika E. Polańska, Filip Logist (Eds.)

PSE PRESS

# High-pressure Membrane Reactor for Ammonia Decomposition: Modeling, Simulation and Scale-up using a Python-Aspen Custom Modeler Interface.

**Leonardo A. C. Avilez, Antonio E. Bresciani, Claudio A. O. Nascimento, and Rita M. B. Alves***

Universidade de São Paulo, Escola Politécnica, Departament of Chemical Engineering, São Paulo, SP, Brazil.
* Corresponding Author: rmbalves@usp.br

## ABSTRACT

One of the current challenges for hydrogen-related technologies is its storage and transportation. The low volumetric density and low boiling point require high-pressure and low-temperature conditions for effective transport and storage. A potential solution to these challenges involves storing hydrogen in chemical compounds that can be easily transported and stored, with hydrogen being released through decomposition processes. Ammonia stands out as a promising hydrogen carrier due to its high hydrogen content (17.8% by weight), relatively mild liquefaction conditions (~10 bar at 25°C), and the availability of a well-established storage and transportation infrastructure. The objective of this study was to develop a mathematical model to analyze and design a membrane fixed-bed reactor (MFBR) for large-scale ammonia decomposition. The kinetic model for the Ru-K/CaO catalyst was obtained from the literature and validated using the experimental data reported in the original study. This catalyst was selected due to its effective performance under high-pressure conditions, which increases the drive force for hydrogen permeation in the membrane reactor. The model was developed in Aspen Custom Modeler (ACM) using a 1D pseudo-homogeneous approach. The governing equations for mass, energy, and momentum conservation were discretized via a first-order backward finite difference method. The effectiveness factor was incorporated to account for intraparticle mass transfer limitations, which are prevalent with the large particle sizes typically employed in industrial applications. The study further investigated the influence of sweep gas ratio, temperature, relative pressure, and space velocity on ammonia conversion and hydrogen recovery, employing response surface methodology generated through an ACM-Python interface. The proposed multi-tubular membrane reactor achieved approximately 94% ammonia conversion and 90% hydrogen recovery, operating at an inlet temperature of 380°C and a pressure of 40 bar. Under comparable conditions of temperature, pressure, and WHSV, the membrane reactor demonstrated an approximately 41.7% higher ammonia conversion compared to a conventional fixed-bed reactor. Furthermore, the developed model is easily transferable to Aspen Plus, facilitating subsequent process conceptual design and economic analyses.

**Keywords**: Hydrogen, Ammonia decomposition, Membrane reactor, Reactor design, Modeling and simulation

## INTRODUCTION

Hydrogen ($H_2$) is a key player in the transition to renewable energy sources due to its high energy density and $CO_2$-emission-free combustion [1]. However, hydrogen volumetric density is low compared to other conventional fuels such as gasoline, ethanol and natural gas [2]. Consequently, its storage and transportation present challenges, requiring energy-intensive methods like high-pressure compression and cryogenic liquefaction.

Currently, hydrogen is most stored as a compressed gas at 150-700 bar [3]. Another approach is liquid-phase storage, which offers a higher energy density but requires extremely low temperatures (-253°C at 1 bar)[4]. A novel potential solution involves storing hydrogen in chemical compounds that can be easily transported and

stored. Ammonia is a promising hydrogen carrier due to its high hydrogen content (17.8% by weight) and its moderate liquefaction conditions (~10 bar, 25°C), reducing transportation and storage [5].

For the strategy of using ammonia as a hydrogen carrier to be feasible, it is essential to study the decomposition process and develop more efficient reaction systems. Membrane fixed-bed reactors (MFBRs) offer advantages over conventional fixed-bed reactors, such as enabling operation at lower temperatures by selectively removing hydrogen, driving higher ammonia conversion, and reducing the costs associated with hydrogen purification. This study aimed to develop a mathematical model to analyze and design an MFBR for large-scale ammonia decomposition, using a Python-Aspen Custom Modeler (ACM) framework.

## METHODS AND MODELING

A simplified schematic of the reactor is presented in Figure 1. The multi-tubular membrane fixed-bed reactor proposed in this study is based on conventional steam methane reformer (SMR) furnaces.

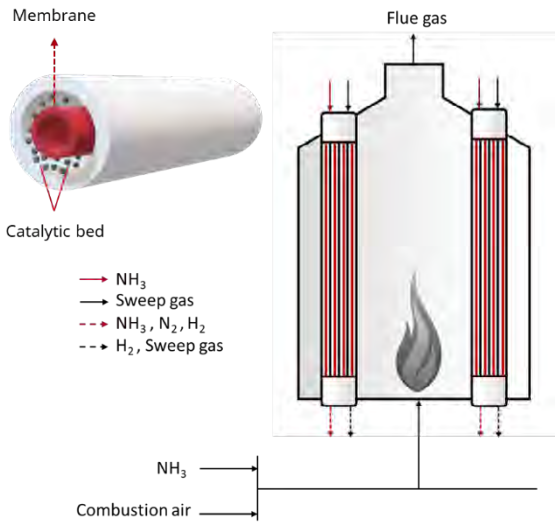



**Figure 1.** Simplified scheme of the multi-tubular membrane reactor.

The reaction system consists of two concentric tubes: an outer tube and an inner tube with a selective palladium membrane. The annular space between these tubes is filled with a Ru-based catalyst, where hydrogen is produced. This hydrogen permeates through the Pd membrane into the inner tube, allowing for selective separation from the reaction mixture. A sweep gas is fed into the inner tube to reduce the partial pressure of permeated hydrogen, enhancing the driving force for separation. The heat is provided to the reaction by flame using the combustion of ammonia itself, a COx-free process.

### Mathematical modeling

The membrane fixed-bed reactor model was developed using a pseudohomogeneous, one-dimensional approach in Aspen Custom Modeler v.12. The main hypotheses of the model are:

1. Steady-state condition;
2. Plug-flow both in reaction and permeation zone due to the high ratio of length to diameter;
3. Negligible axial dispersion due to high calculated Peclet number;
4. Negligible pressure drop in permeation tube;
5. Constant porosity;
6. Membrane 100% selective for hydrogen.

The mass balance for each component in the annular catalytic region is described by Equation 1, while Equation 2 presents the material balance for each component in the permeation tube [6].

$$\frac{dF_{i,a}}{dz} = \eta\, r_i\, \rho_b \pi (R_2{}^2 - R_1{}^2) - 2\pi\, R_1\, J_i \quad (1)$$

$$\frac{dF_{i,t}}{dz} = 2\pi\, R_1\, J_i \quad (2)$$

where $F_{i,a}$ is the component molar flow in the annular region, $\eta$ is the effectiveness factor, $r_i$ is the component reaction rate, $\rho_b$ is the bulk density, $R_2$ is outer tube radius, $R_1$ is the inner tube radius, $F_{i,t}$ is the component molar flow in the permeation region, and $J_i$ is the component permeation flux through the membrane.

The kinetic model for the Ru-K/CaO catalyst, along with its parameters, was obtained from Sayas et al. [7]. The $H_2$ permeation flux was calculated based on Sievert's law, utilizing parameters estimated for a Pd-Ag membrane [8]. The corresponding equations for the reaction rate and $H_2$ permeation flux are presented in the equations 3 and 4.

$$r_{NH_3} = k\, P_{NH_3}{}^a\, P_{H_{2,a}}{}^b \left(1 - \frac{1}{K_{eq}}\left(\frac{P_{N_2}\, P_{H_{2,a}}{}^3}{P_{NH_3}{}^2}\right)\right) \quad (3)$$

$$J_{H_2} = \frac{B_H}{\delta}\left(P_{H_{2,a}}{}^{1/2} - P_{H_{2,t}}{}^{1/2}\right) \quad (4)$$

where $r_{NH_3}$ is the ammonia consumption rate, $k$ is rate constant, $P_{NH_3}$ is the ammonia partial pressure, $P_{H_{2,a}}$ and $P_{H_{2,t}}$ represent the hydrogen partial pressures on the annular and permeate sides, respectively, $P_{N_2}$ is the nitrogen partial pressure, $K_{eq}$ is the thermodynamic equilibrium constant, $J_{H_2}$ is the hydrogen permeation flux, $B_H$ is the permeability, and $\delta$ is the membrane thickness.

For the effectiveness factor calculation, the kinetic

model was mathematically transformed into a pseudo-first-order kinetics, following the Pacheco et al. [9] framework. This transformation allows the Thiele modulus and the effectiveness factor to be calculated analytically.

Equations 5 and 6 present the energy balances for annular region and permeation tube [6]. It was considered that the membrane surface in contact with the reaction zone has the same temperature as the reaction itself. This assumption is reasonable because the metallic components of the membrane structure have high thermal conductivity, making their thermal resistance negligible [6].

$$\left(\sum_{i=1}^{3} F_{i,a}\, c_{p,i}\right)\frac{dT}{dz} = 2\pi\,[R_2(U_1(T_w - T)) - R_1(U_2(T - T_p))] + \pi\,(R_2{}^2 - R_1{}^2)\,\rho_b\,\eta\,r_{rxn}(-\Delta H_{rxn}) \quad (5)$$

$$\left(\sum_{i=1}^{2} F_{i,p}\, c_{p,i}\right)\frac{dT_p}{dz} = 2\pi\; R_1[U_2(T - T_p) - J_{H_2}[h_{H_2}(T_p) - h_{H_2}(T)]] \quad (6)$$

where $c_{p,i}$ is the component molar specific heat, $T$ is the temperature in the reaction region, $T_p$ is the temperature in the permeation region, $T_w$ is the wall temperature, $U_1$ is the overall heat transfer coefficient between the reactor's outer wall and the annular reaction zone, $U_2$ is the overall heat transfer coefficient between the reaction and permeation zones, $r_{rxn}$ is the ammonia decomposition rate, and $h_{H_2}$ is the specific enthalpy of hydrogen.

The overall heat transfer coefficient between reaction tube outer wall and reaction mixture ($U_1$) is calculated using Dixon correlation [10], whereas the overall heat transfer coefficient between the annular region and the permeation ($U_2$) is considered fixed with the value of 8.64 kJ/m²·h·K [11].

For the annular catalytic region, the pressure drop along the reactor's length is calculated using the Ergun equation, as shown in Equation 7.

$$-\frac{dp}{dz} = 150\,\frac{(1-\varepsilon)^2}{\varepsilon^3}\,\frac{\mu\,u}{{d_p}^2} + 1.75\,\frac{1-\varepsilon}{\varepsilon^3}\,\frac{u^2\rho_f}{d_p} \quad (7)$$

where $p$ is the pressure of the annular reaction zone, $\mu$ is the mixture viscosity, $u$ is the fluid superficial velocity, $d_p$ is the spherical equivalent particle diameter, $\varepsilon$ is the bed porosity, and $\rho_f$ is the fluid density.

Physical properties, including mixture density, dynamic viscosity, molar specific heat, and hydrogen specific enthalpy, were calculated using internal procedures within ACM, based on the PR-BM thermodynamic property package. This package employs the Peng-Robinson equation of state with Boston-Mathias modifications to determine the main thermodynamic properties.

The governing equations for mass, energy, and momentum conservation were discretized via first-order backward finite difference method and solved using a nonlinear equation solver. The reactor parameters are detailed in Table 1.

**Table 1:** Parameter setting of the ammonia cracking membrane reactor.

| Parameter | Value | Reference |
|---|---|---|
| Tube length (m) | 12 | [12] |
| Reactor internal diameter (m) | 0.1016 | [13] |
| Membrane diameter (m) | 0.0508 | Adopted |
| Membrane thickness (μm) | 7.5 | [8] |
| Catalyst particle diameter (mm) | 10 | [14] |
| Bed voidage (Estimated) | 0.404 | [15] |

## Sensitivity analysis: Python-ACM interface

ACM enables an automated interface with Python via the comtypes module, facilitating model analysis and response surface generation. Python controls model variables and parameters, sending commands to ACM to perform simulations and record responses. The output data are processed in Python, allowing for the generation of response surfaces and detailed sensitivity analysis.

First, an isothermal reactor was considered and the effect of temperature, space velocity, permeation tube pressure and sweep gas ratio in the ammonia conversion and hydrogen recovery. After establishing the operational conditions, the rigorous model of a non-isothermal reactor was then simulated.

# RESULTS

This section presents the isothermal reactor analysis to evaluate operational variables and define preliminary conditions, followed by the results for the non-isothermal model.

## Effect of pressure and temperature

Figure 2 shows the effect of the tube and reaction pressures on ammonia conversion at temperatures of 350°C, 400°C, and 450°C. The results demonstrate that increasing temperature enhances ammonia conversion, consistent with the endothermic nature of the reaction. At 450°C, near-complete conversion is achieved under favorable pressure conditions (low tube pressure and high reaction pressure).

Higher reaction pressures reduce ammonia conversion due to thermodynamic limitation; however, they also enhance the driving force for hydrogen permeation through the membrane, partially compensating for this limitation. Conversely, higher tube pressures reduce the driving force for hydrogen removal, which can lower conversion efficiency. Nonetheless, they provide the ad-

vantage of delivering pressurized hydrogen, thereby reducing recompression costs.

Another important metric to evaluate is hydrogen recovery (HR), defined as the ratio of the amount of hydrogen separated through the membrane to the total amount of hydrogen produced in the reaction. Figure 3 shows the effect of tube and reaction pressures on HR at temperatures of 350°C, 400°C, and 450°C.

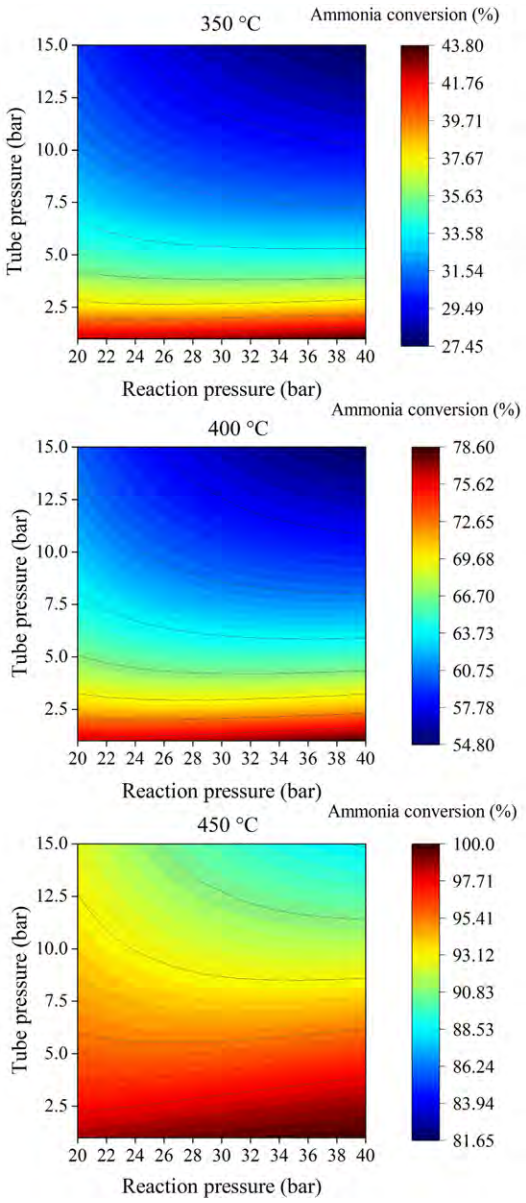



**Figure 2.** Effect of tube and reaction pressure at temperatures of 350°C, 400°C, and 450 °C on ammonia conversion (WHSV = 1000 g/L·h , sweep gas ratio = 0.25).

As expected, HR is enhanced by increasing the pressure difference between the reaction zone and the tube, which acts as the driving force for hydrogen permeation. Temperature also positively influences HR, as it increases the permeation rate of hydrogen. At a pressure difference of 30 bar and a temperature of 350 °C, HR is approximately 56.9%. In contrast, at 450 °C under the same pressure conditions, HR increases significantly, reaching 73.4%.

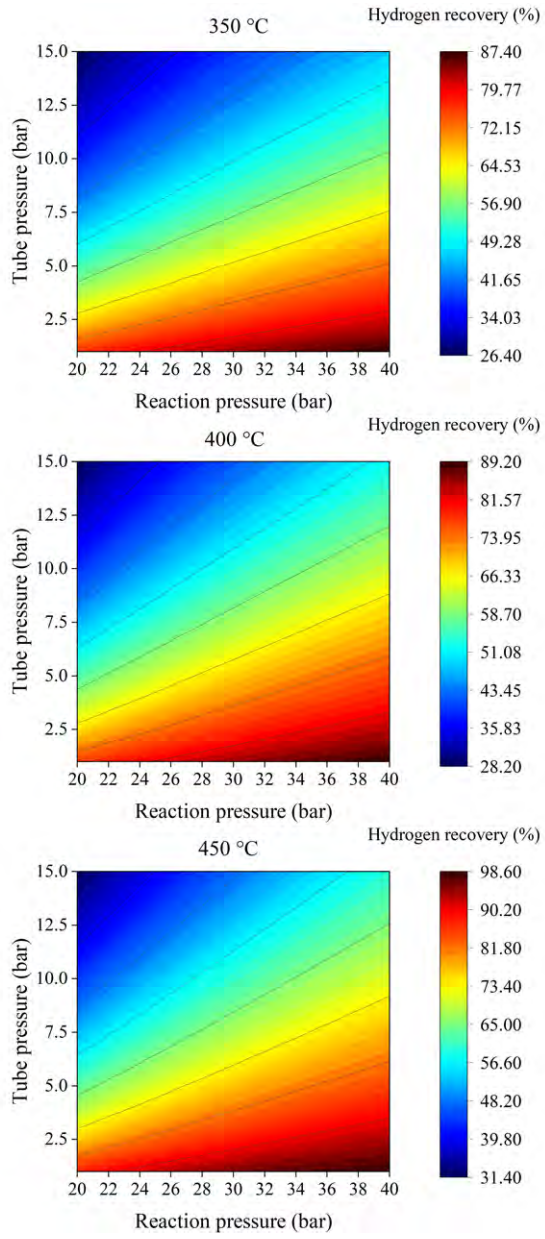



**Figure 3.** Effect of tube and reaction pressure at temperatures of 350°C, 400°C, and 450 °C on hydrogen recovery (WHSV = 1000 g/L·h , sweep gas ratio = 0.25).

## Effect of space velocity and sweep gas ratio

Figure 4 presents the effect of WHSV (weight hourly space velocity) and sweep gas ratio (SGR) on ammonia conversion for 400 and 450°C, while also comparing the performance of the membrane fixed-bed reactor design

(MFBR) with a conventional fixed-bed reactor. The SGR, defined as the molar ratio of sweep gas to feed ammonia, influences the driving force for hydrogen permeation by reducing the partial pressure of hydrogen on the permeation side of the membrane.

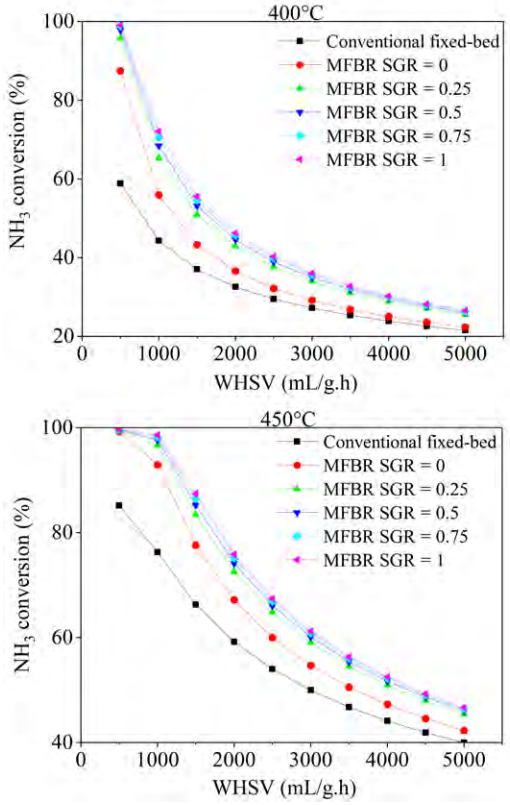



**Figure 4.** Effect of WHSV and sweep gas ratio (SGR) at temperatures of 400 and 450 °C on ammonia conversion (tube pressure = 5 bar, reaction zone pressure = 40 bar).

The results presented in Figure 4 indicated that the conversion gain of MFBR compared to the conventional fixed-bed reactor is more pronounced at lower WHSV values. For instance, at a WHSV of 500 mL/g·h, 400°C, and SGR of 0.25, the conversion increase is approximately 63%. In contrast, at a WHSV of 1500 mL/g·h under the same conditions, the conversion gain drops to 37%. When the temperature increases from 400 to 450 °C, overall ammonia conversion improves for both reactors due to enhanced reaction kinetics. However, at low WHSV values, the relative conversion gain of the MFBR compared to the conventional reactor reduces at 450 °C.

Additionally, increasing the SGR from 0 to 0.25 leads to considerable improvement in ammonia conversion. However, further increases in SGR beyond 0.25 yield only slight gains in conversion.

## Complete model and reactor design

A reactor configuration was proposed based on the analysis of key operating variables. To better represent industrial performance, the model was extended to include non-isothermal behavior and intraparticle mass resistance. Table 2 summarizes the selected operating conditions for the complete model and reactor design.

**Table 2:** Operating conditions for the MFBR Simulation.

| MFBR operating conditions | Value |
|---|---|
| Inlet reactor temperature (°C) | 380 |
| Sweep gas ratio | 0.25 |
| Reaction and tube pressures (bar) | 40/5 |
| WHSV (mL/g·h) | 500 |

Figure 5 compares ammonia conversion and reaction zone temperature profiles along the reactor length for MFBR and conventional fixed-bed reactors under the same operating conditions.

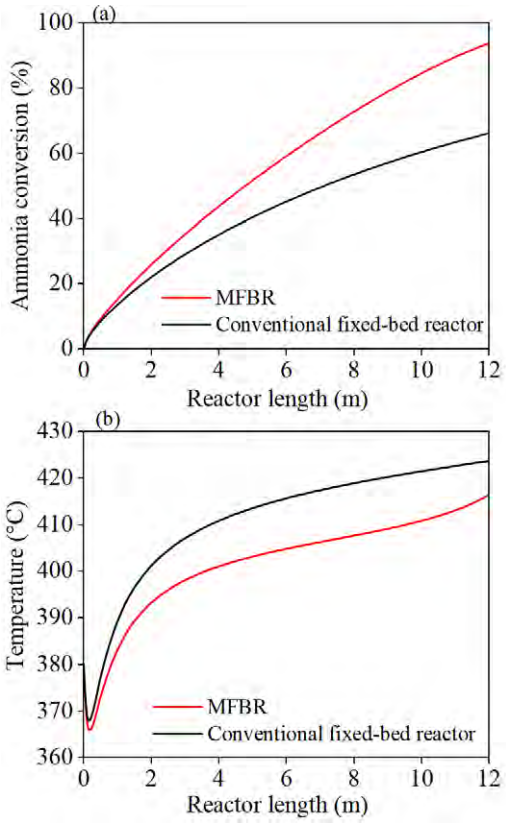



**Figure 5.** Profiles of ammonia conversion (a) and reaction zone temperature (b) along the reactor length for MFBR and conventional fixed-bed reactors ($T_w$ = 430 °C).

The proposed MFBR demonstrated an approximately 41.7% higher ammonia conversion compared to a conventional fixed-bed reactor. The conversion profile indicates that the reaction occurs along the entire reactor

length, ensuring effective utilization of the reactor volume without underutilized sections.

Regarding the temperature profile, an initial drop is observed in both reactors. This behavior can be explained by the reaction's endothermic nature, where a higher reaction rate near the reactor inlet, driven by the elevated partial pressure of ammonia, results in significant heat consumption. Despite the same fixed wall temperature for both reactors, the MFBR exhibits a lower temperature profile along the reactor length due to its higher ammonia conversion.

Considering a large-scale ammonia decomposition unit with the production of 200 tons per day of hydrogen, the proposed reactor would require 1017 tubes.

## CONCLUSION

A unidimensional pseudohomogeneous model describing a multi-tubular membrane reactor for ammonia decomposition was developed. The proposed reactor configuration achieves 94% ammonia conversion and 90% hydrogen recovery, representing a 41.7% higher conversion compared to the traditional reactor. These results are promising and provide a foundation for scaling up the ammonia decomposition process in membrane reactors.

Overall, the MFBR offers several advantages compared to the traditional fixed-bed reactor. It enables operation at lower temperatures due to its higher conversion rates and avoids the need for costly hydrogen separation steps, resulting in potential environmental and economic benefits. In future work, a more detailed 2D model incorporating radial dispersion effects will be developed and the results of both models will be compared.

## ACKNOWLEDGEMENTS

The authors gratefully acknowledge the support of the São Paulo Research Foundation (FAPESP) (#2022/15230-5, #2024/08858-9) and Petronas for the financial support and ANP (Brazilian National Oil, Natural Gas, and Biofuels Agency) for the strategic importance of its support through the R&D levy regulation.

## REFERENCES

1. Huang X, Lei K, Mi Y, Fang W, Li X. Recent progress on hydrogen production from ammonia decomposition: technical roadmap and catalytic mechanism. *Molecules* 28:5245 (2023).
2. Lee JE, Lee J, Jeong H, Park Y-K, Kim B-S. C. Catalytic ammonia decomposition to produce hydrogen: A mini-review. *Chem Eng J* 475:146108 (2023).
3. Hjeij D, Biçer Y, Koç M. Hydrogen strategy as an energy transition and economic transformation avenue for natural gas exporting countries: Qatar as a case study. *Int J Hydrogen Energy* 47:4977-5009 (2022).
4. Züttel A. Hydrogen storage methods. *Naturwissenschaften* 91:157-172 (2004).
5. Spatolisano E, Restelli F, Pellegrini LA, Cattaneo S, De Angelis AR, Lainati A, Roccaro E. Liquefied hydrogen, ammonia and liquid organic hydrogen carriers for harbour-to-harbour hydrogen transport: A sensitivity study. *Int J Hydrogen Energy* 32: 1424-1431 (2024).
6. De Falco M, Dipaola L, Marrelli L. Heat transfer and hydrogen permeability in modelling industrial membrane reactors for methane steam reforming. *Int J Hydrogen Energy* 32: 2902–2913 (2007).
7. Sayas S, Morlanés N, Katikaneni SP, Harale A, Solami B, Gascon J. High pressure ammonia decomposition on Ru–K/CaO catalyst. *Catal Sci Technol* 10:5027–5035 (2020).
8. Basile A, Paturzo L, Vazzana A. Membrane reactor for the production of hydrogen and higher hydrocarbons from methane over $Ru/Al_2O_3$ catalyst. *Chem Eng J* 93:31-39 (2003).
9. Pacheco M, Sira J, Kopasz J. Reaction kinetics and reactor modeling for fuel processing of liquid hydrocarbons to produce hydrogen: isooctane reforming. *Appl Catal A Gen* 250:161-175 (2003).
10. Dixon AG. An improved equation for the overall heat transfer coefficient in packed beds. *Chem Eng Process* 35:323-321 (1996).
11. Madia GS, Barbieri G, Drioli E. Theoretical and experimental analysis of methane steam reforming in a membrane reactor. *Can J Chem Eng* 77:698-706 (1999).
12. Caballero JJB, Zaini IN, Yang W. Reforming processes for syngas production: A mini-review on the current status, challenges, and prospects for biomass conversion to fuels. *Appl Energy Combust Sci* 10:100064 (2022).
13. Li P, Chen L, Xia S, Kong R, Ge Y. Multi-objective optimal configurations of a membrane reactor for steam methane reforming. *Energy Reports* 8:527-538 (2022).
14. Pedernera MN, Piña J, Borio DO, Bucalá V. Use of a heterogeneous two-dimensional model to improve the primary steam reformer performance. *Chem Eng J* 94:29-40 (2003).
15. Benyahia F, O'Neill KE. Enhanced Voidage Correlations for Packed Beds of Various Particle Shapes and Sizes. *Particulate Science and*

*Technology* 23:169-177 (2005).

© 2025 by the authors. Licensed to PSEcommunity.org and PSE Press. This is an open access article under the creative commons CC-BY-SA licensing terms. Credit must be given to creator and adaptations must be shared under the same terms. See https://creativecommons.org/licenses/by-sa/4.0/



Systems & Control Transactions

**Research Article - Peer Reviewed Conference Proceeding**
ESCAPE 35 - European Symposium on Computer Aided Process Engineering
Ghent, Belgium. 6-9 July 2025
Jan F.M. Van Impe, Grégoire Léonard, Satyajeet S. Bhonsale,
Monika E. Polańska, Filip Logist (Eds.)

PSE PRESS

# A 2D Axisymmetric Transient State CFD Modelling of a Fixed-bed Reactor for Ammonia Synthesis

**Leonardo Bravo[a], Camilo Rengifo[b], Martha Cobo[a], Manuel Figueredo[a]***

[a] Energy, Materials and Environment Laboratory, Faculty of Engineering, Universidad de La Sabana, Campus Universitario Puente del Común, Km. 7 Autopista Norte, Bogotá, Colombia.
[b] Department of Mathematics, Physics and Statistics, Universidad de La Sabana, Campus Universitario Puente del Común, Km. 7 Autopista Norte, Bogotá, Colombia.
* Corresponding Author: manuel.figueredo@unisabana.edu.co.

## ABSTRACT

Power-to-Ammonia technology offers sustainable pathways for energy storage and chemical production, with fixed-bed reactors being critical components for efficient synthesis. Understanding reactor dynamics under varying conditions is essential for optimizing these systems, particularly when integrated with intermittent renewable energy sources. This study aims to develop and validate a 2D axisymmetric CFD model for analysing the dynamic response of a ruthenium-catalysed ammonia synthesis reactor to thermal perturbations. The model incorporates detailed reaction kinetics, multicomponent mass transport, and heat transfer mechanisms to predict system behaviour under transient conditions. Results reveal that a step increase in wall temperature from 400°C to 430°C enhances $NH_3$ concentration by 136% (from 2.2 to 5.1 vol.%), with rapid system stabilization achieved within 0.5 seconds. The thermals response maintains consistent heat transfer patterns, exhibiting ~400K differentials between inlet and maximum temperature zones

**Keywords**: Ammonia Synthesis, Process Intensification, Computational Fluid Dynamics, Alternative Fuels, Dynamic Modelling.

## INTRODUCTION

Power-to-Ammonia (PtA) technology offers a sustainable and efficient solution by integrating renewable energy sources with carbon-neutral fuel production. This approach allows energy to be stored in the form of ammonia, which can serve as a fuel, energy carrier, or key ingredient in fertilizers [1]. The core of the PtA process lies in its reaction system, featuring a packed-bed reactor (PBR) where ammonia is synthesized from hydrogen ($H_2$) produced via water electrolysis and nitrogen ($N_2$) captured from the atmosphere. Nevertheless, the synthesis process poses intricate multiscale challenges related to flow, heat, and mass transfer, largely driven by the highly exothermic nature of the reaction . Advanced modeling techniques, such as Computational Fluid Dynamics (CFD), are essential to address these challenges, enabling optimization of reactor performance, catalyst utilization, and overall energy efficiency [2].

Several studies have focused on CFD simulation of the PBR reactor in steady state. Gu et al. [4] explored decentralized ammonia synthesis for hydrogen storage and transport using a CFD model, focusing on a small-scale Haber-Bosch reactor with Ruthenium-based catalysts optimized for mild conditions. The model's accuracy was validated against experimental data and parametric studies were conducted to assess the impact of key operational parameters. The results showed that temperature is the most influential factor affecting ammonia production and pressure primarily affects the chemical equilibrium. Furthermore, the study identified an optimal gas hourly space velocity (GHSV) of 1.8·10^5 h^(-1) for efficient ammonia synthesis. Nikzad et al. [5] compared the performance of three different reactor configurations to find the optimal design to enhance nitrogen conversion and reduce pressure drops. The study used CFD simulations to analyze and compare the mass, energy and momentum conservation in a two-dimensional geometry of the three reactor types. The spherical reactors, particularly the spherical axial flow (SAF) configuration, were more efficient than conventional tubular reactors for

ammonia synthesis. Tyrański et al.[3] investigated the ammonia synthesis process in an axial-radial bed reactor using CFD focusing on understanding the influence of catalyst bed parameters, such as particle size and geometry modifications, on the efficiency of the reactor. The simulations demonstrated that smaller catalyst particles (1-2 mm) provided a higher ammonia formation rate, while larger particles show a slower reaction rate spread throughout the bed. Moreover, modifications in bed geometry could reduce the bed volume by half without losing efficiency.

However, in PtA systems, the intermittent nature of renewable energy sources, such as hydrogen production via electrolysis, introduces additional complexities in reactor performance. Boundary conditions and external disturbances, like variations in hydrogen flow or temperature fluctuations, can significantly impact key process variables, including reaction rates, heat transfer, and overall system stability. Therefore, understanding the reactor's transient response under such dynamic conditions is crucial.

This study focuses on developing a 2D axisymmetric transient CFD model for ammonia synthesis within a fixed-bed reactor, specifically analyzing the dynamic response to thermal perturbation at the reactor wall. By evaluating these transient states, the research aims to provide insights into reactor thermal behavior under temperature fluctuations that may occur in PtA systems.

# MATHEMATICAL MODELING

## Governing Equations

**Table 1:** Governing equations for the catalytic region.

| Description | Mathematical Expression | Eq. |
|---|---|---|
| Transport of concentrated species | $\rho\frac{\partial\omega_i}{\partial t}+\nabla\cdot\mathbf{j_i}+\rho(\mathbf{u}\cdot\nabla)\omega_i=R_i$ | (1) |
| | $\mathbf{j_i}=-\left(\rho D_i^m\nabla\omega_i+\rho\omega_i D_i^m\frac{\nabla M_n}{M_n}-\mathbf{j}_{c,i}\right)$ | (2) |
| Heat transfer in porous media | $(\rho C_p)_{eff}\frac{\partial T}{\partial t}+\rho C_p\mathbf{u}\cdot\nabla T+\nabla\cdot\mathbf{q}=Q$ | (3) |
| | $(\rho C_p)_{eff}=\theta_s\rho_s C_{p,s}+\epsilon_p\rho_f C_{p,f}$ | (4) |
| | $\mathbf{q}=-k_{eff}\nabla T$ | (5) |
| | $k_{eff}=\theta_s k_s+\epsilon_p k_f$ | (6) |
| Brinkman-Forchheimer extended Darcy equation | $\frac{1}{\epsilon_p}\rho\frac{\partial\mathbf{u}}{\partial t}+\frac{1}{\epsilon_p}\rho(\mathbf{u}\cdot\nabla)\mathbf{u}\frac{1}{\epsilon_p}=\nabla\cdot[-p\mathbf{I}+\mathbf{K}]-\left(u\kappa^{-1}+\beta\epsilon_p\rho\lvert\mathbf{u}\rvert\right)\mathbf{u}$ | (7) |
| | $\mathbf{K}=\mu\frac{1}{\epsilon_p}(\nabla\mathbf{u}+(\nabla\mathbf{u})^T-\frac{2}{3}\mu\frac{1}{\epsilon_p}(\nabla\cdot\mathbf{u})\mathbf{I}$ | (8) |
| Continuity equation | $\frac{\partial\epsilon_p\rho}{\partial t}+\nabla\cdot(\rho\mathbf{u})=0$ | (9) |

**Table 2:** Governing equations for the free fluid region.

| Description | Mathematical Expression | Eq. |
|---|---|---|
| Transport of concentrated species | $\rho\frac{\partial\omega_i}{\partial t}+\nabla\cdot\mathbf{j_i}+\rho(\mathbf{u}\cdot\nabla)\omega_i=0$ | (10) |
| | $\mathbf{j_i}=-\left(\rho D_i^m\nabla\omega_i+\rho\omega_i D_i^m\frac{\nabla M_n}{M_n}-\mathbf{j}_{c,i}\right)$ | (11) |
| Heat transfer in porous media | $\rho C_p\frac{\partial T}{\partial t}+\rho C_p\mathbf{u}\cdot\nabla T+\nabla\cdot\mathbf{q}=0$ | (12) |
| | $\mathbf{q}=-k\nabla T$ | (13) |
| Navier-Stokes equation | $\rho\frac{\partial\mathbf{u}}{\partial t}+\rho(\mathbf{u}\cdot\nabla)\mathbf{u}=\nabla\cdot[-p\mathbf{I}+\mathbf{K}],$ | (14) |
| | $\mathbf{K}=\mu(\nabla\mathbf{u}+(\nabla\mathbf{u})^{\mathrm{T}})-\frac{2}{3}\mu(\nabla\cdot\mathbf{u})\mathbf{I}.$ | (15) |
| Continuity equation | $\frac{\partial\rho}{\partial t}+\nabla\cdot(\rho\mathbf{u})=0$ | (16) |

The governing equations describing the behaviour of the fixed-bed reactor for ammonia synthesis can be divided into two main regions: the catalytic region and the free fluid region.

## Kinetic Model for Ammonia Synthesis

The reaction follows a rate-limiting mechanism in which the dissociation of nitrogen is the lowest and most energy-intensive step. The overall reaction is represented as:

$$N_2(g)+3H_2(g)\rightarrow 2NH_3(g) \tag{17}$$

The reaction rate for ammonia synthesis on a ruthenium (Ru)-based catalyst is governed by a modified Temkin kinetic expression, which includes $H_2$ and $NH_3$ adsorption terms [4]. The rate expression is given by:

$$\frac{d\eta}{dt}=k\lambda(q)\left[\frac{(a_{N_2})^{0.5}\left[\frac{(a_{H_2})^{0.375}}{(a_{NH_3})^{0.25}}\right]-\frac{1}{Ka}\left[\frac{(a_{NH_3})^{0.75}}{(a_{H_2})^{1.125}}\right]}{1+K_{H_2}(a_{H_2})^{0.3}+K_{NH_3}(a_{NH_3})^{0.2}}\right] \tag{18}$$

The term $d\eta/dt$ represents the rate at which the limiting reactant is consumed, expressed in $mol\cdot h^{-1}\cdot dm_{cat}^3$. The kinetic constant for the reverse reaction (ammonia decomposition) is denoted as $k$, while $K_a$ refers to the equilibrium constant for the reaction [5].The activities of the reactants and product are indicated by $a_i$. The stoichiometric coefficient, $\lambda(q)$, is set to 1 or 3 depending on whether the $H_2/N_2$ feed ratio is 3 or 1.5, respectively [6]. The absorption equilibrium constants of reactants $K_{H_2}$ and $K_{NH_3}$ are expressed by [7]. The activity of the ith species ($NH_3, H_2$ *or* $N_2$) $a_i$ can be calculated as follows,

$$a_i=y_i\phi_i P \tag{19}$$

Where $P$ indicates the total pressure (atm), $y_i$ and $\phi_i$ denotate the mole fraction and fugacity coefficient of the ith species, respectively. The fugacity coefficients for the reactants and product are fitted by temperature (K) and

pressure (atm) using the equations in expressed by [5].

## RESULTS AND DISCUSSION

### Model Validation and Mesh Independence

A mesh independence study was conducted with four mesh configurations, as illustrated in Figure 1. The $NH_3$ production rate showed minimal variation between coarse (35.802 $kg \cdot m^{-3} \cdot s^{-1}$) and medium (35.825 $kg \cdot m^{-3} \cdot s^{-1}$) meshes (0.064% difference). The fine mesh (36.087 $kg \cdot m^{-3} \cdot s^{-1}$) was adopted, achieving an average element quality of 0.8155. Element quality, a dimensionless metric ranging from 0 to 1, evaluates the regularity of mesh element shapes, with values closer to 1 indicating optimal shape regularity and values near 0 signifying highly distorted or degenerated elements. This measure ensures numerical stability, geometric aligment, and computational accuracy. The selected mesh showed excellent agreement with experimental data from literature (35.5 – 36.5 $kg \cdot m^{-3} \cdot s^{-1}$) [7].

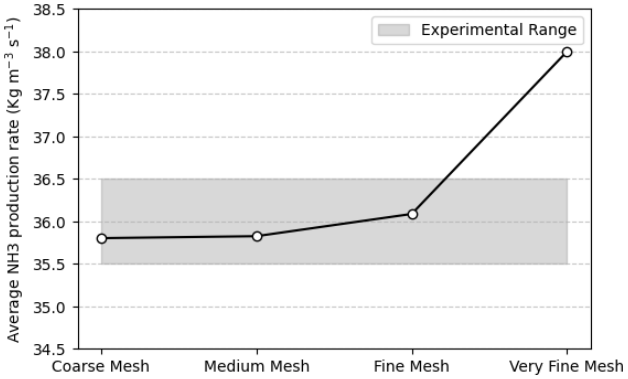



**Figure 1:** Effect of the mesh refinement on average $NH_3$ concentration under standard operating conditions (T=430 ℃, $P = 100$ bar, $GHSV = 180.000\ h^{-1}$).

### Reaction Kinetic and Thermodynamic Response

The kinetic response to the wall temperature step change from 400℃ to 430℃ resulted in a rate constant enhancement factor of 2.08, as shown in Figure 2(a). The relative low activation energy of the Ru/C catalyst (23 kcal/mol) compared to traditional Fe-based catalyst (32 – 35 kcal/mol) accounts for this significant kinetic enhancement, explaining why the $NH_3$ concentration rapidly increased from 2.2 vol.% to 5.1 vol.% after the temperature perturbation. As shown in Figure 2(b), the equilibrium constant (Ka) decreased by approximately 35% at higher temperature, which thermodynamically favours the reverse reaction. However, the observed increase in $NH_3$ production (136%) demonstrates that the kinetic enhancement dominated over the equilibrium constraints in this temperature range. The surface chemistry evolution, depicted in Figure 2(c), shows that the absorption constants for both $H_2$ and $NH_3$ decreased with increasing temperature.

### Thermal Dynamic Response Analysis

The dynamic behavior of the ammonia synthesis reactor under thermal disturbance was systematically investigated to evaluate its response to a step perturbation in the wall temperature. This analysis was conducted maintaining constant operating conditions of 70 bar pressure, GHSV of 180.000 $h^{-1}$, and $H_2/N_2$ feed ratio of 3.0, which represent steady-state operation parameters with the major production rates [7]. Figure 2(d) illustrates the magnitude of the wall temperature step, which was set to 30K based on the high sensitivity of Ru catalyst kinetics to temperature changes in this range, as demonstrated in previous studies [4], [6], [7]. This temperature step is also practically relevant, as it sits within the typical operating window (370-460℃) where Ru catalysts show high activity while avoiding excessive thermal stress on the reactor system.

### $NH_3$ Production

The system's response to the temperature perturbation reveals significant insights into the reactor's dynamic behavior, Figure 2(d). Initially, the $NH_3$ concentration rapidly increases from 0 to approximately 2 vol.% during the first 0.5 seconds showing the system's quick response to the initial operating temperature of 400℃. This is followed by a brief stabilization period where the concentration remains steady at around 2.2 vol.%. At t = 1.0 s, when the step increase in temperature from 400℃ to 430℃ is implemented, the $NH_3$ concentration exhibits a sharp response, rising from 2.2 vol.% to approximately 5.1 vol.%. This dramatic increase, representing a 136% improvement in $NH_3$ production, demonstrates the strong temperature dependence of the reaction kinetics. The smooth transition and stable final concentration suggest that the reactor maintains operational stability despite the sudden temperature change, which is crucial for practical applications in industrial settings.

### Thermal Distribution Evolution

The spatial temperature distributions before and after the step perturbation provide insights into the reactor's thermal behavior. Figure 3(a) shows the temperature field at t = 0.8 s, prior to the step change, where the wall temperature is maintained at 673.15 K (400℃). At this condition, the temperature ranges from 280 K at the inlet to 679 K near the reactor wall, displaying a significant thermal gradient characteristic of the exothermic ammonia synthesis process.

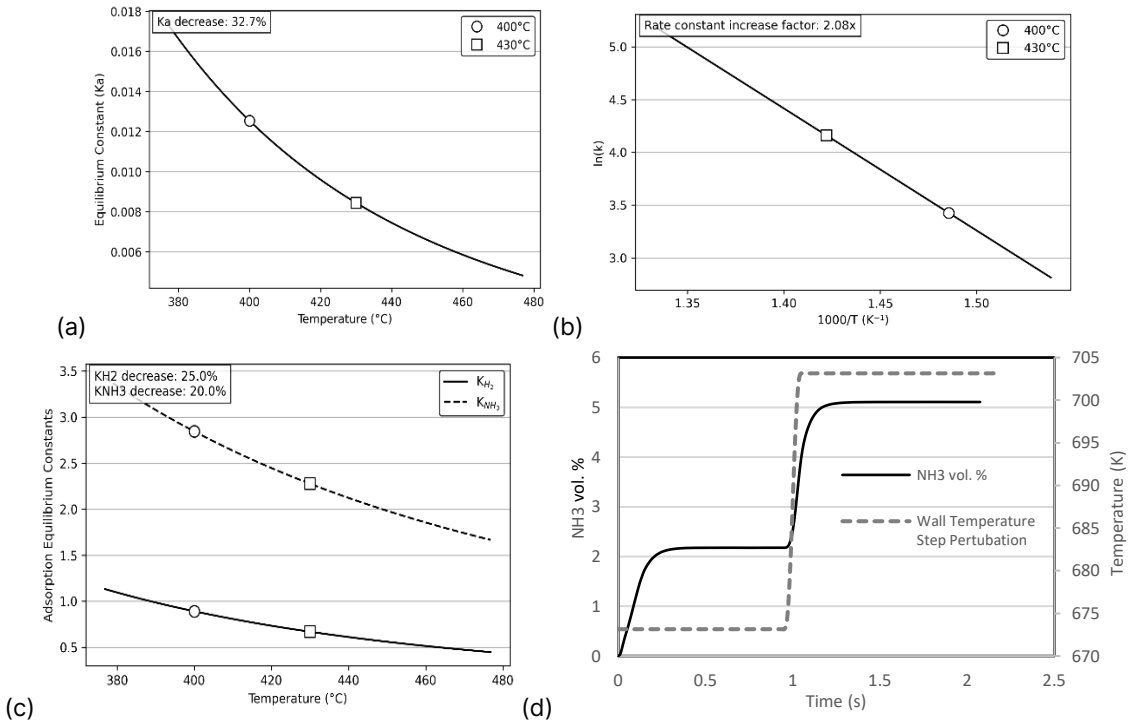



**Figure 2:** Thermal Dynamic Response of the Ammonia Synthesis Reactor. (a) Impact of temperature change on equilibrium constant. (b) Arrhenius behavior of $NH_3$ synthesis rate constant. (c) Temperature step change on adsorption constants. (d) Temperature step perturbation at the reactor walls and Dynamic respon of $NH_3$ volumetric concentration.

After the step perturbation (Figure 3(b), t = 2.0s), the system reaches a new thermal equilibrium with the elevated wall temperature of 703.15 K (430℃). The temperature distribution shows a similar pattern bit with higher overall values, ranging from 277 K at the inlet to 719 K in the reaction zone. The comparison between both states reveals that while the absolute temperatures have increased, the fundamental heat transfer characteristics remain consistent. The effective heat conduction through the catalyst bed is evidenced by the smooth temperature transitions, and the radial temperature distribution indicates significant wall-to-center heat transfer.

A notable observation is the persistence of steep temperature gradients near the inlet in both cases, with a temperature difference of approximately 400 K between the inlet and maximum temperature zones. This consistency in temperature differential, despite the step change in wall temperature, suggests robust heat transfer mechanisms within the reactor. The similarity in the thermal patterns before and after the perturbation indicates that the reactor design effectively manages heat distribution under changing thermal conditions, an essential characteristic for industrial applications where temperature fluctuations may occur.

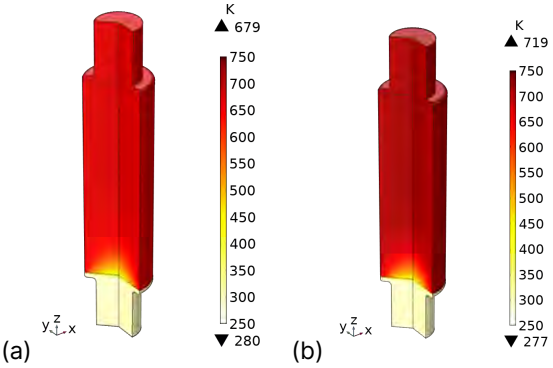



**Figure 3**. Temperature distribution in the reactor at (a) t = 0.8 s with wall temperature of 673.15 K (400℃) and (b) t = 2.0 s after step increase to 703.15 K (430℃).

## $NH_3$ Concentration Evolution

The evolution of $NH_3$ concentration over time, as depicted in Figure 3, clearly represents the fixed-bed reactor's response to a step change in wall temperature, with critical phases occurring at t=0.9 s, t=0.9s, t=1.07 s, and t=2.0 s.

At t=0.9 s, Figure 4(a), prior to the temperature step

change, the wall temperature is maintained at 400°C. During this phase, localized ammonia formation is observed near the reaction zone. This reflects the catalytic activity at the steady-state baseline operating conditions, where the reactor exhibits a controlled and predictable $NH_3$ synthesis rate driven by the Ru/C catalyst's kinetics at the lower temperature.

At t=1.07 s, Figure 4(b), the step temperature change is introduced, rapidly elevating the wall temperature from 400°C to 430°C. This thermal perturbation triggers an immediate enhancement in the reaction rate, as the Ru/C catalyst demonstrates strong sensitivity to temperature increases. The resulting $NH_3$ concentration begins to expand radially, highlighting the acceleration of catalytic activity throughout the reactor. This phase represents the transitional behavior of the system as it responds dynamically to the external thermal input, aligning with the thermal response observed in Figure 1(b).

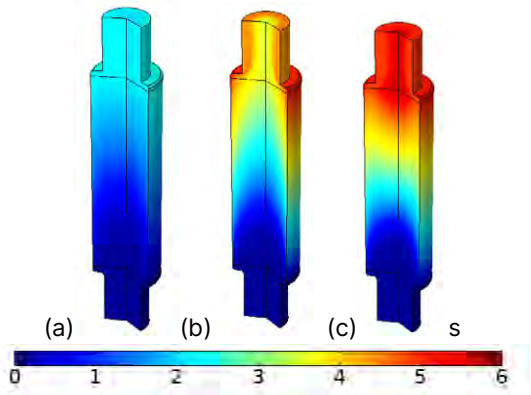



**Figure 4.** Temporal evolution of $NH_3$ concentration profiles at key time points. (a) Concentration profile at t = 0.9 s. (b) Concentration profile at t = 1.07 s. (c) Concentration profile at t = 2 s.

Finally, by t=2.0 s, the reactor achieves stabilization, characterized by a uniform $NH_3$ concentration distribution across the core of the reactor. This indicates that the system has reached a new dynamic equilibrium at the elevated temperature of 430°C. The smooth and rapid stabilization, coupled with a significant increase in $NH_3$ concentration compared to the initial conditions, demonstrates the reactor's efficiency in managing transient thermal changes. This behavior underscores the role of effective heat transfer and robust catalytic performance in maintaining stability despite fluctuating operating conditions.

These findings validate the transient modeling approach and highlight the reactor's capability to adapt quickly to external thermal disturbances. The results provide valuable insights for optimizing the design and operation of ammonia synthesis reactors in Power-to-Ammonia applications, particularly under the variable conditions imposed by intermittent renewable energy sources.

## CONCLUSION

This study developed and validated a 2D axisymmetric transient CFD model to analyze the dynamic response of a fixed-bed ammonia synthesis reactor under thermal perturbations. The results demonstrate a significant enhancement in $NH_3$ concentration (2.2 to 5.1 vol.%) following a temperature step increase from 400°C to 430°C, with rapid stabilization within 0.5 s. The kinetic advantage of Ru/C catalysts at moderate temperatures was found to outweigh thermodynamic limitations, contributing to increased ammonia production. Spatial temperature distributions exhibited consistent heat transfer patterns, maintaining ~400K differentials between inlet and maximum temperature zones.

Future work will address the broader impact of process conditions by extending the sensitivity analysis to include variations in pressure, gas composition, and flow rates. Additionally, a comparative evaluation of alternative reactor configurations and catalyst materials is under investigation to contextualize the advantages and trade-offs of the proposed system. Further assessment of industrial feasibility and scalability, including potential challenges in commercial implementation, will be explored to enhance the model applicability for Power-to-Ammonia applications. These ongoing efforts aim to refine the predictive capabilities of the model and provide deeper insights for optimizing ammonia synthesis under dynamic operating conditions

## ACKNOWLEDGEMENTS

This project is funded by Ministry of Science, Technology, and Innovation (Minciencias, Patrimonio Autónomo del FONDO NACIONAL DE FINANCIAMIENTO PARA LA CIENCIA, LA TECNOLOGÍA Y LA INNOVACIÓN, FRANCISCO JOSÉ DE CALDAS) through the contract 441-2023 and Universidad de La Sabana through the project ING-284-2021. Bravo also acknowledges the support of Universidad de La Sabana through his research assistant position.

## NOMENCLATURE

*Latin letters*

| | |
|---|---|
| $p$ | pressure, [Pa] |
| $Q$ | heat rate per unit volume, [W m-3] |
| $t$ | time, [s] |
| $T$ | temperature, [K] |
| $\mathbf{u}$ | fluid velocity vector, [-] |
| $\mathbf{j}$ | mass flux, [kg m-2 s-1] |

| | |
|---|---|
| $\mathbf{q}$ | heat flux, [W m-2] |
| $\mathbf{I}$ | identity matrix, [-] |
| $R$ | molar reaction rate, [mol gcat-1 s-1] |
| $M_n$ | molar mass, [g mol-1] |
| $D_i^m$ | mixture-average diffusion coefficient, [$m^2$ s-1] |
| $k_{eff}$ | effective thermal conductivity of the porous medium, [K m-1 K-1] |
| $C_p$ | specific heat capacity, [J kg-1 K-1] |

*Greek letters*

| | |
|---|---|
| $\rho$ | density, [kg m-3] |
| $\omega_i$ | species mass fraction, [-] |
| $\mu$ | fluid dynamic viscosity, [Pa s] |
| $\varepsilon_p$ | catalyst bed porosity. [-] |
| $\kappa$ | heat transport coefficient, [W m-1 K-1] |
| $\theta$ | void fraction, [-] |
| [–] | refers to without units or to dimensionless |

*Superscripts*

| | |
|---|---|
| $m$ | mixture |
| $T$ | Transpose operator |

*Subscripts*

| | |
|---|---|
| $i$ | chemical species: {N2, H2, NH3} |
| $eff$ | effective |

*Abbreviations*

| | |
|---|---|
| CFD | Computational Fluid Dynamic |
| GHSV | Gas Hourly Space Velocity |

## REFERENCES


1. P. Berwal, S. Kumar, and B. Khandelwal, "A comprehensive review on synthesis, chemical kinetics, and practical application of ammonia as future fuel for combustion," *Journal of the Energy Institute*, vol. 99, pp. 1743–9671, 2021, doi: 10.1016/j.joei.2021.10.001.
2. A. G. Dixon and B. Partopour, "Computational Fluid Dynamics for Fixed Bed Reactor Design," *Annu Rev Chem Biomol Eng*, vol. 11, no. 1, 2020, doi: 10.1146/annurev-chembioeng-092319-075328.
3. M. Tyrański, J. M. Bujalski, W. Orciuch, and Ł. Makowski, "Computational Fluid Dynamics of Ammonia Synthesis in Axial-Radial Bed Reactor," *Energies 2023, Vol. 16, Page 6680*, vol. 16, no. 18, p. 6680, Sep. 2023, doi: 10.3390/EN16186680.
4. I. Rossetti, N. Pernicone, F. Ferrero, and L. Forni, "Kinetic study of ammonia synthesis on a promoted Ru/C catalyst," *Ind Eng Chem Res*, vol. 45, no. 12, 2006, doi: 10.1021/ie051398g.
5. D. C. Dyson and J. M. Simon, "A kinetic expression with diffusion correction for ammonia synthesis on industrial catalyst," *Industrial and Engineering Chemistry Fundamentals*, vol. 7, no. 4, pp. 605–610, Nov. 1968, doi: 10.1021/I160028A013/ASSET/I160028A013.FP.PNG_V03.
6. A. Tripodi, M. Compagnoni, E. Bahadori, and I. Rossetti, "Process simulation of ammonia synthesis over optimized Ru/C catalyst and multibed Fe + Ru configurations," *Journal of Industrial and Engineering Chemistry*, vol. 66, 2018, doi: 10.1016/j.jiec.2018.05.027.
7. T. Gu, S. S. Araya, C. Yin, and V. Liso, "Exploring decentralized ammonia synthesis for hydrogen storage and transport: A comprehensive CFD investigation with experimental validation and parametric study," *Energy Convers Manag*, vol. 295, p. 117604, Nov. 2023, doi: 10.1016/J.ENCONMAN.2023.117604.



© 2025 by the authors. Licensed to PSEcommunity.org and PSE Press. This is an open access article under the creative commons CC-BY-SA licensing terms. Credit must be given to creator and adaptations must be shared under the same terms. See https://creativecommons.org/licenses/by-sa/4.0/




Systems & Control Transactions

**Research Article - Peer Reviewed Conference Proceeding**
ESCAPE 35 - European Symposium on Computer Aided Process Engineering
Ghent, Belgium. 6-9 July 2025
Jan F.M. Van Impe, Grégoire Léonard, Satyajeet S. Bhonsale,
Monika E. Polańska, Filip Logist (Eds.)

PSE PRESS

# Kernel-based estimation of wind farm power probability density considering wind speed and wake effects due to wind direction

**Samuel Martínez-Gutiérrez[a]*, Daniel Sarabia[a], and Alejandro Merino[a]**

[a] University of Burgos, Department of Digitalization, Area of Systems Engineering and Automatic Control, Burgos, Burgos, Spain
* Corresponding Author: samuel.martinez@ubu.es.

## ABSTRACT

This study compares the probability density function (PDF) of the power generated by a wind farm obtained analytically with the PDF considering the wake effect between wind turbines, a phenomenon that reduces the power generation capacity of wind farms. Instead of considering the wake effect in the analytical method, which is complex and difficult to solve, it has been proposed to use kernel estimators to obtain the PDF. To calculate it, a wind farm power output data set has been used. This data set was generated using historical wind speed and direction data and the Katic multiple wake model. Discrepancies between the analytical PDF and PDF fitted with the kernel estimators, can lead to an overstatement of the annual available energy by 4 an 9 %, depending on the complexity of the wind farm layout. These inconsistencies can have significant implications for production planning, wind farm design, and integration of wind power into the grid. Therefore, this analysis underscores the necessity of incorporating the wake effect in wind farm modelling, to guarantee more precise projections of generation and energy availability.

**Keywords**: Wake effect, wind farm power distribution, kernel estimators

## INTRODUCTION

When planning wind farm projects, it is crucial to quantify and assess the wind resource of the candidate site. This assessment is typically conducted using the wind energy density [1], also called wind power density [2], which requires the probability distribution of wind speed $f_V(v)$ and the power curve of a wind turbine $P_{WT}(v)$ to calculate it. Furthermore, based on $f_V(v)$, $P_{WT}(v)$ and using the change-of-variable technique, it is possible to obtain the probability density function of a wind turbine power output, $f_{PWT}(P_{WT})$, which provides additional insight into the energy that can be produced [3].

However, to optimize the management of a wind farm, it is necessary to know the probability density function of the power generated by the entire wind farm, $f_{PWF}(P_{WF})$. This function enables the estimation of the variability and availability of the power generated by the wind farm, facilitating production planning over a given period. It also ensures the integration of wind energy into the electricity grid by allowing the determination of the probability of achieving a specific power output. This probability-based approach supports optimal decision making [4]. One way to obtain $f_{PWF}(P_{WF})$ is through the probability distribution of wind speed $f_V(v)$, and the wind farm's power curve, $P_{WF}(v)$, as described before for the single turbines. This requires a simple analytical expression of the wind farm power curve $P_{WF}(v)$, which allows the change-of-variable technique to be used. For example, the power produced by a wind farm can be approximated as the power output of a single wind turbine multiplied by the number of turbines, $P_{WF}(v)=n_{turb}\cdot P_{WT}(v)$.

However, this approach has the disadvantage of not considering a significant source of power loss such as the wake effect (turbines shading each other) due to wind direction. A first alternative to consider the wake effect is to use a wind probability density function and a wind farm power curve that depend on wind speed ($v$) and direction ($\theta$): $f_{V,\Theta}(v,\theta)$, $P_{WF}(v,\theta)$. Nevertheless, deriving these expressions and applying the change-of-variable technique to bivariable distribution functions is highly complex.

For this reason, some authors have tried to keep the

$P_{WF}(v)=n_{turb}\cdot P_{WT}(v)$ approximation and add a wake coefficient term [5], simplifying a wake model such as Jensen's [6], but this approximation is only valid for wind farms with *nxm* rectangular geometry.

This paper proposes generating a sample of wind farm power output data based on historical wind speed and direction data from a given location. The Katic wake model [7] is used to calculate the effective incident velocity for each wind turbine. Subsequently, the power generated by each turbine, $P_{WT}(v)$, is determined, and the total wind farm power is obtained by summing the individual contributions. Finally, the wind farm power probability density function, $f_{PWF}(P_{WF})$, is estimated using kernel method. A similar application of kernel estimators to model the probability density function of a group of wind farms is described in [8]; however, their approach also neglects the wake effect.

The paper is structured as follows. Section 2 explains the two alternatives proposed to obtain $f_{PWF}(P_{WF})$ and the wake model used; section 3 gives a brief description of the data used; section 4 shows the results; and section 5 ends with some brief conclusions.

## MODELLING

This section begins with an explanation of the wake effect in wind farms and how it has been modelled in this work. Next, subsection *Theoretical wind farm power PDF* explains how the probability density function of the wind farm power is obtained theoretically. Finally, subsection *Wind farm power PDF considering wake effect* presents our proposal, based on kernel estimators, to obtain the probability density function of the wind farm power considering the wake effect.

### Wake effect

The wake effect is a phenomenon whereby wind turbines located geographically behind others in relation to the wind front will see their capacity to produce electrical energy diminished due to the loss of energy and increased turbulence that the wind undergoes after passing through a turbine.

Jensen's model is the simplest model to describe this phenomenon [6]. It is based on the assumption that there are no deterministic or periodic vortices immediately behind the turbine, but that the air behaves as a turbulent fluid (the particles move disorderly and the particle trajectories meet to form aperiodic vortices). This model also considers that within the wake, the velocity is constant rather than following a Gaussian or other distribution. As shown in Figure 1, the wake behind the turbine starts at the diameter of the turbine and opens linearly with distance, forming a cone.

In the case of wind farms where there may be more wakes that may also partially affect a turbine, the Jensen's multiple wake model or Katic's model [7] is applied.

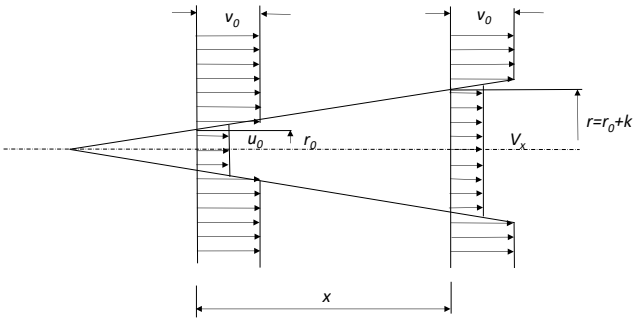



**Figure 1.** Wake generated by the turbine on the left at distance x downstream.

There are many ways to incorporate in a turbine *j* the wake effect of all other turbines *i* upstream. One possibility is to assume that the kinetic energy deficit in turbine *j*, attributable to a mixture of wakes with respect to the undisturbed wind $v_0$, is equal to the sum of the kinetic energy deficits in turbine *j* due to each individual wake of turbine *i* with respect to the undisturbed wind $v_0$, see equation (1).

$$\left(v_0 - v_j\right)^2 = \sum_{i=1}^{n}\left(v_0 - v_{ij}\right)^2 \tag{1}$$

Considering equation (1), together with the Katic's multiple wake model, equation (2) is derived.

$$v_j = v_0\left[1 - \sqrt{\sum_{i=1}^{n}\left(1-\sqrt{1-C_T}\right)^2\left(\frac{r_i}{r_i(x_{ij})}\right)^4\left(\frac{A_{sh,i}}{A_j}\right)^2}\right] =$$

$$v_0\left[1 - \sqrt{\sum_{i=1}^{n}\delta_{ij}^2\left(\frac{A_{sh,i}}{A_j}\right)^2}\right] \tag{2}$$

Where subscript *i* refers to the wind turbines generating a wake on a given wind turbine *j*, $v_0$ is the undisturbed velocity affecting the wind farm (at a position sufficiently far from all turbines), $C_T$ is the thrust coefficient of the wind turbine, $A_{sh,i}$ is the overlapping wake area of wind turbine *i* on wind turbine *j*, and $A_j$ is the swept area of the blades of wind turbine *j*. Finally, $r_i(x_{ij})$ is the radius of the wake of wind turbine *i* (wake generator) at the height of wind turbine *j* (affected by the wake), which can be calculated using equation (3) in terms of the radius of the wind turbine generating the wake, $r_i$, and the wake decay coefficient (4).

$$r_i\left(x_{ij}\right) = r_i + k\cdot x_{ij} \tag{3}$$

The wake decay coefficient is a function of the height of the wind turbine hub, *h*, and the roughness of the terrain, $z_0$.

$$k = \frac{0.5}{ln\left(\frac{h}{z_0}\right)} \tag{4}$$

Considering the different cones generated by the turbines, some of which do not necessarily fully affect the downstream wind turbines, the overlap area $A_{sh,I}$ can be calculated according to three situations:

- If the swept area $A_j$ is outside of the wake area, or wind turbine *i* is stopped, then $A_{sh,i} = 0$.
- If the swept area $A_j$ is completely inside the wake area, and wind turbine *i* is running, then $A_{sh,i} = A_j$.
- If the swept area $A_j$ is partially inside the wake area, and wind turbine *i* is running, then $A_{sh,i}$ is calculated using equation (5).

$$A_{sh,i} = \left[r_i(x_{ij})\right]^2 cos^{-1}\left(\frac{L_{ij}}{r_i(x_{ij})}\right) + r_j^2 \cos^{-1}\left(\frac{d_{ij}-L_{ij}}{r_j}\right) - L_{ij}\sqrt{r(x_{ij})^2 - L_{ij}^2} - (d_{ij}-L_{ij})\sqrt{r_j^2-(d_{ij}-L_{ij})^2} \quad (5)$$

Being $L_{ij}$ described in equation (6).

$$L_{ij} = \frac{r_i^2(x_{ij}) - r_j^2 + d_{ij}^2}{2\,d_{ij}} \quad (6)$$

## Analytical PDF of wind farm power

As mentioned in the introduction, the PDF of the wind farm power $f_{PWF}(P_{WF})$ can be obtained theoretically from the PDF of the wind speed $f_v(v)$ and from the power curve of a wind farm $P_{WF}(v)$, using the change-of-variable technique described in [3].

The power curve of a wind farm, if all wind turbines in the wind farm are equal, can be expressed in megawatts, according to equation (7) and the number of turbines *n_turb*.

$$P_{WF}(v) = \frac{n_turb}{10^6} \cdot P_{WT}(v) \quad (7)$$

The power curve of a wind turbine, $P_{WT}(v)$, establishes the relationship between the wind speed and the power generated by a wind turbine. It can be expressed theoretically as a piecewise function (8), whose parts are defined by $v_{in}$, which is the lower wind speed at which power can be extracted, $v_r$ is the wind speed at which the nominal power of the wind farm ($P_{RWT}$) can be obtained, and $v_{off}$ is the wind speed at which the wind turbine must be stopped in order to prevent damage. Between $v_{in}$ and $v_r$ the power extracted by the wind turbine is a function of the air density $\rho$, the radius $R$ of the area swept by the wind turbine blades, and the power coefficient $Cp$. This coefficient, in turn, is a function of the turbine rotation speed and the pitch angle. The value of this coefficient depends on the turbine model, and its maximum value is set by the Betz limit at 0.593 [9]. In this study, a fixed value has been calculated based on the rated speed of the wind turbine, the rated power of the turbine, and the mean air density at the location of the wind farms.

$$P_{WT}(v) = \begin{cases} 0 & 0 \le v < v_{in} \\ \frac{1}{2}\cdot\pi\cdot R^2\cdot\rho\cdot v^3\cdot Cp & v_{in} \le v < v_r \\ P_{RWT} & v_r \le v < v_{off} \\ 0 & v \ge v_{off} \end{cases} \quad (8)$$

The probability distribution function (PDF) of the wind speed is commonly modelled with a Weibull distribution [1], as it is shown in equation (9).

$$f_v(v) = \begin{cases} \frac{k}{C}\left(\frac{v}{C}\right)^{k-1}\cdot e^{-\left(\frac{v}{C}\right)^k} & v \ge 0 \\ 0 & v < 0 \end{cases} \quad (9)$$

Where *C* and *k* are the scale and the shape parameters, respectively.

Once $f_v(v)$ and $P_{WF}(v)$ are defined, it is possible to obtain the PDF of the wind farm power $f_{PWF}(P_{WF})$, which is described in the equation (10).

$$f_{PWF}(P_{WF}) = \begin{cases} \left(1 + e^{-\left(v_{off}/c\right)^k} - e^{-\left(v_{in}/c\right)^k}\right)\cdot\delta(P_{WF}) & P_{WF} = 0 \\ 0 & 0 < P_{WF} < P_{INWF} \\ \frac{k'}{C'}\cdot\left(\frac{P_{WF}}{C'}\right)^{k'-1}\cdot e^{-\left(P_{WF}/C'\right)^{k'-1}} & P_{INWF} \le P_{WF} < P_{RWF} \\ \left(e^{-\left(v_r/c\right)^k} - e^{-\left(v_{off}/c\right)^k}\right)\cdot\delta(P_{WF}-P_{RWF}) & P_{WF} = P_{RWF} \\ 0 & P_{WF} > P_{RWF} \end{cases} \quad (10)$$

Where $P_{WF}$ is the wind farm power, $P_{INWF}$ is the wind farm power to $v_{in}$, $P_{RWF}$ is the wind farm rated power, $\delta$ is Dirac's delta, and $K''$ and $C''$ are parameters that depend on the previous scale and shape parameters, $k'' = k/3$ and $C'' = (C^3\cdot\pi\cdot R^2\cdot Cp\cdot n_turb)/(2\cdot10^6)$.

Finally, the cumulative distribution function (CDF) of the wind farm power $F_{PWF}(P_{WF})$ is obtained by integrating the PDF of the wind farm (10) between zero and infinity, resulting in (11).

$$F_{PWF}(P_{WF}) = \begin{cases} \left(1 + e^{-\left(v_{off}/c\right)^k} - e^{-\left(v_{in}/c\right)^k}\right) & 0 < P_{WF} < P_{INWF} \\ 1 - e^{-\left(P_{WF}/C'\right)^{k'-1}} & P_{INWF} \le P_{WF} < P_{RWF} \\ 1 - e^{-\left(P_{WF}/C'\right)^{k'-1}} + e^{-\left(v_r/c\right)^k} - e^{-\left(v_{off}/c\right)^k} & P_{WF} = P_{RWF} \\ 1 & P_{WF} > P_{RWF} \end{cases} \quad (11)$$

## PDF of wind farm power considering wake effect

The PDF of the wind farm power obtained previously does not consider the wake effect in any way. In this paper it is proposed to use kernel estimators to estimate the PDF of the wind farm power including the wake effect $f_{PWF_WE}(P_{WF_WE})$. For this purpose, historical wind speed and wind direction data are used to calculate the incident wind speed at each wind turbine ($v_i$) of a wind farm using a valid wake model. In this study, Katic's model is used,

but another model could also be applied while the methodology and conclusions of this paper remain valid. Then, the power generated by each turbine is calculated using $P_{WT}(v)$. Finally, the power of the wind farm is obtained as the sum of the power generated by each turbine (12).

$$P_{WF_WE}(v) = \sum_{j=1}^{n_turb} P_{WT}(v_j) \quad (12)$$

Once the wind farm power data set has been generated, kernel estimators, whose basic equation is shown in equation (13), are used to fit the function $f_{PWF_WE}(P_{WF_WE})$. However, since the power of a wind farm is constrained between 0 and $P_{RWF}$, and the conventional kernel estimator does not consider this constraint, it is necessary to modify it. In this case, the reflection method [10] has been employed, as it is the approach implemented in the kdensity() function of the Statistics and Machine Learning Toolbox [11] from Matlab™ [12], and that will be used to perform the fitting.

$$\hat{f}(x) = \frac{1}{nh}\sum_{i=1}^{n} K\left(\frac{x-x_i}{h}\right) \quad (13)$$

Finally, $f_{PWF_WE}(P_{WF_WE})$ and $F_{PWF_WE}(P_{WF_WE})$ are described in equation (14) and (15) respectively.

$$f_{PWF_WE}(P_{WF_WE}) = \frac{1}{nh}\sum_{i=1}^{n}\left[K\left(\frac{x-2L+x_i}{h}\right) + K\left(\frac{x-x_i}{h}\right) + K\left(\frac{x-2U+x_i}{h}\right)\right] \quad (14)$$

$$F_{PWF_WE}(P_{WF_WE}) = \frac{1}{n}\sum_{i=1}^{n}\left[G\left(\frac{x-2L+x_i}{h}\right) + G\left(\frac{x-x_i}{h}\right) + G\left(\frac{x-2U+x_i}{h}\right)\right] - \frac{1}{n}\sum_{i=1}^{n}\left[G\left(\frac{-L+x_i}{h}\right) + G\left(\frac{L-x_i}{h}\right) + G\left(\frac{x-2U+x_i}{h}\right)\right] \quad (15)$$

Where $n$ is the number of power samples, $L = 0$, $U = P_{RWF}$, $K(\cdot)$ is the kernel estimator, $G(\cdot)$ is the cumulative of $K(\cdot)$, and $x = P_{WF_WE}$.

## Data

The comparison of the two methods will be carried out using simulated data from the New European Atlas [13], [14]. On the NEWA website [15] it is possible to access, free of charge, the time series of wind speed and direction at a given site at different heights (50, 75, 100, 150, 200, 250 and 500 metres), from 2005 to 2018 at half-hourly intervals, a total of 245424 data, of which 195 are missing.

The study is carried out with all data from 2005 to 2018 for two different sites, corresponding to the Rabinaldo wind farm (WF1), located in the province of Burgos (latitude 42° 35' 28.6", longitude -3° 42' 19.7"), and Las Panaderas (WF2) in the province of Valladolid (latitude 41° 47' 21.6", longitude -5° 1' 36.3"). Starting from the velocity time series at the heights available in NEWA, Hellman's law [16] is used to generate the velocity series at the heights of the wind turbine hubs (78 and 114 metres respectively).

However, for the wind direction data series, the NEWA height closest to the hub height (75 and 100 metres respectively) is chosen, since there is no simple analytical expression that relates the variability of the wind direction with height. Information on the wind farms comes also from various official sources. Figure 2 shows the resulting wind roses for each wind farm at wind turbine hub height.

In order to calculate the wake effect, it is also necessary to know the spatial distribution of the wind turbines in each wind farm, which are shown in Figure 3.

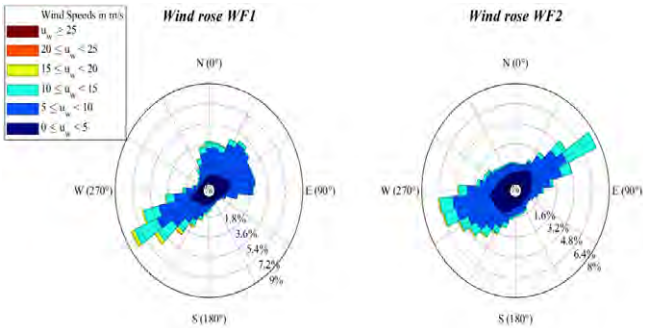



**Figure 2.** Wind roses of wind farms.

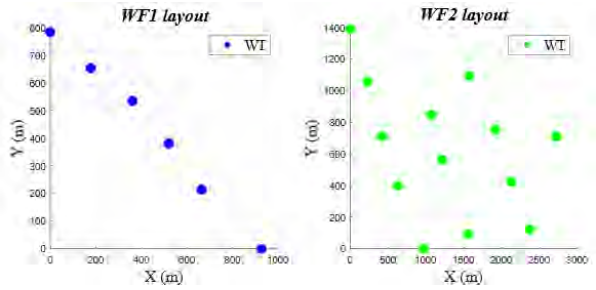



**Figure 3.** Wind farms layouts.

## RESULTS AND DISCUSSION

In this section, the probability density and cumulative distribution functions of the wind farms without taking into account the wake effect, $f_{PWF}(P_{WF})$ and $F_{PWF}(P_{WF})$, are compared with those that consider the wake effect, $f_{PWF_WE}(P_{WF_WE})$ and $F_{PWF_WE}(P_{WF_WE})$. For this comparison, a Gaussian kernel and the plug-in method were used as the optimal bandwidth selection method. The results can be seen in the Figure 4.

The first relevant result is that the bandwidth required to adequately represent $f_{PWF_WE}(P_{WF_WE})$ and $F_{PWF_WE}(P_{WF_WE})$ has very small values, being 2.8209E-4 for WF1 and 8.2103E-5 for WF2. This level of detail is crucial for capturing specific features, such as the zone of $f_{PWF}(P_{WF}) = 0$ between $P_{WF} > 0$ and $P_{WF} < P_{INWF}$, described in the theoretical approach. However, for the estimation with kernels, this $f_{PWF_WE}(P_{WF_WE}) = 0$ zone is smaller, because with the wake effect, $P_{INWF}$, is reduced. This can be clearly seen in Figure 5, an amplified view of the two PDFs

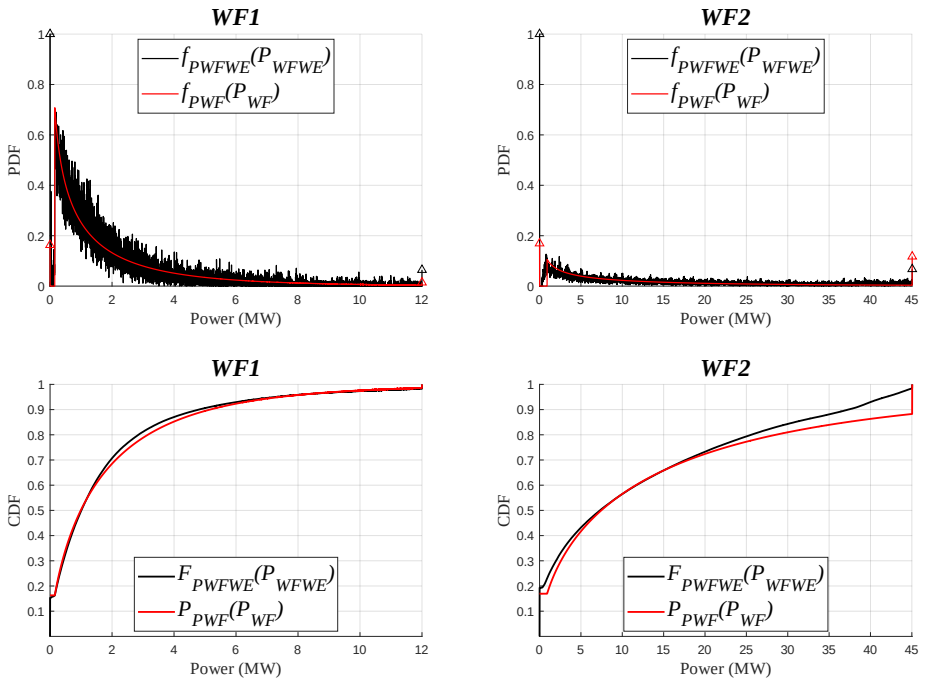



**Figure 4.** Probability density functions and cumulative distribution functions obtained analyticaly without wake effect $f_{PWF}(P_{WF})$ and $F_{PWF}(P_{WF})$ vs $f_{PWF_WE}(P_{WF_WE})$ and $F_{PWF_WE}(P_{WF_WE})$ with wake effect obtained using kernel estimators both for WF1 and WF2.

of WF1, which shows that for $f_{PWF}(P_{WF})$, $P_{INWF}$ is equal to 0.18 MW but for $f_{PWF_WE}(P_{WF_WE})$, $P_{INWF}$ is only 0.02 MW.

**Table 1.** Annual energy (AE) estimation using PDF without including wake effect and including it.

| | AE without wake effect | AE with wake effect | Overestimation |
|---|---|---|---|
| WF1 | 16,935 MWh | 16,250 MWh | 4 % |
| WF2 | 123,061 MWh | 111,813 MWh | 9.1 % |

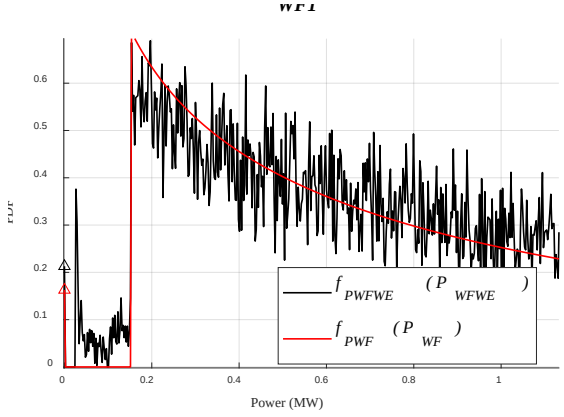



**Figure 5.** Zoom view of the PDFs of WF1.

Then, the annual energy generated by the wind farm (AE), which is simply the expected value of the probability distributions multiplied by the number of hours of the year, 8760, is calculated using $f_{PWF}(P_{WF})$ or $f_{PWF_WE}(P_{WF_WE})$ for WF1 and WF2. It can be seen in Table 1 that for WF1, which has a fairly simple layout and is properly oriented with respect to the prevailing wind directions (northeast-southwest) (Figure 2 and 3), the annual energy without considering the wake effect is 16,935 MWh, while taking the wake effect into account reduces it to 16,250 MWh, overestimating the producible energy by the wind farm by only 4%. The difference is small because along the predominant wind direction there is no wake effect, due to the specific layout of the wind farm. However, for WF2, which has a more complex layout with several wind turbines behind others even towards the prevailing wind direction (northeast-southwest) (Figure 2 and 3), the annual energy is 123,061 MWh without considering the wake effect, and 111,813 MWh with it, overestimating the wind farm's producible power by 9.1%.

There are also discrepancies for both wind farms between $F_{PWF}(P_{WF})$ and $F_{PWF_WE}(P_{WF_WE})$. This implies incorrectly estimating the probability of occurrence of the different power values or power intervals, which can have a negative effect on long-term production decisions. For example, for WF2, the wind farm most affected by the wake effect, the probability of $P_{WF}$ being less than 4 MW is 0.38 for $f_{PWF}(P_{WF})$ and 0.4 for $f_{PWF_WE}(P_{WF_WE})$. Although

this difference may seem small, it can have a large impact on energy production planification in the long run, as its effect is multiplied by the time interval of the decision period. These results highlight the importance of including the wake effect in the analysis because inadequate modelling can underestimate the available power density.

## CONCLUSIONS

In this study, it has been proposed to model the PDF of the power generated by a wind farm taking into account the wake effect, $f_{PWF_WE}(P_{WF_WE})$, and has been compared with the analytical modelling (without wake effect) of the PDF of the power of a wind farm $f_{PWF}(P_{WF})$. To model $f_{PWF_WE}(P_{WF_WE})$ it has been proposed to use a historical wind speed and direction data set and the Katic multiple wake model to generate a data set of wind farm power output, and then use kernel estimators to model the PDF.

A comparison of the two distributions shows that ignoring this effect can result in an overestimation of the available energy of up to 9.1% for wind farms with more complex layouts. The differences seen in PDF modelling also have an effect on the CDF, again proving how a competitive layout can have large differences in cumulative contributions in the low and high-power ranges. These discrepancies can have important implications for production planning and wind farm grid integration, highlighting the importance of incorporating the wake effect into wind farm modelling to ensure more accurate projections of generation and energy availability.

## ACKNOWLEDGEMENTS

The paper is part of the projects 'Optimal Real-Time Management of the Power-to-H2-to-Power cycle (OptiMaPH2P)', TED2021-131220B-I00, funded by MCIN/AEI and by the European Union 'NextGenerationEU', 'Optimal real-time management under uncertainty for digital twins (OptiDit)', PID2021-123654OB-C33, funded by MCIN and by the European Union 'FEDER'. This paper is also part of the Doctoral Thesis of Samuel Martínez-Gutiérrez, funded with a pre-doctoral contract for University Teacher Training (FPU), call 2022, awarded by the MUNI of Spain.

## REFERENCES

1. Mathew S. Wind energy: Fundamentals, resource analysis and economics. Springer Berlin Heidelberg (2007) https://doi.org/10.1007/3-540-30906-3
2. Herrero-Novoa C, Pérez IA, Sánchez ML, García MÁ, Pardo N, Fernández-Duque B. Wind speed description and power density in northern Spain. Energy 138:967–976 (2017) https://doi.org/10.1016/J.ENERGY.2017.07.127
3. Villanueva D, Feijóo A. Wind power distributions: A review of their applications. Renew Sustain Energy Rev 14:1490–1495 (2010) https://doi.org/10.1016/J.RSER.2010.01.005
4. Louie H. Characterizing and modeling aggregate wind plant power output in large systems. IEEE PES General Meeting, PES 2010. (2010) https://doi.org/10.1109/PES.2010.5589286
5. Feijoo A, Villanueva D. Wind farm power distribution function considering wake effects. IEEE Trans Power Syst 32:3313–3314 (2017) https://doi.org/10.1109/TPWRS.2016.2614883
6. Jensen NO. A note on wind generator interaction. Risø National Laboratory, vol. No 2411. (1983) Accessed: Feb. 15, 2023.
7. Katic I, Højstrup J, Jensen NO. A simple model for cluster efficiency. In: EWEC'86. Proceedings. Vol. 1. Ed: Raguzzi A, Palz W, Sesto E. (1987) pp. 407–410.
8. Sobolewski RA, Feijóo AE. Estimation of wind farms aggregated power output distributions. Int J Electr Power Energy Syst 46:241–249 (2013) https://doi.org/10.1016/J.IJEPES.2012.10.032
9. Betz A. Das Maximum der theoretisch möglichen Ausnützung des Windes durch Windmotoren. Z für das gesamte Turbinenwesen 26:307–309 (1920)
10. Jones MC. Simple boundary correction for kernel density estimation. Stat Comput 3:135–146 (1993) https://doi.org/10.1007/BF00147776/METRICS
11. The MathWorks Inc, "Statistical and Machine Learning Toolbox version: 24.1 (R2024a)," 2024.
12. The MathWorks Inc., "MATLAB version: 24.1 (R2024a)," 2024, The MathWorks Inc., Natick, Massachusetts, United States.
13. Hahmann AN, et al. The making of the New European Wind Atlas - Part 1: Model sensitivity. Geosci Model Dev 13:5053–5078 (2020) https://doi.org/10.5194/GMD-13-5053-2020
14. Dörenkämper M, et al. The Making of the New European Wind Atlas - Part 2: Production and evaluation. Geosci Model Dev 13:5079–5102 (2020) https://doi.org/10.5194/GMD-13-5079-2020
15. New European Wind Atlas. https://map.neweuropeanwindatlas.eu/
16. Hellman G. Über die Bewegung der Luft in den untersten Schichten der Atmosphere. Meteorol Z 273:34 (1916)

© 2025 by the authors. Licensed to PSEcommunity.org and PSE Press. This is an open access article under the creative commons CC-BY-SA licensing terms. Credit must be given to creator and adaptations must be shared under the same terms. See https://creativecommons.org/licenses/by-sa/4.0/



Systems & Control Transactions

**Research Article - Peer Reviewed Conference Proceeding**
ESCAPE 35 - European Symposium on Computer Aided Process Engineering
Ghent, Belgium. 6-9 July 2025
Jan F.M. Van Impe, Grégoire Léonard, Satyajeet S. Bhonsale,
Monika E. Polańska, Filip Logist (Eds.)

PSE PRESS

# Thermo-Hydraulic Performance of Pillow-Plate Heat Exchangers with Streamlined Secondary Structures: A Numerical Analysis

**Reza Afsahnoudeh[a], Julia Riese[a], Eugeny Y. Kenig[a]***

[a] Paderborn University, Chair of Fluid Process Engineering, Paderborn, Germany
* eugeny.kenig@upb.de.

## ABSTRACT

Pillow-plate heat exchangers (PPHEs) represent a viable alternative to conventional shell-and-tube and plate heat exchangers. The waviness of their channels intensifies fluid mixing in the boundary layers and facilitates heat transfer. Applying secondary surface structuring can further enhance the overall thermo-hydraulic performance of PPHEs, thus increasing their competitiveness against conventional heat exchangers. In this work, streamlined secondary structures applied on the PPHE surface were studied numerically to explore their potential in enhancing near-wall fluid mixing. Computational fluid dynamics (CFD) simulations of single-phase turbulent flow in the inner PPHE channel were performed and pressure drop, heat transfer coefficients, and overall thermo-hydraulic efficiency were determined. The simulation results clearly demonstrate a favourable influence of secondary structuring on the heat transfer performance of PPHEs.

**Keywords**: Computational Fluid Dynamics, Surface structuring, Heat transfer intensification

## INTRODUCTION

Pillow-plate heat exchangers (PPHEs) are a promising alternative to conventional shell-and-tube and plate heat exchangers. PPHEs are formed by assembling multiple pillow plates (PPs) into a single unit. These PPs are manufactured by spot-welding two steel sheets and seam-welding along the edges, followed by hydroforming, resulting in characteristic pillow-like surfaces (see Fig. 1).

Piper et al. [2] conducted a CFD-based study of turbulent fluid flow in the inner channels (IC) of PPs. Their simulation results revealed that a fully developed turbulent flow in PPs is characterized by two zones: a recirculation zone arising in the wake of a welding spot and a core flow confined by the wall and the recirculation zones. The recirculation zones increase pressure drop and are characterized by slow heat transfer. By reducing the size of these zones, the performance of the PPHEs can be improved; thus, optimization of the PPHE geometry is possible. Therefore, Piper et al. [2] investigated the effect of the form and size of welding spots on the thermo-hydraulic performance of PPHE inner channels. They reported a 37% efficiency increase for a PPHE with streamlined oval-shaped welding spots in a longitudinal-type PP. Shirzad et al. [3] found that with increasing inflation height of the channel, Nusselt number increased while pressure drop decreased.

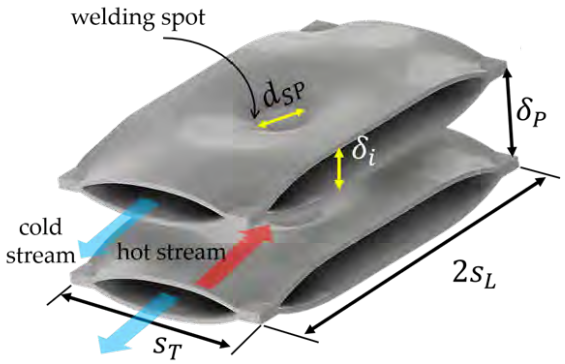



**Figure 1:** A digital image with the characteristic geometry parameters of PPs. Cold fluid flows through inner channels, hot fluid flows through outer channels [1].

Secondary structuring of surfaces has emerged as a method to further enhance PPHE performance. Djakow

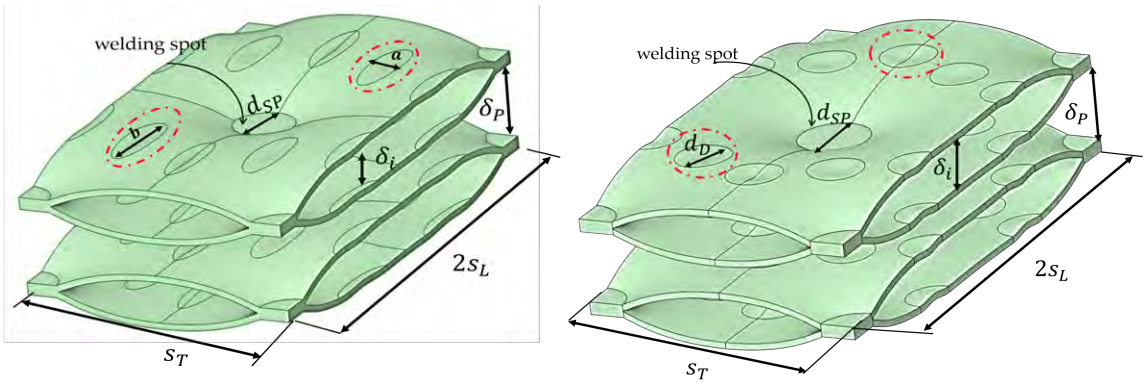



**Figure 2:** Digital images of the studied PPHEs with secondary structures: streamlined-ellipsoidal (left) and streamlined-spherical (right). Red dashed lines denote the secondary structures.

et al. [4] used electro-incremental hydroforming (EIHF) to apply dimples on PP surfaces; based on numerical simulations, they showed a 24% increase in heat transfer coefficient in an IC of the studied PPHE. Piper et al. [5] demonstrated that dimpled surfaces in the outer channels reduced the negative impact of the recirculation zones and improved efficiency. Afsahnoudeh et al. [1] extended this analysis to a wider range of secondary structures and found that streamlined secondary structures in the outer channels increased thermo-hydraulic efficiency by up to 6%.

Despite these promising results, applying secondary structures on PP surfaces presents challenges, as this method is mainly suitable for simple geometries while surface altering requires a substantial amount of energy (see [6]). Considering these limitations and considering that the main heat transfer resistance can be located in the inner channels [2,3], this work focuses on simple streamlined secondary structures that achieve a balance between performance, manufacturability, and cost. Detailed numerical simulations are conducted to evaluate the effect of secondary structures on flow characteristics and heat transfer efficiency.

## GEOMETRY GENERATION AND SURFACE STRUCTURING

To accurately simulate fluid dynamics and heat transfer in the ICs of PPHEs, a realistic digital representation of the PP geometry, which defines the computational domain, is necessary. We employed a forming simulation method detailed in [7] to generate the basic PP geometry. This geometry does not contain secondary structures and serves as a benchmark for the comparison with secondary structured PP. The benchmark has already been optimized with respect to the thermo-hydraulic performance (see [2, 3]).

In our previous work [1], we explored the thermo-hydraulic behavior of the outer channel with different secondary structures. It was found that the PPs with ellipsoidal secondary structures that resulted in a larger volume of the outer channel were most effective in reducing pressure drop and form drag. This geometry, in which both the arrangement and shape of the individual secondary structures are streamlined (Fig. 2, left) is denoted as *streamlined-ellipsoidal*. In [1], we also found that spherical (dimple) secondary structures were most effective in increasing heat transfer, yet with higher pressure drop. Therefore, in this work, we studied two competing PP geometries, the streamlined-ellipsoidal one and the *streamlined-spherical* geometry in which ellipsoidal forms are replaced by spherical forms. The digital images of the two studied secondary structured PPs are shown in Figure 2. In Table 1, the dimensions of the studied PPs are summarized.

**Table 1:** Geometrical parameters of the studied PPHEs (all dimensions in mm).

| $d_{SP}$ | $s_L$ | $s_L$ | $\delta_i$ | $a$ | $b$ | $d_D$ |
|---|---|---|---|---|---|---|
| 10 | 36 | 42 | 7 | 4.72 | 14.2 | 8.2 |

## CFD MODELING

### Model and solution method

The numerical simulations were carried out with the commercial software Fluent 24.1 by ANSYS. The fluid flow was modeled as incompressible, single phase and turbulent, with constant fluid phase properties.

Due to the formation of recirculation zones downstream of the welding spots in an IC and the potential additional recirculation caused by secondary structures, it is crucial to select a turbulence model capable of accurately resolving flow separation. Additionally, the boundary layer separation is expected to induce laminar-turbulent transition. Therefore, to simulate the flow in the IC of the studied PPHEs, we employed the SST model combined with $\gamma$ (intermittency) transition model [8]. Here, $\gamma$

defines the extent of turbulence production in the flow. It has a value of zero for laminar flow, one for fully turbulent flow, and is between zero and one for the transitional flow. The turbulence production term in the SST model equations is multiplied by $\gamma$, which allows a smooth transition between laminar and turbulent regimes based on local flow conditions. This model is well suited for resolving separation-induced and crossflow-induced laminar-turbulent transition in complex geometries [8].

The simulation domain and boundary conditions are illustrated in Fig. 3. To reduce the computational effort, we made use of the flow and geometry symmetry by applying symmetric boundary conditions at $y = 0$ and $y = 0.5\, s_T$ (see Fig. 3). No-slip and constant temperature boundary conditions were set at the wall. Additionally, periodic boundary condition was applied at the inlet ($x = 0$) and outlet ($x = 2\, s_L$) boundaries of the channel, while prescribed values of mass flow and constant bulk temperature were given at $x = 0$. Using periodic boundary condition inherently restricts the investigation to the (periodically) fully developed region. Fluent 24.1 utilizes the method introduced by Patankar et al. [9] for simulating problems with periodic boundary conditions.

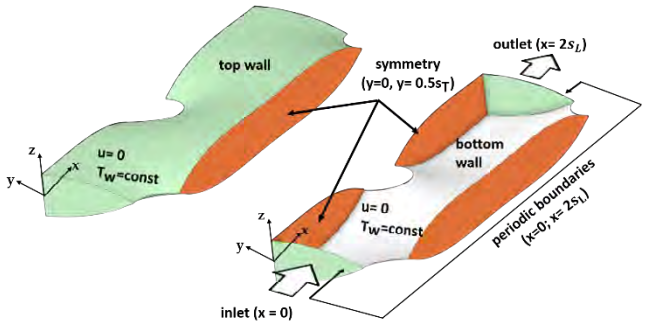



**Figure 3**: Computational domain and boundary conditions of the PP inner channel.

## Grid generation

The grid used was an unstructured poly-hexacore mesh generated with the Fluent-Meshing tool. A grid independence study was performed for all the investigated geometries. Depending on the specific geometry, different grids were generated. The grid was considered finalized when doubling the number of cells resulted in only negligible differences in pressure drop and heat transfer coefficient (less than 0.1%). The number of grid cells ranged between 36 and 42 million. For the finalized grid, the maximum value of the dimensionless wall distance ($y^+$) was about 0.05.

# THERMO-HYDRAULIC EVALUATION CRITERIA

To assess the thermo-hydraulic characteristics of the flow in PPs, the following criteria were used.

The Darcy friction factor ($\xi_{\Delta p}$) can be estimated by the Darcy-Weisbach equation:

$$\xi_{\Delta p} = \frac{2 d_h |\Delta p|}{\rho u_m^2 2 s_L} \quad (1)$$

where $u_m$ is the mean velocity in the IC, $d_h$ is its hydraulic diameter, which can be calculated by the method proposed in [7], and $\Delta p$ is the overall pressure drop, calculated as the difference between the surface-averaged pressure values at the inlet and outlet boundaries.

Using the Fanning friction factor ($\xi_R$), determined as

$$\xi_R = \frac{8 \tau_w}{\rho u_m^2} \quad (2)$$

the drag coefficient ($\xi_D$) is obtained by subtracting Eq. (2) from Eq. (1):

$$\xi_D = \xi_{\Delta p} - \xi_R \quad (3)$$

The Nusselt number is defined by:

$$Nu = \frac{h_m d_h}{\lambda} \quad (4)$$

where $\lambda$ is thermal conductivity, and $h_m$ represents the surface-averaged heat transfer coefficient which can be calculated as:

$$h_m = \frac{\dot{q}_w}{T_w - T_{bulk}} \quad (5)$$

In Eq. (5), $\dot{q}_w$ is the heat flux in the direction normal to the wall and $T_{bulk}$ is the bulk temperature:

$$T_{bulk} = \frac{\int_{A_{CS}} u T dA}{\int_{A_{CS}} u dA} \quad (6)$$

The thermo-hydraulic efficiency $\varepsilon$ is defined as a ratio of the transferred heat per unit time to the pumping power:

$$\varepsilon = \frac{\dot{Q}_w}{\dot{V} \Delta p} \quad (7)$$

where $\dot{V}$ is the volumetric flow rate, and $\dot{Q}_w$ is area-averaged wall heat flux.

The evaluation of the heat transfer coefficient and thermo-hydraulic efficiency of the studied secondary structured PPs is based on the relative deviation of these quantities from the relevant benchmark quantities:

$$Z^* = \frac{Z\,(secondary\ structures) - Z\,(benchmark)}{Z\,(benchmark)} \times 100\% \quad (8)$$

# MODEL VALIDATION

The validation of the CFD model was carried out for the benchmark geometry (PPHE without secondary structures). The comparison of the numerical results was performed with the correlations for the Darcy friction factor ($\xi_{\Delta p}$) and the Nusselt number ($Nu$) from [10].

As can be seen in Fig. 4, $\xi_{\Delta p}$ values obtained from

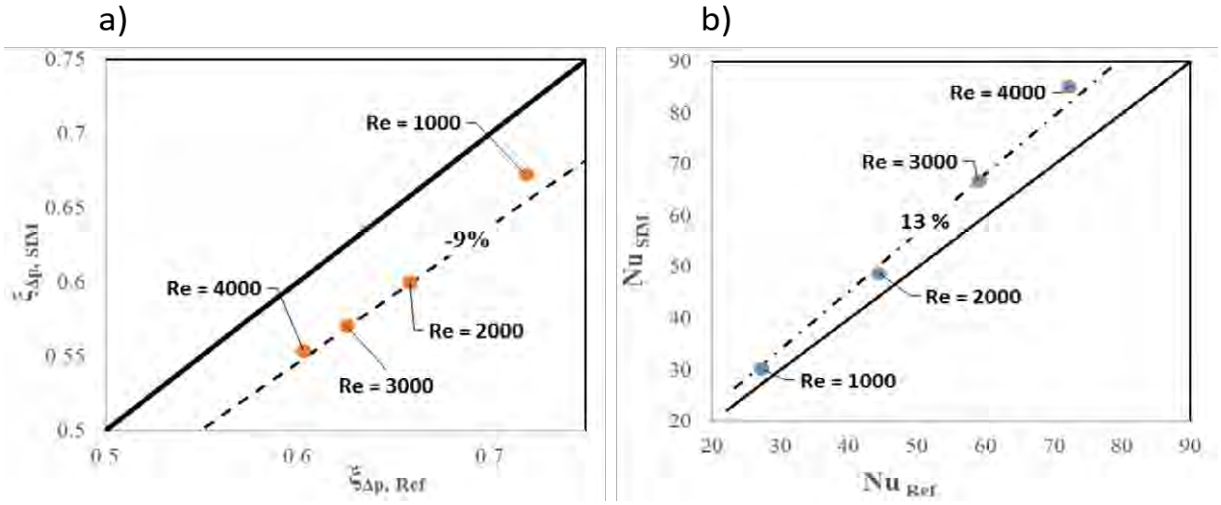



**Figure 4:** Comparison of simulated Darcy friction factor (a) and Nusselt number (b) with data obtained by correlations from [10].

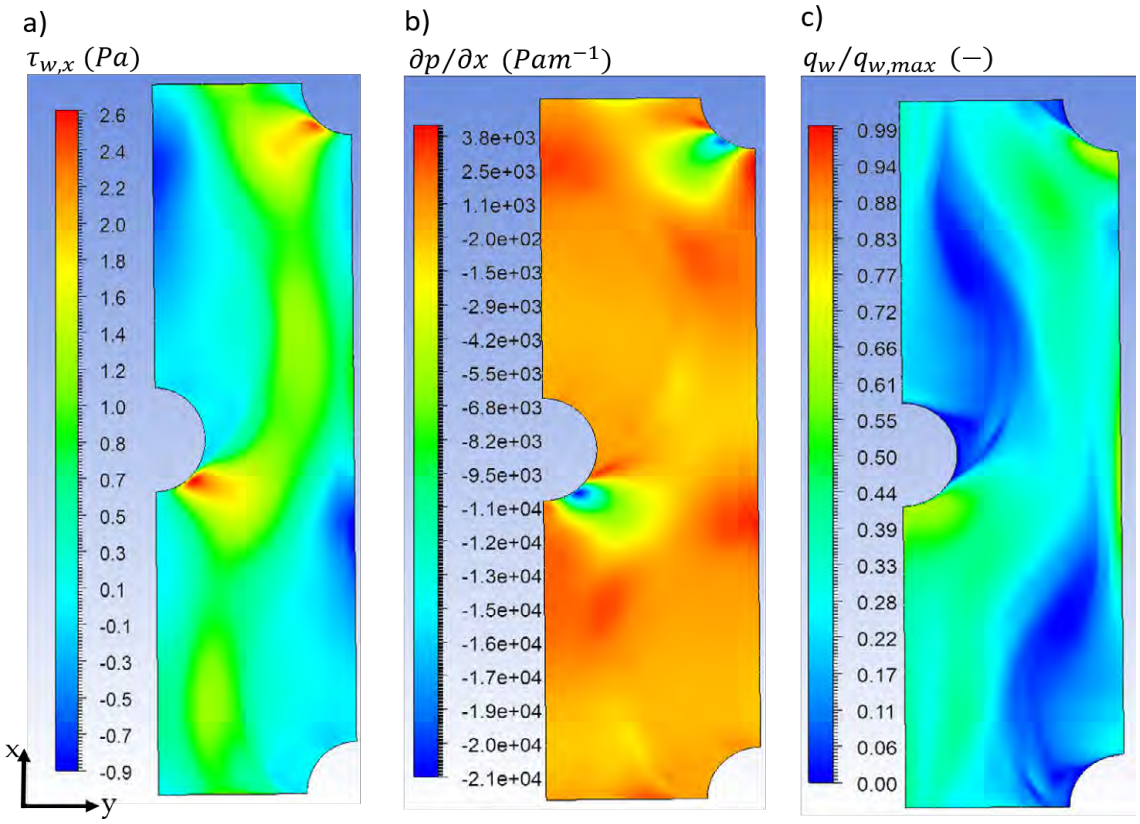



**Figure 5:** Local wall quantities: shear stress (a), pressure gradient in flow direction (b) and normalized heat flux (c).

the simulation are about 9% lower than the correlation data (Fig. 4a), while $Nu$ values are overestimated by about 13% (Fig. 4b) except for Re = 4000 which shows a higher deviation. Considering that the correlations taken from [10] have an accuracy of ±6% for the Darcy friction factor and ±15% for the Nusselt number, it can be concluded that the simulation results are within the accuracy of the correlations and, hence, the CFD model is validated.

## RESULTS AND DISCUSSION

With the validated CFD model, simulations were conducted to investigate the effect of secondary

structures on the flow characteristics and heat transfer. Results were obtained for Reynolds numbers ranging from 1000 to 3000.

In Figure 5, the simulation results of the benchmark IC are shown. The continuous variation in the cross-sectional area of the IC leads to frequent accelerations and decelerations of the flow, resulting in significant changes in wall shear stress (Fig. 5a) along the main flow direction (x-direction). At the maximum inflation height (largest cross-sectional area), the static pressure increases, leading to a positive pressure gradient in the flow direction (Fig. 5b). This causes boundary layer separation and increased form drag. As the flow approaches the welding spot, the cross-sectional area narrows, causing acceleration, a decrease in static pressure, and the development of a negative pressure gradient. The latter reaches its minimum at the stagnation point on the welding spot. Downstream of this point, another boundary layer separation occurs on the welding spot, forming recirculation zones. These zones are the primary contributors to form drag in the IC of the PP. As can be seen in Figure 5c, heat transfer in these recirculation zones is very slow, further emphasizing their detrimental impact on the overall performance.

Figure 6 shows the pressure gradient for the secondary structured PPs. These structures are located in such a way that they are aligned on the maximum inflation height. This alignment mitigates the pressure gradient variations along the main flow, resulting in milder accelerations and decelerations. Consequently, wall friction (Fanning friction factor) and form drag caused by boundary layer separation on the PP surface are reduced. As a result, the overall pressure drop for both secondary-structured PPs is lower than that of the benchmark. This reduction is demonstrated in Figure 7, which shows the Darcy friction factor defined by Eq. (1).

The secondary structures of the streamlined-ellipsoidal PP were most effective in reducing the pressure drop. For a better analysis of the impact of the secondary structures, Figure 8 depicts the Fanning friction factor and drag coefficient. It is evident that the streamlined-ellipsoidal structures primarily influence form drag. The ellipsoidal secondary structures are stretched along the flow direction, which smoothens variations in pressure gradient. This leads to lower wall shear stress (reducing Fanning friction) and minimizes regions with a positive pressure gradient, thereby mitigating boundary layer separation. The latter effect is particularly significant, as the drag coefficient for the streamlined-ellipsoidal PP is approximately 10% lower than that of the benchmark. The results for the streamlined-spherical PP reveal a different behavior compared to the streamlined-ellipsoidal design. While the Fanning friction factor remains nearly the same as for the benchmark, the drag coefficient is reduced by approximately 4%. For both secondary structured PPs, the drag coefficient was lowest at $Re = 2000$.

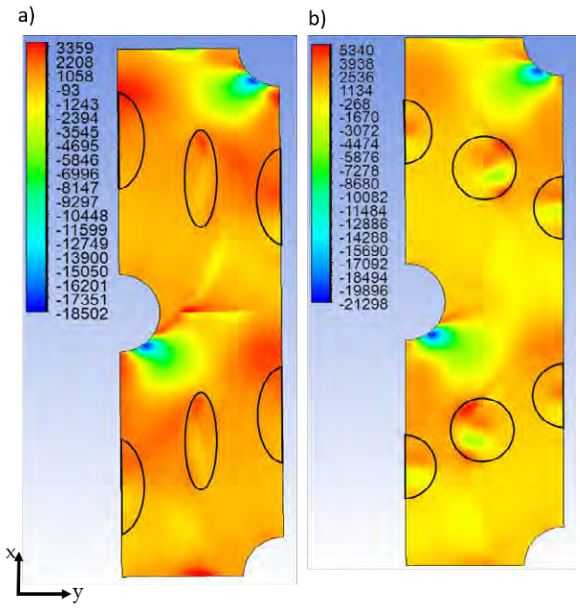



**Figure 6:** Pressure gradient in flow direction for different PPs: streamlined-ellipsoidal (a); streamlined-spherical (b). The secondary structures are denoted with black contours.

In Figure 9, the heat transfer coefficients of the secondary-structured PPs relative to the benchmark ($h^*$) are shown. While the streamlined-ellipsoidal PP effectively reduced the pressure drop, its heat transfer coefficient was lower due to lower wall friction and fluid mixing in the boundary layer. In contrast, the streamlined-spherical PP achieved higher heat transfer rate by enhancing fluid mixing in the boundary layer.

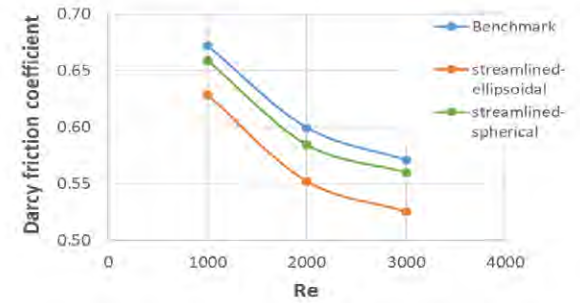



**Figure 7:** Darcy friction factor for studied PPHEs

From an industrial perspective, the thermo-hydraulic efficiency $\varepsilon$ defined by Eq. (7) provides a more meaningful performance evaluation. As shown in Figure 10, the streamlined-ellipsoidal PP consistently achieves a significant enhancement of thermo-hydraulic efficiency relative to benchmark ($\varepsilon^*$) across the entire range of studied Reynolds numbers. This indicates that the "more streamlined" secondary structures are more effective and show a high potential for optimizing the thermo-hydraulic

efficiency of PPHEs.

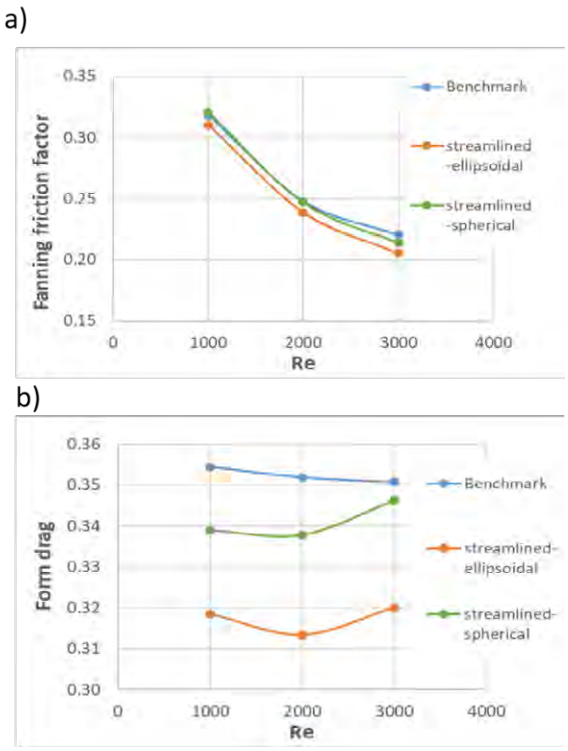



**Figure 8**: Friction coefficients: Fanning friction factor (a) and drag coefficient (b) for studied PPHEs.

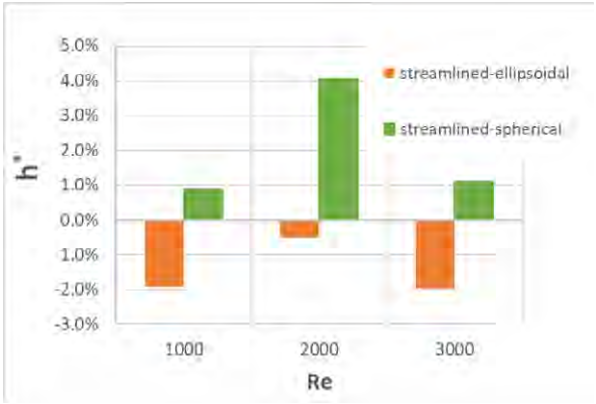



**Figure 9**: Heat transfer coefficient of the studied structured PPs relative to benchmark.

## CONCLUSION

In this work, a CFD-based study was conducted to analyse fluid flow and heat transfer in the inner channel (IC) of pillow-plate heat exchangers (PPHEs) with streamlined secondary structuring. Two designs, streamlined-ellipsoidal and streamlined-spherical, were compared with a benchmark representing an optimized PPHE geometry without secondary structures.

The streamlined-ellipsoidal design resulted in a significantly reduced pressure drop by minimizing boundary layer separation and levelling out pressure variations along the main flow direction. However, its streamlined shape resulted in lower near-wall mixing, and hence, lower heat transfer coefficient compared to the benchmark. In contrast, the streamlined-spherical design enhanced heat transfer by improving near-wall mixing but offered a lower reduction in pressure drop.

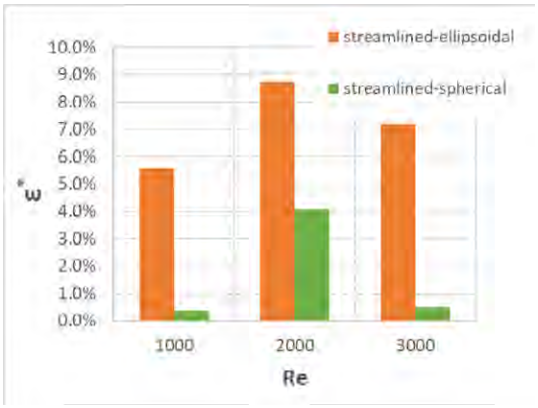



**Figure 10:** Thermo-hydraulic efficiency of the studied structured PPs relative to benchmark.

The overall performance was evaluated using thermo-hydraulic efficiency. The streamlined-ellipsoidal design outperformed both the benchmark and the streamlined-spherical design for all studied Reynolds numbers. This clearly highlights the potential of the streamlined secondary structures in optimizing the performance of the PPHEs.

Future work will focus on investigating the combined impact of secondary structuring on both inner and outer PPHE channels to allow a comprehensive optimization.

## ACKNOWLEDGEMENTS

The authors are grateful for the financial support from the German Research Foundation (DFG, Project number KE 837/46-1). Furthermore, the authors gratefully acknowledge the funding of this project by computing time provided by the Paderborn Center for Parallel Computing ($PC^2$).

## REFERENCES

1. Afsahnoudeh R., Wortmeier A., Holzmüller M., Gong Y., Homberg W., Kenig E.Y. Thermo-hydraulic performance of pillow-plate heat exchangers with secondary structuring: A numerical analysis, *Energies* 16(21):7284 (2023)
2. Piper M., Zibart A., Tran J.M., Kenig E.Y. Numerical investigation of turbulent forced convection heat transfer in pillow plates, *Int. J. Heat Mass Transfer*, 94:516–527 (2016)
3. Shirzad M., Mousavi Ajarostaghi S. S., Aghajani

Delavar M., Sedighi K. Improve the thermal performance of the pillow plate heat exchanger by using nanofluid: Numerical simulation, *Adv. Powder Technol.* 30:1356-1365 (2019)
4. Djakow E., Springer R., Homberg W., Piper M., J Tran J.M, Zibart A., Kenig E.Y. Incremental electrohydraulic forming - A new approach for the manufacturing of structured multifunctional sheet metal blanks, Proc. of the 20th International ESAFORM Conference on Material Forming (2017)
5. Piper M., Zibart A., Djakow E., Springer R., Homberg W., Kenig E. Y. Heat transfer enhancement in pillow-plate heat exchangers with dimpled surfaces: A numerical study. *Appl. Therm. Eng*. 153:142–146 (2019)
6. Hosford W.F., Caddell R.M. Metal Forming Mechanics and Metallurgy, Cambridge University Press (2011)
7. Piper M., Olenberg A., Tran J.M., Kenig E.Y. Determination of the geometric design parameters of pillow-plate heat exchangers *Appl. Therm. Eng.* 91:1168–1175 (2015)
8. Menter F.R., Smirnov P.E., Liu T., Avancha R. A one-equation local correlation-based transition model, *Flow Turbulence Combust* 95:583–619 (2015).
9. Patankar S. V., Liu C. H., Sparrow E. M. Fully developed flow and heat transfer in ducts having streamwise-periodic variations of cross-sectional area, *ASME J. Heat Transfer* 99:180-186 (1977)
10. Piper M., Zibart A., Tran J.M., Kenig E.Y. New design equations for turbulent forced convection heat transfer and pressure loss in pillow-plate channels *Int. J. Therm. Sci.* 120:459-468 (2017)

© 2025 by the authors. Licensed to PSEcommunity.org and PSE Press. This is an open access article under the creative commons CC-BY-SA licensing terms. Credit must be given to creator and adaptations must be shared under the same terms. See https://creativecommons.org/licenses/by-sa/4.0/



Systems & Control Transactions

**Research Article - Peer Reviewed Conference Proceeding**
ESCAPE 35 - European Symposium on Computer Aided Process Engineering
Ghent, Belgium. 6-9 July 2025
Jan F.M. Van Impe, Grégoire Léonard, Satyajeet S. Bhonsale,
Monika E. Polańska, Filip Logist (Eds.)

PSE PRESS

# Optimisation of Biomass-Energy-Water-Food Nexus under Uncertainty

**Md Shamsul Alam[a], I. David L. Bogle[a], Vivek Dua[a]***

[a] Department of Chemical Engineering, The Sargent Centre for Process Systems Engineering, University College London, Torrington Place, WC1E 7JE, London, UK
*Corresponding author: v.dua@ucl.ac.uk.

## ABSTRACT

The three systems, water, energy and food, are intertwined since the effect of any of these systems can affect others. This study proposes a mathematical model incorporating uncertain parameters in the biomass energy-water-food nexus system. The novel aspects of this work include formulating and solving the problem as a mixed-integer linear program and addressing the presence of uncertain parameters through a two-stage stochastic mathematical programming approach. Taking maximising economic benefit as an objective function, this work compares the results of the deterministic model with the results computed by incorporating uncertainty in the model parameters. The results indicate that incorporation of uncertainty gives rise to reduced profitability, but increased greenhouse gas emission (GHG) as compared to the deterministic model. On the other hand, when minimisation of GHG emission is considered as an objective function, a significantly greater reduction in the profitability is observed for both, stochastic and deterministic, models. The model results are used for allocating optimal resources, reducing carbon footprint, increasing economic potential and managing resources sustainably in the whole system.

**Keywords:** biomass energy, optimisation, uncertain parameters

## INTRODUCTION

The biomass energy-water-food nexus concept represents a complex interaction in managing limited resources in an innovative way [ 3, 4,11]. However, production of energy through fossil fuels is linked to global warming [1]. Achieving CO2 emission reduction target-2050 requires that the renewable energy share in electricity generation globally be increased from 29% in 2020 to over 60% in 2030 and to nearly 90% in 2050 [5]. Several studies postulate bioenergy as a cost effective and sustainable way to mitigate climate change [10,12]. Therefore, this study aims to create a mathematical model of biomass energy-water-food-nexus in the presence of uncertain parameter for optimal resource allocation. There are few studies reported on biomass-energy-water-food nexus incorporating uncertain parameters. Li *et al.* proposed a multi-objective optimisation model with a view to determining optimal policy options for the trade-off between financial benefit and environmental impact in the water-land-energy-livestock context with uncertain parameters in the nexus system [6]. Similarly, Lopez-Diaz *et al.* proposed an optimisation model to create efficient supply chain using material flow analysis among watershed, wastewater flown towards watershed, production and distribution of feedstocks, grains and biofuel [7]. Peña-Torres *et al.* proposed a multi-objective optimisation model with five different demands of resources with respect to water-food-energy nexus with a view to maximising economic benefits (EB) and reducing greenhouse gas emission (GHG) [9]. After analysing the literature, this study introduces novelties in the nexus which are described in the methods section.

## METHODS

This study incorporates two mono-objective functions: maximising economic benefit (EB) and minimising greenhouse gas (GHG) emissions. Novel aspects of this research include the addition of effluent treatment plants (ETP), the integration of rainwater harvesting systems and the implementation of solar power generation

systems across all sectors in the superstructure (figure 1). Moreover, this study has incorporated two-stage stochastic mathematical programming for managing uncertainty in the parameter. The superstructure of the system includes water subsystem comprised of water sources from power plants, aquifers, dams, rainwater and ETP. Moreover, fertiliser industry is included in the nexus for supplying fertiliser to agriculture sectors and external market.

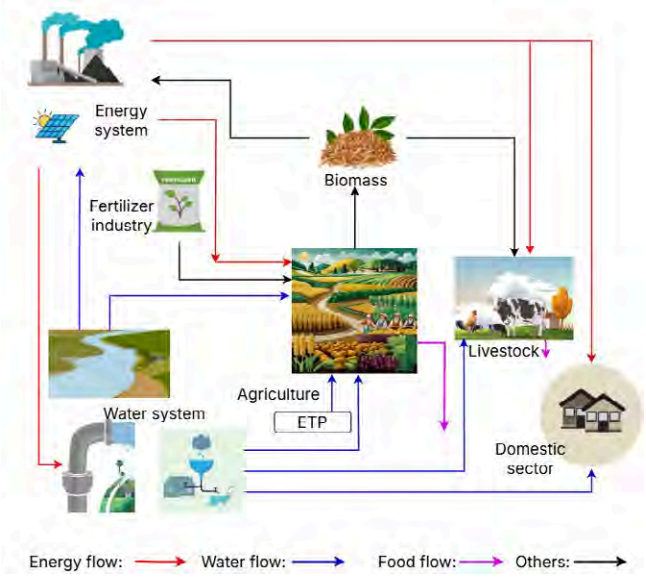



**Figure 1**: Superstructure of Biomass energy water food nexus

The energy subsystem mainly includes existing and new power plants, which utilise biomass, gasification gas and natural gas for producing electricity. On the other hand, electricity from the solar systems in each sector is used in the respective sector.

In this paper, we have generated results for each objective function separately instead of generating results for multi-objective function. The key features of the mathematical model are presented as follows:

**Objective function 1**: Maximising EB

$$Max\ EB = Revenue - TAC \quad (1)$$

**Objective function 2:** Minimising GHG

$$Min\ GHG = sum\ of\ GHG\ in\ all\ sectors \quad (2)$$

**Water mass balance:**

Amount of water remained in the sources within two time periods is equal to the sum of amount distributed and amount that already existed.

$$F_{o,t}^{Wsource} - F_{o,t-1}^{Wsource} = F_{o,t}^{existing} + \sum_A F_{o,A,t}^{Wsource-Actor} \quad (3)$$

Amount of water in actors is equal to the amount of water sent from water sources and the amount of water generated in rainwater harvesting systems.

$$F_{A,t}^{to-Actor} = \sum_o F_{o,A,t}^{WSource-Actor} + F_{A,t}^{Rain-Actor} \quad (4)$$

$$F_{A,t}^{Rain-Actor} = ARW_A . F_{A,t}^{precip} \quad (5)$$

**Energy balance:**

Amount of energy generation in unit is expressed in terms of amount of water utilised for this purpose in power plants.

$$GE_{g,t}^{Esource} = \epsilon^{fuel} . F_{g,t}^{Sea-Esource} \quad (6)$$

$$F_{g,t}^{Sea-Esource} = \omega^{water} . \left[NG_{g,t}^{Esource} + \sum_a AgWaste_{a,g,t}^{Esource} + \sum_h Gas_{h,g,t}^{Esource}\right] \quad (7)$$

Total energy in consuming bodies (actors) is equal to amount of energy flow from generation units to actor and the amount of solar energy generated in that sector.

$$E_{A,t}^{to-Actor} = \sum_g E_{g,A,t}^{Esource-Actor} + GE_{A,t}^{Solar-Actor} \quad (8)$$

$$GE_{A,t}^{Solar-Actor} = AsolarSector_A . SR_t \quad (9)$$

Domestic waste is used to produce gasification gas, which is sent to power plants for energy production and external market.

$$GGasDomWaste_{h,t} = \sum_g Gas_{h,g,t} + Gas_{h,t}^{ext} \quad (10)$$

**Food mass balance in agriculture and livestock sectors:**

Crops from agriculture sectors and meat from livestock sectors are sources of food which are distributed to domestic sectors and external markets.

$$AgL_{al,h,t}^{dom} = FoodDemand_{h,t}^{dom} \quad (11)$$

$$GRfood_{al,t}^{AgL} = AgL_{al,h,t}^{dom} + AgL_{al,t}^{ext} \quad (12)$$

**Mathematical equations related to two-stage stochastic program:**

Food demand in domestic sectors is considered as an uncertain parameter. The general formulation of two-stage stochastic program [2] is:

$$Max\ C^T x + \sum_k p_k q_k^T y_k \quad (13)$$

s.t. Ax=b

$$T_k x + W_k y_k = h_k \quad \forall k$$

$$x \geq 0, y_k \geq 0 \quad \forall k$$

Where $p_k$ is probability of occurrence of uncertain parameters, $x$ and $y_k$ are first and second stage decision variables respectively.

The following equation (14) represents that raw food flow from agriculture and livestock sectors to domestic

sector in time t is equal to uncertain food demand in domestic sector for scenario s.

$$AgL_{al,h,t}^{dom} = FoodDemand_{h,t,s}^{dom} \quad (14)$$

Similarly, total amount of food production in agriculture and livestock sectors is equal to amount sent to domestic sectors and external market for scenario s.

$$GRfood_{al,t}^{AgL} = FoodDemand_{h,t,s}^{dom} + AgL_{al,t,s}^{ext} \quad (15)$$

In this study, all decision variables, except variables related to uncertain parameter, are placed in the first stage. Ten scenarios of uncertain food demand in the domestic sectors are considered. The uncertainty is modelled through normal distribution with 20% standard deviation from the mean value. Distribution is done on twelve individual months of a year with 10 scenarios over three domestic sectors. The second stage decision variables are amount of food sent to domestic sectors and amount of food sent to the external market. The data for the base-case, deterministic model, is taken from Pena Torres *et al.* (2024) and Núñez-López, Rubio-Castro and Ponce-Ortega (2021). Both mathematical models are coded in GAMS software with CPLEX v. 22.1.0.0 solver for the MILP.

## RESULTS

This section presents results of both deterministic and two-stage stochastic solutions. Optimal solutions are presented for four cases such as deterministic solution for maximising EB, stochastic solution for maximising EB, deterministic solution for minimising GHG emission and stochastic solution for minimising GHG emission. Running the model with taking objective function as maximising EB, the stochastic solution provides 11.14% less profit (figure 2) and 3.85% higher GHG emission (figure 3) than deterministic solution. The risk associated with uncertainty is the main cause of such differences. Similarly, for minimising GHG emission cases, the stochastic solution provides 33.46% less profit (figure 2) than deterministic solution but nearly same amount of GHG emission in both models (figures 3). In four types of models, the main profit contributing agent in the system is fertiliser industry. For model with objective function 1, the revenue from fertiliser industry for stochastic solution is 4.93% higher than deterministic solution while running the model with objective function 2, it generates same amount of revenue in the fertilizer industry for both deterministic and stochastic programs (figure 4, tables 1 and 2). In the following tables and figures, monetary values are expressed in million USD and mass quantities in million tons, except for crop distribution in stochastic solution, which is expressed in tons.

**Table 1:** Optimal solution for first objective function

| Variables | Deterministic solution | Stochastic solution |
|---|---|---|
| EB | 8.54E+3 | 7.59E+3 |
| GHG | 2.27E+6 | 2.36E+6 |
| Crop supplied to domestic sectors | 2.13E-1 | second stage decision |
| Crop supplied to market | 4.23 | second stage decision |
| Revenue from fertilizer industry | 5.33E+4 | 5.59E+4 |

**Table 2:** Optimal solution for second objective function

| Variables | Deterministic solution | Stochastic solution |
|---|---|---|
| EB | 1.49E+3 | 9.91E+2 |
| GHG | 1.65E+6 | 1.65E+6 |
| Crop supplied to domestic sectors | 1.11 | second stage decision |
| Crop supplied to market | 0.00 | second stage decision |
| Revenue from fertilizer industry | 4.93E+4 | 4.93E+4 |

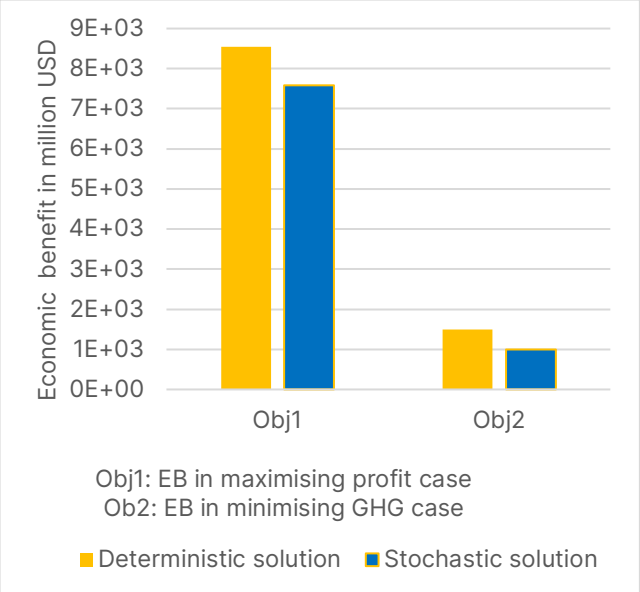



**Figure 2.** Economic benefit (EB) in two different mono-objective cases

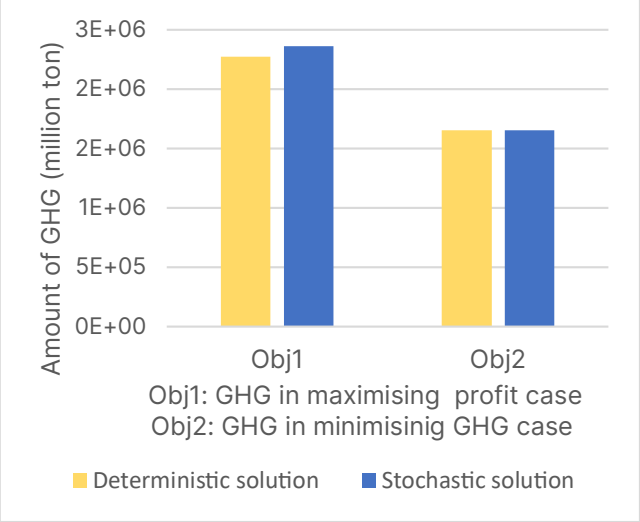



**Figure 3.** GHG emission in two different mono-objective cases

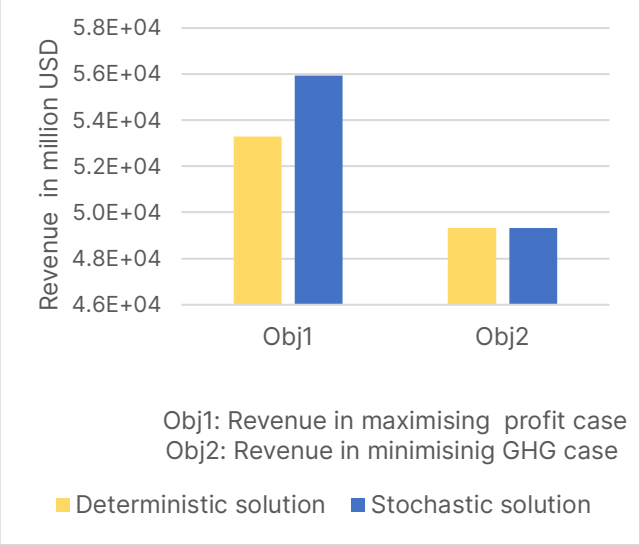



**Figure 4.** Revenue from fertilizer industry in two different mono-objective cases

Optimal number of installation decision has also been generated in this model for the four cases. The optimal number of installation decision of new power plant, gasification plant, rainwater harvesting system and solar panel for deterministic solution for maximising EB and minimising GHG emission cases are 0,0,1, 1 and 0,3,2,3 respectively; the increased number is due to focus on minimisation of GHG in the system. On the other hand, in the first stage of stochastic solution with maximising EB objective function case, the optimal number of installation decision of new power plant, gasification plant, rainwater harvesting system and solar panels are 0,0,1 and 3 respectively. However, the installation decision values become 0,3,2 and 3 respectively for minimising GHG objective function for stochastic solution. The second stage decision variables for stochastic solution are: amount of food, produced in agriculture and livestock sectors, sent to domestic sectors and amount of food sent to external market.

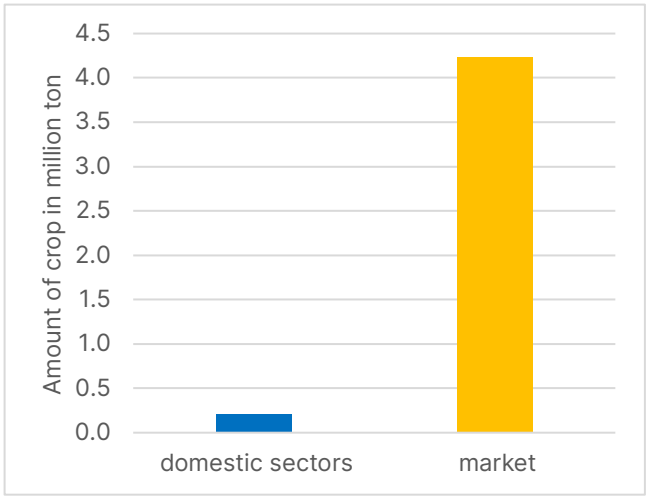



**Figure 5.** Deterministic solution: Crop supply from agriculture sectors to domestic sector and market (maximising EB case)

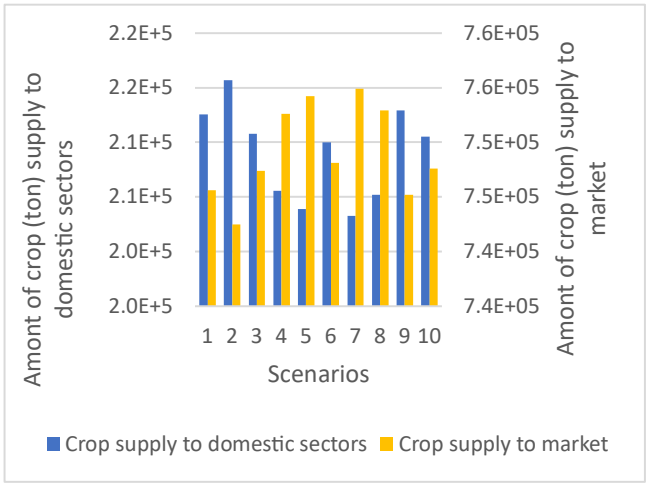



**Figure 6.** Stochastic solution: Crop supply from agriculture sectors (maximising EB case)

For all models, optimal solutions of meat production in livestock sectors are zero. For deterministic solution (scenario independent), it is found that the amount of food sent to external market is much higher than that sent to domestic sectors (figure 5). In the second stage, as soon as the demand scenario is realized, the distribution of food to domestic sectors and external market can be decided (figure 6 and 7). From the figures, it can be observed that the amount of food sent to market for the first mono objective function case is significantly higher than that amount of food sent to domestic sectors compared to second mono objective function case. Conversely, in first mono objective case, the amount of food

sent to domestic sectors is significantly lower compared to second mono objective function case (figure 6, figure 7).

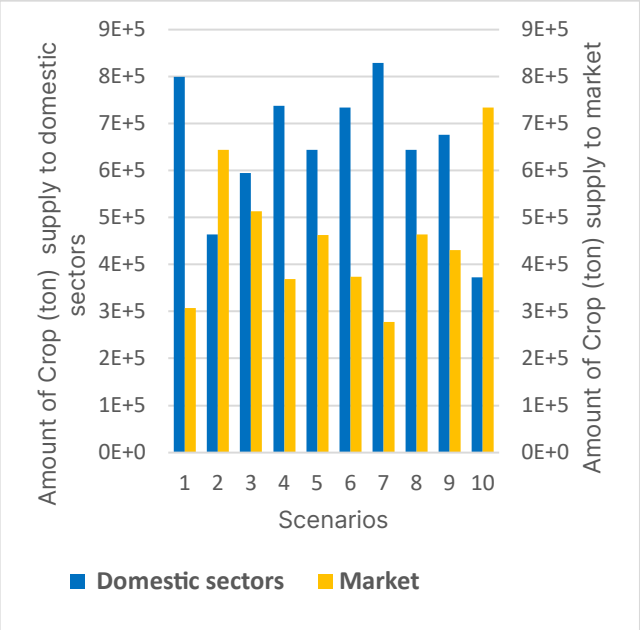



**Figure 7.** Stochastic solution: Crop supply from agriculture sectors (minimising GHG case)

## CONCLUSIONS

First and second mono objective function of this study are maximisation of economic benefit and minimisation of greenhouse gas emission respectively. Both deterministic and stochastic model have been constructed based on the first and second objective functions in the context of optimisation of biomass energy water food nexus. Running the models with objective function 1 and 2 separately, optimal solutions have been generated for four types of cases which are 1) deterministic solution for maximising EB 2) deterministic solution for minimising GHG emission 3) stochastic solution for maximising EB and 4) stochastic solution for minimising GHG emission. The obtained results are then compared. For objective function 1, two-stage stochastic program generates 11.14% less profit than deterministic solution but greenhouse gas emission is increased by 3.85% as there are risks involved in the stochastic solution due to uncertain food demand parameter. Conversely, the model incorporating objective function 2 resulted in significantly lower profit accompanied by a substantial reduction in GHG emission across both deterministic and stochastic solutions. Moreover, optimal installation decisions are different in different cases. In stage two, amount of food distribution decision is determined as soon as the demand parameter is realized. In this study, the optimal solutions of the decision variables in second stage are generated and analysed for objective functions 1 and 2.

## NOMENCLATURE

| Index | Description |
|---|---|
| o | Sources of water |
| a | Agriculture sectors |
| c | Livestock sectors |
| m | Livestock types |
| v | Crop types |
| h | Domestic sectors |
| t | Time period in months |
| A | Actor (water and energy consuming bodies) |
| g | Energy generation units other than solar panels |
| sc | Sectors such as livestock, domestic, industry, agriculture |
| al | Agriculture and livestock sector |

| Acronym | Description |
|---|---|
| AgLI | Agriculture, livestock, fertiliser industry |
| $ARW_A$ | Effective area for rainwater harvesting in the sectors |
| $AsolarSector_A$ | Effective area for solar radiation in the sectors |
| $AgL_{al,h,t}^{dom}$ | Raw food sent to domestic from agriculture and livestock sector |
| $AgL_{al,t}^{ext}$ | Raw food sent to market from agriculture and livestock sector |
| $AgL_{al,t,s}^{ext}$ | Raw food sent to market from agriculture and livestock sector in scenario s |
| EB | Economic benefit in USD |
| Esource | Electricity producing system such as power plants |
| $\epsilon^{fuel}$ | Fuel efficiency coefficient for energy production |
| $F_{A,t}^{Rain-Actor}$ | Water harvested in all sectors such as domestic, livestock |
| $F_{A,t}^{precip}$ | Rainwater precipitation flux in the sectors |
| $FoodDemand_{h,t}^{dom}$ | Amount of food required in domestic sector |
| $FoodDemand_{h,t,s}^{dom}$ | Amount of food required in domestic sector under scenario s |
| $F/E_{index}^{acronym}$ | Input variable such as water/energy flow to a system |
| GHG | Greenhouse gas emission (carbon equivalent in ton) |
| $GRfood_{al,t}^{AgL}$ | Production of raw food such as crop from agriculture and meat from livestock |

| | |
|---|---|
| $GGasDomWaste_{h,t}$ | Amount of gasification gas generated in domestic sector h |
| $Gas_{h,g,t}$ | Amount of gasification gas sent to power generation unit |
| $Gas_{h,t}^{ext}$ | Amount of gasification gas sent to external market |
| $GE_{g,t}^{Esource}$ | Energy generation in any unit |
| $GE_{A,t}^{Solar-Actor}$ | Solar energy generation in the sectors |
| $SR_t$ | Solar radiation flux in month t |
| TAC | Total annualised cost in USD |
| Wsource | Water source such as dam, deep well, aquifer, effluent treatment plant (ETP) |
| $\omega^{water}$ | Water efficiency coefficient for energy generation |

## ACKNOWLEDGEMENTS

This research is supported by "Strengthening Government through Capacity Development of the BCS Cadre Officials (Phase-II)" project implemented under the Ministry of Public Administration, Government of Bangladesh.

## REFERENCES

1. Ahmad M, Khan I, Khan MQS, Jabeen G, Jabeen HS, Isık C. Households' perception-based factors influencing biogas adoption: Innovation diffusion framework. *Energy* 263:126155 (2023). https://doi.org/10.1016/j.energy.2022.126155
2. Birge JR, Louveaux F. Introduction to Stochastic Programming. 2nd Edition. Springer Science & Business Media(2011) ISBN-13978-1461402367.
3. Chamas Z, Najm M, Hindi M, Yassine A, Khattar R. Sustainable resource optimisation under water-energy-food-carbon nexus. *J. Clean. Prod* 278: 123894 (2021). https://doi.org/10.1016/j.jclepro.2020.123894
4. Hooda PS, Edwards AC, Anderson HA, Miller AA. Review of water quality concerns in livestock farming areas. *Sci. Total Environ* 250:143-167(2000). https://doi.org/10.1016/S0048-9697(00)00373-9
5. International Energy Agency (IEA). Net Zero by 2050: A Roadmap for the Energy Sector. 3rd Edition. (2021). https://iea.blob.core.windows.net/assets/beceb956-0dcf-4d73-89fe-1310e3046d68/NetZeroby2050-ARoadmapfortheGlobalEnergySector_CORR.pdf.
6. Li M, Fu Q, Singh VP, Liu D, Li J. Optimisation of sustainable bioenergy production considering energy-food-water-land nexus and livestock manure under uncertainty. *Agricultural Syst* 184:102900(2020). https://doi.org/10.1016/j.agsy.2020.102900
7. Lopez-Diaz D, Lira-Barragan LF, Rubio-Castro E, Serna-Gonzalez M, El-Halwagi MM, Ponce-Ortega JM. Optimisation of biofuels production via a water–energy–food nexus framework. *Clean Technol and Environ Policy* 20:1443-1466(2018). https://doi.org/10.1007/s10098-017-1395-0
8. Núñez-López JM, Rubio-Castro E, Ponce-Ortega JM. Involving resilience in optimizing the water-energy-food nexus at macroscopic level. *Process Saf and Environ Protection* 147:259-273(2021). https://doi.org/10.1016/j.psep.2020.09.037
9. Peña-Torres D, Boix M, Montastruc L. Multi-objective optimisation and demand variation analysis on a water-energy-food nexus system. *Computers and Chemical Eng* 180:108473(2024). https://doi.org/10.1016/j.compchemeng.2023.108473
10. Van Vuuren DP, Bellevrat E, Kitous A, Isaac M. Bioenergy use and low stabilization scenarios. *The Energy J* 31:193–221(2010).
11. Wicaksono A, Jeong G, Kang D. Water, energy and food nexus: review of global implementation and simulation model development. *Water Policy* 19:440–462(2017). https://doi.org/10.2166/wp.2017.214
12. Zhang J, Wang S, Pradhan P, Zhao W, Fu B. Mapping the complexity of the food-energy-water nexus from the lens of sustainable development goals in China. *Resour, Conserv and Recycl* 183:106357(2022). https://doi.org/10.1016/j.resconrec.2022.106357

© 2025 by the authors. Licensed to PSEcommunity.org and PSE Press. This is an open access article under the creative commons CC-BY-SA licensing terms. Credit must be given to creator and adaptations must be shared under the same terms. See https://creativecommons.org/licenses/by-sa/4.0/

Systems & Control Transactions

**Research Article - Peer Reviewed Conference Proceeding**
ESCAPE 35 - European Symposium on Computer Aided Process Engineering
Ghent, Belgium. 6-9 July 2025
Jan F.M. Van Impe, Grégoire Léonard, Satyajeet S. Bhonsale,
Monika E. Polańska, Filip Logist (Eds.)

PSE PRESS

# A Century of Data: Thermodynamics and Kinetics for Ammonia Synthesis on Various Commercial Iron-based Catalysts

**Hilbert Keestra[a,b,*], Yordi Slotboom[a], Kevin H.R. Rouwenhorst[b,c], Derk W.F. Brilman[a]**

[a] Sustainable Process Technology, Faculty of Science and Technology, University of Twente, PO Box 217, 7500 AE Enschede, The Netherlands
[b] Catalytic Processes & Materials, MESA+ Institute for Nanotechnology, University of Twente, PO Box 217, 7500 AE Enschede, the Netherlands
[c] Ammonia Energy Association, 77 Sands Street, 6th Floor, Brooklyn, NY 11201, USA
* Corresponding Author: h.keestra@utwente.nl

## ABSTRACT

This work presents an improved thermodynamic model, an equilibrium model, and a unified kinetic model for ammonia synthesis. The thermodynamic model accurately describes the non-ideality of the reaction system up to 1000 bar using a modified Soave-Redlich-Kwong Equation-of-State. The developed Langmuir-Hinshelwood kinetic model accurately describes ammonia synthesis on iron-based catalysts by incorporating N* and H* surface species, whereas H* species are mainly relevant below 400°C. The model fits an extensive dataset across diverse conditions (251-550°C, 1-324 bar, $H_2/N_2$ ratios 0.33-8.5, and space velocities of 1-1800 $Nm^3$ kg-$cat^{-1}$ $h^{-1}$) and accounts for catalyst activity variations through a Relative Catalytic Activity factor.

**Keywords**: Ammonia, Steady-state kinetics, iron catalyst

## INTRODUCTION

Ammonia, with a global demand of 185 Mt in 2020 [1], serves as both a crucial fertilizer component and a promising zero-carbon fuel and hydrogen carrier [2, 3]. Its production via the Haber-Bosch process (Equation 1) relies on iron-based catalysts operating at 350-500°C and 100-300 bar [4]. These catalysts, derived from magnetite ($Fe_3O_4$) or wüstite ($Fe_{1-x}O$) precursors, incorporate electronic promoters ($K_2O$) and structural promoters ($Al_2O_3$, MgO, $SiO_2$, CaO) to enhance activity and stability [5, 6].

$$3H_2 + 1N_2 \leftrightarrow 2NH_3 \;\; with \;\; \Delta H_r^\circ = -92\ \mathrm{kJ/mol} \qquad (1)$$

While various kinetic models exist for ammonia synthesis [7–10], they are typically based on single-catalyst datasets. This work introduces a comprehensive kinetic model applicable across commercial catalysts at diverse conditions (251-550°C, 1-324 bar), utilizing 11 datasets [7, 8, 10–14] spanning both magnetite and wüstite precursors. The model assumes that despite varying active site densities, the underlying reaction mechanism remains the same across catalysts, with differences in activity addressed through a Relative Catalytic Activity (RCA) correction factor.

Several optimization algorithms were evaluated to fit the kinetic parameters, including Particle Swarm Optimization (PSO), Differential Evolution (DE), Nelder-Mead, compact Genetic Algorithm (cGA), Cobyla, and Powell. The Covariance Matrix Adaptation Evolution Strategy (CMA-ES) proved superior, being the only algorithm to consistently converge to the global minimum across multiple initialization points, likely due to its mechanism to escape local minima in the complex parameter landscape of the kinetic model.

The datasets include various $H_2/N_2$ ratios and space velocities, making it particularly relevant for renewable ammonia plants with fluctuating hydrogen feedstock. In addition to the kinetic model, a simplified Arrhenius-type equilibrium description is presented for industrial temperature ranges (300-550°C), employing a modified Soave-Redlich-Kwong Equation-of-State with the Mathias alpha function using a polarity correction factor of 0.2368 for ammonia.

## THERMODYNAMICS

At high pressures, accurate ammonia synthesis thermodynamics requires an Equation of State (EoS) to account for gas non-ideality [15]. While the Soave-Redlich-Kwong (SRK) EoS is widely used, it poorly describes the polarity of molecules like ammonia at high pressures [16]. This work employs a modified SRK with a polarity correction factor, based on the Mathias alpha function [17], to overcome this limitation.

Existing alternatives to describe the non-ideality, such as Dyson and Simon's polynomials [18] or other EoS [19, 20], lack universal applicability because they are either difficult to implement in commercial flowsheeting software or are inaccurate at high pressures. To address this, a nested fitting method was developed to determine the polarity correction factor in the Mathias alpha function for the SRK EoS. The method was applied to equilibrium data in the range of 300-1100 °C and up to 1000 bar from multiple literature sources.

The resulting equilibrium expression uses a second-order polynomial for reaction enthalpy, simpler than previous higher-order approaches. For practical implementation in software like Aspen HYSYS, we also derived a simplified Arrhenius-type equation valid for 300-550 °C:

$$ln(K_f) = \frac{1}{R}\left(-33.415 - \frac{-4.4401 \cdot 10^4}{T} - 10.578\, ln(T)\right) \quad (2)$$

$$K_f = 1.3632 \cdot 10^{-6} e^{\left(-\frac{-5.1110 \cdot 10^4}{RT}\right)} \quad (3)$$

$$\frac{1}{K_f^2} = 5.3809 \cdot 10^{11} e^{\left(-\frac{1.0222 \cdot 10^5}{RT}\right)} \quad (4)$$

The fitting procedure employs the COBYLA algorithm [21] to optimize the polarity correction factor by minimizing Mean Squared Error, with convergence defined as no improvement beyond the 10th decimal place after 10 iterations.

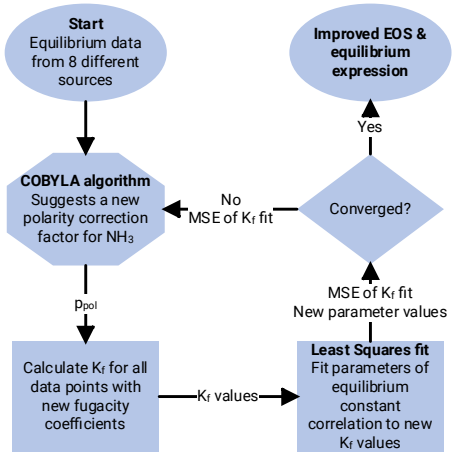



**Figure 1.** Schematic for the nested fitting method to obtain the polarity correction factor for NH3 and to fit the parameter values of the temperature-dependent equilibrium constant correlations.

The polarity correction factor for $NH_3$ was fitted to -0.2368 while the polarity factor of the other molecules were kept at zero.

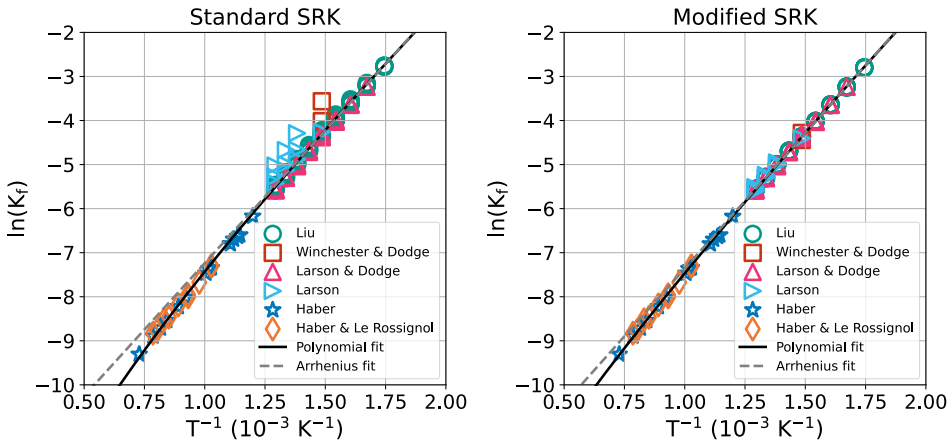



**Figure 2:** Equilibrium constant prediction by the polynomial (fitted to 300-1100 °C data) and Arrhenius type equation (fitted to 300-550 °C data) without (left) and with (right) polarity correction.

## KINETIC MODELLING

### Model derivation

The dissociation of surface-adsorbed dinitrogen to atomic nitrogen (Reaction 2 in Table 1) is the rate-determining step for ammonia synthesis on iron-based catalysts [22–24].

**Table 1:** The microkinetic reactions for ammonia synthesis.

| Number | Microkinetic reactions |
|---|---|
| 1 | $N_2(g) + * \leftrightarrow N_2*$ |
| 2 | $N_2* + * \leftrightarrow 2N*$ |
| 3 | $N* + H* \leftrightarrow NH* + *$ |
| 4 | $NH* + H* \leftrightarrow NH_2* + *$ |
| 5 | $NH_2* + H* \leftrightarrow NH_3* + *$ |
| 6 | $NH_3* \leftrightarrow NH_3(g) + *$ |
| 7 | $H_2(g) + 2* \leftrightarrow 2H*$ |

Molecular nitrogen dissociation (reaction 2 in Table 1) was taken as the rate-determining step, and N* and H* were taken as the most abundant surface species on the active sites of the catalyst [25]. A correction factor ($b_{cat}$) for activity differences between different catalysts was implemented. The derived kinetic model is given in Equation 5,

$$r_{NH_3} = b_{cat} k_{NH_3} f_{N_2} \left(1 - \frac{1}{K_f^2} \frac{f_{NH_3}^2}{f_{N_2} f_{H_2}^3}\right) \left(1 + \frac{f_{NH_3}}{K_N f_{H_2}^{1.5}} + \sqrt{K_H f_{H_2}}\right)^{-2} \quad (5)$$

where $f_i$ stands for the fugacity of a component which is calculated using the modified SRK with the unit bar. $K_f$ is the equilibrium constant calculated using Equation 3. And $r_{NH_3}$ is expressed in mol kg$^{-1}$ s$^{-1}$. $K_N$ and $K_H$ are adsorption constants for the N* and H* surface species. The adsorption constants and $k_{NH_3}$ follow an Arrhenius relationship and contain, thus, two parameters each.

### Modelling procedure

11 datasets found in Refs. [7, 8, 10, 11, 13, 14, 26] with a total of 1019 data points were fitted to the model in Equation 5, over a wide range of temperatures (251-550°C), pressures (1-324 bar), space velocities (1-1800 Nm$^3$ kg-cat$^{-1}$ h$^{-1}$ at NTP (25 °C and 1 atm)), and $H_2/N_2$ ratios (0.33-8.5). Only the gas-hour space velocity data were reported for the Fixed Nitrogen No. 660, Temkin & Phyzev, and Fixed Nitrogen Cat. A catalysts. Therefore, the density of those catalysts was assumed to be 3 g cm$^{-3}$.

The reactor was modelled as an isothermal plug-flow reactor. Due to the wide range of conditions and different orders in magnitude in measured $NH_3$ molar fractions, a type of normalisation was applied to the objective function. The objective function for the fitting is defined in Equation 6 and 7.

$$\chi^2 = \sum_{j=1} \sigma_j \left(\frac{y_{NH_3,j} - \hat{y}_{NH_3,j}}{y^d_{NH_3,\max}}\right)^2 \quad (6)$$

$$\sigma_j = \frac{1}{N_n} \; with \; j \in N_n \quad (7)$$

Where $y^d_{NH_3,\max}$ is the maximum value of the molar fraction in the dataset. Datasets were equally taken into account by calculating a weight ($\sigma_j$) so that the sum of all the weights in a sub-dataset ($N_n$) was equal to 1. Therefore, there is no bias towards larger datasets.

To improve the predictive capabilities of the model, 5-fold cross-validation was applied. Furthermore, the cross-correlation between parameters was reduced by applying the reference temperature approach by Schwaab et al. [27, 28].

### Optimization algorithm selection

Various optimization algorithms were tested to fit the kinetic parameters, including Particle Swarm Optimization (PSO), Differential Evolution (DE), Nelder-Mead, the compact Genetic Algorithm (cGA), COBYLA, and Powell. Among them, the Covariance Matrix Adaptation Evolution Strategy (CMA-ES) with a scale factor of 2.5 demonstrated superior performance, consistently converging to the global minimum across multiple initialization points. This performance is due to its ability to escape local minima in the complex parameter landscape of the kinetic model. The settings for the other algorithms followed the default configurations provided by the Nevergrad [29] optimization package from Meta Inc.

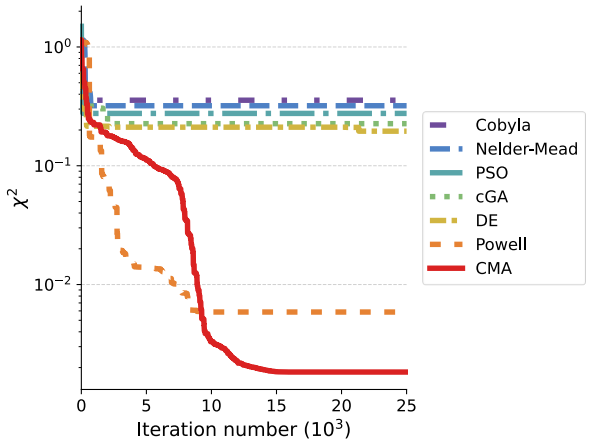



**Figure 3.** Progression of the optimization algorithms. The displayed error represents the lowest error found up to and including the corresponding iteration number.

### Overall fitting results

The calculated parameters for $k_{NH_3}$, $K_N$ and $K_H$ for the kinetic model are listed in Table 2. And the parameters for the Relative Catalytic Activity factors are found in

Figure 4.

**Table 2:** Calculated parameters with 95% confidence interval for the kinetic model.

| Parameter | Value | ± 95% CI | Unit |
|---|---|---|---|
| $k_{NH_3,A}$ | 2.215E+13 | 7.624E+13 | mol kg-cat$^{-1}$ bar$^{-1}$ s$^{-1}$ |
| $k_{NH_3,B}$ | 1.007E+05 | 7.876E+03 | J mol$^{-1}$ |
| $K_{N,A}$ | 2.455E-08 | 6.474E-08 | bar$^{-0.5}$ |
| $K_{N,B}$ | -1.795E+04 | 3.365E+03 | J mol$^{-1}$ |
| $\sqrt{K_{H,A}}$ | 3.276E+02 | 4.271E+02 | bar$^{-0.5}$ |
| $\sqrt{K_{H,B}}$ | -4.948E+03 | 4.887E+03 | J mol$^{-1}$ |

A parity plot comparing the experimental and predicted $NH_3$ mole fractions, based on the kinetic model in Equation 5 and the parameters from Table 2, is presented in Figure 4 (Left). This plot incorporates data from 11 datasets featuring different metal oxide precursors, including magnetite and wüstite. The strong agreement between experimental and predicted $NH_3$ mole fractions supports the hypothesis that all iron-based catalysts reported in literature exhibit similar behavior under operational conditions with respect to temperature and pressure. The primary variations arise from differences in the density of active sites and the effectiveness of promoters, which can be accounted for using a correction factor $b_{cat}$ for catalytic activity.

Multiple models were fitted using the same procedure, and their fitting quality metrics are presented in Table 3. The modified Temkin model, as described by Dyson and Simon [18], features the fewest parameters but exhibits the lowest fit quality, making it more suitable for a narrow operating range. When the model in Equation 5 assumes only N* species, it closely aligns with the model proposed by Nielsen et al. [7]. Substituting partial pressures for fugacities, as implemented by Sehested et al. [8], reduces the fit quality by approximately 20%.

**Table 3:** Statistical results for the fitted models.

| Model | Surface species | MSE | $\chi^2$ |
|---|---|---|---|
| Temkin (modified) | - | 2.55E-04 | 3.75E-03 |
| This work | N | 1.27E-04 | 1.67E-03 |
| This work (partial pressure) | N, H | 4.83E-05 | 7.77E-04 |
| This work | N, H | 4.05E-05 | 6.11E-04 |

## CONCLUSION

The modified Soave-Redlich-Kwong Equation-of-State, incorporating a polarity correction factor of -0.2368 for $NH_3$, effectively accounts for polarity effects at high pressure and accurately describes equilibrium up to 1000 bar. The developed Arrhenius-type equilibrium model and the unified Langmuir-Hinshelwood kinetic model are easily implemented in all commercial flowsheeting software.

The kinetic model successfully describes all available data using a single rate expression and a Relative Catalytic Activity factor per catalyst, capturing variations in active site density and promoter effects. This suggests that ammonia synthesis follows a highly similar mechanism for all iron-based catalysts, regardless of precursor, promoter, or preparation method. The model accurately predicts ammonia synthesis across a broad range of

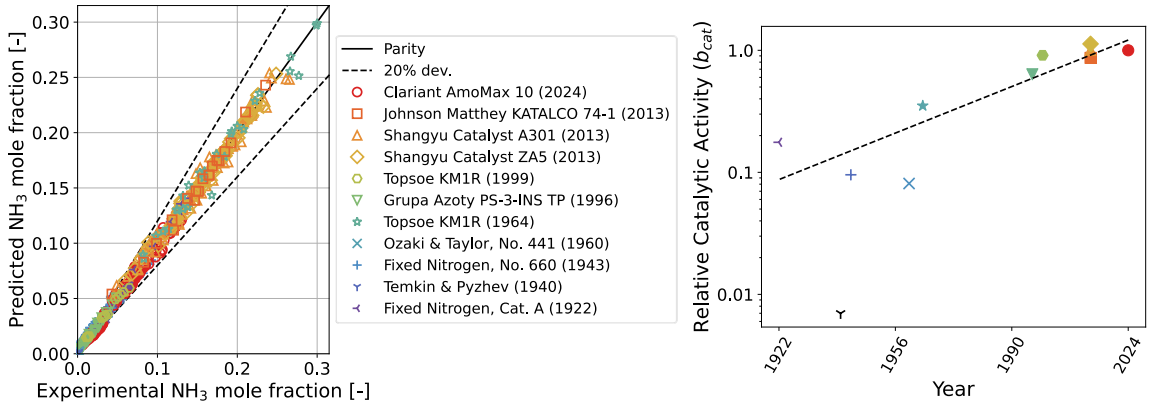



**Figure 4:** Left: Parity plot of the experimental $NH_3$ mole fraction in the outlet from Refs. [7, 8, 10, 11, 13, 14, 26] versus predicted $NH_3$ mole fraction for the same conditions using the model in Equation 5. Right: The calculated Relative Catalytic Activity ($b_{cat}$) for various datasets. The regression line excludes the Temkin & Pyzhev catalyst because this was the only non-promoted iron catalyst.

conditions (251–550 °C, 1–324 bar, $H_2/N_2$ ratios of 0.33–8.5, and space velocities of 1–1800 $Nm^3\ kg\text{-}cat^{-1}\ h^{-1}$). The inclusion of H* surface species are necessary to extrapolate to lower temperatures (<400 °C).

To optimize kinetic parameters, various algorithms were tested, with CMA-ES outperforming others by consistently converging to the global minimum due to its ability to escape local minima in the complex parameter landscape.

This work consolidates over a century of equilibrium and kinetic data for ammonia synthesis using iron-based catalysts with improved and more robust thermodynamic and kinetic models.

## ACKNOWLEDGEMENTS

The authors thank the PROVE-IT consortium (RVO MOOI42014) for providing the financial grants for this research. The authors thank Aayan Banerjee, Jimmy Faria, Leon Lefferts, and Sascha Kersten from the University of Twente for the valuable discussions. Furthermore, Tim van Schagen is thanked for their input on the modeling framework.

## REFERENCES

1. IRENA, Ammonia Energy Association (2022) Innovation Outlook: Renewable Ammonia. https://doi.org/978-92-9260-423-3
2. Rouwenhorst KHR, Van Der Ham AGJ, Mul G, Kersten SRA (2019) Islanded ammonia power systems: Technology review & conceptual process design. Renewable and Sustainable Energy Reviews. https://doi.org/10.1016/j.rser.2019.109339
3. IRENA (2021) Innovation Outlook: Renewable Methanol.
4. Liu H (2014) Ammonia synthesis catalyst 100 years: Practice, enlightenment and challenge. Cuihua Xuebao/Chinese Journal of Catalysis 35:1619–1640
5. Nielsen A (1995) Ammonia: Catalysis and Manufacture, 1st ed. Springer-Verlag, Berlin Heidelberg
6. Liu H, Han W (2017) Wüstite-based catalyst for ammonia synthesis : Structure , property and performance. Catal Today 297:276–291
7. Nielsen A, Kjaer J, Hansen B (1964) Rate equation and mechanism of ammonia synthesis at industrial conditions. J Catal 3:68–79
8. Sehested J, Jacobsen CJH, Törnqvist E, Rokni S, Stoltze P (1999) Ammonia Synthesis over a Multipromoted Iron Catalyst: Extended Set of Activity Measurements, Microkinetic Model, and Hydrogen Inhibition. J Catal. https://doi.org/10.1006/jcat.1999.2628
9. Temkin M, Pyzhev V (1940) Kinetic of Ammonia Synthesis on Promoted Iron Catalysts. Acta Physicochimica URSS 12:327–356
10. Ozaki A, Taylor H, Boudart M (1960) Kinetics and Mechanism of the Ammonia Synthesis. Proceedings of the Royal Society A: Mathematical, Physical and Engineering Sciences 258:47–62
11. Liu H (2013) Ammonia Synthesis Catalysts: Innovation and Practice. https://doi.org/10.1142/8199
12. Aparicio LM, Dumesic JA (1994) Ammonia synthesis kinetics: Surface chemistry, rate expressions, and kinetic analysis. Top Catal. https://doi.org/10.1007/BF01492278
13. Cholewa T, Steinbach B, Heim C, Nestler F, Nanba T, Güttel R, Salem O (2024) Reaction kinetics for ammonia synthesis using ruthenium and iron based catalysts under low temperature and pressure conditions. Sustain Energy Fuels 8:2245–2255
14. Emmett PH, Kummer JT (1943) Kinetics of Ammonia Synthesis. Ind Eng Chem 35:677–683
15. Soave G (1972) Equilibrium constants from a modified Redlich-Kwong equation of state. Chem Eng Sci 27:1197–1203
16. Graboski MS, Daubert TE (1979) A Modified Soave Equation of State for Phase Equilibrium Calculations. 3. Systems Containing Hydrogen. Industrial and Engineering Chemistry Process Design and Development 18:300–306
17. Mathias PM (1983) A Versatile Phase Equilibrium Equation of State. Industrial and Engineering Chemistry Process Design and Development 22:385–391
18. Dyson DC, Simon JM (1968) Kinetic Expression with Diffusion Correction for Ammonia Synthesis on Industrial Catalyst. Industrial & Engineering Chemistry Fundamentals 7:605–610
19. Beattie JA, Bridgeman OC (1928) A New Equation of State for Fluids. Proceedings of the American Academy of Arts and Sciences 63:229
20. Peng DY, Robinson DB (1976) A New Two-Constant Equation of State. Industrial and Engineering Chemistry Fundamentals 15:59–64
21. Powell MJD (1994) A Direct Search Optimization Method That Models the Objective and Constraint Functions by Linear Interpolation. Advances in Optimization and Numerical Analysis 51–67
22. Aika K-I (2017) Role of alkali promoter in ammonia synthesis over ruthenium catalysts—Effect on reaction mechanism. Catal Today 286:14–20
23. Mortensen JJ, Hansen LB, Hammer B, Nørskov JK (1999) Nitrogen Adsorption and Dissociation on Fe(111). J Catal 182:479–488
24. Ertl G, Lee SB, Weiss M (1982) Adsorption of nitrogen on potassium promoted Fe(111) and (100) surfaces. Surf Sci 114:527–545

25. Sehested J, Jacobsen CJH, Törnqvist E, Rokni S, Stoltze P (1999) Ammonia Synthesis over a Multipromoted Iron Catalyst: Extended Set of Activity Measurements, Microkinetic Model, and Hydrogen Inhibition. J Catal 188:83–89
26. Kowalczyk Z (1996) Effect of potassium on the high pressure kinetics of ammonia synthesis over fused iron catalyst. Catal Letters 37:173–179
27. Schwaab M, Pinto JC (2007) Optimum reference temperature for reparameterization of the Arrhenius equation. Part 1: Problems involving one kinetic constant. Chem Eng Sci 62:2750–2764
28. Schwaab M, Lemos LP, Pinto JC (2008) Optimum reference temperature for reparameterization of the Arrhenius equation. Part 2: Problems involving multiple reparameterizations. Chem Eng Sci 63:2895–2906
29. Bennet P, Doerr C, Moreau A, Rapin J, Teytaud F, Teytaud O (2021) Nevergrad. ACM SIGEVOlution 14:8–15

© 2025 by the authors. Licensed to PSEcommunity.org and PSE Press. This is an open access article under the creative commons CC-BY-SA licensing terms. Credit must be given to creator and adaptations must be shared under the same terms. See https://creativecommons.org/licenses/by-sa/4.0/



Systems & Control Transactions

**Research Article - Peer Reviewed Conference Proceeding**
ESCAPE 35 - European Symposium on Computer Aided Process Engineering
Ghent, Belgium. 6-9 July 2025
Jan F.M. Van Impe, Grégoire Léonard, Satyajeet S. Bhonsale,
Monika E. Polańska, Filip Logist (Eds.)

PSE PRESS

# Reaction Pathway Optimization Using Reinforcement Learning in Steam Methane Reforming and Associated Parallel Reactions

**Martín Rodríguez-Fragoso[a], Octavio Elizalde-Solis[a], and Edgar Ramírez-Jiménez[a]***

[a] Department of Chemical Petroleum Engineering, ESIQIE, Instituto Politécnico Nacional, Mexico City, 07738, Mexico
* Corresponding Author: eramirezj@ipn.mx.

## ABSTRACT

This study presents the application of a Q-learning algorithm to optimize the selection of chemical reactions for methane reforming processes. Starting with a set of 11 candidate reactions, the algorithm identified three key reactions. These reactions effectively represent the experimental data while aligning with the underlying physics of the process and previously reported findings. The algorithm employed an epsilon-greedy policy to balance exploration and exploitation during the training process. Furthermore, simulations based on the identified reactions revealed trends consistent with experimental data. This work highlights the efficiency and adaptability of Q-learning in modeling complex catalytic systems and provides a framework for further exploration and optimization of methane reforming processes.

**Keywords**: Methane Reforming, Machine Learning, Optimization, Reaction Engineering, Reinforce Learning

## INTRODUCTION

Methane reforming is one of the key technologies for hydrogen production, an essential energy carrier in the transition toward cleaner energy systems. This process involves a series of simultaneous and coupled chemical reactions, among which Methane Steam Reforming (MSR) and the Water Gas Shift (WGS) reaction are particularly noteworthy. However, the complex and highly nonlinear nature of these reactions poses a significant challenge for process modeling and optimization.

Traditionally, kinetic models used to describe such processes are based on a fixed set of reaction rate equations derived from the Arrhenius equation. While this approach has proven effective in many cases, it can be limited when dealing with systems where operating conditions or predominant reaction pathways change significantly, such as in catalytic reforming in refineries, hydrodesulfurization, and fluid catalytic cracking (FCC). In this context, there is a need for tools capable of dynamically identifying the most relevant combinations of reactions to represent experimental data [1].

Reinforcement learning algorithms, such as Q-learning, offer a novel and powerful approach to tackle this problem [2]. These techniques enable the exploration and exploitation of potential solution spaces, iteratively learning optimal decisions based on a defined reward function. For methane reforming, the use of Q-learning facilitates the selection of reactions that best describe experimental data under varying temperature conditions, while simultaneously optimizing the associated kinetic constants.

This work describes the implementation of a Q-learning algorithm to identify the key reactions within an initial set of 11 reactions considered relevant for methane reforming. Based on this selection, the algorithm fits the experimental data using a model grounded in the Arrhenius equation.

This methodology not only contributes to a better understanding of the most significant reaction pathways but also opens new possibilities for optimizing the design and operation of complex catalytic processes.

## METHODOLOGY

### Q-Learning Framework

To optimize reaction pathways, a framework based on

reinforcement learning is adopted, utilizing a Q-learning process, as illustrated in Fig. 1. A $\epsilon$-greedy policy is defined due to its ability to balance exploration and exploitation. This approach allows the agent to explore new actions with a probability controlled by the epsilon ($\epsilon$) parameter while prioritizing actions with known rewards as learning progresses. This helps avoid suboptimal solutions that could arise from premature exploitation of the environment.

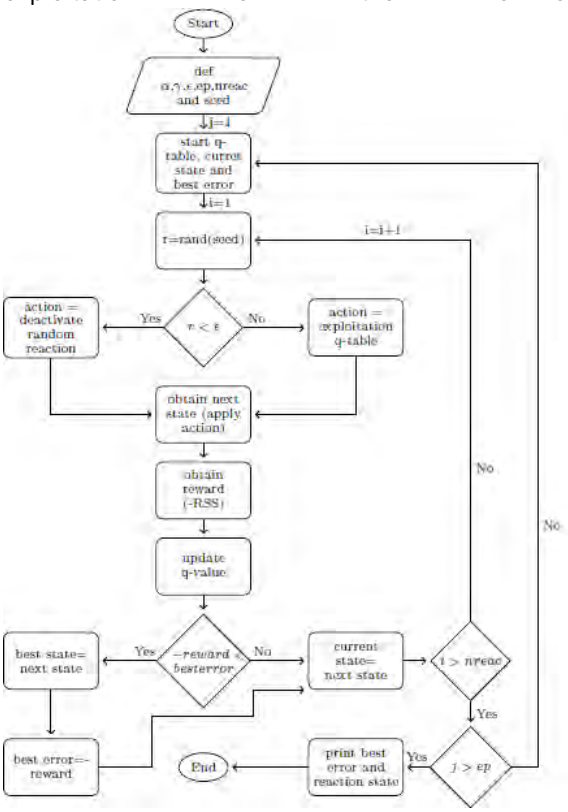



**Figure 1.** Proposed Methodology to select reactions.

This method relies on the iterative updating of Q values using the equation:

$$\mathrm{Q(s,a)} \leftarrow \mathrm{Q(s,a)} + \alpha\left[\mathrm{r} + \gamma \max_{\mathrm{a'}} \mathrm{Q}\,(\mathrm{s'},\mathrm{a'}) - \mathrm{Q(s,a)}\right] \quad (1)$$

Based on this equation, the parameters $\alpha$, $\gamma$, and $\epsilon$ must be defined considering the following criteria:

The learning rate ($\alpha$) controls how much the $Q(s,a)$ values are updated in each iteration. A low $\alpha$ ensures that updates are gradual, reducing the risk of abrupt oscillations in $Q(s,a)$. However, this may slow down convergence. This parameter directly affects the adjustment term:

$$\alpha\left[r + \gamma \max_{a'} Q\,(s',a') - Q(s,a)\right] \quad (2)$$

The parameter $\epsilon$ defines the exploration probability. At the beginning of the learning process, a high $\epsilon$ encourages exploration of the state space to avoid suboptimal local solutions. During training, the value of $\epsilon$ is dynamically adjusted according to:

$$\epsilon_{i+1} = \begin{cases} \epsilon_i * 0.99, & i < 10 \\ 0.1, & i \geq 10 \end{cases} \quad (3)$$

This adjustment allows for a controlled transition from an intensive exploration phase to more consistent exploitation in the final stages of training.

The discount factor ($\gamma$) determines the weight of future rewards. A high $\gamma$ prioritizes long-term rewards, favoring globally optimal strategies. This parameter affects the term:

$$\alpha\gamma \max_{a'} Q\,(s',a') \quad (4)$$

The values of the parameters used in this work for the Q-learning algorithm are summarized in Table 1.

**Table 1:** Q-learning Selected Parameters.

| Parameter | Value |
|---|---|
| Episodes | 30.00 |
| α | 0.10 |
| $\varepsilon_{in}$ | 0.95 |
| $\gamma$ | 0.90 |

This parameter configuration is designed to achieve a balance between learning stability, initial exploration, and efficient exploitation in advanced stages.

## Experimental Data

The experimental data used in this work were reported by Akers et al. [3] This dataset consists of five runs. The first four runs were conducted at the same temperature, varying the methane-to-water feed ratio. The experiments were performed at different reaction times. The reaction time for methane is directly proportional to the amount of catalyst and inversely proportional to the methane feed rate. This reaction time is expressed as a time factor, defined as the weight of the catalyst divided by the natural gas feed rate, expressed in moles per second.

**Table 2:** Experimental Sets Conditions

| *Set* | T [K] | Input molar ratio $\left(\frac{H_2O}{CH_4}\right)$ | W/F$_{max}$ $\left[\frac{kg \cdot s}{mol}\right]$ |
|---|---|---|---|
| 1 | 910 | 10:1 | 1.10× $10^{-3}$ |
| 2 | 910 | 5:1 | 7.00× $10^{-4}$ |
| 3 | 910 | 3.5:1 | 7.00× $10^{-4}$ |
| 4 | 910 | 2.5:1 | 7.00× $10^{-4}$ |
| 5 | 609 | 3:1 | 3.00× $10^{-4}$ |
| 6 | 671 | 3:1 | 3.00× $10^{-4}$ |
| 7 | 723 | 3:1 | 3.00× $10^{-4}$ |
| 8 | 779 | 3:1 | 3.00× $10^{-4}$ |

The fifth run aims to highlight the effect of temperature. For this purpose, the feed ratio and reaction time

were kept constant, while the temperature varied. A summary of the experimental data is presented in Table 2.

Since the catalyst was not used for more than 5 hours, its activity is assumed to remain constant for all runs conducted at the same temperature.

A total of 188 experimental data points is available, corresponding to the partial pressures of the components ($CH_4$, $H_2O$, $CO_2$, $H_2$, and CO). While this may appear to be a relatively small dataset, the use of first-principles models in combination with Q-learning algorithms is expected to yield optimal results. Moreover, the use of experimental data reduces potential errors associated with simulated data points and ensures that the selection of reaction pathways is not biased by the predefined conditions of simulated datasets.

## Kinetics Model

In the methane reforming process, a detailed kinetic model is essential to understand the reaction dynamics. This model considers a network of 11 reactions

The equilibrium constant for each reaction is determined as a function of temperature. Specifically, for each reaction $j$, the equilibrium constant is expressed as:

$$K_{\mathrm{eq},j} = A_j \cdot \exp\left(-\frac{\Delta H_j^{\circ}}{RT}\right) \tag{5}$$

where $A_j$ is a pre-exponential factor related to the standard entropy change ($\Delta S_j^{\circ}$), $\Delta H_j^{\circ}$ is the standard enthalpy change, $R$ is the universal gas constant, and $T$ is the temperature in Kelvin. The data for the equilibrium constants used in this model are compiled in Table 3, which includes values reported by various authors [3-8].

The reaction rate for each reversible reaction $j$ is given by:

$$r_j = k_{f,j} \prod_i P_i^{\nu_{i,j}} - k_{r,j} \prod_i P_i^{\nu'_{i,j}} \tag{6}$$

where $k_{f,j}$ and $k_{r,j}$ are the forward and reverse rate coefficients, respectively, and $P_i$ is the partial pressure of component $i$. The term $\nu_{i,j}$ represents the stoichiometric coefficients of the reactants, while $\nu'_{i,j}$ represents those of the products in reaction $j$. The forward rate constant $k_{f,j}$ is calculated using the Arrhenius equation:

$$k_{f,j} = A_{f,j} \cdot \exp\left(-\frac{E_{f,j}}{RT}\right) \tag{7}$$

where $A_{f,j}$ is the pre-exponential factor and $E_{f,j}$ is the activation energy for the forward reaction. These parameters $A_{f,j}$ and $E_{f,j}$, which are crucial for determining the forward reaction rates, are calculated through an optimization process, as described in the "Parameter Estimation" section of this work.

The reverse rate constant $k_{r,j}$ is related to the forward rate constant and the equilibrium constant $K_{\mathrm{eq},j}$ by:

$$k_{r,j} = \frac{k_{f,j}}{K_{\mathrm{eq},j}} \tag{8}$$

The rate law thus accounts for both the forward and reverse reactions, and the overall reaction rate depends on the partial pressures of the species involved in each reaction.

To maintain mass balance across the system, the rate of change of the partial pressure of any component $i$ is described by a mass balance equation:

$$\frac{dP_i}{d\left(\frac{W}{F_{\mathrm{CH_4}}}\right)} = \sum_{j=1}^{11} \nu_{i,j} r_j \tag{9}$$

where $W$ is the catalyst mass, $F_{\mathrm{CH_4}}$ is the molar flow rate of methane, and $\nu_{i,j}$ is the stoichiometric coefficient of component $i$ in reaction $j$. The set of equations for all components is solved simultaneously to predict the evolution of the partial pressures over time and catalyst mass.

Additionally, a Q-learning algorithm is used to optimize the reaction set. This optimization process dynamically selects which reactions from the set of 11 should be included or excluded from the kinetic model. The goal is to identify the reactions that best represent the methane reforming phenomena, based on experimental or simulated data.

## Parameter Estimation

**Table 3:** Reaction set and its Equilibrium Function [8].

| *I* | Reaction | $K_{pi}$ | Dimensions |
|---|---|---|---|
| 1 | $CH_4 + H_2O \leftrightarrow CO + 3H_2$ | $1.1669 \times 10^{13} \exp(-26380/T)$ | $(atm)^2$ |
| 2 | $CO + H_2O \leftrightarrow CO_2 + H_2$ | $1.767 \times 10^{-2} \exp(4400/T)$ | $(atm)^0$ |
| 3 | $CH_4 + 2H_2O \leftrightarrow CO_2 + 4H_2$ | $2.0620 \times 10^{11} \exp(-22430/T)$ | $(atm)^2$ |
| 4 | $CH_4 + CO_2 \leftrightarrow 2CO + 2H_2$ | $6.6038 \times 10^{14} \exp(-31230/T)$ | $(atm)^2$ |
| 5 | $CH_4 + 3CO_2 \leftrightarrow 4CO + 2H_2O$ | $2.1136 \times 10^{18} \exp(-40030/T)$ | $(atm)^2$ |
| 6 | $CH_4 \leftrightarrow C + 2H_2$ | $4.1066 \times 10^{5} \exp(-10614/T)$ | atm |
| 7 | $2CO \leftrightarrow C + CO_2$ | $5.8201 \times 10^{-10} \exp(20634/T)$ | $(atm)^{-1}$ |
| 8 | $CO + H_2 \leftrightarrow C + H_2O$ | $3.215 \times 10^{-8} \exp(16318/T)$ | $(atm)^{-1}$ |
| 9 | $CO_2 + 2H_2 \leftrightarrow C + 2H_2O$ | $1.7762 \times 10^{-6} \exp(12002/T)$ | $(atm)^{-1}$ |
| 10 | $CH_4 + 2CO \leftrightarrow 3C + 2H_2O$ | $4.2455 \times 10^{-10} \exp(22022/T)$ | $(atm)^{-1}$ |
| 11 | $CH_4 + CO_2 \leftrightarrow 2C + 2H_2O$ | $0.730 \exp(1388/T)$ | $(atm)^0$ |

The parameter estimation process involves solving the system of differential equations that describe the methane reforming reactions and adjusting the model parameters to best fit the experimental data. In particular, the activation energy ($E_a$) and the pre-exponential factor ($A$) of the forward reaction rate constants were estimated through optimization. To solve this system, it was used the `odeint` function from the `scipy.integrate` package in `Python`, with the `LSODA` integrator.

The objective function used to guide the optimization process is the residual sum of squares (RSS) of the partial pressures. The RSS is calculated as:

$$\mathrm{RSS} = \sum_{j=1}^{M} \sum_{i=1}^{N} \left( P_{i,j}^{\mathrm{exp}} - P_{i,j}^{\mathrm{calc}} \right)^2 \tag{10}$$

where $P_{i,j}^{\mathrm{exp}}$ and $P_{i,j}^{\mathrm{calc}}$ are the experimental and calculated partial pressures of component $i$ in condition $j$, respectively, and $N$ is the number of components, while $M$ is the number of conditions. This function serves as the reward function for the Q-learning process, where the goal is to minimize the discrepancy between experimental and model-predicted partial pressures.

The optimization process is carried out using the `minimize` function from the `scipy.optimize` library, with the `L-BFGS-B` algorithm [9-10].

The initial values for the parameters $\boldsymbol{A}$ and $\boldsymbol{E_a}$ are defined based on the literature. Moreover, the values of $\boldsymbol{A}$ and $\boldsymbol{E_a}$ are constrained to be positive, as negative values are physically meaningless in the context of reaction kinetics.

In addition to the parameter optimization, a mechanism is incorporated to optimize a set of parameters defined by a vector that activates or deactivates the reactions to be considered in the kinetic model, it ensures that the optimizer adjusts only the parameters corresponding to the active reactions. This is advantageous because it reduces the dimensionality of the parameter space, allowing the optimizer to focus on the relevant reactions.

This approach is particularly useful as the Q-learning algorithm subsequently refines the reaction set, selecting the most appropriate reactions based on experimental data.

# RESULTS & DISCUSSION

## Evaluation of Reaction Set Combinations

All possible reaction subsets were evaluated, covering every combination from single reactions to the full set of 11 reactions, leading to a total of 2048 cases.

The evaluation of all these combinations provides a comprehensive analysis of the different reaction sets, enabling the identification of the most suitable configuration to describe the methane reforming process. By evaluating every possible combination, it is possible to directly assess the performance of each reaction set based on how well it matches the experimental data. However, this exhaustive approach comes with significant computational costs, especially as the number of reactions increases.

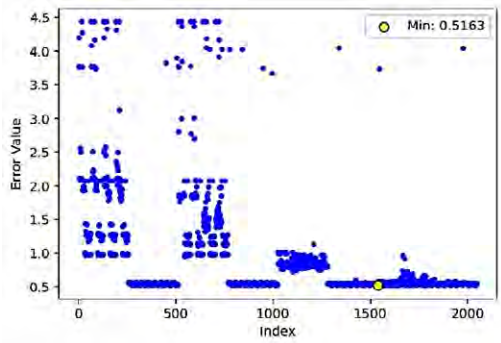



**Figure 2.** Combinatorial Errors from Reaction Set.

The Fig. 2 shows the evaluation of 2048 reaction set combinations, with each combination indexed on the x-axis and the corresponding residual sum of squares (RSS) on the y-axis. The RSS value indicates the accuracy of the model, with lower values representing a better fit to the experimental data.

The yellow-highlighted combination, with an RSS of 0.5163, is the optimal set, providing the best fit to the data. This combination represents the most accurate model of the methane reforming process among all evaluated sets.

The variation in RSS values illustrates the differing performance of the reaction sets, with most combinations yielding higher RSS values, indicating poorer fits. This emphasizes the importance of selecting the correct reaction set to accurately model the system.

## Q-Learning Optimization Results

Fig.3 illustrates the evolution of the best error achieved during the Q-learning training as a function of the number of iterations (11 iterations per episode). It is observed that the best error is reached after approximately 40 iterations, after which no further improvements are identified.

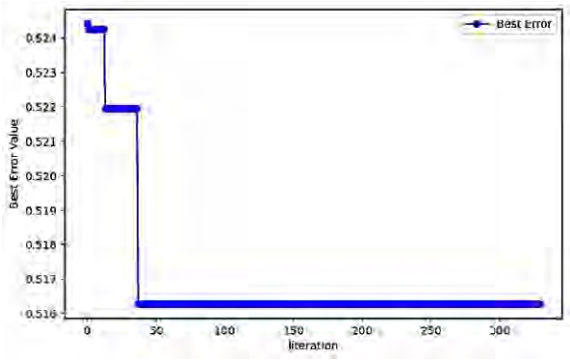



**Figure 3.** Best Error in training Q-learning.

This behavior suggests that the algorithm converges to the optimal set of reactions during the early stages of training, coinciding with episodes where the epsilon parameter (exploration) is high. As training progresses and epsilon decreases, the algorithm prioritizes exploiting the learned solutions, explaining the absence of better error values beyond this point.

The early convergence indicates that the method is efficient in rapidly identifying the most representative reaction combinations, offering significant advantages in terms of computational time and resource requirements

The Q-learning algorithm identified three key reactions from the initial set of 11 that best describe the methane reforming process reported in table 5.

**Table 4:** Active Reaction Selected by Q-learning.

| Reaction | Active Value |
|---|---|
| $CH_4 + H_2O \leftrightarrow CO + 3H_2$ | 1 |
| $CO + H_2O \leftrightarrow CO_2 + H_2$ | 1 |
| $CH_4 + CO_2 \leftrightarrow 2C + 2H_2O$ | 1 |

The first selected reaction is the Methane Steam Reforming (MSR) reaction, which serves as the primary pathway for hydrogen production by breaking down methane in the presence of steam. It is an endothermic reaction that sets the foundation for subsequent reaction pathways, the second is known as the Water Gas Shift (WGS) reaction, this exothermic reaction increases hydrogen yield while reducing carbon monoxide levels. It plays a crucial role in balancing the overall hydrogen and carbon species in the system, the third selected reaction leads to the formation of carbon deposits while consuming hydrogen and carbon dioxide. Its activation highlights the algorithm's ability to capture critical secondary effects that may influence the overall process, especially in systems prone to carbon formation.

The selection of these reactions demonstrates the algorithm's effectiveness in capturing the fundamental and secondary processes necessary for accurately modeling the methane reforming system. These reactions collectively represent the dominant pathways for hydrogen generation and associated carbon transformations under the studied conditions.

The Table 5 presents kinetic constants for the forward and reverse reactions of steam methane reforming (SMR), the water-gas shift reaction (WGS), and the reaction of carbonization. The analysis reveals trends consistent with thermodynamic expectations.

For SMR, the equilibrium shifts towards hydrogen production as temperature increases, aligning with the reaction's endothermic nature. For WGS, the equilibrium shifts towards reactants with increasing temperature. This behavior is expected for an exothermic reaction, were higher temperatures disfavor product formation, as predicted by Le Chatelier's principle.

For the carbonization reaction, the equilibrium similarly shifts to the left at higher temperatures. The reaction's exothermic nature favors the formation of carbon and water at lower temperatures.

## Simulation

The Fig. 4 is a parity plot comparing the calculated partial pressures to experimental values for all species. The results reveal a consistent underestimation of water conversion at higher temperatures and elevated methane feed ratios. This behavior is likely due to limitations in the kinetic model, which does not account for adsorption effects on the catalytic surface. Despite this underestimation, the general production trends for all species remain consistent with experimental data, suggesting the model captures the qualitative behavior.

The Fig. 5 presents a simulation of partial pressures as a function of W/F, which is analogous to reaction time. The model demonstrates a tendency to underestimate water conversion throughout the reaction path, consistent with the observations in the parity plot. In contrast, hydrogen production is overestimated, particularly at intermediate and high W/F values. This discrepancy

**Table 5:** Kinetic Coefficients from Selected Reactions.

| T(K) | $\left[\frac{\text{mol}}{\text{atm}\cdot\text{kg}\cdot\text{s}}\right]$ | SMR | WGS | Carbonization |
|---|---|---|---|---|
| 609.26 | $\mathbf{k_f}$ | $1.209 \times 10^{3}$ | $4.007 \times 10^{4}$ | $5.767 \times 10^{1}$ |
| | $\mathbf{k_r}$ | $6.601 \times 10^{8}$ * | $1.656 \times 10^{3}$ | $8.095 \times 10^{0}$ |
| 671.48 | $\mathbf{k_f}$ | $1.429 \times 10^{3}$ | $4.007 \times 10^{4}$ | $5.767 \times 10^{1}$ |
| | $\mathbf{k_r}$ | $1.412 \times 10^{7}$ * | $3.234 \times 10^{3}$ | $9.997 \times 10^{0}$ |
| 723.15 | $\mathbf{k_f}$ | $1.607 \times 10^{3}$ | $4.007 \times 10^{4}$ | $5.767 \times 10^{1}$ |
| | $\mathbf{k_r}$ | $9.586 \times 10^{5}$ * | $5.166 \times 10^{3}$ | $1.159 \times 10^{1}$ |
| 779.26 | $\mathbf{k_f}$ | $1.792 \times 10^{3}$ | $4.007 \times 10^{4}$ | $5.767 \times 10^{1}$ |
| | $\mathbf{k_r}$ | $7.734 \times 10^{4}$ * | $8.006 \times 10^{3}$ | $1.331 \times 10^{1}$ |
| 910.92 | $\mathbf{k_f}$ | $2.198 \times 10^{3}$ | $4.007 \times 10^{4}$ | $5.767 \times 10^{1}$ |
| | $\mathbf{k_r}$ | $7.112 \times 10^{2}$ * | $1.811 \times 10^{4}$ | $1.721 \times 10^{1}$ |

$*\rightarrow \left[\frac{\text{mol}}{\text{atm}^3\cdot\text{kg}\cdot\text{s}}\right]$

may arise from the same model limitations, including the omission of adsorption dynamics and potential inaccuracies in reaction rate parameters.

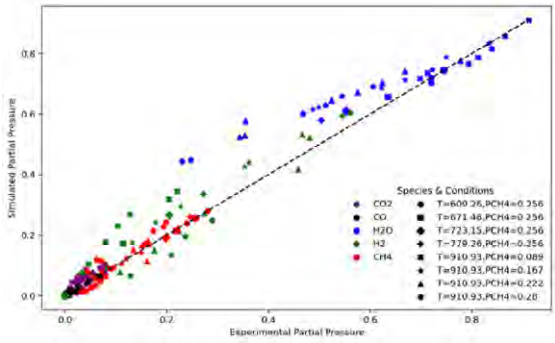



**Figure 4.** Parity Plot of Simulated Partial Pressures.

Nevertheless, the shapes of the curves and their evolution with W/F align with experimental trends, indicating the model adequately predicts the system's dynamic behavior. These results suggest that while the model requires refinement to improve quantitative accuracy, it reliably captures the qualitative aspects of methane reforming and hydrogen production under varying conditions.

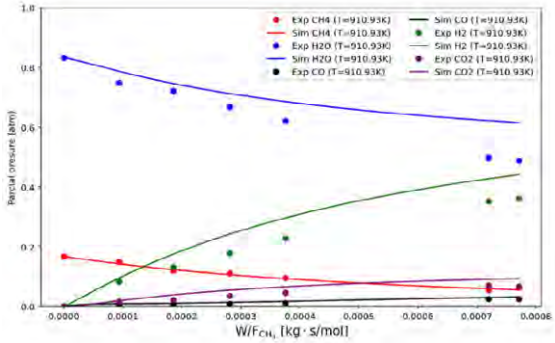



**Figure 5.** Simulation process with Active Reactions.

## CONCLUSIONS

The implementation of the Q-learning algorithm successfully identified the most relevant reactions to describe the methane reforming process. The selected reactions not only align with the physical principles of the process but also agree with previously reported studies, demonstrating the consistency and reliability of the approach. While the model accurately follows experimental trends, it exhibits a tendency to underestimate water conversion and overestimate hydrogen production at high temperatures and higher methane feed ratios. This limitation suggests that exploring alternative models could further enhance representativeness and predictive accuracy.


## ACKNOWLEDGEMENTS

The authors thank the National Council for Humanities, Science and Technology (CONAHCyT) of Mexico for the scholarship granted to Martín Rodríguez-Fragoso.


## REFERENCES


1. Chen K, Zhao Y, Feng D, Sun S. The intrinsic kinetics of methane steam reforming over a nickel-based catalyst in a micro fluidized bed reaction system. Int J Hydrogen Energy 45: 1615-1628 (2020) https://doi.org/10.1016/j.ijhydene.2019.11.080
2. Sutton RS., Barto. AG. Reinforcement Learning: An Introduction. The MIT Press (2014)
3. Akers WW, Camp DP. Kinetics of the methane-steam reaction. J AIChE 1:471-475 (1955) https://doi.org/10.1002/aic.690010415
4. Allen DW , Gerhard ER, Likins MR. Kinetics of the Methane-Steam Reaction. Ind Eng Chem Process Des Dev 14:256-259 (1975) https://doi.org/10.1021/i260055a010
5. Ross JR, Steel MC. Mechanism of the Steam Reforming of Methane over a Coprecipitated Nickel-Alumina Catalyst. J Chem Soc 69: 10-21(1973) https://doi.org/10.1039/F19736900010
6. Dirksen HA, Riesz CH. Equilibrium in the Steam Reforming of Natural Gas. Ind Eng Chem 45:1562-1565 (1953) https://doi.org/10.1021/ie50523a053
7. Jianguo X, Gilbert FF. Methane Steam Reforming, Methanation and Water-Gas Shift: 1. Intrinsic Kinetics. J AIChe 1: 88-96(1989) https://doi.org/10.1002/aic.690350109
8. Hou K, Hughes R. The kinetics of methane steam reforming over a Ni/α-$Al_2O$ catalyst. J Chem Eng 82: 311-328 (2001 ) https://doi.org/10.1016/s1385-8947(00)00367-3
9. Zhu C, Byrd RH, Lu P, Nocedal J. Algorithm 778: L-BFGS-B: Fortran subroutines for large-scale bound-constrained optimization. ACM Trans Math Softw 23:550-560 (1997) https://doi.org/10.1145/279232.279236
10. Byrd RH, Lu P, Nocedal J, Zhu C. A Limited Memory Algorithm for Bound Constrained Optimization. J SIAM Sci Comput 16:1190-1208 (1995) https://doi.org/10.1137/0916069



© 2025 by the authors. Licensed to PSEcommunity.org and PSE Press. This is an open access article under the creative commons CC-BY-SA licensing terms. Credit must be given to creator and adaptations must be shared under the same terms. See https://creativecommons.org/licenses/by-sa/4.0/

Systems & Control Transactions

**Research Article - Peer Reviewed Conference Proceeding**
ESCAPE 35 - European Symposium on Computer Aided Process Engineering
Ghent, Belgium. 6-9 July 2025
Jan F.M. Van Impe, Grégoire Léonard, Satyajeet S. Bhonsale,
Monika E. Polańska, Filip Logist (Eds.)

PSE PRESS

# Integration of Yield Gradient Information in Numerical Modeling of the Fluid Catalytic Cracking Process

**Wenle Xu[a,b], Baohua Chen[a,c], and Tong Qiu[a,b]***

[a] Tsinghua University, Department of Chemical Engineering, Beijing, China
[b] Tsinghua University, State Key Laboratory of Chemical Engineering, Beijing, China
[c] PetroChina Guangxi Petrochemical Company, Qinzhou, Guangxi, China
* Corresponding Author: qiutong@tsinghua.edu.cn.

## ABSTRACT

Fluid catalytic cracking is a crucial process in the refining industry, capable of converting lower-quality feedstocks into higher-value products. Due to the variability in feedstock properties and fluctuations in product market prices, timely adjustment and optimization of the FCC unit are essential. In this context, data-driven models have garnered increasing attention for their capacity to handle the complex, nonlinear reactions involved in the FCC process. However, on account of the limited operating range of the plants and the black-box nature of data-driven models, relying solely on these models for optimization may lead to contradictory decisions in optimization processes. To address these challenges, we integrate gradient information of product yields with respect to key variables derived from the mechanistic model Petro-SIM, into the training process of data-driven models. To mitigate the high computational demands of the Petro-SIM model, we propose the use of active learning methods for efficient sampling and thereby constructing a surrogate model. The results demonstrate that the active learning approach reduces the required sampling size by 25%. More importantly, the data-driven model trained with gradient information improves the accuracy of trend direction prediction by 34.6%, significantly enhancing its effectiveness in supporting the optimization process. The code will be available at https://github.com/xwl514/fcc-hybrid-loss.

**Keywords**: Fluid Catalytic Cracking, Machine Learning, Data-Driven Model, Active Learning, Gradient Information

## 1. INTRODUCTION

Fluid catalytic cracking (FCC) is a crucial process in petroleum refining, converting heavy oils into lighter fuels, such as gasoline and diesel. This process enhances the utilization efficiency of crude oil, reduces resource waste, and meets market demand for light fuels, making it indispensable in both petroleum refining and the chemical industry. Fluctuations in upstream processes and market prices of FCC products necessitate timely adjustments and optimization of the catalytic cracking process conditions to maximize efficiency and profitability. Achieving such optimization depends on accurate modeling of the process, which enables the prediction of key variables directly linked to profitability in response to changes in operating conditions [1].

Modeling of the FCC process can be categorized into mechanism-based and data-driven approaches. Mechanistic models are founded on fundamental physical laws, such as mass conservation, energy conservation, and chemical reaction kinetics. However, due to the complexity of feedstock composition and reaction pathways in FCC, establishing a strict model is challenging. One common simplification is the lumped kinetic model, which consolidates numerous individual compounds into several virtual components based on their similar properties. Reaction pathways are then established for these virtual lumps, and the rate constants are calibrated using plant data. The earliest application in the FCC domain is a three-lump model, which predicts the conversion rate and product distribution under varying reaction conditions, thereby enabling the selection of an optimal operating mode based on production demands [2]. Subsequently, more detailed lumped models have been

developed, offering a more refined description of feedstock and product compositions [3, 4]. However, these traditional lumped models do not account for the molecular structure of the components and are not based on actual reaction mechanisms. In contrast to traditional lumping methods, the structure-oriented lumping (SOL) approach decomposes complex hydrocarbon molecules into molecular fragments or structural groups [5]. This method facilitates the modeling of reactant and product compositions at the molecular level and more closely aligns with the true reaction mechanisms of catalytic cracking, offering improved extrapolation capabilities. However, mechanistic models often require simplifications, which can lead to a loss of accuracy. Furthermore, the development and calibration of these models involve large-scale parameter estimation, a process that is time-consuming and demands high-quality data.

With the advancement of machine learning technologies, data-driven modeling methods have increasingly been applied to the modeling of the FCC process. Machine learning methods, especially deep learning techniques, possess strong nonlinear modeling capabilities and can demonstrate higher accuracy in FCC modeling. However, due to the typically limited operating range, the extrapolation capability of these models is constrained. Although several hybrid modeling approaches have been proposed, these methods often focus primarily on the interpretability and extrapolation of the predicted yield values [6, 7]. However, they do not directly account for the gradient information of product yield with respect to operational variables. Factors such as noise in the factory data can cause the model to unintentionally learn distorted gradient information, potentially leading to incorrect optimization directions.

To address these issues, this study aims to directly integrate the gradient information into the data-driven modeling process, thereby enhancing the model's effectiveness in optimizing the FCC process. The primary innovations of this study are as follows:

1. Active learning for mechanistic sampling: employ active learning methods to sample data from the mechanistic model, Petro-SIM. This approach significantly reduces the time and computational costs associated with data sampling.
2. Gradient calculation via surrogate model: utilize samples from the mechanistic model to construct a surrogate model. The gradient information of yield variables with respect to

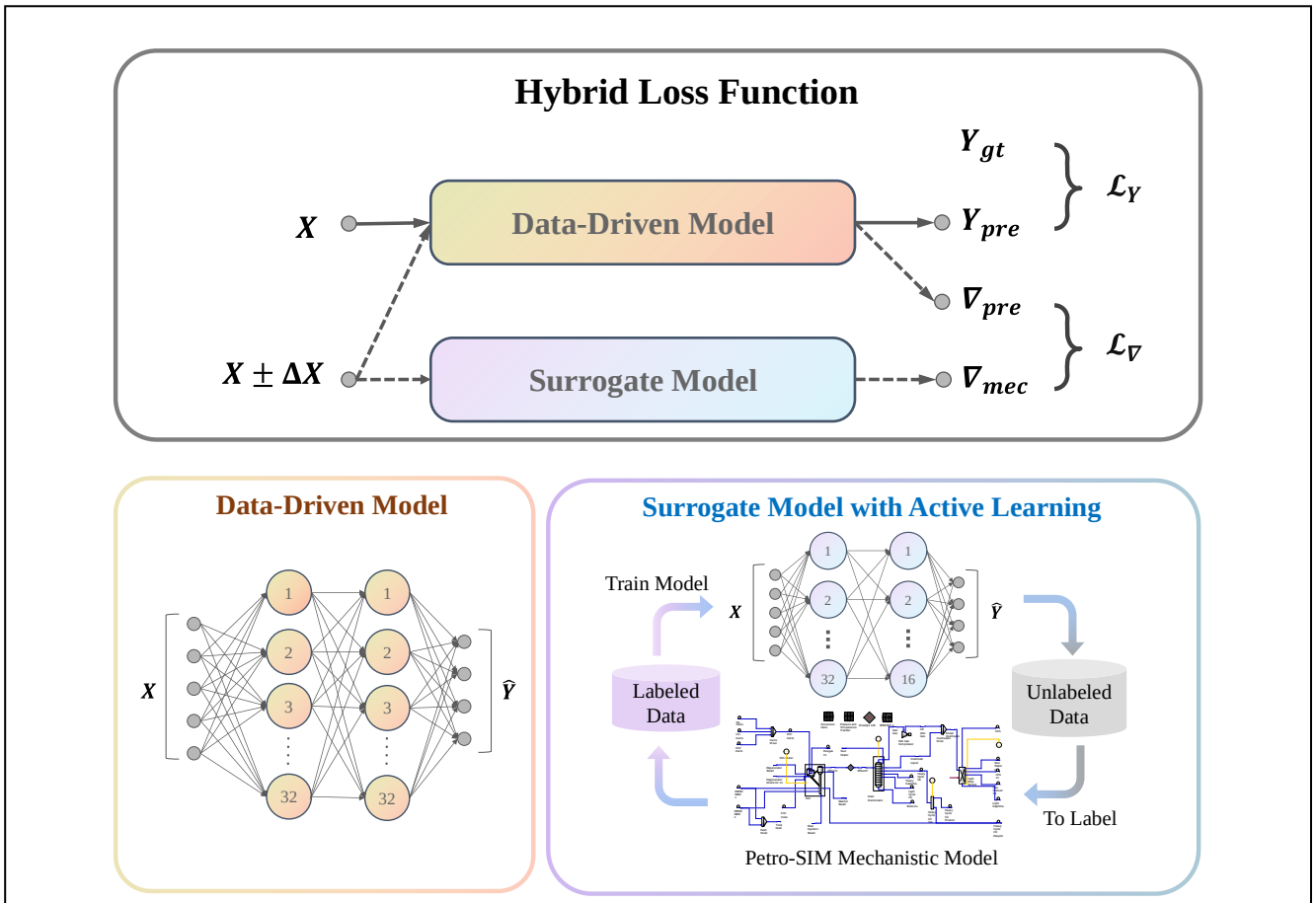



**Figure 1:** Overview of our hybrid loss function framework.

operational variables at plant sample points is computed using the central difference method.

3. Gradient loss function: introduce a novel product yield gradient loss function tailored for the FCC process. This function enables the training of data-driven models and enhances their reliability in optimization tasks.

## 2. METHODS

An overview of our method is shown in Figure 1. First, we apply active learning techniques to sample data from the mechanistic model and use the labeled samples to construct a surrogate model. Next, we develop a data-driven model, and during its training, we not only minimize the deviation between the model's output and the true values, but also minimize the gradient differences between the data-driven model and the surrogate model. A detailed explanation of these components is provided in the following sections.

### 2.1 Surrogate Model with Active Learning

In our hybrid loss function framework, we incorporate the gradient information of target variables with respect to operating variables. However, conducting response tests on operating variables over a wide range during plant operation is impractical, making it challenging to obtain accurate gradient information directly from factory data. To address this limitation, we leverage the mechanistic model, which is based on real reaction kinetics and provides reliable gradient information that reflects actual reaction kinetics.

However, computing the gradient information for each data point using the mechanistic model during every training epoch is computationally prohibitive, especially for the large plant data. When the training set consists of 100,000 points, training a single epoch could take hundreds of hours, making such a workload impractical. To overcome this challenge, we adopt a two-step strategy. First, we utilize active learning methods to sample data from the mechanistic model. By selectively sampling the most informative data points, we significantly reduce the number of required samples. Then, we construct a surrogate model to calculate the gradient information. This integrated approach ensures computational feasibility while maintaining high accuracy in gradient estimation.

We select the key operational variables as input variables and those that significantly influence economic performance as output variables, as shown in Table 1. These variables serve as inputs and outputs for the mechanistic model, surrogate model, and data-driven model.

**Table 1:** Key process input and output variables.

| Variable | Description | Unit |
|---|---|---|
| $x_1$ | Feed flowrate | ℃ |
| $x_2$ | Feed preheat temperature | ℃ |
| $x_3$ | Reflux flowrate | ℃ |
| $x_4$ | Reactor temperature | t/h |
| $x_5$ | Regenerator temperature | t/h |
| $y_1$ | Dry gas yield | wt% |
| $y_2$ | Liquefied gas yield | wt% |
| $y_3$ | Diesel yield | wt% |
| $y_4$ | Gasoline yield | wt% |

#### 2.1.1 Mechanistic Model

The mechanistic model we use is the FCC-SIM model from Petro-SIM (KBC Advanced Technologies Ltd., Walton-on-Thames, UK), which is widely used for the design and optimization of FCC units [7]. We develop an FCC model and calibrate it using factory data to ensure better alignment with the plant's operational conditions. The mechanistic model simulates the FCC process based on input variables and outputs the yields of key products, such as gasoline and diesel, which are the primary variables of interest.

#### 2.1.2 Active Learning

Building a surrogate model requires sampling from the mechanistic model. To reduce the time consumption associated with this sampling, we propose using active learning methods. By selecting the most valuable data for labeling based on criteria such as uncertainty or diversity, this approach minimizes the labeling effort, thereby improving both learning efficiency and model performance. The active learning sampling framework is illustrated in Figure 2.

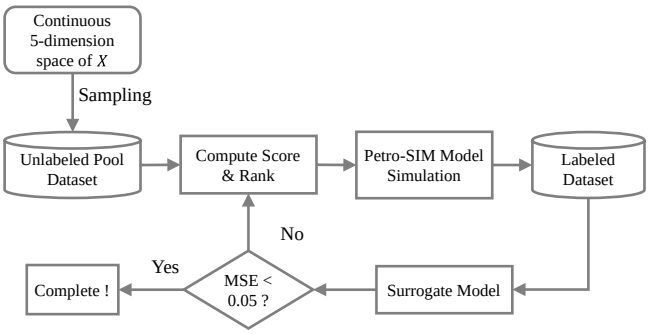



**Figure 2:** Framework of our active learning method.

Since the space of the operating variables is a continuous 5-dimensional space, we begin by performing sampling to obtain a discrete set of sample points. We randomly select 10,000 data points for simulation calculations, which serve as the validation set to verify the accuracy of the surrogate model. Initially, 3,000 samples

are randomly chosen to train the initial surrogate model. In each active learning iteration, we randomly select 10,000 samples from the unlabeled pool, evaluate them using our predefined active learning metric, and rank them according to their scores. The two active learning metrics are described below. The top 300 samples with the highest scores are then selected as inputs for the mechanistic model simulation. Once the outputs from the mechanistic model are obtained, we update the surrogate model with these new samples and decide whether to terminate the process based on the error on the validation set.

We design two active learning metrics, one based on the diversity of $X$ and the other based on the prediction' s uncertainty. For the active learning method based on the diversity of $X$, we query the nearest $k$ labeled samples to a selected unlabeled sample and take the average of their distances as the score for the unlabeled sample. This method identifies unexplored regions by evaluating the distance between unlabeled data points and labeled samples, thereby promoting more effective exploration of the variable space. It helps minimize redundant local exploration and ensures that the model samples more diverse areas of the operational variable space. The pseudocode for the process is as follows:

```
Strategy - X diversity:
Randomly select 10000 samples from the Unla-
beled_Pool
for each sample in selected_samples do
   Compute distances between the sample and
all samples in Labeled_Pool
   Sort the distances and select the small-
est k distances
   Diversity_score ← average of the k small-
est distances
End for
```

For the uncertainty metric, the variance of the model's predictions for an unlabeled point is used to quantify its uncertainty. We perform $T$ inference runs on a selected unlabeled sample using the surrogate model, incorporating Monte Carlo (MC) dropout during the inference process [8]. While dropout is typically disabled during standard inference, the key idea behind MC dropout is to enable dropout during the inference phase as well. This approach allows for the estimation of prediction variance through multiple forward passes, facilitating the assessment of uncertainty. High uncertainty for an unlabeled point suggests that the model has not adequately explored the surrounding space. Such data points are precisely the ones that need to be labeled. The pseudocode for the calculation process is as follows:

```
Strategy - Uncertainty:
Randomly select 10000 samples from Unla-
beled_Pool
for each sample in selected_samples do
   Perform T times inference with dropout
enabled
   Uncertainty_score ← variance of the T
predictions
End for
```

### 2.1.3 Surrogate Model

The surrogate model is based on a multi-layer perceptron (MLP) with two hidden layers. The model is trained using mean squared error (MSE) as the loss function, with a learning rate of 0.001. Each active learning iteration involves training the model for 100 epochs.

## 2.2 Hybrid Loss Function

For data-driven models used in FCC, the loss function typically includes mean squared error, mean absolute error, or other similar loss functions that quantify the deviation between predicted outputs and true values. However, for optimization tasks, solely considering the deviation between predicted values and true values is insufficient. Due to factors such as noise in factory data and overfitting, focusing only on errors in the yield variable during training can result in inaccurate gradients during the FCC optimization process. Therefore, it is crucial to integrate gradient information into the training process.

Consequently, we design a hybrid loss function to train the data-driven model, which not only considers the deviation between predicted values and true values of target variables but also accounts for the discrepancy in gradient directions between the data-driven model and the mechanistic model. The hybrid loss function is as follows:

$$\mathcal{L}_{Hybrid} = w_1\mathcal{L}_Y + w_2\mathcal{L}_\nabla \tag{1}$$

Where $\mathcal{L}_Y$ represents the deviation between the predicted values and the true values of the target variables, and $\mathcal{L}_\nabla$ is the loss function for the gradient component. $w_1$ and $w_2$ are the weights assigned to the two components.

### 2.2.1 Gradient Loss Function

We propose a gradient loss function to quantify the discrepancy between the data-driven model and the mechanistic model. In each epoch, for each training sample, we use the central difference method to compute the gradient of the yield with respect to the operational variables under the given conditions. The calculation formula is as follows:

$$\boldsymbol{\nabla} = \frac{\text{Model}(\boldsymbol{X}+\varepsilon\boldsymbol{I}) - \text{Model}(\boldsymbol{X}-\varepsilon\boldsymbol{I})}{2\varepsilon} \tag{2}$$

Where $\boldsymbol{I}$ is an $m \times m$ identity matrix, with $m$ referring to the number of operational variables. The above formula is used to compute the gradient of a given training

point for both the data-driven model and the surrogate model of the mechanistic model, denoted as $\boldsymbol{\nabla_{pre}}$ and $\boldsymbol{\nabla_{mec}}$. The loss function for the gradient component is computed as follows:

$$\mathcal{L}_{\nabla} = softsign\left(\boldsymbol{\nabla_{pre}} \cdot \boldsymbol{\nabla_{mec}}\right) \cdot \boldsymbol{\nabla_{mec}} \tag{3}$$

We use a sign function as a criterion to determine the directionality of the two gradients. When the directions of the gradients from the data-driven model align with those of the mechanistic model, the sign function yields zero, resulting in a loss function value of zero. This indicates that no correction is needed for the data-driven model. Conversely, when the gradients of the data-driven model and the mechanistic model point in different directions, the sign function returns 1. The subsequent product term $\boldsymbol{\nabla_{mec}}$ serves as a weight term, which increases the importance of points with large gradients and incorrect gradient directions. We use the hyperbolic tangent function because its gradient during the backpropagation process is smoother. The scaling factor $a$ affects the steepness of the hyperbolic tangent function. The $softsign$ formula is as follows:

$$softsign(x) = 0.5 \times \left(1 - \tanh(\alpha \cdot x)\right) \tag{4}$$

The accuracy of gradient direction determination for yield variables with respect to operational variables (denoted as $Acc_{\nabla}$) is also considered in the evaluation of our model, and is defined as follows:

$$Acc_{\nabla} = \frac{\sum_{i=1}^{m}\sum_{j=1}^{n} \mathbb{1}_{(\nabla_{pre}\cdot\nabla_{mec})_{ij}>0}}{m \times n} \times 100\% \tag{5}$$

Where $m$ refers to the number of operational variables and $n$ refers to the number of target variables. It calculates the proportion of gradient directions for all $y$ with respect to all $x$ that are consistent between the data-driven model and the mechanistic model, using the indicator function.

### 2.2.2 Data-Driven Model

Our hybrid loss function does not impose restrictions on the model type. In our experiments, we select an MLP model. The factory data is divided into training, validation, and test sets in a 0.6:0.2:0.2 ratio. The total size of the training set is 79,496 samples, while the validation and test sets each contain 26,499 samples. During the training process, we use our hybrid loss function.

## 3. RESULTS AND DISCUSSIONS

### 3.1 Active Learning Results

The MSE loss on the validation set for each iteration of the two active learning strategies is shown in Figure 3. A random labeling strategy is also included as a baseline. With the same number of labeled samples, the models trained using the active learning approaches show superior performance on the validation set compared to the random labeling strategy. Upon reaching the stopping criterion, the diversity-based and uncertainty-based strategies require only 5,400 and 5,700 labeled samples, respectively, while the random selection method demands 7,200 samples. These findings demonstrate that by leveraging our active learning strategies, it is possible to identify the most informative samples for simulation more efficiently, reducing labeling time by up to 25%.

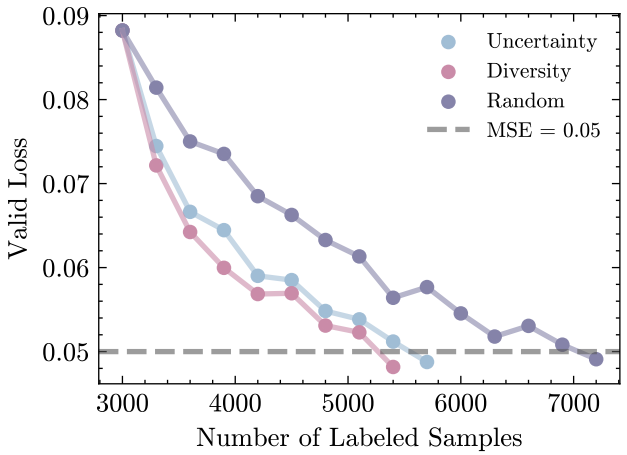



**Figure 3:** The MSE loss on the validation set for each iteration of active learning.

### 3.2 Surrogate Model Results

We select the model built using the diversity-based active learning strategy as our surrogate model. Its prediction performance on the validation set is shown in Figure 4. The accuracy of the surrogate model for the mechanistic model is high enough to ensure its reliability for subsequent precise gradient calculations.

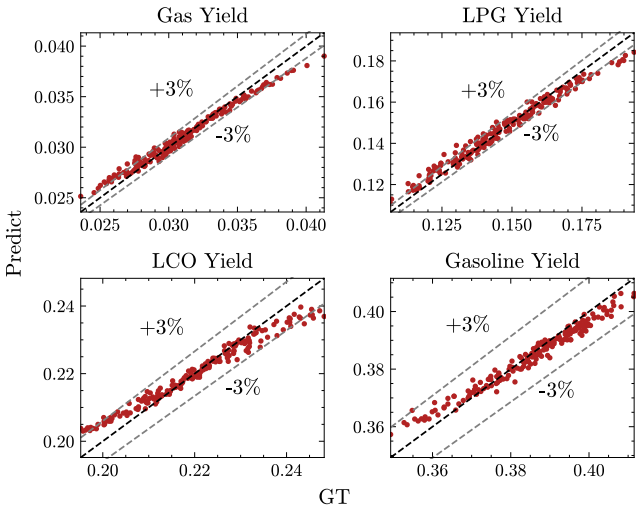



**Figure 4:** The prediction and Ground Truth (GT) on validation set of the surrogate model.

## 3.3 Data-Driven Model Results

The $\mathcal{L}_{MSE}$, $\mathcal{L}_{\nabla}$, and $Acc_{\nabla}$ of the data-driven model trained with the hybrid loss function on the training and validation sets are shown in the Figure 5. During the training process, we first train the model using only the MSE loss. After 50 epochs, we gradually increased the weight of the gradient loss component to $w_2$.This training strategy ensures a more stable training process. It is observed that when the model is trained solely using the MSE loss function, the loss on both the training and validation sets consistently decreases as training progresses. However, the $Acc_{\nabla}$ metric shows no improvement during the training processes. When the hybrid loss function is applied, $\mathcal{L}_{\nabla}$ decreases continuously as training progresses, and the gradient direction accuracy on both the training and validation sets shows consistent improvement. Furthermore, as the weight $w_2$ increases, the $Acc_{\nabla}$ on the validation set improves correspondingly.

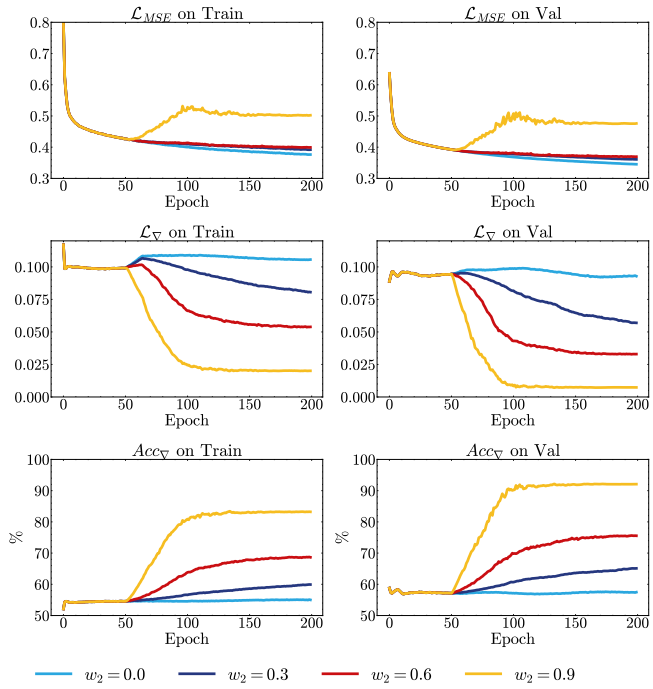



**Figure 5:** The $\mathcal{L}_{MSE}$, $\mathcal{L}_{\nabla}$, and $Acc_{\nabla}$ of the training process.

**Table 2:** The $\mathcal{L}_{MSE}$, $\mathcal{L}_{\nabla}$, and $ACC_{\nabla}$ on the test set.

| $w_2$ | $\mathcal{L}_{MSE}$ | $\mathcal{L}_{\nabla}$ | $Acc_{\nabla}$ % |
|---|---|---|---|
| 0.0 | **0.332** | 0.082 | 57.4 |
| 0.3 | 0.360 | 0.055 | 65.6 |
| 0.6 | 0.371 | 0.037 | 75.4 |
| 0.9 | 0.480 | **0.008** | **92.0** |

The $\mathcal{L}_{MSE}$, $\mathcal{L}_{\nabla}$, and $ACC_{\nabla}$ on test set are shown in the Table 2. The use of the hybrid loss function results in a significant increase on the $ACC_{\nabla}$ metric. When $w_2$ is set to 0.9, the gradient direction accuracy reached 92.0%, representing a 34.6% improvement compared to the model trained solely with the MSE loss function.

In addition, we randomly select 5 data points and visualize $\boldsymbol{\nabla_{pre}}$, as shown in Figure 6. Compared to the $\nabla_{pre}$ of the model trained using only MSE, the $\boldsymbol{\nabla_{pre}}$ of the model trained with the hybrid loss function aligns better to $\boldsymbol{\nabla_{mec}}$. The alignment with the mechanism model's gradient information enhances the reliability of the model, making it more suitable for optimization tasks.

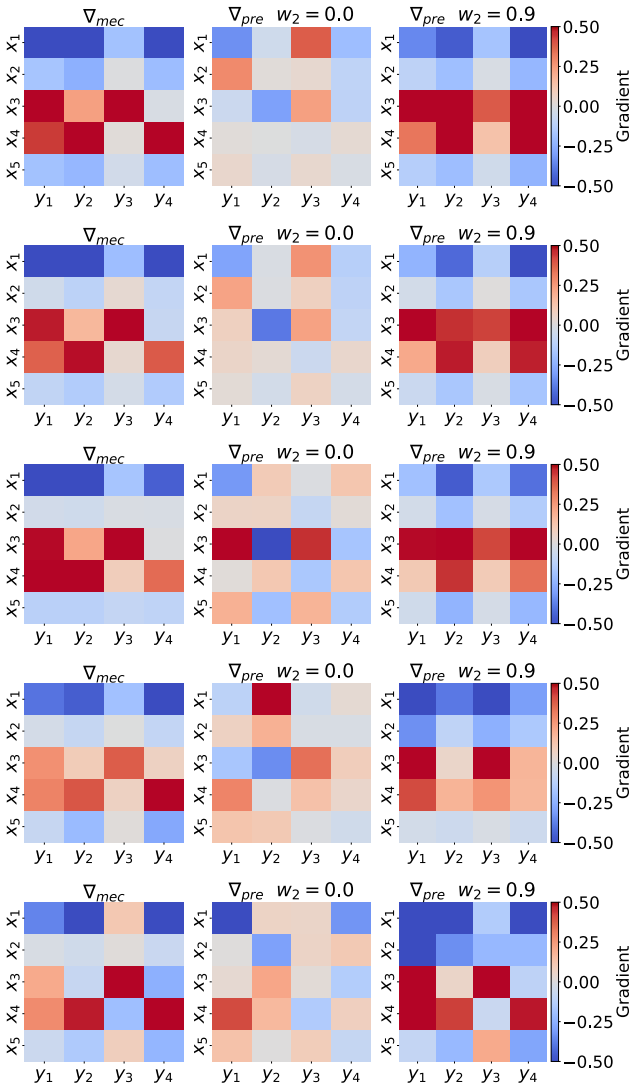



**Figure 6:** The $\boldsymbol{\nabla_{mec}}$ and $\boldsymbol{\nabla_{pre}}$ of the models with different loss function weights of different samples (each row).

## 4. Conclusions

We propose an active learning method based on diversity and uncertainty, significantly reducing the time and computational resources required for sampling from mechanistic models. By constructing a surrogate model from the sampled data, we can efficiently compute the gradient information for plant sample points. By incorporating the consistency of gradient information between

the data-driven model and the mechanistic model into the loss function, the accuracy of the gradient directions is improved by 34.6%. This loss function directly incorporates gradient information offers a novel approach to integrating mechanistic and data-driven models. It facilitates a more effective application of machine learning techniques to optimize operations in industrial plants.

## REFERENCES


1. Wang, Z., Yang, B., Chen, C., Yuan, J., Wang, L. Modeling and optimization for the secondary reaction of FCC gasoline based on the fuzzy neural network and genetic algorithm. *Chemical Engineering and Processing: Process Intensification*. 46, 175–180 (2007). https://doi.org/10.1016/j.cep.2006.05.011
2. Weekman Jr., V.W., Nace, D.M. Kinetics of catalytic cracking selectivity in fixed, moving, and fluid bed reactors. *AIChE Journal*. 16, 397–404 (1970). https://doi.org/10.1002/aic.690160316
3. Hagelberg, P., Eilos, I., Hiltunen, J., Lipiäinen, K., Niemi, V.M., Aittamaa, J., Krause, A.O.I. Kinetics of catalytic cracking with short contact times. *Applied Catalysis A: General*. 223, 73–84 (2002). https://doi.org/10.1016/S0926-860X(01)00744-X
4. Dasila, P.K., Choudhury, I.R., Singh, S., Rajagopal, S., Chopra, S.J., Saraf, D.N. Simulation of an Industrial Fluid Catalytic Cracking Riser Reactor Using a Novel 10-Lump Kinetic Model and Some Parametric Sensitivity Studies. *Ind. Eng. Chem. Res*. 53, 19660–19670 (2014). https://doi.org/10.1021/ie5006433
5. Ghosh, P., Andrews, A.T., Quann, R.J., Halbert, T.R. Detailed Kinetic Model for the Hydro-desulfurization of FCC Naphtha. *Energy Fuels*. 23, 5743–5759 (2009). https://doi.org/10.1021/ef900632v
6. Long, J., Li, T., Yang, M., Hu, G., Zhong, W. Hybrid Strategy Integrating Variable Selection and a Neural Network for Fluid Catalytic Cracking Modeling. *Ind. Eng. Chem. Res.* 58, 247–258 (2019). https://doi.org/10.1021/acs.iecr.8b04821
7. Li, H., Zhao, Q., Wang, R., Xu, W., Qiu, T. Integrated Hybrid Modelling and Surrogate Model-Based Operation Optimization of Fluid Catalytic Cracking Process. *Processes*. 12, 2474 (2024). https://doi.org/10.3390/pr12112474
8. Gal, Y., Ghahramani, Z. Dropout as a Bayesian Approximation: Representing Model Uncertainty in Deep Learning. *Proceedings of The 33rd International Conference on Machine Learning*. pp. 1050–1059 (2016).



© 2025 by the authors. Licensed to PSEcommunity.org and PSE Press. This is an open access article under the creative commons CC-BY-SA licensing terms. Credit must be given to creator and adaptations must be shared under the same terms. See https://creativecommons.org/licenses/by-sa/4.0/




Systems & Control Transactions

**Research Article - Peer Reviewed Conference Proceeding**
ESCAPE 35 - European Symposium on Computer Aided Process Engineering
Ghent, Belgium. 6-9 July 2025
Jan F.M. Van Impe, Grégoire Léonard, Satyajeet S. Bhonsale,
Monika E. Polańska, Filip Logist (Eds.)

PSE PRESS

# Hybrid Modelling for Reaction Network Simulation in Syngas Methanol Production

**Harry Kay[a], Fernando Vega-Ramon[a], and Dongda Zhang[a]***

[a] Department of Chemical Engineering, University of Manchester, Manchester, M13 9PL, UK.
* Corresponding Author: dongda.zhang@manchester.ac.uk.

## ABSTRACT

Sustainability is a thriving global topic of concern and following the advancement of technological progress and increased standards of living, the demands for energy, fuels, chemicals and other requirements have increased significantly. Methanol is one such chemical which has seen increases in demand due to its importance as a precursor in the development of widely used chemicals such as formaldehyde. In order to gain insight into the reaction mechanisms driving the process, it is beneficial to develop kinetic models that accurately describe the system for several reasons: (i) to develop process understanding; (ii) to facilitate control and optimisation; (iii) to reduce experimental burdens; and (iv) to expedite scale up and scale down of processes. Two commonly used kinetic reaction rate models are the power law and Langmuir-Hinshelwood expressions, however the strong assumptions made when developing such models may limit their predictive performance through the introduction of inductive bias (i.e. model structural uncertainty). A solution to counter these drawbacks is known as hybrid modelling where, the inauguration of a data-driven component within the kinetic modelling framework allows for any complex, less understood kinetics to be instead learnt from historical data by a machine learning model. In order to identify the pros and cons associated with each kinetic and hybrid modelling strategy for chemical reaction network modelling, a thorough comparison was made using syngas methanol production as a case study. It was shown that hybrid models offered increased predictive accuracy, robust uncertainty quantifications, and improved generalisability under limited data availability.

**Keywords**: Kinetic modelling, Hybrid modelling, Uncertainty estimation

## INTRODUCTION

Increases in global population and standards of living have intensified the demand for bulk and specialty chemicals, however growing sustainability concerns and economic pressures necessitate further process design innovations, and for optimisation of current production facilities. In order to combat such issues, advanced modelling techniques are required that describe bulk and specialty chemical reaction systems under industrial operation, allowing for the precise estimation of key process variables and reaction performance indicators. Typically, first principle based kinetic models are constructed in order to represent the reaction network of interest due to their inherent interpretability and capacity for proving deep kinetic insight when used to discriminate between reaction mechanisms with two of the most popular applied strategies being the Langmuir-Hinshelwood and power law models.

The Langmuir-Hinshelwood expression finds prominent application within heterogeneous catalysis, specifically for gas phase reactants on solid catalyst surfaces [1], however the model is also used for other catalytic reactions. In comparison, the power law model finds much broader application being employed within catalytic reactions [2], non-catalytic reactions [3], and within fields beyond kinetic modelling. Although kinetic models are interpretable and may be used to offer kinetic insight, it is often the case that many chemical reactions are governed by complex underlying physics, so the identification of a correct structure is challenging, typically required simplifications to be made which may be limiting and reduce generalisability. Because of this, model parameters will exhibit large uncertainties, preventing any

use for control and optimisation.

To address the challenges inherent to kinetic modeling, data driven models have gained significant attention within the literature in recent years. Machine learning based black-box models leverage the availability of extensive experimental datasets and do not require a detailed understanding of the underlying reaction mechanism, thus showing advantages in areas where complex phenomena are present. Machine learning has shown great potential in many fields such as (bio)chemical reaction kinetics predictions [4] and soft-sensing, however they are known to be inhibited by various disadvantages including the requirement for large volumes of data and a lack of interpretability, which hinders their ability to provide mechanistic insights.

In recent years, hybrid modelling has emerged as a potential solution to overcome the challenged associated with kinetic and data driven modelling through the combination of a mechanistic backbone with data-driven knowledge. The mechanistic backbone leverages available prior knowledge whilst the data-driven component accommodates for information not captured through the mechanistic structure. In this manner, the interpretability of the kinetic model is retained without the introduction of large inductive bias, and any available data can be exploited to quantify unknown kinetics that are not described by the kinetic structure. The advantages of hybrid modelling are shown clearly with its successful application in predicting complex reaction kinetics [5], boasting accurate predictions and robust uncertainty estimations.

Another crucial benefit of hybrid modelling stems from their reliable uncertainty quantification, which is especially important when encountering complex bio(chemical) reactions where large process variability or historical dependencies may be present. Typically, kinetic models may suffer with large parameter uncertainties and fail to account for historical dependencies, whereas data driven models may overfit when large batch to batch variability occurs, both of which prevent their application under such conditions. However, this is not true of hybrid modelling which has exhibited the capability to accurately describe process dynamics whilst maintaining narrow uncertainty ranges [6]. Even though the value of using hybrid modelling has been demonstrated, little research has focused on investigating its use within the field of chemical reaction kinetics nor on the effects of the kinetic component on model performance.

Therefore, in this work we present a study to explore the application of hybrid models for predictive modeling of chemical reaction kinetics. A key focus of this study is the role of the mechanistic backbone in hybrid model performance. Specifically, we investigate how the selection of different kinetic model structures influences the predictive accuracy and uncertainty quantification of hybrid models. To this end, two hybrid models were developed using the Langmuir-Hinshelwood and power-law rate expressions as their physical components, respectively. To demonstrate the potential of hybrid models for industrial applications, the methanol synthesis reaction from syngas, coupled with the water-gas shift reaction was chosen as a case study. The reliability of the hybrid models was evaluated from their uncertainty estimations and predictions across a broad range of operating conditions. Lastly, the study evaluated the potential of hybrid models to uncover new physical insights.

### Case study

In this work, the case study is an industrial reaction system consisting of the water-gas shift reaction and syngas methanol synthesis reaction [7]. The reaction system was catalysed by a $Cu/ZnO/Al_2O_3$ catalyst, and the reactions were conducted within fixed-bed, integral-operation microreactors. In total, 38 experiments were carried out, each containing the measurements of 5 states (i.e. reactants and products) at 4 equidistant points along the reactor length. The experiments were conducted under varying feedstock conditions with $CO$ to $CO_2$ ratios of 3:3, 3:1, and 3:0.3; reaction temperatures of 453 K, 463 K, 473 K, 483 K, and 493 K, and reaction pressures of 15 bar, 25 bar, 35 bar. Further details regarding the experimental setup and procedures are provided in [7]. The three possible reactions occurring under such conditions are shown in reactions 1, 2 and 3 below

$$CO_2 + \mathrm{H}_2 \rightleftharpoons CO + H_2O \quad (1)$$

$$CO_2 + 3\mathrm{H}_2 \rightleftharpoons CH_3OH + H_2O \quad (2)$$

$$CO + 2\mathrm{H}_2 \rightleftharpoons CH_3OH \quad (3)$$

where reaction 1 is the reverse water gas shift (RWGS) reaction, and reactions 2 and 3 are methanol synthesis from $CO$ and $CO_2$ respectively.

In this study, it is assumed that CO serves as the primary source of carbon for methanol synthesis. Whilst it is also possible to assume $CO_2$ as the primary carbon source for producing methanol, this choice is not expected to impact model performance because the hybrid models, developed in this work, are designed to incorporate unknown process knowledge through their data-driven components, enabling them to adapt and accurately represent the underlying system dynamics.

## METHODOLOGY

In this section, we will outline the development of two hybrid models based on different mechanistic backbones as shown in Figure 3. In previous literature, Langmuir-Hinshelwood kinetic structures have been proposed to describe reactions 1-3, however due to their

complexity, these often lead to high errors under broad operating conditions, and high parameter uncertainties [7]. Thus, to remove inductive bias, we simplify the equations by lumping complex kinetics into few parameters to be learnt and estimated by a data-driven component.

The second kinetic backbone adopts a power law structure as shown in Figure 3, however since the classical power law expression does not satisfy the thermodynamic constraint at equilibrium conditions [2], a modification has been made. This will ensure that, under equilibrium, the ratio of forward to reverse reaction rate constants are directly equal to the ratio of products to reactants raised to their stoichiometric coefficients.

Due to the complexity of the reaction network under a broad operating range, it is to be expected that some kinetic parameters may contain lumped information and therefore effectively be functions of the operating conditions and input states. Therefore, to construct an accurate and generalisable hybrid model, it is necessary to determine the minimum number of parameters that are dependent on reaction conditions which will be subsequently estimated by the data-driven component. To accomplish this, all parameters were initially assumed condition dependent and parameter estimation, using a modified least squares expression, was conducted to classify parameters as condition-dependent or condition-invariant.

A hybrid model was then constructed, using an artificial neural network (ANN), to estimate the identified condition dependent parameters given their respective operating conditions as shown in Figure 1. The input features to the ANN include $P_T, P_{CO}, P_{CO_2}, P_{H_2}, \frac{P_{CO}}{P_{CO_2}}, \frac{P_{CO}+P_{CO_2}}{P_{H_2}}$ and $T$ where $P_x$ refers to the partial pressure of species $x$, $P_T$ is the total operating pressure, and $T$ is the temperature of the experiment. To ensure high-quality solutions, Bayesian optimisation was employed for hyperparameter optimisation for the ANN.

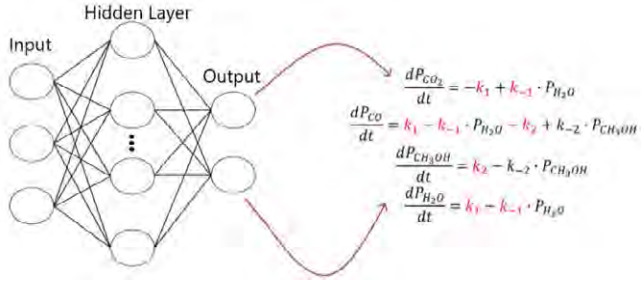



**Figure 1.** Schematic of the hybrid modelling framework using the Langmuir-Hinshelwood mechanistic backbone. The red highlights indicate condition dependent parameters estimated by the ANN.

In this study, the uncertainty of the hybrid model stems predominantly from the condition varying parameters, and hence the ANN's predictions. This is because, during parameter estimation, it was found that the condition invariant parameters show little change across all experiments. Thus, it is paramount that the uncertainty of the ANN is estimated. To accomplish this, a bootstrapping framework was employed to generate a number of ANN's which, when integrated with the mechanistic backbone to attain the corresponding hybrid models, can be used to generate a mean prediction and its respective standard deviation as shown in Figure 2.

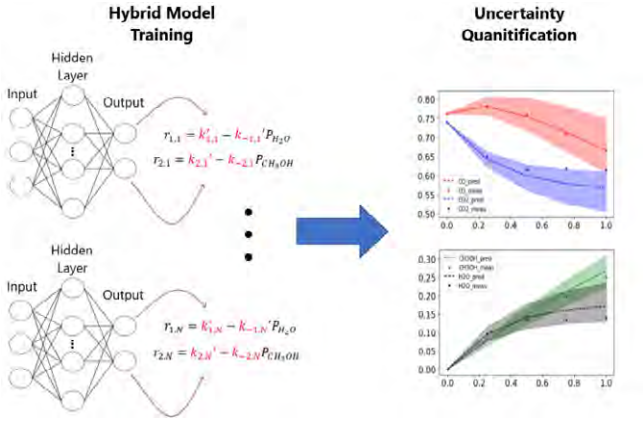


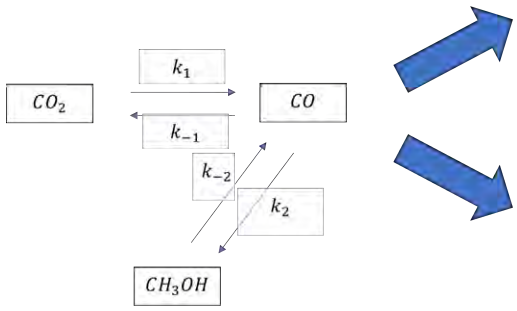

**Figure 2.** Schematic of the bootstrapping framework to estimate the hybrid models uncertainty where $N$ refers to the number of hybrid models constructed. The red highlights indicate condition dependent parameters estimated by the ANN.

## RESULTS AND DISCUSSION

### Results of the Langmuir-Hinshelwood based hybrid model

In the methanol synthesis reaction case study, hydrogen was always provided in excess thus exhibiting hydrogen partial pressure 100-10000 times greater than those of other species. As a result of the excess hydrogen, its consumption and production throughout the process is negligible (i.e., there are little changes in $P_{H_2}$). Consequently, after parameter estimation was conducted, it was found that further model reduction is required from the Equations shown in Figure 3. More specifically, $K_{H_{2,1}}$ and $K_{H_{2,1}}$ were estimated to be zero, and the products $k_1 P_{H_2}$ and $k_2 P_{H_2}$ needed to be lumped as one apparent kinetic constant to overcome identifiability issues. Additionally, $K_{CH_3OH} \cdot P_{CH_3OH}$ and $K_{H_2O} \cdot P_{H_2O} \ll 1$, and $K_{CO_2} \cdot P_{CO_2}$, $K_{CO,1} \cdot P_{CO}$, $K_{CO,2} \cdot P_{CO} \gg 1$, thus either dominating or having a negligible effect on the denominator of the kinetic model.

After model reduction, the Langmuir-Hinshelwood




**Langmuir-Hinshelwood model structure**

$$r_1 = k_1 \frac{P_{CO_2} P_{H_2}}{1 + K_{CO_2} P_{CO_2} + K_{H_{2,1}} P_{H_2}}$$

$$r_{-1} = k_{-1} \frac{P_{CO} P_{H_2O}}{1 + K_{CO,1} P_{CO} + K_{H_2O} P_{H_2O}}$$

$$r_2 = k_2 \frac{P_{CO} P_{H_2}}{1 + K_{CO,2} P_{CO} + K_{H_{2,2}} P_{H_2}}$$

$$r_{-2} = k_{-2} \frac{P_{CH_3OH}}{1 + K_{CH_3OH} P_{CH_3OH}}$$

**Power law model structure**

$$r_1 = k_1 P_{CO_2}^{\alpha_{CO_2,1}} P_{H_2}^{\alpha_{H_2,1}} P_{CO}^{\alpha_{CO,1}} P_{H_2O}^{\alpha_{H_2O}}$$

$$r_{-1} = k_{-1} P_{CO_2}^{-1+\alpha_{CO_2,1}} P_{H_2}^{-1+\alpha_{H_2,1}} P_{CO}^{1+\alpha_{CO,1}} P_{H_2O}^{1+\alpha_{H_2O}}$$

$$r_2 = k_2 P_{CO}^{\alpha_{CO,2}} P_{H_2}^{\alpha_{H_2,2}} P_{CH_3OH}^{\alpha_{CH_3OH}}$$

$$r_{-2} = k_{-2} P_{CO}^{-1+\alpha_{CO,2}} P_{H_2}^{-2+\alpha_{H_2,2}} P_{CH_3OH}^{1+\alpha_{CH_3OH}}$$

**Figure 3:** Thermodynamics inspired power law and simplified Langmuir-Hinshelwood models for the given reaction network where $P_j$, $K_j$, and $\alpha$ are the partial pressure, adsorption equilibrium constants, and reaction orders of species $j$, and $k_i$ and $k_{-i}$ are the forward and reverse reaction rate constants for reaction $i$. The red highlights indicate key process parameters that are modelled using a data-driven component.

expression devolved into a basic power law structure as seen in Figure 1, where the apparent rate constants contain lumped kinetics, and will therefore be estimated by an ANN. As described in the methodology, the condition dependent parameters were identified as $k_1$, $k_{-1}$, and $k_2$ where $k_1$ and $k_2$ are functions of $P_{H_2}$ because of any $H_2$ effects being combined into them, and $k_{-1}$ is a function of $P_{CO}$:$P_{CO_2}$ which is intuitive as it describes the forward water gas shift reaction where $CO$ and $CO_2$ are influential.

The results of the parameter estimation were then used to train the ANN such that the hybrid model can make its predictions on unseen data. In order to quantify the uncertainty predictions of all models, we use the relative percentage uncertainty (RPU) calculated as shown in Equation 4:

$$RPU\% = \frac{100}{N} \cdot \sum_{n=1}^{N} \frac{X_{UB,n} - X_{LB,n}}{X_n} \quad (4)$$

where $X_n$, $X_{UB,n}$ and $X_{LB,n}$ are the nominal, upper bounds and lower bound predictions of species $X$ at experiment $n$.

In total 16 training experiments were used and 22 testing experiments yielding percentage errors of 3.6% and 9.5%, respectively and an average testing RPU of 17%. The hybrid model prediction and uncertainty bounds are shown in Figure 4.

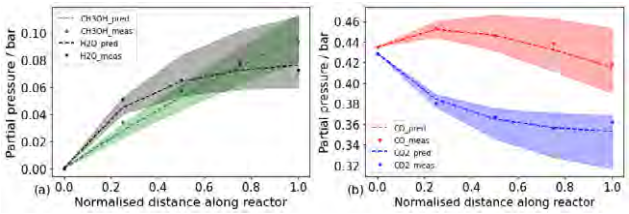



**Figure 4.** Plots showing the uncertainty and testing predictions of the Langmuir-Hinshelwood based hybrid model. (a) shows the predictions for $CH_3OH$ and $H_2O$ and (b) shows the predictions for $CO$ and $CO_2$. The scatter points and dotted lines refer to measured data and predictions, respectively.

It can be seen that the data-driven component has correctly learnt missing information from the simplified mechanistic backbone leading to the hybrid model possessing high accuracies. Furthermore, the similar testing and training performance indicates a high level of generalisability displaying the potential of hybrid modelling for use in chemical reaction kinetics prediction.

Although the Langmuir-Hinshelwood based hybrid model exhibits good predictive accuracy and uncertainty quantifications, it is limited due to it not conforming to well known physics and equilibrium constraints. It is known that kinetic constants are solely functions of temperature typically expressed using an exponential relationship, however it was discovered that, because of the lumped kinetics in the apparent rate constants of the

simplified kinetic model, the exponential temperature dependency was not observed. An example can be seen in the values of $k_1$ where, at temperatures of 453K, 463K, 473K, 483K and 493K, the lumped kinetic constants values are 0.004, 0.0047, 0.0027, 0.012, and 0.005 bar kg$^{-1}$, respectively.

A second limitation derives from the definition of the reaction equilibrium constant where, under equilibrium conditions, the ratio of forward to reverse rate constants should be equal to the ratio of products to reactants raised to their stoichiometric coefficients. As can be seen in Equations 5 and 6, this constraint does not hold true. This inconsistency limits the interpretability and insight that the Langmuir-Hinshelwood based hybrid model may offer, especially under equilibrium conditions.

$$\frac{k_1}{k_{-1}} = \frac{P_{H_2O}}{1} \tag{5}$$

$$\frac{k_2}{k_{-2}} = \frac{P_{CH_3OH}}{1} \tag{6}$$

## Results of the power law based hybrid model

Using the same methodology as for the Langmuir-Hinshelwood based hybrid model construction, parameter estimation was first used to classify condition dependent and condition invariant parameters using the thermodynamics inspired power law defined in Figure 3. Due to the excessive quantities of $H_2$ present in the system, $\alpha_{H_{2,1}}$and $\alpha_{H_{2,2}} = 0$ showing that $H_2$ has no effect on the forward reactions but instead inhibits the reverse reactions.

The exponents, $\alpha_{CO,1}$, $\alpha_{CO,2}$ and $\alpha_{CO_2}$ were found to be equal to 1, which can be reasoned by the large magnitudes of $P_{CO}$ and $P_{CO_2}$ in comparison to $P_{CH_3OH}$ and $P_{H_2O}$, thus any changes are less influential. Therefore, the only condition dependent exponents were $\alpha_{CH_3OH}$ and $\alpha_{H_2O}$. $\alpha_{H_2O}$ took negative values becoming less negative as temperature increased indicating that the role of water changes from inhibiting reaction $r_1$ (RWGS) to promoting the reverse reaction.

Further insight can be gained from the values of the reaction order of $CO$. Since the exponents, $\alpha_{CO,1}$, $\alpha_{CO,2} = 1$, from Figure 3 we can see that, as a product of the reverse water gas shift reaction, $CO$ facilitates the forward reaction. This can be explained by the fact that the use of $CO$ may remove adsorbed oxygen on the Cu catalyst which would ordinarily passivate it. Therefore, any metallic sites that would typically be unavailable for $CO_2$ activation, are now available. An alternative explanation is that the $CO$ may act to remove water from the reaction network which is beneficial because, on a Cu based catalyst, water can inhibit the methanol synthesis reaction from $CO_2$ to $CH_3OH$.

All reaction rate constants within the power law model were found to be condition dependent being solely functions of temperature. Additionally, the trends of the rate constants with respect to temperature all followed the Arrhenius expression as shown in Figure 5. This provides additional confidence into the power law based hybrid model as the results appear to conform to the underlying physics present without any constraints to enforce this and thus, the results are more likely to hold physical significance.

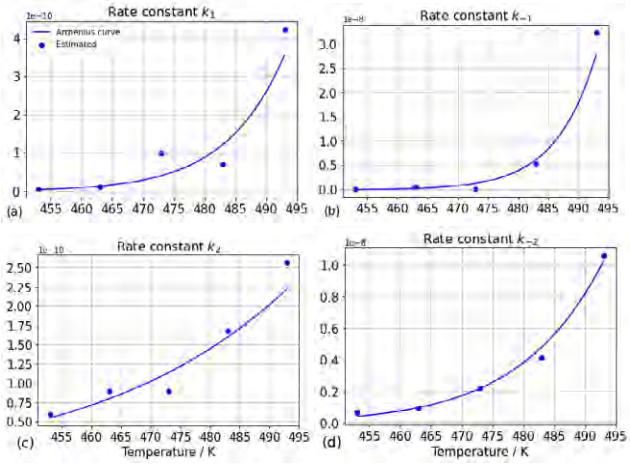



**Figure 5.** Plots showing the rate constants at different temperatures. The scatter points and lines represent the estimated parameter values and the values through fitting an arrhenius curve, respectively.

The results of parameter estimation were then used to train the ANN component in order to correlate the operating conditions and input states to the condition dependent parameters. The completed power law based hybrid model yielded average fitting and testing errors of 3.7% and 6.7%, respectively and an average relative percentage uncertainty of 13.0%. The similar training and testing performance proves the developed model is generalisable, whilst also boasting low prediction errors across a broad range of operating conditions. The hybrid model prediction and uncertainty bounds are shown in Figure 6.

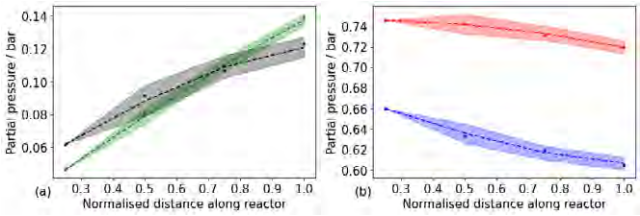



**Figure 6.** Plots showing the uncertainty and testing predictions of the power law based hybrid model. (a) shows the predictions for $CH_3OH$ and $H_2O$ and (b) shows the predictions for $CO$ and $CO_2$.

The fitting and testing results for both the power law based and Langmuir-Hinshelwood based hybrid model are similar with a slight increase in performance for the

former as well as a slight decrease in overfitting. The same conclusion can be drawn about uncertainty where both hybrid structures provide robust estimations that cover the majority of measured datapoints. However, the Langmuir-Hinshelwood based hybrid model holds less interpretability as the apparent kinetic constants are functions of the operating conditions and states whereas, it is widely known that the rate constants should be functions solely of temperature. This phenomenon has been successfully described by the power law based hybrid model, meaning that the results are more likely to hold physical significance. Additionally, we can gain kinetic understanding from the reaction orders of the power law structure.

## CONCLUSION

This study highlights the potential of hybrid modeling to address the limitations of traditional kinetic and data-driven approaches for complex chemical reaction systems. By combining mechanistic insights with the adaptability of data-driven models, the hybrid models developed provided interpretable structures with high predictive accuracy, and reliable uncertainty estimates without the requirement for large quantities of experimental data.

Two hybrid models based on Langmuir-Hinshelwood and power law rate expressions were constructed, demonstrating the flexibility of this approach, with the power law based model offering additional kinetic insights. These findings underscore the promise of hybrid modeling for industrial applications, particularly in process control and optimisation, where accuracy and uncertainty quantification are critical. Overall, this work emphasises the value of hybrid modeling in advancing our modelling capabilities and understanding in reaction engineering, especially for systems with incomplete mechanistic knowledge.

## REFERENCES


1. E. A. Nakajima *et al.*, "Kinetics of dry reforming of methane catalyzed by Ni/Si-MCM-41," *Int J Hydrogen Energy*, vol. 48, no. 83, pp. 32331–32341, Oct. 2023, doi: 10.1016/J.IJHYDENE.2023.05.010.
2. M. Zhu and I. E. Wachs, "Iron-Based Catalysts for the High-Temperature Water-Gas Shift (HT-WGS) Reaction: A Review," *ACS Catal*, vol. 6, no. 2, pp. 722–732, Feb. 2016, doi: 10.1021/ACSCATAL.5B02594/ASSET/IMAGES/LARGE/CS-2015-02594J_0002.JPEG.
3. C. Mendoza-Covarrubias, C. E. Romero, F. Hernandez-Rosales, and H. Agarwal, "N 2 O Formation in Selective Non-Catalytic NO x Reduction Processes," *J Environ Prot (Irvine, Calif)*, vol. 2, pp. 1095–1100, 2011, doi: 10.4236/jep.2011.28126.
4. X. He and M. Yan, "GraphKM: machine and deep learning for KM prediction of wildtype and mutant enzymes," *BMC Bioinformatics*, vol. 25, no. 1, pp. 1–12, Dec. 2024, doi: 10.1186/S12859-024-05746-1/FIGURES/6.
5. A. W. Rogers, Z. Song, F. V. Ramon, K. Jing, and D. Zhang, "Investigating 'greyness' of hybrid model for bioprocess predictive modelling," *Biochem Eng J*, vol. 190, p. 108761, Jan. 2023, doi: 10.1016/J.BEJ.2022.108761.
6. G. Wang, H. Xing, Y. Chen, and Y. Liu, "A dynamic exploratory hybrid modelling framework for simulating complex and uncertain system," *Journal of Safety Science and Resilience*, vol. 5, no. 2, pp. 167–178, Jun. 2024, doi: 10.1016/J.JNLSSR.2024.03.001.
7. S. K. Wilkinson, L. G. A. Van De Water, B. Miller, M. J. H. Simmons, E. H. Stitt, and M. J. Watson, "Understanding the generation of methanol synthesis and water gas shift activity over copper-based catalysts – A spatially resolved experimental kinetic study using steady and non-steady state operation under CO/CO2/H2 feeds," *J Catal*, vol. 337, pp. 208–220, May 2016, doi: 10.1016/J.JCAT.2016.01.025.



© 2025 by the authors. Licensed to PSEcommunity.org and PSE Press. This is an open access article under the creative commons CC-BY-SA licensing terms. Credit must be given to creator and adaptations must be shared under the same terms. See https://creativecommons.org/licenses/by-sa/4.0/




Systems & Control Transactions

**Research Article - Peer Reviewed Conference Proceeding**
ESCAPE 35 - European Symposium on Computer Aided Process Engineering
Ghent, Belgium. 6-9 July 2025
Jan F.M. Van Impe, Grégoire Léonard, Satyajeet S. Bhonsale,
Monika E. Polańska, Filip Logist (Eds.)

PSE PRESS

# Data-Driven Chance-Constrained Mixed Integer Nonlinear Bi-level Optimisation Via Copulas: Application To Integrated Planning And Scheduling Problems

**Syu-Ning Johnn[a], Hasan Nikkhah[b,c], Meng-Lin Tsai[d], Styliani Avraamidou[d], Burcu Beykal[b,c] and Vassilis M. Charitopoulos[a]***

[a] University College London, Department of Chemical Engineering, The Sargent Centre for Process Systems Engineering, London, WC1E 7JE, UK
[b] University of Connecticut, Department of Chemical & Biomolecular Engineering, Storrs, CT, USA
[c] University of Connecticut, Center for Clean Energy Engineering, Storrs, CT, USA
[d] University of Wisconsin-Madison, Department of Chemical & Biological Engineering, Madison, WI, USA
* Corresponding Author: v.charitopoulos@ucl.ac.uk

## ABSTRACT

Planning and scheduling are integral components of process supply chains. The presence of data correlation, particularly multivariate demand data dependency, can pose significant challenges to the decision-making process. This necessitates the consideration of dependency structures inherent in the underlying data to generate good-quality, feasible solutions to optimisation problems such as planning and scheduling. This work proposes a chance-constrained optimisation framework integrated with copulas, a non-parametric data estimation technique to forecast uncertain demand levels in accordance with specified risk thresholds in the context of a planning and scheduling problem. We focus on the integrated planning and scheduling problem following a bi-level optimisation formulation. The estimated demand forecasts are subsequently utilised within the Data-driven Optimisation of bi-level Mixed-Integer NOnlinear problems (DOMINO) framework to solve the integrated optimisation problem, and derive decisions with guaranteed demand satisfaction rates. Computational experiments demonstrate that our proposed copula-based chance-constrained optimisation framework can incorporate demand correlation and achieve higher joint demand satisfaction rate, lower total costs with higher efficiency.

**Keywords**: Planning & Scheduling, Derivative Free Optimization, Bi-level Optimization, Copula Theory, Data-driven optimization.

## INTRODUCTION

In real-world applications, many optimisation problems are inherently difficult to find feasible solutions due to the lack of exact information, the presence of noisy data distributions, data correlations, and parameter uncertainties. As a result, data-driven optimisation approaches are increasingly adopted to efficiently explore solution spaces and identify improved outcomes [2]. Chance-constrained programming (CCP) is an optimisation-based approach that ensures stochastic constraints are met with a predetermined probability of satisfaction amongst all possible scenarios [5, 17]. Numerous studies have successfully integrated CCP within various optimisation problems [3]. However, the applicability of CCP to general optimisation problems is limited by the need of strict assumptions regarding the stochastic nature of the parameters studied. To this end, data-driven variants of CCP have gained increasing attention [15]. Copulas are data-driven coupling functions that capture the dependence structure between multiple uncertain parameters with inherent correlations. Incorporating copula formulations into CCP has the advantage of better modelling dependencies between variables under different scenarios when the underlying data exhibits complex distributions or non-trivial dependencies, such as correlated risks, thereby improving the accuracy of decision-making in optimisation problems with the presence of

uncertain parameters. In recent years, the integration of copula and CCP has shown significant promise. [16] formulated/employed joint chance constraints to address the capacity requirement in a multi-commodity network flow problem, using an Archimedean copula to estimate the dependencies between different capacity coefficient variables. [14] used a copula to model the dependency between resource consumptions of a stochastic resource-constrained shortest path problem. [11] proposed a joint chance-constrained method that integrates the best-performing copula from a set of widely applied bivariate copulas to characterise the uncertain probability distributions and the correlated nature of multi-period, multi-zone residential waste data.

In this work, we propose a data-driven chance-constrained optimisation framework to estimate the demand level within the context of planning and scheduling by leveraging the capabilities of copulas, which helps to achieve good efficiency and accuracy in estimating the multivariate demand data dependency structure. Moreover, we integrate our proposed framework with the DOMINO (Data-driven Optimisation of bi-level Mixed-Integer NOlinear problems) framework [2], which is a data-driven grey-box algorithm for addressing bi-level optimisation problems with various formulations at the lower levels [1].

# METHODOLOGY

## Copula Theory

A copula is a function that joins or "couples" multiple univariate marginal distributions to form a multivariate distribution. This enables the construction of any multivariate distribution using specified marginal distributions and the chosen copula, regardless of whether the underlying real distribution is fully understood. At a higher level, copulas are essential statistical tools for comprehensively analysing the dependency structures that exhibit in multiple random variables, effectively bypassing the marginal behaviour from joint dependence. By focusing on the joint cumulative distribution of marginal quantiles, copulas can capture complex, non-linear, and tail dependencies (extreme events) that traditional correlation metrics may often overlook [4].

The mathematical foundation of a copula is derived from Sklar's Theorem, which states that for any $n$-dimensional cumulative distribution function $F$ with marginal distributions $F_1, F_2, \dots F_n$, there exists a copula $C$ that models and encapsulates the dependency structure:

$$F(x_1, x_2, \dots x_n) = C(F_1(x_1), F_2(x_2), \dots F_n(x_n)) \quad (1)$$

where $x_1, x_2, \dots x_n$ are realisations of the random variables from each distribution, and the marginal distributions $F_i(x_i), i \in \{1, \dots n\}$ represent the individual variable behaviour. A few commonly applied copula models include Gaussian copula [18], t-copula [7], and Archimedean copula [13], each tailored to specific types of dependency structures.

## Chance constrained programming

Chance-constrained programming (CCP) is an optimisation technique that formulates probabilistic constraints to model uncertainty in decision-making problems [17]. This approach addresses uncertainty by allowing specific constraint(s) to be satisfied with a predetermined probability level, thus offering controlled flexibility to manage risk and account for the inherent variabilities in decisions related to demand, resource, or time availability. As a result, CCP provides a structured way to accommodate unpredictable conditions for many real-world problems in fields like energy production [23], finance [6], and supply chain management [19].

An individual probabilistic constraint, known as an individual chance constraint (ICC), requires that the constraint be met with a certain confidence level, denoted as a probability term $(1-\alpha)\%$, where $\alpha$ represents the risk level [5]. For example, setting $\alpha = 0.05$ means that the constraint must hold with at least $95\%$ probability while allowing for a $5\%$ risk tolerance for potential constraint violation. The formulation of a basic ICC can be represented as follows in the context of a production problem.

$$P[x_i \geq D_i] \geq 1 - \alpha_i, \;\; i \in \{1, \dots, n\} \quad (2)$$

where for each production constraint $i$, the production level decision variable $x_i$ must fulfil the uncertain demand parameter $D_i$ for at least $(1-\alpha_i)\%$ of the time. Joint chance constraint (JCC) is a variation of ICC, stressing that multiple constraints must be satisfied simultaneously with a given confidence level. Similarly, the JCC formulation can be expressed mathematically as:

$$P[x_i \geq D_i, i \in \{1, \dots, n\}] \geq 1 - \alpha \quad (3)$$

where the production level $x_i$ in all production scenarios $n$ must be sufficient to meet uncertain demand collectively with a joint confidence level of $(1-\alpha)\%$. As a result, JCCs impose stricter limitations on the feasible region of the solution space, making the problem generally more complex to solve.

The cumulative distribution function (CDF) provides a foundational basis for CCP in accumulating probabilities and facilitates the probabilistic guarantee of constraint satisfaction up to a given threshold. On the contrary, the quantile function, calculated as the inversed CDF, pinpoints a target probability level to the corresponding minimum production value required to meet the specified probability threshold.

## Data-driven chance constrained programming via copulas

In real-life applications, formulating chance constraints is generally challenging because the probability

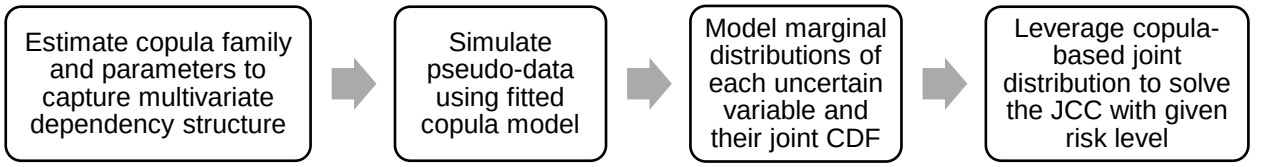



**Figure 1.** Logic flow for the proposed data-driven JCC framework with copula.

distribution of the uncertain parameters is often unknown or difficult to model with limited observed data. The difficulty of estimating an unknown distribution by existing parametric distributions (e.g., Gaussian distribution) is pronounced in high-dimensional or nonlinear contexts with no closed-form formulations, which often necessitates approximation or data-driven methods to adequately capture the distribution. This challenge becomes even more complex with JCCs, in which the dependency structure among the marginal demand distributions introduces correlation in the data. To tackle this issue, integrating the copulas technique into the modelling of JCCs offers a data-driven approach based on empirical data that models the marginal distributions of uncertain variables and their dependency structure to construct joint distributions.

We propose a data-driven framework that integrates copulas into data-driven JCC optimisation, as illustrated in Figure 1. We first employ pyvinecopulib [20] to fit the copulas to existing demand data using maximum likelihood estimation to estimate the best-fitting dependency structure and determine the copula family as well as its parameters. The selection of specific copulas family and dependency structure are based on optimising the AIC, BIC and log likelihood statistics using the pyvinecopulib package. Then, we use the fitted copula to construct a surrogate model that simulates correlated pseudo data while preserving the same dependency structure. The simulated pseudo data offers the advantage of scalability and enhancement by generating complete datasets with dependency structure when the original data may contain real-world data biases or missing values. Then, we can estimate the marginal distributions via non-parametric methods such as kernel density estimation [5] and in this approach, we adapt the built-in function in pyvinecopulib to estimate the marginal distributions and the joint CDF. Lastly, once the copula and marginal distributions are defined, the joint distribution can be estimated via (1) and utilised for approximating the quantile function and the risk level.

Following the data-driven copula framework above, we evaluate the JCC using Monte Carlo simulation. Each scenario generated from the copula-based quantile function is employed to compute the probability of constraint satisfaction across all realisations. By adjusting the number of empirical simulations, the confidence level for the JCCs can be calibrated to meet the desired level of risk tolerance $\alpha$.

### Data-driven mixed integer nonlinear bi-level optimisation

Historical production demand data of an integrated planning and scheduling problem is utilised to compute the copula-estimated demand set corresponding to a particular risk level following the procedure shown in Figure 1. The generated demand set can then be utilised as a demand scenario of integrated planning and scheduling optimisation problems [8, 10, 12] to be solved using the DOMINO framework. DOMINO is a data-driven strategy for solving general constrained bi-level optimisation problems which transform bi-level problems into single-level grey-box optimisations, utilising advanced data-driven techniques and deterministic solvers [22]. We refer the interested reader to [2] for a detailed description of the DOMINO framework and its application to solve integrated planning and scheduling problems under demand uncertainty in [1]. Figure 2 illustrates the workflow between the copulas and DOMINO framework. CCP offers a simplified uncertainty estimation approach based on risk level, which is more efficient compared to alternative methods such as stochastic programming, as originally proposed in [1], which requires explicit representation of all scenarios and since an increasing number of scenarios gives us a better understanding, incurs computational burden for high-dimensional problems.

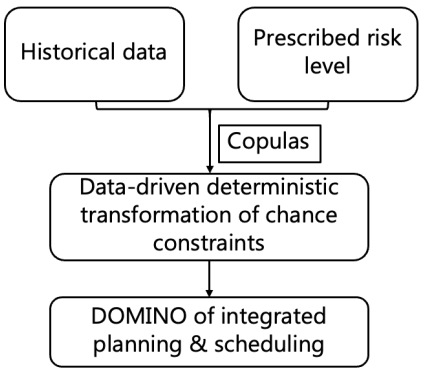



**Figure 2.** Integrated copulas-DOMINO solution workflow

## CASE STUDY

### Experimental setup

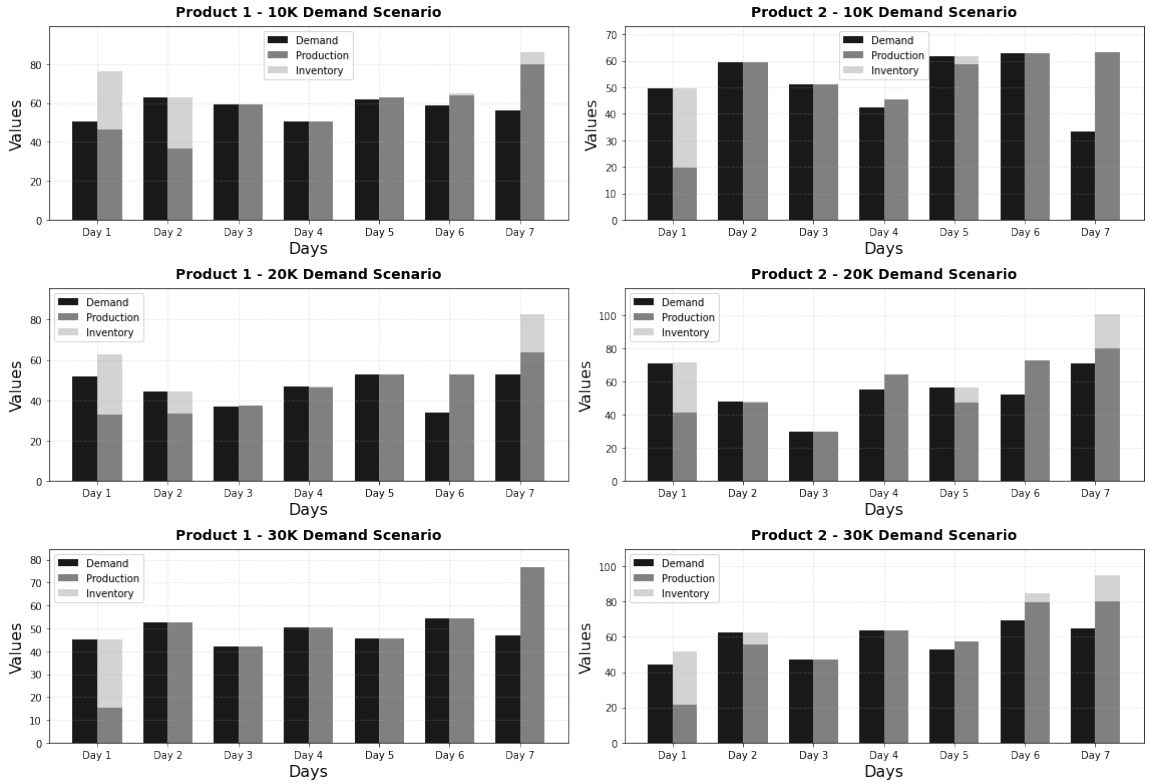



**Figure 3.** Production and inventory levels for the 2-product 7-day instance with copula-generated demand level under a specific number of scenarios (10, 20 or 30K). Planning cost values (scenario sizes): $7,085 (10K), $7,009.5 (20K). $6,850 (30K).

We employ our proposed approach to tackle the integrated planning and scheduling problem under product demand uncertainty. We consider a continuous single stage process with 2 products and 7 days, each with a 24hr duration. Firstly, we define the desired risk level and generate the corresponding demands, which are input as production targets into the DOMINO framework to tackle data-driven optimisation of the production level and evaluate the demand satisfaction rate via a simulation-based evaluation process. Throughout the experiment, two independent sets of scenario-based demands are generated: the first set is utilised to train the copula model designed to predict the empirical CDF and determine the quantile function for the joint chance constraint on demands. The second set serves as an evaluation benchmark during the simulation process to compute the demand satisfaction rate.

We employ the DOMINO framework for the solution of a bi-level optimisation problem case study with linear production planning and mixed-integer nonlinear scheduling from [21], and linear programming planning and scheduling case study from [1], respectively. Specifically, the nonlinear aspects of the integrated problem stem from the variable transition times in the scheduling of continuous manufacturing processes [9]. The case study is executed 10 times on a High-Performance Computing (HPC) machine using Red Hat Enterprise Linux 8.9 (Ootpa). The NOMAD algorithm within the DOMINO framework is executed serially using 1 core per node with 48GB RAM, starting from a random initial point.

## Results

We compute the copula-estimated demand set and input it into the DOMINO framework, wherein the integrated planning and scheduling problem is addressed. The production and inventory level outcomes are presented in Figure 3.

In our experimental design, we aim for 99% demand satisfaction during the generated production schedules. To evaluate, we will assess how the actual performance (a posteriori) in a real-world environment compares to our initially established reliability level (a priori) based on the copula-generated production target. That is, we calculate a fixed schedule derived from the copula-estimated demand level and aim to fix this target as a baseline. Subsequently, we employ copula to simulate the demand and evaluate the frequency with which the simulated demand satisfies all predefined scenarios.

The discrepancy between the a priori and a posteriori performance can arise because the copula method is data-driven and non-parametric. Since we do not require any prior assumption about the underlying distribution for

**Table 1:** Computational time and satisfaction rates for scenario sizes (averaged of 5 computational rounds).

| Products | Weeks | Scenarios | Compute Time (sec) | Multiplication of Individual Satisfaction Rates | Copula-estimated Joint Satisfaction Rates |
|---|---|---|---|---|---|
| 1 | 1 | 10k | 78 | 99.4% | 100% |
| 1 | 1 | 20k | 255 | 98.8% | 100% |
| 1 | 1 | 30k | 486 | 99.1% | 100% |
| 2 | 1 | 10k | 81 | 98.5% | 99.9% |
| 2 | 1 | 20k | 234 | 98.3% | 100% |
| 2 | 1 | 30k | 585 | 98.1% | 100% |
| 4 | 1 | 10k | 109 | 96.4% | 98.6% |
| 4 | 1 | 20k | 281 | 96.2% | 99.1% |
| 4 | 1 | 30k | 527 | 96.3% | 99.3% |
| 6 | 1 | 10k | 372 | 93.1% | 96.4% |
| 6 | 1 | 20k | 516 | 94.0% | 96.8% |
| 6 | 1 | 30k | 842 | 93.8% | 97.0% |

the demand data, we rely on the copula model to estimate the CDF of joint and individual demands. To analyse the impact of this discrepancy, we conduct the following experiment to evaluate the extent to which the scenario size employed during the copula model training influences the accuracy of prediction regarding demand satisfaction. Specifically, we utilise the joint and individual demand satisfaction rates as metrics to assess the quality of copula-generated demand under a certain risk level. The joint satisfaction rate represents the proportion of simulated scenarios for which all product demand targets are met. In contrast, the marginal satisfaction rate for each demand is individually independent, and the multiplication of these rates gives the independently joint satisfaction level, assuming all demands are individually met without considering any intercorrelation.

Table 1 showcases the satisfaction rate and computational time required to solve the offline copula model for different instance and scenario sizes with 7 days. Results demonstrate that the copula model, which assumes correlation among demands, yields higher joint satisfaction rates than the multiplication of individual rates, highlighting the copula model's capacity to capture the collective behaviour of demand data. Moreover, a higher joint satisfaction rate produced by copula suggests that interactions between demand levels may confer additional value. Incorporating these interactions could be crucial in increasing the overall demand satisfaction rate among all products. Furthermore, Table 1 shows a monotonic increase in the joint satisfaction rate when the total number of training scenarios increases from 10k to 30k for all instance sizes. This suggests that increasing the number of scenarios used to train the copulas model can enhance the accuracy of the estimated CDF, resulting in generating a fixed production level that ultimately raises the likelihood of demand satisfaction. The average computational time required for DOMINO to solve the integrated planning and scheduling problem is approximately 6 hours for the case study of 2 products and 7 days. This underscores the significance of managing uncertainty in an offline manner, as advocated by our proposed data-driven copulas framework. Additionally, our proposed copula approach requires estimating the CDF and solving the model only once, hence further enhancing its efficiency.

To summarise, we notice the advantages of our copula method are that the copula-generated plan (as an input to DOMINO) will be feasible for every possible scenario realisation for 99% of the times. Moreover, instead of solving the scenarios iteratively (as in [1]) and being very time-consuming, we can compute the copula-estimated CDF offline to massively save time at the cost of being slightly conservative (risk averse) with the actual demand satisfaction.

## Concluding remarks

We present a joint chance-constrained optimisation framework with data-driven copulas functions to effectively capture and model the multivariate demand data dependency structure for an integrated planning and scheduling problem. Our approach ensures feasible decision-making within a defined risk threshold. We validated the data-driven copulas-generated production targets using the DOMINO framework and tackled the data-driven optimisation. Our experiments demonstrate that the proposed approach is capable of identifying robust solutions that result in higher joint satisfaction rates for products and near-optimal performance, all while significantly reducing computational time compared to exact or stochastic optimisation methods. Plans for future research involve validating the efficiency and effectiveness of our approach through a number of case studies across an extended range of optimisation problems.

## ACKNOWLEDGEMENTS

Financial support from the UK EPSRC grants EP/V051008/1 and EP/W003317/1, U.S. National

Institutes of Health (NIH) grant P42 ES027704, and ACS Petroleum Research Fund Doctoral New Investigator Grant PRF # 66086-DNI9 is gratefully acknowledged.

## REFERENCES


1. Beykal B, Avraamidou S, Pistikopoulos EN. Data-driven optimization of mixed-integer bi-level multi-follower integrated planning and scheduling problems under demand uncertainty. Comput. Chem. Eng., 156,107551 (2022).
2. Beykal B, Avraamidou S, Pistikopoulos IP, Onel M, Pistikopoulos EN. Domino: data-driven optimization of bi-level mixed-integer nonlinear problems. J. Glob. Optim., 78:1-36 (2020)
3. Bianco L, Caramia M, Giordani S. A chance constrained optimization approach for resource unconstrained project scheduling with uncertainty in activity execution intensity. Comput. Ind. Eng., 128:831-836 (2019)
4. Bounitsis GL, Papageorgiou LG, Charitopoulos VM. Stable optimisation-based scenario generation via game theoretic approach. Comput. Chem. Eng., .185:108646 (2024)
5. Calfa BA, Grossmann IE, Agarwal A, Bury SJ, Wassick JM. Data-driven individual and joint chance-constrained optimization via kernel smoothing. Comput. Chem. Eng., 78:51-69 (2015)
6. Charnes A, Thore S. Planning for liquidity in financial institutions: The chance-constrained method. J. Fin., *21*(4):649-674 (1966)
7. Chan JC, Kroese DP. Efficient estimation of large portfolio loss probabilities in t-copula models. Eur. J. Oper. Res., 205(2):361-367 (2010)
8. Charitopoulos VM, Dua V, Papageorgiou LG. Traveling salesman problem-based integration of planning, scheduling, and optimal control for continuous processes. Ind. Eng. Chem. Res. 56(39):11186-205 (2017)
9. Charitopoulos VM, Papageorgiou LG, Dua V. Multi-parametric mixed integer linear programming under global uncertainty. Comput. Chem. Eng., 116:279-95 (2018)
10. Charitopoulos VM, Papageorgiou LG, Dua V. Closed-loop integration of planning, scheduling and multi-parametric nonlinear control. Comput. Chem. Eng., 122:172-92 (2019)
11. Chen F, Huang GH, Fan YR, Wang S. A copula-based chance-constrained waste management planning method: An application to the city of Regina, Saskatchewan, Canada. J. Air Waste Manag., 66:307-328 (2016)
12. Chu Y, You F, Wassick JM, Agarwal A. Integrated planning and scheduling under production uncertainties: Bi-level model formulation and hybrid solution method. Comput. Chem. Eng., 72:255-72 (2015)
13. Genest C, Nešlehová J, Ziegel J. Inference in multivariate Archimedean copula models. Test 20:223-256 (2011)
14. Hosseini Nodeh Z, Babapour Azar A, Khanjani Shiraz R, Khodayifar S, Pardalos PM. Joint chance constrained shortest path problem with Copula theory. J. Comb. Optim., 40:110-140 (2020)
15. Jiang R, Guan Y. Data-driven chance constrained stochastic program. Math. Prog. 158(1):291-327 (2016)
16. Khezri S, Khodayifar S. Joint chance-constrained multi-objective multi-commodity minimum cost network flow problem with copula theory. Comput. Oper. Res., 156,106260 (2023)
17. Li P, Arellano-Garcia H, Wozny G. Chance constrained programming approach to process optimization under uncertainty. Comput. Chem. Eng., 32:25-45 (2008)
18. Masarotto G, and Varin C. Gaussian copula marginal regression. E. J. Stat., 1517-1549 (2012)
19. Mitra K, Gudi RD, Patwardhan SC, Sardar G. Midterm supply chain planning under uncertainty: A multiobjective chance constrained programming framework. Ind. Eng. Res. Des.., 47(15):5501-11 (2008)
20. Nagler T, Vatter T. pyvinecopulib (version 0.6.8)
21. Nikkhah H, Charitopoulos VM, Avraamidou S, Beykal B. Bilevel optimization of mixed-integer nonlinear integrated planning and scheduling problems using the DOMINO framework. Comput. Aid. Chem. Eng., 53:1909-1914 (2024)
22. Nikkhah H, Aghayev Z, Shahbazi A, Charitopoulos VM, Avraamidou S, Beykal B. Bi-level data-driven enterprise-wide optimization with mixed-integer nonlinear scheduling problems. Dig. Chem. Eng., 100218 (2025)
23. Zhang H, Li P. Chance constrained programming for optimal power flow under uncertainty. IEEE Trans. Pow. Sys. 26(4):2417-2424 (2011)


© 2025 by the authors. Licensed to PSEcommunity.org and PSE Press. This is an open access article under the creative commons CC-BY-SA licensing terms. Credit must be given to creator and adaptations must be shared under the same terms. See https://creativecommons.org/licenses/by-sa/4.0/



Systems & Control Transactions

**Research Article - Peer Reviewed Conference Proceeding**
ESCAPE 35 - European Symposium on Computer Aided Process Engineering
Ghent, Belgium. 6-9 July 2025
Jan F.M. Van Impe, Grégoire Léonard, Satyajeet S. Bhonsale,
Monika E. Polańska, Filip Logist (Eds.)

PSE PRESS

# Diagnosing Faults in Wastewater Systems: A Data-Driven Approach to Handle Imbalanced Big Data

**M. Zadkarami[a], K.V. Gernaey[b*], A.A. Safavi[a], and P. Ramin[b]**

[a] School of Electrical and Computer Engineering, Shiraz University, Iran
[b] Process and Systems Engineering Center (PROSYS), Department of Chemical and Biochemical Engineering, Technical University of Denmark (DTU), Denmark
* Corresponding Author: kvg@kt.dtu.dk

## ABSTRACT

Process monitoring is essential in industrial settings to ensure system functionality, necessitating the identification and understanding of fault causes. While a substantial body of research focuses on fault detection, fault diagnosis has received significantly less attention. Typically, faults originate either from abnormal instrument behavior, indicating the need for calibration or replacement, or from process faults, signaling a malfunction within the system. A primary objective of this study is to apply the proposed fault diagnosis methodology to a benchmark that closely mirrors real-world conditions. Specifically, we introduce a fault diagnosis framework for a wastewater treatment plant (WWTP) that effectively addresses the challenges posed by imbalanced big data commonly encountered in large-scale systems. In our study, four distinct fault scenarios were investigated: fault-free conditions, process faults only, sensor faults only, and simultaneous sensor and process faults. To enhance our research, we explored various techniques and approaches to optimally address the fault diagnosis problem. Implementing an undersampling technique based on clustering and determining appropriate hyperparameters proved challenging, alongside deciding the most effective approach for undersampling. Additionally, advanced time-series models, including Long Short-Term Memory (LSTM) and Bidirectional LSTM (BiLSTM), were employed, with particular emphasis on identifying the correct regularization factor and number of epochs being critical. When optimal model parameters are selected, each fault scenario achieves an accuracy of at least 90%, and the maximum simulation time does not exceed 15 minutes. Furthermore, we developed a Python-based GUI for this study to enable users to fully explore the capabilities of the proposed fault diagnosis algorithm.

**Keywords**: Artificial Intelligence, Big Data, Wastewater, Industry 4.0, Process Monitoring

## INTRODUCTION

Today, process monitoring has become an increasingly critical task in industries, driven by cutting-edge technologies capable of handling large volumes of data. This advancement has introduced new challenges, particularly related to big data aspects. In scientific literature, "big data" typically refers to datasets that exhibit at least two of the following characteristics, collectively known as the 5V: Volume, indicating a substantial quantity of data samples; Velocity, reflecting a high sampling rate of incoming data; Veracity, which denotes significant uncertainty and noise within the data; Variety, meaning the dataset is composed of smaller datasets of different types and formats; and Variability, referring to the degree of complexity in the data, such as noticeable fluctuations and peaks in data patterns. It is important to note that whether a dataset is classified as big data also depends on the specific application [1].

Deep learning architectures have emerged as an effective approach for handling big data in process monitoring. Their primary advantage lies in their ability to perform feature analysis systematically, enabling the efficient extraction of key information from large datasets without the need for designing and implementing separate feature extraction mechanisms. However, utilizing deep learning architectures presents certain challenges. Tuning the hyperparameters of these deep structures is

often time-consuming and complex. Additionally, due to their extensive layers and intricate structures, these models are highly susceptible to the vanishing gradient problem, which can lead to inaccurate and erroneous results [2].

In real-world applications, normal operating conditions occur more frequently than faulty ones. From an engineering perspective, process monitoring in such settings constitutes an imbalanced classification problem, where the majority class represents normal conditions. Most statistical and neural network models are typically designed for balanced or nearly balanced classification scenarios, making them ineffective for highly imbalanced tasks. This is because, in imbalanced datasets, the majority class tends to dominate the decision-making process of these models.

One common approach to addressing the imbalanced classification problem is undersampling the majority class, which involves removing samples from the majority class [3]. A straightforward method is to randomly eliminate samples from the majority class. However, this simplistic approach is often naive, as it can result in the loss of important information pertaining to the majority class.

A recent study on fault detection in wastewater treatment plants (WWTPs) utilized an undersampling technique based on Gaussian Mixture Models (GMMs) [3]. The core idea of their research was to cluster the majority class and remove samples associated with the smallest clusters. This method achieved promising fault detection results by effectively balancing the removal of samples while preserving key information and the inherent behavior of the majority class.

In this study, four distinct scenarios for fault diagnosis were generated for a typical WWTP using Benchmark Simulation Model No.2 (BSM2). The research addresses a complex multi-class imbalanced big data problem, which poses significant challenges in accurately identifying and diagnosing faults within the system. To tackle this issue, we expanded our investigation to explore various undersampling techniques, advanced time-series models, and hyperparameter tuning strategies. These approaches aim to enhance the performance of fault diagnosis by effectively managing the imbalance in the dataset and improving the robustness of the models. Furthermore, we developed a Python-based Graphical User

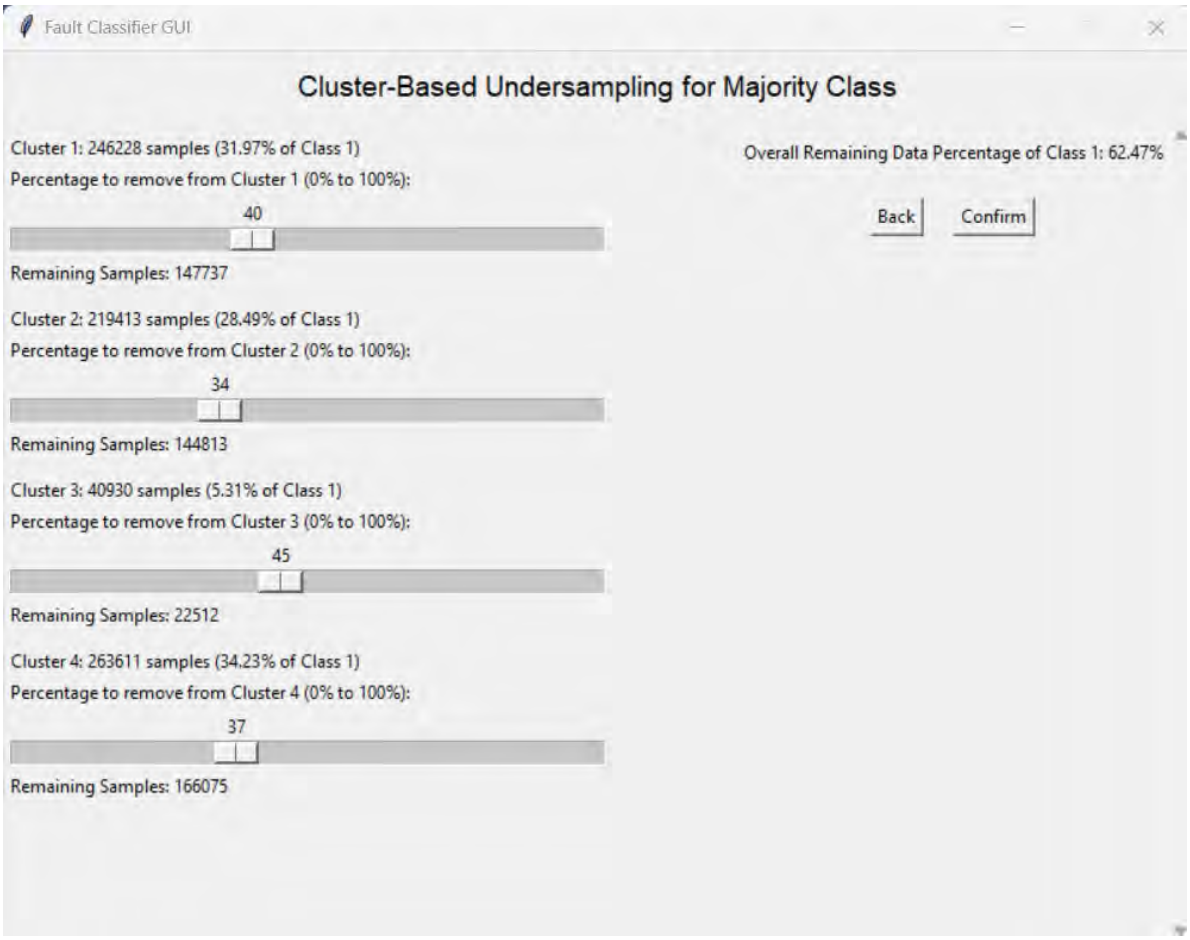



**Figure 1:** The second GUI window

Interface (GUI) to facilitate user interaction with the proposed models. The GUI allows users to deliberately select different models and their corresponding parameters, providing flexibility and ease of use. Additionally, it offers the option to save each modification made during the analysis process, ensuring that users can efficiently track and manage their experiments. The complete code for this study is publicly available on GitHub.

The structure of this paper is organized as follows. Section 2 presents the case study along with the generated data. Section 3 details the proposed fault diagnosis approach and its GUI. In Section 4, the process monitoring results are analyzed. Finally, Section 5 provides the conclusions of the study.

## CASE STUDY

The design of fault scenarios in this study is the same as the methodology outlined in [3, 4]. The faults are carried out on BSM2, closely simulating a real-world WWTP, containing process units listed as: a primary clarifier, activated sludge reactors, a secondary clarifier, a thickener, and a dewatering unit [3, 4]. Data acquisition is performed using 31 easily measurable variables, such as flow rate, Total Suspended Solids (TSS), Volatile Fatty Acids (VFA), among others, collected from various process units. The simulation duration of this plant-wide is 609 days with a sampling time of 1 minute, resulting in 876960 sample points. Therefore, for each fault scenario, a big dataset including 876960 sample points over 31 different measurements is investigated. To ensure the case study aligns more closely with real-world scenarios, the simulation period for normal operating conditions is set to be significantly longer than that for faulty conditions, resulting in an imbalanced big data distribution. The four fault scenarios and their contribution percentage is listed in Table 1.

As illustrated in Table 1, the majority class in this study, which is the normal operation condition, consists of 770182 samples and is designated as Class 1. Independent sensor faults and process faults are labeled as Class 2 and Class 3, respectively, each accounting for approximately 6% of the entire dataset. In this study, the process faults refer to the sludge bulking phenomenon and sensor faults represent an abnormality in the aerated reactors related the airflow. Lastly, only 330 samples (i.e. less than 0.1% of the dataset) indicate the simultaneous occurrence of both sensor and process faults, which are categorized as Class 4.

The aim of this study is to develop a fault diagnosis approach that by analyzing the 31-measurements anticipates which fault scenario is occurring. The primary challenge of this research work is to handle imbalance big datasets while striking a meaningful balance between the accuracy and the computational burden. Although the case study utilized in this research is identical to those presented in [3] and [4], the focus is on fault diagnosis, a multi-class classification problem, rather than fault detection, which is addressed as a binary classification problem. Moreover, aspects of big data must be considered when selecting appropriate parameters to ensure the effectiveness of the proposed approach. Finally, a GUI was developed for the proposed fault diagnosis algorithm, enabling users to easily select the desired model and adjust its parameters. Additionally, the GUI provides the capability to save the results of each stage of the algorithm independently.

**Table 1:** Fault Scenarios

| Stream | Description | Percentage |
|---|---|---|
| Class 1 | Normal | 87.82 |
| Class 2 | Only Sensor Fault | 6 |
| Class 3 | Only Process Fault | 6.14 |
| Class 4 | Both Sensor and Process Fault | 0.04 |

## FAULT DIAGNOSIS APPROACH

The proposed fault diagnosis workflow initiates by loading and preprocessing the dataset, generated by the update version of BSM2 [5], followed by identifying the majority and minority classes. The user is then prompted to input the desired number of clusters, after which the majority class data is segmented into the specified clusters. For each cluster, relevant information is displayed to the user, who determines the percentage of samples to remove. Based on this input, the appropriate number of samples is calculated and removed from each cluster. Subsequently, the undersampled majority class is combined with the minority classes, and the updated class distribution is presented. The user has the option to save the newly balanced dataset before proceeding to the modeling phase, thereby completing the preprocessing sequence.

The subsequent subsections present each window of the proposed fault diagnosis GUI designed to manage multi-class imbalanced big data distributions.

### The First Window: Data information

In the initial window, detailed information is presented, including the sample size of each class and the various imbalance ratios relative to the majority class (Class 1) for the generated fault scenarios of BSM2. In other words, the first window of the GUI displays the number of samples corresponding to each fault scenario: Class 1 contains 770,182 samples, Class 2 contains 52,583 samples, Class 3 includes 53,865 samples, and Class 4 has only 330 samples. Furthermore, the imbalance ratios (IR) are calculated to quantify the degree of class imbalance, yielding $IR_1$ = Class 1 / Class 2 = 14.65,

$IR_2$ = Class 1 / Class 3 = 14.30, and $IR_3$ = Class 1 / Class 4 = 2,333.88. More importantly, users have the option to select the number of clusters into which the majority class should be segmented. In this study, the diagnosis performance were studies for 2 to 6 clusters.

## The Second Window: Undersampling

In the second GUI window, the majority class is segmented based on the number of clusters selected in the preceding window. This window presents detailed information for each cluster, including the cluster size and its contribution percentage. The undersampling technique employed in this study involves initially clustering the majority class and subsequently removing samples randomly from each cluster. The removal percentage for each cluster can be determined through various methods: applying a uniform elimination percentage across all clusters, removing all samples from the smallest clusters sequentially until a predetermined overall removal percentage is achieved, or allowing the user to specify the removal percentage for each cluster individually. Figure 1 illustrates the second window of the developed fault diagnosis GUI.

## The Third Window: Confirmation

In this window, users can view the updated sample size of the majority class along with the revised imbalance ratios. To illustrate, the undersampling percentage applied to each cluster within the majority class (i.e., Class 1) is based on the values presented in Figure 1. As a result, the modified Class 1 is reduced to 481,137 sample points, leading to updated imbalance ratios of $IR_1$ = 9.15, $IR_2$ = 8.93, and $IR_3$ = 1,457.99. Although the dataset does not achieve a fully balanced distribution among the classes, removing the less informative samples from the majority class effectively reduces the degree of imbalance. Additionally, users have the option to save comprehensive information, including input measurements and output labels, for both the modified dataset and the removed samples. If the user is unsatisfied with the current elimination strategy, they can navigate back to the previous window to make adjustments. Otherwise, they can confirm and proceed to the next window.

## The Fourth Window: Time-Series Modelling

In this window, users can select their deep learning time-series model from Long Short-Term Memory (LSTM) and Bidirectional LSTM (BiLSTM). Upon selecting a model, users can adjust various model parameters, including learning rate, batch size, number of epochs, regularization factor, number of LSTM units, and dropout rate. Selecting appropriate values for epochs and the regularization factor is particularly challenging, as it requires balancing accuracy with computational efficiency. It is important to note that selecting lower values for the L2 regularization parameter can significantly increase the computational effort, improving the accuracy. On the other hand, increasing the number of epochs will extend the simulation time without necessarily guaranteeing an improvement in the classification accuracy for each class. Figure 2 illustrates the fourth window of the developed fault diagnosis GUI.

## The Fifth Window: Training Phase

In the fifth GUI window, the model begins training based on the previously provided information, while simultaneously displaying the ongoing simulation time. Monitoring the training time allows the user to terminate the process if the simulation duration exceeds expected limits.

## The Sixth Window: Results

In the final window, once the training phase is completed, the results are displayed, including simulation time, overall accuracy, confusion matrices, and class-specific accuracies for both training and testing datasets. Additionally, users have the option to save these results. It is important to note that overall accuracy may not be a reliable indicator for imbalanced data distributions; instead, ensuring high accuracy for each individual class is crucial. Figure 3 illustrates the last window of the developed fault diagnosis GUI.

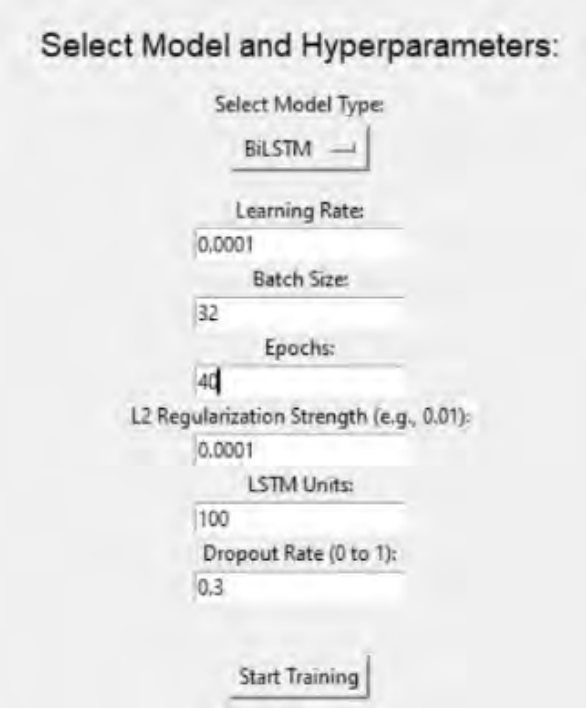



**Figure 2.** The fourth GUI window

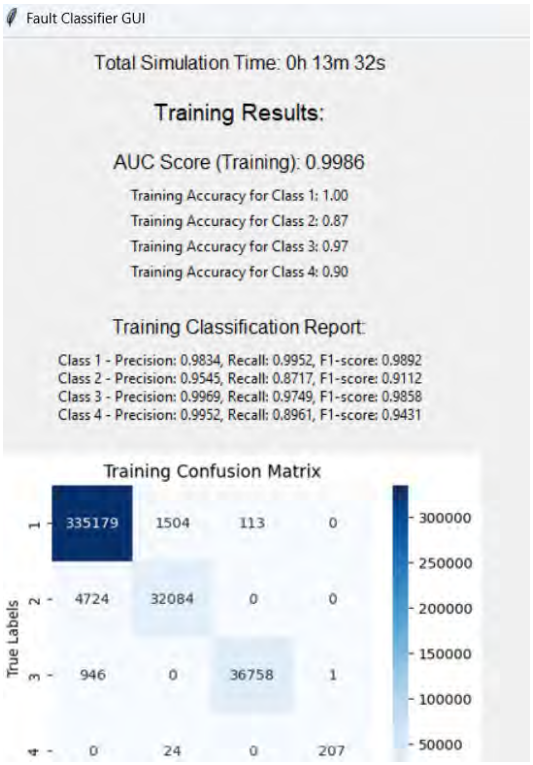



**Figure 3.** The sixth GUI window

## RESULTS AND DISCUSSION

As previously discussed, the regularization factor is crucial for obtaining optimal results. A regularization factor closer (L2) to zero typically enhances accuracy but also increases simulation time. Initially, we examine a fault detection algorithm that does not incorporate any undersampling techniques (Table 2), thereby directly inputting the imbalanced data into either an LSTM or BiLSTM model. In this setup, the parameters are configured with 40 epochs and a dropout rate of 30%.

**Table 2:** No undersampling approach (C denotes here as Class Accuracy)

| L2 | Model | C1 | C2 | C3 | C4 | Time(min) |
|---|---|---|---|---|---|---|
| 0.001 | BiLSTM | 99 | 43 | 76 | 0 | 17 |
| 0.001 | LSTM | 99 | 44 | 77 | 0 | 14 |
| 0.0005 | BILSTM | 99 | 60 | 84 | 0 | 20 |
| 0.0005 | LSTM | 99 | 58 | 84 | 0 | 16 |
| 0.0001 | BiLSTM | 99 | 80 | 95 | 94 | 20 |
| 0.0001 | LSTM | 99 | 80 | 94 | 91 | 18 |

**Table 3:** Comparing different epoch values (C denotes here as Class Accuracy)

| Epoch | C1 | C2 | C3 | C4 | Time (min.) |
|---|---|---|---|---|---|
| 100 | 100 | 91 | 98 | 96 | 34 |
| 40 | 99 | 89 | 97 | 91 | 14 |

According to Table 2, a regularization factor of 0.0001 is considered the highest acceptable value (L2 ≤ 0.0001), as exceeding this threshold leads to the accuracy of Class 4 dropping to zero or near zero.

With an established regularization factor of 0.0001, we proceed to identify the optimal number of epochs that achieves promising performance while minimizing computational time. The parameters fixed for this analysis are as follows: an undersampling rate of 40% (preserving 60% of the majority class) with 3 clusters for the majority class, a BiLSTM model configured with 100 units and a 30% dropout rate. Table 3 presents the classification accuracy for each class at epoch counts of 40 and 100, along with the corresponding simulation times.

Upon analyzing Table 3, it is evident that while the class accuracy of the model trained for 100 epochs is slightly higher than that of the model trained for 40 epochs, the computational cost is significantly greater for the 100-epoch model. Specifically, the fault diagnosis model with 100 epochs requires an additional 20 minutes of simulation time compared to the 40-epoch model. Therefore, it is reasonable to conclude that the 40-epoch configuration is more suitable in terms of both accuracy and computational efficiency.

With the L2 regularization value and the number of epochs established, we can now focus on investigating the number of clusters, determining the undersampling technique, and selecting a time-series model (LSTM or BiLSTM). Table 4 illustrates an undersampling rate of 40% applied uniformly across all clusters, whereas Table 5 demonstrates an undersampling rate of 40% achieved by eliminating the smallest clusters. Please note that in the simulation of Table 4 and 5, the L2 regularization value is 0.0001, drop out is 30%, batch size is 32, number of epoch is 40, the learning rate is 0.0001, and the employed LSTM units is 100.

**Table 4:** Uniformly removing samples from the clusters of the majority class (C denotes here as Class Accuracy)

| Cluster | Model | C1 | C2 | C3 | C4 | Time(min) |
|---|---|---|---|---|---|---|
| 2 | BiLSTM | 99 | 88 | 97 | 91 | 14 |
| 2 | LSTM | 99 | 87 | 96 | 86 | 11 |
| 3 | BILSTM | 99 | 89 | 97 | 91 | 14 |
| 3 | LSTM | 99 | 87 | 97 | 90 | 11 |
| 4 | BiLSTM | 99 | 87 | 97 | 89 | 13 |
| 4 | LSTM | 99 | 87 | 97 | 86 | 11 |
| 5 | BiLSTM | 99 | 87 | 97 | 89 | 13 |
| 5 | LSTM | 99 | 87 | 97 | 87 | 10.5 |
| 6 | BiLSTM | 99 | 88 | 97 | 94 | 11 |
| 6 | LSTM | 99 | 87 | 97 | 83 | 10.5 |

According to Tables 4 and 5, time-series models based on LSTM generally exhibit shorter computational times, averaging approximately three minutes. In contrast, fault diagnosis models utilizing BiLSTM achieve

higher accuracy values. Regarding the undersampling technique, uniformly removing samples from each cluster results in better accuracy compared to the approach of eliminating the smallest clusters. Additionally, the number of clusters has minimal impact on the performance of the proposed fault diagnosis algorithm.

**Table 5:** Removing samples from small clusters of the majority class (C denotes here as Class Accuracy)

| Cluster | Model | C1 | C2 | C3 | C4 | Time(min) |
|---|---|---|---|---|---|---|
| 2 | BiLSTM | 99 | 88 | 97 | 96 | 14.5 |
| 2 | LSTM | 99 | 88 | 98 | 83 | 11.5 |
| 3 | BILSTM | 99 | 87 | 96 | 91 | 13 |
| 3 | LSTM | 99 | 87 | 97 | 88 | 11 |
| 4 | BiLSTM | 99 | 87 | 96 | 96 | 14 |
| 4 | LSTM | 99 | 87 | 97 | 92 | 10.5 |
| 5 | BiLSTM | 99 | 89 | 97 | 85 | 13 |
| 5 | LSTM | 99 | 87 | 97 | 84 | 10.5 |
| 6 | BiLSTM | 99 | 87 | 98 | 99 | 13 |
| 6 | LSTM | 99 | 87 | 97 | 96 | 11 |

Finally, some implementation challenges related to parameter selection for the proposed fault diagnosis approach is highlighted. The total undersampling ratio is critical, as excessive removal of majority class samples may cause information loss. A 40% undersampling rate is recommended, retaining 60% of the majority class (i.e. class 1) samples [3]. For clustering, although the number of clusters has minimal effect, setting three or four clusters and uniformly removing 40% of samples from each cluster prevents losing essential data. Furthermore, both LSTM and BiLSTM models perform similarly, with suggested hyperparameters: learning rate of 0.0001, dropout rate of 0.3, batch size of 32, and 100 LSTM units. These parameters have limited effect on accuracy and simulation time. However, the L2 regularization parameter has a highly significant impact on model performance. Specifically, values greater than 0.0001 prevent the model from correctly identifying fault scenarios associated with Class 4, while values smaller than 0.0001 introduce a substantial computational burden. Additionally, the recommended number of training epochs ranges between 40 and 60. Increasing the number of epochs beyond this range does not necessarily improve classification accuracy but will considerably increase computational cost.

## CONCLUSION

This study presents a fault diagnosis framework specifically for a wastewater treatment plant, addressing the challenges of imbalanced big data typical in large-scale systems. It investigates four fault scenarios: fault-free conditions, process faults, sensor faults, and simultaneous sensor and process faults. The research utilizes clustering-based undersampling and optimizes hyperparameters, employs advanced time-series models such as LSTM and BiLSTM with careful regularization and epoch selection, and develops a Python-based GUI to allow users to effectively explore the fault diagnosis algorithm. The objective is to apply this methodology to benchmarks that closely reflect real-world conditions, enhancing the reliability and efficiency of industrial process monitoring. For future research, the development of an advanced optimization algorithm could be pursued to systematically and more effectively tune hyperparameters.

## DIGITAL SUPPLEMENTARY MATERIAL

The Python code for the proposed fault diagnosis GUI developed in this study is publicly available at https://github.com/Zadkarami/ESCAPE-2025.

## REFERENCES


1. Gandomi A, Haider M. Beyond the hype: Big data concepts, methods, and analytics. International journal of information management. 2015 Apr 1;35(2):137-44.
2. Zadkarami M, Safavi AA, Taheri M, Salimi FF. Data driven leakage diagnosis for oil pipelines: An integrated approach of factor analysis and deep neural network classifier. Transactions of the Institute of Measurement and Control. 2020 Oct;42(14):2708-18.
3. Zadkarami M, Safavi AA, Gernaey KV, Ramin P. A Process Monitoring Framework for Imbalanced Big Data: A Wastewater Treatment Plant Case Study. IEEE Access. 2024 Sep
4. Zadkarami M, Gernaey KV, Safavi AA, Ramin P. Big Data Analytics for Advanced Fault Detection in Wastewater Treatment Plants. InComputer Aided Chemical Engineering 2024 Jan 1 (Vol. 53, pp. 1831-1836). Elsevier.
5. Ramin P, Flores-Alsina X, Topalian SO, Jeppsson U, Gernaey K. Fault detection in a benchmark simulation model for wastewater treatment plants. InComputer Aided Chemical Engineering 2022 Jan 1 (Vol. 49, pp. 1363-1368). Elsevier.



© 2025 by the authors. Licensed to PSEcommunity.org and PSE Press. This is an open access article under the creative commons CC-BY-SA licensing terms. Credit must be given to creator and adaptations must be shared under the same terms. See https://creativecommons.org/licenses/by-sa/4.0/




Systems & Control Transactions

**Research Article - Peer Reviewed Conference Proceeding**
ESCAPE 35 - European Symposium on Computer Aided Process Engineering
Ghent, Belgium. 6-9 July 2025
Jan F.M. Van Impe, Grégoire Léonard, Satyajeet S. Bhonsale,
Monika E. Polańska, Filip Logist (Eds.)

PSE PRESS

# Modelling of a Heat Recovery System (HRS) Integrated with Steam Turbine Combined Heat and Power (CHP) Unit in a Petrochemical Plant

**Daniel Sousa[a]*, Miguel Castro Oliveira[a,b], and Maria Cristina Fernandes[a]**

[a] Instituto Superior Técnico, Universidade de Lisboa, Department of Chemical Engineering, Lisboa, Portugal
[b] Instituto de Soldadura e Qualidade, Research, Development and Innovation, Porto Salvo, Oeiras, Portugal
* Corresponding Author: danielrsousa@tecnico.ulisboa.pt.

## ABSTRACT

This study models a Heat Recovery System (HRS) within a petrochemical plant, assessing its economic and environmental viability. The system integrates four combustion processes and a condensing steam turbine combined heat and power (ST-CHP) generation unit, along with waste heat recovery technologies to reduce the plant's energy use. The developed system-based approach extends a previous methodology, initially focused on reducing energy consumption in production processes, to encompass energy supply systems (in which CHP is included) as well. Simulation models were developed for two improvement scenarios regarding the integration of the ST-CHP into the HRS: preheating either the combustion air stream or the inlet water of the ST-CHP's boiler. The latter demonstrated greater potential for reducing energy-related operational costs, thus an NLP optimisation model was developed based on that scenario. Both simulation and optimisation models were created resorting to the capabilities of the ThermWatt computational tool (comprising Modelica and Python languages). A payback period of about 2 years and 3 months and a reduction in equivalent carbon dioxide emissions of 5.14 kt $CO_{2,eq}$/year were estimated for the final system, which are significantly reasonable in comparison to benchmark values.

**Keywords**: Heat Recovery System, Combined heat and power, ThermWatt computational tool

## INTRODUCTION

In light of the ever-increasing emphasis on environmental protection, the European Union (EU) has introduced various policies and strategic frameworks aimed at fostering sustainable development across all member states. Central to this effort are the multiannual Environmental Action Programmes (EAPs), which have guided the EU's environmental policy since 1973 [1]. The most recent, the 8th EAP, came into effect in May 2022 and sets the legally binding framework for the EU's environmental goals until 2030. Building on the European Green Deal, it reiterates the EU's long-term vision to 2050 of living well and within planetary boundaries and outlines six priority objectives for 2030, along with measures to reach them. Among these objectives is meeting the 2030 greenhouse gas emissions reduction target, which seeks to cut the EU's emissions by 55% compared to 1990 levels [2]. Motivated by the substantial effort still required to meet the proposed targets and guided by the principles of the EU Energy System Integration Strategy (namely its first pillar, dealing with the promotion of the nexus between energy efficiency and circular economy) this work addresses the application of waste heat recovery practices aimed at reducing energy consumption of industrial plants, while delivering both economic and environmental benefits, primarily by reducing operational costs and lowering pollutant emissions.

The Heat Recovery Systems (HRSs) conceptualised in this work explore principles of waste heat recovery and expand a previous methodology (Water and Energy Integration Systems) [3,4], initially focused on reducing energy consumption in production processes, to encompass combined heat and power (CHP) generation systems, which fall under energy supply systems. The application of a unified heat recovery approach is based on

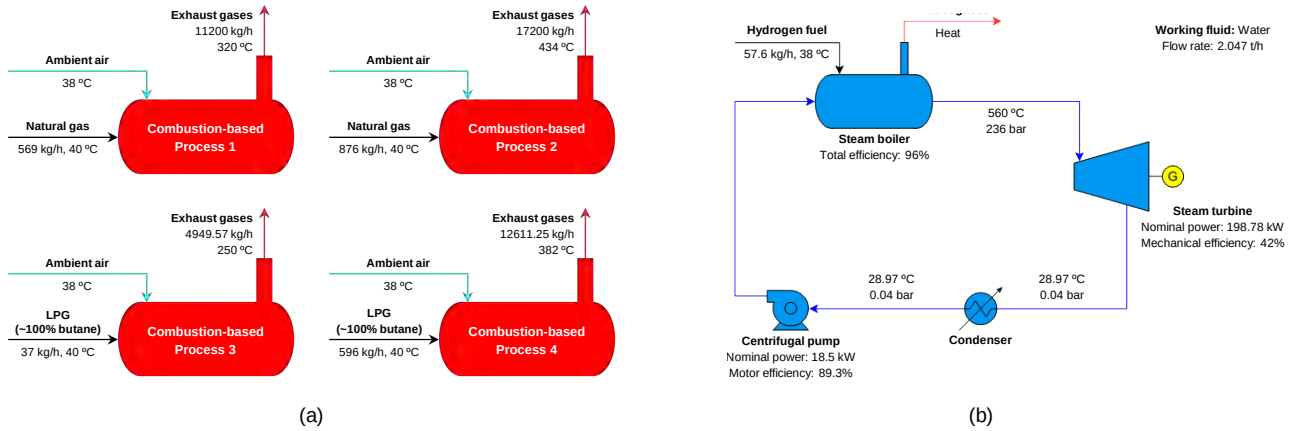



**Figure 1:** Information provided by the plant's stakeholders on the four CBPs (a) and the ST-CHP system (b).

the structural similarities and shared technologies between the two types of systems. This work uses the ThermWatt computational tool (owned by ISQ – Instituto de Soldadura e Qualidade [4]) to simulate and optimise an HRS integrated within a petrochemical plant.

## METHODOLOGY AND TOOLS

The methodological framework associated to this work begins with a clear problem definition, setting specific objectives and understanding the plant's processes. Based on this foundation:

1. The HRS for the targeted plant is designed, making an appropriate choice of heat recovery technologies to be installed in the plant and designing the superstructure of recirculated streams;
2. The ThermWatt computational tool is used to simulate and optimise the proposed HRS through a structured process:
   - 2.1 First, initial simulation models are developed to enable a preliminary analysis of improvement scenarios;
   - 2.2 Next, the most promising scenario is optimised to maximise total energy-related operational cost savings;
   - 2.3 Finally, the optimisation results are integrated back into the simulation model to achieve the system's final model.
3. The project's viability is assessed by calculating specific economic and environmental indicators, which are then compared against industry benchmarks for the chemical sector.

The Heat Recovery Systems are based on the steady-state thermal process subsystem of the Water and Energy Integration Systems (WEISs) [3,4] and seek to contribute with new processes and recirculation points to the existing conceptualised superstructure of WEISs. The HRS comprises N combustion-based processes (CBPs), each receiving fuel and air inputs and producing waste heat streams with recirculation potential (such as exhaust gas and hot air). A superstructure is designed accounting for all recirculation points, directing the mentioned heat streams back to the same CBP, to the other N – 1 CBPs, or to a thermodynamic cycle (TC) for electricity generation. Recirculated heat streams routed to a CBP merge into a single stream and transfer heat to incoming ambient air, either directly by mixing or indirectly via a heat exchanger, depending on the stream composition. For indirect heat recovery, the stream exits to the environment after the heat exchange. All the components and recirculation points mentioned thus far were already part of the WEISs. CHP systems are incorporated into the HRSs aiming to extend the scope of the WEISs to include the reduction of energy input in energy supply systems.

## CASE STUDY CHARACTERISATION

The case study approached in this work examines the implementation of a Heat Recovery System in a petrochemical plant. The plant is not yet operational, although the constituent unit operations have already been planned in terms of operational conditions and overall energy consumption levels. It is set to be located in Sines, Portugal and to operate for 7824 hours annually. The processes of the plant included in the case study are four CBPs and one condensing steam turbine CHP system (ST-CHP). Figure 1 displays information provided by the plant's stakeholders on the five processes. Currently, there is an interest of the plant's stakeholders on reducing consumption levels of natural gas and LPG, as well as on decreasing the use of hydrogen fuel in the ST-CHP

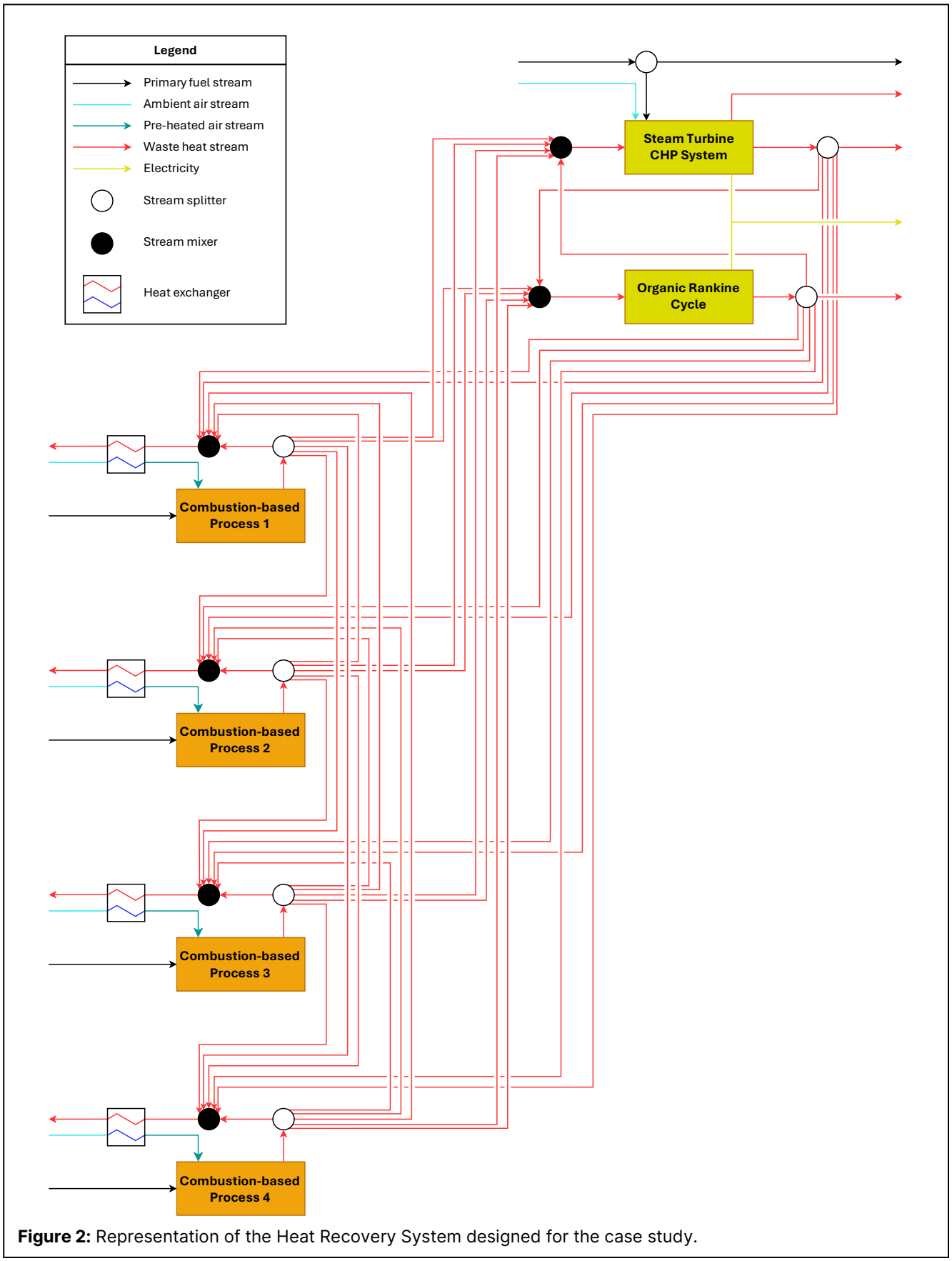



**Figure 2:** Representation of the Heat Recovery System designed for the case study.

system with the goal of reallocating the non-used hydrogen for other applications. The conceptualised HRS superstructure considering the planned energy-using units of the plant is illustrated in Figure 2.

Additional remarks for the implementation of the HRS include the assumption of 95 ºC as the minimum allowed temperature for the exhaust gas streams, ensuring these remain above the dew point. Furthermore, the air-fuel mass ratio was assumed constant. A reasonable maximum combustion air temperature of 300 ºC has been defined.

## SIMULATION

Two approaches have been exploited regarding the integration of the ST-CHP unit into the HRS, leading to two improvement scenarios:

- Scenario 1 involves installing an air preheater to preheat the steam boiler's combustion air to a maximum of 300 ºC, following the same approach applied to the CBPs;
- Scenario 2 proposes installing an economiser to preheat the steam boiler's pressurised feedwater to a maximum of 373.94 ºC, which corresponds to the critical temperature of water (the water in the steam boiler transitions directly to a supercritical state).

In this prospect, two simulation models were developed, one for each scenario, in order to assess which presents the greatest potential for reducing energy-related operational costs. The ORC model incorporated into the simulation models was adapted from one developed in prior work for implementing a WEIS in an industrial plant [4]. Table 1 presents key simulation results, showing that a basis for comparing both scenarios was successfully established, as the results between them differ only in terms of hydrogen consumption.

**Table 1:** Comparison of fuel costs and ORC-generated electricity savings (thus negative values) between the base case and both improvement scenarios, in M€/year.

| Energy vector | Base | Scenario 1 | Scenario 2 |
|---|---|---|---|
| Natural gas | 6.577 | 6.215 | 6.215 |
| LPG | 6.249 | 5.657 | 5.657 |
| Hydrogen | 1.911 | 1.747 | 1.209 |
| Electricity | – | -0.089 | -0.089 |
| Total | 14.737 | 13.530 | 12.992 |

Although the combustion air and inlet water of the steam boiler experienced similar temperature increases (an outlet temperature of 300 ºC was specified for both), the economiser in scenario 2 achieved a heat recovery rate of 2.418 GJ/h, which is 4.22 times higher than that of the boiler's air preheater in scenario 1. Consequently, scenario 2 resulted in significantly greater hydrogen savings. This difference is due to water's higher heat capacity compared to air. Furthermore, the heat recovery rate achieved by the boiler's air preheater of scenario 1 corresponds to its maximum value, as the combustion air temperature cannot exceed 300 ºC, while the economiser's recovery rate can be even higher, with the boiler feedwater capable of being preheated an additional 73.94 ºC. Given these aspects, scenario 2 indubitably offers greater potential for energy-related operational cost savings due to its superior capacity for overall energy consumption reduction. As a result, scenario 2 is the only one submitted to the optimisation procedure.

## OPTIMISATION

The system-level optimisation model of the second improvement scenario was formulated, for the most part, using the same set of parameters, variables and governing equations of the corresponding simulation model (refer to [5]). A few simplifications were applied, namely not calculating the composition of the streams, reducing the ST-CHP to the economiser and steam boiler, as well as simplifying the ORC system to a net efficiency parameter. The two streams recirculating heat between the ST-CHP and ORC had to be removed as they created an interdependency that made it impossible formulating the optimisation problem. The objective function was defined as the maximisation of energy-related operational cost savings. The resulting optimisation model is nonlinear, hence the use of open-source IPOPT solver.

A value of 6.07% was attributed to the ORC net efficiency parameter, aligning with the efficiency of the system adapted from the literature [4] initially implemented into the simulation model. The optimisation results showed that maximum heat recovery was achieved, as all the exhaust gas streams leaving the HRS had reached the minimum allowable temperature of 95 ºC, and that reducing fuel consumption was favoured over additional electricity generation. A sensitivity analysis, present in Figure 3, demonstrated that this preference occurred independently of the value attributed to the ORC net efficiency, within its feasible range (5-20%).

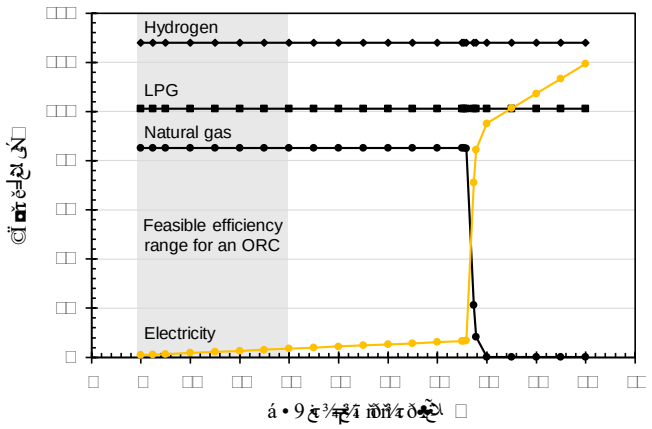



**Figure 3:** Results of the sensitivity analysis on the ORC net efficiency's impact on fuel and electricity savings.

Consequently, the optimised heat recovery rate of the ORC was significantly lower than the original design specifications of the simulated ORC system, failing to completely vaporise the working fluid, so it had to be resized prior to using the OpenModelica Python Package for incorporating the optimisation results into the simulation model. This was accomplished by adjusting the working fluid mass flow rate and pump outlet pressure via a parametric study, while also aiming for a new net efficiency of 12.5%.

Table 2 indicates that the final HRS reduced total energy-related operational costs by 16.9% compared to the base case and by an additional 42.3% compared to that obtained from the simulation of scenario 2.

**Table 2:** Energy consumption (TJ/year), costs (M€/year) and emissions (kt $CO_{2,eq}$/year) resulting from fuel consumption in the final HRS. The ORC-generated electricity savings (negative values) are also represented.

| Energy vector | Energy | Costs | Emissions |
|---|---|---|---|
| Natural gas | 458.29 | 5.912 | 29.38 |
| LPG | 198.13 | 5.458 | 12.49 |
| Hydrogen | 25.52 | 0.900 | – |
| Electricity | -0.53 | -0.017 | -0.03 |
| Total | – | 12.253 | 41.84 |

The final HRS flowsheet and detailed simulation results are provided as supplementary material. The optimisation resulted in no flow rate assigned to the ORC outlet purge stream, rerouting the high-temperature exhaust gas stream to the four CBPs. A similar outcome was observed for the exhaust gases at the outlet of the ST-CHP economiser, though a residual flow rate was still purged. The minimisation of purged high-temperature exhaust gas illustrates how these two recirculation points (exhaust gas stream splitters leaving the ORC and ST-CHP), which were absent in the WEISs, enhance the system's flexibility.

## VIABILITY ASSESSMENT

The economic and environmental indicators used to assess the final HRS project viability are the payback period ($PBP$) and the absolute reduction in equivalent carbon dioxide emissions ($Red.\ CO_{2,eq}$), which are calculated using Eq. (1) and (2).

$$PBP = \frac{Sav}{CAPEX} \quad (1)$$

$$Red.\ CO_{2,eq} = CO_{2,eq}^{BaseCase} - CO_{2,eq}^{HRS} \quad (2)$$

The total energy-related operational costs savings ($Sav$) is calculated using Eq. (3), while the equivalent carbon dioxide ($CO_{2,eq}$) emissions is determined via Eq. (4).

$$Sav = \sum_i \left(EC_i^{BaseCase} - EC_i^{HRS}\right) \cdot Price_i \quad (3)$$

$$CO_{2,eq} = \sum_i EC_i \cdot EF_i \quad (4)$$

In Eq. (3) and (4), $EC_i$, $Price_i$ and $EF_i$ represent the annual energy consumption, price and emission factor of the energy vector $i$ (electricity and fuels).

The capital expenditure ($CAPEX$) is determined as the sum of direct and indirect costs associated with the heat recovery technologies added to the base case. First, the equipment cost is estimated using correlations found in the literature [6,7] and adjusted to the current year using the CEPCI indexes. Then, the remaining direct and indirect expenditures are approximated as percentages of the installed equipment cost [8].

A payback period of less than 3 years is considered reasonable for an investment in waste heat recovery technologies within the industrial sector of the European Union [9]. Furthermore, a project conducted in a fertiliser industry in Norway achieved a reduction of $CO_{2,eq}$ emissions of 12-19 kt/year by increasing energy efficiency through the replacement of old electric motors with newer and more efficient ones [10]. If the estimated values are reasonable in comparison with these benchmarks, then the final HRS project is deemed viable.

Using the previously outlined procedure, the total CAPEX for the four air preheaters, economiser, and ORC system was estimated at 5.464 M€. Based on Tables 1 and 2, the total savings achieved by the final HRS amount to 2.484 M€, leading to a payback period of 2.20 years, or roughly 2 years and 3 months.

The final HRS achieved a reduction in $CO_{2,eq}$ emissions of 5.14 kt/year. While it falls short of the benchmark interval mentioned earlier, it is important to note that this comparison is based on absolute values, which does not consider several factors such as the size of the facility where the project used as a reference was implemented, the extent of the modifications and Norway's electrical energy mix (which influences the emission factor associated with electricity generation). Nevertheless, the final HRS results in a substantial 8.9% reduction in emissions

compared to the base case.

Taking into account the comparison between the estimated results for both indicators and the reference benchmarks, it may be considered that the engineering project associated to the conceptualised HRS presents a significant economic and environmental viability.

## CONCLUSIONS

This work represents an initial step in the design phase of an industrial project, in which a preliminary technical, economic and environmental assessment has been carried out. By exploring the capabilities of the ThermWatt computational tool it was possible to virtually integrate the conceptualised Heat Recovery Systems within a real plant and conclude that the final project not only enhances energy efficiency but also shows promising potential to improve the sustainability and competitiveness of the industrial plant in question. The addition of two new equipment-level models to the ThermWatt Modelica Library signified the further expansion of its capabilities, highlighting its versatility. Overall, this study shows the importance of waste heat recovery in promoting the principles of the circular economy within industrial operations by reducing waste and decreasing reliance on external energy sources through the reuse of thermal energy that would otherwise be lost.

## DIGITAL SUPPLEMENTARY MATERIAL

Digital supplementary material is available at https://psecommunity.org/LAPSE:2025.0007, including basic information regarding the involved energy vectors (lower heating value, prices and emission factors), the validation results of the new steam boiler model and the flowsheets and detailed simulation results of both improvement scenarios and final HRS.

## ACKNOWLEDGEMENTS

This work was funded through the base funding component of the Center for Technology and Innovation — ISQ, under the terms defined in AAC nº 03/C05-i02/2022, and CERENA, under grant UIDB/04028/2020_UIDP/04028/2020.

## REFERENCES

1. Halmaghi E-E. Environmental action programmes of the European Union. *Scientific Bulletin* 21:87–90 (2016) https://doi.org/10.1515/BSAFT-2016-0040
2. European Commission. Stepping up Europe's 2030 climate ambition. EUR-Lex 2020
3. Oliveira MC, Iten M, Matos HA. Review on water and energy integration in process industry: water-heat nexus. *Sustainability* 14(13):7954 (2022) https://doi.org/10.3390/su14137954
4. Oliveira MC. Simulation and Optimisation of Water and Energy Integration Systems (WEIS): An Innovative Approach for Process Industries. Doctoral Thesis: Instituto Superior Técnico (2023) https://doi.org/10.5281/ZENODO.13119500
5. Sousa D. Modelling and Optimisation of Heat Recovery Systems (HRS) using the ThermWatt Computational Tool. Master's Thesis: Instituto Superior Técnico (2024) https://scholar.tecnico.ulisboa.pt/records/GJb4JcFXjCuigP8tziDo2bnXLPznCgq2F3J5
6. Turton R, Shaeiwitz J, Bhattacharyya D, Whiting W. Analysis, Synthesis, and Design of Chemical Processes. Prentice Hall (2018)
7. Lemmens S. Cost engineering techniques & their applicability for cost estimation of organic Rankine cycle systems. *Energies* 9(7):485 (2016)
8. Peters MS, Timmerhaus KD. Plant Design and Economics For Chemical Engineers. McGraw-Hill (1990)
9. Tello P, Weerdmeester R. Spire Roadmap (2013) https://www.aspire2050.eu/sites/default/files/pressoffice/spire-roadmap.pdf
10. ABB. Energy efficiency opportunities in chemical manufacturing (2023)

© 2025 by the authors. Licensed to PSEcommunity.org and PSE Press. This is an open access article under the creative commons CC-BY-SA licensing terms. Credit must be given to creator and adaptations must be shared under the same terms. See https://creativecommons.org/licenses/by-sa/4.0/



Systems & Control Transactions

**Research Article - Peer Reviewed Conference Proceeding**
ESCAPE 35 - European Symposium on Computer Aided Process Engineering
Ghent, Belgium. 6-9 July 2025
Jan F.M. Van Impe, Grégoire Léonard, Satyajeet S. Bhonsale,
Monika E. Polańska, Filip Logist (Eds.)

PSE PRESS

# Integrating Thermodynamic Simulation and Surrogate Modeling to Find Optimal Drive Cycle Strategies for Hydrogen-Powered Trucks

**Laura Stops[a]*, Alexander Stary[a], Johannes Hamacher[a], Daniel Siebe[a], Thomas Funke[b], Sebastian Rehfeldt[a], and Harald Klein[a]**

[a] Technical University of Munich, TUM School of Engineering and Design, Department of Energy and Process Engineering, Institute of Plant and Process Technology, Garching, Germany
[b] Cryomotive GmbH, Grasbrunn, Germany
* Corresponding Author: laura.stops@tum.de.

## ABSTRACT

Hydrogen-powered heavy-duty trucks have a high potential to significantly reduce $CO_2$ emissions in the transportation sector. Therefore, efficient hydrogen storage onboard vehicles is a key enabler for sustainable transportation, as achieving high storage densities and extended driving ranges is essential for the competitiveness of hydrogen-powered trucks. Cryo-compressed hydrogen ($CcH_2$), stored at cryogenic temperatures and high pressures, emerges as a promising solution. This study presents a comprehensive dynamic thermodynamic model that is capable of simulating the tank system across all operating conditions and, therefore, enables thermodynamic analysis of drive cycles. The core of the model is a differential-algebraic equation system that describes the thermodynamic state of the hydrogen in the tank. Additionally, surrogate models based on artificial neural networks are applied to efficiently describe quasi-steady-state heat exchangers integrated into the tank system. Several use cases are explored to demonstrate the model's ability to simulate the thermodynamic behavior and to find optimal operating strategies. The optimal hydrogen density, when to stop driving and refuel the tank to maximize overall driving ranges, is investigated both in ideal and real operation, taking into account the limited availability of refueling stations in early market applications. Further, driving range and venting losses are considered for longer periods of dormancy. These results provide insights into how operational strategies can be tailored to maximize driving range, minimize hydrogen losses, and improve overall system efficiency, ultimately supporting the adoption of hydrogen in long-haul transportation.

**Keywords**: Hydrogen, Dynamic Modeling, Surrogate Model, Process Operations, Matlab

## INTRODUCTION

To reduce $CO_2$ emissions in transportation, hydrogen-powered heavy-duty trucks are a promising solution. Thereby, cryo-compressed hydrogen ($CcH_2$), stored at cryogenic temperatures and high pressures, is an efficient way for onboard hydrogen storage, as it achieves the highest storage densities [1]. In the CryoTRUCK project, funded by the German Federal Ministry of Digital and Transport (BMDV), such a $CcH_2$ storage is being developed. For optimal utilization of the stored hydrogen, good knowledge of the thermodynamic processes within the tank is essential. Thus, in previous works, thermodynamic models and computational fluid dynamics (CFD) analyses studying the heat exchangers of the tank system have been introduced [1-5]. This study applies and combines the thermodynamic models of the tank system to analyze and investigate optimal vehicle operation.

Therefore, surrogate models based on artificial neural networks (ANNs) are used to efficiently simulate the heat exchangers integrated into the system, enhancing simulation speed and reducing model complexity. This model reduction allows the export of the tank model in a compact way for integration into large vehicle models or

even for onboard simulations. Several use cases are explored in this study, focusing on optimal operation to maximize driving range or avoid hydrogen losses.

## METHODOLOGY

The applied model consists of a dynamic thermodynamic tank model and surrogate component models of two heat exchangers that will be discussed hereafter.

### Thermodynamic Tank Model

The considered $CcH_2$ tank is depicted in Figure 1. It consists of an aluminum liner wrapped in carbon fiber and insulated by vacuum and multi-layer insulation. Two heat exchangers are included in the system: an inner (iHEX) and an outer (oHEX) heat exchanger. The latter one heats up the cryogenic hydrogen that is discharged from the tank (mass flow rate $\dot{M}_{\mathrm{disch}}$) before the warm hydrogen is fed to the truck's fuel cell (FC). The iHEX is used to control the pressure in the tank by heating the tank (heat flow $\dot{Q}_{\mathrm{disch}}$). Therefore, hydrogen that has already been heated up in the oHEX is redirected via a three-way valve to the iHEX. After passing the iHEX, the hydrogen flows through the oHEX once more towards the FC.

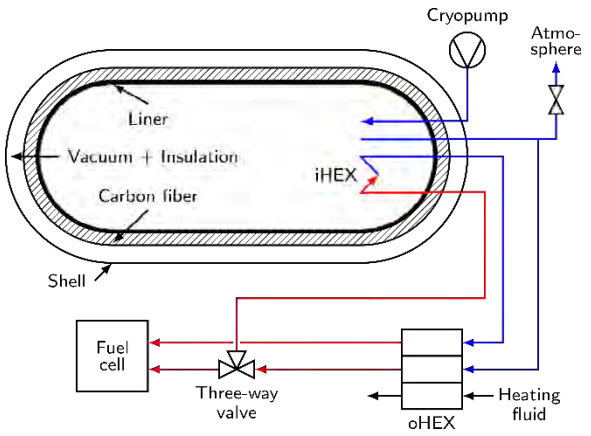



**Figure 1**. CcH2-Tank [2]

Three operating scenarios are considered in this study: discharge (or driving), refueling, and dormancy. In this study, it is assumed that in the refueling scenario, $CcH_2$ is always refueled with a constant mass flow rate $\dot{M}_{\mathrm{fuel}} = 60\ \mathrm{g/s}$ as described in [2]. Further, when the truck is parked for a long time, the pressure may rise above the venting pressure $p_{\mathrm{vent}} = 450\ \mathrm{bar}$ due to heat inleak from the ambiance (heat flow $\dot{Q}_{\mathrm{amb}}$), which requires venting hydrogen with the mass flow rate $\dot{M}_{\mathrm{vent}}$ to maintain the pressure $p_{\mathrm{vent}}$. It is assumed that exactly the amount required to maintain the pressure is vented.

When simulating a discharge process, a constant mass flow rate of $\dot{M}_{\mathrm{disch}} = 1\ \mathrm{g/s}$ is considered. As shown in previous work [1,2], the temperature and pressure in the tank decrease during driving. When the minimum pressure $p_{\mathrm{min}} = 15\ \mathrm{bar}$ required by the FC system is reached, the iHEX is turned on. [1] and [2] assume that the iHEX delivers exactly the heat required for maintaining the pressure $p_{\mathrm{min}}$, which will be referred to as *ideal iHEX*. In this study, it is assumed that the three-way valve in Figure 1 acts as on-off control, meaning that either all discharged hydrogen is passed through the iHEX or none. When the iHEX is on, the temperature and pressure in the tank rise. As soon as an upper threshold is reached, the iHEX is shut off again. Here, the upper threshold is set to 35 bar. The heat flow generated by the iHEX is calculated from surrogate models that will be discussed in the next section. This setup is hereafter referred to as *real iHEX*.

Thus, the $CcH_2$ tank is characterized by the mass and energy balance in Equation (1) and (2). For the sake of simplicity, no index is used for all variables describing the hydrogen within the tank.

$$\frac{\mathrm{d}M}{\mathrm{d}t} = \dot{M}_{\mathrm{fuel}} - \dot{M}_{\mathrm{disch}} - \dot{M}_{\mathrm{vent}} \tag{1}$$

$$\frac{\mathrm{d}U}{\mathrm{d}t} = \dot{M}_{\mathrm{fuel}} \cdot h_{\mathrm{fuel}} - \dot{M}_{\mathrm{disch}} \cdot h - \dot{M}_{\mathrm{vent}} \cdot h + \dot{Q}_{\mathrm{amb}} + \dot{Q}_{\mathrm{disch}} \tag{2}$$

As it is assumed that the hydrogen is ideally mixed, the hydrogen taken from the tank has the same temperature and pressure and, therefore, specific enthalpy $h$ as the hydrogen in the tank. The specific enthalpy $h_{\mathrm{fuel}}$ of the refueled hydrogen results from an isentropic compression from the refueling station pressure to the tank pressure $p$ with the efficiency $\eta_{\mathrm{pump}} = 0.78$ until the fill pressure $p_{\mathrm{fill}} = 400\ \mathrm{bar}$ is reached [2]. Further, only the hydrogen as well as the solid aluminum and carbon fiber parts are considered, while other solid components of the tank are neglected. As the solids are in good thermal contact with the hydrogen, a uniform temperature is assumed [1,2]. Based on the balances and several algebraic equations, a differential-algebraic equation system is defined in [1] and [2], describing the thermodynamic state of the hydrogen in the tank for all operation modes. All parameters used for this study are taken from [2].

### Surrogate Component Models

Within the CryoTRUCK project, rigorous component models of the two heat exchangers in the tank are being developed, based on thermodynamic correlations and CFD simulations [4,5]. Combining these models with the dynamic thermodynamic tank model would highly increase calculation time and model complexity. However, using the model for real drive cycle optimizations, integration into large vehicle models, or usage onboard the truck for driver assistance systems and tank state monitoring requires real-time calculations and low complexity. Thus, surrogate models of the heat exchangers are generated and integrated into the tank model. It is assumed that both heat exchangers are in a quasi-steady state in relation to the dynamics of the $CcH_2$ tank.

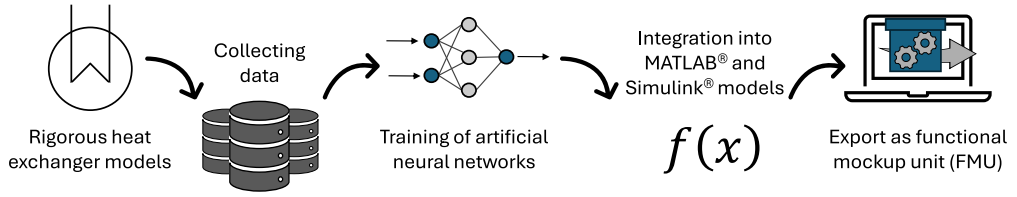



**Figure 2**. Workflow of building the surrogate models.

The workflow of generating these surrogate models is shown in Figure 2. The rigorous heat exchanger models are used to collect datasets of input-output relations for the steady-state heat exchanger characteristics. The inputs are chosen across the operation range using Latin hypercube sampling [6]. The data is used to train, validate, and test ANNs, which take all inputs of the respective rigorous models and return the hydrogen state at the outlet of the heat exchanger and the transferred heat flows. When the ANNs are inserted into the MATLAB® system model, the resulting reduced model includes only two differential equations and accurately represents the overall system while having low model complexity. Additionally, by integrating the ANNs into a Simulink® tank model and exporting it as a functional mockup unit (FMU), the model can be included in other simulation platforms and possibly run onboard a truck.

## RESULTS

This section investigates drive cycles with the ideal and real heat exchanger models. Further, two case studies of typical operating strategy problems are conducted.

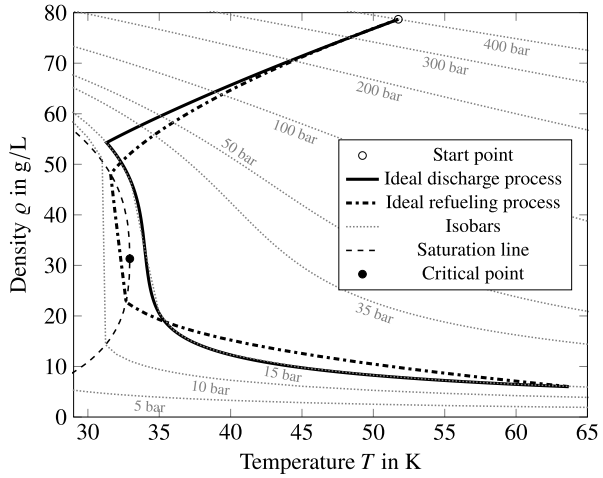



**Figure 3.** Drive cycle with ideal iHEX

Figure 3 shows an ideal cycle of discharge and refueling with the ideal iHEX within a $(T, \varrho)$-diagram. At the beginning of the discharge, temperature and pressure decrease. When reaching $p_{\min}$, the iHEX is switched on and delivers exactly the heat flow required to follow the $p_{\min}$-isobar. As soon as a minimum density, also called stop density $\varrho_{\text{stop}}$, is reached, the truck is stopped and refueled up to $p_{\text{fill}}$, ending up at the same thermodynamic state as at the beginning of the idealized cycle.

The real discharge process, deploying the real iHEX simulated with the surrogate models and the on-off control, is depicted in Figure 5(a) alongside the ideal process. Generally, the real process follows the ideal one, however, due to the on-off control, a zigzag pattern is visible. When $p_{\min}$ is reached and the iHEX is turned on, more heat than required is transferred. Thus, temperature and pressure rise. When the iHEX is shut off at 35 bar, temperature and pressure fall back to the path of the ideal process. At the end of the discharge, much more heat is required to keep the pressure, and the intervals of heating become larger. However, the heating intervals highly depend on the mass flow rate and the starting conditions.

These findings are relevant when considering the influence of $\varrho_{\text{stop}}$ on the usable density $\Delta\varrho_{\text{use}}$ and the fill density $\varrho_{\text{fill}}$, which are plotted over the stop density in Figure 4 for the ideal process, assuming that refueling is possible at any time [2]. The fill density is defined as the density that results from refueling up to $p_{\text{fill}}$, starting from the thermodynamic state at the end of the discharge defined by $\varrho_{\text{stop}}$. The usable density $\Delta\varrho_{\text{use}} = \varrho_{\text{fill}} - \varrho_{\text{stop}}$ relates the current stop density to the subsequent fill density and, thus, to the potential driving range of the next drive cycle.

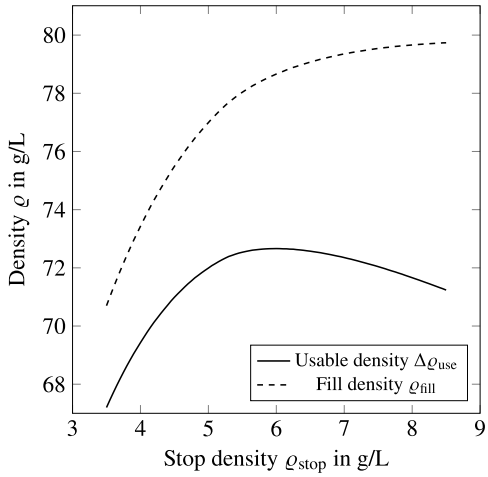
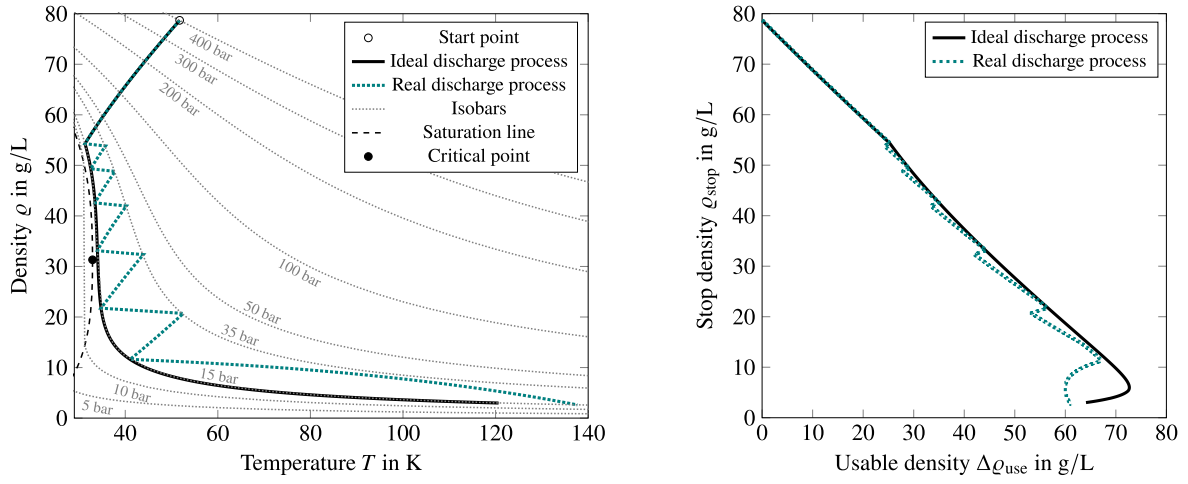



**Figure 4.** Usable and fill density as a function of the stop density




(a) Discharge process (b) Usable density

**Figure 5**. Discharge process and corresponding usable densities for refueling anytime during the discharge

The fill density highly depends on $\varrho_{\mathrm{stop}}$, as at the end of the discharge, the temperature rises fast when the $p_{\mathrm{min}}$-isobar slope becomes small (see Figure 3). For the following refueling process, however, low temperatures in the tank are preferable to achieve higher storage densities. Consequently, the fill density increases in Figure 4 for higher stop densities. Since stopping too early would not exploit the capacity of the tank, the usable density has a clear maximum. Thus, for the ideal process, an optimal stop density, at which it is best to stop and refuel for the maximum driving range, can be found by optimizing $\Delta\varrho_{\mathrm{use}}$. Therefore, the MATLAB® function `fminbnd` is applied to maximize $\Delta\varrho_{\mathrm{use}} = f(\varrho_{\mathrm{stop}})$. The underlying objective function calculates $\Delta\varrho_{\mathrm{use}}$ by simulating a refueling process, starting from the thermodynamic tank state defined by $\varrho_{\mathrm{stop}}$ and $p_{\mathrm{min}}$. The resulting optimal stop density is $\varrho_{\mathrm{stop}}^{\mathrm{ideal}} = 6.025\,\mathrm{g/L}$, which corresponds to a fill state of $\varrho_{\mathrm{fill}} = 78.69\,\mathrm{g/L}$, $T_{\mathrm{fill}} = 51.75\,\mathrm{K}$, and $p_{\mathrm{fill}} = 400\,\mathrm{bar}$. This is used as starting point for all remaining simulations.

When, instead, the real iHEX, including the on-off control, is considered, a different behavior is observed. Figure 5(b) shows the usable density that would be achieved when the truck is stopped and refueled at any time during the ideal and real discharge processes in Figure 5(a). Thereby, the thermodynamic state corresponding to each stop density in Figure 5(b) equals a state in Figure 5(a). The results of the ideal iHEX process are in accordance with the course in Figure 4 and show an optimum at $\varrho_{\mathrm{stop}} = 6.025\,\mathrm{g/L}$. The usable densities simulated with the real iHEX, however, are highly influenced by the peaks due to the on-off iHEX control. Whenever the iHEX is on and the temperature in the tank is high, refueling would be less efficient. Thus, the usable density is best when refueling just before the iHEX is turned on again. At the theoretical optimal stop density, the real process course for the considered starting conditions and mass flow rate is at the peak of a heating period, which is most unfavorable for refueling. Consequently, the real iHEX process would have roughly 5 g/L less maximal usable density compared to the ideal case. When still stopping at the theoretical optimal stop density, 12 g/L of maximal usable density is lost.

While this approach allows calculating optimal stop densities for the real system and could, thus, be used to recommend when to refuel, an even better approach to maximize the usable density would be to alter the iHEX control before refueling. When the truck operator provides the tank system with knowledge of the next refueling point, the iHEX could be turned off to ensure low temperature and pressure when refueling takes place.

## Case Study 1: Refueling Station Scarcity

In this section, the ideal and real discharge processes are investigated, considering that during early market entry, only limited hydrogen refueling stations exist. Two cases are defined: refueling stations are located (a) every 100 km, or (b) every 50 km. It is assumed that a truck has two tanks as defined in [2] and that a hydrogen truck consumes roughly 7 kg per 100 km [7]. Figure 6 highlights all options for refueling during the discharge process in a $(T, \varrho)$-diagram. The resulting usable densities at all refueling stations are depicted in Figure 7(a) and Figure 7(b) for the cases where refueling stations are located every 100 km or every 50 km. Most deviations between the ideal and real iHEX operation occur after long driving ranges because, for the considered mass flow rate and starting conditions, the drive cycle ends with a long period of heating of the real iHEX, which is non-ideal for the subsequent refueling.

In the 100 km case, the last two fuel stations lead to almost the same usable density in the real discharge

process, even though the last tank stop is located at the peak of the last heating period. The non-ideal refueling conditions at the last stop are balanced out by refueling too early at the second last option, not exploiting the usable density.

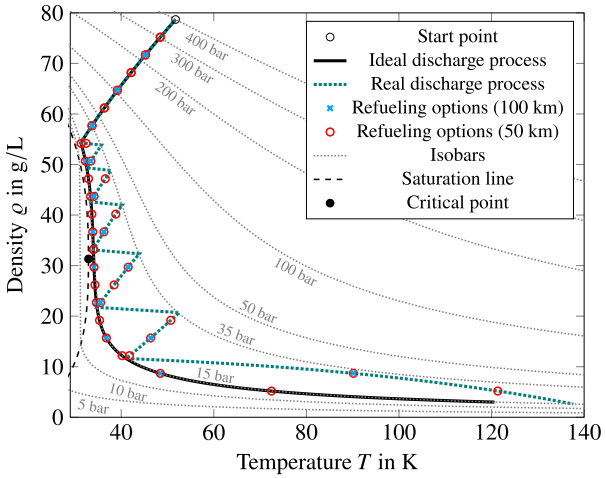



**Figure 6.** Discharge process with markers for refueling stations which are located every 100 or 50 km.

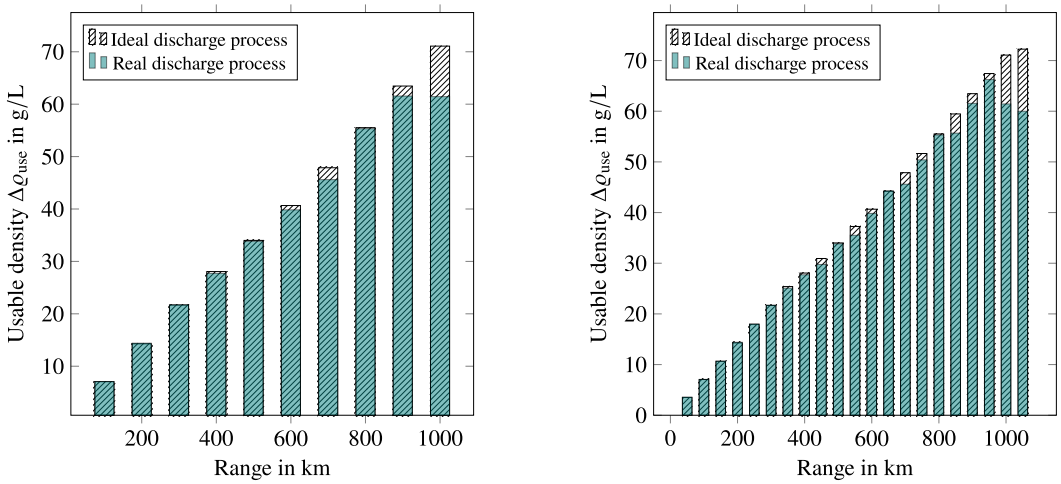
In the 50 km case, the third last stop option is the preferred one. Here, the refueling stop happens just before the next heating period starts. Thus, almost the usable density of the ideal iHEX process is reached. Stopping at the last option, however, would even be worse than the fourth last stop in terms of usable density.

## Case Study 2: Long Dormancies

In a second study, the effect of longer dormancies, e.g., when the truck is parked for the weekend, on the drive cycle operation is investigated. First, the truck is driving until the stop density $\varrho_{\mathrm{stop}} = 6.025\ \mathrm{g/L}$ is reached. Then, it can either be refueled before being parked for the weekend for 62 h (A), or afterward, before starting the next drive after the weekend (B). Figure 7(a) shows both options in a $(T, \varrho)$-diagram.

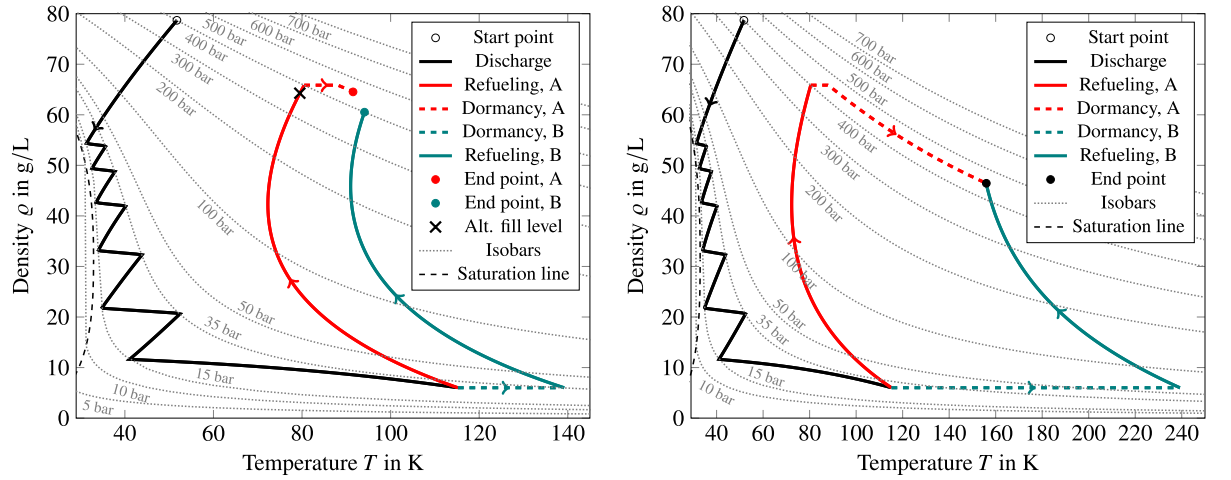
In both cases, temperature and pressure rise during dormancy due to heat leaking into the tank. When, in (A), the pressure reaches the venting pressure $p_{\mathrm{vent}}$ after more than 36 h, hydrogen is vented. Further, since the stop density is reached during a heating period, the refueling process is not ideal. Nevertheless, at the end of the cycle, the tank in (A) is fuller than in (B), where the empty truck is parked for the weekend and refueled after the dormancy, which prevents venting. In (B), the refueling conditions are worse than in (A) as the tank has warmed up during dormancy. Additionally, the temperature increases faster in an empty tank. Thus, even though in (A) 1.27 g/L of fill density is lost due to venting, a 4.06 g/L higher fill density is achieved. With a consumption of 7 kg per 100km, this translates to roughly 30 km extended range, enabling higher route flexibility and less refueling stops. However, as venting also means economic loss, an economically optimal operation can only be determined if all economic parameters are known.

For longer dormancy, the difference between the endpoints of (A) and (B) becomes smaller, and eventually, there is a turnover point. As it is assumed that in (B) the truck starts driving right after refueling, it could be filled, as compared to (A), to the venting pressure $p_{\mathrm{vent}}$. Considering this procedure, the turnover point is calculated by minimizing the difference in storage density at the end of (A) and (B) with `fminbnd`. Figure 7(b) shows the drive cycle with a dormancy of the calculated turnover point (27.5 days). At this point, 19.4 g/L are vented for case (A). Consequently, depending on whether venting should be prevented or the driving range maximized, an operation strategy can be chosen.




(a) Refueling stations located every 100 km (b) Refueling stations located every 50 km

**Figure 7**. Usable density for limited availability of refueling stations.




(a) Drive cycle with 62 h dormancy

(b) Drive cycle at turnover point (27.5 days)

**Figure 8**. Drive cycles of real iHEX consisting of (A) discharge, refueling, and dormancy, and (B) discharge, dormancy, and refueling.

Alternatively, by refueling slightly less than the fill pressure, venting can be fully avoided while still ensuring high fill density. For the 62 h dormancy, this could be achieved by filling to 369.2 bar instead of 400 bar, resulting in a fill density of 64.27 g/L slightly below the final density of case (A) (64.58 g/L). The alternative fill density is marked in Figure 7(a).

## CONCLUSION

The presented study combines a dynamic thermodynamic model of a $CcH_2$ tank for trucks with surrogate quasi-steady-state heat exchanger models based on ANNs. Therefore, this model allows for fast and low-complexity simulations. The resulting system model is used for several case studies, demonstrating the influence of driving strategies on driving ranges and boil-off losses.

## ACKNOWLEDGEMENTS

The authors gratefully acknowledge the financial support of the joint project “CryoTRUCK” by the German Federal Ministry of Digital and Transport (BMDV, FKZ 03B10411E) and the project supervision by the project management organization Projektträger Jülich (PtJ).

## REFERENCES

1. Stops L, Siebe D, Stary A, Hamacher J, Sidarava V. Rehfeldt S, Klein H. Generalized thermodynamic modeling of hydrogen storage tanks for truck application. *Cryogenics* 139. (2024) https://doi.org/10.1016/j.cryogenics.2024.103826
2. Hamacher J, Stary A, Stops L, Siebe D, Kapp M, Rehfeldt S, Klein H. Modeling the thermodynamic behavior of cryo-compressed hydrogen tanks for trucks. *Cryogenics* 135. (2023) https://doi.org/10.1016/j.cryogenics.2023.103743
3. Hamacher J, Stary A, Stops L, Siebe D, Rehfeldt S, Klein H. Novel thermodynamic model for cryo-compressed-hydrogen tanks. In: Proceedings of the 17th CRYOGENICS 2023 IIR International Conference. (2023)
4. Hamacher J, Al-Zoubi A, Stary A, Stops L, Siebe D, Rehfeldt S, Klein H. Wärmeübergangskoeffizienten bei der Anwärmung von kryogenem Wasserstoff. In: Jahrestreffen 2024 der DECHEMA Fachgruppen Wärme- und Stoffübertragung und Trocknungstechnik. (2024)
5. Stary A, Al-Zoubi A, Hamacher J, Siebe D, Stops L, Rehfeldt S, Klein H. Freie Konvektion an einem horizontalen Zylinder in einem kryo-komprimierten Wasserstofftank. In: Jahrestreffen 2024 der DECHEMA Fachgruppen Wärme- und Stoffübertragung und Trocknungstechnik. (2024)
6. Stein M. Large sample properties of simulations using latin hypercube sampling. *Technometrics* 2:29. (1987)
7. Basma H, Rodríguez F. Fuel cell electric tractor-trailers: Technology overview and fuel economy. (2022) https://theicct.org/publication/fuel-cell-tractor-trailer-tech-fuel-jul22/ (accessed 25 Nov 2024)

© 2025 by the authors. Licensed to PSEcommunity.org and PSE Press. This is an open access article under the creative commons CC-BY-SA licensing terms. Credit must be given to creator and adaptations must be shared under the same terms. See https://creativecommons.org/licenses/by-sa/4.0/

Systems & Control Transactions

**Research Article - Peer Reviewed Conference Proceeding**
ESCAPE 35 - European Symposium on Computer Aided Process Engineering
Ghent, Belgium. 6-9 July 2025
Jan F.M. Van Impe, Grégoire Léonard, Satyajeet S. Bhonsale,
Monika E. Polańska, Filip Logist (Eds.)

PSE PRESS

# Wind Turbines Power Coefficient Estimation Using Manufacturer's Information and Real Data

**Carlos Gutiérrez Ortega[a]*, Daniel Sarabia Ortiz[a], and Alejandro Merino Gómez[a]**

[a] University of Burgos, Department of Digitalisation, Area of Systems Engineering and Automatic Control, Burgos, Spain
* Corresponding Author: cgortega@ubu.es.

## ABSTRACT

Dynamic modelling of wind turbines and their simulation is a very useful tool for studying their behaviour. One of the key elements concerning the physical models of wind turbines is the power coefficient *Cp*, which acts as an efficiency in the extraction of power from the wind. Unfortunately, this coefficient is often unknown a priori, as it does not usually appear in the information provided by manufacturers. This paper first describes a methodology for obtaining the power coefficient parameters of a commercial wind turbine model using the power curve provided by the manufacturer, which indicates the theoretical power that the wind turbine can produce at each wind speed. To achieve this, a parameter estimation problem is formulated and solved to determine the power coefficient parameters. Nevertheless, this information is often insufficient, requiring additional knowledge, such as operational data, to improve the fit. Finally, a new parameter estimation is performed using only real data measured from the process, validating the proposed methodology. The operational dataset was obtained from the SMARTEOLE project in France and corresponds to the pitch-controlled variable-speed Senvion MM82/2050 wind turbine.

**Keywords**: Modelling, Optimization, Wind, Renewable and Sustainable Energy, Pyomo.

## INTRODUCTION

As the world shifts towards renewable energy production, wind power has become a key player in reducing our dependence on fossil fuels. Wind turbines and their control systems are now more sophisticated than ever; however, they still face challenges such as wind fluctuations, maintenance costs, and the integration of wind power into the electricity market. To address these issues, digital twin technology is emerging as a promising solution, offering real-time virtual models that optimise wind turbine performance and reliability. This approach aligns with the WindEurope [1] roadmap for the digital wind sector in 2030, which defines the digital technologies to be implemented and aims to develop a comprehensive digital twin. A digital twin is essentially a virtual replica of a physical wind turbine (or a wind farm), continuously updated with real-world data [2]. This technology allows operators to monitor performance in real-time, predict failures before they occur, and adjust operations for maximum efficiency. This study explores a methodology on how to use the measured data to improve wind turbine models for dynamic simulation, which is the basis of a digital twin, specifically the power coefficient behaviour in different scenarios of wind speed, rotor speed, and blade pitch angles for a commercial wind turbine model. One of the most significant variables in the development of a macroscopic mathematical model of a wind turbine is its power coefficient. This coefficient, which will be described later, is crucial for calculating the electrical power supplied by the turbine; nonetheless, it is not typically provided by turbine manufacturers.

This study first describes the methodology for estimating the wind turbine power coefficient using data typically provided by turbine manufacturers, followed by the fitting procedure used when real data are available. The fitting results are then presented for three cases: (Fit 1) based only on real manufacturer data, (Fit 2) using manufacturer data corrected with certain knowledge from process measurements, and (Fit 3) relying solely on real process measurements, which improves the accuracy of the power estimations and validate the proposed methodology. Finally, the results are discussed, followed by

the conclusions and suggestions for future work.

## $C_P$ ESTIMATION WITH MANUFACTURER'S DATA

In the majority of cases, the information we can obtain from the wind turbine manufacturer's data is limited. Usually, we only have the power curve and some design characteristics of the turbine, such as the length of the blades, the wind speed range in which the wind turbine operates, the type of control system used to limit the generated power or regulate the rotor speed, the mechanical and electrical efficiency, or the air density. The power curve in Figure 1 relates the evolution of the electrical power generated by the turbine to the different wind speeds between the cut-in wind speed (the one from which the turbine starts to generate power) and the cut-out speed (the one from which the turbine is braked to preserve the integrity of its elements).

Even so, with this limited information, a family of power coefficient curves *Cp*() can be obtained for implementation in our models to perform dynamic simulations of wind turbines and wind farms. The power coefficient can be understood as the efficiency of the turbine in extracting the power contained in the wind and depends, among other variables, on the commercial model of the turbine or the characteristics of the wind in the area where the turbine is installed.

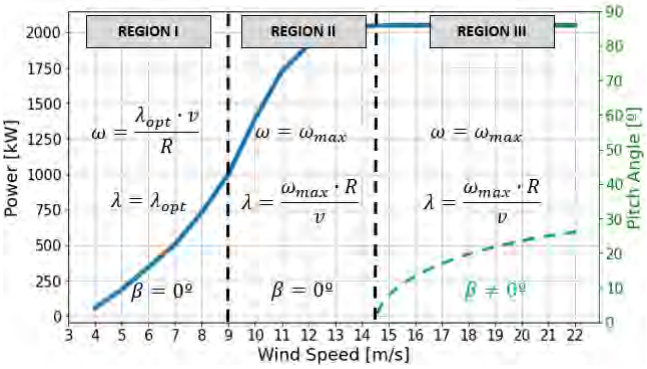



**Figure 1.** Power curve for the Senvion MM82/2050 turbine model [3].

However, the variables that affect the power coefficient can be reduced to two: the specific speed coefficient (or tip-speed ratio) $\lambda$, which is the quotient between the linear speed at the tip of the blades and the speed of the wind speed upstream of the turbine rotor, and the pitch angle $\beta$ (in the case that the turbine has a pitch control system), which is the angle formed by the blades with their rotation plane. This angle can be modified to reduce or increase the blades' resistance to the wind (and therefore, reduce or increase the power generated).

$$\lambda = \omega_r \cdot R / v \tag{1}$$

where $\omega_r$ is the rotor speed in rad/s, $R$ is the rotor radius in meters, and $v$ is the wind speed upstream of the rotor in m/s.

The theoretical limit for the power coefficient, known as the Betz limit, is 0.59 [4]. That is, for an ideal turbine, it is possible to harness only 59% of the power contained in the wind upstream of the rotor. In real turbines, this amount is always less, as will be shown later. The power coefficient can be modelled in three ways: following a polynomial equation, a sinusoidal equation, or an exponential one. The exponential equation has been found to work well for turbines with variable pitch and speed control [5], which is the type of turbine that is the focus of this study [6-7].

$$C_p(\lambda,\beta) = C_1\left(\frac{C_2}{\lambda_i} - C_3\beta - C_4\beta^{C_5} - C_6\right)e^{\frac{-C_7}{\lambda_i}} \tag{2}$$

$$\frac{1}{\lambda_i} = \left(\frac{1}{\lambda + C_8\beta}\right) - \left(\frac{C_9}{\beta^3+1}\right)$$

The generated power can be calculated by Equation (3) in terms of wind speed, power coefficient, and air density $\rho$ in kg/m$^3$.

$$\hat{P} = \frac{1}{2}\rho\pi R^2 v^3 C_P(\lambda,\beta) \tag{3}$$

The idea is to estimate the $C_k$ parameters of power coefficient (2) that make that curve replicate the behaviour of a given turbine for different $\lambda$ and $\beta$ values, which in turn will result in the power calculated with (3) replicating the actual power generated. The parameter estimation problem was formulated as a nonlinear optimisation problem, as described below, and solved using Pyomo 6.4.2 [8] in a Python environment using the IPOPT solver.

The aim of the optimisation problem (4) is to minimise, for each wind speed $v_i$, the error between the theoretical power of the manufacturer's curve $P_i$ and the power calculated using (3).

$$\min_{\{c_k,\beta_j\}} \sum_i \left(P_i - \hat{P}_i(\lambda_i,\beta_i)\right)^2 \tag{4}$$

To establish the constraints, it must be understood how the power curve behaves for each range of wind speeds. As shown in Figure 1, power curves can be divided into at least three regions owing to different operation conditions based on the wind speed value at each moment. Region I extends from the cut-in wind speed to the speed at which the rotor reaches the maximum speed. In region I, the pitch angle equals zero and the tip-speed ratio value is optimal as a consequence of *the maximum power point tracking* system (MPPT) [9]. Region II extends from the wind speed in which the maximum rotor speed is reached to the rated wind speed, when the generated power reaches its rated value. This region is characterised by a constant rotor speed (at its maximum value); therefore, the tip-speed ratio only varies with wind speed, and the pitch angle is still zero.

Region III extends from the rated wind speed to the cut-off wind speed, and between them there is an increase in the pitch angle, with the rotor speed value being constant at its maximum value.

The optimal tip-speed ratio for a pitch angle of $\beta$ = 0 (with wind speed values below the rated wind speed) is obtained by deriving expression (2) and equalling it to zero. The result is a relationship between the parameters $C_k$, as shown in (5). Moreover, this value must be equal to that obtained by calculating the tip-speed ratio with the rated rotor speed and the wind speed at which the maximum power coefficient is reached, which can be determined by clearing *Cp* from expression (3) and substituting *P* for the value obtained from the theoretical curve (assuming an ideal generator efficiency of 1 and standard air density of 1.225 kg/m$^3$).

$$\lambda_{opt} = \frac{C_2 * C_7}{C_2 + C_6 * C_7 + C_2 * C_7 * C_9} = \frac{\omega_{max} \cdot R}{v_{C_{p,i,max}}} \quad (5)$$

Pitch angle $\beta$ is zero for wind speed values less than the rated speed (6) but positive and increasing values with wind speed for wind speed above rated speed.

$$\beta_j = 0 \; \forall \; v_i \leq v_{rated}; \; 0 < \beta_j < \beta_{j+1} \; \forall \; v_i > v_{rated} \quad (6)$$

In addition, certain parameters $C_k$ must have positive values (7) to enable equality (5) to be true and to maintain the structure of term $\beta^{C_5}$ of equation (2).

$$[C_2, C_5, C_6, C_7, C_9] > 0 \quad (7)$$

There is no a priori information on how the pitch angle $\beta$ grows with wind speed. Only the moment when it starts increasing and the final pitch angle value at the cut-off wind speed are fixed, assuming typical wind turbine values.

## $C_P$ ESTIMATION WITH MEASURED DATA

The data used for this study belong to the SMARTEOLE project, which studied a wind farm in France with seven wind turbines [10], whose layout is shown in Figure 2. The manufacturer's data and the power curve of the Senvion MM82/2050 wind turbine model are presented in Table 1 and Figure 1, respectively. The objective of that project was to study the interactions between the different turbines that make up the wind farm in order to develop a wake-steering control system, which consists of misaligning the rotor of the turbines that are first affected by the wind in order to deflect the wakes that appear behind the rotor so that the downstream turbines are affected by them as little as possible, resulting in an overall increase in the available power in the wind farm. Data were recorded between 17 February and 25 May 2020 with a resolution of 1 min.

This study focuses on the SMV1 turbine because it is close enough to the *WindCube V1* measurement system, as will be explained later.

The necessary measured data to perform the calculations are *active power*, *blade pitch angle*, *wind speed*, *wind direction*, *nacelle position*, and *generator speed*. However, the rotor speed, which is the one we are interested in to obtain $\lambda(1)$, is not measured, but the generator rotational speed is measured, and the gear ratio is known. Therefore, under the assumption that the transmission is ideal (without losses), the rotor speed can be obtained as the quotient (8) between the generator speed $\omega_g$ and gear ratio *N*.

$$\omega_r = \omega_g / N \quad (8)$$

Next, the raw data are filtered to ensure that the dataset contains adequate and reliable information using the following criteria: i) The misalignment (*yaw error*) must be less than 0.1, to consider only situations where the turbine is fully aligned with the wind direction. ii) The generator speed must be positive. iii) The measured wind speed must fall within the turbine's operating range ($v_{cut\text{-}in} < v < v_{cut\text{-}off}$). iv) The generated power (active power) should be positive. As a result, the filtered dataset contains 1,131 points instead of the initial 134,661.

In addition to this filter, all negative but near-zero values of the pitch angle $\beta$ were replaced with zero, considering them as measurement errors, preventing errors in the calculation of the power coefficient.

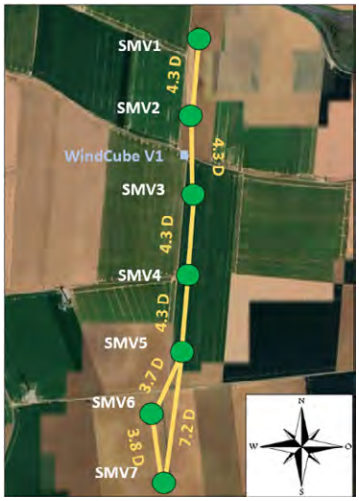



**Figure 2.** Wind farm layout [11].

An initial hypothesis is that the wind speed measured at the turbine is downstream of the rotor and, therefore, does not correspond to the upstream wind speed (with which the manufacturer's power curves are represented) but to a lower speed resulting from the decrease in wind power as it passes through the rotor.

To discard this initial hypothesis, a new filter is added to the data to have only west wind directions between 250º and 290º, so that the wind speeds measured by the *WindCube V1* system and at the turbine are not

affected by the wakes of other turbines. As shown in Figure 3, it is not clear whether one wind speed measurement is higher or lower than the other. Therefore, it is assumed that the wind speed measured at the turbine has been corrected to represent the upstream wind speed values. For calculation purposes, this corrected wind speed was used.

**Table 1:** Senvion MM82/2050 parameters.

| Parameter | Value | Units |
|---|---|---|
| Rated Power | 2050 | kW |
| Rotor Diameter | 82 | m |
| Power Control System | Pitch | |
| Min. rotor speed | 8.5 | rpm |
| Max. rotor speed | 17.1 | rpm |
| Cut-in wind speed | 4 | m/s |
| Rated wind speed | 14.5 | m/s |
| Cut-off wind speed | 22 | m/s |
| Gear ratio (*N*) | 106 | |
| Generator type | DFIG | |
| Max. Generator speed | 1800 | rpm |

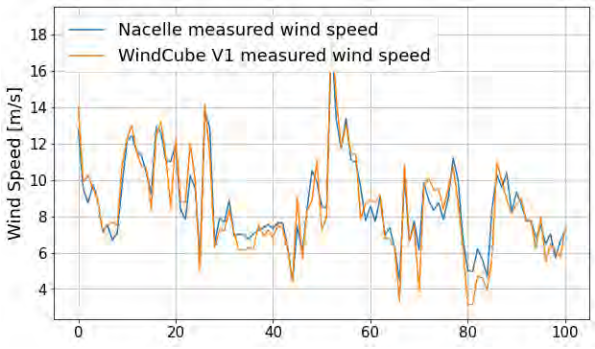



**Figure 3.** Measured wind speeds between 250° and 290° wind directions.

A crucial difference with respect to the previous estimation problem is the availability of pitch angle $\beta^m$ and wind generator speed $\omega_g^m$ measurements for each wind speed; therefore, it will not be necessary to approximate its behaviour using any of the constraints from Fit 1 and 2. Thus, the estimation problem was formulated as the optimisation problem (9) subject to (10), where the only decision variables are the $C_k$ parameters of the power coefficient curve (2). $P_i^m$ and $v_i^m$ represent the active power and wind speed measurements for each point *i* out of the 1131 points in the dataset, respectively.

$$\min_{\{C_k\}} \sum_i \left(P_i^m - \hat{P}_i(\lambda_i, \beta_i^m)\right)^2 \tag{9}$$

subject to:

*Power Coefficient Curve (2)*

$$\hat{P}_i = \frac{1}{2}\rho\pi R^2 (v_i^m)^3 C_P(\lambda_i, \beta_i^m)$$

$$\omega_{r,i} = \omega_{g,i}^m / N; \;\; \lambda_i = \omega_{r,i} \cdot R / v_i^m \tag{10}$$

$$[C_2, C_5, C_6, C_7, C_9] > 0$$

As mentioned before, the rotor speed is known at all times and is calculated using (8) so that the tip-speed ratio λ can be calculated directly using (1).

## RESULTS

The results of the three parameter estimation problems are shown below: using theoretical manufacturer's data (Fit 1), using theoretical manufacturer's but corrected data (Fit 2), and using measured real data (Fit 3).

### Parameter estimation with theoretical manufacturer's data (Fit 1)

Using the data from the theoretical power curve and those in Table 1, optimisation problem (4) was solved. The parameters of the power coefficient are shown in Table 2, and the family of power coefficient curves for different combinations of λ and *β* is shown in Figure 4. The maximum *Cp* value of 0.578 was reached at λ = 13 for *β* = 0. It can then be said that for *β* = 0, the optimal λ is 13. From this maximum, as both λ and *β* vary, *Cp* decreases. Moreover, if the *Cp* curve is divided into two regions for each pitch angle (to the left of optimal λ, and to the right of optimal λ), the turbine will generally work in the left region, since the opposite would imply that λ is higher than the optimal for wind speeds lower than rated, or that the rotor speed keeps increasing its speed from the rated one for wind speeds equal to or higher than rated (which does not happen, the rotor speed remains constant at its rated value from the moment it reaches it).

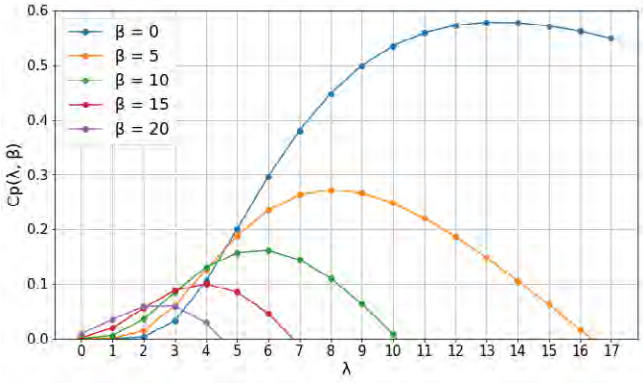



**Figure 4.** Power coefficient curves for Fit 1.

However, looking at the measured data in Figure 5, it is clear that some of the assumptions made do not correspond to the actual wind turbine behaviour. For example, the pitch angle starts to increase between 11 and 12 m/s, whereas initially this was assumed to occur from 14.5 m/s (rated wind speed $v_{rated}$). On the other hand, the rotor speed stabilises at its maximum value of 17 rpm for winds above 8 m/s, being the initial assumption that this occurred at 5.5 m/s.

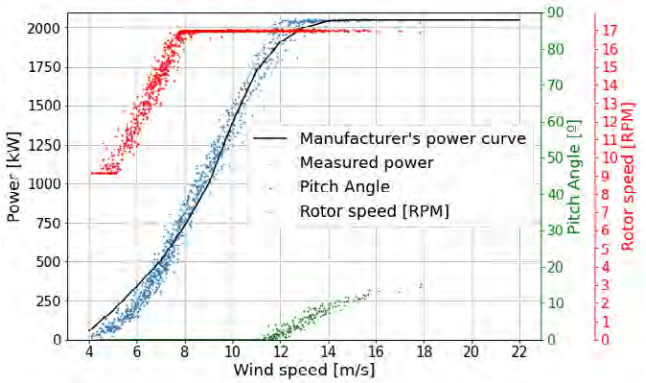



**Figure 5.** Actual power, pitch angle, and rotor speed data.

## Parameter estimation with theoretical manufacturer's corrected data (Fit 2)

Therefore, a second fitting is made by changing to 8 m/s the value of the wind speed at which the rated rotor speed is reached, and indicating that the pitch angle should start to grow from a wind speed of 12 m/s. The new family of power coefficient curves for different combinations of $\lambda$ and $\beta$ is shown in Figure 6, and the parameters of the power coefficient are also shown in Table 2.

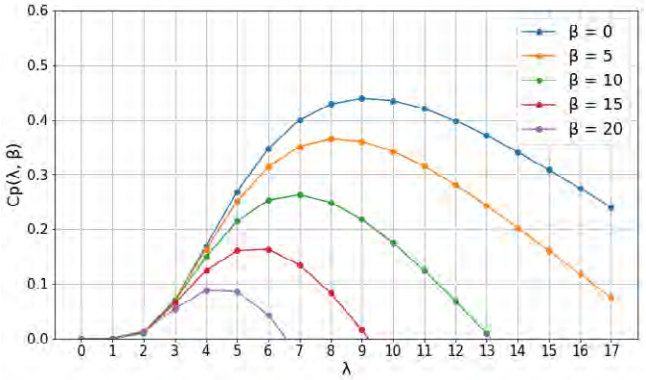



**Figure 6.** Power coefficient curves for Fit 2.

The solutions of the first problem and the new one are compared in Figure 7. In both cases, the pitch angle for the cut-off wind speed has been forced to be 20º (looking at the measured data, this seems reasonable). It can be observed that the new fitting is better than the first one owing to the incorporation of additional turbine performance information obtained from measured data.

## Parameter estimation with measured real data (Fit 3)

Using the measured real data and those in Table 1, the optimisation problem (9) is solved. Table 2 shows the solution for the $C_k$ parameters of the power coefficient curve. Next, Figure 8 shows how the family of power coefficient curves complies with all mentioned in the previous sections and also takes lower values than those of the case with theoretical data (Fit 1). By obtaining the curves from the measured data, all the inefficiencies that occur in the actual operation are included.

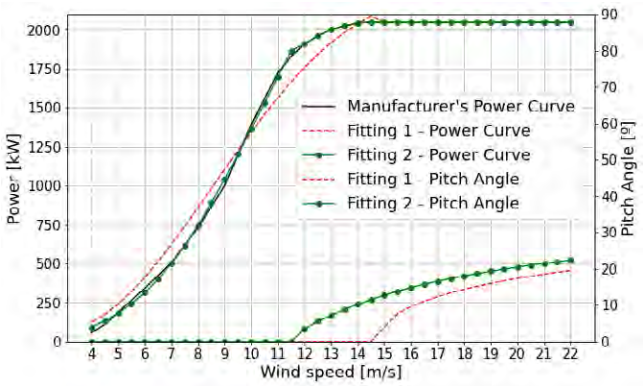



**Figure 7.** Fit 1 and 2 power curve comparison.

Figure 9 shows a comparison between the measured power, the power calculated with the coefficients of Figure 8, and the manufacturer's power curve, as well as the measured pitch angles. The fit is quite good in general, being worse at the starting zone (between 4 and 7 m/s), caused among other reasons by not having considered the changes in air density (all calculations have been made with a standard density of 1.225 kg/m$^3$) and by the influence of transient periods during braking of the turbines at low wind speeds or starting the turbines when the wind speed is again above the cut-in speed ($v_{in}$).

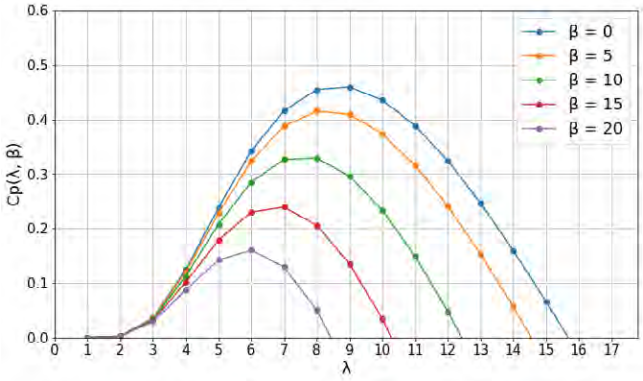



**Figure 8.** Power coefficient curves for Fit 3.

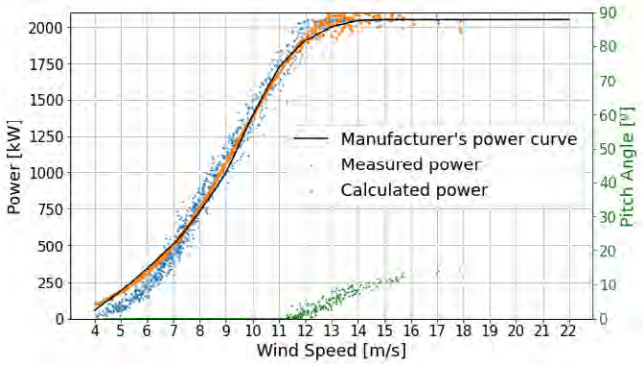



**Figure 9.** Calculated (fit 3), measured and theoretical power curves, and measured pitch angle.

**Table 2:** Power coefficient parameters for the three fits

| Decision variables | Initial values | Fit 1 values | Fit 2 values | Fit 3 values |
|---|---|---|---|---|
| $C_1$ | 1.0148 | 0.109 | 0.077 | 0.00029 |
| $C_2$ | 417.108 | 345.896 | 410.740 | 281927.469 |
| $C_3$ | 0.918 | 1.497 | 0.436 | 7.547e-08 |
| $C_4$ | 0.0021 | 3.540 | 0.071 | 97.864 |
| $C_5$ | 2.569 | 0.436 | 2.103 | 1.689 |
| $C_6$ | 37.058 | 5.702 | 16.491 | 17884.972 |
| $C_7$ | 28.642 | 17.868 | 14.739 | 19.278 |
| $C_8$ | 0.048 | 0.127 | 0.0032 | 0.0 |
| $C_9$ | 0.0 | 0.0024 | 0.00097 | 0.00033 |

## CONCLUSIONS AND FUTURE WORK

In this study, a methodology was developed to obtain power coefficients for use in digital twins. The methodology was tested with different levels of available information. After performing the three fits with different information, some conclusions can be drawn.

The first fitting, only with theoretical data from the manufacturer, can be useful to implement in a turbine model for dynamic simulations, since, roughly speaking, the power behaviour is being replicated with more or less accuracy. As for the pitch angle, those are obtained that make all the other constraints met, so they would also be useful, even though they may not be exactly the actual pitch angles. From the discrepancies observed between the initial assumptions and the measured real data of the turbine, the theoretical data are adjusted by correcting the wind speed value at which the rated rotor speed is reached and the wind speed at which the pitch angle starts to grow. It can be seen how the fitting improves, since the information it incorporates is more similar to that obtained from a real operating turbine. It can also be seen in the power coefficient curve families that the values reached for different pitch angles in fit 2 are closer than those in fit 1 curves to those obtained in fit 3, where wind turbine operating data are incorporated into the estimation problem. Finally, the solution to this new estimation problem enables an accurate estimation of the power coefficient *Cp* of a real wind turbine, which can then be included, for example, in a detailed dynamic simulation of a wind farm.

A future line of work is to implement these curves in wind turbine and wind farm models for dynamic simulation, which are intended to be fed with real operating data to update these models with new information. Just as the transition from Fit 1 to Fit 2 has been greatly improved by including more data, the idea is that by gradually incorporating more information into the model, it will become more precise in representing reality. It is also necessary to test this methodology in situations where the measured wind speed that appears in the data is the downstream wind speed without any correction, when the upstream wind speed is unknown, and also when the wind turbines are misaligned to the wind direction.


## ACKNOWLEDGEMENTS

This work is part of the project “Optimal real-time management under uncertainty for digital twins (Opti-Dit)”, PID2021-123654OB-C33, funded by the MCIN/AEI and by the European Union “FEDER”.


## REFERENCES


1. Klonari V, Papachristos G, Fraile D. Wind energy digitalisation towards 2030, Wind Europe (2021).
2. de Prada C, Galán-Casado S, Pitarch JL, Sarabia D, Galán A, Gutiérrez G. Gemelos digitales en la industria de procesos, *RIAI* 19(3): 285–296 (2022).
3. The Wind Power. https://www.thewindpower.net/turbine_en_464_senvion_mm82-2050.php
4. Rodríguez JL, Burgos JC, Arnalte S. Sistemas Eólicos de Producción de Energía Eólica. Rueda S.L (2003).
5. Castillo OC, Andrade VR, Rivas JJR, González RO. Comparison of power coefficients in wind turbines considering the tip speed ratio and blade pitch angle. *Energies* 16(6):2774 (2023).
6. Manyonge AW, Ochieng RM, Onyango FN, Shichikha JM. Mathematical modelling of wind turbine in a wind energy conversion system: power coefficient analysis. *AMS* 6(91): 4527–4536 (2012).
7. Ackermann T. Wind Power in Power Systems. John Willey & Sons (2005).
8. Pyomo Documentation. https://pyomo.readthedocs.io/en/6.4.2/
9. Pande J, Nasikkar P, Kotecha K, Varadarajan V. A review of maximum power point tracking algorithms for wind energy conversion systems. *JMSE* 9(11): 1187 (2021).
10. Duc T, Smiley E. SMARTEOLE wind farm control open dataset. https://doi.org/10.5281/zenodo.7342466
11. Simley E, Fleming P, Girard N, Alloin L, Godefroy E, Duc T. Results from a wake steering experiment at a commercial wind plant: investigating the wind speed dependence of wake steering performance. *WES* 6: 1427-1453 (2021).



© 2025 by the authors. Licensed to PSEcommunity.org and PSE Press. This is an open access article under the creative commons CC-BY-SA licensing terms. Credit must be given to creator and adaptations must be shared under the same terms. See https://creativecommons.org/licenses/by-sa/4.0/

Systems & Control Transactions

**Research Article - Peer Reviewed Conference Proceeding**
ESCAPE 35 - European Symposium on Computer Aided Process Engineering
Ghent, Belgium. 6-9 July 2025
Jan F.M. Van Impe, Grégoire Léonard, Satyajeet S. Bhonsale,
Monika E. Polańska, Filip Logist (Eds.)

PSE PRESS

# Leveraging Pilot-Scale Data for Real-Time Analysis of Ion Exchange Chromatography

**Søren Villumsen[a], Jesper Frandsen[a], Jakob Kjøbsted Huusom[a], Xiaodong Liang[a], Jens Abildskov[a]**

[a] Dept. of Chemical and Biochemical Engineering, Technical University of Denmark, Søltofts Plads, Building 228A, 2800 Kgs. Lyngby, Denmark
* Corresponding Author: soevi@kt.dtu.dk

## ABSTRACT

This study evaluates the potential for computer-aided real-time monitoring and decision-making in pilot-scale ion-exchange chromatography operations using only historical data from the pilot-scale facility. Historical data of flow and conductivity were utilized from students running pilot-scale ion exchanges that resemble industrial ion exchange processes. A Lumped Rate Model (LRM) with a Steric Mass Action (SMA) isotherm was implemented and parameterized to characterize the fixed-bed column. The Discontinuous Galerkin Spectral Element Method (DGSEM), implemented in CADET-Julia, enabled efficient simulation and parameter estimation. Using DGSEM, the LRM with SMA was solved in less time than the sensor measurement frequency. This development allows for the prediction of batch evolution in real time for operators of the ion-exchange column. Despite challenges related to data preprocessing and manual operation inconsistencies, the results demonstrate the feasibility of integrating real-time analysis into pilot-scale operations.

**Keywords**: Ion-exchange chromatography, Real-time analysis, Pilot-scale, Computer-aided, Modelling, DGSEM

## 1. INTRODUCTION

Chromatography constitutes an important part of downstream bio-manufacturing, where it is used to separate valuable products of upstream production. Precise control over chromatographic processes aids in increasing product yield. Current conservative operational strategies sometimes lead to product loss, which may be remediable with real-time process insights [1].

Batch-to-batch variations in feed composition and operating conditions further complicate achieving optimal yields [2]. Improved understanding and monitoring of separation processes could enable operators to account for batch-to-batch variation, increasing yields without sacrificing product quality [2].

The complexity of chromatographic processes arises from their underlying mechanisms, which can be described using partial differential equations (PDEs) that model advection, diffusion, mass transfer, and adsorption. To enable real-time applications involving systems governed by PDEs, fast discretization methods are essential for solving these equations accurately and efficiently.

This study investigates the potential for real-time process analysis using a pilot-scale ion exchange column at the Technical University of Denmark (DTU) pilot facility. For more details on this facility, see [3]. Here, an ion exchange fixed-bed column equipped with sensors is used as a teaching instrument. The column and the exercises run on it resemble operations encountered in industrial ion exchange operations. The system is equipped with sensors that automatically log measurements every two seconds.

There exist historical data sets of these sensor measurements for experiments run by students from 2019 onwards. In this case, students use the data to perform calculations relating to upscaling the process. Beyond this, the data is not employed for other purposes. This has some resemblance to industrial process systems, where sensors are placed on systems for monitoring and quality control purposes, and process optimization using historical data is an afterthought. This study will evaluate whether the fixed-bed column can be characterized solely by historical data and whether such data provides a sufficient foundation for real-time process applications.

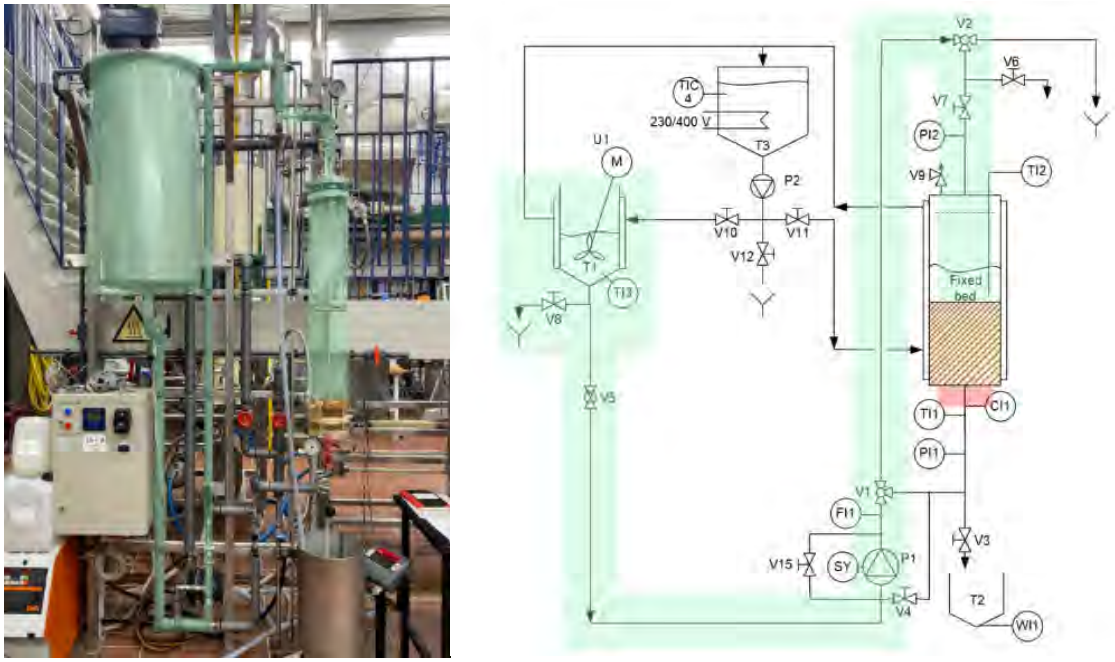



**Figure 1:** (Left) An image of the pilot-scale fixed-bed ion exchange column and (right) P&I diagram for the pilot-scale ion exchange fixed-bed column [8]. The green, orange, and red sections on both the image and the P&I diagram represent the in-flow pipes, the fixed-bed column, and the out-flow pipes, respectively.

## 2. METHODOLOGY

### 2.1 Scoping

There are two subjects of interest in this study. First is the ability to simulate operation of the ion-exchange system based entirely on historical data. The historical data gathered by students was not intended for applications such as those suggested in this study but rather as data to support other investigations. Here, this study investigates the degree to which this data can be repurposed for column characterization and process simulation.

Secondly, the study will investigate if, by using computationally fast numerical schemes, the ion-exchange breakthrough process can be simulated in less time than the measurement frequency of every two seconds. Achieving this would support the development of real-time applications, as the numerical scheme could be solved uniquely for each data point that is gathered. A real-time application of interest in this setting would be the prediction of the breakthrough profile, enabling feedback to the operators of the system as they operate the system.

### 2.2 Experimental Methods

The data used for this study stems from exercises performed by chemical engineering students at DTU [8]. The goal of the exercise is for students to evaluate breakthrough curves during the operation and regeneration of an ion-exchange system, and to determine isotherms and resin properties for scaling up a pilot plant unit.

#### Pilot Plant Setup

The experimental setup features a 10 cm diameter, 1 m tall column occupied by a fixed-bed ion exchange resin. In Figure 1, a piping and instrumentation (P&I) diagram for the system can be seen. The feed solution, stored in a 100 L tank (T1), is pumped through the column. The system includes the following instrumentation:

- Flow-through cell (CI1): Measures conductivity
- Magnetic flow indicator (FI1): Measures flow rate
- Pt100 sensors (TI1 & TI2): Monitor temperature
- Manometer (PI1): Records pressure

Data for time, flow, conductivity, temperature, and pressure are logged automatically every 2 seconds. The resin used is Amberjet 1200 in H-form. The operator must manually control the system by configuring the pump spend and configure valve settings.

#### Experimental Procedure

30 L of 0.1 N $NaNO_3$ feed solution is prepared by dissolving $NaNO_3$ in water, mixing thoroughly for homogenization, and transferring it to the feed tank.

Next, The feed solution of $NaNO_3$ is pumped through the column at a flow rate of 50-80 L/h. Exit flow and conductivity were recorded automatically. The process continued until an S-shaped curve was observed in the conductivity.

Finally, 10 L of water is pumped through the system and column to remove any $NaNO_3$ in the mobile phase.

During all operations, the operator must manually adjust flow rates and the water height inside the column by adjusting valve V3. This is to ensure the resin is always submerged, and to limit excess water in the column.

## 2.3 Modelling

To describe the ion-exchange chromatography process, the Lumped Rate Model (LRM) with the Steric Mass Action (SMA) was used. The LRM and the SMA isotherm are given for each component $i \in \{1, \dots, N_C\}$ in eq. (1)-(2).

$$\frac{\partial c_i}{\partial t} = D_{\text{ax}} \frac{\partial^2 c_i}{\partial z^2} - u \frac{\partial c_i}{\partial z} - \frac{1-\varepsilon}{\varepsilon} \frac{\partial q_i}{\partial t}, \tag{1}$$

$$\frac{\partial q_i}{\partial t} = k_{\text{kin},i}\left(k_{\text{eq},i} c_i \bar{q}_0^{\nu} - q_i c_0^{\nu}\right). \tag{2}$$

Here, $t$ is time, $c_i$ is the mobile phase concentration of component $i$, $q$ is the corresponding stationary phase concentration, $z$ is the spatial coordinate, $D_{\text{ax}}$ is the axial dispersion coefficient, $\varepsilon$ is the total porosity, $k_{\text{eq}}$ is the equilibrium adsorption constant, $k_{\text{kin}}$ is a kinetic constant, $\overline{q_0} = q_0 - \Sigma_j^{N_c} \sigma_j q_j$ is the number of free binding sites where $q_0$ is the bound salt concentration and $\sigma$ is the steric hindrance factor. The bound salt concentration is given by electroneutrality as $q_0 = \Lambda - \Sigma_j^{N_c} \nu_j q_j$ where $\Lambda$ is the ionic capacity and $\nu$ is the characteristic charge. The boundary conditions are given in eq. (3)-(4), respectively.

$$uc_{\text{in},i} = \text{uc}_i(t,0) - D_{\text{ax}} \frac{\partial c_i(t,0)}{\partial z}, \tag{3}$$

$$\frac{\partial c_i(t,L)}{\partial z} = 0, \tag{4}$$

where $L$ is the column length and $c_{\text{in}}$ is the inlet concentration. If assuming isotherm equilibrium, the equations eq. (1)-(2) must be discretized and solved as a differential algebraic equations system, setting eq. (2) equal to 0. Alternatively, one can set a large $k_{\text{kin}}$, value to approximate the equilibrium and still discretize and solve the system as an ordinary differential equation (ODE) system [4]. To solve the PDEs in eq. (1)-(4), the spatial domain of eq. (1) was discretized using the Discontinuous Galerkin Spectral Element Method (DGSEM) derived by Breuer et al [5]. The resulting system of ODEs was solved using the QNDF solver which is a stiff backwards differentiation formula solver using DifferentialEquations.jl [6,7].

### Column Characterization

To model the pilot-scale ion exchange fixed-bed column, CADET-Julia was used [4]. In Table 1, all values used for simulating the ion exchange system can be seen. The system was represented as three serially connected segments: the in-flow pipes, the ion exchange column itself, and the out-flow pipes. In Figure 1, this segmentation can be seen with respect to the physical system. Approximate measurements of pipe length and radii were used for the in-flow and out-flow sections. For the simulation, the value of the axial diffusion coefficient in the pipes, $D_{\text{ax, pipes}}$, was set to $10^{-3}$ $m^2/s$. This value was heuristically chosen to balance minimizing diffusion in the pipes while avoiding an excessively stiff system that would significantly increase the computational time.

For each batch, the median flow rate was calculated and applied as a constant flow in the simulated runs. The median flow was chosen to make the data cleaning more robust towards transmitted values that were deemed outliers. In some cases, pump start-ups were modelled by fitting flow profiles with second- or third-order polynomials, before transitioning to a constant flow profile.

The historical data of the washes were used to characterize the axial diffusion coefficient, $D_{\text{ax}}$, and resin porosity, $\varepsilon$. Parameter estimation was done by fitting a single value of $D_{\text{ax}}$ and a single value of $\varepsilon$ across all batches, ensuring they remain constant. Conductivity was converted to concentration by assuming the initial and final conductivity corresponded to concentrations of 0.1 and 0 N $NaNO_3$, respectively.

**Table 1:** Overview of variables used in simulation of the ion-exchange fixed-bed column using CADET-Julia.

| Symbol | Description | Value Used |
|---|---|---|
| $L_{\text{pipes, in}}$ | In-flow pipes length | 6.74 m |
| $L_{\text{pipes, out}}$ | Out-flow pipes length | 0.19 m |
| $L$ | Fixed-bed column length | 0.095 m |
| $r_{\text{pipes}}$ | Pipe radius | 0.005 m |
| $r_{\text{column}}$ | Column radius | 0.055 m |
| $D_{\text{ax, pipes}}$ | Axial diffusion coefficient in the pipes | $10^{-3}$ $m^2/s$ |
| $\sigma_{H^+}/\sigma_{Na^+}$ | Shielding factor | 0 / 0 |
| $\nu_{H^+}/\nu_{Na^+}$ | Characteristic charge | 1 / 1 |
| $k_{\text{kin}}$ | Kinetic coefficient | $10^8$ |

Subsequently, historical breakthrough curve data were used to fit the SMA model parameters: the ionic capacity, $\Lambda$, and the equilibrium coefficient, $k_{\text{eq}}$. Parameter estimation was done by fitting a single value of $\Lambda$ and a single value of $k_{\text{eq}}$ across all batches, ensuring they remain constant.

The ParticleSwarm algorithm from the Optim.jl package was utilized to perform global parameter searches, using the mean absolute error between simulated runs and historical data as the optimization metric [9].

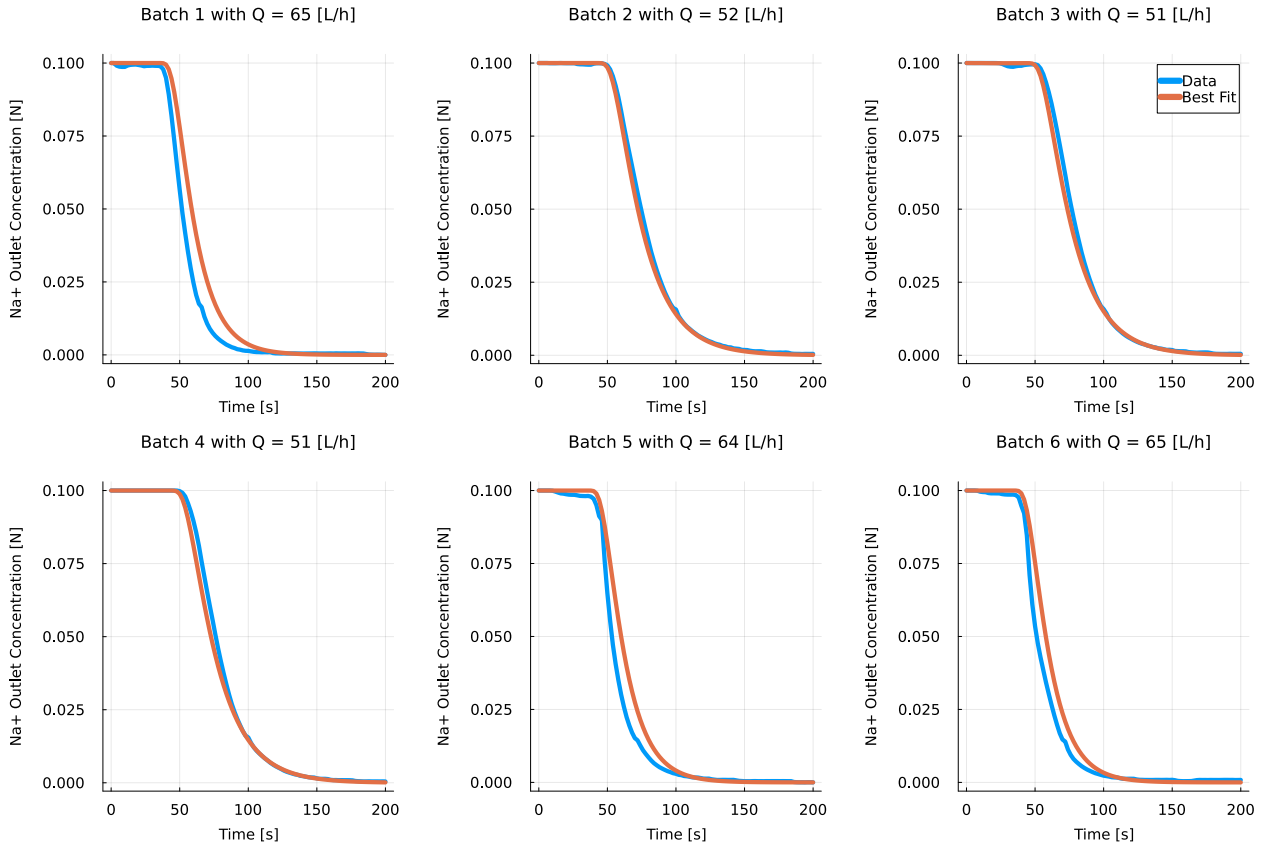



Figure 2: The six batch washes used for estimation of the axial diffusion coefficient, $D_{ax}$ and porosity, $\varepsilon$, alongside simulated runs using best-fit values. Q denotes the median flow rate of the batch.

# 3. RESULTS & DISCUSSION

## 3.1 Parameter Estimation

The batches of wash data were analyzed to estimate the best-fit values for the $D_{ax}$ and $\varepsilon$, which were determined to be $7 \times 10^{-5}$ m$^2$/s and 0.6, respectively. Using these parameter values, Figure 2 illustrates the experimental wash curves alongside their simulated counterparts.

Subsequently, the SMA isotherm parameters $\Lambda$ and $k_{eq}$ were estimated from breakthrough data, which yielded values of 4 eq/L and 3, respectively. Figure 3 presents the experimental breakthrough curves and corresponding simulations.

The LRM with SMA isotherm produces strong fits for both wash data and the breakthrough data. The simulations predict the timing of the initial break of the curve well and follow the same evolution as the observed data.

### Discussion

In Figure 2 and Figure 3, it can be observed that the simulations predict a delayed breakthrough when flow rates (Q) are higher, i.e. Q ≈ 65 L/h, compared to those with lower flow rates, i.e. Q ≈ 51 L/h. This indicates there may be some flow-dependent mechanisms present in the process not entirely explained by the LRM model.

Discrepancies between the simulated and experimental results may stem from uncertainties in the historical data and inconsistent execution across batches. Variations in how operators controlled the water height in the column could have affected the observed conductivity. Additionally, the exact concentration of the $NaNO_3$ solution is unknown; the concentration 0.1 N $NaNO_3$ is assumed based on the exercise instructions. Furthermore, measurement uncertainties in the flow meter and conductivity sensors further contribute to discrepancies between historical data and simulations.

When preprocessing the data, it was observed that parameter estimation was highly sensitive to the choice of $t = 0$, defined as when flow from the feed tank to the column begins. As $t = 0$ was not always clearly discernable, in some batches, it was approximated based on other batches where it was easier to identify. Horizontal translations of the wash curves significantly affected the converged values of the parameter estimation process.

The quality of the available datasets varied noticeably when evaluating historical data for parameter

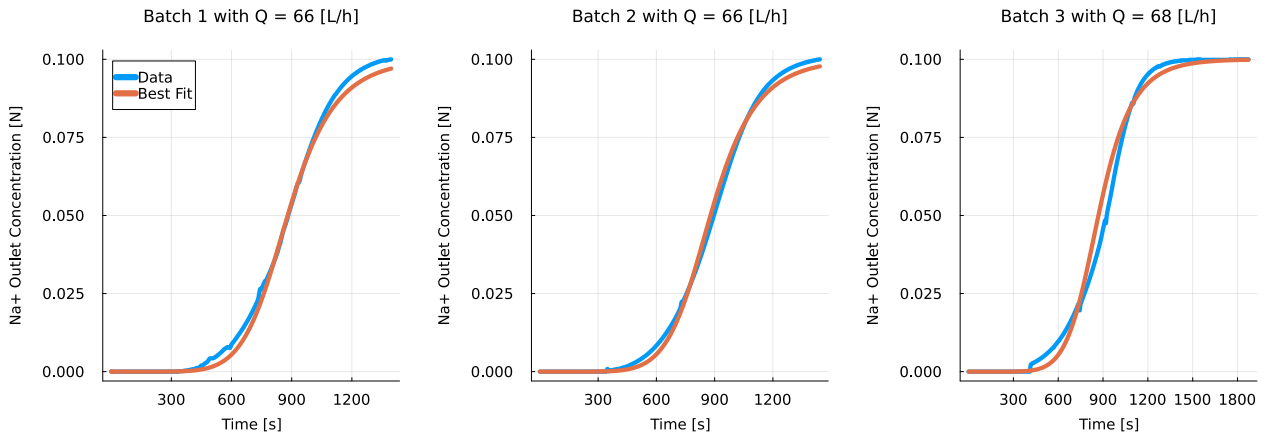



Figure 3: The three batch breakthroughs used for estimation of ionic capacity, $\Lambda$ and equilibrium constant, $k_{\mathrm{eq}}$, alongside simulated runs using best-fit values. Q denotes the median flow rate of the batch.

estimation. Smooth, undisrupted runs were critical to enabling parameter estimation. In this regard, some historical datasets were not considered for parameter estimation, and those used had to be preprocessed to make modeling feasible. The datasets most applicable to parameter estimation were those run by experienced operators conducting experiments for their research. "Data gathered by first-time operators often exhibited signs of process disruption and were rarely as directly usable for parameter estimation, compared to data produced with dedication to the purpose.

## 3.2 Computational Efficiency

In this study, the PDEs described in eqs. (1)–(4) were solved efficiently using DGSEM in CADET-Julia. On an i5-1345U processor (1.60 GHz), the equations were discretized and solved in under two seconds, below the measurement frequency. This was true for both the wash data, each consisting of approximately 100 data points, and the breakthrough data, containing up to 1000 points.

The global parameter searches for all washes and breakthroughs were completed in less than 10 minutes each. Notably, accounting for the inherent uncertainties in the system, adequate parameter values were identified already within the first 1–2 minutes. Additional search iterations refined these values, but the improvements exceed the level of accuracy achievable given the uncertainties present.

### Discussion

The ability to solve the LRM with the SMA isotherm within the 2-second measurement frequency showcases the model's potential for real-time computer-aided applications. In its current the state, the model can predict breakthrough profiles at a speed that enables it to be deployed in real-time. By connecting the model to live data feeds of the flow in the column, the model can alter its predicted breakthrough profile for every new data point.

Currently, the model predicts the entire breakthrough profile from $t = 0$ to the end of the data series, up to some 30 minutes in the future. The computation time can be further reduced by optimizing the routine to avoid redundant calculation on already-past data. The prediction horizon can also be limited, and more powerful hardware can be used to perform calculations.

This may bring the computation time below one second, and effort could then be spent in reducing the sensor measurement frequency to similarly match that. This naively ignores any time taken to retrieve data from the system.

The global parameter search can currently be completed in 1–10 minutes. To further accelerate this, an approach could be employing a local search algorithm with a well-informed initial guess. With tactics like this, the parameter estimation procedure could be reduced to sub-minute computation times.

This may enable real-time parameter adjustment, allowing the system to dynamically adapt to batch-to-batch variations. While it makes little sense for variables like, $D_{\mathrm{ax}}$, $\varepsilon$, $k_{\mathrm{eq}}$, or $\Lambda$ to change between batches, other parameters could be introduced to explain the effects of operating conditions and batch-to-batch variation.

## 3.3 Perspectives

The developed tool can be implemented directly to approximate breakthrough duration during operation. By evaluating the model in real-time, operators can see the impact of adjusting flow on the breakthrough profile.

To enhance the modeling capabilities demonstrated in this study, additional metadata on the process would be beneficial. Specifically, this includes:

- Timestamps for $t = 0$ as the precise point when all the flow from the T1 feed tank is directed into the column.

- Measured concentrations of the $NaNO_3$ solution used for breakthrough.
- Some indication of the operator's ability to maintain the water height within the column.

These lacking metadata mirror challenges frequently faced in industrial systems, where incomplete metadata, missing signals, and absent critical sensors hinder effective modeling.

The investigation has demonstrated the feasibility of characterizing pilot-scale equipment from historical data that mirrors industrial operational data. The methods employed here can be applied to historical data from industrial systems. Using fast numerical schemes or other methods, real-time computer-aided process insights and predictions could be granted to process operators. Parameter search optimizations can be employed for real-time determination of factors that vary from batch to batch.

The approach adopted in this study—leveraging historical data to identify areas of improvement—provides a framework for addressing these challenges. Drawing a clear connection between historical data and its value in developing real-time applications makes it possible to prioritize investments in metadata collection, new sensors, or dsata processing tools. These investments would provide a return in the improved ability to conduct real-time decision-making during operation to increase product yield.

Additional historical data and process understanding could be used to monitor the long-term health and efficiency of the system. In the case of ion-exchange, it could be used to quantify resin degradation and better schedule replacements.

## 4. CONCLUSION

This study demonstrates the potential for real-time analysis of ion-exchange chromatography using historical pilot-scale data of a fixed-bed ion exchange column. Despite challenges such as incomplete metadata and variability in manual operations, the findings confirm that the system can be accurately characterized using only operational historical data

By employing fast computational techniques, the study shows that the system can be modeled in real time, simulating entire breakthrough profiles within the two-second measurement frequency of the system. These findings underscore the potential of using historical data to develop valuable real-time computer-aided process applications in pilot and industrial-scale settings.

## ACKNOWLEDGEMENTS

The authors of this work acknowledge the efforts of students and staff at courses in experimental unit operations at the Department of Chemical and Biochemical Engineering for making data. Additionally, the authors would like to express gratitude to the Novo Nordisk Foundation for their support for the digital infrastructure of pilot facilities through grant NNF19SA0035474.

## REFERENCES

1. Kozorog M, et al. Model-based process optimization for mAb chromatography. Sep Purif Technol 2023;305:122528.
2. Kumar V, and and Lenhoff AM. Mechanistic Modeling of Preparative Column Chromatography for Biotherapeutics. Annu Rev Chem Biomol Eng 2020;11:235–55.
3. Jones MN et al. Pilot Plant 4.0: A Review of Digitalization Efforts of the Chemical and Biochemical Engineering Department at the Technical University of Denmark (DTU). Comput. Aided Chem. Eng., vol. 49, Elsevier; 2022, p. 1525–30.
4. Frandsen J, et al. CADET-Julia: Efficient and versatile, open-source simulator for batch chromatography in Julia. Comput Chem Eng 2025;192:108913.
5. Breuer JM, et al. Spatial discontinuous Galerkin spectral element method for a family of chromatography models in CADET. Comput Chem Eng 2023;177:108340.
6. Shampine LF, and Reichelt MW. The MATLAB ODE Suite. SIAM J Sci Comput 1997;18:1–22.
7. Rackauckas C, and Nie Q. DifferentialEquations.jl – A Performant and Feature-Rich Ecosystem for Solving Differential Equations in Julia. J Open Res Softw 2017;5:15.
8. Large-Scale Exercises in Process Technology and Chemical Unit Operations. Danish Technical University, Department of Chemical and Biochemical Engineering, Pilot Plant; 2024.
9. K Mogensen P, and N Riseth A. Optim: A mathematical optimization package for Julia. J Open Source Softw 2018;3:615.

© 2025 by the authors. Licensed to PSEcommunity.org and PSE Press. This is an open access article under the creative commons CC-BY-SA licensing terms. Credit must be given to creator and adaptations must be shared under the same terms. See https://creativecommons.org/licenses/by-sa/4.0/



Systems & Control Transactions

**Research Article - Peer Reviewed Conference Proceeding**
ESCAPE 35 - European Symposium on Computer Aided Process Engineering
Ghent, Belgium. 6-9 July 2025
Jan F.M. Van Impe, Grégoire Léonard, Satyajeet S. Bhonsale,
Monika E. Polańska, Filip Logist (Eds.)

PSE PRESS

# Model Based Flowsheet Studies on Cement Clinker Production Processes

**George Melitos[a,b], Bart de Groot[a]*, Fabrizio Bezzo[b]**

[a] Siemens Industry Software Limited, 26-28 Hammersmith Grove, W6 7HA London, United Kingdom
[b] CAPE-Lab (Computer-Aided Process Engineering Laboratory), Department of Industrial Engineering, University of Padova, 35131 Padova PD, Italy
* Corresponding Author: b.degroot@siemens.com

## ABSTRACT

Clinker is the main constituent of cement, produced in the pyroprocessing section of the cement plant. This comprises some high temperature and carbon intensive processes, which are responsible for the vast majority of the $CO_2$ emissions associated with cement production. This paper presents first-principles mathematical models for the simulation of the pyroprocess section; more specifically the preheating cyclones, the calciner and the rotary kiln. The models incorporate material and energy balances, the major heat and mass transport phenomena, reaction kinetics and thermodynamic property estimation models. These mathematical formulations are implemented in the gPROMS® Advanced Process Modelling Environment and the resulting index-1 DAE (Differential Algebraic Equation) system can be numerically solved for various reactor geometries and operating conditions. The process models developed for each unit are then used to build a cement pyroprocess flowsheet model. The flowsheet model is validated against published data, demonstrating the ability to predict accurately operating temperatures, degree of calcination, gas and solid compositions, fuel consumption and overall $CO_2$ emissions. The substitution of conventional coal with more sustainable fuels is also investigated, to evaluate the potential for avoiding $CO_2$ emissions by replacing part of the fossil-based coal fuel (used as a reference case). Trade-offs between different process KPIs (f.e. calcination efficiency, specific $CO_2$ emissions per tonne of clinker) are identified and evaluated for each fuel utilization scenario.

**Keywords**: Mathematical Modelling, Cement Production, Simulation, Alternative Fuels, Decarbonisation

## INTRODUCTION

The share of cement and concrete value chain to global $CO_2$ emissions is estimated at 6-7% [1]. These emissions originate from a series of several industrial activities. The first step is the extraction and mining of the raw materials, followed by the preparation and processing of them for the production of clinker, the main component of cement. Once clinker is formed, it is cooled and subsequently ground with gypsum and other additives to produce cement. Cement is then mixed with several aggregates, admixtures and water to form concrete. The stage responsible for the vast majority of the $CO_2$ emissions is the thermal processing (pyroprocessing) of the raw materials for the production of clinker.

The pyroprocessing section of a typical cement plant consists of four main processes: the preheating cyclones, the calciner, the rotary kiln and the grate cooler. From these processes, the calciner and the rotary kiln are responsible for almost 90% of the total emissions [2]. These two processes facilitate the chemical transformation of the raw materials into clinker. Specifically, in the calciner calcium carbonate (limestone) is decomposed into calcium oxide (lime) and carbon dioxide. This reaction is responsible for 60% of the total emissions, the so-called process emissions [1]. These emissions are unavoidable in principle since calcium oxide is the most important intermediate in the clinker formation process. After calcium oxide is formed it reacts with all the remaining raw materials (silicon dioxide, ferric oxide, alumina oxide) to form the final clinker product inside the rotary kiln. Most of the chemical reactions described above are endothermic and require a substantial amount of heat, which is provided to the process by internal combustion

of a solid fuel. The emissions due to fuel combustion are responsible for the remaining 40% of the carbon dioxide emissions [1].

The most common fuels used in the calciner, and the rotary kiln are the fossil-based pulverized coal or petcoke. However, the utilization of solid recovered fuels (SRF) is becoming a common practice in cement industry. These fuels originate from municipal solid waste processing and can play a crucial role in the mitigation of the direct $CO_2$ emissions of a cement plant. This is due to the high biogenic carbon content of such fuels, which emissions during combustion are considered neutral [3]. Based on their source and nature, alternative fuels have different chemical and mechanical properties which affect directly their performance upon combustion [4].

The chemical and physical phenomena occurring in the clinker production processes are rather complex and to this day, these processes have mostly been studied and modelled in literature as standalone unit operations. As a result, there is a lack of holistic model-based approaches on flowsheet simulations of cement plants in literature.

This work sets out to investigate the performance of the clinked production process in a holistic manner, utilizing mechanistic mathematical models. These are used to simulate a reference coal-fired cement plant, validated from literature data. Once the predictive ability of the models is verified, several case studies are presented in which different alternative fuels are used to replace coal, investigating the potential effect of fuel subtitution in the plant's emissions and performance.

# METODOLOGY

## Pyroprocess System Description

The pyroprocess system of a cement plant consists of the preheating cyclones, the calciner, the rotary kiln and the grate cooler. The solid raw meal feedstock is being heated inside the cyclones up to 800°C, then calcined in the calciner and finally converted into clinker reaching 1450°C inside the rotary kiln, while thermal energy from the hot clinker exiting the kiln is recovered in the cooler and recycled back to the former processes by the secondary air (to the kiln) and tertiary air (to the calciner) streams. A visual representation of the pyroprocessing system is presented in Figure 1. The mathematical modelling framework that has been developed and used to perform the simulations will be explained briefly. Given the greater potential for emission reduction, the study focuses on the carbon intensive processes (calciner, kiln) and the $CO_2$ reduction potential from alternative fuel combustion. These models are then used in a flowsheet simulation and the results are presented in the following Chapter.

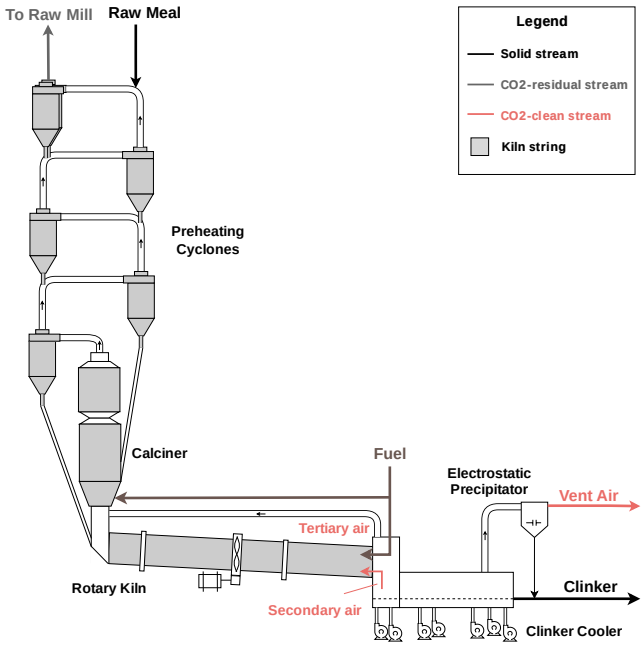



**Figure 1:** Cement Pyroprocess Plant (modified from [5]).

## Preheating Cyclones

The preheating cyclones are modelled as a direct heat exchange process, in which the hot exhaust gas is mixed with the cold solid. The two streams exchange heat inside the cyclones and then are separated in the underflow (solids) and the overflow of the cyclone (gas with dust). Assuming steady state operation the material balance for the solid (1) and gas phase (2) and the energy balance (3) for each cyclone are written as:

$$m_{s,j-1} + m_{es,j+1} = m_{s,j} + m_{es,j} - m_{m,j} \quad \forall\, j \in 1, N \quad (1)$$

$$m_{g,j} = m_{g,j-1} + m_{fa,j} + m_{m,j} \quad \forall\, j \in 1, N \quad (2)$$

$$m_s C_{p,s} T\big|_{j-1} + m_{es} C_{p,s} T\big|_{j+1} + m_g C_{p,g} T\big|_{j-1} + m_{fa,j} C_{p,a} T_a = m_s C_{p,s} T\big|_j + m_{es} C_{p,s} T\big|_j + m_g C_{p,g} T\big|_j \quad \forall\, j \in 1, N \quad (3)$$

Where $m_{i,j}$ (kg/s) is the mass flowrate of the phase *i* out of cyclone *j*, $Cp_{i,j}$ (J/kg*K) is the specific heat capacity of the phase *i* in cyclone *j* and $T_j$ (K) is the temperature inside cyclone *j*. Regarding the phases *i*, s refers to the solid phase, *g* refers to the gas phase, *es* refers to the solids entrained by the gas, *m* refers to the moisture of the raw meal and *fa* refers to the false air that is entering each cyclone.

Except for the mass and energy balances reported above, sub-models for the estimation of the heat losses and pressure drops around each cyclone are included as well, following approaches from relevant literature works [6-7].

## Calciner

The basis of the calciner model were general material and energy conservation balances:

$$\frac{dm_i(z)}{dz} = A_{calciner} * \sum_j R_{i,j}(z) \;\; \forall\, i \in solid, fuel, gas \;(4)$$

$$\frac{dH_t(z)}{dz} = A_{calciner} * (\Delta H_{cal} * R_{cal}(z) + \sum_c \Delta H_c * R_c(z)) \;(5)$$

where $m_i(z)$ (kg/s) is the specific mass flowrate of the component $i$ in the axial position $z$, $A_{calciner}$ (m$^2$) is the cross sectional area of the calciner, $H_t$ (kW) is the enthalpy of the mixture in the axial position $z$ and $R_{ij}(z)$ (kg/m$^3$*s) is the volumetric reaction rate of component $i$ in reaction $j$.

The rate expression for calcination reaction reads:

$$\mathrm{CaCO_3(s) \rightarrow CaO(s) + CO_2(g)}, \qquad \Delta \mathrm{H_{cal}} = 178 \frac{\mathrm{kJ}}{\mathrm{mole}}$$

$$R_{cal}(z) = k(z) * A_{CaCO_3}(z) * \rho_{CaCO_3} * \left(\frac{P_{eq}(z) - P_{CO_2}(z)}{P_{eq}(z)}\right) \;(6)$$

where $k(z)$ (kg/m$^2$) is the global calcination reaction constant, incorporating chemical and physical limitation terms [8], $A_{CaCO3}$ (m$^2$/kg) is the specific surface area of the solids as a function of conversion [9], $\rho_{CaCO3}$ (kg/m$^3$) is the solids density, $P_{eq}(z)$ (Pa) is the calcination equilibrium pressure [9] and $P_{CO2}$ (Pa) the $CO_2$ partial pressure.

Regarding fuel combustion, there are multiple heterogeneous and homogeneous reaction steps occurring. The first step is the evaporation of the fuel moisture, followed by the devolatization of the volatile part of the fuel, leaving the solid particle with just char and ash. The rate expression $R_{i,dev}(z)$ for the devolatization follows an Arrhenius type behaviour:

$$R_{dev}(z) = A_{dev} * e^{-\frac{E_{dev}}{R*T_p}} \quad (7)$$

where $T_p$ (K) is the particle temperature, $R$ (kJ/mole*K) is the ideal gas constant and $A_{dev}$ (1/s) and $E_{dev}$ (kJ/mole) are the kinetic parameters, which are different for different types of solids fuels, like coal and SRF [5]. After the release of the volatiles in the gaseous phase, the volatile mixture that consists of $CH_4$, $C_2H_4$, $H_2$, CO, $O_2$, $N_2$ and $S_2$ is oxidized though homogeneous gas phase reactions to produce the oxidized form of these gases ($CO_2$, $H_2O$, NO, $SO_2$) and provide heat to the system. The kinetic rate expressions for each reaction are extracted from relevant literature [9]. The remaining char is reacting with oxygen according to the following reaction with the respective reaction rate $R_{char}(z)$:

$$\mathrm{C(s) + xO_2(g) \rightarrow yCO(g) + zCO_2(g)}$$

$$R_{char}(z) = \frac{A_p}{V_p} \frac{k_{chem}(z) * k_{phys}(z)}{k_{chem}(z) + k_{phys}(z)} P_{O_2}(z) \quad (8)$$

where x, y, z are temperature dependent coefficients, $A_p$ (m$^2$) and $V_p$ (m$^3$) are the particle's surface and volume, $P_{O2}$ (Pa) is oxygen's partial pressure, and $k_{chem}(z)$ and $k_{phys}(z)$ (kg/m$^2$*Pa*s) are reaction constants, that are evaluated through expressions from literature [4,10].

## Rotary Kiln

For the rotary kiln system, the process model is divided into three sub-models that refer to: a) the motion of solid bed inside the rotating drum, b) the heat transfer phenomena between the solid bed, gas phase and rotating wall and shell, c) the chemical reactions occurring during clinkerization and fuel combustion. The first sub-model is used to calculate accurately the height of the bed, the residence time and velocity of the solids inside the kiln and the cross sectional and contact areas between the bed-gas-wall system, that are essential for the heat transfer model calculations. Due to page limitations the equations of these sub-models will not be displayed here, however the reader is referred to relevant literature works for both the bed motion [11] and heat transfer models [12-13]. For the chemical reaction sub-model, the four main clinker formation reactions were assumed, with the following kinetic rate expressions [13]:

$$2\mathrm{CaO(s) + SiO_2}(s) \rightarrow Ca_2SiO_4(s)\;(C_2S)$$

$$R_{C_2S}(z) = \rho_{bed} * k_{C_2S}(z) * y_{CaO}^2 * y_{SiO_2}$$

$$\mathrm{Ca_2SiO_4(s) + CaO}(s) \rightarrow Ca_3SiO_5(s)\;(C_3S)$$

$$R_{C_3S}(z) = \rho_{bed} * k_{C_3S}(z) * y_{C_2S} * y_{Cao}$$

$$3\mathrm{CaO(s) + Al_2O_3}(s) \rightarrow Ca_3Al_2O_7(s)(C_3A)$$

$$R_{C_3A}(z) = \rho_{bed} * k_{C_3A}(z) * y_{CaO}^3 * y_{Al_2O_3}$$

$$\mathrm{4CaO(s) + Al_2O_3(s) + Fe_2O_3(s) \rightarrow Ca_4Al_2Fe_2O_{10}(s)(C_4AF)}$$

$$R_{C_4AF}(z) = \rho_{bed} * k_{C_4AF}(z) * y_{CaO}^4 * y_{Al_2O_3} * y_{Fe_2O_3}$$

where $\rho_{bed}$ (kg/m$^3$) is the bed density, and $k_i$ (1/s) and $y_i$ (-) are the kinetic constants and mass fractions.

Following the common notation for the clinker phases in cement science, $C_2S$, $C_3S$, $C_3A$ and $C_4AF$ refer to $Ca_2SiO_4$, $Ca_3SiO_5$, $Ca_3Al_2O_7$ and $Ca_3Al_2Fe_2O_7$ respectively.

# RESULTS & DISCUSSION

## Base Case Coal Fired Simulation Results

In this part of the study, the models presented above will be solved simultaneously in a flowsheet simulation and the results will be validated against published data from a relevant work that is based on a cement process simulator developed by VDZ (Association of German Cement Works) [14]. The specification of all the inlet conditions were tuned in accordance with the literature source that was used to validate the results. The inlet conditions and properties of the raw meal and fuel inlet streams are presented in Table 1. The equipment design was taken identical as the one from the reference source [14]. The preheating tower string consists of 5 cyclones

and a calciner with a diameter of 3.88m and a length of 45m, while the kiln is 57m long with a diameter of 4.04m.

The results obtained from the simulation environment of gPROMS® were compared with the reference dataset, and the most important information is summarised in Table 2 and Figure 2. Starting from Table 2, the temperature predictions of the solid and gas streams around the cyclones-calciner string seem to align with the literature data, while the degree of calcination in the calciner is predicted accurately with a relative error of 0.5%.

**Table 1:** Raw Meal & Fuel Inlet Conditions.

| **Raw Meal Conditions** | | |
|---|---|---|
| Temperature (°C) | 60 | |
| Mass Flowrate (kg/s) | 55.2 | |
| $CaCO_3$ (wt.% dry basis) | 78.7 | |
| $SiO_2$ (wt.% dry basis) | 13.6 | |
| $Al_2O_3$ (wt.% dry basis) | 4.3 | |
| $Fe_2O_3$ (wt.% dry basis) | 2.4 | |
| CaO (wt.% dry basis) | 0.0 | |
| Moisture (wt.%) | 1.0 | |
| **Fuel Conditions** | **Coal** | **SRF** |
| Temperature (°C) | 60 | 60 |
| Mass Flowrate to Calciner (kg/s) | 2.42 | 2.85 |
| Mass Flowrate to Rotary Kiln (kg/s) | 1.40 | - |
| Fixed Carbon (wt.% wet basis) | 51.0 | 10.0 |
| Volatile Matter (wt.% wet basis) | 32.0 | 69.3 |
| Ash (wt.% wet basis) | 16.5 | 13.8 |
| Moisture (wt.% wet basis) | 0.5 | 6.9 |
| C (wt.% dry basis) | 69.5 | 45.2 |
| H (wt.% dry basis) | 4.0 | 7.0 |
| O (wt.% dry basis) | 9.0 | 33.0 |
| S (wt.% dry basis) | 0.5 | 0.1 |
| N (wt.% dry basis) | 0.5 | 0.0 |

**Table 2:** Comparison of Model Predictions from Literature Data [14].

| **Variables** | **gPROMS** | **VDZ** |
|---|---|---|
| Flue Gas Temperature (°C) | 315 | 314 |
| Preheated Solids Temperature (°C) | 762 | 760 |
| Calciner Gas Temperature (°C) | 865 | 864 |
| Kiln Feed Loss on Ignition (%) | 2.9 | 3.2 |
| Degree of Calcination (%) | 94.5 | 94.0 |

Moving onto the kiln system, it can be observed from Figure 2 that the prediction of the clinker phases composition is quite close to the reference data. Specifically, the mass fractions of $C_3S$ and free lime are predicted precisely, while the simulated mass fractions of $C_2S$, $C_3A$ and $C_4AF$ deviate from the reference data with relative errors of 3.5%, 3.9% and 4.5% respectively.

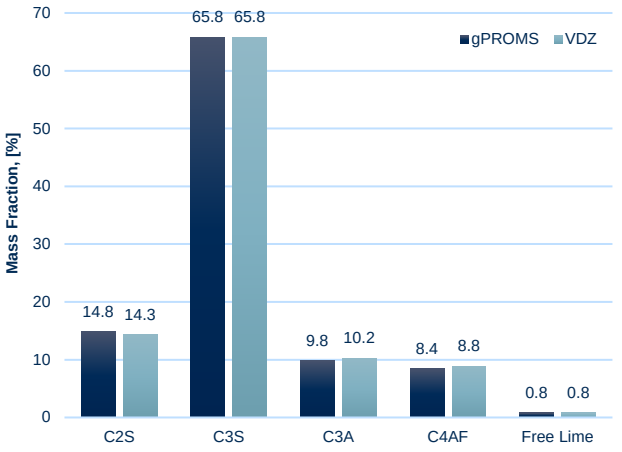



**Figure 2:** Model Predictions of Clinker Compositon.

## Coal Substitution with Solid Recovered Fuels

The chemical (ultimate analysis, composition) and physical (proximate analysis, particle size) characteristics of the simulated SRF were extracted from relevant literature works and are presented in Table 1 [5,14]. Two different case studies were investigated, in which different average particle sizes were assumed. In the first case (SRF-1) a very fine SRF was assumed with an average particle size of 250 μm [5]. In the second case (SRF-2) a SRF with average particle size of 750 μm was assumed [12]. The target is to re-design the calciner system, by modifying the residence time, in order to achieve complete fuel combustion and reach the same temperature and degree of calcination in the outlet of the reactor, since these two variables are the most important KPIs for the operation of the calciner. The biogenic content of the SRFs is assumed to be 80%.

As presented in Figure 3, the temperature and calcination profiles for the three cases are quite different, since the fuels used in each case have different properties that result to different combustion behaviour. That being said, it is important to highlight that no matter the variability of the temperature and calcination distributions for each case study, the values of the variables in the outlet of the calciner have been kept almost the same by modifying the residence time from 2.9 seconds for the base case to 3.3 seconds and 4.1 seconds for the SRF-1 and 2 cases respectively. This translates to a larger calciner with an increased cross-sectional area (diameter), since the length of the calciner is kept constant due to design restrictions.

Table 3 presents the conditions of the flue gas out of the calciner and the preheating tower for the coal and

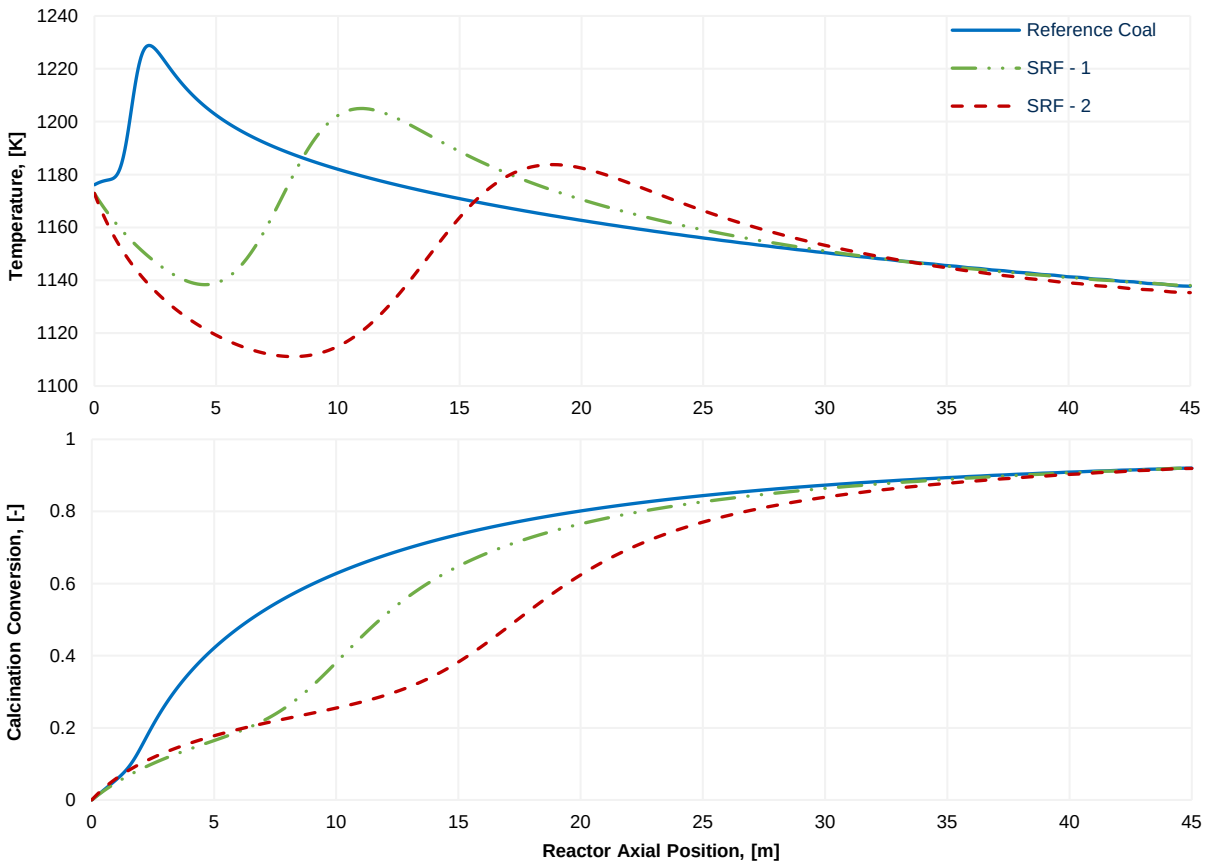



**Figure 3:** Comparison of temperature and conversion calciner profiles for the reference coal (50μm), SRF-1 (250μm) and SRF-2 (750 μm).

the SRF cases respectively. The concentration of $CO_2$ in the SRF-case flue gas is lower than the base case, while the oxygen and water concentrations are significantly higher. This is attributed to the very high moisture content of the SRF (7% in comparison with 0.5% for coal) which is transferred to the gas phase and the increased hydrogen to carbon ratio. In addition, the oxygen content of the SRF (33%) is significantly higher in comparison with coal (9%). It is also important to note that the total mass flowrate of flue gas is higher, since more moisture and oxygen are transferred from the solid fuel to the gas phase.

Table 4 summarises and compares the most important KPIs for both the calciner and the kiln systems in terms of specific $CO_2$ intensity. It is important to note that the fossil-fuel emissions in the calciner for the SRF cases are reduced by 78%. Moreover, it should be borne in mind that even though the substitution rate of coal in the calciner is 100%, there are still some fossil emissions related to the non-biogenic part of the Solid Recovered Fuel (around 20%). The overall plant's emissions are reduced by 18.5%.

**Table 3**: Exhaust Gas Conditions for Coal and SRF Cases.

| **Calciner Exhaust Gas** | **Coal** | **SRF** |
|---|---|---|
| Mass Flowrate (kg/s) | 63.3 | 64.0 |
| Temperature (°C) | 865 | 864 |
| $O_2$ (v/v wet basis) | 2.8 | 4.4 |
| $N_2$ (v/v wet basis) | 59.2 | 57.4 |
| $CO_2$ (v/v wet basis) | 33.1 | 30.6 |
| $H_2O$ (v/v wet basis) | 4.9 | 7.5 |
| **Preheating Tower Exhaust Gas** | **Coal** | **SRF** |
| Mass Flowrate (kg/s) | 66.2 | 66.8 |
| Temperature (°C) | 315 | 323 |
| $O_2$ (v/v wet basis) | 3.4 | 5.0 |
| $N_2$ (v/v wet basis) | 58.9 | 57.3 |
| $CO_2$ (v/v wet basis) | 31.4 | 29.0 |
| $H_2O$ (v/v wet basis) | 6.2 | 8.7 |

**Table 4**: Important KPIs.

| **Calciner** | **Coal** | **SRF** |
|---|---|---|
| Process Emissions ($kg_{CO2}$ / $ton_{clinker}$) | 510.3 | 510.3 |
| Fossil-Fuel Emissions ($kg_{CO2}$ / $ton_{clinker}$) | 181.3 | 26.2 |
| **Rotary Kiln** | **Coal** | **SRF** |
| Process Emissions ($kg_{CO2}$ / $ton_{clinker}$) | 35.0 | 35.0 |
| Fossil-Fuel Emissions ($kg_{CO2}$ / $ton_{clinker}$) | 112.3 | 112.3 |
| Total Emissions ($kg_{CO2}$ / $ton_{clinker}$) | 838.9 | 683.8 |

## CONCLUSIONS

This study highlights the importance of process modelling and simulation to accurately predict and evaluate the performance of a cement plant burning sustainable biogenic fuels instead of the conventional pulverized coal. Even though the quality (moisture, particle size, heating value) of such fuels is rather poor and the thermal performance of the plant decreases significantly, the overall $CO_2$ emissions showed a reduction of around 18.5%, just by replacing the fuel in the calciner. Apart from the energy penalty due to the significantly higher moisture content of the SRFs, the implementation of such a technology would also require increased capital investments, since SRF requires higher residence times (equipment) to combust completely. The flue gas out of an SRF-fired calciner has lower $CO_2$ and higher $H_2O$ and $O_2$ content, making it more difficult to capture in a post-combustion unit.

## ACKNOWLEDGEMENTS

This work has been funded by the European Union's Horizon Europe research and innovation programme under the Marie Sklodowska-Curie Grant Agreement No 101073547 "CO2Valorize".

## REFERENCES

1. Fennell, P., Driver, J., Bataille, C., & Davis, S. J. (2022). Cement and steel—nine steps to net zero. *Nature*, *603*(7902), 574-577.
2. Bhatty, J. I., Miller, F. M., & Bohan, R. P. (2011). *Innovations in Portland Cement Manufacturing* (2nd ed.). Portland Cement Association. Skokie, Illinois
3. Schneider, M., Hoenig, V., Ruppert, J., & Rickert, J. (2023). The cement plant of tomorrow. *Cement and Concrete Research*, *173*, 107290.
4. Wang, G., Silva, R. B., Azevedo, J. L. T., Martins-Dias, S., & Costa, M. (2014). Evaluation of the combustion behaviour and ash characteristics of biomass waste derived fuels, pine and coal in a drop tube furnace. *Fuel*, *117*, 809-824.
5. Varnier, L., d'Amore, F., Clausen, K., Melitos, G., de Groot, B., & Bezzo, F. (2025). Combined electrification and carbon capture for low-carbon cement: techno-economic assessment of different designs. *Journal of Cleaner Production*, 145029.
6. Mujumdar, K. S., Ganesh, K. V., Kulkarni, S. B., & Ranade, V. V. (2007). Rotary Cement Kiln Simulator (RoCKS): Integrated modeling of pre-heater, calciner, kiln and clinker cooler. *Chemical Engineering Science*, *62*(9), 2590-2607.
7. Gupta, A. V. S. S. K. S., & Nag, P. K. (2000). Prediction of heat transfer coefficient in the cyclone separator of a CFB. *International journal of energy research*, *24*(12), 1065-1079.
8. Mikulčić, H., Von Berg, E., Vujanović, M., Priesching, P., Perković, L., Tatschl, R., & Duić, N. (2012). Numerical modelling of calcination reaction mechanism for cement production. *Chemical engineering science*, *69*(1), 607-615.
9. Iliuta, I., Dam-Johansen, K., & Jensen, L. S. (2002). Mathematical modeling of an in-line low-NOx calciner. *Chemical engineering science*, *57*(5), 805-820.
10. Mikulčić, H., Von Berg, E., Vujanović, M., Wang, X., Tan, H., & Duić, N. (2016). Numerical evaluation of different pulverized coal and solid recovered fuel co-firing modes inside a large-scale cement calciner. *Applied energy*, *184*, 1292-1305.
11. Bisulandu, B. J. R. M., & Huchet, F. (2023). Rotary kiln process: An overview of physical mechanisms, models and applications. *Applied Thermal Engineering*, *221*, 119637.
12. Pieper, C., Liedmann, B., Wirtz, S., Scherer, V., Bodendiek, N., & Schaefer, S. (2020). Interaction of the combustion of refuse derived fuel with the clinker bed in rotary cement kilns: A numerical study. *Fuel*, *266*, 117048.
13. Csernyei, C., & Straatman, A. G. (2016). Numerical modeling of a rotary cement kiln with improvements to shell cooling. *International Journal of Heat and Mass Transfer*, *102*, 610-621.
14. Campanari, S., Cinti, G., Consonni, S., Fleiger, K., Gatti, M., Hoppe, H., Martínez, I., Romano, M., Spinelli, M., & Voldsund, M. (2016). *Design and performance of CEMCAP cement plant without $CO_2$ capture. CEMCAP Deliverable D4.1.*

© 2025 by the authors. Licensed to PSEcommunity.org and PSE Press. This is an open access article under the creative commons CC-BY-SA licensing terms. Credit must be given to creator and adaptations must be shared under the same terms. See https://creativecommons.org/licenses/by-sa/4.0/



Systems & Control Transactions

**Research Article - Peer Reviewed Conference Proceeding**
ESCAPE 35 - European Symposium on Computer Aided Process Engineering
Ghent, Belgium. 6-9 July 2025
Jan F.M. Van Impe, Grégoire Léonard, Satyajeet S. Bhonsale,
Monika E. Polańska, Filip Logist (Eds.)

PSE PRESS

# Techno-economic analysis of a novel small-scale blue $H_2$ and $N_2$ production system

**Adrian R. Irhamna[a,b], and George M. Bollas[a]***

[a] Department of Chemical and Biomolecular Engineering, Pratt & Whitney Institute for Advanced Systems Engineering, University of Connecticut, 159 Discovery Dr, Storrs, CT, 06269, USA.
[b] Faculty of Mechanical and Aerospace Engineering, Institut Teknologi Bandung, Jalan Ganesa 10, Bandung, Jawa Barat, 40132, Indonesia
* Corresponding Author: george.bollas@uconn.edu.

## ABSTRACT

This study presents an economic analysis of a blue $H_2$-$N_2$ production system, using a novel intensified reformer system with a hydrogen production efficiency of 80%. The system's ability to produce both high-purity $H_2$ and $N_2$ creates opportunities for small-scale blue $H_2$ and distributed ammonia production. The system consists of three identical, optimized fixed-bed reforming reactors, a heat recovery system, and shift reactors. A dynamic model was developed to simulate three small-scale $H_2$ production systems: 2.8 tpd, 7.1 tpd, and 17.1 tpd, enabling an evaluation of their economic viability. The results indicate that the cost of $H_2$ production ranges from 2.7 to 3.1 USD/kg$H_2$. Sensitivity analysis reveals that natural gas and $CO_2$ transportation costs have a significant impact on the variability of $H_2$ price. This research provides valuable insights into the economic feasibility of small-scale blue hydrogen production, offering a pathway to support the broader adoption of hydrogen technologies in advancing a cleaner energy future.

**Keywords**: Dynamic Modelling, Process Intensification, Process Design, Technoeconomic Analysis, Hydrogen, Nitrogen.

## INTRODUCTION

The use of hydrogen is critical for decarbonization efforts, serving as a replacement for fossil fuels. Approximately 80% of the projected future hydrogen demand stems from emerging applications, with around 27% attributed to the transportation sector [1]. Hydrogen use in medium- and heavy-duty vehicles, maritime shipping, aviation, and rail is among top priorities of the US Clean Hydrogen Strategy and Roadmap [2]. Manufacturers are already transitioning towards hydrogen-powered heavy-duty trucks, utilizing either fuel cells or internal combustion engines [3]. To support the widespread adoption of hydrogen, ensuring its availability and the development of infrastructure at points of use is essential.

However, centralized hydrogen production requires transporting and storing hydrogen, which has proven to be challenging and a significant bottleneck in hydrogen implementation. One proposed solution is blending hydrogen with the current natural gas infrastructure [4]. However, this practice has faced criticism due to safety concerns. Another approach under consideration involves storing hydrogen in the form of ammonia or methanol. This method is considered more economical for larger scale applications, such as continental export and import, given the long supply chain to the point of use [5].

An alternative strategy is smaller, distributed hydrogen tailored to the specific local needs. This approach aligns with hydrogen implementation in the transportation sector, which requires numerous hydrogen refuelling stations along vehicle routes. On-site hydrogen production can be achieved through either green hydrogen or blue hydrogen, depending on the location characteristics and the availability of energy sources and materials. Green hydrogen, while more environmentally friendly, is less cost-effective compared to blue hydrogen [5]. Locations with access to natural gas, biogas or limited renewable energy resources, should consider blue hydrogen technology as a more cost-effective solution for hydrogen production.

The discussion regarding blue hydrogen technology has predominantly focused on large-scale industrial

applications. Steam methane reforming with carbon capture storage (SMR-CCS), the most mature blue $H_2$ technology, continues to face challenges in achieving $CO_2$ capture rates above 80% [6], primarily due to $CO_2$ dilution in the flue gas stream. However, emerging technologies like chemical looping (CL) hydrogen production, show promising potential for blue hydrogen production, as they can achieve higher $CO_2$ concentrations in the downstream process, thereby facilitating more efficient carbon capture [7].

Our previous research demonstrated an optimized fixed-bed reactor for chemical looping hydrogen production that generates high concentrations of hydrogen while simultaneously producing concentrated streams of $CO_2$ and $N_2$ in three separate streams [7]. Our following work presented an optimized control strategy for an integrated multi-reactor system, incorporating heat recovery system and shift reactor components, specifically designed for small-scale hydrogen and nitrogen production [8].

This study presents a techno-economic analysis of a novel blue hydrogen and nitrogen production system designed to meet local demands. Prior studies primarily focused on large-scale hydrogen production, whereas this work provides cost estimates for small-scale distributed H2 production. Thus, it provides valuable insights for stakeholders assessing the feasibility and economic viability of small-scale hydrogen deployment, enabling more informed decision-making on investment and implementation.

# METHODOLOGY

## Small-scale Definition

First, the scale of $H_2$ production must be defined. Most studies on CL-based $H_2$ production plants focus on capacities above 60 tons/day [9-13]. Consequently, we define $H_2$ production of less than 20 tons/day as small-scale. This scale is intended for local applications, such as supporting hydrogen refuelling stations [14].

## The Blue $H_2$-$N_2$ Production System

Figure 1 illustrates the novel blue $H_2$-$N_2$ production system discussed in this work. The system consists of three major subsystems: (i) a train of reforming reactors, (ii) a heat recovery system, and (iii) a gas purification system. The reactor system uses the intensified reforming reactor discussed in [7], operating on the chemical-looping reforming (CLR) principle, with successive oxidation (OX), reduction (RED), and reforming (REF) stages. A minimum of three reactors operates simultaneously at different CLR stages to ensure a continuous product stream. In each stage the reactors produce three different streams: a N2-rich stream from OX, a CO2-rich stream from RED, and a H2-rich stream from REF.

The heat recovery system includes preheaters and steam generators installed along each downstream path to preheat the reformer feed. The hot streams used in the heat recovery system originate from the product streams of the multi-reformer system.

The gas purification system is designed to purify the primary product of each stream. In the $N_2$-rich stream, a methanator converts remaining CO and $CO_2$ into methane. In the $CO_2$-rich stream, a condenser removes steam to ensure a high $CO_2$ concentration output suitable for capture. For the $H_2$-rich stream, a water gas shift reactor converts remaining CO into $H_2$, and a pressure swing adsorption (PSA) separates $H_2$ from the other gases.

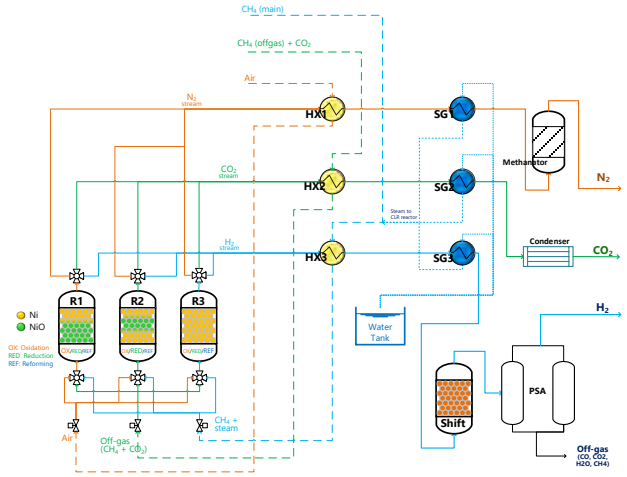



**Figure 1.** Simplified flowchart of the blue $H_2$-$N_2$ production system discussed in this work.

## Modeling and Simulation

The fixed bed reactors for the reforming and shift reactors were modeled using a 1D heterogeneous model, that incorporates mass, energy, and momentum balances, reaction kinetics, and mass-heat transfer correlations. The kinetics of the CL reformer is documented in [7], while that for the shift reactor is provided in [8]. The heat recovery system was modeled as a counter-current heat exchanger, incorporating mass and energy balance equations. The system's compressor was modeled as a two-stage compressor with intercoolers, operating with a mechanical and polytropic efficiency of 90%.

Details on the integrated blue $H_2$-$N_2$ production model, along with its validation and dynamic optimization can be found in [8]. The system is comprised of a set of Differential-Algebraic Equations (DAEs), which were solved using the equation-based process modeling platform gPROMS Process 2023.2.0 [15], with the DAEBDF solver.

To simulate systems of different scales, the reactor's length-to-diameter (L/D) ratio was maintained, while the inlet molar flow rate and reactor volume were

adjusted. Key system parameters, such as the steam-to-methane ratio, the $CO_2$-to-fuel ratio during the reduction stage, and the steam distribution across the steam generators, were kept constant.

## Economic Analysis

This techno-economic analysis covers from the purchase of natural gas to the downstream treatment of the $CO_2$ by product. The analysis was conducted following the framework outlined by DOE/NETL [16], as presented in Table 1.

**Table 1:** Methodology for techno-economic analysis used to estimate $H_2$ production cost based on the framework by DOE/NETL [16].

| Components | Formula |
|---|---|
| Capital Cost | |
| - Bare Erected Cost of j-components ($BECj$) | $\sum BEC_j$ |
| Total $BEC$ | |
| Engineering Procurement and Construction ($EPC$) | $10\%\ (BEC)$ |
| Contingency ($CON$) | $20\%(BEC\ +\ EPC)$ |
| Total Plant Cost ($TPC$) | $BEC + EPC + CON$ |
| Owner Cost & Other Financial Cost ($O\&OFC$) | $20\%\ (BEC)$ |
| Total Overnight Cost ($TOC$) | $TPC + O\&OFC$ |
| Total as spent Cost ($TASC$) | $TOC + 18\%TOC$ |
| Capital Cost per Year ($TASCpa$) | $TASC\ \times\ CCF$ |
| Annual Operation and Maintenance Cost ($O\&M$) | $O\&M$ |
| Total Annual Cost ($TAC$) | $TASCpa + O\&M$ |
| $H_2$ cost (USD/kg) | ${}^{TAC}/_{H2prod.}$ |

The capital cost was determined by summing the costs of the individual reactor components, incorporating additional costs such as Engineering, Procurement, and Construction (EPC), contingency, and overnight costs, resulting in the Total as Spent Cost (TASC). The annual capital cost was then calculated by multiplying the TASC by a capital charge factor (CCF) of 0.159, which assumes an interest rate of 10% and a plant lifetime of 20 years [17]. Component costs for the blue $H_2$ and $N_2$ production system were estimated using reference costs provided by DOE/NETL [16], as summarized in [11], and scaled using the exponential scaling formula shown in Eq. (1). The required capacity of each equipment for this cost estimation was obtained from simulation. Additionally, a balance of plant cost – piping, instruments, controls, and facilities – was included and assumed to be 0.8 of the total equipment cost [17], except for the CL reactor component.

$$\text{Cost}_j = \text{Cost}_{ref}\left(\frac{\text{Capacity}_j}{\text{Capacity}_{ref}}\right)^f \quad (1)$$

The annual operating and maintenance (O&M) costs were estimated by combining fixed and variable costs based on assumptions from [11]. Labor costs were assumed to be 90,000 USD/year/person. The O&M costs also accounted for the transportation of $CO_2$ to local storage sites or for utilization. The transportation cost was based on estimates from [18] for 1 million tons $CO_2$ per year transported within a 100-mile distance. Table 2 summarizes the key assumptions for estimating operating expenses.

**Table 2:** Assumptions for the calculation of the operation and maintenance (O&M) costs.

| Components | Formula |
|---|---|
| Fixed Costs | |
| Labor [USD/person/year] | 90,000 |
| Maintenance | $0.7\%\ TASC$ |
| Insurance | $1.5\%\ TASC$ |
| Variable Costs | |
| Oxygen carriers [USD/kg] | 20 |
| Shift catalyst [USD/kg] | 50 |
| Desulphurization/methanator catalyst [USD/kg] | 15 |
| Lifetime oxygen carriers [years] | 2 |
| Lifetime catalyst [years] | 5 |
| Natural gas cost [USD/$GJ_{LHV}$] | 6.5 |
| Steam cost [USD/$ton_{steam}$] | 0.13 |
| $CO_2$ transportation for 1 Mtpa, <100 miles distance, with low monitoring [USD/ton$CO_2$] | 16.5 |
| Electricity cost [USD/MWh] | 55 |

## RESULT AND DISCUSSIONS

We selected the proposed blue $H_2$-$N_2$ production system with three $H_2$ production scales: 2.8, 7.1, and 17.1 tons of $H_2$ per day. These production scales represent the potential demand for medium-sized hydrogen refuelling stations [14]. Simulation results for each scale were used to extract key parameters for the main equipment in the integrated system, as shown in Table 3. These parameters were subsequently used to estimate equipment costs using Eq. (1) and the points discussed in the previous section.

The techno-economic analysis was conducted using the methodology previously described, with the results summarized in Table 4. The analysis shows that the cost of blue $H_2$ for the proposed small-scale system ranges between 2.73 – 3.04 USD/kg$H_2$, with smaller scales incurring higher costs.

In terms of component costs, the CL reforming reactor accounts for the largest cost, comprising for 45-60% of the total equipment cost. Other significant components include the PSA unit, the heat recovery system, and $CO_2$ compressors.

Operational costs are dominated by the expense of natural gas followed by labor, electricity, and $CO_2$ transportation. However, natural gas costs are highly dependent on global market prices. Similarly, $CO_2$ transportation costs may vary based on the availability of local $CO_2$ utilization options, storage facilities, or reservoirs. Limited storage availability or longer transportation distances can increase costs. Although the cost of the oxygen carrier is relatively minor, it remains subject to variability depending on operational practices. The expense of oxygen carrier replacement may rise if the material demonstrates low durability, especially since CL technology still needs extensive field validation.

Figure 2 presents a sensitivity analysis of blue $H_2$ pricing with respect to potential changes in the natural gas prices, oxygen carrier price/lifetime, and $CO_2$ transportation costs. The analysis reveals that natural gas and $CO_2$ transport costs have the most significant impact on overall $H_2$ price. While natural gas prices are dictated by global market fluctuations, $CO_2$ transport costs depend on the availability and readiness of $CO_2$ storage and transportation infrastructure. Notably, the upper bound of \$88.9/ton$CO_2$ applies to scenarios involving small-scale $CO_2$ transport over long distances (500 miles) with extra monitoring for storage – conditions that are unlikely to be developed [18]. Previous studies suggest a practical cost range of \$4 to \$45/ton$CO_2$ for the transport and storage of $CO_2$ in Tier-1 countries such as the U.S [18]. In contrast, the cost of the oxygen carrier has a relatively minor impact on $H_2$ price unless its lifetime is short, necessitating more frequent replacement.

Figure 3 compares the price of the proposed blue $H_2$-$N_2$ production system with that of other CL-based $H_2$ production systems studied in the literature. Our proposed small-scale system is generally more expensive than the other technologies with larger $H_2$ production capacities. This discrepancy can be attributed to the much smaller production scale of our system, operating at two to three orders of magnitude below those reported in other studies. Additionally, this techno-economic analysis includes the cost of $CO_2$ transportation, which is often excluded in other studies. Despite these differences, Figure 3 reveals a general trend, offering valuable insights into alternatives for blue $H_2$ production at smaller scales.

## CONCLUSIONS

This paper presents a techno-economic analysis based on the dynamic model of a novel blue $H_2$-$N_2$ production system designed for small-scale applications. Utilizing the innovative CL principle, the estimated $H_2$ price is around 3.0 USD/kg$H_2$, which is more expensive than that of larger-scale plants. However, this small-scale approach reduces the need for long-distance hydrogen transportation, as required in centralized scenarios. It is important to emphasize that this scenario depends heavily on the natural gas infrastructure, which has been under scrutiny due to its fugitive methane emissions. Furthermore, ensuring access to local $CO_2$ utilization options and storage reservoirs is critical to minimize $CO_2$ treatment costs, enhancing the system's economic viability.

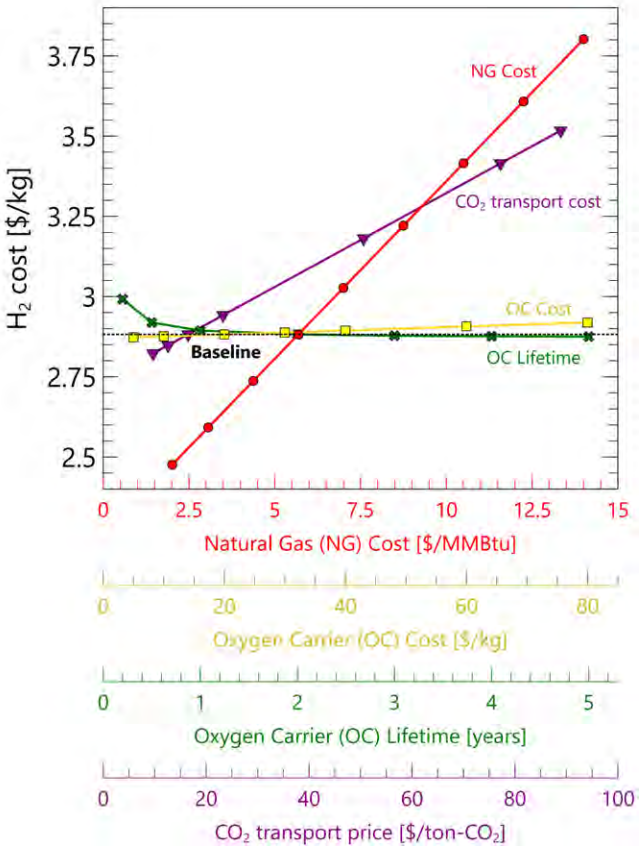



**Figure 2.** Sensitivity analysis of blue $H_2$ price relative to variations in natural gas prices, oxygen carrier (OC) price/lifetime, and $CO_2$ transport costs for the proposed system with 7.1 ton$H_2$ per day production rates.

**Table 3:** The key parameters for equipment price estimation. These values were obtained from the simulation of the proposed system at three different $H_2$ production rates: 2.8-, 7.1-, and 17.1-ton $H_2$ per day.

| Equipment | Scaling parameter | $H_2$ production rate | | |
|---|---|---|---|---|
| | | **2.8 tpd** | **7.1 tpd** | **17.1 tpd** |
| CL Reformer Reactor | Volume [$m^3$] | 5.39 | 15.71 | 47.99 |
| Shift Reactor | Shift gas flow [kg/s] | 0.22 | 0.59 | 1.42 |
| Heat recovery system | Heat duty per temp. [kW/K] | 1.346 | 3.428 | 7.675 |
| PSA | $H_2$ stream flow [m^3/s] | 0.08 | 0.27 | 0.64 |
| Desulphurizer | Methane feed [kg/s] | 5.88 | 14.71 | 35.31 |
| Methanator | $CO_2$ in $N_2$-rich stream [g/s] | 1.615 | 3.533 | 10.164 |
| Air Blowers | Total air flow [kg/s] | 0.47 | 1.18 | 2.83 |
| $CO_2$ compressors | Power [kW] | 130 | 290 | 720 |
| Heat rejection unit | Amount of heat [kW] | 165.4 | 412.9 | 907 |

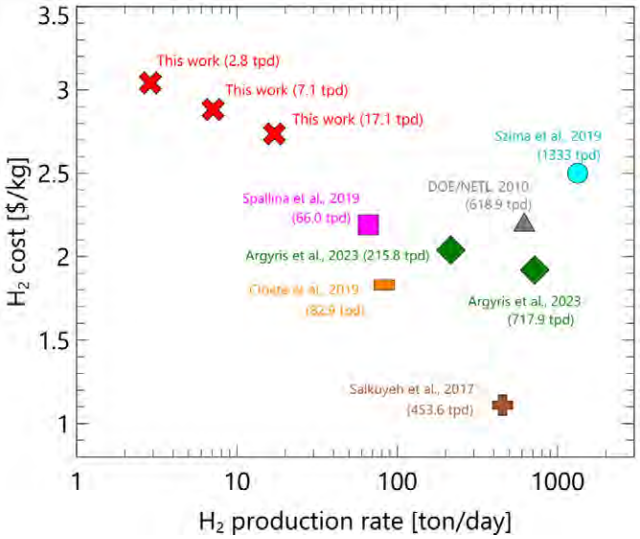



**Figure 3.** Comparison of $H_2$ prices for the proposed blue $H_2$-$N_2$ production system (red cross) with other blue $H_2$ technologies based on CL reforming principles from the literature [9-13], except DOE/NETL[16], which uses SMR-CCS.

## REFERENCES


1. International Energy Agency (IEA), "Global hydrogen demand by sector in the Sustainable Development Scenario, 2019-2070," Paris, 2020.
2. "US National Clean Hydrogen Strategy and Roadmap," 2023.
3. Cummins, "Daimler Truck North America and Cummins collaborate to drive hydrogen fuel cell trucks forward in North America," May 2022.
4. A. Islam, T. Alam, N. Sheibley, K. Edmonson, D. Burns, and M. Hernandez, "Hydrogen blending in natural gas pipelines: A comprehensive review of material compatibility and safety considerations," *Int. J. Hydrogen Energy*, vol. 93, no. November, pp. 1429–1461, 2024, doi: 10.1016/j.ijhydene.2024.10.384.
5. Bloomberg NEF, "Hydrogen Economy Outlook," *Bloom. New Energy Financ.*, p. 12, 2020.
6. D. Schlissel and A. Juhn, "Blue Hydrogen: Not Clean, Not Low Carbon, Not a Solution," 2023. Accessed: Jun. 06, 2024.
7. A. R. Irhamna and G. M. Bollas, "Intensified reforming reactor for blue hydrogen and nitrogen production," *Int. J. Hydrogen Energy*, 2024, doi: 10.1016/j.ijhydene.2024.05.428.
8. Irhamna, A. R., & Bollas, G. M. Enhancing Hydrogen Infrastructure for Domestic Use: A Small-scale Blue Hydrogen and Nitrogen Production System (in preparation)
9. Y. Khojasteh Salkuyeh, B. A. Saville, and H. L. MacLean, "Techno-economic analysis and life cycle assessment of hydrogen production from natural gas using current and emerging technologies," *Int. J. Hydrogen Energy*, vol. 42, no. 30, pp. 18894–18909, 2017, doi: 10.1016/j.ijhydene.2017.05.219.
10. S. Cloete, M. N. Khan, and S. Amini, "Economic assessment of membrane-assisted autothermal reforming for cost effective hydrogen production with CO2 capture," *Int. J. Hydrogen Energy*, vol. 44, no. 7, pp. 3492–3510, Feb. 2019, doi: 10.1016/j.ijhydene.2018.12.110.
11. V. Spallina, G. Motamedi, F. Gallucci, and M. van Sint Annaland, "Techno-economic assessment of an integrated high pressure chemical-looping process with packed-bed reactors in large scale hydrogen and methanol production," *Int. J. Greenh. Gas Control*, vol. 88, pp. 71–84, Sep. 2019, doi: 10.1016/j.ijggc.2019.05.026.
12. S. Szima et al., "Gas switching reforming for flexible power and hydrogen production to balance variable renewables," *Renew. Sustain. Energy Rev.*,

**Table 4:** The techno-economic analysis results for the proposed small-scale blue $H_2$ and $N_2$ production system at three different H2 production rates: 2.8-, 7.1-, and 17.1-ton $H_2$ per day (tpd).

| Cost Items | Price (in thousands USD) | | |
|---|---|---|---|
| | **2.8 tpd** | **7.1 tpd** | **17.1 tpd** |
| Capital Cost | | | |
| Main equipment | | | |
| Reformer system | 1993.2 | 5811.0 | 17752.8 |
| Shift reactor | 96.9 | 222.7 | 455.3 |
| Heat recovery system | 587.6 | 721.8 | 861.8 |
| Pressure swing adsorption (PSA) | 869.6 | 2912.5 | 6952.4 |
| Desulphurizer | 102.5 | 217.2 | 445.3 |
| Methanator | 18.4 | 34.4 | 80.1 |
| Air Blowers | 14.2 | 27.6 | 51.8 |
| $CO_2$ compressor | 530.1 | 942.7 | 1799.5 |
| Cooling plant/ heat rejection unit | 185.3 | 342.0 | 579.7 |
| Balance of plant: piping/instrument/control/facilities | 1923.7 | 4336.7 | 8980.7 |
| Total Plant Cost (TPC) | 7328.3 | 18048.3 | 44005.4 |
| Owner cost & other cost (O&OFC) | 1465.7 | 3609.7 | 8801.1 |
| Total Overnight Cost (TOC) | 8794.0 | 21658.0 | 52806.4 |
| Total as spent Cost (TASC) | 10376.9 | 25556.4 | 62311.6 |
| Capital charge rate factor (CCF) | 0.159 | 0.159 | 0.159 |
| TASC per year = CCF x TASC | 1649.9 | 4063.5 | 9907.5 |
| Operating Cost | | | |
| Fixed | | | |
| Labor | 450 | 810 | 1350 |
| Maintenance | 11.5 | 28.4 | 69.4 |
| Insurance | 24.7 | 61.0 | 148.6 |
| Variables | | | |
| Oxygen carrier replacement | 15.6 | 31.9 | 67.1 |
| Catalyst replacement | 13.3 | 38.9 | 118.8 |
| Electricity | 218.8 | 486.8 | 862.9 |
| Natural gas feedstock | 660.0 | 1650.0 | 3959.9 |
| $CO_2$ transport | 153.0 | 379.5 | 574.8 |
| Total operating cost per year | 1550.2 | 3495.3 | 7178.1 |
| Total annual cost | 3200.1 | 7558.8 | 17085.7 |
| $H_2$ production rate [ton$H_2$ per year] | 1052.0 | 2622.5 | 6244.1 |
| **Cost of $H_2$ [USD/kg$H_2$]** | **3.042** | **2.882** | **2.736** |
| Cost of $CO_2$ avoidance [USD/ton$CO_2$] | 149.8 | 137.3 | 125.9 |


vol. 110, pp. 207–219, Aug. 2019, doi: 10.1016/j.rser.2019.03.061.

13. P. A. Argyris, J. Wong, A. Wright, L. M. C. Pereira, and V. Spallina, "Reducing the cost of low-carbon hydrogen production via emerging chemical looping process," *Energy Convers. Manag.*, vol. 277, Feb. 2023, doi: 10.1016/j.enconman.2022.116581.
14. B. Heid, C. Martens, and M. Wilthaner, "Unlocking hydrogen's power for long-haul freight transport," 2022.
15. Process Systems Enterprise, "gPROMS." 2024.
16. US-DOE & NETL, "Assessment of hydrogen production with CO2 capture volume 1: baseline state-of- the-art plants," US-Department Energy/National Energy Tech. Lab., vol. 1, 2011.
17. G. Towler and R. A. Y. Sinnott, Chemical Engineering Design: Principles, Practice and Economics of Plant and Process Design. 2013.
18. E. Smith, J. Morris, H. Kheshgi, G. Teletzke, H. Herzog, and S. Paltsev, "The cost of CO2 transport and storage in global integrated assessment modeling," *Int. J. Greenh. Gas Control*, vol. 109, p. 103367, 2021, doi: 10.1016/j.ijggc.2021.103367.

© 2025 by the authors. Licensed to PSEcommunity.org and PSE Press. This is an open access article under the creative commons CC-BY-SA licensing terms. Credit must be given to creator and adaptations must be shared under the same terms. See https://creativecommons.org/licenses/by-sa/4.0/



Systems & Control Transactions

**Research Article - Peer Reviewed Conference Proceeding**
ESCAPE 35 - European Symposium on Computer Aided Process Engineering
Ghent, Belgium. 6-9 July 2025
Jan F.M. Van Impe, Grégoire Léonard, Satyajeet S. Bhonsale,
Monika E. Polańska, Filip Logist (Eds.)

PSE PRESS

# A Comparative Evaluation of Complexity in Mechanistic and Surrogate Modeling Approaches for Digital Twins

**Shreyas Parbat[a]*, Isabell Viedt[a,c], Leon Urbas[a,b,c]**

[a] Technische Universität Dresden, Process-to-Order Group, Process Systems Engineering Group, Dresden, Germany
[b] Technische Universität Dresden, Process-to-Order Group, Chair of Process Control Systems, Dresden, Germany
[c] Technische Universität Dresden, Process-to-Order Group, Process-to-Order Lab Learning Factory, Dresden, Germany
* Corresponding Author: shreyas.parbat@tu-dresden.de.

## ABSTRACT

A Digital Twin (DT) is a purposeful digital representation of a physical entity that employs data, algorithms, and software to enhance operations, making it possible to e.g., forecast failures, or evaluate new designs through the simulation of real-world scenarios. DTs are enablers for real-time monitoring, simulation, and optimization. However, traditional simulation DTs often rely on complex, non-linear mechanistic models with high computational demands, complex structures, and a large number of specific parameters and thus pose quite a challenge to maintainability. Surrogate models, on the other hand, are simplified approximations of more complex, higher-order models. These approximations are typically built using data-driven approaches, such as Random Forest Regression, facilitating faster simulations, simpler adaptation, and quicker deployment. This study analyzes the complexity of mechanistic and surrogate modeling approaches in the context of DTs to aid model selection. A model with reduced complexity enhances computational efficiency, simplifies implementation, and supports real-time monitoring and predictive maintenance. Complexity analysis evaluates metrics such as analytical, structural, space, behavioral, training, and prediction complexity, resulting in an overall complexity score for model selection. However, the decision involves trade-offs, such as balancing high fidelity with low complexity or prioritizing high explainability over structural simplicity. Addressing these trade-offs is essential in selecting a model that balances the accuracy, usability, and efficiency of DTs. Using a stirred tank reactor as a use case, the mechanistic model is compared to a surrogate model to quantify complexity scores and select a less complex model for DT development.

**Keywords**: Surrogate Model, Digital Twin, Complexity metric, Complexity Score, Mechanistic Model

## INTRODUCTION

Modeling and simulations provide the mathematical and conceptual foundation for Digital Twins (DTs) [1]. Multiple industries, including pharmaceuticals, manufacturing, chemicals, and food processing, heavily rely on modeling and simulations. One of the important aspects of the model-building process is model selection [2].

Mechanistic models are a critical foundation for DTs [3]. These mechanistic models are non-linear, time-consuming, expensive, and sometimes complex [4]. In such cases, surrogate models are used to approximate or regress the input-output relationships of a more complex, computationally demanding model [5] to reduce complexity by focusing on key elements and interactions, sacrificing some accuracy for efficiency and ease of use. Thermodynamic models for distillation and extraction processes, partial differential equations (PDEs), and computational fluid dynamics (CFD) simulations are examples of complex computational systems. Surrogate modeling techniques can effectively approximate these systems, reducing computational cost while preserving reasonable accuracy [6].

However, defining the complexity of such models is a crucial metric for supporting decision-making and selecting the most beneficial and optimal model for a particular process. The complexity level of a model is determined by its components, which depend on factors such as resolution, scope, size, and the interactions within the model. Assessing the complexity of a model is valuable

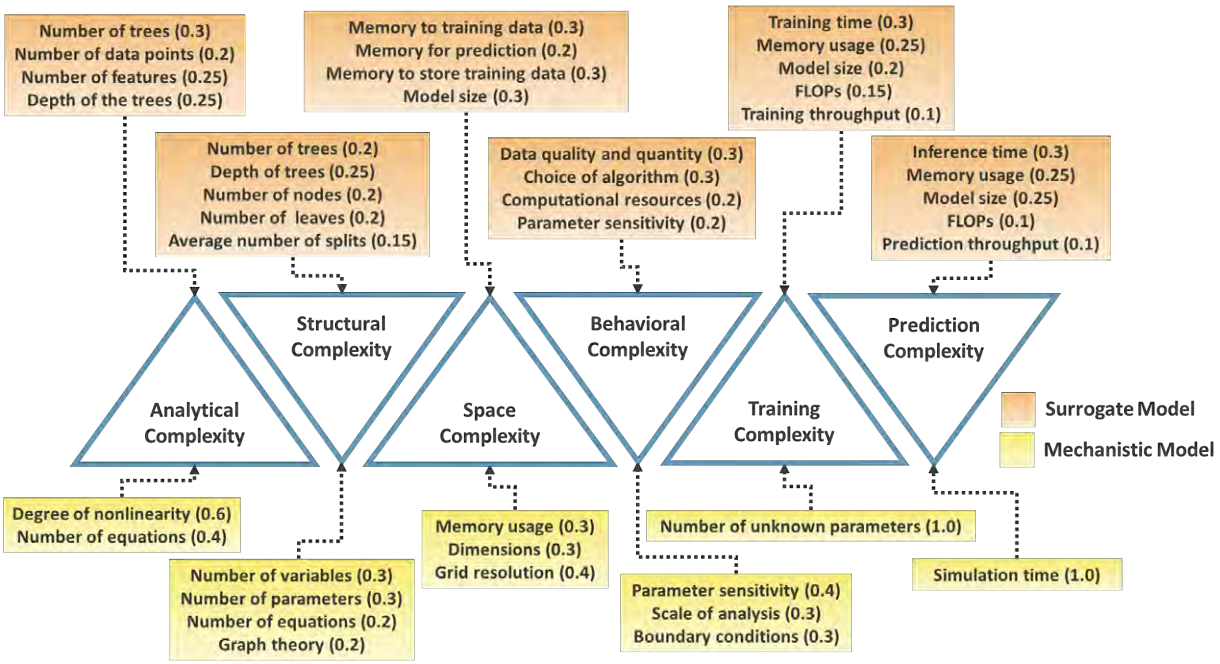



**Figure 1:** Complexity Metrics (analytical, structural, space, behavioral, training, and prediction complexity) and complexity contributors with individual weights

for several applications and is guided by several core principles that process engineers should consider [7]. For example, a Continuous Stirred Tank Reactor (CSTR) model may suffice for quick reactor analysis, but a CFD model might be needed for detailed heat or mass transfer studies. Process engineers must align model complexity with the application, data availability, and computational resources.

In this research, various complexity measures for mechanistic and surrogate models are investigated. The following section defines the different types of complexities associated with simulation models and analyzes their dependencies on several factors. The methodology for calculating complexity scores is presented, along with the rationale for assigning weights. A later section focuses on a simple use case of a stirred tank reactor, analyzing the complexities of both models in terms of reactor temperature. This case study illustrates the approach used to analyze model complexity, and the concept of the complexity score is then applied to these models. Finally, conclusions are drawn based on the proposed case study, and future work is discussed.

## MODEL COMPLEXITY

Complexity can be defined as the state or quality of being intricate [8], with several components and their interactions within a system helping to determine its complexity. Thompson defines model complexity as "The aggregation of a model's detail, external interactions and logical dependencies, and in many contexts its instantiation (input parameter settings) in a specific simulation scenario execution" [7]. In contrast, simple models are easier to understand, faster to implement, easier to verify and validate, more flexible, and simpler to modify [9]. However, some models are not easy to formulate, follow, validate, or verify, and such models can be classified as complex. In Modeling and Simulation, complexity can arise from the model itself or the software used to implement it [8].

### Complexity Metrics

In this work, complexity metrics are defined based on analytical, structural, space, behavioral, training, and prediction complexity. Table 1 outlines several complexities associated with models. Fig. 1 shows the components and contributors of these complexities, highlighting their dependencies on several factors for the models, along with the individual weights of contributors.

Complexities discussed in Table 1 are essential as they cover the entire model lifecycle, from the structure and theoretical foundation to practical implementation and application. Each complexity type addresses a specific challenge in developing, deploying, and maintaining a model, making them collectively crucial for ensuring the overall effectiveness and applicability of the model.

**Table 1:** Complexity Metrics and Definitions.

| Complexity metric | Definition |
|---|---|
| Analytical Complexity | Theoretical analysis of model complexity based on structure and operations |
| Structural Complexity | The complexity of the model architecture itself |
| Space Complexity | Memory required to store the model and data structures during the training and prediction phases |
| Behavioral Complexity | Complexity arising from how the model learns, adapts to data inputs, and responds to varying conditions |
| Training Complexity | Computational resources (time and space) required for model training |
| Prediction Complexity | Computational resources required for making predictions with a trained model |

As Hu et al. [10] discuss, model complexity encompasses various dimensions critical to ensuring models are effective and scalable. These dimensions include analytical complexity, ensuring the theoretical foundation of a model is sound and aligned with its purpose, as unreliable designs can hinder scalability. Structural complexity addresses the model's architecture, balancing interpretability and usability with the risks of impracticality in overly complex designs. Space complexity focuses on memory usage, critical for deploying models in resource-constrained environments like edge devices or real-time systems. Behavioral complexity assesses how the model adapts to varying inputs, ensuring robustness and reliability in dynamic real-world conditions. Training complexity evaluates the computational cost and time needed for model development, especially important in large-scale or iterative applications. Prediction complexity highlights the need for efficient real-time performance in applications such as performance monitoring, optimization, and control systems. These complexities collectively ensure a model is effective, scalable, and practical.

## Complexity Score

The simplest and most straightforward way to create an overall complexity score is the weighted aggregation of the individual complexity metrics. The overall complexity score and the individual complexity scores are calculated using Equations 1 and 2, respectively.

$$CS = \sum_{j=1}^{m} \left( (CS_{ind})_j \cdot W_j \right) \quad (1)$$

$$CS_{ind} = \sum_{i=1}^{n} C_i \cdot w_i \quad (2)$$

$$C_i = \frac{Observed\ Value - Min\ Value}{Max\ Value - Min\ Value} \quad \forall\ i = 1 \ldots n \quad (3)$$

where $CS$ is the overall complexity score, $CS_{ind}$ is the individual complexity score, $C$ is the normalized complexity contributor value (e.g. Number of equations for the mechanistic model and Number of trees for the surrogate model) obtained using the min-max scaling normalization formula (Equation 3), $w$ is the weight for the complexity contributors and $W$ is the weight for the complexity.

## Assignment of Weights to Complexity Metrics

The weights for the individual complexity metrics play an important role in determining the overall complexity score for a given model. These weights represent the relative contribution of each factor to the overall complexity of the model or system, determined primarily through logical reasoning and expert judgment. Table 2 provides the weights ($W$) assigned to the developed complexity metrics shown in Fig. 1.

**Table 2:** Weights ($W$) for Complexity Metrics.

| Complexity metric | Weight |
|---|---|
| Analytical Complexity | 0.15 |
| Structural Complexity | 0.2 |
| Space Complexity | 0.2 |
| Behavioral Complexity | 0.15 |
| Training Complexity | 0.15 |
| Prediction Complexity | 0.15 |

These weights ($W$) are selected based on the relative importance of each metric in the context of evaluating a model's overall complexity and considering the importance of each metric and contributor. Structural and space complexity metrics are weighted higher (0.2 each) because they have a more direct impact on the practical feasibility of the model, particularly in terms of usability, deployment, and hardware requirements [11]. Analytical, behavioral, training, and prediction metrics are equally weighted at 0.15, reflecting their secondary yet significant contributions [12]. They ensure the model is robust, adaptable, and efficient, but are less dominant than structural and space considerations in most applications.

Fig. 1 provides the weights ($w$) for individual contributors of model complexity, which are determined based on their relative contributions, primarily guided by logical reasoning and expert judgment. For mechanistic models, dominant contributors such as nonlinearity (analytical complexity) and grid resolution (space complexity) are assigned higher weights due to their significant anticipated computational impact [13]. In surrogate models, factors like tree depth and training time are prioritized, reflecting their expected influence on scalability and efficiency [11]. The weights are applied to ensure fair consideration of relevant factors, without allowing any single factor to disproportionately influence the outcome. Overlap, such as tree depth affecting both analytical and structural complexity, is mitigated through careful weight

calibration. This approach ensures the complexity metrics highlight the most impactful aspects of each model.

## COMPLEXITY EVALUATION – CASE OF A STIRRED TANK REACTOR

### Reactor Temperature Modeling

To monitor and optimize energy consumption and loss in an insulated Stirred Tank Reactor (STR), a DT for energy Key Performance Indicators (eKPIs) needs to be developed. Understanding energy dynamics is crucial and can be done by analyzing the temperatures of the reactor and jacket. By determining the temperature gradient, the heat loss and process energy consumption between the reactor and the jacket can be calculated. Modular plants are known for their flexibility [14], relying on historical or statistical data for model development is often not feasible. Generating synthetic data enables the creation of more accurate and adaptive models. This case study applies the proposed complexity evaluation concept to guide model selection by comparing a mechanistic and a surrogate model, illustrating how the methodology aligns the model with system requirements and operational constraints.

Modeling of the STR is conducted using the mechanistic and a surrogate model. As shown in Fig. 2, the feed enters the reactor at a specified temperature. The reactor, with a volume of 4L, is agitated at a certain speed and equipped with a water-heated jacket. The fluid properties and the heat transfer coefficient are assumed to be constant, and there is no fouling. Energy balances (Equations 4 and 5) are used to obtain the temperature trajectories for both the reactor and the jacket.

$$\frac{dT_r}{dt} = \frac{1}{V_r \rho_r C_{pr}} * (kA(T_j - T_r)) \quad (4)$$

$$\frac{dT_j}{dt} = \frac{1}{V_j \rho_j C_{pj}} * (m_j C_{pj}(T_{jin} - T_j)) - (kA(T_j - T_r)) \quad (5)$$

Where, $T_r$ is the reactor temperature, $T_j$ is the jacket temperature, $V_r$ is the reactor volume, $\rho_r$ is the reactant density, $C_{pr}$ is the reactant heat capacity, $k$ is the heat transfer coefficient, $A$ is the heat transfer area, $V_j$ is the jacket volume, $\rho_j$ is the jacket fluid density, $C_{pj}$ is the jacket fluid heat transfer capacity, $m_j$ is the jacket fluid mass and $T_{jin}$ is the jacket inlet temperature. The initial temperature of reactor ($T_r$) and jacket ($T_j$) of 293.15 K and jacket inlet temperature ($T_{jin}$) of 283.15 K. The gPROMS simulation results, obtained after nine minutes of reaction time, are shown in Fig. 3. The generated data is used to train a Random Forest Regressor as the surrogate model. The reactor temperature predictions from the surrogate model (Mean Squared Error = 0.015) are shown in Fig. 4.

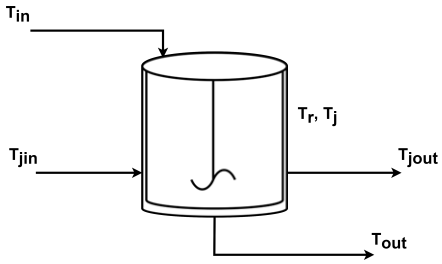



**Figure 2.** Stirred tank reactor: Energy flow.

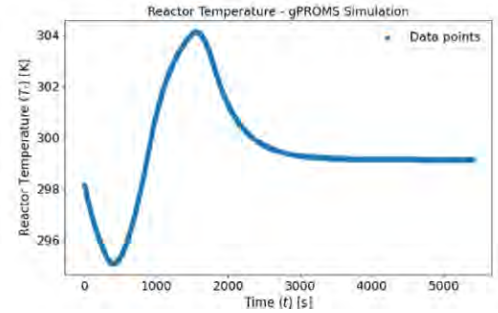



**Figure 3.** Reactor temperature: gPROMS simulation.

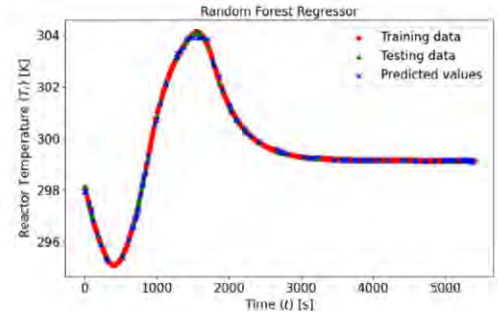



**Figure 4.** Reactor temperature: Random Forest model.

### Complexity Analysis for the STR Case

The models are analyzed for complexity using the developed complexity metrics. In this study, a surrogate model was developed to enable a direct comparison of its complexity with that of the mechanistic model. The surrogate model would not always be developed unless complexity analysis identifies it as the more appropriate choice. A detailed analysis has been conducted to evaluate analytical, structural, space, behavioral, training, and prediction complexities.

#### Analytical Complexity

The analytical complexity of the mechanistic model is minimal due to its linear nature, with two equations and a constant heat transfer coefficient assumed in this study. This simplicity ensures computational efficiency. In contrast, the analytical complexity of the surrogate model arises from parameters like the number of trees (T=300), data points (N=440), features per split (F=1), and tree depth (D=7). While the surrogate model captures nonlinear behaviors effectively, this comes at a higher computational cost. This trade-off highlights the suitability of mechanistic models for systems with well-

understood dynamics and the strength of surrogate models in handling complex, data-driven relationships.

### Structural Complexity

The structural complexity of the mechanistic model is determined by ten parameters, two variables, two equations, and three boundary conditions, with a graph representation of twelve nodes and two edges. This ensures low complexity, simplicity, and interpretability. In contrast, the surrogate model exhibits considerably higher structural complexity, consisting of 300 trees with an average depth of seven. It contains 46,016 nodes, 23,158 leaves, and an average of 153.39 splits per tree. While this allows for greater flexibility and detailed system representation, it also increases storage and computational demands. This comparison highlights the suitability of mechanistic models for lightweight and interpretable applications, whereas surrogate models are ideal for capturing complex systems with detailed requirements.

### Space Complexity

The space complexity of the mechanistic model is minimal, requiring storage for a 2×2 Jacobian matrix and a grid resolution of 1000 for discretization in two dimensions. For the surrogate model, space complexity includes memory for training data (0.006 MB), predictions (0 MB), and the model itself (3.25 MB), driven by the storage of tree structures. The low storage requirements of the mechanistic model make it ideal for resource-constrained, real-time applications. In contrast, the higher memory demands of the surrogate model may limit scalability but enable the handling of more complex systems with adequate computational infrastructure.

### Behavioral Complexity

The behavioral complexity of the mechanistic model depends on system dynamics, parameter variability, and boundary conditions, making it reliable but less flexible for unknown dynamics. The surrogate model relies on data quality, algorithm choice, and computational resources to capture complex patterns. Parameter sensitivity and hyperparameter tuning also impact their performance. Mechanistic models are ideal for data-scarce systems due to their physical foundation, while surrogate models excel in handling high-variability behaviors, offering adaptability in data-rich scenarios. Synthetic data from mechanistic models can mitigate data scarcity and reduce the behavioral complexity of surrogate models.

### Training Complexity

Training complexity for the mechanistic model is negligible since all parameters are known. For the surrogate model, training complexity is crucial, with metrics such as training time (117.32 s), peak memory usage (5.57 MB), model size (3.25 MB), and computational effort (924,000 FLOPs). With a throughput of 3.75 samples/second, the surrogate model demands considerable resources for data processing and hyperparameter tuning, making it the sole contributor to training complexity.

### Prediction Complexity

In mechanistic models, simulation time depends on system dynamics, with this study reporting 2.2 s. Complex systems, though efficient, may have higher computational costs due to detailed calculations. The surrogate model, with a 0.02 s inference time, excels in rapid predictions. It uses 0 MB of memory, has a model size of 3.25 MB, a computational complexity of 2100 FLOPs, with a prediction throughput of 6850.39 predictions/seconds. Here, the mechanistic model is slower and more computationally expensive, while the surrogate model provides faster predictions with lower computational demands, making it ideal for high-throughput applications.

## Complexity Score for the STR Case

Table 3 presents the individual complexity scores ($CS_{ind}$) for both modeling approaches, evaluated using Equation 2, along with dedicated weights for contributors and complexity metrics from Fig. 1.

**Table 3:** Individual complexity score of all complexities

| Complexity Metric | Mechanistic Model | Surrogate Model |
|---|---|---|
| Analytical Complexity | 0.4 | 0.533 |
| Structural Complexity | 0.9 | 1.0 |
| Space Complexity | 0.85 | 0.301 |
| Behavioral Complexity | 0.9 | 0.834 |
| Training Complexity | 0.0 | 0.95 |
| Prediction Complexity | 1.0 | 0.75 |

The complexity evaluation of both the mechanistic and surrogate models highlights the trade-offs between simplicity and flexibility. The mechanistic model scores higher in terms of space, behavioral, and prediction complexities, reflecting the efficiency and ease of implementation of the surrogate model. In contrast, the surrogate model exhibits higher analytical, structural, and training complexity, indicating that the mechanistic model is better suited to handle more complex behaviors.

Overall complexity scores (CS) for both models are determined using Equation 1, based on the individual complexity scores from Table 3 and their weights from Table 2. The overall complexity score shows that the surrogate model, with a CS of 0.72, exhibits higher complexity as compared to the mechanistic model, which has a

CS of 0.69 in this case study. This suggests that the surrogate model, while offering greater flexibility for complex scenarios, requires more resources, making the mechanistic model more suitable for simpler applications. These complexity scores enable developers to make informed choices based on the specific needs of the DT.

## CONCLUSION AND OUTLOOK

The complexity of modeling for the simulation DT is analyzed using the developed complexity metric and score, applied to both mechanistic and surrogate models. The evaluation framework helps identify model components, gather requirements, and inform decisions on model selection, which is crucial for DT development. In the STR case, the surrogate model exhibits a higher complexity score than the mechanistic model. The mechanistic model benefits from simplicity due to its analytical foundation and minimal training requirements, while the increased complexity of the surrogate model arises from structural and training demands. While surrogate models may not always be the final choice, their development offers strategic flexibility and valuable insights, particularly in complex or data-driven scenarios. Dual-model approaches, though rare in real-world plants, improve model selection by addressing diverse challenges, making them valuable in complex, specialized applications.

Future work will focus on enhancing the model selection framework with accuracy and stability analyses. Efforts will aim at reducing surrogate model complexity, improving computational efficiency, and enabling real-time monitoring and predictive maintenance. Temperature-dependent parameters will introduce nonlinearity to the mechanistic model, and surrogate modeling will serve as an alternative if complexity increases. These ongoing developments will provide refined tools for model selection and further optimize DT applications.

## ACKNOWLEDGEMENT

As part of the “Energy Efficiency in Industry”, research funding is provided by the Federal Ministry for Economic Affairs and Climate Action of Germany (BMWK) and Project Management Jülich (PtJ) under the title of project REUNION (FKZ 03EN2100C).

## REFERENCES

1. Parbat S, Iqbal I, Viedt I, Urbas L. Architecture of digital twin for automating waste and recycling material sorting process. *2024 IEEE 29th International Conference on Emerging Technologies and Factory Automation (ETFA)* :1–4 (2024) https://doi.org/10.1109/ETFA61755.2024.10710670
2. Asprion N. Modeling, simulation, and optimization 4.0 for a distillation column. *Chemie Ingenieur Technik* 92:879–89 (2020) https://doi.org/10.1002/cite.202000001
3. Bárkányi Á, Chován T, Németh S, Abonyi J. Modelling for digital twins—potential role of surrogate models. *Processes* 9 (2021) https://doi.org/10.3390/pr9030476
4. Beisheim B, Rahimi-Adli K, Krämer S, Engell S. Energy performance analysis of continuous processes using surrogate models. *Energy* 183:776–87 (2019) https://doi.org/10.1016/j.energy.2019.05.176
5. McBride K, Sundmacher K. Overview of surrogate modeling in chemical process engineering. *Chemie Ingenieur Technik* 91:228–39 (2019) https://doi.org/10.1002/cite.201800091
6. Winz J, Nentwich C, Engell S. Surrogate modeling of thermodynamic equilibria: applications, sampling and optimization. *Chemie Ingenieur Technik* 93:1898–906 (2021) https://doi.org/10.1002/cite.202100092
7. Thompson JS, Hodson DD, Grimaila MR, Hanlon N, Dill R. Toward a simulation model complexity measure. *Information* 14 (2023) https://doi.org/10.3390/info14040202
8. Zhao X, Gray J. Towards a metrics suite for the complexity analysis of labview systems models. *Science of Computer Programming* 227:102931 (2023) https://doi.org/10.1016/j.scico.2023.102931
9. Robinson S. Exploring the relationship between simulation model accuracy and complexity. *Journal of the Operational Research Society* 74:1992–2011 (2023) https://doi.org/10.1080/01605682.2022.2122740
10. Hu X, Chu L, Pei J, Liu W, Bian J. Model complexity of deep learning: a survey. *Knowledge and Information Systems* 63:2585–619 (2021) https://doi.org/10.1007/s10115-021-01605-0
11. Paleyes A, Urma R-G, Lawrence ND. Challenges in deploying machine learning: a survey of case studies. *ACM Comput. Surv.* 55 (2022) https://doi.org/10.1145/3533378
12. Forrester AIJ, Bressloff NW, Keane AJ. Optimization using surrogate models and partially converged computational fluid dynamics simulations. *Proceedings of the Royal Society A: Mathematical, Physical and Engineering Sciences* 462:2177–204 (2006) https://doi.org/10.1098/rspa.2006.1679
13. Blondel VD, Tsitsiklis JN. A survey of computational complexity results in systems and control. *Automatica* 36:1249–74 (2000) https://doi.org/10.1016/S0005-1098(00)00050-9
14. Mädler J, Rahm J, Viedt I, Urbas L. A digital twin-concept for smart process equipment assemblies

supporting process validation in modular plants. *Computer Aided Chemical Engineering* 51:1435–40 (2022) https://doi.org/10.1016/B978-0-323-95879-0.50240-X

© 2025 by the authors. Licensed to PSEcommunity.org and PSE Press. This is an open access article under the creative commons CC-BY-SA licensing terms. Credit must be given to creator and adaptations must be shared under the same terms. See https://creativecommons.org/licenses/by-sa/4.0/



Systems & Control Transactions

**Research Article - Peer Reviewed Conference Proceeding**
ESCAPE 35 - European Symposium on Computer Aided Process Engineering
Ghent, Belgium. 6-9 July 2025
Jan F.M. Van Impe, Grégoire Léonard, Satyajeet S. Bhonsale,
Monika E. Polańska, Filip Logist (Eds.)

PSE PRESS

# Co-gasification of Crude Glycerol and Plastic Waste using Air/Steam Mixtures: A Modelling Approach

**Bahizire Martin Mukeru[a], Bilal Patel[a]***

[a] University of South Africa, Institute for Catalysis and Energy Solutions, Florida, Gauteng, RSA
* Corresponding Author: patelb@unisa.ac.za

## ABSTRACT

This study evaluated the air/steam co-gasification of crude glycerol (CG) and linear low density polyethylene (LLDPE). It was demonstrated that operating the process using air or a mixture of air and steam has significant implications for carbon conversion efficiency (CCE), cold gas efficiency (CGE), lower heating value (LHV) gasifier output temperature and syngas concentration. The CCE reached a maximum value of 100% at equivalence ratio (ER) of 0.3 for 25% LLDPE and an ER of 0.35 for 75% LLDPE when air was used. When steam was introduced in the gasifier at a fixed rate (SFR =0.5), the CCE of 100% was maximised at ER of 0.25 for 25% LLDPE and 0.3 for 75% LLDPE content. An increase in the steam to feedstock ratio (SFR) did not alter the CCE for 25% LLDPE at a constant ER, but for that of 75% LLDPE, a CCE was maximized at an SFR of 0.25. In the case of CGE, a maximum value of 79.24% and 78.12% was reached at ER of 0.3 and 0.35 for 25% LLDPE and 75% LLDPE respectively when pure air was used. Keeping the SFR constant, the CGE slightly increased to 81.33 and 81.45% at ER of 0.25 and 0.3, respectively for 25% LLDPE and 75% LLDPE. The LLDPE content did not significantly alter the syngas LHV at a fixed ER or SFR. The gasifier temperature increased with an increase in ER but decreased when steam was fed into the gasifier. Furthermore, the syngas ratio ($H_2$:CO) achieved in this study can be useful for the synthesis of methanol and dimethyl ether.

**Keywords**: Syngas, Modelling and simulation, Co-gasification, Plastic waste

## INTRODUCTION

There has been unprecedented growth in the production of plastic waste, and current management techniques such as landfilling and incineration are unsustainable, particularly due to the environmental impact associated with these practices. Gasification is considered to be one of the most sustainable ways not only to address these issues, but also to produce energy from waste plastics. However, challenges such as tar and coke formation, and softening are associated with plastic waste gasification which reduces syngas quality[1].

Another typical waste in huge quantities is crude glycerol, with low value, which is a by-product of biodiesel production. The cost involved in its purification is exceedingly high; therefore, this limits its applications as a purified product. Co-feeding plastic waste with crude glycerol for syngas production cannot only address issues related to plastic gasification, but also allows the utilization of crude glycerol and improve syngas quality[2].

Co-gasification is an energy intensive process because it requires high temperatures to convert a blend of different feedstocks into syngas. To sustain the co-gasification process, heat is supplied to the gasifier autothermally [3]. In this case, endothermic reactions are driven by heat from the partial oxidation or substoichiometric combustion of a portion of the feedstock blend or syngas using air or pure oxygen. One of the key parameters pertaining to autothermal processes is the equivalence ratio (ER), which is defined as the ratio between the actual and stoichiometric air/oxygen mass flow rate. Increasing the ER increases the gasifier temperature. In an Aspen Plus simulation, the gasifier temperature is considered an output parameter. Depending on the ER value, the heat supplied to the gasifier can be equal to or greater than the required heat. Preferably, the heat supplied to the gasifier should be equal to the heat required

to avoid irreversibility. In other words, the gasifier should run adiabatically (Q = 0).

The co-gasification of crude glycerol and plastic wastes has not received significant attention in the literature. Mukeru and Patel [4] have recently investigated the co-gasification of glycerol and polyethylene plastic wastes for syngas production using a stoichiometric targeting model. The model was compared with the Aspen Plus simulation. Although the study provided a starting point for crude glycerol and plastic co-gasification, there is still potential for improvements in terms of operational mode. The authors only investigated the co-gasification process in Aspen Plus at different steam to feedstock ratios and the temperature was set to 1000K which does not represent real processes and cannot be used as a guide for pilot and full-scale experimental investigations for the co-gasification of crude glycerol and low linear density polyethylene. Therefore, it is important to develop an air and air-steam co-gasification model whereby the gasifier temperature (GT) is considered as an output parameter along with the syngas concentration based on an autothermal process.

## METHODOLOGY

In this study, a model to evaluate the performance of air and air-steam co-gasification of crude glycerol and polyethylene plastic for hydrogen-rich syngas production, which is developed using Aspen Plus as shown in figure 1. Co-gasification performance indicators such as lower heating value (LHV), carbon conversion efficiency (CCE) and cold gas efficiency (CGE) are used for the evaluation. Equations (1), (2) and (3) were used to calculate these performance indicators [5,6].

$$LHV = 10.78x_{H_2} + 12.63x_{CO} + 35.8x_{CH_4} \quad (1)$$

$$CCE = 100 * \frac{C_{syngas}}{C_{feed}} \quad (2)$$

$$CGE = 100 * \frac{Q_{syngas} * LHV}{LHV_{feed}} \quad (3)$$

Where LHV, CCE, CGE, Q, C and $x_i$ ,the lower heating value (MJ/Nm$^3$), carbon conversion efficiency, cold gas efficiency, syngas flow rate (Nm$^3$/h) the carbon flow rate (mol/s) and mole fraction, respectively.

The first step was to specify all components involved in the simulation, such as crude glycerol, polyethylene plastic waste, $H_2$, $CO_2$, C (solid), CO, $CH_4$, $H_2O$, etc. Crude glycerol and polyethylene were added in Aspen Plus as non-conventional on the basis of their ultimate and proximate analyses [7], [8]. Once the components were specified, the next step was to select a suitable thermodynamic property. Given the fact that crude glycerol and polyethylene plastic waste co-gasification requires high temperatures, Peng-Robinson with Boston-Mathias modifications was selected as a thermodynamic property method [5]. The model developed is depicted in figure 1. The feed stream contains a mixture of crude glycerol and polyethylene plastic waste at standard conditions that is fed to the dryer (R-01) for moisture removal. The dryer is modelled as a stoichiometric reactor operating at 100 ℃. The dried mixture is separated from water vapour using a separator (SEP) and fed to a yield reactor (R-02) whereby it is decomposed into elements according to the ultimate analysis before being fed to the gasifier (R-03). The gasifying agent, air or air-steam mixture is fed to the gasifier whereby partial oxidation/sub-stoichiometric combustion takes place. The product from the gasifier (PROD) consists of gases ($H_2$, CO, $H_2O$, $CO_2$, $CH_4$, $N_2$) and solid (char + ash). A cyclone (CY-01) is used to separate the gases from the solid stream (char and ash). The heat streams Q-1 and Q-2 show the heat integration between the three unit operations (R-01, R-02 & R-03).

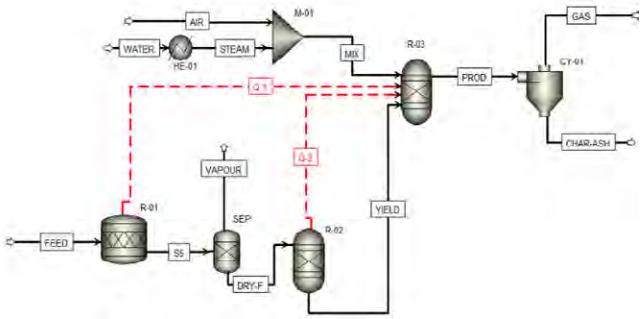



**Figure 1**: Actual Aspen Plus model development

## RESULTS AND DISCUSSIONS

### Effect of equivalent ratio on syngas concentration

Figure 2 shows the effect of ER on the syngas composition (dry basis) and GT for air co-gasification of crude glycerol and LLDPE. In figure 2, it is shown that an increase in ER initially increases CO concentration until it attains a maximum value at an ER of 0.3 and 0.35, respectively, for 25 and 75% LLDPE. The increase in CO concentration is due to partial oxidation of carbon content in the feedstock. However, as the ER was further increased beyond 0.3 and 0.35, the trend of CO concentration decreases. This implies that when more air is supplied in the gasifier, the combustion reaction is favoured over partial oxidation, thus decreasing CO concentration and increasing that of $CO_2$. $H_2$ concentration also decreased with an increase in ER for 25% LLDPE. This is because there is more oxygen available for the oxidation of $H_2$ to form $H_2O$. In the case of 75% LLDPE, increasing the ER to 0.1, $H_2$ concentration initially increased slightly due to low oxygen and high hydrogen content in the feedstock. At an ER of 0.1, the air supplied to the gasifier

promotes methane reforming reaction, thus increasing $H_2$ concentration. Beyond an ER of 0.1, $H_2$ concentration from the gasification of 75% LLDPE followed a trend similar to that of 25% LLDPE. Because an increase in ER increases the gasifier temperature, and favours combustion reactions, $CH_4$ concentration showed a significant decrease. Similar trends were observed for the air co-gasification of biomass (casuarina wood) and polyethylene plastic waste [5] and air gasification of municipal solid waste [9]. Syngas ratio ($H_2$/CO) is an important parameter for downstream processes. Methanol and dimethyl ether (indirect synthesis) require a minimum $H_2$/CO of 2. In this study, a syngas ratio of 2.02 is attained at an ER of 0.2 (GT= 697℃) for 75% LLDPE. DME synthesis (direct route) requires a $H_2$/CO of 1. 25% LLDPE achieves a $H_2$/CO of 1.06 at an ER of 0.35 (GT =932℃) while 75% LLDPE attains 1.01 at the same ER of 0.35 (GT=837℃).

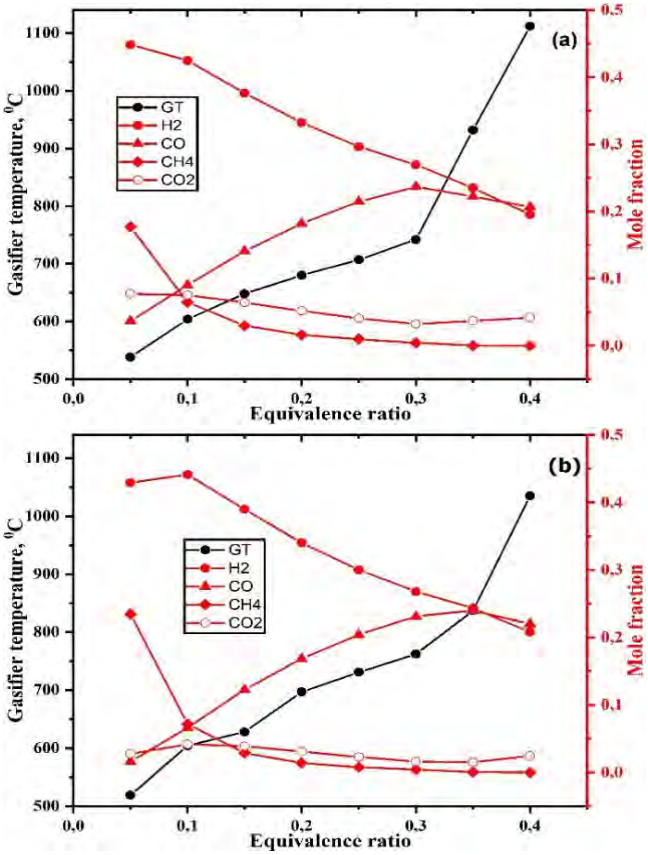



**Figure 2.** Effect of ER on syngas concentration for air co-gasification, (a): 25% LLDPE, (b): 75% LLDPE

## Effect of the equivalence ratio on syngas concentration at a SFR of 0.5

Figure 3 shows the effects of ER on crude glycerol and LLDPE co-gasification at a fixed steam to feedstock ratio (SFR) of 0.5. As ER increased from 0.05 to 0.4, the GT increases but at a lower rate than air co-gasification. This is because steam will absorb a portion of heat generated by exothermic reactions, thus reducing the GT. As summarized in figure 3 a &b, $H_2$ concentration slightly increases when the ER was increased from 0.05 to 0.1. Given the fact that the amount steam introduced in the gasifier is not sufficient to promote steam reforming reactions, $H_2$ concentration decreases with an increase in ER. In other words, $H_2$ starts to oxidize to form $H_2O$. However, the presence of steam in the system results in higher $H_2$ concentration than using air only. Due to lack of sufficient steam, the carbon content in the feedstock still undergoes partial oxidation to form CO when the ER is increased and thus decreases $CO_2$. On the other hand, $CH_4$ concentration is higher at low ER due to insufficient air and low GT but decreases with an increase in the ER. A syngas ratio of 2.03 was achieved at an ER of 0.25 for 25% LLDPE.

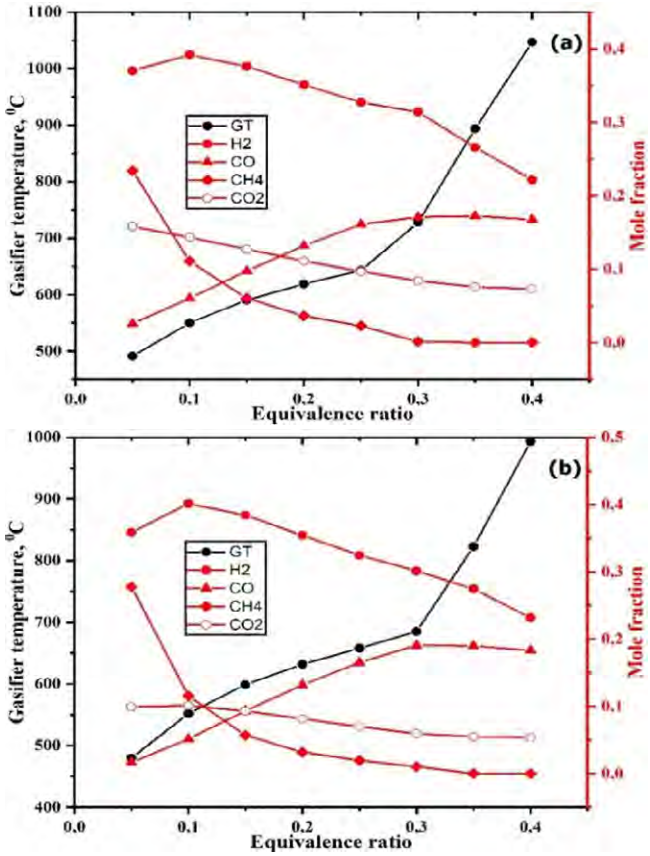



**Figure 3**: Effectof ER on syngas concentration at a fixed SFR of 0.5, (a): 25% LLDPE content, (b): 75 % LLDPE content

## Effect of steam to feedstock ratio (SFR) at a fixed ER

When steam is introduced in the gasifier at a fixed ER of 0.3, the behaviour of GT and syngas concentration differ as shown in figure 4 a & b. An increase in SFR reduces the GT. This implies that the heat generated by the

exothermic reactions during the co-gasification process is used to supply energy to the endothermic steam reforming reactions and since there is no enough energy available the GT drops. An increase in SFR promotes methane steam reforming and water gas shift reactions which results in high $H_2$ and $CO_2$ concentration as shown in figure 4. CO concentration was expected to increase as steam reforming reactions are favoured but it will be consumed by the water has shift reaction, which reduces its concentration with an increase in SFR. A syngas ratio of 2.19 and 2.28 was achieved at SFR of 0.75 and 1 for 25% LLDPE and 75% LLDPE content, respectively which is favourable for downstream applications. The concentration of $CH_4$ remained almost unchanged when the SFR was increased from 0 to 2 at a constant ER value of 0.3 for 25% LLDPE. However, increasing the LLDPE content to 75%, resulted in a slight increase in $CH_4$ concentration at an SFR of 0.5. This rise is due to the methanation reaction, whereby the high carbon content in the feedstock reacts with $H_2$ to form $CH_4$. However, increasing the SFR further, favours methane steam reforming and subsequently reduces $CH_4$ concentration.

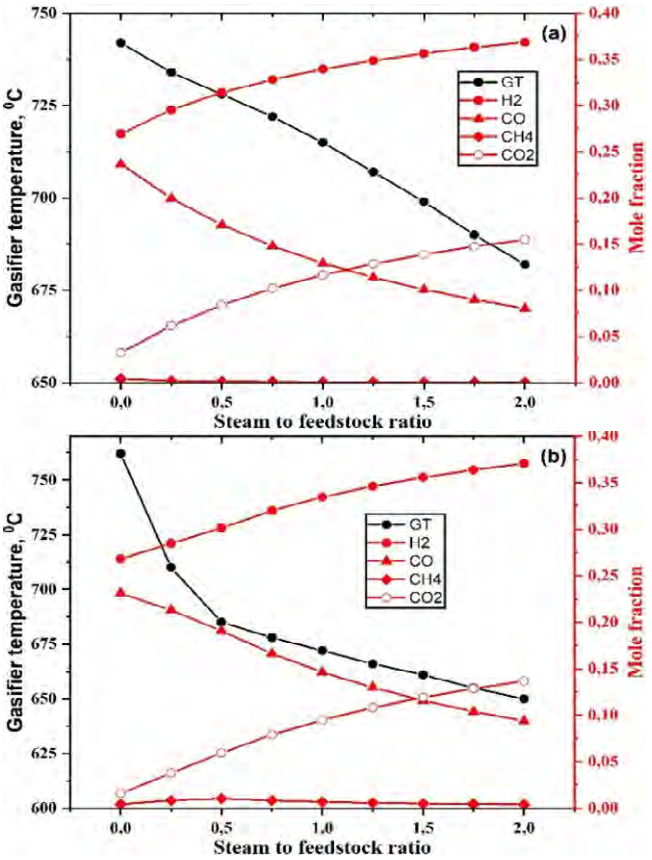



**Figure 4**: Effect of SFR on syngas concentration and GTat a fixed ER of 0.3 (a): 25% LLDPE, (b): 75% LLDPE

## Performance indicators

The lower heating value (LHV) of syngas on a dry basis, carbon conversion efficiency (CCE), and cold gas efficiency (CGE) were used as performance indicators for the co-gasification of CG and LLDPE as depicted in figure 5 (using air), figure 6 & figure 7 (mixture of air and $H_2O$). From 5, it is evident that the CCE increases with an increase in ER until it attains a maximum value at an ER of 0.3 and 0.35 for 25 and 75 % LLDPE respectively due to accelerated oxidation of carbon content in the feedstock. This is in line with figure 2 whereby the CO concentration attained a maximum value at an ER of 0.3 (for 25% LLDPE) and 0.35 (for 75% LLDPE). An opposite trend is observed for LHV whereby it decreases with an increase in the ER. The LHV is significantly reduced at lower ER due to a decrease in $H_2$ and $CH_4$ concentrations. In an ER range of 0.15-0.4, the syngas LHV decreases slightly. However, the decrease in LHV in this range is less for 75% LLDPE. The CGE attains its peak at the point where all the carbon in the feedstock has been converted into CO or $CO_2$, thus maximum CCE (ER =0.3 for 25% LLDPE and ER =0.35 for 75% LLDPE) as presented in figure 4. Beyond an ER value of 0.3 and 0.35, the CGE starts to decrease because the system starts to transit into a combustion regime. The performance indicators from this study are in line with those reported in the literature for the air gasification of municipal solid waste [10].

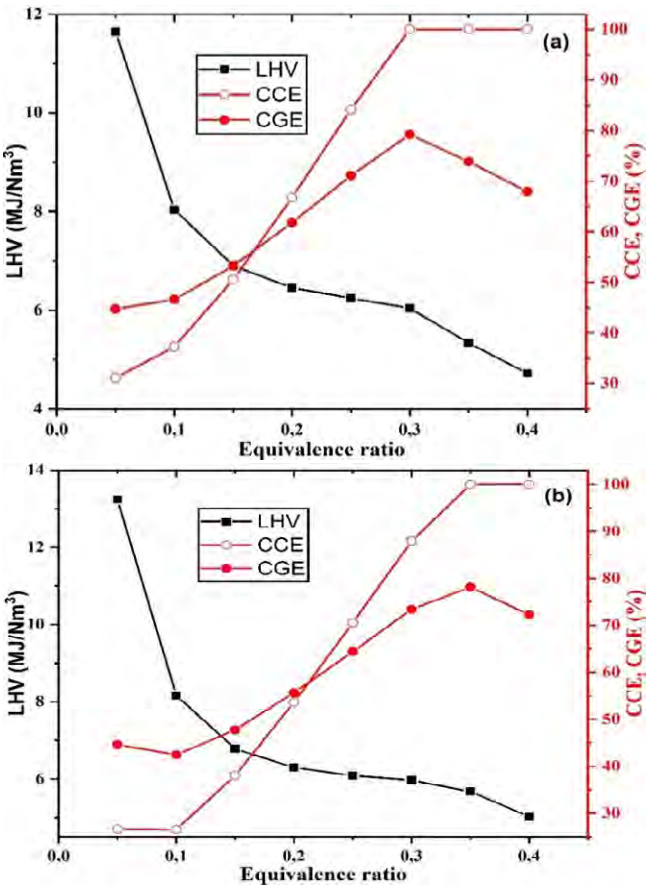



**Figure 5.** Effects of ER on CCE, CGE and LHV for air-cogasification, (a): 25% LLDPE, (b): 75% LLDPE

Figure 6 (a &b) summarizes the effect of ER on CCE, CGE and syngas LHV at a fixed SFR.These performance indicators follow a pattern similar to that of air co-gasifcation. The addition of steam to the gasifier at a constant rate decreases the syngas LHV but remains higher than that of air gasification.The main reason for the decrease in syngas LHV is the decrease of $H_2$ and $CH_4$ concentration,which largely contributes to LHV when the ER was increased. Figure 6 (a &b) shows further that, the presence of steam in the gasifier reduces the amount of air required to achieve a maximum CCE and CGE. Additionally, steam enhances the CGE by promoting steam reforming reactions.

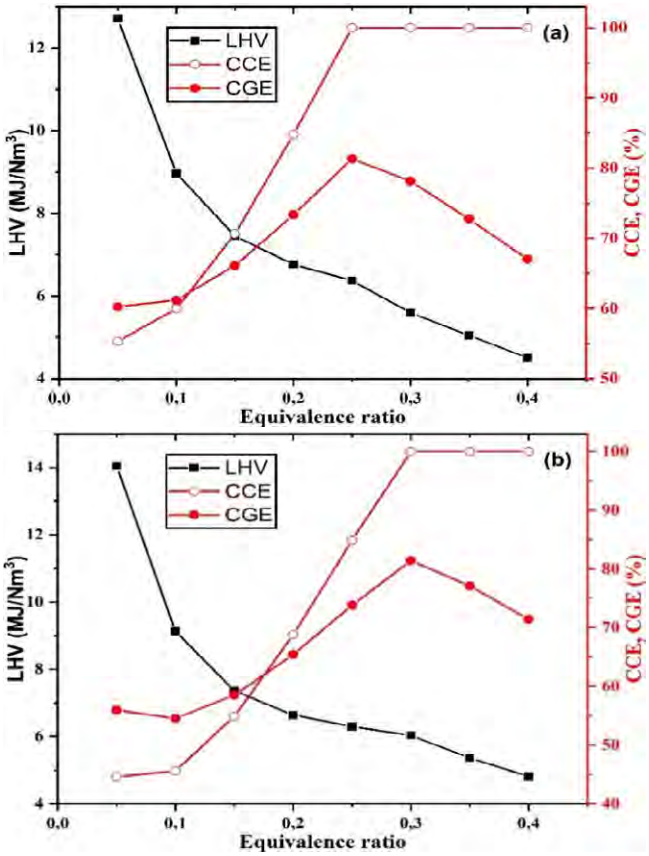



**Figure 6**: Effects of ER on CCE, CGE and LHV at fixed SFR of 0.5, (a): 25% LLDPE, (b): 75% LLDPE

The effect of SFR on syngas LHV, CCE and CGE at a fixed ER is also shown in figure 7 a& b. An increase in SFR increases $H_2$ and $CO_2$ concentration but decreases that of CO and $CH_4$. Since $CH_4$ and CO have lower heating values higher than $H_2$ per unit volume and $CO_2$ has no energy content, this will result in a slight reduction in syngas LHV as presented in figure 7a. As the LLDPE content is increased to 75% (figure 7b), the syngas LHV intially increases with an increase in the SFR.This is because $CH_4$ concentration slightly increased with an increase in SFR due to high carbon and hydrogen content of the feedstock which results in $CH_4$ formation via methanation reaction. As the SFR is further increased, the syngas LHV slightly decreases due to a decrease in $CH_4$ concentration caused by methane steam reforming reactions.The CCE for 25% LLDPE was not influenced by an increase in SFR as it has already attained a maximum value at an ER of 0.3. This resulted in a slight decrease in the CGE when the SFR was increased from 0 to 2. In the case of 75% LLDPE, the CCE increased and attained a maximum value at an SFR of 0.5. Thus, the CGE also attained its maximum value at the same SFR of 0.5.

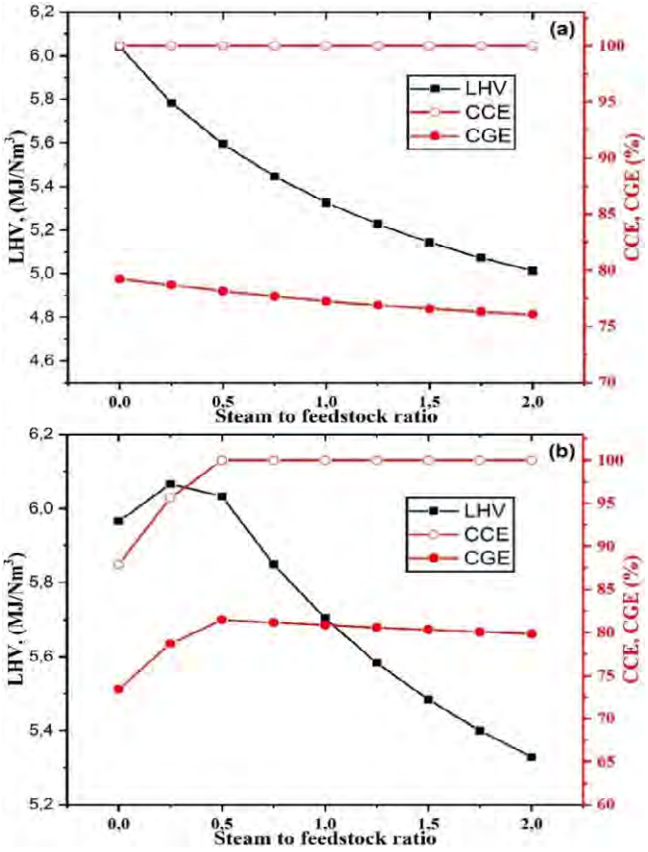



**Figure 7**: Effects of SFR on CCE, CGE and LHV at fixed ER value of 0.3, (a): 25% LLDPE, (b): 75% LLDPE

## CONCLUSION

This study evaluated the air and air/steam co-gasification of crude glycerol and LLDPE using Aspen Plus. Results indicated that an increase in ER or SFR significantly influenced the co-gasification product behaviour. For air co-gasification process, an increase in ER raised the GT and increased CO concentration until it reached a maximum value at an ER of 0.3 (25% LLDPE) and 0.35 (75% LLDPE). At the same time, $H_2$ and $CH_4$ concentration decreased which resulted in a decrease of syngas LHV. Furthermore, the CCE and CGE increased with an increase in ER and attained their maximum values at the CO concentration peak. The introduction of steam in the gasifier at a constant rate reduced the amount of air required

for the gasification process and subsequently enhanced not only the syngas composition, LHV but also the CGE. Additionally, when steam was introduced in the gasifier at a constant ER, the GT decreased significantly with an increase in SFR. Also, as the SFR increased, $H_2$ and $CO_2$ concentration increased but that of CO and $CH_4$ decreased due to steam reforming reactions which resulted in a moderate syngas LHV and CGE. Furthermore, the air gasification of 75% LLDPE achieved a flexible syngas ratio ($H_2$/CO) at an ER of 0.2 for the synthesis of methanol while syngas ratio from 25% LLDPE can be used useful for the synthesis of dimethyl ether. 25% LLDPE achieved a syngas ratio of approximately 2.03 when steam was introduced in the gasifier but 75% LLDPE did not achieve a desirable syngas ratio. When the SFR was increased at a constant ER, the syngas ratio increased and both 25% LLDPE and 75% LLDPE achieved a syngas ratio of 2.19 and 2.28, respectively at an SFR of 0.75 and 1. Therefore, this study offers a sustainable solution for waste management and promotes a circular economy by converting crude glycerol and LLDPE into valuable products. Future work should investigate the environmental and economic feasibility for crude glycerol and LLDPE co-gasification.

## ACKNOWLEDGEMENTS

This work was supported by the University of South Africa (UNISA).

## REFERENCES

1. Erdem, K., Han, D.G & Midilli, A. A parametric study on hydrogen production by fluidized bed co-gasification of biomass and waste plastics. *Int J Hydrog Energy*, 52:,1434–1444 (2023)
2. Chunakiat P, Panarmasar N, Kuchonthara P. Hydrogen production from glycerol and plastics by sorption-enhanced steam reforming. *Ind Eng Chem Res* 62 (49):21057–66(2023) https://doi.org/10.1021/acs.iecr.3c02072.
3. Gómez-Barea, A. & Leckner, B. Modeling of biomass gasification in fluidized bed. *Prog Energy Combust Sci*, 36 (4). 444–509 (2010) doi: 10.1016/j.pecs.2009.12.002.
4. Mukeru, B.M & Patel, B. Co-gasification of glycerol and linear low density polyethylene (LLDPE) for syngas production: A thermodynamic targeting approach. *Fuel*, 381: 133648(2025) doi: 10.1016/j.fuel.2024.133648.
5. Ranjan, N., Yadav, N., Singh, H., Kumar, Kumar, S. Mahajani, S.M. "Modelling and simulation of autothermal downdraft co-gasification of biomass and plastic wastes using Aspen Plus. *Energy Convers Manag*, 297. 117714 (2023). https://doi.org/10.1016/j.enconman.2023.117714
6. Kihedu, J. H., Yoshiie, R., & Naruse, I. Performance indicators for air and air–steam auto-thermal updraft gasification of biomass in packed bed reactor. *Fuel Processing Technology*, *141*, 93–98. (2015). https://doi.org/10.1016/j.fuproc.2015.07.015
7. Manara, P. & and Zabaniotou, A. Co-pyrolysis of biodiesel-derived glycerol with Greek lignite: A laboratory study. *J Anal Appl Pyrolysis*, 100166–172 (2013) doi: 10.1016/j.jaap.2012.12.013.
8. Farooq A, Moogi S, Jang SH, Kannapu HPR, et al. Linear low-density polyethylene gasification over highly active Ni/$CeO_2$-$ZrO_2$ catalyst for enhanced hydrogen generation. *J Ind Eng Chem* 94:336–42 (2021) https://doi.org/10.1016/j. jiec.2020.11.005
9. Niu, M., Huang, Y., Jin, B., & Wang, X. Simulation of Syngas Production from Municipal Solid Waste Gasification in a Bubbling Fluidized Bed Using Aspen Plus. *Ind Eng Chem Res 52*:14768–14775 (2013). https://doi.org/10.1021/ie400026b
10. Arena, U. Process and technological aspects of municipal solid waste gasification. A review. Waste Manag 32:625-639 (2012).https://doi.org/10.1016/j.wasman.2011.09.025

© 2025 by the authors. Licensed to PSEcommunity.org and PSE Press. This is an open access article under the creative commons CC-BY-SA licensing terms. Credit must be given to creator and adaptations must be shared under the same terms. See https://creativecommons.org/licenses/by-sa/4.0/



Systems & Control Transactions

**Research Article - Peer Reviewed Conference Proceeding**
ESCAPE 35 - European Symposium on Computer Aided Process Engineering
Ghent, Belgium. 6-9 July 2025
Jan F.M. Van Impe, Grégoire Léonard, Satyajeet S. Bhonsale,
Monika E. Polańska, Filip Logist (Eds.)

PSE PRESS

# Automated Identification of Kinetic Models for Nucleophilic Aromatic Substitution Reaction via DoE-SINDy

**Wenyao Lyu[a], Federico Galvanin[a]***

[a] University College London, Department of Chemical Engineering, London, United Kingdom

* Corresponding Author: f.galvanin@ucl.ac.uk.

## ABSTRACT

Nucleophilic aromatic substitutions (SNAr) are key chemical transformations in pharmaceutical and agrochemical synthesis, yet their complex mechanisms (concerted or two-step) complicate kinetic model identification. Accurate kinetic models for SNAr are essential for scale-up, optimization, and control of the reaction process, but conventional methods struggle with mechanism uncertainty driven by substrates, nucleophiles, and reaction conditions, with data collection being difficult due to its source-intensive nature. We address this using DoE-SINDy, a data-driven framework for generative modelling without complete theoretical understanding. A benchmark study on the SNAr reaction of 2,4-difluoronitrobenzene with morpholine in ethanol was conducted, incorporating parallel and consecutive side-product formation. Ground-truth kinetic models validated in prior studies were used to generate in-silico data under varying noise levels and sampling intervals. DoE-SINDy successfully identified the true kinetic model with minimal runs, quantifying the impact of key design factors such as inlet concentrations, residence time, sample size and experimental budget on model identification.

**Keywords**: Modelling and Simulations, Reaction Engineering, System Identification, Machine Learning, Model Structure Generation, Design of Experiment

## 1. INTRODUCTION

Nucleophilic aromatic substitution (SNAr) reactions play a crucial role in synthesizing natural products, pharmaceuticals, and agrochemicals. Accurate kinetic model identification is essential for optimizing SNAr reaction conditions, improving process efficiency, and enabling predictive control in manufacturing [1]. SNAr reactions can proceed via a classical two-step pathway or a concerted mechanism (cSNAr), with the preferred pathway influenced by substrate, nucleophile, leaving group, and environmental conditions such as solvation and fluid dynamics. These factors complicate kinetic identification, especially at process scales [2].

While quantum chemical methods like DFT offer detailed mechanistic insights, they are computationally intensive. Molecular descriptors provide a user-friendly alternative but require broader datasets for generalization [3]. Integrating solvent, fluid dynamics, and operational factors is essential for process-scale simulations, which requires computational-experimental approaches [2]. Obtaining reliable experimental data is resource-intensive, especially when integrating multiple effects [4]. Though recent innovations in continuous-flow platforms and experimental design have improved data collection efficiency [2,4–6], their reliance on predefined kinetic models limits the application to systems with incomplete mechanistic understanding. Recently, automated model-building approaches, such as such as AI-DARWIN [7], PySR [8] and SINDy [9], have been developed to rapidly identify interpretable models with minimal data requirements and without requiring fully predefined model expressions.

Motivated by these challenges, a systematic model identification framework named DoE-SINDy is employed in this paper to simultaneously generate mechanistic model structures and estimate model parameters from a small dataset [10], with the ultimate objective to provide

a robust and accurate representations of concentration profiles in SNAr reactions.

## 2. METHODOLOGY

### 2.1 DoE-SINDy framework

A dynamic model of a chemical reaction system can be formulated as a set of differential-algebraic equations (DAEs) as:

$$\begin{cases} \mathbf{f}(\dot{\mathbf{x}}, \mathbf{x}, \mathbf{u}, t, \boldsymbol{\theta}) = 0 \\ \hat{\mathbf{x}} = \mathbf{h}(\mathbf{u}, t, \boldsymbol{\theta}) \end{cases} \quad (1)$$

where $\mathbf{f}$ and $\mathbf{h}$ are sets of model equations, $\mathbf{x}$ is the observable state variable vector, $\mathbf{u} \in \mathrm{U}$ the control variable vector, $t$ time and $\boldsymbol{\theta}$ the parameter vector, and $\hat{\mathbf{x}}$ the predicted measurable state variables. This research focuses on simultaneously identifying the model structure $\mathbf{f}$, and parameters $\boldsymbol{\theta}$.

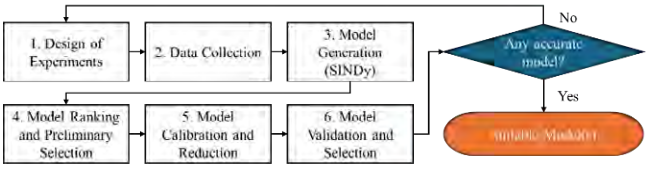



**Figure 1.** Framework of DoE-SINDy for identifying the most suitable models from experimental data [10].

Sparse identification of nonlinear dynamical systems (SINDy) [9] is a sparse regression-based approach that derives nonlinear models from a user-defined candidate term library and reaction profiles data. Assuming a process model is governed by a few key terms, SINDy ensures both accuracy and physical interpretability of the identified models. Building upon SINDy, Lyu & Galvanin proposed an iterative model identification framework named DoE-SINDy to address variability in model generation and enhance identifiability and reliability of identified models [10]. The procedure is articulated in steps illustrated in Figure 1.

In block (1), the DoE-SINDy framework begins with a preliminary design of experiments (DoE) using the minimum number of required runs to explore conditions underlying physical constraints. Step (2) requires the collection of time-varying state variable measurements, the numerical approximation of time derivatives and data splitting into training and testing subsets. In the model generation step (3), the SINDy algorithm, developed in [11,12], is called to build multiple candidate models from subsets of the training dataset. The resulting models are ranked by complexity, and the simplest candidates are selected (4). To improve parameter robustness, maximum likelihood estimation using the full training dataset is performed during the model calibration step (5), followed by model refinement to eliminate non-significant terms that minimally impact reaction profiles, further reducing unnecessary complexity. A sensitivity-based practical parameter identifiability analysis is integrated before and after calibration to ensure that only identifiable models are retained. Calibrated models then undergo model validation for statistical adequacy and check whether the models pass user-defined stopping criteria (6). If no model meets the stopping criteria, the framework iteratively returns to step (1), generating new candidate models using expanded datasets. This iteration continues until at least one model meets the stopping criteria or the experimental budget is exhausted. When the iteration stops, the output will be the statistically acceptable models or the models from the final iteration sorted in terms of Akaike Information Criterion (AIC).

The framework for DoE-SINDy is established in Python. ***PySINDy (v1.7.5)*** is the primary package used for model generation and numerical approximation of time derivatives [11,12]. Additionally, ***scipy*** is employed for ODE integration, parameter estimation, and statistical evaluations, including $\chi^2$ test, normality test and $t$ test.

### 2.2 Assessment criteria for DoE-SINDy identified models

The DoE-SINDy framework evaluates identified models using three main criteria. The first check is if the model is **statistically acceptable.** Goodness-of-fit test evaluates whether a model adequately represents experimental data considering measurement noise. A two-tailed $\chi^2$ test assesses if residuals between predictions and measurements align with assumed noise distribution, detecting underfitting or overfitting cases [13]. However, since DoE-SINDy focuses on identifying promising model structures with limited data, precise parameter estimates are not guaranteed at this stage. A normality test, as a less strict alternative, checks if residuals follow a zero-mean Gaussian distribution [14], allowing inclusion of models that may subsequently improve through refined parameter estimation and additional data. Four options for user-defined stopping criteria are possible:1) passing both tests ('and') 2) passing only $\chi^2$ test ('chi2'); 3) passing only normality test ('normality'), or 4) passing either ('or'). These are ranked from the most to the least strict, and determines when the iteration will stop, with models passing the chosen criterion labelled as "statistically acceptable".

To assess if the identified models successfully recover the ground-truth model structures, the second and the third criteria check if the model is **structurally promising,** as defined in Equation (2), or matches the **ground-truth**, as defined in Equation (3)**:**

$$\mathcal{I}(\boldsymbol{\theta}^{true}) \subset \mathcal{I}(\hat{\boldsymbol{\theta}}) \quad (2)$$

$$\mathcal{I}(\boldsymbol{\theta}^{true}) = \mathcal{I}(\hat{\boldsymbol{\theta}}) \quad (3)$$

where $\boldsymbol{\theta}^{true}$ and $\hat{\boldsymbol{\theta}}$ represent coefficient matrices of

**Table 1:** Potential scenarios for the models identified by DoE-SINDy.

| Performance | Statistically acceptable | Structurally promising | Structurally Ground-truth | Circumstance |
|---|---|---|---|---|
| Best | T | T | T | Statistically acceptable and structurally ground-truth model identified |
| Good | T | T | F | Statistically acceptable and structurally promising model identified |
| Poor | T | F | F | Statistically acceptable but missing term(s) in the ground-truth model |
| | F | T | T | Structurally ground-truth but poor fit |
| | F | T | F | Structurally promising but poor fit |
| Worst | F | F | F | Poor fit and missing terms(s) in the ground-truth model |

ground-truth and identified models, respectively. Each matrix has dimensions corresponding to the number of equations by the size of candidate term library. A non-zero entry in these matrices indicates the presence of a specific term in the model, with its value representing estimated parameters of that term. The notation $\mathcal{I}(\cdot)$ denotes the set of position indices of non-zero elements in the coefficient matrix of each identified model. For example, if the true and identified coefficients matrix of the differential equation for component A are $\theta_{c_A}^{true} = [2\ 0\ 0\ 3\ 0\ 0]$ and $\hat{\theta}_{c_A} = [2\ 0\ 0\ 3\ 1\ 0]$, the true and identified coefficient indices are $\mathcal{I}(\theta_{c_A}^{true}) = \{1,4\}$ and $\mathcal{I}(\hat{\theta}_{c_A}) = \{1,4,5\}$. The model is structurally promising since $\{1,4\} \subset \{1,4,5\}$, meaning that the identified structure contains all terms from the ground-truth model but with additional terms. It is structurally ground-truth if its structure exactly matches the true underlying model, even if parameter uncertainty is still present. For example, a model with the coefficient matrix $\hat{\theta}_{c_A} = [1.8\ 0\ 0\ 3.2\ 0\ 0]$ is considered structurally ground-truth because all the model terms are correctly identified.

## 2.3 Scenarios for DoE-SINDy identified models

Based on the assessment criteria defined in Section 2.2, labels are assigned to each identified model, as summarized in Table 1. The most desirable scenario is 'TTT,' where the identified model is both statistically acceptable and structurally ground-truth. Scenario 'TTF' is also acceptable, as the identified model contains all the ground-truth terms, with extra terms removable after additional data collection and parameter re-estimation. In practice, 'TFF' models are selected for their statistical adequacy when the ground-truth is unknown but may be eliminated through model discrimination techniques [15]. Scenarios 'FTT', 'FTF' and 'FFF' occur when no acceptable model is generated within the available experimental budget. In such cases, redefining the library of candidate terms or adjusting DoE-SINDy setting is recommended before conducting additional experiments.

# 3. CASE STUDY AND IMPLEMENTATION

## 3.1 In-silico data generation

A benchmark case study evaluated the performance of DoE-SINDy in identifying the rate models for the nucleophilic aromatic substitution (SNAr) of 2,4-difluoronitrobenzene 1 with morpholine in ethanol. The reaction produce a mixture of desired product *ortho*-substituted 3 and side products *para*-substituted 4 and *bis*-adduct 5 through parallel and consecutive elementary reaction steps as shown in Figure 2 [5,6].

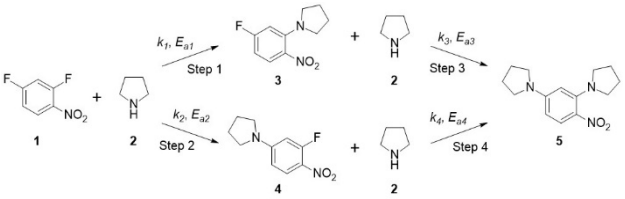



**Figure 2**. Assumed mechanism scheme for SNAr [5,6].

Data was generated through in-silico experiments simulating an automated continuous-flow reactor system with controlled linear flow ramps as in Hone *et al.* [5] and Agunloye *et al.* [6]. The residence time $\tau$ was manipulated through volumetric flow rate changes within a fixed-length reactor. The range of the time axis is equal to the residence time of the experiment with the longest operation time among the set of experiments in the ramp. The three experimental design variables in this system are: 1) initial concentrations; 2) sample size of the concentration-time profile; 3) experimental budget. The molar balance equations for the system, based on the reaction scheme are:

$$\frac{dc_1}{d\tau} = -(k_1 + k_2)c_1c_2 = \theta_1 c_1 c_2$$

$$\frac{dc_2}{d\tau} = -(k_1 + k_2)c_1c_2 - k_3c_2c_3 - k_4c_2c_4$$

$$= \theta_2 c_1 c_2 + \theta_3 c_2 c_3 + \theta_4 c_2 c_4 \quad (4)$$

$$\frac{dc_3}{d\tau} = k_1 c_1 c_2 - k_3 c_2 c_3 = \theta_5 c_1 c_2 + \theta_6 c_2 c_3$$

$$\frac{dc_4}{d\tau} = k_2 c_1 c_2 - k_4 c_2 c_4 = \theta_7 c_1 c_2 + \theta_8 c_2 c_4$$

Experiments were conducted for 2.4 minutes at 130°C, with ground-truth reaction rate constants were defined as $k_1, k_2, k_3, k_4 = [1.21, 0.21, 0.0, 0.057]$. Identifying dynamic models via DoE-SINDy requires multiple trajectories of time-varying states variables. Thus, design of experiment technique, Latin Hypercube Sampling, is applied to design multiple sets of initial concentrations within the experimental design space (Table 2). Notably, the initial concentration of $c_2(0)$ was defined as $c_2(0) = c_1(0) \cdot c_2^{equiv}(0)$.

**Table 2**: Experimental design space for control variables, initial concentrations, employed in the case study [6].

| Limits | $\boldsymbol{c_1(0)}$ (M) | $\boldsymbol{c_2^{equiv}(0)}$ | $\boldsymbol{c_3(0)}$ (M) | $\boldsymbol{c_4(0)}$ (M) |
|---|---|---|---|---|
| Lower | 0.0967 | 0.2054 | 0 | 0 |
| Upper | 1.6917 | 2.5400 | 0.5000 | 0.5000 |

In-silico data were generated by adding random normally distributed noise with zero mean and given standard deviation to the noise-free simulated values of state variables. Subsequently, the time derivatives of the noisy state variables (concentrations) were numerically approximated using Kalman derivative as the measurement errors are assumed to follow a standard normal distributions [12].

The performance of DoE-SINDy in identifying models achieving specific target scenarios was evaluated using a metric, *Target Scenario Achievement Rate (TSAR)*, which is defined as:

$$\text{TSAR} = \frac{\text{Number Of Datasets with Models Meeting the Target Scenario}}{\text{Total Number Of Datasets}} \quad (5)$$

The robustness of DoE-SINDy was tested across three different experimental budgets (10, 15, and 20 experiments), three noise levels ($\sigma = [0.1\%, 1\%, 10\%]$), ten sample sizes (8, 12, 16, 18, 20, 24, 30, 36, 48, 60), and 50 sets of initial concentrations.

## 3.2 Application of DoE-SINDy for model identification

The DoE-SINDy implementation utilized the collected measurements and their time derivatives for model identification. In the model generation step (3), the candidate term library is constructed with the following set of features: $\boldsymbol{g}(\boldsymbol{c}) = [c_1c_2, c_1c_3, c_1c_4, c_2c_3, c_2c_4, c_3c_4]$. The Stepwise Sparse Regressor (SSR) is employed to generate models from data. In step 4 of the proposed procedure, the top three simplest models are selected for further analysis. four different stopping criteria were evaluated to assess their impact on model identification performance.

# 4. RESULTS

This section compares DoE-SINDy example models for the SNAr reaction rate, evaluating the TSAR for achieving 'TTT' and 'TTF' scenarios using four stopping

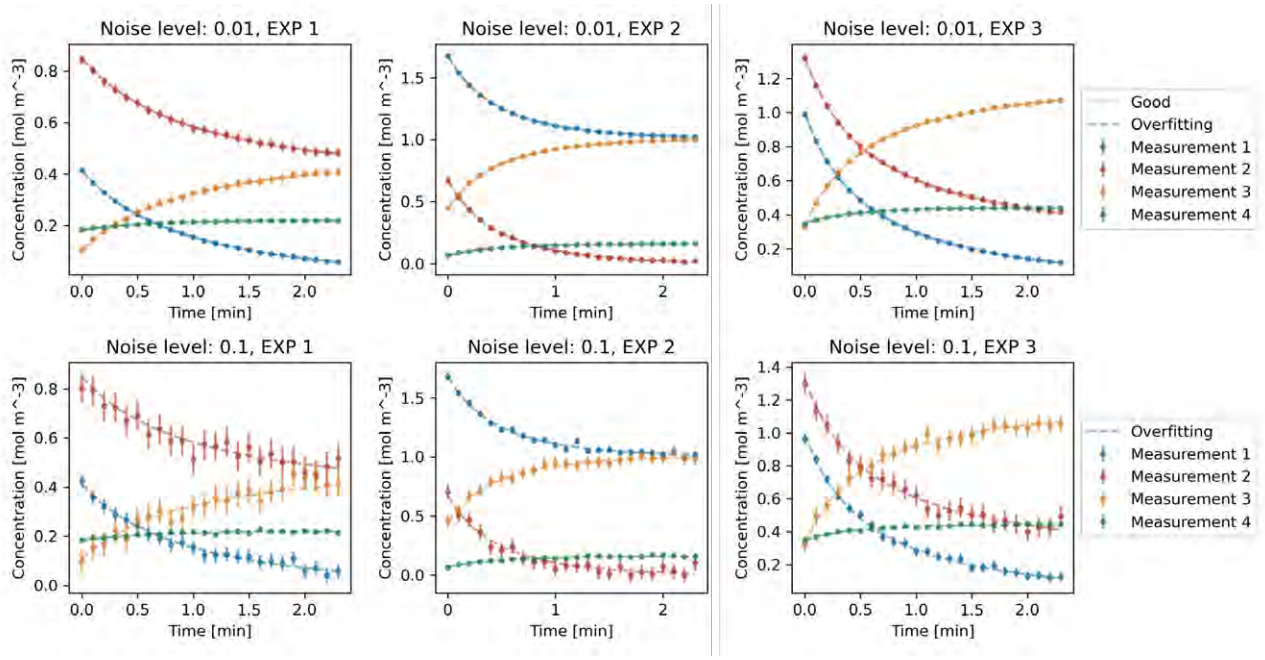



**Figure 3:** Simulations for example 'TTT' scenario models tested as good fit or overfitting based on the $\chi^2$ test, under varying initial conditions and noise levels ($\sigma$=0.01 and 0.1, sample size=24, budget=20 experiments).

**Table 3:** Estimated coefficients ($\hat{\theta}$) and corresponding $t$-values of models achieving 'TTT' scenario (sample size=24, budget=20). Results are presented for three noise levels ($\sigma = 0.1\%, 1\%\ and\ 10\%$).

| | $\theta_{i,ref}$ ($M^{-1}min^{-1}$) | $\hat{\theta}_{i,\sigma=0.1\%}$ | $t\ (t_{ref}(95\%) = 1.97)$ | $\hat{\theta}_{i,\sigma=1\%}$ | $t\ (t_{ref}(95\%) = 1.97)$ | $\hat{\theta}_{i,\sigma=10\%}$ | $t\ (t_{ref}(95\%) = 1.97)$ |
|---|---|---|---|---|---|---|---|
| $\theta_1$ | $-1.42$ | $-1.42$ | $2.06 \times 10^{-3}$ | $-1.41$ | $2.05 \times 10^{-3}$ | $-1.43$ | $2.08 \times 10^{-3}$ |
| $\theta_2$ | $-1.42$ | $-1.42$ | $2.06 \times 10^{-3}$ | $-1.42$ | $2.06 \times 10^{-3}$ | $-1.43$ | $2.07 \times 10^{-3}$ |
| $\theta_3$ | 0.00 | 0.00 | - | 0.00 | - | 0.00 | - |
| $\theta_4$ | $-0.057$ | $-0.056$ | $1.07 \times 10^{-4}$ | $-0.071$ | $1.29 \times 10^{-4}$ | $-0.064$ | $1.23 \times 10^{-4}$ |
| $\theta_5$ | 1.21 | 1.21 | $1.75 \times 10^{-3}$ | 1.20 | $1.73 \times 10^{-3}$ | 1.21 | $1.76 \times 10^{-3}$ |
| $\theta_6$ | 0.00 | 0.00 | - | 0.00 | - | 0.00 | - |
| $\theta_7$ | 0.21 | 0.21 | $3.09 \times 10^{-4}$ | 0.21 | $3.10 \times 10^{-4}$ | 0.21 | $3.11 \times 10^{-4}$ |
| $\theta_8$ | $-0.057$ | $-0.057$ | $1.13 \times 10^{-4}$ | $-0.055$ | $1.26 \times 10^{-4}$ | $-0.057$ | $1.22 \times 10^{-4}$ |

criteria ('and', 'chi2', 'normality', 'or') under varying experimental designs and data conditions.

## 4.1 Identified SNAr reaction rate models

Figure 3 shows simulated reaction profiles for models achieving the 'TTT' scenario under varying noise levels. When $\sigma = 0.01$, the profiles of the good-fit and overfitting models overlap, indicating similar prediction performance. At $\sigma = 0.1$, no good-fit models are identified but the overfitting model aligns perfectly with the observations. These graphical results suggest that both good-fit and overfitting models perform well in representing the dynamic system when the 'TTT' scenario is achieved.

Scenario 'TTT' is the most desirable outcome, where the identified models are statistically acceptable and aligned with the ground-truth. DoE-SINDy successfully identifies 'TTT' models with at least 7 experiments.

We examine three 'TTT' models identified using data with a sample size of 24 and an experimental budget of 20 noise levels of $\sigma$=0.1%, 1% and 10%. As shown in Table 3, the estimated parameter values ($\hat{\theta}_i$) are generally consistent with reference values ($\theta_{i,ref}$), and close to the reference at higher noise levels ($\sigma$=1% and 10%). Figure 3 shows that these models reflect the system dynamics well, even when some parameters deviate slightly from the reference. Parameter $\theta_3$ and $\theta_6$ consistently yield zero estimates, indicating that Step 3 is inactivated in the reaction network, consistent with the assumed reaction mechanism as shown in Figure 2 [5,6].

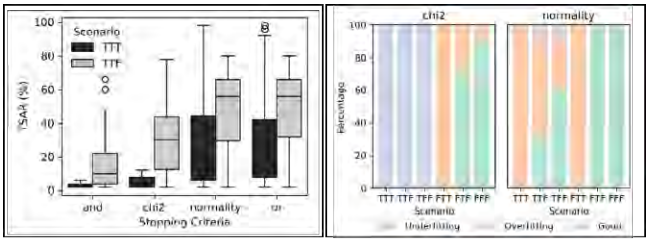
Although the models represent the system well, they might be statistically inadequate due to overfitting as indicated by the $\chi^2$ test. Furthermore, small $t$ values for all parameters suggest significant uncertainty in the estimates, pointing to the need for more informative data to improve parameter precision.

## 4.2 TSAR comparison across stopping criteria

The comparison of TSAR values across stopping criteria provides critical insights into DoE-SINDy's effectiveness in identifying suitable models for the SNAr reaction system. Higher TSAR indicates better performance in achieving specific scenarios.

Figure 4(a) shows that the strictness of stopping criteria significantly affects model identification. For the 'TTT' scenario, the 'normality' criterion achieves the highest average TSAR (over 20%), whereas 'chi2' achieves less than 5%, and 'and' nearly zero. This highlights 'normality' as the most effective criterion for identifying structurally and statistically adequate models. For the 'TTF' scenario, relaxing criteria from 'and' to 'or' improves TSAR from around 10% to 55%, with 'normality' and 'or' performing similarly. Less stringent criteria enable better identification of statistically adequate models, balancing efficiency and reliability.

The box plots reveal high dispersion in TSAR across datasets, reflecting the sensitivity of DoE-SINDy to data quality and experimental design. This underscores the importance of high-quality data and well-designed experiments for reliable model identification.




(a) (b)

**Figure 4:** (a) TSAR distribution for 'TTT' and 'TTF' scenarios under different stopping criteria across various data conditions; (b) Scenario distribution based on the $\chi^2$ test using 'chi2' or 'normality' stopping criteria.

The distribution patterns observed in Figure 4(b) demonstrate the goodness-of-fit of the models categorised in each scenario. Notably, for the 'FTT' scenario under both the 'chi2' and 'normality' criterion, most models correctly identify the ground-truth structure but are excluded as overfitting. These models, with parameter re-estimation, are highly likely to achieve 'TTT'. Using 'normality' as the stopping criterion is more likely to retain such models compared to using 'chi2', explaining higher TSAR values of 'normality' shown in Figure 4(a). Its reliability is supported by Figure 3, where overfitting models passing the normality test align with experimental data under varying noise levels and experimental conditions.

## 5. CONCLUSION

This study demonstrates the effectiveness of DoE-SINDy in identifying kinetic models for SNAr reaction, successfully reconstructing statistically acceptable and structurally ground-truth models with as few as 7 experiments. Adopting the 'normality' stopping criterion allows to achieve the highest TSAR for identifying promising 'TTT' models, while stricter criteria, such as 'chi2' and 'and', tend to reject structurally accurate models due to overfitting.

However, the performance of DoE-SINDy varies under different experimental designs and data conditions. Further investigations into the impact of experimental design variables are necessary to optimize model identification and reduce experimental demands. The significant uncertainty in estimated parameters highlights the need for integrating techniques as model-based design of experiments (MBDoE) in the framework to improve parameter precision [16].Finally, as the ground-truth model is typically unknown in practice, further model discrimination is required to identify the most accurate representation of the system.

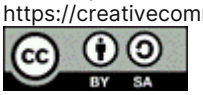
## ACKNOWLEDGEMENTS

The authors gratefully acknowledge the funding support from UCL EPSRC DTP (EP/R513143/1 and EP/W524335/1).

## REFERENCES

1. Rohrbach S, Smith AJ, Pang JH, Poole DL, Tuttle T, Chiba S, et al. Concerted Nucleophilic Aromatic Substitution Reactions *Angew Chem Int Ed* 58(46):16368–88 (2019) https://doi.org/10.1002/anie.201902216
2. Kim J, Hayashi Y, Badr S, Okamoto K, Hakogi T, Furukawa H, et al. Kinetic Study and Model-Based Design Space Determination for a Drug Substance Flow Synthesis Using an Amination Reaction via Nucleophilic Aromatic Substitution *Org Process Res Dev* 28(5):1793–805 (2024) https://doi.org/10.1021/acs.oprd.3c00380
3. Lu J, Paci I, Leitch DC. A broadly applicable quantitative relative reactivity model for nucleophilic aromatic substitution (SNAr) using simple descriptors *Chem Sci*. 13(43):12681–95 (2022) https://doi.org/10.1039/D2SC04041g
4. Hone CA, Boyd A, O'Kearney-McMullan A, Bourne RA, Muller FL. Definitive screening designs for multistep kinetic models in flow *React Chem Eng*. 4(9):1565–70 (2019) https://doi.org/10.1039/C9RE00180H
5. Hone CA, Holmes N, Akien GR, Bourne RA, Muller FL. Rapid multistep kinetic model generation from transient flow data *React Chem Eng*. 2(2):103–8 (2017) https://doi.org/10.1039/C6RE00109B
6. Agunloye E, Petsagkourakis P, Yusuf M, Labes R, Chamberlain T, Muller FL, et al. Automated kinetic model identification via cloud services using model-based design of experiments *React Chem Eng*. 9(7):1859–76 (2024) https://doi.org/10.1039/D4RE00047A
7. Chakraborty A, Sivaram A, Venkatasubramanian V. AI-DARWIN: A first principles-based model discovery engine using machine learning *Comput Chem Eng*. 154:107470 (2021) https://doi.org/10.1016/j.compchemeng.2021.107470.
8. Servia MÁ de C, Sandoval IO, Hii KK (Mimi), Hellgardt K, Zhang D, Chanona EA del R. The automated discovery of kinetic rate models – methodological frameworks *Digit Discov*. 3(5):954–68 (2024) https://doi.org/10.1039/D3DD00212H.
9. Brunton SL, Proctor JL, Kutz JN, Bialek W. Discovering governing equations from data by sparse identification of nonlinear dynamical systems *Proc Natl Acad Sci U S A*. 113(15):3932–7 (2016) https://doi.org/10.1073/pnas.1517384113
10. Lyu W, Galvanin F. DoE-integrated Sparse Identification of Nonlinear Dynamics for Automated Model Generation and Parameter Estimation in Kinetic Studies *Comput Chem Eng*. 53:169-174 (2024) https://doi.org/10.1016/B978-0-443-28824-1.50029-6
11. de Silva BM, Champion K, Quade M, Loiseau JC, Kutz JN, Brunton SL. PySINDy: A Python package for the Sparse Identification of Nonlinear Dynamics from Data *J Open Source Softw*. 5(49):2104–2104 (2020) https://doi.org/10.21105/joss.02104
12. Kaptanoglu AA, Silva BM de, Fasel U, Kaheman K, Goldschmidt AJ, Callaham J, et al. PySINDy: A comprehensive Python package for robust sparse system identification *J Open Source Softw*. 7(69):3994 (2022) https://doi.org/10.21105/joss.03994
13. Silvey SD. Statistical Inference. Routledge (1975)
14. D'Agostino R, Stephens MA. Goodness-of-Fit-Techniques. Routledge (1986)
15. Asprey SP, Macchietto S. Statistical tools for optimal dynamic model building *Comput Chem Eng*. 24(2):1261–7 (2000) https://doi.org/10.1016/S0098-1354(00)00328-8
16. Franceschini G, Macchietto S. Model-based design of experiments for parameter precision: State of the art *Chem Eng Sci*. 63(19):4846–72 (2008) https://doi.org/10.1016/j.ces.2007.11.034.

© 2025 by the authors. Licensed to PSEcommunity.org and PSE Press. This is an open access article under the creative commons CC-BY-SA licensing terms. Credit must be given to creator and adaptations must be shared under the same terms. See https://creativecommons.org/licenses/by-sa/4.0/



Systems & Control Transactions

**Research Article - Peer Reviewed Conference Proceeding**
ESCAPE 35 - European Symposium on Computer Aided Process Engineering
Ghent, Belgium. 6-9 July 2025
Jan F.M. Van Impe, Grégoire Léonard, Satyajeet S. Bhonsale,
Monika E. Polańska, Filip Logist (Eds.)

PSE PRESS

# System analysis and optimization of replacing surplus refinery fuel gas by coprocessing with HTL bio-crude off-gas in oil refineries.

**Erik Lopez-Basto[a,b*], Eliana Lozano Sanchez[c], Samantha Eleanor Tanzer[a], and Andrea Ramirez Ramirez[d]**

[a] Department of Engineering Systems and Services, Faculty of Technology, Policy and Management, Delft University of Technology, Delft, The Netherlands
[b] Cartagena Refinery. Ecopetrol S.A., Colombia
[c] Department of Energy, Aalborg University, Aalborg, Denmark
[d] Department of Chemical Engineering, Faculty of Applied Sciences, Delft University of Technology, Delft, The Netherlands

* Corresponding author: e.lopezbasto@tudelft.nl (E. Lopez Basto).

## ABSTRACT

This study evaluates the introduction of Carbon Capture and Utilization (CCU) process in two Colombian refineries, focusing on their potential to reduce $CO_2$ emissions and their associated impacts under a scenario aligned with the Net Zero Emissions by 2050 Scenario defined in the 2023 IEA report. The work uses a MILP programming tool (Linny-R) to model the operational processes of refinery sites, incorporating a net total cost calculation to optimize process performance over five-year intervals. This optimization was constrained by the maximum allowable $CO_2$ emissions. The methodology includes the calculation of surplus refinery off-gas availability, the selection of products and CCU technologies, and the systematic collection of data from refinery operations, as well as scientific and industrial publications. The results indicate that integrating surplus refinery fuel gas (originally used for combustion processes) and HTL bio-crude off-gas (as a source of biogenic $CO_2$) can significantly lower scope 1 and 2 $CO_2$ emissions, aligning with long-term decarbonization goals. However, these advantages carry additional costs due to significant increases in utility demands. In the high-complexity refinery, electricity consumption increases by a factor of 10, and steam demand and water usage each increase by a factor of 2.5 and 3, respectively. Similarly, in the medium-complexity refinery, electricity consumption rises by a factor of 11, steam demand by a factor of 4, and water usage by a factor of 6. The renewable energy requirements for water electrolyzers and $CO_2$ capture units primarily drive these increases. Furthermore, despite achieving $CO_2$ neutrality in scope 1 and 2 emissions by 2050, scope 3 emissions increase due to additional $CO_2$-based methanol production. Economic analyses highlight profit opportunities in the long term. The production costs of $CO_2$-based methanol are lower than the forecasted cost of production of fossil-based methanol, enhancing their economic viability in the long term. The study emphasizes the critical influence of refinery complexity levels on the scale and timeline for implementing these technologies to achieve short- and long-term $CO_2$ reduction targets. However, further evaluation is necessary to align these results with national electrical grid capacity, water supply availability, and expansion plans.

**Keywords**: Modelling and Simulations, Optimization, Refining, Biofuels, Process Design.

## INTRODUCTION

Reducing $CO_2$ emissions and reaching $CO_2$ neutrality in the long term are the objectives of this study, which focuses on two oil refineries that together contribute with more than 50% of their Scope 1&2 $CO_2$ emissions from

Ecopetrol (the Colombian state oil and gas industry). The process heating requirements via refinery fuel gas are responsible for 50 to 60% of the total scope 1 emissions.

Previous studies on this topic have found that for reducing $CO_2$ emissions, refineries require a portfolio of technologies, including low-carbon hydrogen (Low-C H2), sustainable energy, carbon capture, utilization, and storage (CCUS), bio-feedstocks, and product changes. Colombia's biomass resources offer opportunities for deploying advanced biofuel technologies like Hydrothermal Liquefaction (HTL) in the refineries. HTL produces biocrude compatible with the existing refinery infrastructure; however, co-processing with fossil streams is challenging and is a topic of ongoing research [1]

Alongside biocrude production, the process delivers a rich-biogenic $CO_2$ gas stream with untapped potential to be used in CCU processes. This research is grounded on the opportunity to repurpose the surplus refinery fuel gas that is generated by switching into more sustainable fuels such as Low-C H2, and utilize this refinery fuel gas and (HTL) biocrude off-gas in a conversion processes to produce more valuable and sustainable products, such as Methanol (see Figure 1 for the simplified system block diagram).

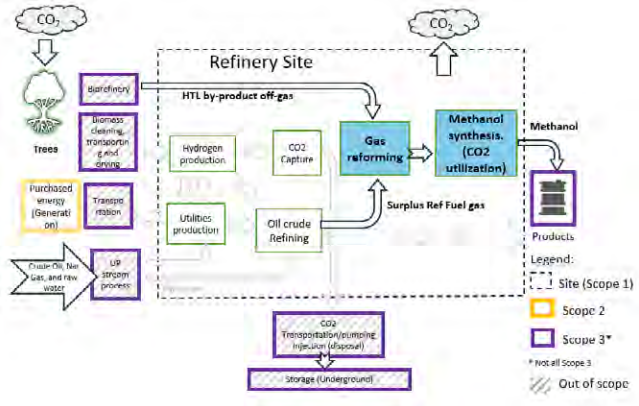



**Figure 1.** Simplified system block diagram.

This research aims to evaluate the impact of introducing CCU processes for methanol synthesis using alternative carbon sources and by-products as feedstock on the refinery performance, considering both short and long-term targets.

## METHODS

This research evaluates the future integration of alternative feedstock in methanol production /CCUS/biogenic C from biomass into two Colombian refineries and redirecting their $CO_2$ to storage. A simplified process flow diagram of the system evaluated is presented in Figure 1.

The methodology comprised five steps. In the first step, surplus refinery fuel gas was estimated. Note that HTL bio-crude off-gas was selected as the source of biogenic $CO_2$ from a biorefinery, which we assume to be installed next to the refinery and converted via thermocatalytic processes into methanol based on a previous study [2]. Second, potential CCU technologies were screened, which resulted in the selection of steam reforming and thermocatalytic hydrogenation to convert refinery fuel gas and biocrude off-gas into methanol.

Next, data was collected. The techno-economic data was sourced from literature and Aspen Plus simulations, therefore, a detailed techno-economic assessment [2] was used as input for this study. Lozano's work identified that up to 44 % of HTL Bio off-gas can be mixed with Refinery fuel gas without an external $H_2$ supply. Furthermore, this research uses data from two refineries owned by Ecopetrol. The two refineries, one with a medium level of process complexity and one with a high level of process complexity, process 7.7 Mtpd and 11.5 Mtpd of crude oil, respectively. The main characteristics of the two refineries are shown in Table 1.

**Table 1:** Main characteristics of the refinery case study

| | | Cartagena | Barrancabermeja |
|---|---|---|---|
| | **Unit** | **Value** | **Value** |
| Complexity level [1] | | High | Medium |
| Crude oil Capacity | Mt/y | 7.7 | 11.9 |
| Annual $CO_2$ emissions | Mt $CO_2$-eq /y | 2.5 | 3.4 |
| Gas fuel consumption | PJ/y | 19.8 | 30.4 |
| Electricity production | PJe/y | 3.2 | 4.9 |
| Steam production | PJth/y | 16.8 | 25.3 |
| Hydrogen production | kt/y | 84 | 28.7 |
| Total Conversion Yield | % | 96.7 % | 77 % |

**1:** The refinery complexity is defined by the Nelson Complexity Index, which quantifies the type of process units in a refinery and their capacity relative to the atmospheric distillation unit by assigning a factor [3].

In the fourth step, a mixed-integer linear programming (MILP) in Linny-R software was used to model and evaluate techno-economic and environmental parameters and energy and material balances at the system level (see Figure 2). Linny-R works with the Gurobi solver for minimizing the system costs under $CO_2$ emission constraints over time. The model was built based on previous work that optimized the basket of low-carbon H2 production technologies and CCS for the two Colombian refineries to achieve the $CO_2$ reduction emissions targets [4]. In the final step, the results were analyzed.

We evaluated this system under a favorable decarbonization scenario aligned with the Net Zero Emissions by the 2050 Scenario (NZE Scenario) defined in the 2023 IEA report [5]. In this scenario, the world moves towards decarbonization by significantly reducing fossil fuel use, having fewer incentives to explore and produce natural gas, and promoting the adoption of renewable energy sources. The parameters defined in the scenario are summarized in Table 2.

The mass and energy balances obtained from the model were compared to the refineries' 2020 material and energy balances. The model results varied less than 5% from real-world data. The model performs a single objective optimization aiming to achieve the largest total cash flow through total cost minimization in every period. In this work, every period involves 5 years. To minimize the total cost (eq 1).

$$\text{Objective function} = \min \; OC_t = \left(\sum_{p=1}^{n}[C_o - C_i]p\right)_t , \quad (1)$$

Where, OC is the overall costs [€], Co is cost output [€], Ci is cost input [€], p is a process in the refinery, and t is the time period.

Cost input is the sum of all cost, including the cost of raw materials, feedstocks, utilities, and Capex and Opex and maintenance of the new technologies, as well as an carbon taxes/penalties that increase as in the IEA scenario[5]; while the cost output category is the sum of the income associated with selling the products. Furthermore, Net margin is calculated as total cash flow divided by crude oil processing throughput. Techno-economic parameters and the calculation of annualized Capex and Opex are described in detail in the supplementary data document [6].

There are some assumptions in this work. First, the processing capacity of the Cartagena refinery will be expanded from 155 kbbl to 205 kbbl in the period between 2020-2025, according to existing plans. Additionally, to be able to use the maximum capacity for both oil refineries, there is a plan to expand the H2 production capacity in the medium term. In the short term, there is a project to interconnect the refineries to the Colombian electric grid through a 70 MW line to reduce their carbon footprint. The Colombian electrical grid has a lower carbon footprint compared with the auto-generated electricity generated at the refineries through natural gas power combined cycles because 70% of Colombian electricity is hydropower. Additionally, as a consequence of the increase in energy efficiency initiatives, there is a goal to achieve the best performance in the peer group (North and South America) in 2035. Thus, the Cartagena refinery will reduce 11% of energy consumption, and Barrancabermeja will reduce 9% of total energy consumption [7] in the short and medium term horizons.

The methanol production is expected to be expanded to fulfill the demand in modules of 500 t/d of methanol.

## RESULTS AND DISCUSSION

The results show that using HTL biocrude off gas (as a source of $CO_2$) with surplus refinery gas utilization (as a source of $H_2$) can significantly reduce scope 1 $CO_2$ emissions. Table 3 shows that the refinery's fuel gas consumption is projected to decrease significantly by 2050 by down to 0% and 39% of the 2020 levels for high-complexity and medium-complexity refineries, respectively. This substantial reduction is due to the substitution of conventional refinery fuel gas with low-carbon hydrogen produced within both refineries. The hydrogen demand for fuel uses would account for 41% and 85% of the total hydrogen requirement by 2050 in the high-complexity and medium-complexity refineries, respectively.

The results show significant reductions in Site direct and Indirect $CO_2$ emissions ( Scope 1&2) for both refinery types, as detailed in Figure 3. However, when use of products $CO_2$ emissions (scope 3) are taken into account, the results show an increase in net emissions due to the introduction of CCU processes, which produce methanol from a external source of mass (HTL biocrude off gas) and the use of refinery fuel gas changes from scope 1 (combustion) to products (scope 3)—as shown in Figure 3.

Furthermore, utilizing surplus refinery fuel gas and coprocessing with HTL bio-crude off-gas significantly increases resource demand in both refineries. Electricity demand rises by 10 and 11 times, respectively, primarily due to the reliance on renewable electricity to power water electrolyzers for the additional low-carbon hydrogen. Consequently, water demand increases by 3 and 6 times for the high-complexity and medium-complexity refinery, respectively. In addition, steam demand increases by 2.5 and 4 times for high-complexity and medium-complexity refineries, respectively, which is driven by the requirements of the $CO_2$ capture units integrated with the steam methane reforming (SMR) and biomass combustion and gasification for Low-C H2 production.

The optimized solution identified for both refinery sites can achieve the long-term $CO_2$ emissions reduction targets regarding scopes 1 and 2, as shown in Figure 3. However, this result is accompanied by a significant Underground storage capacity demand of 33 Mt for the HC refinery and 57 Mt CO2 for the MC refinery at 2050. Furthermore, the net margin is reduced in the order of 34% (high complexity) and 65% (medium complexity) over the long term.

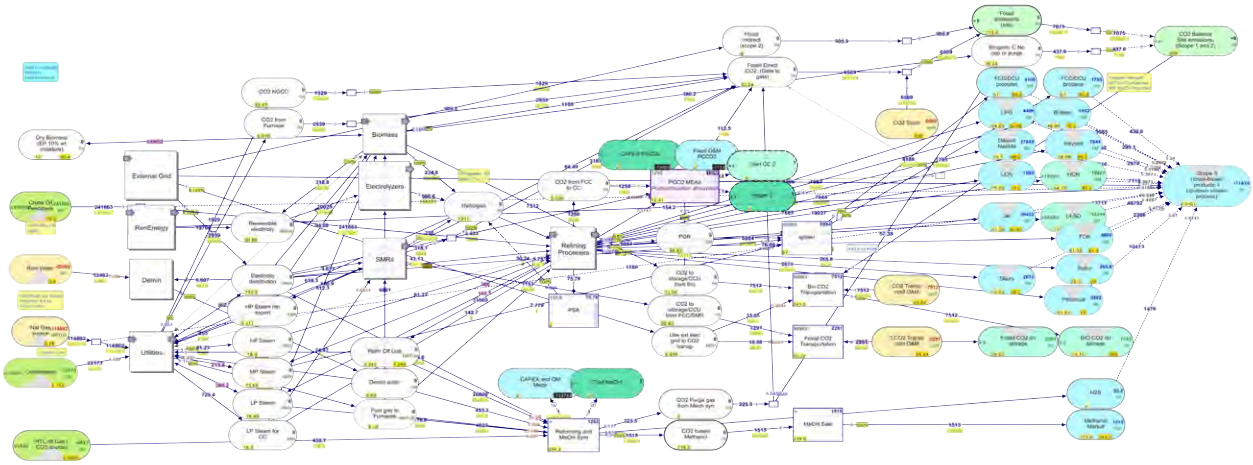


**Figure 2.** Modeled system in Linny-R. Main Layer view High complex refinery. Numbers displayed correspond to optimization result by 2050. Detailed layers in the supplementary material Apendix A.

**Table 2:** Parameters considered in the scenario of evaluation

| Parameter | 2020 | 2030 | 2040 | 2050 | Source |
|---|---|---|---|---|---|
| Natural Gas price, €/GJ | 4.5 | 8.6 | 9.2 | 9.8 | HC and MC Based on [8] |
| $CO_2$ market price, €/t | 0 | 90 | 160 | 200 | |
| $CO_2$ transport, pumping, and injection Cost, €/t | 26.7 | 3% LR | | | Based on [11] |
| $CO_2$ reduction target (scope 1 &2 minus carbon removals). | 0% | 25% | | Neutrality | Based on Ecopetrol targets and [12] |
| Syngas production via SMR | € 6850/t H2 based on [9] | | 1% LR | | Based on [11] |
| CCU. $CO_2$ to Methanol; Catalytic process. Capex | € 582/t based on source:[13] | 5% LR | | | Based on [14] and [15] |
| CCU. $CO_2$ to Methanol; Catalytic process. Yield | 51% Current | | | 60% (2050) | Based on [16] and [17] |

LR: Learning Rate. PV: Photovoltaic. €: 2020 euros

**Table 3:** Impacts on utility balance

| High Complexity | 2020 | 2030 | 2050 |
|---|---|---|---|
| Oil refinery throughput, kbld | 155 | 196 | 196 |
| Kty | 7718 | 9749 | 9749 |
| Refinery offgas as fuel, TJd | 24 | 0 | 0 |
| **Total Hydrogen Demand, t/d** | **221** | **306** | **518** |
| As feedstock, t/d | 221 | 306 | 306 |
| As fuel, t/d | 0 | 0 | 212 |
| **Total electricity demand, MWh** | **100** | **861** | **1007** |
| Renewables, MWh | 0 | 494 | 626 |
| **Total steam demand, kt/d** | **15** | **35** | **37** |
| **Raw water demand, kt/d** | **15** | **36** | **38** |
| **Dry Biomass, TJd** | **0** | **0** | **58** |

| Medium Complexity | 2020 | 2030 | 2050 |
|---|---|---|---|
| Oil refinery throughput, kbld | 240 | 242 | 242 |
| Kty | 11931 | 12034 | 12034 |
| Refinery offgas as fuel, TJd | 59 | 56 | 23 |
| **Total Hydrogen Demand, t/d** | **104** | **111** | **733** |
| As feedstock, t/d | 104 | 111 | 111 |
| As fuel, t/d | 0 | 0 | 622 |
| **Total electricity demand, MWh** | **157** | **210** | **1665** |
| Renewables, MWh | 0 | 12 | 1178 |
| **Total steam demand, kt/d** | **8** | **7** | **34** |
| **Raw water demand, kt/d** | **13** | **13** | **46** |
| **Dry Biomass, TJd** | **0** | **0** | **63** |

**Figure 3.** $CO_2$ emissions Balance. Sankey diagram

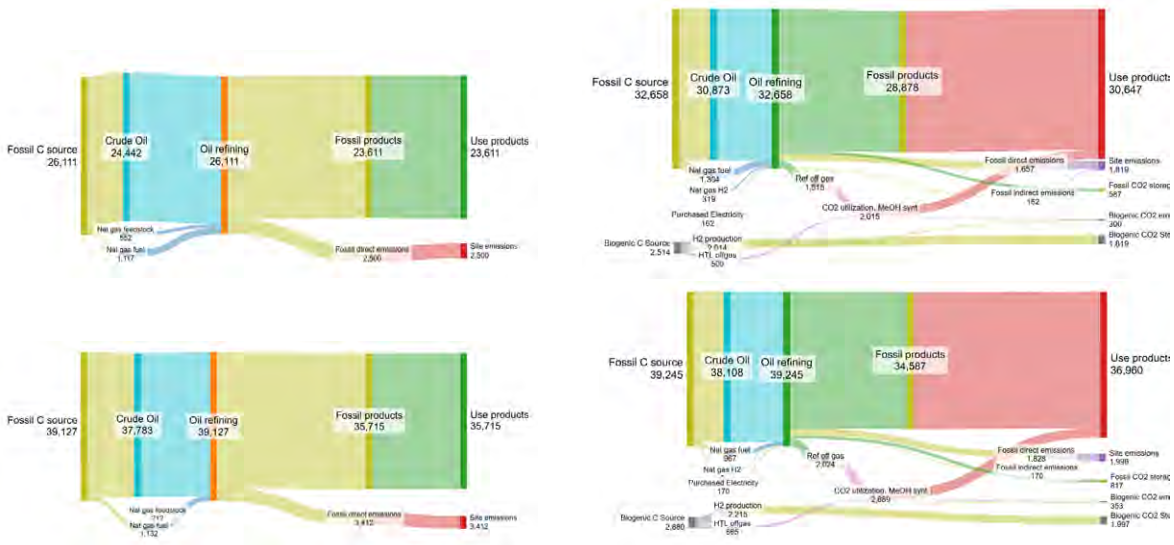



**Table 4:** CCU. Methanol production

| | High Complexity | | | | | Medium Complexity | | | | |
|---|---|---|---|---|---|---|---|---|---|---|
| | **2020** | **2025** | **2030** | **2040** | **2050** | **2020** | **2025** | **2030** | **2040** | **2050** |
| Net margin, €/bbl | 5.9 | 4.1 | 1.4 | 2.8 | 3.9 | 5.2 | 4.0 | 2.5 | 2.0 | 1.8 |
| MeOH synthesis production, t/d | 0 | 614 | 1291 | 982 | 1291 | 0 | 401 | 168 | 1024 | 1689 |
| Cost of methanol production. €/t | - | 339 | 333 | 311 | 307 | - | 335 | 338 | 354 | 366 |
| Cost of fossil-methanol production. €/t | 200 to 340 | *250 to 400 | 300 to 450 | 350 to 500 | †450 to 600 | | | | | |

€ euros 2020. * depending on natural gas prices and location. †due to carbon taxes and limited availability of fossil fuels.
Current Methanol cost of production. 307 €/t. Methanol, EUR (Europe): Methanol, export contract price, fob, Netherlands. [10]

Table 4 also highlights a potential profit opportunity, as the current cost of methanol production is competitive, falling within the same range of fossil-based methanol. In the middle and the long-term, our methanol is expected to be cheaper than the fossil-based methanol due to increasing carbon taxes [5] and the expected limited availability of fossil fuels, particularly in the region of this case study [8] and [9]; however, the current production cost is higher than the European cost ( +10% compared to Europe Methanol, export contract price, fob, Netherlands)[10].

## CONCLUSIONS

In this study, we conducted a comprehensive system analysis and optimization of introducing a CCU technology to produce methanol and olefins using surplus refinery fuel gas and HTL/FP off biogas in two Colombian oil refineries operating at different levels of complexity. The results revealed the significant impact of the refinery's complexity level on the scale and timeline required for implementing these technologies to achieve the committed $CO_2$ emissions reduction goals in the short and long term.

As shown in the results, the introduction of CCU technologies using surplus refinery fuel gas and biogenic CO2 source ( HTL/FP off biogas) enables long-term $CO_2$ emissions reduction for refineries. However, this transition generates a substantial financial cost, with a significant decrease in Net Margin (34% for high-complexity refineries and 65% for medium-complexity refineries). Furthermore, the adoption of CCU technologies significantly increases electricity demand, primarily due to renewable electricity requirements for water electrolyzers producing low-carbon hydrogen as a substitute for refinery fuel gas. Water and steam demand also rise considerably, driven by $CO_2$ capture units.

The results also indicate that both refineries can achieve scope 1 and scope 2 $CO_2$ neutrality by 2050 as modeled, assuming a favorable scenario. However, scope 3 $CO_2$ emissions increase due to the production of additional products like methanol through CCU processes. However, in contrast to the increased emissions associated with scope 3, the production of CO2-based methanol can result in a modest profit opportunity,

The production costs of the $CO_2$-based methanol presented in this study align with the projected cost range of electrochemical-methanol and are lower than current fossil-based methanol in the long term, thereby enhancing its economic competitiveness.

Finally, the results should be further verified against the existing capacities of the national electrical grid and

water supply in these specific areas, as well as the national expansion plans for both. Additionally, uncertainty analysis should be included in further works to evaluate the impact of it on the results.

## DIGITAL SUPPLEMENTARY MATERIAL

The supplementary material can be consulted at http://PSEcommunity.org/LAPSE with the LAPSE ID LAPSE:2025.0041

## ACKNOWLEDGEMENTS

The authors would like to thank Ecopetrol S.A., Instituto Colombiano del Petroleo y Energias de la Transition (ICPET), and VILLUM FONDEN (Danish research grant VIL51464) for the information provided and financial support. The views expressed in this paper do not necessarily reflect those of Ecopetrol S.A or the University.

## REFERENCES

1. C. Lindfors, D. C. Elliott, W. Prins, A. Oasmaa, and J. Lehtonen, "Co-processing of Biocrudes in Oil Refineries," *Energy and Fuels*, vol. 37, no. 2, pp. 799–804, 2023, doi: 10.1021/acs.energyfuels.2c04238.
2. E. Lozano Sanchez, E. López-Basto, and A. Ramírez, "TEA of co-processing refinery fuel gas and by-product gas from biomass thermochemical conversion for methanol synthesis," in *Escape 35*, 2025, p. 6.
3. M. J. Kaiser, "A review of refinery complexity applications," *Pet. Sci.*, vol. 14, no. 1, pp. 167–194, 2017, doi: 10.1007/s12182-016-0137-y.
4. E. L. Basto, G. Korevaar, and A. R. Ramírez, *Impact assessment of CO2 capture and low-carbon hydrogen technologies in Colombian oil refineries*, vol. 53. Elsevier Masson SAS, 2024. doi: 10.1016/B978-0-443-28824-1.50062-4.
5. IEA, "Global Energy and Climate Model," 2023.
6. E. López-Basto, G. Korevaar, S. E. Tanzer, and A. Ramírez, "Assessing the impacts of low-carbon intensity hydrogen integration in oil refineries," *Clean. energy Syst.*, vol. 9, no. October, 2024.
7. Solomon studies, "Ecopetrol refineries Solomon study," 2018.
8. Unidad de Planeación Minero Energética (UPME)., "ESTUDIO TÉCNICO PARA EL PLAN DE ABASTECIMIENTO DE GAS NATURAL," no. 69, 2020.
9. Boston Consulting Group, "Estrategia de Neutralidad de Carbono," 2021.
10. INTRATEC, "https://www.intratec.us," 2024. https://www.intratec.us
11. Ioannis Tsiropoulos, Dalius Tarvydas, and Andreas Zucker, *Cost development of low carbon energy technologies*, no. January. 2018. doi: 10.2760/490059.
12. EPA, "Scope 1 and Scope 2 Inventory Guidance," 2023.
13. J. T. Manalal, M. Pérez-fortes, and I. Gonzalez, "Evaluation of alternative carbon based ethylene production in a petrochemical cluster : Technology screening & value chain impact assessment," in *3rd European Symposium on Computer Aided Process Engineering*, 2023, vol. 52, pp. 2453–2458. doi: 10.1016/B978-0-443-15274-0.50390-5.
14. A. Babarit, J. Gilloteaux, and J. francois Hetet, "Energy and economic performance of the FARWIND energy system for sustainable fuel production from the far-offshore wind energy resource," in *2019 Fourteenth International Conference on Ecological Vehicles and Renewable Energies (EVER)*, 2019, no. April.
15. R. J. Detz, C. J. Ferchaud, A. J. Kalkman, and M. V Shinde, "Electrochemical CO2 conversion technologies: state-of-the-art and future perspectives," *Sustain. Energy Fuels*, 2023, doi: 10.1039/D3SE00775H.
16. T. Ren, M. K. Patel, and K. Blok, "Petrochemicals from oil , natural gas , coal and biomass : Production costs in 2030 – 2050," *Resour. Conserv. Recycl.*, vol. 53, pp. 653–663, 2009, doi: 10.1016/j.resconrec.2009.04.016.
17. M. R. Gogate, "Methanol-to-olefins process technology : current status and future prospects," *Pet. Sci. Technol.*, vol. 37, no. 5, pp. 559–565, 2019, doi: 10.1080/10916466.2018.1555589.

© 2025 by the authors. Licensed to PSEcommunity.org and PSE Press. This is an open access article under the creative commons CC-BY-SA licensing terms. Credit must be given to creator and adaptations must be shared under the same terms. See https://creativecommons.org/licenses/by-sa/4.0/



Systems & Control Transactions

**Research Article - Peer Reviewed Conference Proceeding**
ESCAPE 35 - European Symposium on Computer Aided Process Engineering
Ghent, Belgium. 6-9 July 2025
Jan F.M. Van Impe, Grégoire Léonard, Satyajeet S. Bhonsale,
Monika E. Polańska, Filip Logist (Eds.)

PSE PRESS

# Surrogate Model-Based Optimization of Pressure-Swing Distillation Sequences with Variable Feed Composition

**Laszlo Hegely*, Peter Lang**

Budapest University of Technology and Economics, Department of Building Services and Process Engineering, Budapest, Hungary
* Corresponding Author: hegely.laszlo@gpk.bme.hu.

## ABSTRACT

Pressure-swing distillation (PSD) is a frequently applied method to separate pressure-sensitive azeotropic mixtures; however, its energy demand is very high. In continuous mode, PSD is performed in a system consisting of a high- and a low-pressure column. If the composition of the feed is between the azeotropic compositions at the two pressures, it can be introduced into any of the columns, leading to two possible column sequences. Depending on the feed composition, one of the sequences is optimal whether in terms of energy demand or total annual cost (TAC). In the present work, surrogate model-based optimization is applied to determine the optimal TAC value as a function of the feed composition between the azeotropic ones. As a first step, the column sequence with feeding into the high-pressure column is studied here. The mixture to be separated consists of water and ethylenediamine, which form a maximum-boiling azeotrope. The columns are modeled separately and a large number of simulations are performed in points generated by Latin hypercube sampling, then, algebraic surrogate models are fitted to the simulation results. The resulting surrogate optimization problem is solved for different feed composition values and the accuracy of the models is verified by rigorous simulations, as well. The energy cost and TAC has a maximum as a function of the composition. The error of the estimation of TAC remains under 6 % except at the lowest water concentration studied.

**Keywords**: Distillation, Machine Learning, Modelling and Simulations, Optimization, Surrogate Model

## INTRODUCTION

For separating azeotropic mixtures, special distillation methods must be used, such as pressure-swing (PSD), extractive or heteroazeotropic distillation. The advantage of PSD is that it does not require the addition of a new component. However, it can only be applied if the azeotrope is pressure-sensitive, and its energy demand can also be high. The configuration of the system depends on not only the type of the homoazeotrope but also the feed composition (z). If z is between the azeotropic compositions at the pressures of the columns, the feed can be introduced into either the low- (LP-HP sequence) or the high-pressure column (HP-LP sequence). Depending on the value of z, one of the sequences will be optimal, whether with respect to energy demand or total annual cost (TAC).

Optimization of PSD systems is typically performed either by local methods (e.g. [1]) that might fail in finding the global optimum or by global, evolutionary algorithms (e.g. genetic algorithm, GA), which, however, require a large number of simulations. A potential approach to reduce the computational intensity is surrogate model-based optimization (SMBO), where the objective function is estimated with surrogate models fitted to the results of simulations. To the best of our knowledge, SMBO was only applied to optimize PSD systems by Bubel et al. [2] and Karaman et al. [3].

Bubel et al. [2] minimized the total energy demand of the separation of the maximum-boiling azeotropic mixture acetone-chloroform. They applied artificial neural networks as surrogate models, but did not consider the geometrical parameters (numbers of trays, feed locations) as optimization variables, only the operational ones. Two SMBO approaches were tested: fitting the models to individual columns or to the whole flow-sheets, with the first approach showing better results.

Karaman et al. [3] studied the separation of a maximum-boiling azeotropic mixture water-ethylenediamine by PSD, where z (35 mol% water) was between the azeotropes at 0.1 and 2.02 bar. The TAC of both sequences was minimized without and with heat integration. The LP-HP sequence was more favorable at this composition. The optimization was performed by two methods: a GA and SMBO. By SMBO, algebraic surrogate models were fitted to simulation results of the whole flow-sheet by the ALAMO software [4] and the resulting optimization problem was solved. Different decomposition techniques were tested with the models fitted (1) to elements of TAC (heat duty of LPC, column diameters), (2) to capital and energy costs or (3) to TAC itself. The best results were achieved with the highest level of decomposition. Although the TAC obtained by SMBO was lower than that of GA only once, the difference was always within 5 %.

In this work, our aim is to (1) improve the accuracy of surrogate models, thus, the performance of SMBO and (2) study the influence of z on the optimum of the HP-LP sequence, using the case study of Karaman et al. [3]. The first goal is achieved by fitting the models to the results of the single columns instead of the two-column system. Achieving the second goal requires repeated optimization at different feed compositions, which would be very time-consuming with conventional optimization methods. However, an advantage of SMBO is that z can be included as an input variable of the models. This enables quickly finding the optimum for any feed composition. By performing the optimization for the LP-HP in a future work, it will be possible to determine for both column sequences the range of z where the given sequence is optimal.

The novelty of our work consists of determining the optimal PSD system for the first time as a function of the feed composition by SMBO. Additionally, this is the first work that uses ALAMO to fit the models to be used in the optimization to the individual columns since Karaman et al. [3] fitted them to the two-column system. While Bubel et al. [2] did the model fitting to the individual columns, they only considered operational parameters as optimization variables.

## PROCESS DESCRIPTION

Water(A) and ethylenediamine(B) form a maximum-boiling azeotrope below 4-4.5 bar. The azeotrope is pressure-sensitive, with its A content decreasing from 44.1 mol% at 0.10 bar to 25.6 % at 2.02 bar. The phase equilibrium calculations were performed by UNIQUAC [3].

The flow rate of the feed is F=100 kmol/h; its pressure and temperature are 2.02 bar and 46.85 °C, respectively. Its composition is assumed to be able to vary roughly between the two azeotropic compositions: $0.27 \leq z \leq 0.44$. Both components must be recovered with a purity of 99.5 %.

The feed is introduced into either the high- (HPC, 2.02 bar) or the low-pressure column (LPC, 0.101 bar), leading to the two column sequences HP-LP and LP-HP (Figure 1). Both columns have a pressure drop of 2.74 mbar/tray. (Note that Karaman et al. [3] used constant pressure drop values of 0.2407 and 0.0492 bar for HPC and LPC, respectively.) A is obtained as the distillate of HPC ($D_{HP}$). The bottom product's composition is close to the azeotropic one at the column pressure, and it is fed into LPC, where B is produced as distillate ($D_{LP}$). The bottom product is then led to HPC. The distillate flow rates can be calculated from the material balances written for the feed and the distillates as linear functions of z:

$$D_{HP} = F - D_{LP} \tag{1}$$

$$D_{LP} = F \frac{x_{DHP} - z}{x_{DHP} - x_{DLP}} \tag{2}$$

According to the purity specifications, the concentration A in $D_{HP}$ and $D_{LP}$ is $x_{DHP}$=0.995 and $x_{DLP}$=0.005, respectively.

In the present work, since only the HP-LP sequence is studied, the bottom product of LPC can be considered as a recycle stream ($F_{rec}=W_{LP}$).

## CALCULATION METHOD

Simulation of the individual columns or the whole PSD process is performed with the professional flowsheet simulator CHEMCAD 7.

The total annual cost (TAC) is calculated from the total capital (TCC) and total energy cost (TEC) [1, 5]:

$$TAC = \frac{TCC}{PBP} + TEC \tag{3}$$

where PBP=3 y is the payback period. The capital cost includes the cost of the columns, condensers and reboilers. The energy cost is the cost of the low- and middle-pressure heating steam used to heat the reboiler of LPC and HPC, respectively. A detailed description of the cost calculation is given in Ferchichi et al. [5].

Apart from the numbers of theoretical trays ($N_{HP}$, $N_{LP}$), which are input parameters, the following results are needed for the calculation of TAC: the column diameters ($Di_{HP}$, $Di_{LP}$), the condenser ($Q_{cHP}$, $Q_{cLP}$) and reboiler heat duties ($Q_{rHP}$, $Q_{rLP}$) and temperature of the bottom products ($T_{WHP}$ and $T_{WLP}$). (The temperatures of the distillates are also required to calculate the condenser areas, but they are constant due to the specified purities.) Therefore, surrogate models are fitted to the above results to calculate an estimation of TAC.

Contrary to our previous work [3], the two columns are modelled separately for the fitting of the surrogate models. An overview of the surrogate model system is

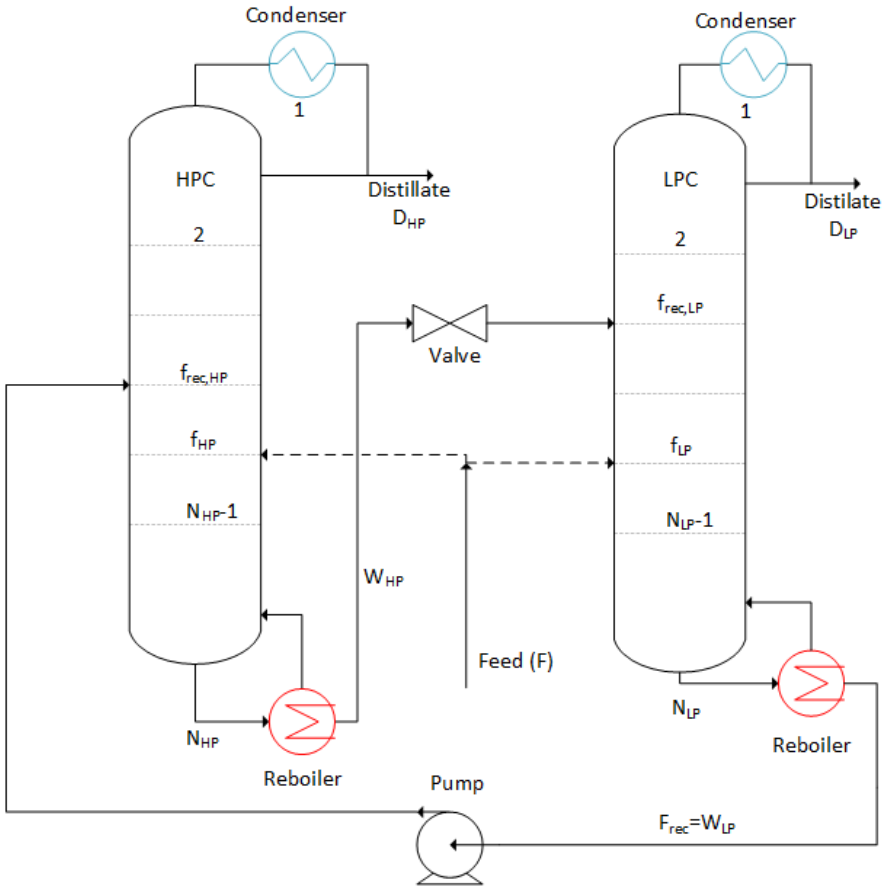



**Figure 1:** Common flow-sheet of the column sequences HP-LP and LP-HP. Depending on the sequence, the feed is either introduced into HPC or LPC (shown by dashed line)

shown in Figure 2. Symbols with * denote values calculated from surrogate models. The input variables for both columns are the number of trays, $F_{rec}$, the composition of the bottom product of LPC ($x_{WLP}$) and z. The flow rate ($W_{HP}$) and composition ($x_{WHP}$) of the feed of LPC are calculated by material balances from $F_{rec}$, $x_{WLP}$ and $D_{LP}$. For both columns, 500-500 points are generated in the four-dimensional space of the input variables by using Latin hypercube sampling (LHS). The ranges of the input variables are given in Table 1. In each point, the column is simulated with the distillate composition and bottom product flow rate as column specifications. For the given input variables, the optimal feed locations are determined by minimizing the reboiler heat duty. Initial locations are set as $f_{rec}=0.1324 \cdot N_{HP}$, $f_{HP}=0.8971 \cdot N_{HP}$, and $f_{rec,LP}=0.2778 \cdot N_{LP}$ based on the optimal values of Karaman et al. [3]. The feed locations are then varied (in the case of HPC, one by one) until reaching the minimum of the heat duty. This procedure guarantees optimal feed locations while eliminating them as input variables, thereby reducing the dimensionality of the surrogate models.

By using ALAMO, algebraic surrogate models are fitted to $Q_{rHP}$, $Di_{HP}$, $Q_{cLP}$, $Q_{rLP}$ and $Di_{LP}$ as functions of the four input variables by minimizing the Bayesian information criterion or, in the case of the mean square error. ALAMO is permitted to select, apart from a constant value, linear, exponential, logarithmic and polynomial functions of the variables, as well as different powers of the binary or tertiary products and ratios of the variables. Models of the diameters are forced to be integer or half-integer values in feet, as CHEMCAD calculates discrete values of diameters. $Q_{cHP}$ is expressed as a linear function of $Q_{rHP}$. In order to be able to estimate the bottom product temperatures of the columns, it is also necessary to describe them by surrogate models. 400 boiling point values are generated by combining 20 pressure and 20 water concentration values. The pressure range is determined by calculating the minimum and maximum possible pressure drops from the range of N used. The concentration ranges used are $0.26 \leq x_{WHP} \leq 0.34$ and $0.40 \leq x_{WLP} \leq 0.44$. ALAMO is then used to fit models to the boiling points.

With the surrogate models, it is possible to calculate TAC*, an estimation of TAC, and minimize it for different values of z. The optimization problem can be written as:

$$\min_{N_{HP},N_{LP},F_{rec},x_{WLP}} TAC^*(N_{HP},N_{LP},F_{rec},x_{WLP},z) \qquad (4)$$

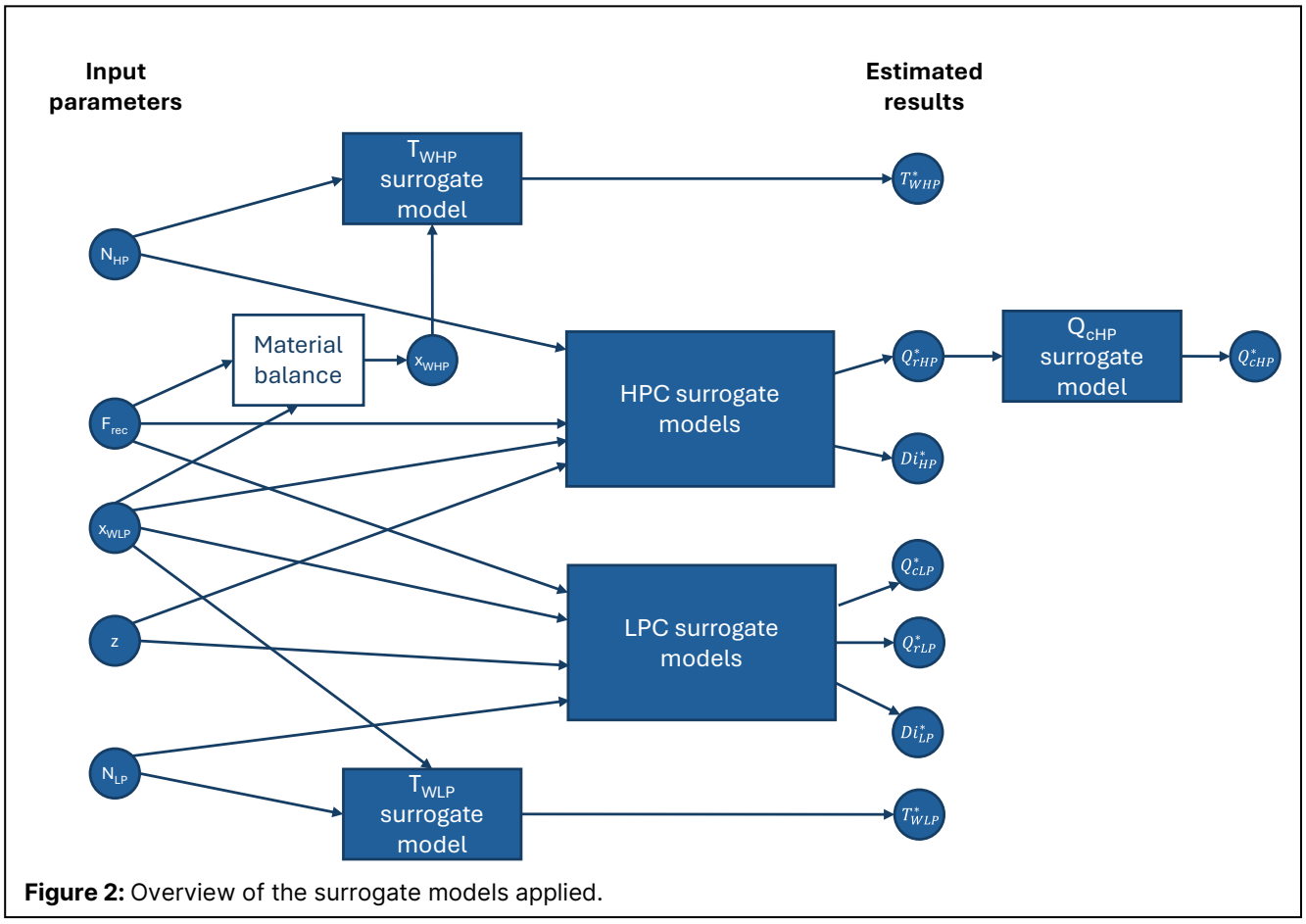



**Figure 2:** Overview of the surrogate models applied.

**Table 1:** Ranges of the input variables used for surrogate model fitting.

| Variable | Minimum | Maximum |
|---|---|---|
| $N_{HP}$ | 50 | 100 |
| $N_{LP}$ | 15 | 60 |
| $F_{rec}$, kmol/h | 80 | 220 |
| $x_{WLP}$ | 0.42 | 0.44 |
| z | 0.27 | 0.43 |

The only constraints of the problem are the lower and upper bounds of the variables (Table 1) to avoid extrapolation with the surrogate models. The optimization problem is solved by sequential quadratic programming in Maple.

After solving the surrogate optimization problem, it is necessary to check the results by creating a three-dimensional plot of TAC* as the function of two variables. This can also help with the identification of local optima, but its most important aim is the following. It often occurs that the value of one or more variables is on the lower or upper bound. This might mean that the (constrained) optimum is truly on said bound, indicating that it is necessary to extend the range of the variable as the true optimum lies outside the current range. However, this can also be an artefact of the surrogate models, which can have a large error close to the bounds, where the concentration of simulation points is lower. If the direction of the errors improves the objective function, an erroneous optimum can be found. This can be prevented by the above graphical analysis and, if necessary, the application of a constraint to exclude the problematic region.

## RESULTS

Karaman et al. [3] optimized the process at z=0.35 both by using a GA and SMBO (Table 2). The SMBO process was followed by determining the optimal feeding locations, as well. Note that the results are not completely comparable to the ones obtained here since they used constant pressure drop values.

In the present work, out of the 500 simulations, 408 converged in the case of HPC and 264 in the case of LPC. The size (number of elements), the adjusted coefficients of determination ($\bar{R}^2$) and root mean square error (RMSE) of the models are given in Table 3.

The linear model of $Q_{cHP}$ and those of the bottom temperatures have a very good fit. The $\bar{R}^2$ values of the other heat duties are relatively high, as well. The least good fit occurs by the column diameters. However, for the majority of the data points, the error of the diameter is only one or two sizes.

**Table 2:** Optimization results of Karaman et al. [3] for z=0.35.

| | GA | SMBO |
|---|---|---|
| $N_{LP}$ | 68 | 72 |
| $F_{rec}$, kmol/h | 161.1 | 184.8 |
| $N_{LP}$ | 36 | 35 |
| $x_{WLP}$ | 0.435 | 0.424 |
| TCC, $10^6$ $ | 1.901 | 1.992 |
| TEC, $10^6$ $/y | 1.989 | 2.045 |
| TAC, $10^6$ $/y | 2.622 | 2.709 |

**Table 3:** Ranges of the input variables used for surrogate model fitting.

| Variable | Model size | $\bar{R}^2$ | RMSE |
|---|---|---|---|
| $Q_{cHP}$ | 2 | 0.998 | 296 MJ/h |
| $Q_{rHP}$ | 37 | 0.962 | 1100 MJ/h |
| $Di_{HP}$ | 21 | 0.679 | 0.122 m |
| $Q_{cLP}$ | 24 | 0.909 | 980 MJ/h |
| $Q_{rLP}$ | 26 | 0.896 | 981 MJ/h |
| $Di_{LP}$ | 11 | 0.635 | 0.177 m |
| $T_{WHP}$ | 7 | 1.00 | $2.93 \cdot 10^{-4}$ °C |
| $T_{WLP}$ | 13 | 1.00 | $6.34 \cdot 10^{-5}$ °C |

The optimization problem is solved for 9 different z values. Table 4 shows the optimal values of the optimization variables. $N_{HP}$ and $F_{rec}$ do not show a monotonous variation; their values are notably higher at z≥0.35. $F_{rec}$ gradually decreases above this value, but both variables clearly show a decrease when approaching z=0.43. $N_{LP}$ always equals 25 except for z=0.35. It must be noted that it was necessary to use a constraint of $N_{LP}$≥20 to avoid false optima at 15, the lower bound $N_{LP}$. $x_{WLP}$ also reached its lower bound at z≤0.29 and z≥0.37. However, this seems not to be due to a particularly high error of TAC*, indicating that it would be necessary to decrease the lower bound of $x_{WLP}$ when performing LHS. As shown in Figure 3 for z=0.35, it seems that two local optima exist, one at $x_{WLP}$=0.42 and another around $x_{WLP}$≈0.43. One of these is found at every z value.

**Table 4:** Optimal values of the optimization variables as a function of z, determined by SMBO.

| z | $N_{HP}$ | $F_{rec}$, kmol/h | $N_{LP}$ | $x_{WLP}$ |
|---|---|---|---|---|
| 0.27 | 68 | 156.8 | 25 | 0.42 |
| 0.29 | 69 | 155.4 | 25 | 0.42 |
| 0.31 | 65 | 148.8 | 25 | 0.4296 |
| 0.33 | 65 | 152.8 | 25 | 0.4296 |
| 0.35 | 75 | 189.9 | 26 | 0.4295 |
| 0.37 | 75 | 187.4 | 25 | 0.42 |
| 0.39 | 76 | 179.9 | 25 | 0.42 |
| 0.41 | 71 | 169.4 | 25 | 0.42 |
| 0.43 | 67 | 150.1 | 25 | 0.42 |

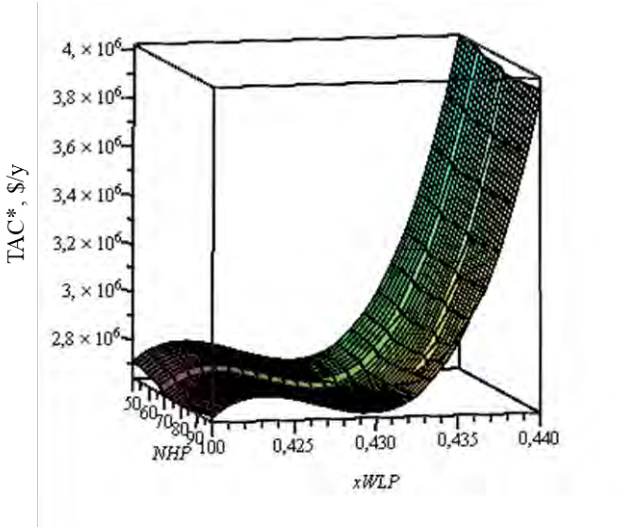



**Figure 3.** TAC* as a function of $N_{HP}$ and $x_{WLP}$ at z=0.35, $F_{rec}$=189.9 kmol/h and $N_{LP}$=26.

Figure 4 shows the costs calculated with the surrogate models in the optima given in Table 4 with dashed curves. At each z value, a simulation is also performed with the optimal values, and the costs are also calculated from the simulation results (shown with continuous curves). TCC* has a maximum as a function of z at z=0.35, but it hardly changes between 0.35 and 0.41. TEC* also has a maximum, but at a much higher value: z=0.41. Below z=0.33, a considerable increase can be observed on the increase of z. Due to the small changes in TCC*, the behavior of TAC* is similar to that of TEC* with a maximum at z=0.41.

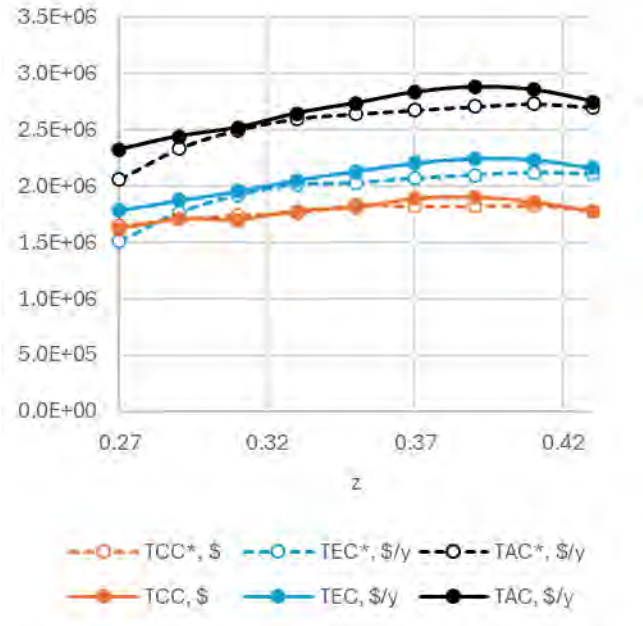



**Figure 4.** Estimated and rigorously calculated costs in the determined optima as functions of z.

The rigorously calculated TCC also shows a limited variation only, mostly explained by changes in $Di_{HP}$, and a maximum of z=0.39. Both TEC and TAC behave similarly to their estimated values, but their maxima are more pronounced and occur at a lower z value, also at z=0.39. The maximum in TEC, and thus in TAC, can be explained by the fact as z increases, more distillate has to be produced in HPC and its heat duty increases, while that of LPC decreases. It must be noted that these TAC values are probably not optimal, only approximations of the optima.

Comparing the estimated and rigorously calculated cost, it can be seen that the error of TCC is relatively low at all z values, with a maximum of 4 % at z=0.39. The error of TEC is low around z=0.32 and 0.43, and it is always below 7 % except at z=0.27 (15 %). The accuracy of TAC is similar to that of TEC. Its error is 11 % at z=0.27, but lower than 6 % otherwise. TEC and TCC are always underestimated by the surrogate models, but this is the case by TCC.

The values of $N_{HP}$ and $F_{rec}$ determined by Karaman et al. [3] by SMBO (Table 2) are close to the ones obtained here, while the values by GA are similar to those calculated for z ≤0.33. $N_{LP}$ is considerably higher by both methods. The $x_{WLP}$ value obtained here is between that of GA and SMBO. Karaman et al. [3] achieved a TAC lower by 1.0 % by SMBO and 4.2 % by GA. The error of TAC estimated by the surrogate models was 3.7 % compared to 3.5 % in this work.

## CONCLUSIONS

The separation of maximum-boiling azeotropic mixture, water-ethylenediamine by pressure-swing distillation (PSD) was studied. The feed composition (z) was between the azeotropic compositions at the pressures of the columns. From the two possible column sequences, the HP-LP one is studied, where the feed is introduced into the high-pressure column (HPC). The total annual cost (TAC) of the PSD system was previously minimized by Karaman et al. [3] for a given feed composition (z=35 mol% water) using a genetic algorithm and surrogate-model based optimization (SMBO). By the latter method, surrogate models were fitted to a large number of simulation results of the two-column system.

In the present work, SMBO was applied by fitting the models to the results of the individual columns. Another novelty was that z was now included as an input variable of the models. The other input variables were the numbers of trays of the columns and the molar flow rate and water content of the bottom product of the recycle stream, that is, the bottom product of the low-pressure column. Using the surrogate models, it was possible to estimate TAC. The resulting surrogate optimization was solved for different values of z. The accuracy of the estimated TAC was verified by rigorous simulations, as well. The energy cost (TEC) and TAC had a maximum as a function of the composition. The capital cost was estimated with a maximal error of 4 %. The errors were higher for TEC and TAC. In the case of TAC, the error of the estimation of TAC remained under 6 % except at the lowest water concentration studied. The minimal TAC at z=35 % found in this work is only by 1 % higher than the SMBO result of Karaman et al. [3] and 4 % than the optimal value found by the genetic algorithm. In conclusion, the accuracy of the SMBO method is acceptable.

In the future, the SMBO of the LP-HP sequence will be performed, as well. This will make it possible to determine for both column sequences the range of z where the given sequence is optimal.

## ACKNOWLEDGEMENTS

This research was funded by the National Research Development and Innovation Fund of Hungary (grant numbers TKP2021-EGA-02, OTKA FK-143059).

## REFERENCES

1. Li R, Ye Q, Suo X, Dai X, Yu H. Heat-Integrated Pressure-Swing Distillation Process for Separation of a Maximum-Boiling Azeotrope Ethylenediamine/Water. *Chem Eng Res Des* 105:1-15 (2016) https://doi.org/10.1016/j.cherd.2015.10.038
2. Bubel M, Ludl PO, Seidel T, Asprion N, Bortz M. A Modular Approach for Surrogate Modeling of Flowsheets. *Chem Ing Tech* 93:1987–1997 (2021) https://doi.org/10.1002/cite.202100077
3. Karaman ÖF, Lang P, Hegely L, Optimisation of pressure-swing distillation of a maximum-azeotropic mixture with heat integration. *Energy* 320:135190 (2025) https://doi.org/10.1016/j.energy.2025.135190
4. Cozad A, Sahinidis NV, Miller DC. Learning surrogate models for simulation-based optimization. *AIChE J* 60:2211–2227 (2014) https://doi.org/10.1002/aic.14418
5. Ferchichi M, Hegely L, Lang P, Economic and environmental evaluation of heat pump-assisted pressure-swing distillation of maximum-boiling azeotropic mixture water-ethylenediamine. *Energy* 239:122608 (2022) https://doi.org/10.1016/j.energy.2021.122608

© 2025 by the authors. Licensed to PSEcommunity.org and PSE Press. This is an open access article under the creative commons CC-BY-SA licensing terms. Credit must be given to creator and adaptations must be shared under the same terms. See https://creativecommons.org/licenses/by-sa/4.0/



Systems & Control Transactions

**Research Article - Peer Reviewed Conference Proceeding**
ESCAPE 35 - European Symposium on Computer Aided Process Engineering
Ghent, Belgium. 6-9 July 2025
Jan F.M. Van Impe, Grégoire Léonard, Satyajeet S. Bhonsale,
Monika E. Polańska, Filip Logist (Eds.)

PSE PRESS

# Economic Evaluation of Solvay Processes for Sodium Bicarbonate Production with Brine and Carbon Tax considerations

**Dina Ewis, Zeyad M. Ghazi, Sabla Y. Alnouri*, Muftah H. El-Naas**

Gas Processing Center, College of Engineering, Qatar University, Doha, Qatar
* Corresponding Author: sabla@qu.edu.qa

## ABSTRACT

Reject brine discharge and high $CO_2$ emissions from desalination plants are major contributors to environmental pollution. Managing reject brine involves significant costs, mainly due to the energy-intensive processes required for brine dilution and disposal. In this context, Solvay process represents a mitigation scheme that can effectively reduce reject brine salinity and sequestering $CO_2$ while producing sodium bicarbonates simultaneously. The Solvay process represents a combined approach that can effectively manage reject brine and $CO_2$ in a single reaction while producing an economically feasible product. Therefore, this study reports a systematic techno-economics assessment of conventional and modified Solvay processes, while incorporating brine and carbon tax. The model evaluates the significance of implementing a brine and $CO_2$ tax on the economics of conventional and $Ca(OH)_2$ modified Solvay compared to industries expenditures on brine dilution and treatment before discharge to the sea. The results show that the conventional Solvay process becomes profitable after applying a brine tax of 1 dollar per meter cube of brine and a $CO_2$ tax of 42 dollars per tonne $CO_2$ —both figures lower than the current costs associated with brine treatment and existing carbon taxes. Moreover, the profitability of the $Ca(OH)_2$-modified Solvay process increases even further with minimal brine and $CO_2$ taxes. The findings highlight the significance of adopting modified Solvay process as an integrated solution for sustainable brine management and carbon capture.

**Keywords**: Solvay Process, Brine Management, Carbon Dioxide Capture, Carbone Tax.

## INTORODUCTION

Carbon dioxide ($CO_2$) is a major contributor to climate change that is responsible for the considerable temperature rise. Considering the current fossil fuels consumptions, it is expected that by 2050, the $CO_2$ emission would reach 50 gigiatons per years that would cause the global temperature to increase by 2.5 °C [1]. However, implementing carbon pricing policies and technologies would limit the temperature increase to 1.5 and the $CO_2$ emission to 20 gigatons per year [2]. In addition, desalination plants produce tremendous amounts of reject brine of a concentration of 70 g/L, which is 20 times higher than the natural seawater concentration. This would cause direct harm to the aquatic species leading to serious consequences for the marine environment. In this context, Solvay process is a combined approach that can effectively mitigate $CO_2$ and reject brine in a single reaction. The traditional method involves the reaction of $CO_2$ and reject brine in the presence of Ammonia ($NH_3$) as a reagent to produce sodium bicarbonates ($NaHCO_3$). Then, $NH_3$ is recovered from the reactor effluents through the effluent reaction with calcium hydroxide $Ca(OH)_2$. The traditional Solvay process can effectively reduce the water salinity and $CO_2$ content by more than 30% and 80%, respectively [3]. The traditional Solvay process reactions are shown by equations 1 and 2.

$$NaCl + NH_3 + CO_2 + H_2O \leftrightarrow NaHCO_3 + NH_4Cl \quad (1)$$

$$2NH_4Cl + Ca(OH)_2 \rightarrow CaCl_2 + 2NH_3 + 2H_2O \quad (2)$$

Despite that, the traditional Solvay process utilizes $NH_3$ as a reagent, which is an environmentally hazardous

chemical besides it is high recovery cost. To mitigate this problem, El-Naas et al [4] proposed the use of $Ca(OH)_2$ as a reagent instead of NH3 to minimize the environmental footprint and the process cost (equation 3). The proposed $Ca(OH)_2$ modified Solvay process showed a $CO_2$ and reject brine salinity reduction percentages of 99% and 35%, respectively.

$$2NaCl + 2CO_2 + Ca(OH)_2 \leftrightarrow 2NaHCO_3 + CaCl_2 \quad (3)$$

In this work, the economic feasibility of the conventional and $Ca(OH)_2$ modified Solvay are evaluated. The model evaluates the influence of different brine salinity on the process performance in terms of $CO_2$ and salinity reduction, product production, and process profitability. Furthermore, the process profitability with implementing carbon and brine taxes is investigated.

## METHODOLOGY

Reject brine is mixed with an alkaline reagent in a mixer. The mixer is introduced into a bubble column (BR) in the case of conventional Solvay; Whereas in case of $Ca(OH)_2$ modified Solvay, the mixture is fed into a novel inert particle spouted bed reactor (iPSBR) developed by Muftah et al.[5]. Inside the reactor, the $CO_2$ is reacted with the mixture to produce $NaHCO_3$ and byproducts. The effluent from the reactor is introduced into filter to separate $NaHCO_3$ from low salinity water. However, in case of conventional Solvay, the effluent is introduced into a recovery reactor to recover $NH_3$ through the reaction of the effluent with $Ca(OH)_2$, which is an energy intensive process. The block flow diagram of the two processes is shown in Figure 1. The mathematical model of the conventional and $Ca(OH)_2$ modified Solvay processes including mass balance, energy consumption, and costing are shown in our previous study[3].

## Constraints and assumptions

The process is considered to be steady stead without any side reactions taking [4]. Also, flue gas is assumed to be ideal gas, and the main constituent of the brine is sodium (Na). Moreover, the plant lifetime is set to 20 years. Table 1 shows the parameter used in the model obtained from experimental data [4, 6]. The current market chemical price for $NH_3$, $Ca(OH)_2$ and $NaHCO_3$ are around 9.81$/kg, 0.11 $/kg and 0.28 $/kg, respectively [7].

**Table 1.** List of experimental parameters used in the model.

| Parameters | Conventional Solvay | $Ca(OH)_2$ modified Solvay |
|---|---|---|
| Brine mass flow rate (kg/min) | 1000 | |
| Reagent wt% | 25 | 2 |
| Flue gas wt% | 17 | 17 |
| BR/iPSBR conversion | 0.86 | 0.6 |
| Reactor temperature (°C) | 20 | |
| $NH_3$ recovery unit conversion | 1 | - |
| Reactor resistance time (minutes) | 20 | |
| Reagent to sodium ratio | 0.03 $NH_3$: NaCl (Mass ratio) | 0.3 $Ca(OH)_2$: NaCl (Molar ratio) |
| Recovery molar ratio | 2 $Ca(OH)_2$: $NH_4Cl$ | - |

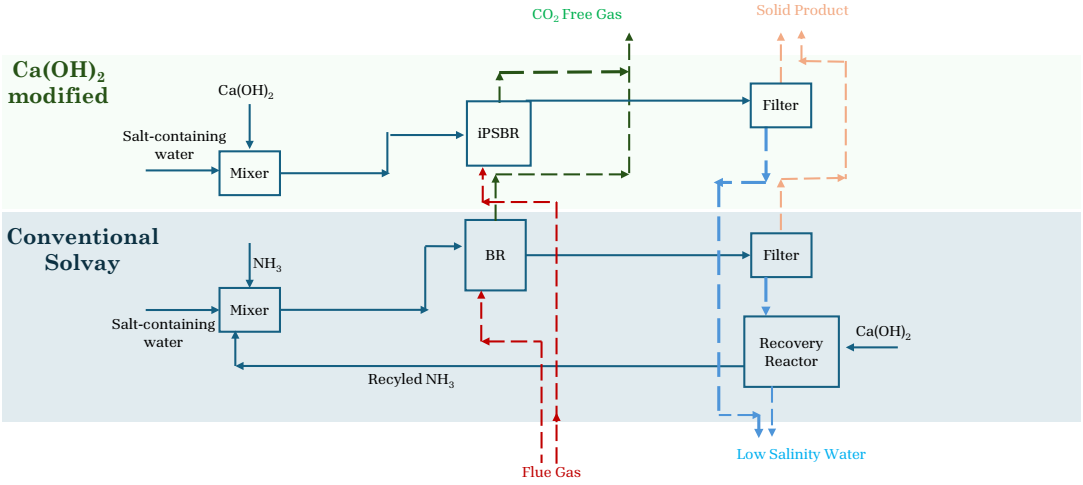



**Figure 1**. Block flow diagram of Conventional and $Ca(OH)_2$ modified Solvay processes.

## RESULTS AND DISCUSSION

The $CO_2$ and sodium reduction percentages as well as the associated profit at different brine water salinities for conventional and $Ca(OH)_2$ modified Solvay processes are shown in Figure 2. It can be observed from Figure 2a that the CO2 removal percentage at brine salinity of 30 g/L, which is sea water quality, attain a CO2 and sodium removal of around 33% and 30%, respectively. The associated expenses is around 10 $\$/m^3_{of\ brine}$ which is mainly due to the low amount of $NaHCO_3$ produced at the indicated water salinity. At water salinity 70 g/L and 90 g/L, the $CO_2$ removal percentage is constant at around 80%, while the sodium removal percentage decreases from around 33% to 22%. In addition, the associated profit is negative and constant at -6 $\$/m^3_{of\ brine}$, which indicates that the conventional Solvay requires expenses to be operated. The constant profit value is mainly due to the constant production rate of $NaHCO_3$ that is also confirmed by the constant consumption of $CO_2$.

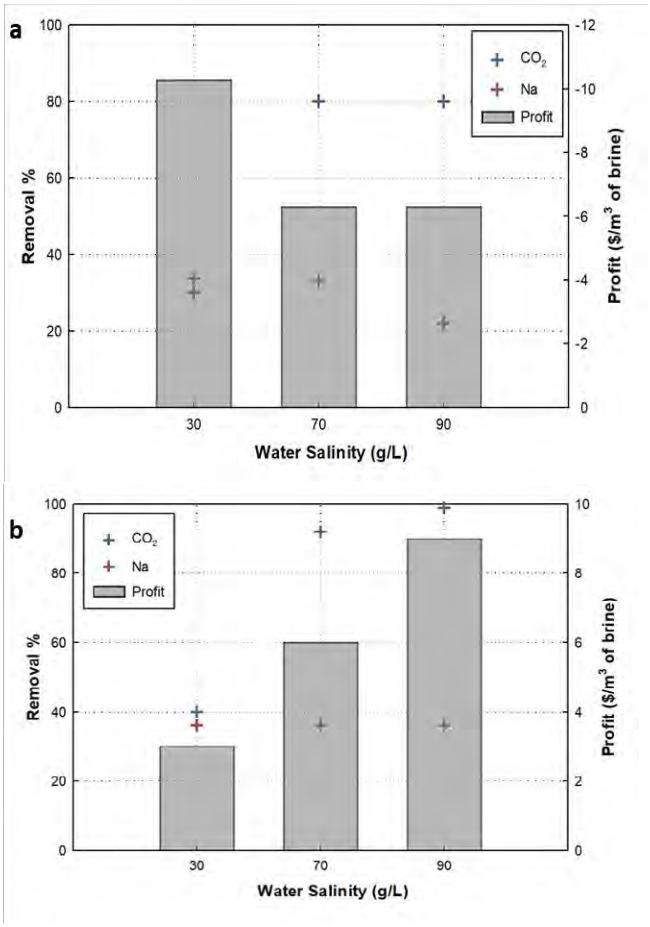



**Figure 2.** The Sodium, $CO_2$ reduction and process profitability of (a) conventional (b) $Ca(OH)_2$ modified Solvay.

On the other hand, it can be seen from Figure 2b that the $Ca(OH)_2$ modified Solvay that $CO_2$ removal increases from 40% to around 99% as the water salinity increases from 30 g/L to 90 g/L; yet the sodium removal is constant at 36%. This is due to the fact that the experimental data utilized the optimized $Ca(OH)_2$:NaCl molar ratio for the maximum sodium removal as indicated in Table 1. Yet, the associated profit is positive and increases from 3 $\$/m^3_{of\ brine}$ to around 9 $\$/m^3_{of\ brine}$. This is mainly due to the rise in $NaHCO_3$ production rate as the brine salinity increases and this is confirmed by the increase in $CO_2$ removal%. These results underscore the economic viability of the $Ca(OH)_2$ modified Solvay besides its high sodium and $CO_2$ reduction percentages for different water quality that varies from sea level salinity up to reject brine salinity level.

The results demonstrated above confirmed the economic feasibility of $Ca(OH)_2$ modified Solvay besides it superb $CO_2$ and sodium reduction percentage. Therefore, implementing $CO_2$ and/or brine tax will further increase the process profitability. Thus, herein, the influence of $CO_2$ and brine tax on the conventional Solvay profitability is investigated. The study considered brine tax values that ranges from 0 $\$/m^3_{of\ brine}$ to 6 $\$/m^3_{of\ brine}$ and $CO_2$ tax values that ranges from 0 \$/tonne $CO_2$ to 120 \$/tonne $CO_2$. Those values covers the range of the implemented tax in countries including Europe, Canada, and Mexico [8]. In fact, the economy of carbon tax is huge; It estimated that in 2023 that the world revenues from carbon tax and Emission Trading Systems (ETSs) are around 29.3 and 75 billion US dollars, respectively, as shown in Figure 3.

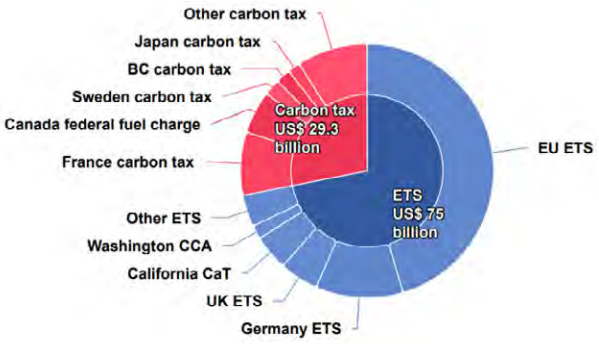



**Figure 3.** Countries contribution to carbon tax and ETSs [8].

Figure 4 shows the 3D plot of the combined effect of brine and $CO_2$ tax on the conventional Solvay process profitability. It is obvious that brine tax has a negligible influence on the Conventional Solvay profitability, whereas carbon tax influences the process profitability significantly. The figure clrearly shows that the conventional Solvay requires a considerable amount of expense. However, implementing carbon and brine tax reduces the expenses required and eventually the process reaches

the breakeven point. Table 2 demonstrates that considering a zero-brine tax, the conventional solvay reaches the breakeven point after implementing carbon tax of 42.5 $/tonne $CO_2$. While the optimum profit is obtained at the maximum implemnted carbon and brine tax.

**Table 2.** Conventional Solvay profitability.

| Parameter | Brine tax | Carbon tax | Profit |
|---|---|---|---|
| Optimum Profit | 7.03 | 116.56 | $6.21x10^6$ |
| Conventional Solvay breakeven | 0 | 42.5 | 0 |

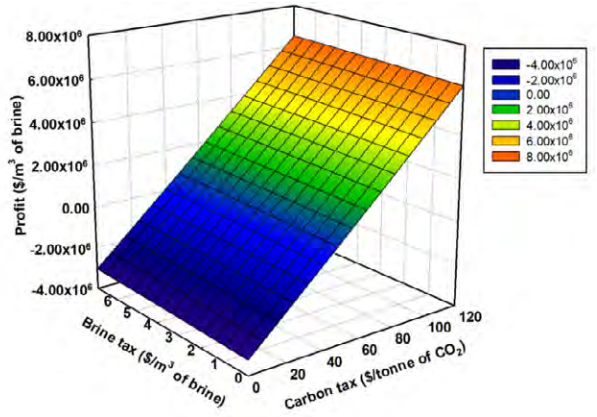



**Figure 4** 3D plots of the combined effect of carbon and brine tax on the Conventional Solvay profitability.

Table 3 shows a summary of the conventional and $Ca(OH)_2$ modified Solvay process performance from experimental and the model used in this study. It is evident that the $CO_2$ and sodium reduction percentages obtained from the model are close to the experimental data, which confirms the validity of the model. In addition, it can be seen that without the implementation of carbon tax, the $Ca(OH)_2$ modified Solvay generates profit of around 3.68 million dollars per year, while conventional Solvay requires expenses of 3.32 million dollars per year. Nevertheless, after implementing a carbon tax of 50 $/tonee $CO_2$, Conventional Solvay generates a profit of 0.6 million dollars per year, while $Ca(OH)_2$ modified Solvay becomes more profitable. This carbon tax value is much lower than the current value implemented in Europe countries and Canada, while is similar to the current value implemented in countries including Hungary, and Iceland. Figure 4 shows the carbon tax implemented in different countries in 2024. It is evident that, adopting conventional Solvay in those countries could contribute to carbon tax reduction if implemented the tax is implemented on industries as it in returns produces a considerable profit. More importantly, implementing the $Ca(OH)_2$ modified Solvay process could significantly reduce the carbon tax burden on both industries and individuals, as the process generating substantial profits from $NaHCO_3$ production, all without necessitating the imposition of a carbon tax. As a result, reducing carbon taxes for industries potentially leads to increased profit margins and enhanced competitiveness in both domestic and international markets. However, this could also result in poor investment in clean energy; therefore, it is substantial to implement a reasonable carbon tax value to ensure long term economic and environmental benefits.

**Table 3.** Summary of the experimental and model results.

| Parameter | Experimental | | Model | |
|---|---|---|---|---|
| | Conventional | $Ca(OH)_2$ modified | Conventional | $Ca(OH)_2$ modified |
| Brine concentration (mg/L) | 71,700 | | 70,000 | |
| Inlet $CO_2$ wt% | 17% | | | |
| Reagent wt% | 25% | 2% | 25% | 2% |
| $CO_2$ removal % | 83 | 99 | 82 | 92 |
| Na removal % | 29 | 35 | 33 | 36 |
| Profit ($/m$^3$ of brine) (without tax) | - | - | $-3.32x10^{-6}$ | $3.68x10^6$ |
| Profit with carbon tax ($/m$^3$ of brine)(50 $/tonne $CO_2$) | - | - | $6.20x10^5$ | $7.62x10^6$ |

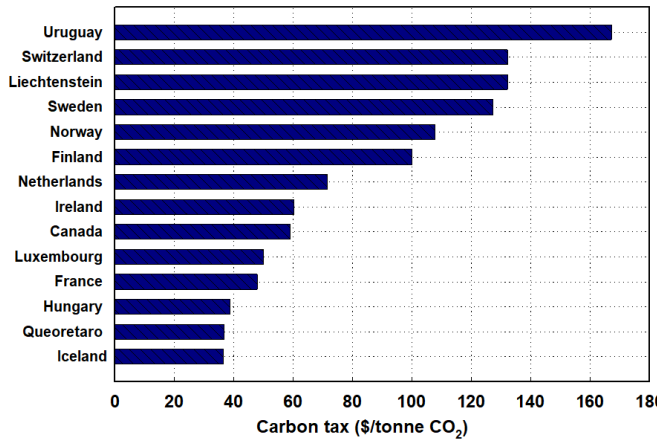



**Figure 4.** The implemented carbon tax in different countries in 2024 [8].

## CONCLUSION

This work demonstrated a systematic techno-economic assessment of Conventional and $Ca(OH)_2$ modified Solvay process considering different brine salinities and brine and carbon tax. The results indicated that $Ca(OH)_2$ modified Solvay sodium and $CO_2$ reduction capability outperform conventional Solvay for all studied brine salinity values that varies from seawater to reject brine salinity level. In addition, conventional Solvay requires considerable expenses, but it becomes profitable after implementing a carbon tax of 50 $/tonne $CO_2$, while $Ca(OH)_2$ modified Solvay is profitable without any carbon tax implementation. These results underscore the economic viability of $Ca(OH)_2$ modified Solvay process besides being an environmentally friendly process compared to conventional Solvay.

## ACKNOWLEDGEMENTS

The authors would like to acknowledge the support of Qatar National Research Fund (a member of Qatar Foundation) through Grant # NPRP 12S-0215-190090. The findings achieved herein are solely the responsibility of the authors.

## REFERENCES

1. *Global challenges*. Available from: https://www.theworldcounts.com/challenges/climate-change/global-warming/global-co2-emissions.
2. Speizer, S., et al., *Integrated assessment modeling of a zero-emissions global transportation sector.* Nature Communications, 2024. **15**(1): p. 4439.
3. Ewis, D., S.Y. Alnouri, and M.H. El-Naas, *A techno-economic assessment of conventional and modified Solvay processes for CO2 capture and reject brine desalination.* Journal of Cleaner Production, 2024. **468**: p. 143087.
4. El-Naas, M.H., et al., *A new process for the capture of CO2 and reduction of water salinity.* Desalination 2017. **411**: p. 69-75.
5. El-Naas, M.H., et al., *Evaluation of a novel gas-liquid contactor/reactor system for natural gas applications.* Journal of Natural Gas Science and Engineering, 2017. **39**: p. 133-142.
6. Mohammad, A.F., et al., *Optimization of a solvay-based approach for CO2 capture.* Int. J. Chem. Eng. Appl, 2016. **7**(4): p. 230.
7. 2023; Available from: https://www.icis.com/explore/.
8. *State and Trends of Carbon Pricing Dashboard*. 2024; Available from: https://carbonpricingdashboard.worldbank.org/.

© 2025 by the authors. Licensed to PSEcommunity.org and PSE Press. This is an open access article under the creative commons CC-BY-SA licensing terms. Credit must be given to creator and adaptations must be shared under the same terms. See https://creativecommons.org/licenses/by-sa/4.0/

Systems & Control Transactions

**Research Article - Peer Reviewed Conference Proceeding**
ESCAPE 35 - European Symposium on Computer Aided Process Engineering
Ghent, Belgium. 6-9 July 2025
Jan F.M. Van Impe, Grégoire Léonard, Satyajeet S. Bhonsale,
Monika E. Polańska, Filip Logist (Eds.)

PSE PRESS

# Application of K-means for Identification of Multiphase Flows Based on Computational Fluid Dynamics

**Patrick S. Lima[a*], Leonardo S. Souza[b], Leizer Schnitman[b], Idelfonso B. R. Nogueira[a]**

[a] Norwegian University of Science and Technology, Department of Chemical Engineering, Trondheim, Trøndelag, Norway
[b] Universidade Federal da Bahia, Salvador, Bahia, Brazil
* Corresponding Author: Patrick.lima@ntnu.no.

## ABSTRACT

This study explores multiphase flow dynamics with a focus on the annular flow regime using Computational Fluid Dynamics (CFD) simulations. The methodology included defining the physical model, generating the computational mesh, and analyzing flow patterns. The Volume of Fluid (VOF) model captured fluid interactions, while the k-ω SST turbulence model ensured accurate flow predictions. Simulations examined mixture density behavior and identified optimal configurations. A dataset was generated and analyzed using k-means clustering to classify flow patterns effectively. The results demonstrate the reliability of this approach for improving multiphase flow systems, with applications in oil-water processes.

**Keywords**: Multiphase Flow, Computational Fluid Dynamics, k-Means Clustering, Flow Pattern Classification

## INTRODUTION

Multiphase flows play an essential role in various industrial sectors, being characterized by the interaction of two or more phases, such as liquid, gas, or solid, moving together.

This phenomenon is present in applications ranging from oil and gas extraction and transportation processes to refrigeration systems and sediment transport in rivers. A detailed understanding of these flows is fundamental for optimizing processes, reducing operational costs, and ensuring safety in industrial operations.

In the oil and gas industry, for instance, multiphase flows are frequently associated with the transportation of mixtures of oil, gas, and water in pipelines. The efficiency of these operations directly depends on understanding the interactions between phases, as well as the ability to predict behaviors such as bubble formation, flow patterns, and pressure gradients [1,2].

Among the various regimes of multiphase flow, core annular flow (CAF) stands out as a highly relevant configuration. One example of this regime can be seen in Figure 1, a central phase, core in red, is surrounded by another phase, annulus in blue, offering significant advantages in applications such as the transportation of high-viscosity fluids. In the oil and gas industry, core-annular flow is widely employed for transporting ultra-viscous oil through pipelines. By surrounding the viscous oil with a layer of less viscous water, this regime reduces wall friction, allowing the fluid to be transported more efficiently and economically [3,4].



**Figure 1**. Example of CAF.

The identification of multiphase flow patterns in real systems has been a critical area of research, given its impact on industrial process optimization and safety.

Traditional experimental methods, such as high-speed imaging, electrical capacitance tomography (ECT), and pressure drop analysis, have been widely employed for flow visualization and pattern classification. For instance, Hewitt (1978) provided a foundational approach to visualizing flow regimes in horizontal and vertical pipes, emphasizing the role of flow characteristics such as velocity, phase distribution, and interfacial dynamics in defining patterns [5]. Another notable contribution was made by Soleimani et al. (2006), who demonstrated the effectiveness of ECT in reconstructing real-time images of multiphase flows, offering a non-intrusive method to map flow patterns accurately [6].

While these methods provide valuable insights, they often require sophisticated equipment and are limited by

operational constraints in high-pressure or high-temperature environments.

Another approach to address these challenges, advanced tools like Computational Fluid Dynamics (CFD) have emerged as powerful approaches. CFD enables the precise simulation of complex flows, providing detailed insights into critical variables such as flow patterns and pressure gradients. However, the detailed analysis of the data generated by these simulations requires methods for identifying and classifying flow regimes.

This article explores the application of the K-means algorithm to identify flow regimes applied data generated by CFD in the context of core-annular flow systems for transporting ultra-viscous oil.

## METHODOLOGY

The methodology was divided into three main stages. In the first stage, the physical model used for the simulation was defined. Subsequently, the process of mesh generation for the system was developed, where the control volumes were defined. These volumes are the elements where the mass and momentum balance equations of the system are solved. Furthermore, in this stage, the models of viscosity, turbulence, and interface governing the interactions between fluids with different properties were established.

In the second stage, individual simulations of different flow patterns were performed, based on the previously constructed geometry and mesh. During these simulations, the behavior of the mixture's density over time was observed, with the objective of understanding and identifying the most suitable approaches for identifying the system.

Finally, in the third stage, 24 simulations were conducted to generate a dataset, which was analyzed using the k-means clustering method. This procedure evaluated the efficiency of the technique in identifying flow patterns, enabling conclusions about its applicability. The resume methodology of this work can be seen in Figure 2.




**Figure 2.** Resume of methodology.

## PHYSICAL STRUCTURE MESH AND MODEL

To induce annular flow, it is common to use a nozzle that allows the simultaneous injection of oil and water through separate orifices. An example of such a setup can be seen in Figure 3.

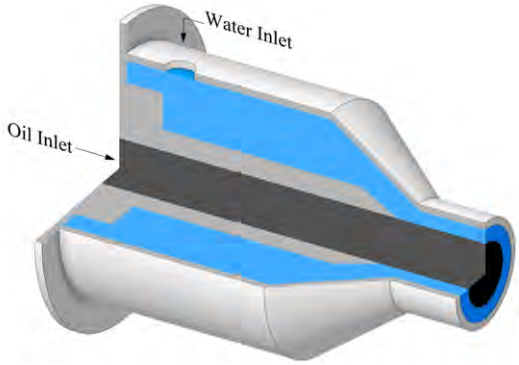



**Figure 3.** Example of nozzle.

To simplify the system's geometry and make the computational cost of the simulation more reasonable, the structure was adapted to a two-dimensional system, as shown in Figure 4.




**Figure 4.** Simplification of nozzle inlet.

This geometry features a centralized inlet of 40 mm for oil injection, along with two additional inlets of 5 mm for water injection. Connected to this inlet structure is a straight horizontal tube with a length of 1000 mm.

In general, any simplification that reduces the dimensionality of a problem results in lower computational effort at the cost of potentially minimizing certain three-dimensional effects. However, the two-dimensional simulations conducted in this study proved to be sufficiently representative in describing the classic multiphase flow patterns reported in the literature.

After preparing the geometry, a mesh was created to solve the partial differential equations for mass balance and the Navier-Stokes equations. The mesh consists of around 10000 elements and can be visualized in Figure 5.a and Figure 5.b with zoom.



**Figure 5.a.** Mesh of system.

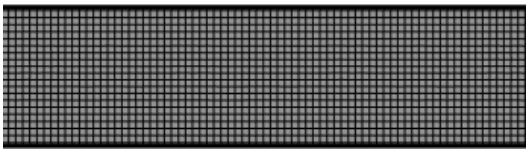


**Figure 5.b.** Mesh of system with zoom.

The mesh scale was determined based on a heuristic approach, and it was considered reasonable when it successfully represented flow patterns closely resembling those already established in the literature.

Since the primary objective of this work was to explore a strategy for identifying flow patterns rather than performing a numerical validation of simulations against real experiments, the choice of a cost-effective mesh was prioritized.

From a rigorous perspective, creating a dedicated numerical mesh for each type of flow pattern would be necessary, but this was not within the scope of the study. Instead, a balanced approach was adopted to ensure computational efficiency while still achieving meaningful results.

The model that was used to simulate the system was Volume of Fluid (VOF). The VOF model was employed to simulate the interfaces between immiscible fluids in the system. This model is well-suited for resolving complex interfacial dynamics, as it uses a single set of momentum equations for the domain and tracks the volume fraction of each fluid. This approach allows for an accurate representation of the interactions between fluids with different properties and is widely used in multiphase flow simulations [7].

During the simulation, an isothermal system was considered, where the physicochemical properties of the fluids water and oil remained constant.

The water density was assumed to be 998.2 kg/m³, while the oil density was set to 854 kg/m³. The dynamic viscosity was defined as 0.001 Pa·s for water and 0.62 Pa·s for oil, with an interfacial tension of 0.032 N/m between the fluids [8].

Another fundamental part of one CFD simulation is the turbulence model. For this application, we use k-ω SST turbulence model due capability to handle flows with adverse pressure gradients and boundary layer separation. It combines the advantages of the k-ω model near walls with the k-ε model in free-stream regions, providing reliable performance across a wide range of flow regimes [9].

## REPRODUCTION OF PATTERN FLOW

In this section, classic flow patterns reported in the literature were simulated [3]. To enhance visualization, oil was represented in red and water in blue, with the transition between colors indicating the interface between the two fluids.

Additionally, the average fluid density at the pipe outlet was monitored over time. It is important to note that the pipe was initially filled entirely with water. As a result, during the early stages of the simulation, the time signal often closely resembled the density of water, as some time was required for the oil to travel from the pipe inlet to its outlet.

The first flow pattern simulated was the oil in water dispersion. This pattern is characterized by small oil droplets dispersed within the water. As shown in Figure 6, the fluid density over time remains close to the density of water, with minor oscillations caused by droplets of varying sizes passing through the pipe outlet.

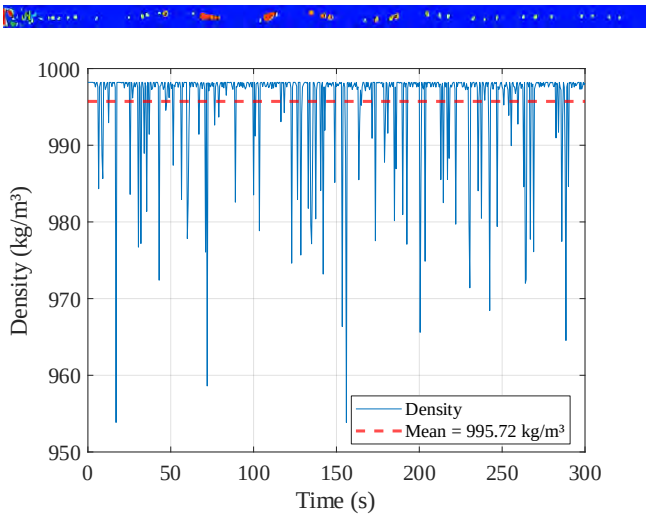



**Figure 6.** Oil in water dispersion signal in the time.

The second simulated flow pattern was the bubbly flow, where the droplets observed in the oil in water dispersion evolve into larger bubbles. This transition leads to a slightly lower average density compared to the previous pattern as shown in Figure 7.

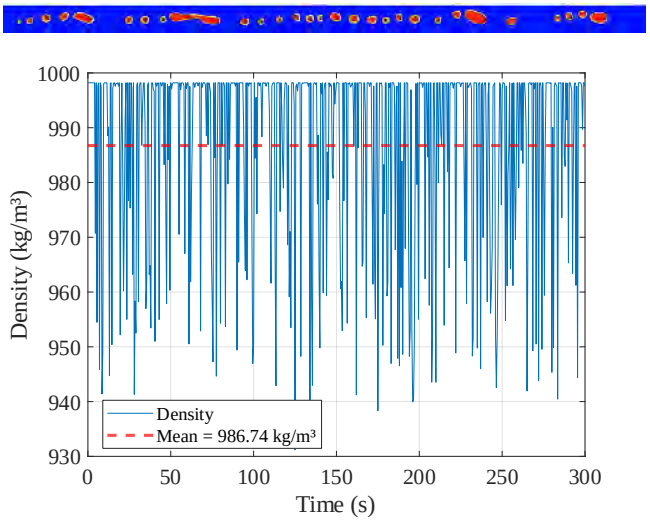



**Figure 7.** Bubble signal in the time.

The third simulated flow pattern was slug flow, which follows a similar progression to bubbly flow. In this regime, the increased volume of oil promotes the coalescence of bubbles, forming elongated oil slugs. These slugs occupy significant portions of the pipe cross-

section, resulting in a further reduction of the average fluid density over time. As depicted in Figure 8, the density signal exhibits larger and more pronounced oscillations, reflecting the alternating passage of oil slugs and water segments at the pipe outlet. This pattern highlights the impact of bubble coalescence on flow dynamics and density distribution.

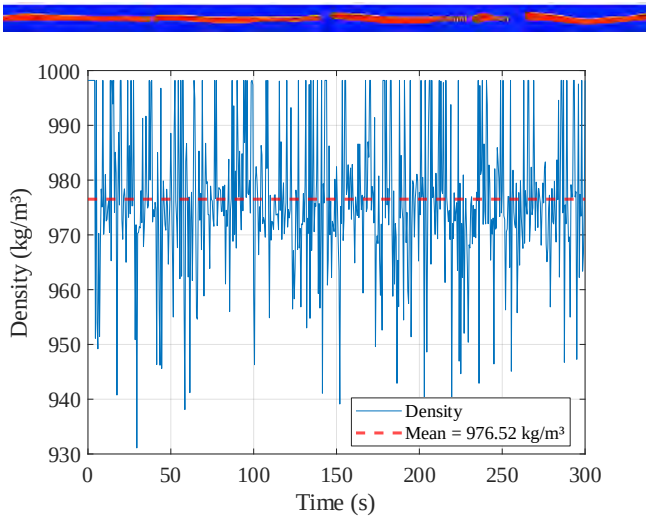



**Figure 8**. Slug signal in the time.

The fourth simulated flow pattern was stratified flow, characterized by oil and water flowing in distinct layers along the pipe. In this regime, the oil does not achieve sufficient velocity to traverse the pipe effectively. As a result, buoyancy forces become significantly relevant, allowing the oil mass to accumulate at the top of the pipe. This behavior increases the likelihood of oil deposition on the pipe walls, leading to fouling over time. As shown in Figure 9, the density signal stabilizes at a lower average value due to the layered separation of the fluids and the reduced mixing between phases. This pattern emphasizes the importance of managing flow conditions to minimize fouling risks in pipeline systems.

The fifth simulated flow pattern was annular flow, that can be seen in Figure 10, which exhibited the lowest average density among all patterns. This observation aligns with expectations, as annular flow contains the highest volume of oil within its cross-section. A notable characteristic of this pattern is the smooth and consistent behavior of the density signal, which contrasts with the noisier signals observed in other patterns. This is attributed to the well-defined interfaces between oil and water, resulting in reduced fluctuations at the pipe outlet. The stability and distinct separation of phases in annular flow highlight its unique dynamics and emphasize the importance of precise modeling for accurate system analysis.

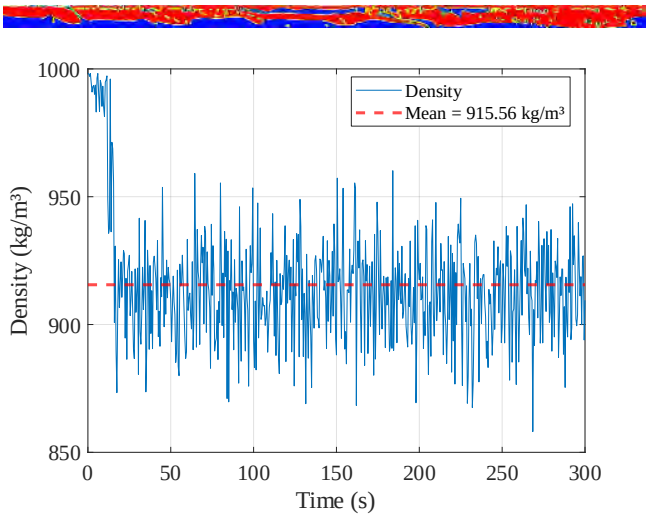



**Figure 9.** Stratified flow signal in the time.

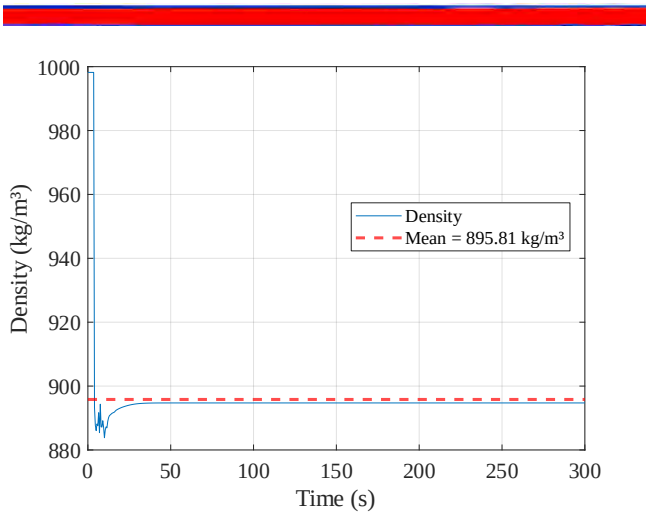



**Figure 9.** Annular Flow sign al in the time

## CLUSTERING AND IDENTIFICATION

To analyze the flow patterns, a one-dimensional k-means clustering was performed, considering the average density of the time signal as the primary variable. To minimize the impact of transient effects in the system, the first 50 seconds of each simulation were excluded from the analysis. This adjustment ensured that the calculated average density more accurately reflected the steady-state behavior of each flow pattern.

A total of 25 simulations were conducted, each running for 300 seconds under varying boundary conditions. This approach allowed for the evaluation of a wide range of scenarios, capturing the diversity in flow dynamics. The use of average density as a clustering metric provided a straightforward yet effective means of distinguishing between patterns, particularly in cases where differences were more pronounced, such as with

core-annular flow.

The Figure 10 shows the results of clustering performed using the k-means method with five clusters based on the average density of the time signal for 25 simulations conducted under different boundary conditions. Each point in the graph represents a specific simulation, while the dashed lines indicate the cluster centers identified by the algorithm.

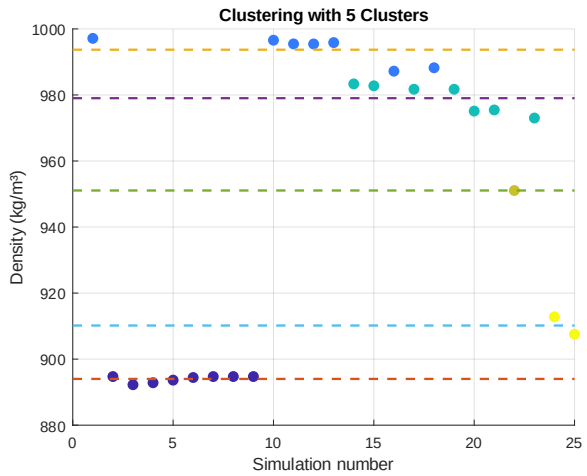



**Figure 10.** Results of K-means

The clusters are well defined and distributed along the density axis, reflecting the differences in the simulated flow patterns. Most points are closely grouped around their respective cluster centers, suggesting that average density was an effective parameter for distinguishing between the different patterns. Additionally, the low variation within each cluster indicates that this parameter reliably captures the general behavior of the flow patterns.

The cluster with the lowest density, located below 900 kg/m³, corresponds to the annular flow pattern, characterized by the highest volume of oil in the pipe's cross-section. This significantly reduces the average density of the signal and shows a clear separation from the other clusters.

On the other hand, the intermediate clusters, such as those around 920 kg/m³ and 940 kg/m³, represent patterns like slug flow and stratified flow, where there is greater interaction between phases. In these cases, some overlap in average density values can be observed, indicating that the boundaries between these patterns may not be perfectly distinct depending on the boundary conditions.

The cluster with the highest density, near 1000 kg/m³, is associated with patterns such as oil in water dispersion, where the amount of oil in the mixture is smaller, and the behavior is dominated by the characteristics of water. This cluster is well-separated from the others, emphasizing the uniqueness of this pattern in terms of average density.

Overall, the results presented in the image demonstrate that the k-means method was effective in identifying flow patterns based on average density. However, the overlap of values observed between some intermediate clusters highlights the need to explore more complex approaches in future studies. These approaches could include the use of multiple variables or the consideration of temporal relationships to improve the discrimination of patterns with very similar characteristics.

## CONCLUSIONS

The strategy of identifying multiphase flow patterns using the k-means clustering method has proven to be promising, as it allowed for a reasonable clustering of results. This approach was particularly effective for core annular flow, which exhibits a highly distinct behavior compared to other patterns due to its low density oscillations over time. However, for other flow patterns, some challenges may arise. Depending on the boundary conditions, there can be an overlap of values between patterns that are very similar, making differentiation more difficult.

Despite these limitations, this study successfully demonstrated a functional method, aligning with its premise of developing a simple approach for flow pattern identification. At the same time, it opens the door for further research into more advanced clustering techniques or methodologies. Future approaches could explore grouping data across multiple dimensions and incorporating temporal relationships, moving beyond reliance on a single variable to achieve more robust and comprehensive results.

## REFERENCES

1. Ishii M, Hibiki T. Thermo-fluid dynamics of two-phase flow. Springer Science & Business Media (2011).
2. Brennen CE. Fundamentals of multiphase flow. Cambridge University Press (2005).
3. Joseph DD, Bai R, Chen K, Renardy Y. Core-annular flows. Annu Rev Fluid Mech 29:65-90 (1997). https://doi.org/10.1146/annurev.fl.29.010197.00043
4. Bannwart AC. Modeling aspects of core-annular flows. J Pet Sci Eng 32:127-143 (2001). https://doi.org/10.1016/S0920-4105(01)00155-5
5. Hewitt GF. Flow regimes. Int J Multiphase Flow 4:89-114 (1978). https://doi.org/10.1016/0301-9322(78)90002-3
6. Soleimani M, Caunce J, Peyton AJ. Imaging of two-phase flows using electrical capacitance tomography. Meas Sci Technol 17:1926-1936 (2006). https://doi.org/10.1088/0957-0233/17/8/037

7. Hirt, C. W., & Nichols, B. D. (1981). Volume of fluid (VOF) method for the dynamics of free boundaries. Journal of Computational Physics, 39(1), 201–225.
8. Lima, P., Nogueira, I., Schnitman, L., Mendes, T. P. G., Costa, E., & Skogestad, S. (2023). Harnessing Feedback Control Strategy for Improved Core Annular Flow Stability in Heavy Oil Transportation. AIChE Annual Meeting, Computing and Systems Technology Division. Orlando, FL.
9. Menter, F. R. (1994). Two-equation eddy-viscosity turbulence models for engineering applications. AIAA Journal, 32(8), 1598–1605.

© 2025 by the authors. Licensed to PSEcommunity.org and PSE Press. This is an open access article under the creative commons CC-BY-SA licensing terms. Credit must be given to creator and adaptations must be shared under the same terms. See https://creativecommons.org/licenses/by-sa/4.0/



Systems & Control Transactions

**Research Article - Peer Reviewed Conference Proceeding**
ESCAPE 35 - European Symposium on Computer Aided Process Engineering
Ghent, Belgium. 6-9 July 2025
Jan F.M. Van Impe, Grégoire Léonard, Satyajeet S. Bhonsale,
Monika E. Polańska, Filip Logist (Eds.)

PSE PRESS

# A New Method to Assess Performance Loss due to Catalyst Deactivation in Fixed- and Fluidized-bed Reactors

**M. Andrea Pappagallo[a,b], Tilman J. Schildhauer[a], Oliver Kröcher[a,b], and Emanuele Moioli[a,c]***

[a] Paul Scherrer Institut, Center for Energy and Environmental Sciences, Villigen, Switzerland
[b] École Polytechnique Fédérale de Lausanne, Institute of Chemical Sciences and Engineering, Lausanne, Switzerland
[c] Politecnico di Milano, Dipartimento di Chimica, Materiali e Ingegneria Chimica 'Giulio Natta', Milano, Italy
* Corresponding Author: emanuele.moioli@polimi.it

## ABSTRACT

A new methodology for the assessment of the performance loss in catalytic reactors due to deactivation was developed and applied to fixed- and fluidized-bed CO methanation, with catalyst subject to coking. The methodology is based on the solution of heat and mass balances, by decoupling the reactor and deactivation dynamics. This is possible by using consecutive 1D, steady-state calculations for the characterization of the reactor performance. In this way, the progressively lower values of catalyst activity along the time on stream are computed with the integration of a dedicated dynamic model. This method has shown promising results in the characterization of the loss of performance of the reactor over time. The model correctly describes a progressive deactivation of the catalyst in fixed-bed reactors, while it shows that the decrease in activity is sudden for the whole reactor volume in fluidized bed reactors and occurs after a critical time-on-stream. Besides, it was observed that the fluidized bed reactor is in general more resistant to deactivation by CO, with the time needed to reach 25% conversion being 1.5 to 2 orders of magnitude higher than for a fixed bed in similar conditions – for example around 250 hours against 50 for a fixed bed at 300°C. This will allow optimizing the reactor with respect to deactivation, hinting the modifications possible in the conditions or in the reactor geometry to maximise the time-on-stream prior to loss in the product quality.

**Keywords**: Catalyst deactivation, Reactor modelling, Fixed-bed reactors, Fluidized-bed reactors

## INTRODUCTION

The increasing amount of anthropogenic greenhouse gases in the atmosphere is a major driver for the development of new technologies that can abate such gas emissions. A widely investigated option to address this challenge is the production of fuels from unconventional and renewable feedstocks, like $CO_2$ from carbon capture processes, biomass, and green waste. This option shows the advantage of emitting the same amount of $CO_2$ that was naturally captured during the production of such feedstocks [1–3], making the overall cycle carbon-neutral. However, these carbon-containing streams are usually contaminated by various additional molecules. In particular, the presence of CO and other organic molecules, which are natural constituents of such feedstock, may lead to catalyst deactivation by decomposition of such molecules and consequent coking of the surface. This may strongly hinder the rate of the reactive steps of the process over time [4]. The development of methods that minimize the impact of coking in these reactions is therefore a key to ensure the efficiency of the whole process and its long-term performance and competitiveness. For this scope, it is crucial to model these deactivation phenomena, both in terms of their intrinsic kinetics and of their impact on the reactor performance. These models should target the optimization of the operating conditions in the reactor to reduce the impact of deactivation.

The main difficulty in modelling catalyst deactivation in catalytic reactors is caused by the different characteristic time scales of the phenomena involved: while the reaction has characteristic times below the order of magnitude of seconds, and the same is valid for the transport phenomena in the reactor, the deactivation by coking has

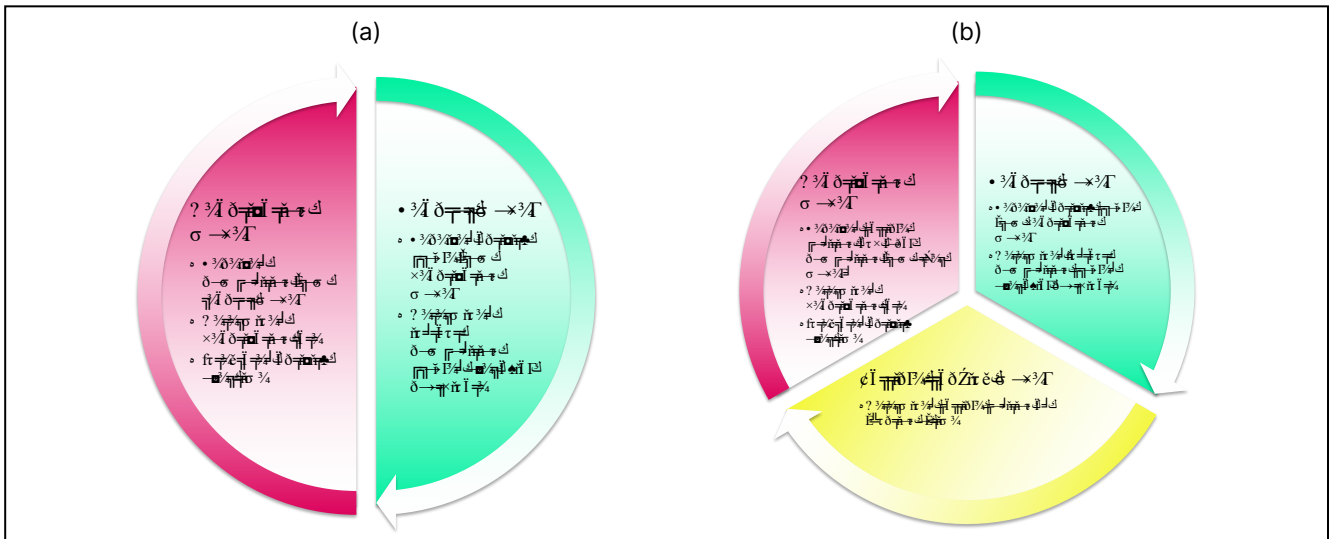



**Figure 1:** Model structure for the (a) pseudo-dynamic model in case of a fixed bed and (b) moving observer model in case of fluidized bed.

a visible impact on the reactor performance only after hours to days [5]. In the case of a fluidized-bed reactor, an additional modelling difficulty is originated by the chaotic movement of particles [6], which has a decisive impact on the deactivation, as the position of the particle at each given instant determines the amount of coke precursors in the gas around it. It is, however, too computationally cumbersome to model this motion for the entirety of the particles in a fluidized bed of a commercially usable scale [7]. This study develops a new methodology that unifies in a single model the information on the effects of catalyst deactivation at different scales, resulting in a computationally affordable model. This model can predict the decrease in the activity of the catalyst over time, the effect of particle motion in fluidized bed reactors on catalyst deactivation and the evolution of the concentration profiles over time. Thanks to the prediction of these various indicators, the model can be used to predict the time the reactor can operate before the outlet concentration is not in line anymore with the requirements of the system in which it is installed. To contextualize the methodology in a case of practical interest, the methanation of syngas is considered as case study for this work.

## METHODS

This work focuses on the development of a model for the evaluation of the impact of catalyst deactivation on chemical reactors. The time scales of the phenomena determining the operation of the reactor and the deactivation of the catalyst are significantly different and can thus be decoupled. The resulting model characterizes the conversion in the reactor in one spatial dimension, and the activity of the catalyst in time, plus one spatial dimension for the fixed-bed case.

The activity of the catalyst is defined in Equation (1), where $r$ represents the local rate of reaction and $r_0$ the rate of the same reaction at the same local conditions of pressure, temperature and composition of $r$, but calculated assuming the catalyst is unaffected by deactivation.

$$a = r/r_0 \tag{1}$$

**Figure 1** shows a schematic representation of the workflow leading to the complete deactivation models for the two reactor types (fixed- and fluidized-bed).

The deactivation model for the fixed-bed reactor has been labelled as pseudo-dynamic model due to its constitution as a series of consecutive steady-state calculations to model the performance loss in time. Starting from a time t=0 and an initial activity a=1, the pseudo-dynamic model follows this procedure for each time step:

1. It calls the steady-state model of the reactor, which solves the model equations for the current steady state,
2. it determines the composition profiles and the partial pressures of the two main components involved in deactivation (CO and $H_2O$),
3. it calculates the deactivation rate from the partial pressures, obtaining the rate of loss of activity as a function of the position in the reactor $da/dt = f(z)$,
4. it integrates the loss of activity and moves to the next step.

The deactivation model for the fluidized bed is referred here as moving observer model because it follows the average catalyst particle through its motions in the bed through a Eulerian-Lagrangian approach. It shows similitudes with the pseudo-dynamic model, with the addition of a model for the position of the particle as a function of time. The activity is therefore no longer calculated as a function of the position, but as a value relative to the single catalyst particle. It is then assumed to be the same throughout the whole reactor due to the very fast mixing inside the system.

## Case study

The methanation of CO is used as case study. The fixed-bed model is based on a plate-cooled fixed-bed reactor with 1 m of length, 50 cm of width and 5 cm of spacing between the plates [8]. The channels between the plates are alternatively filled with the catalyst bed and with the cooling medium (boiling water) at the same temperature of the reactor inlet. The reactor is operated with a stoichiometric inlet stream (3:1 $H_2$/CO) at a pressure of 8 bar and inlet temperatures between 300 and 360°C.

The fluidized-bed model is instead based on a reactor of 2.5 m of length, 22.4 cm diameter and cooled by an inner coil where a cooling oil is circulated. This reactor is also operated with a stoichiometric inlet stream (3:1 $H_2$/CO), at a pressure of 8 bar and uniform reactor temperatures between 300 and 360°C.

The kinetic model used is obtained from the work of Kopyscinski et al. [9] for the methanation of CO and Koschany et al. [10] for the methanation of $CO_2$ (Sabatier reaction), and it consists of three reactions, outlined in **Table 1**.

**Table 1:** Reactions in the kinetic model for CO methanation [9,10].

| Reaction | Equation |
|---|---|
| CO methanation | $CO + 3H_2 \rightleftharpoons CH_4 + 2H_2O$ |
| $CO_2$ methanation | $CO_2 + 4H_2 \rightleftharpoons CH_4 + 3H_2O$ |
| Water-gas shift | $CO + H_2O \rightleftharpoons CO_2 + H_2$ |

The effect of the Boudouard reaction, i.e., the decomposition of CO to coke (assumed as elemental carbon, C) and $CO_2$, leading to coking of the catalyst, has not been taken into account in the reaction kinetics due to its low extent in the residence time of the system (few seconds). Future works might explore this aspect further.

## Fixed-bed reactor digital twin

The fixed-bed digital twin was developed on a 1D pseudohomogeneous assumption, i.e., the catalyst and the gas were modelled as a single pseudophase and gradients were neglected in any direction other than that of the gas flow. Equations (2) and (3) are the component and energy balance for the reactor, respectively. The activity term $a(t)$ is calculated from the deactivation model, as explained in the dedicated subsection.

Component balance

$$\frac{dF_i}{dz} = \rho_c(1-\varepsilon)Aa(t)\sum_{j=1}^{NR}\nu_{ij}r_j \quad (2)$$

Heat balance

$$\frac{dT}{dz} = -\frac{\rho_c(1-\varepsilon)A}{\dot{m}\hat{c}_P}a(t)\sum_{j=1}^{NR}\Delta h_{Rj}r_j - \frac{2W}{\dot{m}\hat{c}_P}U(T-T_e) \quad (3)$$

This digital twin was developed according to state-of-the art models for the calculation of steady-state profiles in fixed beds [11]. The model consists of NC+1 ordinary differential equations, where NC is the number of species considered. The equations were solved in MATLAB via built-in solvers which integrate them in the axial reactor coordinate $z$.

## Fluidized-bed reactor digital twin

For the fluidized bed, a two-phase model was chosen, dividing the reactor in two pseudophases being the bubble and the emulsion or dense phase [4]. The bubble is assumed to contain no catalyst – therefore no reaction happens in it – and to be in a plug-flow regime. The emulsion is instead considered to carry out the reaction since it contains the catalyst, and to be perfectly stirred by the continuous recirculation operated by the bubbles. For the same reason, the reactor is considered isothermal. The component balances for each phase are shown in Equations (4) and (5).

Component balance – bubble phase

$$\frac{dF_i^B}{dz} = -K_i A_B\left(\frac{F_i^B}{Q_B} - \frac{F_i^D}{Q_D}\right) \quad (4)$$

Component balance – dense phase

$$0 = F_i^{D,IN} - F_i^D + \int_0^L K_i A_B\left(\frac{F_i^B}{Q_B} - \frac{F_i^D}{Q_D}\right)dz + V(1-\delta)(1-\varepsilon_{mf})\rho_c\sum_{j=1}^{NR}a(t)\nu_{ij}r_j \quad (5)$$

This digital twin was also developed from state-of-the-art models for fluidized-bed systems [12]. Due to the presence of an integral term, the model could not be solved by numerical integration and must instead be converted to a nonlinear algebraic system by discretization of the derivatives. Such system was then solved via built-in solvers in MATLAB for algebraic equations.

## Particle motion model

A model for particle motion has been derived from the experimental data obtained by Lefebvre et al. [13], normalized on the dimensions of the reactor studied in this work. The wave of the position of the particle in time has been decomposed according to a Fourier transform in the attempt to divide it into components accounting for gross and local circulation phenomena. The advantage of the Fourier transform over other tested approaches (i.e.,

artificial neural networks) is that it conserves the periodicity of the function. Wave components with a negligible impact on the particle position have been filtered out to make the function simple. The goal of the function is not to reproduce accurately the data, but more to learn the trend relative to the time an average particle spends at each height in the reactor.

## Deactivation model

The deactivation model was developed in this work and is based on a reparameterization of a model by Sun et al. [4]. The new parameters were obtained from the catalyst deactivation data during CO methanation reported by Zhang et al. [5], and the resulting model is based on the following equations:

| | | |
|---|---|---|
| Deactivation rate | $\frac{da}{dt} = -r_d a$ | (6) |
| Kinetic equation | $r_d = k_d P_{CO}^{\alpha} f_{H_2O}$ | (7) |
| Temperature dependence (Arrhenius) | $k_d = k_d^0 \exp\left(-\frac{E_d}{RT}\right)$ | (8) |
| Correction factor for water | $f_{H_2O} = \frac{x_{H_2O}-1}{(1-c)x_{H_2O}-1}$ | (9) |

The correction factor is used to account for the hindering effect that a high concentration of water has on the deactivation rate. Water is in fact known to be able to prevent the formation of coke on catalyst particles, slowing down their deactivation [4]. The correction factor in Equation (9) is empirical. The effect of water on deactivation will be studied in more detail in future works.

# RESULTS

The results show the prediction of deactivation profiles in the two reactor types by application of the models described in the methods section.

## Pseudo-dynamic model – fixed-bed

**Figure 2** and **Figure 3** illustrate the results of a simulation of the deactivation effects in the fixed-bed reactor conducted with the pseudo-dynamic model. The evolution of the activity and conversion profiles in time shows that, in the initial moments of the simulation, the activity decreases significantly only at the inlet of the reactor, to then generate a wave of decreasing activity that propagates through the catalyst bed in the axial direction. This is in line with what is expected in fixed bed reactors, where the first layers of catalyst operate as 'filter' for the impurities [4]. The deactivation wave reaches the end of the reactor after about 40 h of operation, when the CO conversion at the outlet starts decreasing from an initial value close to 100%. After 50 h, the catalyst has lost most of its activity throughout all the reactor, which leads to a final conversion of 25% and a hotspot temperature of around 420°C (130°C milder compared to the values during effective operation). This decrease in the hotspot temperature is due to the different distribution of the reaction rate on a partially deactivated catalyst. This reduces the reaction rate at the reactor inlet, hence distributing the conversion over a larger area of the reactor than at the operation start.

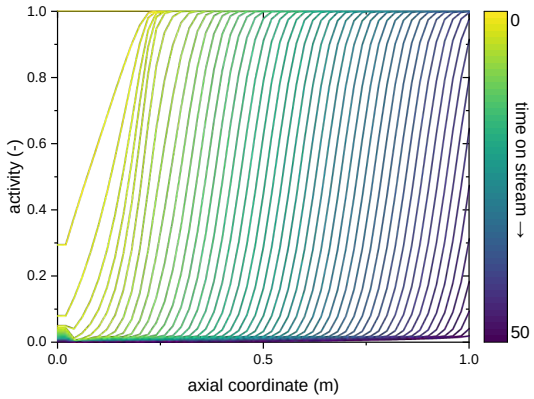



**Figure 2:** Results of the pseudodynamic model for stoichiometric inlet, $T_{in}$ = 300°C, p = 3 bar – deactivation wave.

The different deactivation velocity appears to be mostly due to the difference in temperature throughout the reactor shown in **Figure 4**: as the deactivation rate strongly depends on the temperature through the Arrhenius equation, the deactivation is much faster in the temperature hotspot. The hotspot itself is moving as a result of the wave of decreasing activity, since the less active catalyst in the initial portions of the bed leads to significantly slower reaction rates and therefore to a less prominent heat release. The reaction rate strongly increases once the reactants reach a portion of the bed where the catalyst is still active, and this leads to the generation of a new hotspot there. Both the decrease in activity and the moving hotspot are coherent with experimental observations for similar systems [4].

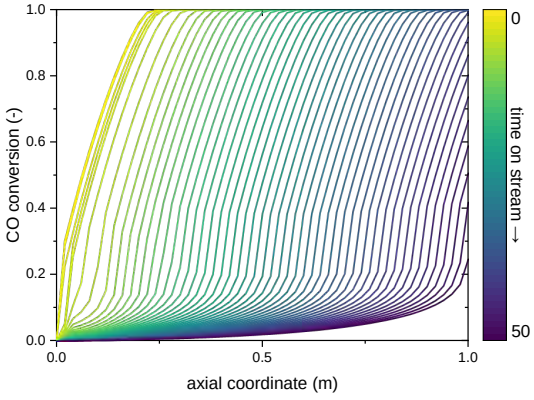


**Figure 3:** Results of the pseudodynamic model for stoichiometric inlet, $T_{in}$ = 300°C, p = 3 bar – conversion profile.

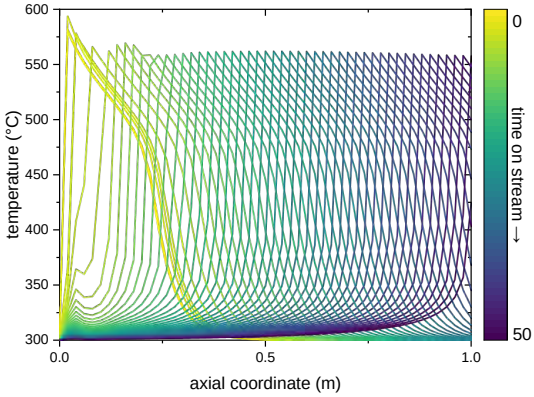



**Figure 4:** Results of the pseudodynamic model for stoichiometric inlet, $T_{in}$ = 300°C, p = 3 bar – moving hotspot.

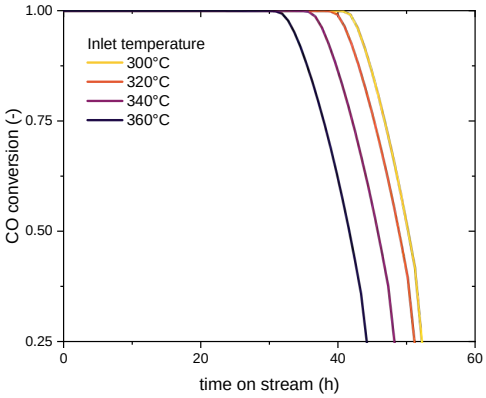



**Figure 5:** Results of the pseudodynamic model for stoichiometric inlet, p = 3 bar – effect of inlet temperature.

**Figure 5** shows the CO conversion at the reactor outlet over time. As expected in fixed-bed reactors operating the $CO_x$ hydrogenation, the conversion remains high until the deactivation wave reaches the terminal part of the reactor (see **Figure 2**). The figure also shows the effect of an increasing inlet temperature on the time required for significant loss of performance of the reactor. A higher inlet temperature leads to higher temperatures throughout the whole reactor, which increase the rate of deactivation as per Equation (8). This leads to a faster propagation of the deactivation wave and consequently to an earlier loss of performance.

## Moving observer model – fluidized-bed

The results of the integration of the moving observer model are shown here. **Figure 6** reports the decrease in conversion over time. In the fluidized-bed reactor, the conversion loss does not follow a wave form, but it is uniform over the axial coordinate. This is an effect of the assumption of perfect mixing for the dense phase. The deactivation is limited to a small portion of the reactor, in the initial section, prior to the full consumption of CO. However, the constant and quick motion of the particles throughout the bed ensures that the particles can be assumed to deactivate all at the same rate. The effect of the zones at low CO concentration is, in turn, prevalent due to their significant size compared to the CO-rich ones, which results in an overall slower deactivation. The time on stream required for a significant loss of performance is therefore longer and the CO conversion curve over time takes a different shape than in the fixed-bed reactor.

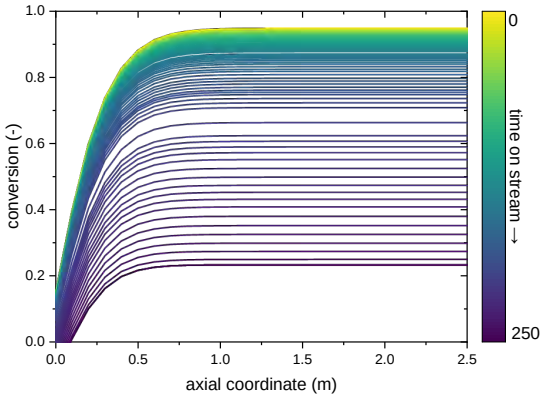



**Figure 6:** Results of the moving observer model for stoichiometric inlet, T = 300°C, p = 8 bar – conversion profile.

These conversion terms are shown in **Figure 7**. The general behaviour is the same as for the fixed-bed case, but the effect of the temperature is reversed: higher temperatures lead here to slower deactivation and loss of performance. Additionally, the drop in CO conversion occurs more suddenly in the fluidized bed reactor, because deactivation is distributed over the catalyst volume, so that when the critical activity of the catalyst dropping the CO conversion is reached, this is reflected by the entire dense phase. This is challenging for the operation of a fluidized-bed reactor, as the conversion drop is sudden and more difficult to predict than in the fixed-bed reactor.

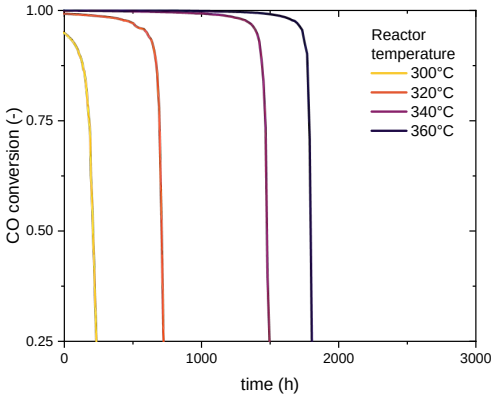



**Figure 7:** Results of the moving observer model for stoichiometric inlet, p = 8 bar – effect of reactor temperature on conversion.

**Figure 8** shows instead the evolution of the catalyst activity over time. The slower deactivation at higher temperatures is due to the faster consumption of CO, which reduces the length of bed in which a significant amount of CO is present and leaves the rest of the bed with low amounts of CO and high amounts of water. This results in a shorter contact time between the particle and a CO-rich gas, therefore a slower deactivation.

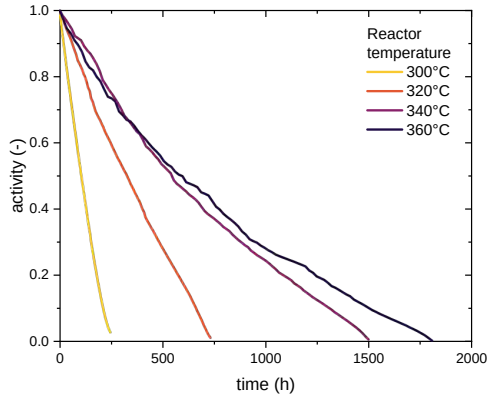



**Figure 8:** Results of the moving observer model for stoichiometric inlet, p = 8 bar – effect of reactor temperature on activity.

The higher temperature also leads to a stronger impact of the position of the particle on the deactivation rate, as shown by the profile at 360°C being less smooth than that at 300°C. This is due to the sharper variations in composition throughout the reactor at higher temperatures, which amplify the variation of the deactivation rate with the particle position.

## CONCLUSIONS

This paper developed a new methodology to describe the reactor deactivation due to coking in fixed- and fluidized-bed reactors. Deactivation can be modelled in fixed-bed reactors by coupling a reliable steady-state model for the calculation of the composition profiles in given conditions, with a model for the deactivation of the catalyst as a function of the local operating conditions (temperature, gas phase composition). The same is possible for fluidized-bed reactors with the addition of a particle tracking model that can express the position of the average catalyst particle as a function of time. Such models are effective in characterizing the loss of performance along the time on stream as a function of key operating conditions of the reactor like the inlet composition, the inlet/operating temperature, pressure etc., and therefore provide the possibility for optimization of such conditions with respect to productivity and minimizing the effect of deactivation. The impact of the operating conditions can in fact be studied in detail with the help of this model, which allows the selection of those sets of conditions that minimize the long-term impact of deactivation on reactor performance.

In the specific case analyzed we observed the behavior of both reactor types at the four temperature values of 300, 320, 340, and 360°C. We considered the catalyst deactivated when a conversion of CO of 25% was reached at the outlet, at which point the simulation was stopped. The most relevant result is the slower deactivation for the fluidized bed, by 1.5 to 2 orders of magnitude.

Future works will be focused on improving the model. Aging experiments will be run on the catalyst, with the goal to gather more deactivation data and improve the model parameters and structure to better characterize the catalyst deactivation and its dependence on temperature and composition. A deeper investigation will also be conducted on particle behavior in the fluidized bed, with the aim of refining the existing model, for example by adding a term accounting for stochasticity.

## ACKNOWLEDGEMENTS

The authors acknowledge the support from the Swiss National Science Foundation (SNSF) Ambizione project: 'Moving catalyst vs. multi-catalyst: determination of the best reactor for the processing of unconventional feedstock' with grant number No. 20912.

## REFERENCES

1. Pearson RJ, Eisaman MD, Turner JWG, Edwards PP, Jiang Z, Kuznetsov VL, et al. Energy storage via carbon-neutral fuels made from CO2, Water, and Renewable Energy. Proceedings of the IEEE. 2012;100(2):440–60.
2. Choi YH, Jang YJ, Park H, Kim WY, Lee YH, Choi

SH, et al. Carbon dioxide Fischer-Tropsch synthesis: A new path to carbon-neutral fuels. Appl Catal B [Internet]. 2017;202:605–10. Available from: http://dx.doi.org/10.1016/j.apcatb.2016.09.072
3. Moioli E, Schildhauer T. Negative CO2 emissions from flexible biofuel synthesis: Concepts, potentials, technologies. Vol. 158, Renewable and Sustainable Energy Reviews. Elsevier Ltd; 2022.
4. Sun D, Khan FM, Simakov DSA. Heat removal and catalyst deactivation in a Sabatier reactor for chemical fixation of CO2: Simulation-based analysis. Chemical Engineering Journal [Internet]. 2017;329:165–77. Available from: http://dx.doi.org/10.1016/j.cej.2017.06.160
5. Zhang J, Fatah N, Capela S, Kara Y, Guerrini O, Khodakov AY. Kinetic investigation of carbon monoxide hydrogenation under realistic conditions of methanation of biomass derived syngas. Fuel [Internet]. 2013;111:845–54. Available from: http://dx.doi.org/10.1016/j.fuel.2013.04.057
6. Lefebvre S, Chaouki J, Guy C. Solid Phase Hydrodynamics of Three-Phase Fluidized Bed Reactors – A Convective / Dispersive Phenomena Solid Phase Hydrodynamics of Three-Phase Fluidized Bed Reactors – A Convective / Dispersive Phenomena. International Journal of Chemical Reactor Engineering. 2007;5.
7. Uglietti R, Bracconi M, Maestri M. Development and assessment of speed-up algorithms for the reactive CFD-DEM simulation of fluidized bed reactors. React Chem Eng. 2020 Feb 1;5(2):278–88.
8. Moioli E, Senn P, Østrup S, Hütter C. Results from the operation of an efficient and flexible large-scale biogas methanation system. Energy Advances. 2023;3(1):131–42.
9. Kopyscinski J, Schildhauer TJ, Vogel F, Biollaz SMA, Wokaun A. Applying spatially resolved concentration and temperature measurements in a catalytic plate reactor for the kinetic study of CO methanation. J Catal. 2010 May 4;271(2):262–79.
10. Koschany F, Schlereth D, Hinrichsen O. On the kinetics of the methanation of carbon dioxide on coprecipitated NiAl(O)x. Appl Catal B [Internet]. 2016;181:504–16. Available from: http://dx.doi.org/10.1016/j.apcatb.2015.07.026
11. Chemical Reaction Engineering - Octave Levenspiel - Google Libri [Internet]. [cited 2025 Mar 5]. Available from: https://books.google.ch/books?hl=it&lr&id=vw48EAAAQBAJ&oi=fnd&pg=PP1&dq=chemical+reaction+engineering+levenspiel&ots=5y-Zju7O2B&sig=YIACK-vHrl0cYXzPPt9B0wjeS6ww&redir_esc=y#v=onepage&q=chemical%20reaction%20engineering%20levenspiel&f=false
12. Abashar MEE, Al-Rabiah AA. Investigation of the efficiency of sorption-enhanced methanol synthesis process in circulating fast fluidized bed reactors. Fuel Processing Technology [Internet]. 2018;179(July):387–98. Available from: https://doi.org/10.1016/j.fuproc.2018.07.028
13. Lefebvre S, Guy C, Chaouki J. A convective/dispersive solid phase mixing model for three-phase fluidized bed reactors: Effect of dimensionless numbers. Chem Eng Sci. 2007;62(18–20):4954–62.

© 2025 by the authors. Licensed to PSEcommunity.org and PSE Press. This is an open access article under the creative commons CC-BY-SA licensing terms. Credit must be given to creator and adaptations must be shared under the same terms. See https://creativecommons.org/licenses/by-sa/4.0/



Systems & Control Transactions

Research Article - Peer Reviewed Conference Proceeding
ESCAPE 35 - European Symposium on Computer Aided Process Engineering
Ghent, Belgium. 6-9 July 2025
Jan F.M. Van Impe, Grégoire Léonard, Satyajeet S. Bhonsale,
Monika E. Polańska, Filip Logist (Eds.)

PSE PRESS

# Enhancing hydrodynamics simulations in Distillation Columns Using Smoothed Particle Hydrodynamics (SPH)

**Rodolfo Murrieta-Dueñas[a], Jazmín Cortez-González[a], Roberto Gutiérrez-Guerra[b], Juan Gabriel Segovia Hernández[c], Carlos E. Alvarado-Rodríguez[c,d]**

[a] Tecnológico Nacional de México / Campus Irapuato, Department of Chemical Engineering, Irapuato, Guanajuato, México
[b] Universidad Tecnológica de Leon, Sustainability for Development Department, León, Guanajuato, México
[c] Universidad de Guanajuato, Department of Chemical Engineering, Guanajuato, Guanajuato, México.
[d] Secretaría de Ciencias, Humanidades, Tecnología e Innovación, Ciudad de México, México
* Corresponding Author: rodolfo.md@irapuato.tecnm.mx

## ABSTRACT

This study presents a numerical simulation of the liquid-vapor (L-V) equilibrium stage in a sieve plate distillation column using the Smoothed Particle Hydrodynamics (SPH) method. To simulate the equilibrium stage, periodic temperature boundary conditions were applied. The column design was carried out in Aspen One, considering an equimolar benzene-toluene mixture and an operating pressure ensuring a condenser cooling water temperature of 120°F. The Chao-Seader thermodynamic model was employed for property calculations. Key outputs included liquid and vapor velocities per stage, mixture viscosity and density, operating pressure, and column diameter. The geometry of the distillation column stage and sieve plate was developed using SolidWorks, and Computational Fluid Dynamics (CFD) simulations were performed using the DualSPHysics code. The results demonstrate the influence of sieve plate design on velocity and temperature distributions within the stage, providing insights for enhancing stage design and operational efficiency.

**Keywords**: CFD, Simulation of distillation, hydrodynamics, SPH, Sieve tray

## 1. INTRODUCTION

Distillation remains the most widely utilized unit operation in Chemical Engineering due to its exceptional capability for product purification. However, conventional distillation processes are often associated with significant inefficiencies, driving the pursuit of alternative strategies to improve thermodynamic efficiency in equipment design and operation. While many of these alternatives have been evaluated using MESH equations and sequential simulators, less attention has been given to their modeling using Computational Fluid Dynamics (CFD), primarily due to its inherent complexity.

CFD employs either Eulerian or Lagrangian approaches. Eulerian methods rely on mesh-based discretization of the medium, producing spatially averaged results at the interfaces between fluids. Examples include the finite volume and finite element methods, with the former being widely adopted for simulating hydrodynamics, mass transfer, and momentum within distillation columns (Haghshenas et al., 2007; Lavasani et al., 2018; Zhao, 2019; Ke, 2022). However, Eulerian methods face limitations, including challenges in interface modeling, achieving convergence, and selecting appropriate turbulence models to accurately simulate turbulent flows.

In contrast, Lagrangian methods provide detailed insights into interfacial phenomena by discretizing the continuous medium into mesh-free points. This approach enables precise evaluation of flow, concentration, and temperature distributions within a system. Smoothed Particle Hydrodynamics (SPH) is a Lagrangian method particularly suited for modeling discontinuous media and complex geometries. It replaces the need for mesh generation by representing the medium with particles, making it applicable to a wide range of scenarios, including microbial growth (Martínez-Herrera et al., 2022), sea wave dynamics (Altomare et al., 2023), and stellar phenomena (Reinoso et al., 2022), demonstrating its flexibility and robustness.

Building on these advantages, this study presents a numerical simulation of a liquid-vapor (L-V) thermal equilibrium stage within a tray distillation column using the SPH method. The study focuses on Sieve trays, incorporating periodic temperature conditions to facilitate the simulation of the equilibrium stage.

## 2. METHODOLOGY

In this work a methodology for the simulation of the hydrodynamics and thermal equilibrium of tray distillation columns is proposed. This methodology consists of 3 stages: rigorous design of the distillation column in Aspen Plus, 3D design of the column - sieve trays and hydrodynamic analysis of the columns using the SPH method.

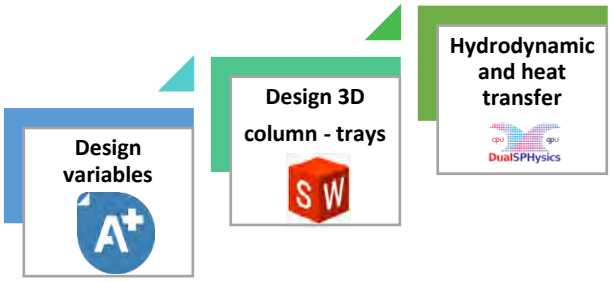



**Figure 1.** Methodology for the numerical simulation of the hydrodynamics and equilibrium of distillation columns.

### 2.1. Rigorous design of the distillation column

The column's sizing was conducted using Aspen One, considering an equimolar mixture of Benzene-Toluene and an operational pressure guaranteeing a condenser cooling water temperature of 120°F. The thermodynamic model applied was Chao-Seader, and sieve trays were employed. The column featured ten stages, with stage 5 designated for feeding, and both components assumed a 98% purification and recovery rate. This information yielded crucial data, including liquid and vapor velocities per stage, mixture viscosity and density, operating pressure, and column diameter. Three-dimensional CAD files of the distillation column and the sieve tray were developed using SolidWorks. Subsequently, these files were imported into DualSPHysics (Domínguez et. al., 2022) for CFD numerical simulation to ascertain flow and temperature profiles at an equilibrium stage. Stage 7 was selected for analysis, given their position below the feed stage.

The design of the distillation column was performed by rigorous methods, solving the MESH equations. **M** represents the total mass balance and the mass balance per component. **E** represents the equilibrium ratios present in the distillation process. **S** represents the sum of the mole fractions of the components of the mixture. **H** represents the total heat balance of the distillation column. This model is represented by equations 1 to 4.

Mass balance:

$$\frac{dM_j}{dt} = L_{j-1} + V_{j+1} + F_j^L + F_j^V - (L_j + U_j) - (V_j + W_j) \quad (1)$$

Equilibrium relationships:

$$Y_{i,j} = K_{i,j} X_{i,j} \quad (2)$$

Summation constraints:

$$\sum_{i=1}^{NC} K_{i,j} X_{i,j} - 1.0 = 0 \quad (3)$$

Energy balance:

$$\frac{d(M_j \overline{U}_{i,j})}{dt} = L_{j-1}\overline{h}_{j-1} + V_{j+1}\overline{H}_{j+1} + F_j^L \overline{h}_j^L + F_j^V \overline{H}_j^V - (L_j + U_j)\overline{h}_j - (V_j + W_j)\overline{H}_j + Q_j \quad (4)$$

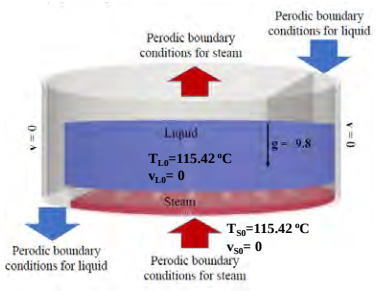
### 2.2. Column and sieve tray sizing

The 3D design of the column and trays was carried out in SolidWorks. The design parameters used were: column diameter, effective and downspout areas, obtained in Aspen Plus. The distance between trays was proposed to be 0.15m. Stainless steel 316L was chosen as construction material. Figure 2 shows, the 3D design of the tray, the stage and the initial conditions.



a) 3D Sieve tray design

b) stage design




c) initial conditions of simulation

**Figure 2.** Sieve tray design to simulation.

**Table 1.** Results of the rigorous simulation of the distillation column in Aspen Plus.

| Parameter | Líquid | Vapor |
|---|---|---|
| **Density (kg/m$^3$)** | 783.8023 | 4.0206 |
| **Viscosity (Ns/m$^2$)** | 2.5x10$^{-4}$ | 9.5x10$^{-6}$ |
| **Temperature (°C)** | 105.99 | 115.42 |
| **Mass fraction** | 0.5886 | 0.5405 |
| **Velocity (m/s)** | 0.0261 | 0.0214 |
| **Coefficient of thermal diffusivity (m$^2$/s)** | 7.9247x10$^{-8}$ | |
| **Surface tension** | 0.018 N/m | 0.018 N/m |

## 2.3. Hydrodynamics and heat transfer

Smoothed Particle Hydrodynamics (SPH) is a Lagrangian, meshless method with applications in the field of Computational Fluid Dynamics. Originally invented for astrophysics in the 1970s (Monagan J, 1992) it has been applied in many different fields, including fluid dynamics (Alvarado-Rodríguez C.E. et al., 2019). The method uses points named particles to represent the continuum and these particles move according to the governing equations in the fluid dynamic. When simulating free-surface flows, no special surface treatment is necessary due to the Lagrangian nature of SPH, making this technique ideal for studying violent free-surface motion.

For the numerical simulation the conservation equations of mass (Eq. 5), momentum (Eq. 6) and energy (Eq. 7) in Lagrangian formalism are considered.

$$\frac{d\rho}{dt} = -\rho\nabla\cdot\mathbf{v} \tag{5}$$

$$\frac{d\mathbf{v}}{dt} = \frac{-1}{\rho}\nabla \mathrm{P} + \frac{\mu}{\rho}\nabla^2\mathbf{v} + \mathbf{g} + \mathbf{F}^{\boldsymbol{B}} \tag{6}$$

$$\frac{dT}{dt} = \frac{1}{\rho C_p}\nabla\cdot(k\nabla T) \tag{7}$$

where $\rho$ is the density, $t$ is the time, $\mathbf{v}$ is the velocity vector, $P$ is the pressure, $\mu$ is the viscosity, g is the gravitational acceleration vector, $T$ is the temperature, $Cp$ is the heat capacity and $k$ is the thermal conductivity coefficient.

The motion of the fluid due to the change in temperature is provided by Boussinesq approximation (Eq. 8):

$$\mathbf{F}^{\boldsymbol{B}} = -\boldsymbol{g}\beta(T - T_r) \tag{8}$$

where $\beta$ is the thermal coefficient of volumetric expansion, and $T_r$ is the reference temperature of the fluid.

The momentum, continuity and energy equations can be discretized using the SPH formalism and gives:

$$\frac{d\rho_a}{dt} = -\rho_a\sum_b^n m_b\frac{\mathbf{v}_b}{\rho_b}\cdot\nabla W_{ab} \tag{9}$$

$$\frac{d\mathbf{v_a}}{dt} = -\sum_b^n m_b\left(\frac{P_b}{\rho_b^2}+\frac{P_a}{\rho_a^2}\right)\nabla_a W_{ab} + \sum_b^n m_b\frac{4\upsilon\, r_{ab}\cdot\nabla W_{ab}}{(\rho_a+\rho_b)({r_{ab}}^2+\varepsilon^2)}\mathbf{v}_{ab} + \boldsymbol{F}^{\boldsymbol{B}} \tag{10}$$

$$\frac{dT}{dt} = \frac{1}{C_p}\sum_b^n \frac{m_b}{\rho_a\rho_b}\frac{(k_a+k_b)r_{ab}\cdot\nabla_a W_{ab}}{{r_{ab}}^2+\varepsilon^2}(T_a - T_b) \tag{11}$$

Equations (Eq. 9)-(Eq. 11) are coupled by the Tait state equation (Eq. 12)

$$P = B\left[\left(\frac{\rho}{\tilde{\rho}}\right)^{\gamma} - 1\right] \tag{12}$$

where $P$ is the pressure, $\tilde{\rho}$ is the reference density, $B = c^2\rho/\gamma$, $\gamma = 7$ = 7 for liquids and $\gamma = 1.4$ for gases.

Different approaches and methods have been proposed to simulate multiphase flows (Tartakovsky & Meakin, 2006; Monaghan & Kocharyan, 1995; Sigalotti et al., 2014). In this work several new approaches are added to the standard formalism. These features permit to properly simulate multiphase flows, where the main contribution lies in the improved management to interphase with highly nonlinear deformations.

The instability and artificial surface tension produced in a multiphase flow using the standard SPH has been reported by (Colagrossi & Landrini, 2003, and Gómez Gesteira et al, 2010). For this work we have replaced the Eq. (10) used in the standard SPH formulation by the Eq. (13) which to permit that higher density ratios in simulations avoiding the artificial surface tension (Colagrossi & Landrini, 2003). The method is rather robust, even for large free-surface fragmentation and folding, efficient and relatively easy-to-code and results stable and capable to easily treat a variety of density ratios.

$$\frac{d\mathbf{v_a}}{dt} = -\sum_b^n m_b\left(\frac{P_b+P_a}{\rho_a\rho_b}\right)\nabla_a W_{ab} + \sum_b^n m_b\frac{4\upsilon\, r_{ab}\cdot\nabla W_{ab}}{(\rho_a+\rho_b)({r_{ab}}^2+\varepsilon^2)}\mathbf{v}_{ab} + \boldsymbol{F}^{\boldsymbol{B}} \tag{13}$$

Higher density ratios can be simulated with the use of this expression avoiding the artificial surface tension.

According to (Colagrossi & Landrini, 2003) the pressure of each phase is calculated using the equation of state (14), which is calculated using appropriate parameters according to each phase reference density. So, the equation of state (14) is calculated for each phase using:

$$P_\alpha = B_\alpha\left[\left(\frac{\rho}{\tilde{\rho}_\alpha}\right)^{\gamma_\alpha} - 1\right] \tag{14}$$

where the subscripts $\alpha$ denote the phase

The constant $B_\alpha$ is chosen form the liquid phase to permit a small compressibility of the higher density fluid, that is $v_{max\alpha} = c_\alpha \ll 1$ 1, where $v_{max\alpha}$ is the maximum velocity of the fluid with higher density expected in the considered problem. Then $B_\alpha$ must be matched to the liquid and gas phases in the equation of state for the fluid with lower density to create a stable pressure at the interphase. This formulation allows the simulation of high-density ratios (e.g. 1:1000, which is like the air-water ratio).

This method was implemented for the numerical analysis of the distillation columns under the following considerations: periodic conditions were used to perform the hydrodynamic and equilibrium analysis. The initial properties of the fluids are shown in Table 1. In all cases, no-slip boundary conditions were considered in the interaction between fluid and boundary particles using the dynamic particle method.

## 3. DISCUSSION OF RESULTS

From the results obtained using the SPH method in numerical simulations, it is possible to analyze the velocity profile and the temperature profile inside the stage. In addition, it is possible to approximate the time it requires for the stage to reach equilibrium under the initial conditions established.

The simulation was performed with a total of 7,261,750 particles of which 1,386,940 are bound, 4,230,940 are liquid and 1, 643,870 are vapor. 60 seconds of real time were simulated. The simulation was completed in a total of 17.5h on the GPU NVIDIA GeForce 3060 of ITESI.

In Figure 3 is shown the evolution of velocity field obtained in the simulation. A higher velocity is obtained in the area where the fluid enters from the downspout, the velocity distribution is not completely homogeneous, however, there are not dominant streamlines in the stage, meaning a good distribution of the flow in the stage.

In Figure 4 the evolution of the temperature in the stage is shown, which due to the good flow get the equilibrium temperature in the simulated time. It is observed that in the downcomer section the fluid velocity is the highest and that the velocity distribution is uniform throughout the tray.

In Figure 5 is shown the distribution of the temperature from a top perspective at 22.5 seconds. The dsitribution of the temperature is almost homogeneus at this time. The liquid temperature and vapor temperature are very nearly at equilibrium. In addition, vapor accumulation zones can be observed which show very high temperatures and therefore no interaction between liquid and vapor.

In Figure 6 is shown a Reynolds map from a top perspective calculated from the average velocity shown in the Figure 3. This figure shows that the highest Reynolds values occur in the holes of the deck area and are consistent with the thermal behavior of Figure 5. This shows that the greater the interaction of the liquid with the vapor, the greater the heat transfer.

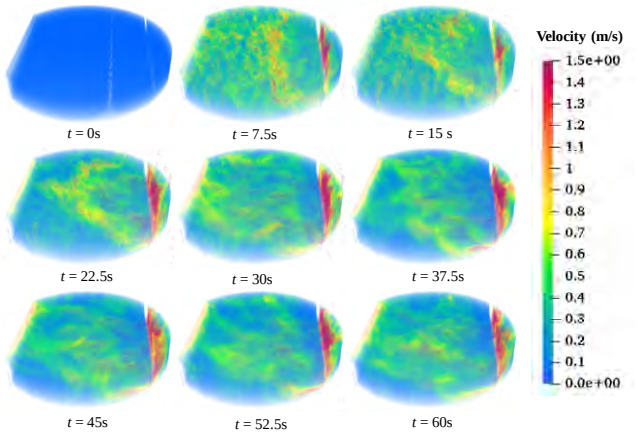



**Figure 3.** 3D perspective of the velocity field evolution in the stage.

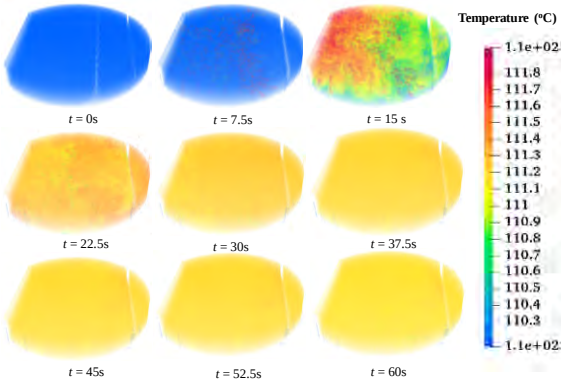



**Figure 4.** 3D perspective of the temperature field evolution in the stage.

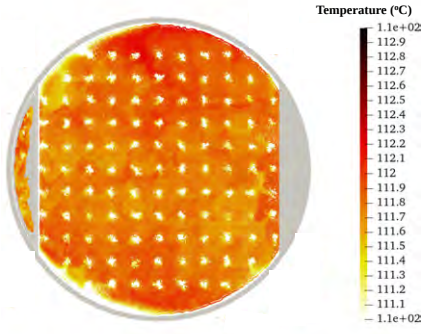



**Figure 5.** Top perspective of the temperature distribution .

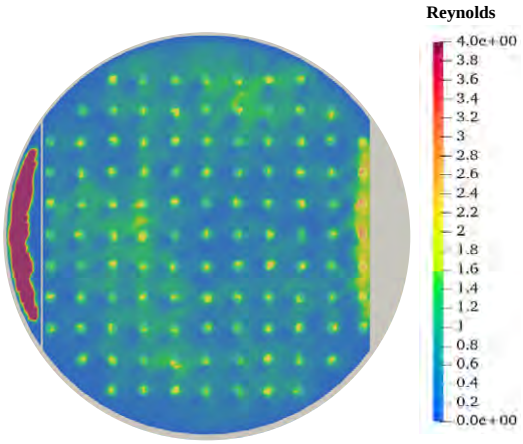



**Figure 6.** Top perspective of the Reynolds map calculated from the average velocity shown in Figure 3.

## 4. CONCLUSIONS

This study presents the CFD numerical simulation of a stage within a distillation column. The column and tray geometries were designed in SolidWorks and subsequently exported to DualSPHysics to carry out simulations based on parameters obtained from rigorous simulations in Aspen Plus. The numerical simulations provide detailed insights into the flow and heat transfer within the stage, accounting for the interaction between the vapor and liquid phases and their respective temperature variations. This data enables the development of a novel methodology for calculating the global heat transfer coefficient in the stage, which can be leveraged to enhance tray design and facilitate comparative analyses of different tray types. In conclusion, the results highlight the effectiveness of applying initial and boundary conditions to simulate thermal equilibrium in distillation columns. Additionally, the SPH method proves to be a powerful and flexible tool for numerical simulations of fluid dynamics and thermal equilibrium, offering valuable contributions to the design and optimization of distillation equipment.

## ACKNOWLEDGEMENTS

We are in agreement with the National Technological Institute of Mexico for the support provided for this research.

## REFERENCES

1. Altomare C, Scandura P, Cáceres I, van der A D, Viccione G. 2023. Large-scale wave breaking over a barred beach: SPH numerical simulation and comparison with experiments. Coastal Engineering, 185, 104362. doi:10.1016/j.coastaleng.2023.104362
2. Alvarado-Rodríguez, C. E., Klapp, J., Domínguez, J. M., Uribe-Ramírez, A. R., Ramírez-Minguela, J. J., & Gómez-Gesteira, M. (2019, March). Multiphase Flows Simulation with the Smoothed Particle Hydrodynamics Method. In International Conference on Supercomputing in Mexico (pp. 282-301). Springer, Cham.
3. Domínguez JM, Fourtakas G, Altomare C, Canelas RB, Tafuni A, García-Feal O, Martínez-Estévez I, Mokos A, Vacondio R, Crespo AJC, Rogers BD, Stansby PK, Gómez-Gesteira M. (2021), DualSPHysics: from fluid dynamics to multiphysics problems. Computational Particle Mechanics.
4. Haghshenas Fard, M., Zivdar, M., Rahimi, R., Nasr Esfahani, M., Afacan, A., Nandakumar, K., & Chuang, K. T. (2007). CFD simulation of mass transfer efficiency and pressure drop in a structured packed distillation column. Chemical Engineering & Technology: Industrial Chemistry-Plant Equipment-Process Engineering-Biotechnology, 30(7), 854-861. Martínez-
5. Herrera, G., Cortez-González, J., Murrieta-Dueñas, R., Uribe-Ramírez, A. R., Pérez-Segura, T., & Alvarado-Rodríguez, C. E. (2022). Smoothed particles hydrodynamics simulations of microbial kinetic in a stirred bioreactor with proximity impellers. Computational Particle Mechanics, 1-13.
6. Ke, T. (2022). CFD simulation of sieve tray hydrodynamics using openfoam.
7. Lavasani, M. S., Rahimi, R., & Zivdar, M. (2018). Hydrodynamic study of different configurations of sieve trays for a dividing wall column by using experimental and CFD methods. Chemical Engineering and Processing-Process Intensification, 129, 162-170.
8. Reinoso, B., Leigh, N. W., Barrera-Retamal, C. M., Schleicher, D., Klessen, R. S., & Stutz, A. M. (2022). The mean free path approximation and stellar collisions in star clusters: numerical exploration of the analytic rates and the role of perturbations on binary star mergers. Monthly Notices of the Royal Astronomical Society, 509(3), 3724-3736.
9. Zhao, H., Li, Q., Yu, G., Dai, C., & Lei, Z. (2019). Performance analysis and quantitative design of a flow- guiding sieve tray by computational fluid dynamics. AIChE Journal, 65(5), e16563
10. Martínez-Herrera, G., Cortez-González, J., Murrieta-Dueñas, R., Uribe-Ramírez, A. R., Pérez-Segura, T., & Alvarado-Rodríguez, C. E. (2022). Smoothed particles hydrodynamics simulations of microbial kinetic in a stirred bioreactor with proximity impellers. Computational Particle Mechanics, 9(5), 1017-1029.
11. Tartakovsky, A., Meakin, P.: Pore scale modeling of immiscible and miscible fluid flows using smoothed particle hydrodynamics. Adv. Water Resour. 29,

1464–1478 (2006).
12. Monaghan, J.J., Kocharyan, A.: SPH simulation of multi-phase flow. Comput. Phys. Commun. 87, 225–235 (1995).
13. Sigalotti, L.D.G., Troconis, J., Sira, E., Peña-Polo, F., Klapp, J.: Diffuse-interface modeling
14. of liquid-vapor coexistence in equilibrium drops using smoothed particle hydrodynamics.
15. Phys. Rev. E 90, 013021 (2014).
16. Colagrossi, A., Landrini, M.: Numerical simulation of interfacial flows by smoothed particle hydrodynamics. J. Comput. Phys. 191, 448–475 (2003)
17. Gómez-Gesteira, M., Rogers, B.D., Dalrymple, R.A., Crespo, A.J.C.: State of the art of classical SPH for free-surface flows. J. Hydrau. Res. 48, 6–27 (2010).

© 2025 by the authors. Licensed to PSEcommunity.org and PSE Press. This is an open access article under the creative commons CC-BY-SA licensing terms. Credit must be given to creator and adaptations must be shared under the same terms. See https://creativecommons.org/licenses/by-sa/4.0/



Systems & Control Transactions

**Research Article - Peer Reviewed Conference Proceeding**
ESCAPE 35 - European Symposium on Computer Aided Process Engineering
Ghent, Belgium. 6-9 July 2025
Jan F.M. Van Impe, Grégoire Léonard, Satyajeet S. Bhonsale,
Monika E. Polańska, Filip Logist (Eds.)

PSE PRESS

# Kinetic Modelling and Optimisation of $Co_2$ Capture and Utilisation to Methane on Dual Function Material

**Meshkat Dolat[a], Andrew D. Wright[b], Mohammadamin Zarei[a], Melis S. Duyar[a,c], and Michael Short[a,c]***

[a] School of Chemistry and Chemical Engineering, University of Surrey, Guildford, Surrey GU2 7XH, UK
[b] Department of Chemical Engineering, School of Engineering, The University of Manchester, UK
[c] Institute for Sustainability, University of Surrey, Guildford, Surrey GU2 7XH, UK
* Corresponding Author: m.short@surrey.ac.uk

## ABSTRACT

Dual function materials (DFMs) integrate $CO_2$ capture and conversion, offering a streamlined approach to Power-to-Gas (PtG) processes. This study develops a cyclic steady-state model for the DFM-based methanation of $CO_2$ using the finite difference method. The model captures the adsorption, purge, and methanation stages and incorporates a semi-implicit numerical scheme for stability and accuracy. Bayesian optimisation is used to explore operational and design parameters to maximise methane productivity, $CO_2$ conversion, and product purity. Multi-objective optimisation reveals key trade-offs among these metrics, while the impact of pressure, hydrogen concentration, DFM weight, geometry and cycle times is systematically evaluated. Results reveal that lower flow rates enhance recovery and purity, while higher flow rates improve productivity. Extended adsorption times favour purity, whereas longer methanation times significantly benefit recovery and productivity. Multi-objective optimisation, presented through Pareto fronts, highlight trade-offs among performance metrics. Variations in hydrogen pressure, DFM mass, and $H_2$ concentration further emphasise their impact on the system's efficiency. This work provides a scalable, reproducible framework for optimising DFM-based PtG systems, advancing their potential for sustainable energy storage and decarbonisation.

**Keywords**: Kinetic Modeling, Dual Function Material, Process Optimization, Power-To-Gas, Carbon Capture and Utilization, Cyclic Steady State Simulation

## INTRODUCTION

Power-to-Gas (PtG) technology offers a transformative solution for mitigating the intermittency of renewable energy sources by converting surplus electricity into synthetic natural gas (SNG). This process uses renewable hydrogen to react with $CO_2$ via the Sabatier reaction, enabling decarbonisation of downstream sectors, reducing reliance on fossil fuels, and promoting renewable energy adoption in traditionally hard-to-electrify domains like heating and heavy transport. It can also integrate with anaerobic digestion (AD) plants to capture $CO_2$ from biogas, converting it into additional bio-methane and enhancing its emission reduction potential. In future, hydrogen injection into natural gas pipelines will further decarbonise sectors such as residential heating and industrial applications, with a portion also supporting PtG processes for efficient renewable energy storage [1]. While PtG offers dual benefits of $CO_2$ utilisation and energy storage, challenges like high $CO_2$ capture costs, thermodynamic and kinetic barriers in methanation, and reactor heat and mass transfer management must be addressed to enhance economic and technical viability.

A notable advancement in this field is the development of dual function materials (DFMs), which integrate $CO_2$ capture and hydrogenation into a single operational unit [2]. This novel approach simplifies the process flow by eliminating the need for energy-intensive intermediate purification steps. DFMs, typically composed of an alkaline component for $CO_2$ adsorption and a catalytic metal for methanation, enable direct conversion of $CO_2$ from dilute streams into methane under operating conditions conducive to both capture and conversion. Previous studies [3] have demonstrated the feasibility of these materials, highlighting their ability to facilitate cyclic $CO_2$ adsorption and hydrogenation operations without

significant performance degradation.

Very few studies have explored the modelling and optimisation of DFM processes. So far there is one dynamic kinetic model developed to describe the $CO_2$ adsorption and hydrogenation on Ru-$Na_2CO_3$/$Al_2O_3$ catalysts [4] which focuses on reaction kinetics and surface coverage through unsteady material balance equations. Mass transfer limitations were neglected in their setup, simplifying their model while limiting its application to scenarios where similar conditions hold. However, the study lacks detailed experimental parameters, making it difficult to extrapolate; it does not investigate cyclic performance systematically; and it does not incorporate systematic optimisation techniques to explore the optimal process conditions and the effect of many important features of the DFM cycle design. Furthermore, the model's software implementation is neither open-source nor clearly detailed.

One recent study [5] adopted a relevant approach, focusing on the methanation step. They employed Computational Fluid Dynamics (CFD) to simulate the performance of a packed-bed reactor, based on calculations of physical parameters such as active surface area and external mass transfer coefficients. However, their study primarily examines the methanation stage, leaving gaps in the cyclic analysis of adsorption and purge phases.

### Contribution

Building on these foundations, this study develops an advanced finite difference model (FDM) in Python, leveraging a semi-implicit numerical approach to address the shortcomings in prior studies. For the first time, cyclic performance of DFMs is systematically designed and analysed, providing a comprehensive understanding of adsorption, purge, and methanation stages in an integrated manner. Furthermore, Bayesian optimisation is applied to identify optimal process parameters, yielding deeper insights into trade-offs between methane productivity, $CO_2$ conversion efficiency, and the product purity. This work addresses existing gaps by offering a reproducible, open-source framework that enhances the design, scalability, and efficiency of PtG systems based on DFM technology.

## METHODOLOGY

The modeling of the DFM process involves the formulation of a system of partial differential equations (PDEs) to describe the dynamics of gas-phase and surface-phase interactions within the reactor. These equations capture the temporal evolution of species concentrations and the coverage of adsorption sites across the reactor length and during the four stages of adsorption, purge, hydrogenation and final purge. The model builds upon the frameworks established in recent studies [4], extending them to incorporate a more efficient open-source numerical approach. This enhanced methodology explicitly incorporates cyclic operations and is tailored for advanced optimisation methods, enabling systematic exploration of optimal operational and design parameters.

### Dynamic DFM simulation model

The model is based on an experimental setup featuring a packed bed reactor loaded with DFM on granular alumina precursors. During the adsorption phase, a mixture of $CO_2$ and inert gas ($N_2$) is introduced into the column, where $CO_2$ is adsorbed onto the active sites of the DFM. Pure $N_2$ is employed during the purging stages, while a mixture of $H_2$ and $N_2$ is used during the hydrogenation phase. In this stage, the introduced $H_2$ aids the removal of adsorbed $CO_2$, driving its hydrogenation into methane. A final purge with pure nitrogen sweeps off the remaining gas components and facilitates the system condition for the next cycle.

### Assumptions

The following assumptions are made in formulating the mathematical model and solving the pertinent equations:

- The process operates isothermally, with the reactor temperature held constant at feasible hydrogenation temperature during all four stages of the process.
- Radial gradients are neglected, assuming uniform distribution of species and properties across the reactor cross-section.
- External and internal mass transfer limitations are considered negligible with similar conditions outlined in the reference study.
- The ideal gas law applies to describe the gas-phase behaviour.
- The reactor column is in thermal equilibrium with its surroundings and the entering feed. Positioned within the flue gas environment, heat transfer between the column and its surroundings is negligible.
- Pressure drop along the length of the reactor is considered negligible.

### Governing equations

The gas-phase concentrations of $CO_2$, $H_2O$, $H_2$, $CH_4$ and $N_2$ are governed by a PDE model assuming plug flow with axial dispersion. The temporal changes to the concentration of component $i$ ($C_i$) in the gas phase is calculated according to the below equation:

$$\frac{\partial C_i}{\partial t} = -\frac{u}{\varepsilon}\frac{\partial C_i}{\partial x} + \frac{D}{\varepsilon}\frac{\partial^2 C_i}{\partial x^2} + \frac{\rho R_i}{\varepsilon} \quad (1)$$

Where, $u$ is the gas linear velocity and $D$ is the axial

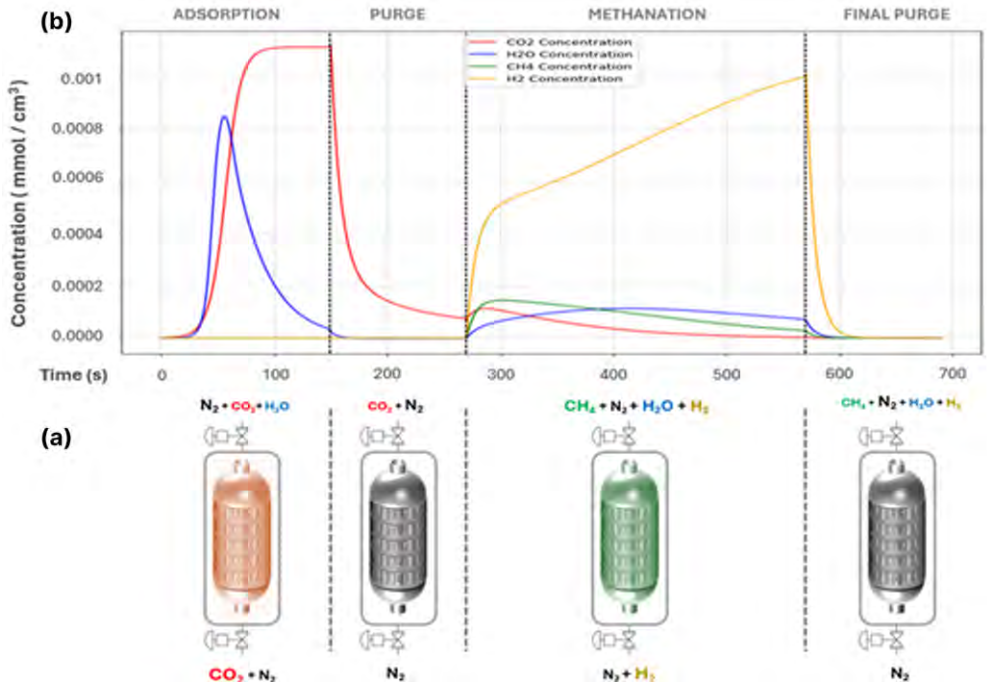



**Figure 1:** (a) The schematic diagram of the 4-stage carbon capturing and methanation in DFM process. (b) The base-case simulation column outlet concentration profile for $CO_2$ (red), $H_2O$ (blue), $CH_4$ (green) and $H_2$ (orange) curves for adsorption, purge 1, hydrogenation and purge 2.

dispersion coefficient. The parameters $\rho$ and $\varepsilon$ are the bed density and void fraction.

The unsteady state component mass balance in the sorbent phase can be expressed in terms of temporal changes to the fraction of the sorbent surface area covered with the component ($\theta_j$) according to Equation 2:

$$\frac{\partial \theta_j}{\partial t} = \frac{R_i}{\Omega_j} \tag{2}$$

Where, $\Omega_j$ is the adsorption capacity of carbon dioxide on the DFM and $R_i$ is the rate of formation for component $i$ which can be expressed in terms of the coverage area ($\theta_j$), stoichiometric coefficient of the component present in the reaction and the intrinsic rate of reaction which are outlined in the reference work [4]. Each rate expression corresponds to a specific chemical reaction within the $CO_2$ capture and conversion mechanism.

Equation (2) is only applied to $CO_2$ and $H_2O$ assuming the adsorption of other gaseous components negligible.

## Bespoke cyclic steady-state model

The PDE system is discretised along the axial direction using finite differences. Central differences are used for spatial derivatives, and backward differences are employed for temporal integration to ensure numerical stability. Also, Danckwert boundary conditions are used at the reactor outlet to ensure mass conservation under convective and diffusive fluxes. The resulting system of ordinary differential equations is solved using a semi-implicit scheme, with convergence criteria set for species concentrations and surface coverages.

The kinetic parameters, including rate constants and activation energies, were determined by fitting the developed PDE model to reference work experimental data using the least squares method. The concentration profiles at the reactor outlet were used for this estimation, with adjustments made to account for the delayed response of the analyser. Following the parameter identification, the bespoke model was applied iteratively to simulate the cyclic performance of the DFM process. The simulation was designed to achieve cyclic steady-state (CSS), defined as the point where consecutive cycles exhibit negligible variation in species concentrations and surface coverages. The CSS was modelled by systematically iterating the cyclic stages—adsorption, purge, hydrogenation, and final purge—until a stable operational pattern was observed. This validated model was then employed for process optimisation to improve system efficiency and performance.

Figure 1 depicts the four stages of DFM process and showcases the concentration profile for each of the components exiting the reactor at each stage after reaching CSS condition. The key design and operational parameters related to this base line model is specified in Table 1.

## Surrogate model optimisation

To optimise the performance of the DFM cyclic process, Bayesian optimisation was employed using Optuna, a robust open-source optimisation library in Python. The optimiser directly evaluates the developed PDE-based kinetic model, treating it as a black-box surrogate within the search space. Unlike traditional grid or random search methods, Optuna employs a tree-structured Parzen estimator (TPE) which models the distribution of hyperparameters that yield favourable outcomes and samples from this distribution in subsequent trials. This allows for a more efficient and adaptive exploration of the parameter space for computationally expensive surrogate models [6].

The developed kinetic model was integrated with Optuna to maximise methane productivity, $CO_2$ conversion efficiency, and purity. The optimisation encompassed a range of design and operational variables, including stage durations, flow rates, reactor geometry, and feed compositions. Multi-objective optimisation was performed to generate Pareto fronts, providing insights into trade-offs among key performance metrics.

**Table 1:** Base-case reactor model parameters for simulating the 4-staged DFM process.

| Parameter | Value |
|---|---|
| Bed density, $\rho$ (g/cm$^3$) | 1.4 |
| Column inner diameter, $d_i$ (mm) | 10.3 |
| DFM weight, $W_{DFM}$ (g) | 3.0 |
| Gas overall flowrate, $F_{gas}$ (mL/min) | 20 |
| Max. adsorption capacity, $\Omega$ (mmol/g) | 0.38 |
| Porosity, ε | 0.35 |
| Temperature, $T$ (K) | 623 |
| Hydrogenation Pressure, $P_{hyd}$ (atm) | 1.0 |
| $CO_2$ ads. feed gas (Vol.%) | 5.7 |
| $H_2$ hyd. feed gas (Vol.%) | 5.7 |

## Objectives, variables and statistics

In this work, the optimisation objectives are to maximise recovery, productivity, and purity at CSS as defined hereunder:

$$Recovery = \frac{mol_{CH_4}|_{out,hyd}}{mol_{CO_2}|_{in,ads}} \quad (3)$$

$$Productivity = \frac{mol_{CH_4}|_{out,hyd}}{(W_{DFM})(\boldsymbol{t_{cycle}})} \quad (4)$$

$$Purity = \frac{mol_{CH_4}|_{out,hyd}}{mol_{CO_2}|_{out,hyd}+mol_{H_2}|_{out,hyd}} \quad (5)$$

For calculating the total number of moles of component $i$ into or out of a stage $k$ we use:

$$mol_i|_k = \int_0^{t_k} F_{total}\, C_i(t)\, dt \quad (6)$$

The parameters influencing cycle performance include process times for each stage, gas linear velocity, column geometry, overall flue gas flow rate, concentrations of $CO_2$ ($C_{CO2}$) and $H_2$ ($C_{H2}$), DFM weight ($W_{DFM}$) and process conditions such as temperature and pressure. These parameters collectively form the degrees of freedom for the optimisation process (9 degrees of freedom in total).

While the impact of certain parameters, such as hydrogen pressure ($P_{hyd}$), $C_{H2}$ and $W_{DFM}$ (referred to as the first group of variables) is relatively straightforward (e.g., increasing hydrogen concentration or DFM weight directly enhances performance metrics), other parameters, such as stage durations, channel diameter, and gas flow rate (the second group), have less predictable or potentially conflicting effects on performance metrics.

This variability necessitates a series of multi-objective optimisation runs for each parameter in the first group. As a result, for each fixed value set of first-group variables, the optimisation explores a range of values for the second group, resulting in a unique Pareto curve for each case.

Each optimisation run includes 500 iterations per pair of two-objective Pareto points. With a minimum number of time steps of $N_t$ = 1000 for each stage, the optimisation takes 300-400 minutes. Previous trials indicate that changes in species concentrations and surface coverages are typically less than 1% after 5 cycles. To enhance computational efficiency, the maximum number of cycles required to achieve CSS has been limited to 5.

# RESULTS AND DISCUSSIONS

The Pareto fronts resulting from the multi-objective optimisation for maximising (a) Purity vs. Recovery, (b) Purity vs. Productivity, and (c) Productivity vs. Recovery are shown in Figures 2a, 2b, and 2c, respectively. In these figures, the iteration points (grey dots) represent the evaluated solutions generated by the CSS model during each iteration of the optimisation process. The Pareto front points (blue markers) highlight the optimal trade-offs between the respective objectives, such as purity and recovery.

For these results, only the second group of variables was manipulated, while the first group of variables was held constant at their base values. The variation bounds and the optimal values of the second group of variables corresponding to the extreme points on each Pareto curve (indicated by numbers) are detailed in Table 2. For simplicity, time steps were initially allowed to vary independently. However, to optimise the number of columns and ensure continuous operation, time steps will be balanced in future work.

**Table 2:** Optimisation results for pareto front extreme points in figures 2a, 2b, and 2c.

| No. | $t_{ads}$ | $t_{prg1}$ | $t_{hyd}$ | $t_{prg2}$ | $d_i$ | $F_{gas}$ |
|---|---|---|---|---|---|---|
| | s | s | s | s | mm | mL/s |
| **1** | 176 | 42 | 42 | 162 | 8.7 | 5.0 |
| **2** | 27 | 42 | 333 | 162 | 15.2 | 5.0 |
| **3** | 151 | 35 | 42 | 24 | 10.3 | 5.0 |
| **4** | 64 | 35 | 235 | 24 | 9.97 | 15.0 |
| **5** | 21 | 29 | 77 | 20 | 13.7 | 21.0 |
| **6** | 24 | 42 | 328 | 110 | 9.4 | 5.0 |

$20 \leq t_{ads} \leq 200$ ; $20 \leq t_{prg1,2} \leq 180$ ; $20 \leq t_{hyd} \leq 400$ ; $8.0 \leq d_i \leq 20$ ; $5 \leq F_{gas} \leq 30$

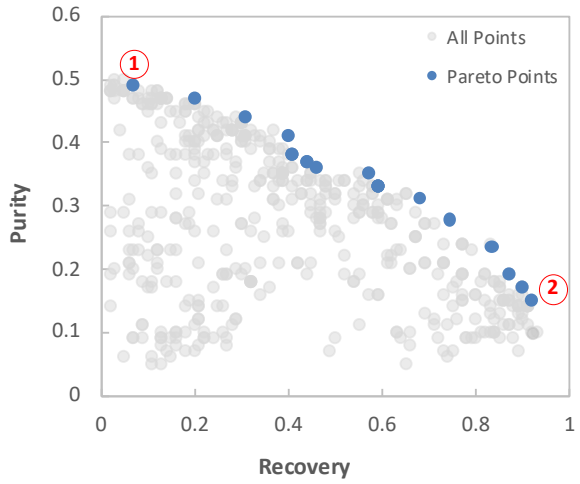



**Figure 2a.** Purity vs. Recovery Pareto Front and iteration points (No. 1 and 2 indicate the extreme points).

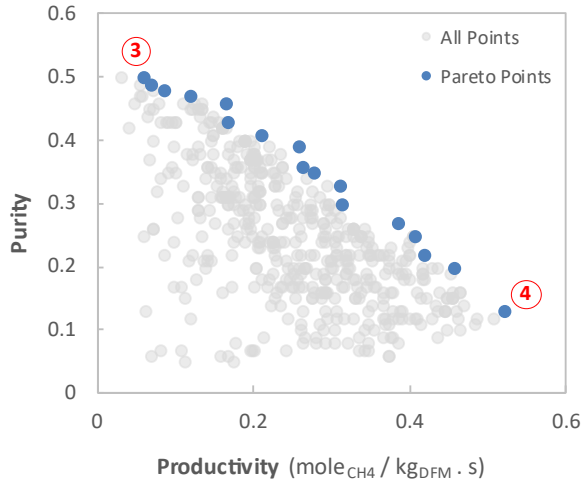



**Figure 2b.** Purity vs. Productivity Pareto Front and iteration points (No. 3 and 4 indicate the extreme points)

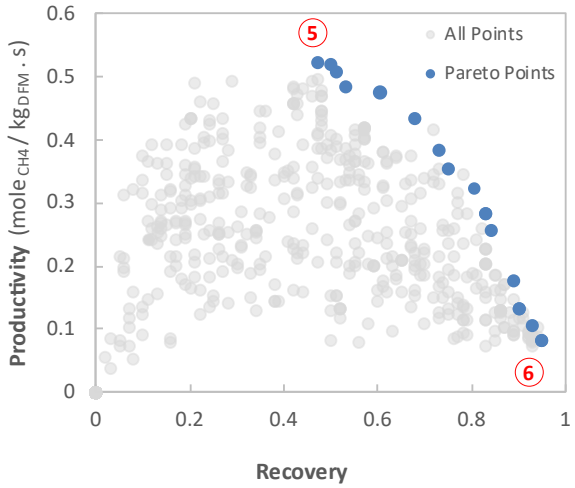



**Figure 2c.** Productivity vs. Recovery Pareto Front and iteration points (No. 5 and 6 indicate the extreme points).

The results reveal that a low gas flow rate is generally preferred when increasing purity and recovery, whereas higher flow rates are favoured for maximising productivity. Both recovery and productivity benefit from extended hydrogenation time ($t_{hyd}$), with recovery showing a stronger preference for longer durations than productivity. Similarly, adsorption time ($t_{ads}$) tends to increase to enhance purity, while the opposite trend is observed for recovery and productivity.

In all cases, the first purging period is reduced toward its lower bound. This is because extended purging times result in greater $CO_2$ loss from the adsorption sites, reducing the surface coverage and consequently diminishing methane production potential during the subsequent hydrogenation stage. Productivity, in particular, minimises this parameter more aggressively than other metrics. The final purge stage has negligible impact on any of the metrics, as the objective function is largely insensitive to its variation. Consequently, purge durations can be minimised to their operational limits, ensuring the removal of residual gases from the previous stage without compromising performance.

The changes to the Pareto curves resulting from variations in the first group of variables are qualitatively predictable. However, to quantitatively illustrate their impact on performance metrics and due to space constraints, only the effects of selected parameters are presented here. Figure 3 demonstrates the influence of two hydrogenation pressure levels, three $H_2$ concentration levels, and two DFM loading weights on the purity-recovery Pareto fronts. In this graph, H10, H30, and H50 represent hydrogen concentrations of 10%, 30%, and 50%, respectively. W6 and W10 indicate DFM weights of 6 g and 10 g, while P5 and P10 correspond to methanation pressures of 5 atm and 10 atm.

Changes to the first group of variables involve

energy and material costs, requiring a detailed analysis to evaluate trade-offs between metric improvements and expenses such as hydrogen compression or purification. Increased DFM weight also leads to higher material costs, pressure drops and longer columns, further impacting costs.

The figure highlights key parameter effects on purity and recovery. For example, increasing hydrogen pressure to 5 atm is more effective than quadrupling the DFM loading, but the scale of performance gains diminishes exponentially with further pressure increases. Similar diminishing returns are observed for other parameters. This further emphasises the necessity for a more detailed cost analysis to derive meaningful techno-economic conclusions.

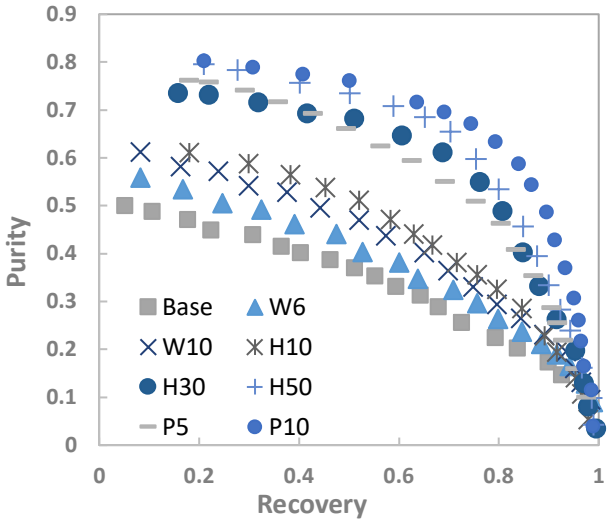



**Figure 3.** changes to Purity vs. Recovery pareto fronts due to step changes to the 1st group of variables.

## CONCLUSIONS AND FUTURE WORK

This study presents a comprehensive cyclic steady-state model for optimising DFMs in PtG applications. Using a semi-implicit numerical approach and Bayesian optimisation, the model systematically evaluates operational parameters, revealing key trade-offs among $CO_2$ conversion, methane productivity, and purity. Results show that lower flow rates enhance recovery and purity, while higher flow rates improve productivity. Extended adsorption times favour purity, while longer methanation times are critical for improving recovery and productivity. Multi-objective optimisation highlights Pareto fronts, illustrating the trade-offs between competing performance metrics. Variations in hydrogen pressure, DFM weight, and $H_2$ concentration demonstrate their substantial influence on system efficiency, with hydrogen pressure showing diminishing returns at higher levels. These insights highlights the importance of optimising both operational and design parameters to achieve industrial scalability. Future work will focus on detailed techno-economic analyses and cost-energy trade-offs to further enhance DFM-based PtG systems. Further fundamental studies on mass transfer, incorporating efficient finite volume approaches, are also recommended.

## DIGITAL SUPPLEMENTARY MATERIAL

The simulation code developed in this study are available in the following GitHub repository: https://github.com/MeshkatD/KinOptCO2CH4

## ACKNOWLEDGEMENTS

We would like to acknowledge that this work was supported by the School of Chemistry and Chemical Engineering at the university of Surrey. It is partly funded by the Engineering and Physical Sciences Research Council (EPSRC) [grant No. EP/X000753/1 and EP/Y005600/1] and Supergene Bioenergy Impact Hub [EP/Y016300/1].

## REFERENCES

1. Liu, W., Wen, F., Xue, Y.: Power-to-gas technology in energy systems: current status and prospects of potential operation strategies. Journal of Modern Power Systems and Clean Energy. 5, 439–450 (2017). https://doi.org/10.1007/S40565-017-0285-0/FIGURES/4
2. Duyar, M.S., Treviño, M.A.A., Farrauto, R.J.: Dual function materials for CO2 capture and conversion using renewable H2. Appl Catal B. 168–169, 370–376 (2015). https://doi.org/10.1016/J.APCATB.2014.12.025
3. Merkouri, L.P., Bobadilla, L.F., Martín-Espejo, J.L., Odriozola, J.A., Penkova, A., Torres-Sempere, G., Short, M., Reina, T.R., Duyar, M.S.: Integrated CO2 capture and dynamic catalysis for CO2 recycling in a microbrewery. Applied Catalysis B: Environment and Energy. 361, 124610 (2025). https://doi.org/10.1016/J.APCATB.2024.124610
4. Bermejo-López, A., Pereda-Ayo, B., González-Marcos, J.A., González-Velasco, J.R.: Modeling the CO2 capture and in situ conversion to CH4 on dual function Ru-Na2CO3/Al2O3 catalyst. Journal of CO2 Utilization. 42, 101351 (2020). https://doi.org/10.1016/J.JCOU.2020.101351
5. Tsiotsias, A.I., Harkou, E., Charisiou, N.D., Sebastian, V., Naikwadi, D.R., van der Linden, B., Bansode, A., Stoian, D., Manos, G., Constantinou, A., Goula, M.A.: Very low Ru loadings boosting performance of Ni-based dual-function materials during the integrated CO2 capture and methanation process. Journal of Energy Chemistry.

(2024). https://doi.org/10.1016/J.JECHEM.2024.11.001
6. Shekhar, S., Bansode, A., Salim, A.: A Comparative study of Hyper-Parameter Optimization Tools. 2021 IEEE Asia-Pacific Conference on Computer Science and Data Engineering, CSDE 2021. (2022). https://doi.org/10.1109/CSDE53843.2021.9718485

© 2025 by the authors. Licensed to PSEcommunity.org and PSE Press. This is an open access article under the creative commons CC-BY-SA licensing terms. Credit must be given to creator and adaptations must be shared under the same terms. See https://creativecommons.org/licenses/by-sa/4.0/



Systems & Control Transactions

**Research Article - Peer Reviewed Conference Proceeding**
ESCAPE 35 - European Symposium on Computer Aided Process Engineering
Ghent, Belgium. 6-9 July 2025
Jan F.M. Van Impe, Grégoire Léonard, Satyajeet S. Bhonsale,
Monika E. Polańska, Filip Logist (Eds.)

PSE PRESS

# Data-Driven Dynamic Process Modeling Using Temporal RNN Incorporating Output Variable Autocorrelation and Stacked Autoencoder

**Yujie Hu[a], Lingyu Zhu[c], Han Gong[d], Xi Chen[a,b]***

[a] State Key Laboratory of Industrial Control Technology, College of Control Science and Engineering, Zhejiang University, Hangzhou, Zhejiang, 310027, China.
[b] Huzhou Institute of Industrial Control Technology, Zhejiang, China.
[c] College of Chemical Engineering, Zhejiang University of Technology, Hangzhou, Zhejiang, 310014, China
[d] Zhejiang Amino-Chem Co., Ltd, Shaoxing, Zhejiang, 312369, China
* Corresponding Author: xi_chen@zju.edu.cn.

## ABSTRACT

Dynamic process modeling in process industries has been extensively studied, especially with the development of deep learning techniques. Recurrent neural networks (RNN) and stacked autoencoders (SAE) are two powerful tools for dynamic modeling and data processing. However, most existing research primarily focuses on extracting features from process input data, often neglecting the temporal autocorrelation of output variables. In this work, a hierarchical model based on time-series RNN structure is proposed. The upper layer employs a long short-term memory (LSTM) network to extract temporal features from process input data. The lower layer uses a gated recurrent unit (GRU) to model the temporal dependencies of output variables across samples. These two parts are concatenated to form the model. Additionally, SAE is utilized to perform dimensionality reduction and reconstruction of process input, seamlessly integrating the reconstruction process with the RNN into a unified framework, termed the AR-SAE-RNN model. Distributed training is employed to effectively learn the model parameters. The proposed AR-SAE-RNN model has been applied to an industrial distillation column. The results demonstrate the model's effectiveness in capturing the dynamic behavior of the system.

**Keywords**: Dynamic process modeling, RNN, SAE

## 1. INTRODUCTION

In recent years, with the rapid advancement of production and information technologies, as well as the shift towards customized and refined product demands, process industries, represented by chemical processes, have become increasingly complex. The various coupled unit operations and energy consumption reduction strategies have made process industry modeling a challenge. On the timescale, process industry modeling can be classified into two categories: steady-state models and dynamic models, with dynamic models playing a dominant role as they better capture the temporal dependencies in real-world production processes. There are generally three approaches to dynamic process modeling: mechanistic-driven, data-driven, and hybrid mechanistic-data-driven models. Among these, mechanistic-driven and hybrid-driven models typically involve the modeling and solving of ordinary differential equations (ODE) or differential-algebraic equations (DAE), which require significant computational resources and time. In contrast, data-driven models, due to their simplicity and low dependence on process-specific backgrounds, have strong potential for application in dynamic modeling.

Data-driven models, in short, involve distinguishing between input and output variables of process data and constructing black-box models between these variables. The burgeoning amount of process data in the process industry has highlighted the advantages of deep learning techniques **[1]**. Among these, structures such as stacked autoencoders (SAE) **[2]**, recurrent neural networks (RNN) **[3]**, and their variants have been widely applied **[4,5]**.

Stacked Autoencoders and their variants are powerful tools for semi-supervised learning and handling missing data. When applied to dynamic modeling, they can perform feature extraction, dimensionality reduction, and denoising on the input data in a semi-supervised manner, making the data more suitable as model inputs **[6-8]**. RNN can extract temporal features from input variables, and variants such as gated recurrent units (GRU) and long short-term memory (LSTM) networks, by introducing gating mechanisms and memory units, further address the issues of vanishing and exploding gradients in traditional RNN, making RNN increasingly powerful in dynamic modeling **[9,10]**.

However, research on the application of RNN to dynamic modeling in process industries has primarily focused on the input process variables **[10,11]**, neglecting the autocorrelation of output variables over time. Specifically, the past states of output variables can also influence the current state. Although some studies **[12]** have included past output variables as inputs, this approach requires the actual values of the output variables from previous time steps, which imposes high demands in practical industrial settings and may introduce delays. Therefore, for dynamic systems with highly autocorrelated output variables, it is crucial to indirectly incorporate the influence of historical states into the RNN model.

Furthermore, most research on the application of SAE and its variants to dynamic modeling typically first uses SAE for input reconstruction, then constructs a dynamic model based on the reconstructed inputs, with the two processes being independent and lacking effective integration. Based on this, this paper proposes a temporal RNN model with an integrated SAE module that considers the autocorrelation of output variables. The model effectively learns the parameters through distributed training, and its effectiveness is validated in a real-world soft sensor case for a distillation column.

## 2. MODEL CONSTRUCTION AND TRAINING

In dynamic modeling, the conventional approach typically involves using RNN models to extract temporal features from input data for each sample, followed by fitting the corresponding output data. However, this approach often neglects the autocorrelation of the output variables or the inter-sample correlations. To address this limitation, we propose a hierarchical model. The upper layer extracts temporal features from input data within each sample, while the lower layer captures temporal dependencies of output data across samples. The features from both layers are concatenated to predict the output variables. Given the complexity of processing high-dimensional input data in the upper layer, we employ the LSTM model for its advanced feature extraction capabilities. In contrast, the lower layer focuses solely on the temporal modeling of output variables, allowing us to simplify the structure by utilizing a GRU model. Additionally, we incorporate a SAE module to reconstruct input data, effectively integrating input reconstruction and model regression into a unified framework. This integrated model is termed the Autoregressive-Stacked Autoencoder-Recurrent Neural Network (AR-SAE-RNN).

### 2.1 Sample Reorganization

Before introducing the AR-SAE-RNN model, we preprocess the standard sample data by reorganizing it. For an input-output dataset ($\boldsymbol{X'}$, $\boldsymbol{Y'}$):

$$X' = [x'_i]_{i=1}^{N} \tag{1}$$

$$Y' = [y'_i]_{i=1}^{N} \tag{2}$$

where $\boldsymbol{N}$ is the total number of samples, $\boldsymbol{x_i}$ represents the input data of the $\boldsymbol{i}$-th sample, and $\boldsymbol{y_i}$ is its corresponding output data. We then reorganize the samples, combining $\boldsymbol{K}$ consecutive original samples into a single new sample:

$$x_j = [x'_i, x'_{i+1}, \cdots, x'_{i+K-1}]_{i=j} \tag{3}$$

$$y_j = [y'_{i+K-1}]_{i=j} \tag{4}$$

To maximize data utilization, we set the sliding step size to 1 during the reorganization process, generating the following reorganized samples:

$$X = [x_j]_{j=1}^{N-K+1} \tag{5}$$

$$Y = [y_j]_{j=1}^{N-K+1} \tag{6}$$

After reorganization, the total number of samples becomes $\boldsymbol{N-K+1}$, effectively discarding the first $\boldsymbol{K-1}$ original samples. In the reorganized dataset, the $\boldsymbol{K}$ input samples are used to predict the output variables of the $\boldsymbol{K}$-th sample.

### 2.2 Model Architecture

The structure of the proposed AR-SAE-RNN model is shown in Fig. 1 and comprises three components:

(1) SAE Module: This module performs dimensionality reduction and reconstruction of the raw input $\boldsymbol{x}$, extracting deep features $\boldsymbol{z}$.

(2) LSTM Module: Using the deep features $\boldsymbol{z}$ extracted from the SAE module as input, this module captures temporal features of the input data within each sample, generating hidden states $\boldsymbol{h_t^k}$.

(3) GRU Module: Taking the hidden state $\boldsymbol{h_T^k}$ of the $\boldsymbol{T}$-th time step of the LSTM unit in each sample as input, this module extracts temporal features of the output variables across samples.

Finally, the hidden state $\boldsymbol{s_{k+K}}$ of the $\boldsymbol{K}$-th sample in the GRU module is concatenated with the hidden state $\boldsymbol{h_T^{k+K}}$ of the $\boldsymbol{T}$-th time step in the LSTM module to predict the output variables of the $\boldsymbol{K}$-th sample.

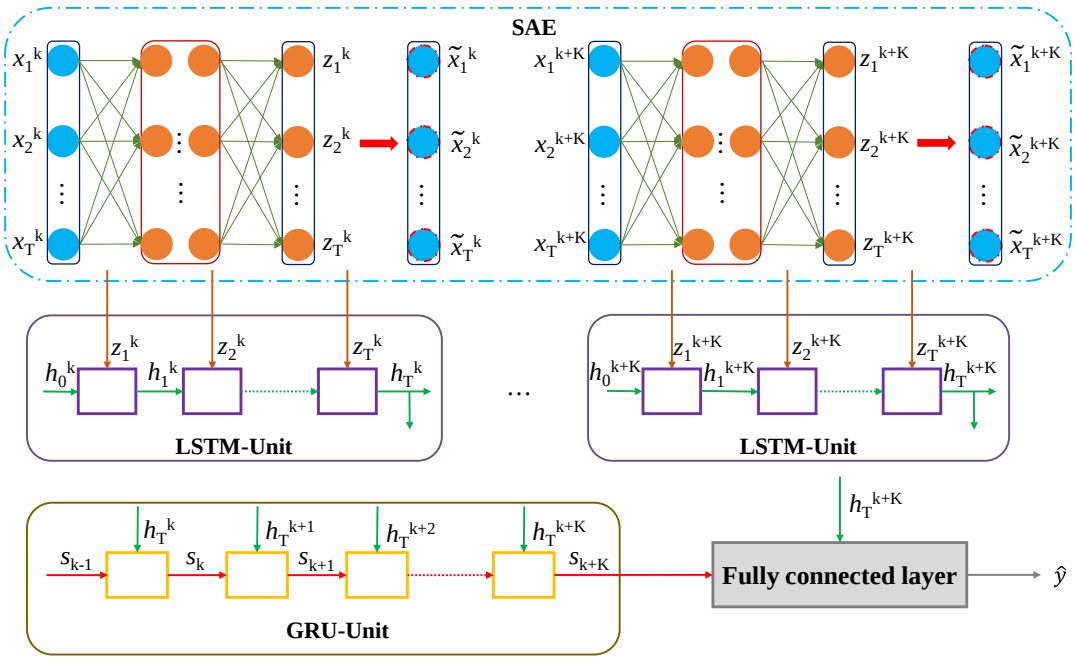



**Figure 1.** AR-SAE-RNN Model Architecture.

Assuming there are ***E*** stacked layers, the SAE module can be expressed as:

$$z^{(0)} = x \tag{7}$$

$$z^{(e)} = \sigma\left(W_{SAE}{}^{(e)} z^{(e-1)} + b_{SAE}{}^{(e)}\right) \tag{8}$$

$$e = 1,2,\cdots,E \tag{9}$$

where $\boldsymbol{W_{SAE}}$ and $\boldsymbol{b_{SAE}}$ are trainable parameters, $\boldsymbol{\sigma}$ is the activation function, and ***E*** is a hyperparameter.

The second component is a standard LSTM unit, except that its input is the deep feature ***z*** from the SAE module instead of the raw input ***x***. The LSTM unit model for the ***k***-th sample at the ***t***-th time step is defined as:

$$f_{(t)} = \sigma\left(W_{fz} z_t^k + W_{fh} h_{t-1}^k + b_f\right) \tag{10}$$

$$i_{(t)} = \sigma\left(W_{iz} z_t^k + W_{ih} h_{t-1}^k + b_i\right) \tag{11}$$

$$o_{(t)} = \sigma\left(W_{oz} z_t^k + W_{oh} h_{t-1}^k + b_o\right) \tag{12}$$

$$\tilde{C}_{(t)} = tanh\left(W_{cz} z_t^k + W_{ch} h_{t-1}^k + b_c\right) \tag{13}$$

$$C_{(t)} = f_{(t)} \odot C_{(t-1)} + i_{(t)} \odot \tilde{C}_{(t)} \tag{14}$$

$$h_t^k = o_{(t)} \odot tanh\left(C_{(t)}\right) \tag{15}$$

$$t = 1,2,\cdots,T \tag{16}$$

where $\boldsymbol{W_{fz}}$, $\boldsymbol{W_{fh}}$, $\boldsymbol{b_f}$, $\boldsymbol{W_{iz}}$, $\boldsymbol{W_{ih}}$, $\boldsymbol{b_i}$, $\boldsymbol{W_{oz}}$, $\boldsymbol{W_{oh}}$, $\boldsymbol{b_o}$, $\boldsymbol{W_{cz}}$, $\boldsymbol{W_{ch}}$, $\boldsymbol{b_c}$ are trainable parameters, $\boldsymbol{\sigma}$ and ***tanh*** are activation functions, and ***T*** is a hyperparameter.

The third component is a standard GRU unit, with its input being the hidden state output by the LSTM module. The GRU model for the ***k***-th sample (considered as the ***k***-th time step in the GRU module) is defined as:

$$r_{(k)} = \sigma\left(W_r h_T^k + U_r s_{k-1}\right) \tag{17}$$

$$gz_{(k)} = \sigma\left(W_{gz} h_T^k + U_{gz} s_{k-1}\right) \tag{18}$$

$$\tilde{s}_k = \varphi\left(W_g h_T^k + U_g\left(r_{(k)} \odot s_{k-1}\right)\right) \tag{19}$$

$$s_k = gz_{(k)} s_{k-1} + (1 - gz_{(k)})\tilde{s}_k \tag{20}$$

$$k = 1,2,\cdots,K \tag{21}$$

where $\boldsymbol{W_r}$, $\boldsymbol{U_r}$, $\boldsymbol{W_{gz}}$, $\boldsymbol{U_{gz}}$, $\boldsymbol{W_g}$, $\boldsymbol{U_g}$ are trainable parameters, $\boldsymbol{\sigma}$ and $\boldsymbol{\varphi}$ are activation functions, and ***K*** is a hyperparameter.

The final prediction of the output variables is given by:

$$\hat{y}_{k+K} = W_{LSTM} h_T^{k+K} + W_{GRU} s_{k+K} \tag{22}$$

where $\boldsymbol{W_{LSTM}}$ and $\boldsymbol{W_{GRU}}$ are trainable parameters. To prevent overfitting on the training set, regularization and dropout modules were incorporated into both the LSTM and GRU models.

## 2.3 Loss Function Design

For general dynamic modeling tasks, the loss function is typically defined as the difference between the predicted output variables and the actual value. In the proposed AR-SAE-RNN model, to effectively integrate input reconstruction and model regression, the loss function includes not only the prediction error of the output variables but also the reconstruction error of the input:

$$l = \alpha \frac{1}{N_{Train} T} \sum_{k=1}^{N_{Train}} \sum_{t=1}^{T} \left(\tilde{x}_t^k - x_t^k\right)^2 + \frac{1}{N_{Train}} \sum_{k=1}^{N_{Train}} (\hat{y}_k - y_k)^2 \quad (23)$$

where $\alpha$ is the hyperparameter representing the weight of the input reconstruction, and $N_{Train}$ denotes the number of training samples. The calculation model for the reconstructed input $\tilde{x}_t^k$ can be referenced from the literature **[6]**.

## 2.4 Model Training and Evaluation

The proposed AR-SAE-RNN model is relatively complex, and training all the parameters simultaneously may lead to divergence. Therefore, a distributed training strategy is adopted: the model parameters are trained sequentially in the order of SAE, LSTM, and GRU. At each step, only the parameters of one module are trained while freezing the others. After all modules are pre-trained, a fine-tuning process is applied to jointly optimize all parameters. Notably, distributed training is also required for the SAE module, and the specific method can be referred to in the literature **[6]**.

After training, the model performance is evaluated using two widely accepted metrics: root mean square error (RMSE) and the coefficient of determination ($R^2$):

$$RMSE = \sqrt{\frac{1}{N_{Train}} \sum_{k=1}^{N_{Train}} (\hat{y}_k - y_k)^2} \quad (24)$$

$$R^2 = 1 - \frac{\sum_{k=1}^{N_{Train}} (\hat{y}_k - y_k)^2}{\sum_{k=1}^{N_{Train}} (\overline{y_k} - y_k)^2} \quad (25)$$

where $\overline{y_k}$ represents the mean value of the output variables in the training set.

# 3. INDUSTRIAL APPLICATION

The industrial case study presented in this paper focuses on the distillation column in the product separation section of the production process, as shown in Fig. 2. In this distillation column, the bottom product stream is composed of heavy key components with a high purity. The top product stream consists of a mixture of various components, which undergo secondary separation downstream.

The purity of the heavy key components in the top liquid product directly influences the purity of the bottom product and the difficulty of the downstream secondary separation. This is a critical indicator in the system, referred to as HKC. Therefore, this study constructs a dynamic model with other process variables as inputs and the HKC purity as the output, aiming to achieve real-time soft sensing of HKC purity.

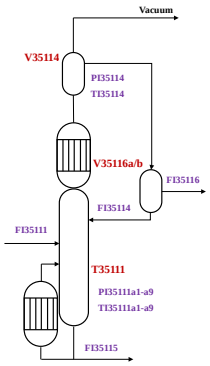



**Figure 2.** Separation Distillation Column.

As shown in Fig. 2, all process variables were sampled at a frequency of 1 minute. The HKC purity was measured online using Raman spectroscopy at a frequency of 10 minutes, which is costly. We collected 70 days of process data for model development. We first applied the 3σ rule to remove outlier samples. For the remaining valid samples, we used cubic spline interpolation to impute missing values in the process data. Finally, to ensure stable training of the neural network model, both the process data and output variables were normalized. Then, the dataset was divided into training, validation, and test sets in a ratio of 5:1:4.

To evaluate the performance of the AR-SAE-RNN model, the standard LSTM model was used as the baseline. Additionally, SAE-LSTM and LSTM-GRU models were included to assess the individual contributions of each module to prediction accuracy. All hyperparameters mentioned in this paper, including training-related parameters such as learning rate, were optimized through grid search.

The prediction performance on the test set is shown in Fig. 3, while the RMSE, $R^2$, and training time are summarized in Table 1. The results of hyperparameter tuning are summarized in Table 2. The standard LSTM model, benefiting from a large amount of training data, achieved accurate predictions for overall trends. However, its local prediction accuracy was suboptimal, with significant errors observed in many regions. By incorporating input dimensionality reduction through SAE, as well as temporal modeling of the HKC purity across samples using GRU, the AR-SAE-RNN model not only maintained accurate overall trend predictions but also significantly improved local prediction accuracy, achieving a 25% improvement in RMSE. Additionally, LSTM is designed to capture long-term dependencies but lacks inherent noise-filtering mechanisms, meaning it learns and propagates both useful patterns and noise through its hidden states. In contrast, the AR-SAE-RNN model integrates a SAE and a GRU, both of which contribute to noise reduction. The SAE compresses and extracts key features from the input data, filtering out irrelevant fluctuations before they

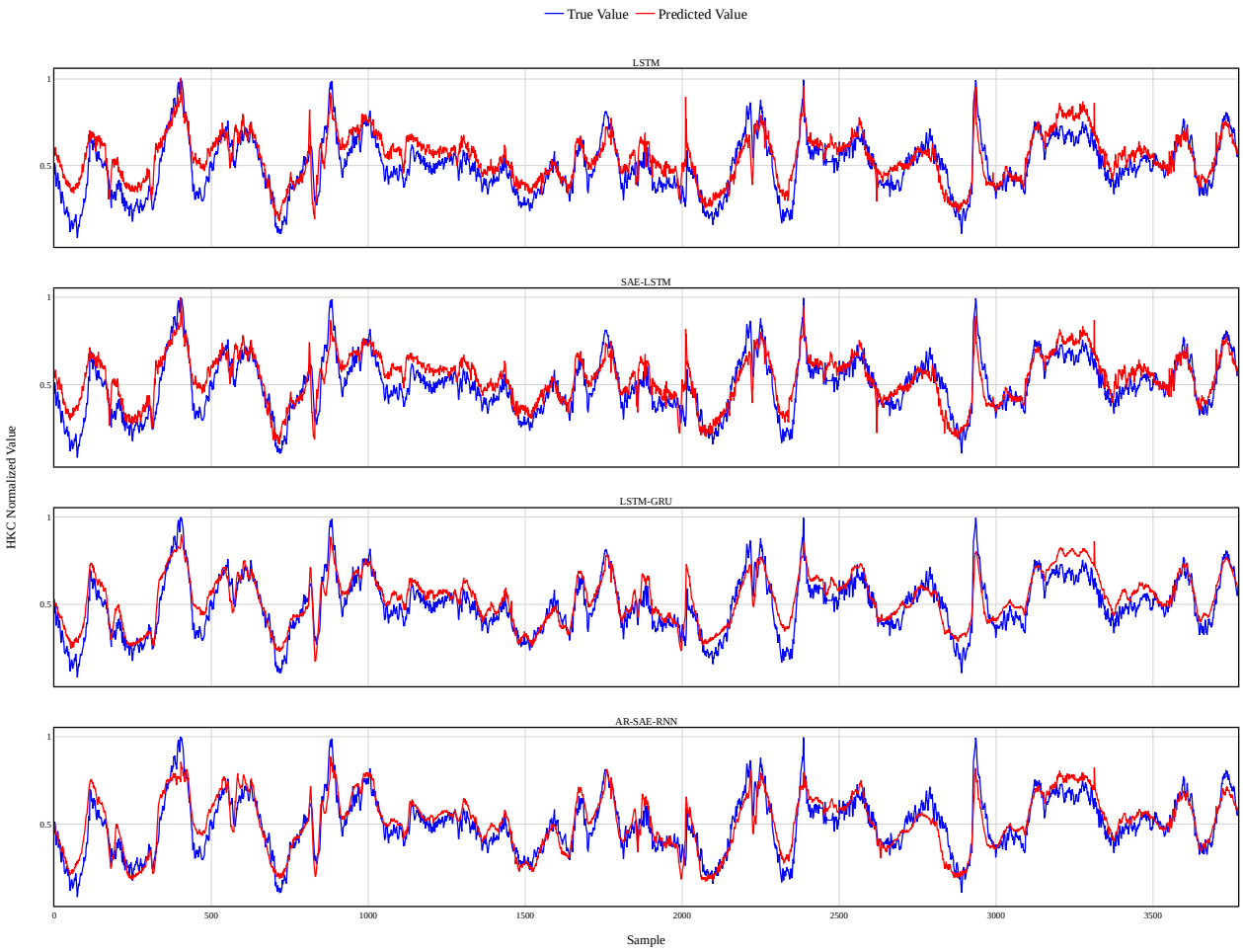



**Figure 3.** Comparison of predicted results and ground truth among four models.

reach the recurrent layers. Additionally, the GRU, with its simpler gating mechanism, is more resistant to noise accumulation, refining the hidden state representations and further attenuating residual noise. As a result, the AR-SAE-RNN model produces smoother and more robust predictions, making it more effective for handling noisy industrial data.

**Table 1:** Summary of Results for Four Models.

| Model | RMSE | $R^2$ | Training-Time(min) |
|---|---|---|---|
| LSTM | 0.09636 | 0.7142 | 0.25 |
| SAE-LSTM | 0.09006 | 0.7503 | 0.97 |
| LSTM-GRU | 0.07764 | 0.8144 | 0.45 |
| **AR-SAE-RNN** | **0.07262** | **0.8377** | **1.38** |

**Table 2:** Hyperparameter Results.

| Hyperparameter | Result |
|---|---|
| $E$ | 3 |
| $T$ | 4 |
| $K$ | 14 |
| $\Gamma$ | 0.3 |
| Lr(Pre-Trained) | 1e-3 |
| Lr(Fine-Tuning) | 1e-6 |
| Batch | 400 |
| LSTM Hidden Size | 64 |
| GRU Hidden Size | 32 |
| Epoch(SAE) | 200 |
| Epoch(LSTM) | 200 |
| Epoch(GRU) | 70 |
| Epoch(Fine-Tuning) | 50 |
| Dropout | 0.2 |

From Table 1 and Fig. 3, it is evident that the GRU module has the most significant impact on improving prediction accuracy. This underscores the importance of considering the autocorrelation of output variables in dynamic modeling. Furthermore, the proposed model does not rely on the actual values of past output variables as inputs, making it more practical for industrial applications.

## 4. CONCLUSION

To address the challenges of dynamic modeling, the proposed AR-SAE-RNN model introduces a novel approach compared to traditional RNN models by effectively accounting for the autocorrelation of output variables. The model integrates temporal modeling of output variables across samples while leveraging SAE to reconstruct input features. This unified framework has demonstrated excellent performance in the soft sensing case study of the distillation column.

Moreover, we aim to enhance our model in three key aspects as part of our future work. First, we will upgrade the SAE to a Variational Autoencoder (VAE), which encodes data as a probability distribution rather than a deterministic value, improving robustness by filtering noise in abnormal process data. Second, we will incorporate an attention mechanism into the GRU modeling of output variable autocorrelation, allowing the model to focus on the most relevant hidden states and improving predictive accuracy. Finally, we aim to integrate a mechanistic model for the distillation unit by constructing a simplified dynamic wave model that captures the temporal and spatial distribution of component compositions along the column height. This framework will decompose the temporal network into three components: sequential modeling of process data, autocorrelation modeling of output variables, and spatial correlation modeling of output variables, which will be combined to enhance predictive performance.

## ACKNOWLEDGEMENTS

The financial support of the "Pioneer" and "Leading Goose" R&D Program of Zhejiang (Grant No. 2024C01028) and the State Key Laboratory of Industrial Control Technology, China (Grant No. ICT2024C04) are gratefully acknowledged.

## REFERENCES

1. Sun Q Q, Ge Z Q. A Survey on Deep Learning for Data-Driven Soft Sensors. *IEEE Transactions on Industrial Informatics*, 17(9):5853-5866 (2021). https://doi.org/10.1109/TII.2021.3053128.
2. Rumelhar D E, Hinton G E, Williams R J. Learning Representations by Back Propagating Errors. *Nature*, 323(6088):533-536 (1986). https://doi.org/10.1038/323533a0.
3. You Y, Nikolaou M. Dynamic process modeling with recurrent neural networks. *AIChE Journal*, 39(10):1654-1667 (1993). https://doi.org/10.1002/aic.690391009.
4. Hochreiter S, Schmidhuber J. Long Short-Term Memory. *Neural Computation*, 9(8):1735-1780 (1997). https://doi.org/10.1162/neco.1997.9.8.1735.
5. Cho K, Merrienboer B V, Gulcehre C, et al. Learning Phrase Representations using RNN Encoder-Decoder for Statistical Machine Translation. *Computer Science*, 1724–1734 (2014). https://doi.org/10.3115/v1/D14-1179.
6. Yuan X, Zhou J, Huang B, et al. Hierarchical Quality-Relevant Feature Representation for Soft Sensor Modeling: A Novel Deep Learning Strategy. *IEEE Transactions on Industrial Informatics*, 2020, 16(6):3721-3730 (2020). https://doi.org/10.1109/TII.2019.2938890.
7. Peng X Y, Wang Y L, Liu C L, et al. Dynamic-static collaborative strategy for industrial data modeling based on hierarchical deep networks. Measurement Science and Technology, 33(12):125010-1-125010-12 (2022). https://doi.org/10.1088/1361-6501/ac86e6.
8. Zhang H, Tang Z H, Xie Y F, et al. ES-net: An Integration Model Based on Encoder–Decoder and Siamese Time Series Difference Network for Grade Monitoring of Zinc Tailings and Concentrate. IEEE Transactions on Industrial Electronics, 70(11):11819-11830 (2023). https://doi.org/10.1109/TIE.2022.3227274.
9. Ma Y, Li H G. GRU-Auto-Encoder neural network based methods for diagnosing abnormal operating conditions of steam drums in coal gasification plants. Computers & Chemical Engineering, 143:107097 (2020). https://doi.org/10.1016/j.compchemeng.2020.107097.
10. Smagulova K, James A P. A survey on LSTM memristive neural network architectures and applications. The European Physical Journal Special Topics, 228:2313-2324 (2019). https://doi.org/10.1140/epjst/e2019-900046-x.
11. Xie C R, Yao R J, Zhu L Y. Soft-Sensor Development through Deep Learning with Spatial and Temporal Feature Extraction of Complex Processes. Industrial & Engineering Chemistry Research, 62:519-534 (2023). https://doi.org/10.1021/acs.iecr.2c03137.
12. Yuan X F, Li L, Wang Y L. Nonlinear Dynamic Soft Sensor Modeling With Supervised Long Short-Term Memory Network. IEEE Transactions on Industrial Informatics, 16(5):3168-3176. https://doi.org/10.1109/TII.2019.2902129.

© 2025 by the authors. Licensed to PSEcommunity.org and PSE Press. This is an open access article under the creative commons CC-BY-SA licensing terms. Credit must be given to creator and adaptations must be shared under the same terms. See https://creativecommons.org/licenses/by-sa/4.0/



Systems & Control Transactions

**Research Article - Peer Reviewed Conference Proceeding**
ESCAPE 35 - European Symposium on Computer Aided Process Engineering
Ghent, Belgium. 6-9 July 2025
Jan F.M. Van Impe, Grégoire Léonard, Satyajeet S. Bhonsale,
Monika E. Polańska, Filip Logist (Eds.)

PSE PRESS

# Real-time carbon accounting and forecasting for reduced emissions in grid-connected processes

**Rafael Castro-Amoedo[a,b,*,+], Alessio Santecchia[b,+], Henrique A. Matos[a] and François Maréchal[c]**

[a] Instituto Superior Técnico, Department of Chemical Engineering, Lisbon, Portugal
[b] Emissium Labs Unipessoal LDA, Alcácer do Sal, Portugal
[c] Industrial Process and Energy Systems Engineering (IPESE), École Polytechnique Fédérale de Lausanne, Sion, Switzerland
[+] The authors contributed equally
* Corresponding Author: rafael.amoedo@emissium.io

## ABSTRACT

Real-time carbon accounting is crucial for advancing policies that effectively meet sustainability objectives. This work introduces a carbon tracking tool specifically designed for the European electricity grid. The tool collects hourly data on electricity consumption and generation, cross-border power exchanges, and weather information to assess the real-time environmental effects of electricity use, employing locally-specific emission factors for the generation sources. It utilizes weather data from various stations across Europe to produce week-ahead forecasts of carbon intensity in the grid. Predictions are created using a random forest regressor, integrated within the optimal controller of an operational industrial batch process. This prediction-based optimizer seeks to reduce total emissions tied to the process schedule's electricity consumption by implementing a rolling horizon strategy. By leveraging enhanced energy flexibility, the controller provides significant opportunities for load shifting and emission reductions, though at a higher cost. An industrial batch process demonstration highlights the potential of this approach, showing environmental savings ranging from 4% in grids with low renewable energy to 32% in nations that incorporate a substantial proportion of renewable energy in their energy mix.

**Keywords**: Energy, Algorithms, Energy Systems, Industry 4.0, Modelling, Grid digitalization, Real-time emissions, Load shifting, Flexible operations

## INTRODUCTION

European countries aim for carbon neutrality by 2050, driving a shift from fossil fuels to renewable energy and widespread electrification. Real-time carbon accounting is critical for effective green policies, while forecasting aids planning and operations [1]. The GHG Protocol [2] introduced a "location-based" method for reporting scope 2 emissions, improving accuracy over the market-based approach. In the same vein, Brander et al. [3] recommended this method to avoid misrepresenting responsibility.

However, the “location-based” method does not reflect real-time consumption emissions. Spork et al. [4] used real-time data to improve carbon reporting in Spain but faced boundary limitations. Significant improvements came from the introduction of input-output lifecycle assessment (IO-LCA) methods, as applied by Claus et al. [5], which expanded system boundaries for better accuracy and highlighted the importance of cross-border carbon transfers. More recently, Tranberg et al. [6] refined this with flow tracing, supporting dynamic carbon taxes.

A major objective with such approach is to be able to schedule operations in periods of low-carbon electricity. However, operational scheduling based on carbon forecasts remains uncommon. Models by Ma et al. [7] and Chen et al. [8] either assumed fixed carbon factors or focused solely on costs. More advanced models, like those by Zhang et al. [9], still lacked real-time carbon integration. Oftentimes, time-dependent carbon data is used in technology design studies, such as in Castro-Amoedo et al. [10].

### Contributions

This study presents a dynamic life-cycle assessment framework for real-time carbon tracking in the

European electricity grid, expanding previous models by including ten more countries and using data from 200+ weather stations for week-ahead carbon forecasts. Key contributions include:

1. Optimized Industrial Operations: Using emission forecasts to control industrial batch processes, enabling load shifting and emission reductions.
2. Grid Digitalization: Emphasizing the need for granular electricity data to support broader carbon reduction strategies.

## METHODOLOGY

The tool uses data provided by the ENTSO-E database [11] to quantify the impact of electricity consumption in each European country. It considers real-time electricity production mixes, electrical power exchanges across borders, and locally differentiated carbon intensities [12] of the energy sources to calculate current or past environmental indicators for each European country with a data granularity of one hour.

The implementation allows interfacing with optimization algorithms in such a way that the data stream indicators can be automatically fed into operation scheduling problems. As a result, the tool provides the basis for carrying out optimization with environmental objectives (i.e. minimization of the carbon footprint associated with production), or, alternatively, it can be used as a post-computation phase to assess the real-time environmental performance of a process by calculating its sustainability indicators. Our methodology includes :

3. Data Acquisition: Fetching real-time data on electricity production, consumption, and cross-border exchanges.
4. Data Validation: Ensuring accuracy by checking production limits, technology mix consistency, and eliminating invalid data.
5. Environmental Indicator Calculation: Computing indicators like carbon footprint, renewable energy share, and ecological impact.

### Mathematical Approach

The carbon intensity arising from the consumption of electricity from the grid in each country is obtained by solving a linear system of equations representing the carbon flows in the European network [6]. The calculated values represent the greenhouse gas footprint of 1 kWh consumed inside a given country. The footprint is measured in $gCO_2$ equivalent, meaning that each greenhouse gas is converted into its carbon dioxide equivalent in terms of climate change potential. For each country $i$, the balance of eq. (1) can be written, where $D_i$ is the total electricity demand, $P_i$ is the total electricity production, and $I_i$ and $E_i$ are the total import and export of electricity, respectively.

$$\mathrm{D}_i = P_i + I_i - E_i \tag{1}$$

By extending eq. (1) to balance the carbon flows of country $i$, one obtains eq. (2), where $x_i$ is the carbon intensity of electricity consumption, $e_{i,r}$ is the carbon intensity of resource $r$ in country $i$, $P_{i,r}$ is the total electricity production using resource $r$, $x_j$ is the carbon intensity of electricity imported from country $j$, $I_{i,j}$ is the electricity import to country $i$ from j, and $E_{i,k}$ is the electricity export from country $i$ to $k$.

$$x_i \mathrm{D}_i = \sum_r e_{i,r}\ P_{i,r} + \sum_j x_j\ I_{i,j} - \sum_k x_i\, E_{i,k} \tag{2}$$

Considering from eq. (1) that $D_i + E_i$ equates to $P_i + I_i$, and writing for each country, the following linear system results (eq. 3).

$$\begin{bmatrix} P_1 + I_1 & \cdots & -I_{1,n} \\ \vdots & \ddots & \vdots \\ -I_{n,1} & \cdots & P_n + I_n \end{bmatrix} \times \begin{bmatrix} x_1 \\ \dots \\ x_n \end{bmatrix} = \begin{bmatrix} \sum_r e_{1,r}\ P_{1,r} \\ \dots \\ \sum_r e_{n,r}\ P_{n,r} \end{bmatrix} \tag{3}$$

Where:

$$\mathrm{P}_1 = \sum_r P_{1,r}\ \ and\ \mathrm{I}_1 = \sum_j I_{1,j} \tag{4}$$

Because the $CO_2$ equivalent emissions of each country depend not only on its own electricity mix but also on that of its neighbours, the $CO_2$ mass flow balance of all countries must be addressed simultaneously. The same procedure was adopted to calculate other environmental indicators, such as renewable energy (RE) share.

The carbon intensities $e_{i,m}$ are location-dependent and specific to each energy resource. Such emission intensities account for the whole life cycle of electricity production, from plant construction and fuel treating, i.e. including all upstream activities, disposal and decommissioning. The impact of each resource $r$ is calculated using all the technologies $m$ associated with such a resource that is available in the country generation mix ($\mathbf{M}^r$). The impact factors $e_{i,m}$ are calculated by weighting each technology by the corresponding market share $s_m$ [12](eq. 5).

$$e_{i,r} = \sum_m^{M^r} s_m \times e_{i,m} \tag{5}$$

### Application to Case Study

A prediction-based optimizer with a weekly (168-hour) horizon is applied to an industrial batch process, simulated over one month with hourly rolling updates. The scheduling model, based on Mixed-Integer Linear Programming (MILP), is solved iteratively. The model is described in Santecchia et al. [13]. Unlike prior studies, this model focuses on minimizing emissions from electricity consumption rather than costs. The objective function is adjusted, extending the scheduling window from 72 to 504 time slots, corresponding to 20-minute intervals.

The predictive controller updates the process

schedule hourly, retrieving electricity and weather data from ENTSO-E and the Visual Crossing API (Fig. 1). This data feeds a random forest regressor to update carbon intensity forecasts. The optimization is solved for each production line to meet minimum environmental impact goals, repeating hourly until the end of the month (N = 720).

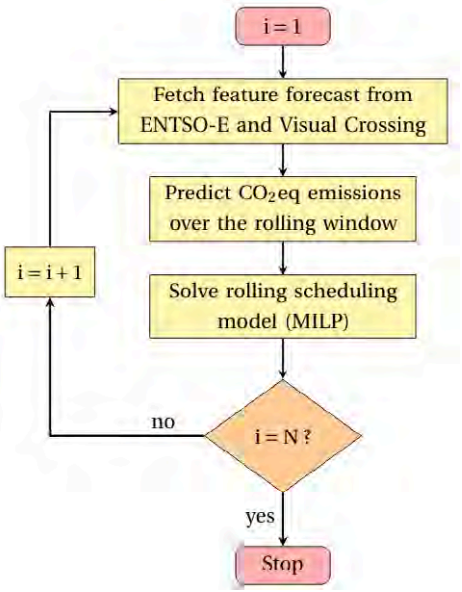



**Figure 1.** Flow diagram of the online scheduling algorithm with MPC approach.

### Feature selection

The framework generates day-ahead and week-ahead carbon emission forecasts using data on projected generation, consumption, solar and wind output, cross-border electricity flows, and day-ahead market prices from the ENTSO-E database. To extend forecasts beyond one day, it integrates weather data (wind speed, direction, temperature, precipitation, cloud cover) from over 200 European weather stations via the Visual Crossing API.

To reduce computational demands, a statistical feature selection method evaluates the relationship between input variables and carbon emissions. This involves constructing a normalized covariance matrix over 1–3 years using Pearson Correlation Coefficients (PCC). Features with strong correlations are flagged as redundant, while weakly correlated ones are removed, ensuring efficient modelling without significant data loss. A PCC of 0.6 was chosen as threshold to distinguish strong and weak correlations, and was not subject to optimization.

### Prediction algorithms

Due to feature selection reducing the dataset - sometimes to as few as two variables - various learning algorithms were tested, including simpler models. These included linear regression with batch and stochastic gradient descent for error minimization, along with LASSO (L1 regularization), Ridge regression (L2 regularization), and their combination through Elastic Net Regression to mitigate overfitting. Multivariate polynomial regression was explored for modeling non-linear relationships, and the RANSAC algorithm was applied to detect outliers.

While these simpler methods aimed to avoid unnecessary complexity, they often lacked sufficient prediction accuracy or failed with high-dimensional data. To address this, advanced models like artificial neural networks (Multi-layer Perceptron, Dense networks) and random forests were implemented. Despite higher computational demands, these models delivered greater accuracy with minimal data pre-processing and tuning. Random forests outperformed other algorithms in early evaluations and were chosen for prediction tasks due to their robustness with complex datasets and resistance to outliers. To further prevent overfitting, hyperparameter tuning was systematically applied using a combinatorial search approach. For random forests, key hyperparameters such as the number of trees, tree depth, and minimum samples per leaf were optimized to balance model complexity and generalization. A grid search and random search were employed to explore different hyperparameter combinations, followed by k-fold cross-validation to evaluate model stability and prevent data leakage. Additionally, cross-validation techniques were employed to assess model performance and ensure that the selected hyperparameters led to robust predictions on unseen data.

## RESULTS

### Accuracy improvements on carbon accounting standards

The real-time carbon tracking method offers greater accuracy than traditional approaches used by organizations for carbon accounting. Typically, impact factors in scope 2 reporting (GHG Protocol Corporate Standard) are based on annual electricity production data. Fig. 3 illustrates the potential improvement of real-time tracking, showing the mean relative error reduction across various time scales (hourly, daily, weekly, monthly). These values estimate the reporting errors in indirect emissions from purchased electricity.

Since the exact real-time environmental impact is unknown, the tool's indicators are treated as accurate. The improvement is assessed using bootstrapping, where random samples from the 2023 environmental impact database are repeatedly drawn to measure deviations from the annual average. This process uses a sample size of 1,000 and is repeated 10,000 times to approximate the accuracy distribution.

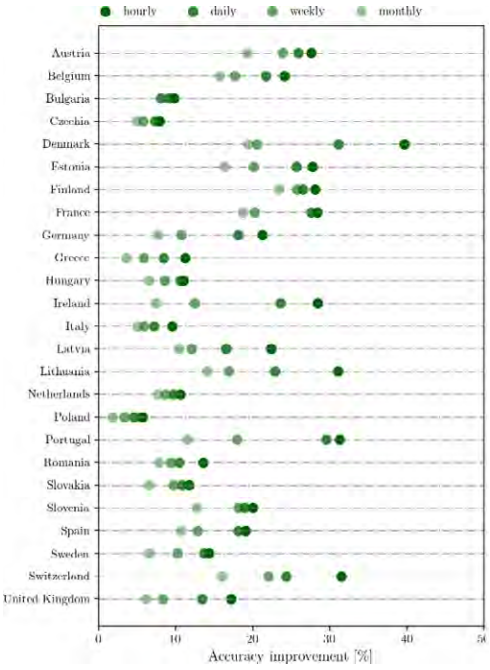



**Fig 3** - Accuracy improvement of real-time carbon tracking compared to current accounting standards, showing average relative improvements across hourly, daily, weekly, and monthly intervals.

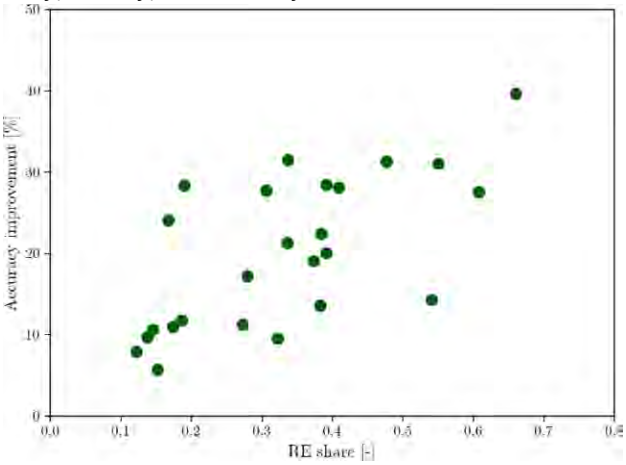



**Fig 4** - Accuracy improvement [%] of the real-time carbon tracking method as a function of the RE share [-] by country.

Hourly accuracy improvements vary by country and are more significant in grids with high renewable energy penetration (Fig. 4). The method shows the smallest benefit in Poland (6%) due to its reliance on coal (15% renewable share) and the largest in Denmark (40%), where renewables account for 66% of electricity. This correlation highlights that greater variability in renewable generation leads to more accurate carbon accounting. Implementing real-time carbon tracking is essential for accurately estimating indirect emissions in renewable-heavy grids, supporting Europe's transition to a decarbonized energy system.

## Emissions forecast with Random Forest

The random forest regressor is trained on the emissions database, split into 80% for training and 20% for testing. While it offers high predictive accuracy, it risks overfitting. A balanced dataset size is essential—too large, and the model overfits past grid data; too small, and it misses key grid patterns. Testing datasets of 1–2 years, closest to the prediction window, ensures optimal accuracy.

Fig. 5 illustrates a week-ahead $CO_2$ prediction (January 1–7, 2023) for Germany. The model accurately tracks carbon intensity trends, with a mean absolute error (MAE) and an R^2 value of 0.86.

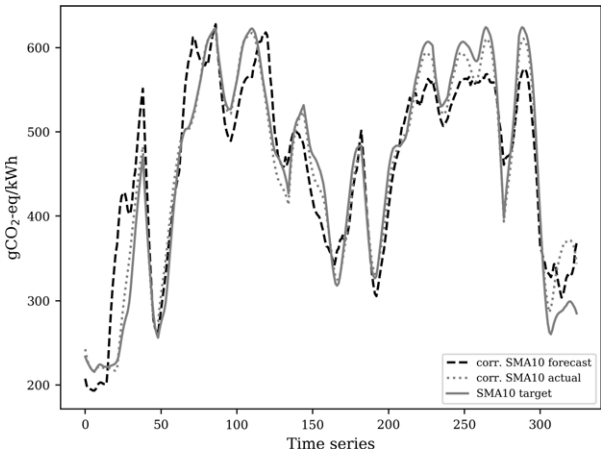



**Fig 5** - Week-ahead prediction trend in Germany (January 1–7, 2023) using a random forest regressor trained on 2020–2022 data. The SMA10 tracks prediction accuracy, with the 'actual' curve showing model output. Key metrics: MAE (19.4 actual, 54.9 forecast) and $R^2$ (0.952 actual, 0.728 forecast).

## Reducing emissions in a batch process

Fig. 6 presents the cumulative average emission profiles for two rolling schedules. In the first scenario (process 1d), emissions are minimized using day-ahead grid carbon intensity predictions with a 24-hour rolling window, limiting the ability to anticipate favorable conditions beyond that period. This approach results in an 11.6% reduction in emissions compared to the baseline scenario (BAU, shown in red).

Extending predictions to a week ahead leads to a greater reduction in emissions. With improved insight into future grid conditions, the optimizer schedules operations more effectively, especially during periods of high carbon intensity (e.g., between 10:00 and 15:00). Unlike the short-term model, the week-ahead schedule shifts energy-intensive tasks to low-emission periods, reducing $CO_2$ emissions by 17.5% compared to BAU and 6.6% compared to the day-ahead scenario.

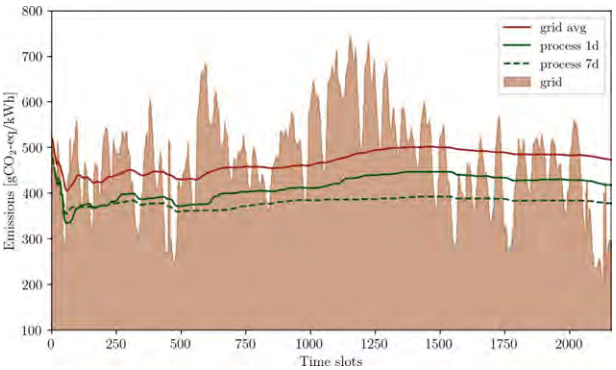



**Fig 6** - Cumulative average emissions of the MPC for an industrial batch process in Germany, comparing day-ahead (solid green) and week-ahead (dashed green) predictions. The shaded area shows hourly grid intensity, and the red line represents the BAU scenario.

## Benefits of optimal operations scheduling with emission targets in Europe

The process was simulated across various European countries using 1-day and 7-day prediction windows. Results in Table 1 show that emission reductions vary by country. Significant improvements occur in nations with high renewable energy use, like Denmark (-28.6%) and Lithuania (-32.4%), while countries reliant on fossil fuels, such as Czechia (-9.2%) and Poland (-4.4%), see smaller gains. This difference stems from the greater variability in carbon intensity within renewable-heavy grids, allowing long-term planning to be more effective. On average, carbon emissions dropped by 15%.

**Table 1:** Results of the MPC simulations by country, showing emission reduction for both the short- (daily) and long-term (weekly) optimizers.

| | Emissions ($gCO_2$/kWh) | | | % |
|---|---|---|---|---|
| Country | Grid | Process 1d | Process 7d | Max reduction |
| Austria | 271.1 | 253.8 | 235.6 | -13.1% |
| Czechia | 763.5 | 731.2 | 692.8 | -9.2% |
| Denmark | 207.0 | 180.4 | 147.8 | -28.6% |
| Estonia | 583.0 | 567.5 | 517.1 | -11.3% |
| Finland | 191.7 | 181.3 | 172.5 | -10.0% |
| Germany | 473.5 | 418.4 | 390.6 | -17.5% |
| Greece | 666.0 | 614.3 | 523.5 | -21.4% |
| Italy | 382.9 | 358.9 | 334.7 | -12.6% |
| Lithuania | 227.9 | 189.3 | 154.1 | -32.4% |
| Poland | 947.4 | 925.4 | 905.3 | -4.4% |
| Spain | 232.5 | 215.6 | 201.3 | -13.4% |
| Sweden | 37.4 | 34.1 | 30.8 | -17.7% |
| UK | 270.8 | 248.3 | 203.1 | -25.0% |

## CONCLUSIONS

This study introduces a real-time carbon tracing method for the electricity grid, using hourly data on electricity consumption, generation, cross-border power flows, and weather conditions to calculate environmental impacts with locally differentiated emission factors. This method improves accuracy over traditional carbon accounting, with emission reporting improvements ranging from 6% in Poland to 40% in Denmark, especially in grids with high renewable energy penetration.

The framework also generates day-ahead and week-ahead carbon emission forecasts based on projected generation, consumption, renewable output, electricity trade, prices, and weather data from ENTSO-E and Visual Crossing APIs. To enhance efficiency, a feature selection algorithm removes redundant data using Pearson Correlation Coefficients.

A random forest algorithm is used for forecasting, with hyperparameter tuning to prevent overfitting. Training the model on one to two years of data achieved reliable carbon intensity predictions ($R^2$ = 0.86).

This model is integrated into a mixed-integer linear programming (MILP) optimizer for an industrial batch process in Germany, reducing emissions by 17.5% and increasing renewable energy use by 9.7 percentage points compared to BAU. Simulations across Europe show greater benefits in countries with high renewable energy shares (-32.4%) and smaller gains in fossil-fuel-dependent countries (-4.4%).

## ACKNOWLEDGEMENTS

Please acknowledge your funders in this section, with grant or funding numbers as appropriate. Note that most funding agencies require this.

## REFERENCES

1. Li, Yaowang et al., A review on carbon emission accounting approaches for the electricity power industry. *Applied Energy* 359, 122681 (2024) https://doi.org/10.1016/j.apenergy.2024.122681
2. Sotos, M. E. GHG Protocol Scope 2 Guidance (2015) https://www.wri.org/research/ ghg-protocol-scope-2-guidance.
3. Brander, M. et al. Creative accounting: A critical perspective on the market-based method for reporting purchased electricity (scope 2) emissions. *Energy Policy* 112, 29–33 (2018). https://www.sciencedirect.com/science/article/pii/S0301421517306213.
4. Spork, C. C., et al. Increasing Precision in Greenhouse Gas Accounting Using Real-Time Emission Factors. *Journal of Industrial Ecology* 19, 380–390 (2015) https://doi.org/10.1111/jiec.12193
5. Clauß, J. et al. Evaluation Method for the Hourly Average CO2eq Intensity of the Electricity Mix and Its Application to the Demand Response of

Residential Buildings. *Energies* 12(7), 1345 (2019). https://doi.org/10.3390/en12071345
6. Tranberg, B. et al. Real-time carbon accounting method for the European electricity markets. *Energy Strategy Reviews* 26, 100367 (2019). https://doi.org/10.1016/j.esr.2019.100367
7. Ma, R., et al. An Economic and low-carbon day-ahead Pareto-optimal scheduling for wind farm integrated power systems with demand response. *Journal of Modern Power Systems and Clean Energy* 3, 393–401 (2015). https://doi.org/10.1007/s40565-014-0094-7
8. Chen, X., et al. The mutual benefits of renewables and carbon capture: Achieved by an artificial intelligent scheduling strategy. *Energy Conversion and Management* 233, 113856 (2021). https://doi.org/10.1016/j.enconman.2021.113856
9. Zhang, N. et al. Unit Commitment Model in Smart Grid Environment Considering Carbon Emissions Trading. *IEEE Transactions on Smart Grid* 7, 420–427 (2016). https://doi.org/10.1109/TSG.2015.2401337
10. Castro-Amoedo, R., et al. The Role of Biowaste: A Multi-Objective Optimization Platform for Combined Heat, Power and Fuel. *Frontiers in Energy Research* 9, 417 (2021). https://doi.org/10.3389/fenrg.2021.718310
11. ENTSO-E. Transparency Platform restful API - Central collection and publication of electricity generation, transportation and consumption data and information for the pan-European market. URL https://transparency.entsoe.eu. (last accessed: 21.10.2024).
12. Wernet, G., Bauer, C., Steubing, B., Reinhard, J., Moreno-Ruiz, E., and Weidema, B. The ecoinvent database version 3 (part I): overview and methodology. *The International Journal of Life Cycle Assessment*, 21(9), pp.1218–1230 (2016). http://link.springer.com/10.1007/s11367-016-1087-8.
13. Santecchia, A., et al. Industrial Flexibility as Demand Side Response for Electrical Grid Stability. *Frontiers in Energy Research* 10 (2022). https://doi.org/10.3389/fenrg.2022.831462

© 2025 by the authors. Licensed to PSEcommunity.org and PSE Press. This is an open access article under the creative commons CC-BY-SA licensing terms. Credit must be given to creator and adaptations must be shared under the same terms. See https://creativecommons.org/licenses/by-sa/4.0/



Systems & Control Transactions

**Research Article - Peer Reviewed Conference Proceeding**
ESCAPE 35 - European Symposium on Computer Aided Process Engineering
Ghent, Belgium. 6-9 July 2025
Jan F.M. Van Impe, Grégoire Léonard, Satyajeet S. Bhonsale,
Monika E. Polańska, Filip Logist (Eds.)

PSE PRESS

# Twin Roll Press Washer Blockage Prediction: A Pulp and Paper Plant Case Study

**Bryan Li[ab], Isaac Severinsen[ab], Wei Yu[ab], Timothy Walmsley[b], and Brent Young[ab]***

[a] Department of Chemical and Materials Engineering, The University of Auckland, Auckland 1010, New Zealand
[b] Ahuora – Centre for Smart Energy Systems, School of Engineering, The University of Waikato, Hamilton 3240, New Zealand
* Corresponding Author: b.young@auckland.ac.nz.

## ABSTRACT

The pulp and paper industry has significant potential to reduce its carbon footprint by optimizing energy and water usage, contributing to global efforts toward net-zero emissions. A critical unit operation in this industry is pulp washing using twin roll press washers, which enhance pulp quality. The filtrate from this unit operation can be concentrated and combusted to generate a significant amount of energy for the plant and nearby industries. However, these washers are prone to blockages that disrupt production and decrease energy efficiency. Despite their importance, models for managing blockages in twin roll press washers are lacking. This study addresses this gap by developing empirical models to predict roll speed based on key process parameters. These models performed well on a case study of un-sanitized data from a real pulp and paper plant, achieving $R^2$ of the order of 0.7. The models can potentially be used by operators to ensure uninterrupted production, and optimize resource usage, supporting the industry's sustainability and decarbonization goals.

**Keywords**: Pulp Washing, Twin Roll Press Washer, Empirical Model

## INTRODUCTION

Achieving net-zero emissions is essential for energy-intensive chemical and process industries to help combat climate change and ensure environmental sustainability. These industries – including mining, iron and steel, aluminum, pulp and paper, chemicals, petrochemicals, cement, and glass – account for approximately 20% of the world's $CO_2$ emissions, totaling 6.2 Gt of $CO_2$ in 2018 [1]. Amongst them, the pulp and paper industry has the potential to reduce its carbon footprint by 30% via reducing its overall energy and water consumption [2].

Pulp washing using twin roll press washers is a crucial unit operation in pulp and paper plants [3]. Pulp washing using twin roll press washers can be compared to an industrial-scale filtration process, similar to squeezing a wet sponge to remove impurities. In this process, wet pulp is combined with hot wash water and passed through the narrow gap (nip) formed by two rotating rolls under high pressure. This action effectively extracts the liquid filtrate, known as weak black liquor, while producing a drier pulp with improved consistency and reduced levels of dissolved organic and inorganic solids. This efficient separation process enhances the overall quality and processability of the pulp in paper manufacturing. The weak black liquor, containing organic and inorganic dissolved solids and a small amount of fiber, is concentrated and combusted for on-site power generation. If the pulp washing process is optimized, the energy generated from the combustion can account for most of the plant's onsite energy consumption and even power neighboring industries. The weak black liquor recoverable from twin-roll press washer is the fifth most significant fuel globally [4], as 1.2 billion tonnes of concentrated black liquor are processed in recovery boilers across the world. This leads to the recovery of 14 million tonnes of cooking chemicals, a decrease in waste, and the generation of 635 million tonnes of steam [5].

Twin roll press washers are prone to blockage issues, which can decrease the plant's energy efficiency, and disrupt operations and productivity. Blockages can be acute and/or chronic. Acute blockage is caused by an inappropriately high dewatering rate, typically due to high roll pressure, high fiber content (pulp consistency),

low pulp flow rate, and low and solid buildup (chronic). Chronic blockage is typically due to the accumulation of pulp fibers, contaminants, or debris within the machinery. When blockages occur, the wash water flow rate is increased in an effort to either rehydrate the pulp or wash off the buildup solids. If this strategy is insufficient, production is ceased, and the solid buildup is manually removed. Disruptions of this process are disastrous, as increasing the wash water flow rate to remove blockages leads to a heavier energy load on the downstream weak black liquor concentrators. Furthermore, pausing the process to address the severe blockage issues leads to not meeting the production demand and reduced power cogeneration.

Fault management studies in the pulp and paper industry have focused on the heat recovery network in thermomechanical pulp process [6], particle formation in recovery boilers [4], and the drying process [7]. Searching "Twin Roll Press Washer" on Scopus yielded one relevant study on its fatigue and failure structure analysis [8], with no first-principles, data-driven machine learning, or hybrid models developed for blockage correlations at all despite its importance. Therefore, this study aims to develop the empirical, machine learning models of the twin roll press washer's roll speed as a function of key process parameters. Successful prediction of roll speed will potentially assist operators in pulp and paper plants to adjust key process setpoints with more certainty. Such an outcome will help prevent blockages by ensuring safe roll speeds, ensuring uninterrupted production, and optimal water and energy usage.

## DATA AND METHODS

Pulp washer plant data was obtained from an operating pulp and paper plant in New Zealand over a 12-month period from the plant's distributed control system. The data was collected at a sampling frequency of 1 minute. Data during plant shutdown periods was manually removed. No denoising algorithms were applied to the industrial data.

Simple linear regression was employed first to identify simple empirical models from the plant data. For these simple empirical models, the first half year of the data was used for model development, while the second half year was used for validation. The first simple empirical model was a model that is only a function of varying roll pressure ($P$) and pulp flow rate ($Q$), while all other process parameters were kept "constant" (within 1% deviation from their setpoints) by filtering the plant data. Since controlled process parameters may deviate from their setpoints, this first model is limited in its accuracy and application. Hence, a second simple empirical model was built which covered a wider range of operating conditions: all ranges of $Q$ and $P$ and larger ranges (within 10% deviation from setpoints) of inlet pulp consistency ($C$) and wash water flow rate (also quantified by dilution factor, $DF$).

A black-box machine learning model was then developed using a feedforward neural network with ReLU activation function to capture complex dependencies and non-linearities in the data better. The model was defined using PyTorch v2.2.2. The model was designed with three hidden layers and employed batch normalization and dropout for regularization. The first hidden layer consisted of 32 neurons, followed by 16 neurons in the second hidden layer, and 4 neurons in the third hidden layer, all equipped with batch normalization. The model was trained using the Adam optimizer with a learning rate of 0.001 and the mean squared error loss function. The above hyperparameters were chosen manually with trial-and-error. A maximum of 100 epochs was allowed. Early stopping was incorporated with a patience of 10 epochs, halting training if the validation loss did not improve. Due to the large numerical difference between variables of different attributes ($Q, P, C, DF$), the dataset was first normalized. Filtered data used to develop the second simple empirical model was used to train, validate, and test the neural network. 70% of the first half year of data was used for training, the remaining 30% of which was used for validation; all of the second half year of the data was used for testing.

## RESULTS AND DISCUSSION

### Simple regression models

Pulp can be likened to a soaked sponge. As the sponge becomes drier, the friction between it and any surface it contacts increases. The dewatering rate of a soaked sponge increases with higher applied pressure and a lower feed rate. Similarly, in the case of pulp, its dryness, and therefore friction, increases with higher roll pressure and lower pulp feed rates, which in turn results in a reduced roll speed. Assuming other process parameters remain constant, this relationship can be mathematically expressed in Equation (1):

$$N = f(Q, P) = k\frac{Q}{P} + b \quad (1)$$

Where $N$ is the twin roll press washer's roll speed, and $k$ and $b$ are the fitted parameters.

Hence, plotting $N$ against $\frac{Q}{P}$ should reveal a straight line, as is indeed is observed in **Figure 1**. The $R^2$ value of the fitted trendline using data from the first half of the year is 0.85, indicating a strong fit. Data from the second half of the year also aligns closely with the trendline, demonstrating that the model remains robust despite seasonal variations and other uncontrollable factors, such as feedstock quality, irregular machine maintenance, and unquantifiable chronic solid buildup. This

provides a solid foundation for developing more practical empirical models that accommodate a broader range of operating conditions.

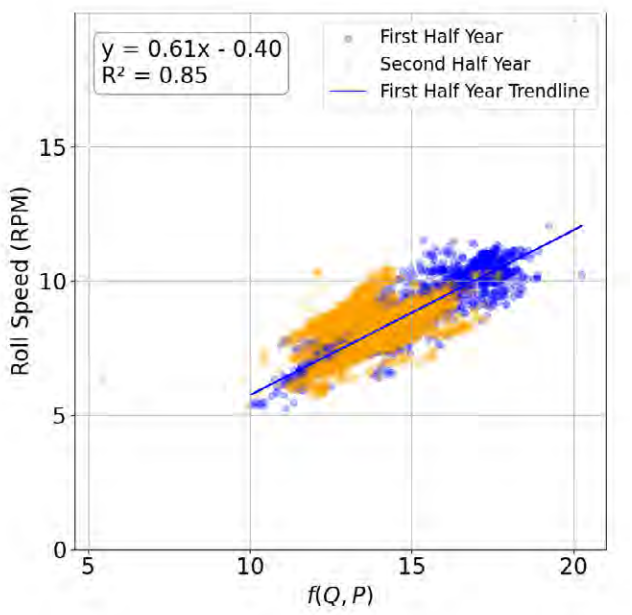



**Figure 1.** The simple first empirical model. Scatter plot of twin roll press washer's roll speed as a function of pulp flow rate and roll pressure, with constant inlet pulp consistency and dilution factor (1% deviation from setpoints).

After introducing data with a 10% variability in the inlet pulp consistency and dilution factor relative to their setpoints, the performance of the initial empirical model declined significantly, achieving an $R^2$ value of only 0.65 (**Figure 2**). This underscores the importance of developing a second empirical model that can maintain robust performance despite such variability.

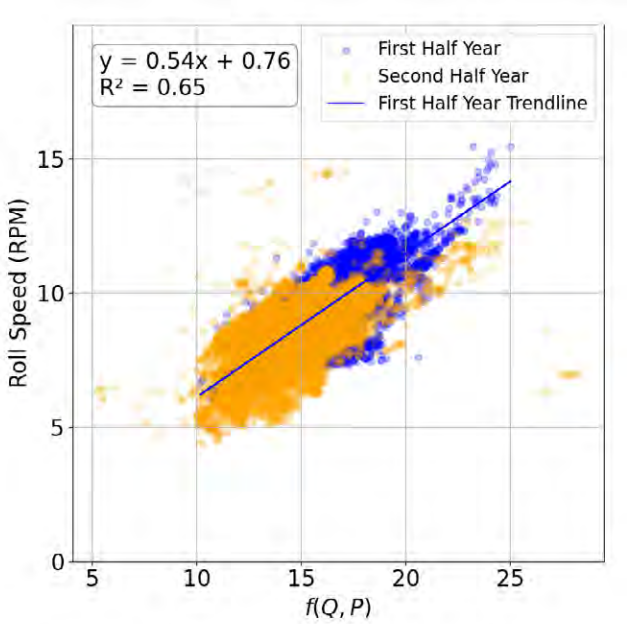



**Figure 2.** The simple first empirical model. Scatter plot of twin roll press washer's roll speed as a function of pulp flow rate and roll pressure, with varying inlet pulp consistency and dilution factor (10% deviation from setpoints).

The second empirical model builds on the first one, and aimed to achieve a better goodness of fit by including the inlet pulp consistency and dilution factor in the Equation (2).

$$N = f(Q, P, C, DF) = k\left(\frac{Q}{P} + m\right) + b \quad (2)$$

Where the correction factor, $m = \frac{Q}{\log P}\sqrt[3]{\frac{DF}{C}}$.

Fitting a trendline between roll speed and $\frac{Q}{P} + m$ yielded an $R^2$ value of 0.7 (**Figure 3**), which suggests that introducing the correction factor was able to improve the model's accuracy. This model can be used to inform the operator that when $\frac{Q}{P} + m$ is smaller than 15, roll speed may be lower than 5 rpm, and the roll pressure setpoint should be lowered to increase $\frac{Q}{P} + m$ and hence the roll speed to prevent blockages.

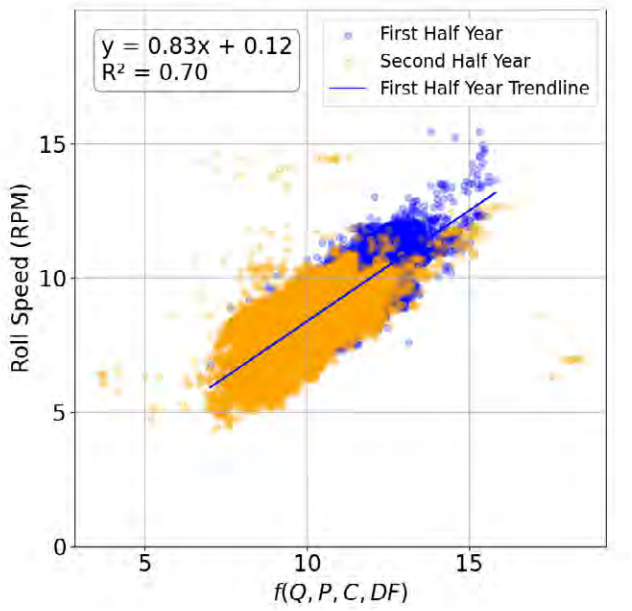



**Figure 3.** The improved second empirical model. Scatter plot of twin roll press washer's roll speed as a function of pulp flow rate and roll pressure, with varying inlet pulp consistency and dilution factor (10% deviation from setpoints).

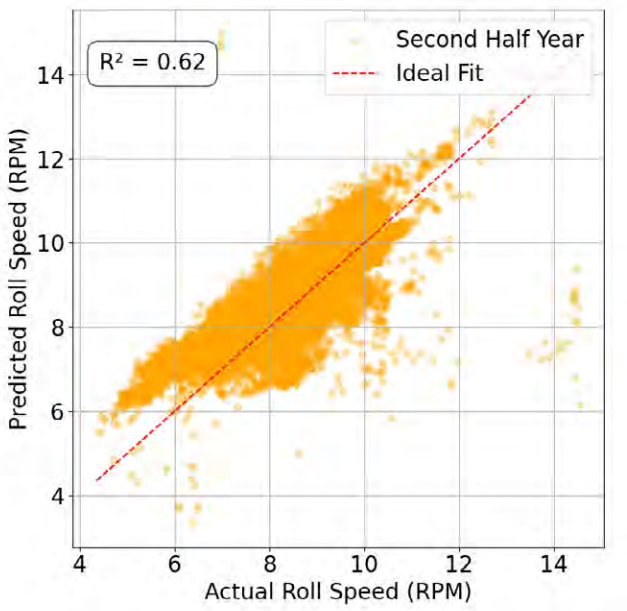



**Figure 4.** The feedforward neural network machine learning model. Scatter plot of predicted vs actual twin roll press washer's roll speed in the test dataset.

### Feedforward neural network model

Given that the simple regression model achieved an $R^2$ of only 0.7 when applied to a broader range of operating conditions, a feedforward neural network was investigated to potentially improve performance. The improvement observed after incorporating the nonlinear correction factor $m$ suggests that the effects of dilution factor and inlet pulp consistency on roll speed are likely nonlinear. Hence, a ReLU activation function was chosen to better capture these relationships. The feedforward neural network model yielded an $R^2$ of 0.62 (**Figure 4**). The low performance can be attributed to the simplicity of the feedforward neural network used in this study, as well as systematic variations over the extended time span between the training and test datasets. These variations include seasonal changes, which can significantly affect the characteristics of wood chips – such as moisture content, density, and composition – ultimately influencing pulp washing performance.

## CONCLUSIONS AND FUTURE WORK

In conclusion, this study successfully developed the first empirical models to predict roll speed in twin roll press washers based on key process parameters. The simple regression models demonstrated strong fits, with the second model being more applicable by incorporating additional variables such as inlet pulp consistency and dilution factor, achieving an $R^2$ value of 0.70. The machine learning model achieved an $R^2$ of 0.62, which may be able to be improved by modifying the feedforward neural network architecture and implementing physics-informed neural networks. However, already, models such as these have the potential to be used by operators to optimize roll speed, prevent blockages, and ensure uninterrupted production, ultimately supporting the pulp and paper industry's goals of sustainability and decarbonization.

Future work could focus on enhancing model adaptability and predictive accuracy by incorporating online learning approaches to continuously update both empirical and machine learning models in response to seasonal variations, machine maintenance, and feedstock quality fluctuations. Additionally, a comparative analysis with alternative modeling techniques such as physics-informed neural networks could provide insights into trade-offs between accuracy, interpretability, and generalization to unseen operating conditions, particularly in roll speed prediction for blockage prevention. Furthermore, a techno-economic analysis could help quantify the trade-offs between maximizing washing efficiency, preventing blockages, and optimizing energy recovery, providing a

holistic view of process improvements.

## DIGITAL SUPPLEMENTARY MATERIAL

The data that has been used is confidential.

## ACKNOWLEDGEMENTS

The authors would like to acknowledge the funding from “Ahuora: Delivering sustainable industry through smart process heat decarbonisation” from the New Zealand Ministry of Business, Innovation and Employment Advanced Energy Technology Strategic Science Investment Fund.

The authors would also like to thank our industrial partner for access to data.

## REFERENCES

1. A. G. Olabi, T. Wilberforce, K. Elsaid, E. T. Sayed, H. M. Maghrabie, and M. A. Abdelkareem, "Large scale application of carbon capture to process industries – A review," *Journal of Cleaner Production,* vol. 362, 2022, doi: 10.1016/j.jclepro.2022.132300.
2. P. Glavič, Z. N. Pintarič, H. Levičnik, V. Dragojlović, and M. Bogataj, "Transitioning towards Net-Zero Emissions in Chemical and Process Industries: A Holistic Perspective," *Processes,* vol. 11, no. 9, 2023, doi: 10.3390/pr11092647.
3. A. W. Krotscheck, "Pulp Washing," in *Handbook of Pulp*, 2006, pp. 511-559.
4. A. Pereira Parente, M. B. de Souza Jr, A. Valdman, and R. O. Mattos Folly, "Data Augmentation Applied to Machine Learning-Based Monitoring of a Pulp and Paper Process," *Processes,* vol. 7, no. 12, 2019, doi: 10.3390/pr7120958.
5. A. K. Singh and R. Chandra, "Pollutants released from the pulp paper industry: Aquatic toxicity and their health hazards," *Aquat Toxicol,* vol. 211, pp. 202-216, Jun 2019, doi: 10.1016/j.aquatox.2019.04.007.
6. M. El Koujok, A. Ragab, H. Ghezzaz, and M. Amazouz, "A Multiagent-Based Methodology for Known and Novel Faults Diagnosis in Industrial Processes," *IEEE Transactions on Industrial Informatics,* vol. 17, no. 5, pp. 3358-3366, 2021, doi: 10.1109/tii.2020.3011069.
7. X. Liang, Q. Zhang, Y. Man, and Z. He, "Toward sustainable process industry based on knowledge graph: a case study of papermaking process fault diagnosis," *Discover Sustainability,* vol. 5, no. 1, 2024, doi: 10.1007/s43621-024-00259-6.
8. J. Zhang, Z. Zhang, H. Yang, and S. Wang, "Fatigue and fracture failure analysis of a twin-roll press," *Engineering Failure Analysis,* vol. 90, pp. 585-596, 2018, doi: 10.1016/j.engfailanal.2018.02.010.

© 2025 by the authors. Licensed to PSEcommunity.org and PSE Press. This is an open access article under the creative commons CC-BY-SA licensing terms. Credit must be given to creator and adaptations must be shared under the same terms. See https://creativecommons.org/licenses/by-sa/4.0/



Systems & Control Transactions

**Research Article - Peer Reviewed Conference Proceeding**
ESCAPE 35 - European Symposium on Computer Aided Process Engineering
Ghent, Belgium. 6-9 July 2025
Jan F.M. Van Impe, Grégoire Léonard, Satyajeet S. Bhonsale,
Monika E. Polańska, Filip Logist (Eds.)

PSE PRESS

# A Novel Bayesian Framework for Inverse Problems in Precision Agriculture

**Zeyuan Song, and Zheyu Jiang***

Oklahoma State University, School of Chemical Engineering, Stillwater, Oklahoma, USA
* Corresponding Author: zheyu.jiang@okstate.edu.

## ABSTRACT

An essential problem in precision agriculture is to accurately model and predict root-zone (top 1 m of soil) soil moisture profile given soil properties and precipitation and evapotranspiration information. This is typically achieved by solving agro-hydrological models. Nowadays, most of these models are based on the standard Richards equation (RE), a highly nonlinear, degenerate elliptic-parabolic partial differential equation that describes irrigation, precipitation, evapotranspiration, runoff, and drainage through soils. Recently, the standard RE has been generalized to time-fractional RE with any fractional order between 0 and 2. Such generalization allows the characterization of anomalous soil exhibiting non-Boltzmann behavior due to the presence of preferential flow. In this work, we focus on inverse modeling of time-fractional RE; that is, how to accurately estimate the fractional order and soil property parameters of the fractional RE given soil moisture content measurements. Specifically, we introduce a novel Bayesian variational autoencoder (BVAE) framework that synergistically integrates our in-house developed fractional RE solver and adaptive Fourier decomposition (AFD) to accurately estimate the parameters of time-fractional RE. Our proposed AFD-enhanced BVAE framework consists of a probabilistic encoder, latent-to-kernel neural networks and convolutional neural networks. The BVAE framework is theoretically explainable and enhanced by the AFD theory, a novel signal processing technique that achieves superior computationally efficiency. Through illustrative examples, we demonstrate the efficiency and reliability of our AFD-enhanced BVAE framework.

Keywords: Artificial Intelligence, Machine Learning, Numerical Methods, Food & Agricultural Processes, Water

## INTRODUCTION

Precision modeling and forecasting of soil moisture are essential for implementing smart irrigation systems and mitigating agricultural drought. Most agro-hydrological models are based on the standard Richards equation [1], a highly nonlinear, degenerate elliptic-parabolic partial differential equation (PDE) with first order time derivative. However, standard RE is limited by its incapability of characterizing preferential flow in anomalous soil exhibiting non-Boltzmann behavior, a common and realistic scenario. To overcome this limitation, time-fractional RE of the following form [2] is developed and employed to model water flow dynamics in real soil systems:

$$\partial_t^{\alpha}\theta + \nabla \cdot \mathbf{q} = S, \tag{1}$$

$$\mathbf{q} = -(C(\theta)\nabla\theta + K(\theta)\nabla z). \tag{2}$$

where $\theta$ denotes the soil moisture content (in, e.g., $m^3/m^3$), $\mathbf{q}$ represents the water flux (in, e.g., $m^3/m^2 \cdot s$), $S$ denotes the sink term measuring water uptake rate by roots, $K(\theta)$ is unsaturated hydraulic water conductivity (in, e.g., $m/s$), $C(\theta)$ is soil moisture diffusivity (in, e.g., $m^2/s$), $t \in [0, T]$ denotes the time (in, e.g., $s$), $z$ corresponds to the vertical depth (in, e.g., $m$), and $\alpha$ is a soil-dependent parameter indicating subdiffusion ($0 < \alpha < 1$) and superdiffusion ($1 < \alpha < 2$) [2]. For unsaturated flow, both $C$ and $K$ are highly nonlinear functions of soil moisture content and soil parameters, thereby posing significant computational challenges for solving the standard Richards equation itself [3]. Thus, most existing research focuses on developing accurate and efficient numerical solvers for the time-fractional RE given soil parameters [2], which is also known as solving the forward problem.

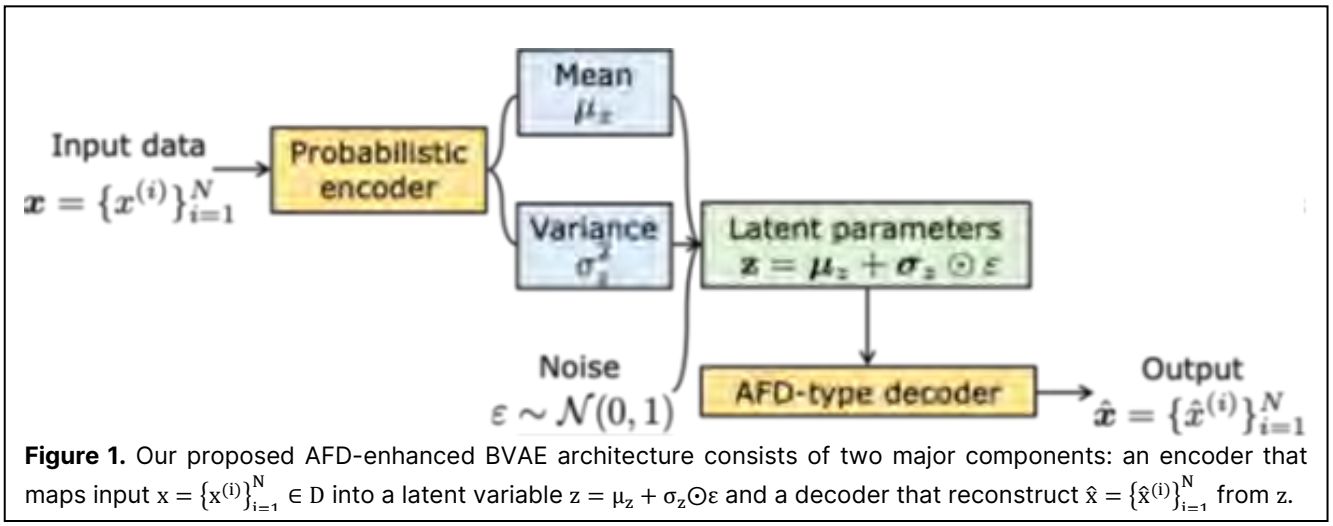



**Figure 1.** Our proposed AFD-enhanced BVAE architecture consists of two major components: an encoder that maps input $x = \{x^{(i)}\}_{i=1}^{N} \in D$ into a latent variable $z = \mu_z + \sigma_z \odot \varepsilon$ and a decoder that reconstruct $\hat{x} = \{\hat{x}^{(i)}\}_{i=1}^{N}$ from $z$.

Meanwhile, an equally important problem, which is to accurately estimate soil parameters given the soil moisture profile, is known as the inverse problem and is often less studied. This is primarily because inverse problems are generally ill-posed due to insufficient and/or inaccurate information (e.g., soil moisture solutions) and thus face significant computational challenges. Nevertheless, with recent advancements in soil sensing technologies and increasing adoption of in situ soil moisture sensors, farmers now have real-time access to massive arrays of root-zone soil moisture data. This poses great need and opportunity to develop more accurate and computationally efficient algorithms for solving inverse problems of time-fractional RE, so that one can extrapolate soil parameters estimated from local in situ soil sensing measurements to model field-wide soil moisture profiles.

Existing approaches to solve inverse problem for standard and/or time-fractional RE can be categorized into deterministic or probabilistic methods. Deterministic methods, which solve the inverse problem as a nonlinear optimization problem [4-6], tend to be trapped in local optima and are sensitive to data noise. Meanwhile, probabilistic methods, such as Markov chain Monte Carlo (MCMC) [7] or variational autoencoder (VAE) [8], can explore the entire solution space. However, state-of-the-art probabilistic methods scale poorly as problem size (e.g., the number of parameters to be estimated) increases, leading to scalability issues [9].

To address these challenges, in this work, we propose a novel Bayesian variational autoencoder (VAE) framework that is built upon our in-house developed time-fractional RE solver [11] and the adaptive Fourier decomposition (AFD) techniques [12,13]. This integration enables precise parameter estimation for time-fractional RE. The AFD-enhanced BVAE framework consists of a probabilistic encoder, latent-to-kernel neural networks, and convolutional neural networks. The probabilistic encoder will map the input data (i.e., soil moisture measurements) to a latent space. To preserve useful mathematical properties and physical insights, we further restrict the latent space to its reproducing kernel Hilbert space (RKHS) via the use of latent-to-kernel neural networks. The AFD-based convolutional neural networks are then applied to the resulting RKHS as decoder for parameter estimation. These neural networks are trained end to end, in which the training data are soil moisture profiles produced by our time-fractional RE solver. Through a simple 3-D time-fractional RE example, we demonstrate the accuracy of our AFD-enhanced BVAE framework in solving inverse problems by comparing it with conventional BVAE approach whose decoder structure is not specially designed.

## AN EXPLAINABLE BAYESIAN FRAMEWORK

### Bayesian VAE framework

Here, we first provide a brief overview of the BVAE framework. The standard variational autoencoder (VAE) is a generative model that learns a structured latent space while reconstructing input data. As shown in Figure 1, VAE consists of two primary components, an encoder that maps input $x \in D$ into a set of latent variables $z$, and a decoder that reconstruct $x$ from $z$.

VAE defines the marginal likelihood as the probability of the observation $x$ under the generative model. Given latent variables $z$, the marginal likelihood is expressed as:

$$p(x) = \int p(x|z)p(z)\,dz, \tag{3}$$

where $p(z)$ is the prior distribution over latent variables (often a standard Gaussian). Since direct computation of the RHS of Equation (3) is intractable, VAE approximates the true posterior $p(z|x)$ using a variational distribution $q(z|x,\phi)$, and maximizes the Evidence Lower Bound (ELBO):

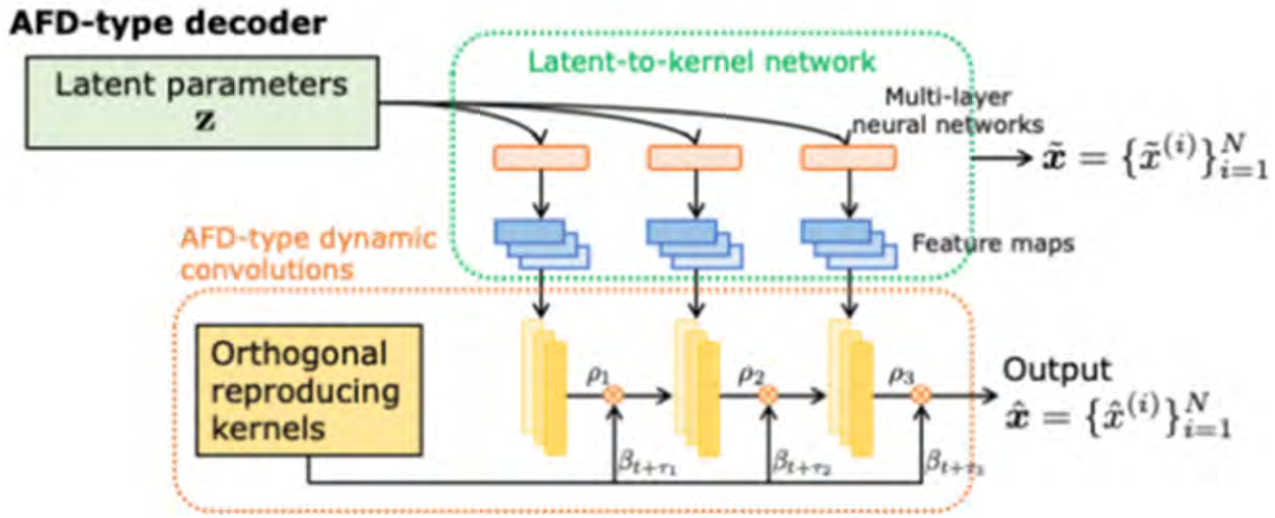



**Figure 2.** The decoder structure of our AFD-enhanced BVAE framework, which consists of two primary components: 1) latent-to-kernel neural networks which will map the latent variables $z$ to $\tilde{x} = \{\tilde{x}^{(i)}\}_{i=1}^{N}$ lying on an RKHS, and 2) dynamic convolutional kernel network that will reconstruct $\hat{x} = \{\hat{x}^{(i)}\}_{i=1}^{N}$.

$$\mathcal{L}_{ELBO} = \sum_{x \in D} \mathcal{L}_{\Theta,\phi}(x), \tag{4}$$

$$\mathcal{L}_{\Theta,\phi}(x) = \mathbb{E}_{q(z|x,\phi)} \log p(x|z,\Theta) - D_{KL}[q(z|x,\phi)\|p(z)] \tag{5}$$

where the first term of Equation (5) ensures accurate reconstruction and the second term regularizes the latent space by minimizing the Kullback-Leibler (KL) divergence between the approximate posterior and the prior distribution.

On the other hand, the BVAE framework extends this by placing priors not only on the latent variables z but also on the model parameters θ, resulting in a Bayesian formulation:

$$p(\Theta|D) \propto p(D|\Theta)p(\Theta). \tag{6}$$

The likelihood function is then defined as:

$$p(x|z,D) = \int p(x|z,\Theta)p(\Theta|D)\, d\Theta \tag{7}$$

and the marginal likelihood as:

$$p(x|D) = \iint p(x|z,D)p(z)\, dz\, p(\Theta|D)\, d\Theta. \tag{8}$$

The BVAE enables more robust parameter estimation and improved uncertainty quantification. Instead of relying on a single point estimate for Θ, BVAE marginalizes over its posterior distribution, leading to better generalization and reliability in low-data regimes. By jointly inferring $p(z|x,D)$ and $p(\Theta|D)$, BVAE offers a fundamental way to incorporate uncertainty into both data representation and model parameters, making it particularly useful for applications requiring high-confidence decision-making.

## A novel, explainable encoder structure in our AFD-enhanced BVAE framework

One common way to enhance the explainability of a neural network is to modify its structure based on the approximation theory (e.g., the universal approximation theorem [14]). In this work, we propose to achieve this by adopting AFD, a novel signal decomposition method that adopts adaptive orthogonal bases and thus leads to higher accuracy and significant computational speedup compared to conventional Fourier decomposition [12,13]. Specifically, as shown in Figure 2, we innovate the decoder structure by combining latent-to-kernel neural network with mathematically interpretable dynamic convolutional kernel network (CKN). In terms of latent-to-kernel network, our proposed structure consists of a multi-layer neural network that will first take the latent parameters $z$ obtained from the encoder and generate $\tilde{x} = \{\tilde{x}^{(i)}\}_{i=1}^{N}$, which belongs to the Hilbert space $H$ of the same manifold $\mathcal{M}$ that $z$ belong to. Next, the latent-to-kernel network consists of feature maps $FM(\tilde{x})$ that project $\tilde{x}$ to its reproducing kernel Hilbert space (RKHS) [15]. This way, our latent-to-kernel network will try to learn the feature maps from $H(\mathcal{M})$ to its nearest RKHS, where the convolutional Kernel is unique and satisfies the reproducing property [16]. This naturally brings in dynamic CKN for local feature extraction, which is mathematically grounded in the RKHS framework. Furthermore, the dynamic CKN structure shown in Figure 2 mathematically resembles AFD in the sense that each dynamic convolutional layer performs cross-correlation between $FM(\tilde{x})$ and the orthogonal reproducing kernels β, i.e., $FM(\tilde{x}) \star \beta_i$. With this, the final output of the dynamic CKN, assuming

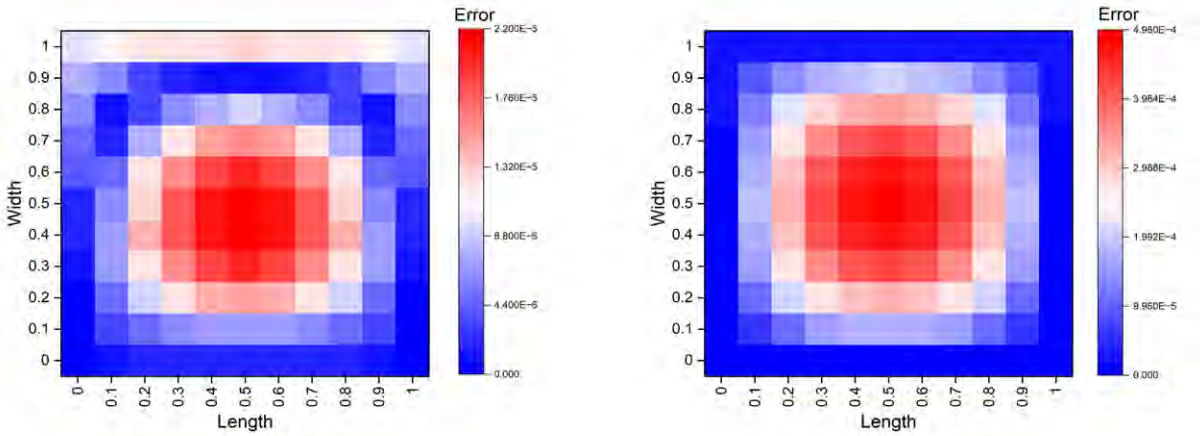



**Figure 3.** The error is obtained by substituting the parameters estimated by our proposed AFD-enhanced BVAE framework (Left) and conventional BVAE (Right) into the time-fractional RE solver [11] and taking the difference the numerical solution with the analytical solution of Equation (12). Ground truth value for the parameters are $\alpha = 0.5$ and $a = 0.001$. The parameters estimated by our proposed AFD-enhanced BVAE framework are $\alpha = 0.496 \pm 0.005$ and $a = 0.00102 \pm 7 \times 10^{-9}$, while those of conventional BVAE are $\alpha = 0.440 \pm 0.004$ and $a = 0.00094 \pm 2 \times 10^{-9}$

that there are a total of $N$ convolutional layers, is given by:

$$\hat{x} = \sum_{i=1}^{N} \rho_i (FM(\tilde{x}) \star \beta_i)\beta_{i+\tau_i}, \qquad (9)$$

where $\rho_i \in (0,1)$ are scaling factors and $\tau_i$ can choose between 0 to $N - i$ for layer $i$. The choices of $\rho_i$ and the orthogonal reproducing kernels must satisfy weak maximal selection principle and convergence theorem [10,12], respectively.

It can be shown that Equation (9) is equivalent to AFD operation [10,12,13]. Thus, with a specially designed structure, the AFD-type dynamic CKN will enjoy significant computational speedup and rigorous performance guarantees just like the AFD. The full AFD-enhanced BVAE model will be trained end to end by minimizing the following total loss function:

$$\mathcal{L} = \|x - \hat{x}\|^2_{H(\mathcal{M})} + \|\tilde{x} - FM(\tilde{x})\|^2_{H(\mathcal{M})} + w D_{KL}[q(z|x,\phi)\|p(z)], \qquad (10)$$

where $w$ is a regularization parameter.

## Using AFD-enhanced BVAE framework to solve inverse problems

Here, we describe the procedure for applying our AFD-enhanced BVAE framework to solve the inverse problem. That is, we would like to reconstruct or estimate the soil-dependent parameters, including $\alpha$ and parameters of hydraulic conductivity function and water retention curve, from soil moisture content profiles through direct sensor measurements. Without loss of generality, we denote those parameters and the corresponding soil moisture content as $\gamma$ and $\theta$, respectively. To train the model, various sets of soil parameters $\gamma$ will be sent to our in-house developed fractional RE solver to generate a set of soil moisture profile solutions. These solutions and their associated soil parameters $\gamma$ will then be sent to the encoder to extract latent parameters $z$, which are then used by the decoder to reconstruct soil parameters $\hat{\gamma}$. During the training process, the total loss function of Equation (10) will be minimized such that the output of the decoder, $\hat{\gamma}$, shall match with the given $\gamma$ as closely as possible.

Once training is complete, our AFD-enhanced BVAE model will only take the actual soil moisture measurements or solution profiles $\theta$ as input and produce the soil-specific parameter estimates $\hat{\gamma}$ as output, which can be used by the fractional RE solver for extrapolation and field-wide soil moisture modeling.

## AN ILLUSTRATIVE EXAMPLE

Here, we present a proof-of-concept example to demonstrate the accuracy enhancement of our proposed AFD-enhanced BVAE framework by considering a simple 3-D time-fractional RE where $K = \theta$ and $C = a(\theta + 1)$. The width, length as well as depth are 1. The boundary conditions are zero at all boundaries and the initial condition is given by:

$$\theta(x, y, z, 0) = (x - x^2)(y - y^2)(z - z^2). \qquad (11)$$

For $a = 0.1$ and $\alpha = 0.5$, the problem has an analytical solution and is given by:

$$\theta(x, y, z, t) = t(x - x^2)(y - y^2)(z - z^2). \qquad (12)$$

Assuming that we do not know the values of $\gamma$ (i.e.,

$\alpha$ and $a$), we generate a total of 10,000 sets of $(\theta, \gamma)$ solutions using our in-house developed fractional RE solver. Both AFD-enhanced BVAE and conventional BVAE models contains three hidden layers and 256 neurons per layer. The Adam optimizer and ReLU activation function are used for training. Figure 3 shows the error of soil moisture profiles between analytical solution and the numerical solution obtained from substituting the estimated soil parameters into our fractional RE solver, where the solution across two dimensions (width and length) are drawn better visualization. For the third dimension (depth), the error employs a similar behavior due to symmetry of this problem. Our AFD-enhanced BVAE model not only produces more accurate parameter estimates, but also enhances the accuracy of our fractional RE solver by at least an order of magnitude compared to conventional BVAE model. This illustrates the synergistic improvement in model accuracy when combining advanced numerical solver (for solving the forward problem) with our AFD-enhanced BVAE model (for solving the inverse problem). Furthermore, the data-driven nature of our proposed framework makes it particularly suitable for integrating in situ soil moisture sensing technologies to equip farmers with accurate tools that will bring "eyes inside the soil".

For comparison, we also implement a simple Kalman filter (KF) algorithm as a benchmark method to solve the same inverse problem. The results of KF are $\alpha = 0.517$ and $a = 0.00114$, which are further away from the ground truth solutions compared to our AFD-enhanced BVAE model.

Lastly, we point out that, unlike MCMC approach, our AFD-enhanced BVAE algorithm does not experience a significant increase in computational time as the number of unknown parameters to be estimated grows. This suggests that the BVAE-type approaches are quite scalable with respect to the dimensionality of the parameter space [17].

## CONCLUSIONS

In this work, we propose a novel AFD-enhanced BVAE framework to accurately solve the inverse problem of time-fractional Richards equation. Our proposed framework synergistically integrates BVAE, neural network, dynamic convolutions, and AFD theory to offer computational speedup and great mathematical explainability. Furthermore, by designing a tailored decoder structure that resembles AFD operation, our new framework significantly improves soil parameter estimation accuracy. In addition, by using this framework in conjunction with our accurate time-fractional RE solver [11], we can achieve synergistic advancement in root-zone soil moisture modeling. Moreover, we remark that our proposed AFD-enhanced BVAE model is a generalized framework that can be leveraged in solving various inverse problems in large-scale and/or complex partial differential equation systems (e.g., convection-diffusion equation, Schrödinger equation, etc.), as well as in other fields such as image processing, data analytics, and so on. We will explore these aspects in our future works.

## ACKNOWLEDGEMENTS

We acknowledge financial support from the startup fund of College of Engineering, Architecture, and Technology at Oklahoma State University.

## REFERENCES

1. Richards LA. Capillary conduction of liquids through porous mediums. Physics 1(5): 318-333 (1931) https://doi.org/10.1063/1.1745010
2. Płociniczak Ł. Analytical studies of a time-fractional porous medium equation: Derivation, approximation, and applications. Commun Nonlinear Sci Numer Simul 24(1-3):169-183 (2015) https://doi.org/10.1016/j.cnsns.2015.01.005
3. Song Z, Jiang Z. A novel numerical method for agro-hydrological modeling of water infiltration in soil. Preprint available at arXiv:2310.02806v3. https://doi.org/10.48550/arXiv.2310.02806
4. Cockett R, Heagy LJ, Haber E. Efficient 3d inversions using the Richards equation. Comput Geosci 116(C):91–102 (2018). https://doi.org/10.1016/j.cageo.2018.04.006
5. Finsterle S, Kowalsky MB. A truncated Levenberg-Marquardt algorithm for the calibration of highly parameterized nonlinear models. Comput Geosci 37(6):731-738 (2011) https://doi.org/10.1016/j.cageo.2010.11.005
6. Haber E. Quasi-newton methods for large-scale electromagnetic inverse problems. Inverse Probl 21(1):305 (2004) 10.1088/0266-5611/21/1/019
7. Dostert P, Efendiev Y, Mohanty B. Efficient uncertainty quantification techniques in inverse problems for Richards' equation using coarse-scale simulation models. Adv Water Resour 32(3): 329-339 (2009). https://doi.org/10.1016/j.advwatres.2008.11.009
8. Lopez-Alvis J, Laloy E, Nguyen F, Hermans T. Deep generative models in inversion: The impact of the generator's nonlinearity and development of a new approach based on a variational autoencoder. Comput Geosci 152:104762 (2021) https://doi.org/10.1016/j.cageo.2021.104762
9. Chen J, Dai Z, Yang Z, Pan Y, Zhang X, Wu J, Reza Soltanian M. An improved tandem neural network architecture for inverse modeling of multi-component reactive transport in porous media.

Water Resour Res 57(12): e2021WR030595 (2021) https://doi.org/10.1029/2021WR030595
10. Qian T, Sprößig W, Wang J. Adaptive Fourier decomposition of functions in quaternionic Hardy spaces. Math Methods Appl Sci 35(1):43-64 (2012) https://doi.org/10.1002/mma.1532
11. Song Z, Jiang Z. A Physics-based, Data-driven Numerical Framework for Anomalous Diffusion of Water in Soil. *Systems and Control Transactions* 4, *in press.* (2025)
12. Song Z, Sun Z. Representing functions in H^2 on the Kepler manifold via WPOAFD based on the rational approximation of holomorphic functions. Mathematics (Basel) 10(15):2729 (2022). https://doi.org/10.3390/math10152729
13. Qian T. Intrinsic mono-component decomposition of functions: An advance of Fourier theory. Math Methods Appl Sci 33(7):880-891 (2010 https://doi.org/10.1002/mma.1214
14. Lu L, Jin P, Pang G, Zhang Z, Karniadakis GE. Learning nonlinear operators via DeepONet based on the universal approximation theorem of operators. Nat Mach Intell 3(3):218-229 (2021). https://doi.org/10.1038/s42256-021-00302-5
15. Shawe-Taylor J, Cristianini N. Kernel Methods for Pattern Analysis. Cambridge University Press (2004)
16. Saitoh S, Sawano Y. Theory of reproducing kernels and applications. Springer (2016)
17. Song Z, Jiang Z. DRW-BO: A Bayesian framework for parameter estimation for fractional Richards equation with applications in precision agriculture. In:2024 AIChE Annual Meeting. AIChE (2024)

© 2025 by the authors. Licensed to PSEcommunity.org and PSE Press. This is an open access article under the creative commons CC-BY-SA licensing terms. Credit must be given to creator and adaptations must be shared under the same terms. See https://creativecommons.org/licenses/by-sa/4.0/



Systems & Control Transactions

**Research Article - Peer Reviewed Conference Proceeding**
ESCAPE 35 - European Symposium on Computer Aided Process Engineering
Ghent, Belgium. 6-9 July 2025
Jan F.M. Van Impe, Grégoire Léonard, Satyajeet S. Bhonsale,
Monika E. Polańska, Filip Logist (Eds.)

PSE PRESS

# Role of process integration and green technologies utilization for the decarbonization of the watchmaking sector.

**Pullah Bhatnagar[a], Daniel Florez-Orrego[a], Vibhu Baibhav[a], Manuele Margni[b], Francois Marechal[a]***

[a] EPFL-Valais, École polytechnic federal de Lausanne, Sion, Switzerland
[b] HES-SO Valais-Wallis, Sion, Switzerland

## ABSTRACT

Decarbonizing the watch industry and improving its sustainability requires enhancing the energy efficiency, intensifying the waste heat recovery and integrating renewable energy resources to significantly reduce the energy consumption and reduce the overall process emissions. The watchmaking industry operates across different periods, each one characterized by own levels of average power demand, plant activity, and duration. While working days (Work D) experience the highest energy demand; other periods, such as weekend (Wend D1, Wend D2 and Wend N), exhibit a substantial drop in energy consumption. It requires a suitable selection of utility systems and an energy planning that can meet the energy requirements regardless of the different operation regimes, reducing the consumption of fossil resources. To this end, this work leverages a systematic framework to perform the techno-economic analysis and explore the feasibility of incorporating alternative energy conversion (e.g. electrification) and storage solutions (for heat) in the watchmaking industry, accounting for the monthly variations of energy demand and environmental conditions.

**Keywords**: Audit, Energy Recovery, Decarbonization Technologies, Optimizing, Operational strategy

## INTRODUCTION

While considerable work had focused on decarbonizing energy-intensive industries like iron and steel, refineries, and chemicals, there has been limited research on non-energy-intensive sectors such as the watchmaking industry.

As governments and international organizations push for net-zero emissions, industries face growing pressure to adopt sustainable practices. The challenges of decarbonizing the watchmaking industry include:

- Limited understanding of the industry
- Multiple decarbonization options to evaluate
- Seasonal effects on energy consumption

Some research has explored energy recovery in batch process industries, considering characteristic power variations (Lin, 2024). Similarly, studies in European textile plants (Zuberi, 2020) identified potential energy savings of 21–43%, depending on time of day and season. However, gaps remain in integrating decarbonization technologies and analyzing their combined effects with seasonal power variation and energy recovery strategies in the luxury and watchmaking industry.

This work aims to evaluate the current operations of the watchmaking industry, emphasizing the role of seasonal and characteristic power variations (also known as characteristic day). It will also explore how energy recovery, building shading, and decarbonization technologies affect the industry's performance under seasonal variations.

## METHODOLOGY

The section there will begin with a brief description of energy audit of the industry, then focusing on energy recovery from CNC(Computer numerical control) and compressor, then analysing the effect of integration of decarbonization technology in the industry and

discussing the methodology to optimize the choice of technology.

## Energy audit

The study begins with an energy audit in a watchmaking industry in the Swiss Jura region. The technologies used in the watchmaking plant are shown in Figure 1. The industrial operation is divided into five characteristic days for the plant operations. Each day is defined by typical average power demand, plant activity, and time. In addition, the changes in the demand in technologies, defines a characteristic day, explained in the Table 1.

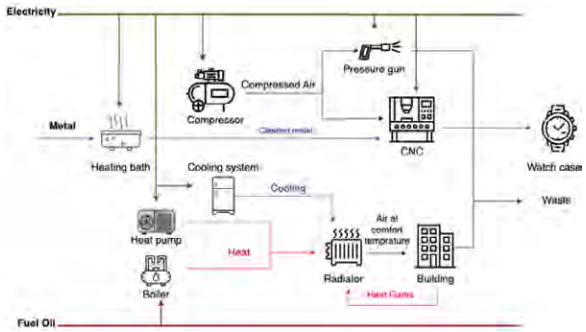



**Figure 1.** Process and utility flow diagram for watchmaking industry.

**Table 1:** Technology power variation depending upon characteristic day ($P_{CNC}$- Max CNC power, $P_{Com}$- Max compressor power and $P_{Bath}$ - Max power heat bath).

| Day | CNC Power (kW) | Compressor Power (kW) | Heat bath (kW) |
|---|---|---|---|
| Work D | $P_{CNC}$ | $P_{Com}$ | $P_{Bath}$ |
| Work N | 0.85* $P_{CNC}$ | 0.79* $P_{Com}$ | $P_{Bath}$ |
| Wend D1 | 0.6* $P_{CNC}$ | 0.56* $P_{Com}$ | $P_{Bath}$ |
| Wend D2 | 0.55* $P_{CNC}$ | 0.51* $P_{Com}$ | $P_{Bath}$ |
| Wend N | 0.55* $P_{CNC}$ | 0.51* $P_{Com}$ | $P_{Bath}$ |

As shown in figure 1, the industry requires two utilities which are electricity and fuel oil(mazout) which helps in meeting all the requirements for the processes. Raw material consumed in industry can be different kind of metals(high qulaity steel, platinum, gold and etc). The materal is heated up in a bath to remove all the impurities and then different machining operation are performed through CNC and Pressure gun. These technology require compressed air, supplied by a compressor. The energy requirement (heating or cooling) of a building depends on the season and the characteristic day. Figure 2 explains the changes in energy requirement for a characteristic day (Work D) depending upon month, and it helps in understanding the changes in building requirement depending upon the month. During winter months there is a heat requirement and during summer month there is a cooling requirement. Figure 3 explains the variation of building energy requirement for a day (beignning with 6h of Work N, 12h of Work D and then again 6 h of Work N) for a month of May.

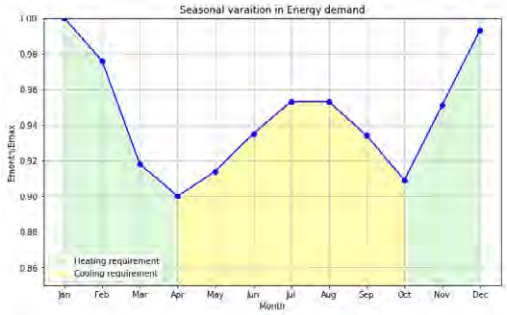



**Figure 2.** Variation in the energy demand for a typical working day in different months.

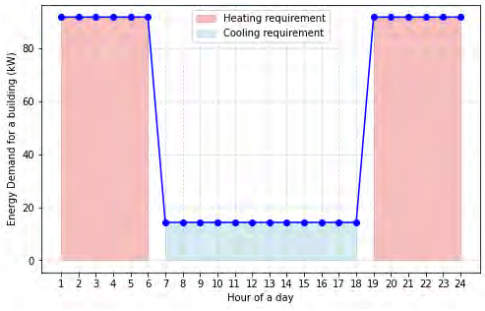



**Figure 3.** Variation in the energy requirement in a day ( beignning with 6h of Work N, 12h of Work D and then again 6 h of Work N) in a month of May.

The energy distribution among different technology is dependent on characteristic day and month. Figure 4 discusses the energy distribution among different technologies for month of December on a characteristic Work D. It is depicted that highest share of energy is going towards the working of CNC and Compressor.

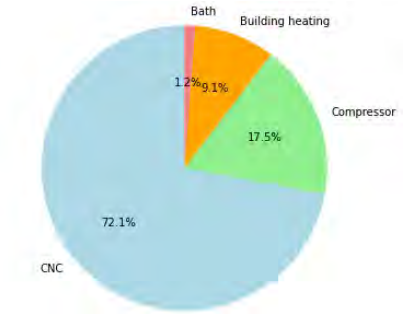



**Figure 4.** Distribution of energy among different technology and building requirement for the month of December.

In the analysis there are certain assumption which are adopted. It is assumed a year has 48 working weeks.

Distribution of characteristic day in a typical week is depicted in figure 5. A typical week consists of 5 Work D and 5 Work N, a characteristic Work D is followed by Work N. After 5 Work N there is Wend D1 for then followed by Wend D2 which is followed by Wend N.




**Figure 5.** Distribution of total number of hours of a week for different characteristic day.

## Energy recovery in CNC and Compressor

An untapped potential for waste heat recovery is observed from the existing energy technologies installed in the watchmaking industry. For instance, the waste heat that can be recovered from compression units depends on the different parameters shown in Eq(1), where , $m_{in}$(kg/s) is the mass flow rate of the compressed air, $Cp_{air}$ (J/kg.K) is the heat capacity of air and $T_{in}$ (K) is the inlet temperature :

$$Q_{rel} = m_{in} * Cp_{air} * (T_{out} - T_{in}) \quad (1)$$

Moreover, the outlet temperature $T_{out}$ is calculated using Eq.(2), where P (-) is the pressure ratio, $T_{in}$ (K) is the inlet temperature ,$\gamma$ is ratio of specific heat capacity, $\eta_{is}$ is the compressor isentropic efficiency. The quality of waste heat depends upon the temperature level which will be computed with the help of Eq (1, 2).

$$T_{out} = T_{in} + \left[\frac{T_{in}*\left(P^{\frac{\gamma-1}{\gamma}}-1\right)}{\eta_{is}}\right] \quad (2)$$

In the case of CNC the waste heat recovery is assumed as 80% of the total power consumption of the CNC machine (Fecko ,2021). The waste heat dissipated in the machining process is recovered with the cooling fluid the temperature of fluid increases from 12.5°C to 17.4°C (Teyu), as per the audit results. Recovering heat these technologies will improve the energy efficiency. As it is reducing the heating requirement for the building and also reducing the excess electricity required for cooling CNC and compressor.

## Shading

For months between April to October, there is a need for cooling to maintain comfort temperature. Cooling requirement can be reduced with installation of shades as it reduces the heat gain.

## Decarbonisation technologies

Some of the technologies which can be incorporated are Photovoltaic system (PV), Solar Thermal (ST) and Thermal Storage. Details of these technologies are discussed below-

## Modeling of the PV for solar electricity production

PV panels can help harvesting the solar energy for producing electricity, therefore reducing the electricity import. The solar irradiance, the temperature of the panel and the area of the panel are important design parameters that can influence the amount of power generated as shown in the Eqs. (3) :

$$T_{panel} = U_{glass} * (T_{ext} + 273.15)/(U_{glass} - \eta_{var} * Irr) + Irr * (f_{glass} - \eta_{ref} - \eta_{var} * T_{ref})/(U_{glass} - \eta_{var} * Irr) \quad (3)$$

where Irr is Irradiance in (W/m$^2$), $U_{glass}$ is the heat transfer coefficient by the glass (W/m$^2$.K) , $\eta_{var}$ (1/K) is efficiency dependent upon the temperature of the panel, and $T_{ref}$(K) and $T_{ext}$(K) are reference and external temperature respectively. The net electricity produced can be calculated with Eq.(4)

$$E_{default} = Irr * A_{real} * (\eta_{ref} - \eta_{var} * (T_{panel} - T_{ref}) \quad (4)$$

where $A_{real}$(m$^2$) is the effective area for the power generation.

### Modelling of the ST for heat production

ST allows producing high grade heat by concentrating solar radiation. The amount of heat can be calculated according to Eqs(5 and 6) The net heat released is sum of $Q_1$ and $Q_2$ which corresponds to heat at two different temperature. The heat is available in two different temperature ranges, $Q_1$ is available between 92°C – 85°C and $Q_2$ is available between 110°C – 92°C.

$$Q_1 = DNI * A_{real} * \eta_1 * 0.9/1000 + 0.0001 \quad (5)$$

$$Q_2 = DNI * A_{real} * \eta_2 * 0.9/1000 + 0.0001 \quad (6)$$

where DNI is Direct Normal Irradiance (W/m$^2$), $A_{real}$ (m$^2$) is the effective solar irradiated area and $\eta_1$ and $\eta_2$ are the efficiency. The value of $\eta_1$ and $\eta_2$ is 0.5 and 0.05 respectively.

## Modelling of the Thermal Storage for storage system

The thermal storage technology helps in storing the heat when there is excess heat generated and supplying when there is a demand for the heat., there are some assumptions the storing fluid is water and the losses are assumed to be nill. The system are modeled using Eqs(7

and 8) respectively:

Charging

$$Q_c = Cp_w * m_w * (T_c - T_h) \quad (7)$$

Discharging

$$Q_d = Cp_w * m_w * (T_h - T_c) - Q_l \quad (8)$$

where $T_c$ (70°C ) and $T_h$ (80°C) are cold or mean initial storing temperature and hot or mean final storing temperature respectively; $m_w$(kg/s) is the mass of the thermal storage fluid ,$Cp_w$(J/kg.K) is the heat capacity of the fluid) and $Q_l$(kW) is the amount of heat lost to the environment during the storage time.

## Optimization strategy for the selection of the energy technology and operation strategy

The optimization process is performed in the OSMOSE (a tool for the design and analysis of integrated energy system performs multi-objective optimization) platform considering all possible technological options (PV, Heat pump, Solar Thermal and Thermal Storage). To this end, OSMOSE solves the Mixed Integer Linear Programming (MILP) problem that selects the energy technologies and operating conditions based on some objective function relevant for the watchmaking industry.

## Objective function

Some of the relevent obejctive function taken in this analysis are discuused below:

CAPEX

It is an economical indicator which helps in evaluating all the investment related decision. It takes care of the money invested in buying the new technology. Investement cost of different technology is taken into consideration are shown in Table 2.

**Table 2:** Cost of decarbonisation technology (TSE 2019), (FSS). (In this $kWh_{st}$ stands for stored amount of energy)

| Technology | Investment Cost |
|---|---|
| PV panel | 400 (CHF/$m^2$) |
| Solar Thermal (ST) | 400 (CHF/$m^2$) |
| Photovoltaic Thermal (PVT) system | 750 (CHF/$m^2$) |
| Thermal storage (TS) system | 630 (CHF/$kWh_{st}$) |

OPEX

It is an economical indicator which helps in evaluating all the resources an industry needs to buy for operation of system The cost of resources for the watchmaking industry taken into consideration are shown in Table 3.

**Table 3:** Cost of resources (Stat, 2024), (Migrol, 2024).

| Resource | Operational Cost |
|---|---|
| Electricity | .304 (CHF/kWh) |
| Mazout | .1174(CHF/kWh) |

TOTEX

It is an economical indicator which helps in determining the total cost incurred by the system . It include both CAPEX and OPEX, it is better to convert CAPEX into annualized cost which can be calculated using, Eq(9):

$$CAPEX_{ANN} = \left[\frac{i*(i+i)^n}{(i+i)^n-1}\right] * CAPEX \quad (9)$$

Where CAPEX(CHF) is the total investement of the technology and $CAPEX_{ANN}$ (CHF/year) is the annualized investment cost, where I is the interest rate and n is total lifetime of technology. The total lifetime of each technology is assumed to be 20 years and interest rate of 8%.

## Operation strategy for thermal storage system

The storage and dispatch strategy depends on month. During extreme winter conditions, like in January and December, maximum heating is required in these months as environmental temperatures is low. Additionally, solar thermal energy generation is minimal in these months because of low irradiance. As a result, heat can only be stored on the characteristic day (Wend D) which has minimum requirement. The characteristic day (Work N and Wend N) where there is no sunlight they use heatpump to full-fill the demand.

In months like February, March, and November, there is potential for storing heat on Work D. As heating demand during these months is lower compared to extreme winter months, and irradiance is slightly higher. However, the stored heat is still insufficient to fully meet nighttime heating demands, so the system continues to rely on a heat pump at night but the cosnumption form the heat pump decreases.

For the rest of the month in the year, solar thermal system is capable of providing all the necessary heat. As a result, heating requirements for all characteristic days will be met using solar thermal energy and thermal storage alone.

# RESULT

The section begins with a discussion of result on improvement in energy efficiency by recovering energy from compressor and CNC, the section also discusses the result on reducing the energy demand by incorporating different decarbonization technology (like PV, Solar Thermal and Thermal Storage). The section is concluded with discussing result of optimization for the industry from the options (like PV, Solar Thermal and Thermal Storage) provided.

## Energy remarks and energy efficiency

In the watchmaking industry, potential sources for waste heat recovery includes compressor intercooling, chemical baths cooling and CNC machines lubricant refrigeration. Heat recovery can reduce fuel oil consumption amount to 1.27 (MWh/year) and decreasing energy consumption by 316 (MWh/year). It is because the heat integration reduces the electricity demand for heat pumps and also reduces fuel oil demand for heating. Shading reduces cooling requirements in summer, cutting annual energy consumption by 120 (MWh/year) by limiting solar heat gains, particularly from April to October. Combining waste heat recovery and building shading improves energy efficiency by 436 (MWh/year). Figure 6 illustrates the monthly impact of these measures on energy efficiency.

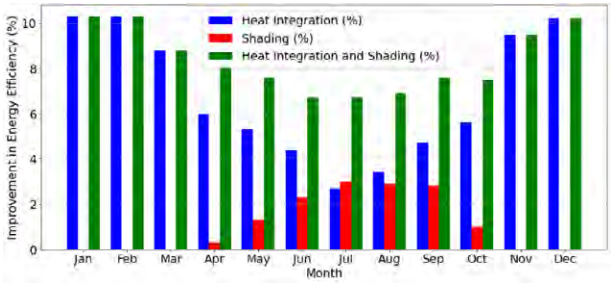



**Figure 6.** Improvement in energy efficiency depending upon the season, blue color corresponds to improvement in efficiency because of heat integration and red corresponds to improvement in efficiency because of shading and green is showing effect of integrating both these technologies.

## Incorporating decarbonisation technology

Implementing technologies like PV and ST can help reducing the grid electricity demand. The area available for these technologies are 3000 $m^2$. Integrating PV entails 700.3 (MWh/year) electricity savings, while ST reduces electricity consumption by 350 (MWh/year), as it offsets heating needs previously met by heat pumps. Integrating both the technologies (which is also called as Photovoltaic-Thermal system (PVT)) decreases the electricity demand by 1050.1 (MWh/year). Thermal storage further reduces energy demand in the watchmaking industry, offering an annual reduction of 580 MWh/year compared to using PVT alone. The cost of the storage technology is 1.2 MCHF. The reductions in the energy demand are most significant from April to October, as heat stored during these months can be used at night for heating purposes (explained in the section operation strategy for thermal storage system). The efficiency of the ST and Thermal Storage depends on the charging and discharging temperature because if the charging temperature is higher than the temperature range in which ST is working then heat from solar storage cannot be used. Therefore, it is important to tune the temperature range such that heat from ST can be used in Thermal Storage. Figures 7 and 8 illustrate the monthly impact of implementing these technologies and the reduction in monthly energy demand.

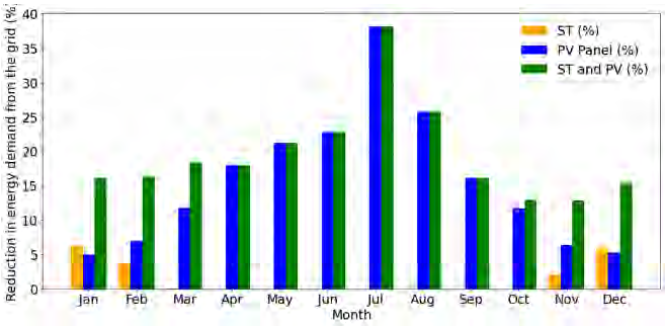



**Figure 7.**Reducing energy demand from the grid depending upon the season and technology installed, blue color corresponds to reducing deamnd from grid because of ST, orange corresponds to reducing deamnd from grid because of PV and green is for PVT technology.

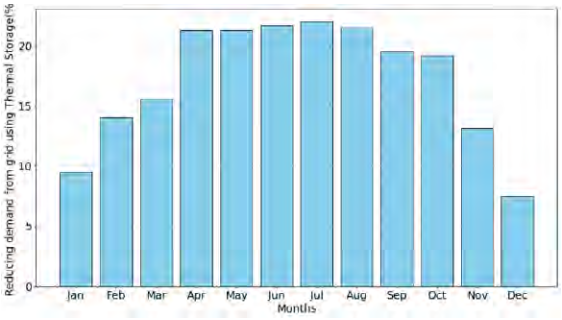



**Figure 8.** Reducing energy demand from the grid depending upon the season and technology installed, blue color corresponds to reducing deamnd from grid because of thermal storage integrated with PVT system.

## Choice of technology

The choice of technology depends upon the type of objective function taken into consideration. There can be multiple function like Total cost, Operational cost, Capital cost and Emissions.

Table 4 helps in estimating how different choices of technology will be affecting the economical indicator. In the

With Capital cost as the objective function the system most optimal solution will be Business As Usual (BAU) case. As the optimizer will try not to install any technology.

If there is a change in the optimizer to Total cost it will try to choose technology where maximum saving is observed it will be PV (without storage) and PVT and TS (with storage).

Now lastly if we keep Optimizer to Operational cost the system will choose PVT system and PVT system with

storage if storage is included.

**Table 4:** Capital cost and savings in operational cost observed for the different technology.

| Technology | CAPEX (kCHF/year) | OPEX savings (kCHF/year) |
|---|---|---|
| BAU | 0 | 0 |
| PV panel | 122 | 219 |
| ST | 122 | 109 |
| PVT system | 229 | 318 |
| TS system | 122 | 166 |

## CONCLUSION

Watchmaking industry are low energy intensive industry. There efficiency can be improved with recovering waste heat released from Compressor and CNC and by reducing the cooling requirement with shading. Incoporating technologies like PV, ST and PVT can help in reducing electricity and heating demand. Incorporating technology like Thermal Storage will help in reducing heating demand in night when there is excess heat in the day. In the consideration if taking total cost as the optimizer chooses to install PV as the savings in total cost will be (97k CHF/year) without considering storage. When considering storage the optimizer chooses to install PVT system with TS as the savings in total cost will be (137k CHF/year).

## ACKNOWLEDGEMENTS

I would like to thank CIRAIG which is helping me in performing such project and analysis.

## REFERENCES

1. (Lin,2024), Chih-Yao Lin and Li Ju Wang. Optimization of heat management and utilization in batch process. *Journal of Cleaner Production* 142707 (2024) https://doi.org/10.1016/j.jclepro.2024.142707
2. (Zuberi, 2020), M Jibran S Zuberi, Don Olsen, Peter Liem, Beat Wellig, and Martin K Patel. Heat integration of a multi-product batch process by means of direct and indirect heat recovery using thermal energy storage. Applied Thermal Engineering, 167:114796, (2020) https://doi.org/10.1016/j.applthermaleng.2019.114796.
3. (Teyu), Teyu, https://www.teyuchiller.com/what-is-the-appropriate-water-temperature-set-for-cnc-spindle-chiller-unit_n1332#:~:text=Well%2C%20the%20temperature%20control%20range,and%20help%20extend%20its%20lifetime.
4. (Fecko,2021), Bransilav Fecko and Tibor Vince. Thermal simulation of CNC Milling machine drives. Acta Electrotechnica et Informatica, Vol 21, 19 -21, DOI: 10.15546/aeei-2021-0015
5. (TSE, 2019), Thunder Said Energy. https://thundersaidenergy.com/downloads/battery-storage-costs-the-economics/
6. (FSS), Free Suns Solar Roofs, https://freesuns.com/en/solar-roof-price-estimate
7. (Stat, 2024), Average monthly electricity wholesale price in Switzerland from January 2019 to September 2024, https://www.statista.com/statistics/1271511/switzerland-monthly-wholesale-electricity-price/
8. (Migrol, 2024), Evolution of fuel Oil prices, https://www.migrol.ch/fr/energie-chaleur/evolution-prix-du-p%C3%A9trole/indice-des-prix/
9. (Sensorfact), Payback period for investments: how and why to calculate it?, https://www.sensorfact.eu/blog/payback-period-for-investments-how-and-why-to-calculate-it/#:~:text=Five%20years%20is%20considered%20an%20excellent%20payback%20period%20for%20an%20investment.

© 2025 by the authors. Licensed to PSEcommunity.org and PSE Press. This is an open access article under the creative commons CC-BY-SA licensing terms. Credit must be given to creator and adaptations must be shared under the same terms. See https://creativecommons.org/licenses/by-sa/4.0/



Systems & Control Transactions

**Research Article - Peer Reviewed Conference Proceeding**
ESCAPE 35 - European Symposium on Computer Aided Process Engineering
Ghent, Belgium. 6-9 July 2025
Jan F.M. Van Impe, Grégoire Léonard, Satyajeet S. Bhonsale,
Monika E. Polańska, Filip Logist (Eds.)

PSE PRESS

# Liquid Organic Hydrogen Carriers: comparing alternatives through $H_2$ equivalent analysis

**Elvira Spatolisano[a]*, Federica Restelli[a], Laura A. Pellegrini[a]**

[a] Politecnico di Milano, Italy
* Corresponding Author: elvira.spatolisano@polimi.it.

## ABSTRACT

Liquid Organic Hydrogen Carriers (LOHCs) represent a promising solution for the efficient transport and storage of hydrogen, addressing critical challenges associated with its low volumetric density and safety concerns in gaseous and liquefied forms. LOHCs are oil-like substance, capable of reversibly binding and releasing hydrogen through catalytic hydrogenation and dehydrogenation. Hydrogenation is performed where renewable energy is extensively available: at the loading terminal, green $H_2$ is produced and is chemically bonded to the LOHC molecule. In this way, the hydrogenated molecule is transported safely under ambient conditions using existing liquid fuels infrastructures. At the delivery site, the dehydrogenation process releases high-purity hydrogen for industrial or mobility applications, with the regenerated LOHC carrier being recycled back to the $H_2$ production site for reuse. In view of highlighting critical issues associated to LOHCs implementation at large scale, this paper explores green $H_2$ transport through toluene and dibenzyltoluene. Considering the overall $H_2$ transport value chain, the performances of these two alternatives are assessed by means of equivalent $H_2$ methodology. As a result, insights are provided on their role in enabling a sustainable and efficient hydrogen economy.

**Keywords**: green H2 transport, LOHC, clean energy, toluene, dibenzyltoluene.

## INTRODUCTION

In the transition towards sustainable energy, green hydrogen has gained attention as a low-emission alternative. However, its transport is hindered by its low volumetric density. To address this challenge, various hydrogen carriers have been proposed as a more practical solution. These hydrogen-bearing compounds can be transported more easily at milder conditions and dehydrogenated upon arrival to release hydrogen. Among all the possible options, liquid organic hydrogen carriers (LOHCs) are considered promising due to their compatibility with existing infrastructures [1]. Various LOHCs have been explored in the literature. While some compounds are more suitable for hydrogenation and dehydrogenation, certain criteria help in identifying optimal candidates. The ideal LOHC should have a low melting point and high boiling point to avoid solidification and volatility issues, respectively, a high hydrogen storage capacity, low dehydrogenation enthalpy, low toxicity and be cost-effective at the same time [2].

Once the hydrogen carrier is selected, a detailed techno-economic assessment of the entire $H_2$ value chain is essential to compare alternatives and demonstrate their feasibility. The $H_2$ value chain typically includes: hydrogenation of the organic molecule exploiting green $H_2$, produced where renewable energy sources are extensively available, transport of the hydrogenated compound to its final destination and, upon arrival, dehydrogenation to release hydrogen.

In this framework, the aim of this work is to present a systematic methodology for comparing different $H_2$ value chains. Toluene (TOL) and dibenzyltoluene (DBT) are selected as representative carriers due to their promising characteristics. A harbor-to harbor scenario is discussed, to study long distance $H_2$ transport. The hydrogenation and dehydrogenation stages were designed in Aspen Plus V11®. Based on process simulations, a detailed technical assessment is provided. Each stage of the value chain (*i.e.*, hydrogenation, seaborne transport, dehydrogenation) is technically discussed. Energy consumptions are expressed in terms of equivalent $H_2$,

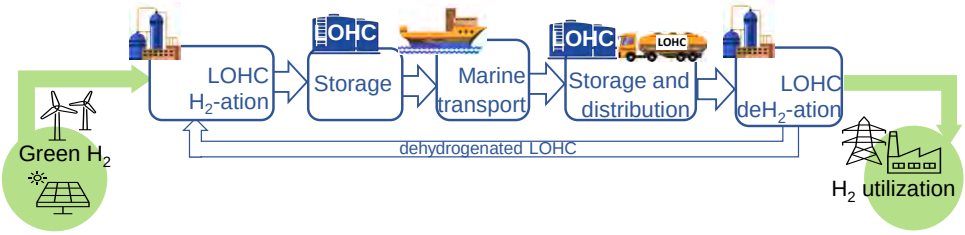



**Figure 1**: Hydrogen value chain exploiting LOHCs as $H_2$ carriers.

which, in the end, lowers the amount of hydrogen delivered at the utilization hub. In this way, the efficiency of each stage can be easily quantified. Weaknesses and drawbacks are pointed out, to pave the way for future process intensification.

## $H_2$ TRANSPORT SCENARIO: BASIS OF DESIGN

The $H_2$ value chain considering LOHCs as $H_2$ carriers is reported in Figure 1.

A harbor-to-harbor $H_2$ transport scenario is assumed. At the loading terminal, a flat $H_2$ production by 100 MW alkaline electrolysers is considered. These electrolysers, operating at 20 bar, are responsible for delivering 20000 $Nm^3/h$ of $H_2$. The assumed production scale of the alkaline electrolysers results in significantly lower $H_2$ production compared to conventional steam reforming plants. This limitation arises because renewable energy-driven industrial sites must align their scale with the land requirements of renewable energy installations.

At the loading terminal, $H_2$ is reacted with an organic carrier through an exothermic hydrogenation process and the resulting hydrogenated compound stored before seaborne transport.

The maritime distance between harbours is 2500 km, with the ship powered by traditional fossil-based fuels (IFO 380 1%S).

Upon arrival at the unloading terminal, the hydrogenated carrier is transported to a $H_2$ valley located 100 km inland via truck.

At the $H_2$ valley, the carrier undergoes a dehydrogenation reaction to release hydrogen. The released hydrogen meets industrial application standards, being produced at 30 bar with a purity exceeding 99.9 mol%.

The conversion and reconversion stages are the core of the whole hydrogen value chain: for this reason, a detailed technical assessment is performed by means of Aspen Plus V11® process simulations, discussed in the following section. Details about the thermodynamic property package are provided elsewhere [4]. On the other hand, for storage, maritime and road transport, reference is made to the available literature [3]. As the organic carriers are oil-like substances, they are compatible with existing oil-handling infrastructure, making their integration seamless.

## SIMULATION OF THE COST-DRIVING PROCESSES

Hydrogenation section for toluene and dibenzyltoluene are reported in Figure 2.

Referring to toluene hydrogenation section, reported in Figure 2a, toluene, both from the unloading terminal and from make-up stream, enters the process unit's battery limits. It is pressurized and heated to the reaction conditions of 20 bar and 210°C [4]. Reactants pre-heating is performed into a process-to-process heat exchanger (PREHEAT in Figure 2a) to recover the high enthalpy of the reaction products. The hydrogenation reaction (1) is highly exothermic: $N_2$ acts as a thermal diluent. Its flowrate is such that its concentration in the reactor inlet stream (REAC-IN in Figure 2a) is approximately 17 mol% [5]. Alongside nitrogen and toluene, green hydrogen produced via water electrolysis (stream $H_2$ in Figure 2a) is also supplied to the battery limits.

$$C_7H_8 + 3H_2 \rightarrow C_7H_{14} \quad (1)$$

The reactor outlet stream (REAC-OUT in Figure 2a), consisting of unreacted hydrogen, nitrogen, and methylcyclohexane, is cooled in the PREHEAT exchanger before proceeding to the separation stages. The separation section, comprising two flash drums in series (FLASH 1 and FLASH 2 in Figure 2a), purifies the reactor output from heavy ends, before and, then, from light ends. The resulting methylcyclohexane (MCH in Figure 2a) is stored and transported by ship to the unloading terminal. Unconverted hydrogen (stream LIGHTEST in Figure 2a) is compressed in COMP and recycled back to the reaction section.

On the other hand, Figure 2b shows the dibenzyltoluene (DBT) hydrogenation process. The organic carrier, H0-DBT in Figure 2b, is sourced from the unloading terminal. Along with a minimal make-up stream, it is routed to the reactor after being pressurized and heated. The reactor (B2 in Figure 2b) is fed with dibenzyltoluene, hydrogen, and nitrogen, with $N_2$ flow rate set identically to that used in the toluene hydrogenation process.

The reactor, operated at 35 bar and 210°C [6], performs DBT hydrogenation as in reaction (2).

$$C_{21}H_{20} + 9H_2 \rightarrow C_{21}H_{38} \quad (2)$$

The reaction products, primarily the hydrogenated species, are cooled and stored for transportation to the unloading terminal. In this case, the separation section downstream of the reactor is simplified, as hydrogen conversion is complete and by-product formation during the reaction is negligible. This characteristic is widely recognized in the literature as a key advantage of dibenzyltoluene as a hydrogen carrier [7]. Additionally, DBT's higher molecular weight compared to toluene enables more effective separation based on vapor-liquid equilibrium, as the larger difference in relative volatilities enhances separation efficiency for lighter compounds.

For the sake of comparison between toluene and dibenzyltoluene hydrogenation, Table 1 reports the thermal energy consumptions and Table 2 provides the electric energy consumptions, retrieved from process simulations.

The dehydrogenation process for both methylcyclohexane and perhydro-dibenzyltoluene (H18-DBT) is shown in Figure 3. As for methylcyclohexane (Figure 3a), it enters the process, it is pressurized and directed to the reaction section. The reactor (REACTOR in Figure 3a) operates at 350°C and is responsible for producing toluene and hydrogen according to reaction (3).

$$C_7H_{14} \rightarrow C_7H_8 + 3H_2 \quad (3)$$

**Table 1:** Thermal energy consumption for hydrogenation sections of Figure 2. Duty is assumed positive when entering the system.

| equipment | $T_{IN}$ [°C] | $T_{OUT}$ [°C] | $Q$ [kW] |
|---|---|---|---|
| *toluene hydrogenation* | | | |
| REACTOR | 146 | 210 | -14557.1 |
| COOLER | 82 | 50 | -3378.5 |
| *dibenzyltoluene dehydrogenation* | | | |
| COOLER | 82.08 | 50 | -482.3 |
| REACTOR | 175.11 | 210 | -16462.3 |

**Table 2:** Electric energy consumption for hydrogenation sections of Figure 2.

| equipment | $P_{IN}$ [°C] | $P_{OUT}$ [°C] | $W$ [kW] |
|---|---|---|---|
| *toluene hydrogenation* | | | |
| PUMP | 1.01 | 20 | 22.05 |
| COMP | 1.01 | 20 | 1271 |
| *dibenzyltoluene dehydrogenation* | | | |
| PUMP | 1.01 | 35 | 47.17 |
| COMPR | 20 | 35 | 550.6 |

The reactor's outlet mixture, composed of minor undesired byproducts (primarily benzene), together with

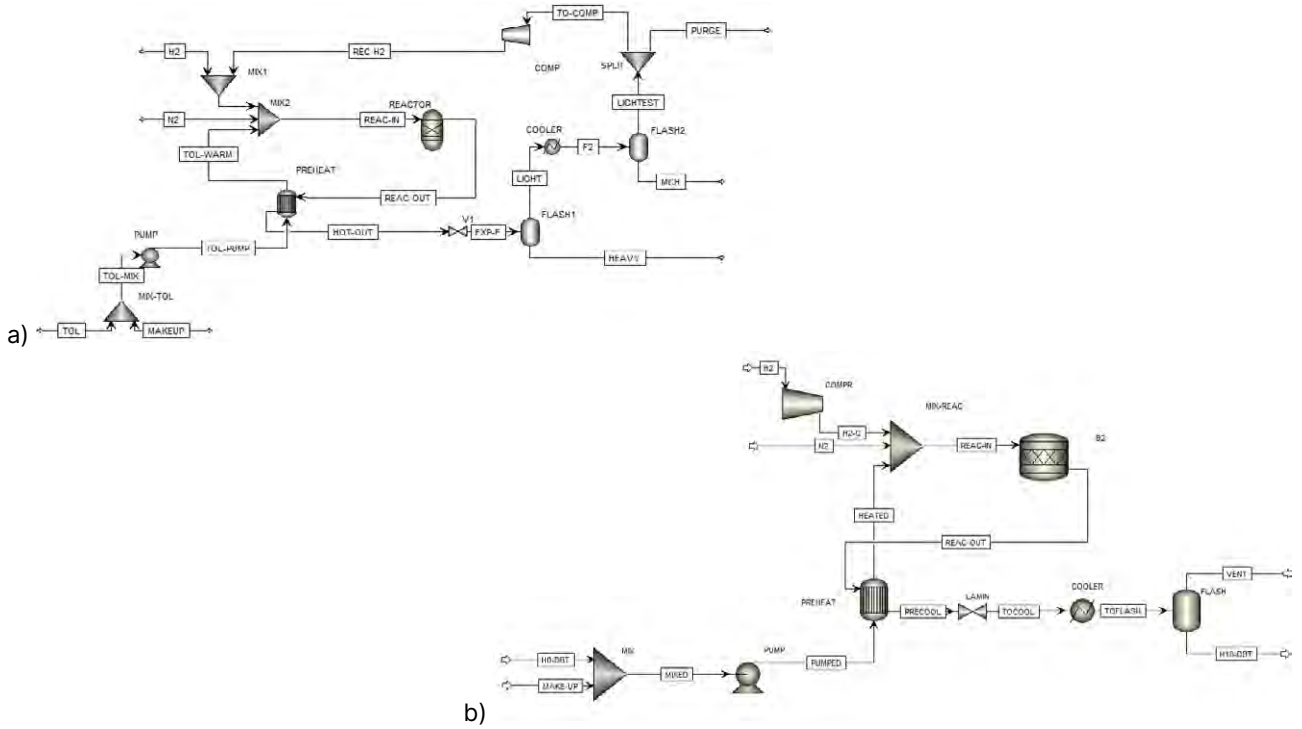



**Figure 2**: Hydrogenation section for: a) toluene and b) dibenzyltoluene. Simulation in Aspen Plus V11®.

toluene and hydrogen, is sent to the downstream separation train. The separated toluene stream (OUT-TOL in Figure 3a) is stored and subsequently routed back to the loading terminal. Hydrogen is purified via pressure swing adsorption (PSA) to achieve the necessary purity specifications for its intended applications.

The dehydrogenation reaction is highly endothermic, requiring a significant heat supply. This heat is provided by burning a portion of the hydrogen produced, along with waste streams (V and VENT in Figure 3a). As a result of this arrangement, the high endothermicity of the dehydrogenation reaction reduces the net amount of hydrogen available for utilization.

In a similar fashion, Figure 3b shows the process simulation performed for the H18-DBT dehydrogenation. The H18-DBT entering the system is pressurized and directed to the reaction section. The reactor (REACTOR in Figure 3b) operates at 320°C and 1.1 bar. In this unit, $H_2$ is obtained according to reaction (4).

$$C_{21}H_{38} \rightarrow C_{21}H_{20} + 9H_2 \quad (4)$$

The reactor's output mixture, consisting of DBT and hydrogen, is processed through a series of separation stages downstream of the reaction section. The recovered DBT (DBT-OUT in Figure 3b) is stored and transported back to the loading terminal, while the hydrogen, which is nearly pure, is compressed and sent to the hydrogen valley for utilization.

Table 3 and Table 4, provide, respectively, the thermal energy consumptions and the electric energy consumptions of the processes depicted in Figure 3.

**Table 3:** Thermal energy consumption for dehydrogenation sections of Figure 3. Duty is assumed positive when entering the system.

| equipment | $T_{IN}$ [°C] | $T_{OUT}$ [°C] | Q [kW] |
|---|---|---|---|
| *methylcyclohexane dehydrogenation* | | | |
| REACTOR | 210 | 350 | 20093 |
| COOL1 | 100 | 50 | -3344.6 |
| COOL2 | 198 | 80 | -996.1 |
| COOL3 | 240 | 50 | -1943.6 |
| *perhydro-dibenzyltoluene dehydrogenation* | | | |
| REACTOR | 306.8 | 320 | 19887.3 |
| COOL1 | 184.8 | 60 | -1002.3 |
| COOL2 | 235.9 | 50 | -1347.0 |
| COOL3 | 220.8 | 50 | -1238.5 |
| COOL4 | 219.9 | 50 | -1234.2 |

**Table 4:** Electric energy consumption for dehydrogenation sections of Figure 3.

| equipment | $P_{IN}$ [°C] | $P_{OUT}$ [°C] | W [kW] |
|---|---|---|---|
| *methylcyclohexane dehydrogenation* | | | |
| PUMP | 1.01 | 3 | 2.62 |
| COMP-1 | 2.9 | 9.3 | 1113.3 |
| COMP-2 | 9.3 | 30 | 1231.2 |
| REC-COM | 2.9 | 3 | 2.17 |
| *dibenzyltoluene dehydrogenation* | | | |
| PUMP | 1.01 | 1.1 | 0.14 |
| COMP1 | 1.01 | 3.15 | 1148 |
| COMP2 | 3.15 | 9.74 | 1081.5 |
| COMP3 | 9.74 | 30 | 1080.2 |
| COMP-R | 1.01 | 1.1 | 5.75 |

To assess the viability of toluene and dibenzyltoluene as $H_2$ carriers and compare their performances, the equivalent $H_2$ methodology is applied, which is described in the following section.

## TECHNICAL ASSESSMENT: EQUIVALENT $H_2$ METHDOLOGY

The Equivalent Hydrogen Methodology (EHM) provides a common metric for evaluating the energy content and efficiency of $H_2$ production, storage and transportation. By calculating the net equivalent hydrogen consumption (*NEHC*) of each energy-consuming process, the Equivalent Hydrogen Methodology enables a more accurate assessment of the total energy required for the full hydrogen cycle, from production to utilization. Then, by subtracting the *NEHC* to the $H_2$ entering the process battery limits, the net equivalent $H_2$ delivered (*NEHD*) to the utilization hub is evaluated, as shown in equation (5).

$$NEHD = F_{H_2,in} - NEHC \quad (5)$$

In this way, this methodology allows to standardize and simplify the comparison of different $H_2$ carriers, in view of identifying the most cost-effective hydrogen solution.

For the evaluation of *NEHC*, heating above the ambient temperature ($NEHC_{h,i}$), cooling below ambient temperature ($NEHC_{c,i}$) and electric power supply ($NEHC_{e,i}$) are accounted for, thus neglecting heating below ambient temperature (< 25°C) and cooling above ambient temperature (> 25°C) [8] (equation (6)).

$$NEHC = \sum_i NEHC_{h,i} + NEHC_{c,i} + NEHC_{e,i} \quad (6)$$

$$NEHC_{e,i} = \frac{W_i}{\eta_{FC} \cdot LHV} \quad (7)$$

In the present case-study, heating above ambient temperature is achieved by process-process heat exchange, when feasible. Otherwise, heating is provided by either burning part of the hydrogen produced, as in the

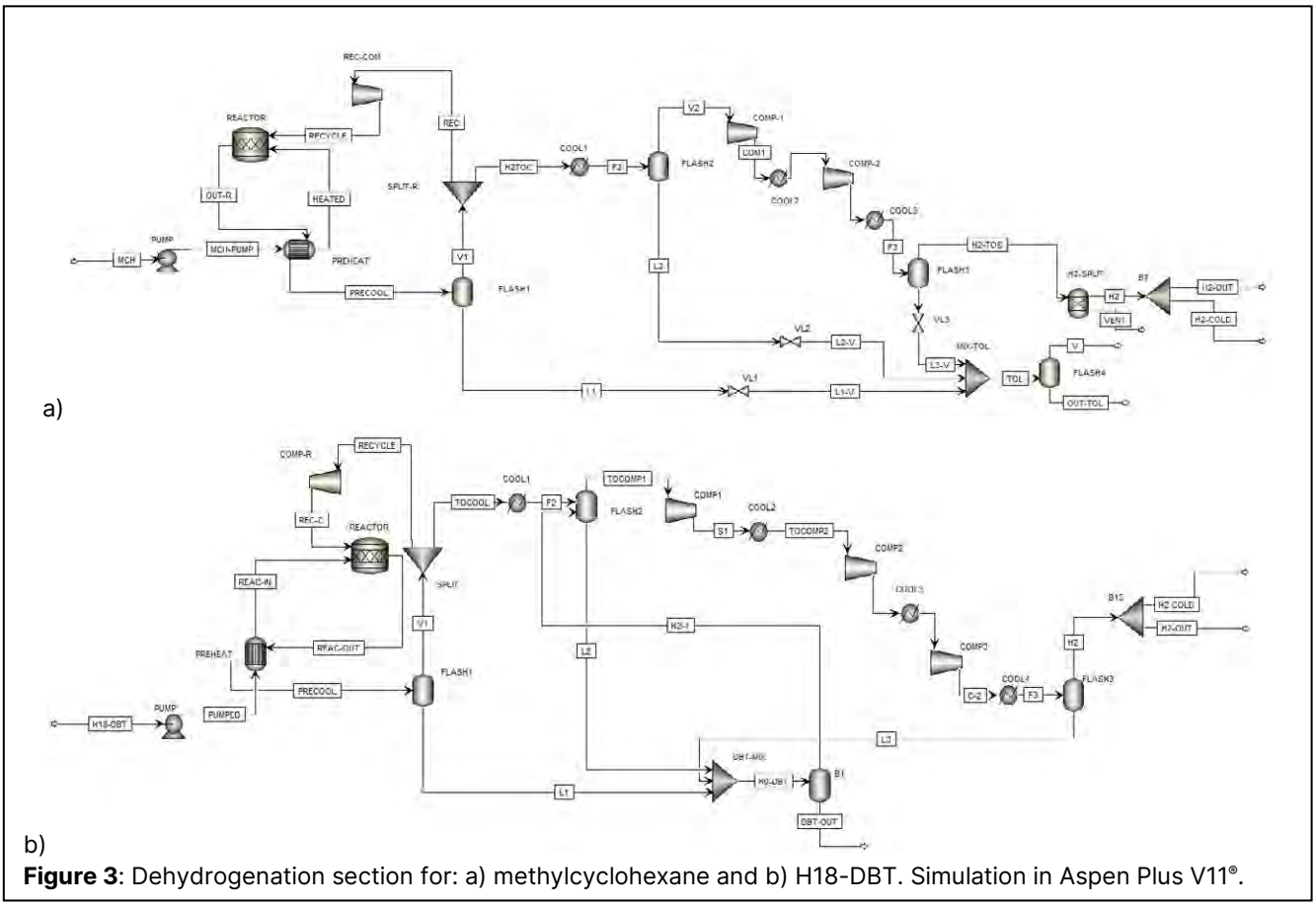



**Figure 3**: Dehydrogenation section for: a) methylcyclohexane and b) H18-DBT. Simulation in Aspen Plus V11®.

dehydrogenation section. In this case, the term $NEHC_{h,i}$ of equation (6) is retrieved from process simulation [3]. In addition, cooling below the ambient temperature is not required considering the value chain of Figure 1. Finally, the Net Equivalent Hydrogen Consumed for supplying electric power ($NEHC_{e,i}$), used for driving compressors and pumps, is calculated according to equation (7), assuming $H_2$ utilization in fuel cells with an efficiency ($\eta_{FC}$) of 60%. In equation (7), $W_i$ is the electric power consumption retrieved from Aspen Plus V11® simulations, while *LHV* is the $H_2$ lower heating value, assumed equal to 120 MJ/kg.

## CONCLUSION

Figure 4 summarizes the results of the equivalent $H_2$ methodology, considering both toluene and dibenzyltoluene as $H_2$ carriers.

As can be observed from Figure 4, dibenzyltoluene is more effective for $H_2$ transport than toluene, allowing for a higher $H_2$ flow rate delivered at the unloading terminal.

In both cases, part of the green hydrogen entering the battery limits is lost in the hydrogenation stage. The toluene hydrogenation stage is more energy-intensive than the dibenzyltoluene one: this is due to the higher electric consumption of the hydrogenation stage, because of the $H_2$ recycle compressor.

As opposite to other $H_2$ carriers (*i.e.*, liquefied hydrogen or ammonia), no $H_2$ losses because of the carrier boil off occur during storage and seaborne transport. One of the main advantages of LOHCs is their capability of storing hydrogen without significant degradation or loss over time, making them ideal for balancing seasonal variations in renewable energy supply. In addition, they are stable under ambient temperature and pressure, reducing the risks associated with hydrogen's volatile and explosive nature.

Regarding the dehydrogenation process, the perhydro-dibenzyltoluene dehydrogenation turns out to be less efficient than the methylcyclohexane one. However, for both of the instances analysed, dehydrogenation processes require significant energy input, which reduces the overall efficiency. A non-negligible amount of the $H_2$ delivered to the unloading terminal is burnt to cope for the endothermicity of the reaction. Moreover, the use of precious metal catalysts (e.g., Pt-based) in hydrogenation and dehydrogenation reactions increases operational costs and catalyst deactivation over time adds to maintenance expenses.

As a result, this assessment confirms that the LOHCs can store significant amounts of hydrogen by

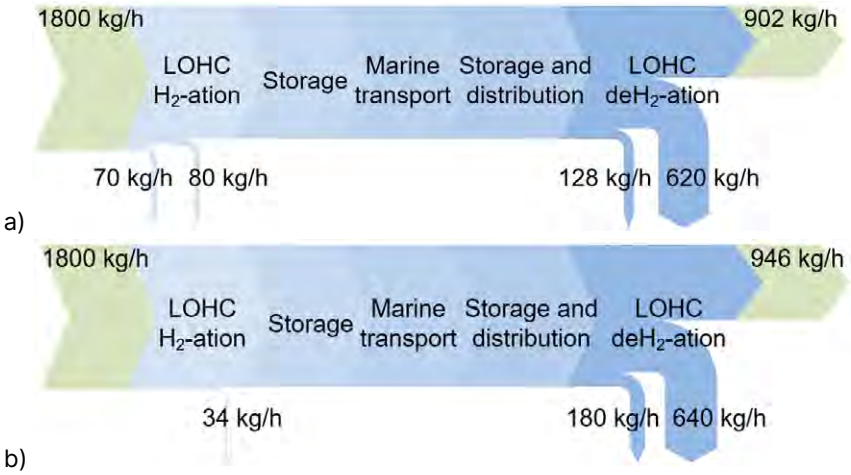



**Figure 4.** Results of the equivalent $H_2$ methodology for: a) toluene and b) dibenzyltoluene as $H_2$ carrier.

chemically binding it, offering high volumetric hydrogen storage density compared to gaseous or cryogenic hydrogen. The liquid-like nature of LOHCs allows them to be transported using existing fuel distribution and storage infrastructure, including pipelines, tanks, and ships.

The carrier molecules can be regenerated and reused for multiple cycles of hydrogenation and dehydrogenation, making LOHC systems sustainable over the long term.

On the other hand, their dehydrogenation is highly energy intensive. For this reason, it is essential to identify species with a lower dehydrogenation enthalpy to enhance the dehydrogenation section energy balance. Also, more active and selective catalysts are needed to enable the dehydrogenation at milder operating conditions.

Finally, it must be noted that both of the LOHC molecules involve fossil-derived feedstocks, raising concerns about the overall environmental footprint if not sustainably sourced, despite the closed cycle realised. Future research should be focus on finding suitable carriers derived from renewable feedstocks, improving the life cycle assessment of the whole value chain.

## REFERENCES


1. Lin A, Bagnato G, Revolutionising energy storage: The Latest Breakthrough in liquid organic hydrogen carriers. *Int J Hydrogen Energy* 63, 315-329 (2024).
2. Pellegrini LA, Spatolisano E, Restelli F, De Guido G, de Angelis AR, Lainati A, Green $H_2$ Transport through $LH_2$, $NH_3$ and LOHC: Opportunities and Challenges. *SpringerBriefs in Applied Sciences and Technology* (2024).
3. Spatolisano E, Restelli F, Matichecchia A, Pellegrini LA, de Angelis AR, Cattaneo S, Roccaro E, Liquefied hydrogen, ammonia and liquid organic hydrogen carriers for harbour-to-harbour hydrogen transport: A sensitivity study. *Int J Hydrogen Energy* 80, 1424-1431 (2024).
4. Spatolisano E, Matichecchia A, Pellegrini LA, de Angelis AR, Cattaneo S, Roccaro E, Toluene as effective LOHC: detailed techno-economic assessment to identify challenges and opportunities. *Comput Aided Chem Eng* 52, 3243-3248 (2023).
5. Imagawa K, Kawai H, Shiraga M, Nakajima Y, Aromatic compound hydrogenation system and hydrogen storage/transport system equipped with same, and aromatic compound hydrogenation method. International patent: WO2015115101A1. (2015).
6. Shi L, Qi S, Qu J, Che T, Yi C, Yang B, Integration of hydrogenation and dehydrogenation based on dibenzyltoluene as liquid organic hydrogen energy carrier. *Int J Hydrogen Energy* 44, 5345-5354 (2019).
7. Raab M, Maier S, Dietrich R-U. Comparative techno-economic assessment of a large-scale hydrogen transport via liquid transport media. *Int J Hydrogen Energy* 46, 11956-11968 (2021).
8. Spatolisano E, Pellegrini LA, $CO_2$-Tolerant Cryogenic Nitrogen Rejection Schemes: Analysis of Their Performances. *Ind Eng Chem Res* 60, 4420–4429 (2021).



© 2025 by the authors. Licensed to PSEcommunity.org and PSE Press. This is an open access article under the creative commons CC-BY-SA licensing terms. Credit must be given to creator and adaptations must be shared under the same terms. See https://creativecommons.org/licenses/by-sa/4.0/

Systems & Control Transactions

**Research Article - Peer Reviewed Conference Proceeding**
ESCAPE 35 - European Symposium on Computer Aided Process Engineering
Ghent, Belgium. 6-9 July 2025
Jan F.M. Van Impe, Grégoire Léonard, Satyajeet S. Bhonsale,
Monika E. Polańska, Filip Logist (Eds.)

PSE PRESS

# Towards the Decarbonization of a Conventional Ammonia Plant by the Gradual Incorporation of Green Hydrogen

**João Fortunato, Pedro M. Castro, Diogo A. C. Narciso, Henrique A. Matos***

Centro de Recursos Naturais e Ambiente, Department of Chemical Engineering, Instituto Superior Técnico, Universidade de Lisboa, Av. Rovisco Pais 1, 1049-001, Lisboa, Portugal
* henrimatos@tecnico.ulisboa.pt

## ABSTRACT

As initiatives to decarbonize societies increase, industry is also being considered for policies to encourage its sustainability. Ammonia ($NH_3$) industry relies entirely on Haber-Bosch (HB) process, consuming fossil fuels for hydrogen production and energy purposes, accounting for more than 1 % of anthropogenic carbon dioxide ($CO_2$) emissions. Emerging technologies such as the electrochemical synthesis of $NH_3$ promise sustainable production from water, air, and renewable energies, but low TRLs are still reported. The electrification of the HB process opens a more viable path for sustainable $NH_3$ production in the near future, where hydrogen ($H_2$) is produced by electrolysis of water, powered from renewable energy sources. Many studies have focused on the production of 100 % green $NH_3$ using only electric HB. In this work, a different approach is presented, which consists of studying the gradual incorporation of green $H_2$ into a conventional $NH_3$ plant. An *Aspen Plus® V14* model of the methane-fed HB process was developed, and the limitations of the process were identified by sequentially incorporating 0 to 10 % green $H_2$. To avoid overheating the equipment in the natural gas reforming stage, a new configuration is suggested for this step. With this modification, the study is extended to incorporating higher percentages of green $H_2$, up to a limit of around 61 %. Finally, the impact of the reforming temperature tolerance on the green $H_2$ incorporation limits for the suggested configuration was studied.

**Keywords**: Ammonia, Haber-Bosch Process, Green Hydrogen

## INTRODUCTION

At the beginning of the 20th century, the agricultural sector was under pressure to find a source of nitrogen allowing the increase of food production in response to the growing population. Until then, nitrogen, one of the most critical needs for crop development, relied on limited natural sources (such as guano). In 1909, Fritz Haber succeeded in fixing atmospheric nitrogen ($N_2$) by synthesizing ammonia ($NH_3$) through its reaction with hydrogen ($H_2$), using an iron-based catalyst (Equation (1)). In 1913, Carl Bosch adapted the process for industrial scale, which is known to this day as the Haber-Bosch Process (HB), considered one of the most important technological developments of humankind [1].

$$N_2 + 3\,H_2 \leftrightarrow 2\,NH_3 \quad (1)$$

Ammonia is currently the second most produced chemical worldwide, with around 85 % of its production used in the nitrogen fertilizer industry (urea, ammonium nitrate, among others). It is estimated that half of the world's current population depends directly on the application of these fertilizers in the agricultural sector. In addition, ammonia also finds uses in the pharmaceutical industry, textiles, explosives production and de$NO_x$ technologies [2].

The global relevance and scale of the HB process makes it responsible for the consumption of 2 % of the final energy consumed and the emission of 1 to 2 % of the world's carbon dioxide ($CO_2$) emissions. This is justified by its high dependence on fossil fuels, not only for process heat, but also as a feedstock for hydrogen production. Around 75 % of $NH_3$ is produced from light hydrocarbons such as natural gas and naphtha. In Europe, almost all plants operate with natural gas consumption, producing $H_2$ by Steam Methane Reforming (SMR), which

is considered the Best Available Technology for its high energy efficiencies and lower emissions. The remaining 25 % is produced using coal and heavy fuel oil, which are consumed mainly by Asian ammonia industry [2,3].

Driven by carbon neutrality and energy independence policies, the ammonia industry is striving for decarbonization. In the European Union, the Renewable Energy Directive III requires that, by 2030, 42 % of the hydrogen consumed in industrial processes should come from renewable sources [4]. The decarbonization of the sector has driven the development of technologies that allow $NH_3$ production to move away from the HB process, which is more decentralized, less carbon and energy intensive, more flexible and with the possibility of fully incorporating renewable energies These include electrochemical, electrocatalytic and plasma synthesis, among others. However, these technologies are still at a low Technology Readiness Level (TRL). The most mature green $NH_3$ production technology relies on the electrification of the HB process, where the SMR process is replaced by water electrolysis – powered via renewables – as the source of hydrogen [1,2].

However, the flexibility of the HB synthesis has yet to be proven, specifically, under the fluctuating supply of $H_2$ when coupled with a renewable power source, which poses major challenges in managing its operation. Many papers have been published on the production of fully green $NH_3$, especially on energy management to ensure the continuous operation of the HB process. The effectiveness of this management is, in most of these works, only achieved by storing hydrogen in tanks or by storing energy in batteries [4]. As the paradigm of $NH_3$ manufacture is changing towards green production, this creates a challenge for the ammonia industry, largely relying on fossil fuels. Namely, this raises questions about how plants will adapt to remain competitive and make the most of the capital invested in the current infrastructure.

The European ammonia industry is starting to adapt and try to position itself in the new reality. Fertiberia, in Spain, and Yara, in Norway, are examples of companies with a long-established position in the ammonia market that have recently begun to introduce green hydrogen into their conventional plants, albeit in small quantities [4]. A single study related to this practice is found in the literature [5], with a maximum green $H_2$ incorporation of around 20 %, limited, among other factors, by overheating of equipment. Inspired by the operating procedures at one real-life plant, this work addresses the challenges of gradually incorporating green $H_2$ into a conventional ammonia production plant and presents a new configuration to achieve higher incorporations.

## GREY TO GREEN AMMONIA

To simulate a conventional methane-fed HB process, an Aspen Plus® V14 model was developed. This model can be divided into two different sections: the SMR section and the HB synthesis section, as shown in Figure 1.

### SMR Section

The SMR section produces hydrogen from natural gas (~$CH_4$), which is initially purified by hydrodesulphurization. The removal of sulphur compounds prevents catalysts' poisoning in multiple process units. This stream is heated, mixed with steam, and fed into a reforming section made up of two separate reactors. In the first reformer, Ref-I, H2 is produced by steam consumption, according to Equations (2) and (3). Steam is supplied in excess to minimize carbon formation reactions and shift the equilibrium towards the products.

$$CH_4 + H_2O \leftrightarrow CO + 3\,H_2 \quad (2)$$

$$CO + H_2O \leftrightarrow CO_2 + H_2 \quad (3)$$

The effluent gas mixture from Ref-I is mixed with compressed hot air and fed into the second reformer, Ref-II, where the conversion of unreacted $CH_4$ is completed ($CH_4$ molar fraction below 0.005). The air stream flowrate ($N_2$ ~0.78, $O_2$ ~0.21, Ar ~0.01 molar fractions) supplied to Ref-II is adjusted to achieve the desired $H_2/N_2$ ratio in the $NH_3$ synthesis section, although simultaneously the oxygen ($O_2$) feed must be fully consumed in this unit according to Equation (4). Argon (Ar) is introduced in this stage and remains as a chemical inert in all process units.

$$CH_4 + 0.5\,O_2 \leftrightarrow CO + 2\,H_2 \quad (4)$$

From Ref-II, the gas mixture is cooled and the carbon monoxide (CO) formed in the reforming stages is converted. This conversion is described by Equation (3) and takes place in two different stages: high-temperature shift (HT) followed by low-temperature shift (LT).

Carbon dioxide is then removed by scrubbing the mixture with an ammonia solution. The removal of $CO_2$ from the syngas stream, as well as all oxygen compounds, is critical to the HB synthesis operation, since these compounds act as poisons to the iron-based catalysts in this stage. The unconverted CO fraction and the uncaptured $CO_2$ undergo a methanation step, consuming a small amount of $H_2$ and generating $CH_4$ and water ($H_2O$), Equations (5) and (6).

$$CO + 3\,H_2 \leftrightarrow CH_4 + H_2O \quad (5)$$

$$CO_2 + 4\,H_2 \leftrightarrow CH_4 + H_2O \quad (6)$$

Like Ar, $CH_4$ is an inert chemical in the HB section and water is separated by molecular sieve adsorbers, ensuring that no oxides are admitted to the HB section. The gas mixture obtained is therefore mostly composed of $H_2$ and $N_2$ in a 3:1 molar ratio, with small amounts of $CH_4$ and

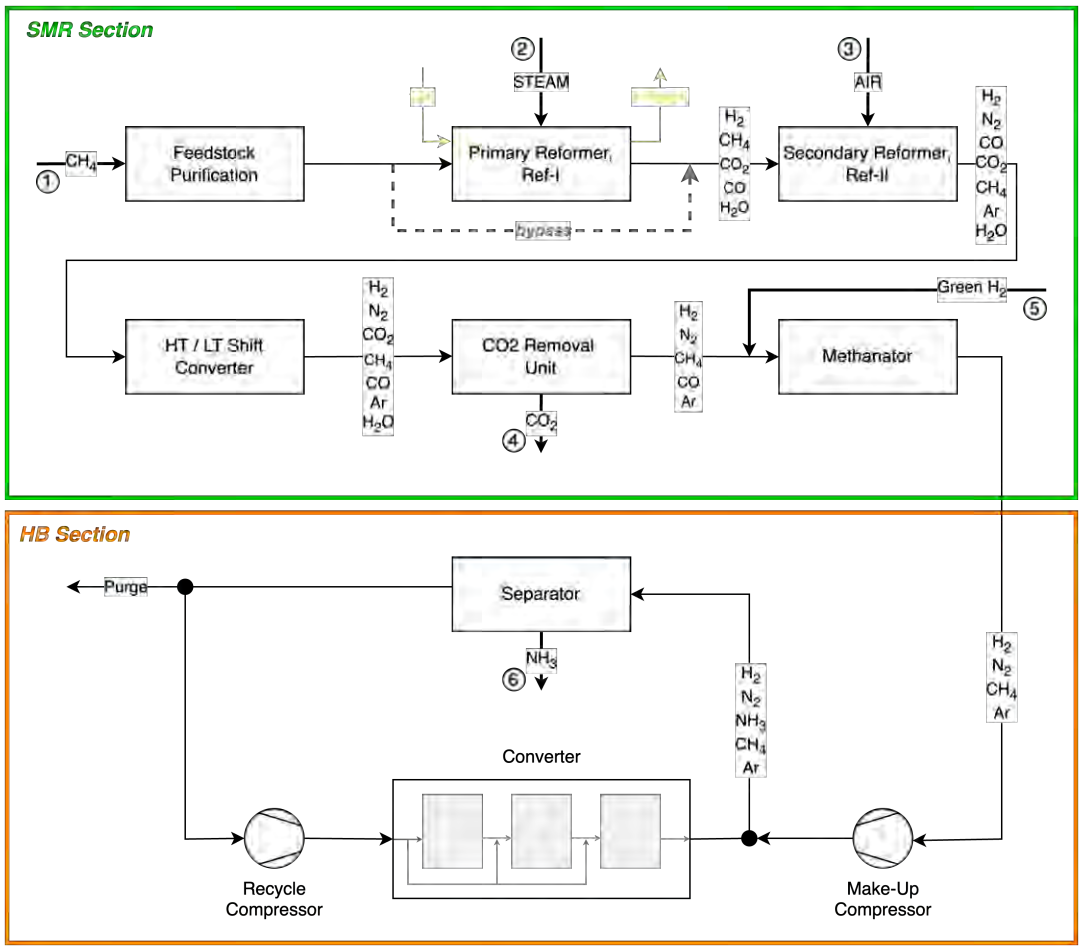



**Figure 1:** Simplified schematics of the model developed, divided into SMR and HB section (adapted from [4]). The first part of this work studies the incorporation of green H2 (stream ⑤) with manipulation of the flow rate of the natural gas stream (stream ①). The second part studies a new configuration of the reforming section, with bypass to primary reforming (as illustrated in dashed line).

Ar. Some metrics of the SMR section are listed in Table 1.

**Table 1:** Main consumptions in the SMR section for hydrogen production of 3 000 kmol/hr, based on the model developed.

| | |
|---|---|
| ① Natural Gas Consumption [ton/hr] | 15.7 |
| ② Steam Consumption [ton/hr] | 51.1 |
| ③ Air Consumption [ton/hr] | 41.2 |

## HB Section

The formation of $NH_3$, according to Equation (1), is highly exothermic and thermodynamically favored by high pressures and low temperatures. However, low temperatures favor low reaction rates. To achieve higher rates, the industry synthesizes $NH_3$ at pressures between 150 and 300 bar and temperatures ranging from 400 to 450 ˚C [4].

Due to the high exothermicity of the synthesis reaction, the reactor is usually divided into three catalytic beds, which promotes a more efficient strategy for effluents' temperature control. This is achieved by splitting the feed stream and introducing it in stages at the entrance to each of the catalytic beds as shown in the HB Section in Figure 1 (Converter).

The conversions achieved per pass are typically low (less than 25 %) and require the recycling of unconverted nitrogen and hydrogen, which must be separated from the $NH_3$ produced to achieve economic viability. Several configurations on the arrangement of reactor beds, stream splits and process units have been reported; the model developed in this work is fully consistent with the process diagram shown in Figure 1.

After leaving the third catalytic bed, the effluent is cooled in a heat exchanger network where the syngas feed is pre-heated and steam is generated (not visible in the diagram). This stream is then mixed with the compressed syngas makeup from the SMR section. Cooling

in the separator stage allows ammonia to be separated from this mixture in the liquid phase, and the gaseous phase is purged to avoid the accumulation of $CH_4$ and Ar. The remaining gas stream is slightly compressed to compensate for the pressure drop, heated, split and admitted to the reaction beds, closing the ammonia synthesis loop. Some indicators of the HB section can be found in Table 2.

**Table 2:** Production and yield achieved in HB section.

| | |
|---|---|
| Ammonia Production [kton/year] | ~200 |
| Ammonia Yield [%] | 93.4 |

## Green Hydrogen Incorporation

The introduction of green $H_2$ into the process was considered immediately upstream of the methanation step (in the SMR section, stream ⑤) and its intake leads to two different operating strategies: S-I and S-II. The S-I reduces the production of grey $H_2$ by reducing natural gas and process steam in the SMR section. The intake of green $H_2$ allows $NH_3$ production to remain fixed. In strategy S-II, grey $H_2$ production remains unchanged, resulting in higher $H_2$ feed to the HB section. By taking in larger quantities of process air, higher $NH_3$ production can be achieved in HB section. Table 3 summarizes the main changes to the process according to the operating strategy considered.

**Table 3:** Effect on the quantities of air, natural gas and steam consumed and on the quantity of $NH_3$ produced with the incorporation of green $H_2$, for S-I and S-II.

| | **Natural Gas** ① | **Steam** ② | **Air** ③ | **$NH_3$ Prod.** ⑥ |
|---|---|---|---|---|
| **S-I** | ↓ | ↓ | = | = |
| **S-II** | = | = | ↑ | ↑ |

Although both strategies lead to a certain degree of decarbonization of $NH_3$ production, it was the authors' decision to focus on the S-I study in this work as it better represents the industrial reality of reaching a certain product capacity to be sold on the market, as well as the effective replacement of grey $H_2$ with green $H_2$. For this study, the input of green $H_2$ by a pure stream ($xH_2 = 1$) was assumed, without modelling the upstream electrolysis process; and full availability of green $H_2$ was considered, with no limit on its supply to the process. The incorporation of green $H_2$ was defined as a function of the total amount of H2 (green + grey) that is supplied to the HB section. To maintain this total amount of $H_2$ unchanged, the natural gas flow (stream ①) is manipulated as the amount of green $H_2$ introduced increases (stream ⑤). To keep the carbon/steam ratio at Ref-I, the steam flow rate (stream ②) is also adjusted.

# RESULTS

## Standard SMR

The incorporation of $H_2$ was considered from 0 to 10 % and the results obtained (Figure 2) show a very similar relationship between the incorporation of green $H_2$ and the reduction in natural gas consumption, as well as with the decarbonization of the process (only the $CO_2$ emissions directly generated by the production of $H_2$ are taken into account, which are those obtained in the $CO_2$ removal unit – stream ④, without the emissions associated with burning natural gas for energy purposes).

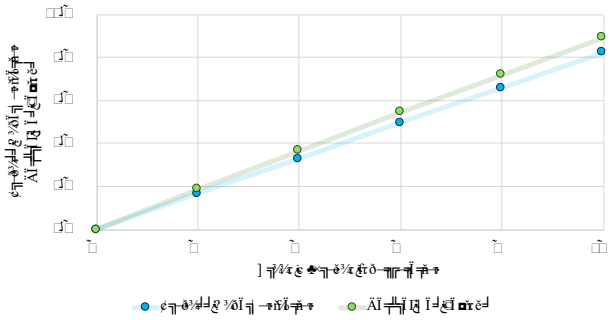


**Figure 2:** Process decarbonization and natural gas savings for an incorporation of green $H_2$ of 0 to 10 %.

Although the reduction in $CH_4$ consumption has an influence on all the stages of the SMR section, the main effects are found in the reforming step, more specifically in Ref-II. Figure 3 shows the results obtained for the $CH_4$ flowrate and the temperature of the Ref-II outlet. These variables are highlighted because they can constrain higher values of green $H_2$ incorporation, due to the possible incomplete consumption of $O_2$ and overheating of the equipment, as explained below.

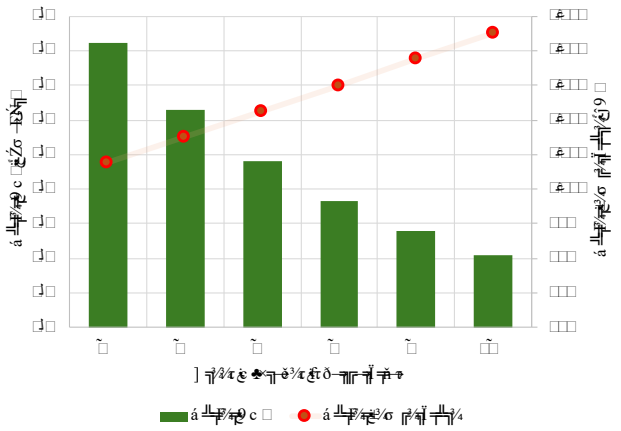


**Figure 3:** $CH_4$ flowrate and effluent temperature of the second reformer for an incorporation of green $H_2$ between 0 to 10 %.

The reduction in the flowrate of $CH_4$ exiting Ref-II is justified by the reduction in natural gas and the requirement to consume the same amount of atmospheric $O_2$. Recalling the importance of this $O_2$ consumption, the declining trend in the amount of CH4 in the effluent may result in incomplete $O_2$ consumption for greater incorporations of green $H_2$. This can lead to $O_2$ being carried over to the HB section and impact on the lifespan of the catalyst used in $NH_3$ synthesis.

The temperature of the effluent is influenced by the exothermicity of the reaction and the heat release is dissipated by a smaller volumetric flow of effluent, due to a lower supply of natural gas. The increase in temperature (around 75 °C for a green $H_2$ incorporation of 10 %) over the already high temperatures of the base case (~1000 °C, 0 % green $H_2$) can lead to equipment overheating, not only of the Ref-II but also downstream. The same results were obtained in a similar study [5], although the variation in temperature obtained by those authors was less sharp than that obtained by the current simulation. The authors also stress the importance of temperature in determining the incorporation of green $H_2$ and limited its variation to a maximum of 100 °C, which resulted in an incorporation of between 15 and 20 % of green $H_2$. Applying the same criteria to this work would result in a maximum limit close to 12 %.

## Adapted SMR

The challenge of introducing green $H_2$, while producing the remaining grey $H_2$, and ensuring the necessary $N_2$ input, total $O_2$ consumption and controlling the temperature of Ref-II is a challenge that could unlock greater incorporations of green $H_2$ and more extensive decarbonization of $NH_3$ production. This can be achieved by a different balance of the fraction of natural gas that is processed in Ref-I and Ref-II. The diverting of $CH_4$ from Ref-I to Ref-II can avoid the obligatory consumption of $CH_4$ per pass in Ref-I, guaranteeing the amount of $CH_4$ necessary for total $O_2$ consumption and grey $H_2$ production and, eventually, temperature control in Ref-II.

To study this possibility, a new configuration was considered for the reforming stage, highlighted by the dashed lines in Figure 4. This new configuration includes a bypass to Ref-I, which gives the model the flexibility it needs to manage $CH_4$ consumption between Ref-I and Ref-II. In this study, the outlet temperature of Ref-II effluent is kept constant and equal to the base case (~1015 °C, 0 % green $H_2$), by adjusting the bypass fraction accordingly.

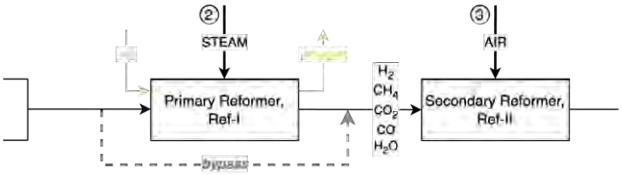



**Figure 4:** New proposed configuration, with Ref-I bypass (detail from **Figure 1**).

For an incorporation of green $H_2$ from 0 to 10 %, Figure 5 shows a similar relationship between the decarbonization of the process and the reduction of natural gas. The same figure shows the results obtained for the bypass fraction, which suggest a linear behavior with the increasing incorporation of $H_2$. For example, introducing 10 % of green $H_2$ means that only around 80 % of the flow is fed to Ref-I. The flow reduction in Ref-I is, however, even more pronounced compared to the base case, since the natural gas flow is already reduced to allow only 90 % of the total hydrogen to be produced.

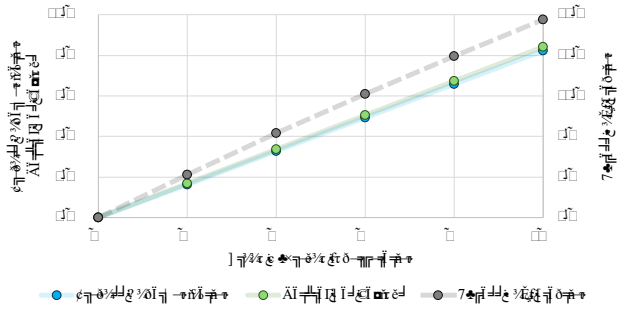


**Figure 5:** Process decarbonization, natural gas savings and bypass fraction for an incorporation of green $H_2$ of 0 to 10 % (adapted SMR with Ref-I bypass).

By analyzing the effluent from Ref-II, whose temperature and molar flow of $CH_4$ are shown in Figure 6, it is possible to identify that temperature control also allows the reduction of $CH_4$ in this stream to be less dependent on green $H_2$ incorporation, possibly leading to a less sudden and delayed depletion of this compound.

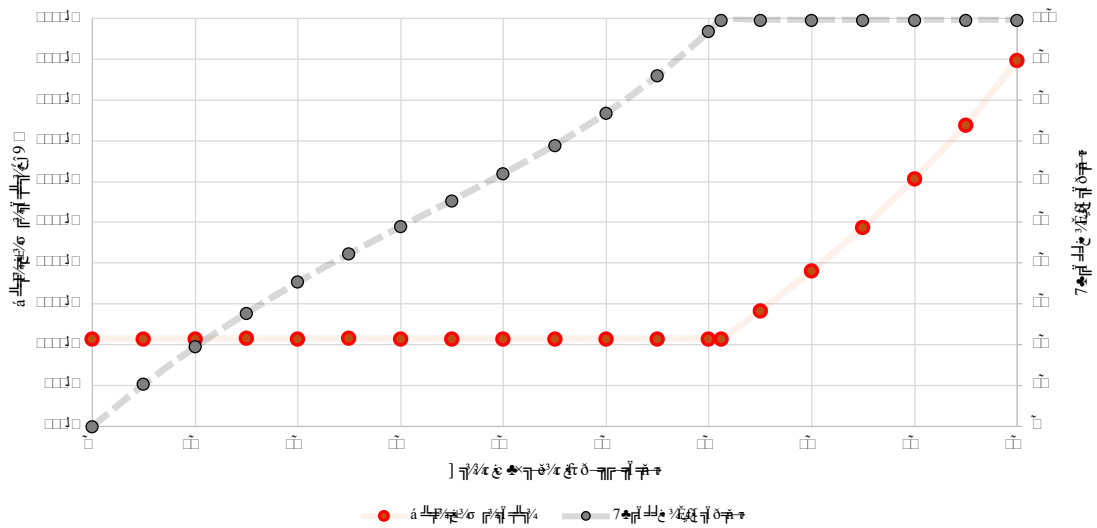


**Figure 7:** Effluent temperature of the second reformer, Ref-II, and bypass fraction for an incorporation of green $H_2$ of 0 to 90 % (adapted SMR with Ref-I bypass).

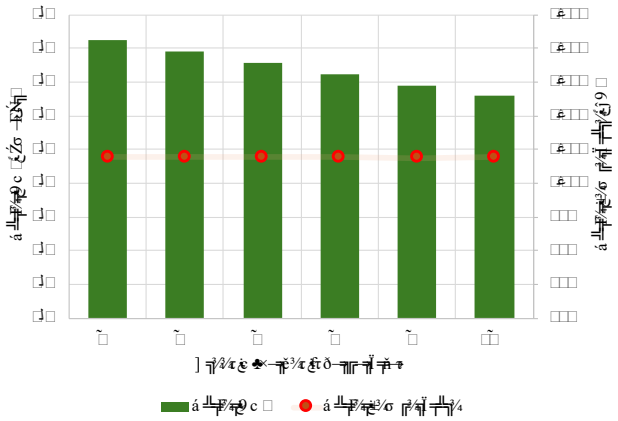


**Figure 6:** $CH_4$ flow rate and effluent temperature of the second reformer for an incorporation of green $H_2$ of 0 to 10 % (adapted SMR with Ref-I bypass).

Once control of the effluent temperature and the presence of enough $CH_4$ to consume $O_2$ were ensured by the new Ref-I bypass configuration, further incorporation of green $H_2$ was studied. Figure 7 shows the behavior of the effluent temperature and the evolution of the bypass fraction for incorporations of 0 to 90 % green $H_2$. Adjustment of the bypass fraction allows the temperature to be controlled up to around 61 % of green $H_2$ intake, at which point the bypass fraction is total, meaning the Ref-I is no longer in operation. This is one of the important points of this analysis, from which the introduction of green $H_2$ is limited by the inability to control the temperature of Ref-II. However, operating at values close to this point implies operating Ref-I with very small flow rates that are far from its nominal capacity.

At this stage, no minimum limit on the volume of gas fed to Ref-I and Ref-II (or any other equipment) has been considered, which could be useful in a future study where the effect of their minimum operating capacities should be addressed. Nevertheless, it is to be expected that the assumption of a minimum capacity value for Ref-I will inevitably result in a limitation of the maximum bypass fraction and, as a result, this limit point will be reached for a smaller incorporation of green $H_2$.

Another important point will be the start of the bypass operation. In this study, the start of operation of the bypass coincides exactly with the start of the green $H_2$ intake because no tolerance to the temperature of the base case (~1015 °C) was considered. Moreover, if it is possible to increase the Ref-II outlet temperature, its effect is found as the % of green $H_2$ incorporated. Assuming a tolerance in that temperature of + 50 and + 100 °C, the start of the bypass becomes increasingly distinct from the start of the incorporation of green $H_2$, and the temperature can be controlled for increasingly higher incorporations. Table 4 summarizes the results obtained.

**Table 4:** Influence of the Ref-II outlet temperature tolerance (ΔT) on the operation of the Ref-I bypass.

| ΔT [°C] | $T_{out}$ [°C] | % Bypass >0 [% Green $H_2$] | % Bypass ~100 [% Green $H_2$] |
|---|---|---|---|
| + 0 | 1015 | 0 | 61 |
| + 50 | 1065 | 7 | 64 |
| + 100 | 1115 | 13 | 67 |

## CONCLUSIONS

The incorporation of green $H_2$ into a conventional

NH3 plant was investigated using a model developed in Aspen Plus® V14. The incorporation of green $H_2$ reduces natural gas consumption and $CO_2$ emissions. It was found that the increase in the temperature of the second reformer could limit extensive incorporation of green $H_2$. A new configuration of the reforming section has been proposed, consisting of a bypass to Ref-I, which allows 61 % of green $H_2$ to be incorporated while maintaining the temperature recorded in conventional operation at 0 %. By studying the influence of the tolerance of this temperature, according to the proposed configuration, it was concluded that greater tolerances make it possible to extend the incorporation of green $H_2$ even further and thus decarbonise the plant to a greater extent.

## DEDICATION

The authors would like to dedicate this article to the memory of Professor Pedro Castro, who was involved in the discussion of this work. His guidance, knowledge and friendship will be greatly missed.

## ACKNOWLEDGEMENTS

Project co-financed by the PRR – Recovery and Resilience Plan by the European Union, in particular, the Mobilizing Agenda "Moving2Neutrality" (Project no. 32, with reference no. C644927397-00000038), by the Fundação para a Ciência e a Tecnologia, I.P/; MCTES through national funds PIDDAC – CERENA (FCT-UIDB/04028/2025 and FCT-UIDP/04028/2025).

## REFERENCES

1. Smith, C., Hill, A. K. & Torrente-Murciano, L. Current and future role of Haber-Bosch ammonia in a carbon-free energy landscape. Energy Environ. Sci 13, 331 (2020).
2. Rouwenhorst, K., Castellanos, G., International Renewable Energy Agency. & Ammonia Energy Association. Innovation Outlook: Renewable Ammonia.
3. IEA International Energy Agency. Ammonia Technology Roadmap - Towards More Sustainable Nitrogen Fertiliser Production. https://www.iea.org/reports/ammonia-technology-roadmap (2021).
4. Narciso, D. A. C. et al. Design and operation of Power-to-Ammonia systems: A review. Energy Convers Manag 327, 119494 (2025).
5. Isella, A., Ostuni, R. & Manca, D. Towards the decarbonization of ammonia synthesis – A techno-economic assessment of hybrid-green process alternatives. Chemical Engineering Journal 486, (2024).

© 2025 by the authors. Licensed to PSEcommunity.org and PSE Press. This is an open access article under the creative commons CC-BY-SA licensing terms. Credit must be given to creator and adaptations must be shared under the same terms. See https://creativecommons.org/licenses/by-sa/4.0/



Systems & Control Transactions

**Research Article - Peer Reviewed Conference Proceeding**
ESCAPE 35 - European Symposium on Computer Aided Process Engineering
Ghent, Belgium. 6-9 July 2025
Jan F.M. Van Impe, Grégoire Léonard, Satyajeet S. Bhonsale,
Monika E. Polańska, Filip Logist (Eds.)

PSE PRESS

# Simulation and Experimental Validation of Biomass Gasification in a Spouted Bed Reactor: Troubleshooting Using DWSIM

**C. Moliner*, V. Carozzo, M. Curti, E. Arato**

Dipartimento di Ingegneria Civile, Chimica e Ambientale (DICCA), Università degli Studi di Genova, Via Opera Pia 15, 16145 Genova (Italy)
* Corresponding Author: cristina.moliner@unige.it

## ABSTRACT

Simulation plays a crucial role in the design and optimization of gasifiers by providing a detailed understanding of the involved physical processes and complex chemical reactions without the need for extensive trial-and-error experiments. It can also serve as a valuable tool for identifying potential technical issues in experimental devices that operate below expected performance. This study presents a comprehensive simulation of biomass gasification using the open-source software DWSIM. The simulated results were compared with experimental data from a pilot-scale spouted bed reactor, featuring a square-based design with a 20 kWth capacity, using pruning of apple tress as feedstock. Experimental results revealed that the reactor operated effectively at temperatures exceeding 850°C, maintaining stable conditions across a wide range of equivalence ratios. However, the distribution of products—particularly hydrogen ($H_2$)—did not match expected results based on both literature and simulations. A joint analysis of experimental data and expected behavior from simulation helped identify the observed inefficiencies and optimize the reactor's performance.

**Keywords**: Biomass, Syngas, Energy Efficiency, Gasification, Spouted Bed

## INTRODUCTION

Simulation-based activities play a crucial role in assessing reactor performance by providing a deeper understanding of underlying processes without the need for costly and time-consuming experiments. Process simulation tools offer a structured approach to modeling chemical reactors, enabling engineers and researchers to analyze, optimize, and predict reactor behavior under various operating conditions, including gasifiers. Among the available simulation platforms, commercial software such as Aspen Plus has long been a standard in chemical engineering, particularly for thermochemical reactions [1], due to its extensive database and robust computational capabilities. However, its reliance on proprietary licenses and limited customization options presents challenges, especially for academic research and collaborative projects.

An alternative to commercial software is the use of open-source process simulators, such as COCO [2], which has been used to simulate the gasification of agricultural residues. Another example is DWSIM, developed by Daniel Medeiros [3], which provides a comprehensive suite of tools for modeling a wide range of chemical engineering processes, including reactors. DWSIM features a freely accessible database with over 1,500 compounds and more than 20 property methods [4].

In this study, a previously developed and validated DWSIM model [4] is used to simulate the gasification of pruning of apple tree in a spouted bed reactor. With an annual availability of 2.23 Mt in Italy [5], along with its renewable nature and favorable properties—such as low to moderate moisture content and high cellulose and lignin levels—apple tree prunings are an ideal feedstock for thermochemical conversion processes.

A 20 kWth spouted bed reactor (SBR) was used for the gasification reactions. An SBR differs from traditional fluidized bed reactors by replacing the perforated base

with a single central gas inlet. This design creates three distinct zones within the reactor: a central spout where the fluidizing agent flows, an annular region surrounding the spout, and a fountain-like region above the bed surface where solids circulate [6]. Due to this configuration, a systematic cyclic circulation of solids is established, enhancing mass and heat transfer rates [7]. SBRs have been successfully applied to the gasification of coal, biomass, and biomass-plastic mixtures [8].

In this study, a previously validated model was used to critically evaluate the experimental results from the spouted bed pilot plant. Specifically, discrepancies in the experimental $H_2$ content were observed, and comparison with the model outputs helped identify the source of the experimental error.

## MATERIALS AND METHODS

### Biomass properties

Pruning of apple trees (PAT) were gasified in a spouted bed reactor [9]. Table 1 summarises their proximate and ultimate analysis and its initial higher heating value (HHV). The moisture content was equal to 8.13 %wt.

**Table 1:** Proximate and ultimate analysis of biomass (% w/w on dry basis, besides for moisture) and HHV (MJ/kg)

| **Proximate Analysis** | | **Ultimate Analysis*** | |
|---|---|---|---|
| Ash | 2.87 | C | 48.88 |
| Fixed carbon | 19.95 | H | 5.71 |
| Volatile matter | 77.18 | O | 42.15 |
| HHV | 18.73 | Ash | 2.87 |

* 0.39%wt of N and S

### Spouted bed reactor and testing conditions

The experimental unit is a pilot plant located in Biella, Italy, designed to operate with a biomass feed rate of 200 g/min, providing a thermal output of 20 kWth. The main components of the plant include a blower, a spouted bed reactor, a biomass feeding system, a gas preheater, and equipment for cleaning the gaseous product stream (filter, scrubber, and cyclone). To enhance mass and energy transfer within the reactor, an inert solid bed is used. This bed consists of 2 kg of silica sand, corresponding to an initial height of 17 cm.



**Figure 1.** Spouted bed reactor

PAT were evaluated under different equivalence ratios (ER). The ER represents the ratio of the actual oxygen supplied to the system to the oxygen needed for full stoichiometric combustion. The air inflow was maintained constant (17 $Nm^3/h$) and the biomass feed was varied to match the ER (Table 2).

**Table 2**: Experimental conditions

| **ER** | **Biomass feed (g/min)** | **Temperature of the bed (°C)** |
|---|---|---|
| 0.42 | 150 | 880 |
| 0.65 | 99 | 911 |

Details on the reactor design, operating procedure, and reaction steps—including preheating, stabilization, and product analysis—are available elsewhere [9].

## Simulation set-up using DWSIM

DWSIM (V8.6.5) was used to simulate the gasification of PAT. A detailed description of the model and its validation using literature data can be found in [4]. In summary, steady-state simulations were performed under isothermal conditions using the Peng-Robinson property method at atmospheric pressure, with no pressure drops considered. The modeled gaseous components included $H_2$, $H_2O$, CO, $CO_2$, $CH_4$, and $N_2$, while char was represented by its main constituents (C(s), O, N, and H) based on experimental data [9].

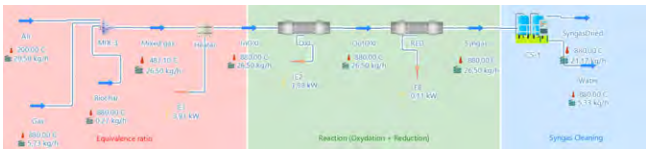


**Figure 2.** DWSIM flowsheet of the gasification plant.

**Table 3**: Kinetic reactions

| | Rate (mol/m³·s) | k (sec⁻¹) | Ea (KJ/mol) |
|---|---|---|---|
| $1.25C(s) + O_2 \rightarrow 0.5CO + 0.75CO_2$ | $r = k \cdot T \cdot e^{(-Ea/RT)} \cdot [O_2]$ | $3.7 \cdot 10^{10}$ | 150 |
| $CH_4 + 0.5O_2 \rightarrow CO + 2H_2$ | $r = k \cdot e^{(-Ea/RT)} \cdot [O_2]^{0.8}[CH_4]^{0.7}$ | $1.58 \cdot 10^{12}$ | 202 |
| $CO + 0.5O_2 \rightarrow CO_2$ | $r = k \cdot e^{(-Ea/RT)} \cdot [O_2]^{0.25}[CO][H_2O]^{0.5}$ | $1.78 \cdot 10^{10}$ | 180 |
| $H_2 + 0.5O_2 \rightarrow H_2O$ | $r = k \cdot e^{(-Ea/RT)} \cdot [O_2]\ [H_2]$ | $1.08 \cdot 10^{7}$ | 108 |
| $C + H_2O \leftrightarrow CO + H_2$ | $r = k \cdot T \cdot e^{(-Ea/RT)} \cdot [H_2O]\ [C]$ | 0.008 | 499 |
| $CO + H_2O \leftrightarrow CO_2 + H_2$ | $r = k \cdot e^{(-Ea/RT)} \cdot [CO]\ [H_2O]$ | 278 | 126 |
| $CH_4 + H_2O \leftrightarrow CO + 3H_2$ | $r = k \cdot e^{(-Ea/RT)} \cdot [H_2O]\ [CH_4]$ | $4.92 \cdot 10^{-11}$ | 125 |
| $C + CO_2 \leftrightarrow 2CO$ | $r = k \cdot e^{(-Ea/RT)} \cdot [C]$ | $1.05 \cdot 10^{13}$ | 135 |
| $CO_2 + H_2 \leftrightarrow CO + H_2O$ | $r = k \cdot e^{(-Ea/RT)} \cdot [CO_2]\ [H_2]^{0.5}$ | 258 | 126 |

The flowsheet is shown in Figure 2. The volatilization stage was modeled using an Excel file (embedded in the program) to calculate the mass balances (Gas and Biochar inlet streams), as described by Pio et al. [10]. The mass balance calculations (yields of pyrolysis products and composition of biochar) were specified, the temperature of decomposition was imported from the input data and the resulting compositions were exported to the corresponding input streams. Successively, the two inlet streams were mixed with the quantity of air (Air) ensuring autothermal conditions, as experimentally specified. Two Plug Flow Reactors (PFRs), with the geometries of the experimental device [9], were used to carry out the oxidation and reduction reactions. Both reactors were considered as isothermal at 880°C and their dimensions were set as 0.3 m of height for the oxidation reactor (corresponding to the bed of particles), 2 m for the reduction reactor (corresponding to the freeboard section) and 0.25 m of internal diameter in both cases. Kinetic reactions (Table 3) and parameters (Table 4) were set according to [11-13] to provide a more accurate representation of the reactor performance for reliable process predictions [14]. Lastly, the cleaning section, corresponding to the removal of moisture and tar before entering the analysing system, was simulated through a compound separator to obtain the final dry syngas stream.

## RESULTS AND DISCUSSION

Table 4 presents the experimental and simulated results of the gasification of PAT under the described operational conditions. The balance term in the analyzer accounts for all products not measured, ensuring the total sums to 100%. In the simulations, this balance term corresponds to the $N_2$ concentration.

**Table 4**: Experimental and simulated results (%vol/vol) at ER=0.42 and ER=0.62

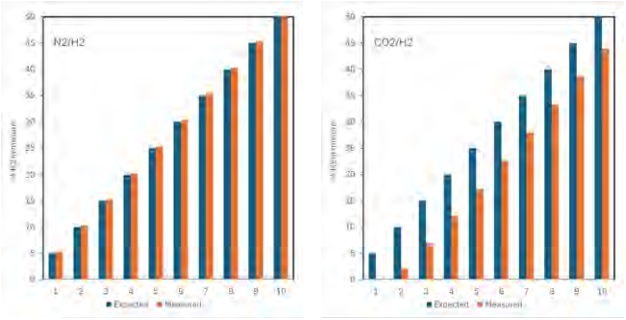
| **ER = 0.42** | **CO** | **$CO_2$** | **$H_2$** | **$CH_4$** |
|---|---|---|---|---|
| Experimental | 10.2 | 19.9 | 4.7 | 2.8 |
| DWSIM | 12.9 | 17.5 | 10 | 4.7 |
| **ER = 0.65** | **CO** | **$CO_2$** | **$H_2$** | **$CH_4$** |
| Experimental | 5.9 | 20.3 | 3.0 | 1.0 |
| DWSIM | 11.3 | 18.1 | 7.2 | 3.5 |

As expected, the CO and $CO_2$ concentrations were estimated with high accuracy, while $CH_4$, and especially $H_2$, were overestimated in the simulations. A consistent trend was observed when comparing the equivalence ratio (ER), with CO increasing and $CO_2$ decreasing as the ER decreased. Additionally, methane and hydrogen concentrations increased as ERs decreased, a trend that was effectively captured by the model. Energy balances were also examined in detail. The measured temperature at the bed of particles was used as the reaction temperature in isothermal conditions to ensure a fixed reaction temperature, as indicated by the experimental setup. According to the simulations, the exothermic contribution was insufficient to sustain the reduction reactions, and it was estimated that around 5 kW would need to be added to the system to achieve autothermal conditions. However, the experimental device performed well, and the gasification reactions occurred in a stable isothermal regime.

An evaluation was conducted to identify the potential experimental reasons for the large discrepancies observed in $H_2$ content and reaction temperature. Possible causes include:

- Unaccounted Heat Losses: Heat losses may reduce reaction efficiency, impacting syngas composition and temperature of reaction.
- Temperature Variations: If the actual operating temperature differs from the model's assumption, it can shift equilibrium reactions (such as the water-gas shift reaction, $CO + H_2O \rightleftharpoons CO_2 + H_2$), which can affect $H_2$ content.
- Unaccounted Side Reactions: Tar formation was not considered due to the lack of experimental data, though its contribution is likely to be significant under real operating conditions.
- Incomplete Mixing or Mass Transfer Limitations: mass transfer limitations, or localized temperature variations are not accounted for in the model.
- Calibration Issues: Gas chromatographs or other analytical instruments may not be properly calibrated, leading to inaccurate measurements.

To ensure consistency between input data, operating conditions, and gas composition measurements, the calibration of the gas analyzer (MCA100 Syn-P, ETG) was first checked. Two gas mixtures—$CO_2/H_2$ and $N_2/H_2$—with known compositions were used to test the instrument calibration. The calibration curve for $N_2$ (Figure 3a) showed perfect alignment between measured and applied compositions. However, the $CO_2/H_2$ calibration curve (Figure 3b) revealed underestimations of about 7%vol of $H_2$ (in average) between the measured and applied compositions, while the contribution from C-based compounds was accurately measured.




(a) (b)

**Figure 3.** Calibration of gas analyser

In summary, by simulating the experimental conditions and comparing the model's predictions with observed data, the study highlighted discrepancies that pointed to specific areas of concern, such as the H2 content in the product stream, led to the critical review of the experimental conditions, as measurement inaccuracies. Modeling is proven to be a powerful troubleshooting tool, enabling researchers to systematically isolate and address these issues, thereby improving the reliability and accuracy of the experimental results. This approach not only enhances the robustness of the current campaign but also provides a framework for optimizing future experimental designs.

## CONCLUSIONS

This study demonstrated the effectiveness of using the open-source software DWSIM to simulate biomass gasification in a spouted bed reactor, providing valuable insights into the process and identifying potential sources of error in the experimental campaign. The simulation results were compared with experimental data from a pilot-scale reactor using pruning of apple tree as feedstock, revealing discrepancies in the hydrogen ($H_2$) content and other gas compositions. The model accurately predicted trends in CO and $CO_2$ concentrations but overestimated $H_2$ and $CH_4$ compositions. Key potential sources of error identified include unaccounted heat losses, temperature variations, side reactions such as tar formation, mass transfer limitations, and calibration issues with analytical instruments. By leveraging the model as a troubleshooting tool, the study successfully pinpointed these inefficiencies, enabling a critical review of experimental conditions and improving the reliability of the results. In successive steps, the other identified sources of error will be studied and analysed for their experimental assessment. This approach not only optimized the current gasification process but also established a robust framework for future experimental designs, emphasizing the importance of integrating simulation with experimental validation to enhance the accuracy and efficiency of biomass gasification systems.

## ACKNOWLEDGEMENTS

EA acknowledges the project “Network 4 Energy Sustainable Transition—NEST” funded under the National Recovery and Resilience Plan (NRRP), Mission 4 Component 2 Investment 1.3—Call for Tender No. 1561 of 11.10.2022 of Ministero dell’Università e della Ricerca (MUR). MC acknowledges PRIN 2022 funded by the European Union—NextGenerationEU.

## REFERENCES

1. Moliner, C., Bove, D., Bosio, B., Ribes, A., & Arato, E. Simulation activities for the pseudo-equilibrium modelling of the gasification of agricultural residues. 24th *European Biomass Conference and Exhibition Proceedings*, 934–940 (2016).
2. Moliner, C., Marchelli, F., Bosio, B., & Arato, E. Simulation of the gasification of agricultural residues using coco simulator. *26th European*

*Biomass Conference and Exhibition Proceedings*, 764–768 (2018).
3. Medeiros, D. *DWSIM simulator*. https://dwsim.org. Last access: 30/1/2025
4. Moliner, C., Carozzo, V., Arato, E. Modelling of biomass gasification: comparison between fre-licensed DWSIM and a commercial software. 32nd *European Biomass Conference and Exhibition Proceedings*, 764–768 (2025)
5. Cotana, F., Calavaglio, G., La valorizzazione energetica delle potature di olivo, Crbnet (2008)
6. K. B. Mathur, P. E. Gishler, J. Chem. Technol. Biot. 5, 624 (1955)
7. Moliner, C., Marchelli, F., Bosio, B., Arato, E. Modelling of Spouted and Spout-Fluid Beds: Key for Their Successful Scale Up. *Energies*, *10*(11), 1729 (2017)
8. Carozzo, V., Arato, E., Moliner, C. Review of Experimental Activities and Recent Developments of Spouted Bed Reactors at Different Operational Scales. *Energies*, *17*(5), 1046 (2024)
9. Bove, D., Moliner, C., Curti, M., Baratieri, M., Bosio, B., Rovero, G., Arato, E. Preliminary tests for the thermo-chemical conversion of biomass in a spouted bed pilot plant. *The Canadian Journal of Chemical Engineering*, *97*(1), 59–66 (2019)
10. Pio, D. T., Tarelho, L. A. C., Matos, M. A. A. Characteristics of the gas produced during biomass direct gasification in an autothermal pilot-scale bubbling fluidized bed reactor. *Energy*, *120*, 915–928 (2017)
11. Martínez González, A., Silva Lora, E. E., Escobar Palacio, J. C., Almazán del Olmo, O. A. Hydrogen production from oil sludge gasification/biomass mixtures and potential use in hydrotreatment processes. *International Journal of Hydrogen Energy*, *43*(16), 7808–7822 (2018)
12. Champion, W. M., Cooper, C. D., Mackie, K. R., Cairney, P. Development of a chemical kinetic model for a biosolids fluidized-bed gasifier and the effects of operating parameters on syngas quality. *Journal of the Air & Waste Management Association*, *64*(2), 160–174 (2014)
13. Puig-Gamero, M., Pio, D. T., Tarelho, L. A. C., Sánchez, P., Sanchez-Silva, L. Simulation of biomass gasification in bubbling fluidized bed reactor using aspen plus®. *Energy Conversion and Management*, *235*, 113981 (2021)
14. Marchelli, F., Moliner, C., Baratieri, M., Bosio, B., Arato, E. From equilibrium to kinetic modelling: The gasification of apple pruning residues in a spouted bed reactor. In Carvalho M.d.G., Scarlat N., Grassi A., & Helm P. (Eds.), 27th *European Biomass Conference and Exhibition Proceedings*, 813–820 (2019)

© 2025 by the authors. Licensed to PSEcommunity.org and PSE Press. This is an open access article under the creative commons CC-BY-SA licensing terms. Credit must be given to creator and adaptations must be shared under the same terms. See https://creativecommons.org/licenses/by-sa/4.0/



Systems & Control Transactions

**Research Article - Peer Reviewed Conference Proceeding**
ESCAPE 35 - European Symposium on Computer Aided Process Engineering
Ghent, Belgium. 6-9 July 2025
Jan F.M. Van Impe, Grégoire Léonard, Satyajeet S. Bhonsale,
Monika E. Polańska, Filip Logist (Eds.)

PSE PRESS

# Identification of Suitable Operational Conditions and Dimensions for Supersonic Water Separation in Exhaust Gases from Offshore Turbines: A Case Study

**Jonatas de O. S. Cavalcante[a]*, Marcelo da C. Amaral[b], Ewerton E. da S. Calixto[a] and Fernando L. P. Pessoa[a,c]**

[a] SENAI CIMATEC University, Salvador, BA, Brazil
[b] CENPES-PETROBRAS, Rio de Janeiro, RJ, Brazil.
[c] Federal University of Rio de Janeiro (UFRJ), Rio de Janeiro, RJ, Brazil.
* Corresponding Author: jonatasosc@hotmail.com.

## ABSTRACT

In offshore environments, where space, weight, and energy efficiency are critical constraints, the effective removal of water from turbine exhaust gases is essential to enhance gas treatment processes. In this context, replacing conventional methods, such as molecular sieves, with supersonic separators (SSRs) emerges as a promising alternative. This study aims to determine the most suitable operating conditions and design parameters for water removal via supersonic separation (SS) in turbine exhaust gases (TxGs) on offshore platforms. Simulations were performed in Aspen HYSYS using a unit operation extension, based on typical TxGs compositions from offshore platforms. Key parameters, including operating conditions, separator dimensions, and shock Mach number, were evaluated to maximize efficiency while minimizing equipment footprint. The results indicated a water capture efficiency of 99.45%, demonstrating that SS technology is not only compact but also a viable and efficient alternative for water removal from exhaust gases, particularly in space-constrained environments.

**Keywords:** Water, Supersonic Separation, Turbine Exhaust Gases, Offshore, Aspen HYSYS

## INTRODUCTION

Climate change is primarily driven by the accumulation of greenhouse gases (GHGs) in the atmosphere, which has increased because of human activities such as deforestation, industrial processes, and fossil fuel consumption. These activities amplify the Earth's natural greenhouse effect, resulting in rising global temperatures, sea level increases, more frequent and severe extreme weather events, and widespread disruptions to biodiversity and ecosystems [1, 2].

In response to these challenges, the development of technologies aimed at mitigating GHG emissions and promoting sustainability has become increasingly urgent. Initiatives such as the Paris agreement and the United Nations' sustainable development goals (SDGs) have spurred significant advances in decarbonization efforts across multiple sectors [3, 4].

Within the oil and gas industry, particularly on offshore platforms, the efficient removal of water from turbine exhaust gases (TxGs) is crucial to enhancing $CO_2$ capture efficiency. Traditional methods, such as molecular sieves, have been widely employed for natural gas (NG) dehydration in production units operating in Pre-salt fields. However, these technologies often involve substantial energy consumption and require large, complex infrastructure, making them less suitable for the spatial and weight constraints typical of offshore operations [5, 6].

In this context, supersonic separators (SSRs) have emerged as a compelling alternative. Utilizing adiabatic expansion, SSRs efficiently cool and condense water and other condensable components without relying on moving parts, thereby reducing maintenance demands. Their compact design, combined with the ability to recover part of the pressure energy lost during the shock, makes

supersonic separation (SS) particularly well-suited to meet the operational and logistical demands of offshore platforms [6, 7].

For $CO_2$ SS in TxGs, the initial removal of water improves process efficiency. Pre-dehydration prevents operational issues such as hydrate formation and reduced $CO_2$ capture efficiency while minimizing moisture impact on downstream equipment [8, 9].

The literature has extensively explored $CO_2$ SS in NG and water SS in NG and TxGs, both through HYSYS simulations and CFD studies. As observed in studies such as those by Saidi and Farokhi, Chen, Arinelli, and Hammer, various approaches have been developed to model SS in different contexts. However, this study is the first to specifically apply supersonic water separation in TxGs using Aspen HYSYS. This novel application demonstrates the feasibility and advantages of SS technology in offshore turbine exhaust processing, addressing an existing gap in the literature [8, 10–13].

Aiming to fill this gap, this study explores the application of SSRs for water removal from TxGs on offshore platforms as an alternative dehydration method and a preparatory step for $CO_2$ capture via SS. The analysis is conducted through process simulation in HYSYS, focusing on the adjusted TxGs compositions from Hammer's study to determine the best operational conditions, as well as the SSR dimensions and shock Mach number. The objective is to increase process efficiency while minimizing equipment size, considering the constraints and specificities of the analyzed case [8].

## METHODOLOGY

The operational scenario was analyzed based on adjusted data from Hammer (Table 1) [8].

**Table 1:** Conditions for the evaluated scenario

| | Unit | Scenario |
|---|---|---|
| Temperature | °C | 87.00 |
| Pressure | bar a | 1.01 |
| Flow rate | t/h | 243.00 |
| $CO_2$ | %mol | 3.24 |
| $N_2$ | %mol | 76.21 |
| $O_2$ | %mol | 13.99 |
| Ar | %mol | 0.92 |
| $H_2O$ | %mol | 5.64 |

Additionally, the following constraints were defined for the process development:

- Compressors must not be used;
- The minimum temperature available for cold utility is 26°C;
- The residual gas stream must contain a maximum of 500 ppm of water;
- The capture stream must contain a maximum of 50 ppm of $CO_2$;
- The SS system must consist of a maximum of 10 and a minimum of 5 SSRs arranged in a battery.

The Peng-Robinson equation of state (PR-EOS) was adopted in this study to model the thermodynamic behavior of the system in Aspen HYSYS. This selection was made due to PR-EOS's well-documented accuracy in predicting phase equilibrium in hydrocarbon and light gas mixtures, including $CO_2$ and water condensation under offshore conditions. Previous studies have demonstrated its suitability for modeling multiphase flows in SSR, reinforcing its application in this study. Its ability to represent water condensation in natural gas has already been demonstrated in previous studies, highlighting its precision in predicting liquid phase composition under condensation conditions. Applications in HYSYS for SS have further reinforced its suitability for modeling $CO_2$ capture in TxGs, emphasizing its applicability to multiphase systems. This performance was expected, considering that the version of PR-EOS implemented in HYSYS has undergone enhancements to handle mixtures containing polar components, such as water, improving its accuracy in non-ideal conditions [8, 13–16].

Considering the previously defined conditions and constraints, the process was modeled in Aspen HYSYS, as shown in Figure 1, outlining the main stages of the SS process. Initially, the TxG stream is cooled in the Cooler "E-1", lowering its temperature to enable effective separation even at low pressures. Next, the flow is split in the Multiplier module "MULT-1", simulating the operation of a SSR battery. The divided stream (FEED) is then directed into the Unit Operation Extension (UOE), where separation occurs, resulting in two distinct streams: "CAPTURE", which contains the captured water, and "PRODUCT", comprising the residual gases.

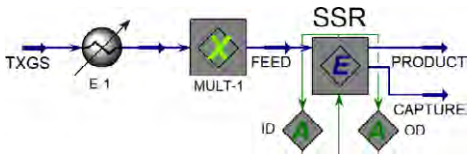



**Figure 1.** Flow diagram for SS modeling of water in TxGs

The UOE used in this study was developed for Aspen HYSYS to enable the modeling of the thermodynamic behavior of SS. This tool was used to assess water removal efficiency under various conditions and refine parameters for offshore applications.

To provide a clear overview of the UOE operation, Figure 2, which illustrates the user interface of the SS model in Aspen HYSYS.

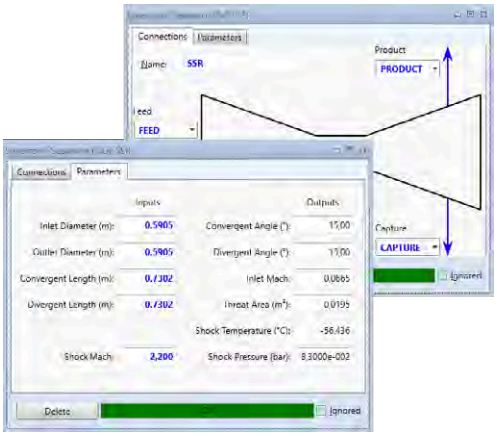



**Figure 2.** User Interface of the SSR UOE

The UOE was validated by reproducing the same input parameters and conditions as those used by Arinelli *et al.*, who applied a rigorous thermodynamic approach to model SS in Aspen HYSYS. The comparison of the obtained results allows for assessing the accuracy of the implemented modeling, ensuring consistency between the predictions of the model used in this study and those presented in the literature [13].

The SSR design adhered to engineering standards to meet the specific requirements of offshore platforms. Inlet and outlet internal diameters were determined using nominal pipe sizes (NPS) and standard thicknesses as defined by the ASME B31.3 and API RP 14E standards [17, 18]. Additionally, the Adjusts "ID" and "OD" (Figure 1) were employed to define the lengths of the convergent and divergent sections, adopting a nozzle angle of 15°, which has been identified in the literature as an efficient design choice for supersonic applications. This configuration balances operational efficiency and compactness, minimizing flow turbulence. The reduced pressure drop and stable supersonic flow contribute to energy efficiency and make the design suitable for space-constrained offshore environments [19].

The simulations evaluated the impact of varying operational and dimensional parameters on the efficiency of water removal in TxGs, while ensuring compliance with the constraints established by the plant. The objective was to systematically assess the trade-offs between maximizing water removal and minimizing $CO_2$ capture during the dehydration stage, considering the interplay between process conditions and equipment dimensions.

The "Case Studies" tool in Aspen HYSYS was utilized to systematically evaluate and determine the most suitable operational conditions and dimensions for the process. In this study, the molar fraction of water in the "PRODUCT" stream and the molar fraction of $CO_2$ in the "CAPTURE" stream were defined as dependent variables, while the temperature of the "FEED" stream and the shock Mach number were adjusted as independent variables. This analysis was conducted across a wide range of scenarios, considering multiple diameter configurations, defined according to the previously mentioned standards, and various multiplier factors whose equivalent divisors were integer values. The "Case Studies" tool was executed for every possible combination of diameter and multiplier factor, ensuring a comprehensive assessment of the process conditions. Table 2 presents the parameters and ranges used in the study.

**Table 2.** Range of variables studied.

| Variable | Unit | Start | End | Step Size |
|---|---|---|---|---|
| FEED Temperature | ºC | 26.0 | 87.0 | 0.1 |
| Shock Mach | - | 1.1 | 2.5 | 0.1 |
| Diameters (NPS) | in | 16.0 | 32.0 | - |
| Multiplier factor | - | 0.1 | 0.2 | - |

Each executed "Case Studies" run was evaluated, and the results were later compared to identify trends and determine the most suitable configuration. To ensure that all variables were comparable and to eliminate the differences in scale between the analyzed parameters, the dependent variables were normalized. This procedure allows variables with distinct units and magnitudes to be evaluated equitably within the performance metric. The normalization was performed using Equation (1):

$$x_{norm,i} = \frac{x_i - x_{min}}{x_{max} - x_{min}} \quad (1)$$

Where $x_i$ represents the original value of the variable, and $x_{min}$ and $x_{max}$ are the minimum and maximum values within the dataset.

After normalization, the Euclidean distance was employed as a proximity criterion between the simulated scenarios and the ideal configuration defined for the study. This method quantifies the similarity between each scenario and the desired condition, enabling the classification of configurations based on their alignment with the established objectives. The Euclidean distance was calculated using Equation (2):

$$d_E = \sqrt{\sum_{i=1}^{n} \left(x_{norm,i} - x_{ideal,i}\right)^2} \quad (2)$$

Where $x_{ideal,i}$ represents the normalized value of the ideal configuration for each variable.

This structured approach allowed for ranking all simulated scenarios from the lowest to the highest distance, facilitating not only the identification of the most suitable configuration for the evaluated conditions but also revealing performance trends, trade-offs between operational parameters, and alternative configurations that could be advantageous depending on specific process constraints.

## RESULTS

The model validation was performed by comparing the simulation results with the numerical data from Arinelli *et al.* The model yielded a shock pressure of 15.20 bar, with an absolute error of 0.99% compared to the reference value (15.05 bar). Similarly, the shock temperature was -38.59°C, resulting in an absolute error of 0.81% compared to the reported value (-38.28°C). These small deviations indicate a strong agreement between the model and the reference data, validating the approach used for the SSR simulation [13].

The total dataset generated by the "Case Studies" tool comprised 439,920 cases. After evaluating the Euclidean distances, the most suitable configuration was identified as the scenario with a diameter of 24 in NPS Std and a multiplier factor of 0.1, corresponding to a battery of 10 SSRs. Within this subset, 9,165 cases were initially considered, of which 7,314 had valid solutions, and 34 met the restrictions defined in the methodology.

The case evaluation revealed key performance trends and trade-offs between operational parameters. The analysis highlighted those configurations with smaller diameters resulted in lower "FEED" stream temperatures and, consequently, higher liquid phase fractions, which could compromise the stability of the supersonic flow. On the other hand, configurations with larger diameters exhibited lower pressure drops, but at the expense of requiring more space, impacting the overall equipment footprint.

The case evaluation indicated that a temperature of 35.20°C in the "FEED" stream and a shock Mach number of 2.2 resulted in the lowest Euclidean distance, therefore representing the most suitable operating conditions. The final simulation results are presented in Table 3.

It is important to highlight that these conditions ensured operation close to the saturation temperature of 35.26°C, resulting in a liquid phase fraction of only 0.02% in the "SSR" feed. This minimal amount does not compromise the stability of the supersonic flow and, consequently, preserves the efficiency of the separation process. Additionally, this operating condition provides a ΔT of approximately 10°C for the cold utility, favoring heat exchange and contributing to the system's energy efficiency [9, 20].

The evaluation of this scenario revealed that a battery of 10 SSRs offers significant advantages. This configuration achieves a well-balanced trade-off between the diameter of each separator, total space occupied by the battery, and modularization required to handle flow rate variations. This balance ensures technical feasibility while providing the operational flexibility needed to adapt to fluctuations in demand.

The TXGS stream contains 3.68 MW of available heat in the "E-1" Cooler, which can be recovered for energy integration. When utilized, this energy can reduce the need for hot utilities, a particularly valuable advantage for offshore platforms.

As expected from the data processed in the spreadsheet, the molar fractions of the "PRODUCT" and "CAPTURE" streams remained within the constraints defined in the methodology. Additionally, the process achieved a water capture efficiency of 99.45%, demonstrating that SS technology is not only a compact and efficient alternative but also a promising solution for TxG dehydration, capable of meeting industry requirements for water

**Table 3.** Operational results and parameters of the simulated scenario

| | Unit | FEED | PRODUCT | CAPTURE |
|---|---|---|---|---|
| Temperature | °C | 35.20 | 131.04 | -56.44 |
| Pressure | bar a | 1.010 | 0.50 | 0.50 |
| Flow rate | t/h | 24.30 | 23.44 | 0.86 |
| Heat Removed (in E-1) | MW | | 3.68 | |
| $CO_2$ | %mol | 3.24 | 3.43 | 45.77 (ppm) |
| $N_2$ | %mol | 76.21 | 80.74 | 19.22 (ppm) |
| $O_2$ | %mol | 13.99 | 14.82 | 2.82 (ppb) |
| Ar | %mol | 0.92 | 0.97 | 0.20 (ppt) |
| $H_2O$ | %mol | 5.64 | 330.22 (ppm) | 99.99 |
| Multiplier Factor | - | | 0.10 | |
| Inlet/Outlet diameter | m | | 0.59 (24 in NPS Std) | |
| Convergent/Divergent Length | m | | 0.81 | |
| Convergent/Divergent Angle | deg | | 15.00 | |
| Shock Mach | - | | 2.20 | |
| Inlet Mach | - | | 0.067 | |
| Throat Area | $m^2$ | | 0.020 | |
| Shock Temperature | °C | | -56.44 | |
| Shock Pressure | bar | | 0.083 | |

removal while providing additional energy integration benefits.

## CONCLUSIONS

This study demonstrated the feasibility and potential of SS as an efficient and compact alternative for water removal from TxGs on offshore platforms. By integrating the Aspen HYSYS simulator with the SSR UOE, a comprehensive analysis of operational and dimensional parameters was conducted, ensuring process efficiency while addressing the spatial and weight constraints typical of offshore environments. The results confirm that the proposed configuration successfully balances technical performance, energy efficiency, and modular adaptability, making SS a competitive alternative to conventional dehydration methods.

The implementation of an SSR battery proved to be viable not only from a technical perspective but also operationally, offering flexibility to accommodate flow variations. The determined "FEED" stream temperature (35.20°C) ensured stability in the supersonic flow, directly contributing to high water removal efficiency while minimizing $CO_2$ co-capture. Furthermore, the study highlighted the significant potential for energy integration, with opportunities to recover and reuse heat from the TxG stream, enhancing the overall sustainability of offshore processing systems.

Beyond its technical feasibility, SS technology aligns with industry demands for lower environmental impact and improved process integration. Its potential to minimize equipment footprint and energy consumption makes it particularly attractive for offshore applications, where operational efficiency is critical. These findings reinforce SS as a promising alternative for TxG dehydration, paving the way for its future application in supersonic $CO_2$ capture.

Further research should focus on detailed economic and environmental assessments to validate large-scale applicability, as well as experimental studies to complement numerical modeling. Additionally, investigating policy incentives and technological advancements, such as enhanced separator designs and hybrid separation strategies, will be essential to accelerate the adoption of SS technology in offshore operations.

## ACKNOWLEDGEMENTS

We would like to thank CENPES-PETROBRAS, ANP and SENAI CIMATEC, whose partnership made the development of this work possible. We also acknowledge the valuable contributions of all collaborators who participated, directly or indirectly, in this research.

## REFERENCES

1. Santana JCS, Ribeiro MEO, Souza PRA, Souza JPS, Peres SM. O uso e produção da energia limpa como método de preservação ambiental sustentável. Epitaya E-Books 1(12):99–111 (2020). https://doi.org/10.47879/ed.ep.2020144p99IPCC.
2. IPCC. Climate Change 2021: The Physical Science Basis. Intergovernmental Panel on Climate Change (2021).
3. UNFCCC. The Paris Agreement. United Nations Framework Convention on Climate Change (2015).
4. UN. Global Sustainable Development Report. United Nations (2015).
5. Cao X, Bian J. Supersonic separation technology for natural gas processing: A review. Chem Eng Process - Process Intensif 136:138–151 (2019). https://doi.org/10.1016/j.cep.2019.01.007
6. Lakzian E, Yazdani S, Salmani F, Mahian O, Kim HD, Ghalambaz M, Ding H, Yang Y, Li B, Wen C. Supersonic separation towards sustainable gas removal and carbon capture. Prog Energy Combust Sci 103:101158 (2024). https://doi.org/10.1016/j.pecs.2024.101158
7. Trotta TAF. Modelagem e Avaliação Técnica de Separador Supersônico para Condicionamento de Gás Natural. Federal University of Rio de Janeiro, School of Chemistry, Program of Chemical and Biochemical Process Engineering (2014).
8. Hammer M, Wahl PE, Anantharaman R, Berstad D, Lervåg KY. CO2 capture from offshore gas turbines using supersonic gas separation. Energy Procedia 63:243–252 (2014). https://doi.org/10.1016/j.egypro.2014.11.026.
9. Medeiros JL de, Arinelli LO, Teixeira AM, Araújo O de QF. Offshore processing of $CO_2$-rich natural gas with supersonic separator: multiphase sound speed, $CO_2$ freeze-out and HYSYS implementation. Springer International Publishing, Cham (2019). https://doi.org/10.1007/978-3-030-04006-2.
10. Saidi, M., Farokhi, G. Modeling and simulation of CO2 removal from CO2-rich natural gas via supersonic separators. Advances in Natural Gas: Formation, Processing, and Applications: Natural Gas Process Modelling and Simul.: Volume 8. pp. 105–143. Elsevier (2024)
11. Chen, J., Gao, Y., Han, X., Li, A., Huang, Z. Supersonic separation benefiting the decarbonization of natural gas and flue gas. Gas Sci. Eng. 129, 205419 (2024). https://doi.org/10.1016/j.jgsce.2024.205419
12. Chen, J., Han, X., Li, A., Xi, G., Huang, Z. Influence of boundary effect on supersonic flows and non-equilibrium condensation in a Laval nozzle for natural gas dehydration. Int. J. Heat Mass Transf.

236, 126302 (2025). https://doi.org/10.1016/j.ijheatmasstransfer.2024.126302
13. Arinelli, L. de O., Trotta, T.A.F., Teixeira, A.M., De Medeiros, J.L., Araújo, O.D.Q.F. Offshore processing of CO2 rich natural gas with supersonic separator versus conventional routes. J. Nat. Gas Sci. Eng. 46, 199–221 (2017). https://doi.org/10.1016/j.jngse.2017.07.010
14. Aspen Technology. Aspen HYSYS Properties and Methods Technical Reference. Aspen Technology, Inc., Burlington, MA, EUA (2013)
15. Peng, D.-Y., Robinson, D.B. A New Two-Constant Equation of State. Ind. Eng. Chem. Fundam. 15, 59–64 (1976). https://doi.org/10.1021/i160057a011
16. Voulgaris, M.E., Peters, C.J., De Swaan Arons, J. Prediction of the Condensation Behavior of Natural Gas: A Comparative Study of the Peng–Robinson and the Simplified-Perturbed-Hard-Chain Theory Equations of State. Ind. Eng. Chem. Res. 37, 1696–1706 (1998). https://doi.org/10.1021/ie970641b
17. API. API Recommended Practice 14E: Design and Installation of Offshore Production Platform Piping Systems, American Petroleum Institute. (2000)
18. LANL. ASME B31.3 Process Piping Guide, Los Alamos National Laboratory (2014).
19. Oliveira M, Possamai TS. Análise numérica de parâmetros de projeto para bocal supersônico utilizado em aplicações aeroespaciais, Federal University of Santa Catarina, Technological Center of Joinville, Aerospace Engineering Program (2017).
20. Bârsan D, Prodea L, Chiș T. Analysis of supersonic techniques for separating water from extracted natural gas. Int J Eng Sci 13(10):50–56 (2024). https://doi.org/10.9790/1813-13105056.

© 2025 by the authors. Licensed to PSEcommunity.org and PSE Press. This is an open access article under the creative commons CC-BY-SA licensing terms. Credit must be given to creator and adaptations must be shared under the same terms. See https://creativecommons.org/licenses/by-sa/4.0/



Systems & Control Transactions

**Research Article - Peer Reviewed Conference Proceeding**
ESCAPE 35 - European Symposium on Computer Aided Process Engineering
Ghent, Belgium. 6-9 July 2025
Jan F.M. Van Impe, Grégoire Léonard, Satyajeet S. Bhonsale,
Monika E. Polańska, Filip Logist (Eds.)

PSE PRESS

# On Optimal Hydrogen Pathway Selection Using the SECA Multi-Criteria Decision-Making Method

**Caroline Kaitano[a], Thokozani Majozi[a]***

[a] School of Chemical and Metallurgical Engineering, University of the Witwatersrand, Johannesburg, Gauteng, South Africa
* Corresponding Author: thokozani.majozi@wits.ac.za

## ABSTRACT

The increasing global population has resulted in the scramble for more energy. Hydrogen offers a new revolution to energy systems worldwide. Considering its numerous uses, research interest has grown to seek sustainable production methods. However, hydrogen production must satisfy three factors, i.e., energy security, energy equity, and environmental sustainability, referred to as the energy trilemma. Therefore, this study seeks to investigate the sustainability of hydrogen production pathways through the use of a Multi-Criteria Decision- Making model. In particular, a modified Simultaneous Evaluation of Criteria and Alternatives (SECA) model was employed for the prioritization of 19 options for hydrogen production. This model simultaneously determines the overall performance scores of the 19 options and the objective weights for the energy trilemma in a South African context. The results obtained from this study showed that environmental sustainability has a higher objective weight value of 0.37, followed by energy security with a value of 0.32 and energy equity with the least at 0.31. Of the 19 options selected, steam reforming of methane with carbon capture and storage was found to have the highest overall performance score, considering the trade-offs in the energy trilemma. This was followed by steam reforming of methane without carbon capture and storage and the autothermal reforming of methane with carbon capture and storage. The results obtained in this study will potentially pave the way for optimally producing hydrogen from different feedstocks while considering the energy trilemma and serve as a basis for further research in sustainable process engineering.

**Keywords**: Hydrogen, Modelling, Optimization, Energy-trilemma, SECA, multi-criteria-decision-making

## INTRODUCTION

Energy is a fundamental component of life and is critical for sustaining modern living standards. Increasing global population and industrialization have driven energy demand to unprecedented levels, placing significant strain on the energy sector [1]. Currently, approximately 85% of energy demand is met by fossil fuels, resulting in substantial $CO_2$ emissions. This has contributed to a 1.1°C rise in global temperatures since the pre-industrial era, with projections of further increases [2].

The energy sector also faces challenges from economic fluctuations, such as those induced by the COVID-19 pandemic, which temporarily reduced global energy demand, emissions, and investment but left renewable energy less affected [3]. As demand pressures persist, governments and organizations are pursuing policies and innovations to transition toward sustainable energy systems emphasizing reliability, environmental sustainability, and affordability [4].

Hydrogen is emerging as a promising clean energy carrier capable of addressing the limitations of traditional renewable energy sources, such as intermittency and lack of inherent storage capacity. With a high energy density (120 $MJ \cdot kg^{-1}$), hydrogen offers versatility in production, storage, and applications, including transportation and grid stabilization [5]. However, the widespread adoption of hydrogen faces challenges related to cost-effective and environmentally sustainable production methods. Current hydrogen generation technologies, primarily reliant on fossil fuels, emit $CO_2$, necessitating a shift toward carbon-free alternatives.

Hydrogen production pathways vary widely in economic, environmental, and technological performance.

Reforming methods are cost-effective but environmentally damaging, while electrolysis, powered by renewable energy, is sustainable but capital-intensive. Multi-criteria decision-making (MCDM) approaches are essential to evaluate and select optimal hydrogen production pathways that balance energy security, equity, and sustainability [6].

This study aims to identify the optimal hydrogen production pathway for South Africa using an MCDM framework. A literature review informs the methodology, followed by an evaluation of the performance of selected processes.

## LITERATURE REVIEW

MCDM methods are effective tools for addressing decision-making problems involving multiple conflicting objectives and stakeholders. Various MCDM techniques have been applied to assess and prioritize hydrogen production technologies. For example, some authors employed the Analytic Hierarchy Process (AHP) [7–8], while others integrated the decision-making trial and evaluation laboratory (DEMATEL) with AHP to improve hydrogen production sustainability [9]. Other studies utilized methods like TOPSIS, VIKOR, and hesitant fuzzy AHP to evaluate hydrogen production pathways based on sustainability criteria[10–11].

Recent advancements in MCDM include integrating fuzzy logic to handle subjective and vague human judgments, such as using the Z-number Best Worst Method (ZBWM) and ELECTRE models [12] or employing fuzzy SWARA and IVIF-WASPAS [13]. Despite these innovations, most methods remain subjective, relying heavily on expert opinions, which introduce inconsistencies and uncertainties. Moreover, these methods typically separate criteria weighting from alternative ranking, thereby limiting integration and efficiency.

Few studies have addressed hydrogen production within the framework of the energy trilemma. Additionally, geographical context, such as the South African unique energy landscape, has received little attention. South African abundant resources and environmental challenges necessitate tailored hydrogen production strategies. However, research gaps persist in addressing the interplay of energy trilemma factors and region-specific conditions.

This study introduces the Simultaneous Evaluation of Criteria and Alternatives (SECA) method, a multi-objective nonlinear programming model that simultaneously calculates criteria weights and ranks alternatives. SECA overcomes the limitations of traditional MCDM methods by optimizing and ranking solutions in a unified framework. The study focuses on identifying the optimal hydrogen production pathway for South Africa, accounting for the complexities of the energy trilemma, thereby filling a critical gap in published literature and offering practical insights for stakeholders in energy policy and planning.

## METHODOLOGY

The study follows three key stages: (1) Defining selection criteria and identifying suitable hydrogen production options, (2) Constructing a decision-making matrix, and (3) Developing a multi-objective nonlinear programming model for optimization.

Environmental sustainability, economic viability, and reliability/availability were chosen as selection criteria, addressing the core challenges in hydrogen production pathway selection. The SECA model [14], a multi-objective nonlinear approach, is applied to determine the optimal method in the South African context. It optimizes three objectives: (1) maximizing overall performance, (2) minimizing deviation in criterion weights within-criterion variation, and (3) minimizing deviation in criterion weights based on between-criterion variation. Unlike traditional methods, SECA does not require expert input for scoring criteria and relies on standard deviation and correlation as reference points for weight minimization.

To enhance model applicability, the study replaces the original SECA normalization method with Min-Max Normalization, addressing the issue of zero-value elements in evaluation matrices. This modification expands the usability of the model across diverse datasets and ensures a more comprehensive assessment framework.

A multi-criteria decision-making (MCDM) problem with *n* alternatives and *m* criteria is represented by the decision matrix:

$$x = \begin{bmatrix} x_{11} & x_{12} & \cdots & x_{1m} \\ x_{21} & x_{22} & \dots & x_{2m} \\ \vdots & \vdots & \ddots & \vdots \\ x_{n1} & x_{n2} & \cdots & x_{nm} \end{bmatrix} \quad (1)$$

Where $x_{ij}$ represents the performance of alternative $i$ alternative on criteria $j$ with $x_{ij} \geq 0$. Normalization is applied based on benefit and cost criteria using Min-Max scaling:

$$x_{ij}^{N} = \begin{cases} \dfrac{x_{ij} - \max x_{ij}}{\max x_{ij} - \min x_{ij}}, j \in BC \\ \dfrac{\max x_{ij} - x_{ij}}{\max x_{ij} - \min x_{ij}}, j \in CC \end{cases} \quad (2)$$

where BC and CC are benefit and cost criteria, respectively.

The SECA model determines criteria weights directly from the decision matrix, using standard deviation $(\sigma_j)$ and correlation $(r_{jl})$. The standard deviation, which indicates the dispersion of data, captures the within-criterion variation. The correlation calculates the contrast intensity in the interaction of the alternatives in each criterion to assess the between-criterion conflict.

$$\sigma_j = \sqrt{\frac{1}{m}\sum_{i=1}^{m}\left(X_{ij} - \overline{X_{ij}}\right)^2}, \quad \pi_j = \sum_{l=1}^{m}\left(1 - r_{jl}\right) \tag{3}$$

The normalized reference points for weight calculation are given by:

$$\sigma_j^N = \frac{\sigma_j}{\sum_{l=1}^{m}\sigma_l} \quad , \quad \pi_j^N = \frac{\pi_j}{\sum_{l=1}^{m}\pi_l} \tag{4}$$

The multi-objective nonlinear programming model consists of three objectives:

1. Maximizing overall performance:

$$\max S_i = \sum_{j=1}^{m} w_j \, x_{ij}^N \qquad \forall_i \in \{1,2,\dots,n\} \tag{5}$$

2. Minimizing deviation from standard deviation-based reference weights:

$$\min \lambda_b = \sum_{j=1}^{m}\left(w_j - \sigma_j^N\right)^2 \tag{6}$$

3. Minimizing deviation from correlation-based reference weights:

$$min\, \lambda_c = \sum_{j=1}^{m}\left(w_j - \pi_j^N\right)^2 \tag{7}$$

Subject to:

$$\sum_{j=1}^{m} w_j = 1 \;\; , \varepsilon \le w_j \le 1 \;\; , \;\; \forall_j \in \{1,2,\dots,m\} \tag{8}$$

where ε is a small positive value (set to $10^{-3}$) ensuring a lower bound on weights.

To transform the multi-objective problem into a single-objective optimization, a weighted sum method is applied:

$$\max Z = \lambda_a - \beta(\lambda_b + \lambda_c) \tag{9}$$

with constraints:

$$\lambda_a \le S_i \;\; , \;\; S_i = \sum_{i=1}^{m} x_{ij}^N \, w_j \, , \quad \forall_i \in \{1,2,\dots,n\} \tag{10}$$

$$\lambda_b = \sum_{j=1}^{m}\left(w_j - \sigma_j^N\right)^2, \;\; \lambda_c = \sum_{j=1}^{m}\left(w_j - \pi_j^N\right)^2 \tag{11}$$

The parameter $\beta$ balances deviations from reference weights, and different $\beta$ values generate alternative rankings. The stability of rankings is evaluated using the Spearman correlation coefficient, ensuring consistency in final rankings.

## CASE STUDY

A pathway database was developed from the literature. The data was collected according to affordability, availability, and environmental sustainability criteria. The affordability was characterized by the cost of hydrogen ($/kg), and the data was adapted from [15].

Environmental sustainability data was collected from different sources in the literature [16–19]. This criterion was characterized by global warming potential (GWP), which is the amount of carbon dioxide produced by the process per amount of hydrogen produced (kg $CO_2$ / kg $H_2$).

Availability is the third criterion, and it measures the raw materials required in a particular process to obtain hydrogen. The measure was rated regarding how much raw material is available. Raw material availability was chosen because neglecting resource availability may cause a model to select a production process that is not well suited to a region of interest. In this research, a rigorous methodology was employed to calculate the availability rating of critical raw materials. The availability rating was determined using the following equation, which was modified from the general efficiency equation:

$$Availability\ rating = \frac{Total\ raw\ material\ available}{Total\ raw\ material\ required} \tag{12}$$

The study considered the total quantities of raw materials required for a 100-year projection assuming stoichiometry. The availability rating for each raw material was calculated individually, offering a detailed assessment of their respective contributions to the overall availability. Furthermore, an average availability rating was computed to provide a holistic perspective on the raw material supply chain. The results reveal a surplus beyond the required quantities, emphasizing the robustness of the production system and its capability to meet demands efficiently. This comprehensive approach to assessing availability contributes valuable insights to the optimization of hydrogen production processes.

A hydrogen demand value of 6 million tons per annum obtained from [20] was used to calculate the amount of raw materials required per pathway. This was done using stoichiometric ratios, assuming 100 % conversion of the limiting reactant. The average raw materials required for a particular pathway were used as the availability rating.

## RESULTS AND DISCUSSION

A decision-making matrix was developed based on a pathway database comprising 19 hydrogen production routes. The matrix was constructed using GAMS modeling software with the Antigone solver to handle the

complex interrelationships and variables within the decision framework.

**Table 1:** The evaluation matrix of the pathway database

| Process | Cost ($/kg) | GWP ($kgCO_2$/ kg $H_2$) | Availability rating |
|---|---|---|---|
| **SMR with CCS (S1)** | 4.84 | 3.40 | 11.65 |
| **SMR without CCS (S2)** | 4.43 | 12.00 | 11.65 |
| **CG with CCS (S3)** | 3.48 | 15.50 | 2.10 |
| **CG without CCS (S4)** | 2.86 | 24.20 | 2.10 |
| **ATR of methane with CCS (S5)** | 3.16 | 3.98 | 7.78 |
| **Methane Pyrolysis (S6)** | 3.18 | 5.00 | 3.02 |
| **Biomass Pyrolysis (S7)** | 3.75 | 2.40 | 6.26 |
| **Biomass Gasification (S8)** | 4.14 | 2.67 | 6.26 |
| **Direct bio Photolysis (S9)** | 3.77 | 0.70 | 6.26 |
| **Indirect bio photolysis (S10)** | 2.51 | 67.00 | 6.26 |
| **Dark Fermentation (S11)** | 4.65 | 16.29 | 6.26 |
| **Photo Fermentation (S12)** | 5.12 | 0.60 | 3.13 |
| **Solar PV Electrolysis (S13)** | 28.23 | 2.00 | 3.13 |
| **Solar thermal electrolysis (S14)** | 15.15 | 2.50 | 3.13 |
| **Wind Electrolysis (S15)** | 12.71 | 0.97 | 3.13 |
| **Nuclear Electrolysis (S16)** | 11.25 | 2.00 | 3.13 |
| **Nuclear Thermolysis (S17)** | 4.66 | 0.63 | 3.13 |
| **Solar Thermolysis (S18)** | 15.91 | 0.68 | 3.13 |
| **Photo-Electrolysis (S19)** | 18.73 | 2.00 | 3.13 |

To ensure consistency, all cost data were standardized to the reference year 2021 using the Chemical Engineering Plant Cost Index (CEPCI). The matrix provides a structured framework for evaluating and comparing pathways against the energy trilemma criteria. **Table 1** presents the evaluation matrix.

## Normalizing the decision-making matrix

The data in **Table 1** were normalized using Equation (2). Affordability and environmental sustainability were identified as cost criteria, given that they need to be minimized. Conversely, availability was identified as a benefit criterion, given that it needs to be maximized.

## Criteria weights analysis

Determining criteria weights is crucial for prioritizing processes. The SECA model was solved for $\beta$ values (0.1, 0.2, 0.3, 0.4, 0.5, 1, 2, 3, 4, 5, 6, 7), extending the initial study by [14] to observe trends beyond $\beta$ = 5. Twelve sets of criteria weights were generated, with variations shown in **Figure 1**. The optimal $\beta$ was selected where consecutive solutions differed by less than 0.01, ensuring near-constant weights.

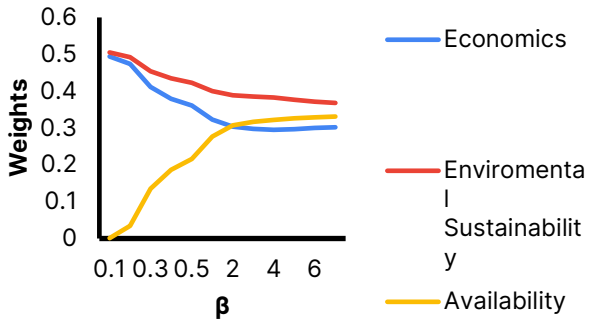



**Figure 1:** The variation of criteria weights related to $\beta$

A clear decrease in the objective function value was observed as $\beta$ increased, as shown in **Figure 2**. The parameter $\beta$ played a critical role in influencing criteria weights, with some criteria gaining importance while others diminished as $\beta$ increased. This dynamic interaction optimized the decision-making process by balancing trade-offs between criteria.

A transition point was identified where criteria weights stabilized, signaling the critical balance of the model. Notably, this stabilization coincided with the maximum value of the objective function, indicating the optimal state of the model. Thus, $\beta$ acted as a lever to achieve a stable and balanced weighting while optimizing the overall objective function.

For $\beta$ values exceeding 3, criteria weights exhibited increased stability, with differences between consecutive weights dropping below 0.01 as $\beta$ approached 5. This indicated a balanced state between decision criteria, leading to the selection of $\beta$ = 5 for determining final weights.

The resulting criteria weights highlighted environmental sustainability as the most significant factor (0.373), emphasizing eco-friendly practices. Availability, particularly of raw materials, ranked second (0.316), underscoring resource reliability. Affordability received the lowest weight (0.310), indicating lower priority in the decision-making process. This prioritization reflects a focus

on sustainability and resource availability.

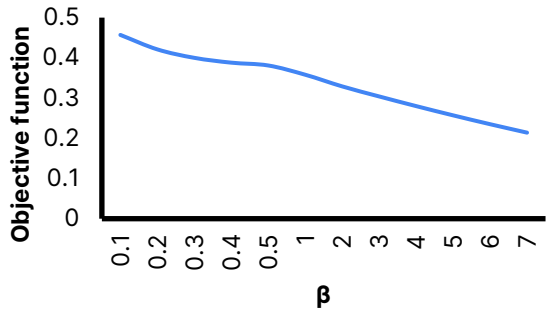



**Figure 2:** Objective function with varying $\beta$

## Analysis of the performance of alternatives

The overall performance of each alternative *Si* was assessed using the SECA model with normalized data and criteria-specific $\beta$ values. The rankings, aligned with the original pathway database (e.g., S1 correspond to "SMR with CCS"), enabled the identification of the most promising pathways based on the three selected criteria.

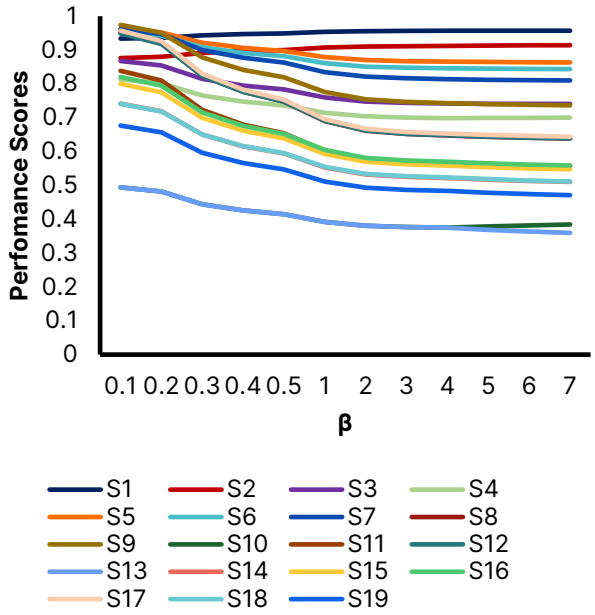



**Figure 3:** Variations in the performance scores related to $\beta$

**Figure 3** provides a graphical representation of performance scores, offering a clear visual understanding of pathway performance and trends for informed decision-making. Rankings were determined based on *Si*, with the highest score indicating superior performance. For $\beta \geq 3$, rankings remained stable (Spearman's correlation coefficient = 1), validating $\beta$ = 5 as the optimal value for final rankings.

Among 19 pathways, steam reforming with CCS emerged as the top option with *Si* = 0.956, balancing energy trilemma criteria due to reduced $CO_2$ emissions, technological maturity, and low raw material costs. This finding aligns with [21], who also identified its robustness using different criteria. Steam reforming without CCS ranked second (*Si*= 0.913), followed by autothermal reforming with CCS (*Si* = 0.845).

Indirect bio-photolysis and solar PV electrolysis were the least preferred pathways, with *Si* values of = 0.448 and 0.400, respectively, primarily due to high economic costs. These results provide a clear framework for selecting the most effective and economically viable hydrogen production pathways, supporting energy sustainability objectives.

## CONCLUSION

In conclusion, this study demonstrated the effectiveness of the SECA multi-criteria decision-making method in optimizing hydrogen production pathway selection within the South African energy landscape, addressing availability, affordability, and environmental sustainability. Using a multi-objective nonlinear programming model, SECA adjusted criteria weights and ranked alternatives, identifying environmental sustainability as the most critical factor, followed by availability and affordability. A $\beta$ value of 5 provided the most stable results, with steam reforming with CCS emerging as the optimal pathway, followed by steam reforming without CCS and autothermal reforming with CCS, while indirect bio-photolysis and solar PV electrolysis ranked lowest due to economic constraints. These insights offer strategic guidance for aligning hydrogen production with sustainability and resource reliability in South Africa.

## ACKNOWLEDGEMENTS

Financial support from the National Research Foundation is gratefully acknowledged.

## REFERENCES

1. DOE. The South African Energy Sector Report (2019).
2. U.S Energy Information Administration. Country Analysis Executive Summary: South Africa. Independent Statistic & Analysis. 1-15 (2021).
3. PWC. COVID-19: What it means for the energy industry. PWC / United Stated, 1-10 (2020). https://www.pwc.com/us/en/library/covid-19/coronavirus-energy-industry-impact.html.
4. EIA. U.S. Energy Facts Explained. Department of Energy. 6 (2023). https://www.eia.gov/energyexplained/us-energy-

facts/.
5. Chih YK, Chen WH, You S, Hsu CH, Lin HP, Raza Naqvi S, Ashokkumar V. Statistical optimization of hydrogen production from bio-methanol steam reforming over Ni-Cu/Al2O3 catalysts. Fuel, 331,125691. (2023). https://doi.org/10.1016/j.fuel.2022.125691.
6. Abdel-Basset M, Gamal A, Chakrabortty RK, Ryan MJ. Evaluation of sustainable hydrogen production options using an advanced hybrid MCDM approach: A case study. International Journal of Hydrogen Energy, 46,4567–4591 (2021). https://doi.org/10.1016/j.ijhydene.2020.10.232.
7. Pilavachi PA, Chatzipanagi AI, Spyropoulou AI. Evaluation of hydrogen production methods using the Analytic Hierarchy Process. International Journal of Hydrogen Energy, 34.5294–5303 (2009). https://doi.org/10.1016/j.ijhydene.2009.04.026.
8. Chung Y, Hong S, Kim J. Which of the technologies for producing hydrogen is the most prospective in Korea?: Evaluating the competitive priority of those in near-, mid-, and long-term. Energy Policy, 65, 115-125 (2014). https://doi.org/10.1016/j.enpol.2013.10.020.
9. Ren J, Manzardo A, Toniolo S, Scipioni A. Sustainability of hydrogen supply chain. Part I: Identification of critical criteria and cause-effect analysis for enhancing the sustainability using DEMATEL. International Journal of Hydrogen Energy, 38, 14159-14171 (2013). https://doi.org/10.1016/j.ijhydene.2013.08.126.
10. Ramazankhani ME, Mostafaeipour A, Hosseininasab H, Fakhrzad MB. Feasibility of geothermal power assisted hydrogen production in Iran. International Journal of Hydrogen Energy, 41,18351–18369 (2016). https://doi.org/10.1016/j.ijhydene.2016.08.150.
11. Acar C, Beskese A, Temur GT. Sustainability analysis of different hydrogen production options using hesitant fuzzy AHP. International Journal of Hydrogen Energy, 43, 18059–18076 (2018). https://doi.org/10.1016/j.ijhydene.2018.08.024.
12. Lin R, Lu S, Yang A, Shen W, Ren J. Multi-criteria sustainability assessment and decision-making framework for hydrogen pathways prioritization: An extended ELECTRE method under hybrid information. International Journal of Hydrogen Energy, 46, 13430–13445 (2021). https://doi.org/10.1016/j.ijhydene.2021.01.018.
13. Seker S, Aydin N. Assessment of hydrogen production methods via integrated MCDM approach under uncertainty. International Journal of Hydrogen Energy, 47, 3171–3184 (2022). https://doi.org/10.1016/j.ijhydene.2021.07.232.
14. Keshavarz-Ghorabaee M, Amiri M, Zavadskas EK, Turskis Z, Antucheviciene J. Simultaneous evaluation of criteria and alternatives (SECA) for multi-criteria decision-making. Informatica (Netherlands), 29, 265–280 (2018). https://doi.org/10.15388/Informatica.2018.167.
15. Nikolaidis P, Poullikkas A. A comparative overview of hydrogen production processes. Renewable and Sustainable Energy Reviews, 67, 597–611 (2017). https://doi.org/10.1016/j.rser.2016.09.044.
16. Mehmeti A, Angelis-Dimakis A, Arampatzis G, McPhail S J, Ulgiati S. Life cycle assessment and water footprint of hydrogen production methods: From conventional to emerging technologies. *Environments - MDPI*, **5**, 1-19 (2018) https://doi.org/10.3390/environments5020024.
17. Acar C, Dincer I. Comparative assessment of hydrogen production methods from renewable and non-renewable sources. International Journal of Hydrogen Energy, 39, 1-12, (2014). https://doi.org/10.1016/j.ijhydene.2013.10.060.
18. Al-Qahtani A, Parkinson B, Hellgardt K, Shah N, Guillen-Gosalbez G. Uncovering the true cost of hydrogen production routes using life cycle monetisation. Applied Energy, 281, 115958 (2021). https://doi.org/10.1016/j.apenergy.2020.115958.
19. Bhandari R, Trudewind C A, Zapp P. Life cycle assessment of hydrogen production via electrolysis - A review. Journal of Cleaner Production, 85, 151-163, (2014). https://doi.org/10.1016/j.jclepro.2013.07.048.
20. DTIC. Green Hydrogen Commercialisation Strategy For South Africa: Executive Summary. 1-26 (2022).
21. Chau K, Djire A, Khan F. Review and analysis of the hydrogen production technologies from a safety perspective. International Journal of Hydrogen Energy, 47, 13990–14007 (2022). https://doi.org/10.1016/j.ijhydene.2022.02.127.

© 2025 by the authors. Licensed to PSEcommunity.org and PSE Press. This is an open access article under the creative commons CC-BY-SA licensing terms. Credit must be given to creator and adaptations must be shared under the same terms. See https://creativecommons.org/licenses/by-sa/4.0/



Systems & Control Transactions

**Research Article - Peer Reviewed Conference Proceeding**
ESCAPE 35 - European Symposium on Computer Aided Process Engineering
Ghent, Belgium. 6-9 July 2025
Jan F.M. Van Impe, Grégoire Léonard, Satyajeet S. Bhonsale,
Monika E. Polańska, Filip Logist (Eds.)

PSE PRESS

# Energy Integration of an Intensified Biorefinery Scheme from Waste Cooking Oil to Produce Sustainable Aviation Fuel

**Ma. Teresa Carrasco-Suárez [a], Araceli Guadalupe Romero-Izquierdo [b]***

[a] Monash University, Faculty of Engineering, Melbourne, Clayton, Australia
[b] Universidad Autónoma de Querétaro, Facultad de Ingeniería, Querétaro, Querétaro, México
* Corresponding Author: araceli.romero@uaq.mx

## ABSTRACT

Sustainable aviation fuel (SAF) is a proven alternative to reduce $CO_2$ emissions in the aviation sector, supporting sustainable growth. However, SAF processes remain economically uncompetitive with fossil-derived jet fuel, prompting interest in strategies to address these challenges. In 2022, Carrasco-Suárez et al. explored process intensification in the SAF separation zone of a biorefinery using waste cooking oil (WCO), achieving a 3.07% reduction in $CO_2$ emissions and lower operational costs for steam and cooling water. Despite these gains, the WCO biorefinery remains economically unviable with high energy demands. This work presents the energy integration of the entire WCO biorefinery addressed from the pinch point methodology, combined with separation zones intensification (EI-PI-S), using the principles of sections movement for distillation columns; these energy efficiency strategies were applied on the biorefinery in Aspen Plus V.10.0 in order to improve the scheme. Key indicators—total annual cost (TAC), energy investment per product energy (EI-P), energy investment per main product mass (EI-MP), and $CO_2$ emissions per main product mass ($CO_2$-MP)—were used to compare the conventional scheme (CS) and the intensified scheme before energy integration (PI-S). The EI-PI-S scheme achieved the best performance, reducing steam and cooling water requirements by 14.34% and 31.06%, respectively, and $CO_2$ emissions by 13.85% and 14.13% compared to CS and PI-S. However, TAC for EI-PI-S was 0.89% higher than PI-S. Despite this, the integrated and intensified WCO biorefinery emerges as a feasible option for SAF production, adhering to energy minimisation principles and improving economic performance.

**Keywords**: WCO biorefinery scheme, SAF, modelling and simulation, energy integration, process intensification

## INTRODUCTION

The aviation industry is increasingly under pressure to reduce its carbon footprint while also trying to recover from the crisis caused by the restrictions of the pandemic brought on by the SARS-CoV-2 virus. In this context, using renewable fuels has proven to be a promising and resilient alternative for the sustainable economic recovery of this sector, which faced its worst year in history in 2020 [1]. Currently, the price of renewable aviation fuel is not competitive compared to its fossil counterpart. One of the strategies to achieve its economic feasibility has been using biorefinery schemes based on residual raw materials, such as WCO. In this biorefinery scheme based on WCO, SAF is obtained as the main product [2]. Then, the separation zone was intensified to improve its economic and environmental competitiveness using the Rong-Errico methodology, achieving up to a 66.95 % reduction in reboiler heat duty through the intensified design [3, 4]. To further improve this biorefinery scheme, this study proposes the intensification of the ethanol recovery zone. Additionally, the energy integration of the scheme aims to utilise the energy from process streams while minimising reliance on external energy sources through the application of pinch point methodology [5]. This study seeks to reduce energy consumption in the

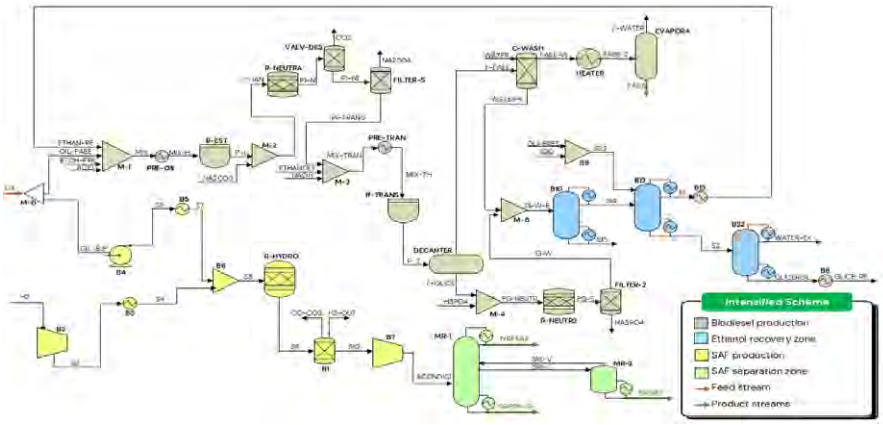



**Figure 1.** Intensified scheme developed by Carrasco-Suárez et al. 2022 [4].

biorefinery, which will contribute to the overall sustainability of the SAF production process.

## METHODOLOGY

The methodology adopted in this work centres on minimising energy consumption within the biorefinery framework by incorporating process intensification and energy integration tools. The following sections will discuss these energy efficiency approaches, alongside an evaluation of their effectiveness using economic-environmental indicators.

### Biorefinery of WCO

The biorefinery scheme developed after intensifying the SAF separation zone, served as the foundation for this work (Figure 1). It processes 2,004.88 kg/h of waste cooking oil (WCO), which consists of 94% triglycerides and 6% free fatty acids [4]. For more detailed information about the feedstock modelling and the base design of the WCO biorefinery, see [4]. The feed (OIL) is divided into two secondary streams, 50% (by weight) for each processing route; the first (OIL-FAEE) is destined for obtaining biodiesel, and the second (OIL-BJF) is to produce SAF.

Biodiesel is produced through two reactive zones in RBatch modules: esterification (R-EST) and transesterification (R-TRANS). The resulting stream (P-2) enters a decanter (DECANTER), producing two streams: F-FAEE (biodiesel) and F-GLICE (glycerol). The biodiesel is washed with a water stream (50% by weight) in the Extract module (C-WASH) to remove impurities. The washed biodiesel (FAEE-W) is dried in a Heater module (HEATER) and purified in a flash tank (EVAPORA) using the Flash2 module. Secondary products (ethanol, water, glycerol) are separated via a train of three RadFrac columns (B10, B12, and B22), with B12 employing glycerol as an extracting agent for recirculation in the biorefinery. The thermodynamic models used are NRTL and UNIFAC for the reactive zones and NRTL for secondary product recovery.

Regarding SAF production, the WCO enters a Pump module (B4) and a heat exchanger (B5) to condition the feed stream to 380 °C and 30 bar. A hydrogen stream at 10 bar enters a compressor (B2) and then to a heat exchanger (B3) to reach 30 bar and 380 °C. Next, both streams enter the hydrotreatment reactor (R-HYDRO), and its output (S10) is sent to a turbine (Compr module B7) to reduce pressure to 1 bar. The output stream (ACONDICI) containing 28 hydrocarbons is divided into three main products: naphtha (NAFTAS), SAF (BIOJET), and green diesel (GREEN-DI). SAF separation is achieved through a distillation train consisting of two columns (RadFrac modules MR-1 and MR-2), producing 306.12 kg/h of SAF with a recovery rate of 99.62% and representing 16.6% of the total products, with biodiesel being the most abundant at 50.1%. The conditioning and reaction zones use Peng-Robinson for thermodynamics, while the separation zone utilises BK10.

### Process Intensification on Separation Zones

Distillation is known for its low thermodynamic efficiency, a significant factor in energy consumption within biorefineries [6]. In this case, distillation accounts for 61.4% of the total energy consumed. This inefficiency requires exploring alternative methods, such as process intensification strategies, to optimise energy use and improve overall performance. Process intensification is a tool in chemical engineering that focuses on designing processes that are more compact, environmentally friendly, safe, and energy-efficient [7]. Using thermally coupled flows instead of traditional heat exchangers in distillation processes has demonstrated a reduction in energy consumption. This improvement enhances heat and mass transfer while meeting recovery and purity goals in distillation sequences [8].

## Intensification of the SAF Separation Zone

A systematic methodology developed by Rong and Errico has been implemented to improve the energy efficiency of the SAF, naphtha, and green diesel separation process, as illustrated in Figure 1. This approach reduced the reboiler heat duty by 66.95 % compared to the conventional one, resulting in a 3.07 % reduction in $CO_2$ emissions. Although the capital cost of the intensified biorefinery is 11.74 % higher than that of the conventional scheme, it offers operating costs that are 2.68 % and 8.13 % lower for steam and cooling water, respectively [4]. These results are promising, indicating that this biorefinery has the potential to meet energy demands sustainably, while significantly reducing emissions and energy requirements. Additionally, the intensification of the ethanol recovery zone could also lead to significant improvements. Thus, both strategies to achieve the complete intensification on the separation zones into the biorefinery scheme could be further improved by using an energy integration tool that utilises process streams and reactive energy zones as energy sources to meet all energy demands in the biorefinery [5].

## Intensification of the Ethanol Recovery Zone

The distillation train illustrated in blue in Figure 1 is designed to recover ethanol with a purity of 99.89%. This high-purity ethanol can subsequently be recirculated back into the biodiesel production process. This part of the biorefinery accounts for 57.7% of the total energy requirements. Thus, implementing energy-saving methodologies is essential for cost reduction, as decreased energy consumption significantly lowers operational expenses and enhances profit margins. Furthermore, such measures mitigate environmental impact by reducing greenhouse gas emissions. This approach is vital for establishing a long-term, viable, and resilient SAF production process, particularly as energy resources become increasingly scarce and expensive.

The conceptual principles of the Rong-Errico methodology were taken as the basis for reducing energy consumption in the ethanol recovery distillation process [3]. It is specifically designed for traditional distillation columns with a single condenser and reboiler, intended for non-azeotropic mixtures. Due to the formation of an azeotrope between ethanol and water, extractive distillation is necessary, utilising glycerol as the extracting agent. Therefore, the distillation train used to recover ethanol, as shown in Figure 1, falls outside the scope of the Rong-Errico approach; however, in order to address this challenge, the conceptual principles of the Rong-Errico methodology were used to enable the creation of intensified configurations.

In this case, a singular simple column configuration (D-SC) exists. The intensification process for this configuration commences with the generation of all possible original thermally coupled configurations (OTC) by substituting the heat exchangers linked to the submixtures S14 and S2 with thermal coupling streams, resulting in three distinct OTCs. These OTCs are the foundation for deriving thermodynamically equivalent structures (TES) by manipulating movable sections. Regarding OTC-2, section 5 cannot be relocated to column B12, as it is not a transport side column. In contrast, TES-1 and TES-3 incorporate a single-section transport side column (B12), while columns B10 and B22 maintain a simple column design. Consequently, ISC-1 and ISC-3 can be generated by omitting column B12 from the configurations.

The modifications to the original methodology for generating the seven intensified configurations involved using the feed stream S14 to define the rectifying and stripping sections in column B12. Additionally, to achieve the desired purity of the products, the feed stage location for stream S22 was modified, along with adjustments to operational parameters such as reflux ratio and mass flux of the thermal coupling streams. The D-SC achieves purities of 99.89% for ethanol, 85.83% for water, and 99.99% for glycerol. Among these configurations, OTC-2 is the only option that meets these requirements, while the other ones present convergence troubles. OTC-2 achieved the required purity specifications by adding glycerol to the top of column B12 to break the azeotrope and introducing thermally coupled flows at the bottom of the column for effective separation. In contrast, in other configurations, the thermally coupled flows in column B10 disrupted the separation process by mixing ethanol, water, and glycerol in the feed with the glycerol needed for column B12. This factor and heat duty savings in the condenser and reboiler were considered when determining the configuration to replace the conventional train. Consequently, OTC-2 was coupled into the biorefinery (Figure 2), which reduced heat duty by 8.17% for the condenser and 5.56% for the reboiler, compared to D-SC.

In the PI-S (Figure 2), designed after intensifying both distillation sequences, the energy requirements for heating and cooling were reduced by 3.10% and 11.81%, respectively, compared to the conventional scheme (CS). $CO_2$ emissions increased by 0.33%. This rise is attributed to the high heat duties in column B22, which has only four stages. Introducing thermal coupling streams (S2-V and S2-L) has negatively affected the column's energy efficiency and performance. With just four stages, the column requires a higher reflux ratio to achieve the necessary purity for glycerol and water. This, in turn, increases the heat duty of the reboiler by 2.76%, meaning the column must work harder to achieve effective separation.

## Energy Integration of an Intensified Biorefinery Scheme

Energy integration is a systematic approach designed to improve the energy efficiency of processes by

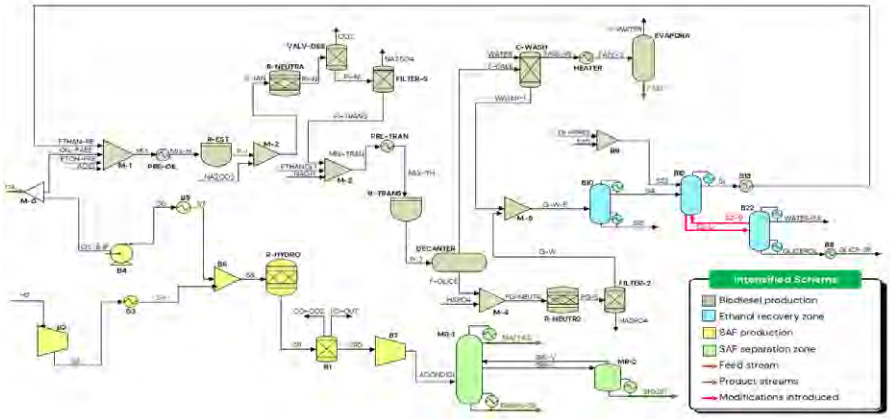



**Figure 2.** Intensified WCO biorefinery scheme

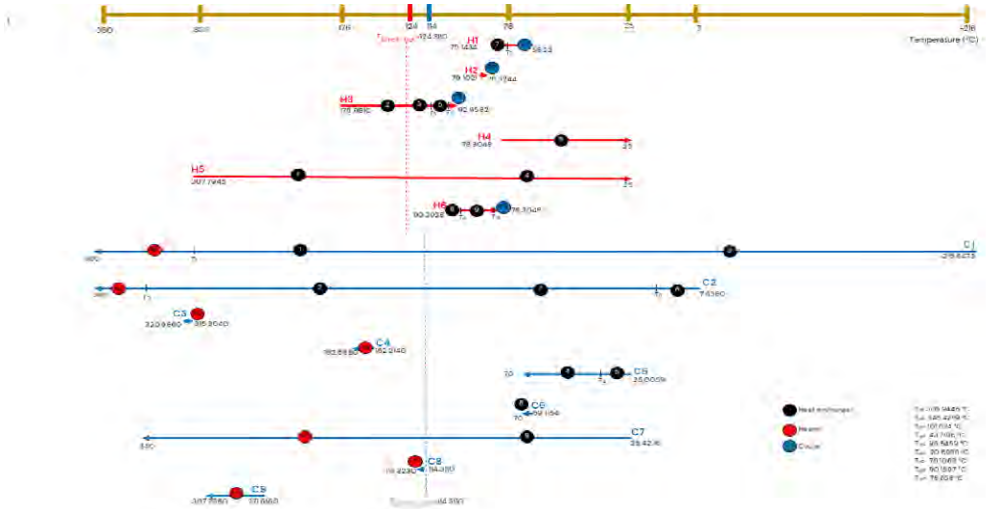


**Figure 3.** HEN designed for the intensified scheme

optimising energy use and recovery within a system. A key technique is pinch point analysis, which minimises energy requirements across the entire biorefinery process[9].

This technique was applied for energy integration of the PI-S, beginning with the collection of data on the energy requirements for both hot and cold process streams, including their temperatures and flow rates, from Aspen Plus V.10.0. This information was then visualised on a temperature-enthalpy (T-H) diagram, where a temperature difference (ΔT) of 10 °C was applied to adjust the temperatures of the hot streams. A heat cascade was employed to identify the pinch point, which was the optimal location for heat recovery, marked by the minimal temperature difference between the hot and cold streams. A heat exchanger network (HEN) was designed to maximise heat transfer around this pinch point while considering thermal constraints. This network aimed to significantly reduce energy consumption, resulting in cost savings and a lower environmental impact [10].

## Biorefinery assessment

The EI-PI-S was evaluated and compared with the CS and PI-S using economic-environmental indicators, defined from the energy and mass requirements of the process. These results quantify the energy performance and the $CO_2$ emissions from the process, as well as its profitability and efficiency. The indicators determined in this work are shown in Table 1.

# RESULTS

In this section are presented the results of energy integration and process intensification, energy efficiency strategies, applied on the WCO biorefinery. Based on the pinch point analysis, the pinch point temperature for hot streams was identified at 124.31 °C, while for cold streams, it was 114.31 °C, using a temperature difference (ΔT) of 10 °C. The calculated minimum heating and cooling requirements, determined through heat cascade analysis are 1126.40 kW and 441.02 kW, respectively.

**Table 1:** Economic-environmental assessment indicators.

| Indicator | Equation and description |
|---|---|
| Total annual cost (TAC) | $TAC\ \left(\frac{USD}{year}\right) = \frac{CC+0.18CC+0.61CC}{n} + OC$ (1)<br>This includes estimating capital (CC) by Aspen Plus and adjusting by CEPCI, as well as the operating costs (OC) and a period of recovery from the investment (5 years) [12,13]. |
| Energy indicator per total energy products (EI-P) | $EI-P\ = \frac{Invested\ energy\ for\ heating}{Energy\ provided\ by\ total\ products}$ (2)<br>It indicates the overall energy efficiency of the biorefinery. |
| Energy indicator per total products (EI-MP) | $EI-MP = \frac{Invested\ energy\ for\ heating}{Mass\ of\ main\ product}$ (3)<br>Similarly to EI-P, this indicator measures how effectively the energy input is converted into SAF, reducing reliance on external energy sources. |
| $CO_2$ emissions indicator per total products ($CO_2$-MP) | $CO_2-MP\ \left(\frac{ton\ CO_2}{kg}\right) = \frac{Total\ \ CO_2\ equivalent\ emissions}{Mass\ of\ main\ product}$ (4)<br>This metric provides insights into the environmental impact and quantifies the emissions relative to the total SAF mass, helping assess the carbon footprint. |

**Table 2:** Estimated indicators

| Scheme | % TAC savings | EI-P (kW/kW) | EI-MP (kW/kg) | $CO_2$-MP (ton $CO_2$/kg) |
|---|---|---|---|---|
| CS | - | 4.2919 | 12.5465 | 9.2918 |
| PI-S | -25.77 % | 4.1394 | 12.1580 | 9.3226 |
| EI-PI-S | -26.90 % | 4.0245 | 11.8202 | 8.0051 |

The designed HEN, shown Figure 3, uses the fewest heat exchangers to maximise savings in steam and cooling water consumption, as well as equipment costs. The energy savings achieved are 14.34% for heating and 31.06% for cooling, compared to the CS. The steam requirement for the EI-PI-S system was 0.67% higher than that of the CS and 0.13% higher than the PI-S. Similar to the PI-S, the ethanol recovery process is responsible for a 2.5% increase in emissions from column B10 in EI-PI-S. This increase occurs because column B10 handles the bulk of the three compounds from the feed, concentrating them into the liquid phase. As a result, higher reboiling energy is needed to generate the vapour phase required for separation, particularly for ethanol and water, which form an azeotrope and thus require additional energy for phase change. Conversely, the amount of cooling water used in the EI-PI-S scheme was reduced by 35.51% compared to the CS and by 8.53% compared to the PI-S.

The results from Table 2 indicate that implementing these methodologies contributed to energy savings and environmental benefits. By combining process intensification and energy integration strategies, the total energy invested is reduced, with the EI-P-S decreasing by 6.23% and the EI-MP decreasing by 5.79% compared to the CS.

Although the amount of vapour required in the EI-PI-S increased, the overall efficiency gains from energy integration led to a reduction in $CO_2$-MP by 13.85% when compared to the CS. The EI-PI-S demonstrates a 26.90% increase in TAC compared to the CS and a 0.89% increase compared to the PI-S.

This suggests that although the EI-PI-S reduces energy consumption and emissions, making it a promising alternative for sustainable biorefineries in the production of SAF, the costs of the equipment and raw materials outweigh the economic benefits gained from energy savings. This presents a challenge to the economic feasibility

of the EI-PI-S scheme, and achieving financial profitability remains a hurdle [11].

## CONCLUSION

In this work, the implementation of the pinch point analysis methodology in an intensified WCO biorefinery scheme to produce SAF was presented, achieving savings of 14.34 % and 31.06 % in heating and cooling requirements, respectively, compared to the conventional scheme. This energy-integrated scheme (EI-PI-S) was evaluated and compared with the conventional (CS) and intensified (PI-S) schemes, reporting savings across the proposed energy-environmental indicators. Thus, the production of SAF in this energetically integrated-intensified biorefinery scheme from WCO represents a promising alternative. Strategies are essential to tackle the challenge of cost competitiveness in biorefineries. Government initiatives and incentives, such as tax credits, grants, and subsidies, can significantly help reduce the capital and operational costs associated with biorefinery investments. Furthermore, promoting stakeholder collaboration is crucial for successfully deploying biorefineries.

## REFERENCES


1. IATA. https://www.iata.org/en/pressroom/pressroom-archive/2021-releases/2021-08-03-01
2. Romero-Izquierdo AG, Gómez-Castro FI, Gutiérrez-Antonio C, Cruz Barajas R, Hernández, S. Development of a biorefinery scheme to produce biofuels from waste cooking oil. *Comput Aided Chem Eng* 46:289-294 (2019) https://doi.org/10.1016/B978-0-12-818634-3.50049-7
3. Rong BG and Errico M. Synthesis of intensified simple column configurations for multicomponent distillations. *Chem Eng and Process: Process Intensif* 62:1-17 (2012) http://dx.doi.org/10.1016/j.cep.2012.10.005
4. Carrasco-Suarez MT, Romero-Izquierdo AG, Gutiérrez-Antonio C, Gómez-Castro FI, Hernández, S. Production of renewable aviation fuel by waste cooking oil processing in a biorefinery scheme: Intensification of the purification zone. *Chem Eng and Process: Process Intensif* 181:109103 (2022) https://doi.org/10.1016/j.cep.2022.109103
5. Villegas-Herrera LA, Gómez-Castro FI, Romero-Izquierdo AG, Gutiérrez-Antonio C, Hernández S. Feasibility of energy integration for high-pressure biofuels production processes. *Comput Aided Chem Eng* 43:1523-1528 (2018) https://doi.org/10.1016/B978-0-444-64235-6.50266-7
6. Jiang Z and Agrawal R. Process intensification in multicomponent distillation: A review of recent advancements. *Chem Eng Res Des* 147:122-145 (2019) https://doi.org/10.1016/j.cherd.2019.04.023
7. Keil FJ. Process intensification. *Rev in Chem Eng* 34(2):135-200 (2018) https://doi.org/10.1515/revce-2017-0085
8. Romero-Izquierdo AG, Gutiérrez-Antonio C, Gómez-Castro FI, Hernández, S. Synthesis and intensification of a biorefinery to produce renewable aviation fuel, biofuels, bioenergy and chemical products from Jatropha Curcas fruit. *IET Renew Powe Gen* 16:2988-3008 (2022) https://doi.org/10.1049/rpg2.12388
9. El-Halwagi MM. Chapter Four – Process Integration for Sustainable Design. In: SUSTAINABILITY IN THE DESIGN, SYNTHESIS AND ANALYSIS OF CHEMICAL ENGINEERING PROCESSES. Ed: Ruiz-Mercado G and Cabezas H. Oxford (2016)
10. Ng, XW. Energy Cascade and Pinch Analysis. In: CONCISE GUIDE TO HEAT EXCHANGER NETWORK DESIGN. Ed: Ng, XW. Springer International Publishing (2021)
11. Makepa DC and Chihobo CH. Barriers to commercial deployment of biorefineries: A multi-faceted review of obstacles across the innovation chain. *Heliyon* 10:1-18 (2024) https://doi.org/10.1016/j.heliyon.2024.e32649
12. Gómez-Castro FI, Segovia-Hernández JG, Hernández S, Rico-Ramírez V, Gutiérrez-Antonio C, Briones-Ramírez A, Cano-Rodríguez I, Gamiño-Arroyo Z. Analysis of alternative non-catalytic processes for the production of biodiesel fuel. *Clean Tech and Env Pol* 17:2041-2054 (2015) https://doi.org/10.1007/s10098-015-0933-x
13. Turton R, Bailie RC, Whiting WB, Shaeiwitz JA, Bhattacharyya D. ANALYSIS, SYNTHESIS, AND DESIGN OF CHEMICAL PROCESSES. Prentice Hall (2012)



© 2025 by the authors. Licensed to PSEcommunity.org and PSE Press. This is an open access article under the creative commons CC-BY-SA licensing terms. Credit must be given to creator and adaptations must be shared under the same terms. See https://creativecommons.org/licenses/by-sa/4.0/




Systems & Control Transactions

**Research Article - Peer Reviewed Conference Proceeding**
ESCAPE 35 - European Symposium on Computer Aided Process Engineering
Ghent, Belgium. 6-9 July 2025
Jan F.M. Van Impe, Grégoire Léonard, Satyajeet S. Bhonsale,
Monika E. Polańska, Filip Logist (Eds.)

PSE PRESS

# A Computational Framework for Cyclic Steady-State Simulation of Dynamic Catalysis Systems: Application to Ammonia Synthesis

**Carolina Colombo Tedesco[a], John R. Kitchin[a], and Carl D. Laird[a]***

[a] Carnegie Mellon University, Chemical Engineering Department, Pittsburgh, Pennsylvania, United States of America
* Corresponding Author: claird@andrew.cmu.edu.

## ABSTRACT

Dynamic or Programmable Catalysis is an innovative strategy to improve heterogeneous catalysis processes by modulating the binding energies (BE) of adsorbates on a catalytic surface. The technique enables the periodic favoring of different reaction steps, overcoming limitations imposed by the Sabatier Principle and allowing for higher overall reaction rates, otherwise unattainable. Previously, we implemented a simultaneous simulation approach using the algebraic modeling language Pyomo and the solver IPOPT to obtain cyclic steady state results for a unimolecular reactive system with up to four-order of magnitude increases in computational performance compared to the previously reported sequential approach. The flexibility of the method allowed for the investigation of the influence of forcing signal parameters on system behavior and provided a framework for waveform design. In this study, we use a hybrid framework that combines the sequential and the simultaneous simulation approaches to find the cyclic steady state of a more complex system, of ammonia synthesis, comprising 19 reversible elementary reaction steps. The framework allowed us to investigate sine wave parameters with approximately 220 times less computational effort compared to the sequential approach alone. With the parameters studied, our findings indicate that frequencies exceeding 1000 Hz and compressive strains greater than 2% can negatively impact the system performance. Future work will focus on expanding the model to include lateral interactions between molecules, using other waveform as forcing signals, and integrating systematic mathematical optimization approaches. These advancements pave the way to establishing a general framework for identifying optimal waveforms across diverse dynamic catalysis systems.

**Keywords**: Simulation, Catalysis, Pyomo, Reaction Engineering, Dynamic Modelling, Dynamic Catalysis, Oscillation, Simultaneous

## INTRODUCTION

In a world facing pressing environmental challenges, disruptive and interdisciplinary solutions need to be explored. To navigate humanity toward sustainable scientific advancements, it is imperative to reinvent catalytic processes used to produce chemicals that are essential for the modern society. In this context, Dynamic or Programmable Catalysis [1] is a novel concept that has been capturing the attention of scientists in the catalysis field.

Research in heterogeneous catalysis has traditionally focused on selecting the ideal catalyst for a specific reaction, or designing the ideal active site within a catalyst, tied to advances of research in materials science and engineering. At its core, heterogeneous catalysis revolves around an important property of catalytic metals: the adsorption or binding energy (BE). Directly related to this property is the concept of the Sabatier Volcano [2, 3], which states that the ideal catalyst for a specific reaction is the one that binds the substrates with a “just-right” energy. Bindings that are too strong or too weak lead to prominent rate-controlling steps, reducing the efficiency of the catalytic process.

Dynamic Catalysis promotes oscillations of the binding energy throughout the duration of a catalytic

process. These oscillations would allow for faster chemical reactions, due to the periodic favoring of otherwise rate-controlling steps.

Figure 1 shows a representation we call the Extended Sabatier Volcano. The volcano-shaped curve in green represents the dependency of the overall reaction rate, commonly expressed as the Turnover Frequency (TOF), with the binding energy. The peak of this curve marks the balance or the compromise between otherwise rate-controlling steps, leading to the higher TOF value. The main goal of Dynamic Catalysis is to overcome the limitations associated to the volcano curve and obtain overall reaction rates that would be unachievable with conventional, or static, heterogeneous catalysis.

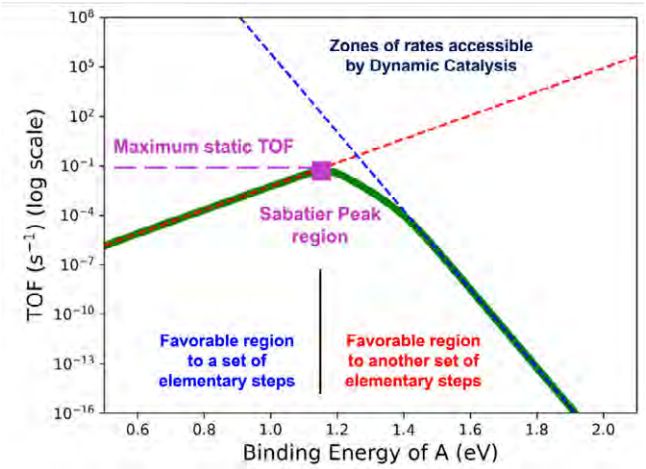



**Figure 1.** The Extended Sabatier Volcano. This is a conceptual figure; axes values are arbitrary and are used for illustration.

Since its introduction, Dynamic Catalysis has sparked significant research interest. On the computational front, researchers have explored several aspects of the concept: using general model reactions to investigate how binding energy (BE) oscillation parameters relate to activity response [1]; introducing conceptual ideas, such as supervolcanoes and molecular pumps derived from energy diagrams [4]; examining product selectivity and reaction pathways [5]; studying surface modulation through applied electric fields [6]; analyzing negative relationships between the BEs of reactants and products [7]; and applying BE modulation to loop reactions [8].

Other computational studies have focused on different simulation methodologies and optimization of forcing signals, including direct limit cycle solutions [9] and Gaussian kernel-based optimization of square wave parameters [10]. Additionally, rate enhancement and computational analysis of oscillation parameters have been applied to more realistic systems, electrocatalytic oxygen evolution reaction over metal oxides, incorporating both fixed overpotential and an additional arbitrary stimulus source [11]; and methane steam reforming under Ru(211) subjected to applied charge [12].

Experimental implementations of Dynamic Catalysis have also demonstrated rate enhancement due to dynamic oscillations. One study utilized pulsed light to control the rate of elementary steps in methanol decomposition [13], while another employed dynamic electrocatalytic modulation for formic acid decomposition [14]. Ongoing research efforts are dedicated to developing techniques and devices capable of inducing the necessary stimuli on catalytic surfaces to promote energetic fluctuations [15]. An interesting advancement is the “catalytic condenser”, a device that applies voltage to the surface, resulting in BE shifts of up to 0.2 eV [16–18]. We recognize that further experimental exploration is essential to validate the approach. Our goal is to have our computational frameworks leveraged to support experimentalists in developing methodologies for experimenting with real-life and industrially relevant reactive systems.

In this context, the present work builds upon our previous research on the simulation and of a unimolecular (“A-to-B”) dynamic catalytic system and the design of a forcing signal waveform [19]. The goal is to extend the framework to a more complex, intricate and industrially relevant system. Specifically, we draw on the work by Wittreich et al [20], who explored dynamic catalysis simulations for the synthesis of ammonia, one of the most important chemicals for modern society.

We use this broadly complex and detailed system as a case study to test and explore frameworks. Ultimately, our goal is to develop generalizable frameworks and tools for simulating dynamic catalysis processes and optimizing the waveform of the forcing signal. These frameworks would enable the identification of decision variables that yield the best outcomes in dynamic catalysis, paving the way for more effective catalytic systems.

The insights gained from results obtained with these frameworks are intended to guide experimentalists in developing techniques and devices for binding energy oscillations, as well as determining conditions for conducting experiments. We see this line of research as a foundational step toward the full application of dynamic catalysis. It lays the groundwork for extensive physical experimentation, progressing toward research on scaling up processes, and ultimately achieving widespread industrial implementation.

## METHODS

### Reactive System and Microkinetic Model

The reactive system for ammonia synthesis comprises 19 reversible reactions involving 16 chemical species. These reactions describe the adsorption and desorption of molecules to the catalytic surface, reactions

between adsorbates and their diffusion across the surface. The microkinetic model considers two distinct types of active sites on the surface, step and terrace sites. The compounds involved include the three gas-phase molecules, nitrogen, hydrogen and ammonia ($N_2$, $H_2$, $NH_3$, respectively), as well as six adsorbates on terrace sites and seven adsorbates on step sites.

In our previous work, we directly investigated the wave parameters of binding energy oscillations. In this study, the oscillation is of the stimulus source - compressive and tensile strain applied to the catalytic surface. The strain is represented by variations in the interatomic distances on the surface, which influence the d-band center of the atoms, leading to both physical and electronic rearrangements [21].

We developed our microkinetic model using Python and Pyomo based on the model developed by Wittreich et al [20] in MATLAB, using the data acquired and provided by the authors. This dataset includes results from energy calculations performed with Density Functional Theory (DFT) for a ruthenium-catalyzed system under three conditions: no strain, +4% compressive strain, and -4% tensile strain. The authors established linear scaling relationships with the data, enabling predictions beyond the specific parameters of the DFT calculations. A comprehensive and detailed description of the methodology used to generate the data is available in the Supporting Information of their publication [20].

The microkinetic model consists of thermodynamic and kinetic calculations to obtain a total of 38 rate constant ($k$) values, corresponding to the forward and reverse rates of each elementary step. Each applied strain value is linked to specific binding energy values, which in turn determine the rate constants. This mechanism explains the periodic favoring of different elementary steps: changes in the applied strain alter the rate constants, thereby influencing the rates at which individual steps occur.

The rate constants are parameters within the coupled system of Ordinary Differential Equations (ODEs) that describe the progression of the reaction over time, with the concentrations of all 16 compounds as the state variables. The complete list of reactions as well as the list of ODEs can be found in the Digital Supplementary Material.

## Sequential and simultaneous simulation workflow

By integrating Python and SciPy [22] with Pyomo.DAE [23] and the IPOPT solver [24], we developed a workflow to identify the cyclic steady-state behavior of the system under different forcing signal conditions and parameters. The unimolecular reactive system used in our previous study was small (four state variables) and simple enough that its solving process and run time were not significantly influenced by the initialization of the problem. However, in this ammonia synthesis system, we have observed that proper initialization is critical to the success of the simulation.

To address this, we developed a cascading framework consisting of the following steps: (1) performing a sequential simulation using Scipy's *integrate.solve_ivp* function until cyclic steady state; (2) using this solution as the initialization for a simultaneous simulation approach, employing the same forcing signal as in the sequential simulation; (3) progressively modifying the input conditions, while using the previous solution from the simultaneous simulation as the initialization for the subsequent iteration. Figure 2 presents a workflow block diagram illustrating the framework.

The sequential approach involves a simulation from initial conditions until cyclic steady state behavior for all the state variables, solving therefore an Initial Value Problem (IVP). Successful integration requires low tolerances and a small maximum step size, and the use of a solver that handles stiff problems, like Radau, LSODA or

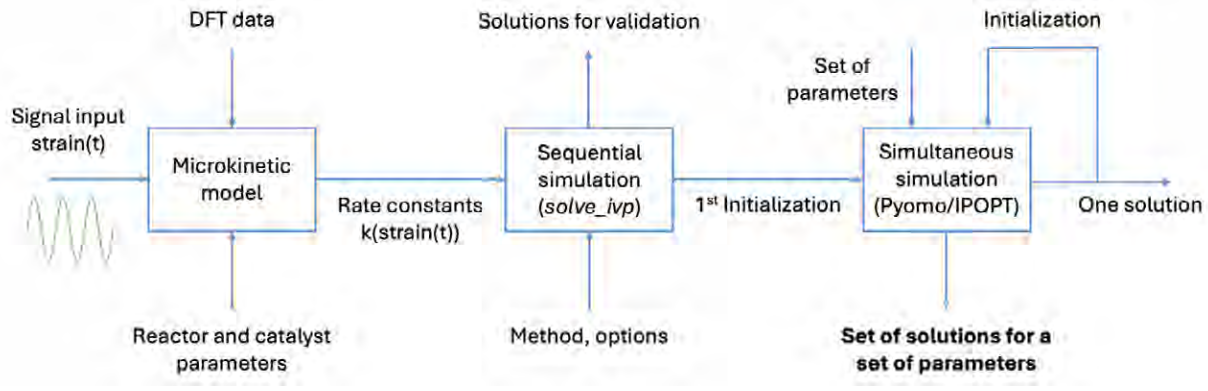



**Figure 2:** Workflow block diagram and systematic view of the simulation procedure.

BDF. Solving a sequence of simulations with this approach involves long computational run times.

The simultaneous simulation approach, in contrast, solves a Boundary Value Problem (BVP), using limit cycle or periodic boundary conditions. These conditions state that the initial and final points of a cycle need to have the same value, which defines the cycle steady state. The ODEs are automatically transcribed into algebraic equations using Pyomo.DAE and IPOPT then solves the square problem for all state variables at all discretized time points simultaneously, outputting a single cycle in the cyclic steady state for all variables [19].

As seen in later figures, the concentrations of the molecules in the reaction medium, which are the state variables, are generally very small, spanning several orders of magnitude - going from around $10^{-4}$ to $10^{-12}$ mol/cm$^3$. These units arise from the many thermodynamic and kinetic calculations that map data to rate constants. Even if the units were converted, the magnitude differences would persist. We explored various manual scaling strategies but found they did not significantly reduce the dependency on initialization or improve solver performance (e.g., reducing memory usage, enabling larger step sizes in the line search, or avoiding the need for restoration mode). However, we observed that scaling the time span (x-axis) had a noticeable impact on solver performance, though it still did not eliminate the dependency to a solid initialization.

In this paper, we focused on the parameters of a sine wave as the forcing signal for the oscillatory system: frequency, amplitude, and offset. The frequency dictates the number of cycles per second, while the amplitude and the offset values define the strain magnitude and its specific values, respectively. The use of strain values beyond those used to obtain the data (+4 and -4%) was done considering the linear scaling relationships can be extrapolated.

# RESULTS AND DISCUSSION

## Simulation framework outcomes

The simulation workflow, which combines initialization via sequential integration and a loop through parameters using the simultaneous approach, significantly reduced computational time compared to running a sequence of forward integrations for each parameter set. The initial single sequential simulation required 26 minutes to generate cyclic steady state results. Afterwards, the simulations for the almost 300 runs with the simultaneous approach were completed in under 10 minutes. Therefore, the total time required for our hybrid algorithm was of approximately 35 minutes. By comparison, if each of these runs had been performed sequentially, with each taking approximately 36 minutes, the total computational time would have been almost 220 times longer.

To validate the framework, several conditions were also simulated using the sequential approach, and the results were consistent with those obtained through the proposed workflow.

## Analysis of wave parameters and responses

The first parameter analyzed was the frequency of the forcing signal. The simulations depicted in Figure 3 were conducted with the default fixed amplitude of 0.04 and offset of 0, corresponding to a strain variation on the catalytic surface from -4% to +4%. From the figure, the average turnover frequency (avTOF) peaks around 500 Hz and declines for higher frequencies. While the absolute changes in values are small, the decrease in avTOF suggests that the rapid transitions between the high and low levels of the wave may not allow sufficient time for an elementary step to be favored in enough extent before the next switch occurs [4]. This result highlights the importance of selecting an appropriate forcing frequency, as operating at excessively high frequencies can also be energy intensive for the process.

Figure 4 was generated by fixing the frequency at 1000 Hz and varying the offset in values of 0.01, 0, and -0.01, individually, while simulating the system across different amplitudes ranging from 0.02 to 0.04. The blue points, representing an offset of 0.01, consistently show the lowest avTOF values for all amplitudes tested, indicating that applying high compressive strain is not favorable. For the default offset of 0, the results reveal an optimal amplitude near 0.024, while the default amplitude of 0.04 results in the lowest avTOF value within this configuration.

This result contradicts the intuitive conclusion drawn in our previous work: that higher amplitudes would lead to higher overall rates by reaching more extreme points of the Sabatier Volcano, where steps would theoretically be highly favorable. As observed for an offset of 0.01, the maximum avTOF occurs when the positive strain reaches the lowest value of 0.02, suggesting that applying excessive compressive strain may be detrimental to the efficacy of the system in achieving high reaction rates.

For an offset of -0.01, represented by the green curve, a maximum avTOF value similar to the one observed with an offset of 0 is achieved, reaching approximately 0.085 1/s for the amplitude of 0.03. The waveform corresponds to a strain oscillation ranging from -0.04 to 0.02. Once again, the analysis suggests that the maximum compressive strain should not exceed 2%. To improve the smoothness of this curve, we ran 100 iterations for this system, instead of 50, as for the others and lowered down the solver's tolerances.

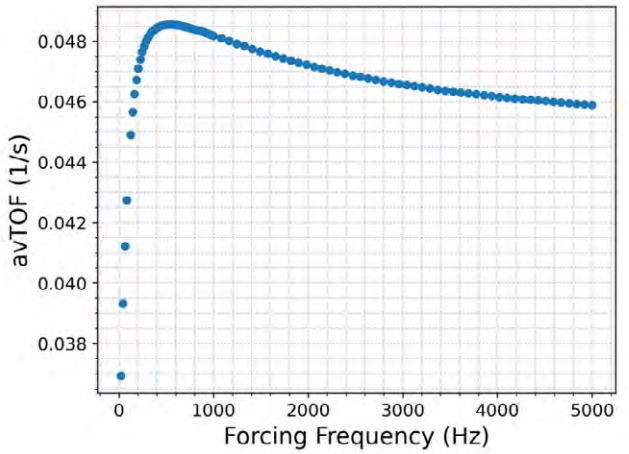



**Figure 3:** Comparison of avTOF results for different frequencies.

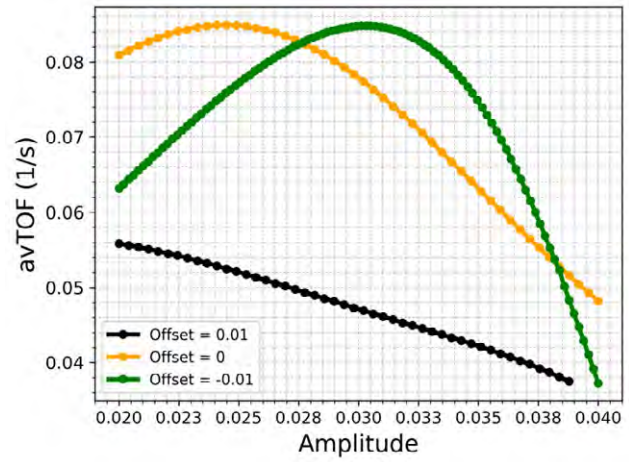



**Figure 4:** Comparison of avTOF results for different amplitudes and offsets - determining the range of strain oscillation.

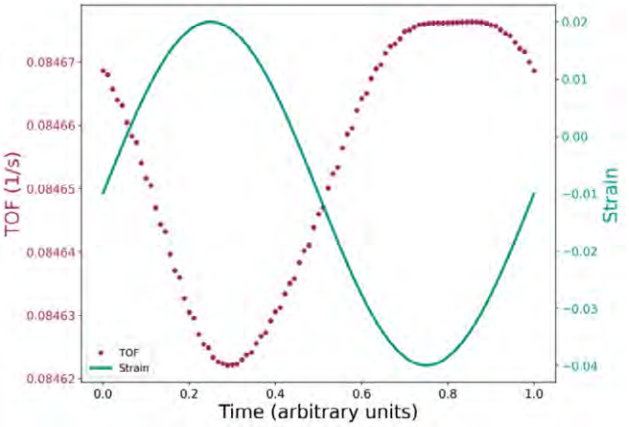



**Figure 5:** Sine wave forcing signal and turnover frequency response over the span of one cycle in cyclic steady state.

Figure 5 shows the shape of the sine wave and the TOF response for the case with higher avTOF for offset of -0.01, for one cycle in cyclic steady state. For this system, the TOF is calculated based on the concentration of reactants and products in the gas phase at each given moment. It is possible to see the mild delay in TOF response after the changes in direction by the sine wave. The first switch, around 0.3 in relative time, is rounder, and the next switch seems to stabilize in the higher value before going down. The causes for such difference are probably intrinsic to the responses of all the other species involved. Plots of the shapes for the concentration of all adsorbates can be found within the Digital Supplementary Material.

For comparison, the TOF of the static system, with no strain applied, is of 0.044 $s^{-1}$. As seen in figures 3 and 4, for some points the use of the oscillatory stimulus results in a lower overall rate than for the static case. This outcome underscores the importance of identifying the ideal wave parameters and carefully designing the forcing signal for dynamic catalysis systems.

As discussed in our previous work [19], analyzing the Extended Sabatier Volcano reveals important considerations for interpreting wave parameters optimality. According to different Sabatier Volcanoes in the literature [20, 26], ruthenium, the catalyst used in the working system, would be in the Sabatier Peak region, suggesting that oscillating symmetrically between either side of the volcano should be favorable. However, the shape of the volcano, which is highly influenced by the Bronsted-Evans-Polanyi relationship, must also be considered.

For instance, in the volcano shown in Figure 1 for the system discussed in our previous paper, the shape of the volcano led to an optimal range of binding energy values that is not symmetrically positioned on either side of the volcano. This observation highlights once again the need of computational investigations and the development of methods for simulating and optimizing input signals. The behavior of complex reactive systems is often non-intuitive and difficult to predict, emphasizing the importance of systematic exploration.

## CONCLUSIONS AND FUTURE WORK

In this work, we expanded on our previous research [19] and the contributions of Wittreich et al [20] to establish a structured and efficient way for simulating ammonia synthesis under Dynamic/Programmable Catalysis. Our approach combines an initialization strategy, based on forward integration results for a default system, with a looped simulation using a simultaneous approach to explore a range of sine wave parameters. The method has shown to improve the efficiency into simulating system with different parameters for forcing signal. Getting the same results solely with the sequential approach would take estimated 220 times more time.

This study represents a foundational step toward further modeling the system and refining the framework.

The next layer of complexity will involve accounting for lateral interactions between adsorbates on the catalytic surface. These interactions affect binding energies and thereby influence the entire dynamic system. With this consideration, the rate constants will depend not only on the applied strain but also on the concentrations of molecules - i.e., the state variables themselves - making the governing ODEs more intricate and their solutions more computationally demanding. To address this, we need to transition the current framework, which integrates Python and Pyomo, into a fully Pyomo-based framework. While this adaptation increases complexity, it will yield a more accurate and reliable microkinetic model by incorporating these essential interactions, which significantly influence the results of the simulations.

We will also extend this workflow to incorporate square wave forcing signals. Square waves, while increasing system stiffness due to their abrupt changes, have the potential for further enhancing the overall reaction rates [1, 4, 19]. From these results, we aim to optimize all wave parameters simultaneously to capture the interdependencies among them. This will require adapting the optimization frameworks from our previous work, particularly in terms of initialization strategies, to ensure convergence.

In parallel, we plan to apply this methodology to a different system, targeting formic acid decomposition (FAD). Like for the ammonia synthesis, the general reaction involves three molecules, but the reaction mechanism is complex and involves many molecules. In the case of FAD, it also involves competing reaction pathways, leading to undesirable products. Leveraging the insights gained from reproducing and adapting the microkinetic model of Wittreich et al [20], we will construct a model for the FAD system. An adjacent part of the work will be using machine learning potentials, trained within the Open Catalyst Project (OCP) [27], to generate input energy data. Our goal is to develop a comprehensive framework that integrates OCP data, microkinetic modeling, simulation, and waveform optimization, not only to enhance reaction rates but also to improve selectivity toward the desired products.

Ultimately, our intention is to develop a general framework for optimizing arbitrary waveforms as forcing signals for general dynamic catalysis reactions. We believe the results from this achievement will provide valuable guidance to experimentalists, enabling them to access the full potential of the promising technique of dynamic catalysis. Such advancements can pave the way for widespread implementation and realization of the benefits of the approach.

## DIGITAL SUPPLEMENTARY MATERIAL

Please access the GitHub repository for code used in this work: https://github.com/ccolomb2/dynamic_catalysis_NH3.git. The repository contains three notebooks that generate the figures presented and two csv files with data necessary to run the code.

## ACKNOWLEDGEMENTS

The authors thank Dr. Gerhard Wittreich for sharing MATLAB files used in previous work [28] and for relevant discussions around the concepts. We also thank Dr. Victor Alves and Laurens Lueg for insights into the work.

## REFERENCES

1. Ardagh MA, Abdelrahman OA, Dauenhauer PJ. Principles of dynamic heterogeneous catalysis: surface resonance and turnover frequency response. ACS Catal 9:6929–6937 (2019) https://doi.org/10.1021/acscatal.9b01606
2. Sabatier P. La catalyse en chimie organique. Librairie polytechnique, Paris (1920)
3. Bligaard T, Nørskov J, Dahl S, Matthiesen J, Christensen C, Sehested J. The Brønsted–Evans–Polanyi relation and the volcano curve in heterogeneous catalysis. J Catal 224:206–217 (2004) https://doi.org/10.1016/j.jcat.2004.02.034
4. Ardagh MA, Birol T, Zhang Q, Abdelrahman OA, Dauenhauer PJ. Catalytic resonance theory: superVolcanoes, catalytic molecular pumps, and oscillatory steady state. Catal Sci Technol 9:5058–5076 (2019) https://doi.org/10.1039/C9CY01258F
5. Gathmann SR, Ardagh MA, Dauenhauer PJ. Catalytic resonance theory: negative dynamic surfaces for programmable catalysts. Chem Catal 2:140–163 (2022) https://doi.org/10.1016/j.checat.2022.01.001
6. Ardagh MA, Shetty M, Kuznetsov A, Zhang Q, Christopher P, Vlachos DG, Abdelrahman OA, Dauenhauer PJ. Catalytic resonance theory: parallel reaction pathway control. Chem Sci 11:3501–3510 (2020) https://doi.org/10.1039/D0SC00752B
7. Shetty M, Ardagh MA, Pang Y, Abdelrahman OA, Dauenhauer PJ. Electric-field-assisted modulation of surface thermochemistry. ACS Catal 10:12867–12880 (2020) https://doi.org/10.1021/acscatal.0c03575
8. Murphy MA, Gathmann SR, Bartel CJ, Abdelrahman OA, Dauenhauer PJ. Catalytic resonance theory: circumfluence of programmable catalytic loops. J Catal 430:115343 (2024) https://doi.org/10.1016/j.jcat.2023.115343
9. Foley BL, Razdan NK. Clarifying mechanisms and kinetics of programmable catalysis. iScience 27:109543 (2024) https://doi.org/10.1016/j.isci.2024.109543

10. Psarellis YM, Kavousanakis ME, Dauenhauer PJ, Kevrekidis IG. Writing the programs of programmable catalysis. ACS Catal 13:7457–7471 (2023) https://doi.org/10.1021/acscatal.3c00864
11. Gathmann SR, Bartel CJ, Grabow LC, Abdelrahman OA, Frisbie CD, Dauenhauer PJ. Dynamic promotion of the oxygen evolution reaction via programmable metal oxides. ACS Energy Lett 9:2013–2023 (2024) https://doi.org/10.1021/acsenergylett.4c00312
12. Vempatti VVR, Wang S, Abdelrahman OA, Dauenhauer PJ, Grabow LC. Catalytic resonance of methane steam reforming by dynamically applied charges. ChemRxiv (2024) https://doi.org/10.26434/chemrxiv-2024-8sxpx
13. Qi J, Resasco J, Robatjazi H, Alvarez IB, Abdelrahman O, Dauenhauer P, Christopher P. Dynamic control of elementary step energetics via pulsed illumination enhances photocatalysis on metal nanoparticles. ACS Energy Lett 5:3518–3525 (2020) https://doi.org/10.1021/acsenergylett.0c01978
14. Gopeesingh J, Ardagh MA, Shetty M, Burke ST, Dauenhauer PJ, Abdelrahman OA. Resonance-promoted formic acid oxidation via dynamic electrocatalytic modulation. ACS Catal 10:9932–9942 (2020) https://doi.org/10.1021/acscatal.0c02201
15. Shetty M, Walton A, Gathmann SR, Ardagh MA, Gopeesingh J, Resasco J, Birol T, Zhang Q, Tsapatsis M, Vlachos DG, et al. The catalytic mechanics of dynamic surfaces: stimulating methods for promoting catalytic resonance. ACS Catal 10:12666–12679 (2020) https://doi.org/10.1021/acscatal.0c03589
16. Onn TM, Gathmann SR, Guo S, Solanki SPS, Walton A, Page BJ, Rojas G, Neurock M, Grabow LC, Mkhoyan KA, et al. Platinum graphene catalytic condenser for millisecond programmable metal surfaces. J Am Chem Soc 144:22113–22127 (2022) https://doi.org/10.1021/jacs.2c09544
17. Onn TM, Gathmann SR, Wang Y, Patel R, Guo S, Chen H, Soeherman JK, Christopher P, Rojas G, Mkhoyan KA, et al. Alumina graphene catalytic condenser for programmable solid acids. JACS Au 2:1123–1133 (2022) https://doi.org/10.1021/jacsau.2c00159
18. Oh K-R, Onn TM, Walton A, Odlyzko ML, Frisbie CD, Dauenhauer PJ. Fabrication of large-area metal-on-carbon catalytic condensers for programmable catalysis. ACS Appl Mater Interfaces 16:684–694 (2023) https://doi.org/10.1021/acsami.3c14623
19. Colombo Tedesco C, Kitchin JR, Laird CD. Cyclic steady-state simulation and waveform design for dynamic/programmable catalysis. J Phys Chem C 128:8993–9002 (2024) https://doi.org/10.1021/acs.jpcc.4c01543
20. Wittreich GR, Liu S, Dauenhauer PJ, Vlachos DG. Catalytic resonance of ammonia synthesis by simulated dynamic ruthenium crystal strain. Sci Adv 8:eabl6576 (2022) https://doi.org/10.1126/sciadv.abl6576
21. Mavrikakis M, Hammer B, Nørskov JK. Effect of strain on the reactivity of metal surfaces. Phys Rev Lett 81:2819–2822 (1998)
22. Virtanen P, Gommers R, Oliphant TE, Haberland M, Reddy T, Cournapeau D, Burovski E, Peterson P, Weckesser W, Bright J. SciPy 1.0: fundamental algorithms for scientific computing in Python. Nat Methods 17:261–272 (2020) https://doi.org/10.1038/s41592-019-0686-2
23. Nicholson B, Siirola JD, Watson JP, Zavala VM, Biegler LT. pyomo.dae: a modeling and automatic discretization framework for optimization with differential and algebraic equations. Math Program Comput 10:187–223 (2018) https://doi.org/10.1007/s12532-017-0127-0
24. Wächter A, Biegler LT. On the implementation of an interior-point filter line-search algorithm for large-scale nonlinear programming. Math Program 106:25–57 (2006) https://doi.org/10.1007/s10107-004-0559-y
25. Ardagh MA, Birol T, Zhang Q, Abdelrahman OA, Dauenhauer PJ. Catalytic resonance theory: superVolcanoes, catalytic molecular pumps, and oscillatory steady state. Catal Sci Technol 9:5058–5076 (2019) https://doi.org/10.1039/C9CY01543D
26. Medford AJ, Vojvodic A, Hummelshøj JS, Voss J, Abild-Pedersen F, Studt F, Bligaard T, Nilsson A, Nørskov JK. From the Sabatier principle to a predictive theory of transition-metal heterogeneous catalysis. J Catal 328:36–42 (2015) https://doi.org/10.1016/j.jcat.2014.12.033
27. Tran R, Lan J, Shuaibi M, Wood BM, Goyal S, Das A, Heras-Domingo J, Kolluru A, Rizvi A, Shoghi N, Sriram A, Therrien F, Abed J, Voznyy O, Sargent EH, Ulissi Z, Zitnick CL. The Open Catalyst 2022 (OC22) Dataset and Challenges for Oxide Electrocatalysts. ACS Catal 13:7457–7471 (2023) https://doi.org/10.1021/acscatal.2c05456
28. Wittreich, G., Vlachos, D. https://github.com/VlachosGroup/NH3-Dynamic-MKM/tree/main

© 2025 by the authors. Licensed to PSEcommunity.org and PSE Press. This is an open access article under the creative commons CC-BY-SA licensing terms. Credit must be given to creator and adaptations must be shared under the same terms. See https://creativecommons.org/licenses/by-sa/4.0/



Systems & Control Transactions

**Research Article - Peer Reviewed Conference Proceeding**
ESCAPE 35 - European Symposium on Computer Aided Process Engineering
Ghent, Belgium. 6-9 July 2025
Jan F.M. Van Impe, Grégoire Léonard, Satyajeet S. Bhonsale,
Monika E. Polańska, Filip Logist (Eds.)

PSE PRESS

# Comparative Analysis of Conventional and Novel Low-Temperature and Hybrid Technologies for Carbon Dioxide Removal from Natural Gas

**Federica Restelli[a]* and Giorgia De Guido[a]**

[a] GASP - Group on Advanced Separation Processes & GAS Processing, Dipartimento di Chimica, Materiali e Ingegneria Chimica "G. Natta", Politecnico di Milano, Piazza Leonardo da Vinci 32, 20133 Milano, Italy
* Corresponding Author: federica.restelli@polimi.it.

## ABSTRACT

Natural gas production is expected to increase, leading to the exploitation of low-quality reserves that contain high levels of acid gases, such as carbon dioxide. The aim of this work is to compare various innovative and conventional technologies for the removal of $CO_2$ from natural gas, considered as a binary mixture of methane and carbon dioxide, with $CO_2$ contents ranging from 10 to 70 mol%. The processes are simulated using Aspen Plus® V9.0 and compared in terms of energy consumption, which is evaluated through the net equivalent methane method. The results show that novel low-temperature and hybrid technologies, which combine distillation and physical absorption, are the most energy-efficient for $CO_2$ removal from natural gas with high acid gas contents, while conventional physical absorption processes are optimal for natural gas with low to moderate acid gas contents.

**Keywords**: natural gas, carbon dioxide removal, physical absorption, hybrid technologies, low-temperature distillation.

## INTRODUCTION

Global electricity consumption is projected to rise in the coming decades. To meet this growing demand sustainably, renewable energy sources and, among fossil fuels, natural gas are expected to see the most significant growth. As natural gas consumption increases, it will also become necessary to extract it from low-quality reserves, which often contain high levels of acid gases, such as carbon dioxide ($CO_2$) and hydrogen sulfide [1].

The aim of this work is to compare various innovative and conventional technologies for the removal of carbon dioxide from natural gas, considered as a binary mixture of methane and carbon dioxide. It first examines the performance of the physical absorption process using propylene carbonate (PC) as a solvent, along with a hybrid process in which it is applied downstream of low-temperature distillation. These results are, then, compared with previously studied technologies, including physical absorption with dimethyl ethers of polyethylene glycol (DEPG), low-temperature distillation, and hybrid processes that combine distillation and absorption [2]. The low-temperature distillation process considered here is the one described by Langé et al. [1]. It consists of two distillation columns operating at different pressures: the bulk $CO_2$ removal is performed in a high-pressure distillation column, typically operated at 50 bar such that $CO_2$ freeze-out is avoided, and the natural gas production at commercial grade is performed in a low-pressure column, typically operated at 40 bar (anyway lower than the critical pressure of methane).

The Fluor Solvent™ process, which uses PC as the solvent, was commercialized by Fluor in the early 1960s. Propylene carbonate is particularly advantageous, as noted by Bucklin and Schendel [3], when hydrogen sulfide is not present in raw natural gas. The bulk distillation + physical absorption finishing with PC is a new process that has been proposed for the first time in a patent by Xu [4]: no other references are in fact present in the literature about combined purification technologies for the natural gas purification in which propylene carbonate is involved.

The PC absorption process and the bulk low-temperature distillation + PC absorption process are

simulated using Aspen Plus® V9.0 [5]. The energy analysis is conducted using the net equivalent methane method. The processes are compared in terms of methane equivalent consumption, methane losses, and net produced purified methane, offering guidance on the optimal process based on the composition of the raw natural gas.

# METHODS

## Inlet and outlet stream conditions

The feed gas conditions are assigned in terms of temperature (35 °C), pressure (50 bar) and total flowrate (5,000 kmol/h). The raw natural gas is assumed to be a binary mixture of methane and carbon dioxide, having a $CO_2$ content ranging from 10 mol% to 70 mol%. When the $CO_2$ molar fraction is below 10 %, amine absorption is known to be a proven and cost-effective technology [1]. A $CO_2$ molar content of 70 % represents a sort of upper limit, indicating a reserve with an extremely low methane content [6].

The conditions for the purified gas are selected based on the requirements for pipeline network application. Therefore, the limit on the $CO_2$ content is set equal to 2 mol% [7]. The temperature of the purified natural gas is set to 25 °C, and the pressure is set to 50 bar, matching the operating pressure of the purification unit in the analyzed processes.

The $CO_2$ product stream is assumed to be injected underground for Enhanced Oil/Gas Recovery or sequestration and the specifications are assigned in terms of temperature (14.06 °C), pressure (50 bar) and maximum limit on hydrocarbons content of 2 mol%.

## Net Equivalent Methane method

The energy analysis is based on the "net equivalent methane" (NEM) method [8], which consists in the evaluation of the equivalent quantity of methane that must be burned to power a specific equipment piece. By using the same basis for the various types of energy, the NEM method allows a fair comparison between different processes. The energy requirements considered include: supplying electric power, heating above ambient temperature, and cooling below ambient temperature. Heating below ambient temperature and cooling above ambient temperature do not consume methane, as service water can be used to provide or remove heat, respectively.

### Supplying electric power

The gas compression and liquid pumping need electric power to be supplied. This electric power is assumed to be obtained by means of a methane-fired combined-cycle power plant. The amount of methane equivalent can be determined according to Eq. (1):

$$NEM = \frac{W}{\eta_{cc} \cdot LHV_{CH4}} \quad (1)$$

where $W$ indicates the mechanical power, $\eta_{cc}$ is the combined-cycle efficiency, assumed equal to 0.55, and $LHV_{CH4}$ is the lower heating value of methane, which is 50 MJ/kg.

### Heating above ambient temperature (> 25 °C)

The supply of heat to the process at temperatures higher than the ambient one is achieved through the use of low-pressure steam. The necessary amount of steam is provided by a boiler fed with methane: the equivalent methane flowrate consumed can be computed according to Eq. (2):

$$NEM = \frac{Q_{hot}}{\eta_b \cdot LHV_{CH4}} \quad (2)$$

where $Q_{hot}$ is the required thermal power, and $\eta_b$ is the boiler efficiency, assumed equal to 0.80.

### Cooling below ambient temperature (< 25 °C)

The removal of heat from the process at temperatures lower than the ambient one requires the use of a proper refrigeration cycle. This refrigeration cycle requires mechanical work to be operated, which is considered to be provided by a combined-cycle plant powered by methane. To calculate the amount of methane equivalent to the required mechanical duty, first it is necessary to compute the coefficient of performance (*COP*) of the refrigeration cycle from Eq. (3):

$$COP = \left(\frac{T_0}{T_f} - 1\right)^{-1} \cdot \eta_{II} \quad (3)$$

In Eq. (3), the term in brackets is the coefficient of performance of an ideal Carnot cycle, that is calculated knowing the temperature of the hot reservoir (the ambient temperature $T_0$ = 25 °C) and that of the cold reservoir (the final temperature reached at the outlet of the cooler, $T_f$). $\eta_{II}$ is the second law efficiency, which is defined as the ratio between the efficiency of the system and the theoretical maximum possible one. $\eta_{II}$ is assumed equal to 0.60.

By definition of the *COP*, the mechanical duty $W$ can be computed given the cooling duty, denoted as $Q_{cold}$, to be removed from the system (Eq. (4)).

$$W = \frac{Q_{cold}}{COP} \quad (4)$$

Therefore, the amount of equivalent methane can be determined according to Eq. (5):

$$NEM = \frac{Q_{cold}}{\eta_{cc} \cdot COP \cdot LHV_{CH4}} \quad (5)$$

# PROCESS SIMULATION

The processes are simulated using Aspen Plus® V9.0 [5]. Physical absorption is modelled with the "Acid gas:

physical solvents" property package, which exploits the PC-SAFT Equation of State (EoS). AspenTech suggests the use of this EoS for simulating physical absorption cleaning processes in the syngas and natural gas industry. To simulate hybrid processes, the flowsheet is divided into two sections. In the first one, related to bulk removal by low-temperature distillation, the Soave-Redlich-Kwong (SRK) Equation of State is selected, while the second section, which corresponds to the physical absorption and subsequent solvent regeneration, is modelled with the PC-SAFT EoS.

To be consistent with the results obtained by De Guido et al. [2], the same simplified assumptions for unit operations are applied: absorbers, distillation columns and heat exchangers provide no pressure drops; isentropic efficiency of compressors and pumps is set equal to the software's default value; the Efficiency Mode is used to simulate the absorption unit, assuming unitary efficiency for each stage. This simplified approach may result in an underestimation of energy consumptions. However, the primary goal of this work is to compare the processes relative to one another, rather than to provide an accurate estimate of methane consumption. Therefore, as long as the assumed values are applied consistently across all considered cases, the comparison remains valid.

After simulating the base configuration of the processes, energy-saving schemes, incorporating heat integration based on pinch analysis, are considered for each process.

## Propylene carbonate absorption process

The Process Flow Diagram (PFD) of the propylene carbonate absorption process is depicted in Figure 1.

The feed gas (FEED) is mixed with recycle streams from the regeneration section (vapors from FLASH-HP and FLASH-MP) and, then, cooled to a proper inlet temperature for the absorption column. To maintain a smooth temperature profile in the absorber, the inlet gas temperature is set equal to the temperature of the rich solvent stream exiting the bottom of the absorber minus 0.3 °C. The absorber has 10 stages: gas is fed at the bottom while propylene carbonate flows in counter-current from the top. It operates at 50 bar, with no assumed pressure drops inside the absorption tower.

According to Burr and Lyddon [9], the operating range for the propylene carbonate solvent is between -18 °C and 65 °C. For this simulation, the PC temperature is set to -15 °C, as reported by Freireich and Klooster [10] for a process in which the pressure of the absorber is 56.2 bar.

The solvent flowrate is determined to achieve a residual $CO_2$ molar content of 2 % in the purified gas.

Regeneration occurs through a series of three flashes at progressively decreasing pressures, with the first two being adiabatic. The pressure levels are chosen based on an example of a real plant reported by Mokhatab et al. [7]. Specifically, the pressure of the first flash is kept equal to 31.7 bar, and the pressure of the second flash is initially set to 13.1 bar, as in the reference example. However, the intermediate flash pressure may need some adjustments to meet the $CO_2$-stream purity requirements for reinjection. Results indicate that this adjustment is necessary when the feed molar $CO_2$ content is below 20 %. Above this threshold, the $CH_4$ molar fraction in the $CO_2$-OUT stream naturally becomes very low due to the reduced amount of methane processed. The last flash operates at atmospheric pressure. After conducting a sensitivity analysis, a pressure of 18 bar, as used by De Guido et al. [2] for absorption with DEPG

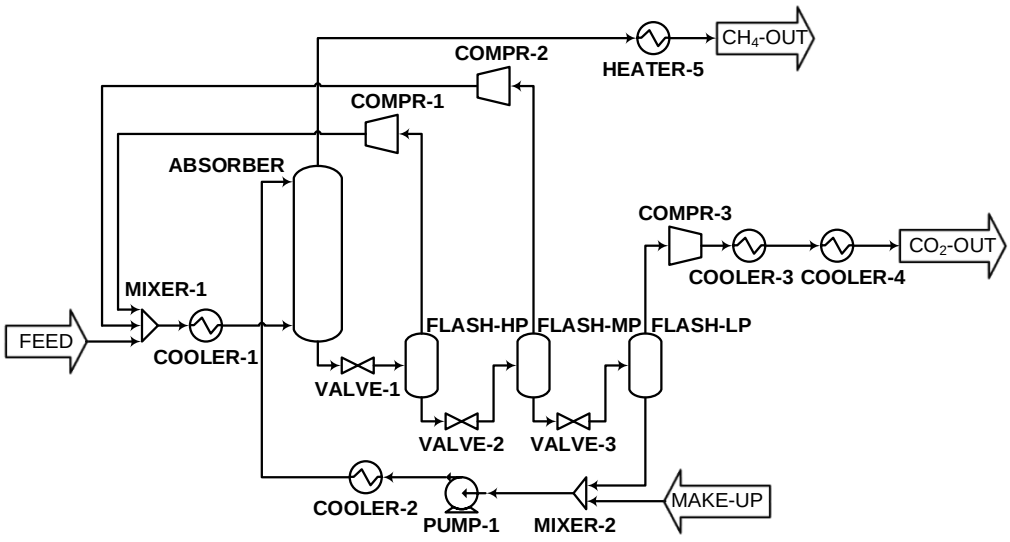



**Figure 1.** PFD of the propylene carbonate absorption process.

solvent, is adopted for the high-pressure vessel when the $CO_2$ molar content is below 20%, as this reduces methane consumption.

The vapor stream from the last flash can be used for reinjection purposes. Atmospheric flash vapors are recompressed to 50 bar in COMPR-3 and, then, cooled down to the bubble point temperature in a battery of two heat exchangers: COOLER-3 and COOLER-4. In the former, the $CO_2$ stream is cooled to ambient temperature (25 °C) using service water, while in the latter the final required temperature of 14.06 °C is reached employing a refrigeration cycle: decoupling these contributions is important, as only the duty related to the last cooler is considered in the energy consumption calculation.

Vapors from the first two flashes are recycled back to the absorber after being recompressed to 50 bar: this recycle is crucial because phase separation at high pressure generates a vapor stream with high methane content, and recycling helps minimize methane losses.

Since the maximum allowed residual $CO_2$ molar content in the purified gas is 2%, the regenerated solvent purity must be at least 98% to provide the necessary driving force for absorption. To ensure an adequate margin, the lean solvent molar purity is set at 98.5%. Solvent purity can be controlled by modifying the FLASH-LP duty.

Solvent losses occur with both $CH_4$-OUT and $CO_2$-OUT streams. Although these losses are small, they are significant enough to require a make-up stream to maintain the circulating solvent flowrate under steady-state conditions. After the introduction of the make-up stream, the regenerated solvent is pumped to 50 bar and cooled to -15 °C in COOLER-2, preparing it for re-entry into the absorber.

## Bulk low-temperature distillation + propylene carbonate absorption process

The PFD of the bulk low-temperature distillation combined with the PC absorption process is illustrated in Figure 2. The distillation unit treats the raw gas to reduce the $CO_2$ content to 20 mol%. The final gas purity is, then, achieved through PC absorption. This process is only simulated for $CO_2$ molar contents greater than 20 % since below this threshold, the process becomes a simple PC absorption operation, eliminating the need for hybrid technology.

The raw gas is expanded to 40 bar and cooled to its dew point in COOLER-6 before being fed into the distillation column (DISTILL-COL). In this column, the specifications are the number of theoretical equilibrium stages (20), the residual $CO_2$ molar fraction in the vapor stream exiting from the top (20 %) and the molar purity of the $CO_2$ product stream obtained at the bottom (99.99 %). The optimal feed tray location, for which the condenser duty is minimized, is immediately above the third tray from the top, independently from the feed composition. Such a high optimal feed location is justified considering that for methane a very rough separation is required (up to 20 mol% residual $CO_2$ in the top product), while at the bottom almost pure carbon dioxide must be obtained.

The separated liquid $CO_2$, with a purity of 99.99 mol%, is pumped to 50 bar and slightly heated to 14.06 °C in HEATER-7 using service water.

The partially purified natural gas is, then, compressed from 40 bar to 50 bar in COMPR-4 before

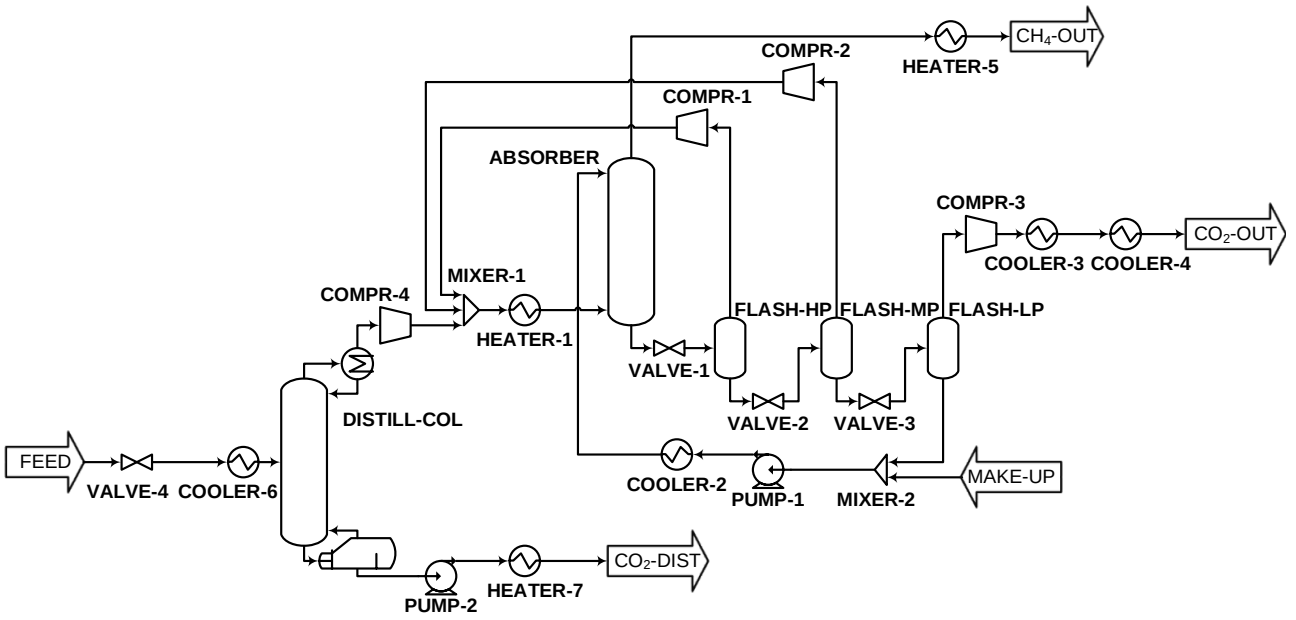



**Figure 2.** PFD of the bulk low-temperature distillation + propylene carbonate absorption process.

entering the absorption section. Absorption is carried out at 50 bar, with a PC feed temperature of -15 °C, consistent with the simple PC absorption process previously discussed. The compressed gas, containing 20 mol% residual $CO_2$, is mixed with vapor recycle streams from the first two flashes in the solvent regeneration section. The resulting stream is heated in HEATER-1 to reach the same temperature, as in the simple PC absorption process. In the absorber, the $CO_2$ content is reduced to 2 mol%.

The $CO_2$-rich solvent exiting the bottom of the absorber is sent to the regeneration section, which operates under identical conditions to those used for the simple PC absorption process when handling a feed stream with 20 mol% initial $CO_2$ content. Vapors from the last flash are recovered for reinjection purposes.

The regenerated lean solvent, with a molar purity of 98.5 %, is pumped back to 50 bar and cooled to -15 °C, preparing it for reuse in the absorption unit.

## RESULTS AND DISCUSSION

The results reported in the following are obtained by applying the NEM method to convert the energy consumptions, retrieved from process simulations, into methane consumptions. To enable a meaningful comparison among the investigated processes, optimized process schemes, incorporating heat integration based on pinch analysis, are considered.

The results in terms of NEM consumption and methane losses in the $CO_2$-rich streams obtained for the PC absorption process and its corresponding hybrid version, together with the technologies studied by De Guido et al. [2], are reported in Figure 3 and Figure 4, respectively. The methane losses in the $CO_2$-rich streams are expressed as a percentage of the methane fed.

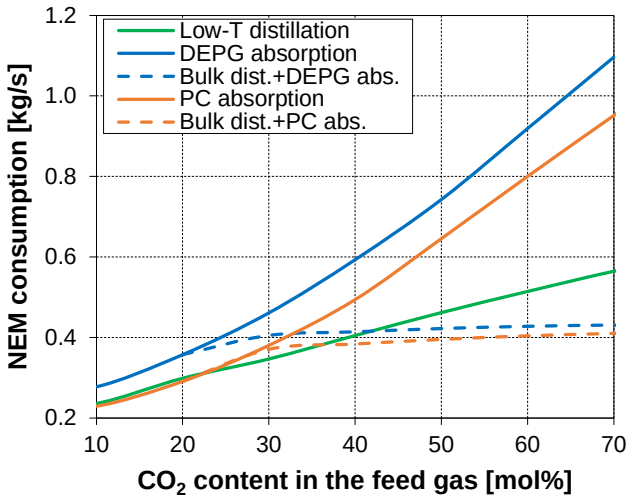



**Figure 3.** Comparison between $CO_2$ removal technologies in terms of NEM consumption.

Looking at Figure 3, it can be observed that physical absorption with PC solvent consumes less energy than with DEPG solvent across the entire range of $CO_2$ contents studied. It also performs slightly better than low-temperature distillation for $CO_2$ concentrations between 10 and 25 mol%. For $CO_2$ contents in the feed gas between 25 and 35 mol%, the process with the lowest energy requirements results to be the one based on low-temperature distillation. Above 35 mol% $CO_2$ in the feed gas, the hybrid process, where the finishing step is carried out using PC physical absorption, becomes more efficient.

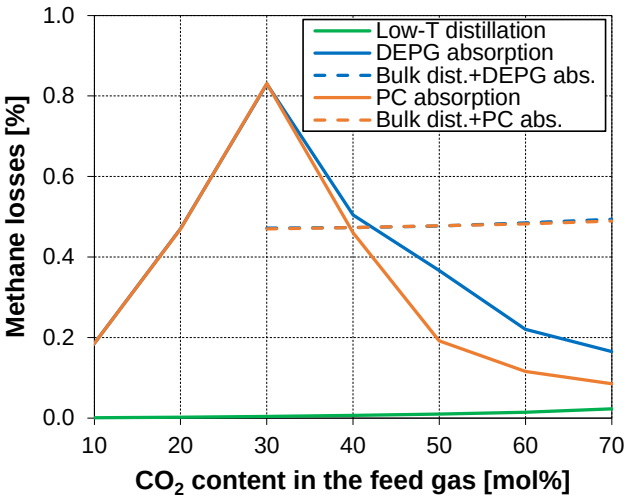



**Figure 4.** Comparison between $CO_2$ removal technologies in terms of methane losses.

From Figure 4 it is possible to notice that up to 30 mol% $CO_2$ content, the methane losses for the two physical absorption technologies considered are the same, due to the imposed specification of 2 mol% methane content in the $CO_2$ product stream. Above a $CO_2$ content in the feed gas of 30 mol%, the percentage of methane lost in this stream falls below the limit of 2 mol % and losses are related to the solubility of methane in physical solvents at atmospheric pressure, which is the pressure set in the last regeneration flash, and at the temperature reached in this non adiabatic flash, which is about 11 °C when PC is used as solvent, and 61 °C when DEPG is used. The propylene carbonate absorption process shows the lowest methane losses because methane's relative solubility in PC is less than in DEPG (0.038 *vs* 0.066 at 25 °C [9]) and due to the lower operating temperature of the FLASH-LP. It is also worth noting that, in the low-temperature distillation process, methane losses are essentially negligible due to the imposed specification on $CO_2$ product purity. For hybrid technologies, methane losses show a flat trend. The lost methane is almost independent of the $CO_2$ content in the feed gas, as the bulk separation is performed in the distillation

section, where a high-purity $CO_2$ stream is removed. Methane losses are similar for both PC and DEPG hybrid technologies.

Net purified methane is defined as the percentage of methane in the raw gas that exits the process in the sales gas, minus the amount of methane burned to operate the process. This parameter takes into account both the equivalent methane consumption, which is a measure of energy requirements, and methane losses, which depend on the nature of the separation process (distillation and/or absorption). Referring to the graph in Figure 5, the best process selection is indicatively:

- PC absorption or low-temperature distillation in the range 10 - 15 mol% $CO_2$;
- low-temperature distillation in the range 15 - 50 mol% $CO_2$;
- hybrid processes, with a slight preference for bulk low-temperature distillation + PC absorption, above 50 mol% $CO_2$.

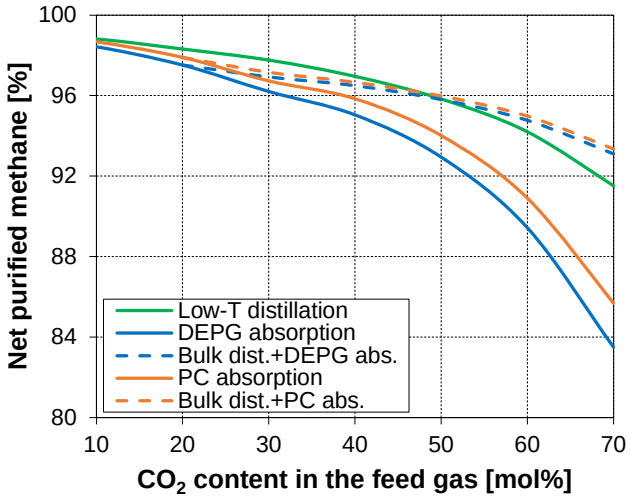



**Figure 5.** Comparison between $CO_2$ removal technologies in terms of net purified methane.

## CONCLUSIONS

The analysis carried out in this work is relevant to the upgrading of low-quality natural gas through $CO_2$ removal and underground storage, offering a climate change mitigation solution by utilizing methane, the cleanest fossil fuel, and securely storing $CO_2$. The focus is on identifying the most energy-efficient $CO_2$ separation technology for natural gas, which mainly contains methane and carbon dioxide, depending on the $CO_2$ content.

For moderate $CO_2$ contents, below 15 mol%, both physical absorption with propylene carbonate and low-temperature distillation are good options, with propylene carbonate outperforming other physical solvents (e.g., DEPG) due to lower $CH_4$ losses with the solvent. For higher $CO_2$ contents, from 15 to 50 mol%, low-temperature distillation is the most convenient process, in fact, by avoiding the use of a solvent, the energy requirements of the plant are less sensitive to the $CO_2$ content in the feed. For very high $CO_2$ concentrations (> 50 mol%), hybrid technologies are optimal, with the propylene carbonate-based process being the most efficient one.

## REFERENCES


1. Langé S, Pellegrini LA, Vergani P, Lo Savio M. Energy and economic analysis of a new low-temperature distillation process for the upgrading of high-$CO_2$ content natural gas streams. *Ind Eng Chem Res* 54(40):9770-9782 (2015) https://doi.org/10.1021/acs.iecr.5b02211
2. De Guido G, Gilardi M, Pellegrini LA. Novel technologies for low-quality natural gas purification. In: Computer Aided Chemical Engineering (50:241-246), Elsevier (2021)
3. Bucklin RW, Schendel RL. Comparison of Fluor Solvent and Selexol processes. *Energy Progress* 4(3):137-142 (1984)
4. Xu J. $CO_2$ capture from $CO_2$-rich natural gas. US Patent 2015/0376527 A1. (2015)
5. AspenTech. Aspen Plus® V9.0. (2016)
6. De Guido G, Fogli MR, Pellegrini LA. Effect of heavy hydrocarbons on $CO_2$ removal from natural gas by low-temperature distillation. *Ind Eng Chem Res* 57(21):7245-7256 (2018) https://doi.org/10.1021/acs.iecr.8b00614
7. Mokhatab S, Poe W, Mak J. Handbook of Natural Gas Transmission and Processing. Principles and Practices. 4th edition. Gulf Professional Publishing (2018)
8. Pellegrini LA, Langé S, Baccanelli M, De Guido G. Techno-economic analysis of LNG production using cryogenic vs conventional techniques for natural gas purification. Offshore Mediterranean Conference and Exhibition, Ravenna, Italy. (2015)
9. Burr B, Lyddon L. A comparison of physical solvents for acid gas removal. Proceedings of the Gas Processors' Association Convention, Grapevine (TX), United States. (2008)
10. Freireich E, Klooster HJ. Treatment of wet natural gas mixtures to recover liquid hydrocarbons. US Patent 3,770,622. (1973)



© 2025 by the authors. Licensed to PSEcommunity.org and PSE Press. This is an open access article under the creative commons CC-BY-SA licensing terms. Credit must be given to creator and adaptations must be shared under the same terms. See https://creativecommons.org/licenses/by-sa/4.0/

Systems & Control Transactions

**Research Article - Peer Reviewed Conference Proceeding**
ESCAPE 35 - European Symposium on Computer Aided Process Engineering
Ghent, Belgium. 6-9 July 2025
Jan F.M. Van Impe, Grégoire Léonard, Satyajeet S. Bhonsale,
Monika E. Polańska, Filip Logist (Eds.)

PSE PRESS

# Development of a virtual CFD model for regulating temperature in a liquid tank

**Jinxin Wang[a], Feng Xu[a], Yuka Sakai[a], Hisashi Takahashi[b], Ruizi Zhang[c], Hiroaki Kanayama[c], Daisuke Satou[c], Yasuki Kansha[a,c]***

[a] Organization for Programs on Environmental Sciences, Graduate School of Arts and Sciences, The University of Tokyo, 3-8-1 Komaba, Meguro-ku, Tokyo 153-8902, Japan
[b] TechnoPro, Inc. TechnoPro R&D Company, Roppongi Hills Mori Tower 35F, 6-10-1 Roppongi, Minato-ku, Tokyo 106-6135, Japan
[c] Technology and Innovation Center, Daikin Industries, LTD., 1-1 Nishi-Hitotsuya, Settsu, Osaka 566-8585, Japan
* Corresponding Author: kansha@global.c.u-tokyo.ac.jp

## ABSTRACT

Temperature regulating in liquid tanks is critical in the chemical industry and conventionally relies on sensor feedback. However, due to the complex thermo-hydrodynamics, unsensed local temperatures can deviate from desired thresholds, underscoring the need for improved tank temperature modeling. The absence of internal thermal or flow data, however, poses significant challenges for the development and validation of effective control strategies. In this study, a virtual model for regulating liquid tank temperature was developed using computational fluid dynamics (CFD). Adaptions were made mainly by involving (1) a simple on-off mechanism of feeding based on a virtual sensor to achieve temperature within the acceptable range and (2) the imposition of unfavorable temperatures on the walls representing ambient influences. Leveraging this virtual system, several new cases were simulated. The simulation results highlighted pronounced temperature non-uniformity, with discrepancies exceeding 2°C between sensor readings and interior points, even leading to inefficiencies of regulatory mechanism. Additionally, the buoyancy was found to significantly influence the internal thermal distributions, and proper outlet position can help alleviate the temperature non-uniformity. Thus, the proposed CFD model serves as a reliable platform for generating comprehensive datasets to support temperature regulation studies in liquid tanks.

**Keywords**: Liquid tank, temperature regulating, CFD, thermal non-uniformity, stratification, buoyancy.

## INTRODUCTION

Liquid temperature non-uniformity is a widespread issue in the chemical industry and thermal management. For instance, maintaining minimal temperature differences within materials should be crucial, as emphasized by the pharmaceutical and food industries, which prioritize thermal uniformity during heating processes [1,2]. Moreover, uneven temperature distribution can cause discomfort for living beings in facilities such as public baths and aquariums.

However, it is impractical to install many physical sensors in the above facilities to measure local temperatures, and current temperature regulation systems often assume uniformity within the unit [3,4]. It is well-established that density variations caused by temperature differences can result in thermal stratification, where buoyancy drives less dense fluid upward. Consequently, sensed temperatures often deviate from actual internal values, leading to less effective control. Fortunately, recent studies have begun addressing this issue through soft-sensor development. Experimental research involving local temperature measurements and flow field visualization has been conducted [4,5]. However, experiments are labor-cost and limited by the availability of facilities.

Computational fluid dynamics (CFD) offers a powerful alternative by providing detailed internal temperature distributions to inform regulation systems. CFD excels at handling complex thermo-hydrodynamics by solving the

Navier-Stokes equations coupled with the energy equation. Control-integrated CFD models have been employed for over a decade to optimize air-conditioning control strategies, despite concerns about computational cost [6]. More recently, CFD has been combined with deep learning frameworks for indoor environmental control [7]. With advancements in computational hardware, CFD is poised to play an increasingly significant role in developing temperature regulation systems.

However, CFD is still underutilized for liquid temperature regulation. A CFD-based model can facilitate system design refinement with quantified insights into thermal field distributions but requires a highly adaptive interface for diverse industrial scenarios and considerable computational resources. Recently, water stratification was investigated thoroughly for energy storage, taking up to 18 days of computation per case [8]. Over the past decade, the open-source CFD software OpenFOAM has gained traction due to its fully adaptable framework, making it a valuable tool for customizing industrial processes. With the rapid expansion of data centers, advancing CFD-based temperature regulation becomes increasingly essential for improving product quality and energy efficiency in industries.

This study aims to bridge the above research gap by introducing the CFD method into the investigation of liquid temperature regulation in a tank. An original CFD model was developed using the OpenFOAM framework and validated against experimental data. The model was adapted as a virtual temperature regulation system, involving ambient temperature influences and integrated with a simple on-off control mechanism. Several regulation scenarios via heating and cooling were simulated and analyzed. The results demonstrated that thermal non-uniformity was well captured, revealing severe temperature discrepancies between interior locations and the virtual sensor. These discrepancies can even disable the regulatory mechanism under severe stratification conditions. The effects of outlet and sensor positions were also investigated in cooling scenarios. Our model enables an in-depth analysis of thermal stratification and regulatory performance, providing a foundation for optimizing system design and control strategies.

## MODELING

### Validation of the original CFD model

In a previous study [5], we encountered stratification issues in a water tank during the development of a soft sensor. Hot water (50 °C) was fed from the top side into a tank filled with cold water (10 °C) at a flow rate of 770 ml/min (or equivalent to 0.1889 m/s at the inlet), which exhibits complexity of natural and forced convections due to strong buoyant influences. Due to the similar main mechanisms existing in our following case study, this original case is suitable to examine our CFD settings. The solver buoyantPimpleFoam in OpenFOAM9 was adopted due to its capability to resolve transient thermo-hydrodynamics. The thermo-physical properties of water were assumed to be temperature-dependent, as described in reference [8], and the same formulations for density, heat conductivity, specific heat capacity, and viscosity were employed. The velocity of 0.1889 m/s was set at the inlet and the gauge pressure=0 Pa was set at the outlet.

Figure 1 (a) illustrates the original CFD model, which conforms to the experimental dimensions. Within the tank, the locations B1M (0.046 m, -0.046 m, 0.0635 m) and C3T (0 m, 0.092 m, 0.127 m) were monitored, consistent with reference [5] where temperature measurements were taken using thermocouples. For subsequent work, we also recorded temperature data from interior locations and a near-outlet sensor, making B1M and C3T suitable validation points. Hybrid mesh system is adopted, with 1.67 million grids in total. Hexa grids are dominant while unstructured grids are near the top to adapt inlet and outlet, as observed at the section X = -0.08 m. As shown in Figures 1(b) and (c), the CFD model results are consistent with experimental data.

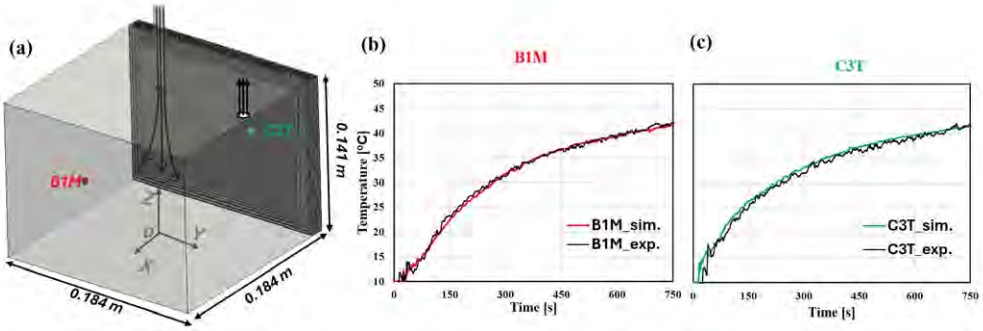



**Figure 1.** (a) The original CFD model used for validation, showing grid distribution at the section X = -0.08 m; temperature variations at (b) B1M and (c) C3T, comparing simulation results with experimental data.

**Table 1.** Case conditions

| Case no. | 1 | 2 | 3 | 4 | 5 |
|---|---|---|---|---|---|
| Target (initial) temperature [°C] | 25 | 20 | 45 | 20 | 20 |
| Fed temperature [°C] | 60 | 10 | 10 | 10 | 10 |
| Ambient temperature [°C] | 15 | 25 | 55 | 25 | 25 |
| Drain nozzle (/sensor) location | top | top | top | Middle | bottom |
| Simulated time [s] | 1200 | 1200 | 1200 | 1200 | 1800 |

*The flow rate is always 770 ml/min (or 0.1889 m/s at the inlet)*

## Adaption and control system integration

The model was adapted by installing the inlet tube on the side of the tank, as shown in Figure 2(a). The inlet velocity and tank size were inherited from the validated CFD model (Figure 1(a)). Hexa-dominant hybrid grids are still adopted with unstructured ones constructed near the side with the inlet and outlet. Another interior location, B2M (0.046 m, 0.046 m, 0.0635 m), was added for temperature monitoring. Notably, three optional outlet positions (diameter = 9 mm) were considered, with center coordinates as follows: top (0 m, 0.078 m, 0.127 m), middle (0 m, 0.078 m, 0.014 m), and bottom (-0.078 m, 0.078 m, 0.0635 m). Corresponding near-outlet sensors (sensorT, sensorM, and sensorB) were positioned 0.014 m from the outlet centerline. When the outlet was at the top or bottom, only half of the domain was simulated using symmetric boundary conditions to save computational cost.

Table 1 summarizes all cases in this study, and Figure 2(b) illustrates the boundary conditions for Case 1 as an example. Unlike the adiabatic wall conditions in the original model (Figure 1(a)), all tank sides were simplified to imposed ambient temperatures, except for the bottom (representing the ground), to simulate environmental influences. The initial tank temperature was set to the target value in all cases. Cases 1 and 2 can be taken as typical regulation scenarios via heating and cooling in winter and summer, respectively. However, regulation issues were identified in Case 2, leading to the design of Cases 3-5 for further analysis. Except for Case 3, the target temperatures were set at 25 °C for heating and 20 °C for cooling.

The on-off control mechanism was implemented using programmable boundary conditions in OpenFOAM via codeStream. The inlet velocity was set to 0.1889 m/s ("On") or 0 m/s ("Off") based on feedback from the virtual sensor. In the heating scenario, the control mechanism was defined as follows:

$$\begin{cases} \boldsymbol{Off},\ T_{sen} \in (T_{targ}+1, +\infty) \\ \boldsymbol{Remain}\ on\ or\ off,\ T_{sen} \in [T_{targ}-1, T_{targ}+1] \\ \boldsymbol{On},\ T_{sen} \in (-\infty, T_{targ}-1) \end{cases} \quad (1)$$

where the $T_{sen}$ represents the sensed temperature, and $T_{targ}$ denotes the target temperature for regulation. In the cooling scenario, the mechanism was reversed, with "On" and "Off" conditions switched in Eq. (1). To account for control system delays in real-world applications, the acceptable temperature range was set to $[T_{targ}-1, T_{targ}+1]$. To illustrate the regulatory mechanism, an additional sensor (sensor0) was embedded to record velocity magnitude at the inlet tube connection, as depicted in Figure 2(b). The temperature at sensorT and the velocity at sensor0 are shown in Figure 2(c), with data after 600 s omitted for brevity due to repetitive patterns. To reach target temperature at sensorT, the water (60 °C) supply was turned off when the temperature at sensorT reached 26 °C and resumed when it dropped below 24 °C, corresponding to "Off" and "On" states, respectively.

# RESULTS AND DISCUSSIONS

## Temperature non-uniformity issue

Significant temperature non-uniformity was observed in Case 1. As shown in Figure 3(a) and (b), the

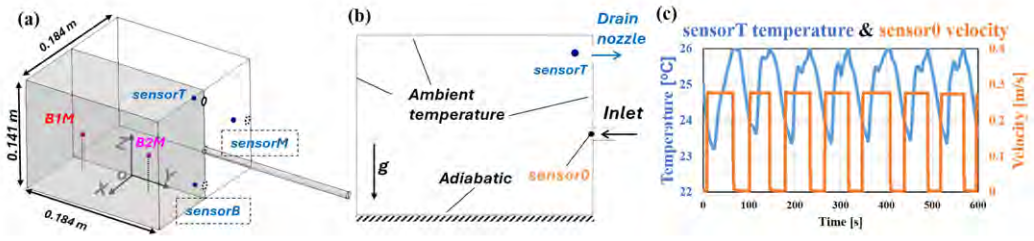



**Figure 2.** (a) Adapted CFD model with monitored points and optional outlet/sensor positions for case study; (b) I illustrations of boundary conditions; (c) the temperature at sensorT and velocity at sensor0 for Case 1.

temperatures at B1M and B2M began to oscillate steadily around certain levels after approximately 600 s. The calculated mean values between 600 s and 1200 s were 22.6 °C, 22.8 °C, and 24.9 °C at B1M, B2M, and sensorT, respectively. These results indicate temperature deviations at interior locations (B1M and B2M) of more than 2 °C from the target (25 °C), even though the control system maintained the sensor's temperature close to the target value. More seriously, as shown in Figure 3(c), at 835 s during the "on" state, temperatures below B1M and B2M were even lower, while some regions near the tank top exceeded 26 °C, further demonstrating stratification.

A more serious issue occurred in the cooling scenario (Case 2), where the regulatory mechanism operated abnormally due to the thermal stratification. As observed in Figure 4(a), the temperature at the sensor could not drop below the acceptable upper limit (21 ˚C) and failed to reach the off-triggering threshold (19 °C) throughout the simulation. Consequently, continuous cooling water feeding caused overcooling inside the tank. As shown in Figure 4(b), the mean temperature at B2M dropped to 17.9 ˚C after 900 s. Additionally, Figure 4(c) reveals that cooler regions persisted below B1M and B2M, indicating severe thermal non-uniformity.

## Analyses on the regulation failure

Stratification in the cooling scenario was characterized by weak mixing effects, which disabled the regulatory mechanism. As shown in Figure 4(c), velocity vectors beneath B1M and B2M (highlighted in red frames) displayed swirling patterns, indicating the difficulty in transporting cold water into regions of retained hot water above. Some upward convection near the wall (black frame) was observed but was insufficient due to heating from ambient temperatures 25 °C imposed on the wall. Consequently, the thermal mixing was weak in Case 2, preventing the "off" state from being triggered.

Buoyancy was found to dominate stratification formation during thermal regulation. Figure 5(a) and (b) present temperature distributions at the central section (X = 0 m) during the "on" state for Cases 1 and 2, respectively. Buoyancy deflected the fed flow along its direction. In Case 3, which shared identical absolute temperature differences with Case 1 ( $|T_{targ} - T_{fed}| = 35$ ˚C, $|T_{amb} - T_{fed}| = 45$ ˚C, $T_{fed}$ and $T_{amb}$ denote the fed and ambient temperatures, respectively), the stratification became more severe compared to Case 2. This ruled out temperature difference as the main factor for regulation failure and emphasized the stronger buoyant effects in Case 3, where greater density differences were present. Unfortunately, Case 3 also failed to trigger the "off" state. Buoyancy in Case 3 redirected the fed flow in the opposite direction of the outlet, contributing to stratification.

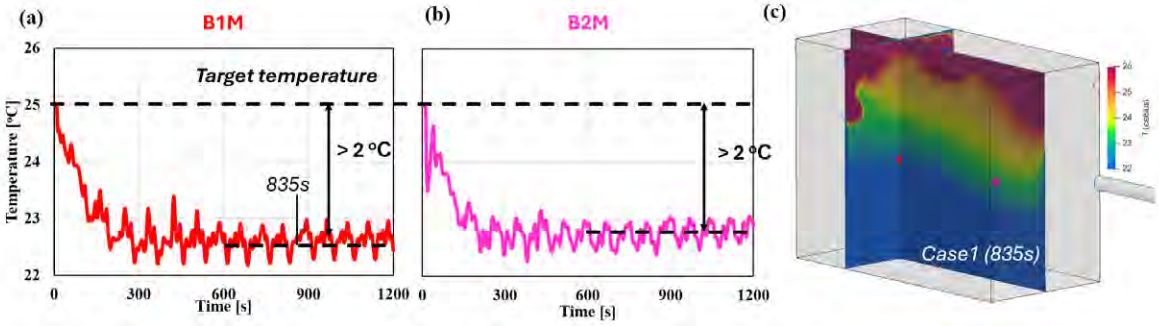



**Figure 3.** Case 1 results: temperature variations at (a) B1M and (b) B2M; (c) temperature contour at 835 s.

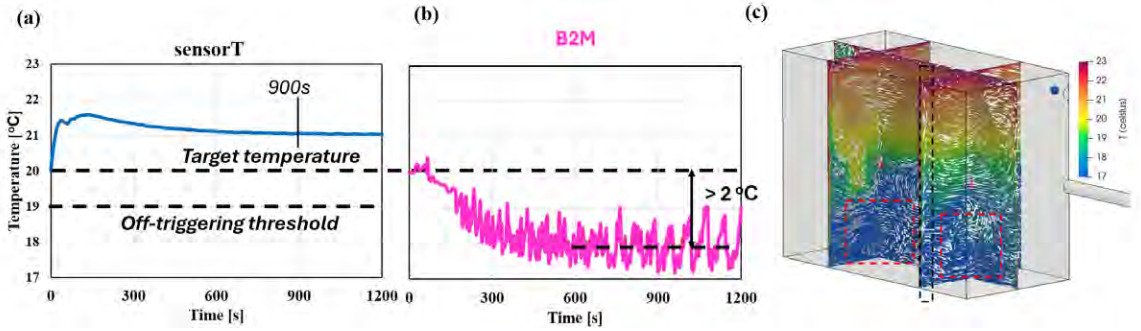



**Figure 4.** Case 2 results: temperature variations at (a) sensorT and (b) B2M; (C) temperature contour with velocity vectors at 900 s.

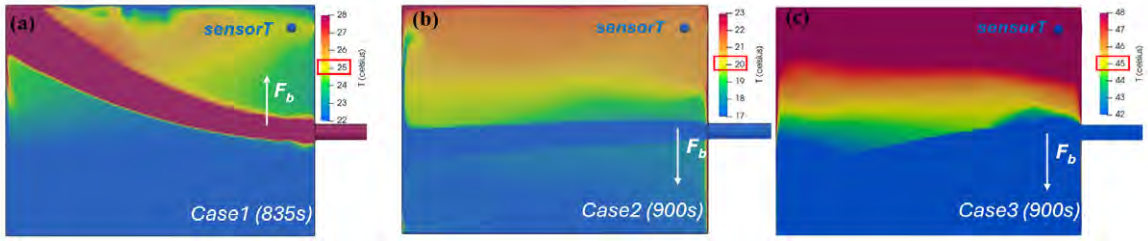



**Figure 5.** Temperature contours at the tank center (section at X = 0 m) for (a) Case 1 (835s) (b) Case 2 at 900 s and (c) Case 3 at 900 s. Framed values on legend indicate target temperatures for corresponding cases.

In contrast, buoyancy in Case 1 aided regulation by pushing fed water toward the outlet, enabling the sensor to detect variations effectively.

## Influences of the outlet position

To activate the "off" state, outlet positions and their corresponding sensors were varied. Cases 4 and 5, sharing identical initial, target, fed, and ambient temperatures with Case 2, positioned outlets in the middle and bottom of the tank, respectively. Notably, Case 4 required simulating the entire domain, unlike the half-domain simulations in other cases, due to symmetry breaking. As shown in Figure 6(a), the middle outlet in Case 4 failed to trigger the "off" state, with sensorM temperatures remaining above 19 ˚C even after 1200 s elapsed. In contrast, Case 5 successfully activated the on-off mechanism (see Figure 6 (d)), but its oscillation cycles (average more than 200 s) were longer than those in Case 2 (average less than 100 s). The simulation for Case 5 was extended to 1800 s to capture steady oscillation patterns while conserving computational resources.

Varying the outlet position cannot eliminate stratification, but it can alleviate non-uniformity severity. As demonstrated in Figure 6 (c), the stratification still exists in Case 4, although temperatures at B2M is nearly stable at the target level (see Figure 6 (b)). In Case 5, despite the mean temperature value at sensorB (Figure 6 (d)) is 20.1 °C between 900 s and 1800 s, the B2M's mean value is 22.1 °C, 2 °C higher than the target level (Figure 6 (e)). Among Cases 2, 4, and 5 (Figure 4(c), Figure 6(c), and Figure 6(f)), the top outlet in Case 2 resulted in the least severe stratification, while Case 5 showed the worst distribution, with over half the regions exceeding 22 °C (Figure 6(f)), despite normal regulatory operation. This can be attributed to the higher-temperature water being retained at higher locations, making it easier to discharge through a top outlet. Conversely, fed cold water tended

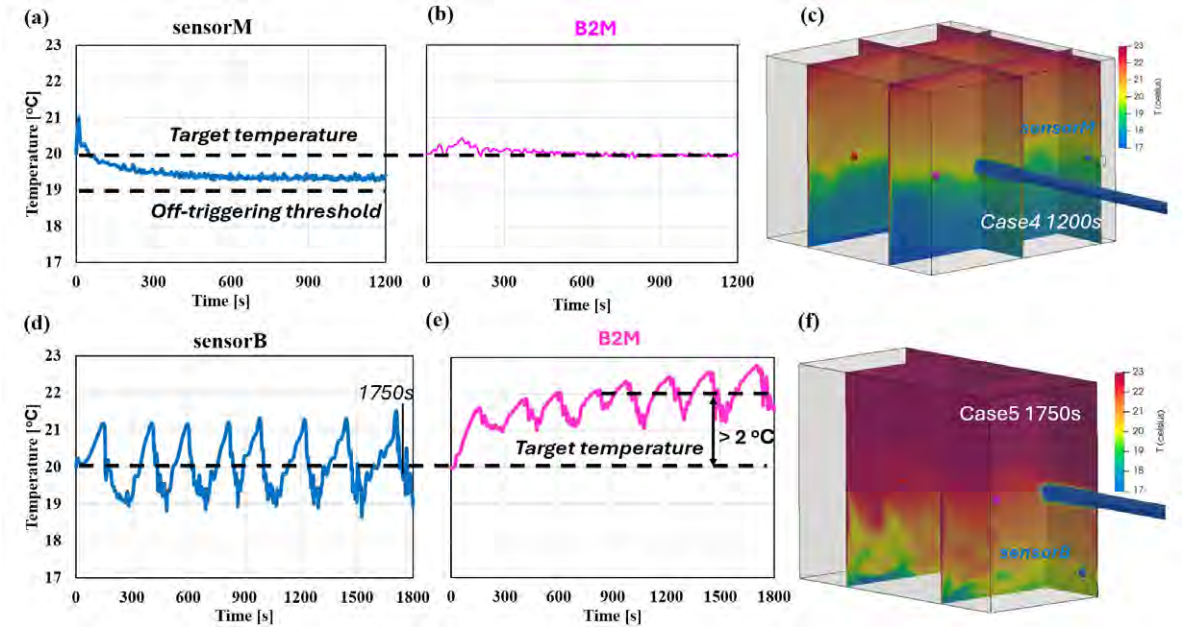



**Figure 6.** Temperature variations in Case 4 at (a) sensorM and (b) B2M; (c) temperature contour of Case 4 at 1200 s; Temperature variations of Case 5 at (d) sensorM and (e) B2M; (f) temperature contour of Case 5 at 1750 s.

to accumulate at lower locations, facilitating its exhaustion through a bottom outlet. Therefore, it is advisable to position the outlet on the side opposite to the buoyancy direction, while the resolving of regulation failure should resort to other strategies except for outlet positions.

### Modifications in future work

In summary, the temperature regulations in this study faced challenges due to stratification and abnormal operations. The single input fluid combined with an on-off control mechanism failed to achieve uniform temperature distribution at the target level. Future strategies can consider adding internal circulation procedure in the regulation mechanism (e.g., the thermo-on/off control in air-conditioning) or using our proposed dual-input systems [9]. Previous research on soft sensors may also provide solutions, particularly given the difficulties in increasing the number of internal sensors [4,5].

## CONCLUSIONS

A CFD-based temperature regulation model for a liquid tank was developed by adapting a validated CFD model. An on-off control mechanism was integrated with $\pm$ 1 °C relative to the target temperature as the acceptable limits. Both heating and cooling regulating scenarios were simulated to investigate the temperature non-uniformity inside the tank. The following conclusions were drawn: (1)buoyancy can induce thermal stratification, leading to interior temperature discrepancies exceeding the acceptable range relative to the target value; (2) thermal stratification can even disable the regulatory mechanism in cooling scenarios, as the conventional near-outlet sensor fails to drop below the "off" triggering threshold (acceptable lower limit) ; (3) Positioning the outlet on the side opposite to the buoyancy direction can mitigate (but not eliminate) thermal non-uniformity by facilitating the removal of retained water.

In summary, our virtual CFD model can provide detailed thermal field information during liquid temperature regulation, offering a controlled environment to explore the system improvement without experimental constraints. The insights gained from the thermal field analysis can guide the development of more effective temperature regulation designs and strategies.

## ACKNOWLEDGEMENTS

This research is financially supported by New Energy and Industrial Technology Development Organization (NEDO), JPNP20004, Japan.

The authors thank the Supercomputer Center, the Institute for Solid State Physics, the University of Tokyo for the use of the facilities.

## REFERENCES

1. Caravella A, Francardi M, Romano S, Prenesti G, Oliverio M. Optimization of temperature distribution in the novel power-to-heat matrix-in-batch OnePot© reactor. *Front. Energy Res.* 10: 964511 (2022)
2. Xu L, Su J, Chen H, Ye J, Qin K, Zhang W, Yang Y, Zhu H. Continuous-flow microwave heating system with high efficiency and uniformity for liquid food. *Innov. Food Sci. Emerg. Technol.* 91: 103556 2024
3. Taler D, Sobota T, Jaremkiewicz M, Taler J. Control of the temperature in the hot liquid tank by using a digital PID controller considering the random errors of the thermometer indications. *Energy* 239: 122771 (2022)
4. Xu F, Sakurai K, Sato Y, Sakai Y, Sabu S, Kanayama H, Satou D, Kansha Y. Soft-Sensor Modeling of Temperature Variation in a Room under Cooling Conditions. *Energies* 16: 2870 (2023)
5. Xu F, Wang J, Sakurai K, Sakai Y, Sabu S, Kanayama H, Zhang R, Satou D, Kansha Y. Soft-sensor model for indoor temperature prediction under heating conditions. *Therm. Sci. Eng. Prog.* 51: 102650 (2024)
6. Sun Z, Wang S. A CFD-based test method for control of indoor environment and space ventilation. *Build. Environ.* 45: 1441–7 2010
7. Sun Y, Zhang Y, Guo D, Zhang X, Lai Y, Luo D. Intelligent Distributed Temperature and Humidity Control Mechanism for Uniformity and Precision in the Indoor Environment. *IEEE Internet Things J.* 9: 19101–15 (2022)
8. Lou W, Baudin N, Roux S, Fan Y, Luo L. Impact of buoyant jet entrainment on the thermocline behavior in a single-medium thermal energy storage tank. *J. Energy Storage* 71: 108017 (2023)
9. Wang Jinxin, Xu Feng, Sakurai Kei, Sakai Yuka, Sabu Shunsuke, Zhang Ruizi, Kanayama Hiroaki, Satou Daisuke, Kansha Yasuki. Investigation of Fluid Dynamics in the Case of Two Higher-temperature Fluid Inputs to Effectively Heat the Vessels *Chem. Eng. Trans.* 114: 271–6 (2024)

© 2025 by the authors. Licensed to PSEcommunity.org and PSE Press. This is an open access article under the creative commons CC-BY-SA licensing terms. Credit must be given to creator and adaptations must be shared under the same terms. See https://creativecommons.org/licenses/by-sa/4.0/



Systems & Control Transactions

**Research Article - Peer Reviewed Conference Proceeding**
ESCAPE 35 - European Symposium on Computer Aided Process Engineering
Ghent, Belgium. 6-9 July 2025
Jan F.M. Van Impe, Grégoire Léonard, Satyajeet S. Bhonsale,
Monika E. Polańska, Filip Logist (Eds.)

PSE PRESS

# Accelerated Process Modelling for Light-Mediated Controlled Radical Polymerization

**Rui Liu[a], Xi Chen[a,b]*, Antonios Armaou[c,d]***

[a] State Key Laboratory of Industrial Control Technology, College of Control Science and Engineering, Zhejiang University 310027, Hangzhou China
[b] National Center for International Research on Quality-targeted Process Optimization and Control, Zhejiang University 310027, Hangzhou China
[c] Chemical Engineering Department, University of Patras, Patras 26504, Greece
[d] Chemical Engineering & Mechanical Engineering Departments, Pennsylvania State University, College Park, PA 16802 USA
* Corresponding Author: xi_chen@zju.edu.cn, armaou@upatras.gr & armaou@psu.edu

## ABSTRACT

Mathematical modelling and simulation are pivotal components in process systems engineering. Focusing on polymerization process systems, identifying microscopic properties of polymers is highly sought after for advancing kinetic comprehension and facilitating industrial applications. Among various computational methods predicting polymeric properties microscopically, kinetic Monte Carlo (kMC) offers a stochastic framework to characterize individual polymer chains and track dynamic system evolution, providing mechanistic insights into complex polymerization kinetics. In this study, an accurately accelerated Superbasin-aided kMC model is developed for enhancing the kinetic understanding of the advanced photo-iniferter RAFT (PI-RAFT) polymerization. The contribution is twofold, presenting advancements in both the mathematical modelling techniques for complex dynamic process systems and the mechanistic understanding of photo-induced polymerizations. Leveraging the increased computational performance and the gained kinetic understanding, batch blending is examined as a viable approach to produce polymers with desired microscopic properties. This work bridges stochastic molecular simulations with scalable polymerization processes, laying groundwork for multiscale modelling in polymer engineering, and also the foundation for process design, control, and optimization.

**Keywords**: Modelling and Simulations, Multiscale Modelling, Polymers, Reaction Engineering, Acceleration.

## INTRODUCTION

Microscopic state variables for describing polymeric structure, including chain length distribution (CLD) and molecular weight distribution (MWD), directly influence the end-use functionalities of polymer products. Mathematical modelling methods for polymerization processes can be categorized into two types: the deterministic method solving mass balance equations and the stochastic simulation using the Monte Carlo (MC) method. For complex polymerizations, like the controlled radical polymerization (CRP) with reverse reaction pairs, it is challenging to derive a rigorous model and solve it with deterministic methods. Direct solution of the underlying ordinary differential equation systems is computationally infeasible due to memory resource limitations and model stiffness. These hurdles can be circumvented via coarse graining and order reduction for computational efficiency, albeit with a trade-off in applicability. In contrast, the kinetic Monte Carlo (kMC) method, based on Gillespie's [1] stochastic simulation algorithm, is conceptually straightforward to implement and insensitive to kinetics complexity, focusing on individual molecules.

In kMC simulations, the system states undergo continuous updates within an event-driven framework. Herein, an "event" refers to one occurrence of any reaction, which leads to the evolution of the system's state. The determination of which events happen is based on a set of probabilities derived from first-principle kinetic-based theory. These probabilities are calculated by evaluating the propensities for all reactions in a chemical system. Through determining events and meticulously

recording all ensuing changes resulting from these events, kMC simulations accurately portray the modelled process system. KMC simulations are straightforward to implement with simple rules; still, their application is limited due to computational inefficiency, particularly for polymerization process with intricate mechanisms.

Events with higher propensities are more frequently observed compared to those with lower propensities. When propensities exhibit significant differences in magnitude, a considerable number of trials must be executed and tracked for stochastic simulation to overcome inherent fluctuation errors and explore rare events with small propensities. For modelling polymerization systems with significant disparities in propensities, the adoption of the Superbasin strategy in stochastic simulation enables computational acceleration through appropriately scaling the propensity values of frequent events [2-3].

Photo-iniferter reversible addition-fragmentation chain-transfer (PI-RAFT) polymerization is a representative technique within the class of CRPs, valued for its ability to produce well-defined polymers in an environmentally friendly way [4]. A defining feature of PI-RAFT is the significant discrepancy in the rates of individual reactions, which involves both frequent and rare reactions. The frequent reactions ensure a controlled polymerization, yielding polymers of uniform chain lengths. Understanding polymerization kinetics and chain growth mechanisms is of great demand in both academia and industrial applications, with mathematical modelling being a viable tool for this purpose. However, challenges remain in accurately modelling the complex PI-RAFT mechanism, particularly with dual chain transfer agents (CTAs) involved, and under varying light irradiation conditions.

In this work, an accelerated Superbasin-aided kMC model is developed, which simulates PI-RAFT polymerization processes with microscopic resolution under different light irradiation conditions. The model successfully captures the full kinetic complexity of the PI-RAFT system, achieving a maximal computational speedup of approximately 50,000 times. Based on the gained accuracy and efficiency from the simulations, batch blending is subsequently investigated as an open topic to provide potential strategies for producing polymers with desired microscopic properties.

This study intents to open new possibilities for further advancements in online control, optimization, and multiscale integrate of dynamic polymerization processes. Specifically, the contributions of this work establish a methodological foundation for developing multiscale models that integrate microscopic insights with macroscopic reactor design. Such integration can be achieved through the developed kMC model by further leveraging techniques such as the computational fluid dynamics (CFD) and data-driven methods.

# METHODOLOGY

## Conventional kinetic Monte Carlo simulation

In the conventional kMC simulation, the reaction propensity for each reaction within the chemical system involving a total of *M* reactions is defined as:

$$R_\mu = k_\mu c_\mu, \forall \mu = 1,2,\dots,M \tag{1}$$

where $k_\mu$ is the kinetic rate constant of the $\mu^{\text{th}}$ reaction, and $c_\mu$ is the concentration of possible molecular sets related to the $\mu^{\text{th}}$ reaction. For a reaction described by:

$$\mathrm{A} + \mathrm{B} \xrightarrow{k_\mu} \mathrm{C} + \mathrm{D} \tag{2}$$

The corresponding sets $c_\mu$ is calculated as:

$$c_\mu = [\mathrm{A}] \cdot [\mathrm{B}] \tag{3}$$

where $[\,\cdot\,]$ represents the concentration of reactants. The probability $\mathbb{P}_\mu$ for the $\mu^{\text{th}}$ reaction to occur is derived by:

$$\mathbb{P}_\mu = \frac{R_\mu}{R_{SUM}} \tag{4}$$

where $R_{SUM}$ is the summation of propensities, given as:

$$R_{SUM} = \sum_{\nu=1}^{M} R_\nu \tag{5}$$

A uniformly distributed random number $rnd_1 \in U(0,1)$ is generated to determine which one reaction event to occurr at the moment based on the rule:

$$\frac{\sum_{\gamma=1}^{\mu-1} R_\gamma}{R_{SUM}} < rnd_1 \leq \frac{\sum_{\gamma=1}^{\mu} R_\gamma}{R_{SUM}} \tag{6}$$

Following the occurrence of the selected event, the molecular set concentration of each reaction is updated. The time between two consecutive events of the chemical system is evaluated by $\tau$, which is determined by:

$$\tau = \frac{\ln(1/rnd_2)}{R_{SUM}} = \frac{-\ln(rnd_2)}{R_{SUM}} \tag{7}$$

where, $rnd_2 \in U(0,1)$. The event selection and system evolution time iterate until a preset simulation step number or desired time is satisfied.

## Accelerated kinetic Monte Carlo simulation

As indicated by (4) and (6), the discrepancy in probability values results in a significant portion of computational effort being consumed by frequent events with high propensities. When frequent reversible events occur ceaselessly during a period of process time, the system is deemed to be trapped, which is called the kinetic trap phenomenon. The system escapes from the entrapment when a rare event occurs. During the entrapment, scaling the propensity of frequent events artificially narrows the occurrence probability gap between frequent and rare reactions. Furthermore, as evidenced by (7), the scaling operation increases the time intervals, reducing the number of simulation steps required to reach the desired time. Therefore, the Superbasin-aided kMC enhances

simulation efficiency. Compared to the conventional kMC, the execution of the Superbasin-aided kMC model involves three additional procedures: (i) identification of frequent and rare events; (ii) feasibility assessment for scaling; and (iii) implementation of the scaling operation.

The flowchart of simulations using the Superbasin-aided kMC model for dynamic PI-RAFT polymerization process considering varying light conditions is presented in Figure 1, wherein the steps corresponding to the conventional kMC are highlighted in blue, the steps corresponding to the Superbasin-aided kMC are highlighted in green. Furthermore, as the photodissociation reactions in PI-RAFT are sensitive to external light sources, the values of the kinetic constants are automatically adjusted in response to the light modulation in the simulations. A light-switch module is designed in this study to implement the varying light irradiation, with the corresponding steps marked in yellow in Figure 1.

## Key procedures in Superbasin-aided kMC model

Focusing on the modelling for the PI-RAFT process, the involved reversible reaction pairs in the form of:

$$\mathrm{E} + \mathrm{F} \xrightarrow{k_{forward}} \mathrm{G} + \mathrm{H} \tag{8}$$

$$\mathrm{G} + \mathrm{H} \xrightarrow{k_{reverse}} \mathrm{E} + \mathrm{F} \tag{9}$$

are classified as frequent events. When the corresponding forward and reverse reactions from a reversible pair exhibit similar propensity values, this reaction pair reaches equilibrium. The successive and abundant occurrences of the forward and reverse reactions from the equilibrium pair leads to a quasi-steady-state (QSSA) system. The molecular concentrations and propensities remain stable as the process moves forward during the QSS period. The occurrences of the other irreversible reactions are classified as rare events, which introduce significant fluctuations into the system.

Frequent events are further categorized as equilibrated or unequilibrated frequent events based on whether the corresponding reaction pairs have reached equilibrium. For a reaction pair $\upsilon$ out of the total $K$ pairs, if the forward and reverse reactions occur $N_f$ times, there is a confidence of $1-\delta_f$ in safely reaching equilibrium if the following rule is satisfied:

$$\left|n_{\upsilon,+} - n_{\upsilon,-}\right| \le \delta_f \cdot N_f, \qquad \forall \upsilon = 1,2,\dots,K \tag{10}$$

$$\eta_{\upsilon,+} + \eta_{\upsilon,-} \ge N_f, \qquad \forall \upsilon = 1,2,\dots,K \tag{11}$$

$$N_f = \left\lceil (\alpha-1)/\delta_f \cdot \ln(\delta_f) \right\rceil \quad \forall \upsilon = 1,2,\dots,K \tag{12}$$

where $n_{\upsilon,+}$ and $n_{\upsilon,-}$ record the occurrence numbers of the forward and reverse reactions over the last $N_f$

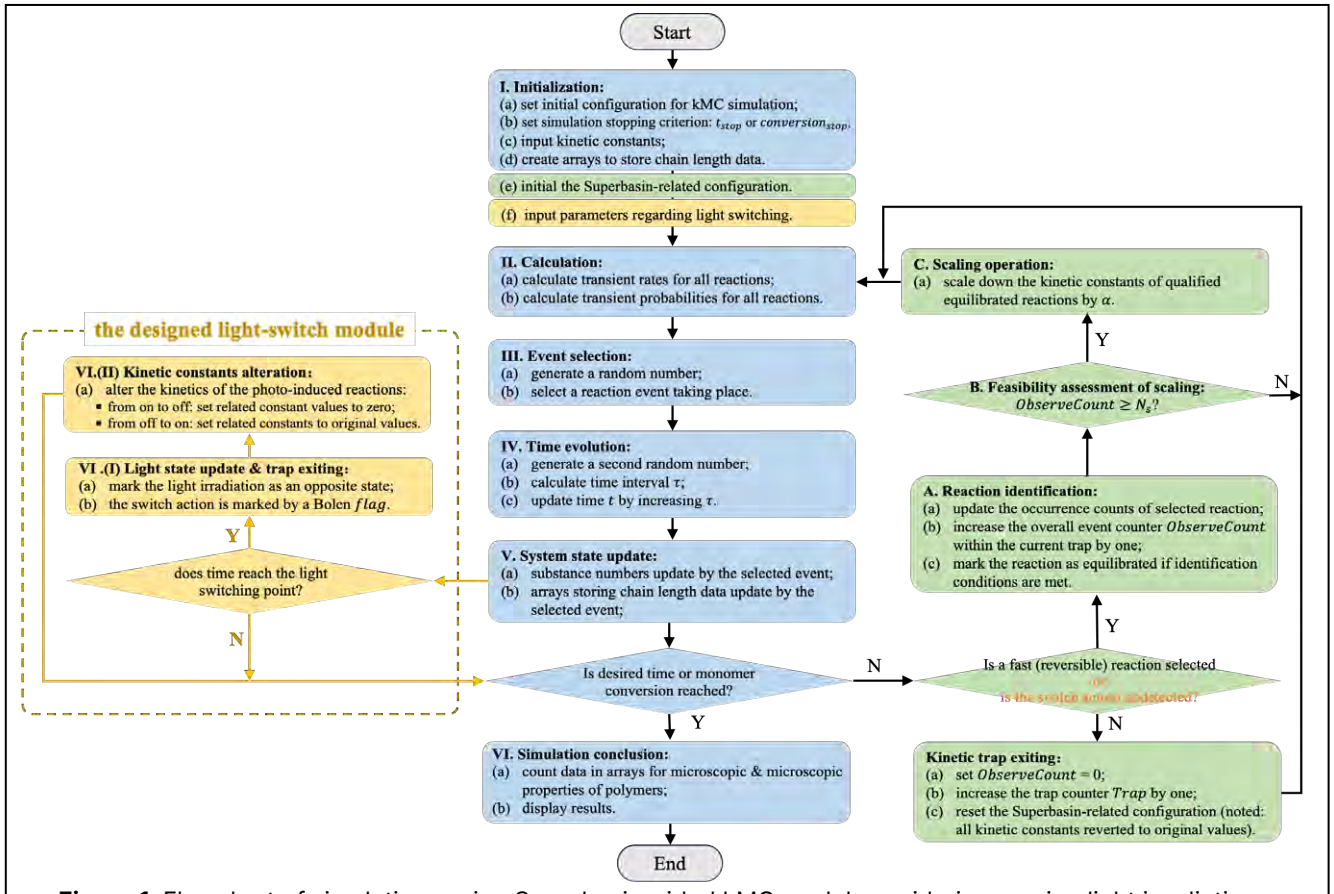



**Figure 1:** Flowchart of simulations using Superbasin-aided kMC model considering varying light irradiations.

reaction events for the reaction pair $\upsilon$. Term $\delta_f \cdot N_f$ calculates a threshold value for reaction identification. Variable $N_f$ is determined by (12) using scaling factor $\alpha$ and $\delta_f$. At the outset of the Superbasin-aided kMC model simulation, all frequent reactions are designated as unequilibrated.

Figure 2 presents the state transition during the Superbasin-aided kMC simulation, considering the complete feasible state space. Following the occurrence of a rare event, a frequent event causes the system to transition from the previous state $S_o$ into a kinetically trapped state $S_i$, as indicated by the leftmost yellow arrow in Figure 2. Two distinct regions comprise region $S_i$: the known ($S_k$) and unknown ($S_u$) regions. The occurrence of an equilibrated event shifts the current system into $S_k$ inside the trap, highlighted in the green area in Figure 2. The occurrence of an unequilibrated event shifts the current system into $S_u$ inside the Superbasin, highlighted in the gray area in Figure 2. A rare event drives the system's exit from the current trap, transitioning it toward $S_o$.

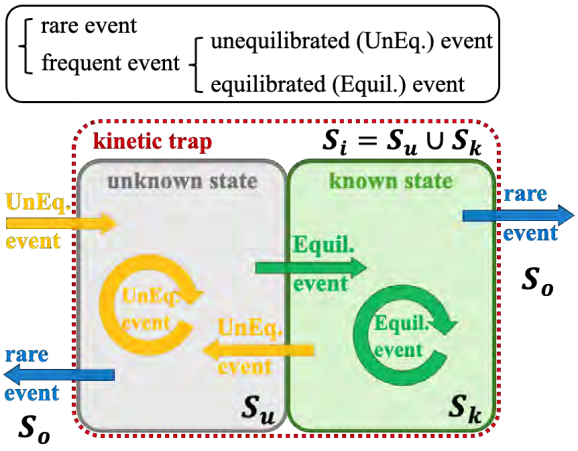



**Figure 2.** System state transformation within the complete possible state space resulting from the occurred reaction event.

When the number of reactions from an equilibrated frequent pair within the current kinetic trap exceeds $N_s$ times, a propensity scaling operation is applied with a confidence of $1 - \delta_f$. The propensity (equivalent to the transient rate) of the corresponding reaction is scaled by a user-defined factor $\alpha$:

$$R'_\mu = \frac{R_\mu}{\alpha},\ \alpha \geq 1 \tag{10}$$

The minimal observed occurrence number is derived as

$$N_s = \left\lceil -\chi \cdot \frac{\alpha - 1}{\delta_f} \cdot \ln(\delta_f) \right\rceil, \chi \geq 1 \tag{11}$$

where $\chi$ is a user-defined parameter determining the minimal observed occurrence number before scaling. For polymerization process modeling, it is critical to accurately capture higher dimensional information such as chain lengths and polymeric structures for individual polymers from diverse polymer species. Parameter $\chi$ facilitates the precise recording of the intricate information associated with polymers.

The scaling operation is applied simultaneously to both forward and reverse reactions of an equilibrated pair, which is recursive, leading to a cumulative effect on the propensity values of fast reactions during simulation. If a reaction pair has been scaled by $\alpha$ once and continues to meet the scaling criteria while within the current kinetic trap, it will undergo further scaling.

## PI-RAFT POLYMERIZATION MECHANISM

The kinetic mechanism of PI-RAFT with two CTA species, $TR$ and $XR$, is tabulated in Table 1. During the polymerization process, different types of CTAs influence the synthesis efficiency, uniformity of polymer chains, and microstructural properties of the resulting polymers. In Table 1, $R^*$, $M$, $T^*$, and $X^*$ denote primary radicals, monomers, and thiocarbonylthio radicals of $T$ and $X$, respectively. $D_n$, $P_n^*$, $TP_n^*$, and $XP_n^*$ represent dead polymers, radical polymers, and inactive polymers of $T$ and $X$ with chain lengths of $n$, respectively. $P_nTR$ and $P_nXR$ are one-arm adduct radicals of $T$ and $X$ with chain lengths of $n$, respectively. $P_nTP_m$ and $P_nXP_m$ are the two-arm adduct radicals of $T$ and $X$ with $n$ and $m$ on each arm. This mechanism involves six micromolecular reactants and eight polymer species, the latter possessing high-dimensional chain structure information that needs to be characterized and recorded in the simulation.

## RESULTS AND DISCUSSIONS ON ONE-SHOT SIMULATION

### Model Accuracy

The simulations were performed on a personal desktop computer with 32 GB RAM and Intel i7-10700 CPU using Python version 3. The initial concentrations of monomers and CTAs are 2 M and 0.04 M, respectively.

Figure 3 presents the Superbasin-aided kMC simulation results as black lines, the conventional kMC simulation results as gray dashed lines for MWDs and method of moments results as gray dashed lines for average information. The results obtained from different methods demonstrate good consistency. The simulated MWDs at 95% monomer conversion for diverse initial CTA concentrations are presented in Figure 3(a)-(b). The evolutions of average chain lengths are presented in Figure 3(c)-(d).

A lower initial feed of $XR$ results in a smaller length disparity of the resulting polymers, and the MWD shape is narrower. A higher $XR$ proportion leads to a faster polymer growth rate at the initial polymerization stage.

**Table 1:** kinetic mechanism for PI-RAFT with two chain transfer agents.

| Number | Reaction | Event type | Equation | Kinetic constant* |
|---|---|---|---|---|
| 1 | ini-propagation | rare | $R^*+M \rightarrow P_1^*$ | $k_{i,R}$=200 M·s$^{-1}$ |
| 2 | propagation | rare | $P_n^*+M \rightarrow P_{n+1}^*$ | $k_p$=200 M·s$^{-1}$ |
| 3 | termination | rare | $R^*+R^* \rightarrow D_0$ | $k_t$=2×10$^4$ M·s$^{-1}$ |
| 4 | termination | rare | $P_n^*+R^* \rightarrow D_n$ | $k_{ts}$=2×10$^4$ M·s$^{-1}$ |
| 5 | combination termination | rare | $P_n^*+P_m^* \rightarrow D_{n+m}$ | $k_{tc}$=10$^4$ M·s$^{-1}$ |
| 6 | disproportionation termination | rare | $P_n^*+P_m^* \rightarrow D_n+D_m$ | $k_{td}$=10$^4$ M·s$^{-1}$ |
| 7 | addition | frequent pair | $TR+P_n^* \rightarrow P_nTR$ | $k_{addT}$=2.857×10$^3$ M·s$^{-1}$ |
| 8 | fragmentation | | $P_nTR \rightarrow TR+P_n^*$ | $k_{-addT}$=5.714×10$^7$ s$^{-1}$ |
| 9 | addition | frequent pair | $TP_n^*+R^* \rightarrow P_nTR$ | $k_{\beta T}$ = 1.333×10$^8$ M·s$^{-1}$ |
| 10 | fragmentation | | $P_nTR \rightarrow TP_n^*+R^*$ | $k_{-\beta T}$ = 2.667×10$^{12}$ s$^{-1}$ |
| 11 | addition | frequent pair | $TP_n^*+P_m^* \rightarrow P_nTP_m$ | $k_{addPT}$=2×10$^3$ M·s$^{-1}$ |
| 12 | fragmentation | | $P_nTP_m \rightarrow TP_n^*+P_m^*$ | $k_{-addPT}$=4×10$^7$ s$^{-1}$ |
| 13 | photodissociation# | frequent pair | $TR \xrightarrow{h\nu} T^*+R^*$ | $k_{bsT1}$=5×10$^{-9}$ s$^{-1}$ |
| 14 | addition | | $T^*+R^* \rightarrow TR$ | $k_{-bsT1}$=5 M·s$^{-1}$ |
| 15 | photodissociation# | frequent pair | $TP_n^* \xrightarrow{h\nu} T^*+P_n^*$ | $k_{bsT2}$=5×10$^{-10}$ s$^{-1}$ |
| 16 | addition | | $T^*+P_n^* \rightarrow TP_n^*$ | $k_{-bsT2}$=5 M·s$^{-1}$ |
| 17 | addition | frequent pair | $XR+P_n^* \rightarrow P_nXR$ | $k_{addX}$=1.7×10$^2$ M·s$^{-1}$ |
| 18 | fragmentation | | $P_nXR \rightarrow XR+P_n^*$ | $k_{-addX}$=3.4×10$^{10}$ s$^{-1}$ |
| 19 | addition | frequent pair | $XP_n^*+R^* \rightarrow P_nXR$ | $k_{\beta X}$=2.267×10$^{10}$ M·s$^{-1}$ |
| 20 | fragmentation | | $P_nXR \rightarrow XP_n^*+R^*$ | $k_{-\beta X}$=4.533 ×10$^{18}$ s$^{-1}$ |
| 21 | addition | frequent pair | $XP_n^*+P_m^* \rightarrow P_nXP_m$ | $k_{addPX}$=68 M·s$^{-1}$ |
| 22 | fragmentation | | $P_nXP_m \rightarrow XP_n^*+P_m^*$ | $k_{-addPX}$=1.36×10$^{10}$ s$^{-1}$ |
| 23 | photodissociation# | frequent pair | $XR \xrightarrow{h\nu} X^*+R^*$ | $k_{bsX1}$=1.2×10$^{-4}$ s$^{-1}$ |
| 24 | addition | | $X^*+R^* \rightarrow XR$ | $k_{-bsX1}$=1×10$^2$ M·s$^{-1}$ |
| 25 | photodissociation# | frequent pair | $XP_n^* \xrightarrow{h\nu} X^*+P_n^*$ | $k_{bsX2}$=9×10$^{-5}$ s$^{-1}$ |
| 26 | addition | | $X^*+P_n^* \rightarrow XP_n^*$ | $k_{-bsX2}$=1×10$^2$ M·s$^{-1}$ |

* Kinetic constants reported in the open literature [4] were used in this work.
# "$h\nu$" indicates reactions triggered by light irradiation.

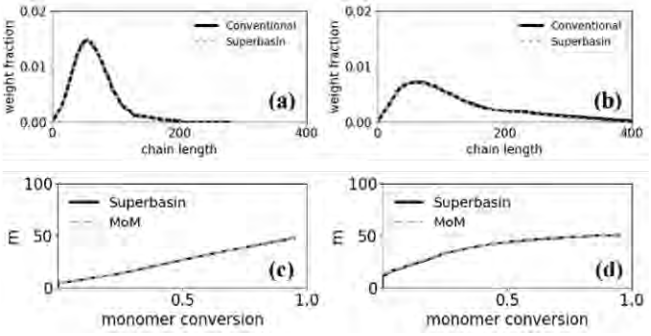



**Figure 3.** Simulated MWDs at 95% conversion and simulated dynamic average chain lengths using $[XR]$:$[TR]$=1:4 and $[XR]$:$[TR]$=4:1, respectively.

## Model Efficiency

The computational time for PI-RAFT processes to 95% monomer conversion with different initial feed ratios of CTAs is shown in Table 2. The developed Superbasin-aided kMC achieves a remarkable thousand-fold acceleration compared to conventional kMC. With a set of alternative user-defined parameters, the simulation has a 48961 times' acceleration from 12.1 days to 21.34 seconds, with a sight compromission on result precision.

**Table 2:** Comparison of computational time.

| Parameter | [XR]:[TR] | Speedup |
|---|---|---|
| $\alpha = 2, \chi = 5.12$ | 1:9 | 205 |
| | 1:4 | 467 |
| | 2:3 | 1182 |
| | 1:1 | 1772 |
| | 4:1 | 3379 |
| | 1:0 | 4729 |
| $\alpha = 1.16, \chi = 1.04$ | 1:0 | 48961 |

# RESULTS AND DISCUSSIONS ON BATCH BLENDING

## Blended molecular weight distribution

Batch blending is an alternative idea in producing polymers with desired microscopic features, which is examined in this study as a strategic approach in the context of PI-RAFT. A schematic representation of the batch blending is presented in Figure 4 to illustrate how the combination of polymers synthesized in distinct batches can achieve a target MWD profile.

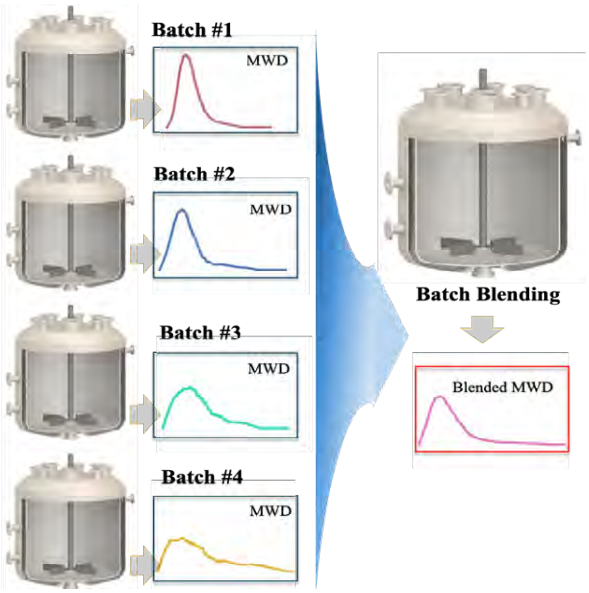



**Figure 4.** Scheme of batch blending.

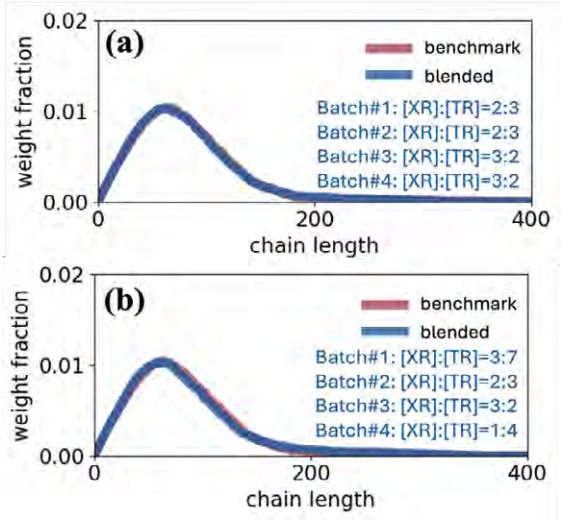



**Figure 5.** The blend MWDs and their comparison with the benchmark distributions (using [XR]:[TR]=1:1) obtained using Superbasin-aided kMC simulation.

The batch blending operation leverages the differences in MWD resulting from the use of varying CTA feeding policies across multiple batch reactors. Figure 5 presents the blended MWDs and their comparison with the benchmark distribution obtained using the feeding policy [XR]:[TR] = 1:1. The results clearly demonstrate the capability of batch blending to closely replicate the benchmark MWD, even with reduced $XR$ usage (with a 16% reduction), as shown in Figure 5(b).

### Prospects of batch blending

Batch blending has advantages in process and production quality optimization. By adjusting the CTA feeding policies in individual batch reactors, the blending operation allows for the achievement of desired MWD profiles without requiring additional polymerization steps. The ability to reduce the feeding of one type of CTA while maintaining target properties further contributes to resource conservation and cost savings. Moreover, with the computational efficiency of the Superbasin-aided kMC model, future studies can explore the effects of varying polymerization conditions, such as temperature, monomer concentration, and irradiation, to further enhance the versatility of batch blending.

## CONCLUSION

Simulating polymerization processes at the microscopic scale presents a significant challenge due to the complex structure of macromolecules. In this study, a Superbasin-aided kMC model was developed to capture microscopic polymeric properties in PI-RAFT processes. The proposed simulation method substantially reduces computational time from weeks to minutes, enabling more efficient exploration of inverse design, online control, and process and production optimization. Additionally, leveraging the efficiency of the simulation, batch blending is introduced as a promising approach to enhance production quality and process optimization. Specifically, one can expand the versatility of the developed Superbasin-aided kMC simulation and the batch blending approach in scale-up strategies and applications under continuous-flow processes for product quality optimization purpose, by combining CFD simulations and real-world data. Ultimately, this computational framework aims to bridge the gap between lab-scale mechanistic insights and industrial scalability in practical applications.

## ACKNOWLEDGEMENTS

The authors acknowledge the support of the National Key Research and Development Project (Grant No. 2023YFB3307800) and the State Key Laboratory of Industrial Control Technology, China (Grant Nos. ICT2024C04 & ICT2024B08). The third author acknowledges the support by the University of Patras, Medicus program (No. 81816).

## REFERENCES

1. Gillespie DT. Exact stochastic simulation of coupled chemical reactions. *J. Phys. Chem.* 81(25): 2340-2361 (1977) https://doi.org/10.1021/j100540a008
2. Chatterjee A, Arthur FV. Accurate acceleration of kinetic Monte Carlo simulations through the modification of rate constants. *J. Chem. Phys.* 132(19) (2010) https://doi.org/10.1063/1.3409606
3. Dybeck EC, Craig PP, Matthew N. Generalized temporal acceleration scheme for kinetic monte carlo simulations of surface catalytic processes by scaling the rates of fast reactions. *J. Chem. Theory*

*Comput.* 13(4): 1525-1538 (2017) https://doi.org/10.1021/acs.jctc.6b00859
4. Lehnen AC, Johannes G, Alain MB, et al. Xanthate-supported photo-iniferter (XPI)-RAFT polymerization: facile and rapid access to complex macromolecules. *Chem. Sci.* 14(3): 593-603 (2023) https://doi.org/10.1039/D2SC05197D

© 2025 by the authors. Licensed to PSEcommunity.org and PSE Press. This is an open access article under the creative commons CC-BY-SA licensing terms. Credit must be given to creator and adaptations must be shared under the same terms. See https://creativecommons.org/licenses/by-sa/4.0/



Systems & Control Transactions

**Research Article - Peer Reviewed Conference Proceeding**
ESCAPE 35 - European Symposium on Computer Aided Process Engineering
Ghent, Belgium. 6-9 July 2025
Jan F.M. Van Impe, Grégoire Léonard, Satyajeet S. Bhonsale,
Monika E. Polańska, Filip Logist (Eds.)

PSE PRESS

# Plantwide Control of a Green Formic Acid Production Process

**Mohammad Mahdi Ghasemi Aliabadi[a], Alexandros Anagnostou[a], Francia Gallardo Gonzalez[a], Shivam Pandey[a], Farzad Mousazadeh[a], Anton Kiss [a*]**

[a] Delft University of Technology, Department of Chemical Engineering, Delft, the Netherlands
* Corresponding Author: a.a.kiss@tudelft.nl.

## ABSTRACT

This study presents the design and evaluation of a plantwide control (PWC) system for Formic acid (FA) production under unsteady green Hydrogen supply. Starting from a steady-state foundation in Aspen Plus V12, the system was prepared to handle variable inputs and was subsequently transitioned into Aspen Dynamics for real-time responsiveness. The two-level design methodology to build a PWC scheme, which is comprised of equipment-specific and plantwide controllers, effectively managed fluctuations in feed rates ranging up to ±20%, maintaining FA purity and production rate targets. Gradual SRAMP (sinusoidal ramp) adjustments of 1% per hour provided optimal stability. These results confirm the PWC system's effectiveness in maintaining production goals under the variability of throughput.

**Keywords**: Plantwide Control, Dynamic Simulation

## INTRODUCTION

The drive for sustainability is compelling the chemical industry to transition from conventional, non-renewable resources to renewable, green feedstocks. Formic acid (FA), which can be synthesized from green Hydrogen and captured carbon dioxide ($CO_2$), presents a promising approach for mitigating greenhouse gas emissions while also yielding a versatile chemical with widespread industrial applications. Nevertheless, the shift to renewable sources introduces new challenges—most notably, the variability in feed availability inherent to renewable sources. In response, maintaining stable production and product quality under these fluctuations has underscored the need for advanced control systems, with plantwide control (PWC) emerging as essential for operational reliability.

This work seeks to design an effective PWC system for a highly intensified FA production plant, targeting a stable production rate of FA with a purity of 85% by weight. The complete plant design can be seen in the previous work [1]. The main challenges for the PWC design include the COPure™ absorption system, the divided wall column and the 16 recycle streams within the plant.

To address these challenges, the approach taken first involved reinforcing the steady-state flowsheet's robustness within Aspen Plus V12. This required a comprehensive evaluation of sensitivity across process parameters and equipment to ensure flexibility in adapting to variations in feed flow rates.

With this foundation established, the focus shifted to transitioning the model into Aspen Dynamics for dynamic simulations. This conversion required incorporating additional equipment and pressure control elements to facilitate a pressure-driven simulation that reflects real operational conditions.

Following successful initialization in dynamic mode, a two-level design methodology for PWC system was developed. The first control layer focuses on equipment-specific control strategies but was found insufficient for handling significant variations in feed rates. Consequently, a second plantwide control layer was designed to manage throughput fluctuations and sustain product specifications across varying production capacities.

The final PWC configuration demonstrates that despite the complexities introduced by the DWC and multiple recycle loops, the designed control system maintains FA purity and production rates, even under ±20% throughput disturbances, confirming that PWC can play a critical role in stabilizing renewable-driven processes

with inherent variability in feedstock supply.

## PROCESS SIMULATION

### Process Description

The production process of formic acid (FA) is divided into two main sections [1]: the synthesis of carbon monoxide (CO) and its subsequent conversion to FA. The $CO_2$ feed is sourced from the CCUS network at 25 °C and 35 bar, while green hydrogen, supplied at 25 °C and 30 bar, is obtained from an electrolyzer (Figure 1).

In the first section, the reverse water-gas shift (RWGS) reaction converts $CO_2$ and $H_2$ into CO within a tubular reactor. The process operates at 1.2–1.4 bar, with temperatures ranging from 573–600 °C and a $H_2$:$CO_2$ molar ratio of 2.5. Following water removal, the reactor outlet undergoes chemical absorption (COPure™ technology) to isolate CO from unreacted feedstock and impurities. This involves selective chemisorption using a $CuAlCl_4$ complex dissolved in toluene, achieving a CO purity of 99% and a recovery rate of 98%. The CO-$CuAlCl_4$ complex is then dissociated in a stripper for further use.

In the second section, methanol is carbonylated with CO in a continuous stirred-tank reactor (CSTR) at a methanol-to-CO ratio of 5, under conditions of 40 bar and 80 °C. This process yields methyl formate (MF) with high selectivity, achieving moderate per-pass conversions of methanol (14.8%) and CO (74%). Excess methanol is separated and recycled via distillation. The hydrolysis of MF to FA occurs in two stages within packed flow reactors (PFRs). The first reactor operates at 18 bar and 120 °C, with MF reacting with water to produce FA and water, achieving a 10% conversion. The resulting FA acts as a catalyst for further hydrolysis in the second reactor, achieving a 30.5% per-pass conversion with 100% selectivity. The reactor outputs are distilled using a dividing wall column (DWC) to separate FA and water from unreacted methanol and MF, which are recycled. The FA-water mixture is then distilled at 3 bar to overcome the azeotrope, achieving the desired FA purity.

### Process Simulation

From the explained process, the aim of the work was

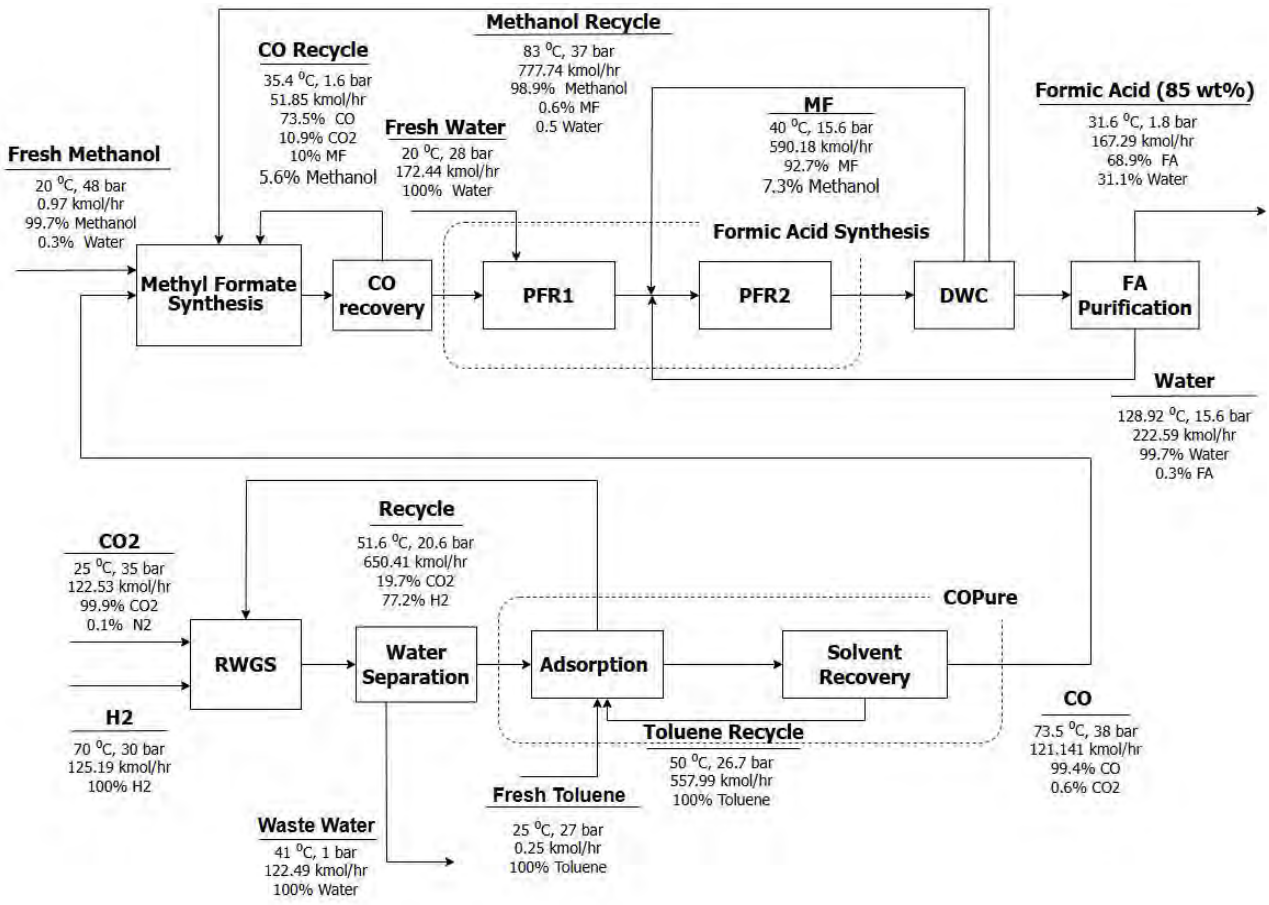



**Figure 1**. Process Block Flow Diagram

to design a PWC system, starting from the development of a robust steady-state model, simulated in Aspen Plus V12.

Two thermodynamic models were chosen to accurately capture the system's phase behavior across diverse conditions. The RWGS reaction and CO separation processes were simulated with the Peng-Robinson equation of state due to their high-pressure and non-polar components, while the UNIQUAC-HOC model was used for MF and FA production to account for complex liquid-phase interactions.

To enhance the simulation's stability and enable responsiveness to feed fluctuations, critical parameters were identified through sensitivity analysis, allowing the model to accommodate a range of operational conditions. Disturbances in feed composition and flow rates were evaluated, ensuring the process could achieve the desired FA purity and throughput across varied conditions. This steady-state simulation serves as the baseline model, supporting the design of a flexible and resilient dynamic model and the foundation for developing an effective plantwide control system in subsequent stages.

The most challenging aspect of achieving robust and flexible steady-state simulation involved the implementation of calculator blocks and flowsheet design specifications. Calculator blocks, along with DesignSpecs at both the flowsheet and equipment levels, were essential for manipulating key process variables to meet the desired product specifications and ensure mass balance closure across the process.

Achieving convergence across multiple disturbance scenarios in steady-state mode proved to be a valuable predictor of smooth operation during dynamic simulation, ultimately ensuring that the system could transition effectively to Aspen Dynamics for plantwide control analysis.

## PWC system Design and Dynamics Simulation

The Integrated Framework of Simulation and Heuristics Method (IFSH) has been widely used for plantwide control (PWC) design [2, 3]. Drawing inspiration from this approach, the methodology begins with defining the objectives of PWC. Plantwide disturbances are then analyzed, and the main throughput variable is identified. Based on these inputs, a two-level control scheme is developed to achieve the desired operational stability and efficiency.

The first control level focuses on stabilizing individual unit operations by implementing primary controllers for critical variables. For example, level control is essential in continuous stirred-tank reactors (CSTRs), where it directly impacts reaction rates. In flash operations and distillation columns, maintaining appropriate liquid levels is equally crucial. The liquid level in flash operations is regulated by adjusting the liquid outlet flow rate, while in distillation columns, the reflux drum and column base levels are controlled via distillate and bottoms flow rates, respectively. Reboiler and condenser temperatures are managed by manipulating their respective heat duties. Similarly, cooler and heater outlet temperatures are controlled by adjusting their thermal inputs. In process-to-process heat exchangers, the temperature on the cold side is regulated by modulating the flow of the hot side through the exchanger. Column and flash pressures are maintained by manipulating the overhead streams and flow controllers manage critical feed streams, including $CO_2$, $H_2$, water, toluene, and methanol.

To ensure optimal performance, a closed-loop autotune variation (ATV) test was conducted with a 1 to 10 percent change in the output range. Based on the outcomes of these tests, the Tyreus-Luyben [4] method was implemented to tune the parameters of the controllers in this first level of the control scheme. The Tyreus-Luyben method was applied primarily; however, in some cases, the Ziegler-Nichols [5] method was used.

These controllers ensure steady operation within each plant section, mitigating localized disturbances and maintaining unit-level stability. However, plantwide disturbance analysis revealed that this layer alone could not adequately address larger fluctuations, particularly those related to variable hydrogen supply. While individual units remained stable, the lack of coordination across sections hindered the system's ability to handle interdependencies effectively.

To manage broader disturbances, a second control level was introduced, focusing on overall production stability, quality targets, and material balance across the plant. This layer employs ratio and mass balance controllers to maintain critical system ratios and regulate material flows, particularly within recycle loops.

Several points of the plant required the implementation of these 2$^{nd}$ level controllers to achieve smooth operation. For example, an important aspect of the reactors is to maintain a constant mole ratio for the reactants. One of them is the ratio for $H_2$ to $CO_2$ entering the RWGS reactor which is dependent on the fresh $H_2$ stream flow. At the same time, a make-up stream of Methanol is adjusted based on the required ratio to CO entering the Methyl Formate synthesis reactor. Additionally, Formic Acid is produced in PFR2, for which the required fresh water is checked by a ratio controller at the inlet of the reactor. Continuing on the topic of ratio control, another highly important ratio controller is the one related to the Toluene solvent in the 1$^{st}$ section. The goal is to keep a constant ratio of gas/liquid entering the adsorption column during transitions, while also compensating for the loss of Toluene in other parts of the plant.

Other, more unique controllers have been implemented in the plant, such as the controller for a main path

valve and compressor in the 1st section, which affects the main path flowrate and consequently the recycle rate towards the RGWS reactor and therefore the extent of the reaction, with the purpose to keep a specific percentage conversion.

In a similar fashion, the conversion of the reaction in the Methyl Formate Synthesis reactor needs to be controlled and this is done by cascading the level controller of the CSTR, which in turn affects the outlet valve opening, the residence time and the conversion rate. For the same reactor, one of the recycle streams entering it is composed of primarily CO and it is controlled to have a specific flow ratio compared to the "fresh" CO entering the 2nd section. Moreover, this unreacted CO is mainly returned due to a flash separation after the CSTR and it is required that a specific percentage of CO exits as the recycle at the top, which is manipulated by the corresponding valve.

The most complicated controller to implement was the one related to methanol build-up in the 2nd section, which is explained in more detail later. Overall, the 2nd level controllers are essential for sustaining continuous, stable operations and achieving the desired purity of FA and separation efficiency, even under varying input conditions.

With the two-level control design methodology established, the transition to dynamic simulation was initiated. Key adjustments were made to ensure consistent pressure conditions, essential for pressure-driven operation throughout the plant. Control valves were configured to maintain a pressure drop of 2–3 bar, enabling precise flow rate control. Furthermore, controlled pressure differentials were introduced between equipment and across battery limits to drive fluid flow and regulate stream entry and exit effectively. Equipment with holdups, such as reactors, flash drums, reflux drum and sump of distillation columns, were sized to accommodate an inventory corresponding to at least 10 minutes of operation. Additionally, a length-to-diameter ratio of 2:1 was assumed [3]. These adjustments were crucial to ensure a stable and responsive dynamic model.

Figure 2 depicts the two-level control design methodology for the Dividing Wall Column (DWC) system. The DWC system is modeled using two RadFrac columns, one equipped with a reboiler and condenser and the other without, simulating the two chambers separated by a dividing wall within a single column. Four intermediate streams are included to represent the vapor and liquid exchange between the chambers. Additionally, pressure gradient equipment has been introduced between these streams to simulate a pressure gradient for modeling purposes [6].

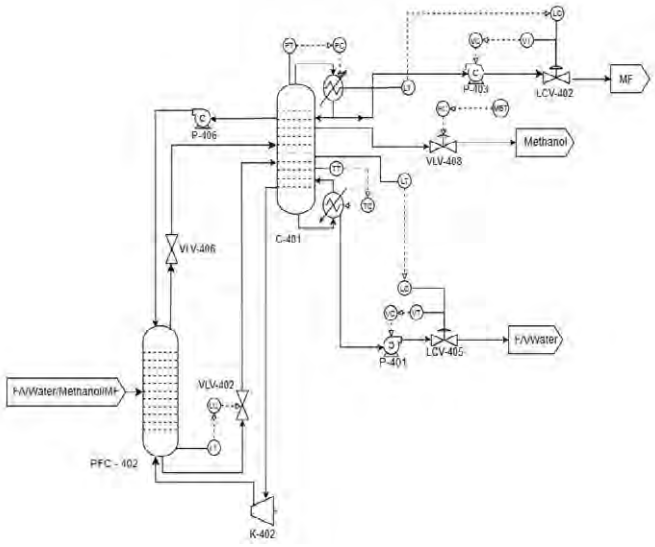



**Figure 2.** Designed PWC for the DWC

The first level of the control scheme for the DWC incorporates level, temperature, and pressure controllers to ensure stable operation. The levels in the reflux drum and the base of the right column are maintained by adjusting the distillate and bottoms flow rates, respectively. Similarly, the base level of the left column is regulated by controlling the liquid exiting from its bottom. Pressure control for the right column is achieved by manipulating the condenser duty, while the reboiler temperature is controlled by manipulating the reboiler duty. Considering the DWC as part of the overall process, the first level of control alone is insufficient to address plantwide operational challenges. This is where the second level of control becomes critical.

At this level, a mass balance controller is introduced to address methanol accumulation within the system. Methanol is the most difficult component to control, because it is consumed at the Methyl Formate Synthesis reactor and generated at the same time in the 2 PFR reactors (Figure 1). These 3 reactors lie in series along the main path of the process and they are also connected end-to-front through a recycle Methanol stream. Simultaneously, fresh make-up methanol enters the system and some of the methanol is purged from the recycle stream coming out of the CO recovery system. All these points of methanol generation and consumption need to be delicately balanced in order to keep its accumulation in the system at 0. The challenge in achieving that is apparent because of the interconnected nature of the plant. However, at a closer glance it can be seen that for a specific amount of CO entering the 2nd section, the fresh methanol is dynamically changed for a specific reactant ratio in the CSTR. As a consequence, the CSTR and PFR1 rates of change stay "locked in" while the purge stream and its contribution is relatively small in the methanol mass balance. This leaves PFR2 as the only variable to

manipulate in order to accomplish 0 accumulation rate. The only way to manipulate the rate of change in PFR2 is by influencing the recycle stream around the reactor composed of unreacted Methyl Formate. This is where the mass balance controller system BC and MBT enter the scene (Figure 2).

To start off, a separate system of logical blocks is used to monitor all the aforementioned points of methanol entry, exit, consumption, and generation across the process and calculates the rate of accumulation of methanol. Its output is used as a process variable in the mass balance controller and set to make it zero. The cascade controller dynamically adjusts the side-draw percentage of the middle stream exiting the DWC column and in continuation it affects the flow of the recycled Methyl Formate stream coming out of the top of the column. By doing so, the mass balance controller effectively minimizes methanol buildup, ensuring a stable material flow and supporting continuous, efficient operation of the process.

During varying throughput scenarios, relying solely on valve adjustments (distillate and bottom flow rates) is insufficient to maintain the levels in the drum and sump. To address this, two additional controllers were implemented to regulate the pump power upstream of the valves. These controllers increase the pump power as needed, providing additional head to the system and ensuring sufficient material flow out of the sump.

## RESULT AND DISCUSSION

To evaluate the performance and resilience of the designed plantwide control (PWC) system, dynamic simulations were conducted by introducing controlled disturbances to the $CO_2$ feed stream as the main throughput manipulator.

These disturbances ranged from a -20% decrease to a +20% increase in throughput flow rate, implemented through a SRAMP function within Aspen Dynamics. The SRAMP function was carefully configured to gradually adjust the $CO_2$ feed rate over a designated time period, thereby simulating fluctuations in green Hydrogen. By systematically varying the feed rate across this spectrum, the control system's ability to maintain consistent Formic acid (FA) production rates and purity levels under both positive and negative disturbances was thoroughly assessed. Each simulation scenario was monitored to capture key performance indicators such as stabilization time, integral absolute error (IAE), and relative absolute error (RAE) in order to assess the designed control scheme.

This approach provided comprehensive insights into how effectively the PWC system could manage and mitigate the impacts of unsteady feed conditions, ensuring operational stability and product quality despite throughput variations.

The analysis revealed that as the magnitude of feed disturbances increased, the time required for the system to transition from one steady state to another also escalated. It is important to note that steady state is achieved when the Relative Absolute Error (RAE) graph drops below 0.1% and remains within this boundary, indicating that the system has stabilized and deviations are effectively minimized. For instance, in simulations with smaller feed fluctuations, the system quickly adapted, achieving a new steady state within 16.7 hours for a +10% feed disturbance and 42.6 hours for a -10% disturbance. However, with larger changes, the time to stabilize increased, as the control system needed to accommodate more significant adjustments throughout the plant (Figure 3 and Figure 4) with transitions taking 33.7 hours for +20% and 59.5 hours for -20% disturbances. Kink points in Figure 3 are primarily due to the challenges of managing material within the recycle loops during capacity changes.

Figure 5 illustrates the FA purity error relative to the target value of 85 wt%, demonstrating that even under significant throughput variations of ±20%, the FA purity remains within a narrow 0.2% range. This error decreases by an order of magnitude for ±10% changes in throughput, indicating improved purity stability under less severe disturbances. However, the error associated with a throughput drop is slightly higher compared to a throughput increase. This variance is likely due to challenges in managing material within the recycle loops during capacity reduction, which may cause slight imbalances and affect the control system's ability to stabilize purity as efficiently. This behavior is further supported by Figure 4, which show that the stabilization time required for the simulation is longer in scenarios involving a throughput drop compared to those with a throughput increase.

To ensure stability and prevent the simulation solver from crashing, tests were conducted with a conservative feed disturbance rate of 1% per hour. Meaning that, while, Figure 6 to Figure 9 indicate that for moderate changes of ±5% or ±10%, this rate could be increased up to 2.5% per hour; the repercussions of doing so led to higher IAE and FA purity Error values, indicating a trade-off between response speed and error minimization. Importantly, a 2.5% rate is unsuitable for extreme 20% changes, as it caused instability in the solver, indicating a control limitation under more severe fluctuations.

Additionally, the relative absolute error and integral absolute error trend remains almost identical, when throughput is either increased or decreased by the same percentage, reflecting symmetrical control behavior for equivalent rises and drops in feed rates period of +10% change in throughput (moderate flow rate changes). This symmetry highlights the robustness of the control strategy in handling feed variability, ensuring consistent error response regardless of the direction of throughput change.

A comparative analysis between the dynamic and steady-state results for the extreme disturbance scenario, demonstrating that, despite deviations from steady-state targets, the plantwide control objectives were largely achieved. Specifically, the control system maintained the desired production rate and adhered to process constraints, even under the harshest fluctuations. When there is a +20% disturbance in the system, the product flow rate, the overall MF production, and the fresh Methanol flow rate deviate by +0.6%, -2.7%, and -1.1% from steady state, respectively.

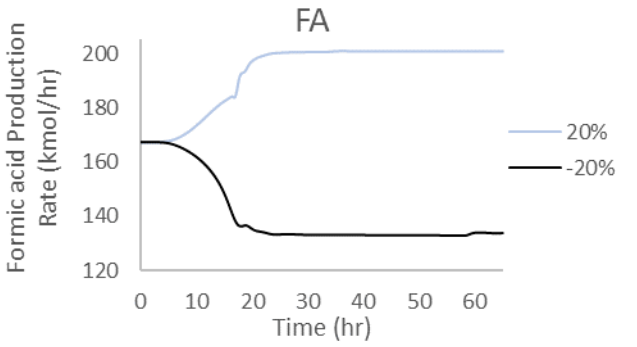



**Figure 3.** FA production rate for +20% and -20% change in throughput

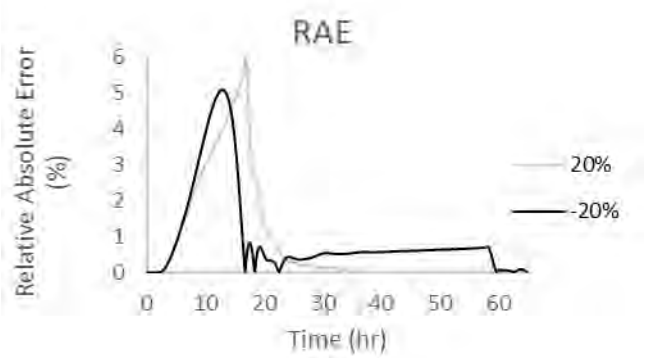



**Figure 4.** Relative Absolute Error (RAE) for +20% and -20% change in throughput

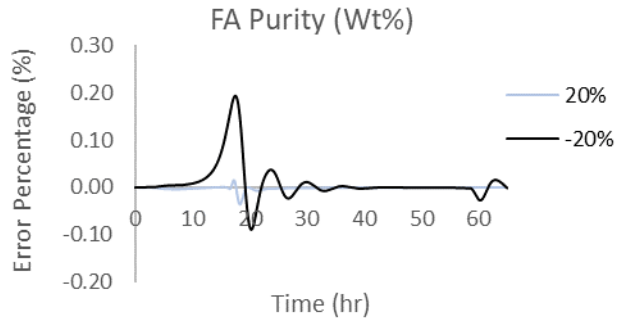



**Figure 5.** FA purity error relative to 85 wt% for +20% and -20% change in throughput

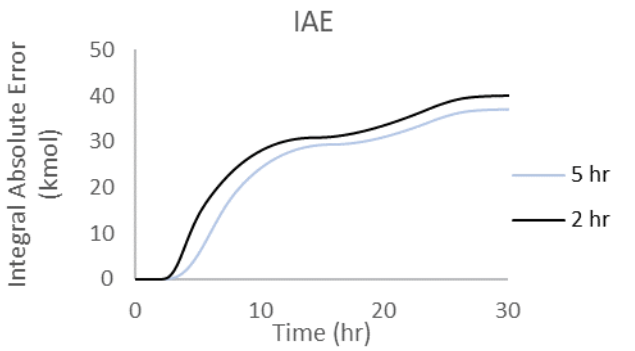



**Figure 6.** Integral Absolute Error (IAE) for 2 and 5 hr ramp period of -5% change in throughput

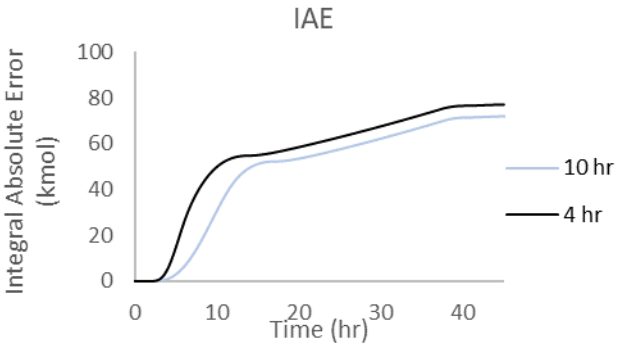



**Figure 7.** Integral Absolute Error (IAE) for 4 and 10 hr ramp period of -10% change in throughput

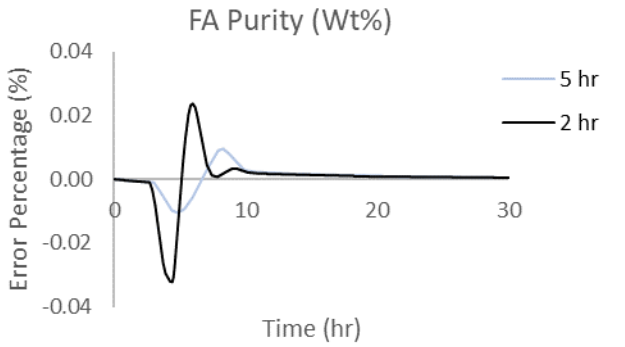



**Figure 8.** FA purity error relative to 85 wt% 2 and 5 hr ramp period of +5% change in throughput

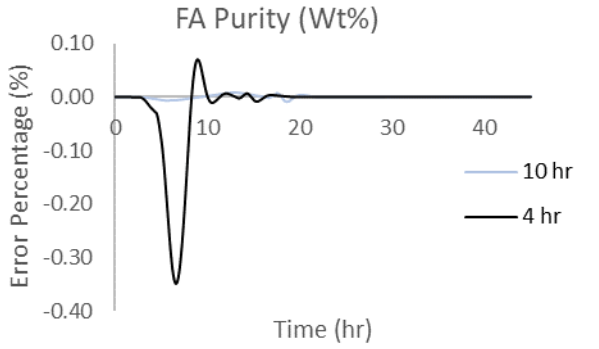



**Figure 9.** FA purity error relative to 85 wt% 4 and 10 hr ramp

Conversely, with a -20% disturbance, the product flow rate, the overall MF production, and the fresh Methanol flow rate deviate by -0.2%, -2.9%, and +1.9% from steady state, respectively. These results confirm the robustness of the PWC system in adapting to significant disturbances, ensuring stable Formic acid output and maintaining operational requirements within acceptable limits.

## CONCLUSION

The designed plantwide control (PWC) system effectively maintained Formic acid (FA) production rates and purity under variable feed conditions caused by unsteady green Hydrogen supplies. The results highlight the impact of the rate of feed changes on the overall control performance, with 1% throughput change per hour identified as a stable rate for maintaining system stability and performance. Despite the complexities of the process, including multiple recycle loops and the divided wall column, the PWC system ensured stable operations. Notably, the FA purity remained within a maximum of 0.2% deviation from the desired 85 wt%, even under the harshest feed flowrate changes of ±20%. The deviation of the FA flow rate in dynamic mode from the steady-state simulation for the +20% and -20% changes in throughput was +0.6% and -0.2%, respectively, further showcasing the robustness of the design. Overall, the evaluation of the PWC design of Formic acid under unsteady Hydrogen supply conditions proved the feasibility of the suggested PWC design on a conceptual level.

## REFERENCES


1. Kalmoukidis N, Barus A, Staikos S, Taube M, Mousazadeh F, & Kiss, A. Novel process design for eco-efficient production of green formic acid from CO2. *IChemE* 210:425-436 (2024) https://doi.org/10.1016/j.cherd.2024.09.001
2. Patle DS, Agrawal V, Sharma S, & Rangaiah G. Plantwide control and process safety of formic acid process having a reactive dividing-wall column and three material recycles. *Comp. Chem. Eng.* 147:107248 (2021) https://doi.org/10.1016/j.compchemeng.2021.107248
3. Patle DS, Gadhamsetti AP, Sharma S, Agrawal V, & Rangaiah G. Plantwide Control of the Formic Acid Production Process Using an Integrated Framework of Simulation and Heuristics. *Ind. Eng. Chem. Res.* 57:13478-13489 (2018) http://dx.doi.org/10.1021/acs.iecr.8b02654
4. M. L. Luyben, B. D. Tyreus, W. L. Luyben. Plantwide Control Design Procedure. *AIChE* 43(12): 3161-3174 (1997) https://doi.org/10.1002/aic.690431205
5. J. G. Ziegler, N. B. Nichols. Optimum Settings for Automatic Controllers. *Dyn. Sys. Meas. Control* 115(2B): 220-222 (1993) https://doi.org/10.1115/1.2899060
6. Wu Y, Zhang G, Xu Z, Qu Z, Wang T, Wang K, Chen K, & Ji L. Enhanced separation of mixing diols by distillation in dividing wall column. *CEP:PI* 149:107859 (2020) https://doi.org/10.1016/j.cep.2020.107859



© 2025 by the authors. Licensed to PSEcommunity.org and PSE Press. This is an open access article under the creative commons CC-BY-SA licensing terms. Credit must be given to creator and adaptations must be shared under the same terms. See https://creativecommons.org/licenses/by-sa/4.0/




Systems & Control Transactions

**Research Article - Peer Reviewed Conference Proceeding**
ESCAPE 35 - European Symposium on Computer Aided Process Engineering
Ghent, Belgium. 6-9 July 2025
Jan F.M. Van Impe, Grégoire Léonard, Satyajeet S. Bhonsale,
Monika E. Polańska, Filip Logist (Eds.)

PSE PRESS

# Energy Water Nexus Resilience Analysis Using Integrated Resource Allocation Approach

**Hesan Elfaki[a,b], Mohammad Lameh[a,b], and Dhabia M. Al-Mohannadi[b,c]***

[a] Texas A&M University, Artie McFerrin Department of Chemical Engineering, College Station, Texas, United States
[b] Texas A&M University at Qatar, Chemical Engineering Program, Education City, Doha, Qatar
[c] Hamad Bin Khalifa University, Education City, Doha, Qatar
* Corresponding Author: dalmohannadi@hbku.edu.qa.

## ABSTRACT

This work presents a macroscopic, high-level representation of the interconnected nexus system, utilizing a resource allocation model to capture the interactions between the power and water subsystems. The model is employed to assess the system's performance under various external stressor impact scenarios, determining the thresholds at which the system can no longer maintain a continuous supply of functional services (i.e. power and water), which reveal the system's vulnerabilities. Resilience metrics are incorporated to interpret these results and characterize the nexus performance. The proposed methodology is generalizable, and its capabilities will be demonstrated through a case study on the energy-water nexus in the Gulf Cooperation Council region.

**Keywords**: Resilience, Energy, Water, Nexus

## INTRODUCTION

Energy and water are essential for societal progress and sustainability, necessitating robust management approaches to address economic, social, and environmental imperatives [1]. The demand for these vital resources rapidly evolves due to population growth, industrial developments, and external events such as climate change and instability. Consequently, the systems producing these resources are subject to multidimensional stressors and must be well-designed and operated to meet these dynamic demands [2]. Energy and water systems, commonly referred to as the Energy-Water Nexus, are interconnected through flows of water, electricity, and heat, which are fundamental to maintaining continuous operation and functional service supply [3]. While distinct in processes and infrastructures, they are highly interdependent, increasing the complexity of the system. Water is needed in energy production for cooling, while energy is essential for pumping, treatment, and desalination. This codependency has guided recent research to view these two systems as a coupled unity with two key directions: "water for energy" and "energy for water" [2,4].

The Gulf Cooperation Council region, GCC, is known for its abundance of energy resources, such as oil and natural gas, making it a global energy hub. However, it faces a severe scarcity of freshwater resources, ranking it among the world's most arid regions [5,6]. As a result, water solutions like desalination plants and wastewater reuse have become the primary strategies in these areas. Seawater desalination, a widely adopted process to address freshwater shortages, is a highly energy-intensive endeavor that requires continuous supplies of heat and/or power, depending on the technology used [7]. Currently, desalination plants account for the majority of the region's freshwater supply, with fossil fuel-based power plants providing the necessary energy input [8]. Wastewater treatment facilities further contribute to the nexus by supplying treated wastewater, primarily for greening, irrigation, and limited agricultural activities [9]. This complex interconnection of power plants, freshwater production plants, and wastewater treatment plants enables the exchange of material and energy resources to support domestic, industrial, and agricultural demands. However, this strong dependency between water and energy systems raises critical concerns about the resilience and sustainability of resource management in the region.

Interconnected Energy-Water Nexus systems face a variety of internal and external events that can disrupt

their operations. These disruptions may decrease the system's efficiency or lead to partial or complete production failure, preventing the system from meeting demand constraints [10]. Potential external factors that may disrupt the operational stability of the nexus include governance frameworks, suboptimal management approaches, resource constraints, and the impacts of climate change [11]. Extreme weather events, policy shifts, geopolitical tensions, or technical failures further intensify nexus vulnerabilities [12]. The inherent uncertainties associated with these events render these critical systems fragile and threaten the continuous provision of essential power and water services. Ensuring resilience to such disruptions is crucial as the unpredictability of these stressors jeopardizes system stability, increasing risks to infrastructure networks and resource security. Climate change, in particular, is one of the primary drivers of instability. Hence, enhancing resilience within the nexus is essential for adaptation [3]. A system's resilience is defined by its ability to withstand, adapt, absorb, and recover from disturbances while maintaining functional service delivery [13].

## Resilience Challenges within the Energy-Water Nexus

Many resilience assessments in energy-water systems focused on evaluating individual subsystems in isolation, limiting their ability to capture the cascading impacts between interconnected components [4,10]. Additionally, some studies rely on static resilience analyses, overlooking the temporal variations in supply and demand that influence real-world infrastructure performance [3]. Emerging research highlights the need for integrated approaches that optimize resource allocation in the energy-water nexus to improve system resilience [14,15]. Process system optimization provides a structured framework for modeling interdependencies and resource flows, enabling cost-efficient decision-making. Adopting these models to the energy-water nexus to represent the subsystems as resource integration networks allows for scenario-based testing and performance evaluation.

A key limitation of current resilience studies is the lack of dynamic modeling to track system behavior over time. Accordingly, introducing a temporal scale into the steady-state resource allocation can bridge this gap by capturing the dynamic behavior of power and water production, as well as fluctuating demands [16]. Resilience must be quantified through scenario analysis to identify deviations from operational targets and expose system vulnerabilities. Incorporating resilience principles into the process system optimization provides a structured decision-making tool for addressing potential disruptions at both design and operation stages [13].

Before implementing resilience planning strategies, it is essential to assess the performance of the existing system and evaluate its vulnerabilities. This pre-assessment allows for optimization-driven solutions tailored to system characteristics and constraints [17]. While such vulnerability assessments have been widely applied in transportation networks and energy supply chains, they remain underutilized in the water-energy nexus domain [18,19].

## Approach and Key Contributions

This study adopts a superstructure-based optimization approach to assess the resilience of an energy-water nexus system under disruption scenarios. The resilience assessment focuses on the measurable impacts of capacity losses on functional service delivery, helping to identify system vulnerabilities and inform resilience enhancement strategies. By simulating disruptions, this approach aids in designing optimal operational adjustments

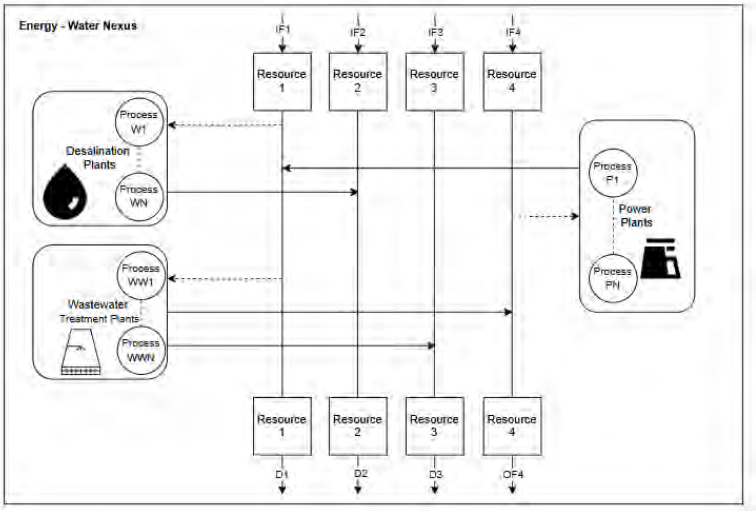



**Figure 1:** Shematic representation of the nexus superstructure

that minimize service interruptions and support system recovery.

To advance resilience modeling, this study introduces a resilience-driven optimization framework that:

- Integrates system-level scenario analysis to investigate cascading disruptions.
- Uses optimization-based resilience assessment to improve resource allocation.
- Incorporates time-dependent resource dynamics, capturing fluctuations in demand and production.
- Identifies key vulnerability thresholds to guide proactive mitigation strategies.

This quantitative approach provides a structured method for evaluating interdependencies and optimizing resource allocation under disruptions. By leveraging scenario-based stress testing, the framework offers actionable insights for policy and infrastructure planning.

# METHODOLOGY

## Energy-Water Nexus Resilience Optimization Framework

The proposed resilience-driven optimization framework integrates system modeling, resource allocation, and resilience quantification. The framework consists of three core stages:

- System Representation & Resource Allocation Modeling: This stage establishes the interconnections between power generation, desalination, and wastewater treatment systems. It defines the material and energy exchange pathways necessary for effective resource allocation and formulates resource balance equations to capture the interdependencies among the subsystems.
- Optimization & Operational Analysis: The second stage implements a cost-minimalization optimization model to balance supply and demand. It incorporates plant capacities, resource availability, and operational flexibility constraints to identify optimal operational configurations under stress scenarios.
- Resilience Assessment & Scenario Testing: The final stage introduces disruption scenarios ranging from partial to complete power losses to evaluate cascading impacts on the nexus. The Resilience

  Index and System Reliability are quantified metrics used to assess the system's performance under stress, revealing key vulnerability thresholds of the nexus.

## System Modeling and Optimization

The energy-water nexus system is represented at a macroscopic, high level in **Figure 1.** The system is modeled using a resource allocation model that captures the interactions between the main components: power plants, desalination plants, and wastewater treatment plants. These components are interconnected through resource lines, where main and auxiliary resources, including materials and energy, are exchanged within the physical constraints imposed by resource availability and plant capacities, adopting the method developed by Ahmed et.al [20]. The model has been advanced to incorporate a temporal scale, which is essential to reflect the dynamic behavior of the energy and water production systems, as well as the dynamic demands for functional services, following the model advances developed by Lameh et.al. and customizing it to the characteristics of the energy-water nexus [16]. The resource balance equation governing the model is:

$$IF(r,t) + \sum \varphi(r,p)CAP(p,t) + OF(r,t) = D(r,t) \quad \forall\, r \in R, p \in P, t \in T \tag{1}$$

Where $IF(r,t), OF(r,t), D(r,t) and\ CAP(p,t)$ are input resource flowrate, output resource flowrate, resource demand rate, and plant capacity respectively.$R, P and\ T$ are the sets of resources, processes and time periods respectively. $\varphi(r,p)$ is a factor that represents the ratio of resource production or consumption to the main resource produced by the process P. The resource allocation model is utilized in an optimization formulation that minimizes the total cost of the integrated system, accounting for components and resources capital and operation cost as given by the objective function:

$$Min\ (C_{CAPEX} + C_{OPEX} - R_{Total}) \tag{2}$$

Where, $C_{CAPEX}, C_{OPEX}, R_{Total}$ are the total capital cost, total operational cost, and total revenues, respectively. The aim is to meet water and electricity system demands at minimum cost. The incorporated subsystems are defined in the model on a technological basis (i.e., technologies for each type of production plant) and incorporate distinctive parameters for each type in terms of CAPEX, OPEX, and minimum and maximum capacities. These parameters are collected from peer-reviewed and reputable literature resources.

## Resilience Analysis

The system's performance is analyzed by observing the optimal solution of the optimization problem. It provides the most optimal operational load at which each production technology must be operated, revealing how much of the total capacity is utilized to meet the demand. The net balance of resources across the network is tracked to indicate the success or failure of the system

to meet the demand. A balance of zero ensures that a demand was met, while a negative balance indicates a shortage. In the later case, the model is directed to provide the needs through virtual, highly costed water and power reservoirs resulting in substantially high overall cost indicating system failure. The study focuses on revealing the nexus's vulnerability to potential losses of power production capacity as an impact of external stressors and how that impact cascades onto water and wastewater plants. Accordingly, disruption scenarios where the model is subjected to gradual losses of power production capacities, ranging from 0% to 100% power losses, are analyzed based on production technology type. This gradual reduction contributes to the loss of plant capacities that are associated with the technology under consideration.

A comparison between the demand variation over time and the system's output of water and electricity is conducted to reveal the system's bottlenecks. The resilience index and reliability of the system are evaluated in each scenario as metrics reflecting the resiliency level, according to the following equations:

$$RI = \frac{D - S_{Op}}{D} \quad (3)$$

$$SR\% = \frac{TD_{met}}{TS_{Op}} \times 100\% \quad (4)$$

where $RI$ is the Resilience index; $D$ is the demand for a functional service; $SR$ is the System reliability, reflecting the system's capability to meet the demand without failure; $TD_{met}$ is the total times the demand is met; and $TS_{Op}$ is the total times the system is operated.

## CASE STUDY

To demonstrate the method, an energy-water nexus system serving an arid region is investigated. The nexus comprises power generation facilities, desalination plants, and wastewater treatment facilities. The power plants produce both electricity and heat to meet external power demands and the needs of the desalination and wastewater treatment processes. The desalination plants generate potable water for domestic and industrial use, while the wastewater treatment facilities produce treated effluent to satisfy water demands for landscaping, irrigation, and limited agricultural activities in the region. The power production facilities incorporate three primary technologies: combined-cycle gas turbine with waste recovery (CCGT-CHP), open-cycle gas turbine (OCGT), and photovoltaic solar panels. The desalination plants employ thermal multi-effect desalination, multi-stage flashing, and reverse osmosis technologies. The wastewater treatment facilities range in scale from medium to large, utilizing secondary and tertiary treatment processes.

**Table 1** and

**Table 2** below summarizes the characteristics of the power plants, the featured nexus subsystem in this study, and the monthly demands for functional services. For demonstration purposes, disruption scenarios in which the production capacity of the dominant power generation technology is subjected to a loss percentage ranging from 0% to 100% are required to evaluate the nexus resilience and reliability to each of these impacts using the resource allocation model.

**Table 1** Power Generation Parameters

| Technology | CAPEX ($/MWh) | Max Capacity (TWh/yr) |
|---|---|---|
| CCGT-CHP | 10.7 | 77.6 |
| OCGT | 9.06 | 17.4 |
| PV | 7.5 | 3.07 |

**Table 2** Monthly demands of functional services

| Month | Power Demand (TWh) | Water Demand ($Mm^3$) | Treated Water Demand ($Mm^3$) |
|---|---|---|---|
| Jan | 2.96 | 52.0 | 11.0 |
| Feb | 2.66 | 47.7 | 10.4 |
| Mar | 3.43 | 54.1 | 12.3 |
| April | 3.98 | 55.9 | 15.7 |
| May | 4.82 | 58.0 | 17.5 |
| Jun | 5.45 | 57.4 | 18.5 |
| Jul | 5.86 | 58.5 | 18.3 |
| Aug | 6.35 | 60.2 | 18.4 |
| Sep | 4.48 | 34.0 | 17.4 |
| Oct | 4.02 | 33.7 | 17.3 |
| Nov | 3.25 | 30.7 | 15.1 |
| Dec | 2.76 | 29.6 | 14.0 |

## RESULTS AND DISCUSSION

The model was employed to examine the impact of losing varying proportions of the power production capacity associated with the predominant technology, the combined cycle gas turbine with waste heat recovery, denoted as T1 in **Figure 1**. This technology accounts for an average of 79% of the total power generation within the existing nexus system. The findings indicate that the nexus can tolerate up to a 20% loss of this technology's capacity, which is equivalent to a 16% reduction in the overall power production capacity of the nexus, while still being capable of meeting the demands for power, water, and treated wastewater effluent. This is demonstrated in **Figure 1(a)** where the resilience index of the system for all of the 3 subsystems involved maintains a value of 1. This is associated with an overall nexus reliability of 100% ensuring the nexus's ability to meet all the demands at all periods despite the impact of the external shocks by

relying on the remaining 84% of total capacity for power generation. As the loss percentage of this technology goes up to 40%, the integrated system succeeds in meeting the demands for both water and treated sewage effluent for all periods while it fails at delivering external power demands for the June to August period. This is reflected by a resilience index that drops to 0.975, 0.9, and 0.825 for these three months, respectively, as shown in **Figure 1(b)**. Alongside the massive loss of generation capacity, another main contributor to the declined system performance is associated with higher demand registered in these summer months. The overall nexus reliability registered for this scenario is 91.7%. **Figure 1(c)** reveals that the impact of losing 60% of T1 production capacity propagates to the water subsystem as reflected by the resilience index drop for this subsystem between the January and September period in addition to the system's inability to meet power demands in May to September. The observed differences in the failure frequencies between the two subsystems potentially hint at cost-based prioritization for power production over water desalination governed by the optimization algorithm, an interesting point that calls for further investigation. In **Figure 1 (d)** 80% loss of T1 led to insufficient power and water supplies for all periods except January and December, where water and power insufficiency altered, respectively bringing the nexus reliability down to 39%. At 100% loss of T1 capacity illustrated in **Figure 1 (e)**, the nexus system 79% of its power generation activities resulted in insufficient supplies of power and water at all periods with resilience indices below 0.6 for the associated subsystems and an overall reliability of 33%. The wastewater treatment subsystem maintained its resilience index at 1 in all scenarios, ensuring that the demand for treated sewage effluent was met. This may be attributed to the relatively lower power requirements and costs associated with the wastewater treatment processes.

## CONCLUSIONS

Using a resource allocation model within an optimization framework is a promising approach to guide decision-making for interconnected energy-water nexus systems. This method has demonstrated the ability to assess the system's resilience against quantified impacts of external stressors. In the examined case, the system could withstand up to a 21% loss of power production capacity before being unable to meet the demand for the interconnected subsystems' functional services. Furthermore, this method facilitates the analysis of each technology's contribution to the overall resilience scheme of the nexus. The optimization component ensures an optimal target is achieved as the system responds to a stressor impact, which may inform strategies that prioritize economic or environmental goals, depending on the set target. Consequently, this method can assist in

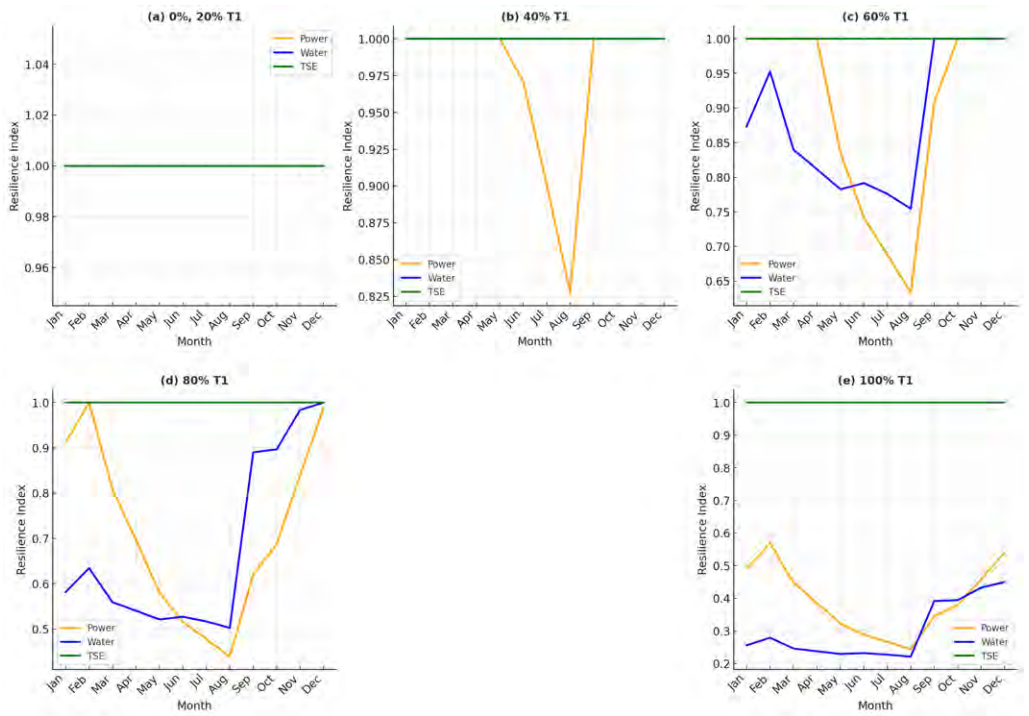



**Figure 1:** Resilience index of the energy-water nexus at various impacts of external stressors (a) 0%,20% T1 capacity loss (b) 40% T1 capacity loss (c) 60% T1 capacity loss (d) 80% T1 capacity loss (e) 100% T1 capacity loss

developing system hardening and emergency response plans to guarantee meeting all or prioritized demands from the nexus. These potential warrants further investigation in future work to help tailor strategies that enhance the resilience of the integrated nexus.

## ACKNOWLEDGEMENTS

The authors gratefully acknowledge the funding provided by the Qatar National Research Fund, Project Number NPRP14C-0920-21001.

## REFERENCES

1. Ghassemi, A., Hu, M. & Zhou, Z. Robust planning decision model for an integrated water system. J. Water Resour. Plan. Manag. 143, 05017002 (2017).
2. Elena, H., Vlad, C. & Marius-daniel, C. Interconnectivity between Energy and Water Supply Systems. Journal of Engineering Sciences and Innovation vol. 7 www.jesi.astr.roTechnology (2022).
3. Núñez-López, J. M., Rubio-Castro, E. & Ponce-Ortega, J. M. Involving resilience in optimizing the water-energy-food nexus at macroscopic level. Process Saf. Environ. Prot. 147, 259–273 (2021).
4. Urban, J. J. Emerging Scientific and Engineering Opportunities within the Water-Energy Nexus. Joule vol. 1 665–688 at https://doi.org/10.1016/j.joule.2017.10.002 (2017).
5. Al-Zu'bi, M. & Keough, N. Water, Energy and Food: The Problematic Aspects of the Transition from 'Silo Approach'to 'Nexus Approach'in the Arab Region. Water, Energy, Food People Across Glob. South 'The Nexus' an Era Clim. Chang. 15–61 (2018).
6. Atilhan, S., Linke, P., Wahab, A. A. & Halwagi, M. M. El. A systems integration approach to the design of regional water desalination and supply networks. Int. J. Process Syst. Eng. 1, 125 (2011).
7. Eke, J., Yusuf, A., Giwa, A. & Sodiq, A. The global status of desalination: An assessment of current desalination technologies, plants and capacity. Desalination 495, 114633 (2020).
8. Al-Saidi, M. & Saliba, S. Water, Energy and Food Supply Security in the Gulf Cooperation Council (GCC) Countries—A Risk Perspective. Water 11, 455 (2019).
9. Qureshi, A. S. Challenges and Prospects of Using Treated Wastewater to Manage Water Scarcity Crises in the Gulf Cooperation Council (GCC) Countries. Water 12, 1971 (2020).
10. Moglen, R. L. et al. A nexus approach to infrastructure resilience planning under uncertainty. Reliab. Eng. Syst. Saf. 230, (2023).
11. Núñez-López, J. M., Cansino-Loeza, B., Sánchez-Zarco, X. G. & Ponce-Ortega, J. M. Involving resilience in assessment of the water–energy–food nexus for arid and semiarid regions. Clean Technol. Environ. Policy 24, 1681–1693 (2022).
12. Sharifi, A. & Yamagata, Y. Principles and criteria for assessing urban energy resilience: A literature review. Renew. Sustain. Energy Rev. 60, 1654–1677 (2016).
13. Ganin, A. A. et al. Operational resilience: concepts, design and analysis. Sci. Rep. 6, 19540 (2016).
14. Zhang, X. & Vesselinov, V. V. Energy-water nexus: Balancing the tradeoffs between two-level decision makers. Appl. Energy 183, 77–87 (2016).
15. Hickman, W., Muzhikyan, A. & Farid, A. M. The synergistic role of renewable energy integration into the unit commitment of the energy water nexus. Renew. Energy 108, 220–229 (2017).
16. Lameh, M., Linke, P. & Al-Mohannadi, D. M. Carbon neutral energy systems: Optimal integration of energy systems with CO 2 abatement pathways. AIChE J. 70, (2024).
17. Ramirez-Marquez, J. E., Rocco, C. M. & Barker, K. Bi-Objective Vulnerability-Reduction Formulation for a Network under Diverse Attacks. ASCE-ASME J. Risk Uncertain. Eng. Syst. Part A Civ. Eng. 3, (2017).
18. Serdar, M. Z. & Al-Ghamdi, S. G. Resilience Assessment of Transportation Networks to Climate Change Induced Flooding: The Case of Doha Highways Network. in 277–284 (2023). doi:10.1007/978-981-99-4101-8_21.
19. Ibrahim, Y., Abraham, E. J. & Al-Mohannadi, D. M. A Systematic Analysis of Economic and Environmental Trade-Offs in Hydrogen Supply Chains with Resilience Considerations. in 2401–2406 (2024). doi:10.1016/B978-0-443-28824-1.50401-4.
20. Ahmed, R., Shehab, S., Al-Mohannadi, D. M. & Linke, P. Synthesis of integrated processing clusters. Chem. Eng. Sci. 227, (2020).

© 2025 by the authors. Licensed to PSEcommunity.org and PSE Press. This is an open access article under the creative commons CC-BY-SA licensing terms. Credit must be given to creator and adaptations must be shared under the same terms. See https://creativecommons.org/licenses/by-sa/4.0/



Systems & Control Transactions

**Research Article - Peer Reviewed Conference Proceeding**
ESCAPE 35 - European Symposium on Computer Aided Process Engineering
Ghent, Belgium. 6-9 July 2025
Jan F.M. Van Impe, Grégoire Léonard, Satyajeet S. Bhonsale,
Monika E. Polańska, Filip Logist (Eds.)

PSE PRESS

# Technoeconomic Analysis of a Novel Amine-Free Direct Air Capture System Integrated with HVAC

**Yasser M. Abdullatif[a,b], Ikhlas Ghiat[a], Riham Surkatti[b] ,Yusuf Bicer[a], Tareq Al-Ansarl[a,b], and Abdulkarem I. Amhamed[b,*]**

[a] College of Science and Engineering, Hamad Bin Khalifa University, Qatar Foundation, Education City, Doha, Qatar.
[b] Qatar Environment and Energy Institute (QEERI), Doha, Qatar.
*Corresponding author's email: aamhamed@hbku.edu.qa

## ABSTRACT

The increasing need for Direct Air Capture (DAC) technologies is driven by the urgent global need to mitigate rising $CO_2$ levels due to climate change. In humid climates, DAC systems face challenges as high humidity increases the energy required for regeneration. This study introduces a novel DAC system integrated within an Air Handling Unit (AHU) that includes a silica gel wheel for air dehumidification before $CO_2$ capture, significantly enhancing physisorbent performance by optimizing conditions for $CO_2$ adsorption. This system, tailored for the AHU of Doha Tower, involves dehumidifying return air, subsequently cooling it for effective CO2 capture. The introduction of the silica gel wheel notably reduced the energy requirements by 81.5% for NbOFFIVE compared to configurations without dehumidification, and the thermal energy cost for NbOFFIVE when integrated with HVAC and silica gel is 70 USD/ $ton_{CO2}$, compared to 160 USD/ $ton_{CO2}$ for SBA-15 + TEPA used alone. Additionally, the thermal energy cost for the HVAC system was reduced from 430 USD/$ton_{CO2}$ to 303 USD/ $ton_{CO2}$. A technoeconomic analysis highlights these improvements as crucial for reducing operational costs and cutting capital expenditures by leveraging existing AHU infrastructure. Despite the higher initial cost of NbOFFIVE, the levelized cost for DAC using NbOFFIVE is estimated at 184 USD per ton of $CO_2$, making it economically advantageous compared to 208 USD per ton for SBA-15.

**Keywords**: DAC, HVAC, Dehumidification, Chemisorption, Physisorption

## INTRODUCTION

Recent data shows a steady increase in global surface temperatures, with a notable 1°C rise since the pre-industrial period, making 2023 the hottest year to date [1]. These changes reflect broader climate shifts that manifest in altered weather patterns and varied precipitation across regions, contributing to environmental strain [2]. Within this context, the built environment emerges as a major energy consumer, responsible for substantial $CO_2$ emissions, particularly from systems like air conditioning that dominate building electricity usage [3, 4]. With projected temperature increases, the demand for cooling is expected to surge, potentially creating a feedback loop that could exacerbate global warming [5].

Direct Air Capture (DAC) technologies represent a promising avenue for mitigating atmospheric $CO_2$ levels. Unlike conventional methods that target emissions at their source, DAC systems capture carbon directly from the air, highlighting their potential in comprehensive climate strategies [6]. However, DAC's effectiveness is tempered by current technological and economic limitations, as evidenced by the modest capacity of existing facilities like the Orca in Iceland [16]. Innovations in material science and system design remain pivotal for enhancing DAC's efficiency and affordability, with costs of carbon removal varying widely [7].

The effectiveness of DAC is heavily influenced by the choice of capture materials—adsorbents and absorbents [8]. Adsorbents, in particular, are advantageous due to their lower energy requirements for regeneration and significant CO2 adsorption capabilities [9]. Developments in materials such as MOFs and amine-functionalized silica have achieved notable $CO_2$ uptake efficiencies

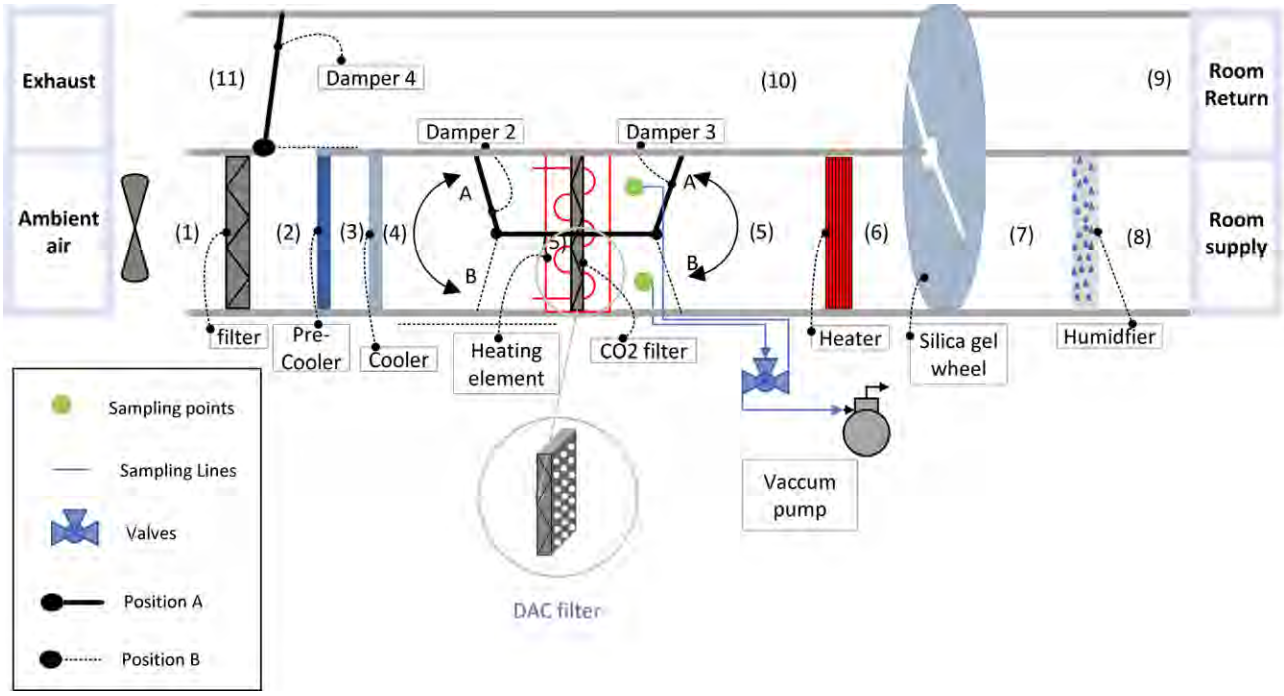



**Figure 1:** System diagram shows the Air handling unit compenents, DAC and silica gel wheel

under ambient conditions [10]. Yet, managing humidity remains a critical challenge, with innovations aimed at mitigating moisture to enhance system performance [11].

In advancing our previous investigations where the integration of DAC within HVAC systems to optimize energy use and $CO_2$ capture in buildings were investigated [12-15]. We examine the technoeconomic aspects of employing a novel physisorbent, NbOFFIVE with silica gel, and compare its performance and cost-effectiveness to a setup using SBA-15 alone, without silica gel. Both scenarios utilize integration within HVAC systems, aiming to establish a comparative understanding of their viability and scalability in urban structures like Doha Tower. This analysis seeks to identify the most efficient and economically feasible solution for large-scale implementation in modern buildings.

## METHODOLGY

### System description

In the configuration shown in Figure 1, return air is first dehumidified by passing through the silica gel wheel at Point 9, which was experimentally proven in our previous work to desorb water without heating, thereby reducing costs associated with water desorption. Following dehumidification, this air is mixed with the required fresh air at Point 2. The mixture is then cooled by the cooling coil to reach the supply temperature of 12°C at Point 3. After cooling, the dry, cooled air enters the Direct Air Capture (DAC) unit at Point 3, where $CO_2$ is captured using NbOFFIVE, a physisorbent free of amines. This material choice not only eliminates the cost of water desorption from DAC but also removes functionalization cost, enhances stability and avoids interactions of amines with air.

This system does not employ full recirculation as studied in [13] which reduces the need for additional filtration to manage airborne particulates, as fresh air is continuously introduced. However, it captures about 50% of ambient $CO_2$ levels due to the filtering of recirculated $CO_2$, with only fresh air and emissions from indoor occupants and appliances contributing to the $CO_2$ load. This setup will be compared to an alternative where SBA-15-TEPA [15] is used without a silica gel wheel and positioned at the beginning of the return stream at Point 9, both integrated within an Air Handling Unit (AHU) in an HVAC system. The comparative analysis aims to evaluate the performance and economic aspects of using NbOFFIVE versus SBA-15.

### Space and AHU design

In designing the AHU setup for a standard office space in Qatar, we considered a room volume of 800 $m^3$ with 30 occupants, aligned with ASHRAE standards for space allocation and ventilation. The AHU is optimized to maintain thermal comfort and indoor air quality, addressing both sensible and latent cooling loads. Our calculations incorporated factors like occupant density, equipment heat gains, and external climatic conditions, with special consideration given to the interaction

between one external wall and the conditioned space. The required supply flow rate was calculated to effectively manage these loads, ensuring stable indoor conditions of 23°C and a specific humidity ratio, by balancing the heat contributions from occupants, equipment, and infiltration.

## Adsorbents analysis

The $CO_2$ and water uptake capacities for SBA-15 functionalized with TEPA were measured using a dynamic adsorption experiments. This chemisorbent, known for its high $CO_2$ capture capacity, was tested under both dry and humid direct air capture (DAC) conditions using a 3P mixSorb analyzer. The rigorous synthesis and detailed characterization of these materials are comprehensively documented in the literature [15]. In contrast, NbOFFIVE, a fluorine-functionalized physisorbent, demonstrates excellent thermal stability with a $CO_2$ capture capacity of 1.3 mmol/g at 298 K in dry conditions. However, under humid conditions, its performance is reduced. The $CO_2$ and water uptake for NbOFFIVE were calculated based on a model outlined in the referenced study, utilizing following equations [16]:

$$q^*_{CO2} = q_s . b . \frac{P_{CO2}}{[1+(b.P_{CO2})^{\omega}]^{\frac{1}{\omega}}} \quad (1)$$

Where $P_{CO2}$ is the $CO_2$ partial pressure. The parameters b and ω describe the affinity and heterogeneity which are function of adsorption temperature and reference temperature, respectively. $q_s$ represents the saturation loading and expressed in temperature dependent form as shown in equation (2). The parameters b and $\omega$ describe the affinity and heterogeneity.

The water isotherm data under equilibrium conditions were fitted using Guggenheim - Anderson - de Boer (GAB) model [16]:

$$q^*_{H2O} = \frac{C_m C_G K_{ads} x}{(1-K_{ads}x)(1+(C_G-1)K_{ads}x)} \quad (2)$$

Here, the relative humidity is represented by x, and Cm, Cg and Kads are fitting parameters.

## Energy calculations

In this study, the energy required for the Thermal Swing Adsorption (TSA) process was estimated by building upon the methodology outlined in our previous work [17]. This involved considering the mechanical work needed for $CO_2$ compression, the heat necessary for desorbing $CO_2$ and $H_2O$, and the energy to facilitate the thermal swing of the sorbent and its adsorbed components. The analysis excluded parasitic losses such as pressure drops and heat dissipation. Energy consumption for sorbent regeneration was quantified, including the power for the vacuum pump operation, calculated as

$$W_{comp} = \frac{R . T_{pump}}{\eta_{pump}} . \ln\left(\frac{P_{amb}}{P_{des}}\right) \quad (3)$$

The sensible heat required to raise the sorbent to the desorption temperature was expressed as

$$Q_{sens} = \left(\frac{c_{p_{sorb}}}{\Delta q_{CO2}} + c_{p_{CO2}} + c_{p_{H2O}} \left(\frac{\Delta q_{H2O}}{\Delta q_{CO2}}\right)\right) . (T_{des} - T_{ads}) \quad (4)$$

The heat inputs for desorption enthalpies of $CO_2$ and H2O were calculated and added to the total heat per mole of separated $CO_2$ (Equations 5 and 6).

$$Q_{des} = \Delta H_{H2O} \left(\frac{\Delta q_{H2O}}{\Delta q_{CO2}}\right) + \Delta H_{CO2} \quad (5)$$

$$Q_{Total} = Q_{des} + Q_{sens} + Q_{cooling} \quad (6)$$

Furthermore, the main components of the AHU, including precooler, cooler, heater, and fan, were modeled using the mass balance equation, the first and second laws of thermodynamics, with the energy balance for each component detailed in [18], represented by

$$\dot{m}_i \times h_i + \dot{Q}_i + \dot{W}_i = \dot{m}_o \times h_o + \dot{Q}_o + \dot{W}_o \quad (7)$$

## Technoeconomic analysis

The levelized cost is calculated using Equation 8, which accounts for capital expenditures (CAPEX), fixed operating costs ($OPEX_{fix}$), variable operating costs ($OPEX_{var}$), and the amount of $CO_2$ captured ($CO_{2,captured}$). The CAPEX includes the base costs of equipment required for the TVSA process in the DAC system, such as the vacuum pump, heat exchanger, heat pump, and the adsorbent filters, as well as the costs associated with equipment delivery and installation. The variable OPEX accounts for utility costs, including electricity requirements for heating, cooling, and vacuum generation. The fixed OPEX covers maintenance, labor, insurance, administrative expenses, and filter replacement costs. The Capital Recovery Factor (CRF), which is used to annualize the capital investment over the project lifetime, is calculated using Equation 9. It is derived from the interest rate and project lifetime.

$$LC = \frac{CAPEX.CRF + OPEX_{fix}}{CO_{2,captured}} + OPEX_{var} \quad (8)$$

$$CRF = \frac{i(1+i)^n}{(1+i)^n - 1} \quad (9)$$

where i is the discount rate (7%) and n is the project lifetime (20 years) [19].

Moreover, a sensitivity analysis is performed to examine the impact of varying discount rates and utility prices, primarily electricity, on the levelized cost of the DAC system.

# RESULTS

Figure 2a displays the thermal energy required for

five different cases concerning HVAC and DAC systems. The first two bars (A and B) represent the cooling load consumption of an HVAC system when operating alone and within an integrated system incorporating DAC and silica gel (as outlined in Figure 1). The significant decrease in energy from A to B demonstrates the efficiency improvement when HVAC is combined with silica gel, which aids in moisture control.

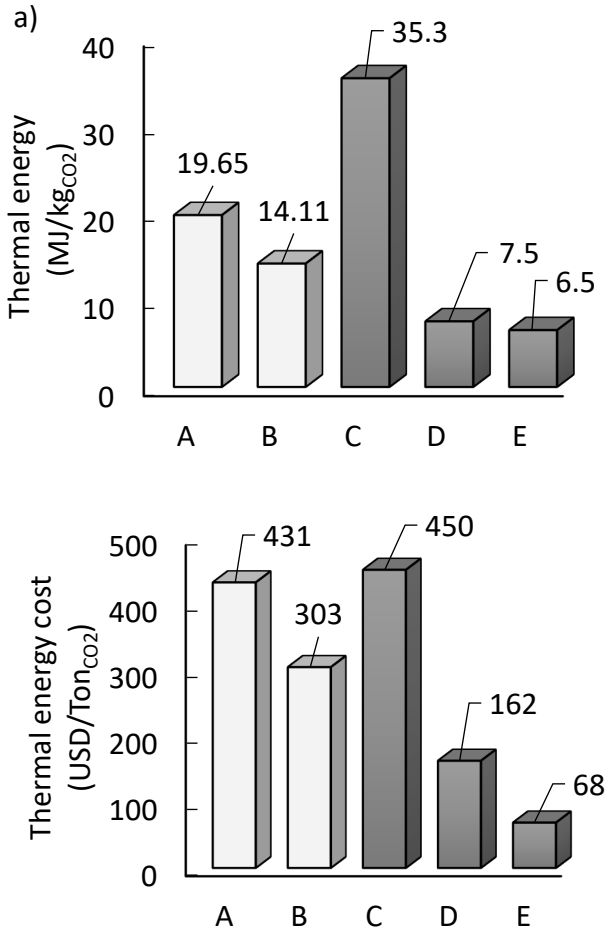



**Figure 2:** 2a) Thermal energy (MJ/kgCO2) and 2b) Thermal energy cost (USD/ $KgCO_2$ ) for (A) HVAC only, (B) HVAC within integration, (C) NbOFFIVE based DAC only, (D) SBA-15 + TEPA based DAC only, (E) NbOFFIVE based DAC within integration.

For bars C to E, it focus on DAC systems. The 'C' bar represents a DAC system using the physisorbent material NbOFFIVE, notable for its sensitivity to humidity, which explains its higher thermal energy consumption. Bar 'D' illustrates the thermal energy for a chemisorption-based DAC system using SBA-15 + TEPA, known for high $CO_2$ uptake efficiencies [15]. Finally, bar 'E' shows the reduced thermal energy consumption for an NbOFFIVE-based DAC system when integrated within the HVAC system incorporating silica gel wheel. This reduction highlights the effectiveness of integrating silica gel for moisture removal and leveraging the cooler air streams from the HVAC system, which significantly lowers thermal energy requirements, making it even more efficient than the SBA-15 + TEPA system.

Figure 2b correlates these thermal energies to their respective costs, normalized by the amount of $CO_2$ captured. The calculated costs incorporate the required electricity for a heat pump (assuming a COP of 2.6) and the local Qatari electricity rates (0.03 USD/kwh). This economic analysis further emphasizes the cost-effectiveness of integrated systems, particularly when using NbOFFIVE within an HVAC setup, due to the synergistic effects of reduced thermal loads and optimized energy use.

This detailed energy and cost analysis provides valuable insights into the selection of HVAC and DAC configurations, guiding towards choices that balance performance with economic feasibility in a climate-sensitive deployment scenario.

The levelized cost of the DAC system in this study is \$190 per ton of $CO_2$, which is within the range of \$88 to \$228 per ton of $CO_2$ estimated by the National Academy of Sciences (NAS) for DAC systems with solid adsorbents. Additionally, TVSA using a magnesium-based solid MOF sorbent has been reported to have a price range of \$60–\$190 per ton of $CO_2$[20].The sensitivity analysis indicates that the levelized cost of the DAC increases with a higher discount rate, reaching \$227 per ton of $CO_2$ at a 15% discount rate (Figure 3, a). Furthermore, utility prices significantly impact the levelized cost, with unsubsidized electricity prices in Qatar potentially driving the DAC's levelized cost up to \$306 per ton of $CO_2$ (Figure 3, b).

For SBA15 the levelized cost is 218 \$/ton $CO_2$. At a discount rate of 15% the cost gets higher to 251\$/ton $CO_2$ and at a high electricity cost of 0.14 \$/kWh the levelized becomes 438 \$/ton $CO_2$.

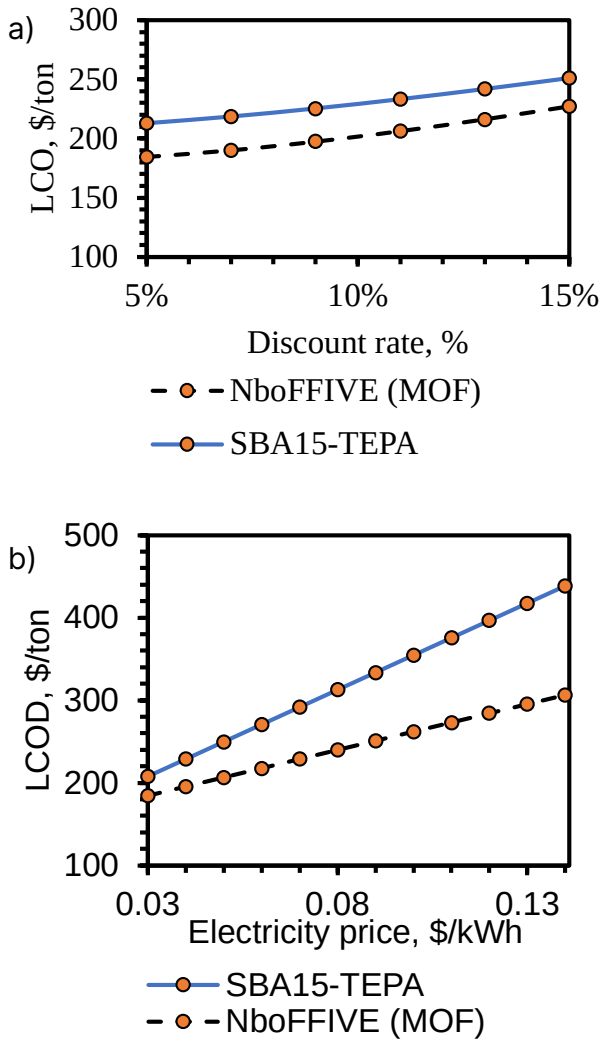



**Figure 3:** Effect of discount rate (a) and electricity price (b) on levelized cost of DAC.

## ACKNOWLEDGEMENTS

Authors acknowledge the financial support from Qatar Environment and Energy Research institute (QEERI), Hamad bin Khalifa University (HBKU) (member of Qatar Foundation). The authors also would like to acknowledge the Core Labs and Hamad Bin Khalifa University for their contribution in the material characterization. This publication was made possible by NPRP 12 grant # (NPRP12C-0821-190017), GSRA8-L-1-0506-21032 from the Qatar National Research Fund (a member of the Qatar Foundation). The findings herein reflect the work and are solely the responsibility of the authors. Open Access funding provided by the Qatar National Library.

### Conclusion

In conclusion, this study demonstrates the significant potential of integrating Direct Air Capture (DAC) technology within an Air Handling Unit (AHU) to effectively mitigate the challenges posed by high humidity in DAC systems. By incorporating a silica gel wheel for air dehumidification before $CO_2$ capture, the system tailored for the AHU of Doha Tower significantly enhances the performance of physisorbents like NbOFFIVE, reducing their energy requirements by 81.5% compared to traditional configurations. This integration not only leads to a substantial decrease in thermal energy costs—from 430 USD/tonCO2 to 303 USD/ton$CO_2$ for the HVAC system and from 160 USD/ton$CO_2$ to 70 USD/ton$CO_2$ for NbOFFIVE—but also notably lowers the levelized cost of DAC to 184 USD per ton of $CO_2$, offering an economic advantage over systems using SBA-15 + TEPA. Furthermore, this innovative integration allows for the utilization of an amine-free system, marking a significant advancement, particularly for indoor applications where health concerns are paramount. The technoeconomic analysis underscores the crucial role of leveraging existing AHU infrastructure to cut operational costs and capital expenditures, making this integrated DAC system a highly attractive solution for large-scale $CO_2$ capture in building environments.

## REFERENCES

1. Esper, J., et al., *The IPCC's reductive Common Era temperature history.* Communications Earth & Environment, 2024. **5**(1): p. 222.
2. Trancoso, R., et al., *Significantly wetter or drier future conditions for one to two thirds of the world's population.* Nature Communications, 2024. **15**(1): p. 483.
3. González-Torres, M., et al., *A review on buildings energy information: Trends, end-uses, fuels and drivers.* Energy Reports, 2022. **8**: p. 626-637.
4. Abdullatif, Y.M., et al., *Thermodynamic analysis of gravity assisted solar-powered reverse osmosis unit for greenhouses situated in a depleted zone.* Case Studies in Thermal Engineering, 2021. **25**: p. 100990.
5. Ghazi, B., R. Przybylak, and A. Pospieszyńska, *Projection of climate change impacts on extreme temperature and precipitation in Central Poland.* Scientific Reports, 2023. **13**(1): p. 18772.
6. McQueen, N., et al., *A review of direct air capture (DAC): scaling up commercial technologies and innovating for the future.* Progress in Energy, 2021. **3**(3): p. 032001.
7. You, T., *Research on the Current Situation and Future Development Trends of Direct Air Capture Technology.* Highlights in Science, Engineering and Technology, 2024. **83**: p. 349-353.
8. Essehli, R., et al., *Single crystal structure, vibrational spectroscopy, gas sorption and antimicrobial properties of a new inorganic acidic*

*diphosphates material (NH4)2Mg(H2P2O7)2•2H2O.* Scientific Reports, 2020. **10**(1): p. 8909.
9. Zavahir, S., et al., *Fluorescent Zn(II)-Based Metal-Organic Framework: Interaction with Organic Solvents and CO2 and Methane Capture.* Molecules, 2022. **27**(12): p. 3845.
10. Lai, J.Y., L.H. Ngu, and S.S. Hashim, *A review of CO2 adsorbents performance for different carbon capture technology processes conditions.* Greenhouse Gases: Science and Technology, 2021. **11**(5): p. 1076-1117.
11. Wilson, S.M. and F.H. Tezel, *Direct dry air capture of CO2 using VTSA with faujasite zeolites.* Industrial & Engineering Chemistry Research, 2020. **59**(18): p. 8783-8794.
12. Abdullatif, Y., et al., *Emerging trends in direct air capture of CO 2: a review of technology options targeting net-zero emissions.* RSC advances, 2023. **13**(9): p. 5687-5722.
13. Abdullatif, Y.M., et al., *Optimizing chemisorption based direct air capture unit efficiency in HVAC systems: A study on the impact of DAC location and adsorption conditions as a response to the climate crisis and indoor air quality.* Energy Conversion and Management, 2023. **291**: p. 117280.
14. Sodiq, A., et al., *A review on progress made in direct air capture of CO2.* Environmental Technology & Innovation, 2023. **29**: p. 102991.
15. Surkatti, R., et al., *Comparative analysis of amine-functionalized silica for direct air capture (DAC): Material characterization, performance, and thermodynamic efficiency.* Separation and Purification Technology, 2025. **354**: p. 128641.
16. Balasubramaniam, B.M., et al., *Process-performance of solid sorbents for Direct Air Capture (DAC) of CO2 in optimized temperature-vacuum swing adsorption (TVSA) cycles.* Chemical Engineering Journal, 2024. **485**: p. 149568.
17. Abdullatif, Y.M., et al., *Optimizing chemisorption based direct air capture unit efficiency in HVAC systems: A study on the impact of DAC location and adsorption conditions as a response to the climate crisis and indoor air quality.* Energy Conversion and Management, 2023. **291**.
18. Abdullatif, Y.M., et al., *Thermodynamic analysis of gravity assisted solar-powered reverse osmosis unit for greenhouses situated in a depleted zone.* Case Studies in Thermal Engineering, 2021. **25**.
19. Fasihi, M., O. Efimova, and C. Breyer, *Techno-economic assessment of CO2 direct air capture plants.* Journal of Cleaner Production, 2019. **224**: p. 957-980.
20. Azarabadi, H. and K.S. Lackner, *A sorbent-focused techno-economic analysis of direct air capture.* Applied Energy, 2019. **250**: p. 959-975.

© 2025 by the authors. Licensed to PSEcommunity.org and PSE Press. This is an open access article under the creative commons CC-BY-SA licensing terms. Credit must be given to creator and adaptations must be shared under the same terms. See https://creativecommons.org/licenses/by-sa/4.0/



Systems & Control Transactions

**Research Article - Peer Reviewed Conference Proceeding**
ESCAPE 35 - European Symposium on Computer Aided Process Engineering
Ghent, Belgium. 6-9 July 2025
Jan F.M. Van Impe, Grégoire Léonard, Satyajeet S. Bhonsale,
Monika E. Polańska, Filip Logist (Eds.)

PSE PRESS

# Exploiting Operator Training Systems in chemical plants: learnings from industrial practice at BASF

**Frederic Cuypers[a], Tom Boelen[a*] and Filip Logist[a]**

[a] BASF Antwerpen NV, Advanced Process Control, Antwerpen, Belgium
* Corresponding Author: Tom.boelen@basf.com

## ABSTRACT

Demographic shifts and increased automation in chemical plants are reducing the experience and skill levels of plant operators. Therefore, BASF has implemented Operator Training Simulators (OTS) to allow operators to practice and improve their skills in this safe and controlled environment. The OTS consists of a dynamic model of the process, a control system and safety logics. This paper describes the learnings from using OTS at BASF, where they are used to train operators in process understanding, optimization, procedural training, and disturbance handling. Benefits include reduced training costs, minimized risks and improved efficiency. Also organizational guidelines are provided to ensure that the mentioned benefits are realized in industrial practice. Additionally, high-accuracy OTS models support HAZOP, debottlenecking, and optimization studies.

**Keywords**: Simulation, Optimization, Modelling and Simulations, Training Systems, Digital Twin, Dynamic Modelling

## INTRODUCTION

The chemical industry is characterized by complex processes and stringent safety requirements, making the training of operators a critical component for ensuring operational efficiency and safety. Traditional training methods, while effective to some extent, often fall short in providing hands-on experience and real-time decision-making skills necessary for modern plant operations.

Furthermore, a significant demographic shift and a surge in automation, has led to a decline in the experience and skill levels. This trend is further exacerbated by the fact that new operators are accustomed to different learning methods compared to their predecessors. Consequently, there is an urgent need for innovative training solutions to bridge the skills gap and ensure operational safety and efficiency.

*Operator Training Simulators* (OTS) (see, e.g., [1-3]) have become indispensable tools within BASF to address these challenges. OTS provide a realistic and immersive training environment where operators can practice and enhance their skills in a safe and controlled setting. Furthermore, the OTS system serves as a *digital twin* of the plant, allowing to test changes in control structure and perform optimisation process studies [4]. These OTS's simulate the dynamic behavior of the chemical plant with a *dynamic first principles model*, replicate the behavior of the *Distributed Control System* (DCS) system including the *Human Machine Interface* (HMI) and process controls and the safety logics, offering a comprehensive training experience.

In this paper, first the different types of OTS systems are discussed, followed by the technical details of how an OTS is set up. Third, insight is given in the way OTS's are embedded in the organization from a management perspective followed by some case studies. Operators trained with OTS exhibit improved problem-solving skills, faster response times, and a better understanding of process safety. Furthermore, the use of OTS has been linked to a reduction in operational errors and incidents, contributing to overall plant safety and efficiency. Finally, a summary is presented including lessons learned.

## TYPES OF OTS SYSTEMS

Industrial OTS systems consist of 3 distinct main parts as depicted in Figure 1:

- a detailed *dynamic model* which accurately describes the plant behavior.

- an emulation of (i) the *Distributed Control System* (DCS), comprising the process controls and logics, and (ii) the *Safety Interlock System* (SIS), comprising the separate safety system.
- a *Human Machine Interface* (HMI), displaying all sensor values on a process diagram and allowing the operator to interact with the process.

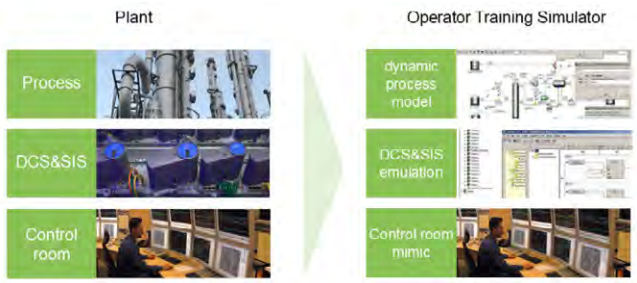



**Figure 1.** Components of an OTS system.

A distinction between 3 classes of OTS's can be made based how accurately the real plant is represented by the OTS and the way the above-mentioned components are implemented: (i)*High Fidelity* (HiFi) OTS, (ii) *Mid Fidelity* (MiFi) OTS and (iii) *Low Fidelity* (LoFi) OTS. Here is HiFi-OTS the most expensive and complex to implement while the other two are a less accurate representation of the plant, but at a significant lower implementation cost and complexity. Below, we will briefly discuss every type. Figures 2 and 3 summarize their features.

The **HiFi OTS** is distinguished by its highly detailed and realistic modeling, designed to closely replicate actual plant operations. This system facilitates comprehensive training, encompassing both the start-up and shut-down processes of the plant, as well as the management of random scenarios. The HiFi OTS employs components for the DCS that are virtually identical to those used in the actual DCS, ensuring that the training environment accurately mirrors the real control system. Furthermore, it features the same HMI as the real DCS, providing operators with a familiar and intuitive interface. The SIS within the HiFi OTS is also an exact replica of the real SIS, enhancing the realism and effectiveness of the training experience. Because this type of OTS matches closely the real plant, the OTS also serves as a digital twin allowing to, e.g., test DCS changes and perform plant optimization and safety studies. A HiFi-OTS is particularly advantageous for plants that experience infrequent shut-downs and where unplanned trips are exceedingly costly. In general, this OTS is considered for larger plants with typically more than 5000 IO's (Input/Output points). By providing a realistic and immersive training environment, the HiFi OTS enables operators to develop and refine their skills, thereby improving operational efficiency and safety.

The **MiFi OTS** is most suited for smaller plants which have more frequent shutdowns, are less complex and have less costly plant trips. For such plants, MiFi OTS offers a better balance between cost and functionality, making it a practical choice for enhancing operator training and plant performance. The development of MiFi OTS was primarily driven by the need to reduce the investment costs associated with a traditional HiFi OTS, thereby allowing a broader adoption across various plants and processes. By simplifying the OTS architecture, MiFi OTS achieves a significant cost reduction. It employs a simpler first principles model, which focuses on fundamental process dynamics rather than the precise replication of real plant behavior. As a result, MiFi OTS typically does not support plant start-up simulations, which are often complex and require much more modelling effort. One of the key cost-saving features of MiFi OTS is the elimination of the substantial expenses linked to the representation of the DCS system and the SIS system. Instead of relying on these complex and licensed systems, MiFi OTS integrates process controls, DCS logic, and SIS logic directly within the first principles model. This integration not only reduces costs but also simplifies the overall system architecture. The graphical interface of the DCS HMI is emulated using a multifunctional graphical software package, ensuring a user-friendly interaction that generally mimics the actual plant HMI environment. MiFi-OTS is generally envisioned for plants with 1000-2000 Input/Output (I/O) points, seeking a cost-effective and less complex OTS, while still enabling training of normal operations, standard scenarios and standard procedures.

**LoFi OTS** (or generic OTS) are designed around standard unit operations to train new operators during their initial weeks. They provide a foundational understanding of basic processes and procedures, aiming to enhance the competence and confidence of new hires.

At BASF Antwerpen, the focus is on MiFi OTS and HiFi OTS. These systems allow for plant specific training with higher effectiveness on different training levels. LoFi OTS is not used often within BASF Antwerpen due to the limited learning experience which is only relevant during the first weeks of onboarding. In this paper we will therefore further focus on HiFi OTS and MiFi OTS.

## BUILDING AN OTS

Different elements are needed to build an OTS. Depending on the type of OTS envisioned and the plant condition, the requirements can change slightly. As mentioned, we focus in this paper on the cases of MiFi and HiFi OTS.

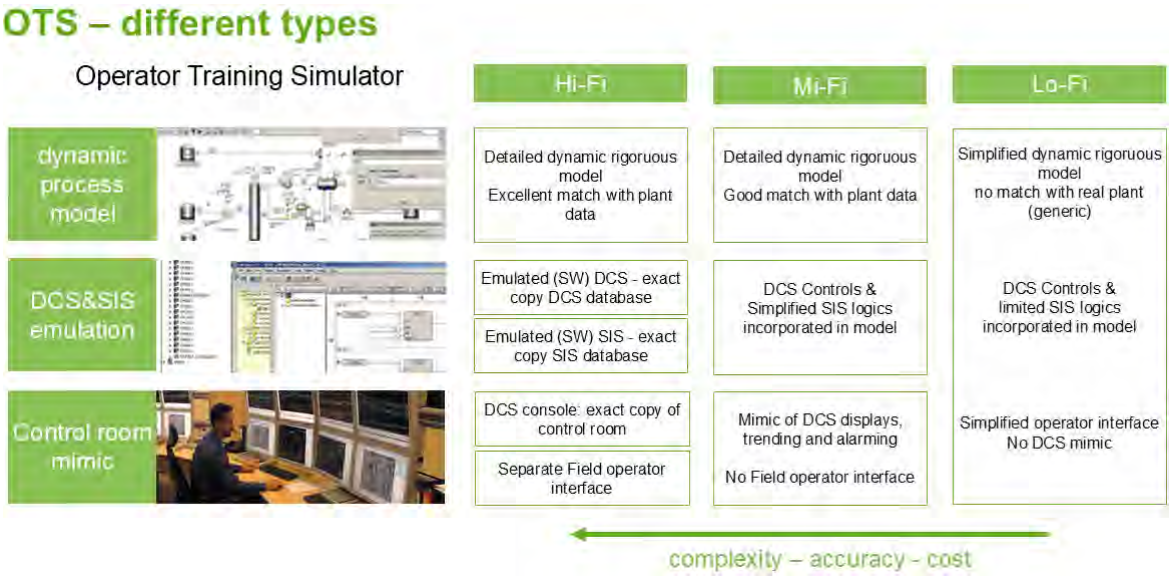



**Figure 2.** Different components of the various types of OTS systems.

| Type | Scope | Training | | | | | Testing | | Cost | |
|---|---|---|---|---|---|---|---|---|---|---|
| | | Training level | Understand process | Defined scenarios | Startup/S hutdown | Random scenarios | DCS/SIS changes | Process changes | Invest | Maintain |
| Hi-Fi | Whole plant (>5000 IO's) | Monitor<br>Operate<br>Master | ✓<br>✓<br>✓ | ✓<br>✓ | ✓ | ✓ | ✓ | ✓ | 1000k€ - 2000k€ | 5-10% |
| Mi-Fi | Section/small plant (250 – 5000 IO's) | Monitor<br>Operate<br>Master | ✓<br>✓<br>✓ | ✓<br>✓ | ✗<br>✗ | ✗ | ✓ limited | ✓ limited | 150k€ - 500k€ | 5-10% |
| Lo-Fi (generic) | Unit operation (<250 IO's) | Monitor<br>Operate<br>Master | ✓<br>✓<br>✓ | ✗<br>✗ | ✗<br>✗ | ✗ | | | 50k€ - 150€ | 5% |

**Figure 3.** Comparison between different types of OTS systems.

## REQUIRED INFORMATION

Different information is needed for the dynamic model of a plant. In view of the general plant set-up this includes (i) process flow diagrams (PFD) for the general plant lay-out (including the material and heat balances), (ii) Piping and Instrumentation Diagrams (P&IDs) for the over-all pipe connections and control design, (iii) equipment design sheets of all equipment (e.g., reactors, columns, tanks, heat exchangers, pumps, valves, compressors, sensors, ….) for the mechanical and thermal behavior, (iv) a scheme describing the relative heights of the different equipment. In view of the chemical and thermodynamical modeling this includes among others reaction kinetics, vapor-liquid equilibrium data. For HiFi OTS detailed information for all items is needed. For MiFi OTS, several aspects of can be simplified (e.g., linear valve curves, lumped kinetics and thermodynamics, and approximated thermal and kinetic equipment inertia). In view of process control functional descriptions of the different control structures are needed. When constructing an OTS, the dynamic simulations must be validated against plant data. Typically, this is performed section by section. For the brownfield OTS projects (where the plant already exists) this can be done against actual plant data. For greenfield OTS projects (where the plant is being constructed) it must be done against the (steady-state) simulation data that was gathered during plant design phase, more specifically the heat and material balance of each unit and stream.

In view of the HMI interface, there is a large difference between MiFi and HiFi OTS. For HiFi OTS the actual DCS configurations and faceplates are needed and have to available. Typically, the actual DCS system will be emulated. For MiFi OTS a selection of the actual DCS features has to programmed using DCS screenshots.

## Modeling and simulation tools

Different dynamic flowsheet simulators exist. At BASF Antwerpen the following ones are used: Aspen HYSYS (AspenTech) for MiFi OTS and DynSim (Aveva) and UniSim (Honeywell) for HiFi OTS. Apart from typical simulation aspects (mass and energy balances), the tools also have to include typical aspects for process control and process safety. This includes PID and possibly MPC controllers as well as alarming features and cause and effect schemes that guarantee the interlock and trip behavior of different equipment.

## Graphical tools

For MiFi OTS specific software is needed to create the HMI layer as the actual DCS screens and faceplates are not being emulated. Instead a mimic of the DCS displays is built covering most the most important functionality and information to be presented to the operator. At BASF Antwerpen the InProcess Infrastructure Suite IIS (InProcess) is used for this purpose.

## Software and hardware set-up

From an ICT point of view, a typical set-up of an OTS will be different for a MiFi and a HiFi OTS.

In Figure 4 a typical example of for the set-up of a HiFi OTS is given. This set-up comprises two virtualized servers hosting the different components of the process control and simulation network. These components are connected via ethernet to a switch. To this switch are also a NAS, the different operator stations as well as the instructor station connected.

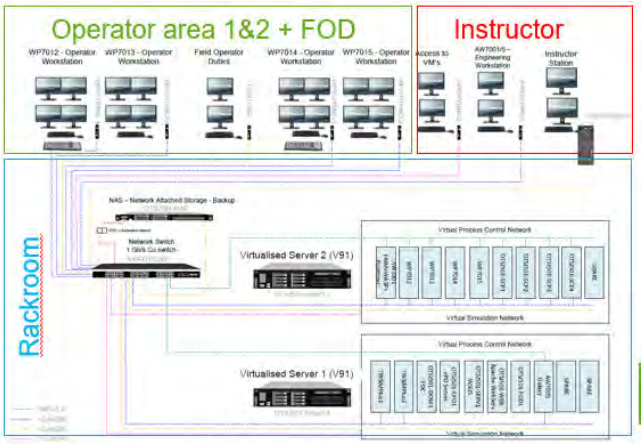



**Figure 4.** ICT components of a HiFi OTS system.

For MiFi OTS the ICT framework is simpler (see Figure 5). It comprises of a single server, where both the simulation and the HMI runs. This server is connected via the local network to an operator and an instructor station. The number of components for a MiFi OTS is low compared to the set-up of HiFi OTS .

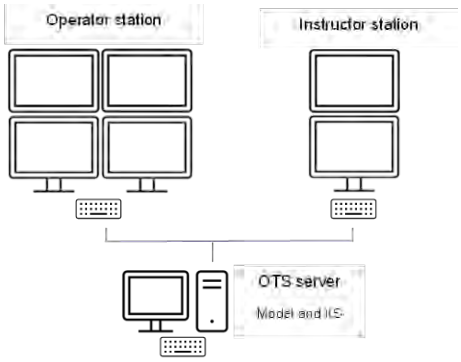



**Figure 5.** ICT components of a MiFi OTS system.

The operator working console should be mimicked as closely as possible in the training room. This means, for instance, that the operator should have sufficient screens to displays trends alongside the DCS screens. The typical quad-head setup is mimicked from the control room. Typically, in the training room there is a console for the trainer, who can interact with the simulation, e.g., by initiating different scenarios and disturbances. A picture of an OTS training room is presented in Figure 6.




**Figure 6.** View of an HiFi OTS training room.

# OTS TRAINING APPROACH

Continuous training of the operators is required to improve and maintain their skill level to assure correct operator actions in case of specific situations. OTS training has become an essential part of this continuous operator training journey within BASF.

Within BASF the skill level of operators is typically increased in three steps:

- *Monitor* level: the operator needs to be able to understand and interpret how the process is working. At this level the operator is not yet allowed to operate the plant/process from the DCS panel.
- *Operate* level: the operator is able to operate the plant from the DCS panel in normal conditions and he is able to act properly to reject smaller disturbances.
- *Master* level: the operator is able to handle the

process properly in all situations including bigger disturbances and full start-up/shut-down.

OTS is an effective training tool to reach the different skill levels mentioned above and/or to sustain the knowledge at the desired level as is depicted in Figure 3:

- *Monitor* level: basic process behavior, dynamic interactions in the plant/section can be explained and illustrated to the trainee on the OTS. The OTS is an ideal environment to explore the information displayed on and demonstrate the functionality of DCS (displays, PID faceplates, trends, alarm lists, control concepts, ...).
- *Operate* level: operators can train on the OTS how to handle the plant during, e.g., load changes or specific disturbances (e.g., smaller equipment failures) can be introduced on the OTS on which the trainee needs to respond in a correct and timely manner.
- *Master* level: the trainee can train full start-up and shut-down. Random disturbances can be introduced on OTS (equipment failures/trips) causing significant disturbances to be handled by the operator.

**HiFi OTS** systems can cover training to reach (or sustain knowledge at) all three levels mentioned above. In large, complex plants where an HiFi OTS is available, it is important to bring operators efficiently to a basic operating skill level but it is equally important to maintain and even deepen the skills of the more experienced operators (operate and master level). An evolution of the registered training of a HiFi OTS at BASF Antwerpen is depicted in Figure 7.

**MiFi OTS** systems are typically more limited in functionality (e.g. limited number of available scenario's). Consequently, they mainly focus on training towards the *monitor* and *operate* level. Typically, the plants/sections for which a MiFi OTS is available, have a smaller scope and lower complexity compared to plants where the choice is made for a HiFi OTS. In such a case (smaller scope, lower complexity plants) intensive training of operators on the *master* level is less crucial as well.

In most plants with an OTS a dedicated training instructor manages and coordinates all the training activities within the plant. The *training instructor* is *key for the success* and effectiveness of the OTS as training tool. In most BASF plants where an OTS is introduced we have a combination of training sessions on OTS performed by the instructor (typically during day time or depending on availability of the instructor) and training sessions without instructor (e.g., during night/weekend). *Instructor-led* training sessions are required to transfer knowledge in a consistent way to the trainees and to give them correct feedback on the actions taken on the OTS. *Instructor-less* training sessions allow the trainee to train on his own (e.g. repeat training sessions/scenarios performed with the instructor). *Instructor-less* training is in some cases supported by definition of kpi's (key performance indicators) to track the operator performance during the execution of a certain task on the OTS: kpi's can be defined as time or process criteria: achieve goals within time limit, while assuring not to exceed certain process parameters.

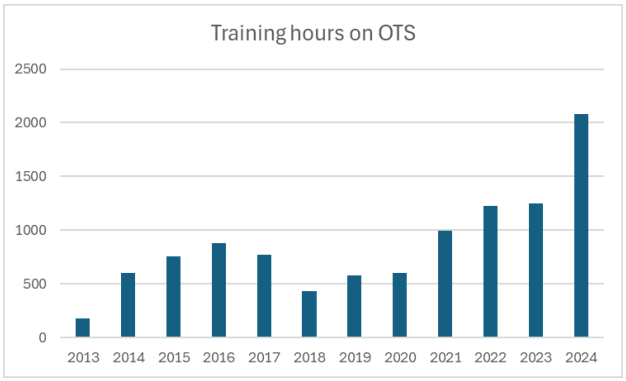



**Figure 7.** Registered training hours for a HiFi OTS at BASF Till 2022 only instructor-led trainings were registered.

## OTS AS A DIGITAL TWIN

The focus for an OTS application is training as described above. However, the rigorous dynamic plant model and the link with the control system (DCS/SIS) allows the OTS to be used for a broader range of applications ranging from process (control) optimization and design to safety studies. Below two examples are given of how OTS can be used as a digital twin to bring substantial benefits by supporting other activities besides training.

### "Parking lot" sequence for the steam cracker plant

For the steam cracker, i.e., the biggest and most complex plant at the BASF Antwerp site, a "parking lot" sequence concept has been developed. The aim of this sequence is to support the operator in case of a serious plant disturbance and to bring the plant quickly to a safe and stable state ("parking lot"). This allows a faster recovery to normal load and avoids a full trip of the plant. When the full "parking lot" sequence is activated around 150 variables (setpoints, valves, ...) are triggered to reach a desired position. The full concept was first implemented on the HiFi OTS to verify its correct operation. The HiFi OTS environment is used as an accurate digital twin allowing for full dynamic response evaluation of the plant in case the sequence is activated. In addition the operators were trained on the OTS on what to expect in case the sequence is activated. Only after these steps, the final version of the "parking lot" sequence was implemented on the real plant. This approach (validation and training on OTS first) assures a "first time right" implementation in the real plant and on top a very high

acceptance of the operators since they feel confident that the sequence and logics will work as expected. In the years the "parking lot" sequence has been implemented it was activated a couple of times working as expected. This allowed the plant to stabilize and recover to normal plant load quicky, minimizing production losses.

### Greenfield OTS: a digital twin for a new plant

Building an OTS for a greenfield plant (greenfield OTS) is especially beneficial to assure a smooth and efficient start-up of the plant due to different reasons.

The OTS can be used to train the operators extensively in order to improve and speed up significantly the understanding of the new process and how to handle it (e.g. start-up/shut-down) before the actual plant is started up. Having the OTS already available before the start-up of the plant will allow the start-up/shut-down procedures to be validated thoroughly and where required adjusted. Having the OTS available in this stage of the project allows as well to validate in detail the control concepts (DCS) and safety logics (SIS) in more detail compared to the typical FAT (factory acceptance testing) protocols applied for the DCS and SIS. The OTS allows full dynamic testing of the interaction of all the controls and logics in all different states of the process. The control concepts and logics can be improved based on the outcome of these detailed dynamic tests. Stable and dynamic behavior of the process is also related to the tuning of the PID controllers in the DCS. The OTS serves as digital twin and is the ideal test bank to provide appropriate initial values for the PID tuning. The PID parameters obtained during the testing and training on the OTS can be transferred to the life system before start-up. Sometimes conceptual design errors are identified during greenfield OTS projects that require equipment changes. An example from one of the greenfield OTS projects is the wrong sizing and positioning of an outlet nozzle on a drum not allowing to collect sufficient liquid in the drum to operate properly in all circumstances.

As illustrated above, the use of a greenfield OTS as a digital twin facilitates the early detection of all kinds of design errors (equipment, controls, procedures, …) which leads to a smoother start-up and significantly reduced start-up times. Due to the OTS training before start-up, operators are familiar with the procedures and feel much more confident to start up their greenfield plant.

## OTS MAINTENANCE

Plants are subject to modifications continuously, either to improve process efficiency or for safety reasons, equipment, piping, controls and logics are changed throughout the lifetime of a plant. Keeping the OTS aligned with the real plant is important for operators to experience the actual plant's state properly on the OTS. Training of operators on an outdated OTS system (OTS not fully in line anymore with the real plant) significantly reduces the effectiveness of the training. To avoid this degradation of the OTS training experience, regular maintenance on the OTS is required. The maintenance includes model changes (to reflect, e.g., equipment and piping changes) as well as control and logic changes (to reflect changes in DCS&SIS). Typically, maintenance is performed by a process control engineer (e.g., model changes, control and logics changes) together with the instructor (validating the applied changes in the OTS). The maintenance frequency depends on the number of plant modifications in the real plant but typically ranges from twice to once a year. Typical bigger maintenance activities on OTS are related to turn around (TAR) activities of the real plant in which major modifications are implemented on the real plant. Again, here the OTS can serve as the perfect test bank (digital twin) for changes to be applied during the TAR by implementing and testing the OTS relevant changes before the TAR takes place.

## CONCLUSION

OTS systems have become a vital tool for training starting as well as experienced operators within BASF. At BASF Antwerpen, the deployment of both High Fidelity (HiFi) and Mid Fidelity (MiFi) OTS has enabled to differentiate and tailor these training tools to different types of plants, enabling a wider adoption. The presence of a dedicated instructor is critical for the effective implementation and utilization of an OTS, ensuring consistent and impactful training. Furthermore, regular maintenance of an OTS is imperative to maintain the alignment with real plant conditions, thereby preserving its relevance and efficacy as training instrument. Beyond their primary training function, OTS also serve as a digital twins, facilitating the testing and validation of modifications in the DCS&SIS or the plant itself of both green/brownfield plants.

## REFERENCES


1. DS Patle, Z Ahmad, GP Rangaiah. Operator training simulators in the chemical industry: review, issues, and future directions. *Rev Chem Eng* 30: 199-216 (2014) https://doi.org/10.1515/revce-2013-0027
2. DS Patle, D Manca, N Salman, S Swapnil. Operator training simulators in virtual reality environment for process operators: a review. *Virtual Reality* 23: 293-311 (2018). http://dx.doi.org/10.1007/s10055-018-0354-3
3. R Kallakuri, PC Bahuguna. Role of Operator Training Simulators in Hydrocarbon Industry – a Review. *Int J Sim Mod* 20: 649-660 (2021) https://doi.org/10.2507/ijsimm20-4-575.
4. G Yang, Z Xu, Z Shao, H Liao, M Yu. Dynamic load

change operation education in air separation processes using a multivariable and nonlinear model. *J Proc Control* 116: 93-113 (2022) https://doi.org/10.1016/j.jprocont.2022.05.009

© 2025 by the authors. Licensed to PSEcommunity.org and PSE Press. This is an open access article under the creative commons CC-BY-SA licensing terms. Credit must be given to creator and adaptations must be shared under the same terms. See https://creativecommons.org/licenses/by-sa/4.0/



Systems & Control Transactions

**Research Article - Peer Reviewed Conference Proceeding**
ESCAPE 35 - European Symposium on Computer Aided Process Engineering
Ghent, Belgium. 6-9 July 2025
Jan F.M. Van Impe, Grégoire Léonard, Satyajeet S. Bhonsale,
Monika E. Polańska, Filip Logist (Eds.)

PSE PRESS

# Comparative Assessment of Aspen Plus Modeling Strategies for Biomass Steam Co-gasification

**Usman Khan Jadoon[a*], Ismael Díaz[a], Manuel Rodríguez[a]**

[a] Departamento de Ingeniería Química Industrial y del Medioambiente, Escuela Técnica Superior de Ingenieros Industriales, Universidad Politécnica de Madrid, Madrid, Spain
* Corresponding Author: uk.jadoon@upm.es

## ABSTRACT

The urgent need for sustainable energy drives the exploration of biomass and plastic waste co-gasification, a promising route for producing clean fuels and chemicals, reducing greenhouse gas emissions, and minimizing fossil fuel dependence. Modeling and simulation are vital for optimizing this process, particularly syngas yield, yet comparative studies on Aspen Plus modeling techniques for steam co-gasification are limited. This research addresses this gap by comparing three Aspen Plus strategies: thermodynamic equilibrium modeling (TEM), restricted thermodynamic modeling (RTM), and kinetic modeling (KM), for simulating the co-gasification of pine sawdust and polyethene (PE) with steam in bubbling fluidized bed gasifier (BFBG). The primary objective is to evaluate the effectiveness of each strategy in predicting the syngas composition under varying conditions. Three models were developed in Aspen Plus on the basis of each strategy, and their predicted syngas compositions were compared with published experimental data. A detailed sensitivity analysis was performed within the RTM framework to obtain optimized values of the approach temperatures to enhance predictive accuracy. The results showed that RTM provided the highest precision, with an average root mean square error (RMSE) of 0.0296, while TEM showed the lowest precision with RMSE of 0.1234. KM performed moderately with an RMSE of 0.0929. These findings demonstrate that RTM is superior for predicting the syngas composition for this co-gasification process, and its optimized solution presents a viable alternative when detailed kinetic data are lacking, thus reducing computational expense.

**Keywords**: Aspen Plus, Syngas prediction, Equilibrium modeling, Kinetic modeling

## INTRODUCTION

The escalating global climate crisis, coupled with concerns regarding energy security and dependence on finite fossil fuel resources, has spurred a critical need for the development and implementation of sustainable energy alternatives [1]. In this context, steam co-gasification of biomass and plastic waste in BFBGs emerges as a promising technology, offering a dual benefit of renewable energy generation and waste valorization. This thermochemical conversion process effectively transforms these feedstocks into syngas, a valuable intermediate product for producing clean fuels, sustainable aviation fuels, and various chemicals such as methanol, ethanol, and dimethyl ether. By utilizing renewable biomass sources and mitigating the environmental impact of plastic waste, steam co-gasification holds the potential to significantly reduce greenhouse gas emissions and lessen reliance on fossil-based energy systems [2]. Therefore, the precise analysis and optimization of this process are vital for its widespread adoption and contribution to a sustainable energy future.

In this regard, some researchers have explored high-temperature steam gasification to enhance $H_2$ production. For instance, Chang et al. (2011) reported that steam gasification of agricultural waste in a fluidized bed reactor at 1000 °C and an equivalence ratio of 0.2 yielded a maximum bio$H_2$ of 29.5%, CO at 23.6%, and $CO_2$ at just 10.9% [3]. Ahmed et al. (2009) compared pyrolysis and steam gasification of paper, varying temperatures from 400 to 700 °C for pyrolysis and 600 to 1000 °C for gasification [4]. Numerous experimental studies have been

published in literature show that steam gasification has the ability to produce the medium heating value of up to 16 MJ/Nm$^3$ and $H_2$ concentration in syngas up to 60% [5-7].

However, accurate modeling and simulation of thermochemical processes are indispensable tools for gaining a fundamental understanding of their behavior and for optimizing gasification performance. Specifically, for gasification, modeling is crucial in predicting syngas yield, composition, and process efficiency under varying operating conditions. Syngas, as the primary product of gasification, serves as a versatile building block for numerous energy and chemical applications, making a reliable prediction of its composition very important. This requires the development and comparative analysis of different modeling strategies, each with its unique capabilities and limitations.

Although various modeling techniques have been proposed in the literature for gasification processes, there remains a noticeable gap in comprehensive comparative assessments, particularly concerning different Aspen Plus modeling approaches for steam co-gasification of biomass and plastic waste. This gap highlights the need for further investigation to identify the most effective and accurate modeling strategies for this specific process. Recognizing the limitations mentioned above in the existing literature, this study focuses on a comparative evaluation of three distinct Aspen Plus modeling strategies: thermodynamic equilibrium modeling (TEM), restricted thermodynamic modeling (RTM), and kinetic modeling (KM) for simulating steam co-gasification of pine sawdust and polyethene in a bubbling fluidized bed reactor.

## METHODOLOGY

In this article experimental study was adopted from Pinto et al. (2002) for the pine and polyethylene (PE) co-gasification in BFBG by steam [5]. The reactor configuration is given in the article along with the ultimate and approximate analysis of the feedstocks. Modeling was carried out in 100% Pine, 10% PE and 90% pine mix, 40% PE and 60% pine, and 60% PE and 40% pine at varying temperature, while the steam-to-biomass ratio remains at 0.8kg/kg-feedstock. This study employed Aspen Plus V.14.0 to model the steam co-gasification process and predict syngas composition under various operating conditions, and both equilibrium and kinetic modeling strategies were implemented. In Aspen Plus platform all models began with the definition of biomass, PE, ash, and char as non-conventional components, using proximate and ultimate analyses from the ULTANAL and PROXANAL models, respectively. The built-in property database of Aspen Plus was utilized for the calculations, with the HCOALGEN and DCOALIGT models providing enthalpy and density data, respectively, based on biomass combustion and composition. Heat of combustion was derived from biomass combustion using the HCOALGEN model and elemental analysis, while density was determined using the DCOALIGT model, which is based on the IGT correlation and utilizes ultimate analysis data. The Peng-Robinson thermodynamic package with the Boston-Mathias function was chosen for its suitability in high-temperature gasification simulations.

### Equilibrium Modeling

Thermodynamic Equilibrium Model (TEM) and Restricted Thermodynamic Model (RTM). TEM, a non-stoichiometric approach, determines the equilibrium composition by minimizing Gibbs free energy, requiring only the elemental composition derived from ultimate analysis. This makes it computationally efficient and useful for preliminary assessments. However, TEM does not incorporate reaction kinetics or stoichiometric constraints, leading to discrepancies in syngas predictions, particularly in underestimating syngas composition.

RTM, a stoichiometric approach, improves upon TEM by incorporating temperature-dependent constraints on chemical equilibria. Real-world gasification processes often do not reach complete equilibrium due to kinetic limitations, and RTM accounts for this by restricting selected reactions to better match experimental conditions. By restricting reaction equilibria to temperatures above or below the actual reactor temperature, accounting for stoichiometric constraints. This approach is designed to provide a more realistic representation of the gasification process, since the reactions in the reactor may not necessarily reach the true thermodynamic equilibrium. By incorporating temperature-based constraints, it improves the accuracy of syngas composition predictions and other performance metrics. A similar approach was previously applied to air gasification by Jadoon et al., (2025) this study implemented strategy for the steam gasification to improve the precision for optimizing operating conditions and improving the overall efficiency of predicting the syngas composition [6].

In this study the Aspen Plus model developed by Acar et al., (2019) for gasification, was adopted, using both TEM and RTM [7]. Biomass and plastic waste were first decomposed in the RYIELD reactor (DECOMP) into constituent elements based on its ultimate and proximate analyses. Ash was then separated from the other components using a separator (SEP1). The elemental components were mixed with steam and then fed to an RGIBBS reactor. The gasifier (EQIL) simulates the TEM approach, while another reactor (R-GASI) models RTM. Syngas is then separated from other byproducts in separators (SEP2 for R-GASI and SEP3 for EQIL) as shown in Figure 1.

Following Acar et al. (2019), four key reactions

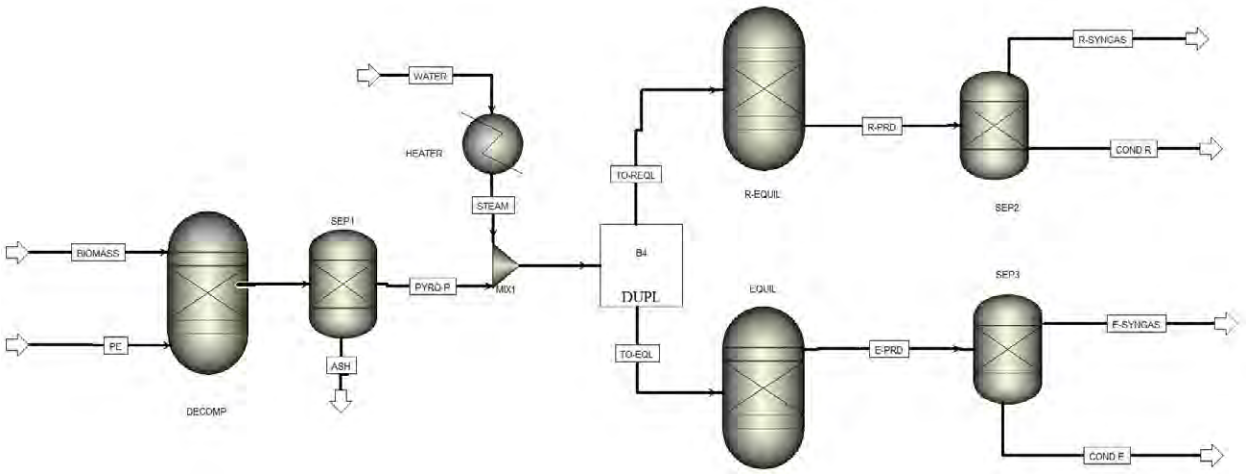



**Figure 1:** Process flowsheet of Equilibrium model

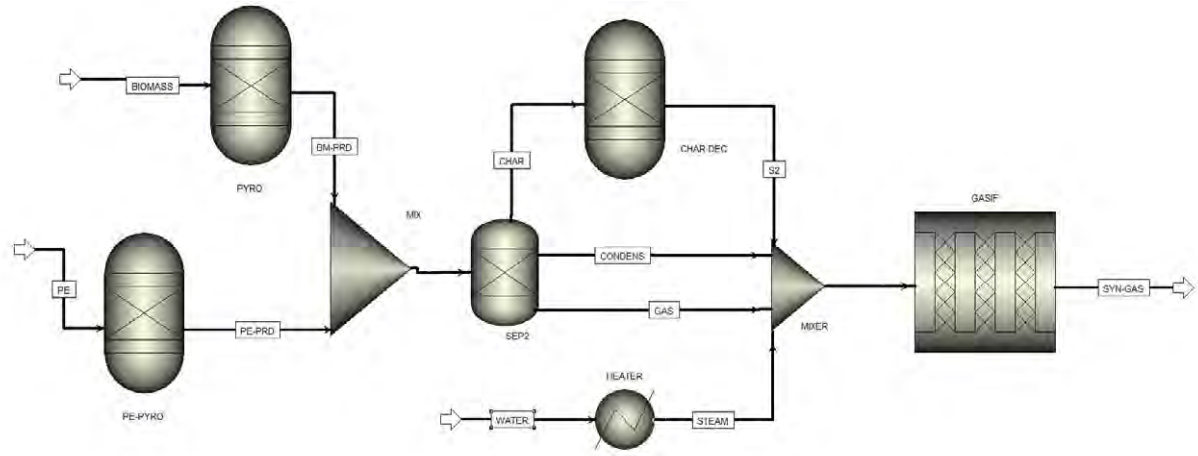



**Figure 2:** Process flowsheet of kinetic model

(listed in Table 1) were selected to constrain the chemical equilibrium within the RTM framework. A sensitivity analysis was performed for each of the 17 experimental instances by varying the approach temperature of individual reactions. Each sensitivity analysis consisted of 22,500 cases, and the case with the smallest absolute difference between experimental and predicted values was selected. The absolute difference between the molar fractions of the predicted and experimental syngas composition was calculated using Equation 1, where ME represents the minimum error, *e* is the experimental value, *p* is the predicted value, and *i* denotes the *i*-th case in the sensitivity analysis.

$$(ME)_i = |H_2^e - H_2^p|_i + |CO^e - CO^p|_i + |CO_2^e - CO_2^p|_i + |CH_4^e - CH_4^p|_i \quad (1)$$

Table 1: Reactions used in RTM

| No. | Reaction | ΔHr (kJ/mol) |
|---|---|---|
| R1 | $C + H_2O \rightarrow CO + H_2$ | 131 |
| R2 | $C + 0.5O_2 \rightarrow CO$ | -111 |
| R3 | $CO + H_2O \rightarrow CO_2 + H_2$ | -41.2 |
| R4 | $CH_4 + H_2O \rightarrow CO + 3H_2$ | 206 |

## Kinetic Modeling

A KM was developed within the Aspen Plus environment to simulate the co-gasification feedstocks, explicitly representing the complex thermochemical reactions occurring within BFBG. The model's flowsheet, depicted in Figure 2, utilizes several interconnected unit operation blocks. Initial decomposition of biomass in the RYIELD reactor (PYRO) was modeled using empirical equations from Neves et al. (2011) [8]. In contrast, plastic waste decomposition (PE-PYRO) was based on its ultimate and proximate analyses, reflecting the primary and secondary depolymerization processes that occur at high temperatures. The resulting pyrolysis products were then separated by a separator (SEP2) into gaseous, condensable, and char fractions. The char fraction was further decomposed into elemental carbon, sulfur (if present), and ash

within another RYIELD reactor (CHAR-DEC). These decomposition products were then combined with the gasifying medium in a mixer (MIX2) before entering the gasification reactor. A plug flow reactor was opted for modeling the final gasification process to convert the pyrolysis products and gasifying medium into syngas. Kinetic models use rate equations to quantify the rates of various chemical reactions that occur during gasification. The reactions and kinetic data used in the gasification step are given in **Table 2** and **Table 3** [9].

**Table 2:** Chemical reactions and rate expressions

| Reaction | Rate expression |
|---|---|
| $C + 0.5O_2 \rightarrow CO$ | $r_1 = k_1 \cdot \exp\left(\frac{E}{RT}\right)[O_2]^{0.78}$ |
| $H_2 + 0.5O_2 \rightarrow H_2O$ | $r_2 = k_2 \cdot \exp\left(\frac{-E}{RT}\right)[H_2][O_2]$ |
| $CO + 0.5O_2 \rightarrow CO_2$ | $r_3 = k_3 \exp\left(\frac{-E}{RT}\right)[CO][O_2]^{0.5}[H_2O]^{0.}$ |
| $C + H_2O \rightarrow CO + H_2$ | $r_4 = k_4 \cdot \exp\left(\frac{-E}{RT}\right)[C][H_2O]$ |
| $C + CO_2 \rightarrow 2CO$ | $r_5 = k_5 \cdot \exp\left(\frac{-E}{RT}\right)[CO_2]$ |
| $CH_4 + H_2O \rightarrow CO + 3H_2$ | $r_6 = k_6 \cdot \exp\left(\frac{-E}{RT}\right)[CH_4][H_2O]$ |
| $CO + H_2O \rightarrow CO_2 + H_2$ | $r_7 = k_7 \cdot \exp\left(\frac{E}{RT}\right)[CO][H_2O]$ |
| $C + 2H_2 \rightarrow CH_4$ | $r_8 = k_8 \cdot \exp\left(\frac{-E}{RT}\right)[H_2]$ |
| $C_{10}H_8 \rightarrow 7.38C + 0.275C_6H_6 + 0.94CH_4 + 1.235H_2$ | $r_9 = k_9.\exp\left(\frac{-E}{RT}\right)[C_6H_6O]^{1.6}[H_2]^{-0.5}$ |
| $C_6H_6 + 2H_2O \rightarrow 1.5C + 2.5CH_4 + 2CO$ | $r_{10} = k_{10}.\exp\left(\frac{-E}{RT}\right)[C_6H_6]^{1.3}[H_2O]^{0.2}[$ |
| $C_6H_6O + 3H_2O \rightarrow 4CO + 0.5C_2H_4 + CH_4 + 3H_2$ | $r_{11} = k_{11}.\exp\left(\frac{-E}{RT}\right)[C_6H_6O]$ |

**Table 3:** Kinetic parameters

| Reactions | k | E (J/mol) |
|---|---|---|
| $r_1$ | $5.70 \cdot 10^{11}$ | $5.50 \cdot 10^{4}$ |
| $r_2$ | $2.20 \cdot 10^{9}$ | $1.08996 \cdot 10^{6}$ |
| $r_3$ | $1.00 \cdot 10^{10}$ | $1.2599 \cdot 10^{5}$ |
| $r_4$ | 200 | $4.9887 \cdot 10^{4}$ |
| $r_5$ | 4.364 | $2.48123 \cdot 10^{5}$ |
| $r_6$ | $3.00 \cdot 10^{3}$ | $1.2471 \cdot 10^{5}$ |
| $r_7$ | $2.20 \cdot 10^{-2}$ | $3.473 \cdot 10^{4}$ |
| $r_8$ | $2.43 \cdot 10^{-4}$ | $1.30 \cdot 10^{4}$ |
| $r_9$ | $1.70 \cdot 10^{14}$ | $3.50 \cdot 10^{5}$ |
| $r_{10}$ | $2.00 \cdot 10^{16}$ | $4.43 \cdot 10^{5}$ |
| $r_{11}$ | $1.00 \cdot 10^{7}$ | $1.00 \cdot 10^{5}$ |

The syngas molar fraction predicted by each model is evaluated using RMSE, which measures the square root of the average squared differences between predicted and observed values. RMSE can be computed by equation 2.

$$RMSE = \sqrt{\frac{1}{n}\sum_{i=1}^{n}(y_i - \hat{y}_i)^2} \quad (2)$$

## RESULTS AND DISCUSSION

Aspen Plus models utilizing TEM, RTM, and KM were developed to simulate steam co-gasification in a BFBG. For RTM, a detailed sensitivity analysis was conducted to align the syngas composition as closely as possible with experimental values. This analysis, performed using Aspen Plus's built-in sensitivity tool by changing the temperature for each reaction given in Table 1. The temperature limit for the reactions R3 and R4 are zero to 1000 °C and -1 to -500 °C, respectively. A total of 22,500 sensitivity instances were computed for each sensitivity analysis, and this analysis was performed for all seventeen experimental cases. The absolute error was calculated for every instance, and then minimum absolute error was determined using equation 1. The syngas composition corresponding to this minimum error was selected as the final syngas composition in RTM framework.

**Table 4**: RMSE of different Aspen Plus models

| | RTM | KM | TEM |
|---|---|---|---|
| $H_2$ | 0.0363 | 0.1705 | 0.2101 |
| CO | 0.0533 | 0.0953 | 0.1184 |
| $CO_2$ | 0.0208 | 0.0374 | 0.0365 |
| $CH_4$ | 0.0079 | 0.0682 | 0.1285 |
| Average | 0.0296 | 0.0929 | 0.1234 |

RMSE values for different modeling strategies—RTM, TEM, and KM—are presented in **Table 4**. These results highlight notable differences in the predictive performance of the models for co-gasification. RTM demonstrated the most favorable performance overall, achieving the lowest RMSE values across all outputs compared to the other models. The average RMSE for RTM is 0.0296, significantly outperforming TEM and KM, who's average RMSE values were 0.1234 and 0.0929, respectively.

Unlike the TEM model the RTM model accounts for kinetic constraints that influence reaction rates. This is particularly relevant in non-equilibrium conditions where factors such as heat and mass transfer limitations affect the reaction progress. Additionally, while the KM model includes kinetic mechanisms, its predictive capability is restricted by predefined reaction pathways and rate expressions that may not fully represent the complexities of co-gasification, especially for varying feedstock compositions. The RTM framework, by contrast, fine-tunes

reaction temperatures through sensitivity analysis, ensuring improved alignment with experimental data.

When examining individual syngas components, RTM consistently exhibited the lowest RMSE values. For CO, RTM achieved the lowest RMSE of 0.0533, followed by KM at 0.0953, while TEM performed poorly with RMSE values of 0.1184. A similar trend was observed for $CO_2$, where RTM had an RMSE of 0.0208, followed by KM at 0.0374 and TEM at 0.0365. For $CH_4$, RTM again excelled with the lowest RMSE of 0.0079 while KM and TEM have 0.0682 and 0.1285, respectively.

The predictions obtained from different models were analyzed and plotted to evaluate their performance. **Figure 3** illustrates the comparison between experimental and predicted $H_2$ values across various feedstock compositions. Among the models, the RTM demonstrates exceptional predictive accuracy, with blue data points closely aligning with the experimental values for all percentages of polyethylene (PE). The minimal error observed in RTM predictions underscores its reliability and effectiveness. In contrast, the KM model performs well for feedstocks containing 100% pine and mixtures with 80% pine + 20% PE, but its accuracy significantly deteriorates for feedstocks with 40% or 60% PE, where it tends to overpredict $H_2$ values. This decline in performance suggests that the KM model is less suitable for feedstocks with higher PE content. The TEM model, on the other hand, consistently overpredicts $H_2$ values across all feedstock compositions, likely due to limitations in Gibbs free energy estimations for syngas constituents, as highlighted by Ajorloo et al. (2022) [10].

**Figure 4** illustrates the prediction of CO in Aspen Plus model's environment in comparison to the experimental values. The RTM model again demonstrates strong predictive accuracy, with blue data points aligning closely with experimental values across all percentages of PE, reaffirming its robustness in predicting CO concentrations. The KM model provides reasonable predictions for feedstocks with low PE content, such as 100% pine and 20% PE. However, as the PE content in the feedstock exceeds 40%, the KM model begins to underpredict CO concentrations, indicating its limited applicability for feedstocks with higher PE proportions. In contrast, the TEM model shows improved accuracy in predicting CO for feedstocks with 40% or more PE, suggesting that its performance improves with increasing PE content. As the PE content is increasing, 40% and above, in feedstock the TEM prediction tends to accurately predict it.

For $CO_2$ predictions, depicted in **Figure 5**, the RTM model once again delivers the most accurate results. However, predictions by the TEM and KM models exhibit similar trends and complement each other, as evidenced by their comparable RMSE values in **Table 4**. This alignment suggests that both models can provide reasonable $CO_2$ predictions under certain conditions, though they remain less accurate than the RTM model.

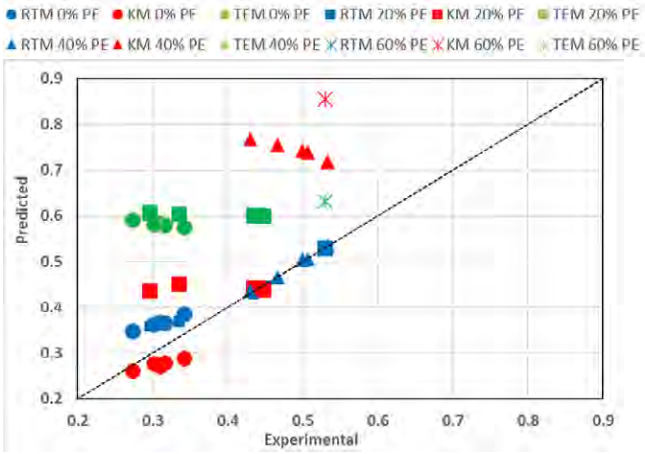



**Figure 3:** Experimental and Predicted mole fraction of $H_2$

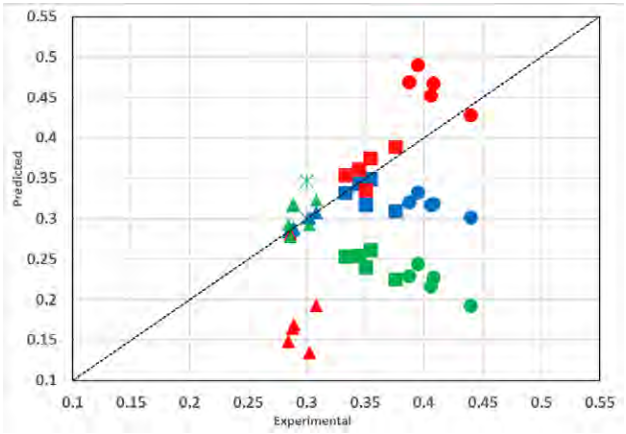



**Figure 4:** Experimental and predicted mole fraction of CO

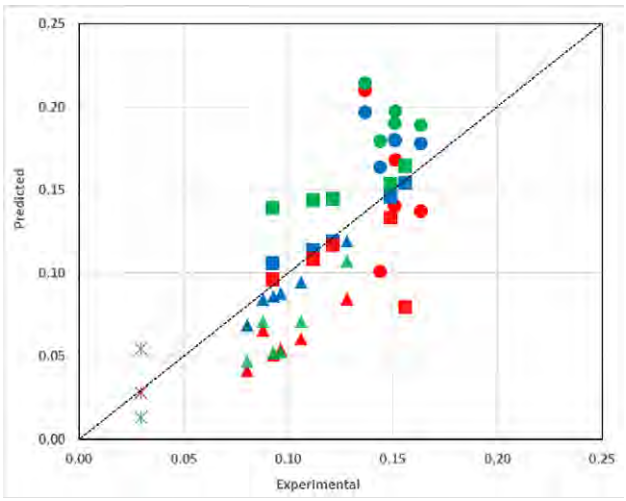



**Figure 5:** Experimental and Predicted mole fraction of $CO_2$

From the **Figure 6** $CH_4$ predictions further emphasize the superior performance of the RTM model, which consistently provides accurate results. In contrast, the

TEM model struggles significantly, often underpredicting $CH_4$ concentrations. The KM model performs adequately for feedstocks with low PE content, but its accuracy declines sharply as the PE proportion increases, resulting in poor predictions for higher PE feedstocks.

In this study the RTM model demonstrated exceptional predictive capabilities for molar concentration of $H_2$, CO, $CO_2$, and $CH_4$ across all feedstock compositions, making it the most reliable model overall. While the KM and TEM models exhibit some strengths in specific scenarios, their accuracy diminishes as the PE content in the feedstock increases, highlighting the importance of model selection based on feedstock composition.

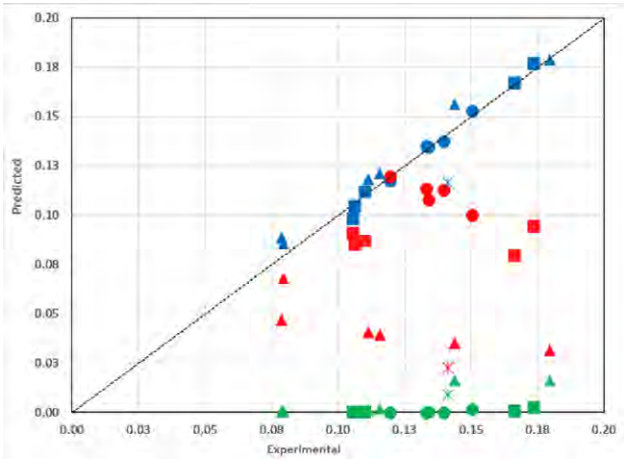



**Figure 6:** Experimental and Predicted mole fraction of $CH_4$

## CONCLUSIONS

Pine and plastic steam co-gasification offers a promising route for renewable energy production; however, accurately predicting syngas composition remains a significant challenge. This study provides a comprehensive comparative analysis of three modeling approaches—TEM, RTM, and KM—in a BFBG. Among these models, RTM demonstrated the highest accuracy in predicting syngas composition, with an average RMSE of 0.0296. In contrast, the TEM model showed the lowest performance consistently overestimated or underestimated syngas composition, with an RMSE of 0.1234, while the KM model exhibited intermediate performance with an RMSE of 0.0929. The KM model's performance notably declined as the proportion of PE in the feedstock increased, further limiting its reliability for feedstocks with higher plastic content. In comparison, RTM proved to be the most robust and accurate, making it a strong candidate for future research on syngas composition across different technologies and fuel mixtures, including agricultural, forestry, and municipal solid wastes with steam or steam-$O_2$ gasification.

## ACKNOWLEDGEMENTS

This research has received funding from the European Union's Horizon 2020 research and innovation program under the Marie Skłodowska-Curie grant agreement No. 945139

## REFERENCES

1. Osman, A.I., et al., Cost, environmental impact, and resilience of renewable energy under a changing climate: a review. Environmental chemistry letters, 2023. **21**(2): p. 741-764.
2. Lee, U., J.N. Chung, and H.A. Ingley, High-Temperature Steam Gasification of Municipal Solid Waste, Rubber, Plastic and Wood. Energy & Fuels, 2014. **28**(7): p. 4573-4587.
3. Chang, A.C.C., et al., Biomass gasification for hydrogen production. International Journal of Hydrogen Energy, 2011. **36**(21): p. 14252-14260.
4. Ahmed, I. and A.K. Gupta, Syngas yield during pyrolysis and steam gasification of paper. Applied Energy, 2009. **86**(9): p. 1813-1821.
5. Pinto, F., et al., Co-gasification study of biomass mixed with plastic wastes. Fuel, 2002. **81**(3): p. 291-297.
6. Jadoon, U.K., I. Díaz, and M. Rodríguez, Comparative analysis of aspen plus simulation strategies for woody biomass air gasification processes. Biomass and Bioenergy, 2025. **194**: p. 107626.
7. Acar, M.C. and Y.E. Böke, Simulation of biomass gasification in a BFBG using chemical equilibrium model and restricted chemical equilibrium method. Biomass and Bioenergy, 2019. **125**: p. 131-138.
8. Neves, D., et al., Characterization and prediction of biomass pyrolysis products. Progress in Energy and Combustion Science, 2011. **37**(5): p. 611-630.
9. Cao, Y., Y. Bai, and J. Du, H2-rich gas production from co-gasification of biomass/plastics blends: A modeling approach. Journal of the Energy Institute, 2024. **112**: p. 101454.
10. Ajorloo, M., et al., Recent advances in thermodynamic analysis of biomass gasification: A review on numerical modelling and simulation. Journal of the Energy Institute, 2022. **102**: p. 395-419.

© 2025 by the authors. Licensed to PSEcommunity.org and PSE Press. This is an open access article under the creative commons CC-BY-SA licensing terms. Credit must be given to creator and adaptations must be shared under the same terms. See https://creativecommons.org/licenses/by-sa/4.0/

Systems & Control Transactions

**Research Article - Peer Reviewed Conference Proceeding**
ESCAPE 35 - European Symposium on Computer Aided Process Engineering
Ghent, Belgium. 6-9 July 2025
Jan F.M. Van Impe, Grégoire Léonard, Satyajeet S. Bhonsale,
Monika E. Polańska, Filip Logist (Eds.)

PSE PRESS

# Enhancing the Technical and Economic Performance of Proton Exchange Membrane Fuel Cells Through Three Critical Advancements

**Željko Penga[a]*, Jure Penga[b], Yuanjing Zhao[c], Lei Xing[c]**

[a] Faculty of Electrical Engineering, Mechanical Engineering and Naval Architecture, University of Split, Croatia
[b] University of Defense and Security Dr. Franjo Tuđman, Croatia
[c] University of Surrey, UK
* Corresponding Author: zpenga@fesb.hr

## ABSTRACT

Proton Exchange Membrane (PEM) fuel cells are gaining traction in automotive applications due to their efficiency and environmental benefits, but they face challenges such as high costs, degradation rates, and limited hydrogen availability. To address these issues, novel operational methods have been developed, focusing on customized designs rather than traditional uniform configurations. These advancements include the variable temperature flow field, which maintains high relative humidity without external humidification by leveraging internally generated water and heat, and graded catalyst loading, which enhances current density distribution. Additionally, complex flow fields have been designed using 3D metal printing to mitigate liquid water accumulation. These innovations have shown significant performance improvements, particularly when combined, demonstrating a 260% increase in current density at 0.6 V. These advancements hold promise for overcoming the limitations of conventional PEM fuel cell designs and enhancing their viability for commercial applications.

**Keywords**: PEM fuel cells, Computational Fluid Dynamics, Variable Temperature Flow Field, Graded Catalyst Design, 3D Metal Printed Flow Field

## INTRODUCTION

Proton exchange membrane (PEM) fuel cells are steadily gaining momentum in automotive applications. Besides their formidable benefits such as low operating temperature, high efficiency, zero emissions and low noise, there are several drawbacks such as high price, unreliable degradation rates and very limited availability of hydrogen, as well as poor dynamic power output. To tackle these issues, we have developed several novel methods for operation of PEM fuel cells. There methods are based on designing the PEM fuel cell in a custom way to fit the application, instead of using uniform design with fully humidified reactants which is common practice. Throughout our research over a span of several years we have started to address the issue of liquid water accumulation and transport inside the cell, which is consequence of cell operating at the constant temperature with usage of fully humidified hydrogen at the anode and air at the cathode. The humidification of reactants was thought to be a necessity, since the proton conductivity of the Nafion membrane is directly proportional to its water content. However, since PEM fuel cell generates large quantities of water during operation at elevated current densities, using fully humidified reactants is detrimental to its performance since the generated water remains in liquid form and is unable to evaporate and thus accumulates in the diffusion layers and sometimes in the reactant channels, which causes uneven current density and heat transfer distribution. The first method we have developed to tackle these issues is variable temperature flow field, shown in references [1-3]. This method is based on usage of ambient air and dry hydrogen for feeding of the cell. High relative humidity is achieved by establishing and maintaining a precise temperature profile along the cell which in ensures almost 100% humidified reactant gases along the active area of the cell using water generated by the cell. To establish and maintain this specific

temperature profile coolant fluid is used. Coolant enters the cell at temperature of 30°C and gradually increases its temperature to 60°C while absorbing internally generated heat. Variable temperature flow field has shown that it is possible to achieve higher performance using this method and basically dry reactants contrary to the isothermal operation with fully humidified reactants, which indicates its potency towards the development for commercial applications. This method was further enhanced together with another method, which was developed by Xing et al. research group [4,5], utilizing graded catalyst loading which further enhances the current density distribution of the cell by controlling of the chemical rates of reaction along the active area of the cell. Graded catalyst design was combined with variable temperature flow field in [4] and compared to fully humidified isothermal operation. It was demonstrated experimentally that using variable temperature flow field combined with graded catalyst design leads to 260% increase in current density at 0.6 V which was astounding. Our research also focused in the direction of developing complex flow fields which utilize pressure gradients to expel the liquid water, which tends to accumulate near the cathode outlet. This method has also demonstrated that it is possible to achieve significant improvements in the performance at elevated current densities. We call these three methods - three critical advancements. They are described in more details in the continuation of this work.

## 1 CRITICAL ADVANCEMENTS

### Coolant Induced Variable Temperature Flow Field

Traditional Proton Exchange Membrane (PEM) fuel cell operation relies on maintaining an isothermal temperature profile across the cell, which necessitates external humidification systems to ensure high membrane water content. However, this conventional approach introduces increased system complexity, higher parasitic energy losses, and greater cost. The critical challenge in PEM fuel cell operation is maintaining optimal membrane hydration while preventing flooding that can block reactant transport pathways. Conventional isothermal approaches struggle to achieve the delicate balance between membrane hydration and preventing excess water accumulation in the gas diffusion layer (GDL) and catalyst layer (CL). This excess water can block oxygen transport to reaction sites, especially at higher current densities, leading to reduced performance. External humidification has been the standard solution but introduces significant system complications.

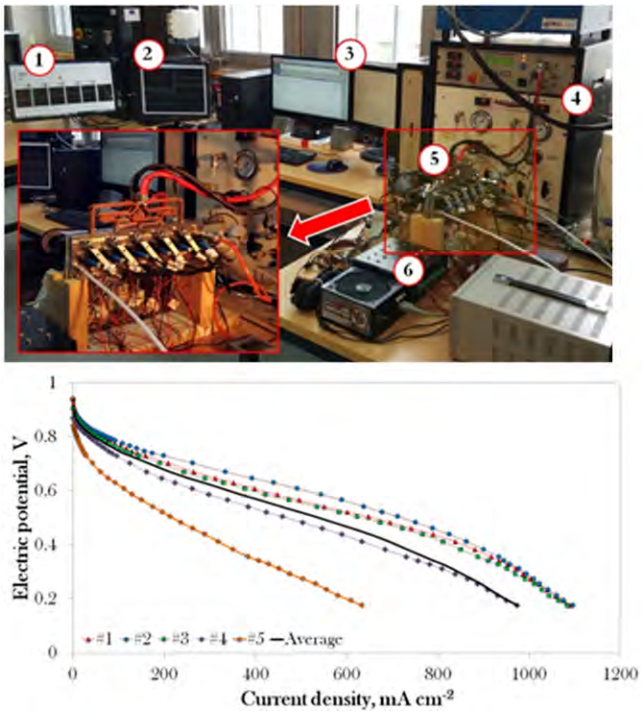



**Figure 1.** Experimental investigation of variable temperature flow field and polarization curves for each segment.

Željko Penga's innovative variable temperature flow field (VTFF) concept represents a significant advancement in addressing these challenges. The VTFF approach creates a controlled temperature gradient along the flow field by gradually increasing the coolant temperature as it passes through the PEM fuel cell. This strategic temperature management leverages internally generated water and heat to maintain relative humidity close to 100% along the entire flow field of both anode and cathode sides without requiring external humidification. The VTFF concept operates on the principle that water generated during fuel cell operation can be effectively utilized for internal reactant humidification when properly managed with a temperature gradient. By carefully controlling the temperature profile, the water vapor partial pressure can be maintained just below saturation pressure throughout the reactant channels. This prevents liquid water condensation while ensuring high membrane hydration, effectively addressing the dual challenges of membrane drying and electrode flooding that plague conventional designs. Penga validated this concept through extensive computational fluid dynamics (CFD) modeling and experimental testing using a custom-designed segmented PEM fuel cell setup, shown in Figure 1. The experimental apparatus provided critical insights into membrane water transport, temperature distribution on current collectors and inside channels, and current density distribution along the cell. This segmented approach allowed for precise monitoring of conditions at different

positions along the flow field, confirming the theoretical predictions of the VTFF concept. The experimental results demonstrated that PEM fuel cells operating with dry reactants under the VTFF concept achieved performance comparable to or better than conventional isothermal configurations with fully humidified reactants. Polarization curve comparisons revealed that the VTFF approach particularly excelled in reducing mass transport losses at higher current densities. This improvement stems from the VTFF's ability to maintain optimal hydration while preventing liquid water accumulation by evaporating generated water into the reactant streams. The most significant contribution of the VTFF concept is its ability to eliminate the need for external humidification while simultaneously enhancing high-current performance.

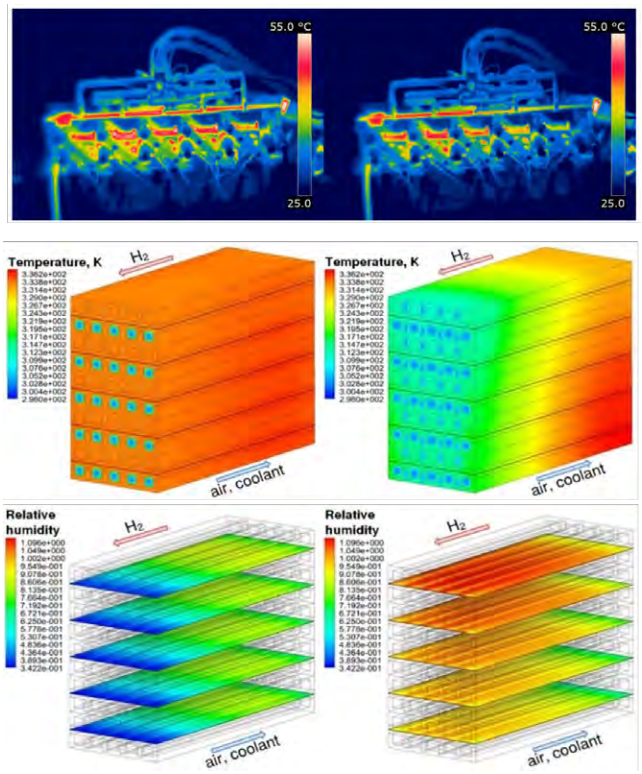



**Figure 2.** Isothermal (left) vs. variable temperature flow field (right) operation. Exp. vs. CFD results (above vs below) for temperature and relative humidity distributions.

By maintaining high relative humidity without condensation, the VTFF concept minimizes the problematic accumulation of liquid water that typically restricts reactant transport at higher current densities. This results in extended operational ranges and improved overall efficiency. Furthermore, the VTFF concept offers substantial system-level benefits, including reduced complexity, lower parasitic power losses, and decreased weight and volume requirements due to the elimination of external humidifiers. This makes the approach particularly valuable for mobile and portable applications where system simplicity and efficiency are paramount. The concept has been demonstrated to be applicable to PEM fuel cell stacks, as shown in Figure 2, further extending its practical utility for commercial applications.

## Variable Temperature Flow Field with Graded Catalyst Design

Traditional Proton Exchange Membrane (PEM) fuel cell designs typically employ a uniform distribution of functional components throughout the membrane electrode assembly (MEA), including consistent platinum catalyst loading, ionomer content, and porosity distributions. However, this uniform approach fails to account for the highly non-uniform distribution of current density, reactant concentration, and water content that naturally occurs during operation. This mismatch between uniform design and non-uniform operating conditions leads to suboptimal performance, excessive platinum utilization in low-activity regions, and heterogeneous degradation patterns. The cost of platinum-based catalysts remains a significant barrier to widespread PEM fuel cell adoption, with catalyst layers accounting for approximately 40% of the total system cost. Additionally, the durability issues stemming from non-uniform current distribution continue to impede commercial deployment. These challenges create a pressing need for more sophisticated design approaches that can optimize material utilization and performance simultaneously. Lei Xing's research has pioneered the concept of functionally graded porous electrode design, which strategically varies the distribution of key components along both through-plane and in-plane directions. This approach recognizes that different regions of the MEA experience vastly different local conditions during operation, requiring tailored properties to optimize performance. By creating spatial gradients of functional components such as platinum loading, ionomer content, and porosity, the graded design approach can significantly enhance performance while reducing material usage. The graded design strategy addresses the trilemma of performance, durability, and cost that has long challenged PEM fuel cell commercialization. For cells operated under varying loads, different regions require different catalyst activities and mass transport rates due to non-uniform reactant and product distribution. A rational graded design helps reduce precious material usage, improve overall cell performance, and achieve more uniform distributions of current density and heat generation.

A key innovation in Xing's work is the development of sophisticated hybrid modeling approaches that combine physics-based simulation with machine learning techniques. This methodology first establishes detailed multi-physics models that capture the complex interactions between electrochemical reactions, heat transfer, and mass transport. After experimental validation, these

models generate comprehensive databases that inform data-driven machine learning algorithms, creating powerful surrogate models capable of rapid multi-objective optimization. This hybrid approach overcomes the limitations of purely physics-based or purely data-driven methods. The physics-based foundation ensures accurate representation of fundamental processes, while the machine learning integration enables efficient exploration of vast design spaces that would be computationally prohibitive with traditional methods. This combination has proven particularly effective for optimizing multiple interconnected variables involved in graded electrode design. Xing's research has demonstrated significant improvements through graded catalyst designs, particularly in homogenizing current density distribution and enhancing performance at high current densities. By strategically varying platinum loading and gas diffusion layer porosity along in-plane directions, these designs achieve more uniform reaction rates and improved reactant transport to under-represented regions. The optimized graded designs have shown superior performance compared to uniform designs while using less platinum catalyst overall. Multi-objective optimization techniques have been employed to balance competing performance metrics such as maximum power density, platinum utilization efficiency, and current density homogeneity. These approaches have identified optimal grading profiles that represent the best compromises between different objectives, providing valuable design guidelines for practical implementation. The research has clearly established that properly designed graded structures can simultaneously address cost, performance, and durability challenges. By using a combination of variable temperature flow field and graded catalyst design, it was demonstrated that at 0.6 V the current density can be 260% higher when compared to isothermal operation with constant catalyst loading which is highly favourable for wide range of fuel cell applications because it addresses most of its current issues. The experimental rig where variable temperature flow field and graded catalyst design were used is shown in Figure 3.

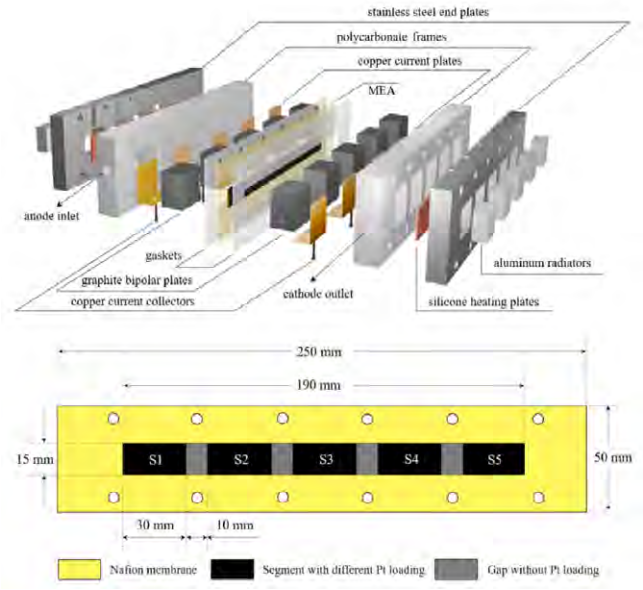



**Figure 3.** Segmented fuel cell with temperature control of each segment and segmented membrane-electrode assembly with different catalyst layer concentration on each segment.

## 3D Metal Printed Flow Fields

Conventional flow field designs in PEM fuel cells face significant challenges related to reactant distribution and water management, particularly in regions directly beneath the ribs of bipolar plates. These under-the-rib areas typically suffer from lower oxygen concentration and more severe water flooding than areas beneath the channels, creating performance bottlenecks that limit overall cell efficiency. The design of flow field geometry thus becomes critical for optimizing the balance between electrical conductivity and mass transport. Traditional manufacturing methods have imposed significant constraints on flow field designs, often limiting innovation to simple channel geometries that fail to address these under-the-rib transport issues. The emergence of advanced manufacturing techniques, particularly three-dimensional (3D) metal printing, has opened new possibilities for creating complex flow field geometries previously impossible to fabricate using conventional methods. Research by Penga, Xing, and colleagues has explored innovative flow field designs that leverage 3D metal printing capabilities to address under-the-rib transport limitations. These designs feature auxiliary channels equipped with through-plane arrayed holes strategically positioned to improve oxygen transport and water removal from under-the-rib regions. The auxiliary channels create additional pathways for reactant delivery and product removal, while the through-plane holes facilitate direct transport between the main channel and the electrode surface beneath the rib. These novel designs represent sophisticated modifications of traditional

serpentine and parallel flow field patterns. By integrating auxiliary structures without compromising the mechanical integrity or electrical conductivity of the bipolar plate, these designs achieve a careful balance between competing requirements. The number, placement, and dimensions of auxiliary channels and holes have been systematically optimized to maximize performance benefits while minimizing pressure drop penalties.

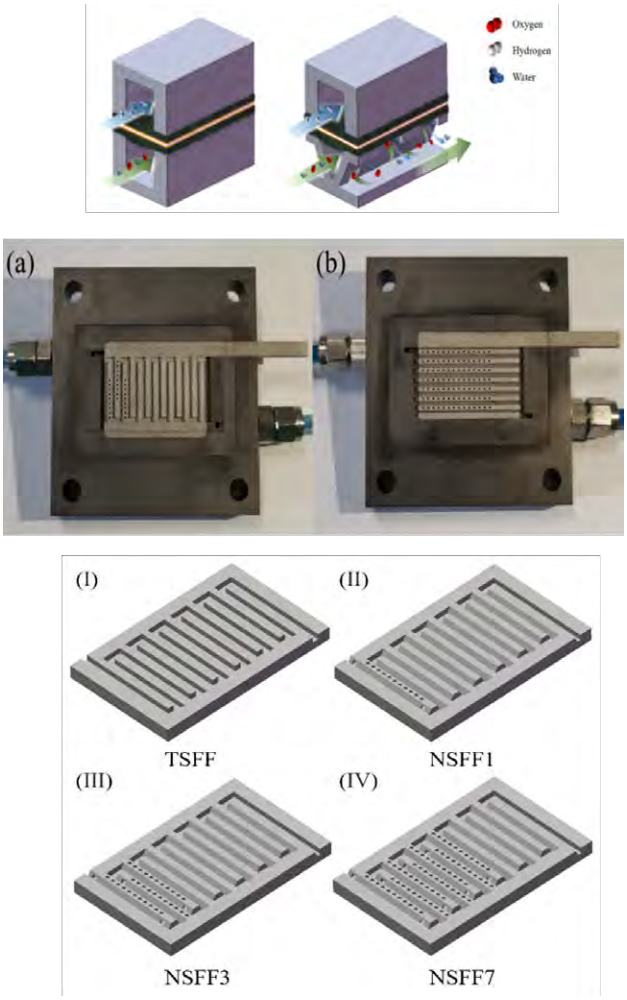



**Figure 4.** Isothermal (left) vs. variable temperature flow field (right) operation. Exp. vs. CFD results (above vs below) for temperature and relative humidity distributions.

The implementation of these complex flow field designs has been enabled by advances in 3D metal printing technology, as shown in Figure 4, which allows for the fabrication of intricate features with high precision. This additive manufacturing approach overcomes the limitations of traditional machining methods, enabling the creation of structures with internal passages, overhanging features, and precise dimensional control that would be difficult or impossible to achieve through conventional means. The 3D printing process for these flow fields involves selective laser melting of metal powders, building the structure layer by layer according to a digital design. This approach offers significant advantages in terms of design freedom,

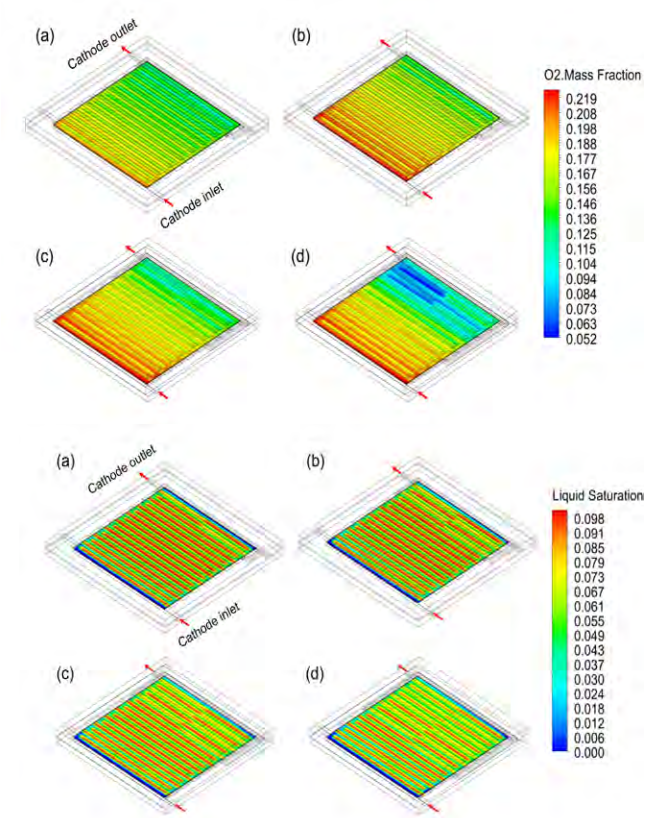



**Figure 5.** Isothermal (left) vs. variable temperature flow field (right) operation. Exp. vs. CFD results (above vs below) for temperature and relative humidity distributions.

The technology has reached sufficient maturity to produce functional bipolar plates with the required dimensional accuracy, surface finish, and material properties for practical fuel cell applications. Experimental and numerical evaluations, Figure 5, of the 3D printed novel flow fields have demonstrated significant performance improvements, particularly at high current densities where mass transport limitations typically dominate. Cells equipped with optimized auxiliary channel designs showed reduced ohmic resistance and enhanced mass transport capabilities compared to conventional designs. The performance gains were achieved through the improved oxygen supply and water removal from under-the-rib regions, preventing local flooding and reactant starvation. Perhaps most significantly, these novel flow field designs successfully address what the researchers describe as the "trilemma" of performance, pressure

drop, and manufacturability. Conventional designs typically force compromises between these competing factors, but the combination of innovative geometry and advanced manufacturing technology has enabled solutions that excel in all three dimensions. The optimal designs achieve enhanced performance without excessive pressure drop penalties, while the 3D printing approach makes their manufacture commercially viable.

## CONCLUSIONS

The innovations in variable temperature flow fields, graded catalyst designs, and 3D metal printed flow structures represent significant advancements in PEM fuel cell technology. Željko Penga's variable temperature flow field concept eliminates the need for external humidification while maintaining optimal membrane hydration and reducing mass transport losses. Lei Xing's graded catalyst approach optimizes material utilization and performance through strategic variation of functional components guided by sophisticated hybrid modeling. The collaborative work on 3D metal printed flow fields addresses critical under-the-rib transport limitations through novel geometries enabled by advanced manufacturing techniques. Together, these innovations address key barriers to widespread PEM fuel cell adoption by enhancing performance, reducing cost, increasing durability, and simplifying system design. The integration of these approaches offers a promising pathway toward more efficient, cost-effective, and commercially viable PEM fuel cell systems for a variety of applications, from transportation to stationary power generation. As these technologies continue to mature, they will likely play an increasingly important role in the transition to clean energy systems and contribute significantly to global decarbonization efforts. In this work, we have demonstrated that the performance of conventional PEM fuel cell designs—characterized by isothermal operation, constant catalyst loading, and standard flow field configurations—can be significantly enhanced through the application of our proposed methods. The integration of these approaches has the potential to enable the development of a novel class of PEM fuel cells, tailored in every aspect to meet specific application requirements. However, the combination of these methods introduces a vast array of input and output parameters, necessitating the development of an advanced AI model to guide and optimize this process, which will be the focus of our future research.

## REFERENCES


1. Penga Ž, Radica G, Barbir F, Nižetić S. Coolant Induced Variable Temperature Flow Field for Improved Performance of Proton Exchange Membrane Fuel Cells. *International Journal of Hydrogen Energ*, 44 (2019), 20; 10102-10119 https://doi.org/10.1016/j.ijhydene.2018.10.237
2. Penga Ž, Pivac I, Barbir F. Experimental Validation of Variable Temperature Flow Field Concept for Proton Exchange Membrane Fuel Cells. *International Journal of Hydrogen Energy*, 42 (2017), 41; 26084-26093 https://doi:10.1016/j.ijhydene.2017.08.135
3. Penga Ž, Tolj I, Barbir F. Computational fluid dynamics study of PEM fuel cell performance for isothermal and non-uniform temperature boundary conditions. *International Journal of Hydrogen Energy*, 41 (2016), 39; 17585-17594 https://doi:10.1016/j.ijhydene.2016.07.092
4. Xing L, Yuanxiang X; Penga Ž, et. al. A segmented fuel cell unit with functionally graded distributions of platinum loading and operating temperature. *Chemical Engineering Journa*l, 406 (2021), 126889, 16 https://doi:10.1016/j.cej.2020.126889
5. Gaojian C, Xing L, Penga Ž, et al. Improvement of under-the-rib oxygen concentration and water removal in PEMFCs through 3D metal printed novel flow fields. *AIChE Journal* 68:e17758 (2022) https://doi.org/10.1002/aic.17758



© 2025 by the authors. Licensed to PSEcommunity.org and PSE Press. This is an open access article under the creative commons CC-BY-SA licensing terms. Credit must be given to creator and adaptations must be shared under the same terms. See https://creativecommons.org/licenses/by-sa/4.0/




Systems & Control Transactions

**Research Article - Peer Reviewed Conference Proceeding**
ESCAPE 35 - European Symposium on Computer Aided Process Engineering
Ghent, Belgium. 6-9 July 2025
Jan F.M. Van Impe, Grégoire Léonard, Satyajeet S. Bhonsale,
Monika E. Polańska, Filip Logist (Eds.)

PSE PRESS

# Cell culture process dynamics and metabolic flux distributions using hybrid models

**Rajiv Kailasanathan[a,b], Abhishek Sivaram[a], and Seyed Soheil Mansouri[a]***

[a] Department of Chemical and Biochemical Engineering, Technical University of Denmark
[b] The Novo Nordisk Foundation Center for Biosustainability, Technical University of Denmark
* Corresponding Author: seso@kt.dtu.dk.

## ABSTRACT

Cell culture processes play a central role in the production of various therapeutic compounds. These processes are multiscale and highly complex, making them challenging to describe comprehensively using fully mechanistic models. In this study, we employ an integrated hybrid machine learning and first principles model to predict the viable cell density, product titer, and metabolite concentration profiles. We employ the concept of degree of hybridization, where we create a family of hybrid models each with increasing degree of process knowledge. Predictions from the feasible hybrid architecture were integrated with a genome scale metabolic model to evaluate the flux distribution of reactions related to the central carbon metabolism of the cell throughout the process duration. We demonstrate that the current approach not only reasonably predicts the bioprocess profile but also provides biologically relevant information that can uncover dynamics of intracellular metabolism which can open opportunities for new optimization strategies.

**Keywords**: Modelling and Simulations, Machine Learning, Hybrid Modelling, Metabolic flux distribution

## INTRODUCTION

Mathematical modelling of mammalian cell based biomanufacturing process is now at the heart of academic and industrial research due to quality-by-design standards[1] that are recommended by regulatory agencies as well as its potential in optimizing the processes driven by global sustainability demands[2]. Mechanistic (or knowledge-driven, first principles) and statistical (or data-driven) are two ends of a spectrum of modelling strategies. Knowledge-driven models are preferred when fundamental knowledge of the underlying process is available. But, construction of fully mechanistic models for bioprocesses is extremely challenging, as the knowledge available to describe the biology of the process is limited or too complex for practical applications[3]. Hence, conventional mechanistic models attempt to achieve a trade-off between the process knowledge they attempt to describe using the experimental data available and the computational complexity of a robust model.

On the other hand, data-driven models are preferred when there is limited understanding of the underlying process. Statistical and machine learning techniques are employed to infer non-linear relationships between process variables. While these models are often simple to generate and use, they often cannot extrapolate, and a large quantum of training data is required to adequately capture process dynamics.

An attractive combination of mechanistic and data-driven techniques to integrate the advantages of both approaches is being increasingly investigated over the past decades. Several architectures of hybrid models have been built which are described in detail in [4]. In our study, we use a serial architecture in which we establish a mechanistic backbone that is derived from the principle of conservation of mass and use a data-driven model to estimate the unknown parts of the equation. We investigate the concept of 'degree of hybridization'[5], [6] to identify the optimal level of process knowledge that can be described by the hybrid model. To achieve this, we construct a family of hybrid models with varying levels of process knowledge and evaluate their predictive capability.

A connection between macro-scale process model and microscale metabolic behaviour can provide scientific

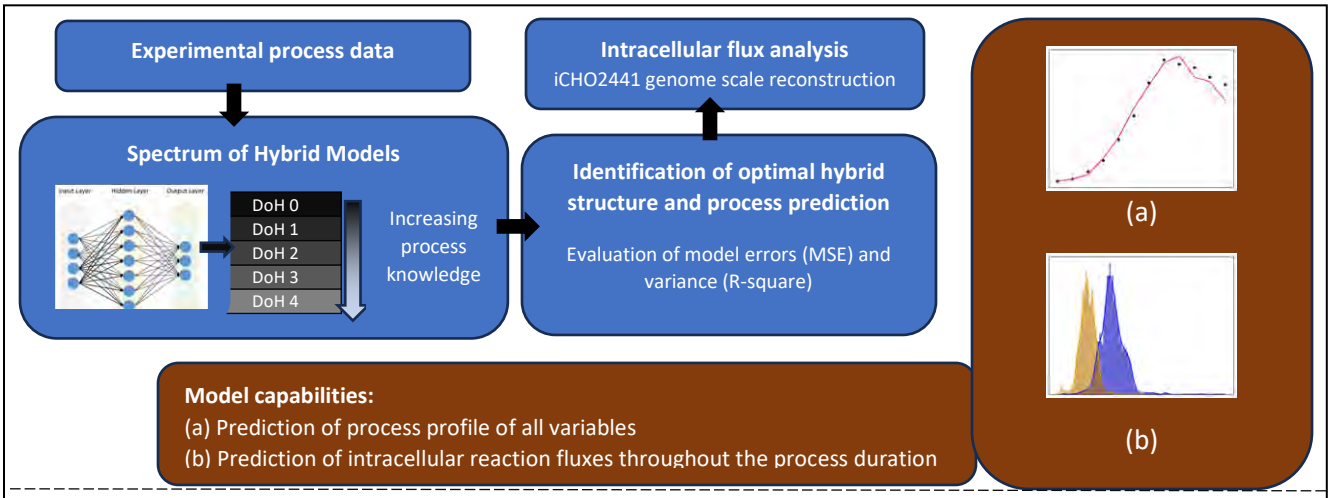



**Figure 1:** Hybrid modelling framework outline.

understanding of the biological process and uncover new strategies for optimization. Genome scale metabolic models are a mathematical representation of all known metabolic reactions for an organism and are a valuable tool to understand the interplay between various cellular pathways. Usually these models are expressed as an underdetermined system of equations and the flow of metabolites through the network is studied by optimizing the fluxes to achieve a 'cellular objective'[7], which results in an infinite solution space that satisfies the cellular objective as well as other enforced constraints that are determined through experimental and theoretical knowledge. Flux sampling is another powerful method that allows us to study the steady state distribution of fluxes throughout the feasible solution space without assuming a cellular objective[8] and as a result eliminates observer bias. In this study we harness the power of both hybrid process models and genome scale metabolic models to simultaneously model the process dynamics of CHO cell cultures and describe the intracellular behaviour that drives the observed process. The overall modelling framework is outlined in Figure 1. First, we demonstrate the concept of degree of hybridization and use it to determine the optimal level of process knowledge that accurately describes the process dynamics. Subsequently, we use the predictions of the hybrid process model to determine the distributions of important reactions belonging to the TCA cycle and pentose phosphate pathway of CHO cell metabolism using a recent genome scale reconstruction to study the intracellular behaviour throughout the fed-batch process. We demonstrate that the optimal hybrid model makes predictions that are not only accurate, but also biologically relevant. This framework can be a useful tool in building process monitoring tools and developing optimization strategies.

# METHODS

## Family of hybrid models

The family of hybrid models are constructed as described by Narayanan[5], where they define the degree of hybridization (DoH) as a measure of the process knowledge that is described explicitly by the mechanistic part of the hybrid model. This strategy was adopted to determine the optimal degree of hybridization that best describes the process dynamics of the cell culture under study. A family of 5 models with increasing degree of hybridization were constructed. The purely data-driven model (DoH =0) has no process knowledge incorporated and is tasked with predicting the process variables directly. The succeeding model (DoH=1) attempts to learn the rate of accumulation of the process variables, and the mechanistic part of the model calculates the value of the process variable at the next time step by integrating the system of differential equations. Here, the data driven part, a neural network, must learn to close the mass balance. The next hybridized model (DoH=2) is tasked with learning only the rates of production or consumption of the process variables, because the mechanistic model describes the mass balance through inflow and outflow rates of the process variables.

Further knowledge is added in the next model (DoH = 3) by encoding the proportionality of the reaction rates to the viable cell density. This allows the data-driven model to learn the specific reaction rates of the various process variables. The final model of this study (DoH = 4) incorporates the phenomenon of cell death, which is also modelled as a reaction proportional to the viable cell density. In all models, we employ only shallow neural networks as the data-driven part of the hybrid model. It is also assumed that the reactor is fully mixed with a homogenous cell population. Table 1 describes the model equations of the family of hybrid models.

## Datasets for modelling

| Degree of Hybridization (DoH) | Process knowledge described | Mechanistic model | Data-driven model |
|---|---|---|---|
| **0** | - | - | $[Z, Y_{t-1}, F] \xrightarrow[ANN]{} Y_t$ |
| **1** | Rate of accumulation | $\frac{d\boldsymbol{Y}}{dt} = \boldsymbol{\alpha}$ | $[Z, Y_{t-1}, F] \xrightarrow[ANN]{} \boldsymbol{\alpha}$ |
| **2** | Mass balance | $\frac{d\boldsymbol{Y}}{dt} = \boldsymbol{\beta} + \boldsymbol{F}_{in} - \boldsymbol{F}_{out}$ | $[Z, Y_{t-1}, F] \xrightarrow[ANN]{} \boldsymbol{\beta}$ |
| **3** | Cell specific reaction rate | $\frac{d\boldsymbol{Y}}{dt} = \boldsymbol{\gamma} * X_v + \boldsymbol{F}_{in} - \boldsymbol{F}_{out}$ | $[Z, Y_{t-1}, F] \xrightarrow[ANN]{} \boldsymbol{\gamma}$ |
| **4** | Cell specific reaction rates, growth and death rates | $\frac{dX_v}{dt} = \boldsymbol{\mu_g} * X_v - \boldsymbol{\mu_d} * X_v + \boldsymbol{F}_{in} - \boldsymbol{F}_{out}$<br>$\frac{d\boldsymbol{Y}}{dt} = \boldsymbol{\gamma} * X_v + \boldsymbol{F}_{in} - \boldsymbol{F}_{out}$ | $[Z, Y_{t-1}, F] \xrightarrow[ANN]{} \boldsymbol{\mu_g}, \boldsymbol{\mu_d}, \boldsymbol{\gamma}$ |

**Table 1:** Description of family of hybrid models explored in this study. In all hybrid structures, the data-driven part and mechanistic part are sequentially connected and the data driven part is tasked with learning a different phenomenon for each model. $\boldsymbol{\alpha}$ describes the rate of accumulation, $\boldsymbol{\beta}$ describes rate of production/consumption, $\boldsymbol{\gamma}$ describes cell specific reaction/growth rates, $\boldsymbol{\mu_g}$ is the specific growth rate, and $\boldsymbol{\mu_d}$ is specific death rate. *Z*: process conditions (feed concentrations of glucose and glutamine), *Y*: Response variables measured daily, *F*: Feeding profile and feed rate.

The dataset consists of 33 fed-batch shake flask cultivations that were collected and provided publicly by Bayer et al[9]. In brief, the cultivations were carried out with defined process conditions designed using Design of Experiments (DoE). The 4 important process conditions that were varied in the DoE were glucose concentration in the feed, glutamine concentration in the feed, rate of bolus feed, and the feeding profile. The cultivations were sampled once per day, the response variables (Viable and dead cell density, concentrations of glucose, glutamine, ammonia, lactate, and product) were analytically determined.

## Model training and evaluation

The family of hybrid models were constructed and trained in Python using the package PyTorch (2.5.1). The data driven part of the models had similar structure with only 1 hidden layer composed of 10 nodes activated by a *tanh* function. Of the 33 fed batch runs, 5 batches were set aside for testing and the rest were split into a ratio of 80:20 for training and validation after normalization.

The performance of the different models was compared using mean squared error for the test data:

$$MSEP = \frac{1}{N_time \cdot N_var} \sum_{i=1}^{N_var} \sum_{t=1}^{N_time} \left( C_{i,t}^{meas} - C_{i,t}^{pred} \right)^2$$

In addition, R-squared values were computed for each process variable in the test data for each model, to assess the ability of the model in capturing the variance in the dataset.

## Metabolic flux distribution

The metabolic flux analysis part of this multiscale framework is developed using iCHO2441, a genome scale metabolic model of Chinese Hamster Ovary cell[10]. Transport fluxes which carry metabolites in and out of the cell are determined by the hybrid process model described previously. The cell-specific reaction rates of glucose, glutamine, ammonia, and lactate are incorporated in the metabolic model as the transport fluxes. In addition, cell specific growth rate was also used to constrain the 'biomass transport flux'. The assumption of a pseudo-steady state results in equation (2):

$$\boldsymbol{S v_t} = 0, \tag{2}$$

$$\boldsymbol{v_t^{trans}} = \boldsymbol{r_i^{hybrid}}, \quad i \in \{Glc.Gln, Lac, Amm, Biomass\} \tag{3}$$

In equation (2), $\boldsymbol{S}$ corresponds to the stoichiometric matrix of the genome scale model, which is composed of the stoichiometric coefficient of every metabolite in every equation. $\boldsymbol{v_t}$ refers to the flux of every reaction at time **t**. This equation imposes the pseudo-steady state by ensuring that there is no intracellular accumulation of metabolites. The metabolic network is subject to the constraints imposed by equation (3) on the extracellular transport fluxes $\boldsymbol{v_t^{trans}}$, which correspond to the specific exchange reaction rates $\boldsymbol{r_i^{hybrid}}$ that are determined by the hybrid process model. Equation (2) and (3) will result

in infinite possible solutions for $\boldsymbol{v_t}$, as the number of variables is much higher than the number of equations in the model. Biologically, this means that the flow of metabolites can be re-routed in infinitely possible ways to satisfy the requirements of the cell. To study the solution space generated by equations (2) and (3), we perform uniform sampling of the solution space using an artificial centering hit-and-run sampling implemented in Python[11]. By generating 10000 samples of the metabolic network at each time step, we analysed the changes in the distribution of fluxes of reactions belonging to the central carbon metabolism (TCA cycle and Pentose Phosphate Pathway).

## RESULTS AND DISCUSSION

### Identification of optimal hybrid architecture

Figure 2 compares the predictive performance of the family of hybrid models in the test data set. The purely data driven model exhibits the lowest performance both in terms of mean squared error of the predictions and the coefficient of determination.

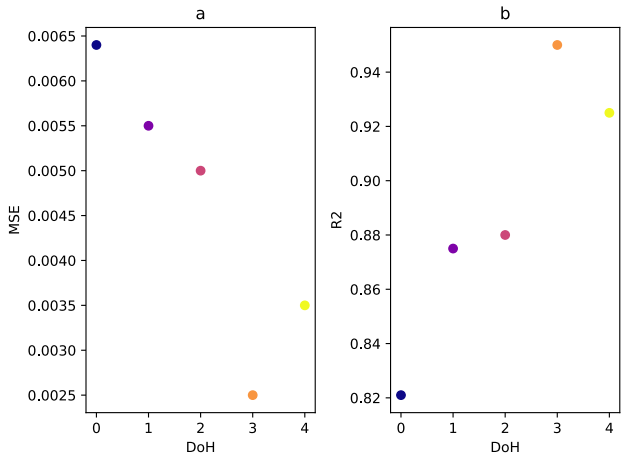



**Figure 2**: MSE (a) and coefficient of determination (b) of the family of hybrid models applied on the test data set. DoH=3 shows the best performance interms of least error ($2.5 \times 10^{-3}$) and highest R2 (0.95).

Addition of the first layer of process knowledge (DoH = 1) brings the MSE down by about 14% to $5.5 \times 10^{-3}$. This trend continues in the next two steps, where the MSE lowers to $5.0 \times 10^{-3}$ for the model with DoH = 2 and further down to a minimum of $2.5 \times 10^{-3}$ for the model with DoH = 3. Interestingly, the DoH=4 model does not follow this trend. Addition of process knowledge about cell death increased the MSE error of DoH=4 model to $3.5 \times 10^{-3}$. A similar trend is seen in the coefficient of determination (Fig 2B), where the highest R squared value is observed for the model with DoH = 3. It is important to note that despite the addition of further process knowledge from DoH =3 to 4, the predictive performance of the hybrid model decreases. This observation underlines the trade-off between the generalizability of the hybrid model and the degree of freedom imposed by the hybrid architecture. Based on these observations, DoH=3 was selected to be the optimal level of hybridization.

### Intracellular flux distributions

The selected optimal hybrid model provides biologically interpretable information in terms of cell specific uptake and secretions of Glucose, Glutamine, Lactate, and Ammonia. In addition, it is also able to describe the specific growth rate of the cells. The profile of the cell specific exchange fluxes predicted by the hybrid model for a test data set throughout its process profile is shown as illustrative example in Figure 4.

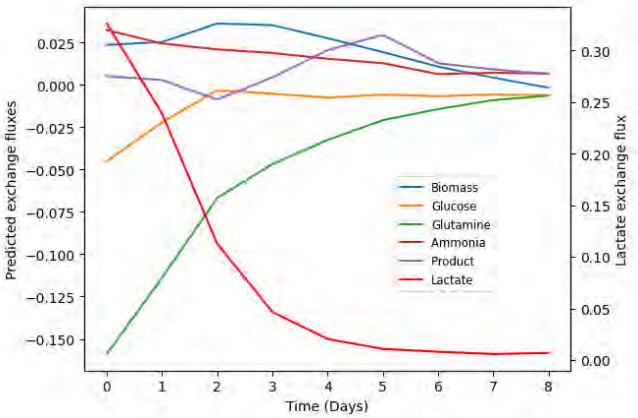



**Figure 4:** Cell specific uptake and secretion fluxes predicted by the hybrid process model. All fluxes except biomass are expressed in $mmol\,(10^6\,cells)^{-1}day^{-1}$. Biomass flux is expressed conventionally in $day^{-1}$ .

The exchange fluxes predicted by the hybrid process model describe a rapid proliferation/growth phase between days 1-3, and a production phase between days 4-7. In the growth phase, the cells have a high uptake rate of glutamine and glucose. As expected, the secretion flux of lactate is also high, to account for the ATP generation required to meet the cells energy demand. In the production phase, as secretion flux of lactate is low, the carbon flux is directed towards the product.

To understand the intracellular metabolism that underlies the observed process, a genome scale metabolic reconstruction of CHO cell was employed. This reconstruction, iCHO2441[10], has been reported to have improved intracellular predictive performance. By using the predictions from the hybrid model as constraints, 10000 points were sampled from the solution space generated by assuming a pseudo-steady state at each time step. The sampled fluxes were used to visualize the difference in cellular metabolism between the growth phase and the

stationary/production phase.

### TCA cycle

The distribution of fluxes of 2 important reactions belonging to TCA cycle is visualized in Figure 5. It is observed that the activity of reactions in the TCA cycle is higher in the production phase than in the growth phase.

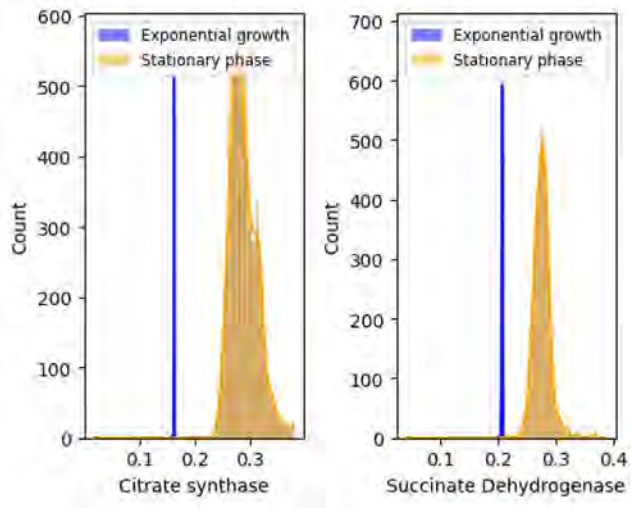



**Figure 5:** Distribution of fluxes of reaction in TCA cycle (in $mmol\ (10^6\ cells)^{-1} day^{-1}$).

This has been previously verified through experimental approaches through $^{13}C$ metabolic flux analysis[12]. In the growth phase, lactate production is preferred as it is faster but energetically less efficient route for ATP synthesis. But in the production phase, TCA cycle is favoured to generate ATP. A possible reason for this phenomenon is the inhibiting nature of the accumulated lactate[13].

Pentose Phosphate Pathway

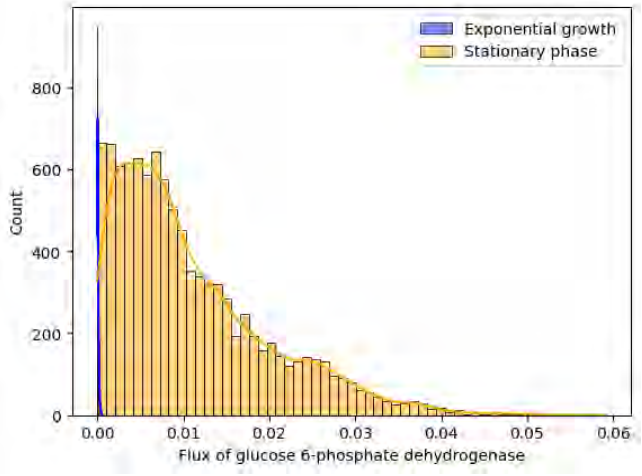



**Figure 6:** Distribution of flux of G6PDH reaction in the oxidative PP pathway in the exponential and stationary phase.

Oxidative pentose phosphate pathway (oxPPP) flux was significantly higher after the growth phase, while it was close to zero during the growth phase. The flux of glucose-6-phosphate dehydrogenase (G6PDH) increased during production phase even as the uptake fluxes of glucose and glutamine fell considerably when compared to the growth phase. The distribution of G6PDH is visualized in figure 6. This phenomenon of increased oxPPP activity during post growth phase has been reported previously[14]. It has been suggested that the increased flux towards PPP is a result of increased antibody production, which requires constant supply of NADH for protein folding[15].

## CONCLUSION AND OUTLOOK

In this study, we demonstrate that for the cell culture process described by the dataset, hybrid architectures work much better than purely data-driven models and that the introduction of fundamental process knowledge greatly improves the predictive capability of the model. By constructing a family of hybrid models with increasing degree of hybridization, we observe that the predictive accuracy of the hybrid model increases as long as the process knowledge introduced does not introduce a bias in the model. There exists a trade-off between the model parameters and the fundamental process knowledge to be added, as a more complex model needs more data points for robust training. In this case, a model with moderate degree of hybridization (DoH=3) was found to be the optimal model by comparing the error and predictive accuracy across the family of models. This model can efficiently learn the cell specific uptake/secretion/growth rates of the cell culture process, which aids in both macro-scale process monitoring as well as understanding of biologically relevant phenomena. While the hybrid process model shows good accuracy within the dataset, it will be interesting to test the capabilities of the model in extrapolating with respect to the process operating conditions. This

A cellular scale understanding of the cell culture process is achieved by employing a genome scale metabolic reconstruction of CHO metabolism constrained by the predictions of the hybrid model. By performing flux sampling, we capture the distribution of the entire feasible solution space of the metabolic network within these predicted constraints. This allows us to study the flux distribution without the assumption of metabolic objectives, which cannot be experimentally determined at most time steps. The captured flux distributions match well with previously available experimental data and provides a micro-scale understanding of the bioprocess. This hybrid framework opens avenues for further process optimization strategies by targeting cellular level processes; for example, a glucose feeding profile that directs carbon

flux towards the TCA cycle instead of the energetically inefficient lactate synthesis.

Overall, the outlined hybrid framework has the ability to combine data-driven techniques with fundamental process knowledge to simultaneously predict macroscale process profile and biologically relevant process information that can provide microscopic information about cellular behaviour. This strategy is particularly relevant for advanced modelling and simulation of cell cultures for process monitoring and optimization.

## ACKNOWLEDGEMENTS

This work was funded by the Novo Nordisk Foundation through grant number NNF20CC0035580.

## REFERENCES

1. Q. Su *et al.*, "A perspective on Quality-by-Control (QbC) in pharmaceutical continuous manufacturing," *Comput. Chem. Eng.*, vol. 125, pp. 216–231, Jun. 2019, doi: 10.1016/j.compchemeng.2019.03.001.
2. K. Pandey, M. Pandey, V. Kumar, U. Aggarwal, and B. Singhal, "Bioprocessing 4.0 in biomanufacturing: paving the way for sustainable bioeconomy," *Syst. Microbiol. Biomanufacturing*, vol. 4, no. 2, pp. 407–424, Apr. 2024, doi: 10.1007/s43393-023-00206-y.
3. S. Craven, N. Shirsat, J. Whelan, and B. Glennon, "Process model comparison and transferability across bioreactor scales and modes of operation for a mammalian cell bioprocess," *Biotechnol. Prog.*, vol. 29, no. 1, pp. 186–196, 2013, doi: 10.1002/btpr.1664.
4. D. Solle *et al.*, "Between the Poles of Data-Driven and Mechanistic Modeling for Process Operation," *Chem. Ing. Tech.*, vol. 89, no. 5, pp. 542–561, 2017, doi: 10.1002/cite.201600175.
5. H. Narayanan, M. Luna, M. Sokolov, A. Butté, and M. Morbidelli, "Hybrid Models Based on Machine Learning and an Increasing Degree of Process Knowledge: Application to Cell Culture Processes," *Ind. Eng. Chem. Res.*, vol. 61, no. 25, pp. 8658–8672, Jun. 2022, doi: 10.1021/acs.iecr.1c04507.
6. "Hybrid Models Based on Machine Learning and an Increasing Degree of Process Knowledge: Application to Capture Chromatographic Step | Industrial & Engineering Chemistry Research." Accessed: Nov. 11, 2024. [Online]. Available: https://pubs.acs.org/doi/10.1021/acs.iecr.1c01317
7. J. D. Orth, I. Thiele, and B. Ø. Palsson, "What is flux balance analysis?," *Nat. Biotechnol.*, vol. 28, no. 3, pp. 245–248, Mar. 2010, doi: 10.1038/nbt.1614.
8. [8] H. A. Herrmann, B. C. Dyson, L. Vass, G. N. Johnson, and J.-M. Schwartz, "Flux sampling is a powerful tool to study metabolism under changing environmental conditions," *Npj Syst. Biol. Appl.*, vol. 5, no. 1, pp. 1–8, Sep. 2019, doi: 10.1038/s41540-019-0109-0.
9. B. Bayer, M. Duerkop, R. Pörtner, and J. Möller, "Comparison of mechanistic and hybrid modeling approaches for characterization of a CHO cultivation process: Requirements, pitfalls and solution paths," *Biotechnol. J.*, vol. 18, no. 1, p. 2200381, 2023, doi: 10.1002/biot.202200381.
10. B. Strain, J. Morrissey, A. Antonakoudis, and C. Kontoravdi, "How reliable are Chinese hamster ovary (CHO) cell genome-scale metabolic models?," *Biotechnol. Bioeng.*, vol. 120, no. 9, pp. 2460–2478, Sep. 2023, doi: 10.1002/bit.28366.
11. W. Megchelenbrink, M. Huynen, and E. Marchiori, "optGpSampler: An Improved Tool for Uniformly Sampling the Solution-Space of Genome-Scale Metabolic Networks," *PLOS ONE*, vol. 9, no. 2, p. e86587, Feb. 2014, doi: 10.1371/journal.pone.0086587.
12. J. Dean and P. Reddy, "Metabolic analysis of antibody producing CHO cells in fed-batch production," *Biotechnol. Bioeng.*, vol. 110, no. 6, pp. 1735–1747, 2013, doi: 10.1002/bit.24826.
13. O. Pennington, S. Espinel Ríos, M. T. Sebastian, A. Dickson, and D. Zhang, "A multiscale hybrid modelling methodology for cell cultures enabled by enzyme-constrained dynamic metabolic flux analysis under uncertainty," *Metab. Eng.*, vol. 86, pp. 274–287, Nov. 2024, doi: 10.1016/j.ymben.2024.10.013.
14. N. Templeton, J. Dean, P. Reddy, and J. D. Young, "Peak antibody production is associated with increased oxidative metabolism in an industrially relevant fed-batch CHO cell culture," *Biotechnol. Bioeng.*, vol. 110, no. 7, pp. 2013–2024, 2013, doi: 10.1002/bit.24858.
15. S. Chakravarthi, C. E. Jessop, and N. J. Bulleid, "The role of glutathione in disulphide bond formation and endoplasmic-reticulum-generated oxidative stress," *EMBO Rep.*, vol. 7, no. 3, pp. 271–275, Mar. 2006, doi: 10.1038/sj.embor.7400645.

© 2025 by the authors. Licensed to PSEcommunity.org and PSE Press. This is an open access article under the creative commons CC-BY-SA licensing terms. Credit must be given to creator and adaptations must be shared under the same terms. See https://creativecommons.org/licenses/by-sa/4.0/



Systems & Control Transactions

**Research Article - Peer Reviewed Conference Proceeding**
ESCAPE 35 - European Symposium on Computer Aided Process Engineering
Ghent, Belgium. 6-9 July 2025
Jan F.M. Van Impe, Grégoire Léonard, Satyajeet S. Bhonsale,
Monika E. Polańska, Filip Logist (Eds.)

PSE PRESS

# Development and Integration of a Co-Current Hollow Fiber Membrane Unit for Gas Separation in Process Simulators Using CAPE-OPEN Standards

**Loretta Salano[a], Ilaria Dagna[a], Mattia Vallerio[a], and Flavio Manenti***

[a] Politecnido di Milano, Dipartimento di Chimica, Materiali ed ing. Chimica "G.Natta", p.zza
* Corresponding Author: flavio.manenti@polimi.it

## ABSTRACT

Process simulation is essential for optimizing chemical processes, offering a cost-effective alternative to the experimental approach. This study presents a co-current hollow fibre membrane model for $CO_2$ separation, integrated into Aspen HYSYS® using the CAPE-OPEN standard. A one-dimensional boundary value problem (BVP) is solved through the shooting method, ensuring accuracy for complex gas separation processes. The unit is implemented in C++, facilitating interoperability, error handling, and optimization of key performance indicators like energy consumption and separation efficiency. Appropriate output variables are employed in the Aspen HYSYS® environment to enable direct sensitivity analysis and optimization within the process simulator. Results Sensitivity analysis results demonstrate that the co-current hollow fiber membrane unit improves methane recovery compared to a pressure swing water absorption (PSWA) column for biogas upgrading to biomethane. While membrane technology showed a 24% reduction in energy consumption for biomethane production, PSWA exhibits higher efficiency for biomethanol production. This study not only demonstrates the value of CAPE-OPEN standards in implementing custom unit operations but also lays the groundwork for future developments in process simulation using advanced mathematical modelling and optimization techniques.

**Keywords**: CAPEOPEN, Biogas, Modelling, C++

## INTRODUCTION

Sustainable process alternatives in the chemical industry have emerged to comply with the reduction of greenhouse gases (GHG). The main molecule to mitigate among GHG is $CO_2$. A valid mitigation strategy involves the substitution of thermal energy sources with renewable electrical ones, capture and storage technologies (CCS) and capture and utilization (CCU) technologies. Among carbon neutral sources, there is biogas: a mixture of gases produced by anaerobic digestion of either agricultural, animal or municipal waste. Composition is typically formed by 55-60 % of methane and 38-40 % of $CO_2$, with different amounts of impurities, depending on the feedstock [1]. The high tenor of methane allows for biomethane production or implementation in fuel production applications, as reported by many in the literature [2], [3], [4]. Membrane technology, particularly hollow fiber membranes, has gained increasing importance in industries for its energy efficiency, scalability, and suitability for applications in biogas upgrading, where either all or part of the total carbon dioxide is removed [5].

Process simulation is an essential tool for the design, control and optimization of chemical processes. It allows for detailed analysis of individual unit operations and entire processes under different operating conditions, providing a valid alternative to costly and time-consuming laboratory experiments, without risking any plant damage. While common unit operations are already implemented in the database of commercial process simulation software, non-conventional units can only be externally included as custom units. This work focuses on the implementation of a nonstandard co-current hollow fiber membrane unit for gas separation in Aspen HYSYS V11®, using C++ programming and the CAPE-OPEN (Computer Aided Process Engineering - Open Standard),

a standard that offers interoperability and communication between different process simulation software tools [6]. The procedure for integrating a custom unit in a process simulator begins with validating a suitable mathematical model found in the literature or derived from experimental data, which accurately describes the behaviour of the unit operation. The validated model is then integrated into a C++ code for CAPE-OPEN units, where the material port and parameter collection of the unit are also defined. Once implemented, the custom unit is applied in process simulation case studies to compare layouts and find optimal operating conditions.

# METHODOLOGY

## Solution-diffusion model

As a common practice in literature, the solution-diffusion model is implemented to predict gas permeation through the polymer membrane. The model implies gas separation through the membranes to occur according to both gas molecular size and gas-polymer interaction: the gas dissolves into the polymer, diffuses through it, and desorbs on the other side. The fundamental equation of the solution-diffusion model is Fick's law, which expresses the gas diffusion at a steady state of species i ($J_i$) through a polymeric membrane of thickness l as a function of its diffusivity ($D_i$) and its gradient of concentration ($c_i$), Eq. (1).

$$J_i = -D_i \frac{dc_i}{dl} \tag{1}$$

In an ideal system where solubility ($S_i$) is independent of concentration, Henry's law relates gas concentration to its solubility and pressure. Integrating Fick's law across the membrane thickness ($l$) yields total flux:

$$J_i = \frac{D_i S_i (x_i P_f - y_i P_p)}{l} \tag{2}$$

where $x_i$ is the retentate side mole fraction, $y_i$ is the permeate side mole fraction, $P_f$ is the feed side pressure and $P_p$ is the permeate-side pressure. Moreover, ($D_i \cdot S_i$) is the membrane permeability, which indicates how effectively the membrane allows gas to pass through. Permeance, defined as the ratio of permeability and thickness of the membrane, is used in modelling hollow fibre membranes.

## Mathematical model

Hollow fibre membranes allow for a compact configuration, where multiple fibres are bundled in a shell due to their small diameter (1 mm). This technology is one of the most diffused in the industry. Operation can be co-current or counter current, differing by the flow direction of the permeate flux direction. A co-current hollow fibre membrane modulus can be schematically represented as a horizontal cylinder with one closed end (**Figure 1**). The gas is fed on the shell side, where, by passing through the tiny hollow fibres, it is separated from the feed into a permeate and a retentate stream.

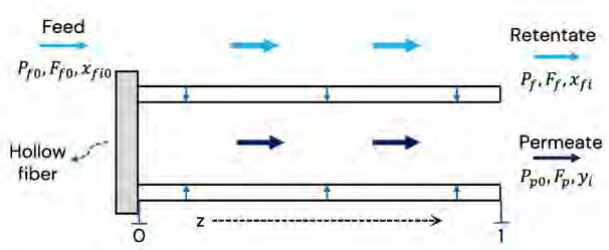



**Figure 1**. Simplified representation of a hollow-fiber co-current membrane.

The axial domain is normalized along the $z$ coordinate, and the following assumptions are taken under consideration:

- the model is one-dimensional;
- the Hagen-Poiseuille equation describes pressure drop on the permeate side;
- the pressure at the retentate side is constant and equal to the feed pressure;
- the gas presents laminar behaviour in both the retentate and permeate sides;
- properties and structure of the membrane are not influenced by pressure. Hence, permeances are assumed constant along the membrane;
- the unit is isothermal, thus no energy balance is needed to describe its thermal behaviour;
- the unit works at steady state conditions;
- membrane porosity does not oppose any resistance to the gas;
- no mixing occurs between permeate fluxes of different compositions along the length of the membrane.

Given the stated assumptions, the molar balance for the $i^{th}$ component along the membrane is expressed as reported in Eq. (3)

$$\frac{dF_{fi}}{dz} = -2\pi r_0 N_f L K_i \left(x_i P_f - y_i P_p\right) \tag{3}$$

where $F_{fi}$ is the molar is the feed side flowrate of the component, $N_f$ represents the number of fibres and is calculated as the ratio between the total membrane area $A$ and the external area of a single cylindrical fibre $2\pi r_0 L$. $K_i, x_i, y_i, P_f, P_p$ are, respectively, the permeance, the molar fraction and pressure feed and permeate side.

The pressure drop is described by the Hagen-Poiseuille equation Eq. (4), where R is the universal gas

constant, $r_{in}$ the inner radius of the hollow fibre, $\mu_m$ is the viscosity of the mixture and $F_p$ is the flowrate on the permeate side.

$$\frac{dP_p}{dz} = -\frac{8RTL\mu_m F_p}{\pi r_{in}^4 N_f P_p} \quad (4)$$

Appropriate boundary conditions are applied to both balances, Eq. (5) and Eq. (6), given the inlet feed flowrate $(F_{f0}, x_{f0})$ and downstream pressure $P_{p0}$.

$$\begin{cases} F_f(z=0) = F_{f0} \\ x_i(z=0) = x_{f0} \end{cases} \quad (5)$$

$$P_p(z=1) = P_{p0} \quad (6)$$

The mathematical problem to be solved is a so-called Boundary Value Problem (BVP), given the boundary conditions on different ends of the domain. The system is composed by the total number of molar components, NC+1 equations. A BVP can be solved by an iterative procedure that simplifies the problem to an Initial Value Problem (IVP) by guessing initial conditions and integrating to check if boundary conditions are met. If the error does not comply with the accepted tolerance $\varepsilon$, set equal to 1e-4, a new guess is given to the IVP. To ensure a decreasing trend in the total error, the initial guess is updated at each iteration by a relaxation factor $\alpha$, equal to 0.1 (Eq. (7)).

$$x_{j+1} = x_j - \alpha|error| \quad (7)$$

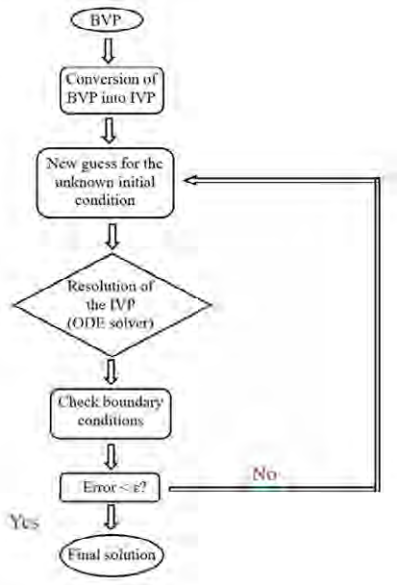



**Figure 2**-Scheme of the shooting methodology for the resolution of a boundary value problem.

The described method is commonly referred to as the *shooting method* [7], a scheme representation is reported in **Figure 2**. The mathematical model is first validated against data from the literature [8], [9], [10] in Matlab® and successively implemented in Aspen HYSYS®. It is highly relevant to provide feasible physical guesses to the unit to ensure convergence in the process simulator. For the validation results, experimental data were available to test, but for process operation, the choice is to consider the pressure higher at z=0, as pressure drops are present along the membrane.

$$P_p(z=1) = P_{p0} \quad (6)$$

A counter current implementation requires numerically to modify the boundary values. The permeate side would migrate in opposite direction from the feed, exiting at x=0. The assumptions stated are valid, the sign in front of Eq. (4) becomes a plus sign and the boundary condition for the permeate pressure becomes:

$$P_p(z=0) = P_{p0} \quad (9)$$

## Case studies in the simulation environment

The study investigates the application of the hollow fiber membrane in biogas processing, for its upgrading to biomethane (Case A), or partial $CO_2$ separation for methanol synthesis application (Case B). Both systems treat 24.5 kmol/h of biogas with 60% tenor of methane and 40% of carbon dioxide, supposing to collect it from pretreatment facilities where impurities such as $H_2S$, siloxanes or volatile components are removed. A block scheme diagram is reported in **Figure 3,** it shows both configuration unit operations.

Case A studies the production of biomethane for grid injection (purity of 98% and 13 bars according to Italian standards) by comparing a pressure swing water absorption (PSWA) column performance to a three hollow fibre co current membrane system at 20 bars [11]. In the latter configuration, the first membrane recovers most of the methane, the retentate is sent to a second membrane where the specifications for biomethane are met. A third membrane is necessary to further recover the methane present in the permeate P-2, as reported in

**Figure 4.**

In Case B, the stream undergoes a partial removal of $CO_2$ to prepare for methanol synthesis. The optimal operating conditions are reached with syngas with a stoichiometric ratio (SN) equal to 2, Eq. (8).

$$SN = \frac{y_{H_2} - y_{CO_2}}{y_{CO} + y_{CO_2}} \quad (10)$$

In this case, separation by membrane was achieved with a two-membrane setup [11]. Case A is only concerned by the $CO_2$ removal, while case B undergoes a steam reforming unit, which produces hydrogen and CO, that after condensation of water, enters the methanol synthesis reactors and purification by a two-distillation columns system. The reforming reactor operates at 900°C with a feed steam to carbon ratio of 3 and 15 bars. Methanol synthesis operates at 61 bars, 250 °C and with a 5% purge when recycling the unreacted syngas.

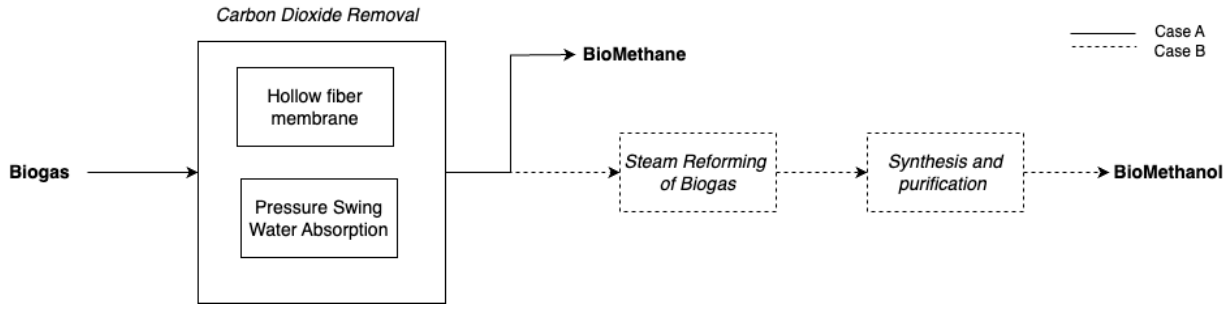



**Figure 3** - Block scheme for the case studies simulated in Aspen HYSYS®. Case A compares the carbon dioxide removal technologies for biomethane as the final product, while case B removes only partially CO2 to use the product for biomethanol production.

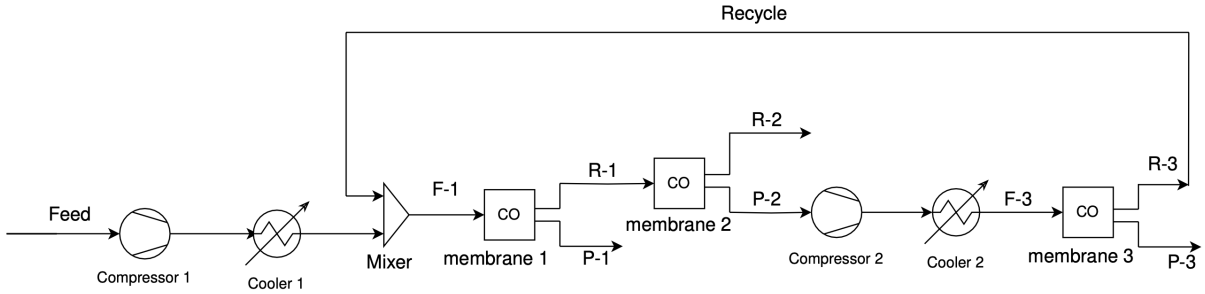



**Figure 4 -** Three membrane configuration for biomethane production from biogas.

**Table 1** - Membrane input parameters implemented in process simulations in Aspen HYSYS®

| Parameter | Unit | Case A | Case B |
|---|---|---|---|
| *L* | m | 4 | 2 |
| *A* | *m*2 | 800 | 90 |
| *rin* | *μ*m | 40 | 40 |
| $r_o$ | *μ*m | 100 | 100 |
| $xf,CO_2$ | - | 0.40 | 0.40 |
| $xf,CH_4$ | - | 0.60 | 0.60 |
| $K_{CO2}$ | mol/m$^2$/s/Pa | 7.86e-9 | 1.34e-8 |
| $K_{CH4}$ | mol/m$^2$/s/Pa | 6.77e-10 | 3.72e-10 |

**Table 2-** KPIs for the two case studies

| KPI | Formulation | Unit | Case A | | Case B | |
|---|---|---|---|---|---|---|
| | | | PSWA | Membrane | PSWA | Membrane |
| $EC_{bioCH4/bioMeOH}$ | $\frac{Q_{compr}+Q_{pumps}}{\dot{m}_{bioCH_4/bioMeOH}}$ | *kWh/kg* | 0.75 | 0.57 | 0.18 | 0.22 |
| $EC_{BG}$ | $\frac{Q_{compr}+Q_{pumps}}{\dot{m}_{BG}}$ | $kWh/kg_{BG}$ | 0.31 | 0.25 | 0.12 | 0.15 |
| $EC_{CO2}$ | $\frac{Q_{compr}+Q_{pumps}}{\dot{m}_{CO_2,out}}$ | $kWh/kg_{CO2}$ | 0.35 | 0.44 | 0.41 | 0.68 |
| $R_{bioCH4/bioMeOH}$ | $\frac{\dot{m}_{bioCH_4/bioMeOH}}{\dot{m}_{BG}}$ | $kg_{bioCH4}/kgBG$ | 0.41 | 0.43 | 0.68 | 0.66 |

Both scenarios are compared in terms of key performance indicators (KPI), reported in the results (**Table 2**), to evaluate which technology suits best each application.

The key steps of the implementation procedure include creating both material port connections (the feed, retentate and permeate ports) and parameter collections

(the main features to define the membrane unit), including the equations of the mathematical model and transferring data between the simulation environment and the custom unit.

The code is then compiled into a DLL (Dynamic Linked Library) file, which is registered in the Windows operating system to enable the use of its final version within Aspen HYSYS®. In particular, the input parameters to be provided by the user, and chosen for the cases under study, are reported in **Table 1**.

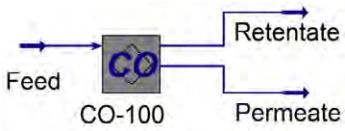



**Figure 5**-CAPEOPEN unit implemented in the process simulator

## RESULTS AND DISCUSSION

### Model validation

**Figure 6** shows both model results and experimental data in the three reference cases: the molar fraction of the species of interest in the permeate decreases when stage-cut increases and a maximum relative error lower than 14% demonstrates a good accuracy of the mathematical model. Further on, convergence is met after few iterations (in the order of 5), given a first guess from the available literature data.

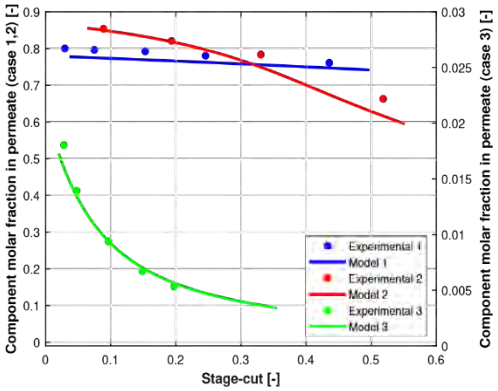



**Figure 6** - Model performance against the collected experimental data from the literature [8], [9], [10].

### Case studies result in Aspen HYSYS®

Once the mathematical model is validated, the co-current hollow fiber membrane unit can be integrated in Aspen HYSYS® using the CAPEOPEN Unit Operation in its "model palette" of the simulator, which is directly connected to a DLL. developed in C++.

The goal of the simulation is to find the most suitable operational unit for biomethane and biomethanol production from biogas. The implementation of the CAPEOPEN unit allows for carrying out a sensitivity analysis in the process simulator and obtaining reliable results. The most relevant results are summarized in **Table 2**. In Case A biomethane is the main product to be injected into the Italian national grid at 13 bars. The three-membrane system shows a lower methane slip when compared to the column, with a recovery term $R_{bioCH4}$ of 0.43 rather than 0.41, which has a strong impact if considering product revenues. Energy costs are evaluated directly from electrical demand from compressors and pumps (of water recirculation in the absorption column) given equal operating conditions. The membranes allow for lower costs in biomethane production, even if, to ensure low slip values, two compressors' stages are required between each recycle (**Figure 4**). The PSWA low efficiency is associated with the high amount of water and carbon dioxide recirculated in the system. Around 57 tons per hour of water are necessary to reach 98% purity in methane. The operating pressure is highly relevant in the PSWA, increasing its values strongly affects the $CO_2$ removal, for this case study a value of 21 bar is chosen after appropriate operational case studies.

The second application frames the CAPEOPEN unit in a complex process simulation from biogas to biomethanol composed by a steam reforming section, methanol synthesis section and finally, a purification section. Results are evaluated on the base of biomethanol rather than biomethane. In this case, the PSWA shows lower consumption as a lower amount of $CO_2$ must be separated to reach biomethanol synthesis optimal conditions, even if in this configuration the membranes can only take advantage of two units and one intermediate compression. The constraint provided is in fact to reach an SN value of 2±0.1.

Further on, the two-membrane layout allows for a slightly higher methane slip, reducing the recovery term and producing slightly lower methanol than the PSWA configuration. Another relevant aspect regards the operating pressure required by both configurations, the membrane require 30 bar to reach the specifics, while the PWSA is operated at 23 bars, to avoid an extra compression step before the reformer, which works at the same conditions. The choice of higher-pressure operation is due to the methanol synthesis necessary further compression step.

## CONCLUSIONS

In the study, a custom co-current hollow fiber membrane model for $CO_2$ separation was successfully developed and integrated into Aspen HYSYS® simulation environment using the CAPE-OPEN standard. The mathematical model was first validated against experimental data, demonstrating high accuracy with a relative error below 14%. Comparative case studies highlight the versatility of

the membrane unit in biogas upgrading applications, showing its capability to produce biomethane with reduced methane slip and lower energy costs compared to a column water absorption technology. For biomethanol production, the PSWA shows lower energy consumption and higher productivity, due to the low amount of CO2 that must be separated to reach an SN equal to 2 in the synthesis section. The simulations show the advantages of membrane technologies in biogas processing, including their adaptability to various product specifications and their ability to reduce operational energy demands. Additionally, the CAPE-OPEN framework has proven to be a powerful tool for integrating and optimizing novel unit operations within standard process simulation environments. It can be concluded that while membranes are more energy-efficient for high-purity biomethane production, a comprehensive comparison should also consider the cost associated with each layout, as membranes require higher maintenance but allow for compact systems. Further optimizations and evaluations can be carried out directly in the process simulator environment thanks to the CAPEOPEN output variables provided. The methods developed for co-current hollow fibre membranes can be applied to other custom unit operations in process simulation, offering versatility for future applications.

## REFERENCES


1. X. Y. Chen, H. Vinh-Thang, A. A. Ramirez, D. Rodrigue, and S. Kaliaguine, “Membrane gas separation technologies for biogas upgrading,” 2015, *Royal Society of Chemistry*. doi: 10.1039/c5ra00666j.
2. G. Bozzano, C. Pirola, C. Italiano, R. Pelosato, A. Vita, and F. Manenti, “Biogas: a Possible New Pathway to Methanol?,” in *Computer Aided Chemical Engineering*, vol. 40, Elsevier B.V., 2017, pp. 523–528. doi: 10.1016/B978-0-444-63965-3.50089-1.
3. M. Beil and W. Beyrich, “Biogas upgrading to biomethane,” in *The Biogas Handbook: Science, Production and Applications*, Elsevier Inc., 2013, pp. 342–377. doi: 10.1533/9780857097415.3.342.
4. I. Angelidaki *et al.*, “Biogas upgrading and utilization: Current status and perspectives,” *Biotechnol Adv*, vol. 36, no. 2, pp. 452–466, Mar. 2018, doi: 10.1016/J.BIOTECHADV.2018.01.011.
5. L. Salano, M. M. Bozzini, S. Caspani, G. Bozzano, and F. Manenti, “Integration of an Autothermal Outer Electrified Reformer Technology for Methanol Production from Biogas : Enhanced Syngas Quality Production and CO 2 Capture and,” 2024.
6. J. Van Baten and M. Pons, “Cape-open: Interoperability in industrial flowsheet simulation software,” *Chem Ing Tech*, vol. 86, no. 7, pp. 1052–1064, 2014, doi: 10.1002/cite.201400009.
7. M. R. Osborne, “On shooting methods for boundary value problems,” *J Math Anal Appl*, vol. 27, no. 2, pp. 417–433, 1969, doi: 10.1016/0022-247X(69)90059-6.
8. S. H. Choi, M. M. B. Sultan, A. A. Alsuwailem, and S. M. Zuabi, “Preparation and characterization of multilayer thin-film composite hollow fiber membranes for helium extraction form its mixtures,” *Sep Purif Technol*, vol. 222, no. March, pp. 152–161, 2019, doi: 10.1016/j.seppur.2019.04.036.
9. M. Sidhoum, A. Sengupta, and K. K. Sirkar, “Asymmetric cellulose acetate hollow fibers: Studies in gas permeation,” *AIChE Journal*, vol. 34, no. 3, pp. 417–425, 1988, doi: 10.1002/aic.690340309.
10. C. Fabiani, L. Bimbi, and F. Carta, “Gas Separation in a Membrane Unit: Experimental Results and Theoretical Predictions,” *Sep Sci Technol*, vol. 24, no. 14, pp. 1207–1226, 1989, doi: 10.1080/01496398908049898.
11. G. Aguilloso, K. Arpia, M. Khan, Z. A. Sapico, E. Clyde, and R. Lopez, “Recent Advances in Membrane Technologies for Biogas Upgrading †,” 2024.



© 2025 by the authors. Licensed to PSEcommunity.org and PSE Press. This is an open access article under the creative commons CC-BY-SA licensing terms. Credit must be given to creator and adaptations must be shared under the same terms. See https://creativecommons.org/licenses/by-sa/4.0/




Systems & Control Transactions

**Research Article - Peer Reviewed Conference Proceeding**
ESCAPE 35 - European Symposium on Computer Aided Process Engineering
Ghent, Belgium. 6-9 July 2025
Jan F.M. Van Impe, Grégoire Léonard, Satyajeet S. Bhonsale,
Monika E. Polańska, Filip Logist (Eds.)

PSE PRESS

# A Comparative Study of Aspen Plus and Machine Learning Models for Syngas Prediction in Biomass-Plastic Waste Co-gasification

**Usman Khan Jadoon[a]*, Ismael Díaz[a], Manuel Rodríguez[a]**

[a] *Departamento de Ingeniería Química Industrial y del Medioambiente, Escuela Técnica Superior de Ingenieros Industriales, Universidad Politécnica de Madrid, Madrid, Spain*
* Corresponding Author: uk.jadoon@upm.es

## ABSTRACT

The co-gasification of biomass and plastic waste offers a promising pathway for sustainable syngas production, necessitating precise prediction of its composition to optimize efficiency. This study compares the performance of Aspen Plus models, including the thermodynamic equilibrium model (TEM) and restricted thermodynamic equilibrium model (RTM), with machine learning (ML) techniques, focusing on the support vector regression (SVR) for syngas prediction during steam and air co-gasification. Aspen Plus simulations provided valuable mechanistic insights, while the ML model demonstrated superior predictive accuracy. The SVR, enhanced by principal component analysis (PCA), significantly improved performance, achieved $R^2$ values of 0.879 for $H_2$, 0.856 for CO, 0.859 for $CO_2$, and 0.744 for $CH_4$ on the testing dataset. It also outperformed other models in terms of RMSE, achieving exceptional precision for $CH_4$ (0.0087), CO (0.0193), and $H_2$ (0.0194). In contrast, RTM exhibited moderate accuracy with minimal deviations, while TEM showed the highest RMSE values across all predictions, indicating its limited reliability for real-world applications. This study advances gasification technologies by demonstrating the advantages of ML models, particularly SVR, in predicting syngas composition and supporting the global transition toward sustainable energy systems.

**Keywords**: Biomass, Aspen Plus, Modeling and Simulations, Plastic wastes, Syngas prediction

## INTRODUCTION

The transition to sustainable energy production necessitates the optimization of thermochemical conversion processes, with co-gasification of biomass and plastic waste emerging as a promising route for syngas generation. Accurate prediction of syngas composition is crucial for efficient process design and operation. Traditional modeling approaches, primarily thermodynamic equilibrium and kinetic models implemented in process simulation software like Aspen Plus, have served as the foundation for gasification studies. These models leverage fundamental principles of thermodynamics and reaction kinetics to simulate the complex interactions within the gasifier. However, they often struggle to capture the non-linearities and intricate phenomena inherent in these processes, especially when dealing with mixed feedstocks [1].

Machine learning (ML) is increasingly being explored as a complementary or alternative approach, offering the potential to enhance predictive accuracy. ML techniques, such as random forest, artificial neural networks (ANNs), and support vector machines (SVMs) can learn complex relationships directly from data, bypassing some of the limitations of purely mechanistic models [2]. ML's capacity to learn from high-dimensional data and capture non-linear relationships has made them a popular choice for modeling complex systems. Significant research has focused on both Aspen Plus modeling and ML-based modeling of gasification. For example, Aspen Plus studies often focus on the effects of different operating conditions such as temperature, air/steam to fuel ratio on syngas composition . ML studies, on the other hand, tend to concentrate on developing predictive models that are trained

using either experimental data or output from process simulation software [3]. The comparison of these two approaches and the exploration of their potential synergy, however, is less well-explored in the current literature.

While both Aspen Plus and ML techniques have individually contributed to understanding and predicting syngas production from gasification, the direct comparative analysis of these methods, particularly in the context of co-gasification, is lacking. This research directly addresses this gap by comparing the predictive performance of Aspen Plus models, TEM and RTM, and surrogate ML model, SVM, for the co-gasification of biomass and plastic waste, and exploring the advantages each technique bring. The novelty of this study lies in the integration of these approaches and offers a comprehensive comparison of their prediction accuracy in prediction of syngas compositions. While conventional gasification methods and simulation tools like Aspen Plus have been widely used to study biomass and plastic waste gasification, this study will also explore how ML model trained on experimental data can overcome limitations in mechanistic models for predicting syngas outputs [4]. This approach has the potential to contribute towards a more accurate and data-driven approach to design and optimization of co-gasification plants.

## METHODOLOGY

Experimental data on steam-$O_2$ biomass plastic gasification, based on a mixture of rice husk (RH), polyethylene PE, polyethylene terephthalate (PET), and tyres, was collected from the published articles by Brachi et al. (2014), Pinto et al. (2002), and Pinto et al. (2016) [5-7]. Experiments were performed on a bench scale with varying temperature and steam-to-biomass ratio. To conduct the ML model training, the eleven input features selected were ash, moisture, volatile matter, and fixed carbon from the proximate analysis. From the ultimate analysis, carbon, hydrogen, nitrogen, and oxygen were selected, and from the process variables, reactor temperature, steam-to-biomass ratio (S/B), and equivalence ratio (ER) were included. The dependent features are the molar fraction of the syngas composition $H_2$, CO, $CO_2$ and $CH_4$. The dataset consists of 40 rows with eleven input and four output features, so PCA was applied to reduce dimensionality before training the ML model to avoid possible overfitting. The data was then standard scaled, and 10-fold cross-validation was performed, splitting the data into an 80/20 ratio for training and testing purposes.

### Equilibrium Modeling

This study employed Aspen Plus V.14.0 to model steam co-gasification and predict syngas composition under various conditions, utilizing both equilibrium and kinetic modeling strategies. Biomass, PE, and char were defined as non-conventional components using proximate and ultimate analyses from the ULTANAL and PROXANAL models, with enthalpy and density data provided by HCOALGEN and DCOALIGT models, respectively, based on biomass combustion and composition. Ash was treated as inert, and the Peng-Robinson thermodynamic package with the Boston-Mathias function was selected for high-temperature gasification simulations. Two equilibrium models were used: the TEM, which minimizes Gibbs free energy to predict product composition but neglects reaction kinetics and often overestimates or underestimates syngas, and the RTM, which incorporates temperature-dependent constraints to better reflect real-world gasification by minimizing Gibbs free energy based on elemental composition without requiring detailed kinetic data.

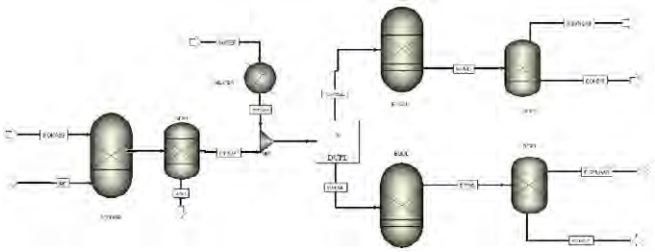


**Figure 1:** Aspen Plus modeling of TEM and TRM

In this study the Aspen Plus model structure developed by Acar et al., (2019) for gasification, was adopted, using both TEM and RTM [8]. Biomass and plastic waste were decomposed in a RYIELD reactor (DECOMP) into constituent elements based on ultimate and proximate analyses, with ash separated using a separator (SEP1). The components were mixed with steam and fed into an RGIBBS reactor, where the gasifier (EQIL) simulated the TEM approach and another reactor (R-GASI) modeled RTM. Syngas was separated from byproducts using separators (SEP2 for R-GASI and SEP3 for EQIL), as illustrated in Figure 1. Following Acar et al. (2019), four key reactions (Table 1) were used to restrict chemical equilibrium in RTM, and sensitivity analysis was conducted for each of the 40 experimental instances by varying the approach temperature of individual reactions, generating 22,500 cases per instance. The absolute difference between the molar fractions of the predicted and experimental syngas composition was calculated using Equation 1, where ME represents the minimum error, *e* is the experimental value, *p* is the predicted value, and *i* denotes the *i*-th case in the sensitivity analysis [9].

$$(ME)_i = |H_2^e - H_2^p|_i + |CO^e - CO^p|_i + |CO_2^e - CO_2^p|_i + |CH_4^e - CH_4^p|_i \quad (1)$$

**Table 1:** Reactions used in RTM

| No. | Reaction | ΔHr (kJ/mol) |
|---|---|---|
| R1 | $C + H_2O \rightarrow CO + H_2$ | 131 |
| R2 | $C + 0.5O_2 \rightarrow CO$ | -111 |
| R3 | $CO + H_2O \rightarrow CO_2 + H_2$ | -41.2 |
| R4 | $CH_4 + H_2O \rightarrow CO + 3H_2$ | 206 |

## Dimensionality Reduction

In order to address the curse of dimensionality and possible multicollinearity among the input variables and also to represent independent variables with minimal redundancy, PCA has been used, which can find feature components that have low and high variance in a given data set [10]. PCA is a multivariate technique that allows one to transform a series of correlated variables into a set of uncorrelated variables known as principal components (PCs). The PCs of a data set *x* are obtained by solving an eigenvalue–eigenvector problem. In this regard, the covariance matrix can be computed by equation 2. Where *n* is total number of samples in the data set and $\overline{x_i} = \frac{1}{n}\sum_{i=1}^{n} x_i$.

$$M_c = \frac{1}{n-1}\sum_{i=1}^{n}(x_i - \overline{x_i})(x_i - \overline{x_i})^T \quad (2)$$

## Machine learning

SVR is a powerful supervised learning algorithm based on the principles of Support Vector Machines (SVMs). Unlike traditional regression models, SVR aims to find a function that not only minimizes error but also avoids overfitting by balancing complexity and predictive performance. SVR achieves this by defining a margin of tolerance within which predictions are considered acceptable deviations from the actual data points. In SVR, the objective is to find a hyperplane that best fits the data points, allowing for some deviations. The SVR function can be expressed in equation 3, where w is weight vector, x is input feature vector, and b is bias term.

$$f(x) = [w, x] + b \quad (3)$$

## Performance Evaluation

The accuracy and reliability of the surrogate models were evaluated using Coefficient of Determination ($R^2$), RMSE, and Mean Absolute Error (MAE) for both training and testing datasets. $R^2$, as defined by Equation 4 measures how well the model explains variance in the target variable. RMSE, defined by Equation 5, quantifies the average prediction error with greater sensitivity to outliers. In addition, MAE, as described in Equation 6, provides a straightforward measure of overall error magnitude. These evaluation metrics were specifically applied to the molar fractions of syngas components—$H_2$, CO, $CO_2$, and $CH_4$—where $y_i$ is the observed value, $\hat{y}_i$ is the predicted value, $\overline{y}_i$ is the mean of the observed values, and *n* is the number of data points.

$$R^2 = 1 - \frac{\sum_{i=1}^{n}(y_i - \hat{y}_i)^2}{\sum_{i=1}^{n}(y_i - \overline{y}_i)^2} \quad (4)$$

$$RMSE = \sqrt{\frac{1}{n}\sum_{i=1}^{n}(y_i - \hat{y}_i)^2} \quad (5)$$

$$MAE = \frac{1}{n}\sum_{i=1}^{n}|y_i - \hat{y}_i| \quad (6)$$

## RESULTS AND DISCUSSION

SVR with a radial basis function kernel was employed to develop a predictive model based on the eleven input features, utilizing MultiOutputRegressor to handle multiple output variables. The model was configured with an RBF kernel, a regularization parameter of 1.0, and an epsilon value of 0.1, which defines the margin of tolerance for error. The model's accuracy was assessed using $R^2$, RMSE, and MAE for both training and testing datasets. The results are summarized in **Table 2**, values in parentheses representing the test dataset. The results indicate that the SVR model performed well in capturing the variance in the training set, with $R^2$ values exceeding 0.78 across all outputs. However, a decrease in $R^2$ for the testing set shows overfitting.

**Table 2:** Performance matrix of train(test) based on real input features

| | $R^2$ | RMSE | MAE |
|---|---|---|---|
| $H_2$ | 0.894(0.652) | 0.022(0.040) | 0.016(0.030) |
| CO | 0.966(0.862) | 0.015(0.031) | 0.012(0.025) |
| $CO_2$ | 0.936(0.779) | 0.023(0.043) | 0.015(0.031) |
| $CH_4$ | 0.784(0.577) | 0.013(0.019) | 0.008(0.014) |

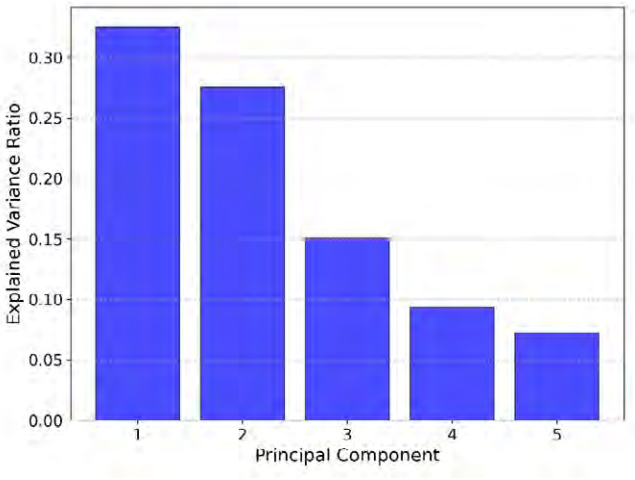



**Figure 2:** Explained variance for every PC

To address potential overfitting and improve model performance, PCA was applied to reduce the dimensionality of the input features while retaining essential information. The dataset, sourced from published studies, was first standardized using the Standard Scaler to

ensure uniform scaling across variables. PCA was then performed, and cumulative explained variance analysis showed that five principal components captured over 90% of the total variance. This transformation effectively simplified the data structure while preserving key patterns, allowing for a refined input representation for subsequent modeling steps. The cumulative explained variance, shown in **Figure 2**, further highlights the efficiency of PCA in retaining maximum information. The bars in the graph indicate that the first PC accounts for over 30% of the variance, the second PC captures approximately 28%, and the third PC retains around 15%, with the first three PCs collectively preserving more than 75% of the total variance. This finding provides a solid foundation for further analysis using the reduced dataset, ensuring computational efficiency without compromising data integrity. Elmaz et al., (2020) applied PCA to reduce input dimensionality in a downdraft biomass gasification study before training SVR, DTR, and MLP models for prediction [11].

**Table 3** presents the performance metrics ($R^2$, RMSE, and MAE) for each syngas component, with values in parentheses representing the testing dataset. These results are based on PCA-reduced input features, which significantly improved model performance. $H_2$ exhibits the highest $R^2$ values for both training (0.977) and testing (0.853), along with favorable RMSE and MAE values, indicating superior predictive accuracy. CO demonstrates comparable training performance ($R^2$ = 0.950) but surpasses $H_2$ in testing ($R^2$ = 0.878), suggesting improved generalization. While CO's training RMSE (0.0191) is lower than that of $H_2$ (0.0240), its other error metrics remain slightly below $H_2$. $CO_2$ and $CH_4$ show lower $R^2$ values in both training and testing datasets, with $CH_4$ exhibiting the lowest $R^2$ (0.744) for testing. However, $CH_4$ also has the lowest RMSE and MAE, indicating relatively small errors despite lower variance capture. The improvements observed in these results highlight the effectiveness of PCA in reducing dimensionality while preserving essential information, thereby enhancing the SVR model's predictive capabilities. The performance variations across syngas components may stem from differences in their formation mechanisms or disparities in the quality and quantity of available training data. Further investigation into these factors could refine model accuracy even further.

**Table 3:** Performance matrix of train(test) based on PCA reduced features

| | $R^2$ | RMSE | MAE |
|---|---|---|---|
| $H_2$ | 0.977(0.853) | 0.0240(0.038) | 0.016(0.029) |
| CO | 0.950(0.878) | 0.0191(0.035) | 0.014(0.027) |
| $CO_2$ | 0.942(0.805) | 0.0223(0.040) | 0.015(0.028) |
| $CH_4$ | 0.944(0.744) | 0.0135(0.018) | 0.008(0.013) |

*Performance matrix for SVR is given as train(test)

**Table 4** presents the predicted values from all models, clearly showing that SVR consistently outperformed the other techniques across all syngas components by achieving the lowest RMSE values. Among the predictions, the most accurate prediction by SVR was for $CH_4$, with an exceptionally low RMSE of 0.0137, signifying high precision. Similarly, SVR also demonstrated strong predictive performance for CO and $CO_2$, with RMSE values of 0.0197 and 0.0238, respectively. Although the RMSE for $H_2$ (0.0242) was slightly higher than that of RTM (0.0238), SVR still outperformed the remaining models by a considerable margin.

**Table 4:** RMSE values of different modeling techniques

| | RTM | TEM | SVR |
|---|---|---|---|
| $H_2$ | 0.0238 | 0.1971 | 0.0242 |
| CO | 0.0391 | 0.0911 | 0.0197 |
| $CO_2$ | 0.0539 | 0.1038 | 0.0238 |
| $CH_4$ | 0.0488 | 0.1125 | 0.0137 |

In comparison, the RTM showed commendable prediction accuracy, though not as precise as SVR. It achieved moderately low RMSE values for $H_2$ (0.0238), CO (0.0391), $CO_2$ (0.0539), and $CH_4$ (0.0488), making it a viable alternative in some scenarios. However, its performance for the $H_2$/CO ratio, with an RMSE of 0.2569, was less accurate compared to SVR. Conversely, TEM performed the weakest among the three techniques, with significantly higher RMSE values across all predictions. For example, the RMSE for $H_2$ was 0.1971, almost ten times higher than that of SVR, while the RMSE values for CO (0.0911), $CO_2$ (0.1038), and $CH_4$ (0.1125) further highlighted its lack of precision.

In this Study the predictions obtained from different models were analyzed and plotted to evaluate their performance. **Figure 3** illustrates the comparison between experimental and predicted $H_2$ values across various feedstock compositions and process variables. Among the models, the SVR demonstrates exceptional predictive accuracy, with green data points closely aligning with the experimental values for all the experimental values. The minimal error observed in SVR predictions underscores its reliability and effectiveness. In contrast, the RTM also performed well for the $H_2$ concentration above 35%. The TEM model, on the other hand, consistently overpredicts $H_2$ values across all feedstock compositions, likely due to limitations in Gibbs free energy estimations for syngas constituents, as highlighted by Ajorloo et al. (2022) [1].

The predictions of all models for CO against the experimental values are given in the **Figure 4**. Just like the predictions of H2 the SVR also has excelled in predicting the CO in this study. The SVR model consistently demonstrates superior predictive performance, with the predicted values (green points) closely matching the experimental results. The RTM model performs relatively well

in predicting CO values at lower concentrations but exhibits slight deviations at higher concentrations. Conversely, the predictions by TEM model are quite diverse as shown by the red points, reflecting potential inaccuracies in the equilibrium modeling of CO. This is also evident by the RMSE values from the **Table 4** where TEM has highest RMSE among other models.

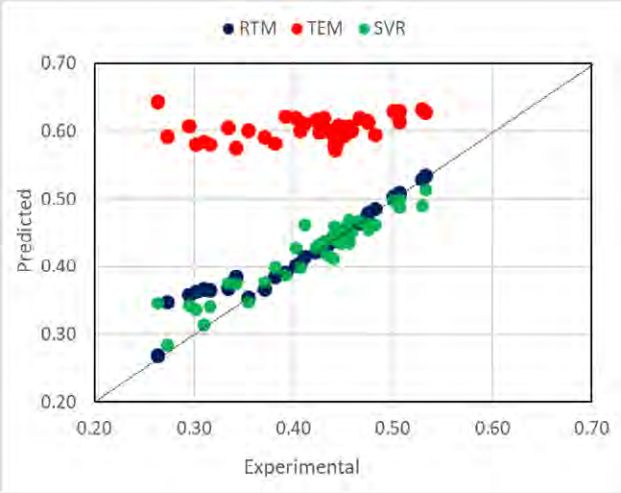



**Figure 3:** Experimental and predicted mole fraction of $H_2$

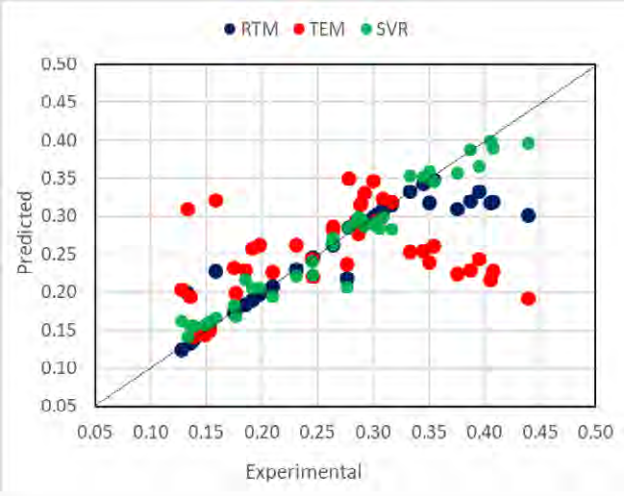



**Figure 4:** Experimental and predicted mole fraction of CO

Figure 5 and Figure 6 shows the predicted values by the models for CO2 and CH4 respectively. Similar to the predictions of $H_2$ and CO, the SVR model demonstrates excellent agreement with experimental data, as the predicted values align closely with the experimental results. On the other hand The RTM model shows reasonable accuracy for higher $CO_2$ concentrations but fails to maintain the same precision for predicting $CH_4$. The TEM model, however, systematically underpredict $CO_2$ values in Figure 5 and predictions for the $CH_4$ are quite lower below 1% even sometimes the predicted values for $CH_4$ are like $10^{-5}$ which raises serious question mark on the predictive accuracy and use of TEM for the real world scenario. SVR remained most accurate predicting model which shows that data based modeling outperforms the Aspen Plus, TEM and RTM, modeling strategy.

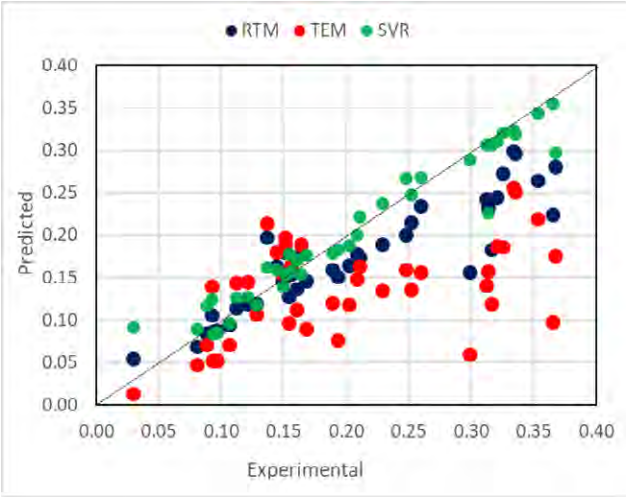



**Figure 5:** Experimental and predicted mole fraction of $CO_2$

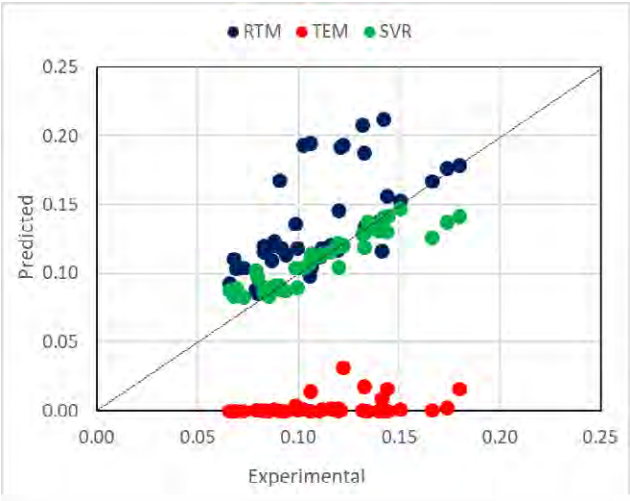



**Figure 6:** Experimental and predicted mole fraction of $CH_4$

## CONCLUSIONS

In this study, a comparative analysis of Aspen Plus models and machine learning techniques was conducted to evaluate their performance in predicting syngas composition during the co-gasification of biomass and plastic wastes. The results clearly demonstrate that the SVR, in accurately capturing the non-linearities of the gasification process. Without the use of PCA, the SVR model achieved high performance in training dataset, particularly for syngas components like CO and $CH_4$, with RMSE values as low as 0.0197 and 0.0137, respectively, across training and testing datasets. However, the application of

PCA to reduce the dimensionality of the input features resulted in substantial improvements in model accuracy. For instance, after applying PCA, the RMSE for $CH_4$ further decreased to 0.0135, while the $R^2$ for $H_2$ increased from 0.894 to 0.977 for training and 0.652 to 0.853 for testing, indicating better generalization.

While the SVR model with PCA consistently outperformed the other techniques across all syngas components, achieving notably low RMSE values, the RTM showed commendable accuracy, although not as precise as SVR. The RTM model achieved moderately low RMSE values for $H_2$ (0.0238), CO (0.0391), $CO_2$ (0.0539), and $CH_4$ (0.0488), but fell behind SVR in terms of predictive precision. The TEM model, on the other hand, performed the weakest, with significantly higher RMSE values for all components. For example, the RMSE for $H_2$ was 0.1971, almost ten times higher than that of SVR, underscoring the strength of SVR in handling non-linear relationships and high-dimensional data.

These findings highlight the importance of dimensionality reduction through PCA when applying machine learning to predict complex systems such as syngas composition. The superior performance of the PCA-enhanced SVR model, coupled with its ability to generalize better across different feedstock compositions and operating conditions, emphasizes its potential as a robust predictive tool in renewable energy technologies. Furthermore, this study underscores the potential of ML models to complement traditional mechanistic models like Aspen Plus, providing valuable insights into syngas production processes, thus advancing the transition toward more sustainable energy systems.

## ACKNOWLEDGEMENTS

This research has received funding from the European Union's Horizon 2020 research and innovation program under the Marie Skłodowska-Curie grant agreement No. 945139

## REFERENCES

1. Ajorloo, M., et al., Recent advances in thermodynamic analysis of biomass gasification: A review on numerical modelling and simulation. Journal of the Energy Institute, 2022. **102**: p. 395-419.
2. Wen, H.-T., J.-H. Lu, and M.-X. Phuc, Applying artificial intelligence to predict the composition of syngas using rice husks: A comparison of artificial neural networks and gradient boosting regression. Energies, 2021. **14**(10): p. 2932.
3. Mutlu, Ö.Ç. and T. Zeng, *Challenges and opportunities of modeling biomass gasification in Aspen Plus: A review.* Chemical Engineering & Technology, 2020. **43**(9): p. 1674-1689.
4. Xue, P., et al., Prediction of syngas properties of biomass steam gasification in fluidized bed based on machine learning method. International Journal of Hydrogen Energy, 2024. **49**: p. 356-370.
5. Brachi, P., et al., Fluidized bed co-gasification of biomass and polymeric wastes for a flexible end-use of the syngas: Focus on bio-methanol. Fuel, 2014. **128**: p. 88-98.
6. Pinto, F., et al., Effect of gasification agent on co-gasification of rice production wastes mixtures. Fuel, 2016. **180**: p. 407-416.
7. Pinto, F., et al., Co-gasification study of biomass mixed with plastic wastes. Fuel, 2002. **81**(3): p. 291-297.
8. Acar, M.C. and Y.E. Böke, Simulation of biomass gasification in a BFBG using chemical equilibrium model and restricted chemical equilibrium method. Biomass and Bioenergy, 2019. **125**: p. 131-138.
9. Jadoon, U.K., I. Díaz, and M. Rodríguez, Comparative analysis of aspen plus simulation strategies for woody biomass air gasification processes. Biomass and Bioenergy, 2025. **194**: p. 107626.
10. Jolliffe, I.T. and J. Cadima, *Principal component analysis: a review and recent developments.* Philosophical transactions of the royal society A: Mathematical, Physical and Engineering Sciences, 2016. **374**(2065): p. 20150202.
11. Elmaz, F., Ö. Yücel, and A.Y. Mutlu, Predictive modeling of biomass gasification with machine learning-based regression methods. Energy, 2020. **191**: p. 116541.

© 2025 by the authors. Licensed to PSEcommunity.org and PSE Press. This is an open access article under the creative commons CC-BY-SA licensing terms. Credit must be given to creator and adaptations must be shared under the same terms. See https://creativecommons.org/licenses/by-sa/4.0/



Systems & Control Transactions

**Research Article - Peer Reviewed Conference Proceeding**
ESCAPE 35 - European Symposium on Computer Aided Process Engineering
Ghent, Belgium. 6-9 July 2025
Jan F.M. Van Impe, Grégoire Léonard, Satyajeet S. Bhonsale,
Monika E. Polańska, Filip Logist (Eds.)

PSE PRESS

# Multiscale Modeling of Internal Reforming in Solid Oxide Fuel Cells: A Study of Electrode Morphology and Gradient Microstructures

**Hamid Reza Abbasi[a], Masoud Babaei[a], and Constantinos Theodoropoulos[a,b]***

[a] Department of Chemical Engineering, The University of Manchester, Manchester, M13 9PL, UK
[b] Department of Chemical Engineering, National Technical University of Athens, Athens, 15772, Greece
* Corresponding Author: k.theodoropoulos@manchester.ac.uk.

## ABSTRACT

This work presents a comprehensive multiscale model for Solid Oxide Fuel Cells (SOFCs), integrating microscale and macroscale simulations to analyze internal reforming and its impact on overall cell performance. The microscale model [1], [2] captures the intricate mass and charge transport phenomena at the pore scale of porous electrodes, resolving electrochemical reactions at the triple-phase boundaries and modeling chemical reactions at pore spaces. Simultaneously, the macroscale model provides a broader view of the entire cell's behavior by solving the same transport equations on a coarser computational mesh. The multiscale approach is particularly useful for addressing the challenges posed by simultaneous chemical and electrochemical reactions at the anode, which complicate the modeling of internal reforming. To overcome these challenges, a novel approach is introduced [3], spatially separating the regions of chemical and electrochemical activity in the pore scale domain by taking the electrochemical active layer thickness into consideration. The integrated multiscale model is applied to a complete internal reforming SOFC to explore how electrode morphology, particularly the use of gradient microstructures, influences cell performance.

**Keywords**: SOFC, Multiscale Model, Microscale Model, Internal Reforming, Gradient Microstructure

## INTRODUCTION

Fuel cells are electrochemical devices that convert the chemical energy of a fuel directly into electricity, heat, and water through a reaction with oxygen, typically without combustion. They are highly efficient, scalable, and environmentally friendly, making them suitable for various applications, including power generation, transportation, and portable energy solutions. Among the different types of fuel cells, the choice depends on factors such as operating temperature, efficiency, and fuel flexibility.

Solid Oxide Fuel Cells (SOFCs) are a type of high-temperature fuel cell that operates at temperatures between 600°C and 1000°C. They use a solid ceramic electrolyte to conduct oxygen ions from the cathode to the anode, where they react with a fuel—such as hydrogen, natural gas, or biogas—to generate electricity. SOFCs are known for their high efficiency, fuel flexibility, and ability to use waste heat for additional power generation in combined heat and power (CHP) systems [4].

To use hydrocarbon fuels like methane ($CH_4$) in SOFCs, a reforming process, such as steam reforming, converts them into hydrogen-rich gas. SOFC high operating temperatures enable internal reforming, which simplifies system design and improves efficiency but requires careful management to prevent carbon deposition and ensure stable operation.

Internal reforming can be categorized into indirect and direct methods. Indirect reforming places the reformer outside the fuel cell but in thermal contact, using SOFC-generated heat to drive the reaction and minimizing carbon deposition risks [5]. Direct reforming occurs within the anode, where fuel and steam react together, streamlining the system and boosting efficiency but demanding precise control of temperature gradients to

prevent material degradation.

SOFCs exhibit defining features across various length scales, from the microscale structure of the porous electrodes to the macroscale design of the entire system. To predict their performance, different types of models have been developed, each focusing on a specific length scale. Microscale models focus on reactions and mass transport processes within the porous anode and cathode. At the macroscale, models address the transport phenomena within a single cell. By combining these models, researchers can better understand and enhance the performance of SOFCs across all relevant scales.

The microstructure design of the porous electrodes plays a critical role in defining the performance of SOFCs. Electrochemical reactions primarily occur at the triple-phase boundary (TPB), where the electrolyte, electrode, and gas phase meet. A high TPB density is essential for maximizing reaction sites and enhancing performance. Additionally, the tortuosity of the porous structure significantly affects gas and ion diffusion [6]. High tortuosity can hinder mass transport by increasing the effective path length for reactants and ions, leading to concentration gradients and performance losses. Optimizing the microstructure to balance TPB density and tortuosity is crucial for achieving efficient gas diffusion, ionic conductivity, and overall cell performance.

A multiscale model combines the strengths of these individual models to assess SOFC performance more comprehensively. By integrating physics across different length scales, such a model can capture detailed electrochemical and transport processes at the microscale while also considering cell-level features at the macroscale.

In the current study, a direct internal reforming SOFC is modelled using a multiscale framework. The model solves transport, chemical reactions, and electrochemical reactions at the microstructure level and transport equations, and chemical reactions at the cell level, syncing information between these two scales. Different microstructure configurations—conventional, lattice, and fibrous—are tested for both the anode and cathode to evaluate the benefits of each design.

## METHODOLOGY

The methodology employs a multiscale framework that integrates two distinct models: a microscale model and a macroscale model. The microscale model focuses on the processes occurring within the porous microstructure of the electrodes. The macroscale model captures the transport behaviour at the cell level, addressing overall performance metrics. The computational domain is schematically shown in figure 1.

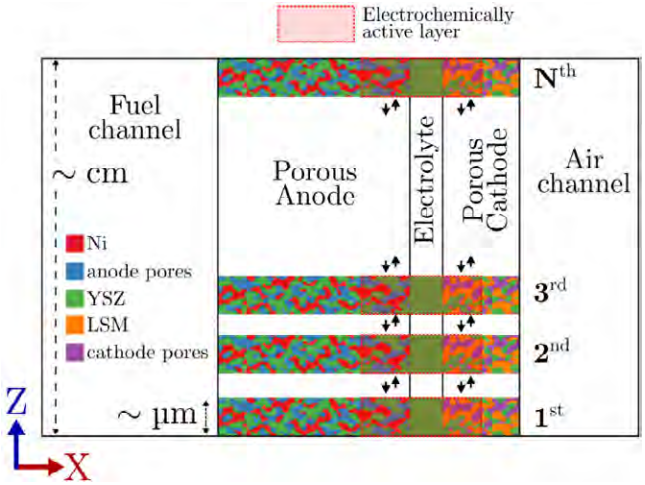



**Figure 1.** Schematic domain of the problem (microstructures and the entire cell)

Here only small "patches" of the microstructural domain are actually solved, as in the gap-tooth scheme [7,8] to reduce computational cost. The vertical arrows in fig 1 represent the fluxes between the microstructure patches.

To ensure consistency between the two scales, an iterative algorithm is employed. This algorithm minimizes discrepancies between the outputs of the microscale and macroscale models by iteratively adjusting parameters in the macroscale model. More specifically, the electrochemical reaction rates in the macroscale model are modified to better align with the detailed microscale predictions since there is a more fundamental definition for the kinetics of electrochemical reactions at the microscale. To describe the rate of electrochemical reactions at microscale we have used a lineal exchange current density, which is per length of TPB. Whereas for the macroscale model the kinetics of electrochemical reactions could only be described based on area or volume. Since electrochemical reactions are essentially heterogeneous and take place on the TPB lines in space (as opposed to a homogeneous reaction that take place in space) a lineal exchange current density is fundamentally more accurate than an area-averaged or volume-averaged definition.

By iterating between the models, the framework converges to a solution that harmonizes the behaviour across scales. This idea is explained in more detail in our recent work [2].

The convective and diffusive mass transport is dictated by the following equation:

$$\overbrace{\nabla \cdot \left(D_i^{\text{eff}} \nabla C_i\right)}^{\text{diffusive}} - \overbrace{\nabla \cdot (\vec{V} C_i)}^{\text{convective}} + S_i = 0 \qquad (1)$$

Here, $D_i^{\text{eff}}$ is the effective diffusivity of component $i$ into the gaseous mixture, $C_i$ is mass density of $i_{th}$ gaseous component, $V$ is fluid velocity. The term $S_i$ is the non-

linear source term that exists due to chemical and electrochemical reactions that consume or produce a particular component in the mixture. In the microscale model the convective term is disregarded due to the small pore sizes in the porous electrodes.
The ion conduction is modeled using this equation:

$$\nabla \cdot \left(\sigma_{\text{ion}}^{\text{eff}} \nabla \phi_{\text{ion}}\right) + S_{\text{ion}} = 0 \quad (2)$$

Here, $\sigma_{\text{ion}}^{\text{eff}}$ is the effective diffusivity of ions in the ion conductive material and $S_{\text{ion}}$ is the non-linear source term due to electrochemical reactions.

The two main chemical reactions considered for internal reforming are Steam-Methane Reforming (SMR) and the Water-Gas Shift (WGS) reaction. In SMR, methane reacts with steam to produce hydrogen and carbon monoxide: $CH_4 + H_2O \rightarrow CO + 3H_2$. The WGS reaction further converts carbon monoxide and steam into additional hydrogen and carbon dioxide: $CO + H_2O \rightarrow CO_2 + H_2$. These reactions are crucial for generating the hydrogen necessary for electrochemical reactions at the anode. The following equations describe the rate of SMR and WGS [9]:

$$r_{\text{SMR}} = k_{\text{SMR}} p_{\text{CH4}} \, exp\left(-\frac{E_{\text{SMR}}^{A}}{RT}\right) \quad (3)$$

$$r_{\text{WGS}} = k_{\text{WGS}} p_{\text{CO}} \left(1 - \frac{p_{\text{CO2}} p_{\text{H2}} / p_{\text{CO}} p_{\text{H2O}}}{K_{eq}}\right) \quad (4)$$

Here, $E_{\text{SMR}}^{A}$ is the SMR reaction activation energy, $k_{\text{SMR}}$ is pre-exponential factor of SMR. For WGS, $k_{\text{WGS}}$ is the reaction rate constant, and $K_{eq}$ is the equilibrium constant.

Modelling internal reforming presents a significant challenge when it comes to simultaneously simulating chemical and electrochemical reactions. These two processes occur in tandem, but their interplay complicates the formulation of the problem. One specific issue is the modelling of concentration overpotential, which is traditionally defined in terms of the bulk pressure of hydrogen. In the case of internal reforming SOFCs, if the hydrogen pressure at the inlet is zero, the concentration overpotential would theoretically become infinite, which is physically unrealistic and resulting in zero-division error. This presents a fundamental problem because it suggests an unbounded overpotential. To address this, we propose a solution that involves artificially separating the regions where electrochemical and chemical reactions occur.

In our model, the anode side of the microstructure is divided into two distinct zones: the region closer to the electrolyte, where electrochemical reactions dominate, is treated as an electrochemical-only zone, while the region farther away from the electrolyte, where chemical reactions dominate, is treated as a chemical-only zone. This separation allows us to avoid the unphysical infinite concentration overpotential by ensuring that each region is simulated with the appropriate reaction mechanism. This is schematically shown in Figure 2.

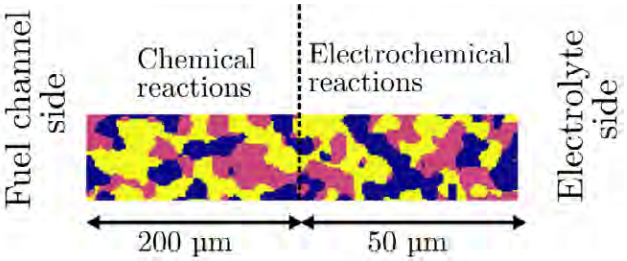



**Figure 2.** Separation of anode side into two regions

Electrochemical reactions are dominant in a very thin layer close to the electrolyte called the "electrochemical active layer". The length of this layer is reported to be smaller than $50\ \mu\text{m}$ [10]. The concept is that the rate of electrochemical reactions is negligible on the left side of Figure 2, while the rate of chemical reactions is negligible on the right side. Therefore, it is assumed that these negligible rates are effectively zero.

Different microstructure designs tested in this study are shown in Figure 3. The reasoning behind why each design is selected is further explained in our recent manuscript [11].

## RESULTS AND DISCUSSION

### Model Validation

The model is firstly validated against experimental measurements of Rogers et al.12]. The polarization curve is selected for the basis of the comparison, and it is shown in Figure 4. In this figure the experimental data points are shown with black dots, and results of the macroscale and multiscale models are shown with red and green lines, respectively. The red area shows the region where the polarization curve varies with a ±10% change in the calibration parameter of macroscale model.

From figure 4, it is obvious that both the calibrated macroscale model, and multiscale model, are capable of explaining the polarization curve of the cell. However, the two models differ in terms of calibration requirements. The macroscale model requires calibration using experimental data, with the calibration parameter being the area-averaged exchange current density, which accounts for the overall electrochemical activity in the cell. In contrast, the multiscale model does not require such calibration. This is because it uses a more fundamental definition of exchange current density, namely the lineal exchange current density. As a result, the multiscale model offers a more fundamental approach without the need for calibration, while the macroscale model relies on fitting to ample experimental data to accurately represent the system's behaviour.

It is also important to note that the point of using a multiscale model is not to achieve a better match with experimental results for a given set of datapoints on the polarization curve. Rather, the goal here is to explore

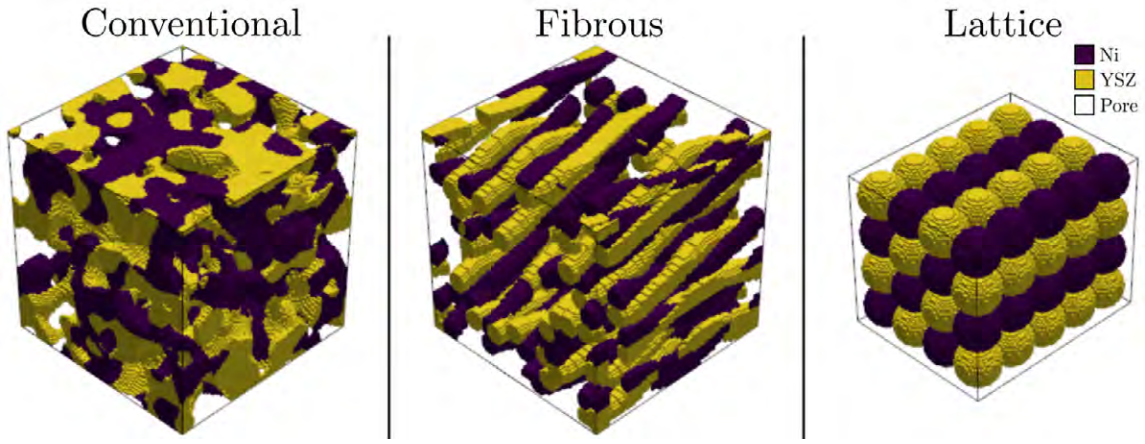



**Figure 3.** Different microstructure designs

different designs with varying microscopic and macroscopic features, especially for which no measured experimental data is available. This allows for the investigation of new designs and configurations that are not constrained by the existing experimental dataset.

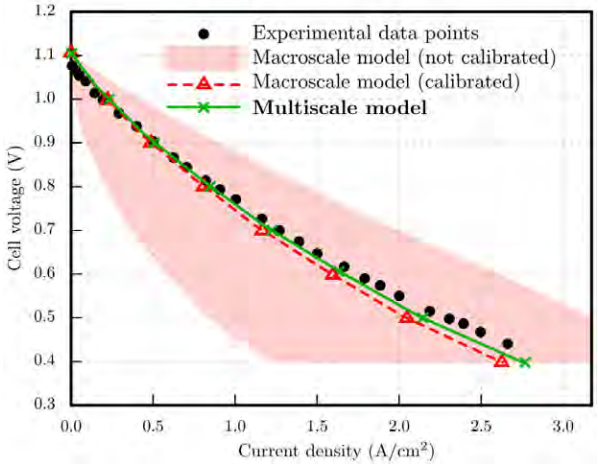



**Figure 4.** Polarization curve of different models compared with experimental measurements [9]

## Spatial Distribution of Field Variables Across the Anode

Variation of concentration of different components across the anode is shown in figure 5. This figure is for the case of conventional microstructure (refer to figure 2). Five different components exist in the gaseous mixture in the anode side.

At the anode inlet, only $CH_4$ and $H_2O$ have non-zero concentrations. Due to SMR, the concentration of $CH_4$ decreases monotonically toward the electrolyte side. Based on the chemical reactions, the concentration of $H_2O$ would be expected to decrease monotonically because it is consumed in both SMR and WGS. However, due to the production of $H_2O$ in the electrochemically active layer, its concentration levels off as it approaches this layer and then begins to increase. A similar explanation, but with the opposite reasoning, applies to the hydrogen concentration. Due to SMR and WGS, its concentration increases as it approaches the electrochemically active layer, only to level off and then decrease upon entering this layer.

To validate the assumption of a negligible chemical reaction rate near the electrolyte and a negligible electrochemical reaction rate in the remaining of the porous anode, these rates are compared in Figure 6, which is based on the case of a conventional microstructure. It can be observed that the rate of electrochemical reactions levels off after the first $50\ \mu m$ near the electrolyte. This occurs because the electrochemical activity becomes limited by the availability of reactants in this region. Similarly, the rate of the SMR reaction drops significantly as it approaches this region, which can be attributed to the limited availability of $CH_4$ approaching the electrochemically active layer.

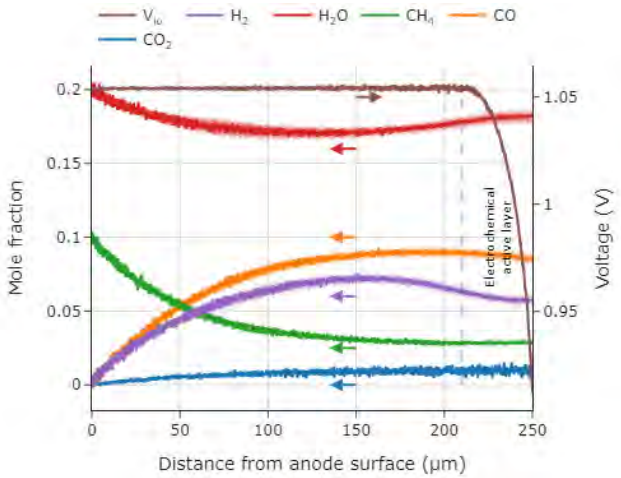



**Figure 5.** Concentration of different species across the anode

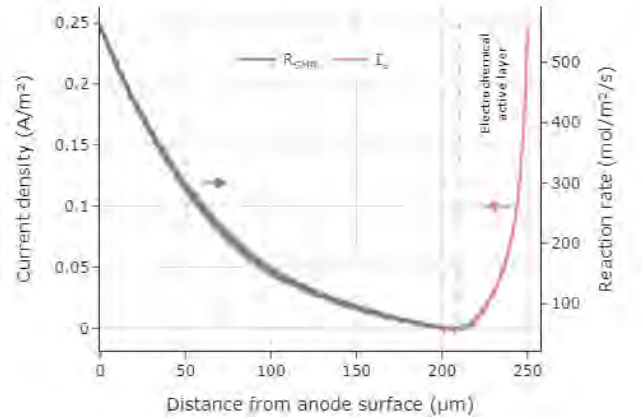



**Figure 6.** Comparison of electrochemical and chemical reactions rates

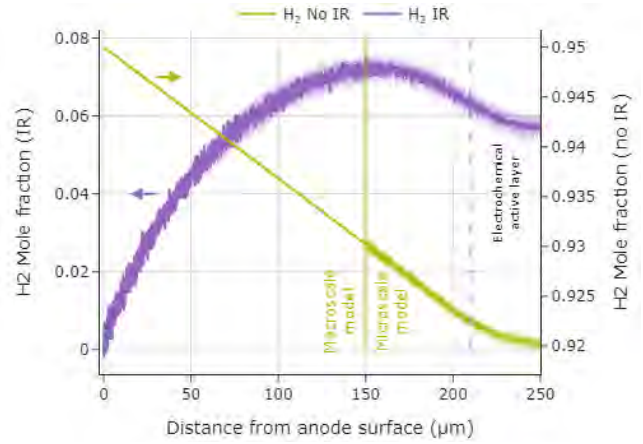



**Figure 7.** Evolution of hydrogen mole fraction across the width of the anode surface for the case of no IR and IR.

## Different Morphologies and Gradient Microstructures

Gradient microstructures are designed so that the volume fraction of the ion-conducting phase (YSZ, in this case) linearly decreases as we move further from the electrolyte. If the volume fraction of the ion-conducting phase behaves in the opposite manner, the resulting microstructure does not offer any benefits. This phenomenon is discussed in more detail in our recent manuscript [11]. Gradient microstructures have been synthetically generated using the framework discussed in our previous work [11] with $f_G$ being defined as $f_G = \frac{\overline{v_f^{\mathrm{YSZ}}} - v_f^{\mathrm{YSZ}}(x = x_{\mathrm{electrolyte}})}{\overline{v_f^{\mathrm{YSZ}}}}$.

The results in figure 8 shows the TPB density and current density of IR cell performing under $V = 0.4\ [V]$. The figure indicates that a microstructure with a stronger gradient of volume fraction leads to a greater reduction in TPB density. This occurs because, at both ends of a gradient microstructure, the volume fractions of the three phases deviate significantly from each other. Such imbalance makes the microstructure less optimal for TPB formation, as TPB density in conventional designs is maximized when the volume fractions of the three phases are nearly equal. While TPB density decreases as the gradient strength increases, the current density (a measure of the cell's overall performance) initially rises (in the $G^+$ region) before eventually declining (in the $G^-$ region). The decrease in current density in the $G^-$ region corresponds to the drop in TPB density. However, the initial rise in current density in the $G^+$ region, despite the reduction in TPB density, can be explained by improved ion conduction. This enhanced ion conduction promotes higher rates of electrochemical reactions at the remaining TPB sites, leading to better overall performance initially.

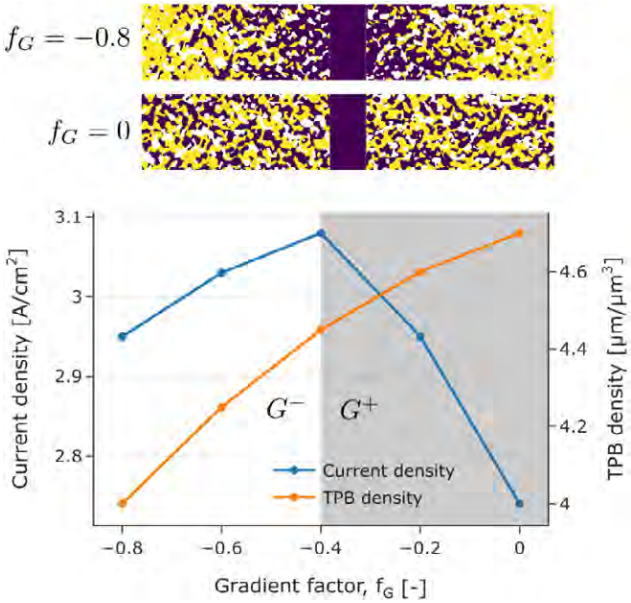



**Figure 8.** Performance of gradient microstructures

Different designs are tested for the microstructure of porous anode and cathode. Each design is tested for both sides of the cell—anode and cathode. In other words, the microstructural designs of the anode and cathode are assumed to be identical. To compare the performance of different designs, current density was measured at an operating voltage of 0.4 volts. Results indicate that the fibrous design increased current density by approximately 48%, from 2.74 A/cm² (conventional design) to 4.05 A/cm². In contrast, lattice structures significantly enhanced performance, increasing current density by roughly 4.4 times, from 2.74 A/cm² to 12.05 A/cm². It is important to acknowledge that the lattice structures depicted in Figure 3 represent a highly optimized theoretical design. Current state-of-the-art fabrication techniques cannot achieve the precise, highly ordered placement of nanoparticles required to realize these structures.

## CONCLUSIONS

This study employed a multiscale model to predict the performance of direct internal reforming solid oxide fuel cells, eliminating the need for calibration typically required with macroscale models. The model was used to evaluate various microstructure designs, including gradient microstructures, to assess their potential benefits. Results demonstrate the successful application of the multiscale model in predicting the polarization curve of a complete cell. Furthermore, the study revealed that certain gradient microstructures can outperform the counterpart non-gradient designs.

## ACKNOWLEDGEMENTS

The project is implemented within the framework of the National Recovery and Resilience Plan "Greece 2.0" and has been financed by the European Union (NextGeneration EU)

## REFERENCES

1. Abbasi, H. R., Babaei, M., Rabbani, A., & Theodoropoulos, C. Multi-scale model of solid oxide fuel cell: enabling microscopic solvers to predict physical features over a macroscopic domain. In *Computer Aided Chemical Engineering* (Vol. 52, pp. 1039-1045). Elsevier. (2023)
2. Abbasi, H. R., Babaei, M., & Theodoropoulos, C. Multiscale Modeling of Solid Oxide Fuel Cells Using Various Microscale Domains Across the Length of the Cell. In *Computer Aided Chemical Engineering* (Vol. 53, pp. 2317-2322). Elsevier.H. (2024)
3. Abbasi, H., Babaei, M., & Theodoropoulos, C. Multiscale Simulation of Internal Reforming Solid Oxide Fuel Cells to Capture Complex Reaction Phenomena. In *Electrochemical Society Meeting Abstracts prime2024* (No. 48, pp. 3310-3310). The Electrochemical Society, Inc. (2024, November)
4. Singh, M., Zappa, D., & Comini, E. Solid oxide fuel cell: Decade of progress, future perspectives and challenges. *International Journal of Hydrogen Energy*, *46*(54), 27643-27674. (2021)
5. Fan, L., Li, C. E., Aravind, P. V., Cai, W., Han, M., & Brandon, N. Methane reforming in solid oxide fuel cells: Challenges and strategies. *Journal of Power Sources*, *538*, 231573. (2022)
6. Tseronis K, Bonis I, Kookos IK, Theodoropoulos C, Parametric and transient analysis of non-isothermal, planar solid oxide fuel cells. *International journal of hydrogen energy* 37 (1), 530-547 (2012)
7. Kevrekidis I.G., Gear W.C., Hyman J,M., Kevrekidis P.G, Runborg O. & Theodoropoulos C. Equation-free, coarse-grained multiscale computation: Enabling mocroscopic simulators to perform system-level analysis. Commun. Math. Sci. 1(4) 715-762 (2003).
8. Armaou A., Kevrekidis IG, Theodoropoulos C. Equation-free gaptooth-based controller design for distributed complex/multiscale processes. Comput. Chem. Eng. 29(4), 731-740 (2005).
9. Tseronis, K., Fragkopoulos, I. S., Bonis, I., & Theodoropoulos, C. Detailed Multi-dimensional Modeling of Direct Internal Reforming Solid Oxide Fuel Cells. *Fuel Cells*, *16*(3), 294-312. (2016)
10. Kishimoto, M., Iwai, H., Saito, M., & Yoshida, H. Quantitative evaluation of solid oxide fuel cell porous anode microstructure based on focused ion beam and scanning electron microscope technique and prediction of anode overpotentials. *Journal of Power Sources*, *196*(10), 4555-4563. (2011)
11. Abbasi, H., Rabbani, A., Babaei, M., & Theodoropoulos, C. A pore-scale computational framework for enhancing solid oxide fuel cell performance through the design of anode porous configurations. *Journal of The Electrochemical Society. In press* https://doi.org/10.1149/1945-7111/adbfc4 (2025).
12. Rogers, W. A., Gemmen, R. S., Johnson, C., Prinkey, M., & Shahnam, M. Validation and application of a CFD-based model for solid oxide fuel cells and stacks. In *International Conference on Fuel Cell Science, Engineering and Technology* (Vol. 36681, pp. 517-520). (2003, January)

© 2025 by the authors. Licensed to PSEcommunity.org and PSE Press. This is an open access article under the creative commons CC-BY-SA licensing terms. Credit must be given to creator and adaptations must be shared under the same terms. See https://creativecommons.org/licenses/by-sa/4.0/



Systems & Control Transactions

**Research Article - Peer Reviewed Conference Proceeding**
ESCAPE 35 - European Symposium on Computer Aided Process Engineering
Ghent, Belgium. 6-9 July 2025
Jan F.M. Van Impe, Grégoire Léonard, Satyajeet S. Bhonsale,
Monika E. Polańska, Filip Logist (Eds.)

PSE PRESS

# Process simulation and thermodynamic analysis of newly synthesized pre-combustion $CO_2$ capture system using novel Ionic liquids for $H_2$ production

**Sadah Mohammed[a], Fadwa Eljack[a]***

[a] Qatar University, Department of Chemical Engineering, College of Engineering, P.O. Box 2713, Doha, Qatar
*Corresponding Author: Fadwa.Eljack@qu.edu.qa

## ABSTRACT

This paper evaluates the thermodynamic efficiency of a newly synthesized large-scale pre-combustion $CO_2$ capture process using a novel ionic liquid (IL) 1-octyl-2,3-methylimidazolium thiocyanate [OMMIM][SCN] for blue $H_2$ production. In addition, the potential eco-toxicity of the selected IL was assessed using the ADMETlab 2.0 web tool. The results of these analyses were compared to those of an established IL 1-butyl-2,3-dimethylimidazolium bis(trifluoromethyl sulfonyl)imide [BMMIM][TF2N]. The eco-toxicity assessment confirmed that [OMMIM][SCN] is less environmentally toxic than [BMMIM][TF2N]. Thermodynamic analysis of the novel system shows the COOLER unit accounts for the highest energy demand; however, the [OMMIM][SCN] system demonstrates a 7.45% reduction in energy consumption in the COOLER unit compared to [BMMIM][TF2N]. The system experienced the highest exergy losses (irreversibilities) in the COOLER unit for [BMMIM][TF2N] (12982 kW) and in the flash separator unit for [OMMIM][SCN] (8256 kW). The thermodynamic efficiency was analyzed within a specified IL inlet temperature range (25°C – 75°C) and absorption pressure range (7 - 16 bar). The results show that the [OMMIM][SCN] system outperforms [BMMIM][TF2N] with higher IL inlet temperature but decreases at higher absorption pressure, while [BMMIM][TF2N] maintains constant energy efficiency. The exergy efficiency of the [OMMIM][SCN] system shows better performance across the studied conditions but decreases beyond the peak temperature range of 50–60°C. These findings highlight the potential of [OMMIM][SCN] as an excellent alternative solvent for pre-combustion $CO_2$ capture applications.

**Keywords**: Hydrogen, Carbon Dioxide Capture, Energy Efficiency, Exergy Efficiency, Aspen Plus

## INTRODUCTION

Hydrogen ($H_2$), a non-carbonaceous fuel abundant on earth in its oxidized form, has emerged as a promising pathway for deep decarbonization in various sectors, such as power generation and transportation [1]. However, the majority of the $H_2$ is produced from reforming fossil fuels, with steam methane reforming (SMR) accounting for 50% of the total production, without carbon capture, resulting in high $CO_2$ emissions (89.1 $gCO_2/MJ$) [2]. Blue $H_2$ is a viable solution with lower carbon intensity (22.4 $gCO_2/MJ$) and offers a feasible route to sustain reliance on fossil fuels [3]. Therefore, developing an economically viable and sustainable $CO_2$ capture system with a low environmental footprint is imperative. The pre-combustion $CO_2$ capture system has been widely explored in $H_2$ production units for its effectiveness in handling high-pressure streams with high $CO_2$ concentrations. In this context, solvent selection is essential for designing the $CO_2$ removal system by considering various factors, encompassing eco-toxicity, minimizing irreversibility, and increasing energy efficiency. Ionic liquids (ILs) have shown exceptional performance in reducing energy regeneration compared to conventional solvents such as Monoethanolamine (MEA), making ILs well-suited for pre-combustion applications [4]. Nevertheless, their tunability makes it challenging to synthesize the optimal IL from numerous possibilities.

This work conducts a comprehensive thermodynamic analysis of a newly synthesized pre-combustion

$CO_2$ capture process for large-scale $H_2$ production. The analysis aims to evaluate its energy and exergy performance and identify process irreversibilities. A novel IL 1-octyl-2,3-methylimidazolium thiocyanate [OMMIM][SCN], designed in our previous work using a predictive deep learning model [5], was utilized as a physical absorbent in this study (see **Figure 1**). The IL was defined in the simulation software Aspen Plus, following the integrated modified translation-rotation-internal coordinate (TRIC) system with the COSMO-based/Aspen approach developed in our previous work [6]. An eco-toxicity analysis was carried out using the ADMETlab 2.0 web tool [7] to evaluate the environmental suitability of [OMMIM][SCN]. Finally, the performance of [OMMIM][SCN] was compared to an established IL, 1-butyl-2,3-dimethylimidazolium bis(trifluoromethyl sulfonyl)imide [BMMIM][TF2N] to assess their relative effectiveness in the process and their environmental suitability.




**Figure 1.** Molecular structure of novel IL [OMMIM][SCN] [5]

# METHODOLOGY

## Eco-Toxicity assessment

The ADMETlab 2.0 web tool evaluated the selected ILs' eco-toxicity, leveraging its robust framework for accurate toxicity predictions. By providing the SMILES (Simplified Molecular Input Line Entry System) representation of the IL as input to the platform, the molecular structure is processed to predict different properties using the advanced quantitative structure-property relationship (QSPR) model. The platform assesses different endpoints, such as environmental toxicity. It evaluates carcinogenicity, eye and skin irritation, and respiratory toxicity. The results of the assessment are shown as numerical scores. These scores range from 0 to 1 and then are categorized using an empirical decision scale, as indicated in **Table 1**.

**Table 1**: Empirical decision score based on ADMETlab 2.0 framework [7].

| Empirical decision | Category |
|---|---|
| 0.0-0.3 | "Non-toxic" |
| 0.3-0.7 | "Slightly toxic" |
| 0.7-1.0 | "Toxic" |

## Large-scale pre-combustion $CO_2$ capture simulation

Following the TRIC system with the COSMO-based/Aspen approach, the novel IL [OMMIM][SCN] was successfully defined in the simulation software Aspen Plus V12 as a pseudocomponent. A steady-state large-scale pre-combustion $CO_2$ capture process was then developed, as depicted in **Figure 2**. This process was designed to capture 90% of the $CO_2$ and achieve an $H_2$ purity of 97%. It treats $H_2$ produced from a large-scale steam methane reformer (SMR), generating a 6.98x104 kg/h flow of syngas stream with the following compositions: 16.27% $CO_2$, 4.63% CO, 75.61% $H_2$, 3.05% $CH_4$, 0.24% $H_2O$, and 0.2% $N_2$. The syngas flow specifications were obtained from the IEAGHG report [8]. The proposed configuration comprises four main components: absorption columns, pumps, flash drums, heat exchangers, and compressors. The process specifications suggested by Hospital-Benito et al.[9], were used to develop the large-scale pre-combustion process in Aspen Plus. During the process development, the number of stages was adjusted and it was only 10 stages required to achieve the specified $CO_2$ removal target of (90%).

The syngas stream enters a flash separator (F-101) to separate the water content from the gas stream. The dry gas stream (S4) then enters a "RADFRAC" packed bed absorber column at 35°C and 26 bar, where the $CO_2$ is absorbed by the IL counter currently within the column. The stream "PURE $H_2$" exists from the column overhead, whereas the $CO_2$-rich stream (S6) leaves from the bottom of the column and enters the flash drum (F-102) to remove and recycle $H_2$ back to the absorber. Before the regeneration stage, the $CO_2$-rich stream (S8) is heated by a heat exchanger (HEATER) to a temperature suitable for effective separation. Then, the heated stream (S9) enters two flash separators arranged in series for the regeneration of IL, where the streams that contain mostly $CO_2$ leave the top of the flash columns (F-103 and F-104) and are combined via a mixer (M-102). The regenerated IL (S15) from F-104 is cooled via a heat exchanger (COOLER) and recirculated back (LEANIN) to the absorber.

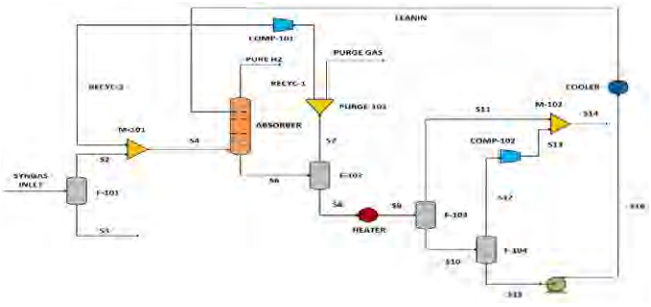



**Figure 2.** Large-scale pre-combustion $CO_2$ capture process scheme

## Energy and exergy analysis

Evaluating the thermodynamic efficiency via process system engineering aspects, such as energy and exergy, is essential for optimizing pre-combustion $CO_2$ capture and achieving maximum $CO_2$ capture efficiency and $H_2$ purity.

The energy-consuming equipment in the suggested process scheme includes heat exchangers, compressors, and flash separators. The equipment's energy duty (kW) values were obtained from Aspen Plus.

The overall thermal efficiency ($\eta$) of the $CO_2$ capture process can be evaluated using equation (1) [10]:

$$\eta = \frac{\sum \dot{Q}_{useful} + \sum \dot{W}_{out} + \sum \dot{m}_{useful} h_{useful}}{\sum \dot{Q}_{in} + \sum \dot{W}_{in} + \sum \dot{m}_{in} h_{in}} \quad (1)$$

Where $\dot{Q}_{useful}$ is the useful thermal energy output, $\dot{W}_{out}$ refers to the useful mechanical energy output, $\dot{Q}_{in}$ and $\dot{W}_{in}$ represent the total thermal energy and the mechanical energy inputs to the system, respectively, $\dot{m}_{useful}$ indicates the mass flow rate of useful products, specifically the pure $H_2$ stream, and the captured $CO_2$, $\dot{m}_{in}$ refers to the inlet mass flow rate, $h_{useful}$ and $h_{in}$ represent the enthalpy of useful and input streams, respectively.

The exergy flow rate $\dot{E}x$ of a material stream can be calculated using equation (2) [10]:

$$\dot{E}x = \dot{m}[(h_i - h_o) - T_o(s_i - s_o)] \quad (2)$$

$h_i$ and $s_i$ denote the stream's specific molar enthalpy and entropy in a certain state, $h_o$ and $s_o$ refer to specific molar enthalpy and entropy in the reference state ($T_o$ = 25°C, $P_o$ = 1 bar), and $T_o$ represents the reference temperature. The exergy destruction rate ($\dot{E}x_d$) can be calculated from the exergy balance equation of the main processing equipment as given by equation (3) [10]:

$$\sum \dot{m}_{in}\dot{E}x_{in} + Q_{consumption}\left(1 - \frac{T_o}{T}\right) + \dot{W}_{consumption} = \sum \dot{m}_{out}\dot{E}x_{out} + \dot{Q}_{generation}\left(1 - \frac{T_o}{T}\right) + \dot{W}_{generation} + \dot{E}x_d \quad (3)$$

Where the term $Q\left(1 - \frac{T_o}{T}\right)$ denotes the rate of exergy destruction associated with heat transfer. $\dot{E}x_{in}$ and $\dot{E}x_{out}$ refer to the inlet and outlet exergy flow rate mass, $\dot{E}x_d$ is the exergy destruction, $\dot{W}_{consumption}$ work consumed by the system, and $\dot{W}_{generation}$ generated by the system

The overall exergy efficiency of the proposed process configuration can be calculated using equation (4) [10]:

$$\varepsilon = \frac{\sum Ex(\dot{Q}_{useful}) + \sum \dot{W}_{out} + \sum \dot{m}_{useful} Ex_{useful}}{\sum Ex(\dot{Q}_{in}) + \sum \dot{W}_{in} + \sum \dot{m}_{in} Ex_{in}} \quad (4)$$

# RESULTS AND DISCUSSION

## Eco-toxic evaluation of selected ILs

The toxicity evaluation for both ILs, [OMMIM][SCN] and [BMMIM][TF2N], was conducted using the ADMETlab 2.0 web tool. The results of the assessment are summarized in Table 2. The toxicological profiles of IL [OMMIM][SCN] and [BMMIM][TF2N] differ noticeably. For instance, [OMMIM][SCN] is classified as slightly toxic for carcinogenicity (0.478), whereas [BMMIM][TF2N] is toxic (0.944), indicating a higher risk. However, despite these differences, both ILs exhibit high toxicity in respiratory effect, with [BMMIM][TF2N] demonstrating a slightly higher value (0.986) compared to [OMMIM][SCN] (0.882). Overall, the newly designed IL [OMMIM][SCN] shows less toxicity across multiple properties, suggesting that the IL is relatively safer and environmentally suitable.

**Table 2**: Probability of eco-toxicity assessment parameters

| Property | [OMMIM][SCN] | [BMMIM][TF2N] |
|---|---|---|
| **Carcinogenicity** | 0.478 (slightly toxic) | 0.944 (toxic) |
| **Eye Corrosion** | 0.257 (nontoxic) | 0.003 (nontoxic) |
| **Eye Irritation** | 0.434 (slightly toxic) | 0.032 (nontoxic) |
| **Skin Sensitization** | 0.156 (nontoxic) | 0.325 (slightly toxic) |
| **Respiratory Toxicity** | 0.882 (toxic) | 0.986 (toxic) |

## Thermodynamic analysis

The energy performance of the large-scale pre-combustion $CO_2$ capture process was analyzed, targeting a 90% $CO_2$ removal rate, and the results are shown in **Figure 3**. The COOLER demonstrates the highest energy demand for both ILs, with the [OMMIM][SCN] system requiring slightly less energy by 7.45% (33985 kW) than [BMMIM][TF2N] (36722 kW). On the other hand, the energy consumption associated with the HEATER, P-101, Comp-101, and Comp-102 is nearly identical for the two ILs. A noticeable difference is observed in energy demand for F-104, where [OMMIM][SCN], at 1080 kW, requires less energy than [BMMIM][TF2N] (2743 kW). In contrast, the total energy demand in F-102 (4785 kW) is slightly larger for [OMMIM][SCN] compared to [BMMIM][TF2N] (3748 kW).

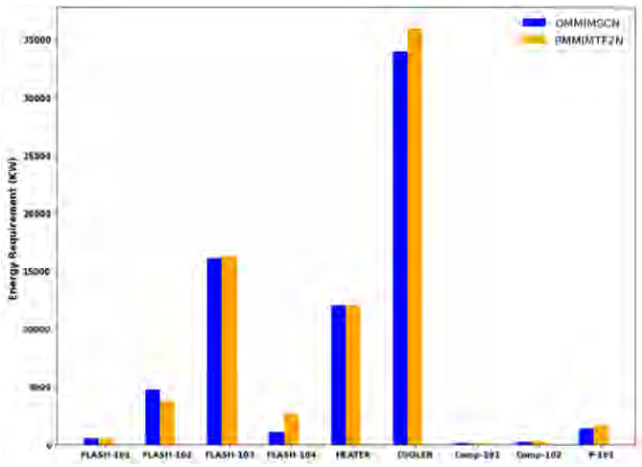



**Figure 3**. Comparisons of energy requirement for different equipment for both ILs.

Each unit's irreversibility (exergy loss) is calculated using equations (2) and (3), and the results are highlighted in **Figure 4**. The analysis shows that in the [BMMIM][TF2N] system, the COOLER component is the largest contributor to exergy loss, accounting for 47% (12982 kW) of the total exergy loss of the entire system. Conversely, the energy destruction in the [OMMIM][SCN] system is much lower (4690 kW), indicating that [OMMIM][SCN] operates with higher thermodynamic efficiency in the COOLER unit. In the separation stage (C-101), exergy loss in the [OMMIM][SCN] system is higher at 4048 kW compared to 2431 kW for the [BMMIM][TF2N] system. As for the regeneration stage, the exergy loss is greater in both units F-102 (1383 kW) and F-103 (8256 kW) in the [OMMIM][SCN] system compared to [BMMIM][TF2N], while [OMMIM][SCN] experiences less exergy loss in F-104, at 646 kW, than [BMMIM][TF2N] system.

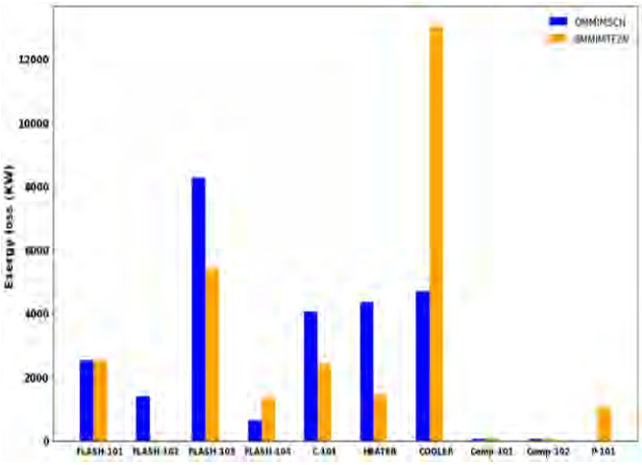



**Figure 4.** Exergy loss comparison across various equipment for both ILs.

## Parametric analysis

This section examines the impact of system parameters like the IL inlet temperature and absorption pressure on the thermodynamic efficiency of the proposed pre-combustion $CO_2$ capture process configuration. The effect was studied within the temperature range of 25°C to 75°C and pressure absorption range of 7 to 22 bar and 7 to 16 bar for energy and exergy efficiency, respectively.

### Effect of IL inlet temperature

Using equation (1), the total energy efficiency of the entire process was calculated within the specified temperature range, and the result is depicted in **Figure 5**. The system's energy efficiency decreases as the inlet temperature increases. The highest energy efficiency for both systems, [OMMIM][SCN] and [BMMIM][TF2N], occurs at 25°C. However, [OMMIM][SCN] demonstrates higher energy efficiency (91.2%) at 25°C than [BMMIM][TF2N] (90.6%). Additionally, the difference in energy efficiency between the two systems decreases across the temperature range, with the [OMMIM][SCN] system achieving higher energy efficiency. This trend continues throughout the temperature range, suggesting that the [OMMIM][SCN] system consumes less energy and, therefore, is more energy-efficient.

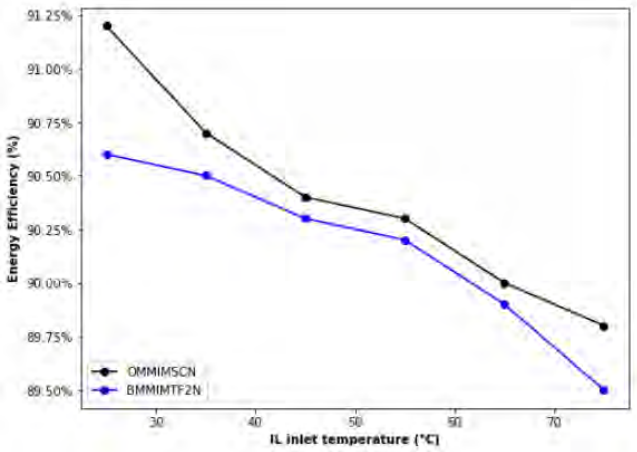



**Figure 5**. Effect of IL inlet temperautre on Energy Efficiecny (%).

Equations (2), (3), and (4) are used to calculate the overall exergy efficiency. **Figure 6** illustrates the exergy efficiency for both systems across the specified range for IL inlet temperature. As depicted from the graph, both IL systems demonstrate a significant increase in exergy efficiency as the temperature rises. The [OMMIM][SCN] system exhibited a higher exergy efficiency than [BMMIM][TF2N] throughout the temperature range, indicating that the [OMMIM][SCN] system experiences fewer irreversibilities. The maximum exergy efficiency occurs at 50-60°C, where [OMMIM][SCN] has slightly higher exergy efficiency (73.24%) compared to [BMMIM][TF2N]

(71.1%). Beyond this optimal range, the efficiency declines for both systems to around 57% at 75°C.

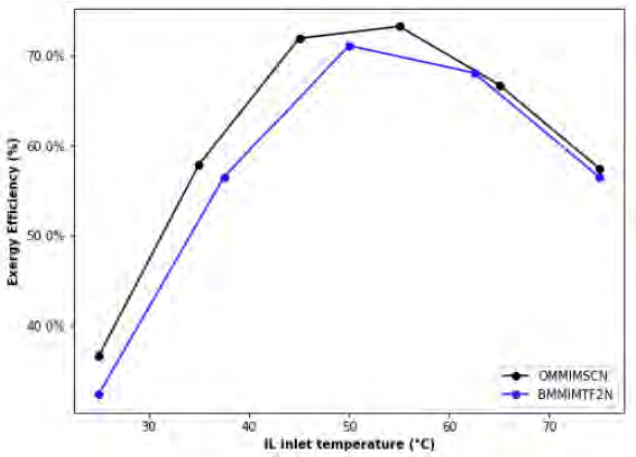



**Figure 6**. Effect of IL inlet temperautre on Exergy Efficiecny (%).

## Effect of absorption pressure

The impact of varying the absorption pressure on the overall energy efficiency was also calculated. As seen in **Figure 7**, the [OMMIM][SCN] system demonstrates a decline in efficiency as the pressure increases, whereas [BMMIM][TF2N] maintains energy efficiency close to 89.9% throughout the pressure range. While, [OMMIM][SCN] shows higher energy efficiency (91%) at 7 bar compared to [BMMIM][TF2N] (89.9%), the efficiency of [OMMIM][SCN] decreases by 1% within the limited pressure range of 10-16 bar. Given that physical absorption generally favors higher pressures for better $CO_2$ removal, [BMMIM][TF2N] is more suitable for higher absorption pressures.

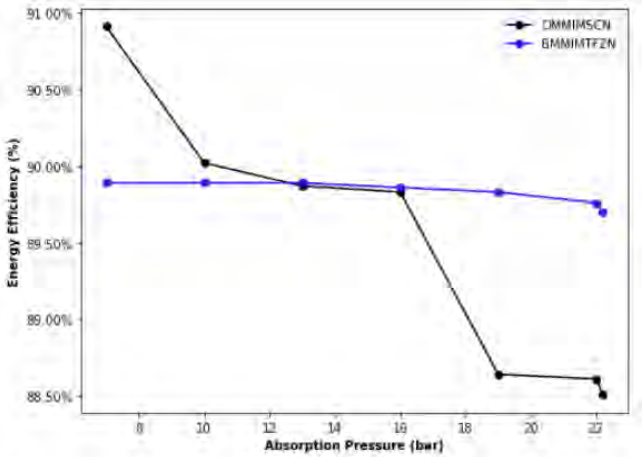



**Figure 7**. Effect of absorption pressure on Energy Efficiency (%)

Similarly, the parametric analysis was conducted to calculate the exergy efficiency within the specified pressure range. As illustrated in **Figure 8**, both IL systems experience a significant increase in efficiency as the pressure rises. The [OMMIM][SCN] system achieves higher efficiency across the pressure range compared to [BMMIM][TF2N], increasing from 25% to 37%. In contrast, the exergy efficiency for [BMMIM][TF2N] increases from 21% to 33%.

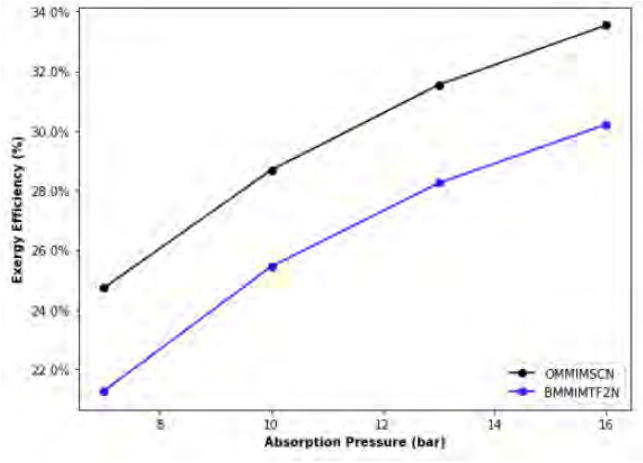



**Figure 8**. Effect of absorption pressure on Exergy Efficiency (%)

## CONCLUSIONS

This study evaluates the thermodynamic efficiency of a large-scale pre-combustion $CO_2$ capture process using two IL systems: novel IL [OMMIM][SCN] and established IL [BMMIM][TF2N]. Alongside the thermodynamic performance, the toxicity analysis of ILs using ADMETlab 2.0 was evaluated. The results indicate that [OMMIM][SCN] is less toxic across the studied properties, indicating that the IL is environmentally safer compared to [BMMIM][TF2N]. The results of the thermodynamic analysis conducted at a 90% $CO_2$ removal rate reveal that the highest energy consumption for both IL systems occurs at the “COOLER” units, while [BMMIM][TF2N] requires slightly more energy duty. Moreover, the “F-104” exhibits a larger energy demand in the [BMMIM][TF2N] system, whereas the energy consumption for [OMMIM][SCN] is marginally larger in “F-102”. Similarly, the exergy destruction results demonstrate that the “COOLER” in the [BMMIM][TF2N] contributes the highest system irreversibility. Conversely, [OMMIM][SCN] experiences higher exergy loss in F-102 and F-103 compared to [BMMIM][TF2N]. In terms of efficiency, the results highlight that the [OMMIM][SCN] system is more energy efficient when IL inlet temperature increases. However, its efficiency declines at higher absorption pressure, whereas the energy efficiency of the [BMMIM][TF2N] system remains constant. As for the exergy efficiency,

the [OMMIM][SCN] system shows higher exergy efficiency than [BMMIM][TF2N] throughout the studied temperature and pressure ranges. However, a decline in exergy efficiency is observed beyond the peak point temperature range of 50-60°C. This indicates that [OMMIM][SCN] exhibits better performance than established IL [BMMIM][TF2N], confirming its potential as a promising alternative for large-scale pre-combustion $CO_2$ capture process for blue $H_2$ production. However, while computational toxicity predictions using ADMETlab 2.0 provide valuable insights, experimental validation of [OMMIM][SCN] is crucial to evaluate its practical feasibility in industrial applications. In addition to toxicity assessment, further evaluation encompassing scalability and cost should be addressed to determine its large-scale implementation. Also, additional study is needed to optimize the [OMMIM][SCN] system to reduce irreversibility in process equipment and increase energy efficiency.

## ACKNOWLEDGEMENTS

The authors acknowledge the paper was made possible by grant QUHI-CENG-22-23-465 from Qatar University. The statements made herein are solely the responsibility of the author[s].

## REFERENCES

1. P. R. Yaashikaa, P. Senthil Kumar, S. J. Varjani, and A. Saravanan, "A review on photochemical, biochemical and electrochemical transformation of CO2 into value-added products," *J. CO2 Util.*, vol. 33, no. May, pp. 131–147, 2019, doi: 10.1016/j.jcou.2019.05.017.
2. F. Birol, "The Future of Hydrogen – Analysis - IEA," *Technology report*, 2019. https://www.iea.org/reports/the-future-of-hydrogen (accessed Mar. 13, 2021).
3. C. E. Regulator, "Market Snapshot: How hydrogen has the potential to reduce the CO2 emissions of natural gas," *Canada Energy Regulator*, 2020. https://www.cer-rec.gc.ca/en/data-analysis/energy-markets/market-snapshots/2020/market-snapshot-hydrogen-potential.html (accessed Nov. 19, 2022).
4. M. Aghaie, N. Rezaei, and S. Zendehboudi, "A systematic review on CO 2 capture with ionic liquids : Current status and future prospects," vol. 96, no. December 2017, pp. 502–525, 2018, doi: 10.1016/j.rser.2018.07.004.
5. S. Mohammed, F. Eljack, M. K. Kazi, and M. Atilhan, "Development of a deep learning-based group contribution framework for targeted design of ionic liquids," *Comput. Chem. Eng.*, vol. 186, no. January, p. 108715, 2024, doi: 10.1016/j.compchemeng.2024.108715.
6. S. Mohammed, F. Eljack, S. Al-Sobhi, and M. K. Kazi, "Simulation and 3E assessment of pre-combustion CO2 capture process using novel Ionic liquids for blue H2 production," *Comput. Aided Chem. Eng.*, vol. 53, pp. 517–522, Jan. 2024, doi: 10.1016/B978-0-443-28824-1.50087-9.
7. G. Xiong *et al.*, "ADMETlab 2.0: An integrated online platform for accurate and comprehensive predictions of ADMET properties," *Nucleic Acids Res.*, vol. 49, no. W1, pp. W5–W14, 2021, doi: 10.1093/nar/gkab255.
8. DOE/NETL, "IEAGHG Techno - Economic Evaluation of SMR Based Standalone (Merchant) Hydrogen Plant with CCS, 2017," 2022. [Online]. Available: https://eur-lex.europa.eu/legal-content/EN/TXT/?uri=CELEX:52020DC0301%0Ahttp://www.irena.org/publications%0Ahttp://ieaghg.org/exco_docs/2017-02.pdf.
9. D. Hospital-Benito, I. Díaz, and J. Palomar, "Technical performance and environmental assessment of an ionic liquid-based CCS process for hydrogen production," *Sustain. Prod. Consum.*, vol. 38, no. May, pp. 283–294, 2023, doi: 10.1016/j.spc.2023.04.017.
10. H. Alyasi, A. AlNouss, Y. Bicer, and G. Mckay, "A biomass-based integrated energy system for urea and power production: Thermodynamic analysis," *Int. J. Hydrogen Energy*, vol. 91, no. October, pp. 1365–1375, 2024, doi: 10.1016/j.ijhydene.2024.10.113.

© 2025 by the authors. Licensed to PSEcommunity.org and PSE Press. This is an open access article under the creative commons CC-BY-SA licensing terms. Credit must be given to creator and adaptations must be shared under the same terms. See https://creativecommons.org/licenses/by-sa/4.0/



Systems & Control Transactions

**Research Article - Peer Reviewed Conference Proceeding**
ESCAPE 35 - European Symposium on Computer Aided Process Engineering
Ghent, Belgium. 6-9 July 2025
Jan F.M. Van Impe, Grégoire Léonard, Satyajeet S. Bhonsale,
Monika E. Polańska, Filip Logist (Eds.)

PSE PRESS

# Mechanistic and Data-Driven Models for Predicting Biogas Production in Anaerobic Digestion Processes

**Rohit Murali[a,b], Benaissa Dekhici[a], Tao Chen[a,b], Dongda Zhang[c] , Michael Short[a,b,*]**

[a] School of Chemistry and Chemical Engineering, University of Surrey, Guildford, GU2 7XH, United Kingdom
[b] Surrey Institute for People-Centred Artificial Intelligence, University of Surrey, Guildford, GU2 7XH, United Kingdom
[c] Department of Chemical Engineering, The University of Manchester, Manchester, M13 9PL, United Kingdom
* Corresponding Author: m.short@surrey.ac.uk

## ABSTRACT

Accurately predicting biogas production for real-time applications remains a challenge in anaerobic digestion (AD) due to the process's complexity and dynamic nature. While mechanistic models are essential for understanding and modelling AD processes, however they are highly non-linear and depend on detailed feedstock characterisation and parameter calibration. In contrast, data-driven models do not rely on predefined equations and rather use process data to capture the system's underlying dynamics. This study compares mechanistic and data-driven models for biogas prediction using lab-scale data. A state estimation framework with a rolling window was used for the mechanistic model, based on biomass and substrate concentrations with Haldane kinetics, achieved an accuracy of ($R^2$ = 0.91). A Long Short-Term Memory (LSTM) model with Bayesian Optimisation for hyperparameter optimisation, trained on the same data showed superior performance ($R^2$ = 0.93–0.98) and captured temporal dependencies inherent to the AD process. The LSTM model was further applied to industrial data, maintaining high accuracy ($R^2$ = 0.95–0.97) and demonstrating its scalability. Its strong predictive capabilities, combined with practicality for real-time applications, make it a promising tool for optimising operations in large-scale AD plants.

**Keywords**: Anaerobic Digestion, Mechanistic Modelling, Data Driven Modelling, Long Short-Term Memory

## INTRODUCTION

Anaerobic digestion (AD) is a biological process where microorganisms decompose organic matter in the absence of oxygen, producing biogas (primarily $CH_4$ and $CO_2$) and nutrient-rich digestate. This sustainable process supports waste management and renewable energy generation, aligning with global net-zero carbon emission goals [1]. Modelling AD is critical for optimising its performance and addressing its inherent complexity. Mechanistic models, such as the Anaerobic Digestion Model No. 1 (ADM1), simulate the biochemical and physicochemical processes in AD systems, offering detailed insights. However, these models often require extensive parameterisation where parameters can be difficult to identify uniquely along with high computational resources [2]. In contrast, simplified AD models focus on key system parameters which tend to be more identifiable and provide faster predictions but may compromise accuracy. Data-driven models from machine learning (ML) offer an alternative by capturing nonlinear relationships and dynamics directly from data [2]. Identifying the most suitable and accurate model for predictions is important to enhance system performance, enabling real-time control and decision-making for efficient AD operation.

Current approaches often prioritise either mechanistic accuracy or computational simplicity, limiting the ability to dynamically adapt to real-world scenarios. ADM1 remains widely used in AD modelling, but its application is constrained by insufficient measurements of state variables during AD operations [3]. Compared to physics-based models, ML has gained attention for advantages [4] including ease of implementation, generalisability, and faster execution times [5]. ML models can map inputs to outputs without requiring an understanding of underlying physical processes, making them particularly suitable for AD prediction and optimisation [6]. However, algorithms, such as Support vector machines and artificial neural networks, often struggle to capture sufficient information from sequential data to provide

accurate predictions [7]. The digester's performance is influenced by previous feeding where hydraulic retention time (HRT) is a crucial parameter affecting AD performance [6]. A Long Short-Term Memory (LSTM) network is a form of recurrent neural network (RNN), developed to solve the vanishing gradient problem of RNNs by retaining or discarding the data over long sequences. LSTMs excel due to their rapid learning capabilities and ability to retain long-term dependencies within sequential data, making them effective in improving the accuracy of biogas production predictions while considering HRTs [7-8]. LSTMs have demonstrated significant potential in AD with promising results, such as predicting biogas yields, optimising feed rates, process parameters and resulting in methane production enhanced by up to 25% [6-7]. [6] applied LSTMs on a wastewater site, while [7] applied LSTMs on limited food waste data which was extended using a synthetic minority over-sampling technique, however nobody has applied LSTMs on energy crops and waste co-digestion data from laboratory and Industrial plant with varying HRTs.

Therefore, this study compares a practical mechanistic model and a purely data-driven model with Bayesian optimisation for hyperparameter tuning for predicting biogas production using solid AD feedstocks at the laboratory level. The data-driven model's applicability is extended to industrial datasets, demonstrating its potential for real-time site-level predictions.

## METHODS

### Experimental Set-up and Data Collection

This study first uses a kinetic model proposed by [9] to simulate and fit parameters related to substrate degradation, biomass growth, and methane production. In a lab-scale AD system, experimental data were collected over time for various state variables, such as substrate concentration, biomass concentration, and biogas (methane) production. The lab-scale digester was fed with roughly 10% maize silage and 12% dried maize, 14% rye silage, 18% wheat grain, 25% pig slurry and 11% water in a % fresh weight basis, with the setup shown in **Figure 1**.

Experimental data was obtained from the laboratory from a small scale 5-liter AD reactor which mimicked an industrial site's operation using anaerobic co-digestion.

### Mechanistic Model Development

Interpreting the experimental data to predict system behaviour under different conditions for control and fast predictions across wider input space requires a simplified model. The model used simplifies the AD process by reducing it to two main state variables: substrate concentration ($ST$), biomass concentration ($XT$) and output of methane production ($Q$). By fitting the model represented in **Figure 2** to experimental data using optimisation techniques, the goal is to identify key kinetic parameters maximum specific growth rate ($\mu_{max}$), half-saturation constant ($K$), inhibition constant ($K_i$), substrate conversion coefficient ($k$), and methane production coefficient ($K_m$) , to accurately predict biogas production.



**Figure 1.** Semi-continuous AD experiment set-up.

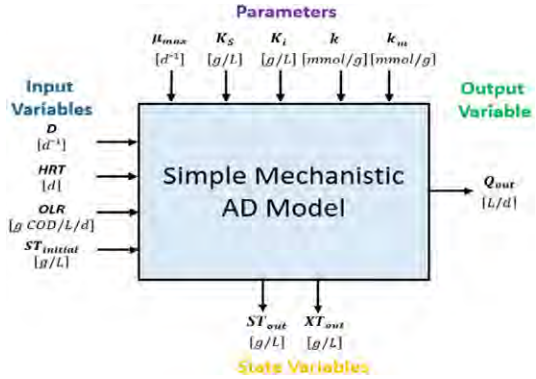



**Figure 2:** Simple Mechanistic AD Model Superstructure

The following steps outline the methodology used to model, simulate, and optimise the AD process in a lab-scale reactor using a simplistic mechanistic model. The model simulates the system's behaviour over time by integrating the differential equations which represent the mass balances for the substrate and biomass. The model parameters are optimised to minimise the difference between the model's predictions and the experimental data. The model uses a set of nonlinear differential equations to describe the interaction between these state variables, including substrate degradation and biomass growth as functions of substrate availability and microbial growth. The system of ordinary differential equations (ODEs) that governs the dynamics of the substrate concentration ($ST$), biomass concentration ($XT$), and methane production rate ($QT$). A rolling-window state estimation approach is used, instead of integrating the entire system from the initial to the final time. The rolling-window method divides the simulation horizon into sequential, overlapping segments. At each time step $t_i$, the state vector is re-initialised using the most recent measurements by setting $ST(t_i)$ and $QT(t_i)$ to their corresponding measured values while $XT(t_i)$ is propagated from the

previous prediction.

$$x(t_i) = \begin{bmatrix} ST(t_i) \\ XT(t_i) \\ QT(t_i) \end{bmatrix} \quad (1)$$

The rate of change of substrate concentration is represented by:

$$\frac{dST}{dt} = D \cdot (ST_{in} - ST) - k \cdot \mu \cdot XT \quad (2)$$

There are several growth rate equations available in literature such as Monod kinetics, first order kinetics, etc. For this model the specific growth rate ($\mu$) is modelled using Haldane kinetics, which accounts for both substrate saturation and inhibition:

$$\mu = \mu_{max} \frac{ST}{ST + K_S + \frac{ST^2}{K_i}} \quad (3)$$

The rate of change of biomass concentration is represented by:

$$\frac{dXT}{dt} = (\mu - D) \cdot XT \quad (4)$$

The methane production rate is calculated directly from the biomass concentration and the specific growth rate:

$$Q = k_m \cdot \mu \cdot XT \quad (5)$$

The objective function to be minimised is Sum of Squared Errors (SSE) between the model's predictions and the experimental data is defined as:

$$\text{Objective} = \sum_{i=1}^{n} \left(\frac{ST_{sim,i} - ST_{out,i}}{ST_{out,i}}\right)^2 + \sum_{i=1}^{n} \left(\frac{Q_{sim,i} - Q_i}{Q_i}\right)^2 \quad (6)$$

Where:

$ST_{sim,i}$: Simulated substrate concentration at time $i$
$ST_{out,i}$: Measured substrate concentration at time $i$
$Q_{sim,i}$: Simulated methane production rate at time $i$
$Q_i$: Measured methane production rate at time $i$
$n$: Number of data points

The integration over each small interval is performed using numerical solvers, yielding predicted states at $t_{i+1}$. Prior to the next integration step, the states are reset such that:

$$\begin{aligned} ST_{initial}(t_{i+1}) &= ST_{measured}(t_{i+1}) \\ XT_{initial}(t_{i+1}) &= XT_{measured}(t_{i+1}) \\ QT_{initial}(t_{i+1}) &= Q_{measured}(t_{i+1}) \end{aligned} \quad (7)$$

This approach reduces integration errors and offsets model mismatches by aligning the simulation with recent empirical data. A window size of 30 is the period during which new measurements replace older ones which was used based of average HRTs.

## Data-Driven Modelling Approach

### LSTM Model Development

Two LSTM neural networks were developed to predict total biogas production using input features from biogas plants and experimental data. The first model (LAB-LSTM) was applied to lab-scale reactor data of 150 sample points to evaluate performance on smaller datasets. The second (IND-LSTM) was applied to an industrial AD plant's historical data of 600 days to assess its capability for plant-level predictions. Feature selection was performed using Recursive Feature Elimination (RFE), which eliminates less relevant features based on model performance [6,8]. For the industrial case study, the top five parameters and any site-controllable variables were kept for control applications. Selecting the optimal hyperparameters is challenging for neural networks and trial and error can be long and expensive. Hyperparameters which were focussed on were LSTM units, batch size, epoch and learning rate (LR). The number of LSTM units determines the model's capacity to capture patterns, while batch size and learning rate balance computational efficiency and model accuracy. Epochs were adjusted to prevent overfitting, with training monitored to stop when validation loss increased. Bayesian Optimisation (BO) was employed for hyperparameter tuning, outperforming traditional methods like grid or random search by strategically minimising error through iterative adjustments [6-8]. The error measurement was performed using 5-fold cross-validation with the Mean Absolute Error (MAE) objective function to ensures a reliable evaluation of the model by averaging performance across multiple subsets of the data, reducing the risk of overfitting due to specific data splits. For each fold 80% of the data was used for training and 20% for testing. BO allowed for efficient exploration of parameter spaces, such as LSTM units (10-50), batch size (4-32), and LR (0.0001-1), ensuring a balance between performance and computational demands. The LSTM model predicts the next time step (t+1) based on a look-back window corresponding to the average HRT (t-average HRT) of 30 days. Since HRT represents the time required for feedstock to break down and produce biogas, this approach aligns predictions with the system's natural kinetics. Additionally, it enhances interpretability for operators and supports process optimisation by linking predictions to real-world process dynamics. In this study for all LSTM models, the number of iterations for the optimised hyperparameters was set to 25 to lower computational demands. All models were implemented using Python. Libraries included Pandas and NumPy for data preparation, Scikit-learn for feature selection and performance metrics, TensorFlow's `Keras` was for model development, and the `bayes_opt` library was used for hyperparameter tuning, and Matplotlib was used for data visualisation. The overall model architecture for the two LSTM models and optimised hyperparameters are outlined in **Table 1**.

**Table 1:** Model Architecture of each LSTM case study

| Model | Input Layer | LSTM Layer | | Output Layer | | Compilation | | Training Details | | |
|---|---|---|---|---|---|---|---|---|---|---|
| | Features | Units | Activation Function | Dense Layer | Activation Function | Loss Function | Optimiser | Epochs | LR | Batch Size |
| **IND** | Feedstock Quantities Tempera-ture, HRT, HLR, OLR & Stirrer Speeds | 24 | Hyperbolic tangent | Total Biogas | Linear | MAE | Adam | 70 | 0.003 | 14 |
| **LAB** | Feed, HRT & OLR | 35 | | Total Biogas Produc-tivity | | | | 100 | 0.005 | 10 |

# RESULTS AND DISCUSSION

## Performance Evaluation

To assess the accuracy of the model, the following error metrics are calculated:

a) Root Mean Squared Error (RMSE):

$$RMSE = \sqrt{\frac{1}{n}\sum_{i=1}^{n}(y_{sim,i} - y_{obs,i})^2} \quad (8)$$

b) Coefficient of Determination ($R^2$):

$$R^2 = 1 - \frac{\sum_{i=1}^{n}(y_{obs,i} - y_{sim,i})^2}{\sum_{i=1}^{n}(y_{obs,i} - \bar{y}_{obs})^2} \quad (9)$$

Where:

$y_{sim,i}$: Simulated value at time $i$

$y_{obs,i}$: Observed (measured) value at time $i$

$\bar{y}_{obs}$: Mean of the observed values

## Optimised Mechanistic Model

The parameter fitting was carried out using the Nelder-Mead method, which iteratively adjusts the parameter values to minimise SSE to a final value of 0.1204. After optimisation, the following parameters were obtained and shown in **Table 2**.

**Table 2:** Optimised Parameters from Mechanistic Model

| Parameter | Value | Unit |
|---|---|---|
| $\mu_{max}$ | 0.067 | 1/day |
| $K_S$ | 927 | g/L |
| $K_i$ | 265.5 | g/L |
| $k$ | 2796 | mmol/g |
| $K_m$ | 13.25 | mmol/g |

The model fits the experimental data shown in **Figure 3.**

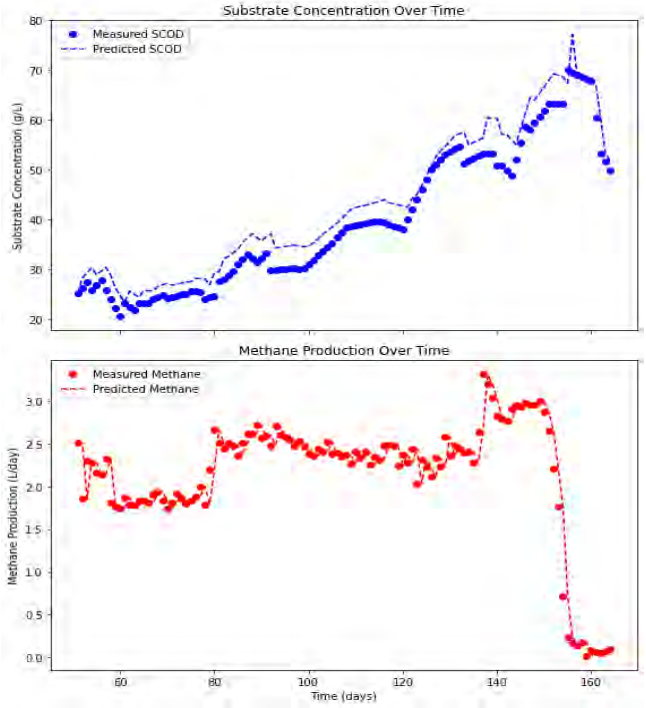



**Figure 3.** Substrate concentration and Methane production over time.

Mechanistic models rely on well-defined equations that represent the underlying biochemical and physical processes. However, these models are particularly sensitive to non-steady state conditions, as such variability may not be captured by the simplified model. The selected time points from the dataset used was days 50-162 where measurements of the substrate concentrations were made available. The optimised model was evaluated using RMSE and R2 values. The model fits the experimental data reasonably well, particularly for methane production. The RMSE and R2 values for substrate concentration (RMSE = 3.927, R2 = 0.87) and methane production (RMSE = 0.2089, R2 = 0.91) indicate that the model effectively captures the general trends in the data,

including both the dynamic nature of substrate degradation and methane yield over time. The model effectively captures oscillatory behaviour in substrate concentration, indicating it accurately reflects the dynamic relationship between substrate consumption and biomass growth. This is achieved using Haldane kinetics, which accounts for substrate inhibition, particularly at higher organic loading rates (OLRs).

This model is useful for early-stage predictions and lab-scale experiments, providing initial estimates for substrate concentration, biomass growth, and methane production. The model is flexible enough to incorporate key biological processes such as substrate inhibition and microbial growth, which are important at higher OLRs and help in planning and designing lab-scale experiments. This understanding aids in optimising processes, such as adjusting feed rates or HRTs, to maximise biogas yield.

## LSTM Results and Model Performance

The LAB-LSTM was developed using data from the lab scale AD reactor. For IND-LSTM, operation and feeding data from industrial partners where both LSTMs' capabilities to predict the total biogas produced was assessed. Since data-driven models do not require prior assumptions about the system's behaviour and can adapt to both steady and non-steady state conditions the entire dataset was used. The output is shown in **Figure 5**. The two LSTM models reveal consistent accuracy in predicting biogas production across different datasets and contexts. Each model, while designed with unique inputs and variable output, effectively captures the under-lying patterns in the AD process, showing their use in practical applications. Across both models, the $R^2$ values achieved in training and testing of 0.90-0.98 indicate strong predictive capabilities. This high level of accuracy shows that the models can effectively learn the relationships between the input features and their respective output variables, whether it is total biogas production or productivity. The close alignment between actual and predicted values in visual plots highlights the effectiveness of the models. **Figure 6** presents the error distributions of both models to provide further insights into model performance across different datasets.

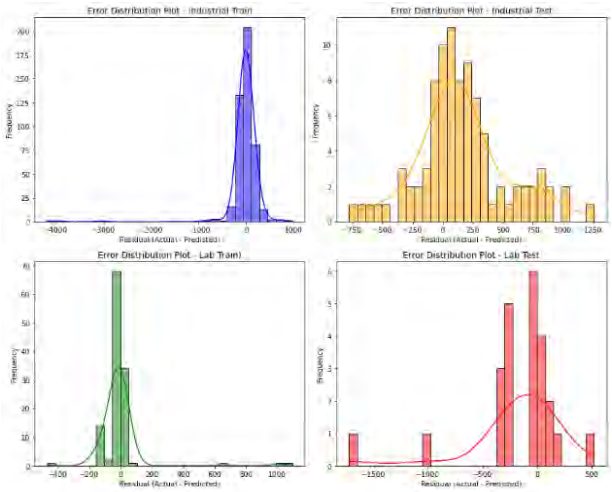



**Figure 6.** Model Error Distribution for Train and Test for Lab and Industrial Datasets.

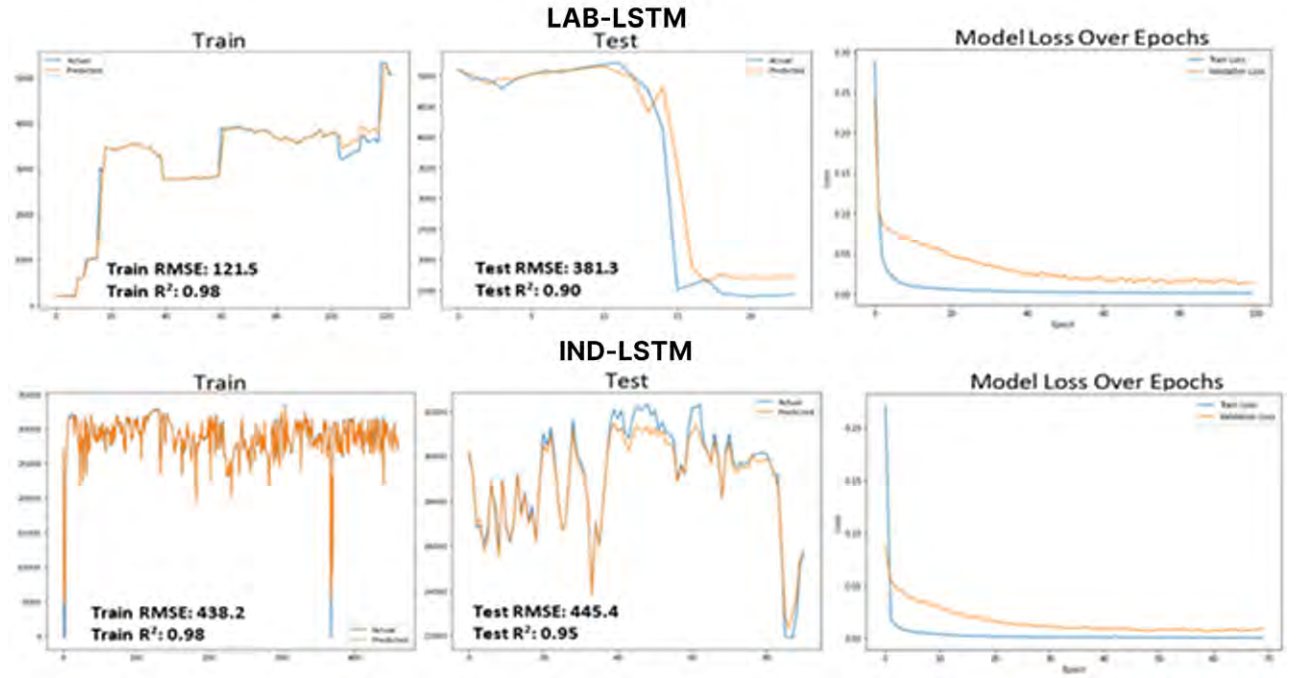



**Figure 5a-f:** Test, Train and Loss and Epoch plots of both laboratory scale data and industrial data LSTM Models.

The industrial dataset showed a near-normal residual distribution in training, indicating a well-fitted model, while the test set showed slightly higher variance, suggesting minor overfitting. In contrast, the lab-scale dataset had tightly clustered training residuals but a more skewed test distribution with higher variance, highlighting generalisation challenges. However, minor discrepancies, particularly during sharp changes, suggest a need for further refinement to improve responsiveness to dynamic transitions particularly on lab scale data which may be a result of the small dataset used.

## CONCLUSION

Both mechanistic and data-driven models demonstrated strong predictive capabilities for AD. The mechanistic model performed well at predicting substrate degradation and methane production in lab-scale systems with simpler feedstocks and OLRs, offering valuable insights for process control and early experimentation. However, enhancing the model with more advanced kinetics, additional states, and considerations for inhibitory factors such as ammonia, volatile fatty acids, and variables such as temperature and pH could improve its industrial applicability. The state estimation framework for the mechanistic model with the rolling window can also be explored further in future works. The use of Unscented Kalman Filter (UKF) can be explored and integrate integrated into the state estimation framework to enhance real-time prediction accuracy for the AD processes. Unlike the rolling-window approach, which relies on periodic re-initialisation from measurements, the UKF) continuously updates state estimates in real-time.

The LSTM models outperformed the mechanistic model across all datasets and scaling effectively to industrial datasets with higher $R^2$ values ranging between 0.90-0.98. While the LSTM model contains a larger number of trainable parameters compared to the first-principle model, this is necessary to capture complex temporal dependencies and non-linear interactions that are not explicitly represented in mechanistic equations. To mitigate the risk of overfitting, BO was employed to optimise the hyperparameters, ensuring a balance between model complexity and performance. LSTMs could be extended from predictions and be integrated into control systems for real-time monitoring and dynamic adjustments to parameters such as feed and loading rates, enhancing process stability and efficiency. Developing hybrid models that combine LSTMs with mechanistic approaches offers a promising forward direction. Such physics-informed models would integrate mechanistic constraints with LSTM's learning capabilities, providing accurate and interpretable results for improved decision-making and process optimisation.


## ACKNOWLEDGEMENTS

This work was kindly supported and funded by the Surrey Institute for People-Centred AI (PAI) and by the Engineering and Physical Sciences Research Council EP/Y005600/1 (AI for Net Zero programme).


## REFERENCES


1. Huang X. The promotion of anaerobic digestion technology upgrades in waste stream treatment plants for circular economy in the context of "dual carbon": Global status, development trend, and future challenges. Water (Switzerland) 2024.
2. Onu P, Mbohwa C, Pradhan A. An analysis of the application of machine learning techniques in anaerobic digestion. Institute of Electrical and Electronics Engineers (IEEE) 2023:1–6.
3. Meola A, Weinrich S. Hybrid modelling of dynamic anaerobic digestion process in full-scale with LSTM NN and BMP measurements (2024)
4. Andrade Cruz I, Chuenchart W, Long F, Surendra KC, Renata Santos Andrade L, Bilal M, et al. Application of machine learning in anaerobic digestion: Perspectives and challenges. Bioresour Technol 345 (2022).
5. Dekhici B, Belkaid AB. Data-Driven Modeling, Order Reduction and Control of Anaerobic Digestion Processes (2024). https://doi.org/10.13140/RG.2.2.27352.26883.
6. Salamattalab MM, Hasani Zonoozi M, Molavi-Arabshahi M. Innovative approach for predicting biogas production from large-scale anaerobic digester using long-short term memory (LSTM) coupled with genetic algorithm (GA). Waste Manage 175:30–41 (2024).
7. Han Y, Du Z, Hu X, Li Y, Cai D, Fan J, et al. Production prediction modeling of food waste anaerobic digestion for resources saving based on SMOTE-LSTM. Appl Energy 352 (2023).
8. Jeong K, Abbas A, Shin J, Son M, Kim YM, Cho KH. Prediction of biogas production in anaerobic co-digestion of organic wastes using deep learning models. Water Res 205 (2021).
9. Bernard O, Chachuat B, Hélias A, Rodriguez J. Can we assess the model complexity for a bioprocess: Theory and example of the anaerobic digestion process. Water Sci Technol 53:85–92 (2006).



© 2025 by the authors. Licensed to PSEcommunity.org and PSE Press. This is an open access article under the creative commons CC-BY-SA licensing terms. Credit must be given to creator and adaptations must be shared under the same terms. See https://creativecommons.org/licenses/by-sa/4.0/




Systems & Control Transactions

**Research Article - Peer Reviewed Conference Proceeding**
ESCAPE 35 - European Symposium on Computer Aided Process Engineering
Ghent, Belgium. 6-9 July 2025
Jan F.M. Van Impe, Grégoire Léonard, Satyajeet S. Bhonsale,
Monika E. Polańska, Filip Logist (Eds.)

PSE PRESS

# Dynamic analysis for prediction of flow patterns in an oscillatory baffled reactor using machine learning

**Hideyuki Matsumoto[a]*, Yuma Kambayashi[a], Shiro Yoshikawa[a], and Shinichi Ookawara[a,b]**

[a] Institute of Science Tokyo, Department of Chemical Science and Engineering, Tokyo, Japan
[b] Yasuda Women's University, Department of Aesthetic Design and Technology, Hiroshima, Japan
* Corresponding Author: matsumoto@mct.isct.ac.jp

## ABSTRACT

In the present paper, we come up with application of machine learning using data for flow visualization as a method for predicting unsteady flow patterns in oscillatory baffled reactors (OBRs). Application of the proper orthogonal decomposition (POD) is investigated for dynamic analysis of spatio-temporal data acquired by particle image velocimetry (PIV) to determine inputs and outputs for neural network model. It has demonstrated that three sets of modes and time-varying mode coefficients extracted by the POD could be useful for dynamic analysis and prediction of time-variant flow patterns in OBR. Also it is shown that decomposition of the time-series data for the mode coefficients by Fourier series expansion was effective for deriving reduced order model.

**Keywords**: Oscillatory baffled reactor, Proper orthogonal decomposition, Neural network model

## INTRODUCTION

An oscillatory baffled reactor (OBR) [1] is a type of flow reactor, and is generally structured with equally spaced baffles arranged inside a circular tube. In this reactor, the fluids in the reactor are mixed by periodically oscillating the fluids or the baffles. Tubular reactors and continuous stirred tank reactors (CSTRs) have been widely used as conventional flow reactors. Tubular reactor is a type of reactor in which the fluids flow continuously in one direction with reaction, and has a simple structure. However, it requires a large flow rate to sufficiently promote the mixing of the fluids, which results in a problem of consuming a lot of power. In addition, for long tube reactors that are applicable to slow reaction, there are limitations for implementation in terms of installation space and cost. On the other hand, CSTRs have the advantage that the fluids are sufficiently mixed in each stirred tank, but in order to attain a uniform residence time distribution, a large number of stirred tanks must be connected in series, which causes the system to become complicated.

OBRs are attracting attention for their process intensification effects, such as high mixing performance at low flow rates and long residence time due to the vortices generated by the interaction between the oscillating flow and the baffles. Due to high performances for mixing and mass transfer, the OBRs are applied to various process systems. For example, for applications of OBRs to gas-liquid reactions, the reaction efficiency could be enhanced by increase in the contact area between the gas and liquid that is caused by oscillating flow. For liquid-liquid reactions, OBRs could be applied to achieve uniform mixing of two phase flow. Also, for application of OBRs to solid-liquid reactions, it has been observed that oscillating flow between baffles performs well-dispersion of solid particles, which leads to intensification of the reaction process. Due to the above-mentioned process intensification effects, OBRs are being put to practical use in various industrial fields, such as fine chemicals, pharmaceuticals and biodiesel productions [2-3].

In design of the oscillatory baffled reactors, optimal reactor performance could be achieved through complex interactions among multiple design parameters. The design parameters for OBR are related to geometry of baffle, structure of reactor and operation for generation of oscillating flow, so that they influence flow pattern inside reactor. The design of the flow in OBR is evaluated by several dimensionless numbers, including the oscillatory Reynolds number), the Strouhal number (St), the velocity ratio and so on.

The oscillatory Reynolds number (Reo) [1] is an

index representing the mixing intensity inside the OBR, and is expressed by the following formula.

$$Re_o = \frac{2\pi f x_0 \rho d}{\mu} \quad (1)$$

where $f$ is the frequency of oscillation, $x_0$ is the amplitude of oscillation, $\rho$ is the density of the fluid, and $\mu$ is the viscosity of the fluid. When $Re_O \leq 250$, the flow is axially symmetric and is defined as laminar flow. In a case when $250 < Re_O < 2000$, the flow is in the transition region, and the flow where $Re_O \geq 2000$ is generally considered as turbulent. In our previous study for application of OBR to three-phase hydrogenation of 3-butyn-2-ol by using $Pd/Al_2O_3$ catalyst, OBR has demonstrated higher reaction performance than the conventional packed bed reactor (PBR), and at the same $Re_O$, OBR with lower amplitude attained higher conversion [4].

As shown Figure 1, it was considered that the difference in $f$ and $x_0$ influenced the flow pattern inside the reactor and behavior of the reaction process (e.g. conversion $X$) for a case when frequency and amplitude differ with the same $Re_O$. As a result of flow visualization, since the generation of vortices was remarkably observed in the vicinity of the loaded catalyst when the amplitude $x_0$ was smaller, it was thought that analysis and prediction of the time-dependent changes in the local circulating flow in the region between the baffles would lead to more efficient design of OBR.

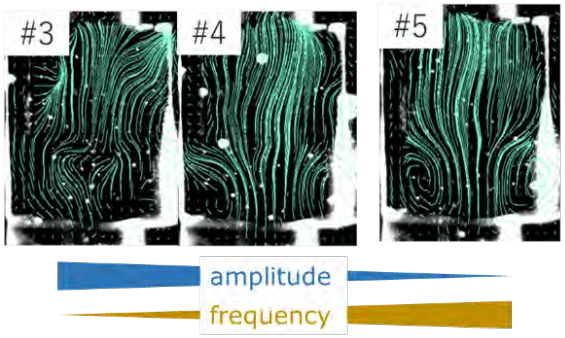



**Figure 1.** Comparison of streamlines that was obtained by PIV (#3: $x_0 = 15mm, X = 36.4\%$, #4: $x_0 = 10mm, X = 43.9\%$,#5: $x_0 = 5mm, X = 52.2\%$).

Although it is well known that computational fluid dynamics simulations [5-6] are effective in analysis and prediction of the flow patterns, there is a problem in that calculations for unsteady processes require a high computational load. Therefore, we came up with application of machine learning using data for flow visualization as a method for predicting unsteady flow patterns. In the present paper, we investigated methods for dynamic analysis of spatiotemporal data acquired by Particle Image Velocimetry (PIV) to determine inputs and outputs for neural network model.

# METHODOLOGIES

## Acquisition and analysis of flow visualization data

Figure 2 shows a schematic diagram of the oscillatory baffled reactor used in the flow visualization experiment using particle image velocimetry (PIV). The reactor is an acrylic tube type with an inner diameter of 26 mm. Baffles with a diameter of 25 mm and an opening area of 25% are placed in the reactor at equal intervals of 35 mm. The center part of the reactor tube with a length of 250 mm is covered by a rectangular vessel that is filled with water to eliminate distortion due to light refraction.

The flow rate of the steady flow was controlled by a plunger pump (FLOM, KP-22), and the oscillatory flow was generated from the bottom of the reactor using a syringe pump (Hamilton, PSD/6). Polyamide particles KP-050 (Kato Koken), which have a specific gravity almost the same as that of water, were used as tracer particles. The flow was visualized by irradiating the tracer particles with a green laser sheet formed by a PIV laser G2000 (Kato Koken). The motion of the tracer particles was recoded by using a high-speed camera (Kato Koken, k-8HD), and the obtained image data was analyzed by PIV software (Kato Koken, Flow Expert).

Table 1 shows operating conditions for acquisition of flow visualization data. Oscillatory Reynolds number $Re_O$, the flow rate of the steady flow $Q$, the amplitude of oscillation of syringe pump $x_0$, and the frequency of oscillation of syringe pump $f$ were changed in the present experiments.

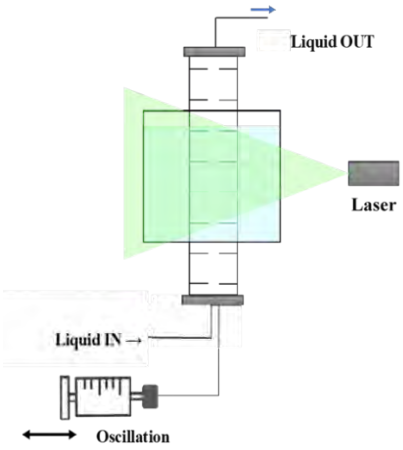



**Figure 2.** Schematic diagram of flow visualization experiment systems including OBR.

**Table 1:** Operating conditions for flow visualization experiments.

| | |
|---|---|
| $Re_O$ [-] | 762, 595, 293, 142, 40 |
| $Q$ [ml/min] | 8.3, 16.6 |
| $x_O$ [mm] | 5, 10, 15 |
| $f$ [Hz] | 0.02 – 1.06l |

## Application of the proper orthogonal decomposition (POD)

Recently, in the fields of computational fluid dynamics simulation, an approach that integrates the reduced order modeling (ROM) with machine learning technology has been investigated [7]. The major ROM techniques include the principal component analysis (PCA) and the proper orthogonal decomposition (POD) [8]. Application of the he ROM techniques can efficiently extract important information from phenomena by reducing the dimensionality of high-dimensional data, enabling accurate learning and highly accurate modeling of even highly nonlinear phenomena, enabling advanced prediction and analysis.

In the present paper, we investigate applicability of POD to reduced order modeling of spatiotemporal PIV data for OBRs. As mentioned above, POD is a modal decomposition method widely used in the field of fluid dynamics, which is used to efficiently reduce the dimensionality of huge amounts of data and extract the dominant structures in the flow field. POD is effective for analysis of unsteady flow, and is known as a method to clarify the essential characteristics of complex flow phenomena. POD calculates a spatially accommodating structure called "mode" based on a given data set, sorts the modes in order of contribution, and reduces the dimensionality of the data by selecting the dominant mode from the top.

In POD analysis, flow field data is decomposed based on the following formula.

$$\boldsymbol{q}(\boldsymbol{\xi},t)-\overline{\boldsymbol{q}}(\boldsymbol{\xi})=\sum_{j=1}^{r}a_j(t)\boldsymbol{\phi}_j(\boldsymbol{\xi}) \quad (2)$$

where $\boldsymbol{q}(\boldsymbol{\xi},t)$ is the time- and space-dependent flow field data, $\overline{\boldsymbol{q}}(\boldsymbol{\xi})$ is the time-averaged flow field data, $a_j(t)$ is the time-varying coefficient corresponding to each mode, $\boldsymbol{\phi}_j(\boldsymbol{\xi})$ is the spatial eigenmode, and $r$ is the total number of modes. In this decomposition, the spatial modes $\boldsymbol{\phi}_j(\boldsymbol{\xi})$ are obtained by solving the eigenvalue problem of the covariance matrix.

$$\boldsymbol{R}\boldsymbol{\phi}_j=\lambda_j\boldsymbol{\phi}_j \quad (3)$$

where $\boldsymbol{R}$ is the covariance matrix, and $\lambda_j$ is the eigenvalue indicating the contribution of each mode.

The covariance matrix $\boldsymbol{R}$ is defined as follows:

$$\boldsymbol{R}=\sum_{i=1}^{m}\boldsymbol{x}(\boldsymbol{t}_i)x^T(t_i) \quad (4)$$

The time-varying mode coefficients $a_j(t)$ represent the contribution of each POD mode at a particular time. The time-varying coefficients are calculated by the following equation:

$$a_j(t)=\langle\boldsymbol{q}(\boldsymbol{\xi},t)-\overline{\boldsymbol{q}}(\boldsymbol{\xi}),\boldsymbol{\phi}_j(\boldsymbol{\xi})\rangle \quad (5)$$

On the other hand, singular value decomposition (SVD) is sometimes used to calculate POD analysis, and is expressed as follows for a data matrix $\boldsymbol{X}$:

$$X=\boldsymbol{\phi}\sum\boldsymbol{\psi}^{\boldsymbol{T}} \quad (6)$$

where $\boldsymbol{X}$ is the data matrix, $\boldsymbol{\phi}$ is the left singular vector representing the spatial mode, $\sum$ is the singular value representing the contribution, and $\boldsymbol{\psi}$ is the right singular vector representing the time-varing coefficient indicating the temporal change of each mode.

# RESULTS AND DISCUSSION

## POD analysis of PIV data for OBR

Figure 3 shows time variation of streamlines that were obtained by PIV analysis when $Re_O$ was 762, $Q$ was 8.3 mil/min, and $x_O$ was 5 mm. It was observed that the flow pattern changes in this order: at the moment the oscillating flow became a push-out flow, vortices are generated on both sides of the lower part. The vortices then disappeared and the vertical flow occurred. At the moment when the flow became pull-out flow, vortices were generated on both sides of the upper part, and then the vertical flow was seen again. For the same oscillatory Reynolds number ($Re_O = 762$), when $x_O$ was 15 mm, it was seen that the vortices generated at the bottom and top moved up and down respectively, and the vortices remained. It was also observed that the axial symmetry of the flow was broken.

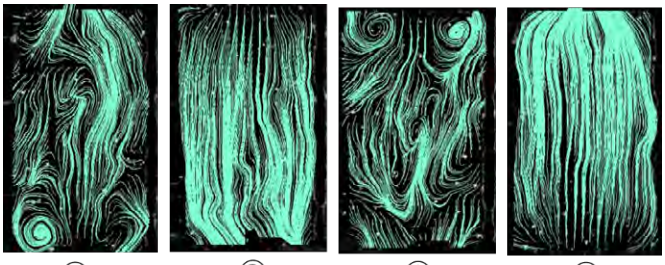



**Figure 3.** Time variation of streamlines that were obtained by PIV analysis.

As a result of POD analysis of the above-mentioned PIV data, the cumulative contribution of modes 1 to 3, which have the largest contribution, was about 80% (Figure 4 ). Figure 5 shows images of flow vectors that were reconstructed for three modes with the highest contribution which were selected from the more than 200 modes, for a case when $Re_O$ was 762, $Q$ was 8.3 mil/min, and $x_O$

was 5 mm. It was considered that the flow pattern for mode 1 represents profile of vertical flow and the flow pattern for mode 2 represents profile of generation of vortices in the upper and lower parts. Then Figure 6 plots change in calculated values of the time-varying mode coefficients $a_j(t)$. The trend in the time variation of $a_j(t)$ shows that POD could derive the reduced order model with characteristics of periodic changes in the flow pattern.

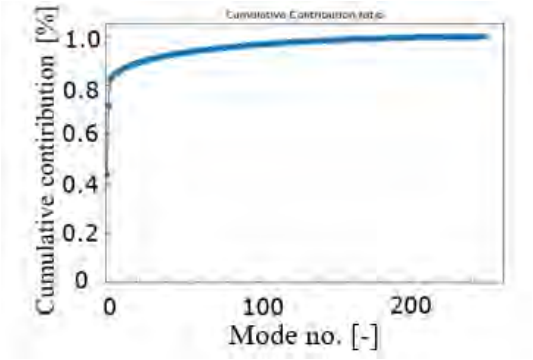



**Figure 4.** Variation of the cumulative contribution with increase in number of modes.

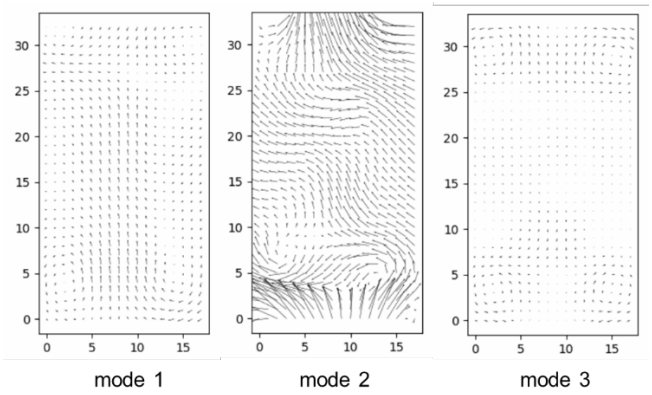



**Figure 5** Images of flows of vector fields that were reconstructed for principal three modes.

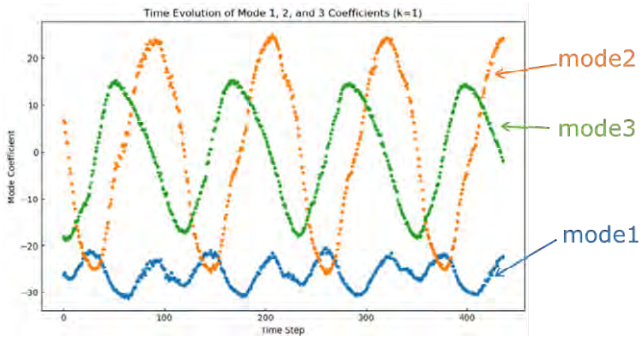



**Figure 6** Time-series plots for time-varying mode coefficients.

Cases that the profile of vertical flow was extracted as mode 1 were seen when the amplitude $x_O$ was larger. Even when the oscillatory Reynolds number $Re_O$ was small and the flow rate of the steady flow $Q$ was large, it was distinguished that the flows of vector fields for mode 1 showed profile of vertical flow. In addition, we analyzed the PIV data that were acquired by changing baffles with the different opening. When the baffle with small opening (16%) were used, it was experimentally observed position of generated vortices was upper part than cases of using the abovementioned baffles with 25% of opening. In application of POD analysis, the flows of vector fields with profile of generation of vortices in the upper and lower parts were extracted as mode 1, for case when the baffles with smaller opening.

## Application of neural network modeling for prediction of flows of vector fields in OBR

We developed the multi-layered neural network model with three outputs of mode 1 – 3 that were extracted above, by using the no-code AI analysis platform "Multi-Sigma" (AIZOTH Inc.). In the modeling, oscillatory Reynolds number, amplitude and frequency of oscillation of syringe pump, velocity ratio for oscillatory flow and local velocity vectors were set as inputs. When training was implemented by changing the number of hidden layers from 1 to 10 and the number of hidden nodes from 3 to 96. As shown in Figure 7, results with high predictive performance were obtained for the generation, size, and movement of vortices. On the other hand, poor predictive performance was observed when $Re_O$ was lower.

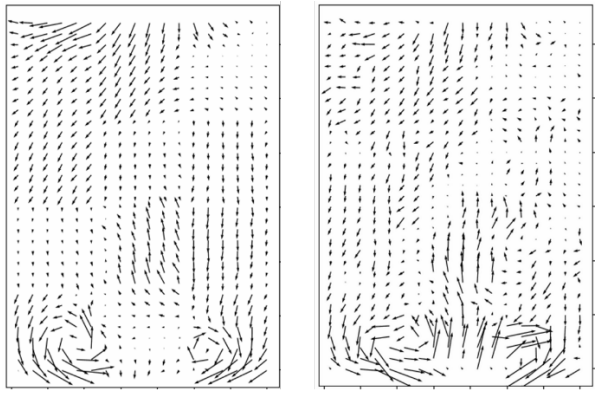



**Figure 7** Recall of flows of vector fields by using the trained neural network model.

Next, methods for prediction of time-varying mode coefficients for the above mentioned three modes were investigated. In order to reduce dimensionality of data for the mode coefficients, we investigated application of decomposition of the time-series data for the mode coefficients into periodic integrals by Fourier series expansion:

$$f(t) = \frac{a_0}{2} + \sum_{n=1}^{\infty}(a_0 \cos(nt) + b_n \sin(nt)) \quad (7)$$

Parameters $(a_0, a_1, \ldots, a_n b_1, \ldots, b_n)$ that were calculated by Eqs. (8) and (9) was used as outputs for multi-layered neural network model for prediction of the time-varying mode coefficients.

$$a_n = \frac{2}{T}\int_0^T f(t)\cos(nt)\,dt \tag{8}$$

$$b_n = \frac{2}{T}\int_0^T f(t)\sin(nt)\,dt \tag{9}$$

Combination of two types of neural network model for prediction of three mode (flows of vector fields) and for prediction of Fourier series expansion parameters related to the time-varying mode coefficients has demonstrated to show high predictive performance for time-varying streamlines in OBR.

While the proposed modeling approach has demonstrated the potential of black-box modeling for prediction of flow patterns, it was considered that the reliance on data-driven modeling without explicit physical insights may limit its generalizability across different reactor conditions. In future, it is necessary to focus on bridging machine learning models with first-principles approaches, ensuring a more interpretable and robust predictive framework for industrial OBR applications.

## CONCLUSIONS

In the present paper, we investigated application of POD for dynamic analysis of spatio-temporal data acquired by PIV to determine inputs and outputs for neural network model. It was demonstrated that three sets of modes and time-varying mode coefficients extracted by the POD could be useful for dynamic analysis and prediction of time-variant flow patterns in OBR. Also it was shown that decomposition of the time-series data for the mode coefficients by Fourier series expansion was effective for deriving reduced order model.

In future, we will apply this proposed method to machine learning modeling based on CFD simulation data to clarify its superiority over CFD simulation. Furthermore, by clarifying the correlation between the feature quantities extracted from the CFD simulation data and the structural parameters of the reactor, it is expected that the I/O structure of a machine learning model could ensure a more interpretable and robust predictive performance for a wider range of reactor conditions.

## ACKNOWLEDGEMENTS

This paper is based on results obtained from a project, JPNP19004, commissioned by the New Energy and Industrial Technology Development Organization (NEDO).

## REFERENCES

1. Avila M., Kawas B., Fletcher D.F., Poux M., Xuereb C., Aubin J., Design, performance characterization and applications of continuous oscillatory baffled reactors. *Chem. Eng. Process.* 180: 108718 (2022)
2. McGlone T., Briggs N.E., Clark C.A., Brown C.J., Sefcik J., Florence A.J., Oscillatory Flow Reactors (OFRs) for Continuous Manufacturing and Crystallization. *Org. Process Res. Dev.* 19: 1186–1202 (2015)
3. Harvey A.P., Machley M.R. Seliger T., Process intensification of biodiesel production using a continuous oscillatory flow reactor. *J. Chem. Technol. Biot.* 78: 338–341 (2003)
4. Nabeshima M., Matsumoto H., Hamzah A.B., Yoshikawa S., Ookawara S., Analysis of Dynamic Behavior of Gas Bubbles and Solid Particles in an Oscillatory Baffled Reactor and Its Application to Design of Hydrogenation Processes. *Chem. Eng. Trans.* 94: 967-972 (2022)
5. Ni X., Jian H., Fitch A.W., Computational fluid dynamic modelling of flow patterns in an oscillatory baffled column. *Chem. Eng. Sci.* 57: 2849–2862 (2002)
6. Mazubert A., Fletcher D.F., Poux M., Aubin J., Hydrodynamics and mixing in continuous oscillatory flow reactors—Part I: Effect of baffle geometry. *Chem. Eng. Process.* 108: 78–92 (2016)
7. Shin J.H., Cho K.W, Comparative study on reduced models of unsteady aerodynamics using proper orthogonal decomposition and deep neural network. *J. Mech. Sci. Technol.* 36: 4491–4499 (2022)
8. Ooi C., Le Q.T., Dao M.H., Nguyen V.B., Nguyen H.H., Ba T., Modeling transient fluid simulations with proper orthogonal decomposition and machine learning. *Int. J. Numer. Meth. Fl.* 93: 396–410 (2021)

© 2025 by the authors. Licensed to PSEcommunity.org and PSE Press. This is an open access article under the creative commons CC-BY-SA licensing terms. Credit must be given to creator and adaptations must be shared under the same terms. See https://creativecommons.org/licenses/by-sa/4.0/



Systems & Control Transactions

**Research Article - Peer Reviewed Conference Proceeding**
ESCAPE 35 - European Symposium on Computer Aided Process Engineering
Ghent, Belgium. 6-9 July 2025
Jan F.M. Van Impe, Grégoire Léonard, Satyajeet S. Bhonsale,
Monika E. Polańska, Filip Logist (Eds.)

PSE PRESS

# Comparative Analysis of PharmHGT, GCN, and GAT Models for Predicting LogCMC in Surfactants.

**Gabriela C. Theis Marchan[a], Teslim Olayiwola[a], Jose Romagnoli[a]***

[a] Louisiana State University, Department of Chemical Engineering, Baton Rouge, Louisiana 70803, United States
* Corresponding Author: jose@lsu.edu.

## ABSTRACT

Predicting the critical micelle concentration (CMC) of surfactants is essential for optimizing their applications in various industries, including pharmaceuticals, detergents, and emulsions. In this study, we investigate the performance of graph-based machine learning models, specifically Graph Convolutional Networks (GCN), Graph Attention Networks (GAT), and a graph-transformer model, PharmHGT, for predicting CMC values. We aim to determine the most effective model for capturing the structural and physicochemical properties of surfactants. Our results provide insights into the relative strengths of each approach, highlighting the potential advantages of transformer-based architectures like PharmHGT in handling molecular graph representations compared to traditional graph neural networks. This comparative study serves as a step towards enhancing the accuracy of CMC predictions, contributing to the efficient design of surfactants for targeted applications.

**Keywords**: Graph Neural Networks, Critical Micelle Concentration, Surfactants, Machine Learning, Molecular Property Prediction.

## INTRODUCTION

Surfactants are versatile chemical compounds utilized across various industries, including cosmetics,(*1*) pharmaceuticals, detergents,(*2*) and enhanced oil recovery.(*3*) Their unique amphiphilic structure, containing both hydrophilic and hydrophobic components, enables them to interact with immiscible phases by reducing interfacial tension.(*4*) A key property influencing surfactant behavior is the critical micelle concentration (CMC), defined as the minimum concentration at which micelles begin to form spontaneously.

Traditional methods for CMC determination, such as surface tension measurements(*5, 6*) and fluorescence spectroscopy,(*7*) while accurate, are time-consuming and require specialized equipment. Computational approaches, including quantitative structure-property relationship (QSPR) models(*8*) and molecular dynamics simulations,(*9*) offer alternatives but face limitations in accuracy or computational efficiency. Recent advances in graph-based neural networks present promising opportunities for molecular property prediction, offering potentially faster and more accurate predictions while capturing complex structure-property relationships.

This study compares three graph-based deep learning architectures—PharmHGT, GCN, and GAT—for predicting LogCMC values. We aim to evaluate their relative strengths in capturing molecular features and their potential for accelerating surfactant design and optimization.

## METHODOLOGY

### Model Architectures

#### PharmHGT Model

Our work adapts the Pharmacophoric-constrained heterogeneous graph transformer (PharmHGT) architecture, originally developed by Jiang et al.(*10*) for molecular property prediction, to specifically address the unique challenges of surfactant modeling and LogCMC prediction. While maintaining the core heterogeneous graph architecture of PharmHGT, we introduce several key modifications to handle surfactant-specific characteristics such as amphiphilic structure, head group chemistry, and tail group interactions.

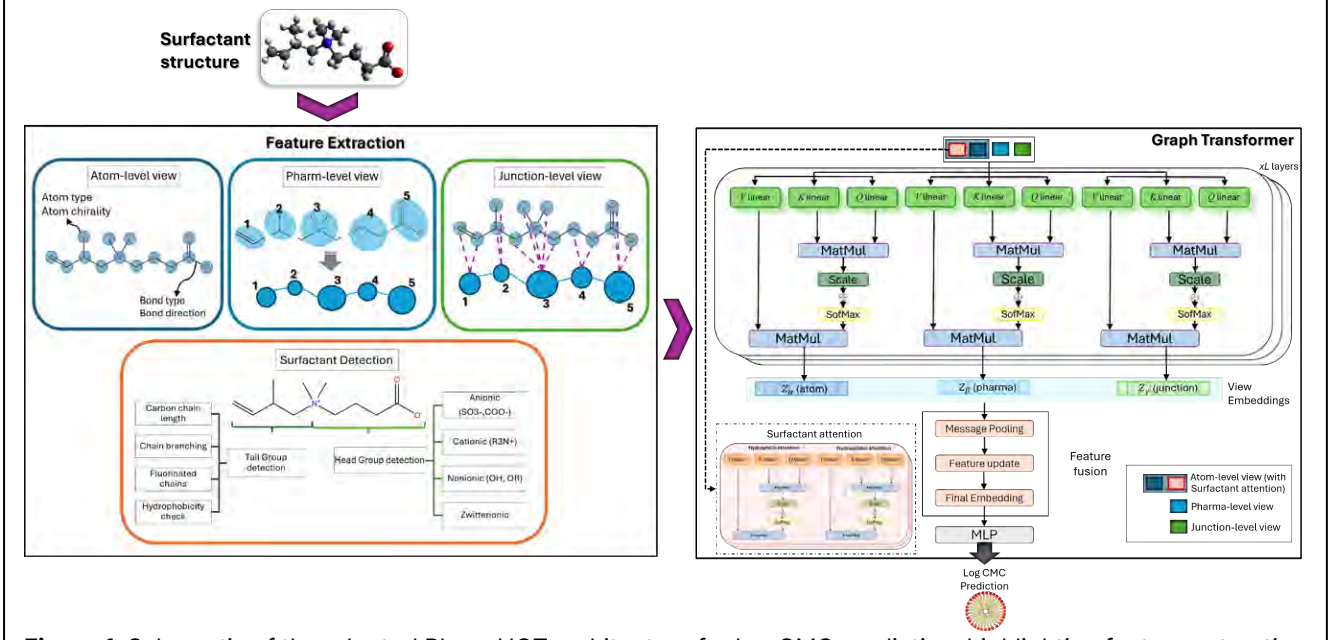



**Figure 1:** Schematic of the adapted PharmHGT architecture for LogCMC prediction, highlighting feature extraction (atom-level, pharmacophore-level, and junction-level), the surfactant detection module, attention mechanisms, and hierarchical feature fusion.

While the original PharmHGT framework was designed for capturing pharmacophoric structures through heterogeneous graph representation, we found it initially struggled to recognize the unique molecular structures of surfactants due to their unique amphiphilic nature and the interactions between hydrophilic and hydrophobic regions. However, the framework's underlying architecture for heterogeneous graph learning provided a valuable foundation. Our adaptation enhances this framework by incorporating surfactant-specific features and attention mechanisms, enabling it to effectively capture the distinct functional regions that significantly influence surfactant properties.

The adapted PharmHGT represents surfactants as heterogeneous graphs $G = (V, E)$, where $V$ is the set of nodes representing molecular components (e.g., atoms or functional groups) and $E$ is the set of edges representing chemical bonds or interactions. Node types are mapped using $\phi: V \to O$, and edge types are mapped using $\psi: E \to P$. This representation integrates three complementary views of the molecular structure:

The atom-level view ($G_\alpha$), which captures atomic features such as atomic number, chirality, and bonding patterns. Additionally, it encodes surfactant-specific information, such as whether an atom belongs to a hydrophilic head group or hydrophobic tail group.

The pharmacophore-level view ($G_\beta$), which focuses on functional groups and their interactions, especially tail-head relationships. Pharmacophoric features are derived using MACCS keys and chemical feature detection.

The junction-level view ($G_\gamma$), which combines atom-level and pharmacophoric information to provide a comprehensive molecular representation.

These three complementary views are illustrated in Figure 1 in the feature extraction section, which provides an overview of the adapted PharmHGT model and its surfactant-specific enhancements.

The model employs a multi-head attention mechanism to dynamically learn the importance of different molecular features across atom-level, pharmacophore-level, and junction-level views. The attention mechanism is mathematically expressed as:

$$Attention(Q, K, V) = \sum_{p \in P} \Omega_p \cdot \sigma\left(\frac{Q_p K_p^T}{\sqrt{d_k}}\right) \cdot V_p \qquad (1)$$

where Q, K, and V are the query, key, and value matrices; $\Omega_p$ is a learnable weight matrix specific to view p; and σ represents the SoftMax function. This mechanism prioritizes interactions unique to surfactants, such as those between hydrophilic head groups and hydrophobic tail regions, achieved through dedicated attention modules. Feature propagation through the graph is governed by a multi-view message-passing framework (MVMP), expressed as Eq. 2:

$$M^{(t)}(X_v) = \sum_{u \in N(v)} Attention\left(H^{(t-1)}(X_v)W_Q, H^{(t-1)}(X_u)W_K, H^{(t-1)}(X_u)W_V\right) \qquad (2)$$

where $M^{(t)}(X_v)$ is the updated feature of node v at

step t; $N(v)$ represents the neighbors of node v; $H^{(t-1)}(X_v)$ is the feature of v from the previous step; and $W_Q$,$W_K$,$W_V$ are learnable projection matrices. The MVMP framework integrates attention mechanisms to dynamically aggregate and prioritize molecular interactions, effectively capturing the diverse structural and functional relationships unique to surfactants.

After integrating surfactant-specific features into the atom-level embeddings, the model combines all structural views (atom-level, pharmacophore-level, and junction-level) through a hierarchical Readout Attention mechanism:

$$Z_{\gamma\beta} = ReadOutAttention(Z_\gamma, Z_\beta) \quad (3)$$

where $Z_\gamma$ and $Z_\beta$ are the feature embeddings from the junction-level and pharmacophore-level views, respectively. The resulting embedding $Z_{\gamma\beta}$ is further integrated with atom-level features using Eq. 4:

$$Z = ReadOutAttention(Z_\alpha, Z_{\gamma\beta}) \quad (4)$$

where Z_α is the atom-level embedding. Finally, the LogCMC prediction is obtained through a multi-layer perceptron (MLP), expressed as Eq. 5:

$$\hat{y} = MLP(Z) \quad (5)$$

### GCN Model

Our GCN architecture consists of two graph convolutional layers followed by a three-layer fully connected regression network as we defined in our previous work.(*11*) The model processes molecular graphs by iteratively updating node features based on their local neighborhood information.(*11, 12*) Each node's feature vector encodes atomic properties and surfactant-specific characteristics. The first convolutional layer maps input features to a hidden representation, while the second layer refines these representations. A global mean pooling operation then aggregates node-level features into a graph-level representation, which is processed through the regression network for final prediction. This architecture effectively captures local molecular structure and chemical bonding patterns while maintaining computational efficiency.

### GAT Model

The GAT architecture enhances the basic graph neural network framework by incorporating attention mechanisms that dynamically weight the importance of different atomic interactions.(*13*) Our implementation uses a dual-layer architecture with four attention heads in the first layer and a single consolidating head in the second layer. This multi-head attention allows the model to capture different aspects of molecular structure simultaneously. Each attention head computes importance weights for neighboring atoms, enabling the model to focus on the most relevant structural features for LogCMC prediction. The model combines local atomic features with global molecular context through a series of attention-weighted transformations, followed by a global pooling operation and regression layers.

### Data and Implementation

Our study utilized two carefully curated datasets of surfactants compiled from literature sources.(*14-19*) Data1 consists of 285 non-ionic surfactants, providing a focused dataset for evaluating model performance on a single surfactant class. Unlike Data1, Data2 encompasses 365 surfactants with a broader chemical diversity: 285 non-ionic, 35 cationic, 34 anionic, and 11 zwitterionic surfactants. This diverse dataset enables the assessment of model generalization across different surfactant types.

For molecular representation, we used RDKit(*20*) to generate comprehensive feature sets for each surfactant. Atomic features included atomic number, formal charge, hybridization state, aromaticity, and surfactant-specific properties such as head/tail group identification. Bond features captured bond type, conjugation, and ring membership. For the PharmHGT model, additional pharmacophoric features were extracted using MACCS keys(*21*) and chemical feature detection.

In creating the regression models, we adopted the PyTorch(*22*) for neural network components and the Deep Graph Library (DGL)(*23*) for efficient graph operations. For model training and evaluation, we systematically divided the available experimental datasets (containing the chemical structure and their corresponding logCMC values) into training (70%), testing (20%), and validation (10%) sets, maintaining the consistent distribution of surfactant types across splits. Hyperparameter optimization was conducted using Optuna, running 100 trials per model. Table S1 in the digital supplementary material presents the optimal hyperparameters for each model-dataset combination. All models were trained using early stopping with patience ranging from 20-40 epochs (monitoring validation loss without improvement) to prevent overfitting while ensuring convergence. Data splitting was performed using stratified random sampling to maintain a consistent distribution of surfactant types across training, testing, and validation sets. (see Table S2 in the digital supplementary material)

## RESULTS AND DISCUSSION

We evaluated the performance of PharmHGT, GCN, and GAT models on two distinct datasets (Data1 and Data2) using root mean square error (RMSE) and mean absolute error (MAE) as primary metrics. The comparative analysis reveals notable differences in predictive capabilities across model architectures and dataset compositions.

For Data1, which consists exclusively of non-ionic

surfactants (n=285), all three models demonstrated strong predictive capabilities, albeit with varying degrees of accuracy. As shown in Table 1, the PharmHGT model achieved the highest performance, with a test MSE of 0.090 and MAE of 0.207, followed by the GCN model (MSE: 0.238, MAE: 0.340) and the GAT model (MSE: 0.314, MAE: 0.369). Notably, the training metrics in Table 1 indicate strong learning capacity across all models, with PharmHGT showing the lowest training MSE (0.017) and highest training $R^2$ (0.990).

The superior performance of PharmHGT can be better understood by examining the structural complexity of Data1. Despite focusing solely on non-ionic surfactants, Data1 exhibits considerable structural diversity at both atomic and pharmacophoric levels. Quantitative diversity analysis reveals five unique atom types (C: 72.55%, O: 25.64%, N: 0.92%, F: 0.59%, S: 0.31%) with significant variance in key atom features (mean-variance: 0.036). At the pharmacophoric level, molecules contain a wide range of functional fragments (1-84 per molecule, average: 9.14±10.24) with varied fragment sizes (1-22 atoms, average: 3.38±3.68). Feature similarity analysis identifies multiple distinct structural clusters, indicating that the dataset encompasses diverse molecular scaffolds despite focusing on non-ionic surfactants. This structural complexity particularly benefits PharmHGT's heterogeneous graph representation, which better captures the varying importance of different structural features compared to the more uniform approaches of GCN and GAT.

**Table 1**: Model Performance on Data1 (Non-ionic Surfactants)

| Model | MSE | | $R^2$ | | MAE | |
|---|---|---|---|---|---|---|
| | Train | Test | Train | Test | Train | Test |
| GAT | 0.075 | 0.314 | 0.955 | 0.845 | 0.158 | 0.369 |
| GCN | 0.042 | 0.238 | 0.974 | 0.883 | 0.091 | 0.340 |
| PharmHGT | 0.017 | 0.090 | 0.990 | 0.943 | 0.098 | 0.207 |

Figure 2 presents scatter plots comparing predicted versus experimental values for all three models on Data1 in the top row. The PharmHGT model exhibits the tightest clustering around the diagonal line ($R^2$ = 0.943), indicating superior prediction accuracy across the full range of CMC values. The GCN model shows good correlation ($R^2$ = 0.883), while the GAT model demonstrates slightly lower but still substantial predictive power ($R^2$ = 0.845). Both models show increased scatter at extreme CMC values compared to PharmHGT. The outlier non-ionic surfactants in Figure 2 feature: (1) extreme ethoxylation patterns (very short or very long chains), (2) highly branched hydrophobic tails, and (3) atypical oxygen atom distributions throughout the molecule rather than concentrated in head groups. PharmHGT's superior handling of these challenging structures (reducing prediction error by up to 31% compared to GAT) demonstrates the advantage of heterogeneous graph representation and transformer-based attention mechanisms for capturing complex structure-property relationships in surfactants with

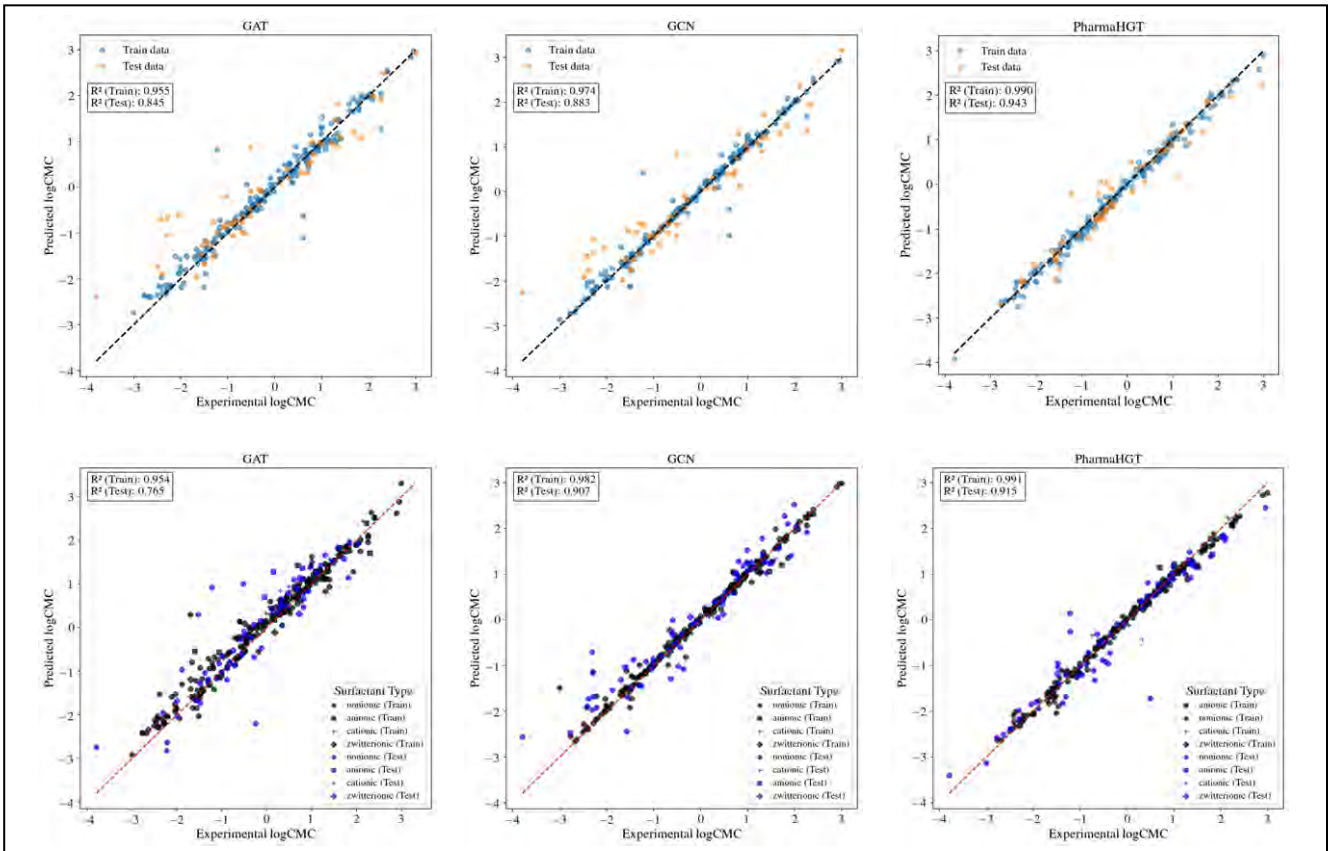



**Figure 2:** Scatter Plots of Predicted Vs. Experimental LogCMC Values for the top row representing Data Set 1 and the bottom row representing Data Set 2.

unconventional features.

The more diverse Data2 dataset (n=365), containing a mixture of non-ionic, cationic, anionic, and zwitterionic surfactants, presented a more challenging prediction task. As detailed in Table 2, the performance differences between models became more pronounced. The PharmHGT model maintained robust performance (MSE: 0.171, MAE: 0.250), demonstrating effective handling of diverse surfactant types. The GCN model showed comparable performance (MSE: 0.182, MAE: 0.307), while the GAT model exhibited higher prediction error (MSE: 0.318, MAE: 0.369). The training metrics in Table 2 reveal particularly strong learning capacity for both PharmHGT (training MSE: 0.014, $R^2$: 0.991) and GCN (training MSE: 0.027, $R^2$: 0.982), suggesting effective feature extraction from the more complex dataset.

Figure 2 illustrates the prediction performance on Data2 through scatter plots in the bottom row. The PharmHGT model maintains a strong correlation ($R^2$ = 0.915) despite the increased chemical diversity. The GCN model shows similar performance ($R^2$ = 0.907), while the GAT model ($R^2$ = 0.765) shows more substantial scatter across surfactant types. All models display some deviation from the ideal prediction line for surfactants with extreme LogCMC values, though this effect is least pronounced in the PharmHGT predictions.

**Table 2**: Model Performance on Data2 (Mixed surfactants)

| Model | MSE | | $R^2$ | | MAE | |
|---|---|---|---|---|---|---|
| | Train | Test | Train | Test | Train | Test |
| GAT | 0.078 | 0.318 | 0.954 | 0.765 | 0.190 | 0.369 |
| GCN | 0.027 | 0.182 | 0.982 | 0.907 | 0.083 | 0.307 |
| Pharm HGT | 0.014 | 0.171 | 0.991 | 0.915 | 0.080 | 0.250 |

Tables 1-2 report results from a single stratified random split (70/20/10) with fixed random seeds to ensure reproducible partitioning. To evaluate the impact of model configuration on performance, we first assessed all models with identical default parameters on the same data split, then performed systematic hyperparameter optimization using Optuna (100 trials per model). Notably, PharmHGT with default parameters ($R^2$ = 0.925 on Data1) outperformed both GCN and GAT even before optimization ($R^2$ = 0.862 and 0.814 respectively), demonstrating

that its superior performance is not merely an artifact of hyperparameter tuning. While performance may vary slightly with different splits, the consistent ranking of models across both default and optimized configurations confirms the robustness of our findings with respect to data partitioning and parameter selection.

### Analysis of Model Strengths

Based on the two dataset types studied in this work, it was discovered that PharmHGT performs better than GCN and GAT and the GAT model showing the least accuracy. The PharmHGT model's superior performance can be attributed to its sophisticated architecture that combines transformer-based attention mechanisms with heterogeneous graph representation. Its consistent performance across both datasets suggests effective capture of both local molecular features and global structural patterns. The GCN model showed robust performance, particularly on Data2, where it achieved comparable results to PharmHGT. This suggests that its message-passing mechanism effectively captures essential molecular features for LogCMC prediction. Lastly, the GAT model's performance revealed limitations in handling diverse surfactant types, with accuracy decreasing notably for the mixed surfactant dataset. This suggests that simple attention mechanisms may not fully capture the complex interactions present in diverse surfactant systems.

## CONCLUSION

In this study, we conducted a comprehensive comparison of three graph-based deep learning architectures (PharmHGT, GCN, and GAT) for predicting LogCMC values of surfactants. Our investigation using two distinct datasets, one focused on non-ionic surfactants and another encompassing diverse surfactant types, revealed several important findings about the capabilities and limitations of each architecture.

The PharmHGT model demonstrated superior performance across both datasets, achieving the highest prediction accuracy ($R^2$ = 0.943 for non-ionic surfactants and $R^2$ = 0.915 for mixed surfactant types) and the most consistent generalization behavior. The model's ability to maintain high accuracy when transitioning from non-ionic to mixed surfactant types (with only minimal performance degradation) highlights its robustness in handling diverse molecular structures. This effectiveness stems from its sophisticated architecture that combines transformer-based attention mechanisms with heterogeneous graph representation.

The GCN model showed surprisingly strong performance, particularly for the mixed surfactant dataset where it achieved results comparable to PharmHGT ($R^2$ = 0.907). This suggests that well-designed message-passing mechanisms can effectively capture the essential molecular features governing surfactant behavior. The GAT model, while performing adequately for non-ionic surfactants ($R^2$ = 0.845), showed limitations in handling the increased complexity of mixed surfactant types ($R^2$ = 0.765), indicating that simple attention mechanisms may not fully capture the complex interactions present in diverse surfactant systems.

Future work could explore several promising directions. First, the models could be extended to predict additional surfactant properties beyond LogCMC, such as surface tension or aggregation numbers. Second, the architecture could be modified to incorporate explicit handling of environmental factors such as temperature, pH, and ionic strength, which significantly influence surfactant behavior. Finally, the strong performance of these models suggests potential applications in inverse design problems, where the goal is to generate novel surfactant structures with desired properties.

## DIGITAL SUPPLEMENTARY MATERIAL

The digital supplementary material includes Table S1 detailing optimal hyperparameters for all models (batch size, learning rate, hidden units, epochs, and model-specific parameters); Table S2 showing Hyperparameter Ranges for GAT, GCN, and Graph Transformers. This information supports findings regarding model optimization, reproducibility, and result robustness. The supplementary material is available at https://psecommunity.org/LAPSE:2025.0036v1.

## ACKNOWLEDGEMENTS

This work was supported by the U.S Department of Energy, Office of Science, under the Office of Basic Energy Science Separation Science program under Award No. DE-SC0022304. The authors gratefully acknowledge the computer time allotted by the high-performance computing center (HPC) at LSU and the Louisiana Network initiative.

## REFERENCES

1. B. Bhattacharya, T. K. Ghosh, N. Das, Application of bio-surfactants in cosmetics and pharmaceutical industry. Sch. Acad. J. Pharm 6, 320-329 (2017).
2. C. Ceresa, L. Fracchia, E. Fedeli, C. Porta, I. M. Banat, Recent advances in biomedical, therapeutic and pharmaceutical applications of microbial surfactants. Pharmaceutics 13, 466 (2021).
3. C. Negin, S. Ali, Q. Xie, Most common surfactants employed in chemical enhanced oil recovery. Petroleum 3, 197-211 (2017).
4. M. J. Rosen, J. T. Kunjappu, Surfactants and interfacial phenomena. (John Wiley & Sons, 2012).

5. M. Bielawska, A. Chodzińska, B. Jańczuk, A. Zdziennicka, Determination of CTAB CMC in mixed water+ short-chain alcohol solvent by surface tension, conductivity, density and viscosity measurements. Colloids and Surfaces A: Physicochemical and Engineering Aspects 424, 81-88 (2013).
6. S. F. Burlatsky et al., Surface tension model for surfactant solutions at the critical micelle concentration. Journal of colloid and interface science 393, 151-160 (2013).
7. M. M. Mabrouk, N. A. Hamed, F. R. Mansour, Spectroscopic methods for determination of critical micelle concentrations of surfactants; a comprehensive review. Applied Spectroscopy Reviews 58, 206-234 (2023).
8. A. R. Katritzky, L. Pacureanu, D. Dobchev, M. Karelson, QSPR study of critical micelle concentration of anionic surfactants using computational molecular descriptors. Journal of chemical information and modeling 47, 782-793 (2007).
9. A. P. Santos, A. Z. Panagiotopoulos, Determination of the critical micelle concentration in simulations of surfactant systems. The Journal of chemical physics 144, (2016).
10. Y. Jiang, S. Jin, X. Jin, Pharmacophoric-constrained heterogeneous graph transformer model for molecular property prediction. Communications. Chemistry 6, (2023).
11. P. Naghshnejad, G. Theis Marchan, T. Olayiwola, R. Kumar, J. Romagnoli, Graph-Based Modeling and Molecular Dynamics for Ion Activity Coefficient Prediction in Polymeric Ion-Exchange Membranes. Industrial & Engineering Chemistry Research, (2024).
12. D. Deng et al., XGraphBoost: extracting graph neural network-based features for a better prediction of molecular properties. Journal of chemical information and modeling 61, 2697-2705 (2021).
13. P. Velickovic et al., Graph attention networks. stat 1050, 10-48550 (2017).
14. M. Nnadili et al., Surfactant-Specific AI-Driven Molecular Design: Integrating Generative Models, Predictive Modeling, and Reinforcement Learning for Tailored Surfactant Synthesis. Industrial & Engineering Chemistry Research 63, 6313-6324 (2024).
15. S. Qin, T. Jin, R. C. Van Lehn, V. M. Zavala, Predicting critical micelle concentrations for surfactants using graph convolutional neural networks. The Journal of Physical Chemistry B 125, 10610-10620 (2021).
16. R. A. Saunders, J. A. Platts, Correlation and prediction of critical micelle concentration using polar surface area and LFER methods. Journal of physical organic chemistry 17, 431-438 (2004).
17. S. Lee, J. Lee, H. Yu, J. Lim, Synthesis of environment friendly nonionic surfactants from sugar base and characterization of interfacial properties for detergent application. Journal of Industrial and Engineering Chemistry 38, 157-166 (2016).
18. L. Chaveriat, I. Gosselin, C. Machut, P. Martin, Synthesis, surface tension properties and antibacterial activities of amphiphilic D-galactopyranose derivatives. European Journal of Medicinal Chemistry 62, 177-186 (2013).
19. C. Yan, G. Li, The rise of machine learning in polymer discovery. Advanced Intelligent Systems 5, 2200243 (2023).
20. G. Landrum, RDKit: Open-source cheminformatics. 2006. Google Scholar, (2006).
21. J. L. Durant, B. A. Leland, D. R. Henry, J. G. Nourse, Reoptimization of MDL keys for use in drug discovery. Journal of chemical information and computer sciences 42, 1273-1280 (2002).
22. A. Paszke et al., Pytorch: An imperative style, high-performance deep learning library. Advances in neural information processing systems 32, (2019).
23. M. Wang et al., Deep graph library: A graph-centric, highly-performant package for graph neural networks. arXiv preprint arXiv:1909.01315, (2019).

© 2025 by the authors. Licensed to PSEcommunity.org and PSE Press. This is an open access article under the creative commons CC-BY-SA licensing terms. Credit must be given to creator and adaptations must be shared under the same terms. See https://creativecommons.org/licenses/by-sa/4.0/



Systems & Control Transactions

**Research Article - Peer Reviewed Conference Proceeding**
ESCAPE 35 - European Symposium on Computer Aided Process Engineering
Ghent, Belgium. 6-9 July 2025
Jan F.M. Van Impe, Grégoire Léonard, Satyajeet S. Bhonsale,
Monika E. Polańska, Filip Logist (Eds.)

PSE PRESS

# Short-Cut Correlations for $CO_2$ Capture Technologies in Small-Scale Applications

**So-mang Kim[a]*, Joanne Kalbusch[a], and Grégoire Léonard[a]**

[a] University of Liège, Department of Chemical Engineering, Liège, Belgium
* Corresponding Author: sm.kim@myuliege.be

## ABSTRACT

The escalating urgency to address climate change has driven carbon capture (CC) technologies into the spotlight, particularly for large-scale emitters, which benefit from economies of scale. However, small-scale emitters account for a significant share of $CO_2$ emissions, yet such applications remain largely overlooked in the literature. While CC cost is often used as a key performance indicator (KPI) for CC technologies, the lack of standardized cost estimation methods leads to inconsistencies, complicating comparisons, and hindering the deployment of CC systems. This study addresses these challenges by developing flexible short-cut correlations for selected CC technologies, providing estimates of the total equipment cost (TEC) and energy consumption specific to small-scale applications across various $CO_2$ inlet concentrations (mol%) and capture scales (10 – 100 kt/y). The flexibility of the correlations enables the integration of various cost estimation methods available in the literature and case-specific assumptions (e.g., utility prices), enhancing their consistency and applicability across various scenarios. This approach provides decision-makers with a practical yet simple method for assessing the technical and economic viability of CC systems without conducting extensive simulations or detailed techno-economic assessments (TEAs). Ultimately, this work aims to improve the accessibility of CC technologies for small-scale industries, facilitating their broader application and contributing to the overall goal of reducing greenhouse gas emissions across various sectors.

**Keywords**: Carbon Capture, Technoeconomic Analysis, Short-cut correlations, Small-scale capture

## 1. INTRODUCTION

Carbon capture (CC) is crucial for achieving net-zero emissions and mitigating climate change. Despite its critical importance, the current deployment of CC technologies remains insufficient to meet the climate target, indicating an urgency to increase the number of CC applications [1]. Emission sources vary significantly in capture scale, with large-scale emitters benefiting from economies of scale, while smaller-scale applications are often neglected. However, to reach net-zero emissions, CC applications at various emission levels are necessary [2].

While many studies on CC technologies highlight capture cost as a key performance indicator (KPI), there is currently no standardized method in the literature to estimate the cost of CC [3, 4], leading to inconsistencies and incomparable results. This makes it challenging for decision-makers to fairly compare and identify suitable CC options based on the literature results, holding back the deployment of CC units. In addition, conducting detailed simulations and Techno-Economic Assessments (TEAs) to identify viable capture options across various scenarios can be time-consuming and requires significant effort.

To address the aforementioned challenges, this work develops short-cut correlations describing the total equipment cost (TEC) and energy consumption of selected CC technologies for small-capture scale applications. This will allow exploration of the role of CC in small-scale industries and offer a practical means of evaluating the technical and economic viability of various CC systems. Heat integration is not considered due to case-specific waste heat availability.

The goal of this paper is to provide an efficient approach for decision-makers to estimate the cost of CC

without the need for extensive simulations and detailed TEAs while ensuring consistent assumptions and cost estimation methods are applied across comparison studies. Also, the correlations are flexible, allowing for various cost estimation methods and case-specific assumptions to fine-tune the analyses for various scenarios.

## 2. MODELLING

In this paper, Aspen Plus models were developed to study chemical absorption and membrane separation processes which are among the promising CC technologies available today for small-scale applications [2]. The system boundary includes capturing units and $CO_2$ compressions as presented in Figure 1. Data related to pretreatment, transportation, and sequestration or utilization are excluded from the current study.

While $CO_2$-containing gases often include impurities like $NO_x$ and $SO_x$, it is assumed that the inlet feed gas is free from these impurities. The flue gas temperature is maintained at 170°C to avoid condensation of acid gases. Typically, flue gases contain between 5.5% and 15% $H_2O$ [5] and this study uses a default value of 11% $H_2O$. The common range for $O_2$ content is 2-8%, and this study adopts a value of 6.4%, with the remainder of the feed gas assumed to be $N_2$. A capture rate of 90% was attained across various $CO_2$ concentrations (5–70 mol%) and feed gas flow rates (corresponding to capture scales between 10 and 100 kt/y), with the minimum purity of the $CO_2$ product stream established at 95% or higher. Heat integration is not covered in this study due to the availability and characteristics of waste heat is highly case-specific. However, one of the outcomes of this research is to evaluate energy needs, which could be beneficial for future heat integration studies. The captured $CO_2$ is compressed to 150 bar for transportation through a multi-stage compression system (3 compressors plus a pump) equipped with intercoolers [6].

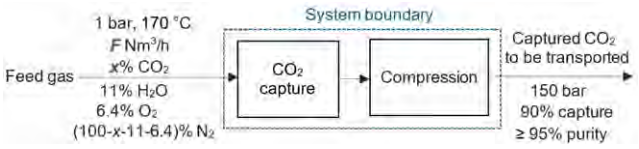



**Figure 1.** System boundary for $CO_2$ capture technologies

### 2.1 Chemical absorption process

Monoethanolamine (MEA) process is one of the widely studied capture technologies where lean solvent (30 wt.% in water) selectively absorbs $CO_2$ from flue gases and is then sent to the stripper for regeneration (100-140°C at 1 atm). In Aspen Plus, the electrolyte-NRTL thermodynamic package, in conjunction with the ideal gas law, is employed, and the design of the absorber is executed first using equilibrium calculations, subsequently changed to rate-based calculations to accurately model both equilibrium and kinetic reactions occurring within the absorber. A design specification was used to attain a 90% capture rate by adjusting the necessary reboiler duty in the stripper. For the compression loop, the Peng Robinson property package was used. This study employs vendor estimates from the paper of Nwaoha et al. for equipment cost estimation [7]. Other process parameters and cost data as well as detailed validations are presented in the work of current authors [8].

### 2.2 PolyActive membrane

Membrane CC represents a beneficial alternative technology compared to conventional solvent methods. A membrane separates gas mixture based on varying permeation rates. Membrane separation operates on partial pressure principles and is most effective with high-pressure gas streams [9]. Current advancements indicate that polymeric membranes dominate commercial membrane CC applications and the PolyActive membrane is selected in this study. This paper adopts a two-stage membrane system [9] to achieve enhanced capture rate and product stream purity.

Aspen Custom Modeller (ACM) was used to create a cross-flow membrane module, which was integrated into Aspen Plus as a block component. The process was assumed to be isothermal with negligible pressure drop, ideal gas behavior, and constant permeabilities. The module was divided into 100 cells, where feed conditions were set at the first cell inlet. The retentate ($F_{Ret,k}$) serves as the feed for the subsequent cell, while the permeate ($F_{perm,k}$) is combined with other streams and exits through the last cell. Mass balance calculations are conducted for each cell to determine the permeate flow rate and compositions as described in Equations 1 and 2.

$$F_{Ret,k-1} = F_{Ret,k} + F_{perm,k} \quad (1)$$

$$F_{Ret,k-1} \cdot ZRet_{comp,k-1} = F_{Ret,k} \cdot ZRet_{comp,k} + F_{perm,k} \cdot Zperm_{comp,k} \quad (2)$$

where $ZRet_{comp,k}$ and $Zperm_{comp,k}$ are the molar fractions of each component in each cell for retentate and permeate streams respectively. The permeances [$Nm^3m^{-2}h^{-1}bar^{-1}$] of the PolyActive membrane as well as other process and economic parameters are summarized in the supporting document, Tables S1–S2.

## 3. METHODOLOGY FOR CORRELATION DEVELOPMENT

This study aims to evaluate the performance of selected CC technologies, specifically MEA and the Polymeric membrane systems, under varying $CO_2$ concentrations ($x_{co_2}$, mol%) and flow rates ($F$, $Nm^3/h$). To overcome the limitations of literature-based cost comparisons

which are often fixed at specific flue gas characteristics and a selected CapEx/ OpEx estimation method, a flexible correlation is developed [8]. The correlation format of Equation 3 was adopted from the work of Hasan et al. [5] and various CapEx estimation methods can be applied to the TEC (total equipment cost) obtained from this correlation. A summary of the CapEx/ OpEx estimation method applied throughout this study is presented in Table S3, in the supporting document.

$$\text{TEC [M€]} = \alpha + (\beta \cdot {x_{co_2}}^{n} + \gamma) \cdot F^{m} \quad (3)$$

$$\text{Energy requirement} = \alpha \cdot e^{n x_{co_2}} + \beta \cdot e^{m x_{co_2}} \quad (4)$$

Where $\alpha$, $\beta$, $\gamma$, $n$ and $m$ are fitting parameters and to develop these parameters, several steps were followed: (1) a validated Aspen Plus model [8] was assessed across various $CO_2$ concentrations and feed gas flow rates generated from the Latin Hypercube Sampling (LHS) at a 90% capture rate; (2) these data points were connected to an Excel-based cost model to evaluate the TEC and specific energy consumptions; (3) results from the Excel model were imported to Matlab for multivariable regressions. The data points used in the correlation development can be found in the supporting document (Tables S4 and S5). The specific energy consumptions were found to be independent of capture scales [8], leading to a correlation format (Equation 4) based on the $CO_2$ inlet concentration only.

# 4. RESULTS AND DISCUSSION

## 4.1 Correlations for CC processes

The developed correlation parameters are presented in Table 1. These correlation results can be used to estimate capture costs relative to $CO_2$ concentrations and flue gas flow rates within defined ranges. The rule of six-tenths can be utilized for the TEC estimations beyond these boundaries.

In the PolyActive systems, the total membrane area showed a linear correlation with fixed $CO_2$ inlet concentration. To minimize inconsistencies in cost scaling, the specific membrane cost [€$_{2023}$/t] is separated from other membrane TEC. Therefore, the TEC correlation parameters in Table 1 solely reflect the aggregate process equipment costs, without the total membrane cost. A separate correlation was developed for the membrane cost [€/t] as a function of $CO_2$ inlet concentration, following a power law due to economies of scale.

$$\text{TEC}_{PolyActive}\left[\frac{€}{t}\right] = 2.6726\left(x_{co_2}\right)^{-1.298} \quad (5)$$

## 4.2 Correlations for $CO_2$ compressions

The specific TEC of the compression loop depends on the capture scale ($S$, in t/h) as the flue gas $CO_2$ concentration does not affect the $CO_2$ product stream. Equations 6 and 7 present the developed correlations for each CC technology.

$$\text{TEC}_{Comp,\ MEA}\left[\frac{\text{M€}}{\text{t/h}}\right] = 0.3957\ (S)^{-0.602} \quad (6)$$

$$\text{TEC}_{Comp,\ PolyActive}\left[\frac{\text{M€}}{\text{t/h}}\right] = 0.4634\ (S)^{-0.642} \quad (7)$$

Also, the electrical and cooling duties of the compression loop for MEA and PolyActive membrane are presented in Table 2 below. For MEA, the purity of the product stream stayed ≥ 99% and therefore, the specific energy consumptions across the $CO_2$ inlet concentrations and capture scale remained constant.

**Table 2:** Energy consumptions of the compression loops

| Compression Loop for: | Electrical duty [kWh/t] | Cooling duty [GJ/t] |
|---|---|---|
| MEA | 87.56 | 0.594 |
| PolyActive | 106.53[*] | 0.613[*] |

[*] The table lists average energy consumption for the PolyActive membranes at ≥ 95% purity.

**Table 1:** Correlation parameters for estimating the performances of small-scale $CO_2$ capture (10-100 kt/y)

| Process | $\alpha$ | $\beta$ | $\gamma$ | $n$ | $m$ | $x_{co_2}$ [mol%] | $F$ [1000 Nm³/h] |
|---|---|---|---|---|---|---|---|
| | | | | TEC [M€$_{2023}$] | | | |
| MEA | 1.0160 | 1.3364 | -0.0123 | 0.4486 | 0.7022 | $5 \le x_{co_2} \le 50$ | $1.30 \le F \le 128.80$ |
| PolyActive | 5.3843 | 0.0071 | 0.8840 | -0.8785 | 0.4915 | $5 \le x_{co_2} \le 70$ | $0.92 \le F \le 128.80$ |
| | | | | Specific Cooling Duty $\left[\frac{GJ}{t_{co2}}\right]$ | | | |
| MEA | 9.0860 | 2.8623 | — | -31.5148 | 0.2572 | $5 \le x_{co_2} \le 50$ | $1.30 \le F \le 128.80$ |
| PolyActive | 21.1248 | 3.3077 | — | -22.9241 | -1.9204 | $5 \le x_{co_2} \le 70$ | $0.92 \le F \le 128.80$ |
| | | | | Specific Reboiler Duty $\left[\frac{GJ}{t_{co2}}\right]$ | | | |
| MEA | 1.6315 | 3.5678 | — | -38.4307 | -0.0199 | $5 \le x_{co_2} \le 50$ | $1.30 \le F \le 128.80$ |
| | | | | Specific Electrical Duty $\left[\frac{kWh}{t_{co2}}\right]$ | | | |
| MEA | 9.4061 | 2.2475 | — | -21.6650 | -1.2483 | $5 \le x_{co_2} \le 50$ | $1.30 \le F \le 128.80$ |
| PolyActive | 1227.2 | 263.27 | — | -18.9830 | -0.9304 | $5 \le x_{co_2} \le 70$ | $0.92 \le F \le 128.80$ |

In this work, average values are presented in Table 2 when the purity is ≥ 95% as a simplified approach to estimate the energy consumption.

## 4.3 Correlations and relative errors

The relative errors between the correlation results and the data points obtained from detailed TEAs for the selected CC technologies are presented in Table 3.

**Table 3:** Relative errors of the capture technologies

| MEA | Average relative error [%] | Min/ Max relative error [%] | $R^2$ |
|---|---|---|---|
| TEC | 4.28 | 0.014/ 8.50 | 0.975 |
| Reboiler duty | 0.12 | 0.002/ 0.40 | 0.996 |
| Electrical duty | 2.87 | 0.03/ 8.59 | 0.997 |
| Cooling duty | 1.38 | 0.19/ 7.54 | 0.997 |
| **PolyActive** | | | |
| TEC | 1.90 | 0.004/ 4.92 | 0.999 |
| Electrical duty | 2.57 | 0.42/ 8.77 | 0.999 |
| Cooling duty | 3.95 | 0.24/ 8.67 | 0.999 |

Given the scarcity of real CC project data for small-scale applications in the public domain, it is important to clarify that these errors do not represent the uncertainty of a real CC unit but rather deviations between the correlation and TEA data used in this study. For CapEx/ OpEx, uncertainties as high as 10 to 20% are common during a process scale-up [5] and therefore, the average error as well as the maximum errors depicted in the correlations can be considered within the expected variations. Correlation development is iterative and more data points can be added to improve the correlation results. The validity of the developed correlations is demonstrated through the case studies.

## 4.2 Case study

### 4.2.1 Cement industry CC (20.5 mol%, 111 kt/y)

In this section, correlations from this study are applied to case studies presented by IEAGHG [2], starting with a small-scale cement plant. The CapEx estimation method used in the case study is presented in the supporting document. Key assumptions and input data are presented in Table 4. Note that natural gas is used to generate steam required by the MEA process while for the PolyActive membrane, no steam is required. Detailed breakdowns of the MEA capture cost retrieved from IEAGHG [2] as well as the correlation results for the MEA and PolyActive membranes are presented in Figure 2. CapEx is one of the dominant factors and accounts for close to 50% of the capture cost for small-scale application. Comparing the MEA correlation CapEx to the literature value, a difference of 6% was observed while the NG fuel costs showed a deviation of 5%. In the case of electricity costs, the report extracted electrical energy consumption from a coal-fired power plant case study treating a flue gas at 4.1 mol% $CO_2$ concentration without conducting a detailed simulation. As indicated in Table 8, the flue gas considered in this case study has a high

**Table 4:** Case study process/ economic inputs and assumptions [2] for the small-scale cement plant

| Parameters | Values | Parameters | Values |
|---|---|---|---|
| $CO_2$ concentration | 20.5 mol% | Operating hours | 7451 h/y |
| Capture scale | 111.3 kt/y | CEPCI (2024 April) | 799.5 |
| Process lifetime | 25 y | Electricity | 132.31 $/MWh |
| Discount rate | 10% | Natural gas (NG) price | 22.82 $/MWh |

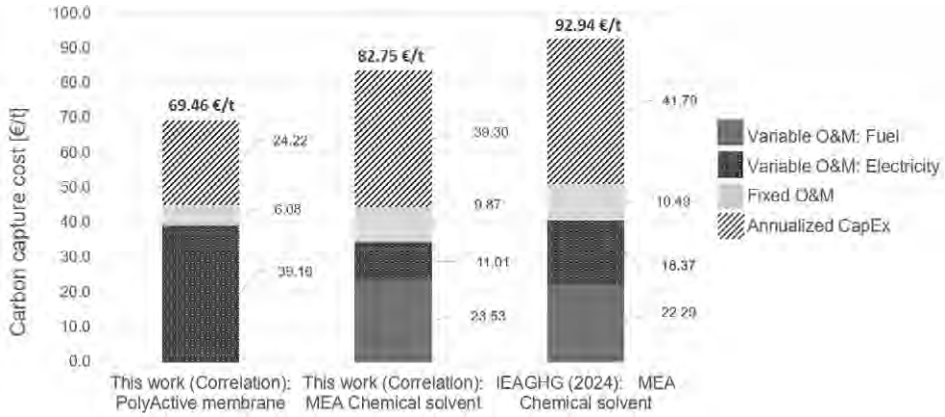



**Figure 2.** Detailed breakdown of carbon capture and compression cost [€/t]: Case study 1

concentration of 20.5 mol%. At low $CO_2$ concentrations (e.g., 4.1 mol%), high flue gas volumes will pass through a blower and more power will be required. Also, the study reported 1.58 $MW_{el}$ for the compression of $CO_2$ product which is higher than the power consumption considered in this study (1.11 $MW_{el}$), but no details about product compression was given. In addition, higher solvent pump power consumptions were considered in the literature by accounting for pressure drop in pipelines (a pump head of 10 bar) which was not considered in this study. These differences in the assumptions lead to a deviation of 45% in electricity costs. Overall, the MEA correlation showed a capture cost of 82.75 €/t with a difference of 11% compared to the reported value which is within the expected deviation defined by AACE [10]. Assuming more accurate power consumptions were applied in the literature result, the difference in capture costs for MEA process could be even lower which shows a good applicability of the correlations.

The capture cost obtained using the PolyActive correlations was found to be 69.46 €/t which is lower than the MEA process. This is possible since the membrane process can be less CapEx intensive and more cost-effective at high $CO_2$ concentrations. Also, membranes are well-suited for small-scale applications due to their modularity. However, 56.3% of the capture cost arises from the electricity cost and therefore, sources of electricity will be an important criterion to be considered.

### 4.2.2 Energy from Waste (EfW) (10 mol%, 90 kt/y)

An EfW plant with a capture scale of 90 kt/y was considered in the second case study where process parameters and assumptions are outlined in Table 5. The EfW plant without a CC unit produces 7.7 $MW_{el}$ and 8.1 $MW_{th}$. Note that NG cost is not considered since all the steam needed for solvent regeneration is assumed to be supplied by the steam turbine from the EfW plant. Based on this, a steam turbine loss of 3.89 $MW_{el}$ was assumed in the literature [2] and applied in the correlation results as well. Since the EfW plant produces electricity, a wholesale electricity price of 56.85 $/MWh was retrieved from the literature [2] and applied in this case study. The detailed breakdowns of capture costs are shown in Figure 3.

As observed in the first case study, the CapEx is the main contributor to the capture costs (54% for the literature MEA results and 59% for the MEA correlation result). For the annualized CapEx, a difference of 12% was observed between the correlations and the literature, while for the electricity cost, a difference of 22% was observed. As explained in Section 4.2.1, much higher power consumption for the compression loop and the solvent pumps are used in the literature [2]. Overall, a capture cost of 82.92 €/t was obtained from the MEA correlations with a difference of 3.54% compared to the literature value of 79.98 €/t. In the case of the PolyActive membrane, a capture cost of 71.48 €/t was obtained using the correlations with the same assumptions, which is a cheaper CC option than the conventional MEA CC in the EfW case as well.

**Table 5:** Case study process/ economic inputs and assumptions [2] for EfW process

| Parameters | Values | Parameters | Values |
|---|---|---|---|
| $CO_2$ concentration | 10.0 mol% | Operating hours | 7451 h/y |
| Capture scale | 90.0 kt/y | CEPCI (2024 April) | 799.5 |
| Process lifetime | 25 y | Electricity | 56.8 $/MWh |
| Discount rate | 10% | Natural gas (NG) price | NA |

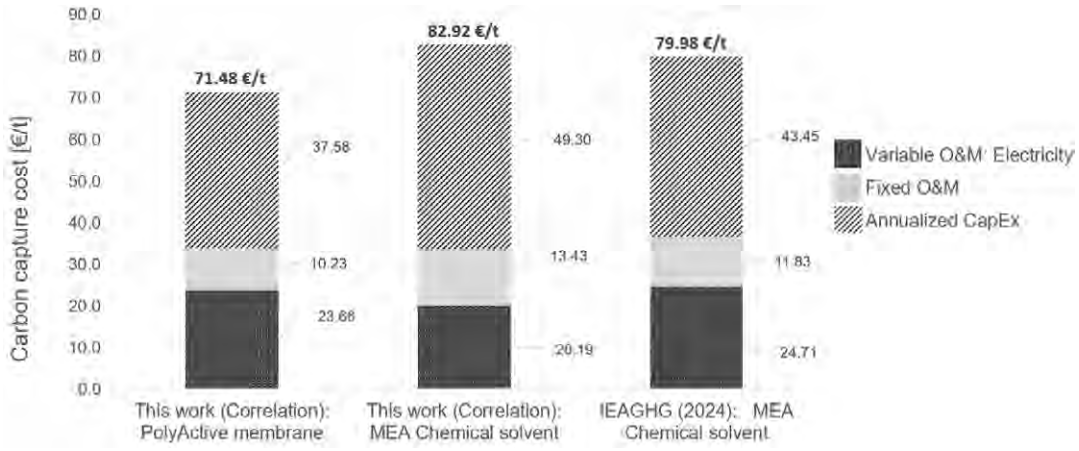



**Figure 3.** Detailed breakdown of carbon capture and compression cost [€/t]: Case study 2

## CONCLUSION AND PERSPECTIVES

In this paper, small-scale correlations for the MEA and the PolyActive membrane CC technologies are developed and the applicability is demonstrated in the case studies. These correlations can be applied across various $CO_2$ inlet concentrations (between 5 and up to 70 mol%) and capture scales (10-100 kt/y). Also, a consistent CapEx/ OpEx estimation method can be applied throughout the comparison studies to minimize discrepancies. More importantly, case-specific utility costs can be applied to the correlation results to fine-tune the capture costs depending on the considered case studies. As a benchmark CC process, MEA correlations are presented in this work which is one of the well-suited CC options for large-scale applications. However, small-scale CC processes are CapEx intensive due to the absence of economies of scale, leading to higher costs per ton of $CO_2$ captured. Therefore, technologies with a lower CapEx intensity (e.g., membranes) will have higher potential for small-scale emitters. Also, modularity and installation area of technologies will be crucial KPIs for small-scale applications due to often limited space availabilities. In the perspectives, new emerging technologies such as advanced chemical absorption or cryogenic CC can be studied to enrich small-scale CC applications in the literature.

Overall, these easy-to-use small-scale correlations are envisioned to assist with decision-making processes for small-scale CC and improve deployment of CC units by providing a framework to fairly compare various CC technologies.

## DIGITAL SUPPLEMENTARY MATERIAL

The supplementary materials can be found at: https://psecommunity.org/LAPSE:2025.0031

## ACKNOWLEDGEMENTS

The authors are grateful to the Belgian Federal Public Service Economy and to the Belgian Energy Transition Fund which support this research within the project PROCURA.

## REFERENCES

1. Page, B., Turan, G., Zapantis, A., Burrows, J., Consoli, C., Erikson, J., Havercroft, I., Kearns, D., Liu, H., Rassool, D., others, 2020. The global status of CCS 2020: vital to achieve net zero. GCCSI.
2. IEAGHG, 2024, Baseline Techno-Economic Assessment of Small-Scale Carbon Capture for Industrial and Power Systems, IEAGHG Technical Report 2024-03.
3. Rubin, E.S., 2012. Understanding the pitfalls of CCS cost estimates. Int. J. Greenh. Gas Control 10, 181–190.
4. Roussanaly, S., Berghout, N., Fout, T., Garcia, M., Gardarsdottir, S., Nazir, S.M., Ramirez, A., Rubin, E.S., 2021. Towards improved cost evaluation of Carbon Capture and Storage from industry. Int. J. Greenh. Gas Control 106, 103263.
5. Hasan, M.F., Baliban, R.C., Elia, J.A., Floudas, C.A., 2012. Modeling, simulation, and optimization of post combustion $CO_2$ capture for variable feed concentration and flow rate. 1. Chemical absorption and membrane processes. Ind. Eng. Chem. Res. 51, 15642–15664.
6. DECARBit, 2011. European best practice guidelines for assessment of $CO_2$ capture technologies. SINTEF Trondheim Nor.
7. Nwaoha, C., Beaulieu, M., Tontiwachwuthikul, P., Gibson, M.D., 2018. Techno-economic analysis of CO2 capture from a 1.2 million MTPA cement plant using AMP-PZ-MEA blend. Int. J. Greenh. Gas Control 78, 400–412.
8. Kim, S., and Léonard, G., $CO_2$ Capture Technologies and Shortcut Cost Correlations for Different Inlet $CO_2$ Concentrations and Flow Rates. 1. Chemical Absorption. Available at SSRN: http://dx.doi.org/10.2139/ssrn.4967576
9. Wang, Y., 2020. Techno-economic assessment of hybrid post-combustion carbon capture systems in coal-fired power plants and steel plants. PhD thesis. Forschungszentrum Jülich
10. AACE, 2011. Cost Estimate Classification system-as applied in engineering, procurement, and construction for the process industries. AACE Int. Recomm. Pract. 18R-97, 1–9.

© 2025 by the authors. Licensed to PSEcommunity.org and PSE Press. This is an open access article under the creative commons CC-BY-SA licensing terms. Credit must be given to creator and adaptations must be shared under the same terms. See https://creativecommons.org/licenses/by-sa/4.0/

Systems & Control Transactions

**Research Article - Peer Reviewed Conference Proceeding**
ESCAPE 35 - European Symposium on Computer Aided Process Engineering
Ghent, Belgium. 6-9 July 2025
Jan F.M. Van Impe, Grégoire Léonard, Satyajeet S. Bhonsale,
Monika E. Polańska, Filip Logist (Eds.)

PSE PRESS

# Numerical Modelling of Carbon Dioxide Adsorption in Dual Function Materials: An CFD approach.

**Andrés F. Soto-Cañón[a], Rodinson R. Arrieta-Peréz[a], Camilo Rengifo[b], Martha Cobo[a] and Manuel Figueredo[a,*]**

[a] Universidad de La Sabana, Department of Chemical Engineering, Chía, Cundinamarca, Colombia
[b] Universidad de La Sabana, Department of Mathematics, Physics and Statistics, Chía, Cundinamarca, Colombia
* Corresponding Author: manuel.figueredo@unisabana.edu.co

## ABSTRACT

Integrated Carbon Capture and Conversion (ICCC) technologies offer an efficient alternative to conventional Carbon Capture, Utilization, and Storage (CCUS) methods by simultaneously capturing and converting $CO_2$ into value-added chemicals. Dual-function materials (DFMs) are particularly promising due to their capability to integrate adsorption and catalysis in a single step, thereby reducing both energy consumption and associated costs. This study models the dynamic behavior of $CO_2$ adsorption within a laboratory-scale packed-bed reactor employing DFMs. The mathematical model incorporates momentum, mass, and heat transfer equations, implemented using COMSOL Multiphysics v5.6, and evaluates various axial dispersion models (ADMs) and mass transfer coefficients (MTCs). The results indicate that the Rastegar-Gu ADM, combined with an MTC of $8.3 \times 10^{-2}$ $s^{-1}$, provides the most accurate representation of breakthrough and saturation times, as well as the total quantity adsorbed. Furthermore, relative errors associated with this model are consistently lower than those observed in alternative models. These findings offer valuable insights for the scaling-up of ICCC technologies, underscoring the significance of precise Computational Fluid Dynamics (CFD) simulations in advancing sustainable $CO_2$ capture and conversion solutions.

**Keywords**: Adsorption, Carbon Capture, Computational Fluid Dynamics, DFMs

## INTRODUCTION

ICCC technologies represents an advancement over conventional CCUS methods[1]. The ICCC technologies are based on the *in-situ* conversion of the captured carbon into high-value chemical products, such as methane and methanol, thus eliminating the need for costly compression and transport processes [1]. Among these technologies, DFMs emerge as a promising solution, facilitating the integration of $CO_2$ adsorption (capture) and methanation (conversion), while simultaneously reducing energy consumption [2].

However, there remains a gap between the research and development of DFMs and their industrial implementation [1, 2]. As a result, both numerical simulation and CFD are pivotal in the optimal design and scale-up of these processes.

In the context of carbon dioxide adsorption, the numerical simulation incorporates the three primary transport phenomena – momentum, mass and heat transfer- coupled with equilibrium and kinetic adsorption models [3]. This approach is suitable for a range of adsorbent materials and their modifications [4]. Additionally, numerical simulation offers a rigorous framework for the design and optimal mathematical description for cyclic carbon capture processes, such as Pressure Swing Adsorption (PSA) and Temperature Swing Adsorption (TSA) [5].

The dynamic behavior of the adsorption column is typically described by a “breakthrough curve”. This curve is generated as the mass transfer zone advances through the column and reaches the exit [6]. The shape of the mass transfer zone and, consequently the breakthrough curve, depends on the isotherm model, axial dispersion model, and mass transfer model [7].

Both the axial dispersion coefficient and the mass transfer coefficient are key parameters influencing the adsorption dynamic behavior [8]. Axial dispersion arises from turbulent mixing and molecular diffusion [4, 6]

The mass transfer coefficient reflects the rate at which the adsorbate is transferred from the gas phase to the solid phase within the particles. It may also account for the resistance effects associated with diffusion into the solid materials [6].

In this study, the dynamic behavior of carbon dioxide adsorption from a nitrogen mixture using a $Ru/Na_2O_3/Al_2O_3$ DFM in a laboratory-scale packed bed is simulated using COMSOL Multiphysics v5.6. The momentum, mass, and heat transfer phenomena are modeled and integrated through various physics modules. Furthermore, several axial dispersion models (ADM) and mass transfer coefficients (MTCs) are evaluated.

## MATHEMATICAL MODELS

This section presents the formulation of the mathematical model. It outlines the assumptions, the geometry implemented in the software, and the physics modules, along with the equations utilized.

### Assumptions

For simplicity, several assumptions have been made regarding the mathematical model. First, it is assumed that only carbon dioxide is adsorbed onto the DFM, and the linear driving force model is implemented to account for mass loss. Additionally, the gas mixture is considered ideal. Finally, the energy balance model is assumed to be homogeneous.

### Geometry

To replicate the experimental system, a one-dimensional geometry was created in COMSOL along de *x*-axis. Two subdomains were defined: quartz wool and DFM. Figure 1 illustrates the final geometry implemented in the CFD model, while Image 1 depicts the laboratory-scale reactor used in the experiment.

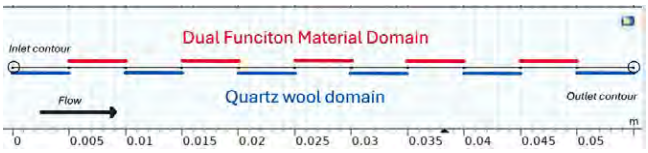



**Figure 1**. One-dimensional geometry employed in COMSOL.



**Image 1**. Laboratory-scale DFM packed reactor employed.

## Governing transport phenomena equations

### Momentum Balance

For the momentum balance, Darcy's *Law* physics module was implemented. This module includes both the continuity equation and the Darcy's law equation for pressure drop. The equation is expressed as follows:

$$\frac{\partial(e_{cat}\rho_f)}{\partial t} + \frac{\partial}{\partial x}\rho_f u = 0 \quad (1)$$

$$u = -\frac{\varkappa}{\mu}\frac{\partial P}{\partial x} \quad (2)$$

Where: $u$ is the Darcy velocity (m/s), $e_{cat}$ is the DFM porosity, $\rho_f$ and $\mu$ represent the gas phase density (kg/m$^3$) and viscosity (Pa·s), respectively. Finally, $\varkappa$ is the permeability (m$^2$), which was calculated using the integrated Kozeny-Carman equations and $P$ is pressure (Pa).

### Mass Balance

The Mass balance equations were modeled using *transport of diluted species* physics modules. The equation is expressed as follows.

$$\frac{\partial C_i}{\partial t} - D_L\frac{\partial^2 C_i}{\partial x^2} + u\frac{\partial C_i}{\partial x} = \mathrm{R}_i \quad (3)$$

Where $C_i$ denotes the gas phase concentration of each species (mol/m$^3$), $D_L$ represents the axial dispersion coefficient (m$^2$/s), and $\mathrm{R}_i$ refers to the reaction or sink term (mol/m$^3$·s).

### Adsorption term

To simulate the adsorption phenomenon, the linear driving force equation was implemented as a *domain ordinary differential equation* module, applied exclusively to the DFM subdomain.

$$\frac{\partial q}{\partial t} = k(q_e - q) \quad (4)$$

In this equation, $q$ represents the quantity of carbon dioxide adsorbed onto the solid material (mol/kg), $q_e$ is the equilibrium quantity (mol/kg), and $k$ is the mass transfer coefficient (1/s).

Thus, the mass balance for carbon dioxide is expressed as follows:

$$\frac{\partial C_{CO_2}}{\partial t} - D_L\frac{\partial^2 C_{CO_2}}{\partial x^2} + u\frac{\partial C_{CO_2}}{\partial x} = -\frac{1-e_{cat}}{e_{cat}}\rho_s\frac{\partial q}{\partial t} \quad (5)$$

For nitrogen, $\mathrm{R}_i$ is equal to zero.

### Adsorption equilibrium

The Langmuir isotherm model was used to represent the equilibrium quantity (equation 6). To ensure an accurate depiction of these phenomena, the model was fitted to experimental data obtained with a Micromeritics ASAP 2020+ at pressures up to 760 mmHg and 320 °C for $Na_2O/Al_2O_3$, a precursor to DFM. Table 1 presents the obtained parameters values.

$$q_e = \frac{q_{sat}K_L P_{CO_2}}{1+K_L P_{CO_2}} \quad (6)$$

**Table 1:** Langmuir isotherm model parameters.

| Stream | Description | Value |
|---|---|---|
| $q_{sat}$ | Saturated quantity | 0.193 mol/kg |
| $K_L$ | Equilibrium constant | $73x10^{-5}$ $Pa^{-1}$ |

## Energy Balance

The energy balance was modeled using the *heat transfer on porous media* physics module. The equation is expressed as follows:

$$A_c(\rho C_p)_{eff}\frac{\partial T}{\partial t} + A_c\rho_f C_{p,f} u\frac{\partial T}{\partial x} - A_c k_{eff}\frac{\partial T^2}{\partial x^2} = Q_{ads} \quad (7)$$

Where: $T$ is the system temperature (K), $A_c$ the cross-sectional area ($m^2$), $k_{eff}$ represents the effective heat transfer coefficient (W/m·K), and $Q_{ads}$ denotes the heat of adsorption ($W/m^3$).

## Boundary conditions

The equations for the boundary conditions at the boundaries of the geometry (Figure 1) are expressed as follows:

$$\boldsymbol{n}\cdot(\rho_f u) = \rho_f U_0 \quad (8)$$

$$\boldsymbol{n}\cdot\left(-D_L\frac{\partial C_i}{\partial x} + uC_i\right) = \boldsymbol{n}\cdot(uC_{i,0}) \quad (9)$$

$$-\boldsymbol{n}\cdot\left(-A_c k_{eff}\frac{\partial T}{\partial x}\right) = A_c\rho_f\Delta H(\boldsymbol{n}\cdot u) \quad (10)$$

Equations (8-10) represent the Danckwerts form for the inlet conditions for the momentum, mass, and energy balance, respectively. Here, $U_0$ is the initial Darcy velocity, $C_{i,0}$ the initial concentration of each gas in the inlet mixture (calculated using ideal gas equation), and $\Delta H$ the sensible enthalpy (KJ/mol) [9]

$$\boldsymbol{n} * (\rho_f u) = p_0 \quad (11)$$

$$\boldsymbol{n} * \left(-D_L\frac{\partial C_i}{\partial x}\right) = 0 \quad (12)$$

$$-\boldsymbol{n} * \left(-A_c k_{eff}\frac{\partial T}{\partial x}\right) = 0 \quad (13)$$

On the other hand, equations (11-13) describe the outlet boundary conditions. Here, $p_0$ represents the barometric pressure at the outlet, defined as zero. This condition ensures that *Darcy's Law* physics module calculates the barometric pressure drop [9].

## Initial values

The initial values for each of the main transport equations are presented as follows:

$$p_{t=0} = p_{op} \quad (14)$$

$$C_{CO_2,t=0} = 0 \qquad C_{N_2,t=0} = \frac{p_{op}}{R*T_{op}} \quad (15)$$

$$q_{CO_2,t=0} = 0 \quad (16)$$

$$T_{t=0} = T_{op} \quad (17)$$

Where: $p_{op}$ is the initial barometric pressure and $T_{op}$ is the initial temperature.

## Mixture properties calculation

The mixture properties, including density, viscosity, heat capacity and thermal conductivity, were calculated using a thermodynamics module. Each property was modeled as a function of temperature, pressure, and molar composition. However, to reduce computational time, these calculations were based on the inlet mixture compositions and a constant inlet barometric pressure.

## Computational aspects

As previously mentioned, COMSOL Multiphysics v5.6 CFD software was used. A mesh of ninety-nine (99) elements was created in conjunction with the one-dimensional geometry. A dynamic study was conducted from 0 to 540 seconds. MATLAB was employed as complemented software to perform various calculations.

# METHODOLOGY

## Axial dispersion coefficient models

Several models were evaluated to identify the most suitable for representing the dynamic behavior of the adsorption process. These models, along with their respective equations, are presented in the table below:

**Table 2**: Axial dispersion models evaluated.

| Model | Equation |
|---|---|
| No model (NM) | $D_L = D_m$ |
| Wakao-Funazkri (WF)[6] | $D_L = \frac{D_m}{e_{cat}}(20 + 0.5ScRe)$ |
| General model (GM) [6] | $D_L = 0.7D_m + 0.5dp_{cat}u$ |
| Rastegar-Gu (RG) [4] | $D_L = \frac{d_{p,cat}u}{Pe_z}$ <br> $\frac{1}{Pe_z} = \frac{0.7D_m}{Lu} + \frac{d_{p,cat}}{L}\frac{e_{cat}}{0.18+0.008Re^{0.59}}$ |

## Mass transfer coefficient constants

Table 3 represents a list of evaluated mass transfer coefficient (MTC) constants.

**Table 3:** Mass transfer constants evaluated.

| Reference | Value |
|---|---|
| [10] | $2.2\cdot10^{-2}$ [1/s] |
| [11] | $6.7\cdot10^{-2}$ [1/s] |
| [11] | $8.3\cdot10^{-2}$ [1/s] |

The evaluation of both axial dispersion models (ADM) and mass transfer coefficient constants (MTC) were performed simultaneously by pairing each model

with its MTC. As a result, twelve tests were conducted, divided into three sets of simulations.

**Table 4**: Sets of simulations performed.

| Set | Description |
|---|---|
| A | $k = 2.2 \cdot 10^{-2}$ [1/s]; with all ADM evaluated. |
| B | $k = 6.7 \cdot 10^{-2}$ [1/s]; with all ADM evaluated. |
| C | $k = 8.3 \cdot 10^{-2}$ [1/s]; with all ADM evaluated. |

## Breakthrough and saturation times

Two key design parameters for adsorption columns are the breakthrough $t_b$ and saturation time $t_s$. These parameters correspond, respectively, to the time when the mass transfer zone reaches the end of the column and the time when the column is fully saturated or in equilibrium with the flowing gas [12].

These parameters will be compared to verify that the mathematical model can be extrapolated to the design and optimization of an industrial scale reactor.

## Total quantity adsorbed

In addition to the $t_b$ and $t_s$ parameters, the total quantity adsorbed ($q_{total}$) is considered to assess the mathematical model and its relevance. Equation 18 presents the mathematical formula for its calculation [12].

$$q_{total} = \frac{F_{op} C_{i,in}}{m_{cat}} \int_0^{t_s} 1 - \frac{C_{i,out}(t)}{C_{i,in}} \partial t \quad (18)$$

Where: $F_{op}$ is the volumetric flow (m³/s), $\frac{C_{i,out}(t)}{C_{i,in}}$ represents the breakthrough curve, and $m_{cat}$ is the total mass of DFM inside the reactor (kg). To facilitate the rapid calculation of $q_{total}$, the breakthrough curve data for each run were first fitted to the Thomas model, as shown in Equation 19.

$$\frac{C(t)}{C_i} = \frac{1}{\exp\left(\frac{k_T q_T m_b}{F_{op}} - k_T C_i t\right) + 1} \quad (19)$$

By using the non-linear fitting tools in MATLAB, the values of $k_T$ and $q_T$ were determined. Subsequently, numerical integration was performed.

# RESULTS

## Breakthrough and saturation time

The breakthrough and saturation times obtained from the experimental set are presented in Table 5, while the results for each simulation set are shown in Tables 6-8.

To assess the accuracy of the simulation results, the relative error (RE) was calculated by comparing the simulated data with the corresponding experimental measurements. This comparison offers a quantitative evaluation of the model's predictive capability and underscores its potential reliability under the tested conditions.

**Table 5:** Experimental breakthrough and saturation times.

| Set | $t_b$ (min) | $t_s$ (min) |
|---|---|---|
| Experimental | 3.27 | 4.32 |

A comparison between the simulation results without the implementation of the ADM and the general model shows that the breakthrough and saturation times are closely aligned, both displaying similar trends of decreasing relative error as other mass transfer coefficient constants (MTC) are evaluated.

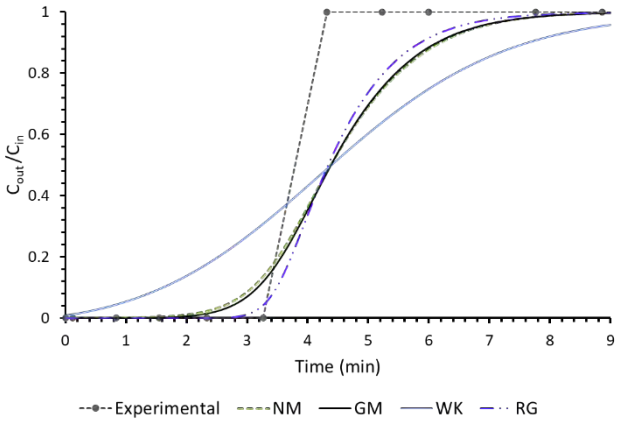



**Figure 2.** Axial dispersion model comparison. Set A

**Table 6:** Breakthrough and saturation times. Set A.

| ADM | $t_b$ (min) | RE $t_b$ (%) | $t_s$(min) | RE $t_s$ (%) |
|---|---|---|---|---|
| No Model | 1.08 | 66.9 | 8.16 | 89.0 |
| General Model | 1.32 | 59.6 | 8.15 | 88.8 |
| WK | 0.017 | 99.5 | 11.1 | 157.1 |
| RG | 2.53 | 22.6 | 7.72 | 78.8 |

In contrast, the Rastegar-Gu model demonstrates a significant improvement over the previously discussed models. The application of this model results in more closely spaced breakthrough and saturation times, leading to a steeper breakthrough curve. This corresponds to a shorter mass transfer zone, a characteristic that must be accurately represented in a DFM-packed bed, as observed in the experimental breakthrough curves (Figure 2-4). Furthermore, the Rastegar-Gu model consistently exhibits the lowest relative error for both breakthrough and saturation times across all three simulation sets, offering superior predictive capability under the evaluated conditions.

The application of the Wakao-Funazkri model

results in a broader breakthrough curve, characterized by breakthrough times of less than 0.20 minutes and saturation times exceeding 9 minutes. Moreover, this model shows significantly high relative errors, approaching 100% when compared to experimental data. These results suggest that the model lacks the precision required to accurately represent the dynamics observed in the experimental setup.

From a different perspective, the use of mass transfer coefficient constants of $6.7 \cdot 10^{-2}$ $s^{-1}$ and $8.3 \cdot 10^{-2}$ $s^{-1}$ leads to a significant reduction in the relative error associated with both breakthrough and saturation times. For example, for the general model, the relative error in saturation time is reduced by half, as observed in the simulation without an implemented model. Moreover, the relative error for breakthrough times decreases substantially by nearly one-third for the case without any model implemented and by one-sixth for the general model.

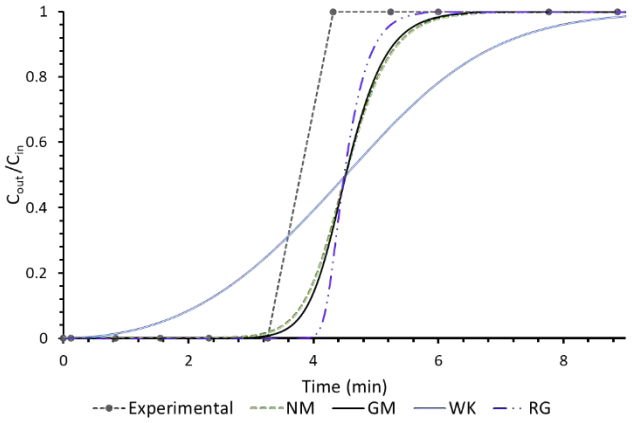



**Figure 3.** Axial dispersion model comparison. Set B

**Table 7:** Breakthrough and saturation times. Set B.

| ADM | $t_b$ (min) | RE $t_b$ (%) | $t_s$(min) | RE $t_s$ (%) |
|---|---|---|---|---|
| No Model | 2.48 | 24.1 | 6.30 | 45.9 |
| General | 2.75 | 15.8 | 6.13 | 42.0 |
| WK | 0.12 | 96.3 | 9.33 | 116.1 |
| RG | 3.88 | 18.8 | 5.58 | 29.3 |

The most favorable results are obtained with a mass transfer coefficient constant of $8.3 \cdot 10^{-2}$ $s^{-1}$, combined with the Rastegar-Gu axial dispersion model. This combination demonstrates superior consistency, yielding comparable reductions in relative error for both breakthrough and saturation times.

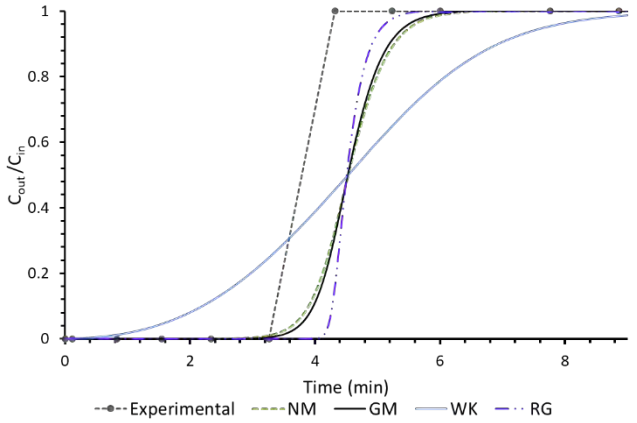



**Figure 4.** Axial dispersion model comparison. Set C

**Table 8:** Breakthrough and saturation times. Set C.

| ADM | $t_b$ (min) | RE $t_b$ (%) | $t_s$(min) | RE $t_s$ (%) |
|---|---|---|---|---|
| No Model | 2.67 | 18.3 | 6.08 | 40.8 |
| General | 2.93 | 10.3 | 5.93 | 37.4 |
| WK | 0.18 | 94.5 | 9.20 | 113.1 |
| RG | 4.03 | 23.4 | 5.42 | 25.6 |

## Total quantity adsorbed

**Table 9:** Experimental total quantity adsorbed.

| Set | $q_{total}$(mmol/g) |
|---|---|
| Experimental | 0.1645 |

The results for $q_{total}$, representing the total quantity adsorbed are presented in Table 9 for the experimental data and in Table 10 for each set of simulation runs. Due to the high relative errors observed, the Wakao-Funazkri axial dispersion model was excluded from the evaluation of $q_{total}$. This decision highlights the model's limitations in accurately representing the adsorption dynamics under the tested conditions, rendering it unsuitable for further analysis in this context.

**Table 10:** Results for the total quantity adsorbed for every set of runs.

| Set | A | B | C |
|---|---|---|---|
| ADM | | $q_{total}$(mmol/g) | |
| No model | 0.1894 | 0.1926 | 0.1929 |
| General | 0.1893 | 0.1926 | 0.1929 |
| Rastegar-Gu | 0.1883 | 0.1920 | 0.1925 |

**Table 11:** Results for the relative error, comparison between experimental and simulated $q_{total}$.

| Set | A | B | C |
|---|---|---|---|
| **ADM** | | Relative error (%) | |
| No model | 15.12 | 17.12 | 17.30 |
| General | 15.16 | 17.10 | 17.28 |
| Rastegar-Gu | 14.46 | 16.75 | 17.04 |

For all three simulation sets, the total quantity adsorbed exhibits only minor variations, with relative errors consistently around 15%. Regarding breakthrough and saturation times, the general model shows no significant improvement compared to simulations conducted without an implemented model. However, the Rastegar-Gu model remains the best option. In contrast to the behavior observed for breakthrough and saturation times, the relative error for $q_{total}$ increases in simulation sets B and C. Despite this, the combination of the Rastegar-Gu axial dispersion model and a mass transfer coefficient constant of $8.3 \cdot 10^{-2}$ $s^{-1}$ still provides the most accurate results in this context.

## CONCLUSION

This study compares various axial dispersion models and mass transfer constants used in the mass balance model of a packed-bed adsorption column. Additionally, it provides valuable insights into the CFD simulation of the carbon dioxide adsorption process utilizing DFMs. The general model does not demonstrate significant improvement, as its results are comparable to those obtained from the simulation set where no axial dispersion coefficient model was applied.

The findings indicate that the Rastegar-Gu axial dispersion model, combined with MTC of $8.3 \cdot 10^{-2}$ $s^{-1}$, provides an effective approach for accurately replicating the adsorption behavior of DFMs. These results represent a crucial starting point for the design, optimization, and scaling of dual-function reactors, facilitating their further development in $CO_2$ capture and utilization technologies.

## ACKNOWLEDGEMENTS

This project is funded by Ministry of Science, Technology, and Innovation (Minciencias, Patrimonio Autónomo del Fondo Nacional de Financiamiento Para la Ciencia, La Tecnología y la Innovación, Francisco José de Caldas) through the contract 441-2023.

## REFERENCES

1. Bin S, et al. CO2 capture and in-situ conversion: recent progresses and perspectives. *GreenChE* 3:189-198 (2022) doi: 10.1016/j.gce.2021.11.009.
2. Han L, et al. Progress in reaction mechanisms and catalyst development of carbon dioxide methanation. *J CO2 Util* 84: 102845 (2024), doi: 10.1016/j.jcou.2024.102845.
3. Shuangjun L, et al. Mathematical modeling and numerical investigation of carbon capture by adsorption: Literature review and case study," *Appl Energy* 221: 437–449 (2018) doi: 10.1016/j.apenergy.2018.03.093.
4. Francisco J G O, Manuel B R, Ralph T Y. Modeling of fixed-bed columns for gas physical adsorption. *Chem. Eng. J* 378:121985 (2019) doi: 10.1016/j.cej.2019.121985.
5. Toluleke E A, Phebe L B P, Meihong W. Experimental studies, molecular simulation and process modelling\simulation of adsorption-based post-combustion carbon capture for power plants: A state-of-the-art review. *Appl Energy* 317:119156 (2022) doi: 10.1016/j.apenergy.2022.119156.
6. Douglas M. R, PRINCIPLES OF ADSORPTION AND AD-SORPTION PROCESSES. Wiley-Interscience, (1984).
7. Ralph T Y, GAS SEPARATION PROCESS BY ADSORPTION PROCESSES. Butterworth Publishers, (1987).
8. Motoyuki S. ADSORPTION ENGINEERING. Elsevier science (1990).
9. COMSOL Reference Manual https://www.comsol.com
10. Mingheng L. Dynamics of CO2 adsorption on sodium oxide promoted alumina in a packed-bed reactor. *Chem Eng Sci* 66:5938–5944 (2011) doi: 10.1016/j.ces.2011.08.013.
11. K. B. Lee, M. G. Beaver, H. S. Caram,S. Sircar. Chemisorption of carbon dioxide on sodium oxide promoted alumina. *AIChE Journal* 53:2824–2831, (2007) doi: 10.1002/aic.11312.
12. Alan G. Adsorption basics: part 1. *AIChE CEP* 48–53 (2017).

© 2025 by the authors. Licensed to PSEcommunity.org and PSE Press. This is an open access article under the creative commons CC-BY-SA licensing terms. Credit must be given to creator and adaptations must be shared under the same terms. See https://creativecommons.org/licenses/by-sa/4.0/



Systems & Control Transactions

**Research Article - Peer Reviewed Conference Proceeding**
ESCAPE 35 - European Symposium on Computer Aided Process Engineering
Ghent, Belgium. 6-9 July 2025
Jan F.M. Van Impe, Grégoire Léonard, Satyajeet S. Bhonsale,
Monika E. Polańska, Filip Logist (Eds.)

PSE PRESS

# Design Considerations for Hardware Based Acceleration of Molecular Dynamics

**Joseph Middleton[a], Joan Cordiner[a*]**

[a] The University of Sheffield, School of Chemical, Biological and Materials Engineering, Sheffield, United Kingdom
* Corresponding Author: j.cordiner@sheffield.ac.uk

## ABSTRACT

As demand for long and accurate molecular simulations increases so too does the computation demand. Beyond using new, enterprise scale processor developments - such as the ARM neoverse chips – or performing simulations leveraging Graphics Processing Unit compute, there exists a potentially faster and more power efficient option in the form of custom hardware. Using hardware description languages it is possible to transform existing algorithms into custom, high performance hardware layouts. This can lead to faster and more efficient simulations but compromises on the required development time and flexibility. In order to take the greatest advantage of the potential performance gains, the focus should be on transforming the most computationally expensive parts of the algorithms. When performing molecular dynamics simulations in a polar solvent like water, non-bonded electrostatic calculations dominate each simulation step, as the interactions between the solvent and the molecular structure are calculated. However, simply developing a non-bonded electrostatics co-processor may not be enough, as transferring data between the host program and the Field Gate Programable Arrays itself incurs a significant time delay. For any changes to be made, competitive to existing calculation solutions, the number of data transfers must be reduced. This could be achieved by simulating multiple time-steps between memory transfers, which may impact accuracy, or performing more calculations in the custom hardware.

**Keywords**: Modelling, Algorithms, FPGA, Molecular Dynamics, Optimisation

## INTRODUCTION

Molecular dynamics is the process of simulating molecular interactions at an atomic level, this allows researchers to divine information from chemical mechanisms that cannot be easily observed or measured. Depending on the configuration, simulations can be used to determine the reaction specific parameters such as the activation and Gibbs free energy of complex or expensive experimental processes in a way that may not be obtainable in a lab. As the simulations comprise of many bound and free atoms, the workloads are a prime candidate for parallelisation as the simulation space can be divided up into smaller chunks. This allows for the simulations to be run in supercomputers, which may have thousands of nodes, rather than just a few very fast machines. The majority of the simulations are run using either Central Processing Units or using Graphics Processing Units either as co-processors to the CPU or self-contained. CPU based calculations can be offloaded across one node by running multiple threads or across many nodes by utilising libraries like OpenMP. Simulations on a GPU backend are more complex, as they require the node to communicate and synchronize data especially if the simulation is running on a single-node, multi-GPU system, or on multi-node, multi-GPU systems. This also introduces the problem of communications latency between the co-processor – in this case, the GPU – and the host which must be taken into account when running very large scale or long simulations. This communications latency can be eliminated by performing all of the calculations within the GPU, which has been developed by AMBER using the PNEND backend. Whilst coming at the cost of scalability, as this method lacks inter-node communication, calculations are performed fast enough for that to be of limited benefit.

The CPU and GPU are not the only hardware available, however, Field Programmable Gate Arrays (FPGAs) are available for commercial purchase. They allow developers to design, prototype and deploy custom hardware layouts to chips in order to perform calculations in a time defined and massively parallel way. Designing a standalone FPGA molecular dynamics solver is outside the scope of this work, and has already been achieved though it did not act as a co-processor to an existing molecular dynamics program [8, 7, 9]. The aim here is to determine, for large simulations involving the In-Vitro Transcription (IVT) process, what parts of the simulation would be best handed off to a custom hardware environment.

## Molecular Dynamics

There are two varieties of Molecular modeling, molecular dynamics and quantum dynamics. Both have their distinct advantages and disadvantages. Quantum Dynamics is the most computationally demanding, with it realistically being limited to small molecules, but provides the most information and most accurate capture of real phenomena. Molecular dynamics on the other hand can be used to simulate large systems with reasonable accuracy in timescales of nano and microseconds. It achieves this by abstracting the difficult calculations performed by QM systems, into lookup tables which can be later adjusted to better replicate experimental results for the research area the force field has been tuned to. Prominent force-fields are both CHARMM-39 and AMBER, with both being tuned for bio-molecules and their associated structures [12]. The sometimes-extensive parameterisation into these force fields represents a major drawback to molecular simulations, as optimised force-fields struggle to accurately model molecular behaviour outside of the target domain [1]. Approaches exist that both attempt to mitigate this and to increase the scope of molecular simulations by allowing for non-ground state simulations, with the methods allowing for good accuracy whilst maintaining reasonable calculation speeds [2]. Many other abstractions are made to MD simulations to make them more performant, one of the most prominent is the treatment of solvents in large simulation domains. Due to the nature of a solvent, its presence within the simulation is typically the dominant force, and without further abstractions or clever modelling methods - such as periodic boundaries, the simulation of the solvent can take up a large portion of the compute time taken to simulate each timestep. In simulation domains that use Particle Mesh Ewald (PME), the number of atoms scales in line with Equation 1. Where N is a real number of elements within the simulation and where the equation models the growth in compute complexity for N.

$$Cost(N) = \mathrm{N}\log(\mathrm{N}) \tag{1}$$

Because the solvent particles are not numerous, it is necessary to simplify the structure and define the number of electrostatic interactions, with the most common water solvent model being TIP3P, which has a fixed charge and 3 polar interaction sites [4]. Even with this abstraction, when simulating large biomolecules, establishing periodic boundaries may only have a limited effect on the number of solvent molecules. An alternative is to replace the individual solvent molecules with a continuum dielectric model which is sampled to generate the electrostatic forces, These implicit solvent models can offer significant performance benefits, up to 100 times faster for specific simulations with the AMBER implementation of Generalised Born (GB) [10]. Despite the improvements in simulation speed, the scaling of strict GB computation complexity is worse than that for explicit methods, Equation 2. Where *n* is the real number of elements within the simulation solvent.

$$Cost(n) = n^2 \tag{2}$$

Despite the worse computational complexity implicit simulation methods can sample the solvent space faster. Though this faster simulation speed becomes more prominent when compared against explicit models with large solvent volumes. Using GB models also increases the design considerations of the simulation, as just as not all force-fields will produce accurate results, not all GB models are able to produce the same results in different simulation environments [3]. In addition, in order to facilitate the fast conformal sampling desired the collision frequency of the solvent is reduced, meaning that using implicit models necessitates the loss of viscosity modelling [10].

## Simulation Hardware

The majority of modern simulations are no longer performed on the CPU, both because of an increase in complexity and because there are alternative calculation methods in the form of consumer and datacenter GPUs which offer significantly better parallel performance. Instead, CPUs are used to orchestrate the management of the processes, and in multi-node simulations, to handle internode communication. There are two primary methods of GPU integration, the standalone method discussed already, AMBER PNEND manages all of the simulation steps on the GPU. Alternatively, the CPU will correlate and propagate the simulation timesteps, whilst the GPU performs all of the calculations on the data. This method is beneficial as it allows for the coordination of more resources, with simulations being able to be performed over multi-nodeGPU systems, though has a significant drawback in that the data is not available instantly. The primary method for connecting CPU and GPU systems is the PCIe bus, which has a non-trivial multi mi-

crosecond latency [13], especially between complex devices. This connection lag becomes more problematic as GPUs become more powerful, essentially meaning that devices are sitting idle for longer, increasing the amount of time required to run the simulation. New hardware designs such as Heterogeneous System Architecture can be used to mitigate this latency, which allows both devices to have a unified memory pool, eliminating the need to transfer the data. Other GPU bound processes also experience this problem, and other Host-Device communication protocols exist, which have lower latencies, such as NVLink for use in SXM socket GPUs.

As might be expected from CPUs, they are designed for general purpose compute tasks, GPUs whilst being specifically tuned for graphics operations, at least originally, are capable of doing a great many things. Though when performing computational work, the specific area of interest is typically the floating point mathematical operations they can carry out in parallel. This means that only a section of each chip will be operating, whilst the entire chip is powered on and operating. This presents a problem, as the throughput of the chip is limited by the number of physical compute cores and the operating speed of the chip. Increases in the chip speed lead to higher power consumption, including powered on components, such as memory banks, that are not being used. Additionally, in order to focus on Artificial Intelligence workloads like training and inference, manufacturers are reducing the amount of single and double precision floating point computing to dedicate more chip space to half and float8 workloads, though there are ways to recover some of this loss, and it is more prevalent in consumer grade chips [5].

In cases where standalone or co-processor GPU workloads are not supported, CPUs need to be used, at a significant performance penalty. This can be mitigated by using high core count chips, such as the Neoverse series of ARM chips, which are capable of scaling to 128 individual cores and performing 16 Fused Add Multply operations per cycle [6].

Instead of taking the general purpose approach to hardware, it is possible to use FPGAs, which sit in between the general purpose hardware solutions and completely custom Application Specific Integrated Circuits (ASICs), a category which both CPUs and GPUs fall into. As discussed earlier they allow for the design and implementation of custom hardware designs, which can be entire algorithms and allow for complete flexibility in their implementation; at least within the bounds of the FPGA manufacturer. The designs are typically limited in speed to the MHz range, which when compared to modern CPU and GPUs appears to be a significant performance reduction. FGPA designs are specific to the desired task, minimising the amount of general purpose overhead the chips must perform, and the large number of onboard components allows for them to maintain many data processing pipelines, which encourages parallel operation. Having the physical program laid out in the hardware allows for data to be processed at every step along it, rather than just at the instruction pointer like in a CPU. As well as MD solvers for FGPAs as mentioned earlier, solvers have also been created for ASICs, in the form of ANTON and MDGrape [14, 15]. With the FPGA hardware solutions holding their own against contemporary GPU hardware and the ASIC solutions capable of performing multi microsecond simulations per day. However, ASIC development costs are extraordinarily high, being in the region of Millions of USD, which places them out of the scope of many developers. In addition to this cost, because of the fixed nature of the designs, hardware must be extensively tested to ensure there are no bugs, with this verification typically being performed in FPGA based hardware. Both custom hardware solutions have significant efficiency benefits over complete GPUs however, which can consume up to 500W. This can be a critical factor, especially if simulations are being performed over a significant length of time, and helps to reduce the overall cost of the simulations, as whilst both custom solutions have a higher setup cost, the running costs can be significantly less.

## SIMULATION

Molecular Dynamics is a very capable tool for investing bio-molecules, as they are typically very complex and consequently reactions are not well understood. This is why simulation techniques must be implemented to investigate what cannot be observed directly. As such predicting protein physical properties and interactions with other molecules are important problems to the development of better healthcare. Whilst also being difficult to observe, some interesting but complex processes are also very expensive to investigate. One of these being mRNA, which even in research grade environments can easily consume USD$10,000 to USD$100,000 in materials over a set of experiments. mRNA investigation has gained significant traction after the pandemic, due largely to the fact that it uses the bodies own protein synthesis mechanisms to deliver the designed biological payloads, whether these be vaccines or therapeutic payloads. The process of mRNA manufacturing is an area of intense development, and in many cases determining specific reaction kinetics, such as the Activation Energy, Gibbs Free Energy and reaction coordinate diagrams would allow for the production of better higher order models. Which in turn would allow for experiments to be planned to both corroborate results and plot out the manufacturing space.

T7RNA transcriptase is a relatively large protein, and

the DNA molecular structures and mRNA chains are long, which prevents the use of tight periodic boundaries within the simulation. Not all of the reactions that involve these species are appropriate, the interaction of covalent bonds cannot be modeled using MD, and instead a mixed QM/MD approach must be used. Simulations that break ionic bonds however, are not restricted. This leads to the use of large solvent volumes which must be solved for each timestep. If a correlation between the simulation temperature and the Gibbs free energy was desired then an explicit solver would need to be used. Though in the case of the reaction coordinate diagram, a faster implicit solver could be used. Knowing that it is likely that the simulation run time will largely be dominated by electrostatic forces, the electrostatic interaction algorithm could make an impactful first target for transition to a FPGA based co-processor.

## Approaching electrostatic interactions.

In order to take advantage of the hardware co-processor being a part of the system, both the general purpose electrostatic algorithm, which supports both the explicit solvent model and inter-atomic electrostatic interactions, and the implicit solvent model should be implemented. As discussed previously, the hardware designs take up physical space on the FGPA, this is in antithesis to how CPUs work, which operate on information at the instruction pointer and is not dissimilar to how GPUs are designed, though the embedded pipelines tend to be more general. In order to take the greatest advantage of the physical nature of the design, most FGPA designs operate like pipes, taking data and using the design to transform it into the desired output, which allows for more data to be processed at a time. The downside of the physical layout is that there are finite resources available onboard, and increasingly complex pipelines reduce the number that can be fit in parallel onboard, which in turn reduces the calculation throughput.

### Designing

Since the idea is to use this as a co-processor to assist in calculations being performed on a host, it makes sense to convert parts of an existing simulation program to ensure maximum compatibility. This also allows for comparisons to be made between the co-processor and original code, to help eliminate any calculation drift or bugs that were introduced in the transfer. It is possible to convert the existing code almost directly into a Hardware Description Language (HDL) through a process known as High Level Synthesis (HLS). Though this approach is almost entirely automated, it can struggle to develop performant designs both due to the existing code semantics being designed for a general purpose architecture. The most performant option would be to port the algorithms by hand to HDL, which would allow for them to be tightly coupled to the physical resources onboard the FPGAs as it allows for complete control over the physical hardware implementation. This process is very labour intensive and requires all of the support infrastructure to be instantiated manually, such as the memory controllers. Though most importantly, especially so for long, mathematically intensive algorithms, it would require that all of the floating point units be designed and linked up by hand.

### Mitigation

Laying out the structure of the floating point operations manually in the hardware represents a significant amount of work, not only does it involve instantiating the hardware, but also determining how the data will flow through it. In order to do this in a scalable way, a semi-supervised automation approach is suggested as it would be easier to manage than a fully automated approach that would inherit the same problems as HLS. In this semi-supervised approach, the algorithm would be broken down into a graph representation, where nodes represent individual calculation steps, and the connections between them the flow of the data.

Once the pipeline is in this format, the physical layout can be organised by a series of optimisation algorithms, which determine where the most low-latency operations would be required, and where calculations are able to take longer to resolve. Once the fast and slow data paths have been determined, the configuration of the nodes can be transformed into instantiated floating point units, before being placed onto the FPGA fabric. This approach allows for designs to be optimised by configurable constraints, which supports flexible designs without having to rewrite large sections of the hardware design.

## CONCLUSION

Both FPGA and ASIC solutions are very competitive against modern hardware when running in stand-alone configurations, and will likely compare well in comparison to co-processor designs as they are all equally limited by the latency of the PCIe bus. Even outside of a speed comparison, FPGA solutions are more energy efficient than the alternatives making them a compelling choice. Though compared to stand-alone solutions an electrostatic co-processor is limited, it could potentially be beneficial for large solvent volumes within transcription simulations, and further developing a semi-supervised process for designing floating point algorithms would be helpful when expanding the design to become a self-sufficient solution.

## ACKNOWLEDGEMENTS

I would like to acknowledge Crina-Maria Pricop for helping me write this paper, her patience was enormously

helpful. I would like to thank Joan Cordiner for being an excellent supervisor.

## REFERENCES


1. V. Zapletal et al., “Choice of Force Field for Proteins Containing Structured and Intrinsically Disordered Regions,” Biophysical Journal, vol. 118, no. 7, pp. 1621–1633, Feb. 2020, doi: https://doi.org/10.1016/j.bpj.2020.02.019.
2. A. Warshel and M. Levitt, “Theoretical studies of enzymic reactions: Dielectric, electrostatic and steric stabilization of the carbonium ion in the reaction of lysozyme,” Journal of Molecular Biology, vol. 103, no. 2, pp. 227–249, May 1976, doi: https://doi.org/10.1016/0022-2836(76)90311-9.
3. A. V. Onufriev and D. A. Case, “Generalized Born Implicit Solvent Models for Biomolecules,” Annual Review of Biophysics, vol. 48, no. 1, pp. 275–296, May 2019, doi: https://doi.org/10.1146/annurev-biophys-052118-115325.
4. C. Vega and E. de Miguel, “Surface tension of the most popular models of water by using the test-area simulation method,” The Journal of Chemical Physics, vol. 126, no. 15, p. 154707, Apr. 2007, doi: https://doi.org/10.1063/1.2715577.
5. Hiroyuki Ootomo and R. Yokota, “Recovering single precision accuracy from Tensor Cores while surpassing the FP32 theoretical peak performance,” International Journal of High Performance Computing Applications, vol. 36, no. 4, pp. 475–491, Jun. 2022, doi: https://doi.org/10.1177/10943420221090256.
6. ARM Holdings, “Neoverse V1 introduction,” Jun. 2021. Accessed: Jan. 04, 2025. [Online]. Available: https://teratec.eu/library/pdf/forum/2021/A05-03.pdf
7. Brahim Betkaoui, D. B. Thomas, and W. Luk, “Comparing performance and energy efficiency of FPGAs and GPUs for high productivity computing,” Dec. 2010, doi: https://doi.org/10.1109/fpt.2010.5681761.
8. C. Yang et al., “Fully integrated FPGA molecular dynamics simulations,” arXiv (Cornell University), Nov. 2019, doi: https://doi.org/10.1145/3295500.3356179.
9. P. Hamm, “Toward an FPGA-based dedicated computer for molecular dynamics simulations,” The Journal of Chemical Physics, vol. 162, no. 5, Feb. 2025, doi: https://doi.org/10.1063/5.0248834.
10. R. Anandakrishnan, A. Drozdetski, Ross C. Walker, and Alexey V. Onufriev, “Speed of Conformational Change: Comparing Explicit and Implicit Solvent Molecular Dynamics Simulations,” Biophysical Journal, vol. 108, no. 5, pp. 1153–1164, Mar. 2015, doi: https://doi.org/10.1016/j.bpj.2014.12.047.
11. Wilfred and A. E. Mark, “Validation of molecular dynamics simulation,” vol. 108, no. 15, pp. 6109–6116, Apr. 1998, doi: https://doi.org/10.1063/1.476021.
12. K. Vanommeslaeghe et al., “CHARMM general force field: A force field for drug-like molecules compatible with the CHARMM all-atom additive biological force fields,” Journal of Computational Chemistry, vol. 31, no. 4, pp. 671–690, Mar. 2010, doi: https://doi.org/10.1002/jcc.21367.
13. N. Zilberman *et al.*, “Where Has My Time Gone?” Accessed: Mar. 14, 2025. [Online]. Available: https://api.repository.cam.ac.uk/server/api/core/bitstreams/b0e91ca7-9b3b-4f31-b1d8-05c6668c8a66/content
14. D. E. Shaw *et al.*, “Anton, a special-purpose machine for molecular dynamics simulation,” *ACM SIGARCH Computer Architecture News*, vol. 35, no. 2, pp. 1–12, Jun. 2007, doi: https://doi.org/10.1145/1273440.1250664.
15. Itta Ohmura, G. Morimoto, Y. Ohno, A. Hasegawa, and Makoto Taiji, “MDGRAPE-4: a special-purpose computer system for molecular dynamics simulations,” vol. 372, no. 2021, pp. 20130387–20130387, Aug. 2014, doi: https://doi.org/10.1098/rsta.2013.0387.


© 2025 by the authors. Licensed to PSEcommunity.org and PSE Press. This is an open access article under the creative commons CC-BY-SA licensing terms. Credit must be given to creator and adaptations must be shared under the same terms. See https://creativecommons.org/licenses/by-sa/4.0/



Systems & Control Transactions

**Research Article - Peer Reviewed Conference Proceeding**
ESCAPE 35 - European Symposium on Computer Aided Process Engineering
Ghent, Belgium. 6-9 July 2025
Jan F.M. Van Impe, Grégoire Léonard, Satyajeet S. Bhonsale,
Monika E. Polańska, Filip Logist (Eds.)

PSE PRESS

# An Automated $CO_2$ Capture Pilot Plant at ULiège: A Platform for the Validation of Process Models and Advanced Control

**Cristhian Molina-Fernández[a]*, Patrick Kreit[a], Brieuc Beguin[a], Sofiane Bekhti[a], Cédric Calberg[a], Joanne Kalbusch[a], and Grégoire Léonard[a]**

[a] University of Liège, Department of Chemical Engineering, Sart-Tilman, Liège, Belgium
* Corresponding Author: cmolinafernandez@uliege.be.

## ABSTRACT

The deployment of $CO_2$ capture technologies at a large scale will largely benefit from the knowledge acquired during pilot testing. A mobile $CO_2$ capture pilot unit is currently being designed at the University of Liège. Here, the pilot plant is introduced, and the column sizing results are presented. The sizing was performed with a process model built in Aspen Plus. Overall, the pilot installation is expected to serve for process model validation, data collection and technology de-risking while assisting Belgian industries in their transition towards carbon neutrality.

**Keywords**: CO2 capture, MEA, pilot, ASPEN PLUS

## INTRODUCTION

As the European Union accelerates its efforts to decarbonize society, pilot installations play a pivotal role in validating both emerging and established technologies within the field of carbon capture (CC) [1]. Numerous CC pilot projects have been carried out in European countries such as the Netherlands, UK, Norway, Poland, Germany, Denmark, and Switzerland. This extensive testing has yielded parametric studies, validation of steady state and dynamic models, characterization of process emissions, determination of solvent corrosion behavior and degradation, comparison of different solvents, testing of different analytical tools, improved process modifications, and studies on control strategies [2,3]. Nevertheless, the high uncertainty across the whole $CO_2$ value chain prevents the large-scale deployment of such technologies.

Currently, supported by the European Union's Recovery and Resilience Facility, the Products, Environment, and Processes (PEPs) group at the University of Liège (ULiège) in Belgium is leading the construction of several key pilot installations, including a mobile $CO_2$ capture pilot plant, a $CO_2$-to-kerosene conversion unit, and a direct air capture (DAC) test bench.

The mobile $CO_2$ capture pilot plant will utilize chemical absorption to capture about 1 ton of $CO_2$ per day. The unit has been designed to operate with the benchmark solvent monoethanolamine (MEA). However, other solvents such as carbonates can be employed too. As shown in Figure 1, the installation is housed within three 20-foot shipping containers to support easy transport and deployment at various industrial locations. Two adjacent maritime containers enclose most of the process equipment as well as part of the electric cabinets. From these containers protrude the main columns. To render the unit more flexible, it comprises a gas pretreatment section that includes dust, $NO_x$, and $SO_x$ removal by bag filters, selective catalytic reduction, and alkaline scrubbing, respectively. These pretreatment steps are crucial to ensure the long-term performance of the unit by mitigating solvent degradation [1]. The plant is fully electrified, and its maximal power consumption is estimated to be 100 kW. Moreover, a heat pump is integrated into the system to enhance energy efficiency by recovering heat from the condenser and upgrading it for reboiler use. The automation and control system are centralized in the third container. The unit features a high degree of automation for remote and extended operation. This level of automation supports continuous data collection, which is essential for validating computational models and applying advanced control strategies, such as

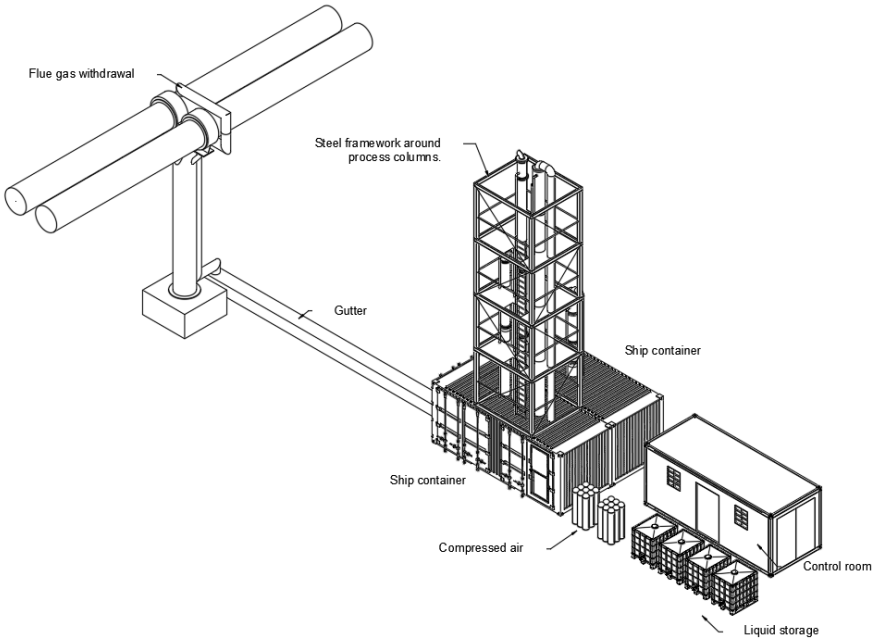



**Figure 1.** 3D plan of the $CO_2$ capture unit and its connection to the flue gas pipelines of the central heating station of the Sart-Tilman campus.

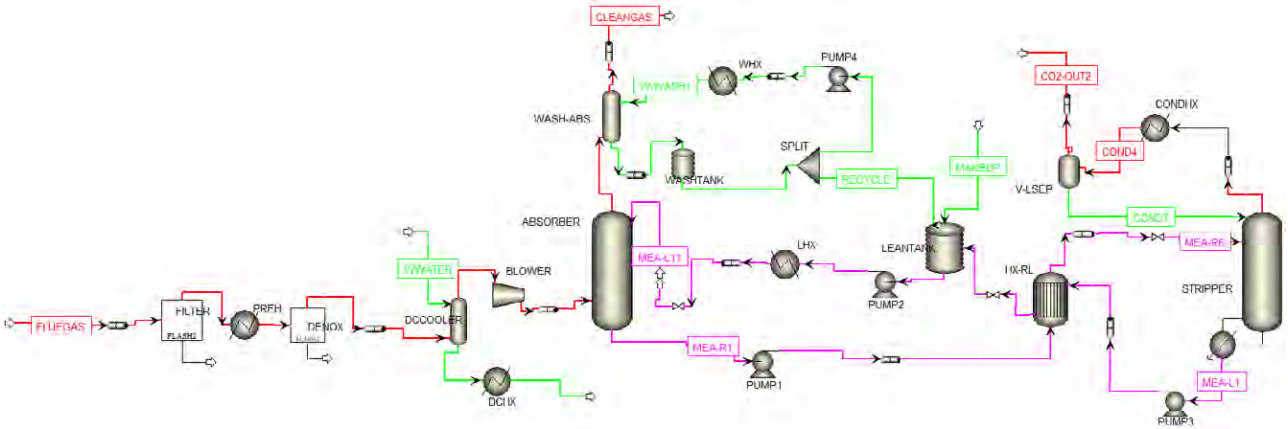



**Figure 2.** $CO_2$ capture pilot model in Aspen Plus.

machine learning algorithms [4,5]. Extended operation provides critical information to test solvent stability, understanding corrosion behavior, and refining steady state and dynamic process models—key factors for scaling up CC technology.

Commissioning and the first experimental campaigns are expected to take place at the central heating station at the Sart Tilman campus of ULiège in early 2026. Here, the pilot plant will treat a slipstream of the flue gases produced by a 7 $MW_{th}$ biomass cogeneration unit. All details of the unit, including the simulation files, PFD, P&ID, 3D plans, HAZOP tables and equipment, accessories, and instrumentation specifications will be made available after the commissioning and first experimental tests to facilitate the quick deployment of similar installations.

This work aims at introducing the model used to design the pilot and the main sizing results.

## MODEL DESCRIPTION

A model was built in Aspen Plus V11 to perform the basic engineering, see Figure 2. The thermodynamic model was set as the standard ENRTL-RK method [6]. Direct contact cooler, absorber (absorption and washing sections), and stripper (desorption and washing sections) were simulated using Rate-based modeling [6]. To simulate the reaction of $CO_2$ with the solvent, the following set of reactions were considered [6].

$$CO_2 + MEA + H_2O \rightarrow MEACOO^- + H_3O^+ \quad (1)$$

$$MEACOO^- + H_3O^+ \rightarrow CO_2 + MEA + H_2O \quad (2)$$

$$CO_2 + OH^- \rightarrow HCO_3^- \quad (3)$$

$$HCO_3^- \rightarrow CO_2 + OH^- \quad (4)$$

$$MEA + H_3O^+ \leftrightarrow MEAH^+ + H_2O \quad (5)$$

$$HCO_3^- + H_2O \leftrightarrow CO_3^{2-} + H_2O^+ \quad (6)$$

$$2H_2O \leftrightarrow H_3O^+ + OH^- \quad (7)$$

Reactions 1-4 are kinetic reactions whereas the rest are fast enough to consider them equilibrium reactions. Two different sets of values of the pre-exponential factors and activation energies were used for the absorber and stripper [6]. Some parameters of the rate-based model were tuned following the recommendations from [7] while the rest were left with the default values. A discretized film was only considered for the liquid phase. The number of discretization points was 5, whose thicknesses were fixed with a discretization ratio (ratio of film thickness between two adjacent discretization regions) of 10. Segments closer to the gas-liquid interface are thinner. The selected type of discretization option is geometric as it is expected to provide a better reproduction of $CO_2$ concentration profiles in the reactive film with fewer points. The reaction condition factor was 0.9 because of the fast reaction rate between $CO_2$ and MEA. The flow model was set to mixed to improve conversion.

The washing section of the absorber was modeled separately. Despite being inside the same vessel, this is consistent with the actual process as the washing section features a liquid collector with total draw-off to avoid mixing washing water and solvent inside of the absorber. On the other hand, the washing section of the stripper is modeled in the same block because of the presence of a collector-distributor above the first desorption bed. Both absorber and stripper were modeled using 20 stages while the direct contact cooler and the absorber washing section with only 10.

To facilitate conversion, the solvent loop is broken in the model. Consequently, the lean solvent loading fed to the absorber was fixed to the optimal value (determined by a sensitivity analysis using Equilibrium-based modeling) and a Design Spec (DS) was utilized to vary the lean solvent flow rate to achieve a given capture rate (usually 90%). Another DS was introduced to vary the reboiler duty of the stripper so that the amount of $CO_2$ recovered matches that captured in the absorber. Similarly to [8], the water balance in the solvent loop was kept by varying the temperature of the water fed to the washing section of the absorber. Thanks to these three DS, the composition of the lean solvent at both sides of the broken loop was very similar.

The model also includes most of the process pumps, piping, and gas filters. Due to the limited temperature of the gases fed to the pilot, an electric gas heater is going to be installed to ensure the effectiveness of the SCR filters. Finally, the $CO_2$ purification and compression sections are excluded from the model because they are not currently present in the pilot design.

## MODEL VALIDATION

Firstly, the reliability of the thermodynamic model was challenged by examining the prediction of the $CO_2$-MEA-$H_2O$ equilibrium at temperatures relevant for the absorber and desorber. As shown in Figure 3, the model provided an accurate determination of the $CO_2$ loading in MEA solutions in the required temperature range.

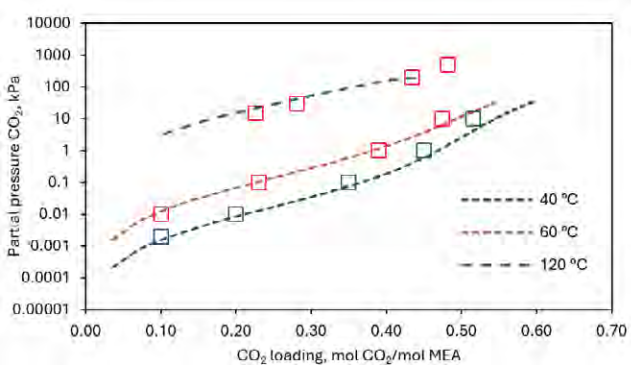



**Figure 3.** Validation of $CO_2$-MEA-$H_2O$ equilibrium. Experimental data (□) was obtained from [9].

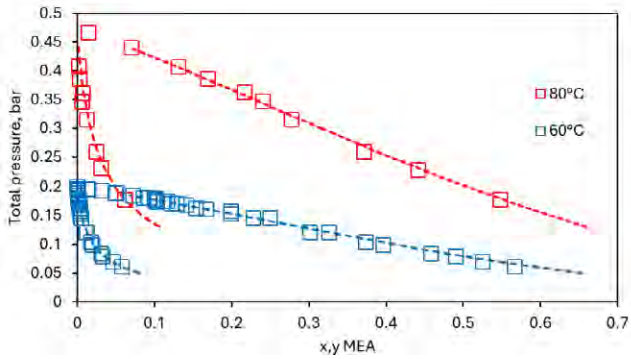



**Figure 4.** Validation of the MEA-$H_2O$ VLE equilibrium. Experimental data (□) was retrieved from [10,11].

MEA emissions are a concern from both an economic and safety point of view. Amine losses must be compensated by an MEA make-up stream. Additionally, MEA is a hazardous chemical for human health. The main points of solvent emission in the plant are the gaseous streams leaving the top of the absorber and stripper. A common solution to tackle the emissions is to install a water-wash section and a demister on the top of both columns. Experimental data from the MEA-water vapor-liquid equilibrium (VLE) was validated with the simulation tool before addressing the sizing of washing sections. Two temperatures were examined, 60 and 80°C. For both, there is a good agreement between the

experimental data and the model, see Figure 4. To further evaluate the capacity of the simulator to predict the emissions of the absorber and stripper, a literature survey has been conducted to identify MEA emission data from pilot plant installations. Measurements of total emitted MEA (in the form of vapor MEA, entrained droplets, and aerosols) were performed at the TNO's $CO_2$ capture pilot plant [12]. The MEA emission values were around 407-466 mg/STP $m^3$ (dry gas) right after the absorber. A water wash step and a conventional demister can reduce the total emissions to about 46%. A Brownian Demister Unit was necessary to further diminish the emissions to ~99%. From the total emissions encountered at the absorber outlet (before the water washing), it is expected that about 200 mg/STP $m^3$ are due to vapor MEA (gas temperature 30-40°C). This value is in the same range as the experimental volatility data when applied to the absorber top conditions, i.e., a concentration of vapor MEA of 285 mg/$Nm^3$ (50°C, 0.25 mol $CO_2$/mol MEA for the lean solvent loading) [13]. It is difficult to validate the data from the TNO's $CO_2$ capture pilot plant as the lean solvent loading is not provided and certain data must be traced from different documents. Nevertheless, a few simulations indicated that the predicted vapor MEA emissions on top of the absorber are in the same range.

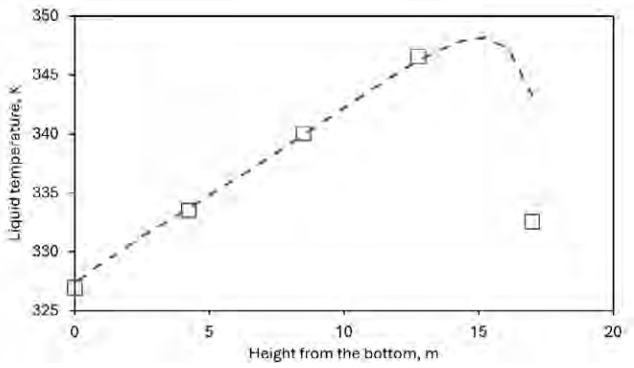



**Figure 5.** Validation of temperature profile in the absorber. Experimental data (□) was obtained from [15].

**Table 1:** Validation of absorber outputs. Data from [14].

| | Experimental | Model |
|---|---|---|
| $pCO_2$ in, kPa | 2.69 | 2.62 |
| $pCO_2$ out, kPa | 1.13 | 1.22 |
| Rich loading, mol/mol | 0.40 | 0.40 |
| T gas out, °C | 54.4 | 54.5 |

The capacity of the model to predict the behavior of the absorber was evaluated by comparing experimental data from pilot installations to simulated results. Two sets of data were utilized for the validation: Run 12 by Tobiesen et al. at Gløshaugen pilot (SINTEF-NTNU), Norway [14] and Run 1-A2 by Razi et al. at the large-scale Esbjerg CESAR pilot plant, Denmark [15]. Particularly, the absorber outputs and the temperature profiles along the column. The data shows the typical temperature bulb in the absorber temperature profiles caused by the exothermic $CO_2$ absorption.

Similarly, for the desorption unit, the simulation was validated employing data from two different installations: Run 1 by Tobiesen et al. at Gløshaugen pilot (SINTEF-NTNU), Norway [4], and Run 47 by Dugas at the pilot plant from the University of Texas at Austin [16]. The data from the latter pilot was retrieved from [7].

As portrayed in Figures 5 and 6 and Tables 1 and 2, the model was able to reproduce the experimental results to a certain extent. Increasing the number of column segments, the number of liquid thin film discretization points or changing the flow model did not improve the results significantly, indicating that the uncertainty could be coming mainly from the reliability of the kinetic data or the quality of the inputs for the modeling validation.

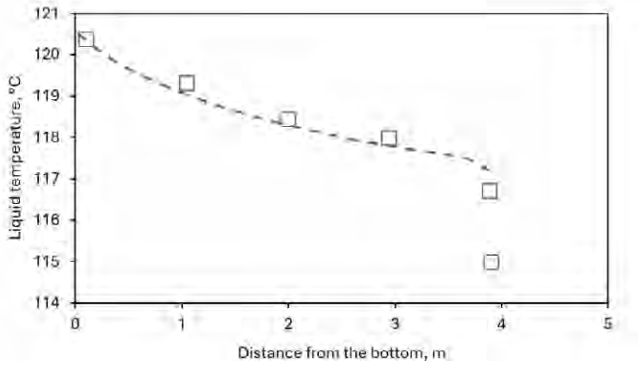



**Figure 6.** Validation of temperature profile in the stripper. Experimental data (□) was obtained from [4].

**Table 2:** Validation of stripper outputs. Data from [7].

| | Experimental | Model |
|---|---|---|
| $CO_2$ product, kg/h | 92 | 101 |
| Lean loading mol/mol | 0.29 | 0.24 |

Because of the limitations on data availability, validation results were obtained by modeling standalone equipment instead of the complete flowsheet. However, the latter was employed for the results discussed in the following sections.

## COLUMN SIZING

Packed columns typically operate in the range between 30-80% of the gas flooding velocity. The range of flue gas flow rates fed to the absorber was determined based on the desired capture scale (1 ton $CO_2$/day) and the $CO_2$ concentration encountered in the fumes produced by the biomass boiler of the Sart Tilman campus (about 10%$_{V\ dry}$). Considering the design (maximum) flue gas flow rate, 360 kg/h, and the available ASME pipes,

the absorber diameter has been fixed to 0.25 m allowing the column to operate at a flooding capacity between 50-85% in a broad range of solvent flow rates, 300-1000 kg/h. The gas flow rate could be varied between 180-360 kg/h without flooding the column (780 Kg/h solvent). Note that the flooding conditions are default parameters in Aspen Plus. The diameter of the stripper is equal to the absorber. In this regard, the stripper is oversized. However, this guarantees a larger flexibility of the vessel and the possibility of operating it under a slight vacuum.

To determine the required absorber height, the lean solvent concentration has been set to 5%$_w$ $CO_2$ (~0.23 mol $CO_2$/mol MEA) which is close to the optimum observed in the literature [17,18]. With the specified lean solvent conditions, a smaller column height can deliver the same performance at the expense of higher solvent flow rates than a taller one. Since the amount of solvent affects the reboiler duty, larger columns would lead to lower energy requirements in the stripper. Thus, there is a trade-off between CAPEX and OPEX. Similarly, a shorter stripper would require more energy to regenerate the solvent. The required packing height in both absorber and stripper was estimated by a sensitivity study. As shown in Figure 7, increasing the packing height reduces the specific reboiler duty. However, once a certain value is attained, further increases only lead to marginal improvement. Although it was not considered in the model, in practice, to limit the overall height of the pilot, the required packing in the absorber was distributed in two vessels. Thus, there are two absorbers connected in series in the pilot unit. The desorber height influences the required reboiler duty mildly, see Figure 8. As indicated in the figure, the diminution in energy consumption becomes marginal after 5 m of height.

In the model, the packing of both columns was the commonly employed Sulzer Mellapak™ 250.Y [6].

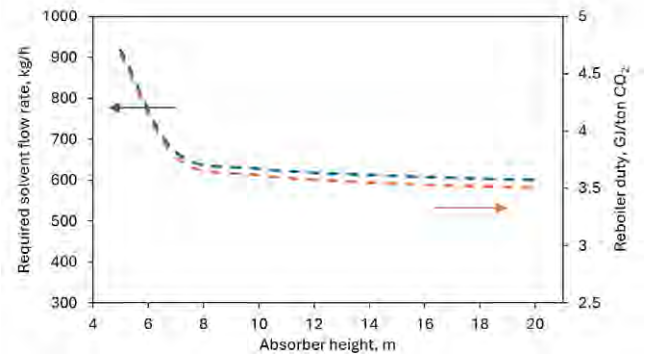



**Figure 7.** Effect of packing height in the absorber column on the specific reboiler duty.

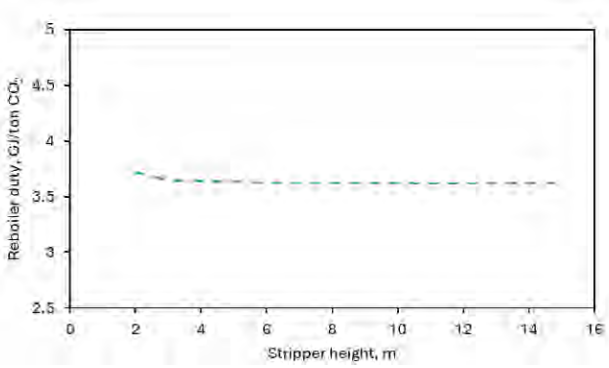



**Figure 8.** Effect of packing height in the stripper column on the specific reboiler duty.

At the top of the second absorber is the washing section which has the same diameter. The washing section fulfills two objectives: to control the water balance and to reduce MEA volatile emissions. As shown in Figure 9, both washing water temperature and flow rate can be used to keep the water balance. On the other hand, the packing height was determined using a sensitivity analysis on the recovery of volatile MEA, see Table 3. As indicated in the table, the washing water temperature and flow rate have a minor effect in comparison to the packing height.

For the stripper washing section, since the amount of volatile amine in the $CO_2$ product was fairly small after the condenser, the packing height was kept to 1 m.

**Table 3:** Sensitivity analysis on the recovery of volatile amine (%) by the water washing section on top of the absorber.

| | | Packing height, m | | | |
|---|---|---|---|---|---|
| **Water temperature, °C** | **Water flow rate, kg/h** | 0.5 | 1 | 1.5 | 2 |
| 30 | 1000 | 75.9 | 87.1 | 92.0 | 95.4 |
| 40 | 1000 | 75.7 | 87.0 | 91.9 | 94.5 |
| 40 | 500 | 75.0 | 96.5 | 91.6 | 94.2 |

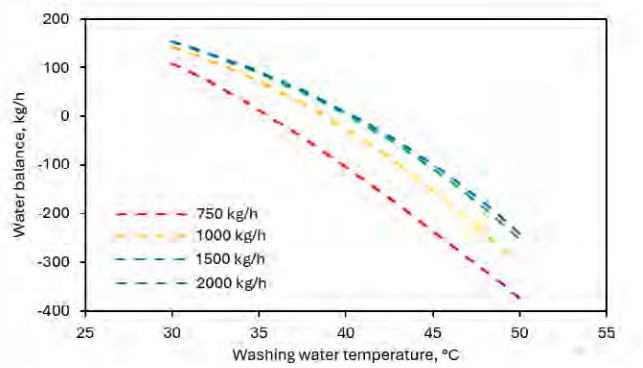



**Figure 9.** Water balance as a function of washing water flow rate and temperature in the washing section of the absorber.

## CONCLUSIONS

A 1 ton/day $CO_2$ mobile capture pilot is being designed at ULiège, Belgium. The main process equipment, notably the columns, have been sized utilizing a model built in Aspen Plus. From a sensitivity study, it was determined that the required absorber and stripper packed bed heights. Beyond those points, further increments in height did not cause a significant reduction in the reboiler duty. The effect of increasing the height is more marked for the absorber. The washing section of the absorber was set to ensure substantial recovery of volatile amines. Cooling washing water flow rate and temperature had minor effects on the separation. Being less relevant, the washing section of the stripper was shorter. Ongoing work will provide more details about the basic and detailed engineering of this project. Moreover, the models will be validated after the first experimental campaigns.

## ACKNOWLEDGEMENTS

The authors want to thank the organizations who are supporting this project and the coauthors of the present paper. In particular, the European Union Recovery and Resilience Facility is supporting the experimental developments. The authors were supported by diverse Walloon Region projects, a FEDER project (DECARBOWAL), as well as by a FNR-FNRS FRIA grant (for Brieuc Beguin).

## REFERENCES

1. Buvik, V. et al. A review of degradation and emissions in post-combustion $CO_2$ capture pilot plants. *International Journal of Greenhouse Gas Control* 106: 103246 (2021) https://doi.org/10.1016/j.ijggc.2020.103246
2. Idem, R. et al. Practical experience in post-combustion $CO_2$ capture using reactive solvents in large pilot and demonstration plants. *International Journal of Greenhouse Gas Control* 40:6-25 (2015) https://doi.org/10.1016/j.ijggc.2015.06.005
3. Nessi, E. et al. A review of research facilities, pilot and commercial plants for solvent-based post-combustion $CO_2$ capture: Packed bed, phase-change and rotating processes. *International Journal of Greenhouse Gas Control* 111:103474 (2021) https://doi.org/10.1016/j.ijggc.2021.103474
4. Tobiesen, F. A. et al. Experimental validation of a rigorous desorber model for $CO_2$ post-combustion capture. *Chemical Engineering Science* 63(10):2641–2656 (2008) https://doi.org/10.1016/j.ces.2008.02.011
5. Li, F. et al. Modelling of a post-combustion $CO_2$ capture process using neural networks. *Fuel* 151:156-163 (2015) https://doi.org/10.1016/j.fuel.2015.02.038
6. Li, BH. et al. Simulation and analysis of $CO_2$ capture process with aqueous monoethanolamine solution. *Applied Energy* 161:707-717 (2016) https://doi.org/10.1016/j.apenergy.2015.07.010
7. Madeddu, C. et al. $CO_2$ CAPTURE BY REACTIVE ABSORPTION-STRIPPING: MODELING, ANALYSIS AND DESIGN. *Springer* (2019)
8. Liu, F. et al. Evaluation on water balance and amine emission in $CO_2$ capture. *International Journal of Greenhouse Gas Control* 112:103487 (2021) https://doi.org/10.1016/J.IJGGC.2021.103487
9. Aronu, E. et al. Solubility of $CO_2$ in 15, 30, 45 and 60 mass% MEA from 40 to 120°C and model representation using the extended UNIQUAC framework. *Chemical Engineering Science* 66:6393-6406 (2011)
10. Kim, I. et al. Ebulliometric determination of vapor-liquid equilibria for pure water, monoethanolamine, N-methyldiethanolamine, 3-(methylamino)-propylamine, and their binary and ternary solutions. *Journal of Chemical and Engineering Data* 53(11): 2521-2531 (2008) https://doi.org/10.1021/je800290k
11. Pinto, D. et al. Vapor Liquid Equilibrium Measurements of Two Promising Tertiary Amines for $CO_2$ Capture. *Processes* 7(12):951 (2019) https://doi.org/10.3390/PR7120951
12. Khakharia, P. et al. Field study of a Brownian Demister Unit to reduce aerosol based emission from a Post Combustion $CO_2$ Capture plant. *International Journal of Greenhouse Gas Control* 28:57-64 (2024) https://doi.org/10.1016/j.ijggc.2014.06.022
13. Nguyen, T. et al. Amine volatility in $CO_2$ capture. *International Journal of Greenhouse Gas Control* 4(5):707-715 (2010) https://doi.org/10.1016/j.ijggc.2010.06.003
14. Tobiesen, F. A. et al. Experimental validation of a

rigorous absorber model for $CO_2$ postcombustion capture. *AIChE Journal* 53(4):846–865 (2007) https://doi.org/10.1002/aic.11133
15. Razi, N. et al. Validation of mass transfer correlations for $CO_2$ absorption with MEA using pilot data. *International Journal of Greenhouse Gas Control* 19:478–491 (2013) https://doi.org/10.1016/J.IJGGC.2013.10.006
16. Dugas, R. E. Pilot plant study of carbon dioxide capture by aqueous monoethanolamine. (2006)
17. Sanchez del Rio, M. et al. On the retrofitting and repowering of coal power plants with post-combustion carbon capture: An advanced integration option with a gas turbine windbox. *International Journal of Greenhouse Gas Control* 58:299–311 (2017) https://doi.org/10.1016/j.ijggc.2016.09.015
18. Xue, F. et al. A comparative study of MEA and DEA for post-combustion $CO_2$ capture with different process configurations. *International Journal of Coal Science & Technology* 4:15-24 (2017)

© 2025 by the authors. Licensed to PSEcommunity.org and PSE Press. This is an open access article under the creative commons CC-BY-SA licensing terms. Credit must be given to creator and adaptations must be shared under the same terms. See https://creativecommons.org/licenses/by-sa/4.0/



Systems & Control Transactions

**Research Article - Peer Reviewed Conference Proceeding**
ESCAPE 35 - European Symposium on Computer Aided Process Engineering
Ghent, Belgium. 6-9 July 2025
Jan F.M. Van Impe, Grégoire Léonard, Satyajeet S. Bhonsale,
Monika E. Polańska, Filip Logist (Eds.)

PSE PRESS

# New Directions and Software Tools Within the Process Systems Engineering Ecosystem

**S. Burroughs[a], B. Lincoln[b], A. Adeel[a], I. Severinsen[c], A. Lee[d,e], O. Amusat[f], D. Gunter[f], B. Nicholson[g], M. Apperley[a], B. Young[c], J. Siirola[g], and T. G. Walmsle[b*]**

[a] Ahuora – Centre for Smart Energy Systems, Department of Software Engineering, University of Waikato, Hamilton 3240, New Zealand
[b] Ahuora – Centre for Smart Energy Systems, School of Engineering, University of Waikato, Hamilton 3240, New Zealand
[c] Department of Chemical and Materials Engineering, University of Auckland, 5 Grafton Road, Auckland, 1010, New Zealand
[d] National Energy Technology Laboratory, Pittsburgh, PA 15236, United States of America
[e] NETL Support Contractor, Pittsburgh, PA 15236, USA
[f] Lawrence Berkeley National Laboratory, Berkeley, CA 94720, United States of America
[g] Center for Computing Research, Sandia National Laboratories, Albuquerque, NM, 87185, United States of America
* tim.walmsley@waikato.ac.nz

## ABSTRACT

Process Systems Engineering (PSE) provides the advanced conceptual framework and software tools to formulate and optimise well-considered integrated solutions that could accelerate the sustainability transition within the industrial sector. The landscape of advanced PSE is poised to undertake a considerable transformation with the rise in popularity of open-source and script-based software platforms with predictive modelling capabilities based on modern mathematical optimization techniques. This paper highlights three leading equation-based platforms—IDAES[1], Modelica[2], and GEKKO[3] — that are increasingly utilised for the modelling, simulation, and optimisation of complex systems within the advanced PSE domain, alongside the strengths and limitations of each approach. Following this, we present a framework through which emerging techniques within the domain of Software Engineering could be leveraged to address these limitations, with a vision of improving the accessibility and flexibility of complex modelling tools for industrial partners.

**Keywords**: Pyomo, Industry 4.0, Process Design, Simulation, Process Synthesis

## INTRODUCTION

Process Systems Engineering (PSE) emphasises the ability to appropriately model, analyse, and optimise systems that relate to the design, retrofit, and operation of processes throughout its life cycle. Chemical plants often comprise multiple interacting processes, each of which involves complex, non-linear dynamics. Accurate models are necessary to establish the economic viability and chemical feasibility of processes of a plant and any changes. This is particularly relevant when considering the increase in global regulation requiring adherence to specific targets for greenhouse gas emissions and pollution reduction and the integration of renewable energy.

From the inception of PSE as a field of study, mathematical models often based on first-principles relationships have been developed to capture the complex interactions within unit operations and between components of plants. Relationships can also be data-driven using classical regression or modern machine learning methods, such as physics-informed neural networks (PINN) [1-2]. These models form systems of equations involving

[1] https://idaes.org/
[2] https://modelica.org/
[3] https://machinelearning.byu.edu/

integer variables, continuous variables, convex/non-convex relationships, and so on, that can be simultaneously solved to find the simulated solution (DOF=0) or optimal (and near-optimal) solution (DOF>0).

The PSE modelling approach is now well established and continues to progress with new advancements. Of particular note, several solvers have been developed specifically to solve formulated mathematical modelling problems, with both open source (e.g., IPOPT) and commercial solutions (e.g., BARON, Gurobi) accessible to researchers and industry [3]. These solvers represent verified programmes that enable practitioners to focus more on developing representative models, and less on the mechanics of how they are solved.

In a further step, Algebraic Modelling Languages (AML)s have also emerged to facilitate the faster development of models through systematic methods for expressing the equations using familiar mathematical notion and language. GAMS in the 1970's pioneered this level of abstraction, creating a comprehensive framework for capturing algebraic expressions. Similar open-source libraries built within modern programming languages are now seeing an upswing in use [4]. Of particular focus within this paper are the IDAES, Modelica, and GEKKO frameworks, each of which adopts an object-oriented approach to define properties and behaviours of modelled components, although with differing levels of abstraction [4-8]. To this end, IDAES and GEKKO are developed as open-source packages within Python, with components following a class structure that allows for the complex development of a system through the creation of modelled objects. In contrast, Modelica utilises a stand-alone language that follows the Modelica language specification.

The advance of AMLs has increased the accessibility of mathematical modelling, as demonstrated by the broad range of libraries developed within the Modelica community. However, broad adoption of such approaches is still limited by learning curve required to gain familiarity with the axioms and syntax of each respective framework, as well as broader experience in formulating models well suited to optimisation and proficiency with programming languages. Models are also constrained by the computational resources that are available to the solver.

At the opposite end of the abstraction spectrum lies process simulators such as Aspen Plus, Aspen HYSYS, gPROMS, CadSIM, DW Sim, and many more. Each of these simulators provide a "drag and drop" approach to adding/removing/modifying operations to a flowsheet while in the background models are being generated and solved. Advanced users can customise nearly all aspects of the flowsheet but not the mathematical model. Furthermore, once a complex flowsheet is built, there is no possibility to export the mathematical model to form a light-weight representation that could be solved independently.

In this paper, we discuss the IDAES, Modelica, and GEKKO frameworks and propose that advances within the domain of Software Engineering can be leveraged to better address current deficiencies in abstraction, computational resourcing, and modern software application development practices. Nearly all simulators predate modern software engineering practices (e.g., only DW Sim has an interactive web-based platform). As a result, their adoption of such practices and advances are constrained. To this end, we present a framework through which complex modelling capabilities can be enhanced and integrated into a unified and accessible software tool that follows a modular architecture, allowing for the integration of individual capabilities, developed as stand-alone modules, into a central system. This framework has a focus on User Experience (UX) based design, with data structures that are obscured from the user behind a UI, allowing for information to be stored in a standardised form that can be filtered for use across multiple analysis modules. Significantly, this framework leverages containerisation and cloud orchestration technologies to improve accessibility and performance by removing conflicts that arise when producing software solutions for heterogeneous hardware configurations and Operating Systems.

## MATHEMATICAL OPTIMISATION FRAMEWORKS

The frameworks explored within this paper are free-to-use and have established their capacity for the modelling, analysis, and optimisation of complex systems via the formulation of mathematical models created via an abstract AML syntax that are then passed to open source and commercial solvers. While the specifics of how this is accomplished differs between frameworks, as does the domain focus and accessibility model, there are strengths and limitations that are common across all approaches and speak to the broader need to improve accessibility and extendibility such that the benefits of mathematical models can be fully leveraged by those within the chemical process engineering domain.

IDAES and GEKKO are standalone packages, with modelling components developed within the Python programming language. GEKKO utilises its own AML formulation to achieve this, while the IDAES Core Modelling Framework (IDAES CMF) is built on top of Pyomo, a general-purpose Python AML. As Python packages, the creation of models within GEKKO and IDAES is achieved via the instantiation of defined classes as modelling objects. Models are specified as high level objects, from which complex behaviours can be captured through the incorporation of defined constants, parameters, and variables.

The intra-connectivity of models is established by relating model components through connections, intermediates, and equations in the case of GEKKO and arcs, expressions, and constraints in the case of IDAES. Once defined, models are optimised for a given objective function [9-11,6,8].

Modelica in contrast utilises its own language with a standardised approach for defining variables and behaviour. There are inherent trade-offs between these approaches. On the one hand, a proprietary syntax like that developed for tools within the Modelica framework ensures the consistency of modelled components and the compatibility of analysis techniques. Conversely, the Python based approach of IDAES and GEKKO presents a lower barrier to entry for users who are already familiar with the underlying syntax and concepts within Python as a higher level programming language, while also retaining the ability to integrate broader functionality within the Python ecosystem into the modelling process.

A key distinguishing feature between the frameworks is the primary use cases that they support. GEKKO is intended primarily for the dynamic optimisation and control of linear and non-linear systems, with an APMonitor executable providing solving capabilities. Specific libraries can be imported into GEKKO to extend this base functionality to incorporate Deep Learning and Machine Learning, as well as a chemical library that defines a flowsheet class, chemical compounds and thermodynamic properties. The relationship between GEKKO and its chemical library extension is somewhat analogous to that of IDAES and Pyomo, with Pyomo as a domain agnostic optimisation package and IDAES as a standalone library that leverages Pyomo capabilities to model problems within the domain of chemical engineering [12]. A core difference is that as a standalone modelling package, IDAES is much more feature-rich and comprehensive, with the core library providing capabilities to model unit operations and properties within chemical processes [8]. Specific libraries are also available for domain specific processes such as power generation, materials processing, and water purification, as well as further modelling extensions that support surrogate modelling and parameter estimation approaches and the incorporation of deep learning models trained through standard frameworks such as PyTorch and Keras [13]. As a well-established stand-alone modelling language, the ecosystem that has developed around Modelica is broad. Modelica has thus emerged as a framework for use in simulation of multi-domain dynamic systems, with libraries adhering to the Modelica specification released under both open source and commercial licences. This reflects the core strength of Modelica, being the ability to integrate dynamics across multiple domains into a single model for a given system [5,7,14].

While there are specific applications for which each framework is well suited - real-time optimisation and control for GEKKO, chemical process systems for IDAES, and multi-domain system modelling for Modelica – there are broader strengths and limitations that are applicable to all EOM frameworks. An obvious strength is the comparative performance of mathematical modelling approaches vs traditional simulation, due largely to the commercial and open source solvers that are available for computing solutions for well formulated models [3]. This is particularly relevant when considering the non-linear relationship between model complexity and solution space, for which the solving performance of traditional first principles based simulation engines becomes a clear bottleneck [15]. More significantly for chemical process engineering is the degree of customisation and extensibility that is available to an end user through mathematical modelling. Within traditional simulation engines, users are generally unable to access the expressions that govern the behaviour of modelled components. Furthermore, it is challenging to define and integrate new components. In contrast, using an AML it is possible to build new unit operations or property packages to suit the individual needs of a modelled system. This is exemplified within IDAES through their modular property package and reaction frameworks, as well as their generic *UnitModelBlockData* class, each of which can be implemented with custom configurations. In cases where dynamics are unknown for a given component within a system, surrogate models can be developed through machine learning techniques to capture the desired behaviours [16].

Common underlying limitations for all frameworks can broadly be captured under the scope of usability, accessibility, and extendibility. While the adoption of programming language-like syntax has greatly improved the usability of EOM frameworks, users are still faced with a steep learning curve to master the syntax and implementation of each AML, as well as the broader concepts and logic associated with the use of programming languages and environments. This is particularly challenging when considering IDAES wherein multiple layers of inheritance are implemented on top of base Pyomo classes, requiring a high degree of familiarity with the underlying source code to gain the full benefits. Furthermore, upon mastering the syntax and concepts of each AML, there is still a significant effort required to ensure that models are adequately specified with the correct number of degrees of freedom and can be initialised [17]. This limitation is recognised, with frameworks implementing approaches to abstract away the complexity of the underlying AML behind a User Interface (UI). In the case of GEKKO and IDAES this is limited to visualising and manipulating flowsheets after they have already been defined programmatically, although IDAES has also taken steps to provide users with Command Line Interface (CLI) diagnostics [17]. Modelica has open source and commercial tools to

provide a UI, however the open source UI of OpenModelica is somewhat unintuitive and outdated, while access to commercial versions is naturally constrained by cost. This issue of commercial vs open source development is also a core consideration for accessibility and extendibility. While the Modelica language specification has contributed to the development of an ecosystem of analysis packages, the creation of multi-domain models is predicated on the willingness and ability of the end user to pay for each of the commercial libraries that they require. Furthermore, to gain the best user experience when using these libraries, further costs must be borne to access relevant commercially developed UIs. Consequently, while the established nature of Modelica as a framework and its standardisation as an AML contributes to its extendibility, accessibility and collaboration is limited by its inherent commercial realities. GEKKO and IDAES are less established as frameworks but are entirely open source in their development, meaning that functionality is well suited to customisation and extension for user specific cases. Furthermore, the Python based nature of GEKKO and IDAES means that they are inherently compatible with other libraries that exist within the Python ecosystem, which is immense.

As a result of these observations, there is clear scope for the development of a generalised and intuitive, user experience-driven platform that is framework agnostic. Such an approach would provide the usability benefits of traditional process simulators, while retaining the extendibility and performance provided by mathematical frameworks. There are clear benefits that would result from such development, foremost of which is the ability to leverage the strengths of each framework and compare the resultant analysis for a given model. This benefit is not limited to EOM frameworks, as data within such a platform could be stored in a traditional database rather than existing explicitly within the context of any individual AML. Consequently, further forms of analysis that are not EOM based (such as Pinch Analysis or Heat Exchanger Network synthesis) could be performed on the same data, allowing for greater access to and integration of insights from such techniques. This would be of great benefit to chemical engineers seeking to design or analyse processes, as it would remove a lot of the time that is spent manually creating models across different frameworks and updating each with the results of another, as is the case in the current status quo.

## FRAMEWORK FOR A COMPREHENSIVE PLATFORM

There are two broad classes of problems that present bottlenecks to the uptake of robust equation-based modelling techniques: usability and compatibility. The modelling frameworks explored within this paper are all reliant on the user's familiarity with programming languages and development environments. Furthermore, each framework has its own respective axioms and syntaxes, with sophisticated capabilities inaccessible without significant legwork on the part of the user. This has contributed to the lack of extensive adoption of such frameworks outside of the research space.

Compatibility challenges extend beyond the scope of equation-based modelling, reflecting an issue that is more fundamental to modelling and optimisation in general: multiple forms of analysis and degrees of abstraction are often desirable, and it is difficult to integrate the insights from one approach into the formulation of another without considerable effort on the part of the end user. We propose a solution to these issues in the form of a comprehensive platform developed along software engineering methodologies.

### Addressing Usability Concerns

The fundamental issue at the core of usability challenges is the barrier to entry presented by the complex and abstract nature of modelling frameworks and syntax, as well as the inherent challenges in debugging models and interpreting results. We propose that to address this, a UX-focused UI should be developed independently from any single modelling framework. Interfaces should also be designed with a view of integrating further analysis and modelling functionality in the future, ensuring that the final solution does not suffer from the clutter that is associated with frequent retroactive additions. To this end, the design process should begin with initial consultation with intended users to elicit functional requirements and identify pain points with existing approaches, from which multiple draft prototypes should be developed to capture functionality and workflows. These steps should be repeated to select and refine the implementation, following which components should be developed from final prototypes.

The separation of concerns between front-end UI and backend data structures and modelling logic is part of a higher-level modular architecture that is a core feature of this framework. The modular components fall into the following three categories: front-end UIs, analysis, and data structures and APIs. UIs and analysis modules are developed independently of each other. The Front-end should have a focus on intuitive design and data interpretation, while analysis modules should be standalone packages. The link between front and back-end elements is established through a final module, which defines data structures and APIs.

Data structures can capture an exhaustive amount of information about a given system component beyond the scope of any individual modelling framework or form of analysis and can be informed by live sensor data. As further functionality is integrated into the platform,

additional properties can be added to the existing data structures as required, with new APIs managing the communication between the new module and the database. It is thus possible to retroactively integrate new features or properties without breaking existing models. Model data can also be filtered to display different abstractions or engage in multiple analysis functionalities, with each of them manipulating and modifying a shared data source, providing the user with a level of control over the detail and complexity of the UI, allowing for use by both basic and advanced users.

A modular architecture is further beneficial for maintaining code as modifications to the functionality of one module will not break the functionality of another. This supports a 'plug and play' approach for developing additional functionality. Each module is developed as a standalone package with a defined set of required parameters and accompanying tests to verify functionality. Database migrations are applied to integrate new properties into models, with UI components developed to manage interactions with the new module and an API layer developed to facilitate the communication of data between the database and the module.

## Leveraging Cloud Computing Strategies

The outlined modular architecture is well suited to deployment across a distributed system in the form of a microservice architecture [18]. This is achieved through a containerisation approach, which packages a process alongside its dependencies into a lightweight container image. Container images also define an Operating System (OS) that is required for the process, enabling processes with different OS requirements to run on the same system. In a microservice architecture, a complex application is separated into its constituent modular elements, each of which is then packaged as a containerised process. Containerisation has several benefits compared to more traditional monolithic application architectures [19]:

- Resource utilisation can be handled at a more granular level as each containerised process has its own respective allocations.
- The number of replicas for a containerised process can be increased or decreased. Requests can be handled by any replica.
- The impact of any given process failing is greatly reduced. functional replicas will automatically take up the jobs assigned to a failed container. Furthermore, containers can be quickly recreated as needed.

Kubernetes is a container orchestration platform that facilitates the management of containerised applications across a cluster of networked computational resources by encapsulating them within a higher-level "pod". This is achieved through a self-adaptive approach that leverages a control approach to match the running state of the application to an expected state. In practice, this means that Kubernetes allows for self-healing behaviour, wherein failed processes are automatically restarted, and autoscaling, where the number of container replicas for a given process will automatically increase and decrease in response to dynamic demand. A microservice architecture deployed to a Kubernetes cluster is visualised within figure 1.

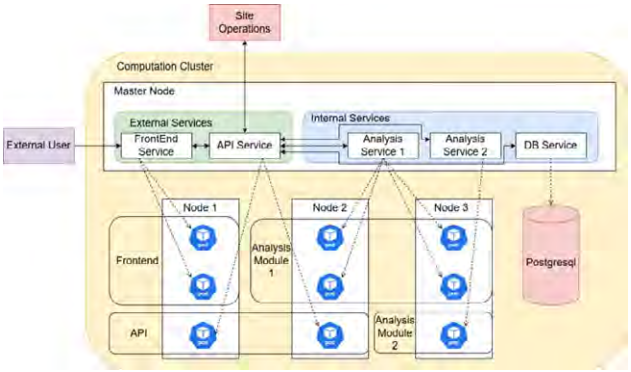



**Figure 1:** Microservice architecture deployed on Kubernetes.

As data is created or modified within the front-end, information is created or updated within the linked database. Upon engaging analysis functionalities, API calls extract relevant information from the database and send it to the relevant module. The results of the analysis are then returned to the database and displayed within the associated UI component. All interactions between a user and data within the platform are managed via UI components, with the actual data handling managed through APIs.

The integration of Kubernetes allows for an economic model that supports simultaneous commercial and open access releases, without limiting accessibility to core functionality. This can be achieved through the release the end software as a standalone containerised application that can be run on a local machine, or the release of standalone modules that could be integrated into other custom software. Conversely, more advanced users that wish to collaborate with others over shared models or require additional access to computational resources for parallel analysis could pay for access to the Kubernetes version, which is hosted externally. Such a financial model would support the continued development and maintenance of the software, while also ensuring that libraries remain open source and core capabilities are accessible.

## Key Directions for Future Research and Development

To adequately fulfil the vision that our presented

framework represents, the software platform must achieve the following outcomes:

- UI development should center around user experience, with primary consideration given to intuitive workflows.
- The platform should be agnostic with regard to modelling frameworks. Backend analysis modules should be able to automatically generate, export, and solve models using a framework chosen by the user.
- It should be freely available for research and development, with modules released as standalone, open source packages.
- It should leverage cloud computing paradigms such as containerisation to achieve optimal performance through scaling actions and avoid conflicts of OS or hardware configurations.

We envisage that such a platform would naturally fill a gap within the existing modelling ecosystem, improving accessibility to such tools and potentially extending in future to include multi-domain level analysis through the integration of additional modules.

## CONCLUSIONS AND FUTURE VISION

This paper has outlined the development of abstracted modelling within the process engineering domain, from initial verbose mathematical models to modern process simulation software and mathematical modelling frameworks. Three mathematical frameworks were chosen for their relevance to the chemical process engineering domain, as well as their individual implementation. Strengths and weaknesses for each framework were outlined, establishing advantages of mathematical modelling for performance and customisation while also highlighting the usability concerns associated with the steep learning curves required to gain proficiency. We then presented a framework through which the strengths of traditional process simulators can be combined with the powerful functionality of equation-oriented modelling via the adoption of modern software engineering concepts and methodologies for the development of a comprehensive software solution that allows for the integration of independent modules behind a single UI.

The vision we present for a software solution that follows the implementation path of our proposed framework is that of a centralised, comprehensive platform that serves as an intuitive interface through which users can access complex functionality. This platform would greatly contribute to the accessibility of advanced modelling capabilities by removing the requirements of familiarity with AML syntaxes and programming environments. Furthermore, the abstract nature of the data structures within this platform would also contribute to the integration of multiple disparate forms of analysis into a single shared knowledge base, greatly increasing the ability for engineers to integrate insights from multiple sources into a single model.

## ACKNOWLEDGEMENTS

This research has been supported by the program “Ahuora: Delivering sustainable industry through smart process heat decarbonisation”, an Advanced Energy Technology Platform, funded by the Aotearoa New Zealand Ministry of Business, Innovation and Employment.

This project was funded by the United States Department of Energy, National Energy Technology Laboratory, in part, through a site support contract. Neither the United States Government nor any agency thereof, nor any of their employees, nor the support contractor, nor any of their employees, makes any warranty, express or implied, or assumes any legal liability or responsibility for the accuracy, completeness, or usefulness of any information, apparatus, product, or process disclosed, or represents that its use would not infringe privately owned rights. Reference herein to any specific commercial product, process, or service by trade name, trademark, manufacturer, or otherwise does not necessarily constitute or imply its endorsement, recommendation, or favoring by the United States Government or any agency thereof. The views and opinions of authors expressed herein do not necessarily state or reflect those of the United States Government or any agency thereof. Sandia National Laboratories is a multimission laboratory managed and operated by National Technology and Engineering Solutions of Sandia LLC, a wholly owned subsidiary of Honeywell International Inc. for the U.S. Department of Energy's National Nuclear Security Administration under contract DE-NA0003525. This material is based upon work supported by the U.S. Department of Energy, Office of Science, under Contract No. DEAC02-05CH11231.

## REFERENCES

1. Daoutidis, P., Lee, J. H., Rangarajan, S., Chiang, L., Gopaluni, B., Schweidtmann, A. M., ... & Georgakis, C. (2024). Machine learning in process systems engineering: Challenges and opportunities. Computers & Chemical Engineering, 181, 108523.
2. Bishnu, S. K., Alnouri, S. Y., & Al-Mohannadi, D. M. (2023). Computational applications using data driven modeling in process Systems: A review. Digital Chemical Engineering, 8, 100111.
3. Lavezzi, G., Guye, K., Cichella, V., & Ciarcià, M. (2023). Comparative Analysis of Nonlinear Programming Solvers: Performance Evaluation, Benchmarking, and Multi-UAV Optimal Path

Planning. Drones, 7(8), 487.
4. Hedengren, J., & Nicholson, B. (2022). Open-Source Modeling Platforms (No. SAND2022-12379C). Sandia National Lab.(SNL-NM), Albuquerque, NM (United States).
5. Ploch, T., von Lieres, E., Wiechert, W., Mitsos, A., & Hannemann-Tamás, R. (2020). Simulation of differential-algebraic equation systems with optimization criteria embedded in Modelica. Computers & Chemical Engineering, 140, 106920.
6. Beal, L. D., Hill, D. C., Martin, R. A., & Hedengren, J. D. (2018). GEKKO optimization suite. Processes, 6(8), 106.
7. Fritzson, P., Pop, A., Abdelhak, K., Asghar, A., Bachmann, B., Braun, W., ... & Ostlund, P. (2022). The OpenModelica integrated environment for modeling, simulation, and model-based development. Mic.
8. Lee, A., Ghouse, J. H., Eslick, J. C., Laird, C. D., Siirola, J. D., Zamarripa, M. A., ... & Miller, D. C. (2021). The IDAES process modeling framework and model library—Flexibility for process simulation and optimization. Journal of advanced manufacturing and processing, 3(3), e10095.
9. Hall, K. K., Walmsley, T. G., Nemet, A., & Walmsley, M. (2022, September). Open-source tool for heat exchanger network synthesis. In PRES'22.
10. Udugama, I. A., Hall, K. K., Bayer, C., Young, B. R., & Walmsley, T. G. (2023). Real-time control and scheduling decision making in fermentation-based food process operations. In Computer Aided Chemical Engineering (Vol. 52, pp. 2381-2386). Elsevier.
11. Eslick, J. C., Zamarripa, M. A., Ma, J., Wang, M., Bhattacharya, I., Rychener, B., ... & Miller, D. C. (2022). Predictive modeling of a subcritical pulverized-coal power plant for optimization: Parameter estimation, validation, and application. Applied Energy, 319, 119226.
12. Nicholson, B., Siirola, J. D., Watson, J. P., Zavala, V. M., & Biegler, L. T. (2018). pyomo. dae: A modeling and automatic discretization framework for optimization with differential and algebraic equations. Mathematical Programming Computation, 10, 187-223.
13. Ceccon, F., Jalving, J., Haddad, J., Thebelt, A., Tsay, C., Laird, C. D., & Misener, R. (2022). OMLT: Optimization & machine learning toolkit. Journal of Machine Learning Research, 23(349), 1-8.
14. Ding, H., Li, W., Duan, C., Xu, H., Ding, P., Zhang, Y., & Hong, G. (2021). A thermal-hydraulic analysis model of printed circuit heat exchangers for system simulation using Modelica. Journal of Nuclear Science and Technology, 58(12), 1296-1307.
15. Valmari, A. (1996, September). The state explosion problem. In Advanced Course on Petri Nets (pp. 429-528). Berlin, Heidelberg: Springer Berlin Heidelberg.
16. Amusat, O. O., Atia, A. A., Dudchenko, A. V., & Bartholomew, T. V. (2024). Modeling Framework for Cost Optimization of Process-Scale Desalination Systems with Mineral Scaling and Precipitation. ACS Es&t Engineering, 4(5), 1028-1047.
17. Lee, A., Parker, R., Poon, S., Gunter, D., Dowling, A., & Nicholson, B. (2024). Model Diagnostics for Equation Oriented Models: Roadblocks and the Path Forward. National Energy Technology Laboratory (NETL), Pittsburgh, PA, Morgantown, WV, and Albany, OR (United States).
18. Pahl, C., Jamshidi, P., & Zimmermann, O. (2020). Microservices and containers.
19. Amaral, M., Polo, J., Carrera, D., Mohomed, I., Unuvar, M., & Steinder, M. (2015, September). Performance evaluation of microservices architectures using containers. In 2015 ieee 14th international symposium on network computing and applications (pp. 27-34). IEEE.

© 2025 by the authors. Licensed to PSEcommunity.org and PSE Press. This is an open access article under the creative commons CC-BY-SA licensing terms. Credit must be given to creator and adaptations must be shared under the same terms. See https://creativecommons.org/licenses/by-sa/4.0/



# Section 2

## Sustainable Product Development and Process Design

Systems & Control Transactions

**Research Article - Peer Reviewed Conference Proceeding**
ESCAPE 35 - European Symposium on Computer Aided Process Engineering
Ghent, Belgium. 6-9 July 2025
Jan F.M. Van Impe, Grégoire Léonard, Satyajeet S. Bhonsale,
Monika E. Polańska, Filip Logist (Eds.)

PSE PRESS

# Steady-State Digital Twin Development for Heat and Shaft-Work Integration in a Dual-Stage Pressure Nitric Acid Plant Retrofit

**Stanislav Boldyryev[a]* and Goran Krajačić[a]**

[a] University of Zagreb Faculty of Mechanical Engineering and Naval Architecture, Zagreb, Croatia
* Corresponding Author: stanislav.boldyryev@fsb.unizg.hr.

## ABSTRACT

This study focuses on enhancing heat and shaft power integration within existing nitric acid production processes to optimize waste heat recovery and identify opportunities to improve process efficiency. A digital twin of the operational plant is utilized, which features a dual-stage pressure nitric acid production process with a capacity of 50 tons/h of $HNO_3$ (100% equivalent). The authors conducted a simultaneous analysis of the thermal energy potential and the expansion capacity of tail gases to effectively fulfil the primary process's heating, cooling, and power requirements while increasing steam generation through waste heat recovery, all without compromising plant throughput. The proposed process modifications lead to a 23.8% reduction in cooling water usage and a 35.6% decrease in $CO_2$ equivalent emissions while achieving a 13.1% increase in steam generation. These utility savings culminate in a 10.2% enhancement in plant throughput.

**Keywords**: Energy Efficiency, Heat Exchanger Network, Modelling and Simulations, Process Synthesis.

## INTRODUCTION

Ammonia production contributes approximately 1.8% of global annual $CO_2$ emissions, equivalent to 439 million tons of $CO_2$ [1]. Nitric acid is produced through three well-established methods, with ongoing process improvements focusing on reducing nitrogen oxides ($NO_x$) in tail gases and enhancing productivity and energy efficiency. The mono-pressure process has been extensively studied; for instance, optimizations conducted in the ProSimPlus environment have led to a 55% reduction in NOx emissions and an 18% increase in productivity. However, this method necessitates cooling water at 5 °C, which requires additional energy for cooling [2]. A significant area of research remains centred on reducing nitrous oxide emissions in tail gases [3]. Recently, Clariant reported a reduction of $N_2O$ emissions by 690 kilotons per year of $CO_2$ equivalent using a new catalyst [4]. Catalyst ageing seriously challenges operating costs and $N_2O$ emissions, prompting extensive research efforts [5]. An exergy destruction analysis conducted on Ostwald-based plants indicated a high potential for improving energy efficiency [6]. Exergy analysis has been utilized for environmental impact assessments [7] and has subsequently been enhanced by sustainability evaluations, resulting in a 3% improvement in exergy efficiency through adjustments in compressor pressure [8]. Simulations of nitric acid plants have primarily focused on identifying optimal process parameters [9] and have been conducted using Aspen HYSYS [10] and Aspen Plus [11] commercial software to explore process parameter modifications and increase the concentration of final products. Some researchers have also implemented a pinch-based approach to improve nitric acid plants' heat exchanger network, highlighting a potential utility savings of 14%, excluding specific process changes and utilities [12].

Despite extensive research focused on optimizing nitric acid production processes, there remains a notable deficiency in the investigation of plants employing a dual-pressure method. Furthermore, energy consumption and emissions challenges continue to pose significant issues as society shifts towards circular production and consumption models. This study presents the findings from an investigation into dual-pressure nitric acid production through simulations of an existing facility. It analyzes energy and emission savings potential by integrating heat

and shaft work power. The theoretical potential and specific process modifications are examined using a simulation model, and the economic viability of these enhancements is also assessed.

## MATERIALS AND METHODS

The approach employed in this study is based on simulating the existing processes of a dual-pressure nitric acid plant coupled with a thermodynamic analysis of energy utilization. This approach aims to identify process modifications that can enhance the plant's overall performance. The integration of simultaneous thermal and shaft work power is evaluated while adhering to the existing equipment's constraints and the proposed solutions' economic viability. A comprehensive workflow outlining this approach is shown in Fig. 1.

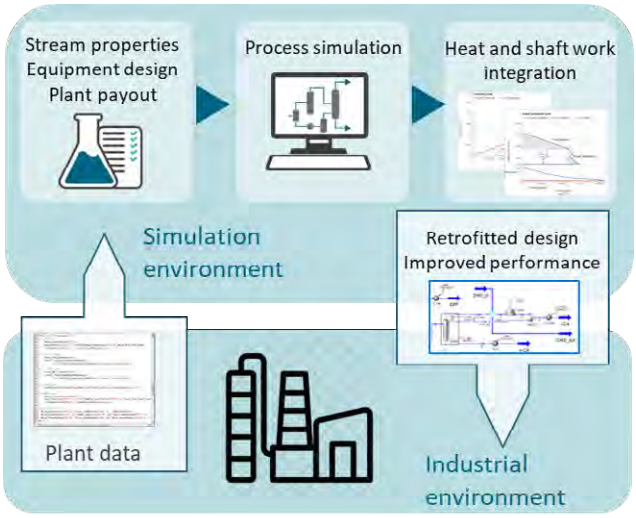



**Figure 1.** General workflow of the proposed method.

The investigated nitric acid plant was simulated utilizing UniSim Design software [13], and the simulation process flow diagram (PFD) is shown in Fig. 2.

### Simulation model set-up:

Materials are ammonia, air (feedstock), and nitric acid with a concentration of 60%wt in water (product). Fluid packages are extended NRTL and PRSV [14].

#### Chemical reactions

Ammonia conversion (conversion)

$$4NH_3 + 5O_2 \rightarrow 4NO + 6H_2O \ (-227 \ \frac{MJ}{kmole \ NH_3}) \quad (1)$$

$$4NH_3 + 3O_2 \rightarrow 2N_2 + 6H_2O \ (-317 \ \frac{MJ}{kmole \ NH_3}) \quad (2)$$

$$2NH_3 + 2O_2 \rightarrow N_2O + 3H_2O \ (-276 \frac{MJ}{kmole \ NH_3}) \quad (3)$$

Cooling and absorption of $NO_x$ (equilibrium)

$$2NO + O_2 \rightleftarrows 2NO_2 \ (-56.6 \frac{MJ}{kmole \ NO}) \quad (4)$$

$$2NO_2 \rightleftarrows N_2O_4 \ (-29.3 \frac{MJ}{kmole \ NO_2}) \quad (5)$$

$$3NO_2 + H_2O \rightleftarrows 2HNO_3 + NO \ (-12.7 \frac{MJ}{kmole \ NO_2}) \quad (6)$$

$$3N_2O_4 + 2H_2O \rightleftarrows 4HNO_3 + 2NO \ (33.3 \frac{MJ}{kmole \ N_2O_4}) \quad (7)$$

Tail gas treatment (catalytic)

$$2H_2 + O_2 \rightarrow 2H_2O (-484 \frac{MJ}{kmole \ O_2}) \quad (8)$$

$$2N_2O \rightarrow 2N_2 + O_2 \ (-81.6 \frac{MJ}{kmole}) \quad (9)$$

$$CH_4 + 2O_2 \rightarrow 2H_2O + CO_2 (-802 \frac{MJ}{kmole \ N_2O}) \quad (10)$$

$$CH_4 + 2NO_2 \rightarrow N_2 + 2H_2O + CO_2 \ (-435 \frac{MJ}{kmole \ NO_2}) \quad (11)$$

$$CH_4 + 4NO \rightarrow 2N_2 + 2H_2O + CO_2 \ (-291 \frac{MJ}{kmole \ NO}) \quad (12)$$

$$2CH_4 + 3O_2 \rightarrow 2CO + 4H_2O \ (-519 \frac{MJ}{kmole \ CH_4}) \quad (13)$$

$$CO + H_2O \rightarrow CO_2 + H_2 \ (-41.4 \frac{MJ}{kmole \ CO}) \quad (14)$$

$$NO + H_2 \rightarrow NH_3 + H_2O \ (-378 \frac{MJ}{kgmole \ NO}) \quad (15)$$

#### Specific variables

- $CO_2$ emission (Nat. gas) is 0.201 kg/kWh;
- $CO_2$ emissions of electricity (nat. gas) is 0.490 kg/kWh;
- nat. gas price is 0.110 €/kWh;
- calorific of natural gas is 42,000 kJ/m$^3$;
- electricity price is 0.24 €/kWh;
- nitric acid price is 0.23 €/kg;
- interest rate is 10%; project lifetime 5 years.

The following utilities are used: steam (2.2 MPa), electricity, cooling water, natural gas (97.4% $CH_4$, 2.6% $N_2$), and $N_2/H_2$ mixture (75% $H_2$, 25% $N_2$).

#### Process units' simulation methods

- Ammonia conversion: conversion reactor;
- Cooling: chemical equilibrium and heat transfer;
- Heat exchangers: sizing-based rating;
- Absorbers: rate-based radfrac model;
- Rotating units working curve-based rating.

The main modelling assumptions are feedstock flow rate is constant, heat losses not accounted, steady-state simulation mode, pipe pressure drop is not considered.

### Heat and shaft work power integration

The energy utilization efficiency in the simulated nitric acid production facility is evaluated in terms of thermal energy and mechanical power output. As detailed in work [15] and refined by various researchers, a systematic graphical methodology is implemented to identify

opportunities for optimizing heat recovery within the current process. This approach also aims to improve mechanical power generation, as suggested by Varbanov et al. [16], through strategic modifications to the process. The method leverages the thermodynamic potential of tail gas to produce mechanical power, which is subsequently harnessed for compressor operations. The proposed enhancements are scrutinized against the operational constraints of turbines and compressors. The maximum energy recovery potential is quantified while ensuring the plant maintains a consistent output level in alignment with the established baseline scenario. The analysis of capital costs for heat exchangers is conducted following the guidelines in [17]. In contrast, the capital costs for steam turbines and system upgrades are assessed according to results in [18], incorporating factors related to materials, pressure, and temperature. The integrated solution developed is evaluated for its capacity to enhance plant throughput by optimizing nitric acid production while adhering to the performance limitations of the existing equipment and the realized energy savings. The results from this analysis are contrasted with the baseline scenario, with particular emphasis on key performance indicators relevant to the plant's operation.

## CASE STUDY

The nitric acid production process under investigation commences with the catalytic conversion of ammonia to nitrogen monoxide through the oxidation of ambient air at low-pressure conditions. The resulting nitrogenous gases are directed to a waste heat recovery system, where steam is generated at a pressure of 4 MPa. Following this, the $NO_x$-rich gas is cooled using cooling water before entering a gas washer, where it is treated to eliminate by-products via the condensation of nitric acid. Upon washing, the $NO_x$-containing gas is subjected to high-pressure compression and subsequently routed into an absorption unit, where nitrogen oxides are absorbed by demineralized water, producing nitric acid. Thermal energy from gas cooling and absorption processes is recovered using cooling water in the main absorber and associated heat exchangers. The resulting nitric acid is funnelled to a purge column, where nitrogen oxides are purged, producing a final product with a concentration of approximately 60% (mass).

**Table 1:** Mass balance of the simulated nitric acid plant.

| | |
|---|---|
| **Feed streams (kg/h)** | |
| Ammonia | 14,801 |
| Air to conversion | 261,850 |
| Water to absorption | 18,742 |
| Feed water | 74,800 |
| Natural gas to fire heater | 1,140 |
| Air to fire heater | 22,237 |
| $N_2/H_2$ mixture to gas treatment | 80 |
| Steam-to-gas treatment | 10,000 |
| Natural gas to gas treatment | 1,280 |
| Steam to turbine (2 MPa) | 31,400 |
| Total | 436,331 |
| **Product streams (kg/h)** | |
| Nitric acid (final product) | 88,094 |
| Steam (4 MPa) | 64,134 |
| Boiler purging | 10,666 |
| Cooling air to turbines | 5,075 |
| Condensate | 31,400 |
| Total | 436,331 |

The tail gas that leaves the absorber is conveyed to a gas treatment unit designed to reduce $NO_x$ emissions and capitalize on the energy potential for operating oxygen and nitrogen gas compressors. The PFD for the simulation and the corresponding mass balance are

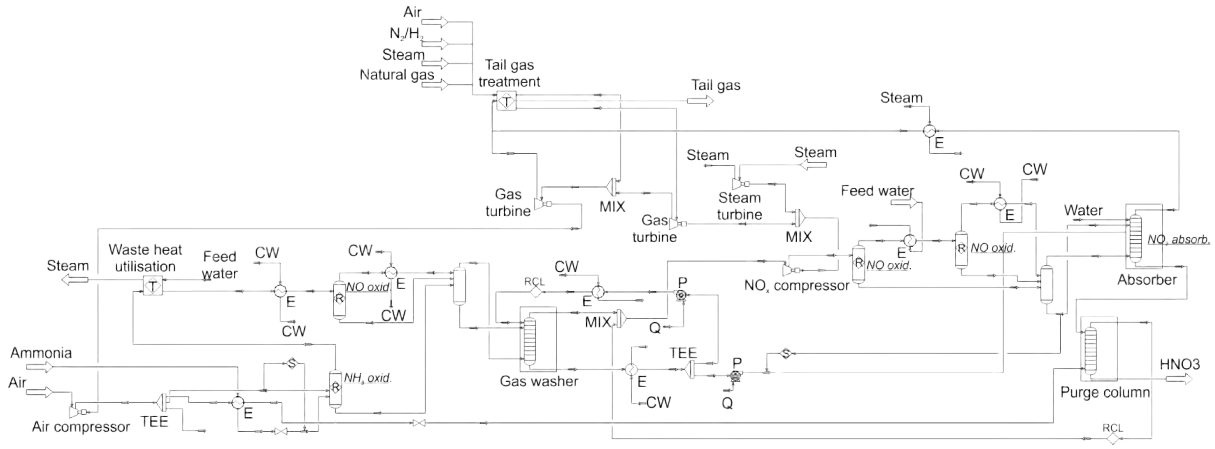



**Figure 2:** Simulation PFD of the current dual-pressure nitric acid plant. A – adjust of parameters; CW – cooling water; E – heat exchanger; MIX – stream mixer; TEE – stream splitter; P – pump; Q – power; R – reactor; RCL – process recycle; S – parameter set; T – sub-flowsheet.

presented in Fig. 2 and Table 1, respectively. Table 2 outlines the primary process parameters of the simulated nitric acid plant, highlighting deviations from the actual measured data from the existing operational plant.

**Table 2:** Process parameters of nitric acid plant.

| Parameter | Measured at plant | Simulated |
|---|---|---|
| Conversion reactor temperature (°C) | 868 | 859 |
| Ammonia/air ratio (%vol.) | 9.90 | 9.91 |
| Conversion ratio (%mol.) | 96.00 | 96.00 |
| Absorption ratio (%mol.) | 99.02 | 99.12 |
| Low-pressure level (kPa) | 418 | 418 |
| High-pressure level (kPa) | 1,072 | 1,072 |
| $O_2$ at absorber top (%mol.) | 2.40 | 2.40 |
| $NO_x$ in tail gas (ppm) | 224 | 181 |
| Tail gas temperature (°C) | 237 | 260 |
| $HNO_3$ concentration (%mass.) | 59.20 | 59.17 |
| Plant yield (t/h 100% $HNO_3$) | 51.90 | 52.12 |

## RESULTS AND DISCUSSION

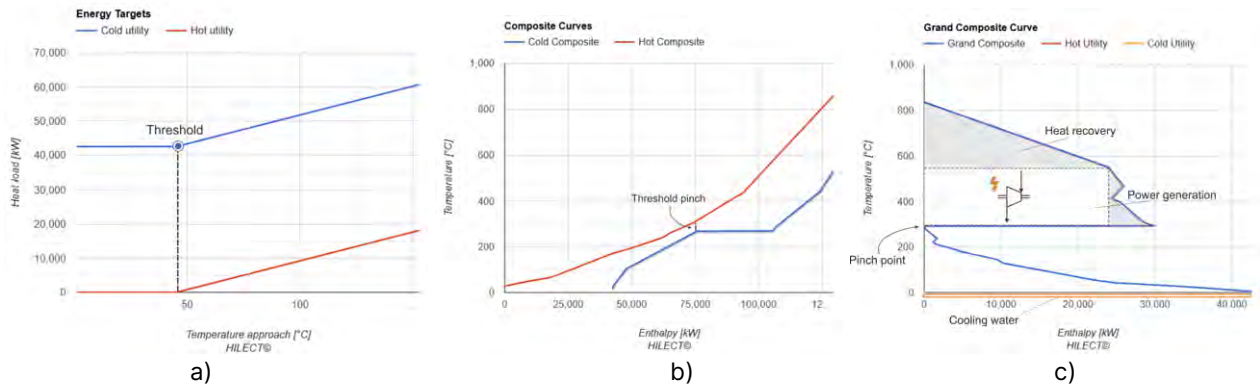
### Energy performance

The analysis of the energy performance of the nitric acid plant revealed significant potential for energy savings that can be incrementally achieved by enhancing heat recovery within the existing process. The thermodynamic potential for energy savings reaches up to 18.1 MW for both cooling and heating applications, which can be realized by optimizing the heat recovery network. The relationship between energy savings and the minimum temperature approach is illustrated in Fig. 3a. A bottleneck inhibits further energy reductions, which the threshold pinch point can explain. This threshold pinch point is identified at a minimum temperature difference ($\Delta T_{min}$) of 46 °C, as shown in Fig. 3b. However, this bottleneck can be mitigated by the addition of steam generation at 2.2 MPa, necessitating an increase in the heat transfer area and a revamp of the existing network. Additionally, there exists further cogeneration potential within the investigated plant, with a theoretical power production potential of 4.5 MW, as illustrated in Fig. 3c. The realization of the identified energy efficiency potential necessitates an upgrade of the process through the retrofitting of the feed water heater, waste heat recovery unit, and heat exchanger associated with tail gas treatment. To fully exploit the $NO_x$ gas's heat recovery potential and preheat the untreated tail gas, two new heat exchangers are required to replace the existing gas coolers. Additionally, a new steam turbine is necessary to capitalize on the cogeneration potential of the waste heat unit, assuming a polytropic efficiency of 69% for the new turbine, which is pertinent for mid-sized units [19].

The simulation of the retrofitted process flowsheet facilitates the assessment of the potential increase in plant throughput resulting from the conservation of energy resources. In addition to energy savings and enhanced throughput, the retrofitted process design contributes to a reduction in harmful emissions. This is achieved by lowering natural gas consumption for the fire heater of the tail gas treatment unit, reducing cooling water requirements, and increasing the efficiency of the cogeneration facility. The process flow diagram (PFD) of the retrofitted system, reflecting the increased yield, is provided in Fig. 4, and the key performance indicators of the process are detailed in Table 3.

### Process electrification and low-grade heat

The utilization of the energy-saving potential within the nitric acid plant demonstrates that all heating requirements can be internally satisfied, while any surplus heat necessitates additional cooling capacity. This cooling demand is met by the cooling water cycle, which is powered




a) b) c)

**Figure 3:** Graphical interpretation of energy targets for analysed nitric acid, threshold $\Delta T_{min}$=46 °C: a) energy targets; b) composite curve; c) grand composite curve.

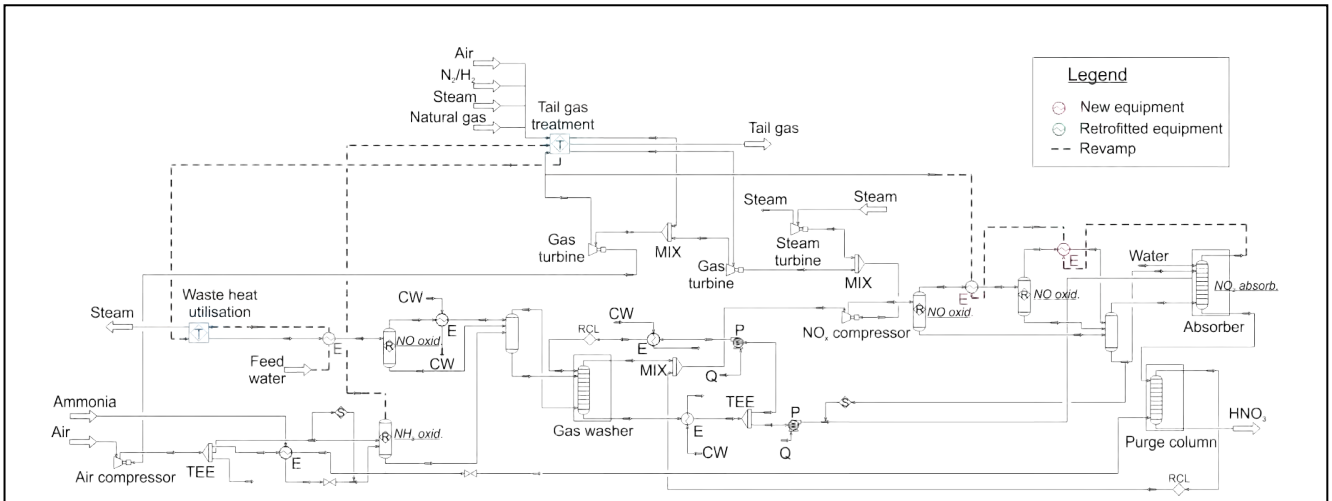



**Figure 4:** Simulation PFD of retrofitted dual-pressure nitric acid plant. A – adjust of parameters; CW – cooling water; E – heat exchanger; MIX – stream mixer; TEE – stream splitter; P – pump; Q – power; R – reactor; RCL – process recycle; S – parameter set; T – sub-flowsheet.

by electricity. However, the combustion of natural gas and a nitrogen/hydrogen ($N_2/H_2$) mixture continues to be employed for tail gas treatment. To facilitate a transition towards a fully electrified process with energy surplus capabilities, further investigation into the electrification of this part of the process is required. Despite the aforementioned process updates, there remains potential for further improvements within the investigated plant. According to the targeting procedure, a total of 42.6 MW of heat must be dissipated from the process through cooling. As illustrated in Fig. 3c, the temperature profile indicates that approximately 20 MW of this thermal energy can be utilized for district heating or other applications, with the remainder being addressed by the cooling water system. A thorough analysis of the effective utilization of this potential is warranted to capitalize on all available opportunities fully.

### Main limitations and future works

Future investigations may concentrate on the two previously mentioned issues and further alleviate the bottleneck associated with tail gas treatment caused by environmental regulations. Additionally, an analysis of the plant's operational lifespan in relation to the benefits of retrofit design should be conducted to assist plant owners in making informed decisions regarding the retrofitting of existing facilities. Moreover, the impact on the global fertilizer supply chain and other commodities should also be examined. The primary limitation to consider is the existing equipment design and plant layout, which significantly constrain any process updates or theoretical advancements. Furthermore, these types of processes typically have a limited operational lifespan, necessitating a trade-off decision between extending the facility's lifetime or investing in new structures.

**Table 3:** Main results of the nitric acid plant retrofit.

| Performance indicator | Base case | Improved process |
|---|---|---|
| Natural gas, $m^3/h$ | 3,528 | 2,239 |
| Cooling water, $m^3/h$ | 7,253 | 5,529 |
| $N_2/H_2$ mixture, t/h | 79.7 | 87.7 |
| Power generation, MW | 0.0 | 3.1 |
| Steam generation (4 MPa), t/h | 61.1 | 70.3 |
| $CO_2$ emissions, kt/y | 73.4 | 47.3 |
| Yield (100% $HNO_3$), t/h | 52.1 | 57.4 |
| Retrofit cost, € | - | 11,039,207 |
| Utility cost saving, €/y | - | 11,075,228 |
| Increased capacity, €/y | - | 9,995,800 |
| Payback period, y | - | 0.57 |

## CONCLUSIONS

The research findings highlight that existing dual-pressure plants still possess significant energy recovery potential. This potential was evaluated by developing a simulation model based on the actual operational processes of the plant, which was subsequently assessed and updated to integrate thermal energy and shaft work power effectively. Energy targets were established, and corresponding process modifications were proposed and simulated to validate the feasibility of these updates.

The primary outcome indicates that plant capacity can be enhanced by 10.2% through the debottlenecking of the energy system and improved utility efficiency. An analysis of capital expenditure recovery revealed a payback period of 7 months, assuming a 10% interest rate and a project lifespan of 5 years. Furthermore, the

environmental impact of the existing plant can be reduced by approximately 26.1 kt$CO_2$ per year. The results of this study are valuable for assessing the decarbonization potential within the fertilizer industry and for facilitating the electrification of existing processes during the transition to new sustainable chemical processes.

## ACKNOWLEDGEMENTS

This research is supported by the European Commission under the LIFE programme, project 101119793 – LIFE22-CET-SET_HEAT and HORIZON Europe programme, project 101136775 INITIATE.

## REFERENCES

1. Bouramdane AA. Multi-Criteria Evaluation of Carbon Capture Technologies in Steel, Cement, Petrochemical, and Fertilizer Industries: Insights for Emerging and Developed Countries. *Sci. Total Environ.* 957:177754 (2024) https://doi.org/10.1016/j.scitotenv.2024.177754
2. Nascimento GRO, Dangelo JVH. Operating Parameters Analysis of a Nitric Acid Plant to Increase Production and Reduce NOx Gases Emission. *Chem. Eng. Process. - Process Intensif.* 196:109662 (2024) https://doi.org/10.1016/j.cep.2024.109662
3. Pérez-Ramírez J, Kapteijn F, Schöffel K, Moulijn JA. Formation and Control of $N_2O$ in Nitric Acid Production. *Appl. Catal. B Environ.* 44:117–151 (2003) https://doi.org/10.1016/S0926-3373(03)00026-2
4. Clariant EnviCat N2O-S Catalyst to Cut CO2eq by 690,000 Tonnes/y at Hengli's Nitric Acid Plant in China. *Focus Catal.* 2024:6 (2024) https://doi.org/10.1016/j.focat.2024.11.063.
5. Aging of Industrial Fe-Zeolite Based Catalysts for Nitrous Oxide Abatement in Nitric Acid Production Plants. *Catal. Sci. Technol.* 12:7308–7321 (2022) https://doi.org/10.1039/d2cy01486f.
6. Buelvas Hernández A, Fajardo JG, Barreto D, Carrillo Caballero GE, Cárdenas Escorcia Y, Vidal Tovar CR, Gordon Hernández Y. Conventional and Advanced Exergoeconomic Indicators of a Nitric Acid Production Plant Concerning the Cooling Temperature in Compression Train's Intermediate Stages. *Case Stud. Therm. Eng.* 27:101214 (2021) https://doi.org/10.1016/j.csite.2021.101214.
7. Kirova-Yordanova Z. Application of the Exergy Method to the Environmental Impact Estimation: The Nitric Acid Production as a Case Study. *Energy* 36:3733–3744 (2011) https://doi.org/10.1016/j.energy.2010.12.039
8. Abbasian Hamedani E, Abdalisousan A, Khoshgard A, Nazari M. Energy, Exergy, and Sustainability Analysis of an Industrial Nitric Acid Plant. *Energy Sources Part Recovery Util. Environ. Eff.* 45:10952–10970 (2023) https://doi.org/10.1080/15567036.2023.2253762
9. Chatterjee IB, Joshi JB. Modeling, Simulation and Optimization: Mono Pressure Nitric Acid Process. *Chem. Eng. J.* 138:556–577 (2008) https://doi.org/10.1016/j.cej.2007.07.064
10. Abbasian Hamedani E, Hamidzadeh Z, Mousavi SA, Kariman A, Mahnesaei A. Simulation of a Nitric Acid Production Unit in Aspen Hysys, 9th International Conference on Technology and Energy Management, Behshahr, Mazandaran, Iran (2024)
11. Mukhitdinov D, Sattarov O, Akhmatov A, Abdullayeva D, Bekchanov E. Computer Simulation and Optimization of the Oxidation Process in the Production of Nitric Acid in the Aspen Plus Environment. *E3S Web Conf.* 417:05004 (2023) https://doi.org/10.1051/e3sconf/202341705004
12. Ivaniš G, Lazarevic M, Radovic I, Kijevcanin M. Energy Integration of Nitric Acid Production Using Pinch Methodology. *Hem. Ind.* 69:39–39 (2014) https://doi.org/10.2298/HEMIND140204039I
13. UniSim Design Suite. https://process.honeywell.com/us/en/products/industrial-software/process-optimization/unisim-design-suite
14. UniSim Design, Simulation Basis, Reference Guide, Release 492. Honeywell (2022)
15. Klemeš JJ, Varbanov PS, Alwi SRW, Manan ZA, Fan YV, Chin HH. Sustainable Process Integration and Intensification: Saving Energy, Water and Resources. Walter de Gruyter (2023)
16. Varbanov PS, Doyle S, Smith R. Modelling and Optimization of Utility Systems. *Chem. Eng. Res. Des.* 82:561–578 (2004) https://doi.org/10.1205/026387604323142603
17. Smith R. Chemical Process Design and Integration. Wiley (2016)
18. Peters MS, Timmerhaus KD. Plant Design and Economics for Chemical Engineers. McGraw-Hill (1980)
19. Liu M, Shi Y, Fang F. Combined Cooling, Heating and Power Systems: A Survey. *Renew. Sustain. Energy Rev.* 35:1–22 (2014) https://doi.org/10.1016/j.rser.2014.03.054

© 2025 by the authors. Licensed to PSEcommunity.org and PSE Press. This is an open access article under the creative commons CC-BY-SA licensing terms. Credit must be given to creator and adaptations must be shared under the same terms. See https://creativecommons.org/licenses/by-sa/4.0/



Systems & Control Transactions

**Research Article - Peer Reviewed Conference Proceeding**
ESCAPE 35 - European Symposium on Computer Aided Process Engineering
Ghent, Belgium. 6-9 July 2025
Jan F.M. Van Impe, Grégoire Léonard, Satyajeet S. Bhonsale,
Monika E. Polańska, Filip Logist (Eds.)

PSE PRESS

# Simulation of Decarbonization of Natural Gas to Methanol Conversion Process Using Microwave-Assisted Dry Reforming with Integrated Chemical Looping for Hydrogen Production

**Omar Almaraz[a], Srinivas Palanki[a], and Jianli Hu[a]***

[a] 1Department of Chemical and Biomedical Engineering, West Virginia University, Morgantown, WV 26506, USA
* Corresponding Author: srinivas.palanki@mail.wvu.edu

## ABSTRACT

In this research, a chemical looping scheme is combined with dry reforming of natural gas in a novel microwave reactor to produce industrial quantity of methanol. Simulation results show that the chemical looping scheme can produce all the hydrogen required by the methanol reactor as well as a significant portion of the carbon dioxide required for the syngas reactor. A heat exchanger network is developed to substantially reduce the hot and cold utility usage. A technoeconomic analysis indicates a significant positive net present value along with a substantial reduction in carbon dioxide emissions as well as a reduction in energy consumption.

**Keywords**: Microwave-assisted dry reforming, Chemical looping, Carbon-neutral methanol synthesis, $CO_2$ utilization, Decarbonization technologies

## INTRODUCTION

Methanol is valued for its versatility as a feedstock and energy carrier. As a key component in producing formaldehyde, acetic acid, and methyl tert-butyl ether (MTBE), it supports a wide array of industries, including plastics, textiles, and automotive. Methanol also plays a growing role in renewable energy solutions, such as biodiesel production and as a hydrogen carrier for fuel cells. Global demand for methanol estimated to be $41.91 billion by 2026 [1], driven by expanding applications in petrochemicals and clean energy technologies. As global efforts toward sustainability intensify, methanol's importance as a low-carbon fuel alternative is set to rise. While methanol can be produced from different feedstocks, the most common feedstock is natural gas, primarily because it is available in abundant quantities at a cost-effective price [2]. In this process natural gas (primarily methane) is reformed into synthesis gas (syngas), a mixture of carbon monoxide, carbon dioxide, and hydrogen via steam methane reforming (SMR), where natural gas reacts with steam at high temperatures (700–1,000°C) and in the presence of a nickel-based catalyst. Alternatively, autothermal reforming (ATR) or partial oxidation can be used, especially in large-scale plants. The resulting syngas is then passed through a methanol synthesis reactor under high pressure (50–100 bar) and moderate temperatures (200–300°C), where it reacts over a copper-based catalyst to form methanol. The crude methanol is subsequently distilled to remove water and other impurities, yielding high-purity methanol. This process accounts for the majority of global methanol production, leveraging natural gas as a cost-effective and abundant feedstock. However, this process is highly energy intensive and contributes to greenhouse gases (carbon dioxide) to the atmosphere. As a result, there is significant interest to explore alternative pathways for methanol production that are more energy-efficient and environmentally sustainable.

One promising method is the microwave-assisted conversion of natural gas to methanol via dry reforming. This method uses electromagnetic waves to activate the natural gas molecules and create reactive species that can react with oxygen or carbon dioxide to form methanol. The advantages of this method include operation at lower temperatures and pressures, reduced number of

process steps, enhanced selectivity, and yield of methanol, and the utilization of carbon dioxide as a raw material [3]. However, dry reforming requires a source of hydrogen and it important to consider the energy cost and environmental impact of hydrogen production when considering dry reforming of methane as an alternative route for producing methanol.

In this paper, we explore the use of a chemical looping scheme that produces two separate streams of hydrogen and carbon dioxide that are then utilized in the production of methanol via dry reforming. The overall objective of this research is to develop a simulation model of a novel decarbonized microwave-assisted dry reforming process integrated with chemical looping for methanol production. Specifically, three key objectives are pursued: (1) investigate the impact of replacing the conventional syngas reactor with a microwave reactor for dry reforming of methane, (2) explore the feasibility of utilizing chemical looping for utilizing methane to produce the required hydrogen for methanol production, and (3) conduct a techno-economic analysis to evaluate the viability of the integrated process.

## REACTION CHEMISTRY AND REACTOR DESIGN CONSIDERATIONS

The current industrial approach to produce methanol involves steam reforming of methane to produce syn gas followed by catalytical conversion of syn gas to methanol [4]:

$$CH_4 + H_2O \rightarrow CO + 3H_2 \quad (1)$$

Some of the carbon monoxide reacts further with steam to form carbon dioxide via the water-as shift reaction:

$$CO + H_2O \rightarrow C0_2 + H_2 \quad (2)$$

An alternative method to produce syn gas is via methane dry reforming (MDR), Which uses carbon dioxide as a reactant, making advantageous for reducing greenhouse gas emissions [5]. The MDR reaction can be represented by the following equation:

$$CH_4 + CO_2 \leftrightarrow 2CO + 2H_2 \quad (3)$$

The MDR reaction is thermodynamically favorable at high temperatures (800-1000 °C) and low pressures, but it requires a suitable catalyst to overcome the kinetic limitations and avoid the formation of carbon deposits. Once syn gas is produced, it is possible to utilize this intermediate to produce methanol [4]:

$$CO + 2H_2 \leftrightarrow CH_3OH \quad (4)$$

The hydrogen to carbon monoxide ratio needs to be adjusted to a 2:1 ratio. Typically, the dry reforming process does not produce sufficient hydrogen, and so additional hydrogen needs to be added to the feed stream of the methanol reactor. This provides the motivation to utilize a chemical looping reactor system that converts methane and steam into separate streams of hydrogen and carbon dioxide. The hydrogen is sent to the methanol reactor feed, and the excess carbon dioxide is recycled back to the syngas reactor for dry reforming.

## PROCESS MODELING

### Methodological Framework

This research is divided into the following sections: (1) steady-state model development, (2) heat exchanger network (HEN) design, and (3) techno-economic analysis. In the first step, a comprehensive process model is developed for the integrated microwave-assisted dry reforming (MDR) and chemical looping processes, followed by methanol synthesis and product purification. The purpose of incorporating chemical looping is to generate additional hydrogen, compensating for the lower stoichiometric ratio ($H_2$ - $CO_2$) / (CO + $CO_2$) produced in conventional dry reforming. The goal is to achieve the target ratio of 2, which is optimal for methanol synthesis. Chemical looping provides a steady hydrogen source through an indirect oxidation process, using metal oxides to facilitate controlled oxygen transfer and ensure the required stoichiometric balance. Key process information, reaction kinetics, and operating conditions are taken from recent studies on chemical looping and microwave-assisted MDR5, with feed specifications aligned with the commercial Natgasoline process [4]. The steady-state simulation, developed in Aspen Plus v11, includes syngas production, methanol synthesis, and product purification. Next, a detailed HEN is designed using Aspen Energy Analyzer (AEA) v11.0 software. The HEN design targets energy optimization by creating a network that maximizes heat recovery and minimizes utility consumption. This configuration balances utility costs with capital. The resulting HEN grid meets targeted utility requirements, capital constraints, and optimal surface area, enabling efficient heat integration both in the microwave-assisted and chemical looping processes. Finally, a techno-economic analysis (TEA) is conducted using Aspen Process Economic Analyzer (APEA) v11 to account for capital and operating costs based on the Aspen Plus simulation specifications. Key economic indicator such as net present value (NPV) is calculated to evaluate the profitability of this novel methanol production process.

Figure 1 shows a schematic of the novel microwave-assisted dry reforming process. While the process development closely follows the flowsheet that is utilized commercially at Natgasoline LLC, two major changes are made to the process. First, the steam is replaced by carbon dioxide in the feed to the syn gas reactor and

secondly, an additional hydrogen stream, which is produced by chemical looping, is added to the inlet of the methanol reactor to have the correct carbon monoxide to hydrogen ratio. The carbon dioxide produced via chemical looping is recycled to the syngas reactor feed. In addition, there is a change in the process equipment where the conventional multi-tubular syn gas reactor is replaced by a microwave reactor. The separation train of distillation columns are essentially the same type as those found in the Natgasoline process; however, since the flow rates of some of the gaseous components are different, these distillation columns are sized appropriately. The final product stream is 14,201 lbmol/h of 99.9% pure methanol, which is the same as that produced via the conventional Natgasoline process.

## ASPEN PLUS Modeling

The methanol production process is modeled in two integrated subplants: Subplant 1, which handles hydrogen generation through chemical looping, and Subplant 2, where syngas is synthesized using a microwave reactor, supplemented by the $H_2$ stream from Subplant 1. The thermodynamic package RK-SOAVE is used for the syngas part while NRTL is used for the methanol production part and PENG-ROBINSON is used for the chemical looping. In Subplant 1, the chemical looping process is configured as a three-reactor, countercurrent setup to enable hydrogen production and $CO_2$ capture, based on the conditions outlined in the work of Riley et al [5]. The looping system uses $CaFe_2O_4$ as an oxygen carrier, which alternates between oxidized and reduced forms to facilitate methane and steam conversion in a controlled series of reduction and oxidation cycles. Process feed conditions and specifications for this setup are summarized in Table 1. Conditions such as temperature, pressure, and gas flow rates, are adapted from Riley et al. [5], but are further adjusted to meet the specific $H_2$ demand of our methanol synthesis setup.

The chemical looping system operates as follows: Natural gas is introduced into the fuel reactor (FR) to react with the oxidized $CaFe_2O_4$, producing $CO_2$ and $H_2O$ while reducing the oxygen carrier. This stage is conducted at elevated temperatures, allowing efficient conversion of methane into products that can be further processed. In the air reactor (AR), the reduced $CaFe_2O_4$ is re-oxidized by reacting with air, regenerating the oxygen carrier. In the steam reactor (SR) the re-oxidized $CaFe_2O_4$ interacts with steam, producing $H_2$ and $H_2O$. The operating conditions for each reactor in the chemical looping process are shown in Table 2. The $H_2$ generated in this stage is directed to Subplant 2 to supplement the syngas stream, achieving the necessary $H_2$ ratio for methanol synthesis. In Subplant 2 the methanol production process utilized in this research is modeled similarly to the commercial setup at Natgasoline LLC, with adjustments to the syngas production, feed conditions, and reactor configurations [6]. The syngas feed for methanol synthesis is through a microwave-assisted dry reforming reactor, where methane ($CH_4$) and recycled carbon dioxide ($CO_2$) are converted into a syngas stream. This process is conducted at 800°C and 1 bar and is modeled as a stoichiometric reactor. The $H_2$ ratio in the syngas is optimized by supplementing it with hydrogen generated from the chemical looping process in Subplant 1. The operating specifications for the microwave-assisted syngas production are provided in Table 2. The conditioned syngas is then compressed to approximately 76 bar and distributed across two parallel methanol synthesis reactors, each operating at 254°C and 76 bar. Here, CO and $CO_2$ undergo hydrogenation in the presence of a Cu/Zn-based catalyst to produce methanol and water. The product gas from reactors is then preheated by exchanging heat with the reactor feed stream before undergoing a final conversion step in an additional reactor operated

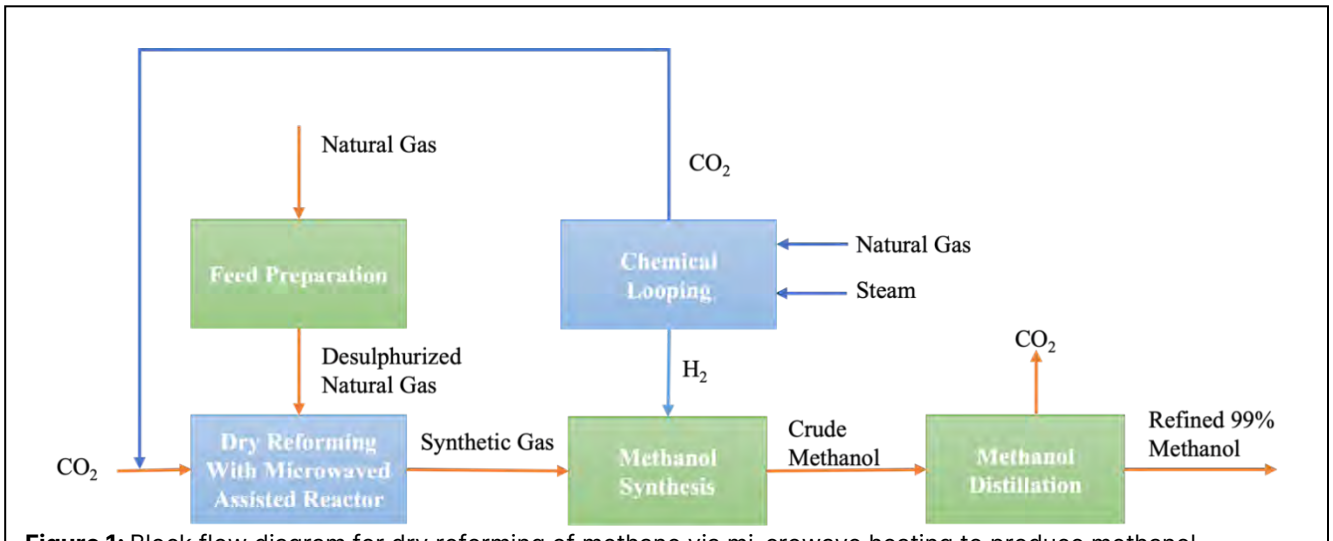



**Figure 1:** Block flow diagram for dry reforming of methane via mi-crowave heating to produce methanol.

**Table 1:** Feed Specifications for Syngas and Chemical Looping Processes

| | Natural Gas | | | Water | $CO_2$ | CAFE | Air |
|---|---|---|---|---|---|---|---|
| **Stream** | NG | NG-CL | NG-HEAT | STM-SR | CO2 | CAFE | AIRFEED |
| **Temperature (°C)** | 30 | 25 | 25 | 230 | 30 | 970 | 25 |
| **Pressure (bar)** | 1 | 2 | 1 | 2 | 1 | 2 | 1 |
| **Flow Rate [kmol/h]** | 2648 | 3320 | 100 | 8597 | 1168 | 71297 | 133446 |

**Table 2:** Reactor Operating Conditions in Chemical Looping and Methanol Synthesis

| Reactor | Subplant | Function | Temperature (°C) | Pressure (bar) |
|---|---|---|---|---|
| Fuel Reactor (TOP-FR) | 1 | Reduce Oxygen Carrier | 960 | 2 |
| Fuel Reactor (BTM-FR) | 1 | | 870 | 2 |
| Air reactor (AR) | 1 | Oxygen Carrier Regeneration | 928 | 2 |
| Steam Reactor (SR) | 1 | H2 Production | 875 | 2 |
| R-1 | 2 | Hydrodesulphurization | 375 | 1 |
| Microwaved Reactor (R-MW) | 2 | Syngas Production | 800 | 1 |
| R-2 | 2 | Methanol Production | 254 | 76 |
| R-3 | 2 | | 254 | 76 |
| R-4 | 2 | | 220 | 71 |

at 220°C and 71 bar. This additional reactor stage helps maximize methanol yield by enhancing the conversion of residual CO and $CO_2$. The reactor outlet gas, containing methanol, water, and unreacted gases ($H_2$, CO, $CO_2$, $CH_4$, and inert gases like $N_2$), is directed to a separator, where crude methanol is separated at 40°C and 67 bar. A portion of the unreacted gases is recycled back to the reactors to improve process efficiency, while a portion is purged.

The purification of crude methanol is achieved through a series of steps involving a flash tank and three distillation columns. First, crude methanol is depressurized in the flash, allowing off-gas, which mainly consists of $CO_2$, $H_2$, and $CH_4$, to be vented. The liquid phase is directed to the first column for initial purification. This column separates residual $CO_2$ and trace gases, which are flared, while the methanol-rich bottom stream is pumped into the second column for further separation. Here, methanol of approximately 99.99% purity is collected as the distillate, while the remaining mixture of methanol and water proceeds to the third column, where the final methanol product with a purity of 99.99 mol% is produced. The data from the steady-state simulation in Aspen Plus was imported to Aspen Energy Analyzer (AEA) v11 to design and optimize the Heat Exchanger Network (HEN) for maximum energy recovery. The HEN was designed separately for each subplant, with a larger HEN configuration applied to the microwave-assisted dry reforming process in Subplant 2 and a smaller HEN configured for the chemical looping process in Subplant 1.

## RESULTS

The steady-state simulation results for the integrated chemical looping and microwave-assisted reforming process demonstrate effective syngas production, hydrogen supplementation, and methanol synthesis, achieving high efficiency and purity. In Subplant 1, the chemical looping process is configured to produce a hydrogen stream of 22,299 lbmol/h, meeting the precise hydrogen requirement for the syngas production in Subplant 2. The chemical looping configuration also produces 7,163 lbmol/h of carbon dioxide. However, the syngas production reactor in Subplant 2 requires 9,746 lbmol/h of carbon dioxide. This additional amount of carbon dioxide (2,583 lbmol/h) has to be purchased separately or obtained from a separate decarbonization campaign in another part of the chemical plant. In Subplant 2, the microwave-assisted dry reforming reactor achieved a methane conversion rate of 97%. The resulting syngas composition is 40.3% $H_2$, 41.5% CO, 17% $CO_2$, and 0.57% $CH_4$, with an $H_2$ ratio of 0.971. This ratio is then optimized by supplementing the syngas with the hydrogen stream from Subplant 1 to achieve the ideal stoichiometric conditions for methanol synthesis. Moreover, the microwave-assisted dry reforming process reduced natural gas feed requirements by 12% and steam feed

consumption by 6%, demonstrating the process's enhanced resource efficiency compared to conventional methods. The methanol produced reaches 14,201 lbmol/h with a high purity of 99.9%, aligning with commercial methanol production rate and quality. The process overall achieves a net $CO_2$ utilization rate of -1,117 lbmol/h, indicating that it consumes $CO_2$ rather than emitting it. Compared to a baseline emission rate of 575 lbmol/h in conventional steam reforming processes, this setup achieves a $CO_2$ emission reduction of 294.3%. This reduction highlights the environmental benefits of integrating $CO_2$ into the process, furthering the goal of sustainable and decarbonized methanol production. The HEN design employed a mixed-integer linear programming (MILP) approach to achieve optimal heat recovery, thus, the utility requirements showed substantial reductions: Hot utility demand dropped from 2923 MMBTU/hr to 478 MMBTU/hr, representing an 83.6% reduction. Cold utility demand decreased from 3968 MMBTU/hr to 1482 MMBTU/hr, achieving a 62.7% reduction. The integration of HEN not only reduces operational costs but also aligns with decarbonization goals by lowering the environmental impact through reduced energy consumption.

Capital costs for standard equipment items were estimated by mapping the equipment items from the Aspen Plus plant-wide model to Aspen Process Economic Analyzer (APEA) V11. Costs for the microwave-assisted reactor (MW-reactor) was estimated separately as quoted equipment in APEA, broken down into the magnetron (including other electrical ancillaries) and pressure vessel. The magnetron cost, including electrical ancillaries, accounts for components such as the cavity, generator, controls, transformers, switches, installation, and setup, obtained from a vendor based on the power (kW) rating. The pressure vessel cost was estimated using correlations from Turton et al [7]., considering the material of construction and operating pressure. Additional costs, such as assembly, commissioning, and markup, were accounted for with escalations, given the novel state of MW-assisted reactor technology. Utilities such as electricity, cooling water, steam, and flow rates of raw materials were obtained from the Aspen Plus process model. The economic analysis of the proposed methanol production process shows that the integrated process achieves a TCI of $515.68 million, annual operating costs of $486.13 million and a combined NPV of $1439 million. The integrated design leverages the strengths of both subplants, offering significant economic potential through high methanol production and $CO_2$ utilization.

An additional amount of carbon dioxide (2,583 lbmol/h) is required to operate the syngas reactor, and this carbon dioxide cost can affect the NPV. The economic analysis presented in Table 3 assumes a cost of carbon dioxide as $38.59/ton. To assess the impact of key cost variables on the operating expenses (OPEX), a sensitivity analysis was conducted on electricity price (ranging from 0.01 to 0.12 cents/kWh) and methane price (ranging from 0.1 to 2 $/MMBtu).

**Table 3:** Economic Summary for Integrated Process.

| Parameter | Integrated Process |
|---|---|
| Total capital cost ($MM) | 515.68 |
| Total Operating Cost ($MM/year) | 486.13 |
| Raw Material Cost ($MM/year) | 162.25 |
| Utility Cost ($MM/year) | 279.14 |
| Methanol Production (lb/year) | $3.99x10^9$ |
| NPV ($MM) | 1,439 |

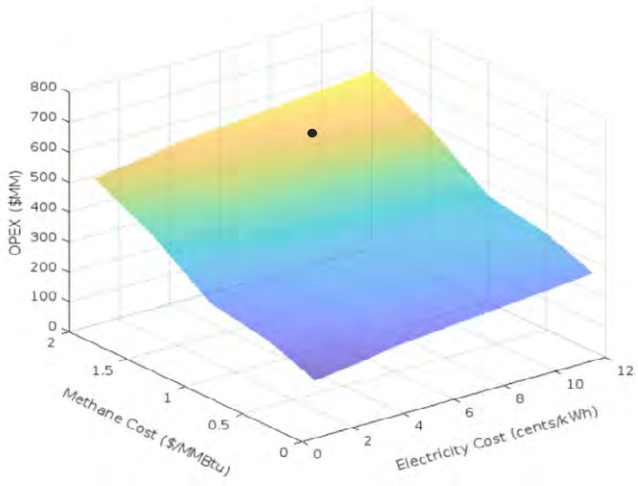



**Figure 2.** Sensitivity Analysis of OPEX to Electricity and Methane Costs

Figure 2 shows that OPEX increases with both electricity and methane costs, with a stronger sensitivity observed toward methane pricing. The lowest OPEX value, $160.84 MM, occurs at the lowest electricity and methane cost combination, whereas the highest OPEX, $592.20 MM, corresponds to the most expensive conditions. The black marker in the plot highlights the current cost scenario (electricity = 8.72 cents/kWh, methane = $1.8/MMBtu), which results in an OPEX of $486.13 MM. The findings emphasize that while both variables impact operational costs, controlling methane costs presents the most effective strategy for cost optimization in the proposed process.

## CONCLUSION

Current industrial practice for methanol is very energy intensive and produces a large amount of carbon dioxide. The use of a novel microwave-assisted conversion of natural gas to methanol via dry reforming has the potential to reduce energy costs and reduce carbon dioxide

emissions. However, this method requires the use of hydrogen. It is shown via simulation studies in this research that the hydrogen required for methanol production can be generated via chemical looping. Furthermore, chemical looping also produces a pure stream of carbon dioxide that can be utilized in the dry reforming step. Technoeconomic analysis indicates that this integrated plant has the potential to be profitable.

While the use of microwave reactors is promising and moves the chemical industry in the direction of electrification of process energy, further research is needed to make commercial-scale microwave reactors at a price comparable to traditional jacketed reactors that operate using hydrocarbon combustion. The scale-up of microwave reactors using multiple units of pilot-scale equipment and the effect of reactor cost on the manufacturing cost of methanol is being evaluated [8]. Another factor under consideration is the stability of the catalyst under microwave conditions, which is an area of active research [9]. While chemical looping is shown to be feasible for producing the necessary hydrogen for dry reforming, this method requires the transport of solids, which require special pneumatic handling techniques for smooth long-term operation. These issues, along with a quantitative comparison with current industry methods will be addressed in a future publication.

## ACKNOWLEDGEMENTS

This study was supported by the United States Department of Energy.

## REFERENCES

1. Market Research (2023). Methanol Market by Feedstock (Natural Gas, Coal, Biomass), https://www.marketresearch.com/MarketsandMarkets-v3719/Methanol-Feedstock-Natural-Gas-Coal-30408866/ (accessed 04.04.23)
2. G. Aimiuwu, E. Osagie and O. Omoregbe (2020) Process simulation for the production of methanol via CO2 reforming of methane route. Chemical Product and Process Modeling. 17:69-79.
3. T. T. P. Pham, K. S. Ro, L. Chen, D. Mahajan, T. J. Siang, U. P. M. Ashik, J. Hayashi, D. P. Minh, D. N. Vo (2020). Microwave-assisted dry reforming of methane for syngas production: a review. Environmental Chemistry Letters 18(6): 1987-2019.
4. M. E. Haque, N. Tripathi, and S. Palanki (2021). Development of an Integrated Process Plant for the Conversion of Shale Gas to Propylene Glycol. Industrial & Engineering Chemistry Research. 60 (1):399-411
5. Riley, J., Bobek, M., Atallah, C., Siriwardane, R., Bayham, S. "Syngas and $H_2$ Production from Natural Gas using $CaFe_2O_4$ Looping: Experimental and Thermodynamic Integrated Process Assessment," U.S. Department of Energy, National Energy Technology Laboratory, Morgantown, WV, USA
6. Almaraz, O., Palanki, S., & Hu, J. (2024). Process Design of Carbon-Neutral Routes for Methanol Synthesis. *Computer Aided Chemical Engineering, 53,* 97-102. https://doi.org/10.1016/B978-0-443-28824-1.50017-X
7. Turton R, Shaeiwitz JA, Bhattacharyya D, Whiting WB. Analysis, synthesis, and design of chemical processes. fifth ed. Pearson Education; 2018.
8. Almaraz, O. & Palanki, S., Decarbonization of Methanol Production Process. *International Congress on Sustainability Science and Engineering (*ICOSSE) 2025, Auckland, NZ, February 20-22, 2025
9. Huang, Q., Wang, Y., & Zhu, X. (2021). "Microwave-assisted dry reforming of methane to syngas: A review of catalyst development and process optimization." *Renewable and Sustainable Energy Reviews*, vol. 138, Article 110520.

© 2025 by the authors. Licensed to PSEcommunity.org and PSE Press. This is an open access article under the creative commons CC-BY-SA licensing terms. Credit must be given to creator and adaptations must be shared under the same terms. See https://creativecommons.org/licenses/by-sa/4.0/



Systems & Control Transactions

**Research Article - Peer Reviewed Conference Proceeding**
ESCAPE 35 - European Symposium on Computer Aided Process Engineering
Ghent, Belgium. 6-9 July 2025
Jan F.M. Van Impe, Grégoire Léonard, Satyajeet S. Bhonsale,
Monika E. Polańska, Filip Logist (Eds.)

PSE PRESS

# Modeling and Simulation of a Novel Process that Converts Low Density Polyethylene to Ethylene

**Xiaoyan Wang[a], Omar Almaraz[a], Jianli Hu[a] and Srinivas Palanki[a*]**

[a]Department of Chemical and Biomedical Engineering, West Virginia University,
Morgantown, WV 26506, USA
* Corresponding Author: srinivas.palanki@mail.wvu.edu

## ABSTRACT

In this research, a novel process is developed that utilizes low density polyethylene from plastic waste to produce ethylene. In this process, waste polyethylene is reacted in a microwave reactor to produce ethylene. A conceptual flowsheet based on this reactor is developed in the ASPEN Plus environment. Heat integration tools are utilized to reduce the hot and cold utilities used in this process. This novel design is compared with the conventional process of making ethylene from ethane via cracking. A technoeconomic analysis is conducted to demonstrate the economic feasibility of this process.

**Keywords**: Ethylene, Process Design, Process Development

## INTRODUCTION

Plastics are used in a wide variety of products and have displaced other materials – such as wood, metal, and glass – that were previously used for applications that plastics are currently used. The worldwide annual production of plastics has increased nearly 200-fold to 400.3 million metric tons in 2022 from 2 million metric tons in 1950 [1]. While plastic products have a service-life of around 10 years, plastics can take up to 500 years to decompose, depending on their composition and disposal. Most of the plastic waste generated is either landfilled or incinerated. It takes a long time for landfilled plastic waste to degrade, and incinerated plastic waste generates harmful air pollutants. Mismanaged plastic waste is mainly disposed of at illegal dumpsites or burned in open pits, while a considerable amount also leaks into rivers and oceans. From 1970 to 2019, an estimated 30 million metric tons of plastics have accumulated in the ocean, while more than 100 million tons have accumulated in rivers and lakes [1]. Such large amounts of plastic waste pollution in waterways can have a devastating impact on marine life and ecosystems.

In this research, a novel process is developed in which waste low-density polyethylene (LDPE) is converted into ethylene using a microwave reactor. A conceptual flowsheet for this reactor-based process is developed in the ASPEN Plus environment that is at industrial-scale. Heat integration tools are applied to optimize the use of hot and cold utilities in the process. This innovative design is compared with the current industrial production method of ethylene via ethane steam cracking to evaluate the cost constraints of the microwave reactor.

## PRODUCTION OF ETHYLENE

While ethylene was traditionally produced via steam cracking of petroleum (naphtha) at 800–900°C (1,470–1,650°F), followed by separation to isolate ethylene from the resulting gas mixture, there is an increasing trend to use ethane, derived from natural gas, to produce ethylene via steam cracking [2]. Ethane forms a major component of natural gas liquids (NGL) that is obtained from shale gas while purifying methane. This NGL feed stream is pre-heated by a heat exchanger, mixed with steam, and then further heated to its incipient cracking temperature (500°C to 680°C). At this point, it enters a reactor (typically, a fired tubular reactor) where it is heated to cracking temperatures, 750°C to 875°C. After cracking reaction, cracked gas mixture leave the furnace at 750°C to 875°C. The gases must be cooled immediately in the quench tower to preserve the current composition of the gas and prevent undesirable side reactions. After the

cracked gas mixture has been cooled in the quench tower and compressed, it is sent to the fraction section at a pressure of 464 to 551 psi (32-38 bar) for further separation into different products and fractions at specified qualities. This is done through a series of distillation columns and results in the separation of ethylene from the unreacted ethane, as well as the side products propylene, hydrogen and methane. Steam cracking of ethane is an energy intensive process due to the high reaction temperature (> 800°C). Furthermore, this process generates a significant amount of greenhouse gas (GHG) emissions and utilizes a non-renewable hydrocarbon feed resource. The process generally results in approximately 1.2 to 1.6 tons of $CO_2$-equivalent ($CO_2e$) per ton of ethylene produced [2,3].

The availability of a large amount of plastic waste provides the motivation to develop technologies to convert this waste product to ethylene instead of using ethane from non-renewable sources to produce ethylene. Tertiary recycling uses chemical and thermochemical methods to recover various components of waste plastic into monomers or fuels. This type of recycling is called “upcycling” as the waste plastic is converted back to monomeric forms of molecules that can be further processed into useful forms (polymeric or otherwise). The depolymerization process involved in upcycling of plastics can be enhanced by the use of catalysts, which promote deep cracking of primary products and accelerate the breaking of C–C and C–H bonds, resulting in high yields of liquid products with enhanced combustion performance and high-quality fuel production in a shorter time and at lower temperatures (280–500°C) compared to pure pyrolysis [4]. The products from catalyzed depolymerization processes include a mix of gasoline hydrocarbons (C5-C12), aromatics, light olefins, and other chemical feedstocks. Suitable catalysts and process conditions can be chosen for commercial applications to target the recovery of specific desired products.

The depolymerization process requires energy and different forms of thermal energy can utilized. The efficiency of this thermal energy utilization can vary significantly depending upon the type of energy. There is current interest in the use of microwave heating as a source of energy for depolymerization reactions. Microwave is a form of electromagnetic wave with perpendicular oscillating electric field and magnetic field that result in heat generation via (1) dielectric heating, (2) Joule heating, and (3) inductive heating. Compared with traditional hydrocarbon-based jacketed reactors as well as more novel resistive-heating reactors, microwave heating provides advantages in utilization efficiency, rapid heating, and lower bulk temperatures during reaction. For instance, it has been shown in laboratory-scale experiments that microwave-enhanced ethane catalytic cracking can produce the same conversion of ethane as conventional thermally heated cracking at an average temperature that is 150-200°C lower [5,6].

This provides the motivation to develop a process that utilizes polyethylene as a feed source in a microwave reactor to produce polymer-grade ethylene.

## PROCESS MODELING

### Conventional Production of Ethylene via Ethane Steam Cracking

A process simulation model is developed for the conversion of ethane to ethylene based on current industry practice [7]. This model is used as a basis of comparison for studying the advantages and disadvantages of the novel microwave-enhanced process for producing ethylene from LDPE. Ethylene is produced via thermal steam cracking of ethane gas. A process flow diagram based on industrial practice is shown in Figure 1.

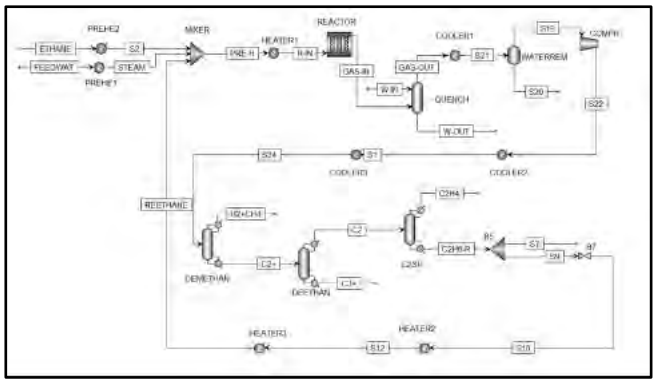



**Figure 1**: Process Flow Diagram for Ethane Cracking

The feed to the production process is ethane gas that comes from an ethane gas pipeline. Fresh ethane gas is fed into the process at a rate of 149 tons/h. The ethane gas is mixed with 50 tons/h of process steam to achieve a steam to hydrocarbon ration of 0.33 by mass and passed through the thermal stream cracking reactor at inlet conditions of 700 °C and 3.2 bar. The reaction conditions are 840 °C and 3.2 bar in the reactor. Under these conditions, the thermal steam cracking reaction occurs in the absence of a catalyst, converting the ethane feedstock into a gas mixture containing primarily ethylene, methane, hydrogen, and residual ethane. The exit gases from the reactor are cooled and sent through a flash unit to remove water. The organic vapors are compressed and sent through a series of three distillation columns. The top product of the last column is polymer-grade ethylene.

A simulation model is developed in ASPEN Plus v11 for this process. The feed specifications are listed in Table 1. The reaction kinetics [7] used in this model are shown in Table 2 and the reactor specifications are shown in Table 3. The Grayson thermodynamic property

model is used for this module. The flash unit and the three distillation columns utilize the Soave-Redlich-Kwong thermodynamic property model and rigorous modeling tools are used (e.g. RADFRAC) to model these separation units.

**Table 1**: Feed Specifications for Ethane Cracking

| Component | Ethane | Steam | Initiator |
|---|---|---|---|
| Pressure (bar) | 3.21 | 3.21 | 2,010.00 |
| Temperature (°C) | 700.00 | 700.00 | 0.00 |
| Flow Rate (kmol/hr) | 3,259.77 | 2,517.82 | 0.84 |
| Flow Rate (tons/hr) | 149 | 50.00 | 0.20 |

**Table 2:** Kinetics of Ethane Cracking

| No | Reaction | Order | Forward Reaction | Reverse Reaction |
|---|---|---|---|---|
| | | | A [$s^{-1}$ ] or [L (mol s)$^{-1}$] | A [L (mol s)$^{-1}$] |
| | | | E [kJ mol$^{-1}$ ] | E [kJ mol$^{-1}$ ] |
| 1 | $C_2H_6 \leftrightarrow C_2H_4 + H_2$ | 1 | A = 4.6 x $10^{13}$ E = 272.8 | A = 8.49 x $10^{8}$ E = 136.5 |
| 2 | $C_3H_6 \leftrightarrow C_2H_2 + CH_4$ | 1 | A = 7.2 x $10^{12}$ E = 274.2 | A = 3.81 x $10^{8}$ E = 147.2 |
| 3 | $C_2H_2 + C_2H_4 \rightarrow C_4H_6$ | 2 | A = 1.0 x $10^{15}$ E = 172.6 | |
| 4 | $C_2H_4 + C_4H_6 \rightarrow C_6H_6 + 2H_2$ | 2 | A = 8.3 x $10^{9}$ E = 144.6 | |
| 5 | $C_3H_8 \leftrightarrow C_3H_6 + H_2$ | 1 | A = 5.8 x $10^{10}$ E = 214.6 | A = 9.03 x $10^{5}$ E = 93.5 |
| 6 | $C_3H_8 + C_2H_4 \rightarrow C_2H_6 + C_3H_6$ | 2 | A = 2.5 x $10^{13}$ E = 247.1 | |
| 7 | $2C_3H_6 \rightarrow 3C_2H_4$ | 1 | A = 7.3 x $10^{12}$ E = 268.5 | |
| 8 | $2C_2H_6 \rightarrow C_3H_8 + CH_4$ | 1 | A = 3.8 x $10^{11}$ E = 273.0 | |
| 9 | $C_4H_{10} \leftrightarrow C_4H_8 + H_2$ | 1 | A = 1.6 x $10^{12}$ E = 260.9 | A = 1.78 x $10^{7}$ E = 135.1 |
| 10 | $C_2H_4 + C_2H_6 \rightarrow C_3H_6 + CH_4$ | 2 | A = 7.0 x $10^{13}$ E = 252.8 | |
| 11 | $C_3H_6 + C_2H_6 \rightarrow C_4H_8 + CH_4$ | 2 | A = 1.0 x $10^{14}$ E = 251.8 | |

**Table 3**: Ethane Cracking Reactor Specifications

| Reactor Specifications | |
|---|---|
| Pressure (bar) | 3.2 |
| Temperature (°C) | 840 |
| Length (m) | 10.5 |
| Diameter (m) | 0.085 |
| No. of Tubes | 240 |
| Heat Duty MW | 132.81 |

The product gas from the reactor unit is 40.35 mol% ethylene, 41.75mol% hydrogen, 3.97 mol% methane, 11.67 mol% unreacted ethane and with slight impurities of other products. The results closely align with the industrial data available in literature [8] as shown in Table 4. The outlet gas of the cracking reactor is cooled down to 10 °C with the help of a quench tower. The condensed water vapor is separated from the bottom in a flash separator. Vapor products from the flash separator are compressed to 8 bars and then cooled down to -100 °C. This stream is sent to the demethanizer column where methane and hydrogen are separated as top products.

**Table 4**: Comparison of Simulation with Industrial Data

| Main Products | Product Yield [mol %] | | |
|---|---|---|---|
| | Simulation | Industrial Data | % Diff. |
| $H_2$ | 37.47 | 36.49 | 2.69 |
| $CH_4$ | 4.75 | 8.42 | 43.59 |
| $C_2H_4$ | 34.41 | 33.07 | 4.05 |
| $C_2H_6$ | 19.89 | 18.86 | 5.46 |

The bottom products are sent to the deethanizer column, where ethane and ethylene flow out of the top of the column while the remaining (undesired) products are separated from the bottom of the column. Finally, the top product stream is sent to the final column where ethylene is separated as the top product from ethane. The purified ethylene (99.97mol%) is recovered at 8 bar and -58.4 °C. The unreacted ethane is recovered from the bottom of the column and recycled back to the feed stream. The columns specification for ethylene separation are listed in Table 5.

**Table 5:** Column Specifications

| | Columns | | |
|---|---|---|---|
| | DEMETHAN | DEETHAN | C2SPLIT |
| Purpose | Distillation | Distillation | Distillation |
| No. of Stages | 10 | 24 | 50 |
| Feed Stage | 5 | 10 | 27 |
| Feed Temperature (°C) | -100 | -50.8 | -42.68 |
| Pressure (bar) | 8 | 8 | 8 |
| Reflux Ratio | 1.4 | 0.38 | 4.05 |
| Condenser Duty (MW) | -18.17 | -5.85 | -28.73 |
| Condenser Temperature (°C) | -156.89 | -42.68 | -58.4 |
| Distillate Rate (kmol/h) | 3068.65 | 4126.49 | 2492.85 |
| Reboiler Duty (MW) | 19.70 | 20.51 | 22.57 |
| Reboiler Temperature (°C) | -50.80 | 82.87 | -39.02 |
| Bottom Rate (kmol/h) | 4194.48 | 67.99 | 1631.33 |
| Tray Spacing (m) | 0.8 (2-4) | 0.6 (2-9) | 0.85 (2-26) |
| | 1 (5-10) | 0.8 (10-23) | 0.85 (27-49) |
| Tray Type | Sieve | Sieve | Sieve |
| Column Diameter (m) | 3.3 (2-4) | 3.1 (2-9) | 4.5 (2-26) |
| | 3.5 (5-10) | 3.5 (10-23) | 3.6 (27-49) |

Figure 2 shows the temperature and composition profiles of ethane and ethylene in the final distillation column. Since the reactor outlet matches industrial data closely and the final product results in polymer-grade ethylene, this simulation model is of high-fidelity and can be used in a technoeconomic analysis to compare with the economics of producing ethylene via a novel microwave process that utilizes LDPE.

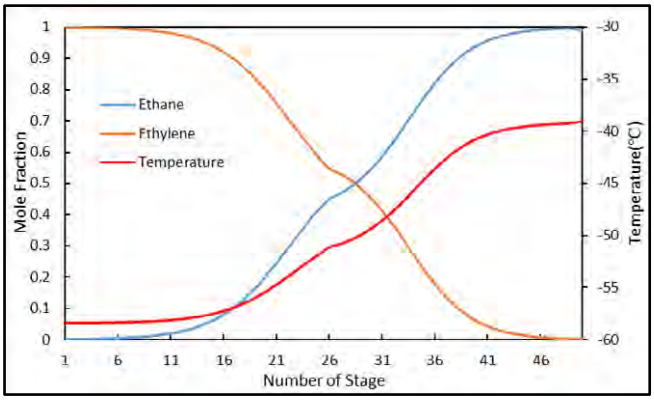



**Figure 2**: Temperature and Composition Profiles for Ethylene and Ethane in column C2SPLIT

## Microwave Enhanced Catalytic Conversion of LDPE to Ethylene

The focus of this section is the development of an ASPEN Plus simulation for the microwave-enhanced process to convert LDPE to ethylene. The objective is to match the same ethylene production as the conventional ethane cracking process in terms of quantity as well as product purity. A process flow diagram of the microwave process under consideration is shown in Figure 3. The reactor in the conventional process is replaced by a microwave reactor and a suitable distillation train is designed to recover the ethylene.

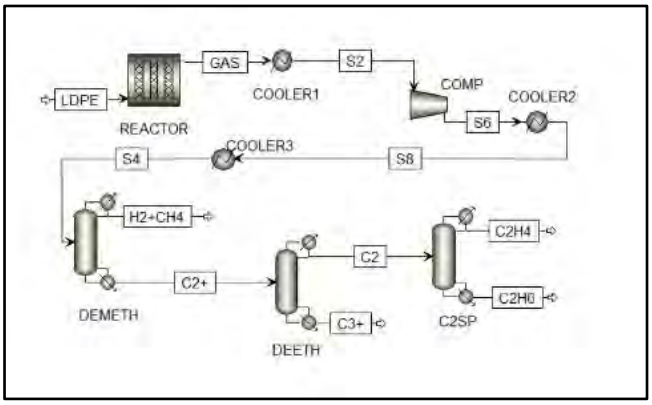



**Figure 3**: Flow Diagram of Microwave Enhanced Process for Converting LDPE to Ethylene

Preliminary data from laboratory-scale microwave reactor experiments [9] indicates that the product composition of the reactor under microwave heating with LDPE as feed is not the same as the product composition of conventional heating with ethane as feed as shown in Table 6. In particular, the microwave reactor produces a significant amount of propylene, which is also a valuable product, in addition to ethylene. This implies that the separation train specifications for the microwave process will be different from that of the conventional ethane-to-ethylene process. If propylene is included as a target product, additional costs for distillation to recover propylene, as well as the associated profits, will need to be considered. If the cost of recovering propylene is not competitive, it is necessary to redesign the microwave reactor to produce more ethylene and less propylene.

**Table 6:** Reactor Outlet Composition

| Gas components (ton/h) | $LDPE/N_2$ | Ethane |
|---|---|---|
| | MW | Conventional |
| | 400°C | 840°C |
| Hydrogen | 2.06 | 6.05 |
| Methane | 16.58 | 6.10 |
| Ethylene | 77.29 | 77.29 |
| Ethane | 16.21 | 47.90 |
| Acetylene | 0.09 | 0.00 |
| Propane | 8.42 | 0.99 |
| Propylene | 54.37 | 7.87 |
| C4 and higher | 39.15 | 2.81 |

In the novel microwave process, it is necessary to determine the feed rate of LDPE as well as the separation train design that results in the same amount of polymer-grade ethylene as the conventional process (77 tons/h). This allows for a comparison of capital cost, operating cost and life-cycle cost for the two processes. It was determined that a feed of 214 tons/hour of LDPE was required to produce the required amount of ethylene (77 tons/h) in the microwave reactor. The reactor is modeled as a yield reactor that has the same outlet composition as shown in Table 6. The reactor is assumed to operate at a temperature of 400 °C and a pressure of 1 bar. The outlet of the reactor is cooled and sent to a demethanizer column, followed by a deethanizer column, and finally to an ethylene column, similar to the separation process used in conventional ethane steam reforming product separation. In addition, an extra column is designed to recover propylene. The columns specifications for this process are listed in Table 7. Figure 4 shows the temperature and composition profile of ethylene from the C2 splitter.

## ECONOMIC EVALUATION

Aspen Energy Analyzer (AEA) V11 is used to develop and optimize a HEN for both the conventional as well as the novel process. The software employs a pinch analysis technique in the optimization algorithm to compute overall matches with heat load, surface area and cost target. The objective function of the HEN is to minimize utility cost, which is formulated as a mixed integer linear programming (MILP) problem. The solution consists of the

best set of matches rather than a single match.

**Table 7**: Column Specifications for Microwave Enhanced Process

| | Columns | | |
|---|---|---|---|
| | **DEMETHAN** | **DEETHAN** | **C2SPLIT** |
| Purpose | Distillation | Distillation | Distillation |
| No. of Stages | 15 | 24 | 60 |
| Feed Stage | 6 | 10 | 31 |
| Feed Temperature (°C) | -100 | -40.85 | -54.52 |
| Pressure (bar) | 8 | 8 | 8 |
| Reflux Ratio | 0.74 | 0.47 | 2.39 |
| Condenser Duty (MW) | -3.14 | -4.67 | -19.09 |
| Condenser Temperature (°C) | -142.54 | -54.52 | -58.4 |
| Distillate Rate (kmol/h) | 1864.76 | 2991.49 | 2501.02 |
| Reboiler Duty (MW) | 9.3 | 17.35 | 17.38 |
| Reboiler Temperature (°C) | -40.85 | 22.85 | -39.29 |
| Bottom Rate (kmol/h) | 4960.87 | 1969.38 | 490.47 |
| Tray Spacing (m) | 0.6 (2-5) | 0.6 (2-9) | 1 (2-30) |
| | 1 (6-14) | 0.9 (10-23) | 1 (31-59) |
| Tray Type | Sieve | Sieve | Sieve |
| Column Diameter (m) | 1.7 (2-4) | 2.7 (2-9) | 3.85 (2-30) |
| | 2.6 (5-10) | 3.2 (10-23) | 3 (31-59) |

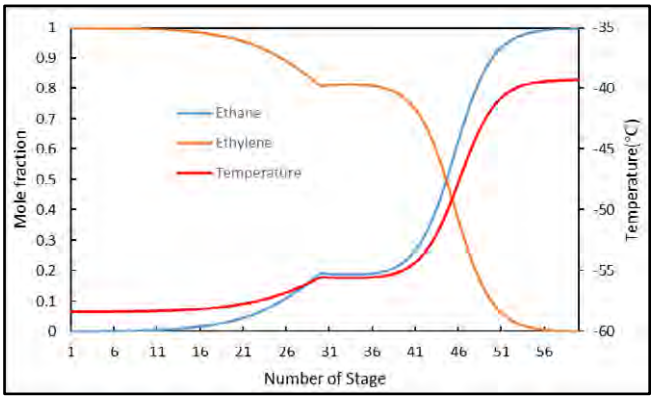



**Figure 4**: Temperature and Composition Profiles for Ethylene, Ethane in C2 splitter

Capital costs for standard equipment items were estimated by mapping the equipment items from the Aspen Plus plant-wide model to Aspen Process Economic Analyzer (APEA) V11. Costs for the microwave-assisted reactor (MW-reactor) was estimated separately as quoted equipment in APEA, broken down into the magnetron (including other electrical ancillaries) and pressure vessel. The magnetron cost, including electrical ancillaries, accounts for components such as the cavity, generator, controls, transformers, switches, installation, and setup, obtained from a vendor based on the power (kW) rating [10]. The pressure vessel cost was estimated using correlations from Turton et al [11]., considering the material of construction and operating pressure. Additional costs, such as assembly, commissioning, and markup, were accounted for with escalations, given the novel state of MW-assisted reactor technology. Utilities such as electricity, cooling water, steam, and flow rates of raw materials were obtained from the Aspen Plus process model.

A comparison of capital cost, operating cost, and utility cost between conventional steam reforming and microwave-enhanced LDPE upcycling (excluding the reactor component) is conducted as shown in Table 8. The objective of this comparison is to estimate the cost constraints of the microwave reactor necessary to ensure that the microwave-enhanced LDPE upcycling process is economically comparable to the conventional ethylene production process.

**Table 8**: Comparison of Capital and Operating Costs

| Scenario | Capital Cost (USD/Year) | Operating Cost (USD/Year) | Utility Cost (USD/Year) | Product |
|---|---|---|---|---|
| Conventional Ethane Steam Reforming | 36,557,700 | 48,770,700 | 42,463,100 | Ethylene |
| LDPE Conversion (MW/ excluding reactor) | 18,313,500 | 5,063,400 | 2,921,440 | Ethylene |

Currently a microwave reactor at industrial scale is not available for the proposed LDPE microwave enhanced conversion process and hence it is difficult to estimate its cost accurately. A rough estimate the microwave reactor cost based on magnetron price and reactor materials can be used as a first step. The LDPE feed rate of 214 ton/h is required to meet the ethylene production rate of 77 ton/h to match the ethylene production in the conventional ethane-to-ethylene process. The overall cost of the microwave reactor systems depends on the number of magnetron units needed to generate the necessary power requirement. As the batch time lowered down, the magnetron cost declines proportionally. When the batch time is 10 minutes, the magnetron cost is approximately $11 million as shown in Table 9. As this time is lowered, the cost of the microwave reactor systems falls further. Table 9 shows that if the batch time for the microwave-enhanced LDPE conversion process is reduced to less than 10 minutes, it has the potential to be competitive with conventional ethylene production.

**Table 9**: Cost Estimation of Microwave Reactor

(Magnetron Power: 100kW/module, Magnetron Price: 113872.82$/module, Power Needed: 66921420.69W)

| Batch time(min) | 0.5 | 1 | 2 | 5 | 10 |
|---|---|---|---|---|---|
| Batch volume($m^3$) | 8.45 | 16.89 | 33.79 | 84.47 | 168.94 |
| Microwave reactor power | 557678.51 | 1115357.01 | 2230714.02 | 5576785.06 | 11153570.11 |
| Magnetron needed(unit) | 5.58 | 11.15 | 22.31 | 55.77 | 111.54 |
| Total cost of Magnetron ($) | 683,236.92 | 1,366,473.84 | 2,732,947.68 | 6,376,877.92 | 12,753,755.84 |

## CONCLUSION

Simulation of industrial-scale production of ethylene via two distinct routes, ethane steam cracking and polyethylene upcycling, were considered. While the product compositions at the reactor outlet differ between the two processes, the feed rate of the reactants has been

adjusted to achieve the same ethylene production capacity. The novel microwave-enhanced process demonstrates the potential to produce both ethylene and propylene. The economic viability of using microwave reactors for LDPE conversion depends on the balance between the high efficiency and selectivity of the process against capital and operating costs. Technoeconomic analysis indicates that this integrated plant has the potential to be profitable.

## ACKNOWLEDGEMENTS

This study was supported by the United States Department of Energy grant DE-EE0010838.

## REFERENCES

1. Geyer, R., Jambeck, J.R., Law, K.L., Production, Use, and Fate of All Plastics Ever Made, Sci. Adv., 3 (7) (2017) e1700782
2. Ren, T., Patel, M.K., Blok, K. Olefins from Conventional and Heavy Feedstocks: Energy Use in Steam Cracking and Alternative Processes, Energy, 33(6), 817-833 (2008)
3. Yao, Y., Graziano, D.J., Riddle, M., Cresko, J., Masanet, E., Understanding Variability To Reduce the Energy and GHG Footprints of U.S. Ethylene Production, Environ. Sci. Technol., 49, 14704–14716 (2015)
4. Peng, Y., Wang, Y., Ke, L., Dai, L., Wu, Q., Cobb, K., Zeng, Y., Zou, R., Liu, Y., Ruan, R., A Review on Catalytic Pyrolysis of Plastic Wastes to High-Value Products, Energy Conversion and Management, 254, 115243 (2022)
5. Robinson, B., Caiola, A., Bai, X., Abdelsayed, V., Shekhawat, D., Hu, J., Catalytic Direct Conversion of Ethane to Value-Added Chemicals Under Microwave Irradiation, Catalysis Today, 356 3–10 (2020)
6. Wang, X., Wang, Y., Robinson, B., Caiola, A., Hu, J., Selectivity Modulated Oxidative Dehydrogenation of Ethane with CO2 under Microwave Catalytic Processing, Catal. Sci. Technol.,13, 3499-3504 (2023)
7. Sundaram, K. M., Froment, G. F., Modeling of Thermal Cracking Kinetics —I: Thermal Cracking of Ethane, Propane and their Mixtures, Chem. Eng. Sci., 32,601 (1977)
8. Ranjan, P., Kannan, P., Al-Shoaibi, A., Srinivasakannan, C., Modeling of Ethane Thermal Cracking Kinetics in a Pyrocracker. Chemical Engineering Technology, 1093-1097 (2012)
9. Wang, X., Modeling and Simulation of a Process for Upcycling Of Low-Density Polyethylene Plastic Waste To Ethylene, Doctoral Research Proposal, West Virginia University (2024)
10. Ogunniyan, O., Haque, M. E., Wang, Y., Bhattacharyya, D., Hu, J., Low-Pressure Microwave-Assisted Ammonia Synthesis: Evaluation of Novel Separation Technologies, Plant-Wide Process Design, and Techno-Economic Analysis." Applied Energy, 373, 123877 (2024)
11. Turton R., Shaeiwitz J.A., Bhattacharyya D., Whiting W.B., Analysis, Synthesis, and Design of Chemical Processes. fifth ed. Pearson Education, 2018

© 2025 by the authors. Licensed to PSEcommunity.org and PSE Press. This is an open access article under the creative commons CC-BY-SA licensing terms. Credit must be given to creator and adaptations must be shared under the same terms. See https://creativecommons.org/licenses/by-sa/4.0/



Systems & Control Transactions

**Research Article - Peer Reviewed Conference Proceeding**
ESCAPE 35 - European Symposium on Computer Aided Process Engineering
Ghent, Belgium. 6-9 July 2025
Jan F.M. Van Impe, Grégoire Léonard, Satyajeet S. Bhonsale,
Monika E. Polańska, Filip Logist (Eds.)

PSE PRESS

# A global sensitivity analysis for a bipolar membrane electrodialysis capturing carbon dioxide from the air

**Grazia Leonzio[a,b*], Alexia Thill[b], and Nilay Shah[b]**

[a] Department of Mechanical, Chemical and Materials Engineering, University of Cagliari, via Marengo 2, 09123 Cagliari, Italy
[b] Sargent Centre for Process Systems Engineering, Department of Chemical Engineering, Imperial College London, London SW7 2AZ, UK
* Corresponding Author: grazia.leonzio@unica.it

## ABSTRACT

Bipolar membrane electrodialysis are receiving the attention of the research community in the last years because they can help the electrification and the spread of direct air capture systems. In this work, a mathematical model of a bipolar membrane electrodialysis cell for carbon dioxide recovery is carried out in order to find the most significant parameters on efficiency through a global sensitivity analysis. The electrochemical cell can be integrated into an absorption column capturing carbon dioxide from the air. Results show that the most important parameter over all investigated figures of merit (specific energy consumption, costs, carbon dioxide desorption efficiency, potassium transport number, removal ratio of potassium cation and carbon) is the potassium cation concentration in the rich solution feeding the cell. A trade-off between energy efficiency, process speed and operational cost is suggested. Future research should be conducted in order to apply the global sensitivity analysis to the overall integrated system considering the whole carbon cycle between the bipolar membrane electrodialysis and absorption column.

**Keywords**: Direct air capture, Global sensitivity analysis, Mathematical modelling, Bipolar membrane electrodialysis, Simulation, Optimization

## INTRODUCTION

Global warming and climate change are two critical and current global challenges, due to continuous greenhouse gas (GHG) emissions that characterize the history after the industrial revolution. After the pandemic period, carbon dioxide ($CO_2$) emissions (one of the most important and abundant GHG in the earth atmosphere today) started rising again to a value of 37.79 billion ton on 2023 [1]. There is simultaneously an increase of temperature due to the trapping role of $CO_2$, so that the Intergovernmental Panel on Climate Change (IPCC) decided to restrict the global average temperature increase to within 2 °C above preindustrial levels [2].

The achievement of this objective will not be easy, as it will require a drastic reduction in $CO_2$ emissions by 2030 and net zero emissions by 2050 [3].

Within this context, it is becoming increasingly imperative to invent not only efficient but also cost-effective technologies for controlling and reducing the atmospheric $CO_2$ concentration. So that, in addition to the conventional capture of $CO_2$ from flue gases and industrial processes, new solutions to capture $CO_2$ from the air have been proposed and investigated among the literature and new emerging companies, during the last decades. It is evident that, direct air capture (DAC) technology is one of the most important process to achieve negative $CO_2$ emissions. The annual capture of $CO_2$ should reach more than 85 Mton in 2030 and more than 980 Mton in 2050 in order to control the 13% of global $CO_2$ emissions by 2050 [4].

Absorption, adsorption, ion exchange resin, mineral carbonation, membrane, photocatalysis, cryogenic separation, electrochemical approach and electrodialysis approaches have discussed and presented in the literature as potential alternative to this mentioned capture solution [4, 5, 6, 7]. Each reported technology has disadvantages and advantages and a defined value of technology readiness level (TRL) [8]. Among DAC companies, it is possible to find the main known and important such as Climeworks and Global Thermostat (based on adsorption), Carbon Engineering (based on absorption), Mission

Zero Technology (based on bipolar membrane electrodialysis (BPMED)) [8].

The BPMED is receiving a greater attention as a DAC technology in the last year, because it is based only on the use of electrical energy with the advantages to be modular, work in an isotherm modality, desorb $CO_2$ at an ambient or higher pressure and with the minimum efficiency losses compared to a temperature or pressure swing adsorption solution, if renewable energy is used.

In particular, a BPMED stack is used to regenerate the hydroxide based-solved (mostly NaOH or KOH water solution) coming from an absorption column and capturing $CO_2$ from the air [9]. In this way, it is possible to recycle the solvent to the column and release the captured $CO_2$ for its storage or utilization.

$CO_2$ separation through BPMED has already been analyzed in the literature with mathematical models [4, 9, 10, 11, 12] and experimental works [13] find a cost even higher than 1000 \$/ton$CO_2$ and energy consumption up to 1451 kJ/mol$CO_2$ in not optimal operating conditions.

A high separation cost is due to a high membrane cost, large electricity consumption, and uncertainties on the lifetime of the materials [9]. For this reason, the process optimization through the use of a mathematical model is therefore useful to support design and development through the identification of the best operating conditions and parameters along with a Global Sensitivity Analysis (GSA) with the aim of suggesting significant operating parameters on costs, energy consumptions and efficiency.

In this research, a mathematical model for a BPMED capturing $CO_2$ from the air is proposed to conduct a GSA to identify the most effective parameters for total costs and energy consumptions alongside with others figures of merit, as the considered Key Performance Indicators (KPIs).

# MODELLING

## Description of the technology

The scheme of the analyzed BPMED system is reported here and shown in Figure 1. The single cell has an acidic and alkaline compartment separated by a cation exchange membrane (CEM) in addition to a bipolar membrane for water dissociation. The acidic side is feed by a rich solution of carbonates and bicarbonates coming from the DAC absorption column. Here, the influx of protons ($H^+$) produced from the electro-dissociation of water inside the bipolar membrane reduces the pH, converting the carbonate ions to dissolved carbon dioxide. At the same time, $K^+$ ions are transported across the CEM to the alkaline compartment. $CO_2$ is finally recovered in a knock-out vessel, where an expansion induces a drastic reduction in solubility. On the other hand, the liquid stream, which is very diluted in KOH and $CO_2$, is fed to the alkaline compartment, where it receives the influx of $K^+$ from the acidic compartment and $OH^-$ from the bipolar membrane. The alkaline hydroxide solution is then regenerated and can be recycled in the absorption column.

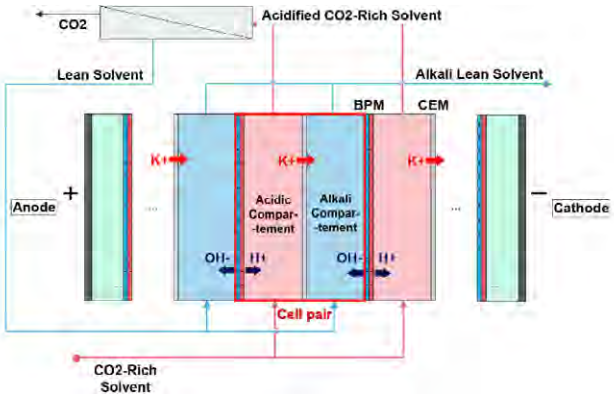



**Figure 1** Scheme of the investigated BPMED

In this work, a mathematical model for the BPMED unit inside the capture process is developed.

## Mathematical models

A model based on gas–liquid equilibria and mass balances has been carried out in MATLAB to evaluate the performance of the BMED-CEM system, considering the following assumptions: well-mixed compartments, ideal membrane behaviour without interfacial perturbations at its surface, absence of transport for neutral species through the membranes, steady-state conditions [11]. The liquid solution is described by the acid-base equilibrium equations for $H_2CO_3$, $HCO_3^-$, $CO_3^{2-}$ and $H_2O$ in addition to the electroneutrality of the solutions. In the acidic side, the liquid solution is in equilibrium with the gas phase (pure $CO_2$) with an absolute pressure of 0.6 bar so that the dissolved $CO_2$ concentration ($H_2CO_3$) can be estimated by the Henry's Law. In the alkaline compartment, there is no exchange of $CO_2$ with other parts of the system, so that the total concentration of $H_2CO_3$, $HCO_3^-$, and $CO_3^{2-}$ remains the same as in the acidic solution. In order to define the $K^+$ concentration in the acidic compartment the following correlations are used and linked to equilibrium equations (Eqs. 1-2) [11]:

$$J_{tot} = J_{k^+} + J_{H^+} = \frac{i}{F} \quad (1)$$

$$J_{k^+} = \frac{V_{rich}}{A_m} \times ([k^+]_{rich} - [k^+]_{acid}) \quad (2)$$

with $J_{tot}$ the total flux of cations ($K^+$ and $H^+$) across the CEM (mol/s•m$^2$), $J_K$+ and $J_H$+ the flux of $K^+$ and $H^+$ across the CEM respectively (mol/s•m$^2$), $V_{rich}$ the volumetric flow rate of rich solution (L/s), $A_m$ the CEM area (m$^2$), i the current density (A/m$^2$) and F the Faradaic constant (96485 C/mole-). Similarly, the amount of desorbed $CO_2$ ($J_{CO2}$ in mol/s•m$^2$) is evaluated by the following equation (see Eq. 3) [11]:

$$J_{CO2} = \frac{V_{rich}}{A_m} \times ([C_t]_{rich} - [C_t]_{acid}) \quad (3)$$

With $Ct_{rich}$ and $Ct_{acid}$ the total carbon concentration in the rich and acidic solutions.

The following figures of merit (removal ratio of $K^+$ ($R_{k+}$ in Eq. 4), removal ratio of carbon ($R_{ct}$ in Eq. 5), potassium transport number ($t_{k+}$ in Eq. 6), $CO_2$ desorption efficiency ($\eta_{CO2}$ in Eq. 7)) are considered to evaluate the efficiency of the electrodialysis process [11]:

$$R_{k^+} = \frac{[k^+]_{rich} - [k^+]_{acid}}{[k^+]_{rich}} \quad (4)$$

$$R_{C_t} = \frac{V_{CO2,g}}{V_{rich} \times [C_t]_{rich} \times V_m} \quad (5)$$

$$t_{k^+} = \frac{V_{rich} \times ([k^+]_{rich} - [k^+]_{acid}) \times F}{i \times A_m \times N} \quad (6)$$

$$\eta_{CO2} = \frac{V_{CO2,g} \times F}{i \times A_m \times N \times V_m} \quad (7)$$

With $V_{CO2,g}$ the $CO_2$ flow rate exiting the regeneration stage (L/s), $V_m$ the molar volume of $CO_2$ in standard conditions (22.4 L/mol), N the number of cell pairs.

It is possible to define, in addition, the carbon loading as the ratio between the total carbon concentration in the solution coming from the absorption column and the $K^+$ concentration in the same solution.

On the other hand, the load ratio is defined as the fraction electrical current to moles of $K^+$ ions supplied to the system (see Eq. 8) [11]:

$$L_{k^+} = \frac{i \times A_m \times N}{V_{rich} \times [k^+]_{rich} \times F} \quad (8)$$

In our model, at a fixed value of $K^+$ concentration, from Eq.8, we found the value of $V_{rich}$ that is able to provide the minimum positive value of load ratio. In this way the system equation is well determinate.

## Energy consumption

The specific energy consumption of the process is evaluated according to the following equation (Eq. 9) [11]:

$$SEC = \frac{U_{cell} \times i}{J_{CO2}} \quad (9)$$

With $U_{cell}$ the potential drop over N cell pairs calculated as (see Eq. 10):

$$U_{cell} = (N + 1) \times U_{BPM} + N \times U_{CEM} + N \times U_{ohmic} \quad (10)$$

where $U_{BPM}$ and $U_{CEM}$ are related to the overall potential drop over the bipolar membranes and CEMs while $U_{ohmic}$ considers the voltage for acidic and alkaline solutions. Their correlations are reported in the work of Castano et al. [11] taking into account the formation of $CO_2$ gas bubbles in the acidic solution.

## Economic analysis

A simple economic analysis has been performed for the BPMED stack system. The capture cost ($/ton$CO_2$) is provided by the following correlation (see Eq. 11) [9]:

$$Capture\ cost = \frac{TOC \times CRF + C_{O\&M}^{fix} + C_{O\&M}^{var} \times h_{eq}}{F_{CO2} \times h_{eq}} \quad (11)$$

with TOC as the total overnight cost, $F_{CO2}$ the overall captured flow rate ($J_{CO2} \bullet A_m$), CRF the capital recovery factor, $h_{eq}$ the plant ability. The TOC is evaluated as 2.6 times the bare erected cost (BEC) equal to 233 $/m$^2$, the fixed cost is a percentage of TOC (4.5%) while variable costs are evaluated considering a price for electricity, BPM and CEM respectively of 0.06 $/kWh, 750 $/m$^2$ and 75 $/m$^2$ [9-10].

## Global sensitivity analysis

A GSA has been conducted by quantifying the overall uncertainty in the KPIs of interest (specific energy consumption, capture cost, $CO_2$ desorption efficiency, removal ratio of $K^+$ and carbon, potassium transport number) and by simultaneously varying all of the uncertain factors through their entire range. The uncertain factors assume an uniform distribution, as reported in Table 1.

**Table 1.** Definition of uncertainty parameters in the GSA

| Uncertainty parameter | Lower bound | Higher bound |
|---|---|---|
| Current density (A/m$^2$) | 150 | 1000 |
| $K^+$, Rich concentration (M) | 0.5 | 2 |
| Membrane area (m$^2$) | 0.008 | 0.012 |
| Number of cell pairs | 3.2 | 4.8 |
| $CO_2$ partial pressure in the gas phase (bar) | 0.3 | 0.9 |

The GSA is conducted using the software Sobol-GSA, which constructs high dimensional model representation (HDMR) surrogates by drawing 1000 Sobol samples [14] from the uncertainty distribution and reevaluating the process model, then estimates total-order Sobol sensitivity indices [15] for each KPIs. The mentioned indices are evaluated in order to consider also interactions among parameters.

# RESULTS AND DISCUSSION

The developed mathematical model has been validated with data reported in Castano et al. [11]. The GSA provides 1000 values of input operating parameters reflecting on the distribution of the considered figures of merit and energy consumption and costs as reported in Figure 2. In Figure 2a, values of specific energy consumption are comparable with those reported in the literature [11] as well as for costs [9,10] in Figure 2b. Low values of $CO_2$ desorption efficiency in Figure 2c are due to the high load ratio caused by DAC operation or to a quite weak pH swing (driving force). Values of carbon removal ratio (Figure 2d), potassium removal ratio (Figure 2e) and

potassium transport number (Figure 2f) are similar to that reported in the literature [11].

Total-order Sobol sensitivity indices are evaluated and reported in Table 2: values higher than 5% suggest that the considered input is significant for the analyzed output [16].

The main specific energy consumption drivers seem to be the potassium cations concentration and the number of cell in the BPMED stack.. The cation concentration on rich solution has the highest impact on this response.

For the total cost, current density, $K^+$ concentration in the rich solvent and number of cell pairs are significant. The current density has the highest impact on costs while the number of cell pairs has the lowest impact on economy.

Minimal costs and energy consumptions are obtained at low potassium concentration. At lower current density, the system may experience lower losses due to reduced heat generation, less resistance in the system, and more efficient ion transport.

The concentration of $K^+$ in the feed and number of cells significantly affect the $CO_2$ desorption efficiency with a more effect for the cation concentration.

The concentration of $K^+$ cation in rich solvent is significant for the carbon and potassium removal ratio. The same input in addition to the number of cells significantly affect the potassium transport number. Here the number of cell pairs has a lower effect compared to the potassium concentration in the feed.

From the results, it is evident that membrane area does not affect the analyzed KPIs. This can be explained by the fact that the considered range values for the membrane area is not wide enough to be significant on cost or energy consumption, as reported in Sabatino et al. (2020). Moreover, as the $CO_2$ partial pressure does not affect each of the considered output, lower operating pressure are preferred to reduce costs and energy consumptions.

It is possible to see that the $K^+$ concentration is affecting all analyzed outputs and in a higher measure the carbon removal ratio. On the other hand, $K^+$ concentration has a lowest effect on the potassium transport number.

It is important to underline that these results are obtained considering a single electrodialysis cell not integrated into an absorption column so that the potassium cation concentration is fixed a priori and it is not a result from the absorption unit where the chemical absorption of $CO_2$ occurs. For this reason, values of load ratio higher than that reported in the literature in Castano et al. [11] are obtained in our results, as reported in Figure 3 where the potassium removal ratio as a function of load ratio is shown with $K^+$ concentration as parameter.

These results suggest that the optimal operation of the electrodialysis cell can be obtained only with an optimal operation of the absorption column that provides the optimal potassium concentration in the rich solution able to maximize efficiency and minimize costs.

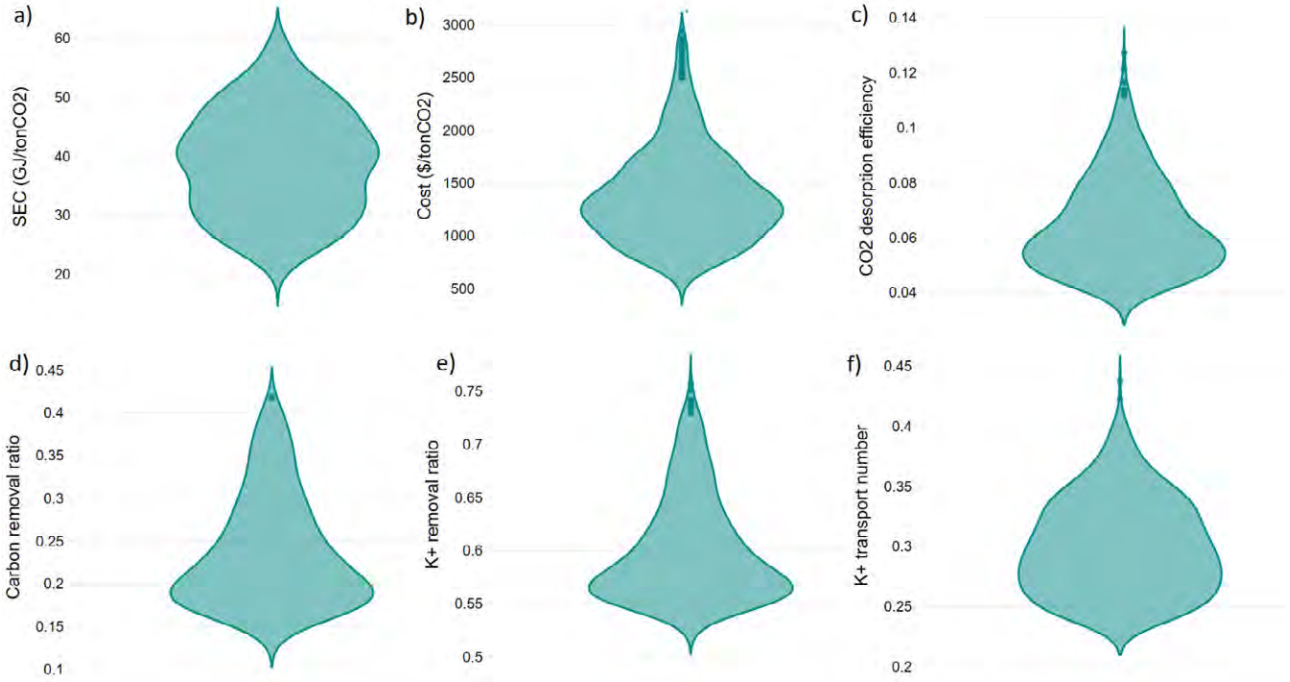



**Figure 2:** Distribution of a) SEC; b) Cost; c) $CO_2$ desorption efficiency; d) Carbon removal ratio; e) Potassium removal ratio; f) Potassium transport number.

**Table 2** Results of the Total-order Sobol sensitivity indices

| | SEC ($GJ/tonCO_2$) | Cost ($/tonCO_2$) | $\eta_{CO2}$ | $R_{CO2}$ | $tn_{K^+}$ | $R_{K+}$ |
|---|---|---|---|---|---|---|
| Current density ($A/m^2$) | 0.0003 | 0.4910 | 0.0001 | 0.0001 | 0.0000 | 0.0001 |
| $[K^+]_{rich}$ (M) | 0.8589 | 0.4597 | 0.8250 | 0.9976 | 0.2067 | 0.9817 |
| Membrane area ($m^2$) | 0.0005 | 0.0003 | 0.0002 | 0.0002 | 0.0000 | 0.0001 |
| Number of cell pairs | 0.1404 | 0.0732 | 0.1819 | 0.002 | 0.7960 | 0.0012 |
| $CO_2$ partial pressure in the gas phase (bar) | 0.0043 | 0.0021 | 0.0043 | 0.0002 | 0.0005 | 0.0196 |

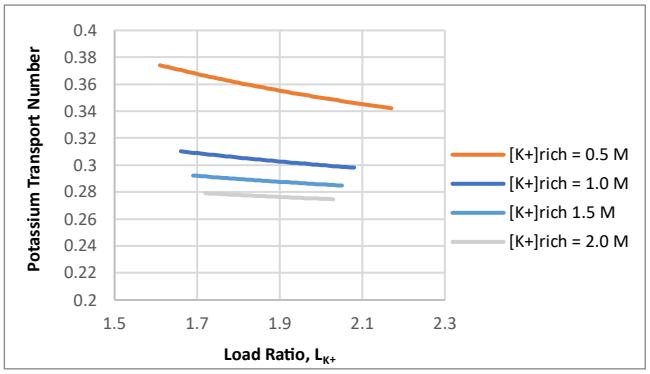



**Figure 3.** Potassium transport number as a function of load ratio and potassium concentration as a parameter

The optimization results interestingly highlight the trade-off between energy efficiency, process speed, and operational costs. Lower process costs are obtained at a higher current intensity due to an improved membrane utilization, the system operating at a more optimal voltage and current conditions. This may reduce the need for more frequent membrane replacements or over-sizing of the system, which can reduce long-term operational costs. Moreover, although higher current densities lead to higher specific energy consumption and lower efficiency, they can reduce overall costs by increasing the production rate or reducing the time required to process a given amount of $CO_2$. This faster operation could mean lower fixed costs for labour, equipment, and maintenance per ton of processed $CO_2$.

## CONCLUSIONS

This work analyzes the performances of a BPMED system for an absorption DAC. In particular a mathematical model has been developed considering equilibrium equations and material balances. In this way, a GSA is carried out to find significant parameters on the main figures of merit. Results show that the main important factor is the potassium concentration in the rich solvent affecting energy consumption, cost, $CO_2$ desorption efficiency, potassium and carbon removal ratio and potassium transport number.

A trade-off between energy efficiency, process speed, and operational costs could be achieved to have to optimal operating conditions.

In future research, an overall integrated system considering the absorption column and the cell must be considered for a better analysis.

## ACKNOWLEDGEMENTS

The authors would like to thank the University of Cagliari and Imperial College London.

## REFERENCES

1. Ourworldindata, 2024, https://ourworldindata.org/co2-and-greenhouse-gas-emissions#all-charts, accessed on 13 November 2024.
2. Cao, T.N.D., Snyder, S.W., Lin, Y.I., Lin, Y.J., Negi, S., Pan, S.Y., Unraveling the Potential of Electrochemical pH-Swing Processes for Carbon Dioxide Capture and Utilization, Ind. Eng. Chem. Res. 62, 20979−20995 (2023)
3. Allen, M.; Dube, O. P.; Solecki, W.; Aragón-Durand, F.; Cramer, W.; Humphreys, S.; Kainuma, M.; Kala, J.; Mahowald, N.; Mulugetta, Y.; et al. Global Warming of 1.5°C; An IPCC Special Report on the Impacts of Global Warming of 1.5°C above Pre-Industrial Levels and Related Global Greenhouse Gas Emission Pathways, in the Context of Strengthening the Global Response to the Threat of Climate Change, Sustainable Development, And Efforts to Eradicate Poverty; IPPC, 2018.
4. Liu, G., Yang, A., Darton, R.C., Numerical Modeling and Comparative Analysis of Electrolysis and Electrodialysis Systems for Direct Air Capture, ACS Sustainable Chem. Eng. 12, 3951−3965, (2024)
5. Leonzio, G., Fennell, P.S., Shah, N., Analysis of Technologies for Carbon Dioxide Capture from the Air, Appli. Sci., 12(16), 8321 (2022)

6. Xu, H., Yu, L., Chong, C., Wang, F., 2024. A comprehensive review on direct air carbon capture (DAC) technology by adsorption: From fundamentals to applications, Energy Convers. Manag. 322, 119119 (2024)
7. Sodiq, A., Abdullatif, Y., Aissa, B., Ostovar, A., Nassar, N., El-Naas, M., Amhamed, A., A review on progress made in direct air capture of CO2, Environmental Technology & Innovation 29, 102991 (2023)
8. Bisotti, F., Hoff, K.A., Mathisen, A., Hovland, J., Direct Air capture (DAC) deployment: A review of the industrial deployment, Chem. Eng. Sci. 283, 119416 (2024)
9. Sabatino, F., Mehta, M., Grimm, A., Gazzani, M., Gallucci, F., Kramer, G.J., and Annaland, M., Evaluation of a Direct Air Capture Process Combining Wet Scrubbing and Bipolar Membrane Electrodialysis, Ind. Eng. Chem. Res. 59, 7007–7020, (2020).
10. Sabatino, F., Gazzani, M., Gallucci, F., Annaland, M., Modeling, Optimization, and Techno-Economic Analysis of Bipolar Membrane Electrodialysis for Direct Air Capture Processes, Ind. Eng. Chem. Res. 61, 12668–12679 (2022).
11. Vallejo Castano, S., Shu, Q., Shi, M., Blauw, R., Loldrup Fosbøl, P., Kuntke, P., Tedesco, M., Hamelers, H.V.M., Optimizing alkaline solvent regeneration through bipolar membrane electrodialysis for carbon capture, Chem. Eng. Journal 488, 150870, (2024).
12. Young, J., McQueen, N., Charalambous, C., …, Renforth, P., Garcia, S., van der Spek, M., The cost of direct air capture and storage can be reduced via strategic deployment but is unlikely to fall below stated cost targets, One Earth 6, 899–917, (2023).
13. Eisaman, M. D., Alvarado, L., Larner, D., Wang, P., Littau, K.A. CO2 desorption using high-pressure bipolar membrane electrodialysis, Energy Environ. Sci. 4 (10), 4031 (2011).
14. IM Sobol, Global sensitivity indices for nonlinear mathematical models and their Monte Carlo estimates, Mathematics & Computers in Simulation 55, 271 – 280, (2001)
15. H Rabitz, OF Alis, General foundations of high-dimensional model representations, J. Math. Chem., 25, 197–233, (1999).
16. Zhang, X.Y., Trame, M.N., Lesko, L.J., Schmidt, S., Sobol sensitivity analysis: a tool to guide the development and evaluation of systems pharmacology models. CPT Pharmacometrics Syst. Pharmacol. 4 (2), 69–79 (2015).

© 2025 by the authors. Licensed to PSEcommunity.org and PSE Press. This is an open access article under the creative commons CC-BY-SA licensing terms. Credit must be given to creator and adaptations must be shared under the same terms. See https://creativecommons.org/licenses/by-sa/4.0/



Systems & Control Transactions

**Research Article - Peer Reviewed Conference Proceeding**
ESCAPE 35 - European Symposium on Computer Aided Process Engineering
Ghent, Belgium. 6-9 July 2025
Jan F.M. Van Impe, Grégoire Léonard, Satyajeet S. Bhonsale,
Monika E. Polańska, Filip Logist (Eds.)

PSE PRESS

# Intensified Alternative for Sustainable Gamma-Valerolactone Production from Levulinic Acid

**Brenda Huerta-Rosas[a], Melanie Coronel-Muñoz[a], Juan José Quiroz-Ramírez[c], Carlos Rodrigo Caceres-Barrera[a], Gabriel Contreras-Zarazua[b], Juan Gabriel Segovia-Hernández[a] , Eduardo Sánchez-Ramírez[a]**

[a] Universidad de Guanajuato, Noria Alta s/n, Guanajuato 36050, Mexico, eduardo.sanchez@ugto.mx
[b] Área de Ingeniería Química, IPH, Universidad Autónoma Metropolitana-Iztapalapa, Av. FFCC R. Atlixco 186, 09340 Iztapalapa, Ciudad de México, México.
[c]CONACyT – CIATEC A.C. Centro de Innovación Aplicada en Tecnologías Competitivas, Omega 201, Col. Industrial Delta, 37545 León, Gto. México.
* Corresponding Author: eduardo.sanchez@ugto.mx

## ABSTRACT

An intensified approach to γ-valerolactone (GVL) production is achieved using a reactive distillation column. Conventional methods require multiple units, leading to high energy consumption, costs, and limited scalability. The proposed technology integrates reaction and separation into a single unit, enhancing process efficiency for biomass-derived chemicals. A multiobjective optimization framework balances economic, environmental, and operational goals, reducing total annual cost (TAC) by 43% and environmental impact (EI99) by 45% compared to conventional processes. Additionally, energy consumption drops by 63%, while GVL production increases by 25%, highlighting the potential of reactive distillation for improved efficiency and sustainability.

**Keywords**: Process Intensification, Optimization, Distillation, Life Cycle Analysis, Biomass

## INTRODUCTION

The rise of Industry 4.0 is transforming manufacturing through digital integration, automation, and smart systems, fostering sustainability and efficiency [1]. Traditional biofuel production, such as bioethanol and biobutanol, faces challenges in cost and energy efficiency, prompting a shift towards high-value bio-based chemicals like γ-valerolactone (GVL) [2]. GVL, derived from levulinic acid via catalytic hydrogenation, serves as a green solvent, biofuel additive, and precursor for biofuels [2]. Despite its potential, conventional GVL production methods are energy-intensive and costly, requiring high pressures and temperatures, limiting scalability [2-3]. Process Intensification (PI) offers a solution by integrating chemical reactions and separation, reducing energy consumption and enhancing efficiency [5]. Reactive distillation, which combines reaction and distillation into a single unit, has successfully improved processes like biodiesel production, reducing energy use by 40% [6]. This study proposes a sustainable, intensified approach to GVL production using reactive distillation, compared with conventional methods under a multi-objective optimization framework evaluating total annual cost (TAC) and environmental impact [7]. This novel strategy aligns with Industry 4.0 and sustainability goals, enhancing GVL production efficiency and viability.

## PROBLEM STATEMENT AND CASE STUDY

Biocompounds derived from renewable biomass present a sustainable alternative to petrochemical-based products. However, conventional production methods are highly energy-intensive, often diminishing their environmental advantages. Typical processes involve multiple stages, including feedstock pretreatment, chemical or biochemical conversion, and product purification. Each stage contributes significantly to energy demand, with steam explosion consuming up to 15% of the total process energy, fermentation requiring 10-15%, and distillation accounting for 35-40% in ethanol production [7].

To address these inefficiencies, Process Intensification (PI) has emerged as a promising strategy,

integrating multiple unit operations to enhance mass and heat transfer, reduce equipment size, and minimize energy consumption. By leveraging PI, biocompound production can achieve improved economic feasibility and environmental performance [8].

In the case of γ-valerolactone (GVL) production, catalytic hydrogenation of levulinic acid (LA) has been widely studied [8]. demonstrated that a Cu–$ZrO_2$ nanocomposite catalyst achieves over 90% selectivity under optimal conditions (473 K, 3–4 MPa $H_2$ pressure), with excellent recyclability and low metal leaching, making it suitable for industrial applications. Later, [7]. implemented this process in a multi-product biorefinery, producing GVL alongside levulinic acid, furfural, and hydroxymethylfurfural using conventional reaction and separation technologies. However, their study revealed that GVL production accounted for 41% of the total energy demand of the process, highlighting a need for further optimization.

This study proposes the integration of a reactive distillation column as an intensified alternative to replace conventional reactor-separation schemes. By merging reaction and separation into a single unit, energy consumption is reduced, operational efficiency is enhanced, and process sustainability is improved. The proposed intensified process will be systematically compared against its conventional counterpart using multi-objective optimization, evaluating total annual cost (TAC) and environmental impact (EI99) as key performance indicators. The conceptual approach for process intensification applied to GVL production is illustrated in Figure 1.

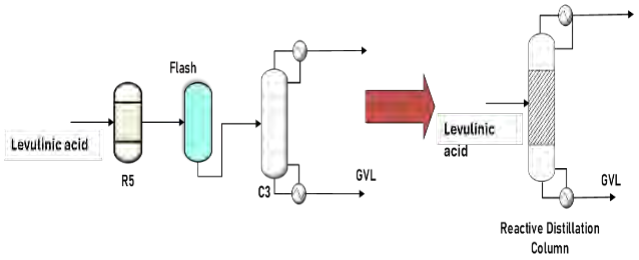



**Figure 1:** Process intensification applied to GVL production.

## PERFORMANCE ASSESSMENT

### Economic and Environmental Evaluation

A multi-objective optimization framework is used to evaluate both economic and environmental performance. The total annual cost (TAC) [9]. and environmental impact (EI99) [1]. serve as key indicators:

TAC Calculation:

$$TAC\ (\$/y) = \frac{\sum_{i=1}^{n} C_{TM,i}}{n} + \sum_{j=1}^{n} C_{ut,j} \qquad (1)$$

where TAC represents the total annual cost, CTM stands for the capital cost of the plant, n signifies the payback period, and $C_{ut}$ represents the utility cost.

Environmental Impact Evaluation (EI99):

To ensure a robust assessment, the system boundaries were carefully defined to encompass the entire life cycle of the process, from raw material input to product output. The analysis considers both direct and indirect environmental impacts associated with the production and operation of the proposed technology. Specifically, it includes the environmental footprint of the materials used for equipment construction, the energy required for heating, and the utilities needed for process operation. In particular, the impact of steel used for the fabrication of the equipment is incorporated into the analysis, considering its extraction, processing, and eventual disposal. Additionally, the steam utilized for process heating is accounted for, as it represents a major contributor to energy consumption. The evaluation also includes the electricity required for pumping operations, which reflects the indirect energy demand necessary for fluid transport and process continuity.

$$EI99 = \sum_b \sum_d \sum_{k \in K} \delta_d \omega_d \beta_b \alpha_{b,k} \qquad (2)$$

Here, $\beta_b$ denotes the total quantity of chemical b released per unit of reference flow due to direct emissions, $\alpha_{b,k}$ represents the damage caused by category k per unit of chemical b released into the environment, $\omega_d$ is the weighting factor for damage in category d, and $\delta_d$ is the normalization factor for damage in category d. This approach considers the impact of steel used for construction, steam used for heating, and electricity used for pumping.

## METHODOLOGY

### Kinetic Parameter Determination

The kinetic model for GVL production was developed using experimental data from [8]. with reaction kinetics adapted for a Cu–$ZrO_2$ catalyst. The catalyst parameters were optimized using the kinetic parameter estimation framework proposed by [9]. The process follows a two-step hydrogenation reaction: first, hydrogen peroxide decomposes into hydrogen and carbon dioxide. Then, levulinic acid undergoes hydrogenation in the presence of hydrogen gas, yielding γ-valerolactone (GVL) and water. Finally, an intramolecular cyclization step completes the formation of GVL, a high-value bio-based chemical with diverse industrial applications:

$$CH_2O_2 \rightarrow H_2 + CO_2 \qquad (3)$$

$$C_5H_8O_3 + H_2 \rightarrow C_5H_8O_2 + H_2O \qquad (4)$$

### Process Simulation and Modeling

The intensified alternatives were developed based on the optimization of the conventional GVL production process. The previously reported scheme [7]. was replicated to ensure a fair comparison, as detailed in Table 1 and illustrated in Figure 2, which highlights the key process stages. At the inlet of reactor R5, the feed stream rich in levulinic acid undergoes conversion, primarily yielding γ-valerolactone (GVL). The Aspen Plus process simulator was used to model both conventional and intensified processes, ensuring accurate process representation. Thermodynamic modeling was performed using the Non-Random Two-Liquid (NRTL) model for phase equilibrium, providing reliable predictions of separation efficiencies and component interactions.

**Table 1:** Design parameters conventional design [7].

| Column C3 | Value | Reactor R5 | Value |
|---|---|---|---|
| Stages | 39 | Flow rate (l/min) | 12.188 |
| Feed Stage | 22 | Volume ($m^3$) | 0.731 |
| Reflux ratio | 0.039 | Diameter (m) | 0.677 |
| Distillate flow (kmol/h) | 7.296 | Pressure (kPa) | 101.32 |
| Diameter (m) | 0.992 | Temperature (°K) | 473 |
| Condenser Duty (Watt) | 91280 | | |
| Reboiler Duty(Watt) | 138022 | | |
| Height (m) | 22.55 | | |

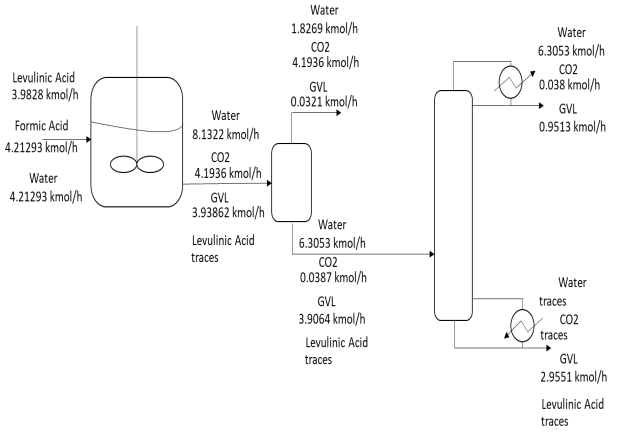



**Figure 2:** Mole balance of the conventional technology for GVL production.

## Reactive Distillation Design and Optimization

The optimization of the reactive distillation column design combines empirical heuristics with a hybrid optimization approach, integrating Aspen Plus with Differential Evolution with Tabu List (DETL) [12]. This method effectively handles nonlinear, nonconvex processes by preventing the re-evaluation of previously assessed points, enhancing search efficiency. The objective function minimizes both total annual cost (TAC) and environmental impact (EI99), ensuring an optimal balance between economic and environmental performance.

The design process starts with defining key parameters such as column dimensions, catalyst type, number of stages, and feed conditions, which are initialized using empirical rules and refined through Aspen Plus simulations. To ensure feasibility, the operating conditions of reaction and separation must align. Factors such as temperature, pressure, and relative volatility are critical, as mismatches between reaction kinetics and separation efficiency can compromise performance [11].

The multi-objective optimization integrates Aspen Plus with Excel via Dynamic Data Exchange (DDE). The DETL algorithm, implemented in Visual Basic, iteratively adjusts decision variables (e.g., reflux ratio, reboiler duty, and feed stage locations) based on process simulations. Optimization parameters include 200 individuals, 1000 generations, a tabu list size of 50%, a tabu radius of $1\times10^{-6}$, and crossover/mutation rates of 0.8 and 0.6, derived from previous studies [12]. The objective function minimizes both TAC and EI99:

$$Min(TAC, EI99) = f(N_{tn}, N_{fn}, R_{rn}, F_{rn}, R_{sn}, D_{cn}) \quad (5)$$

$$\text{Subject to } \vec{x_m} > \vec{y_m}$$

where $N_{tn}$ is the total number of column stages, $N_{fn}$ is the feed stages in the column, $R_{rn}$ is the reflux ratio, $F_{rn}$ is the distillate/bottoms flux, $R_{sn}$ is the reactive stages, and $D_{cn}$ is the column diameter. $y_m$ and $x_m$ are the vectors of both obtained and required purities for the $m_{th}$ components, respectively. The minimum purity targets were fixed as 98.5 %wt for GVL.

Decision variables such as reflux ratio, reboiler duty, feed stage locations, and catalyst distribution are identified and optimized with respect to a multi-objective function that incorporates economic, environmental, and operational goals (See Table 2).

**Table 2:** Decision Variables in the multi-objective optimization problem

| Variable | Type | Search Range |
|---|---|---|
| Number of Stages | Discrete | 5-100 |
| Feed Stages | Discrete | 4-99 |
| Reactive stages range | Discrete | 4-99 |
| Reflux Ratio | Continuous | 0.1-5 |
| Bottoms Rate | Continuous | 3.5 - 4 (kmol h-1) |
| Diameter | Continuous | 0.9-5 (meters) |

## RESULTS AND DISCUSSION

### Kinetic Model Validation

**Figure 3** shows a strong correlation between experimental and predicted outflows in the reactor, with a **99.9% GVL yield**. The close agreement between red (experimental) and blue (predicted) bars across all components validates the kinetic model's accuracy, confirming its reliability for process optimization.

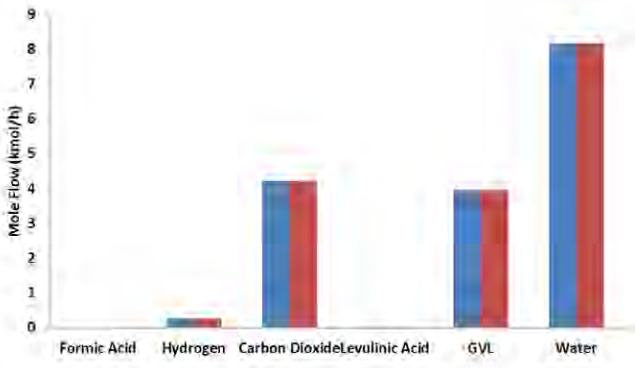



**Figure 3:** Experimental (red) and predicted (blue) outflows in the reactor

**Table 3** presents the kinetic parameters for key reactions in GVL production. The decomposition of **formic acid ($CH_2O_2 \rightarrow H_2 + CO_2$)** has a high rate constant and activation energy, indicating a fast, energy-intensive step. In contrast, the **hydrogenation of levulinic acid to GVL** occurs at a slower rate, suggesting it is the limiting step. These findings emphasize the need for optimized catalysts and conditions to enhance conversion efficiency

**Table 3:** Caption for the table. Multi-line table captions will be fully justified. The style is **PSE_TableCaption**.

| Reaction | k | E (cal/mol) |
|---|---|---|
| $CH_2O_2 \rightarrow H_2 + CO_2$ | 29513.430 | 3399.005 |
| $C_5H_8O_3 + H_2 \rightarrow C_5H_8O_2 + H_2O$ | 552.581 | 1703.585 |

### Process Optimization and Comparison

Reactive distillation column for GVL production was optimized using Differential Evolution with Tabu List (DETL), minimizing total annual cost (TAC) and environmental impact (EI99). The Pareto front (Figure 4) highlights designs that meet GVL purity constraints, demonstrating the trade-off between economic and environmental objectives.

Reducing equipment costs favors smaller, compact designs, but these require higher reflux ratios or reboiler duties, increasing operational costs. Conversely, minimizing steel usage reduces environmental impact but can lead to higher energy consumption. The optimal design, marked in Figure 4, balances TAC and EI99, ensuring an efficient and sustainable reactive distillation process.:

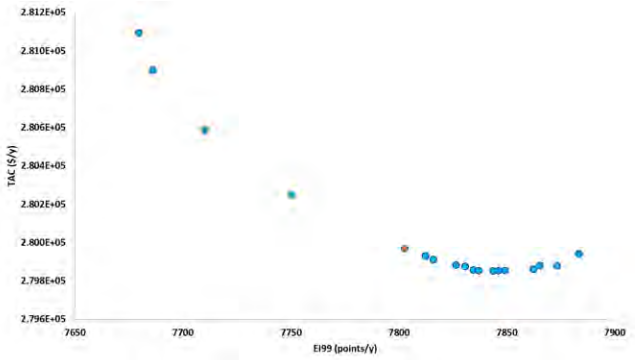



**Figure 4.** Pareto front for the reactive distillation column for GVL production.

A Pareto front analysis identified optimal designs that balance total annual cost (TAC) and environmental impact (EI99), demonstrating the advantages of the intensified process over the conventional approach. The intensified design achieved a 43% reduction in TAC, a 45% decrease in EI99, and a 63% reduction in energy consumption, while increasing GVL production by 25%. Compared to the conventional process, these improvements highlight the effectiveness of integrating reaction and separation into a single unit, significantly enhancing efficiency and sustainability.

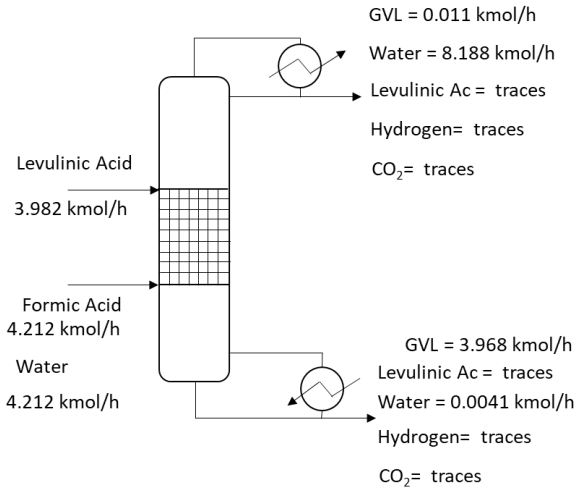



**Figure 5:** Flowsheet of the reactive distillation column.

Figure 5 presents the complete flowsheet of the intensified process, emphasizing the integration of reaction and separation within a single unit to enhance efficiency and sustainability. When contrasted with the Pareto front shown in Figure 4, the optimized design achieves a significant reduction in total annual cost (TAC) and environmental impact (EI99). The highlighted optimal point in the Pareto front confirms that the intensified

process configuration successfully balances economic and environmental objectives, reinforcing the advantages of reactive distillation over conventional multi-unit approaches.

**Table 4:** Optimal design parameter of the reactive distillation for GVL production.

| Reactive Column | | | |
|---|---|---|---|
| Number of stages | 12 | Distillate flowrate (kmol h-1) | 12.64 |
| Reflux ratio | 0.322 | Condenser duty (kcal h-1) | -15.66 |
| Feed stage | 5 and 9 | Reboiler duty (Watt) | 9.89 |
| Reactive stages | 5 to 9 | Operative pressure (kPa) | 101.32 |
| Hold Up (cum) | 0.668 | GVL production (kmol/h) | 3.968 |

Table 4 presents the complete flowsheet of the intensified process, emphasizing the integration of reaction and separation within a single unit to enhance efficiency and sustainability. This optimized design, when contrasted with the Pareto front in Figure 5, demonstrates a substantial reduction in total annual cost (TAC) and environmental impact (EI99). The highlighted optimal point in the Pareto front confirms that the intensified configuration effectively balances economic and environmental objectives. The key design parameters, such as the number of stages, reflux ratio, and reboiler duty, were optimized to maximize GVL yield while minimizing energy consumption. This reinforces the advantages of reactive distillation over conventional multi-unit approaches, offering a more sustainable and cost-effective alternative for GVL production.

The results clearly demonstrate the advantages of process intensification in γ-valerolactone (GVL) production. As shown in **Figure 6**, the intensified process significantly reduces Total Annual Cost (TAC) and environmental impact (EI99) while maintaining a lower heat duty compared to the conventional approach. This indicates improved energy efficiency and economic feasibility. Furthermore, **Figure 7** illustrates the molar composition profile along the reactive distillation column, where levulinic acid is effectively converted into GVL, with water as a major byproduct. The presence of formic acid and carbon dioxide suggests minor side reactions, while hydrogen formation in intermediate stages aligns with catalytic hydrogenation mechanisms. Overall, these findings validate the effectiveness of reactive distillation in optimizing GVL production, offering a more sustainable and cost-efficient alternative to conventional multi-unit processes.

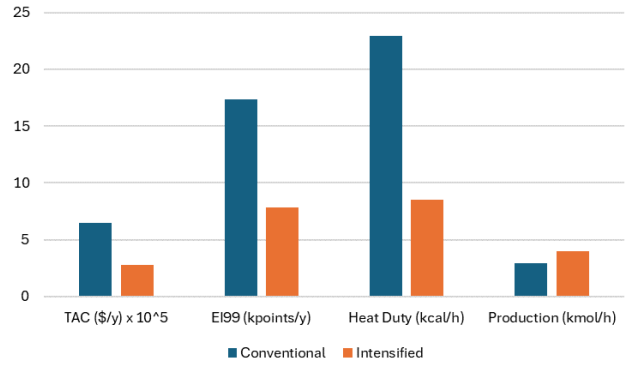



**Figure 6:** Comparison of the performance of technologies in GVL production

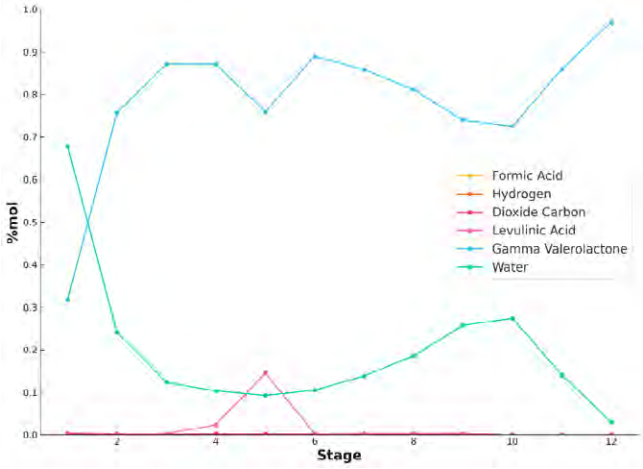



**Figure 7:** Molar composition profile at the reactive distillation column for GVL production

## CONCLUSION

This study introduces an intensified reactive distillation process for γ-valerolactone (GVL) production, significantly improving efficiency over conventional methods. By integrating reaction and separation in a single unit, energy consumption is reduced to 37% of the traditional process, enhancing sustainability. The approach aligns with Industry 4.0 principles, emphasizing process integration, automation, and resource efficiency, demonstrating its potential to drive economic and environmental benefits in modern industrial practices.

## ACKNOWLEDGEMENTS

Please acknowledge your funders in this section, with grant or funding numbers as appropriate. Note that most funding agencies require this.

## REFERENCES

1. Lasi H, Fettke P, Kemper HG, Feld T, Hoffmann M.

Industry 4.0. Bus Inf Syst Eng 6:239–242 (2014) https://doi.org/10.1007/S12599-014-0334-4
2. Pereira AA, Vera FPS, Coelho HCP, Tessaro I, Chandel AK. Renewable carbon in Industry 4.0: Toward the sustainable bioeconomy. Green Energy and Technology Part F2511:1–27 (2024) https://doi.org/10.1007/978-3-031-51601-6_1
3. Horváth IT, Mehdi H, Fábos V, Boda L, Mika LT. γ-Valerolactone—a sustainable liquid for energy and carbon-based chemicals. Green Chem 10:238–242 (2008) https://doi.org/10.1039/B712863K
4. Tang Y, Fu J, Wang Y, Guo H, Qi X. Bimetallic Ni-Zn@OMC catalyst for selective hydrogenation of levulinic acid to γ-valerolactone in water. Fuel Process Technol 240:107559 (2023) https://doi.org/10.1016/J.FUPROC.2022.107559
5. López-Guajardo EA, Delgado-Licona F, Álvarez AJ, Nigam KDP, Montesinos-Castellanos A, Morales-Menendez R. Process intensification 4.0: A new approach for attaining new, sustainable, and circular processes enabled by machine learning. Chem Eng Process Process Intensif 180:108671 (2022) https://doi.org/10.1016/J.CEP.2021.108671
6. Kiss AA, Omota F, Dimian AC, Rothenberg G. The heterogeneous advantage: Biodiesel by catalytic reactive distillation. Top Catal 40:141–150 (2006) https://doi.org/10.1007/S11244-006-0116-4
7. Caceres CR, Sánchez-Ramirez E, Segovia-Hernández JG. Design and optimization of a sustainable process for the transformation of glucose into high added value products. Comput Aided Chem Eng 53:73–78 (2024) https://doi.org/10.1016/B978-0-443-28824-1.50013-2
8. Hengne AM, Rode CV. Cu–$ZrO_2$ nanocomposite catalyst for selective hydrogenation of levulinic acid and its ester to γ-valerolactone. Green Chem 14:1064–1072 (2012) doi.org/10.1039/C2GC16558A
9. Goedkoop M, Spriensma R. Eco-indicator 99 Manual for Designers. PRe´ Consultants, Amersfoort, The Netherlands (2000)
10. Sánchez-Ramírez E, Huerta-Rosas B, Quiroz-Ramírez JJ, Suárez-Toriello VA, Contreras-Zarazua G, Segovia-Hernández JG. Optimization-based framework for modeling and kinetic parameter estimation. Chem Eng Res Des 186:647–660 (2022) https://doi.org/10.1016/J.CHERD.2022.08.040
11. Shah M, Kiss AA, Zondervan E, De Haan AB. A systematic framework for the feasibility and technical evaluation of reactive distillation processes. Chem Eng Process 60:55–64 (2012) https://doi.org/10.1016/j.cep.2012.05.007
12. Srinivas M, Rangaiah GP. Differential evolution with tabu list for global optimization: Evaluation of two versions on benchmark and phase stability problems. Adv Process Syst Eng 6:91–127 (2017) https://doi.org/10.1142/9789813207523_0004

© 2025 by the authors. Licensed to PSEcommunity.org and PSE Press. This is an open access article under the creative commons CC-BY-SA licensing terms. Credit must be given to creator and adaptations must be shared under the same terms. See https://creativecommons.org/licenses/by-sa/4.0/



Systems & Control Transactions

**Research Article - Peer Reviewed Conference Proceeding**
ESCAPE 35 - European Symposium on Computer Aided Process Engineering
Ghent, Belgium. 6-9 July 2025
Jan F.M. Van Impe, Grégoire Léonard, Satyajeet S. Bhonsale,
Monika E. Polańska, Filip Logist (Eds.)

PSE PRESS

# Environmental assessment of the catalytic arabinose oxidation

**Mouad Hachhach[a,b*], Dmitry Yu. Murzin[a], and Tapio Salmi[s]**

[a] Laboratory of Industrial Chemistry and Reaction Engineering (TKR), Johan Gadolin Process Chemistry Centre (PCC), Åbo Akademi University, FI-20500 Turku-Åbo, Finland
[b] National Thematic Institute for Scientific Research-Water, Ibn Zohr University, Agadir, Morocco
* Corresponding Author: mouad.hachhach@abo.fi.

## ABSTRACT

Oxidation of arabinose to arabinoic acid is an innovative way to valorize local biomass to a high add value product. Previously done experiments on oxidation of arabinose to arabinoic acid with molecular oxygen were used to determine the optimum reaction conditions, scale-up the process and analyse the techno-economic aspects. These results were utilized to analyse the environmental impact of the scaled-up process during its lifetime using the life cycle assessment (LCA) methodology. SimaPro software combined with the impact assessment method IMPACT 2002+ were applied. The results revealed that heating seems to be the largest contributor to the environmental impact even if the reaction is performed under rather mild conditions (70°C). This highlights the importance of reducing the energy consumption via efficient heat integration.

**Keywords**: Catalyst, LCA, Biomass

## INTRODUCTION

The global transition toward sustainable chemical processes has underscored the importance of assessing the environmental impacts of emerging industrial technologies. One such process, the catalytic oxidation of arabinose to arabinoic acid, has gained attention for its diverse applications in the pharmaceutical, cosmetic, and food industries due to the functional properties of arabinoic acid as a platform chemical [1, 2].

Gold-based catalysts have been shown to be effective in achieving high sugar conversion and sugar acid selectivity under optimal conditions, especially in a slightly basic environment [3]. However, the environmental impact of scaling up this process needs to be carefully investigated. This is especially true with respect to energy-intensive operations such as heat generation and wastewater treatment.

Life Cycle Assessment (LCA) is a well-established framework for evaluating the environmental performance of chemical processes by systematically analyzing their impact across categories such as human health, ecosystem quality, climate change, and resource use. The IMPACT 2002+ methodology, a widely recognized LCA framework [4], integrates midpoint and endpoint impact categories, enabling a detailed analysis of environmental trade-offs associated with chemical processes. By applying this methodology, the present study aims to evaluate the environmental impact of catalytic oxidation of arabinose to arabinoic acid, focusing on critical hotspots such as heat generation and wastewater treatment.

This research employs a large-scale process model designed in Aspen Plus to simulate the production of arabinoic acid, offering insights into energy consumption, material flows, and waste streams. Specifically, the study investigates the contributions of heat generation and wastewater treatment to the overall environmental footprint of the process, identifying opportunities for optimization and mitigation. The results will pave a way for developing strategies for reducing emissions, minimizing resource depletion, and improving the sustainability of arabinoic acid production, thereby contributing to the broader goal of sustainable industrial chemistry and process technology.

## METHODOLOGY

### Oxidation of Arabinose

The selective oxidation of arabinose over gold

catalysts has been studied extensively to optimize reaction conditions. The process was carried out isothermally at atmospheric pressure in a semi-batch mode, with variations in temperature, pH, and catalytic properties to achieve the best results.

The primary product, arabinoic acid, is obtained via the intermediate arabinolactone. This final product, the sugar acid, and its derivatives are valuable compounds finding applications in the cosmetic, food, and pharmaceutical industries, offering a competitive price and versatility. Figure 1 illustrates the reaction pathway, highlighting the transformation of arabinose to arabinoic acid via arabinolactone.

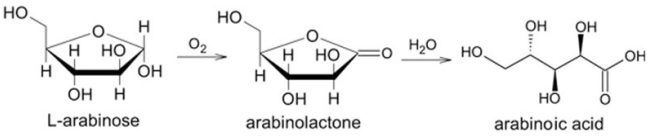



**Figure 1.** The reaction scheme for selective catalytic oxidation of arabinose (adapted from [5]).

The experimental studies reported in [6, 7] demonstrated that in acidic media, the reaction resulted in only 23% conversion of arabinose after 200 minutes, with 46% selectivity towards the desired product, arabinoic acid. Significant amounts of the intermediate compound, arabinolactone, were formed under these conditions. In contrast, slightly basic conditions (pH 8–9) led to the complete conversion and total selectivity for arabinoic acid within the same time frame. The temperature elevation was observed to enhance reaction activity but also promoted formation of the undesired byproducts.

Utilization of a continuous reactor can be challenging because the pH control is not easy, however, it was shown in [8] showed that continuous sugar oxidation could be carried out in a plug-flow reactor without the need for a pH control alongside the whole reactor. Moreover, it was reported that selectivity in the plug-flow reactor was similar to that in the batch reactor, 94% and 99%, respectively.

## Process Design and Modeling

Process design and modeling were conducted in Aspen Plus V11, following the methods used in similar studies previously [9–11]. As the properties of some compounds were not available in the Aspen database, Aspen Properties module was used to estimate the required parameters. The Peng-Robinson equation of state (EoS) was applied to calculate the phase equilibrium [13]. The reactor was modeled using Aspen PFR blocks, in accordance with Ranade et al. [12], who applied plug flow models for trickle bed reactors. Arabinoic acid properties, unavailable in the database, were added via the user-defined compound wizard after their estimation with the Joback method [13], while other parameters were computed with Aspen Properties. The developed flowsheet is

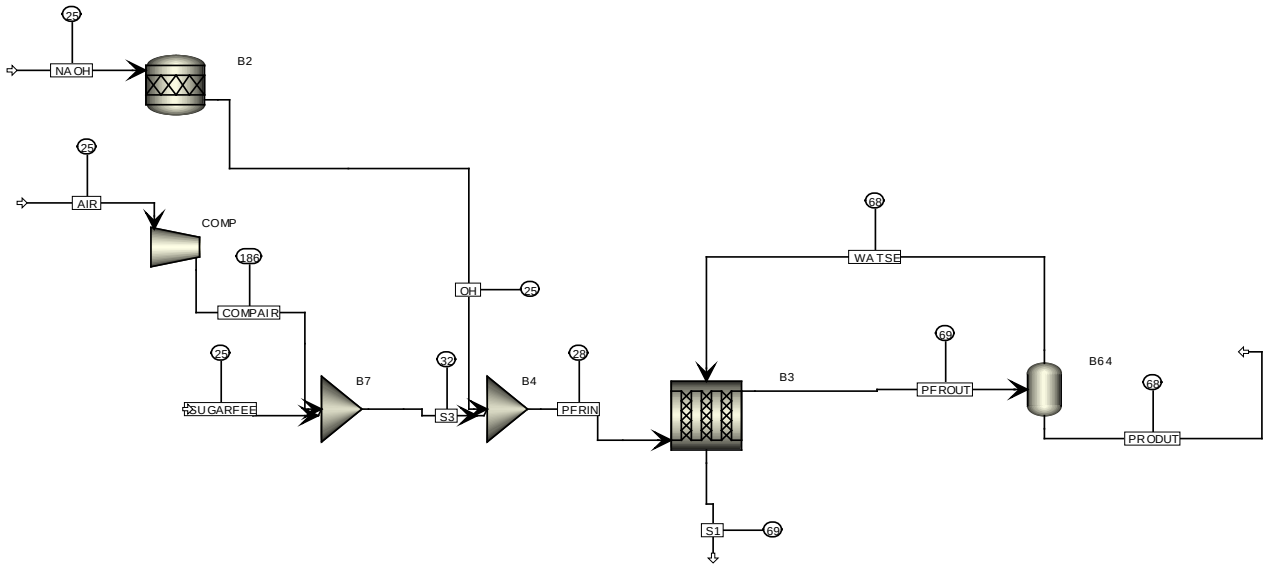



**Figure 2.** Flowsheet of arabinoic acid production via catalytic oxidation of arabinose

**Table 1.** Summary of the main operating conditions

| pH | Residence time (min) | Temperature (°C) | Pressure (atm) |
|---|---|---|---|
| 8 | 29 | 60 | 1 |

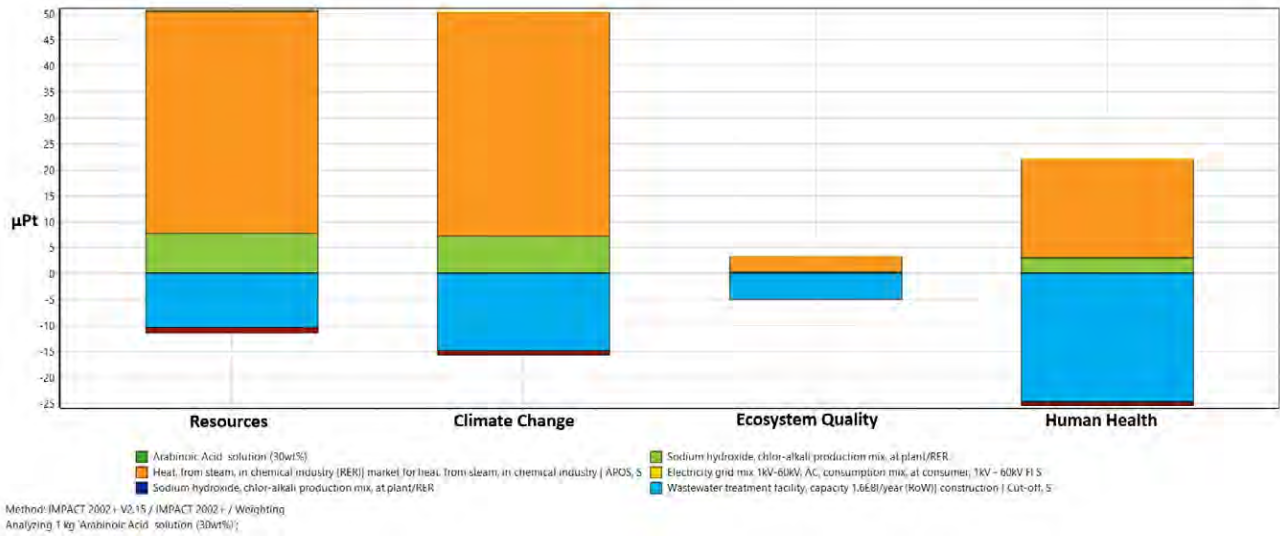



**Figure 3.** LCA normalized results for the arabinose oxidation.

presented in Figure 2.

## Goal and scope

The goal of this study is to investigate the environmental impact of the catalytic oxidation of the arabinose sugar on a supported gold catalyst. This assessment is based on the data generated from the large-scale process model developed using Aspen Plus [10]based on the experimental results generated in laboratory scale [6, 14–16]. In this study, the annual processing capacity of 10 kt of arabinose solution (30 wt%) was considered. The functional unit was taken as 1 kg of arabinoic acid solution (30 wt%). The system boundaries followed a cradle-to-gate approach. SimaPro software was used for this work.

## Life Cycle Inventory and Life Cycle Impact Assessment

The life cycle inventory (LCI) data for the system (i.e. chemicals, energy, reactants' consumption) consists of the mass, heat balance, and energy consumption from the simulations using Aspen Plus. The details are reported in our previous publication [10].

Life Cycle Impact Assessment (LCIA) is a phase in the Life Cycle Assessment process where the potential environmental impact associated with a product or process is evaluated. The impact assessment was performed using the impact 2002+ method, originally developed in [4].

# RESULTS AND DISCUSSIONS

Figure 3 highlights the environmental impact of arabinose oxidation across four damage assessment categories: Human Health, Ecosystem Quality, Climate Change, and Resource Use, with contributions from specific sources represented as stacked bars.

Heating used in the process emerges as a major contributor to negative impacts in all categories. In the Human Health category, industrial heat processes significantly affect health outcomes, primarily due to emissions and resource-intensive operations. Similarly, for Climate Change, heat generation from industrial sources is the dominant factor driving adverse impacts, reflecting high greenhouse gas emissions associated with these processes. In Resource Use, the production and use of heat in industrial activities lead to substantial resource depletion, further emphasizing its environmental burden. Conversely, the impact of heat-related processes on Ecosystem Quality is relatively minor, though still present.
Wastewater treatment processes generally have a mixed impact. In the Human Health category, they show a slight mitigating effect, likely due to their role in reducing pollutants that would otherwise harm human populations. Similarly, in the Climate Change category, wastewater treatment contributes modestly to mitigating greenhouse gas emissions, though its overall impact is small compared to industrial processes like heat generation.

However, in the Resource Use category, wastewater treatment has a slightly negative impact, most likely due to the energy and materials required for facility operation. The effects on Ecosystem Quality are minimal, indicating that the wastewater treatment has a limited but generally a positive role in addressing ecosystem-related concerns.

The analysis, conducted using the IMPACT 2002+ methodology, underscores the significant role of heat generation in driving environmental and health impacts,

particularly in resource use and climate change. This highlights an urgent need for improving the energy efficiency, adopting renewable energy sources for heat generation, and exploring alternative, lower-impact materials in industrial processes to mitigate these effects. Prioritizing these strategies can significantly reduce the environmental footprint of heat-related activities.

## CONCLUSIONS

The obtained LCA results show that heat generation is the leading cause of environmental impact across all the major categories, especially resource use and climate change. This emphasizes the urgent need to transition to more energy-efficient systems and integrate renewable energy sources into industrial processes. Heat integration and optimization also play an important role in reducing the energy consumption, thus decreasing greenhouse gas emissions and improving the overall process efficiency.

Wastewater treatment, while essential for mitigating pollution and safeguarding public health, also presents opportunities for further optimization. Enhancing the energy efficiency of treatment systems and integrating renewable energy, such as solar or wind power, into their operation can help offset the environmental burdens associated with these processes.

## ACKNOWLEDGEMENTS

Financial support from Academy of Finland (Academy Professor grants 319002, 320115, 345053 (T. Salmi)), from Finnish Cultural Foundation in Finland and from Lieto Savings Bank Foundation is gratefully acknowledged (M. Hachhach).

## REFERENCES

1. Worgul B, Freites Aguilera A, Vergat-Lemercier C, et al (2022) Sugar acid production on gold nanoparticles in slurry reactor: Kinetics, solubility and modelling. Chem Eng Sci 260:. https://doi.org/10.1016/j.ces.2022.117948
2. Fricke PM, Hartmann R, Wirtz A, et al (2022) Production of l-arabinonic acid from l-arabinose by the acetic acid bacterium Gluconobacter oxydans. Bioresour Technol Rep 17:100965. https://doi.org/10.1016/J.BITEB.2022.100965
3. Correia LS, Grénman H, Wärnå J, et al (2019) Catalytic oxidation kinetics of arabinose on supported gold nanoparticles. Chemical Engineering Journal 370:952–961. https://doi.org/10.1016/j.cej.2019.03.241
4. Jolliet O, Margni M, Charles RR, et al (2003) IMPACT 2002+: A New Life Cycle Impact Assessment Methodology Olivier. The International Journal of Life Cycle Assessment volume 8:324–330. https://doi.org/10.1007/BF02978505
5. Franz S, Shcherban ND, Bezverkhyy I, et al (2021) Catalytic activity of gold nanoparticles deposited on N-doped carbon-based supports in oxidation of glucose and arabinose mixtures. Research on Chemical Intermediates 47:2573–2587. https://doi.org/10.1007/s11164-021-04426-6
6. Kusema BT, Mikkola J-PP, Murzin DY (2012) Kinetics of L-arabinose oxidation over supported gold catalysts with in situ catalyst electrical potential measurements. Catal Sci Technol 2:423–431. https://doi.org/10.1039/c1cy00365h
7. Kusema BT, Campo BC, Mäki-Arvela P, et al (2010) Selective catalytic oxidation of arabinose - A comparison of gold and palladium catalysts. Appl Catal A Gen 386:101–108. https://doi.org/10.1016/j.apcata.2010.07.037
8. Van Der Klis F, Gootjes L, Van Haveren J, et al (2018) From batch to continuous: Au-catalysed oxidation of d-galacturonic acid in a packed bed plug flow reactor under alkaline conditions. React Chem Eng 3:540–549. https://doi.org/10.1039/c8re00047f
9. Sladkovskiy DA, Godina LI, Semikin K V., et al (2018) Process design and techno-economical analysis of hydrogen production by aqueous phase reforming of sorbitol. Chemical Engineering Research and Design 134:104–116. https://doi.org/10.1016/j.cherd.2018.03.041
10. Hachhach M, Sladkovskiy DA, Salmi T, Murzin DY (2021) Selective Oxidation of Arabinose on Gold Catalysts: Process Design and Techno-economic Assessment. Chem Eng Technol 1–9. https://doi.org/10.1002/ceat.202100211
11. Murzin DYu, Daigue E, Slotte R, et al (2020) Techno-economic analysis for production of L-arabitol from L-arabinose. Chem Eng Technol 43:1260–1267. https://doi.org/10.1002/ceat.202000125
12. Ranade V, Chaudhari R, Gunjal PR (2011) Trickle Bed Reactors. Elsevier
13. Joback KG, Reid RC (1987) ESTIMATION OF PURE-COMPONENT PROPERTIES FROM GROUP-CONTRIBUTIONS. Chem Eng Commun 57:233–243. https://doi.org/10.1080/00986448708960487
14. Kusema BT, Murzin DY (2013) Catalytic oxidation of rare sugars over gold catalysts. Catal Sci Technol 3:297–307. https://doi.org/10.1039/C2CY20379K
15. Simakova IL, Hachhach M, Aho A, et al (2023) Arabinose oxidation in a fixed bed of extrudates and solid foams containing gold nanoparticles. Chemical Engineering Journal 474:145659.

https://doi.org/10.1016/J.CEJ.2023.145659
16. Herrero Manzano M, Eranen K, Freites Aguilera A, et al (2021) Interaction of intrinsic kinetics, catalyst durability and internal mass transfer in the oxidation of sugar mixtures on gold nanoparticle extrudates. Ind Eng Chem Res 60:6483–6500. https://doi.org/10.1021/acs.iecr.0c05305

© 2025 by the authors. Licensed to PSEcommunity.org and PSE Press. This is an open access article under the creative commons CC-BY-SA licensing terms. Credit must be given to creator and adaptations must be shared under the same terms. See https://creativecommons.org/licenses/by-sa/4.0/



Systems & Control Transactions

**Research Article - Peer Reviewed Conference Proceeding**
ESCAPE 35 - European Symposium on Computer Aided Process Engineering
Ghent, Belgium. 6-9 July 2025
Jan F.M. Van Impe, Grégoire Léonard, Satyajeet S. Bhonsale,
Monika E. Polańska, Filip Logist (Eds.)

PSE PRESS

# Green Industrial-Scale Plant Design for Syngas Fermentation to Isopropyl Alcohol and Acetone: Economic and Environmental Sustainability Assessment

**Gijs J.A. Brouwer[1†], Tamara Janković[1†], Adrie J.J. Straathof[1], Anton A. Kiss[1]*, and John A. Posada[1,2]**

[1] Delft University of Technology, Department of Biotechnology, Delft, South-Holland, The Netherlands
[2] Universidad ECCI, Postgraduate Department, Bogotá 111311, Colombia
[†] Equal contributions
* Corresponding author: tonykiss@gmail.com, A.A.Kiss@tudelft.nl

## ABSTRACT

Steel mill off gas fermentation presents a promising green alternative to petrochemical isopropyl alcohol (isopropanol, IPA) and acetone production while potentially reducing greenhouse gas emissions. A pilot-scale study stated negative global warming potential (GWP) at 85% gas conversion and 90% product selectivity. However, industrial-scale plant design including detailed techno-economic assessment (TEA) and life cycle assessment (LCA) remain undescribed. Therefore, this study modelled a heat-integrated 47.5 kton/ year gas fermentation process to IPA and acetone, based on pilot-scale data. The downstream processing was designed using vacuum distillation and heat-pump integrated (extractive) distillation to purify the 50 $g_{product}$/ L broth with biomass and acetate as byproducts, to obtain 41.8 kton/ year of 99.6 wt. % IPA and 5.64 kton/ year of 99.0 wt. % acetone. Notably, no steam is consumed and 2.6 MWh of electricity is generated by utilising the energy from the steel mill off gas. The estimated unit production cost (UPC; 0.57 \$/$kg_{product}$) is significantly below market prices (1.65 \$/ $kg_{IPA}$ and 1.45 \$/ $kg_{acetone}$). Moreover, the cradle-to-gate LCA gave GWPs of -1.42 $kg_{CO2-eq}$/ $kg_{IPA}$ and -1.25 $kg_{CO2-eq}$/ $kg_{acetone}$, mainly due to avoided steel mill emissions. Other environmental impacts studied were also lower than for petrochemical production. Only the freshwater use is higher (70 L/ $kg_{IPA}$ and 62 L/ $kg_{acetone}$) compared to petrochemical production (16 L/ $kg_{IPA}$ and 28 L/ $kg_{acetone}$). Future research should study the impact of IPA and acetone selectivity and titer on the economic and environmental sustainability of steel mill off gas fermentation to IPA and acetone.

**Keywords**: Syngas fermentation, Isopropanol, Techno-economic assessment (TEA), Life Cycle Assessment (LCA), Product selectivity, Vacuum distillation, *Clostridium autoethanogenum*

## INTRODUCTION

Syngas fermentation of steel mill off gas can provide both (1) a sustainable alternative to petrochemical isopropyl alcohol (isopropanol, IPA) and acetone production and (2) reduce greenhouse gas emissions from the steel industry. Syngas fermentation using *Clostridium autoethanogenum* can convert the energy-rich steel mill off gas (50% CO, 10% $H_2$, 20% $CO_2$, 20% $N_2$) to ethanol on an industrial-scale [1]. Recently, a 120 L pilot producing mainly either isopropyl alcohol (IPA), or acetone or a mixture of both was published [2]. Liew *et al.*, (2022) even claimed negative global warming potential (GWP) for the production of IPA and acetone from steel mill off gas. However, the industrial-scale plant design and its potential techno-economic and environmental performance is yet unknown. Therefore, this study aims to design and model an economically and environmentally sustainable industrial-scale syngas fermentation to produce 47.5 kton/year of >99 wt. % isopropyl alcohol and acetone. Previous work has modelled the syngas fermentation to IPA at a 46 kton/year scale and described the dilution rate, volumetric mass transfer of CO, product selectivity and gas conversion as key sustainability parameters [3]. Besides, an eco-efficient downstream processing has been modelled and described for a gas fermentation

broth containing an IPA and acetone mixture [4]. This study fully-integrates the upstream and downstream process design including heat integration and wastewater treatment (anaerobic digestion, CHP and water recycle). Then a techno-economic assessment (TEA) and life cycle assessment (LCA) were performed. Not only considering GWP but also assessing stratospheric ozone depletion, fine particulate matter formation, freshwater eutrophication, marine eutrophication, human carcinogenic toxicity, land use, and freshwater use.

# METHODS

## Process modelling

The process was modelled in Aspen Plus V12.0 for a total production of IPA and acetone of 47.5 kton/y (see Figure 1). Whereas, the gas fermentation was modelled as previously described [3] using the 120 L pilot data [2], with adaptation of the (optimistic) CO volumetric mass transfer rate to 14.9 g/L/h. A CO volumetric mass transfer up to 8.5 g/L/h was deemed feasible for ethanol [5] at a lower overhead pressure (1.1 bar vs 1.4 bar). Additionally, IPA decreases the bubble size already at lower concentrations [6]. This resulted in a product titer of about 50 g/L, which can give a ~33% lower biomass growth rate [7]. The downstream processing was modelled based on [4]. Vacuum distillation was employed to capture volatile products while recycling the broth back to the fermenter. The product stream was further purified using heat pump-assisted distillation, incorporating heat integration from the hot steel mill off-gas. Additionally, Combined Heat and Power (CHP) generation and wastewater treatment with recycling were implemented [8]. All decisions during process design were made to minimise energy requirements.

## Techno-economic assessment (TEA)

The techno-economic assessment was performed according to the National Renewable Energy Laboratory (NREL) methodology to determine the capital expenses (CAPEX) and operating expenses (OPEX) [9]. The CAPEX includes the equipment and installation costs as well as indirect costs for home office and construction, field expenses, proratable expenses, project contingency, working capital, site development, additional piping, warehouse and initial water and solvent costs. The installed costs for the equipment, except the bioreactor was determined according to [10], [11] and using the Marshall & Swift cost index value of 1773.4 (end of 2021). Whereas the bioreactor (external-loop gas lift reactor) installed costs were determined based on a direct quotation, a scaling factor of 0.60, an installation factor of 2.00 [9], and a Chemical Engineering Plant Cost Index (CEPCI) of 800.3 (2024). In principle, the assessment was done for a plant located in the US. The assumed plant lifetime was 10 years.

For the OPEX, the costs for the steel mill off gas were assumed 14.64 $/ton based on low-pressure steam costs (7.78 $/GJ) for replacing the otherwise captured heat from flaring (38% efficiency) and the CHP costs were assumed 2.1 $/MWh (2024) [12]. The costs of wastewater treatment for recycle was done using data from [8]. The unit production costs (UPC) were calculated in US$ per kg of product (isopropyl alcohol or acetone) and the profit margin was calculated based on the market prices (1.65 $/ $kg_{IPA}$ and 1.45 $/ $kg_{acetone}$).

## Life cycle assessment (LCA)

The Life Cycle Assessment was performed cradle-to-gate (see Figure 1) using the ReCiPe 2016 Midpoint Hierarchical method (V1.04) and the US life cycle impacts from the Ecoinvent database V3.11. Including scope 1, 2, and 3 emissions. The assessed midpoint indicator categories are: (I) Global warming potential (GWP in $kg_{CO2\text{-}eq}$/ $kg_{product}$), (II) Stratospheric ozone depletion (SOD in $kg_{CFC11\text{-}eq}$/ $kg_{product}$, (III) Fine particulate matter formation (FPMF in $kg_{PM2,5\text{-}eq}$/ $kg_{product}$), (IV) Freshwater eutrophication (FWE in $kg_{P\text{-}eq}$/ $kg_{product}$), (V) Marine eutrophication (ME in $kg_{N\text{-}eq}$/ $kg_{product}$), (VI) Human Carcinogenic Toxicity (HCT in $kg_{1,4\text{-}DCB\text{-}eq}$/ $kg_{product}$), (VII) Land use ($m^2_{crop\text{-}eq}$/ $kg_{product}$), and (VIII) Freshwater use ($m^3$/ $kg_{product}$).

The environmental impacts are economically allocated to IPA and acetone based on their market price. Besides, production of other byproducts (i.e., biomass as a feed and electricity generation) is accounted for using substitution.

# RESULTS AND DISCUSSION

## Process

IPA and acetone are produced from the hot steel mill off gas (syngas) through gas fermentation (see Figure 1) at a capacity of 5,278 $kg_{IPA}$/h of 99.57 wt. % IPA and 706 $kg_{Ac}$/h of 99 wt. % acetone. After the gas fermentation followed the broth and the volatile products are separated and purified through vacuum distillation (C1), acetone distillation (C2), pre-concentration (C3), and extractive distillation with ethylene glycol (C4 and C5). The heat pump integration of the distillation columns and the utilisation of the heat from the syngas feed showed that the process at a CO conversion of 85%, product selectivity of 90% and a product titer (IPA + acetone) of about 50 g/L is utilising no steam and producing net 2.6 MWh of electricity. Whereas, Liew *et al.* [2] reported ~5 $MJ_{electricity}/kg_{product}$ for both products and for IPA the need for 6.28 $MJ_{steam}/kg_{IPA}$. Thus, the modelled process is more energy efficient than the model used for the 120 L pilot [2], possibly due to the optimistic CO volumetric mass transfer rate of 14.9 g/L/h resulting in a 50 g/L product titer in

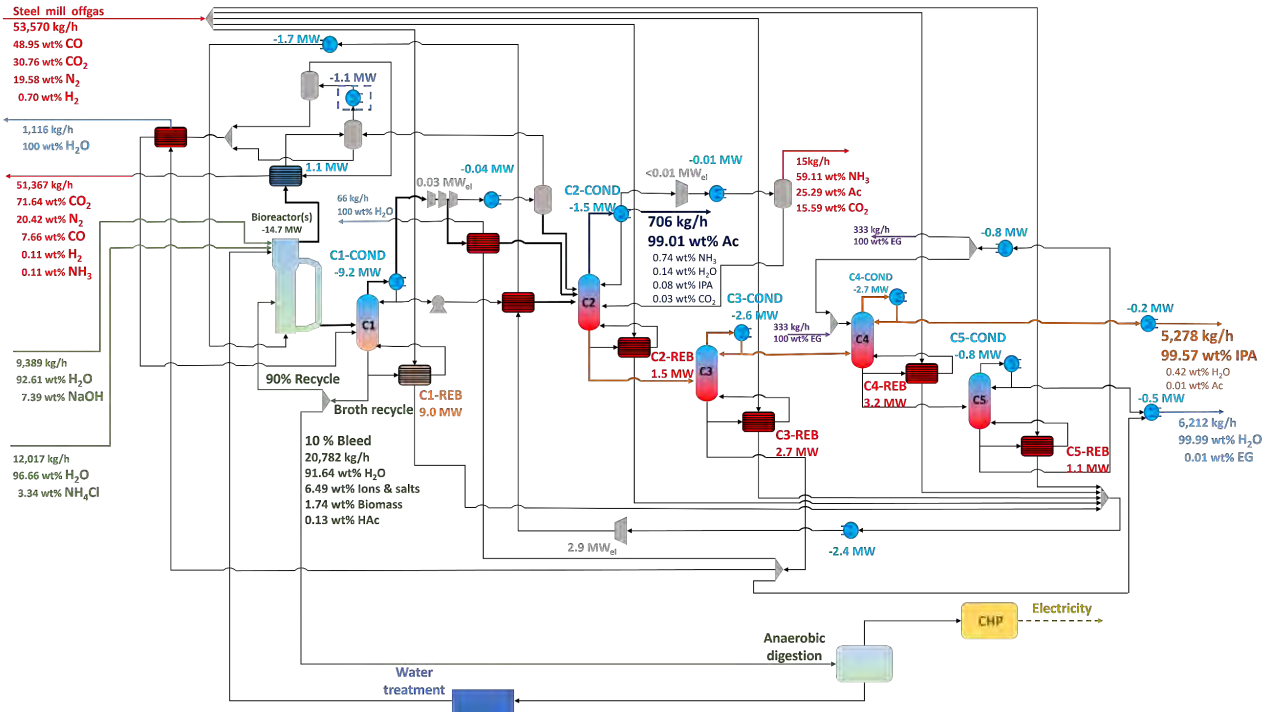



**Figure 1:** Overview of the 47.5 kton/year syngas fermentation (41.8 $kton_{IPA}$/y, 5.64 $kton_{acetone}$/y). The green inflows to the bioreactor are the pH control and nitrogen source, whereas the red in- and outflows are the gas streams. The inflowing syngas (at 1373 K/ 1100 °C) is used for heat exchange before it is compressed (3.84 bar) and fed to the bioreactor. Multi-stage heatpump integrated distillation is used to obtain 99.01 wt. % Ac (C2, dark blue) and 99.57 wt. % IPA (C4, orange). First the broth is separated from the volatile products (C1) by vacuum distillation. Followed by acetone distillation (C2), pre-concentration of IPA (C3), extractive distillation of IPA with ethylene glycol (EG) (C4), and EG recovery (C5). The anaerobic digestion, combined heat and power generation (CHP), and water treatment to demiwater are included within the system boundaries for the economic and environmental assessment.

combination with the energy-efficient DSP design.

## Techno-economic assessment (TEA)

### Capital Expenses (CAPEX): Bioreactor as main cost component and minimal expenses for the distillation columns

The NREL method [9] gave a factor of 1.84 for the modelled syngas fermentation process to get to the CAPEX of 103.7 M$, from the total installed equipment costs (56.3 M$, see Figure 2A). At a plant lifetime of 10 years, the **CAPEX** is about **0.22 $/kg$_{product}$**. The total installed equipment costs are dominated by the bioreactor costs (57.9%, see Figure 2A) which were estimated to have a working volume of 565 $m^3$ [5]. Besides the bioreactor, the compressors (17.8%) and the combined heat and power generation (CHP, 13.4%) contribute most to the total installed equipment costs. 38% of the compressor CAPEX are to compress the gas feed to 3.84 bar before fermentation. Whereas, all distillation columns only make up 5.5% of the CAPEX, because of separating the volatile products directly from the broth through vacuum distillation [4]. This reduces the mass flow to the distillation columns by 88.4%.

### Operating Expenses (OPEX): Minimised through heat integration of the hot steel mill off gas

The **OPEX** (see Figure 2B) are only 16.82 M$/y, which is **0.35 $/kg$_{product}$**. Traditional fermentation processes have OPEX dominated by feedstock expenses. However, the use of the steel-mill "waste" off-gas only contributes 0.04% to the OPEX. The steel mill off gas costs were assumed based on the otherwise obtained heat from flaring. In addition, no consumption of heat utilities and the net generation of 2.6 MWh electricity greatly reduce the OPEX. Moreover, the efficient recycle of the broth and components due to vacuum distillation allows for 90 % broth recycle as well as efficient downstream processing of the products. Therefore, typically minor expenses like labour and pH control together contribute to 67% of the OPEX.

### Overall economics

The estimated **unit production costs (UPC)** are only

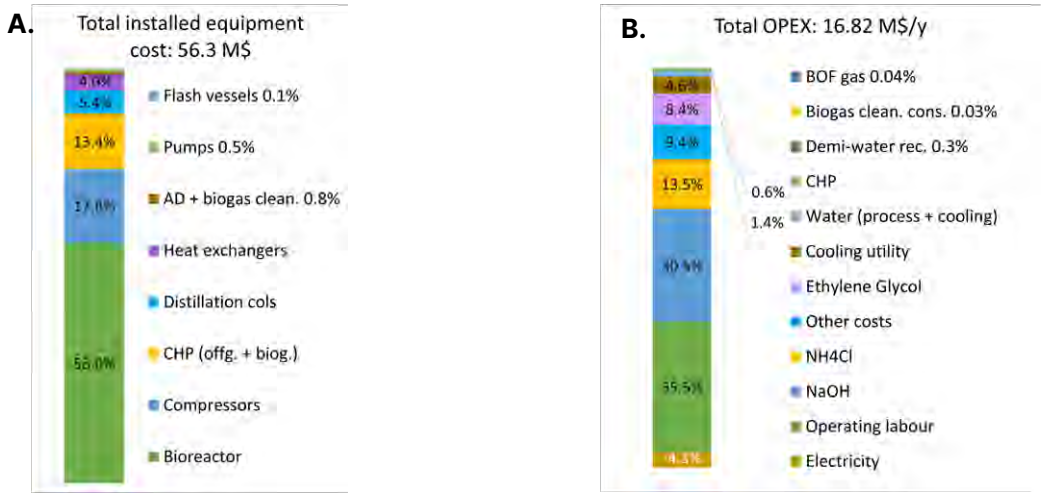



**Figure 2:** Economic assessment of the modelled syngas fermentation to 47.5 kton/y of isopropyl alcohol and acetone process. The calculated CAPEX is 103.7 M$ assuming a plant lifetime of 10 years of which 54.3% is the total installed equipment costs (A), the operating expenses are 16.82 M$/year (B). The excess energy produced from the CHP is assumed to be sold as electricity to the grid. AD is anaerobic digestion, CHP is combined heat and power generation, and BOF gas is the steel mill offgas (basic oxygen furnace gas) from the steel mill.

**0.57 $/kg$_{product}$** (isopropyl alcohol or acetone). whereas the market price for these products is 1.65 $/kg$_{IPA}$ and 1.45 $/kg$_{Ac}$ [13]. This leaves a margin between the production costs and the 2024 market price of 1.08 $/kg$_{IPA}$ (65.6%) and 0.88 $/kg$_{Ac}$ (60.8%), respectively. Thus, having an estimated **margin** of **over 60%** using the modelled, heat-integrated, gas fermentation process. Moreover, when the biomass byproduct is not anaerobically digested but sold as an animal feed, the overall UPC decreases with an additional 8.8% (0.05 $/kg$_{product}$).

## Cradle-to-gate life cycle assessment (LCA)

### The global warming potential can be net zero when considering the converted steel mill off gas as prevented emissions

The cradle-to-gate LCA gave net zero GWP for IPA and acetone production, when considering it as preventing the steel mill off gas related emissions (see Figure 3 & Table 1). The environmental impacts are economically allocated to the products and gave GWPs similar to the pilot-scale study [2] (see Figure 3). However, the results for acetone of Liew *et al.* [2] are on the high acetone selectivity (~85%), whereas this study uses high IPA selectivity with only 12 wt. % acetone produced. Besides, comparison of the GWPs from this study to the petrochemical IPA and acetone production indicates a potential GWP reduction of 160% for IPA and 147% for acetone. Still, the GWP is dependent on the mitigated $CO_2$ emissions by converting steel mill off gas into IPA and acetone. Additionally, utilising both the latent energy of the steel mill off gas before gas fermentation and combusting the residual off gas enables lower GWPs because of zero steam consumption and net electricity production (see Table 1). Additionally, the gas fermentation process prevents the direct use of fossil fuels for IPA and acetone production.

**Table 1:** Global Warming Potential (GWP) contributions for the modelled syngas fermentation to 47.5 kton-$_{prod}$/year of >99 wt. % isopropyl alcohol (IPA) and acetone (Ac).

| | **Isopropy alcohol** ($kg_{CO2\text{-}eq}/kg_{IPA}$) | **Acetone** ($kg_{CO2\text{-}eq}/kg_{Ac}$) |
|---|---|---|
| Process emissions | 7.64 | 6.70 |
| Heat replacement | 0.636 | 0.558 |
| NaOH | 0.147 | 0.129 |
| Ethylene Glycol | 0.120 | 0.105 |
| NH4Cl | 0.090 | 0.079 |
| Water | 0.069 | 0.061 |
| NaCl | $8.87x10^{-4}$ | $7.79x10^{-4}$ |
| Steam | 0.000 | 0.000 |
| Electricity (produced) | -0.255 | -0.224 |
| CO2 prevented from flaring | -9.86 | -8.66 |
| **Total** | **-1.42** | **-1.25** |

## Other environmental impacts most relevant to fermentation processes

Comparison of the modelled syngas fermentation process with conventional petrochemical production (see Table 2) also gave lower impacts for the stratospheric ozone depletion, marine eutrophication human carcinogenic toxicity. In addition, the calculated fine particulate

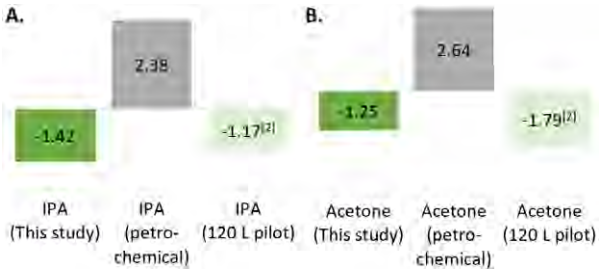



**Figure 3:** The cradle-to-gate global warming potential of the modelled syngas fermentation to 47.5 kton/year of >99 w% isopropyl alcohol and acetone (left, dark green) compared to the GWP of petrochemical-derived IPA (middle, grey) from ECOINVENT V3.11, and the reported 120 L pilot-scale based LCA [2]. Both this study and [2] assumed the steel mill offgas to be prevented carbon emissions.

matter formation and land use are about one order of magnitude smaller for the syngas fermentation process. On top of that, the freshwater eutrophication could be net zero due to the prevented steel mill emissions and net electricity generation. A common concern for fermentation processes is the high fresh water use. However, for the modelled gas fermentation process the freshwater use is only about threefold that of the petrochemical processes, ranging from 62-70 L/$kg_{product}$ (see Table 2). The designed process already has about maximum fresh water recycle and reuse. Therefore, efficient water management is important for developing more sustainable chemical production through (syngas) fermentation.

## CONCLUSIONS

- Converting steel mill off gas through (syn)gas fermentation at a product titer of 50 g/L and 85% gas conversion can produce high purity (>99 wt. %) isopropyl alcohol (isopropanol, IPA) and acetone. This process is both economically sustainable (unit production costs ≈ 1/3 market price) and environmentally sustainable, potentially achieving net zero GWP.
- Effective downstream processing of the volatile products, isopropyl alcohol (isopropanol, IPA) and acetone, can be obtained through vacuum distillation with broth recycling, followed by acetone distillation, pre-concentration, and extractive distillation of IPA with ethylene glycol.
- Effective heat integration, utilising both the latent and chemical energy of the steel mill off gas, results in net zero steam consumption and net electricity generation (2 MWh) in the modelled syngas fermentation process, producing 47.5 $kton_{product}$/ year.
- The method of accounting for the environmental impacts and substitution, when utilising a waste stream or generating a byproduct, respectively, is crucial to the LCA outcome. When the steel mill off gas is considered as prevented emissions, the modelled syngas fermentation process can have a net zero GWP.

**Table 2:** Environmental impacts, besides the global warming potential for the cradle-to-gate LCA of the modelled syngas fermentation of steel mill off gas to 47.5 kton/year of >99 wt. % isopropyl alcohol (IPA) and acetone (Ac).

| Product: | **Isopropyl alcohol** (This study) | **Petrochemical IPA** (ECOINVENT V3.11) | **Acetone** (This study) | **Petrochemical Acetone** (ECOINVENT V3.11) |
|---|---|---|---|---|
| Stratospheric ozone depletion ($kg_{CFC11\text{-}eq}$ / $kg_{product}$) | 4.17E-07 | 4.60E-07 | 3.66E-07 | 3.24E-07 |
| Fine particulate matter formation ($kg_{PM2.5\text{-}eq}$ / $kg_{product}$) | 3.23E-04 | 2.77E-03 | 2.84E-04 | 3.31E-03 |
| Freshwater eutrophication ($kg_{P\text{-}eq}$ / $kg_{product}$) | -2.89E-05 | 4.15E-04 | -2.54E-05 | 4.28E-04 |
| Marine eutrophication ($kg_{N\text{-}eq}$ / $kg_{product}$) | 9.12E-05 | 2.59E-05 | 8.01E-05 | 2.33E-05 |
| Human carcinogenic toxicity ($kg_{1,4\text{-}DCB\text{-}eq}$ / $kg_{product}$) | 0.021 | 0.057 | 0.018 | 0.061 |
| Land use ($m^2_{crop\text{-}eq}$ / $kg_{product}$) | 4.94E-03 | 1.81E-02 | 4.34E-03 | 1.61E-02 |
| Water consumption ($m^3$ / $kg_{product}$) | 0.070 | 0.016 | 0.062 | 0.028 |

## RECOMMENDATIONS

- To evaluate the effect of titer and product selectivity on the downstream process design, techno-economic performance and environmental sustainability of syngas fermentation, future work should look into both lower isopropyl alcohol and acetone product titer and higher acetone selectivity.
- To study the influence of different (volatile) by-products on the process performance.
- To perform experimental studies on the effect of isopropyl alcohol concentration on the volumetric mass transfer.

## ACKNOWLEDGEMENTS

This work is funded by the TU Delft Department of Biotechnology as a part of the Zero Emissions Biotechnology consortium.

## REFERENCES

1. Köpke M, Simpson SD. Pollution to products: recycling of 'above ground' carbon by gas fermentation. Curr Opin Biotechnol 1;65:180–189 (2020) https://doi.org/10.1016/J.COPBIO.2020.02.017
2. Liew FE, Nogle R, Abdalla T, Rasor BJ, Canter C, Jensen RO, et al. Carbon-negative production of acetone and isopropanol by gas fermentation at industrial pilot scale. Nat Biotechnol 40(3):335–344 (2022) https://doi.org/10.1038/s41587-021-01195-w
3. Brouwer GJA, Shijaz H, Posada JA. Modelling and Parametric Analysis for Improving Technical Performance of Industrial-Scale Basic Oxygen Furnace Gas Fermentation to Isopropyl Alcohol. In: Manenti F, Reklaitis G V, editors. Computer Aided Chemical Engineering 403–408 (2024) https://doi.org/10.1016/B978-0-443-28824-1.50068-5.
4. Janković T, Straathof AJJ, Kiss AA. Advanced purification of isopropanol and acetone from syngas fermentation. Journal of Chemical Technology and Biotechnology 99(3):714–726 (2024) https://doi.org/10.1002/jctb.7576.
5. Puiman L, Abrahamson B, van der Lans RGJM, Haringa C, Noorman HJ, Picioreanu C. Alleviating mass transfer limitations in industrial external-loop syngas-to-ethanol fermentation. Chem Eng Sci 259:117770 (2022) https://doi.org/10.1016/j.ces.2022.117770
6. Keitel G, Onken U. The effect of solutes on bubble size in air-water dispersions. Chem Eng Commun 17(1–6):85–98 (1982)
7. Koepke M, Simpson S, Liew F, Chen W. Fermentation process for production isopropanol using a recombinant microorganism. US patent 2,012,252,083A1. (2012)
8. Kehrein P, Jafari M, Slagt M, Cornelissen E, Osseweijer P, Posada J, et al. A techno-economic analysis of membrane-based advanced treatment processes for the reuse of municipal wastewater. Water Reuse. 11(4):705–725 (2021) https://doi.org/10.2166/wrd.2021.016
9. Humbird D, Davis R, Tao L, Kinchin C, Hsu D, Aden A, et al. Process Design and Economics for Biochemical Conversion of Lignocellulosic Biomass to Ethanol: Dilute-Acid Pretreatment and Enzymatic Hydrolysis of Corn Stover. NREL. (2011) http://www.osti.gov/bridge
10. Mantingh J, Kiss AA. Enhanced process for energy efficient extraction of 1, 3-butadiene from a crude C4 cut. Sep Purif Technol. 267:118656A (2021)
11. EIA, "U.S. power plants' O&M costs by type 2022." https://www.statista.com/statistics/519144/power-plant-operation-and-maintenance-costs-in-the-us-by-technology/
12. United Nations. UN Comtrade. https://comtradeplus.un.org/TradeFlow

© 2025 by the authors. Licensed to PSEcommunity.org and PSE Press. This is an open access article under the creative commons CC-BY-SA licensing terms. Credit must be given to creator and adaptations must be shared under the same terms. See https://creativecommons.org/licenses/by-sa/4.0/



Systems & Control Transactions

**Research Article - Peer Reviewed Conference Proceeding**
ESCAPE 35 - European Symposium on Computer Aided Process Engineering
Ghent, Belgium. 6-9 July 2025
Jan F.M. Van Impe, Grégoire Léonard, Satyajeet S. Bhonsale,
Monika E. Polańska, Filip Logist (Eds.)

PSE PRESS

# Energy Efficient Process Designs for Acrylonitrile Production by Propylene Ammoxidation

**Qing Li[a], Alexandre C. Dimian[b], and Anton A. Kiss[a]***

[a] Delft University of Technology, Department of Chemical Engineering, Delft, The Netherlands
[b] University Politehnica of Bucharest, Department of Chemical and Biochemical Engineering, Bucharest, Romania
* Corresponding Author: a.a.kiss@tudelft.nl.

## ABSTRACT

Acrylonitrile is a critical commodity chemical used to produce a variety of industrial polymers, such as carbon fibers, plastics, etc. Currently 90% of the global acrylonitrile production is based on propylene ammoxidation. However, there is no literature reporting the whole process holistically in detail, and which also looks into the energy utilization of the whole process including the reaction heat as well as the energy demands of the downstream separation. This original study provides a rigorous process design of the full process from a holistic viewpoint, covering 7 sections of acrylonitrile production (reaction, acid quenching, absorption-desorption, hydrogen cyanide recovery, acrolein recovery, acrylonitrile-acetonitrile-water separation, acetonitrile recovery sections). In order to further improve the energy efficiency, three energy integration strategies are proposed (1) Energy integrated downstream processing; (2) Systematic heat integration utilizing the heat of reaction; (3) Power generation by process surplus heat. Design 1 employs a direct heat exchanger network, recovering 30.1 MW heat through multiple heat exchanges, saving 86.91% fuel gas, 17.38% low pressure steam and 43.96% cooling utilities. Design 2 and 3 recovers 58.39 MW heat, and 12.20 MW low pressure steam is output as waste heat recovery in design 2, whereas 11.06 MW low pressure steam and 7.8 MW electricity are generated in design 3. The pro/con each options are also discussed for further guidance. As the first comprehensive description of the design of the entire acrylonitrile production process, this work highlights the potential for improved energy efficiency in the acrylonitrile production.

**Keywords**: Process Design, Process Intensification, Distillation, Energy Efficiency, Heat Exchanger Network

## 1. INTRODUCTION

Acrylonitrile (AN) is a widely used commodity chemical in industry, primarily as a monomer for the production of acrylic fibers, acrylonitrile-butadiene-styrene (ABS) resins, adiponitrile, acrylamide, nitrile rubbers, and carbon fibers. Driven by the increasing demand for acrylonitrile from end-use industries, such as construction,, the global acrylonitrile market size valued at USD 11.87 billion in 2021 is expected to grow at a compound annual growth rate (CAGR) of 1.3% from 2022 to 2030 [1].

Over 90% of the world's acrylonitrile is commercially manufactured via the propene ammoxidation process, described by Equation 1:

$$CH_2{=}CHCH_3 + NH_3 + 3/2O_2 \rightarrow CH_2CHCN + 3H_2O \quad (1)$$

However, this global reaction involves a complex reaction mechanism and is accompanied with the formation of acetonitrile, hydrogen cyanide, acroleine, acrylic acid, carbon oxides (COx), and large amounts of water. Therefore, to separate the products, the whole process can be described as the following sections, according to the descriptions given by Dimian and Bildea [2]: (1) reactor, (2) acid-quench, (3) absorption-desorption, (4) removal of hydrogen cyanide (5) separation of acrolein, (6) separation of acrylonitrile, (7) separation of acetonitrile.

The reaction is performed at temperatures of 400-510°C and pressures of 1.5-3 bar. The high exothermicity of the reactions involved ($\triangle H = -123$ kcal/mol) requires very efficient cooling to maintain the reaction temperature in the desired range. The downstream separation and purification of AN involves several distillation

columns, which are very energy intensive, however, energy costs and environmental concerns associated with energy consumption were not critical in the past, the energy consumption and the improvement of the energy usage and integration did not draw much attention. Thus, in the current climate, better utilization of the energy for the whole process is essential, and before investigating this, a detailed design of the whole process is also necessary.

The objectives of this study are: (1) to develop an optimized complete process flowsheet using thermodynamic analysis and literature information, (2) to implement process intensification technologies for downstream processing (DSP), such as dividing wall columns, exploring also the mechanical vapor recompression heat-pumping potentials, (3) to explore heat integration potentials by heat exchanger network design, utilizing the heat from reactions for the whole process, (4) to evaluate and compare different designs in terms of the energy intensity of each process.

## 2. PROBLEM STATEMENT

Acrylonitrile production process by propylene ammoxidation involves high exothermicity reactions, multi co-products which need to be separated, and complex downstream separation and purification processes. Developing a comprehensive flowsheet involving both reactions and separations to understand the whole process is essential, and energy integrated options should be considered in order to develop more energy-efficient flowsheets. Different designs should be evaluated and compared based on key performance parameters such as economics and sustainability, and suggestions are given based on the different advantages and disadvantages of each design.

## 3. DESIGN AND SIMULATION APPROCH

### 3.1 Process design

Aspen Plus V12 is used for rigorous simulations in this work. According to the process proposed by Dimian and Bildea [2], fifteen components are present in the process: acetonitrile, acrolein, acrylic acid, acrylonitrile, ammonia, ammonium sulphate, carbon dioxide, carbon monoxide, hydrogen cyanide, nitrogen, oxygen, propane, propylene, sulfuric acid, and water. The UNIQUAC-RK model is selected in Aspen Plus as suitable property model to calculate all physical properties required for the process simulation. The stoichiometric reactor model is used to model the reactions based on the activity data for a molybdenum/bismuth-modified catalyst reported in the patent (US 6,596,897 B1, 2003 [3]), in order to achieve a reliable description of the conversion of reactants into products, co-products, and other impurities. The simulation is developed based on VLE data, ternary diagrams combined with RCM, reaction conditions, separation specifications, and product purity requirements. Plant production capacity is 120 ktpy (acrylonitrile 99.4 wt% purity, 99.9 wt% recovery) with a corresponding reactor production rate of 272.34 kmol/h acrylonitrile.

### 3.2 Energy integration methodology

#### 3.2.1 Process intensification opportunities for DSP to enhance energy efficiency

Process intensification (PI) technologies are considered to have great potential in reducing the high costs and energy requirements of the separation and purification step, enhancing productivity while improving process safety, reducing waste without sacrificing product quality. The intensified distillation technologies considered in this work include dividing wall column (in which one column shell with the middle wall is used to replace the conventional two columns and avoid re-mixing effect); and heat pump assisted distillation (in which the overhead vapor can be upgraded and re-used to heat the bottom reboiler), which addresses heat transfer bottlenecks by increasing the temperature of cold streams to create a feasible temperature driving force, thereby expanding heat transfer opportunities for integration.

#### 3.2.2 Heat exchanger network (HEN) design to utilize the heat of the process

The HEN is synthesized by a stage-wise superstructure optimization approach, integrating systematically direct heat integration and heat pumps. In addition, it allows the integration of multiple hot utility options, waste heat recovery, and mechanical heat pump applications, to enhance energy efficiency and reduce costs. Direct stream-stream transfer, indirect transfer via heat pumps, and utility-mediated heat transfer for waste heat are automatically selected for each heat transfer match. Heat exchangers are positioned at optimal locations between hot and cold streams, enabling efficient heat recoveries. A detailed description of this HEN synthesis method can be found in literature [4]. Initial and target temperatures of the streams, heat capacities, and stream film heat transfer coefficients are required for a new HEN design. The superstructure formulation is modelled as a mixed-integer nonlinear program (MINLP) and solved by BARON/GAMS, the objective function of this model is minimizing the total annualized cost (TAC). The fixed and area costs of heat exchangers, compressor size costs, and utility costs are considered as the cost-related parameters. The capital costs related to heat exchangers are taken from the literature [5]. The minimum approach temperature difference for heat transfer is set at 10°C.

## 4. RESULTS AND DISCUSSIONS

### 4.1 Base case design

Figure 1 presents the base-case flowsheet comprising the reaction and separation section. The fluid-bed reactor operates at 2.0 bar and 440°C. The reactants - propylene, ammonia, and air - are separately fed in the molar ratio 1, 1.2, 9.8 to fulfill reaction chemistry and safety constraints. After cooling at 220°C, the reaction mixture enters the quench column A-Q operated at 1.9 bar with a view to removing the excess ammonia as ammonium sulphate through neutralization with sulfuric acid (30 mol%). The bottom stream is sent to the recovery of ammonium sulphate that is a co-product of this process. After acid quenching and cooling at 30°C, the cleaned gas enters the absorption/desorption section. First, the column ABS equipped with 24 stages and operating at 1.6 bar, separates non-condensable components ($N_2$, $O_2$, $CO_2$, CO and propene) by absorption in water at 5°C. Next, the recovery of acrylonitrile from the aqueous bottom stream is sent to the column REC (36 stages). Top-vapor condensation at 30°C followed by liquid-liquid splitting in the DECANT1 ensures the recovery of the organic components (acrylonitrile, acetonitrile, hydrogen cyanide, and acrolein) in the organic phase and recycles the aqueous phase to the stripper.

The organic phase enters the column ACR for splitting the mixture in acrylonitrile/acetonitrile and HCN / acrolein fractions (1.1 bar). In the hydrogen cyanide section, hydrogen cyanide is recovered from the hydrogen cyanide-acrolein overhead (1.01 bar). The product stream leaving the bottom of the acrolein section is fed to the acrylonitrile-acetonitrile-water section, operating around atmospheric pressure, targeting the recovery of acrylonitrile as desired product. An extractive distillation is performed using water as mass-separating agent. The feed stream from the previous separation is combined with the aqueous stream from the decanter and the entrainer water stream to form the combined stream. The combined stream is separated in the first column to obtain a near-azeotropic distillate at the top, water at the bottom, and an acetonitrile-water mixture as a side stream. The organic phase from the decanter is sent to a second column (C2) to obtain a near-azeotropic distillate at the top and pure acrylonitrile at the bottom.

Finally, the side stream from the acrylonitrile-acetonitrile-water section is fed to the acetonitrile recovery section, which performs a pressure-swing distillation. Extractive distillation has good performance for recovering acetonitrile from water, yet there is only 4% acetonitrile in the feed resulting in low absolute value of the separating duties. Therefore the difference between different separation methods is small. Pressure swing distillation does not require introducing a third component so this is preferable. The pressure of the columns are 4.4 bar and 1.1 bar respectively. Overall 48.42 MW hot utilities and 43.15 MW cold utilities are needed by the process (after the heat recovery by HX1, 11.88 MW). Of the total 43.15 MW cold utility requirement, 3.39 MW of refrigerant is needed to cool the “ABS-H2O” stream in the absorption-desorption section (25°C–5°C), while 0.16 MW of chilled water is required for HCN column condenser (25.7°C–24.7°C). The remaining cooling duties are covered by cooling water. As the temperatures of ABS-H2O stream and the HCN condenser are too low for heat integration, they are excluded from the heat exchanger network (HEN) optimization process but re-added as cooling utilities in the optimized solution. Thus the refrigerant and chilled water requirements remain constant across all designs.

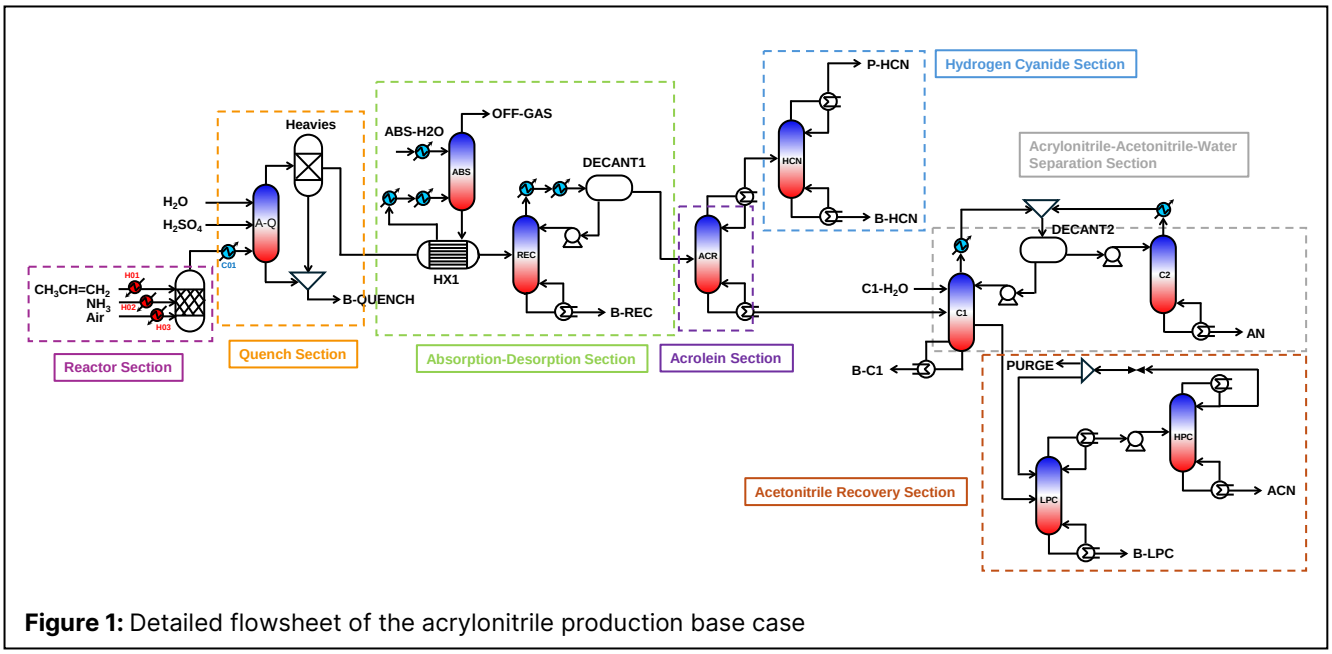



**Figure 1:** Detailed flowsheet of the acrylonitrile production base case

## 4.2 Process Energy integration

Propylene ammoxidation is an exothermic reaction - the reactor operates at 440°C and generates surplus heat amounting to 59.74 MW, which must be removed using a heat medium to ensure process stability. The heat can be removed directly by cooling medium to ensure effective cooling *(Section 4.2.1)*, the focus of the energy integration is then on the downstream separations; or the heat of the reaction can also be integrated into the process *(Section 4.2.2)*, by transferring its heat to a utility stream (hot oil, 400°C), and a heat exchanger network is developed by utilizing the reaction heat as well as the process to process heat integration;

Alternatively, the heat generated from the reaction can be utilized to produce power (very high pressure (VHP) steam to a steam turbine) and low-pressure (LP) steam. The generated power can be exported, while the LP steam serves as a hot utility within the process. The optimal heat integration solutions are presented through a HEN, as detailed in *(Section 4.2.3)*.

### 4.2.1 Energy integration of DSP taking into account process intensification options – Design 1

As heat pump assisted distillation has great potential to be able to enhance the energy efficiency, it is involved in the systematic heat integration approach. Taking vapor recompression as an example, the overhead vapor from the distillation column is compressed to a higher pressure, and used as heat source for the reboiler. However, when the process in complex (e.g., has multiple heat exchangers as well, providing heat integration potentials), a systematic heat exchanger network design is necessary, as an effective process to process heat transfer could also be potentially more effective than using heat pumps.

For heat pump assisted distillation, the lower the temperature lift (i.e., the temperature difference between the overhead vapour and the condenser), the higher the coefficient of performance [6,7]. When analysing the process, there are three potentials opportunities by integrating heat pumps in the acrylonitrile production process: (1) The overhead vapour from the recovery column (89°C) and the reboiler of the ACR column (81°C); (2) The overhead vapor of the first column of ACN/AN/$H_2O$ separation section (BD-C1, 76°C) to its reboiler (113°C); (3) The overhead vapor of second column of ACN/AN/$H_2O$ separation section (BD-C2, 76°C) to its reboiler (82°C).

However, an effective process to process heat integration might integrate the heat well without heat pumps, therefore a systematic heat exchanger network design (described in Section 3.2.2) is carried out, which includes the flexibility of choosing to use heat pumps is it brings more benefits. **Figure 2** presents the optimal heat exchanger network design of the process, and shows that in this case no heat pumps are needed. The target HEN configuration includes 10 hot streams, 11 cold streams, and two hot utilities: fuel gas and low-pressure steam. The heat exchanger HX1 (11.88 MW) in the conventional design was released as a degree of freedom in the new HEN design. Cooling water (20-25°C) and chilled water (5-15°C) refrigerant (-20°C) are employed to meet the cooling demands of system [8]. 10 heat exchangers are installed with a total heat transfer area of 3706 m², strategically placed within the network.

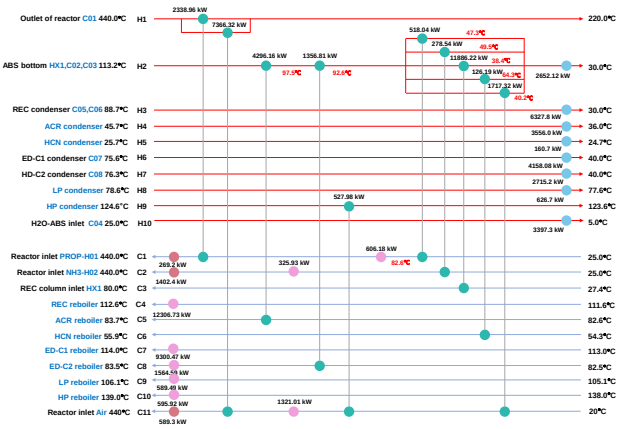



**Figure 2.** Heat exchanger network design via systemetic energy utilization for downstream processing without reaction-separation integration

These exchangers enable heat recovery of 30.41 MW, comparing to the conventional process. 28.87 MW hot utilities are needed (2.26 MW fuel gas, 26.61 MW LP steam), and 23.60 MW cold utilities are needed. Overall 20.60 MW hot utilities and 20.60 MW cold utilities are saved comparing to the conventional process, effectively utilizing heat from the reactor outlet stream (H1) and the ABS bottom stream (H2). The number and ratio of stream splits are shown in the HEN, maximizing the use of temperature driving forces to efficiently transfer heat to multiple cold streams. LPS is placed at the intermediate stage of cold stream C1, C2 and C11 by multiple utility optimization, to avoid the extra usage of fuel gas.

Note that the option of using dividing wall columns in this process does not bring benefits after calculations, therefore it will not be discussed further.

### 4.2.2 Systematic heat integration utilizing the heat of reaction – Design 2

Differently, the surplus heat from the reaction can also be first utilized to preheat the reactor feed inlets - propylene, NH3, and air - from 420°C to 440°C. The remaining surplus heat is then transferred to generate hot oil (200°C–400°C, 301.8 t/h), which is introduced as a new hot stream. The use of hot oil allows the HEN to operate with single-phase heat transfer, avoiding operational challenges associated with phase-change heat transfer in steam networks. A new HEN synthesis is

proposed in **Figure 3**, incorporating the hot oil stream. This design problem involves 11 hot streams, 11 cold streams, and two hot utilities. Additionally, LPS is used as a cold utility for automated waste heat recovery (steam generation). The LPS generated by the hot oil stream is exported from the system, further increasing energy benefits and enhancing overall efficiency.

**Figure 3** illustrates the optimal HEN design, which includes a total of 16 heat exchangers with a total heat transfer area of 2308 m². This improves process energy efficiency by achieving 58.39 MW of heat recovery compared to Section 4.2.1. The hot oil (59.74 MW) heat transferred by the reaction surplus heat covers all the hot utilities needed in this process, and additionally 12.20 MW LPS is generated/output as a form of waste heat recovery. 43.15 MW cold utilities are needed.

The previous design relied on a complex HEN with stream branches to utilize H1 and H2, yet the HEN in this section focuses on maximizing cost efficiency by utilizing the hot oil stream (H11). Half of the heat exchangers are placed in the hot oil stream, recovering 47.54 MW to cold streams. Overall, this HEN achieves complete heat integration without requiring any hot utility input, showcasing efficient energy utilization and cost-effectiveness.

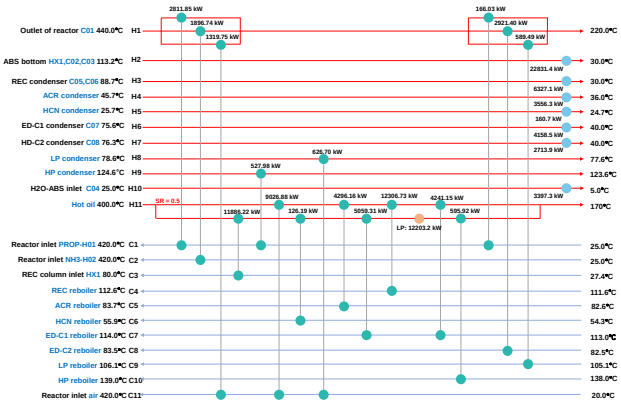



**Figure 3.** Reaction-separation integration via hot oil (to take the reaction surplus heat for integration) and systematic heat exchanger network design

### 4.2.3 Taking the reaction heat to generate power – Design 3

A steam network is established to generate electricity and provide heating for cold streams. The surplus heat (59.74 MW) from the reactor is first used to generate VHP steam (40 barg, 251.8°C), with 1.40 MW of heat transferred to the reaction inlet (air, C3) stream. The remaining VHP steam (58.35 MW) is passed through a steam turbine to generate electricity and produce LP steam (6 barg, 160°C) for process heating requirements. A partial HEN is synthesized using an optimization approach, incorporating only H1, C1, C2, and C11 within a multiple utility system. The remaining cold streams are directly heated by the steam network, simplifying the overall configuration while ensuring efficient energy utilization.

In this case, the steam network sufficiently meets the main heating requirements of 42.02 MW for cold streams C3–C10. Cold streams C1, C2, and C11 require an additional 5.28 MW from the steam network, while H1 compensates for the remaining 9.71 MW of heating. Overall 58.39 kW heat recovery can be achieved by this HEN. The key advantage of this solution is that the steam network not only meets heating demands but also generates 7.8 MW of electricity and 11.06 MW of LP steam as waste heat recovery. The turbine is simulated in Aspen Plus V12, with isentropic efficiency of 0.85 and mechanical efficiency of 0.98. However, integrating a steam network into the whole design introduces added complexity, particularly regarding control and safety considerations.

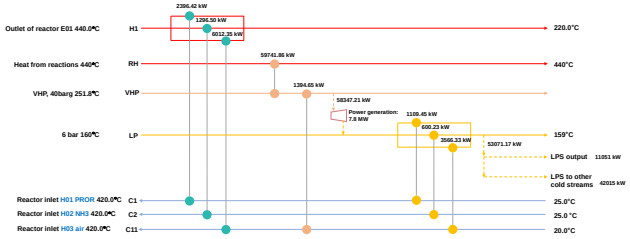



**Figure 4.** Reaction-separation integration via steam network and power generation (to take the reaction surplus heat for integration) by systematic heat exchanger network design; Hot (cold) streams that are directly cooled (heated) are not included in this diagram.

## 4.3 Comparisons of different design cases

The comparison of the different design cases is shown in Table 1 and 2. Overall, Design 1 employs a direct HEN that recovers 30.1 MW through multiple heat exchangers, balancing network investment and energy efficiency. This solution requires multiple stream splits to maximize the utilization of driving forces, resulting in a more complex network. Compared to the non heat integrated case, all the heat is needed by the fuel gas (assuming that no multiple-utility is used in heat exchangers), however in Design 1 (see figure 2), part of the heat is provided by heat recovery, therefore less fuel gas is required.

Design 2 introduces a hot oil stream to heat cold streams, enabling single-phase heat exchange and increasing heat recovery to 58.39 MW. This substantial improvement demonstrates that incorporating alternative heat transfer fluids can significantly enhance energy efficiency by extracting energy from exothermic reactions. Design 3 integrates a steam network to achieve multifunctional energy utilization. It generates both electricity and low-pressure steam while meeting the primary heating demands, offering a comprehensive solution for energy recovery and utilization.

Both Design 2 and 3 meet the heating requirements

for cold streams while generating low-pressure steam (LPS) of 12.2 MW and 11.06 MW, respectively. However, Design 3 relies on a steam turbine and high-pressure systems, which introduce additional complexities in control, safety, and integration with existing process streams, despite its ability to generate 7.8 MW electricity. In contrast, Design 2 includes additional equipment, such as hot oil loops and associated heat exchangers. This approach simplifies the challenges associated with phase-change heat transfer, offering a more straightforward and manageable solution for heat integration.

**Table 1:** Comparison between the conventional design and the Design 1 (downstream separations only)

| | Conv. | Design 1 | Savings |
|---|---|---|---|
| CU for reactor (MW) | 59.74 | 59.74 | - |
| Fuel gas (MW) | 17.26 | 2.26 | 86.91% |
| LP steam (MW) | 32.21 | 26.61 | 17.38% |
| CU (MW) | 44.20 | 23.60 | 43.96% |
| Area ($m^2$) | - | 3706 | - |
| No. HEx | - | 10+19 | - |
| Power Gen. (MW) | - | - | - |
| Energy ($kWh/kg_{AN}$) | 3.42 | 1.99 | 41.81% |

**Table 2:** Comparison between the Design 2 and 3 (including the reactions surplus heat)

| | Design 2 | Design 3 |
|---|---|---|
| Hot oil (t/h) | 301.8 | - |
| HU (MW) | 0 | 0 |
| CU (MW) | 43.15 | 44.30 |
| Area ($m^2$) | 2308 | 3036.2 |
| No. HEx | 16+8 | 3+12 |
| LPS Gen. (MW) | 12.20 | 11.06 |
| Power Gen. (MW) | - | 7.8 |
| Energy ($kWh/kg_{AN}$) | -0.84 | -1.30 |

**Note:** HU - hot utility required; CU – cold utilities required; Area – heat exchangers area; No. HEx – Number of heat exchangers, the number of heat exchangers for utilities is underlined; LPS Gen – low pressure steam generated; Power Gen. – power generated; AN production 120 ktpy

## 5. CONCLUSIONS

The comprehensive process developed in this study demonstrates the efficiency of integrated process design, coupling rigorous reaction modeling with thermodynamically and economically optimized separation strategies. Systematic heat integration can save around a half of the utility requirements compared to the conventional design. When utilizing the surplus reaction heat, generating LP steam and associated power has the lowest energy intensity, comparing to taking the reaction heat by heat oil and use it again as a hot stream in the process. However, relying on steam turbines and high-pressure systems might not be favorable due to the additional complexities. The energy integration strategies proposed in this research can be chosen based on different needs.

Including different designs and the quantification of their associated trade-offs ensure reliable performance and applicability in industrial processes. The flexibility of the resulting heat exchanger networks and utility configurations ensures that the findings can be appropriate to specific operational requirements. The results not only bridge an important knowledge gap in acrylonitrile production design but also offer a solution for optimizing similar exothermic processes characterized by complex product distributions and energy-intensive separations.

## REFERENCES


1. G. V. Research, "Acrylonitrile Market Growing Demand and Trends 2023 to 2028.," [Online]. https://www.grandviewresearch.com/industry-analysis/acrylonitrile-acn-market. [Accessed 01 January 2025].
2. Dimian AC, Bildea CS. Chemical Process Design: Computer-Aided Case Studies. John Wiley & Sons (2008), pp. 313-338.
3. Guan X, Chen X, Wu L. Catalysts for Producing Acrylonitrile. US Patent 6,596,897 B1. (2003)
4. Yang Z, Zhang N, Smith R. Enhanced superstructure optimization for heat exchanger network synthesis using deterministic approach. *Front. Sustain.* 3:976717 (2022) https://doi.org/10.3389/frsus.2022.976717
5. Zhai J, Chen X, Xie H, Sun X, Zhao P, Liu Y. Improving the economic saving, environmental sustainability, and energy efficiency of separating acetone/n-heptane mixture via heat pump-assisted extractive dividing wall column with heat exchanger network. *Chem. Eng. Process.: Process Intensif.* 187:109354 (2023) https://doi.org/10.1016/j.cep.2023.109354
6. Kiss AA, Ferreira CAI. Heat Pumps In Chemical Process Industry. CRC Press (2016).
7. Li Q, Somoza-Tornos A, Kiss AA. A systematic selection and decision matrix for energy-efficient intensified distillation technologies. *Chem. Prod. Process Model.* (2024) https://doi.org/10.1515/cppm-2024-0035
8. Turton R, Bailie RC, Whiting WB, Shaeiwitz JA. Analysis, Synthesis and Design of Chemical Processes. Pearson Education (2018).



© 2025 by the authors. Licensed to PSEcommunity.org and PSE Press. This is an open access article under the creative commons CC-BY-SA licensing terms. Credit must be given to creator and adaptations must be shared under the same terms. See https://creativecommons.org/licenses/by-sa/4.0/




Systems & Control Transactions

**Research Article - Peer Reviewed Conference Proceeding**
ESCAPE 35 - European Symposium on Computer Aided Process Engineering
Ghent, Belgium. 6-9 July 2025
Jan F.M. Van Impe, Grégoire Léonard, Satyajeet S. Bhonsale,
Monika E. Polańska, Filip Logist (Eds.)

PSE PRESS

# Optimizing the Selection of Solvents for the Dissolution and Precipitation of Polyethylene

**Riccardo Standish[a], Jian Yin[b], Mirjana Minceva[b], Jakob Burger[c], Amparo Galindo[a], George Jackson[a] and Claire S. Adjiman[a]***

[a] Department of Chemical Engineering, Sargent Centre for Process Systems Engineering, South Kensington Campus, Imperial College London, London SW7 2AZ, UK
[b] Biothermodynamics, TUM School of Life Sciences, Technical University of Munich, Freising, Germany
[c] Technical University of Munich, Campus Straubing for Biotechnology and Sustainability,94315 Straubing, Germany
* Corresponding Author: c.adjiman@imperial.ac.uk.

## ABSTRACT

Plastic recycling is prevalently mechanical, which is inefficient at removing contaminants and produces low-grade materials. Solvent-based polymer dissolution and precipitation is emerging as a low-energy alternative to mechanical recycling when tackling highly contaminated plastic waste streams. We present a computer-aided molecular and process design (CAMPD) formulation for the selection of optimal solvents and process temperatures for polymer recycling via a dissolution and precipitation process. A mixed-integer nonlinear programming (MINLP) model is proposed to minimize the energy requirement for the dissolution of commercial low-density polyethylene, a ubiquitous polymer in industrial and municipal plastic waste, while minimizing the solvent viscosity and toxicity through multiobjective optimization. We integrate the SAFT-$\gamma$ Mie group-contribution equation of state in the optimization framework to predict key thermodynamic properties and to ensure that the desired phase behaviour is achieved. A ranked list of solvents and the corresponding process temperatures is obtained using integer cuts. Two polyethylene molecular weights are considered. In each case, we construct a Pareto front to quantify the trade-offs between the energy requirements of the process and the selected solvent properties. Furthermore, we investigate the simultaneous design of the dissolution and cooling precipitation to analyse the effect of varying the precipitation temperature on the energy of dissolution. The current study provides valuable insights into selecting optimal solvents for polyethylene dissolution, advancing the design of more efficient plastic recycling processes.

**Keywords**: Plastic recycling, CAMPD, SAFT-$\gamma$ Mie.

## INTRODUCTION

The recycling of plastics via solvent-based processes is an emerging alternative to the more established mechanical recycling technologies, particularly when addressing highly contaminated and multilayer plastic waste, and targeting high-quality recycled polymers [1]. Amongst solvent-based recycling technologies, physical recycling processes, that do not involve any chemical modifications of the molecular species, lead to significantly less carbon dioxide ($CO_2$) emissions compared to chemical recycling, which requires the energy-intensive cleavage of polymer bonds to produce monomers, the building blocks of polymers [2]. This is particularly the case when considering polyolefins like polyethylene and polypropylene, which have highly unreactive carbon-carbon bonds. However, dissolution and precipitation methods are more energy intensive than mechanical recycling and are often not suitable to produce food-grade recycled polymers due to the use of toxic solvents [3], which also pose general concerns with respect to environmental impact. Identifying new solvents and improved process designs is therefore key to advancing solvent-based dissolution and precipitation to levels comparable with mechanical recycling and to make it competitive with virgin polymer production.

Polymer solubility experiments are expensive and time consuming, so that the availability of predictive tools

for relevant properties to make informed decisions about the process and solvent choice is critical. The selection of solvents based on Hansen solubility parameters (HSPs) has been proposed [4]. While HSPs are useful for rapid solvent screening, they do not provide the required properties for process optimization, such as the solubility or the enthalpy at different process conditions. Recently, COSMO-RS, which can account for polymer–solvent molecular detail, has been used to predict the solubility of polymers in solvents for dissolution applications [5]. However, the prediction of the solubility of the polymer with COSMO-RS is computationally expensive, requiring molecular simulation to identify representative polymer conformations. Furthermore, there has been limited validation of the approach in terms of the polymer molecular weight and of the temperature range. The SAFT-γ Mie [6,7] equation of state offers an alternative route to predict solid–liquid equilibrium and liquid–liquid demixing in polymer-solvent mixtures, as well as other thermodynamic properties. It has been shown to deliver accurate properties of complex mixtures, including polymers and solvents [6-8], and, as a group-contribution method, it is naturally suited for use in solvent (molecular) design. It has for example recently been used in computer-aided molecular and process design (CAMPD) to identify better solvents and process conditions for pharmaceutical manufacturing [9] and for $CO_2$ capture [10]. Crystallization processes in drug manufacturing also depend heavily on solubility (solid–liquid equilibrium), providing a foundation for the model-based design of dissolution-precipitation processes. The use of SAFT-γ Mie to support the design of physical recycling processes is investigated in our current study, building on previous work on multiobjective optimization (MOO) to understand the tradeoffs between different objective functions, such as the solvent toxicity [11], the crystal yield and the solvent consumption [9].

The CAMPD framework is applied for the first time to solvent-based dissolution and precipitation recycling of plastics. As case studies, we explore the selection of optimal solvents and process conditions that minimize the energy requirements for the recycling of two types of low-density polyethylene (LDPE) while ensuring a homogeneous liquid polymer–solvent mixture is formed. This scenario is relevant to a plastic recycling problem where LDPE is mixed with solid waste impurities, such as secondary plastics and the presence of metals or cardboard [12]. We provide a ranked list of optimal solvents and process conditions and explore the trade-offs between the energy requirements and two key solvent properties: toxicity and viscosity. Furthermore, we analyse the relationship between the objective function and the precipitation temperature.

## DESIGN METHODOLOGY

### Problem definition

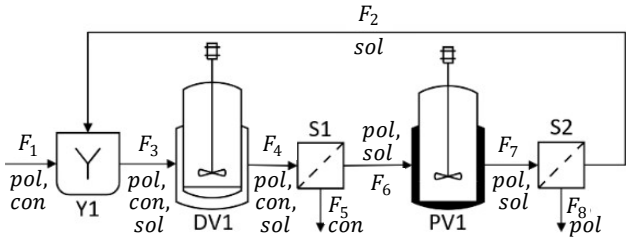



**Figure 1:** Schematic of an idealised polyethylene dissolution and cooling precipitation flowsheet.

In the CAMPD problem we focus on a general approach to designing a polymer dissolution and precipitation system. This involves identifying the optimal solvent molecules, weight fractions, and process temperatures to minimize the performance objective, which in this case is the energy of dissolution. The process configuration is shown in Figure 1, assuming perfect separation in each unit. A stream of plastic waste consisting of LDPE ($pol$) and a solid contaminant ($con$), with a flowrate $F_1$ , is mixed with a solvent ($sol$) recycle stream $F_2$ in a mixer Y1. The two-phase slurry $F_3$ is fed to a dissolution vessel DV1, where heat is provided through a heating jacket to dissolve the solid polymer. The outlet of DV1 is passed through a filtration unit S1, where the undissolved solid contaminants are filtered out. The filtrate $F_6$ then enters a precipitation vessel PV1, where the polymer–solvent mixture is cooled down to obtain solid polymer. Finally, the solvent is recovered in filter S2, and the purified

**Table 1:** Key model equations.

| Description | Equation | |
|---|---|---|
| Energy consumption | $Q = Q_{pol} + \left[F_4^L\, h^L(T_4, P_4, x_4^L) - F_3^L x_{3,pol}^L h_{pol}^L(T_3, P_3) - F_3^L x_{3,sol}^L h_{sol}^L(T_3, P_3)\right]$ | (1) |
| Heat required to obtain a liquid polymer at $T_3$ | $Q_{pol} = F_3^s x_{3,pol}^s [c_{P,pol}^S (T_{pol}^{\text{fus}} - T_3) + \Delta h_{pol}^{\text{fus}}] + F_3^L x_{3,pol}^L [h_{pol}^L(T_3, P_3) - h_{pol}^L(T_{pol}^{\text{fus}}, P_3)]$ | (2) |
| Solid–liquid equilibrium model | $\ln \boldsymbol{x}_{i,pol}^L + \ln \gamma_{i,pol}(T_i, P_i, \boldsymbol{x}_i^L) = -\frac{\Delta h_{pol}^{\text{fus}}}{R}\left[\frac{1}{T_i} - \frac{1}{T_{pol}^{\text{fus}}}\right],\ i = 4{,}7,\ 0 \le w_{7,pol}^L \le 10^{-6}$ | (3) |
| Polymer and solvent form a single stable liquid phase | $\tilde{S}_l\ (T_4, P_4\ , x_4^L) = 1$ | (4) |

polymer leaves S2 in stream $F_8$.

## Model formulation

All separations are assumed to be perfect. The polymer is a solid in streams $1, 3, 7,$ and $8$, and in the liquid phase in streams $4$ and $6$. Stream $2$ is pure solvent, stream $5$ pure solid contaminant and stream $8$ pure polymer. The material balances for the system are easily derived and not shown.

Other key model equations are shown in Table 1. $Q$ is the energy consumption in dissolution vessel DV1, neglecting any energy required for agitation as well as the enthalpy change due to the solid contaminant. It is derived from an energy balance around DV1, given as Equations (1) and (2) in Table 1, where $F_i^L$ denotes the liquid flowrate in stream $i$, $F_i^S$ the corresponding solid flowrate, and $h_i^L(T_i, P_i, \boldsymbol{x}_i^L)$ the liquid-phase enthalpy of stream $i$ at temperature $T_i$, pressure $P_i$ (here assumed to be atmospheric throughout) and mole fraction vector $\boldsymbol{x}_i^L$. $h_{i,pol}^L$ and $h_{i,sol}^L$ denote the pure component liquid-phase enthalpies for the polymer and the solvent, respectively. $\boldsymbol{x}_{i,k}^L$ denotes the mole fraction of component $k$ ($pol$ or $sol$) in the liquid phase in stream $i$, while $\boldsymbol{x}_{i,pol}^S$ denotes the corresponding solid-phase mole fraction. $Q_{pol}$ is the enthalpy change of the polymer on going from solid to liquid. $c_{P,pol}^S$ is the solid-phase molar heat capacity of the polymer, $T_{pol}^{\text{fus}}$ is the melting temperature of the polymer, and $\Delta h_{pol}^{\text{fus}}$, its enthalpy of fusion at $T_{pol}^{\text{fus}}$.

Solid–liquid equilibrium must hold in DV1 and PV1. This is enforced by Equation (3). $\gamma_{i,pol}(T_i, P_i, \boldsymbol{x}_i^L)$ is the activity coefficient of the polymer at the specified conditions, and $R$ is the ideal gas constant. In addition, the mass fraction of polymer in the liquid phase in PV1 (i.e., in $F_7^L$) is set to be very close to zero to ensure full precipitation.

Finally, in order to ensure that the polymer and solvent form a single stable liquid phase in DV1, a logical stability function $\tilde{S}_l$ $(T_4, P_4, \boldsymbol{x}_4^L)$ is constrained to $1$. A value of $1$ indicates that a temperature-pressure flash calculation at the specified conditions does not detect a second liquid phase or a vapour, while 0 indicates the presence of another fluid phase.

SAFT-$\gamma$ Mie is used to calculate the activity coefficients and the liquid-phase enthalpies with group interaction parameters taken from [8] or combining rules [8] where no group parameters have been developed.

## CAMPD formulation

The model equations are integrated within a Mixed Integer Nonlinear Programming (MINLP) that takes as input a list $\mathcal{L}$ of candidate solvents. Each solvent $l$ is characterized by a set of functional group numbers, $n_{g,l}$, $g \in G$, where $G$ is the set of SAFT-$\gamma$ Mie groups, as well as its toxicity $\tau_l$, taken as $\text{LC}_{50}$ from [16], and an experimental viscosity $\eta$ at $298\ \text{K}$, taken from the DETHERM database [17]. A binary variable $y_l$ is introduced to denote whether solvent candidate $l$ is selected and is defined such that only one solvent can be chosen:

$$\sum_{l \in \mathcal{L}} y_l = 1. \tag{5}$$

Assignment constraints are used to set the values of the SAFT-$\gamma$ Mie group numbers, the toxicity, and the viscosity to be those of the selected solvent. The number of groups of type $g$ in the solvent is given by

$$n_g = \sum\nolimits_{l \in \mathcal{L}} y_l n_{g,l}, \tag{6}$$

and the toxicity and viscosity are given by

$$\tau = \sum\nolimits_{l \in \mathcal{L}} y_l \tau_l; \quad \eta = \sum\nolimits_{l \in \mathcal{L}} y_l \eta_l \tag{7,8}$$

A constraint is also imposed on the maximum mass fraction of polymer in DV1, to prevent the formation of gel.

The problem is formulated using up to two objectives that must be minimized, one of which is always $Q$ and the other $\tau$ or $\eta$.

# CASE STUDIES

## Case study description

LDPE is one of the most widely present polyolefins in plastic products and is highly valued for its durability and versatile nature. However, its durable qualities make its recycling challenging and energy intensive. Two molecular weights of polymer are considered, $270\ \text{kg mol}^{-1}$ and $4\ \text{kg mol}^{-1}$, and the designs are developed on a basis of $1\ \text{kg}$ of polymer. The primary objective of the design problems considered is to identify optimal solvents and corresponding process conditions to minimize the energy consumption, $Q$, in a process to remove a solid contaminant from LDPE via dissolution-precipitation. A secondary objective is also considered in some cases, chosen as either the minimization of the toxicity $\tau$ or of the viscosity $\eta$.

The specific heat capacity $c_{P,pol}^S$ is assumed to be independent of molecular weight and set equal to the experimental value measured at $1\ \text{atm}$ and $298\ \text{K}$, $46.5\ \text{J mol}^{-1}\ \text{K}^{-1}$ [15]. The experimental values for $T_{pol}^{\text{fus}}$ values are either obtained through differential scanning calorimetry (DSC) in our current work or from [13], and the experimental values for $\Delta h_{pol}^{\text{fus}}$ are obtained from [14] (see Table 2).

Polythermal solubility measurements are conducted for selected polymer-solvent mixtures, corroborating the reliability of the SAFT-$\gamma$ Mie model.

**Table 3:** Ranking of optimal solvents generated with integer cuts for both polymers considered. Energy consumption ($Q$), polymer mass fraction ($w$), dissolution temperature ($T_4$), mixture stability ($\tilde{S}_l$), solvent toxicity ($\tau$) [16], and viscosity ($\eta$) [17] at the solution of the CAMPD problem with $T_7$ =298.15 K.

| LDPE | Rank | Solvent selected? | $Q$/kJ | $w_{pol}$ | $T_4$ /K | $\tau(-\log[\mathrm{LC}_{50}])$ | $\eta$ / (mPa s) |
|---|---|---|---|---|---|---|---|
| 4 kg mol$^{-1}$ | 1 | Decalin | 366.03 | 0.3 | 341.05 | 3.88 | 2.47 |
| | 2 | Mesitylene | 401.38 | 0.3 | 343.42 | 4.19 | 0.66 |
| | 3 | Xylene | 404.74 | 0.3 | 344.17 | 3.81 | 0.61 |
| | 4 | Toluene | 420.01 | 0.3 | 346.41 | 3.42 | 0.55 |
| | 5 | Benzene | 455.88 | 0.3 | 351.21 | 3.61 | 0.82 |
| 270 kg mol$^{-1}$ | 1 | Decalin | 439.04 | 0.3 | 356.07 | 3.88 | 2.47 |
| | 2 | Mesitylene | 458.70 | 0.3 | 356.33 | 4.19 | 0.66 |
| | 3 | Xylene | 462.83 | 0.3 | 357.31 | 3.81 | 0.61 |
| | 4 | Toluene | 479.05 | 0.3 | 359.85 | 3.42 | 0.55 |
| | 5 | Cymene | 582.59 | 0.3 | 373.93 | 3.61 | 0.82 |

**Table 2:** Molecular weight and melting properties of the polymers of interest [14]. [*] denotes the property is measured in our current work.

| | **Short LDPE** | **Long LDPE** |
|---|---|---|
| $\boldsymbol{M_w/(\mathrm{kg\ mol^{-1}})}$ | 4 | 270 |
| $\boldsymbol{u}$ /(-) | 142 | 9623 |
| $\boldsymbol{T_i^{\mathrm{fus}}/\mathrm{K}}$ | 375.15 [*] | 389.15 [13] |
| $\boldsymbol{\Delta h_i^{\mathrm{fus}}/(\mathrm{kJ\ mol^{-1}})}$ | 8.22$u$ [14] | 8.22$u$ [14] |

To construct the list of candidate solvents we conduct an HSP analysis to identify solvents that exhibit low relative energy difference (RED) values with LDPE, using a threshold of 0. The solvents used in dissolution and precipitation experimental studies reported by Li et al. [1] and Ügdüler et al. [4] are considered. This results in 17 candidate molecules. To evaluate the effects of the precipitation temperature ($T_7$) on the design problem, ten design scenarios are considered with different allowed temperature differences between DV1 and PV1.

## Results and discussion

The formulation is implemented in gPROMS Process version 2023.1.0 and solved using the MINLPOA (outer approximation) local solver. The built-in stability function is used for Equation (4).

The ranked list of optimal solutions shown in Table 3, obtained for a base case of $T_7 = 298.15$ K, indicates that decalin, mesitylene, xylene, toluene, benzene and cymene are promising solvent candidates that require the least energy to dissolve LDPE. The first four solvents are the same for both polymer samples, while benzene and cymene rank fifth for the $4\ \mathrm{kg\ mol^{-1}}$ LDPE and 270 kg mol$^{-1}$ LDPE, respectively. The polymer solubility ($w_{pol}$) reaches the $0.30$ upper bound in each iteration, indicating that high solubility and, thus, low solvent use minimizes the energy requirements of the process. Trade-offs between $Q$ and $\tau$, and between $Q$ and $\eta$, are explored by solving bi-objective problem using the $\varepsilon$-constraint

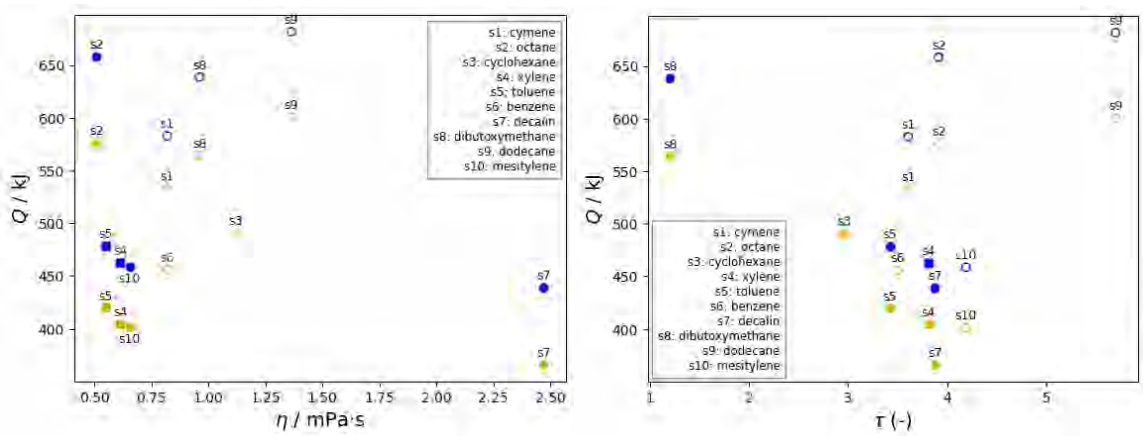



**Figure 2:** Pareto optimal solutions (filled circles) obtained when solving the optimization problem with two competing objectives: energy consumption $Q$ and solvent viscosity $\eta$ (left), and energy consumption $Q$ and solvent toxicity $\tau$ (right). Empty circles depict feasible solvents. The colour indicates the type of polymer: 270 kg mol$^{-1}$ polyethylene (blue) and 4 kg mol$^{-1}$ polyethylene (orange). Note that the filled circles denote Pareto points found via the $\varepsilon$-constraint method and the filled squares Pareto points found only via integer cuts due to the $\varepsilon$ steps.

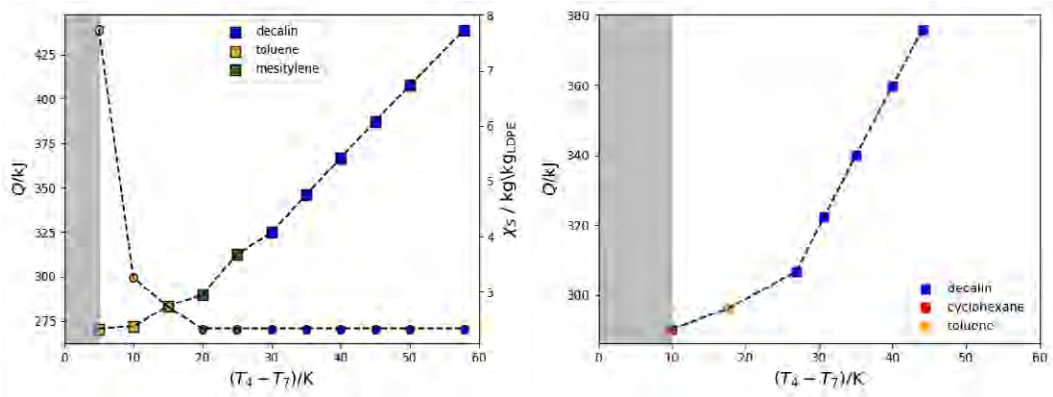



**Figure 3:** Minimum energy requirement $Q$ as a function of the minimum allowed temperature difference between dissolution and precipitation $(T_4 - T_7)$ for 270 kg mol$^{-1}$ LPDE (left plot) and 4 kg mol$^{-1}$ LPDE (right plot). $\chi_S$ indicates the solvent inventory. The point with the largest value of $(T_4 - T_7)$ corresponds to the temperature difference when $T_7$ =298.15 K. Gray shading indicates infeasible regions. The dashed curves are included to aid visualisation.

method for 10 equally spaced $\varepsilon$ values. Pareto optimal solvents are depicted in Figure 2, together with feasible solvents. These were obtained by adding integer cut inequality constraints to the optimization problem. According to the Multi Objective Optimization (MOO) solutions, mesitylene may be a more suitable solvent to dissolve polyethylene than decalin due to its significantly lower $\eta$ with only a slightly higher $Q$. A solvent with a lower viscosity is desirable as it may offer faster dissolution and lower processing costs due to a lower energy input for pumping and mixing. On the other hand, no solvent offers a significantly lower toxicity than decalin without a large increase in energy requirements. However, toxicity may be considered less critical than viscosity if the polymer is fully recovered and the solvent is efficiently recycled, minimizing solvent loss to the environment. Employing cymene, a bio-derived solvent that ranks fifth (cf. Table 3) for $270\ \mathrm{kg\ mol^{-1}}$ LDPE, offers a potentially sustainable alternative to conventional organic solvents by reducing the reliance on fossil feedstocks for solvent production—aligning with the core objective of polymer recycling to promote environmental sustainability. On the other hand, a high recycling efficiency can reduce the greenhouse gas emissions associated with the need for fresh solvent input, potentially justifying the use of conventional organic solvents, particularly if they contribute to lower overall process energy demands. A broader lifecycle analysis is required to quantify these trade-offs. Dibutoxymethane, the least toxic solvent considered is associated with a high energy consumption, likely due to its polarity. An expanded solvent design space may help us to identify additional feasible solvents and explore the empty regions of the multiobjective spaces shown in Figure 2. This could be achieved by allowing the design of solvent mixtures [18].

The impact of the precipitation temperature, $T_7$, on the energy consumption is investigated by varying the temperature limit constraint. As shown in Figure 3, by reducing the extent of cooling in PV1, the optimal solvent, toluene for $270\ \mathrm{kg\ mol^{-1}}$ LDPE and cyclohexane for $4\ \mathrm{kg\ mol^{-1}}$ LDPE, can be supplied to DV1 at a higher temperature and thus the energy consumption decreases. This trend is a result of the steep decrease in solubility of LDPE as a function of temperature in the vicinity of the pure solvent limit. Based on the analysis in Figure 3, the optimal operating temperatures for PV1 are $347.19\ \mathrm{K}$ for $270\ \mathrm{kg\ mol^{-1}}$ LDPE and $342.54\ \mathrm{K}$ for $4\ \mathrm{kg\ mol^{-1}}$ LDPE when a margin of at least 5 K between $T_4$ and $T_7$ is enforced. These guarantee $100\%$ LDPE precipitation and energy requirements of $283.32\ \mathrm{kJ}$ and $290.37\ \mathrm{kJ}$ for $270$ and $4\ \mathrm{kg\ mol^{-1}}$ LDPE, respectively. The operating point for $270\ \mathrm{kg\ mol^{-1}}$ LDPE offers a good compromise between $Q$ and a solvent inventory ($\chi_S$) equal to $3.26$. While for all $4\ \mathrm{kg\ mol^{-1}}$ LDPE points a $\chi_S$ of $2.33$ is achieved.

## CONCLUSIONS

We have developed a general formulation for the optimal process and solvent design for solvent-based dissolution and precipitation recycling of plastics based on a CAMPD framework with a simple initial process model and rigorous thermodynamics. In this framework, the optimal solvent candidate, the polymer solubility, and the dissolution (and precipitation) temperatures required to minimize the energy consumption can be obtained simultaneously. The general model is applied to the dissolution and precipitation of two types of LDPE, for which separate ranked lists of optimal solvents are produced. In both cases, only apolar solvents appear in the solvent rankings, with decalin identified as minimizing the energy consumption. MOO is employed to consider the trade-offs between the energy consumption and toxicity or viscosity of the solvent. Mesitylene is found to have a lower viscosity and similar $Q$ when compared to decalin. The

simultaneous optimization of the dissolution and precipitation temperatures leads to improved results when compared to the case where the precipitation temperature is fixed and highlight the impact on the solvent inventory, which also has implications on the cost and environmental impact of the process and have not yet been quantified.

The current study provides a foundation for optimizing the dissolution-precipitation process, to make this recycling technology both economically viable and environmentally friendly. In future work, we plan to extend the design formulation to treat multilayer plastic waste, including polyethylene mixed with polypropylene, and solvent mixtures. We also aim to include a technoeconomic and lifecycle analysis for a more advanced flowsheet of the physical recycling process.

## ACKNOWLEDGEMENTS

The authors gratefully acknowledge financial support from the Joint Academy of Doctoral Sciences and the EPSRC DTP grant (Grant Ref: EP/W524323/1).

## REFERENCES

1. H. Li et al. Expanding plastics recycling technologies: chemical aspects, technology status and challenges, *Green Chem.* 24:8899–9002 (2022) 10.1039/D2GC02588D
2. I. Vollmer et al. Beyond Mechanical Recycling: Giving New Life to Plastic Waste, *Angewandte Chemie International Edition* 59:15402–15423 (2020) 10.1002/anie.201915651
3. T. Uekert et al. Technical, Economic, and Environmental Comparison of Closed-Loop Recycling Technologies for Common Plastics. *ACS Sustainable Chem. Eng.* 11:965–978 (2023) 10.1021/acssuschemeng.2c05497
4. S. Ügdüler et al. Challenges and opportunities of solvent-based additive extraction methods for plastic recycling. *Waste Management* 104:148–182 (2020) 10.1016/j.wasman.2020.01.003
5. K. L. Sánchez-Rivera et al. Reducing Antisolvent Use in the STRAP Process by Enabling a Temperature-Controlled Polymer Dissolution and Precipitation for the Recycling of Multilayer Plastic Films. *ChemSusChem.* 14: 4317–4329 (2021) 10.1002/cssc.202101128
6. V. Papaioannou et al. Group contribution methodology based on the statistical associating fluid theory for heteronuclear molecules formed from Mie segments. *The Journal of Chemical Physics* 140:054107 (2014) doi: 10.1063/1.4851455
7. S. Dufal et al. Prediction of Thermodynamic Properties and Phase Behavior of Fluids and Mixtures with the SAFT-γ Mie Group-Contribution Equation of State. *J. Chem. Eng. Data* 59:3272–3288 (2014) 10.1021/je500248h.
8. A. J. Haslam et al. Expanding the Applications of the SAFT-$\gamma$ Mie Group-Contribution Equation of State: Prediction of Thermodynamic Properties and Phase Behavior of Mixtures. *J. Chem. Eng. Data* 65:5862–5890 (2020) 10.1021/acs.jced.0c00746
9. O. L. Watson et al. Computer Aided Design of Solvent Blends for Hybrid Cooling and Antisolvent Crystallization of Active Pharmaceutical Ingredients. *Org. Process Res. Dev.* 25:1123–1142 (2021) 10.1021/acs.oprd.0c00516
10. Y. S. Lee et al. Enabling the direct solution of challenging computer-aided molecular and process design problems: Chemical absorption of carbon dioxide. *Computers & Chemical Engineering* 174:108204 (2023) 10.1016/j.compchemeng.2023.108204
11. S. Jonuzaj et al. Computer-aided design of optimal environmentally benign solvent-based adhesive products. *Computers & Chemical Engineering* 130:106518 (2019) 10.1016/j.compchemeng.2019.106518
12. Association of Plastic Recyclers. https://plasticsrecycling.org/. Accessed: Dec. 17, 2024.
13. Merck. https://www.sigmaaldrich.com/DE/en. Accessed: Dec. 23, 2024.
14. B. Wunderlich et al. Thermodynamic Properties of Polymers. *Encyclopedia of Polymer Science and Engineering* 16:767–807 (1989)
15. D. W. Van Krevelen and K. Te Nijenhuis. Chapter 5 - Calorimetric Properties. In Properties of Polymers (Fourth Edition). Ed: D. W. Van Krevelen and K. Te Nijenhuis. Elsevier (2009)
16. T. M. Martin and D. M. Young. Prediction of the Acute Toxicity (96-h LC50) of Organic Compounds to the Fathead Minnow (Pimephales promelas) Using a Group Contribution Method. *Chem. Res. Toxicol.* 14:1378–1385 (2001) 10.1021/tx0155045
17. Physical Sciences Data science Service. https://www.psds.ac.uk/. Accessed: Dec. 17, 2024.
18. S. Jonuzaj et al. The formulation of optimal mixtures with generalized disjunctive programming: A solvent de-sign case study. *AIChE Journal* 62:1616–1633, (2016) 10.1002/aic.15122

© 2025 by the authors. Licensed to PSEcommunity.org and PSE Press. This is an open access article under the creative commons CC-BY-SA licensing terms. Credit must be given to creator and adaptations must be shared under the same terms. See https://creativecommons.org/licenses/by-sa/4.0/



Systems & Control Transactions

**Research Article - Peer Reviewed Conference Proceeding**
ESCAPE 35 - European Symposium on Computer Aided Process Engineering
Ghent, Belgium. 6-9 July 2025
Jan F.M. Van Impe, Grégoire Léonard, Satyajeet S. Bhonsale,
Monika E. Polańska, Filip Logist (Eds.)

PSE PRESS

# Sustainable Downstream Process Design for HMF Conversion to Value-Added Chemicals

**Norbert B. Mihály[a]*, Miruna Prodan[a], Vasile M. Cristea[a] and Anton A. Kiss[b]**

[a] Babes-Bolyai University of Cluj-Napoca, 1 Mihail Kogalniceanu Street, 400028 Cluj-Napoca, Romania
[b] Delft University of Technology, van der Maasweg 9, 2629 HZ Delft, Netherlands
* Corresponding Author: norbert.mihaly@ubbcluj.ro

## ABSTRACT

Biomass conversion to chemical derivatives and essential intermediates is regarded as a long-term strategy for the chemical sector. Among the numerous valuable chemicals obtained from biomass, 5-hydroxymethylfurfural (HMF) is considered an industrially relevant compound due to its capacity to be converted into a variety of value-added chemicals. Compared to conventional catalytic synthesis, bio-catalysis has emerged as a potential greener substitute for HMF conversion to value-added compounds. HMF conversion through bio-catalysis, although more sustainable, seldom leads to the production of a single derivative. Thus, the development of efficient purification and separation processes of several products are crucial to scalability. The downstream process for the novel enzymatic conversion of HMF to high value-added chemicals (i.e., 1-phenylethylamine, 2,5-bis(hydroxymethyl)furan, 1-phenylethylalcohol, and 5-(aminomethyl)-2-furanmethanol) was designed by means of rigorous simulations in Aspen Plus®. The proposed process resulted in product streams with 97 wt% or larger for their respective component, and at least 95% product recovery is attained for each value-added HMF derivative. The global greenhouse gas emissions for the manufacture of a kg of product is 2.26 $kg_{CO_2e}$/ $kg_{product}$, while 0.086 $m^3_{wastewater}$/ $kg_{product}$ is generated. The proposed downstream sequence offers an overview of the feasibility for the scalability of the enzymatic process, crucial in developing sustainable bioprocesses.

**Keywords**: Modelling and Simulations, 5-hydroxymethylfurfural, Separation and purification, Sustainability

## 1. INTRODUCTION

Sustainable development is a concept that responds to the challenges posed by the needs of a rapidly growing population and rapidly increasing industry demands for petroleum-based carbon sources for energy and chemical synthesis [1].

Biomass has become an attractive carbon-neutral resource (as its emissions are of biogenic origin) due to its widespread availability (approximately 18 trillion tons on land and 4 billion tons of aquatic biomass) and renewable nature [2]. One particularly valuable chemical produced from glucose or fructose obtained from biomass is HMF [3]. Due to fructose's high cost and low availability, glucose can replace fructose as a feedstock to synthesise HMF. This process requires an additional step for the isomerisation of glucose to fructose. Current research focuses on biowaste and lignocellulosic biomass as feedstock for HMF synthesis due to their low cost, lack of impact on the food chain supply, and carbon-neutral nature. Processes starting from biowaste employ a pretreatment step followed by hydrolysis to liberate glucose from the starting polysaccharides [4,5].

HMF is an important intermediate in synthesising renewable polymers, pharmaceuticals, resins, solvents, fungicides and fuels. HMF is composed of a furan ring on which hydroxymethyl and formyl functional groups are grafted. Hence, complex chemicals can be obtained from simple chemical reactions such as oxidation, reduction, esterification or condensation [6]. As such, HMF has been evaluated in the Top 10 biobased chemicals by the U.S. Department of Energy [1].

The chemical synthesis of HMF derivatives typically involves metal-based catalysts (Pd, Ru, Pt, Mn, V and Au), elevated reaction temperatures and pressures, and organic solvents like dimethyl sulfoxide,

dimethylformamide, or toluene [5,7].

In contrast, enzymes are recognized as an alternative to chemical catalysis due to their alignment with the twelve principles of green chemistry. These biocatalysts require mild reaction conditions for temperatures and pressures and utilize water as a solvent. Additionally, enzymes demonstrate high specificity, which helps eliminate the need for protection and deprotection steps. They are also characterized by low toxicity and generate less harmful waste, primarily in the form of wastewater [8].

The oxidative products, including 5-hydroxymethyl-2-furancarboxylic acid, 2,5-diformylfuran, 5-formyl-2-furancarboxylic acid, and 2,5-furandicarboxylic acid, find applications in the polymer industry (such as polyurethanes, polyesters, copolyesters, polyamides, polyimides, and epoxy resins) [7]. Compounds such as 2,5-dihydroxymethylfuran and 2,5-bis(hydroxymethyl)furan (BHMF) are derived from HMF through hydrogenation, and both are valuable in polymer synthesis, particularly for polyurethanes, polyesters, and polycarbonates [7,9]. BHMF could also be utilized as a fuel source[9].

Various enzymatic oxidase systems, have been evaluated for their ability to produce oxidative products from HMF. These enzymatic systems showcase high conversion rates of HMF, however, in most cases several products are obtained. As such, product separation and purification play an essential role in scalability [10].

Chemical synthesis already produces value-added derivatives of MHF at an industrial scale [11]. For the feasibility of enzymatic synthesis on an industrial scale, downstream techniques that are both cost-effective and process-efficient need to be developed [9]. In conclusion, the viability of enzymatic synthesis as a green alternative is reliant on developing efficient downstream processes. The plethora of studies that aimed to develop new and effective enzymatic catalysts seldom researched or discussed the downstream processes necessary to separate and purify the obtained products.

The current study aims to bridge the mentioned gap and design a sustainable downstream process considering a novel enzymatic pathway for the conversion of HMF to value-added chemicals. The separation and purification process of a mixture of four products obtained from an enzymatic conversion of HMF to value-added products was designed in Aspen Plus®. To the best of the authors' knowledge the separation of 1-phenylethylamine (PEAM), BHMF, 1-phenylethylalcohol (PEA), and 5-(aminomethyl)-2-furanmethanol (HMFA) has yet to be discussed in the literature.

## METHODOLOGY

The enzymatic conversion of HMF and 1-phenylethylamine (PEAM) was studied which results in a mixture of BHMF, 1-phenylethylalcohol (PEA), PEAM and 5-(aminomethyl)-2-furanmethanol (AMFM).

For the separation of alcohols and amines that come from the bioreactor, ion exchange was opted for. Mineral acid (i.e., HCl) solution is added to the mixture until pH of 2 is reached in order to form the salts of the amines, while the alcohols remain in a neutral state. As such, a cation exchange material can be utilized to form an ionic bond with the amines while the alcohols pass through the ion exchange separator.

The amines can then be recovered when regenerating the cation exchange material, which involved the use of a mineral bases (i.e., NaOH). As a result, NaCl would form in the mixture which was removed before continuing with other product purification processes. In order to eliminate the mineral salt from the solution, their crystallization was considered by evaporation of the mixture to obtain an oversaturated solution of higher temperature. This solution, when cooled results in the crystallization of said mineral salt that was filtered from the aqueous solution.

The next steps in the downstream process relate to the separation and purification of the products. In case of the stream containing the alcohol products, BHMF can be separated from the aqueous solution through distillation. As PEA forms a well-known azeotrope with water (Figure 1), these compounds cannot be separated in the same manner, a liquid-liquid extraction process was opted for. Hexane was utilized as the solvent, as it was demonstrated to be the most efficient in similar systems [12]. This is further separated from hexane by a distillation column.

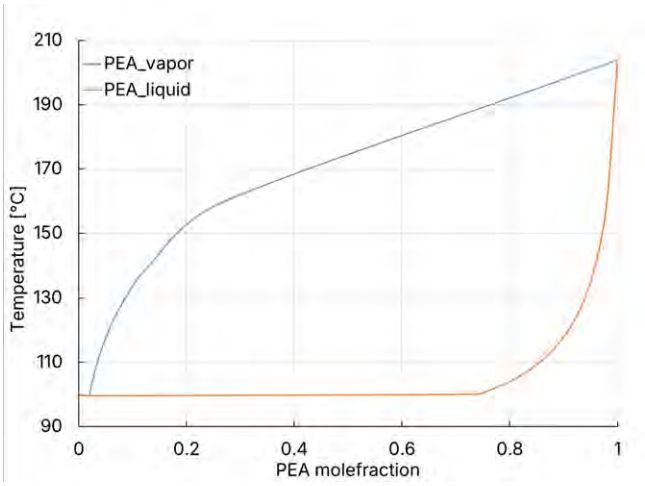



**Figure 1.** T-xy diagram of the PEA and water binary system.

On the other side, the aqueous solution containing the amine products goes through a crystallization process similar to the above mentioned to rid the solution of the mineral salts. In this case the separation of each

individual product from the aqueous solution can be performed by distillation. However, the intensification of these processes can be achieved through fractional distillation. The previously described downstream separation and purification processes are presented in Figure 2.

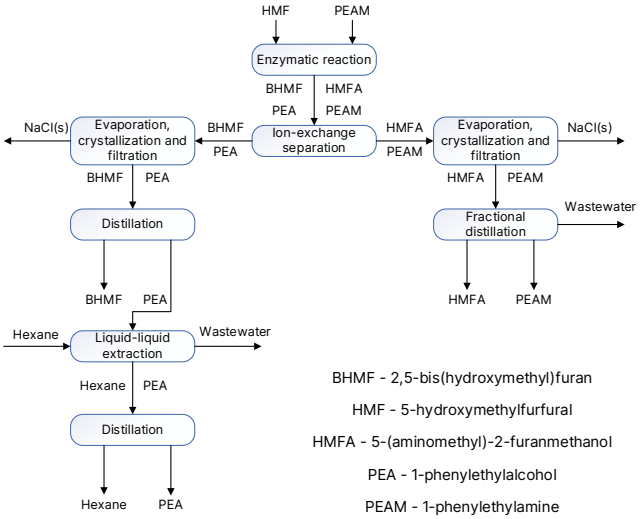



**Figure 2.** Simplified flowsheet of the HMF biocatalytic transformation to value-added products, their separation and purification.

The design of the separation and purification processes took into account laboratory scale experimental results, as well as the following assumptions. Firstly, full conversion of HMF is considered resulting in an equimolar mixture of BHMF, PEA, PEAM and HMFA. Secondly, the separation of amines and alcohols was assumed to be ideal in the ion exchange system. Thirdly, the solubility of the mineral salt was considered to be solely influenced by the water's mass fraction of the solution.

## RESULTS AND DISCUSSION

The proposed downstream process (Figure 3) was simulated in Aspen Plus® V11 software environment. The ion-exchange separation process (IEX) is presented in a simplified form as it was not the main focus of the current study. ELECNRTL and SOLIDS property methods were utilized to model the various processes involved. ELECNRTL was used as it is the most flexible property technique since it can handle both very low and high concentrations of aqueous and mixed solvent systems. The same method cannot be used to compute the characteristics of both solids and fluid phases. Therefore, for computations involving solid components, the SOLIDS property approach was employed. The incoming, purified and other relevant material streams of the simulation are summarized in Table 1.

It can be observed that the salt (i.e., NaCl) could not be fully removed through crystallization and filtration, and it will influence the purity of the bottom product streams of the first distillation process both for the amine and alcohol products (i.e., AMFM and BHMF).

In both cases, the process occurs under vacuum

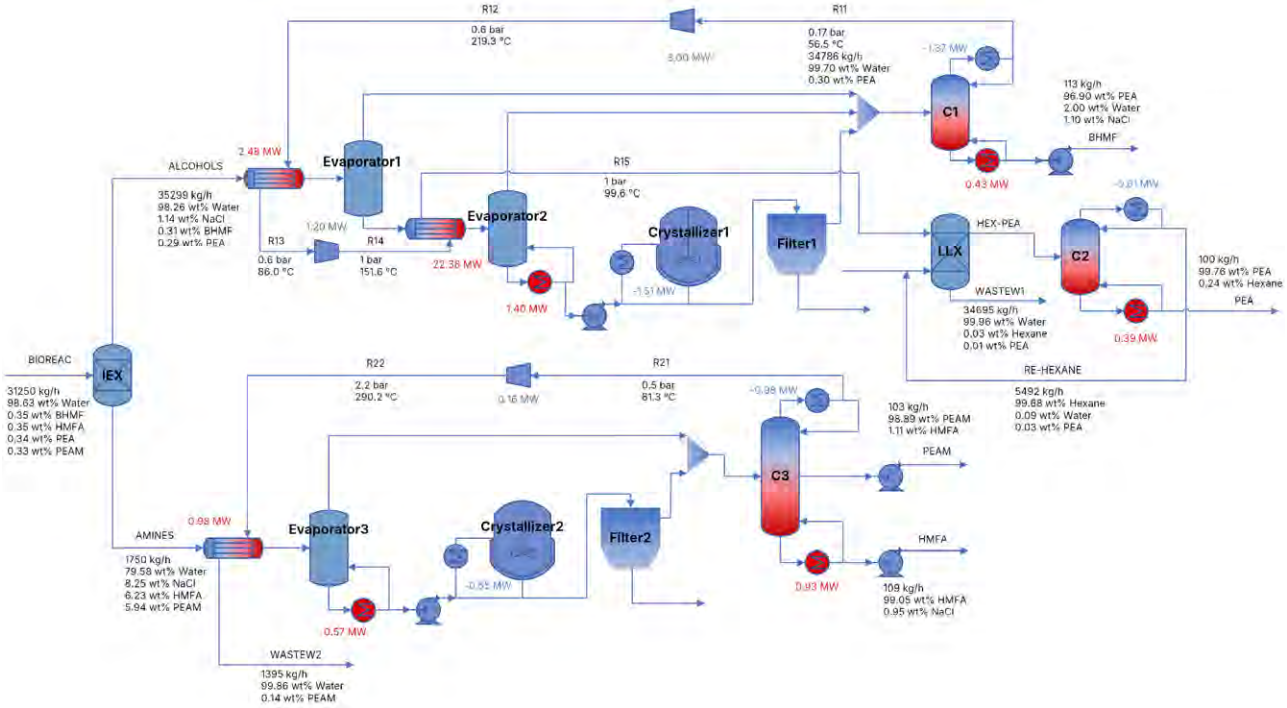



**Figure 3:** Schematic of product separation and purification processes implemented in the Aspen Plus® simulation

**Table 1:** Parameters and composition results of the most important streams from Figure 3.

| Stream | BIOREAC | HMFA | BHMF | PEA | PEAM | RE-HEXANE | HEX-PEA |
|---|---|---|---|---|---|---|---|
| **Temperature [°C]** | 30 | 228.2 | 117.3 | 197.1 | 134.7 | 57.2 | 110.9 |
| **Pressure [bar]** | 1 | 1 | 1 | 1 | 1 | 1 | 1 |
| **Flowrate [kg/h]** | 31250 | 109 | 113 | 100 | 103 | 5492 | 5592 |
| **Mass fractions** | | | | | | | |
| **HMFA** | 3.50E-03 | 9.91E-01 | 0.00E+00 | 0.00E+00 | 1.11E-02 | 0.00E+00 | 0.00E+00 |
| **BHMF** | 3.50E-03 | 0.00E+00 | 9.69E-01 | 0.00E+00 | 0.00E+00 | 0.00E+00 | 0.00E+00 |
| **Water** | 9.86E-01 | 0.00E+00 | 2.00E-02 | 0.00E+00 | 0.00E+00 | 9.00E-04 | 9.00E-04 |
| **PEA** | 3.40E-03 | 0.00E+00 | 0.00E+00 | 9.98E-01 | 0.00E+00 | 3.00E-04 | 1.81E-02 |
| **PEAM** | 3.30E-03 | 0.00E+00 | 0.00E+00 | 0.00E+00 | 9.89E-01 | 0.00E+00 | 0.00E+00 |
| **Hexane** | 0.00E+00 | 0.00E+00 | 0.00E+00 | 2.40E-03 | 0.00E+00 | 9.99E-01 | 9.81E-01 |
| **NaCl** | 0.00E+00 | 9.50E-03 | 1.10E-02 | 0.00E+00 | 0.00E+00 | 0.00E+00 | 0.00E+00 |

conditions in order to maintain the obtained products in their reported thermal stability range. In regards to BHMF, the streams containing this compound were kept at temperatures below 120 °C [13]. A partial-vapor condenser was set for both columns (i.e., C1 and C3) in order to ensure the desired reflux ratio, as well as to utilize the vapor distillate in a heat pump system to preheat the respective streams before the evaporation process. As the streams containing BHMF had to be maintained at lower temperatures, this thermal integration could only be realized in two steps, as it can be observed in Figure 2.

The optimal conditions for each unit operation were searched for by conducting sensibility analysis for each design parameter that applied to the respective unit operation (e.g.., reflux ratio, heat duty, number of stages, feed stage, by-product stage, etc.). In this manner, the desired product purity of 97 wt% or higher was obtained for all three products that could be separated in the first distillation steps (i.e., BHMF, PEAM and HMFA). Higher purity product can be obtained by evaporating a larger portion of water, thus improving the crystallization process of NaCl. However, the trade-off with the thermal energy required for the evaporation has to be considered, and the temperature constraints should also be taken into account. In case of the amine products, a single fractional distillation column was utilized for their separation and purification. The parameters of this ternary system were defined based on the study by Wen et al. 2017 [14].

The separation and purification of PEA further required a liquid-liquid extraction due to the azeotrope it forms, and a distillation process afterwards. Hexane was utilized for the extraction of PEA, based on its reported close to ideal recovery rate of PEA, also validated by the ternary diagram shown in Figure 4. The proposed process extracted more than 95% of PEA from the aqueous solution. A more efficient extraction can be achieved with a larger quantity of hexane, however that would also imply an increase in the reboiler duty of the distillation column that follows. Although the usage of an organic solvent influences the sustainability of the process, it is recovered in a high purity stream which can be recycled. In this manner, high purity PEA is obtained with a weight percent of 99.

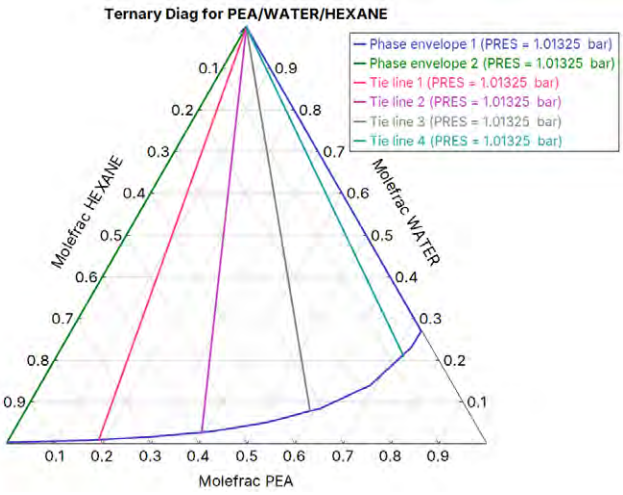



**Figure 4:** Ternary diagram with tie lines for the PEA-water-hexane system at atmospheric pressure.

Other than the purity of product streams, It is also important to note that the four compounds of interest are recovered from the reaction mixture in 98.9%, 99.8%, 95.3% and 96.4% for HMFA, BHMF, PEA and PEAM, respectively. To measure the sustainability of the downstream process, the specific material intensity, energy intensity, wastewater intensity, greenhouse gas (GHG) emissions, toxic emissions and pollutant emissions were calculated for a unit of output. The unit of output was

considered as a kg of product (i.e., HMFA, BHMF, PEA and PEAM).

The material intensity refers to the mass of wasted materials per unit of output. The non-recovered products were considered as wasted material resulting in a value of 0.020 $kg_{wasted}/kg_{product}$. The energy intensity criterion took into account both thermal and electric energy consumers (e.g., pumps, reboilers, etc.). The proposed process requires 4.36 MW electrical energy and 3.72 MW thermal energy. The overall energy requirement was calculated utilizing an electrical-to-thermal conversion factor of 2.5 [15] resulting in a value of 34.88 kWh/ $kg_{product}$. This value is mostly due to the low concentration of the mixture after reaction, the incoming stream containing 30.82 tonnes of water. The significant energy intensity does not thwart the feasibility of the process as the prices of the obtained products range from 0.5$/kg to 50$/kg.

In the calculation of wastewater intensity water that requires wastewater treatment per kilogram of product was considered (i.e., stream WASTEW1 and WASTEW2) resulting in 86.04 $kg_{wastewater}$/ $kg_{product}$. The large wastewater intensity can be attributed to the enzymatic process, which leads to a mixture of products from 20 to 30 mM. In addition, the usage of less concentrated solutions in the downstream process necessary to avoid the formation of Bronsted acids/bases (e.g., 2M NaOH) increases both the processes' energy and wastewater intensity.

For the calculation of GHG emissions, only off-site emissions were considered as there are no gaseous emission in the designed process. The off-site emissions considered were those related to electricity and steam generation. For calculations, the data from 2023 regarding EU-27 GHG emissions intensity for electricity generation used, i.e., 0.21 $kg_{CO_2e}$/kWh [16]. The emission factor for steam generation was considered as 19.46 $kg_{CO_2e}$/MWh [17]. The GHG emissions value per unit of output is 2.26 $kg_{CO_2e}$/ $kg_{product}$. These emissions could be reduced utilizing regenerable energy sources, however a more in-depth study is required to investigate the trade-off with other sustainability indices.

Toxic emissions were calculated as the mass of toxics and hazardous materials for the operating personnel present in the output streams per unit of output, other than the intended product streams. The compounds' toxicity was determined based on their material safety data sheet, as such, toxic emissions value of 0.042 $kg_{toxic}$/ $kg_{product}$ was obtained. Pollutants were considered as the non-toxic material present in the output streams, except the four product streams. In this manner, pollutant emissions were calculated as $2.00 \square 10^{-5}$ $kg_{pollutant}$/ $kg_{product}$. The negligible amount of pollutants is due to the toxicity of most materials present in the system, therefore special attention should be paid towards the treatment of generated wastewater.

## CONCLUSIONS

The proposed downstream process concerning the four value-added HMF derivatives (HMFA, BHMF, PEA and PEAM) showed that each product can be separated with purities of at least 97 wt% comparable to those found on the market, obtained through non-enzymatic pathways. This efficient downstream configuration presents an overall recovery of over 98% of the value-added derivatives.

The studied process is suitable for production of natural chemicals, which can be essential taking into account the use of the obtained products such as food and pharmaceutical industry. Although high value-added products are obtained in the studied system, an economic assessment is required to investigate the influence of the proposed separation and purification process on the feasibility of the industrial scale from an economic standpoint, which is the scope of future work.

## ACKNOWLEDGEMENTS

This study was supported from the project "Advanced (multi)-enzymatic synthesis and purification processes for bio-based furan derivatives – ASPIRE" (CF 25/14.11.2022).

## REFERENCES

1. van Putten R.-J., van der Waal J.C., de Jong E., Rasrendra C.B., Heeres H.J., de Vries J.G., Hydroxymethylfurfural, A Versatile Platform Chemical Made from Renewable Resources. *Chem Rev* 113:1499–1597 (2013) https://doi.org/10.1021/cr300182k
2. Tursi A., A review on biomass: importance, chemistry, classification, and conversion. *Biofuel Res J* 6 :962–979 (2019) https://doi.org/10.18331/BRJ2019.6.2.3
3. Rosatella A.A., Simeonov S.P., Frade R.F.M., Afonso C.A.M., 5-Hydroxymethylfurfural (HMF) as a building block platform: Biological properties, synthesis and synthetic applications. *Green Chem* 13:754 (2011) https://doi.org/10.1039/c0gc00401d
4. Bin Abdul Rani M.A.A., Karim N.A., Kamarudin S.K., Recent reaction systems for the syn-thesis of 5-hydroxymethylfurfural (HMF) from carbohydrates with process development analysis: A review. *Int J Energy Res* 46:18996–19050 (2022) https://doi.org/10.1002/er.8545
5. Jiang Z., Zeng Y., Hu D., Guo R., Yan K., Luque R., Chemical transformations of 5-hydroxymethylfurfural into highly added value

products: present and future. *Green Chem* 25:871–892 (2023) https://doi.org/10.1039/D2GC03444A
6. Wang Y., Brown C. A., Chen R., Industrial production, application, microbial biosynthesis and degradation of furanic compound, hydroxymethylfurfural (HMF). *AIMS Microbiol* 4:261–273 (2018) https://doi.org/10.3934/microbiol.2018.2.261
7. Kucherov F.A., Romashov L. V., Galkin K.I., Ananikov V.P., Chemical Transformations of Biomass-Derived C6-Furanic Platform Chemicals for Sustainable Energy Research, Materials Science, and Synthetic Building Blocks. *ACS Sustain Chem Eng* 6:8064–8092 (2018) https://doi.org/10.1021/acssuschemeng.8b00971
8. Sheldon R.A., Woodley J.M., Role of Biocatalysis in Sustainable Chemistry. *Chem Rev* 118:801–838 (2018) https://doi.org/10.1021/acs.chemrev.7b00203
9. Saikia K., Rathankumar A.K., Kumar P.S., Varjani S., Nizar M., Lenin R., George J., Vaidyanathan V.K., Recent advances in biotransformation of 5-Hydroxymethylfurfural: challenges and future aspects. *J Chem Technol Biotechnol* 97:409–419 (2022) https://doi.org/10.1002/jctb.6670
10. Vaidyanathan V.K., Saikia K., Kumar P.S., Rathankumar A.K., Rangasamy G., Dattatraya G.S., Advances in enzymatic conversion of biomass derived furfural and 5-hydroxymethylfurfural to value-added chemicals and solvents. *Bioresour Technol* 378:128975 (2023) https://doi.org/10.1016/j.biortech.2023.128975
11. Davidson M.G., Elgie S., Parsons S., Young T.J., Production of HMF, FDCA and their derived products: a review of life cycle assessment (LCA) and techno-economic analysis (TEA) studies. *Green Chem* 23:3154–3171 (2021) https://doi.org/10.1039/D1GC00721A
12. Kamkar J., Bagher R. M., Razieh A., Someyeh F., Mahdi Y., Shahrokh K., Firoozeh H., A Major Loss of Phenyl Ethyl Alcohol by the Distillation Procedure of Rosa damascene Mill. *Int J Med Plants By-Prod* 1:1–10 (2023) https://doi.org/10.22034/jmpb.2023.358636.1473
13. Post C., Maniar D., Voet V.S.D., Folkersma R., Loos K., Biobased 2,5-Bis(hydroxymethyl)furan as a Versatile Building Block for Sustainable Polymeric Materials. *ACS Omega* 8:8991–9003 (2023). https://doi.org/10.1021/acsomega.2c07629
14. Wen L., Zhang N., Li H., Huang Q., Wu X., Hao X., Wu M., Ban C., Zhao J., Ternary Liquid–Liquid Equilibrium for Mixtures of Water + (±)α-Phenylethylamine + n -Hexane at T = 298.2, 318.2, and 333.2 K. *J Chem Eng Data* 62:1819–1824 (2017) https://doi.org/10.1021/acs.jced.6b01064
15. Janković T., Sharma S., Straathof A.J.J., Kiss A.A., Adaptable downstream processing design for recovery of butanediols after fermentation. *Chem Eng Res Des* 213 210–220 (2025) https://doi.org/10.1016/j.cherd.2024.12.011
16. European Environment Agency, Greenhouse gas emission intensity of electricity generation in Europe. https://www.eea.europa.eu/en/analysis/indicators/greenhouse-gas-emission-intensity-of-1?activeAccordion=ecdb3bcf-bbe9-4978-b5cf-0b136399d9f8
17. U.S. Environmental Protection Agency, Emission Factors for Greenhouse Gas Inventories. https://www.epa.gov/sites/default/files/2021-04/documents/emission-factors_apr2021.pdf

© 2025 by the authors. Licensed to PSEcommunity.org and PSE Press. This is an open access article under the creative commons CC-BY-SA licensing terms. Credit must be given to creator and adaptations must be shared under the same terms. See https://creativecommons.org/licenses/by-sa/4.0/



Systems & Control Transactions

**Research Article - Peer Reviewed Conference Proceeding**
ESCAPE 35 - European Symposium on Computer Aided Process Engineering
Ghent, Belgium. 6-9 July 2025
Jan F.M. Van Impe, Grégoire Léonard, Satyajeet S. Bhonsale,
Monika E. Polańska, Filip Logist (Eds.)

PSE PRESS

# Solar Desalination and Porphyrin Mediated Visible-Light Photocatalysis in Decolouration of Dyes as Biological Analogues Applied in Advanced Water Treatment

**Evans M. N. Chirwa*, Bezza F. Andualem, Osemeikhain Ogbeifun, Shepherd M. Tichapondwa, Wesley Lawrence and Bonhle Manoto**

University of Pretoria, Department of Chemical Engineering, Pretoria, Gauteng, South Africa
* Corresponding Author: evans.chirwa@up.ac.za

## ABSTRACT

Engineering can be made simple and more impactful by observing and understanding how organisms in nature solve eminent problems. For example, scientists around the world have observed green plants thriving without organic food inputs using the complex photosynthesis process to kick-start a self-sustaining biochemical food chain. In this study, two biological analogues for advanced water treatment, i.e., visible-light photocatalysis using porphyrin-$Bi_{12}O_{17}Cl_2$ and $BiOIO_3$ compounds and interfacial solar desalination by a by Reduced Graphene Oxide-Black $TiO_2$ (rGO-Black $TiO_2$) were investigated. For the visible-light photocatalytic process for dye decolouration, a porphyrin@$Bi_{12}O_{17}Cl_2$ system was applied to successfully degrade Rhodamine B dye in batch experiments, achieving up to 79% degradation within 240 minutes. These results show that more advances and more efficient engineered systems can be achieved by observing nature and how these systems have survived over billions of years. The rGO-Black $TiO_2$ system achieved increases in temperature for 25oC to 60oC in less than 5 seconds. Based on these observations, the research group from the Water Utilisation Group at the University of Pretoria have studied and developed fundamental processes for the degradation and remediation of unwanted compounds such as disinfection byproducts (DBPs), volatile organic compounds (VOCs) and pharmaceutical products from water.

**Keywords**: solar desalination, heterogenous photocatalysis, 3D-printed Graphene Oxide, advanced water treatment, biological analogues.

## INTRODUCTION

### Desalination

The crucial demand for sustainable and eco-friendly desalination technologies propelled by renewable energy is essential for overcoming global water scarcity. Solar desalination has been recognised as a prominent technology as it exploits solar energy to produce clean water through sufficient thermal management and the localisation of heat using a solar absorber [1].

Currently, Reverse osmosis (RO) is the most broadly used process for saline water treatment, as well as industrial and drinking water. Roughly 53 % of the feed water for RO systems is seawater followed by mostly brine, fresh water, and treated wastewater. The multi-stage flash (MSF) and multi-effect distillation (MED) are the second and third most used technologies, respectively. Reverse osmosis, MED and MSF technologies constitute 94 % of the overall desalinated water produced. Solar-powered desalination via photovoltaic desalination and solar thermal evaporation constitute less than 1 %. Of the global freshwater desalinated, membrane-based processes account for 71 % of the total capacity produced and thermal processes make up the other 29 %. This displays the historical mass application of membrane-based desalination technologies. The advantage of utilising seawater RO or brackish water RO is due to the total energy costs of seawater RO (3 – 4 kWh·m-3) and brackish water RO (0.5 – 2.5 kWh·m-3) desalination being lower than the energy required for thermal desalination

technologies such as MSF (14 – 25.5 kWh·m-3) and MED (6.5 – 11 kWh·m-3) which requires the use of electrical and thermal energy. The energy cost difference between seawater RO and brackish water RO is due to brackish water having a substantially lower osmotic pressure compared to seawater and thus requiring less energy. The high salinity concentration of seawater limits the osmosis process due to affecting the osmosis pressure, requiring more energy. However, the economic cost of seawater desalination using MSF or MED is proportionate to that of RO as a result of the lower investment costs. The availability and cost of energy account for more than 30 % of the total desalination cost. It is estimated that the present global desalination capacity roughly consumes a minimum of 75.2 TWh annually, which is equivalent to 0.4 % of the global electricity usage.

Solar-driven absorbers generally involve a mono or bi-layer design, comprising a solar-light absorber and a floating substrate. The solar absorber converts incident light into heat energy, while the floating substrate facilitates water transfer to the active vapour generation site and minimising heat energy loss through conduction [2].

The ongoing challenge of salt accumulation on the surface of the solar absorber as a result of the high salt concentration in the bulk water body leads to the obstruction of light absorption, subsequently hindering freshwater vapour release and efficient photothermal efficiency [1].

Recent research motivated by the modification of natural saline inhabiting vegetation (halophyte plants) has been employed to embrace the biomimetic principle for numerous engineering practices such as freshwater steam generation and salt rejection [3] Naturally, plants possess inherent capabilities which harness solar energy and groundwater in the photosynthesis process to create oxygen and carbohydrates. For example, trees make use of their trunk and leaves for continuous nutrient and water transfer for nourishment. This principle has inspired wood-based solar absorbers for solar steam generation. For example, carbon nanotube-modified flexible wood membranes [4] and graphite-coated wood solar absorbers [5] have demonstrated great potential.

Sun *et al.* proposed a three-dimensional (3D) solar evaporator inspired by the outer shell structure of Vasticardium vertebratum, demonstrating a 95% evaporation efficiency and a superb evaporation rate of 1.73 kg/m$^2$·h while effectively preventing salt accumulation [3]. Furthermore, mangrove-inspired configurations [6] provide promising potential aimed at bio-mimicking solar absorbers. This is driven by the inherent water transfer and salt-tolerant characteristics of mangrove trees which regulate water and ion absorption [6]. Solar absorbers utilising a graphene oxide-reduced graphene oxide (GO-rGO) lotus leaf-inspired Janus film [7] or mangrove-mimicked designs have displayed efficient photothermal conversion performance and high evaporation rates of seawater [8].

Black titanium dioxide ($TiO_2$) has the ability to absorb immense ultraviolet-visible (UV-Vis) light for chemical or electrical energy conversion owing to the enhanced photocatalytic performance from the introduction of lattice disorder. Black $TiO_2$ can be obtained by establishing oxygen vacancies and $Ti^{3+}$ doping into the $TiO_2$ lattice using chemical reduction [9]. The combination of carbon-based materials such as GO with $TiO_2$ has displayed a synergistic effect between the two constituents as the photoactive $TiO_2$ integrates with the adsorption potential imparted by carbon. Carbon can assist in charge separation and obstruct electron-hole recombination in $TiO_2$ [10] .

The bio-inspired structural fabrication of rGO was designed for water and heat transfer abilities similar to that of plant root cells. Black $TiO_2$ can be utilised to minimise light reflection and efficiently absorb light across the UV-near infrared region, inspired by black snake scales.

## Photocatalysis

Recently, photocatalysis has garnered attention for pollution mitigation. The technology is amenable to visible light activation which make up 42%–43% of the solar spectrum [11]. To cut down on greenhouse gases emission, the leaning towards solar-driven processes is unavoidable. Solar energy is renewable and abundant.

In Photocatalytic process semiconductor photocatalyst, materials are activated by sufficient photon to generate electrons ($e^-$) and holes ($h^+$) [12]. The $e^-$ and $h^+$ in subsequent reaction with dissolved $O_2$ and $H_2O$ produce superoxide anion radicals ($\bullet O_2^-$) and hydroxyl radicals (.OH), with the ability to destroy adsorbed pollutant on the photocatalyst [13-15].

Generation of abundant $e^-$ and $h^+$, separation and boosting redox ability is crucial for material performance. These have been achieved via plasmon resonance effect [16]heterojunction formation [17], ion doping [18], photosensitization effect [19] and other strategies. In photosensitization strategy light sensitive or absorbing material such as porphyrin are apply to photocatalyst enhance visible light utilization [20], and ultimately the photocatalytic ability of photocatalyst.

Porphyrins are organic molecules are similar to the structure of chlorophyll in plant. They are efficient absorber of visible light, producing a photochemical reaction [21]. Porphyrin can be modified into different shapes sucha s rods, hexagonal, hollow spheres, tubes [22]. The complexity of versatility of in terms of assembly of the molecules make them useful in various application including photocatalysis. Porphyrin have been combined with graphite carbon nitrides [23]; $Fe_3O_4$ [24]; $TiO_2$ [25], BiOCl [26], ZnO nanofiber composite [27], graphene [28] and $Bi_{12}O_{17}Cl_2$ [29], where they demonstrated enhanced

photodegradation in comparison with individual porphyrin and the inorganic photocatalyst components.

Solar desalination is viewed as one of the most sustainable ways of dealing with the global energy challenge with emerging technological advancements. The technology is highly efficient in that the solar energy is targeted at the interface between a water surface and solar absorbing material to achieve evaporation with minimal energy losses. In addition, notable innovations can be found in adsorption desalination and energy-efficient freeze desalination. The work outlined here has been patented by several leading researchers around the world but no full-scale plant has not yet been built to demonstrate the economic feasibility of this technology at the date of publication of this article.

## APPLICATIONS AND PERFORMANCES OF MATERIALS

### Performance of $TiO_2$/rGO in Desalination

Excellent solar absorption potential across the UV-Vis solar spectrum for solar absorbers is crucial for achieving efficient desalination [30]. As presented in Figure 1, the black $TiO_2$/rGO composite exhibited remarkable light absorption potential across the ensure UV-Vis region in comparison to white $TiO_2$ which displayed good UV light absorption with almost no visible light absorption and rGO showed excellent visible light absorption, however, the light absorption across the UV spectrum was similar to that of white $TiO_2$. Therefore, demonstrating the enhanced light absorption performance of the composite where the beneficial attributes of each component act synergistically.

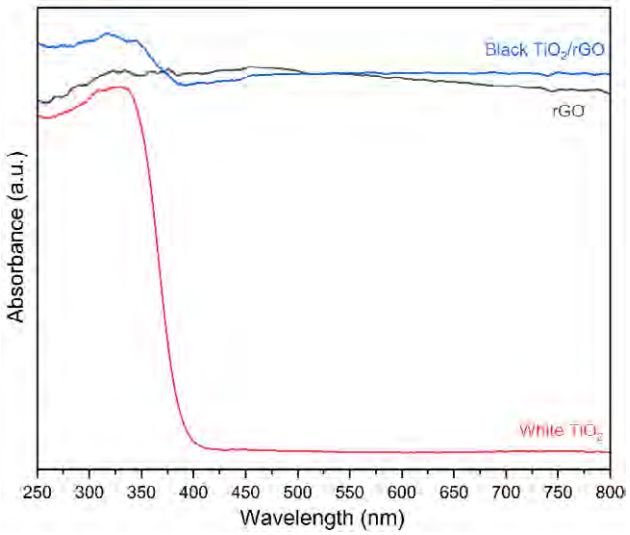



**Figure 1.** UV-Vis DRS spectra of rGO, white $TiO_2$, and black $TiO_2$/rGO.

In solar-driven desalination, the water evaporation rate can be determined using [31].

$$v = \frac{\Delta m}{A \times t} \quad (1)$$

Where v is the evaporation rate (kg/m²·h), Δm is the change in mass due to water evaporation (kg), A represents the evaporation area (m²), and t is the duration of the evaporation process (h). The photothermal conversion or steam generation efficiency, $\eta$, can be determined using [5] :

$$\eta = \frac{v \cdot H_{LV}}{P} \quad (2)$$

$$H_{LV} = h_v + C\Delta T \quad (3)$$

Where $H_{LV}$ is the total liquid-vapour phase change enthalpy, P is the solar power density (1 kW/m²), $h_v$ represents the latent heat of vaporisation (kJ/kg), C is the specific heat capacity of water (4.2 kJ/kg·K), and ΔT is the temperature increase of water (K). The freshwater vapour generation (Figure 2b) was determined to be 1.19 kg/m²·h with an 82.38% photothermal conversion efficiency. The solar absorber displayed a surface temperature increase of 23.8°C (Figure 2a) within 120 min of commencing the desalination test. Furthermore, the bio-inspired solar absorber demonstrated effective salt rejection of the surface owing to the small interlayer spacings and the negatively charged surface of the rGO nanopores.

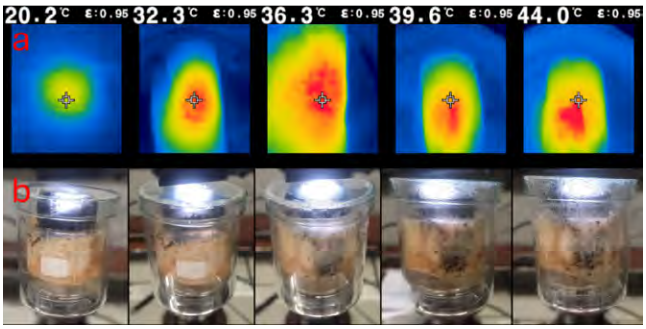



**Figure 2.** IR thermal images of the black $TiO_2$/rGO solar absorber (a) and photos of the solar desalination test (b) taken every 30 min.

### Performance of Porphyrin/$Bi_{12}O_{17}Cl_2$ in Pollutant Degradation

Tetrakis (4-carboxyphenyl) porphyrin (TCPP), a member of porphyrin, coupling with $Bi_{12}O_{17}Cl_2$ improved its performance. First, TCPP was modified to a rod shape and applied to $Bi_{12}O_{17}Cl_2$ to form composites.

The degradation study was carried out using Rhodamine as a model pollutant. The experiment involved a simple batch degradation study in a beaker, where TCPP-Bi12O17Cl2 composite was dispersed in the solution of Rhodamine dyes. The reaction was sufficiently stirred in

the dark to achieve absorption-desorption equilibrium. Thereafter, it was irradiated with visible light to initiate the photocatalytic degradation of the dye. The result of dye degradation overtime on the materials 0.02%wtTCPP-$Bi_{12}O_{17}Cl_2$,0.4%wtTCPP-$Bi_{12}O_{17}Cl_2$ 1%wtTCPP-$Bi_{12}O_{17}Cl_2$, $Bi_{12}O_{17}Cl_2$, TCPP are presented in Figure 3. Within 240 min, the 52%, 68%, 79%, 40% and 20% degradation were achieved.

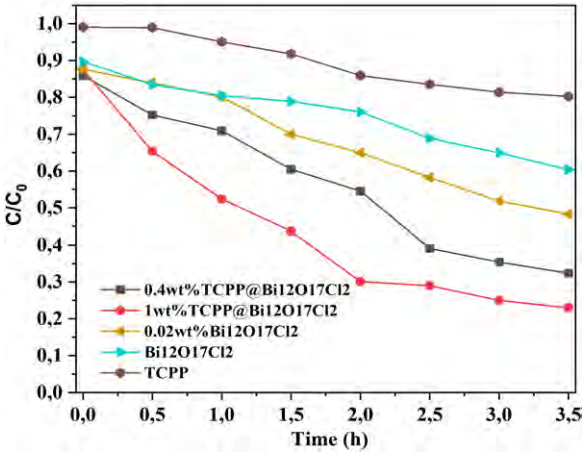



**Figure 3**. Photocatlytic decolourization of Rhodamine B dye

The performance of the TCPP/$Bi_{12}O_{17}Cl_2$ was attributed to the expanded visible light response and composite/heterojunction formation. Figure 4(a) shows the shift of the absorption edge of pristine $Bi_{12}O_{17}Cl_2$ with the introduction of TCPP. The enhanced visible light response favoured increased electrons and hole generation from the sufficient capture of the visible light by the porphyrin molecules. Figure 4(b) shows the material's Electrochemical impedance spectroscopy (EIS). Data from EIS provide transport and separation of electrons and holes. A smaller semi-circle observed with TCPP-load $Bi_{12}O_{17}Cl_2$ indicates superior transport and separation of the photogenerated electron and hole, the reason for the strengthened photodegradation activity of the dye.

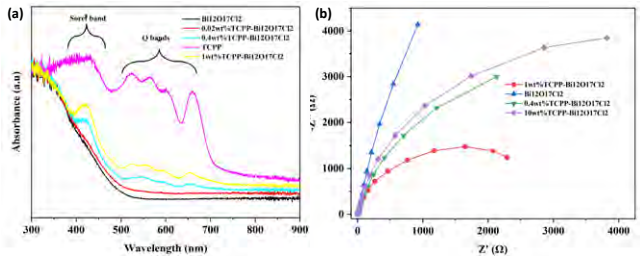



**Figure 4**. UV vis DRS (a) and EIS spectra of material (b)

When porphyrin-$Bi_{12}O_{17}Cl_2$ is exposed to visible light, electrons are excited from the highest occupied molecular orbital (HOMO) to the lowest unoccupied molecular orbital (LUMO) [32]. These excited electrons in the LUMO are subsequently transferred to the conduction band (CB) of the host material [25], effectively separating them from the corresponding holes [33]. This separation enhances the photocatalytic efficiency of the system.

## CONCLUSION AND FUTURE WORK

In summary, the bioinspired 3D black $TiO_2$/rGO solar absorber demonstrated efficient freshwater evaporation and photothermal conversion efficiency. This can be attributed to the successful mimicking of plant root cells for water transfer and the light absorption ability of black snake scales. These results show the promising potential for further advancing bioinspired photothermal solar absorbers.

Also, using porphyrin, a biological analogue of chlorophyll, proved advantageous for visible light capture in the porphyrin-$Bi_{12}O_{17}Cl_2$ system for pollutant degradation.

This work reported on one example of the porphyrin-$Bi_xO_yX_z$ system, TCPP-$Bi_{12}O_{17}Cl_2$. The porphyrin-$Bi_xO_yX_z$ system is diverse considering the many forms of porphyrin structures and morphologies available, as well as $Bi_xO_yX_z$. Further exploration of the combinations, therefore, in the system holds potential in photocatalysis. Porphyrin-$BiOIO_3$ is also proposed, where the visible light absorption of $BiOIO_3$ enhancement is envisaged. Comparatively, $BiOIO_3$ has good electron and hole separation upon activation. However, it cannot be activated due to the wide gap energy, hence the proposed composite with porphyrin.

## ACKNOWLEDGEMENTS

The study was funded by the National Research Foundation (NRF) through Grant No's. SRUG2204072544 and EQP180503325881 and Rand Water Company, through Grant No. RW01413/18 awarded to Prof E.M.N. Chirwa, and The NRF Thuthuka Fund Grant No. TTK18024324064 awarded to Prof S.M. Tichapondwa at the University of Pretoria

## REFERENCES

1. Wu L, Dong Z, Cai Z, Ganapathy T, Fang NX, Li C, Yu C, Zhang Y, Song Y, 2020. Highly efficient three-dimensional solar evaporator for high salinity desalination by localized crystallization. *Nature Communications*. 11:521. 10.1038/s41467-020-14366-1 (2020)
2. Dai X, Guan H, Wang X, Wu M, Jiang P, Chai Y, Wang X, 2024. Apple leaf-inspired bilayered Janus wood evaporator with decoupled light-vapor interfaces for high-efficiency solar steam generation. *Chem Eng J*. 499:155796.

https://doi.org/10.1016/j.cej.2024.155796 (2024)
3. Sun S, Shi C, Kuang Y, Li M, Li S, Chan H, Zhang S, Chen G, Nilghaz A, Cao R, Tian J, 2022. 3D-printed solar evaporator with seashell ornamentation-inspired structure for zero liquid discharge desalination. *Water Res.* 226:119279. https://doi.org/10.1016/j.watres.2022.119279 (2022)
4. Liu H, Chen C, Chen G, Kuang Y, Zhao X, Song J, Jia C, Xu X, Hitz E, Xie H, Wang S, Jiang F, Li T, Li Y, Gong A, Yang R, Das S, Hu L, 2018. High-Performance Solar Steam Device with Layered Channels: Artificial Tree with a Reversed Design. *Advanced Energy Materials.* 8:1701616. https://doi.org/10.1002/aenm.201701616 (2018)
5. Li T, Liu H, Zhao X, Chen G, Dai J, Pastel G, Jia C, Chen C, Hitz E, Siddhartha D, Yang R, Hu L, 2018. Scalable and Highly Efficient Mesoporous Wood-Based Solar Steam Generation Device: Localized Heat, Rapid Water Transport. *Adv Funct Mater.* 28:1707134. https://doi.org/10.1002/adfm.201707134 (2018)
6. Wang Y, Lee J, Werber JR, Elimelech M, 2020. Capillary-driven desalination in a synthetic mangrove. *Science Advances.* 6:eaax5253. doi:10.1126/sciadv.aax5253 (2020)
7. Han D-D, Chen Z-D, Li J-C, Mao J-W, Jiao Z-Z, Wang W, Zhang W, Zhang Y-L, Sun H-B, 2020. Airflow Enhanced Solar Evaporation Based on Janus Graphene Membranes with Stable Interfacial Floatability. *ACS Applied Materials & Interfaces.* 12:25435-25443. 10.1021/acsami.0c05401 (2020)
8. Abdelsalam MA, Sajjad M, Raza A, AlMarzooqi F, Zhang T, 2024. Sustainable biomimetic solar distillation with edge crystallization for passive salt collection and zero brine discharge. *Nature Communications.* 15:874. 10.1038/s41467-024-45108-2 (2024)
9. Tudu BK, Gupta V, Kumar A, Sinhamahapatra A, 2020. Freshwater production via efficient oil-water separation and solar-assisted water evaporation using black titanium oxide nanoparticles. *J Colloid Interface Sci.* 566:183-193. https://doi.org/10.1016/j.jcis.2020.01.079 (2020)
10. Ghumro SS, Lal B, Pirzada T, Qazi MA, Ali A, Altaf AA, Thebo KH, Kazi M, 2025. Exploring the hetero-catalytic proficiencies of pristine and carbon-doped titania nanocatalysts in dye degradation and their synergetic profiles against bacteria. *J Mol Struct.* 1319:139462. https://doi.org/10.1016/j.molstruc.2024.139462 (2025)
11. Hassaan MA, El-Nemr MA, Elkatory MR, Ragab S, Niculescu V-C, El Nemr A, 2023. Principles of Photocatalysts and Their Different Applications: A Review. *Top Curr Chem.* 381:31. 10.1007/s41061-023-00444-7 (2023)
12. Khan K, Tareen AK, Aslam M, Sagar RUR, Zhang B, Huang W, Mahmood A, Mahmood N, Khan K, Zhang H, Guo Z, 2020. Recent Progress, Challenges, and Prospects in Two-Dimensional Photo-Catalyst Materials and Environmental Remediation. *Nano-Micro Letters.* 12:167. 10.1007/s40820-020-00504-3 (2020)
13. Arumugam M, Choi MY, 2020. Recent progress on bismuth oxyiodide (BiOI) photocatalyst for environmental remediation. *Journal of Industrial and Engineering Chemistry.* 81:237-268. https://doi.org/10.1016/j.jiec.2019.09.013 (2020)
14. Wang Y, Shi Z-q, Fan C-m, Hao X-g, Ding G-y, Wang Y-f, 2012. Synthesis of BiOCl photocatalyst by a low-cost, simple hydrolytic technique and its excellent photocatalytic activity. *International Journal of Minerals, Metallurgy, and Materials.* 19:467-472. 10.1007/s12613-012-0581-7 (2012)
15. Lal M, Sharma P, Singh L, Ram C, 2023. Photocatalytic degradation of hazardous Rhodamine B dye using sol-gel mediated ultrasonic hydrothermal synthesized of ZnO nanoparticles. *Results in Engineering.* 17:100890. https://doi.org/10.1016/j.rineng.2023.100890 (2023)
16. Zhang M, Bi C, Lin H, Cao J, Chen S, 2017. Construction of novel Au/Bi12O17Cl2 composite with intensive visible light activity enhancement for contaminants removal. *Mater Lett.* 191:132-135. https://doi.org/10.1016/j.matlet.2016.12.089 (2017)
17. Bi C, Cao J, Lin H, Wang Y, Chen S, 2016. BiOI/Bi12O17Cl2: A novel heterojunction composite with outstanding photocatalytic and photoelectric performances. *Mater Lett.* 166:267-270. https://doi.org/10.1016/j.matlet.2015.12.089 (2016)
18. Yang Y, Zeng Y, Jin T, Zhang X, Teng H, Wang S, Chen H, 2022. Construction of oxygen vacancy on Bi12O17Cl2 nanosheets by heat-treatment in H2O vapor for photocatalytic NO oxidation. *Journal of Materials Science & Technology.* 123:234-242. https://doi.org/10.1016/j.jmst.2022.02.018 (2022)
19. Ye L, Su Y, Jin X, Xie H, Zhang C, 2014. Recent advances in BiOX (X = Cl, Br and I) photocatalysts: synthesis, modification, facet effects and mechanisms. *Environmental Science: Nano.* 1:90-112. 10.1039/C3EN00098B (2014)
20. Zheng H, Chen G, Zhang A, Tan Z, Wang R, Wang H, Mei Y, Zhang X, Ran J, 2021. Enhanced photocatalytic activity of Bi24O31Br10 microsheets constructing heterojunction with AgI for Hg0 removal. *Sep Purif Technol.* 262:118296. https://doi.org/10.1016/j.seppur.2020.118296 (2021)

21. Joseph M, Haridas S, 2020. Recent progresses in porphyrin assisted hydrogen evolution. *Int J Hydrogen Energy.* 45:11954-11975. https://doi.org/10.1016/j.ijhydene.2020.02.103 (2020)
22. Medforth CJ, Wang Z, Martin KE, Song Y, Jacobsen JL, Shelnutt JA, 2009. Self-assembled porphyrin nanostructures. *Chem Commun.* 7261-7277. 10.1039/B914432C (2009)
23. Mei S, Gao J, Zhang Y, Yang J, Wu Y, Wang X, Zhao R, Zhai X, Hao C, Li R, Yan J, 2017. Enhanced visible light photocatalytic hydrogen evolution over porphyrin hybridized graphitic carbon nitride. *J Colloid Interface Sci.* 506:58-65. https://doi.org/10.1016/j.jcis.2017.07.030 (2017)
24. Rabbani M, Rafiee F, Ghafuri H, Rahimi R, 2016. Synthesis of Fe3O4 nonoparticles via a fast and facile mechanochemicl method: Modification of surface with porphyrin and photocatalytic study. *Mater Lett.* 166:247-250. https://doi.org/10.1016/j.matlet.2015.12.087 (2016)
25. Wang H, Zhou D, Wu Z, Wan J, Zheng X, Yu L, Phillips DL, 2014. The visible light degradation activity and the photocatalytic mechanism of tetra(4-carboxyphenyl) porphyrin sensitized TiO2. *Mater Res Bull.* 57:311-319. https://doi.org/10.1016/j.materresbull.2014.06.017 (2014)
26. Zhao P, Huang Y, Chen J, Shao S, Miao H, Xia J, Jia C, Hua M, 2020. Preparation of meso-tetraphenyl porphyrin modified defect-rich BiOCl with enhanced visible-light photocatalytic activity for antibiotic degradation and mechanism insight. *Journal of Photochemistry and Photobiology.* 3-4:100014. https://doi.org/10.1016/j.jpap.2020.100014 (2020)
27. Vo HT, Nguyen AT, Tran CV, Nguyen SX, Tung NT, Pham DT, Nguyen DD, La DD, 2021. Self-Assembly of Porphyrin Nanofibers on ZnO Nanoparticles for the Enhanced Photocatalytic Performance for Organic Dye Degradation. *ACS Omega.* 6:23203-23210. 10.1021/acsomega.1c02808 (2021)
28. La DD, Rananaware A, Salimimarand M, Bhosale SV, 2016. Well–dispersed assembled porphyrin nanorods on graphene for the enhanced photocatalytic performance. *ChemistrySelect.* 1:4430-4434. https://doi.org/10.1002/slct.201601001 (2016)
29. Ogbeifun O, Tichapondwa SM, Chirwa EMN, 2023. Self-assembled micro and nano rod-shaped porphyrin@Bi12O17Cl2 composite as an efficient photocatalyst for degradation of organic contaminants. *Discover Nano.* 18:137. 10.1186/s11671-023-03915-4 (2023)
30. Bezza FA, Iwarere SA, Brink HG, Chirwa EMN, 2024. Design and fabrication of porous three-dimensional Ag-doped reduced graphene oxide (3D Ag@rGO) composite for interfacial solar desalination. *Scientific Reports.* 14:13793. 10.1038/s41598-024-62987-z (2024)
31. Liu X, Zhu Q, Qian Y, Wu W, 2025. Enhanced photothermal interface evaporation via coupling of Ag-GO aerogel with thermal insulation substrate. *Sep Purif Technol.* 360:131080. https://doi.org/10.1016/j.seppur.2024.131080 (2025)
32. Moshari M, Rabbani M, Rahimi R, 2016. Synthesis of TCPP–Fe3O4@S/RGO and its application for purification of water. *Res Chem Intermed.* 42:5441-5455. 10.1007/s11164-015-2378-6 (2016)
33. Zhang Z, Liu H, Xu J, Zeng H, 2017. CuTCPP/BiPO4 composite with enhanced visible light absorption and charge separation. *Journal of Photochemistry and Photobiology A: Chemistry.* 336:25-31. https://doi.org/10.1016/j.jphotochem.2016.12.020 (2017)

© 2025 by the authors. Licensed to PSEcommunity.org and PSE Press. This is an open access article under the creative commons CC-BY-SA licensing terms. Credit must be given to creator and adaptations must be shared under the same terms. See https://creativecommons.org/licenses/by-sa/4.0/



Systems & Control Transactions

**Research Article - Peer Reviewed Conference Proceeding**
ESCAPE 35 - European Symposium on Computer Aided Process Engineering
Ghent, Belgium. 6-9 July 2025
Jan F.M. Van Impe, Grégoire Léonard, Satyajeet S. Bhonsale,
Monika E. Polańska, Filip Logist (Eds.)

PSE PRESS

# Technical Assessment of direct air capture using piperazine in an advanced solvent-based absorption process

**Shengyuan Huang[a], Olajide Otitoju[a], Yao Zhang[a], Meihong Wang[a]***

[a] School of Chemical, Materials and Biological Engineering, The University of Sheffield, Sheffield S1 3JD, UK
* Corresponding Author: meihong.wang@sheffield.ac.uk.

## ABSTRACT

Climate and environmental problems caused by increasing $CO_2$ concentration in the atmosphere make the direct air capture (DAC) technology having great prospects for development. As the widely used solvent in carbon capture based on chemical absorption processes, MEA still fails to address the issues of high energy consumption and high costs when used in DAC process. In this study, piperazine (PZ) was used as the new solvent for DAC process. The new configuration was simulated in Aspen Plus® V11 and the model was validated through experimental data and model comparison. It is followed by investigation of the potential for energy efficiency and cost reduction. The standard DAC-PZ configuration could reduce the reboiler duty from 10.7 GJ/t$CO_2$ to 8.9 GJ/t$CO_2$ for DAC-MEA process. Economic analysis will be carried out through Aspen Process Economic Analyzer®. Further analysis (e.g. sensitivity analysis for different parameters and optimisation) will be performed to further reduce the energy consumption and cost for the DAC-PZ process with different configurations.

**Keywords**: direct air capture, chemical absorption, process simulation

## INTRODUCTION

### Background and motivation

The concentration of $CO_2$ in the atmosphere is increasing for several decades. In November 2024, it has reached 423 ppm [1]. Carbon capture is essential to combat the ecological problems such as global warming associated with increased carbon emissions. Among all the carbon capture technologies, direct air capture (DAC), as a negative emission technology, has great potential for development to capture 980Mt $CO_2$ in 2050 according to the IEA Net Zero Emissions Scenario.

In the conventional solvent-based carbon capture process, MEA is the most commonly used solvent [2]. Nevertheless, MEA has a series of disadvantages which affects the improvement of the performance for carbon capture process. In comparison, PZ offers better performance and is more economical. Replacing MEA with PZ in the DAC process provides a new alternative for the DAC process to reduce energy consumption and costs.

### Literature review

The solvent-based carbon capture process is widely used. The process is based on chemical reactions between solvent and carbon dioxide which enables selective capture of specific components from the flue gas. In Canepa et al. [3], a solvent-based carbon capture process using MEA solvent was integrated with a combined cycle gas turbine (CCGT) power plant. Exhaust gas recirculation (EGR) technology was proposed to reduce the energy consumption for solvent regeneration. Luo and Wang [4] combined the solvent-based carbon capture process with nature gas combined cycle (NGCC) power plant. In addition to the traditional power plants, Hu et al. [5] applied the carbon capture process using MEA for treating flue gas from thermal cracking furnace in ethylene manufacturing. By recovering the excess heat from the gasoline fractionator, the energy consumption and capture cost could be reduced.

With minor modification of solvent-based carbon

capture, it can be used for DAC. Kiani et al. applied a conventional carbon capture process using MEA solvent for DAC. An economic performance analysis of the whole system confirmed the potential of this approach to reduce the cost of DAC [6]. Michailos integrated the air absorber with a traditional post-combustion carbon capture (PCC) absorber column to reduce the energy consumption for DAC. [7].

PZ is a better replacement of MEA in carbon capture studies due to its higher absorption capacity and heat degradation resistance. The performance parameters of two different concentrations of PZ comparing with MEA are presented in Table 1. Otitoju et al. used PZ in PCC process for NGCC power plant. PZ with higher performance could reduce the total energy consumption from 5.34GJ/t$CO_2$ with 30wt% MEA to 3.56GJ/t$CO_2$ with 30wt% PZ [8]. Ma et al. also used PZ instead of MEA in the carbon capture process for the ethylene plant. With flue gas heat recovery, the energy consumption could be reduced by 37.71% compared to the standard MEA configuration, while costs can be lowered by 36.76% [9]. These highlighted the significant potential of PZ solvents in the carbon capture field.

**Table 1:** Performance parameters of different solvents [8]

| Parameter | 30wt% MEA | 30wt% PZ | 40wt% PZ |
|---|---|---|---|
| $K_L$@313K (mol/s Pa $m^2$) | 4.3 | 11.3 | 8.5 |
| Viscosity (Pa s) @313K | 0.0025 | 0.003 | 0.011 |
| $CO_2$ capacity ($mol_{CO2}/mol_{amine}$) | 0.5 | 0.63 | 0.79 |
| Thermal stability $T_{max}$ (K) | 393 | 436 | 436 |
| Max. regeneration Pressures (bar) | 2.2 | 14.3 | 14.3 |

## Novelty of this study

Several studies on the DAC process use packed bed column as shown in the literature review part. High energy consumption and high cost remain significant challenges to the commercial deployment of DAC technology. However, use of PZ solvent in DAC process offers the possibility to optimize the process. In this study, PZ was selected as solvent for DAC process inside a packed bed column. Through simulation, new results on energy consumption and capture cost will be obtained. In future work, sensitivity analysis for different process parameters and optimisation will be performed to further reduce the energy consumption and cost for the DAC.

## PROCESS DESCRIPTION

The process of standard solvent-based absorption process for DAC process using PZ solvent is shown in Fig. 1. The process contains absorber, stripper, splitter, pump and heat exchanger. The absorber and stripper are all packed bed column using Mellapak 250X packing. In contrast to the PCC process, since $CO_2$ concentration in the air is much lower than in the flue gas from power plants or chemical plants, the rich solvent from absorber needs to be diverted by a splitter. Majority of the solvent is returned to the top of absorber for re-absorption. This is to increase the liquid/gas ratio in absorber to meet the design requirements of a conventional packed bed column. The remaining small portion goes to the stripper for solvent regeneration. The regenerated solvent from stripper then undergoes a heat exchange process with the small portion rich solvent to decrease the energy penalty.

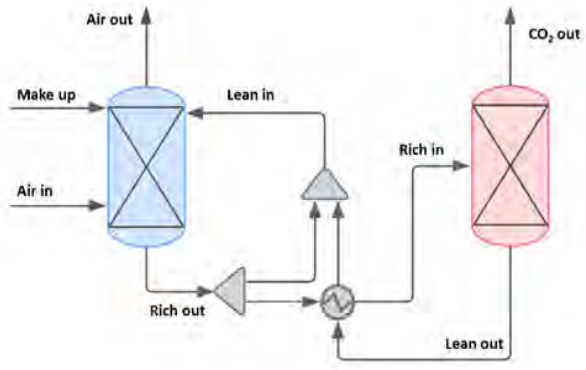



**Figure 1.** The process of standard DAC process using PZ.

## MODEL DEVELOPMENT

In this study, the DAC process using PZ was developed in Aspen Plus ® V11. The absorber and stripper are all rate-based models using RadFrac Block in the software. The rate-based model was used for reactions and physical properties. The liquid phase was calculated with Electrolyte Non-Random Two-Liquid (ElecNRTL) method. The vapour phase was calculated with the Redlich-Kwong equation of state. Equations (1) -(7) are equilibrium reactions for describing chemistry of $CO_2$ absorption with PZ solvent.

$$2H_2O \rightleftharpoons H_3O^+ + OH^- \quad (1)$$

$$CO_2 + 2H_2O \rightleftharpoons HCO_3^- + H_3O^+ \quad (2)$$

$$H_2O + HCO_3^- \rightleftharpoons CO_3^{2-} + H_3O^+ \quad (3)$$

$$PZH^+ + H_2O \rightleftharpoons PZ + H_3O^+ \quad (4)$$

$$PZ + HCO_3^- \rightleftharpoons PZCOO^- + H_2O \quad (5)$$

$$H^+PZCOO^- + H_2O \rightleftharpoons PZCOO^- + H_3O^+ \quad (6)$$

$$PZCOO^- + HCO_3^- \rightleftharpoons PZ(COO^-)_2 + H_2O \quad (7)$$

The equilibrium constants ($K_{eq}$) was calculated by equation (8) based on molar concentration scale. All

these chemical reactions and coefficients of the equilibrium constant are coming from reference studies [8].

$$In\ K_{eq} = A + \frac{B}{T} + C\ In\ T + DT \quad (8)$$

Equations (9) -(14) are kinetically controlled reactions for describing the rate of absorption.

$$CO_2 + OH^- \rightarrow HCO_3^- \quad (9)$$

$$HCO_3^- \rightarrow CO_2 + OH^- \quad (10)$$

$$PZ + CO_2 + H_2O \rightarrow PZCOO^- + H_3O^+ \quad (11)$$

$$PZCOO^- + H_3O^+ \rightarrow PZ + CO_2 + H_2O \quad (12)$$

$$PZCOO^- + CO_2 + H_2O \rightarrow PZ(COO^-)_2 + H_3O^+ \quad (13)$$

$$PZ(COO^-)_2 + H_3O^+ \rightarrow PZCOO^- + CO_2 + H_2O \quad (14)$$

The power law is described in equation (15) which determines the reaction rates ($k_j$). All parameters pre-exponential factor $k_j^o$ and activation energy $E_j$ for calculating the reaction rates of kinetically controlled reactions (9)-(14) are shown in Table 2.

$$k_j = k_j^o exp\left(-\frac{E_j}{RT}\right)\prod_N^{i=1} C_i^{aij} \quad (15)$$

**Table 2:** Kinetic parameters for reactions (9) -(14)

| Reaction No. | $k_j^o$ (m³/kmol s) | $E_j$ (kJ/kmol) |
|---|---|---|
| 9 | 4.32 e + 13 | 5.55 e + 4 |
| 10 | 2.38 e + 17 | 1.23 e + 5 |
| 11 | 4.14 e + 10 | 3.36 e + 4 |
| 12 | 7.94 e + 21 | 6.69 e + 4 |
| 13 | 3.62 e + 10 | 3.36 e + 4 |
| 14 | 5.56 e + 25 | 7.69 e + 4 |

## MODEL VALIDATION AND COMPARISON

Model validation is essential to verify the accuracy of the model. For this case, there is no experimental data for DAC process using PZ solvent. The model validation and comparison is divided into two parts: (a) The accuracy of PZ solvent for $CO_2$ capture is validated using experimental data from pilot plant at the University of Texas at Austin as presented in [10]. (b) The accuracy of the DAC process simulation using MEA is verified by comparing the simulation results of a DAC process using MEA solvent with those presented in [6].

### Model validation for Carbon Capture process using PZ solvent

The validation part for PZ used pilot plant data to test the model prediction accuracy for the absorber-only process. The pilot plant data is from the University of Texas at Austin. The flue gas mass flow rate is 0.165 m³/s. The $CO_2$ concentration in flue gas is 12vol%. The height of absorber is 6.1m, diameter is 0.427m and packing material is chosen as Mellapak 2X [10].

In this part, 5 cases were chosen with different concentration of PZ, L/G ration and lean loading as input. Two model prediction outputs: rich loading and capture level are compared with the experimental results. The relative error for different cases are shown in Table 3. By comparing model prediction results with experimental data, the errors across different cases were all kept within 10%. It proved that the model can simulate the performance of $CO_2$ absorption by PZ in the absorber.

### Model comparison for DAC process using MEA solvent

The DAC process using MEA solvent is simulated. The MEA concentration is chosen as 30 wt%. The capture level from air is set as 50%. The inlet air mass flowrate is 943t/h and $CO_2$ concentration in the air is assumed as 400 ppm. The ratio of rich solvent recirculation splitter is set the same to reach 2.54 L/G ratio (kg/kg) for absorber [6]. The impact of lean loading on the reboiler duty for DAC was considered and used as results for comparison. The simulation results compared with Kiani et al. [6] are shown in Figure 2. The simulation results have the same trend as Kiani et al. [6]. The relative error range is setting as 10% in the figure.

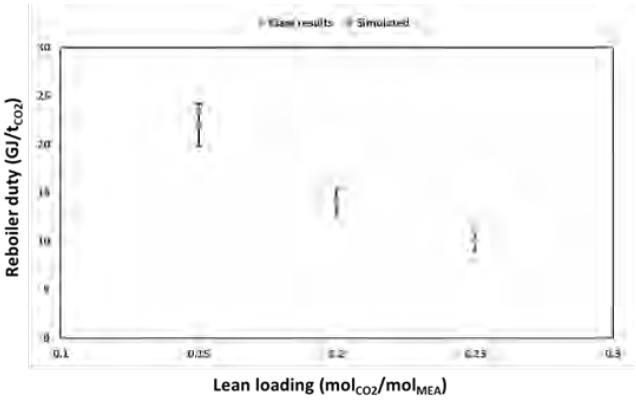



**Figure 2.** Comparison of simulation results with reference [6] on DAC process.

## CASE STUDY TO DETERMINE PZ SOLVENT CONCENTRATION

As we mentioned in the literature review, PZ has better performance as a replacement for MEA. Since the DAC-PZ process is different from other conventional PZ-based carbon capture studies, it is essential to determine the optimal PZ concentration.

This case study compared 30wt% PZ with 40wt% PZ in the absorber only DAC process. The lean loading was setting as 0.2 mol $CO_2$/mol alkalinity, the capture level of $CO_2$ from air was setting as 50%. The sensitivity analysis

**Table 3:** Validation results of comparing 5 experimental cases to model prediction values with relative error

| Input | | | Output 1 | | | Output 2 | | |
|---|---|---|---|---|---|---|---|---|
| PZ wt% | L/G (mol/mol) | Lean loading | Experimental Rich loading | Prediction Rich loading | Relative error | Experimental Capture level % | Model prediction Capture level % | Relative error |
| 30 | 5.5 | 0.257 | 0.360 | 0.391 | 8.6% | 78.3 | 82.4 | 5.3% |
| 30 | 6.8 | 0.274 | 0.360 | 0.386 | 7.2% | 88.6 | 90.2 | 1.8% |
| 40 | 5.5 | 0.285 | 0.340 | 0.355 | 4.4% | 85.9 | 88.6 | 3.2% |
| 40 | 6.7 | 0.267 | 0.340 | 0.334 | 1.9% | 92.2 | 91.3 | 1.0% |
| 40 | 5.5 | 0.308 | 0.370 | 0.358 | 3.2% | 66.6 | 61.1 | 8.3% |

of solvent flowrate on rich loading for 30wt% and 40wt% is shown in Figure 3. The solubility of aqueous solutions of PZ is also labelled in the right side. As indicated by the orange dashed line in Figure 3, excessively high or low loading can lead to solid formation in PZ solvent. 40wt% PZ has significantly narrow operational range compared to 30 wt% PZ although it has a higher $CO_2$ capacity. Meanwhile, the higher mass transfer rate and lower viscosity of 30 wt% PZ make it more suitable for the DAC-PZ process.

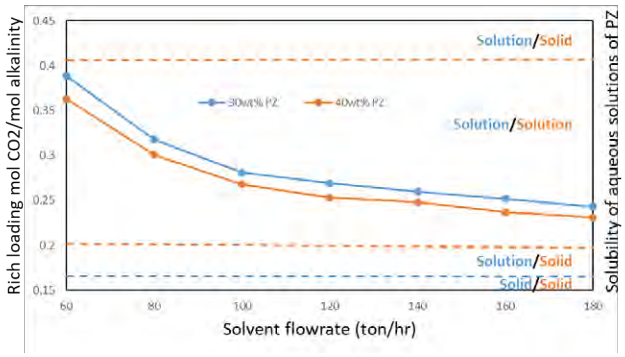



**Figure 3.** Sensitivity analysis of different solvent flowrate on rich loading with solubility area.

## CASE STUDY OF STANDARD DAC-PZ PROCESS

The standard DAC-PZ process was simulated as the closed-loop model. The operating parameters were listed in the Table 4. Due to the higher absorption capacity of PZ solvent compared to MEA, the rich solvent entering the stripper has a higher rich loading. The impact of solvent flowrate to stripper on the reboiler duty is shown in Figure 4 through sensitivity analysis. When the solvent flowrate is too low to the stripper, the rich loading of solvent will be above the highest operating range for PZ. When the solvent flowrate is too high, the reboiler duty will increase significantly because of the increasing heat requirement for water in solvent. In this case, the separation ratio of the splitter controlling the solvent circulation is different to DAC-MEA, with a different L/G ratio as 2.03 and liquid flowrate to stripper as 8.81 ton/hr.

**Table 4:** Operating conditions

| Operating conditions | |
|---|---|
| Inlet air temperature (K) | 298 |
| Air relative humidity (%) | 100 |
| $CO_2$ concentration in inlet air (ppm) | 400 |
| $CO_2$ captured (ton/hr) | 0.291 |
| $CO_2$ capture efficiency (%) | 50 |
| Flow rate of air (ton/hr) | 943 |
| PZ concentration (wt%) | 30 |
| L/G ratio in absorber (ton/ton) | 2.03 |
| Flooding capacity of absorber/stripper (%) | 70/65 |
| Packing type (Absorber and Stripper) | Mellapak 250X |
| Absorber pressure (bar) | 1 |
| Stripper pressure (bar) | 2 |
| Absorber diameter (m) | 9.8 |
| Absorber packing height (m) | 4 |

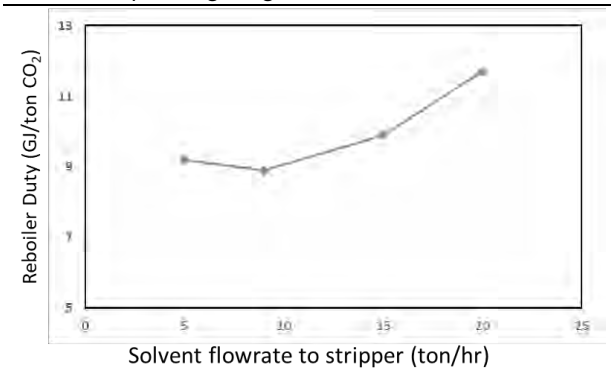



**Figure 4.** Impact of solvent flowrate to the stripper on reboiler duty.

The simulation results were presented in the Table

5. At a $CO_2$ production rate of 0.289 ton/hr, the reboiler duty is 8.9 GJ/t$CO_2$, which is 16.8% lower than the reboiler duty of 10.7 GJ/t$CO_2$ observed in the DAC process using MEA.

**Table 5:** Compare of simulation results between DAC-PZ and DAC-MEA process.

| Simulation results | DAC-PZ | DAC-MEA |
|---|---|---|
| Absorption liquid flow to stripper (ton/hr) | 8.81 | 9.12 |
| Absorber recirculation liquid flow (ton/hr) | 1905 | 2396 |
| $CO_2$ lean loading ($mol_{CO2}/mol_{alk}$) | 0.2 | 0.2 |
| $CO_2$ rich loading ($mol_{CO2}/mol_{alk}$) | 0.4 | 0.35 |
| Reboiler temperature (K) | 394 | 396.2 |
| $CO_2$ production (ton/hr) | 0.289 | 0.288 |
| Reboiler duty (GJ/hr) | 2.57 | 3.08 |
| Reboiler duty (GJ/t$CO_2$) | 8.9 | 10.7 |

## CONCLUSION AND FUTURE WORK

Using PZ solvent to replace MEA solvent in standard configuration of DAC process, the reboiler duty could reduce 16.8%. As a more efficient solvent with lower energy consumption, this study demonstrates that the application of PZ in the DAC process is promising.

Due to page limitations, the economic analysis of the standard DAC-PZ process is not presented in this paper. This part will be addressed in future work which will be carried out through Aspen Process Economic Analyzer®. Building on the standard configuration, this study will conduct further analyses, such as examining the impact of the separation factor of the circulating solvent on this system and the effect of different $CO_2$ concentration in the atmosphere on DAC-PZ process. Through different configurations, such as utilizing advanced flash stripper(AFS) and rich-split process, this study will perform energy and economic optimizations for the DAC-PZ system. Optimal design and operation for DAC process using PZ can be achieved.

## ACKNOWLEDGEMENTS

The authors would like to acknowledge the financial support of the EU RISE project OPTIMAL (Ref 101007963).

## REFERENCES

1. CO2.Earth (2024), https://www.co2.earth/
2. Wang, M., Lawal, A., Stephenson, P., Sidders, J. and Ramshaw, C. (2011). Post-combustion CO2 capture with chemical absorption: A state-of-the-art review. Chemical Engineering Research and Design, 89(9), pp.1609–1624. https://doi.org/10.1016/j.cherd.2010.11.005.
3. Canepa, R., Wang, M., Biliyok, C. and Satta, A. (2012). Thermodynamic analysis of combined cycle gas turbine power plant with post-combustion CO2 capture and exhaust gas recirculation. Proceedings of the Institution of Mechanical Engineers, Part E: Journal of Process Mechanical Engineering, [online] 227(2), pp.89–105. https://doi.org/10.1177/0954408912469165.
4. Luo, X. and Wang, M. (2016). Optimal operation of MEA-based post-combustion carbon capture for natural gas combined cycle power plants under different market conditions. International Journal of Greenhouse Gas Control, 48, pp.312–320. https://doi.org/10.1016/j.ijggc.2015.11.014.
5. Hu, G., Li, X., Liu, X., Hu, J., Otitoju, O., Wang, M., Du, W., Ye, Z., Long, J. and Qian, F. (2023). Techno-economic evaluation of post-combustion carbon capture based on chemical absorption for the thermal cracking furnace in ethylene manufacturing. 331, pp.125604–125604. https://doi.org/10.1016/j.fuel.2022.125604.
6. Kiani, A., Jiang, K. and Feron, P. (2020). Techno-Economic Assessment for CO2 Capture From Air Using a Conventional Liquid-Based Absorption Process. Frontiers in Energy Research, 8. https://doi.org/10.3389/fenrg.2020.00092.
7. Michailos, S., Samson, A., Lucquiaud, M. and Gibbins, J. (2022). A performance modelling study of integrating a MEA direct air capture unit with a CCGT absorber. SSRN Electronic Journal. https://doi.org/10.2139/ssrn.4283821.
8. Otitoju, O., Oko, E. and Wang, M. (2021). Technical and economic performance assessment of post-combustion carbon capture using piperazine for large scale natural gas combined cycle power plants through process simulation. Applied Energy, 292, p.116893. https://doi.org/10.1016/j.apenergy.2021.116893.
9. Ma, J., Dong, Z., Otitoju, O., Wang, M., Du, W. and Qian, F. (2024). Heat integration, process design and techno-economic assessment of post-combustion carbon capture using piperazine for large-scale ethylene plant. Chemical Engineering Science, 284, pp.119531–119531. https://doi.org/10.1016/j.ces.2023.119531.
10. J. M. Plaza and G. T. Rochelle, “Modeling pilot plant results for CO2 capture by aqueous piperazine,” Energy Procedia, vol. 4, pp. 1593–1600, 2011, doi: https://doi.org/10.1016/j.egypro.2011.02.029.

© 2025 by the authors. Licensed to PSEcommunity.org and PSE Press. This is an open access article under the creative commons CC-BY-SA licensing terms. Credit must be given to creator

and adaptations must be shared under the same terms. See https://creativecommons.org/licenses/by-sa/4.0/



Systems & Control Transactions

**Research Article - Peer Reviewed Conference Proceeding**
ESCAPE 35 - European Symposium on Computer Aided Process Engineering
Ghent, Belgium. 6-9 July 2025
Jan F.M. Van Impe, Grégoire Léonard, Satyajeet S. Bhonsale,
Monika E. Polańska, Filip Logist (Eds.)

PSE PRESS

# Valorization of refinery fuel gas and biogenic gases from thermochemical conversion into low-carbon methanol

**Eliana Lozano Sanchez[a]*, Erik Lopez-Basto[b,c], and Andrea Ramirez Ramirez [d]**

[a] Department of Energy, Aalborg University, Aalborg, Denmark
[b] Cartagena Refinery. Ecopetrol S.A., Colombia
[c] Department of Engineering Systems and Services, Faculty of Technology, Policy and Management, Delft University of Technology, Delft, The Netherlands
[d] Department of Chemical Engineering, Faculty of Applied Sciences, Delft University of Technology, Delft, The Netherlands
* Corresponding author: els@energy.aau.dk.

## ABSTRACT

By-product fuel gases from refinery operations are a major heat source in fossil refineries and their availability poses a challenge to the deployment of low-carbon heat sources. This study evaluates the valorization of refinery fuel gases (RFG) into low-carbon methanol via co-processing with residual biogenic gas streams from biomass thermochemical conversion. Results from techno-economic analysis indicate that up to 44 wt.% of biogenic blend is possible without the need for external hydrogen supply, while electricity and heat requirements per tonne of methanol change by -4 % and + 80% respectively. Nevertheless, at the 44 wt.% blend, the estimated methanol cost increases only by 2.4 % (0.43 EUR/kg), while the reduction in methanol carbon intensity is approximately 40 %. This highlights promising benefits that can contribute to the integration of bio-oils producing technologies within fossil refineries.

**Keywords**: Technoeconomic Analysis, Biomass, Refining, Biofuels, Process Design.

## INTRODUCTION

Heat decarbonization is a major strategy for fossil refineries to achieve emission reductions in the short/medium term. Direct electrification and other low carbon heat sources are expected to play a key role, however, availability of surplus refinery fuel gases (RFG) – a mixture of residual gases rich in hydrocarbons used for on-site heat generation - may limit decarbonization efforts if alternative uses for surplus RFG are not explored.

Excessive production of RFG and the challenge it brings for the implementation of energy reduction projects in refineries is not a new topic. Over the years, increasing emphasis on higher energy efficiency and lower emissions has resulted in less fuel consumption, making energy reduction projects less attractive in cases where these could result in flaring the RFG produced [1]. Some options discussed in literature to reduce RFG disposition are to increase hydrogen recovery in PSA/membrane units, improve liquid recovery in separators to reduce $C_{3+}$ components in the gas, optimize fuel system control to minimize fuel imports, or include co-generation units that use RFG to produce additional heat and power [1–3]. Nevertheless, there is a lack of studies that explore further utilization options, particularly in the context of the integration of biomass technologies that represent a valuable source of renewable carbon for refineries.

In recent years, there has been increasing interest in biomass thermochemical conversion technologies and particularly in bio-oil producing technologies such as fast pyrolysis (FP) and hydrothermal liquefaction (HTL) due to their potential to deliver drop-in biofuels that can be integrated within existing refinery infrastructure. Although co-processing of bio-oils has been extensively discussed in literature [4–6], there is a lack of studies that explore the integration of by-products within a refinery context to increase biogenic carbon conversion into valuable products.

This study presents a techno-economic assessment of co-processing by-product gases from biomass thermochemical conversion with RFG to produce methanol, a key chemical with high demand in industry and as shipping fuel. The impact of co-feeding HTL gas or FP gas

with RFG is evaluated in terms of overall carbon efficiency to methanol, energy requirements, methanol production cost and carbon intensity.

# METHODS

## Process description

A simplified process flow diagram of the system evaluated is presented in Figure 1. A mixture of surplus RFG and HTL or FP gas is converted into methanol following a two-step process: steam reforming to produce syngas and methanol synthesis via $CO_2$/CO hydrogenation. The RFG and HTL/FP gases are by-products of the refinery and biomass thermochemical conversion processes, respectively and are the starting point of this analysis.

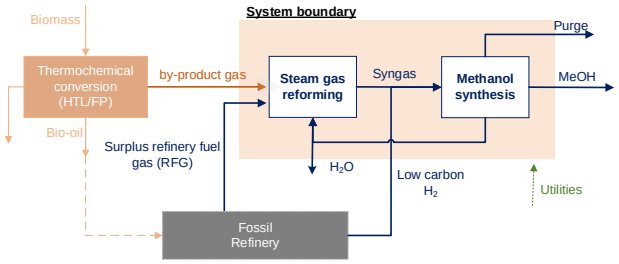



**Figure 1.** Simplified diagram of integrated biomass liquefaction in refinery context with co-processing of by-product gases for methanol synthesis.

**Table 1:** Composition of refinery fuel gas (RFG) and by-product gases from hydrothermal liquefaction (HTL) and fast pyrolysis (FP) of forestry residues (dry basis).

| | RFG | HTL gas | FP gas |
|---|---|---|---|
| Temperature [C] | 40 | 30 | 30 |
| Pressure [bar a] | 5.15 | 1 | 1 |
| Composition [mol%] | | | |
| $CO_2$ | 1.50 | 90.20 | 34.72 |
| Hydrogen | 38.22 | 0.90 | 0.00 |
| CO | 2.21 | 0.00 | 45.94 |
| Methane | 33.85 | 3.00 | 12.82 |
| Ethane | 16.44 | 2.50 | 1.50 |
| Ethylene | 0.00 | 0.00 | 5.02 |
| $C_3$ | 2.18 | 1.90 | - |
| $C_4$ | 2.23 | 1.50 | - |
| $C_{5+}$ | 1.78 | - | - |
| $H_2S$ | 1.59 | - | - |
| LHVstd [MJ/kg] | 46.96* | 3.30* | 9.99* |

The process is modelled in Aspen HYSYS V12.1 assuming a fixed RFG input of 25 tonne/h, which corresponds to an estimated RFG surplus in a refinery case study after initial emission reduction measures. The impact of gas co-processing is evaluated for increasing ratios of HTL gas or FP gas blended with RFG, from 0% (RFG case) to 100% (full biogenic carbon case), in terms of hydrogen requirement, carbon conversion to methanol, overall water balance and energy consumption. The analysis is performed for the HTL gas and FP gas separately. The composition of the input gas streams is presented in Table 1. The main process steps are briefly described in the following sections.

## Steam gas reforming (SMR)

The feed gases are pressurized to 30 bar, mixed with steam (steam/carbon ratio S/C= 4), pre-heated to 400 ℃ to enter the pre-reformer, and sent to the main steam reformer at 900 ℃. In the pre-reformer, conversion of $C_{2+}$ hydrocarbons to methane and hydrogen is favored at relatively lower temperatures, while endothermic steam reforming reactions are favored at higher temperatures in the main reformer. The produced syngas is cooled down to 30 ℃ to condense water that is reused for steam generation. The reformer is simulated as a furnace and a Gibbs reactor, so the heat requirement is the sum of the furnace duty and the reaction heat at 900 ℃. This configuration allows heat integration between the flue gases, reformer products and feeds, including the furnace fuel ($CH_4$) and air, resembling typical SMR configurations. Removal of $H_2S$ upstream the reactor is required to avoid catalyst poisoning and it is implemented for the RFG via caustic wash with NaOH; however, this step is not included for the HTL/FP gases since $H_2S$ was not reported in the data consulted [8].

## Methanol synthesis

Methanol is produced via catalytic hydrogenation of $CO_2$ and CO, in which a minimum ratio between hydrogen and carbon oxides is required (stoichiometric number, $SN=H_2-CO_2/CO_2+CO=2$). After reforming, the SN of the syngas is calculated and, if required, hydrogen is added to satisfy the minimum SN. The adjusted syngas is pressurized to 60 bar and preheated to 220 ℃ to enter the methanol synthesis reactor (Gibbs reactor) in which a reaction temperature of 250 ℃ is specified based on [7]. The reactor products are cooled down to 30 ℃ and separated at high pressure, with the unreacted gases being recirculated and the liquid products sent to distillation to obtain high purity methanol. A purge of 3% is included to avoid accumulation of inerts (unconverted hydrocarbons) in the system, and its potential use as fuel in the reformer furnace is evaluated (85 % furnace efficiency). Water obtained as by-product (99.9 mol%) is recirculated to the reforming process to decrease external water consumption for steam generation.

## Economic evaluation

An economic evaluation is conducted to assess the impact of co-processing in the methanol minimum selling price at increasing HTL/FP gas ratios. Capital and

operational expenses are estimated using the cost parameters in Table 2. In terms of Capex, purchase equipment costs of the SMR (including the heat supply system) and methanol production process reported in literature with reference year 2020 are adjusted to 2021 euros (EUR) and scaled to the required size using the CEPCI index and a scaling factor of 0.7. Fixed (FCI) and total capital investment (TCI) are estimated from the total purchase equipment costs (TPE) multiplied by a factor of 4.8 and 5.8 respectively [9]. In terms of feedstock, there is no reported selling price of RFG, HTL or FP gases since these are not traded as products but used (or expected to be used) for heat purposes. Consequently, their price is assumed to be proportional to the price of methane times the LHV ratio. Operation and maintenance (O&M) and other fixed costs (local taxes, insurance, plant overhead and administrative costs) are estimated based on detailed methodology in literature [10]. The methanol price is then estimated using a net present value (NPV) analysis with a 10% discount rate, straight line depreciation and a plant lifetime of 25 years.

**Table 2:** Cost parameters and assumptions used in the economic evaluation.

| | Base case | Low case | High case |
|---|---|---|---|
| **Equipment cost** | | | |
| SMR [$MEUR_{2020}$] [11] | 24.5 | -- | -- |
| (kt/d feed [a]) | (9.9) | | |
| MeOH synthesis [$MEUR_{2020}$] [12] | 15.7 | -- | -- |
| (kt/d MeOH) | (0.3) | | |
| **Variable costs** | | | |
| Natural gas (NG) price [EUR/GJ] [13] | 6.63 | 5.43 | 7.54 |
| RFG price [b] [EUR/GJ] | 6.23 | 5.10 | 7.08 |
| HTL gas price [b] [EUR/GJ] | 0.44 | 0.36 | 0.50 |
| FP gas price [b] [EUR/GJ] | 1.33 | 1.09 | 1.51 |
| Low carbon $H_2$ price [EUR/kg] | 2.50 [c] | 2.20 [d] | 4.60 [e] |
| Electricity price [EUR/MWh] [f] | 60.00 | 40.00 | 68.00 |
| Demineralized water price [EUR/$m^3$] | 0.51 | -- | -- |
| Cooling water price [EUR/$m^3$] | 0.42 | -- | -- |
| **Other parameters** | | | |
| Scaling factor | 0.70 | -- | -- |
| Hourly labor cost | 31.40 | -- | -- |
| Operators per shift | 6 | -- | -- |
| Furnace efficiency | 0.85 | -- | -- |
| Annual operation hours | 8000 | -- | -- |

a. SMR including heat supply system, scaled based on total feed mass flow (steam + natural gas).
b. Price estimated based on the gas calorific value relative to natural gas ($LHV_{gas}/LHV_{NG} * NG_{price}$).
c. Blue $H_2$ (NG SMR with carbon capture) based on natural gas price of 5.4 EUR/GJ [13].
d. Produced via electrolysis based on an electricity consumption of 53 kWh/kg H2 and capex of 315 EUR/kW [13]
e. Produced via electrolysis based on an electricity consumption of 59 kWh/kg H2 and capex of 575 EUR/kW [13]
f. Price range in line with wholesale electricity prices reported in Denmark and The Netherlands in 2021 [16]

## Carbon intensity of methanol

The impact of co-processing biogenic streams in the methanol carbon intensity is evaluated based on the main scope 1 emission reported in Table 3. $CO_2$ emissions from the RFG are calculated based on the carbon content, while no $CO_2$ equivalent is allocated to the HTL/FP gases. This assumption is considered reasonable since these are by-products of the bio-oil production process with very low energetic or economic value and would only yield biogenic $CO_2$ if they were to be used for heat purposes in the upstream process. Regarding the electricity and $H_2$ contributions, low and high emission scenarios are considered due to the well-known impact of the hydrogen source in the carbon intensity of synthetic fuels. An electricity carbon intensity between 50 and 250 kg $CO_2$eq/MWh is considered based on 2023 data for European countries such as France, Denmark and Netherlands [14]. Natural gas is assumed as make-up heating source, but up-stream leakage is not included in the analysis. The methanol carbon intensity is then estimated as the sum of the listed contributions for 0% to 100% biogenic blends with RFG.

**Table 3:** Scope 1 emission sources included in methanol carbon intensity estimation.

| Emission source | Base case | Low case | High case |
|---|---|---|---|
| Refinery fuel gas (RFG) [kg $CO_2$eq/h] | 65.48 | 65.48 | 65.48 |
| HTL/FP gas [kg $CO_2$eq/h] | 0.00 | 0.00 | 0.00 |
| Heating (Natural gas) [kg $CO_2$eq/MWh] | 15.58 | 15.58 | 15.58 |
| Electricity [kg $CO_2$eq/MWh] | 150.00 | 50.00 | 250.00 |
| Low carbon $H_2$ [kg $CO_2$eq/kg $H_2$] | 3.00[a] | 2.65[b] | 3.38[c] |

a. Defined in EU taxonomy based on GHG emission savings of 73.4% in comparison to the fossil fuel comparator of 94 g $CO_2$eq/MJ (https://ec.europa.eu/sustainable-finance-taxonomy/faq).
b. Calculated for electrolytic hydrogen based on an electricity consumption of 53 kWh/kg $H_2$ and carbon intensity of 50 kg $CO_2$eq/MWh.
c. Threshold in RFNBO regulation of 70 % reduction relative to fossil comparator of 94 g $CO_2$eq/MJ.

# RESULTS

## Impact of co-processing in mass balance

Figure 2 shows the distribution of reactants and products for increasing shares of HTL gas in the feed (see results of the FP gas case in the supplementary material). Regarding the reactants, there is a steady decrease in water consumption due to a combined effect of less hydrocarbons in the feed gas that reduce the steam input for SMR, plus increased water production from the methanol synthesis that gets recirculated. The reduction in the hydrocarbons content results in less $H_2$ in the syngas until SN=2 at 42.8 wt% blend, above which make-up

$H_2$ is required. This condition is met at a 44 wt% blend with FP gas due to its higher hydrocarbon content, however, for simplicity, the neutral-$H_2$ blend used for both cases is 44% in the rest of the discussion.

In terms of products, methanol production drops at increasing HTL gas shares, going from 41.2 t/h in the RFG case to 18.9 t/h in the HTL gas case (23.8 t/h for FP). This is a direct result of less carbon in the gas blend by increasing the $CO_2$ content. Although the carbon conversion is estimated between 84 and 90%, future studies including reaction kinetics are recommended for a more detailed assessment of the impact in conversion.

Figure 3 shows the overall mass balance for the $H_2$ neutral blend of 42.8 % HTL gas. Despite of not being within scope of the present study, the indirect biomass consumption for bio-oil production in the HTL process is estimated in 1.5 kt/d, being in the range of relatively large biomass conversion plants (2.2 kt/d in the FP gas). More detailed information on streams composition and process conditions can be found in the supplementary material.

## Impact of co-processing in energy needs

Electricity and heat requirements are summarized in Table 4 for 0%, 44 % and 100 % HTL gas blend with RFG. Overall, the total electricity use in the 44% case is the lowest evaluated due to a lower syngas flow, absence of external hydrogen, and thus less work required for compression (see details in supplementary material). Nevertheless, the specific electricity consumption is approximately the same as in the RFG case (0.2 MWh/t MeOH) due to the lower methanol production. The full biogenic cases exhibit much higher specific electricity consumption (0.44 and 0.39 MWh/t MeOH respectively) despite having about the same total requirement as the RFG case due to reduced methanol throughput.

**Table 4:** Energy consumption in 0%, 44 % and 100 % HTL gas blend with RFG.

| | 0 % | 44 % | 100 % |
|---|---|---|---|
| **Heat [MW]** | | | |
| Total heat requirement | 135.2 | 87.7 | 27.5 |
| Heat potential vent (LHV) | 111.1 | 35.3 | 12.3 |
| Net Heat requirement | 40.8 | 57.7 | 17.1 |
| Specific heat [MWh/t MeOH] | 1.0 | 1.9 | 0.9 |
| **Electricity [MW]** | | | |
| Total electricity requirement | 8.2 | 5.6 | 8.3 |
| Specific electricity [kWh/t MeOH] | 198.3 | 189.3 | 440.9 |

In terms of heat, the total demand decreases with increasing biogenic gas share due to less steam needed to maintain the same SMR S/C ratio. For all three cases, the unconverted gases have potential to reduce the SMR fuel input significantly; however, the specific heat required is substantial, being almost twice in the 44% blend (+82.8 % in the FP blend). Process modifications such as electrified SMR [15] or advanced distillation concepts for methanol production [7] are recommended in future studies to lower the heat requirement.

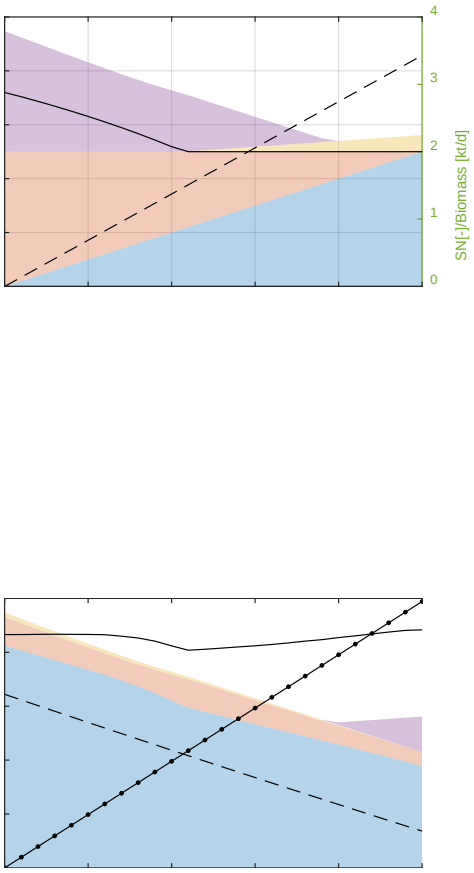



**Figure 2.** Change in mass flows with increasing share of HTL gas in blend with RFG (% in mass basis).

## Methanol production costs and carbon intensity

The results in Figure 4 show the trade-off between methanol cost and carbon intensity at increasing ratios of the biogenic carbon feeds. Co-processing of HTL gas increases the methanol production cost from 0.42 EUR/kg to 0.71 EUR/kg in the full HTL gas case. However, as observed in the plot, the increase is only marginal until 44% blend (+2.4 %) and becomes significant from this point onwards due to the growing $H_2$ requirement. The FP gas case shows the same trend, but the increase in cost is

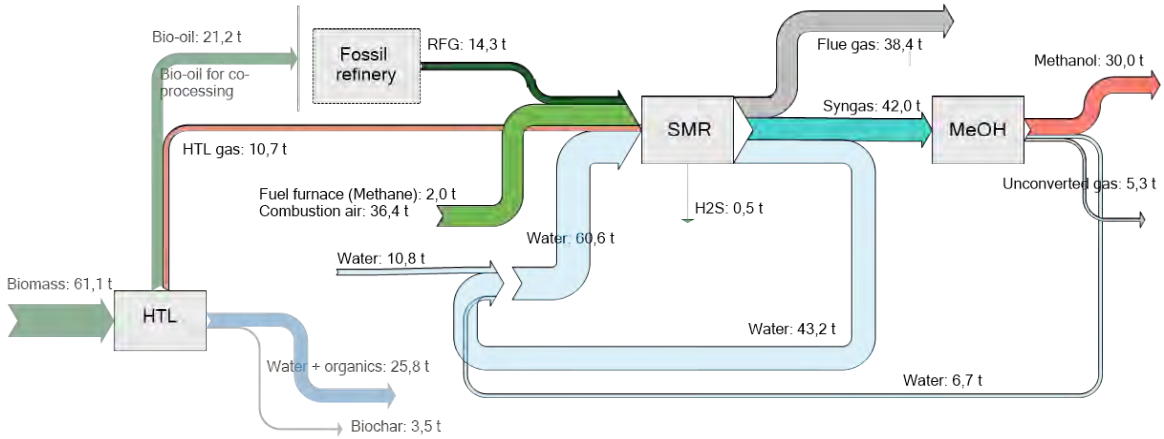



**Figure 3.** Mass Sankey diagram of HTL gas co-process with RFG (42.8 % case).

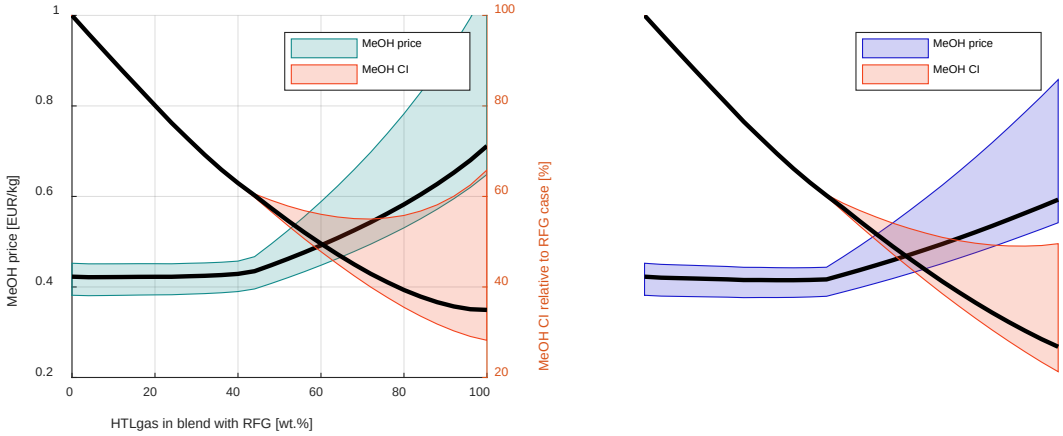



**Figure 4.** Mass Sankey diagram of HTL gas co-process with RFG (42.8 % case).

lower than for HTL due to slightly lower hydrogen needs and higher methanol production.

In the full biogenic feed cases, the estimated methanol carbon intensity is 27 and 36 kg $CO_2$eq/GJ, being in the range of the 65 % GHG reduction target by the REDIII relative to the fossil comparator (35.6 kg $CO_2$eq/GJ methanol). In these results, $H_2$ has by far the largest carbon footprint contribution followed by the electricity, causing variations in the estimated carbon intensity between -5% and + 30 % in the low and high scenarios considered. These could result in even higher emissions of the full biogenic case compared to the co-processing route, represented by the shadow areas in Figure 6. Lower variations in price and carbon footprint are observed up to the 44% blend since the $H_2$ impact is avoided. A life-cycle assessment of the integrated system is recommended in future studies for a more detailed evaluation of environmental impacts.

## CONCLUSIONS

- Co-processing by-product gases from thermochemical biomass conversion is deemed as a favorable strategy to valorize surplus RFG into low-carbon methanol, adding to the potential benefits of integrating bio-oil producing technologies within oil refineries.
- Co-processing 44% biogenic gas is identified as a suitable strategy that avoids the need of external $H_2$ supply. At this point, the estimated methanol cost is only 2.4 % higher than the RFG reference (0.43 EUR/kg), while the reduction in carbon intensity is approximately 40 %.
- The main impact of co-processing rich $CO_2$ streams with RFG is the reduction in methanol throughput. Although this increases the specific heat consumption (+89.5 %), the methanol cost is not affected significantly and the increased share of biogenic carbon in the product has a dominant positive impact.
- Detailed kinetics and LCA studies are recommended in the future to address the limitations of this study and further improve the analysis.

## DIGITAL SUPPLEMENTARY MATERIAL

The supplementary material can be consulted in http://PSEcommunity.org/LAPSE:2025.0014.

## ACKNOWLEDGEMENTS

This contribution was supported by a Danish research grant (VIL51464) from VILLUM FONDEN.

## REFERENCES

1. Rossiter, A. P. & Jones, B. P. Energy Management and Efficiency for the Process Industries. (John Wiley & Sons, Inc., Hoboken, New Jersey, 2015). doi:10.1002/9781119033226.
2. Nazerifard, R., Mohammadpourfard, M. & Zeinali Heris, S. Design, thermodynamic and economic evaluation, and optimization of gasoline production from refinery furnaces flue gas. Energy Convers Manag 293, 117492 (2023).
3. Zhou, L. et al. Energy configuration and operation optimization of refinery fuel gas networks. Appl Energy 139, 365–375 (2015).
4. Lindfors, C., Elliott, D. C., Prins, W., Oasmaa, A. & Lehtonen, J. Co-processing of Biocrudes in Oil Refineries. Energy & Fuels 37, 799–804 (2023).
5. Sharma, K., Pedersen, T. H., Toor, S. S., Schuurman, Y. & Rosendahl, L. A. Detailed Investigation of Compatibility of Hydrothermal Liquefaction Derived Biocrude Oil with Fossil Fuel for Corefining to Drop-in Biofuels through Structural and Compositional Analysis. ACS Sustain Chem Eng 8, 8111–8123 (2020).
6. van Dyk, S., Su, J., Mcmillan, J. D. & Saddler, J. (John). Potential synergies of drop-in biofuel production with further co-processing at oil refineries. Biofuels, Bioproducts and Biorefining 13, 760–775 (2019).
7. Vaquerizo, L. & Kiss, A. A. Thermally self-sufficient process for cleaner production of e-methanol by CO2 hydrogenation. J Clean Prod 433, 139845 (2023).
8. Tews, I. J. et al. Biomass Direct Liquefaction Options. TechnoEconomic and Life Cycle Assessment. https://www.osti.gov/biblio/1184983 (2014) doi:10.2172/1184983.
9. Seider, W. D., Seader, J. D. & Lewin, D. R. Product and Process Design Principles: Synthesis, Analysis, and Evaluation. (Wiley, 2004).
10. de Jong, S. et al. Cost optimization of biofuel production – The impact of scale, integration, transport and supply chain configurations. Appl Energy 195, 1055–1070 (2017).
11. Oni, A. O., Anaya, K., Giwa, T., Di Lullo, G. & Kumar, A. Comparative assessment of blue hydrogen from steam methane reforming, autothermal reforming, and natural gas decomposition technologies for natural gas-producing regions. Energy Convers Manag 254, 115245 (2022).
12. Vaquerizo, L. & Kiss, A. A. Thermally self-sufficient process for cleaner production of e-methanol by CO2 hydrogenation. J Clean Prod 433, 139845 (2023).
13. López-Basto, E., Korevaar, G., Tanzer, S. E. & Ramírez, A. R. Assessing the impacts of low-carbon intensity hydrogen integration in oil refineries. Cleaner Energy Systems 9, 100161 (2024).
14. Statista. Carbon intensity of the power sector in the European Union in 2023, by country. https://www.statista.com/statistics/1291750/carbon-intensity-power-sector-eu-country/#:~:text=Power%20sector%20carbon%20intensity%20in%20the%20European%20Union%202023%2C%20by%20country&text=Poland's%20power%20sector%20had%20the,just%20over%20530%20gCO%E2%82%82%2FkWh. (2024).
15. From, T. N. et al. Electrified steam methane reforming of biogas for sustainable syngas manufacturing and next-generation of plant design: A pilot plant study. Chemical Engineering Journal 479, 147205 (2024).
16. EMBER. https://ember-energy.org/data/european-electricity-prices-and-costs/

© 2025 by the authors. Licensed to PSEcommunity.org and PSE Press. This is an open access article under the creative commons CC-BY-SA licensing terms. Credit must be given to creator and adaptations must be shared under the same terms. See https://creativecommons.org/licenses/by-sa/4.0/



Systems & Control Transactions

**Research Article - Peer Reviewed Conference Proceeding**
ESCAPE 35 - European Symposium on Computer Aided Process Engineering
Ghent, Belgium. 6-9 July 2025
Jan F.M. Van Impe, Grégoire Léonard, Satyajeet S. Bhonsale,
Monika E. Polańska, Filip Logist (Eds.)

PSE PRESS

# System scale design and mesoscale modeling for natural gas dehydration process

**Zhehao Jin[a], Zhongde Dai[b], and Yiyang Dai[a]***

[a] Sichuan University, School of Chemical Engineering, Chengdu, Sichuan Province, China.
[b] Sichuan University, School of Carbon Neutrality Future Technology, Chengdu, Sichuan Province, China.
* Corresponding Author: daiyy@scu.edu.cn.

## ABSTRACT

Triethylene glycol (TEG) or mono-ethylene glycol (MEG) absorption are the commercial technologies for natural gas dehydration processes. Nevertheless, the necessity of regenerating solvents under high temperatures results in environmental footprint and complex operation. Membrane with advantages in small footprint and high feasibility operation in hostile conditions is considered as promising technology for natural gas dehydration processes. In this work, system scale design and mesoscale modelling are synchronously adopted to optimize natural dehydration process design. Aspen HYSYS with ChemBrane extension is used for natural gas dehydration process. Taking pressure ration, membrane area and sweep gas flowrate as decision variables for minimizing specific process cost is optimized through NSGA-II algorithms. The minimum specific cost of < $3.06\times10^{-2}$ \$/m$^3$ natural gas is estimated to achieve the separation requirement of <100 ppm. Then, the module length, and membrane thickness of the hollow fiber membrane design is investigated using Computational fluid dynamics (CFD), which better configures the simulation results and concentration, velocity profile to analyze the simulation results. The system scale engineering design and mesoscale modelling provide an in-depth insight into natural gas dehydration process.

**Keywords**: Natural gas dehydration, System scale design, Mesoscale design

## 1. INTRODUCTION

Natural gas (NG) proves to be a notably secure energy commodity during its transportation, storage and utilization processes [1]. Natural gas must be dried before enters distribution pipelines, otherwise it may corrode pipelines or form hydrocarbon [2]. Triethylene glycol (TEG) or mono-ethylene glycol (MEG) absorption are the commercial method for NG dehydration. However, the volatile organic compounds especially benzene, toluene, ethylbenzene, and xylenes will vent during absorption processes [3] and complex operating and control system restrict its application in remote and harsh environment [4,5]. Gas separation membrane with small footprint and no necessity for frequent parameter adjustments [6,7] is an attractive alternative for natural gas dehydration.

At the laboratory scale, the selectivity of water/methane can reach several thousand or even tens of thousands [8–12]. The gutter layer exists in membrane shows significant resistance to water vapor permeation which leads to the disparity in selectivity between laboratory-scale and pilot-scale conditions[13]. Lin et al. [13]evaluated a spiral-wound module for natural gas dehydration processes, results show that a low selectivity of 47 at 30-60 bar under field testing. However, the optimization of crucial parameters such as pressure ratio, sweep gas flowrate, and membrane area was not addressed in the aforementioned researches. He et al. conducted a hybrid membrane process for natural gas dehydration and sweeting, sensitivity analysis taking outlet pressure of each stage membrane as decision variable to minimize the specific NG processing cost. The research gap exists in the impact of flow and diffusion patterns of membrane is not been fully conducted.

In this work, a system scale design using Aspen HYSYS software with ChemBrane [14,15] extensions is used for natural gas dehydration process modeling, and pressure ratio, sweep gas flowrate, membrane area as decision variables to minimize the processing cost. The fluid

dynamic simulation of gas separation membranes is modeled by coupling laminar flow module and transport of concentrated species module. The effect of velocity distribution field and concentration field at the mesoscale on membrane efficiency are discussed.

## 2. METHODLOGY

### 2.1 Simulation basis

The natural gas produced from a natural gas processing plant in Qinghai Province, China. The natural gas with a total molar flowrate of 2571.29 kmol/h in water saturated at 308K, 4500kPa. The water content in the residue side of the gas separation membrane system must below 100ppm. Aspen HYSYS in conjunction with ChemBrane [15] was used to simulate the process conditions. The membrane used has a water vapor permeance of 983 gpu and water/methane selectivity of 47, the detailed information of other components permeance is shown in Table 2. The system scale design minimizes the specific cost of the natural gas dehydration process, taking pressure ratio, membrane area, and sweep gas flowrates as decision variables. Furthermore, the mesoscale design delves into the influence of parameters such as the inner and outer diameter and aspect ratio of the membrane on its performance. By examining the influence of different parameters across two distinct scales on membrane performance, aim to provide enhanced guidance for membrane structural design and industrial parameter selection.

**Table 1.** Typical compositions of gas streams at natural gas processing plant.

| Component | Molar flowrate(kmol/h) | Molar fraction (%) |
|---|---|---|
| Methane | 2502.5 | 0.9733 |
| Ethane | 1.77 | 0.0007 |
| Propane | 0.64 | 0.0003 |
| Hydrogen | 0.10 | 0.00004 |
| Water | 3.74 | 0.0015 |
| Carbon dioxide | 18.61 | 0.0072 |
| Nitrogen | 36.05 | 0.014 |
| Helium | 0.15 | 0.00006 |
| Oxygen | 7.70 | 0.003 |

**Table 2.** Gas permeance of membranes.

| Component | Gas permeance(mol(STP)/($m^2$·h·kPa)) |
|---|---|
| Methane | 0.023 |
| Ethane | 0.046 |
| Propane | 0.071 |
| Water | 1.217 |

### 2.2 System scale Design

#### 2.2.1 Process description

Natural gas dehydration process was conducted by HYSYS integrated with ChemBrane unit. The natural gas with saturated water content is gradually condensed through the cooler and then introduced into a gas-liquid separator to remove condensed water and heavy hydrocarbons. Subsequently, sent to the dehydration membrane unit, where the nitrogen gas used as sweep gas. The membrane unit operated in counter-current form and outlet natural gas water content need be less than 100 ppm. By system design, the appropriate pressure ratio, membrane area, and sweep gas flowrates can be determined to maximize the process economics. However, the system design is unable to determine parameters such as the inner and outer diameter thickness, aspect ratio, and distribution form of the membrane.

#### 2.2.3 Process parameters optimization

The most critical parameters in gas separation membranes unit are pressure ratio, sweep gas flowrate, and membrane area, as these factors directly determine the hydrocarbon loss and cost associated with dehydration processes. The membrane cost of \$50 per $m^2$ was used to estimate the dehydration membrane unit cost and a life time of the membrane was 5 years [14]. The cost functions regarding the heat exchanger, and separator are neglected. An annual interest rate of 7% was used for the calculation of annual capital cost. The price of electricity is 0.05\$/kWh used for operating cost of the compressors. The specific process cost model is shown in equation (1) [16].

$$CC^s = \frac{Capital\ related\ cost + OPEX}{Total\ NG\ production} \quad (1)$$

Figure 1. displays the schematic diagram of the optimization process. The range of variables is initially obtained through sensitivity analysis. Subsequently, generate the initial values of variables and input into the Aspen HYSYS software. Optimize the specific process cost while ensuring outlet natural gas water content is below 100 ppm. Provided that the obtained values do not meet the pre-defined criteria, the new parameters will be generated for next iteration.

### 2.3 Mesoscale modeling

#### 2.3.1 Computational fluid dynamic (CFD) simulation model

To date, the CFD simulation about natural gas dehydration process through membrane technology has not been reported. The optimized parameter values obtained through system design are incorporated into CFD model. In system design, the calculation can be performed by inputting the defined membrane area. At the CFD scale, the impact on membrane performance can be investigated by adjusting parameters such as the inner and outer

diameters, aspect ratio, and distribution of individual hollow fiber membranes. Modeling the mass transfer process and flow pattern of natural gas dehydration using the COMSOL software. Figure 2. illustrates the membrane structure in the simulations, encompassing the feed gas side, selective membrane, porous layer, and permeate side. The simulation process is conducted with the utilization of laminar flow module and transported of the concentrated spices. Given that the flow patterns and diffusion characteristics of the gas significantly influence this process, it is crucial to preserve the reliability of the flow pattern and diffusion mechanisms while simplifying the model. The following assumptions are considered during modeling.

1. The modeling is under steady-state conditions and in adiabatic conditions;
2. The diffusion mechanism is Fick's law;
3. The simulated fluid is Newtonian-type fluid and adheres to the ideal gas assumption;
4. The driving force for the transportation is pressure difference between feed and permeate side;
5. Hollow fiber membrane has uniform outer and inner diameters.

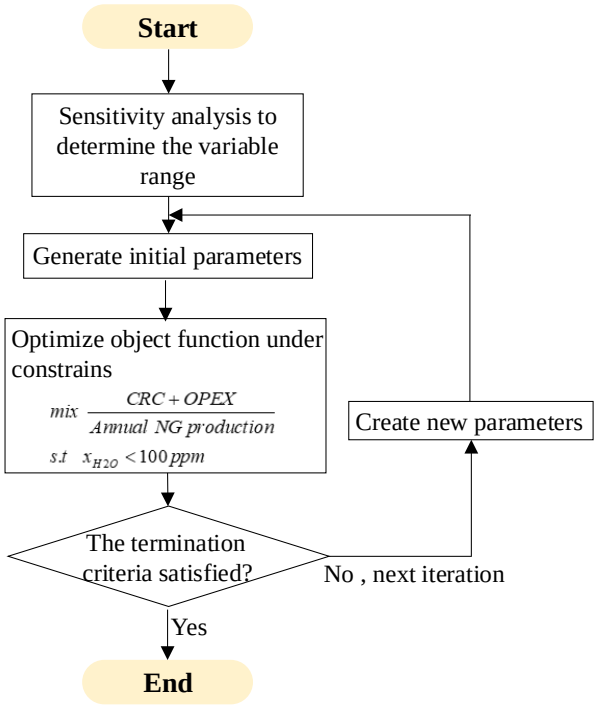



**Figure 1.** Schematic diagram of optimization process.

### 2.3.2 Numerical methods

The natural gas dehydration membrane modeling governing equation with the boundary conditions were solved utilizing COMSOL Multiphysics (6.2) software with the finite element method. Figure 2. displays the detailed mesh partitioning of the modeling, encompassing 404,487 degrees of freedom. The time required to solve a set of governing equations is 180 seconds. Table 3. presents pivotal parameters in CFD simulations, including the temperature and pressure distribution in both side of the membrane [17].

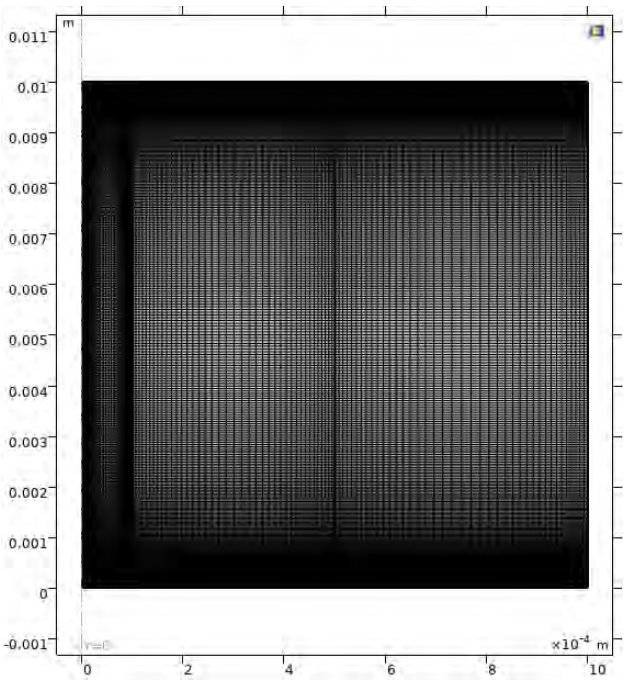



**Figure 2.** Mesh partitioning of the proposed model.

**Table 3.** The key input parameters for the proposed model.

| Parameters | Value | units |
|---|---|---|
| Temperature of inlet gas | 323 | K |
| Pressure of feed | 45 | Bar |
| Pressure of sweep gas | 0.8 | Bar |
| Permeance of $CH_4$ | 0.023 | mol(STP)/($m^2$·h·kPa) |
| Permeance of $H_2O$ | 1.217 | mol(STP)/($m^2$·h·kPa) |
| Diffusion coefficients of $CH_4$ | $2.32\times10^{-5}$ | $m^2/s$ |
| Diffusion coefficients of $H_2O$ | $1.66\times10^{-5}$ | $m^2/s$ |
| Dynamic viscosity of $CH_4$ | $1.058\times10^{-5}$ | Pa·s |
| Dynamic viscosity of $H_2O$ | $1.3\times10^{-5}$ | Pa·s |

## 3. RESULTS AND DISCUSSION

### 3.1 Process parameters optimization results

The optimization process selects specific costs as the objective function, using pressure ratio, membrane area, and sweep gas usage as decision variables, and applies the NSGA-II algorithm for optimization. The optimization range of decision variables is determined based on the results of sensitivity analysis.

**Table 4.** Decision variables ranges of the optimization process.

| Decision variables | Optimization range |
|---|---|
| Pressure ratio | [30,60] |
| Membrane area | [650,950] |
| Sweep gas flowrate | [150,300] |

The optimization process involves selecting the point with the minimum process cost to be incorporated into the operation. In this case, the permeate pressure is 0.8 bar, the membrane area is 850 $m^{2,}$ and the amount of sweep gas used is 150 kmol/h.

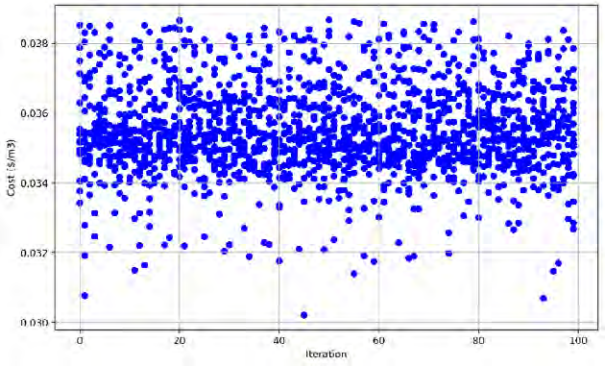



**Figure 3.** Optimization process scatter distribution.

At 4500 kPa, saturated natural gas passes through heat exchanger 1 (HX-1) and heat exchanger 2 (HX-2) to gradually lower the temperature before being sent to the gas-liquid separator (Sep). After removing condensate water and some heavy hydrocarbons, the gas is warmed up by HX-1 and then directed into a gas separation membrane unit for deep dehydration. By incorporating optimized parameters into the model, the water content in the outlet natural gas is 96 ppm, meeting the dehydration requirements, with a hydrocarbon loss rate of 3.00% and the specific cost of the process is 0.0306 $/$m^3$.

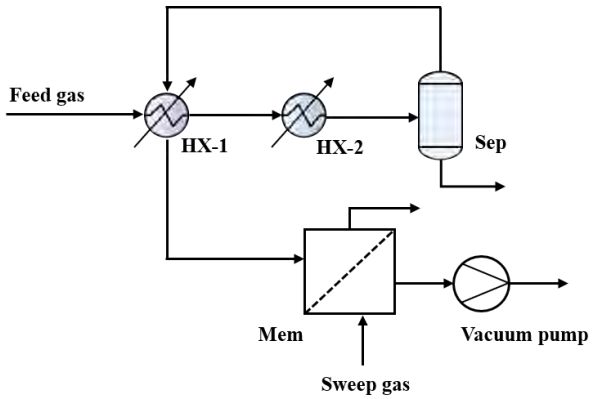



**Figure 4.** The flowchart of the natural gas dehydration process.

### 3.2 CFD simulation results

The velocity field and concentration field of water profile in the gas separation membrane are shown in Figures 5-6.

The velocity profile exhibits a parabolic distribution form, with the maximum flow velocity of 0.063m/s at the center of the pipe, while the velocity is reduced to 0.023m/s at the pipe wall due to the frictional force acting between the membrane selective layer. Furthermore, it is evident that the velocity remains undeveloped at the entrance zones of the feed side, with full development occurring as distance from the entrance increases. This observation underscores the significance of inlet effects on fluid flow hydrodynamics on the feed side. The velocity distribution on the shell side is determined through the solution of the Navier-Stokes equations and material balance equations.

Figure 6. describes the water concentration in the feed side of the feed side. The molar concentration of water in the natural gas feedstock decreased from 1.2 $mol/m^3$ to 0.18 $m^3/s$ at the outlet, successfully meeting the dehydration requirement of less than 100 ppm in the outlet natural gas. Moreover, the dehydration process exhibited a rational design as evidenced by the gradient changes in concentration curve, which showed good consistency with simulations performed using Aspen HYSYS software.

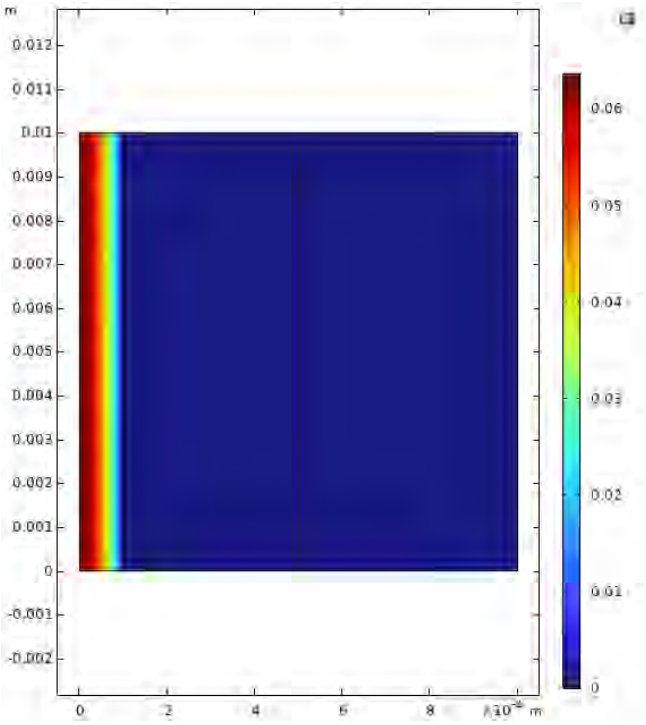


**Figure 5.** Field of velocity in the gas separation membrane

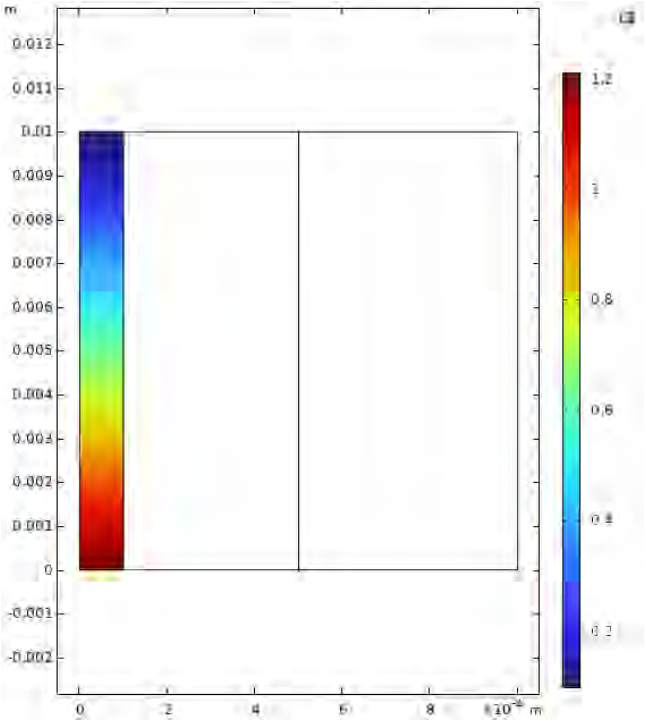


**Figure 6.** Concentration field of water in the feed side of the gas separation membrane.

## 4 CONCLUSION

The study employs a simultaneous approach of system scale design and mesoscale modeling to enhance the efficiency of natural dehydration process design. The natural gas dehydration process is conducted using Aspen HYSYS with ChemBrane extension. Decision variables such as pressure ratio, membrane area, and sweep gas flowrate are considered to minimize the specific process cost through optimization with NSGA-II algorithms. A minimum specific cost of 3.06×10-2 $/m$^3$ natural gas is projected to meet the separation requirement of 100 ppm. Subsequently, Computational Fluid Dynamics (CFD) is utilized to analyze the hollow fiber membrane design from the velocity and concentration profile, resulting in improved simulation outcomes. The integration of system scale engineering design and mesoscale modeling offers a comprehensive understanding of the natural gas dehydration process.

## ACKNOWLEDGEMENTS

The authors would like to thank the Sichuan Science and Technology Program for their financial support (Grant No. 2021YFH0116).

## REFERENCES

1. S. Faramawy, T. Zaki, A.A.-E. Sakr, Natural gas origin, composition, and processing: A review, Journal of Natural Gas Science and Engineering 34 (2016) 34–54. https://doi.org/10.1016/j.jngse.2016.06.030.
2. X. He, I. Kumakiri, M. Hillestad, Conceptual process design and simulation of membrane systems for integrated natural gas dehydration and sweetening, Separation and Purification Technology 247 (2020) 116993. https://doi.org/10.1016/j.seppur.2020.116993.
3. K. Ohlrogge, J. Wind, T. Brinkmann, Membrane Technology for Natural Gas Processing, in: 2002: p. SPE-75505-MS. https://doi.org/10.2118/75505-MS.
4. K. Dalane, Potential applications of membrane separation for subsea natural gas processing: A review, Journal of Natural Gas Science and Engineering (2017).
5. H. Lin, S.M. Thompson, A. Serbanescu-Martin, J.G. Wijmans, K.D. Amo, K.A. Lokhandwala, T.C. Merkel, Dehydration of natural gas using membranes. Part I: Composite membranes, Journal of Membrane Science 413–414 (2012) 70–81. https://doi.org/10.1016/j.memsci.2012.04.009.
6. R.W. Baker, K. Lokhandwala, Natural Gas Processing with Membranes: An Overview, Ind. Eng. Chem. Res. 47 (2008) 2109–2121. https://doi.org/10.1021/ie071083w.
7. R.W. Baker, Future Directions of Membrane Gas Separation Technology, Ind. Eng. Chem. Res. 41 (2002) 1393–1411. https://doi.org/10.1021/ie0108088.

8. M. Mulder, Basic principles of membrane technology, Springer science & business media, 2012.
9. V. Barbi, S.S. Funari, R. Gehrke, N. Scharnagl, N. Stribeck, SAXS and the Gas Transport in Polyether-b lock-polyamide Copolymer Membranes, Macromolecules 36 (2003) 749–758.
10. S.J. Metz, M.H.V. Mulder, M. Wessling, Gas-permeation properties of poly (ethylene oxide) poly (butylene terephthalate) block copolymers, Macromolecules 37 (2004) 4590–4597.
11. T. Watari, H. Wang, K. Kuwahara, K. Tanaka, H. Kita, K. Okamoto, Water vapor sorption and diffusion properties of sulfonated polyimide membranes, Journal of Membrane Science 219 (2003) 137–147.
12. J.S. Chiou, D.R. Paul, Gas permeation in a dry Nafion membrane, Industrial & Engineering Chemistry Research 27 (1988) 2161–2164.
13. H. Lin, S.M. Thompson, A. Serbanescu-Martin, J.G. Wijmans, K.D. Amo, K.A. Lokhandwala, B.T. Low, T.C. Merkel, Dehydration of natural gas using membranes. Part II: Sweep/countercurrent design and field test, Journal of Membrane Science 432 (2013) 106–114. https://doi.org/10.1016/j.memsci.2012.12.049.
14. X. He, Y. Chu, A. Lindbråthen, M. Hillestad, M.-B. Hägg, Carbon molecular sieve membranes for biogas upgrading: Techno-economic feasibility analysis, Journal of Cleaner Production 194 (2018) 584–593. https://doi.org/10.1016/j.jclepro.2018.05.172.
15. D. Grainger, Development of carbon membranes for hydrogen recovery, (2007).
16. Y. Chu, X. He, Process Simulation and Cost Evaluation of Carbon Membranes for CO2 Removal from High-Pressure Natural Gas, Membranes 8 (2018) 118. https://doi.org/10.3390/membranes8040118.
17. D.J. Jasim, T.J. Mohammed, H.N. Harharah, R.H. Harharah, A. Amari, M.F. Abid, Modeling and Optimal Operating Conditions of Hollow Fiber Membrane for CO2/CH4 Separation, Membranes 13 (2023) 557. https://doi.org/10.3390/membranes13060557.

© 2025 by the authors. Licensed to PSEcommunity.org and PSE Press. This is an open access article under the creative commons CC-BY-SA licensing terms. Credit must be given to creator and adaptations must be shared under the same terms. See https://creativecommons.org/licenses/by-sa/4.0/



Systems & Control Transactions

**Research Article - Peer Reviewed Conference Proceeding**
ESCAPE 35 - European Symposium on Computer Aided Process Engineering
Ghent, Belgium. 6-9 July 2025
Jan F.M. Van Impe, Grégoire Léonard, Satyajeet S. Bhonsale,
Monika E. Polańska, Filip Logist (Eds.)

PSE PRESS

# Digital Twin supported Model-based Design of Experiments and Quality by Design

**Amy Koch[a,b*], Jessica Ebert[a], Isabell Viedt[a,b], Andreas Bamberg[d], Leon Urbas[a,b,c]**

[a] Technische Universität Dresden, Process-to-Order Group, Process Systems Engineering
[b] Technische Universität Dresden, Process-to-Order Group, Process-to-Order Lab Learning Factory
[c] Technische Universität Dresden, Process-to-Order Group, Chair of Process Control Systems
[d] Merck Electronics KGaA
* Corresponding Author: amy.koch@tu-dresden.de.

## ABSTRACT

The pharmaceutical and specialty chemical industries are challenged with the requirement of faster time-to-process to meet market demands. Here, Modular Plants made up of predesigned process equipment assemblies (PEAs) are advantageous. Moreover, equipment-based Digital Twins of these modules can further reduce the time-to-process when combined with methods such as Quality by Design (QbD) and model-based design of experiments (MBDoE) to reduce uncertainty. This paper presents a lab scale-based workflow using an equipment-based Digital Twin, which applies QbD and MbDoE methods to identify the Design Space in the lab scale which can be transferred to production scale equipment as part of a Digital Twin based workflow for scale-up in Modular Plants.

**Keywords**: Digital Twins, Model-based Design of Experiments, Quality by Design, Scale-up

## MOTIVATION

In the specialty chemical and pharmaceutical industries, faster time-to-process is a significant measure of success. Here the use of predesigned modules according to VDI 2776 [1] are advantageous. Additional benefit can be derived by creating equipment-based Digital Twins of these modular process equipment assemblies which can be combined with multiple product descriptions. This further supports and expedites the process development phase in multipurpose plants by providing Digital Twin supported prior knowledge of equipment capabilities with multiple product descriptions. In addition to these Digital Twins, another method to support faster time-to-process is reducing experimental efforts in the process development phase using model-based methods. Here, Digital Twin workflows which incorporate methods such as Quality by Design (QbD), Global System Analysis, model-based design of experiments (MBDoE), and the identification of the Design Space as well as leveraging prior knowledge of the equipment capabilities can be utilized to reduce the experimental load [2]. Prior knowledge of equipment capabilities and limits is supplied by the Digital Twin and is used to pre-screen combinations of Critical Process Parameters (CPP), Critical Material Attributes (CMA), and model parameters to identify suitable parameter combinations for inclusion in the MBDoE optimization problem [3].

In this paper, the relevant methodology and background is presented. Then, a Digital Twin workflow in the using a Capability Model of a Digital Twin of the lab scale equipment is introduced, explained, and applied using the process simulation tool gPROMS® for the specific example of an esterification process in a stirred tank reactor module. The use case highlights the benefits of combining these methodologies such as improved reduced experimental effort compared to traditional DoE and increased knowledge of Critical Process Parameters. We conclude this work with a critical evaluation of the applied methods and an outlook to future work.

## METHODOLOGY

### Digital Twins in Modular Plants

Modular Plants (MPs) are defined in the VDI 2776 [1] and VDI 2658 [4] set of specifications and consist of Functional Equipment Assemblies (FEAs) grouped into

reusable and adaptable Process Equipment Assemblies (PEAs). The functional capabilities of the PEAs are described by services, which can be orchestrated into recipes in the process orchestration layer (POL)[5].

For the context of this paper, a Digital Twin is defined as a semantically linked collection of digital artifacts [6]. These digital artifacts can be organized into partial models following a Product-Process-Resource-Model [7]. For Modular Plants, the Digital Twin is created from knowledge that is shared between PEA manufacturers and owner/ operator (O/O). The PEA manufacturer knowledge is a **Capability Model** describing the equipment capabilities independent of the product. The owner/operator knowledge is a **Transformation Model**, which is equipment independent and product specific. The Digital Twin combines these two models to form an **Operation Model**, which is used for recipes and process optimization. Similar separation-of-concern approaches are discussed in the domain of discrete manufacturing with a focus on standardized description of tasks and skills of machinery, e.g. [8], [9], [10]. For this purpose of this work, the Digital Twin is an equipment-based Digital Twin of a PEA which should be understood as a well characterized **Capability Model** that can be flexibly combined with a **Transformation Model** and uncertainties of a new product.

## Quality by Design

The Quality by Design (QbD) methodology is outlined in the ICH Q8 - 10. The QbD methodology combines different scientific methods such as Design Space identification, design of experiments, and risk management with the result of guaranteed product quality [11]. The two most relevant sub-concepts in QbD methodology are statistical DoE and the Design Space (DS). Statistical DoE is used to identity which experiments must be run to collect data required to describe the Knowledge Space. From the Knowledge Space, the Design Space can be identified. The Design Space describes the relationship between Critical Process Parameters (CPPs) and Critical Material Attributes (CMAs) which are inputs to a process and the acceptable ranges of Critical Quality Attributes (CQAs) of the product.

## Model-based Design of Experiments

As an alternative to statistical design of experiments, Model-based Design of Experiments (MBDoE) is a methodology which integrates differential and algebraic equation (DAE) type models and Design of Experiments (DoE). Here, the goal is to select the experiment variables with the highest sensitivities to the model parameters, yielding improved information from experiments [12], [13]. Prior knowledge (model structure from the Capability Model and initial parameter estimates from the Transformation Model) are used to design an experiment [14]. The result is quick identification of optimum process conditions based on the Critical Process Parameters for experiments, this aims to reduce experimental load as the information obtained from experiments increases. This is advantageous in process development workflows where time-to-process is critical and with additional benefit of supporting situations where experiment budget is limited.

## Digital Twin Workflow

The application of QbD and MBDoE methodologies into smart PEAs to reduce uncertainty in the process qualification phase has been explored by [3], [15] . The workflow presented in Figure 1 extends the workflow from [15] and is intended for scale-up based on a Digital Twin as shown in [2], [16]. This work focuses on the pre-

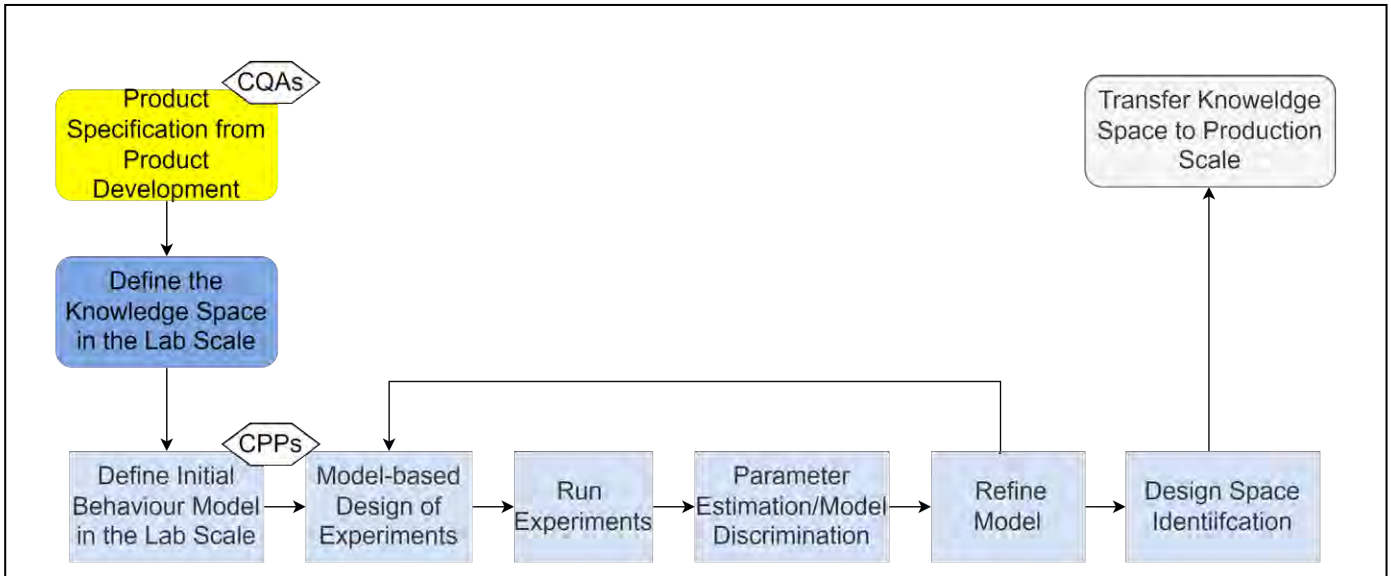



**Figure 1:** Digital Twin based workflow using the equipment-based Digital Twin in the lab scale with input from product specification and CQAs from product development.

screening using Global System Analysis, MBDoE, and identification of the Design Space in the lab scale using a Digital Twin of a PEA. This Digital Twin in this work combines a Capability Model [7] of the PEA with a Transformation Model of the product yielding an Operation Model. In the workflow in Figure 1, first Critical Quality Attributes are identified based on a product specification provided by product development. Then the Digital Twin of the lab scale is utilized. Using this Operation Model of the lab scale equipment, first Global System Analysis and variance-based sensitivities are used identify Critical Process Parameters and Critical Material Attributes based on the identified Critical Quality Attributes from the product specification. Critical model parameters for the MBDoE optimization problem are also identified.

Next, model-based design of experiments combines the prior knowledge of the CPPs from the Capability Model to identify the ideal set of process conditions to yield the maximum amount of information from experiments. The model parameters can be divided according to the PPR model [7], where the product specific parameters (i.e. activation energy, $k_\infty$, heat of reaction) are described by the Transformation Model and resource specific parameters (i.e. heat transfer coefficients, mixing time) are described by the Capability Model. Here, it is assumed that the uncertainty regarding the Transformation Model is significantly higher than model parameters which are described by the Capability Model, which has been characterized and validated from characterization experiments and previous processes run in the equipment. Following the MBDoE, experiments are run, and the experimental data is used to improve the parameter estimates in the model. These improved parameter estimates are then implemented into the model and validated with experimental data which has not been used for the parameter estimation. If the predictive capabilities of the model are sufficiently accurate based on the validation data, the model can be used to define the Knowledge Space. The final step of the workflow in Figure 1 in the lab scale is to use the CQAs to identify the Design Space from the Knowledge Space. Based on the identified Design Space, the relevant model parameters and uncertainty from the Transformation Model are transferred from the Operation Model of the lab reactor to the Capability Model of the production equipment. This yields an Operation Model of the production equipment which is then used to characterize the Knowledge Space and subsequently identify the Design Space in the production scale.

# CASE STUDY

## Application Example

To illustrate the methods of the workflow presented in Figure 1, an esterification reaction in a 2 L stirrer tank reactor was selected. The butyl acetate synthesis [17] is a homogeneously catalysed reaction. The catalyst in this example is sulfuric acid. The CQA for the product specification is the concentration $C_{butyl\ acetate} \geq 0.5\ mol/L$ of the target product butyl acetate the outlet of the reactor.

$$butanol + acetic\ acid \leftrightarrow butyl\ acetate + water \quad (1)$$

The kinetic behavior of the process can be described with the following set of equations:

$$r = c_{sulfuric\ acid}\,(k_1 * c_{butanol} * c_{acetic\ acid} - k_2 * c_{butyl\ acetate} * c_{water}) \quad (2)$$

$$K_{eq} = k_1/k_2 \quad (3)$$

$$k_i = k_{i,\infty} \exp\left(\frac{-E_{A,i}}{R\,T}\right) \quad (4)$$

To mimic the real conditions in process development, initial estimates for the kinetic parameters and uncertainties was estimated by fitting real experimental data from [17] to Arrhenius' law given by Equation 4.

$$E_{A,1} = 36281\ \frac{J}{mol};\ k_{1,\infty} = 31.5\,\frac{L^2}{min \cdot mol^2}$$

$$E_{A,2} = -478.34\ \frac{J}{mol};\ k_{2,\infty} = 1.6E^{-5}\ \frac{L^2}{min \cdot mol^2}$$

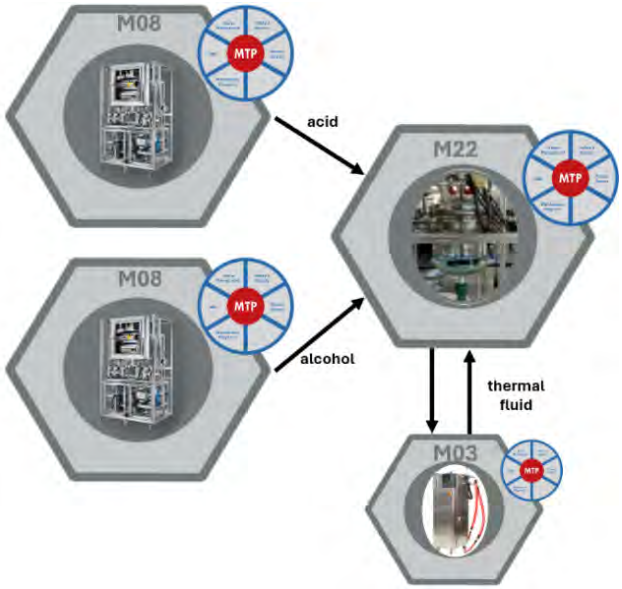



**Figure 2.** Modular plant configuration for butyl acetate synthesis.

Figure 2 provides an overview of the modular configuration which is used to carry out the esterification process. Here, three different modules are used:

- M08 is a doubling dosing module which is used to store and supply the reactants to the reactor

- M22 is a 2 L stirred tank reactor which is used to carry out the reaction
- M03 is a thermostat module used to supply mono ethylene glycol to the M22 reactor jacket.

We can describe our system with the following set of variables:

- **x** describes the state of the system at time ($t$)
- $\mathbf{u}_{CMA}$ describes independent inputs related to CMAs
  - Purity of the reactants ($x_{Acid,1}, x_{Alcohol,2}$)
- $\mathbf{u}_{CPP}$ describes independent inputs related to CPPs
  - Reactor temperature ($T$) controlled by the Temperature of the heating medium $T_{HM}$ with the Service *Tempering*
  - Feed ratio of reactants ($\dot{n}_{Alcohol}, \dot{n}_{Acid}$) controlled by the *Dosing* Services
  - Mixing speed $n_{Stirrer}$ controlled by the *Stirring* Service
- $\boldsymbol{\theta}_{TM}$ describes the parameter values related to the Transformation Model of the product:
  - Activation energy ($E_{A,1}, E_{A,2}$)
  - Pre-exponential factor ($k_{inf,1}, k_{inf,2}$)
- $\boldsymbol{\theta}_{CM}$ describes the parameters contained in the Capability Model of the PEA:
  - Heat transfer coefficient ($k_D$)

In the system described by the variable set, the significant uncertainty in the model is the Transformation Model parameters ($\boldsymbol{\theta_{TM}}$) as outlined in the methodology.

To better understand the effect that the uncertainty of the estimated model parameters in the Transformation Model $\boldsymbol{\theta_{TM}}$ has on the predictive capabilities of the Digital Twin, a Global System Analysis is carried out with respect to $\boldsymbol{u}_{CPP}$ the described by the resources model and $\boldsymbol{u}_{CMA}$ described by the product model. The parameter screening uses the GSA tool in gPROMS®, which combines a Monte-Carlo-Simulation and Sensitivity analysis based on variance-based indices. The result of the pre-screening is a series of scatter plots that serve two purposes: (1) identify relationships between CPPs $u_{CPP}$ and CMAs $u_{CMA}$ and model parameters $\boldsymbol{\theta_{TM}}$ and (2) identify relationship between model parameters $\boldsymbol{\theta_{TM}}$ and the CQAs. A selection of two GSA scatter plots is shown in Figure 3. The effects of model parameter from the Transformation Model $\theta_{TM}(E_{A,1})$ and CPP from the resource model $u_{CPP}(T_{HM})$ are shown. Here, it is evident that the estimated value of model parameter of the activation energy of the forward reaction $E_{A,1}$ has a significant influence on the target CQA, while the CPP of the temperature of the heating medium $T_{HM}$ does not have a clear effect.

## MBDoE Problem

To describe the Knowledge Space prior knowledge from the equipment capabilities from the PEA manufacturer is combined with initial parameter estimates provided by the owner/operator. These initial parameter estimates can be obtained with short cut models or group contribution estimation methods. This yields a Digital Twin built from combined knowledge of a characterized equipment model with less characterized product model.

Using this behavior model of the Digital Twin, MBDoE methods [14] are applied for parameter estimation and for model discrimination.

$$y_i = m(u_i, \boldsymbol{\theta}_{TM}) + \epsilon_i \quad (5)$$

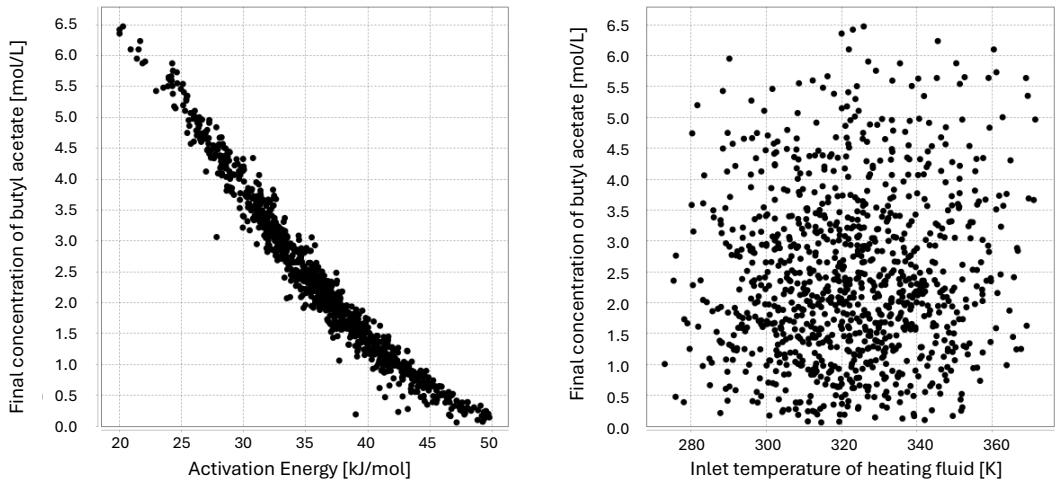



**Figure 3:** Influence of the Transformation Model parameter of Activation Energy $\theta_{TM}(E_{A,1})$ on the CQA ($C_{butyl\ acetate}$) (left). Influence of the CPP of temperature of the heating medium $u_{CPP}(T_{HM})$ on the the CQA ($C_{butyl\ acetate}$) (right).

Here, $y_i$ are the measurements (concentration samples), $m$ is the DAE model, $\theta_{TM}$ is the set of model parameters to be optimized ($E_{A,1}$, $k_{1,\infty}$ ), $u_i$ are the control variables based on the service specification and parameterization of the module which can be manipulated in the optimization problem. For the MBDoE optimization problem, the experimental budget was determined to be six experiments: five for model-based experiments and one for model validation. The data collected during these experiments is used to estimate parameters in the Transformation Model $\boldsymbol{\theta}_{TM}$ including uncertainty estimates, applying e.g., the maximum likelihood method [14].

## Identification of the Design Space from the Knowledge Space

Once the model has been revised with the parameter estimates from the experiment data. The design spec can be identified. To describe the Knowledge Space a system of nonlinear algebraic equations (NAEs) based on the previously described set of variables is proposed:

$$\mathbf{0} = \boldsymbol{h}(\boldsymbol{x}, \boldsymbol{u}_{\mathrm{CMA}}, \boldsymbol{u}_{\mathrm{CPP}}, \boldsymbol{\theta}_{\mathrm{TM}}, \boldsymbol{\theta}_{\mathrm{CM}}) \quad (6)$$

To identify the Knowledge Space, prior knowledge is required. The prior knowledge of CPPs is based on the resource model, specifically the operational limits of the model and the service specification described by the Capability Model of the Digital Twin. Then, the model according to Equation (1) is revised with the improved estimates of the model parameters. To identification of the Design Space from a Knowledge Space described in Equation (6), an Extended Flexibility Analysis approach such as described by [18] and illustrated in [3], [15] is applied. In the Flexibility Analysis, the range of the CQAs are described by the feasibility function

$$\boldsymbol{g}_{\boldsymbol{j}}(\boldsymbol{x}, \boldsymbol{u}_{\mathrm{CMA}}, \boldsymbol{u}_{\mathrm{CPP}}, \boldsymbol{\theta}_{\mathrm{TM}}, \boldsymbol{\theta}_{\mathrm{CM}}) \leq 0 \quad (7)$$

An example of the Knowledge Space according to Equation 6 as well as the identification of the Design Space from the Knowledge Space as part of the flexibility analysis applying Equation 7 is shown in Figure 4.

# DISCUSSION

The Digital Twin workflow based on the Capability Model of the lab scale equipment presented in the methodology and illustrated using the application example of the esterification process shows how application of MBDoE methods reduces the required number of experiments required to estimate new parameter values to improve the prediction accuracy of the lab scale model. In the example here, an experimental budget of six experiments was selected, whereas statistical plans to describe the Knowledge Space require a minimum of nine or more experiments. Although real experimental data was used to generate initial estimates for the model parameters, the experimental data for the MbDoE optimization problem was simulated using models based on the real equipment geometry and capabilities. The incorporation of real experimental data into MBDoE step of the workflow would strength the results of the use case. However, the benefit of the workflow is still illustrated by the presented results. Moreover, metrics based on heuristics are needed to compare the results of this method both in terms of time saved as well as information gained.

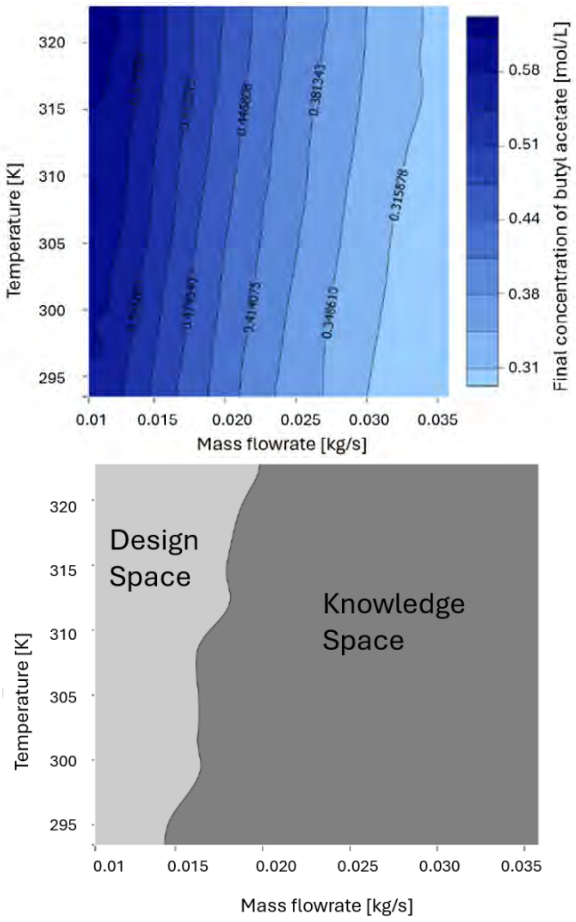



**Figure 4.** Identification of the Knowledge Space (top), identification of the Design Space from the Knowledge Space based on the CQA criteria from the product model (bottom).

# CONCLUSION AND OUTLOOK

This paper presented a Digital Twin based workflow using a Capability Model of a lab scale PEA incorporating MBDoE and QbD methodology for simultaneously increasing information about the Knowledge Space and resulting Design Space, while using model-based methods to reduce experimental load in the process development phase resulting in a faster time-to process. In a next step, the workflow should be illustrated using real experimental data. Future work will also focus on the specific

challenges in scaling-up between dimensions as well as the benefits of scale-up in Modular Plants where the advantages of process intensification can be retained. A specific challenge is to integrate the identified parameter values from Transformation Model along with uncertainty factors into the Capability Model of the production scale equipment. These Capability Models are for equipment that is functionally similar, but of different scales and different PEA Manufacturers.

## ACKNOWLEDGEMENTS

The authors would like to thank our partners Merck Electronics KGaA and Siemens AG in the industrial research project Lab2Plant for the fruitful discussions as well as P2O-Lab Learning Factory at TU Dresden's Process-to Order Group for the information about their modules M02, M08, and M22.

## REFERENCES

1. VDI 2776 Blatt 1, Process engineering plants - Modular plants - Fundamentals and planning modular plants. 2020.
2. A. Koch, J. Mädler, A. Bamberg, and L. Urbas, "Digital Twins for Scale-Up in Modular Plants: Requirements, Concept, and Roadmap," in Computer Aided Chemical Engineering, vol. 52, Elsevier, 2023, pp. 2063–2068. doi: 10.1016/B978-0-443-15274-0.50328-0.
3. J. Mädler, A. Koch, A. Bamberg, and L. Urbas, "Process Validation in Modular Plants considering the Scale-Up and Prior Knowledge," in Computer Aided Chemical Engineering, vol. 52, A. C. Kokossis, M. C. Georgiadis, and E. Pistikopoulos, Eds., Elsevier, 2023, pp. 2057–2062. doi: 10.1016/B978-0-443-15274-0.50327-9.
4. VDI/VDE/NAMUR 2658-1:2019, Automation engineering of modular systems in the process industry - General concept and interfaces, Oct. 2019.
5. A. Klose et al., "Anforderungen an die Orchestrierung modularer Prozessanlagen," 2019, doi: 10.25532/OPARA-29.
6. R. Rosen, J. Fischer, and S. Boschert, "Next Generation Digital Twin: an Ecosystem for Mechatronic Systems?," IFAC-Pap., vol. 52, no. 15, pp. 265–270, Jan. 2019, doi: 10.1016/j.ifacol.2019.11.685.
7. A. Bamberg, L. Urbas, S. Bröcker, M. Bortz, and N. Kockmann, "The Digital Twin – Your Ingenious Companion for Process Engineering and Smart Production," Chem. Eng. Technol., vol. 44, no. 6, pp. 954–961, 2021, doi: 10.1002/ceat.202000562.
8. M. Schleipen, A. Lüder, O. Sauer, H. Flatt, and J. Jasperneite, "Requirements and concept for Plug-and-Work: Adaptivity in the context of Industry 4.0," - Autom., vol. 63, no. 10, pp. 801–820, Oct. 2015, doi: 10.1515/auto-2015-0015.
9. J. Pfrommer, D. Stogl, K. Aleksandrov, S. Escaida Navarro, B. Hein, and J. Beyerer, "Plug & produce by modelling skills and service-oriented orchestration of reconfigurable manufacturing systems," - Autom., vol. 63, no. 10, pp. 790–800, Oct. 2015, doi: 10.1515/auto-2014-1157.
10. J. Pfrommer et al., "An ontology for remanufacturing systems," - Autom., vol. 70, no. 6, pp. 534–541, Jun. 2022, doi: 10.1515/auto-2021-0156.
11. S. Chatterjee, C. M. V. Moore, and M. M. Nasr, "An Overview of the Role of Mathematical Models in Implementation of Quality by Design Paradigm for Drug Development and Manufacture," in Comprehensive Quality by Design for Pharmaceutical Product Development and Manufacture, 2017, pp. 9–24. doi: 10.1002/9781119356189.ch2.
12. D. M. Bates and D. G. Watts, Eds., Nonlinear Regression Analysis and Its Applications. in Wiley Series in Probability and Statistics. Hoboken, NJ, USA: John Wiley & Sons, Inc., 1988. doi: 10.1002/9780470316757.
13. N. Asprion et al., "Implementation and Application of Model-Based Design of Experiments in a Flowsheet Simulator," J. Chem. Eng. Data, vol. 65, no. 3, pp. 1135–1145, 2020a, doi: 10.1021/acs.jced.9b00494.
14. G. Franceschini and S. Macchietto, "Macchietto, S.: Model-based design of experiments for parameter precision: State of the art. Chemical Engineering Science 63(19), 4846-4872," Chem. Eng. Sci., vol. 63, pp. 4846–4872, Oct. 2008, doi: 10.1016/j.ces.2007.11.034.
15. J. Mädler, Smarte Process Equipment Assemblies für die Unterstützung der Prozessvalidierung in modularen Anlagen, Als Manuskript gedruckt. in VDI Fortschritt-Berichte Reihe 20, Rechnerunterstützte Verfahren, no. Nr. 480. Düsseldorf: VDI Verlag GmbH, 2023.
16. A. Koch, J. Madler, A. Bamberg, and L. Urbas, "Towards PEA Matching from Simulation as Part of a Digital Twin Concept for Scale-Up in Modular Plants," in Computer Aided Chemical Engineering, vol. 53, Elsevier, 2024, pp. 595–600. doi: 10.1016/B978-0-443-28824-1.50100-9.
17. R. Soni and G. Jyoti, "Kinetics of esterification of acetic acid with n-butanol over different homogeneous acid catalysts," Int. J. Chem. Kinet., vol. 56, no. 2, pp. 96–104, Feb. 2024, doi: 10.1002/kin.21694.

18. M. P. Ochoa, S. García-Muñoz, S. Stamatis, and I. E. Grossmann, “Novel flexibility index formulations for the selection of the operating range within a design space,” Comput. Chem. Eng., vol. 149, p. 107284, 2021, doi: https://doi.org/10.1016/j.compchemeng.2021.107284.

© 2025 by the authors. Licensed to PSEcommunity.org and PSE Press. This is an open access article under the creative commons CC-BY-SA licensing terms. Credit must be given to creator and adaptations must be shared under the same terms. See https://creativecommons.org/licenses/by-sa/4.0/



Systems & Control Transactions

**Research Article - Peer Reviewed Conference Proceeding**
ESCAPE 35 - European Symposium on Computer Aided Process Engineering
Ghent, Belgium. 6-9 July 2025
Jan F.M. Van Impe, Grégoire Léonard, Satyajeet S. Bhonsale,
Monika E. Polańska, Filip Logist (Eds.)

PSE PRESS

# Sustainable Development Goals Assessment of Alternative Acetic Acid Synthesis Routes

**Juan D. Medrano-García[a], Sachin Jog[a], Abhinandan Nabera[a] and Gonzalo Guillén-Gosálbez[a]***

[a]Institute for Chemical and Bioengineering, Department of Chemistry and Applied Biosciences, ETH Zurich, Vladimir-Prelog-Weg 1, 8093 Zurich, Switzerland
* Corresponding Author: gonzalo.guillen.gosalbez@chem.ethz.ch.

## ABSTRACT

Acetic acid is an important bulk chemical and one of the major downstream products of methanol. However, it has received less attention from an environmental sustainability perspective. Here, we evaluate the absolute sustainability of several acetic acid synthesis routes, considering both fossil and renewable feedstocks. More specifically, we studied the business-as-usual (BAU) methanol carbonylation and the novel, low technology readiness level (TRL) methane carboxylation and semi-artificial photosynthesis routes. Using process simulation and life cycle assessment (LCA), our results reveal that the alternative routes have the potential to outperform the fossil BAU in at least 14 out of the 16 evaluated impact categories. However, despite the overall improvements, their performance in SDGs 3, 6, 13, 14 and 15 remains poor in any of the studied scenarios, which could potentially be addressed by hybridizing fossil and renewable feedstocks. All in all, our analysis underscores the importance of absolute sustainability to contextualize the environmental footprint of alternative chemical synthesis pathways, going beyond climate change to embrace a broader sense of categories relative to absolute thresholds.

**Keywords**: green acetic acid, alternative chemical synthesis pathways, semi-artificial photosynthesis (SAP), sustainable development goals (SDGs), absolute environmental sustainability assessment (AESA)

## 1. INTRODUCTION

Identifying pathways to replace fossil carbon with renewable carbon (i.e., captured $CO_2$, chemical waste and biomass) in chemical production is one of the most sought-after solutions for mitigating the greenhouse gas emissions associated with the chemical industry [1]. However, while this shift to renewable carbon often reduces $CO_2$ emissions, it can also lead to burden shifting, where improvements in one environmental category come at the expense of worsening others [2].

Acetic acid is an important chemical with an annual demand of over 17 Mt and serves applications, including the synthesis of plastics, dyes, insecticides and drugs. The standard route to synthesize acetic acid relies on fossil natural gas-based methanol and carbon monoxide in the so-called Cativa process, involving four energy-intensive reaction steps [3]. In the context of sustainable acetic acid synthesis, existing environmental studies are scarce and primarily focus on carbon footprint, rarely addressing other impact categories [4-7]. Moreover, current studies employ conventional life cycle assessment (LCA), which evaluates the relative differences against a benchmark, often set by the standard fossil-based process. While this methodology is useful for comparing technologies, it fails to capture the true environmental implications of the assessed processes at an Earth-system level. Consequently, absolute environmental sustainability assessment (AESA) methods are gaining popularity [8]. These methods are built on the concept of planetary boundaries (PBs), which define the safe operating space (SOS) for humanity to interact with the planet, enabling direct comparisons with the Earth's carrying capacity [9].

To address this research gap, here we compare the environmental performance of alternative, more efficient, single-step acetic acid synthesis routes with both fossil and green-based conventional processes. Moreover, for the first time, we assess the absolute sustainability level of these synthesis pathways based on the Sustainable

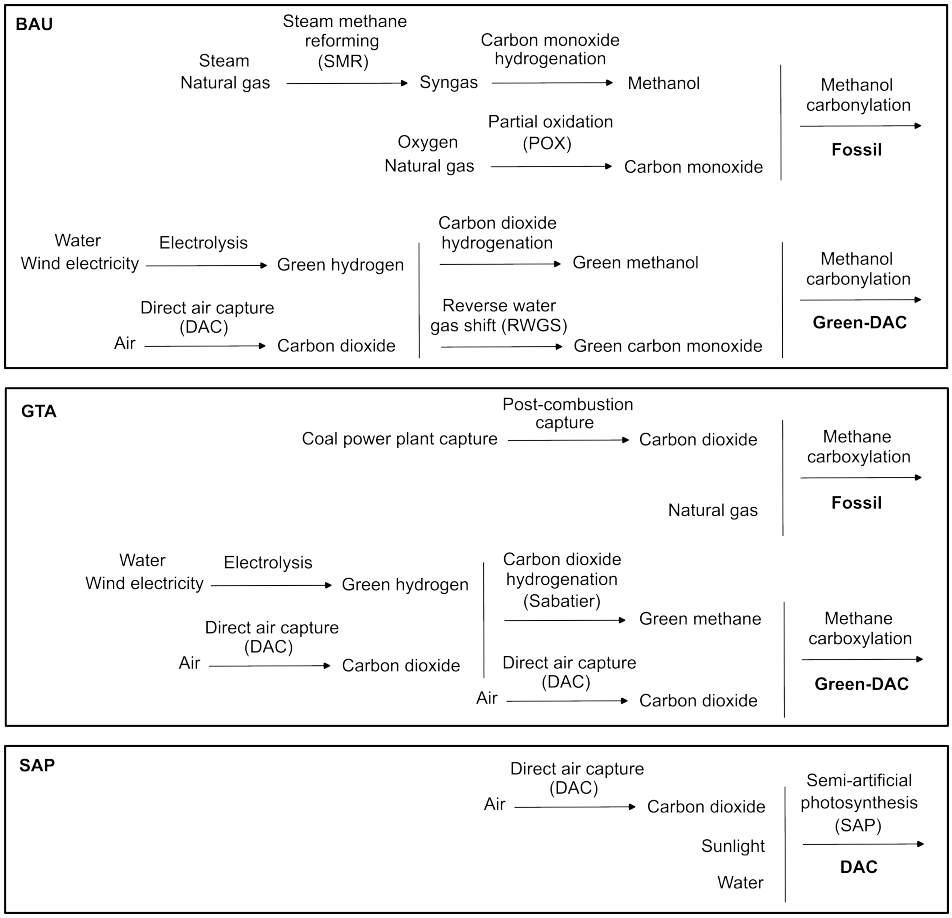



**Figure 1:** Assessed acetic acid synthesis scenarios.

Development Goals (SDGs), which are computed considering the transgression levels attained relative to the PBs [10].

Our results uncover that despite significantly improving climate change impacts, in addition to other 13 impact categories, none of the studied alternative acetic acid synthesis routes can simultaneously stay within the SOS of the impact categories connected to the SDGs. Moreover, we highlight the potential of hybridizing the feedstocks to enhance their environmental performance.

## 2. METHODOLOGY

We study five acetic acid synthesis pathways from an absolute sustainability perspective (Figure 1). These scenarios combine three different technologies (business-as-usual, BAU; gas-to-acid, GTA and semi-artificial photosynthesis, SAP), with two different feedstocks: fossil-based (natural gas, coal power plant captured $CO_2$) and renewable (wind-powered electrolytic green H2 and direct air captured (DAC) $CO_2$). We use process simulation (Aspen Plus v12) and literature data to model all proposed scenarios. An overview of the routes is shown in Figure 1.

For the life cycle assessment (LCA), we follow the guidelines of the ISO 140040/44 framework [11]. We perform a cradle-to-gate assessment with a cut-off attributional approach for acetic acid synthesis, with a functional unit of 1 kg of acetic acid. The foreground system is based on energy and material streams extracted from process simulations developed using Aspen Plus v12, and was retrieved from a previous work [4]. The background system is defined from the Ecoinvent v3.9.1 [12] database and includes all upstream activities related to electricity, energy and raw material production. The life cycle impact assessment (LCIA) is computed with Brightway2 v2.4.6 [13] using the EF v3.1 (15 impact categories) and LANCA v2.5 (land use) methods for the analysis.

The AESA is carried out following the methodology developed by Sala and collaborators [10]. Using Eq.(1), we quantify the transgression level (TL) of category $i$ ($TL_i$) based on the environmental impact of category $i$ per kg of acetic acid ($impact_i$) and the global demand of acetic acid in 2022 ($market^{acetic}$, 17.48 Mt). This calculation is performed relative to the PB of said category i ($PB_i$),

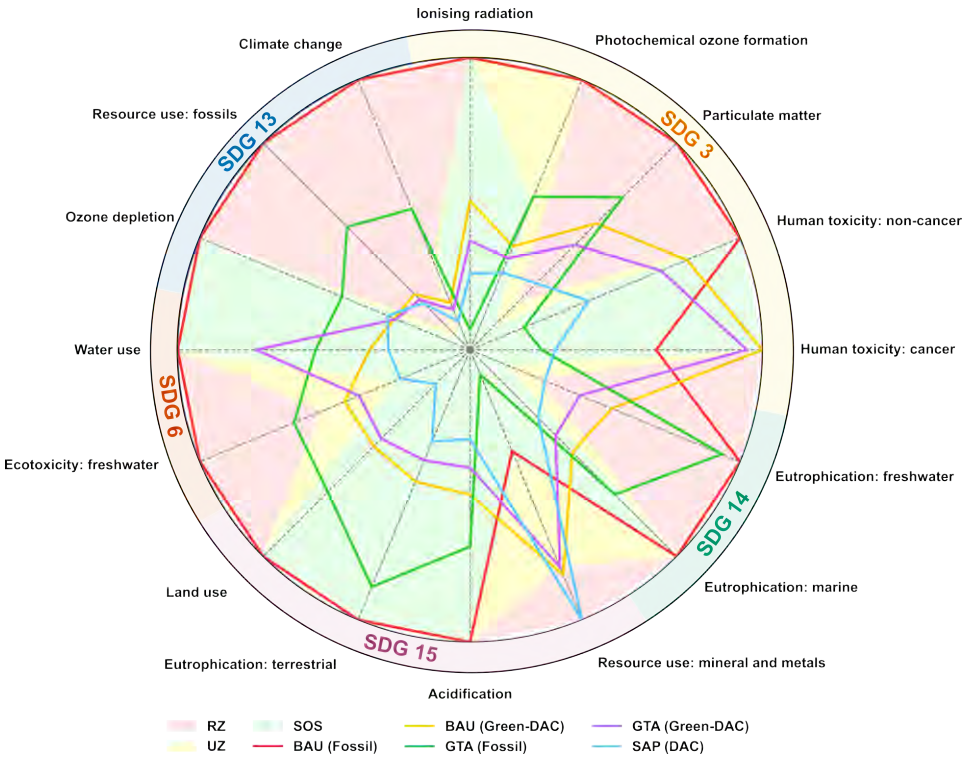



**Figure 2:** Overview of the absolute sustainability results for the studied scenarios. The background colors showcase the level of transgression: SOS, safe operating space (green), UZ, uncertainty zone (yellow); RZ, risk. zone (red). Scenarios are defined in Figure 1.

and is multiplied by a downscaling factor ($DF$). This downscaling factor (Eq.(2)) allocates a fraction of the total PBs to acetic acid production based on some sharing principles [14]. Here, we adopt a utilitarian approach based on the global market value of acetic acid in 2022 ($GVA^{acetic}$, 14.15 B$) and the world ($GVA^{world}$, 88570 B$) gross value added (GVA) for the same year. Finally, we link the TL of each impact category to the SDGs following the guidelines outlined in Sala et. al [10].

$$TL_i = \frac{impact_i \cdot market^{acetic}}{PB_i \cdot DF} \quad \forall\, i \in I \tag{1}$$

$$DF = \frac{GVA^{acetic}}{GVA^{world}} \tag{2}$$

We consider that the level of impact on an SDG is within the associated thresholds when the TL of every impact category associated with that SDG is below one, that is, it operates within the allocated fraction of the PB, also referred to as the SOS [15, 16]. Values of the TL between one and two are considered within the so-called uncertainty zone, while values over two belong to the risk zone.

## 3. RESULTS

As seen in Figure 2, the fossil BAU scenario is outperformed in 14 out of the 16 studied categories by all the proposed alternative synthesis routes, while the fossil GTA and the SAP scenarios perform better in 15 of them. Overall, most of the synthesis pathways are unable to operate within all the thresholds of all the impact categories linked to an SDG, except for the fossil BAU and GTA in SDG 15 (life on land), and SAP attaining SDG 6 (clean water and sanitation). Across scenarios, SDG 3 (good health and well-being) is hindered by high impacts, well into the risk zone, of particulate matter; SDG 6 is affected by high freshwater ecotoxicity levels; SDG 13, (climate action) suffers from high fossil resource use; SDG 14 (life below water) is adversely affected by freshwater eutrophication levels and, finally, the SOS associated with SDG 15 is transgressed from high mineral and metals resource use.

Despite the fossil BAU scenario performing worse in most cases, it already operates within the SOS in 9 out of 16 categories: ionizing radiation, non-cancer human toxicity, cancer human toxicity, marine eutrophication, mineral and metals resource use, acidification, terrestrial eutrophication, land use, water use and ozone depletion. In contrast, it transgresses the SOS (uncertainty zone) for photochemical ozone formation, and it is well into the risk zone in the remaining five categories: particulate matter, freshwater eutrophication, freshwater ecotoxicity, fossil

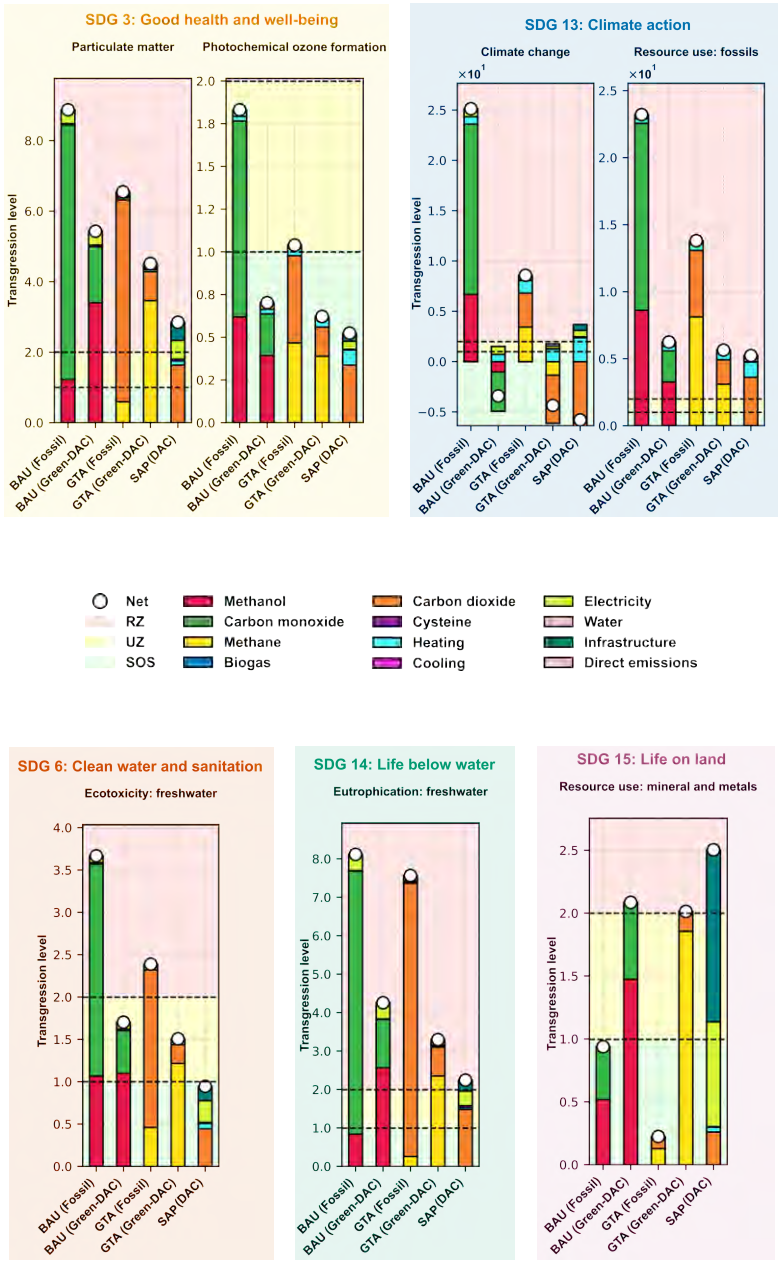



**Figure 3:** Transgressed impact categories process contributions.

resource use and climate change.

By switching the feedstock to green methanol and carbon monoxide synthesized from DAC $CO_2$ and renewable electricity, the green-DAC BAU scenario shows improvements over its fossil analog in all categories except cancer human toxicity and mineral and metals resource use. However, it is worth noting that the absolute sustainability assessment reveals that for cancer human toxicity, this collateral damage occurs within the limits of the SOS. Despite these overall improvements, the green-DAC BAU scenario is still unable to stay within the SOS of any SDG, as the impacts on particulate matter, freshwater eutrophication, mineral and metals resource use, freshwater ecotoxicity and fossil resource use, associated with SDGs 3, 6, 15, 14 and 13, respectively, transgress the maximum threshold.

The fossil GTA, that is, the direct synthesis of acetic acid from methane (natural gas) and coal power plant-captured $CO_2$, outperforms the fossil BAU in all categories due to the reduced energy and material requirements of the one-step process compared to the four steps required for the standard synthesis. However, despite this

excellent performance, SDGs 3, 6, 13 and 14 lie still outside the SOS due to high impacts in the categories cited above. On the other hand, SDG 15 is within the SOS due to a particularly low mineral and metals resource use impact compared to the other scenarios. The green variant of the GTA, which uses DAC $CO_2$ and renewable energy, performs slightly better than the green-DAC BAU scenario but also transgresses the SOS in all categories studied.

Finally, the SAP using DAC $CO_2$ as a carbon source emerges as one of the best-performing synthesis routes, being the only pathway to operate within the SOS in freshwater ecotoxicity and thus attaining SDG 6. Conversely, this scenario also exhibits the highest impact on mineral and metal resource use due to the utilization of solar power, batteries and specialized infrastructure, as detailed below.

Figure 3 shows the material and energy contributions of the transgressed impact categories for all evaluated scenarios. Overall, the main sources of impact in all categories for the fossil BAU are the raw materials, methanol and carbon monoxide, followed by very small contributions from process heating and electricity. From these results, it is evident that fossil carbon monoxide singlehandedly prevents staying within the SOS of SDGs 3, 6, 13 and 14, while the contribution from methanol is much lower. On the contrary, for the green-DAC BAU scenario, green methanol shows overall higher impacts than green carbon monoxide, especially in mineral and metals resource use (SDG 15), particulate matter (SDG 3), freshwater ecotoxicity (SDG 6) and freshwater eutrophication (SDG 14). These results suggest that partially shifting to green carbon monoxide from renewable electricity and captured $CO_2$ could significantly improve the performance of the BAU. More specifically, this hybrid configuration could help operate within the SOS of SDG 6, particularly for photochemical ozone formation, without causing significant burden-shifting (i.e., the collateral damage remains below the SOS).

The GTA process shows some parallelism with the BAU. The main impact contributions of the fossil variant of the GTA are the raw materials, methane from natural gas and $CO_2$ captured from a coal power plant, with negligible contributions from energy. However, $CO_2$ dominates in most of the transgressed categories (particulate matter, photochemical ozone formation, climate change, freshwater ecotoxicity and eutrophication). In contrast, the green-DAC GTA suffers from high impacts from synthetic methane. Hence, shifting to a hybrid natural gas with DAC $CO_2$ GTA could potentially help the technology operate within the SOS of SDGs 6, 14 and 15 despite still using fossil methane as feedstock.

Finally, the SAP scenario behaves differently depending on the impact category with DAC $CO_2$ being the most important contribution in air, water and fossil resource use-related categories. However, renewable solar electricity and the borosilicate/aluminum photochemical reactor account for over 90% of the impacts on mineral and metal resource use.

From these results, we can infer that the hybridization of fossil and renewable feedstocks could potentially help operate within the SOS of a higher number of SDGs, such as SDGs 6, 14 and 15. More specifically, using fossil methanol with green carbon monoxide in the BAU, or fossil methane with DAC $CO_2$ in the GTA, could minimize the trade-offs derived from using electrolytic hydrogen and renewable electricity of a hypothetical complete shift to renewable energy sources.

## 4. CONCLUSIONS

In this work, we studied the absolute sustainability of alternative acetic acid synthesis routes and compared them to the BAU using fossil methanol and carbon monoxide. Our results show that all evaluated acetic acid synthesis pathways outperform the fossil BAU in terms of climate change impact and 13 other categories. However, burden-shifting still manifests in two categories: human toxicity, and minerals and metals resource use. The AESA reveals that the human toxicity collateral damage occurs within the SOS, rendering it less important. Despite the overall improvements in most impact categories, all the evaluated scenarios transgress at least one of the impact categories associated with the assessed SDGs. However, hybridization of the feedstocks could help in balancing the trade-offs, with a fossil-renewable hybrid GTA scenario potentially operating within the SOS of SDGs 6, 14 and 15. All in all, we show how it is possible to improve the sustainability level of acetic acid synthesis and demonstrate that AESAs provide very valuable insights in the evaluation of alternative synthesis pathways.

## ABBREVIATIONS

AESA, absolute environmental sustainability assessment; BAU, business-as-usual; DAC, direct air capture; GTA, gas-to-acid; LCA, life cycle assessment; LCIA, life cycle impact assessment; SAP, semi-artificial photosynthesis; SDGs, sustainable development goals; SOS, safe operating space; TL, transgression level; TRL, technology readiness level

## ACKNOWLEDGEMENTS

Funded by the European Union. The work described in this publication was subsidized by Horizon Europe (HORIZON) framework by the Grant Agreement Number 101069357.

## REFERENCES

1. Otto, A.; Grube, T.; Schiebahn, S.; Stolten, D. Closing the Loop: Captured $CO_2$ as a Feedstock in the Chemical Industry. Energy Environ. Sci., 8 (11), 3283–3297 (2015). https://doi.org/10.1039/c5ee02591e.
2. Medrano-García, J. D.; Charalambous, M. A.; Guillén-Gosálbez, G. Economic and Environmental Barriers of $CO_2$-Based Fischer-Tropsch Electro-Diesel. ACS Sustain. Chem. Eng., 10 (36), 11751–11759 (2022). https://doi.org/10.1021/acssuschemeng.2c01983.
3. Le Berre, C.; Serp, P.; Kalck, P.; Torrence, G. P. Acetic Acid. In: Ullmann's Encyclopedia of Industrial Chemistry; Wiley-VCH Verlag GmbH & Co. KGaA: Weinheim (2022). https://doi.org/10.1002/14356007.a01_045.pub3.
4. Medrano-García, J. D.; Calvo-Serrano, R.; Tian, H.; Guillén Gosálbez, G. Win-Win More Sustainable Routes for Acetic Acid Synthesis. ACS Sustain. Chem. Eng., (2025). (Accepted 6 January 2025). https://doi.org/10.1021/acssuschemeng.4c07324
5. Budsberg, E.; Morales-Vera, R.; Crawford, J. T.; Bura, R.; Gustafson, R. Production Routes to Bio-Acetic Acid: Life Cycle Assessment. Biotechnol. Biofuels, 13 (1), 1–15 (2020). https://doi.org/10.1186/s13068-020-01784-y.
6. Petrescu, L.; Cormos, C. M. Classical and Process Intensification Methods for Acetic Acid Concentration: Technical and Environmental Assessment. Energies, 15 (21) (2022). https://doi.org/10.3390/en15218119.
7. Medrano-García, J. D.; Ruiz-Femenia, R.; Caballero, J. A. Revisiting Classic Acetic Acid Synthesis: Optimal Hydrogen Consumption and Carbon Dioxide Utilization. Comput. Aided Chem. Eng., 46, 145–150 (2019). https://doi.org/10.1016/B978-0-12-818634-3.50025-4.
8. Galán-Martín, Á.; Tulus, V.; Díaz, I.; Pozo, C.; Pérez-Ramírez, J.; Guillén-Gosálbez, G. Sustainability Footprints of a Renewable Carbon Transition for the Petrochemical Sector within Planetary Boundaries. One Earth, 4 (4), 565–583 (2021). https://doi.org/10.1016/j.oneear.2021.04.001.
9. Rockström, J.; W. Steffen; K. Noone; Å. Persson; F. S. Chapin; E. F. Lambin; T. M. Lenton; M. Scheffer; C. Folke; H. J. Schellnhuber; B. Nykvist; C. A. de Wit; T. Hughes; S. van der Leeuw; H. Rodhe; S. Sörlin; P. K. Snyder; R. Costanza; U. Svedin; M. Falkenmark; L. Karlberg; R. W. Corell; V. J. Fabry; J. Hansen; B. Walker; D. Liverman; K. Richardson; P. Crutzen; J. A. Foley. A Safe Operation Space for Humanity. Nature 461, 472–475 (2009). https://doi.org/10.1038/461472a.
10. Sala, S.; Crenna, E.; Secchi, M.; Sanyé-Mengual, E. Environmental Sustainability of European Production and Consumption Assessed against Planetary Boundaries. J. Environ. Manage., 269 (2020). https://doi.org/10.1016/j.jenvman.2020.110686.
11. ISO 14044. International Standard Organisation, 14044, Environmental Management - Life Cycle Assessment - Requirement and Guidelines. 61010-1 © Iec2001 2014, 2014, 13.
12. Wernet, G.; Bauer, C.; Steubing, B.; Reinhard, J.; Moreno-Ruiz, E.; Weidema, B. The Ecoinvent Database Version 3 (Part I): Overview and Methodology. Int. J. Life Cycle Assess., 21 (9), 1218–1230 (2016). https://doi.org/10.1007/s11367-016-1087-8.
13. Mutel, C. Brightway: An Open Source Framework for Life Cycle Assessment. J. Open Source Softw., 2 (12), 236 (2017). https://doi.org/10.21105/joss.00236.
14. Ryberg, M. W.; Andersen, M. M.; Owsianiak, M.; Hauschild, M. Z. Downscaling the Planetary Boundaries in Absolute Environmental Sustainability Assessments – A Review. J. Clean. Prod., 276 (2020). https://doi.org/10.1016/j.jclepro.2020.123287.
15. Negri, V.; Charalambous, M. A.; Medrano-García, J. D.; Guillén-Gosálbez, G. Sustainable Development Goals Assessment of Carbon Capture On-Board; Elsevier Masson SAS, 2023; Vol. 52. https://doi.org/10.1016/B978-0-443-15274-0.50466-2.
16. Jog, S.; Vázquez, D.; Santos, L. F.; Medrano-García, J. D.; Guillén-Gosálbez, G. Sustainable Development Goals-Based Prospective Process Design Using Hybrid Modeling. Ind. Eng. Chem. Res. 2025. (Accepted 3 January 2025). https://doi.org/10.1021/acs.iecr.4c03563.

© 2025 by the authors. Licensed to PSEcommunity.org and PSE Press. This is an open access article under the creative commons CC-BY-SA licensing terms. Credit must be given to creator and adaptations must be shared under the same terms. See https://creativecommons.org/licenses/by-sa/4.0/



Systems & Control Transactions

**Research Article - Peer Reviewed Conference Proceeding**
ESCAPE 35 - European Symposium on Computer Aided Process Engineering
Ghent, Belgium. 6-9 July 2025
Jan F.M. Van Impe, Grégoire Léonard, Satyajeet S. Bhonsale,
Monika E. Polańska, Filip Logist (Eds.)

PSE PRESS

# Synergies Between the Distillation of First- and Second-Generation Sugarcane Ethanol for Sustainable Biofuel Production

**Luiz M. Costa[ab], Abhay Athaley[c], Zach Losordo[d], Adriano P. Mariano[a], John Posada[be], and Lee R. Lynd[df]***

[a] Faculdade de Engenharia Química, Universidade Estadual de Campinas, Campinas, SP, Brazil
[b] Department of Biotechnology, Delft University of Technology, Delft, the Netherlands
[c] National Renewable Energy Laboratory, Golden, TX, USA
[d] Terragia Biofuel Incorporated, Hanover, NH, USA
[e] Postgraduate Department, Universidad ECCI, Bogotá, Colombia
[f] Thayer School of Engineering, Dartmouth College, Hanover, NH, USA
* Corresponding Author: lee.r.lynd@dartmouth.edu.

## ABSTRACT

This work investigated synergies for improved energy efficiency between integrated first- (1G) and second-generation (2G) sugarcane ethanol distillation, an energy-intensive unit operation, especially for stand-alone 2G ethanol. For this investigation, integrated and separated 1G2G distillation simulations were conducted using Aspen Plus v.10 assuming a dilute 2G fermentation beer with titer varying from 5 to 40 g/L. The results were then assessed in heating energy demand savings for distillation, and it was measured the potential of saved bagasse (boiler fuel) for valorization in either electricity or 2G ethanol. A life cycle assessment was also performed for a consequential approach to carbon emission reductions from energy savings. As our main result, distillation integration can maintain the heat demand of a stand-alone 1G mill, regardless of the 2G ethanol beer titer. This means energy savings between 9 and 15% in total ethanol heat demand, and between 46 and 92% in 2G ethanol heat demand. The savings are due to the reflux ratio associated with 2G ethanol distillation becoming close to the host 1G distillation process. However, although the energy savings may result in economic gains, not assessed in this study, by using saved bagasse for either electricity (between 0.14 and 0.23 $MJ_{Electricity}/kg_{Ethanol}$) or 2G ethanol production (between 6.8 and 4.1 $g_{2G\ Ethanol}/kg_{Ethanol}$), the boiler fuel savings do not significantly decrease carbon emissions of ethanol production (less than 1%). Nonetheless, the lower energy demand has the potential to debottleneck the operational cost challenge of distillation for 2G ethanol production without associated trade-offs.

**Keywords**: biorefinery, distillation, sugarcane ethanol, process integration, life cycle assessment

## INTRODUCTION

Achieving a sustainable future requires shifting from non-renewable to renewable energy sources. Among several strategies for energy decarbonization, biofuels are of economic and environmental interest because they produce energy while being carbon-negative if the production process is integrated with carbon capture technologies [1]. Ethanol is one of the most studied biofuels, being produced commercially in Brazil mainly by fermenting sugars from sugarcane juice (first-generation ethanol) and sugarcane bagasse (second-generation ethanol), resulting in fermentation beer containing mostly ethanol and water.

Among many technologies for ethanol separation, distillation is the traditional choice in industry. However, distillation is also known for being energy-intensive and thermodynamically inefficient [2]. Such energy waste creates unnecessary emissions and costs to the production of ethanol. Although this inefficiency can be

improved by heat integration strategies, such as side heat exchangers and heat pumps [2], first-generation (1G) sugarcane ethanol has already achieved commercial viability in Brazil. Meanwhile, the production scale of second-generation (2G) bagasse ethanol increases yearly with the opening of new mills in Brazil by Raízen [3].

Despite this growth, 2G bagasse ethanol is more energy inefficient than its 1G counterpart because 2G ethanol fermentation beer has lower ethanol titer, increasing heat duty and production costs per ethanol mass produced [4]. This increased production cost can become a limiting factor for 2G bagasse ethanol economic viability in titers below 40 g/L, which is the case of most 2G ethanol fermentation technologies, in stand-alone mills [4]. For this reason and because of the logistics involving transporting sugarcane bagasse, 2G bagasse ethanol is currently commercially produced in plants annexed to 1G ethanol plants, and this configuration can likely become one path of evolution for ethanol production in Brazil.

In the context of 1G2G integrated sugarcane ethanol plants, mixing ethanol fermentation beer from both processes may reduce the production costs of 2G ethanol (personal communication with a 2G ethanol producer). Another approach is to perform an initial stripping of 2G ethanol and then integrate the resulting vapor into a host 1G distillation column. However, the energy advantages of this integrated model compared to its stand-alone counterparts remain unclear. Thus, a preliminary comparison with rigorous simulations is needed to measure the benefits of integrating the distillation of 1G and 2G ethanol from an energy efficiency point of view, as well as the consequences from potential energy savings for the reduction of carbon emissions and residue (boiler fuel) valorization.

## METHODOLOGY

This investigation presents an integrated distillation approach that utilizes a first-generation (1G) distillation column for processing second-generation (2G) ethanol. In this proposed configuration, it is crucial that the rectification section, particularly its condenser duty, remains unaffected by the addition of diluted ethanol.

Whereas the integration can be accomplished through a single-column system that processes beer from both 1G and 2G processes, this work proposes a two-column system, featuring a dedicated column for stripping the 2G beer. The vapor generated in this column is then directed to an integrated column that processes the 1G beer. This dual-column configuration is favored for economic reasons, as it allows for the separation of 1G and 2G bottoms (i.e. stillage), facilitating potential residue valorization through other processes.

This investigation does not compare its findings with other energy-saving distillation strategies, such as double-effect and heat-pumped distillation. A comprehensive comparison would necessitate an in-depth analysis of the technical, economic, and environmental metrics, given the differing theoretical frameworks of these strategies.

Simulations of separated (Figure 1) and integrated (Figure 2) 1G2G distillation were conducted using Aspen Plus v.10. The nonrandom two-liquid (NRTL) thermodynamic model was used to represent the liquid-vapor equilibrium. The separated distillation configuration comprised two RadFrac columns designed to distill the fermentation beer from both first-generation (1G) and second-generation (2G) processes until reaching near azeotropic levels. In contrast, the integrated distillation setup features an initial column that strips the 2G beer into a vapor phase, followed by an integrated column that distills both the 2G vapor and the 1G fermentation beer until they also reach azeotropic levels. The RadFrac distillation columns were simulated with 40 stages for operation near the minimum reflux condition and to isolate changes in energy demand for only interactions between distillation columns and not due to possible distillation inefficiencies by additional feeds. The RadFrac 2G stripping column was simulated with 20 stages for the same reasons as the distillation columns. In both integrated and separate situations, the final distillate is assumed to be in the vapor phase for the subsequent dehydration step in the ethanol mill. For the purpose of the preliminary analysis reported here, it was assumed that both mixtures enter the columns as saturated liquids, comprising primarily water and ethanol to facilitate a generalized analysis. Additionally, other components, such as residues from the fermentation process, were not included in this assessment. This exclusion is based on the typically low mass fractions of these residues, which can vary depending on the fermentation conditions, and their minimal impact on the overall energy demand of the process.

The distillation system operates at 1 atm, and the 1G beer titer was kept at 100 g/L to represent a typical 1G sugarcane fermentation and the 2G fermentation beer titer was varied from 5 to 40 g/L to study and compare the energy impacts for low titer 2G beer. This analysis assumes that the annexed 2G plant is smaller than the host 1G plant, so it was proposed to use a proportion of 3 kg of 1G to 1 kg of 2G fermentation beer. The mass flow of 1G fermentation beer was assumed to be 500 t/h to be in the same order of magnitude as real ethanol biorefineries [5], but this value will not affect the results because they are measured on a distilled ethanol basis. Additionally, the adopted ethanol mass fraction of distillate was 92.5%wt and of stillage (bottoms) was 0.05% wt to match industrial specifications [5]. Finally, while the proposed distillation system employs a simplified approach, note that there are studies that utilize rigorous simulations of simplified water-ethanol systems specifically for the

energy analysis of distillation [6].

An energy analysis based on the heating energy demand was conducted to quantify and compare the reboilers' duty and distilled ethanol production. In the case of the 1G2G integrated arrangement, the 2G ethanol net duty was considered to be the sum of the 2G rectification column with the heat duty change of the 1G distillation column compared to the separated counterpart.

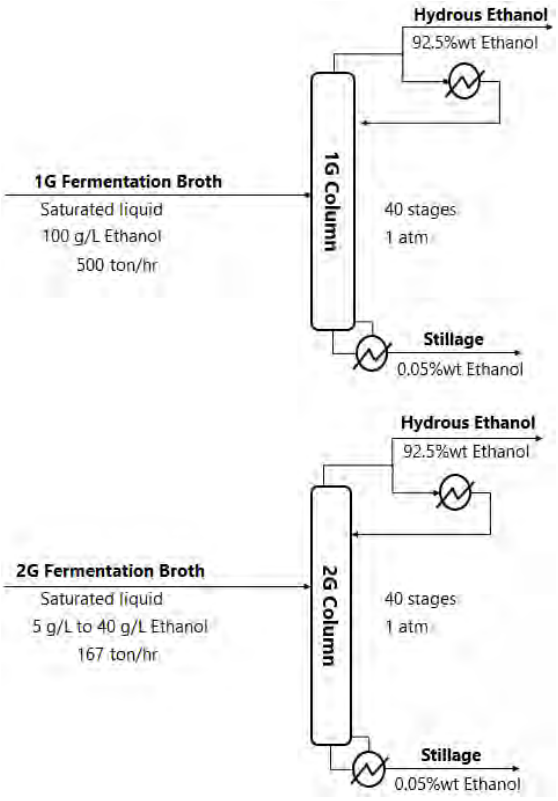



**Figure 1.** Schematic diagram for separated distillation configuration.

The results of the energy analysis were evaluated in terms of biomass demand required to generate the necessary distillation utilities. In other words, the amount of bagasse needed for cogeneration to meet distillation's steam demand. For an accurate estimation, a conversion factor between steam production and bagasse combustion was obtained using the cogeneration spreadsheet model developed for a modern 1G sugarcane ethanol biorefinery boiler system by Bonhivers *et al.* [7].

By estimating the amount of bagasse saved due to energy savings in the distillation, valorization of the saved bagasse was assessed in terms of either electricity production by cogeneration or 2G ethanol production by fermentative route. Whereas electricity production was calculated using a conversion factor obtained from the previously mentioned cogeneration spreadsheet model [7], 2G ethanol production was calculated using a conversion factor between bagasse and 2G ethanol in an integrated 1G2G sugarcane biorefinery simulated by Bonomi *et al.* [8]. Table 1 contains the conversion factors used in this work.

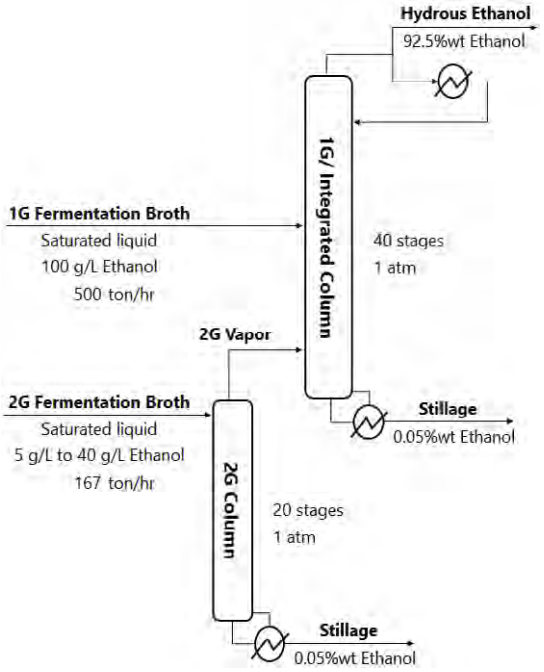



**Figure 2.** Schematic diagram for integrated distillation configuration.

**Table 1:** Conversion factors to calculate dry bagasse saving and its possible valorization (adapted from [7] and [8]).

| Conversion factor | Unit | Value |
|---|---|---|
| Bagasse to steam production | $MJ_{Steam}/kg_{Bagasse}$ | 9.97 |
| Saved bagasse to electricity | $MJ_{Electricity}/kg_{Bagasse}$ | 4.12 |
| Saved bagasse to 2G ethanol | $kg_{2G\ Ethanol}/kg_{Bagasse}$ | 0.12 |

Furthermore, considering the energy savings in distillation, a life cycle assessment was conducted using a consequential approach to evaluate carbon emissions associated with bagasse (boiler fuel) consumption reduction, following the ISO 14040 standard [9]. The adopted system boundary was the boiler and distillation system considering bagasse entering the boiler as an input and distilled ethanol from distillation as output. This system was chosen because it would link steam savings by energy demand reductions in the distillation integration with steam generation by bagasse in the boiler unit. As an observation, the fermentation beers were not considered as input due to not changing in the consequential approach. The functional unit used was 1 kg of distilled ethanol due to ethanol being the product of interest. Multifunctionality was not addressed because there was no

generation of other products. The 2016 ReCiPe Methodology (Hierarchist) was used, the impact category measured was "Climate change", and it was used the greenhouse gas (GHG) emissions inventory for bagasse for a Brazilian 1G sugarcane boiler by Capaz *et al.* [10].

## RESULTS AND DISCUSSION

From a column operation point of view, distillation integration allows the stripping of 2G beer and the distillation of 1G2G ethanol without efficiency loss when compared with the separated scenario (Figures 3 and 4). Considering a dilute 2G beer feed, the operating lines of the integrated distillation column and the pure 1G column are overlapping, meaning that the reflux ratio does not change. It may be because the 2G ethanol vapor entering the integrated column does not have sufficient mass flow to disrupt the column's operating line. Therefore, the reflux ratio is comparable to that of a standalone first-generation (1G) distillation system, enabling substantial energy savings in the distillation of second-generation (2G) ethanol, particularly at initial low ethanol concentrations.

Note that the rectification section of the 2G column does not operate in the integrated scenario. In this configuration, the reboiler duty is primarily linked to the vaporization of the feed, and there is no additional heat requirement associated with the condensing process at the top stage. However, this does not imply that the overall energy demand of the column is significantly reduced compared to a complete distillation process. The stripped vapor has a considerably higher mass flow rate that must be processed, owing to a lower concentration of ethanol.

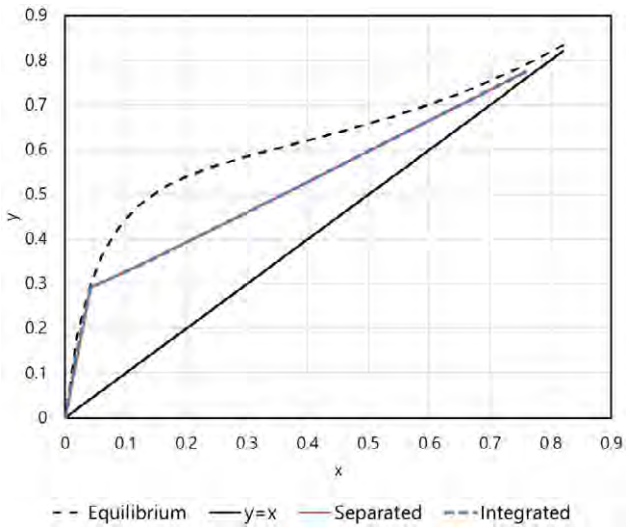



**Figure 3.** Operating lines for distillation in a stand-alone 1G column (Separated) or an integrated column with 1G fermentation beer and 2G ethanol vapor (Integrated).

Distillation integration is a viable strategy for the energy demand to remain close to a 1G ethanol plant. 1G2G integration resulted in an overall heating energy demand for ethanol distillation at a near-constant value of 3.30 $MJ/kg_{Ethanol}$, regardless of the 2G ethanol titer (Figure 5). Furthermore, the energy demand of the integrated scenario differs by only 0.4% compared to the calculated 1G fermentation beer (3.29 $MJ/kg_{Ethanol}$). Meanwhile, the energy demand of the separated scenario ranges from 3.64 (at 40 g/L 2G beer titer) to 3.85 (at 5 g/L 2G beer titer) $MJ/kg_{Ethanol}$, resulting in energy savings of 9.3% to 14.6%, respectively (Figure 5). The main reason for this result is that the energy demand for distilling 2G ethanol decreases in the integrated 1G2G column due to the reflux ratio being similar to that of a stand-alone 1G system. This alignment with the 1G distillation conditions contributes to enhanced energy efficiency. However, note that the reflux ratio and energy demand of the integrated 1G2G distillation system may vary based on the proportion of 1G to 2G beer and the ethanol titer of the 1G process. This could be observed by a slight increase in energy demand within the integrated system as the ethanol titer rises, specifically around 0.4% when moving from 5 to 40 g/L. This increase is attributed to the higher volume of 2G vapor, which has a subtle impact on the overall operation of the column by increasing the reflux ratio.

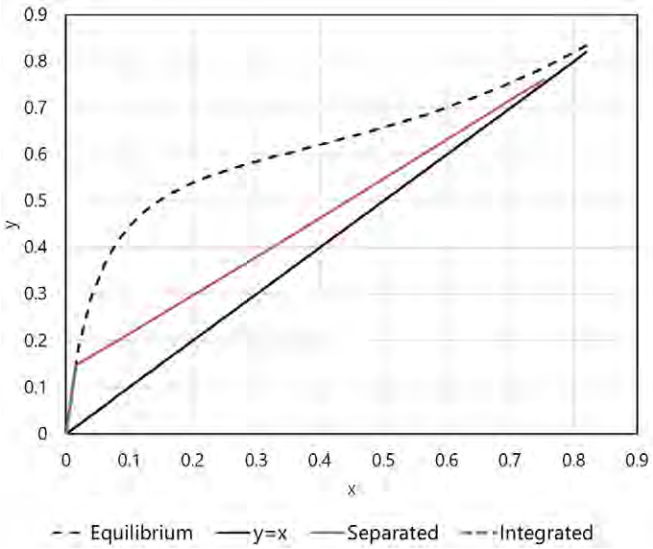



**Figure 4.** Operating lines for distillation in a stand-alone 2G column (Separated) or a 2G stripping-only column (Integrated).

The new reflux ratio condition leads to increased energy savings in the distillation of 2G ethanol. While in the separate scenario, the heat demand varies from 6.34 (at 40 g/L 2G beer titer) to 41.52 (at 5 g/L 2G beer titer) $MJ/kg_{Ethanol}$, the demand is near constant at 3.45 $MJ/kg_{Ethanol}$ in the integrated scenario (Figure 6). The corresponding energy savings range from 91.5 to 45.9%, respectively which are significant values in the context of cellulosic ethanol distillation. Additionally, the energy demand

of the integrated scenario is close to the energy demand of 1G ethanol. The relative difference between the integrated 2G ethanol energy demand and 1G ethanol is around 4%, making the operational costs of 2G ethanol distillation close to the stand-alone 1G operation, regardless of the 2G beer titer. Thus, the integration may significantly decrease the typical high distillation operating costs of 2G ethanol production.

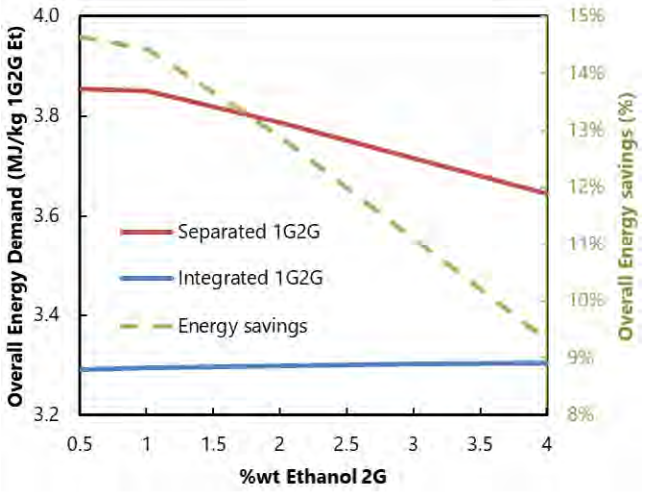



**Figure 5.** Overall energy demand and energy savings comparison between separated and integrated 1G2G distillation.

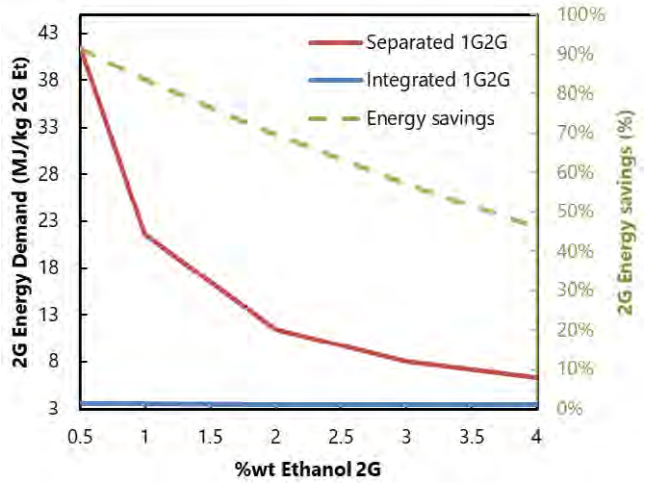



**Figure 6.** 2G ethanol energy demand and energy savings comparison between separated and integrated 1G2G distillation.

The decrease in energy demand obtained with integration results in savings of bagasse (boiler fuel), which can potentially increase either the electricity or 2G ethanol production (Figure 7). The bagasse savings can vary from 57 (at 5 g/L 2G beer titer) to 34 $kg_{Bagasse}/ton_{Ethanol}$ (at 40 g/L 2G beer titer) and it could generate 0.23 and 0.14 $MJ_{Electricity}/kg_{Ethanol}$, respectively. This electricity production represents an increase of approximately 5% in electricity output in 1G2G sugarcane ethanol plants, which typically produce 3.29 $MJ_{Electricity}/kg_{Ethanol}$ [8]. Equally interesting, the bagasse available could produce 6.8 and 4.1 $g_{2G\ Ethanol}/kg_{Ethanol}$.

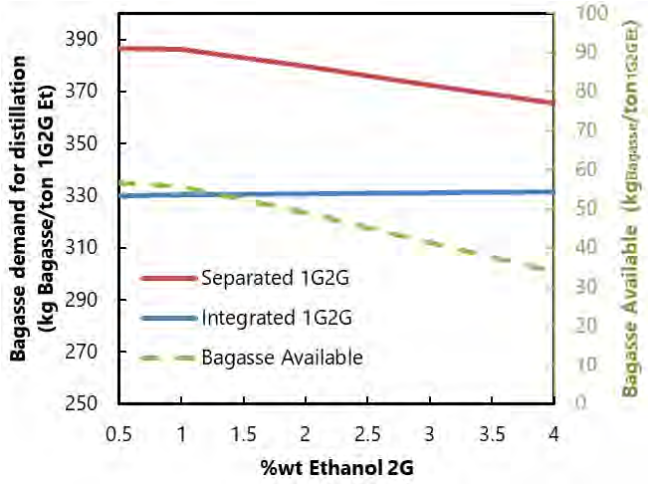



**Figure 7.** Comparison between bagasse demand for distillation in the separated and integrated 1G2G scenario.

Despite the robust energy savings, the environmental performance is not altered significantly (Figure 8). The corresponding decrease in bagasse demand for cogeneration decreases the GHG emissions by nearly 1 $gCO_2eq/kg_{Ethanol}$, which is a small amount compared to typical values of sugarcane ethanol production in Brazil [761 (integrated 1G2G ethanol) and 241 $gCO_2eq/kg_{Ethanol}$ (stand-alone 2G ethanol)] [11]. This result was expected because the bagasse used to provide heat for distillation is a renewable fuel and corresponds to a small portion of the environmental profile of sugarcane ethanol production. Nonetheless, in the context of processes with a more energy-intensive distillation that uses fossil fuels such as natural gas in corn ethanol mills in the United States, the energy savings could provide a more significant reduction in the product's emission profile.

## CONCLUSIONS

The integration of distillation processes for first- and second-generation sugarcane ethanol significantly reduces the overall energy demand for distillation, achieving reductions between 10% and 15%. Furthermore, it significantly decreases the heat duty required for distilling second-generation ethanol, with reductions ranging from 47% to 92%. Under the conditions examined, characterized by dilute second-generation feeds, the low concentration of second-generation ethanol led to an integrated distillation setup with both reflux ratio and heat demand closely aligned with the standalone first-generation (1G) conditions, irrespective of the 2G

ethanol titer. Although potential economic benefits may be realized by converting the saved bagasse into electricity or additional ethanol, it is important to note that these energy savings have a limited impact on the carbon emissions associated with sugarcane ethanol production.

Finally, unlike other energy integration strategies such as heat pumps and double-effect distillation, distillation integration offers a straightforward process integration method that achieves energy savings without significant trade-offs.

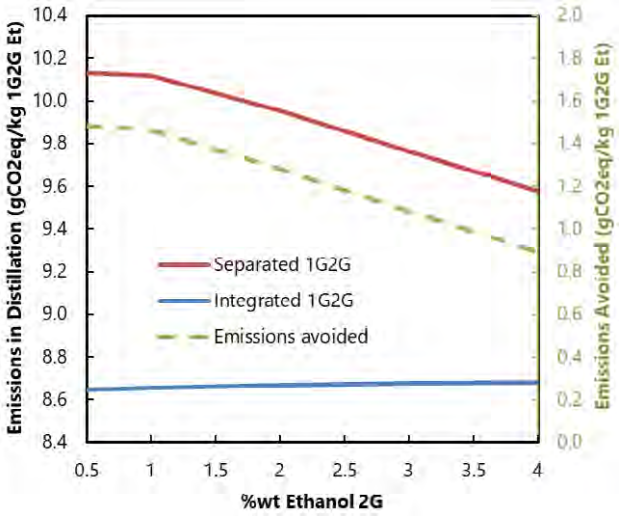



**Figure 8.** Comparison between greenhouse gas emissions for distillation in the separated and integrated 1G2G scenario.

## ACKNOWLEDGEMENTS

We acknowledge the provision of a PhD scholarship (TNW23.160) from the Department of Biotechnology at the Delft University of Technology as part of a Dual Degree PhD project under the agreement between Unicamp and TU Delft. This study was financed, in part, by the São Paulo Research Foundation (FAPESP), Brazil - Process Number 18/25682-0.

## REFERENCES

1. Smith P, House JI, Bustamante M, Sobocká J, Harper R, Pan G, West PC, Clark JM, Adhya T, Rumpel C, Paustian K, Kuikman P, Cotrufo MF, Elliott JA, McDowell R, Griffiths RI, Asakawa S, Bondeau A, Jain AK, Meersmans J, Pugh TAM. Global change pressures on soils from land use and management. *Global Change Biology* 22:1008-1028 (2015) https://doi.org/10.1111/gcb.13068
2. Ozcan Konur. Bioethanol Fuel Production Processes. II. CRC Press (2023).
3. Raízen. https://ri.raizen.com.br/en/e2g/
4. Lynd LR, Beckham GT, Guss AM, Jayakody LN, Karp EM, Maranas CD, McCormick RL, Amador-Noguez D, Bomble YJ, Davison BH, Foster C, Himmel ME, Holwerda EK, Laser MS, Ng CY, Olson DG, Román-Leshkov Y, Trinh CT, Tuskan GA, Upadhayay V, Vardon DR, Wang L, Wyman CE. Toward low-cost biological and hybrid biological/catalytic conversion of cellulosic biomass to fuels. *Energy Environ. Sci.* 15:938-990 (2022) https://doi.org/10.1039/D1EE02540F
5. National Renewable Energy Laboratory (NREL). Process design and economics for biochemical conversion of lignocellulosic biomass to ethanol: dilute-acid pretreatment and enzymatic hydrolysis of corn stover. Technical Report NREL/TP-5100/47764. (2011)
6. Bonomi A, Cavalett O, Cunha MP, Lima MAP. Virtual Biorefinery. Springer (2016)
7. Bonhivers JC, Maciel MRW, Reddick C, Zemp R, Mariano AP, Filho RM. The E-S-T method based on the grande composite curve links energy consumption with number of stages and stage temperature for binary mixture distillation. *Process Integr Optim Sustain* 5:919-946 (2021) https://doi.org/10.1007/s41660-021-00189-0
8. Bonhivers JC, Ortiza PAS, Reddick C, Rossel CEV, Mariano AP, Filho RM. Graphical analysis of plant-wide heat cascade for increasing energy efficiency in the production of ethanol and sugar from sugarcane. *Process Integr Optim Sustain* 5:335-359 (2021) https://doi.org/10.1007/s41660-020-00149-0
9. International Organization for Standardization (ISO). ISO 14040: Environmental Management - Life Cycle Assessment - Principles and Framework. (2006)
10. Capaz RS, Posada JA, Osseweijer P, Seabra JEA. The carbon footprint of alternative jet fuels produced in Brazil: exploring different approaches. *Resources, Conservation & Recycling* 166 (2021) https://doi.org/10.1016/j.resconrec.2020.105260
11. Maga D, Thonemann N, Hiebel M, Sebastião D, Lopes TF, Fonseca C, Gírio F. Comparative life cycle assessment of first- and second-generation ethanol from sugarcane in Brazil. *Int J Life Cycle Assess* 24:266-280 (2019) https://doi.org/10.1007/s11367-018-1505-1

© 2025 by the authors. Licensed to PSEcommunity.org and PSE Press. This is an open access article under the creative commons CC-BY-SA licensing terms. Credit must be given to creator and adaptations must be shared under the same terms. See https://creativecommons.org/licenses/by-sa/4.0/

Systems & Control Transactions

**Research Article - Peer Reviewed Conference Proceeding**
ESCAPE 35 - European Symposium on Computer Aided Process Engineering
Ghent, Belgium. 6-9 July 2025
Jan F.M. Van Impe, Grégoire Léonard, Satyajeet S. Bhonsale,
Monika E. Polańska, Filip Logist (Eds.)

PSE PRESS

# Superstructure as a Communication Tool in Pre-Emptive Life Cycle Design Engaging Society: Findings from Case Studies on Battery Chemicals, Plastics, and Regional Resources

**Yasunori Kikuchi[abcd]*, Ayumi Yamaki[a], Aya Heiho[ce], Jun Nakatani[df], Shoma Fujii[ad], Ichiro Daigo[dg], Chiharu Tokoro[hi], Shinsuke Murakami[dj], and Satoshi Ohara[acdg]**

[a] the University of Tokyo, Institute for Future Initiatives, Bunkyo-ku, Tokyo, Japan
[b] the University of Tokyo, Department of Chemical System Engineering, Bunkyo-ku, Tokyo, Japan
[c] the University of Tokyo, Presidential Endowed Chair for "Platinum Society", Bunkyo-ku, Tokyo, Japan
[d] the University of Tokyo, UTokyo LCA Center for Future Strategy, Meguro-ku, Tokyo, Japan
[e] Tokyo City University, Department of Environmental Management and Sustainability, Setagaya-ku, Tokyo, Japan
[f] the University of Tokyo, Department of Civil Engineering, Bunkyo-ku, Tokyo, Japan
[g] the University of Tokyo, Research Center for Advanced Science and Technology, Tokyo, Japan
[h] Waseda University, Department of Creative Science and Engineering, Shinjuku-ku, Tokyo, Japan
[i] the University of Tokyo, Department of Systems Innovation, Bunkyo-ku, Tokyo, Japan
[j] the University of Tokyo, Department of Technology Management for Innovation, Bunkyo-ku, Tokyo, Japan
* Corresponding Author: ykikuchi@ifi.u-tokyo.ac.jp.

## ABSTRACT

Emerging technologies require sophisticated design and optimization due to their rapid advancement and potential to alter material flows and life cycles. However, their future development remains uncertain due to sociotechnical factors such as regulations, infrastructure, and market dynamics. Multiple technologies are often considered simultaneously, but their interactions and synergies are not systematically evaluated. This study addresses pre-emptive life cycle design in social challenges by integrating emerging technologies into superstructures, which help visualize alternative candidates for design problems. Case studies on battery chemistry, plastics, and regional resource circulation demonstrate this approach. For battery technology, nickel-manganese-cobalt lithium batteries have dominated over lithium iron phosphate alternatives. Superstructures were developed to assess recycling technologies and were refined through communication with managers of Japanese national battery projects. In plastics, system designs integrating biomass-derived and recycled carbon sources were explored, and scenario planning with life cycle assessment (LCA) was shared with stakeholders. Regional resource circulation was studied through technological integration and local stakeholder engagement, leading to demonstration tests. Findings suggest that superstructures and technology assessments enhance understanding of applicable technologies and their trade-offs. Given the critical role of social acceptance in technology implementation, computer-aided process engineering (CAPE) tools should facilitate discussions on socio-technical and socio-economic aspects of process systems engineering.

**Keywords**: Life cycle assessment, Co-creation, Scenario planning, Social engagement, Policy making

## INTRODUCTION

The rapid advancement of emerging technologies [1] necessitates a comprehensive approach to their design and optimization, incorporating considerations of social systems and regulatory frameworks. These

technologies possess the potential to transform material flows and life cycles; however, their future development remains highly uncertain due to the evolving sociotechnical landscape, including regulatory policies, societal infrastructure, and market dynamics [2]. The concurrent exploration of multiple technological solutions for a given challenge further complicates the assessment of their respective boundaries and potential synergistic interactions. A systematic evaluation framework is, therefore, imperative to ensure the effective integration of emerging technologies into optimized systems.

In this study, we address the pre-emptive life cycle design (LCD) of emerging technologies within the context of societal challenges, focusing on case studies in battery chemistry, plastics, and regional resource management. To achieve this, we construct comprehensive frameworks that encapsulate a range of technological alternatives and facilitate the visualization of potential design pathways by superstructures. These superstructures, developed in collaboration with industrial stakeholders and national initiatives, serve as the basis for modeling life cycle scenarios using life cycle assessment (LCA) methodologies.

## MATERIALS AND METHODS

### Framework Development of Pre-Emptive LCD

Pre-emptive LCD requires the steps of process systems engineering, e.g., alternative generation, analysis, evaluation and optimization, and sensitivity analysis. Forward-looking LCA has become an important tool for examining the future applicability of emerging technologies considering the scenarios in line with shared socioeconomic pathways [3]. New technologies are constantly being developed, and while they may solve one particular problem, they can also cause other problems, which can have a complex impact on the processing system. In this situation, it can be effective to use superstructure-based visualization to support communication while implementing forward-looking LCA and designing the life cycle, while proposing appropriate alternative solutions.

In the case study described below, we conducted pre-emptive LCD based on the individual problems and conditions. The extracted works and functions of pre-emptive LCD are framed and visualized as a model represented in integrated definition type 0 modeling language (IDEF0) [4].

### Case Examples of Pre-Emptive LCD

In the alternative generation of pre-emptive LCDs, we consider not only technology candidates that have reached a certain level of technological maturity, as evidenced by patents and academic papers, but also cutting-edge technological development issues that are currently being addressed in national projects. Even for technology candidates with low technological maturity, it is possible to consider the impact on the life cycle in advance using future LCA combined with computer-aided process engineering (CAPE) [3]. This makes it possible to design the life cycle appropriately, taking into account resource recycling, environmental impact, socio-economics, and socio-technical regimes. At this time, it is important to consider the elements of the life cycle other than the target technology, even in projects that are developing elemental technology, and there is a possibility that an appropriate evaluation range and purpose can be set by building a superstructure.

The superstructure in this study encompasses all potential pathways in cradle-to-grave life cycles of target functions. Concerning the cases below, both technological options and socio-economic/technical options could influence the future performance of these life cycles. Wherever possible, such options were gathered from national projects, experts, and relevant government officials.

#### Circulation of battery chemicals

In the realm of battery chemistry, nickel-manganese-cobalt (NMC) lithium-ion batteries (LiB) have emerged as the dominant technology, although lithium iron phosphate (LFP) batteries remain a viable alternative. Superstructures were formulated to evaluate recycling technologies, incorporating insights from Japanese national battery technology initiatives [5]. The required data was obtained from industries and authorized LCA databases. The mathematical models from the previous studies [5] were applied.

#### Plastic life cycles with renewable carbon sources

In the plastics sector, the transition to biomass-derived and recycled carbon sources necessitates systematic design considerations. Scenario planning and LCA based on superstructure-based analyses were conducted and shared with stakeholders to inform sustainable carbon strategies [6, 7]. The required data was obtained from industries and authorized LCA databases. The mathematical models from the previous studies [9] were applied. The social situation was obtained from surveys, e.g., on bioplastics [9].

#### Circulated use of regionally available resources

A shift from imported fossil fuels to local renewable resources and empowering rural areas is crucial for regional sustainability. Regionally available resources, e.g., biomass from agriculture and forestry, renewables such as solar and wind, and wastes to be treated, have been examined with technologies for their valorization. In this regard, however, not individual use but combined application of such regional resources is effective [10]. Superstructure-based analysis supported by technology

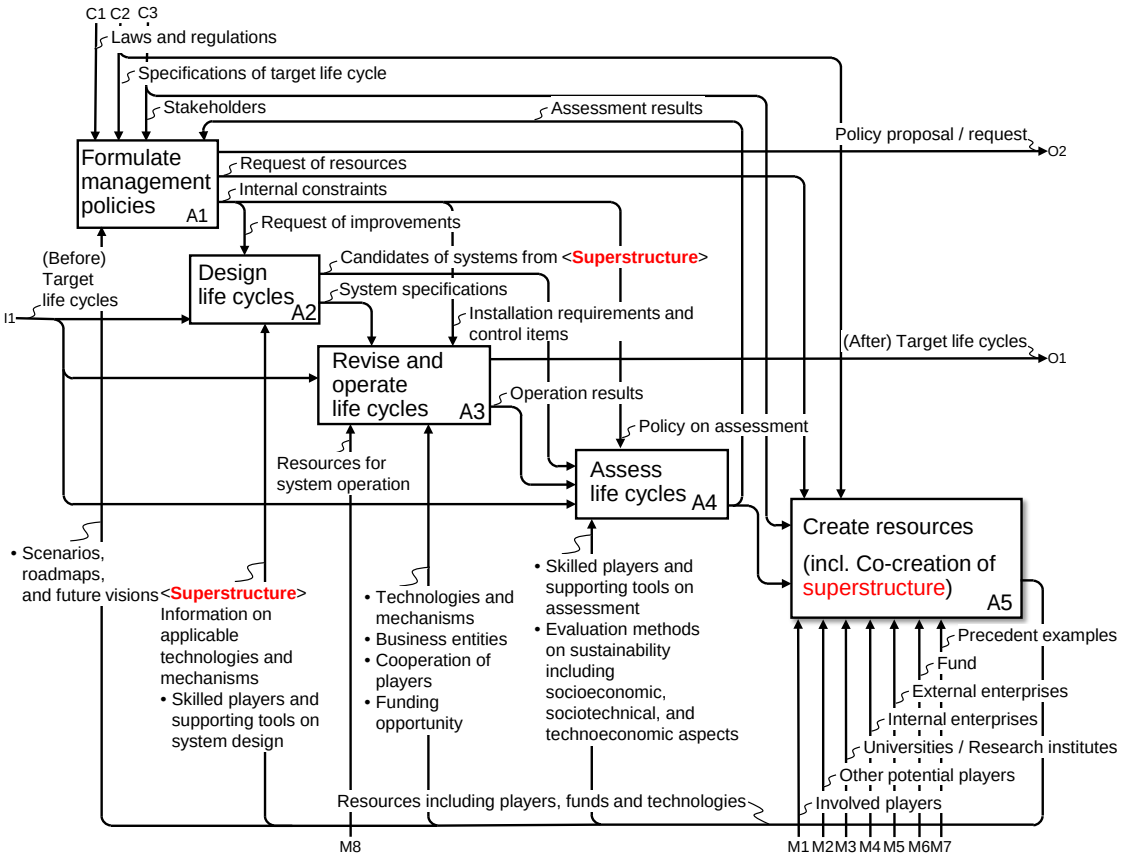



**Figure 1:** Activities and information flows associated with the utilization of superstructure model in pre-emptive life cycle design represented in IDEF0 manner.

assessments such as LCA and consumer surveys is needed to address stakeholder concerns and reveal the socioeconomic impacts of technology options. As a regional case study, regional resource circulation in a remote island, Tanegashima, was explored through the integration of multiple technologies, with demonstration tests conducted in collaboration with local communities and stakeholders [10].

## RESULTS AND DISCUSSION

### Pre-Emptive LCD with Superstructure

Figure 1 shows the activities and information flows associated with the utilization of the superstructure model in pre-emptive LCD, represented in an IDEF0 manner. The framework consists of five activities (A1–A5) that follow a continuous improvement cycle similar to the plan-do-check-act model. A1 (planning) and A2 (acting) define policies and generate alternative solutions, while A3 (doing) implements system revisions, and A4 (checking) assesses outcomes. A5 provides necessary resources and supports stakeholder engagement.

A1 formulates regional policies based on external and internal feedback. A2 generates alternative systems in response to improvement requests and assesses their socioeconomic, technoeconomic, and sociotechnical impacts. A3 converts current life cycles into revised ones by integrating specifications from A2 and assessment results from A1. A4 examines operated systems and feeds back insights for further refinement. A5 serves as an open platform, supplying resources and fostering co-learning among stakeholders.

Assessment methods such as socioeconomic and technoeconomic evaluations guide decision-making. Stakeholder involvement in A5 ensures inclusive development, similar to biodiversity conservation and community-based participation models. The framework facilitates social transformation in target life cycles by continuously improving system operations and stakeholder collaboration.

The superstructure can be seen as a source of design information in the pre-emptive LCD shown in Figure 1. The superstructure itself is expanded and strengthened through co-creation, but here it is adapted to the characteristics of the lifecycle in each case study.

### Findings in Battery Systems Case

A comprehensive superstructure was developed to

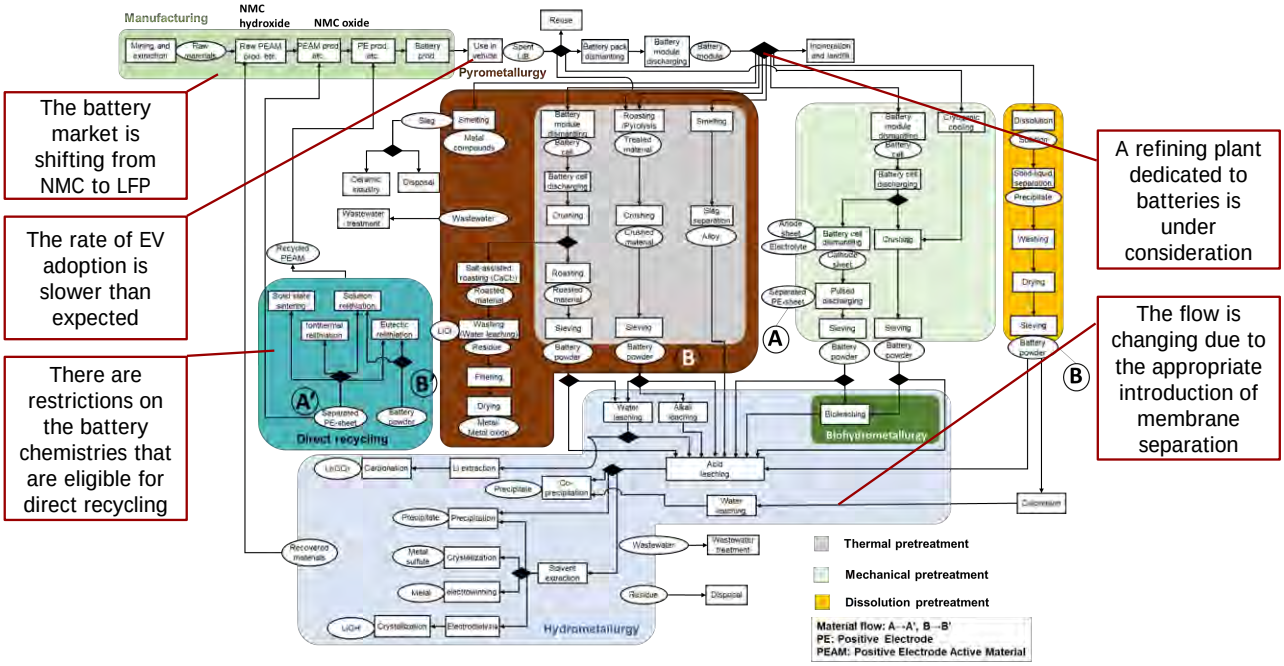



**Figure 2:** Superstructure constructed in a previous study [5]. The comments were examples of the content discussed through co-creation with stakeholders of LiB life cycles.

visualize the potential life cycle of LiBs and serve as a decision-support tool for life cycle design as shown in Figure 2. This study constructs the superstructure for LiB cathode recycling through an integrative approach, incorporating a systematic literature review, bibliometric analysis, and expert discussions. The literature review identified key technological pathways for LiB end-of-life (EoL) management, including landfill/incineration and resource recovery via recycling. Cathode recycling processes are classified into pyrometallurgical, hydrometallurgical, and direct recycling techniques. Pyrometallurgy involves smelting, pyrolysis, and roasting [11], whereas hydrometallurgy encompasses leaching and solvent extraction [12]. Direct recycling, in contrast, enables the regeneration of cathode materials without complete metal separation, utilizing processes such as sintering [13]. Through co-creation with national projects and stakeholders of LiBs in Japan, it was found that the superstructure that had been constructed could be used to gain a common understanding of the issues in the LiB life cycle and to consider countermeasures. Some of these are shown in Figure 2. With regard to LiBs, there is a great deal of uncertainty as an emerging technology, and the infrastructure for recycling is also incomplete. Therefore, we must be aware that the optimization of the current life cycle will become a constraint in future designs, narrowing down the options.

## Findings in Plastic Systems Case

Figure 3 illustrates the production flow of petroleum-derived plastics, detailing oil refining and petrochemical processes. At the end of the plastic life cycle, waste plastics are managed through resource recycling methods such as mechanical recycling, monomerization, and catalytic cracking, or alternative disposal routes, including energy recovery (ER), gasification, and metallurgical reduction processes.

As shown in Figure 3, crude oil is refined into naphtha, which undergoes petrochemical processing to yield basic chemicals such as olefins and BTX. Catalytic cracking converts waste plastics into hydrocarbons resembling conventional refinery products through solvent mixing, cracking reactions, and distillation, which are categorized by carbon chain length: Product A (C1–C4) serves as a raw material for cryogenic separation, Products B (C5–C7) and C (C8–C9) substitute for naphtha, and Product D (>C10) undergoes further cracking via fluid catalytic cracking (FCC).

We carried out co-creation with the relevant parties regarding the plastic system based on the constructed superstructure. There are many different materials used in plastics, and the manufacturing methods are complex, but at the same time, there is a lot of interest from consumers, and they are also recognized as being able to be used as alternatives to paper and metal. For this reason, in addition to raw materials, manufacturing technology, applications and recycling, it is a system that also involves consumer preferences, and the superstructure was effective for visualizing the overall picture of plastics.

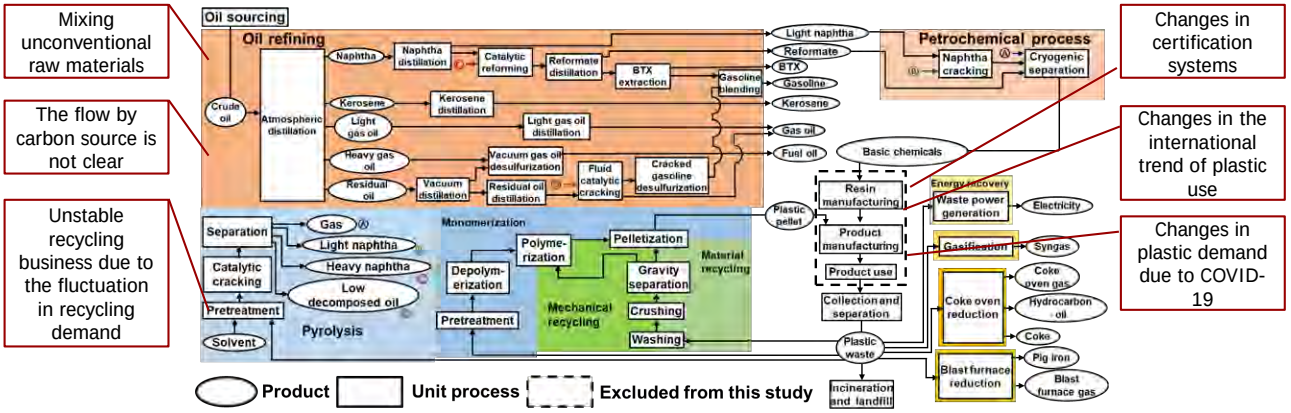



**Figure 3:** Superstructure constructed in a previous study [9]. The comments were examples of the content discussed through co-creation with stakeholders of LiB life cycles.

## Findings in Regional Systems Case

Tanegashima hosts a diverse range of agricultural, forestry, and livestock industries, with sugarcane cultivation playing a central role in regional culture and economy. The sugar industry, which processes locally grown sugarcane into raw sugar, is a key economic driver. Historically, sugarcane bagasse has been utilized as fuel within sugar mills, but previous studies indicate that the available bagasse-derived energy exceeds the demand for sugar production, presenting an underutilized resource [14]. Additionally, the island's forests suffer from aging tree populations and a low proportion of high-quality timber suitable for sawmilling. Expanding the use of woody biomass for energy could simultaneously reduce reliance on fossil fuels and improve forest health [15]. Industrial symbiosis is emerging as a transformative strategy for fostering fossil-free resource utilization in agricultural and forestry regions. The combined application of bagasse and woody biomass has the potential to serve as a stable biomass feedstock for fuel production via torrefaction [16]. Furthermore, advances in sugarcane cultivar breeding could enhance industrial sustainability, as confirmed by rigorous assessments of potential impacts on sugar production [17].

Based on such regional problems and conditions, the superstructure of regional-resource circulated systems was proposed [10, 18] and used for the co-creation with regional stakeholders. Regional residents may not have a comprehensive understanding of the potential of the regional resources, and it can be said that they were motivated by the possibility of simultaneously achieving regional revitalization, de-fossilization, and green transformation. At the same time, we also found that clarifying the challenges that require reform also creates friction regarding the details.

## CONCLUSION

The findings of this study highlight the critical role of superstructure-based technology assessments in facilitating a comprehensive understanding of technological feasibility, trade-offs, and viable implementation pathways. As technological adoption is intrinsically influenced by social acceptance, it is imperative that computer-aided process engineering (CAPE) tools are designed to integrate sociotechnical and socio-economic dimensions within process systems engineering frameworks. By embedding these considerations, CAPE can enhance decision-making processes, promote stakeholder engagement, and support the development of sustainable and resilient technological solutions. This interdisciplinary approach is essential for advancing the practical implementation of emerging technologies in complex industrial and regional systems.

## ACKNOWLEDGEMENTS

This work was supported by MEXT/JSPS KAKENHI (Grant Number JP21H03660, JP23K11521, and JP22K18061), JST COI-NEXT JPMJPF2003, JST PRESTO (Grant Number JPMJPR2278), the Environment Research and Technology Development Fund (Grant Number JPMEERF20213R01 and JPMEERF20243004) of the Environmental Restoration and Conservation Agency of Japan, the New Energy and Industrial Technology Development Organization (NEDO) (Grant number JPNP21026 and JPNP20012), and the Nippon Foundation. Activities of the Presidential Endowed Chair for “Platinum Society” at the University of Tokyo are supported by Mitsui Fudosan Corporation, Sekisui House, Ltd., the East Japan Railway Company, and Toyota Tsusho Corporation.

## REFERENCES

1. Rotolo D, Hicks D, Martin BR. What is an emerging technology? *Res. Policy*, 44(10): 1827-1843 (2015) https://doi.org/10.1016/j.respol.2015.06.006
2. Geels FW, Sovacool BK, Sorrell S. Sociotechnical transitions for deep decarbonization. *Science* 357: 1242–1244 (2017) http://dx.doi.org/10.1126/science.aao3760
3. van der Giesen C, Cucurachi S, Guinée J, Kramer FJ, Tukker A. A critical view on the current application of LCA for new technologies and recommendations for improved practice, *J Clean Prod*, 259: 120904 (2020) https://doi.org/10.1016/j.jclepro.2020.120904
4. IDEF Family of Methods, https://www.idef.com/
5. Yonetsuka T, Yamaki A, Heiho A, Kanematsu Y, Teah HY, Kikuchi Y. Superstructure Modeling of Lithium-Ion Batteries for an Environmentally Conscious Life-Cycle Design, *Comput Aid Chem Eng*, 53: 1417-1422 (2024) http://dx .doi.org/10.1016/B978-0-443-28824-1.50237-4
6. Meng F, Wagner A, Kremer AB, Kanazawa D, Leung JJ, Goult P, Guan M, Herrmann S, Speelman E, Sauter P, Lingeswaran S, Stuchtey MM, Hansen K, Masanet E, Serrenho AC, Ishii N, Kikuchi Y, Cullen JM. Planet compatible pathways for transitioning the chemical industry, *Proc Natl Acad Sci*, 120(8): e2218294120 (2023) https://doi.org/10.1073/pnas.2218294120
7. Kanazawa D, Wagner A, Kremer AB, Leung JJ, Lingeswaran S, Goult P, Herrmann S, Ishii N, Kikuchi Y. Scope 1, 2, and 3 Net Zero Pathways for the Chemical Industry in Japan. *J Chem Eng Jpn* 57 (1) (2024) https://doi.org/10.1080/00219592.2024.2360900.
8. Nakamura T, Fujii S, Heiho A, Teah HY, Kanematsu Y, Kikuchi Y. Assessment of Plastic Recycling Technologies Based on Carbon Resource Circularity Considering Feedstock and Energy Use, *Comput Aid Chem Eng*, 53: 799-804 (2024) http://dx .doi.org/10.1016/B978-0-443-28824-1.50134-4
9. Cao Y, Otsuka A, Teah HY, Kanematsu Y, Kikuchi Y. Consumers' knowledge, perceptions, and preferences regarding bioplastics: Evidence from a survey in Japan. Sustain Prod Consum, 55, 1-10(2025) https://doi.org/10.1016/j.spc.2025.02.003
10. Kikuchi Y, Nakai M, Kanematsu Y, Oosawa K, Okubo T, Oshita Y, Fukushima Y. Application of technology assessments into co-learning for regional transformation: A case study of biomass energy systems in Tanegashima, *Sustain Sci*, 15: 1473-1494 (2020) https://doi.org/10.1007/s11625-020-00801-1
11. Makuza B, Tian Q, Guo X, Chattopadhyay K, Yu D. Pyrometallurgical options for recycling spent lithium-ion batteries: A comprehensive review, *J Power Sources*, 491: 229622 (2021) http://dx.doi.org/10.1016/j.jpowsour.2021.229622
12. Meshram P, Pandey BD, Mankhand TR. Extraction of lithium from primary and secondary sources by pre-treatment, leaching and separation: A comprehensive review, *Hydrometallurgy*, 150: 192-208 (2014) https://doi.org/10.1016/j.hydromet.2014.10.012 .
13. Xu P, Tan DHS, Jiao B, Gao H, Yu X, Chen Z. A Materials Perspective on Direct Recycling of Lithium-Ion Batteries: Principles, Challenges and Opportunities, *Adv Funct Mater*, 33: 2213168 (2021) https://doi.org/10.1002/adfm.202213168
14. Kikuchi Y, Kanematsu Y, Ugo M, Hamada Y, Okubo T. Industrial Symbiosis Centered on a Regional Cogeneration Power Plant Utilizing Available Local Resources: A Case Study of Tanegashima, *J Ind Ecol*, 20(2): 276-288 (2016) http://dx.doi.org/10.1111/jiec.12347
15. Kanematsu Y, Oosawa K, Okubo T, Kikuchi Y. Designing the scale of a woody biomass CHP considering local forestry reformation: a case study of Tanegashima, Japan, *Appl Energ*, 198: 160-172 (2017) https://doi.org/10.1016/j.apenergy.2017.04.021
16. Corradini LL, Heiho A, Kanematsu Y, Shimono R, Ohara S, Kikuchi Y. Simulation-based design of regional biomass thermochemical conversion system for improved environmental and socio-economic performance, *Comput Aided Chem Eng*, 52: 2361-2366 (2023) http://doi.org/10.1016/B978-0-443-15274-0.50375-9
17. Ouchida K, Kanematsu Y, Fukushima Y, Ohara S, Sugimoto A, Hattori T, Terajima Y, Okubo T, Kikuchi Y. Coordinated Integration of Agricultural and Industrial Processes: A Case Study of Sugarcane-Derived Production, *Process Integra Optim Sustain*, 7: 1191-1209 (2023) https://doi.org/10.1007/s41660-023-00337-8
18. Kikuchi Y, Kurishima H, Kanematsu Y, Kasai T, Fujii S, Oshita Y, Ishida T, Ohara S, Prospective life-cycle design of regional resource circulation applying technology assessments supported by CAPE tools, *Comput Aid Chem Eng*, 53: 2251-2256 (2024) http://dx .doi.org/10.1016/B978-0-443-28824-1.50376-8

© 2025 by the authors. Licensed to PSEcommunity.org and PSE Press. This is an open access article under the creative commons CC-BY-SA licensing terms. Credit must be given to creator and adaptations must be shared under the same terms. See https://creativecommons.org/licenses/by-sa/4.0/



Systems & Control Transactions

**Research Article - Peer Reviewed Conference Proceeding**
ESCAPE 35 - European Symposium on Computer Aided Process Engineering
Ghent, Belgium. 6-9 July 2025
Jan F.M. Van Impe, Grégoire Léonard, Satyajeet S. Bhonsale,
Monika E. Polańska, Filip Logist (Eds.)

PSE PRESS

# Integration of renewable energy and reversible solid oxide cells to decarbonize secondary aluminium production and urban systems

**Daniel Flórez-Orrego[a]*, Dareen Dardor[a,b], Meire Ellen Ribeiro Domingos[a], Reginald Germanier[c], Francois Marechal[a]**

[a] Industrial Process and Energy Systems Engineering, EPFL, Sion, 1950, Switzerland
[b] Institute of Sustainable Energy, University of Applied Sciences and Arts Western (HES-SO), Sion, Switzerland
[c] Novelis Switzerland S.A.
* Corresponding Author: daniel.florezorrego@epfl.ch

## ABSTRACT

This study explores an energy transition strategy that leverages reversible solid oxide cells (rSOC), power-to-gas (PtG) conversion, and $CO_2$ management to enhance the efficiency and sustainability of secondary aluminum production. A comparative analysis between conventional and integrated energy scenarios highlights the benefits of multi-technology integration. The results indicate that the integrated system increases total energy demand by 27% due to additional energy conversion steps, but eliminates natural gas consumption, reducing dependency on fossil fuels. Additionally, net $CO_2$ emissions are reduced more than fivefold, demonstrating the potential of carbon capture and utilization strategies. The seasonal storage of synthetic natural gas (SNG) and biogenic $CO_2$ further enhances system flexibility, allowing excess renewable electricity to be converted into storable fuels for winter use. Despite higher capital expenditures, the operational costs of the integrated system are 11% lower than the conventional approach due to improved energy efficiency and $CO_2$ taxation savings. These findings underscore the importance of process integration, energy storage, and renewable electricity utilization in achieving a low-carbon, resilient aluminum industry and urban heating networks.

**Keywords**: Secondary aluminum, renewable energy integration, power-to-gas, reversible solid oxide cells, $CO_2$ utilization, process optimization.

## INTRODUCTION

Aluminium industry relies on fossil natural gas and emits 2% of global industrial emissions [1]. To reduce this dependency, an increased use of renewable energy and advanced conversion systems is aimed. Due to the intermittency of renewable energy, a set of technologies is needed to improve the energy integration and enhance the process resiliency in the heavy industry. Another untapped savings potential is waste heat [2], which can be recovered from stack gases or casting water. Aluminium is processed in semi-batch steps with metallurgical and technical constraints, adding complexity to waste heat valorization. To tackle this issues, advanced technologies including storage units, oxycombustion furnaces, carbon abatement and power-to-gas systems, biomass thermochemical conversion systems, as well as electrified annealing furnaces [3, 4] can be integrated to handle seasonal renewable energy storage, targeting its utilization during periods of high electricity and natural gas prices. Meanwhile, high temperature reversible solid oxide cells can meet the energy balance of the overall system, while increasing exergy efficiency of the integrated facility. Power-to-gas-to-power systems can use renewable electricity and biogenic $CO_2$ to produce synthetic natural gas [5] to replace fossil fuels in the aluminium plant and supply the necessary power to other industrial and urban systems. In this way, a cyclic fuel production and utilization in an integrated aluminium remelting plant behaves as an industrial battery, which can use firstly high-grade waste heat for industrial applications, followed by air and

scrap metal preheating [2, 6], to finally cascade the low-grade waste heat to an urban system [7, 8]. In this work, a scenario of waste heat valorization and renewable energy integration is presented, in which the high-temperature waste heat from the aluminium processing plant is used to reduce the energy consumption in the power-to-gas and biomass energy conversion systems. Those systems facilitate the energy and $CO_2$ management and offset the problem of renewable energy resources intermittency. The performance of the decarbonization route is analyzed in the light of thermal, economic and environmental indicators and compared to a conventional setup based on fossil fuel furnaces and biomass boilers.

## METHODOLOGY

Waste heat from the aluminium furnaces and the biomass energy conversion favors the integration of high temperature reversible solid oxide cells (rSOC). The post-combustion of the tail gas from the rSOC can partly supply the heat needed in the melter furnace, whereas the electricity generated in the cell can be used elsewhere, such as in electrical furnaces, rolling process, ancillary demands, and heat pumping systems of district heating network. Integration of renewable energy resources and technologies, such as gasification, has shown promising potential to attain net negative emissions when combined with electrification, power-to-gas systems, and carbon sequestration methods, adding flexibility to the energy and carbon management systems [9, 10,11].

In the aluminium plant, pure aluminium ingots are preheated from 25°C to 250°C. Next, the pure aluminium is mixed with scrap aluminium and sent to a melting furnace at 660°C. A holder furnace operates as a buffer for the subsequent direct chill casting process (DCC), where aluminium solidifies into ingots using groundwater. This hot water (50 °C) is rejected to the environment. In an improved scenario, the casting water is a heat sink integrated to a $CO_2$ network to supply heating requirements to a city. In the rolling plant, ingots are surface-polished and heated up to 550°C in pusher furnaces, before they go through a hot rolling process followed by an intercooling step and a subsequent cold rolling process powered by electricity. Some coils are sent to an annealing continuous line (ACL), wherein they are chemically and thermally treated.

In the gasification section, biomass moisture is reduced to 10% in a rotary dryer before is chipped consuming ~ 3% of biomass energy (LHV) [12]. In the gasifier (900°C), biomass is converted into syngas rich in CO, $H_2$, $CO_2$ and $CH_4$, among other components, using steam as the gasification agent (S/B ratio 0.75). Syngas is cooled to 400 °C and water-scrubbed to remove impurities and compressed to 35 bar. Downstream water gas shift reactors increase hydrogen content. Syngas can be used for producing hydrogen or synthetic natural gas, whereas gasification waste heat is used for combined heat and power production instead of merely burning biomass. In addition, waste heat is used to produce the steam necessary to feed a solid oxide electrolysis cell (SOEC). As a result, an oxygen-rich stream is also produced. SOEC technology operates typically between 600 °C and 850 ºC, which brings about higher thermodynamic efficiency and faster kinetics [13]. SOEC is operated at a thermoneutral voltage of 1.29 V and electricity consumption of 35 kWh/kgH2. In the context of sustainable energy transition, SOECs are expected to play a role in harvesting and transforming renewable electricity into storable chemicals and fuels [14,15]. The reversible electrolysis cell also works as fuel cell (SOFC) consuming hydrogen and oxygen or air to produce electricity, which requires preheating reactants up to 850 ºC [16]. The inefficiency of SOFC is exploited to harvest waste heat in a downstream post-combustion system using oxygen to drive high temperature aluminium melting furnaces. Meanwhile, the produced electricity can be used to drive other heating furnaces and appliances in the aluminium plant, as well as heat pumps of the district heating network. All in all, the integration of an rSOC enables energy storage and power generation [17], facilitated carbon separation, post-combustion carbon capture, and waste heat valorization. It occurs first at high-temperature for the melting of the aluminium, and later for the low-temperature $CO_2$ district heating network, composed of a closed loop of $CO_2$ that harvests waste heat from the industrial, biomass conversion and power-to-gas systems. $CO_2$ evaporates at 50 bar (~14°C) and can later release the condensation enthalpy in a heat pump that supplies space heating or domestic hot water to a nearby urban system. A superstructure used to provide the energy demands of the aluminium and the urban agglomeration also include heat pumps; gasification, methanation and gas treatment systems; $CO_2$ abatement units, electrification technologies, storage units and cogeneration cycles (Figure 1).

In view of multiple technological options and trade-offs between electricity, gas or biomass import, a systemic approach is developed to evaluate the most cost-efficient configuration to supply combined heat and power to the aluminium remelting process. OSMOSE platform [11] is used to solve a minimum energy requirements (MER) of the overall process. Subsequently, this framework handles the mixed integer linear programming problem (MILP) that works out the best energy technologies and their operating conditions. Aspen Plus® software is used to simulate different energy conversion systems. In this regard, the number of decarbonization options increases, calling for a systemic study to evaluate the most suitable processes and carbon neutral technologies to

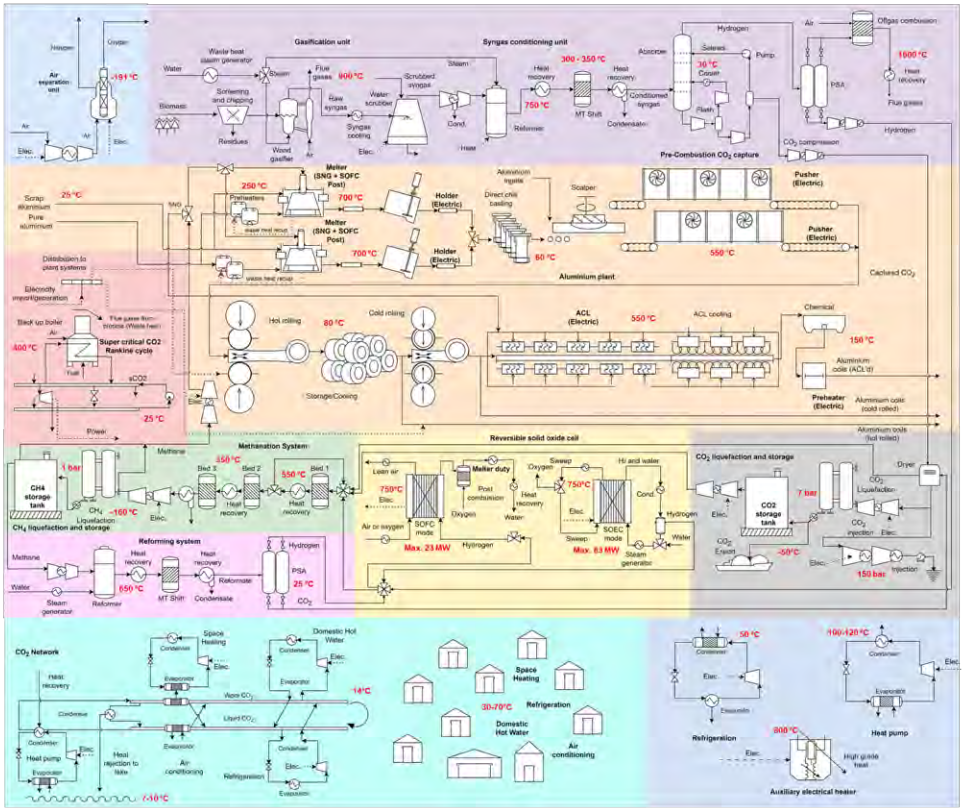



**Figure 1:** Integrated aluminium production plant and potential utility and decarbonization technologies.

supply the energy requirements to aluminium industry without significantly impacting the operational settings and process reliability. To this end, a mixed integer linear problem is conducted using OSMOSE platform [11] to maximize waste heat recovery and define the most economically, thermodynamic and environmentally favorable configurations to integrate the aluminium plant, the biomass conversion units and the grid into the urban system, considering the temporal variation of the prices and energy demands. The solver minimizes the total operating cost, Eq. (1), where Cop1 and Cop2 represent the fixed and variable operating costs of a unit (u) and Cinv1 and Cinv2 are the fixed and variable investment costs of a unit (u). $Y_u$ is a binary variable related to the presence or absence of a unit (u), while $M_u$ is its respective continuous load factor.

$$\min C_{tot} = \sum_{u\in U}\left[\sum_{t\in T}\left(Cop1_u \cdot Y_{u,t} + Cop2_u \cdot M_{u,t}\right)\cdot \Delta t + Cinv1_u \cdot Y_u + Cinv2_u \cdot M_u\right] \quad (1)$$

This objective function is subject to multiple constraints including unit existence and load conditions:

$$Y_{u,t} \cdot Fmin_u \le M_{u,t} \le Y_{u,t} \cdot Fmax_u \;;\; \forall u \in U,\ \forall t \in T \quad (2)$$

$$M_{u,t} \le M_u \quad (2)$$

$$Y_{u,t} \le Y_u \quad (3)$$

Mass and energy balance constraints:

$$\sum m_{\text{Input streams}} = \sum m_{\text{Output streams}}\;; \qquad \forall T \quad (5)$$

Power production or consumption constraints:

$$\sum_{w=1}^{N_w} M_w \cdot w_{w,utilities} + \sum_{Processes} W + W_{import} - W_{export} = 0\,, \forall T \quad (6)$$

Heat cascade constraints and balance at the temperature interval r:

$$\sum_{w=1}^{N_w} M_w \cdot q_{w,r} + \sum_{i=1}^{N} Q_{i,r} + R_{r+1} - R_r = 0\;;\ \forall r = 1 \ldots . N \quad (7)$$

And solution feasibility:

$$R_1 = 0, R_{N+1} = 0, \qquad R_r \ge 0\,; W_{import} \ge 0, \quad W_{export} \ge 0 \qquad \forall r = 1 \ldots . N \quad (8)$$

where;

- *N* is the number of temperature intervals based on supply and target temperatures of streams [-]
- *Q* is the heat exchanged between process streams [kW],
- *R* is the heat cascaded from higher (r+1) to lower

(r) intervals of temperature [kW],

- $N_w$ is the number of utility units available [-],
- $q_{w,r}$ is the specific heating or cooling flow supplied by a utility unit *w* within an interval *r* [kW],
- *W* is the power produced or consumed by the utilities and process units, or the grid [kW].

The mathematical formulation of the problem can be solved using any open-source mixed integer linear programming solver, compatible with AMPL® community edition. The costs of the commodities are assumed based on the current European market and are set as 3.50 Eur/m$^3$ for water, 0.15 Eur/kWh winter - 0.05 Eur/kWh summer for electricity, 0.08 Eur/kWh winter - 0.06 Eur/kWh summer for biomass, 0.07 Eur/kWh for natural gas, and 100 Eur/t for the $CO_2$ tax.

## RESULTS AND DISCUSSION

Table 1 compares the energy consumption of the conventional scenario (i.e. only natural gas-fired furnaces and biomass combustion-based district heating network) and the integrated solution proposed to decarbonize the aluminium plant and the city demands. The energy consumption in advanced integrated scenario is 27% higher than that of the conventional scenario since biomass needs to be converted internally in the battery limits of the integrated aluminium plant and urban system. However, the conventional scenario is strongly dependent on the consumption of fossil gas, which is subject to volatile market conditions and increasing surveillance due to associated direct and indirect atmospheric emissions. Also, it is worth noting an opportunity to increase the share of renewable input in aluminium industry and urban systems by importing nine times more electricity from the grid, which has lower associated indirect emissions than the fossil gas. In the rSOC, the power consumption during the electrolysis mode averages 57 MW, whereas the fuel cell power generation is 15 MW.

The rSOC together with the storage systems help managing the $CO_2$ and SNG streams. $CO_2$ produced and captured in the reformer, the auxiliary oxy-furnace, and syngas pre-treatment (see Table 3) can be later used to generate SNG that is stored in the summer season and consumed later on the winter season. By harnessing renewable electricity in summer, total biomass energy consumption can be reduced to 25% of the total amount consumed in less efficient biomass boilers for space heating and domestic hot water production. Yet, the most striking outcome is the complete replacement of fossil natural gas by renewable energy resources, such as biomass and electricity. Table 2 summarizes the $CO_2$ emissions balance including direct and indirect emissions for both conventional and integrated scenarios. Net $CO_2$ emissions of the conventional scenario can be reduced more than five times if an integrated carbon management and sequestration system is employed. Captured and injected biogenic $CO_2$ allows offsetting indirect emissions associated to the supply chains of electricity and biomass

In the integrated scenario, total energy demand is around 30% higher, and total incremental cost is about 35% higher due to the additional investment (~22 MEur/y). Carbon tax associated to fossil direct and indirect $CO_2$ emissions in the conventional scenario adds a penalty of more than 4 MEur/y.

**Table 1.** Energy consumption remarks of decarbonization solutions for the aluminium remelting and the district heating network.

| Parameter | Conventional solution | Integrated solution |
|---|---|---|
| Biomass consumption [GWh/y][1] | 218.04 | 51.95 |
| Electricity import [GWh/y] | 70.00 | 570.28 |
| Natural gas import [GWh/y] | 200.00 | 0.00 |
| Total energy demand [GWh/y] | 488.04 | 622.23 |
| Electricity export [GWh/y] | 0.00 | 0.00 |

1. In the conventional case, biomass is only consumed in a decentralized hot water boiler (eff. 70%) for district heating purposes

**Table 2.** Direct and indirect emissions $CO_2$ emissions for conventional and integrated aluminium plant and the district heating network.

| Parameter | Conventional solution | Integrated solution |
|---|---|---|
| Direct $CO_2$ emissions from natural gas consumption [kt/y] | 40 | 0 |
| Indirect $CO_2$ emissions from electricity consumption [kt/y][2,3] | 1.60 | 13.30 |
| Indirect $CO_2$ emissions from biomass consumption [kt/y] [1,2] | 2.00 | 0.467 |
| Indirect $CO_2$ emissions from natural gas consumption [kt/y][2] | 9.90 | 0 |
| $CO_2$ injection (biogenic sequestered) [kt/y] | 0 | -5.19 |
| Net $CO_2$ emissions to environment [kt/y] | 53.50 | 8.58 |

1. Biogenic $CO_2$ emissions are considered as circular emissions and they do not contribute to the net $CO_2$ emission to environment if eventually released. 2. Specific indirect emissions of biomass 0.0025 $g_{CO2}/kJ_{biowood}$; Specific indirect emissions of electricity 23.32 $g_{CO2}/kWh_{elec}$, Specific indirect emissions of natural gas 0.0138 $g_{CO2}/kJ_{CH4}$; 3. Maximum electrolyzer capacity 85 MW.

Figure 2 illustrates seasonal storage profiles for SNG and $CO_2$ gases. Loading of SNG tanks occurs during summer season when surplus electricity from renewable energy resources is available. It renders more attractive to harvest electricity and store it in the form of fuel to be

used later in the colder season. Biomass resource harvested during the summer season can be used to produce syngas or synthetic natural gas consumed in the SOFC. The $CO_2$ gas is used to refill the storage tanks that store $CO_2$ until is reacted in a methanation section to produce SNG in summer season. The benefit to store renewable energy in the form of gas is twofold: biomass consumption is drastically reduced and biogenic $CO_2$ produced is used to offset the $CO_2$ losses. Annualized investment and operational costs calculated for the conventional and integrated systems, are summarized in Table 3. Total cost of advanced technologies is 28% higher than for the conventional route, due to twenty times higher annualized investment. Yet, the annualized operational expenditure of the conventional solution is higher (11%) than for the integrated approach, due to cheaper biomass resources and use of electricity during the summer season to produce and store fuel using biogenic $CO_2$.

**Table 3.** Annualized investment and operational costs.

| Cost [Eur/y] | Conventional solution | Integrated solution |
|---|---|---|
| Electricity consumption cost | 6,074,580 | 31,861,130 |
| Biomass consumption cost | 15,537,550 | 4,155,900 |
| Natural gas consumption cost | 13,648,440 | 0 |
| Fossil $CO_2$ emissions taxation | 5,313,070 | 518,640 |
| Annualized operational cost | 40,573,650 | 36,535,680 |
| Annualized capital cost | 1,456,350 | 21,869,870 |
| Total annualized cost | 42,030,000 | 58,405,550 |

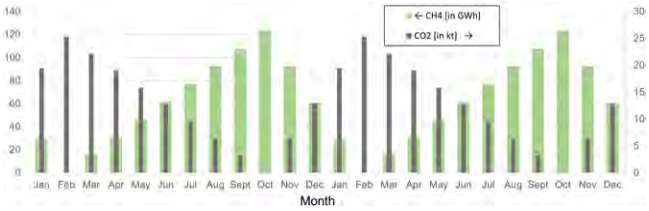
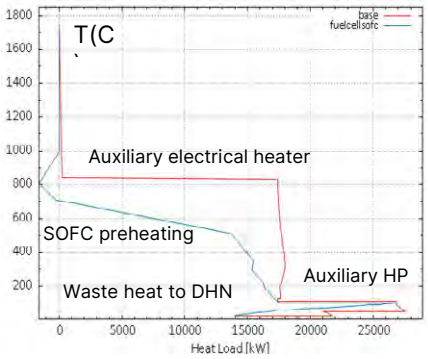
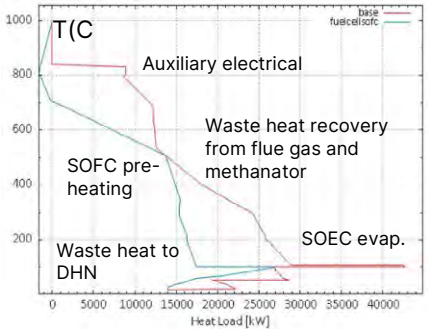



**Figure 2:** Seasonal gas storage

Figure 3 shows the integrated curves of the integrated aluminium plant, including the biomass energy conversion units, the power-to-gas system and the seasonal storage demands. These plots are useful to quantify the amount of waste heat available at different temperature levels, as well as to point out more rational energy uses and integration solutions, such as prioritizing the utilization of high-grade chemical and thermal energy in applications running at high temperatures, and only cascading waste heat down to lower temperatures after the high temperature energy demands have been meet. In this way, the irreversibility of the overall energy system is minimized, and other energy technologies, such as heat pump systems, can be rather activated at the adequate temperature levels of heat supply. According to Figures 3a and b, the waste heat recovery from flue gases, gasifier effluent, SOFC tail gas combustors, as well as auxiliary oxy-furnaces allows integrating the aluminium plant and the biomass conversion processes to the power-to-gas system. The solid oxide cell operates at elevated temperatures in order to increase the process efficiency and minimize the electrochemical losses, thus an internal waste heat recovery is fundamental to reduce the external energy imports. In summary, the high-grade chemical energy of the valuable biomass resource is used firstly at high temperatures in the most suitable applications, such as the aluminium melting process and the solid oxide cell, to be next cascaded down for being used at lower temperatures, such as in space heating and domestic hot water production. In this regard, the heat cascading efficiency principle allows reducing the biomass consumption, which otherwise would be burnt in a biomass boiler to merely produce hot water below 70 °C.




(a)




(b)

**Figure 3:** Integrated curves of the integrated aluminium plant (a) SOFC integrated curve in winter, (b) SOFC integrated curve in summer.

## CONCLUSIONS

In this work, the advantages and challenges of the use of renewable energy resources and more advanced energy technologies for process integration and decarbonization of an aluminium remelting plant and a district heating network are presented. As a result, the energy consumption in more advanced integrated scenario is 30% higher than that of the conventional scenario based on natural gas. It can be explained by the fact that biomass needs to be converted internally in the

battery limits of the integrated scenario. The power-to-gas-to-power and the renewable energy storage systems also entail inherent inefficiencies while aiming to internalized fuel supply and emissions management. On the other hand, in the integrated aluminium decarbonization scenario, the direct fossil fuel consumption is completely avoided, despite the fact that indirect emissions linked to electricity mix are still significant, especially if electricity from the grid is partly composed of a non-renewable share at different scopes. In any case, the net CO2 emissions of the conventional scenario using natural gas and biomass boilers achieve values higher than 50 kt/y, which is roughly 0.2 tCO2/tAl. This value can be reduced by more than three times if an integrated carbon management and sequestration system is implemented. A district heating network can help to distribute the waste heat available through all the industrial process, but only after the high-grade chemical, electrical and thermal energy has been used at high temperature in the melting furnaces and solid oxide cells. The post-combustion of the tail gas from the SOFC cell can supply the heat needed in the melter furnace, whereas the electricity generated in the cell can be used elsewhere in the plant, such as in other electrical furnaces, rolling processes, ancillary power demands, and heat pumping systems of the district heating network.

## ACKNOWLEDGEMENTS

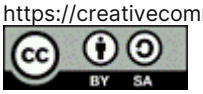
The authors would like to thanks the Swiss Federal Office of Energy and Suisse Energie for funding this research work within the NetZero Lab Consortium.

## REFERENCES

1. IAI. Aluminium Sector GHG Pathways to 2050, Available at: https://international-aluminium.org/resource/aluminium-sector-greenhouse-gas-pathways-to-2050-2021/ Accessed 25 March 2023.
2. Kumar RA, Prabhuram K, Subrammaniyan V, et al. A Method for Recovering the Waste Heat to Achieve Overall Energy Conservation in Aluminum Casting Industries. In: Narasimhan NL, Bourouis M, Raghavan V (eds) Recent Advances in Energy Technologies. Singapore: Springer Nature Singapore, pp. 331–342.
3. Yu M, Gudjonsdottir MS, Valdimarsson P, et al. Waste Heat Recovery from Aluminum Production. In: Sun Z, Wang C, Guillen DP, et al. (eds) Energy Technology 2018. Cham: Springer International Publishing, pp. 165–178.
4. Clos DP, Andresen T, Nekså P, et al. Enabling Efficient Heat Recovery from Aluminium Pot Gas. In: Ratvik AP (ed) Light Metals 2017. Cham: Springer International Publishing, pp. 783–791.
5. Borge-Diez D, Rosales-Asensio E, Açikkalp E, et al. Analysis of Power to Gas Technologies for Energy Intensive Industries in European Union. Energies 2023; 16: 538.
6. Arink T, Hassan MI. Metal Scrap Preheating using Flue Gas Waste Heat. Energy Procedia 2017; 105: 4788–4795.
7. Bertrand A, Mian A, Kantor I, et al. Regional waste heat valorisation: A mixed integer linear programming method for energy service companies. Energy 2019; 167: 454–468.
8. Stijepovic MZ, Linke P. Optimal waste heat recovery and reuse in industrial zones. Energy, Volume 36, Issue 7, pp 4019-4031.
9. Florez-Orrego DA, Ribeiro Domingos M. E.G D, Dardor D, et al. Renewable Energy Integration and Waste Heat Recovery for the Production of Sustainable Jet Fuel and Decarbonization of Industrial Heating Applications. In: Proceedings of the 2023 AIChE Annual Meeting. Orlando (FL), United States: American Institute of Chemical Engineering, 2023.
10. Florez-Orrego D. A systemic study for enhanced waste heat recovery and renewable energy integration towards decarbonizing the aluminium industry. 36th International Conference on Efficiency, Cost, Optimization, Simulation and Environmental Impact of Energy Systems - ECOS 2023, June 25th – 30th, Las Palmas de Gran Canaria, Spain.
11. Flórez-Orrego D, Ribeiro Domingos M., Maréchal F. A systematic framework for the multi-time integration of industrial complexes and urban systems, 7th International Conference on Contemporary Problems of Thermal Engineering - CPOTE 2022, Warsaw, Poland, 20th-23th September, 2022
12. Flórez-Orrego D, Maréchal F, de Oliveira Junior S. Comparative exergy and economic assessment of fossil and biomass-based routes for ammonia production. Energy Conversion and Management 2019; 194: 22–36.
13. Fan L, Li C, Van Biert L, et al. Advances on methane reforming in solid oxide fuel cells. Renewable and Sustainable Energy Reviews 2022; 166: 112646.
14. Flórez-Orrego D, Dardor D, Ribeiro Domingos ME, et al. Renewable energy integration and waste heat valorization in aluminum remelting mills for the co-production of kerosene and methanol. 34rd European Symposium on Computer Aided Process Engineering – ESCAPE 34 and International Symposium on Process Systems Engineering – PSE 24, June 2 to June 6, 2024. Florence, Italy.

15. Domingos MEG, Florez-Orrego D, Dardor D, et al. Sustainable Methanol Production Using a Multi-Time Energy Integration and CO2 Management Approach as an Energy Carrier for Synthetic Natural Gas Synthesis. In: Proceedings of 2023 AIChE Annual Meeting. Orlando (FL), United States: American Institute of Chemical Engineering, 2023.
16. Salomone F, Giglio E, Ferrero D, et al. Techno-economic modelling of a Power-to-Gas system based on SOEC electrolysis and CO2 methanation in a RES-based electric grid. Chemical Engineering Journal Volume 377, 2019, pp 120233.
17. Jensen SH, Graves C, Mogensen M, et al. Large-scale electricity storage utilizing reversible solid oxide cells combined with underground storage of CO2 and CH 4. Energy & Environmental Science 2015; 8: 2471–2479

© 2025 by the authors. Licensed to PSEcommunity.org and PSE Press. This is an open access article under the creative commons CC-BY-SA licensing terms. Credit must be given to creator and adaptations must be shared under the same terms. See https://creativecommons.org/licenses/by-sa/4.0/



Systems & Control Transactions

**Research Article - Peer Reviewed Conference Proceeding**
ESCAPE 35 - European Symposium on Computer Aided Process Engineering
Ghent, Belgium. 6-9 July 2025
Jan F.M. Van Impe, Grégoire Léonard, Satyajeet S. Bhonsale,
Monika E. Polańska, Filip Logist (Eds.)

PSE PRESS

# Assessing the economic viability of green methanol production: The critical role of $CO_2$ purity in green methanol production

**Franc González-Cazorla[a,b]*, Jordi Pujol[a], Oriol Martínez[a], Lluis Soler[b], and Moisès Graells[b]**

[a] GasN2, Carrer Roure Gros, 23, Sentmenat, Barcelona, 08181, Spain
[b] Chemical Engineering Department, Universitat Politècnica de Catalunya, Escola d'Enginyeria de Barcelona Est (EEBE), Av. Eduard Maristany, 16, 08019, Barcelona, Spain
* Corresponding Author: fgonzalez@gasn2.com.

## ABSTRACT

The growing concern over climate change and rising carbon dioxide ($CO_2$) emissions have spurred the development of strategies to upcycle greenhouse gases. One promising solution is the synthesis of green methanol via catalytic hydrogenation of captured $CO_2$ using renewable hydrogen ($H_2$). This provides a versatile chemical feedstock for fuels and industrial processes while reducing $CO_2$ levels. Recent advancements in $CO_2$ capture technologies achieve purities ranging from 83% to 98% (v/v), enabling a sustainable integration with green hydrogen for methanol production. While research has largely focused on $CO_2$ purities above 96%, such models overlook the variability and lower purities typical of industrial carbon capture streams. Addressing this gap, this study examines the economic impacts of $CO_2$ purity on methanol synthesis. Using Aspen Hysys V14, the hydrogenation process is simulated to assess the effects of varying $CO_2$ purities on operational costs, yield, and profitability, providing a realistic evaluation under actual industrial conditions. The results reveal that even slight changes in $CO_2$ purity markedly influence both costs and profitability, highlighting the importance of studying $CO_2$ capture technologies for methanol production. This study quantifies the relationship between $CO_2$ purity and operational cost, contributing critical insights for process operation. By emphasizing the role of $CO_2$ purity in enhancing both sustainability and economic feasibility, it advances the understanding of green methanol production as a viable strategy for climate change mitigation.

**Keywords**: $CO_2$ hydrogenation, Green methanol production, Techno-Economic Analysis.

## INTRODUCTION

Anthropogenic emissions of carbon dioxide ($CO_2$) have surged dramatically in the past century, becoming a central focus of climate change mitigation efforts. The overwhelming scientific consensus indicates that the increase in atmospheric $CO_2$ concentration is strongly correlated with the rise in global temperatures, prompting the development of technologies to capture and utilize $CO_2$ [1]. Among these, the conversion of $CO_2$ into value-added products has garnered significant attention as a strategy to mitigate emissions while supporting the transition to a circular carbon economy.

Approximately 35% of global anthropogenic $CO_2$ emissions stem from industrial processes and power generation reliant on fossil fuels [2]. While capturing $CO_2$ from these sources is technically feasible, the associated costs remain high due to the energy-intensive nature of capture and compression processes [3]. Integrating $CO_2$ utilization into this framework offers an opportunity to offset costs by transforming $CO_2$ into marketable products, such as methanol, thereby enhancing the economic viability of carbon capture initiatives.

Methanol is a key platform chemical widely used in the production of formaldehyde, acetic acid, and methyl tert-butyl ether. It is also an alternative fuel with excellent combustion properties, presenting fewer environmental pollutants compared to conventional fossil fuels [4].

The quality of the CO2 feedstock is crucial for the upcycling process. Research has largely focused on $CO_2$

purities above 96% (v/v) [5]. However, recent advancements in $CO_2$ capture technologies achieve purities ranging from 83% to 98% (v/v) [6]. Hence, this study aims to evaluate the impact of $CO_2$ purity on the production of fuel-grade methanol, considering the technical and economic implications of integrating $CO_2$ capture and utilization processes efficiently. By focusing on the catalytic hydrogenation of $CO_2$ under varying purity levels, the research quantifies the potential for emission abatement and economic feasibility, thus contributing to the broader adoption of sustainable methanol synthesis technologies.

## Methanol production process

Traditionally, methanol is synthesized from synthesis gas—a mixture of carbon monoxide (CO), $CO_2$, and $H_2$—derived predominantly from natural gas via steam methane reforming [7]. The increasing emphasis on sustainability has driven interest in alternative feedstocks and processes for methanol production. Among these, the production of methanol from captured $CO_2$ through catalytic hydrogenation using renewable hydrogen ($H_2$) represents a genuinely green alternative, offering a pathway to reduce dependency on fossil fuels while enabling the recycling of $CO_2$ into valuable chemicals.

The direct hydrogenation of $CO_2$ to methanol in a single reaction step is simpler and more efficient [8] This method eliminates the need for intermediate processes, such as syngas production, required by traditional methods. Streamlining the reaction pathway not only reduces energy consumption but also lowers process complexity, improving overall economic feasibility and making it more suitable for large-scale applications. Additionally, it avoids the complex handling of CO and $CO_2$, which further enhances its compatibility with carbon capture and storage technologies [9].

This process not only facilitates $CO_2$ recycling but also contributes to the substitution of fossil feedstocks in methanol production, reducing the overall carbon footprint of the chemical industry. This process typically employs $Cu/ZnO/Al_2O_3$ catalysts, which operate under moderate conditions (210–270°C, 50–100 bar) with high selectivity (<99%) for methanol [10].

Yet, the economic and environmental impact of this process is highly dependent on the purity of the captured $CO_2$ and the energy used for hydrogen production.

## $CO_2$ hydrogenation

Methanol can be synthesized from $CO_2$ through two main pathways: a one-step process or a two-step process. The one-step pathway involves the direct hydrogenation of $CO_2$ to methanol, while the two-step process first converts $CO_2$ to CO via the Reverse Water Gas Shift (RWGS) reaction, followed by hydrogenation of CO to methanol. In this study, the one-step hydrogenation of $CO_2$ was selected as the conversion method.

The $CO_2$ utilized in these processes can be sourced from flue gases emitted by thermal power plants (e.g., coal or natural gas-based), as well as from industrial facilities such as steel mills, cement plants, and other significant $CO_2$ emitters.

The hydrogen required for this reaction must be produced sustainably, for instance, via biological methods using algae or through water electrolysis powered by carbon-neutral electricity sources [11].

The production of methanol is achieved through highly exothermic reactions (Eqs. 1, 2), while the RWGS reaction (Eq. 3) may also proceed in parallel. These reactions collectively enable the valorization of $CO_2$ into a versatile chemical with broad industrial applications.

$$CO_{(g)} + 2H_{2\,(g)} \leftrightarrow CH_3OH_{(l)} \quad \Delta H_{298K} = -128\ \frac{kJ}{mol} \tag{1}$$

$$CO_{2\,(g)} + 3H_{2\,(g)} \leftrightarrow CH_3OH_{(l)} + H_2O_{(l)} \quad \Delta H_{298K} = -87\ \frac{kJ}{mol} \tag{2}$$

$$CO_{2\,(g)} + H_{2\,(g)} \leftrightarrow CO_{(g)} + H_2O_{\,(l)} \quad \Delta H_{298K} = 41\ \frac{kJ}{mol} \tag{3}$$

The hydrogenation of $CO_2$ to produce methanol has garnered significant attention in recent years. Joo et al. investigated a two-step methanol production process and observed higher yields compared to the one-step alternative [12]. Mignard et al. proposed a process that synthesizes methanol from $CO_2$ captured from coal-fired power plant flue gases, using electrolytic hydrogen. Their findings highlighted that the availability of waste heat from the power plant is crucial to supply the thermal energy needed for substantial $CO_2$ abatement [13]. Without this thermal integration, $CO_2$ mitigation is negligible.

Methanol production emerged as the most energy-efficient route. Pontzen et al. compared the performance of $CO_2$-based methanol production over a $Cu/ZnO/Al_2O_3$ catalyst with conventional synthesis gas processes, finding that the $CO_2$-based process exhibited lower productivity levels [14].

Soltanieh et al. conducted an economic analysis for co-producing methanol and electricity from captured $CO_2$ and carbon-free hydrogen, emphasizing the potential for integrated systems [15]. Van Der Ham et al. proposed a $CO_2$-to-methanol process utilizing a fluidized-bed membrane reactor, which achieved significant $CO_2$ reduction [16]. However, the process faced challenges related to economic feasibility.

These studies collectively underscore both the technical promise and the economic hurdles associated with methanol production from $CO_2$ hydrogenation.

# METHODOLOGY

Operational analysis and simulation were carried out using Aspen HYSYS V14 with stoichiometric feed conditions tailored to the methanol synthesis reaction. Thermodynamic properties of high-pressure streams (>10

bar) were modeled using the Redlich-Kwong-Soave equation of state, while the NRTL model was employed for streams at lower pressures (<10 bar). These thermodynamic models ensure robust and reliable process representation, optimizing performance across varying conditions. Sensitivity analysis of $CO_2$ purity were carried out for a given operational case study in methanol hydrogenation, evaluating its impact on process performance and efficiency. The simulated data obtained were used for the subsequent economic analysis. Hence, a relationship between feed purity and overall process economics was set by correlating these data with operating costs.

## Case study

The process utilizes $CO_2$ sourced from any industrial facility emitting significant amounts of $CO_2$, coupled with hydrogen produced via water electrolysis, as feedstock for methanol synthesis. A schematic representation of the process is shown in **Figure 1**.

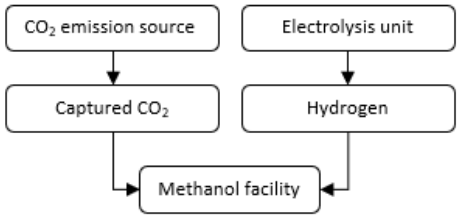



**Figure 1.** Scheme of methanol synthesis.

Water electrolysis is powered by carbon-free electricity sources such as renewables (e.g., hydroelectric, wind, solar, or biomass) or nuclear power. The entire system, including both hydrogen production and methanol synthesis, is designed to operate as an integrated unit, minimizing energy losses and simplifying logistics. This integration ensures that the hydrogen generated is directly utilized within the methanol synthesis process, avoiding storage and transportation challenges.

### Water electrolysis unit

The production of hydrogen via water electrolysis (Eq. 4) requires an energy input of 60 kWh/kg $H_2$ [17]. The hydrogen exits the electrolyzer at 6 bar and 25 °C, ready for direct use in the methanol synthesis process.

$$H_2O_{(l)} \rightarrow H_{2\,(g)} + 0.5\,O_{2\,(g)} \quad (4)$$

Electrolysis also produces a significant quantity of oxygen as a by-product. This oxygen could be internally used in the power plant for oxycombustion, enhancing $CO_2$ concentration in flue gases and lowering the energy requirements for its capture. Alternatively, it can be marketed. This study analyses the first option.

### $CO_2$ capture unit

The $CO_2$ capture unit considered in this paper relies on physical adsorption using adsorbents materials. In this process, $CO_2$ is captured from flue gases of industrial sources through its interaction with the adsorbent.

Flue gases containing $CO_2$ are first compressed to offset the pressure drop in the adsorption system. These gases are then introduced into the adsorbent bed, where the $CO_2$ is physically adsorbed due to the adsorbent's microporous structure. The system operates by cycling the pressure, with $CO_2$ being adsorbed at higher pressures. Once the zeolite becomes saturated with $CO_2$, the desorption process is initiated. This is achieved by reducing the pressure or increasing the temperature, which allows $CO_2$ to be released and collected for further utilization.

The adsorbent material can be regenerated after each cycle by applying pressure or temperature swing adsorption (PSA/TSA) methods [18], allowing it to be reused multiple times without significant loss of efficiency. The desorbed $CO_2$ is then captured and fed to the methanol synthesis unit, where it is combined with hydrogen.

The overall performance of the system depends on the adsorption capacity of the adsorbent, the frequency of regeneration cycles, and the efficiency of the desorption process [19].

$CO_2$ capture performance and associated energy use are influenced by the purity of the incoming $CO_2$ stream. Typically, the purity of captured $CO_2$ in industrial applications ranges from 83% to 98%. For $CO_2$ with a purity of 83%, the energy consumption for $CO_2$ capture can range between 1.00 kWh and 1.20 kWh/kg $CO_2$ [20]. When the $CO_2$ purity increases to 98%, the energy consumption for the same processes increases, typically between 1.50 kWh and 2.00 kWh/kg $CO_2$ [6], due to the need for higher efficiency in separating and adsorbing the $CO_2$ at greater purity levels. Estimations from industrial practice are shown in **Figure 2**. $CO_2$ is fed to the methanol plant at 6 bar and 25°C.

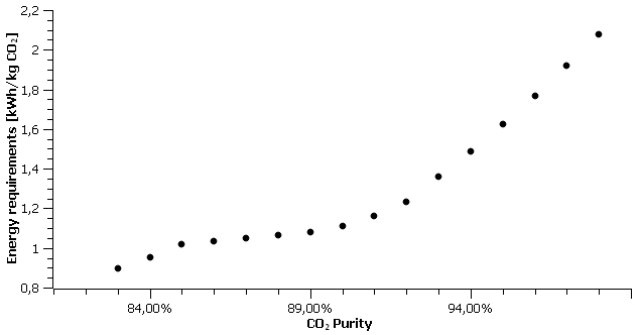



**Figure 2.** Energy demand for $CO_2$ purification.

## Methanol synthesis and purification unit

The process flowsheet is presented in **Figure 3**. To analyze the operating modes of methanol production via $CO_2$ hydrogenation, a process flowsheet was developed for the methanol synthesis and purification stages. The conversion process utilizes a conversion reactor for $CO_2$

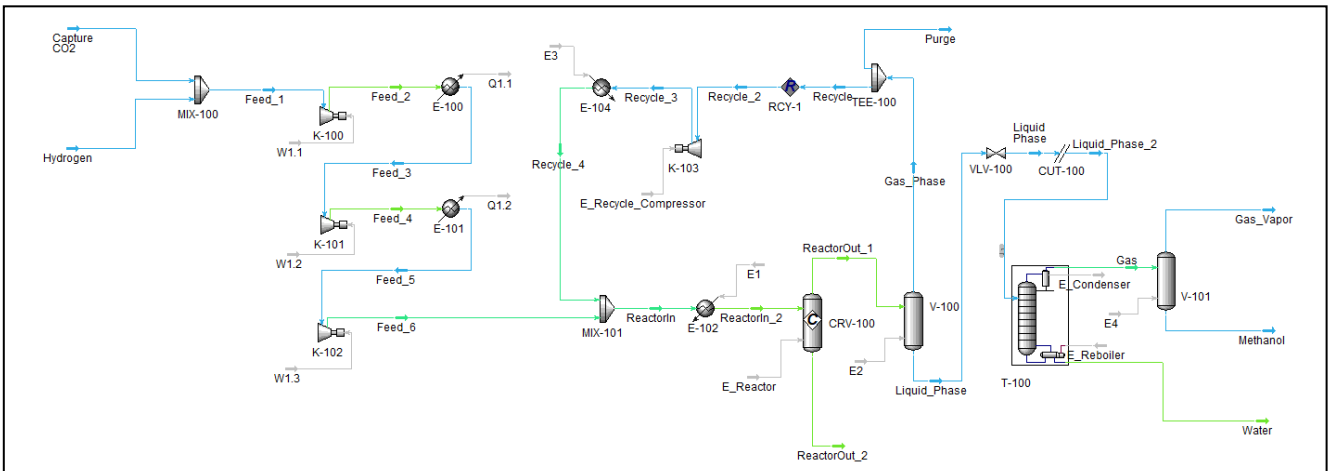



**Figure 3.** Flowsheet of the process for green methanol production from captured $CO_2$ and renewable hydrogen.

hydrogenation. Conversion reactor used for production of methanol works with 17.25 % of $CO_2$ conversion and the pressure is 60 bar [21].

The economic analysis assumes a base price of 50€/MWh for the energy cost [22]. Production cost is measured in kWh per kilogram of feed, reflecting the efficiency of the process and the energy requirements for transforming raw materials into the final product.

### Process description

$CO_2$ and hydrogen is fed into the system at 6 bar, both at an initial temperature of 25 °C. The feed undergoes compression to the reaction pressure of 60 bar through a series of compressors with intercooling. The two compressed gases are initially mixed in MIX-100 and subsequently combined with the recycle stream.

The mixed stream is heated in E-102 to the desired reaction temperature (215ºC) before being introduced into the conversion reactor system. In these reactors, methanol synthesis occurs via the catalytic hydrogenation of $CO_2$. Heat generated during the reaction is managed through the reactor heat exchanger (E-Reactor).

The reactor outlet stream is sent to a flash separation unit (V-100), where it is divided into two phases. The gas phase, composed of non-reacted gases and by-products, is split into two streams: a small fraction is purged (5%) to prevent the accumulation of inerts and by-products, while the majority is compressed (K-103) and recycled back into the process, ensuring efficient use of unreacted reactants.

The liquid phase, containing methanol and water, is sent to the distillation column (T-100) for further purification. The crude methanol mixture undergoes pressure reduction via a valve system (VLV-100). The water by-product exits from the bottom of the column, while purified methanol vapor exits the top, where it is cooled and condensed to liquid form for collection.

## RESULTS & DISCUSSION

The influence of $CO_2$ purity on the methanol synthesis process was analyzed, focusing on energy requirements (kWh/kg methanol), productivity (kg/h), recycle ratio, and production cost (€/kg methanol). Results are shown in **Figure 4**.

The recycle ratio decreases as $CO_2$ purity increases. At lower purities, higher amounts of inerts are recycled for the methanol synthesis, leading to increased operational demands on the system. Conversely, higher purities reduce recycle ratio, minimizing the energy for recycling equipment and improving overall system efficiency.

Methanol productivity increases proportionally with $CO_2$ purity. From an economic perspective, this increase in productivity directly offsets operational costs, making higher-purity $CO_2$ streams more favorable despite the potential increase in capture costs.

Lower purities result in greater energy demand due to the recycling of inert gases and increased compression requirements. As purity rises, energy consumption decreases significantly. This energy efficiency translates directly into reduced operational costs, particularly for systems where energy-intensive recycling and compression are dominant expenses.

The results highlight a non-linear relationship between $CO_2$ purity and methanol production costs. At lower purities, the cost remains relatively stable, suggesting that impurities within this range do not significantly impact the overall process economics.

As purity increases towards 89%, production costs rise and then fall for higher purities (>92%). This trend can be attributed to the balance between purification expenses and process efficiency. Intermediate purities like-

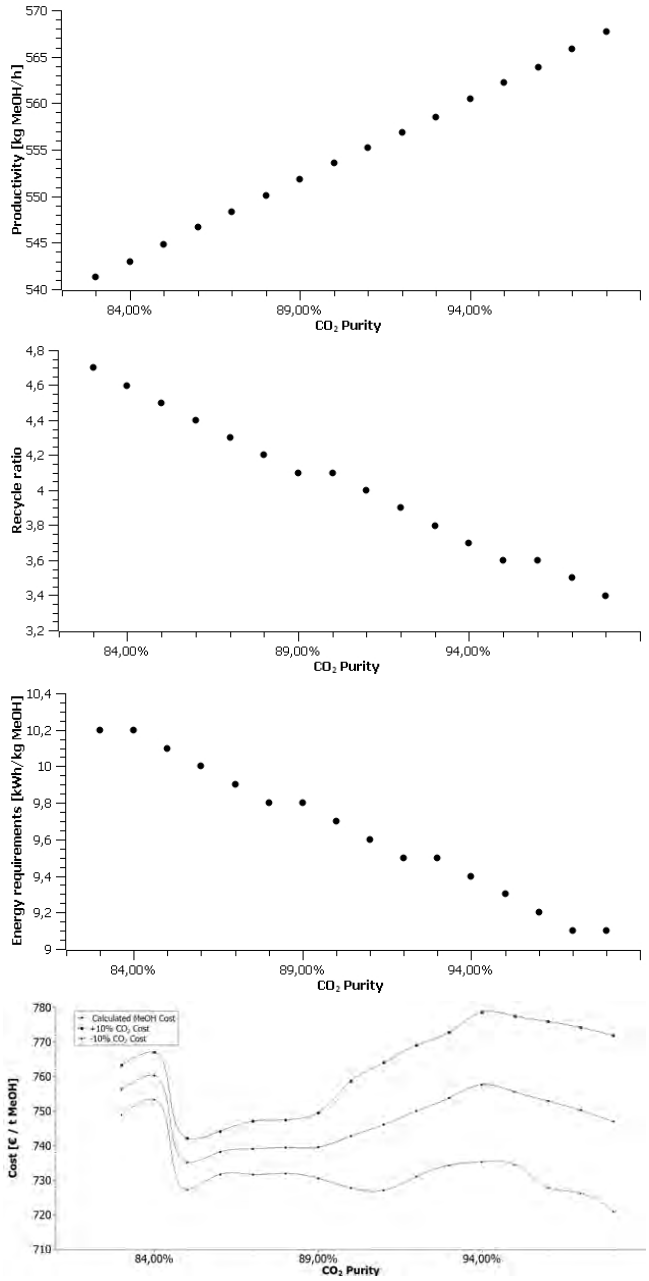



**Figure 4**. Effect of $CO_2$ purity on 1) Methanol productivity 2) Recycle ratio 3) Energy requirements 4) Cost of methanol production.

ly require additional separation steps, increasing operational costs. In contrast, at higher purities, methanol productivity increases while the energy requirements per unit of methanol decrease, leading to a reduction in overall production costs. As $CO_2$ purity increases toward 89%, production costs rise and can reach 770–780 €/t MeOH, indicating a local maximum. The ±10% cost lines bracket this baseline scenario, revealing how incremental shifts in $CO_2$ capture expenses can shift the overall cost curve by approximately 10–15 €/t.

$CO_2$ purity emerges as a decisive factor influencing operational costs. Lower purities introduce inefficiencies across multiple aspects of the process. Higher purities not only enhance productivity but also reduce operational costs, particularly in energy-intensive systems. The trade-off lies in balancing the cost of achieving higher $CO_2$ purity against the operational savings realized during methanol synthesis.

## CONCLUSION

This study highlights the critical impact of $CO_2$ purity on green methanol production through catalytic hydrogenation, addressing a key gap in existing research focused primarily on high-purity $CO_2$ streams (>96%). Results demonstrates that higher $CO_2$ purity leads to reduced energy consumption, streamlined operational dynamics, and lower production costs, enabling optimal process performance. In contrast, lower $CO_2$ purities increase inert loads, energy demand, and recycle ratios, while excessively high purities elevate upstream costs, resulting in diminishing economic returns despite improved yields. These findings highlight the critical role of energy-efficient $CO_2$ capture technologies in enhancing the sustainability and economic viability of methanol synthesis. Moreover, it provides a foundation for further investigation into system optimization, supporting the development of green methanol production as a viable strategy for climate change mitigation.

This work contributes to the broader discourse on climate change mitigation by offering actionable insights into the interplay between $CO_2$ capture, purification, and utilization technologies.

## ACKNOWLEDGEMENTS

This work was supported by the Generalitat de Catalunya (AGAUR projects 2021-SGR-01061 and 2024 DI 00011 - UPCO2FUEL) and the projects PID2021-124572OB-C31, PID2020-116051RB-I00 and CEX2023-001300-M funded by MCIN/AEI/10.13039/501100011033 and "ERDF A way of making Europe". L.S. is grateful to the MICINN Ramon y Cajal program (grant RYC2019-026704).

## REFERENCES

1. Liu Z, Deng Z, Davis SJ, Giron C, Ciais P. Monitoring global carbon emissions in 2021. Nat Rev Earth Environ 3:217-219 (2022) https://doi.org/10.1038/s43017-022-00285-w
2. International Energy Agency (IEA). World Energy Outlook 2022. IEA (2022).
3. Koytsoumpa EI, Bergins C, Kakaras E. The CO2 economy: review of CO2 capture and reuse technologies. J Supercrit Fluids 132:3-16 (2018) https://doi.org/10.1016/j.supflu.2017.07.029

4. Olah GA, Goeppert A, Prakash GS. Chemical recycling of carbon dioxide to methanol and dimethyl ether: from greenhouse gas to renewable, environmentally carbon neutral fuels and synthetic hydrocarbons. J Org Chem 74:487-498 (2008) https://doi.org/10.1021/jo801260f
5. Bhadola A, Patel V, Potdar S, Mallick S. Technology scouting - carbon capture: from today's to novel technologies. Report no. 18/20. Concawe, Brussels (2020).
6. Gutiérrez Ortega AE, Nomen i Ribé R, González Olmos R. Carbon dioxide capture and utilization by VPSA: a sustainable development. Universitat Ramon Llull (2019).
7. Nestler F, Krüger M, Full J, Hadrich MJ, White RJ, Schaadt A. Methanol synthesis – industrial challenges within a changing raw material landscape. Chem Ing Tech 90:1409-1418 (2018) https://doi.org/10.1002/cite.201800026
8. Marlin DS, Sarron E, Sigurbjörnsson Ó. Process advantages of direct $CO_2$ to methanol synthesis. Front Chem 6:446 (2018). https://doi.org/10.3389/fchem.2018.00446
9. Farahiyah Abdul Rahman, Md Maniruzzaman A. Aziz, R. Saidur, Wan Azelee Wan Abu Bakar, M.R Hainin, Ramadhansyah Putrajaya, Norhidayah Abdul Hassan. Pollution to solution: Capture and sequestration of carbon dioxide ($CO_2$) and its utilization as a renewable energy source for a sustainable future. Renew Sustain Energy Rev 71:112-126 (2017). https://doi.org/10.1016/j.rser.2017.01.011
10. Ullmann's Encyclopedia of Industrial Chemistry. Sixth ed. Wiley-VCH Verlag GmbH & Co. KGaA (2002).
11. Demirci UB, Miele P. Overview of the relative greenness of the main hydrogen production processes. J Clean Prod 52:1-10 (2013) https://doi.org/10.1016/j.jclepro.2013.03.025
12. Joo O-S, Jung K-D, Moon I, Rozovskii AY, Lin GI, Han S-H, Uhm S-J. Carbon dioxide hydrogenation to form methanol via a reverse-water-gas-shift reaction (the CAMERE process). Ind Eng Chem Res 38:1808-1812 (1999) https://doi.org/10.1021/ie9806848
13. Mignard D, Sahibzada M, Duthie JM, Whittington HW. Methanol synthesis from flue-gas CO2 and renewable electricity: a feasibility study. Int J Hydrogen Energy 28:455-464 (2003) https://doi.org/10.1016/S0360-3199(02)00082-4
14. Pontzen F, Liebner W, Gronemann V, Rothaemel M, Ahlers B. CO2-based methanol and DME – Efficient technologies for industrial scale production. Catal Today 171:242-250 (2011) https://doi.org/10.1016/j.cattod.2011.04.049
15. Soltanieh M, Mahmoodi Azar K, Saber M. Development of a zero emission integrated system for co-production of electricity and methanol through renewable hydrogen and CO2 capture. Int J Greenhouse Gas Control 7:145-152 (2012) https://doi.org/10.1016/j.ijggc.2012.01.008
16. Van-Dal ÉS, Bouallou C. Design and simulation of a methanol production plant from CO2 hydrogenation. J Clean Prod 57:38-45 (2013) https://doi.org/10.1016/j.jclepro.2013.06.008
17. Genovese M, Blekhman D, Dray M, Fragiacomo P. Multi-year energy performance data for an electrolysis-based hydrogen refueling station. Int J Hydrogen Energy 52:688-704 (2024) https://doi.org/10.1016/j.ijhydene.2023.04.084
18. Plaza MG, García S, Rubiera F, Pis JJ, Pevida C. Post-combustion CO2 capture with a commercial activated carbon: comparison of different regeneration strategies. Chem Eng J (2010) https://doi.org/10.1016/j.cej.2010.07.030
19. Choi WK, Kwon TI, Yeo YK, Lee H, Song H, Na BK. Optimal operation of the pressure swing adsorption (PSA) process for CO2 recovery. Korean J Chem Eng 20:617-623 (2003) https://doi.org/10.1007/BF02706663
20. Ishibashi M, Ota H, Akutsu N, Umeda S, Tajika M, Izumi J, Yasutake A, Kabata T, Kageyama Y. Technology for removing carbon dioxide from power plant flue gas by the physical adsorption method. Energy Convers Manag 37:929-933 (1996) https://doi.org/10.1016/0196-8904(95)00279-0
21. Chatake VS, Rambhia HV, Bhalerao SS, Korpale VS, Ahire JP, Pandit AB. Process simulation and optimization of methanol production and utilization for electricity generation. Waste Manag Bull 2:56-63 (2024) https://doi.org/10.1016/j.wmb.2024.09.005
22. Martin-Valmayor MA, Gil-Alana LA, Infante J. Energy prices in Europe: evidence of persistence across markets. Resour Policy 82:103546 (2023) https://doi.org/10.1016/j.resourpol.2023.103546

© 2025 by the authors. Licensed to PSEcommunity.org and PSE Press. This is an open access article under the creative commons CC-BY-SA licensing terms. Credit must be given to creator and adaptations must be shared under the same terms. See https://creativecommons.org/licenses/by-sa/4.0/



Systems & Control Transactions

**Research Article - Peer Reviewed Conference Proceeding**
ESCAPE 35 - European Symposium on Computer Aided Process Engineering
Ghent, Belgium. 6-9 July 2025
Jan F.M. Van Impe, Grégoire Léonard, Satyajeet S. Bhonsale,
Monika E. Polańska, Filip Logist (Eds.)

PSE PRESS

# Gate-to-Gate Life Cycle Assessment of $CO_2$ Utilisation in Enhanced Oil Recovery: Sustainability and Environmental Impacts in Dukhan Field, Qatar

**Razan Sawaly, Ahmad S. Abushaikha, and Tareq Al-Ansari***

College of Science and Engineering, Hamad Bin Khalifa University, Qatar Foundation, Doha, Qatar
*Corresponding author: talansari@hbku.edu.qa

## ABSTRACT

This study presents a gate-to-gate Life Cycle Assessment (LCA) evaluating the sustainability and environmental impacts of utilising $CO_2$ for Enhanced Oil Recovery (EOR) in Dukhan Field. The assessment employs a detailed model that encompasses $CO_2$ capturing, transportation, injection, and oil production processes. Utilising Gabi software, the study assesses $CO_2$ emissions across different stages of the EOR process and evaluates the environmental efficiency using two functional units: '1 kg of $CO_2$ captured' and '1 kg of oil produced'. Results indicate that Post-Combustion Capture (PCC) contributes the highest emissions, accounting for 76% of the total Global Warming Potential (GWP), while transportation pipelines and separators contribute only 2% and 4%, respectively. By Year 21, emissions drop by over 98%, with a corresponding GWP reduction from 4.73 billion $kgCO_2e$ in Year 1 to 94.97 million $kgCO_2e$. Emission rates for $CO_2$ capture and oil production also decrease significantly, reaching 0.01 $kgCO_2e$ per kg of $CO_2$ captured and 0.03 $kgCO_2e$ per kg of oil produced. These findings highlight the transformative potential of closed-loop $CO_2$ management, where recycling reduces reliance on external $CO_2$ sources and enhances the sustainability of EOR operations. This study provides actionable insights for optimising $CO_2$-EOR systems, contributing to both economic and environmental sustainability goals.

**Keywords**: Life Cycle Analysis, Carbon Dioxide, Carbon Capture, Optimisation, Environment.

## INTRODUCTION

Global $CO_2$ emissions have risen significantly, reaching 37.9 Gt in 2018, contributing over 75% of total greenhouse gases (International Energy Agency, 2023). The oil and gas sector alone accounts for 10% of these emissions (Kamkeng et al., 2021). Carbon Capture and Utilisation (CCU) is a promising approach to mitigating these emissions by capturing $CO_2$ and repurposing it for Enhanced Oil Recovery (EOR).

The environmental performance of CCU technologies has been widely evaluated in literature through the Life Cycle Assessment (LCA); a holistic approach that examines both resource consumption and pollutant release across all phases of a product's life cycle (Faber et al., 2022). Building on established LCA frameworks, Müller et al., (2020) introduced guidelines tailored to CCU in collaboration with over 40 experts, aiming to quantify the environmental benefits of CCU products and processes relative to conventional fossil-based alternatives. One key challenge when applying LCA to CCU arises from its multifunctional nature: $CO_2$ serves both as a waste product and a valuable resource. This dual role creates a direct link between $CO_2$ emission sources and its subsequent use in CCU, making the assessment more complex. To address this, the guidelines recommend a systematic approach aligned with ISO 14040/44 standards, which involves segmenting the process, expanding the assessment scope, and allocating impacts based on chemical or physical criteria. This methodology helps navigate the complexities introduced by CCU's multifunctionality.

Several studies have critically evaluated $CO_2$-EOR using LCA, highlighting both its potential and limitations as a carbon sequestration strategy. Jaramillo et al. (2009) examined lifecycle emissions from $CO_2$ capture at power

plants through to the combustion of the produced oil, questioning $CO_2$-EOR's net benefits for carbon sequestration. In contrast, Jensen et al. (2018) compared $CO_2$ EOR with conventional oil and natural gas production, illustrating that $CO_2$ EOR could reduce lifecycle greenhouse gas emissions, with outcomes heavily influenced by factors such as $CO_2$ capture rate and oil recovery efficiency.

Morgan et al. (2021) conducted a gate-to-gate LCA over a decade of $CO_2$-EOR operations, using 100% anthropogenic $CO_2$. The study demonstrated that $CO_2$-EOR has the potential to achieve net-negative emissions, citing a 92% storage rate for injected $CO_2$ and identifying operational improvements as key to enhancing environmental outcomes.

Similarly, Abuov et al. (2022)'s study indicated that $CO_2$-EOR can yield lower GHG emissions than conventional oil production, particularly under favorable carbon pricing and when $CO_2$ is sourced from coal-fired or NGCC power plants, thereby maintaining economic viability while reducing emissions.

Despite extensive research on $CO_2$-EOR, most studies focus on short-term assessments of $CO_2$ capture, injection, and sequestration, with limited analysis of long-term environmental performance. The transition from external $CO_2$ supply to a closed-loop recycling system remains underexplored, particularly in oil reservoirs in Qatar, such as the Dukhan Field.

Existing evaluations do not comprehensively quantify the long-term emissions reduction potential, sequestration efficiency, or overall sustainability of such systems. A systematic, long-term assessment of $CO_2$-EOR operations is essential to address this gap, providing critical insights into emissions dynamics, sequestration effectiveness, and the feasibility of achieving a self-sustaining carbon management approach.

## Study Objectives

This study aims to fill that gap by focusing on a detailed, gate-to-gate LCA that examines the environmental impacts of direct $CO_2$ injection for oil recovery, offering new insights into emissions reductions over an extended timeline. It also evaluates the operational efficiency of $CO_2$ sequestration under specific conditions unique to Dukhan Field, thereby contributing to a more targeted understanding of EOR's sustainability potential. To achieve this, the objectives of this research are to:

- Evaluate the environmental impacts of direct $CO_2$ injection for EOR using LCA.
- Quantify emissions and environmental efficiencies through two functional units: '1 kg of $CO_2$ captured' and '1 kg of oil produced.'
- Simulate operational efficiency and emissions reductions over 21 years, transitioning from external $CO_2$ to recycled $CO_2$.
- Analyse the feasibility of closed-loop $CO_2$ management in achieving long-term emissions reductions of over 90%.
- Provide recommendations to policymakers and industry leaders for implementing sustainable $CO_2$-EOR practices.

# METHODOLOGY

Building on the $CO_2$ reinjection closed-loop model developed by (Sawaly et al., 2022) for Dukhan Field, this study evaluates the feasibility and environmental impact of direct $CO_2$ injection for Enhanced Oil Recovery (EOR) in Dukhan Field, Qatar, without prior water injection. Initially, the model depends on externally sourced $CO_2$ but progressively transitions to recycling recovered $CO_2$ from previous cycles, with the potential to operate solely on reinjected $CO_2$ by the 21st year (Figure 1).

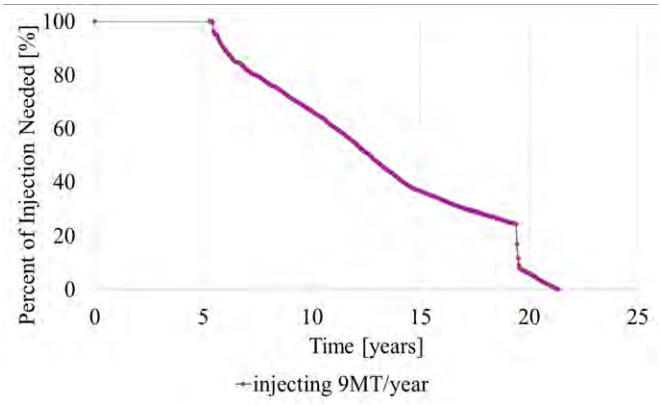



**Figure 1:** $CO_2$ utilisation process with reinjection.

## Model description

This gate-to-gate Life Cycle Assessment (LCA) examines the $CO_2$-EOR process from capture through oil production, excluding downstream refining and end-of-life emissions. Gabi software is used for environmental impact assessment, quantifying emissions and energy use. The system boundary extends from the flue gas stream exiting the source to crude oil production, incorporating $CO_2$ capture, compression, transportation, injection, separation, and reinjection to form a closed-loop system. The field specifications and production rate over time are detailed in (Sawaly et al., 2022). The model simulates a progressive transition from externally sourced $CO_2$ to internally recycled $CO_2$ over the 21-year period. As $CO_2$ recycling efficiency increases, the need for additional $CO_2$ purchases declines, and the production rate is adjusted dynamically based on reservoir performance and injection efficiency. The $CO_2$ composition of the produced stream is also accounted for through changes in

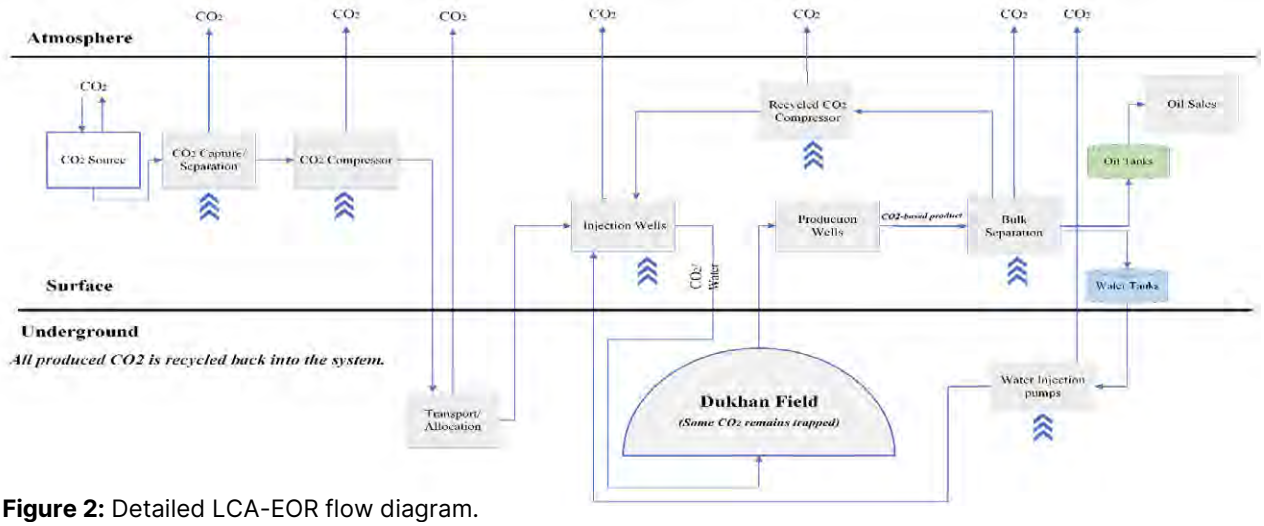



**Figure 2:** Detailed LCA-EOR flow diagram.

**Table 1:** Key operational and environmental metrics.

| Category | Term | Value | Unit | Reference |
|---|---|---|---|---|
| **Operational Metrics** | Feed Flowrate | 9000000 | t/y | (Sawaly et al., 2023) |
| | Production Rate | 0.2 | tonOil/ton$CO_2$ | (Sawaly et al., 2023) |
| | Distance | 100 | km | (Sawaly et al., 2023) |
| **Energy Metrics** | Capture | 3.32 | GJ/ton$CO_2$ | (Azzolina et al., 2017) |
| | Compression and transportation *(pipeline, 100km)* | 1.3 | kWh/ton$CO_2$ | (Azzolina et al., 2017) |
| | Injection Well | 64.5 | kWh/ton$CO_2$ | (Azzolina et al., 2017) |
| | Uplift (pump) production | 20 | kWh/bbl of oil | (Azzolina et al., 2017) |

separation efficiency and reinjection rates over time. These dynamic changes are integrated into the model to reflect realistic long-term operational scenarios.

Two functional units are used: '1 kg of $CO_2$ captured', assessing emissions per unit of injected $CO_2$, and '1 kg of oil produced', quantifying the carbon footprint of recovered oil. As illustrated in Figure 2, $CO_2$ is initially captured and purified at the source, compressed, and transported to injection wells, where it enhances oil recovery while storing $CO_2$ underground. During production, $CO_2$ resurfaces with oil and water, is separated, recompressed, and reinjected, minimising reliance on fresh $CO_2$ and maximising sustainability and efficiency. This approach supports a low-carbon oil recovery strategy, demonstrating the long-term potential of EOR as an emissions-reduction solution.

## Available data and assumptions

This section outlines the key operational and environmental parameters used to simulate the Enhanced Oil Recovery (EOR) process and assess its environmental impacts. These parameters include $CO_2$ capture emissions, energy consumption during capture, transportation, and injection, as well as $CO_2$ production rates and oil recovery yields.

$CO_2$ is captured using amine-based Post-Combustion Capture (PCC) technology with a 90% purity assumption, ensuring less than 10% impurities for efficient processing. The capture process requires both electricity and heat—electricity powers pumps and mechanical components, while heat regenerates the amine solvents in a desorption cycle, allowing solvent reuse and improving process sustainability. Emissions at this stage include direct emissions from PCC operations and indirect emissions linked to energy consumption, depending on the carbon intensity of the power source.

After capture and purification, $CO_2$ is transported via pipeline to the EOR site, requiring electricity-powered pumps to maintain flow and pressure. This ensures efficient delivery while minimising pressure losses. Emissions stem from pump and compressor operations, as well as energy consumption associated with transport. At the Dukhan Field, $CO_2$ is injected directly into the reservoir to enhance oil recovery, displacing hydrocarbons and reducing viscosity. This stage requires electricity to power injection pumps, as well as energy for drilling and completing wells. Emissions at this phase include direct emissions from drilling operations and indirect emissions from power consumption. Oil extraction involves drilling and well operations, requiring energy to operate lifting

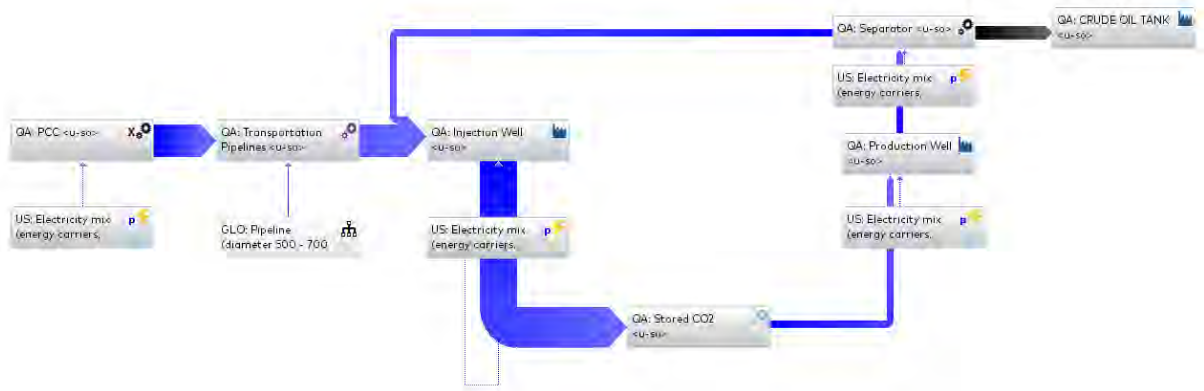



**Figure 3:** Gabi Screenshot of the model.

systems and production pumps. Emissions from this stage stem from both direct drilling activities and indirect energy use. Post-production, $CO_2$ is separated from oil and water using thermal and mechanical processes, requiring heat for thermal separation and electricity for compression and mechanical separation. Recovered $CO_2$ is then recompressed and reinjected, minimising the need for additional $CO_2$ purchases and supporting a closed-loop EOR system. Emissions include direct emissions from separation and indirect emissions from energy use. The emissions for each stage were calculated by multiplying the energy consumed at that stage by the $CO_2$-intensity factor for Qatar's electricity generation, which is primarily based on natural gas. The $CO_2$ intensity of Qatar's electricity grid is approximately 0.111 $tCO_2/GJ$ (or ~0.40 $tCO_2/MWh$)(IEA, 2019). This value represents the emissions released per unit of power generated in a natural gas system. In the case of pipeline transportation, a direct emission factor of 0.0001986 t $CO_2$/t $CO_2$ transported (per 100 km) is applied, as reported by Azzolina et al. (2017). This value reflects fugitive or operational emissions—such as small leaks and routine venting—rather than emissions from the electricity used to operate pumps or compressors.

The methodology acknowledges that brine is excluded from the analysis due to a lack of specific data, which is a recognised limitation of the current LCA scope. Table 1 summarises the key operational and environmental metrics, providing essential data for assessing the sustainability and efficiency of $CO_2$-EOR in Dukhan Field.

## RESULTS AND DISCUSSION

This section presents the key findings from the gate-to-gate LCA of the $CO_2$-EOR process in Dukhan Field. The analysis evaluates the environmental and operational impacts of $CO_2$ injection, focusing on enhanced oil recovery, reduced emissions, and the benefits of closed-loop recycling to support optimisation and sustainable development.

The LCA provides a detailed assessment of various operational scenarios over several years. The system boundaries extend from $CO_2$ extraction from the flue gas stream to oil production, excluding the life cycle impacts of crude oil products and upstream LNG production. Figure 3 illustrates the model employed in this assessment, highlighting the interactions between key variables and processes involved in $CO_2$-EOR.

Figure 4 presents a breakdown of the Global Warming Potential (GWP) across different stages of the $CO_2$-EOR process, offering critical insights into environmental performance. The stages include the injection well, post-combustion capture (PCC), the separator, transportation pipelines, and the total cumulative impact. The chart also shows the emission rates per kilogram of $CO_2$ captured and per kilogram of oil produced, providing a comprehensive view of the environmental footprint at each stage.

The PCC stage is the most emission-intensive, with a GWP of 1.20 billion $kgCO_2e$, highlighting the high energy demand of $CO_2$ capture, particularly when powered by non-renewable sources. In contrast, the injection well demonstrates a relatively low GWP of 0.29 billion $kgCO_2e$, indicating efficient $CO_2$ utilisation in oil recovery with minimal contribution to overall emissions. Emissions from the separator and transportation pipelines are significantly lower, at 0.07 billion $kgCO_2e$ and 0.02 billion $kgCO_2e$, respectively, reflecting effective management of these processes to minimise environmental impact. The total GWP across all stages is 1.58 billion $kgCO_2e$, with emission rates of 0.53 $kgCO_2e$ per kilogram of oil produced. This underscores the challenge of managing emissions throughout the $CO_2$-EOR process while identifying PCC as a critical area for potential improvement to reduce overall emissions.

Figure 5 illustrates the evolution of $CO_2$ utilisation and its impact on environmental performance over time through four distinct scenarios, each representing different stages of the $CO_2$-EOR process at Dukhan Field. These scenarios, spanning from Year 1 to Year 21, demonstrate the shift from external $CO_2$ sourcing to increased internal recycling. Each scenario reflects varying proportions of $CO_2$ sourced from external versus

internally recycled $CO_2$, highlighting the system's progression toward greater sustainability and efficiency. The gradual reduction in $CO_2$ allocation from external sources, combined with increased recycling and reinjection of $CO_2$ produced during oil extraction, emerges as a pivotal factor in enhancing the environmental and operational performance of the entire process.

As shown in Figure 5, in Year 1, when 100% of the required $CO_2$ is sourced externally, the system exhibits a high Global Warming Potential (GWP) of 4.73 billion $kgCO_2e$, reflecting the substantial environmental impact associated with early reliance on external $CO_2$ sources. However, as internal recycling mechanisms are adopted, the need for external $CO_2$ supply diminishes progressively. By Year 21, when no $CO_2$ is sourced externally, the GWP drops to 94.97 million $kgCO_2e$, representing a reduction of over 98% compared to Year 1. This decline underscores the success of the closed-loop $CO_2$ management strategy, wherein most of the $CO_2$ required for EOR operations is derived from recycled sources. Consequently, the emission rates per kilogram of $CO_2$ captured and per kilogram of oil produced decrease to 0.01 $kgCO_2e$ and 0.03 $kgCO_2e$, respectively, further demonstrating the efficiency gains achieved through internal $CO_2$ recycling.

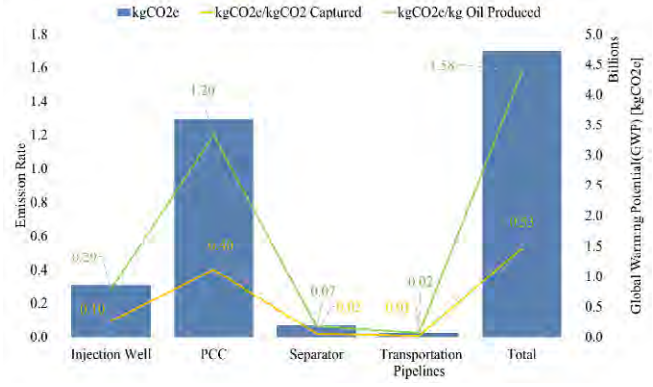



**Figure 4:** GWP of the base case scenario (year 1).

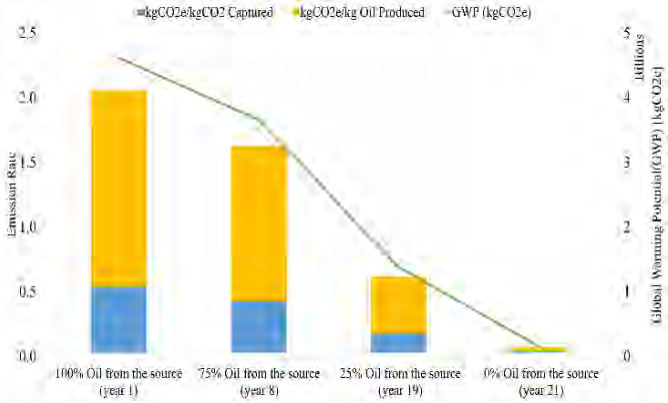



**Figure 5:** Comparison of 3 GWP Scenarios for 4 different years.

By improving $CO_2$ utilisation and reducing reliance on external supply, the system enhances oil production while simultaneously lowering emissions, thereby optimising the need for additional $CO_2$ input and improving the overall carbon efficiency of the EOR process. The reduction in PCC-related emissions over time reinforces the broader environmental benefits of transitioning towards a more self-sustaining $CO_2$-EOR operation. Overall, the results highlight the significant potential of internal $CO_2$ recycling to enhance the sustainability and environmental performance of $CO_2$-EOR operations. By reducing reliance on external $CO_2$ sources and optimising internal recycling processes, the system achieves substantial reductions in emissions while supporting a more economically viable and environmentally responsible oil recovery process.

The findings of this study align closely with those of previous $CO_2$-EOR LCA studies. Nuñez-López et al. (2017) reported an emission rate of 2.7 $kgCO_2e$ per kilogram of oil produced, which is consistent with the overall trend observed in this analysis. Slight variations may stem from differences in reservoir properties, energy sources, and operational conditions. Despite these variations, both studies underscore the potential of $CO_2$-EOR to enhance oil recovery while managing environmental impacts.

## CONCLUSION

This This study presents a detailed gate-to-gate Life Cycle Assessment (LCA) of $CO_2$ utilisation in Enhanced Oil Recovery (EOR) at Dukhan Field, Qatar, demonstrating the environmental and operational benefits of direct $CO_2$ injection without water flooding. The results show that implementing internal $CO_2$ recycling can reduce net emissions by over 90% by Year 21, confirming the effectiveness of closed-loop $CO_2$ management in cutting the carbon footprint of EOR operations. This reduction is primarily driven by the progressive replacement of externally sourced $CO_2$ with recycled $CO_2$, decreasing reliance on external carbon inputs.

The analysis evaluates $CO_2$ capture, transportation, injection, and recycling using functional units ("1 kg of $CO_2$ captured" and "1 kg of oil produced") to provide objective performance benchmarks. The findings underscore that Post-Combustion Capture (PCC) is the most emission-intensive stage, contributing approximately 76% of the total Global Warming Potential (GWP) in Year 1. Improving PCC energy efficiency and exploring alternative capture technologies, such as membrane-based systems or cryogenic separation, could significantly reduce the overall carbon footprint of $CO_2$-EOR.

While the findings highlight the potential of $CO_2$-EOR in reducing emissions and enhancing oil recovery, the study's scope is limited to the specific geological and

operational characteristics of Dukhan Field. This may restrict the direct applicability of the results to other fields with different reservoir conditions. Future research should extend the system boundaries to include downstream emissions from refining and combustion and assess the impact of $CO_2$ purity and reservoir pressure on sequestration efficiency and oil recovery rates. Comparative studies across different reservoir profiles would strengthen the generalisability of these findings.

The demonstrated reduction in emissions through internal $CO_2$ recycling also enhances economic feasibility by lowering the need for external $CO_2$ supply. This reinforces the strategic role of $CO_2$-EOR in supporting a transition toward low-carbon oil production, providing a viable path for balancing energy security with environmental responsibility.

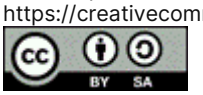
## ACKNOWLEDGEMENTS

The authors acknowledge the support of Qatar National Research Fund (a member of Qatar Foundation) provided by GSRA grants no. GSRA9-L-1-0531-22069.

## REFERENCES

1. Abuov, Y., Serik, G., & Lee, W. (2022). Techno-Economic Assessment and Life Cycle Assessment of CO2-EOR. Environmental Science and Technology, 56(12). https://doi.org/10.1021/acs.est.1c06834
2. Azzolina, N. A., Hamling, J. A., Peck, W. D., Gorecki, C. D., Nakles, D. V., & Melzer, L. S. (2017). A Life Cycle Analysis of Incremental Oil Produced via CO2 EOR. Energy Procedia, 114, 6588–6596. https://doi.org/10.1016/j.egypro.2017.03.1800
3. Giordano, L., Roizard, D., & Favre, E. (2018). Life cycle assessment of post-combustion CO2 capture: A comparison between membrane separation and chemical absorption processes. International Journal of Greenhouse Gas Control, 68. https://doi.org/10.1016/j.ijggc.2017.11.008
4. Ho, H. J., Iizuka, A., & Shibata, E. (2019). Carbon Capture and Utilization Technology without Carbon Dioxide Purification and Pressurization: A Review on Its Necessity and Available Technologies. Industrial and Engineering Chemistry Research, 58(21). https://doi.org/10.1021/acs.iecr.9b01213
5. Jaramillo, P., Griffin, W. M., & Mccoy, S. T. (2009). Life cycle inventory of CO2 in an enhanced oil recovery system. Environmental Science and Technology, 43(21). https://doi.org/10.1021/es902006h
6. Jensen, M. D., Azzolina, N. D., Schlasner, S. M., Hamling, J. A., Ayash, S. C., & Gorecki, C. D. (2018). A screening-level life cycle greenhouse gas analysis of CO2 enhanced oil recovery with CO2 sourced from the Shute Creek natural gas-processing facility. International Journal of Greenhouse Gas Control, 78. https://doi.org/10.1016/j.ijggc.2018.08.010
7. Kamkeng, A. D. N., Wang, M., Hu, J., Du, W., & Qian, F. (2021). Transformation technologies for CO2 utilisation: Current status, challenges and future prospects. In Chemical Engineering Journal (Vol. 409). https://doi.org/10.1016/j.cej.2020.128138
8. Morgan, A., Grigg, R., & Ampomah, W. (2021). A gate-to-gate life cycle assessment for the co2-eor operations at farnsworth unit (Fwu). Energies, 14(9). https://doi.org/10.3390/en14092499
9. Müller, L. J., Kätelhön, A., Bachmann, M., Zimmermann, A., Sternberg, A., & Bardow, A. (2020). A Guideline for Life Cycle Assessment of Carbon Capture and Utilization. Frontiers in Energy Research, 8. https://doi.org/10.3389/fenrg.2020.00015
10. Nuñez-López, V., Gil-Egui, R., Gonzalez-Nicolas, A., & Hovorka, S. (2017). Carbon Balance of CO2-EOR for NCNO Classification. Energy Procedia, 114. https://doi.org/10.1016/j.egypro.2017.03.1803
11. Sawaly, R., Alherbawi, M., & Alansari, T. (2023). Development of 'Green' LNG through a CO2 allocation procedure within a CO2 utilisation network in Qatar. In Computer Aided Chemical Engineering (Vol. 52). https://doi.org/10.1016/B978-0-443-15274-0.50347-4
12. Sawaly, R., Ghiat, I., Mohamed, A., Abushaikha, A., & Al-Ansari, T. (2022). Optimal CO2 allocation for enhanced oil recovery operations within carbon utilisation networks in Qatar. In Computer Aided Chemical Engineering (Vol. 51). https://doi.org/10.1016/B978-0-323-95879-0.50083-7

© 2025 by the authors. Licensed to PSEcommunity.org and PSE Press. This is an open access article under the creative commons CC-BY-SA licensing terms. Credit must be given to creator and adaptations must be shared under the same terms. See https://creativecommons.org/licenses/by-sa/4.0/



Systems & Control Transactions

**Research Article - Peer Reviewed Conference Proceeding**
ESCAPE 35 - European Symposium on Computer Aided Process Engineering
Ghent, Belgium. 6-9 July 2025
Jan F.M. Van Impe, Grégoire Léonard, Satyajeet S. Bhonsale,
Monika E. Polańska, Filip Logist (Eds.)

PSE PRESS

# Sustainable Two-Column Design for the Separation of Ethyl Acetate, Methanol, and Water

**Prakhar Srivastava[a], and Nitin Kaistha[a]***

[a] Indian Institute of Technology, Department of Chemical Engineering, Kanpur, India
* Corresponding Author: nkaistha@iitk.ac.in

## ABSTRACT

This study investigates the design of a two-column distillation (TCD) process to separate a dilute ternary Ethyl Acetate (EtAc)-Methanol (MeOH)-water waste solvent into nearly pure components. The separation is complicated by the presence of a homogeneous EtAc-MeOH azeotrope and a heterogeneous EtAc-water azeotrope, creating a distillation boundary that divides the ternary composition space into two distinct regions. To address this, the proposed flowsheet incorporates liquid-liquid phase separation to cross the distillation boundary, enabling feasible separation. Additionally, the pressure sensitivity of the distillation boundary is exploited to reduce the recycle rate, enhancing energy efficiency. The basic TCD flowsheet consists of a decanter, a high-pressure simple column, and a low-pressure divided-wall column (DWC). Heat integration (HI) is achieved using external process-to-process heat exchangers and vapor recompression (VR)-driven reboilers. The resulting energy-efficient HIVR-TCD configuration is more cost-effective and energy-efficient than existing designs in the literature. Specifically, the total annualized cost (TAC) of the proposed HIVR-TCD process is 15.4% lower than the literature best design, with reductions in energy consumption and $CO_2$ emissions of 34.3% and 31.4%, respectively, representing a significant improvement.

**Keywords**: Sustainable, Azeotrope, DWC, Distillation

## INTRODUCTION

Spent solvents are widely generated in the pharmaceutical industry. Due to rising sustainability concerns and stricter waste disposal rules, there is a growing emphasis on recovering, recycling, and reusing the organic compounds within these solvents. Achieving minimal waste discharge requires addressing challenges such as azeotropes that limit simple distillation. Advanced techniques like pressure swing, extractive, and azeotropic distillation are utilized to efficiently recover and purify components based on the solvent mixture's composition.

Ethyl acetate (EtAc) and methanol (MeOH) are frequently used solvents in pharmaceutical manufacturing. Spent solvents typically contain a mixture of EtAc, MeOH, and water. However, minimum boiling binary azeotropes like EtAc-$H_2O$ and EtAc-MeOH hinder the recovery of pure components from this ternary mixture. Therefore, an advance distillation-based sequence is required to efficiently separate these components.

**Table 1**: Normal boiling point of components

| Component | Boiling Point ($^oC$) |
|---|---|
| MeOH/EtAc azeotrope | 62.3 |
| MeOH | 64.5 |
| Water/EtAc azeotrope | 70.8 |
| EtAc | 77.2 |
| Water | 100 |

In the literature various designs for separating EtAc-MeOH-water mixtures have been proposed, with Yang's design [1] proving most efficient. It uses a liquid-liquid phase split to overcome distillation boundaries and features a heterogeneous triple-column distillation (HTCD) system with a decanter and three columns. Energy efficiency is enhanced through heat integration (HI) and heat pump–vapor recompression (HP-VR), forming the hybrid-HTCD process. This design reduces total annual cost by 16% and 11% compared to HTCD and HI-HTCD systems, respectively, making it the most economical option.

The azeotropes of EtAc-water and MeOH-EtAc are known to be pressure-sensitive, with EtAc showing limited solubility in water and MeOH being fully miscible with both. This results in a significant liquid-liquid phase separation region in the ternary composition diagram. Thus, exploring pressure-swing distillation and liquid-liquid phase splitting offers a potential pathway to cross distillation boundaries and develop a more efficient flowsheet for separating MeOH-EtAc-water mixtures into pure components. This study focuses on achieving this goal.

This work employs residue-curve maps (RCMs) to design a distillation process with a decanter and two columns operating at different pressures, one of which is a divided-wall column (DWC), to separate a dilute MeOH-EtAc-water mixture. Energy efficiency is enhanced through process-to-process heat exchange and vapor recompression for column reboil. An economic steady-state design is developed and compared to existing flowsheets, evaluating energy consumption, $CO_2$ emissions, and total annualized cost (TAC) to quantify savings. The work concludes by highlighting its key contributions.

## PROCESS MODELLING

Aspen plus is used for steady state simulation the thermodynamic properties are modelled by NRTL equation for liquid phase activity coefficient and vapor phase is modelled as an ideal gas. The binary interaction parameters as well as liquid phase envelope data is provided in the NIST database based on that a regressed NRTL parameter are provided in the Table 2 below.

**Table 2**: Regressed NRTL interaction parameter

| Comp i | Comp j | $A_{ij}$ | $A_{ji}$ | $B_{ij}$ | $B_{ji}$ | $C_{ij}$ |
|---|---|---|---|---|---|---|
| MeOH | Water | 3.65 | -2.47 | -1556.8 | 1460.8 | 0.13 |
| MeOH | EtAc | 4.56 | -5.52 | -1196.9 | 2216.8 | 1.11 |
| Water | EtAc | -3.8 | -3.64 | 2229.9 | 1699.1 | 0.36 |

## FLOWSHEET SYNTHESIS

This study examines a dilute mixed solvent with a mole fraction of [0.05, 0.05, 0.90] for EtAc–MeOH–water, similar to Yang et al. Figure 1 displays residue-curve maps (RCMs) at different pressures, showing EtAc and water as stable nodes, MeOH as a saddle, and two minimum boiling binary azeotropes: a homogeneous MeOH–EtAc azeotrope and a heterogeneous EtAc–water azeotrope, both unstable nodes. Table 1 provides the boiling points of the pure components and azeotropes. A distillation boundary between the azeotropes divides the ternary composition space into two distinct distillation regions.

Figure 1 illustrates that azeotrope positions are pressure-dependent, with the distillation boundary shifting leftward as pressure increases. This shift, along with the liquid-liquid phase split enabling spontaneous separation, allows for energy-efficient separation. The dilute fresh feed, within the liquid-liquid phase envelope, can be decanted at 1 bar to cross the boundary, producing an EtAc-rich organic layer in region II and a water-rich aqueous layer in region I. The organic stream is stripped to obtain pure EtAc, while the overhead vapor near the boundary is condensed and recycled for further phase separation.

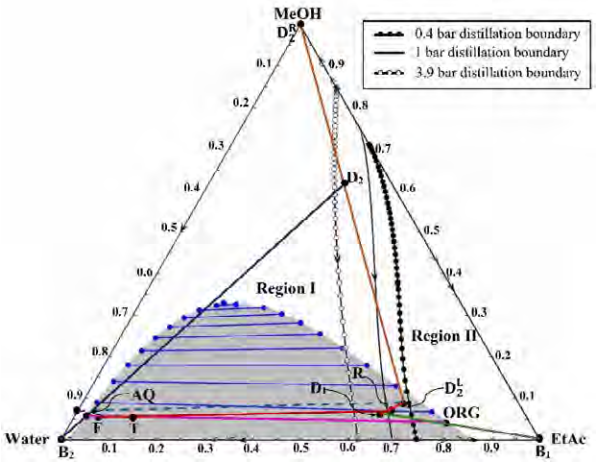



**Figure 1:** RCM at different pressure

As the distillation boundary and the overhead condensate composition shift leftward with increasing column pressure, the separation should occur at a moderate pressure above 1 bar, such as 4 bar. This increases the gap between the overhead condensate and bottom compositions, reducing the recycle rate to the decanter according to the lever rule.

The aqueous stream from the decanter, with a composition in region I, can be stripped to produce an EtAc-free bottom product near the MeOH–water binary edge and an overhead ternary vapor within the liquid-liquid envelope in region I, close to the distillation boundary. This vapor can be condensed and recycled to the decanter. The EtAc-free MeOH–water bottoms can then be distilled to obtain pure MeOH distillate and a water bottom product. To maximize relative volatility and reduce energy consumption, aqueous separations should be performed at low pressure.

The basic TCD flowsheet includes a decanter and two distillation columns: the high-pressure (HP) stripper. Figure 1 displays the material balance lines for each unit operation based on the recommended design and operating conditions. The decanter tie-line (magenta) indicates the compositions of the organic (ORG) and aqueous (AQ) phases. The $C_1$ bottoms ($B_1$) are at the EtAc vertex, while the distillate ($D_1$) lies in region II, near the 3.9 bar distillation boundary, along the line connecting the organic phase and EtAc vertex.

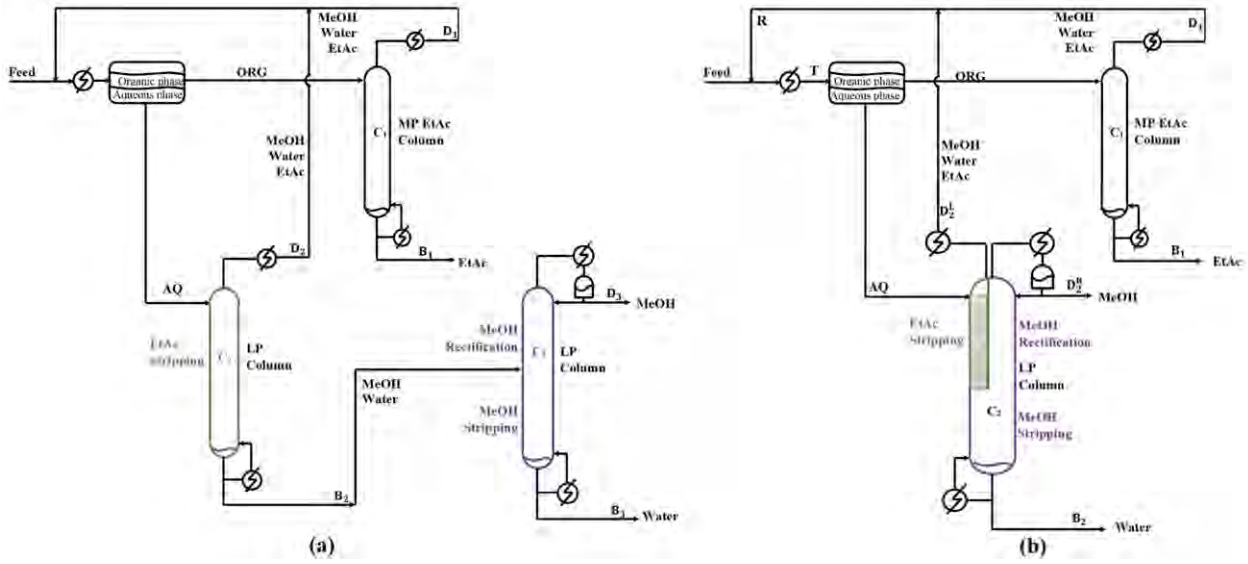



**Figure 2**: Synthesis of a) Conventional distillation scheme b) Intensified two column distillation scheme

Column $C_2$ separates the aqueous stream into nearly pure water bottoms ($B_2$), pure MeOH distillate ($D_2^R$), and ternary left distillate ($D_2^L$). The intersection of the $B_2$-AQ and $D_2^R$-$D_2^L$ lines defines the total overhead product ($D_2$). The distillates from $C_1$ ($D_1$) and $C_2$ ($D_2^L$) form the mixed recycle stream (R), with the tie-line intersection of the fresh feed (FF) and R determining the total feed (T) to the decanter. The HP and LP columns shift the distillation boundaries, reducing the recycle rate and improving energy efficiency. The boundary is crossed through liquid-liquid phase separation in the decanter. The next step is to develop the economic steady-state design.

## ECONOMIC STEADY-STATE DESIGN

An economic steady-state design for the TCD process, shown in Figure 2b, uses a fresh feed rate of 100 kmol/h with a composition of [5, 5, 90] mol % MeOH–EtAc–water, as per Yang et al.'s [1] conditions. The desired product purities are 99.91 mol % for EtAc, 99.9 mol % for MeOH, and 99.99 mol % for wastewater, matching those in Yang et al.'s most economical hybrid-HTCD [1] design for comparison.

For a fully specified fresh feed, the process has four steady-state operating degrees of freedom (DOFs) and seven equipment design DOFs. These are optimized to minimize the total annual cost (TAC), which is defined as:

$$TAC = \frac{TCC}{PBP} + YOC$$

where TCC represents the total capital cost, PBP is the payback period, and YOC refers to the yearly operating cost. A typical PBP value of 3 years is used, with cost correlation and pricing data adapted from Turton [2] and Luyben [3].

Minimizing TAC using the available degrees of freedom (DOFs) is a mixed-integer nonlinear programming (MINLP)problem, solvable with an optimization algorithm. In this case, MATLAB's Mult objective genetic algorithm (MOGA) is used, with Aspen Plus as the steady-state flowsheet solver. The two objectives for minimization are TCC/PBP (the first term of TAC) and YOC (the second term of TAC).

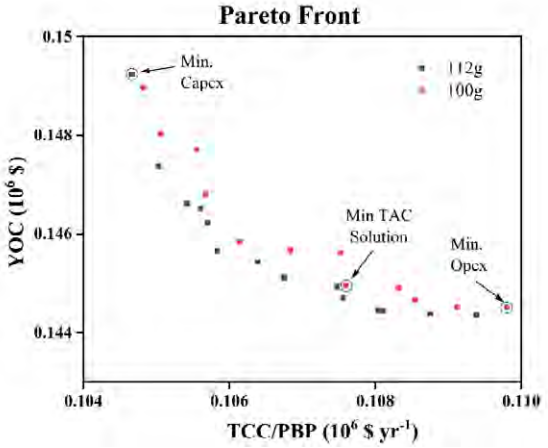



**Figure 3**: Pareto optimal front for TCD process

Among the 11 DOFs, three are fixed by product purity and one by the decanter temperature, leaving seven DOFs. The geometric constraint of equal trays on both sides of the DWC reduces this to six DOFs for optimization. These are optimized using MOGA, with bounds for the decision variables. For brevity, the details of the variables are omitted here. The optimization uses MATLAB's

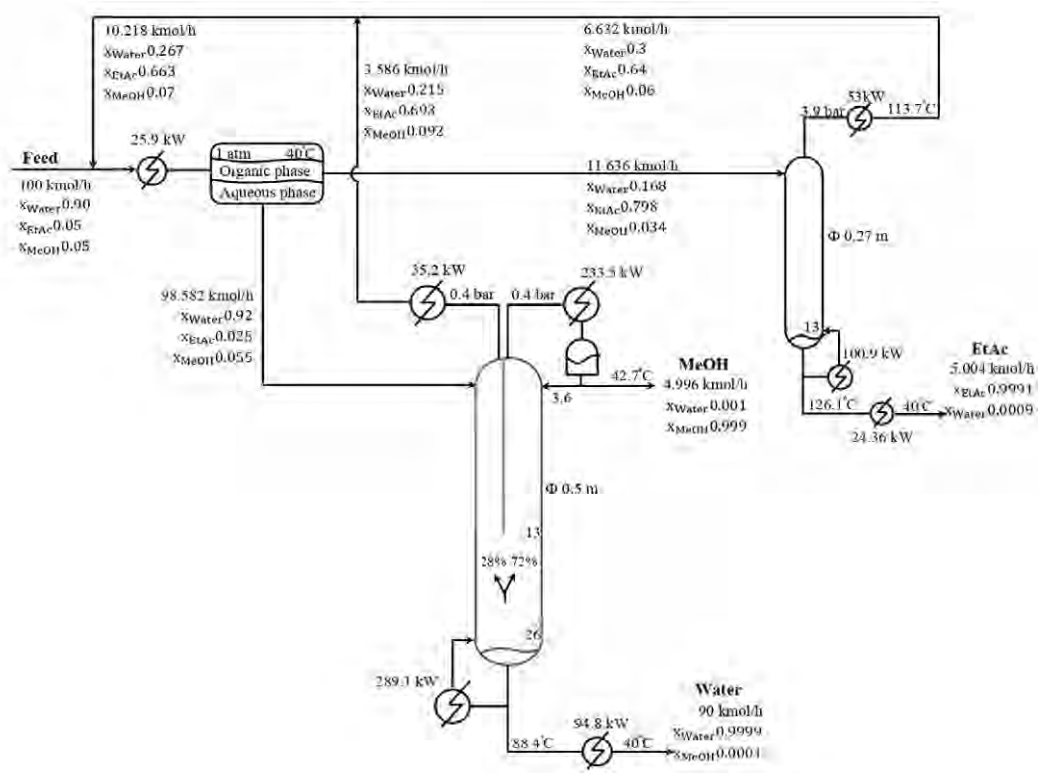



**Figure 4**: Nominal design and operating condition of TCD process

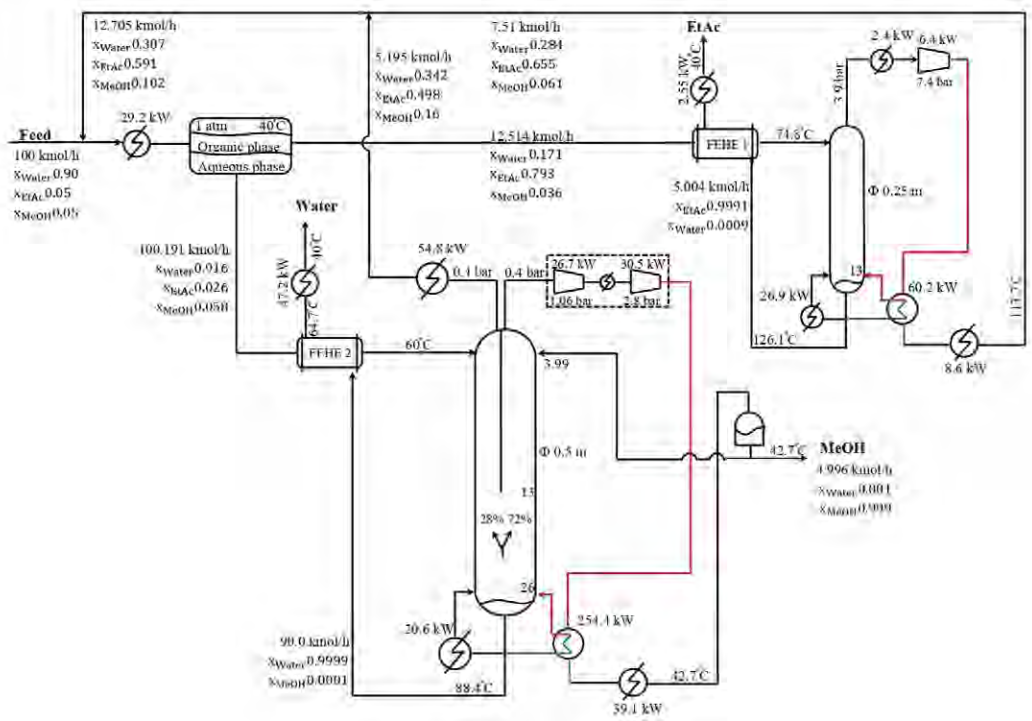



**Figure 5**: Nominal design and operating condition of Hybrid TCD process

*gamultiobj* function with a population size of 50 and a maximum of 200 generations. The converged Pareto optimal front after 112 generations is shown in figure 3, with the minimum TAC solution indicated.

The key steady-state conditions for the recommended basic TCD process design are shown in Figure

4, with an optimum TAC of \$0.252 × $10^6$ per year.

### Heat Integrated Hybrid TCD

Condensing the overhead vapor for reboil in both columns enhances the energy efficiency of the basic TCD flowsheet. Vapor recompression (VR) is effective when the coefficient of performance (COP) between the reboiler and condenser is high. Studies suggest VRHI is unsuitable for COP < 5, ideal for COP > 10, and requires further evaluation between 5 and 10. In our design, the COP values for the high-pressure column ($C_1$) and low-pressure dividing wall column ($C_2$) are 31.2 and 6.91, respectively. Applying VRHI to $C_2$ resulted in a significant TAC reduction, prompting its implementation in both columns along with feed-effluent heat exchangers (FEHEs), greatly improving energy efficiency.

In implementing vapor recompression (VR), process limitations are considered [4], including a maximum compressor outlet temperature of 190°C and a maximum compression ratio of 4. The overhead vapor is pressurized so that the bubble point of the condensed liquid exceeds the reboiler temperatures by 20–25°C, ensuring sufficient heat transfer. As a result, the overhead vapor from columns $C_1$ and $C_2$ are compressed to pressures of 7.4 bar and 2.8 bar, respectively. Due to the high compression ratio of 7, $C_2$'s overhead vapor undergoes two-stage compression with interstage cooling.

The final proposed design and operating conditions for the near-optimal flowsheet are shown in Figure 5. This design achieves a total annual cost (TAC) of \$0.198 × $10^6$ per year, marking a 21% reduction compared to the basic TCD design, with a notable 70% reduction in energy consumption.

## COMPARISON WITH LITERATURE DESIGN

We compare the energy consumption, $CO_2$ emissions, and total annual cost (TAC) of the most energy-efficient hybrid-TCD design with the best design from Yang's work, the hybrid heterogeneous triple column distillation (HTCD), shown in Figure 6. The hybrid-HTCD process includes a decanter and three columns. In this setup, the aqueous phase undergoes distillation to produce a MeOH-EtAc-water ternary distillate with reduced water content and an EtAc-free MeOH-water bottoms stream. The bottoms stream is further distilled to separate pure MeOH and water, while the organic layer is distilled to recover pure EtAc and recycle a MeOH-lean distillate to the decanter.

To improve energy efficiency, vapor recompression is applied to all three columns, along with feed-effluent heat exchange, as shown in Figure 6. Similar to our proposed flowsheet, a multi-objective genetic algorithm was used to minimize the TAC of the literature flowsheets. The figures display key design and operating parameters of the optimized hybrid-HTCD processes derived from this approach.

The Table 3 compares the total energy consumption, $CO_2$ emissions, and TAC of the alternative process designs. For the hybrid-HTCD process, energy consumption and $CO_2$ emissions are 172.8 kW and 69.59 kg/h, respectively, while the hybrid-TCD process developed in this study achieves 113.5 kW and 47.64 kg/h. This shows that the hybrid-HTCD process consumes 52.2% more energy and produces 45.9% higher $CO_2$ emissions than the proposed hybrid-TCD design.

The superior energy efficiency and lower $CO_2$ emissions of the hybrid-TCD design are due to its reduced total recycle rate, leverage of azeotrope pressure sensitivity, integration of process-to-process heat exchange, and use of vapor recompression-driven column reboil. Additionally, the proposed hybrid-TCD design is 15.4% more cost-effective than the best-in-literature hybrid-HTCD design.

The quantitative analysis shows that, from both economic and sustainability perspectives, the proposed hybrid-TCD process design is a significant improvement over existing literature designs for separating a dilute EtAc-MeOH-water mixed solvent into its pure components. This advancement is due to several factors, including the use of spontaneous liquid-liquid phase splitting to overcome distillation limitations, exploitation of azeotrope pressure sensitivity to reduce the total recycle rate, energy savings from process-to-process heat exchange, and enhanced energy efficiency through vapor recompression-driven column reboil. Additionally, the integration of a divided wall column (DWC) further boosts the process's efficiency and effectiveness.

## CONCLUSION

**Table 3**: Ecconomic and sustainability metric for alternate designs

| Metric | Hybrid-TCD | Hybrid-HTCD |
|---|---|---|
| Total Energy (kW) | 113.5 | 172.84 |
| $CO_2$ emission (kg/h) | 47.64 | 69.59 |
| TAC×$10^6$ (\$/yr) | 0.198 | 0.2341 |

This study presents an environmentally friendly, two-column compact flowsheet for separating a dilute EtAc-MeOH-water solvent into its pure components. The basic flowsheet incorporates a decanter and two columns, utilizing liquid-liquid phase separation to overcome distillation limitations and the pressure sensitivity of azeotropes to minimize the total recycle rate. Enhancements include process integration with a divided wall column (DWC) and energy optimization through process-to-process heat exchange, along with condensing compressed overhead vapor to supply a substantial

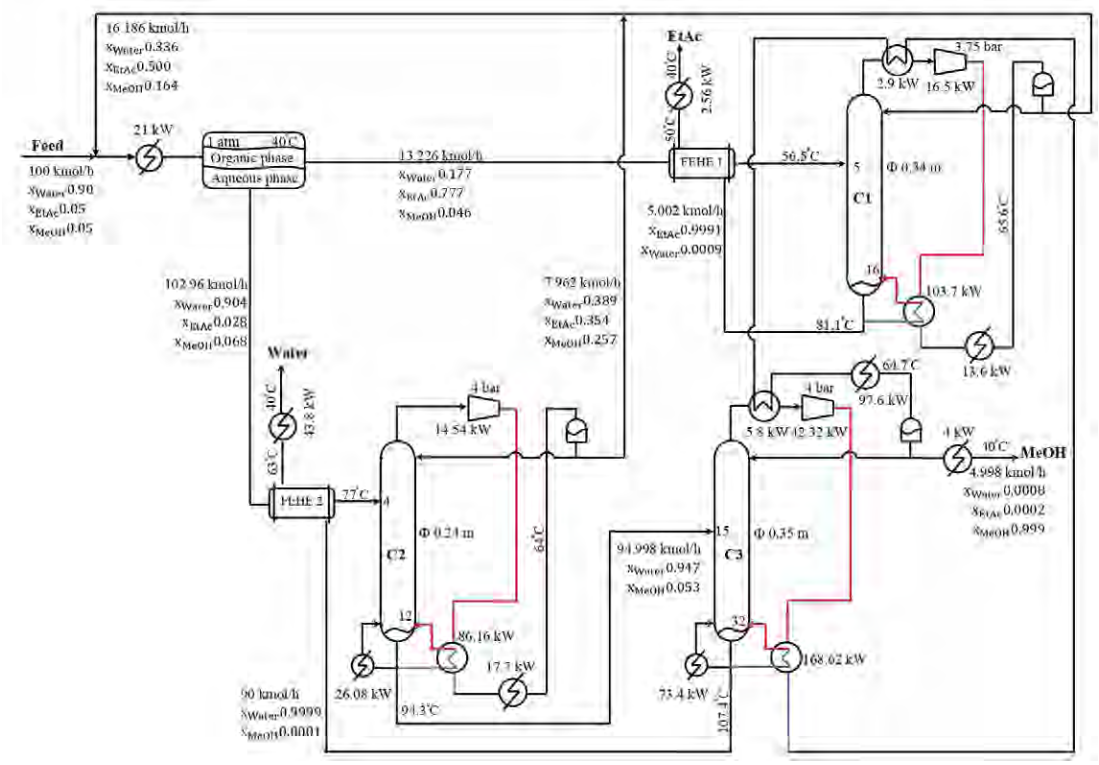



**Figure 6:** Nominal design and operating condition of Hybrid HTCD process

portion of the reboiler duty in both columns, resulting in an economically and energy-efficient design.

A quantitative comparison with the best existing design, the hybrid heterogeneous triple column distillation (hybrid-HTCD), reveals that the proposed hybrid two column distillation (hybrid-TCD) design reduces TAC by 15.4%, while also cutting energy consumption and $CO_2$ emissions by 34.3% and 31.4%, respectively. Thus, the developed hybrid-TCD process marks a significant advancement over the current state-of-the-art for separating a dilute EtAc-MeOH-water mixed solvent.

## ACKNOWLEDGEMENTS

We sincerely acknowledge the financial support provided by the Government of India.

## REFERENCES

1. A. Yang, S. Sun, Z. Y. Kong, S. Zhu, J. Sunarso, W. Shen: Energy-efficient heterogeneous triple-column azeotropic distillation process for recovery of ethyl acetate and methanol from wastewater. *Comput. Chem. Engg.* 183:108618 (2024) https://doi.org/10.1016/j.compchemeng.2024.108618 .
2. R Turton, R. C. Bailie, W. B. Whiting, A. J. Shaeiwitz: Analysis, synthesis and design of chemical processes. Pearson Education (2008).
3. W.L. Luyben: Design and control of the ethyl benzene process *AIChE journal* 57,665-670 (2011) https://doi.org/10.1002/aic.12289
4. W.L. Luyben: Compressor heuristics for conceptual process design *Industrial and Engineering Chemistry Research* 50,13984-13989 (2011) https://doi.org/10.1021/ie202027h

© 2025 by the authors. Licensed to PSEcommunity.org and PSE Press. This is an open access article under the creative commons CC-BY-SA licensing terms. Credit must be given to creator and adaptations must be shared under the same terms. See https://creativecommons.org/licenses/by-sa/4.0/

Systems & Control Transactions

**Research Article - Peer Reviewed Conference Proceeding**
ESCAPE 35 - European Symposium on Computer Aided Process Engineering
Ghent, Belgium. 6-9 July 2025
Jan F.M. Van Impe, Grégoire Léonard, Satyajeet S. Bhonsale,
Monika E. Polańska, Filip Logist (Eds.)

PSE PRESS

# Robust Flowsheet Synthesis for Ethyl Acetate, Methanol and Water Separation

**Aayush Gupta[a], Kartavya Maurya[a], and Nitin Kaistha[a]***

[a] Indian Institute of Technology, Kanpur, Uttar Pradesh, India
* Corresponding Author: nkaistha@iitk.ac.in

## ABSTRACT

This work presents a robust flowsheet design for the recovery and purification of waste solvent streams containing ethyl acetate (EtAc), methanol (MeOH), and water. Separation of this mixture is challenging due to the presence of two azeotropes: a homogeneous EtAc-MeOH azeotrope and a heterogeneous EtAc-water azeotrope. These azeotropes create a distillation boundary that divides the ternary composition space into two distinct regions, making separation via conventional distillation difficult. Additionally, the wide variability in waste solvent compositions requires a versatile design, as flowsheets optimized for dilute mixtures may not be feasible for concentrated ones. The key to this design is using a liquid-liquid extractor (LLX) with recycled water as the solvent, ensuring the mixture remains within the liquid-liquid equilibrium (LLE) split region, which facilitates spontaneous separation across the distillation boundary and promotes energy-efficient separation. The raffinate composition lies near the EtAc-water edge in the EtAc-rich region and is stripped to recover pure EtAc, while the extract phase is processed to yield pure MeOH and water. Converged designs are developed for equimolar, EtAc-rich, MeOH-rich, and water-rich compositions, with the proposed robust structure validated for all four compositions. This study represents a significant advancement in sustainable solvent recovery by eliminating the need for separate designs tailored to specific compositions, offering a unified, robust solution for separating various solvent feed mixtures.

**Keywords**: Liquid Liquid Envelope, Liquid Liquid Extractor, Azeotropes, Robust Flowsheet

## INTRODUCTION

Ethyl acetate (EtAc) and methanol (MeOH) are widely used solvents in the pharmaceutical, textile, dyes, and paints industries [1,2]. Significant volumes of organic waste streams containing EtAc and MeOH are generated varying composition based on the specific processes and conditions. Stricter waste discharge regulations and sustainability concerns now mandate the complete recovery, recycling, and reuse of organic solvents. The global shift towards sustainable practices and circular economy principles has intensified the focus on waste minimization, making solvent recovery and recycling from industrial waste streams essential for both environmental and economic reasons.

The separation and recovery of organic solvents from water are challenging due to the presence of two azeotropes—a homogeneous EtAc-MeOH azeotrope and a heterogeneous EtAc-water azeotrope. A line connecting these azeotropes creates a distillation boundary that divides the ternary composition space into two regions, complicating the separation process and making conventional distillation ineffective.

Separation facilities that process waste streams into pure components often face significant variability in EtAc, MeOH, and water concentrations, depending on the source process and operational parameters. This variability poses a design challenge, as flowsheets optimized for dilute compositions may not be suitable for concentrated ones, while those designed for concentrated mixtures may be too costly for dilute streams. Traditional solutions typically involve multiple processing units for different compositions or frequent adjustments to operating conditions, both of which can compromise the economic viability of the recovery process.

Industrial plants typically operate with fixed

equipment configurations, such as the number of trays, column diameter, and heat exchangers, which cannot be easily modified once installed. As a result, there is a pressing need for robust flowsheet designs that ensure operational feasibility across the full range of potential feed compositions. Developing such flowsheet structures requires careful consideration of operational constraints and innovative approaches to process synthesis and design. The goal of this work is to design a robust flowsheet capable of handling substantial variability in feed composition for the separation of EtAc-MeOH-water.

The article is organized as follows: the next section discusses the thermodynamics of the process, followed by the synthesis of a flowsheet for MeOH rich feed composition. We then present a near-optimal economic design for that composition. Finally, we explore the robust design that effectively handles variations across all ranges and conclude the article with its main findings.

## PROCESS MODELLING

Aspen Plus is used for steady-state simulation, with thermodynamic properties modeled using the NRTL equation for the liquid-phase activity coefficient and the vapor phase treated as an ideal gas. The binary interaction parameters are adapted from the work of Srivastava et al. [3]. Steady-state designs are developed for an inlet feed stream flow rate of 100 kmol/h, considering four distinct feed compositions. These compositions (all in molar percentages) represent different mixture: (1) 33.34% EtAc, 33.33% MeOH, 33.33% Water; (2) 80% EtAc, 10% MeOH, 10% Water; (3) 10% EtAc, 10% MeOH, 80% Water; and (4) 10% EtAc, 80% MeOH, 10% Water. The targeted purities are 99.5% for EtAc and MeOH, and 99.9% for Water.

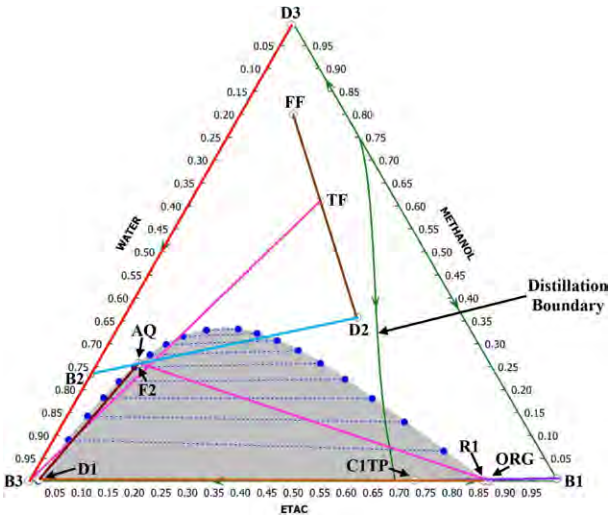



**Figure 1**: Residue Curve Map at 1 bar

## PROCESS FLOWSHEET SYNTHESIS

Figure 1 shows the Residue Curve Map (RCM) for the MeOH rich feed composition, revealing the presence of a Liquid-Liquid Envelope (LLE) and two minimum boiling azeotropes: EtAc/MeOH and EtAc/Water. We leverage the LLE to design the separation process flowsheets. In systems with LLE, the efficient method is to use a decanter to cross the distillation boundary and obtain pure products. However, the RCM indicates that the feed point lies outside the LLE. To address this, we propose using a Liquid-Liquid Extractor (LLX) with recycled water as a solvent to bring the feed point into the LLE. The proposed design is shown in Figure 2.

The fresh feed, mixed with the recycle stream (D2), is fed into the LLX as a total feed (TF) from the bottom, with recycled water introduced from the top in a counter-current manner. This setup brings the feed point within the LLE split region, as shown in Figure 1. The mixture then spontaneously separates into an EtAc-rich organic phase (ORG) and a water-rich aqueous phase (AQ), crossing the distillation boundary without any external energy input. The organic phase is fed into Column 1 (C1), where pure EtAc is recovered at the bottom (B1). The distillate composition (C1TP) remains within the LLE region and is decanted in an adjacent decanter, separating it into an organic phase (R1) and an aqueous phase (D1). The EtAc-rich organic phase (R1) is refluxed back into C1, while the water-rich aqueous phase (D1) is mixed with the aqueous stream (AQ) from LLX.

The resulting F2 stream is fed into Column 2 (C2), which prevents EtAc leakage into the bottom stream

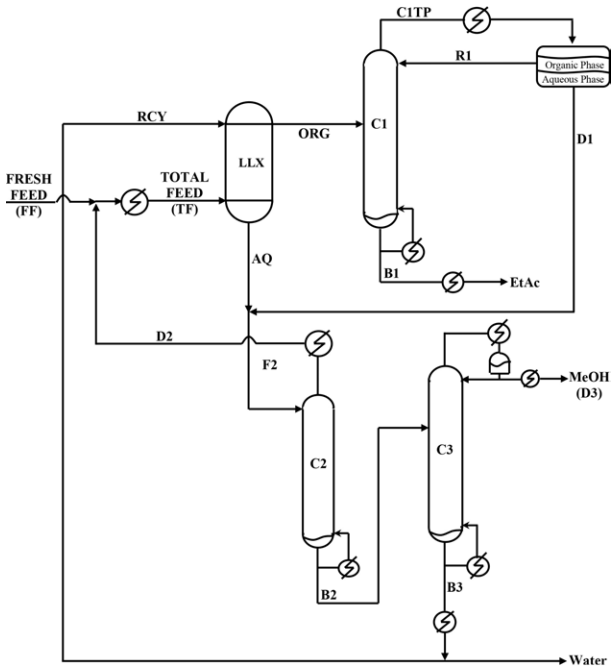



**Figure 2**: Proposed flowsheet structure

**Table 1**: Degrees of Freedom and Specifications

| S.N. | Degrees of Freedom | Equimolar | EtAc rich | MeOH rich | Water rich |
|---|---|---|---|---|---|
| | **Steady State DoFs** | | | | |
| 1 | Fresh feed rate (kmol/hr) | 100 | 100 | 100 | 100 |
| 2,3 | EtAc and MeOH product mole fraction | 0.995 | 0.995 | 0.995 | 0.995 |
| 4 | Water product mole fraction | 0.999 | 0.999 | 0.999 | 0.999 |
| 5 | C2 bottom stream EtAc impurity (ppm) | 24 | 74 | 20 | 160 |
| 6 | Water recycle rate (kmol/hr) | 98 | 104 | 252 | 14.71 |
| 7 | LLX operating temperature (°C) | 40 | 40 | 40 | 40 |
| 8,9,10 | Product temperature (°C) | 40 | 40 | 40 | 40 |
| | **Design DoFs** | | | | |
| 1,2,3,4 | LLX and Column pressure (bar) | 1 | 1 | 1 | 1 |
| 5 | Number of stages in LLX | 5 | 6 | 4 | 5 |
| 6 | Number of trays in column C1 | 18 | 18 | 18 | 18 |
| 7 | Number of trays in column C2 | 12 | 9 | 12 | 9 |
| 8 | Number of trays in column C3 | 27 | 30 | 27 | 30 |
| 9 | Feed tray location in column C1 | 9 | 11 | 11 | 11 |
| 10 | Feed tray location in column C3 | 12 | 14 | 12 | 14 |

(B2). The distillate (D2) lies outside the envelope, so it is recycled back to the LLX for further separation. The methanol-water bottoms (B2) are then distilled in Column 3 (C3) to produce pure methanol distillate (D3) and pure water bottoms (B3). A portion of the bottoms is recirculated to the LLX as the solvent feed. In the next section we will discuss the economic steady state design of the proposed process.

## ECONOMIC STEADY STATE DESIGN

The proposed design, depicted in Figure 2, has 20 degrees of freedom (DoFs), comprising 10 steady-state DoFs and 10 design DoFs. These DoFs are adjusted to minimize the Total Annualized Cost (TAC), resulting in an economic steady-state design.

$$TAC = \frac{TCC}{PBP} + \text{YOC}$$

where TCC is the Total Capital Cost, PBP is the Payback Period, and YOC is the Yearly Operating Cost. A payback period of 3 years is used.

We have used engineering heuristics to fix these DoFs, with details provided in Table 1. However, the economically dominant DoFs are optimized for minimizing the TAC using the Aspen Plus *sensitivity analysis* tool. For the MeOH-rich feed composition design, we identified three economically dominant DoFs among the 20: the total number of trays in the LLX ($N_{LLX}$), the EtAc impurity $x_{EtAc}$ in the C2 bottom stream (B2), and the water flow rate $F_{Water}$ for the recycled water to the LLX.

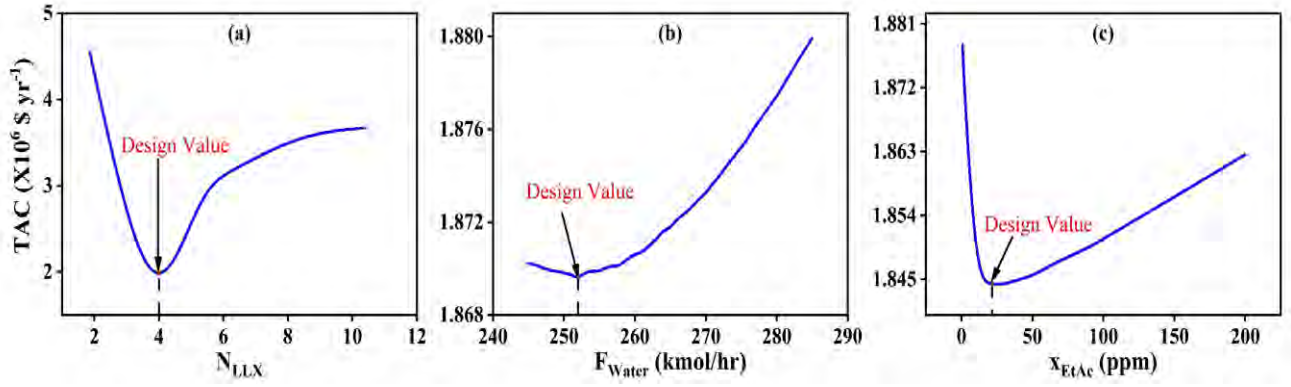



**Figure 3:** Optimization parameters for MEOH rich composition (a) Number of stages in LLX (b) Water recycle rate to LLX (c) EtAc impurity in B2 stream

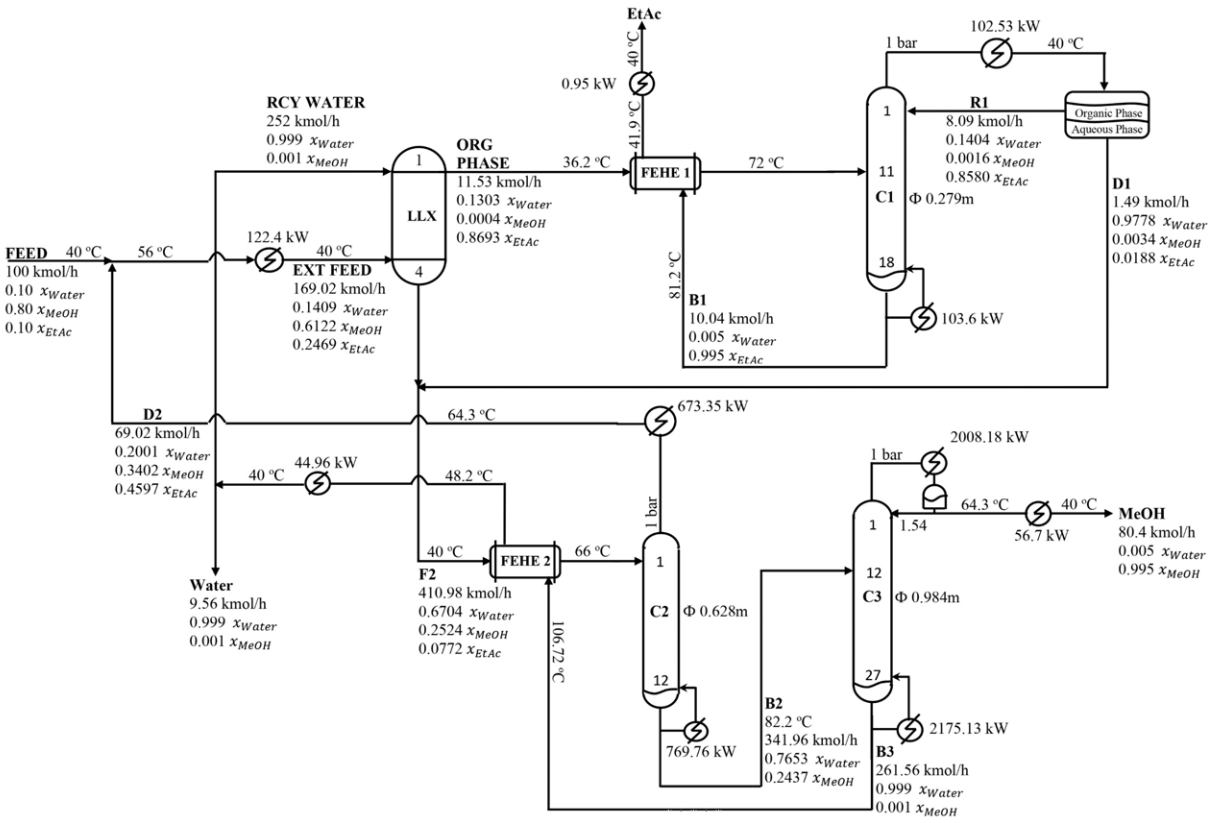



**Figure 4:** Nominal Design and Operating Condition for MeOH rich Feed

Figure 3 illustrate the variation of TAC with respect to the recommended design values corresponding to the optimum TAC. The optimum $N_{LLX}$ was determined to be 4. Above this value, TAC increases due to the higher capital cost of the LLX, while below it, TAC rises because of the increased water recycle rate needed to maintain the feed point in the LLE region, which increases the total reboiler duty. The optimum $x_{EtAc}$ is set at 20 ppm; exceeding this value leads to higher TAC due to increased reboiler duty in the C3 column, whereas falling below this value raises TAC due to the increase in reboiler duty of the C2 column. The optimum water flow rate $F_{Water}$; above this value, TAC increases due to a higher solvent water recycle rate, which elevates the reboiler duties of both C2 and C3. Conversely, below this optimum, TAC rises because of the increased reboiler duty in the C1 column, resulting from higher recycling associated with the C1 column.

Similarly, the other three steady-state designs can be developed. For brevity, the details are omitted here, but the DoFs are provided in Table 1. In the next section, we will synthesize the robust flowsheet.

## SYNTHESIS OF ROBUST FLOWSHEET

Based on the insights from Table 1, the robust flowsheet is designed by selecting the maximum stage or tray requirement for each unit to ensure effective separation across all compositions. In the LLX unit, the number of stages varies from 4 for MeOH-rich feeds to 6 for EtAc-rich feeds; therefore, 6 stages are incorporated into the robust design to maintain separation efficiency in all scenarios. For column C1, 18 trays are optimal across all compositions, which is retained in the robust configuration. In column C2, 12 trays are selected to facilitate effective separation across all four compositions. Similarly, for column C3, 30 trays are selected in the robust design to ensure reliable performance under all operating conditions. In the LLX, the liquid level corresponds to the dispersed phase, which has a low volume fraction. As seen from Table 1, the water flow rate has a low flow rate, which is why it is considered the dispersed phase here, except for the MeOH-rich composition, where it is the continuous phase. Therefore, the liquid level is in the aqueous phase for all compositions, except for the MeOH-rich case, where the level is in the organic phase. As the composition shifts from MeOH-rich to any other case, the LLX level changes from organic to aqueous, which is not feasible in the design. To address this, the water flow rate is maintained as the continuous phase for all composition cases to ensure effective separation. Thus, the water is in a ratio with the total feed to the LLX ($F_{LLX}$), which varies from 0.14 to 1.46. We selected the

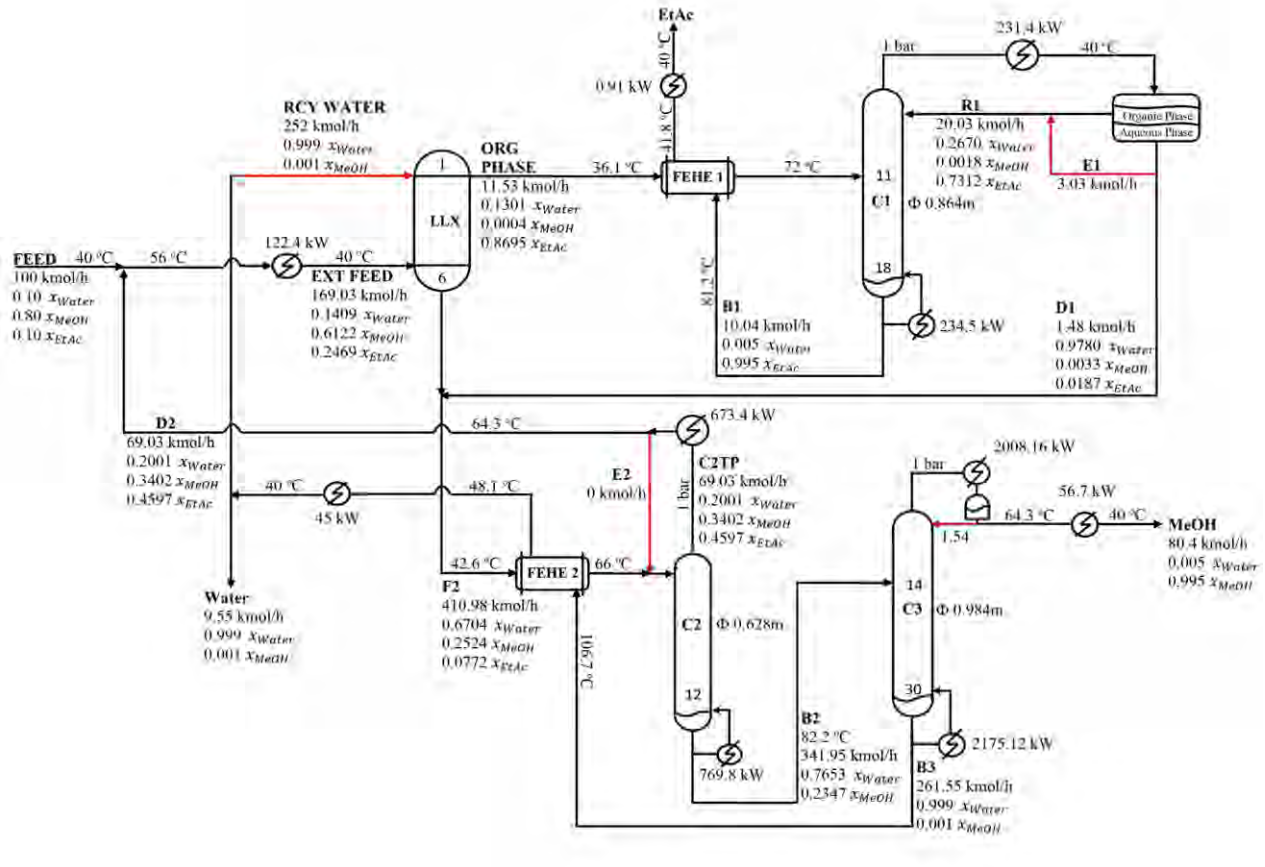



**Figure 5:** Robust Design and Operating Condition for MeOH rich Feed

highest ratio of 1.46 for the robust design to ensure effective extraction while maintaining operational efficiency across all scenarios.

Having established the basic design parameters, it was crucial to address the operational challenges posed by feed composition variations. As the composition changes from EtAc-rich to MeOH-rich, the feed to column C1 decreases while the feed to columns C2 and C3 increases. These variations significantly impact the reboiler duties required for the desired separation. Increased duties in columns C2 and C3 may lead to flooding, while the decreased duty in column C1 risks low boil-up rates, which can result in weeping and reduced tray efficiency. If the vapor rate falls below a critical point, it may trigger the low vapor boil-up limit, leading to weeping, which adversely affects tray efficiency and separation. The minimum allowable boil-up rate is determined using the turndown ratio, defined as the ratio of normal operating vapor throughput to the minimum allowable vapor throughput. We chose bubble cap trays for their 8:1 turndown ratio [4,5], which offers greater operational flexibility compared to sieve and valve trays. To

**Table 2**: Economic and sustainability metric for alternative feed composition

| Metric | Equimolar | | EtAc rich | | MeOH rich | | Water rich | |
|---|---|---|---|---|---|---|---|---|
| | Optimized Design | Robust Design | Optimized Design | Robust Design | Optimized Design | Robust Design | Optimized Design | Robust Design |
| Energy (kW) | 1601.4 | 1703.2 | 1437 | 2112.6 | 3048.5 | 3189.8 | 648.4 | 1048.8 |
| TCC×$10^6$ ($/yr) | 1.73 | 2.56 | 1.90 | 2.56 | 2.12 | 2.56 | 0.99 | 2.56 |
| YOC×$10^6$ ($/yr) | 0.60 | 0.64 | 0.54 | 0.79 | 1.14 | 1.19 | 0.24 | 0.39 |
| TAC×$10^6$ ($/yr) | 1.18 | 1.50 | 1.17 | 1.64 | 1.85 | 2.04 | 0.57 | 1.24 |

determine the minimum vapor throughput, we compared the vapor throughput across all four flowsheets and selected the highest value for each column as its design basis. While the 8:1 turndown ratio theoretically permits operation down to 12.5% of normal throughput, operating at this boundary risks weeping conditions. Therefore, we set 25% of normal throughput as the lower operational limit during turndown conditions to maintain a safety margin against weeping. Consequently, the reboiler duties in all columns can safely be reduced to this limit during operation, as required for different feed compositions.

To maintain the minimum vapor throughput of 25%, an additional degree of freedom (DoF) is required for each column to prevent weeping when the feed composition shifts from one composition to the other. In column C1, this involves partial recycling of the D1 stream back into the column, effectively maintaining minimum vapor rates while preserving separation efficiency. Column C2 employs a similar strategy by partially recycling the top product stream. For column C3, separation performance is sustained by carefully adjusting the reflux ratio, which ensures both product purity and operation above the minimum vapor rate limits. The detailed robust flowsheet, incorporating these strategies, is depicted in Figure 5, illustrating the design modifications and their alignment with operational requirements.

Table 2 presents an economic and energy comparison between the optimized flowsheet and the robust flowsheet for all considered feed compositions. As shown in the table, the robust design incurs a higher TCC than the optimized design due to the addition of an extra DoF and changes in design conditions. For a fair comparison, the TAC of the robust design should be compared with the sum of the TAC values for each optimized design. The cumulative TAC of all four optimized designs is **$4.77 \times 10^6$ $/yr**, whereas the TAC of the robust design—calculated as **(TCC/3 + YOC of individual feed composition)**—is **$3.86 \times 10^6$ $/yr**, which is **20% lower**. Thus, the robust design demonstrates a lower TAC while offering enhanced operational flexibility and reliability across varying feed compositions. This contributes to the sustainability of the overall process by ensuring long-term efficiency and minimizing the need for frequent process adjustments.

## CONCLUSION

This work presents a robust flowsheet design for the recovery and purification of waste solvent streams containing EtAc, MeOH, and water. The design effectively addresses challenges such as azeotropes and the variability in feed compositions. Crux to the design is the use of LLX, with recycled water as the solvent. This ensures that the total feed mixture remains within the LLE split region, regardless of the fresh feed composition. This enables spontaneous separation across the distillation boundary. The design has been validated across a wide range of feed compositions, including equimolar, EtAc-rich, MeOH-rich, and water-rich mixtures.

The robust design shows significant TAC savings of 20% than the cumulative TAC of all four optimized design and also offers greater flexibility in handling diverse feed mixtures. Additionally, it eliminates the need for multiple, composition-specific designs, leading to significant savings in land costs. Ultimately, the proposed design enhances operational flexibility and supports more scalable separation processes, representing a significant advancement in waste solvent recovery technology.

## ACKNOWLEDGEMENTS

We sincerely acknowledge the financial support provided by the Government of India.

## REFERENCES

1. Constable, David JC, Conchita Jimenez-Gonzalez, and Richard K. Henderson. "Perspective on solvent use in the pharmaceutical industry." Organic process research & development 11, no. 1 (2007): 133-137. https://doi.org/10.1021/op060170h
2. Cybulski, Andrzej, M. M. Sharma, R. A. Sheldon, and J. A. Moulijn. FINE CHEMICALS MANUFACTURE: TECHNOLOGY AND ENGINEERING, Gulf Professional Publishing (2001).
3. Srivastava, Prakhar, Aayush Gupta, and Nitin Kaistha. "Synthesis and Integrated Design of a Compact Azeotropic Process for EtAc–MeOH–Water Separation." *Industrial & Engineering Chemistry Research* 63, no. 49 (2024): 21466-21478. https://doi.org/10.1021/acs.iecr.4c03880
4. Lockett, M. J., and D. R. Summers. "Aspects of distillation column design for high turn-down applications in nitrogen rejection units." *Gas Separation & Purification* 3, no. 2 (1989): 71-74. https://doi.org/10.1016/0950-4214(89)85004-2
5. Bahadori, Alireza. NATURAL GAS PROCESSING: TECHNOLOGY AND ENGINEERING DESIGN. Gulf Professional Publishing (2014).

© 2025 by the authors. Licensed to PSEcommunity.org and PSE Press. This is an open access article under the creative commons CC-BY-SA licensing terms. Credit must be given to creator and adaptations must be shared under the same terms. See https://creativecommons.org/licenses/by-sa/4.0/



Systems & Control Transactions

**Research Article - Peer Reviewed Conference Proceeding**
ESCAPE 35 - European Symposium on Computer Aided Process Engineering
Ghent, Belgium. 6-9 July 2025
Jan F.M. Van Impe, Grégoire Léonard, Satyajeet S. Bhonsale,
Monika E. Polańska, Filip Logist (Eds.)

PSE PRESS

# Environmental Impacts of Trichlorosilane: Process Optimization, Life Cycle Assessment, and the Importance of Processing History

**Ethan Errington*[a], Deniz Etit[b], Tom Vinestock[a], Jaewook Lee[a], Jerry Heng[b], and Miao Guo[a]**

[a] King's College London, Department of Engineering, London, WC2R 2LS, UK
[b] Imperial College London, Department of Chemical Engineering, London, SW7 2AZ, UK
* Corresponding Author: ethan.errington@kings.ac.uk.

## ABSTRACT

Trichlorosilane (TCS) is a platform chemical used in the manufacture of silicon metals, silicones, and functional silanes. Despite this, very little information is available on the environmental impact (EI) associated with its manufacture. This work addresses this gap by developing estimates for the EI of reagent grade TCS (RG-TCS) based on a combination of process modelling & optimisation and life cycle assessment (LCA). Two production methods are considered: 1) direct chlorination (DC) producing RG-TCS as a main product, and 2) the Siemens process (SP) producing RG-TCS as a co-product. Results of a bi-objective process optimization suggest that the DC approach provides consistently better pareto-optimal (PO) trade-offs between the global warming potential (GWP) of RG-TCS and process profit; predicted GWPs are 3.2 to 3.3 $kgCO_2$-eq/kg for DC-derived RG-TCS and 3.8 to 4.9 $kgCO_2$-eq/kg for SP-derived PO designs. This suggests that processing history is important when considering the EI of RG-TCS. Nonetheless, further discussions of model uncertainty stress that these GWP estimates should be considered as preliminary, with improvements to modelling being required to refine EI predictions of RG-TCS in the future.

**Keywords**: Life Cycle Assessment, Process Modelling, Process Optimization, Trichlorosilane, Silicon

## INTRODUCTION

Trichlorosilane (TCS) is a platform chemical used in the manufacture of silicon metals, silicones, and functional silanes. Knowing the environmental impact (EI) of TCS is thus key to understanding the EI of many products, ranging from electronics to adsorbent materials.

Despite the importance of TCS, very little information is available on the environmental impact (EI) of TCS manufacturing. Thus, it is difficult to understand the EI of producing TCS, and TCS-derived products.

One reason for the lack of EI information may be variable production history. For example, reagent grade TCS (RG-TCS, 98wt%) can be produced as a main product of the direct chlorination (DC) of metallurgical grade silicon (MG-Si) [1], or as a co-product of the Siemens process (SP) for high purity silicon metal (≥99.9999 wt%) [2].

While both the DC and the SP rely on the chlorination of MG-Si, they differ in their energy intensity. This suggests the possibility of an importance of processing history in governing the EI of RG-TCS.

One way in which the EI of RG-TCS could be established is through Life Cycle Assessment (LCA). Nonetheless, this would require knowledge of material and energy use associated with gate-to-gate production of RG-TCS. In the absence of real plant data, prior research suggests that process modelling may be the preferred approach for accurately gathering this kind of information [3].

Herein, process modelling-informed LCA models are developed to quantify the EI of RG-TCS with the aim of:

1) detailing typical process designs by which RG-TCS is produced by DC and the SP,
2) identifying pareto optimal (PO) trade-offs in the EI and profitability of DC and the SP designs.
3) establishing the importance of processing history on the EI of RG-TCS products.

This has been done with modelling specific to China given its large share in global SG-Si production [2].

# METHODS

## Process Description

### Direct Chlorination

In the DC method (Figure 1a), hydrogen chloride (HCl) is produced through the reaction of hydrogen ($H_2$) and chlorine (Cl2) in reactor R1 (Equation 1). HCl is then reacted with MG-Si to produce chlorosilanes in R2 (Equation 2 and 3) [1].

$$H_2 + Cl_2 \rightarrow 2HCl \quad (1)$$

$$3HCl + Si_{MG} \rightarrow SiCl_3H + H_2 \quad (2)$$

$$4HCl + Si_{MG} \rightarrow SiCl_4 + 2H_2 \quad (3)$$

Chlorosilanes in the effluent of R2 are then separated by flash condensation in unit F1 and refined into RG-TCS and silicon tetrachloride (STC, 98wt%) products by distillation in C1 [2]. Residual gases leaving F1 are separated into chlorosilanes and hydrogen in adsorption column (A1) [4]. Recovered hydrogen is recycled and the chlorosilanes are fed to C1 [2].

### Siemens Process

The SP (Figure 1b) extends the DC method by further purifying TCS in columns C2 and C3, yielding an RG-TCS product (C2 tops), an ultra-high purity TCS (C3 tops, 99.99 wt%) and residual waste (C3 bottoms) [2]. The TCS from C3 is heated in a furnace (E5) and reduced using hydrogen (3:1 $H_2$:TCS mole ratio [2]) in reactor R3 to produce solar grade silicon (SG-Si, 99.9999 wt%) according to Equations 4 and 5 [2]. The resulting gases are recycled and STC is hydrogenated to form TCS in R4 [2] (Equation 6); R4 effluent is fed to column C4 for material recovery.

$$SiCl_3H + H_2 \rightarrow Si_{SG} + 3HCl \quad (4)$$

$$2SiCl_3H + HCl \rightarrow SiCl_4 + H_2 \quad (5)$$

$$Si_{MG} + 2H_2 + 3SiCl_4l \rightarrow 4SiCl_3H \quad (6)$$

## Process Modelling

Models for the DC and SP methods were built in the Aspen Plus V11 software according to process flow diagrams shown in Figure 1. Vapour-liquid equilibria was modelled using the NRTL-RK method. Equipment with fixed operating conditions are listed in Table 1.

Reaction performance associated with each process was based on patent and academic literature (Table 2). Compressor performance was modelled according to isentropic compression. Distillation was modelled according to the MESH equations.

The production scale of both DC and the SP was based on a 24.1 kmol/hr feed of HCl to reactor R2 [6].

It was assumed that 75% of heat generated by reactors R1 and R2 could be recovered as steam.

**Table 1:** Thermodynamic information for equipment assumed to have fixed conditions.

| Unit | Temperature, C | Pressure, bar | Ref. |
|---|---|---|---|
| R1 | 250 | 2.5 | [7] |
| R2 | 350 | 5.0 | [8] |
| R3 | 1100 | 1.1 | [6] |
| R4 | 500 | 36.0 | [9] |
| A1 | 25 | 1.1 | - |
| E3 | 25 | 1.1 | - |
| E4 | 25 | 1.1 | - |
| E5 | 400 | 1.1 | [6,10] |
| E6 | 25 | 1.1 | - |
| E7 | 500 | 1.1 | [9] |

**Table 2:** Summary of reaction performance assumed during reaction modelling.

| Unit | Equation | Yield, % | Basis (w.r.t) | Ref. |
|---|---|---|---|---|
| R1 | 1 | 100 | $H_2$ | [7] |
| R2 | 2 | $^{13}$90 | Si | [6,10] |
| | 3 | $^{13}$10 | Si | [6,10] |
| R3 | 4 | $^{14}$30 | $SiCl_3H$ | [6,12] |
| | 5 | $^{14}$70 | $SiCl_3H$ | [6,12] |
| R4 | 6 | $^{11}$25 | $SiCl_4$ | [6,8] |

## Process Optimization

The NSGA-II algorithm [16] (100 individuals, PYMOO package [17]) was used to find PO frontiers for maximisation of the total annualised process profit, $TAP$ ($/yr), and minimization of the Global Warming Potential of RG-TCS ($GWP$, kg$CO_2$-eq/kg) for DC and the SP. In each case, optimization was run until a minimum of 4000 profitable designs were found.

$$\min\ [-TAP,\ GWP] \quad (7)$$

$$\text{given: } TAP = f_1(x) \quad (8)$$

$$GWP = f_2(x) \quad (9)$$

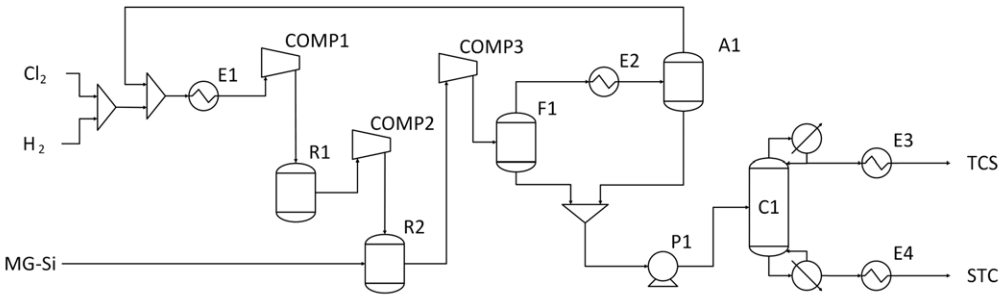
$$\text{s.t.: } g(x) \leq 0 \quad (10)$$

$$x^{lb} \leq x \leq x^{ub} \quad (11)$$

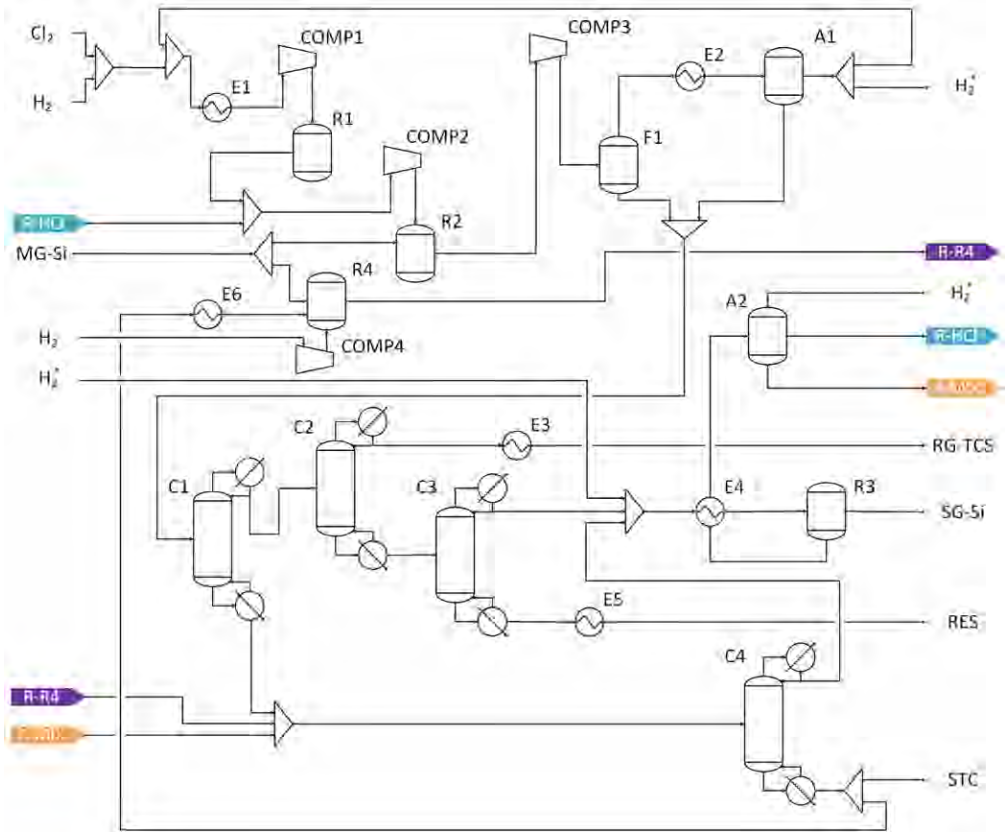
Where $g(x)$ is a black-box function based on the underlying process model, Equation 10 represents practical constraints associated with product purity in the black box model, and $x^{lb}$ and $x^{lu}$ represent the lower and upper bounds associated decision vector $x$. Minimum purities of 98 wt% were set for sale of RG-TCS and STC. A minimum purity of 99.99 wt% TCS was set for the top product of column C3 used to produce SG-Si in the SP method [6].

## Process Economics

The $TAP$ of each process was calculated by subtracting the sum of total annualised capital and operational expenditures, $TAC$ and $TAO$ ($/yr), from the total annualised revenue, $TAR$ ($/yr), as shown in Equation 12.




**(a)**




**(b)**

**Figure 1:** Process flow diagrams for production of trichlorosilane by the direct chlroination (top) and Siemens process (bottom) methods. TCS: trichlorosilane, STC: silicon tetrachloride, RES: residual waste chlorosilanes, MG-Si: metallurgical grade silicon, SG-Si: solar grade silicon, $H_2$: reagent grade hydrogen; $H_2^*$: high purity hydrogen.

It was assumed that costs reflected the implementation of a grass-roots plant based on the year 2019.

$$TAP = TAR - (TAC + TAO) \quad (12)$$

## Total Annual Revenue

$TAR$ was calculated based on product sales according to Equation 13 and Table 3.

$$TAR = \sum_p P_p \dot{m}_p \quad (13)$$

Where $P_p$ is the sale price of product $P_p$ ($/kg) and $\dot{m}_p$ is the annual production amount of product $p$ ($/kg).

## Total Annual Capital Expenditure

$TAC$ was calculated using Equation 14, considering costs associated with compressor, heat exchanger, pump, and distillation units only.

$$TAC = \frac{\sum_e CAPEX_e}{A} \quad (14)$$

Where $CAPEX_e$ is the capital expenditure of unit $e$ ($), and $A$ is an annualization factor (yr) assuming a 30-year payback period and 3% interest rate. $CAPEX$ calculation included bare module costs [15], materials choice [16], and geographic location [16].

**Table 3:** Assumed material and utility fuel source prices

| Material | Price, $/unit | Unit | Ref. |
|---|---|---|---|
| MG-Si | 1.75 | kg | [18] |
| $Cl_2$ | 0.28 | kg | [19] |
| $H_2$[a] | 0.15/4.00 | kg | [19,20] |
| RG-TCS | 1.00 | kg | [21] |
| STC | 1.00 | kg | [21] |
| SG-Si | 12.00 | kg | [18] |
| Electricity | 0.088 | kWh | [22] |
| Coal[b] | 4.022 | GJ | [22] |

[a] prices reflect 98 and 99.99 wt% hydrogen product purities, [b] assuming energy conversion factor of 30 GJ/tonne of coal

### Total Annual Operational Expenditure

$TAO$ was calculated including consideration for feedstock use (Table 2), utility use and waste handling (Table 3, as per [17]), and operator labour (as per [15]) according to Equation 15.

$$TAO = \sum P_f \dot{m}_f + \sum P_u \dot{Q}_u + \sum P_w \dot{Q}_w + 4.8 P_{OL} \quad (15)$$

Where $P_f$ and $\dot{m}_f$ are the price ($/kg) and annual usage (kg/yr) of feedstock $f$, and $P_u$ and $\dot{Q}_u$ are the price ($/kJ) and annual usage (KJ/yr) of utility, $u$; $P_w$ and $\dot{Q}_w$ are the price of waste treatment ($/kg) and annual amount of waste produced (kg/yr); and $P_{OL}$ is the price of labor four process operators each with a 36,000 $/yr salary.

### Life Cycle Assessment

#### Goal and Scope Definition

The goal of LCA in this work is to estimate the EI of RG-TCS produced by DC and the SP. An attributional LCA approach was used, considering a cradle-to-gate scope, with 1 kg of RG-TCS as a functional unit.

#### Inventory Modelling

Life cycle inventories were generated using material and energy use estimates from process modelling & optimization. The EcoInvent Database (v3.10, APOS) [23] was used to model background life cycle activity.

#### Impact Assessment

The EI of RG-TCS has been estimated using the ReCiPe 2016 (H) method [24] considering the GWP ($kgCO_2$-eq) as a proxy for EI. Calculations include a cut-off factor of 0.1%. Co-product impacts have been allocated according to the mass of product produced.

## RESULTS AND DISCUSSION

Results of bi-objective optimization are shown in Figure 2. This data includes three expected trends.

Firstly, results for both processes display a positive correlation between the GWP and profitability of PO process designs for DC and the SP – reflecting the presence of a trade-off between process profit and product GWP.

Secondly, the GWP of SP-derived RG-TCS is observed to be consistently larger than that of DC-derived

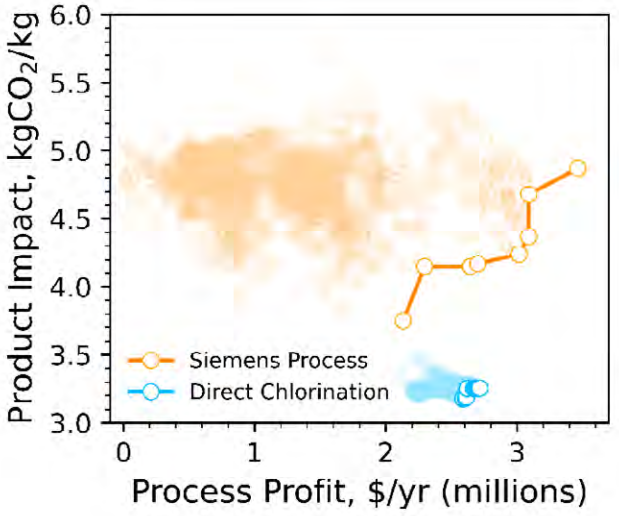



**Figure 2:** Trade-offs in global warming potential and profitability identified during design optimization. Solid lines outline pareto-optimal designs. Dull markers represent other feasible, non pareto-optimal designs.

RG-TCS for all pareto optimal designs. This is intuitive given the high energy intensity of distillation and production of SG-Si in the SP (see Figure 1).

Thirdly, the PO frontier of DC designs covers a small range of profitability, which may be attributed to the simplicity of DC and lack of competition between reducing EI and maximising profit during design.

On the contrary, Figure 2 also shows two unexpected results.

Firstly, PO designs of the SP cover a very similar range of possible profitability when compared to that of PO DC designs. This is unexpected given the high value of SG-Si produced by the SP method (see Table 3) and complexity of the SP (see Figure 1), which may lead to the expectation of greater return in process profit.

Secondly, the GWP of RG-TCS produced by PO designs of DC and the SP are found to be relatively similar (i.e. 3.2 to 3.3 and 3.8 to 4.9 kg $CO_2$-eq/kg respectively). This may contradict the expected scale of GWP associated with energy intensity of SG-Si production in the SP.

### Relation to Trichlorosilane Yield

To explain unexpected results in Figure 2, further consideration is needed for process designs of PO solutions. Results in Figure 3 illustrate the relationship of RG-TCS yield and process profit for DC and SP designs.

Surprisingly, results for both DC and the SP show designs with high RG-TCS yields (90 to 92 % and 76 to 91 % respectively). This is intuitive for DC designs as the yield of RG-TCS does not compete directly with the yield of STC (see Figure 1), making high yields of RG-TCS likely to reflect materially efficient design implementations.

Conversely, high RG-TCS yields are counterintuitive

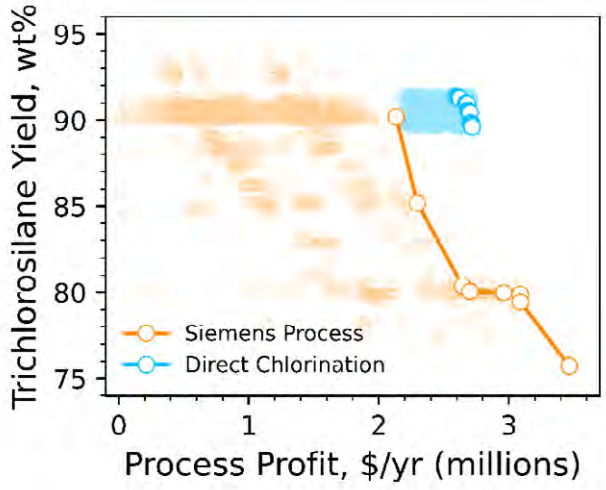



**Figure 3:** Relationship of trichlorosilane yield and process profit identified during design optimization. Solid lines highlight the location of pareto-optimal designs shown in Figure 2. Dull markers represent other feasible designs.

for the SP - given that the yield of RG-TCS competes directly with the yield of SG-Si (Figure 1). Consequently, the observed PO SP designs must minimise the production of SG-Si - the intended main product of the SP.

To understand why this is, three aspects of the modelling method used must be further considered.

## Relation to Impact Allocation Method

One way in which the observed PO SP designs may tend toward maximising RG-TCS yield is through an inherent bias introduced by using a mass-based impact allocation method during LCA. This is because of the relatively high molar mass of TCS (135 g/mol) when compared to Si (28 g/mol), which suggests that the conversion of feedstock to RG-TCS in high yield is likely to minimise the GWP of RG-TCS products by maximising the total mass of products produced by the SP.

## Relation to Optimization Algorithm

Another reason why the observed PO SP designs may tend to maximise RG-TCS yield is because of limitations in the optimization algorithm used. Specifically, the optimizer used may have failed to identify regions of the search space in which feasible high-profit, high-impact designs exist - e.g. as a result of maximizing SG-Si yield at the expense of RG-TCS yield and GWP.

This may be corroborated by the fact that multiple high-profit, high-impact SP designs were observed during the early stages of optimization but lost as optimization proceeded due to violating constraints associated with RG-TCS (≥98 wt%). Such designs may have failed to evolve toward feasible solutions due to the use of a strict "feasibility first" constraint handling approach, which prioritises feasible designs over search diversity [17].

Thus, it is possible that the PO frontiers visualised in Figure 3 represent only the low-impact, low-profit subset of the true PO design space available to the SP.

Further research is needed to explore the SP design space more rigorously.

## Relation to Process Modelling Uncertainties

Finally, four major sources of uncertainty in process modelling must be considered when interpreting data.

Firstly, the SP modelled (Figure 1) considers only one method for recycling of the chlorosilane-rich effluent which arises after the deposition of SG-Si (see R4, Figure1) [2]. Thus, the reported GWP of SP-derived RG-TCS may not accurately reflect the GWP of RG-TCS produced by SP designs using different material recycling methods.

Secondly, the SP modelled does not consider the possibility of thermally integrating distillation columns. This can cause up to a 50% reduction in energy requirements associated with distillation in the SP [2] – suggesting that reported GWPs may be overestimated in this regard.

Thirdly, the effect of impurities on distillation efficiency has not been modelled. This may cause the GWP to be underestimated due to inaccuracy in material and energy estimates associated with distillation in the SP.

Fourthly, the separation of chlorosilanes, hydrogen and hydrogen chloride via adsorption (see Figure 1) has not been modelled rigorously in this work. This may cause the GWP to be underestimated due to failing to account completely for energy and material efficiency in both DC and SP designs.

# CONCLUSIONS

Understanding the environmental impact of trichlorosilane (TCS) is crucial in enabling the impact assessment of many products. Consequently, this work has set out to establish estimates for the impact of reagent grade TCS (RG-TCS) produced according to two approaches - direct chlorination (DC), and the Siemens process (SP) for manufacturing solar-grade silicon (SG-Si).

Using global warming potential (GWP) as a proxy for impact, bi-objective optimization suggests that the impact of SP-derived TCS (3.8 to 4.9 kg $CO_2$-eq/kg) is larger than that of DC-derived TCS (3.2 to 3.3 kg $CO_2$-eq/kg). This suggests that the processing history of RG-TCS may be an important factor governing the impact of RG-TCS.

Interestingly, it is also observed that results of the work tend to highlight PO SP designs which prioritise the production of RG-TCS in high yield over SG-Si. This is despite SG-Si being the intended main-product of the SP. This is explained as arising from three main factors affecting modelling and optimization: 1) the use of a mass-basis of impact allocation (which biases PO SP designs to SP designs with high TCS yield), and 2) limitations in the

optimization method used, which has possibly failed to identify PO SP designs of high-impact and high-profit, and 3) uncertainty in process modelling, particularly in the case of modelling designs of the SP.

Consequently, though results suggest that processing history is important in governing the impact of RG-TCS, the absolute value of GWP reported for SP-derived RG-TCS should be considered to be a preliminary estimate with room for future improvement. Findings of the work may be of interest to individuals working to produce chlorosilane materials and TCS-derived products.

## ACKNOWLEDGEMENTS

This work has been made possible by funding provided by Scottish Water, the UK EPSRC SSCP Doctoral Training Program, and UKRI Innovate UK. EE also thanks Alex Durkin and Benjamin Lyons of Imperial College London for formative discussions on process systems engineering (inc. process modelling and optimization).

## REFERENCES

1. Simmler, W. 2000. Silicon Compounds, Inorganic. In: Ullmann's Encyclopedia of Industrial Chemistry. Wiley-VCH. (2000).
2. Yan D. Siemens Process. In: Handbook of Photovoltaic Silicon. Ed: Yang D. Springer. (2019).
3. Parvatker AG and Eckleman MJ. Comparative evaluation of chemical life cycle inventory generation methods and implications for life cycle assessment results. *ACS Sus. Chem. & Eng.* 7(1):350-367. (2019).
4. Xiqun W, Li T. Pressure swing adsorption system for separation of mixed gas including hydrogen and chlorosilane and/or chlorine hydride. CN Patent 202,620,982U. (2012).
5. Del Coso, G *et al*. Temperature homogeneity of polysilicon rods in a Siemens reactor. *J. Cryst. Growth*. 299(1): 165-170. (2007).
6. Ramírez-Márquez C, *et al*. Process design and intensification for the production of solar grade silicon. *J. of Clean. Prod.* 170: 1579-1593. (2018).
7. Benoit J and Mellard J. Facility and reactor for directly synthesizing hydrochloric acid from hydrogen and chlorine with heat recovery. US Patent No. 9,414,364 B2 (2011).
8. Chee Y and Kunimune T. Hybrid TCS-siemens process equipped with 'turbo charger' FBR; method of saving electricity and equipment cost from TCS-siemens process polysilicon plants of capacity over 10,000 MT/YR. US Patent No. 20,120,114,546 A1. (2010).
9. Erickson CE, and Wagner GS. Hydrogenation of halogenosilanes. U.S. Patent No. 2,595,620. (1952).
10. Diez E, *et al*. Distillation assisted heat pump in a trichlorosilane purification process. *Chem. Eng. Process*. 69: 70-76. (2013).
11. Kotzsch HJ, *et al*. Process for the hydrochlorination of elemental silicon. U.S. Patent No. 4,044,109. (1977).
12. Jain MP *et al*. Studies on hydrochlorination of silicon in a fixed bed reactor. *Ind. Chem. Eng.* 53(2):61-67. (2011).
13. Deb K. *et* al. A fast and elitist multiobjective genetic algorithm: nsga-II. *Trans. Evol. Comp*. 6(2):182–197. (2002).
14. Blank J and Deb K. pymoo: Multi-Objective Optimization in Python. *IEEE Access*. 8: 89497-89509. (2020).
15. van Amsterdam MF. Factorial techniques applied in chemical plant cost estimation: A comparative study based on literature and cases. [Thesis Work]. *TU Delft.* (2018).
16. Sinnott R and Towler G. Chemical Engineering Design. 6th Ed. Elsevier. (2020).
17. Ulrich GD. And Vasudevan PT. Chemical Engineering Process Design and Economics. 2nd Ed. Process Publishing Co. (2004).
18. Jarkin VN, *et al*. Methods of trichlorosilane synthesis for polycrystalline silicon production. Part 2: Hydrochlorination and redistribution. *Modern Elec. Mats.* 7(2): 33-43. (2021).
19. Business Analytiq. https://businessanalytiq.com/. [Accessed 31-Jan-2025]. N.B.: “Hydrogen price index” and “Chlorine price Index”.
20. Global Insight Services. High Purity Hydrogen
21. Alibaba. https://www.alibaba.com/. [Accessed 31-Jan-2025]. N.B.: “Trichlorosilane” and “tetrachlorosilane”. Market Analysis and Forecast to 2034. (2025).
22. Statista. https://www.statista.com. [Accessed 31-Jan-2025]. N.B.: “Business electricity price china “ and “South china coal price”.
23. Wernet, G *et al*. The ecoinvent database version 3 (part I): overview and methodology. *Int. J. of LCA*. 21(9): 1218–1230. (2016).
24. Huijbregts, MAJ, *et al*. ReCiPe 2016: a harmonized life cycle impact assessment method at midpoint and endpoint level report I: characterization. (2016).https://rivm.openrepository.com/

© 2025 by the authors. Licensed to PSEcommunity.org and PSE Press. This is an open access article under the creative commons CC-BY-SA licensing terms. Credit must be given to creator and adaptations must be shared under the same terms. See https://creativecommons.org/licenses/by-sa/4.0/



Systems & Control Transactions

**Research Article - Peer Reviewed Conference Proceeding**
ESCAPE 35 - European Symposium on Computer Aided Process Engineering
Ghent, Belgium. 6-9 July 2025
Jan F.M. Van Impe, Grégoire Léonard, Satyajeet S. Bhonsale,
Monika E. Polańska, Filip Logist (Eds.)

PSE PRESS

# Sodium bicarbonate production from $CO_2$ captured in Waste-to-Energy plants: an Italian case-study

**Elvira Spatolisano[a,*], Giorgia De Guido[a], Laura A. Pellegrini[a], Elena Riva Redolfi[b], Mauro Corradi[b], Davide Alberti[c], Adriano Carrara[c]**

[a] Politecnico di Milano, Milan, Italy
[b] Acinque Ambiente Srl, Italy
[c] a2a SpA, Italy
* Corresponding Author: elvira.spatolisano@polimi.it.

## ABSTRACT

As anthropogenic $CO_2$ emissions continue to drive global warming, innovative approaches to repurpose $CO_2$ into valuable products emerge as pivotal solutions to mitigate its environmental impact. $CO_2$ utilization encompasses a range of technologies, including its conversion into fuels, chemicals, and materials, leveraging $CO_2$ as a resource rather than treating it solely as a waste. This shift not only reduces greenhouse gas emissions but also supports the circular economy by integrating industrial processes with carbon capture and storage technologies. Specifically, in the Waste-to-Energy (WtE) context, sodium bicarbonate production can be an attractive solution, considering that it is required in the plant for $SO_x$ and acidic gases abatement. In this work, the carbon dioxide utilization to give sodium bicarbonate in a WtE context is analyzed. With reference to an existing waste-to-energy plant in Italy, the potential of this $CO_2$ utilization method is highlighted by means of process simulation. A preliminary feasibility study is presented, based on heat and material balances retrieved from Aspen Plus® V14, properly set for the accurate modeling of the system's behaviour. Process performances are discussed, in view of the pilot plant engineering and construction.

**Keywords**: CO2 utilization, NaHCO3, waste-to-energy, CO2 emissions, carbon neutrality.

## INTRODUCTION

Waste-to-energy (WtE) plants play a dual role in modern waste management, generating energy and reducing landfill dependency at the same time. Nevertheless, they significantly contribute to greenhouse gas emissions [1]. Therefore, the integration with $CO_2$ capture and utilization technologies can enhance sustainability, enabling for both waste reduction and climate change mitigation [2]. When $CO_2$ is captured from the flue gas, it can be eventually converted into high value-added products, following the circular economy principles. $CO_2$ utilization technologies hold promise particularly where the waste-to-energy plant is far away from the injection point for $CO_2$ sequestration, such that its transportation becomes costly. Key conversion technologies include chemical, electrochemical or biological methods for $CO_2$ valorization to methanol, syngas, plastics, minerals or fuels. However, challenges remain about the cost-effective implementation of these solutions at the commercial scale.

One promising application is the production of sodium bicarbonate ($NaHCO_3$). $NaHCO_3$ is often used for waste-to-energy flue gas treatment to abate various harmful pollutants, as sulfur oxides ($SO_x$) and acidic gases as hydrogen chloride (HCl). Therefore, bicarbonate production *in situ* from captured $CO_2$ can be interesting for simultaneously lowering the plant environmental impact and improving the economic balance.

To explore sodium bicarbonate as an alternative for the carbon dioxide chemical fixation, its production from sodium carbonate ($Na_2CO_3$) is analyzed within an existing waste-to-energy context in Italy [3-4]. In view of performing a preliminary feasibility study, the thermodynamic framework has been properly set up in Aspen Plus® V14, taking into account the vapor-liquid and liquid-solid

equilibria involved in the system. The process scheme has been designed to minimize wastes and water demand. $CO_2$ coming from the carbon capture section, with traces of $N_2$ and $O_2$, is fed at the battery limits, together with solid $Na_2CO_3$. Sodium carbonate powder has to be dissolved in water, such that a solution at 30 wt.% of $Na_2CO_3$ is fed to the reaction section. Inlet $CO_2$ flowrate is fixed to guarantee a bicarbonate output of about 30% of the annual need of the waste-to-energy plant. $NaHCO_3$ is produced in the form of a slurry to be dried in the downstream section. Process performances are technically discussed referring to heat and material balances. As a result, the technology feasibility is analyzed, in view of the pilot plant engineering and construction.

This research project, the result of a collaboration between A2A SpA, Acinque Ambiente Srl and the GASP (Group on Advanced Separation Processes & GAS Processing) of Polytechnic University of Milan, is part of a broader vision of research activities to achieve the decarbonization objectives of A2A SpA.

## THERMODYNAMIC FRAMEWORK

### Chemical and physical equilibrium

For process simulation purposes in Aspen Plus® V14, the thermodynamic framework has to be carefully set up. Many species are available in the system, not only in the vapor phase ($N_2$, $O_2$, $H_2O$, $CO_2$) or liquid phase ($H_2O$), but also as ionic species ($HCO_3^-$, $CO_3^{2-}$, $Na^+$, $H_3O^+$, $OH^-$) and solids (the main ones are $NaHCO_3$, $Na_2CO_3$, however several hydrates can exist).

The process thermodynamics involves both physical (liquid-vapor and liquid-solid phase equilibria) and chemical (liquid phase reactions) equilibrium. The approach used for modeling purposes is schematized in Table 1.

**Table 1:** Schematization of the thermodynamic package as specified in Aspen Plus® V14.

| **physical equilibrium** | |
|---|---|
| thermodynamic quantities | $\Delta G_f^0$, $\Delta H_f^0$ for solid species |
| liquid phase activity coefficient model | ELECNRTL |
| vapor phase EoS | Kwong (RK) |
| **chemical equilibrium** | |
| ionic dissociation | 1a) $H_2O + HCO_3^- \rightleftharpoons CO_3^{2-} + H_3O^+$<br>2a) $2\ H_2O + CO_2 \rightleftharpoons HCO_3^- + H_3O^+$<br>3a) $2\ H_2O \rightleftharpoons OH^- + H_3O^+$ |
| salt formation | 1b) $Na_2CO_3 \rightleftharpoons CO_3^{2-} + 2\ Na^+$<br>2b) $NaHCO_3 \rightleftharpoons HCO_3^- + Na^+$ |

For the vapor-liquid equilibrium in the presence of ionic species, a γ/φ approach (2° group) is used. Accordingly, the activity coefficient has been evaluated with the ELECNRTL model, while the fugacity coefficient is calculated by means of the Redlich-Kwong equation of state (RK EoS). $CO_2$, $N_2$ and $O_2$ have been defined as Henry components.

As for the liquid-solid equilibrium, it has been accounted for as in equation (1), in which the solid phase fugacity is calculated through thermodynamic quantities referred to the solid phase. To ensure a reliable estimation, $\Delta G_f^0$, $\Delta H_f^0$ for solid species available in the simulation software have been compared with literature [5], finding a good agreement for all the values (the maximum relative deviation was found to be 0.25% for $NaHCO_3$).

$$x_i \gamma_i f_i^0 = f_i^0 \exp\left(\frac{\Delta h_{i,fus}}{R}\left(\frac{1}{T_{fi}} - \frac{1}{T}\right) + \frac{c_{pi}^L - c_{pi}^S}{R}\left(\frac{T_{fi}}{T} - 1 - \ln\left(\frac{T_{fi}}{T}\right)\right)\right) \quad (1)$$

Considering the chemical equilibrium, both ionic dissociation and salt formation reactions have been introduced, each one with its equilibrium constant. There are two different approaches to evaluate the equilibrium constant, as shown in equations (2) and (3). In the approach 1, as in equation (2), $K_{eq}$ is evaluated from the Gibbs free energy of the reaction.

$$lnK_{eq} = \frac{\Delta G_R^0}{RT} \quad (2)$$

$$lnK_{eq} = A + \frac{B}{T} + \mathrm{ClnT} + \mathrm{DT} \quad (3)$$

On the other hand, the approach 2, as in equation (3), involves a built-in correlation for the $K_{eq}$ calculation, whose constants are specified in Table 2 for each reaction.

**Table 2:** Constants for the ionic dissociation and salt formation reactions of Table 1.

| reaction | A | B | C | D |
|---|---|---|---|---|
| 1a | 216.050 | -12431.7 | -35.4819 | 0 |
| 2a | 231.465 | -12092.1 | -36.7816 | 0 |
| 3a | 132.899 | -13445.9 | -22.4773 | 0 |
| 1b | -30.468 | 6566.26 | 0 | 0 |
| 2b | -63.4345 | -1296.96 | 11.9061 | -0.029058 |

The values *A*, *B*, *C* for the dissociation reactions 1a, 2a, 3a are in line with literature [6].

Regarding the carbonate and bicarbonate formation reactions (1b and 2b of Table 1), to select the most accurate approach for $K_{eq}$ evaluation, Figure 1 shows the

comparison between equilibrium constants from literature [7] and Aspen Plus® V14 predictions according to equations 2 and 3. As can be observed from Figure 1, the $K_{eq}$ evaluated using equation 2 in Aspen Plus® are much closer to the literature data. Therefore, this approach was chosen for the calculation of the equilibrium constants for carbonate and bicarbonate production from ionic species.

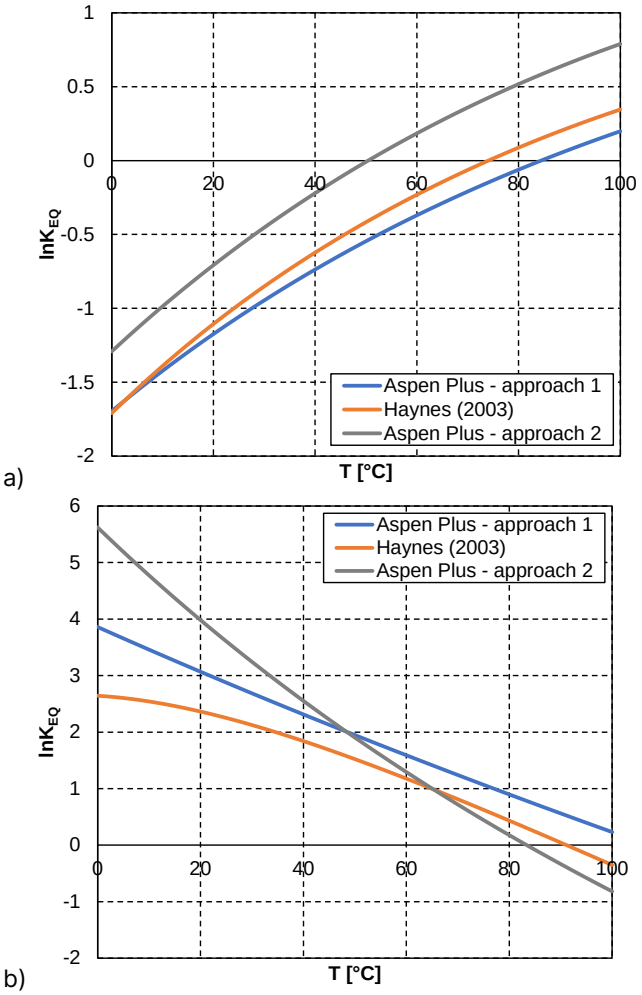



**Figure 1.** ln $K_{eq}$ for the production of: a) bicarbonate and b) carbonate as a function of temperature ($T$). Comparison between literature models and Aspen Plus® V14 models predictions according to approach 1 (blue) and approach 2 (grey).

## Solubility analysis

To verify the predictions of the simulation software, the Aspen Plus® solubility analysis tool was used. This tool evaluates the solid species solubility in liquid, gaseous and supercritical solvents. Firstly, solubility of single salts (*i.e.*, $NaHCO_3$ and $Na_2CO_3$) in $H_2O$ has been calculated as a function of temperature. The obtained results have been compared with the available literature [8], once again obtaining a good agreement. Then, the effect of the presence of one salt on the solubility of the other was assessed. This analysis allows to get an idea of the possible critical issues related to the precipitation of carbonate and bicarbonate. With reference to the specific case study, the soda ash carbonation reaction (4) proceeds consuming $Na_2CO_3$ to produce $NaHCO_3$.

$$Na_2CO_3 + H_2O + CO_2 \leftrightarrow 2\ NaHCO_3 \quad (4)$$

The concentration of $Na_2CO_3$ in solution, at the beginning equal to 30 wt.%, decreases as the reaction proceeds in the range of 0-30 wt.%. Assuming complete conversion for $Na_2CO_3$, the mass fraction of $NaHCO_3$ in solution (*i.e.*, the maximum possible) is almost equal to 50 wt.%.

For this reason, to analyse the precipitation equilibria of the system, the $Na_2CO_3$ solubility and $NaHCO_3$ solubility have been considered, respectively, at variable $NaHCO_3$ concentration in solution in the range 0-50 wt.% and at variable $Na_2CO_3$ in solution in the range 0-30 wt.%. Since bicarbonate must be recovered in solid phase, it is necessary for $NaHCO_3$ to precipitate, while $Na_2CO_3$ must be kept in solution.

Results are plotted in Figure 2: from Figure 2a, as the $Na_2CO_3$ content increases, the solubility of $NaHCO_3$ decreases. On the other hand, Figure 2b shows the solubility of $Na_2CO_3$ in $H_2O$ at different concentrations of $NaHCO_3$: as the $NaHCO_3$ content increases, the solubility of $Na_2CO_3$ decreases significantly.

Referring to reaction (4), it is possible to determine, at a fixed $Na_2CO_3$ conversion, the produced $NaHCO_3$ and the residual $Na_2CO_3$ in solution.

Table 3 shows the mass fraction of $Na_2CO_3$ and $NaHCO_3$ in solution depending on the $Na_2CO_3$ conversion. Comparing the concentrations of Table 3 with the curves of Figure 2b, there are no critical issues regarding the precipitation of $Na_2CO_3$ if the conversion of $Na_2CO_3$ is > 85%: in this case, the residual $Na_2CO_3$ in solution is within the solubility limit. At lower conversions, the possible precipitation of $Na_2CO_3$ together with that of $NaHCO_3$ is to be verified in the simulation phase.

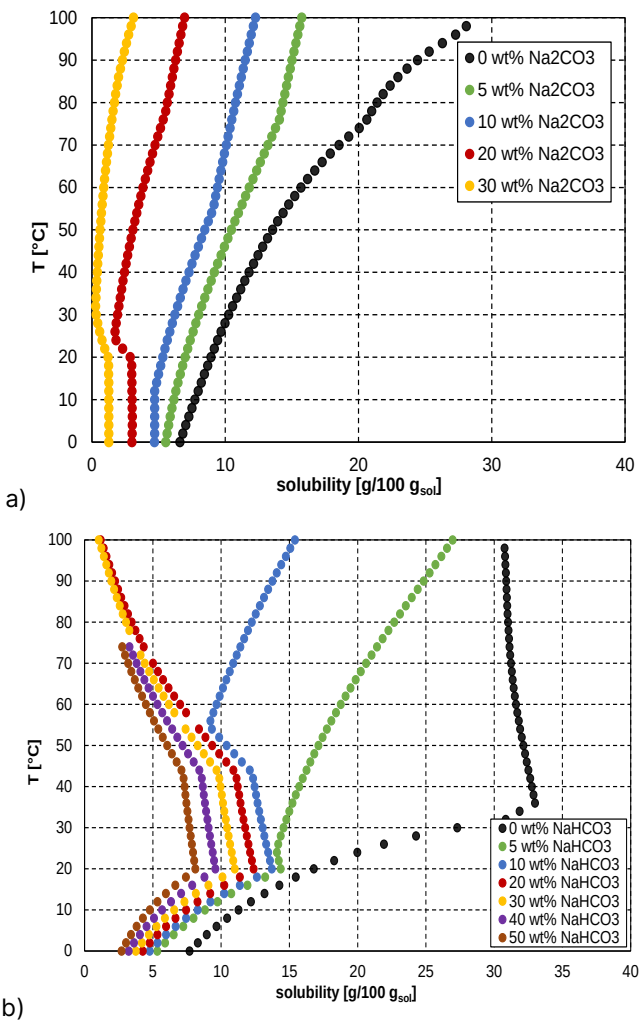



**Figure 2.** Solubility of: a) $NaHCO_3$ in $H_2O$ at different $Na_2CO_3$ concentrations and b) $Na_2CO_3$ in $H_2O$ at different $NaHCO_3$ concentrations.

**Table 3:** Conversion of $Na_2CO_3$ and corresponding mass fractions of $Na_2CO_3$ and $NaHCO_3$.

| conversion [%] | $Na_2CO_3$ [wt.%] | $NaHCO_3$ [wt.%] |
|---|---|---|
| 100 | 0.0 | 47.55 |
| 85 | 4.5 | 40.42 |
| 70 | 9.0 | 33.28 |
| 55 | 13.5 | 26.15 |
| 40 | 18.0 | 19.02 |
| 25 | 22.5 | 11.89 |
| 10 | 27.0 | 4.75 |

## PRELIMINARY FEASIBILITY STUDY

Set up and validated the thermodynamic package, the process simulation has been performed.

Figure 3 shows the process scheme for $NaHCO_3$ production as simulated in Aspen Plus® V14. The scheme is composed of different sections, each of them described in the following.

- Preparation of $Na_2CO_3$ solution. Solid $Na_2CO_3$ is dissolved into fresh $H_2O$ (stream 13 in Figure 3) and recycled (stream 11 in Figure 3). The make-up water flow rate was modulated to guarantee a $Na_2CO_3$ solution concentration of 30 wt.%. This value is close to the solubility limit at the operating temperature of the process. The dissolution of $Na_2CO_3$ in $H_2O$ is exothermic: Aspen Plus® V14 predicts a temperature increase up to about 50 °C: it is, therefore, necessary to provide a jacketed tank with cooling water.
- Reaction. The $CO_2$ from the carbon capture section, together with the sodium carbonate solution, react in T-101, which is the carbonation tower operated at constant temperature and pressure. The $CO_2$ flow rate is fixed to guarantee, at complete

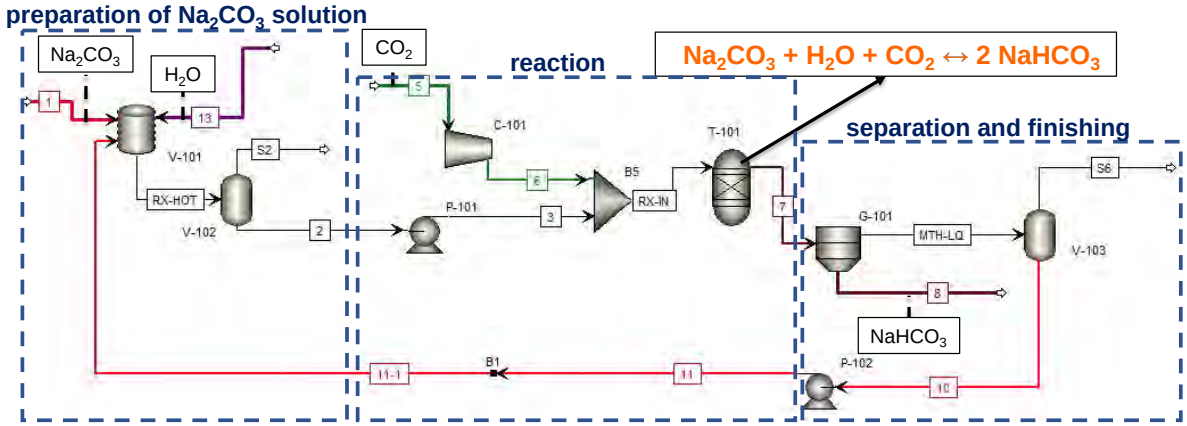



**Figure 3.** Process scheme for $NaHCO_3$ production. Simulation in Aspen Plus® V14

conversion, the productivity detailed in the Introduction. Pressure, temperature and $CO_2$ composition are defined by the upstream capture section. On the other hand, the $Na_2CO_3$ flow rate entering the process battery limits is stoichiometric to the inlet carbon dioxide. The operating pressure for the carbonation reactor is in the range 1.5-2.5 bar from literature [9-10]. Since the reaction is in the liquid phase, pressure has no influence on the kinetics, but on the $CO_2$ solubility only (*i.e.*, on the transfer of carbon dioxide from the gas phase to the liquid phase). $P$ = 1.8 bar has been fixed and kept constant for simulation purposes. As for the operating temperature, it is in the range 35-60 °C from the literature [9-10]. Temperature has an effect on reaction thermodynamics and kinetics: it must be limited to avoid decomposition of $NaHCO_3$ (left-shifted equilibrium in reaction (4)), favored at high temperatures. $T$ = 40 °C has been fixed for simulation purposes. The carbonation reaction is exothermic: it is necessary to provide a reactor jacketed with cooling water for isothermal operation. A bicarbonate slurry is produced, which must be separated and dried before storage.

- Separation and finishing. The solid-liquid separation is carried out in a centrifuge (G-101 in Figure 3). The fraction of liquid retained by the solid, preliminarily assumed to be 15% [10], depends on the specifications of the downstream dryer. For the drying unit operation, the most suitable equipment (which cannot be simulated in Aspen Plus®) must be chosen on the basis of experience and experimental tests. The mother liquor is recycled to the preparation of the $Na_2CO_3$ solution section.

The heat and material balances for the process of Figure 3 are reported in Table 4, Table 5 and Table 6.

**Table 4:** Cooling duty for the process of Figure 3.

| Equipment | $T_{in}$ [°C] | $T_{out}$ [°C] | $Q$ [kW] |
|---|---|---|---|
| V-101 + V-102 | 52.84 | 40 | -1.270 |
| T-101 | 62.47 | 40 | -4.226 |

**Table 5:** Electric power consumption for the process of Figure 3.

| Equipment | $P_{in}$ [bar] | $P_{out}$ [bar] | $W$ [kW] |
|---|---|---|---|
| P-101 | 1.0 | 1.8 | 0.0064 |
| P-102 | 1.7 | 1.8 | 0.0008 |
| C-101 | 1.8 | 3.0 | 0.1194 |

The performances of the process are good: no thermodynamic limitations or particular critical issues were detected. From Table 6, it can be noted that the outlet $CO_2$ in gas phase (stream S6 in Figure 3) is negligible. Cooling is all to be carried out with cooling water as a utility. Electric power consumption is negligible and is due to liquid and gas circulation only.

In addition to the electric power and cooling duty retrieved from process simulation, it is necessary to consider the power consumption of the G-101 centrifuge and the heating duty of the dryer.

## CONCLUSIONS

The integration of sodium bicarbonate production from captured $CO_2$ into waste-to-energy plants represents an innovative synergy between waste management and carbon utilization. By leveraging emissions to create a high-demand product, WtE plants can enhance their economic and environmental performance. This approach holds significant promise for transforming WtE facilities into more sustainable and resource-efficient operations while contributing to global efforts to combat climate change.

In this work, the $CO_2$ to $NaHCO_3$ conversion is explored with reference to an existing waste-to-energy plant in Italy. A preliminary feasibility study is presented, based on heat and material balances retrieved from Aspen Plus® V14, properly set for the accurate modeling of the system's behaviour. Process performances are discussed, in view of the pilot plant engineering and construction.

Due to the encouraging outcomes and the easy implementation to the existing infrastructures, the potential of carbon dioxide conversion to bicarbonate is demonstrated, proving that it can became a feasible $CO_2$ utilization choice within the waste-to-energy context.

Although the potential benefits are significant, challenges such as managing operational costs and optimizing the chemical process for scalability must be addressed. For this reason, future developments of this work will regard:

1. a sensitivity study, depending on the reactant ratio $CO_2/Na_2CO_3$ fed to the battery limits, to identify optimal operating conditions;
2. the pilot plant sizing and layout, to evaluate its footprint;
3. the economic assessment and the overall $CO_2$ emissions evaluation, both direct and indirect, to establish the real process feasibility at the industrial level.

The deepening of these three aspects will provide a

**Table 6:** Material balance for the process of Figure 3.

| | UoM | 5 | 1 | 13 | 8 | | 10 | S6 |
|---|---|---|---|---|---|---|---|---|
| **Temperature** | °C | 30 | 25 | 40 | 40 | 40 | 40 | 40 |
| **Pressure** | bar | 1.8 | 1 | 1.8 | 1.8 | 1.8 | 1.8 | 1.7 |
| **Phase** | | G | S | L | L | S | L | G |
| **Molar Flow rate** | kmol/hr | 0.2219 | 0.2219 | 0.4441 | 0.2472 | 0.4193 | 4.6964 | 0.0005 |
| **Mass Flow rate** | kg/hr | 9.6342 | 23.5141 | 8.0000 | 5.2853 | 35.2249 | 100.395 | 0.0177 |
| **Mass composition** | | | | | | | | |
| **$Na_2CO_3$** | | 0.0000 | 1.0000 | 0.0000 | 0.0000 | 0.0000 | 0.0000 | 0.0000 |
| **$H_2O$** | | 0.0089 | 0.0000 | 1.0000 | 0.7108 | 0.0000 | 0.7108 | 0.0220 |
| **$CO_2$** | | 0.9900 | 0.0000 | 0.0000 | 0.0008 | 0.0000 | 0.0008 | 0.4268 |
| **$NaHCO_3$** | | 0.0000 | 0.0000 | 0.0000 | 0.0000 | 1.0000 | 0.0000 | 0.0000 |
| **$HCO_3^-$** | | 0.0000 | 0.0000 | 0.0000 | 0.1398 | 0.0000 | 0.1398 | 0.0000 |
| **$CO_3^{2-}$** | | 0.0000 | 0.0000 | 0.0000 | 0.0543 | 0.0000 | 0.0543 | 0.0000 |
| **$Na^+$** | | 0.0000 | 0.0000 | 0.0000 | 0.0943 | 0.0000 | 0.0943 | 0.0000 |
| **$N_2$** | | 0.0008 | 0.0000 | 0.0000 | 0.0000 | 0.0000 | 0.0000 | 0.4268 |
| **$O_2$** | | 0.0002 | 0.0000 | 0.0000 | 0.0000 | 0.0000 | 0.0000 | 0.1244 |

more reliable answer to the effectiveness of this $CO_2$ utilization technology.

## REFERENCES


1. Kearns DT, Waste-to-Energy with CCS: A pathway to carbon-negative power generation. ©Global CCS Institute (2019).
2. Otgonbayar T, Mazzotti M, Modeling and assessing the integration of $CO_2$ capture in waste-to-energy plants delivering district heating. *Energy* 290, 130087 (2024).
3. Moioli S, De Guido G, Pellegrini LA, Fasola E, Redolfi Riva E, Alberti D, Carrara A, Techno-economic assessment of the $CO_2$ value chain with CCUS applied to a waste-to-energy Italian plant. *Chem Eng Sci* 287, 119717 (2024).
4. Moioli S, De Guido G, Pellegrini LA, Fasola E, Alberti D, Carrara A. Case Study for the Application of CCUS to a Waste-to-Energy Italian Plant. In Acid Gas Injection. Field, Data, Simulation. Ed: Carroll JJ, Wu Y, Hao M, Zhu W. Scrivener Publishing (2024).
5. Barin I. Thermochemical Data of Pure Substances. 2nd Edition, VCH Verlagsgesellschaft, Weinheim, Basel (1993).
6. Edwards TJ, Maurer G, Newman J, Prausnitz JM, Vapor-Liquid Equilibria in Multicomponent Aqueous Solutions of Volatile Weak Electrolytes. *AIChE J* 24(6): 966-976 (1978).
7. Haynes H W Jr. Thermodynamic solution model for trona brines. *AIChE J* 49(7): 1883-1894 (2003).
8. Thieme, 2000. Sodium Carbonates. In Ullmann's Encyclopedia of Industrial Chemistry.
9. Yoshi HCMH, Silva AB, de Souza M, de Faria SHB, Bernardo A, Bonfim-Rocha L, Multi-criteria assessment of sodium bicarbonate optimized production through CO2 utilization strategies. *J Clean Prod* 349, 131419 (2022).
10. Lee JH, Lee WD, Kwak C, Kang KJ, Lee JH, Technoeconomic and Environmental Evaluation of Sodium Bicarbonate Production Using $CO_2$ from Flue Gas of a Coal-Fired Power Plant. *Ind Eng Chem Res* 58: 15533–15541 (2019).



© 2025 by the authors. Licensed to PSEcommunity.org and PSE Press. This is an open access article under the creative commons CC-BY-SA licensing terms. Credit must be given to creator and adaptations must be shared under the same terms. See https://creativecommons.org/licenses/by-sa/4.0/

Systems & Control Transactions

**Research Article - Peer Reviewed Conference Proceeding**
ESCAPE 35 - European Symposium on Computer Aided Process Engineering
Ghent, Belgium. 6-9 July 2025
Jan F.M. Van Impe, Grégoire Léonard, Satyajeet S. Bhonsale,
Monika E. Polańska, Filip Logist (Eds.)

PSE PRESS

# Modelling of the Co-precipitation of Ni-Mn-Co Hydroxides.

**Erik G. Resendiz-Mora[a], and Solomon F. Brown[a]***

[a] University of Sheffield, Department of Chemical and Biological Engineering, Sheffield, South Yorkshire, United Kingdom
* Corresponding Author: s.f.brown@sheffield.ac.uk.

## ABSTRACT

A simple mathematical model of the co-precipitation of Ni-Mn-Co hydroxides is developed and applied to investigate the effect of pH, initial concentration of ammonia in the solution, concentration of the ammonia feed, nucleation rate constant and exponent, growth rate constant and growth exponent over the model output. The model is shown to produce a correct representation of the precipitation variables, and the general trends obtained for different sets of parameters are found in agreement with results presented elsewhere. A sensitivity analysis is carried out and the sensitivity indices are calculated. It is found that pH, initial concentration of ammonia and growth rate constant are the input parameters with the most relevant effect over the model input.

**Keywords**: Aspen Custom Modeler, Co-precipitation modeling, Ni-Mn-Co hydroxide, Cathode precursor.

## INTRODUCTION

As the world transitions to cleaner energy sources like solar and wind, which are inherently intermittent, lithium-ion batteries have emerged as a suitable solution due to their high energy density, versatility, and long cycle life. Li-ion batteries excel in storing excess energy generated during periods of high production and releasing it when supply falls short, enabling a stable and reliable energy supply. Widely used in portable electronics, electric vehicles, and stationary energy storage systems [1-4], lithium-ion batteries also play a pivotal role in the electrification of transportation, significantly reducing reliance on fossil fuels and lowering greenhouse gas emissions. Their integration into energy systems not only facilitates the adoption of renewable energy but also supports global efforts to achieve net-zero carbon goals. By bridging the gap between energy production and consumption, lithium-ion batteries are indispensable in building a sustainable and resilient energy future.

The widespread adoption of batteries in daily life faces significant challenges, particularly regarding performance, cost, and sustainability. A key hurdle lies in optimizing cathode materials, which critically influence a battery's energy density, lifespan, and overall efficiency [5, 6]. These properties are largely inherited from the chosen materials for cathode's precursors and from the synthesis route, which determines relevant features of the particles such as their mean size, PSD, porosity and morphology.

Ni-Mn-Co hydroxides can be synthesized by different methods, e.g. solvo/hydrothermal, solid state, or co-precipitation [5, 7, 8]. The latter involves the mixing of stoichiometric amounts of transition metal salts with a complexing agent (e.g. ammonia) and a precipitating agent (e.g. sodium hydroxide) under controlled reaction conditions to produce quasi-spherical particles and tailor the particle morphology and density. Key parameters to optimize such particle properties are the reaction environment pH, stirring velocity, temperature and reaction time [5, 9, 10].

The optimization of the parameters mentioned above can be troublesome, particularly because the precipitation environment is very scale-dependent and an observed behaviour at a lab facility might not be reproduced at an industrial precipitator, hence, following an experimental route may prove costly and ineffective [11]. To tackle this problem, it is useful to turn to mathematical models that can produce a fair representation of the phenomena at a low cost. Because of that, in this investigation we develop a mathematical model of a semi-batch precipitator to study the effect of input parameters in the response of the model regarding the particle size distribution (PSD), the supersaturation and the particle mean

sizes $d_{4,3}$ and $d_{3,2}$. A few studies regarding the modelling of co-precipitation of Ni-Mn-Co hydroxides are available in the open literature. Barai et al. [2] developed a multi-scale model considering nucleation, growth and aggregation of particles and simulated a continuous stirred tank crystallizer to study the effect of pH and ammonia concentration over the PSD and mean particle size. Shiea et al. [1] applied a CFD-PBE modelling approach to a multi-inlet vortex micromixer and simulated the effect of varying the flowrate and concentration of the feed, they reported a decrease in mean particle size as the feed concentration and flowrate increase. Para et al. [3] applied the same approach to simulate a similar system and fitted the model output to experimental datapoints of mean particle size. Mugumya et al. [12] investigated the co-precipitation of NMC111; their modelling work was limited to solving the equilibrium conditions and did not include any description of the formation and growth of crystals. Querio et al. [13] compared the computational performance of the CFD-PM approach versus a compartment model and found that the latter approach render less accurate, yet less computationally expensive qualitatively correct predictions. In this work, we utilize a simple transient model of a semi-batch crystallizer to study the sensitivity of the response of the model to the variation of relevant operating parameters like pH and ammonia concentration, but also to the changes of the kinetic parameters of crystal nucleation and growth. The intent of this work is to obtain a simple, representative model capable of producing a reliable output regarding PSD and particle size, which will be integrated in the context of a whole manufacturing plant model in future work.

# METHODS

## System description

The system to be modelled is a stirred crystallizer operating in a semi-batch mode as illustrated in Figure 1. The crystallizer is initially charged with a solution of aqueous ammonia prepared according to the specifications outlined in Table 1. During the process, a 2M transition metal solution containing an 8:1:1 ratio of nickel, manganese and cobalt is gradually introduced into the reactor, along with a 10M sodium hydroxide solution and an aqueous ammonia solution with concentration varying from 1.14 – 5.7M. The operating parameters of the crystallizer are summarized in Table 1.

## Model assumptions.

The development of the crystallizer model is based on the following key assumptions, which simplify the representation of the system while maintaining its relevance to practical applications:

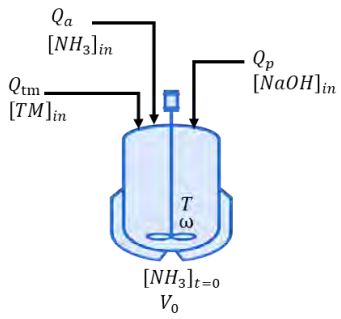



**Figure 1.** Schematic representation of the modelled crystallyzer.

**Table 1:** Operating conditions of the crystallizer.

| Param. | Description | Value |
|---|---|---|
| $T$ | Temperature | 60°C |
| $\omega$ | Stirring velocity | 1000 rpm |
| $V_0$ | Initial solution volume | 0.0008 $m^3$ |
| $[TM]$ | Molar concentration of the transition metal solution. | 2M |
| $[NaOH]$ | Molar concentration of the precipitating agent. | 10M |
| $Q_{TM}$ | TM solution volumetric flowrate | $4.8x10^{-5}$ $m^3$ $h^{-1}$ |
| $Q_a$ | Chelating agent sol. volumetric flowrate | $2.4x10^{-5}$ $m^3$ $h^{-1}$ |
| $Q_p$ | Precipitating agent sol. volumetric flowrate. | $1.92x10^{-5}$ $m^3$ $h^{-1}$ |
| $t_a$ | Reagent addition time. | 10.4h |

1. Crystal particles are modeled as having spherical geometries to streamline the mathematical treatment of shape-dependent phenomena.
2. The formation of transition metal hydroxides is considered negligible. The primary reaction pathway is assumed to involve the formation of transition metal ion complexes, followed by their conversion into combined transition metal hydroxides.
3. The reaction rates for both ionic complex formation and hydroxide formation are assumed to be fast. As a result, the rate-controlling processes are the nucleation and growth of crystals.
4. Aggregation and breakage of crystals are neglected, focusing the model on the nucleation and growth mechanisms.
5. The crystallizer is assumed to operate isothermally, with a consistent and uniform temperature maintained throughout the process.
6. It is assumed that no seed crystals are present in the feed entering the crystallizer.

## Model development.

The particle size distribution is mathematically described by the population balance equation (PBE). For a semi-batch crystallizer, the PBE is [14]:

$$\frac{\partial Vn}{\partial t} + G\frac{\partial Vn}{\partial L} = 0 \quad (1)$$

Where $V$ is the crystallizer volume, $n$ is the number density, $t$ is the batch time, $L$ is the crystal size and $G$ is the crystal growth rate. Equation (1) neglects the agglomeration and breakage of particles in the crystallizer. Since the crystallization process starts from a clear solution, the following initial condition applies to Equation (1):

$$n(0, L) = 0 \quad (2)$$

Additionally, the following boundary condition is applied depending on the level of supersaturation of the desired product in the crystallizer:

$$n(t, 0) = \begin{cases} 0 \; if \; S \leq 1 \\ \frac{B}{G} \; if \; S > 1 \end{cases} \quad (3)$$

Where $S$ is the supersaturation and $B$ is the nucleation rate; the supersaturation, and by extension the nucleation and growth rates relate to the equilibrium concentration of the ions of nickel ($[Ni^{2+}]_{eq}$), manganese ($[Mn^{2+}]_{eq}$), cobalt ($[Co^{2+}]_{eq}$), and hydroxyl ions ($[OH^-]$) and are defined as:

$$S = \left( \frac{[Ni^{2+}]_{eq}^{x}[Mn^{2+}]_{eq}^{y}[Co^{2+}]_{eq}^{z}[OH^-]_{eq}^{2}}{K_{sp}^{Ni_xMn_yCo_z(OH)_2}} \right)^{1/3} \quad (4)$$

$$B = k_B(S-1)^b \quad (5)$$

$$G = k_G(S-1)^g \quad (6)$$

Where $k_B$ is the nucleation kinetic constant, $k_G$ is the growth kinetic constant, $b$ is the nucleation exponent, $g$ is the growth exponent and the exponents $x$, $y$ and $z$ are determined by the desired stoichiometry of the combined hydroxide; for the case of NMC811, these values are $x = 0.8$, $y = 0.1$ and $z = 0.1$. The equilibrium concentrations of the ionic species in the solution are calculated by solving the complex chemical equilibrium relationships expressed in Equations (7) – (13):

$$[Ni^{2+}] = [Ni^{2+}]_{eq} + \sum_{i=1}^{6}\left[Ni(NH_3)_n{}^{2+}\right]_{eq} \quad (7)$$

$$[Mn^{2+}] = [Mn^{2+}]_{eq} + \sum_{i=1}^{4}\left[Mn(NH_3)_n{}^{2+}\right]_{eq} \quad (8)$$

$$[Co^{2+}] = [Co^{2+}]_{eq} + \sum_{i=1}^{6}\left[Co(NH_3)_n{}^{2+}\right]_{eq} \quad (9)$$

$$[NH_3] = [NH_3]_{eq} + [NH_4^+]_{eq} + \sum_{n=1}^{6} n\left[Ni(NH_3)_n{}^{2+}\right]_{eq} + \sum_{n=1}^{4} n\left[Mn(NH_3)_n{}^{2+}\right]_{eq} + \sum_{n=1}^{6} n\left[Co(NH_3)_n{}^{2+}\right]_{eq} \quad (10)$$

$$K_n^{M^{2+}} = \frac{\left[M(NH_3)_n{}^{2+}\right]_{eq}}{[M^{2+}]_{eq}[NH_3]_{eq}^{n}} \quad (11)$$

$$K_w = [H_3O^+]_{eq}[OH^-]_{eq} \quad (12)$$

$$K_b = \frac{[NH_4^+]_{eq}[OH^-]_{eq}}{[NH_3]_{eq}} \quad (13)$$

Where the equilibrium constants of the coordination of transition metal ions with ammonia ($K_n^{M^{2+}}$), the dissociation of water ($K_w$), and dissociation of ammonia ($K_b$) are taken from [15]. To solve Equations (7) – (13) the total concentrations of nickel ($[Ni^{2+}]$), manganese ($[Mn^{2+}]$), cobalt ($[Co^{2+}]$), and ammonia ($[NH_3]$) are required; the concentration of these species evolve dynamically throughout the process and are given by:

$$\frac{d[Ni^{2+}]V}{dt} = Q_{tm}[Ni^{2+}]_{in} - \frac{0.8Vk_v\rho_c}{MW_c}\frac{dm_3}{dt} \quad (14)$$

$$\frac{d[Mn^{2+}]V}{dt} = Q_{tm}[Mn^{2+}]_{in} - \frac{0.1Vk_v\rho_c}{MW_c}\frac{dm_3}{dt} \quad (15)$$

$$\frac{d[Co^{2+}]V}{dt} = Q_{tm}[Co^{2+}]_{in} - \frac{0.1Vk_v\rho_c}{MW_c}\frac{dm_3}{dt} \quad (16)$$

$$\frac{d[SO_4^{2-}]V}{dt} = Q_{tm}[SO_4^{2-}]_{in} \quad (17)$$

$$\frac{d[NH_3]V}{dt} = Q_a[NH_3]_{in} \quad (18)$$

$$\frac{d[Na^+]V}{dt} = Q_p[Na^+]_{in} \quad (19)$$

$$\frac{dV}{dt} = Q_s + Q_a + Q_p \quad (20)$$

$$\frac{dm_3}{dt} = 3Gm_2 \quad (21)$$

$$m_2 = \int_0^{\infty} n\,L^2 dL \quad (22)$$

Where $Q_s$, $Q_a$, and $Q_p$ are the volumetric flowrates of transition metal solution, ammonia and precipitant agent; $k_v$ is the volumetric factor, $\rho_c$ is the crystal density, $MW_c$ is the precipitate molecular weight, $m_2$ and $m_3$ are the second and third moments of the particle size distribution.

## Model solution.

The model equations were implemented and solved using the method of lines in Aspen Custom Modeler. A total of 250 simulations were conducted, varying key parameters, including the initial concentration of ammonia, the ammonia concentration fed to the crystallizer, the solution pH, and the crystallization kinetics parameters for crystal nucleation and growth. These variables were randomly sampled using the Latin hypercube sampling method, ensuring efficient exploration of the parameter space within the ranges specified in Table 2.

# RESULTS

The results of the simulation of four selected cases for key variables like supersaturation, mean particle sizes and particle size distribution are presented in Figures 2 through 5. As mentioned before, the input parameters

utilized for these simulations were randomly sampled, and for quick reference are presented in Table 3.

**Table 2:** Parameter ranges utilized to simulate the co-precipitation of Ni-Mn-Co hydroxides.

| Param. | Description | Value |
|---|---|---|
| $[NH_3]_{t=0}$ | Initial ammonia conc. | 0.3–1.5M |
| $[NH_3]_{in}$ | Ammonia feed conc. | 1.14–5.7M |
| $pH$ | Solution pH | 9.5–11.5 |
| $k_B$ | Nucleation constant | $10^4$–$10^{10}$ |
| $b$ | Nucleation exponent | 1–5 |
| $k_G$ | Growth constant | $10^{-6}$–$10^{-10}$ |
| $g$ | Growth exponent | 0.5 – 2.5 |

**Table 3:** Input parameters utilized to generate the results presented in this paper.

| Param | Units | (a) | (b) | (c) | (d) |
|---|---|---|---|---|---|
| $[NH_3]_{t=0}$ | mol $m^{-3}$ | 1.17 | 0.51 | 0.74 | 0.63 |
| $[NH_3]_{in}$ | mol $m^{-3}$ | 3.32 | 1.66 | 2.43 | 3.79 |
| $pH$ | - | 11.4 | 9.9 | 9.8 | 10.2 |
| $k_B x10^{-6}$ | $m^{-3}\,h^{-1}$ | 0.014 | 22.3 | 0.057 | 0.131 |
| $b$ | - | 4.5 | 2.8 | 4.7 | 4.0 |
| $k_G x10^{10}$ | $m\,h^{-1}$ | 81.7 | 27.0 | 3.7 | 3.44 |
| $g$ | - | 1.0 | 1.5 | 2.4 | 1.7 |

Figure 2 presents multiple supersaturation profiles generated by the model using different sets of input parameters. As anticipated for a semi-batch system initially containing only one of the reacting species, the supersaturation levels increase over time, reaching a peak before gradually declining until the end of the process.

In all cases, an initial induction period is observed at the start of the run, marking the addition of reagents to the crystallizer. After this phase, supersaturation breaks through and builds up at a rate dictated by crystallization kinetics and reactant concentrations. The magnitude of supersaturation is determined by the availability of transition metal and hydroxyl ions in the solution [1], with the highest levels in Figure 2 corresponding to simulation cases with the highest pH. Conversely, the position of the supersaturation peak is influenced by crystallization kinetics, particularly the crystal growth rate, which governs how quickly reactants are consumed to form Ni-Mn-Co hydroxide crystals.

Figures 3 and 4 are plots of the evolution of the volume-weighted mean size and the surface-weighted mean size, respectively. In both cases, the growth of the NMC particles breaks trough after 3 hours which coincides with the development of the supersaturation curves discussed above. For Case (a), both the volume- and surface-weighted mean sizes seem to have an initially fast growth but then plateau at the lowest mean size of the four cases. Conversely, for case (c) the growth is sustained for longer, yielding the highest mean particle sizes among all of them. This behaviour seems obvious given the rapid decline of the supersaturation for case (a), which in turn renders a decline of the crystal growth rate. On the other hand, for case (c), even when the supersaturation does not reach very high values, its decline is less severe and, in addition, the value of the growth exponent magnifies the crystal growth rate.

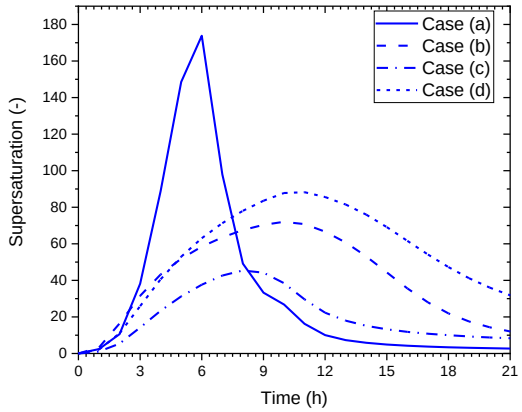



**Figure 2.** Supersaturation of Ni-Mn-Co hydroxide at different operating conditions of pH and ammonia concentration, and with different sets of kinetic parameters.

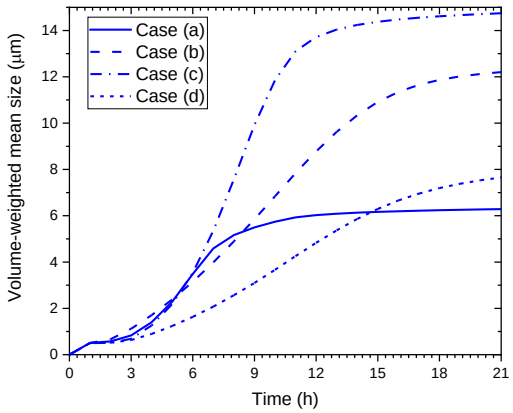



**Figure 3.** Volume-weighted mean size of the selected numerical experiments simulated.

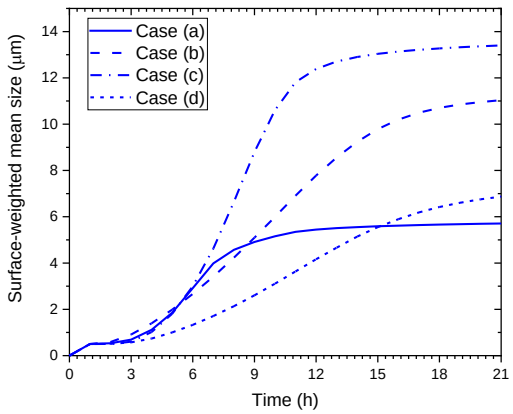



**Figure 4.** Surface-weighted mean size of the selected numerical experiments simulated.

Figure 5 displays the particle size distribution (PSD) for simulation cases (a), (b), (c), and (d), highlighting the significant impact of varying input parameters. All PSD curves exhibit unimodal distributions skewed toward the smaller particle size range, with a decreasing coefficient of variation as pH increases. The coefficient of variation refers to the 'width' of the distribution and it reflects the degree of polydispersity in crystal size; in the results presented here, the most uniform product is achieved at pH 11.5, albeit with the smallest particle size. The trends identified align with previous studies [2], albeit the optimal pH condition depend upon the desired product to be synthesized [5].

Determining the importance of the input parameters is complex due to the interplay among factors both physically and in the mathematical model. To support the investigation of the relevance of the input parameters, the sensitivity indices were calculated and are presented in Table 4. This analysis was carried out considering the mean sizes $d_{4,3}$ and $d_{3,2}$ as the outputs of interest. By inspecting the values summarized in Table 4, it is evident that the $k_G$, $g$, $pH$ and $[NH_3]_{t=0}$ have a strong influence over the output of the model.

**Table 4:** Sensitivity indices of the investigated parameters.

| Parameter | Indices |
|---|---|
| $[NH_3]_{t=0}$ | 0.1341 |
| $[NH_3]_{in}$ | 0.0036 |
| $pH$ | 0.0809 |
| $k_B$ | 0.0001 |
| $b$ | 0.0023 |
| $k_G$ | 0.6378 |
| $g$ | 0.1413 |

## CONCLUSIONS

A simple mathematical model of a semi-batch crystallizer has been presented. The model has been solved by the method of lines utilizing the commercial solver contained in Aspen Custom Modeler® and applied to conduct a sensitivity and uncertainty analysis to verify the effect of pH and ammonia concentration, and the kinetics of nucleation and growth over the particle size distribution and mean particle sizes.

Despite the simplicity of the model, it produces a fair representation of the precipitation variables, and the prediction of relevant particle properties agrees with the observations of previous work conducted for this type of system. The model can be enhanced by incorporating the

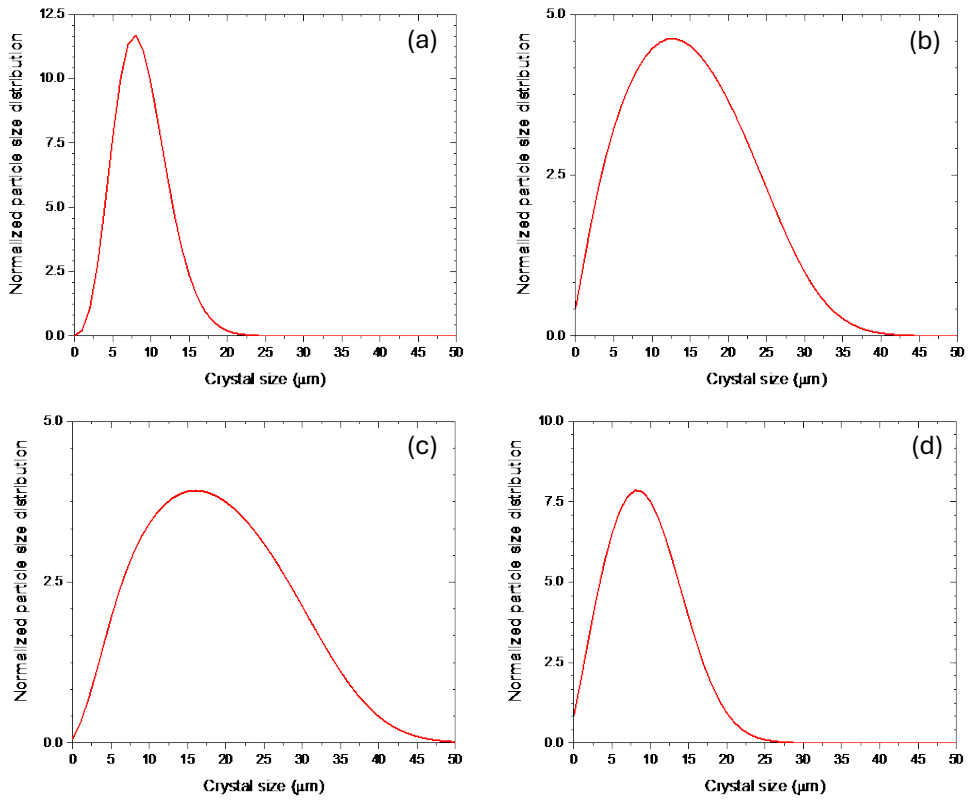



**Figure 5:** Particle size distribution (PSD) curves of selected numerical experiments simulated in this work.

aggregation/breakage phenomena into the PBE and by incorporating the thermal effects over the crystallization kinetics.

The sensitivity analysis indices indicated that the crystallization of Ni-Mn-Co hydroxides with stoichiometry 0.8:0.1:0.1 is primarily sensitive to the growth kinetics, the solution pH and the initial concentration of ammonia. Less relevant is the kinetics of nucleation, whereas the concentration of ammonia feed seems to be irrelevant.

## FUTURE WORK

The resulting model is to be improved by incorporating the agglomeration/breakage term to the population balance. Similarly, the effect of temperature over the crystallization kinetics was not incorporated in this work, this is an important piece to enable a better understanding and optimization of the process. This model will be used to conduct studies regarding the kinetics of crystallization.

## ACKNOWLEDGEMENTS

The authors would like to thank the UK Engineering and Physical Sciences Research Council (EPSRC) for funding the SuMMa project, grant reference EP/W018950/1.

## REFERENCES

1. Shiea, M., et al., CFD-PBE modelling of continuous Ni-Mn-Co hydroxide co-precipitation for Li-ion batteries. Chemical Engineering Research & Design, 2022. 177: p. 461-472.
2. Barai, P., et al., Multiscale Computational Model for Particle Size Evolution during Coprecipitation of Li-Ion Battery Cathode Precursors. Journal of Physical Chemistry B, 2019. 123(15): p. 3291-3303.
3. Para, M.L., et al., A modelling and experimental study on the co-precipitation of Ni<sub>0.8</sub>Mn<sub>0.1</sub>Co<sub>0.1</sub>(OH)<sub>2</sub> as precursor for battery cathodes. Chemical Engineering Science, 2022. 254.
4. Wu, Z.W., et al., Investigating the effect of pH on the growth of coprecipitated Ni0.8Co0.1Mn0.1(OH)2 agglomerates as precursors of cathode materials for Li-ion batteries. Ceramics International, 2023. 49(10): p. 15851-15864.
5. Entwistle, T., et al., Co-precipitation synthesis of nickel-rich cathodes for Li-ion batteries. Energy Reports, 2022. 8: p. 67-73.
6. Enasel, E. and G. Dumitrascu, Storage solutions for renewable energy: A review. Energy Nexus, 2025. 17.
7. Breddemann, U. and I. Krossing, Review on Synthesis, Characterization, and Electrochemical Properties of Fluorinated Nickel-Cobalt-Manganese Cathode Active Materials for Lithium-Ion Batteries. Chemelectrochem, 2020. 7(6): p. 1389-1430.
8. Pardikar, K., et al., Status and outlook for lithium-ion battery cathode material synthesis and the application of mechanistic modeling. Journal of Physics-Energy, 2023. 5(2).
9. Han, Q.Y., et al., Study on the Effect of Coprecipitation Conditions on the Growth and Agglomeration of Ni<sub>0.8</sub>Co<sub>0.1</sub>Mn<sub>0.1</sub>(OH)<sub>2</sub> Particles. Industrial & Engineering Chemistry Research, 2024. 64(1): p. 283-300.
10. Lee, M.H., et al., Synthetic optimization of Li Ni<sub>1/3</sub>Co<sub>1/3</sub>Mn<sub>1/3</sub> O<sub>2</sub> via co-precipitation. Electrochimica Acta, 2004. 50(4): p. 939-948.
11. Mou, M.Y., et al., Scalable Advanced Li(Ni0.8Co0.1Mn0.1)O2 Cathode Materials from a Slug Flow Continuous Process. Acs Omega, 2022. 7(46): p. 42408-42417.
12. Mugumya, J.H., et al., Synthesis and Theoretical Modeling of Suitable Co-precipitation Conditions for Producing NMC111 Cathode Material for Lithium-Ion Batteries. Energy & Fuels, 2022. 36(19): p. 12261-12270.
13. Querio, A., et al., Comparison between Compartment and Computational Fluid Dynamics Models for Simulating Reactive Crystallization Processes. Industrial & Engineering Chemistry Research, 2024. 63(50): p. 21991-22004.
14. Jha, S.K., S. Karthika, and T.K. Radhakrishnan, Modelling and control of crystallization process. Resource-Efficient Technologies, 2017. 3(1): p. 94-100.
15. van Bommel, A. and J.R. Dahn, Analysis of the Growth Mechanism of Coprecipitated Spherical and Dense Nickel, Manganese, and Cobalt-Containing Hydroxides in the Presence of Aqueous Ammonia. Chemistry of Materials, 2009. 21(8): p. 1500-1503.

© 2025 by the authors. Licensed to PSEcommunity.org and PSE Press. This is an open access article under the creative commons CC-BY-SA licensing terms. Credit must be given to creator and adaptations must be shared under the same terms. See https://creativecommons.org/licenses/by-sa/4.0/



Systems & Control Transactions

**Research Article - Peer Reviewed Conference Proceeding**
ESCAPE 35 - European Symposium on Computer Aided Process Engineering
Ghent, Belgium. 6-9 July 2025
Jan F.M. Van Impe, Grégoire Léonard, Satyajeet S. Bhonsale,
Monika E. Polańska, Filip Logist (Eds.)

PSE PRESS

# A System-Dynamics Based Approach for Modeling Circular Economy Networks: Application to the Polyethylene Terephthalate (PET) Supply Chain

**Daniel Pert[a], Ana Inés Torres[a]***

[a] Carnegie Mellon University, Department of Chemical Engineering, Pittsburgh, PA, USA
* Corresponding Author: aitorres@cmu.edu.

## ABSTRACT

The transition to a circular economy (CE) requires agents in circular supply chain (SC) networks to take a variety of different initiatives, many of which are dynamic in nature. We use a system dynamics (SD)-based approach to develop a generic framework for dynamic modeling of CE networks and propose a prototypical circular SC network by combining dynamic models for five actors: a manufacturer, consumer, material recovery facility (MRF), recycling facility, and the Earth. We apply this framework to the supply chain for Polyethylene Terephthalate (PET) plastic packaging by considering different scenarios over a 65-year time horizon in the US. We include both "slow-down-the-loop" initiatives (i.e., those that extend product use time through demand reduction or reuse) and "close-the-loop" initiatives (i.e., those that reintroduce product to the supply chain through recycling) by the consumer, as well as sorting and recycling capacity expansion. We find that, given the current recycling infrastructure in the U.S., "slow-down-the-loop" initiatives are more effective than "close-the-loop" initiatives for improving circularity and minimizing environmental impact. However, combining the two initiatives eliminates the need for capacity expansion and leads to the highest circularity in the shortest amount of time.

**Keywords**: Dynamic Modelling, Circular Economy, Plastic recycling

## INTRODUCTION

The current "take-make-use-dispose" paradigm of the current extractive "linear economy" has led to unnecessary waste, pollution, and extraction of natural resources. The "circular economy" (or CE) paradigm aims to eliminate waste, pollution, and resource extraction through restorative circular flows [1].

Circular *initiatives* are actions that an *actor* (e.g. a firm or consumer) in a supply chain (SC) network can take to improve their level of "circularity." Initiatives can be categorized into those that "slow down the loop" by using products for longer, "narrow the loop" by using fewer resources per product, or "close the loop" by reintroducing the product to the SC through recycling [2].

Since most frameworks for studying CE networks operate at steady state and do not include the time dimension, they cannot consider the time-delayed effects of CE initiatives on upstream and downstream actors or time-dependent initiatives such as those that extend product use time. Thus, dynamic models that incorporate the time dimension are needed to model CE networks.

The use of system dynamics (SD), a framework that, in addition to stocks and flows, incorporates auxiliary variables, coflows, and nonlinear feedback mechanisms [3], would enable a more detailed understanding of what external driving forces are needed to enable these changes and any possible unintended consequences of CE initiatives. Previous studies have already begun to use SD to study various aspects of CE transitions [4-7]. However, none of these studies are systematic in nature or provide clear mathematical models of CE initiatives at the actor level.

The main objective of this work is to develop a modular SD-based framework that can be used to study the effects of CE initiatives taken by different actors. First, we develop a dynamic model for a generalized actor and propose a systematic method for quantifying material

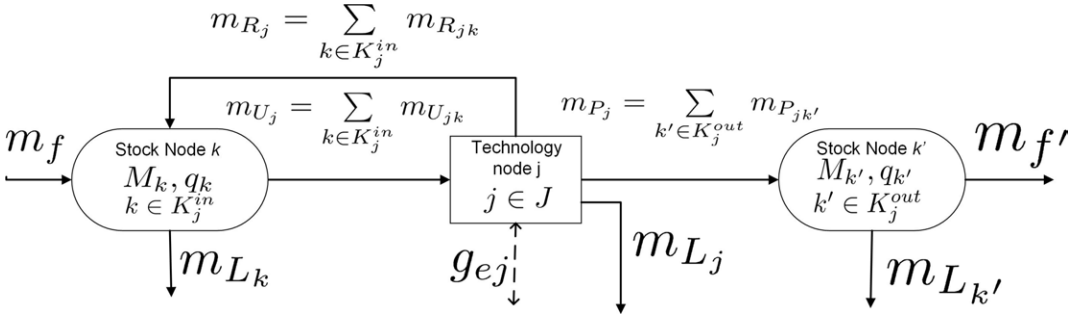



**Figure 1:** Stock-and-flow diagram for a generalized actor in a circular SC network, including technology node $j \in J$ and stock nodes $k \in K$. $m_{L_k}$ is the rate of disposal from stock node $k$, $m_{U_{jk}}$ is the rate of usage of material from stock node $k$, $m_{P_{jk'}}$ is the rate of production of output $k'$, and $m_{R_{jk}}$ is the rate of recirculation of input $k$. Environmental impact flows ($g_{ej}$) and denoted by the dashed arrow.

quality loss. Then, we combine different actors in a prototypical circular SC to form a synthetic "block" network and formulate a dynamic model governing the network on multiple time scales. Finally, we apply this framework to compare the long-term effects of different CE initiatives on the PET plastic packaging SC.

## GENERIC MODEL FOR AN ACTOR

The stock-and-flow diagram for a generalized actor is shown in **Figure 1**. Each actor exchanges material with other actors, performs a composition transformation on the material via a *technology node*, and stores material as inventory in one or more *stock nodes*. Let *F* be the set of material flows *J* be the set of technology nodes, *K* be the set of stock nodes, $K_j^{in}$ (and $K_j^{out}$) be the sets of stock nodes that feed into (and are fed to) by node $j \in J$, $F_j^{in}$ (and $F_j^{out}$) be the sets of flows entering (and exiting) node *j*, $F_k^{in}$ (and $F_k^{out}$) be the sets of material flows entering (and exiting) stock *k*, *E* be the set of environmental impact flows (e.g., natural resource inputs and pollution), $g_{ej}$ be the rate at which technology node *j* contributes to environmental impact *e*, $M_k$ be the quantity of material stored in stock node *k* at a given time, $m_f$ be the material flow rate of flow *f*, and $q_k$ (and $q_f$) be the material qualities of stock node *k* and flow *f*. Material quality is modeled as a coflow and discussed below.

Using this notation, the material balances on stock node *k* and technology node *j* are given by **Equations 1-2**. The total rates of material input and production of technology node *j* are denoted by $m_{U_j}$ and $m_{P_j}$, which are related by the process yield $\eta_j$ (**Equation 3**). The remainder of the input is either discarded at a rate of $m_{L_j}$or recirculated at a rate of $m_{R_j}$.

$$\frac{dM_k}{dt} = \sum_{f \in F_k^{in}}(m_f) - \sum_{f' \in F_k^{out}}(m_{f'}) \quad \forall k \in K \tag{1}$$

$$m_{U_j} = m_{P_j} + m_{L_j} + m_{R_j} \quad \forall j \in J \tag{2}$$

$$m_{P_j} = \eta_j m_{U_j} \quad \forall j \in J \tag{3}$$

Material stocks (or flows) may also have some quality attributes, such as desirable physical properties, and they are modeled using the co-flow structure [3]. We normalize quality to be between zero and one, with virgin material having a quality of one and increasing quality being more desirable. We assume quality follows a linear mixing rule; that is, the quality of a mixture of two streams is given by the mass flow-weighted average of their qualities. The quality of stock node $k$ is governed by **Equation 4,** while **Equation 5** specifies that technology node $j$ reduces material quality by some constant factor ($\omega_j$).

$$\frac{dq_k}{dt} = \frac{1}{M_k}\sum_{f \in F_k^{in}} m_f [q_f - q_k] \quad \forall k \in K \tag{4}$$

$$q_{P_j} = \omega_j q_{U_j} \quad \forall j \in J \tag{5}$$

We assume $m_{U_j}$, the rate of material input to technology node *j*, is limited by some maximum processing capacity ($Capacity_j$). If the rate of material influx exceeds the maximum capacity or downstream demand for material produced by the node, any excess inventory may be discarded at a rate of $m_{L_k}$.

To adjust to increased (or decreased) demand or inflow, an actor may expand the capacity of a technology node. However, capacity expansion requires planning and construction, leading to a time delay ($\theta_j$) between the time that capacity expansion is initiated and completed. The time scale ($\tau$) on which capacity expansion occurs is much longer than the time scale (t) on which production does. If $Inst_j(\tau)$ is the rate of initiation of capacity expansion at time $\tau$, the installed capacity of technology node *j* and the quantity of capacity currently under construction ($Con_j$) are governed by **Equations 6** and **7**.

$$\frac{dCapacity_j}{d\tau} = Inst_j(\tau - \theta_j) \quad \forall j \in J \tag{6}$$

$$\frac{dCon_j}{d\tau} = Inst_j(\tau) - Inst_j(\tau - \theta_j) \quad \forall j \in J \tag{7}$$

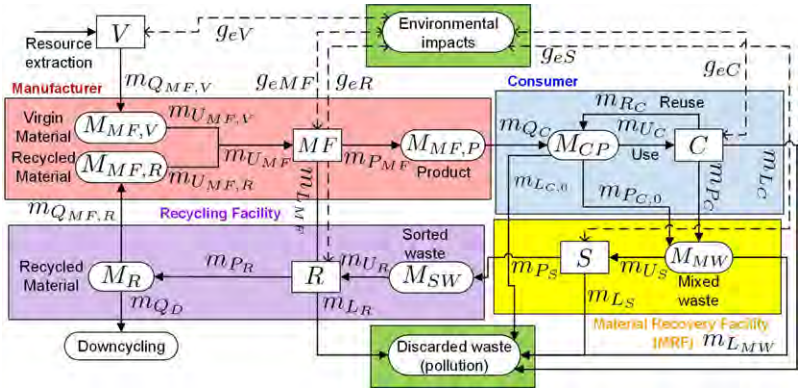



**Figure 2:** Schematic of CE network for PET packaging SC with manufacturer (red), consumer (blue), MRF (yellow), recycling facility (purple), and the Earth (green). Blocks represent technology nodes and ovals represent stock nodes. The flow rate associated with each flow f is denoted by $m_f$ and shown by a solid arrow, and the rate at which technology node j contributes to environmental impact e (i.e. resource use or pollution) is denoted by $g_{ej}$ and shown by a dashed arrow.

We assume capacity expansion is governed by a proportional control-like policy (**Equation 8**). That is, the rate of initiation of capacity expansion is proportional to the difference between $m_{j,in}$, the total inlet flow rate to stock nodes that feed into node $j$ from outside the system boundary of the actor and the current capacity plus the capacity currently under construction (**Equation 9**):

$$Inst_j(\tau) = \max\{0, \kappa_j[m_{j,in} - Capacity_j(\tau) - Con_j(\tau)]\} \quad (8)$$

$$m_{j,in} = \sum_{f \in F_k^{in}} \sum_{k \in K_j^{in}} (m_f) - m_{R_j} \quad (9)$$

Here $\kappa_j$ is a proportional control parameter, which we assume is inversely proportional to construction time $\theta_j$ required to install new capacity: $\kappa_j = 1/\theta_j$.

## SYNTHETIC CIRCULAR SUPPLY CHAIN NETWORK

**Figure 2** shows a stock-and-flow diagram for a synthetic CE network including a manufacturer, who produces a product from raw material, a consumer who uses product and generates waste material, a material recovery facility (MRF) who collects and sorts mixed post-consumer waste into purified waste streams, a recycling facility who converts these purified waste streams into useful products, and the Earth, who supplies virgin material and is a sink for disposed waste.

The manufacturing process (technology node *MF*) requires a single input, which may be sourced from virgin material extracted and produced via technology node *V* or recycled material produced via technology node *R*. The manufacturing process requires a minimum quality of $q_{min}$. We assume none of the actors recirculate processing waste except for the consumer, who recirculates product for reuse at a rate of $m_{R_C}$. The fraction of end-of-life product recycled by the consumer is given by the "recycle rate" $r_C$. The recycling facility produces recycled material at a rate of $m_{P_R}$, which reduces quality by a constant factor of $\omega_R$. Any unpurchased recycled material is downcycled at a rate of $m_{Q_D}$.

### Sustainability Assessment

To quantify absolute environmental sustainability, or the extent to which the environmental impact of a CE network exceeds the restorative capacity of the Earth [8], we use the planetary boundaries (PBs) framework [9], which proposes a "safe operating space" for humanity by defining threshold values (i.e., planetary boundaries) for different "control variables" describing human impacts on nine "Earth-system processes" beyond which there is increasing risk of environmental destabilization.

The Earth system impact metric (ESIM) measures the aggregated impact of a network on multiple Earth-system processes while accounting for current levels of global PB transgression [10]. For the sake of space, details on the calculation of the ESIM are not shown here and are left for a full journal publication.

### Circularity Assessment

The circularity of a CE network is quantified using the Material Circularity Indicator (MCI) proposed by the Ellen MacArthur Foundation [1, 11]. The MCI is given by **Equation 15** and is a function of the Linear Flow Index (LFI), or the fraction of material flowing in a linear fashion (**Equation 16**), and the product utility $\overline{\chi}$ (the mean utility, or number of uses) relative to the industry average ($\chi_{av}$). Here $m_{L_{tot}}$ is the total rate of discarded waste.

$$MCI = 1 - \frac{LFI}{\overline{\chi}/\chi_{av}} \quad (15)$$

$$LFI = \frac{m_{Q_{MV}} + m_{L_{tot}}}{2m_{U_M}} \quad (16)$$

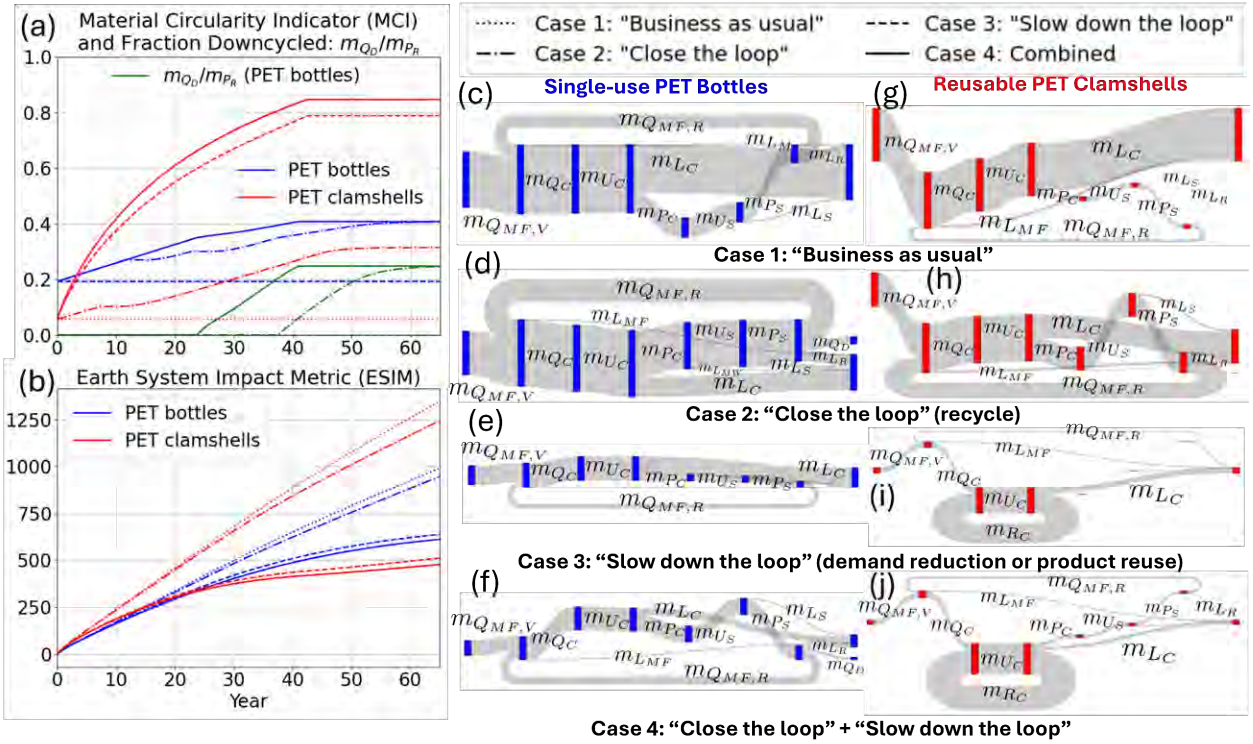



**Figure 3:** Behavior of PET packaging supply chain over 50-year horizon under four scenarios described above. (a) Evolution of Material Circularity Indicator (MCI) and fraction of recycled PET bottles that are downcycled to textiles ($m_{Q_D}/m_{P_R}$) in green. No PET clamshells are downcycled to textiles. The MCI for bottles and clamshells are shown in blue and red, respectively. (b) Evolution of Earth System Impact Metric (ESIM) for PET bottle and clamshell SCs in blue and red, respectively. In (a-b), the four scenarios are shown by the dotted, dashdotted, dashed, and solid lines, as indicated by the legend. (c-j) Sankey diagrams comparing the relative values of the different material flow rates for cases 1-4 for PET bottles (c-f) and clamshells (g-j).

## CASE STUDY: PET SUPPLY CHAIN

We apply the generic model described above to the supply chain for single-use polyethylene terephthalate (PET) bottles and reusable PET clamshell packaging (a type of thermoform) in the U.S. We choose PET since it is relatively easy to recycle yet suffers from low recycling rates in the U.S., representing an opportunity for improved circularity [12]. In addition, a wide variety of circular pathways can be applied to PET, including reuse or repurposing of packaging [13], downcycling to textiles [14], and conversion to pyrolysis oil [15].

Given the current recycling infrastructure in the U.S., we assume the recycling facility uses mechanical recycling; the maximum capacities of the MRF and recycling facility are based on current recycling infrastructure in the U.S. [19]. Since most recyclers only accept PET bales with up to 10% thermoform content, we assume the maximum capacity for clamshell recycling is 10% of total recycling capacity [20]. As a measure of PET material quality, we use the intrinsic viscosity (IV) of the polymer melt, which determines what applications it can be used for [14] and is reduced by mechanical recycling [16].

## RESULTS AND DISCUSSION

The dynamic model for the PET SC network was implemented in Python using the JiTCDDE package [17] and simulated for a 65-year time horizon, from 2022 to 2087, with parameters initialized at their current baseline values. We consider four scenarios: case 1 ("business as usual"), with recycling rates remaining at their current levels of 9% and 29% for clamshells and bottles and with no consumer reuse, case 2 ("close-the-loop" initiatives), or a recycle rate increase of 1% per year for 41 years, case 3 ("slow-down-the-loop" initiatives), or an increase in the fraction of clamshells reused of 2% per year until reaching 85% and a decrease in bottle demand of 1% per year, and case 4 (a combination of "close-the-loop" and "slow-down-the-loop" initiatives). For simplicity, we consider the SCs for PET clamshells and bottles separately. The behavior of the PET bottle and clamshell SC over the 50-year horizon for the four scenarios described above

is shown in **Figure 3**. Panels (a-b) show the temporal evolution of the Material Circularity Indicator (MCI), Earth System Impact Metric (ESIM), and fraction of recycled PET that is downcycled to textiles ($m_{Q_D}/m_{P_R}$) over the simulation. Sankey diagrams with line widths proportional to the final values of the different material flow rates are shown in panels (c-f) and (g-j) for bottles and clamshells, respectively. Case 1 ("Business as usual") results in both the lowest circularity and highest environmental impacts, while case 3 ("slow-down-the-loop") is significantly more effective than case 2 ("close-the-loop") for both increasing circularity and lowering environmental impact.

This is illustrated by the Sankey diagrams. Product reuse (i) results in significantly more circular flow than increased clamshell recycling (h), and demand reduction (e) reduces the amount of linear flow more than increased bottle recycling (d). The difference in environmental impact between cases 2 and 3 is even greater since product reuse is less resource-intensive than recycling and preserves the value of the product, not just its material. Additionally, due to quality loss, a product can be reused far more times than it can be recycled.

For PET bottles, although both cases 2 and 4 achieve the highest final circularity (MCI), the MCI increases faster in case 4 due to the time delay associated with capacity expansion in case 2. Nonetheless, it is important to note that since the LFI is normalized by total product flow, the MCI is insensitive to demand reduction, unless such a reduction is reflected by an increase in product utility (as with product reuse). These results demonstrate that more holistic circularity indicators are needed to account for "slow-down-the-loop" and "narrow-the-loop" initiatives such as a reduction in consumer demand or the mass per unit of product.

However, due to quality loss, mechanically recycled PET must be blended with virgin PET to meet the minimum intrinsic viscosity requirements of the manufacturing process, which puts an upper bound on the fraction of product that can be sourced from mechanically recycled PET. As a result, once the bottle recycles rate exceeds a threshold of around 50%, the manufacturer does not purchase any additional recycled PET, and it must be downcycled to textiles. This was not observed in the PET clamshell results since the minimum quality requirement for clamshell manufacturing is lower than for bottles, although it would be observed for a recycle rate above 85%. Mitigating this effect would require more costly and resource-intensive chemical recycling techniques that produce virgin-grade PET resin [18].

## CONCLUSIONS

Here, we developed a generic framework for dynamic modeling of circular economy networks, which can be used to better understand the effects of circular initiatives taken by individual actors in a supply chain on upstream and downstream actors, including the Earth. We start by developing a dynamic model for a generic actor and then combine different actors into a synthetic CE network. We use the planetary boundaries framework to quantify the absolute environmental sustainability of the network. We apply this framework to study the supply chain for PET clamshells and bottles in the U.S. by comparing the effects of different initiatives.

We find that "slow-down-the-loop" initiatives like consumer reuse and demand reduction are more effective than "close-the-loop" initiatives like recycling. Additionally, increased recycling associated with the "close-the-loop" scenario requires recycling capacity expansion and an associated time delayed circularity increase. However, when combined with "slow-down-the-loop" initiatives, the need for capacity expansion, and thus the time delay, is reduced or eliminated.

However, even with increased consumer reuse, recycling, and capacity expansion, closed-loop circularity is still limited by the quality loss associated with the mechanical recycling process widespread in the U.S. Thus, although "slow-down-the-loop" initiatives are more promising short-term solutions, investments in chemical or solvent-based recycling technologies that reduce or eliminate quality loss are needed in the long term to maximize circularity.

Since the framework is modular, it can easily be extended to other supply chain structures by constructing alternative networks to the one considered here. For example, such a network could include multiple product manufacturers and recyclers or additional actors such as a government agency, who regulates the network, a "repairer," who extends product lifetime by making repairs, and a "refurbisher," who converts end-of-life products to alternative applications through refurbishment.

In future work, we aim to extend the framework to combine the supply chains for multiple PET products, including bottles, clamshells, and textiles. We hope this framework will enable the identification of which initiatives favor win-win scenarios by maximizing circularity while balancing trade-offs among different actors' objectives and avoiding burden-shifting.

## ACKNOWLEDGEMENTS

This material is based upon work supported by the National Science Foundation under Award No. 2339068 (NSF CAREER Award PI AI Torres).

Disclaimer: Any opinions, findings, and conclusions or recommendations expressed in this material are those of the author(s) and do not necessarily reflect the views of the National Science Foundation.

## REFERENCES

1. MacArthur E. Towards the circular economy. *J. Ind. Ecol* 2(1):23-44 (2013) https://www.werktrends.nl/app/uploads/2015/06/Rapport_McKinsey-Towards_A_Circular_Economy.pdf
2. Bocken NMP, de Pauw I, Bakker C, van der Grinten B. Product design and business model strategies for a circular economy. *J. Ind. Prod. Eng* 33(5):308-320 (2016) https://doi.org/10.1080/21681015.2016.1172124
3. Sterman J. System Dynamics: Systems Thinking and Modeling for a Complex World. McGraw-Hill (2000).
4. Franco MA. A system dynamics approach to product design and business model strategies for the circular economy. *J. Clean. Prod.* 241:118327 (2019) https://doi.org/10.1016/j.jclepro.2019.118327
5. Guzzo D, Pigosso DCA, Videira N, Mascarenhas, J. A system dynamics-based framework for examining circular economy transitions. *J. Clean. Prod.* 333:129933 (2022) https://doi.org/10.1016/j.jclepro.2021.129933
6. Bassi AM, Bianchi M, Guzzetti M, Pallaske G, Tapia C. Improving the understanding of circular economy potential at territorial level using systems thinking. *Sustain. Prod. Consum*. 27:128–140 (2021) https://doi.org/10.1016/j.spc.2020.10.028
7. Alamerew YA, Brissaud D. Modelling reverse supply chain through system dynamics for realizing the transition towards the circular economy: A case study on electric vehicle batteries. *J. Clean. Prod.* 254: 120025 (2020) https://doi.org/10.1016/j.jclepro.2020.120025
8. Hjalsted AW, Laurent A, Andersen MM, Olsen KH, Ryberg M, Hauschild M. Sharing the safe operating space: Exploring ethical allocation principles to operationalize the planetary boundaries and assess absolute sustainability at individual and industrial sector levels. *J. Ind. Ecol* 25(1):6-19 (2021) https://doi.org/10.1111/jiec.13050
9. Steffen W, Richardson K, Rockström J, Cornell SE, Fetzer I, Bennett EM, Biggs R, Carpenter SR, de Vries W, de Wit CA, Folke C, Gerten D, Heinke J, Mace GM, Persson LM, Ramanathan V, Reyers B, Sörlin S. Planetary boundaries: Guiding human development on a changing planet. *Science* 347( 6223):1259855 (2015) https://doi.org/10.1126/science.1259855
10. Lade SJ, Fetzer I, Cornell SE, Crona B. A prototype Earth system impact metric that accounts for cross-scale interactions. *Environ. Res. Lett.* 16(11):115005 (2021) https://doi.org/10.1088/1748-9326/ac2db1
11. Ellen MacArthur Foundation. Circularity Indicators: An approach to measuring circularity. https://www.ellenmacarthurfoundation.org/material-circularity-indicator
12. Smith RL, Takkellapati S, Riegerix RC. Recycling of plastics in the United States: plastic material flows and polyethylene terephthalate (PET) recycling processes. *ACS Sustain. Chem. Eng.* 10(6):2084–2096 (2022) https://doi.org/10.1021/acssuschemeng.1c06845
13. Hitt C, Douglas J, Keoleian G. Parametric life cycle assessment modeling of reusable and single-use restaurant food container systems. *Resour. Conserv. Recycl.* 190:106862 (2023) https://doi.org/10.1016/j.resconrec.2022.106862
14. Ewell J. Chemical recycling: Making fiber-to-fiber recycling a reality for polyester textiles. https://greenblueorg.s3.amazonaws.com/smm/wp-content/uploads/2018/05/Chemical-Recycling-Making-Fiber-to-Fiber-Recycling-a-Reality-for-Polyester-Textiles-1.pdf
15. Ragaert K, Delva L, Van Geem K. Mechanical and chemical recycling of solid plastic waste. *Waste Management* 69:24–58 (2017) https://doi.org/10.1016/j.wasman.2017.07.044
16. Jang JY, Sadeghi K, Seo J. Chain-Extending Modification for Value-Added Recycled PET: A Review. *Polymer Reviews* 62(4):860–889 (2022) https://doi.org/10.1080/15583724.2022.2033765
17. Ansmann G. Efficiently and easily integrating differential equations with JiTCODE, JiTCDDE, and JiTCSDE. *Chaos* 28(4):043116 (2018) https://doi.org/10.48550/arXiv.1711.09886
18. Chaudhari US, Lin Y, Thompson VS, Handler RM, Pearce JM, Caneba G, Muhuri P, Watkins D, Shonnard DR. Systems analysis approach to polyethylene terephthalate and olefin plastics supply chains in the circular economy: A review of data sets and models. *ACS Sustain. Chem. Eng.* 9(22):7403–7421 (2021) https://doi.org/10.1021/acssuschemeng.0c08622
19. NAPCOR. 2020 PET Recycling Report. https://napcor.com/wp-content/uploads/2023/12/NAPCOR_2020RateReport_FINAL.pdf
20. Dimino R, Goodall C. Thermoform recycling realities. https://resource-recycling.com/recycling/2021/07/20/thermoform-recycling-realities/

© 2025 by the authors. Licensed to PSEcommunity.org and PSE Press. This is an open access article under the creative commons CC-BY-SA licensing terms. Credit must be given to creator and adaptations must be shared under the same terms. See https://creativecommons.org/licenses/by-sa/4.0/



Systems & Control Transactions

**Research Article - Peer Reviewed Conference Proceeding**
ESCAPE 35 - European Symposium on Computer Aided Process Engineering
Ghent, Belgium. 6-9 July 2025
Jan F.M. Van Impe, Grégoire Léonard, Satyajeet S. Bhonsale,
Monika E. Polańska, Filip Logist (Eds.)

PSE PRESS

# Sustainable production of L-lactic acid from lignocellulosic biomass using an alternative buffer system: Process development and techno-economic and environmental analysis

**Donggeun Kang, Donghyeon Kim, Dongin Jung, Siuk Roh, and Jiyong Kim***

Sungkyunkwan University (SKKU), Department of Chemical Engineering, Suwon, Republic of Korea
* Corresponding Author: jiyongkim@skku.edu.

## ABSTRACT

L-lactic acid (L-LA), a key monomer in biodegradable plastics, is a sustainable alternative that can be derived from LCB. The L-LA production process typically involves various technologies such as fermentation, filtration, and distillation. In the L-LA production process, large amounts of buffers are used to maintain proper pH during fermentation, so conventional buffers (e.g., $CaCO_3$) are often selected because of their low cost. However, these buffers cannot be recycled efficiently, and the potential for alternative buffers remains uncertain. In this work, we aim to develop and evaluate novel processes for sustainable L-LA production using the alternative buffer (i.e., KOH). The processes involve a series of different unit operations such as pretreatment, fermentation, extraction, and electrolysis. An efficient buffer regeneration process using membrane electrolysis is implemented to recycle the buffer with minimal energy input. Then, we evaluated the viability of the proposed processes compared to the conventional process based on minimum selling price (MSP), and global warming potential (GWP). The MSP for L-LA was evaluated to be 0.83 USD /kg L-LA, and the GWP was assessed to be 2.93 kg $CO_2$-eq/kg L-LA. These results represent a 25% reduction in MSP and a 32% reduction in GWP compared to the conventional process. Additionally, a sensitivity analysis was performed to identify the major cost drivers of MSP, such as interest rate, and the price of biomass. The proposed process, as a cost-effective and eco-friendly process, promotes biotechnology practices for sustainable production of L-LA.

**Keywords**: L-lactic acid, lignocellulosic biomass, alternative buffer, process development, techno-economic analysis

## INTRODUCTION

Climate change and food security remain critical challenges for sustainable development [1]. The global dependence on petroleum-based chemicals continues to drive environmental degradation and climate change [2]. To address these challenges, there is growing interest in producing chemicals and materials from renewable resources. Lignocellulosic biomass (LCB) offers a promising sustainable alternative to produce various bio-based materials [3]. One significant LCB-based chemical is lactic acid (LA), which has emerged as a key platform chemical, particularly important in the production of biodegradable plastics [4]. LA exists in two enantiomeric forms, with L-lactic acid (L-LA) being crucial for industrial applications due to its influence on the mechanical and thermal properties of polylactic acid (PLA) [5]. Consequently, numerous studies on LA microbial fermentation technologies focusing on high enantiomeric purity of L-lactic acid (L-LA) have been published, demonstrating the potential to improve the quality and application potential of LA-based products across various industries.

Microbial fermentation is widely used to produce L-LA with a high enantiomeric purity. As with other fermentation processes, the L-LA fermentation process requires various feedstocks, including fermentation medium and

other necessary materials. Buffers are particularly important for maintaining an optimal pH level to ensure the efficiency and yield of the process [6]. Notably, calcium-based buffers (e.g., $Ca(OH)_2$ and $CaCO_3$) are commonly preferred in commercial L-LA production due to their cost-effectiveness. However, using these buffers typically results in solid byproducts, such as gypsum ($CaSO_4$), which require disposal and create waste management challenges [7]. Therefore, an alternative buffer system could potentially address these issues by reducing waste and improving the sustainability of the L-LA production process.

In this work, we aim to develop and evaluate novel approaches for sustainable L-LA production using an alternative buffer (i.e., KOH). To achieve this goal, we first established a conventional L-LA production process as a baseline and developed a KOH recycling-based L-LA production (KRL) system incorporating buffer recycling technologies. We then evaluated the economic and environmental impacts of the proposed KRL systems and compared them with those of the conventional process. Additionally, sensitivity analysis was conducted to identify major cost drivers of proposed processes for cost reduction.

## TECHNOLOGY OVERVIEW AND ANALYSIS METHODS

### Process configuration

Fig. 1(a) represents the baseline L-LA production process, which uses $Ca(OH)_2$ as a buffer in the fermentation stages. After fermentation, $H_2SO_4$ is mixed to convert L-lactate to L-LA, and the gypsum is filtered out by centrifugation. Crude L-LA is separated and purified by reactive distillation units coupled with the synthesis and hydrolysis of methyl lactate. This baseline process demonstrates the established methodology and operational simplicity of the purification method. However, the generation of gypsum causes significant waste management problems.

In this study, we propose two novel KOH recycling-based L-LA production (KRL) configurations that incorporate advanced buffer recovery and regeneration technologies, as shown in Fig. 1(b) and (c). In the fermentation steps, KOH is used as a buffer to maintain the optimal condition for microbials. $H_2SO_4$ is substituted with HCl to convert L-lactate to L-LA. The use of HCl allows the KOH to be regenerated using alternative downstream processes. Solvent extraction and back-extraction units are employed for buffer recovery, L-LA separation, and purification. Solvent extraction effectively separates the impurities from the L-LA, while KCl releases the salts. The distillation unit purifies L-LA to high concentration by removing water and residual impurities while operating under vacuum conditions. The stream containing KCl is subjected to membrane filtration for conditioning. Alkaline water electrolysis decomposes KCl and water to regenerate KOH. This reaction also produces hydrogen ($H_2$) and chlorine ($Cl_2$) gases as byproducts. In addition, the first alternative configuration (KRL #1) employs gas treatment units to clean the byproduct gases. The purified byproduct gases can be sold, contributing to the economic potential of the process.

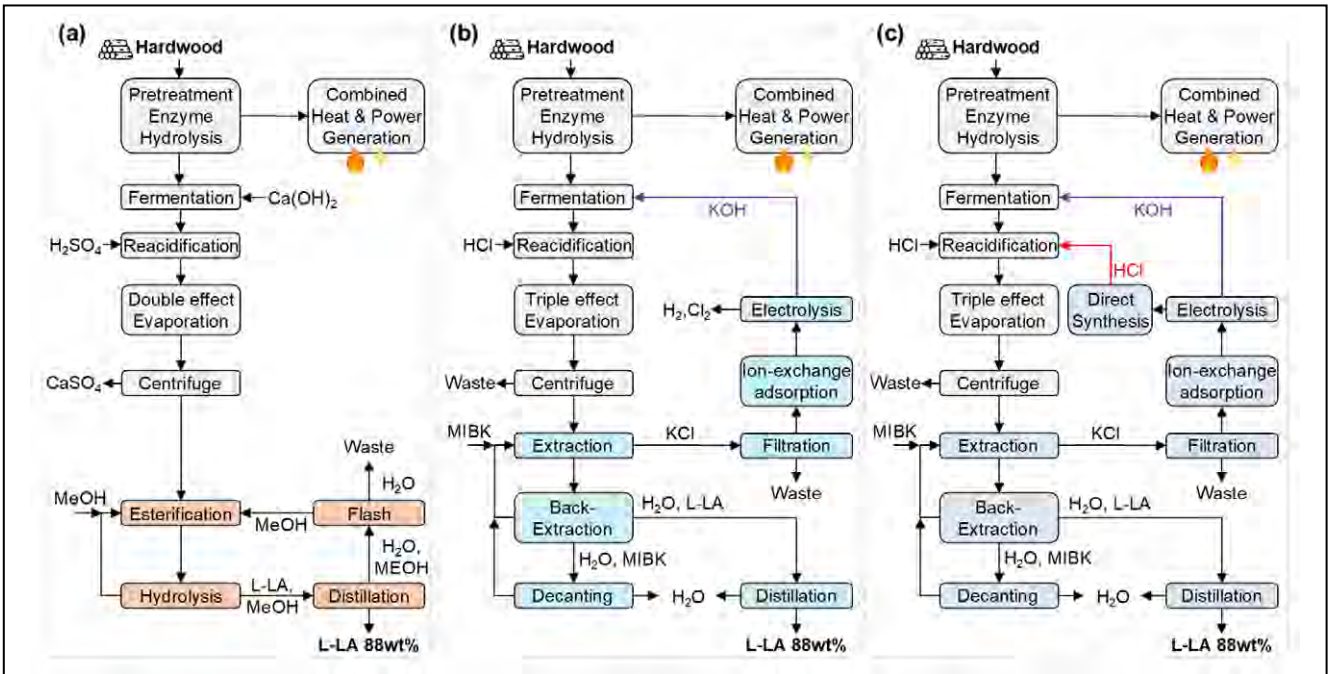



**Figure 1:** Block diagrams of the L-lactic acid production from lignocellulosic biomass. (a) baseline process; (b) KRL #1: KOH recycling-based process; (c) KRL #2: KOH and HCl recycling-based process.

On the other hand, as shown in Fig. 1(c), the second alternative configuration (KRL #2) includes HCl regeneration steps where $H_2$ and $Cl_2$ gases are reacted to produce an HCl solution. This HCl solution is then used in the reacidification unit to enhance the recycling loop. Accordingly, the novel KRL system offers key advantages over the conventional process through integrated recycling technologies. These improvements minimize raw material consumption and waste generation, thereby enhancing both economic viability and environmental sustainability.

## Technology overview

### Pretreatment and enzymatic hydrolysis

Pretreatment converts hemicellulose to sugars, degrading LCB for efficient enzymatic hydrolysis. In this area, LCB is treated in high-temperature dilute $H_2SO_4$ for degradation. It is then neutralized with ammonia to pH 5 for optimal enzymatic hydrolysis. This technique directly conditions the entire hydrolysate slurry without the need for solid-liquid separation, thereby improving sugar recovery [8]. Table S1 in Digital Supplementary Information (SI) presents the major reactions and process conditions.

In this study, the feedstock for the process is 1000 dry tons/day of Eastern cottonwood, a hardwood species. Hardwoods are widely used in bioprocessing due to their high cellulose and hemicellulose content and low inhibitor content compared to other biomass species. The composition of Eastern cottonwood is provided in Table S2 in SI. This composition is implemented in Aspen Plus V12.0 software using an in-house physical property NREL database to ensure an accurate representation of the biomass components [9].

### L-LA fermentation

Microbial fermentation is a preferred method for L-LA production due to its ability to achieve high optical purity. In this process, sugars derived from LCB are converted to L-LA by microbial metabolism. As a microbial strain, thermophilic Bacillus coagulans was used in this study due to its capability to co-utilize hexose and pentose sugars efficiently [10,11]. This co-utilization of carbon sources minimizes by-product formation and maximizes L-LA yield. The fermentation process uses $Ca(OH)_2$ or KOH as a buffer to maintain optimal pH levels. The buffer reacts with the L-LA released by the microbes to form L-lactate. This ensures stable microbial activity and improves L-LA productivity.

### Separation and purification

After fermentation, insoluble cellular material is first separated from the broth by centrifugation. Then, the crude L-lactate mixture is treated with a strong acid to convert L-lactate to L-LA in the acidification reactor. The crude L-LA stream is concentrated via a multi-effect evaporator unit. The conventional process employs the reactive distillation units to separate other impurities and purify L-LA. L-LA in the concentrated stream is converted into methyl L-lactate by esterification coupled with a distillation. Then, another reactive distillation unit for hydrolysis is used to decompose methyl L-lactate into L-LA and purify L-LA. The raw L-LA is purified to over 88wt% in the distillation column.

The novel configurations (KRL #1 and KRL #2) employ liquid-liquid extraction units with methyl isobutyl ketone (MIBK) as the extraction solvent to effectively remove heavy impurities from the concentrated stream. The extracted solution is back-extracted with water to transfer the L-LA and ions to the aqueous phase, leaving the light impurities to remain in the solvent. The MIBK solvent is then recovered by decanting and distillation. Finally, the aqueous L-LA stream is further concentrated and purified by evaporation and distillation to achieve the L-LA product of over 88wt% purity.

### Alkaline water electrolysis and acid gas synthesis

The regeneration of KOH is achieved through an integrated system involving the electrolysis of KCl. In the alkaline water electrolysis step, a fluorinated cation exchange membrane was used to decompose water and KCl. The membrane enables high current efficiency and low voltage operation, achieved through its selective ion transport properties and enhanced chemical stability under alkaline conditions [12]. Additionally, the electrolysis reaction also generates $H_2$ and $Cl_2$ gases as byproducts. In KRL #1, these by-product gases are purified and prepared for sale as chemical products. The $H_2$ gas from the alkaline water electrolysis achieves 99.97% purity through pressure swing adsorption using a molecular sieve hierarchical adsorbent. The adsorption columns operate at 30°C-35°C with pressure cycling up to 34 bar, resulting in the $H_2$ recovery of 91.9% [13]. The chlorine gas is dried through desorption using concentrated sulfuric acid, which effectively removes moisture to achieve a final purity of 99.99%. These high-purity byproducts provide a significant source of revenue. By contrast, KRL #2 uses these gases directly in the acid gas synthesis unit. The $H_2$ and $Cl_2$ gases react to form dry HCl gas. This gas is absorbed into deionized water to make an aqueous HCl solution, which is used in the reacidification unit.

## Process analysis method

The proposed processes were simulated and modeled using Aspen Plus V.12 software. We evaluated the economic and environmental impacts of the developed process with mass and energy balances obtained from the process simulation. In this study, the viability of the proposed process was evaluated against the conventional process based on minimum selling price (MSP), and global warming potential (GWP).

For the economic evaluation of the L-LA production

processes, the MSP was used as a primary indicator of economic viability. The MSP represents the product's sale price at the break-even point, where total revenue matches total expenses. The total revenue is generated from the sales of L-LA, while the total expenses include the annualized return on investment (ROI), fixed operating costs, and taxes.

The ROI was determined based on the total project investment (TPI), the interest rate, and the process lifetime, as in Eq. (1).

$$ROI = TPI \times \frac{i \times (1+i)^r}{(1+i)^r - 1} \quad (1)$$

where $i$ represents the interest rate, and $r$ denotes the lifetime of the process. The TPI, which includes both direct and indirect costs, was determined using cost estimation and scaling methods applied to simulation results. In addition, mass and energy balance data obtained from the process simulation were used to estimate the fixed and variable operating costs. Depreciation was calculated using Eq. (2). Income tax was determined based on the net income and applicable tax rate, as detailed in Eq. (3).

$$Depreciation = \frac{TPI}{Lifetime} \quad (2)$$

$$Tax = (Profit - Depreciation) \times Tax\ rate \quad (3)$$

Finally, the MSP was calculated by dividing the sum of the annualized ROI, total operating expenses, and taxes by the total amount of L-LA produced annually, as shown in Eq. (4).

$$MSP = \frac{ROI + Expense + Tax}{The\ amount\ of\ L\text{-}LA} [\$/kg_{L-LA}] \quad (4)$$

The GWP was assessed as an environmental performance metric through life cycle assessment (LCA) methodology, representing the total $CO_2$ equivalent emissions per unit of L-LA produced. The system boundary encompasses raw material extraction, transportation, utility, and waste treatment from manufacturing operations. The GWP analysis quantifies direct $CO_{2eq}$ emissions from process vent streams and indirect $CO_{2eq}$ emissions from utility consumption. It also takes account of emissions associated with waste disposal, input material production, and transport. The assessment followed ISO 14040 and 14044 standards, with inventory factors sourced from the Greenhouse gases, Regulated Emissions, and Energy use in Technologies (GREET) model [14].

## RESULTS AND DISCUSSION

### Simulation results

In this section, key operational parameters are discussed to provide a detailed understanding of the performance of each process. The operability of the proposed processes was assumed to be 7980 h operation per year. The baseline L-LA production process can produce 88wt% L-LA of 178,752 tons/year. The supplied amount of $Ca(OH)_2$ is 78,204 tons/year on a dry basis and then gypsum waste of 152,418 tons/year is removed via centrifugation after the reacidification unit. The downstream esterification and hydrolysis steps demonstrated a recovery efficiency of 94.9%.

Both KRL #1 and KRL #2 processes achieved an annual production of 197,673 tons/year of 88wt% L-LA. The supplied amount of KOH is 11,387 tons/year on a dry basis. The liquid-liquid extraction steps efficiently removed impurities, with an L-LA recovery efficiency of 85.7%. Separation and electrolysis units regenerated over 96.5% of the KOH supplied to the fermenters. The electrolysis units in KRL #1 produced byproduct gases, $H_2$ and $Cl_2$, at rates of 2,394 tons/year and 84,588 tons/year, respectively. In KRL #2, the HCl recovery rate exceeded 87.0% of the HCl supplied to the reacidification reactor,

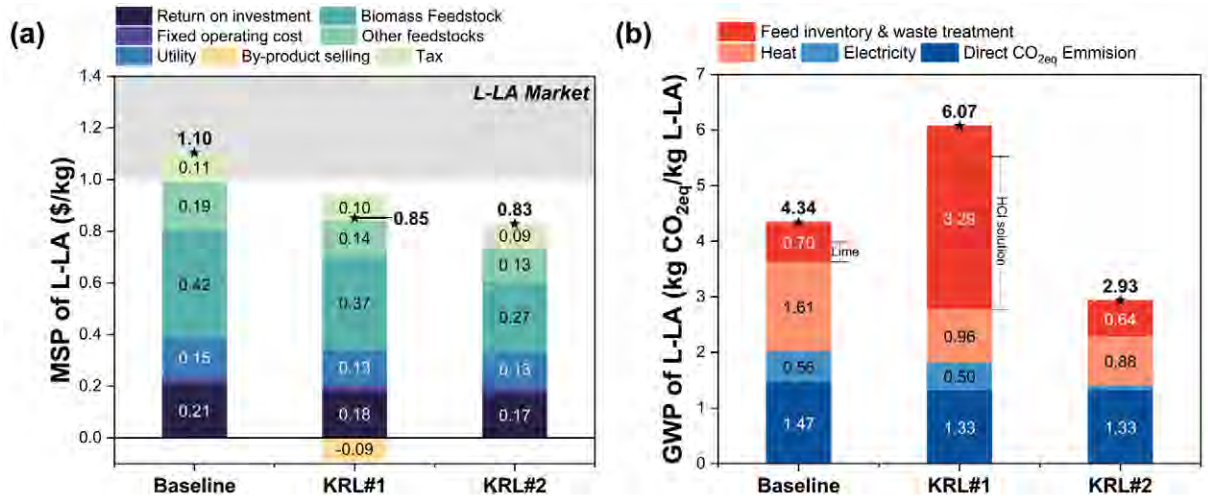



**Figure 2.** (a) MSP and (b) NCE of produced L-LA via the baseline and proposed processes

reducing the reliance on external inputs.

## Techno-economic and environmental analysis

The economic and environmental performance of the developed processes were evaluated using the MSP and GWP as key indicators. As shown in Fig. 2, the proposed KRL system leads to a decrease in the MSP of L-LA. One of the major drivers of this cost reduction was the higher L-LA production rate in the KRL processes compared to the baseline process. Additionally, the introduction of KOH, together with the implementation of advanced buffer recycling technologies, reduced the cost of buffer materials and waste disposal. The favorable results of KRL #2 can be attributed to the integration of effective regeneration and reuse of KOH, which are also present. These elements were further enhanced in KRL #2 through the integration of the HCl recycling loop, optimizing material utilization and reducing production costs. As a result, KRL #2 achieved an MSP of 0.83 $/kg, representing a 25% reduction compared to the baseline MSP of 1.10 $/kg.

In terms of environmental performance, the baseline process demonstrated a relatively higher GWP compared to KRL #2, attributed to the substantial use of $Ca(OH)_2$ and the indirect emissions from utility consumption. KRL #1 exhibited a GWP of 3.45 kg $CO_{2\text{-eq}}$/kg L-LA, which represents an increase of 40% compared to the baseline process. This is due to the energy-intensive electrolysis and high consumption of HCl. Conversely, KRL #2 exhibited the lowest GWP of 2.93 kg $CO_{2\text{-eq}}$/kg L-LA, showing a reduction of 51% relative to the baseline process. The recycling of HCl in KRL #2 significantly reduced material consumption, reducing the $CO_{2eq}$ inventory of raw materials.

## Sensitivity analysis

A sensitivity analysis was performed to identify the key economic parameters influencing the MSP of L-LA. The sensitivity analysis evaluated how much MSP of L-LA would change if the economic parameters varied by ±20%, as presented in Fig. 3. The detailed values of major economic parameters used in the sensitivity analysis are provided in Table S3 in SI. For the baseline process, the interest rate was the most sensitive factor on MSP, affecting a change of up to +4.69%. The biomass feedstock price was the second largest influential factor, with a ±2.63% variation. For the KRL processes, the interest rate was also the most sensitive factor, with a change of up to 5.20%. Biomass feedstock is another sensitive factor, causing a variation of ±3.08% and ±3.17% in KRL #1 in KRL #2, respectively. Consequently, we identified the interest rate and biomass feedstock price as the main cost drivers influencing the MSP of the developed processes. These results indicate the importance of optimizing these parameters to improve the economic viability of L-LA production.

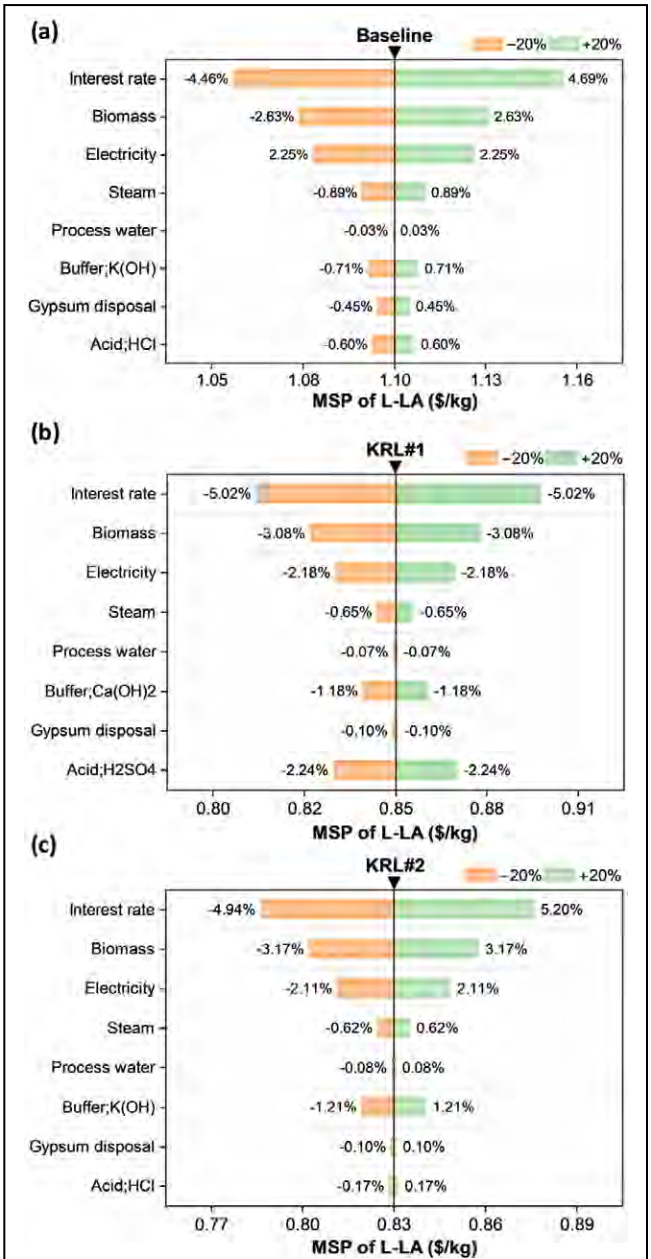



**Figure 3.** Sensitivity of the major economic parameters on the MSP

## CONCLUSIONS

This study developed the conventional L-LA production process and the novel KOH recycling-based L-LA production system for producing high enantiomeric purity of L-LA from LCB. Then we evaluated the economic and environmental performances of the developed

processes. Then we evaluated the economic and environmental performances of the developed processes. In economic evaluation, KRL #1 exhibited improved economics due to cost reduction from buffer recycling and byproduct utilization. KRL #2 demonstrated the best improvements in economic performance by incorporating HCl solution synthesis units. The MSP of L-LA was 0.83 $/kg for KRL #2 and 0.89 $/kg for KRL #1, representing cost reductions of 23% and 25%, respectively, compared to the baseline process. However, the environmental performance of KRL #1 was limited by the significant electricity demand and the extensive use of HCl. Conversely, the GWP of L-LA via KRL #2 was 2.93 kg $CO_{2\text{-eq}}$/kg, representing a 51% reduction compared to the baseline process. Furthermore, the sensitivity analysis revealed that the interest rate and biomass feedstock price are the main cost drivers. Addressing these key economic drivers will be essential to further enhance the viability of the developed L-LA production processes. This study highlights the potential of integrating advanced recycling technologies to achieve both economic and environmental benefits, promoting biotechnology practices for sustainable production of L-LA.

## DIGITAL SUPPLEMENTARY MATERIAL

The following materials are available in the Living Archive for Process Systems Engineering (LAPSE:2025.0021): These materials provide comprehensive information for reproducing the results presented in this study.

## REFERENCES


1. Wheeler, Tim, and Joachim Von Braun. "Climate change impacts on global food security." *Science* 341.6145:508-513 (2013)
2. Lopez, Gabriel, et al. "From fossil to green chemicals: sustainable pathways and new carbon feedstocks for the global chemical industry." *Energy & Environmental Science* 16.7:2879-2909 (2023)
3. Isikgor, Furkan H., and C. Remzi Becer. "Lignocellulosic biomass: a sustainable platform for the production of bio-based chemicals and polymers." Polymer chemistry 6.25:4497-4559 (2015)
4. de Oliveira, Regiane Alves, et al. "Polymer grade l-lactic acid production from sugarcane bagasse hemicellulosic hydrolysate using Bacillus coagulans." Bioresource Technology Reports 6:26-31 (2019)
5. Klotz, Silvia, et al. "Biotechnological production of enantiomerically pure d-lactic acid." Applied microbiology and biotechnology 100.22:9423-9437 (2016)
6. Abdel-Rahman, Mohamed Ali, et al. "Efficient homofermentative L-(+)-lactic acid production from xylose by a novel lactic acid bacterium, Enterococcus mundtii QU 25." Applied and environmental microbiology 77.5:1892-1895 (2011)
7. Huang, Xing, et al. "Time-resolved transcriptomic and proteomic profiling of Heyndrickxia coagulans during NaOH-buffered L-lactic acid production." Frontiers in Microbiology 14): 1296692 (2023)
8. Humbird, Davis, et al. Process design and economics for biochemical conversion of lignocellulosic biomass to ethanol: dilute-acid pretreatment and enzymatic hydrolysis of corn stover. No. NREL/TP-5100-47764. National Renewable Energy Lab.(NREL), Golden, CO (United States), (2011)
9. Wooley, Robert J., and Victoria Putsche. Development of an ASPEN PLUS physical property database for biofuels components. No. NREL/TP-425-20685. National Renewable Energy Lab. (NREL), Golden, CO (United States), (1996)
10. van der Pol, Edwin C., Gerrit Eggink, and Ruud A. Weusthuis. "Production of l (+)-lactic acid from acid pretreated sugarcane bagasse using Bacillus coagulans DSM2314 in a simultaneous saccharification and fermentation strategy." Biotechnology for biofuels 9:1-12 (2016)
11. Ma, Kedong, et al. "Highly efficient production of optically pure L-lactic acid from corn stover hydrolysate by thermophilic Bacillus coagulans." Bioresource technology 219:114-122 (2016)
12. Suhara, Manabu, and Yoshio Oda. "Electrolysis of aqueous solution of potassium chloride." U.S. Patent No. 4,261,803. (1981)
13. Luberti, Mauro, et al. "Design of a H 2 PSA for cogeneration of ultrapure hydrogen and power at an advanced integrated gasification combined cycle with pre-combustion capture." Adsorption 20: 511-524 (2014).
14. The Greenhouse Gases, Regulated Emissions, and Energy Use in Transportation Model (GREET). Argonne National Laboratory. https://greet.es.anl.gov/.



© 2025 by the authors. Licensed to PSEcommunity.org and PSE Press. This is an open access article under the creative commons CC-BY-SA licensing terms. Credit must be given to creator and adaptations must be shared under the same terms. See https://creativecommons.org/licenses/by-sa/4.0/




Systems & Control Transactions

**Research Article - Peer Reviewed Conference Proceeding**
ESCAPE 35 - European Symposium on Computer Aided Process Engineering
Ghent, Belgium. 6-9 July 2025
Jan F.M. Van Impe, Grégoire Léonard, Satyajeet S. Bhonsale,
Monika E. Polańska, Filip Logist (Eds.)

PSE PRESS

# Potential of chemical looping for green hydrogen production from biogas: process design and techno-economic-environmental analysis

**Donghyeon Kim, Minseong Park, Donggeun Kang, Dongin Jung, Siuk Roh, and Jiyong Kim***

Sungkyunkwan University (SKKU), Department of Chemical Engineering, Suwon, Republic of Korea
* Corresponding Author: jiyongkim@skku.edu.

## ABSTRACT

Hydrogen ($H_2$), as the promising alternative to fossil fuel-based energy carriers, faces the critical challenge of diversifying its sources and lowering production costs. Biogas, produced from organic waste, offers a renewable and carbon-neutral option for $H_2$ production, but its high $CO_2$ content requires a pre-separation process of $CO_2$ from $CH_4$ or specialized catalysts for use in existing reforming processes. Chemical looping reforming (CLR), as an advanced $H_2$ production process, uses an oxygen carrier (OC) as the oxidant, allowing raw biogas to be used directly in the reforming process. Recently, numerous studies on CLR design and analysis have demonstrated their growing economic feasibility. However, deploying the CLR process in the biogas treatment industry requires further research to analyze its technical, economic, and environmental performance under target capacities and $H_2$ purity. This study proposes biogas-based CLR processes and analyzes the capability of the processes from techno-economic and environmental perspectives: i) chemical looping partial oxidization (CLPO), ii) chemical looping steam reforming (CLSR), iii) chemical looping water splitting (CLWS), and iv) chemical looping $CO_2$ splitting (CLCS). Evaluation metrics include energy efficiency, exergy efficiency, unit production cost (UPC), and net $CO_2$ equivalent emission (NCE) to compare technical, economic, and environmental performance, respectively. Each process is simulated in Aspen Plus to obtain mass and energy balance data. The heat exchanger network (HEN) is optimized to maximize heat recovery and achieve autothermal conditions. As a result, we comparatively analyze the economic and environmental capability of the proposed processes by identifying the major cost drivers and $CO_2$ emission contributors.

**Keywords**: Renewable and Sustainable Energy, Process Synthesis, Hydrogen, Chemical Looping, Technoeconomic Analysis.

## INTRODUCTION

As the demand for sustainable energy systems intensifies, hydrogen ($H_2$) has emerged as a significant energy carrier capable of decarbonizing in heavy industry and long-distance transportation [1]. Currently, most of the global $H_2$ production relies on fossil fuel-based processes, notably steam methane reforming (SMR), which emits substantial amounts of $CO_2$ into the atmosphere [2]. While water electrolysis powered by renewable energy offers a carbon-neutral alternative, its widespread implementation faces significant economic and logistical barriers, particularly due to the high cost and the intermittent availability of renewable energy sources [3]. As such, innovative reforming technologies that achieve a balance between cost-effectiveness and environmental sustainability are needed to enable a smooth energy transition.

Biogas, a renewable energy source produced through the anaerobic decomposition of organic waste, presents an attractive feedstock for sustainable $H_2$ production [4]. Unlike natural gas, biogas is composed primarily of $CH_4$ and $CO_2$. The high $CO_2$ content of biogas poses technical challenges for conventional reforming technologies, requiring either costly pre-separation of $CO_2$ from $CH_4$ or advanced systems capable of directly

processing $CO_2$-rich feedstocks [5][6]. However, when its $CO_2$ content is effectively utilized, biogas can offer a carbon-neutral pathway. Therefore, the need for reforming technologies that can efficiently exploit the potential of biogas without incurring additional separation costs is increasing.

Chemical looping reforming (CLR) has emerged as a next-generation $H_2$ production technology capable of overcoming many of the limitations associated with traditional reforming technologies. In CLR processes, a solid metal oxygen carrier (OC) facilitates redox reactions, enabling the direct utilization of raw biogas without the need for prior $CO_2$ removal [7]. This innovative process can achieve autothermal conditions that improve both energy and operational efficiencies while integrating inherent $CO_2$ capture capabilities that reduce carbon management costs. These combined advantages make CLR processes a cost-competitive pathway for sustainable $H_2$ production [8].

Despite the promising characteristics of CLR process, its practical application in the biogas industry remains limited. Further research is necessary to evaluate the performance of CLR processes under various configurations and operating scales. This study aims to evaluate the performance of four different CLR process configurations: i) chemical looping partial oxidation (CLPO), ii) chemical looping steam reforming (CLSR), iii) chemical looping water splitting (CLWS), and iv) chemical looping $CO_2$ splitting (CLCS). Through a comprehensive analysis of their technical, economic, and environmental performance, this research seeks to identify viable processes for integrating CLR processes into sustainable $H_2$ production systems, while also identifying key cost drivers and key environmental impact variables.

## TECHNOLOGY OVERVIEW AND METHODOLOGY

### Technology overview

### Chemical looping partial oxidization (CLPO)

The CLPO process consists of two reactors: a reducer and a combustor. In the reducer, biogas is partially oxidized with the OC, producing syngas while reducing the OC. The reduced OC is then transported to the combustor, where it is fully regenerated with air, releasing significant heat. This heat is used to sustain the endothermic reactions in the reducer as the OC circulates back, ensuring efficient heat transfer. The overall thermal balance is maintained by an optimized heat exchanger network (HEN). The reducer employs a moving bed reactor design, which facilitates countercurrent contact between the biogas and the OC, thereby enhancing reaction efficiency and maximizing syngas yield [9]. Conversely, the combustor utilizes a fluidized bed reactor to ensure uniform temperature distribution and efficient heat transfer [10]. Downstream of the reducer, the syngas undergoes a water-gas shift (WGS) reaction to increase its $H_2$ content. A monoethanolamine (MEA)-based $CO_2$ absorption process is then used to capture $CO_2$ and reduce greenhouse gas emissions, followed by pressure swing adsorption (PSA) is employed to produce high-purity $H_2$.

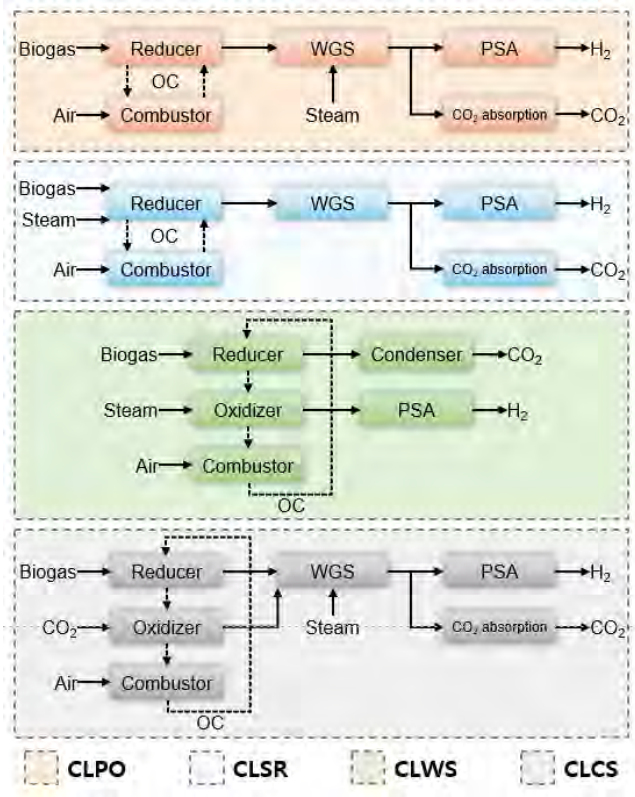



**Figure 1.** Process flow diagram of CLR processes.

Key reactions in the CLPO process:

Reducer:

$$Fe_2O_3 + CH_4 \rightarrow Fe/FeO_{0.947} + CO + H_2, \Delta H > 0 \quad (1)$$

Combustor:

$$Fe/FeO_{0.947} + O_2 \rightarrow Fe_2O_3, \Delta H < 0 \quad (2)$$

WGS reactor:

$$CO + H_2O \rightarrow CO_2 + H_2, \Delta H < 0 \quad (3)$$

### Chemical looping steam reforming (CLSR)

Building on the CLPO configuration, the CLSR process introduces steam into the reducer to enable simultaneous SMR reaction. While the addition of steam requires more energy, it substantially increases the $H_2$ yield due to the SMR reaction. The reduced OC is subsequently regenerated in the combustor, as in CLPO, while the syngas undergoes WGS to enhance $H_2$ content, MEA-based $CO_2$ absorption for carbon capture, and PSA for $H_2$ purification. Similar to CLPO, the CLSR process uses a

moving bed reducer for enhanced biogas and steam reactions, paired with a fluidized bed combustor for efficient heat recovery.

Key reaction in the CLSR process:

SMR reaction in reducer:

$$CH_4 + H_2O \rightarrow CO + 3H_2, \Delta H > 0 \quad (4)$$

## Chemical looping water splitting (CLWS)

In addition to the reducer and combustor, the CLWS process introduces a third reactor, the oxidizer. In the reducer, the biogas undergoes complete oxidization with the OC, producing flue gas containing only $N_2$, $CO_2$ and $H_2O$. The water in the flue gas is removed by condensation, leaving $CO_2$, which is then captured at a relatively low quality. The reduced OC is partially re-oxidized with steam in the oxidizer, directly producing $H_2$. By enabling water splitting, the CLWS process eliminates the need for a WGS and MEA-based $CO_2$ absorption process and simplifies the downstream $H_2$ purification steps to just a condenser and a PSA unit. The oxidizer is designed as a moving bed reactor, ensuring an efficient water splitting reaction. The OC is fully regenerated in the combustor before being returned to the reducer.

Key reactions in the CLWS process:

Reducer:

$$Fe_2O_3 + CH_4 \rightarrow FeO_x + CO_2 + H_2O, \Delta H > 0 \quad (5)$$

Oxidizer:

$$FeO_x + H_2O \rightarrow FeO_y + H_2, \Delta H < 0 \quad (6)$$

Combustor:

$$FeO_y + O_2 \rightarrow Fe_2O_3, \Delta H < 0, (x \leq y \leq 1.33) \quad (7)$$

## Chemical looping $CO_2$ splitting (CLCS)

The CLDR process, like the CLWS process, consists of a reducer, oxidizer, and combustor, but differs in that $CO_2$ is used as the oxidant in the oxidizer, allowing for a $CO_2$ splitting reaction. In the reducer, biogas goes through partial oxidation, to produce syngas, while $CO_2$ in the oxidizer partially regenerate the OC, producing CO. The resulting syngas and CO are sent to the WGS reactor along with steam, which increases the $H_2$ production by converting $H_2O$ and CO into $H_2$ and $CO_2$. The $H_2$-rich stream undergoes MEA-based $CO_2$ absorption for carbon capture, followed by PSA for further $H_2$ purification. Unlike other CLR processes, the CLDR process involves a highly endothermic $CO_2$ splitting reaction, using $CO_2$ as an oxidant in the oxidizer. Thus, to maintain autothermal conditions, heat generated in the combustor is recovered and transferred to the oxidizer through a jacketed reactor. This ensures that the energy required for oxidizer is supplied efficiently, providing stable and energy-efficient operation.

Key reaction in the CLDR process:

Oxidizer:

$$FeO_x + CO_2 \rightarrow FeO_y + CO, \Delta H > 0, (x \leq y \leq 1.33) \quad (8)$$

## Model description

For process simulation and optimization, the commercial process simulator Aspen Plus is used as the primary modeling tool. The Peng-Robinson-Boston-Mathias (PR-BM) equation of state is selected to accurately represent the thermodynamic properties of all units. The CLR reactions are simulated using the Gibbs free energy minimization method, to achieve equilibrium-based calculations for the redox reactions. The CLR reactors are designed to operate near atmospheric pressure. All processes are designed to operate under heat-neutral conditions. To ensure thermal balance and enhance $H_2$ yield, heat integration is performed using an optimized HEN. The HEN is designed using Aspen Energy Analyzer to ensure efficient energy recovery and the autothermal operating conditions. Product specifications are set for high-purity $H_2$ and $CO_2$ streams at industrially relevant pressures. In all configurations, biogas and other feed streams, such as water and air, are preheated to the same temperature before entering the reforming reactors to ensure consistent evaluation criteria, with feedstock and OCs also having identical compositions.

## Evaluation method

The performance of the CLR processes is evaluated from three perspectives: thermodynamic efficiency, economic performance, and environmental impact. From a thermodynamic perspective, energy efficiency and exergy efficiency are calculated to assess the ability of the process to convert input energy to useful $H_2$ with minimal losses. Energy efficiency, expressed as $\eta_{energy}$, is defined as the ratio of the chemical energy in the $H_2$ product to the total energy input, including feedstock and external utilities.

$$\eta_{energy} = \frac{\dot{P}_i \times LHV_i}{\sum(\dot{F}_i \times LHV_i) + \sum U_j} \quad (9)$$

Here, $\dot{P}_i$ represents the molar flow rate of the $H_2$ product, while $LHV_i$ denotes the lower heating value of each material. Similarly, $\dot{F}_i$ corresponds to the molar flow rate of the feedstock, and $\sum U_j$ indicates the total external energy input.

Exergy efficiency, denoted as $\eta_{Exergy}$, measures the capacity of the process to minimize the loss of energy during the conversion processes.

$$\eta_{Exergy} = \frac{\dot{E}x_{in,total} - \dot{E}x_{des,total}}{\dot{E}x_{in,total}} = \frac{\dot{E}x_{out,total}}{\dot{E}x_{in,total}} \quad (10)$$

In eq. 10, $\dot{E}x_{in,total}$ is the total input exergy, $\dot{E}x_{out,total}$, is the total output exergy, and $\dot{E}x_{des,total}$ represents the exergy destroyed within the process.

The economic performance of the processes is evaluated using the unit production cost (UPC) of $H_2$. The total investment cost includes both capital expenditure (CAPEX) and operating expenditure (OPEX). CAPEX is calculated from the annualized capital investment (ACI), which is derived from the total capital investment (TCI). TCI comprises direct plant cost (DC), indirect plant cost (IDC), and working capital (WC). The capital recovery factor (CRF), calculated using Eq. 11, is used to annualize the capital costs.

$$CRF = \frac{i \times (1+i)^r}{(1+i)^r - 1} \tag{11}$$

Where $i$ is the interest rate and $r$ is the plant lifetime. Using the CRF, the ACI is calculated based on eq. 12.

$$ACI = TCI \times CRF \tag{12}$$

OPEX accounts for both variable operating costs (VOC) and fixed operating costs (FOC). Finally, the UPC of $H_2$ is determined by dividing the total annualized cost by the annual $H_2$ production ($P_{H_2}$).

$$UPC = \frac{ACI + VOC + FOC}{P_{H_2}} \tag{13}$$

From an environmental perspective, the processes are analyzed based on their net $CO_2$ equivalent emission (NCE), which reflects the total $CO_2$ emissions per kilogram of $H_2$ produced. NCE includes direct $CO_2$ emissions (DCE) from the process, indirect $CO_2$ emissions (ICE) associated with energy inputs, and carbon credits (CC). The CC is calculated as the net difference between the $CO_2$ reduction effect of biomass and the $CO_2$ emissions from biogas production [11]. The NCE is calculated using eq. 14.

$$NCE = \frac{DCE + ICE - CC}{P_{H_2}} \tag{14}$$

## RESULT AND DISCUSSION

### Techno-economic and environmental analysis

The energy and exergy efficiencies of the four CLR processes are shown in Fig. 2. The CLSR process demonstrates the highest thermodynamic performance, achieving energy and exergy efficiencies of 49% and 47%, respectively, due to its high $H_2$ yield from SMR reaction and effective heat recovery strategies via the HEN. Closely following CLSR, the CLCS process achieve comparable efficiencies of 48% and 47%. Although its high $H_2$ production contributes significantly to performance, the strong heat demands of the $CO_2$ splitting reaction slightly limits its overall efficiency. In contrast, the CLPO process shows the lowest performance, with efficiencies of 23% and 22%, mainly due to the imbalance between endothermic heat in the reducer and excessive heat generation in the combustor, resulting in significant thermal losses. The CLWS process shows intermediate performance, with efficiencies of 43% and 42%, respectively. While its effective heat recovery strategy supports reasonable performance, its lower $H_2$ yield limits its thermodynamic efficiency compared to CLSR and CLCS.

Taken together, the CLR processes, except CLPO, exhibit similar process efficiencies due to HEN designs optimized for autothermal conditions. The CLPO process exhibits lower efficiency due to heat imbalance, suggesting that advanced heat recovery strategies such as combined heat and power plant can effectively address this limitation and improve performance.

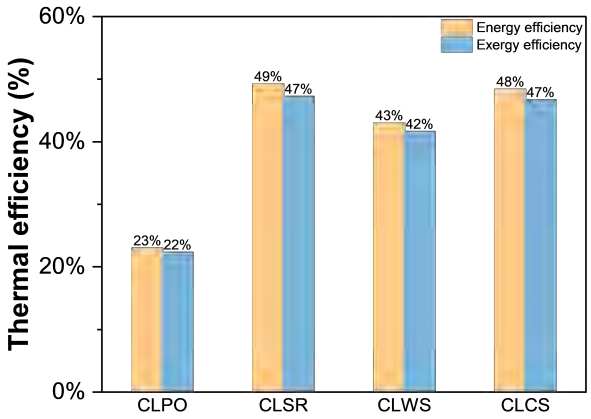



**Figure 2.** Thermal efficiencies of CLR processes.

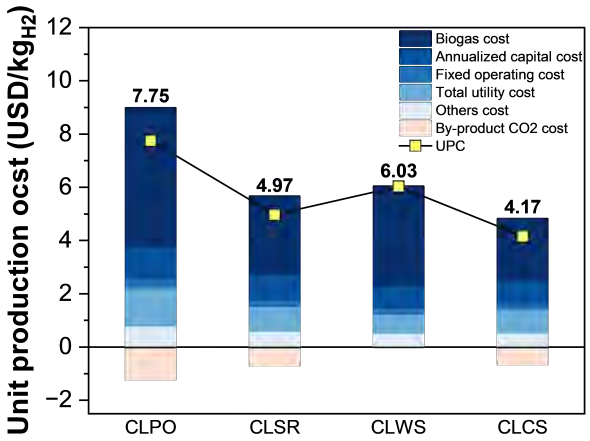



**Figure 3.** Unit production costs of CLR processes.

The economic performance of the four CLR processes is evaluated based on their UPC (USD/kg$_{H_2}$), as shown in Fig 3. Among the processes, the CLCS process achieves the lowest UPC of 4.17 USD/kg$_{H_2}$, benefiting from reduced biogas cost by producing additional $H_2$ through the utilization of CO. In contrast, the CLPO process has the highest UPC at 7.75 USD/kg$_{H_2}$, primarily due to its higher operating energy requirements and lower $H_2$ yield. The CLSR and CLWS processes show mid-range

UPC of 4.97 USD/$kg_{H_2}$ and 6.03 USD/$kg_{H_2}$, respectively. The relatively lower cost of CLSR can be attributed to the integration of steam reforming, which enhances the $H_2$ yield. On the other hand, the CLWS process has higher UPC due to a lack of by-product $CO_2$ credit, attributed to the relatively low-quality of the captured $CO_2$. A comprehensive evaluation of the results shows that biogas cost, energy inputs, and capital expenditures emerge as the primary cost drivers for all processes.

The environmental performance of the CLR processes is evaluated based on their NCE ($kg_{CO_2eq}/kg_{H_2}$), as shown in Fig. 4. Among the processes, the CLWS process demonstrates the most environmentally favorable

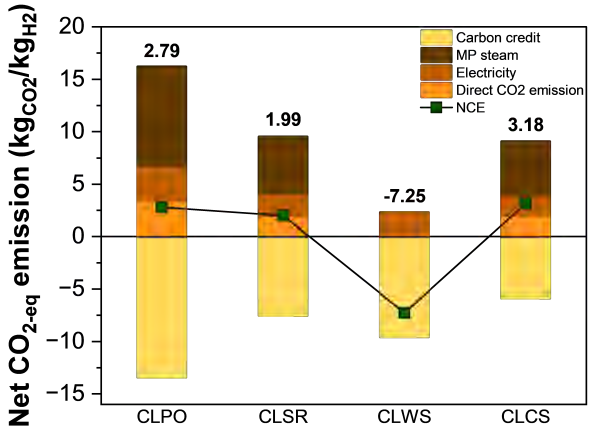



**Figure 4.** Net $CO_2$ equivalent emissions of CLR processes.

outcome, achieving a negative emission of -7.25 $kg_{CO_2eq}/kg_{H_2}$. This carbon-negative result stems from the ability to capture $CO_2$ internally without the need for an MEA-based $CO_2$ absorption process, thereby significantly reducing both indirect and direct $CO_2$ emissions. In contrast, the CLCS process exhibits the highest emissions at 3.18 $kg_{CO_2eq}/kg_{H_2}$, primarily due to the significant thermal energy required for $CO_2$ capture. The CLSR and CLPO processes show moderate results, with net emissions of 1.99 $kg_{CO_2eq}/kg_{H_2}$ and 2.79 $kg_{CO_2eq}/kg_{H_2}$, respectively. The results highlight the significant environmental benefits of the CLWS process and demonstrate its potential for carbon-negative $H_2$ production. It is also observed that the presence or absence of an MEA-based $CO_2$ absorption process has the greatest impact on the overall $CO_2$ equivalent emissions of the process. Therefore, further in-depth research on $CO_2$ separation technologies is essential to improve the environmental performance of CLR processes.

## Sensitivity analysis

A comprehensive techno-economic assessment of the four CLR processes identify biogas cost, energy inputs, and capital expenditures as critical factors influencing the UPC of $H_2$. To quantify their economic impact, a sensitivity analysis is conducted on key parameters, including biogas price, interest rate, plant lifetime, and utility prices.

The sensitivity analysis results for the four CLR processes (Fig. 5) highlight that biogas price is the most

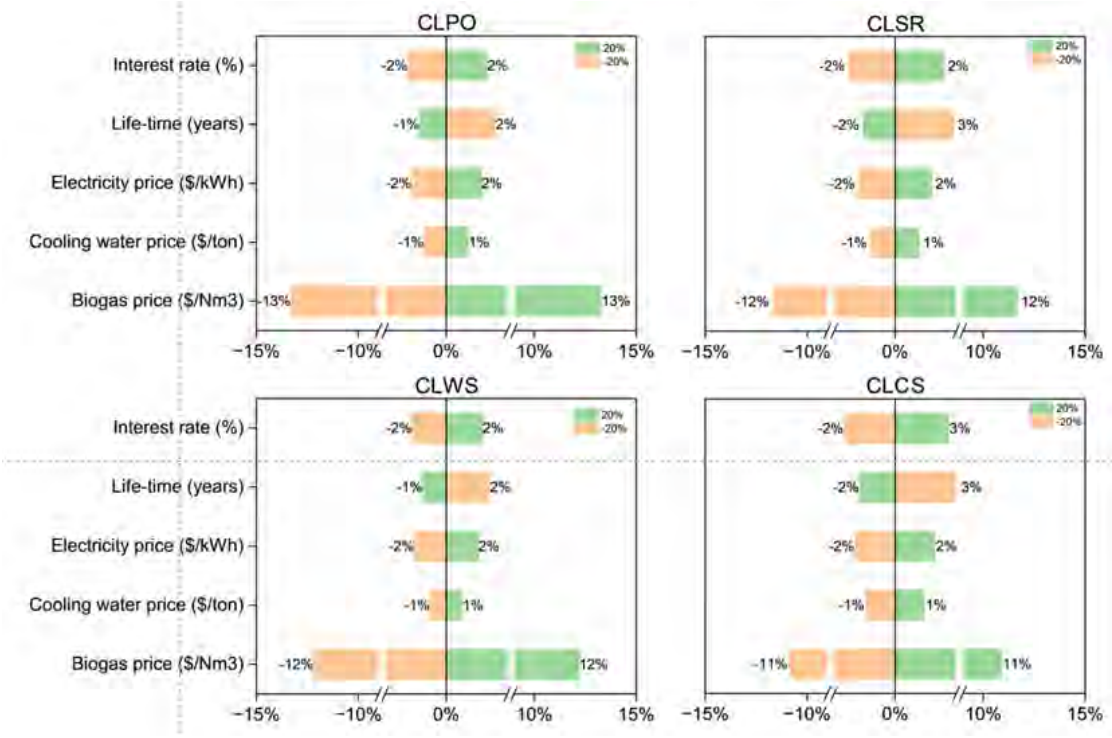



**Figure 5.** Sensitivity anlaysis results of CLR processes.

influential factor affecting the UPC of $H_2$. A 20% increase in the biogas price leads to a corresponding UPC rise of approximately 11-13% across all processes, highlighting the critical role of the biogas price in the economics of $H_2$ production. Moreover, capital related parameters such as interest rate and plant lifetime have an impact. A 20% increase in the interest rate increases UPC by about 2% while extending the plant lifetime by 5 years decreases it by 2%. Similarly, operational parameters such as electricity price and cooling water price show effects, with UPC variations of ±2% and ±1%, respectively. The analysis identify biogas price, capital related parameters, and utility prices as the dominant factors influencing the economics of CLR processes. Prioritizing strategies to reduce biogas costs and optimize capital and operating expenditures will be essential for improving economic viability of CLR processes.

## CONCLUSION

This study evaluated four CLR processes: CLPO, CLSR, CLWS, and CLCS for $H_2$ production from biogas, focusing on their techno-economic and environmental performance. Among the processes, CLCS emerged as the most promising option, offering a balanced performance with thermal efficiency and economic benefits due to effective $CO_2$ utilization and reduced biogas costs. The CLSR process showed strong potential with competitive production costs and high $H_2$ yields. The CLWS process achieved carbon reduction, demonstrating its potential as a negative carbon emission technology, although its higher cost remains a challenge. In contrast, the CLPO process had the lowest performance across all criteria, indicating the need for further advancement to enhance its feasibility and performance. To enable the industrial application of CLR processes in the biogas industry, advances in $CO_2$ capture technologies, heat integration, and process optimization are essential. This study demonstrates the feasibility of biogas-based CLR processes for scalable, sustainable $H_2$ production, providing a pathway toward carbon-neutral energy solutions.

## REFERENCES


1. He G, Mallapragada DS, Bose A, Heuberger-Austin CF, Gençer E. Sector coupling via hydrogen to lower the cost of energy system decarbonization. Energy Environ. Sci. 14:4635–4646 (2021). https://doi.org/10.1039/D1EE00627D
2. Dincer I, Acar C. Review and evaluation of hydrogen production methods for better sustainability. Int J Hydrogen Energy 40:11094–11111 (2015) https://doi.org/10.1016/j.ijhydene.2014.12.035
3. Schmidt O, Gambhir A, Staffell I, Hawkes A, Nelson J, Few S. Future cost and performance of water electrolysis: an expert elicitation study. Int J Hydrogen Energy 42:30470–30492 (2017) https://doi.org/10.1016/j.ijhydene.2017.10.045
4. Angelidaki I, Xie L, Søndergaard T, Ahring BK, Cavinato C, et al. Biogas upgrading and utilization: current status and perspectives. Biotechnol Adv 36:452–466 (2018) https://doi.org/10.1016/j.biotechadv.2018.01.011
5. Abatzoglou N, Boivin S. A review of biogas purification processes. Biofuels Bioprod Biorefin 3:42–71 (2009) https://doi.org/10.1002/bbb.117
6. Scarlat N, Dallemand JF, Fahl F. Biogas: developments and perspectives in Europe. Renew Energy 129:457–472 (2018) https://doi.org/10.1016/j.renene.2018.03.006
7. Hossain MM, de Lasa HI. Chemical-looping combustion (CLC) for inherent CO2 separations—a review. Chem Eng Sci 63:4433–4451 (2008) https://doi.org/10.1016/j.ces.2008.05.028
8. Lu Y, Zhang X, Wang S, Chen H. Current challenges and prospects of water electrolysis for hydrogen production: from materials to system engineering. Int J Hydrogen Energy (2023) https://doi.org/10.1016/j.ijhydene.2023.10.212
9. Adánez J, Abad A, García-Labiano F, Gayán P, de Diego LF. Progress in chemical-looping combustion and reforming technologies. Energy Fuels 26:718–733 (2012) https://doi.org/10.1021/ef3020475
10. Santos JC, Soares JBP, Secchi AR. Modeling and simulation of polyethylene production in a fluidized bed reactor. Braz J Chem Eng 24:237–250 (2007) https://doi.org/10.1590/S0104-66322000000200004
11. S. Lehtoranta, E. Tampio, S. Rasi, J. Laakso, K. Vikki, and S. Luostarinen, The implications of management practices on life cycle greenhouse gas emissions in biogas production, J. Environ. Manage. 366, 121884 (2024). https://doi.org/10.1016/j.jenvman.2024.121884



© 2025 by the authors. Licensed to PSEcommunity.org and PSE Press. This is an open access article under the creative commons CC-BY-SA licensing terms. Credit must be given to creator and adaptations must be shared under the same terms. See https://creativecommons.org/licenses/by-sa/4.0/




Systems & Control Transactions

**Research Article - Peer Reviewed Conference Proceeding**
ESCAPE 35 - European Symposium on Computer Aided Process Engineering
Ghent, Belgium. 6-9 July 2025
Jan F.M. Van Impe, Grégoire Léonard, Satyajeet S. Bhonsale,
Monika E. Polańska, Filip Logist (Eds.)

PSE PRESS

# Decarbonized Hydrogen Production: Integrating Renewable Energy into Electrified SMR Process with $CO_2$ Capture

**Joohwa Lee[a], Haryn Park[a], Bogdan Dorneanu[b], Jin-Kuk Kim[a]*, and Arellano-Garcia Harvey[b]***

[a] Hanyang University, Department of Chemical Engineering, Seoul, Republic of Korea (South Korea)
[b] Brandenburgische Technische Universitat Cottbus-Senftenberg, FG Prozess- und Anlagentechnik, Cottbus, Land Brandenburg, Germany
* Corresponding Author: jinkukkim@hanyang.ac.kr, arellano@b-tu.de

## ABSTRACT

Electrified steam methane reforming has emerged as a promising technology for electrifying the hydrogen production process industries. Unlike conventional fossil fuel-based steam methane reforming, the electrified steam methane reforming process relies exclusively on electrical heating, eliminating the need for fossil fuel combustion. Beyond that, however, significant amounts of electricity required for the electrified process should be imported from the renewable energy-based system rather than fossil fuel-based grid electricity to have an environmental advantage over the conventional process. This study suggests a framework for integrating renewable energy systems into the electrified process for decarbonized hydrogen production. Considering the variability of renewable energy, wind and solar power are supplemented by battery storage, to facilitate a stable electricity supply to the electrified hydrogen production process. A Mixed-Integer Linear Programming (MILP) model is developed to optimally size and operate both the renewable system and potential grid imports. Case studies under various carbon tax scenarios, using historical weather data from a region in Germany, are conducted, followed by a techno-economic assessment to estimate the Cost of Hydrogen (COH). The results show that higher carbon taxes and reduced capital costs for wind, solar, and storage technologies significantly increase the share of renewable-based electricity. These findings highlight the importance of more stringent carbon taxation and improvements in the technology readiness level (TRL) of renewable energy are critical for accelerating large-scale, clean hydrogen production and industrial decarbonization.

**Keywords**: Hydrogen, Renewable energy, Electrification

## 1. INTRODUCTION

Interest in sustainable hydrogen production has increased as hydrogen becomes more widely recognized as a clean energy source and a vital chemical feedstock. Among the different strategies for producing hydrogen, furnace heated steam methane reforming (SMR) is widely regarded as an economic solution for large-scale hydrogen production. However, it requires significant heat energy, which results in a large amount of $CO_2$ emissions. To address these challenges, Wismann et al. [1], in collaboration with Haldor Topsoe, developed an innovative "Electric Heating Steam Methane Reformer", providing a promising eco-friendly alternative to the conventional fossil fuel-based furnace heating technology.

Several studies were investigated, regarding the process design and economic analysis of electrified hydrogen production [2-5]. However, these studies mainly focused on the electrified hydrogen production process itself, with relatively limited consideration of feasibility about introducing renewable energy sources at a commercial scale of the electrified process. Nava et al. [6] considered renewable energy integration for hydrogen production process, but it mainly focused on biogas-based hydrogen production and a relatively small scale of the process [7].

This study provides conceptual guidelines for the clean and sustainable production of hydrogen through

renewable-powered electrification, contributing to the decarbonization of the hydrogen industry and the global energy transition.

## 2. METHODOLOGY

Building upon our previous work on process guidelines and techno-economic analysis for large-scale electrified hydrogen production hydrogen production [5], this study introduces a renewable energy system (RES) model to supply electricity for the process. The integration of renewable energy sources, such as solar and wind, into hydrogen plants requires systematic consideration of their intermittent characteristics due to their dependence on weather conditions.

To ensure a reliable energy supply for the electrified hydrogen plant, battery storage systems and grid are introduced to store any surplus energy or supplement energy in deficit. To effectively manage these fluctuations, a system-wide optimization approach is employed to integrate renewable energy systems, ensuring reliable energy supply and high energy efficiency.

The proposed framework includes process modelling and simulation for the electrified hydrogen plant (**Figure 1**) is developed, with a focus on renewable energy integration. Case studies are conducted to investigate configurational and operational changes of renewable energy systems integrated with electrified hydrogen production process. A techno-economic assessment for these case studies is to estimate the Cost of Hydrogen (COH), which enhances our understanding on the economic feasibility of renewable-based electrification for hydrogen production.

## 3. PROBLEM DEFINITION

In this study, among various configurations of the electrified hydrogen production, the most cost-effective $CO_2$ capture integrated electrified hydrogen production process alternative is selected. Heat integration is applied throughout the electrified hydrogen production process, and an electric boiler is used to provide the additional low-pressure steam required for the $CO_2$ capture process. Based on simulation results using Aspen HYSYS, the estimated total power consumption for this large-scale electrified hydrogen production process is 424.1 MWe. The techno-economic analysis of the large-scale electrified hydrogen production process was conducted, assuming that an unlimited and consistent supply of renewable energy is available at a given renewable energy-based electricity cost. A break-even point of the renewable electricity cost was identified, at which the electrified hydrogen production option might be more economical than the conventional hydrogen production process.

However, in practical circumstances, it is difficult to continuously provide 424.1 MWe of renewable-based power [8]. Therefore, in this study, the large-scale electrified hydrogen production process is reduced in size to a tenth of its initial size, requiring 42.4 MWe of constant power, which is still a commercial-scale hydrogen plant, as shown in **Table 1**.

The main objective of this study is to develop a model of a renewable energy system (RES) employing an optimized combination of wind turbines (WT), solar photovoltaic (PV) arrays, and electrical energy storage (EES), with grid electricity support, to provide the steady power required for the electrified hydrogen production process.

The 2023 annual weather data for the German region of Freiburg im Breisgau, including wind speed and solar radiation, is adopted for the case study [9]. By using realistic weather data, the time-dependent characteristics of solar and wind power generation are fully considered in the RES model. The capacity of each renewable power generation facility, including WT, PV, and EES, and their hourly operating conditions, are determined using an optimization framework to minimize the COH.

COH breakdown of the electrified hydrogen production hydrogen plant, without electricity and the carbon tax is shown in **Table 1**. The utility cost, including natural gas and grid electricity, has been updated to 2023 German industrial price of 41€/MWh and 95.18 €/MWh, respectively [10-11]. The other economic parameters used are referred to the previous study [5]. The COH for electricity and carbon tax is estimated in the case study section that provides a full breakdown based on the modeling and simulation results of renewable energy system.

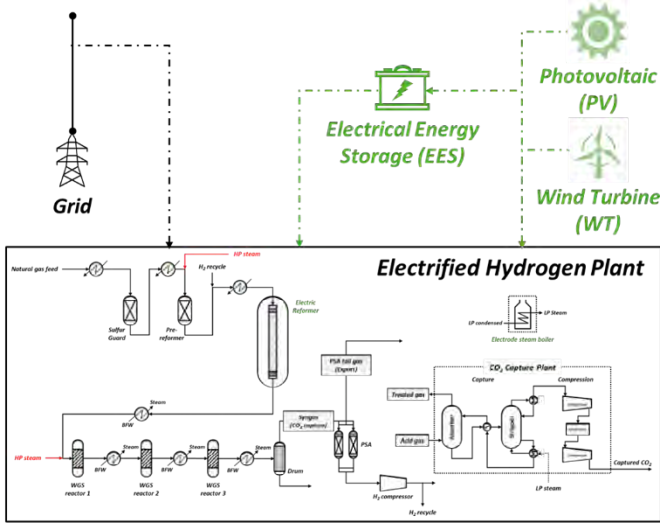



**Figure 1.** An electrified hydrogen production hydrogen plant integrated with renewable energy and grid

**Table 1:** Key Process Performance Data & Cost of Hydrogen Breakdown for the Electrified Hydrogen Production Process

| | Unit | Ref. [5] | Case study |
|---|---|---|---|
| **Performance** | | | |
| Natural gas | t/h | 63.9 | 6.4 |
| Power consumption | $MW_e$ | 424.1 | 42.4 |
| $H_2$ Production | t/h | 22.8 | 2.3 |
| **Cost of Hydrogen** | | | |
| Capital | $/kg | 0.26 | 0.82 |
| Fixed O&M | $/kg | 0.09 | 0.31 |
| Variable O&M | $/kg | 0.07 | 0.15 |
| Natural gas | $/kg | 1.81 | 1.81 |
| Electricity (RES) | $/kg | 1.91 | TBD |
| Carbon tax | $/kg | - | TBD |
| Total | $/kg | 4.14 | TBD |

## 4. OPTIMIZATION MODEL

A mathematical model is developed for a renewable energy system (RES) to provide electricity required for the electrified hydrogen production process. The values of design parameters of the RES model are presented in **Table 2**.

**Table 2:** Design Parameters of RES

| Parameter | Description | Value |
|---|---|---|
| $\eta$ | PV efficiency | 0.19 [12] |
| $\theta$ | Static loss of EES | 0.05 [13] |
| $\chi$ | Charge rate | 0.1 [13] |
| $\Delta\chi$ | Discharge rate | 0.15 [13] |
| $Demand$ | Electricity demand (MWh) | 42.4 [5] |
| $Rad(t)$ | Solar radiation (kWh/m$^2$) | Hourly data [9] |
| $v(t)$ | Wind Speed (m/s) | Hourly data [9] |
| $I_{POA}(Rad)$ | Plane of array irradiance (kWh/m$^2$) [12] | |
| $uE_{WT}(v)$ | Power performance of unit wind turbine [14] | |

The resulting MILP model of the RES is shown below. The equations regarding wind turbine and solar power generation are (1)-(3), and equations regarding electrical energy storage are (4)-(10). When the amount of renewable energy produced exceeds the demand for the electrified hydrogen production process, the renewable energy system is designed to use the generated renewable energy directly ($E_{DU}$) for the electrified hydrogen production process and store the remaining electricity in electrical energy storage (StoreIn) (Equations (4)-(6)). Static loss, charge rate, and discharge rate are all taken into consideration with the State of Charge (SOC) of the electrical energy storage (Equations (8)-(9)). Additionally, it is designed to have the same initial and final SOC, considering multiple-period operation (Equation (10)).

$$E_{WT}(t) = N_{WT} \cdot uE_{WT}(v(t)) \quad (1)$$

$$E_{PV}(t) = A_{PV} \cdot I_{POA}(Rad(t)) \cdot \eta \quad (2)$$

$$E_{Ren}(t) = E_{WT}(t) + E_{PV}(t), \quad \forall t \quad (3)$$

$$StoreIn(t) = E_{Ren}(t) - E_{DU}(t), \quad \forall t \quad (4)$$

$$Demand(t) = StoreOut(t) + Grid(t) + E_{DU}(t), \quad \forall t \quad (5)$$

$$SOC(t+1) = (1-\theta) \cdot SOC(t) + (1-\chi) \cdot StoreIn(t+1) - \frac{StoreOut(t+1)}{1-\Delta\chi}, \quad \forall t \quad (6)$$

$$SOC(t) \le CAP_{EES}, \quad \forall t \quad (7)$$

$$(1-\theta) \cdot SOC(t) + (1-\chi) \cdot StoreIn(t+1) \le CAP_{EES}, \quad \forall t \quad (8)$$

$$\frac{StoreOut(t+1)}{1-\Delta\chi} \le (1-\theta) \cdot SOC(t), \quad \forall t \quad (9)$$

$$SOC(0) = SOC(8760) \quad (10)$$

To determine the optimal design and operating condition of the renewable energy system, the cost of hydrogen (COH) is defined as an objective function of optimization. As shown in equations (11)-(20), the cost of hydrogen (COH), is estimated considering the total annual cost (TAC) and the annual hydrogen production ($Prod_{H2}$). Capital expenditures (CAPEX) considering maximum capacity for WT, PV systems, and electrical energy storage (EES), as well as operating expenditures (OPEX) for these facilities are included in TAC. Grid electricity import and carbon tax considering $CO_2$ emission factors for each technology are also included in TAC. All the costing parameters for the COH estimation of renewable energy system are shown in **Table 3**. The optimal set of design variables for the renewable energy system is determined by using the MATLAB optimization solver "intlinprog" to minimize COH while considering the set of constraints (Equations (1)-(10)).

**Table 3:** Costing parameters of RES

| Parameters | Unit | Values [15] |
|---|---|---|
| Natural gas price | €$_{2023}$/MWh | 41 [10] |
| Grid power unit price ($GP$) | €$_{2023}$/MWh | 95.18 [11] |
| $CO_2$ emission factor ($EF$) | g$CO_{2e}$/kWh | 13 (WT) [16]<br>43 (PV) [16]<br>744 (Grid) [16] |
| WT capital cost ($CC_{WT}$) | $$_{2023}$/kW | 1010.2 (Advanced)<br>1809.6 (Current) |
| WT O&M cost ($AOC_{WT}$) | $$_{2023}$/kWyr | 16.394 (Advanced)<br>32.252 (Current) |
| PV capital cost ($CC_{PV}$) | $$_{2023}$/kW | 562.6 (Advanced)<br>1610.9 (Current) |
| PV O&M cost ($AOC_{PV}$) | $$_{2023}$/kWyr | 11.381 (Advanced)<br>22.219 (Current) |
| EES capital cost ($CC_{EES}$) | $$_{2023}$/kW | 190.5 (Advanced)<br>520.1 (Current) |
| EES O&M cost ($AOC_{EES}$) | $$_{2023}$/kWyr | 15.879 (Advanced)<br>47.674 (Current) |
| Plant lifetime | yr | 30 [7] |
| Fixed charge rate ($FCR$) | 1/yr | 0.0586 [7] |
| Capacity factor | % | 90 [7] |
| Unit carbon tax ($CTAX_{unit}$) | $$_{2023}$/t$CO_2$ | 0 - 180 |

$$TAC = FCR \cdot (\sum CAPEX) + \sum(OPEX + CTAX) \quad (11)$$

$$CAPEX_{PV} = CC_{PV} \cdot \max_t E_{PV}(t) \quad (12)$$

$$CAPEX_{WT} = CC_{WT} \cdot \max_t E_{WT}(t) \quad (13)$$

$$CAPEX_{EES} = CC_{EES} \cdot CAP_{EES} + SOC(0) \cdot (GP + EF_{Grid} \cdot CTAX_{unit}) \quad (14)$$

$$OPEX_{PV} = AOC_{PV} \cdot \sum_t E_{PV}(t) / 8760 \quad (15)$$

$$OPEX_{WT} = AOC_{WT} \cdot \sum_t E_{WT}(t) / 8760 \quad (16)$$

$$OPEX_{EES} = AOC_{EES} \cdot \sum_t StoreOut(t) / 8760 \quad (17)$$

$$OPEX_{Grid} = EC_{Grid} \cdot \sum_t Grid(t) \quad (18)$$

$$CTAX_{total} = CTAX_{unit} \cdot (\sum_t E_{PV}(t) \cdot EF_{PV} + \sum_t E_{WT}(t) \cdot EF_{WT} + \sum_t Grid(t) \cdot EF_{Grid}) \quad (19)$$

$$COH_{total} = TAC / Prod_{H2} \quad (20)$$

## 5. CASE STUDY RESULTS

In this contribution, a total of eight case studies are conducted by varying the carbon tax (0 - 180 $/tCO$_2$) under two different scenarios: one reflects the comparatively high capital and operating costs corresponding to the current state of renewable energy (WT, PV, and EES) technical maturity, while the other reflects the potential expenses in 2050, when renewables will be expected to be advanced and more economical. For each case study, the mathematical model of the RES determines the optimal solution for combination of WTs, PV system, EES, and grid electricity imports. The optimized annual operating conditions of RES & Grid for each case study are shown in **Figure 2**.

The optimization results for each case study are presented in **Tables 4** and **Table 5**, with a breakdown of the grid's and the renewable energy facility's performance and cost of hydrogen. In the current technology scenario without carbon tax, the most economical option to supply the electrified hydrogen production power demands is to rely mainly on grid electricity while 27% of the total demand is supplied by the renewable energy systems. However, as the carbon tax increases, the renewable energy system introduction is encouraged by increasing tax on indirect $CO_2$ emissions from grid electricity. When the carbon tax is increased to $180/tCO$_2$, the renewable energy ratio increases from 27% to 51%. As technological maturity increases and the unit cost related to renewable energy system decreases, the ratio of renewable energy increases from 27% to 56%, even without the carbon tax. Furthermore, if the carbon tax is increased to $180/tCO$_2$, the renewable energy ratio increases to 72%.

As shown in **Table 5**, the overall cost of hydrogen varies from 1.78-3.27 $/kgH$_2$ depending on the carbon tax when the technical maturity is at its current level. However, the overall cost of hydrogen is expected to vary from 1.38-2.28 $/kgH$_2$, when the technical maturity reaches the advanced level in the future, indicating a cost reduction of 22.5-30.3% can be achieved depending on the carbon tax.

**Table 4:** Optimal Solution for Renewable Energy Supply

| Carbon tax | | 0 | 60 | 120 | 180 |
|---|---|---|---|---|---|
| **Current state** | | | | | |
| Capacity | WT [MW] | 23 | 39 | 47 | 51 |
| | PV [MW] | 37 | 50 | 63 | 71 |
| | EES [MWh] | 5 | 74 | 135 | 178 |
| Annual power gen. [GWh] | WT | 34 | 60 | 71 | 78 |
| | PV | 54 | 73 | 92 | 103 |
| | EES | 0 | 2 | 7 | 12 |
| | Grid | 246 | 203 | 176 | 163 |
| Renewable ratio | | 0.27 | 0.39 | 0.47 | 0.51 |
| **Advanced state** | | | | | |
| Capacity | WT [MW] | 53 | 62 | 69 | 74 |
| | PV [MW] | 85 | 126 | 132 | 137 |
| | EES [MWh] | 246 | 467 | 518 | 572 |
| Annual power gen. [GWh] | WT | 80 | 94 | 106 | 113 |
| | PV | 124 | 184 | 192 | 199 |
| | EES | 20 | 46 | 53 | 58 |
| | Grid | 147 | 108 | 100 | 94 |
| Renewable ratio | | 0.56 | 0.68 | 0.70 | 0.72 |

**Table 5:** Economic Results of Cost of Hydrogen (COH)

| Carbon tax [$/tCO$_2$] | | 0 | 60 | 120 | 180 |
|---|---|---|---|---|---|
| **Current state cost of hydrogen (COH) [$/kgH$_2$]** | | | | | |
| CAPEX | WT | 0.14 | 0.25 | 0.29 | 0.32 |
| | PV | 0.21 | 0.28 | 0.35 | 0.40 |
| | EES | 0.01 | 0.13 | 0.24 | 0.32 |
| OPEX | WT | 0.01 | 0.01 | 0.01 | 0.02 |
| | PV | 0.01 | 0.01 | 0.01 | 0.01 |
| | EES | 0.00 | 0.00 | 0.00 | 0.00 |
| | Grid | 1.41 | 1.16 | 1.01 | 0.93 |
| CTAX | | 0.00 | 0.52 | 0.91 | 1.26 |
| Total COH | | 1.78 | 2.36 | 2..84 | 3.27 |
| **Advanced state cost of hydrogen (COH) [$/kgH$_2$]** | | | | | |
| CAPEX | WT | 0.19 | 0.22 | 0.24 | 0.26 |
| | PV | 0.17 | 0.25 | 0.26 | 0.27 |
| | EES | 0.16 | 0.31 | 0.34 | 0.38 |
| OPEX | WT | 0.01 | 0.01 | 0.01 | 0.01 |
| | PV | 0.01 | 0.01 | 0.01 | 0.01 |
| | EES | 0.00 | 0.00 | 0.01 | 0.01 |
| | Grid | 0.84 | 0.62 | 0.57 | 0.54 |
| CTAX | | 0.00 | 0.30 | 0.56 | 0.80 |
| Total COH | | 1.38 | 1.72 | 2.01 | 2.28 |

These case studies suggest that either an aggressive carbon tax to reduce grid-based electricity use or a significant reduction in capital costs accompanied by the technological innovation of RES is required to increase the use of renewable energy for the commercial-scale, low-carbon hydrogen production process.

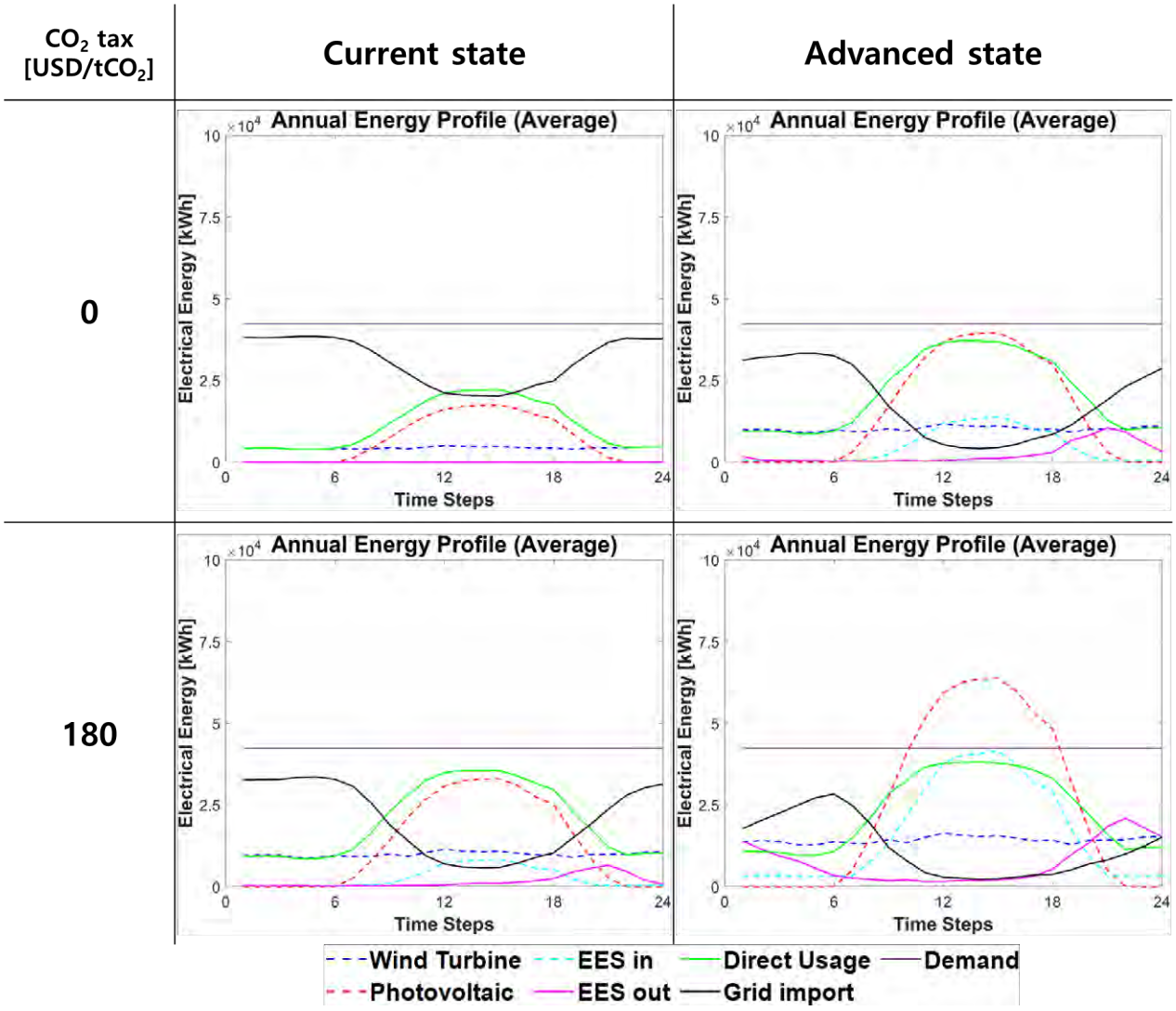



**Figure 2:** Annual Everage Electricity Supply Profiles of Renewable Energy System & Grid

## 6. CONCLUSION

This study proposes a comprehensive framework to determine the optimal design and operation of a combined renewable energy system & grid electricity supply for the electrified hydrogen production process. The MILP model is designed to optimize the operating conditions of the electricity supply system and to minimize the total cost including capital and operating costs of the renewable energy system, grid electricity costs, and carbon tax. The case studies investigated show that the optimized combination of the electricity mix is significantly influenced by the carbon tax levels and that the reducing capital costs with advanced technological maturity is crucial for the economic feasibility of the renewable energy system integration.

Future work will extend this framework to scenarios where the electrified hydrogen production process requires additional thermal energy, thereby exploring integrated renewable heat and power supply systems. Time-varying operational strategies that optimize both electricity and heat requirements under different policy conditions would further enhance understanding of the potential pathways toward large-scale, low-carbon hydrogen production.

## ACKNOWLEDGEMENTS

This work was supported by the National Research Foundation of Korea (NRF) grant funded by the Korean government (MSIT) (RS-2025-00515836) and under the framework of international cooperation program managed by the NRF (No. 1711200829, FY2023) and the German Research Foundation (DFG) under the OPTIMGRID project (AE707 5-1).

## NOMENCLATURE

| Abbreviation | Description |
|---|---|
| $AOC$ | Unit annual operating cost |
| $CAPEX$ | Capital expenditure |
| $CC$ | Unit capital cost |
| $COH$ | Cost of hydrogen |
| $CTAX$ | Carbon tax |
| $EES$ | Electrical energy storage |
| $EF$ | Emission factor |
| $FCR$ | Fixed charge ratio |
| $GP$ | Grid power unit price |
| $MILP$ | Mixed-Integer linear programming |
| $OPEX$ | Operating expenditure |
| $PV$ | Photovoltaic |
| $RES$ | Renewable energy system |
| $WT$ | Wind turbine |

| $\boldsymbol{Variable}$ | Description | Unit |
|---|---|---|
| $Independent$ | | |
| $A_{PV}$ | Area of solar PV panels | $m^2$ |
| $CAP_{EES}$ | Capacity of electrical energy storage | kWh |
| $E_{DU}$ | Direct usage of renewable electricity | kWh |
| $Grid$ | Grid import | kWh |
| $N_{WT}$ | Number of wind turbine | - |
| $SOC$ | State of charge | kWh |
| $StoreIn$ | Electricity from renewables to EES | kWh |
| $StoreOut$ | Electricity discharged from the EES | kWh |
| $Dependent$ | | |
| $E_{PV}$ | Total PV power generation | kWh |
| $E_{Ren}$ | Renewable power generation | kWh |
| $E_{WT}$ | Total WT power generation | kWh |

## REFERENCES


1. Sebastian Thor Wismann et al. Electrified methane reforming: A compact approach to greener industrial hydrogen production. *Science* 364:756-759 (2019) DOI:10.1126/science.aaw8775
2. Huchao Song et al. Energy, environment, and economic analyses on a novel hydrogen production method by electrified steam methane reforming with renewable energy accomodation. *Energy Convers. Manag.* 258:115513 (2022) https://doi.org/10.1016/j.enconman.2022.115513
3. Thai Ngan Do et al. Carbon-neutral hydrogen production from natural gas via electrified steam reforming: Techno-economic-environmental perspective. *Energy Convers. Manag.* 279:116758 (2023) https://doi.org/10.1016/j.enconman.2023.116758
4. Diego Maporti et al. Towards sustainable hydrogen production: Integrating electrified and convective steam reformer with carbon capture and storage. *Chem. Eng. J.* 499:156357 (2024) https://doi.org/10.1016/j.applthermaleng.2024.125274
5. Joohwa Lee et al. Process design and integration for the electrification of a SMR-based hydrogen plant with absorption-based $CO_2$ capture. *Appl. Therm. Eng.* 262:125274 (2025) https://doi.org/10.1016/j.applthermaleng.2024.125274
6. Andrea Nava et al. Carbon-negative "emerald hydrogen" from electrified steam methane reforming of biogas: System integration and optimization. *Int. J. Hydrogen Energy* 88:1237-1255 (2024) https://doi.org/10.1016/j.ijhydene.2024.09.171
7. Eric Lewis et al. Comparison of commercial, state-of-the-art, fossil-based hydrogen production technologies. DOE/NETL-2022/3241 (2022)
8. IRENA. Renewable power generation costs in 2022. International Renewable Energy Agency. Abu Dhabi (2023)
9. Open-Meteo. https://open-meteo.com/en/docs/historical-forecast-api
10. Bundesnetzagentur. https://www.bundesnetzagentur.de/SharedDocs/Pressemitteilungen/EN/2024/20240104_Gasversorgung2023.html#:~:text=The%20average%20day%2Dahead%20price,%2Drueckblick2023%20(in%20German).
11. Bundesnetzagentur. https://www.bundesnetzagentur.de/SharedDocs/Pressemitteilungen/EN/2024/20240103_SMARD.html
12. SAM Photovoltaic Model Technical Reference Update. NETL/TP-6A20-67399 (2018)
13. Tim Sidnell et al. Optimal design and operation of distributed energy resources systems for residential neighbourhoods. *Smart Energy* 4:100049 (2021)
14. Power Performance Test Report for the U.S. Department of Energy 1.5-Megawatt Wind Turbine. NREL/TP-5000-63684 (2015)
15. NREL. https://atb.nrel.gov/electricity/2024/technologies
16. NREL. Life Cycle Greenhouse Gas Emissions from Electricity Generation: Update. NREL/FS-6A50-80580 (2021)



© 2025 by the authors. Licensed to PSEcommunity.org and PSE Press. This is an open access article under the creative commons CC-BY-SA licensing terms. Credit must be given to creator and adaptations must be shared under the same terms. See https://creativecommons.org/licenses/by-sa/4.0/




Systems & Control Transactions

**Research Article - Peer Reviewed Conference Proceeding**
ESCAPE 35 - European Symposium on Computer Aided Process Engineering
Ghent, Belgium. 6-9 July 2025
Jan F.M. Van Impe, Grégoire Léonard, Satyajeet S. Bhonsale,
Monika E. Polańska, Filip Logist (Eds.)

PSE PRESS

# Assessing the Synergies of Thermochemical Energy Storage with Concentrated Solar Power and Carbon Capture

**Nitin Dhanenjey R[a] and Ishan Bajaj[a]***

[a] Indian Institute of Technology Kanpur, Department of Chemical Engineering, Kanpur, Uttar Pradesh, India
* Corresponding Author: ibajaj@iitk.ac.in

## ABSTRACT

As greenhouse gas emissions continue to increase worldwide, the growing energy demand must be met using low-carbon technologies. Renewable energy and carbon capture and storage are the two important technologies that can mitigate $CO_2$ emissions. The two technologies have been primarily developed independently. However, their hybridization can offer complementary benefits and lower the costs of greenhouse gas abatement. Accordingly, in this article, we develop a novel carbon-neutral process that combines concentrated solar power (CSP) and fuel-based combustor with redox-based thermochemical energy storage (TCES) materials. The TCES materials are used for energy storage and as a source of oxygen ($O_2$) for combusting fuel. We optimize the process' economic performance considering variability in solar irradiance by developing a two-stage stochastic programming model. We illustrate that compared to the CSP-TCES process employing the $Mn_2O_3/Mn_3O_4$ TCES system, the proposed hybrid process has a 25% lower levelized cost of electricity (LCOE) for an 80% capacity factor. We also compare the economic performance of our process with another hybrid configuration containing CSP-TCES, boiler for fuel combustion, and air separation unit (ASU) to produce $O_2$, which is then used to combust fuel. We conclude that the LCOE of the proposed process is 11.5% lower than the LCOE of the process with an ASU.

**Keywords**: Concentrated solar power, energy storage, stochastic programming, carbon capture and storage, hybrid energy systems

## 1. INTRODUCTION

As the energy demand continues to increase, there is an urgent need to develop technologies to reduce $CO_2$ emissions. Two classes of technology that can mitigate $CO_2$ emissions are carbon capture and storage (CCS) and renewable energy generation from sources such as solar and wind. While CCS aims to prevent $CO_2$ from being released into the atmosphere, renewable energy generation technologies avoid $CO_2$ emissions. While using a combination of photovoltaic (PV) or wind power with battery can provide reliable electricity, another promising strategy to deliver cost-effective, reliable, and dispatchable renewable power is integrating concentrated solar power (CSP) with thermal energy storage (TES). Among various TES technologies, thermochemical energy storage (TCES) is reported to be especially appealing for the next generation CSP plants because of their high energy density and ability to deliver heat at a high temperature (> 1000 °C). A recent material screening study concluded that due to the low energy density of TCES materials, even the most economically favorable reaction system leads to more than 50% higher levelized cost of electricity (LCOE) than the monthly average electricity retail price [1]. This is mainly due to a lower energy density of the TCES materials. Thus, hybridizing CSP with energy-dense fossil fuel power plants equipped with carbon capture can reduce the cost of producing clean power.

Attempts have been made to integrate solar thermal energy into post-combustion $CO_2$ capture (PCC). Parvareh et al. [2] showed that by utilizing solar thermal energy to support the thermal demand of the stripper, the energy penalty can be reduced, and more power can be produced. Qadir et al. highlighted the potential of

dynamic, flexible operation to reduce $CO_2$ capture costs [3]. Hong and Jin used solar thermal energy as a heat source to drive the endothermic reaction of a metal oxide with $CH_4$ [4] and reported that solar energy can be converted to chemical energy at a low temperature and released at a higher temperature. Jafarian et al. [5] proposed the use of metal oxide for thermal energy storage and reported a lower fuel consumption and reduced $CO_2$ emissions by 50% compared to natural gas combined cycle with carbon capture.

Kumar and Tiwari summarized the potential of solar thermal energy in coal-fired power plants retrofitted with a PCC system. Specifically, they discussed various PCC and solar thermal integration techniques, economic and environmental impacts, benefits and challenges [6]. Dalvi et al. indicated that solar thermal systems can be easily integrated into Rankine-cycle power plants. They further showed that solar heat can offset up to 50% of fossil fuel consumption and this strategy is more economical than installing CCS for mitigating an equivalent amount of GHG emissions [7]. Most previous studies focussed on the feasibility aspect of hybridizing renewable energy and carbon capture, often ignoring the optimization of both the design and operational decisions.

While there is consensus on the economic and environmental benefits of integrating solar thermal heat and carbon capture technologies, no previous work has sought to employ TCES materials for energy storage and as a source of oxygen for fuel combustion. Accordingly, in this article, we develop a novel carbon-neutral process referred to as CSP-TCES-OFC. The process combines CSP and fuels-based combustor to generate power and redox-based TCES materials for energy storage and a source of oxygen, which is used to combust fuel, like an oxy-fuel combustion (OFC) process. The process has three advantages. First, the power cycle can be operated at a higher temperature during the night compared to a standalone CSP-TCES process, wherein the reversible reaction temperature limits the temperature of the power cycle. This would lead to higher overall efficiency of the CSP-TCES-OFC process compared to CSP-TCES. Second, oxygen separation occurs using thermal energy, a low-grade energy source compared to electricity, the primary energy source for an air separation unit used in a traditional OFC process. Third, the process enables energy storage and carbon capture simultaneously. We develop a stochastic programming-based optimization model that considers variability in solar irradiance to minimize the levelized cost of electricity (LCOE). We also compare the economic performance of our processes with other processes and show that our process results in a lower LCOE.

## 2. SYSTEM DESCRIPTION

Figure 1(A) shows the schematic of the CSP-TCES-OFC process. The system operates as follows. During the day, the collector focuses sunlight onto a receiver, where photons are absorbed, and the heat transfer fluid (HTF) is heated. The flow of HTF is split such that a part of it flows through the reactor (R1) to provide heat to the forward endothermic decomposition reaction ($M_xO_z \leftrightarrow M_xO_y + \frac{z-y}{2}O_2$), and the remaining flows through the power block to provide heat to the working fluid (WF). The oxygen ($O_2$) released due to the forward endothermic reaction is compressed and stored. It is then used for fuel combustion when solar energy is unavailable. Since $O_2$ from R1 is at a high temperature and compressing a gas at a lower temperature results in a lower power consumption, its sensible heat is extracted using a sensible heat storage unit. A multistage compressor is employed to compress $O_2$. An intercooler is used after each compressor so that the temperature of $O_2$ after each stage is 35 °C. The compressed $O_2$ is stored underground or in a pressure vessel.

During the night, the reverse exothermic reaction occurs in the presence of air to regenerate the metal oxide in a higher oxidation state. The heat stored in the sensible heat storage unit is used to increase the temperature of air entering R2. The energy from the high-pressure $O_2$ is recovered using a pressure recovery turbine (PRT) such that the pressure of $O_2$ entering the combustor is 1 atm. In the combustor, $O_2$ is combusted with fuel to produce heat. In this article, we consider natural gas as the fuel. Thus, energy is obtained during the night operation by reversible exothermic reaction, combusting fuel, and recovery energy from compressed $O_2$ using PRT. After exchanging heat with the combustor and R2, WF is sent to a power cycle to generate electricity. Since natural gas is combusted in the presence of $O_2$, the exhaust from the combustor mainly contains $CO_2$ and $H_2O$. The $CO_2/H_2O$ stream is at a high temperature, and the stored $O_2$ is at a lower temperature. We employ a heat exchanger to increase the $O_2$ stream temperature and decrease the $CO_2/H_2O$ stream temperature because increasing the $O_2$ temperature will result in a higher PRT efficiency, and decreasing the $CO_2/H_2O$ stream temperature will aid in separating $CO_2$ and $H_2O$. The $CO_2/H_2O$ stream temperature is further decreased to room temperature and separated using a flash column. The $CO_2$ stream is then compressed to 150 bar by four multistage compressors with intercoolers. The compressed $CO_2$ is then transported and stored underground.

## 3. ALTERNATIVE PROCESSES

We compare the economic performance of CSP-TCES-OFC with two alternative processes. The first process is the CSP-TCES with redox-based TCES material, illustrated in Figure 1(B). There are two key differences

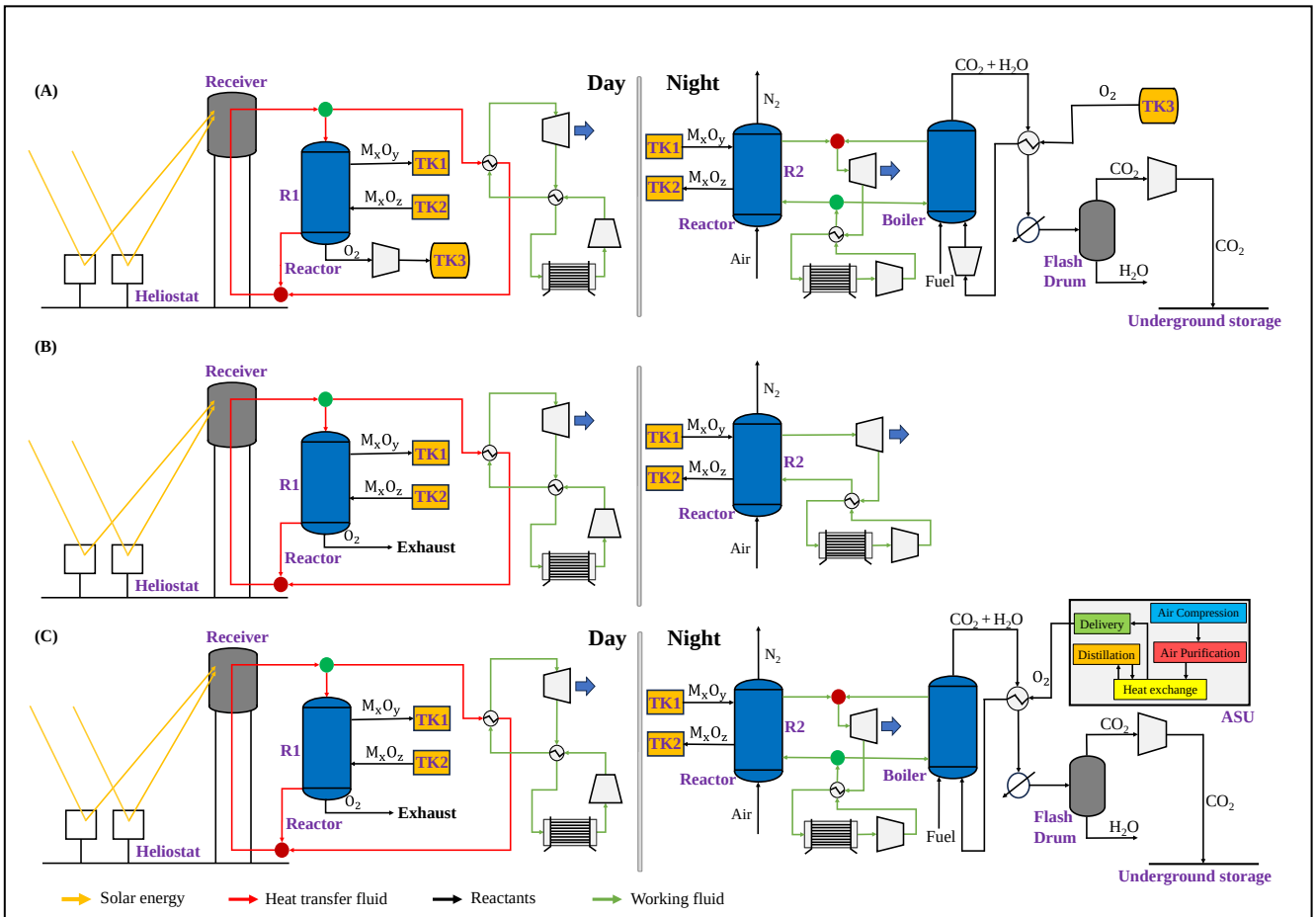



**Figure 1.** Schematic of (A) CSP-TCES-OFC, (B) CSP-TCES, (C) CSP-TCES-ASU processes.

between the CSP-TCES and CSP-TCES-OFC processes. First, oxygen is not stored, and second, no fuel is combusted. The proposed process has several advantages over the CSP-TCES process. First, the power cycle can be operated at a higher temperature at night than a standalone CSP-TCES process. Second, oxygen separation occurs using thermal energy, a low-grade energy source compared to electricity, which is the primary energy source for an air separation unit used in a traditional OFC process. Third, the process enables energy storage and carbon capture simultaneously. Fourth, there is no direct contact between metal oxide and $CO_2$, thus avoiding the carbonation of the metal oxide and improving reversibility.

The schematic of the second process, referred to as CSP-TCES-ASU, is shown in Figure 1(C). Instead of storing oxygen formed during the forward endothermic reaction, an ASU produces oxygen needed to combust fuel during the night. We assume that 250 kWh of electricity is needed to produce 1 tonne of $O_2$.

## 4. METHODOLOGY

We evaluate the techno-economic performance of the CSP-TCES-OFC process via optimization of the energy system design, considering variability in solar irradiance. We develop a stochastic programming (SP) model to account for variability in solar irradiance. Based on the previous works [1,8], we extend the SP model developed for CSP-TCES to CSP-TCES-OFC. The inputs required by the model are (1) solar irradiance data, (2) plant capacity, (3) TCES and combustion reactions and properties (reaction enthalpy, equilibrium temperature), and (4) cost parameters.

We selected the plant location as Daggett, California. We used its solar irradiance data from the National Solar Irradiance Database and use k-means clustering to obtain six representative scenarios. We assume that the plant operates in day and night modes. The plant capacity is chosen to be 100 MW. The TCES system is $Mn_2O_3/Mn_3O_4$ because it is one of the most well-studied systems, and we assume that natural gas is combusted using $O_2$. The objective of the model is to minimize the LCOE subject to the constraints that include the physical model of the plant components (i.e., collector, receiver, TCES reactors, storage tanks, compressors, combustor, power cycle), unit mass and energy balances, equipment sizing, and cost correlations. The model solution results

in optimal design and scenario-dependent operating variables. The overall framework is given in Figure 2. The resulting model is a mixed integer nonlinear programming model formulated and solved using Gurobi's Python API. The cost parameters and complete model equations for CSP-TCES-OFC and CSP-TCES-ASU can be found in the

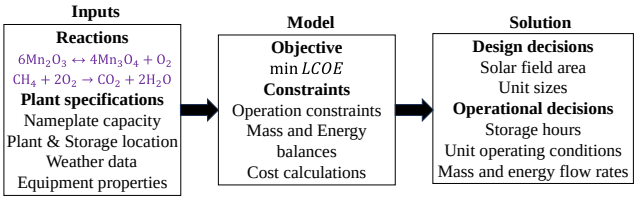



**Figure 2.** Overwiew of the optimization model for CSP-TCES-OFC process.

supplementary material, and the model for CSP-TCES can be found in the ESI of Bajaj et al. [1].

## 5. RESULTS

We consider two sets of cost parameters for transporting and storing $CO_2$ and $O_2$, which are given in Table 1. The two cases for $CO_2$ storage and transportation costs are the typical values given in the literature. The case 1 for storing $O_2$ corresponds to pressure vessel and case 2 corresponds to underground storage. Figure 3 shows the LCOE distribution for the three processes, and Table 2 lists the important decision variables. The subscript 'h' and 'l' denote the higher and lower cost parameters (case 1 and case 2), respectively. The LCOE of the CSP-TCES-OFC process ranges between 8.66 – 9.67 ¢/kWh, and lowest among the three processes, suggesting that the proposed integrated process synergistically combines energy storage and carbon capture. The capital investment required for CSP-TCES-OFC, CSP-TCES, and CSP-TCES-ASU are $ 605.18 million, $ 658.8 million, and $ 711.9 million, respectively. The total electricity produced is 870 GWh, 649 GWh, and 897 GWh, respectively.

**Table 1**: Cost of storage and transportation of gases for CSP-TCES-OFC model considered for different cases.

| Case | $CO_2$ storage price ($/ton) | $CO_2$ transportation price ($/km ton) | $O_2$ storage price ($/m$^3$) |
|---|---|---|---|
| 1 | 15 | 2 | 5700 |
| 2 | 5 | 1 | 50 |

For all the processes, the solar field/collector and receiver are the main contributing factors to LCOE, followed by the power block. Compared to the CSP-TCES process, the LCOE contribution of solar field and receiver is lower for the CSP-TCES-OFC process because of their lower sizes (Table 2). This is primarily due to (1) the higher efficiency of the power cycle during the night due to a higher working fluid temperature (Table 2) and (2) energy production from low-cost and energy-dense natural gas and compressed $O_2$. The power cycle operates at a lower temperature in the CSP-TCES process because the thermal energy is provided by the reversible exothermic reaction, which due to thermodynamic limitations, can only occur at a temperature lower than the equilibrium temperature. Although the cost of the power block is the same for all the processes, its contribution to CSP-TCES-OFC is lower because of higher electricity production.

The TCES material requirement is the lowest for the CSP-TCES-OFC process due to additional lower-cost energy production sources (methane and compressed $O_2$) at night. This also results in lower reactor and solid storage tank costs. The operating cost is higher for the CSP-TCES-OFC process due to natural gas and cooling requirements. Additionally, the CSP-TCES-OFC requires compressors and gas storage infrastructure to store $O_2$ and $CO_2$. The LCOE contributions for both CSP-TCES-OFC and CSP-TCES-ASU processes differ mainly by the capital expenses needed for the air separation unit in the latter and the $O_2$ compressor and storage in the former. However, the cost associated with compressing and storing $O_2$ is much lower than that of an ASU. The analysis illustrates that it is more economical to use redox-based TCES materials for both energy storage and a source of $O_2$ for fuel combustion.

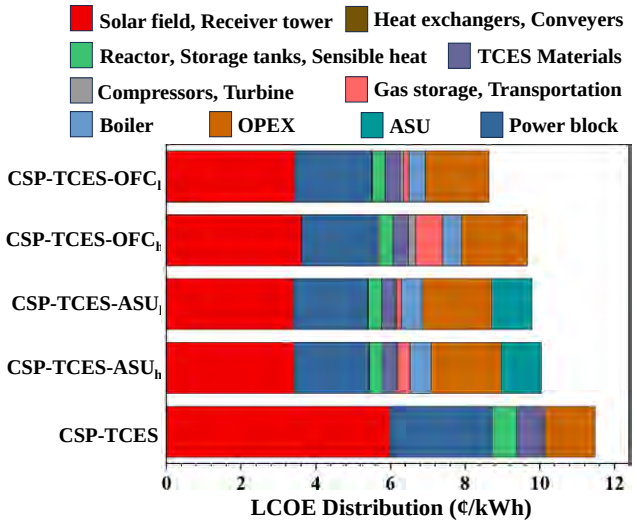



**Figure 3**. LCOE distribution for various processes.

A key decision variable is the storage pressure of $O_2$. While high storage pressure results in a lower tank cost and more power production by PRT, it also produces higher power consumption during the day and a higher compressor cost. We can observe from Table 2 that $O_2$ storage pressure is higher when $O_2$ is stored in a pressure

**Table 2:** Comparison of key decision variables of the three processes.

| Decision variables | CSP-TCES-OFC$_l$ | CSP-TCES-OFC$_h$ | CSP-TCES | CSP-TCES-ASU$_l$ | CSP-TCES-ASU$_h$ |
|---|---|---|---|---|---|
| Power cycle temperature during day (TIT) (K) | 1377.1 | 1382.5 | 1415.3 | 1385.2 | 1394.4 |
| Power cycle temperature during night (TIT) (K) | 1048.1 | 1048.3 | 967.3 | 1017.5 | 1007.8 |
| Receiver temperature (K) | 1273.3 | 1276.7 | 1314.3 | 1280.9 | 1284.1 |
| Collector area ($m^2$) | 913.1 | 955.4 | 1182.3 | 927.2 | 929.2 |
| Receiver size ($MWh_t$) | 493.7 | 514.9 | 635.5 | 497.9 | 500.3 |
| CF (%) | 79.8 | 78.9 | 74.1 | 81.1 | 80.8 |
| Oxygen storage pressure (bar) | 5.3 | 39.3 | - | - | - |
| Yearly $CH_4$ consumption ($10^3$ tonnes) | 25.9 | 27.6 | - | 33.4 | 33.6 |
| Yearly $O_2$ consumption ($10^3$ tonnes) | 103.6 | 110.5 | - | 133.6 | 134.1 |
| Power generated at night (MW) | 42.3 – Combustion<br>59.3 – Reactor<br>1.9 - PRT | 44.1 – Combustion<br>62.7 – Reactor<br>3.6 - PRT | 100.0 – Reactor | 54.7 – Combustion<br>56.7 - Reactor | 54.2 – Combustion<br>62.2 - Reactor |
| Power consumed at night (MW) | 1.7 - Compressor | 1.8 - Compressor | - | 2.1 – Compressor<br>8.0 - ASU | 2.2 – Compressor<br>8.1 - ASU |

vessel (case 1), resulting in the production of a higher amount of power.

Capacity factor (CF) is the ratio of the actual amount of energy produced by the plant to the amount of energy that could have been produced by that plant when operated at its full power rating during the same period. Mathematically, CF is defined as follows:

$$CF = \frac{\sum_{t\in T} \pi_t \left(DT_t^c + NT_t^d\right)}{\sum_{t\in T} 24 \times \pi_t}$$

where $\pi_t$ is the probability of occurrence of scenario $t$, $DT_t^c$ is the charging time, and $NT_t^d$ is the discharging time.

Figure 4 shows the variation of LCOE with CF. The LCOE of the CSP-TCES-OFC process is the lowest among the three processes for CF varying between 60 – 85%. The difference in LCOE between the CSP-TCES and CSP-TCES-OFC processes becomes larger as CF increases to more than 80%. The cost of the CSP-TCES process increases more with CF because as CF increases, power needs to be produced during low DNI scenarios, which requires a larger collector and receiver. Furthermore, increasing CF requires more energy storage to provide power during nighttime, resulting in more TCES material requirements, larger reactors, and storage tanks. The optimal CF for CSP-TCES, CSP-TCES-ASU, and CSP-TCES-OFC processes are given in Table 2. The corresponding charging and discharging times for the three processes are shown in Figure 5.

We observe that the charging time for the CSP-TCES process in all the scenarios is the highest, whereas the discharging time is the lowest. This occurs because of the lower energy density of TCES materials. However, the amount of material stored is still insufficient to provide power for longer discharging times. The presence of an additional source of energy (natural gas combustion) in CSP-TCES-OFC and CSP-TCES-ASU results in longer discharging times, resulting in a higher overall CF for the two processes.

## 6. CONCLUSIONS

We proposed a hybrid process that combines concentrated solar thermal and fossil-fuel-based power production with redox-based TCES materials for energy storage and carbon capture. We develop a stochastic programming-based optimization model that considers the variability in solar irradiance to evaluate the economics of the process. We compare the economic performance of our process with CSP-TCES and show that the optimal LCOE of our process is 15.9% – 24.6% lower. This illustrates that the redox-based TCES materials enable synergistic energy storage and carbon capture, reducing overall electricity production costs at higher capacity factors. Our analysis provides critical insights into the benefits of redox-based TCES materials, and we hope more experimental studies will follow to elucidate the $O_2$ formation and energy storage capabilities of TCES materials.

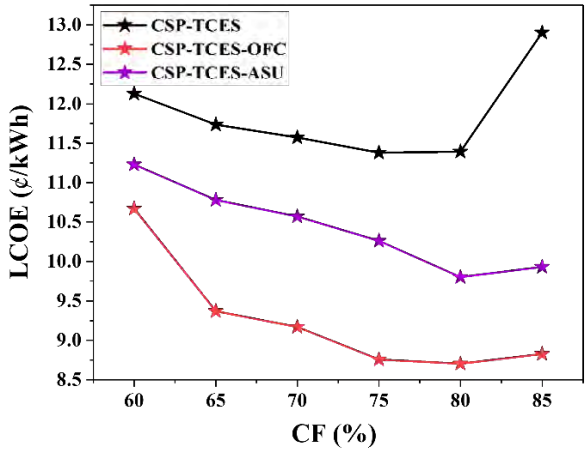



**Figure 4.** LCOE variation for different CF for the three processes.

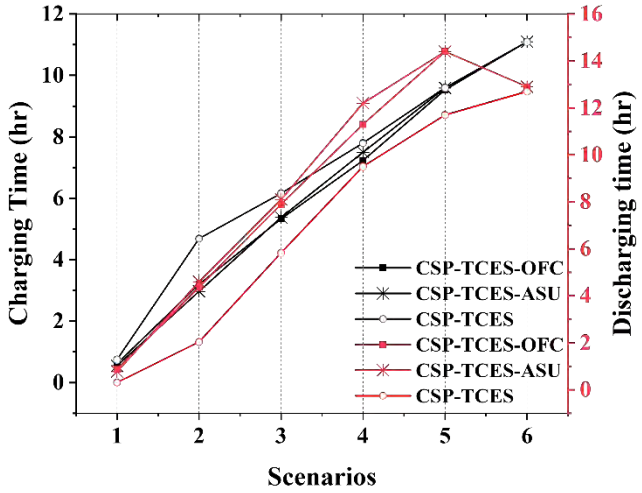



**Figure 5.** Charging and discharging times during various scenarios for the three processes.

## DIGITAL SUPPLEMENTARY MATERIAL

The complete SP model for the CSP-TCES-OFC and CSP-TCES-ASU processes and CSP-TCES-ASU can be found in the Living Archive for Process Systems Engineering using the ID LAPSE:2025.0025v2

## REFERENCES


1. I. Bajaj, X. Peng, C.T. Maravelias, Screening and property targeting of thermochemical energy storage materials in concentrated solar power using thermodynamics-based insights and mathematical optimization, RSC Sustainability 2 (2024) 943–960. https://doi.org/10.1039/d3su00244f.
2. F. Parvareh, M. Sharma, A. Qadir, D. Milani, R. Khalilpour, M. Chiesa, A. Abbas, Integration of solar energy in coal-fired power plants retrofitted with carbon capture: A review, Renewable and Sustainable Energy Reviews 38 (2014) 1029–1044. https://doi.org/10.1016/j.rser.2014.07.032.
3. A. Qadir, M. Sharma, F. Parvareh, R. Khalilpour, A. Abbas, Flexible dynamic operation of solar-integrated power plant with solvent based post-combustion carbon capture (PCC) process, Energy Convers Manag 97 (2015) 7–19. https://doi.org/10.1016/j.enconman.2015.02.074.
4. H. Hong, J. Hongguang, A Novel Solar Thermal Cycle with Chemical Looping Combustion, Int J Green Energy 2 (2005) 397–407.
5. M. Jafarian, M. Arjomandi, G.J. Nathan, A hybrid solar chemical looping combustion system with a high solar share, Appl Energy 126 (2014) 69–77. https://doi.org/10.1016/j.apenergy.2014.03.071.
6. A. Kumar, A.K. Tiwari, Solar-assisted post-combustion carbon-capturing system retrofitted with coal-fired power plant towards net-zero future: A review, Journal of CO2 Utilization 65 (2022). https://doi.org/10.1016/j.jcou.2022.102241.
7. V. Dalvi, S. Panse, J. Joshi, Solar thermal technologies as a bridge from fossil fuels to renewables, Nat Clim Chang 5 (2015) 1007–1013.
8. X. Peng, I. Bajaj, M. Yao, C.T. Maravelias, Solid-gas thermochemical energy storage strategies for concentrating solar power: Optimization and system analysis, Energy Convers Manag 245 (2021) 114636. https://doi.org/10.1016/j.enconman.2021.114636.



© 2025 by the authors. Licensed to PSEcommunity.org and PSE Press. This is an open access article under the creative commons CC-BY-SA licensing terms. Credit must be given to creator and adaptations must be shared under the same terms. See https://creativecommons.org/licenses/by-sa/4.0/

Systems & Control Transactions

**Research Article - Peer Reviewed Conference Proceeding**
ESCAPE 35 - European Symposium on Computer Aided Process Engineering
Ghent, Belgium. 6-9 July 2025
Jan F.M. Van Impe, Grégoire Léonard, Satyajeet S. Bhonsale,
Monika E. Polańska, Filip Logist (Eds.)

PSE PRESS

# Modelling of Wood Biomass Gasification for Process Optimization

**Yu Hui Kok, Yasuki Kansha***

The University of Tokyo, Organization for Programs on Environmental Sciences, Graduate School of Arts and Sciences, 3-8-1 Komaba, Meguro-ku, Tokyo 153-8902, Japan
* Corresponding Author: kansha@global.c.u-tokyo.ac.jp

## ABSTRACT

Biomass gasification is a promising technology for sustainable energy production. To date, extensive research has been conducted on biomass gasification, particularly focusing on the reaction models of the process. However, existing models are too complex to apply to the control system or to optimize the process operating conditions effectively, limiting their practical use for industrial applications. To address this, a simple reaction model for biomass gasification was developed and validated. A steady state simulation of the biomass gasification process is conducted to analyze gasifier behavior and provide insights into reaction dynamic. The findings in this study align well with existing literature, confirming the reliability of the approach. This simulation serves as a foundation for further study in process control and optimization. Future work will include experimental validation to enhance model accuracy and applicability.

**Keywords**: Biomass, Modelling and Simulations, Gasification

## INTRODUCTION

The urgency to tackle environmental challenges such as climate change, pollution, and resource depletion has become increasingly evident. As a result of the consequences of unsustainable practices, technology offering innovative solutions to mitigate environmental degradation and foster long-term resilience has garnered significant public attention.

Biomass gasification appears to be such a technological innovation, offering a sustainable alternative to traditional energy generation methods. It is one of the most effective technologies which has great potential for biomass energy recovery. Biomass gasification converts biomass into syngas ($CH_4$, CO, $H_2$ and $CO_2$) which can be further converted into electricity and biofuel [1], [2]. This technology aligns with the global shift toward sustainable development by promoting waste utilization and reducing carbon footprint.

There is a wide variety of biomass feedstock, including agriculture, forestry residue and municipal waste. Among all these biomass, woody biomass has shown great potential as a good-quality feedstock due to its high energy content and relatively high fixed carbon content [3]. Japan's forest covers about 25 million hectares, which accounts for two-thirds of the country's land. Approximately 40% of the forest planted, predominantly with Japanese cedar (Cryptomeria japonica), is valued for its adaptability and growth, but its pollen causes allergies affecting 40% of the population. Thus, Japan government implement measures in 2024 to reduce pollen dispersal by promoting sustainable wood utilization [4].

With the growing interest in biomass gasification, numerous studies have been conducted to study this multifaceted and complicated process focusing on areas such as modelling, optimization, process analysis and gasifier design [5]. Mathematical models can be an effective tool to evaluate the plant's performance, optimize its operation and improve its efficiency [6]. These reaction models enable more computationally efficient predictions of the yield and composition of various gas and tar species, making it feasible to simulate complex reactor configurations without compromising accuracy. Most of the simulation studies focus on thermodynamic equilibrium modelling. Many researchers have found a high degree of similarity between modelling and theoretical predictions based on equilibrium modelling [7]–[9].

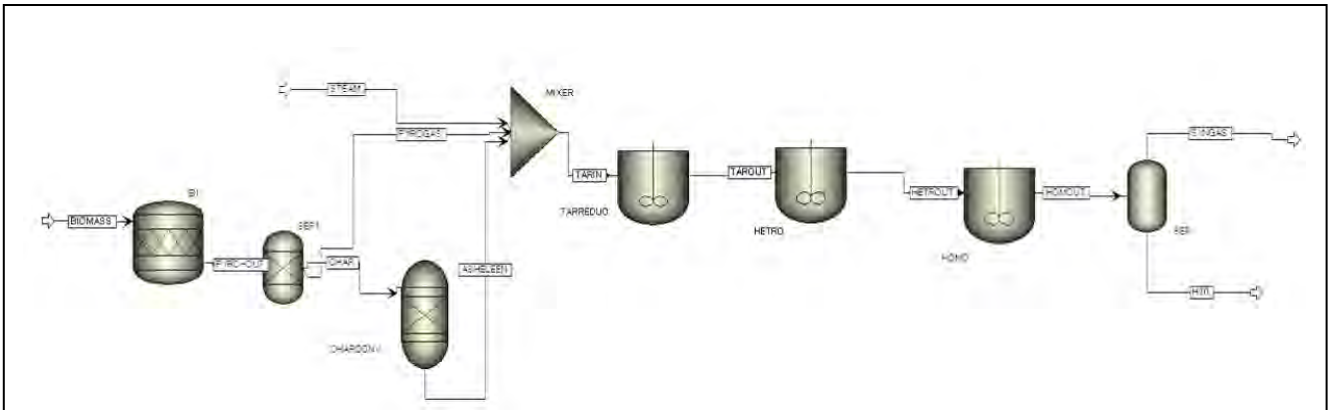



**Figure 1:** Flow chart of biomass gasification simulation using Aspen Plus

However, for dynamic simulations and control applications, a model which able to capture the time-dependent behaviour of the process is necessary. This model needs to employ reaction kinetic to capture the time-dependent evolution of the process.

Several authors discuss the kinetic model of steam gasification on wood biomass especially on pyrolysis [10] - [14]. However, the existing models are too complex and not suitable to apply to the control system or to optimize the process operating conditions effectively, limiting their practical use for industrial applications.

To overcome this limitation, the present paper aims to bridge this gap by creating a kinetic model to investigate wood biomass gasification.

## MATERIALS AND METHOD

### Biomass samples

Japanese waste wood was chosen as a feedstock for this biomass gasification simulation. The proximate and ultimate value of the biomass used in this research is presented in Table 1.

**Table 1**: Proximate and ultimate analysis of feedstock

| **Proximate analysis wt.%** | **Japanese Waste Wood [10]** |
|---|---|
| Moisture Content (as determined basis) | 21.8 ± 7.5 |
| Volatile Material (dry basis) | 84 ± 4.1 |
| Fixed Carbon (dry basis) | 51.4 ± 2 |
| **Ultimate analysis, wt.% (dry ash free basis)** | |
| C | 51.4 ± 0.2 |
| H | 6.2 ± 0.3 |
| N | 0.3 ± 0.3 |
| O | 42.2 ± 2.1 |
| **HHV, MJ/kg** | 21.1 ± 0.9 |

### Process Assumption

There are a few assumptions considered in this process modelling:

- Temperature and pressure drop in processes are neglected.
- Ash is inert and does not participate in the reaction.

### Modelling and Simulation Software

The biomass gasification discussed in this paper is based on uncoupling the downdraft biomass gasifier into different parts based on the main reactions, biomass pyrolysis and reduction. These parts are linked with different types of reactors in Aspen Plus version 14.

The Peng-Robinson-Boston-Mathias (PB-RM) property method is used in this simulation. This method is recommended for hydrocarbon processing applications such as gas processing in all temperatures and pressures [16]. Biomass, Char and Ash were defined as non-conventional components in this process. The enthalpy and density models used for the non-conventional components were DCOALIGT and HCOALGEN. The stream classes defined as MIXCINC.

### Aspen Plus Model Description

The wood biomass gasification flowsheet has been developed as shown in Figure 1 while the unit operation blocks used in the flowsheet are summarized and presented in Table 2.

The feed stream “Biomass” was dry basis biomass, specified as a non-conventional stream with the proximate and ultimate analysis value as shown in Table 1. The mass flow rate was set as 50kg/hr. The biomass was directly fed to pyrolysis reactor “B1” as the temperature of the feed stream was higher than the wood drying temperature [17]. Pyrolysis is a complicated thermochemical process. It can be modelled by a stoichiometric reactor to simulate the reaction based on the following empirical equations in Table 3 where $Y_i = aT^2 + bT + c$, [kg h$^{-1}$] is a

**Table 2:** Reactor block description used in the simulation

| Default ID | Assigned ID | Operating Condition | Description |
|---|---|---|---|
| RStoic | B1 | 1 atm<br>850 °C | Stoichiometric reactor - model the reactor with specified reaction extends or conversion |
| SEP2 | SEP1 | 1 atm<br>850 °C | Separator – separate char from pyrolysis gases |
| | SEP | 1 atm<br>850 °C | Separator – separate water from syngas |
| RYield | CHAR-CONV | 1 atm<br>850 °C | Yield reactor – convert char into its conventional element according to yield distribution data |
| Mixer | MIXER | 1 atm<br>850 °C | Mixer - Mixing steam and gases |
| RCSTR | TARREDUC | 1 atm<br>850 °C | Continuous stirred tank reactor – tar reduction take place |
| | HETRO | 1 atm<br>850 °C | Continuous stirred tank reactor – heterogenous gasification take place |
| | HOMO | 1 atm<br>850 °C | Continuous stirred tank reactor – homogenous gasification take place |

**Table 3**: Empirical correlations of wood chips pyrolysis [18]

| i | a | b | c |
|---|---|---|---|
| $CH_4$ | $-4.341 \times 10^{-5}$ | $10.12 \times 10^{-2}$ | -51.08 |
| $H_2$ | $1.362 \times 10^{-5}$ | $-2.517 \times 10^{-2}$ | 12.19 |
| CO | $-3.524 \times 10^{-5}$ | $9.770 \times 10^{-2}$ | -24.93 |
| $CO_2$ | $3.958 \times 10^{-5}$ | $-9.126 \times 10^{-2}$ | 64.02 |
| $C_2H_4$ | $-6.873 \times 10^{-5}$ | $14.94 \times 10^{-2}$ | -76.89 |
| $C_2H_6$ | $8.265 \times 10^{-6}$ | $-2.105 \times 10^{-2}$ | 13.38 |
| $C_6H_6$ | $-3.134 \times 10^{-5}$ | $7.544 \times 10^{-2}$ | -42.72 |
| $C_7H_8$ | $-4.539 \times 10^{-5}$ | $0.687 \times 10^{-2}$ | 1.462 |
| $C_6H_6O$ | $1.508 \times 10^{-5}$ | $-3.662 \times 10^{-2}$ | 22.19 |
| $C_{10}H_8$ | $-8.548 \times 10^{-6}$ | $1.882 \times 10^{-2}$ | -9.851 |
| $H_2O$ | $5.157 \times 10^{-5}$ | $11.86 \times 10^{-2}$ | 84.91 |

mass yield of pyrolysis product, T [K] is a reaction temperature, and a [kg $h^{-1}$ $K^{-2}$], b [kg $h^{-1}$ $K^{-1}$], and c [kg $h^{-1}$] are coefficients obtained from experimental data. This empirical model can be applied for the reactor temperature between 700 and 1000 °C [18]. This empirical equation is a simplified method to present the yield of pyrolysis including the primary and secondary tar. The char mass yield is calculated based on mass balances after other product determinations. The pyrolysis gas is then introduced into a separator "SEP 1" to separate the char. The char is turned into conventional elements according to its yield distribution data at "CHARCONV" reactor. The gas produced is mixed with pyrolysis gases and steam at "MIXER". The gases undergo tar reduction with the reaction R3 listed in Table 4. Following tar treatment, the gases were introduced into the 'HETRO' reactor to undergo a heterogeneous gasification process at 850 °C and 1 bar, facilitated by reaction R1. Subsequently, homogenous gasification was conducted under the same pressure and temperature at "HOMO" reactor with reaction R2.

**Table 4:** List of reactions involved

| No | Reaction | Kinetic | Source |
|---|---|---|---|
| R1 | $C + CO_2 \leftrightarrow 2CO$ | $4.4Te^{(\frac{-1.62\times10^8}{RT})}[CO_2]^{0.6}$ | [1] |
| | $C + H_2O \leftrightarrow CO + H_2$ | $1.33Te^{(\frac{-1.47\times10^8}{RT})}[H_2O]^{0.6}$ | [1] |
| R2 | $CH_4 + H_2O \rightarrow CO + 3H_2$ | $3.0\times10^5 e^{(\frac{1.25\times10^8}{RT})}[CH_4]^1[O_2]^1$ | [23] |
| | $CO + H_2O \rightarrow CO_2 + H_2$ | $2.78\times10^6 e^{(\frac{-1.26\times10^7}{RT})}\left([CO][H_2O] - \frac{[CO][H_2O]}{k_p(T)}\right)$ $k_p(T) = 0.0265e^{(\frac{4.55\times10^7}{RT})}$ | [1] |
| R3 | $C_6H_6 + 2H_2O \rightarrow 3C + 2CH_4 + 2CO$ | $4.0\times10^{16} e^{(\frac{-4.43\times10^5}{RT})}[C_6H_6]^{1.3}[H_2]^{-0.4}[H_2O]^{0.2}$ | [18] |
| | $C_7H_8 + H_2 \rightarrow C_6H_6 + CH_4$ | $1.04\times10^{12} e^{(\frac{-2.47\times10^5}{RT})}[C_7H_8]^1[H_2]^{0.5}$ | [18] |
| | $C_6H_6O \rightarrow CO + 0.4C_{10}H_8 + 0.15C_6H_6 + 0.1CH_4 + 0.75H_2$ | $10^7 e^{(\frac{10^5}{RT})}[C_6H_6O]^1$ | [18] |
| | $C_{10}H_8 \rightarrow 9C + 0.16667C_6H_6 + 3.5H_2$ | $3.4\times10^{14} e^{(\frac{3.5\times10^5}{RT})}[C_{10}H_8]^{1.6}[H_2]^{-0.5}$ | [18] |

## RESULT AND DISCUSSION

### Effect of temperature on syngas composition

Figure 2 presents the effect of temperature on the syngas composition at a steam-to-biomass ratio of 3. The temperature was varied in the range of 750 ˚C to 1050 ˚C as the suitable temperature for gasification to occur is more than 750 ˚C [19].

Raising the temperature increases the yield of $H_2$ and decreases the contents of $CO_2$ and $CH_4$. H2 has increased 36% from 750 ˚C to 1050 ˚C. This result is almost consistent with the results by Talero et al. in 2022 [15]. In particular, similar CO synthesis trend was also reported in several previous papers [9], [20], [21].

From the R1 and R2 reactions listed in Table 4, only the water gas shift reaction is exothermic. When increasing the temperature of the gasification, Boudourd reaction, water gas reaction and steam methane reforming which are endothermic reactions favour the forward reaction, resulting in an increase in $H_2$ and CO composition and decreasing in $CH_4$ and C composition. The exothermic properties of the water gas shift reaction hinder the production of $H_2$ and $CO_2$.

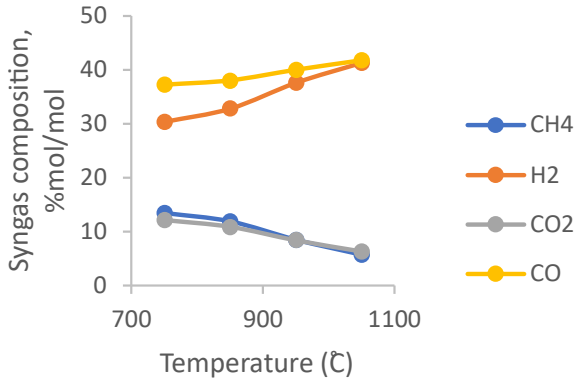



**Figure 2:** Effect of temperature on syngas composition

### Effect of steam to biomass ratio on syngas composition

The effect of steam to biomass ratio is one of the critical parameters that affect gasification efficiency, syngas composition and reaction mechanism. Figure 3 shows the effect of steam to biomass ratio on the syngas composition at a gasification temperature of 850 ˚C. There is a slight increase in the $H_2$ value when increasing the steam-to-biomass ratio. This can be explained according to Le Chatelier's Principle as the increase in the

steam will favour the $H_2$ formation reaction, especially in steam methane reforming and water gas reaction. $CH_4$ and CO will decrease to maintain the equilibrium of the reaction. A similar result is obtained by Huang where the syngas composition is studied from the range of 0.5 to 3.0 [22] whereas a similar increasing trend is also discussed by Paiva and Florin with lower steam-to-biomass ratio [7], [21].

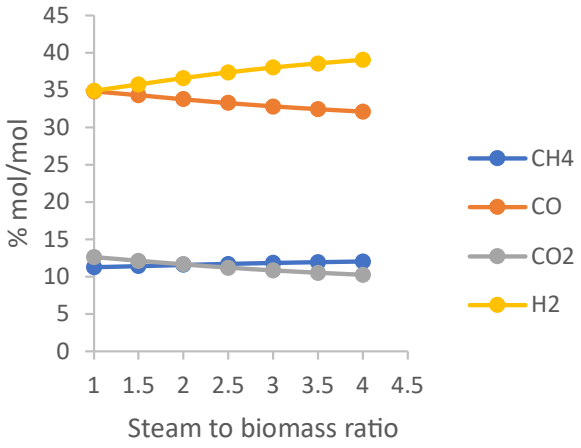



**Figure 3:** Effect of steam to biomass ratio on syngas composition

The introduction of steam during the gasification process promotes the further pyrolysis and gasification of tar and coke. This can improve the syngas quality as shown in Figure 4.

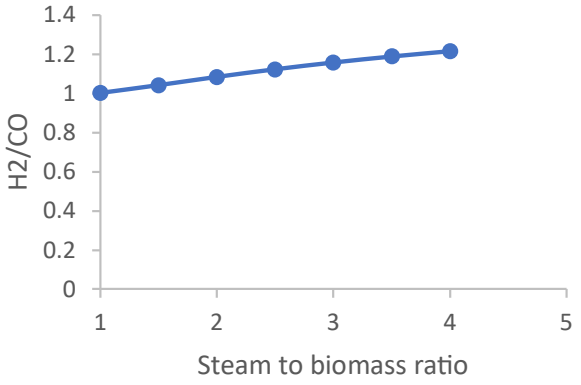



**Figure 4:** Effect of steam to biomass ratio on H2/CO ratio

It can be seen that the proposed kinetic biomass gasification models showed the consistent results with the previous research. From these results, the authors concluded that the proposed models capture the characteristics of the gasification reaction, although the proposed models are much simpler than others counterparts. Furthermore, it can be said that the control system can be designed based on these models for optimizing the process operation.

## CONCLUSION

A simple kinetic biomass gasification model is developed in the Aspen Plus simulator to discuss the syngas production during the steam gasification of Japan waste wood. Each kinetic reaction captured in the model affects the biomass gasification process.

In this study, we compared our simulation model with those presented in previous research to assess its relative performance and validity. This study helps develop a control system in future studies which able to capture the complex interactions between the factors that influence the performance of gasifiers and optimize them for improved efficiency and scalability in industrial applications.

While our current analysis is based on simplified models, we recognize the importance of validating these findings through experimental data. Therefore, in future work, we plan to conduct experiments which will allow us to rigorously compare our simplified models with experimental outcomes, ensuring greater accuracy and reliability in our conclusions.

## REFERENCES


1. W. C. Yan *et al.*, "Model-based downdraft biomass gasifier operation and design for synthetic gas production," *J. Clean. Prod.*, vol. 178, pp. 476–493, 2018, doi: 10.1016/j.jclepro.2018.01.009.
2. N. Gao and A. Li, "Modeling and simulation of combined pyrolysis and reduction zone for a downdraft biomass gasifier," *Energy Convers. Manag.*, vol. 49, no. 12, pp. 3483–3490, 2008, doi: 10.1016/j.enconman.2008.08.002.
3. A. Anniwaer *et al.*, "Steam co-gasification of Japanese cedarwood and its commercial biochar for hydrogen-rich gas production," *Int. J. Hydrogen Energy*, vol. 46, no. 70, pp. 34587–34598, 2021, doi: 10.1016/j.ijhydene.2021.08.032.
4. Forestry Agency, "Annual Report on Forest and Forestry in Japan. Fiscal Year 2023 (Summary)," *Minist. Agric. For. Fish.*, vol. 2023, 2023.
5. A. Kushwah, T. R. Reina, and M. Short, "Modelling approaches for biomass gasifiers: A comprehensive overview," *Sci. Total Environ.*, vol. 834, no. April, p. 155243, 2022, doi: 10.1016/j.scitotenv.2022.155243.
6. K. Atsonios, A. Nesiadis, N. Detsios, K. Koutita, N. Nikolopoulos, and P. Grammelis, "Review on dynamic process modeling of gasification based biorefineries and bio-based heat & power plants," *Fuel Process. Technol.*, vol. 197, no. March 2019, p.

106188, 2020, doi: 10.1016/j.fuproc.2019.106188.
7. M. Paiva, A. Vieira, H. T. Gomes, and P. Brito, “Simulation of a downdraft gasifier for production of syngas from different biomass feedstocks,” *ChemEngineering*, vol. 5, no. 2, 2021, doi: 10.3390/chemengineering5020020.
8. M. Fernandez-Lopez, J. Pedroche, J. L. Valverde, and L. Sanchez-Silva, “Simulation of the gasification of animal wastes in a dual gasifier using Aspen Plus®,” *Energy Convers. Manag.*, vol. 140, pp. 211–217, 2017, doi: 10.1016/j.enconman.2017.03.008.
9. L. P. R. Pala, Q. Wang, G. Kolb, and V. Hessel, “Steam gasification of biomass with subsequent syngas adjustment using shift reaction for syngas production: An Aspen Plus model,” *Renew. Energy*, vol. 101, pp. 484–492, 2017, doi: 10.1016/j.renene.2016.08.069.
10. D. Cerinski, A. I. Ferreiro, A. I. Baleta and M. Costa, Modelling the biomass updraft gasification process using the combination of a pyrolysis kinetic model and a thermodynamic equilibrium model, *Energy Reports*, 2021.
11. P. E. A. Debiagi, G. Gentile, M. Pelucchi, A. Frassoldati, A. Cuoci, T. Faravelli and E. Ranzi, "Detailed kinetic mechanism of gas-phase reactions of volatiles released from biomass pyrolysis," *Biomass and Bioenergy*, vol. 93, pp. 60-71, 2016.
12. D. Humbird, A. Trendewicz, R. Braun and A. Dutta, "One-Dimensional Biomass Fast Pyrolysis Model with Reaction Kinetics Integrated in an Aspen Plus Biorefinery Process Model," *ACS Sustainable Chemistry and Engineering*, vol. 5, pp. 2463-2470, 2017.
13. J. F. Peters, S. W. Banks, A. V. Bridgwater and J. Dufour, "A kinetic reaction model for biomass pyrolysis processes in Aspen Plus," *Applied Energy*, vol. 188, pp. 595-603, 2017.
14. M. Calonaci, R. Grana, E. Barker Hemings, G. Bozzano, M. Dente and E. Ranzi, "Comprehensive kinetic modeling study of bio-oil formation from fast pyrolysis of biomass," *Energy and Fuels*, vol. 24, pp. 5727-5734, 2010.
15. G. Talero and Y. Kansha, “Simulation of the Steam Gasification of Japanese Waste Wood in an Indirectly Heated Downdraft Reactor Using PRO/II™: Numerical Comparison of Stoichiometric and Kinetic Models,” *Energies*, vol. 15, no. 12, 2022, doi: 10.3390/en15124181.
16. A. Plus, A. Properties, A. E. Suite, A. Technology, T. C. Park, and O. Systems, “Part Number : Aspen Physical Property System 11 . 1 September 2001,” *Engineering*, pp. 2–18, 2001, [Online]. Available: http://www.aspentech.com.
17. Y. Cheng, Z. Thow, and C. H. Wang, “Biomass gasification with CO2 in a fluidized bed,” *Powder Technol.*, vol. 296, pp. 87–101, 2016, doi: 10.1016/j.powtec.2014.12.041.
18. S. M. Beheshti, H. Ghassemi, and R. Shahsavan-Markadeh, “Process simulation of biomass gasification in a bubbling fluidized bed reactor,” *Energy Convers. Manag.*, vol. 94, pp. 345–352, 2015, doi: 10.1016/j.enconman.2015.01.060.
19. L. J. R. Nunes, “Biomass gasification as an industrial process with effective proof-of-concept: A comprehensive review on technologies, processes and future developments,” *Results Eng.*, vol. 14, no. April, p. 100408, 2022, doi: 10.1016/j.rineng.2022.100408.
20. A. Inayat, M. M. Ahmad, S. Yusup, and M. I. A. Mutalib, “Biomass steam gasification with in-situ CO2 capture for enriched hydrogen gas production: A reaction kinetics modelling approach,” *Energies*, vol. 3, no. 8, pp. 1472–1484, 2010, doi: 10.3390/en3081472.
21. N. H. Florin and A. T. Harris, “Hydrogen production from biomass coupled with carbon dioxide capture: The implications of thermodynamic equilibrium,” *Int. J. Hydrogen Energy*, vol. 32, no. 17, pp. 4119–4134, 2007, doi: 10.1016/j.ijhydene.2007.06.016.
22. F. Huang and S. Jin, “Investigation of biomass ( pine wood ) gasification : Experiments and Aspen Plus simulation,” no. October 2018, pp. 1178–1187, 2019, doi: 10.1002/ese3.338.
Z. Yang *et al.*, “Numerical Study on the Steam Gasification of Biomass in a 100 kW Dual Fluidized Bed Gasifier,” *Energy and Fuels*, vol. 38, no. 5, pp. 4273–4289, 2024, doi: 10.1021/acs.energyfuels.3c04754.

© 2025 by the authors. Licensed to PSEcommunity.org and PSE Press. This is an open access article under the creative commons CC-BY-SA licensing terms. Credit must be given to creator and adaptations must be shared under the same terms. See https://creativecommons.org/licenses/by-sa/4.0/



Systems & Control Transactions

**Research Article - Peer Reviewed Conference Proceeding**
ESCAPE 35 - European Symposium on Computer Aided Process Engineering
Ghent, Belgium. 6-9 July 2025
Jan F.M. Van Impe, Grégoire Léonard, Satyajeet S. Bhonsale,
Monika E. Polańska, Filip Logist (Eds.)

PSE PRESS

# Optimal Design and Analysis of Thermochemical Storage and Release of Hydrogen via the Reversible Redox of Iron Oxide/Iron

**Richard Yentumi[a,b], Constantin Jurischka[a], Bogdan Dorneanu[a], and Harvey Arellano-Garcia[a]***

[a] FG Prozess-und Anlagentechnik, Brandenburgische Technische Universität, Cottbus, Germany
[b] Department of Engineering & Maintenance, Ghana National Gas Company (GNGC), Accra, Greater Accra, Ghana
* Corresponding Author: arellano@b-tu.de

## ABSTRACT

In this contribution, a thermodynamic model-based approach for the optimal design of a solid-state hydrogen storage and release system utilizing the reversible iron oxide/iron thermochemical redox mechanism is presented. Existing storage processes using this mechanism face significant limitations, including low hydrogen conversion, high energy input requirements, limited storage density, and slow charging/discharging kinetics. To address these challenges, a custom thermodynamic model using NIST thermochemistry data is developed, enabling an in-depth analysis of redox reaction equilibria under different conditions. Unlike previous studies, this approach integrates a multi-objective optimization framework that explicitly balances competing objectives: maximizing hydrogen yield while minimizing thermal energy demand. By systematically identifying optimal trade-offs, the study provides new insights into improving process efficiency and reactor design for thermochemical hydrogen storage. These findings contribute to advancing energy-efficient and scalable hydrogen storage technologies.

**Keywords**: Hydrogen, Hydrogen Fuel Cells, Energy Storage, Modelling and Simulations, Optimisation, Thermochemical storage, Green hydrogen

## INTRODUCTION

As the European Union (EU) aims to reach net zero emissions by 2050, green hydrogen ($H_2$) has emerged as a clean alternative to existing mainstream hydrocarbon fuels and even unabated hydrogen. One of the major challenges with hydrogen, however, is that it is relatively difficult to store at large scale. Moreover, gaseous and liquefied hydrogen storage processes are energy intensive and expensive [1]. More recently, there has been growing interest in the development of cost-effective and energy-efficient solid-state processes for hydrogen storage. Thermochemical storage (TCS) is emerging as a promising method. As defined by De Rosa et al. [2], thermochemical storage is any storage method based on reversible chemical reactions in which heat is stored and released during the forward endothermic and reverse exothermic reactions respectively. The principle behind thermochemical hydrogen storage is the reversible reduction and oxidation of a metal oxide/pure metal pair. The balanced chemical equation for this reaction is written as:

$$Fe_3O_4\,(s) + 4H_2\,(g) \rightleftharpoons 3Fe\,(s) + 4H_2O\,(g)$$

In the forward endothermic reaction, the solid metal oxide ($Fe_3O_4$) is reduced to a pure metal (Fe) with hydrogen acting as the reducing agent. The hydrogen feed is thus converted to steam. In the reverse exothermic reaction, the pure metal (Fe) is re-oxidised to a metal oxide ($Fe_3O_4$) with water/steam acting as the oxidising agent. Essentially, hydrogen is stored in the reduction reaction and the metal oxide acts a solid-state storage medium. The stored hydrogen may be recovered in the reverse oxidation reaction. Figure 1 shows the schematic of a thermochemical storage system.

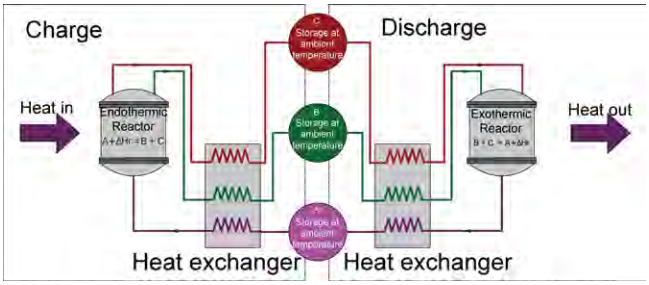


Figure 1. Schematic of a thermochemical storage system

To underscore the suitability $Fe_3O_4$/Fe pair, Brinkman et al. [3] evaluated various other metal oxide/pure metal candidate pairs such as ZnO/Zn, $SnO_2$/Sn, $GeO_2$/Ge, $WO_{2.722}$/W, $MoO_2$/Mo, for use as solid-state storage mediums for hydrogen. Considering evaluation criteria such as process conditions, energy requirements, material costs, and storage density, they identified $Fe_3O_4$/Fe as the optimal candidate pair. However, it is important to note that Otsuka et al. [4] were the first to propose this storage method for hydrogen fuel cell vehicles (FCVs). Brinkman et al. [3] highlighted that the strict performance requirements - such as energy density, process conditions, and charging/discharging response times - make it unlikely that this cyclical storage method will adequately meet the demands of FCV applications. Conversely, they suggested that for large-scale, long-term storage applications, where cost and safety are the primary concerns, the hydrogen TCS method could serve as a viable alternative.

From this perspective, chemical reactor design, a vital step in the development of hydrogen TCS processes, is the overall aim of this work. Different reactor types being studied include fixed bed or fluidised bed reactors.

In this contribution, Section 2 presents a novel fixed-bed single reactor concept. Additionally, it outlines a custom thermodynamic model developed using the NIST Standard Reference Database 69: *NIST Chemistry WebBook* [5] and details its model-based optimisation. Section 3 presents and discusses the results. Finally, conclusions are drawn in Section 4.

# 2. METHODOLOGY

## 2.1 Single-Reactor Concept

Most research on hydrogen TCS has been carried out based on a two-reactor system (Figure 1) – an endothermic reactor for reduction and an exothermic reactor for oxidation [3]. To maximise energy efficiency, such systems include heat exchangers and other equipment units. Thus, overall, the CAPEX and OPEX outlays for these systems are high. Thus, a fixed bed type single reactor concept is proposed that combines the endothermic and exothermic reactors into a single unit with the primary aim of minimising energy input through heat integration. The proposed concept consists of four main operating modes that include: standby/factory mode; storage process; cold storage mode; and release process. Figure 2 illustrates the proposed operating modes.

In *standby mode*, the outer shell of the reactor is packed with beds of Fe while the inner shell is packed with beds of $Fe_3O_4$. In the *storage process*, a green hydrogen feed which is available to be stored, flows into the inner shell for reduction of the metal oxide while steam is introduced into the outer shell to oxidise the pure metal into a metal oxide. A portion of the thermal energy released from the exothermic oxidation reaction in the outer shell meets the heat input requirements of the endothermic reduction reaction in the inner shell. Once almost all the pure gaseous products of hydrogen from the outer shell and the steam from the inner shell are removed, the storage process completes, and the unit may be allowed to cool down and enter a *cold storage mode* which theoretically may be long term durations. It is important to note that once the storage process is complete, the outer shell shall consist of beds of $Fe_3O_4$ while the inner shell contains Fe. To initiate the hydrogen *release mode*, on-site hydrogen is fed to the outer shell for reduction of $Fe_3O_4$ to Fe while steam is fed to the inner shell for oxidation of Fe to $Fe_3O_4$. A portion of the thermal energy released from this exothermic oxidation reaction thus, feeds the endothermic reaction in the outer shell. The net effect of these alternating redox reactions in the outer and inner shells results in the minimisation of the overall energy input required for hydrogen TCS.

Moreover, besides the comparative advantage of lower costs, this proposal offers several other advantages such as the potential for miniaturisation for mobile applications such as in FCVs. Some potential challenges with this concept may include maintainability problems, challenges with its dynamic operations nature, temperature controllability challenges, heat transfer management between shells, special high temperature materials requirement, and so on.

## 2.2 Thermodynamic Model

The objective of the proposed model is to predict the reaction temperature that maximises equilibrium conversion. Integration of thermodynamic and chemical reaction equilibrium yields this powerful model; to predict the reaction equilibrium constant and other key thermodynamic physical properties (temperature, pressure, etc.) as well as thermodynamic functions such as enthalpy, entropy and Gibbs free energy of the reacting system. This algebraic thermochemical equilibrium model is given as:

$$\Delta_r G^o(T) = -RT\ ln\ K_{eq} \quad (1)$$

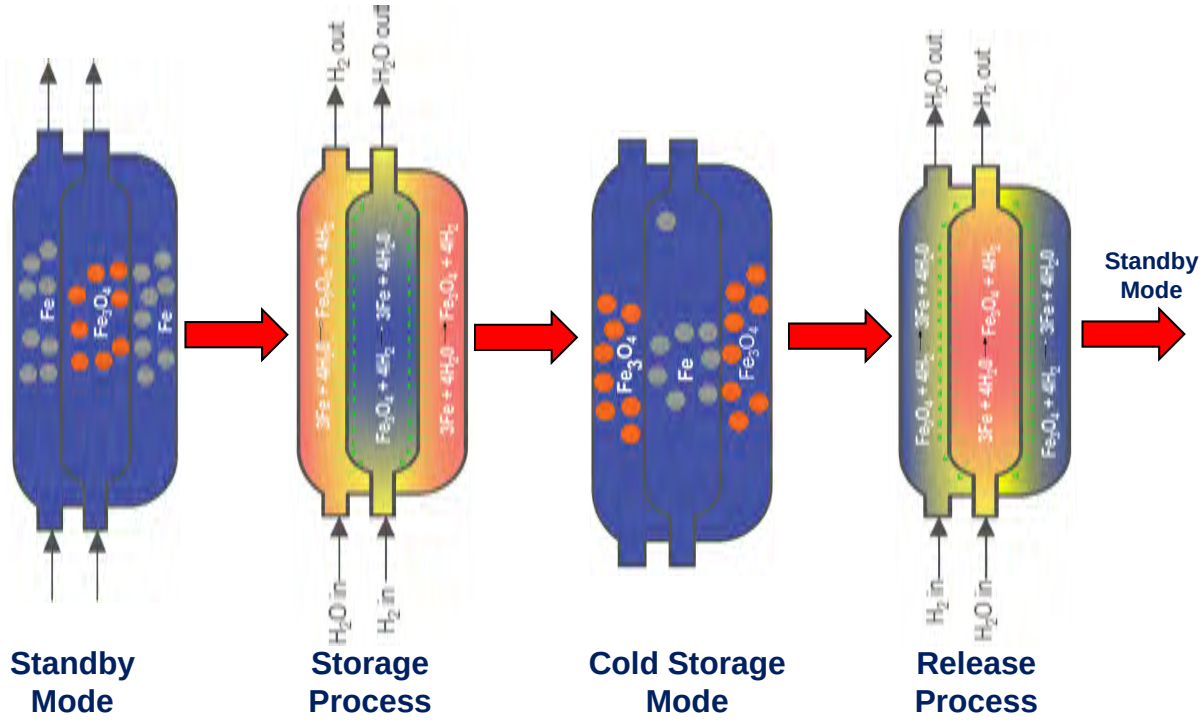



**Figure 3.** Operating modes of a proposed single reactor concept for thermochemical storage

The standard change in Gibbs free energy, $\Delta_r G^o$, at a fixed temperature and pressure is estimated from the relation:

$$\Delta_r G^o(T) = \Delta_r {H_f}^o - T\Delta_r S^o \quad (2)$$

From the NIST Thermochemistry data [5], the magnitude of the standard enthalpy change of a reaction $\Delta_r H_f^o$ is the sum of the standard enthalpies of formation of the products, each multiplied by its appropriate coefficient, minus the sum of the standard enthalpies of formation of the reactants, also multiplied by their coefficients. The standard entropy change of a reaction, $\Delta_r S^o$, is estimated similarly. The equilibrium constant as a function of the reaction temperature, $T$, for each reaction is estimated from the relation:

$$K_{eq}(\mathrm{T}) = exp^{\left(-\frac{\Delta_r G^o(T)}{RT}\right)} \quad (3)$$

Brinkman et al. [3] reported that under the idealisations similarly applied for this work, varying the reactor pressure had no significant effect on equilibrium conversion ($x$).

The equilibrium conversion ($x$) in dimensionless units and as a function of temperature is thus, estimated as follows:

$$x_{H_2}(\mathrm{T}) = \left(\frac{SC_{H_2}}{SC_{H_2O}}\right) \cdot \frac{\left[K_{eq}(\mathrm{T}).q_{n,H_{2-in}}\right]}{\left[q_{n,H_{2-in}} + K_{eq}(\mathrm{T}).q_{n,H_{2-in}}\right]} \quad (4)$$

$$x_{H_2O}(\mathrm{T}) = \left(\frac{SC_{H_2O}}{SC_{H_2}}\right) \cdot \frac{\left[K_{eq}(T).q_{n,H_2O-in}\right]}{\left[q_{n,H_2O-in} + K_{eq}(T).q_{n,H_2O-in}\right]} \quad (5)$$

Where SC is the stoichiometric coefficient (dimensionless); $K_{eq}(T)$is equilibrium constant (dimensionless) and $q_{n,}$ is molar flow rate (kmol/hr). The heat flow for the forward reduction reaction, $Q_f(T)$ and that for the reverse oxidation reaction, $Q_r(T)$, both in kW, are estimated from the relations.

$$Q_f(\mathrm{T}) = Q_{products}(\mathrm{T}) - Q_{reactants}(T) \quad (6)$$

$$Q_r(\mathrm{T}) = Q_{products}(\mathrm{T}) - Q_{reactants}(T) \quad (7)$$

Where the heat flow for the products or reactants may be determined from the relation:

$$Q_i = \sum_{i=1}^{n} q_{n,i} \cdot \Delta {h_i}^o(T) \quad (8)$$

Where $n$ is the number of chemical components. The total enthalpy in kJ/kmol of the reactant and product streams are estimated from the relation:

$$\Delta h^o(\mathrm{T}) = \sum y_i \cdot \left[{h_{f,i}}^o + h^o(T)\right] \tag{9}$$

The temperature dependent enthalpies $h^o(T)$ for each chemical component are estimated from the component specific NIST thermochemistry data heat capacity (Shomate equation).

## 2.3 Optimisation Model

The purpose of the optimisation study is to identify optimal operating conditions in the presence of trade-offs between conflicting objectives; maximisation of equilibrium conversion and minimisation of energy input in both the reduction and oxidation processes. The presence of these conflicting objectives gives rise to a multi-objective optimisation problem (MOOP).

Eq. (10) shows the general structure of a MOOP for the forward reduction reaction with the reaction temperature, $T$, as the decision variable.

Equation (1) sets thermodynamic boundaries on the total energy changes occurring during the reactions. Equation (2) establishes feasibility limits on the composition of the reaction system at equilibrium.

The decision variable, $T$, was constrained to operate within a range of 25°C and bounded at approximately 80% of the melting point temperature of iron (Fe) reported by [6]. In practical terms, this helps prevent melting and other forms of physical degradation of the solid particles, such as sintering, agglomeration, and so on.

MOOP differs from a single objective optimisation problem (SOOP), in that two or more objective functions are required to be solved within the specified constraints simultaneously. Moreover, whereas a unique optimal solution may exist for SOOPs, a set of trade-off solutions may typically exist for MOOPs.

$$\begin{gathered} max \;\; f_1(T) = x_{\mathrm{H2}}(T) \\ min \;\; f_2(T) = Q_f(T) \\ s.t. \\ Eqn.(1) \\ Eqn.(3) \\ T^{LB} \leq T \leq T^{UB} \end{gathered} \tag{10}$$

Several methods currently exist for solving MOOPs. The epsilon($\varepsilon$)-constrained method (ECM) first proposed by Haimes et al. [7] was applied in this study as it yields the set of exact Pareto-optimal solutions efficiently. In applying the ECM, a so-called primary objective function is selected to be optimised while the other remaining objective functions are converted into constraints with predefined upper bounds $\varepsilon_i$. The $\varepsilon_i$-values were selected based on industrial-scale constraints to guarantee feasible solutions.

Notwithstanding, it is essential to highlight that all objectives hold the same level of importance, in that, no weights of preference are assigned to the objective functions as with some other methods. However, in general, the successful implementation of ECM requires careful specification of feasible $\varepsilon_i$ values and consideration of computational efficiency.

In the reduction step, equilibrium conversion of hydrogen was specified as the primary objective function in the description of the MOOP in ECM form as shown in Eq. (11).

$$\begin{gathered} min \;\; -f_1(T) = -x_{\mathrm{H_2}}(T) \\ s.t. \\ f_2(T) = Q_f(T) \leq \varepsilon \\ Eqn.(1) \\ Eqn.(3) \\ T^{LB} \leq T_f \leq T^{UB} \end{gathered} \tag{11}$$

Similarly, the ECM form for the reverse oxidation reaction is shown in Eq. (12):

$$\begin{gathered} min \;\; -f_1(T) = -x_{\mathrm{H_2O}}(T) \\ s.t. \\ f_2(T) = Q_r(T) \leq \varepsilon \\ Eqn.(1) \\ Eqn.(3) \\ T^{LB} \leq T_r \leq T^{UB} \end{gathered} \tag{12}$$

The gradient-based MATLAB nonlinear solver fmincon was used to solve the resulting SOOPs within the practical bounds of the decision variable (reaction temperature) and by systematically varying the constraints which includes the $\varepsilon_i$ values.

The results generated from solving the MOOP is a set of non-dominated or Pareto-optimal solutions of the entire feasible decision space. The superiority of the final solution (best compromised solution) over the other solutions is determined by the decision-maker mostly based on a combination of technical and economic considerations.

In this work, the fuzzy based method as proposed by Yalcin & Erginel [8] was used to identify the best compromised solutions out of the set of Pareto efficient solutions for each of the objective functions. For each reaction, the optimum is a set of solutions that define the best trade-off between the competing maximisation (Eq. 13)

and minimisation (Eq. 14) objective functions.

$$\mu_k(T) = \frac{f_k(T) - f_k^*}{f_k^* - f_k'} \quad (13)$$

$$\mu_k(T) = \frac{f_k' - f_k(T)}{f_k' - f_k^*} \quad (14)$$

Maximum and minimum values of the maximization and minimisation objectives are calculated from Eqs. (15) and (16) under the problem constraints, respectively.

$$f_k^* = max\big(f_k(T)\big), \quad f_k' = min\big(f_k(T)\big) \quad (15)$$

$$f_k^* = min\big(f_k(T)\big), \quad f_k' = max\big(f_k(T)\big) \quad (16)$$

The best compromised solution being the first solution point with the largest numerical value for $\mu_k(T)$.

## 3. RESULTS & DISCUSSION

Figure 3 shows a plot of the model predicted equilibrium conversion vs. reaction temperature for the reduction (red curve) and the oxidation (blue) curves.

The reduction step is favoured by high temperatures; equilibrium conversion of hydrogen in the range $0.50 \leq x_{H_2} \leq 0.9999$ were predicted to occur within operating temperature range of $792\ \text{K} \leq T_f \leq 1307\ \text{K}$, respectively.

Conversely, the oxidation step is favoured by lower temperatures; such that within similar equilibrium conversion bounds for steam ($x_{H_2O}$), the predicted temperature range is $792\ \text{K} \leq T_r \leq 568\ \text{K}$, respectively.

Although the results suggest that conducting the reduction step at high temperatures enhances conversion rates, it is essential to account for the drawbacks of high operating temperatures, including safety risks, increased energy consumption, higher costs, and other related factors. Moreover, Spreitzer and Schenk [9] have reported, referencing the Baur-Glassner diagram, that at reduction temperatures > 570 °C, $Fe_3O_4$ is first reduced to wüstite (an intermediate oxide) before being further reduced to pure Fe. While the chemical thermodynamic effects of wüstite formation was ignored in this work, it may be important to characterise its overall effect on the model.

To identify optimum operating conditions for the redox reactions, Pareto front diagrams, the boundary marked out by the set of all points plotted from the Pareto-optimal set were developed.

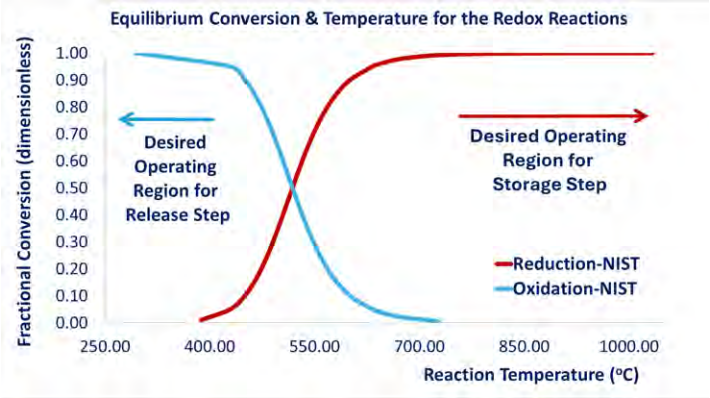



**Figure 3.** Equilibrium equilibrium conversion vs temperature of the redox reactions

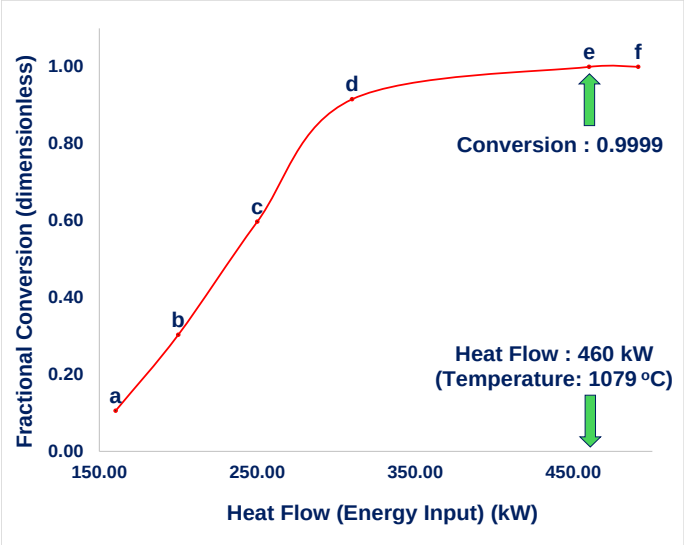



**Figure 4**. Pareto front diagram showing the best compromised solution for reduction

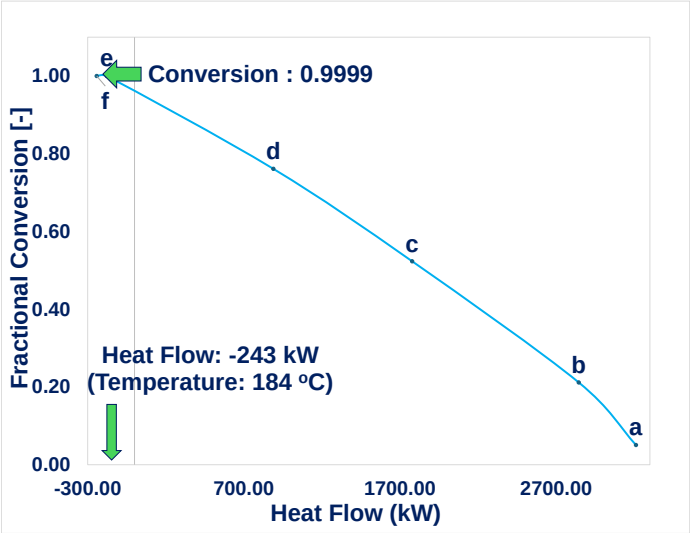



**Figure 5.** Pareto front diagram showing best compromised solution for oxidation

Figure 4 shows the Pareto front considering heat flow (energy input) and equilibrium conversion for the endothermic forward reduction reaction, while Figure 5 illustrates the Pareto front considering heat flow and equilibrium conversion for the exothermic reverse oxidation reaction.

Furthermore, the best compromised solutions for the endothermic reduction and exothermic oxidation reactions were determined and spot-lighted in Figures 4 and 5, respectively, using the fuzzy-based method.

Overall, the results obtained show that for once-through process storage step, reduction should be conducted at a temperature of about 1079 °C while oxidation for the release step should be conducted at about 184 °C. The results obtained also show potential for energy savings owing to configuration of the single reactor concept through heat integration.

As highlighted by Smith [10], it is important to note that the predicted equilibrium conversion values are independent of the reactor design and represent the absolute maximum conversions of reactants in a reversible reaction mixture at a given temperature and pressure.

## 4. CONCLUSIONS

In this work, the thermo-chemical feasibility of a reactor concept for hydrogen storage and release has been established. Through thermodynamic modeling and optimization, ideal operating conditions have been identified, maximizing hydrogen conversion while minimizing energy input. The proposed reactor concept demonstrates the potential for significantly lower specific energy requirements compared to conventional compressed and liquefied hydrogen storage methods, offering a promising alternative for efficient hydrogen storage.

To further refine the system, detailed kinetic studies using the shrinking core model have been conducted to determine lab-scale charging and discharging times. Ongoing experimental work is focused on assessing the long-term stability of the $Fe_3O_4$/Fe system and exploring performance enhancements through the incorporation of metal oxide/metal pairs as structural supports.

Future work includes the development of a dynamic distributed parameter model to capture spatial and temporal variations within the reactor. Further efforts will focus on improving energy efficiency, optimizing key performance metrics, and advancing the scalability of this storage technology for practical applications.

## ACKNOWLEDGEMENTS

The project has been funded by Bundesministerium für Wirtschaft und Klimaschutz (BMWK) under grant number 03EI3102C. The authors would also like to thank the CEO of GNGC, Ben K.D Asante, PhD, for his visionary investments in this research work.

## REFERENCES

1. Raman R, Nair VK, Prakash V, Patwardhan A, Nedungadi P, Green-hydrogen research: What have we achieved, and where are we going? Bibliometrics analysis, *Energy Reports*, 8, 9242–9260 (2022)
2. De Rosa M, Afanasevab O, Fedyukhinc AV, Bianco V, Prospects and characteristics of thermal and electrochemical energy storage systems, *Journal of Energy Storage*, 44, 103443 (2021)
3. Brinkman L, Bulfin B, Steinfeld A, Thermochemical hydrogen storage via the reversible reduction and oxidation of metal oxides, *Energy Fuels*, 35, 18756-18767 (2021)
4. Otsuka K, Yamada C, Kaburagi T, Takenaka S, Hydrogen storage and production by redox of iron oxide for polymer electrolyte fuel cell vehicles, *International Journal of Hydrogen Energy*, 28, 335-342 (2003)
5. NIST Chemistry WebBook, SRD 69 (webpage), https://webbook.nist.gov/chemistry/
   Condensed Phase Thermochemistry Data for: $Fe_3O_4$ and Fe.
   Gas Phase Thermochemistry Data for $H_2$ and $H_2O$.
6. Desai P.D, Thermodynamic properties of iron and silicon, *Journal of Physical and Chemical Reference Data*, 15, 967-983 (1986)
7. Haimes Y, Lasdon L, Wismer D, On a bicriterion formulation of the problems of integrated system identification and system optimization, *IEEE Transactions on Systems, Man, and Cybernetics*, 1:296-297 (1971)
8. Yalcin GD, Erginel N, Determining weights in multi-objective linear programming under fuzziness, *World Congress on Engineering*, Vol II (2011)
9. Spreitzer D, Schenk J, Reduction of iron oxides with hydrogen—A review, *Steel Research Int.*, 90,1900108 (2019)
10. Smith R, Chemical Process Design and Integration, 2nd Edition, John Wiley & Sons Ltd (2016)

© 2025 by the authors. Licensed to PSEcommunity.org and PSE Press. This is an open access article under the creative commons CC-BY-SA licensing terms. Credit must be given to creator, and adaptations must be shared under the same terms. See https://creativecommons.org/licenses/by-sa/4.0/



Systems & Control Transactions

**Research Article - Peer Reviewed Conference Proceeding**
ESCAPE 35 - European Symposium on Computer Aided Process Engineering
Ghent, Belgium. 6-9 July 2025
Jan F.M. Van Impe, Grégoire Léonard, Satyajeet S. Bhonsale,
Monika E. Polańska, Filip Logist (Eds.)

PSE PRESS

# Robust pharmaceutical tableting process through combined probabilistic design space and flexibility analysis

**Ashish Yewale[a], Xuming Yuan[a] and Brahim Benyahia[a]***

[a] Department of Chemical Engineering, Loughborough University, Leicestershire, UK
* Corresponding Author: b.benyahia@lboro.ac.uk

## ABSTRACT

This study investigates the development of a probabilistic design space (DS) for a tableting process, focusing on the uncertainty in critical model parameters. A an empirical model is used to assess the impact of critical process parameters (CPPs), including lubrication extent and porosity, on tablet tensile strength (CQA). By incorporating Monte Carlo and Bayesian techniques, the uncertainty of five model parameters is propagated, allowing the estimation of feasibility probabilities for achieving CQAs with a reliability greater than 0.95. The resulting probabilistic DS provides manufacturers with a tool to assess the likelihood of meeting CQAs under varying production conditions. The findings indicate that specific combinations of lubrication rate and porosity define a robust DS within the acceptable operating region, ensuring consistent tableting performance even in the presence of uncertainties. This approach emphasizes the importance of probabilistic DS in optimizing manufacturing processes and delivering built-in quality assurance.

**Keywords**: Probabilistic design space, Tableting process, Bayesian inference, Operational flexibility, Acceptable Operating Region, Nominal Operating Point inference

## 1. INTRODUCTION

Pharmaceutical manufacturing operates under stringent regulatory constraints, requiring a thorough understanding of the interplay between raw material attributes, process parameters, and product quality[1–3]. To meet these requirements, Quality by design (QbD) has emerged as a key approach to achieve consistent, high-quality production by identifying critical material attributes (CMAs) and critical process parameters (CPPs) that impact critical quality attributes (CQAs). The International Council for Harmonization (ICH) introduced the QbD initiative through guidelines ICH Q8–12, emphasizing a scientific and risk-based approach over traditional quality-by-testing methods[4,5]. This transformation in pharmaceutical development has enabled the development of robust process designs through the concept of design space (DS), which allows for safe operation without the need for additional regulatory approvals. DS can be identified using various strategies, such as empirical models, data-driven models, response surface methodologies, multivariate experimental design, and high-dimensional model representation, all grounded in existing literature, prior experiences, and process knowledge. However, conventional DS models often assume constant model parameters, overlooking the inherent uncertainty in both model parameter and the manipulated variables[6]. By incorporating these uncertainties, which typically can be captured by probabilistic distributions, the DS evolves from a deterministic framework to a probabilistic DS. This transformation provides a more realistic and adaptable approach to ensuring consistent product quality under variable conditions.

Bayesian approaches have been used to identify probabilistic DSs, in various process such as spray drying processes[7], crystallization of casopitant mesylate[8], and solid oral dosage form[9]. The DS is a subset of the knowledge space, which represents the operating envelope explored, studied, and well understood. To effectively characterize the probabilistic DS, computational methods are crucial, particularly in addressing uncertainties within model parameters[10]. Sampling algorithms

method discretizes the model parameter space by generating samples that account for probabilistic distributions of uncertainties. Techniques such as uniform gridding or (quasi) Monte Carlo simulations are commonly employed to propagate uncertainty and ensure all quality constraints are met with the desired level of reliability. This sampling-based approach is particularly effective in capturing the complexities of probabilistic DS offering robust solution for compliance with quality requirements. As number of parameters increases, these sampling methods suffer from the "curse of dimensionality", making them computationally expensive. In addition, these methods distribute samples uniformly, wasting computational resource on low-probability regions while undersampling high-probability areas.

To address these challenges, a Monte Carlo technique based on nested sampling method was developed in conjunction with a Bayesian inference based parameter estimation. The algorithm works by progressively sampling within nested contours of increasing likelihood, maintaining a dense sample in high-likelihood regions. This adaptive approach helps overcome the limitations of traditional methods, allowing particularly the handling of multimodal posteriors and high-dimensional spaces. Additionally, it allows for flexible adjustment of feasibility probability thresholds to meet industrial reliability requirements. Nested sampling integrates seamlessly with Bayesian parameter estimation, providing a unified probabilistic approach to probabilistic DS characterization. Overall, nested sampling provides a more efficient, flexible, and accurate tool for ensuring robust product quality in pharmaceutical manufacturing.

## 2. METHOD

### 2.1 Case study: Tablet Lubrication process

Lubrication plays a critical role in tablet manufacturing, particularly in direct compression process, as it enhances tablet ejection during compression. However, the extent of lubrication must be carefully controlled, as it significantly impacts the overall quality and efficacy of the drug product. The interaction between lubrication and compression processes influences key quality attributes, such as tablet tensile strength. An increase in lubrication may lead to a reduction in tensile strength, a challenge that can potentially be mitigated by increasing compaction pressure.

Kushner and Moore (2010)[11] developed an empirical model to capture lubrication and compaction performance across various blending conditions and scales, given by:

$$\sigma = \sigma_{sf=0.85,0}\big((1-\beta)+\beta exp(-\gamma k)\big) \quad (1)$$

where $\sigma_{sf=0.85,0}$ is the initial tensile strength at 0.85 solid fraction, $\beta$ is the total fraction of tensile strength that can be lost due to lubrication, and $\gamma$ is the lubrication rate constant of the blend.

Based on this initial approach, Nassar et al. (2022)[12] proposed a simplified model that relates the Kushner model parameters ($\sigma_{sf=0.85,0}$, and β) with the porosity:

$$\sigma_{sf=0.85,0} = a_1 exp\big(b_1(1-sf)\big) \quad (2)$$

$$\beta = a_2(1-sf)+b_2 \quad (3)$$

This model involves five unknown parameters: $\theta = [a_1(MPa);\ b_1(-);\ a_2(-);\ b_2(-);\ \gamma(dm^{-1})]$ and captures the effects of solid fraction and lubrication extent on tablet tensile strength which are identified as CPPs, while tablet tensile strength is regarded as a CQA.

### 2.2 Bayesian parameter estimation

In this study, the uncertainty associated with model parameters ($\theta$) is quantified using Bayesian inference. Experimental data published by Kushner et al. (2012)[13] for the Turbula mixer was utilized to estimate these parameters and identify the uncertainties in the model relationships. This dataset includes tensile strength measurements under varying conditions of lubrication and compaction, providing a reliable basis for parameter estimation.

Bayesian methods provide a powerful framework for parameter estimation, incorporating prior knowledge and experimental data to obtain a posterior distribution for each model parameter. This distribution provides the most likely values of the parameters and quantifies the associated uncertainty, which is crucial for model validation and identifying the robust design space.

Bayes' Theorem combines prior knowledge about the model parameters with the experimental data to update the probability distribution of the parameters. This approach is mathematically expressed as:

$$p(\theta|D) = \frac{\mathcal{L}(D|\theta)\varphi(\theta)}{P(D)} \quad (4)$$

Here, $\varphi(\theta)$ is the prior knowledge about the true value of the model parameters, $p(\theta|D)$ is the posterior distribution representing an updated belief about model parameter value after observing the experimental data. $\mathcal{L}(D|\theta)$ is likelihood distribution and $P(D)$ is marginal likelihood, which normalizes the posterior. The posterior distribution offers not only the most likely parameter values but also quantifies the uncertainty surrounding these estimates.

### 2.3 Nested sampling

The mathematical model describing the relationship between the CPPs, CMAs and CQAs is expressed as:

$$CQAs = f(x,\theta) \quad (5)$$

Here $x$ represents the vector of CPPs within the knowledge domain ($\chi$) in real space ($R^s$), while $\theta$ is the uncertain model parameter defined in $m$-dimensional real

space ($R^m$) with a probability density function (pdf).
The constraints on the CQAs, which can be combined with additional process constraints, are given as

$$G(x,\theta) := g(x, f(x,\theta)) \geq g^* \tag{6}$$

where $g^*$ represents a vector of predefined bounds for the CQAs. If the uncertainty in the model parameter is disregarded, the nominal DS is designed as

$$DS_{nom} := \{x \in \chi | g(x, G(x,\theta_{nom})) \geq g^*\} \tag{7}$$

where $\theta_{nom}$ represents a specific nominal value of the model parameter. However, since $\theta$ is inherently uncertain, whether due to limitation in parameter estimation or to the nature of modeling and data, ignoring this uncertainty may lead to oversimplified DS representations.

To address this, a probabilistic DS is expressed as

$$DS = \{x \in \chi | E_\theta[p(CQAs \in \Lambda) | X = x, \theta] \geq \alpha\} \tag{8}$$

According to equation (8), the DS is a subset of the knowledge space ($\chi$), mapping a set of CPPs ($x$) where the probability of CQAs satisfying the specified limit ($\Lambda$) exceeds a specified reliability value ($\alpha$), while accounting for the uncertainty in the model parameter $\theta$. The reliability value should be kept between $0 < \alpha \leq 1$.
A Bayesian framework addresses this challenge by treating $\theta$ as a random variable with joint probability distribution $p(\theta)$, representing the belief about its potential value of $\theta$. For example, $p(\theta)$ can be estimated from experimental data using Bayesian inference. In this framework, the model is primarily used to predict the probability that the manufacturing process is feasible for a given set of conditions.

$$\mathbb{P}[G(x,\cdot) \geq g^* | p(\theta)] := \int_{\{\theta: G(x,\theta) \geq g^*\}} p(\theta) d\theta \tag{9}$$

Hence, the probabilistic DS can be presented as

$$DS = \{x \in \chi | [\mathbb{P}[G(x,\cdot) \geq g^* | p(\theta)]] \geq \alpha\} \tag{10}$$

In general, at fixed manipulated variable $x,\cdot$ sampled from $S_d$, the probability of meeting CQA constraint is estimated via an ensemble of simulation over uncertainty scenario in $S_\theta$.

$$\hat{\mathbb{P}}[G(x_i,\cdot) \geq g^* | S_\theta] := \sum_{(\theta_j,\omega_j) \epsilon S_\theta} \mathbb{I}[G(x_i,\theta_j)]\omega_j \tag{11}$$

where $\mathbb{I}[\cdot]$ is an indicator function, which takes the value 1 if the constraint is satisfied, and 0 if they are not satisfied. The model parameters $\theta_i$ with corresponding weights $\omega_i$ are sampled from the posterior distribution function $p(\cdot)$. This method requires running full model $N_d \times N_\theta$ times, where $N_d$ and $N_\theta$ are the number of sample points taken from $S_d$ and $S_\theta$ space, respectively, which can be exceedingly costly for practical test cases.

In Nested sampling, the posterior distribution $p(\theta)$ can be derived using Bayes' theorem, which was explained earlier. The equation for the posterior distribution in the context of nested sampling is:

$$\left.\begin{aligned} p(\theta) &= \frac{\mathcal{L}(\theta)\varphi(\theta)}{\mathrm{Z}} \\ \mathrm{Z} &:= \int \mathcal{L}(\theta)\varphi(\theta)\, d\theta \end{aligned}\right\} \tag{12}$$

where Z is referred to as the Bayesian evidence, and it represents the integral of the likelihood weighted by the prior. Unlike the traditional Markov Chain Monte Carlo (MCMC) methods, which aim primarily to approximate the posterior distribution $p(\theta)$, nested sampling focuses on directly estimating Z as its primary target. This is achieved by iteratively sampling within nested contours of increasing likelihood, ensuring a systematic exploration of the parameter space. As a result, regions of high likelihood are densely sampled, enabling accurate estimation of Z. This feature is particularly advantageous for Bayesian model selection, as the evidence Z quantifies the overall fit of a model to the data while accounting for model complexity.

To implement nested sampling in DS characterization, $N_L$ points in the set of live points ($S_L$), can be initialized via uniform sampling in the design space. Nested sampling begins by estimating the feasibility probability at each of these points, according to equation (12), which calculates the likelihood of meeting the CQA constraints as described in equation (11). Estimating the feasibility probability for a given live point requires process model runs for the uncertainty set $S_\theta$. The number of models run for $N_\theta$ parameters in the uncertainty set $S_\theta$ is a critical computational cost of the algorithm.

During each iteration, the worst point $x$, having the lowest feasibility probability, is identified. This point is determined by calculating minimum feasibility probability ($\hat{\mathbb{P}}_{min}$) across all the live points, as shown in equation (13):

$$\hat{\mathbb{P}}_{min} = min_i\{\hat{\mathbb{P}}[G(x_i,\cdot) \geq g^* | S_\theta] : i \in S_L\} \tag{13}$$

The corresponding live point $x$ is the one that minimizes this probability is identified using equation (14), expressed as:

$$x = argmin_i\{\hat{\mathbb{P}}[G(x_i,\cdot) \geq g^* | S_\theta] : i \in S_L\} \tag{14}$$

Once the worst point is identified, it is replaced by a new point selected from the set of replacement point ($N_R$). To accelerate the process, the evaluation of a replacement candidate can be interrupted if the cumulative feasibility probability mass and the remaining samples are below a certain threshold. This strategy reduces unnecessary computations by rejecting unlikely candidates early. Rejected points are not added to the result set, ensuring that the focus remains on finding $N_L$ points with feasibility probabilities greater than or equal to the target reliability ($\pi$).

The replaced live points, along with their associated feasibility probabilities, are then stored in the result set for further analysis. The main iteration concludes when all live points meet or exceed the target probability. These points are then added to the result set, which may

also include dead points. If multiple replacements occur during the final iteration, the result set may exceed $N_L$. Conversely, if the set of live points becomes empty, the algorithm stops prematurely. This situation can be detected by monitoring the rate of improvement in feasibility over several iterations, ensuring that the algorithm doesn't waste resources when progress slows, or the reliability threshold is set too high.

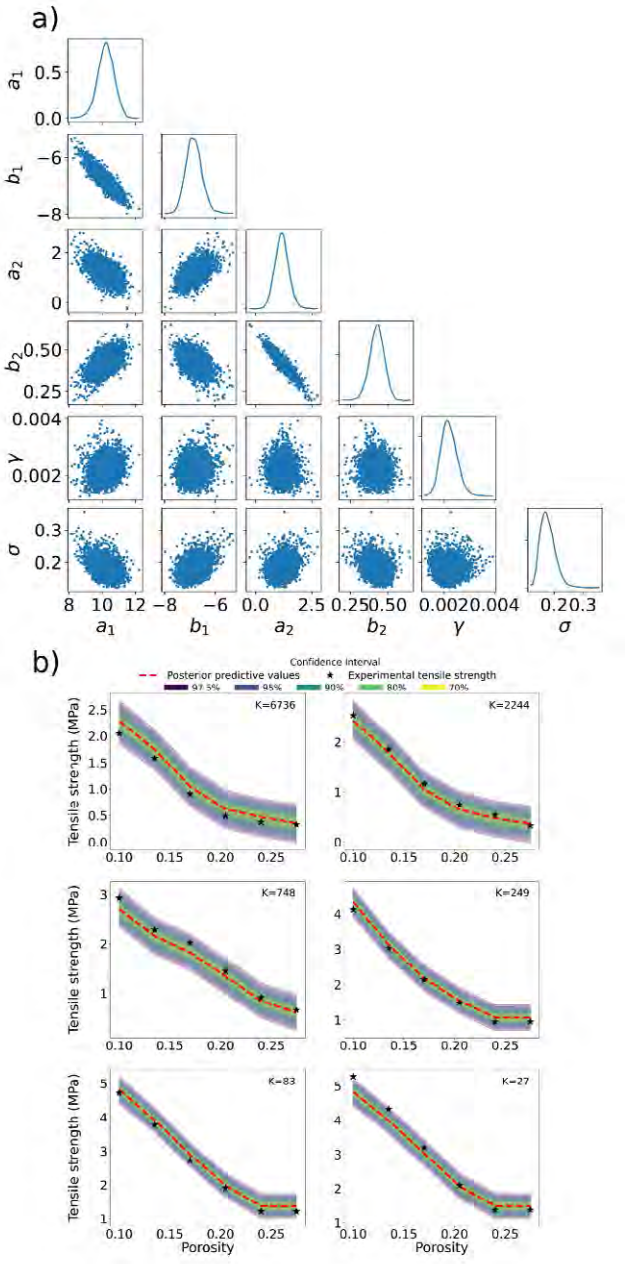



**Figure 1.** (a) Pair-wise plots of posterior distributions and (b) Model predictions with the confidence bands based on Bayesian inference.

The total number of process model runs ($N_{total}$), which is required for $N_{iter}$ iterations of nested sampling, can be expressed as:

$$N_{total} = N_\theta(N_L + N_{iter}N_R) \quad (15)$$

where, $N_L$ is total number of live points, $N_R$ is total number of replacement points, and $N_{iter}$ number of nested sampling iterations.

### 2.4 Flexibility Analysis and the Acceptable Operating Range (AOR)

The flexibility of a system is dictated by the size and shape of its Acceptable Operating Range (AOR) around the Nominal Operating Point (NOP). A larger AOR indicates greater flexibility, allowing the system to operate effectively across a wider range of conditions, while a smaller AOR reflects more constrained operating conditions, limiting the system's ability to adapt to variations[14]. The AOR is identified through a bisection search starting from a NOP and expanding uniformly in all directions until one of its vertices hits the boundary of the design space. The selection of points is entirely dependent on the constraints and nature of the problem. The algorithm terminates when either the maximum number of iterations is reached or when all vertices in the expansion are within the acceptable operating range, and the difference between the upper and lower bounds is smaller than the specified bisection tolerance. If the algorithm reaches the maximum number of iterations before convergence, it may indicate that the vertices haven't expanded sufficiently or the bisection tolerance hasn't been met, in which case increasing the number of iterations may help achieve better convergence.

## 3. RESULTS

The proposed Bayesian parameter estimation framework was implemented using experimental data from Kushner et al. (2012)[13] to quantify the uncertainties in the model parameters described in Sections 2.1 and 2.2. The pair-wise plot for all five model parameters ($\theta = [a_1, b_1, a_2, b_2, \gamma]$ constructed using the posterior samples obtained from Markov Chain Monte Carlo (MCMC), is illustrated in Figure 1(a). The plot shows the marginal posterior distributions along the diagonal as kernel density estimates and joint distributions of parameter pairs as contour plots below the diagonal. The sharpness of the marginal posterior probability density functions (PDFs), along with small coefficients of variation (CV), indicates that the parameter uncertainties are well quantified. The contour plots also provide key insights into the correlations between model parameter pairs [15], which are further explained by the Pearson correlation matrix in figure 2. For example, a strong negative correlation was observed between certain parameter pairs, such as $a_1$ & $b_1$, and $a_2$ & $b_2$. The covariance matrix, which captures these relationships, provides a more realistic measure of model uncertainty, as it reflects the actual behavior of the

system based on the posterior samples. Table 1 presents the sample mean, standard deviation, and CV values of the posterior MCMC samples. Furthermore, figure 1(b) shows the posterior predictive simulations (PPS), generated using the values of $\theta$ and $\sigma$ obtained during the inference. The mechanistic model used for the PPS is the same as the one used for the inference, facilitating direct comparison with the "experimental" data. The PPS confidence ranges are shown by the colored areas in figure 1(b), while the "experimental" values are indicated by the black stars overlaid on the prediction plots.

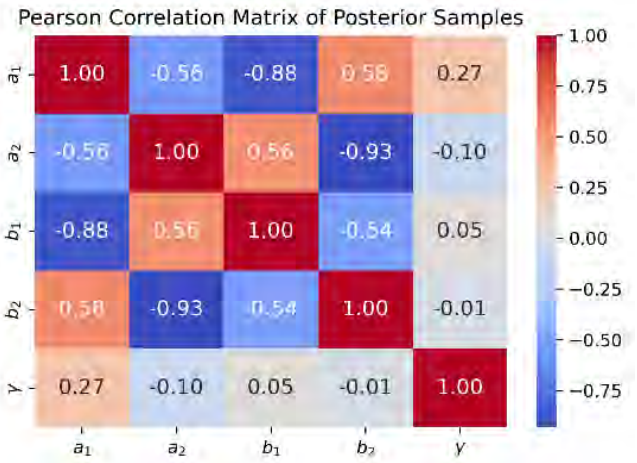



**Figure 2.** Pearson correlation matrix of model parameters. (Darker shades indicate stronger correlations).

**Table 1**. Summary of the Bayesian inference posterior statistics for all model parameters

| Model parameter | Mean | Std deviation | coefficients of variation (CV) |
|---|---|---|---|
| $a_1$ | 10.2268 | 0.508 | 0.0497 |
| $b_1$ | -6.83272 | 0.3116 | -0.045 |
| $a_2$ | 1.1765 | 0.3126 | 0.265 |
| $b_2$ | 0.4268 | 0.0492 | 0.115 |
| $\gamma$ | 0.00222 | 0.00033 | 0.150 |

The knowledge space for this analysis is defined in terms of two CPPs: (i) the lubrication extent $k(dm^{-1}) \in [27, 7000]$, and (ii) porosity, $\mathcal{E} \in [0.01, 0.31]$. The feasible operating region is further constrained by the CQA limits for 8 mm flat faced tablets, $Ts(MPa) \in [2,\ 6]$, ensuring the tableting tensile strength delivers the required quality attributes. The CQA constraints provide essential constraints, limiting the parameter space and ensuring that the system remains within acceptable performance limits. Next, the impact of uncertainty is captured by the probabilistic design space by propagating the model parameter uncertainties, represented as a set of weighted samples $\{\theta_j, \omega_j\}_{j=1,\dots N_\theta}$.

A nested sampling algorithm with a reliability target value of α=0.95 is implemented to focus on higher likelihood samples. To ensure the sufficiently high sample density, 500 live points and 100 uncertainty model descriptions, each with equal weights, are drawn from the posterior density function. The resulting samples are depicted in different colors according to their reliability membership, providing a clear visualization of the probabilistic design space and highlighting areas of high and low reliability in figure 3. On comparison with quasi MCMC, it is observed that nested sampling method efficiently focusing on high-probability region of knowledge space and eliminate the least-probability sampling points. This targeted approach not only enhances the precision of the estimates but also significantly reduces the computational resources required compared to more exhaustive sampling methods.

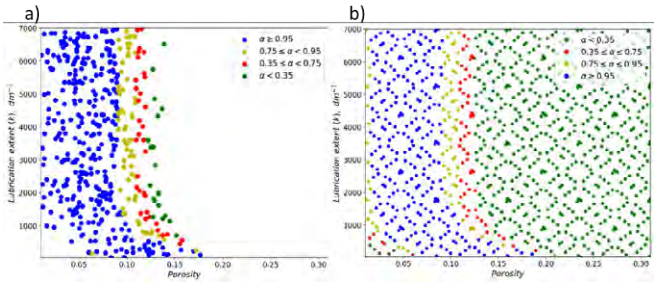



**Figure 3.** Probabilistic design space identified using (a) Nested sampling and (b) Quasi MCMC for the tableting process

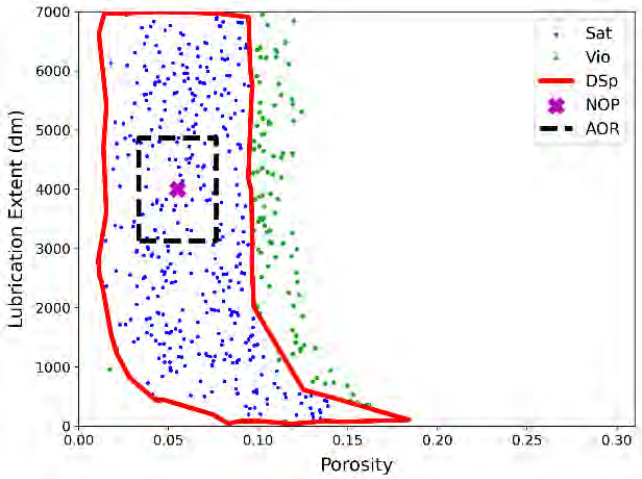



**Figure 4.** Acceptable Operating Region and Nominal Operating Point. 4

To visualize the AOR, probabilistic design space is segmented into satisfied (blue) and violated (green) regions, as shown in figure 4. The black line represents the AOR, encompassing the range of porosity and lubrication extent values that satisfy predefined constraints. The NOP, marked by a purple star at [0.055, 4000], serves as a reference for optimal system performance. The red line

indicates the DS boundary, beyond which the system may exhibit undesirable behavior. . A bisection search method is applied to expand a uniform square region outward from the NOP in all directions until one of the vertices reaches the boundary, ensuring that the AOR remains within acceptable design constraints. The final AOR size of 0.0625 $dm^{-1}$, derived from this iterative process, represents the largest feasible region centered around the NOP's lubrication extent and porosity values. This indicates improved process flexibility and robustness without violating constraints, providing a systematic approach to assess the system's operational limits under varying conditions.

## 4. CONCLUSION

This study successfully developed a probabilistic design space for a pharmaceutical tableting process using Bayesian inference and nested sampling. The approach effectively quantified and propagated uncertainties in model parameters, ensuring consistent tablet tensile strength (CQA) with over 95% reliability. The nested sampling method efficiently identified high-probability regions, reducing computational costs and enhancing precision. The acceptable operating range analysis demonstrated significant process flexibility and robustness. This work underscores the value of probabilistic DS in optimizing manufacturing processes and maintaining regulatory compliance, offering a powerful tool for consistent product quality and operational robustness. Future research will explore extending this methodology to other processes and parameters, with a focus on using iterative selection of nominal points to further explore process robustness and identify optimal operating conditions.

## ACKNOWLEDGEMENTS

The authors acknowledge funding from the UK Engineering and Physical Sciences Research Council (EPSRC), for Made Smarter Innovation – Digital Medicines Manufacturing Research Centre (DM2), EP/V062077/1.

## REFERENCES

1. Campbell, T. J. S.; Rielly, C. D.; Benyahia, B. Digital Design and Optimization of an Integrated Reaction-Extraction-Crystallization-Filtration Continuous Pharmaceutical Process. Comput.-Aided Chem. Eng. 2022, 51, 775–780.
2. Benyahia, B.; Brumano, L. P.; Pessoa, A.; Santos da Silva, F. V. Biopharmaceutical Development, Production, and Quality. In New and Future Developments in Microbial Biotechnology and Bioengineering: Microbial Biomolecules: Properties, Relevance, and Their Translational Applications; Elsevier, 2020; pp 69–89. https://doi.org/10.1016/B978-0-444-64301-8.00003-2.
3. Benyahia, B. Applications of a Plant-Wide Dynamic Model of an Integrated Continuous Pharmaceutical Plant: Design of the Recycle in the Case of Multiple Impurities. In Computer Aided Chemical Engineering; Elsevier B.V., 2018; Vol. 41, pp 141–157. https://doi.org/10.1016/B978-0-444-63963-9.00006-3.
4. Peterson, J. J.; Yahyah, M. A Bayesian Design Space Approach to Robustness and System Suitability for Pharmaceutical Assays and Other Processes. Stat Biopharma Res 2009, 1 (4), 441–449. https://doi.org/10.1198/sbr.2009.0037.
5. Peterson, J. J. A Bayesian Approach to the ICH Q8 Definition of Design Space. J Biopharm Stat 2008, 18 (5), 959–975. https://doi.org/10.1080/10543400802278197.
6. Bouchkira, I.; Benyahia, B. Multi-Objective Optimization Approach for Enhancing Flexibility of a Pharmaceutical Process. In Proceedings of the 34th European Symposium on Computer Aided Process Engineering / 15th International Symposium on Process Systems Engineering (ESCAPE34/PSE24), June 2-6, 2024, Florence, Italy; 2024; pp 1271–1278.
7. Lebrun, P.; Boulanger, B.; Debrus, B.; Lambert, P.; Hubert, P. A Bayesian Design Space for Analytical Methods Based on Multivariate Models and Predictions. J Biopharm Stat 2013, 23 (6), 1330–1351. https://doi.org/10.1080/10543406.2013.834922.
8. Tabora, J. E.; Lora Gonzalez, F.; Tom, J. W. Bayesian Probabilistic Modeling in Pharmaceutical Process Development. AIChE Journal 2019, 65 (11). https://doi.org/10.1002/aic.16744.
9. Sano, S.; Kadowaki, T.; Tsuda, K.; Kimura, S. Application of Bayesian Optimization for Pharmaceutical Product Development. J Pharm Innov 2020, 15 (3), 333–343. https://doi.org/10.1007/s12247-019-09382-8.
10. Yuan, X.; Benyahia, B. A Holistic Approach for Model Discrimination, Multi-Objective Design of Experiment and Self- Optimization of Batch and Continuous Processes. In Proceedings of the 34th European Symposium on Computer Aided Process Engineering / 15th International Symposium on Process Systems Engineering (ESCAPE34/PSE24), June 2-6, 2024, Florence, Italy; 2024; pp 391–396.
11. Kushner, J.; Moore, F. Scale-up Model Describing the Impact of Lubrication on Tablet Tensile Strength. Int J Pharm 2010, 399 (1–2), 19–30.

https://doi.org/10.1016/j.ijpharm.2010.07.033.
12. Nassar, J.; Williams, B.; Davies, C.; Lief, K.; Elkes, R. Lubrication Empirical Model to Predict Tensile Strength of Directly Compressed Powder Blends. Int J Pharm 2021, 592. https://doi.org/10.1016/j.ijpharm.2020.119980.
13. (Kushner IV, J. Incorporating Turbula Mixers into a Blending Scale-up Model for Evaluating the Effect of Magnesium Stearate on Tablet Tensile Strength and Bulk Specific Volume. Int J Pharm 2012, 429 (1–2), 1–11. https://doi.org/10.1016/j.ijpharm.2012.02.040.
14. Sachio, S.; Kontoravdi, C.; Papathanasiou, M. M. A Model-Based Approach towards Accelerated Process Development: A Case Study on Chromatography. Chemical Engineering Research and Design 2023, 197, 800–820. https://doi.org/10.1016/j.cherd.2023.08.016.
15. Benyahia, B.; Latifi, M.A.; Fonteix, C.; Pla, F. Emulsion copolymerization of styrene and butyl acrylate in the presence of a chain transfer agent. Part 2: Parameters estimability and confidence regions 2013, 90, 110–118. https://doi.org/10.1016/j.ces.2012.12.013.

© 2025 by the authors. Licensed to PSEcommunity.org and PSE Press. This is an open access article under the creative commons CC-BY-SA licensing terms. Credit must be given to creator, and adaptations must be shared under the same terms. See https://creativecommons.org/licenses/by-sa/4.0/



Systems & Control Transactions

**Research Article - Peer Reviewed Conference Proceeding**
ESCAPE 35 - European Symposium on Computer Aided Process Engineering
Ghent, Belgium. 6-9 July 2025
Jan F.M. Van Impe, Grégoire Léonard, Satyajeet S. Bhonsale,
Monika E. Polańska, Filip Logist (Eds.)

PSE PRESS

# Separation Sequencing in Batch Distillation: An Extension of Marginal Vapor Rate Method

**Prachi Sharma[a], Sujit S. Jogwar[a]***

[a] Indian Institute of Technology Bombay, Department of Chemical Engineering, Mumbai, Maharashtra, India
* Corresponding Author: jogwar@iitb.ac.in

## ABSTRACT

Multi-component batch distillation, wherein multi-component mixtures are separated using a single column, is a crucial separation technique in the chemical industry. Traditionally, the components are separated in the descending order of volatility (direct sequence). Similar to continuous distillation, a specific separation sequence can optimize batch distillation. This work aims to generate such optimal sequence for a batch distillation in a computationally efficient manner. Specifically, the proposed approach extends the marginal vapor rate method, which is used for sequencing continuous distillation to multi-cut batch separation. The approach addresses challenges arising due to dynamic nature of batch distillation. The proposed methodology is validated using simulation case studies.

**Keywords**: Batch Distillation, Separation Sequencing, Marginal Vapor Method

## INTRODUCTION

Batch distillation is an important separation technique which is used in the fine and specialty chemical, pharmaceutical, biochemical and food industries. With batch distillation, separation of multi-component mixture can be achieved using a single column where products are recovered in a particular sequence (also known as multi-cut operation). Conventionally, the feed is added in the reboiler and products are withdrawn as distillate in the decreasing order of their volatilities (direct sequence, Figure 1 (a)). On the other hand, in an inverse configuration, the feed is added in the reflux drum and the products are withdrawn from the bottom in the increasing order of volatility (indirect sequence, Figure 1 (b)). Although these sequences can yield the products with the same purity, they require different capital and operating costs. A key question in the design of batch distillation processes is to obtain the optimal sequence of separation. As the number of components to be separated increases, the number of potential separation sequence alternatives increase drastically, necessitating a systematic approach to obtain the best sequence. Optimal sequencing leads to reduced cost and improved efficiency in industrial distillation operations. However, very few studies address this aspect of batch distillation [1-3].

On the other hand, there are numerous studies published in literature discussing design of continuous distillation separation sequences [4-9]. These articles deal with choosing of split sequences to separate a multi-component feed stream into relatively pure, typically single component, product streams making up the majority of the design decisions. Most of

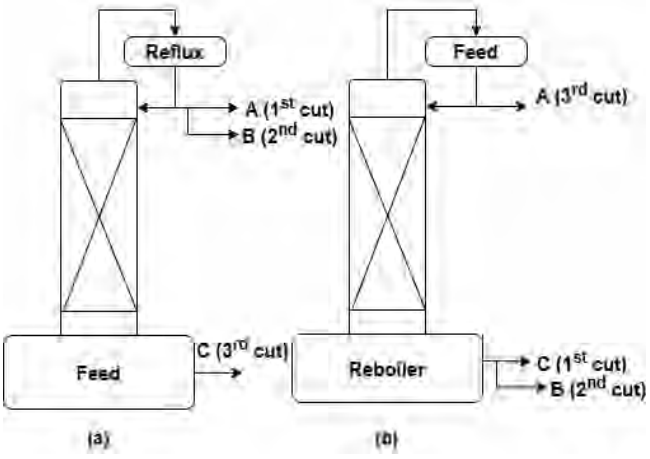



**Figure 1.** Batch distillation sequences (a) direct, (b) indirect for a ternary mixture

these articles either uses heuristics or rigorous optimization. Heuristic approaches offer rapid and low-data requirements for investigation, but often have one dominant rule, leading to miscalculations or contradictory rules. Employing these rules in a structured way is challenging. Mathematical programming methods employ optimization strategies to create ideal separation structures, offering rigorous and optimal solutions. However, they are usually computationally inefficient [9]. One of the most popular methods for continuous distillation column sequencing is marginal vapor rate method [10]. In this method, marginal vapor accounts for capital cost (column diameter) as well as the operational cost (reboiler duty). The sequence with the lowest marginal vapor rate is considered to be optimal.

This article extends this marginal vapor method to solve the sequencing problem for batch distillation. This extension faces two significant challenges. Firstly, in batch distillation, the feed and product compositions vary over time, in contrast to steady state operation in continuous distillation. Secondly, there are material balance limits on total moles rather than molar flow rate. These two challenges are addressed in this work by approximating the batch distillation as a sequence of continuous distillation tasks with varying feed composition [11]. Multiple simulation studies are used to demonstrate and validate performance of the proposed method.

## SEPARATION SEQUENCING

Separation sequencing refers to the process of determining the most efficient order of separating different components of a mixture based on their boiling points or volatility. This study investigates how a specific separation sequence can be employed in a batch distillation column to separate a mixture of N components (A, B, C, etc.) into N relatively pure single component products. N components can be separated into pure components using the number of sequences ($N_s$) provided by Thompson and King [7]:

$$N_s = \frac{[2(N-1)]!}{N!\,(N-1)!} \quad (1)$$

Consider a quaternary mixture of A, B, C and D, where A being the most volatile component and D the least. There are five potential sequences (Table 1) and their respective configurations are shown in Figure 2. Table 1 shows the labelling used to assign numbers to the five sequences. For example, in sequence 1, the first task is to separate the most volatile component A as the first cut. The second tasks is to separate component B as the second cut and the last separation task is perform separation between C and D to obtain C as the third cut. The last product D is collected in the reboiler. Kindly note that only main product cuts are listed in these sequence. In many cases, intermediate slop cuts are also taken during multi-cut separation. The objective of separation sequencing is to find the optimal separation sequence among these alternatives.

**Table 1**: Possible sequences for separation of quaternary mixture

| Sequence | Task I | Task II | Task III |
|---|---|---|---|
| 1 | A/BCD | B/CD | C/D |
| 2 | A/BCD | BC/D | B/C |
| 3 | AB/CD | A/B | C/D |
| 4 | ABC/D | A/BC | B/C |
| 5 | ABC/D | AB/C | A/B |

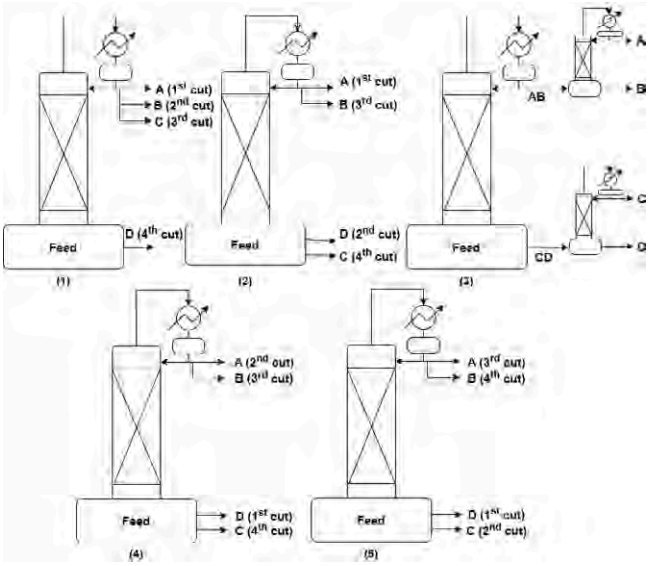



**Figure 2**: Possible configurations for separation of quaternary mixture

## MARGINAL VAPOR METHOD FOR CONTINUOUS DISTILLATION SEQUENCING

Westerberg introduced the marginal vapor method which finds its motivation from marginal price, for solving the sequencing problem for multi-component ideal mixtures in continuous distillation column. Marginal price (annualized cost) assesses the cost of performing a split in the presence of non-key components [10]. The marginal annualized cost (MAC) is evaluated as the cost difference between separation in the presence and absence of non-key components. The MAC is used to select tasks which are least affected by the presence of non-key components. Those separations most affected by the presence of non-key components are operated after the non-keys are no longer present. They demonstrated that MAC can be estimated from the marginal vapor rate

(MVR). Since vapor rate is a key determinant of column diameter, reboiler and condenser areas, and reboiler and condenser duties, it can be a cost metric accounting for the estimate.

Marginal vapor (MV) is the difference in vapor flow (V) of a distillation column in the presence and absence of non-key components. The marginal vapor of a separation task $l \ldots lk/hk..h$ is given by:

$$MV(l \ldots lk/hk..h) = V(l \ldots lk/hk..h) - V(lk/hk) \quad (2)$$

where $V(l \ldots lk/hk..h)$ is the vapor rate of the separation task $l \ldots lk/hk..h$ in the presence of non-key components, and $V(lk/hk)$ is the vapor rate of the separation task $lk/hk$. For example, MV of a quaternary mixture (A, B, C and D) where component A is separated from component B in the presence of other two non-key components will be:

$$MV(A/\mathrm{BCD}) = V(\mathrm{A/BCD}) - V(A/B) \quad (3)$$

Marginal vapor method is based on Underwood's equation. To compute marginal vapor for a separation task, the vapor flow for the column is calculated first using Underwood's equation which assumes constant molar overflow in the column. The Underwood's equations for a distillation column are given by:

$$\sum_{i=l}^{h} \frac{\alpha_i d_i}{\alpha_i - \emptyset} = D(R_{min} + 1) \quad (4)$$

$$\sum_{i=l}^{h} \frac{\alpha_i f_i}{\alpha_i - \emptyset} = F(1 - q) \quad (5)$$

where $l$ is the lightest component in the feed, $h$ is the heaviest component, $F$ and $D$ are feed and distillate flow rates respectively, $\alpha_i$ is the relative volatility of component $i$, $d_i$ is its quantity in the distillate, $f_i$ is its amount in the feed, $R_{min}$ is the minimum reflux ratio of the column, $\emptyset$ is the root of the Eq. (5), and $q$ is the thermal condition of the feed, which is equal to 1 for a saturated liquid. The actual reflux ratio of a column is given by:

$$R = \beta R_{min} \quad (6)$$

where $\beta > 1$ and typically taken as 1.2-1.3. The vapor rate in a column, $V$, is given by:

$$V = D(R + 1) \quad (7)$$

where $D$ is distillate flow rate and $R$ is the reflux ratio.

These equations are solved to estimate vapor flows $V(l \ldots lk/hk..h)$ and $V(lk/hk)$. Then, using Eq. (2), marginal vapor rate for the separation task $(l \ldots lk/hk..h)$ is computed. Subsequently, the MV for entire sequence is computed by adding MV of each separation task in that sequence. Lastly, the sequence with the least MV is considered to be optimal.

## MARGINAL VAPOR METHOD FOR BATCH DISTILLATION SEQUENCING

In the proposed approach, the MV method for continuous distillation as described above is extended for batch separation. This extension faces two significant challenges. Firstly, there are material balance limits on total moles rather than molar flow rate (feed $F$ and products $D$ are specified in total mol instead of molar flow rate). Secondly, in batch distillation, the feed $(x_{fi})$ and product $(x_{di})$ compositions vary over time, in contrast to steady state operation in continuous distillation. This results in varying $R_{min}$ and vapor flow, $V$, during the batch period. To address these challenges, it is considered that batch distillation is equivalent to continuous distillation with varying feed composition [11]. Therefore, by calculating the variation in feed composition as a function of time, the variation in vapor rate during batch distillation can be estimated. Subsequently, this vapor rate profile is integrated along the batch to compute the total vapor required for a given separation task. Lastly, instead of computing marginal vapor rate, marginal total vapor is computed for a separation task. Marginal total vapour is the difference between total vapor required for a given batch separation task in the presence and absence of non-key components. The analytical equations enabling the calculation of this marginal total vapor are presented below.

The first step is to derive equations capturing dynamic evolution of feed composition. Consider a multicomponent mixture (A, B, C....N) separation in a traditional batch distillation, where feed is introduced at the reboiler with A being the most volatile component. Assuming negligible tray and reflux drum holdup, the overall material balance for the column is given as:

$$\frac{dH_F}{dt} = -D \quad (8)$$

where $H_F$ is the total holdup in the still at any time instant and $D$ is the product withdrawal rate. The component mass balance for the $i^{th}$ component in the reboiler is given by:

$$\frac{d[H_F x_{Fi}]}{dt} = -\mathrm{D}x_{Di} \quad \forall\, i \in \mathrm{A, B, C \ldots N} \quad (9)$$

where $x_{Fi}$ and $x_{Di}$ are the composition of component $i$ in the still and distillate respectively. Integrating Eq. (8) over time with $F_0$ being the initial feed amount at the start of operation, for constant distillate flow rate, $D$, the variation of $H_F$ with time is given by:

$$H_F = F_0 - Dt \quad (10)$$

Assuming sharp separation and that the components are collected into pure streams without any slop-cuts (i.e. $x_{DA} = 1, x_{Dj} = 0\ \forall\, i \in \mathrm{B, C, D \ldots N}$), and substituting Eq. (8) in Eq. (9), the Eq. (9) can be rearranged as:

$$\frac{dx_{FA}}{dt} = \frac{D(x_{FA} - 1)}{H_F} \quad (11)$$

Integrating Eq. (11), the relation of $x_{FA}$ with time is given by:

$$x_{FA} = \frac{F_0(z_{FA} - 1)}{F_0 - Dt} + 1 \quad (12)$$

where $z_{FA}$ is the initial feed composition of component A. Similarly, the compositions of all the other components are given by:

$$x_{Fi} = \frac{F_0(z_{Fi})}{F_0 - Dt} \qquad \forall\, i \in \mathrm{B, C, D \ldots} \quad (13)$$

The Underwood's equations (Eq. (4) and (5)) are reformulated in terms of compositions of the components:

$$\sum_{i=l}^{h} \frac{\alpha_i x_{di}}{\alpha_i - \emptyset} = (R_{min} + 1) \quad (14)$$

$$\sum_{i=l}^{h} \frac{\alpha_i x_{fi}}{\alpha_i - \emptyset} = (1 - q) \quad (15)$$

The feed compositions computed by Eq. (12) and (13) are used to find the roots of Eq. (15) at each time instant, $t$. Accordingly, $R_{min}$ and $V$ variations as a function of time are obtained.

For an indirect sequencing of the same mixture in an inverted batch column, feed is introduced at the top of the column and the least volatile product (N) is withdrawn first from the reboiler. The overall material balance is:

$$\frac{dH_F}{dt} = -L \quad (16)$$

where $H_F$ is the total holdup in the reflux drum at any time instant and $L$ is the product withdrawal rate. Integrating Eq. (16) over time with $F_0$ being the initial feed amount at the start of operation for constant withdrawal rate, $L$ , the relation of $H_F$ with time can be written as:

$$H_F = F_0 - Lt \quad (17)$$

The component mass balance for the $i^{\text{th}}$ component in the reflux drum is given by:

$$\frac{d[H_F x_{Fi}]}{dt} = -L x_{Bi} \qquad \forall\, i \in \mathrm{A, B, C \ldots N} \quad (18)$$

where $x_{Bi}$ and $x_{Fi}$ are the composition of component $i$ in the still and reflux drum respectively. Assuming sharp separation i.e. $x_{Bj} = 0\ \forall\, j \in \mathrm{A, B, \ldots N-1}$ and $x_{BN} = 1$, the composition profiles for the components are given by:

$$x_{FN} = \frac{F_0(z_{FN} - 1)}{F_0 - Lt} + 1 \quad (19)$$

$$x_{Fi} = \frac{F_0(z_{Fi})}{F_0 - Lt} \qquad \forall\, i \in \mathrm{A, B, \ldots N-1} \quad (20)$$

where $z_{Fi}$ is the initial feed composition of component $i$. For each time instant, the amount of vapor produced is computed similarly to the direct sequencing approach but in a reverse manner. The total amount of vapor is then integrated over time.

Eventually, marginal vapors for each separation task in a sequence are added together to obtain its marginal total vapor. Lastly, the sequence with the lowest marginal total vapor is recommended as the optimal sequence.

## CASE STUDIES

Let us now consider few case studies to illustrate and validate the proposed approach.

### Case study 1: Pentane-Hexane-Heptane

In the first case study, a mixture of pentane (A), hexane (B), and heptane (C) is to be separated into pure components. Using the above-mentioned methodology, marginal total vapor is estimated for the direct and indirect sequences.

**Table 2**: Data for case study 1

| Component | α | $z_F$ |
|---|---|---|
| Pentane | 7.1352 | 0.25 |
| Hexane | 2.6292 | 0.50 |
| Heptane | 1.0000 | 0.25 |

In the direct sequence, consider the separation A/BC where pentane is separated first from hexane in the presence of heptane. Using the initial feed conditions shown in Table 2, variation of $x_F$ with time is computed using Eq. (12) and Eq. (13) for a constant distillate rate (D) of 1.5 mol/min. These $x_F$ values are then used to find the roots ($\emptyset$) of Eq. (15) to calculate the reflux ratio of the column which is further used to estimate the vapor generated at each time instant.

Figure 3 shows the vapor rate at each time instant for A/BC and A/B respectively. The vapor generated is integrated over batch time to compute the total vapor for the column ($V(\mathrm{A/BC})$) which comes out to be 3627 mol. In a similar way, the total vapor required for binary separation of pentane and hexane ($V(\mathrm{A/B})$) is computed as 2853 mol. The marginal total vapor for the direct sequence is 774 mol.

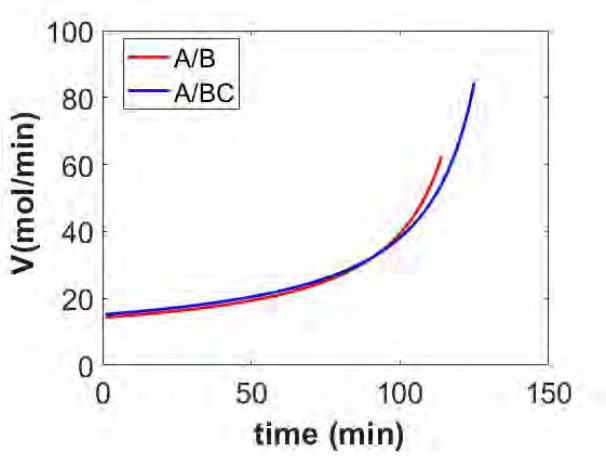



**Figure 3**: Vapor flow for the separation task A/BC and A/B

Alternatively, for the indirect sequence, heptane is separated first from hexane in the presence of pentane. Using the same initial conditions used for the direct sequencing method (Table 2), the total vapor is calculated for both ternary $V(\mathrm{AB/C})$ and binary separation $V(\mathrm{B/C})$. The corresponding values are 5772 mol and 2804 mol, respectively. Thus the marginal total vapor is 2968 mol. It is clearly evident that the direct sequence is better than the indirect sequence.

In order to validate this claim, dynamic simulations are performed for this batch distillation in both conventional (direct sequence) and inverted (indirect sequence) configurations. The operating conditions required for this simulation are specified in Table 3 and Table 4 respectively. For the direct sequence, the time required to separate pentane from hexane in the presence of heptane is 150 minutes. As the simulation used a constant vapor rate of 20 mol/min, the total vapor required is 3000 mol. Similarly, total vapor required for the separation of binary mixture (pentane-hexane) is 2220 mol. Thus, marginal total vapor for direct sequence based on dynamic simulation is 780 mol.

Similarly, for the indirect sequence, the time required to separate hexane from heptane in the presence of pentane is 203 minutes, and the total vapor required is 4060 mol. Total vapor required for the corresponding binary separation (hexane-heptane) is 1140 mol. This results in marginal total vapor of 2920 mol.

**Table 3**: Operating conditions for case study 1 in a direct sequence

| Separation | A/BC | A/B |
|---|---|---|
| No. of trays | 42 | 42 |
| Feed (mol) | 1000 | 750 |
| $Z_F$ | [0.25 0.50 0.25] | [0.333 0.667] |
| V (mol/min) | 20 | 20 |

**Table 4**: Operating conditions for case study 1 in an indirect sequence

| Separation | AB/C | B/C |
|---|---|---|
| N | 42 | 42 |
| Feed(mol) | 1000 | 750 |
| Z | [0.25 0.50 0.25] | [0.667 0.333] |
| V(mol/min) | 20 | 20 |

Table 5 shows the marginal vapor for the sequences as calculated from the proposed approach and simulations. The differences in the values of marginal total vapor are because of the assumption of negligible tray holdup as during simulations, 5% of the initial feed amount was taken as total tray holdup.

**Table 5**: Marginal total vapor for case study 1

| Sequence | Proposed (mol) | Simulation (mol) |
|---|---|---|
| Direct | 774 | 780 |
| Indirect | 2968 | 2920 |

It can be seen from the table above that the marginal vapor of the direct sequence is less than that of the indirect sequence and hence, the direct sequence is the optimal separation sequence for this mixture. As the simulation study used constant vapor rate, smaller total vapor for direct sequence also corresponds to smaller batch time as compared to indirect sequence.

The concentration profiles of three components in the still and reflux drum over time for a traditional batch column (direct sequence) are displayed in Figure 4 (a) and (b). There are five phases to the operation. Phase 1 involves operating the column under total reflux circumstances until the reflux holdup achieves a certain level of purity. The pure product is then gathered in phase 2. Phase 3 involves the withdrawal of an impure mixture of A and B called slop cut. Pure product B is gathered in the following stage, and the process is finished when the holdup in the still is pure C. Similarly, Figure 4 (c) and (d) shows the concentration profile of three components in the reflux drum and the still respectively over time for an inverted batch column (indirect sequence). The product is removed from the bottom and the reboiler holdup is maintained constant. Here also there are 5 operational phases with product C removed in phase 2, product B in phase 4 and product A in the fifth phase. For Figure 4, it can again be seen that the direct sequence is faster than the indirect sequence. This further validates the conclusion drawn from the proposed approach.

## Case study 2: Benzene-Toluene-o-Xylene

Similar study is performed for a mixture of Benzene-

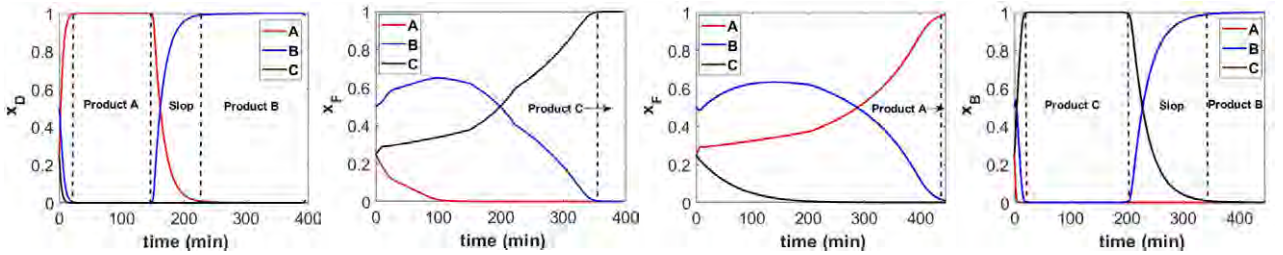



**Figure 4:** Concentration profile of case study 1 in (a) reflux drum, (b) still in direct sequence and (c) reflux drum, (d) still in an indirect sequence

Toluene-o-Xylene with a different set of operating conditions. The information for the problem specification of this mixture is given in Table 6.

**Table 6**: Data for case study 2

| Component (i) | α | $z_F$ |
|---|---|---|
| Benzene | 6.2314 | 0.2 |
| Toluene | 2.6436 | 0.6 |
| o-Xylene | 1.0000 | 0.2 |

The application of the proposed approach results in marginal total vapor of 1047 mol for indirect sequence and 2890 mol for direct sequence. Thus, indirect sequence (inverted configuration) is better for this mixture. This was validated using simulation study where direct sequence required almost three times the amount of total vapor as compared to indirect sequence.

**Table 7:** Marginal total vapor for case study 2

| Sequence | Proposed (mol) | Simulation (mol) |
|---|---|---|
| Direct | 2890 | 2880 |
| Indirect | 1047 | 1060 |

## Quaternary Mixture

Lastly, let us consider a four-component alkane mixture of i-Butane (A), n-Butane (B), i-Pentane (C), and n-Pentane (D) with operating conditions given in Table 8 [9]. Each of the five alternate sequences with ten different separation tasks are indicated in Table 1. Table 9 lists the marginal total vapor values for this mixture using simulation and the proposed approach. The five sequences are then ranked, where the sequence with least marginal total vapor value is ranked first and the sequence with the highest value is ranked the last.

Sequence 3 which is an intermediate sequence is ranked first based on proposed approach as well as dynamic simulation. This sequence is favored as the separation of n-Butane from i-Pentane is easier than that from i-Butane or n-Pentane according to the relative volatility difference.

**Table 8**: Data for quaternary mixture

| S. NO. | Component | $z_F$ | α |
|---|---|---|---|
| 1 | i-Butane | 0.2 | 2.0 |
| 2 | n-Butane | 0.3 | 1.8 |
| 3 | i-Pentane | 0.2 | 1.2 |
| 4 | n-Pentane | 0.3 | 1.0 |

**Table 9**: Marginal total vapor for quaternary mixture

| Sequence | Proposed (mol) | Simulation (mol) | Rank |
|---|---|---|---|
| 1 | 1410 | 1492 | 5 |
| 2 | 1200 | 1251 | 4 |
| 3 | 570 | 596 | 1 |
| 4 | 1050 | 1042 | 3 |
| 5 | 870 | 874 | 2 |

Based on these three case studies, it can be argued that the marginal total vapor method proposed in this work correctly captures the optimal separation sequence for batch distillation.

## CONCLUSION

In this article, we have effectively extended the marginal vapor rate method for optimal sequencing of continuous columns to batch column operations for ideal systems. By applying this method to batch columns, we can deduce the optimal separation sequence in a computationally efficient manner. The proposed approach offers computational advantage over rigorous optimization as well as helps identifying optimal non-trivial separation sequences. The methodology is validated with simulation case studies involving separation of ternary and quaternary mixtures.

In the current form, the work can be directly applied to zeotropic systems. In order to extend this to non-ideal mixtures, one needs to check the feasibility of a separation task before evaluating the separation sequences.

One of the popular approaches to this end is the residue curve maps (RCM) [12]. Thus, the extension of the proposed work to non-ideal mixtures will involve using RCM to identify feasible regions for separation and subsequently determine the optimal sequence of distillation steps. This work is under progress in our group.

## REFERENCES


1. Bernot C., Doherty F. M., Molone F. M. Feasibility and separation sequencing in multicomponent batch distillation. *Chemical Engineering Science* 46 :1311–1326 (1991)
2. Safrit B. T., Westerberg A. W. Synthesis of Azeotropic Batch Distillation Separation Systems. *Ind. Eng. Chem. Res.* 36: 1841-1854 (1997)
3. Jain S., Kim J., Smith R. Process synthesis of batch distillation systems. *Ind. Eng. Chem. Res.* 52.24 :8272-8288 (2013)
4. Lockhart F. J. Multi-column distillation of natural gasoline. *Pet. Refin*. 26.8:14 (1947)
5. Rod V., Marek J. Separation sequences in multicomponent rectification. *Collect. Czech. Chem. Commun.*, 24.10: 3240-3248 (1959)
6. Nishimura H., Hiraizumi Y. Optimal system pattern for multi-component distillation systems. *Int. Chem. Eng.* 11, 188. (1971)
7. Thompson R. W., King C. J. Systematic synthesis of separation schemes. *AIChE J.* 18.5, 941-948 (1972)
8. Agrawal R. Synthesis of distillation column configurations for a multicomponent separation, *Ind. Eng. Chem. Res.* 35.4:1059–1071 (1996)
9. Giri A. P., Yogesh S. M., Separation Task Based Marginal Vapor Rate (MVR) Approach for Optimal Column Sequencing of Multicomponent Mixtures. *Theoretical foundations of Chemical Engineering* 57:360–368 (2023)
10. Modi A. K., Westerberg A. W. Distillation Column Sequencing Using Marginal Price. *Ind. Eng. Chem. Res.* 31:839-848 (1992)
11. Diwekar U. Batch Distillation: simulation, optimal design, and control. *CRC Press* (1995).
12. Malone M. F., Doherty M. F. Separation system synthesis for nonideal liquid mixtures. In AIChE Symposium Series, 91.304:9-18 (1995).



© 2025 by the authors. Licensed to PSEcommunity.org and PSE Press. This is an open access article under the creative commons CC-BY-SA licensing terms. Credit must be given to creator and adaptations must be shared under the same terms. See https://creativecommons.org/licenses/by-sa/4.0/




Systems & Control Transactions

**Research Article - Peer Reviewed Conference Proceeding**
ESCAPE 35 - European Symposium on Computer Aided Process Engineering
Ghent, Belgium. 6-9 July 2025
Jan F.M. Van Impe, Grégoire Léonard, Satyajeet S. Bhonsale,
Monika E. Polańska, Filip Logist (Eds.)

PSE PRESS

# Steel Plant Electrification: A Pathway to Sustainable Production and Carbon Reduction

**Rachid Klaimi[a], Sabla Y. Alnouri[b]*, Vladimir Stijepovic[c], Aleksa Miladinovic[c] and Mirko Stijepovic[c]**

[a] Chemical Engineering Program, Mechanical Engineering Department, Notre Dame University-Louaize, PO Box: 72, Zouk Mosbeh, Lebanon
[b] Gas Processing Centre, College of Engineering, Qatar University, P.O. Box 2713, Doha, Qatar
[c]University of Belgrade, Faculty of Technology and Metallurgy, Karnegijeva 4, 11000 Belgrade, Serbia
* Corresponding Author: sabla@u.edu.qa

## ABSTRACT

Traditional steel processes are energy-intensive and rely heavily on fossil fuels, contributing to significant greenhouse gas emissions. By adopting electrification technologies, such as electric boilers and compressors, particularly when powered by renewable energy, steel plants can reduce their carbon footprint, enhance process flexibility, and lower long-term operational costs. This transition also aligns with increasing regulatory pressures and market demand for greener practices, positioning companies for a more competitive and sustainable future. This work investigates the potential of replacing conventional steam crackers in a steel plant that relies on the use of fossil fuels, with electrically driven heating systems powered by renewable energy sources. The overall aim was to significantly lower greenhouse gas emissions by integrating electric furnaces and heat pumps into the steel production process. This study evaluates the potential carbon savings from the integration of solar energy in a steel plant with a production capacity of 300,000 tons per month. The solar field required for this integration was found to span an area ranging from 122,142 to 362,360 m², while the wind field area required is estimated at 550.373 m2. By incorporating solar power into the plant's energy mix, the analysis reveals a significant reduction in carbon emissions, with an estimated saving of 707,597 tons of $CO_2$ per year.

**Keywords**: Electrification, Steel, Carbon Reduction, Optimization, GHG, additional keywords separated by commas

## INTRODUCTION

The steel industry is among the most energy-intensive sectors globally, with traditional processes heavily dependent on fossil fuels. This reliance not only drives significant greenhouse gas (GHG) emissions but also poses challenges in meeting evolving environmental regulations and market expectations for sustainability. With the increasing availability of renewable energy and advancements in electrification technologies, steel plants have a transformative opportunity to decarbonize their operations.

Electrification of key processes, such as heating systems, using technologies like electric boilers, compressors, and heat pumps, offers a pathway to significantly reduce carbon emissions. These systems, when powered by renewable energy, not only lower the carbon footprint but also enhance process efficiency and flexibility, positioning companies for long-term economic and environmental sustainability. Furthermore, transitioning to electric systems aligns with the growing demand for greener practices. Wei, McMillan and de la Rue du Can [1] reviewed the latest research on the potential for industry electrification to support decarbonization efforts. Sun, Wang [2] analysed carbon emission reduction strategies in the industry through the interconnection of carbon, electricity, and hydrogen, highlighting potential development directions. Hadera, Harjunkoski [3] developed a continuous-time scheduling model to incorporate energy-awareness, optimizing electricity purchases and load commitments. Luh, Budinis [4] used a global energy system simulation to assess the impacts of $CO_2$ reduction measures, including fuel

switching, electrification, and Carbon Capture and Storage (CCS), on investment and operations. Several scenarios that evaluate the role of $CO_2$ pricing as a policy tool for decarbonizing the industrial sector were presented. Sun, Harjunkoski and Castro [5] used the Resource Task Network (RTN) examined the effect of fluctuating electricity prices on production scheduling the economic benefits of the steel plant's participation in incentive-based demand-side management (iDSM) programs. This study explores the feasibility of replacing conventional fossil-fuel-based steam crackers in steel production with electrically driven heating systems powered by renewable energy. The focus is on integrating electric furnaces and heat pumps into the steelmaking process to achieve substantial reductions in greenhouse gas emissions.

## METHODOLOGY

Electrification offers a promising pathway to reduce carbon footprints by replacing fossil-fuel-based technologies with electric-driven alternatives powered by renewable energy sources such as wind, solar, or hydroelectric power. This paper explores the integration of electrification technologies, including electric furnaces, heat pumps, and renewable energy systems, like solar PV, wind, or CSP, into the steel production process. (**Figure 1**) By optimizing energy consumption and incorporating sustainable power sources, the methodology aims to significantly reduce greenhouse gas emissions and enhance operational efficiency. A critical aspect includes evaluating the feasibility of these technologies, assessing their environmental benefits, and performing cost analyses to ensure economic viability

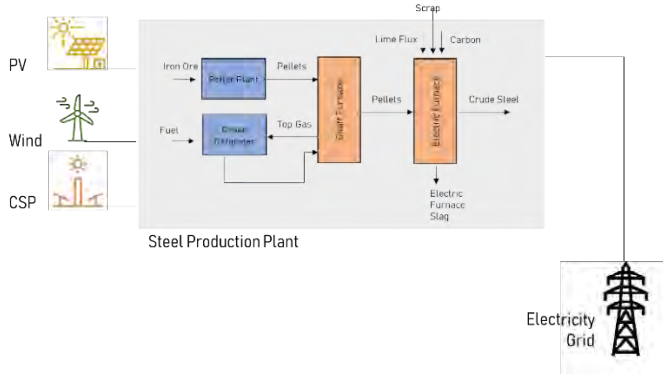



**Figure 1.** The integration of solar PV, wind, and CSP, into steel production

In this paper, a comprehensive approach to assessing the electrification options for a steel plant was made. **Figure 2** below summarizes the approach that was utilized in this work. First, the plant's current energy demand, including the total consumption, peak load, and base load, was evaluated to identify how much can be replaced by renewable sources. This was then followed by an analysis of local renewable energy resources, such as wind and solar, based on site-specific conditions like wind speeds and solar irradiance, to estimate the potential energy generation from wind and photovoltaic (PV) systems. The feasibility of integrating these renewable sources into the plant's electrical system is then assessed, considering factors like land availability, grid connectivity, and required infrastructure upgrades. Economic modeling was then conducted by calculating the Levelized Cost of Electricity (LCOE) for both wind and PV technologies, factoring in CAPEX and OPEX expenditures. Additionally, the environmental impact of the steel plant was then evaluated after electrification options were introduced, focusing on the reduction of greenhouse gas emissions through the adoption of renewable energy. Finally, the most cost-effective and sustainable mix of wind and PV systems that supply the plant's energy needs while meeting the environmental constraints was identified.

## CASE STUDY INFORMATION

The steel plant that was considered in this case study is a high-capacity facility with significant energy demands. The plant's operations require 186.264 MW of electrical power for various industrial processes, including smelting, rolling, and ancillary systems, which rely on a continuous and stable electricity supply. Additionally, the plant consumes 522.5 tons per hour of low-pressure (LP) steam at 3 bars, utilized for processes such as heating, drying, and maintaining operational conditions in different stages of steel production. To meet these intensive energy requirements sustainably, the proposed energy alternatives come from renewable energy sources, including solar PV, wind, and CSP, alongside advanced energy storage and conversion technologies. A lead-acid battery storage system is included to buffer the variability inherent in renewable energy generation, providing grid stability and ensuring uninterrupted power delivery during periods of low generation [6]. This is very important for processes that demand consistent power, as fluctuations can disrupt operations and reduce efficiency. Moreover, in order to meet the plant's steam requirements, electric boilers are incorporated to convert any surplus electricity into thermal energy, hence producing the required low-pressure steam for the plant's operation.

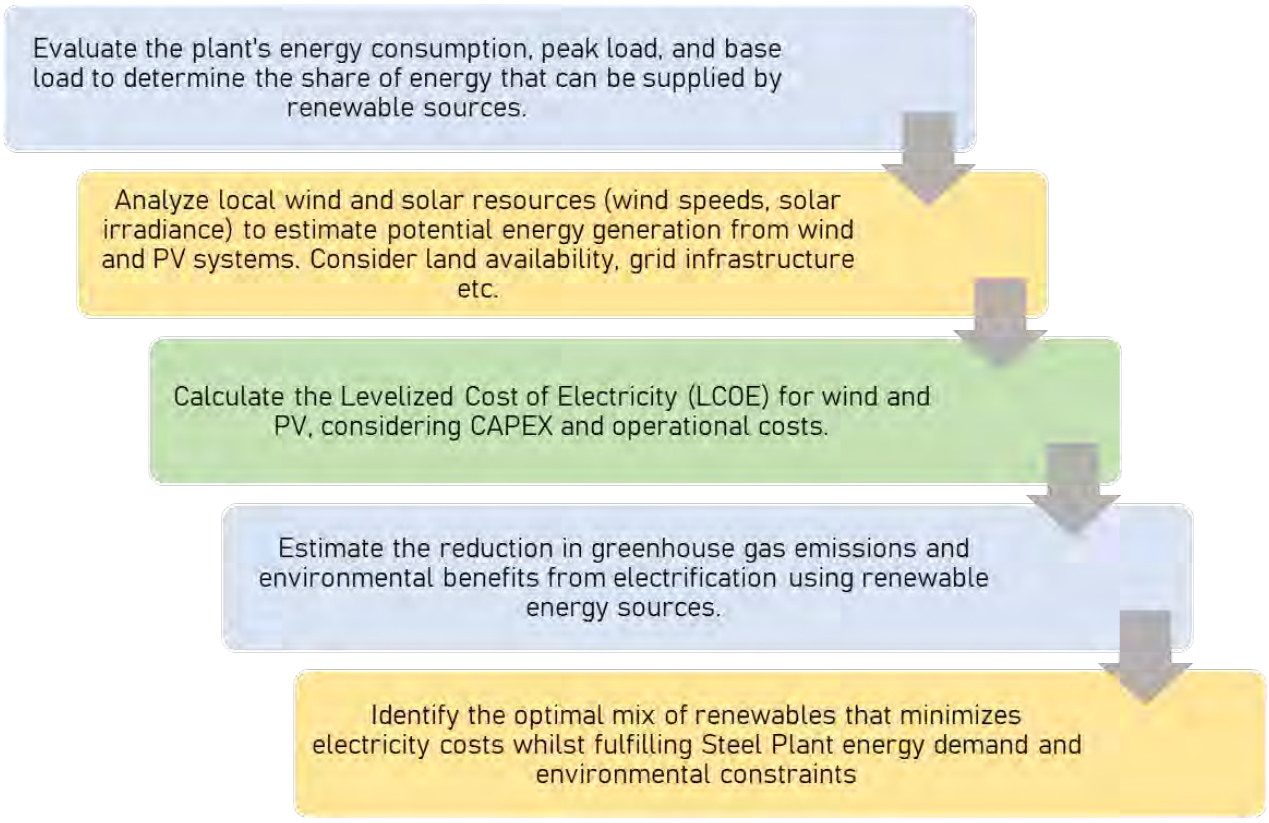



**Figure 2:** Summary of Research Framework

## RESULTS AND DISCUSSION

The results of the study are summarized in **Table 1,** which highlights the differences in land use, energy cost, and CO2 savings for each renewable energy option

**Table 1:** Summary of Parameters associated with CSP, PV and wind energy

| Parameter | CSP | PV | Wind |
|---|---|---|---|
| Land Area ($m^2$) | 122,142 | 362,360 | 550,373 |
| No. Panels /Turbines | - | 181,180 | 272 |
| Cost (USD/kWh) | 0.165 | 0.096 | 0.055 |
| $CO_2$ Savings (tons/y) | 629,868 | 569,413 | 675,930 |

CSP systems use solar thermal technology to generate electricity and heat, making them an ideal candidate for dual production of electricity and steam. In this study, CSP requires a land area of 122,142 m² to meet the plant's energy demands. Although CSP inherently supports thermal energy storage, the integration of Pb-acid batteries ensures continuous operation during periods of low solar irradiance. The levelized cost of energy (LCOE) for CSP was calculated at $0.165/kWh, the highest among the technologies evaluated. PV systems are assessed for their cost-effectiveness and scalability. Covering an area of 362,360 m², the PV system includes 181,180 panels to generate the required power. Since PV systems produce only electricity, electric boilers are incorporated to fulfill the steam demand. The LCOE for PV is $0.096/kWh with storage and $0.049/kWh without storage, showcasing its competitive advantage. However, the dependency on battery storage for consistent operation poses challenges related to cost and efficiency. Wind turbines were evaluated at an average wind speed of 7 m/s. To meet the plant's energy requirements, 272 turbines occupying 550,373 m² were proposed. With an LCOE of $0.055/kWh, wind energy proves to be the most economical option with storage. The cost drops further to $0.032/kWh when storage is excluded. Interestingly, if wind speeds increase to 9 m/s, the LCOE reduces to $0.047/kWh, demonstrating the high sensitivity of wind energy costs to wind conditions. Despite the variance in cost and land area, the CO2 emissions reduction from operation is identical across the three technologies and estimated at 707,597 tons/y. This uniformity arises

from the complete replacement of natural gas with renewable sources. However, when considering the $CO_2$ life cycle assessment (LCA) of each technology, the actual net emissions reduction differs due to the embedded emissions in manufacturing, transportation, installation, maintenance, and decommissioning. CSP, with a lifecycle emission factor of 27 g $CO_2$/kWh, achieves a reduction of 629,868 tons/year. PV, having a higher emission factor of 48 g $CO_2$/kWh, results in a slightly lower reduction of 569,413 tons/year. On the other hand, wind energy, with the lowest lifecycle emissions at 11 g $CO_2$/kWh, leads to the highest reduction of 675,930 tons/year [7]. These results highlight the importance of considering full life cycle emissions when assessing the environmental impact of renewable technologies. While all three sources significantly reduce emissions compared to fossil fuels, wind energy emerges as the most effective in minimizing $CO_2$ footprint, followed by CSP and then PV.

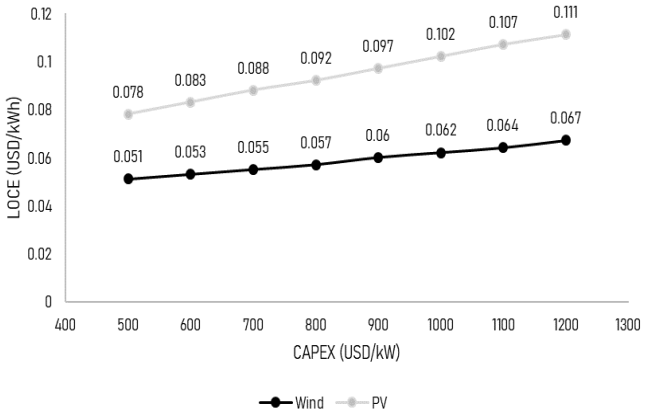



**Figure 3.** Optimal costs attained for Steel Electrification via PV and Wind technologies

The use of electric boilers is a pivotal adaptation for PV and wind systems, as these technologies generate electricity exclusively. This ensures that the steel plant's LP steam requirements are met without compromising its operational integrity. The integration of Pb-acid batteries across all systems addresses intermittency issues, though the added cost impacts overall feasibility. From an economic standpoint, wind energy emerges as the most viable option, particularly in regions with high average wind speeds. The reduced LCOE at higher wind speeds further enhances its competitiveness. However, the extensive land requirement for wind turbines and PV systems poses logistical challenges, especially in densely populated or land-constrained areas. CSP, while requiring less land, is the most expensive option and may be less attractive unless thermal energy storage provides significant operational advantages. Further studies could explore alternative storage technologies, such as lithium-ion batteries, which may offer improved efficiency and lower costs. Additionally, hybrid solutions that combine CSP with PV or wind could optimize resource utilization and mitigate individual technology limitations.

A sensitivity analysis was performed to assess the impact of the capital expenditure on the levelized cost. **Figure 3** shows the results that were attained for wind and PV energy systems. The results indicate that as CAPEX increases from 500 to 1200 units, the LCOE for both wind and PV systems also increases. For wind, the LCOE increases from 0.051 to 0.067 USD/kWh, while for PV, it increases from 0.078 to 0.111 USD/kWh.

It is evident that PV systems have a higher LCOE compared to wind systems at all CAPEX levels, reflecting higher costs for generating electricity from PV systems under these conditions. The rate of increase in LCOE appears consistent for both technologies, suggesting a proportional relationship between CAPEX and operational costs. Moreover, while wind energy appears more cost-effective for the steel plant in this case study, regional factors such as resource availability, land use, and grid infrastructure can influence the decision-making process.

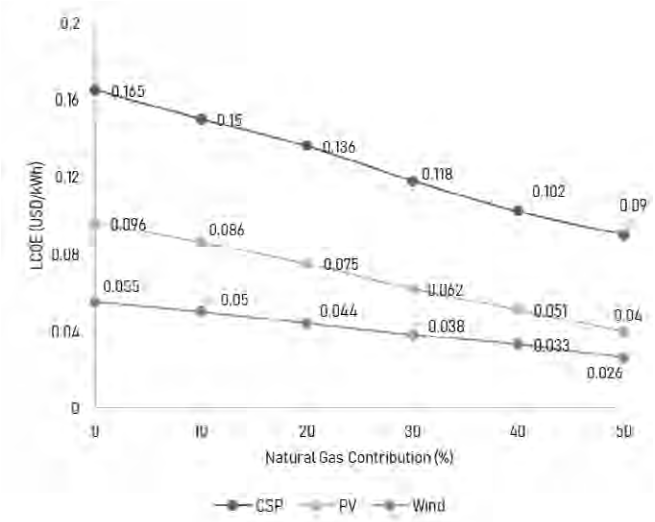



**Figure 4.** Natural gas (NG) proce sensitivity on the levelized cost of electricity (LCOE) for CSP, PV and wind

**Figure 4** demonstrates the sensitivity analysis conducted on the effect of natural gas (NG) contribution on the levelized cost of electricity (LCOE) for CSP, PV, and wind technologies. A clear tread is observed; increasing the share of NG in the energy mix leads to a reduction in LCOE across all three renewable technologies. This trend is expected since NG is typically a lower-cost generation source compared to renewable technologies, especially when considering the high capital expenditure (CAPEX) of CSP and PV systems.

At 0% NG contribution (i.e., fully renewable operation), CSP exhibits the highest LCOE (0.165 $/kWh), followed by PV (0.096 $/kWh), and wind (0.055 $/kWh). As NG contribution increases to 50%, the LCOE for all

technologies decreases significantly, reaching 0.09 $/kWh for CSP, 0.04 $/kWh for PV, and 0.026 $/kWh for wind. This reduction can be attributed to the lower cost of NG electricity production and the reduced reliance on high-capital-cost renewable infrastructure. Among the three technologies, CSP experiences the most significant absolute decrease in LCOE (from 0.165 $/kWh to 0.09 $/kWh), reflecting its higher initial cost and greater sensitivity to hybridization with conventional power sources. On the other hand, wind, which starts with the lowest LCOE, exhibits the least reduction, dropping from 0.055 $/kWh to 0.026 $/kWh, indicating that its cost structure is already competitive with NG.

These findings highlight the economic advantage of incorporating a certain percentage of NG into renewable energy systems to reduce costs. However, the trade-off between cost reduction and carbon emissions should be carefully considered when optimizing the energy mix for sustainability goals.

## CONCLUSIONS

The adoption of electrification technologies, particularly when combined with renewable energy sources, offers a promising pathway for decarbonizing the energy-intensive steel industry. This study demonstrates the potential of replacing conventional fossil-fuel-based steam crackers with electrically driven heating systems, such as electric furnaces and heat pumps, powered by solar or wind energy. The integration of wind and solar power into the steel plant's energy mix resulted in a substantial reduction in carbon emissions, with an estimated annual savings of 2,831 tons of $CO_2$. By integrating renewable energy sources like CSP, wind, or PV, steel plants can easily shift from fossil fuel dependence to cleaner electricity, reducing their environmental impact.

## REFERENCES


1. Wei, M., C.A. McMillan, and S. de la Rue du Can, Electrification of Industry: Potential, Challenges and Outlook. Current Sustainable/Renewable Energy Reports, 2019. 6(4): p. 140-148.
2. Sun, C., et al., Process Path for Reducing Carbon Emissions from Steel Industry—Combined Electrification and Hydrogen Reduction. Processes, 2024. 12(1): p. 108.
3. Hadera, H., et al., Steel Production Scheduling Optimization under Time-sensitive Electricity Costs, in Computer Aided Chemical Engineering, J.J. Klemeš, P.S. Varbanov, and P.Y. Liew, Editors. 2014, Elsevier. p. 373-378.
4. Luh, S., et al., Decarbonisation of the Industrial Sector by means of Fuel Switching, Electrification and CCS, in Computer Aided Chemical Engineering, A. Friedl, et al., Editors. 2018, Elsevier. p. 1311-1316.
5. Sun, L., I. Harjunkoski, and P. Castro, Resource-Task Network Based Approach for Industrial Demand Side Management of Steel Production, in Computer Aided Chemical Engineering, A. Kraslawski and I. Turunen, Editors. 2013, Elsevier. p. 259-264.
6. Gupta R, Soini MC, Patel MK, Parra D. Levelized cost of solar photovoltaics and wind supported by storage technologies to supply firm electricity. Journal of Energy Storage. 2020 Feb 1;27:101027.
7. IPCC Working Group III – Mitigation of Climate Change, Annex III: Technology - specific cost and performance parameters - Table A.III.2 (Emissions of selected electricity supply technologies (gCO 2eq/kWh))" (PDF). IPCC. 2014. p. 1335.



© 2025 by the authors. Licensed to PSEcommunity.org and PSE Press. This is an open access article under the creative commons CC-BY-SA licensing terms. Credit must be given to creator and adaptations must be shared under the same terms. See https://creativecommons.org/licenses/by-sa/4.0/




Systems & Control Transactions

**Research Article - Peer Reviewed Conference Proceeding**
ESCAPE 35 - European Symposium on Computer Aided Process Engineering
Ghent, Belgium. 6-9 July 2025
Jan F.M. Van Impe, Grégoire Léonard, Satyajeet S. Bhonsale,
Monika E. Polańska, Filip Logist (Eds.)

PSE PRESS

# Conceptual design of energy storage systems for continuous operations in renewable-powered chemical processes

**Andrea Isella[a], Alfonso Pascarella[a], Angelo Matichecchia[b], Raffaele Ostuni[b], and Davide Manca[a]***

[a] PSE-Lab, Process Systems Engineering Laboratory, Dipartimento di Chimica, Materiali e Ingegneria Chimica "Giulio Natta", Politecnico di Milano, Piazza Leonardo da Vinci 32, 20133 Milano, Italy
[b] Casale SA, Via Giulio Pocobelli 6, 6900 Lugano, Switzerland
* Corresponding Author: davide.manca@polimi.it.

## ABSTRACT

This work aims to develop an energy storage system that allows fluctuating energy inputs (*i.e.* from process sections driven by renewable sources) to power two process units that are operated continuously at different temperatures. The system consists of two vessels storing diathermal mediums: one for the hotter- and the other for the colder-energy fluxes. The investigated solutions include sensible-heat-, latent-heat-, and thermochemical-TES (thermal energy storage). Organic Rankine cycles (ORCs) with lithium-ion batteries and thermoelectric generators were also assessed. Indeed, all these technologies allow the exploitation of low-temperature thermal energy to supply the high-temperature unit during periods of energy scarcity. Both vessels aim for total self-sufficiency; however, the option to rely on external utilities has been included to meet the energy demand of both units when sufficient process-side power is unavailable. Two energy profiles were investigated to assess the proposed storage systems' performance: one showing only solar energy inputs and the other showing only wind energy inputs. Finally, an optimization problem was formulated to estimate the optimal size of both storage vessels. Indeed, increasing their capacities would lead to higher capital expenses (CAPEX) and lower operating expenses (OPEX). As a result, the assessed process-integrated configurations (*i.e.* those featuring any energy storage system) proved competitive with the non-integrated solution (*i.e.* the one fully relying on external sourcing of electricity) only if referring to high electric energy prices (300 USD/MWh). Conversely, when considering an electricity price of 100 USD/MWh, all the assessed process-integrated configurations proved more expensive than the non-integrated solution.

**Keywords**: Energy storage, Heat recovery, Process integration, Renewable energy, Solar power, Wind power.

## INTRODUCTION

Powering the chemical industry with renewable energy represents a significant challenge for process engineers today. The primary obstacle to achieving a fully integrated green solution lies in harmonizing inherently intermittent energy production with processes that require predominantly continuous operation. Energy storage has emerged as a highly effective approach to address this challenge, with various methods aiming to regulate oscillatory renewable energy inputs for processes requiring operational steadiness. Scientific literature offers several innovative energy storage methods, such as fluid heating via electrical resistances [1], or storage by batteries [2] or reversible reactions (being exothermic or endothermic according to the direction taken) [3], *i.e.* electrochemical storage. Other technologies involve evaporating liquefied air to drive turbines for electricity generation during the discharge phase, complemented by compression cycles during the energy storage charging phase [4]. Lastly, even Brayton cycles and subsequent storage of working fluids may play a role in continuous electricity production [5]. This work aims to model and optimize the heat recovery system powering two different process units (*aka* "users") relying entirely on the thermal energy recovered from upstream process sections exposed to significant

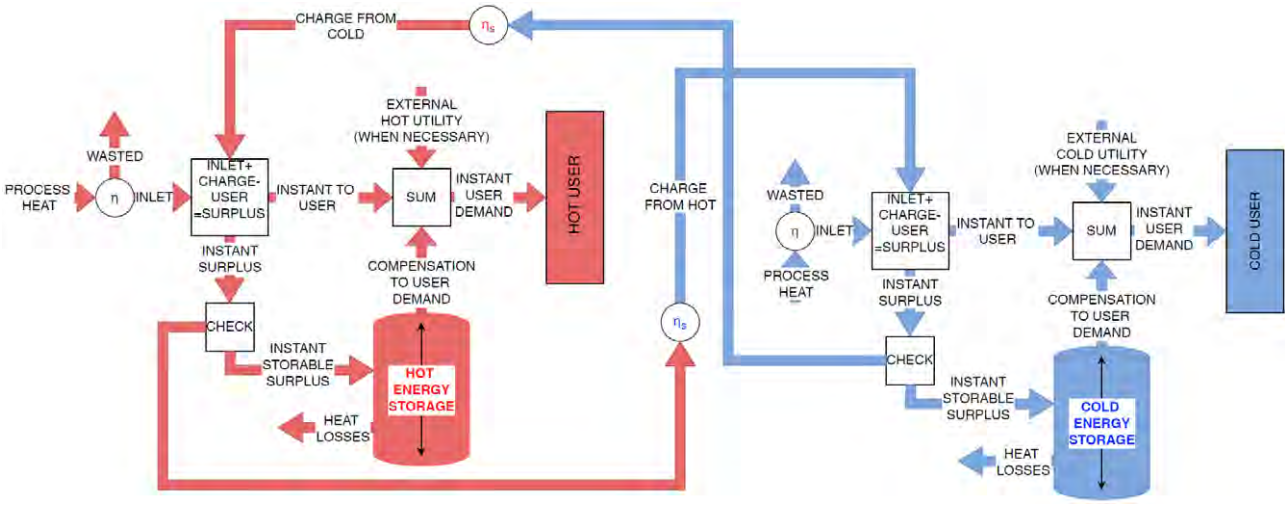



**Figure 1:** Block flow diagram of the integrated system model.

thermal load fluctuations due to renewable energy inputs. To ensure the continuous operation of the investigated process units, it is crucial to identify the optimal configuration according to the technologies employed and the storage capacities to be installed (as it concerns the CAPEX). Also, such an integrated solution should minimize the reliance on external utilities (as it concerns the OPEX).

## METHODOLOGY

Operating at two different temperatures, the two users are supplied by two streams at distinct temperatures: the "hot" (*i.e.* 185 °C) and the "cold" (*i.e.* 95 °C) one. The system incorporates two storage tanks amidst the users' incoming energy inputs and departing energy demands. Both tanks are interconnected to optimize energy integration, allowing energy transfer between them in cases where a surplus exceeds the storage capacity. In this regard, the "hot-to-cold" energy transfer efficiency is approximately 90% [6]. Conversely, the "cold-to-hot" energy transfer efficiency significantly changes according to the technologies employed for energy conversion.

Three distinct energy storage technologies are evaluated: latent-heat-, sensible-heat-, and thermochemical-TES (thermal energy storage). On the other hand, an organic Rankine cycle (ORC), combined with an electric resistance and a battery to manage short-term fluctuations and ensure the continuous operation of the turbine, has been assessed to convert cold thermal energy into hot thermal energy. Also, a process configuration featuring a thermoelectric reactor coupled with thermal resistance has been considered. **Figure 1** illustrates how the system was modeled. To run the optimization problem, the sizes of the storage tanks act as degrees of freedom. Larger tanks would increase capital investment costs but reduce external energy purchases. Conversely, smaller tanks would reduce investment costs but increase operational costs and emissions, as they require more external energy, which might also be associated with a high carbon footprint. Going into the modeling details of both energy storage systems (*i.e.* the "hot" and the "cold" ones), $Instant\ Surplus$ is a variable of key importance, accounting for the difference between the energy demand of the users and the energy supplied by the heat recovery system (plus any eventual energy coming from the other vessel). Accordingly, it is defined as:

$$InstantSurplus(t) = Inlet(t) \cdot \eta - User(t) + ChargeFromSystem(t) \cdot \eta_c \quad (1)$$

where $\eta$ accounts for the energy losses due to storage, and $\eta_c$ is the conversion efficiency (*i.e.* "hot-to-cold" or "cold-to-hot"). Hot-to-cold energy transfers typically feature near-unity efficiencies, while cold-to-hot energy transfers generally show much lower efficiencies due to thermodynamical and conversion limitations. Hereafter, the $ChargeFromSystem$ variable is defined as:

$$ChargeFromSystem(t) = max\big(InstantSurplus(t) - \big(MAXEnergyStorage - EnergyStorage(t)\big), 0\big) \quad (2)$$

Equation 2 quantifies the energy that can be transferred between the systems when immediate use or storage is not possible, according to the installed capacity of the storage system ($MAXEnergyStorage$). The $EnergyStorage$ variable tracks the filling and emptying of storage vessels over time, incorporating heat losses:

$$EnergyStorage(t) = \min(\max(EnergyStorage(t-1) + InstantSurplus(t), 0), MAXEnergyStorage) \cdot (1 - HeatLosses) \quad (3)$$

This ensures full compliance with physical and operating limitations in both storage systems. When neither stored

**Table 1:** The proposed technologies for energy storage and conversion.

| Technology | Medium (hot and cold storage) | Plant section | Efficiency | Lifetime | Ref. |
|---|---|---|---|---|---|
| Latent heat | $KNO_3$ KOH<br>$H_2C_2O_4$ | Energy storage | $\eta$ = 90%<br>Heat losses = 1%/h | 15 y | [7] |
| Sensible heat | $NaNO_3$ NaOH<br>$H_2C_2O_4$ | Energy storage | $\eta$ = 90%<br>Heat losses = 1%/h | 15 y | [7] |
| Thermochemical | $CaAl_{0.02}Mn_{0.8}O_{2.68}+0.16O_2$<br>$\leftrightarrow CaAl_{0.02}Mn_{0.8}O_3$<br>[Unfeasible] | Energy storage | $\eta$ = 90%<br>Heat losses = 1%/h | 15 y | [8] |
| ORC + Battery | – | Energy conversion | $\eta_c$ = 30% | 20 y | [9] |
| Thermoelectric generator | – | Energy conversion | $\eta_c$ = 5% | 12 y | [10] |

nor transferred energy is enough to meet the users' demand, any remaining imbalance is compensated by the $ExternalUtility$ variable, calculated as:

$$\boldsymbol{if}\ InstantSurplus < 0 \quad AND \quad |InstantSurplus(t)| > EnergyStorage(t)$$

$$ExternalUtility(t) = |InstantSurplus(t)| - EnergyStorage(t)$$

$$\boldsymbol{else}$$

$$ExternalUtility(t) = |InstantSurplus(t)| - EnergyStorage(t) \quad (4)$$

Thus, the optimizer iteratively adjusts the maximum hot and cold storage capacities ($MAXEnergyStorage$) through an exhaustive grid-search to identify the configuration minimizing the total costs. Such calculations, based on the energy demand vs. production profiles, describe the storage dynamics, the power needed for the conversion technology, and the utility requirements accounted for by the objective function. The maximum storage size matches to $MAXEnergyStorage$, the maximum required conversion power corresponds to the highest value by the $ChargeFromSystem$ time-array, and the total external utility demand comes from integrating the $ExternalUtility$ vector throughout the assessed time frame.
Two distinct objective functions have been considered. The former distributes the investment costs over the lifetime ($LT$) of each process unit:

$$\Phi_{OBJ}^{(1)} = HotMediumCost/LT_{HotMedium} + HotTankCost/LT_{HotTank} + ColdMediumCost/LT_{ColdMedium} + ColdTankCost/LT_{ColdTank} + \left(\sum_{t=1}^{t_{end}} ColdUtility(t) + \sum_{t=1}^{t_{end}} HotUtility(t)\right) \cdot ElectricityCost + EnergyConversionCost/LT_{conversion} \quad (5)$$

The latter incorporates a Capital Recovery Factor ($CRF$), calculated as $\frac{IR(1+IR)^{LT-1}}{(1+IR)^{LT}-1}$, with an 8% interest rate ($IR$) to account for the time value of money. Several factors may influence the interest rate, including project risk (higher perceived risk results in higher interest rates), financial market considerations, and the type of financing used (as equity and debt involve different costs). Consequently, a range between 5% and 8% (hence the 8% choice has a conservative nature) is suggested for the interest rate as green projects often benefit from incentives and more favorable conditions compared to traditional sectors, though frequently facing major risks related especially to technological innovation or regulatory variability.

$$\Phi_{OBJ}^{(2)} = HotMediumCost \cdot CRF_{HotMedium} + HotTankCost \cdot CRF_{HotTank} + ColdMediumCost \cdot CRF_{ColdMedium} + ColdTankCost \cdot CRF_{ColdTank} + \left(\sum_{t=1}^{t_{end}} ColdUtility(t) + \sum_{t=1}^{t_{end}} HotUtility(t)\right) \cdot ElectricityCost + EnergyConversionCost \cdot CRF_{conversion} \quad (6)$$

For both objective functions (defined in Equations 5 and 6, respectively), an operating time of 8760 hours per year (*i.e.* assuming non-stop plant operations) was assessed. Indeed, as the upstream process sections (*i.e.* those providing the "process heat" reported in **Figure 1**) are powered by renewable energy inputs, they typically exhibit large oscillations throughout the year, especially due to solar and wind seasonal trends. In this regard, **Table 1** reports all the technologies proposed for the investigated system and their respective efficiencies and lifetimes. Finally, the optimization problem was assessed through a brute-force but exhaustive grid-search routine in MATLAB™ R2024a. As mentioned above, this problem shows two continuous degrees of freedom (*i.e.* decision variables): the installed capacity of the hot and the cold energy storage systems.

## RESULTS AND DISCUSSION

The model underwent two distinct input thermal-

**Table 2:** The investigated process configurations.

| # | Hot storage | Cold storage | Energy conversion |
|---|---|---|---|
| 1 | Sensible | Sensible | ORC + Battery |
| 2 | Latent | Sensible | ORC + Battery |
| 3 | Thermochemical | Sensible | ORC + Battery |
| 4 | Sensible | Sensible | TEG |
| 5 | Latent | Sensible | TEG |
| 6 | Thermochemical | Sensible | TEG |
| 7 | Sensible | Latent | TEG |
| 8 | Latent | Latent | TEG |
| 9 | Thermochemical | Latent | TEG |
| 10 | Sensible | Latent | ORC + Battery |
| 11 | Latent | Latent | ORC + Battery |
| 12 | Thermochemical | Latent | ORC + Battery |

energy profiles, "A" and "B", based on solar (the former) and wind (the latter) energy inputs. In both cases, the primary purpose of the optimization process is to identify the most effective process-integration technique and determine whether energy storage is more cost-effective than relying on external utilities. Please note that both objective functions disregard carbon emissions entirely. However, integrated heat recovery systems typically reduce carbon intensity due to their lower dependence on external utilities (which usually are highly carbon-intensive, especially those used for heating).

The technologies listed in **Table 2** were combined to assess the three storage methods for both (*i.e.* "hot" and "cold") tanks with the proposed two conversion methods. Considering all possible combinations, 18 configurations (*i.e.* = 3·3·2) were obtained. However, excluding those 6 featuring thermochemical energy storage for the cold tank (since the investigated scientific literature does not report any storage medium available at such temperatures) resulted in 12 viable and technically feasible configurations.

From the proposed optimization problem, one can expect two opposite scenarios: the former, minimizing the OPEX, almost nullifies the need for external utilities by contemplating heavy energy transfer from the cold to the hot tank through a conversion technology; the latter, minimizing the CAPEX, rejects any integrated conversion feature: *i.e.* it increases reliance on external utilities (thus potentially leading to higher emissions) but also reduces investment costs and spatial requirements associated with the energy conversion system.

Another critical aspect of the analysis concerns the competitiveness of the process integration compared to purchasing external energy whenever needed to mitigate renewable energy fluctuations. Therefore, even buying electrical energy from an external power grid has been evaluated as a reference benchmark (such configuration has been referred to as "NI", *i.e.* "non-integrated"). Accordingly, we assumed an electricity cost equal to 100 USD/MWh. However, we also performed a parallel estimation referring to the European peak electric price of 300 USD/MWh, as reported by Eurostat [11] for the last decade, to account even for scenarios with high energy prices.

**Figure 2** shows the results for those two different electricity prices in the case of Profile A. The first couple of columns report the costs associated with the non-integrated configuration. In this context, when the instantaneous energy supply is insufficient to meet user requirements, any deficit is compensated by purchasing electricity from the grid. A similar trend can be observed when referring to Profile B. While Profile A leads to process configurations ranging between 118.1 kUSD/y and 707.7 kUSD/y (100 USD/MWh) and 200.2 kUSD/y and 795.6 kUSD/y (300 USD/MWh), Profile B leads to process configurations ranging between 125.1 kUSD/y and 543.5 kUSD/y (100 USD/MWh) and 262.3 kUSD/y and 695.2 kUSD/y (300 USD/MWh). Concerning Profile A, when referring to 100 USD/MWh, all the assessed energy storage technologies lead to higher costs than the non-integrated configuration (NI). However, when considering 300 USD/MWh, all the configurations except #4, #5, and #6 are cheaper than NI. Concerning Profile B, when referring to 100 USD/MWh, all the assessed energy storage technologies lead to higher costs than the non-integrated configuration (NI). However, when considering 300 USD/MWh, only the #8 and #11 configurations are cheaper than NI.

Therefore, the assessed case study does not show remarkable economic benefits from integrating energy storage systems into the process compared to external sourcing of electricity (*e.g.*, from the power grid) unless significant electric energy price increases.

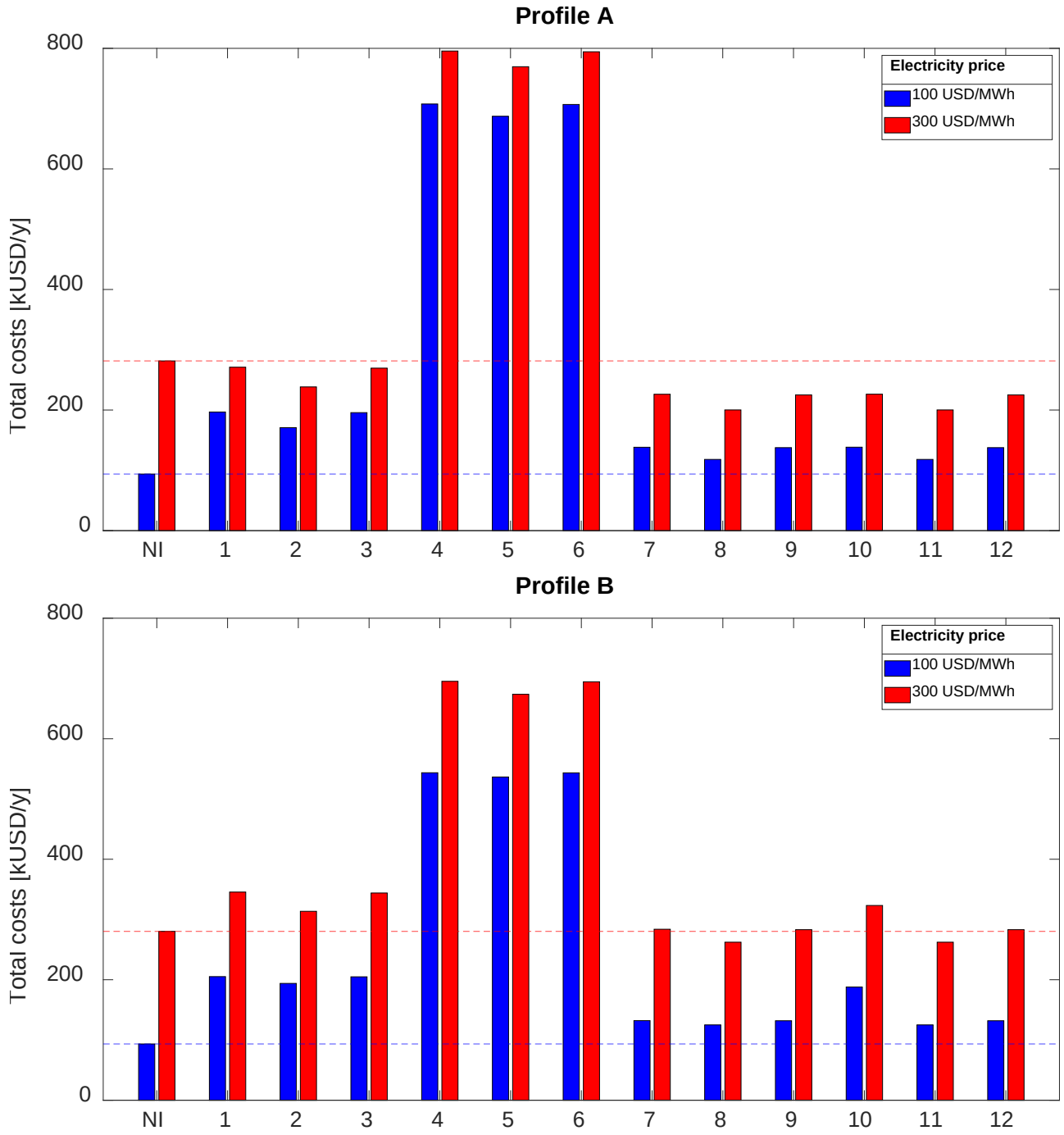



**Figure 2:** Annual total costs ($\Phi_{OBJ}^{(2)}$) by the 12 assessed configurations (see **Table 2**) compared to the non-integrated one (NI) when referring to Profile A (Panel A, top) or Profile B (Panel B, bottom).

## CONCLUSIONS

This study highlights the critical role of energy storage in improving both economic and environmental outcomes in chemical plants. Process integration and energy storage systems allow for reducing carbon emissions and even operating costs when energy prices are particularly high. The results underscore that large-scale integration of renewable energy into chemical processes is only feasible through effective storage systems that consistently outperform external energy purchases during peak demand and production shortfalls. Also, higher economic benefits are expected due to the environmental benefits

of process integration (*e.g.*, less dependence on external electricity and/or heat sourcing, which is typically carbon-intensive).

The presented optimization demonstrated the potential benefits of process-integrated energy storage solutions. While this work performed a sensitivity analysis of electricity prices, dynamic conceptual design techniques accounting for price variations over time may provide additional insights. Nevertheless, including energy storage consistently resulted in reduced external utility consumption when renewable energy sources were used.

An innovative aspect of this study lies in assessing energy conversion between two interconnected tanks whose sizes are to be optimized. Although promising, the feasibility of this method depends heavily on energy profiles and economic factors, as shown by the different results obtained with the two objective functions, two profiles, and two electricity prices. As such, industrial-scale implementation of energy conversion must be rigorously evaluated, accounting for several techno-economic assumptions.

Lastly, this work proves that coupling renewable energy inputs with energy storage systems allows for the operation of large-scale chemical processes according to the need for smooth variations in mass and energy flows by only calling for minor modifications to existing units. This approach aligns with process sustainability goals, especially the transition to greener industrial solutions.

## ACKNOWLEDGEMENTS

A.I. acknowledges the contribution of the Italian Ministry of University and Research (MUR) under the PON Research and Innovation 2014-2020 program (Action IV.5 – Doctorates on green topics).

## REFERENCES

1. Al-Maliki WAK, Alobaid F, Keil A, Epple B. Dynamic Process Simulation of a Molten-Salt Energy Storage System. *Appl. Sci.* 11(23):11308 (2021) https://doi.org/10.3390/app112311308
2. Isella A, Manca D. A framework for the design of battery energy storage systems in Power-to-X processes. *J. Energy Storage* (Under Review)
3. Stitou D, Mazet N., Mauran S. Experimental investigation of a solid/gas thermochemical storage process for solar air-conditioning. *Energy* 41(1):261-270 (2012) https://doi.org/10.1016/j.energy.2011.07.029
4. Rabi AM, Radulovic J, Buick JM. Comprehensive Review of Liquid Air Energy Storage (LAES) Technologies. *Energies* 16(17):6216 (2023) https://doi.org/10.3390/en16176216
5. Wang H, Zhang Y, Jin P, Cai X, Du J, Zhang W, Wang H, Li R. Dynamic thermodynamic performance analysis of a novel pumped thermal electricity storage (N-PTES) system coupled with liquid piston. *J. Energy Storage* 84:110836 (2024) https://doi.org/10.1016/j.est.2024.110836
6. Magaldi. https://www.magaldigreenenergy.com/en
7. Da Cunha JP, Eames PC. Thermal energy storage for low and medium temperature applications using phase change materials – A review. *Appl. Energy* 177:227-238 (2016) https://doi.org/10.1016/j.apenergy.2016.05.097
8. Sandia National Laboratories. https://www.sandia.gov/ess-ssl/wp-content/uploads/2020/12/ESHB_Ch12_Thermal_Ho.pdf
9. Pantaleo AM, Simpson M, Rotolo G, Distaso E, Oyewunmi OA, Sapin P, De Palma P, Markides CN. Thermoeconomic optimisation of small-scale organic Rankine cycle systems based on screw vs. piston expander maps in waste heat recovery applications. *En. Conv. Man.* 11:112053 (2019) https://doi.org/10.1016/j.enconman.2019.112053
10. Li K, Garrison G, Zhu Y, Horne R, Petty S. Cost estimation of thermoelectric generators. In: Proceedings of the 46th Workshop on Geothermal Reservoir Engineering. Stanford University (2021).
11. Eurostat. https://ec.europa.eu/eurostat/statistics-explained/index.php?title=Electricity_price_statistics

© 2025 by the authors. Licensed to PSEcommunity.org and PSE Press. This is an open access article under the creative commons CC-BY-SA licensing terms. Credit must be given to creator and adaptations must be shared under the same terms. See https://creativecommons.org/licenses/by-sa/4.0/



Systems & Control Transactions

**Research Article - Peer Reviewed Conference Proceeding**
ESCAPE 35 - European Symposium on Computer Aided Process Engineering
Ghent, Belgium. 6-9 July 2025
Jan F.M. Van Impe, Grégoire Léonard, Satyajeet S. Bhonsale,
Monika E. Polańska, Filip Logist (Eds.)

PSE PRESS

# Olefins production through sustainable pathways: techno-economic and environmental assessment

**Oktay Boztaş[a*], Meire E. G. R. Domingos[a], Daniel A. Flórez-Orrego[a] and François Maréchal[a]**

[a] Industrial Process and Energy Systems Engineering, EPFL, Sion, Valais, Switzerland
* Corresponding Author: oktay.boztas@epfl.ch.

## ABSTRACT

This study presents a comparative analysis of various configurations for sustainable olefins production via chemical recycling of plastic/biomass wastes, integrating $CO_2$ capture, storage and management technologies. The co-gasification, methanol synthesis and methanol-to-olefins process models were developed on the Aspen Plus® software. Optimization of processing conditions is achieved through the OSMOSE Lua platform, for minimizing the total cost of operation while accounting for seasonal variability in the electricity prices. $CO_2$ valorization processes have been shown to increase carbon efficiency from 55% up to 97% compared to steam naphtha cracking, making chemical recycling of plastics an appealing alternative. In addition, direct $CO_2$ emissions can be fully eliminated, resulting in up to 70% lower net $CO_2$ emissions even when fossil-based plastic waste is used as feedstock. Seasonal $CO_2$ storage can extend the economic benefits by acting as a buffer against high electricity costs and serving as a feedstock for $CO_2$ valorization processes when excess renewable electricity is available. The benefits of the proposed configurations are expected to become increasingly significant with the decarbonization of the electricity generation, relying more on renewable resources.

**Keywords**: Plastic Waste, Light Olefins, Gasification, Renewable and Sustainable Energy, Process Integration, Circular Economy

## INTRODUCTION

Currently, plastic usage exceeds 400 Mt and with continued economic growth, the production is expected to triple in volume by 2060 [1]. Steam cracking is the dominant method for producing olefins, with naphtha—derived from oil refineries—as the primary feedstock in Europe. This process, however, is highly energy-intensive, as cracking furnaces use fossil fuel combustion to provide the necessary reaction energy. Annually, 400 Mt $CO_2$ is emitted to produce light olefins, which represents 30% of the emissions of the chemicals sector[2]. Chemical recycling of plastic waste offers an alternative that fosters a circular economy, reduces emissions, and enhances resource efficiency. Waste plastic gasification, followed by methanol synthesis and methanol-to-olefins (MTO), is one of the alternative pathways that can promote waste valorization, minimizing the need for virgin plastics. $CO_2$ capture and storage, when combined with processes such as methanation, rWGS, and co-electrolysis, can broaden the benefits of sustainable chemical recycling. This study presents a comparative analysis of various configurations for sustainable light olefins production, accounting for the changing electricity prices driven by renewable energy availability.

## METHODS

### Process Modeling and Simulation

The superstructure for olefins production based on plastics and biomass wastes is presented in Figure 1. The inputs to the overall process are represented by High-Density Polyethylene (HDPE) for the waste plastics and pinewood for the biomass (see Table 1). The downdraft co-gasifier is modeled in Aspen® Plus, featuring 4 main stages, namely internal drying, pyrolysis, tar reforming, and reduction. Modeling of pyrolysis of plastic waste is based on experimental data at 500-550 °C, yielding 11% gas, 47% oil, and 42% wax, which is further broken down

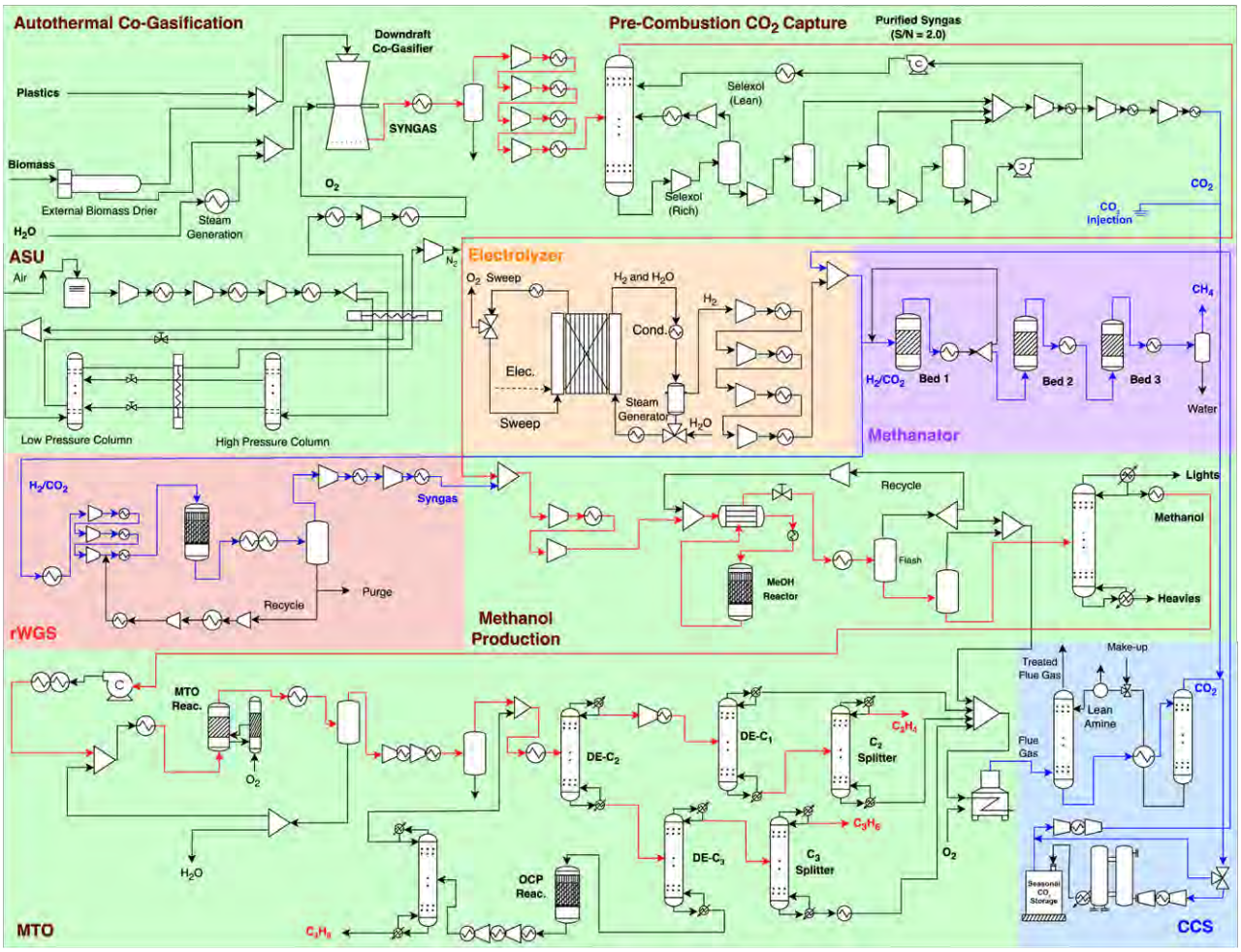



**Figure 1:** Superstructure for olefins production from plastic and biomass wastes mixture through gasification, methanol synthesis and MTO process.

in the tar reforming stage into solid carbon, CO, $CO_2$, and $H_2$ [3]. Biomass pyrolysis yields are determined by temperature-dependent empirical relations using FORTRAN subroutines [4]. The steam reduction stage is modeled using a REquil reactor with water-gas, water-gas-shift(WGS), and steam methane reforming reactions, for which the approach-to-equilibrium (ATE) temperature difference is tuned through sensitivity analysis compared with the experimental data [5]. The model exhibits a relative error of 4.7% and a root-mean square error (RMSE) of 2.2 under operating temperature of 850 °C, pressure of 1 bar, steam-to-feed ratio of 1.0, and plastics-to-feed ratio of 0.5 (dry mass basis). The gasifier is autothermal and the heat is supplied by combustion of char and syngas with $O_2$ supplied from the air separation unit. The dry molar composition of the syngas is 58.4% $H_2$, 18.0% CO, 22.7% $CO_2$, and 0.5% $CH_4$. The stoichiometric number, defined as:

$$SN = (x_{H_2} - x_{CO_2})/(x_{CO} + x_{CO_2})$$

which favors methanol synthesis when slightly > 2.0. This condition is met by $CO_2$ removal via physical absorption using Selexol® solvent at 30 bar, resulting in a syngas composition of 69.2% $H_2$, 21.2% CO, 9.9% $CO_2$, and 0.1% $CH_4$.

**Table 1:** Proximate and ultimate analysis of biomass and plastic feedstocks (dry mass basis)[6]

| Composition | | Pinewood | HDPE |
|---|---|---|---|
| Proximate Analysis [%] | M | 11.5 | 0.02 |
| | FC | 15.4 | 0.30 |
| | VM | 84.2 | 99.7 |
| | Ash | 0.45 | 0 |
| Ultimate Analysis [%] | C | 51.4 | 84.9 |
| | H | 4.90 | 15.1 |
| | N | 0.90 | 0 |
| | O | 42.4 | 0 |

Methanol synthesis is modeled based on Lurgi's Mega-Methanol® technology and the kinetic modeling by

Kiss et al., occurring at 210°C and 90 bar [7, 8]. The process could reach 96% methanol yield (depending on $CO_2$ content in the feed), including a recycle loop with a purge stream that is combusted with pure oxygen, releasing $CO_2$. After the distillation step providing >99.5% w/w purity methanol, it is sent to MTO process for light olefins synthesis.

This stage consists of a MTO reactor integrated with a catalyst regenerator that uses pure $O_2$ to combust deposited coke, an olefin cracking reactor for breaking down $C_4$+ olefins into valuable light olefins, and a series of cryogenic distillation columns to produce polymer-grade final product. The MTO reactor is modeled with a RYield reactor based on experimental data[9]. The yields based on infeed methanol are 19.0% for polymer-grade ethylene and 19.5% for polymer-grade propylene. $H_2O$ formed within the MTO reactor is recycled back into the process as steam. The undesired organic products, such as alkanes and out-of-spec natural gas are combusted with pure oxygen to recover waste heat, whereas $CO_2$ in the flue gas is captured and valorized after heat recovery.

$CO_2$ abatement and other energy technologies are integrated to improve process efficiency and offset emissions. The two possible routes for capturing $CO_2$ are pre-combustion carbon capture, operated at 30 bar using Selexol® solvent, where $CO_2$-rich solvent is decompressed, flushed and recycled, and post-combustion carbon capture, with 90% efficiency, using chemical absorption in an absorber-desorber column configuration with a di-ethanol amine (DEA) solvent, which enables a high adsorption rate while reducing desorber energy requirements [10]. Pre- and post-combustion captured $CO_2$ can either be injected for permanent geological storage, upgraded into $CH_4$, or used as feedstock for syngas production to enhance olefins production. The possible configurations considered in the scope of this work are given bellow:

1. **pre-combustion carbon capture and injection (preCCS & Inj):** Pre-combustion $CO_2$ captured during the syngas treatment is injected for geological storage, while combustion gases are released into the environment, therefore no $CO_2$ upgrading is considered. Seasonal $CO_2$ storage is not implemented in this configuration.

2. **methanation-based:** Both pre-combustion and post-combustion captured $CO_2$ is seasonally stored in liquid form or upgraded with methanation process depending on the electricity prices.

3. **reverse water gas shift-based (rWGS):** Both pre-combustion and post-combustion captured $CO_2$ is seasonally stored in liquid form or upgraded with rWGS process for syngas production depending on the electricity prices.

4. **co-electrolysis-based (co-SOEC):** Both pre-combustion and post-combustion captured $CO_2$ is only seasonally stored in liquid form or upgraded with co-electrolysis process for syngas production depending on the electricity prices.

5. **steam naphtha cracking (SNC):** steam fossil naphtha cracking without CCS unit.

Permanent $CO_2$ storage is considered only in configuration 1, as $CO_2$ is already captured as a requirement for methanol synthesis. Unlike other configurations that aim to increase olefins production by eliminating $CO_2$ emissions, no additional technologies for $CO_2$ capture from flue gases are included in configuration 1.

The necessary $H_2$ for configurations 2 and 3 is supplied with a solid oxide electrolyzer (SOEC), which operates at 800°C and 1 bar, with a specific electricity consumption of 35.2 kWh/kg$H_2$ [11, 12]. In terms of $CO_2$ and energy management, since most configurations entail high electricity consumption, they are vulnerable to fluctuations in electricity prices. As an alternative to buffer against these costs, $CO_2$ can be seasonally stored in liquid form at 7 bar and -50 °C during periods of high electricity prices, and processed when prices are lower [13]. A steam network system is also considered to recover waste heat for electricity generation.

## Optimization Problem Definition

The process integration of the proposed configurations is handled by Osmose Lua platform [14]. It works out the optimal operating conditions of the technologies of the superstructure, based on an objective function that minimizes the total cost.

$$\min Cost_{tot} = \sum_{u \epsilon Units} \left[ \sum_{t \epsilon Time} \left[ \left( Cop1_u \cdot Y_{u,t} + Cop2_u \cdot M_{u,t} \right) \Delta t + Cinv1_u \cdot Y_u + Cinv2_u \cdot M_u \right] \right]$$

- $Cop1_u$ [EUR/h]: fixed operating cost of unit u,
- $Cop2_u$ [EUR/kWh or EUR/kg]: variable operating cost of unit u,
- $Y_{u,t}$ [-]: integer variable standing for the activation of the unit u at a time t,
- $M_{u,t}$ [kg/h or kW]: continuous variable standing for the load of the unit u at a time t,
- $Cinv1_u$ [EUR/y]: fixed annualized cost of unit u,
- $Cinv2_u$ [EUR/kWh or EUR/kg]: variable annualized cost of unit u,
- $Y_u$ [-]: integer variable for the activation of the unit u, maximum value of $Y_{u,t}$,
- $M_u$ [kg/y or kWh/y]: maximum load of the unit.

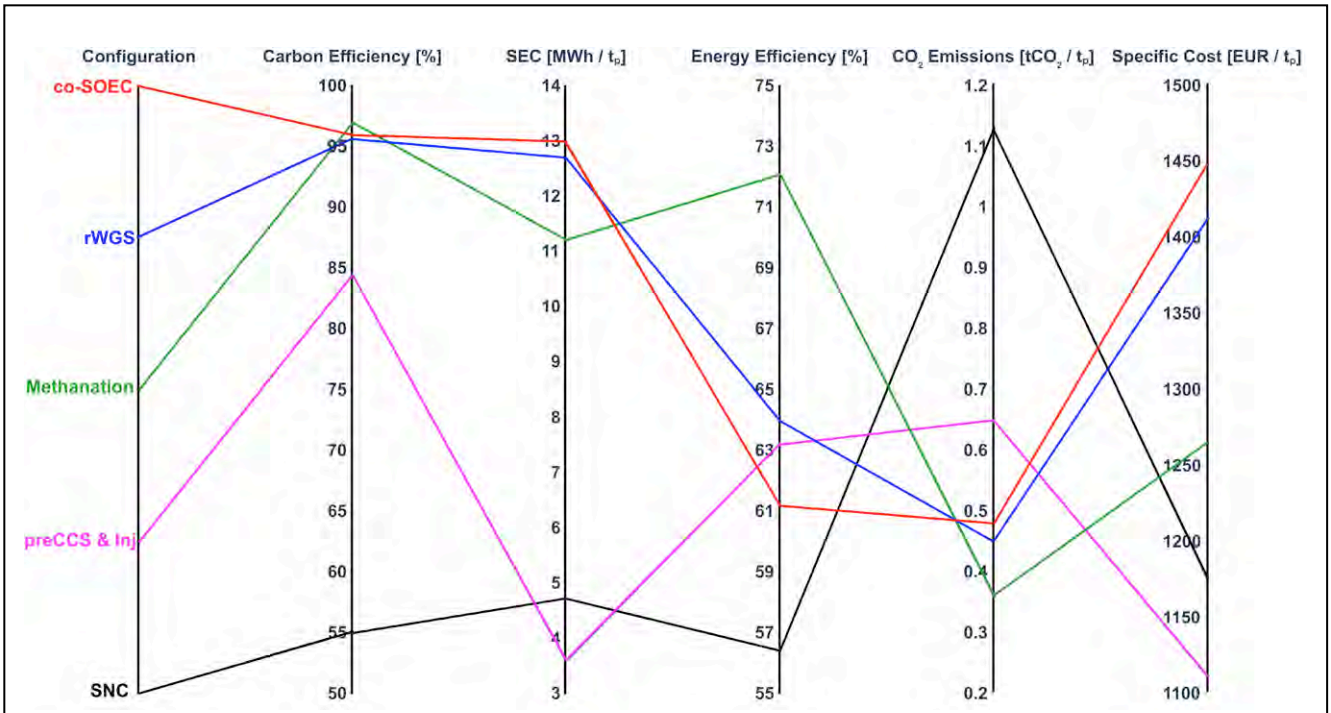



**Figure 2:** Key performance indicators for process configurations. $t_p$: tonne of products.

The defined problem is solved over an entire year (8760 h), divided into 12 monthly periods. Based on the availability of renewable electricity throughout the year, the electricity cost is set at 0.05 EUR/kWh from March to October and 0.15 EUR/kWh from November to February. The energy mix is based on the Swiss grid, with an environmental impact of 0.048 $kgCO_2e/kWh$. A carbon tax of 120 $EUR/t_{CO2}$ is assumed. The prices set for the main products and raw materials are as follows: ethylene at 1,200 EUR/t, propylene at 1,100 EUR/t, butene at 1,000 EUR/t, $CH_4$ at 0.07 EUR/kWh, permanently stored $CO_2$ with a carbon permit valued at 8.4 EUR/t, plastic waste at 454 EUR/t, and biomass at 73 EUR/t.

## Key Performance Indicator Definitions

For comparing the proposed configurations, several key performance indicators (KPIs) are established. These are carbon efficiency (CE), specific energy consumption (SEC), process energy efficiency ($\eta_{Energy}$), environmental impact ($CO_2e$), and specific cost (SC). The definitions of the established KPIs are provided below:

- CE [%] = $\frac{Carbon\ in\ products}{Carbon\ in\ feedstock}$
- SEC $\left[\frac{kWh}{kg}\right] = \frac{E_{el}}{m_{products}}$
- $\eta_{Energy}[\%] = \frac{m_{products} \cdot LHV_{products}}{m_{feed} \cdot LHV_{feed} + E_{el}}$
- $CO_2e\ \left[\frac{kgCO_2e}{kg}\right] = \frac{Direct\ CO_2\ . + Indirect\ CO_2\ . - \text{Avoided } CO_2}{m_{products}}$
- SC$\left[\frac{EUR}{t}\right] = \frac{CAPEX + OPEX}{m_{products}}$

Where $E_{el}$ is the electricity consumption of the overall process within a year [MWh]; m is the total mass within a year [kg or t], LHV refers to the total lower heating value within a year [MWh]. For calculation, the considered specific LHVs are: 5.42 kWh/kg for biomass, 9.47 kWh/kg for HDPE, 13.1 kWh/kg for $C_2H_4$, 12.7 kWh/kg for $C_3H_6$, 12.6 kWh/kg for $C_4H_8$ and 13.9 kWh/kg for $CH_4$. The considered impact factors are: 0.048 $kgCO_2e/kWh$ for electricity, 1.6 $kgCO_2e/kg$ for HDPE and 0.05 $kgCO_2e/kWh$ for pinewood. The total products could consist of olefins, and $CH_4$ depending on the configuration.

The carbon content within biomass, is biogenic, therefore capture of biogenic carbon within product or with injection, it is counted towards avoided(negative) emissions, however since carbon content within plastic is fossil based, it cannot contribute to negative emissions. It is also assumed that, initially the carbon content within plastics is consumed for product formation and injection. After all the fossil carbon is accounted for, additional carbon is considered to be consumed from biogenic source. Therefore, if the carbon contents within the product is exceeds the carbon content of plastics, all emitted $CO_2$ should incorporate biogenic carbon, leading to zero direct $CO_2$ emissions. For indirect $CO_2$ emissions, the impact of electricity, fossil HDPE production and biomass supply chain are accounted.

## RESULTS AND DISCUSSION

The key performance indicators of the optimal configurations are provided in Figure 2. By integrating $CO_2$

management technologies, the carbon efficiency can reach up to 97%, nearly doubling the produced amount of olefins considering the same amount of feedstock.

## $CO_2$ Emissions, Capture and Utilization

As shown in Table 2, none of the alternative configurations entails direct $CO_2$ emissions. Moreover, the net $CO_2$ emissions for the proposed setups are 40-70% lower compared to 5. SNC process. Particularly, in the 2. methanation configuration, lowest $CO_2$ emissions are reached, due to capturing the highest amount of biogenic carbon within the products.

Since the feedstock consists of waste plastics derived from fossil resources, indirect $CO_2$ emissions are significant for all configurations. The impact associated with plastics waste accounts for 60-80% of the emissions depending on the studied configurations. The introduction of SOEC introduces an additional impact of 0.5-0.6 $tCO_2/t_p$ due to the high electricity consumption. However, the increased process carbon efficiency offset the impact of raw materials, leading to lower indirect $CO_2$ emissions in the configurations with SOEC when compared to the 1. preCCS & Inj case.

**Table 2:** Fossil $CO_2$ emissions balance for the process configurations[15].

| **$CO_2$ emission** ($t_{CO2}/t_p$) | **1** | **2** | **3** | **4** | **5** |
|---|---|---|---|---|---|
| Direct | 0 | 0 | 0 | 0 | 0.50 |
| Indirect | 2.21 | 1.46 | 1.58 | 1.63 | 0.63 |
| Avoided (-) | 1.57 | 1.10 | 1.14 | 1.14 | - |
| **Net** | **0.64** | **0.36** | **0.44** | **0.49** | **1.13** |

Figure 3 highlights that the optimal strategy during high electricity price periods is to store liquid $CO_2$, which can later be used to enhance syngas production capacity when electricity prices drop.

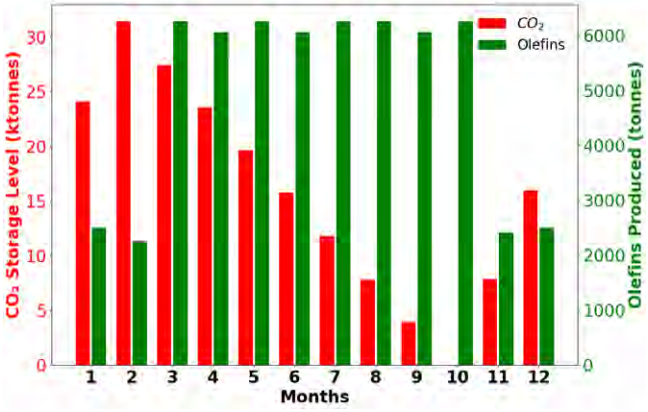



**Figure 3:** Monthly storage level and olefins production capacity for co-SOEC configuration.

## Energy Input and Management

The integration of SOEC causes an increase in energy consumption, making up 60-70% of the overall electricity demand. On the other hand, SOEC boosts the carbon efficiency by 75% compared to 5. SNC and 15% compared to the 1. preCCS & Inj configuration while the energy efficiency is improved by 4 to 16 percentage points with respect to 5. SNC. 1. PreCCS & Inj configuration shows the lowest SEC, due to not leveraging SOEC, and a good integration of the steam network, which provides 78% of the electricity demand of the process. Meanwhile, this power self-generation ratio is limited to 15-20% for the other configurations. None of the processes requires heat from combustion and are autothermal in meeting their heating demands thanks to extensive internal waste heat recovery.

## Economic Evaluation

The specific cost of production for SOEC-integrated processes show an increase of 20-50% compared to the 5. SNC. The 1. preCCS & Inj setup has the lowest SC (1111 EUR/$t_p$), while 4. co-SOEC exhibits the highest cost (1450 EUR/$t_p$). Operating expenditures (OPEX), account for 65-75% of the total specific cost, mainly due to electricity costs, leading to higher impact for all SOEC-integrated configurations. The capital expenditure (CAPEX) is annualized for 40 years with an interest rate of 6%. The highest CAPEX is linked to the 3. rWGS configuration (504 EUR/$t_p$), and the lowest cost is that of the 1. preCCS & Inj configuration (318 EUR/$t_p$).

# CONCLUSIONS

This study proposes and analytically compares various routes for the chemical upgrading of plastic wastes to olefins, integrating $CO_2$ management and energy technologies. This approach offers a globally applicable process that consumes plastic wastes as a widely available feedstock and reduces the dependency on fossil fuels. Furthermore, these configurations not only prevent direct $CO_2$ emissions but also cut down the emissions linked to the virgin plastic production and the treatment of plastic waste, establishing the foundations of plastics circular economy.

The alternative configurations evaluated using high temperature electrolyzers (SOEC) require a significant amount of seasonal, renewable electricity. However, seasonal $CO_2$ storage can address this issue by optimizing the process for both process efficiency and operational costs, increasing the production capacity by 40%. In the long term, with increased share of renewable electricity mixes, these routes are expected to economically outperform traditional processes of plastics manufacturing and plastics waste treatment.

## REFERENCES


1. OECD (2022) Global Plastics Outlook: Policy Scenarios to 2060. OECD Publishing, Paris
2. Flores-Granobles M, Saeys M (2023) Quantitative analysis of CO2 emissions reduction potential of alternative light olefins production processes. Green Chem 25:6459–6471
3. Jiang G, Wang J, Al-Salem SultanM, Leeke GA (2020) Molten Solar Salt Pyrolysis of Mixed Plastic Waste: Process Simulation and Technoeconomic Evaluation. Energy Fuels 34:7397–7409
4. Trninic M, Stojiljkovic D, Manic N, Skreiberg Ø, Wang L, Jovovic A (2020) A mathematical model of biomass downdraft gasification with an integrated pyrolysis model. Fuel 265:116867
5. Ajorloo M, Ghodrat M, Scott J, Strezov V (2022) Modelling and statistical analysis of plastic biomass mixture co-gasification. Energy 256:124638
6. Pinto F, Franco C, André RN, Miranda M, Gulyurtlu I, Cabrita I (2002) Co-gasification study of biomass mixed with plastic wastes. Fuel 81:291–297
7. Kiss AA, Pragt JJ, Vos HJ, Bargeman G, Groot MT de (2016) Novel efficient process for methanol synthesis by CO2 hydrogenation. Chemical Engineering Journal 284:260–269
8. Domingos MEGR, Flórez-Orrego D, Santos MT dos, Oliveira S de, Maréchal F (2022) Techno-economic and environmental analysis of methanol and dimethyl ether production from syngas in a kraft pulp process. Computers & Chemical Engineering 163:107810
9. Hannula I, Arpiainen V (2015) Light olefins and transport fuels from biomass residues via synthetic methanol: performance and cost analysis. Biomass Conversion and Biorefinery 5:63–74
10. Flórez-Orrego DA, Domingos MEGR, Nakashima RN, Santos MT dos, Junior S de O (2023) Chapter 2 - Syngas purification by common solvents. In: Rahimpour MR, Makarem MA, Meshksar M (eds) Advances in Synthesis Gas : Methods, Technologies and Applications. Elsevier, pp 27–72
11. Domingos MEGR, Flórez-Orrego D, Sfeir S, Maréchal F (2024) Integration of biodigestion, gasification, renewable energy, reversible solid oxide cell and CO2 management strategies for sustainable natural gas production.
12. Flórez-Orrego D, Dardor D, Domingos MEGR, Germanier R, Maréchal F (2024) Integration of renewable energy and reversible solid oxide cells towards decarbonizing the secondary aluminium production and urban systems.
13. Domingos MEGR, Flórez-Orrego D, Santos MT dos, Júnior S de O, Maréchal F (2023) Multi-time integration approach for combined pulp and ammonia production and seasonal CO2 management. Computers & Chemical Engineering 176:108305
14. Dardor D, Flórez-Orrego D, Terrier C, Ribeiro Domingos ME, Platteau C, da Silva JC, Lopez M, Maréchal F (2024) ROSMOSE: A web-based decision support tool for the design and optimization of industrial and urban energy systems. Energy 304:132182
15. Young B, Hawkins TR, Chiquelin C, Sun P, Gracida-Alvarez UR, Elgowainy A (2022) Environmental life cycle assessment of olefins and by-product hydrogen from steam cracking of natural gas liquids, naphtha, and gas oil. Journal of Cleaner Production 359:131884



© 2025 by the authors. Licensed to PSEcommunity.org and PSE Press. This is an open access article under the creative commons CC-BY-SA licensing terms. Credit must be given to creator and adaptations must be shared under the same terms. See https://creativecommons.org/licenses/by-sa/4.0/




Systems & Control Transactions

**Research Article - Peer Reviewed Conference Proceeding**
ESCAPE 35 - European Symposium on Computer Aided Process Engineering
Ghent, Belgium. 6-9 July 2025
Jan F.M. Van Impe, Grégoire Léonard, Satyajeet S. Bhonsale,
Monika E. Polańska, Filip Logist (Eds.)

PSE PRESS

# Integrating Chemical Recycling into Brownfield Processes: Waste Polyethylene Pyrolysis and Naphtha Steam Cracking

**Marc Caballero, Thanyanart Sroisamut, Anton A. Kiss, and Ana Somoza-Tornos***

Delft University of Technology, Department of Chemical Engineering, Delft, The Netherlands
* Corresponding Author: A.SomozaTornos@tudelft.nl.

## ABSTRACT

In this study, we evaluate the economic and environmental impacts of integrating waste polyethylene (PE) pyrolysis with naphtha-based steam cracking for 660 Mt/y ethylene production. We compare six integration scenarios to both business-as-usual (BAU) steam cracking and greenfield waste PE pyrolysis plant. We perform process simulations and equipment design in Aspen Plus® V12, followed by a techno-economic analysis (TEA) and a life-cycle assessment (LCA. The integration capacity we considered corresponds to one full-capacity PE pyrolysis furnace, reducing naphtha feed by 7% in BAU steam cracking. Through the TEA, we identify the most cost-effective scenario by merging the PE pyrolysis gas with the steam cracker furnace outlet after preheating the PE feed. This integration reduces production costs by 6.46MM€/y, improving costs a 0.3% compared to BAU and 30% compared to the pyrolysis greenfield design. LCA results show that the greenfield pyrolysis plant achieves the lowest global warming potential (GWP), reducing emissions by 14% compared to BAU. Among the integration scenarios, lowest GWP occurs when PE pyrolysis gases, also with feed pre-heating, merge before the main compressor train, obtaining a 0.12% GWP reduction compared to BAU. This analysis highlights the potential of introducing circular technologies in existing plants to progressively shift from fossil fuel usage.

**Keywords**: process integration, circular economy, ethylene, sustainable feedstock, chemical recycling

## INTRODUCTION

Circularity in the chemical industry is essential for achieving sustainability, especially as the sector moves away from linear, fossil-based production models. Circular processes aim to minimize waste, optimize resource use, and closing carbon loops by utilizing renewable and waste resources. This approach is a key strategy to address both environmental and economic challenges [1].

Plastics account for the largest share of oil usage outside fuel production [2]. Their widespread use has led to vast global waste accumulation, particularly from single-use packaging. In the European Union, packaging represents approximately 40% of plastic demand, generating large volumes of waste that often escape effective management systems [3].

Compared to disposal methods like landfilling and incineration, recycling faces challenges related to cost and material quality. Mechanical recycling is one of the least energy-intensive options, but it is limited by the number of cycles the material can endure [4]. In contrast, chemical recycling is a more expensive alternative but avoids degradation by breaking plastics down into their monomers [5].

In Europe, the most produced polymer is the polyethylene (PE) families of plastics, with a share of 22% of the production [3]. Given that PE is the most widely produced plastic and is predominantly used in single-use packaging, it represents the most promising candidate for chemical recycling.

Among the diverse chemical recycling methods, pyrolysis is the most researched since it converts plastic into lower molecular weight products [5], which allows the recovery of monomers and the closure of carbon loops.

Waste PE Pyrolysis plants are already existing at a commercial scale, and many companies have announced collaborations between projected pyrolysis plants and their refineries [5]. However, repurposing existing infrastructure for circular processes offers a more cost-

**Table 1:** Integration scenarios summary

| Scenario | Integration concept | Pyrolysis product feed location |
|---|---|---|
| 1.a | Waste LDPE pyrolysis integrated without the need of additional equipment | Outlet of naphtha furnace reactor |
| 2.a | - Increase the heat recovery of pyrolysis gas to generate power. The absence of heavy component in the product gas, allows more efficient cooling. Heat exchanger(s) EX1-P perform this task.<br>- Duty reduction in primary fractionator (T1), bypassing the unit since pyrolysis gas contains no heavy components | After primary fractionator |
| 3.a | - All from 2.a<br>- Reduce the energy requirements of the distillation units for light components by separating the $C_4$+ components prior to integration. Flash separator SEP3-P performs this task, with the aid of compressor C2-P to reach the adequate pressure for the integration point, and heat exchanger EX2-P to lower the gas temperature to allow gas to condense in the flash drum. | Intermediate stage compressor and T7 feed |
| 1.b, 2.b, 3.b | Use heat from the pyrolysis gas to preheat waste PE feed in the first pyrolysis (low temperature) reactor | To corresponding scenario (1.a-3.a) |

effective and resource-efficient solution [6]. This study explores different integration strategies for incorporating PE pyrolysis into existing ethylene production. The proposed scenarios are compared against both a greenfield design of waste LDPE pyrolysis plant and naphtha steam cracking.

## APPROACH AND METHODOLOGY

### Integration Strategy

We first replicated the design from Somoza et al. [7] for a greenfield ethylene plant based on waste PE pyrolysis, and the design from Spallina et al. [8] for a brownfield olefins plant based on naphtha steam cracking (SC). As reference for pyrolysis of PE, we used the conversion and yields from Kannan et al. [9], whose experiments focused on maximizing the ethylene yield in the flash pyrolysis of waste low density polyethylene (LDPE).

Both designs share a substantial similarity, due to their comparable main reactor outlets, since both processes' main products are polyolefins. Both plants can be briefly described with their major common elements by having the high-temperature reactor, a following cooling stage, a compressor train to raise the pressure enough to enable the separation of the light hydrocarbons and the consequent distillation column cascade. The SC contains additional processes, such as a removal of water and $C_9$+ fraction preceding the compression train, and intermediate reaction steps between the cascade distillation, with the aim to increase the ethylene and propylene yields.

Given these similarities, we developed six integration scenarios to incorporate LDPE pyrolysis into an existing steam cracking process. The goal is to achieve a competitive cost compared to the grass-roots design of a standalone pyrolysis plants, and with the second aim to reduce the cost of ethylene production by steam cracking. A brief summary of the proposed integration scenarios is provided in Table 1.

Figure 1 illustrates the SC layout alongside with the proposed integration scenarios, highlighting the similarities between the SC and the greenfield pyrolysis design. The color coding emphasizes the units that perform equivalent tasks in the waste pyrolysis plant design.

### Simulation and Assessment Methods

We performed process simulations and equipment design for both independent plant designs and the integration scenarios, in Aspen Plus® V12, using PolyNRTL as property package, to enable LDPE to be handled in mass and energy balances.

For each integration scenario, we conducted a comprehensive techno-economic assessment (TEA) and life cycle assessment (LCA) to evaluate both the economic viability and environmental impact of incorporating LDPE pyrolysis into the naphtha steam cracking process.

For the TEA, we followed the cost evaluation guidelines from Towler and Sinnott [10], supplementing with additional sources [8] [11] for equipment not covered in [10].

For the LCA, we applied the ISO 14040:2006 standards for life cycle assessment methodology, using the Ecoinvent3 database in SimaPro software to assess environmental impacts, focusing primarily on Global Warming Potential (GWP).

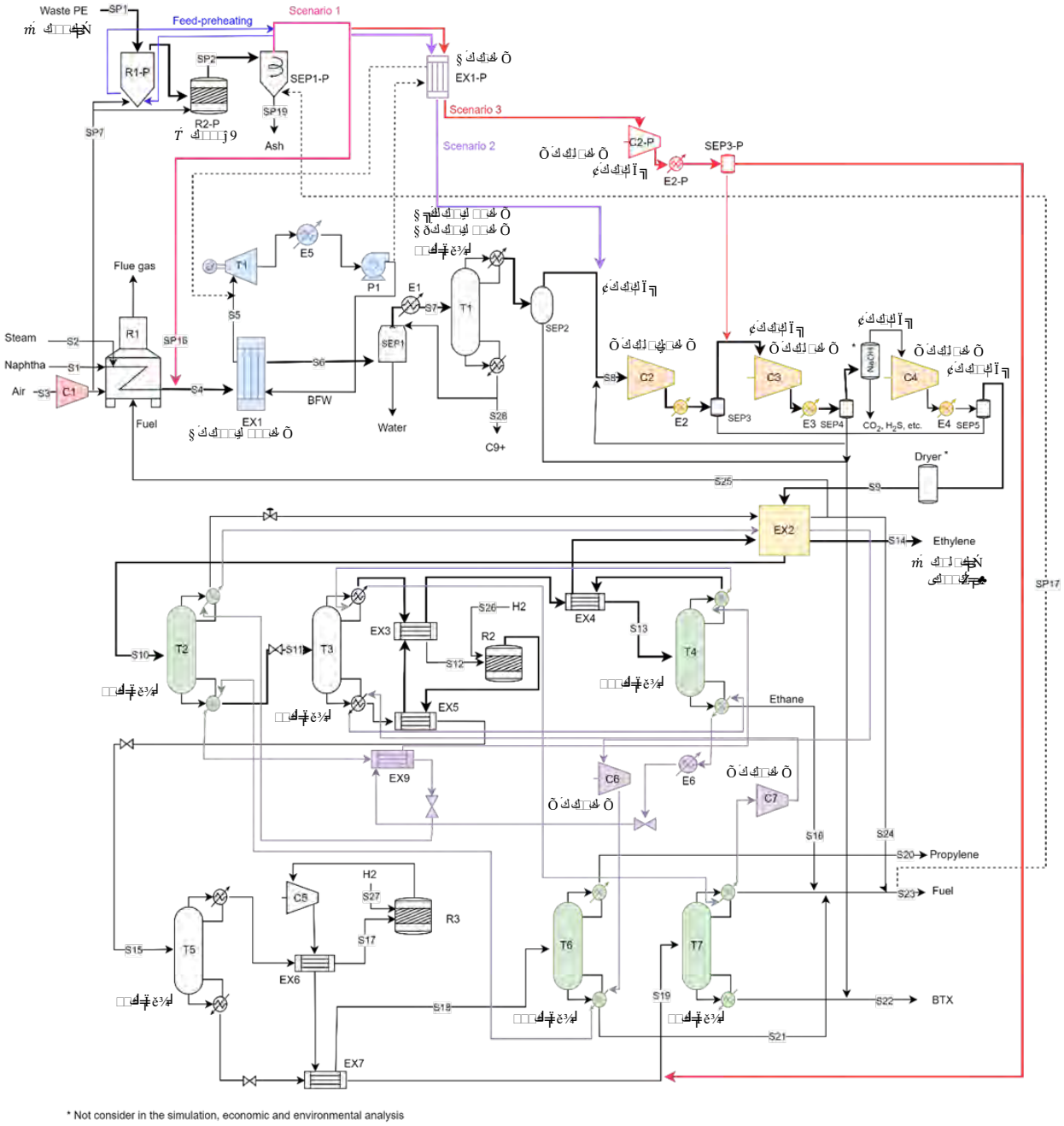



**Figure 1:** Steam Cracking plant layout with PE pyrolysis integration scenarios. Colored units correspond to the coinciding units in a standalone PE pyrolysis plant, highlighted for similarity.

## RESULTS AND DISCUSSION

### Techno-Economic Assessment (TEA)

To compare both standalone plants, we allocated the cost of production per kg of ethylene. The feed from the greenfield design for a waste PE pyrolysis plant, corresponds to one full-capacity pyrolysis furnace, representing approximately a 7% of the steam cracking naphtha feed. Using this cost allocation, we estimate that the standalone waste PE pyrolysis plant produces ethylene at 1.045€/kg of ethylene, while the cost at the steam cracking plant is 0.7429€/kg of ethylene. This significant cost difference is what motivated this study.

For the integration scenarios, we set the ethylene production capacity to 660Mt/y. Introducing one LDPE pyrolysis furnace at full capacity, the naphtha feedstock can be reduced by the aforementioned percentage.

Figure 2 illustrates the cost differences between the average of all integration scenarios and the business-as-usual (BAU) standalone steam cracking process. Since ethylene production remains fixed, this output remains unaltered across all scenarios.

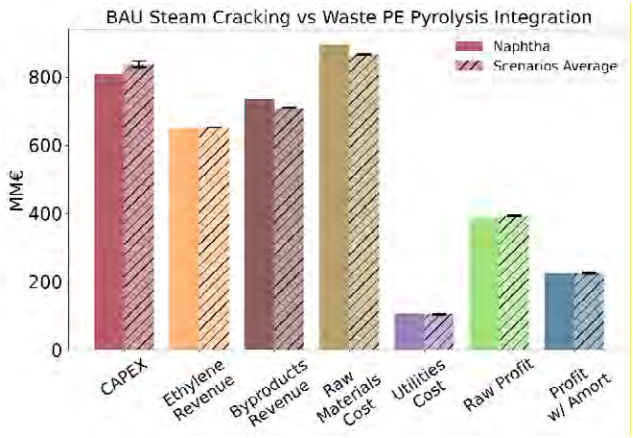



**Figure 2.** Comparison of business as usual steam cracking vs average of integration scenarios.

Figure 3 breaks down the main costs and revenues for each scenario, using the BAU steam cracking as reference. The ethylene production (and revenue) remains

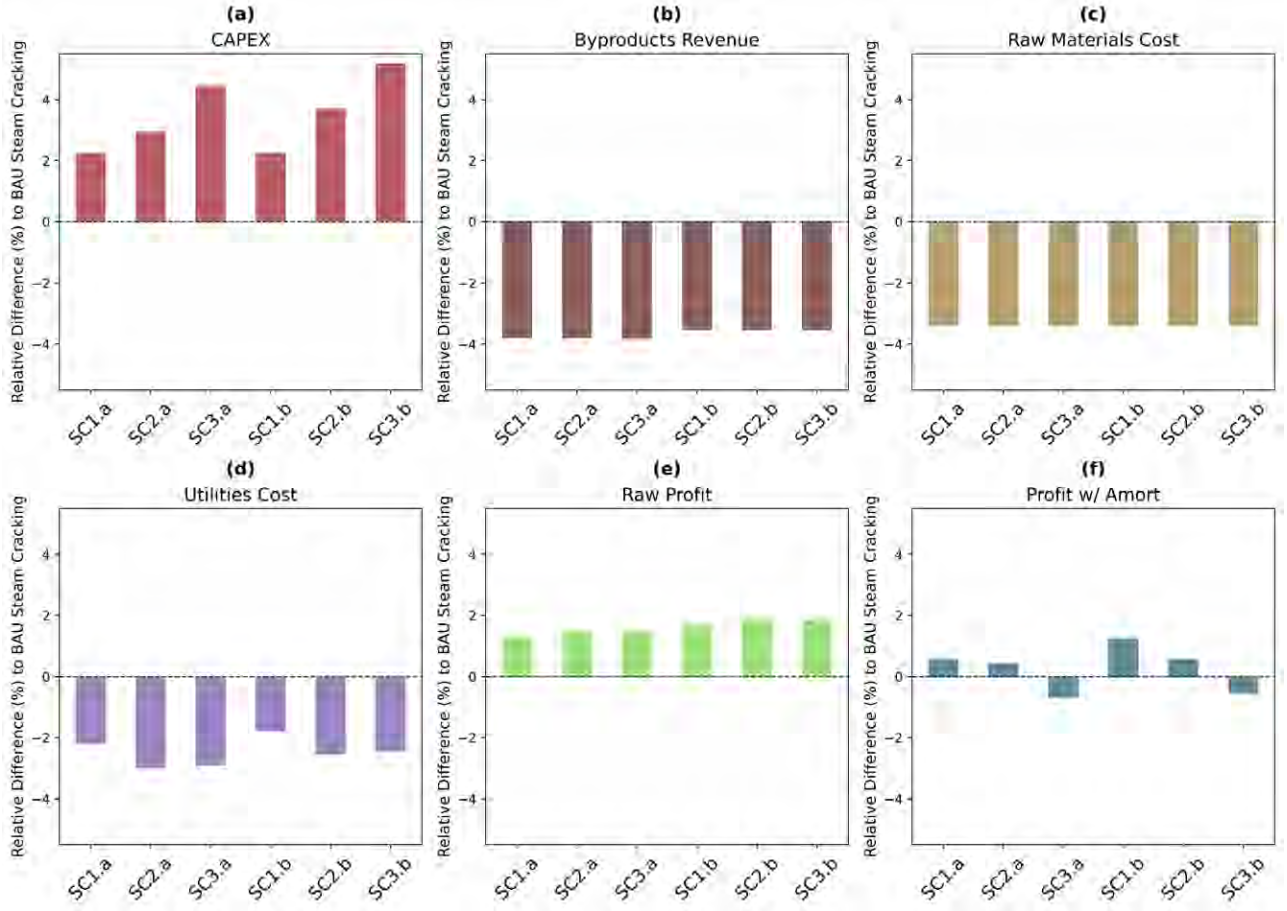



**Figure 3:** Comparison of economic and operational metrics for naphtha-based steam cracking and waste PE pyrolysis scenarios

constant across all scenarios. However, the revenue from other products decreases in all integration cases. This reduction occurs because (high temperature) flash pyrolysis is targeted towards maximizing ethylene yield [9]. Among the byproducts, propylene production is the least affected, with only a 0.82% reduction (2.4M€/y) from the BAU case. The revenue from $C_{9+}$ stream decreases by 7.5% (2.4M€/y), while the BTX revenue drops by 3.3% (7.7M€/y), with minimal differences between the integration cases. Fuel products experience the largest revenue loss, averaging 11% (12.6M€/y) in cases without feed pre-heating and 10% (10.6M€/year) in cases with pre-heating. Overall, the average reduction in revenue across the scenarios is a 3.6% (27M€/y).

Despite revenue losses, utility expenses decrease by approximately 5% (3M€/y) across all integration scenarios. Scenario 2 achieves greater utility savings than Scenario 1, as expected. The utilities reduction for Scenario 3 are, however, lower than Scenario 2, due to the low substitution ratio that hinders the potential energy savings in distillation. This trend applies to both cases with and without feed pre-heating.

Differences in feedstock prices result in a yearly cost reduction of 3.6% (30M€/y) for a 7% of reduction in naphtha consumption. However, revenue losses offset most of this benefit. In the best-performing scenario (Scenario 1 with feed pre-heating), this translates into an overall raw profit increase of 1.67% (6.5M€/y), primarily due to lower utility costs. After accounting for the CAPEX amortization of the equipment and overhead expenses, the final cost of ethylene production drops minimally to 0.7407€/kg, compared to 0.7429€/kg of BAU case.

## Life Cycle Assessment (LCA)

The Life Cycle Assessment (LCA) evaluates the Global Warming Potential (GWP) across different configurations: BAU steam cracking, greenfield plant of waste LDPE pyrolysis, and six integrated scenarios.

As shown in Figure 4 a), the greenfield pyrolysis process has a lower GWP than the BAU naphtha steam cracking (1.243 vs. 1.441 kg $CO_2$ eq./kg ethylene), largely due to reduced reliance on fossil naphtha. In the naphtha steam cracking process, the highest emissions are from fossil feedstock (35% of total) and direct emissions from furnace combustion (28%). In contrast, standalone pyrolysis sees direct emissions contribute approximately 54% of its GWP due to higher energy demand, with electricity also a significant factor (26%).

The integration scenarios, which substitute only 7%

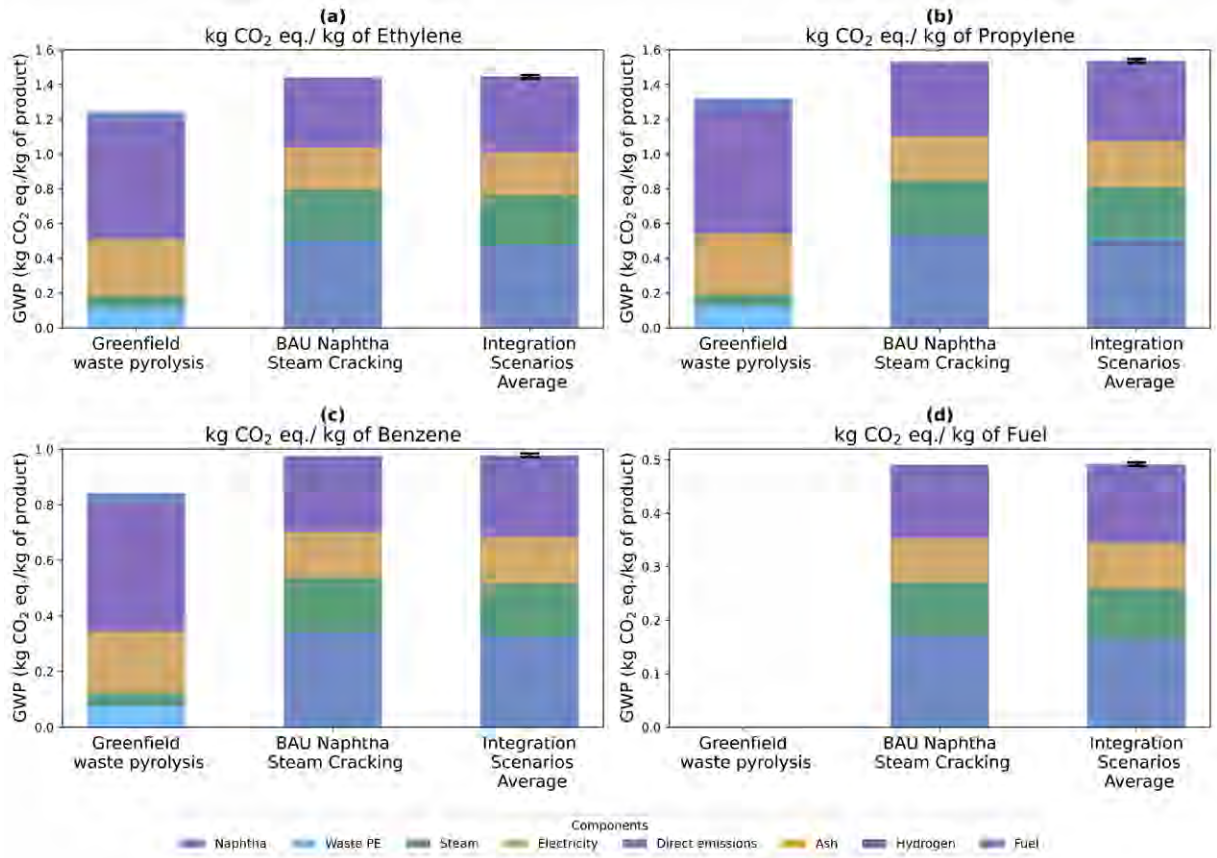



**Figure 4:** Comparison of LCA results of Standalone plants and average of integration scenarios

of naphtha with pyrolysis gas, yield marginal GWP reductions. Although they reduce GWP contributions from naphtha, steam, and hydrogen, these benefits are partially offset by increased direct emissions and electricity use. Among the integration options, Scenario 2.b achieves the lowest GWP (1.439 kg $CO_2$ eq./kg ethylene), demonstrating that preheating lowers emissions. Overall, all products—ethylene, propylene, BTX, and fuel—exhibit similar GWP trends across the processes.

From the rest of the mid-point categories we evaluated in the LCA analysis, fossil resource scarcity is the category most positively impacted by pyrolysis integration scenarios. All of them show a reduction respect to BAU steam cracking, with also Scenario 2.b achieving the highest reduction of a 4.8%(from 1.817 kg of oil eq. to 1.729 kg of oil eq.).

## CONCLUSION

A 7% of substitution of naphtha with pyrolysis gas offers an economically feasible way for the industry to gradually introduce sustainable technology and gain operational experience, however, the cost improvements remain marginal. However, the key factor that makes pyrolysis of waste plastic attractive is the price gap between naphtha and waste plastic.

In this study, we identified Scenario 1 with feed preheating the most economically viable integration option, achieving annual operating cost savings of 6.5 million euros compared to business as usual operation of steam cracking.

From an environmentally perspective, the pyrolysis process has a lower GWP than both naphtha steam cracking and integration scenarios. Among the integration options, Scenario 2 with feed preheating achieves the lowest GWP at 1.439 kg $CO_2$ eq./kg $C_2H_4$, demonstrating that heat integration is key to reduce environmental impact.

The divergence between economic and environmental assessments highlights the challenges of integrating waste plastic pyrolysis at low substitution ratios. Nevertheless, since the factor that determines Scenario 1.b as the best candidate in economic terms is the low CAPEX, a higher substitution ratio might favour Scenario 2.b since it showed the highest raw profits among the integration possibilities.

In addition, LCA indicators support Scenario 2.b as the best candidate, however, since the waste PE pyrolysis is carried at higher temperatures compared to steam cracking, increasing the share of PE pyrolysis integrated might change the preferred integration scenario, and affect sustainability indicators.

Therefore, a study of higher substitution ratios is highly recommended.

## REFERENCES


1. J. Slootweg. Sustainable chemistry: Green, circular, and safe-by-design. OneEarth, 7, 5, 754 – 758 (2024).
2. World Economic Forum, Ellen MacArthur Foundation and McKinsey & Company, The New Plastics Economy: Rethinking the future of plastics (2016).
3. European Green Deal, Putting an end to wasteful packaging, boosting reuse and recycling(2022).
4. J. Garcia, M. Robertson. The future of plastics recycling. Science, 358, 6365 (2017).
5. H. Li, et al. Expanding plastics recycling technologies: chemical aspects, technology status and challenges. Green Chemistry, 24, 8899 – 9002 (2022).
6. K. Télessy, L. Barner, F. Holz. Repurposing natural gas pipelines for hydrogen: Limits and options from a case study in Germany. International Journal of Hydrogen Energy, 80, 821 – 831 (2024).
7. A. Somoza -Tornos, A. Gonzalez-Garay, C. Pozo, M. Graells, A. Espuña, G. Guillén-Gosálbez. Realizing the Potential High Benefits of Circular Economy in the Chemical Industry: Ethylene Monomer Recovery via Polyethylene Pyrolysis. ACS Sustainable Chem. Eng., 8,9, 3561 – 3572 (2020).
8. V. Spallina, I. Campos Velarde, J.A. Medrano Jimenez, H. Reza Godini, F. Gallucci, M. van Sint Annaland. Techno-economic assessment of different routes for olefins production through the oxidative coupling of methane (OCM): Advances in benchmark technologies. Energy Conservation and Management, 154, 244 – 261 (2017).
9. P. Kanan, A. Al Shoaibi, C. Srinivasakannan. Temperature effects on the yield of gaseous olefins from waste polyethylene via flash pyrolysis. Energy & Fuels, 28(5): p/ 3363-3366 (2014).
10. G. Towler, R. Sinnott. Chemical Engineering Design: Principles, Practice and Economics of Plant and Process Design. Ed: Third edition. Butterworth-Heinemann, Elsevier. (2021).
11. R. Turton, J. Shaeiwith, D. Bhattacharyya,W.B. Whiting. Analysis, Synthesis and Design of Chemical Processes. Ed: Fifth Edition (2018).



© 2025 by the authors. Licensed to PSEcommunity.org and PSE Press. This is an open access article under the creative commons CC-BY-SA licensing terms. Credit must be given to creator and adaptations must be shared under the same terms. See https://creativecommons.org/licenses/by-sa/4.0/




Systems & Control Transactions

**Research Article - Peer Reviewed Conference Proceeding**
ESCAPE 35 - European Symposium on Computer Aided Process Engineering
Ghent, Belgium. 6-9 July 2025
Jan F.M. Van Impe, Grégoire Léonard, Satyajeet S. Bhonsale,
Monika E. Polańska, Filip Logist (Eds.)

PSE PRESS

# Integrated LCA and Eco-design Process for Hydrogen Technologies: Case Study of the Solid Oxide Electrolyser

**Gabriel Magnaval[a,b,*], Tristan Debonnet[b], Manuele Margni[a,b]**

[a] CIRAIG, Polytechnique Montréal, Montréal, Canada
[b] HES-SO Valais-Wallis, Sion, Switzerland
* Corresponding Author: gabriel.magnaval@hevs.ch

## ABSTRACT

The Life Cycle Assessment (LCA) of a solid oxide electrolyser (SOE) has been performed using publicly available data. The system for producing 1 kg of hydrogen at 25bar and 99.9% purity is represented by a modular structure, which includes the 20-kW solid oxide stack manufacturing, balance of plant equipment, operation consumables, and end-of-life processes. A parametrized life cycle inventory modeling approach was developed. The results illustrate that SOE performs better than steam methane reforming only if supplied by electricity from renewable or nuclear sources. The operation consumables have been identified as the most contributive life stage (67%-89% of potential impacts), followed by equipment manufacturing (7%-22%) and stack manufacturing (4%-11%). Considering the predominant contribution of electricity supply in the consumables, no compromise should be made on ensuring clean electricity sourcing and on the stack energy conversion efficiency. The lifetime of the stack and the balance of plant equipment, as well as the heat mix have been identified as sensitive parameters to minimize the environmental impact of the hydrogen technology. These LCA results have been used to produce a tailored eco-design process for hydrogen projects: (i) organization of an eco-design workshop to present LCA results & environmental hotspots and related key parameters where to leverage eco-design innovations through an open discussion (brainstorm); (ii) provide an eco-design tool obtained from a simplified version of the LCA model parametrized around a limited number key life cycle inventory parameters, enabling the designers/developers to independently test the environmental performance of their innovations.

**Keywords**: Life Cycle Assessment, Eco-design Process, Solid Oxide Electrolyser, Parametrized Life Cycle Inventory

## INTRODUCTION

Hydrogen technologies are promising solutions for ecological transition in energy and industry. Electrolysers can produce hydrogen through water electrolysis powered by renewable electricity to replace fossil-based hydrogen obtained by Steam Methane Reforming (SMR), providing industrial processes such as steel production and chemical synthesis with low-impact feedstock. Hydrogen can also serve as an energy carrier to facilitate the shift toward a renewable energy mix. Fuel Cell technologies can convert hydrogen back into electricity, so that hydrogen would provide a flexible energy storage to balance the grid [1]. As the fuel cells and electrolysers (FC&EL) are still emerging technologies, they present an opportunity to integrate effective eco-design strategies early in their conception, when the degree of freedom in design choices are higher. Eco-design refers to the objective of minimizing the potential environmental impacts of a technology while conserving its functionalities [2]. To define these eco-design strategies, assessing the potential environmental impact of the FC&EL is crucial. Life Cycle Assessment (LCA) is a methodology for evaluating the environmental impacts of a product or system throughout its entire life cycle, from raw material extraction to disposal. LCA has been widely used for eco-design [3]. It allows identifying the hotspots and key technological parameters that mostly contribute to the potential impacts along the supply chain of the product, and to anticipate unexpected burden shifting between impact

categories.

The hydrogen technologies studied in this paper rely on solid oxide cells (SOCs). The particularity of this technology is the high-temperature operation (500°C-1000°C) and the possible reversibility of the cells (rSOCs) [4]. It means that the same cells can be used either for electrolyser mode (SOE) or for fuel cell mode (SOFC). Few LCA have already been developed for SOFC system [5], [6], [7], for SOE system [8], [9], [10], [11] and for reversible system [12] but they raised some methodological issues. First, the system boundaries of some studies focus solely on the production of one stack (cradle-to-gate), while others include the operation phase (cradle-to-grave) that represents the largest contributor to the overall environmental impact scores (70-100% depending on energy sourcing and technology). Second, the quality of hydrogen produced (purity, pressure) were rarely explicitly defined. Third, modeling of the balance of plant and the end-of-life of the system have been neglected by many studies. Finally, these LCA have been developed for comparative studies (with other FC&EL technologies or SMR) rather than specifically for eco-design process.

This paper aims (1) to develop a consistent LCA modular structure across all hydrogen technologies, facilitating comparability and harmonization in modeling and interpreting their environmental performances; (2) illustrate its application performing the LCA of a SOE from publicly available data; and (3) to support an eco-design process with quantified metrics from these LCA results.

## METHODS

This section describes the methodology followed to compute the LCA of a solid oxide baseline, and to derive eco-design principles from these LCA results. Figure 1 gives a graphical representation of this approach. The LCA has been performed according to ISO 14040 and ISO 14044 standards [13], [14]. The following sections detail each phase of the methodology.

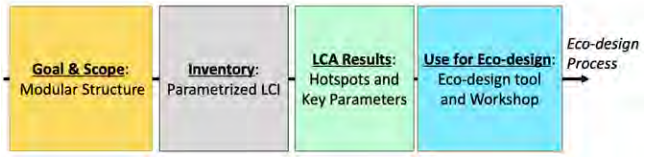



**Figure 1.** Graphical representation of the methodology for developing an eco-design process based on LCA.

### Goal & Scope and Modular Structure

Existing guidelines for the LCA of hydrogen technologies provide valuable guidance for practitioners [2], [15], [16], [17]. However, they lack a standardized framework for defining the goal and scope of hydrogen technologies, limiting the interpretation, comparability of LCA results and hindering interoperability of datasets. This paper offers a first attempt to improve consistency and harmonization defining the LCA scope for H2 technologies: terminology and classification of key processes and their organization in hierarchical supply tiers, providing a structured approach that can be applied across all other hydrogen technologies (Figure 2). This approach requires an explicit functional unit which incorporates pressure and purity conditions, but also the stack power, to enable fair comparisons between systems. For the case study, the functional unit is defined as "producing 1 kg hydrogen @25bar and 99.9% purity, using a 20kW stack, in Europe in 2024". The process tree delivering the functional unit is organized in hierarchical supply tiers. Tier 1 encompasses the following main life cycle stages: the stack manufacturing, the balance of plant equipment, the operation consumables, and the end-of-life of the system. Each of them links to specific upstream supply processes at Tier 2. Typically, the BoP contains standard equipment, and a compressor to ensure the hydrogen is delivered at 25bars (the hydrogen reaches 99.9% at this pressure without additional equipment). Tier 3 maps suppliers of each Tier 2 process, and so on. Tier 4 represents the background system, consisting in processes for which primary data on supply material, energy, and services are not generally available and for which generic datasets are used to estimate cradle-to-gate life cycle inventories of the respective supply chains. Such generic datasets are taken from commercial life cycle inventory databases.

### Parametrized Life Cycle Inventory

The LCI data collection mainly concerns the materials used, the energy consumed, and the amount and type of wastes and emissions generated by each process included in the system boundaries. To ensure reproducibility and adaptability of the study, and to facilitate the eco-design process, a parametrized life cycle inventory (p-LCI) is developed. This practice consists in structuring the inventory with raw parameters linked with explicit equations, instead of introducing computed numbers [18].

The parameters introduced in this p-LCI describe the stack geometry, the stack composition, the industrial processes involved in component production, the operational performance of the electrolyser and the energy mixes. The illustrative case study assumes a 100% renewable electricity mix supply and 65% of heat valorized from waste heat supplied by an industrial site where the SOE is operated. This waste heat is assumed impact free. The remaining 35% of heat is assumed to be provided by electric heaters. Table 1 presents the parameters for calculating Tier 1 process flows.

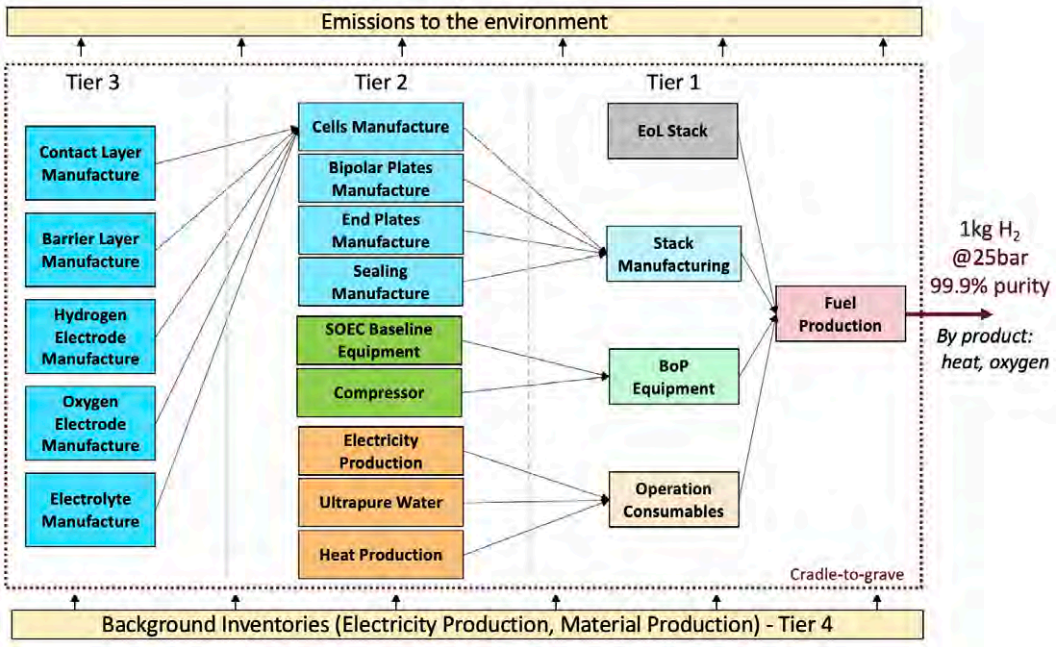



**Figure 2:** System boundaries of the screening LCA to deliver the functional unit, ordered by supply tier. Tier 1 encompasses the main life stages. Each element is further subdivided in common Tier 2 sub processes and so on.

**Table 1:** Main foreground parameters introduced in the study for SOE baseline values.

| Component | Description | Baseline Value | Source |
|---|---|---|---|
| Cell | Active Surface | 0.02 $m^2$ | [7], [8] |
| Stack | Stack Power | 20 kW | FU |
| Stack | Current Density | 1 A/$cm^2$ | [10] |
| Stack | Voltage | 1.3V | [8], [11] |
| Stack | Degradation Rate | 1%/kh | [11] |
| BoP | BoP lifetime | 80,000h | [19] |
| Operation | Beginning of life LHV-based System Efficiency | 85% | [9] |
| Operation | Water Demand | 14 L/$kgH_2$ | [20] |
| Operation | Heat Demand | 9 kWh/$kgH_2$ | [10] |
| Electricity Mix | Wind Power | 75% | [21] |
| | PV Power | 7% | |
| | Hydraulic Power | 18% | |
| Heat Mix | Waste heat available | 65% | [9] |
| | Heaters (electricity) | 35% | |

The complete set of parameters is available in Supplementary Information. Most of secondary data comes from the life cycle inventory (LCI) modules available in the European *Ecoinvent v3.10* database [19].

## LCA results

The impact profile has been computed using the Footprint version of the Impact World+ v2.0 method [22]. Five categories of impacts are assessed: the *Carbon footprint (CC)* in $kgCO_2eq.$, the *Water Scarcity footprint* in $m^3$ world-eq., the *Fossil and Nuclear Energy Use* in MJ deprived, the *Remaining Human Health (Rem. HH)* in DALY and the *Remaining Ecosystem Quality (Rem. EQ)* in PDF.$M^2$.yr. The categories *Remaining of human health* and *of ecosystem quality* exclude the contributions of *climate change* and *water availability,* avoiding double counting. The OpenLCA 2.0.3 software was used to compute the potential impacts associated with the inventoried emissions.

First, the environmental profile of the production of 1kg of $H_2$ (@25bar, 99.9% purity) using the 20-kW stack is performed. The efficiency of the system (78%) is determined as the average efficiency that includes a typical ohmic degradation of the stack over its useful life (based on a 10% maximum degradation) and the energy for compression. A comparison is made with hydrogen production from Steam Methane Reforming (SMR) (@25bar and 99.9% purity). The SMR process is modeled using the *Ecoinvent* database, specifically tailored to the European context. Second, a contribution analysis is performed to take a deep dive into the results. The contribution analysis is made stepwise, by progressively disaggregating the processes following the tiers of the modular structure. This work clarifies which life cycle stages, unit processes, then components mainly contribute to the overall impact scores and therefore identify the hotspots of the SOE baseline layout. Third, sensitivity analyses are

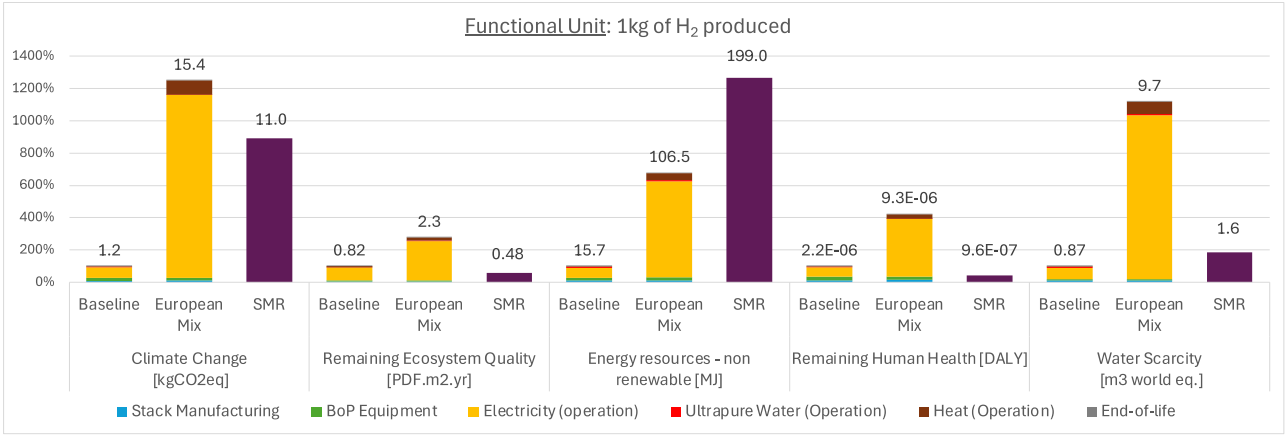



**Figure 3:** Comparative environmental profile of the SOE baseline scenario (Green Mix), the European Mix Scenario (sensitivity analysis) and the production of $H_2$ by SMR. Absolute values of the different indicators are given on the

performed to check the results robustness to the scenarios, and to provide valuable insights on the most critical processes and key parameters for reducing the environmental impacts. The sensitivity to energy mixes, to the purity requirement and to the system size are performed. A systemic sensitivity analysis of the foreground parameters introduced in the p-LCI is also performed.

## Deriving an eco-design process from LCA results

The interpretation of the LCA results provides the foundation for defining the key eco-design messages. The eco-design process relies on two complementary elements. First, an eco-design workshop is organized to translate the LCA findings into actionable design innovations. The workshop initiates with a knowledge-sharing presentation. The principles of life cycle thinking, and the risks of burden shifting are introduced to the project partners. The LCA results are communicated to the participants, emphasizing the most contributive processes, components, and the most sensitive parameters, fostering a collective understanding of the key priorities and key leverages for reducing the environmental impacts. The second part of the workshop aims at stimulating the creativity of the engineers/designers around the innovations aimed to improve the environmental performance of the baseline technology. The eco-design wheel developed by the HEU eGhost, which outlines eight core eco-design principles [2], was used as a step-by-step framework for guiding partners discussions. The second element consists in providing an eco-design tool obtained from a simplified version of the LCA model parametrized around a limited number of key LCI parameters. This tool enables designers to independently test the environmental performance of their innovations, providing immediate feedback on the environmental performance of their ideas and fostering an iterative improvement process.

## RESULTS

The LCA of the SOE baseline has been performed to evaluate the impact scores across the five different categories to produce 1 kg of hydrogen. The 'Baseline' bars in the figure 3 illustrate this environmental profile compared with the SMR impact scores (in purple). The baseline performs better than SMR for *Climate Change* (factor 9), *Energy Resource* (factor 12.5) and *Water Scarcity* (factor 2), while the results are reversed for *Remaining Ecosystem Quality* (factor 2) and *Remaining Human Health* (factor 2) impact scores. An additional comparison using the IW+ expert version, which aggregates the five categories of the footprint version into two damage indicators (*Human Health* and *Ecosystem Quality*), has been performed to clarify the trade-offs illustrated by the footprint version. This work reveals that the SOE baseline outperforms SMR for both indicators (see Supplementary Information).

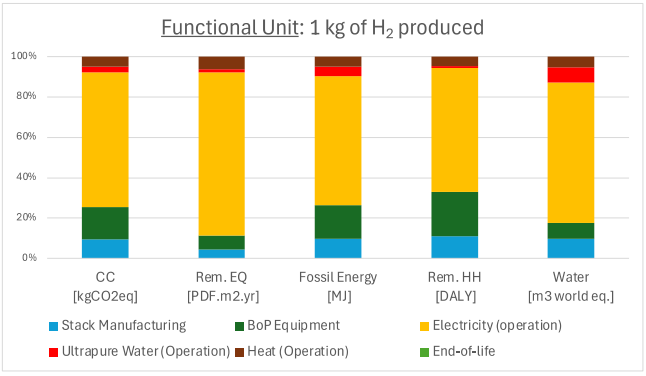



**Figure 4.** Contribution Analysis of the main life stages of the baseline SOE supplied with a 100%-renewable electricity mix. Operation phase is detailed at Tier 2 level.

## Contribution analyses

The contribution analysis shows that the operation phase dominates all impact categories by contributing 67%-89%, followed by the Balance of Plant (7%-22%), while stack manufacturing remains low at 4%-11%, and End-of-Life is negligible (Figure 4).

The Tier 2 analysis of the operation life stage highlights that electricity consumption drives the consumables impact scores (61%-81%), while heat consumption (5-6%) and ultrapure water consumption (1%-7%) are less contributive.

Figure 5 shows the contribution analysis of the stack manufacturing according to two different groupings of processes, with results normalized to the impacts of the production of 1 unit of stack of 20kW (cradle-to-gate).




**Figure 5.** Contribution Analysis of the solid oxide stack manufacturing. The processes are decomposed following (A) the tier 2 of the stack manufacturing and (B) the tier 4 of the stack manufacturing.

The first group (A) corresponds to the Tier 2 elements of the stack as presented in the Figure 2 (SOC, Bipolar Plates, Gasket and End Plates). The second group (B) aggregates the impact scores of the Tier 4 processes (Energy, Material, Chemical and Waste). Figure 5A illustrates that the stack manufacturing impacts are driven by the cells, the bipolar plates, and the end plates productions. The cells manufacturing dominates the *Remaining Ecosystem Quality* and the *Water Scarcity* with respectively 61% and 66% of the impacts of the stack production. The end plates are the largest contributor to *Climate Change* (39%) and *Energy Use* (36%). The bipolar plates dominate the *Remaining Human Health* (36%) category. Moreover, the Figure 5B highlights that the materials used to produce the stack components are the main source of impacts for all categories with a relative contribution of 70-86% of the impact scores. The impact contribution of waste treatments generated during manufacturing are negligible. Energy required for manufacturing is the second highest contributor (15-25%), followed by the chemicals production used as solvent during the manufacturing (2%).

## Sensitivity Analyses Results

The sensitivity analysis on the electricity mix supply illustrates that low-carbon electricity from renewable or nuclear sources is essential for the SOE to outperform the environmental performance of hydrogen production by SMR (Figure 3). Supplying the SOE with the 2024 European electricity grid instead of the 100% renewable mix of the baseline would considerably increase the impacts of hydrogen production, for all impact categories between a factor of 6.5 and 12. Hydrogen produced by the SOE baseline supplied with this 2024 European electricity mix would lead to higher impacts than SMR for all categories except the Energy Resources indicator.

Other sensitivity analyses on heat supply, scalability of the SOE at market scale, hydrogen purity and other key technical parameters are provided in Supplementary information with numerical and graphical results. The use of natural gas to supply heat should be avoided as it increases *Climate Change* and *Energy Resources* scores (factor 2.5-3). As the scalability of SOE is more sensitive to the system size than the stack itself [23], we modeled a scenario scaling the BoP equipment to the power of the system by applying the method developed by Zhang et al. [24]. Scaling up the BoP from 20kW to 20MW may reduce the system's potential impacts by 7-19%. Moving from 99.9% to 99.999% hydrogen purity using a Pressure Swing Adsorption process increases the potential impacts by 9-11%. A systematic sensitivity analysis of key parameters was performed on the *Climate Change* indicator by independently varying each foreground parameter by 10% and calculating the corresponding relative change in impact scores. This analysis highlights stack efficiency being the most critical parameter causing an 8.4% change in impact score, followed by BoP equipment lifetime (1.5%) and stack degradation rate (0.9%). Parameters influencing stack manufacturing are less sensitive: end plates, bipolar plates, and hydrogen electrode thicknesses (around 0.2%).

## Interpretation for eco-design

The results emphasize that no compromises should be made regarding stack efficiency. Achieving a high

energy conversion efficiency is the most critical objective to minimize environmental burdens of hydrogen production. Any innovation that would affect energy efficiency of the stack has a high risk to decrease the environmental performance of the SOE technology. While the stack and the equipment processes are less impactful than the operational phase, their design plays a role in reducing the project's overall impact. Extending the lifespan of equipment and components has also been identified as sensitive eco-design strategies. The materials used, particularly for the cell elements, bipolar plates, end plates, but also for the BoP, are the most contributive processes of the manufacturing of the stack components. Potential solutions include minimizing material use through redesign and exploring alternative low emission materials, if these solutions do not affect system efficiency.

## DISCUSSION

The limitations of both the LCA model and the eco-design process are discussed here. Regarding LCA limitations, as few datasets of the Balance of Plant equipment have been found in the literature, the representativeness of the equipment potential impacts is low, while being quite contributive. Some life stages, such as the maintenance phase, have not been modeled due to lack of accurate datasets in the literature. Future efforts should focus on these processes to improve the completeness of the inventory. Moreover, solid oxide electrolysers are still an emerging technology, and it induces at least three limitations. (a) The background inventories may contain data gaps and uncertainties for the modeling of specific processes, like specific materials production (e.g. Yttrium, Zirconium); (b) A prospective electricity mix needs to be selected to anticipate the grid conditions in which the technology will be used, but this prospective approach is intrinsically associated with uncertainties; (c) As the hydrogen industry is in rapid evolution, the presented inventories may not be representative of state-of-the-art technologies. Finally, the electrolysers are known to consume critical raw material [2], [17]. Yet, the impact assessment methods selected do not offer indicator to assess this environmental issue which is still poorly addressed in LCA [25].

Regarding the eco-design process, three main limitations have been identified. First, economic viability of the innovations was not assessed. Future works should focus on developing a common structure to couple LCA model with economic approaches such as Techno-Economic Assessment (TEA) or Life Cycle Costing (LCC) to identify correlations and trade-offs between environmental and cost dimensions of design choices such as increasing efficiency, reducing the thickness of materials, etc. Second, the influence of the operation context (load range, flexible operation) on the use phase parameters (lifetime, efficiency) are still missing and should be modeled. And third, as a 20kW-stack is not representative of the potential scaled-up technology that would penetrate the market, the model of SOE should be improved by incorporating prospective life cycle inventories, and by considering potential improvements in materials and in manufacturing processes associated with large-scale development.

## DIGITAL SUPPLEMENTARY MATERIAL

Data sheets presenting the LCA model, including the p-LCI, unit processes, and results, are available at LAPSE:2025.0030.

## ACKNOWLEDGEMENTS

The authors thankfully acknowledge the financial support from the European Union projects PRESSHYOUS and SUSTAINCELL under the grant agreement no.101101337 and no.101101479. This work was supported by the Swiss State Secretariat for Education, Research, and Innovation (SERI) under the contract no.23.00267.

## REFERENCES

1. Fuel Cells and Hydrogen 2 Joint Undertaking. Hydrogen roadmap Europe – A sustainable pathway for the European energy transition. Publications Office; 2016.
2. Gramc J, Stropnik R, Hojkar D, Sekavcnik M, Iribarren D, Dufour J, et al. Ecodesign as a key concept for improving the life cycle environmental performance of proton-exchange membrane fuel cells. Int J Hydrogen Energy. 2024 Aug;
3. Bovea MD, Pérez-Belis V. A taxonomy of ecodesign tools for integrating environmental requirements into the product design process. J Clean Prod. 2012 Jan;20(1):61–71.
4. Brisse A, Schefold J, Zahid M. High temperature water electrolysis in solid oxide cells. Int J Hydrogen Energy. 2008 Oct;33(20):5375–82.
5. Mehmeti A, McPhail SJ, Pumiglia D, Carlini M. Life cycle sustainability of solid oxide fuel cells: From methodological aspects to system implications. J Power Sources. 2016 Sep;325:772–85.
6. Bicer Y, Khalid F. Life cycle environmental impact comparison of solid oxide fuel cells fueled by natural gas, hydrogen, ammonia and methanol for combined heat and power generation. Int J Hydrogen Energy. 2020 Jan;45(5):3670–85.
7. Lee YD, Ahn KY, Morosuk T, Tsatsaronis G. Environmental impact assessment of a solid-oxide fuel-cell-based combined-heat-and-power-

generation system. Energy. 2015;79(C):455–66.
8. Häfele S, Hauck M, Dailly J. Life cycle assessment of the manufacture and operation of solid oxide electrolyser components and stacks. Int J Hydrogen Energy. 2016 Aug;41(31):13786–96.
9. Zhao G, Kraglund MR, Frandsen HL, Wulff AC, Jensen SH, Chen M, et al. Life cycle assessment of H2O electrolysis technologies. Int J Hydrogen Energy. 2020 Sep 3;45(43):23765–81.
10. Gerloff N. Comparative Life-Cycle-Assessment analysis of three major water electrolysis technologies while applying various energy scenarios for a greener hydrogen production. J Energy Storage. 2021 Nov 1;43.
11. Wei X, Sharma S, Waeber A, Wen D, Sampathkumar SN, Margni M, et al. Comparative life cycle analysis of electrolyzer technologies for hydrogen production: Manufacturing and operations. Joule. 2024 Dec;8(12):3347–72.
12. Di Florio G, Macchi EG, Mongibello L, Baratto MC, Basosi R, Busi E, et al. Comparative life cycle assessment of two different SOFC-based cogeneration systems with thermal energy storage integrated into a single-family house nanogrid. Appl Energy. 2021 Mar 1;285.
13. ISO. ISO 14040:2006 - Environmental management - Life cycle assessment - Principles and framework. 2006.
14. ISO. ISO 14044:2006 - Environmental management - Life cycle assessment - Requirements and guidelines. 2006.
15. Melideo D, Ortiz Cebolla R, Weidner Ronnefeld E. Life cycle assessment of Hydrogen and Fuel Cell Technologies. Luxembourg; 2020.
16. Lozanovski A, Schuller O, Faltenbacher M. Guidance Document for performing LCAs on Fuel Cells and H2 Technologies . 2011.
17. Bargiacchi E, Puig-Samper G, Iribarren D, Dufour J. D2.2 Definition of FCH-LCA Guidelines. 2022.
18. Cooper JS, Noon M, Kahn E. Parameterization in Life Cycle Assessment inventory data: review of current use and the representation of uncertainty. Int J Life Cycle Assess. 2012 Jul 3;17(6):689–95.
19. Wernet G, Bauer C, Steubing B, Reinhard J, Moreno-Ruiz E, Weidema B. The ecoinvent database version 3 (part I): overview and methodology. International Journal of Life Cycle Assessment. 2016 Sep 1;21(9):1218–30.
20. Simoes SG, Catarino J, Picado A, Lopes TF, di Berardino S, Amorim F, et al. Water availability and water usage solutions for electrolysis in hydrogen production. J Clean Prod. 2021 Sep;315:128124.
21. Santecchia A, Castro-Amoedo R, Nguyen TV, Kantor I, Stadler P, Maréchal F. The critical role of electricity storage for a clean and renewable European economy. Energy Environ Sci. 2023;16(11):5350–70.
22. Bulle C, Margni M, Patouillard L, Boulay AM, Bourgault G, De Bruille V, et al. IMPACT World+: a globally regionalized life cycle impact assessment method. International Journal of Life Cycle Assessment. 2019 Sep 1;24(9):1653–74.
23. Memorial Institute, Fuel Cell Systems for Primary Power and Combined Heat and Power Applications. 2017. Accessed: Mar. 05, 2025. Available:https://www.energy.gov/sites/prod/files/2018/02/f49/fcto_battelle_mfg_cost_analysis_1%20_to_25kw_pp_chp_fc_systems_jan2017_0.pdf
24. X. Zhang, C. Bauer, C. L. Mutel, and K. Volkart, “Life Cycle Assessment of Power-to-Gas: Approaches, system variations and their environmental implications,” Appl Energy, vol. 190, pp. 326–338, Mar. 2017, doi: 10.1016/j.apenergy.2016.12.098.
25. Greffe T, Margni M, Bulle C. An instrumental value-based framework for assessing the damages of abiotic resources use in life cycle assessment. Int J Life Cycle Assess. 2023 Jan 16;28(1):53–69.

© 2025 by the authors. Licensed to PSEcommunity.org and PSE Press. This is an open access article under the creative commons CC-BY-SA licensing terms. Credit must be given to creator and adaptations must be shared under the same terms. See https://creativecommons.org/licenses/by-sa/4.0/



Systems & Control Transactions

**Research Article - Peer Reviewed Conference Proceeding**
ESCAPE 35 - European Symposium on Computer Aided Process Engineering
Ghent, Belgium. 6-9 July 2025
Jan F.M. Van Impe, Grégoire Léonard, Satyajeet S. Bhonsale,
Monika E. Polańska, Filip Logist (Eds.)

PSE PRESS

# Assessing Distillation Processes through Sustainability Indicators Aligned with the Sustainable Development Goals

**Ömer Faruk Karaman*, Peter Lang, and Laszlo Hegely**

Budapest University of Technology and Economics, Department of Building Services and Process Engineering, Budapest, Hungary
* Corresponding Author: karaman@edu.bme.hu.

## ABSTRACT

A generally applicable framework for the evaluation of the sustainability of distillation processes is proposed by aligning indicators directly to selected sustainable development goals (SDGs) created by the United Nations. The indicators are related to the goals good health and well-being (SDG 3), clear water and sanitation (SDG 6), affordable and clean energy (SDG 7), decent work and economic growth (SDG 8), industry, innovation and infrastructure (SDG 9), responsible consumption and production (SDG 12), climate action (SDG 13) and life below water (SDG 14). A total of 12 sustainability indicators, including human toxicity potential, wastewater generation, water consumption, renewable energy share, energy demand, material footprint, profit, waste generation, recycling ratio of waste, greenhouse gas emission, eutrophication potential and acidification potential are assigned to selected SDGs. The application of the indicators is illustrated by two case studies: a batch (BD) and a continuous (pressure-swing) distillation process. Case BD6, where the $CO_2$ emission was minimized, proves to be the most sustainable BD process. It has the lowest greenhouse gas emission, acidification potential and waste generation. Although it has the lowest profit, the variations across the BD cases are minimal. By the pressure-swing distillation, L4 (feeding into low-pressure column, heat integration with optimization) is the best case, with the highest profit and the lowest energy demand, material footprint and greenhouse gas emission values.

**Keywords**: Distillation, Continuous Distillation, Batch Distillation, Environment, Energy, Sustainability

## INTRODUCTION

There has been a growing interest in sustainability in chemical engineering as industries aim to reduce their environmental footprint without compromising economic performance. This research proposes a set of sustainability indicators aligned with the United Nations' Sustainable Development Goals (SDGs) [1] for the evaluation of the sustainability of distillation processes, offering a structured way to assess and improve these systems. The use of these indicators is illustrated in two case studies: (1) a continuous pressure-swing distillation (PSD) of a maximum-azeotropic mixture without and with heat integration and (2) the recovery of acetone from a waste solvent mixture by batch distillation (BD). These processes were selected due to their widespread industrial use, their potential to benefit from improvements in their sustainability, and to show the general applicability of the indicators proposed.

Distillation is one of the most commonly used methods for the separation of liquid mixtures. It is performed in a continuous way when large processing capacities are needed (e.g. refining). Batch distillation is also used frequently (e.g. in the pharmaceutical industry) because of its flexibility in separating mixtures with varying quantity and composition, including waste solvent mixtures. However, distillation is very energy-intensive, leading to high operational costs and greenhouse gas emissions. In fact, distillation stands out as the most energy-consuming process in the chemical industry, using more than 40% of the total energy demand of an industry itself responsible for 30% of industrial energy usage in the US.

This study aims to address these issues by propos-

ing sustainability indicators that account for environmental, economic and social aspects. By aligning these indicators with the SDGs, as globally recognized sustainability standards, the research also aims to encourage industries towards more sustainable practices. To our knowledge, this work is the first to propose sustainability indicators aligned with SDGs in the field of distillation.

The case studies illustrate how to apply the proposed indicators to evaluate the sustainability aspects of distillation processes. In the PSD example [3], the process was optimized without and with heat integration, which led to a significant decrease in both the total annual cost (TAC) and environmental impact ($CO_2$ emission). In the acetone recovery by BD case [4], either the profit or the $CO_2$ emissions were optimized. In this work, we determined how the proposed sustainability indicators improved due to the optimization and heat integration performed in these previous works.

This study focuses on addressing a key gap by aligning the evaluation of distillation processes directly with the SDGs. This ensures that the results contribute not only to advancing methodological approaches but also directly support global sustainability goals. Therefore, in this study, we propose a set of sustainability indicators aligned with SDGs.

Another key novelty of this study is that, while traditional techno-economic analysis (TEA) focuses on economic feasibility and life cycle assessment (LCA) on environmental impact, our approach simultaneously incorporates both dimensions.

This framework could also be applied to any process with well-defined inputs and outputs where emissions and products are generated.

## METHODOLOGY

The following potentially distillation-related SDGs are selected: good health and well-being (3), clean water and sanitation (6), affordable and clean energy (7), decent work and economic growth (8), industry, innovation and infrastructure (9), responsible consumption and production (12), climate action (13), life below water (14). For each SDG, the UN has selected different targets, each of which has one or more numerical indicators assigned. However, these SDG indicators can only be interpreted at regional or higher levels, making them unsuitable for assessment of technological processes. Within the selected SDGs, the following relevant targets are identified: reduction of deaths and illnesses from hazardous chemicals and environmental pollution (3.9), improving water quality by reducing pollution and increasing water-use efficiency across all sectors (6.3 and 6.4), increasing the share of renewable energy in the global energy mix and improvement of energy efficiency by 2030 (7.2 and 7.3), improving global resource efficiency in consumption and production (8.4 and 12.2), added manufacturing value (9.2), reduction of $CO_2$ emission and greenhouse gases (9.4, 13.2), proportion of hazardous waste treated (12.4), recycling rate (12.5), marine pollution by eutrophication (14.1) and acidification (14.3) [1].

After selecting the relevant targets and the more specific SDG indicators proposed by the UN that could be linked to distillation studies, sustainability indicators were aligned to the SDG indicators and defined. The selected SDG indicators and their aligned sustainability indicators can be found in Table 1.

The indicators could be expressed either as absolute or relative (specific) values. In the latter case, which is selected here, they are expressed relative to the total mass or mass flow rate of the product(s) ($m_p$). It must be noted that many of the quantities used for the calculation of the indicators have different units depending on whether the process is batch or continuous. In the former case, masses are used, in the latter, mass flow rates. Nevertheless, the indicators always have the same units.

Human toxicity potential (HTP) [5] weighs thethe masses of potentially toxic components (for components i=1...n, where n is the number of components) in the waste streams with their characterization factor (CF). Wastewater generation (WwG) and water consumption (WC) contain the total wastewater mass flow rate ($m_{ww}$) and the total mass flow rate of water used in the process, respectively. Renewable energy share (RES) is the ratio of total energy from renewable energy sources ($E_r$) to total energy demand (E); the latter value is used in the energy demand (ED).

The material footprint (MF) takes into account the mass of equipment ($m_{eq}$) and additional materials consumed during the operation, such as entrainer or reagents. Since the installation of the equipment only happens once, the mass of additional materials and $m_p$ should be calculated for the lifetime of the plant to ensure a fair comparison. Profit (P) is calculated by net income (I) after the costs (C). I typically includes the value of the products. Waste generation (WG) contains the total mass of liquid waste ($m_{lw}$). Recycling ratio of waste (RRW) is the ratio of the mass of the recycled waste ($m_r$) to $m_{lw}$. The greenhouse gas emission (GHG) [6] expresses the total mass emissions of the process in $CO_2$ equivalents. This value could be calculated with different time horizons of GWP (e.g., 20 y). $CO_2$ emissions as an indicator could be aligned with 9.4.1, but it would be redundant as it is already included in GHG. By the eutrophication potential (EP) [7] the emissions of components in waste streams are weighted by their potency factor (PF). The acidification potential (AP) [6] refers to only the aquatic acidification potential, calculated from the total mass of released $H^+$ ions ($m_{H^+}$), as we assume, as a worst-case scenario from the point of view of aquatic life, that gaseous emissions would be completely absorbed in surface waters.

**Table 1:** Selected UN SDG indicators and their aligned indicators with the equations.

| SDG Indicators | Indicator Name | Indicators | Formula | |
|---|---|---|---|---|
| 3.9.1<br>3.9.3 | Air pollution mortality rate<br>Unintentional poisoning mortality | Human toxicity potential (HTP) | $HTP = \frac{\sum_{i=1}^{n}(m_i \cdot CF_i)}{m_p}$ | (1) |
| 3.9.2<br>6.3.1<br>6.3.2 | Water and sanitation mortality rate<br>Wastewater treated safely<br>Good ambient water quality | Wastewater generation (WwG) | $WwG = \frac{m_{ww}}{m_p}$ | (2) |
| 6.4.1<br>6.4.2 | Water-use efficiency change<br>Water stress level | Water consumption (WC) | $WC = \frac{m_w}{m_p}$ | (3) |
| 7.2.1 | Renewable energy share | Renewable energy share (RES) | $RES = \frac{E_r}{E}$ | (4) |
| 7.3.1 | Energy intensity | Energy demand (ED) | $ED = \frac{E}{m_p}$ | (5) |
| 8.4.1 | Material footprint | Material footprint (MF) | $MF = \frac{m_{eq} + m_a}{m_p}$ | (6) |
| 9.2.1<br>12.2.1 | Manufacturing value added<br>Material footprint | Profit (P) | $\mathrm{P} = \frac{I-C}{m_p}$ | (7) |
| 12.4.2 | Hazardous waste generation | Waste generation (WG) | $\mathrm{WG} = \frac{m_{lw}}{m_p}$ | (8) |
| 12.5.1 | Recycling rate | Recycling ratio of waste (RRW) | $RRW = \frac{m_r}{m_{lw}}$ | (9) |
| 9.4.1<br>13.2.2 | $CO_2$ emission<br>Total GHG emission | Greenhouse gas emission (GHG) | $GHG = \frac{\sum_{i}^{n}(m_{GHG,i} \cdot GWP_i)}{m_p}$ | (10) |
| 14.1.1 | Coastal eutrophication | Eutrophication potential (EP) | $EP = \frac{\sum_{i}^{n}(m_i \cdot PF_i)}{m_p}$ | (11) |
| 14.3.1 | Marine acidity | Acidification potential (AP) | $AP = \frac{m_{H^+}}{m_p}$ | (12) |

RES and WC are not calculated, as renewable energy sources and freshwater were not used in the case studies. However, they were added as indicators to propose a framework that could be applied to all distillation processes.

## CASE STUDIES

### Pressure-swing distillation

A maximum-boiling azeotropic water(A)–ethylenediamine(B) mixture is separated by PSD [3]. The flow rate of the fresh feed is 100 kmol/h with a composition of 35 mol% A. As calculated by the UNIQUAC model, the azeotrope contains 44.1% A at 0.10 bar and 25.6 % A at 2.02 bar, which are the two column pressures. Since the feed composition is between the azeotropic ones, it can enter either the high- (HPC) or the low-pressure column (LPC), resulting in two possible sequences: HP-LP (Figure 1) and LP-HP. The distillate of HPC is A with a purity of 99.5 %. The bottom product of HPC is fed into LPC, where B is produced as distillate in a purity of 99.5 %, and the bottom product, whose composition is near the azeotropic one at the pressure of LPC, is recycled to HPC.

By the PSD cases (Table 2), H and L identify the column sequences HP-LP and LP-HP. H1 and L1 refer to cases without heat integration (NHI) and optimization, and H2 and L2 mean optimized NHI cases. H3 and L3 denote the application of heat integration to the optimal NHI without further optimization, while H4 and L4 refer to optimized heat-integrated cases. TAC was the objective function. Heat integration is achieved by heating the reboiler of the LPC by condensing the top vapor of HPC. The integration is partial in all cases except H4, meaning that an auxiliary condenser is needed to fully condense the vapor. By H4, full heat integration is optimal, where the heat duties of the condenser of HPC and reboiler of

LPC are equal.

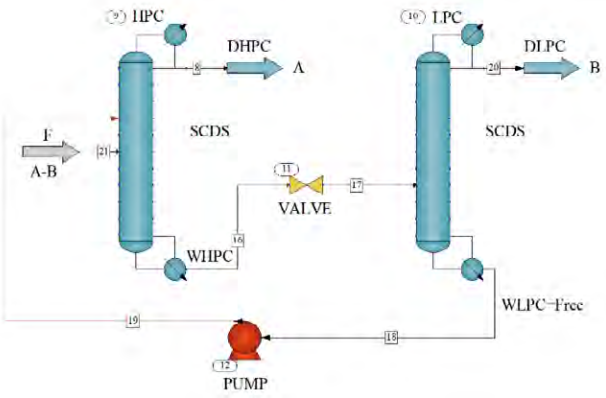



**Figure 1.** ChemCAD flowsheet for the separation of the A-B mixture with feeding into HPC.

By L2, surrogate model-based optimization was used with models fitted to the simulation results by using ALAMO. By H2, H4 and L4, TAC was minimized by an elitist, real-coded genetic algorithm.

HTP is not calculated since CF of B is not available. The only waste stream is the distillate of HPC, and it is considered as wastewater. Thus, WG equals WwG. The total energy demand is the sum of the two reboiler duties. MF takes the shell weight of the columns (calculated by CHEMCAD) into account during their lifetime (assumed to be 10 y), while GHG consists of the $CO_2$ emissions related to the production of heating steam. RRW is zero since there is no waste recycling. AP is also zero because the waste stream is basic. P was calculated as the yearly income minus TAC, the former of which is the mass of the B product and the price of B (1682 US$/t [8]). For the calculation of EP, the mass of B in the waste is multiplied by its COD value and PF of 0.022, as well as its nitrogen content with a PF of 0.42 [9].

## Recovery of acetone by batch distillation

From an aqueous waste solvent mixture containing dichloromethane (A) and methyl tert-butyl ether (B) as pollutants, acetone (C) is recovered by BD [4]. The composition of the feed is 1 mass% A, 1% B, 49% C and 49% water (D). The purity requirements for the acetone product are: ≤0.1 mass% A, ≤0.1% B and ≤ 0.25% D.

The components form three minimum-boiling (A-D, B-C, B-D) and one maximum-boiling (A-B) binary azeotropes, as well as a ternary saddle azeotrope (A-B-C). The VLLE calculations were performed by UNIQUAC.

The recovery of C is performed in a BD column with 25 theoretical trays (not including the reboiler and the condenser) at atmospheric pressure. The volume of the charge is 20 $m^3$ (17,785.9 kg). The reboiler duty is 1800 MJ/h. The steps of the process are as follows:

1. A and the majority of B are removed in Fore-cut1, although with a considerable loss of C due to the B-C azeotrope. This fore-cut is incinerated. The reflux ratio of the step ($R_1$) and its stopping criteria ($Cr_1$) are optimized.

2. Fore-cut2 is taken to remove the remaining amount of B. It is recycled to recover its C content. $R_2$ and $Cr_2$ are parameters optimized.

3. The main cut is high purity C. A relatively high $R_3$ (optimized) is needed due to the C-D tangent azeotrope.

4. The C content of the still residue (wastewater) is decreased to the necessary extent (0.2 %) for biological purification by taking an after-cut. $R_4$ is optimized.

The cases of BD (Table 3) are as follows: by BD1 Fore-cuts 1 and 2 are taken as a single fore-cut. By BD2 the fore-cut is divided into two parts with no other modification. BD3 and BD4, respectively, denote the cases with the highest profit and lowest specific $CO_2$ emission obtained by modifying a single input variable by sensitivity studies. BD5 and BD6 refer to cases with maximum P and minimum $CO_2$, optimized by the complex method.

In HTP, the HCl emission (CF=24) from the incineration of the A content of the fore-cut and the C emission (CF=0.079) in the still residue are taken into account [9]. WwG includes the wastewater from the still residue. MF was calculated by the shell weight of the column (1727 kg) divided by the total mass of the product for the lifetime of the plant (10 y). In WG, the total mass of liquid waste includes the fore-cut(s), the after-cut and the still residue. To calculate RRW, the recycling of the after-cut and second fore-cut was considered. GHG considers the $CO_2$ emissions resulting from the incineration of the fore-cut and that from the generation of heating steam. EP is calculated from the emission of C in the still residue multiplied by its COD value and PF=0.022. For AP, the mass of $H^+$ ions was calculated from the HCl emission.

# RESULTS

## Pressure-swing distillation

Table 2 shows the results of PSD cases. WwG=WG and EP were constant (0.163 kg/kg and 3.10 mg/kg) in all cases as the waste stream and $m_p$ were the same. Therefore, these values are not given in Table 2.

H1 had the highest ED, making it the most energy-intensive case. H1 also had the lowest P and highest GHG. While MF remained high due to larger diameters and shell weight of the columns. These factors indicate that H1 is the least favorable case in terms of overall sustainability. This is due to the fact that it did not benefit either from the heat integration or from the optimization.

L1 performed slightly better than H1 with a reduced ED (by 15%) because of lower heat duties while maintaining a comparable P. It also showed a lower GHG(by 15%) due to its reduced ED, reducing its overall environmental footprint.

By H2, the optimization reduced both the capital cost and the heat duties of the columns. H2 had a much

**Table 2:** Calculated sustainability indicators for PSD cases.

| Indicators | PSD cases | | | | | | | |
|---|---|---|---|---|---|---|---|---|
| | H1 | L1 | H2 | L2 | H3 | L3 | H4 | L4 |
| ED, MJ/kg | 8.71 | 7.38 | 7.26 | 6.97 | 4.60 | 4.20 | 4.44 | 4.18 |
| MF, mg/kg | 285 | 294 | 293 | 240 | 293 | 240 | 269 | 178 |
| P, $/kg | 1.59 | 1.60 | 1.60 | 1.61 | 1.63 | 1.63 | 1.63 | 1.63 |
| GHG, kg/kg | 0.13 | 0.11 | 0.11 | 0.11 | 0.07 | 0.06 | 0.07 | 0.06 |

lower ED (by 17%) than H1 and a slightly higher P. It also had a much lower GHG (by 15%), while its MF increased slightly (by 3%).

L2 had a lower ED (by 5%) and a reduced MF(by 18%) compared to L1. Its P was slightly (by 1%) higher than that of L1, with a similar GHG value. L2 is more favorable than H2 in all respects.

H3 had a much lower ED (by 47% and 17%) compared to H1 and H2 due to the usage of the top vapor of HPC to heat the reboiler of LPC. Thus, compared to H2, it also had a higher P (by 3%) while. its GHG () was significantly (by 36%) reduced, making it one of the better cases. However, MF remained high.

L3 showed further improvement, having a lower ED (by 40%) compared to L2 due to the heat integration. It maintained a high P and a similar MF, as well. With the second lowest GHG, L3 emerges as one of the most environmentally sustainable cases, balancing profitability and reduced emissions.

H4 had an even lower ED (by 3%) than H3, although it was still higher than that of L3. It maintained a high P and its MF was also lower than that of H1 (by 6%) or H2 (by 9%) but still higher than L2. Its GHG was comparable to H3, showing a good sustainability performance.

L4 was the most sustainable case, with the lowest ED (7.86 MJ/kg), MF (178 mg/kg), and GHG (0.06 kg/kg) values, while its P (1.63 $/kg) was the highest. These factors indicated that L4, benefiting from both heat integration and optimization, is the most sustainable option.

## Batch distillation

Table 3 shows the results of BD cases. As it had the highest amount of incinerated fore-cut, BD1 had the highest HTP among all cases. For the same reason, it also had the highest GHG, making it the least sustainable in terms of environmental impact. WwG was 1.12 kg/kg. It had the second lowest P and RRW. It had a high MF and a relatively moderate EP and the highest AP. Additionally, BD1 generated the second most waste and had a high ED, contributing to its lower sustainability profile. These results could be explained by the fact that BD1 had a single fore-cut that was incinerated, thus causing more environmental impact and incineration cost.

BD2 showed a significantly lower HTP (by 14%) since the amount of incinerated material decreased. It had the highest P due to the high $m_p$ and lower incineration cost. The values of WwG, ED, WG, MF, EP, and AP did not change compared to BD1. RRW was the highest among all cases. Its GHG was reduced considerably (by 26%) compared to BD1 because less fore-cut was incinerated. BD3, where $R_2$ was considerably decreased, benefited from the sensitivity study and had slightly lower HTP and WwG values than BD1 and BD2. It had the lowest ED, one of the lowest MF and WG, and performed slightly better in terms of GHG (by 5%) than BD2. P was between BD1 and BD2. It also had a reduced AP (by 6%) and EP (by 3%) compared to BD2, indicating a more sustainable process than BD1 and BD2. These changes can be explained by a higher $m_p$ and lower operation time.

**Table 3:** Calculated sustainability indicators for BD cases.

| Inds. | BD cases | | | | | |
|---|---|---|---|---|---|---|
| | BD1 | BD2 | BD3 | BD4 | BD5 | BD6 |
| HTP, kg/kg | 0.56 | 0.48 | 0.46 | 0.47 | 0.46 | 0.46 |
| WwG, kg/kg | 1.12 | 1.12 | 1.09 | 1.10 | 1.08 | 1.08 |
| ED, MJ/kg | 5.84 | 5.84 | 5.29 | 5.87 | 5.37 | 5.90 |
| MF, mg/kg | 95.3 | 95.3 | 92.5 | 93.7 | 92.1 | 92.4 |
| P, $/kg | 1.18 | 1.21 | 1.19 | 1.20 | 1.19 | 1.17 |
| WG, kg/kg | 1.33 | 1.33 | 1.26 | 1.29 | 1.23 | 1.23 |
| RRW, kg/kg | 0.03 | 0.07 | 0.05 | 0.07 | 0.03 | 0.05 |
| GHG, kg/kg | 0.44 | 0.32 | 0.31 | 0.30 | 0.29 | 0.26 |
| EP, mg/kg | 0.35 | 0.35 | 0.34 | 0.33 | 0.41 | 0.25 |
| AP, mg/kg | 83.0 | 71.0 | 66.9 | 68.6 | 66.3 | 66.7 |

By BD4, R1 was increased compared to its value by BD2. This decreased the mass of both fore-cuts and increased $m_p$. BD4 had a similar HTP to BD3. It also had the second-highest ED value due to a slight increase in the operation time. MF and WwG were both slightly (by 2%) lower than by BD2. It had a lower GHG (by 6%), as well as slightly reduced WG (3%) and AP (by 3%) compared to

BD2. It had the second-highest P and the second-lowest EP.

By BD5, the profit (in $) was maximized. It had the lowest HTP and WG, and the second lowest ED. WwG was relatively low. P was very similar to BD3. Its GHG value was relatively low. While it showed the lowest AP, its EP was the highest. Overall, BD5 is favorable in terms of sustainability.

BD6, where the $CO_2$ emission was minimized, emerged as the most sustainable case. It had the lowest GHG and EP, second-lowest HTP and AP WG values. However, it had the highest ED and lowest P value mostly because of the increased operation time. However, the difference in P among the BD cases was very small.

## CONCLUSIONS

To assess the sustainability of distillation processes, a set of sustainability indicators, directly linked to sustainable development indicators of the United Nations, were proposed. Sustainable development goals (SDGs), targets and, finally, the sustainable development indicators were selected by considering their fit to distillation studies.

8 out of 17 SDGs were selected, and they include good health and well-being, clear water and sanitation, affordable and clean energy, decent work and economic growth, industry, innovation and infrastructure, responsible consumption and production, climate action and life below water.

A set of (12) sustainability indicators aligned with those of UN's included human toxicity potential (HTP), wastewater generation (WwG), water consumption (WC), renewable energy share (RES), energy demand (ED), material footprint (MF), profit (P), waste generation (WG), recycling ratio of waste (RRW), greenhouse gas emissions (GHG), eutrophication potential (EP) and acidification potential (AP).

This framework was applied to a batch (BD) and a continuous (pressure-swing, PSD) distillation case study to evaluate their performance in terms of sustainability. Six cases were studied for BD evaluating the effects of the division of the fore-cut, sensitivity studies and optimization of the profit or the $CO_2$ emissions. PSD cases include scenarios such as no heat integration and no optimization, optimized without heat integration, heat integration without optimization, and optimal heat integration. These scenarios were studied for two column sequences differing in whether the feed was introduced into high- or the low-pressure column.

In the case of PSD, the most sustainable operation was L4 (heat-integrated and optimized by GA, feeding into the low-pressure column). It had the lowest ED, MF and GHG, while the highest P value. Among the BD cases, BD6 (minimized $CO_2$ emission) had the best overall sustainability: lowest GHG, WwG and EP and second lowest HTP, MF, WG and AP values.

## ACKNOWLEDGEMENTS

This research was funded by the National Research Development and Innovation Fund of Hungary (grant numbers TKP2021-EGA-02, OTKA FK-143059).

## REFERENCES

1. United Nations. Global indicator framework for the Sustainable Development Goals and targets of the 2030 Agenda for Sustainable Development (2022)
2. Kiss AA. Rethinking energy use for a sustainable chemical industry. *Chem Eng Trans* 76:13-18 (2019) https://doi.org/10.3303/CET1976003
3. Karaman ÖF, Lang P., Hegely L. Optimisation of Pressure-Swing Distillation of a Maximum-Azeotropic Mixture with Heat Integration. *Energy, 320: 135190* (2025) https://doi.org/10.1016/j.energy.2025.135190
4. Karaman ÖF, Lang P, Hegely L. Economic and Environmental Optimisation of Acetone Recovery by Batch Distillation. In: Proceedings of the 27th Conference on Process Integration, Modelling and Optimisation for Energy Saving and Pollution Reduction. Ed: Varbanov PS, Zeng M, Van Fan Y, Wang X. PRES24.0144 (2024)
5. Li H, Yang S, Qian Y. Life cycle assessment of coal-based methanol. *Comput Aided Chem Eng* 31:530-534 (2012) https://doi.org/10.1016/B978-0-444-59507-2.50098-6
6. Ruiz-Mercado GJ, Smith RL, & Gonzalez MA. Sustainability indicators for chemical processes: I. Taxonomy. *Ind Eng Chem Res 51*(5): 2309–2328 (2012) https://doi.org/10.1021/ie102116e
7. IChemE. The sustainability metrics. The Institution of Chemical Engineers, Rugby (2010)
8. Imarc. https://www.imarcgroup.com/ethylenediamine-pricing-report
9. Hertwich EG, Mateles SF, Pease WS, McKone TE. An update of the human toxicity potential with special consideration of conventional air pollutants. Norwegian University of Science and Technology (2006)

© 2025 by the authors. Licensed to PSEcommunity.org and PSE Press. This is an open access article under the creative commons CC-BY-SA licensing terms. Credit must be given to creator and adaptations must be shared under the same terms. See https://creativecommons.org/licenses/by-sa/4.0/



Systems & Control Transactions

**Research Article - Peer Reviewed Conference Proceeding**
ESCAPE 35 - European Symposium on Computer Aided Process Engineering
Ghent, Belgium. 6-9 July 2025
Jan F.M. Van Impe, Grégoire Léonard, Satyajeet S. Bhonsale,
Monika E. Polańska, Filip Logist (Eds.)

PSE PRESS

# Integrating Direct Air Capture and HVAC Systems: An Economic Perspective on Cost Savings

**Ikhlas Ghiat[a*], Yasser M. Abdullatif[a,b], Yusuf Bicer[a], Abdulkarem I. Amhamed[b], Tareq Al-Ansari[a,b]**

[a] College of Science and Engineering, Hamad Bin Khalifa University, Qatar Foundation, Education City, Doha, Qatar.
[b] Qatar Environment and Energy Institute (QEERI), Doha, Qatar.
* Corresponding Author: ikghiat@hbku.edu.qa

## ABSTRACT

Direct Air Capture (DAC) technology has gained significant attention as a promising solution for mitigating $CO_2$ emissions and meeting climate goals. However, the current challenges of high energy demand, capital costs, and scalability present critical challenges to the widespread deployment of DAC systems. Integrating DAC with Heating, Ventilation, and Air Conditioning (HVAC) systems in buildings offers a potential solution by enhancing indoor air quality while capturing $CO_2$, thus lowering energy consumption and capital investment compared to standalone DAC systems. This study evaluates the techno-economic performance of an integrated DAC-HVAC system against a standalone DAC system. This analysis combines thermodynamic estimation of $CO_2$ and $H_2O$ loadings and energy requirements with an economic evaluation of capital and operating costs to calculate the levelized cost of $CO_2$ capture (LCOD) for both DAC-HVAC and DAC-standalone. A sensitivity analysis explores the effects of varying climatic conditions, specifically temperature and humidity, on the economic performance of the DAC-standalone system. Further sensitivity analysis examines the impact of discount rates and electricity prices on both systems' economic viability. Results show that the DAC-HVAC integration achieves lower energy consumption and capital costs, with an LCOD of approximately 219 \$/ton $CO_2$, compared to the DAC-standalone system, which ranges from 349–429 \$/ton $CO_2$ depending on climatic conditions. In addition to offering a lower levelized cost, the DAC-HVAC system also provides resilience against climate and cost fluctuations. This study demonstrates the significant economic benefits and scalability potential of integrating DAC technologies within existing building infrastructures.

**Keywords**: DAC, CO2 capture, HVAC, Energy efficiency, Techno-economics.

## INTRODUCTION

As the global climate crisis intensifies, the need for effective negative emission technologies (NETs) to remove $CO_2$ from hard-to-abate industries and address historical emissions has become increasingly urgent [1]. Among the various NETs, Direct Air Capture (DAC) with carbon storage is considered a promising complementary solution to meet climate goals, with the potential to significantly reduce atmospheric $CO_2$ levels [2]. However, despite the significant promise of DAC, the energy and economic costs of its implementation remain uncertain, with estimates ranging between \$100 and \$1000 per ton of $CO_2$ captured. Furthermore, DAC is projected to require substantial energy resources if deployed at scale, potentially consuming around 50 EJ annually by 2100 which is more than half of the current global electricity production [2]. This highlights the critical need to explore innovative solutions to reduce the energy requirements associated with DAC systems.

One promising approach is the integration of DAC into existing Heating, Ventilation, and Air Conditioning (HVAC) infrastructures. This coupling offers dual benefits; it not only reduces the energy demands of DAC systems but also enhances the efficiency of HVAC systems by enabling air recirculation and $CO_2$ recycling. Additionally, the integration provides an opportunity to maintain high indoor air quality (IAQ), which is crucial for the well-being of building occupants. Research has shown that $CO_2$ concentrations above 1000 ppm can lead to adverse

health effects, such as the Sick Building Syndrome (SBS), while concentrations below 1000 ppm are generally considered acceptable for IAQ, provided that appropriate ventilation measures are in place [3,4]. Moreover, elevated $CO_2$ levels have been associated with reduced cognitive performance, further emphasizing the importance of maintaining optimal air quality [4].

Although limited studies have examined the integration of DAC with HVAC systems, few have addressed the fluctuations in $CO_2$ and $H_2O$ loadings with varying outside temperatures and humidity, which directly impact the energy requirements of DAC standalone systems [5]. Other studies explored DAC-standalone economics without consideration of varying climatic conditions [6].

The goal of this study is to evaluate the techno-economics of integrating DAC with HVAC systems and compare it with the performance of standalone DAC systems. In standalone DAC, the energy requirements for the Temperature-Vacuum Swing Adsorption (TVSA) process vary with changes in external climate condition such as temperature and humidity, as these factors influence the $CO_2$ and $H_2O$ adsorption capacities. This study aims to assess the fluctuations in $CO_2$ and $H_2O$ loadings in response to changes in outside temperature and pressure and examine how these fluctuations affect energy requirements, and consequently, the operating expenses of the DAC standalone system. This will provide a comprehensive comparison with the proposed DAC-HVAC integration, which remains unaffected by external temperature and humidity conditions.

## SYSTEM DESCRIPTION

The proposed system integrates a direct air capture (DAC) unit into the Heating, Ventilation, and Air Conditioning (HVAC) infrastructure of buildings to optimize energy use during adsorption and desorption while also improving indoor air quality. The DAC-HVAC system is strategically positioned at the exhaust stream, where $CO_2$ concentrations are highest, to maximize the $CO_2$ capture efficiency. This placement within the HVAC system has been shown to optimize $CO_2$ capture for DAC-HVAC integration, when air recirculation is considered [7]. A target $CO_2$ concentration of 400 ppm is assumed for $CO_2$ capture in this study.

Both the DAC-HVAC and DAC-standalone systems operate through temperature vacuum swing adsorption (TVSA) process, which includes vacuum application, heating for desorption, cooling, pressurization, and adsorption. The DAC system operates continuously with two parallel adsorbent filters, one in adsorption mode while the other undergoes desorption. A cooling jacket-type heat exchanger is used to meet the thermal needs of the TVSA process, providing heating and cooling as required.

Lewatit VP OC 1065 is used as the sorbent material in both configurations. While the DAC-HVAC system benefits from utilizing existing HVAC blowers, reducing capital expenditures, the DAC-standalone system requires additional blowers, increasing its capex. The consistent filter design and TVSA process across both systems allow for a direct techno-economic comparison of DAC-HVAC integration versus the standalone DAC system.

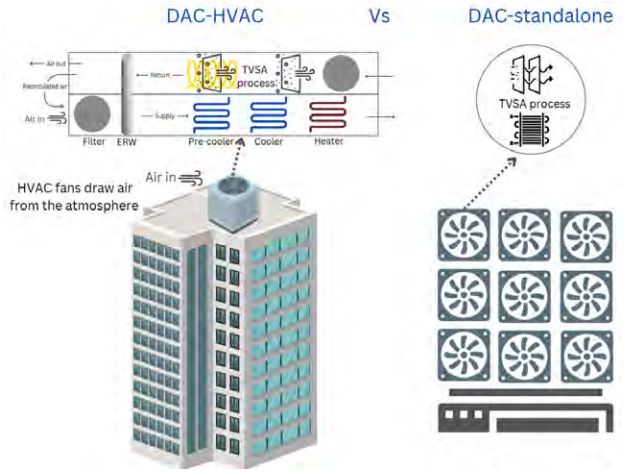



**Figure 1.** Schematic of DAC-HVAC and DAC-standalone systems.

## METHODOLOGY

This study is structured into two key components; a thermodynamic analysis to estimate $CO_2$ and $H_2O$ loadings and assess the energy requirements of the TVSA process and an economic analysis to evaluate capital and operational costs and determine the levelized cost of $CO_2$ capture (LCOD).

### Thermodynamic analysis

This study entails a thermodynamic analysis of the DAC system to evaluate its energy requirements, which include operating the vacuum pump, heating the sorbent during desorption and cooling the sorbent before adsorption. Additionally, blower power is considered to account for the pressure drop from the filters in the system. Equations 1–6 quantify these energy demands, detailing the heating load for desorption (Equations 1–3), the cooling load before adsorption (Equation 4), the vacuum pump work (Equation 5), and the additional blower power required to compensate for pressure drop from the filters (Equation 6). These calculations are essential for estimating the system's variable operational costs in terms of electricity consumption and for determining the appropriate sizing of equipment required. Table 1 presents the various thermodynamic variables utilized in the analysis.

$$\dot{Q}_{heating} = Q_{sens} + Q_{latent} \quad (1)$$

$$\dot{Q}_{sens} = \dot{m}\left(\frac{c_{p,ads}}{\Delta_{qCO2}} + c_{p,CO2} + c_{p,H20}\frac{\Delta_{qH2O}}{\Delta_{qCO2}}\right)(T_{des} - T_{ads}) \quad (2)$$

$$\dot{Q}_{latent} = \dot{m}\left(\Delta H_{H2O}\left(\frac{\Delta_{qH2O}}{\Delta_{qCO2}}\right) + \Delta H_{CO2}\right) \quad (3)$$

$$\dot{Q}_{cooling} = \dot{m}\frac{c_{p,ads}}{\Delta_{qCO2}}(T_{des} - T_{ads}) \quad (4)$$

$$\dot{W}_{pump} = \dot{m}\frac{R.T_{pump}}{\eta_{pump}}\ln\left(\frac{P_{amb}}{P_{des}}\right) \quad (5)$$

$$\dot{W}_{blower} = 2.72 \text{ x } 10^{-5}\frac{\dot{V}_{air}\Delta P}{\eta_{fan}} \quad (6)$$

Where $\dot{Q}_{heating}$ is the total heating load including sensible heat ($Q_{sens}$) and latent heat ($Q_{latent}$). $\dot{Q}_{cooling}$ is the cooling load, $\dot{W}_{pump}$ is the work of the pump, $\dot{W}_{blower}$ is the fan power, $\dot{V}_{air}$ is the incoming air flowrate, $\Delta P$ is the pressure drop, $\eta_{fan}$ is the fan efficiency, and $\dot{m}$ is the $CO_2$ mass flowrate.

Moreover, the water and $CO_2$ adsorption capacities are determined using mechanistic co-adsorption models, which describe the isotherm behavior as outlined in Equations 7 and 8. These models provide a detailed understanding of how the sorbent interacts with both $CO_2$ and $H_2O$, enabling the calculation of adsorption capacities under varying conditions [5].

$$q_{CO2} = \frac{\phi}{\phi_{dry}}\,\mathrm{f}(p_{CO2}, T, \Delta H) \quad (7)$$

$$q_{H2O} = \frac{q_m kcx}{(1-kx)(1+(c-1)kx)} \quad (8)$$

Where $q_{CO2}$ is the $CO_2$ loading, $\phi$, and $\phi_{dry}$ are amine efficiencies under actual and dry conditions, f is the partial pressure ($p_{CO2}$) and temperature dependent isotherm function, and $\Delta H$ is the average heat of adsorption of wet and dry states. $q_{H2O}$is the $H_2O$ loading, $q_m$ is the monolayer loading, x is the humidity and k and c are affinity parameters taken from Young et al. [5].

**Table 1:** Thermodynamic analysis variables.

| Variable | Description | Value |
|---|---|---|
| $c_{p,ads}$ | Specific heat of adsorbent | 1.58 kJ/kg/K |
| $c_{p,CO2}$ | Specific heat of $CO_2$ | 0.03868 kJ/mol/K |
| $c_{p,H20}$ | Specific heat of $H_2O$ | 0.07528 kJ/mol/K |
| $T_{ads}$ | Adsorption temperature | 23.7 °C |
| $T_{des}$ | Desorption temperature | 90 °C |
| $P_{des}$ | Desorption pressure | 25 kPa |
| $\Delta H_{CO2}$ | $CO_2$ heat of desorption | 70 kJ/mol $CO_2$ |
| $\Delta H_{H2O}$ | $H_2O$ heat of desorption | 44.2 kJ/mol $CO_2$ |

## Economic analysis

To evaluate the overall economic performance, the levelized cost of direct air capture (LCOD) is calculated using equation 9. LCOD is a crucial metric for comparing the costs of different DAC technologies. In this study, it is used to compare the DAC-HVAC and DAC-standalone systems by consolidating both fixed and variable operating costs, as well as capital expenditures providing an overall cost comparison between the two systems based on the amount of $CO_2$ captured. The economic analysis of the DAC system involves estimating both capital expenditures (CAPEX) and operating expenditures (OPEX) of both the DAC-HVAC and DAC-standalone systems. Equipment base costs are determined using an exponential method that incorporates capacity-ratio exponents to calculate equipment costs based on their capacity, as previously estimated in the thermodynamic analysis. These equipment costs are then estimated in terms of delivered, installed, and escalated cost projections. The variable operating costs include electricity for heating and cooling, pumping, and additional fan power requirements. The fixed operating cost includes ongoing costs such as maintenance, insurance, labor, and other administrative expenses that remain constant regardless of the system's operation.

$$LCOD = \frac{Capex\,.\,CRF + Opex_{fix}}{CO2} + Opex_{var} \quad (9)$$

Where CAPEX represents the capital expenditures, CRF is the capital recovery factor, $CO_2$ is the annual amount of $CO_2$ captured, and $Opex_{fix}$ and $opex_{var}$ denote fixed and variable operating expenditures, respectively. The CRF is calculated using equation 10.

$$CRF = \frac{i(1+i)^n}{(1+i)^n - 1} \quad (10)$$

In this equation, i is the annual discount rate (7%), and n is the system's lifetime (20 years). The CRF is used to calculate the annualized capital cost, enabling the distribution of CAPEX over the system's lifespan.

A sensitivity analysis is conducted to evaluate the effect of varying temperature and humidity on $CO_2$ and $H_2O$ adsorption capacities, and the resulting changes in LCOD for the DAC-standalone system. This analysis considers humidity ranges between 20-90% and temperatures between 25-45°C. Additionally, actual data points for temperature and humidity from Qatar, based on hourly data collected over four months (May to August), are studied to assess the range of LCOD changes for this case study. This sensitivity analysis, however, is not applicable to the DAC-HVAC system, as it maintains a constant temperature and humidity within the HVAC infrastructure, which helps stabilize conditions and mitigate the fluctuations observed in the standalone system.

Moreover, a sensitivity analysis is performed to evaluate the impact of varying discount rates (5-15%) and electricity prices ($0.30-$0.14/kWh) on the levelized cost of direct air capture (LCOD) for both the DAC-HVAC and DAC-standalone systems. This analysis allows for an assessment of how fluctuations in these key economic factors influence the overall cost-effectiveness of the systems.

## RESULTS AND DISCUSSION

At a discount rate of 7% and an electricity price of 0.0351 $/kWh, the levelized cost of direct air capture (LCOD) for the DAC-HVAC system is 219 $/ton $CO_2$, while the DAC-standalone system has a significantly higher LCOD of $374/ton $CO_2$. This disparity highlights the cost advantages of integrating DAC with HVAC systems.

The DAC-HVAC system benefits from the synergy between the two processes. By utilizing the heating and cooling capabilities of the HVAC system to enhance the $CO_2$ loading and reduce the $H_2O$ loading, the DAC-HVAC system can capture $CO_2$ more cost-effectively. This integration results in improved energy efficiency, reducing the energy consumption per ton of $CO_2$ captured, which is a key driver of its lower LCOD. On the other hand, the DAC-standalone system operates independently and is subject to fluctuations in climate conditions, which influence $CO_2$ and $H_2O$ adsorption capacities, thereby affecting energy requirements and operational expenses. Additionally, the DAC-HVAC system can leverage existing HVAC blowers, while the DAC-standalone system incurs additional capital expenditure due to the need for separate blowers.

The LCOD of the DAC-standalone system is highly sensitive to variations in temperature and humidity due to their impact on $CO_2$ and $H_2O$ adsorption capacities. A contour plot was generated to visualize the fluctuations in LCOD across a range of temperature (4–25°C) and humidity (20–90%) conditions as presented in Figure 2. Additionally, actual hourly temperature and humidity data over four months in Qatar were plotted on the contour map to assess variations in LCOD.

The results indicate that LCOD fluctuates between 349–429 $/ton $CO_2$, with the highest LCOD observed at high temperatures and high humidity levels. This can be attributed to the increased presence of $H_2O$ in the air under these conditions, which competes with $CO_2$ for adsorption on the sorbent material. As a result, $CO_2$ capture efficiency declines, leading to higher energy requirements for desorption and subsequently increasing LCOD. The lowest LCOD values occur at low temperatures and low humidity levels, where $CO_2$ adsorption is more favorable, and less energy is required for regeneration.

For the Qatar case study, the results indicate that when temperature is high, humidity is relatively lower, leading to a maximum LCOD of approximately 405 $/ton $CO_2$. Notably, there are no data points corresponding to conditions where both temperature and humidity are high for the studied dataset of three months, which means the LCOD does not reach the maximum value of 429 $/ton $CO_2$.

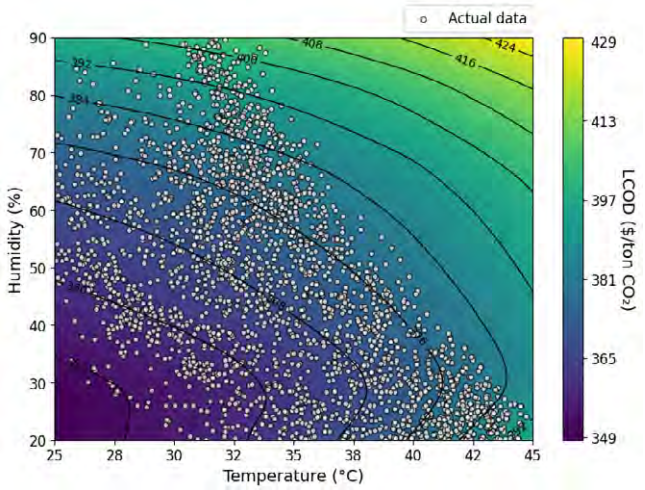



**Figure 2.** Contour plot of LCOD with respect to temperature and humidity for DAC-standalone system.

The sensitivity analysis of LCOD with respect to varying electricity prices and discount rates further illustrates the cost dynamics of both systems. As electricity prices increase, the LCOD for both DAC-HVAC and DAC-standalone systems rises (Figure 3). For example, at an electricity price of 0.14 $/kWh, the LCOD for the DAC-standalone system increases to 536 $/ton $CO_2$, while the DAC-HVAC system reaches 381 $/ton $CO_2$. This significant difference highlights that in regions where electricity prices are volatile or high, DAC-HVAC systems may offer a more cost-effective solution.

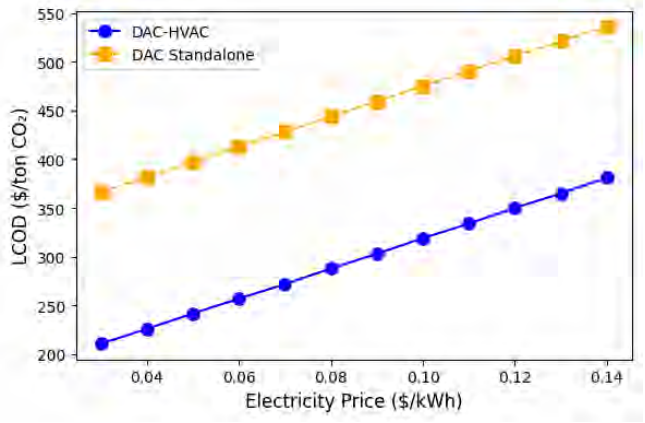



**Figure 3.** Effect of electricity price on LCOD.

Similarly, the LCOD values for both systems are sensitive to changes in the discount rate. While both systems experience a rise in LCOD with higher discount rates, the DAC-HVAC system consistently maintains a lower cost compared to the DAC-standalone system (Figure 4). This suggests that the DAC-HVAC system is more resilient to long-term financial considerations, owing to its lower operational and capital costs, making it a more attractive option for long-term projects.

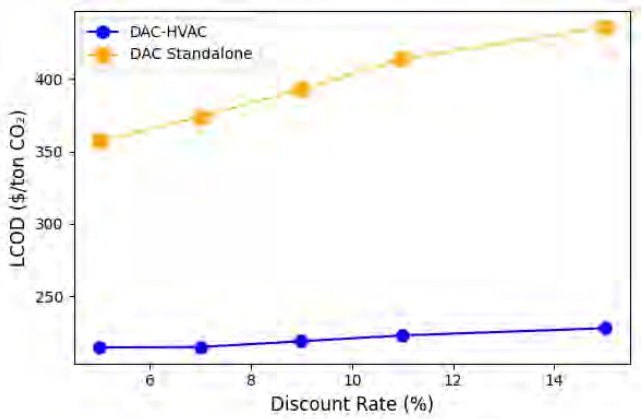



**Figure 4.** Effect of discount rate on LCOD.

The DAC-HVAC integration mitigates several technical and financial barriers of standalone DAC. However, key technical challenges remain, including managing pressure drop from the filters and ensuring efficient adsorbent regeneration, both of which are considered in this study. Financially, DAC-HVAC integration reduces capital and operational costs by leveraging existing HVAC infrastructure, as demonstrated by its economic advantage over standalone DAC.

## CONCLUSION

This study highlights the techno-economic benefits of integrating direct air capture (DAC) with Heating, Ventilation, and Air Conditioning (HVAC) systems compared to standalone DAC. The results show that the levelized cost of direct air capture (LCOD) for the DAC-HVAC system is significantly lower (219 $/ton $CO_2$) than that of the DAC-standalone system (374 $/ton $CO_2$) at an electricity price of 0.0351 $/kWh and a 7% discount rate. This cost reduction is attributed to the synergy between DAC and HVAC, which improves energy efficiency by leveraging existing heating, cooling, and ventilation infrastructure. Additionally, the DAC-HVAC system benefits from more stable operating conditions, avoiding the fluctuations in $CO_2$ and $H_2O$ adsorption capacities that significantly impact the energy requirements of standalone DAC. A sensitivity analysis of the DAC-standalone system further reveals that LCOD is highly dependent on external climate conditions. Temperature and humidity variations influence $CO_2$ and $H_2O$ loadings, leading to LCOD fluctuations between 349 and 429 $/ton $CO_2$.

## ACKNOWLEDGEMENTS

The authors acknowledge the support provided by Hamad Bin Khalifa University and Qatar Environment and Energy Research institute (QEERI) (a member of Qatar Foundation). This publication was made possible by NPRP12C-0821-190017 from Qatar National Research Fund.

## REFERENCES

1. I. Ghiat, T. Al-Ansari, A review of carbon capture and utilisation as a CO2 abatement opportunity within the EWF nexus, J. CO2 Util. 45 (2021) 101432. https://doi.org/10.1016/j.jcou.2020.101432.
2. G. Realmonte, L. Drouet, A. Gambhir, J. Glynn, A. Hawkes, A.C. Köberle, M. Tavoni, An inter-model assessment of the role of direct air capture in deep mitigation pathways, Nat. Commun. 10 (2019) 3277. https://doi.org/10.1038/s41467-019-10842-5.
3. A. Persily, Challenges in developing ventilation and indoor air quality standards: The story of ASHRAE Standard 62, Build. Environ. 91 (2015) 61–69. https://doi.org/10.1016/j.buildenv.2015.02.026.
4. ASHARE, ASHRAE Position Document on Indoor Carbon Dioxide, (2022). www.ashrae.org.
5. J. Young, E. García-Díez, S. Garcia, M. van der Spek, The impact of binary water–CO 2 isotherm models on the optimal performance of sorbent-based direct air capture processes, Energy Environ. Sci. 14 (2021) 5377–5394. https://doi.org/10.1039/D1EE01272J.
6. M. Fasihi, O. Efimova, C. Breyer, Techno-economic assessment of CO2 direct air capture plants, J. Clean. Prod. 224 (2019) 957–980. https://doi.org/10.1016/j.jclepro.2019.03.086.
7. Y.M. Abdullatif, A. Sodiq, T. Al-ansari, N.N. Nassar, I. Amhamed, Optimizing chemisorption based direct air capture unit efficiency in HVAC systems : A study on the impact of DAC location and adsorption conditions as a response to the climate crisis and indoor air quality, Energy Convers. Manag. 291 (2023) 117280. https://doi.org/10.1016/j.enconman.2023.117280.

© 2025 by the authors. Licensed to PSEcommunity.org and PSE Press. This is an open access article under the creative commons CC-BY-SA licensing terms. Credit must be given to creator and adaptations must be shared under the same terms. See https://creativecommons.org/licenses/by-sa/4.0/

Systems & Control Transactions

**Research Article - Peer Reviewed Conference Proceeding**
ESCAPE 35 - European Symposium on Computer Aided Process Engineering
Ghent, Belgium. 6-9 July 2025
Jan F.M. Van Impe, Grégoire Léonard, Satyajeet S. Bhonsale,
Monika E. Polańska, Filip Logist (Eds.)

PSE PRESS

# Insights on $CO_2$ Utilization through Reverse Water Gas Shift Reaction in Membrane Reactors: A Multi-scale Mathematical Modeling Approach

**Zhaofeng Li[a], Anan Uziri[a], Zahir Aghayev[c,d], Burcu Beykal[c,d] and Michael Patrascu[a,b]***

[a] Technion Israel Institute of Technology, Faculty of Chemical Engineering, Technion City, Haifa 3200003, Israel
[b] Technion Israel Institute of Technology, Grand Technion Energy Program, Technion City, Haifa 3200003, Israel
[c] University of Connecticut, Department of Chemical & Biomolecular Engineering, Storrs, CT, USA
[d] University of Connecticut, Center for Clean Energy Engineering, Storrs, CT, USA
* Corresponding Author: michael@technion.ac.il.

## ABSTRACT

The rising levels of carbon dioxide ($CO_2$) in the atmosphere significantly contribute to climate change, highlighting the need for effective $CO_2$ mitigation strategies. While capturing and storing $CO_2$ is important, converting it into useful products offers additional environmental and economic benefits. One promising method is the reverse water gas shift (RWGS) reaction, which transforms $CO_2$ into carbon monoxide (CO). Membrane reactors (MR), which integrate selective membranes with equilibrium limited chemical reactions, have the potential to intensify processes based on the RWGS reaction. In such reactors, by-products like water are removed in-situ from the reaction zone, effectively shifting the reaction equilibrium to favor higher $CO_2$ conversion. This study develops a comprehensive multi-scale mathematical model for RWGS membrane reactors. We integrate the microscale permeance model (for LTA-4A membrane) with the RWGS MR unit scale and the system's scale models. The effectiveness of applying sweep gas has been suggested, and the optimal $H_2$ perm-selectivity is found in the range from 30 to 50. A detailed membrane permeance model for LTA-4A membranes is integrated in the MR model to assess how species permeance changes with varying reactor conditions. We propose a sweep recycle configuration and compare it with the conventional sweeping configuration commonly assumed in most literature. A thermal efficiency analysis is conducted to evaluate the proposed recycling configuration, providing insights into the practical feasibility of membrane reactors for $CO_2$ utilization.

**Keywords**: Multiscale Modelling, Carbon Dioxide, Modelling and Simulations, Membranes, Process Intensification

## INTRODUCTION

Current environmental challenges necessitate the mitigation of $CO_2$ emissions. However, $CO_2$ emissions from certain industries are expected to remain significant in the foreseeable future. $CO_2$ utilization presents an innovative approach to reducing atmospheric $CO_2$ by using it as a feedstock to produce valuable products [1].

Process intensification through steam separation is a promising concept that enables the development of novel $CO_2$ utilization pathways [2], since most $CO_2$ utilization processes produce $H_2O$ as a side product. Water-permeable membranes enable in-situ selective water transfer to shift the reaction forward, according to the Le Chatelier's principle. Membrane reactors (MRs) combine the selective permeable membranes with traditional catalytic processes, enhancing production, separation, and energy efficiency [3].

The core principle of water-permeable membrane reactors lies in their selective permeability, allowing water molecules to pass while retaining other reactants and products. This permeability is typically achieved through the use of hydrophilic membrane [4], made from materials like polymers, ceramics, and composite materials, which exhibit hydrothermal stability, good permeance and perm-selectivity [5]. Among the various types of

membranes, LTA zeolite membranes have garnered significant attention [6]. LTA-4A is well-reported for its high hydrophilicity, small pore size (0.42 nm) comparing to other zeolites (0.735 nm for FAU, 0.65 nm for MOR, 0.51 nm for ZSM-5) [7]. The excellent performance of LTA membranes can be attributed to their unique structural properties, excellent thermal and chemical stability at high temperature and pressure, and high affinity for water. The modeling of gas species permeation in the presence of water through LTA membrane has been investigated [8].

The application of membrane reactors technology to conduct various reactions utilizing $CO_2$ as a reactant have been recently reviewed [7,10,11]. Some key reactions of interest are the conversion of $CO_2$ to CO, methane, methanol and dimethyl ether. Among the various $CO_2$ utilization pathways, the reverse water gas shift (RWGS) reaction, eq. (1), has gained significant attention due to its ability to produce syngas, a mixture of $H_2$ and CO [11]. Syngas serves as a fundamental feedstock for synthesizing a wide array of chemicals and fuels, including methanol, higher alcohols, and hydrocarbons via the Fischer–Tropsch synthesis. Despite its importance, the RWGS reaction has been rarely investigated within MR modeling [12].

$$CO_2 + H_2 \rightleftharpoons CO + H_2O \quad (1)$$

Although a few RWGS MR models exist, they tend to oversimplify membrane characteristics and overlook practical aspects. For example, a $N_2$ stream has frequently been considered as the sweep gas by default [13,14,15], which is not practical in industrial application. The sweep stream will contain $H_2$, which is difficult to recover from $N_2$. The evaluation of sweeping conditions still requires more attention. Additionally, although numerous simulations have been conducted to assess the performance of MRs under the assumption of constant species permeance, the lack of detailed models that accurately represent membrane characteristics has limited the predictive capabilities of these systems. The $H_2O/H_2$ permselectivity has been suggested the value greater than 100, though this remains a topic of debate.

This work provides insights into the use of RWGS MRs for $CO_2$ utilization. We develop a dimensionless MR model and, under the assumption of constant membrane permeance, evaluate reactor performance across various sweeping conditions and species permeance-selectivity. Additionally, we integrate a detailed membrane permeance model for an LTA-4A zeolite membrane to assess how species permeance changes with varying reactor conditions, an area currently under explored in the literature. Furthermore, we propose a recycling configuration and compare it with the conventional sweeping configuration that is commonly assumed in most literature. A thermal efficiency analysis is conducted to examine the proposed recycling configuration.

## MODELING

In this section, the RWGS process is modeled at three different scales: The microscale permeance in LTA-4A membrane and its dependence on local conditions, the RWGS MR unit scale, and the system's scale including recycling.

### Permeance model of the membrane

The LTA-4A membrane is selected to model the species permenace for its good performance in selective permeation of water. Zito et al. propose a validated permeance model for light gases in the presence of water for the 4A zeolite [8]. The trans-membrane flux is given as the sum of surface and gas translation diffusion flux [15] :

$$J_i = \rho C_{\mu s_i} D_{SD} \Gamma \frac{d\theta_i}{dl} + \frac{\epsilon\left(C_{\mu s_i}\right)}{\tau\left(C_{\mu s_i}\right)} \frac{1}{\zeta} \frac{\lambda}{RT} \sqrt{\frac{8RT}{\pi M}} e^{-\frac{E_{GT}}{RT}} \frac{dP_i}{dl} \quad (2)$$

The permeance is described as the ratio between the transmembrane flux and the driving force:

$$Q_i = \frac{J_i}{\left(P^R y_i^R - P^P y_i^P\right)} \quad (3)$$

$$Q_i = \rho C_{\mu s} D_{\mathrm{SD},i} \Gamma_i \frac{\theta_i^R - \theta_i^P}{\left(P^R y_i^R - P^P y_i^P\right) \cdot \delta_{\mathrm{membrane}}} + \frac{\varepsilon\left(C_{\mu s}\right)}{\tau\left(C_{\mu s}\right)} \frac{\lambda}{\zeta \mathrm{RT}} \sqrt{\frac{8\mathrm{RT}}{\pi M_i}} \frac{e^{-\frac{E_{\mathrm{GT}}}{\mathrm{RT}}}}{\delta_{\mathrm{membrane}}} \quad (4)$$

The permeance is then integrated into the MR model proposed in the following section, including the impact on membrane selectivity, $S_i = \frac{Q_{\mathrm{H2O}}}{Q_i}$.

### Membrane reactor model

A packed-bed tubular and concentric membrane reactor is illustrated in Figure 1. In this configuration, the catalyst particles bed is placed in the annular chamber, through which the reactant stream is introduced, serving as the retentate side. Inside the membrane (the tubular chamber) sweeping stream can be introduced in co-current direction with respect to the feed stream. The model obeys the following assumptions: One-dimensional flow, isothermal operation, assuming heat supplied continuously from the furnace, no pressure drops in both retentate and permeate side, assuming pressure regulator implemented to maintain constant pressure,, and absence of internal and external mass transfer resistance. The RWGS reaction kinetic rate expression is taken after Gine et al. 's work for $CuO/Al_2O_3$,[16], the dimensionless component balance equations are given as follows:

$$\frac{d\,\widetilde{F_i^R}}{d\,Pe_m} = \alpha_i B \left(y_{CO_2} y_{H_2} - \frac{y_{CO} y_{H_2O}}{Keq_1}\right) - \frac{1}{S_i}\left(y_i^R - P_r^{-1} y_i^P\right) \quad (5)$$

$$\frac{d\,\widetilde{F_i^P}}{d\,Pe_m} = \frac{1}{S_i}\left(y_i^R - P_r^{-1} y_i^P\right) \quad (6)$$

The dimensionless variables are defined as follows:

$$\widetilde{F_i^R} = \frac{F_i^R}{F_{\mathrm{CO2},0}^R}, \quad \widetilde{F_i^P} = \frac{F_i^P}{F_{\mathrm{CO2},0}^R}, \quad \widetilde{F_{\mathrm{N2}}^P} = \frac{F_{\mathrm{N2}}^P}{F_{\mathrm{CO2},0}^R}, \quad P_r = \frac{P^R}{P^P},$$

$$S_i = \frac{Q_{\mathrm{H2O}}}{Q_i}, Pe_m = \frac{(2\pi R_{\mathrm{in}} Q_{\mathrm{H2O}} P^R)z}{F_{\mathrm{CO2},0}^R}, B = \frac{A^R \rho_s (1-\varepsilon) k_1 C_{FP}}{2\pi R_{\mathrm{in}} Q_{\mathrm{H2O}} P^R}$$

The $F_{\mathrm{CO2},0}^R$ represents the $CO_2$ inlet flow rate. It is assumed that only $CO_2$ and $H_2$ are fed into the reactor, with $n$ is defined as the feed molar ratio between $H_2$ and $CO_2$. $Q_i$ refers to the permeance of species $i$. $P^R$ and $P^P$ are the pressures on the retentate and permeate sides, respectively. $A^R$ is the cross-section area of the retentate side and $R_{in}$ is the radius of inner tube, $k_1$ is the rate constant for the RWGS reaction, $Keq_1$ is the RWGS reaction equilibrium constant, $\rho_s$ is the catalyst solid density, $\varepsilon$ is the void fraction of the catalyst bed, $Q_i$ is the permeance of species $i$, $C_{FP}$ is the reaction correction factor. The conversion of $CO_2$ is expressed as follows:

$$X = \frac{F_{CO_2,0} - F_{CO_2}}{F_{CO_2,0}} = 1 - \frac{F_{CO_2}}{F_{CO_2,0}} = 1 - \widetilde{F_{CO_2}^R} - \widetilde{F_{CO_2}^P} \quad (7)$$

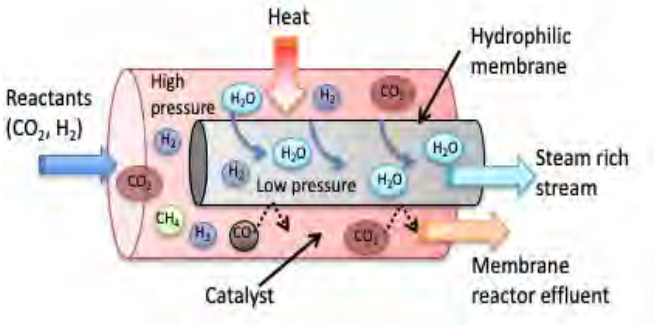



**Figure 1.** Schematic of a membrane reactor utilizing a hydrophilic membrane.

## Reactor system flowsheet

A simple reactor system flowsheet including the upstream and downstream operations is proposed to further evaluate the MR performance. In the conventional design as shown in Figure 2, two streams are fed into the reactor, the compressed feed stream serves as the retentate side while a low pressure pure $H_2$ stream serves as the sweep gas in the permeate side. In Figure 3 we propose a recycle configuration, where instead of using an extra stream for sweeping, the retentate effluent is recycled to the permeate side serving as the sweep gas, after pressure reduction. In both designs, the heat integration is considered, and the product streams are all cooled down and fed to a flash unit for water separation. The feed, sweep and product streams in both configurations are all set to standard conditions for thermal efficiency comparisons. The reactor system is simulated in Aspen Plus, where the detailed MR model developed in MATLAB is embeded.

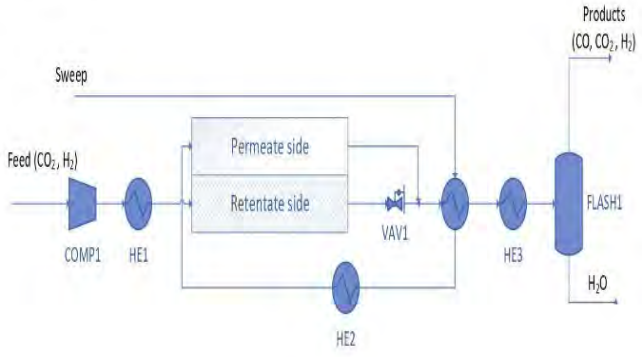



**Figure 2.** The conventional design for MR model with heat integration, $H_2$ stream serves as the sweep gas.

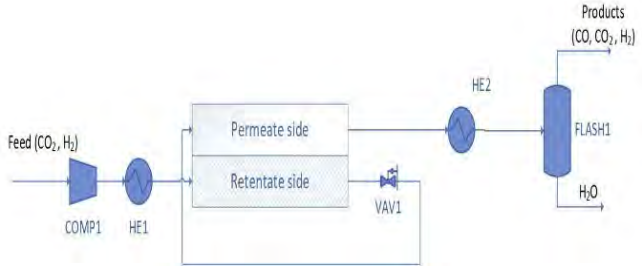



**Figure 3.** The recycle configuration for MR model with heat integration. The outlet of the retentate side serves as the sweep gas.

The thermal efficiency is defined as the ratio between the heating value of the produced syngas to the total used hydrogen and the external heat and power demands for the system, which is defined as:

$$\eta_{en} = \frac{n_{\mathrm{CO}} \cdot \mathrm{LHV_{CO}} + n_{\mathrm{H2,out}} \cdot \mathrm{LHV_{H2}}}{n_{\mathrm{H2,in}} \cdot \mathrm{LHV_{H2}} + E_{MR} + E_{vav1} + E_2 + P_{\mathrm{COMP}}} \quad (8)$$

where LHV is the lower heating value, $n$ is the molar flow rate, $E_i$ represents the required heat for block $i$, $P_{COMP}$ represents the power input for the compressor.

# RESULT AND DISCUSSION

## Membrane reactor performance analysis

The effect of different sweeping scenarios on $CO_2$ conversion, as a function of $H_2$ perm-selectivity and $Pe_m$, is shown in Figure 4. The membrane permeance is assumed constant along the reactor.

In the no-sweep gas scenario (Figure. 4a), increasing $S_{H_2O/H_2}$ initially enhances $CO_2$ conversion, as the removal of reaction product $H_2O$ is more significant than the leaking of reactant $H_2$, which shift the equilibrium toward higher $CO_2$ conversion, according to Le Chatelier's

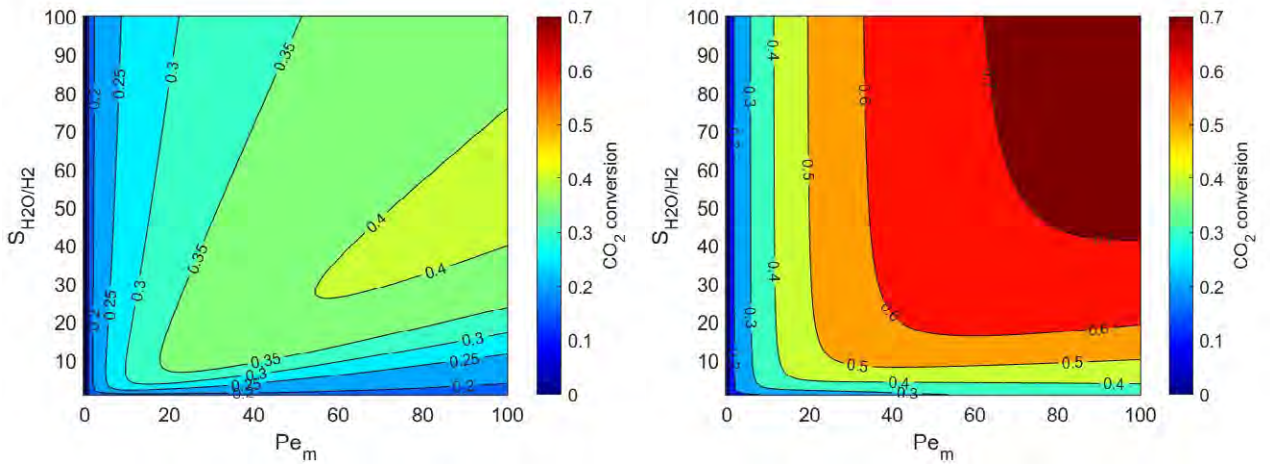



**Figure 4:** Comparison of $CO_2$ conversion varying with $Pe_m$ under different $S_{H_2O/H_2}$ . T = 300°C, $H_2/CO_2$ ratio= 3, pressure ratio Pr = 20, dimensionless number B = 1. The membrane is impermeable to CO and $CO_2$. Co-current configuration. (a) No sweep gas applied in the peremeate side. (b) $H_2$ sweep gas ratio of 10.

principle. However, once the perm-selectivity exceeds a certain threshold, increasing $S_{H_2O/H_2}$leads to a $CO_2$ conversion decline. This is due to reduced $H_2$ leakage to the permeate side, which increases the partial pressure of water in the permeate side. The increased water partial pressure decreases the driving force for the forward reaction, thus limiting the $CO_2$ conversion potential. This effect is more pronounced at low membrane permeances.

In the applied sweep gas scenario (Figure 4b), a high sweep flow rate significantly improves the $CO_2$ conversion for the entire range of $Pe_m$ and $S_{H_2O/H_2}$ values compared to the case represented in Figure 4a. The sweep gas facilitates the continuous removal of $H_2O$, maintaining a favorable partial pressure gradient and preventing water accumulation in the reactor. Nevertheless, there is a threshold value for $S_{H_2O/H_2}$, beyond which further increases do not significantly improve in $CO_2$ conversion. These simulations suggest that high $S_{H_2O/H_2}$ and $Pe_m$ are not always desirable in any cases, applying sweep gas can significantly improve the MR performance.

## Permeance analysis

The detailed permeance model reveals that the permeance of species is also influenced by the differences in their partial pressures, which vary continuously within the reactor. We integrated this permeance model into the MR model to examine how membrane properties change along the reactor as species' partial pressures change.

Figure 5 shows the permeance of different gas species through the LTA-4A membrane as $Pe_m$ increases. The $H_2O$ permeance is the highest and remains nearly constant as $Pe_m$ increases, primarily due to the membrane's strong affinity for water and its hydrophilic nature. $CO_2$ permeance is the lowest and decreases as $Pe_m$ increases. The $H_2$ and CO permeance also declines as $Pe_m$ increases. Additionally, the $H_2$ and CO permeance are similar in value compared to $CO_2$ and $H_2O$. And for $Pe_m$ values smaller than 20, $H_2$ permeance is higher, while the CO permeance becomes higher as $Pe_m$ exceeds 20. This is due to the fact that $H_2$ permeance experiences a larger decline compared to CO permeance as $Pe_m$ increases.

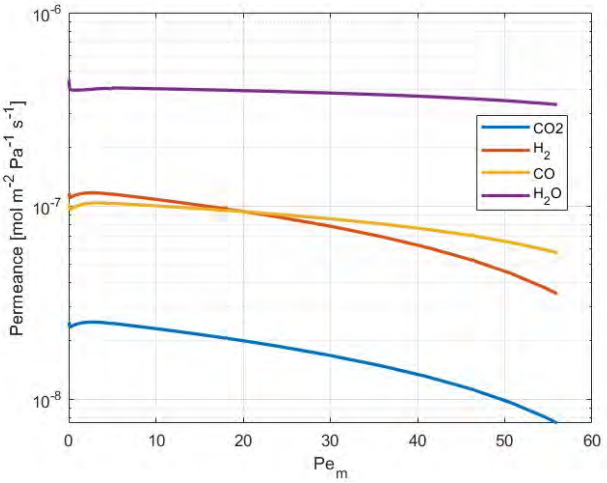



**Figure 5.** The gas species permeance of LTA-4A membrane along the reactor for different gas species. T = 300°C. $H_2/CO_2$ feed ratio = 3, reaction pressure is 10 bar, permeate pressure is 1 bar. Co-current configuration.

The varying permeance of these species plays a critical role in the MR performance. Figure 6 shows that perm-selectivity for all gas species increases as $Pe_m$ increases. $CO_2$ perm-selectivity ranges from 15 to 45 along the whole MR. The large boundary highlights the importance of integrating the permeance model into the MR

model for process simulation. Additionally, CO perm-selectivity shows similar value to $H_2$ perm-selectivity. Since most literature only considers $H_2$ perm-selectivity in simulations, the competing CO perm-selectivity values raise the question of whether it is appropriate to assume only $H_2$ permeation in the MR model.

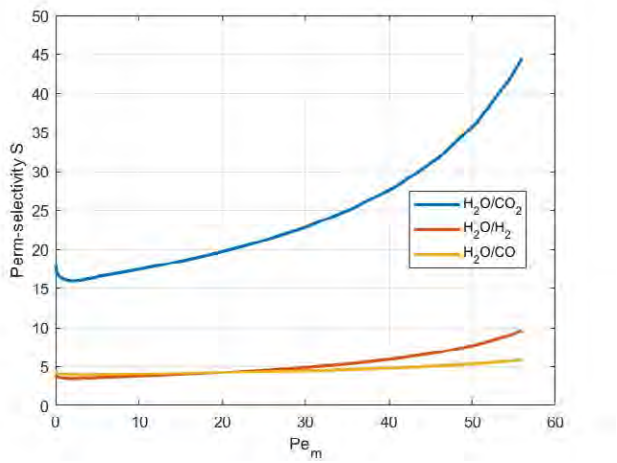



**Figure 6.** The species perm-selectivity of LTA-4A membrane along the reactor for different gas species. T = 300°C. $H_2/CO_2$ ratio=3, reaction pressure is 10 bar, permeate pressure is 1 bar. Co-current configuration.

## Thermal efficiency comparative analysis

Figure 7 shows the thermal efficiency of the RWGS process with varying $CO_2$ conversion in the product stream, achieved by changing the reactor length. The recycling configuration has higher thermal efficiency compared to the conventional one across the entire range of $CO_2$ conversion. Additionally, the efficiency of the recycling configuration remains almost constant as $CO_2$ conversion increases, while that of the conventional design drops. The sweep gas used in conventional design requires a significant amount of heat to maintain the temperature of the sweep gas. This additional heating leads to a decrease in thermal efficiency. As operating pressure increases from 10 bar to 20 bar, thermal efficiency declines for both configurations. This is because higher pressures increase the enthalpy of the flows, requiring more energy to maintain the system's operational temperature. However, the decrease in thermal efficiency for the conventional design is more significantly affected by the increase in operating pressure, showing a reduction of around 15%, while the recycling configuration experiences only about a 5% decrease in thermal efficiency. This suggests that the recycling configuration remains preferable when the system operates at high pressure.

## CONCLUSIONS

This study presents a multi-scale modeling approach to evaluate RWGS performance in MR for CO2 utilization. Through the development of a dimensionless model, integration of a detailed membrane permeance model for LTA-4A zeolite, and the simulation of a simple process system, we provided insights into the performance of membrane reactors under various conditions.

Our findings highlight the importance of optimal sweeping conditions and membrane properties in enhancing $CO_2$ conversion. Specifically, sweep gas improves conversion significantly compared to the no-sweep configuration. The analysis reveals that one can locate the optimal $H_2$ perm-selectivity, beyond which the performance gains diminish. It could be in the range around 30 to 50 for $Pe_m$ smaller than 70. Additionally, the species variable permeance was found to be a critical factor that should be considered in modeling the MR, with

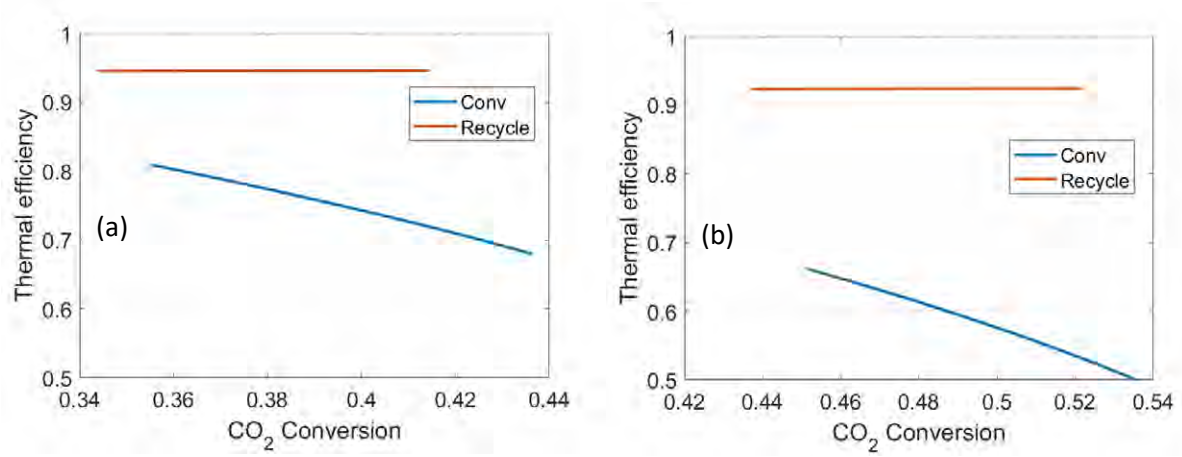



**Figure 7:** Thermal efficiency for different configurations as a function of $CO_2$ conversion. $H_2/CO_2$ feed ratio= 3. T = 300°C. (a) Reaction pressure of 10 bar. (b) Reaction pressure of 20 bar.

$H_2O$ showing the highest permeance, which remained almost constant across the reactor, while CO, $CO_2$ and $H_2$ permeance decreased with increasing reactor length.

Thermal efficiency analysis shows that the recycling configuration outperforms the conventional configuration for all $CO_2$ conversion values, maintaining a more stable thermal efficiency as $CO_2$ conversion increases. This suggests that the recycling design is more energy-efficient, particularly under high-pressure conditions, and offering significant advantages in practical applications.

## ACKNOWLEDGEMENTS

This research was carried out within the framework of the UConn-Technion Energy Collaboration Initiative, supported by the UConn-Technion Leadership Program for Global Energy Sustainability, the Maurice G. Gamze Endowed Fund (at the American Technion Society), Larry Pitt and Phyllis Meloff, the Eileen and Jerry Lieberman UConn/Israel Global Partnership Fund and the Grand Technion Energy Program (GTEP). We also thank the financial support of the Boeing-Technion SAF Innovation Center supported by the Boeing Company.

## REFERENCES

1. M. Genovese et al., "Power-to-hydrogen and hydrogen-to-X energy systems for the industry of the future in Europe," Int. J. Hydrogen Energy, vol. 48, no. 44, pp. 16545–16568, May 2023, doi:10.1016/j.ijhydene.2023.01.194.
2. M. Patrascu, "Process intensification for decentralized production," Chem. Eng. Process. - Process Intensif., vol. 184, p. 109291, Feb. 2023, doi: 10.1016/J.CEP.2023.109291.
3. E. Harkou et al., "Different reactor configurations for enhancement of CO2 methanation," Environ. Res., vol. 236, p. 116760, Nov. 2023, doi: 10.1016/j.envres.2023.116760.
4. J. van Kampen et al., "Steam separation enhanced reactions: Review and outlook," Chem. Eng. J., vol. 374, pp. 1286–1303, Oct. 2019, doi: 10.1016/J.CEJ.2019.06.031.
5. P. F. Zito et al., "Light gases saturation loading dependence on temperature in LTA 4A zeolite," Microporous Mesoporous Mater., vol. 249, pp. 67–77, Sep. 2017, doi: 10.1016/j.micromeso.2017.04.021.
6. Z. Li et al., "High Temperature Water Permeable Membrane Reactors for CO2 Utilization," Chem. Eng. J., vol. 420, p. 129834, Sep. 2021, doi: 10.1016/j.cej.2021.129834.
7. N. Wang et al., "Hydrophilic SOD and LTA membranes for membrane-supported methanol, dimethylether and dimethylcarbonate synthesis," Microporous Mesoporous Mater., vol. 207, pp. 33–38, May 2015, doi: 10.1016/J.MICROMESO.2014.12.028.
8. P. F. Zito et al., "Water vapor permeation and its influence on gases through a zeolite-4A membrane," J. Memb. Sci., vol. 574, pp. 154–163, Mar. 2019, doi: 10.1016/j.memsci.2018.12.065.
9. N. Diban et al., "Membrane reactors for in situ water removal: A review of applications," Ind. Eng. Chem. Res., vol. 52, no. 31, pp. 10342–10354, Aug. 2013, doi: 10.1021/IE3029625/ASSET/IMAGES/IE-2012-029625_M012.GIF.
10. I. G. Wenten et al., "Zeolite membrane reactors: from preparation to application in heterogeneous catalytic reactions," React. Chem. Eng., vol. 6, no. 3, pp. 401–417, Mar. 2021, doi: 10.1039/D0RE00388C.
11. F. Samimi et al., "Green Methanol Production Process from Indirect CO2 Conversion: RWGS Reactor versus RWGS Membrane Reactor," J. Environ. Chem. Eng., vol. 7, no. 1, p. 102813, Feb. 2019, doi: 10.1016/j.jece.2018.102813.
12. S. Dzuryk and E. Rezaei, "Dimensionless analysis of reverse water gas shift Packed-Bed membrane reactors," Chem. Eng. Sci., vol. 250, p. 117377, Mar. 2022, doi: 10.1016/j.ces.2021.117377.
13. E. Rezaei and S. Dzuryk, "Techno-economic comparison of reverse water gas shift reaction to steam and dry methane reforming reactions for syngas production," Chem. Eng. Res. Des., vol. 144, pp. 354–369, Apr. 2019, doi: 10.1016/J.CHERD.2019.02.005.
14. S. Dzuryk and E. Rezaei, "Intensification of the Reverse Water Gas Shift Reaction by Water-Permeable Packed-Bed Membrane Reactors," Ind. Eng. Chem. Res., vol. 59, no. 42, pp. 18907–18920, Oct. 2020, doi: 10.1021/ACS.IECR.0C02213/ASSET/IMAGES/MEDIUM/IE0C02213_M033.GIF.
15. R. Krishna and J. A. Wesselingh, "The Maxwell-Stefan approach to mass transfer," Chem. Eng. Sci., vol. 52, no. 6, pp. 861–911, Mar. 1997, doi: 10.1016/S0009-2509(96)00458-7.
16. M. J. L. Ginés et al., "Kinetic study of the reverse water-gas shift reaction over CuO/ZnO/Al2O3 catalysts," Appl. Catal. A Gen., vol. 154, no. 1–2, pp. 155–171, Jun. 1997, doi: 10.1016/S0926-860X(96)00369-9.

© 2025 by the authors. Licensed to PSEcommunity.org and PSE Press. This is an open access article under the creative commons CC-BY-SA licensing terms. Credit must be given to creator and adaptations must be shared under the same terms. See https://creativecommons.org/licenses/by-sa/4.0/

Systems & Control Transactions

**Research Article - Peer Reviewed Conference Proceeding**
ESCAPE 35 - European Symposium on Computer Aided Process Engineering
Ghent, Belgium. 6-9 July 2025
Jan F.M. Van Impe, Grégoire Léonard, Satyajeet S. Bhonsale,
Monika E. Polańska, Filip Logist (Eds.)

PSE PRESS

# Optimized integration strategies for the PMR-based $H_2$ production with $CO_2$ capture process

**Donghoi Kim[a]*, Zhongxuan Liu[b], Rahul Anantharaman[a], Thijs A. Peters[c], Truls Gundersen[b]**

[a] SINTEF Energy Research, Trondheim, Norway
[b] Norwegian University of Science and Technology (NTNU), Department of Energy and Process Engineering, Trondheim, Norway
[c] SINTEF Industry, Oslo, Norway
* Corresponding Author: donghoi.kim@sintef.no

## ABSTRACT

This work develops process options using a novel protonic membrane reformer (PMR) and liquefaction-based $CO_2$ capture process for low-carbon hydrogen production from natural gas. Several hybrid concepts of the PMR and liquefaction process are suggested based on the strategies to handle the residual gas from the reformer. The process intensification and optimization results indicate that the hybrid system with a water-gas-shift reactor and off-gas recycling guarantees high $H_2$ and $CO_2$ recovery rates for the PMR operating at relatively low $H_2$ recovery. The hybrid concept also has 74% energy conversion efficiency, which is higher than a conventional steam-methane reforming (SMR)-based $H_2$ production with chemical absorption $CO_2$ capture.

**Keywords**: Hydrogen, Carbon Dioxide Capture, Energy Efficiency, Process Design, Process Intensification, proton conducting membrane.

## INTRODUCTION

To achieve low-carbon hydrogen production, a novel protonic membrane reformer (PMR) has been developed that uses electricity to convert natural gas into pure hydrogen while generating a $CO_2$-rich retentate gas [1,2]. This syngas composition enables efficient low temperature-based carbon capture, achieving high $CO_2$ capture rates with reduced complexity and cost [3]. Thus, the PMR system produces hydrogen with a low carbon intensity, which can be further reduced with low-carbon electricity.

For process intensification, the integration of the PMR with $CO_2$ liquefaction offers several potential configurations that optimize energy efficiency and maximize hydrogen and $CO_2$ recovery. In particular, the hybrid concept allows the PMR to operate at relatively low $H_2$ recovery rates with less electricity input, guaranteeing high system throughput at a wide range of operating conditions in the reformer. It should be noted that the PMR stacks can achieve very high $H_2$ recovery rates over 99 % [2], indicating that the PMR-based concepts are not bound to lower recovery scenarios.

This hybrid approach has also been examined in an autothermal reforming (ATR)-based $H_2$ production system [4]. Previous studies, however, have only analyzed a single configuration of this hybrid system in detail [5]. Therefore, this study extends earlier work by proposing several hybrid configurations that explore different approaches integrating hydrogen production and $CO_2$ capture. This comparative analysis aims to identify the optimal configuration that balances energy efficiency, hydrogen and $CO_2$ recovery, and economic viability, covering a wide operating range of the PMR.

## PMR AND HYBRID PROCESS OPTIONS

The focus of this work is on the management of the residual gas from the $CO_2$ liquefaction process, which has a significant impact on system performance. In particular, (1) the residual gas may contain significant amounts of hydrogen, which directly affects the hydrogen recovery rate of the system, and (2) its flow rate affects both power consumption and capital cost when recycled to the PMR for further hydrogen recovery. Based on the two considerations, four possible hybrid process options are suggested.

### Hybrid process without off-gas recycling (Option 1)

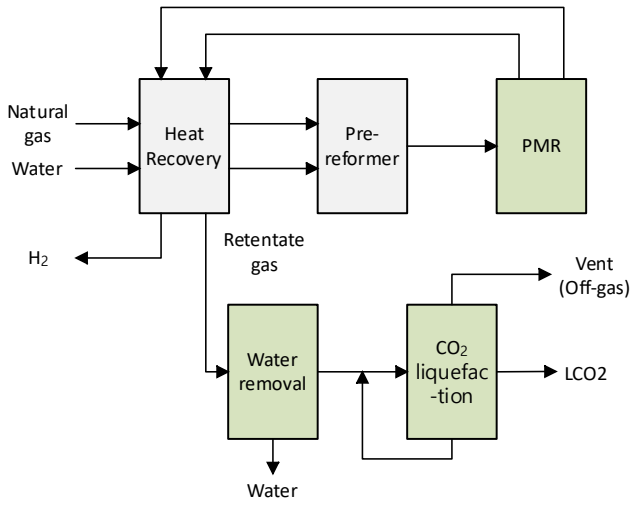



**Figure 1.** Block diagram of the hybrid process without off-gas recycling (Option 1) (white blocks: process without energy input, green blocks: process with energy input).

A simple cascade of the PMR and liquefaction is a promising option for a low process complexity and easy operation. However, other process steps are required for PMR-based $H_2$ production, as presented in Figure 1. The first step is heating the two feed streams (natural gas, water) before sending them to a pre-reformer. The heat duty is supplied by the $H_2$ and retentate gas from the PMR, which has a high temperature. In the pre-reformer, heavier hydrocarbons are converted to methane, which is then fed to the PMR. In the pre-reformer, some $CO_2$ and $H_2$ will also already be produced.

The PMR feed stream is further heated by the heat generated from the PMR and supplied to the membrane reformer. The PMR has a net endothermic reaction with steam-methane reforming (SMR) and water-gas-shift (WGS), which is compensated by heat produced during hydrogen separation and compression through the membrane with electricity input. As a result, high-pressure pure $H_2$ from methane is produced in one step through the PMR while generating a $CO_2$-rich retentate stream. The internal heat exchange also makes the membrane reformer efficient by eliminating the need for external heating, often regarded as the primary loss point for natural gas-based $H_2$ production systems. After delivering heat to the heat recovery unit, the retentate stream is dehydrated and condensed through the liquefaction process to capture high-purity $CO_2$. The impurities in the captured $CO_2$ are removed via off-gas purging.

Although this configuration efficiently produces hydrogen, the overall hydrogen recovery rate of the hybrid system will be limited by the PMR operation at a relatively low-performance region. This is due to the vent stream, which contains considerable amounts of hydrogen. The hydrogen left in the PMR is sent to the liquefaction process through the retentate gas. Since the $H_2$ is not condensed in the $CO_2$ capture process, it is wasted through the vent gas, resulting in a low system hydrogen recovery rate. In addition, the retentate gas from the PMR contains a relatively high CO fraction, which is difficult to separate from $CO_2$ while keeping the $CO_2$ capture rate high in the liquefaction process.

## Hybrid process with off-gas recycling (Option 2)

To minimize the $H_2$ loss of the hybrid system, the off-gas from the liquefaction process can alternatively be recycled to the PMR, as seen in Figure 2. Although recycling will increase the size and capital cost of the system, valuable hydrogen products can be collected from the off-gas, achieving a very high hydrogen recovery rate while maintaining the energy input to the PMR low. However, purging of a part of the recycled off-gas will be required in this configuration to avoid inert gas (such as $N_2$) accumulation in the hybrid system.

Although the recycled off-gas will improve the system performance with a higher $H_2$ recovery rate, the retentate gas from the PMR will still contain a considerable amount of CO. Thus, the possible drawbacks of this configuration are (1) the separation of CO in the liquid $CO_2$ stream will result in a lower $CO_2$ capture rate, (2) a higher content of impurities in the retentate gas will lead to larger specific power consumption of the $CO_2$ capture process and thus the hybrid system.

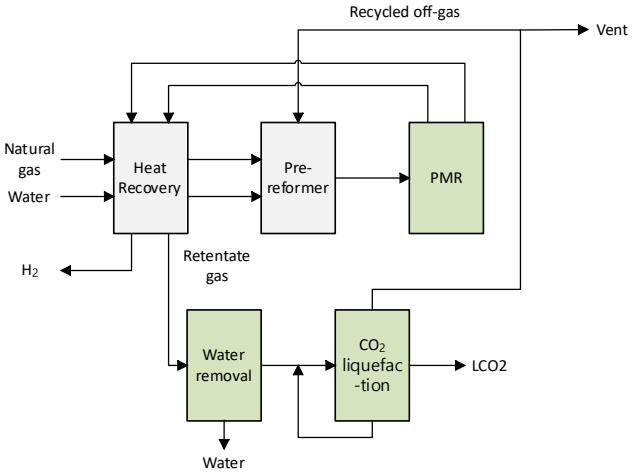



**Figure 2.** Block diagram of the hybrid process with off-gas recycling (Option 2) (white blocks: process without energy input, green blocks: process with energy input).

## Hybrid process with off-gas recycling and extra WGS after liquefaction (Option 3)

To handle the issues of CO, an extra WGS reactor is considered to convert CO to $CO_2$ in the hybrid system. However, the configuration and the performance of the system will vary depending on the location of the extra WGS reactor.

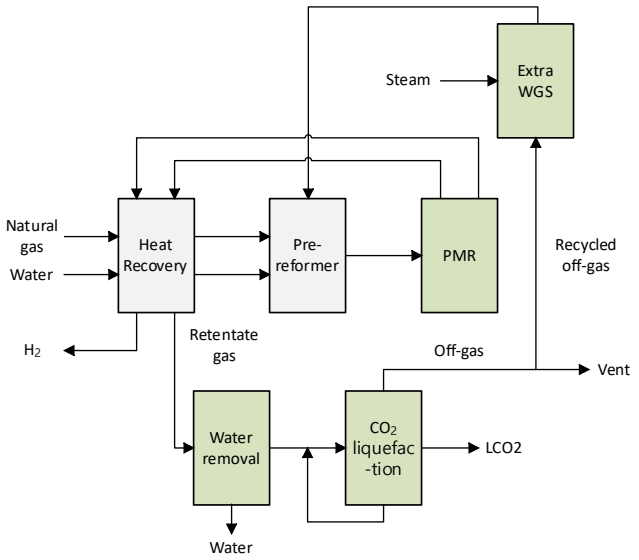



**Figure 3.** Block diagram of the hybrid process with off-gas recycling and extra WGS after liquefaction (Option 3) (white blocks: process without energy input, green blocks: process with energy input).

Possible locations of the extra WGS reactor are either on the recycled off-gas or the retentate gas. The former configuration is Option 3, where the extra WGS is located before the pre-reformer for the recycled off-gas, as illustrated in Figure 3. In this configuration, the size of the extra WGS is minimized as it is only responsible for the recycled off-gas. This option is considered one of the promising options to be evaluated in detail. However, the extra WGS will not handle the CO in the retentate gas, which is fed to the $CO_2$ capture part. Thus, this option will also result in poor performance of the liquefaction process and, hence, the hybrid system. In addition, due to the low temperature of the off-gas from the liquefaction process, an extra heat supply will be needed to preheat the recycled stream, thereby reducing the energy efficiency of the hybrid concept.

### Hybrid process with off-gas recycling and extra WGS after liquefaction (Option 4)

As shown in Figure 4, another possible hybrid configuration with an extra WGS is to place it on the retentate gas in front of the water removal unit to convert the CO in the feed gas to the liquefaction process. Consequently, almost no CO in the retentate gas is sent to the $CO_2$ separation process, giving lower specific power consumption and a higher $CO_2$ capture rate. Another possible advantage is that the vent stream will not require additional equipment to handle the CO. Therefore, this hybrid system will achieve high hydrogen and $CO_2$ capture rates.

However, the size of the extra WGS reactor will be significantly larger than for Option 3, where the extra WGS is only responsible for the recycled off-gas. Nevertheless, the high temperature of the retentate gas will not require any additional heat supply system for the reactor, which is essential for Option 3. Thus, an objective comparison of Options 3 and 4 using economic analysis will be necessary to identify the cost-optimal process for the hybrid concept.

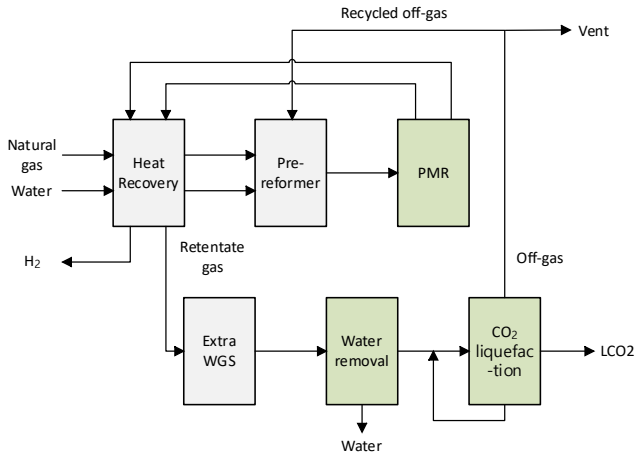



**Figure 4.** Block diagram of the hybrid process with off-gas recycling and extra WGS after PMR (Option 4) (white blocks: process without energy input, green blocks: process with energy input).

## SYSTEM MODELING AND DESIGN BASIS

The hybrid system is modeled using the PMR model in C, which is validated against the data supplied by previous work [1]. The reformer model is integrated with Aspen HYSYS where other process units are modelled to build the hybrid process. This framework uses Matlab to interface the PMR model in C and the HYSYS model. To identify optimal operating conditions for the four different configurations, the hybrid systems are optimized to minimize their specific power consumption (SPC), while the energy conversion efficiency of the system is calculated.

$$SPC_{\mathrm{sys}} = \frac{Power_{\mathrm{net}}}{\dot{m}_{\mathrm{H_2\ product}}} \quad (1)$$

$$\eta_{\mathrm{energy\ conversion}} = \frac{LHV_{\mathrm{H_2\ product}}}{Power_{\mathrm{net}} + LHV_{\mathrm{NG}}} \quad (2)$$

This enables an objective comparison of the different configurations, identifying the most promising option for the hybrid concept. The Particle Swarm Optimization (PSO) algorithm is used for the optimization work as it is a derivative-free approach that can be easily applied to complex or black box models such as this hybrid process.

During the optimization, the system hydrogen recovery rate (HRR) and $CO_2$ capture rate (CCR) are constrained to be larger than or equal to 95 % and 90 %, respectively. It is worth noting that the operating condition of the PMR is set to give 90% of HRR to identify the benefit of the hybrid concept under a relatively mild operating region for the membrane reformer.

$$HRR_{sys} = \frac{\dot{n}_{H_2}}{\dot{n}_{H_2\ pre-reformer} + \dot{n}_{H_2PMR} + \dot{n}_{H_2WGS}} \quad (3)$$

$$CCR_{sys} = \frac{\dot{n}_{CO_2,Captured\ CO_2}}{\sum \dot{n}_{C,Natural\ Gas}} \quad (4)$$

In addition, the $CO_2$ loss from the $CO_2$ capture process is limited to be smaller than or equal to 5 % so that enough $CO_2$ in the retentate gas is either captured through the liquid $CO_2$ or recycled via the off-gas. Considering the trade-off between cost and energy efficiency, the minimum approach temperature of heat exchangers is set differently for heat exchangers operating above (20 °C) and below ambient temperature (3 °C).

For the energy-efficient operation of the hybrid concept, the heat generated from the PMR should be matched with the heat required in the heat recovery part to avoid using external heaters. Thus, the system heat balance is constrained to be equal to or larger than zero, which means the system will always have net surplus heat [6].

The thermodynamic performance of the hybrid concept is also affected by the operating conditions of the PMR (temperature, pressure, current density). Yet, their values are fixed in this work for a comparative analysis of different process configurations.

The hybrid system assumes a natural gas feed rate of 3000 kmol/h, with a lower heating value of 50 MJ/kg, to generate around 500 t/d of $H_2$. $CO_2$ is specified for delivery at 150 bara with a purity of 99 mol% while maintaining CO levels below 0.5 vol% for pipeline transport [7]. Other key design conditions are listed in Table 1.

**Table 1:** Design basis for the PMR and the $CO_2$ capture process [1,5].

| Parameters | Unit | Value |
|---|---|---|
| PMR SC ratio | - | 2.5 |
| PMR temperature | bara | 26 |
| PMR pressure | °C | 800 |
| PMR current density | A/m$^2$ | 7000 |
| PMR retentate pressure | bara | 26 |
| PMR retentate temperature | °C | 800 |
| Pre-reformer temperature | °C | 450 |
| Extra WGS temperature | °C | 200 |
| $H_2$ product pressure | bara | 26 |
| $CO_2$ product pressure | bara | 150 |
| Compressor efficiency | % | 80 |
| Pump efficiency | % | 75 |
| Gas expander efficiency | % | 85 |

## RESULTS

This section compares the performance of the hybrid process with that of a conventional $H_2$ production method with $CO_2$ capture [8]. The conventional process consists of SMR and WGS reactors, a solvent-based $CO_2$ capture process, and a pressure swing adsorption $H_2$ purification step. As seen in Table 2, the hybrid concept gives a higher $H_2$ and $CO_2$ recovery rate than the conventional technology.

In addition, the hybrid concept provides a higher energy conversion efficiency than the conventional process, except for Option 1. Another advantage of the hybrid concept is that $CO_2$ is captured at transport conditions while the conventional system needs purification and compression steps for the captured $CO_2$, requiring extra power. The simple heat integration performed in the hybrid system also means that a detailed study on the heat integration with the surplus heat from the PMR will further increase the energy conversion efficiency. Thus, the hybrid system will be a less carbon-intensive solution for natural gas-based hydrogen production than the conventional method.

Among the four configurations of the hybrid process, Option 1, which is a simple cascade of the PMR and the liquefaction process, cannot meet the minimum HRR and CCR requirements. In Option 2, both the HRR and CCR can be satisfied by recycling 90 % of the off-gas to the PMR. However, the CO content in the pre-reformer and the retentate gas is too high, which can be an operational burden to the PMR and the $CO_2$ capture system.

To handle the potential issues with CO, an extra WGS reactor is considered for the recycled off-gas in Option 3. It is observed that the CO in the recycled off-gas is successfully removed. However, a considerable amount of CO generated in the PMR will still exist in the retentate gas, leading to a poor performance of the $CO_2$ capture process.

In Option 4, an extra WGS reactor is placed after the PMR. The CO in the retentate gas is then removed, and better $CO_2$ capture performance (SPC and CCR) is achieved. The reduced SPC for the CCS also gives the smallest system SPC compared to other alternatives. Although Option 4 has a slight reduction in system HRR, the lowest system SPC and $CO_2$ loss will make it the most promising hybrid concept. The detailed process configuration of Option 4 is presented in Figure 5.

## CONCLUSION

A hybrid process comprising protonic membrane reformer technology and $CO_2$ liquefaction is developed in this work for efficient hydrogen production with integrated carbon capture. The hybrid system without recycling the off-gas can have a smaller equipment size and capital cost while having a significant $H_2$ loss through the off-gas, which is wasted as a vent stream. Therefore, this simple hybrid concept will be practical when the PMR is

**Table 2:** Performance of the PMR-based hybrid process options and a conventional SMR-based $H_2$ production with $CO_2$ capture.

| Parameter | SMR with CCS | Option 1 | Option 2 | Option 3 | Option 4 |
|---|---|---|---|---|---|
| $p_{H2}$ [bara] | 22.3 | 26.0 | 26.0 | 26.0 | 26.0 |
| $p_{CO2}$ [bara] | 1.3 | 150.0 | 150.0 | 150.0 | 150.0 |
| $HRR_{sys}$ [%] | 87.0 | 91.1 | 99.7 | 98.9 | 96.8 |
| $CCR_{sys}$ [%] | 90.0 | 57.8 | 93.2 | 92.6 | 99.1 |
| $SPC_{PMR}$ [MJ/kg$H_2$] | - | 46.4 | 42.5 | 42.6 | 41.8 |
| $SPC_{Liq}$ [MJ/kg$CO_2$] | - | 0.5 | 0.3 | 0.3 | 0.3 |
| $SPC_{sys}$ [MJ/kg$H_2$] | - | 48.2 | 44.2 | 44.2 | 43.9 |
| $\eta_{energy\ conv}$ [%] | 71.1 | 64.0 | 76.4 | 76.6 | 74.3 |

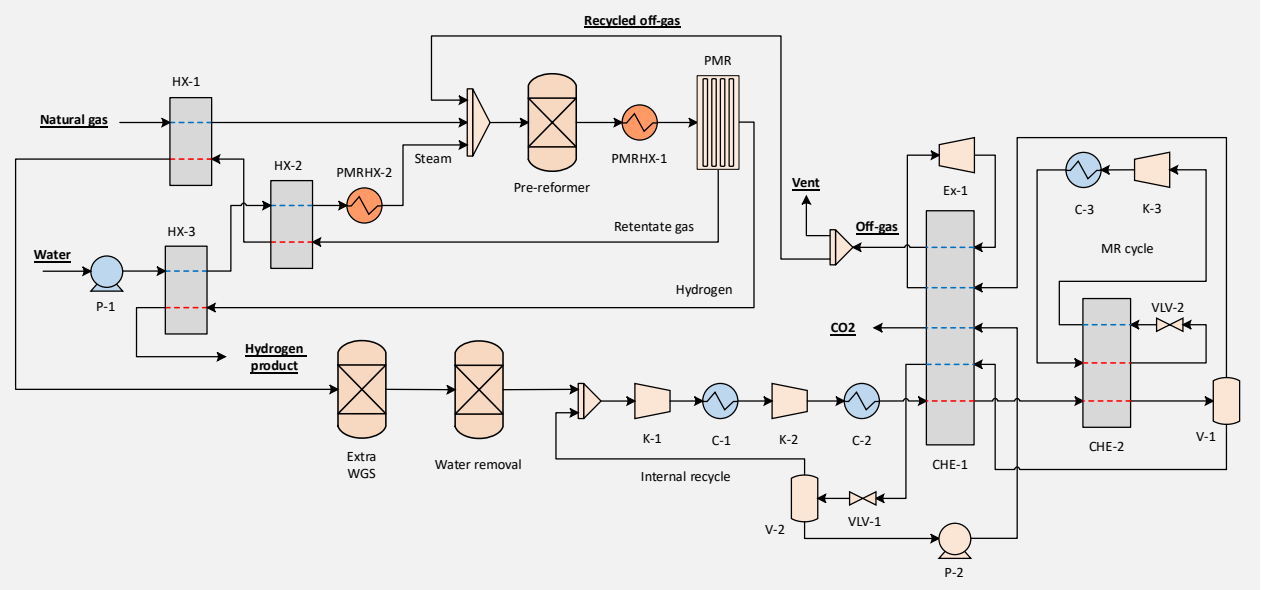



**Figure 5:** Detailed process flow diagram of hybrid process with off-gas recycling and extra WGS after PMR (Option 4).

in a high-performance operating region where hydrogen recovery is high.

Although the configurations recycling the off-gas will minimize the hydrogen loss, it is found that the CO content in the retentate gas needs to be treated for the downstream carbon capture process. Thus, using a WGS reactor with off-gas recycling is deemed necessary to achieve both high $H_2$ recovery and carbon capture rates when the PMR is operated at a lower load condition.

In particular, the configuration with the WGS reactor for the retentate gas is the most promising option as it can effectively remove CO in the liquefaction process feed stream, maximizing the carbon capture rate of the system with reduced energy consumption. Therefore, this hybrid concept is considered for further evaluation to explore its potential and role in the hydrogen economy.

Since the PMR-based hybrid utilizes both heat and electricity, their price and $CO_2$ intensity will be key factors influencing the techno-economic viability. Therefore, a detailed analysis considering uncertainties in energy prices and $CO_2$ intensity will be conducted to characterize the economic performance of the hybrid system.

## ACKNOWLEDGEMENTS

This work was performed within the CLIMIT-KPN MACH-2 project (294629) with support from the NCCS Centre, performed under the Norwegian research program Centres for Environment-friendly Energy Research (FME). The authors acknowledge the following partners for their contributions: Aker Solutions, Ansaldo Energia, Baker Hughes, CoorsTek Membrane Sciences, EMGS, Equinor, Gassco, Krohne, Larvik Shipping, Lundin, Norcem, Norwegian Oil and Gas, Quad Geometrics, Total, Vår Energi, and the Research Council of Norway (257579).

## REFERENCES


1. Malerød-Fjeld H, Clark D, Yuste-Tirados I, Zanón R, Catalán-Martinez D, Beeaff D, et al. Thermo-electrochemical production of compressed hydrogen from methane with near-zero energy loss. Nature Energy 2:923–31 (2017). https://doi.org/10.1038/s41560-017-0029-4.
2. Clark D, Malerød-Fjeld H, Budd M, Yuste-Tirados I, Beeaff D, Aamodt S, et al. Single-step hydrogen production from NH3, CH4, and biogas in stacked proton ceramic reactors. Science 376:390–3 (2022). https://doi.org/10.1126/science.abj3951.
3. Kim D, Berstad D, Anantharaman R, Straus J, Peters TA, Gundersen T. Low Temperature Applications for CO2 Capture in Hydrogen Production. Computer Aided Chemical Engineering 48:445–50 (2020). https://doi.org/10.1016/B978-0-12-823377-1.50075-6.
4. Straus J, Skjervold VT, Anantharaman R, Berstad D. Novel approach for low CO2 intensity hydrogen production from natural gas. Sustainable Energy Fuels 6:4948-4961 (2022). https://doi.org/10.1039/D2SE00862A.
5. Kim D, Liu Z, Anantharaman R, Riboldi L, Odsæter L, Berstad D, et al. Design of a novel hybrid process for membrane assisted clean hydrogen production with CO2 capture through liquefaction. Computer Aided Chemical Engineering 49:127–32 (2022). https://doi.org/10.1016/B978-0-323-85159-6.50021-X.
6. Kim D, Roussanaly S, Anantharaman R, Riboldi L, Odsæter L, Berstad D, et al. Process Design Optimization and Techno-Economic Analysis of a Hybrid Low-Emission Hydrogen Production System. GHGT-16 (2022). https://doi.org/10.2139/ssrn.4286146.
7. Harkin T, Filby I, Sick H, Manderson D, Ashton R. Development of a CO2 Specification for a CCS Hub Network. Energy Procedia 114:6708–20 (2017). https://doi.org/10.1016/j.egypro.2017.03.1801.
8. IEAGHG. Techno-economic evaluation of SMR based standalone (merchant) hydrogen plant with CCS. IEAGHG (2017).



© 2025 by the authors. Licensed to PSEcommunity.org and PSE Press. This is an open access article under the creative commons CC-BY-SA licensing terms. Credit must be given to creator and adaptations must be shared under the same terms. See https://creativecommons.org/licenses/by-sa/4.0/




Systems & Control Transactions

**Research Article - Peer Reviewed Conference Proceeding**
ESCAPE 35 - European Symposium on Computer Aided Process Engineering
Ghent, Belgium. 6-9 July 2025
Jan F.M. Van Impe, Grégoire Léonard, Satyajeet S. Bhonsale,
Monika E. Polańska, Filip Logist (Eds.)

PSE PRESS

# Design and Cost Analysis of a Reactive Distillation Column to Produce Ethyl Levulinate Using Excess Levulinic Acid

**Igor F. Fioravante, Riann de Q. Nóbrega, Rubens Maciel Filho, and Jean F. Leal Silva**

School of Chemical Engineering, University of Campinas (UNICAMP), Campinas, SP, Brazil
* Corresponding Author: jeanf@unicamp.br

## ABSTRACT

Despite the potential of electrification in transportation, diesel will remain one of the main fuels for decades. The replacement of diesel with biodiesel is one of the solutions to decrease the net emissions of diesel engines. However, biodiesel has limited performance in cold weather and requires fuel additives. In this context, choosing additives from non-edible, inexpensive, renewable sources is important. Ethyl levulinate, an ester derived from levulinic acid that can be produced from sugarcane, is a promising option because it improves the cold-flow properties of fuels and reduces soot emissions. In this work, a reactive distillation column was designed to produce ethyl levulinate. Because of the volatility order of the components involved in this reaction, levulinic acid was chosen as the excess reactant. Production cost was calculated based on ethanol price, capital cost, and operating expenses for several scenarios. The results showed that the optimized reactive distillation column using excess levulinic acid provides a production cost 29% lower than that of a similar esterification process with a continuous stirred tank reactor followed by distillation.

**Keywords**: biofuel, process simulation, biodiesel, ethanol, distillation.

## INTRODUCTION

The biochemical biorefinery platform has been a focus of research because of the potential of using cellulosic sugars in fermentation processes [1]. However, in biomass hydrolysis, part of the sugars is lost in dehydration reactions, yielding furans such as 5-hydroxymethylfurfural and furfural [2]. Generally, furans negatively impact fermentation performance by depleting microorganisms of reducing power [3]. Alternatively, the thermolytic transformation of biomass into products such as furans has great economic potential and avoids fermentation problems [4,5]. Therefore, it is key to explore biorefinery processes based on furans.

Hydrolysis of cellulose yields glucose, which, under severe reaction conditions, is dehydrated to 5-hydroxymethylfurfural (HMF) and subsequently rehydrated to yield levulinic acid and formic acid [6]. Levulinic acid is a γ-keto acid widely recognized as a building block: the carbon chain length and the presence of two organic functions open a myriad of applications [7]. Esters of levulinic acid have a great potential in the fuels market, especially ethyl levulinate [8].

Studies demonstrate that ethyl levulinate enhances combustion efficiency and cold-flow properties of diesel and biodiesel. It also reduces soot emissions in diesel engines [9,10]. The effective replacement of fossil fuels by biofuels depends on the production of high-performance biofuel blends that include key biofuel additives [8], such as ethyl levulinate. Despite the growing interest in electrification, liquid fuels are likely to remain the main energy source for transportation around the world up until 2050 [11], and the decrease in $CO_2$ emissions by electric vehicles using current battery technology and non-renewable electricity sources is questionable [12]. Additionally, efforts to decarbonize hard-to-electrify sectors, such as the development of marine biofuels, hold a promising future for ethyl levulinate as a fuel additive [13].

The feasibility of ethyl levulinate production on a large scale depends on the production cost of levulinic acid [8]. Production processes for levulinic acid and ethyl levulinate are not well-established in the industry [7]. Besides the bottlenecks in reactor development, there are many subprocesses with cost reduction potential, such as esterification [8]. Process intensification has demonstrated successful results in the esterification of

carboxylic acids in reactive distillation columns [14]. Another important aspect is that distilling ethyl levulinate and levulinic acid requires high temperature, which could otherwise be used to drive the esterification.

The volatility ranking of species is fundamental to deciding upon feed position and size of the reactive section in reactive distillation columns [15,16]. In the case of autocatalysis, all stages are reacting stages. The volatility ranking for the ethyl levulinate reaction represents the least favorable case since both products are the intermediate keys in the distillation [15]. Therefore, conventional approaches for the design of reactive distillation columns cannot be applied thoroughly in this case. A previous study evaluated this system, but it used the traditional excess alcohol strategy, which ended up contributing to increased cost, thus indicating that the opposite approach might be more suitable [17]. Therefore, this work explores an alternative strategy: excess carboxylic acid.

This work investigated the process design of an autocatalyzed reactive distillation column for ethyl levulinate production, assuming an excess carboxylic acid ratio, coupled with techno-economic analysis. A surrogate model was used to optimize operating conditions to improve economic indicators. The developed process design was then compared to a conventional autocatalyzed esterification process working at similar conditions.

## METHODOLOGY

Process design consisted of three steps: i) initial assessment based on thermodynamics and kinetic limitations; ii) use of design of experiments to obtain a surrogate model for optimization; and iii) simulation and assessment of optimized operating conditions.

Thermodynamic and kinetic analyses were conducted using Aspen Plus 14 (AspenTech, Inc., USA, 2022). Carboxylic acids associate in the vapor phase and lead to a negative deviation in the molar volume, which is accounted for by the Hayden-O'Connell equation of state [18]. The NRTL (non-random, two-liquid) model was chosen for the liquid phase; binary interaction parameters of the water-ethanol pair were obtained from the Aspen Plus 14.0 database, and parameters for the other pairs were obtained from Resk *et al.*, 2014 [18].

The conversion of levulinic acid at equilibrium conditions was calculated using the *REquil* model in Aspen Plus, which considers chemical equilibrium conditions. A similar analysis was carried out considering reaction kinetics using an *RCSTR* model (residence time: 60 min). The esterification reaction is presented in Figure 1, and the kinetics of the autocatalyzed reaction is described by Eq. (1). In this equation, the driving force is the concentration of species on molar basis ($C_{LA}$ for levulinic acid, $C_{EtOH}$ for ethanol, $C_{EL}$ for ethyl levulinate, $C_w$ for water), mediated by the equilibrium constant $K_{eq}$. Other factors include the pre-exponential factor ($k_0$, 100 m³/kmol.s), the activation energy ($E_A$, 49 kJ/mol), the universal gas constant ($R$), and the temperature ($T$) [19].

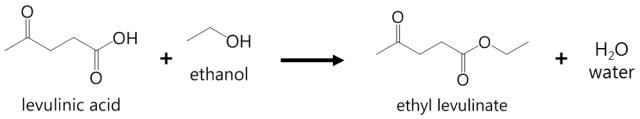



**Figure 1.** Esterification of levulinic acid with ethanol.

$$r = k_0 \exp\left(\frac{-E_A}{RT}\right)\left(C_{LA}C_{EtOH} - \frac{C_{EL}C_w}{K_{eq}}\right) \quad (1)$$

Optimization was carried out using a surrogate model based on a central composite design with face-centered star points to facilitate convergence. This approach also allows the statistical analysis of the process. The following parameters of the reactive distillation column were considered in the surrogate model: weir height ($WH$), ethanol to levulinic acid ratio ($ELA$), number of stages ($NST$), and reboiler temperature ($RT$). The column diameter was calculated in Aspen Plus (Fair correlation). The column diameter and weir height determine the liquid holdup needed for the reaction. The design space (Table 1) was defined based on simulations of distillation columns (shortcut method) for feeds in the conversion range of 10–100% of the reaction depicted in Figure 1.

**Table 1:** Design space used in the process optimization.

| Variable | -1 | 0 | +1 |
|---|---|---|---|
| WH (mm) | 100 | 150 | 200 |
| ELA | 0.2 | 0.6 | 1.0 |
| NST | 20 | 40 | 60 |
| RT (°C) | 160 | 180 | 200 |

The design included 25 cases since there are four factors and the process was simulated (replicates to calculate error are unnecessary). For each case, the cost of ethyl levulinate ($CEL$) was calculated. $CEL$ is defined as the sum of operating and capital expenses divided by the production rate of ethyl levulinate (excluding the cost of levulinic acid), $x$ represents each coded variable, and $c$ represents the coefficients of the surrogate model. Capital cost was calculated according to the literature [20] and added to the $CEL$ after a discount rate of 10% on an equipment life span of 10 years. The material of construction was SS316. The column uses bubble cap trays. The statistical analysis was completed using the software Statistica 13.3 (TIBCO Software Inc., Palo Alto, USA, 2017). Utility cost was estimated according to the literature [21]. Ethanol cost was based on the monthly average from 2019 to 2023 [22]. Data of the 25 cases were regressed into the surrogate model shown in Eq. (2).

$$CEL = c_0 + \sum_{i=1}^{n} c_i x_i + \sum_{i=1}^{n} c_{ii} x_i^2 + \sum_{i=1}^{n} \sum_{j \geq i}^{n} c_{ij} x_i x_j \quad (2)$$

Levulinic acid (recycled and fresh) was fed at 90 °C to the top tray of the reactive distillation column (*RadFrac* block). The levulinic acid to ethanol ratio was adjusted via the Design Spec tool of Aspen Plus according to each simulated case. Ethanol (1.5 bar, 150 °C) was fed at the bottom of the reactive distillation column as vapor. The esterification reaction was set to occur on all stages with kinetics described by Eq. (2). Residence time in each tray was set according to the calculated velocity obtained as a function of the diameter of the column. As a simplification due to the volume of simulations, vapor-liquid equilibrium was reached in any stage of the column.

The bottoms flow rate was fixed via the Calculator tool of Aspen Plus equal to 99.5% of the levulinic acid and ethyl levulinate entering the column. The reflux ratio was varied to recover a bottom product containing 99.9% levulinic acid and ethyl levulinate. The distillate contained water and unreacted ethanol. Ethanol and water were separated using molecular sieves. For this processes, operating conditions and investment were based on data available in the literature [23]. Unreacted ethanol was recycled into the column. The bottom stream of the reactive distillation column was distilled to separate ethyl levulinate and levulinic acid, the latter recycled to the esterification process. This last column was designed using shortcut methods. Ethyl levulinate was obtained at a purity of 99.5 wt%.

Other parameters considered in the process simulation include: pressure in the condenser of the reactive distillation column was varied to attain any specified $RT$ (design variable); stage pressure drop was 4-6 mbar (depending on $RT$); tray spacing of 0.6 m in both the reactive distillation column and second distillation column; residence time in the reflux drum and reboiler sump was 5 min; streams of wastewater, levulinic acid, and ethyl levulinate leaving the second column and the ethanol dehydration were used in heat integration to preheat ethanol, considering a temperature approach of 10 °C in a series of *HeatX* models; streams of ethyl levulinate and wastewater were cooled to 50 °C; service life of molecular sieves used in dehydration of ethanol was equal to the project lifespan (10 years); saturated steam was available at 28 bar and 8 bar (returning as saturated liquid); cooling water was available at 30 °C (returning at 40 °C); chiller water was available at 0 °C (returning at 10 °C). The system was sized to a production rate of 100 kt/y of ethyl levulinate, operating 8000 h per year.

The validity of the surrogate models was attested using the Fisher test with the analysis of variance table. The surrogate model was used as the objective function to minimize $CEL$ using the gradient-based method of the Solver tool of Microsoft Excel. The obtained results were then simulated to validate the optimization, and the reactive distillation column was analyzed in terms of profiles (composition, temperature, etc.).

For the sake of comparison, an esterification via a conventional process composed of a stirred tank reactor followed by a distillation train was simulated as well. The reaction kinetics were the same as Eq. (2). Among the variables of Table 1, only $ELA$ was considered an optimization variable in this scenario. The optimum was searched in the range of 0.6 to 1.4. The reactor temperature was fixed at 200 °C to ensure a high reaction rate, and pressure was chosen to ensure the reactor operated at subcooled conditions. The residence time was varied to attain 99% of the equilibrium conversion at any specified $ELA$ condition.

## RESULTS AND DISCUSSION

### Basis for process design

According to Figure 2a, increasing the $ELA$ from 1 to 2 increases the conversion at equilibrium conditions on average by 13% (temperature range of 0-200 °C). Regarding the kinetics of the autocatalyzed reaction (Figure 2b), increasing the $ELA$ from 1 to 2 increases the conversion in a reaction time of 20 minutes at 200 °C by 31% and at 150 °C by 38%. Different from $ELA$, temperature has little effect over the maximum possible conversion at equilibrium conditions (Figure 2a). However, high temperature is fundamental to achieving desirable conversion in the autocatalyzed reaction (Figure 2b). This scenario – high $ELA$ and high temperature – corresponds to the conditions expected at the bottom of the distillation column since the unreacted levulinic acid is in contact with the total feed of ethanol at the reboiler temperature.

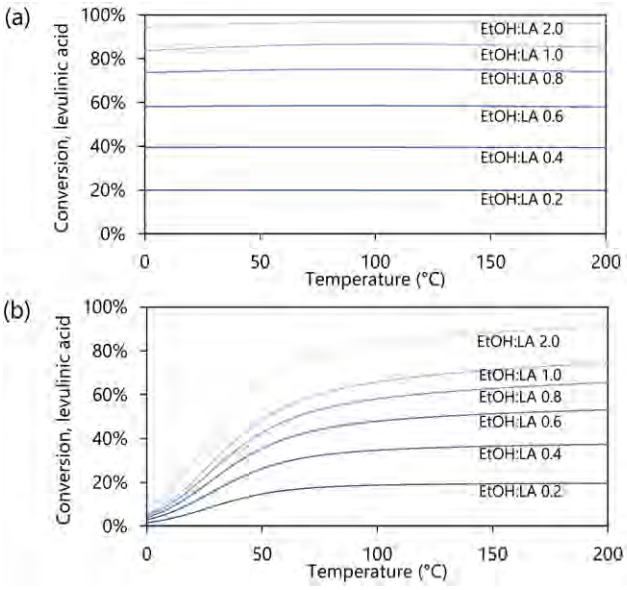



**Figure 2.** Conversion of levulinic acid at equilibrium and at 60 minutes for different temperatures and ethanol to levulinic acid (EtOH:LA, $ELA$) ratios of 0.2 to 2.0.

The absence of an efficient catalyst and the unfavorable volatility ranking (products are intermediate keys) gives rise to a problem: a design to attain complete conversion of reactants is unfeasible. Moreover, other two factors play an important role: i) ethanol and water present an azeotrope, which requires special treatment, and ii) the light key components are considerably more volatile than the heavy key components. Therefore, the design used in this work was based on the potential of contacting a high excess of reactants on both the top and bottom of the column to drive conversion.

## Surrogate model

Simulations were run considering the design of experiments, and the resulting $CEL$ was calculated for each case. Ethanol accounts for 83% of the $CEL$. The data were analyzed with a confidence interval of 95%. The $R^2$ (coefficient of determination) was 0.976. The calculated F-test ratio in both scenarios exceed 10 by a large margin, thus indicating that the surrogate model is useful for prediction and, consequently, can be used in process optimization despite being a simplistic approach. Figure 3 shows the response surfaces obtained from the data.

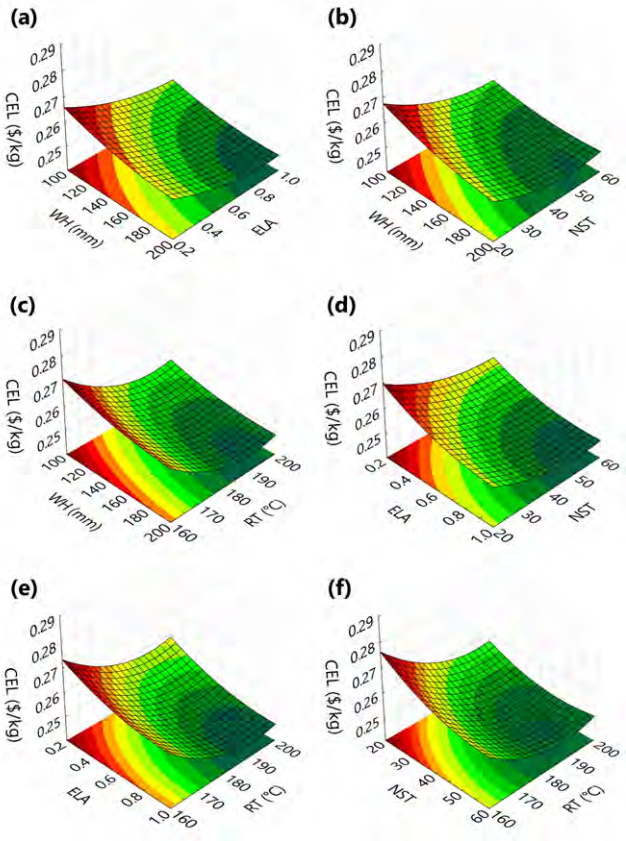



**Figure 3.** Response surfaces: a) $WH$ *vs.* $ELA$, b) $WH$ *vs.* $NST$, c) $WH$ *vs.* $RT$, d) $ELA$ *vs.* $NST$, e) $ELA$ *vs.* $RT$, and f) $NST$ *vs.* $RT$. In each case, values of the other variables were fixed at their central points.

Based on the surrogate model, conditions that minimize CEL are as follows: $WH$ of 185 mm, $ELA$ of 0.93, $NST$ of 46, and $RT$ of 190 °C. The CEL was estimated via process simulation based on these conditions: \$0.243 $kg^{-1}$. The value predicted by the model differs only by 0.26% from the value calculated via process simulation. This demonstrates the potential of the surrogate model in predicting the results of the rigorous model.

Analysis of graphs a, b, and c of Figure 3 shows that $CEL$ decreases when $WH$ is increased (n.b.: the axis direction in some graphs was inverted to aid visualization). High $WH$ means that the column needs to be reinforced to withstand the large liquid holdup, which in turn means an increase in capital cost. However, the obtained increase in residence time as a consequence of the high $WH$ demonstrated to be effective in reducing the $CEL$. The increase in $NST$ also contributes to lower $CEL$, as observed in graphs b, d, and f of Figure 3. However, it can be observed that this effect levels off around 50 stages, with a clear minimum. Similar behavior occurs for $RT$ (graphs c, e, and f of Figure 3) around 190-200 °C. Even though high temperature substantially increases the conversion rate, it demands more corrosion allowance, which increases capital cost.

Graphs a, d, and e of Figure 3 demonstrate the effect of $ELA$. Excess of one reactant is interesting to achieve higher conversion at equilibrium conditions (Figure 1). However, since the reaction is autocatalyzed, the system never reaches near-equilibrium conditions. Therefore, the equilibrium is not a limitation to justify the use of high excess of any reactant. It was observed that the extreme condition of large excess of one reactant implies in a low concentration of the other, which in turn decreases the reaction rate.

## The optimized design

The design of the optimized esterification process is presented in Figure 4. The reaction rate (Figure 5a) averaged 1.9 kmol $h^{-1}$ on column trays. The condenser drum, which operated at low temperature and a residence time of 5 min, presented a reaction rate of 0.001 kmol $h^{-1}$ mainly because of the low levulinic acid concentration (Figure 5b). The reboiler has by far the highest temperature and it presented a reaction rate in the same order as the rest of the column (2.0 kmol $h^{-1}$) despite the low ethanol concentration. Ethanol was fed one stage above and preferentially flows to the upward stages.

Temperature (Figure 5a) grew steadily from top to bottom in almost the entirety of the column, growing rapidly after ethanol concentration in the liquid phase peaks (stages 41-45). The slow increase in temperature is a consequence of volatility and concentration of components along the column. In bottom stages, the concentration of components is ranked as ethyl levulinate, levulinic acid, and ethanol, with the latter (the lightest component)

reaching concentrations up to 9 mol% in the liquid phase (Figure 5b). In the top stages, ethyl levulinate has a low concentration, at the same region where water concentration peaks. Therefore, the change in temperature is both a consequence of column fractionation and reaction, which is an expected behavior. Similar behavior was observed by the other investigators [16].

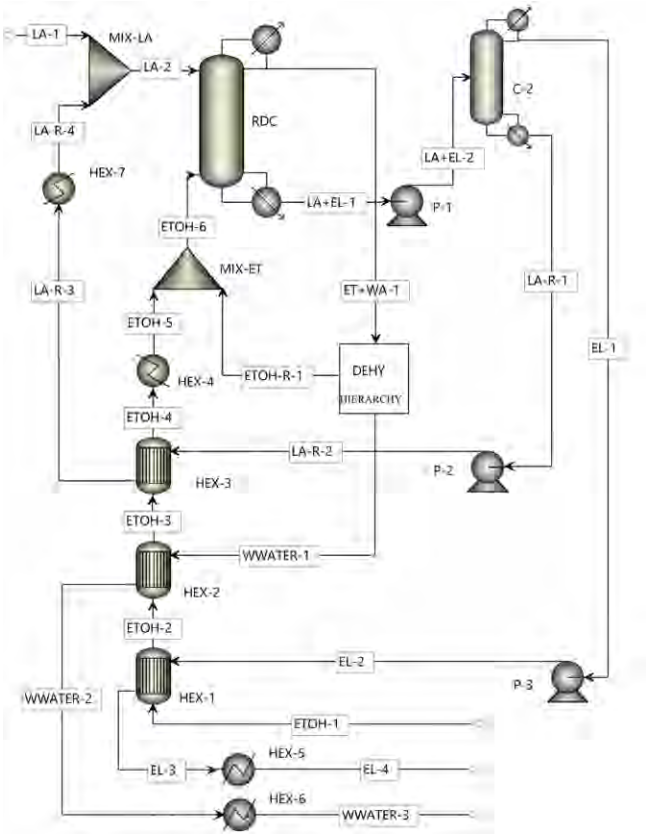



**Figure 4.** Simulation flowsheet of the optimized process.

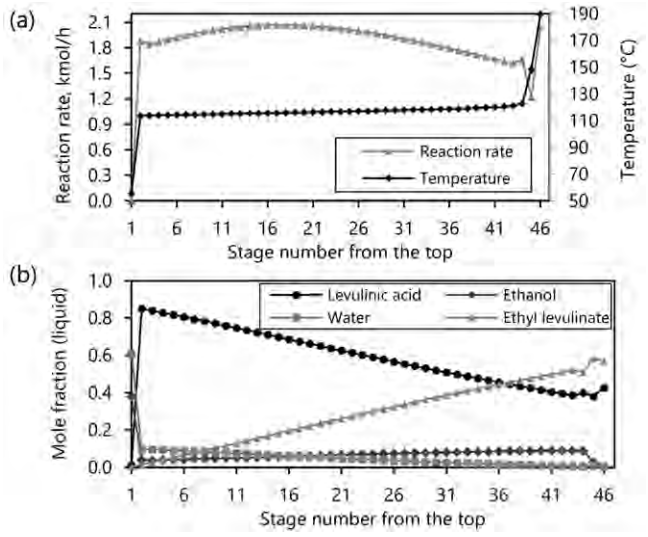



**Figure 5.** Simulation flowsheet of the optimized process.

The reaction rate is almost constant throughout the column, decreasing towards the bottom (stages 18-46). Consequently, concentration profiles (Figure 5b) are nearly straight lines. The concentration profile of levulinic acid in the liquid phase decreases according to the reaction rate because levulinic acid flows downward, its concentration in the vapor phase is too low. As the reaction slows down in the bottom stages, the concentration of levulinic acid tends to become constant.

Stages 45 and 46 have temperatures beyond 130 °C. High temperature is expected at the bottom stages because of the reboiler, thus contributing to a higher reaction rate as the ester product becomes more concentrated. On the other hand, trays on stages 2-40 operate between 110-120 °C. This result suggests that the trays of the upper stages of the column require less corrosion allowance, which could reduce their cost.

## Comparison to other process option

Optimization via a surrogate model of the conventional setup (stirred tank reactor followed by distillation) indicated that an $ELA$ of 1.09 results in a $CEL$ of \$0.253 $kg^{-1}$, 4.05% higher than that of the optimized reactive distillation. Ignoring ethanol cost in both scenarios, the difference regarding equipment cost and operating expenses becomes more evident: the conventional process costs 41% more than the reactive distillation process.

# CONCLUSIONS

This work assessed a reactive distillation column that produces ethyl levulinate via autocatalyzed esterification of levulinic acid. Optimized operating conditions were estimated via a surrogate model obtained via design of experiments. Statistical analysis demonstrated that the quadratic surrogate model has desirable confidence level inside the explored data space. Optimized parameters indicated that the lowest cost of ethyl levulinate was obtained at high reboiler temperature, high number of stages, high liquid holdup, and ethanol to levulinic acid molar ratio slightly lower than one. Single-pass conversion was not feasible because of the low reaction rate and recycle of unconverted reactants showed a large impact on operating costs. Nevertheless, the design was effective: the cost of ethyl levulinate on a conventional set of stirred tank reactor and distillation train excluding ethanol and levulinic acid costs was estimated to be 41.1% higher than the upgrading cost using a reactive distillation column. These results indicate the opportunity of carrying out the esterification of levulinic acid in a reactive distillation column.

# ACKNOWLEDGEMENTS

The authors acknowledge the São Paulo Research

Foundation (#2022/16379-8, #2024/21072-4, and #2024/03409-1) and Coordenação de Aperfeiçoamento de Pessoal de Nível Superior – CAPES/Brazil.

## REFERENCES


1. Leal Silva JF, Nakasu PYS, Costa AC da, Maciel Filho R, Rabelo SC. Techno-economic Analysis of the Production of 2G Ethanol and Technical Lignin via a Protic Ionic Liquid Pretreatment of Sugarcane Bagasse. *Ind Crops Prod* 189:115788 (2022)
2. Clauser NM, Gutiérrez S, Area MC, Felissia FE, Vallejos ME. Small-sized biorefineries as strategy to add value to sugarcane bagasse. *Chem Eng Res Des* 107:137–46 (2016)
3. Sun C, Liao Q, Xia A, Fu Q, Huang Y, Zhu X, et al. Degradation and transformation of furfural derivatives from hydrothermal pre-treated algae and lignocellulosic biomass during hydrogen fermentation. *Renew Sustain Energy Rev* 131:109983 (2020)
4. Leal Silva JF, Mariano AP, Maciel Filho R. Less severe reaction conditions to produce levulinic acid with reduced humins formation at the expense of lower biomass conversion: Is it economically feasible? *Fuel Commun* 9:100029 (2020)
5. Yong KJ, Wu TY, Lee CBTL, Lee ZJ, Liu Q, Jahim JM, et al. Furfural production from biomass residues: Current technologies, challenges and future prospects. *Biomass and Bioenergy* 161:106458 (2022)
6. Lopes ES, Silva JFL, do Nascimento LA, Bohórquez JFC, Lopes MS, Tovar LP, et al. Feasibility of the conversion of sugarcane molasses to levulinic acid: Reaction optimization and techno-economic analysis. *Ind Eng Chem Res* 60:15646–57 (2021)
7. Di Menno Di Bucchianico D, Wang Y, Buvat JC, Pan Y, Casson Moreno V, Leveneur S. Production of levulinic acid and alkyl levulinates: a process insight. *Green Chem* 24:614–46 (2022)
8. Leal Silva JF, Grekin R, Mariano AP, Maciel Filho R. Making Levulinic Acid and Ethyl Levulinate Economically Viable: A Worldwide Technoeconomic and Environmental Assessment of Possible Routes. *Energy Technol* 6:613–39 (2018)
9. Chernyshev VM, Kravchenko OA, Ananikov - VP, Ramanathan NR, K Balasekhar CS, Frigo S, et al. Utilisation of Ethyl Levulinate as Diesel Fuel Additive. *J Phys Conf Ser* 2648:012072 (2023)
10. Wu P, Miao C, Zhuang X, Li W, Tan X, Yang T. Physicochemical characterization of levulinate esters with different alkyl chain lengths blended with fuel. *Energy Sci Eng* 11:164–77 (2023)
11. Dale S, Smith TD. Back to the future: electric vehicles and oil demand BP Group chief economist BP Global Oil Market Economist. London (2016)
12. Qiao Q, Zhao F, Liu Z, Jiang S, Hao H. Cradle-to-gate greenhouse gas emissions of battery electric and internal combustion engine vehicles in China. *Appl Energy* 204:1399–411 (2017)
13. Oppong F, Xu C, Li X, Luo Z. Esters as a potential renewable fuel: A review of the combustion characteristics. *Fuel Process Technol* 229:107185 (2022)
14. Lee H-Y, Hsiao T-L, Ng DKS, Elyas R, Chen C-L, Elms RD, et al. Design and Simulation of Reactive Distillation Processes. Elsevier, p. 311–53, (2017)
15. Tung S-T, Yu C-C. Effects of relative volatility ranking to the design of reactive distillation. *AIChE J* 53:1278–97 (2007)
16. Novita FJ, Lee H-Y, Lee M. Energy-Efficient Design of an Ethyl Levulinate Reactive Distillation Process via a Thermally Coupled Distillation with External Heat Integration Arrangement. *Ind Eng Chem Res* 56:7037–48 (2017)
17. Leal Silva JF, Wolf Maciel MR, Maciel Filho R. Optimization of High Temperature Reactive Distillation for Production of Ethyl Levulinate. *Chem Eng Trans* 69:379–84 (2018)
18. Resk AJ, Peereboom L, Kolah AK, Miller DJ, Lira CT. Phase Equilibria in Systems with Levulinic Acid and Ethyl Levulinate. *J Chem Eng Data* 59:1062–8 (2014)
19. Bankole KS, Aurand GA. Kinetic and Thermodynamic Parameters for Uncatalyzed Esterification of Carboxylic Acid. *Res J Appl Sci Eng Technol* 7:4671–84 (2014)
20. Turton R, Shaeiwitz JA, Bhattacharyya D, Whiting WB. Analysis, Synthesis, and Design of Chemical Processes. Pearson Education (2018)
21. Ulrich GD, Vasudevan PT. How to Estimate Utility Costs. *Chem Eng* April:66–9 (2006)
22. Brazilian Ministry of Economy. Comex Stat. http://comexstat.mdic.gov.br/en/home (accessed May 16, 2024).
23. Kang Q, Huybrechts J, Van der Bruggen B, Baeyens J, Tan T, Dewil R. Hydrophilic membranes to replace molecular sieves in dewatering the bio-ethanol/water azeotropic mixture. *Sep Purif Technol* 136:144–9 (2014)


© 2025 by the authors. Licensed to PSEcommunity.org and PSE Press. This is an open access article under the creative commons CC-BY-SA licensing terms. Credit must be given to creator and adaptations must be shared under the same terms. See https://creativecommons.org/licenses/by-sa/4.0/



# Section 3

## Large Scale Design and Planning/Scheduling

Systems & Control Transactions

**Research Article - Peer Reviewed Conference Proceeding**
ESCAPE 35 - European Symposium on Computer Aided Process Engineering
Ghent, Belgium. 6-9 July 2025
Jan F.M. Van Impe, Grégoire Léonard, Satyajeet S. Bhonsale,
Monika E. Polańska, Filip Logist (Eds.)

PSE PRESS

# Analysis for CFD of the Claus Reaction Furnace with Operating Conditions: Temperature and Excess Air for Sulfur Recovery

**Pablo Vizguerra Morales[a]*, Miguel Ángel Morales Cabrera[b], and Fabian S. Mederos Nieto[a]**

[a] Instituto Politécnico Nacional, Centro Mexicano para la producción más Limpia, Gustavo Madero, Ciudad de Mexico, Mexico
[b] Universidad Veracruzana, Facultad de Ciencias Químicas, Xalapa, Veracruz, Mexico
* Corresponding Author: p.vizguerramorales@ugto.mx.

## ABSTRACT

In this work, a Claus reaction furnace was analyzed in a sulfur recovery unit (SRU) of the Abadan Oil Refinery where the combustion operating temperature is important since it ensures optimal performance in the reactor, this study focused on temperature of control of 1400, 1500 and 1600 K and excess air of 10, 20 and 30% to improve the reaction yield and $H_2S$ conversion. The CFD simulation was carried out in Ansys Fluent in transitory state and in 3 dimensions, considering turbulence model κ -ε standard, energy model with transport by convention and mass transport with chemical reaction using the Arrhenius Finite – rate/Eddy dissipation model for a Kinetic model of destruction of acid gases $H_2S$ and $CO_2$, obtaining a good approximation with experimental results of industrial process of the Abadan Oil Refinery, Iran. The percentage difference between experimental and simulated results varies between 0.5 to 5 % depending on species. The temperature of 1600 K and with excess air of 30% was the best, with one fraction mol of 0.054 of $S_2$ at the outlet and with conversion of the acid gas ($H_2S$) of 97.64%, which is quite good compared to the experimental one.

**Keywords**: CFD, SRU, Claus Reaction, Furnace, Sulfur.

## INTRODUCTION

High concentrations of sulfur and nitrogen are produced in crude oil processing, increasing the formation of hydrogen sulfide ($H_2S$) and ammonia ($NH_3$). Most of the H2S is absorbed by the circulation of an amine solution (DEA process), and much of the ammonia is absorbed, along with proportional amounts of $H_2S$, in the wash with water (stripper of sour waters).

Applying a Claus process, the Sulfur Recovery Unit (SRU) converts $H_2S$ present in sour amine gas and sour NH3 gas to elemental (pure) sulfur. Environmental regulations have become stricter on sulfur dioxide emissions. One of the main strategies to reduce sulfur emissions is to increase the performance of sulfur recovery units (SRU) [1]. The modified Claus process is one of the main processes that convert toxic hydrogen sulfide into elemental sulfur from acid gas during natural gas processing and upgrading the refinery [2]. The main reactions of a sulfur recovery unit occur in two stages:
A highly exothermic reaction occurs in which a large amount of heat is released, and a partially exothermic reaction occurs in which sulfur dioxide ($SO_2$) is produced in the reactor, and unreacted $H_2S$ are burned together to produce sulfur elements [3]. The modified Claus process in which hydrogen sulfide is converted to sulfur can be represented by;

$$H_2S + 0.5O_2 \rightarrow 0.5S_2 + H_2O \quad (1)$$

The sulfur recovery in the modified Claus process is obtained through thermal and catalytic reactions. The first step is thermal, where one-third of the hydrogen sulfide ($H_2S$) is partially oxidized, and Sulfur dioxide ($SO_2$) is produced at very high temperatures. The second step involves the reaction between unreacted hydrogen sulfide and sulfur dioxide over a catalytic bed at lower temperatures:

$$H_2S + 1.5O_2 \rightarrow SO_2 + H_2O \quad (2)$$

$$2H_2S + SO_2 \rightarrow 1.5S_2 + 2H_2O \quad (3)$$

The conversion of $H_2S$ to $SO_2$ in the modified Claus process is carried out in the reaction furnace, which is a cylindrical vessel with a refractory lining. The acid gas stream at a pressure typically ranging from 130 to 180 kPa is fed to the reaction furnace burner along with an appropriate amount of air to oxidize the feed contaminates and results in a 2:1 ratio of $H_2S$:$SO_2$ in the reactor effluent. The combustion of acid gases in the RF is carried out in temperature ranges of 975-1300 °C, and residence times of the gas are 0.5-2.0 s [4]. Another experimental investigation was on the effect of $O_2$ enrichment on the yield of the Claus process. It was observed that the rate of COS formation increased with $O_2$ enrichment due to the availability of higher amounts of CO, while that of $CS_2$ (carbon disulfide) decreased.

A tool that has been used lately is CFD (Computational Fluid Dynamics), where you can work with the kinetics of chemistry and the transport of mass, momentum, and heat, which helps us predict the temperature of combustion, recovery of sulfur and molar fractions of the products. The Abadan Oil Refining Company in Iran has introduced CFD to analyze the effect of $O_2$ enrichment on dry air, combustion temperature, sulfur recovery, and pollutant production [5].

A current study develops a new reduced kinetic model for simulating the destruction of acid gases in the industrial sector in a sulfur recovery unit reaction furnace. The proposed CFD model includes the reactions of the new kinetic mechanism and stationary laminar flamelet model. The relative error of the H2S conversion calculated by CFD, using the new kinetic model, is 9.48% compared to industrial data [6].

The present work has focused on the effects of the operating temperature of the Claus reactor and excess air on the combustion and SRU emission characteristics, using a kinetic model of acid gas destruction (H2S and CO2) with Fluent to improve the reaction yield. The experimental data of a reaction furnace of Abadan Oil Refining Company in Iran was taken as a reference. [7] The kinetic studies Kinetic Modeling and Optimization of the Claus Reaction Furnace by Samane Zarei [8] and the evaluation of kinetic models to simulate Claus reaction furnaces in sulfur recovery units under different feeding conditions. This work has the following objective:

1. Simulate with Fluent the kinetic model of the destruction of acid gases H2S and CO2 and mass transfer in the furnace of the Claus reactor of SRU of the Abadan Oil Refinery. The novelty of this work is the study of different control temperatures 1400, 1500 and 1600 K, with excess air of 10, 20 and 30% to increase and ensure that more reactions occur in the reaction oven, since in other works only modified operating conditions.
2. Use CFD to improve the reaction performance by modifying the operating temperature of the Claus reactor and removing excess air from the combustion.

## METHODOLOGY

The following equations are involved in solving the problem posed by the physical phenomenon to be modelled: Navier-Stokes Reynolds average equation (RANS), turbulence model $(k-\varepsilon)$ standard, equations of state and coupled methods; FLUENT 16TM uses the method of finite volumes as a numerical method to solve the governing equations and those mentioned above [9]. The partial differential equations that describe the phenomenon of mass transport are the following:

The equation of conservation of mass or continuity.

$$\frac{\partial \rho}{\partial t} + \nabla.(\rho \vec{v}) = S_m \quad (4)$$

The conservation equation of momentum or the m mentum theorem in inertial reference frame is;

$$\frac{\partial}{\partial t}(\rho \vec{v}) + \nabla.(\rho \vec{v}\vec{v}) = -\nabla \mathrm{p} + \nabla.(\vec{\tau}) + \rho \vec{g} + \vec{F} \quad (5)$$

Where p is the static pressure, τ is the stress tensor, ρg is the gravitational force and F is the external force.

The stress tensor is given by:

$$\bar{\tau} = \mu\left[(\nabla \vec{v} + \nabla \vec{v}^T) - \frac{2}{3}\nabla.\vec{v} I\right] \quad (6)$$

Where μ is the molecular viscosity, I is the unit tensor and the second term on the right side is the effect of volume expansion.

Standard turbulence model $(k-\varepsilon)$

$$\frac{\partial}{\partial t}(\rho k) + \frac{\partial}{\partial x_i}(\rho k u_i) = \frac{\partial}{\partial x_j}\left[\left(\mu + \frac{\mu_t}{\sigma_k}\right)\frac{\partial k}{\partial x_j}\right] + G_k + G_b - \rho\varepsilon - Y_M \quad (7)$$

$$\frac{\partial}{\partial t}(\rho \varepsilon) + \frac{\partial}{\partial x_i}(\rho \varepsilon u_i) = \frac{\partial}{\partial x_j}\left[\left(\mu + \frac{\mu_t}{\sigma_\varepsilon}\right)\frac{\partial \varepsilon}{\partial x_j}\right] + C_1\frac{\varepsilon}{k}(G_k + C_3 G_b) - C_2\rho\frac{\varepsilon^2}{k} \quad (8)$$

κ is the turbulence kinetic energy, ε is the dissipation rate, $G_k$ represents the generation of turbulence kinetic energy due to the mean velocity gradient, $G_b$ is the generation of turbulence kinetic energy due to buoyancy.

The above equations are considered in Cartesian coordinates, $C_1$, $C_2$, $C_3$, $\sigma_\kappa$, and $\sigma_\varepsilon$ are closure coefficients and the values of these coefficients are: 1.44, 1.92, 0.09, 1.0 and 1.3, respectively for the standard turbulence model (κ - ε) equations 7 and 8 (Launder and Spalding 1972).

The energy conservation equation is given by the

following expression:

$$\frac{\partial}{\partial t}(\rho E) + \nabla \cdot \left(\vec{v}(\rho E + p)\right) = \nabla . \left( k_{eff} \nabla T - \sum_j h_j \bar{J}_j - (\bar{\tau}_{eff} . \vec{v}) \right) + S_h \quad (9)$$

where $k_{eff}$ is the effective conductivity (k + $k_t$, where $k_t$ is the turbulent thermal conductivity, defined according to the turbulence model being used), and $\bar{J}_j$ is the diffusion flux of species j. The combustion process in the Claus reaction furnace was modeled and simulated using Ansys Fluent to study the influence of furnace temperature and keep it under control and from excess intake air for sulfur recovery and pollutant production, The temperatures used were 1400 K, 1500 K and 1600 K, varying various excesses of air 10, 20 and 30 %.

The dimensions of the reaction furnace in SRU of the Abadan Oil Refinery were taken from Abdoli et al. (2018) and a representation is shown in Figure 1. The inner surface of the reaction furnace is covered by refractory to protect its wall.

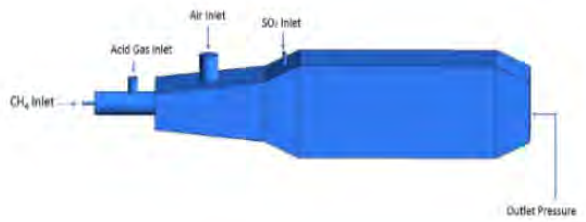



**Figure 1.** Reaction furnace in SRU of the Abadan Oil Refinery.

The reaction furnace consists of 4 inputs: $CH_4$ input, acid gas ($H_2S$) input, air input are located in the burner and $SO_2$ input is in the reaction furnace, there is a product output.

For the simulation the walls were assumed to be adiabatic, the mixture was treated as an incompressible, ideal gas, and there is no slip on the walls.

The furnace produces sulfur, but also oxidizes $H_2S$ to $SO_2$. After the furnace there are catalytic reactors that produce sulfur from $SO_2$, but at lower temperatures than the reaction furnace. Also at the exit of the furnace there is a heat exchanger that cools the gases before the catalytic stage.

The study of hydrodynamics and mass transfer was carried out with CFD tools in Fluent 16.0, which will give us the profile of products obtained. A computer with 16 GB RAM and an Intel (R) Core™ i 7 -2600 CPU was used.

The essential parameters to carry out a study of this type were to obtain an adequate mesh that represents our study area, propose ANSYS models to represent our process, turbulent model, reaction equations.

**Table 1.** shows the input operating conditions of the reagents.

| Mole Fraction | acid gas | air | $SO_2$ | $CH_4$ |
|---|---|---|---|---|
| Inlet temperature (k) | 353.15 | 463.15 | 324.15 | 3113.15 |
| Mass flow (kg/s) | 1.338 | 0.09028 | 0.25167 | 3.1025 |
| Species | | | | |
| $H_2$ | 0.00197 | 0 | 0 | 0 |
| $O_2$ | 0 | 0.19291 | 0 | 0 |
| $H_2S$ | 0.68952 | 0 | 0 | 0 |
| $SO_2$ | 0 | 0 | 0.90728 | 0 |
| $H_2O$ | 0.147 | 0.07948 | 0.09272 | 0 |
| $CH_4$ | 0.00725 | 0 | 0 | 1 |

## Simulation in CFD Preprocessing

Reactor meshing was performed in ANSYS ICEM software and boundary conditions were also entered into the mesh. The mesh was made with a hexahedral structure with a size of 364456 cells (see Figure 2).



**Figure 2.** Mesh generated for the reactor.

## Processing

The simulation in Fluent version 16.0 was performed in 3 dimensions, in transient state, using the viscous model of $k - \varepsilon$ standard, the species transport model and for the reaction the Finite-rate/Eddy - Dissipation model. To simulate the combustion reaction in the Claus SRU furnace, the following reaction mechanism was followed [Amer Mehmood, 2020];

$$H_2S + 1.5O_2 \rightarrow SO_2 + H_2O$$
$$2H_2S + SO_2 \rightarrow 1.5S_2 + 2H_2O$$
$$CH_4 + 2O_2 \rightarrow CO_2 + 2H_2O$$
$$CO_2 + H_2 \rightarrow CO + H_2O$$
$$CO + 0.5S_2 \rightarrow COS$$
$$CH_4 + 2H_2S \rightarrow CS_2 + 4H_2 \quad (10)$$

The transport equation was solved for each species.

## Postprocessing

The profiles and temperature contours were obtained, the profiles of the products will be obtained, as well as those of the acid gas conversion profiles at various temperatures 1400, 1500 and 1600 K with excess air

10, 20 and 30 %, the mathematical model in Fluent will be validated with the experimental data.

## RESULTS

The numerical results of the simulation are presented below, Figure 3 shows the behavior of the molar fraction of $S_2$ along the reactor at a temperature of 1400 K at 10, 20 and 30% excess air at 300 seconds of simulation. The air and acid gas inlets are the same in the reactor causing the concentration to increase in the first 2 meters by 0.032 which is where the chemical reaction takes place the most, the molar fraction of 0.043 at the exit for 10% excess air and a value of 0.045 for 20 and 30% excess air at 1400 K.

Figure 4 shows the profile of the $S_2$ molar fraction in the reactor at a temperature of 1500°K with 10, 20 and 30% excess air at 300 seconds of simulation. The concentration increases in the first 3 meters up to 0.032 because it is where the reaction gases come together and where the greatest reaction takes place and at the end it has a value of 0.042, for 10% excess air and 0.045 for 20% and 0.046 for 30% excess air at 1500°K.

Figure 5 shows the profile of the molar fraction of $S_2$ in the reactor at a temperature of 1600 ° K at 10, 20 and 30% excess air at 300 seconds of simulation. As in the other cases, the concentration increases in the first meters of the reactor length up to 0.042 and at the exit there is less reaction and a value of 0.046 is obtained for 10% excess air and 0.055 for 20% and 0.054 for 30% excess air at 1600 K. It is observed that there is a greater conversion of $S_2$ at 1600 ° K and at 30% excess air.

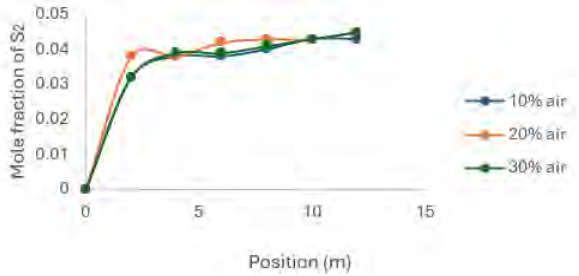



**Figure 3.** Mole fraction profiles of $S_2$ at 1400 K with 10, 20 and 30% excess air in the SRU reaction oven.

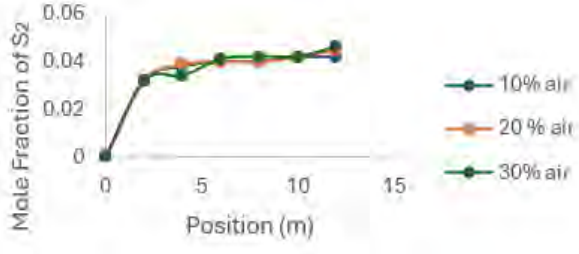



**Figure 4.** Mole fraction profiles of $S_2$ at 1500 K with 10, 20 and 30% excess air in the SRU reaction oven.

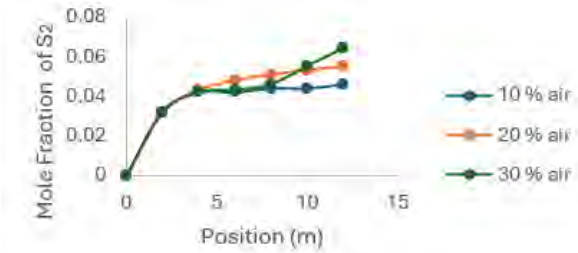



**Figure 5.** Mole fraction profiles of $S_2$ at 1600 K with 10, 20 and 30% excess air in the SRU reaction oven.

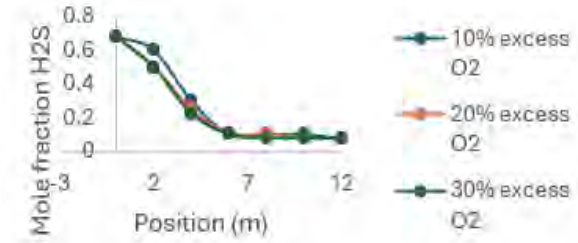



**Figure 6.** Mole fraction profiles of $H_2S$ at 1400 K with 10, 20 and 30% excess air in the furnace at 300 seconds of simulation.

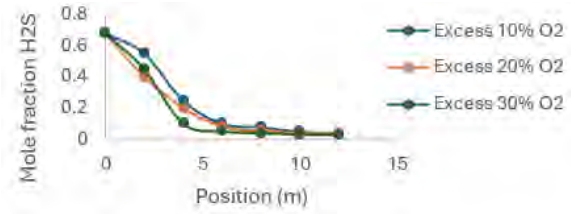



**Figure 7.** Mole fraction profiles of $H_2S$ at 1600 K with 10, 20 and 30% excess air in the furnace at 300 seconds of simulation.

The following results show the acid gas ($H_2S$) conversion profile at the various temperatures 1400, 1500 and 1600 K and with the various excesses of air 10, 20 and 30% respectively. The fluctuations in figures 3, 4 and 5 depend on the reaction turbulence and the equipment design.

Figure 6 shows the H2S conversion profiles in the reactor at 1400 K at different air excesses 10, 20 and 30%, it starts with a value of 0.68 molar fraction of acid gas, after 4 and 5 meters it consumes up to 0.1, and at the reactor exit it reaches a value of 0.075, with a conversion of 89.12%, due to the design of the equipment, it could be raised if there was more contact and turbulence of the reactants.

Figure 7 shows the $H_2S$ conversion profiles in the reactor at 1600 K at different air excesses 10, 20 and 30%, it starts with a value of 0.68 molar fraction of acid gas at the inlet, after 4 and 5 meters it is consumed up to 0.05 is where the reaction takes place, at the reactor outlet it reaches a value of 0.03, a conversion of 97.64% is

obtained, this is similar to the experimental conversion with a value of 97.98%.

The results are presented only as a function of axial position (graph 1-D) to analyze the behavior profiles on action lines in the reactor. No experimental points were added in the figures to show how the model compares to reality, because I do not have all the experimental data from the company, only output results.

The temperature as a function of the molar fraction of $CO_2$, CO and COS, $H_2O$ species with 30% excess air was the best result, compared with the industrial data of Abadan Oil Refining Company. $S_2$, $SO_2$ and $H_20$ species tend to increase at the exit of the Claus furnace, and $CO_2$, COS and CO tend to decrease.

The results of the simulation were compared with the experimental data of the Abadan Oil Refining company. Th results of the simulation for 30% excess air and the experimental data for the species of $S_2$, $SO_2$, CO, $CO_2$, $H_20$, COS and $H_2S$. The relative error with respect to the temperature of 1400, 1500 and 1600 K is 0.02, 0.01 and 0.02% respectively.

## CONCLUSIONS

In this work, the SRU (sulfur recovery unit) process was analyzed to improve the performance of the reaction and sulfur recovery using the CFD tool, a standard k-ϵ turbulence model, an energy model with convective transport and mass transport were used. with chemical reaction using the Finite - rate/Eddy model. - Proposed model for the destruction of acid gases ($H_2S$ and $CO_2$).

This work presents a CFD analysis controlling the temperature and excess air of 10, 20 and 30% to improve the reaction performance, outlet temperature, sulfur recovery. It was obtained a good approximation with the experimental results of the industrial process of the Abadan Oil refinery, Iran. Control temperatures of 1400, 1500 and 1600 K were analyzed, as well as excess air of 10, 20 and 30% respectively. It was found that at the highest temperature of 1600 K and at 30 of excess air there is a higher reaction yield, producing 0.0728 mole fraction of $S_2$, compared to the experimental one of 0.0709, which has an error of 2.6 %.

For the conversion of $H_2S$, a value of 0.03 mole fraction was obtained at the reactor outlet compared to the experimental one, with an error of 4%, a good approximation to the experimental results of the process. was obtained a conversion of the acid gas ($H_2S$) of 95.64%, which is quite good compared to the experimental one. The results of simulation or numerical predictions confirm that, at higher temperatures and higher excess air, the acid gas increases combustion and sulfur conversion. The results confirm that the excess air for combustion and more than 30% and with a temperature of 1600 K improve the recovery of sulfur and reduce the amount of pollutants such as COS and $CO_2$ and CO. The experimental conversion of sulfur was 99.1% and the conversion for the temperature of 1600 K and 30% with excess air was 99.5% with a percentage deviation of 0.4%, for the other temperatures of 1400, 1500 with 30% with excess air conversion was lower with a value of 98%.

## ACKNOWLEDGEMENTS

Acknowledge to the University of Guanajuato and the University of Veracruz for their support in the development of this project and Dr. Fabian Salvador Mederos Nieto for his support in this work, as well as to the research project SIP - IPN- 20231028

## REFERENCES

1. El-Bishtawi, Haimour No' man, Claus recycle with double combustion process. Fuel Process Technol 86:245–260 (2004) https://doi.org/10.1016/j.fuproc.2004.04.001
2. Dowling, N.I., Hyrne, J.B., Moon, D.L., Clark, P.O., Un horno Claus de craqueo térmico de $H_2S$ Modificación Para la Producción de Hidrógeno, Reunión Técnica Anual (1995)
3. Maddox RN, Gas Conditioning and Processing: gas and liquid sweetening. Campbell Petroleum Series, Norman, Oklahoma (1983)
4. Monnery, W.D., Svrcek, W.Y., Behie, L.A., Modelling the modified Claus process reaction furnace and the implications on plant design and recovery, The Canadian Journal of Chemical Engineering, 71, 711-724, (1993) https://doi.org/10.1002/cjce.5450710509
5. Abdoli P, Hosseini SA, Abdul Mujeebu M, Influence of O2 enrichment in dry air on combustion temperature, contaminant production and sulfur recovery, in SRU reaction furnace. Forschung im Ingenieurwesen 82:99–106, (2018). https://doi.org/10.1007/s10010-017-0260-y
6. Bayazid Mahmoodi, A new acid gas destruction kinetic model for reaction furnace of an industrial sulfur recovery unit: A CFD study, Chemical Engineering Science, 256, 117692 (2022). https://doi.org/10.1016/j.ces.2022.117692
7. Pedram Abdoli1, Seyed Amin Hosseini, Muhammad Abdul Mujeebu, Effect of Preheating Inlet Air and Acid Gas on the Performance of Sulfur Recovery Unit—CFD Simulation and Validation, Forsch Ingenieurwesen, 83:81–89 (2019) https://doi.org/10.1007/s10010-019-00299-9
8. Samane Zarei, Hamid Ganji, Maryam Sadi, Mehdi Rashidzadeh, Kinetic Modeling and Optimization of Claus Reaction Furnace, Journal of Natural Gas

Science and Engineering, 747 – 757, (2016) https://doi.org/10.1016/j.jngse.2016.03.086
9. ANSYS, Inc., (2016), ANSYS Fluent User's Guide. Canonsburg, PA, USA. https://www.afs.enea.it/project/neptunius/docs/fluent/html/ug/main_pre.htm

© 2025 by the authors. Licensed to PSEcommunity.org and PSE Press. This is an open access article under the creative commons CC-BY-SA licensing terms. Credit must be given to creator and adaptations must be shared under the same terms. See https://creativecommons.org/licenses/by-sa/4.0/



Systems & Control Transactions

**Research Article - Peer Reviewed Conference Proceeding**
ESCAPE 35 - European Symposium on Computer Aided Process Engineering
Ghent, Belgium. 6-9 July 2025
Jan F.M. Van Impe, Grégoire Léonard, Satyajeet S. Bhonsale,
Monika E. Polańska, Filip Logist (Eds.)

PSE PRESS

# A Transparent Techno-Enviro-Economic Assessment of a Coal-Fired Power Plant: Integrating Biomass Co-Firing and $CO_2$ Sequestration Technology in a Carbon-Priced Environment

**N. F. E. Nor Fadzil[a], N. Abdul Manaf[a*] and N. Shah[b]**

[a] Department of Chemical and Environmental Engineering, Malaysia-Japan International Institute of Technology (MJIIT), Universiti Teknologi Malaysia, Kuala Lumpur, Malaysia
[b] Department of Chemical Engineering, Imperial College London, SW7 2AZ, United Kingdom
* Corresponding Author: norhuda.kl@utm.my

## ABSTRACT

The integration of carbon capture and storage (CCS) into coal and biomass co-firing systems (CBCCS) offers a promising solution for reducing carbon emissions in electricity generation. This study evaluates hypothetical scenarios in Malaysia and Indonesia, focusing on techno-economic-environmental transparency. The analysis shows a negligible change in plant net efficiency (~1%) across biomass co-firing ratios of 5-20% in both countries. The capture penalty increases at higher biomass ratios, particularly at 20% co-firing, due to higher auxiliary power demands and steam extraction. As biomass share increases, net $CO_2$ emissions decrease by an average of 43% in Malaysia and 34% in Indonesia. Economic evaluations show a positive revenue increase for Malaysia at a 20% co-firing ratio, while Indonesia faces a revenue deficit (0.6%) under the same condition, mainly due to an unattractive carbon price and feed-in tariff from 2027 onward. Malaysia faces a higher risk of stranded assets due to earlier retirement plans, compared to Indonesia. As the co-firing ratio increases, the risk of stranded assets decreases by 3% in Malaysia and 0.6% in Indonesia. The present work showcases the intricate and synergistic effects of energy and commodity market dynamics from a micro-sector perspective towards plant revenue. This allows both Indonesia and Malaysia to learn from each other in their quest to achieve energy independence and security. Collaboration in tapping renewable sources is one way the two countries can secure energy for their domestic needs while addressing the challenges of carbon lock-in and the impact of stranded assets.

**Keywords**: Carbon Dioxide Sequestration, Energy, Genetic Algorithm, Matlab, Renewable and Sustainable Energy

## INTRODUCTION

The energy sector remains the largest contributor to global greenhouse gas emissions, with coal accounting for approximately 45% of total emissions from fuel combustion [1]. To address this issue, two promising strategies have been identified, which include cofiring coal with biomass for power generation (CB) and retrofitting coal-fired power plants with carbon capture and storage (CCS) technology. According to the Intergovernmental Panel on Climate Change (IPCC), these strategies play a significant role in supporting the Paris Agreement targets [2]. Many studies have been carried out on the performance of biomass cofiring integrated with CCS system (CBCCS), encompassing both technical and environmental perspectives. For instance, Cebrucean et al. [3] identified that biomass co-firing with a supercritical coal plant equipped with a carbon capture system can enhance energy and environmental performance, achieving a 2.4% increase in net efficiency and a 6% reduction in $CO_2$ emissions compared to conventional subcritical plants. How-

ever, at a 30% co-firing ratio, net plant efficiency is reduced by 1%, negatively impacting the plant's economic viability. In another study, approximately a 14% reduction in net plant efficiency was observed at a 10% biomass co-firing ratio. This significant discrepancy is influenced by the type of biomass and coal plant technology. While co-firing ratios exceeding 10% have been shown to result in net negative $CO_2$ emissions, Yang et al. [4] reported that higher $CO_2$ capture rates are directly associated with significant declines in net plant efficiency, which typically ranges from 28% to 31%. Despite several studies available on the ground, the global commercialization of CBCCS technology remains sluggish. This can be attributed to factors such as the limited availability of biomass resources, socio-economic barriers, the absence of robust policies and regulatory frameworks, and the risk of stranded assets (SA) faced by coal-fired power plants [5-6]. In this paper, we evaluate the techno-enviro-economic performance of the CBCCS system, taking into account carbon price and the impact of stranded assets on the plant's lifetime operation. This work addresses concerns raised by the International Energy Agency (IEA), emphasizing the need for a reliable framework that ensures transparency to support CBCCS technology as one of the carbon dioxide removal solutions[7].

## METHODOLOGY

### An improved genetic algorithm (GA) optimization algorithm

Present work adapts and further enhances a previously developed GA optimization algorithm executed in Mathlab software [8]. The enhancement focuses on biomass co-firing in a supercritical power plant (direct co-firing) integrated with CCS system (i.e. monoethanolamine (MEA) – based post combustion carbon capture)). For this study, it is assumed that the coal plant does not require significant modifications for the carbon capture retrofit or biomass co-firing integration. The analysis also includes the cost of stranded assets, evaluated based on both physical and economic lifetimes, alongside the feed-in tariff (FiT). This approach provides new insights into the financial risks and benefits posed by the evolving power sector.

The objective function of the enhanced GA optimization remains focused on maximizing plant revenue from 2024 to 2034 by optimizing the power plant load ($PP_N$) and $CO_2$ capture rate. Table 1 presents the details of the optimization enhancements. While this paper presents only significant and new information and approaches, readers can reference previous works for comprehensive background information [9-10].

As referenced in Table 1, the revenue formulation is illustrated in the equation (1).

$$Max(Revenue) = \int E\ (Q_e - Q_p)\ dt - \int C\ (Q_c)\ dt - PP_{op} - CCS_{op} - CCS_{cap} + \int F\ (Q_L)\ dt \quad (1)$$

Where *E, C* and *F* represent the electricity price, carbon price and feed-in-tariff for biomass, while $Q_e$, $Q_p$, $Q_c$, $Q_L$ are power plant net load, total power penalty, $CO_2$ emissions and proportion of electricity produced from biomass in co-firing power plant. Since biomass is considered as carbon neutral fuel thus burning biomass is not counted for carbon tax[11-12]. In this work, we consider a stringent and extreme condition, where no free allowance provided to the power plant.

**Table 1:** Detail of the GA optimization enhancement adapted in present study.

| **Items** | **Ref work** [9] | **Present work** |
|---|---|---|
| Power plant (660 MW) | Subcritical | Supercritical |
| Non-linear prediction model | $Q_{reb}$ =f($x_i$)<br>Aux = f($x_i$) | $Q_{reb}$ = -20% *(f($x_i$)[3]<br>Aux = - 8* f($x_i$) [3] |
| Objective function | Revenue (without FiT) | Revenue (with FiT and CCS capital cost) |
| Inequality constraint | $c_1$:$PP_N$ < $PP_G$ | $c_1$: $PP_N$ < $PP_G$<br>$c_2$: $CO_2^E$ < $CO_2^T$ |
| Fuel | Coal | Coal and biomass (palm kernel shell, PKS) |
| Stranded asset | Not evaluated | Evaluated by the influence of power plant load ($x_i$) |

On top of ensuring that the $PP_N$ of the power plant does not exceed the gross load ($PP_G$), present work incorporates carbon neutrality and emission constraints into the enhanced optimization algorithm, as follows.

```
max_CO2_threshold = 0.5
c2 = ((Total_CO2_Emissions/PP_load) -
max_CO2_threshold)
```

This constraint ($c_2$) ensures that the $CO_2$ emissions produced at each interval remain below a specified threshold (max_$CO_2$_threshold) to align with carbon neutrality/emission reduction goals. While a standard methodology (ISO 14068-1) exists for assessing carbon neutrality [13], no specific emission threshold has been formally established yet. Therefore, this work sets the threshold at 0.5 tonnes $CO_2$/MWh, based on China's coal benchmarking for power decarbonization from 2018 to 2030. This value aligns with the averaged benchmark outlined in Sustainable Development Goals (SDGs)[14]. For the evaluation of stranded asset (SA), the calculation was

adapted from [6] as shown in equation (2).

$$SA = OC_{cap} * K * \left(\frac{L_R}{C_{LT}}\right) * LF \quad (2)$$

Where $OC_{cap}$ is an overnight capital cost (USD/kW), *K*, $L_R$ and $C_{LT}$ are the plant capacity, remaining lifetime and coal plant lifetime. This work considers SA based on physical ($SA_{LP}$) and economic lifetimes ($SA_{LE}$). Where physical lifetime is generally longer (standard/technical lifetime) than the economic lifetime (early retirement). In this work, load factor (LF) is being considered to reflect the operational deficiency over the years of co-firing power plant. The LF is dynamically calculated as in equation (3).

$$LF = \frac{PP_N}{700} \quad (3)$$

While other researchers have used intricate and financially detailed methods to evaluate SA[15], this work considers a simple and tactical method as a preliminary approach.

## Scenario setting

Four scenarios representing three ranges of biomass ratios (by low heating value, LHV) are evaluated based on hypothetical situations in Malaysia and Indonesia. As both countries are the major producers of palm oil [16], there is significant potential for the adoption and development of biomass co-firing technology within their energy infrastructure. However, as developing nations with dynamic economic and policy landscapes, both countries face considerable risks of stranded assets and carbon lock-in. Therefore, understanding the technical, environmental and economic implications is critical to effectively evaluate their exposure to stranded asset risks and align with emission reduction targets, particularly for hybrid technologies like the CBCCS system. Table 2 presents the input data used in the enhanced optimization algorithm, including the associated costs for the CBCCS system. Several assumptions were made due to the unavailability of certain data. This study does not consider biomass pre-treatment, assuming that the power plant receives biomass with suitable characteristics for direct use.

**Table 2:** Input data and costs assumptions of CBCCS plant.

| Parameters | Malaysia | Indonesia |
|---|---|---|
| Plant commissioning | Tanjung Bin, 2016 [17] | Cirebon, 2012 [18] |
| PKS ratio (%) | 0, 5, 10, 20 | |
| $PP_G$ (MW) | Similar pattern [19] | |
| FiT (USD/MWh) | 62.60[20] | 60.00[21] |
| Electricity price (USD/MWh) | 2024: [22] 2025-2034 :10% increment[23] | 2024: [24] 2025-2034: 20% increment |
| Coal price (USD/tonne) | 2024 [25] 2025-2034: 12% [26] | 2024: [27] 2026 - 2034: Follow MAS |
| Biomass price (USD/tonne) | 2024: 53.50[28] 2029-2034: 300 [28] | 2024: 140 2025-2034: 150 |
| $OC_{cap}$ (USD/kW) | 6,901 based on 4,759 (2010) [29] | |
| LHH (MJ/kg) | Coal: 24.4, PKS: 20.09 | |
| EF (kg $CO_2$/MJ) | Coal: 0.0959, PKS: 0.112 | |
| $CB_{Lp}$ | 35 [6] | |
| $CB_{LE}$ | 2044 [30] | 2035 [31] |
| CB operating cost (USD) | 1,733,000 | |
| CCS capital cost (USD) | 10,420,657 [8] | |
| $CO_2$ price (USD/tonne) | 8.00 [32] | 2.10 [33] |
| MEA price (USD/tonne) | 1,940[34] | |
| Transportation and storage (USD) | 25[35] | |

# RESULTS AND DISCUSSION

## Technical transparency

The net plant efficiency is a critical indicator of the energy conversion performance of a system. According to Table 3, the analysis reveals a marginal efficiency variation from 29.8% to 31% across the co-firing spectrum (0–20%) for both countries, with an approximate difference of 1% point. This noteworthy phenomenon is attributed to the sensitivity and flexibility of the optimization algorithm, which requires the power plant load to dynamically meet the objective function while adhering to the constraint ($c_1$) at each time interval. This finding is distinct with existing literature, where increasing the biomass co-firing ratio typically leads to a decline in net plant efficiency. Such depreciation is often directly related to the high $CO_2$ capture rate, commonly set at 90% [4]. In contrast, the current work considers a dynamic capture rate influenced by carbon pricing and emission constraints ($c_2$), which we believe more accurately reflects real-world flexible CBCCS operations. This aligns with the findings of [3], which showed that the net efficiency of power plants increases when the capture efficiency is reduced from 90% to 50%. This improvement is primarily due to the reduced steam extraction from the steam cycle to meet the heat requirements of the capture unit, allowing more steam to be available for power generation. Additionally, operating the power plant in a baseload scenario may not generate significant revenue for

plant owners. The $CO_2$ capture energy penalty exhibits an upward trajectory for both nations, with Malaysia's requirements increasing from 9.66 to 11.53 MJ/kg $CO_2$ and Indonesia's from 9.24 to 11.51 MJ/kg $CO_2$ as the biomass ratio escalates. This range is technically accepted since maximum energy penalty associated with MEA-capture system (retrofit with coal plant) can reach up to maximum 8.00[36] to 10.23 MJ/kg $CO_2$ [37]. Where, this escalation in energy penalty is consistent with the technical challenges including increased parasitic loads from auxiliary equipment and reboiler duty from the steam extraction/solvent regeneration [3,38]. Based on the optimization results presented in this study, it is suggested that retrofitting carbon capture technology into a supercritical plant with a co-firing ratio of 5–20% does not impose a significant efficiency penalty, provided the plant is allowed to operate flexibly. This technical transparency highlights a critical trade-off between achieving higher biomass co-firing ratios for enhanced carbon reduction and maintaining optimal plant performance, particularly in the context of emerging economies transitioning to low-carbon energy systems

**Table 3:** Technical performance of CBCCS system under the carbon price regime.

| **Co-firing ratio** | | **0** | **5** | **10** | **20** |
|---|---|---|---|---|---|
| Net plant | MAS | 29.8% | 30.6% | 30.9% | 31.0% |
| eff. (LHV %) | IND | 30.5% | 30.5% | 30.5% | 31.0% |
| $CC_{penalty}$ | MAS | 9.66 | 9.76 | 10.30 | 11.53 |
| (MJ/kg $CO_2$) | IND | 9.24 | 9.78 | 10.23 | 11.51 |

## Environmental transparency

The environmental performance analysis of the CBCCS system reveals distinct $CO_2$ emission patterns across varying co-firing ratios, demonstrating the system's potential for carbon mitigation. As shown in Figure 1, increasing the co-firing ratio results in a notable reduction in net $CO_2$ emissions. At 20% biomass co-firing, the net $CO_2$ emissions account for 43% and 34% of the total $CO_2$ emissions from co-firing plant in Malaysia and Indonesia, demonstrating a trend similar to that observed in [3]. Without co-firing, coal plants generate an average of 65% net $CO_2$ emissions, emphasizing the significant contribution of biomass co-firing to $CO_2$ emission mitigation. However, the total $CO_2$ emissions from the biomass combustion of a biomass co-firing plant increase by 17% compared to a coal plant due to the adoption of co-firing. Since $CO_2$ emissions from biomass combustion are sequestered as biomass regrows, sustainably managed biomass is considered carbon neutral. These findings underscore the effectiveness of biomass co-firing in reducing fossil-based $CO_2$ emissions by substituting a portion of fossil carbon with a renewable carbon source. The total captured $CO_2$ exhibits slight variation across different co-firing ratios, reflecting the complex interaction between maintaining $CO_2$ emissions below a specified threshold ($c_2$) and maximizing plant revenue. This observation aligns with [39] , which identified that biomass co-firing ratios significantly influence carbon capture performance due to variations in fuel composition and combustion characteristics. Notably, under higher carbon pricing scenarios, CBCCS plants in Malaysia tend to reduce their total capture percentage to optimize economic outcomes. The dynamic interplay between these emission components highlights the potential of CBCCS as a viable negative-emission technology, particularly in regions with access to sustainable biomass resources and existing coal power infrastructure.

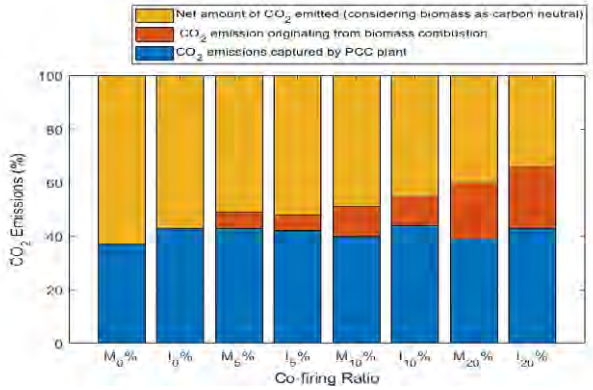



**Figure 1.** Environmental performance of CBCCS system under at various biomass co-firing ratio under carbon price regime

## Economic transparency

Figure 2 illustrates the economic performance of the CBCCS system, focusing on plant revenue, $CO_2$ emission costs, and stranded assets (SA) in Malaysia and Indonesia. In Malaysia, revenue increases modestly from USD 3 billion to USD 3.5 billion as co-firing ratios rise to 20%, while Indonesia sees higher revenue due to its higher electricity prices and low carbon price. Both countries show exponential growth in FiT rates, highlighting the need for financial incentives to offset higher operational costs. The $CO_2$ emission costs decline with higher co-firing ratios, with Malaysia consistently having higher costs due to its higher carbon price. For stranded assets under the physical lifetime, Malaysia shows a higher baseline (USD 2.1 billion) compared to Indonesia (USD 1.8 billion), but both exhibit a slight decline with higher co-firing, suggesting biomass integration helps hedge against future carbon regulations. The economic lifetime SA risk remains stable, though Malaysia consistently faces higher risks. These results indicate that CBCCS systems, while requiring significant initial investment and policy support, offer substantial benefits in reduced carbon costs and stranded asset risk. The differences system, while requiring significant initial investment policy support, offer substantial benefits in reduced and

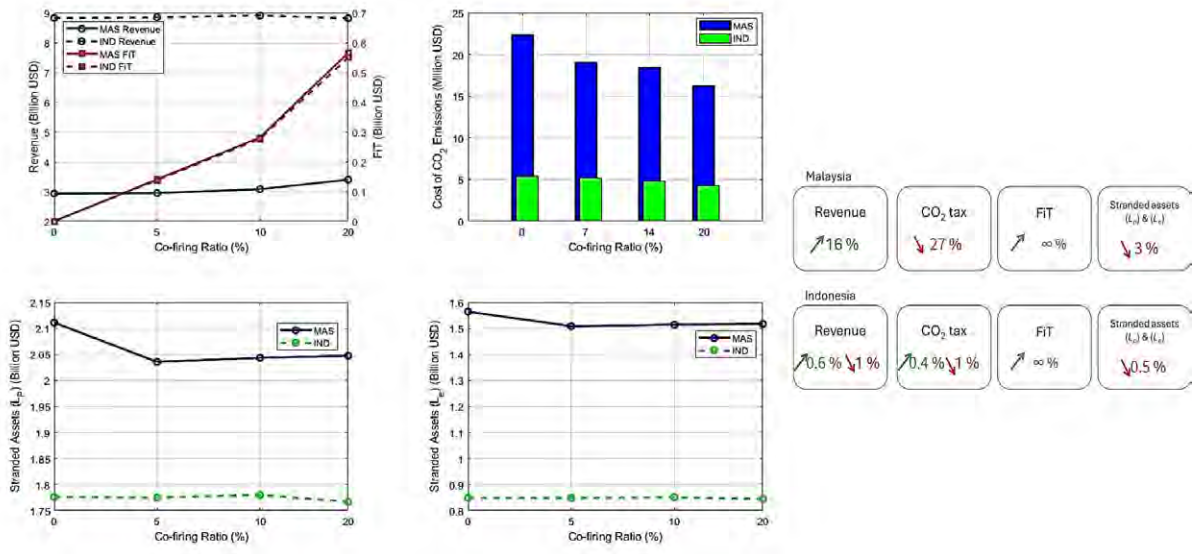



**Figure 2.** Economic performance of CBCSS system at various biomass co-firing ratio under the carbon price regime**.**

between Malaysia and Indonesia are mainly due to infrastructure age, policy frameworks, and market dynamics. The comparative dashboard (Figure 2, right) provides a scalable performance overview from 2024 to 2034, serving as a guideline for future implementation.

## CONCLUSION

Biomass co-firing (5-20%) in Malaysia and Indonesia shows minimal impact on plant efficiency (~1%) but manage to reduce net $CO_2$ emissions (43% Malaysia, 34% Indonesia). At 20% co-firing, Malaysia sees revenue growth even under the high carbon price, while Indonesia faces deficit. This preliminary work shows that Malaysia has higher stranded asset risk, though increased co-firing slightly reduces this risk in both countries**.**

## ACKNOWLEDMENTS

This study was supported by the Ministry of Higher Education under Fundamental Research Grant Scheme (FRGS/1/2024/TK08/UTM/02/17) and Universiti Teknologi Malaysia through the Universiti Teknologi Malaysia Fundamental Research (UTMFR) Grant, project no. Q.K130000.3843.22H31.

## REFERENCES

1. IEA. Greenhouse Gas Emissions from Energy Data Explorer.
2. IPCC. Global Warming of 1.5 ºC —
3. Cebrucean D, Cebrucean V, Ionel I. Modeling and performance analysis of subcritical and supercritical coal-fired power plants with biomass co-firing and CO2 capture. *Clean Technol Environ Policy* 22:153–169 (2020) https://doi.org/10.1007/s10098-019-01774-1
4. Yang B, Wei YM, Hou Y, et al. Life cycle environmental impact assessment of fuel mix-based biomass co-firing plants with CO2 capture and storage. *Appl Energy* 252:113483 (2019) https://doi.org/10.1016/j.apenergy.2019.113483
5. Babin A, Vaneeckhaute C, Iliuta MC. Potential and challenges of bioenergy with carbon capture and storage as a carbon-negative energy source: A review. *Biomass Bioenergy* 146:105968 (2021) https://doi.org/10.1016/j.biombioe.2021.105968
6. Edwards MR, et al. Quantifying the regional stranded asset risks from new coal plants under 1.5 °C. *Environ Res Lett* 17:24029 (2022) https://doi.org/10.1088/1748-9326/ac4ec2.
7. IEA. https://www.iea.org/energy-system/carbon-capture-utilisation-and-storage/bioenergy-with-carbon-capture-and-storage
8. Abdul Manaf N, Milani D, Abbas A. An intelligent platform for evaluating investment in low-emissions technology for clean power production under ETS policy. *J Clean Prod* 317:128362 (2021) https://doi.org/10.1016/j.jclepro.2021.128362
9. Abdul Manaf N, Abbas A. Economic and environmental sustainability of low-carbon power generation: Relevancy in the Malaysia Green Technology Master Plan (GTMP). *J Chem Technol Biotechnol* 94:1425–1432 (2019) https://doi.org/10.1002/jctb.5901
10. Qadir A, Sharma M, Parvareh F, et al. Flexible

dynamic operation of solar-integrated power plant with solvent-based post-combustion carbon capture (PCC) process. *Energy Convers Manag* 97:7–19 (2015) https://doi.org/10.1016/j.enconman.2015.02.074
11. Rahmanta MA, Aprilana A, Ruly, Cahyo N, et al. Techno-economic and environmental impact of biomass co-firing with carbon capture and storage in Indonesian power plants. *Sustainability* 16:83423 (2024) https://doi.org/10.3390/su16083423
12. Huang Q, Feng Q. A bi-level model for coal power decarbonization via biomass co-firing considering CO2 emission trading system. *Energy* 305:132385 (2024) https://doi.org/10.1016/j.energy.2024.132385
13. ISO. https://www.sgs.com/en/services/iso-14068-1-verification-climate-change-management-transition-to-net-zero-carbon-neutrality.
14. IEA. https://www.iea.org/reports/chinas-emissions-trading-scheme.
15. Zhang W, Ren M, Kang J, et al. Estimating stranded coal assets in China's power sector. *Util Policy* 75:101352 (2022) https://doi.org/10.1016/j.jup.2022.101352
16. Papilo P, et al. Palm oil-based bioenergy sustainability and policy in Indonesia and Malaysia: A systematic review and future agendas. *Heliyon* 8:e10919 (2022) https://doi.org/10.1016/j.heliyon.2022.e10919
17. Global Power Journal. https://globalpowerjournal.com/2016/04/11/tanjung-bin-energy-power-plant-malaysia/.
18. Azwar AS. https://www.thejakartapost.com/news/2012/10/19/cirebon-power-plant-stream-java-and-bali.html.
19. Suruhanjaya Tenaga (Energy Commission of Malaysia). https://www.st.gov.my/en/web/general/details/364
20. SEDA. https://www3.seda.gov.my/iframe/.
21. Halstead M, Mikunda T, Cameron L. CONCEPT.
22. Tenaga Nasional Berhad. https://www.tnb.com.my/residential/pricing-tariffs.
23. Ahmad NH, Dahlan NY, Bazin NEN, et al. Modelling base electricity tariff under the Malaysia incentive-based regulation framework using system dynamics. *Int J Electr Comput Eng* 13:2 (2023) http://doi.org/10.11591/ijece.v13i2.pp1231-1240
24. Aditya IA, et al. Biomass power plant prospects in Indonesia's energy transition: IPP and PLN perspectives. *Heliyon* 10:e38970 (2024) https://doi.org/10.1016/j.heliyon.2024.e38970.
25. Market Insiders. https://markets.businessinsider.com/commodities/coal-price.
26. Agnolucci P, Makarenko N, Guerra M. https://blogs.worldbank.org/en/opendata/international-coal-price--higher-for-longer.
27. Ordonez JA, Jakob M, et al. Coal, power and coal-powered politics in Indonesia. *Environ Sci Policy* 123:44–57 (2021) https://doi.org/10.1016/j.envsci.2021.05.007
28. Ahmad SM, Ismail A, Wahab NA, et al. Comparative analysis of current biomass utilization by palm oil mills in Peninsular Malaysia. *J Sustain Sci Manag* 19:166–176 (2024) http://doi.org/10.46754/jssm.2024.07.009
29. EIA. U.S. Energy Information Administration - EIA - Independent Statistics and Analysis
30. Zhai Yun T. https://theedgemalaysia.com/node/716752.
31. ADB. https://www.adb.org/news/new-agreement-aims-retire-indonesia-660-mw-coal-plant-almost-7-years-early.
32. Zhai Yun T. https://theedgemalaysia.com/article/cover-story-getting-ready-carbon-pricing.
33. Andriansyah SHL.. https://amro-asia.org/cap-first-and-then-tax-carbon-pricing-in-indonesia/.
34. Yang B, et al. Life cycle cost assessment of biomass co-firing power plants with CO2 capture and storage considering multiple incentives. *Energy Econ* 96:105173 (2021) https://doi.org/10.1016/j.eneco.2021.105173
35. Ye B, et al. Technical and economic analysis of amine-based carbon capture and sequestration at coal-fired power plants. *J Clean Prod* 222:476–487 (2019) https://doi.org/10.1016/j.jclepro.2019.03.050
36. Gao W, et al. Industrial carbon dioxide capture and utilization: State of the art and future challenges. *Chem Soc Rev* 49:8584–8686 (2020) https://doi.org/10.1039/D0CS00025F
37. Joshi PK. Techno-economic assessment of carbon capture from low concentration streams. (2023)
38. Emenike O, Michailos S, Finney KN, et al. Initial techno-economic screening of BECCS technologies in power generation for a range of biomass feedstock. *Sustain Energy Technol Assess* 40:100743 (2020) https://doi.org/10.1016/j.seta.2020.100743
39. Liu L, et al. Recent advances of research in coal and biomass co-firing for electricity and heat generation. *Circ Econ* 2:100063 (2023) https://doi.org/10.1016/j.cec.2023.100063

© 2025 by the authors. Licensed to PSEcommunity.org and PSE Press. This is an open access article under the creative commons CC-BY-SA licensing terms. Credit must be given to creator and adaptations must be shared under the same terms. See https://creativecommons.org/licenses/by-sa/4.0/



Systems & Control Transactions

**Research Article - Peer Reviewed Conference Proceeding**
ESCAPE 35 - European Symposium on Computer Aided Process Engineering
Ghent, Belgium. 6-9 July 2025
Jan F.M. Van Impe, Grégoire Léonard, Satyajeet S. Bhonsale,
Monika E. Polańska, Filip Logist (Eds.)

PSE PRESS

# Genetic Algorithm-Driven Design of CCUS and Hydrogen Pipeline Networks: Decentralised Expansion with Complex Geographical Constraints

**Joseph Hammond[a] and Solomon Brown[a]***

[a] School of Chemical, Materials, and Biological Engineering, University of Sheffield, Sheffield, S1 3JD, UK
* Corresponding Author: s.f.brown@sheffield.ac.uk

## ABSTRACT

The development of Carbon Capture, Transport, and Storage (CCTS) and hydrogen pipeline networks is crucial for achieving deep decarbonisation in industrial sectors. However, existing network design models often assume perfect foresight, limiting their applicability to real-world infrastructure planning, which is inherently uncertain and iterative. This study introduces a novel rolling-horizon methodology for pipeline network expansion, leveraging a genetic algorithm-based approach that allows for adaptive routing and incremental infrastructure development. By comparing rolling-horizon designs to 2050-optimised networks in a case study of the Humber region in the UK, the analysis highlights the trade-offs between adaptability and cost efficiency. Results indicate that while rolling-horizon approaches better reflect real-world decision-making, they also introduce inefficiencies, increasing capital expenditures by approximately 8% for both hydrogen and CCTS infrastructure. Additionally, the study examines the economic risks associated with transitioning from blue to green hydrogen production, revealing a 20-fold increase in CCTS costs per tonne of $CO_2$ when hydrogen production shifts to green. The findings underscore the importance of integrating uncertainty-aware strategies in infrastructure planning to mitigate inefficiencies while maintaining adaptability to technological and policy changes.

**Keywords**: Carbon capture transport and storage, Hydrogen, GIS, Infrastructure, Rolling-horizon

## BACKGROUND

Transitional pipeline infrastructures, such as Carbon Capture, Transport, and Storage (CCTS) and hydrogen networks, have the potential to facilitate a low-carbon transition in fossil fuel dependent industries, particularly in foundational sectors such as iron and steel, chemicals, and power generation [1]. However, the path to sectoral and site-specific decarbonisation is paved with uncertainties [2]. These challenges arise from the dynamic evolution of technologies, shifting policy priorities, and the need to align stakeholder decisions, all of which complicate the development and long-term adaptability of these infrastructures [3].

Spatially-explicit computational models enable the design and evaluation of pipeline networks by incorporating geographical, technological, and policy-related constraints. To create resilient and adaptive infrastructures, these models must address both spatial and temporal complexities. The spatial aspect involves determining optimal routes while accounting for geographical and environmental constraints, whereas the temporality considers how these networks evolve over time in response to changing demands, technologies, and policy goals.

Static models, offering a snapshot design at a single point in time, determine the optimal topology and specifications of the pipeline infrastructure for a specific configuration of sites. Topological considerations require a spatially-explicit model to ascertain the route. This has mostly been achieved using grid-based methods and pathfinding algorithms, such as the well-known A* algorithm, to develop candidate networks that a subsequent optimisation method can utilise to optimise the infrastructure [4,5]. More recently, Hammond et al. [6] presented a graph-based, multi-stage approach for pipeline

infrastructure design that generates networks across a geographically complex region for a given set of sites. Removing the need for a candidate network structure and optimising the route directly.

While static models provide valuable insights, they fail to capture the dynamic nature of infrastructure development. Temporal dynamism is crucial for understanding the impact of changing conditions over time. Existing models often assume perfect foresight in hydrogen [7,8] and CCTS [9-11] network design, where infrastructure is designed to accommodate a known future state. André et al. applied a backward approach to describe the time development of hydrogen networks, starting with the target year and retrospectively determining the configurations, therefore optimising the infrastructure for the end point. Becattini et al. [10] provided a more advanced perfect foresight approach which leverages the uptake forecast to optimise the CCTS network across all time steps. The study examines a 25-year time horizon using both static and dynamic cases to discover that the optimal dynamic strategy delays the installation of infrastructure to reduce overall costs by leveraging discounted future flows.

These approaches simplify the design process but do not mirror real-world decision-making processes and constraints, limiting its applicability to network strategists and planners. Perfect foresight assumes a level of certainty and coordination that rarely exists in practice, overlooking the iterative, adaptive nature of infrastructure development. Delaying investments risks increased long-term costs, lost opportunities for early adoption, and challenges in stakeholder alignment.

In contrast, rolling-horizon models adopt a myopic approach, where infrastructure is developed incrementally in response to immediate needs and uncertainties. Few pipeline infrastructure network models utilise non-anticipatory rolling-horizons frameworks. Johnson and Ogden [12] demonstrated this approach with their HyPAT model, which simulates hydrogen infrastructure deployment under a staged, rolling-horizon framework. However, the model's broader limitation lies in its flexibility to adapt routing and pipeline design between time steps, reducing its ability to fully explore and optimise network evolution in response to shifting spatial and operational demands.

The advantages of rolling-horizon models are grounded in their capacity to address shortcomings of perfect foresight approaches. First, as Papadimitriou and Fortz [13] argue, rolling-horizon models better reflect real-world decision-making by breaking long-term plans into iterative and manageable stages. Second, they are inherently adaptive, enabling designs to respond dynamically to changes in demand, technology, and policy over time. Third, and central to this study, is the idea that strategic insights derived from perfect foresight models overlook the complexities of real-world uncertainties. Unlike static optimisations models, rolling-horizon models integrate recourse decision-making, where future uncertainties unfold sequentially, allowing adjustments at each stage based on updated information. This aligns with principles of stochastic control and dynamic programming, which highlight the benefits of making decisions that evolve over time rather than relying on fixed, foresight-dependent solutions [14].

Building on these principles, this study introduces a novel rolling-horizon methodology for designing pipeline networks that grow incrementally while addressing complex spatial constraints. Unlike existing models that assume straight-line connections between nodes [7-10] or rely on predefined candidate networks [4,5,11,12], this approach allows the network to evolve freely. By removing the reliance on candidate networks, the methodology accommodates adaptive routing configurations that reflect real geographical constraints.

To demonstrate the applicability of this approach, the study explores the co-design of CCTS and hydrogen infrastructures, with a focus on the transition from blue to green hydrogen production. This transition poses risks such as stranded assets and operational challenges, which the proposed methodology uncovers. As far as the authors are aware, no prior studies have investigated the co-design of these infrastructures with high spatio-temporal resolution and adaptability, further underscoring the novelty of this contribution.

The methodology is described in Section 2, which is applied to the case study described in Section 3. Section 4 discusses the findings and results, and Section 5 concludes this work.

# METHODOLOGY

## Network Design

The proposed methodology is built upon the multi-stage approach presented in Hammond et al. [15] and Hammond et al. [6], where the routing is defined using a modified Steiner tree with Obstacles Genetic Algorithm (StObGA) [16]. The premise is that the network, described by the genome, converges on an optimal network configuration by learning to traverse across the cost surface made up of polygonal obstacles which represent geographic constraints.

This study presents an algorithmic development that enables the rolling-horizon designs of spatially-aware routes across complex terrains. At each time step, the algorithm minimises the weight network length ($L_n^w$), as defined in Equation 1. This is calculated over the set of arcs $A$, where each arc $(i,j)$ consists of obstacle-constrained lengths ($L_{ij,o}^{obs}$) weighted by penalty $w_o$ for obstacles $o \in O$, and obstacle-free lengths ($L_{ij}^{free}$).

$$min(L_n^w) = \sum_{(i,j)\in A}(\sum_{o\in O_{ij}} L_{ij,o}^{obs} \cdot w_o + L_{ij}^{free}) \quad (1)$$

The genetic algorithm's genome, given in Equation 2, describes the infrastructure's network in two parts: 1) the locations of terminal nodes, Steiner points, and bifurcation nodes; and 2) fixed-length binary list that determines which corners points of the polygonal obstacles are activated. Bifurcation nodes are introduced as nodes that are placed along existing arcs to allow for flexible expansion from a previous network structure.

$$\big((x_1, y_1), (x_2, y_2), \dots, (x_s, y_s)\big) + [1\ 0\ 1\ 0\ 0\ 0\ 1\ 1\ 0\ 0] \quad (2)$$

The pipeline design optimisation is a MINLP formulation that minimises the total pipeline costs ($C$) according to the objective function given in Equations 3 and 4. The capital cost ($C_{ij}^C$) for each arc $(i, j)$ in the network is determined by the number of parallel pipelines ($N_{ij}^p$), the outer diameter ($D_{ij}^{po}$), and the weighted pipeline length ($L_{ij}^w$). The network's operating cost is assumed to be 4% of the capital cost annually. Hydraulic, structural, and commercial availability constraints are considered as described in Hammond et al. [6]. The pipeline sizes are oversized to align with the optimal final infrastructure configuration in 2050.

$$\min C = (1 + 0.04) \sum_{i|(i,j)\in A} C_{ij}^C \quad (3)$$

where

$$C_{ij}^C = N_{ij}^p(61e^{2.74D_{ij}^{po}} + 376\big(D_{ij}^{po}\big)^2 + 2290D_{ij}^{po} + 278)L_{ij}^w \quad (4)$$

## Geographic Information System

The Geographic Information System (GIS) created for this study, depicted in Figure 1, is the collation of many constraints collected from publicly available datasets. These constraints are grouped into category penalties, informed by the literature [17], technical reports [18], and confidential discussions with industry experts, presented in Table 1.

**Table 1:** Categories of geographical features with corresponding penalty weighting.

| Penalty category | Geographic features | Penalty weighting |
|---|---|---|
| Untraversable | National parks | ∞ |
| Very high | Rivers | 50 |
| High | Urban areas, conservation areas | 5 |
| Medium | Woodlands, historic landfills | 3 |
| Low | Roads, rails, peaty soils | 1.2 |

## CASE STUDY

The case study explores CCTS and hydrogen infrastructure design in the Humber region of the UK, a significant industrial hub with high emissions density. Two scenarios are compared across six time steps to assess their impact on the economic viability of CCTS infrastructure: 1) Blue hydrogen production plants transition to green hydrogen production in 2040; and 2) Blue hydrogen production plants continue operating without transitioning to green hydrogen.

The purpose of comparing these scenarios is to investigate the impact that this transition has on the economic viability of the CCTS infrastructure.

The study evaluates a network consisting of 9 hydrogen production plants, 45 hydrogen consumers, and

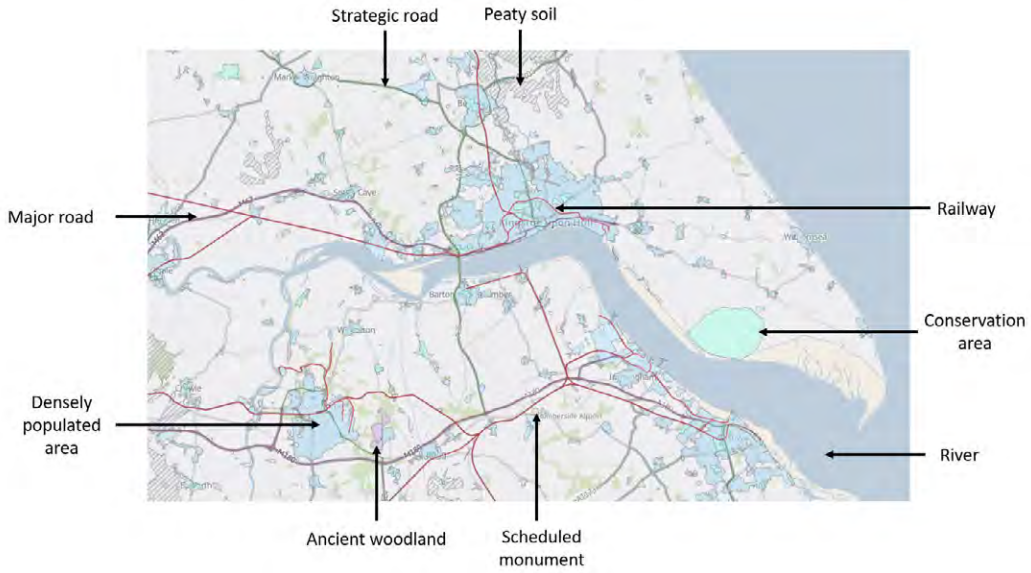



**Figure 1:** Geographical features considered for pipeline routing in the Humber, UK case study.

21 $CO_2$ capture facilities. Captured $CO_2$ is transported to a designated offtake point, where it is considered stored. The model assumes the presence of compressor stations at all sites with fluid outflows and at junctions where multiple pipelines converge. These stations compress hydrogen to 70 bar and $CO_2$ to 35 bar, ensuring efficient transport.

Pipeline design includes 817 unique combinations of inner and outer diameters, ranging from DN6 to DN2300, with a wide range of schedules. This broad range accommodates different operational and economic scenarios, ensuring flexibility in network optimisation.

## RESULTS AND DISCUSSION

### Design analysis

Figure 2 compares the rolling-horizon and 2050-optimised designs for hydrogen and CCTS infrastructure. The rolling-horizon approach (A1, B1) results in an incremental network expansion, with early-stage infrastructure aligning with immediate demand and gradually adapting over time. In contrast, the 2050-optimised design (A2, B2) represents an idealised final-state configuration, assuming perfect foresight of future requirements.

A visual analysis highlights the topological differences that emerge as a result of the iterative nature of rolling-horizon designs. As shown in B1 and B2, the 2050-optimised design takes a route south of the river, whereas the rolling-horizon planning approach follows a northern route. This divergence occurs due to the sequential nature of rolling-horizon planning – the network expands based on immediate cost and connectivity considerations, without foresight of potential long-term inefficiencies. As a result, rolling-horizon designs may lead to routing decisions that, while reasonable given the available information at each stage, may require adjustments as the network evolves.

Figure 3 illustrates the capital investment trends for the hydrogen and CCTS infrastructures over time, comparing rolling-horizon expenditures with the total cost of the 2050-optimised network. The difference in capital investment between these approaches is substantial. Given the high cost of pipeline infrastructure, even small inefficiencies in routing and capacity planning result in significant financial losses. For hydrogen infrastructure, rolling-horizon inefficiencies result in an additional 23.4 million USD in capital expenditures, accounting for approximately 8% of the total investment. Similarly, for CCTS infrastructure, the inefficiency gap amounts to 7.2 million USD, also around 8% of the required investment.

While the 2050-optimised design achieves greater cost efficiency, it assumes perfect foresight which is not attainable in real-world infrastructure planning. Rolling-horizon approaches, by contrast, reflect the iterative design-making process that network designers must navigate. This study highlights not only the financial

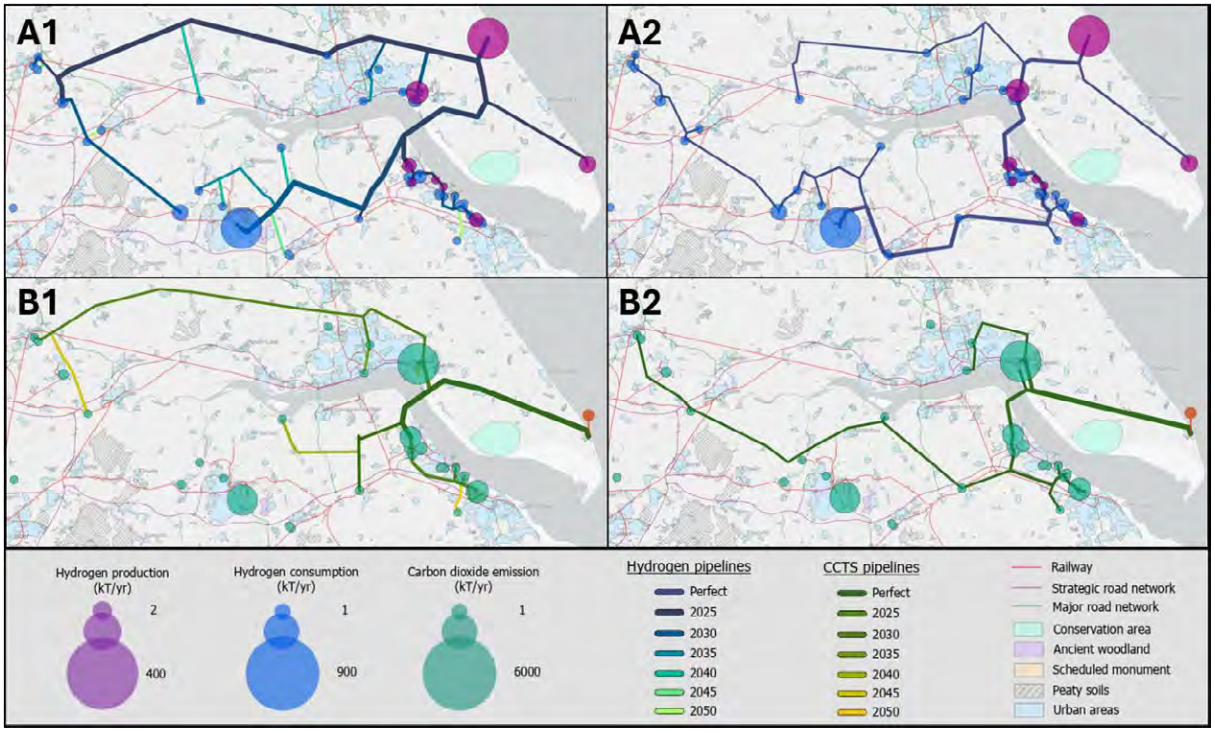



**Figure 2:** Rolling-horizon (A1, B1) vs. 2050-optimised (A2, B2) designs for hydrogen (A) and CCTS (B) infrastructure in the Humber region.

implications of rolling-horizon inefficiencies, but also the importance of developing strategies to mitigate them.
The design tool presented here provides a framework to test rolling-horizon strategies under various potential scenarios. By integrating uncertainty-aware decision-making, future iterations of rolling-horizon planning can minimise inefficiencies while maintaining the flexibility needed to adapt to evolving demands, technological advancements, and policy changes.

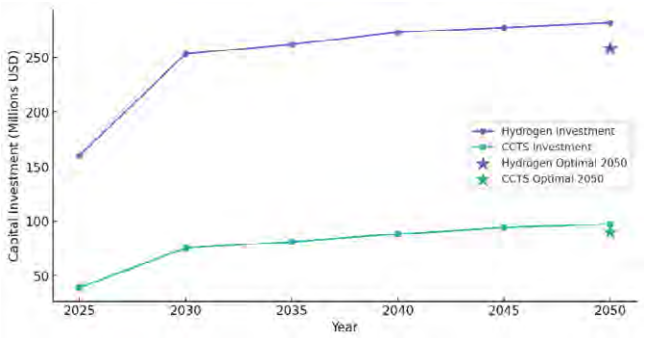



**Figure 3:** Capital investment in hydrogen and CCTS infrastructure over time, comparing rolling-horizon investments with the optimal 2050 configurations.

Table 2 compares the capital investment required per tonne of $CO_2$ saved under the two scenarios. The results indicate a 20-fold increase in CCTS infrastructure costs per tonne of $CO_2$ when blue hydrogen production transitions to green hydrogen. This surge occurs because hydrogen plants, which previously served as major $CO_2$ capture points, no longer contribute to CCTS infrastructure utilisation, reducing overall system efficiency.

It is also worth noting the operational difficulties that will coincide with such a massive reduction in fluid volume in the pipelines.

This finding underscores the interconnected nature of low-carbon infrastructure development. Decisions made in one sector, such as hydrogen production, can have significant economic and operational consequences for another, such as CCTS. As a result, strategic planning must account for cross-sector uncertainties and the evolving role of different infrastructures to avoid cost escalations and stranded assets.

**Table 2:** $CO_2$ Savings Cost ($/Tonne$CO_2$) for Hydrogen & CCTS (2025–2050). Scenario 1: Blue hydrogen; Scenario 2: Transition to green in 2040, increasing CCTS costs.

| Year | Hydrogen Infrastructure ($/Tonne$CO_2$) | CCTS scenario 1 ($/Tonne$CO_2$) | CCTS scenario 2 ($/Tonne$CO_2$) |
|---|---|---|---|
| 2025 | 423 | 128 | 128 |
| 2030 | 30 | 18 | 18 |
| 2035 | 35 | 21 | 21 |
| 2040 | 37 | 25 | 505 |
| 2045 | 42 | 28 | 544 |
| 2050 | 46 | 31 | 597 |

## Critical analysis of the model

Model validation for StObGA in a previous work [6], showed >98% accuracy in predicting route length, confirming its reliability in network design.

Unlike traditional methods, StObGA does not rely on predefined candidate networks but evolves the network by bifurcating existing pipelines. This enhances flexibility and adaptability. The model is highly scalable and provides a framework for incorporating design standards, regulations, and future scenarios testing through rules build into the genetic algorithm, making it valuable for long-term planning.

A key limitation is its inability to anticipate future uncertainties in network expansion, as it optimises only for current constraints. This may limit its effectiveness in dynamic or evolving infrastructure needs.

Simulates were run on a Precision 7875 Tower (AMD Ryzen Threadripper Pro 7945WX, 12 cores, 64 GB RAM), requiring ~2 hours for infrastructure design. Parallelisation improves performance, reducing computation time compared to sequential processing significantly.

## CONCLUSION

This study demonstrates the advantages and limitations of rolling-horizon methodologies for designing hydrogen and CCTS pipeline infrastructure in the context of heavy-industry decarbonisation. While rolling-horizon models offer a more flexible and realistic approach by accommodating evolving spatial and operational constraints, they introduce inefficiencies compared to long-term optimised designs. The case study analysis highlights how incremental infrastructure expansion can lead to higher capital expenditures and suboptimal routing decisions over time. Furthermore, the transition from blue to green hydrogen production presents significant challenges for CCTS infrastructure, with the cost per tonne of $CO_2$ increasing substantially as hydrogen plants cease to contribute to $CO_2$ capture. These findings emphasise the need for hybrid modelling approaches that balance flexibility with long-term cost efficiency. Future work should focus on integrating uncertainty-aware decision-making frameworks into rolling-horizon models to mitigate inefficiencies while ensuring adaptability to emerging technologies, policy shifts, and market dynamics.

## REFERENCES

1. HM Government. Industrial Decarbonisation Strategy. Pages 45–28, March 2021. https://www.gov.uk/government/publications/indus

trial-decarbonisation-strategy
2. Gerres T., Ávila J., Llamas P., et al. A review of cross-sector decarbonisation potentials in the European energy intensive industry. Journal of Cleaner Production (2019). https://doi.org/10.1016/j.jclepro.2019.02.012
3. Rissman J., Bataille C., Masanet E., et al. Technologies and policies to decarbonise global industry: Review and assessment of mitigation drivers through 2070. Applied Energy (2020). https://doi.org/10.1016/j.apenergy.2020.114848
4. Middleton R.S., Kuby M.J., Bielicki J.M. Generating candidate networks for optimisation: The CO2 capture and storage optimisation problem. Computers, Environment and Urban Systems 36(1):18–29 (2012). https://doi.org/10.1016/j.compenvurbsys.2011.08.002
5. Babaei F., Bozorgmehry Boozarjomehry R., Kheirkhah Ravandi Z., Pishvaie S.M.R. A techno-economic analysis framework for power system-aware co-expansion planning of integrated gas transmission networks and chemical industries toward sustainable multi-energy systems. Sustainable Energy, Grids and Networks 32 (2022). https://doi.org/10.1016/j.segan.2022.100893
6. Hammond J., Rosenberg M., Brown S. Understanding costs in hydrogen infrastructure networks: A multi-stage approach for spatially-aware pipeline design. International Journal of Hydrogen Energy 102:430–443 (2025). https://doi.org/10.1016/j.ijhydene.2024.12.273
7. André J., Auray S., Brac J., et al. Design and dimensioning of hydrogen transmission pipeline networks. European Journal of Operational Research 229(1):239–251 (2013). https://doi.org/10.1016/j.ejor.2013.02.036
8. Moreno-Benito M., Agnolucci P., Papageorgiou L.G. Towards a sustainable hydrogen economy: Optimisation-based framework for hydrogen infrastructure development. Computers and Chemical Engineering 102:110–127 (2017). https://doi.org/10.1016/j.compchemeng.2016.08.005
9. Elahi N., Shah N., Korre A., Durucan S. Multi-period least cost optimisation model of an integrated carbon dioxide capture, transportation, and storage infrastructure in the UK. Energy Procedia 63:2655–2662 (2014). https://doi.org/10.1016/j.egypro.2014.11.288
10. Becattini V., Gabrielli P., Antonini C., et al. Carbon dioxide capture, transport and storage supply chains: Optimal economic and environmental performance of infrastructure rollout. International Journal of Greenhouse Gas Control (2022). https://doi.org/10.1016/j.ijggc.2022.103635
11. Middleton R.S., Yaw S.P., Hoover B.A., Ellett K.M. SimCCS: An open-source tool for optimising $CO_2$ capture, transport, and storage infrastructure. Environmental Modelling & Software 124:104560 (2020). https://doi.org/10.1016/j.envsoft.2019.104560
12. Johnson N., Ogden J. A spatially-explicit optimisation model for long-term hydrogen pipeline planning. International Journal of Hydrogen Energy 37(6):5421–5433 (2012). https://doi.org/10.1016/j.ijhydene.2011.08.109
13. Papadimitriou D., Fortz B. A rolling horizon heuristic for the multiperiod network design and routing problem. Networks 66(4):364–379 (2015). https://doi.org/10.1002/net.21663
14. Powell W.B. Reinforcement Learning and Stochastic Optimization: A Unified Framework for Sequential Decisions. John Wiley & Sons, Hoboken (2022).
15. Hammond J., Rosenberg M., Brown S. A genetic algorithm-based design for hydrogen pipeline infrastructure with real geographical constraints. In: Manenti F., Reklaitis G.V. (Eds.), Proceedings of the 34th European Symposium on Computer Aided Process Engineering / 15th International Symposium on Process Systems Engineering (ESCAPE34/PSE24) (2024). https://doi.org/10.1016/B978-0-443-28824-1.50106-X
16. Rosenberg M, French T, Reynolds M, While L. A genetic algorithm approach for the Euclidean steiner tree problem with soft obstacles. In: Proceedings of the genetic and evolutionary computation conference. ACM; 2021. https://doi.org/10.1145/3449639.3459397.
17. van den Broek M., Mesquita P., Carneiro J., Silva J.R., Berghout N., Ramírez A., Gouveia J.P., Seixas J., Cabal H., Martinez R., Rimi A., Zarhloule Y., Sardinha M., Boavida D., Tosato G. Region-specific challenges of a $CO_2$ pipeline infrastructure in the West Mediterranean Sea. Energy Procedia 37:3137–3146 (2013). https://doi.org/10.1016/j.egypro.2013.06.200
18. Scott L., Anyszewekski A. New Pipeline AI Routing. Continuum Industries Technical Report (2022). Retrieved on Nov 2024, but no longer available online.

© 2025 by the authors. Licensed to PSEcommunity.org and PSE Press. This is an open access article under the creative commons CC-BY-SA licensing terms. Credit must be given to creator and adaptations must be shared under the same terms. See https://creativecommons.org/licenses/by-sa/4.0/



Systems & Control Transactions

**Research Article - Peer Reviewed Conference Proceeding**
ESCAPE 35 - European Symposium on Computer Aided Process Engineering
Ghent, Belgium. 6-9 July 2025
Jan F.M. Van Impe, Grégoire Léonard, Satyajeet S. Bhonsale,
Monika E. Polańska, Filip Logist (Eds.)

PSE PRESS

# A Forest Biomass-to-Hydrogen Supply Chain Mathematical Model for Optimizing Carbon Emissions and Economic Metrics

**Frank Piedra-Jimenez[a], Rishabh Mehta[b], Valeria Larnaudie[c], Maria Analia Rodriguez[a*] and Ana Inés Torres[b]**

[a] Universidad Nacional de Córdoba, CONICET, Instituto de Investigación y Desarrollo en Ingeniería de Procesos y Química Aplicada, Córdoba, Córdoba, Argentina
[b] Carnegie Mellon University, Department of Chemical Engineering, Pittsburgh, Pennsylvania, United States
[c] Universidad de la República, Facultad de Ingeniería, Departamento de Bioingeniería, Montevideo, Uruguay
* Corresponding Authors: analia.rodriguez@unc.edu.ar; aitorres@cmu.edu.

## ABSTRACT

This study introduces a mathematical programming approach to optimize biomass-to-hydrocarbon supply chain design and planning, aiming to balance economic and environmental outcomes. The model incorporates a range of residual biomass types from forestry, sawmills, and the pulp and paper industry, with the option to establish various processing facilities and technologies over a multi-period planning horizon. The analysis involves selecting forest areas, identifying biomass sources, and determining the optimal locations, technologies, and capacities for facilities converting wood-based residues into methanol and pyrolysis oil, which can be further refined into biodiesel and drop-in fuels. Using Life Cycle Assessment (LCA) in a gate-to-gate analysis, forest supply chain carbon emissions are estimated and integrated into the optimization model, extending previous research. A multi-objective framework is employed to minimize $CO_2$-equivalent emissions while minimizing present costs, with efficient Pareto points evaluated in a case study focused on the Argentine forest industry.

**Keywords**: Supply Chain, Life Cycle Analysis, Biomass, Optimization.

## INTRODUCTION

Forest supply chains (FSCs) are critical for achieving decarbonization targets [1]. FSCs are characterized by abundant biomass residues, offering an opportunity to add value to processes while contributing to the production of clean energy products. One particularly interesting aspect is their potential integration with oil refineries to produce drop-in fuels, offering a transformative pathway to mitigate traditional refinery emissions [2].

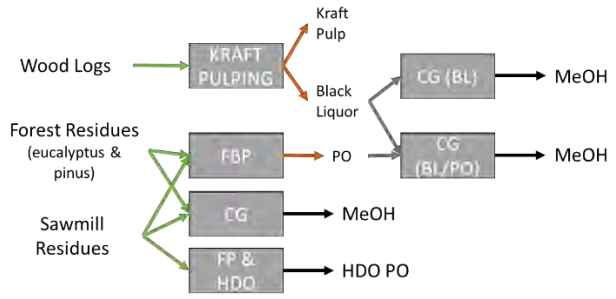
In this article, a disjunctive mathematical programming approach is presented to optimize the design and planning of the FSC for the production of hydrocarbon products from biomass, optimizing both economic and environmental objectives. Various types of byproducts and residual biomass from forest harvesting activities, sawmill production, and the pulp and paper industries are considered. Alternative processing facilities and technologies can be established over a multi-period planning horizon. The design problem scope involves selecting forest areas for exploitation, identifying biomass sources, and determining the locations, technologies, and capacities of facilities that transform wood-based residues into methanol and pyrolysis oil, which are further processed in biodiesel and petroleum refinery plants, respectively. This problem is challenging due to the complexity of the supply chain network, which involves numerous decisions, constraints, and objectives. In particular, in the case of large geographical areas, transportation becomes a crucial aspect of supply chain design and planning because the low biomass density significantly impacts carbon emissions and costs. Thus, the scope of planning the problem includes selecting connections and material flows across the supply chain. A multi-objective approach is proposed to assess economic and environmental objectives. A set of efficient Pareto points is

obtained and compared in a case study of the Argentine forest industry.

## PROBLEM STATEMENT

A supply chain superstructure is considered in this paper formed by three echelons: the feedstock areas where pine and eucalyptus logs, forest residues, and sawmill residues are obtained; the processing facilities, where biomass is converted into fuels and intermediates; and the consumer nodes (biodiesel plants or petroleum refineries). Logs are used for the paper industry, i.e., the kraft pulping process, while residues from all sources are transformed into fuel products. Stand-alone and integrated plants can be selected to produce intermediate or final products (hydrogenated pyrolysis oil for petroleum refineries and methanol for biodiesel plants).

Process alternative pathways are presented in Figure 1.




References: BL: black liquor; CG: catalitic gasification; FBP: fluidised bed pyrolysis; FP: fast pyrolysis; PO: Pyrolysis oil; HDO: Hydroxygenation; HDO PO: Hydroxygenated pyrolysis oil.

**Figure 1.** Process alternatives.

The problem studied can be stated as follows, given: processing, investment and transportation costs; environmental impact of each process, measured in equivalent carbon emissions; products' demand; capacity levels and economy scale factors; biomass availability and allowed capacity expansions in forest nodes; processing yields. The model must select over a multi-period timeframe: (i) The extent of land and types of tree species to be harvested at each forest location and within each time period; (ii) The processing facilities to be established at each location over time, including their technology, scale, and degree of integration; (iii) The output levels for each technology and processing plant in every time period; (iv) The capacity outlines for each supply chain processing facility across the entire timeline; (v) The transport flows of all materials and supply chain linkages across each time period. The goal is to minimize the present costs and the environmental impact of the supply chain.

## MULTI-OBJECTIVE APPROACH

As mentioned, this article extends previous work from Piedra-Jimenez et al. [3], where the supply chain is optimized assuming an economic objective function (minimizing total present costs). The deterministic formulation presented there is reformulated as a bi-objective model to include the minimization of the CO2 equivalent emissions.

The Life Cycle Assessment (LCA) methodology is used to estimate FSC carbon emissions. A gate-to-gate analysis is carried out for each activity in the FSC and combined with the optimization problem to obtain a cradle-to-gate LCA. The predicted LCA results are then integrated as input parameters into a mathematical programming model for FSC design and planning to optimize the bi-objective problem. This formulation is solved by assuming the Ɛ-constraint approach to obtain a set of Pareto optimal points. The total impact is presented in Eq. (1). Transportation emissions are estimated in Eq. (2), and emissions from processing facilities are estimated in Eq. (3). Due to space limitations, the rest of the formulation is not transcribed here, as it can be found in Piedra-Jimenez et al. (2024), resulting in a generalized disjunctive model (GDP) implemented as a mixed integer linear programming (MILP) model using Big M reformulation.

$$CO_2e = TCO_2e + PCO_2e \tag{1}$$

$$TCO_2e = \sum_{(r,s)\in M_{RS}} \zeta 1_{r,s} \cdot \rho 1_{j,k} \cdot F1_{r,s,j,k,m,t} + \sum_{\substack{(i,m)\in M_I \\ (i,m')\in I_M}} \zeta 2_i \cdot \rho 2_{k,k'} \cdot F2_{i,k,m,k',m',t} + \sum_{(o,m)\in M_O} \zeta 3_o \cdot \rho 3_{k,l} \cdot F3_{o,k,m,l,t} \quad \forall\, t \tag{2}$$

$$PCO_2e = \sum_{(r,s)\in M_{RS}} \vartheta 1_{r,s,m} \cdot F1_{r,s,j,k,m,t} + \sum_{\substack{(i,m)\in M_I \\ (i,m')\in I_M}} \vartheta 2_{i,m} \cdot F2_{i,k,m,k',m',t} \tag{3}$$

### Parameters

$\zeta 1_{r,s}$ carbon dioxide equivalent emission for the transportation truck used for raw material (r,s) from sources j to plants k (t CO2 Emission/ t-km)

$\zeta 2_i$ carbon dioxide equivalent emission for the transportation truck used for intermediate product i from plants k to other facilities k (t CO2 Emission/ t-km)

$\zeta 3_o$ carbon dioxide equivalent emission for the transportation truck used for product o from plants k to clients l (t CO2 Emission/ t-km)

$\vartheta 1_{r,s,m}$ carbon dioxide equivalent emission from processing raw material r from tree species using technology m (t CO2 Emission/ t feedstock)

$\vartheta 2_{i,m}$ carbon dioxide emission from processing intermediate product i using technology m (t CO2 Emission/ t feedstock)

$\rho 1_{j,k}$ distance between raw material nodes j and processing plants k (km)

$\rho 2_{k,k'}$ distance between processing plants k and k' (km)

$\rho 3_{k,l}$ distance between processing plants k and clients l (km)

## Positive variables

$F1_{r,s,j,k,m,t}$ amount of raw material r of tree species s from node j to facility node k produced with technology m in period t

$F2_{i,k,m,k',m',t}$ amount of intermediate product i produced from processing node k which applying technology m that is consumed by node k´ for further processing with technology m´ in period t

$F3_{o,k,m,l,t}$ amount of final product o produced with technology m in location k to satisfy demand node l in period t

$TCO_2e$ carbon equivalent emissions from transportation activities

$PCO_2e$ carbon equivalent emissions from processing facilities

$CO_2e$ total carbon equivalent emissions

The resulting formulation is a linear generalized disjunctive model that is reformulated with Big-M relaxation.

# CASE STUDY AND RESULTS

Open LCA and EcoInvent 3.11 were used to estimate the equivalent $CO_2$eq emissions from processes and transportation following ISO 14040 and ISO 14044 [4, 5]. The processes characteristics regarding energy consumptions, efficiency, yields, were obtained from the literature [6 - 13]. Power energy matrix from Argentinean case study is estimated considering reports from the country [14]. A 15-year horizon planning (HP) is assumed.

The resulting emissions from each process and the input and output characteristics are presented in Table 1.

Regarding transportation, EURO 3 truck technology is assumed. The capacity assumed is based on typical cargo transportation options in Argentina (28.5 t for all type of products and an additional limitation of 37 $m^3$ for liquids). Since no data for this country is available in LCA database, the rest of the world (RoW) reported emission from the EcoInvent is assumed. This value is estimated considering an average capacity load of 5.8 t.

In the Argentinean case study, the average load is quite larger than the one reported in the EcoInvent database. Therefore, the transportation emissions per ton-km are estimated according to the Argentinean load factor. This type of procedure is supported, for instance, in [15]. It is assumed that the trucks are used with 90% of the full load of a one-way trip and an empty return is considered. This estimation is presented in the last line of Table 2. For the different products, their density is used to calculate if the capacity restriction is determined by the volume or the weight of the truck. Except for the saw-mill residues, in all cases, the maximal weight is the active limitation. The calculated emission for each type of product is presented in Table 2.

The supply chain nodes considered are located in the northeast and center regions from Argentina as depicted in Figure 2. The FSC superstructure consists of 25 supply sources, 3 operational kraft pulp mills, 13 potential biorefinery locations, and 26 demand nodes (21 soybean-based biodiesel plants and 5 petroleum refineries).

**Table 1:** Process characteristics and estimated emissions from LCA analysis.

| Material Input | Flowrate input (t/h) | Technology | Material Output | Flowrate Output (t/h) | Emission (t CO2eq /t input) |
|---|---|---|---|---|---|
| Saw-mill residues | 43.29 | Fast Pyrolysis | FP Oil | 21.65 | 0.42627 |
| FP Oil | 21.65 | Hydroxgenation (HDO) | HDO Bio-oil | 14.29 | 0.20465 |
| Forest Residues | 52.70 | Catalytic Gasification (1) | Methanol | 22.7 | 0.18654 |
| Forest Residues | 20.90 | Fluidised Bed Pyrolysis | FBP Oil | 7.56 | 0.26788 |
| FBP Oil + Black Liquor | 43.4 + 173.6 | Catalytic Gasification (2) | Methanol | 62.5 | 0.62199 |
| Black Liquor | 173.60 | Catalytic Gasification (3) | Methanol | 40.1 | 0.26254 |

**Table 2:** Estimated emissions for transportation alternative and material.

| Type of truck | Emission* | Saw-mill residues | Forest residues | Forest logs | FBP Oil | HDO Bio-oil | Methanol |
|---|---|---|---|---|---|---|---|
| Euro 3 16-32 Tons | 0.196 | 0.1183 | 0.0885 | 0.0885 | 0.0885 | 0.0885 | 0.0885 |
| Average load in t | | 10 | 13 | 13 | 13 | 13 | 13 |

* Data from EcoInvent Database 3.11 for RoW assuming 5.8 t of average capacity use
All reported units are in (kg CO2eq/t-km)

The model was implemented in GAMS and executed using solver CPLEX on a 32GB RAM machine with Intel Core i9-11900K 3.50GHz CPU. The problem consists of 4,968 integer variables, 88,016 continuous variables and 59,654 constraints. Each iteration (one per Pareto point) was executed to global optimality (gap 0%) in less than 9 minutes.

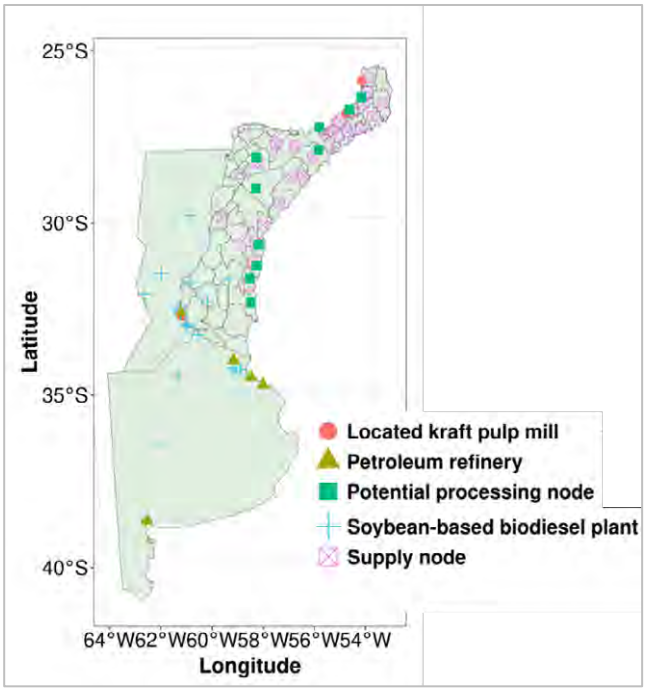



**Figure 2.** Locations for supply chain nodes.

The optimal solutions obtained are depicted in Figure 3, showing the compromise between the two proposed objectives.

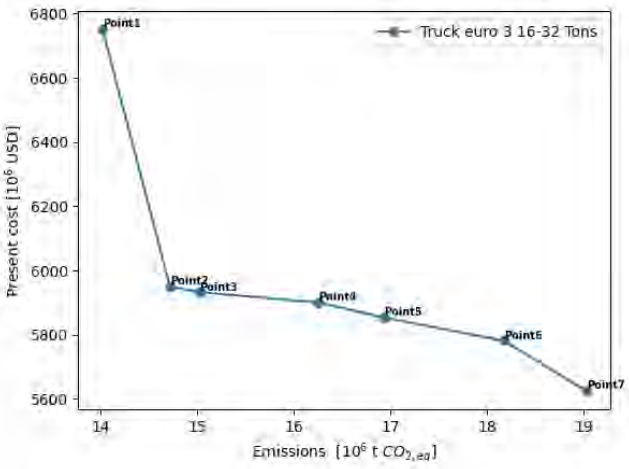



**Figure 3.** Pareto front.

Considering the relative difference between points, the best compromise solution is given in point 2, i.e. a relevant decrease in present cost is shown at an expense of small increment in CO2 emissions. In this point, total emissions for the 15-year HP are 14,719,296 ton of CO2eq while total present costs are USD 5,949,789,094.

Figures 4 and 5 present the environmental and cost functions breakdown, respectively. In all cases, process emissions are larger than the ones from transportation. Particularly, processing forest biomass is the one that most contributes to the CO2 equivalent emissions. Regarding transportation, the larger emission from transportation of final products can be explained by the distances between nodes. Considering all solutions, the main difference in the emissions scheme is observed from point 1 to 2. In the first solution, only sawmill residues and forest biomass are consumed as raw materials. To improve costs, the use of intermediate products (such as black liquor and pyrolysis oil) is increased while sawmill residues consumption diminishes.

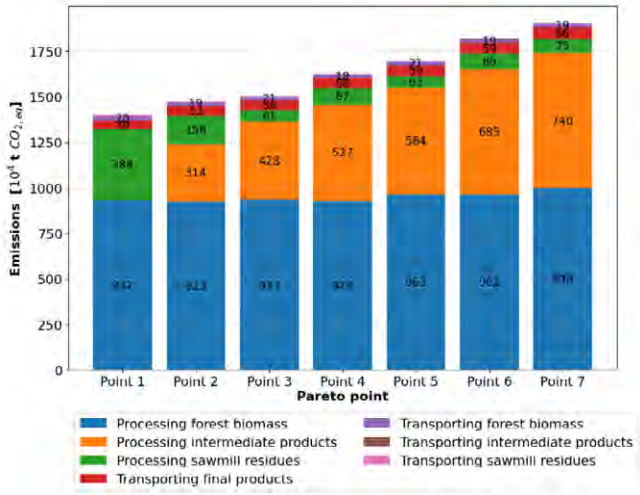



**Figure 4.** Emissions breakdown for all points

In the case of present costs, main component is given by investment cost in new plants followed by the variable cost for processing forest biomass. Except for the first point as mentioned before, the cost breakdown does not significantly change among points.

The selected technologies and plant locations are presented in Figure 6 for point 2 that is considered the best compromise solution. Two plants for producing HDO PO are installed, one located near 3 petroleum refineries and the other placed in the biomass sourcing area. Two plants are integrated to Kraft mills for producing methanol from black liquor via catalytic gasification. Another stand-alone plant is installed for producing methanol from forest residues using catalytic gasification technology.

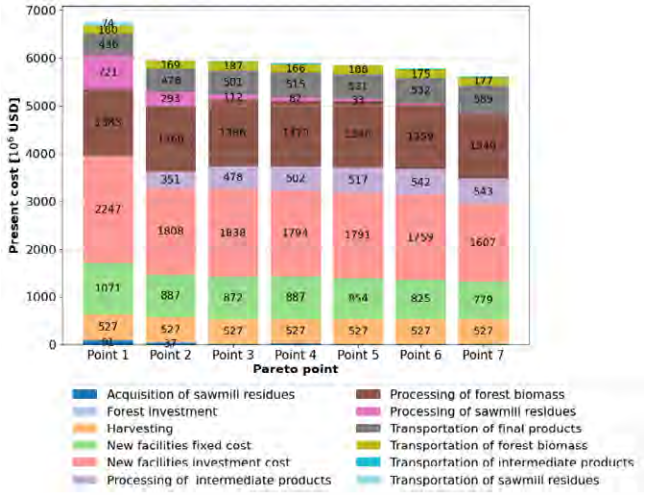



**Figure 5.** Present costs breakdown for all points

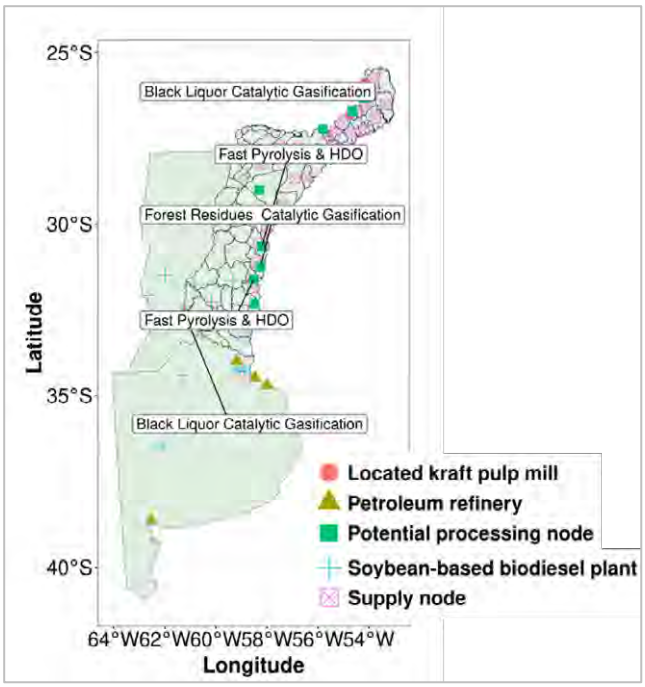



**Figure 6.** Technologies and locations selected.

**Table 3:** Carbon intensity mean values.

| Product | Co2 intensity (ton Co2eq/ton product) | Co2 intensity (g Co2eq/MJ) |
|---|---|---|
| HDO PO | 1.65129 | 55.04 |
| Methanol | 0.98780 | 43.52 |

Table 3 presents the average carbon intensity for the produced bio-methanol and hydroxigenated pyrolysis oil. The fluctuations between points on the Pareto curve in unit emissions for hydrogenated pyrolysis oil are negligible. Only very small changes are observed. In the case of methanol, although there are variations between points, the maximum difference is less than 30%.

## CONCLUSIONS

This article extends previous work by incorporating carbon emissions in the forest supply chain as a second optimization objective. The LCA methodology was applied to assess the environmental emissions of each activity within the supply chain's scope. A clear compromise solution can be selected, maintaining a good balance between present costs and total emissions.

The proposed model serves as a valuable tool for guiding the decision-making process, considering both economic and environmental perspectives in a supply chain that could reshape the wood-based industry in Argentina. The results indicate that residual biomass from this sector can be converted into value-added products, replacing their fossil-based alternatives. Future work includes testing the model computational performance for other instances considering other regions, input data and increasing problem size.

## REFERENCES

1. Santos A, Carvalho A, Barbosa-Póvoa AP, Marques A, Amorim P. Assessment and optimization of sustainable forest wood supply chains – a systematic literature review. *For Policy Econ* 105:112-135 (2019) https://doi.org/10.1016/j.forpol.2019.05.026.
2. Barbosa-Povoa AP, Pinto JM. Process supply chains: perspectives from academia and industry. *Comput Chem Eng* 132:106606 (2020) https://doi.org/10.1016/j.compchemeng.2019.106606.
3. Piedra-Jimenez F, Torres AI, Rodriguez MA. A robust disjunctive formulation for the redesign of forest biomass-based fuels supply chain under multiple factors of uncertainty. *Comp Chem Eng* 181:108540 (2024), https://doi.org/10.1016/j.compchemeng.2023.108540
4. International Organization for Standardization. Environmental management-Life cycle assessment principles and framework (ISO/DIS Standard No. 14040) (2006).
5. International Organization for Standardization. Environmental management-Life cycle assessment Requirements and guidelines (ISO/DIS Standard No. 14044) (2006).
6. Wu L, Wang Y, Zheng L, Wang P, Han X. Techno-economic analysis of bio-oil co-processing with vacuum gas oil to transportation fuels in an existing fluid catalytic cracker. *Ener Conv and*

*Manag* 197:111901 (2019). https://doi.org/10.1016/j.enconman.2019.111901.
7. Carvalho L, Furusjö E, Kirtania K, Wetterlund E, Lundgren J, Anheden M, Wolf J. Techno-economic assessment of catalytic gasification of biomass powders for methanol production. *Biores Tech* 237:167-177 (2017). https://doi.org/10.1016/j.biortech.2017.02.019.
8. Onarheim K, Solantausta Y, Lehto J. Process simulation development of fast pyrolysis of wood using aspen plus. *Ener & Fuels* 29:205-217 (2015). https://doi.org/10.1021/ef502023y.
9. Carvalho L, Lundgren J, Wetterlund E, Wolf J, Furusjö E. Methanol production via black liquor co-gasification with expanded raw material base–Techno-economic assessment. *App Energy*, 225:570-584 (2018). https://doi.org/10.1016/j.apenergy.2018.04.052.
10. Jafri Y, Wetterlund E, Mesfun S, Radberg H, Mossberg J, Hulteberg C, Furusjö E. Combining expansion in pulp capacity with production of sustainable biofuels – Techno-economic and greenhouse gas emissions assessment of drop-in fuels from black liquor part-streams. *Appl Energy* 279:115879 (2020). https://doi.org/10.1016/j.apenergy.2020.115879.
11. Jafri Y, Furusjö E, Kirtania K, Gebart R. Performance of an entrained-flow black liquor gasifier. *Ener Fuel* 30:3175–3185 (2016). https://doi.org/10.1021/acs.energyfuels.6b00349.
12. Qian Z, Zhai R, Feng L, Mei W. Performance analysis of the acid gas removal from syngas based on self-heat recuperation technology. *App Thermal Eng* 219: 119506 (2023). https://doi.org/10.1016/j.applthermaleng.2022.119506.
13. Zhang Z, Delcroix B, Rezazgui O, Mangin P. Methanol production from pyrolysis oil gasification—model development and impacts of operating conditions. *Appl Sci* 10:7371 (2020). https://doi.org/10.3390/app10207371.
14. Secretaría de Energía. Balance Energético Nacional Serie histórica – Indicadores Actualizado al año 2021. https://www.energia.gob.ar/contenidos/archivos/Reorganizacion/informacion_del_mercado/publicaciones/energia_en_gral/balances_2021/sintesisbalancesenergeticos2021v1.pdf
15. Rizet C, Cruz C, Mbacké M. Reducing freight transport CO2 emissions by increasing the load factor. *Procedia - Soc and Behavioral Sci* 48:184–195 (2012). https://doi:10.1016/j.sbspro.2012.06.999.

© 2025 by the authors. Licensed to PSEcommunity.org and PSE Press. This is an open access article under the creative commons CC-BY-SA licensing terms. Credit must be given to creator and adaptations must be shared under the same terms. See https://creativecommons.org/licenses/by-sa/4.0/



Systems & Control Transactions

**Research Article - Peer Reviewed Conference Proceeding**
ESCAPE 35 - European Symposium on Computer Aided Process Engineering
Ghent, Belgium. 6-9 July 2025
Jan F.M. Van Impe, Grégoire Léonard, Satyajeet S. Bhonsale,
Monika E. Polańska, Filip Logist (Eds.)

PSE PRESS

# A Novel Detailed Representation of Batch Processes for Production Scheduling

**Alexandros Koulouris[a]*, Georgios P. Georgiadis[a,b]**

[a] International Hellenic University, Department of Food Science and Technology, Thessaloniki, Greece
[b] Intelligen Inc., Freehold, NJ, USA
* Corresponding Author: akoul@ihu.gr.

## ABSTRACT

Traditional scheduling approaches often rely on simplified process representations to reduce computational complexity, failing to capture the real-world dynamics where tasks often overlap, and their timing depends on finer operational steps. To address these limitations, this paper proposes a novel process representation that breaks down production tasks into smaller, more primitive steps called operations. Unlike traditional methods, this approach provides a more granular depiction of task timing and resource dependencies. Operations can define the start or end of other tasks, utilize shared resources, and incorporate recipe constraints that mandate task sequencing. The proposed representation is utilized to develop two MILP models to address the makespan and the cycle time minimization problems. Finally, the efficiency and practical applicability of the developed models are showcased with a help of a case study from the pharmaceutical industry.

**Keywords**: production scheduling, process representation, mixed integer programming, makespan, cycle time

## INTRODUCTION

The highly competitive industrial landscape enforces companies to strive for profit maximization. In that line, optimal production scheduling plays a significant role in ensuring the efficient utilization of the available resources and the increase of productivity. Effective schedules allow companies to improve important Key Performance Indicators (KPIs) like, customer satisfaction, mitigation of overproduction and overall profitability boost. However, the optimal production scheduling problem remains a significant challenge due to its high combinatorial complexity, arising from the dynamic and interconnected nature of modern manufacturing. More specifically, in chemical process production steps often overlap and their exact timing and duration can be influenced by dependencies between operations and shared resources usage. These production details are often overlooked in traditional process representations for production scheduling, resulting in suboptimal solutions that may not reflect real-world conditions.

A plethora of mathematical optimization models, such as mixed-integer linear programming (MILP) has been proposed to solve the optimal production scheduling problem [1]. Formulating the production scheduling problem as an MILP model requires a coherent representation of the production process. The most used representations are the State-Task-Network (STN) [2] and the Resource-Task-Network (RTN) [3]. These were initially introduced for network production environments and were later extended to include sequential and hybrid environments. Numerous extensions of the STN and the RTN have been proposed by the scientific community, that e.g. include the structural aspects of the plan [4] or consider routing limitations [5]. Recently, the General Material Task System (GMTS) representation has been proposed for systems with multiple production environments and diverse types of processes [6]. However, applying such methods in industrial practice is difficult. Simplified process representations are often used to make scheduling problems computationally feasible, but they fail to capture the complexity and flexibility inherent in production systems. Traditional approaches treat batch processing stages as rigid blocks, with fixed precedence constraints determining the order in which tasks are executed. In a real production environment, the tasks rarely follow strict sequential execution. On the contrary, they often overlap, and their exact timing is driven by

operations that are highly dependent on resource availability and inter-task dependencies. This mismatch between traditional scheduling models and real-world production highlights the need for a more flexible and accurate approach.

To address these limitations, this paper introduces a novel process representation that captures the complex interactions between tasks, their resource requirements, and timing uncertainties inherent in production environments. Tasks are broken down into smaller processing steps called procedures and operations, capturing the interdependencies between tasks and their resource requirements. Operations are tied to recipe constraints that define strict sequencing rules, but timing flexibility can be introduced using dummy operations with variable durations. This approach allows the model to handle timing uncertainties and resource-sharing scenarios more effectively, making it possible to generate optimized schedules that closely reflect real-world production realities. The proposed representation is incorporated into a MILP-based scheduling framework, improving the accuracy and reliability of scheduling decisions without significantly increasing computational complexity. Two MILP models for makespan minimization and cycle time minimization are developed with their applicability and efficiency demonstrated through case study applications.

## MATHEMATICAL FORMULATION

### Process Representation

A batch process consists of processing tasks (*procedures*) each executed in some equipment unit. Within a procedure, more primitive processing steps (*operations*) can be recognized. For example, a fermentation procedure consists of a series of operations such as SIP, loading of materials, heating, fermenting, transferring-out the broth, CIP etc. With the exception of the main equipment unit defined at the procedure level, all other resources (materials, utilities, labor etc.) are consumed at the operation level. Relative timing of all processing tasks is also done at the operation level. This is an important aspect of the proposed formulation which differentiates it from established process representations. Moreover, it offers an intuitive representation for process engineers, as it aligns perfectly with how they conceptualize and structure their process.

In batch processing, the set of all procedures comprises the process *recipe* for the production of a stable product or intermediate. Unlike discrete manufacturing industries, recipes in processing industries are, in general, rigid structures with operations executed in sequence or in parallel with fixed timings. However, in many cases, the execution of certain operations could be delayed if the required resources are not available. For example, a CIP operation can wait up to a certain time (the dirty-hold time) if the required cleaning skid is not available. This kind of flexibility in the execution of operations is introduced in the formulation in the form of flexible shifts which denote the maximum possible delay (positive for forward scheduling, negative for backward scheduling). For consistency with the rest of the representation, flexible shifts are modelled as "dummy" operations with variable duration.

Let $M$ be the set of all operations in a recipe. Each operation, $m$, in this set is given a triplet of variables for its start ($s_m$), duration ($d_m$) and end ($e_m$) which we call "timing elements". Because of the way recipes are executed, all these timing elements are interrelated (e.g. the start of one operation coincides with the end of the previous). Figure 1 shows an example of the proposed representation for a fermentation procedure. A dummy "Flexible Delay" operation has been added to the list of actual operations to represent the possible delay in the execution of the CIP operation if needed. The duration of this dummy operation is considered variable.

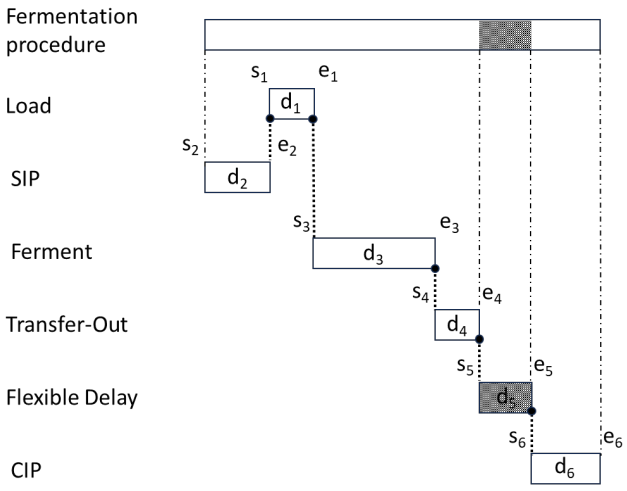



**Figure 1.** Representation of a fermentation procedure.

Let $V$ be the set of all timing elements in the recipe ordered by dependency. Then, it is possible to construct a lower-triangular matrix, $\sigma$, whose entries represent the coefficients in the dependency equations. In other words:

$$V = \sigma \cdot V + \varphi + F \tag{1}$$

In this equation, $\varphi$ is a vector of constant values (e.g. the fixed duration of certain operations) and $F$ is a vector of variable values (e.g. the duration of the dummy flexible shift operations).

The actual execution of a recipe constitutes a *batch*. When scheduling a batch, the objective is to find the appropriate timing values for the execution of all processing tasks and assign all needed resources. The set of processing tasks does not necessarily coincide with the set

of operations which give rise to the vector of timing elements, *V*, since, in scheduling, only tasks (procedures and operations) that consume resources are of interest. However, the timing of these tasks can be determined with the help of the timing elements.

Let *I* be the set of all processing tasks that need to be scheduled. If a task *i* represents a procedure, then its start ($L_i$) is the earliest start time of all contained operations, its end ($C_i$) is the latest end time of all contained operations and its duration ($Dur_i$) is the difference between the two:

$$\begin{aligned} L_i &\le V_n \quad \forall i \in I, n \in S_{i,n} \\ C_i &\ge V_n \quad \forall i \in I, n \in E_{i,n} \\ Dur_i &= C_i - L_i \quad \forall i \in I \end{aligned} \tag{2}$$

where $S_{i,n}$ are the indices *n* of vector *V* that the start $L_i$ of a task *i* depends upon and $E_{i,n}$ are the indices *n* of vector *V* that define the end $C_i$ of a task *i*.

Let *J* be the set of available equipment to be used for the execution of all tasks. Each task *i* (procedure or operation) has a specific pool of candidate equipment to be used for its execution. For this reason, a matrix $IJ_{i,j}$ of binary values is constructed with unary values in the permissible task-equipment pairs.

This framework can be extended to introduce equipment-related durations of operations and also compatibility/connectivity constraints between all equipment. For reasons of brevity, these extensions are not discussed in this paper.

## MILP formulation

The proposed novel production process representation is integrated within a MILP model to address the production scheduling optimization problem. The developed MILP model is based on the general precedence framework, which utilizes binary sequencing variables to indicate optimal task ordering and allows for a flexible and efficient approach to manage complex scheduling constraints. = It is important to note that the proposed process representation is versatile enough to be integrated with other MILP frameworks for optimal production scheduling.

Given a number of batches *B* of processing tasks to be processed in the available equipment *J*, the MILP model generates an optimal production schedule. It should be underlined that the set of processing tasks include all tasks (procedures and operations) that require the use of a resource. Two binary variable sets are employed to describe the allocation $Y_{i,b,j}$ and sequencing decisions $X_{i,b,i',b'}$. Moreover, continuous variables are introduced to model all time-related decisions like start ($L_{i,b}$) and completion ($C_{i,b}$) of tasks, value of timing elements ($V_{n,b}$) and duration of flexible operation shifts ($F_{n,b}$). All constraints of the model are presented below.

### Allocation constraints

According to constraint set (3), exactly one equipment *j* will process each batch *b* of task *i*. The subset $IJ_{i,j}$ represents the equipment capable of processing task *i*.

$$\sum_{j \in IJ_{i,j}} Y_{i,b,j} = 1 \; \forall i \in I, b \in B \tag{3}$$

### Timing constraints

In constraint sets (4), the value of timing elements related to all tasks, that represent a procedure or an operation ($n \notin Flex_n$) are calculated based on their relative timings ($\sigma_{n,n'}$). More specifically, the value of an entity *n* in batch *b* equals the summation of all values of all other entities *n'* of batch *b* that entity *n* depends on. Respectively, constraints (5) calculate the value of timing items related to flexible operation shifts. The difference here is that the duration is not known but it is rather an unknown variable to be optimized. Constraints (6) ensure that the start time of a task will be less than the value of all relative start elements plus the start time of the batch. Similarly, the completion times are calculated in the next constraint set (7). Notice that the inequalities are required since in the case of procedures a task may be comprised by numerous operations and flexible shifts ($n \in Flex_n$). Finally, constraints (8) and (9) denote that the batch *b* of a task *i* will start and finish after the start and completion of the previous batch *b-1*.

$$V_{n,b} = \sum_{n'<n} \left(\sigma_{n,n'} \cdot V_{n',b}\right) \quad \forall n \notin Flex_n, b \in B \tag{4}$$

$$V_{n,b} = \sum_{n'<n} \sigma_{n,n'} \cdot V_{n',b} + F_{n,b} \quad \forall n \in Flex_n, b \in B \tag{5}$$

$$L_{i,b} \le V_{n,b} + L_{i1,b} \quad \forall i \in I, b \in B, n \in S_{i,n} \tag{6}$$

$$C_{i,b} \ge V_{n,b} + L_{i1,b} \quad \forall i \in I, b \in B, n \in E_{i.n} \tag{7}$$

$$L_{i,b} \ge L_{i,b-1} \quad \forall i \in I, b \in B \tag{8}$$

$$C_{i,b} \ge C_{i,b-1} \quad \forall i \in I, b \in B \tag{9}$$

### Sequencing constraints

Constraints (10) and (11) are complementary sequencing constraints that make use of a big-M parameter. In particular, constraint set (10) ensures that if a batch *b* of task *i* is processed before another batch *b'* of task *i'* ($X_{i,b,i',b'}=1$) and both of them are processed in the same equipment ($Y_{i,b,j}=Y_{i',b',j}=1$) then batch *b'* of task *i'* must start after the completion of batch *b* of task *i*. Respectively, constraint set (11) considers the case where batch *b* of task *i* is processed after another batch *b'* of task *i'* ($X_{i,b,i',b'}=0$) in the same equipment. Finally, constraints (12) guarantee that batch *b'* of task *i* will start after the completion of a batch *b*<*b'* of the same task when both are processed in the same equipment.

$$\begin{aligned} L_{i',b'} \ge C_{i,b} - M \cdot (1 - X_{i,b,i',b'}) - M \cdot (2 - Y_{i,b,j} - Y_{i',b',j}) \\ \forall i \in I, i' \in I, b \in B, b' \in B, j \in (IJ_{i,j} \cap IJ_{i',j}) : i < i' \end{aligned} \tag{10}$$

$$L_{i,b} \ge C_{i',b'} - M \cdot X_{i,b,i',b'} - M \cdot (2 - Y_{i,b,j} - Y_{i',b',j})$$

$$\forall i \in I, i' \in I, b \in B, b' \in B, j \in (IJ_{i,j} \cap IJ_{i',j}) : i < i' \quad (11)$$

$$L_{i,b'} \geq C_{i,b} - M \cdot (2 - Y_{i,b,j} - Y_{i,b',j})$$
$$\forall i \in I, b \in B, b' \in B, j \in IJ_{i,j} : b < b' \quad (12)$$

### Objective function

The goal of the mathematical model is to optimize a given objective that is meaningful to the problem under study and can improve significant production KPIs. Some typical examples are the minimization of production makespan, changeover minimization, order earliness/tardiness minimization, profit maximization and changeover minimization. In the context of this model the objective of makespan minimization $C_{max}$ is considered.

$$C_{max} \geq C_{i,b} \qquad \forall i \in I, b = |B| \quad (13)$$

## Extension for Periodic Production Scheduling

The proposed process representation is also utilized to address the cycle time minimization problem in production environments that follow a periodic scheduling approach. Cyclic, and more specifically periodic, scheduling is a very popular production scheme in many industries due to its reduced shop floor nervousness and simple implementation. However, it poses some clear disadvantages mainly related to the tight timing constraints it imposes, which typically negatively affect the production makespan.

A cyclic schedule is characterized as a schedule that is repeated following a specific timing and resource allocation pattern. Timewise this pattern is specified by the cycle time *H*. This means that if the first task *i* in batch b starts at time $L_{i,b}$, then the same task will start in the subsequent batch at $L_{i,b}+H$. In traditional cyclic scheduling, the resource allocation pattern is very limited, since each task is processed by exactly one of the available equipment throughout the schedule. As expected, this significantly reduces flexibility and resource utilization, potentially lower productivity. To address this issue the concept of periodicity has been proposed [7]. For each task *i*, the periodicity $\pi_i$ denotes how often resource allocation decisions are repeated and is equal to the size of the task's equipment pool. For example, if the equipment pool consists of *J1* and *J2*, then all even batches of task *i* {$b_1$, $b_3$, $b_5$, ...} are processed by J1 and all odd ones {$b_2$, $b_4$, $b_6$, ...} by *J2*.

The mathematical formulation developed to tackle this optimization problem is based on the presented detailed process representation and the MILP model introduced in the previous section. However, this needs to be modified to properly address the specifics of the cycle time minimization problem. This also showcases the general applicability of the proposed framework and its ability to optimally deal with a wide range of production scheduling problems.

The following constraints (3') – (7') need to be adapted to the current optimization problem:

$$\sum_{j \in IJ_{i,j}} Y_{i,b,j} = 1 \qquad \forall i \in I, b \in B : b < \pi_i \quad (3')$$

$$V_{n,b} = \sum_{n'<n} (\sigma_{n,n'} \cdot V_{n',b}) \quad \forall n \notin Flex_n, b \in B : b < \pi_n \quad (4')$$

$$V_{n,b} = \sum_{n'<n} (\sigma_{n,n'} \cdot V_{n',b}) + F_{n,b} \qquad \forall n \in Flex_n, b \in B : b < \pi_n \quad (5')$$

$$L_{i,b} \leq V_{n,b} + (b-1) \cdot H \quad \forall i \in I, b \in B, n \in S_{i,n} \quad (6')$$

$$C_{i,b,n} \geq V_{n,b} + (b-1) \cdot H \quad \forall i \in I, b \in B, n \in E_{i.n} \quad (7')$$

Notice that in this case only the batches specified by the periodicity parameter are considered since the allocation decisions are repeated in the cyclic schedule. Since a cyclic scheduling approach is considered, constraints (4) – (7) need to be updated so that the required timing pattern is imposed. More specifically, constraint sets (4') and (5') are only considered for a subset of the total number of batches, which is defined by the periodicity parameter. Notice that the periodicity of a timing element $\pi_n$ is equal to the periodicity of the associated task $\pi_i$. Constraints (6') ensure that the start time of a task will be less than the value of all relative start elements plus the required cycle time. Similarly, the completion times are calculated in the constraint set (7').

### Cyclic heuristic constraints

The constraints described in this subsection are responsible for generating a cyclic rather than a typical production schedule. They ensure a periodic pattern both regarding the timing and the allocation decisions, that is specified by the cycle time and the periodicity parameter.

$$L_{i,b} + H = L_{i,b+1} \forall i \in I : i = 1, b \in B : b < |B| \quad (14)$$

$$Y_{i,b+\pi_i,j} = Y_{i,b,j} \forall i \in I, b \in B, j \in J : b \leq (|B| - \pi_i) \quad (15)$$

$$V_{n,b+\pi_n} = V_{n,b} \forall n \in N, b \in B : b \leq (|B| - \pi_n) \quad (16)$$

$$F_{n,b+\pi_n} = F_{n,b} \forall n \in N, b \in B : b \leq (|B| - \pi_n) \quad (17)$$

$$L_{i,b+\pi_i} \geq C_{i,b} \forall i \in I, b \in B : b \leq (|B| - \pi_i) \quad (18)$$

Constraint set (14) guarantees that the first task *i* of batch *b+1* must start at exactly *H* time units after the start of the same task in the previous batch *b*. It's important to emphasize that this constraint is only valid for the first task of each batch, thus increasing the timing flexibility for the rest of the tasks. The following constraint sets (15) – (18) are tightening constraints that take advantage of the schedule's cyclic nature to improve the model's computational efficiency. In particular, constraints (15) impose that the equipment allocation decisions are repeated for every $\pi_i$ batches. For example, let us assume that task *I1* of batch *B1* is processed in equipment *J1*, and the periodicity of *I1* is 3, then constraint (15) will guarantee that batch *B4* of *I1* will be processed in equipment *J1*. Similarly, constraints (16) and (17) impose the timing constraints of the schedule's cyclic nature utilizing the

periodicity parameter associated with each entity $\pi_n$. Finally, constraint set (18) denotes that task *i* of batch *b*+$\pi_i$ will start after task *i* of batch *b*.

### Cyclic scheduling objective

The goal of the mathematical model is to minimize the production cycle time *H*, which is beneficial for key production metrics, like decreased dead-times and increased throughput.

$$min\ H \tag{19}$$

In summary the mathematical model for the minimization of the cycle time consists of constraints (3') – (7'), (10) – (12), (14) – (18) and the objective function (19).

## CASE STUDY

One case study from the pharmaceutical industry is presented here to illustrate the applicability of the proposed process representation. The case study is solved both for the makespan minimization problem as well as for cyclic time minimization. The case study uses a recipe representing a single step from a multi-step organic synthesis of a small API molecule. The recipe consists of eleven procedures, each requiring several operations. The synthesis steps are executed in two reactors (R-101 and R-102) which utilize two holding tanks (T-101 and T-102) for solution preparation and material holding after each reactor process. A filtration and a drying task complete the recipe. Figure 2 shows a graphical depiction of the reaction and holding procedures and operations with their scheduling links. Blue arrows indicate internal (within a procedure) links while red arrows indicate links across procedures. As it can be seen, there exist complex operation interrelations with various scheduling links.

The reactors execute dedicated tasks; the tanks, however, can be used alternately for any holding task depending on their availability. The transfer of material into a tank from a reactor is considered inflexible but the transferring of material out of the tank to some reactor has a flexible start of 12 hours maximum. In other words, the material can be held in the tank until the destination reactor for the material becomes available.

Figure 3a shows, in the form of a Gantt chart, the optimal schedule of six batches of this process using the makespan minimization objective. For brevity, only the reactor and tank procedures are shown. The batches are identified by different colors in the chart. As seen, the optimal solution makes full utilization of reactor R-101 by inserting tasks of subsequent batch within the gaps between the tasks of each executed batch. This is made possible by the use of flexible shifts in the tank operations that delay the transfer of material to the reactors

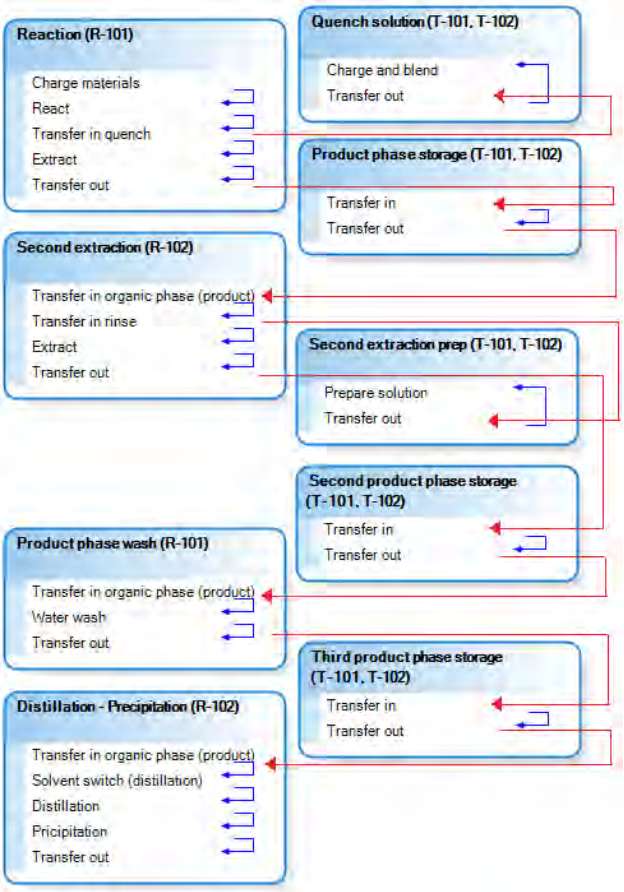



**Figure 2.** Graphical depiction of recipe.

until the latter become available. These flexible shifts are indicated in the charts by the gaps of idle time seen in the operations executed in T-101 and T-102. The optimal make span is calculated at 159 hours.

In the second case shown in Figure 3b, the obtained schedule minimizes the cycle time. In this case, all tasks are executed periodically and all batches are identical. The optimization still makes use of flexible shifts to minimize the cycle time but the shifts have the same value in all batches in order to preserve periodicity. The calculated minimum cycle time is 20.5 hours, but at the expense of increased makespan which is now 171 hours. In an industrial setting, however, a periodic schedule is sometimes favored due to its simplicity in execution.

The SCIP open-source solver [8] was used for the solution of the optimization problems. The recipe representation, formulation of the mathematical optimization problem and visualization of the results were executed in the scheduling software SchedulePro (by Intelligen, Inc.).

## CONCLUSION

In this paper, a novel detailed representation capable of capturing all timing aspects of a production

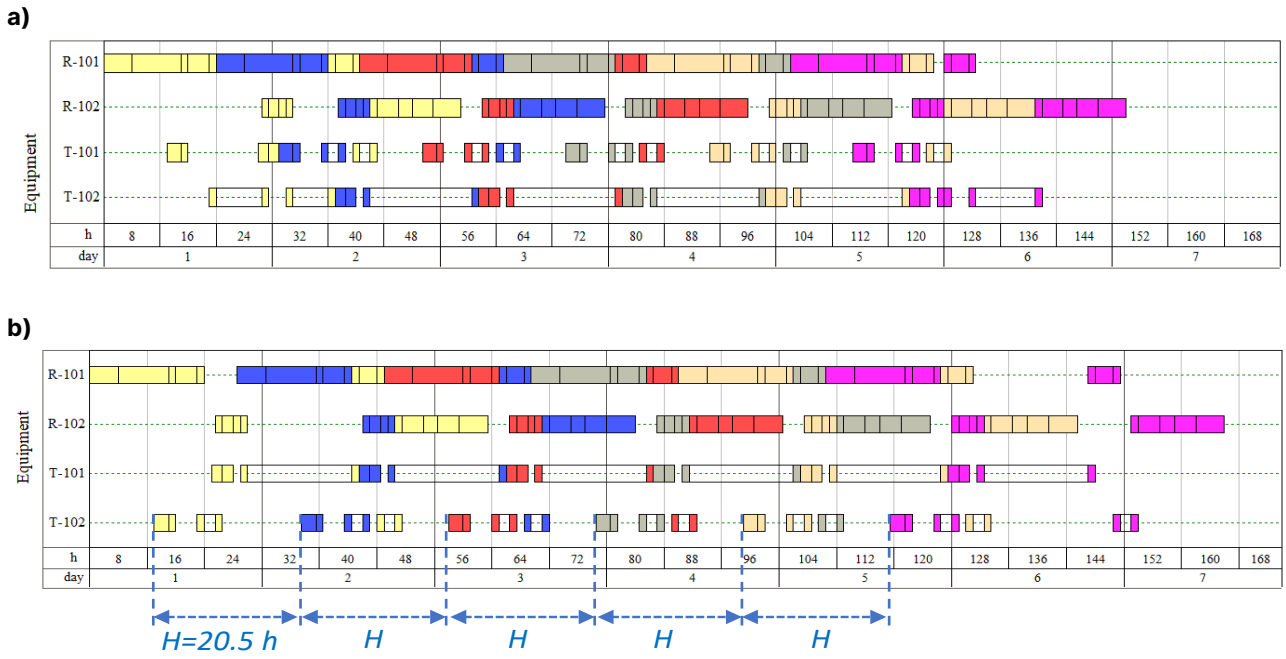



**Figure 3:** Gantt charts for a) makespan minimization and b) cycle time minimization

process is presented. The proposed approach ensures that optimal scheduling decisions even for very detailed recipes can be generated. Based on this representation, two MILP models have been developed - one focusing on makespan minimization and the other on cycle time minimization. The applicability and efficiency of these models are demonstrated through a realistic and complex case study, where optimal schedules are promptly generated. The results highlight the ability of the representation in handling complex production processes facilitating the implementation of optimization-based solutions into real industrial environments, thus reducing the gap between academic research and industrial practice.

## REFERENCES


1. Georgiadis GP, Elekidis AP, Georgiadis MC. Optimization-based scheduling for the process industries: from theory to real-life industrial applications. *Processes* 7:438 (2019) https://doi.org/10.3390/pr7070438
2. Kondili E, Pantelides CC, Sargent RWH. A general algorithm for short-term scheduling of batch operations-I. MILP formulation. *Comput. Chem. Eng.* 17 (2):211-277 (1993) https://doi.org/10.1016/0098-1354(93)80015-F
3. Pantelides, CC. Unified frameworks for optimal process planning and scheduling. *In: Proceedings of the Second Conference on Foundations of Computer Aided Operations. CACHE Publications* 253-274 (1994)
4. Barbosa-Povoa AP, Macchietto S. Detailed design of multipurpose batch plants. *Comput. Chem. Eng.* 18 (11-12):1013-1042 (1994) https://doi.org/10.1016/0098-1354(94)E0015-F
5. Zyngier D, Kelly JD. UOPSS: a new paradigm for modeling production planning & scheduling systems. *In: Proceedings of the Symposium on Computer Aided Process Engineering:* 20 (2012)
6. Samadi A, Maravelias CT. A comprehensive chemical production scheduling representation. *Comput. Chem. Eng.* 181: 108552 (2024) https://doi.org/10.1016/j.compchemeng.2023.108552.
7. Georgiadis GP, Koulouris A. A MILP Model for the Minimization of Cycle Time in Periodic Production Scheduling using Flexible Operation Shifts. *Comput. Aided Chem. Eng.* 53:1651-1656 (2024) https://doi.org/10.1016/B978-0-443-28824-1.50276-3
8. Bestuzheva K, Besançon M, et al. The SCIP Optimization Suite 8.0. arXiv preprint arXiv:2112.08872 (2021)



© 2025 by the authors. Licensed to PSEcommunity.org and PSE Press. This is an open access article under the creative commons CC-BY-SA licensing terms. Credit must be given to creator and adaptations must be shared under the same terms. See https://creativecommons.org/licenses/by-sa/4.0/

Systems & Control Transactions

**Research Article - Peer Reviewed Conference Proceeding**
ESCAPE 35 - European Symposium on Computer Aided Process Engineering
Ghent, Belgium. 6-9 July 2025
Jan F.M. Van Impe, Grégoire Léonard, Satyajeet S. Bhonsale,
Monika E. Polańska, Filip Logist (Eds.)

PSE PRESS

# Enhancing Large-Scale Production Scheduling Using Machine-Learning Techniques

**Maria E. Samouilidou[a], Nikolaos Passalis[a], Georgios P. Georgiadis[a], Michael C. Georgiadis [a,*]**

[a] Aristotle University of Thessaloniki, Department of Chemical Engineering, University Campus, Thessaloniki, 54124, Greece
* Corresponding Author: mgeorg@auth.gr

## ABSTRACT

This study focuses on optimizing production scheduling in multi-product plants with shared resources and costly changeover operations. Specifically, two main challenges are addressed, the unknown changeover behavior of new products and the need for rapid schedule generation after unforeseen events. An innovative framework integrating Machine Learning (ML) techniques with Mixed-Integer Linear Programming (MILP) is proposed for single-stage production processes. Initially, a regression model predicts unknown changeover times based on key product attributes. Then, a representation where distances correlate with changeover times is compiled through multidimensional scaling, allowing constrained clustering to group production orders according to available packing lines. Ultimately, the MILP model generates the production schedule within a constrained solution space, utilizing optimal product-to-line allocation from cluster segmentation. A case study inspired by a Greek construction materials plant is used to validate the proposed approach. The results showed that this framework improves scheduling efficiency by providing rapid solutions, reducing downtime and facilitating the introduction of new products. Overall, a novel scheduling solution is proposed for manufacturing industries that face unknown production data and need quick schedule alternations.

**Keywords**: Scheduling, Optimization, Machine Learning, Industry 4.0, MILP

## 1. INTRODUCTION

As global competition rises and customer expectations increase, manufacturing industries must embrace digital technologies to remain competitive. Fluctuating demands, equipment breakdowns and raw material availability are some challenges that necessitate for schedules to be flexible and to adapt quickly to changing conditions without causing order delays or increased costs. This is particularly difficult in the presence of frequent and expensive product changeovers, since production schedules are typically handled manually and combinatorial complexity of real-life industrial instances does not allow exact methods to deliver optimal solutions quickly.

Recent breakthroughs in Artificial Intelligence (AI) and improvements in algorithms, computational capabilities and data accessibility, are opening up new ways to face challenges in manufacturing [1]. Today, industries have large amounts of data that are not being fully utilized. By applying techniques like ML, they could improve their decision-making processes. ML can help in demand forecasting, optimizing production schedules and managing the workforce efficiently.

Production scheduling is one of the major challenges in manufacturing environments. Fundamental research in production scheduling primarily focused on employing MILP and heuristic approaches. More specifically, Das et al. [2] and Georgiadis et al. [3] focused on reducing changeover times in flexible manufacturing systems. Notable contributions also include MILP formulations for handling sequence-dependent tasks in manufacturing environments [4,5] and decomposition strategies aimed at improving efficiency in scheduling [6,7]. While these scheduling approaches are effective for small and medium-sized problems, they often fail with larger, more complex ones, or when online scheduling is needed, highlighting the need for improvement and development of new rules to optimize solutions.

More recent studies have focused on integrating ML or Reinforcement Learning (RL) into scheduling systems.

Heger et al. [8] improved scheduling efficiency and reduced delays by dynamically adjusting dispatching rules with ML, while Gomes et al. [9] combined ML with optimization to enhance production. Additionally, studies like Hubbs et al. [10] have shown RL's effectiveness in dynamic scheduling environments. While promising, these methods have some critical limitations, including high complexity, overfitting, low data efficiency and long training times, suggesting the need to explore alternative ML approaches. Furthermore, although research on production scheduling has advanced significantly in recent years, its use in real-world industrial settings remains limited.

To overcome such restrictions, this work proposes a hybrid framework for optimizing production scheduling in multi-product, multi-line manufacturing plants that frequently require changeovers. The framework combines ML with a MILP model. Specifically, it creates a representation space where the distance between products correlates with their changeover times. Then the production orders are organized into clusters that match the available packing lines, using constrained k-means clustering. This assignment is introduced into the MILP model to restrict the solution space and allow for quicker schedule generation. Moreover, to address the problem of missing changeover data, the framework includes a ML model that predicts unknown changeover times and identifies infeasible transitions based on key product attributes. The framework is tested on a real-world scenario inspired by a Greek construction materials plant, demonstrating its effectiveness. The proposed approach improves scheduling efficiency, reduces downtime and helps facilities quickly adapt new products to the production.

## 2. PROBLEM STATEMENT

Production scheduling in multi-product industrial plants is a complex task characterized by demand variability and frequent changeovers, which can lead to substantial downtime, resource wastage and operational inefficiencies. For this reason, the establishment of effective scheduling strategies is essential.

The duration of a changeover may vary depending on characteristics of the product such as formulation, quality requirements and physical properties. It is common that the production schedules are altered during the week, thus generating extra changeover operations. Furthermore, changeover data for specific products might be unavailable. Handling changeovers is a complex task, as it requires balancing the need to meet product demand with the goal of reducing inefficiencies and minimizing waste. In response to these dynamic conditions, scheduling approaches that quickly generate optimal solutions are needed.

To address these issues, the integration of ML techniques with MILP models presents a promising approach. Specifically, clustering methods can be utilized to group products with similar changeover requirements, thus narrowing the solution space for scheduling MILP models and facilitating its solution. Moreover, ML-based predictive models can predict changeover times even with incomplete data available. In this way, the production process can become more efficient and responsive.

In this study, a real-world scheduling scenario is examined, based on a construction materials plant in Greece. The facility produces around 240 final products through a two-stage continuous process, including mixing and packaging. There are 4 packing lines available in the facility, which operates 5 days a week. The production process is characterized by frequent changeovers, which vary due to products' properties, making their allocation to the packing lines a challenging task. The production is order driven and organized in a weekly basis.

Particularly, the production process includes the following steps. First, raw materials are weighed according to the product recipe. The weighed materials are fed into a mixing tank. After mixing takes place, the produced mixture is temporarily stored before being packaged by the available packing lines and transferred to the warehouse. It is noted that the whole production process operates in a continuous manner, therefore, production scheduling can be solely focused on the slowest stage, which is the packing stage. This allows for the reduction of the problem size and computational cost.

The problem described is solved using a novel solution framework which combines mathematical modeling and ML, aiming to rapidly create optimal schedules even in the presence of missing changeover data. The aim of this work is not to develop or compare machine learning algorithms but to propose an efficient scheduling solution that addresses the specific challenges of large-scale industries.

## 3. MATHEMATICAL FRAMEWORK

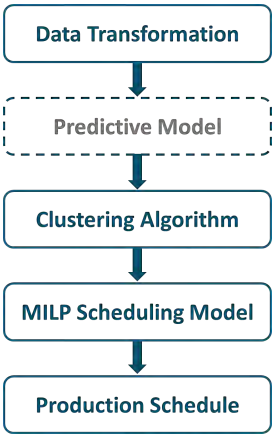



**Figure 1.** Solution strategy.

A hybrid scheduling solution is presented (Figure 1), for manufacturing industries that deal with unknown production data and need quick schedule adjustments. The detailed steps of the model are described in the following subsections.

## 3.1 Data Transformation

The production data must be properly formatted to be utilized in the proposed framework. The data transformation process involves the conversion of raw production data into a standardized format, using numerical and normalized values. Key product features, including raw material type, color, resin content and package size, are compiled into feature vectors, along with changeover duration data. All categorical features were converted into numerical values. For example, raw material type was transformed using one-hot encoding and colors were represented by their corresponding RGB codes. The transformed data serve as inputs for the next steps of the framework.

## 3.2 Predictive Model

This is an optional step, applicable in cases where there are missing data. Unknown changeover data, particularly when new products are introduced or when specific transitions have never been tested, should be predicted for smoother product transitions. ML forecasting models can be employed to estimate the unknown information. Specifically, a data-driven approach is used to predict missing changeover times. The approach uses a pair-based prediction method to estimate changeover times for any two products, whether or not they are part of the training set, based on the feature vectors of the product pair. The objective function for training the model is to minimize the difference between predicted and actual changeover times. To train the model, a regularized predictor is used, in particular Polynomial Regression with L2 Regularization, due to the small size of the dataset available. A third-order polynomial is chosen to capture the non-linear changeover behavior and to avoid excessive variance. L2 regularization is applied to penalize large coefficients and prevent overfitting. If more data were available, more advanced techniques like Deep Learning could be used, however, such models may not perform well with small datasets due to overfitting. The predicted changeover times are used to create practical production schedules.

## 3.3 Clustering Algorithm

The aim is to simplify the complex scheduling problem by decomposing it into smaller sub-problems. This is achieved by clustering products into groups corresponding to the available packing lines. The goal is to identify clusters that minimize the total expected within-cluster changeover time $T_i$, given by equation (1).

$$T_i = \frac{1}{|\mathcal{C}_i|} \sum_{p \in \mathcal{C}_i} \sum_{\substack{p' \in \mathcal{C}_i, \\ p' \neq p}} \min(ch_{p,p'}, ch_{p',p}) \tag{1}$$

Where $|\mathcal{C}_i|$ is the number of products in the $i^{th}$ cluster, and the minimum of $ch_{p,p'}$ and $ch_{p',p}$ represents the best-case changeover time between two products $p$ and $p'$, when changeovers are not symmetrical. Using the average changeover time could overestimate distances, leading to less efficient clustering, whereas using the best-case scenario results in more compact, homogeneous clusters. While $T_i$ does not represent actual changeover times for specific schedules, it serves as an estimator for the average expected changeover time within each cluster.

To facilitate the clustering process, a structured approach is proposed, inspired by clustering-oriented representation learning methods [11]. A new representation space $z_p$ is compiled for each product, where the distance between products reflects their changeover time. Particularly, a distance metric $d(z_p, z'_p)$ is learned to approximate the changeover time between two products. In this representation, products closer to each other have smaller changeover times, making it easier to group them effectively for scheduling purposes. The Euclidean distance is used as the distance metric. Since Euclidean distance is symmetric and cannot handle asymmetry, the approach focuses on the expected changeover time, which is calculated as the minimum changeover time between two products.

The learning objective minimizes the difference between the distance in the new representation space and the expected changeover time as shown in (2).

$$\min \sum_{p \in P} \sum_{\substack{p' \in P \\ p' \neq p}} \left( d(z_p, z'_p) - \min(ch_{p,p'}, ch_{p',p}) \right)^2 \tag{2}$$

This can be interpreted a classical Multidimensional Scaling (MDS) problem with distance targets equal to $\min(ch_{p,p'}, ch_{p',p})$. The application of this method produces a changeover-time driven representation space. K-means clustering can be applied on this space to group the products based on their new representations, minimizing the within-cluster distances $D_i$, which is equivalent to minimizing the expected changeover time $T_i$ within each cluster, as explained in (3).

$$D_i = \frac{1}{|\mathcal{C}_i|} \sum_{p \in \mathcal{C}_i} \sum_{\substack{p' \in \mathcal{C}_i, \\ p' \neq p}} \left|\left| z_p - z_{p'} \right|\right|_2^2 = T_i \tag{3}$$

By grouping products into clusters with small changeover time values, the complexity of the scheduling problem is significantly reduced. In this way, clusters can be assigned to specific production lines and sequencing decisions are only made for the products within a cluster. This approach enhances computational efficiency while

ensuring practical and effective production schedules.

It is noted that the clustering solution also respects production time constraints by ensuring that all products within a cluster can be produced within the available time on each production line. This is done using a constrained k-means approach. To account for the sensitivity of k-means to initial cluster centers, the algorithm is run multiple times with different random initializations, and the best clustering solution is selected after evaluating the total expected within-cluster changeover time.

### 3.4 MILP Scheduling Model

To address the production scheduling challenges described, an immediate precedence MILP model developed within our group [12] is employed. The model incorporates mass balance, assignment, timing and sequencing constraints, using a continuous time frame for precise timing decisions. The objective of the model is to minimize the production's total changeover time. The allocation of products to packing lines given from the previous step of the framework is inserted as a fixed decision into the scheduling model, thus reducing its complexity and facilitating its solution. The mathematical model is implemented in GAMS 42.5.0 and solved using CPLEX 12.0. The following represent the key constraints included in the mathematical model.

$$\sum_{j \in Pj} Y_{p,j} = 1 \quad \forall\, p \tag{4}$$

$$\sum_{p' \neq p, p' \in Pj} X_{p',p,j} \leq Y_{p,j} \quad \forall\, j, p \in Pj \tag{5}$$

$$\sum_{p' \neq p, p' \in Pj} X_{p,p',j} \leq Y_{p,j} \quad \forall\, j, p \in Pj \tag{6}$$

$$\sum_{p \in Pj} \sum_{p' \neq p, p' \in Pj} X_{p,p',j} + 1 = \sum_{p \in Pj} Y_{p,j} \quad \forall\, j \tag{7}$$

$$C_{p,j} + ch_{p,p'} \cdot X_{p,p',j} \leq C_{p',j} - r_{p'} \cdot Y_{p,j} + \omega\left(1 - X_{p,p',j}\right) \quad \forall\, j, p \in Pj, p' \in Pj, p' \neq p \tag{8}$$

$$C_{p,j} \geq (s + r_p) \cdot Y_{p,j} + \sum_{p' \neq p,\, p' \in Pj} ch_{p',p,j} \cdot X_{p',p,j} \quad \forall\, j, p \in P_j \tag{9}$$

$$C_{p,j} \leq \omega \cdot Y_{p,j} \quad \forall\, j, p \in P_j \tag{10}$$

$$\min \sum_{j, p \in Pj} \sum_{p' \neq p, p' \in Pj} ch_{p,p',j} \cdot X_{p,p',j} \tag{11}$$

Constraints (4) guarantee that each product *p* is assigned to a single packing line *j* through the binary allocation variable $Y_{p,j}$. The set $Pj$ introduces the potential assignment of products to processing lines. Constraints (5) and (6) ensure that each product assigned to a processing unit *j* has only one direct predecessor and successor *p'* in the production sequence, using the sequence binary variable $X_{p,p',j}$. Constraints (7) require that the total number of active allocation variables for the packing line must be one greater than the sum of all active sequence binary variables. Constraints (8) dictate that if two products are processed consecutively in a unit, the completion time of the second product $C_{p',j}$ minus its processing time $r_{p'}$ must be greater than the completion time of the first product plus the required changeover time between them $ch_{p,p'}$. Constraints (9) and (10) establish that the completion time of a product is greater than the sum of its setup time $s$, processing time and the required changeover time but does not exceed the available production horizon. Lastly, constraint (11) represents the objective function of the model, which is to minimize the total changeover time across all production lines.

### 3.5 Production Schedule

By implementing data preprocessing, unknown data regression and clustering, the production orders are organized into clusters with minimal changeover times. This assignment is then input into the scheduling MILP model and production schedules characterized by minimum changeover times and efficient use of packing lines are generated. The employment of this framework results in time-efficient production schedules for multi-product industrial plants with frequent changeover operations.

## 4. RESULTS & DISCUSSION

Initially, the prediction of missing changeover data was examined. This is something which can occur either when certain product-to-product transitions have not been tested or when new products are introduced into production. Accurately predicting these changeover times is essential, as selecting an unfavorable or infeasible production sequence can lead to downtime and waste.

To achieve this, key factors that influence changeover times, such as raw material type, color, resin content and package size are used as features in a predictive model. A cubic polynomial regression model is used, with a regularization hyperparameter $\lambda$ set to 0.01, as it was found to provide the best fit to the data. To prevent overfitting, L2 regularization is applied.

Eight case studies were conducted to evaluate the performance of the predictive model (Table 1). In each case, 10-12 products were removed from the initial dataset to serve as the test data, while the remaining data was used for training. Only a small proportion was chosen for testing due to the limited size of the dataset. Testing with larger proportions could potentially compromise the model's ability to learn generalizable patterns.

The model's performance was assessed based on its ability to accurately predict infeasible changeovers (Infeasible Changeover Accuracy % – ICA), as well as its

Mean Squared Error (MSE) and Mean Absolute Error (MAE). As shown in Table 1, the model exhibits high prediction accuracy across both training and testing datasets. On the training data, the model achieves an average ICA of 99.71%, with a MSE of 0.022 and a MAE of 0.072. On the testing data, it demonstrates an ICA of 99.90%, with a MSE of 0.018 and a MAE of 0.074.

**Table 1:** Predictive model metrics.

| | ICA % | | MSE | | MAE | |
|---|---|---|---|---|---|---|
| Case | Train | Test | Train | Test | Train | Test |
| 1 | 99.65 | 99.77 | 0.024 | 0.023 | 0.071 | 0.081 |
| 2 | 99.75 | 100.00 | 0.020 | 0.010 | 0.073 | 0.064 |
| 3 | 99.75 | 99.89 | 0.020 | 0.019 | 0.072 | 0.079 |
| 4 | 99.76 | 100.00 | 0.020 | 0.020 | 0.073 | 0.080 |
| 5 | 99.75 | 99.87 | 0.019 | 0.020 | 0.071 | 0.078 |
| 6 | 99.64 | 99.85 | 0.025 | 0.021 | 0.073 | 0.072 |
| 7 | 99.64 | 99.85 | 0.025 | 0.019 | 0.073 | 0.070 |
| 8 | 99.76 | 100.00 | 0.020 | 0.013 | 0.073 | 0.071 |
| Avg | 99.71 | 99.90 | 0.022 | 0.018 | 0.072 | 0.074 |

With the problem of unknown production data solved, the next part of the study focuses on improving scheduling efficiency by minimizing total changeover time across packing lines in shorter timeframes. In fast-paced industrial settings, production schedules often need to be quickly adjusted multiple times a day due to unforeseen changes. For this reason, the proposed approach was applied to assess the produced schedules and the computational times.

Four scenarios involving 100 to 130 production orders over a 120-hour horizon were investigated, since the problem size and order mixture are expected to have an impact on the production schedules obtained. First, the monolithic MILP model was used to solve the problem, with a CPU time limit of 2 hours. This time restriction was introduced due to the practical limitations of computationally expensive methods in real-world applications. For cases where the MILP model failed to find an optimal solution within this time, the best solution obtained during this period was recorded.

The proposed solution framework (PROP) was then applied to the same scenarios. The framework initially grouped production orders into clusters using the representation and clustering step, ensuring that each packing line handled products with minimal changeover times. Employing the representation step helps to separate the clusters more clearly, as shown in Figure 2. The axes represent the two dimensions of the reduced space obtained through MDS. The product mixture may lead to more dispersed clusters in some case studies, affecting clustering time, which remains minimal, but with little to no impact on optimality.

It is noted that some points may appear to fit better in a different cluster, but they were placed in neighboring clusters due to production line operating time constraints. The allocations were subsequently input into the MILP scheduling model, to reduce the solution space, improving computational efficiency.

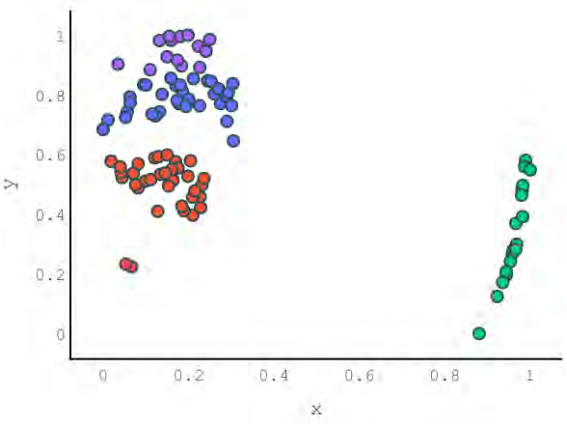



**Figure 2.** Clusters of production orders for case study A.

Table 2 summarizes the results of the case studies examined, organized by the number of weekly orders in ascending order. The two approaches are assessed based on their computational cost and the objective values.

**Table 2:** Comparison between the two approaches.

| | Objective | | | CPU (s) | |
|---|---|---|---|---|---|
| Case | MILP | PROP | Diff% | MILP | PROP |
| A | 17.41 | 14.66 | -15.8 | 7200 | 27.4 |
| B | 19.87 | 15.54 | -21.8 | 7200 | 4.1 |
| C | 24.13 | 17.54 | -27.3 | 7200 | 8.0 |
| D | 25.76 | 18.62 | -27.7 | 7200 | 3.4 |

Combining clustering techniques with optimization methods significantly improved computational efficiency, generating high-quality schedules with the smallest objective values within seconds across all case studies. While the monolithic MILP model failed to find optimal solutions within a 2-hour limit, the proposed framework consistently delivered efficient results, especially for more complex problems which showcased greater improvements. The framework seems to effectively reduce problem complexity, demonstrating its suitability for dynamic industrial environments.

## 5. CONCLUSIONS

This study proposed a framework to optimize production scheduling in multi-product manufacturing plants with parallel production lines, shared resources and frequent changeover operations. The framework integrates ML techniques with MILP to address two main challenges, minimizing product changeover times and predicting unknown changeover durations.

The ML-based predictive model addressed the

issue of missing changeover data by achieving high accuracy in its predictions. It identified infeasible transitions with over 99.6% accuracy and achieved a low prediction error, with an average MSE of 0.02 and MAE of 0.07. These outcomes make it easier to integrate new products into production schedules while minimizing disruptions and inefficiencies. Additionally, the results of the presented framework showed significant improvements in scheduling efficiency. The computational time was cut down by two orders of magnitude. Furthermore, across different case studies, the objective value was reduced by 16% to 28%, highlighting the framework's ability to generate more effective schedules.

The results indicate that the proposed approach is suitable for dynamic real-world industrial environments where changeovers are a major source of downtime and waste. However, the framework does have limitations. Since the approach is not exact, the results can vary depending on the initial clustering configuration and production order combinations. Future work could focus on taking into consideration additional plant constraints, such as due dates and raw material availability, to further improve its applicability. Furthermore, it could focus on extending the model to account for multi-stage production processes and investigating alternative objective functions. Finally, testing advanced ML techniques, like neural network-based solutions, could enhance prediction accuracy and error minimization.

## ACKNOWLEDGEMENTS

The authors would like to thank ISOMAT S.A for inspiring this research and sharing valuable insights into industrial challenges, which helped shape the problem addressed in this study.

## REFERENCES

1. Jiang Z, Yuan S, Ma J, Wang Q. The evolution of production scheduling from Industry 3.0 through Industry 4.0. *Int J Prod Res* 60(11):3534-3554 (2022) https://doi.org/10.1126/science.aaa8415
2. Das K, Baki MF, Li X. Optimization of operation and changeover time for production planning and scheduling in a flexible manufacturing system. *Comput Ind Eng* 56(1):283-293 (2009) https://doi.org/10.1016/j.cie.2008.06.001
3. Georgiadis GP, Pampín BM, Cabo DA, Georgiadis MC. Optimal production scheduling of food process industries. *Comput Chem Eng* 134:106682 (2020) https://doi.org/10.1016/j.compchemeng.2019.106682
4. Nazarian E, Ko J, Wang H. Design of multi-product manufacturing lines with the consideration of product change-dependent inter-task times, reduced changeover and machine flexibility. *J Manuf Syst* 29(1):35-46 (2010) https://doi.org/10.1016/j.jmsy.2010.08.001
5. Velez S, Dong Y, Maravelias CT. Changeover formulations for discrete-time mixed-integer programming scheduling models. *Eur J Oper Res* 260(3):949-963 (2017) https://doi.org/10.1016/j.ejor.2017.01.004
6. Castro PM, Harjunkoski I, Grossmann IE. Greedy algorithm for scheduling batch plants with sequence-dependent changeovers. *AIChE J* 57(2):373-387 (2011) https://doi.org/10.1002/aic.12261
7. Samadi A, Maravelias CT. Computational enhancements of continuous production scheduling MILPs using tightening constraints. *Comput Chem Eng* 184:108609 (2024) https://doi.org/10.1016/j.compchemeng.2024.108609
8. Heger J, Branke J, Hildebrandt T, Scholz-Reiter B. Dynamic adjustment of dispatching rule parameters in flow shops with sequence-dependent set-up times. *Int J Prod Res* 54(22):6812-6824 (2016) https://doi.org/10.1080/00207543.2016.1178406
9. Gomes M, Silva F, Ferraz F, Silva A, Analide C, Novais P. Developing an ambient intelligent-based decision support system for production and control planning. *Intelligent systems design and applications*: 984-994 (2017) https://doi.org/10.1007/978-3-319-53480-0_97
10. Hubbs CD, Li C, Sahinidis NV, Grossmann IE, Wassick JM. A deep reinforcement learning approach for chemical production scheduling. *Comput Chem Eng* 141:106982 (2020) https://doi.org/10.1016/j.compchemeng.2020.106982
11. Passalis N, Tefas A. Information clustering using manifold-based optimization of the bag-of-features representation. *IEEE Trans Cybern* 48(1):52-63 (2016) https://doi.org/10.1109/TCYB.2016.2623581
12. Elekidis AP, Corominas F, Georgiadis MC. Production scheduling of consumer goods industries. *Ind Eng Chem Res* 58:23261–23275 (2019) https://doi.org/10.1021/acs.iecr.9b04907

© 2025 by the authors. Licensed to PSEcommunity.org and PSE Press. This is an open access article under the creative commons CC-BY-SA licensing terms. Credit must be given to creator and adaptations must be shared under the same terms. See https://creativecommons.org/licenses/by-sa/4.0/



Systems & Control Transactions

**Research Article - Peer Reviewed Conference Proceeding**
ESCAPE 35 - European Symposium on Computer Aided Process Engineering
Ghent, Belgium. 6-9 July 2025
Jan F.M. Van Impe, Grégoire Léonard, Satyajeet S. Bhonsale,
Monika E. Polańska, Filip Logist (Eds.)

PSE PRESS

# Multiscale analysis through the use of biomass residues and $CO_2$ towards energetic security at country scale via methane production

**Guillermo Galán[a], Manuel Taifouris[a], Mariano Martín[a]*, and Ignacio E. Grossmann[b]**

[a] University of Salamanca, Department of Chemical Engineering, Salamanca, Salamanca, SPAIN
[b] Carnegie Mellon University, Department of Chemical Engineering, Pittsburgh, PA, U.S.A.
* Corresponding Author: mariano.m3@usal.es.

## ABSTRACT

The growing demand for sustainable energy has driven research into renewable methane production to reduce greenhouse gas emissions and reliance on fossil fuels. Promising feedstocks include lignocellulosic dry residues, wet waste, and captured $CO_2$, converted via gasification, anaerobic digestion, and synthetic processes with renewable hydrogen. This study uses a multiscale approach to compare these sources, incorporating a techno-economic evaluation to identify key performance indicators (KPI) for facilities and renewable energy sources. A facility location problem (FLP) determines plant locations and production capacities, considering material availability and transportation costs. The analysis focuses on the decentralised use of wastes and $CO_2$ from point and diluted sources across Spain, employing an MILP model to optimise waste and $CO_2$ utilisation alongside solar and wind energy systems. Results highlight lignocellulosic dry waste and $CO_2$ captured with MEA from point sources as the most promising options. Sensitivity analysis predicts methane prices between 13.028 €/MWh and 47.216 €/MWh through 2050, requiring substantial investment for full methane self-sufficiency. With carbon taxes, the price could drop to 10.735 €/MWh by 2050, competitive with current natural gas prices.

**Keywords**: DAC, electrolysis, green hydrogen, synthetic natural gas, strategic $CO_2$ and biomass waste valorisation, methane production and distribution

## 1. INTRODUCTION

Industrial and transportation growth has increased atmospheric $CO_2$ levels from 300 ppm in the late 19$^{th}$ century to 425 ppm in 2024, contributing to a 1ºC global temperature rise [1]. The 2015 Paris Agreement aims to limit warming to 1.5ºC, reducing emissions by 55% by 2030 and achieving net zero by 2050 [2].

Meeting these targets requires transitioning to decarbonised energy systems, especially in the energy and chemical sectors. Geopolitical disruptions, mainly the Ukraine conflict, highlight Europe's energy vulnerabilities, emphasising the need for self-reliant solutions. Synthetic methane production offers a promising route to energy resilience and reduced fossil fuel dependence. The $CO_2$ capture methods include biomass growth, which absorbs $CO_2$ naturally and engineered systems that capture emissions from industrial sources and the atmosphere. Biomass can be used to produce bioethanol, DME, methanol [3], and biodiesel, but challenges such as land, water, and fertiliser limit its scalability. Dry wastes such as lignocellulosic raw material are used via gasification to produce synthetic biomethane. Manure, municipal solid waste (MSW), and sludge are processed via anaerobic digestion to produce biogas and biomethane [4], though logistics and environmental issues reduce efficiency, leading to landfill or incineration. Carbon capture, utilisation, and storage (CCUS) technologies are crucial for meeting climate targets by capturing $CO_2$ from industrial sources for storage or conversion. Methods such as physisorption and amine-based chemisorption face challenges in capturing ambient $CO_2$ due to high energy demands. Direct air capture (DAC) technologies, such as alkaline solutions and BPMED, show promise, especially

when combined with renewable hydrogen to produce methanol or synthetic methane [5].

Current research often addresses processes separately from biomass supply chain optimisation, MSW-to-liquid-fuel, and biogas and $CO_2$ utilisation, but few integrate waste, biomass, and $CO_2$ for synthetic methane production [6]. This study fills this gap by offering a multiscale framework to enhance energy security, using an extended Facility Location Problem (FLP) is formulated as a Mixed-Integer Linear Programming (MILP) across 356 Spanish shires to optimise waste utilisation into methane, integrating various feedstocks and technologies for sustainable energy independence.

## 2. METHODOLOGY

This work evaluates renewable resources and biowastes, such as lignocellulosic waste, manure, MSW, sludge, and captured $CO_2$, to reduce fossil fuel dependence. It optimises waste treatment, $CO_2$ capture, hydrogen electrolysis, and methane production, relying on decentralised utilisation powered by PV and wind energy [6].

### 2.1. Process level analysis

This section depicts technologies for waste management, $CO_2$ capture, and methane conversion, focusing on waste recovery, gasification, digestion, hydrogen production, and renewable energy harvesting.

#### 2.1.1. Waste treatment technologies

**Gasification:** This process converts lignocellulosic waste into syngas for biomethane production using an indirect gasifier-combustor. $H_2S$ is removed with ZnO, and methanation produces biomethane, refined by PSA to reduce $CO_2$ to 2% [7].

**Anaerobic digestion**: This technology processes high-water-content biowaste to produce biogas, upgrading it to biomethane with $H_2S$, $CO_2$, $NH_3$, and $H_2O$ removal [7].

#### 2.1.2. $CO_2$ capture technologies

**Point sources:** $CO_2$ is captured using aqueous amine solutions (MEA) at 25-30°C and partial pressures over 0.05 bar, achieving 90-95% removal at 0.1 bar, with a 20% MEA concentration.

**Diluted sources:** $CO_2$ is captured from the air via DAC technology. Fans pass air through KOH-based solutions, where KOH converts $CO_2$ into $HCO_3^-$ and $CO_3^{2-}$ ions. KOH is regenerated with $Ca(OH)_2$, producing $CaCO_3$, which is dried and calcinated with biogas to regenerate $Ca(OH)_2$[6].

#### 2.1.3. Electrolytic hydrogen production

Green hydrogen is produced via water electrolysis using solar or wind power, and purified by condensation, deoxygenation, and zeolite dehydration.

#### 2.1.4. Energy harvesting

**Wind energy:** A GE 1.5sle turbine with a nominal power of 1,500 kW is considered. Installation costs in 2022 are 1,600 €/kW, and operating costs are 0.026 €/kWh. $CO_2$ emissions are 0.012 $kgCO_2$/kWhe.

**Solar energy:** PV panels generate power, with each 4 $m^2$ panel producing 1 kW peak (kWp) at 25% efficiency ($\eta_{PV}$). The total panel surface reaches up to 7 $m^2$ due to installation needs. In 2022 costs are 1,050 €/kWp and 0.042 €/kWh, with $CO_2$ emissions of 0.048 $kgCO_2$/kWhe.

#### 2.1.5. Methane synthesis

e-Methane is produced from $CO_2$ via methanation using renewable hydrogen and captured $CO_2$ at 1-30 bar and 140°C-350°C. Synthetic biomethane is obtained from syngas methanation, while biomethane comes from biogas upgrading. Purification achieves over 95% methane purity.

### 2.2. Process technologies surrogate modelling and process scale-up

The formulation of the FLP requires surrogate input-output models for the waste processing technologies, including manure, 63-368 kt/year, MSW, 20-53 kt/year, and lignocellulosic biomass, 10-820 kt/year, with corresponding CAPEX and OPEX. Up to 50 designs are modelled, yielding 0.012, 0.070, and 0.285 $kg_{Biomethane}$/kg [7].

The $CO_2$ capture modelling includes yields, energy requirements, and linearised CAPEX and OPEX for MEA and conventional DAC systems. CAPEX and OPEX follows Sinnott's methodology, excluding waste disposal. Auxiliary costs (steam, water, energy) are based on mass and energy balances. CAPEX includes equipment sizing for compressors, heat exchangers, filters, and cyclones.

#### 2.3.1. Description of resources

The extended FLP model includes $CO_2$ capture, biomass availability, and processing methods across 356 Spanish shires, limiting surface use by up to 2%. It prioritizes PV panels for renewable power. Gasification processes dry lignocellulosic biomass, while wet wastes require anaerobic digestion. $CO_2$ emissions, measured in $kt_{CO_2}$/year, include industrial, agricultural, livestock, and transport sources using MEA and DAC systems. Solar and wind availability are based on annual averages of solar irradiance, and wind velocity.

#### 2.3.2. Formulation of the FLP problem

Each shire is defined by its capital city's latitude and longitude, evaluating $CO_2$ capture, sun and wind availability, and shire area for PV panels, considering:

1. Biowaste, $CO_2$ captured from point and diluted sources using MEA solutions and DAC technology, solar radiation and wind velocity data, and land availability to

build infrastructures.

2. Surrogate models using first principles such as mass and energy balances, thermodynamic equilibrium and correlations based on predicting yield, production, and costs for $CO_2$ capture, renewable energy, biomass gasification, anaerobic digestion, hydrogen production, and methane synthesis, estimating performance and costs, such as CAPEX and OPEX, based on the last processes facility capacities.

3. Network modelling for biomass, $CO_2$, and hydrogen transportation between production sites and processing installations, optimising the use of decentralised resources to reduce transportation costs.

4. An objective function to maximise $CO_2$ usage within the budget, minimising network costs. The objective is to maximise the $CO_2$ captured within the assigned budget, focusing on minimising network costs through the integration of transportation, processing, and renewable energy generation.

Key variables include selecting biomass and $CO_2$ sources, facility capacities, and locations for $CO_2$ capture, hydrogen, and renewable energy production.

#### 2.3.3. Resolution method and limitations

The resolution method optimises resource integration and cost efficiency, starting with a process-level analysis of waste treatment, $CO_2$ capture, hydrogen production, and energy generation. This is expanded into a multiscale framework that integrates different levels of analysis: a process-level evaluation, which assesses technologies and costs; a resource availability analysis, which considers the spatial distribution of biomass, waste, and $CO_2$ sources; and a country-level optimisation scale, which determines the optimal locations for facilities based on economic and geographic constraints. The FLP is formulated as an MILP model to optimise facility locations and costs, ensuring decentralised production and strategic energy security. Limitations include data availability, uncertainties in technology performance, and external factors like legislative changes, which may impact technology deployment and require further investigation.

## 3. CASE STUDY

### 3.1. General settings, constraints, and assumptions of the case study

The FLP optimisation model is formulated analysing 356 Spanish shires. It considers 29,900 kt/year of dry waste, 121,400 kt/year of manure, 9,500 kt/year of MSW, 3,400 kt/year of sludge, and $CO_2$ emissions from human activities, totalling 93,327 $kt_{CO_2}$/year and 102,250 $kt_{CO2}$/year, from point and diluted sources. Renewable energy data is sourced from Sun and Wind Atlas. The MILP considers a 10,195 M€ MITECO budget, 23,911 equations, and 91,192 variables, and is solved using CPLEX.

### 3.2. Working data, parameters, variables, and evolution over the time horizon

The study analyses waste availability in 2022, 2030, and 2050, with Spain's population of 50–60 million stabilising waste generation through improved consumption, ensuring consistent synthetic biomethane and biogas production. $CO_2$ availability is based on 2022 data, assuming constant emissions despite policy cuts. By 2050, CAPEX for PV panels drops from 1,050 to 297.8 €/kWp, and wind turbines from 1,600 to 1,138.7 €/kW. OPEX falls for PV from 0.042 to 0.009 €/kWh and wind turbines from 0.026 to 0.013 €/kWh. Synthetic methane production integrates $CO_2$ capture, water use, $H_2$ and $O_2$ generation, while carbon taxes rise to 180 €/$t_{CO_2}$.

## 4. RESULTS AND DISCUSSION

This section analyses decentralised methane production from lignocellulosic waste, manure, MSW, and $CO_2$, focusing on costs in MITECO's 2020–2050 budgets. It assesses CAPEX and OPEX, a sensitivity analysis on infrastructure, prices, and carbon tax credits, as well as limitations like data gaps and legislative uncertainty.

### 4.1. Analysis of current state: Year 2022

#### 4.1.1. Use of the different waste materials, $CO_2$ capture, and use

Without a carbon tax, synthetic bio-methane and bio-methane are produced using 26,702 kt/year of lignocellulosic dry biomass, 83,070 kt/year of manure, and 7,775 kt/year of MSW. Waste treatment needs 11,174 M€ as investment and 5,341 M€/year in operating costs. The optimal scenario prioritises lignocellulosic dry waste for its high yield, especially in river-adjacent regions like the Duero, Ebro, and Guadalquivir (Figure 1a). Manure and MSW contribute 2,750 kt/year and 1,790 kt/year of biomethane, respectively. Shires where manure is used are shown in Figure 1b, but sludge is excluded due to its moisture content [7]. $CO_2$ capture reaches 5,858 kt/year, below previous estimates of 10,000–12,500 kt/year [6]. MEA solutions, chosen for low costs, are used in northern Spain and the Balearic Islands. Carbon taxes phase out manure and MSW, cutting costs by over 50%.

#### 4.1.2. Production of renewable energy

The system requires 147 km² of PV panels, approximately 2% of Spain's available area, and 2,465 wind turbines. Combined, investment and operating costs reach up to 28,020 M€ and 2,430 M€/year, generating 7.3 GW, over 6% of Spain's 2022 electricity output. PV panels are prevalent in southeastern Spain, with wind turbines in coastal and mountainous regions (Figures 1e and 1f). With

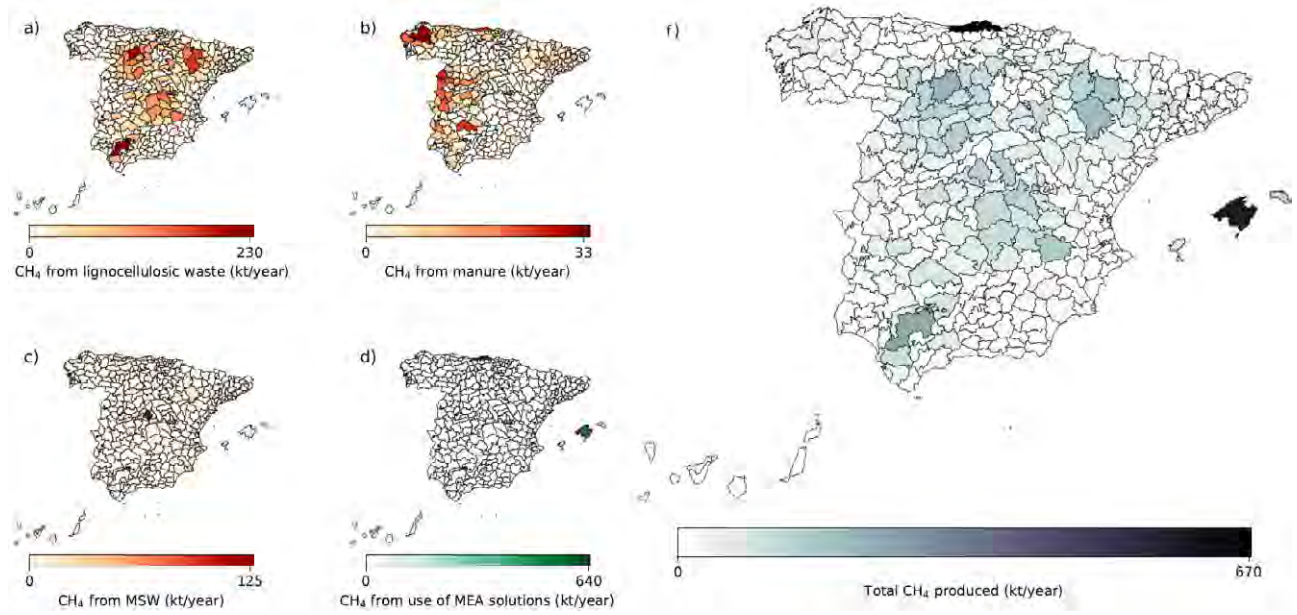



**Figure 1.** Distribution of lignocellulosic dry waste (a), manure (b), MSW (c), sludge (d), and methane production (f) by shires in Spain in 2022, without carbon tax.

a carbon tax, synthetic methane demand doubles the PV panel area to 290 km², representing an increase of almost 100%, while turbine numbers remain stable. Costs rise to 49,355 M€ and 4,282 M€/year, with energy output growing to 12.4 GW. PV panel deployment expands, but turbine locations remain unchanged.

### 4.1.3. Methane production

Synthetic methane production requires 3 $kg_{CO_2}/kg_{CH_4}$ and 0.41 $kg_{H_2}/kg_{CH_4}$ [6]. Without carbon taxes, Spain produces 11,104 kt/year of renewable methane, covering nearly 46% of national consumption in 2022 [7]. Synthetic biomethane comes mainly from lignocellulosic waste, 7,610 kt/year. Investment and operating costs are 14,440 M€ and 5,900 M€/year. Hydrogen needs are 805 $kt_{H_2}$/year, costing 3,202 M€ and 304 M€/year. With a carbon tax, lignocellulosic waste generates 7,610 kt/year of biomethane, 31.5% of consumption, and synthetic methane rises to 3,300 kt/year, with total methane production reaching 10,910 kt/year and costs dropping to 11,989 M€ and 3,284 M€/year.

### 4.1.4. Evolution of self-sufficiency methane percentage, and methane prices

In 2022, methane self-sufficiency without carbon taxes is 30.7%, with lignocellulosic waste contributing 25% of the budget. MEA solutions raise self-sufficiency to 42.9% at 300%, with full self-sufficiency needing 410.4% and methane prices reaching 124.69 €/MWh. With a carbon tax, $CO_2$ capture accelerates, favouring MEA. Lignocellulosic waste provides 31.5% self-sufficiency at 15% of the budget, while MSW replaces manure at 125%, adding 2.1%. Full self-sufficiency requires four times the budget, reducing methane prices to 100.35 €/MWh. By 2030 and 2050, MEA and DAC reduce prices and self-sufficiency.

### 4.1.5. Environmental impact of energy generation: $CO_2$ emissions, minerals required, and water use

Among renewable sources, PV panels emit 2,325 $kt_{CO_2}$/year and wind turbines 188 $kt_{CO_2}$/year, contributing 1.19% and 0.10% to Spain's 2022 $CO_2$ emissions. PV panels are preferred for cost-effectiveness, requiring 55,759 t of minerals, accounting Cu, Ni, Mn, Cr, Mo, Zn, Rare Earths, Si. Mineral extraction emits 321 $kt_{CO_2}$ for PV and 86 $kt_{CO_2}$ for wind, totalling 2,646 $kt_{CO_2}$. Water usage is $1.6 \cdot 10^7$ m³/year for PV, $6.7 \cdot 10^5$ m³/year for wind turbines, and $7.3 \cdot 10^6$ m³/year for hydrogen production. A carbon tax boosts PV panel deployment, increasing emissions from mineral extraction and resource demands. Mineral needs rise to 90,077 t of minerals. The $CO_2$ emissions reach 5,051 $kt_{CO2}$ for PV and 273 $kt_{CO2}$ for wind turbines. Water use is up to $3.06 \cdot 10^7$ m³/year for PV.

## 4.2. Analysis of the future status: Years 2030 and 2050

### 4.2.1. Use of the different waste materials, $CO_2$ capture, and its use

By 2030, lignocellulosic dry waste will produce 25,292 kt/year of synthetic biomethane, a 5.28% decrease from 2022 due to lower technology costs and improved efficiency (Figure 2a). Investment and operating costs will drop to 5,604 M€ and 1,826 M€/year, a

reduction of 49.84% and 65.81%, excluding manure and MSW (Figures 2b, 2c). Point sources will emit 29,378 $kt_{CO_2}$/year, increasing by 400% with lower costs and efficiency gains (Figure 2d). Spain's carbon tax of 150 €/$t_{CO_2}$ will reduce lignocellulosic waste use to 20,328 kt/year, lowering costs to 3,688 M€ and 1,130 M€/year, while MEA solutions capture 32,231 $kt_{CO_2}$/year (Figure 2d).By 2050, lignocellulosic waste use will drop to 24,052 kt/year, with costs at 5,044 M€ and 1,591 M€/year. With a 180 €/$t_{CO_2}$ tax, waste use will fall to 2,719 kt/year, and MEA will capture 42,258 $kt_{CO_2}$/year (Figure 2d).

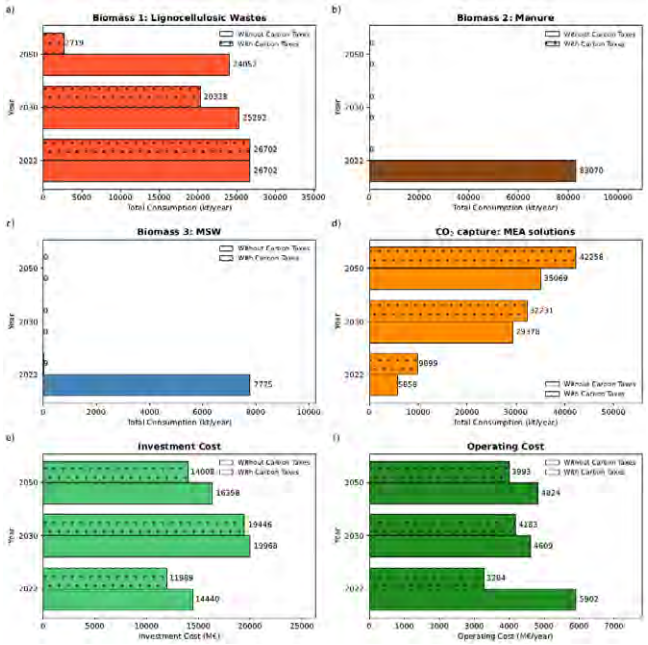



**Figure 2**. se of Lignocellulosic dry waste (a), manure (b), MSW (c), MEA $CO_2$ capture (d), total investment (e) and total operating costs (f) for 100% methane self-sufficiency, without and with carbon taxes, 2022, 2030, 2050.

### 4.2.2. Production of renewable energy

By 2030, energy production will rely on PV panels across Almería, the Canary Islands, and central regions, covering 1,042 km², up from 147 km² in 2022 (Figure 3a). Investment and operating costs will reach 59,956 M€ and 2,892 M€/year, generating 36.7 GW (Figures 3b–3d). A carbon tax boosts synthetic methane production to 40.2 GW, concerning 2022 levels, at costs of 65,910 M€ and 3,173 M€/year (Figures 3b-3d). By 2050, PV panels will cover 1,511 km², generating 52.8 GW at 64,280 M€ (Figures 3a–3c).

### 4.2.3. Methane production

By 2030, synthetic biomethane production will focus on gasifying lignocellulosic dry waste and synthesising methane from $CO_2$ captured via MEA solutions, excluding anaerobic digestion. Output will be 7,208 $kt_{Biomethane}$/year, a 5.29% decrease from 2022. Methane consumption will drop to 18,990 $kt_{CH_4}$/year [6], with synthetic production rising to 9,793 $kt_{CH_4}$/year. Costs will total 19,968 M€ and 4,609 M€/year (Figures 2e, 2f). By 2050, lignocellulosic waste use will decrease by 9.93%, producing 6,855 $kt_{Biomethane}$/year. Domestic methane consumption will drop to 13,815 $kt_{CH_4}$/year [6], while synthetic methane rises to 11,690 $kt_{CH_4}$/year. Costs will total 16,359 M€ and 4,824 M€/year (Figures 2e, 2f).

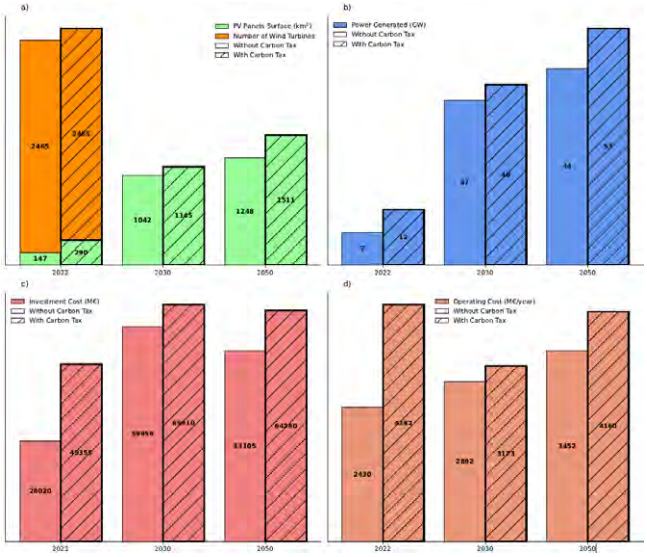


**Figure 3**. PV panel surface, wind turbines (a), power generation (b), investment (c) and operating costs (d), without and with carbon taxes, 2022, 2030, 2050.

### 4.2.4. Evolution of self-sufficiency methane percentage, and methane prices

By 2030, lignocellulosic dry waste and MEA solutions will remain key for cost efficiency. Methane prices, excluding carbon tax, will rise to 17.545 €/MWh when employing lignocellulosic dry waste. Once lignocellulosic dry waste is depleted, MEA solutions for $CO_2$ capture begin to be used until a methane price of 53.547 €/MWh is reached. However, at 100% budget utilisation, the price drops to 43.170 €/MWh. At 300% budget use, lignocellulosic waste will provide 38% of methane self-sufficiency. Carbon taxes will benefit synthetic methane over biomethane, with prices potentially dropping to 23.336 €/MWh. By 2050, advancements will favour MEA solutions. Without a carbon tax, methane will cost 17.545 €/MWh, with MEA solutions at 47.214 €/MWh. At 100% budget utilisation, methane costs 39.577 €/MWh, 40.12% lower than in 2022. Methane self-sufficiency will be achieved with 66.7% of the budget at 35.171 €/MWh, with prices dropping to 12.540 €/MWh at 100% budget use.

### 4.2.5. Environmental impact of energy generation: $CO_2$ emissions, minerals required, and water use

By 2030, PV panels will be the main energy source,

emitting 6,427 $kt_{CO_2}$/year, with 2,095 $kt_{CO_2}$ from mineral extraction, accounting for 29% of $CO_2$ captured by MEA solutions, 29,378 $kt_{CO2}$/year. Mineral requirements are $2.50 \cdot 10^5$ t, accounting for Cu, Ni, Zn, Si. PV panels use $1.06 \cdot 10^8$ $m^3$/year of water, 0.19% of Spain's capacity, while hydrogen production uses $3.64 \cdot 10^7$ $m^3$/year. Carbon taxes increase PV emissions to 7,052 $kt_{CO_2}$/year, contributing 29% of $CO_2$ captured by MEA solutions. By 2050, expanding PV panels will raise emissions, mineral demand, and water usage. PV panels emit 3,836 $kt_{CO_2}$/year, with 2,501 $kt_{CO_2}$ from mineral extraction, totalling 6,337 $kt_{CO_2}$/year, or 18.07% of $CO_2$ captured by MEA solutions, 35,069 $kt_{CO2}$/year. Mineral needs reach $2.98 \cdot 10^5$ t, and water use rises to $1.27 \cdot 10^8$ $m^3$/year.

## 5. CONCLUSIONS

This study examines large-scale renewable synthetic methane production from biomass gasification, anaerobic digestion, and $CO_2$ hydrogenation using green hydrogen. Gasification processes lignocellulosic dry waste, while anaerobic digestion whereas manure, MSW, and sludge, upgrading biogas to biomethane and producing synthetic methane using $CO_2$ captured from point and diluted sources.

Lignocellulosic dry waste gasification is the most efficient due to its high yield and low moisture content. $CO_2$ capture from point sources is preferable to DAC, potentially reducing Spain's industrial emissions by half. A land-use analysis considers decentralised deployment across 356 shires, allocating 2% for PV and wind turbines. By 2050, expanded capacity will ensure energy for $CO_2$ capture and hydrogen production.

Economic integration of lignocellulosic waste gasification with MEA-based $CO_2$ capture shows a potential 134.2% natural gas substitution. Investment costs in waste treatment, $CO_2$ capture, and power generation are projected to decrease, with cumulative costs of 14,008 M€ and 64,000 M€ by 2050.

Synthetic methane production will grow, with emission reductions between 49.8% and 59.6%. The integration of waste treatment, $CO_2$ capture, and hydrogenation offers a promising path for defossilising the energy sector, requiring strategic investments and policies.

## ACKNOWLEDGMENTS

The authors are thankful to the PSEM3 GIR group at USAL and the CAPD at CMU. Fellowship received from the Spanish Government. This work was supported by the Regional Government of Castilla y León (Junta de Castilla y León) and by the Ministry of Science and Innovation MICIN and the European Union NextGenerationEU / PRTR (H2MetAmo project - C17.I01.P01.S21).

## REFERENCES

1. NASA, 2024. Carbon Dioxide. Direct measurements, 1958-Present. https://climate.nasa.gov/vital-signs/carbon-dioxide/?intent=121
2. European Commission, 2020. Climate Action. 2030 Climate Target Plan. https://climate.ec.europa.eu/eu-action/european-green-deal/2030-climate-target-plan_en
3. Martín M, Grossmann IE. Optimal simultaneous production of i-butene and ethanol from switchgrass. *Biomass Bioenergy*. 61: 93–103 (2014) https://doi.org/10.1016/J.BIOMBIOE.2013.11.022
4. Sampat AM, Hicks A, Ruiz-Mercado GJ, Zavala VM. Valuing economic impact reductions of nutrient pollution from livestock waste. *Resources, Conservation and Recycling*. 164: 105199 (2021) https://doi.org/10.1016/j.resconrec.2020.105199
5. Gupta S, Li L. The Potential of Machine Learning for Enhancing $CO_2$ Sequestration, Storage, Transportation, and Utilisation-based Processes: A Brief Perspective. *JOM*. 74: 414–428 (2022). https://doi.org/10.1007/s11837-021-05079-x
6. Galán G, Martín M, Grossmann IE. Multiscale analysis for the utilisation of $CO_2$ towards the production of chemicals at the country level: Case study of Spain. *J Clean Prod.* 47: 140551 (2024) https://doi.org/10.1016/j.jclepro.2023.140551
7. Taifouris M, Martín M. Towards energy security by promoting circular economy: A holistic approach. *Appl Energy*. 333: 120544 (2023) https://doi.org/10.1016/j.apenergy.2022.120544

© 2025 by the authors. Licensed to PSEcommunity.org and PSE Press. This is an open access article under the creative commons CC-BY-SA licensing terms. Credit must be given to creator and adaptations must be shared under the same terms. See https://creativecommons.org/licenses/by-sa/4.0/



Systems & Control Transactions

**Research Article - Peer Reviewed Conference Proceeding**
ESCAPE 35 - European Symposium on Computer Aided Process Engineering
Ghent, Belgium. 6-9 July 2025
Jan F.M. Van Impe, Grégoire Léonard, Satyajeet S. Bhonsale,
Monika E. Polańska, Filip Logist (Eds.)

PSE PRESS

# Integrating Time-Varying Environmental Indicators into an Energy Systems Modeling and Optimization Framework for Enhanced Sustainability

**Marco P. De Sousa[a,b], Rahul Kakodkar[a,b], Betsie M. Flores[a,b], Saatvi Suresh[a,b], Harsh B. Shah[a,b], Dustin Kenefake[a,b], Iosif Pappas[c], Xiao Fu[c], Doga C. Demirhan[d], Brianna Ruggiero[d], Mete Mutlu[d], and Efstratios N. Pistikopoulos[a,b,*]**

[a] Texas A&M University, Artie McFerrin Department of Chemical Engineering, College Station, Texas, USA
[b] Texas A&M University, Texas A&M Energy Institute, College Station, Texas, USA
[c] Shell Global Solutions International B.V., Amsterdam, Netherlands
[d] Shell Global Solutions International B.V., Houston, Texas, USA
* Corresponding Author: stratos@tamu.edu.

## ABSTRACT

Data-driven decision-making is crucial in the transition to a low-carbon economy, especially as global industries strive to meet stringent sustainability goals. Traditional life cycle assessments often rely on static emission factors, overlooking the dynamic nature of the energy grid. As renewable energy penetration increases, grid carbon intensity fluctuates significantly across time and regions, due to the inherent intermittency of renewable sources like wind and solar. This variability introduces discrepancies in emission estimations if time-averaged factors are applied, leading to sub-optimal process operations and unintended environmental consequences. To this end, we present a real-time emission-aware optimization framework, which is implemented through a mixed-integer linear programming formulation that can determine optimal design configurations and operation schedules while simultaneously mitigating emissions by utilizing electricity price forecasts, time-varying emission factors, sporadic weather data, and supply and demand variability. The optimization model integrates life cycle assessment criteria to evaluate various environmental inputs, categorized into direct on-site emissions (Scope 1), indirect emissions from energy use (Scope 2), and upstream, downstream, and construction-related emissions associated with the process system (Scope 3). The framework, demonstrated through a detailed hydrogen production case study, showcases the effect of time-varying emissions by generating a set of optimal solutions that balance the trade-offs between environmentally sustainable and economical operational strategies.

**Keywords**: Real-time carbon accounting, Life cycle assessment, Time-varying indicators, Sustainability, Optimization

## INTRODUCTION

Climate change remains a critical challenge in the 21st century, necessitating comprehensive strategies to mitigate greenhouse gas (GHG) emissions across various sectors. In this context, life cycle assessment (LCA) has emerged as a pivotal tool for evaluating the environmental impacts of products and processes. Central to LCA is the accurate quantification of emissions, which has traditionally relied on static average emission factors (AEFs) [1]. However, growing concerns about the temporal and spatial variability of emissions have highlighted the need for more dynamic approaches, such as the use of marginal emission factors (MEFs) [2]. Marginal emission factors quantify the incremental change in emissions resulting from a unit change in electricity demand or supply. Unlike AEFs, which represent the average emissions over a fixed period, MEFs account for real-time grid conditions and the specific generation mix at a given moment. This distinction is especially critical in regions with a high

share of renewable energy sources, where the marginal electricity emission factor often differs from the average emission factor calculated of the given fuel mix [3]. Consequently, MEFs provide a more accurate representation than AEFs, particularly in grids with diverse renewable sources such as wind and solar, which exhibit high intermittency. The dynamic nature of MEFs provides a more accurate representation of the environmental impact of electricity use, especially in the context of flexible and time-dependent systems like hydrogen production, electric vehicle charging, and energy storage [4]. Adopting MEFs enables policymakers and industry stakeholders to design interventions that align with low-carbon electricity availability, thereby enhancing the efficacy of decarbonization efforts. For instance, scheduling energy-intensive processes during periods of low marginal emissions can significantly reduce overall GHG impacts. Furthermore, MEFs facilitate a better understanding of the interplay between electricity demand patterns and grid emissions, offering valuable insights for optimizing energy transitions [5].

This paper explores the significance and effects of using MEFs instead of static emission factors in an energy systems modeling and optimization framework. By advocating for the adoption of MEFs, this study aims to contribute to a more nuanced and impactful approach to emission accounting, thereby advancing global efforts toward sustainable development.

## SYSTEM UNDER INVESTIGATION

### Goal, Scope, and Boundary System

The objective of this case study is to meet a daily hydrogen demand of 240,000 kg by integrating various hydrogen production technologies. The primary focus is on minimizing costs and emissions, with particular attention to the impact of employing marginal emission factors rather than static emission factors. To highlight the influence of emissions on hydrogen production, the Houston area in Texas has been selected as a representative location for potential hydrogen infrastructure development [6]. A superstructure, illustrated in Figure 3, has been developed to incorporate both conventional steam methane reforming (SMR) and proton exchange membrane (PEM) processes for hydrogen production. The system considers three energy sources: the electrical grid and two renewable power purchase agreements (PPAs), specifically solar and wind energy. The electrical grid comprises multiple energy generation sources, including nuclear, hydropower, solar, wind, natural gas, and coal/lignite, each characterized by distinct global warming potentials. Table 1 presents the global warming potentials, expressed in kg $CO_2$-eq/MWh, which are used to calculate the time-varying emission factors of the electrical grid. Figure 1 illustrates the hourly dynamic behavior of the Electric Reliability Council of Texas (ERCOT), highlighting the contributions of various energy sources to meet hourly energy demand. It is important to note that the energy mix is determined in advance through fuel mix forecasting, as performed by ERCOT. This forecasting relies on predictive models that estimate electricity demand and the availability of renewable energy sources, such as wind and solar, based on weather patterns and historical data. Figure 2 demonstrates the significant variation in emission factors resulting from fluctuations in the contributions of these energy sources. The calculated marginal emission factor of the ERCOT grid ranges from 276.06 to 403.75 kg $CO_2$-eq./MWh, with an average value of 353.80 kg $CO_2$-eq./MWh. This average aligns closely with the emission factor reported by the Environmental Protection Agency (EPA), which is 351.31 kg $CO_2$-eq./MWh [7].

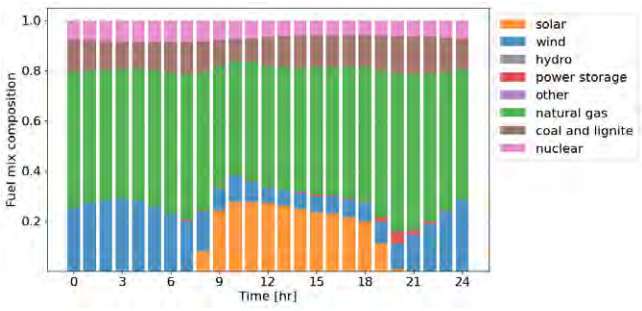



**Figure 1.** Time-varying energy mix of the ERCOT grid.

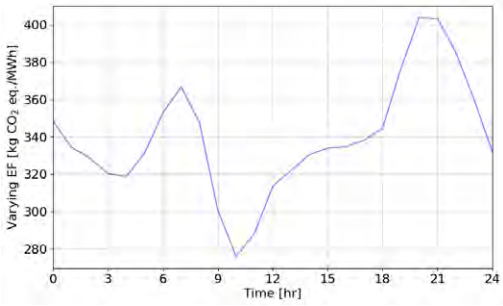



**Figure 2.** Time-varying emission factor of the grid on an hourly resolution.

**Table 1:** Various energy sources generating power within the ERCOT grid – *adapted from Ecoinvent V3.10.*

| Energy Source | GWP 100 [kg $CO_2$ eq./MWh] |
|---|---|
| Coal and lignite | 960.00 |
| Natural gas | 407.00 |
| Nuclear | 50.00 |
| Wind | ≈0.00 |
| Solar | ≈0.00 |
| Hydropower | ≈0.00 |

### Data Sourcing and Assumptions

Operational data for the SMR, and CCS, were

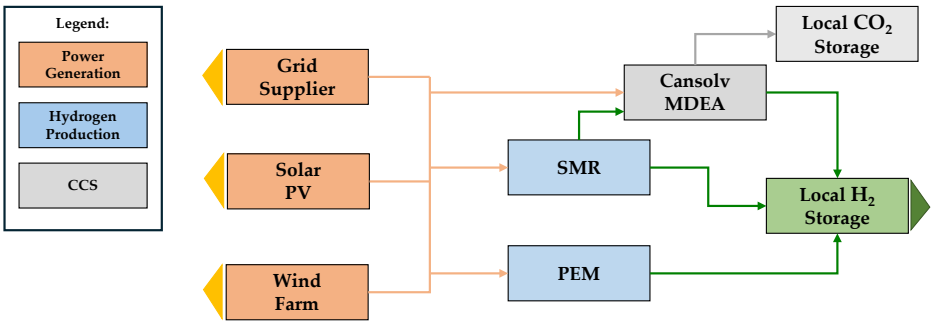



**Figure 3:** Proposed superstructure integrating two renewable energy sources—wind and solar—alongside a grid supplier, a conventional steam methane reformer, and a proton exchange membrane hydrogen production unit. The system operates within a life cycle boundary framework that accounts for both scope 1 and scope 2 emissions.

sourced from the National Energy Technology Laboratory (NETL) and Zang et al., both of which comprehensively discuss the operational aspects of hydrogen production processes [8,9]. Data for the PEM process were obtained from the National Renewable Energy Laboratory's (NREL) report on proton exchange membrane water electrolyzers and Gerloff N. [10,11]. Emission factors for all resources utilized in this study were extracted from Ecoinvent version 3.10, while characterization factors for converting emissions into carbon dioxide equivalent values were derived from the Sixth Assessment Report of the Intergovernmental Panel on Climate Change (IPCC) [12,13]. Lastly, Figure 4 presents the hourly electricity pricing data sourced from ERCOT, along with the capacity factors reflecting solar and wind variability in Texas. These data are integrated into the model to formulate a linear programming problem, enabling the development of economical and environmentally optimized production schedules. The implementation was conducted on a Windows 11 system equipped with a 13th Gen Intel(R) Core(TM) i7-13700 processor and 32 GB of DDR5 RAM, while using Gurobi to solve the optimization problem.

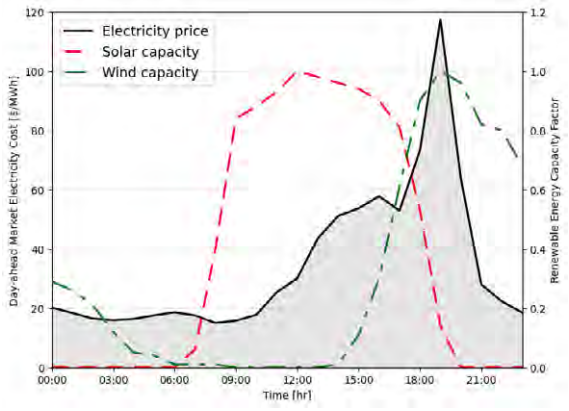



**Figure 4.** Varying day-ahead market electricity prices and renewable energy availability

## Methodology

The proposed framework is designed to be applicable and adaptable over different research sectors, extending beyond the specific case study of hydrogen production. The framework's foundation lies in a resource-process approach, which categorizes system components into resource inputs, conversion processes, and associated outputs [14]. This modular and systematic structure allows the framework to accommodate a wide range of process systems, provided they adhere to this fundamental programming structure.

By decoupling the methodological design from the specifics of any one application, the framework achieves a level of generality suitable for addressing diverse optimization problems in various sectors. Examples include chemical manufacturing, energy systems, and other industrial processes that involve resource transformation and utilization. This adaptability ensures the framework's relevance in solving problems related to cost minimization, and emissions reduction. The generalizable nature of the framework not only enhances its utility for interdisciplinary applications, but also ensures its scalability for future advancements in sustainable process system scheduling and design.

### Time-varying Emission Factor Formulation

To fully encapsulate the time-varying aspect of electrical grid power generation, Eq. 1 is utilized to quantify the varying emission factor. The total energy generation, $E_t$, must be known at each time step, which is multiplied by the contribution percentage, $Co_{r,t}$, of each energy producing source, which is then multiplied with their corresponding global warming potential, $GWP_{r,t}$.

$$EF_t = E_t \times \sum_{r \in R} Co_{r,t} . GWP_{r,t} \quad \forall\, t \in T \tag{1}$$

### Scope-wise Emission Approach

Within this quantification framework, Eq. 2 captures emissions associated with both resource consumption and discharge. The total resource emissions, $em_r$, are

calculated as the sum of emissions from resource consumption and discharge at time, $t \in T_{sch}$. Specifically, the emissions from total resource consumption, $c_{r,t}$, are determined by multiplying the consumed quantity by the corresponding emission factor, $EF_{r,t}$, for the resource, $r$. Similarly, the emissions from resource discharge, $s_{r,t}$, are calculated by multiplying the discharged quantity by its associated emission factor. This formulation ensures a comprehensive accounting of resource-related emissions within the system's lifecycle.

$$em^r = \sum_{t \in T^{sch}} \sum_{r \in R} (EF_{r,t} \cdot c_{r,t} + EF_{r,t} \cdot s_{r,t}) \quad (2)$$

Secondly, on-site emissions, referred to as process emissions, are quantified using Eq. 2. These emissions are determined by the production quantity and the emission factors associated with the resources utilized during the production phase. Specifically, the process emissions at a given location are calculated by summing the emission contributions of each resource used. This is achieved by multiplying the emission factor, $EF_{r,t}$, of a resource by the conversion factor, $\eta_{p,r,t}$, which represents the efficiency of process, $p \in P$, in converting the resource into the desired product. The result is then multiplied by the total production quantity, $p_{p,t}$, of the process at the location of interest. This formulation ensures an accurate representation of emissions directly attributable to production activities at specific locations.

$$em^p = \sum_{t \in T^{sch}} \sum_{r \in R} EF_{r,t} \times \sum_{p \in P} \eta_{p,r,t} \cdot p_{p,r,t} \quad (3)$$

## RESULTS & DISCUSSION

### The Cost Minimization Scenario

When optimizing for cost, the use of time-varying emission factors is found to have no impact on the production schedule as seen in Figure 5. Regardless of the chosen emission quantification approach, the cost-minimized optimal configuration consistently involves using SMR without CCS. This is due to the total emissions generated are not weighted in the optimization process when prioritizing profitability. However, while the production schedules remain identical, the quantification of total emissions differs between the two approaches. Using the time-varying emission factor approach results in total emissions of 2,861 metric tons (MT) of $CO_2$-eq., whereas the constant emission factor approach yields 2,864 MT of $CO_2$-eq.

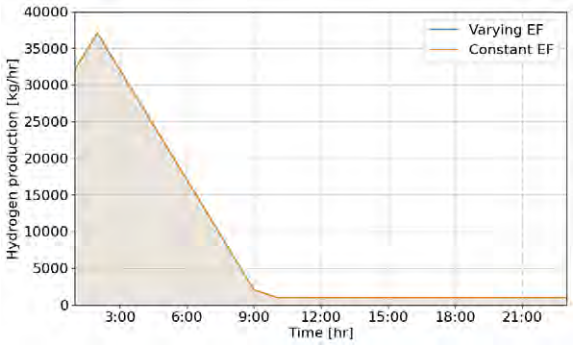



**Figure 5.** Hydrogen production profile using time-varying and constant emission factors while minimizing the cost objective.

This represents a difference of up to 3,000 kg $CO_2$-eq. within a 24-hour period. These findings highlight the influence of a dynamically changing energy mix, demonstrating that specific times of the day may be more favorable for increasing production rates due to lower emission factors. Figure 6 demonstrates that, despite the objective function being focused on cost minimization, the renewable PPAs for solar and wind energy, with fixed rates of $52.69/MWh and $60.11/MWh respectively, are more cost-effective during specific periods of the day. As a result, these renewable energy sources are prioritized over the more volatile grid electricity prices during those times.

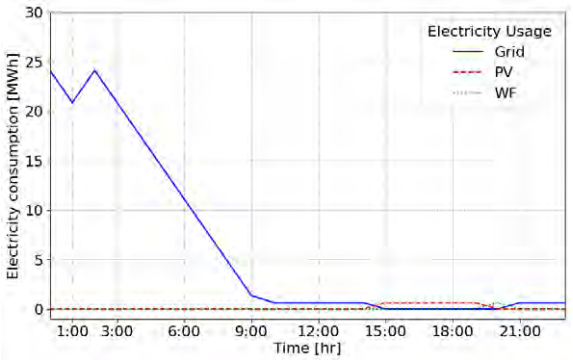



**Figure 6.** Energy consumption from different sources required to produce hydrogen in the cost minimization scenario.

### Emission Minimization Scenario

When the objective function is adjusted to prioritize minimizing total emissions, Figure 7 illustrates a shift in the optimal production schedule when utilizing time-varying emission factors. An important observation is that SMR coupled with CCS is the preferred technology configuration when minimizing emissions. In contrast, PEM is not utilized, as its high energy demand would significantly increase grid power consumption, ultimately leading to higher overall emissions. The Maximum production in Figure 7 is concentrated in the earlier hours of the day,

specifically between 9:00 AM and 12:00 PM, coinciding with the period when the grid's emission factor is at its lowest. During this timeframe, the emission factor ranges from 270 to 300 kg $CO_2$-eq./MWh consumed, highlighting the environmental benefits of strategically aligning production with periods of lower grid emissions.

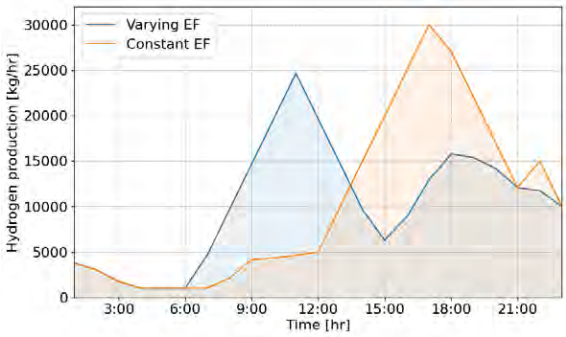



**Figure 7.** The difference in hydrogen production profiles when minimizing the total emission objective.

Table 2 reveals a significant difference in total emissions between the two carbon accounting approaches, with a disparity of 8,365 kg $CO_2$-eq. Additionally, while the change in the levelized cost of hydrogen (LCOH) is minimal, its impact becomes more pronounced when scaled to meet the daily hydrogen demand. Specifically, this minor deviation translates to a $4,800 difference in daily hydrogen value, which would accumulate to an annual difference of $1,752,000.

**Table 2:** Difference in LCOH and total emissions occurring when time-varying emission factors are utilized.

| Scenario | LCOH [kg/$H_2$] | Total Emission [kg $CO_2$ eq.] |
|---|---|---|
| Time-varying EF | 3.85 | 728,722 |
| Average EF | 3.87 | 737,087 |

A comparison of the energy consumption patterns in Figures 8 and 9 reveals that both approaches fully utilize the available solar and wind energy resources. However, the use of the grid supplier distinctly highlights the impact of varying emission factors on the timing and quantity of energy consumption required to meet the daily hydrogen production demand. In Figure 9, grid energy consumption is significantly constrained by the time-varying emission factor. In contrast, under the average emission factor scenario, there are no restrictions on when grid power can be consumed. As a result, the model is only constrained by the ramping and production limitations of the technology utilized. This demonstrates how the dynamic nature of grid emissions influences energy allocation strategies.

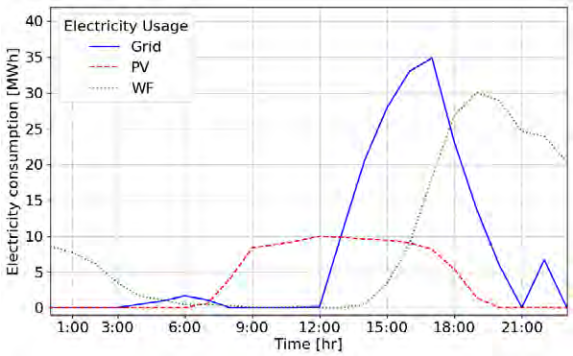



**Figure 8.** The energy consumption of different sources while utilizing an averaged emission factor approach.

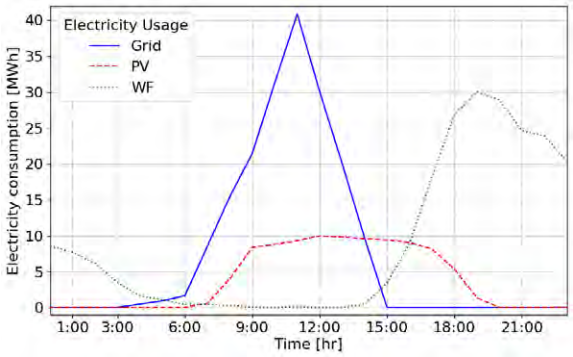



**Figure 9.** The energy consumption of different sources while utilizing a time-varying emission factor approach.

## CONCLUSION & ONGOING WORK

Time-varying environmental indicators provide deeper insights into emission accounting by addressing the uncertainty of major contributors such as grid suppliers. However, this concept can be further expanded to not only cover dynamic energy production, but also create varying emission factors for any resource that is dependent on being produced by using electricity from grid suppliers. Cooperative decision-making between energy suppliers and plant management is also essential to enhance precise and accurate real-time carbon accounting and emission factor calculation. A key area of the ongoing work is to introduce social quantification metrics into the optimization framework to evaluate broader societal impacts and have a triple-bottom-line optimization approach. Furthermore, efforts are put into investigating the temporal dynamics of greenhouse gas residence times and their influence on global warming potential over various time horizons, which could lead to having time-varying global warming potentials that can be used to calculate dynamically changing emissions present in the atmosphere. These efforts aim to refine the framework and facilitate the transition toward a more sustainable and emission-conscious hydrogen production sector.

## DIGITAL SUPPLEMENTARY MATERIAL

The supplementary materials for this study are accessible at Marcopdsousa-TAMUparametric. The data file *"RT 20 August 2024"* includes raw data for Day-Ahead Market (DAM) and natural gas prices, as well as maximum electricity production factors for solar and wind power in the Houston area, which is retrieved from ERCOT. The repository contains the optimization models used in this study. The *"Constant_EF"* model optimizes hydrogen production using the average emission factor approach, as defined by the Environmental Protection Agency (EPA). The *"Time_varying_EF"* model incorporates the calculated time-varying emission factors into the optimization framework. These resources are provided to enhance reproducibility and collaboration on the subject. For further inquiries or assistance, please contact *Marcopdsousa@tamu.edu*.

## ACKNOWLEDGEMENTS

The authors acknowledge the financial support from Shell Global Solutions and the Texas A&M Energy Institute.

## REFERENCES

1. Risner Jamie, Sutherland Anna. Static grid carbon factors–Can we do better? *Building Services Engineering Research and Technology*, 42:257-277 (2021)
2. Schram Wouter, Lampropoulos Ioannis, AlSkaif Tarek, Van Sark Wilfried. On the use of average versus marginal emission factors. *8th International Conference on Smart Cities and Green ICT Systems,* 1:187-193 (2019)
3. Böing Felix, Regett Anika. Hourly $CO_2$ emission factors and marginal costs of energy carries in future multi-energy systems. *Energies,* 12:2260 (2019)
4. Ricks Wilson, Xu Qingyu, Jenkins Jesse D. Minimizing emissions from grid-based hydrogen production in the United States. *Environmental Research Letters*, 18:014025 (2023)
5. Siler-Evans Kyle, Azevedo Ines Lima, Morgan M. Granger. Marginal emissions factors for the US electricity system. *Environmental science & technology* 46:4742-4748 (2012)
6. Gawlick Julia, Beagle Emily A., Webber Michael E., Hamacher Thomas. Assessment of a coupled electricity and hydrogen sector in the Texas energy System in 2050. *Int. J. Hydrogen Energy,* 91:787-799 (2024)
7. Environmental Protection Agency. Emissions & generation resource integrated database (egrid). https://www.epa.gov/egrid
8. Lewis Eric, McNaul Shannon, Jamieson Matthew, Henriksen Megan S., Metthews H. Scott, Walsh Liam, Grove Jadon, Shultz Travis, Skone Timothy J., Stevens Robert. Comparison of commercial, state-of-the-art, fossil-based hydrogen production technologies. *Technical report of the National Energy Laboratory (NETL),* Pittsburgh, PA, Morgantown, West Virginia (2022)
9. Guiyan Zang, Edward J. Graham, Dharik Mallapragada. $H_2$ production through natural gas reforming and carbon capture: A techno-economic and life cycle analysis comparison. *Int. J. Hydrogen Energy,* 49:1288-1303 (2024)
10. Mayyas Ahmad, Ruth Mark, Pivovar Bryan, Bender Guido, Wipke Keith. Manufacturing cost analysis for proton exchange membrane water electrolyzers. *Technical report NREL/TP-6A20-72740.* National Renewable Energy Laboratory, Golden, CO (2018)
11. Gerloff Niklas. Comparative life-cycle-assessment analysis of three major water electrolysis technologies while applying various energy scenarios for a greener hydrogen production. *Journal of Energy Storage,* 43:102759 (2021)
12. Ecoinvent Center, Ecoinvent version 3.10, https://ecoinvent.org/
13. Intergovernmental Panel on Climate Change (Ed.), Climate Change 2021: The physical science basis. Contribution of working group 1 to the sixth assessment report of the intergovernmental panel on climate change, Cambridge University Press, Cambridge, United Kingdom and New York, NY, USA (2021)
14. Allen Richard Cory, Baratsas Stefanos G., Kakodkar Rahul, Avraamidou Styliani, Demirhan Cosar Doga, Heuberger-Austin Clara F., Klokkenburg Mark, Pistikopoulos Efstratios N. A multi-period integrated planning and scheduling approach for developing energy systems. *Journal of Optimal Control Applications and Methods,* 44:335-372 (2023)

© 2025 by the authors. Licensed to PSEcommunity.org and PSE Press. This is an open access article under the creative commons CC-BY-SA licensing terms. Credit must be given to creator and adaptations must be shared under the same terms. See https://creativecommons.org/licenses/by-sa/4.0/



Systems & Control Transactions

**Research Article - Peer Reviewed Conference Proceeding**
ESCAPE 35 - European Symposium on Computer Aided Process Engineering
Ghent, Belgium. 6-9 July 2025
Jan F.M. Van Impe, Grégoire Léonard, Satyajeet S. Bhonsale,
Monika E. Polańska, Filip Logist (Eds.)

PSE PRESS

# Modular and Heterogeneous Electrolysis Systems: a System Flexibility Comparison

**Hannes Lange[a,b*], Michael Große[b,c], Isabell Viedt[a,b], Leon Urbas[b,c]**

[a]TUD Dresden University of Technology, Process-to-Order Group, Process Systems Engineering Group
[b]TUD Dresden University of Technology, Process-to-Order Group, P2O Lab Learning Factory
[c]TUD Dresden University of Technology, Process-to-Order Group, Chair of Process Control Systems
*Corresponding author: hannes.lange1@tu-dresden.de

## ABSTRACT

Green hydrogen will play a key role in the decarbonization of the steel sector via the direct reduction path [1]. To meet the demand side, both a highly efficient numbering-up based scaling strategy for water electrolysis is needed as well as flexible operation strategies that follow the fluctuating electricity load. This paper presents a modularization approach for electrolysis systems that addresses both aspects by combining different electrolysis technologies into one heterogeneous electrolysis system. We present a modular design of such a heterogeneous electrolysis system that can be scaled for large-scale applications. The impact of different degrees of technological and production capacity-related heterogeneity is investigated using system co-simulation to find an optimal solution for the goal-conflict, that the direct reduction of iron for green steel production requires a constant stream of hydrogen while the renewable electricity profile is fluctuating. For this use-case the distribution of technology and production capacity in the heterogeneous plant layout is optimized regarding overall system efficiency and the ability to follow flexible electricity profiles. The simulation results are compared with conventional homogenous electrolyser plant layouts. First results underline the benefits of combining different technologies and production capacities of individual systems in a large-scale heterogeneous electrolyser plant. It is shown that the presented modular electrolysis systems can follow the current flow without losing significant efficiency. However, for a downstream system that requires a constant hydrogen mass flow, supplementary hydrogen storage is required.

**Keywords**: Energy Efficiency, Hydrogen, Process Design, Energy Systems, Renewable and Sustainable Energy, Flexibility, Lange-Große-Coefficient

## BACKGROUND

Hydrogen has a thermal and material application (purpose) in shaft furnaces. On the one hand, hydrogen is used to reduce the iron ore, and on the other hand for combustion and the associated melting of the iron ore. However, an electrolysis system is needed to provide this hydrogen. The electrolysis system presented here is to be modularly constructed and heterogeneously scaled. The concept and structure of individual modular electrolysis systems have already been explained in the past [2–4]. A heterogeneously scaled electrolysis system is understood to be the numbering-up of different electrolysis technologies in different sizes in one overall electrolysis system. That way technology-specific advantages, like high efficiency or increased energy input flexibility, can be harnessed more efficiently [5]. Due to an increasing amount of renewable energy in the grid, the price of electricity is also fluctuating more throughout the day. In general, it can be said that the electricity price is lowest when the proportion of renewable energies in the electricity mix is high [6]. These temporal fluctuations need to be harnessed by designing flexible control strategies for large-scale electrolysis systems, that can follow them. Using heterogeneous electrolysis systems can provide a bigger operational window and higher flexibility for such fluctuating power inputs while maintaining high efficiency of hydrogen production resulting in lower hydrogen cost.

## METHODS & IMPLEMENTATION

### Assumptions

An average fictional steelworks with a production capacity of 125,000 kg/h of briquetted sponge iron was set up as a boundary condition [7–9]. To produce the mass flow of briquetted sponge iron, a minimum of 6364 kg/h of H2 are required. This can be calculated from the stoichiometry in the reduction equation in (1).

$$Fe_2O_3 + 3\,H_2 \rightarrow 2\,Fe + 3\,H_2O\;\Delta H_R = 99{,}5\;kjmol^{-1} \quad (1)$$

This calculated minimum requirement shall define the lower boundary of the demand side. To define the fluctuating energy side, synthetic 'Solar Power Data for Integration Studies' data from the National Renewable Energy Laboratory for the state of New York [10] is used as a initial scenario. The data was created specifically for system integration studies, as in this study. The solar power data consists of 5-minute solar power data with hourly Day-Ahad forecasts and refers to the year 2006. The data generated from the 5-minute data set was developed by NREL using a 'Sub-Hour Irradiance Algorithm' [10]. The first week of January and the first week of July of this 5-minute time-step data were extracted and the data was normalized against the maximum within the sample set to define the operating point inputs between zero load and nominal load of the electrolysis system.

As shown in Table 1 the scaled modular and heterogeneous electrolysis system consists of aggregated blocks of both the electrolysis technologies alkaline electrolysis (AEL) and the proton exchange membrane electrolysis (PEMEL), as these two are the technologies with the highest technology readiness level (TRL). In our design an AEL block consists of eight AEL stack units with an output of 5 MW each that are connected to a lye circulation module. A PEMEL block consists of two PEMEL stack units with an output of 2 MW each that are connected to a DI-water circulation module [3,11]. A DI-water circulation module is a process engineering unit that has been specially developed for the circulation of treated water through the satellite unit. It also takes over the separation of product gases hydrogen and oxygen from the water circuit [3,11]. An efficiency of $\eta_{AEL}$= 0.68 was assumed for the AEL and an efficiency of $\eta_{PEMEL}$= 0.63 for the PEMEL relative to the lower heating value of hydrogen [11].

Another assumption is that at least one AEL block is always operated to ensure a minimum hydrogen volume flow for the subsequent process. This is since AEL cannot react as quickly to power changes and has a higher efficiency than PEMEL, which makes it more interesting for constant operation. The AEL was assumed to have a load gradient of 30 %/s ramp-up and 10 %/s ramp-down while the load gradients of the PEMEL are 50 %/s in ramp-up and 40.6 %/s in ramp-down. [11]

### Optimization problem

The hydrogen mass flow generated can be approximately calculated according to equation (1), where the nominal power of the two electrolysis technologies in hydrogen production are multiplied with their respective system efficiency and divided by the gravimetric calorific value of hydrogen, which is 33.33 kWh kg$^{-1}$ [12].

$$\dot{m}_{max}\,[\frac{kg}{h}] = \frac{A \cdot 8 \cdot 5000[kW] \cdot \eta_{AEL} + B \cdot 2 \cdot 2000[kW] \cdot \eta_{PEM}}{33{,}33\,[\frac{kWh}{kg}]} \quad (1)$$

The variables 'A' and 'B' presented in Formula (2) and (3) are used to calculate the distribution of the AEL and PEMEL. The variable 'A' represents a selected number of AEL blocks, starting with 0 blocks, scaled up step by step to 10 AEL blocks. The variable 'B' represents the corresponding number of PEMEL blocks, which can be calculated with the maximum hydrogen massflow given, using formula (2):

$$B\,[-] = \frac{\dot{m}_{max}[\frac{kg}{h}] \cdot 33{,}33[\frac{kWh}{kg}] - A \cdot 8 \cdot 5000[kW] \cdot \eta_{AEL}}{2 \cdot 2000[kW] \cdot \eta_{PEM}} \quad (2)$$

As boundary conditions, the number of respective technology blocks, A and B, cannot be below a set minimum threshold. For these first evaluations, the threshold has been set to 0.

$$A > A_{min}$$
$$B > B_{\min} \quad (3)$$

**Table 1:** Configurations of aggregated AEL and PEMEL blocks

| Config. | AEL | PEMEL |
|---|---|---|
| 0 | 0 | 109 |
| 1 | 1 | 98 |
| 2 | 2 | 87 |
| 3 | 3 | 76 |
| 4 | 4 | 66 |
| 5 | 5 | 55 |
| 6 | 6 | 44 |
| 7 | 7 | 33 |
| 8 | 8 | 22 |
| 9 | 9 | 11 |
| 10 | 10 | 0 |

As this is to be a heterogeneous electrolysis system,

both electrolysis technologies must be installed in one electrolysis system. The fifrst scaling configuration is an AEL block in conjunction with 91 PEMEL blocks. Based on this, the AEL blocks are now gradually increased up to eight AEL blocks while simultaneously reducing the number of PEMEL blocks to keep the total $H_2$ capacity (1 AEL block equals 11 PEMEL blocks). Table 1 shows the eleven possible configurations of AEL and PEMEL blocks.

The overall efficiency of the electrolysis system is calculated from the number of blocks in the system and the individual efficiencies of the electrolysis technologies using equation (4). The values of the individual efficiencies were taken from [11].

$$\eta_{sys}\,[-] = \frac{A \cdot 8 \cdot 5000[kW] \cdot \eta_{AEL} + B \cdot 2 \cdot 2000[kW] \cdot \eta_{PEM}}{A \cdot 8 \cdot 5000[kW] + B \cdot 2 \cdot 2000[kW]} \quad (4)$$

To evaluate the system flexibility the Expected Unserved Flexible Energy (EUFE) value is calculated for the described input scenario of solar power input in 5-minute time-steps [13]. The power input behavior of the electrolyzer blocks is simplified, using the load gradient parameters for a linear load ramp-up and ramp-down from Lange et al. [11]. The EUFE can now be determined from the specified operating point of the scenario and the actual operating point of the electrolysis system, following the requested load changes of the solar power input profile. Often the EUE value is also used for this, which stands for “Expected Unserved Energy”, but both describe the same thing [14]. According to equation (5), the power of the scenario is subtracted from the power of the actual operating point at each time step and integrated over the period under consideration.

$$EUFE\,[kWh] = \int abs((P_{scenario}(t) - P_{system}(t))dt \quad (5)$$

One problem with the EUFE value is the comparability of different scenarios and systems. As this is a continuous summation of the differences in output, the EUFE value is heavily dependent on the consideration of the time length of the scenario and the system under consideration. Therefore, the authors of this study aim to modify the EUFE value to consider the flexibility of a system that is more independent of the scenario under consideration and the system performance of the system under consideration. For this purpose, the EUFE value is related to the integrated power input of the scenario. The resulting value represents the share of energy in the scenario that cannot be utilized by the system under consideration. This value is referred to below as the “Lange-Große-Coefficient” (LGC) and is calculated using equation (6):

$$LGC = \frac{EUFE}{\int P_{scenario}(t)dt} \quad (6)$$

The Levelized Cost of Hydrogen (LCOH) was also calculated according to [15].

$$M = \begin{cases} y = f(\eta, LGC, LCOH, \dot{m}_{H_2}) \\ s.t.\, LGC \leq 5\% \\ s.t.\, \dot{m}_{H_2} \geq \dot{m}_{max} \end{cases} \quad (7)$$

Equation (7) describes the model of the optimisation problem.

## DISCUSSION

The system configurations listed in Table 1 were simulated in MATLAB/Simulink. The results are summarized in

Figure 2. The dots reflect the LGC (see equation (6)) against the system efficiency, the triangles the calculated LCOH against the system efficiency. The LGC increases linearly with the system efficiency, which is due to the increase in AEL in the overall system. In contrast, the LCOH behaves inversely proportional and decreases with the increase of the AEL in the overall system. If the LGC must not rise above a value of 5%, configurations 7-10 would not apply.

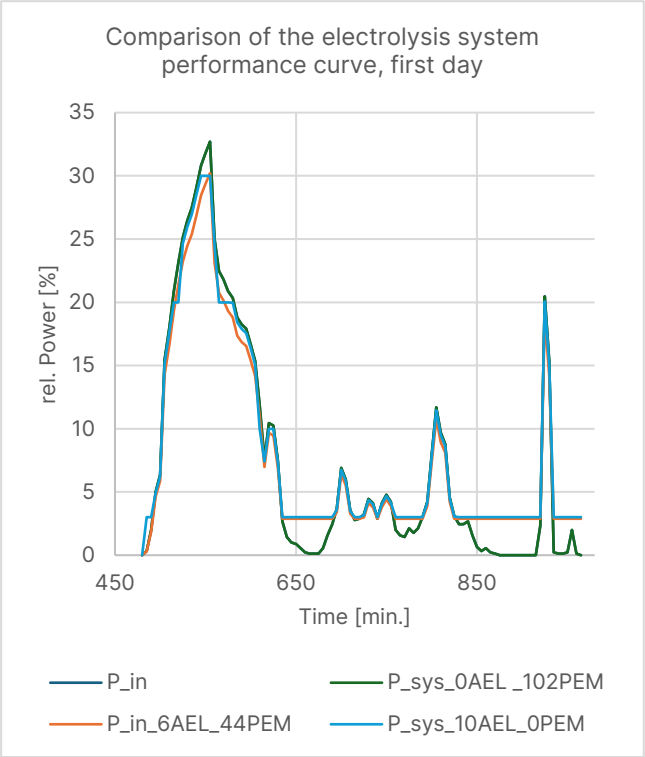



**Figure 1:** Comparison of the system outputs of the optimum case (Con. 6, orange line) and the two marginal cases (Con. 0, green line and Con. 10, blue line) with the outputs entering the electrolysis system to illustrate the ‘start-stop principle’ operating strategy [11,16]. Due to the absence of the AEL and the associated base load in Con. 0, smaller partial load ranges below 3% are also utilised.

Configuration 0 with a 100% share of PEMEL represents the first edge case. In contrast to the systems with AEL blocks there is no base load component in this edge case. As a result, every change in the input power is adopted, which means that the LGC is higher than in configuration 1. This shows, that the LGC needs further adjustments become even more independent of the flexibility requests of the input scenario. With the introduction of the base load by the AEL, the LGC decreases, while at the same time increasing the system efficiency. The second edge case is configuration 10 with a 100% AEL share. Here it is the case that when the minimum load of the AEL is reached, only the start-stop principle is used [11].

The two edge cases consisting of 100% PEMEL (configuration 0) and 100% AEL (configuration 10) are included in the analysis of the modular and heterogeneous electrolysis system. These two modular homogeneous scaling cases show anomalies, as can be seen in Figure 2. For the configuration, the increase in LGC is due to the distribution of power within the system. No minimum load was initially defined for the PEMEL, which enables the PEMEL to follow the power and the associated flexibility signals exactly. Flexibility signals are time steps at which the incoming power into the system changes, to which the system in turn must react. As soon as the AEL is added to the system, flexibility signals that are below the minimum load are ignored and are therefore not included in the calculation of the LGC, which is why the LGC drops in the first configuration.

The second edge case in configuration 10 shows a drop in the LGC. This is since anomalies also occur during system start-up, just as during system shutdown. With a start-stop strategy that only allows the system to be operated at 100% power, flexibility signals that are not sufficient to start up an entire AEL block are ignored. This leads to a reduction in the LGC. This lack of capacity was compensated for by the PEMEL in the previous configuration. One solution could be to shut down an AEL block to start a new one. This must be done on the condition that it is known that the incoming power will continue to increase. One solution could be to shut down an AEL block in order to start a new one. This must be done on the condition that it is known that the incoming power will continue to increase. The shutdown behavior of the system can also be further optimized. Here, several AEL units could initially be run in a partial load range instead of taking entire units out of operation. This would have an additional effect on the efficiency of the system, as the AEL systems are more efficient in the partial load range. Optimisation can still take place for both edge cases, as the same operating strategy was selected for the modular homogeneous systems as for the modular heterogeneous systems to establish comparability.

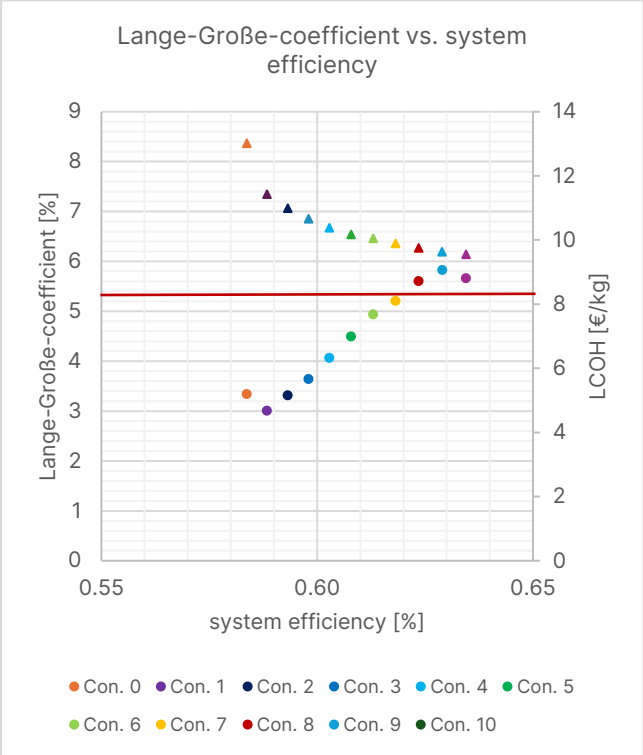



**Figure 2:** Lange-Große-Coefficient (LGC) and Levelised Cost of Hydrogen (LCOH) vs. system efficiency. All modular heterogeneous system configurations from Table 1 (Con. 1-9) are shown, including the two edge cases for modular homogeneous system configurations (Con. 0 and Con 10). The LGC is represented by a dot in the diagram, the LCOH by a triangle, and each configuration has its own colour. Dabei ist ein Abfallen der LCOH mit steigender A drop in the LCOH can be recognised with increasing system efficiency, which is the same for Con. 8 reaches a minimum. The LGC increases linearly with increasing system efficiency, if the two marginal cases are disregarded.

The weighted optimum is the sum of the system efficiency, the LGC and the LCOH. For this purpose, the LCOH is normalised and related to the lowest value. The same is done for the LGC. For both values, a low value is better than a high one. The system efficiency is also normalized to the value. The rule here is that a high system efficiency is better. The sum of these three normalized values can now only be between 0 and 3. As shown in the Figure 3 weighted optimum drops further with each configuration. With the previously established boundary condition that the LGC should not be above 5%, configuration 6 turns out to be the optimal distribution between AEL and PEMEL.

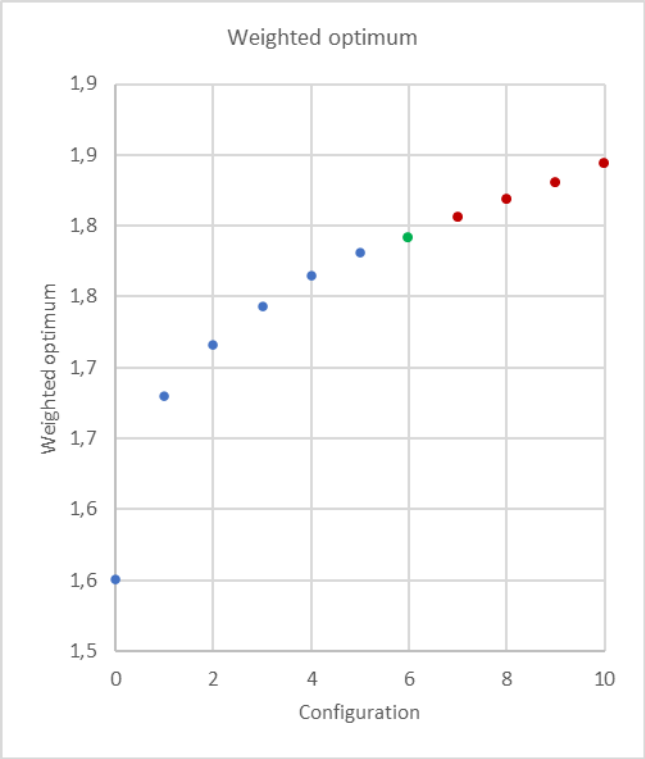



**Figure 3** The weighted optimum for all configurations. Configuration 6 is marked in green, all configurations outside the 5% limit of the LGC are marked with red dots.

## CONCLUSION

As has been shown, a fluctuating current curve can be followed with the modular heterogeneous electrolysis systems shown. This results in an optimum within the distribution of electrolysis technologies. An optimally composed electrolysis system consisting of 58% AEL and 42% PEMEL was determined for the scenario shown for an average fictional steelworks. With this composition, high efficiency at low LCOH can be guaranteed in a system that is able to respond to flexibility signals with an LGC of less than 5%. This system composition is therefore to be favored in operation. While the LCOH between configuration 6 and 10 fluctuate by 0.51 €/kg H2, the LGC between these two configurations fluctuates by 0,75%. To put this into perspective, the LCOH decreases between configurations 1 and 6 by 2.98 €/kg. Although an electrolysis system consisting purely of AEL has lower operating costs of 0.51 €/kg, it cannot react as quickly to power fluctuations. This flexibility advantage can be useful in the future, especially with flexible electricity tariffs.

## OUTLOOK

As shown in the previous section, the LGC must be made even more scenario-independent. No flexibility signals below the minimum load should be ignored. If flexibility signals cannot be served, this must be included in the LGC to ensure full comparability with the marginal cases.

Furthermore, the load distribution within an electrolysis system must be further adapted. As has been shown, the LGC can be reduced even further with a further customized operating strategy. A comparison of different operating strategies in a modular heterogeneous plant design with different electrolysis technologies must be investigated further; the foundations for this have already been laid in [11,16].

Another point is the simulative integration of high temperature electrolysis (HTEL) into a system with AEL and PEM. Here it may be possible to further increase the base load efficiency by extracting heat and the associated vaporization of water for the HTEL.

Furthermore, the relationship between a fluctuating current input and a subsequent process such as direct iron reduction after electrolysis, which requires a constant hydrogen mass flow, is still unclear. At this point, energy storage is required, either on the electricity or the hydrogen side of the process. A suitable method needs to be developed to define the right ratio between electricity and hydrogen storage.

## ACKNOWLEDGEMENTS

We would like to thank the German Federal Ministry of Education and Research and the project management organization Jülich for their financial support within the framework of the eModule research project (FKZ 03HY116A) of the H2Giga lead platform. Furthermore, the P2O-Lab Learning Factory of the TUD Dresden University of Technology is thanked for its support.

## REFERENCES

1. Wietschel M, Zheng L, Arens M, Helbing C, Ranzmeyer O, Schaadt A, et al. Metastudie Wasserstoff – Auswertung von Energiesystemstudien. Studie im Auftrag des Nationalen Wasserstoffrats. Karlsruhe, Freiberg, Cottbus: 2021.
2. Bittorf L, Beisswenger L, Erdmann D, Lorenz J, Klose A, Lange H, et al. Upcoming domains for the MTP and an evaluation of its usability for electrolysis. 2022 IEEE 27th international conference on emerging technologies and factory automation (ETFA), 2022, p. 1–4. https://doi.org/10.1109/ETFA52439.2022.9921280
3. Lange H, Klose A, Beisswenger L, Erdmann D, Urbas L. Modularization approach for large-scale electrolysis systems: a review. Sustainable Energy Fuels 2024:10.1039.D3SE01588B. https://doi.org/10.1039/D3SE01588B

4. Lange H, Schirmer C, Mock M, Viedt I, Klose A, Urbas L. Operation Strategies for Modular Large-Scale Alkaline Electrolysis Systems. 2024 IEEE 22nd International Conference on Industrial Informatics (INDIN), Beijing, China: IEEE; 2024, p. 1–7. https://doi.org/10.1109/INDIN58382.2024.10774361
5. Mock M, Viedt I, Lange H, Urbas L. Heterogenous electrolysis plants as enabler of efficient and flexible Power-to-X value chains. Computer Aided Chemical Engineering, vol. 53, Elsevier; 2024, p. 1885–90. https://doi.org/10.1016/B978-0-443-28824-1.50315-X
6. ISE F. Day-ahead auktion vs. Solar + wind onshore + wind offshore in deutschland, 2022. Energy-Charts 2023.
7. Albrecht U, Ball M, Bünger U, Kutz C, Michalski J. Metastudie zu den technischen, technologischen und wirtschaftlichen Parametern für die Umstellung der deutschen Stahlindustrie auf eine emissionsarme Stahlproduktion auf Basis von grünem Wasserstoff 2022.
8. Hölling M, Weng M, Gellert S. Bewertung der Herstellung von Eisenschwamm unter Verwendung von Wasserstoff (Evaluation of the production of sponge iron using hydrogen). Eisen & Stahl 2017;6:47–56.
9. Nuber D, Eichberger H, Rollinger B. Circored fine ore direct reduction. MILLENNIUM STEEL 2006:37–40.
10. National Renewable Energy Laboratory. Solar Power Data for Integration Studies 2024. https://www.nrel.gov/grid/solar-power-data.html (accessed November 14, 2024).
11. Lange H, Klose A, Lippmann W, Urbas L. Technical evaluation of the flexibility of water electrolysis systems to increase energy flexibility: A review. International Journal of Hydrogen Energy 2023;48:15771–83. https://doi.org/10.1016/j.ijhydene.2023.01.044.
12. VDI e. V., editor. VDI-Wärmeatlas. Berlin, Heidelberg: Springer Berlin Heidelberg; 2013. https://doi.org/10.1007/978-3-642-19981-3
13. Gusain D, Cvetkovic M, Palensky P. Quantification of operational flexibility from a portfolio of flexible energy resources. International Journal of Electrical Power & Energy Systems 2022;141:107466. https://doi.org/10.1016/j.ijepes.2021.107466
14. Fazio J, Hua D. Three probabilistic metrics for adequacy assessment of the Pacific Northwest power system. Electric Power Systems Research 2019;174:105858. https://doi.org/10.1016/j.epsr.2019.04.036
15. European Hydrogen Observatory. Levelised Cost of Hydrogen (LCOH) Calculator 2024.
16. Lorenz J, Klose A, Lange H, Kock T, Urbas L. Flexible Process Control for Scalable Electrolysis Systems. III. International Conference on Electrical, Computer and Energy Technologies (ICECET 2023), Cape Town-South Africa: IEEE; 2023. https://doi.org/10.1109/ICECET58911.2023.10389401.

© 2025 by the authors. Licensed to PSEcommunity.org and PSE Press. This is an open access article under the creative commons CC-BY-SA licensing terms. Credit must be given to creator and adaptations must be shared under the same terms. See https://creativecommons.org/licenses/by-sa/4.0/



Systems & Control Transactions

**Research Article - Peer Reviewed Conference Proceeding**
ESCAPE 35 - European Symposium on Computer Aided Process Engineering
Ghent, Belgium. 6-9 July 2025
Jan F.M. Van Impe, Grégoire Léonard, Satyajeet S. Bhonsale,
Monika E. Polańska, Filip Logist (Eds.)

PSE PRESS

# Methods for Efficient Solutions of Spatially Explicit Biofuels Supply Chain Models

**Phuc M. Tran[ab]*, Eric G. O'Neill[ab], and Christos T. Maravelias[abc]**

[a] Department of Chemical and Biological Engineering, Princeton University, Princeton, NJ 08540, USA
[b] DOE Great Lakes Bioenergy Research Center
[c] Andlinger Center for Energy and the Environment, Princeton University, Princeton, NJ 08540, USA
* Corresponding Author: pt3594@princeton.edu.

## ABSTRACT

The growing size and complexity of energy system optimization models, driven by high-resolution spatial data, pose significant computational challenges. This study introduces methods to reduce model's size and improve computational efficiency while preserving solution accuracy. First, a composite-curve-based approach is proposed to aggregate granular data into larger resolutions without averaging out specific properties. Second, a general clustering method groups geographically proximate fields, replacing multiple transportation arcs with a single arc to reduce transportation-related variables. Lastly, a two-step algorithm that decomposes the supply chain design problems into two smaller, more manageable subproblems is introduced. These methods are applied to a case study of switchgrass-to-biofuels network design in eight U.S. Midwest states, demonstrating their effectiveness with realistic and detailed spatial data.

**Keywords**: Energy and Sustainability, Biofuels, Computation Performance, Solution Quality, Optimization.

## INTRODUCTION

As a renewable energy resource, biofuels are expected to play a vital role in the transition to a low-carbon energy system, particularly in the transportation sector [1]. Although electrification has penetrated the light vehicle fleet, electrifying the heavy-duty vehicle fleet remains quite challenging [2]. In the near future, biomass-derived fuels can help alleviate the sector's reliance on fossil fuels without significantly altering the fleet [1,2].

The limitations of first-generation biofuels, mainly their competition for land use with food crops, have placed greater attention on second-generation biofuels, which are derived from ligno-cellulosic sources [3]. These crops are attractive due to their low net carbon emissions and ability to grow on non-arable lands [4]. Also, agricultural practices associated with these crops mitigate greenhouse gases (GHG) by sequestering atmospheric $CO_2$ in the form of soil organic carbon (SOC) [4,5]. However, the low bulk density of biomass and its dispersed availability often lead to expensive supply chain (SC) networks [6]. Hence, determining the optimal biofuels SC network is vital to making second-generation biofuels viable, both commercially and environmentally.

Detailed SC optimization models, typically in the form of mixed-integer linear programming (MILP) models, have been developed to investigate the economic and environmental performance of large-scale biofuels SC [7,8]. Recently, significant improvements have been made in identifying and characterizing potential fields for ligno-cellulosic crop growth, providing more detailed data on their locations and properties [6]. While highly granular data can improve the solution quality of SC models, they create significant computational issues, resulting in the formulation of models with large numbers of variables and constraints, mainly related to biomass procurement and transportation [7,8].

Spatial aggregation methods that group small fields into larger representative cells have been developed to address this issue. These approaches allow variables to be utilized at a coarser resolution, reducing model complexity. Nevertheless, this practice can reduce the accuracy of the aggregated data. The properties of the aggregated cells are typically the averages of fields' properties, failing to account for any variability in field-specific properties [9]. Furthermore, cells with fixed resolutions (e.g., counties or 25m x 25km) are commonly used for network reduction [8,9]. All fields within a cell are assumed to

share the same distances to facilities. Transportation arcs from these cells are assumed to originate from the cells' centers of mass, which are determined based on fields' locations and biomass availabilities within these cells. Given the dispersed locations of these fields, cells with fixed resolutions can lead to inaccurate transportation arcs. Such inaccuracies can reduce the solution quality of SC models.

In this paper, we propose two methods to reduce the large number of procurement and transportation variables while maintaining the accuracy of SC models: composite curves and location-based clustering. We also put forth a two-step algorithm that breaks large-scale problems into two smaller subproblems, which are solved more efficiently. The remainder of this paper is structured as follows: the Background section presents the necessary background for biofuels SC models and the terminology used in the paper. The Methods section outlines the major approaches and describes the models that can be created using the proposed methods. Lastly, a case study on biofuels SC in the U.S. Midwest is presented in the Case Study section.

## BACKGROUND

A biofuels SC model incorporates a wide range of activities and a complex set of parameters [9]. Depending on the scope and objective, implementation of SC models can help determine decisions at three distinct levels: long-term strategic, medium-term tactical, and short-term operational [9]. Long-term decisions involve facility location, technology selection, and capacity installation. Medium-term decisions include materials procurement and transportation. Short-term decisions pertain to production scheduling.

This work focuses mainly on SC models that consider medium-term decisions variables, which are specifically influenced by the granularity of spatial input data. For consistency, biomass procurement refers to the harvesting of crops at a specific location, while biomass transportation denotes the delivering of this material from a location to dedicated facilities. The cells used for aggregation are denoted as "harvesting sites" (HS).

**Table 1:** Nomenclature

| Symbol | Description |
|---|---|
| *Sets/Subsets* | |
| $f \in \mathbf{F}$ | Fields |
| $i \in \mathbf{I}$ | Compounds in the network |
| $j \in \mathbf{J}$ | Harvesting sites |
| $g \in \mathbf{G} \subset \mathbf{F}\mathbf{x}\mathbf{J}$ | Two-dimensional set of fields $f$ and the HS $j$ containing them |
| | Feedstock (biomass crop) |
| $\mathbf{I^F} \subset \mathbf{I}$ | All fields contained within an HS $j$ |
| $\mathbf{G_j} \subset \mathbf{G}$ | |
| *Parameters* | |
| $\alpha_{i,f}$ | Crop $i$ productivity in field $f$ (Mg/ha) |
| $\iota_{i,f}$ | Land available for crop $i$ in field $f$ (ha) |
| $\lambda_i^{FEED}/\lambda_i^{MAN}$ | Per-mass feedstock/management cost of feedstock $i$ ($/Mg) |
| $\upsilon_i^{HARV}/\upsilon_i^{MAN}$ | GHG emissions from harvesting/managing $i$ ($MgCO_2e/Mg$)/($MgCO_2e/ha$) |
| $\upsilon_{i,f}^{SOC}$ | SOC sequestration potential from $i$ in field $f$ ($MgCO_2e/ha$) |
| $\omega^{SCC}$ | Social cost of carbon ($/$MgCO_2e$) |
| *Variables* | |
| $H_{i,f}/\bar{H}_{i,j}$ | Procurement of $i$ in field $f$/HS $j$ (Mg) |
| $N_{i,f}/\bar{N}_{i,j}$ | Land use for crop $i$ in field $f$/HS $j$ (ha) |
| $C_{i,j}^{PRO}$ | Procurement cost of crop $i$ in field $f$ ($) |
| $J_{i,f}^{PRO}$ | GHG emissions from procuring crop $i$ in field $f$ ($MgCO_2e$) |
| $J_{i,j}^{SOC}$ | SOC sequestration from crop $i$ in HS $j$ ($MgCO_2e$) |
| $C^{TRA}$ | Transportation cost ($) |
| $OBJ$ | Objective – total supply chain cost ($) |

## METHODS

We present two complexity reduction methods and a solution method to solve large-scale SC models.

### Composite Curves

A composite curve depicts the relationship between two decision variables within an HS, such as land use and SOC sequestration, based on an optimized field selection order. This selection order is established using a ranking metric, which can change depending on the objective of the SC model. For instance, if the objective is to minimize land utilization, the ranking metric would prioritize fields based on their biomass productivity.

This leads to a distinctive land use versus biomass procurement curve. At first, the curve has a steep slope due to the use of highly productive fields, gradually flattening as less productive fields are incorporated. Using a composite curve instead of an average productivity value for the HS allows for a more precise representation of the field selection pattern inherent to the SC models. In practice, field-level optimization aims to prioritize the most productive fields to achieve minimal land utilization. Composite curves effectively capture this behavior, ensuring the alignment between field-level decisions and the aggregated outcomes at the HS level.

While the previous example emphasizes land use, which leads to a straightforward ranking metric, SC models often involve complex objectives. Then, it is crucial to systematically analyze how the procurement process contributes to the overall objective function. This involves identifying all the parameters, variables, and constraints pertaining to procurement, and modifying them to gauge how changes in procurement affect the

objective function. This rate of change derived from the analysis effectively serves as our ranking metric. To illustrate this approach, we present a case study from Christian County in Illinois (Figure 2), with an objective to minimize the total network cost, accounting for GHG emissions through the use of social cost of carbon (SCC).

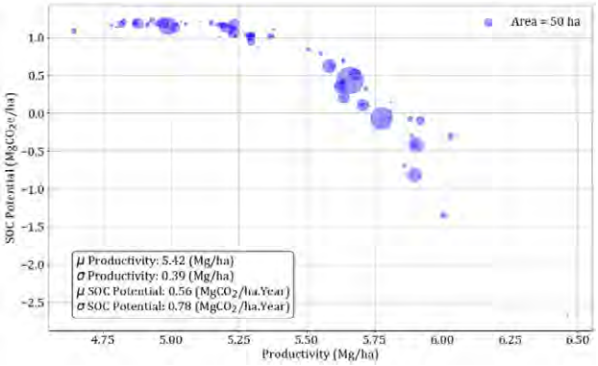



**Figure 2.** Properties of fields within Christian county for switchgrass

We first identify the contributions that biomass procurement makes to the overall network cost: procurement cost, $C_{i,f}^{PRO}$. We then identify all relevant constraints:

$$H_{i,f} = \alpha_{i,f} N_{i,f} \quad (1)$$

$$N_{i,f} \leq \iota_{i,f} \quad (2)$$

$$J_{i,f}^{PRO} = \upsilon_i^{HARV} H_{i,f} + \upsilon_i^{MAN} N_{i,f} - \upsilon_{i,f}^{SOC} N_{i,f} \quad (3)$$

$$C_{i,f}^{PRO} = \lambda_i^{FEED} H_{i,f} + \lambda_i^{MAN} N_{i,f} + \omega^{SCC} J_{i,f}^{PRO} \quad (4)$$

where Equation (1) relates land use decisions to biomass procurement decisions for each field. Equation (2) enforces an upper bound on land use. Equation (3) tracks the GHG emissions from biomass procurement, and Equation (4) calculates procurement costs. To determine how procurement costs scale with biomass procurement, we aim to convert all variables on the right-hand side of Equation (4) into $H_{i,f}$. We can make use of Equation (1):

$$N_{i,f} = \frac{H_{i,f}}{\alpha_{i,f}} \quad (5)$$

and substitute this expression into Equations (3) and (4):

$$C_{i,f}^{PRO} = \left[\lambda_i^{FEED} + \frac{\lambda_i^{MAN}}{\alpha_{i,f}} + \omega^{SCC}\left(\upsilon_i^{HARV} + \frac{\upsilon_i^{MAN}}{\alpha_{i,f}} - \frac{\upsilon_{i,f}^{SOC}}{\alpha_{i,f}}\right)\right] H_{i,f} \quad (6)$$

The rate of change of procurement cost per unit biomass procurement, described by the term in the square brackets of Equation 6, serves as the ranking metric. This ensures that the most cost-effective fields are prioritized. To aggregate field-specific variables, we introduce the following HS-level variables:

$$J_{i,j}^{SOC} = \sum_{f \in \mathbf{G}_j} \upsilon_{i,f}^{SOC} N_{i,f} \quad (7)$$

$$\bar{H}_{i,j} = \sum_{f \in \mathbf{G}_j} H_{i,f} \quad (8)$$

$$\bar{N}_{i,j} = \sum_{f \in \mathbf{G}_j} N_{i,f} \quad (9)$$

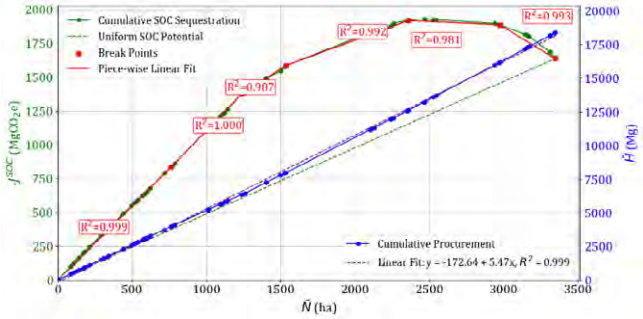



**Figure 3.** $\bar{N} - J^{SOC}$ and $\bar{N} - \bar{H}$ composite curves for Christian county with $\omega^{SCC}$ = \$65/MgCO₂e

Figure 3 displays a non-linear relationship between $\bar{N}_{i,j}$and $J_{i,j}^{SOC}$, and a linear one between $\bar{N}_{i,j}$ and $\bar{H}_{i,j}$. It is evident that we can use an average value in cases where the data has a narrow spread in values. However, composite curves are needed for data with high variability. In this example, composite curves are used to model $J_{i,j}^{SOC}$, while $\bar{H}_{i,j}$ can be assumed to scale linearly with $\bar{N}_{i,j}$.

To effectively approximate $\bar{N} - J^{SOC}$ composite curves while maintaining linearity in our model, we employ piecewise linearization. We develop a technique which seeks to maximize the linear fitting coefficients of determination $R^2$ by discretizing the $\bar{N} - J^{SOC}$ curve into consecutive linear segments. We also limit the number of segments in each curve to a maximum of six.

## Location-based Clustering

We propose using location-based clustering to define HS that better capture the geographical locations of fields for network reduction. The clustering algorithm of choice in this study is the *k*-means algorithm. The *k*-means algorithm partitions a dataset (fields) into a user-defined number *K* of distinct clusters (HS) based on selected properties (longitude and latitude):

$$min \sum_{j=1}^{K} \sum_{x \in \boldsymbol{C}_j} \left|\left|x - \mu_j\right|\right|_2^2 \quad (7)$$

where *K* is the user-defined number of HS; $x$ contains the longitude and latitude of a field; $\boldsymbol{C}_j$ is the set of fields assigned to HS $j$; $\mu_i$ contains the longitude and latitude of the centroid of HS $j$. The algorithm minimizes the within-HS variance by finding the optimal HS centroids and their member fields at the same time. With spatial coordinates as input properties, fields in the same *k*-means HS are spatially proximate, making sure that transportation arcs originating from these centroids are representative of their member fields' locations.

Because the objective function is non-convex, the algorithm is run several times with different initializations,

and the best solution is selected. The use of the *k*-means clustering for network reduction terminates the reliance on Geographical Information System (GIS) software to process geospatial data. Also, the number of HS can be easily adjusted through the parameter *K*, offering flexibility and scalability.

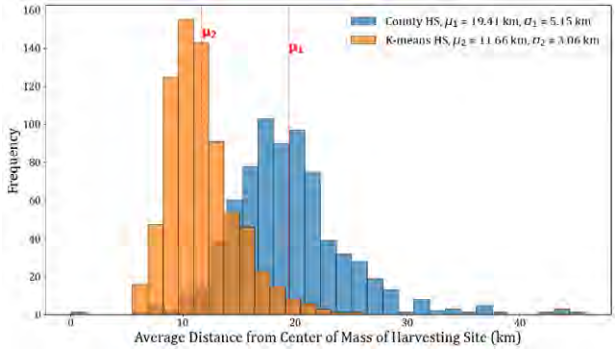



**Figure 4.** Distribution of mean distances between fields and the center of mass/centroid of their HS

To demonstrate, we apply the *k*-means algorithm to our case study, creating *K* = 734 HS. We select this *K* value because the fields in our dataset span across 734 counties in the study area. Figure 4 shows the statistics of the best solutions out of 10 *k*-means runs different initialization. As shown, the mean distances within *k*-means generated HS are more narrowly distributed than those of county-level HS.

## Two-step Algorithm

To balance computational efficiency with spatial granularity, we introduce a two-step algorithm that effectively solves large-scale network design models with high spatial resolution. In Step 1, an MILP model that incorporates at least one of the proposed complexity reduction methods is solved to attain a "coarse" solution of the large-scale model. In Step 2, this solution is refined to a higher resolution. We develop a linear programming (LP) model that takes in the HS-level procurement decisions from the Step 1 solution as parameters and re-optimizes these decisions to a field level. This second step uses field-originating transportation arcs, enabling more precise calculation of transportation costs, which can then be used to re-evaluate the objective function values found in Step 1.

The Step 1 model can have different formulations based on the methods employed, while the Step 2 model always stays unchanged. We refer to all Step 1 models by the letter M. Superscripts denote the resolution of the biomass procurement variables: field-level (*F*) or HS-level (*HS*). Subscripts describe the complexity reduction methods used. For network reduction, we can use fixed-resolution (-) or *k*-means HS (*K*). Composite curves (CC) can also be used.

Four Step 1 models are considered in this study, each having a unique combination of the proposed methods. The baseline model, $\mathrm{M}^{F}_{-,-}$, has a field resolution and uses fixed-resolution (county-level) HS for network reduction. Models $\mathrm{M}^{HS}_{-,CC}$ and $\mathrm{M}^{F}_{K,-}$ use composite curves and *k*-means HS, respectively. Finally, model $\mathrm{M}^{HS}_{K,CC}$ combines both complexity reduction methods.

# CASE STUDY

We use the four developed models to analyze a switchgrass-to-biofuels SC. The area of study includes the 8 states in the US Midwest: Ohio, Indiana, Iowa, Illinois, Michigan, Minnesota, Missouri, and Wisconsin.

All models are implemented for multiple instances. Specifiaclly, $\omega^{SCC}$ values are varied from \$0/MgCO$_2$e to \$25/MgCO$_2$e, with \$5/MgCO$_2$e increments. We also have three levels of biofuels demand, denoted as $\beta$: 500M gallons of gasoline equivalent (GGE), 800 GGE, and 1000M GGE.

We are given (i) the realistic, spatially explicit data on the biomass productivity and SOC potential of each field; (ii) potential biorefinery and preprocessing depot locations and their technology options; (iii) operating and transportation cost parameters. We also have the state-dependent prices and GHG impacts of grid electricity. Model models yield the optimal (i) fields for procurement and land utilization; (ii) facility locations, as well as their technologies and capacities (iii) transportation routing and production planning. The objective function is the minimization of total SC cost, including environmental factors, in net-present dollar amount.

All models in this study are formulated on GAMS Studio 45.7.0 and implemented with Gurobi 10.0.1.

## Effects of Composite Curves

We look into how $J^{SOC}$ values change between Step 1 and Step 2 solutions to investigate the effects of composite curves, as they are used to approximate this variable. Small differences in $J^{SOC}$ are observed between the two steps for $\mathrm{M}^{\mathrm{HS}}_{-,CC}$ in Figure 5a, showing that composite curves are able to capture the behavior of sequestration on a field level. There are, however, notable differences in $J^{SOC}$ values for both steps among models. This is due to the use of average productivity values for the HS in $\mathrm{M}^{HS}_{-,CC}$, which leads to different land use decisions, and thus different sequestration patterns in the models' solutions.

Despite this, $\mathrm{M}^{HS}_{-,CC}$ has great performance, as shown in Figure 6. The y-axis shows the fraction of all instances that are solved to optimality. The multiplier $\varepsilon$ represents how much longer it takes for each model to solve with respect to the fastest one, for that instance. The performance profile of $\mathrm{M}^{HS}_{-,CC}$ starts at y=0.39, indicating that the model is the most efficient for 39% of the instances. The

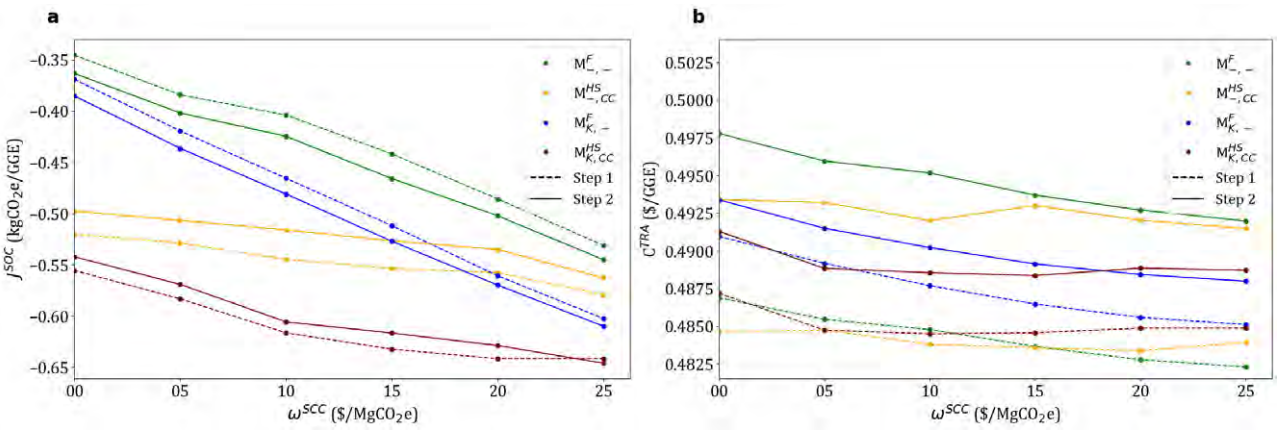



**Figure 5:** Results from the case study for all models, with $\beta$ = 500M GGE and varying $\omega^{SCC}$. a) SOC sequestration, b) transportation cost, normalized to a per GGE basis.

profile also reaches y=1.0 within a small range of $\varepsilon$, meaning that, for the instances that $M^{HS}_{-,CC}$ is not most efficient model, its run times are not significantly longer than those of the fastest model. Overall, composite curves allow us to aggregated field-level variables into HS-level ones in model $M^{HS}_{-,CC}$ without severely degrading solution quality, leading to improved run times compared to models with field-level variables.

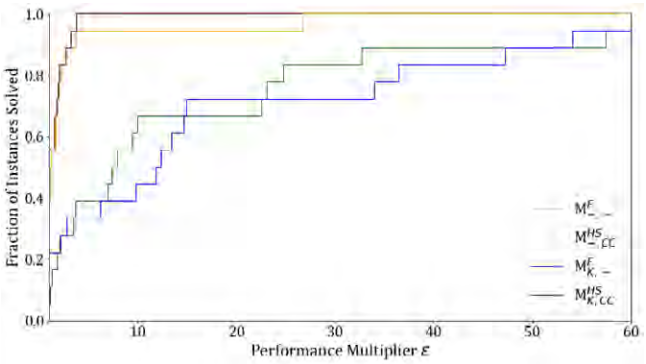



**Figure 6.** Performance chart of all models, with 18 total instances

## Effects of Location-based Clustering

For all instances, Figure 5b showcases that $M^{F}_{K,-}$ has significantly lower $C^{TRA}$ differences between Steps 1 and 2 than those of $M^{F}_{-,-}$ and $M^{HS}_{-,CC}$, which use county-level HS. These lower $C^{TRA}$ differences influence the objective in a meaningful way. For most instances, although $M^{F}_{K,-}$ finds worse $OBJ$ values than $M^{F}_{-,-}$ does, Step 2 solutions then reveal that $M^{F}_{K,-}$, in reality, attains better objective function values when $C^{TRA}$ changes are accounted for. This can lead to differences in optimal configurations. One such instance is where $\omega^{SCC}$= 15/MgCO$_2$e and $\beta$ = 800M GGE. Here, $M^{F}_{K,-}$ finds an optimal configuration that contains one more biorefinery than that of $M^{F}_{-,-}$ (circled in red on Figure 7). This result emphasizes the effects of using location-based clustering to improve the quality and accuracy of model solutions.

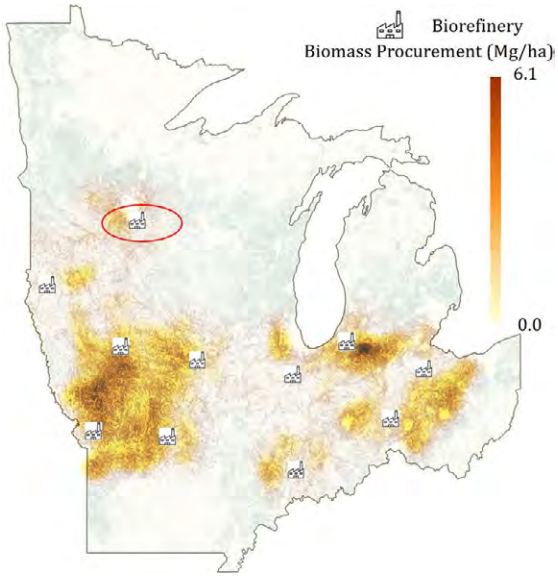



**Figure 7.** Optimal configuration of $M^{F}_{K,-}$ for instance $\omega^{SCC}$ = \$15/MgCO$_2$e and $\beta$ = 800M GGE. All refineries have pyrolysis with hydrogen purchase as the techonology

## Combined Effects

Figure 5a shows that $M^{HS}_{K,CC}$ has small changes in $J^{SOC}$ between Steps 1 and 2, illustrating the ability to capture within-HS procurement patterns of composite curves. Figure 5b exhibits similarly small $C^{TRA}$ differences between $M^{HS}_{K,CC}$ and $M^{F}_{K,-}$, highlighting the importance of *k*-means clustering. Also, $M^{HS}_{K,CC}$ displays short run times that are characteristic of composite curves. Figure 6 shows comparably fast performance between $M^{HS}_{K,CC}$ and $M^{HS}_{-,CC}$. In fact, $M^{HS}_{K,CC}$ slightly outperforms $M^{HS}_{-,CC}$. It is evident that $M^{HS}_{K,CC}$ inherits the characteristics of both

complexity reduction methods. The model maintains the field-level accuracy while using HS-level variables and having improved run times through the use of composite curves. Moreover, $M_{K,CC}^{HS}$ reduces transportation cost changes between Steps 1 and 2 through the use of *k*-means clustering. The combination of both complexity reduction methods enables $M_{K,CC}^{HS}$ to find high-quality solutions within a short amount of time.

## CONCLUSION

We investigated the use of two complexity reduction methods and a solution method, with the goal to increase the performance as well as accuracy of large-scale, spatially explicit SC models in this paper. We first introduced a composite-curves based approach, which creates characteristic curves for HS-level decision variables according to a specific ranking metric for fields. We also presented a framework to determine this ranking metric. Second, we utilized location-based network reduction, which reduces transportation-related variables by assuming the same transportation arc from multiple fields to dedicated facilities. The accurate clustering of fields for network reduction was achieved via the *k*-means algorithm, leading to more realistic transportation arcs. Lastly, a two-step algorithm was designed to decompose large-scale SC models into two more manageable sub-problems. These sub-problems can be solved sequentially and more efficiently. Lastly, we put forth a switchgrass-to-biofuels SC case study in the U.S. Midwest to probe how the proposed complexity reduction methods influence the performance and solution quality of models. Our results suggested that composite curves effectively improve the performance of models while successfully capturing the within-HS fields selection pattern, and *k*- means clustering improves models' accuracy in establishing representative transportation arcs for groups of fields. The combination of both complexity reduction methods led to better objective function value as well as more efficient performance. These ideas can be utilized in SC models that deal with large spatial datasets in order to increase their performance without trading off the accuracy of solutions.

## DIGITAL SUPPLEMENTARY MATERIAL

Additional description of proposed methods, formulation of Step 1 and Step 2 models, parameters and results of the case study can be found at:
https://psecommunity.org/LAPSE:2025.0029

## ACKNOWLEDGEMENTS

This material is based upon work supported by the Great Lakes Bioenergy Research Center, U.S. Department of Energy, Office of Science, Office of Biological and Environmental Research under award number DE-SC0018409.

## REFERENCES

1. Demirbas A. Importance of biodiesel as transportation fuel. Energy Policy 2007;35:4661–70. https://doi.org/10.1016/j.enpol.2007.04.003
2. Geissler CH, Ryu J, and Maravelias CT. The future of biofuels in the United States transportation sector. Renewable and Sustainable Energy Reviews 2024;192:114276. https://doi.org/10.1016/j.rser.2023.114276
3. Naik SN, Goud VV, Rout PK, and Dalai AK. Production of first and second generation biofuels: A comprehensive review. Renewable and Sustainable Energy Reviews 2010;14:578–97. https://doi.org/10.1016/j.rser.2009.10.003
4. Cai X, Zhang X, and Wang D. Land availability for biofuel production. Environmental science & technology 2011;45:334–9. https://doi.org/10.1021/es103338e
5. Martinez-Feria R and Basso B. Predicting soil carbon changes in switchgrass grown on marginal lands under climate change and adaptation strategies. GCB Bioenergy 2020;12:742–55. https://doi.org/10.1111/gcbb.12726
6. Mielenz JR. Ethanol production from biomass: technology and commercialization status. Current Opinion in Microbiology 2001;4:324–9. https://doi.org/10.1016/S1369-5274(00)00211-3
7. He-Lambert L, English BC, Lambert DM, et al. Determining a geographic high resolution supply chain network for a large scale biofuel industry. Applied Energy 2018;218:266–81.
8. O'Neill EG, Martinez-Feria RA, Basso B, and Maravelias CT. Integrated spatially explicit landscape and cellulosic biofuel supply chain optimization under biomass yield uncertainty. Computers & Chemical Engineering 2022;160:107724.https://doi.org/10.1016/j.compchemeng.2022.107724
9. Ng RT, Kurniawan D, Wang H, Mariska B, Wu W, and Maravelias CT. Integrated framework for designing spatially explicit biofuel supply chains. Applied Energy 2018;216:116–31. https://doi.org/10.1016/j.apenergy.2018.02.077

© 2025 by the authors. Licensed to PSEcommunity.org and PSE Press. This is an open access article under the creative commons CC-BY-SA licensing terms. Credit must be given to creator and adaptations must be shared under the same terms. See https://creativecommons.org/licenses/by-sa/4.0/



Systems & Control Transactions

**Research Article - Peer Reviewed Conference Proceeding**
ESCAPE 35 - European Symposium on Computer Aided Process Engineering
Ghent, Belgium. 6-9 July 2025
Jan F.M. Van Impe, Grégoire Léonard, Satyajeet S. Bhonsale,
Monika E. Polańska, Filip Logist (Eds.)

PSE PRESS

# Integrating Carbon Value Vectors in the Energy and Materials Transition Nexus: A Case Study on Mobility Optimization

**Betsie S. M. Montano Flores[a,b], Rahul Kakodkar[a,b], Marco P. De Sousa[a,b], Shayan S. Niknezhad[a,b] and Efstratios N. Pistikopoulos[a,b]***

[a] Artie McFerrin Department of Chemical Engineering, Texas A&M University, College Station, TX, USA
[b] Texas A&M Energy Institute, Texas A&M University, College Station, TX, USA
* Corresponding Author: stratos@tamu.edu.

## ABSTRACT

The ongoing energy transition involves decarbonization across different sectors. Amongst these, the transportation sector contributes significantly owing to its reliance on traditional fossil fuels as feedstock. Attaining decarbonization goals requires the adoption of novel sustainable technologies such as electric vehicles (EVs), and hydrogen fuel cell vehicles (HFCVs), amongst others. The feedstock transition towards electricity and dense energy carriers is challenged by the requirement for additional infrastructure to manage intermittency, power generation, and grid expansion which requires both materials and capital investment. By evaluating and redirecting the role of carbon value vector from fossil fuel production towards the production of carbon-based materials such as polymers to empower the energy transition, we can optimize resource allocation and maintain economic viability, all while reducing environmental impact. In this work, we propose an integrated framework to systematically address energy-materials-mobility transition nexus challenges. The proposed multiscale framework utilizes a resource-task-network (RTN) representation and a life cycle assessment (LCA) step and considers future material demand and production capacities. Its capabilities are demonstrated through a case study on the transition from gasoline-fueled vehicles to EVs, analyzing (i) the role of carbon value vectors in resources and materials production, and (ii) electricity generation, storage, and dispatch using intermittent renewables. The study reveals the interactions between energy, material, and mobility value chains while providing configurations for exploiting such synergies.

**Keywords**: Energy transition, Material transition, Carbon value vectors.

## INTRODUCTION

The energy transition necessitates the adoption of low-carbon technologies, which are inherently capital-intensive and require substantial material inputs [1]. This creates a critical nexus between energy and materials, as the development of new infrastructure demands significant quantities of resources, while the growing energy sector is required to manufacture components such as wind turbines, solar panels, and electric vehicles [2].

Renewable power systems, such as solar photovoltaics (PV), wind farms (WF), and decarbonized transportation technologies, including EVs, rely on materials like metals, rare earth elements, polymers, and concrete. However, the extraction and processing of these materials are energy and emission intensive [3]. Leveraging synergies between distinct value chains offers a pathway to promote decarbonization while managing economic expenditures.

For instance, polymers have the potential to play a pivotal role in the mobility transition, functioning as carbon sinks, and contributing to decarbonization efforts [4]. We are considering that polymers can be produced from fossil fuels and can be carbon sinks since instead of burning fossil fuels, they can be utilized to produce materials. Another case is when polymeric materials are

created from $CO_2$ captured utilizing CCUS technologies for the current BAU production and utilizing it to produce monomers for polymers through technologies such as methanol to olefins and oxidative coupling of methane. Polymers can enhance fuel efficiency by making vehicles lighter, serve as integral components in renewable energy systems and grid infrastructure, and be synthesized using carbon captured from industrial processes [5]. A promising approach to addressing these challenges involves reevaluating the role of carbon as a value vector. Repurposing existing oil and gas infrastructure for polymer production rather than traditional fuel refinement offers an opportunity to reduce carbon emissions in the mobility sector while capitalizing on existing assets [6, 7].

A holistic approach must be taken to achieve cost-effective solutions in the energy-materials-mobility transition nexus, analyzing the current and future scenarios, and considering all three interconnected aspects to ensure sustainable and efficient outcomes. This includes operational carbon footprint as well as those embedded in material extraction, manufacturing, and infrastructure development. The 3 synergetic transitions in energy, materials, and mobility (See Figure 1), face significant challenges, including managing energy storage for intermittent renewables, addressing emissions from diverse sources, optimizing production costs, and coordinating technology transitions across sectors such as power generation, and transportation [8].

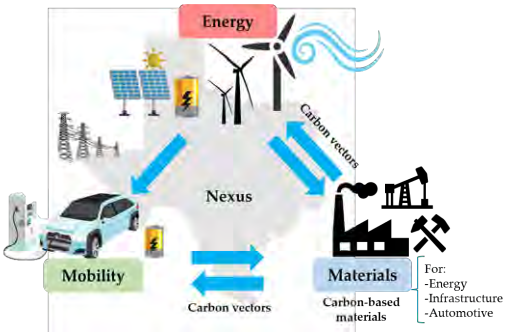



**Figure 1.** The energy-materials-mobility nexus.

This work introduces a multiscale modeling and optimization framework using the resource task network (RTN) representation which integrates network design and operation considering the nexus between energy-materials-mobility transition. A mixed-integer linear programming (MILP) integrates an LCA step for emissions from material synthesis, resource consumption, and infrastructure establishment. A case study on the transition from gasoline-fueled vehicles to EVs highlights the framework's capabilities, focusing on the role of material production and electricity generation, storage, and dispatch. This analysis implemented in energiapy uncovers synergies between energy, material, and mobility value chains, and identifies optimal configurations, and trade-offs across key parameters [9].

## CASE STUDY CONSIDERATIONS

The energy transition is driving a transformation across multiple sectors, including mobility infrastructure, manufacturing technologies, power generation, and material production. These interconnected shifts highlight a crucial nexus between energy, materials, and mobility.

**Energy Transition**: Power generation must expand to meet the increased demand from transportation and manufacturing. Requisite power generation and management systems can be established through different material alternatives. PVs can be made from monocrystalline or polycrystalline silicon, lithium for lithium-ion batteries can be sourced either through rock or brine lithium, and wind farms can be offshore or land-based each with different material requirements. Other materials required for construction include glass, steel, concrete, aluminum, silicon, copper, and cast iron [10-12].

**Material Transition**: Low-carbon technologies necessitate the production of advanced materials, such as those needed for renewable energy systems, batteries, and vehicle components. Polymer production is modeled as High-Density Polyethylene (HDPE) production and the production of vehicle parts through a combination of different methods [11].

Technological pathways for plastic production [13]:

1. Business as usual (BAU): HDPE is produced from fossil feedstock such as natural gas and oil.
2. Carbon capture utilization and sequestration (CCUS): Utilizes resources such as $CO_2$, $H_2$ and $O_2$.

Additionally, two processes are given for olefin production from $CO_2$. The pathways considered for olefin production are [14]:

1. Methanol to Olefins (MTO): Involves synthesizing methanol through $CO_2$ hydrogenation, which is then converted into olefins, primarily ethylene and propylene.
2. Oxidative Coupling of Methane (OCM): In this process, methane derived from $CO_2$ hydrogenation undergoes oxidative coupling to predominantly produce ethylene.

Moreover, the role of oil in producing polymers is introduced as a new concept of carbon value vectors utilization of the carbon-based materials that come from fossil fuel production, in which the current oil use for fuels or manufacturing polymers will change over time.

**Mobility Transition**: This sector involves adopting alternative fuels and transitioning from internal

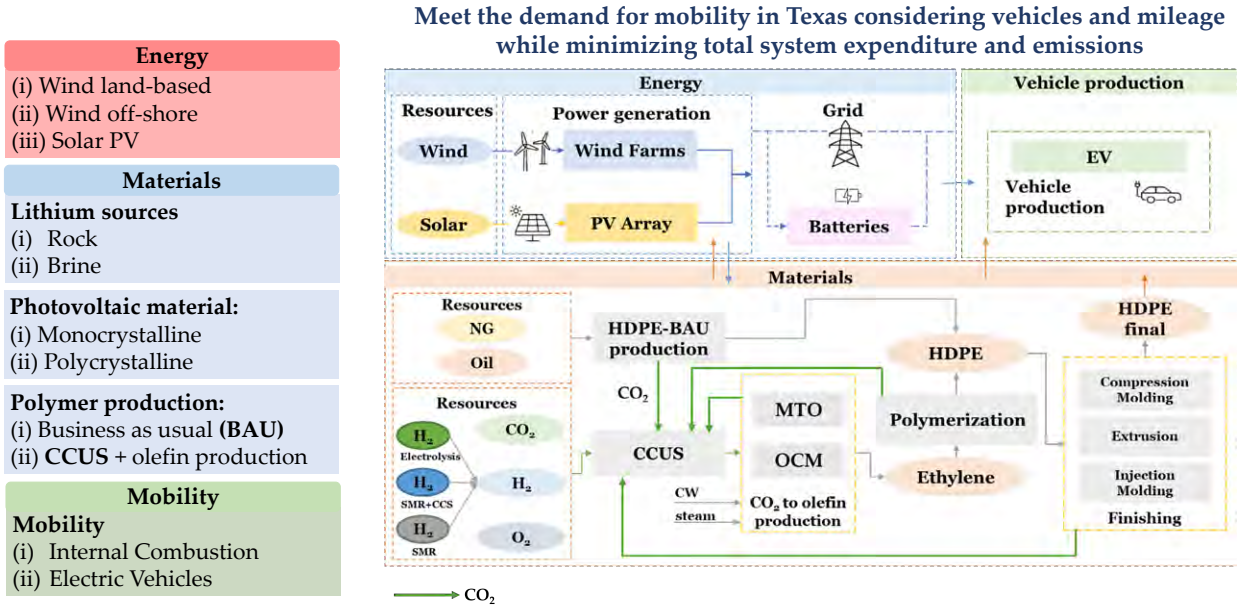



**Figure 2:** Comprehensive schematic of the mobility transition supply chain case study, illustrating the included resources and processes. The diagram comprises three key components: 1) Renewable energy-based power generation. 2) Polymer production via both fossil fuel-based (BAU) and CCUS pathways. 3) Vehicle production, focusing on three HDPE finishing processes for automotive applications.

combustion engine vehicles (ICEVs) to alternatives such as EVs [15]. This requires both new types of vehicles and the infrastructure to support them.

These transitions are highly interdependent, creating a nexus between them. For example, renewable power generation supports manufacturing and transportation, while advanced materials, including carbon-based polymers, enable the development of efficient vehicles and infrastructure. The mobility sector, in turn, influences energy demand and material production needs, creating a feedback loop within this interconnected system. The representation of the system of study is shown in Figure 2, illustrating the key components of the energy-materials-mobility transition nexus.

## METHODOLOGY AND FORMULATION

The framework operates on multiple scales, capturing phenomena that vary across space and time, such as fluctuations in renewable energy availability. Additionally, it integrates operational decisions with network planning into a unified model. The planning horizon is divided into two distinct scales: (1) a broader scale for network-level decisions and (2) a detailed scheduling scale with hourly resolution. The framework integrates the optimization of both network design and process scheduling. Mixed-integer linear programming is employed, binary variables are used for decisions such as process placement and selection of optimal material modes, while continuous variables address mass balance and economic considerations. Key constraints include material balance, emission limits, and network design requirements.

### Sets and definitions

**Table 1:** Sets

| sets | definition |
|---|---|
| $l \in L$ | location |
| $p \in P$ | process |
| $r \in R$ | resource |
| $m \in M$ | material |
| $w \in W$ | material modes |
| $e \in E$ | emissions |
| $t \in T^N$ or $t \in T^S$ | network or scheduling scale |

### Network design constraints

- Process/inventory capacity: Processes and inventories are restricted within specified minimum and maximum capacities ($Cap_{l,p/r,t}^{P/S-min/max}$). The binary variable $x_{l,p/r,t}^{P/S}$ takes a value of 1 if the capacity is expanded during that time and 0 otherwise.

$$Cap_{l,p/r,t}^{P/S-min} \cdot x_{l,p/r,t}^{P/S} \leq Cap_{l,p/r,t}^{P/S} \leq Cap_{l,p/r,t}^{P/S-max} \cdot x_{l,p/r,t}^{P/S} \forall\, l \in L, r \in R, p \in P, t \in T^N \quad (1)$$

- Capacity of material mode: The capacity of a process $Cap_{l,p,w,t}^{P-W}$ is determined by the material mode selected for constructing the process. This

capacity is constrained by the process's minimum and maximum limits. The binary variable $x_{l,p,w,t}^{P-W}$ takes a value of 1 if the material mode is active, and 0 otherwise.

$$Cap_{l,p,t}^{P-min} \cdot x_{l,p,w,t}^{P-W} \leq Cap_{l,p,w,t}^{P-W} \leq Cap_{l,p,t}^{P-max} \cdot x_{l,p,w,t}^{P-W} \forall\, l \in L, w \in W, p \in P, t \in T^N \quad (2)$$

Binary variables $x_{l,p,w,t}^{P-W}$ are introduced for each process and material mode option used. The binary variable $x_{l,p,t}^{P}$ indicates whether a process is active or not and is defined as the sum of the binary variables corresponding to the selected material modes for that process.

$$x_{l,p,t}^{P} = \sum_{w \in W} x_{l,p,w,t}^{P-W} \forall\, l \in L, w \in W, p \in P, t \in T^N \quad (3)$$

## Materials constraints

- Materials to set up a process: This quantity ($Mat_{l,p,m,t}^{P}$). is the sum of the products of material consumption ($Mat_{p,w,m}^{cons}$) for a given process, mode, and material, and the capacity of each process mode ($Cap_{l,p,w,t}^{P-W}$).

$$Mat_{l,p,m,t}^{P} = \sum_{w \in W} \left( Mat_{p,w,m}^{cons} \cdot Cap_{l,p,w,t}^{P-W} \right) \quad \forall\, l \in L, m \in M, p \in P, t \in T^N \quad (4)$$

- Materials utilized at a location: Calculated as the summation of the materials utilized across all processes.

$$Mat_{l,m,t}^{L} = \sum_{p \in P} Mat_{l,p,m,t}^{P} \forall\, l \in L, m \in M, t \in T^N \quad (5)$$

- Materials utilized in the network: Calculated as the sum of the materials utilized across all locations.

$$Mat_{m,t}^{N} = \sum_{l \in L} Mat_{l,m,t}^{L} \forall\, m \in M, t \in T^N \quad (6)$$

## Emissions constraints

Different types of emissions are identified, such as emissions coming from resources, indirect emissions from materials, and direct emissions from processes [10, 11].

- Emissions from materials: The emissions resulting from materials ($Em_{l,e,m,t}^{m}$) are calculated as the product of the emission factor for that material ($EP_{e,}^{m}$) and the amount of the material utilized at a location and time ($Mat_{l,m,t}^{L}$).

$$Em_{l,e,m,t}^{m} = EP_{e,}^{m} \cdot Mat_{l,m,t}^{L} \forall\, l \in L, e \in E, m \in M, t \in T^N \quad (7)$$

Emissions are annualized based on the lifespans of the technologies, materials, and vehicles used in the system. Technologies are designed to last 20 years, while vehicles have a lifespan of 15 years. The total emissions are calculated over the entire lifetime of the system, but for reporting purposes, only the annual emissions corresponding to yearly production are displayed.

- Total emissions at a location: This quantity includes emissions from resources ($Em_{l,e,r,t}^{r}$), materials ($Em_{l,e,m,t}^{m}$), and processes ($Em_{l,e,p,t}^{p}$). The total emissions of the network can be calculated in a similar form to equation 6.

$$Em_{l,e,t}^{L} = \sum_{r \in R} Em_{l,e,r,t}^{r} + \sum_{m \in M} Em_{l,e,m,t}^{m} + \sum_{p \in P} Em_{l,e,p,t}^{p} \forall\, l \in L, e \in E, t \in T^N \quad (8)$$

## Objective functions

Different objectives can be defined based on the decision maker's motivation, such as the minimization of the cost of the network or the environmental impact.

- Cost: Minimize the cost of the network.

$$Min \sum_{t \in T^N} \propto \cdot Capex_t^N + Fopex_t^N + Vopex_t^N \quad (9)$$

- Environmental: Minimize the emissions of the network.

$$Min \sum_{t \in T^N} Em_{e,t}^N \quad (10)$$

# RESULTS AND DISCUSSION

## Polymers for the mobility transition

A base case is established to minimize the system cost for polymer production. The network design for the base case consists of WF, PV, LiI batteries, HDPE production from the BAU pathway, and the finishing processes (Figure 3). With the base case established, the network is optimized for reducing GWP, achieving a maximum emissions reduction of 34.7%. The minimum emissions design favors the WF because it has lower material emissions than PV for energy production and integrates the CCUS with the MTO pathway for polymer production (Figure 4). This reduction corresponds to a 135.63% increase in cost compared to the base case (Figure 5).

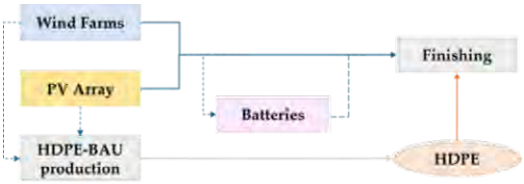



**Figure 3.** Low-cost pathway for HDPE production.

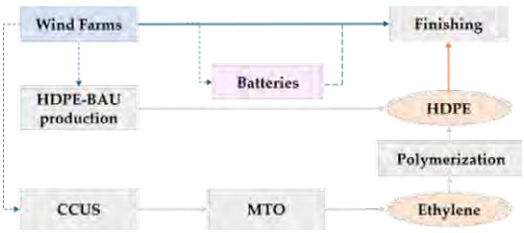



**Figure 4.** Low carbon pathway for HDPE production.

## Integration of materials in the framework

Different studies do not consider the impact of material on the design and scheduling of energy systems, resulting in a more optimistic scenario.

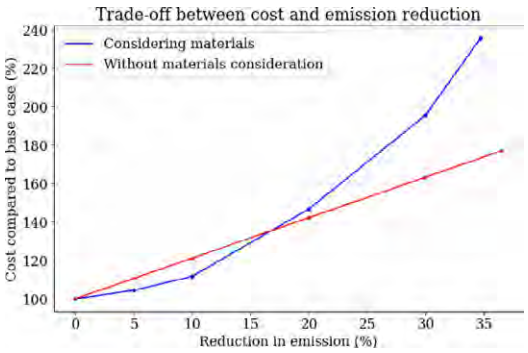



**Figure 5.** Trade-off between cost and emissions reduction for polymer production.

In this example, including materials results in a maximum emissions reduction of 34.7% with a 135.63% cost increase. However, not including the material aspect in the framework achieved a higher maximum emissions reduction of 36.5% and a lower extra cost (77.1%). These findings highlight the need to account for material aspects to achieve accurate outcomes. Additionally, Figure 6 shows the breakdown of emissions for each point in the Pareto curves above, illustrating the types of materials, resources, and processes that generate emissions in the system.

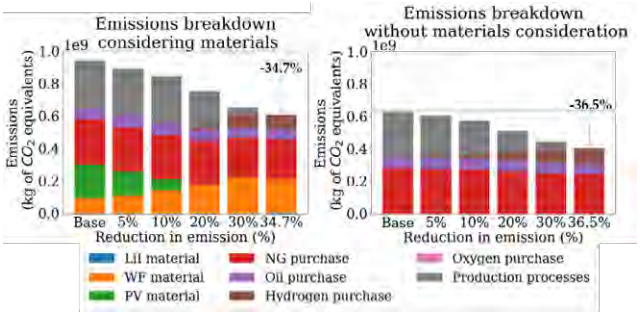



**Figure 6.** Breakdown of emissions for polymer production.

## Analysis of Texas mobility transition through the years

In the last section, only the polymer production for vehicles was considered. Here, the driving phase is also integrated into the case study. For this analysis, the projection of vehicles in Texas was considered with the future demand of cars expected every decade, using a linear model ($y = 305873x - 6 \cdot 10^8$) where $y$ is the number of cars expected in year $x$. Starting in 2025, with about 26 million vehicles, a base case with all ICE cars is considered. Three scenarios for the future are analyzed, with low, medium, and high reductions in oil consumption.

**Table 2:** Scenarios studied for mobility transition subject to reduction in oil consumption and EV adoption results.

| | Maximum oil consumption (%) | | | | | |
|---|---|---|---|---|---|---|
| **Scenario** | **Low (%)** | **EV (%)** | **Medium (%)** | **EV (%)** | **High (%)** | **EV (%)** |
| 2025 | 100 | 0 | 100 | 0 | 100 | 0 |
| 2030 | 95 | 12.3 | 90 | 18.1 | 80 | 29.6 |
| 2040 | 90 | 27.9 | 80 | 37.8 | 60 | 55.7 |
| 2050 a | 85 | 40 | 70 | 52.3 | 40 | 74.8 |
| 2050 b | | | | | 0.1 | 100 |

For each scenario, the objective is to minimize the cost of the system subject to a maximum hourly consumption of oil concerning the base year 2025 (Table 2). An extra scenario with 100% EVs by 2050 was also introduced (2050 b). The constraints in the reduction of oil consumption led to the adoption of EVs (Table 2), the number of EVs shown corresponds to the minimum cost of the network with energy coming from PVs and WFs.

## Cost of the mobility transition

For each scenario, the reduction in oil consumption affected lowering the average emissions per car over the years. Additionally, the average cost per car and yearly emissions were determined as shown in Figure 7. It is shown that the total emissions per car are reduced with a significant cost increase due to the investment in EVs and renewable energy generation. Relying solely on wind farms for power generation incurs higher costs but results in greater emissions reduction due to the lower emissions associated with materials for WFs (Figure 8).

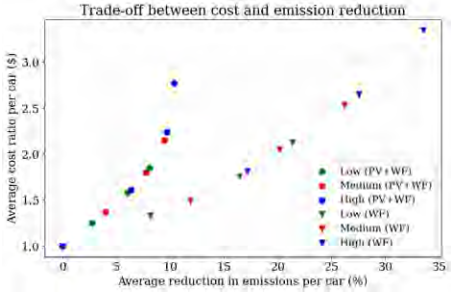



**Figure 7.** Cost vs. emissions of the mobility transition.

## Material impact on the mobility transition

The environmental impact of the mobility transition was quantified by considering materials, resources, and processes, as shown in Figure 8 (for the high reduction in oil consumption scenario). It is important to note that the total emissions of the fleet decrease in cases where all the energy is generated through WF. However, this result depends on the assumption of the fleet projections. For

example, despite the adoption of EVs, emissions may continue to rise if energy production relies on a combination of photovoltaic (PV) systems and WFs due to the material emissions associated with PVs. However, emissions will still be lower than solely relying on gasoline vehicles.

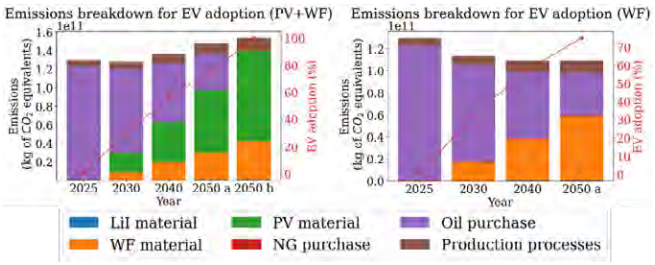



**Figure 8.** Contribution of materials, resources, and processes to emissions for high EV adoption.

## Renewable energy expansion and carbon vectors in the mobility transition

For the given scenarios the total installed capacity of renewable energy was estimated per decade as shown in Figure 9. Additionally, these capacities were compared with the current Texas grid capacity (Table 3), finding that the expansion of renewable energy can be similar to the current installed grid capacity for scenario 2050 b (100% EV).

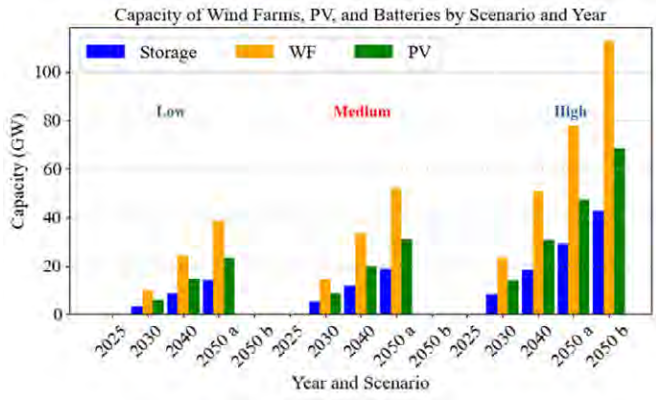



**Figure 9.** Required installed capacity of renewables and storage for the mobility transition.

Moreover, Table 3 evaluates the carbon value vectors of oil used in producing plastics in the column of oil to plastics, quantifying the amount of oil that can be redirected to valuable polymers for vehicles and charging stations over time. Given that this represents a small amount of the current oil consumption in the mobility sector, other applications for this resource can be explored.

**Table 3:** Comparison of the required capacity of WF and PV with the current grid capacity in Texas (145 GW).

| Scenario | WF capacity (%) | PV capacity (%) | Oil to plastics (%) |
|---|---|---|---|
| 2025 | 0.22 | 0.14 | 0.077 |
| 2030 | 16.05 | 9.67 | 0.081 |
| 2040 | 34.96 | 21.11 | 0.090 |
| 2050 a | 53.65 | 32.46 | 0.098 |
| 2050 b | 77.56 | 47.05 | 0.098 |

## CONCLUSIONS AND FUTURE WORK

This study served to realize interconnections between energy and materials, emphasizing the importance of an integrated energy-materials nexus approach for applications in the design of energy systems. Different aspects were addressed with the framework such as the integration of materials and energy requirements and technologies, the trade-offs between cost and emissions reduction, as well as the impact of emerging technologies. Process lifetimes and the circularity of materials can be incorporated for a more comprehensive approach, as well as carbon taxes and future reductions in EV costs.

Besides renewable intermittency, the framework can also accommodate variability in the cost of resources such as natural gas and oil and resource demand. Case studies considering such aspects and the redirection of oil resources will be presented in future publications. The inclusive framework for the Energy-Materials-Mobility Transition Nexus can coordinate options of technologies and materials to determine the minimum cost, minimum emissions scenarios, and tradeoffs. Considering material use for setting up technology infrastructure systems provides realistic emissions reduction and cost scenarios and allows the investigation of material substitution options as carbon sinks through the utilization of carbon value vectors in a circular economy framework.

## ACKNOWLEDGEMENTS

We acknowledge the financial support from Saudi Aramco and the Texas A&M Energy Institute.

## REFERENCES

1. Kirsten Hund, Daniele La Porta, Thao P Fabregas, Tim Laing, and John Drexhage. Minerals for climate action: The mineral intensity of the clean energy transition. The World Bank, 2023.
2. J. Holechek, H. Geli, M. Sawalhah, R. Valdez, A. G. Assessment, Can renewable energy replace fossil fuels by 2050? sustainability 14 (2022) 4792.
3. Takuma Watari, Benjamin C McLellan, Damien Giurco, Elsa Dominish, Eiji Yamasue, and Keisuke Nansai. Total material requirement for the global

energy transition to 2050: A focus on transport and electricity. Resources, Conservation and Recycling, 148:91–103, 2019.
4. R. Kakodkar, B. Flores, M. Sousa, Y. Lin, E. Pistikopoulos, Towards energy and material transition integration-a systematic multi-scale modeling and optimization framework, 2024, pp. 461–468. doi:10.69997/sct.171988.
5. Glenn S Daehn, Katrin E Daehn, and Oliver Kuttner. Environmentally responsi- ble lightweight passenger vehicle design and manufacturing. Automotive Innovation, 6(3):300–310, 2023.
6. Tahir Rasheed, Ahmad Naveed, Jiahang Chen, Bareera Raza, and Jiulin Wang. Re- visiting the role of polymers as renewable and flexible materials for advanced batteries. Energy Storage Materials, 45:1012–1039, 2022.
7. Peng-Cheng Ma and Yi Zhang. Perspectives of carbon nanotubes/polymer nanocomposites for wind blade materials. Renewable and Sustainable Energy Reviews, 30:651–660, 2014.
8. R. Kakodkar, G. He, C. Demirhan, M. Arbabzadeh, S. Baratsas, S. Avraamidou, D. Mallapra-gada, I. Miller, R. Allen, E. Gençer, et al. (2022). A review of analytical and optimization methodologies for transitions in multi-scale energy systems. Renew. Sust. Energ. Rev. 160:112277
9. Rahul Kakodkar and Efstratios Pistikopoulos. Energiapy-an open source python package for multiscale modeling & optimization of energy systems. In 2023 AIChE Annual Meeting. AIChE, 2023.
10. National Renewable Energy Laboratory. https://atb.nrel.gov/electricity/2023/index.
11. Argonne National Laboratory. Greet 2022 net software v1.3.0.13991, 2022. greet life cycle model 2022 argonne, 2022. Available online: 10.11578/GREET-Net-2022/dc. 20220908.2.
12. Ecoinvent Centre. Ecoinvent database. version 3.9.1, 2023. Ecoinvent Centre, St. Gallen.
13. Zhitong Zhao, Jingyang Jiang, and Feng Wang. An economic analysis of twenty light olefin production pathways. Journal of Energy Chemistry, 56:193–202, 2021.
14. Moustafa Ali, Yuhe Tian, Dustin Kenefake, and Efstratios N Pistikopoulos. Process design and intensification of circulating catalytic fluidized bed membrane reactor for oxidative coupling of methane. In Computer Aided Chemical Engineering, volume 52, pages 2031–2036. Elsevier, 2023.
15. Fuel Freedom Foundation. What cars will we be driving in 2050?, n.d. Accessed: 2024- 08-05.

© 2025 by the authors. Licensed to PSEcommunity.org and PSE Press. This is an open access article under the creative commons CC-BY-SA licensing terms. Credit must be given to creator and adaptations must be shared under the same terms. See https://creativecommons.org/licenses/by-sa/4.0/



Systems & Control Transactions

**Research Article - Peer Reviewed Conference Proceeding**
ESCAPE 35 - European Symposium on Computer Aided Process Engineering
Ghent, Belgium. 6-9 July 2025
Jan F.M. Van Impe, Grégoire Léonard, Satyajeet S. Bhonsale,
Monika E. Polańska, Filip Logist (Eds.)

PSE PRESS

# Assessing Operational Resilience Within the Natural Gas Monetisation Network for Enhanced Production Risk Management: Qatar as a Case Study

**Noor Yusuf, Ahmed AlNouss, Roberto Baldacci and Tareq Al-Ansari***

College of Science and Engineering, Hamad Bin Khalifa University, Doha, Qatar
* Corresponding Author: talansari@hbku.edu.qa

## ABSTRACT

The turbulence in energy markets poses risks to energy suppliers, impacting profitability. Whilst risk mitigation is crucial for new projects, adapting existing infrastructure to evolving conditions incurs additional costs. For natural gas dependent economies, the natural gas industry faces exogenous uncertainties represented by demand and price fluctuations, and endogenous risks arising from inadequate proactive planning. This study evaluates the resilience of optimised Qatar's natural gas monetisation infrastructure under different cases by examining the network's ability to meet production targets amid process disruptions and market volatility. The analysed network includes 6 direct and indirect utilisation routes, represented by liquefaction, Haber-Bosch, methanol, gas-to-liquids, MTBE and urea processes to produce 9 products. First, process simulations and market assessments were used to obtain operational and market input data. Second, a mixed-integer linear programming model was used to optimise the natural gas allocation to processes under 9 case studies for a planning horizon of 10 year (2024-2033) with an objective of profitability maximisation. Third, the resilience% of processes and the overall network was estimated as per the model's suggested allocation strategy to evaluate the infrastructure utilisation efficiency. Process resilience below 100% indicates vulnerability to disruptions. Incorporating operational and market data increased network resilience from 74% to at least 82%, highlighting the value of flexibility in planning. Furthermore, allowing dynamic natural gas allocation improved profitability by at least 27% compared to a baseline scenario lacking operational and market considerations. The findings highlight the importance of adaptive strategies in ensuring long-term economic sustainability.

**Keywords**: Natural gas monetisation, Operational flexibility, Resilience, and Flexibility

## INTRODUCTION

The rapid global growth in populations and economies has led to an increase in energy consumption for industrialisation, transportation, urbanisation, food production, and drinking water production. Increased interest for utilising different energy resources has dominated countries for energy generation, including fossil-based fuels and renewable energy resources. However, following the adoption of the Paris Agreement on climate change in 2016, a significant transition toward cleaner energy resources has been observed to mitigate greenhouse gas emissions. Natural gas has been recognised as a cleaner energy resource in national energy and environmental roadmaps until the full transition to renewables. Overall, different chemical and physical natural gas monetisation options have been deployed to produce value-added products wherein each produced commodity has different applications, markets, and pricings. Hence, end-markets play a critical role in shaping the overall economic sustainability and growth of gas-based economies. For the state of Qatar, the country has deployed direct and indirect monetisation routes for monetising its fundamental resource. This includes direct processes, including gas-to-power liquefaction, gas-to-liquids (GTL), Haber-Bosch technology, and the methanol



SLB-Private

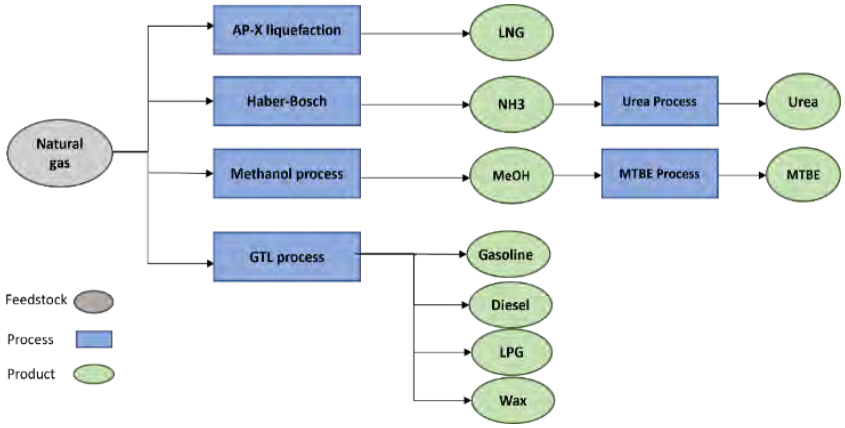



**Figure 1.** Investigated Qatar-based natural gas monetisation network, managed by QatarEnergy.

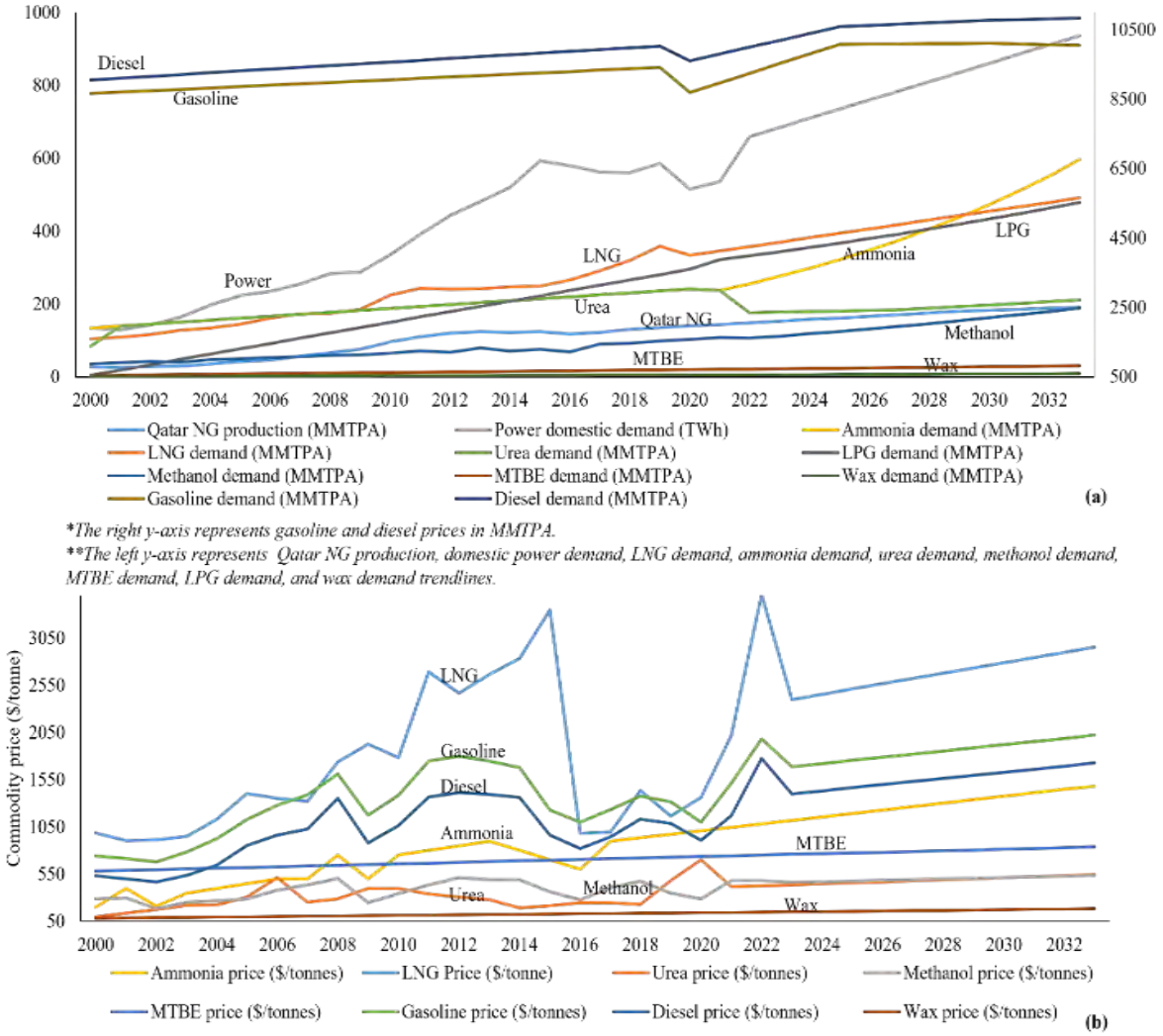



**Figure 2.** Input market data for optimising annual natural gas allocation: (a) demand data and (b) price data.

process, and in-direct routes, such as methanol to methyl tert-butyl ether (MTBE) and ammonia to urea.

With the increased uncertainties imposed on the market due to supply shocks, geopolitical tensions, and pandemics, the influence of uncertainties on existing and planned oil and gas supply became crucial for producers, consumers, and policymakers. Such assessments are especially important given the fluctuation's consequences

in terms of economic disruptions, energy security, and environmental sustainability. In the literature, researchers addressed the effectiveness of quantitative decision-making tools to evaluate the cost-effective utilisation of natural gas under market uncertainties [1,2]. Li et al., [3] utilised mathematical formulation as a decision-making tool and developed two scenario-based two-stage stochastic programming models for investigating optimal natural gas infrastructure development under market uncertainties. Additionally, Attia et. al. [4] developed a multi-objective stochastic mathematical programming model for tactical planning in the downstream sector of the oil and natural gas supply chain, addressing uncertainties in petroleum product prices and demand. On the other hand, managing an existing supply chain under uncertainties represents more challenges due to systems restrictions related to deployed infrastructure. Earlier studies investigated the optimal natural gas allocation to a multi-level network comprising different natural gas monetised products under demand and price uncertainties using quantitative decision-making tools represented by agent-based modelling and mathematical programming [5,6]. Fundamentally, the tools have been deployed for allocation under economic or environmental objectives, considering market data and operational data. The results of the studies provided crucial insights in terms of the economic added value of switching production capacities of different processes within the network based on market performance. Yet, the resilience (i.e., the ability of the network to withstand disruptions) of such a decision was not evaluated as a decision metric. This study addresses the gap in natural gas network optimisation under uncertainty by evaluating the resilience of allocation decisions proposed by decision-making tools. It focuses on optimising annual natural gas distribution within Qatar's multi-level network, considering uncertainties in demand and pricing, as well as operational constraints for flexible operations. This approach enables an understanding of the added value of operational flexibility from economic, environmental, and resilience perspectives in the context of natural gas network planning and management.

## METHODOLOGY AND DATA

This work utilises a data-driven mathematical programming model as a quantitative decision-making approach for the optimisation of natural gas allocation to processes within the Qatari natural gas monetisation network, managed by QatarEnergy. The approach aims to justify the importance of such models in addressing market volatility and enhancing economic attractiveness by adjusting the annual production capacities dynamically, based on demand, prices, and operational constraints. Figure 1 illustrates the Qatar-based natural gas monetisation network, comprising four direct natural gas utilisation processes (i.e., AP-X liquefaction, Haber-Bosch, Methanol process, and GTL process) and two indirect processes (i.e., Urea process and MTBE process) for the production of nine products (i.e., LNG, ammonia, methanol, gasoline, diesel, LPG, wax, urea and MTBE).

### Input Data

The proposed mathematical model integrates projected annual demand and commodity prices with technical data from Qatar's natural gas processes to optimise resource allocation. Demand and price historical and forecasted data for the period between 2000 and 2033 were derived from online sources, with data gaps addressed using interpolation and cross-verification techniques [7-9]. Additionally, the study herein focuses on 10-years planning horizon (2024-2033) to balance practicality and flexibility, minimising long-term forecasts risks. Figure 2 illustrates the price and demand time series associated with different products. In terms of operational data, technically validated operational bounds for the production processes were considered (Table 1).

### Mathematical Model Formulation

With an aim to optimise annual natural gas allocation to the multi-level production network, the model proposed herein is a mixed-integer linear programming model (MILP), formulated and solved using the concept of superstructure. The objective function of the model aims to maximise the overall network's profitability (revenue-cost) by optimising the annual allocation of available natural gas ($M_t$), to a process ($\mathcal{J}_k$) in the process structure $k$. Fundamentally, each product within the network is associated with a revenue that influences the first part of the objective function. While the second part of the objective function is influenced by the fixed process's cost ($\mathrm{F_i}$), the varied operating cost ($C_{it}$), and the natural gas share allocated to a process ( $\mathrm{m_{it}^{in}}$). The model can be summarised as follows:

#### Objective function, Maximise:

$$\sum_{j\in\mathcal{J}_i}\sum_{t\in\tau} R_{jt} m_{jt}^{out} - \left[\sum_{i\in I} F_i + \sum_{i\epsilon\mathcal{J}_k}\sum_{t\epsilon\tau} C_{it} m_{it}^{in}\right] \quad (1)$$

#### Constraints:

The following conservation constraint ensures continuity in flow dynamics for all process structures:

$$m_{kt}^{\circ} = \sum_{i\in\mathcal{J}_k} m_{it}^{in} \qquad \forall k \in \mathcal{K}\ \&\ t \in \tau \qquad (2)$$

For fixed operational conditions (temperature and pressure), the yield ($X_{\mathrm{ij}}$) for converting natural gas (*i*) to a product (*j*) remains the same at time *t*:

$$m_{jt}^{out} = X_{ij} m_{it}^{in} \qquad \forall i \in \mathcal{J}_k, j \in \mathcal{J}_i\ \&\ t \in \tau \ (3)$$

Each process in the network operates within variable boundaries, known as upper and lower limits. The

following constraints ensures that natural gas allocated to a process falls within the upper and lower limits (4)-(5). Additionally, constraint (6) is a non-negativity constraint, while equation (7) ensures that the total natural gas feed allocated to processes is less than or equal to the total allocated feed to the process structure $k$ at time $t$:

$$m_{it}^{in} \leq U_i y_i \qquad \forall i \in \mathcal{I}_k, j \in \mathcal{J}_i \ \& \ t \in \tau \qquad (4)$$

$$m_{it}^{in} \geq L_i y_i \qquad \forall i \in \mathcal{I}_k, j \in \mathcal{J}_i \ \& \ t \in \tau \qquad (5)$$

$$m_{it}^{in} \geq 0 \qquad \forall i \in \mathcal{I}_k, j \in \mathcal{J}_i \ \& \ t \in \tau \qquad (6)$$

$$m_{it}^{in} \leq U_i y_i \qquad \forall i \in \mathcal{I}_k, j \in \mathcal{J}_i \ \& \ t \in \tau \qquad (7)$$

Finally, as the problem focuses on optimising the network based on international market demand, equation (8) ensures that the produced product flow from a process *j* at time *t* is less than the global demand:

$$m_{jt}^{out} \leq D_{jt} \qquad \forall j \in \mathcal{J}_i \ \& \ t \in \tau \qquad (8)$$

The model and the constraints have been explained intensively in Yusuf et. al. [5]. The formulation presented herein was solved using Gurobi optimisation software (Gurobi 11.0) and implemented using python programming language within the Jupyter Notebook environment.

## Case Studies

The MILP presented herein was considered for optimising natural gas allocation in 3 main cases with 7 sub-scenarios (total of 9). Fundamentally, the cases differ based on the consideration of upper and lower limits, forecasted market data, and the decision of whether to allow the model to divert surplus natural gas to other processes. For the description, the cases can be described as the following:

- **Case 1:** considers a business-as-usual scenario wherein the model allocates natural gas to processes.
- **Case 2:** considers natural gas allocation to processes based on forecasted demand and operational limits
- **Case 3.1:** considers planned LNG shutdown for the period of 1 month every two years
- **Case 3.2:** considers planned ammonia shutdown for the period of 1 month every two years
- **Case 3.3:** considers planned GTL shutdown for the period of 1 month every two years
- **Case 3.4A:** considers *planned shutdown* of LNG, ammonia, and GTL for the period of 1 month every two years with no surplus natural gas allocation to other processes
- **Case 3.4B:** considers *planned shutdown* of LNG, ammonia, and GTL processes for the period of 1 month every two years with no surplus natural gas reallocation to other processes
- **Case 3.5A:** Considers *planned shutdown* of LNG, ammonia, and GTL processes for the period of 1 month every two years and *unplanned shutdowns* with no surplus natural gas allocation to other processes
- **Case 3.5B:** Considers *planned shutdown* of LNG, ammonia, and GTL processes for the period of 1 month every two years and *unplanned shutdowns*.

All cases considered demand and price forecasts, in addition to upper and lower limits, except for case 1. The outputs of the allocation were analysed in terms of profitability, resilience%, and production capacity.

# RESULTS AND DISCUSSION

The MILP model was implemented to optimise the allocation to the natural gas network comprising 4 direct and 2 in-direct routes on annual basis for the time horizon of 10 years (2024-2033). The model optimises with the objective of maximising the total profit of the products sales based on market performance by allowing the model to change the production capacity within the upper and lower operational limits. The allocation decision was then evaluated by estimating the resilience of each process and the overall resilience of the network. This, in turn, allows the decision-maker to employ resilience index as a decision-making metric to evaluate the added-value of flexible operations in natural gas network planning. The sub-sections below discuss the results represented by profitability, allocation strategy, and resilience.

## Profitability Assessment

With the objective to maximise profitability based on market performance and flexible allocation, Table 2 summarises the achieved profitability under different cases. Case 1 represents a baseline scenario under a business-as-usual scenario wherein natural gas is allocated to processes regardless of the global market performance and upper operational limits for processes, resulting in the lowest profitability estimate.

The results indicate that introducing market data as input data in the decision-making process have enhanced the allocation strategy by at least 21% by achieving the profitability maximisation targets in cases 2-3.5B. However, the values differed in the cases as per the considered assumptions. For example, in the cases (case 3.4A and 3.5A) where surplus natural gas was restricted for reallocation to other processes, lower profitability values have been achieved. This, in turn, justifies the economic added value of flexible operations in natural gas network planning for enhanced profitability under

dynamic market conditions.

**Table 2:** Maximum profitability estimation for all cases for optimal flexible natural gas allocation to processes.

| Case | Profit ($x10^{12}$ $) | Case | Profit ($x10^{12}$ $) |
|---|---|---|---|
| Case 1 | 2.10 | Case 3.4A | 2.66 |
| Case 2 | 2.91 | Case 3.4B | 2.87 |
| Case 3.1 | 2.87 | Case 3.5A | 2.66 |
| Case 3.2 | 2.87 | Case 3.5B | 2.87 |
| Case 3.3 | 2.91 | | |

## Resilience Assessment

While profitability values could justify the added value of flexible operations in efficiently responding to exogenous uncertainties, resilience index (resilience%) could be another metric to evaluate the added value of flexibility. Fundamentally, resilience reflects the efficiency in utilising existing infrastructure, wherein higher efficiency percentages indicate higher efficiency in utilising the deployed infrastructure. Figure 3 below demonstrates a bar chart summarising the average resilience% estimated for each case study.

For the baseline scenario where flexible boundaries of processes were not considered in the assessment, a resilience index of 74% was achieved for the model's suggested allocation strategy. Additionally, the absence of market data as an input data to the model restricted the model's efficiency in considering the performance of end markets in the decision-making process.

On the contrary, case studies considering flexible boundaries and market input data resulted in higher resilience%, with values between 85-86%, due to the model's suggested allocation strategies. Yet, in the cases (i.e., case 3.4A and 3.5A) where the model was not allowed to divert surplus natural gas feed to processes resulted in a reduced resilience value by 4% compared to the same cases that considered surplus natural gas diversion (i.e., case 3.4B and 3.5B). This justifies the importance of reallocating surplus natural gas during times of disturbance to other processes to enhance the overall network infrastructure utilisation.

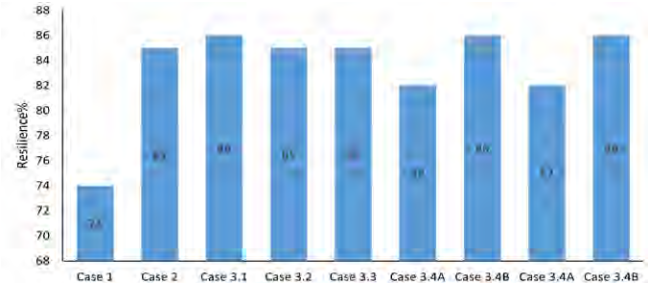



**Figure 3.** Average Resilience% estimated for each case study as per the allocation strategy for maximum achieved profitability.

## Processes assessments

To analyse the allocation strategies suggested by the model for maximising profitability under each case, it crucial to highlight that natural gas is the primary resource to the four direct processes (i.e., liquefaction, Haber-Bosch, methanol, and GTL processes). Hence, this section focuses on the natural gas allocation strategies to the primary processes under each scenario. Figures 4-7 demonstrates the natural gas allocation share% and the achieved resilience% associated with each primary process in the network under the investigated case studies.

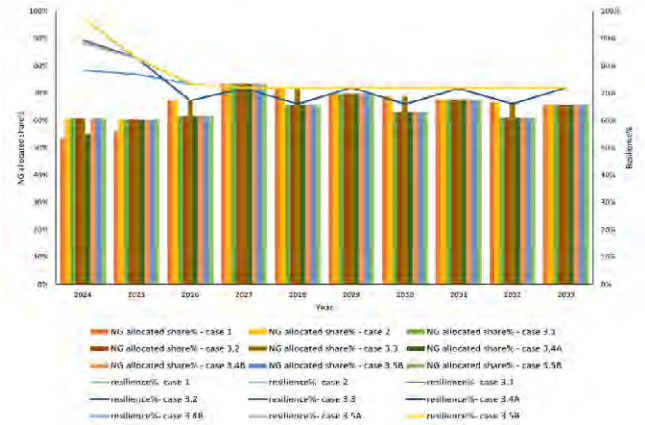


**Figure 4.** Annual natural gas allocated share% and resilience% to the liquefaction process under each case study.

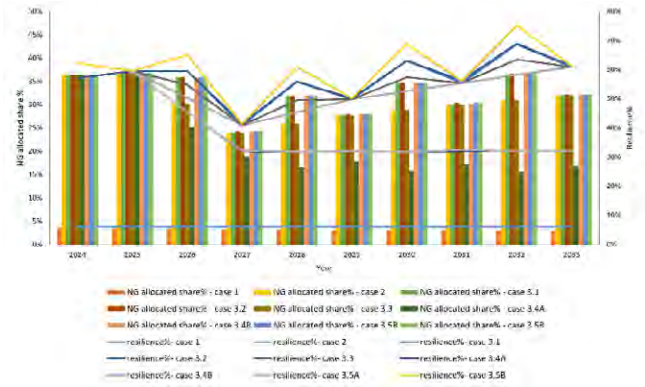


**Figure 5.** Annual natural gas allocated share% and resilience% to the GTL process under each case study.

Given that LNG is the most primary product in the Qatari natural gas portfolio, liquefaction capacities are the largest in the network, with an expected LNG production capacity to reach 142 MTPA, 85% from the current production capacity, by 2030. Hence, due to the infrastructure availability, the model prioritised allocating natural gas to the liquefaction route to meet the lower operational limits throughout the cases, as shown in Figure 4. This in turn justifies the high natural gas allocated share (more than 50%), in addition to the high resilience%. Yet, throughout the planning horizon, the resilience

associated with the cases dropped as influenced by the operational shutdowns.

On the other hand, natural gas allocated to the GTL process was the second highest after liquefaction. This is due to the infrastructure capabilities and the high market demand and prices associated with liquid fuels. Hence, the model favoured allocating natural gas to the GTL process for all process except for case 1 wherein no market data were used as an input to influence the decision-making process. This justifies the efficiency of utilising market data as an input data for informed decision-making.

As shown in Figure 6, the model allocated more than 20% of natural gas to the Haber-Bosch process to produce ammonia in case 1 when no market data and no upper operational limits were considered. This, in turn, resulted in overestimating the achieved resilience% wherein a value of 100% was achieved throughout the planning horizon for case 1. Yet, as more data were introduced to the model under the different case studies, the natural gas allocated share under cases (case2- case 3.5B) remain almost the same by achieving natural gas allocation as per the maximum available capacity, which contributed into high resilience% values.

As the methanol infrastructure in Qatar is limited and constrained by smaller scale plants, the natural gas allocated share to the methanol process was the lowest as shown in Figure 7 wherein less than 1% of the available natural gas was allocated to the methanol process. Additionally, the model allocated even less natural gas to the methanol process in case 1 in the absence of input market data and upper operational limits. Instead, the available natural gas was diverted to other processes, such as Haber-Bosch and liquefaction. For the resilience%, a value of around 85% was achieved throughout the planning period for all cases, except for case 3.4B and case 3.5B where the resilience dropped from 100% at year 2024 and 2025 to 85% at year 2026. This is attributed to the expansion of the liquefaction capacities wherein additional available natural gas share was allocated to produce LNG.

## CONCLUSION

This study highlighted the industry's vulnerability to both market fluctuations and operational disruptions, emphasing the need for proactive planning and flexible resource allocation. Findings showed that the liquefaction process received the highest allocated natural gas share for all optimised case studies due to the established infrastructure, while the methanol process had the lowest due to smaller plant capacities. Integrating operational and market data in cases 2-3.5B improved overall network resilience from 74% to at least 82%, reinforcing the value of adaptive strategies. Additionally, allowing surplus natural gas feed diversion during planned and unplanned shutdowns enhanced the economic profitability by approximately 8% and improved resilience by around 4% from case 3.4A to case 3.4B and from case 3.5A to case 3.5B. Yet, further resilience enhancements could be achieved by increasing the available natural gas feed to ensure the full utilisation of existing infrastructure.

Overall, the results emphasise the importance of resilience-based strategies in infrastructure planning and management. A dynamic natural gas approach enhanced system stability, optimises resource utilisation, and improves economic outcomes. As the global energy landscape evolves, integrating flexibility into decision-making will be key to ensuring resilience, long-term sustainability and profitability of the natural gas industry from the perspective of suppliers.

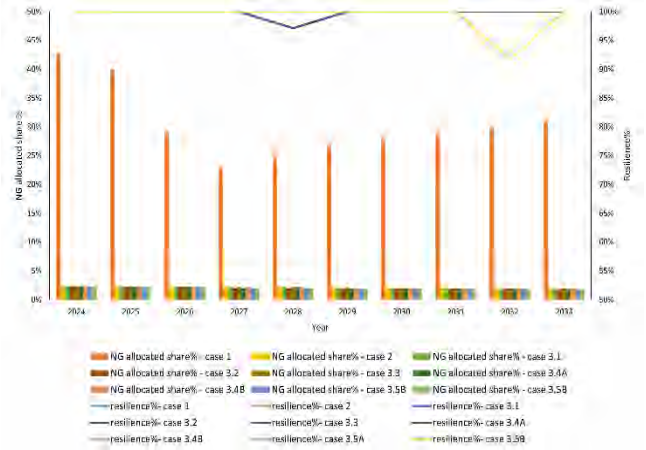


**Figure 6.** Annual natural gas allocated share% and resilience% to the Haber-Bosch process to produce ammonia.

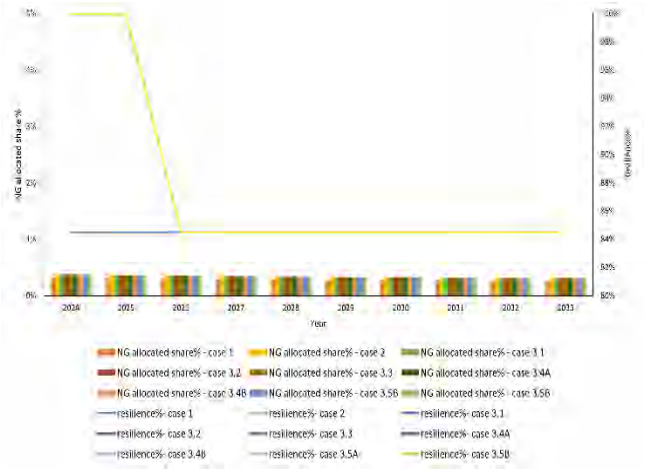


**Figure 7.** Annual natural gas allocated share% and resilience% to the methanol process to produce ammonia.

## ACKNOWLEDGEMENTS

This research would not have been possible without the support of the College of Science and Engineering at Hamad Bin Khalifa University, a member of the Qatar Foundation.

## REFERENCES

1. Behrooz, H. A., & Boozarjomehry, R. B. (2017). Dynamic optimization of natural gas networks under customer demand uncertainties. *Energy*, *134*, 968-983.
2. Yusuf, N., Govindan, R., Al-Fagih, L., & Al-Ansari, T. (2023). Strategic and flexible LNG production under uncertain future demand and natural gas prices. *Heliyon*, *9*(6).
3. Li, X., Tomasgard, A., & Barton, P. I. (2017). Natural gas production network infrastructure development under uncertainty. *Optimization and Engineering*, *18*, 35-62.
4. Attia, A. M., Ghaithan, A. M., & Duffuaa, S. O. (2019). A multi-objective optimization model for tactical planning of upstream oil & gas supply chains. *Computers & chemical engineering*, *128*, 216-227.
5. Yusuf, N., Baldacci, R., AlNouss, A., & Al-Ansari, T. (2024). Multi-period optimisation of flexible natural gas production network infrastructure with an operational perspective: A mixed integer linear programming approach. *Energy Conversion and Management: X*, *24*, 100818.
6. Yusuf, N., AlNouss, A., Baldacci, R., & Al-Ansari, T. (2024). Data-Driven Decision-Making for Flexible Natural Gas Allocation Under Uncertainties: An Agent-Based Modelling Approach. *Energy Conversion and Management: X*, *24*, 100734.
7. Methanex. Methanex Methanol Pricing. Methanol Pricing 2024. https://www.methanex.com/about-methanol/pricing/ (accessed January 5, 2024).
8. Expert Market Research. Global Urea Marke Outlook; 2023.
9. Vantage Market Research. Methanol Market - Global Industry Assessment & Forecast; 2022.

© 2025 by the authors. Licensed to PSEcommunity.org and PSE Press. This is an open access article under the creative commons CC-BY-SA licensing terms. Credit must be given to creator and adaptations must be shared under the same terms. See https://creativecommons.org/licenses/by-sa/4.0/



Systems & Control Transactions

**Research Article - Peer Reviewed Conference Proceeding**
ESCAPE 35 - European Symposium on Computer Aided Process Engineering
Ghent, Belgium. 6-9 July 2025
Jan F.M. Van Impe, Grégoire Léonard, Satyajeet S. Bhonsale,
Monika E. Polańska, Filip Logist (Eds.)

PSE PRESS

# Minimization of Hydrogen Consumption via Optimization of Power Allocation Between the Stacks of a Dual-Stack Fuel Cell System

**Beril Tümer[a], Deniz Şanlı Yıldız[b], and Yaman Arkun[a]***

[a] Koç University, Department of Chemical and Biological Engineering, Istanbul, Turkey
[b] Ford Otosan R&D Center, Istanbul, Turkey
* Corresponding Author: yarkun@ku.edu.tr

## ABSTRACT

A dual-stack fuel cell model was developed to simulate the hydrogen consumption a fuel cell-powered vehicle for a specific drive cycle. Two fuel cell stacks, each consisting of 65 parallel cells at different aging status and thus with different efficiency profiles (i.e., low and high) were considered. A constrained optimization for power distribution between individual stacks was performed where the objective function was to minimize the hydrogen consumption while meeting the total demand. For proper power management each stack has its own power controller which manipulates the stack current to control the stack power at its desired-set point. Computed optimal power values constitute the desired set-points for the local power PID controllers of the individual stacks. Closed-loop simulations were performed by simulating the developed mechanistic model together with optimization and PID controllers in SIMULINK platform. The closed loop simulations demonstrate how well the power demand of the drive cycle is tracked and the hydrogen consumption is minimized. To assess the impact of optimization strategy used, hydrogen consumption is compared to that of equal power sharing and a daisy-chain strategies. The results demonstrate that the optimization strategy effectively reduces the total hydrogen consumption.

**Keywords**: Proton Exchange Membrane Fuel Cells (PEMFC), Hydrogen Consumption Minimization, Power Sharing

## INTRODUCTION

Fuel cells are devices that convert chemical energy into electrical energy via transfer of electrons and protons. They possess key characteristics such as high efficiency, high power density, low corrosion, low emissions and moderate operating temperatures, and those characteristics position them as highly favorable alternative power sources in the automotive industry. To meet the high-power demand of a vehicle numerous individual cells are assembled in series or parallel configurations, forming what are known as "Fuel Cell Stack." For heavy duty vehicle applications, such as trucks and buses, multiple fuel cell stacks can be combined to increase the lifetime of the vehicle and energy efficiency.

Depending on the power management algorithm, each stack can exhibit varying efficiencies over lifetime due to differences in operating conditions and the rate of cell aging. Stack efficiency directly influences the amount of hydrogen consumed by the vehicle. Thus, efficient power distribution across multiple fuel cell stacks is crucial for minimizing total hydrogen consumption while satisfying the vehicle's power requirements.

In this study, we examine a two-stack fuel cell system, with each stack having distinct efficiency profiles (high and low) to mimic different aging status. The number of parallel cells in one stack can vary and is chosen as 65 by the authors in this work. The fuel cell stacks are modeled using first principles and simulated in MATLAB Simulink environment and the effects of aging on power allocation and hydrogen consumption were analyzed. Figure 1 illustrates the architecture of the control model where a given power demand is optimally shared between the two stacks. The local power controllers of the individual stacks manipulate their currents to meet their allocated power demands.

There are several studies in the literature for hydrogen consumption minimization [1], [2] which analyze fuel cell stacks with different efficiency profiles and compare the two common optimization strategies: equal power distribution and daisy-chain configurations. In the daisy-chain strategy, power is distributed sequentially, with one stack supplying the load until it reaches its limit, then the next stack takes over. [3] employed a geometric approach to compute the optimal power distribution and to maximize the power-efficiency. [4] proposed a power allocation strategy based on particle swarm optimization (PSO) and compared its performance with an equal power distribution strategy for two different load profiles. In these studies, the efficiency curves that are utilized in optimization were estimated from the experimental data. In this study, a mechanistic fuel cell model was used to calculate the efficiency curves for investigation of the effect of different designs and operating variables and physical parameters on the optimal power allocation.

## METHODOLOGY

The power and efficiency model for the fuel cell is taken from the work of [5] and the fundamental equations are presented below:

$$E = E^0 - \frac{RT}{nF}\ln\frac{\prod p_{products}^{v_i}}{\prod p_{reactants}^{v_i}} \quad (1)$$

$$E_{oc} = N \times E \quad (2)$$

$$V_{act,loss} = \frac{NRT}{n\alpha F}\ln\frac{j_{fc}}{j_0} \quad (3)$$

$$V_{ohm,loss} = R_{ohm} \times j_{fc} \quad (4)$$

$$V_{conc,loss} = N \times c\ln\frac{j_L}{j_L - j_{fc}} \quad (5)$$

$$V_{fc} = E_{oc} - V_{act,loss} - V_{ohm,loss} - V_{conc,loss} \quad (6)$$

$$P_{fc} = i \times V_{fc} \quad (7)$$

$$\eta_{thermo} = 0.83 \quad (8)$$

$$\eta_{fuel} = \frac{1}{ɻ} \; where \; ɻ = \frac{\frac{i}{nF}}{\dot{v}_{fuel}} \quad (9)$$

$$\eta_{voltage} = \frac{V_{fc}}{E_{oc}} \quad (10)$$

$$\eta = \eta_{thermo} \times \eta_{fuel} \times \eta_{voltage} \quad (11)$$

$$\dot{m}_{H_2} = \frac{Ni(MW_{H_2})}{nF\eta_{fuel}} \quad (12)$$

The partial pressures, $p$ in atm, in Eqn. 1 are calculated from a separate mechanistic model [6], [7].

The objective function for the optimization is to minimize the total hydrogen consumption rate (kgs$^{-1}$) of two fuel cell stacks, formulated as follows:

$$\min_{i_1,i_2} \dot{m}_{H_2,total} = \frac{Ni_1(MW_{H_2})}{nF\eta_{fuel1}} + \frac{Ni_2(MW_{H_2})}{nF\eta_{fuel2}}$$

s.t.

$$8 \le i_1, i_2 \le 300$$

$$P_{fc,1} + P_{fc,2} = P_{demand}$$

The decision variables in this optimization are the fuel cell currents. The usage of the DC-DC converter establishes the minimum current at 8, while the maximum current of 300 is defined by the limiting current density value. The algorithm computes the optimal individual stack currents, and thus the optimal power outputs of each stack, $P_{fc,1}^{opt}$ and $P_{fc,2}^{opt}$ as depicted in Figure 1. Above optimization has a global and unique optimum since the objective function is linear in the decision variables $i_1, i_2$ and the constraints define a closed convex feasible set. We used MATLAB's fmincon function with the Sequential Quadratic Programming (SQP) algorithm to solve the optimization.

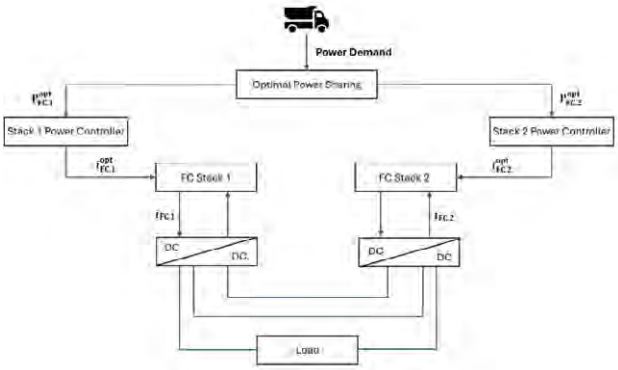



**Figure 1.** Model architecture and control strategy

## RESULTS

Aging and/or degradation are the two key factors that directly impact the lifespan and performance of fuel cell stacks. Degradation can occur in various components of the fuel cell, such as the catalyst, membrane, and gas diffusion layers. Each of these components contributes to performance losses in specific ways, such as reducing the exchange current density, increasing ohmic resistance, or decreasing the limiting current density. Collectively, these effects diminish the power output of the fuel cell stack over time.

In this study, the electron transfer coefficient ($\alpha$) is used to indicate the level of degradation/aging in the fuel cell stack. $\alpha$ values are between 0 and 1; and it is well known that [5] lower values result in increased voltage losses indicative of increased degradation/aging.

In the results to follow, the optimal power values are provided as set-points to the local PID controllers that adjust the currents. Due to the inherently slow response

time of the fuel cell, the stack powers reach their set-points within 100 sec with a smooth response.

## Case 1: Equal Fuel Efficiency and Different Degradation Levels

### Case 1.1: $\alpha_1$=0.6 and $\alpha_2$=0.4, $\lambda_1 = \lambda_2$=1.2

The first case examines the impact of different degradation levels on power distribution and compares hydrogen consumption across three different strategies. For Case 1.1 analysis, $\alpha$ values of 0.6 and 0.4 were chosen for stacks 1 and 2, respectively. The fuel efficiency $\eta_{fuel}$ of each stack is set equal to 0.8333 which corresponds to 20% of excess hydrogen feed ($\lambda_1 = \lambda_2$=1.2). Due to degradation, stack 2 has lower $\alpha$ value, which leads to a decline in power output and efficiency. The superimposed power outputs of both stacks are shown in Figure 2.

In the equal distribution strategy [2], the power produced by each stack is equal, with each contributing half of the total power demand, as shown in Figure 3. Since stack 2 experiences higher degradation compared to stack 1, its current and therefore its hydrogen consumption is higher, as shown in Table 1. In the daisy-chain strategy [8], stack 1 serves as the primary energy source due to its higher power output and efficiency. When the total power demand exceeds the maximum capacity of stack 1, stack 2 compensates for the power gap. Otherwise, stack 2 idles at its minimum power P=637 W, as illustrated in Figure 4. Since stack 1 meets most of the power demand, its hydrogen consumption is significantly higher than that of stack 2 (see Table 1). Optimization approach adjusts the power level for each stack based on the stack efficiency without using any priori rule as in equal power and daisy-chain strategies. Optimal power allocated to each stack is shown in Figure 5. Comparing with Figures 3 and 4, we see that in optimal allocation stack 2 power idles less than daisy-chain; therefore, less power is needed from stack 1. This results in lower currents in stack 1 and less hydrogen consumption, which is proportional to the current. Table 1 shows that optimization gives the least hydrogen consumption (0.4249 kg), for the given drive cycle with duration of 4000 sec. This is a 5.29% improvement over the daisy-chain algorithm. However, the improvement of the optimization strategy over the equal distribution algorithm (0.96%) is not very significant in this scenario. This is because the $\alpha$ values and the performance of the fuel cell stacks are quite similar, and the fuel efficiencies of the stacks are the same. Nevertheless, these small percentage improvements will result in significant hydrogen saving considering the overall lifetime of the vehicle.

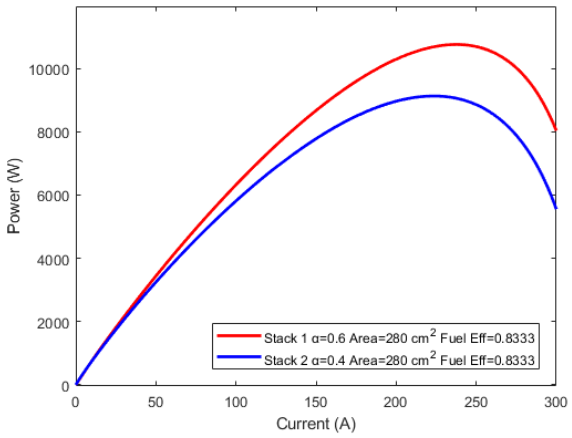



**Figure 2**. Current vs power curves for both stacks.

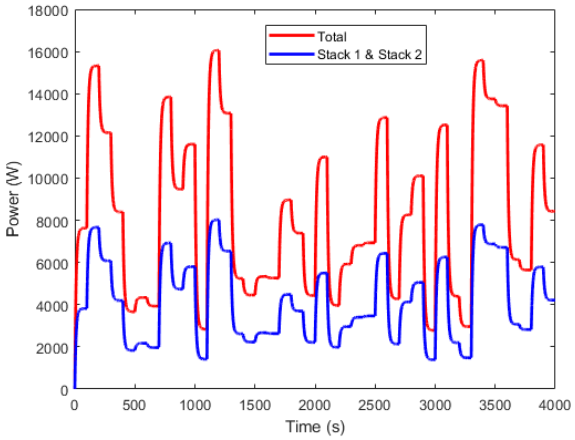



**Figure 3.** Power sharing using equal distribution strategy.

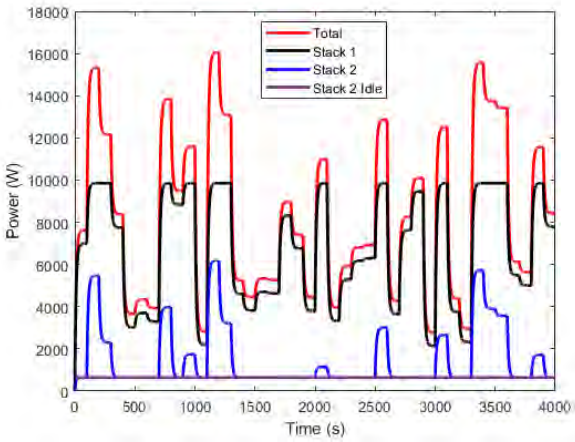



**Figure 4.** Power sharing using daisy-chain strategy.

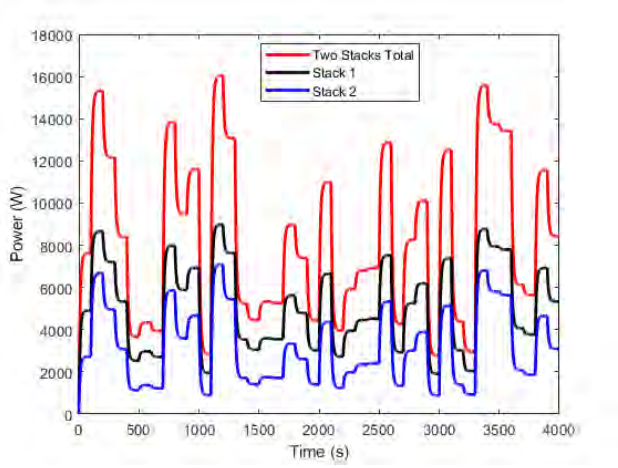



**Figure 5.** Power sharing using optimization strategy.

**Table 1:** Total Hydrogen Consumption of the Stacks with Different Strategies where $\alpha_1$=0.6, $\alpha_2$=0.4 and $\lambda_1$= $\lambda_2$=1.2

| Strategy | Stack 1 $H_2$ Consumption (kg) | Stack 2 $H_2$ Consumption (kg) | Total $H_2$ Consumption (kg) |
|---|---|---|---|
| Equal distribution | 0.2043 | 0.2247 | 0.4290 |
| Daisy-chain | 0.3727 | 0.0759 | 0.4486 |
| Optimization | 0.2582 | 0.1667 | 0.4249 |

### Case 1.2: $\alpha_1$=0.6 and $\alpha_2$=0.25, $\lambda_1$= $\lambda_2$=1.2

For Case 1.2 analysis, the $\alpha$ values were set as 0.6 and 0.25, and thus differences between the power and efficiency curves of the stacks are much larger. The same drive cycle data was used as the power demand input. With the new degradation level, stack 2 can produce a maximum of 6510 W (Figure 6). In the equal distribution scenario, when the power demand for each stack exceeds 6510 W, a power deficit occurs for stack 2 which is set to be met by stack 1. Figure 7 displays that the black and blue lines do not overlap at power demands higher than 6510 watts which is the result of modification in the algorithm. In this case, the equal distribution algorithm consumed the maximum hydrogen (0.4854 kg), as shown in Table 2. Power demand was successfully met in the daisy-chain algorithm. In this scenario, stack 1 again served as the primary power source, while stack 2 mostly operated at its idle power. Compared to the previous scenario, hydrogen consumption for stack 1 remained constant, as its $\alpha$ value did not change. However, the decrease in $\alpha$ value for stack 2 from 0.4 to 0.25 led to an increase in the current required for the same power demand in stack 2 which resulted in operating at lower efficiency. As a result, hydrogen consumption for stack 2 increased in this case (see Tables 1 and 2). Finally, the optimization algorithm successfully met the entire power demand, relying more on stack 1 (higher efficiency) and less on stack 2 (lower efficiency) (Figure 8). The increase in hydrogen consumption for stack 1 is due to the higher power production, and less power was produced by stack 2, resulting in reduced hydrogen consumption compared to the previous scenario. Similar to the previous case, the optimization strategy consumed the lowest hydrogen amount (see Table 2). However, the greater difference in $\alpha$ values made the daisy-chain scenario more favorable than in the previous case. As a result, the improvement of optimization over the daisy-chain scenario decreased but still demonstrated better performance, with 2.15% less hydrogen consumption. The equal distribution scenario showed the worst performance, with the optimization strategy achieving a 6.94% improvement over it.

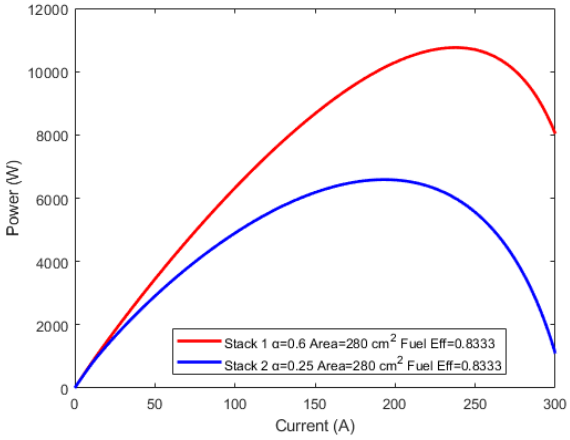



**Figure 6.** Current vs power curves for both stacks incorporating the new degradation level of stack 2.

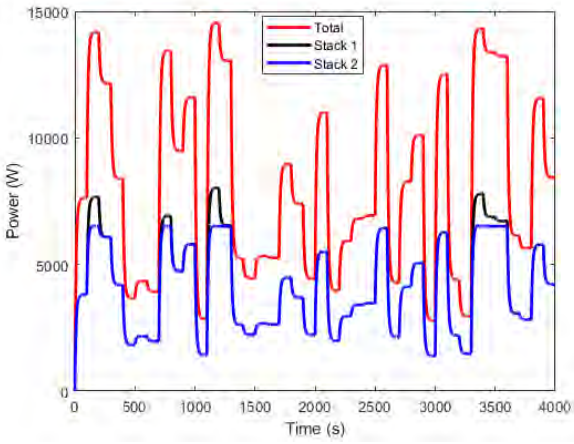



**Figure 7.** Power sharing using modified equal distribution strategy incorporating the new degradation level of stack 2.

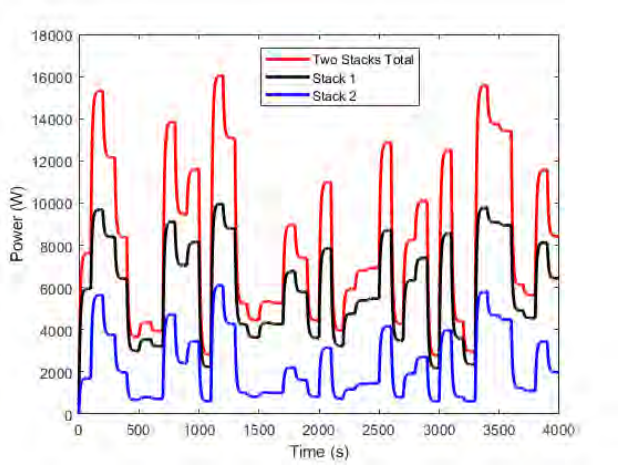



**Figure 8.** Power sharing using optimization strategy incorporating the new degradation level of stack 2.

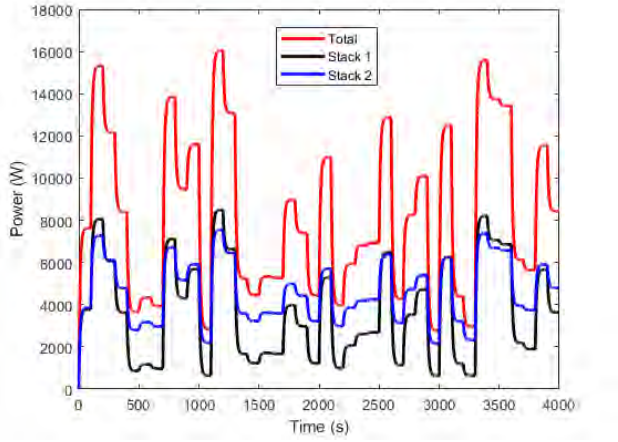



**Figure 9.** Power sharing between stacks using the optimization strategy with $\lambda_1$=1.5 and $\lambda_2$=1.2.

**Table 2:** Total Hydrogen Consumption of the Stacks with Different Strategies where $\alpha_1$=0.6, $\alpha_2$=0.25 and $\lambda_1$=$\lambda_2$=1.2

| Strategy | Stack 1 $H_2$ Consumption (kg) | Stack 2 $H_2$ Consumption (kg) | Total $H_2$ Consumption (kg) |
|---|---|---|---|
| Equal distribution | 0.2043 | 0.2811 | 0.4854 |
| Daisy-chain | 0.3727 | 0.0889 | 0.4616 |
| Optimization | 0.3166 | 0.1351 | 0.4517 |

### Case 2: Different Fuel Efficiencies and Degradation Levels ($\alpha_1$=0.6 and $\alpha_2$=0.4, $\lambda_1$=1.5 and $\lambda_2$=1.2)

Aging results in several changes in the structure of the catalyst layer of fuel cells which can hinder the smooth movement of hydrogen molecules resulting in lower fuel efficiency and higher hydrogen feed excess ratio, $\lambda$. In case study 2, $\lambda_1$ was set to 1.5. Optimal power distributions are shown in Figure 9. Since $\lambda_1$ is higher than $\lambda_2$, the power allocated to stack 2 is increased. As a result, the hydrogen consumption of stack 2 is higher than that of stack 1, as presented in Table 3. Table 3 summarizes the hydrogen consumption across all strategies, showing that the daisy-chain strategy performs the worst, while the optimization strategy achieves the best results.

**Table 3:** Total Hydrogen Consumption of the Stacks with Different Strategies where $\alpha_1$=0.6, $\alpha_2$=0.4 and $\lambda_1$=1.5 and $\lambda_2$=1.2

| Strategy | Stack 1 $H_2$ Consumption (kg) | Stack 2 $H_2$ Consumption (kg) | Total $H_2$ Consumption (kg) |
|---|---|---|---|
| Equal distribution | 0.2553 | 0.2247 | 0.4800 |
| Daisy-chain | 0.4658 | 0.0759 | 0.5417 |
| Optimization | 0.2264 | 0.2512 | 0.4776 |

## CONCLUSION

Minimizing fuel consumption of a vehicle is one of the most crucial tasks for automotive producers to be competitive in the market. Likewise, for a fuel cell-powered vehicle the focus is mainly on minimizing the hydrogen consumption via distributing the demanded power effectively between fuel cell stacks. In this study, three different power allocation strategies, namely equal distribution, daisy-chain, and optimal power sharing, were compared for dual-stack fuel cell system, each stack having different aging levels. For similar aging levels of the stacks, the performance of optimization strategy equal distribution algorithm was similar. However, as the aging levels of the stacks differ, the performance of optimization strategy is superior to that of equal distribution and aligns more closely with the daisy-chain algorithm. Additionally, the impact of fuel efficiency changes, influenced by alterations in the catalyst structure, was analyzed. In all cases, the optimization strategy resulted in the lowest hydrogen consumption.

## NOMENCLATURE

| | |
|---|---|
| $\alpha$ | Electron transfer coefficient |
| $c$ | Constant |
| $E$ | Reversible cell voltage (V) |
| $E^0$ | Ideal reversible voltage (V) |
| $E_{oc}$ | Open circuit voltage (V) |
| $F$ | Faraday's number (C) |
| $i$ | Current (A) |

| | |
|---|---|
| $j_0$ | Exchange current density ($Acm^{-2}$) |
| $j_{fc}$ | Current density ($Acm^{-2}$) |
| $j_L$ | Limiting current density ($Acm^{-2}$) |
| $MW$ | Molecular weight ($kgkmol^{-1}$) |
| $\dot{m}_{H_2}$ | Hydrogen consumption rate ($kgs^{-1}$) |
| $n$ | Number of electrons transferred |
| N | Number of cells |
| $P_{fc}$ | Power (W) |
| R | Gas constant ($Jmol^{-1}K^{-1}$) |
| $R_{ohm}$ | Ohmic resistance (Ω) |
| T | Temperature (K) |
| $\dot{v}_{fuel}$ | Fuel supply rate ($mols^{-1}$) |
| $V_{act,loss}$ | Activation loss (V) |
| $V_{conc,loss}$ | Concentration loss (V) |
| $V_{fc}$ | Fuel cell voltage (V) |
| $V_{ohm,loss}$ | Ohmic loss (V) |
| η | Stack efficiency |
| $\eta_{fuel}$ | Fuel utilization efficiency |
| $\eta_{thermo}$ | Reversible thermodynamic efficiency |
| $\eta_{voltage}$ | Voltage efficiency |
| ג | Fuel stoichiometric factor |

## ACKNOWLEDGEMENT

This work is supported by TÜBİTAK (Project Number :119C176). Financial support from Ford Otomotiv San. AŞ. is also acknowledged.

## REFERENCES

1. Y. F. Liang, Q. C. Liang, J. F. Zhao, and J. N. He, "Minimum hydrogen consumption power allocation strategy for the multi-stack fuel cell (MFC) system based on a discrete approach," *Front Energy Res*, vol. 10, Sep. 2022, doi: 10.3389/fenrg.2022.966852.
2. T. Wang, Q. Li, L. Yin, and W. Chen, "Hydrogen consumption minimization method based on the online identification for multi-stack PEMFCs system," *Int J Hydrogen Energy*, pp. 5074–5081, Feb. 2019, doi: 10.1016/j.ijhydene.2018.09.181.
3. Y. Yan, Q. Li, W. Chen, W. Huang, and J. Liu, "Hierarchical management control based on equivalent fitting circle and equivalent energy consumption method for multiple fuel cells hybrid power system," *IEEE Transactions on Industrial Electronics*, vol. 67, no. 4, pp. 2786–2797, Apr. 2020, doi: 10.1109/TIE.2019.2908615.
4. N. Bouisalmane *et al.*, "Hydrogen consumption minimization with optimal power allocation of multi-stack fuel cell system using particle swarm optimization," in *2021 IEEE Transportation Electrification Conference and Expo, ITEC 2021*, Institute of Electrical and Electronics Engineers Inc., Jun. 2021, pp. 154–160. doi: 10.1109/ITEC51675.2021.9490111.
5. R. P. O'hayre, W. G. Colella, and R. H. Adams, "FUEL CELL FUNDAMENTALS SUK-WON CHA FRITZ B. PRINZ," 2016.
6. J. T. Pukrushpan, H. Peng, and A. G. Stefanopoulou, "CONTROL-ORIENTED MODELING AND ANALYSIS FOR AUTOMOTIVE FUEL CELL SYSTEMS," 2004.
7. B. Tümer, D. Ş. Yıldız, and Y. Arkun, "Water and thermal management in PEM fuel cells using feasible humidity plots and model predictive controllers," *Comput Chem Eng*, vol. 192, Jan. 2025, doi: 10.1016/j.compchemeng.2024.108905.
8. N. Marx, D. C. T. Cárdenas, L. Boulon, F. Gustin, and D. Hissel, "Degraded mode operation of Multi-stack fuel cell systems," *IET Electrical Systems in Transportation*, vol. 6, no. 1, pp. 3–11, Mar. 2016, doi: 10.1049/iet-est.2015.0012.

© 2025 by the authors. Licensed to PSEcommunity.org and PSE Press. This is an open access article under the creative commons CC-BY-SA licensing terms. Credit must be given to creator and adaptations must be shared under the same terms. See https://creativecommons.org/licenses/by-sa/4.0/



Systems & Control Transactions

**Research Article - Peer Reviewed Conference Proceeding**
ESCAPE 35 - European Symposium on Computer Aided Process Engineering
Ghent, Belgium. 6-9 July 2025
Jan F.M. Van Impe, Grégoire Léonard, Satyajeet S. Bhonsale,
Monika E. Polańska, Filip Logist (Eds.)

PSE PRESS

# A Novel Global Sequence-based Mathematical Formulation for Energy-efficient Flexible Job Shop Scheduling Problem

**D. Li[a], and T.C. Zheng[a], and J. Li[a]***

[a] The University of Manchester, Department of Chemical Engineering, Manchester, UK
* Corresponding Author: jie.li-2@manchester.ac.uk

## ABSTRACT

With increasing emphasis on energy efficiency, more researchers are focusing on energy-efficient flexible job shop scheduling problems. Mathematical programming is a commonly used optimization method for such scheduling challenges, offering the advantages of achieving global optima and serving as a foundation for other approaches. However, current mathematical programming formulations face several challenges, including insufficient consideration of various forms of energy consumption and low efficiency, particularly in handling large-scale instances, which struggle to converge. In this study, we propose a novel global sequence-based approach with high computational efficiency. In this model, immediate precedence relationships are identified using constraints, enabling the precise determination of idle durations within any idle slots. The proposed formulation achieves a significant reduction in energy consumption by up to 20% relative to other formulations. Furthermore, it successfully reaches feasible solutions in challenging cases.

**Keywords**: Algorithms, Energy Efficiency, Optimization, Scheduling, Energy

## INTRODUCTION

The job-shop scheduling problem (JSSP) has been widely existing in various fields such as enterprise management [1,2], transportation [3] and aerospace [4,5]. As the demands for small-volume and personalized products increases, enterprises orientate at improving the flexibility of manufacturing processes by introducing parallel machines, which is generally termed as the flexible job-shop scheduling problem (FJSSP) [6]. In this content, assignment of operations to a machine as well as their sequence on the machine should be determined, making it more challenging to solve than JSSP. The inherent flexibility of FJSSP provides potential for significant economic or energy-efficient savings reflected in a schedule solution with the best assignments and sequences. Many approaches have been developed to address FJSSP, including exact algorithms [7-8], heuristics [9], and metaheuristics [10-11]. Several excellent reviews about the development, methodologies, and applications of FJSSP have been provided in the literature [12-13].

The prior research on FJSSP primarily centered around the economic performance or makespan, neglecting the simultaneous consideration of energy consumption. As manufacturing has the predominant contribution to annual industrial energy consumption, constituting the largest share at 76% among four major industry sectors in 2022 [14], the optimal schedule without consideration of energy consumption may lead to large energy wastage. Various forms of energy consumption have been identified, including standby, processing, turn-on/off, and setup energy consumption [8,15]. Notably, it was observed that 65% of the total energy consumption (TEC) in FJSSP is unrelated to actual processing activities. Instead, this substantial portion of energy is expended during periods when processing units are either idle or in standby mode [15]. The separation between economic optimization and energy awareness in production scheduling has significant implications. Production schedules optimized solely for economic goals may inadvertently result in unnecessarily high energy consumption. Consequently, there has been a growing recognition of the importance of incorporating energy considerations into FJSSP, especially due to net-

zero strategies proposed by different countries.

Investigations have been conducted to propose optimization approaches for the energy-efficient FJSSP, which can be broadly categorized into exact methods and approximate methods. Among the exact methods, mathematical programming approaches, such as mixed-integer linear programming (MILP) formulations, are commonly utilized [16]. The MILP formulations excel in generating optimal solutions and serve as a foundation in understanding the characteristics of scheduling problems [17]. Additionally, the development of MILP formulations lays the groundwork for establishing decomposition approaches that are highly effective in handling the complexities of energy-efficient FJSSP.

Researchers [17-22] developed MILP models for energy-efficient FJSSP based on the time-grid representation. [18] and [19] discretized the time horizon into uniform time intervals and introduced binary variables to indicate whether an operation starts processing at a given time point. Unlike discrete-time representations, continuous-time representations divide the time horizon into events with unknown and variable durations. Zhang et al. [20] proposed an event-based MILP model to minimize the TEC, to establish comparison benchmarks for a gene-expression programming approach and to explicitly analyse the problem's features. Followingly, a more efficient event-based unit- specific model was proposed [21], incorporating auxiliary states to link adjacent operations within the same job and ensure their precedence constraints. These aforementioned studies comprehensively consider various forms of energy consumption, including standby energy, switch off/on energy, direct (i.e., processing) energy and indirect energy. However, these exhibit inefficiencies when applied to large-scale energy-efficient FJSSP systems. For example, they struggle to find feasible solutions within hours for problems involving more than 200 operations [20,21]. Further research on MILP models with continuous-time representations can be found in [17,22,23].

In addition to time-grid representation, MILP formulations can be developed based on the precedence relations between operations on machines. For example, [8] and [24] proposed the local-sequence-based formulation, where binary variables indicate whether an operation immediately precedes another on a machine. In contrast, the global-sequence-based formulation focuses on global precedence relations, requiring fewer binary variables, making it more efficient. This is because the binary variable denoting the first or last operations on machines are omitted. [25] presented a novel global sequence-based MILP formulation to optimize the minimization of makespan or TEC. However, they did not account for the selection between standby and switch off-on modes for machines, which is crucial for reducing energy waste during machine idle times. More specifically, their MILP model fails to accurately estimate the specific durations of each idle period on machines.

In this work, a global sequence-based MILP formulation (**MG**) is proposed to minimize TEC, encompassing direct, indirect and unload energy consumption. Its novelty lies in the incorporation of constraints that identify immediate precedence relations between operations and the optimal duration of idle slot between them. Selection between machine modes during idle slots is achieved by introducing a new set of binary variables. The proposed model is compared with MILP models based on time-grid representations and precedence relations as well as a decomposition approach.

## PROBLEM DEFINITION

Fig. 1 illustrates an energy-efficient FJSSP involving a set of jobs $k \in \mathbf{K}$ and machines $j \in \mathbf{J}$. A job $k$ is processed with a sequence of operations $i \in \mathbf{I}_k$. Machines $j$ that can process operation $i$ of job $k$ are included in a set $\mathbf{J}_{ki}$. The processing time for machine $j$ performing operation $i$ of job $k$ is denoted by $P^{\mathrm{T}}_{kij}$, and the cutting power is $P^{\mathrm{C}}_{kij}$. The objective is to minimize $TEC$, encompassing energy consumed by machines during processing operations (i.e., direct energy), idle periods (i.e., unload energy), and by auxiliary facilities (i.e., indirect energy).

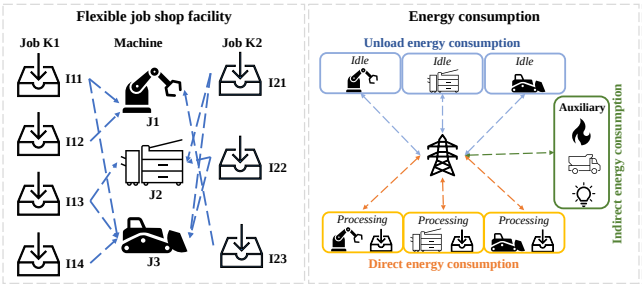



**Figure 1.** A FJSSP considering energy consumption.

To save energy, a machine $j$ can be temporarily switched off or maintain standby after processing (see Figure 2). Its switch off/on energy and unload power are expressed by $E^{\mathrm{O}}_j$ and $P^{\mathrm{U}}_j$, respectively.

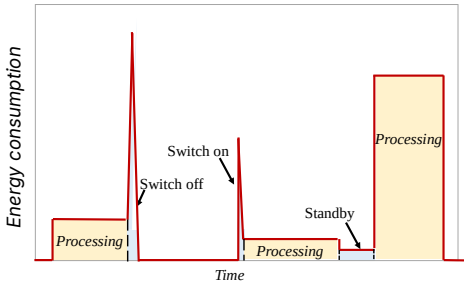



**Figure 2**. Energy consumption profile for a machine

## MATHEMATICAL FORMULATION

In the global sequence-based formulation (**MG**), we define four-index binary variables to denote the global precedence of two operations (e.g. $i$ and $i'$),

$$x_{kik'i'} = \begin{cases} 1 & \text{if } i \text{ in } k \text{ precedes } i' \text{ in } k' \text{ on one machine} \\ 0 & \text{otherwise} \end{cases}$$

Binary variables $w_{kij}$ express the assignment of operations on machines,

$$w_{kij} = \begin{cases} 1 & \text{if } i \text{ in } k \text{ is assigned on a machine } j \\ 0 & \text{otherwise} \end{cases}$$

Any operation $i$ of job $k$ must be assigned on a machine $j$.

$$\sum_{j \in \mathbf{J}_{ki}} w_{kij} = 1 \qquad \forall k, i \in \mathbf{I}_k \tag{1}$$

If operations $i, i'$ are processed on a machine, either $i$ precedes $i'$ or $i'$ precedes $i$. That is if variables $w_{kij} = 1$ and $w_{k'i'j} = 1$, then exactly one of $x_{kik'i'}$ or $x_{k'i'ki}$ should be equal to 1, indicating their precedence on $j$.

$$x_{kik'i'} + x_{k'i'ki} \geq w_{kij} + w_{k'i'j} - 1 \quad \forall k, k', j \in (\mathbf{J}_{ki} \cup \mathbf{J}_{k'i'}), i \in \mathbf{I}_k, i' \in \mathbf{I}_{k'}, (k < k') \cup (k = k' \cap i < i') \tag{2}$$

When two operations $i$ in job $k$ and $i'$ in job $k'$ are performed on different machines (e.g., $w_{kij} = 1$ and $w_{k'i'j} = 0$ ), their corresponding variables $x_{k'i'ki}$ and $x_{kik'i'}$ should be zero. The set $i' \in \mathbf{I}_{ki}^{\mathrm{G}}$ includes operations $i'$ that can share the same machine with $i$ of $k$.

$$w_{k'i'j} \geq w_{kij} + x_{k'i'ki} + x_{kik'i'} - 1 \quad \forall k, k', j \in (\mathbf{J}_{ki} \cup \mathbf{J}_{k'i'}), i \in \mathbf{I}_k, i' \in \left(\mathbf{I}_{k'} \cap \mathbf{I}_{ki}^{\mathrm{G}}\right), [k < k' \cup (k = k' \cap i < i')] \tag{3}$$

$$w_{kij} \geq w_{k'i'j} + x_{k'i'ki} + x_{kik'i'} - 1 \quad \forall k, k', j \in (\mathbf{J}_{ki} \cup \mathbf{J}_{k'i'}), i \in \mathbf{I}_k, i' \in \left(\mathbf{I}_{k'} \cap \mathbf{I}_{ki}^{\mathrm{G}}\right), [k < k' \cup (k = k' \cap i < i')] \tag{4}$$

Continuous variable $T_{ki}$ denotes the start time for operation $i$ of job $k$. An operation $i \in \mathbf{I}_k$, which is the successor of the operation $i' \in \mathbf{I}_k$ in the same job, should start after the completion of operation $i'$.

$$T_{ki} \geq T_{ki'} + \sum_{j \in \mathbf{J}_{ki'}} \left(P_{ki'j}^{\mathrm{T}} \cdot w_{ki'j}\right) \qquad \forall k, i' \in \mathbf{I}_k, i \in \mathbf{I}_k, i = i' + 1 \tag{5}$$

We define binary variables $z_{kij}$ and 0-1 continuous variables $y_{kij}$ to express the machine modes on $j$ after processing an operation $i$ of job $k$.

$$z_{kij} = \begin{cases} 1 & \text{if } j \text{ is switched off after processing } i \text{ in } k \\ 0 & \text{otherwise} \end{cases}$$

$$y_{kij} = \begin{cases} 1 & \text{if } j \text{ remains standby after processing } i \text{ in } k \\ 0 & \text{otherwise} \end{cases}$$

A machine $j$ would remain standby or be switched off after performing $i$ (see eq. 6). It ensures that $y_{kij}$ is 0 or 1 only even it is defined as 0-1 continuous variables.

$$y_{kij} + z_{kij} = w_{kij} \qquad \forall k, i, j \in \mathbf{J}_{ki} \tag{6}$$

Continuous variables $ST_{kij}$ denote the duration of a machine $j$ keeping standby mode after processing $i \in \mathbf{I}_k$. $ST_{kij}$ equals the time interval between the finish of operation $i$ and the start of its immediate precedence operation $i' \in \mathbf{I}_{k'}$ on the identical machine $j$, as handled in Eq. (7) and Eq. (8). Specifically, Eq. (7) handles that if a machine remains standby after performing operation $i$ of job $k$ (i.e., $z_{kij} = 0$), the start time of any subsequent operation $i'$ (i.e., $x_{kik'i'} = 1$) is expected to be later than the finish time of $i$ plus the standby duration.

$$T_{k'i'} \geq T_{ki} + \sum_{j \in \mathbf{J}_{ki}} \left(P_{kij}^{\mathrm{T}} \cdot w_{kij} + ST_{kij} + \frac{E_j^{\mathrm{O}}}{P_j^{\mathrm{U}}} \cdot z_{kij}\right) - M \cdot (1 - x_{kik'i'}) \qquad \forall k, k', (k \neq k') \cup (k = k' \cap i < i'), i \in \mathbf{I}_k, i' \in \left(\mathbf{I}_{k'} \cap \mathbf{I}_{ki}^{\mathrm{G}}\right) \tag{7}$$

The immediate successor $i'$ of operation $i$ on the same machine is identified by Eq. (8), where the number of preceding operations of $i'$ should be one more that of operation $i$. Here, the $M$ indicates a big number, taking the value of 10000 in this work. $N_j^{max}$ is the maximum number of jobs that can be processed on $j$.

$$T_{k'i'} \leq T_{ki} + \sum_{j \in \mathbf{J}_{ki}} \left(P_{kij}^{\mathrm{T}} \cdot w_{kij} + ST_{kij} + \frac{E_j^{\mathrm{O}}}{P_j^{\mathrm{U}}} \cdot z_{kij}\right) + M \cdot \left[\max_j \left(N_j^{max}\right)\right] \cdot (1 - x_{kik'i'}) + M \cdot \left(1 - \sum_{j \in \mathbf{J}_{ki}} y_{kij}\right) + M \cdot \left(\sum_{k''} \sum_{\substack{i'' \in \mathbf{I}_{k'i'}^{\mathrm{G}} \\ (k'' \neq k') \cup (k'' = k' \cap i'' \neq i')}} x_{k''i''k'i'} - \sum_{k''} \sum_{\substack{i'' \in \mathbf{I}_{ki}^{\mathrm{G}} \\ (k'' \neq k) \cup (k'' = k \cap i'' \neq i)}} x_{k''i''ki} - 1\right) \qquad \forall k, k', (k \neq k') \cup (k = k' \cap i < i'), i \in \mathbf{I}_k, i' \in \left(\mathbf{I}_{k'} \cap \mathbf{I}_{ki}^{\mathrm{G}}\right) \tag{8}$$

Standby energy consumption $ES_{ki}$ is calculated using Eq. (9), which is proportional to the duration of standby time and the unload power of the machine $j$. $ST_{kij}$ is enforced as zero if the machine does not remain standby after processing $i \in \mathbf{I}_k$, as indicated in Eq. (10).

$$ES_{ki} = \sum_{j \in \mathbf{J}_{ki}} \left(ST_{kij} \cdot P_j^{\mathrm{U}}\right) \qquad \forall k, i \in \mathbf{I}_k \tag{9}$$

$$ST_{kij} \leq \left[\min\left(M, \frac{E_j^{\mathrm{O}}}{P_j^{\mathrm{U}}}\right)\right] \cdot y_{kij} \qquad \forall k, i, j \in \mathbf{J}_{ki} \tag{10}$$

Makespan should be larger than the finish time of the last operation ($\mathbf{LI}_k$) in all jobs. And it is no less than cumulative processing times of all operations in any job.

$$T_{ki} + \sum_{j \in \mathbf{J}_{ki}} \left(w_{kij} \cdot P_{kij}^{\mathrm{T}}\right) \leq MS \qquad \forall k, i \in (\mathbf{I}_k \cap \mathbf{LI}_k) \tag{11}$$

$$\sum_{i \in \mathbf{I}_k} \sum_{j \in \mathbf{J}_{ki}} \left(w_{kij} \cdot P_{kij}^{\mathrm{T}}\right) \leq MS \qquad \forall k \tag{12}$$

On any $j$, the accumulated time used to process operations and keep standby should be no larger than $MS$.

$$\sum_k \sum_{i \in \mathbf{I}_{kj}} \left(w_{kij} \cdot P_{kij}^{\mathrm{T}} + ST_{kij} + \frac{E_j^{\mathrm{O}}}{P_j^{\mathrm{U}}} \cdot z_{kij}\right) \leq MS \quad \forall j \tag{13}$$

Constraint (14) is the objective function.

$$TEC = \sum_k \sum_i \sum_{j \in \mathbf{J}_{ki}} \left(w_{kij} \cdot P^{\mathrm{T}}_{kij} \cdot P^{\mathrm{C}}_{kij}\right) + \beta \cdot MS + \sum_k \sum_{i \in \mathbf{I}_k} ES_{ki} + \sum_i \sum_k \sum_{j \in \mathbf{J}_{ki}} \left(E^{\mathrm{O}}_j \cdot z_{kij}\right) \quad (14)$$

The start time of an operation $i$ of job $k$ should be always after the minimum required time for all predecessor operations in the same job.

$$T_{ki} \geq \sum_{i' < i, i' \in \mathbf{I}_k} \left\{ \min_{j \in \mathbf{J}_{ki}} \left(P^{\mathrm{T}}_{ki'j}\right) \right\} \quad \forall k, i \in \mathbf{I}_k \quad (15)$$

Upper bounds are imposed on the positive variables $MS$ and $T_{ki}$, as specified by Eq. (16) and Eq. (17).

$$MS \leq M \quad (16)$$

$$T_{ki} \leq M \qquad \forall k, i \quad (17)$$

Moreover, if an operation cannot be performed on a machine $j$ (i.e., $j \notin \mathbf{J}_{ki}$), its corresponding binary variables (e.g., $w_{kij}, y_{kij}$ and $z_{kij}$) should be set to zero.

$$w_{kij} = 0, y_{kij} = 0, z_{kij} = 0 \qquad \forall k, i, j \notin \mathbf{J}_{ki} \quad (18)$$

Precedence between operations of the same job can be confirmed on the same machine. And variables $x_{kik'i'}$ are fixed to zero if $i'$ cannot share any machine with $i$ (i.e., $i' \notin \mathbf{I}^{\mathrm{G}}_{ki}$)

$$x_{ki'ki} = 0 \qquad \forall i \in \mathbf{I}_k, i' \in \mathbf{I}_k, i < i' \quad (19)$$

$$x_{kik'i'} = 0 \qquad \forall k, i \in \mathbf{I}_k, k', i' \in \mathbf{I}_{k'}, i' \notin \mathbf{I}^{\mathrm{G}}_{ki} \quad (20)$$

Finally, equations (21-23) list all the continuous and binary variables in model **MG**. We complete the mathematical model **MG** consisting of constraints (1-23).

$$ES_{ki}, ST_{kij}, MS, T_{ki} \geq 0 \quad (21)$$

$$0 \leq y_{kij} \leq 1 \quad (22)$$

$$z_{kij}, x_{kik'i'}, w_{kij} \in \{0, 1\} \quad (23)$$

## COMPUTATIONAL STUDIES

**Table 1:** Problem size of benchmark examples.

| **Problem size** $(K * I * J)$ | **Example (Ex)** |
|---|---|
| 2*4*2 | 1-5 |
| 2*6*3 | 6-10 |
| 3*6*2 | 11-15 |
| 3*9*3 | 16-20 |
| 6*36*6 | 21 |
| 10*100*10 | 22, 39-43 |
| 10*50*5 | 24-28 |
| 15*75*5 | 29-33 |
| 20*100*5 | 34-38 |
| 15*150*10 | 44-48 |
| 20*200*10 | 49-54 |
| 30*300*10 | 55-58 |

We utilize the proposed **MG** to solve 58 benchmark examples from the literature [20,21] to evaluate its computational performance. These examples are sourced from the Hurink_DATA dataset [20], comprising 20 small-scale and 38 industrial-scale examples. Their respective problem sizes are listed in Table 1. **MG** is benchmarked against MILP-based model formulated using local sequence-based representations (**ML**) [24] and event-based continuous-time representations (**MU**) [21]. Additionally, the solution quality of **MG** is compared with a decomposition approach from Rakovitis *et al.* [21]. All examples are solved using CPLEX22.1.0/GAMS40.3.0 on a desktop computer with AMD RyzenTM 9 5950X 3.40 GHz and 96.0 GB RAM running Windows 10. A time limit of one hour is imposed for all MILP formulations.

### Comparison with mathematical programming models

Comparisons between **MG** and MILP model from literature for the small-size examples are provided in Table 2. All formulations generate identical optimal solutions, which represent the global optimum, with similar computational times of approximately 1 second.

**Table 2: TEC** computational results for small-size examples from **MG**, **MU** and **ML**.

| **Ex** | **MG, MU, ML** | **Ex** | **MG, MU, ML** |
|---|---|---|---|
| *1* | 63.03 | *11* | 166.23 |
| *2* | 122.44 | *12* | 176.75 |
| *3* | 75.74 | *13* | 121.30 |
| *4* | 146.63 | *14* | 156.86 |
| *5* | 78.40 | *15* | 163.20 |
| *6* | 220.74 | *16* | 219.46 |
| *7* | 97.54 | *17* | 306.68 |
| *8* | 146.81 | *18* | 210.60 |
| *9* | 230.66 | *19* | 269.52 |
| *10* | 161.06 | *20* | 274.94 |

**Table 3: TEC** computational time for industrial-size examples from **MG**, **MU** and **ML**

| **Ex** | **MG** | **MU** | **ML** | **Ex** | **MG** | **MU** | **ML** |
|---|---|---|---|---|---|---|---|
| *21* | **183** | 183 | 183 | *40* | **3327** | 3705 | 3715 |
| *22* | 3473 | 3779 | 3393 | *41* | **3344** | 3618 | 3497 |
| *23* | 3639 | 3421 | 3862 | *42* | **3698** | 3731 | 3798 |
| *24* | **1776** | 1776 | 1776 | *43* | **3692** | 3659 | 4173 |
| *25* | **1769** | 1830 | 1800 | *44* | **5052** | 5091 | NA |
| *26* | **1530** | 1623 | 1603 | *45* | 4722 | 4612 | NA |
| *27* | **1647** | 1647 | 1691 | *46* | **5197** | 5225 | NA |
| *28* | **1463** | 1465 | 1495 | *47* | **5314** | 5467 | NA |
| *29* | **2584** | 2584 | 2626 | *48* | **5362** | 5291 | NA |
| *30* | 2404 | 2439 | 2378 | *49* | **6815** | 7582 | NA |
| *31* | **2486** | 2486 | 2568 | *50* | **7772** | 8823 | NA |
| *32* | **2638** | 2638 | 2696 | *51* | **7059** | 8826 | NA |
| *33* | **2522** | 2522 | 2522 | *52* | **7854** | NA | NA |
| *34* | 3744 | 3353 | 3973 | *53* | **7075** | NA | NA |
| *35* | **2996** | 3036 | 3277 | *54* | **14480** | NA | NA |
| *36* | **3162** | 3195 | 3309 | *55* | **13930** | NA | NA |
| *37* | 3473 | 3422 | 3595 | *56* | **19081** | NA | NA |
| *38* | 3457 | 3441 | NA | *57* | **15674** | NA | NA |
| *39* | 3781 | 3800 | 3713 | *58* | **21380** | NA | NA |

Table 3 presents the optimized TEC of industrial-size examples from MILP formulations. If **MG** achieves solutions that are no worse than those from **MU** and **ML**, its TEC results are highlighted in bold. And 'NA' indicates no available solutions are found. Table 3 proves that **MG** outperforms both **MU** and **ML** in examples 25, 26, 28, 35, 36, 40-44, 46, 47, and 49-58. The maximum reduction in TEC is 20% (7059 vs. 8826) in example 51, compared to **MU**. Advantage of **MG** is mainly evident in complicated examples. In detail, for cases with more than 200 operations (e.g., examples 49-58), both **MU** and **ML** fail to find feasible solutions in most instances. However, **MG** successfully provides feasible solutions for these cases.

Some examples converge within a computation time of less than 1 hour. The specific computational times for these examples are presented in Table 4, allowing for a comparison of the computational efficiency of the MILP formulations. Table 4 demonstrates that **MG** achieves shorter computational time relative to **MU** and **ML** in most cases (8 out of 9 examples). The most significant reduction is observed in example 26, where **MG** requires 1/14 of the time (248 seconds vs. 3600 seconds) to reach a better solution (1530 vs. 1623 and 1603).

**Table 4:** Computational times (Seconds) of industrial-size examples from **MG**, **MU** and **ML**.

| Ex | MG | MU | ML | Ex | MG | MU | ML |
|---|---|---|---|---|---|---|---|
| *24* | **5** | 97 | 325 | *32* | **362** | 3600 | 3600 |
| *26* | **248** | 3600 | 3600 | *33* | **218** | 1668 | 3326 |
| *28* | **209** | 3600 | 3600 | *35* | **3336** | 3600 | 3600 |
| *29* | 644 | 206 | 3600 | *36* | **1481** | 3600 | 3600 |
| *31* | **526** | 1136 | 3600 | | | | |

## Comparison with a decomposition algorithm

A decomposition algorithm [21], denoted by **GD**, is proposed to address industrial-scale problems. We compare its performance with the proposed **MG** (see Table 5). Since the computational time for **MG** is currently limited to one hour, making it suitable for real-world applications in complex cases, our focus is primarily on comparing the solution quality between **GD** and **MG**. Table 5 demonstrates the clear superiority of **MG** for examples with no more than 100 operations (i.e., examples 21-43), achieving a maximum TEC reduction of 13.6% (2996 vs. 3467 in example 35). For examples with more than 300 operations, although **MG** is capable of finding feasible solutions, it yields worse optimal solutions relative to **GD**.

## CONCLUSIONS

In this work, we presented a mixed-integer linear programming formulation for energy-efficient flexible job shop scheduling problems. The objective was to minimize total energy consumption, including energy used during processing operations, idle durations, and auxiliary facilities. The formulation was developed based on the global precedence relationships of operations on machines. Since immediate precedence relationships cannot be directly expressed using decision variables, we incorporated novel constraints to identify them. This enabled the precise estimation of idle durations between adjacent operations on machines, which in turn determined the optimal machine modes. Computational studies showed the superiority of the proposed formulation. Its advantages are reflected in reduction in total energy consumption by up to 20%. It successfully provided feasible solutions for all considered examples, including those where existing mathematical formulations failed.

**Table 5: TEC** computational results of industrial-size examples from **MG** and **GD**.

| Ex | MG | GD | Ex | MG | GD |
|---|---|---|---|---|---|
| *21* | **183** | 196 | *40* | **3327** | 3564 |
| *22* | **3473** | 3850 | *41* | **3344** | 3517 |
| *23* | **3639** | 4063 | *42* | **3698** | 3682 |
| *24* | **1776** | 1837 | *43* | **3692** | 3959 |
| *25* | **1769** | 1922 | *44* | **5052** | 5335 |
| *26* | **1530** | 1682 | *45* | **4722** | 4978 |
| *27* | **1647** | 1764 | *46* | 5197 | 5180 |
| *28* | **1463** | 1570 | *47* | 5314 | 4993 |
| *29* | **2584** | 2694 | *48* | **5362** | 5567 |
| *30* | **2404** | 2541 | *49* | **6815** | 7164 |
| *31* | **2486** | 2682 | *50* | 7772 | 7758 |
| *32* | **2638** | 2728 | *51* | 7059 | 6683 |
| *33* | **2522** | 2750 | *52* | 7854 | 7241 |
| *34* | **3744** | 3589 | *53* | **7075** | 7229 |
| *35* | **2996** | 3467 | *54* | 14480 | 8712 |
| *36* | **3162** | 3397 | *55* | 13930 | 9690 |
| *37* | **3473** | 3767 | *56* | 19081 | 9091 |
| *38* | **3457** | 3864 | *57* | 15674 | 8873 |
| *39* | **3781** | 3887 | *58* | 21380 | 10004 |

## ACKNOWLEDGEMENTS

Authors appreciate financial support from China Scholarship Council and The University of Manchester (201908130170, 202106440020) and Engineering and Physical Sciences Research Council (EP/T03145X/1, EP/V051008/1).

## REFERENCES

1. Yang L, Li J, Chao F, Hackney P, Flanagan M. Job shop planning and scheduling for manufacturers with manual operations. Expert Syst 38: e12315 (2021) https://doi.org/10.1111/exsy.12315
2. Liao J, Lin C. Optimization and simulation of job-shop supply chain scheduling in manufacturing enterprises based on particle swarm optimization. Int J Simul Model 18:187-196 (2019)

https://doi.org/10.2507/IJSIMM18(1)C05
3. Nouri HE, Driss OB, Ghédira K. A classification schema for the job shop scheduling problem with transportation resources: state-of-the-art review. Artif Intell Perspect Intell Syst Adv Intell Syst Comput 464:1-11 (2016) https://doi.org/10.1007/978-3-319-33625-1_1
4. Tian Z, Jiang X, Liu W, Li Z. Dynamic energy-efficient scheduling of multi-variety and small batch flexible job-shop: a case study for the aerospace industry. Comput Ind Eng 178:109111 (2023) https://doi.org/10.1016/j.cie.2023.109111
5. Jiang X, Tian Z, Liu W, Suo Y, Chen K, Xu X, Li Z. Energy-efficient scheduling of flexible job shops with complex processes: a case study for the aerospace industry complex components in China. J Ind Inf Integr 27:100293 (2022) https://doi.org/10.1016/j.jii.2021.100293
6. Brucker P, Schlie R. Job-shop scheduling with multipurpose machines. Computing 45:369-375 (1990) https://doi.org/10.1007/BF02238804
7. Demir Y, İşleyen SK. Evaluation of mathematical models for flexible job-shop scheduling problems. Appl Math Model 37:977-988 (2013) https://doi.org/10.1016/j.apm.2012.03.020
8. Ham A, Park MJ, Kim KM. Energy-aware flexible job shop scheduling using mixed integer programming and constraint programming. Math Probl Eng 2021:1-12 https://doi.org/10.1155/2021/8035806
9. Wang S, Yu J. An effective heuristic for flexible job-shop scheduling problem with maintenance activities. Comput Ind Eng 59:436-447 (2010) https://doi.org/10.1016/j.cie.2010.05.016
10. Li X, Gao L. An effective hybrid genetic algorithm and tabu search for flexible job shop scheduling problem. Int J Prod Econ 174:93-110 (2016) https://doi.org/10.1016/j.ijpe.2016.01.016
11. Ding H, Gu X. Improved particle swarm optimization algorithm based novel encoding and decoding schemes for flexible job shop scheduling problem. Comput Oper Res 121:104951 (2020) https://doi.org/10.1016/j.cor.2020.104951
12. Xie J, Gao L, Peng K, Li X, Li H. Review on flexible job shop scheduling. IET Collab Intell Manuf 1:67-77 (2019) https://doi.org/10.1049/iet-cim.2018.0009
13. Coelho P, Pinto A, Moniz S, Silva C. Thirty years of flexible job-shop scheduling: a bibliometric study. Procedia Comput Sci 180:787-796 (2021) https://doi.org/10.1016/j.procs.2021.01.329
14. U.S. Energy Information Administration. https://www.eia.gov/energyexplained/use-of-energy/industry.php (2023) [13 July 2023].
15. Nguyen TAL, Tran LNH, Paris H, Mathieu M. Evaluating energy efficiency of production machine. Appl Mech Mater 889:580-587 (2019) http://doi.org/10.4028/www.scientific.net/AMM.889.580
16. Meng L, Ren Y, Zhang B, Li JQ, Sang H, Zhang C. MILP modeling and optimization of energy-efficient distributed flexible job shop scheduling problem. IEEE Access 8:3032548 (2020) https://doi.org/10.1109/ACCESS.2020.3032548
17. Meng L, Zhang C, Shao X, Ren Y. MILP models for energy-aware flexible job shop scheduling problem. J Clean Prod 210:118289 (2019) https://doi.org/10.1016/j.jclepro.2018.11.021
18. Zhang L, Li Z, Królczyk G, Wu D, Tang Q. Mathematical modeling and multi-attribute rule mining for energy efficient job-shop scheduling. J Clean Prod 241:118289 (2019) https://doi.org/10.1016/j.jclepro.2019.118289
19. Park MJ, Ham A. Energy-aware flexible job shop scheduling under time-of-use pricing. Int J Prod Econ 248:108507 (2022) https://doi.org/10.1016/j.ijpe.2022.108507
20. Zhang L, Tang Q, Wu Z, Wang F. Mathematical modeling and evolutionary generation of rule sets for energy-efficient flexible job shops. Energy 138:101421 (2017) https://doi.org/10.1016/j.energy.2017.07.005
21. Rakovitis N, Li D, Zhang N, Li J, Zhang L, Xiao X. Novel approach to energy-efficient flexible job-shop scheduling problems. Energy 238:121773 (2022)https://doi.org/10.1016/j.energy.2021.121773
22. Dai M, Tang D, Giret A, Salido MA. Multi-objective optimization for energy-efficient flexible job shop scheduling problem with transportation constraints. Robot Comput-Integr Manuf 59:101249 (2019) https://doi.org/10.1016/j.rcim.2019.04.006
23. Cheng L, Tang Q, Zhang L, Meng K. Mathematical model and enhanced cooperative co-evolutionary algorithm for scheduling energy-efficient manufacturing cell. J Clean Prod 326:129248 (2021)https://doi.org/10.1016/j.jclepro.2021.129248
24. Li D, Zheng T, Li J, Teymourifar A. A hybrid framework integrating machine-learning and mathematical programming approaches for sustainable scheduling of flexible job-shop problems. Chem Eng Trans 103:385-390 (2023) https://doi.org/10.3303/CET23103065
25. Gong G, Tang J, Huang D, Luo Q, Zhu K, Peng N. Energy-efficient flexible job shop scheduling problem considering discrete operation sequence flexibility. Swarm Evol Comput 84:101421 (2024) https://doi.org/10.1016/j.swevo.2023.101421

© 2025 by the authors. Licensed to PSEcommunity.org and PSE Press. This is an open access article under the creative

commons CC-BY-SA licensing terms. Credit must be given to creator and adaptations must be shared under the same terms. See https://creativecommons.org/licenses/by-sa/4.0/



Systems & Control Transactions

**Research Article - Peer Reviewed Conference Proceeding**
ESCAPE 35 - European Symposium on Computer Aided Process Engineering
Ghent, Belgium. 6-9 July 2025
Jan F.M. Van Impe, Grégoire Léonard, Satyajeet S. Bhonsale,
Monika E. Polańska, Filip Logist (Eds.)

PSE PRESS

# Materials-Related Challenges of Energy Transition

**Fatemeh Rostami[a], Piera Patrizio[b,c], Laureano Jimenez[a], Carlos Pozo[a]*, and Niall Mac Dowell[b,c]**

[a] Universitat Rovira I Virgili, Department d'Enginyeria Quimica, Tarragona, Spain
[b] Imperial College London, Center for Environmental Policy, London, UK
[C] Imperial College London, Center for Process Systems Engineering, London, UK
* Corresponding Author: Carlos.Pozo@urv.cat.

## ABSTRACT

Transition from fossil fuels to clean energy technologies (CETs) is critical, but material shortages threaten to hinder progress. This study analyzes the potential deficits in 14 key materials – such as lithium, nickel, and cadmium – based on capacity projections for CETs by eight Integrated Assessment Models (IAMs) for 2020-2050. It focuses on technologies including battery storage, concentrated solar power (CSP), electrolyzers, solar photovoltaics (PV), and wind turbines. Our findings show that these materials could face shortages of up to 97% by 2050. To meet rising demand, material production rates must increase sharply, with some materials like cadmium, selenium, and tellurium requiring about 31% increases, peaking in this decade. Immediate actions are needed to accelerate production and improve recycling efforts. However, recycling targets, such as 325% for lithium, seem highly challenging to achieve. Without these measures, material shortages could delay CET deployment, risking Paris Agreement goals. To prevent these disruptions, we call for: (i) revising CET capacity projections, (ii) urgent planning for mining expansion, and (iii) a significant increase in recycling infrastructure to ensure a sustainable energy transition.

**Keywords**: Energy transition, Clean Energy, Integrated Assessment Models, Material Requirements.

## INTRODUCTION

Clean energy technologies are pivotal in reducing fossil fuel consumption, mitigating greenhouse gas (GHG) emissions, and enhancing energy security. However, as CET deployment accelerates, resource extraction grows, presenting significant challenges to meeting the energy sector's rising material demands.

The capacity requirements for CETs are a central focus of climate policies shaped by IAMs [1]. These models are used for guiding policy strategies, driving climate change mitigation, and informing global initiatives [2]. However, IAMs have faced criticism overlooking key factors such as human behaviour [3], socio-technical insights [4], and political neutrality [5]. A particular concern is the absence of materials availability to scale CETs. This undermines the credibility of their capacity projections.

This study evaluates the feasibility of CET capacity projections across 25 scenarios from eight widely used IAMs, aligned with the Paris Agreement temperature target. These scenarios, covering diverse assumptions, increase the reliability of our findings. We assess capacity projections for stationary and Electric Vehicle (EV) batteries, electrolyzers, CSP systems, PV panels, and wind turbines against realistic capacities based on the availability of 14 materials, including critical minerals, rare earth elements, and platinum group metals. Then, we develop an optimization model to identify the gap between IAM projected capacities and realistic estimates constrained by material availability. Also, we calculate the recycling rates required to meet IAM-projected capacities.

## Methodology

First part of this section focuses on estimating the material demand, while the second part introduces a model to evaluate the effect of material unavailability.

### Assessing the feasibility of IAM projections

The materials demand estimation is based on the projected capacity for each technology from 2020 to 2050, using data from 25 scenarios provided by eight widely used IAMs [6], discussed in the following.

#### Overview of selected IAMs

Recognizing that each IAM employs unique scenario designs and technological assumptions, our analysis

incorporates multiple IAMs to provide a comprehensive range of perspectives and account for differences in modelling approaches. Specifically, we include the following IAMs: GCAM 4.2, IMAGE 3.0.1, MERGE-ETL 6.0, MESSAGE-GLOBIOM 1.0, MESSAGEix-GLOBIOM 1.0, POLES ADVANCE, REMIND-MAgPIE 1.7-3.0, and WITCH-GLOBIOM 4.4. These models collectively represent 25 scenarios explained in Rostami et al. [7].

Throughout this study, references to IAMs specifically pertain to the eight models and their respective scenarios selected for analysis.

## Accounting for technology variations

IAMs provide data at a general, archetypal technology level, but in reality, technology designs – and their material requirements – vary significantly. To account for this, our analysis includes seven battery types, three CSP types, two electrolyzer types, three PV panel types, and six wind turbine types. We allocate IAM capacity projections across different technology types using two market contribution scenarios [8]: ***Continued***, which assumes a gradual evolution of existing technologies; and ***Technological Change***, which considers the potential for rapid advancements and shifts in technology design. These scenarios predict how various technology designs will contribute to the overall market. The specific selected technology types and market contribution values are detailed in supplementary information. Furthermore, we will highlight the technology types that are most recommended under materials availability constraints.

## Materials demand estimation

Material consumption per gigawatt (GW), known as material intensity, was sourced from the literature for each technology type [8], [9]. We used two material intensity scenarios: ***Current,*** reflecting present-day intensities; and ***Learning curve,*** accounting for technological advancements that may reduce intensities over time.

The material intensity values used for each technology type are available in supplementary information.

To estimate material demand, we multiplied the projected technology capacities from each of the 25 IAM scenarios by two market contribution trends (*k:"Continued"* and *"Technological Change"*) and two material intensity scenarios (*i:"Current"* and *"Learning Curve"*). This approach, illustrated in Equation 1, results in a total of 100 potential outcomes, providing a comprehensive assessment of material demand under varying assumptions.

$$MD^{T}_{m,t,n,s,k,i} = CC^{T}_{n,s} \cdot MC_{t,n,k} \cdot MI_{m,t,n,i} \quad (1)$$

$$\forall m,n,s,k,i,\ t \in TT_{T},\ T=\{BAT,\ CSP,\ ELECTZ,\ PV,\ WIND\}$$

Here, $MD^{T}_{m,t,n,s,k,i}$ [ton] represents the demand for material *m* , driven by technology type *t* within the broader technology category *T*, for year *n* as determined by IAM scenario *s*, market trend *k*, and material intensity *i*. $CC^{T}_{n,s}$ [GW] denotes the installed capacity for technology category *T* in year *n* according to IAM scenario *s*, while $MC_{t,n,k}$ [%] is the market contribution of technology type *t* in year *n* according to market trend *k*. The relationship between technology types *t* (e.g., crystallin silicon PV panels) and technology categories *T* (e.g., PV panels) is given by set $TT_{T}$, which specifies the types *t* that belong to category *T*. $MI_{m,t,n,I}$ [ton/GW] is the material intensity *i* (*"Current"* or *"Learning Curve"*) of material *m* used in type *t* of technology *T* in year *n*.

To assess the potential material shortages, we compared the material demands estimated over time with their prospective market availability, calculated projecting their current production rates. The details of these comparisons are explained in Equation 2.

$$MSh_{m,n,s,k,i} = \frac{([PR_{m,20} \cdot (1+\alpha)^{r} \cdot Sh^{CETs}_{m,20}] - \sum_{t,T} MD^{T}_{m,t,n,s,k,i}) \cdot 100}{\sum_{t,T} MD^{T}_{m,t,n,s,k,i}} \quad (2)$$

$$(\forall m,n,s,k,i,t \in TT_{T}, r = 0,1,\dots,30)$$

In Equation 2, the first term in the numerator calculates the market availability of material *m* in year *n* for CET development [ton]. Our estimation is based on the production rates for 2020 ($PR_{m,20}$) sourced from the literature [7]. The production rate might remain constant (*α=0*) or grow annually. To account for its variations, we assume an annual growth rate of *α=2.7%*, reflecting the average growth in metal mining [10]. Notably, *r* is the counter of the years in the projection period, starting at *r=0* for 2020 and increasing to *r=30* for 2050. Since materials are not solely used for CET development (i.e., they are also needed in other sectors), we limit the allocation of each material for CETs by applying the 2020 share of CET-driven demand ($Sh^{CETs}_{m,20}$). It represents the proportion of each material´s total production used for CETs in 2020 [%]. This calculation gives the market availability of material *m* for CETs in year *n*. From this, we then subtract the total demand for each material *m* in year *n*, derived by IAM scenario *s*, market trend *k*, and material intensity scenario *i* across all technology types *t* within each category *T* [ton]. The resulting difference, divided by total demand for desired material, provides the shortage in its availability for CETs development ($MSh_{m,n,s,k,i}$).

The required growth rates for material production to meet the IAM capacity projections are determined by forcing the numerator of Equation 2 to be zero, and solving the resulting equation for α.

## Estimating technology capacity shortfalls

To evaluate the impact of material shortages on CET deployment, we aim to estimate the achievable capacities of CETs. This involves developing an optimization

model, formulated and solved in General Algebraic Modeling System (GAMS), to minimize the gap between the capacities projected by IAMs and the realistic capacities constrained by material availability. In the model, variables are *italicized*, and parameters are presented in standard font for clarity throughout the equations.

$$\text{Min} \sum_{T,n,S} Diff_{n,s}^{T} \quad (3)$$

$$\text{s.t:} \quad Diff_{n,s}^{T} = CC_{n,s}^{T,Opt} - \text{CC}_{\text{n,s}}^{\text{T,IAMs}} \quad (4)$$
$$\forall n,s,T=\{BAT, CSP, ELECTZ, PV, WIND\}$$

$$Diff_{n,s}^{T} \geq 0 \quad (5)$$
$$\forall n,s,T=\{BAT, CSP, ELECTZ, PV, WIND\}$$

$$\sum_{k,t,T} CC_{n,s}^{T,Opt} \cdot \text{MC}_{\text{t,n,k}} \cdot \text{MI}_{\text{m,t,n}} \leq \text{PR}_{\text{m,n}} \cdot \text{SHARE}_{\text{m,2020}}^{\text{CETs}} \quad (6)$$
$$\forall m,s,\ n=2021, \ldots, 2050$$

$$\sum_{n,k,t,T} CC_{n,s}^{T,Opt} \cdot \text{MC}_{\text{t,n,k}} \cdot \text{MI}_{\text{m,t,n}} \leq \text{Res}_{\text{m}} \quad \forall m,s \quad (7)$$

$$Diff_{n,s}^{T},\ CCI_{t,n,s}^{T,Opt} \in \text{R}^{+} \quad (8)$$

The objective of the model (Equation 3) is to minimize capacity disparities across technology categories *T* (e.g., PV), IAM scenarios *s*, and years *n*, as denoted by $Diff_{n,s}^{T}$. These disparities are defined in Eq. 4 as the difference between the capacities projected by IAMs ($\text{CC}_{\text{n,s}}^{\text{T,IAMs}}$) and the "realistic" capacities estimated by the model ($CC_{n,s}^{T,Opt}$). For each technology, this difference should be positive to prevent situations where surplus capacity in one technology category offsets deficits in another (Eq. 5). The values for $\text{CC}_{\text{n,s}}^{\text{T,IAMs}}$ are obtained from IAMs, for the corresponding scenario *s* and year *n*. In this context, as discussed in Equation 1, the left-hand side of Equation 6 calculates the demand for material *m* driven by all types of technology *T* developed in year *n*. By incorporating multiple technology types into our models, we can determine which technologies are preferentially selected. The right-hand side reflects the portion of the realistic production rate for material *m* in year *n* ($\text{PR}_{\text{m,n}}$) allocated to CET manufacturing. Indeed, the shares observed in 2020 ($\text{SHARE}_{\text{m,2020}}^{\text{CETs}}$) are used to limit the amount of each material available for CET manufacturing. Notably, production rates for 2020 ($\text{PR}_{\text{m,2020}}$) are sourced from the literature [7]. Future production rates ($\text{PR}_{\text{m,n}}$) are obtained by applying an annual growth rate of α = 2.7%, reflecting the historical average annual growth rate of metals mining [10]. This rate was adjusted to 0.7% and 4.7% for sensitivity analysis, representing the average growth ± 2%. Finally, Equation 7 is used to constrain the cumulative demand for material *m* by year *n,* driven by all the technologies, to remain within the limits of its available reserves ($\text{Res}_{\text{m}}$), as given in literature [11].

To estimate the minimum recycling rates needed to address CET material shortages and achieve IAM capacity projections, we developed a secondary optimization model, deriving from this one. The objective of this second model is to calculate the minimum required recycling rates. The model uses constraints similar to those in the primary model but incorporates recycling as an additional supply source (i.e., recycling is added as a new variable to the right-hand sides of Eqs. 6–7). Due to space limitations, we avoid detailed explanation of this model. Further details can be found in Rostami et al. [7].

For each of the 25 IAM scenarios, we ran the model 12 times, using different combinations of two market trends, two material intensity projections, and three annual production rates (α). This results in a total of 300 (i.e., 25×12) estimates for each material´s recycling rate. Current recycling rates, sourced from various references [11], [12], are used to contextualize the results.

## Results and discussion

### Material shortage

Figure 1 illustrates the potential material shortages for CET development, shown as negative values (red shadow), and the necessary annual production growth rates to address these shortages, represented by positive values (blue shadow). The lines inside each shadow present the median results across 100 scenarios.

The red lines highlight significant material shortages, with materials such as cadmium, graphite, indium, lithium, nickel, and tellurium projected to fall short by up to 97% of demand. Materials like dysprosium, iridium, neodymium, silver, and terbium face comparatively lower deficits, still their shortages remain significant. The steep decline in the red curves indicates that the most severe shortages are likely to occur within this decade, followed by a moderate worsening trend in next decades. An exception is iridium, where based on the median values, shortages are mainly expected after 2040, aligning with the large-scale deployment of electrolyzers. However, when considering all the scenarios (i.e., the red shadow), we might face an iridium shortage starting this decade. Overall, these commodities markets will be so tight that the deployment of CETs at the pace and scale envisioned by IAMs seems impossible. It will likely translate into higher cumulative emissions, which might prevent us from meeting Paris agreement targets.

Addressing these deficits requires urgent and worthy action. Incremental production increases, such as the 2.7% annual growth shown by thin red lines (reflecting historical averages of metal mining annual growth rate), are clearly insufficient. For instance, this growth only marginally reduces lithium shortages from 97% to 93%. Without addressing these material deficits, achieving CET capacities at the scale envisioned may not be feasible. This underscores the importance of integrating material constraints into IAMs to ensure realistic projections.

For most materials, the blue lines, representing the

median of necessary annual production growth rates, start at low values in 2020 and rise sharply during the early years (2020–2025). Materials like cadmium, gallium, indium, selenium, silver, and tellurium exhibit high starting points in 2020, reflecting their early and intensive use in PV panels. Since production of these materials has not increased as necessary in recent years, we expect a challenging period, indicating that more effort will be required in the future to compensate for these shortages and achieve the CET projected capacities by 2050.

Overall, after 2025, the rate of increase slows but remains positive, suggesting that while the urgency for scaling production decreases, steady growth remains necessary. Factors such as technological maturity and improved material intensity likely contribute to this trend. Even in the long term, annual growth rates remain above 5.6%, with this median observed for iridium in 2050.

Furthermore, in the early 2030s, a second peak in the production of cobalt, graphite, and lithium will be necessary to develop batteries for EVs at the projected scale. Similarly, unachieved targets before 2030 will exacerbate the situation beyond that point, if we want to catch up the projections at some point. It is important to note that mine expansion is time-intensive, meaning that material production might not ramp up at the necessary pace in the short term. This highlights the urgency of planning for mining expansion.

Alternatively, CET development could be adjusted to require a steadier material production rate over time. Implementing this requires adjustments in CET projections and offers significant long-term benefits by ensuring more stable material production. For example, it reduces the risk of supply chain bottlenecks, provides more time to incentivize investments in recycling infrastructure, decreases market volatility and price fluctuations, and benefits industries dependent on these materials.

## CET shortfalls and required material recycling

Figure 2 highlights the shortfalls in CET capacities based on IAM scenarios and after implementing constraints on materials availability. Meeting IAM projections for batteries and PV panels is challenging. For batteries, persistent material deficits are expected starting this decade (see cobalt, graphite, lithium, and nickel in Figure 1), potentially resulting in a 94% shortfall, equating to 11.1 TW below the 2050 targets. Similarly, PV panels capacity may fall short by 1.6 TW (94% of projections) due to cadmium, gallium, indium, selenium, and tellurium, shortages.

Electrolyzer deployment appears more feasible under median scenarios. However, under pessimistic condition, iridium shortages could limit output by 752 GW. CSP faces a moderate shortfall, with a median capacity deficit of 10.4 GW by 2050. Still, under ambitious scenarios, the entire 169 GW projected capacity may be unattainable. Wind turbine deployment could also be hindered by dysprosium, neodymium, and nickel shortages, resulting in a median shortfall of 88 GW (54% below the 2050 target). All these highlight the urgent need to modify IAMs by incorporating material availability constraints.

Raw materials are unevenly distributed across the globe, which inherently creates vulnerabilities in supply chains. For instance, a substantial share of gallium reserves is concentrated in China. Therefore, geopolitical

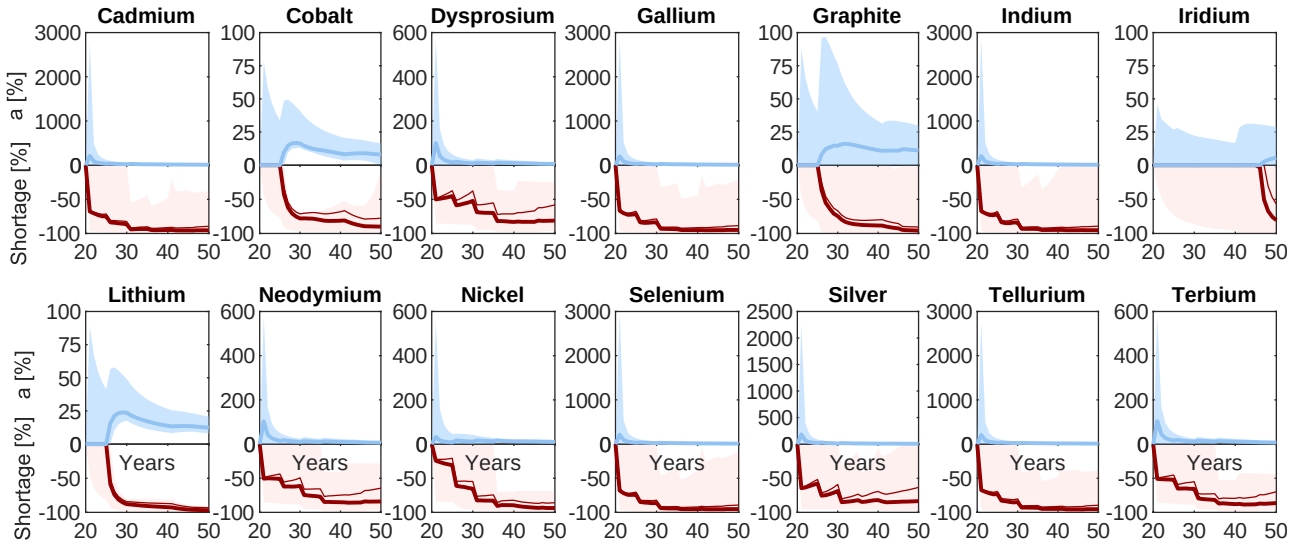



**Figure 1:** Material shortages and required annual production growth rates across 100 evaluated scenarios. The red thick line shows median material shortages (% of annual demand) based on current production rates, while the red thin line reflects shortages assuming a 2.7% annual increase in production. The blue line represents the median of required annual production growth rates. Timeframes: 20 (2020), 30 (2030), 40 (2040), and 50 (2050).

factors may further compound the challenge of securing sufficient raw materials for CETs. In the event of political conflicts, trade restrictions, or economic sanctions, these imbalances could be exacerbated, further reducing the attainable capacity of CETs or driving up their costs.

In Figure 2, the narrow bars above the panels indicate the technology types selected by the model. The findings demonstrate that, due to their unique designs and material requirements, technology types face varying levels of material shortage challenges. While some types are not selected at all, others, such as lithium ferro phosphate batteries, dominate, indicating these designs are strongly favored under materials availability constraints. For the list of technology names, refer to the supplementary information.

The data from Figure 3 underscore the magnitude of the challenge. For materials like lithium, iridium, and terbium, the recycling rates required to meet IAM projections are dramatically higher than current recycling rates. For example, based on median values, by 2050, lithium's recycling rate must reach 325% of its annual production, which indicates the amount of lithium needed for recycling would far exceed what is produced in a single year, pointing to the need for large-scale, long-term strategies for material recovery. This required a massive effort to dismantle existing infrastructure, including outdated technologies, in a feasible and sustainable way.

Materials such as dysprosium, graphite, iridium, and terbium also require substantial increases in recycling rates. For instance, for iridium it should rise from the current 17% to 64%, which highlights the significant gap between current capabilities and future needs.

## Conclusion

This study emphasizes the severe challenges posed by material shortages in the development of CETs, highlighting the urgent need to revise IAM capacity projections and take proactive measures in material production and recycling. The analysis reveals that critical materials such as lithium, nickel, cadmium, indium, and iridium are projected to experience substantial shortages, with some deficits reaching up to 97% of the required demand by 2050, based on IAM projections. For example, lithium shortfalls potentially lead to a deficit of more than 11 TW, which accounts for 94% of the projected battery capacity. Similarly, PV panel deployment could fall short by 1.6 TW (94% of projections) due to the scarcity of materials like cadmium, gallium, and tellurium. The availability of

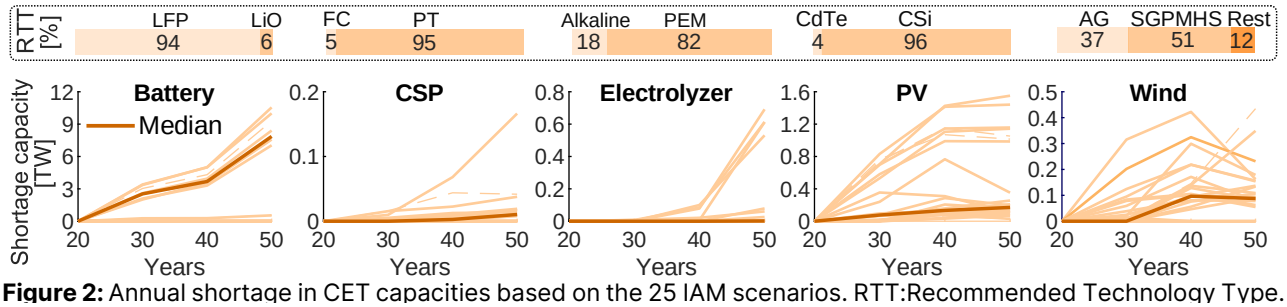



**Figure 2:** Annual shortage in CET capacities based on the 25 IAM scenarios. RTT:Recommended Technology Type.

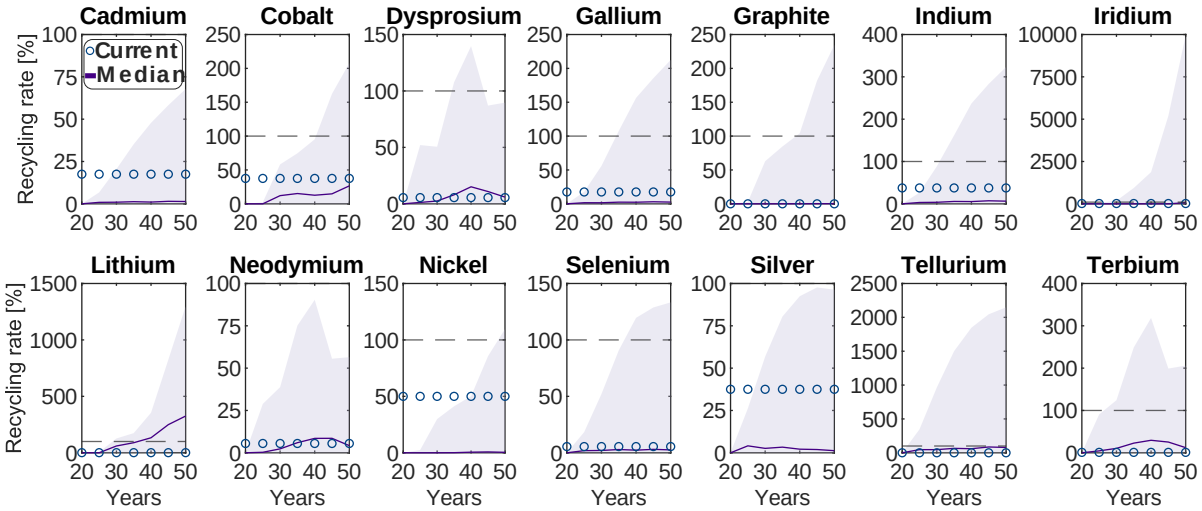



**Figure 3:** Recycling rates required to meet IAM capacity projections. The shaded area represents the range of recycling rates derived from 300 scenarios. Timeframes: 20 (2020), 30 (2030), 40 (2040), and 50 (2050).

materials for electrolyzers, CSP, and wind turbines could also be severely impacted, hindering their development.

To meet the growing material demands for CETs, production rates must increase significantly. Materials such as cadmium, selenium, and tellurium are expected to see a sharp rise in their production rate. However, the pace of production growth may not be able to keep up with this demand, emphasizing the need for immediate and strategic planning to expand mining capacity.

The unequal distribution of raw materials gives countries with domestic access a strategic advantage while disadvantaging others. This underscores the need for a free and open global market, combined with strong international collaboration, to mitigate supply chain risks and ensure that the transition to a sustainable clean energy future is not derailed by geopolitical tensions.

Investing in recycling infrastructure and circular economy initiatives helps to reduce reliance on raw material extraction. For example, by 2050, recycling rates for lithium and iridium will need to reach 325% and 64% of their annual production, respectively – an ambitious target, asking for extra efforts.

Overall, this calls for adjustment of IAMs so as to account for the availability of raw materials, enabling them to provide more realistic guidance for policy makers.

## DIGITAL SUPPLEMENTARY MATERIAL

Supplementary information with record ID: LAPSE:2025.0006 is available in https://psecommunity.org/LAPSE:2025.0006.

## ACKNOWLEDGEMENTS

The authors acknowledge grants PID2021-127713OA-I00, PID2021-123511OB-C33, and PID2021-124139NB-C22 funded by MCIN/AEI/ 10.13039/501100011033 and by "FEDER, UE", grant TED2021-129851B–I00 funded by MCIN/AEI /10.13039/501100011033 by the European Union NextGenerationEU/PRTR, and grant CNS2023-144890 funded by MICIU/AEI/ 10.13039/501100011033 and by the European Union NextGenerationEU/PRTR.

## REFERENCES

1. S. Pauliuk, A. Arvesen, K. Stadler, and E. G. Hertwich, "Industrial ecology in integrated assessment models," Nat Clim Chang, vol. 7, no. 1, pp. 13–20, 2017, doi: 10.1038/nclimate3148.
2. I. Keppo et al., "Exploring the possibility space: taking stock of the diverse capabilities and gaps in integrated assessment models," Environmental Research Letters, vol. 16, no. 5, p. 053006, 2021, doi: 10.1088/1748-9326/abe5d8.
3. D. L. McCollum et al., "Improving the behavioral realism of global integrated assessment models: An application to consumers' vehicle choices," Transp Res D Transp Environ, vol. 55, 2017, doi: https://doi.org/10.1016/j.trd.2016.04.003.
4. M. A. E. van Sluisveld et al., "Aligning integrated assessment modelling with socio-technical transition insights: An application to low-carbon energy scenario analysis in Europe," Technol Forecast Soc Change, vol. 151, p. 119177, 2020, doi: https://doi.org/10.1016/j.techfore.2017.10.024.
5. L. van Beek, J. Oomen, M. Hajer, P. Pelzer, and D. van Vuuren, "Navigating the political: An analysis of political calibration of integrated assessment modelling in light of the 1.5 °C goal," Environ Sci Policy, vol. 133, pp. 193–202, 2022, doi: https://doi.org/10.1016/j.envsci.2022.03.024.
6. D. Huppmann et al., "IAMC 1.5°C Scenario Explorer and Data hosted by IIASA," 2018, Integrated Assessment Modeling Consortium & International Institute for Applied Systems Analysis. doi: 10.22022/SR15/08-2018.15429.
7. F. Rostami, P. Patrizio, L. Jimenez Esteller, C. Pozo Fernandez, and N. MacDowell, "Assessing the Realism of Clean Energy Projections," Energy Environ Sci, p., 2024, doi: 10.1039/D4EE00747F.
8. S. Schlichenmaier and T. Naegler, "May material bottlenecks hamper the global energy transition towards the 1.5 °C target?," Energy Reports, vol. 8, 2022, doi: 10.1016/j.egyr.2022.11.025.
9. S. Carrara, P. Alves Dias, B. Plazzotta, C. Pavel, and P. O. of the E. Union, "Raw materials demand for wind and solar PV technologies in the transition towards a decarbonised energy system," Luxembourg, 2020. doi: 10.2760/160859.
10. N. LePan, "Visualizing the Size of Mine Tailings," Elements. Accessed: Nov. 12, 2023. Available: https://elements.visualcapitalist.com/visualizing-the-size-of-mine-tailings/
11. Mineral commodity summaries 2023, Reston, VA, 2023. Accessed: Apr. 21, 2023. Available: https://pubs.usgs.gov/periodicals/mcs2023/mcs2023.pdf
12. UNEP, "Recycling Rates of Metals - A Status Report," 2011. Accessed: May 04, 2024. Available: https://www.resourcepanel.org/sites/default/files/documents/document/media/e-

book_metals_report2_recycling_130920.pdf

© 2025 by the authors. Licensed to PSEcommunity.org and PSE Press. This is an open access article under the creative commons CC-BY-SA licensing terms. Credit must be given to creator and adaptations must be shared under the same terms. See https://creativecommons.org/licenses/by-sa/4.0/



Systems & Control Transactions

**Research Article - Peer Reviewed Conference Proceeding**
ESCAPE 35 - European Symposium on Computer Aided Process Engineering
Ghent, Belgium. 6-9 July 2025
Jan F.M. Van Impe, Grégoire Léonard, Satyajeet S. Bhonsale,
Monika E. Polańska, Filip Logist (Eds.)

PSE PRESS

# A Modern Portfolio Theory Approach for Chemical Production with Supply Chain Considerations for Efficient Investment Planning

**Mohamad Almoussaoui[a], Dhabia M. Al-Mohannadi[a,b,c]***

[a] Texas A&M University at Qatar, Chemical Engineering Program, Education City, Doha, Qatar
[b] Hamad Bin Khalifa University, College of Science and Engineering, Education City, Doha, Qatar
[c] Texas A&M University, Department of Multidisciplinary Engineering, College Station, Texas, USA
* Corresponding Author: dhabia.al-mohannadi@qatar.tamu.edu.

## ABSTRACT

Commodity chemicals and energy supply chains are an essential part of the hydrocarbon industry in several countries. As these supply chains are susceptible to disruptions caused by various risks, the economies of countries that depend on the hydrocarbon sector as a major source of income might be negatively affected. One major risk is the price fluctuations of the resources used in the multiple stages of the supply chains. Investment decisions in this sector aim to secure the investment portfolio's financial returns against the risk of price fluctuations. This work introduces an adaptation of a portfolio optimization technique, the modern portfolio theory (MPT) to the case of commodity chemicals and energy supply chain investments by considering all supply chain stages in formulating the MPT framework. A case study considering four chemical commodities and three potential importing countries is presented with a sensitivity analysis that studies the impact of changing the costs associated with the several stages of the supply chain on the investment portfolio. Results show the importance of integrating both the chemical production and the shipping stages of the supply chain in developing a portfolio optimization framework and its impact on the optimal investment portfolios. The developed model guides investment planners to target the desired financial returns at a minimum risk.

**Keywords**: Investment Decision, Portfolio Selection, Supply Chain, Modern Portfolio Theory

## INTRODUCTION

Since the outbreak of the COVID-19 pandemic, concerns have risen regarding the importance of sustaining energy supply chains to ensure the energy security of importing countries [1] and the financial security of exporting countries [2]. Such supply chains are susceptible to risks such as economic shocks, geopolitical disruptions, pandemics, etc. [3]. The COVID-19 pandemic has caused the highest energy market volatility [4]. It led to a sudden decrease in demand for energy, chronic disruptions to supply chains, and elevated prices after recovery [5]. Similarly, geopolitical acts and threats could drive the risk of a crash in the prices of natural gas and oil [6]. Fluctuations in the prices of the exported commodity chemicals and fuels or the raw materials used in their production can result in increased financial burdens on importing countries or a significant decrease in exporting countries' profits. The hydrocarbon industry contributes significantly to the financial stability of several countries with significant oil and gas reserves. For example, as the hydrocarbon sector has contributed to over 70% of Qatar's government's total revenue and 80% of the country's total exports since 2014 [7], ensuring the security of this sector against the risk of price fluctuations is a priority for the country. The hydrocarbon industry is very capital-intensive, and the budget for some projects is over one billion US dollars [8]. As investments in this sector require large capital, time, and technology investments, selecting investment portfolios is critical [9]. As such, an investment planning methodology is necessary for the hydrocarbon sector in such countries. Optimizing and diversifying the investment portfolio can help decrease the risk of investment return uncertainty resulting from price

fluctuations. Diversifying the investment portfolio can ensure the security of the hydrocarbon industry's returns as losses from one investment can be compensated by gains from another and portfolio optimization can help in the investment decision-making process as it aims to maximize a portfolio's expected return while minimizing the uncertainty of the return, the portfolio risk [10]. The Modern Portfolio Theory (MPT) developed by Harry Markowitz is an investment portfolio selection tool that aims to guide an investor in determining the optimal investment portfolio [11]. Markowitz formulated a mean-variance optimization problem that results after its solution in a set of Pareto optimal investment portfolios that maximizes the investment portfolio return for a given level of risk, the efficient frontier. In other words, for a portfolio on the efficient frontier, there is no other portfolio with a higher return for a specified level of risk. The theory has been widely used in several fields as a decision-making tool for investment portfolio selection. The Markowitz framework was adapted to optimize the national grain imports by reducing the cost and risk associated with the imports [12]. Due to the price fluctuations of coal, the theory was used to determine the optimal coal purchasing strategy for Taiwan Power Company [13]. The energy security of energy-importing countries also has been studied extensively using the MPT framework. The impact of the fluctuating prices of oil on China's energy import portfolio was studied [14]. Several research works adapted the MPT framework to problems related to the energy security of the exporter. An MPT framework was developed for investment portfolio diversification of major GCC oil-exporting countries [15]. A similar framework was developed to determine the exporting strategy for a natural gas exporting country [16]. The theory was adopted for selecting investment portfolios for the chemical production industry [17, 18]. The decision-making process of hydrocarbon export investments is based on a complex export system. Investors have several options considering the exported chemical commodities, transportation methods, and partner importers. In other words, the problem is of a supply chain scope. The previous adaptations of MPT to the chemical exports problem had several drawbacks: either the development of the framework did not consider a supply chain perspective ignoring the importance of selecting not only the exported commodities but also the partner importers or did not consider the foundations of chemical production and transportation processes This is reflected by disregarding the price fluctuations of all raw materials and utilities used in the export system and considering the price uncertainty of the traded commodities only. A visual representation of the hydrocarbon export problem and the associated price fluctuations is shown in Figure 1. For an exporting country, considering both the production and transportation stages affects the efficient frontier, the set of optimal investment portfolios. To counter the risk of price fluctuations associated with the hydrocarbon exports investments problem, this work develops an MPT framework by considering a supply chain perspective and the foundations of chemical production and transportation as a tool to aid investors in the investment decision-making process. Two efficient frontiers are obtained after solving the Markowitz optimization problem, the first by considering the production stage of the supply chain only and the second by considering both the production and transportation stages.

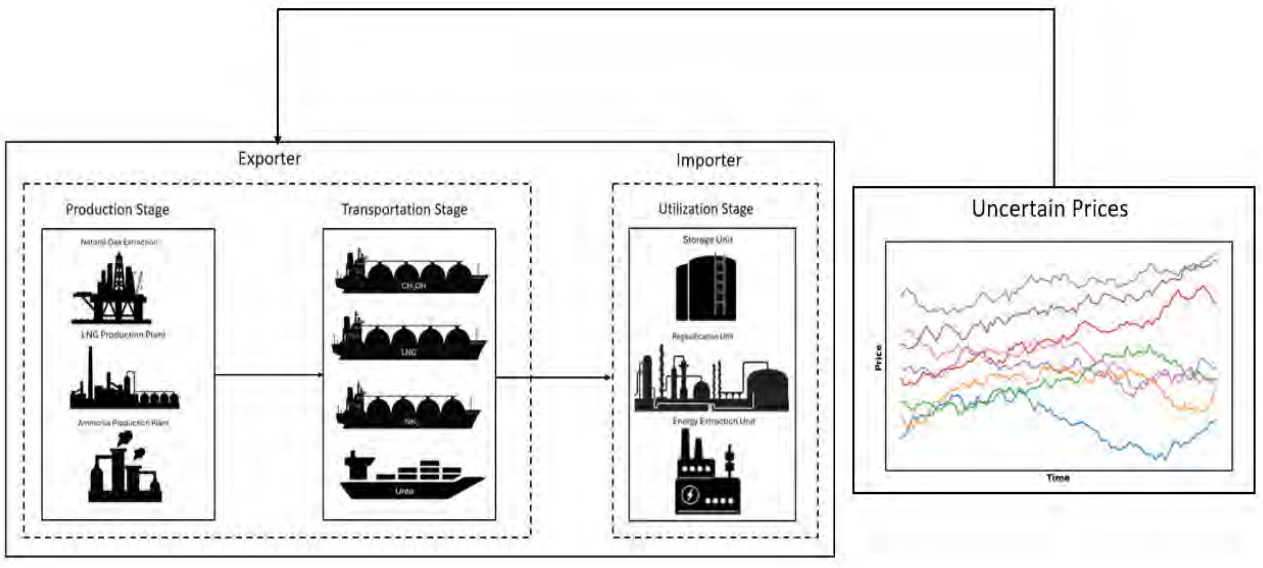



**Figure 1:** The price uncertainty associated with a hydrocarbon export system.

## APPROACH AND PROBLEM STATEMENT

The work aims to develop an MPT framework for energy and commodity chemicals supply chain investments, to determine the investment portfolios with the maximum financial returns at a given level of risk.

Given is a set of commodity chemicals $C = \{c_1, c_2, ..., c_n\}$, $n \in \mathbb{N}$ each produced by a respective production plant from the set $P = \{p_1, p_2, ..., p_n\}$, $n \in \mathbb{N}$. Let $I = \{I_{i,1}, I_{i,2}, ..., I_{i,k_i}\}$, $k_i \in \mathbb{N}$, be the set of potential importing countries of the commodity chemical $c_i$ where $k_i$ is the total number of potential importing countries of $c_i$. $I_{i,j}$ is the j-th importing country of the chemical $c_i$ where j = 1, 2, ...., $k_i$. A supply chain is defined as a combination of a commodity and an importing country. It is represented as $S_{ij} = \{(c_i, I_{i,j})\}$ where i is the index referring to the traded commodity and j is the index referring to the importer of the commodity. The weight of the capital invested in the supply chain asset $S_{i,j}$ is $w_{i,j} \in [0,1]$. The resulting supply chains represent the potential investment assets constituting an investment portfolio. The historical price data for the production plants' inputs and outputs are required. The plant inputs are the raw materials and energy requirements needed to produce the commodity chemical $c_i$, and the latter is the plant output. Further information on the plants' capital, fixed, and variable operating costs is required. Such data ensures the ability to determine the efficient frontier for a chemical production investment problem. Additionally, a transportation mode to export the commodity $c_i$ to the importing country $I_i$ is defined. Information on the distance between the exporter and the importer, the transporting ship type, its speed, capital cost, the bunker fuel, its consumption rate, and cost is required. This information is needed to account for the transportation stage of the supply chain. The total amount of capital to be invested in the supply chain portfolio is given. To be calculated is the return on each supply chain investment over a given period. The variance of the return due to fluctuation of the prices of the supply chain inputs and outputs is calculated over a given period. The standard deviation represents the risk of investing in the asset.

The optimization problem is once formulated considering the production stage of the supply chain only and then by additionally accounting for the transportation stage. Evaluating the optimization problem results in determining the efficient frontier that shows the constituting supply chain investments of an optimal portfolio, their respective return and risk, and the weight of capital allocated for each supply chain investment. The weight reflects the capacity of each production plant $p_i$ and the amount of the commodity $c_i$ that should be exported to the importer $I_i$, using the specified transportation method. The efficient frontier is generated for both cases. The difference between the two obtained efficient frontiers emphasizes the importance of using a supply chain perspective to address the hydrocarbon exports investment selection problem.

A sensitivity analysis is conducted by varying the cost of producing or transporting a commodity, $c_i$, to study the impact of such changes on the efficient frontier's constituting portfolios. The sensitivity analysis can reflect the effect of using new technologies in producing and transporting chemical commodities on the optimal investment portfolios.

## METHODOLOGY

The starting point for formulating the model is the general MPT concepts and equations [19]. Adapting the MPT framework to the commodity chemicals supply chain problem requires calculating each investment portfolio's return and risk. This requires calculating the return on each supply chain investment, $ROI_{supply\ chain,\ year}$, by considering the yearly profit of the supply chain, $Profit_{supply\ chain,\ year}$, and the total capital cost of the supply chain investment, Capital $Cost_{supply\ chain,\ year}$, which are variable over time due to fluctuations in prices as shown in Equation 1:

$$ROI_{supply\ chain,year} = \frac{Profit_{supply\ chain,year}}{Capital\ Cost_{supply\ chain,year}} \forall\ supply\ chain \quad (1)$$

The profit of the supply chain is the supply chain revenue from the sales of the chemical commodity, $Revenue_{supply\ chain}$, after deducting the fixed and variable operating costs and the cost of depreciation designated as Fixed $OPEX_{supply\ chain}$, Variable $OPEX_{supply\ chain}$, and $Depreciation_{supply\ chain}$, respectively, as shown in Equation 2:

$$Profit_{supply\ chain} = Revenue_{supply\ chain} - Fixed\ OPEX_{supply\ chain} - Variable\ OPEX_{supply\ chain} - Depreciation_{supply\ chain} \forall\ supply\ chain \quad (2)$$

However, since it is assumed that the exporter is responsible for the production and shipping stages of the supply chain, both stages contribute to cost calculation as shown in Equation 3, Equation 4, and Equation 5:

$$Fixed\ OPEX_{supply\ chain} = Fixed\ OPEX_{supply\ chain}^{Production} + Fixed\ OPEX_{supply\ chain}^{Shipping} \forall\ supply\ chain \quad (3)$$

Where Fixed $OPEX_{supply\ chain}^{Production}$ and Fixed $OPEX_{supply\ chain}^{Shipping}$ designate the fixed operating costs of the production plant and transporting ship, respectively, accounting for labor and maintenance costs. In Equation 4, Variable $OPEX_{supply\ chain}^{Production}$ and Variable $OPEX_{supply\ chain}^{Shipping}$ designate the variable operating costs of the production plant and transporting ship, respectively. These include the variable costs of raw materials and utilities required for the processing plants and the cost of

shipping fuel.

$$Variable\ OPEX_{supply\ chain} = Variable\ OPEX_{supply\ chain}{}^{Production} + Variable\ OPEX_{supply\ chain}{}^{Shipping}\ \forall\ supply\ chain \quad (4)$$

In Equation 5, $Depreciation_{supply\ chain}{}^{Production}$ and $Depreciation_{supply\ chain}{}^{Shipping}$ designate the costs resulting from the depreciation of the production plant and transporting ship, respectively.

$$Depreciation_{supply\ chain} = Depreciation_{supply\ chain}{}^{Production} + Depreciation_{supply\ chain}{}^{Shipping}\ \forall\ supply\ chain \quad (5)$$

Similarly, the capital cost of a supply chain is the sum of the capital cost of the production plant, $Capital\ Cost_{supply\ chain}{}^{Production}$, and that of the transporting ship, $Capital\ Cost_{supply\ chain}{}^{Shipping}$, as shown in Equation 6:

$$Capital\ Cost_{supply\ chain} = Capital\ Cost_{supply\ chain}{}^{Production} + Capital\ Cost_{supply\ chain}{}^{Shipping}\ \forall\ supply\ chain \quad (6)$$

The weight of the investment capital allocated to each supply chain investment is denoted as $w_{supply\ chain}$. The return of a portfolio, Portfolio Return, is defined as a weighted average of the average return of a supply chain investment over the years, $\overline{ROI_{supply\ chain}}$:

$$Portfolio\ Return = \sum_{supply\ chain} w_{supply\ chain} \times \overline{ROI_{supply\ chain}} \quad (7)$$

The variance of a portfolio is determined as follows:

$$Portfolio\ Variance = \sum_{supply\ chain} w_{supply\ chain} \times Variance\ ROI_{supply\ chain} + 2\sum_{supply\ chain} \rho_{ROI_{supply\ chain}, ROI_{supply\ chain+1}}\ SD_{supply\ chain} SD_{suply\ chain+1} \quad (8)$$

Where $\rho_{ROI_{supply\ chain}, ROI_{supply\ chain+1}}$ is the correlation coefficient between the returns of two supply chain investments and $SD_{supply\ chain}$ is the standard deviation of the investment return. The risk of a portfolio, Portfolio Risk, is defined as the standard deviation of the portfolio's variance:

$$Portfolio\ Risk = \sqrt{Portfolio\ Variance} \quad (9)$$

After developing an MPT framework for the commodity chemicals and energy supply chain problem, the multi-objective optimization problem is presented as follows:

$$\begin{aligned} &Maximize\ Portfolio\ Return \\ &Minimize\ Portfolio\ Risk \\ &Subject\ to\ \sum_{supply\ chain} w_{supply\ chain} = 1 \end{aligned} \quad (10)$$

The problem evaluation results in determining the efficient frontier, a set of Pareto optimal investment portfolios.

As a plant can produce a commodity exported to multiple countries and a ship can transport the commodity to several destinations, an investor should aim for the least number of processing plants and transporting ships required which is considered in the developed model. Moreover, as the supply chains are defined specifically with a single importing country, the capital cost associated with the production and transportation stages of the supply chain is calculated based on the demand share of the importing country.

## CASE STUDY

A case study is designed to test the developed methodology. The four commodities considered in the case study are methanol, ammonia, urea, and LNG, all of which can be produced from natural gas. It is assumed that the exporter is a country in the Middle East with abundant natural gas reserves and the considered importers are India, China, and Singapore. Chemical commodities are to be transported to destinations using ships. The case study considers 12 possible supply chain investments, which is the maximum number of possible combinations of commodities and importing countries. These supply chains are: (Methanol, India), (Methanol, China), (Methanol, Singapore), (Ammonia, India), (Ammonia, China), (Ammonia, Singapore), (Urea, India), (Urea, China), (Urea, Singapore), (LNG, India), (LNG, China), and (LNG, Singapore). The work will be based on the period between 2018 and 2023. The import demand of the countries for these chemical commodities from the exporter is obtained from the World Integrated Trade Solution database of the World Bank [20]. The historical prices of raw materials, utilities, and exported commodities obtained from the Intratec database were used in this case study [21]. After calculating the return on each supply chain investment and its associated risk, the multi-objective optimization problem presented by Equation 10 is solved twice to determine the efficient frontier: first by considering only the costs of the production stage of the supply chain and then by considering the costs associated with both the production and shipping stages. Hence, two efficient frontier curves are determined. Python's Gurobi solver was used to evaluate the optimization problem using the epsilon constraint method [22].

While Figure 2 shows the efficient frontier determined only when considering the production stage of the supply chain, Figure 3 shows the efficient frontier determined when considering both the production and transportation stages. The constituting investment portfolios of the efficient frontier curves of Figure 2 and Figure 3 are shown in Table 1 and Table 2 respectively.

As shown, developing an MPT framework based on all supply chain stages increased the number of optimal

portfolios from five to seven, decreased the maximum possible return due to accounting for transportation costs, and decreased the portfolio risk range due to the increased diversification of the investment portfolios. The constituting supply chains of the optimal portfolios differ between the two efficient frontier curves obtained due to the effect of transportation costs in altering the attractiveness of the supply chain investments. The number of optimal assets in the optimal portfolios of the efficient frontier developed based on the production stage only ranged between one and three. However, introducing a supply chain perspective while developing the MPT framework increased this number where it ranged between one and nine. As such, a supply chain perspective offers a larger number of optimal investment export portfolio options. The portfolio with the highest return in both cases is a one-asset portfolio. It is the supply chain exporting methanol to Singapore which is the asset with the highest return on investment.

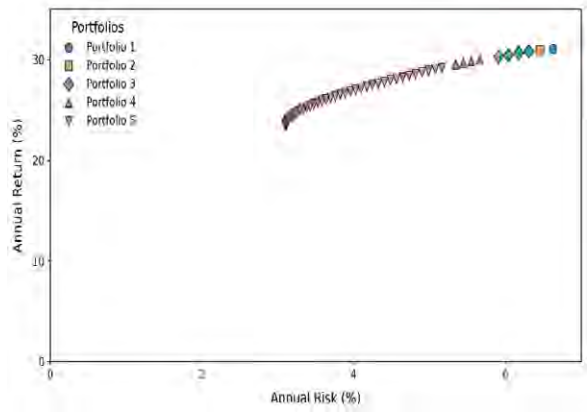



**Figure 2:** Commodity chemicals and energy production processes efficient frontier.

**Table 1:** The constituting investments of the commodity chemicals and energy production processes efficient frontier

| Portfolio | Constituents |
|---|---|
| Portfolio 1 | (Methanol, Singapore) |
| Portfolio 2 | (Methanol, China), (Methanol, Singapore) |
| Portfolio 3 | (Methanol, China), (Methanol, Singapore), (LNG, China) |
| Portfolio 4 | (Methanol, Singapore), (LNG, China) |
| Portfolio 5 | (Methanol, Singapore), (Urea, China), (LNG, China) |

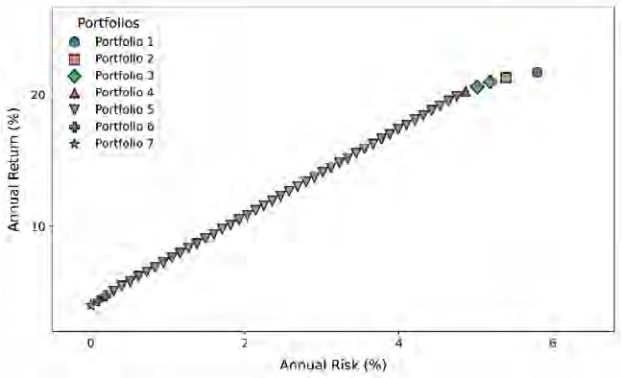



**Figure 3:** Commodity chemical and energy supply chains efficient frontier.

**Table 2:** The constituting investments of the commodity chemicals and energy supply chains efficient frontier.

| Portfolio | Constituents |
|---|---|
| Portfolio 1 | (Methanol, Singapore) |
| Portfolio 2 | (Methanol, India), (Methanol, Singapore) |
| Portfolio 3 | (Methanol, India), (Methanol, China), (Methanol, Singapore), (Ammonia, India) |
| Portfolio 4 | (Methanol, China), (Methanol, Singapore), (Ammonia, India) |
| Portfolio 5 | (Methanol, China), (Methanol, Singapore), (Ammonia, India), (Urea, India), (Urea, China) |
| Portfolio 6 | (Methanol, China), (Methanol, Singapore), (Ammonia, India), (Urea, India), (Urea, China), (Urea, Singapore) |
| Portfolio 7 | (Methanol, India), (Methanol, China), (Methanol, Singapore), (Urea, India), (Urea, China), (Urea, Singapore), (LNG, India), (LNG, China), (LNG, Singapore) |

While LNG production was a constituent of three out of five optimal portfolios in the chemical production efficient frontier, it is only a constituent of one portfolio in the supply chain perspective efficient frontier, the portfolio with the lowest risk. This is a result of the high transportation costs associated with LNG shipping. Methanol was present in all optimal portfolios of the two efficient frontier curves as investments in methanol exports are of the highest return. The production of ammonia is not considered an attractive investment based on the production stage efficient frontier. Similarly, urea is only present in Portfolio 5 of the production stage efficient frontier due to the lower return of this commodity compared to methanol and LNG. For the supply chain perspective efficient frontier, the first two portfolios with the highest returns

include only methanol supply chains. The export of ammonia and urea becomes attractive for portfolios of lower risk and return. The general trend in both cases is that decreasing the risk requires increasing the number of portfolio constituents which reflects the ability of portfolio diversification to decrease the return uncertainty, the investment portfolio risk.

The sensitivity analysis considers four alterations of the base case: twice by decreasing the production capital costs of the considered commodities, and twice by decreasing the shipping capital costs. The analysis shows that reducing all commodities' production or transportation costs increases the number of optimal supply chain portfolios as shown in Table 3. As such, using technologies with lower costs will increase the number of options an investor can consider. The constituting optimal supply chains of the five cases considered in the sensitivity analysis were different. While in the base case supplying LNG to India was an optimal investment in one portfolio only, reducing the transportation cost by 20% made this investment present in five optimal portfolios increasing its attractiveness.

**Table 3:** The impact of the changes in the cost on the number of optimal supply chain investment portfolios

| Case | Number of Optimal Portfolios of the Efficient Frontier |
|---|---|
| Base case | 7 |
| 20% decrease in production costs | 11 |
| 80% decrease in production costs | 12 |
| 20% decrease in transportation costs | 11 |
| 80% decrease in transportation costs | 11 |

## CONCLUSION

In response to the risk of price fluctuations affecting the financial security of hydrocarbon commodities exporters, a framework of MPT, an investment portfolio selection tool, has been developed for the energy and commodity chemicals supply chain problem. The developed model can determine the optimal investment options in terms of the traded commodities, capacities of production plants, partner importers, and the supply volume to each country. As the previous adaptation of MPT to the hydrocarbon exports field did not consider either a supply chain perspective or was not developed based on chemical production and transportation foundations, this work shows the impact of using a supply chain perspective in developing an MPT framework on the portfolio selection process. The developed MPT framework was applied to a case study by considering four commodities with their respective transportation modes and three potential importing countries. The results suggest that the developed framework can provide additional insight into what previous work has shown and act as a decision-making tool to aid investors in the commodity chemicals and energy export sector.

## ACKNOWLEDGEMENTS

The authors have no acknowledgments to disclose.

## REFERENCES

1. Liu, S.Q., Huang, X., Li, X., Masoud, M., Chung, S., Yin, Y. How is China's energy security affected by exogenous shocks? Evidence of China-US trade dispute and COVID-19 pandemic. *Discov Energy* 1 (2021). https://doi.org/10.1007/s43937-021-00002-6
2. Szczygielski, J. J., Brzeszczyński, J., Charteris, A., Bwanya, P. R. The COVID-19 storm and the energy sector: The impact and role of uncertainty. *Energy Econ.* 109 (2022). https://doi.org/10.1016/j.eneco.2021.105258
3. Energy Technology Perspectives 2023. International Energy Agency (2023).
4. Shaikh, I. Impact of COVID-19 pandemic on the energy markets. *Econ Change Restruct* 55: 433–484 (2021). https://doi.org/10.1007/s10644-021-09320-0
5. Energy Technology Perspectives 2024. International Energy Agency (2024).
6. Apergis, N., Fahmy, H. Geopolitical risk and energy price crash risk. *Energy Econ.* 140 (2024). https://doi.org/10.1016/j.eneco.2024.107975
7. International Trade Administration https://www.trade.gov/country-commercial-guides/qatar-market-challenges.
8. Bret-Rouzaut, N. Economics of Oil and Gas Production. In The Palgrave Handbook of International Energy Economics. Palgrave Macmillan Cham, (2022).
9. Lin, Z., Ji, J. The portfolio selection model of oil/gas projects based on real option theory. *ICCS* (2007). https://doi.org/10.1007/978-3-540-72588-6_151
10. Markowitz, H. M. Portfolio Selection: Efficient Diversification of Investments. Yale University Press (1971).
11. Markowitz, H. PORTFOLIO SELECTION*. *J. Finance* 7: 77-91 (1952). https://doi.org/10.1111/j.1540-6261.1952.tb01525.x
12. Karakoc, D.B., Konar, M. Optimization of national grain imports to balance risk and return: a portfolio theory approach. *Environ. Res.: Food Syst.* 1

(2024). https://doi.org/10.1088/2976-601X/ad22d1
13. Huang, Y.-H., Wu, J.-H. A portfolio theory based optimization model for steam coal purchasing strategy: A case study of Taiwan Power Company. *J. Purch. Supply Manag.* 22: 131-140 (2016). https://doi.org/10.1016/j.pursup.2016.03.001
14. Wu, G., Liu, L.-C., Wei., Y.-M. Comparison of China's oil import risk: Results based on portfolio theory and a diversification index approach. *Energy Policy* 37:3557 - 3565 (2009). https://doi.org/10.1016/j.enpol.2009.04.031
15. Bollino, C. A., Galkin, P. Energy security and portfolio diversification: conventional and novel perspectives. *Energies* (2021). https://doi.org/10.3390/en14144257
16. Nowrouzi, A., Panahi, M., Ghaffarzadeh, H., Ataei., A. Optimizing Iran's natural gas export portfolio by presenting a conceptual framework for non-systematic risk based on portfolio theory. *Energy Strat. Rev.* 26 (2019). https://doi.org/10.1016/j.esr.2019.100403
17. Shehab, S., Al-Mohannadi, D.M., Linke, P. Chemical production process portfolio optimization. *Chem. Eng. Res. Des.* 167: 207-217 (2021). https://doi.org/10.1016/j.cherd.2021.01.013
18. Shehab, S., Linke, P., Al-Mohannadi, D.M. Chemical production process portfolio optimization considering resource integration. *Chem. Eng. Res. Des.* 179: 285-297 (2022). https://doi.org/10.1016/j.cherd.2022.01.022
19. J. C. Francis and D. Kim, Assessing Risk. In: Modern Portfolio Theory: Foundations, Analysis, and New Developments. John Wiley & Sons, Incorporated (2013)
20. World Integrated Trade Solution. https://wits.worldbank.org/.
21. Intratec. https://www.intratec.us/.
22. Gurobi Optimization. https://www.gurobi.com/

© 2025 by the authors. Licensed to PSEcommunity.org and PSE Press. This is an open access article under the creative commons CC-BY-SA licensing terms. Credit must be given to creator and adaptations must be shared under the same terms. See https://creativecommons.org/licenses/by-sa/4.0/



Systems & Control Transactions

**Research Article - Peer Reviewed Conference Proceeding**
ESCAPE 35 - European Symposium on Computer Aided Process Engineering
Ghent, Belgium. 6-9 July 2025
Jan F.M. Van Impe, Grégoire Léonard, Satyajeet S. Bhonsale,
Monika E. Polańska, Filip Logist (Eds.)

PSE PRESS

# Optimization models and algorithms for the Unit Commitment problem

**Javal Vyas[a], Carl Laird[a], Ignacio E. Grossmann[a,*], Ricardo M. Lima[b], Iiro Harjunkoski[c], Jan Poland[d]**

[a] Department of Chemical Engineering, Carnegie Mellon University, Pittsburgh, PA 15213, USA
[b] King Abdullah University of Science and Technology, Thuwal 23955-6900, Saudi Arabia
[c] Hitachi Energy Research, Havellandstr. 10-14, Mannheim 68309, Germany
[d] Hitachi Energy Research, Segelhofstr. 7, 5405 Baden-Dättwil, Switzerland
* Corresponding Author: grossmann@cmu.edu.

## ABSTRACT

The unit commitment problem determines the optimal strategy to meet the electricity demand at minimum cost by committing power generation units at each point of time. Solving the unit commitment problem gives rise to a challenging optimization problem due to its combinatorial complexity and potentially long solution time requirements. Our proposed solution approach utilizes a decomposition method in conjunction with alternative models from the EGRET library. Results of this decomposition approach tested against four benchmarking systems show that significant computational speed ups are achieved.

**Keywords**: Scheduling, Energy Systems, Optimization, Rolling Horizon Optimization

## BACKGROUND

The Unit Commitment (UC) problem is a foundational problem in the field of power systems. This problem tackles the decision making for the operation of the grid, defining when to switch on or off generators, and defining their power production levels to meet the forecasted energy demand. Initially it was solved using dynamic programming [1], which moved to a more sophisticated version using the heuristics based on Lagrangean Relaxation and then to mixed-integer linear programming (MILP) formulations[2]. This problem is usually solved for the day-ahead unit commitments, and bids are placed by the operator, the downside to this is that the operator has at most around 3 hours to solve the model and analyze the bids of which the most time is consumed in data verification, network analysis. Thus, the solution time requirement for solving the UC problem should be no more than 10-15 minutes. In practice, the UC problem must be solved repeatedly throughout the day, and the practical time window for the entire decision-making process is often around 20-30 minutes. This creates a stringent need for a faster solution approach. As the number of generation units increases due to the smaller distributed electricity resources (often solar and wind), this also increases the problem complexity significantly.

## PROBLEM STATEMENT

In the context of an electrical grid comprising multiple generation units, this study addresses the security constrained unit commitment (SCUC) problem, which also considers power grid transmission line limitations and other operational constraints such as reserve requirements. The objective is to determine the optimal schedule for generation units over a defined time horizon. Here we deal with the most common day-ahead unit commitment problem, and thus the time horizon remains 24 hours with hourly intervals. The grid's configuration includes the operational parameters of each generation unit, network topology, transmission line limits, and the forecasted energy demands at each node. The aim is to minimize the total generation cost, while satisfying to the energy balance constraints at each node, transmission line capacity limits, and operational limits of the generation units.

As the problem size is expected to rapidly grow due to both the increased number of generation units, as well as a trend to move to 15-minute time intervals, this work specifically focuses on efficient modeling and solution of a large-scale SCUC problem. It excludes considerations of uncertainties associated with renewable energy

sources, as well as the inclusion of energy storage. Here it is assumed that the fuel sources for all generators are non-renewable and thus fully dispatchable.

## PROPOSED METHODOLOGY

Given the extensive body of research on UC problem, this study leverages established tools and methodologies from the literature. We employ the open-source software package EGRET[3], which provides a comprehensive framework for UCP by offering 41 different model formulations drawn from the existing literature.

Among these formulations, we focus on two specific categories of models: those developed by Morales-España et al. [4], Knueven et al. [5], known for their competitive computational performance, and the models identified by Knueven et al. [3], classified as the "Tight" and "Compact" formulations based on their efficiency in computational studies.

However, these models often struggle to close the optimality gap within a reasonable time limit, when applied to larger, more complex systems. To address this limitation, we propose the use of a shrinking horizon method.

### Optimization models

To expand on the available models from the literature, we briefly examine the key characteristics and improvements introduced by each model:

a. Morales-España model (MLR): Building upon the foundational model developed by Carrion and Arroyo[6], the Morales-España model introduces tighter bounds on generation production. The proposed reformulation of the MILP model is both tight and compact, thus making it computationally competitive.

b. Knueven Ostrowski Watson model (KOW): The KOW model refines the Morales-España model by tightening the formulations of both piecewise linear production costs and start-up costs. The proposed model aggregates the thermal generators with identical characteristics into a single unit which reduces the redundancy in search space.

c. Tight Model (T): The tight model, akin to the KOW model improves on the tightness by enhancing the generation limits, tight start-up cost formulation, and it also uses two period ramping from the Damci Kurt et al. [7]. The tight model does lose on the compactness. Here the tightness of the model refers to the search space a solver needs to explore to find the optimal solution. Tighter models would have reduced search space.

d. Compact model (Co): The Compact model, is similar to the MLR model, with the difference being two period ramping from Damci Kurt et. al. [7] and improved reserve production. This formulation loses a bit on the tightness but is compact. Here the compactness of the model refers to the model size. A compact model has fewer number of variables and constraints.

### Shrinking Horizon Method

The Shrinking Horizon method was introduced by Balasubramanian and Grossmann[8], is an iterative method designed to improve computational tractability of multiperiod MILP models, particularly for large-scale systems. In this approach, the time horizon is divided into overlapping windows. During the first iteration, a window spanning from time t=1 to t=h is defined, where binary decision variables are active. For the remaining time-periods t=h+1 to t=n, the binary variables are relaxed. The model is solved within this window, and the binary decisions are recorded.

In subsequent iterations, the binary decisions for the previous window are fixed, and the window is advanced to t=h+1 to t=2h. This process is repeated iteratively, shifting the window forward until the entire time horizon is covered. This method allows for a more manageable and efficient solution process as illustrated in Figure 1.

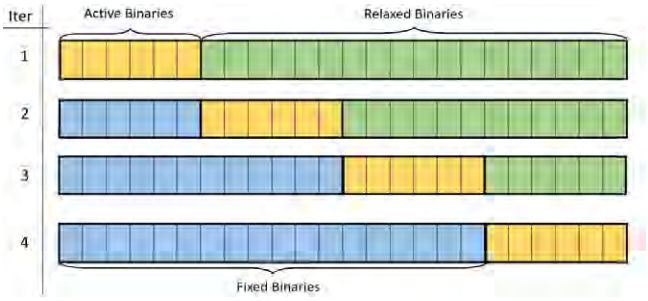



**Figure 1.** Shrinking Horizon Method

The Shrinking Horizon method inherently relies on solving a sequence of optimization problems over progressively shorter horizons, where future time periods are relaxed to facilitate computational tractability. However, the effectiveness of this approach depends on the quality of these relaxations, loose relaxations can lead to poor bounds, increased solution time, and suboptimal intermediate decisions.

Tight Model, mentioned to have the tightest relaxation amongst formulations in the UC literature [3] is particularly well-suited for the Shrinking Horizon method. The tight relaxations offer stronger bounds at each iteration and thus enhances the pruning efficiency of branch-and-cut algorithm, reducing the number of nodes explored in the tree search. Thus, the solvers can converge faster to a high-quality solution.

Furthermore, the Tight model mitigates the myopic effects of the Shrinking Horizon method by ensuring the relaxed future decisions remain closer to their integer counterparts. This reduces the risk of infeasibilities or drastic corrections in subsequent iterations, leading to a stable and efficient optimization process. By leveraging

the Tight Model within the Shrinking Horizon framework, the full computational potential of modern off-the-shelf solvers can be effectively realized.

## CASE STUDY

In this section, we present the results of applying the Shrinking Horizon method across various benchmark case studies, including IEEE118, WP2383, SP3120, and CASE6468RTE, each representing a system of varying size and complexity (Table 1). These case studies range from IEEE118, a relatively small system with 17 generating units, to the largest system, CASE6468RTE, containing 1181 units. 20 instances for each case study using a proprietary code by our collaborators at Hitachi Energy[9]. The analysis focuses on comparing the performance of the Shrinking Horizon method with the traditional monolithic approach, evaluating both computational speedup and solution quality in terms of objective deviation.

All case studies in the monolithic approach were solver to 0.01% optimality gap, except for CASE6468RTE, which was solved to a 1% gap and time limit of 3600

**Table 1:** Network Topology

| Case name | Nodes (Buses) | Lines | Generating Units |
|---|---|---|---|
| IEEE118 | 118 | 179 | 17 |
| WP2383 | 2383 | 2896 | 293 |
| SP3120 | 3120 | 3693 | 452 |
| CASE6468RTE | 6468 | 9000 | 1181 |

**Table 2:** Case6468RTE Analysis

| | Compact Model | | KOW Model | | MLR Model | | Tight Model | |
|---|---|---|---|---|---|---|---|---|
| | Optimalilty Gap % | Speedup factor | Optimalilty Gap % | Speedup factor | Optimalilty Gap % | Speedup factor | Optimalilty Gap % | Speedup factor |
| Min | **0.0000** | **0.5312** | **0.0000** | 0.4834 | **0.0000** | 0.3776 | **0.0000** | 0.4386 |
| Median | 4.2662 | 0.9455 | 6.0975 | 1.7521 | 5.0206 | 0.9491 | **4.1889** | **1.9803** |
| Max | 80.5953 | 1.8351 | 75.7198 | **4.2460** | 71.9478 | 1.9836 | **71.1481** | 2.8829 |
| Std | 17.8190 | 0.3989 | 24.6893 | 0.8674 | 20.6174 | 0.4739 | 20.1230 | 0.6995 |

**Table 3:** SP3120 Analysis

| | Compact Model | | KOW Model | | MLR Model | | Tight Model | |
|---|---|---|---|---|---|---|---|---|
| | Optimalilty Gap % | Speedup factor | Optimalilty Gap % | Speedup factor | Optimalilty Gap % | Speedup factor | Optimalilty Gap % | Speedup factor |
| Min | 0.0006 | 0.4002 | **0.0001** | 0.5539 | 0.0012 | 0.4611 | 0.0149 | **0.6022** |
| Median | **0.0766** | 0.6839 | 0.1967 | 1.2206 | 0.1069 | 0.7399 | 0.1785 | **1.3568** |
| Max | 100.0 | 2.2878 | 0.7198 | 3.9246 | **0.5909** | 2.9072 | 0.6640 | **4.0035** |
| Std | 22.325086 | 0.5263 | 0.1934 | 0.9948 | 0.1961 | 0.6610 | 0.1997 | 1.0178 |

**Table 4:** WP2383 Analysis

| | Compact Model | | KOW Model | | MLR Model | | Tight Model | |
|---|---|---|---|---|---|---|---|---|
| | Optimalilty Gap % | Speedup factor | Optimalilty Gap % | Speedup factor | Optimalilty Gap % | Speedup factor | Optimalilty Gap % | Speedup factor |
| Min | 0.0021 | 0.4455 | 0.0025 | **0.5468** | 0.0021 | 0.4611 | **0.0012** | 0.4653 |
| Median | **0.0594** | 0.6891 | 0.0651 | **1.1884** | 0.0621 | 0.7399 | 0.0792 | 0.8688 |
| Max | 0.2087 | 2.0498 | 0.2433 | **3.6665** | **0.1266** | 2.9072 | 0.2073 | 3.4818 |
| Std | 0.0592 | 0.4092 | 0.067 | 0.8085 | 0.0451 | 0.6443 | 0.0593 | 0.7771 |

**Table 5:** IEEE118 Analysis

| | Compact Model | | KOW Model | | MLR Model | | Tight Model | |
|---|---|---|---|---|---|---|---|---|
| | Optimalilty Gap % | Speedup factor | Optimalilty Gap % | Speedup factor | Optimalilty Gap % | Speedup factor | Optimalilty Gap % | Speedup factor |
| Min | 0.0000 | 0.4044 | **0.0000** | 0.5568 | **0.0000** | **0.6685** | 0.0000 | 0.5058 |
| Median | 0.0002 | 1.0759 | **0** | **2.3391** | **0** | 1.8660 | 0.0185 | 1.4557 |
| Max | 5.7381 | 2.3007 | **1.6808** | **11.0642** | **1.6808** | 3.7002 | 4.3298 | 5.5728 |
| Std | 1.5072 | 0.5464 | 0.3894 | 2.2481 | 0.4074 | 0.9062 | 1.3254 | 1.2035 |

*** Best** values are bold and underlined. Second best values are underlined

seconds. For most part of the CASE6468RTE case study in the monolithic approach, the solver timed out with a median optimality gap of nearly 5%. Notably, the Shrinking Horizon method was solved for 0% optimality gap for each iteration across all case studies, except for CASE6468RTE, where each iteration was solved to 1% optimality gap with a time limit of 3600 seconds per iteration.

The computational study was conducted on a Linux machine equipped with 8 Intel Xeon Gold 6234 CPUs, operating at 3.30 GHz with a total of 8 hardware threads and 1 TB of RAM, all running within an Ubuntu environment. The models were constructed using EGRET's model library and solved with Gurobi v9.5.1 as the solver.

The speedup factor is calculated as:

$$speedup\ factor = \frac{solution\ time\ with\ monolithic\ model}{solution\ time\ with\ SH\ method}$$

The speedup factor reflects the efficiency gained by applying the shrinking horizon method. A factor greater than 1 suggests that the SH method is less effective than solving the problem as a whole.

Similarly, the objective deviation factor is calculated as:

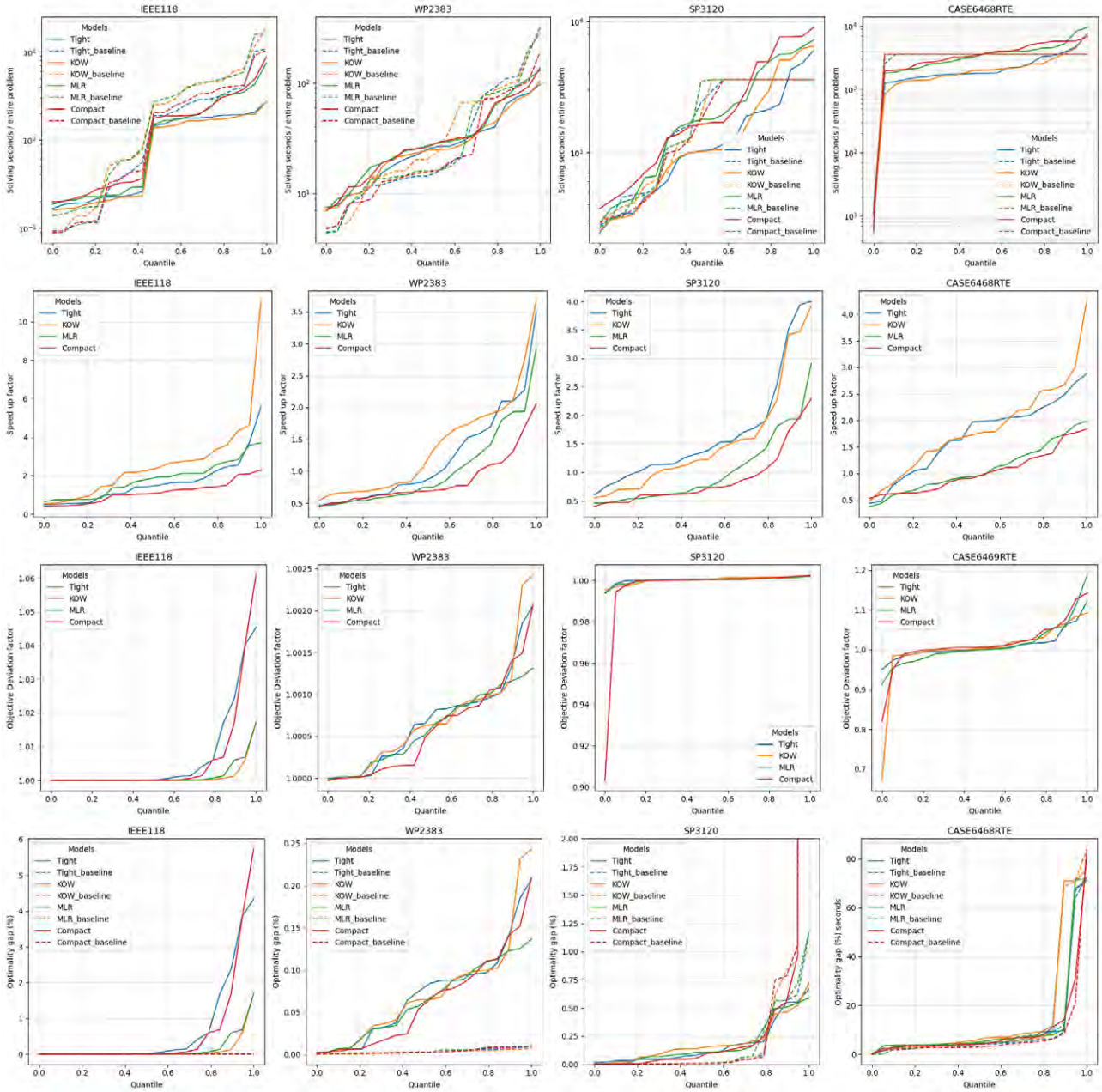
$$Obj\ deviation\ factor\ \% = \frac{Obj\ value\ w/SH}{Obj\ value\ w/o\ SH}$$

This factor behaves conversely to the speedup factor: a higher objective deviation factor indicates a greater deviation from the optimal solution, meaning the SH method is less effective and results in a compromise on the objective value.

Similarly, a higher optimality gap signifies a larger deviation from the optimal solution, implying a greater trade-off in solution quality for the computational efficiency achieved with the shrinking horizon method.

The results demonstrate that the solving times for the shrinking horizon method are consistently lower, and in some cases, significantly lower, for the KOW and Tight models across most case studies (Figure 2). This indicates that these models are more effective under the shrinking horizon method compared to other models. As

**Figure 2.** Casewise analysis of models




a result, they emerge as the preferred formulations for achieving the best speedups.

Additionally, these models maintain near-optimal performance, with minimal compromise on the objective value. For example, the maximum median deviation in the objective value is approximately 0.25% for both the Tight and KOW models for all other cases except case6468rte where the median deviation is 4.18% for Tight model while KOW has 4.26% as the median deviation, demonstrating their ability to balance computational efficiency with solution accuracy.

The advantage of these models becomes even more pronounced when applied to large case studies, where their efficiency and reliability provide substantial benefits. This highlights their suitability for scaling to more complex or computationally demanding scenarios.

## CONCLUSION

In this study, we have proposed and validated a novel approach to solving the UC problem by integrating the Tight, KOW, MLR and compact model with a Shrinking Horizon method.

Our analysis of 20 random instances for each case

study further confirmed the Tight and KOW model's stability and computational efficiency, particularly excelling in larger systems like CASE6468RTE. These results demonstrate that the Tight and KOW model with the Shrinking Horizon method are effective strategies for efficiently solving large-scale UCPs while ensuring computational speedups while not losing much on the solution quality.

Future research should explore this approach's scalability in more complex grid scenarios involving renewable energy sources, storage systems, and uncertainties. Additionally, investigating alternative decomposition techniques could further enhance its performance and applicability.

## ACKNOWLEDGEMENTS

The authors would like to acknowledge the financial support for this research from Hitachi Energy Research and the Center for Advanced Process Decision-making at Carnegie Mellon University.

## REFERENCES

1. O'Neill, R. P., Dautel, T., & Krall, E. (2011). Recent ISO software enhancements and future software and modeling plans. Federal Energy Regulatory Commission, Tech. Rep.
2. Snyder, W. L., Powell, H. D., & Rayburn, J. C. (1987). Dynamic programming approach to unit commitment. IEEE Transactions on Power Systems, 2(2), 339-348.
3. Knueven, B., Ostrowski, J., & Watson, J. P. (2020). On mixed-integer programming formulations for the unit commitment problem. INFORMS Journal on Computing, 32(4), 857-876.
4. Morales-España, G., Latorre, J. M., & Ramos, A. (2013). Tight and compact MILP formulation for the thermal unit commitment problem. IEEE Transactions on Power Systems, 28(4), 4897-4908.
5. Knueven, B., Ostrowski, J., & Watson, J. P. (2017). Exploiting identical generators in unit commitment. IEEE Transactions on Power Systems, 33(4), 4496-4507.
6. Carrión, M., & Arroyo, J. M. (2006). A computationally efficient mixed-integer linear formulation for the thermal unit commitment problem. IEEE Transactions on power systems, 21(3), 1371-1378.
7. Damcı-Kurt, P., Küçükyavuz, S., Rajan, D., & Atamtürk, A. (2016). A polyhedral study of production ramping. Mathematical Programming, 158, 175-205.
8. Balasubramanian, J., & Grossmann, I. E. (2004). Approximation to multistage stochastic optimization in multiperiod batch plant scheduling under demand uncertainty. Industrial & engineering chemistry research, 43(14), 3695-3713.
9. Harjunkoski, I., Giuntoli, M., Poland, J., & Schmitt, S. (2021, October). Matheuristics for Speeding Up the Solution of the Unit Commitment Problem. In 2021 IEEE PES Innovative Smart Grid Technologies Europe (ISGT Europe) (pp. 01-05). IEEE.

© 2025 by the authors. Licensed to PSEcommunity.org and PSE Press. This is an open access article under the creative commons CC-BY-SA licensing terms. Credit must be given to creator and adaptations must be shared under the same terms. See https://creativecommons.org/licenses/by-sa/4.0/



Systems & Control Transactions

**Research Article - Peer Reviewed Conference Proceeding**
ESCAPE 35 - European Symposium on Computer Aided Process Engineering
Ghent, Belgium. 6-9 July 2025
Jan F.M. Van Impe, Grégoire Léonard, Satyajeet S. Bhonsale,
Monika E. Polańska, Filip Logist (Eds.)

PSE PRESS

# Development of a hybrid, semi-parametric Simulation Model of an AEM Electrolysis Stack Unit for large-scale System Simulations

**Isabell Viedt[a,c]*, Michel Große (né Mock)[a,c], and Leon Urbas[a,b,c]**

[a] Technische Universität Dresden, Process-to-Order Group, Process Systems Engineering Group
[b] Technische Universität Dresden, Process-to-Order Group, Chair of Process Control Systems
[c] Technische Universität Dresden, Process-to-Order Group, Process-to-Order (P2O) Lab Learning Factory
* Corresponding Author: isabell.viedt@tu-dresden.de.

## ABSTRACT

A key technology for integrating fluctuating renewable energy into the process industry is the production of green hydrogen through water electrolysis plants. Scaling up electrolysis plant capacity remains a significant challenge for the renewable energy transition. System simulation of large-scale electrolysis plants can support process design, monitoring, optimization, and maintenance scheduling. Hybrid modeling methods are promising for improving simulation reliability by combining process knowledge with process data, addressing gaps in understanding of the underlying processes. These hybrid, semi-parametric models have shown improved accuracy than purely mechanistic models. This study develops a hybrid, semi-parametric model for an anion exchange membrane electrolysis (AEMEL) stack unit. Parameters such as heat loss and heat transfer, which cannot be directly measured, are estimated using real process data. Sensors provide data on lye tank temperature, outlet temperature, and flow rate, enabling estimation of heat transfer coefficients and losses. The hybrid model is validated against operational data from different load settings of the AEMEL stack unit. To test its scalability, a large-scale electrolysis plant configuration is simulated, comprising multiple AEMEL stack units, a water supply module. Performance accuracy and efficiency of the hybrid model are compared with the mechanistic model. This hybrid model lays the foundation for future use in efficient system simulations with surrogate models, potentially enhancing large-scale electrolysis plant performance and renewable energy integration.

**Keywords**: Hydrogen, Modelling and Simulations, System Simulation, Hybrid Modeling, Modular Plants

## INTRODUCTION & BACKGROUND

A crucial technology for integrating variable renewable energy into the process industry is the production of green hydrogen through water electrolysis. Scaling-up electrolysis plant capacity remains a significant challenge in facilitating a successful transition to renewable energy. One potential pathway to successfully scale-up the hydrogen production is the numbering-up of electrolyzer systems using modular plant concepts, according to VDI 2776 [1]. This approach allows for the combination of different electrolysis technologies and electrolyzer scales within one process plant a so-called modular, heterogeneous electrolysis to achieve higher flexibility of start-up, shut-down and operation [2].

With this, the system simulation of these large-scale electrolysis plants can be utilized for process design but also for process monitoring and optimization, and maintenance scheduling [3]. Since the underlying processes for the simulation models are often not completely understood, hybrid modeling methods are a promising approach to combine process knowledge with process data for more reliable and precise simulation models [4]. These hybrid, semi-parametric models

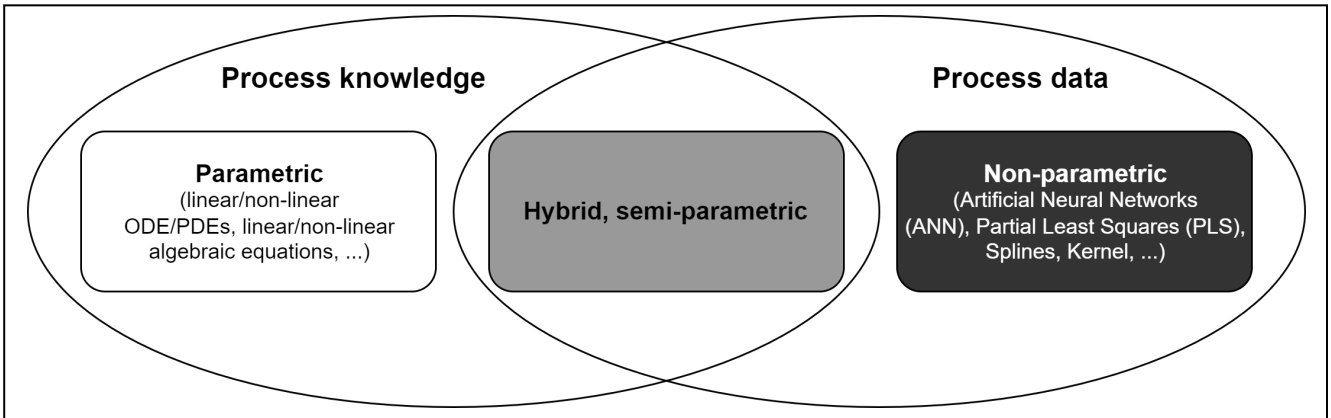



**Figure 1.** Taxonomy of hybrid, semi-parametric models.

achieved better accuracy and prediction quality than knowledge-driven mechanistic models.

In this work a hybrid, semi-parametric model for an anion exchange membrane electrolysis (AEMEL) stack unit is developed. The basis of this model is a mechanistic model of the AEMEL stack unit [5]. To evaluate the applicability of the hybrid, semi-parametric AEMEL model within a large-scale system simulation context, an electrolysis plant configuration is designed including multiple AEMEL stack modules, a water supply module and post-processing steps for the produced hydrogen. This plant configuration is then simulated using both the hybrid, semi-parametric and mechanistic AEMEL models to compare performance accuracy and simulation efficiency of both model types. In future work, this hybrid, semi-parametric model could be the basis for creating more efficient system simulations utilizing surrogate models.

## METHODOLOGY

### Modeling for flexible, heterogenous water electrolysis plants

Simulation models of entire process chains can be used to evaluate plant structures and provide virtual testing capabilities of developed automation and control concepts [6,7]. With the scale-up of water electrolysis plants following modular standards [2], the modeling approach must also follow this approach [3,8].

In the research project eModule this modular, flexible modeling approach is followed to investigate the applicability and operability of these modular heterogenous water electrolysis plants. The project aims to develop open-source model repositories. Dynamic stack unit models were designed for low-temperature electrolysis technologies, namely alkaline electrolysis (AEL), proton exchange membrane electrolysis (PEMEL), as well as anion exchange membrane electrolysis (AEMEL) [5]. Further dynamic models for the balance of plant (BoP) components like e.g., lye circulation and water supply were designed [3,8]. Additionally, a dynamic partial model for solid-oxide high-temperature electrolysis (SOEL/HTEL) was developed as a black-box model [9]. Details on the developed models can be found in [5] and the linked Github repository in the supplementary material.

To ensure accurate estimation and system simulation, process data is used to refine and validate the simulation models resulting in more accurate hybrid, semi-parametric simulation models as compared to the currently existing mechanistic models.

### Hybrid, semi-parametric modeling

Mechanistic models form a broad and transparent class, typically based on fundamental principles such as conservation laws [4]. In contrast, data-driven models rely solely on process data, offering a less transparent modeling approach [10].

Hybrid semi-parametric models, also known as gray-box models, integrate parametric and non-parametric sub-models derived from different knowledge sources. These models offer several advantages over traditional mechanistic or purely data-driven approaches [11]. An overview of hybrid semi-parametric simulation models is presented in Figure 1. Key benefits include a broader knowledge base, greater transparency in modeling, and cost-effective development [10]. In complex process simulations, hybrid approaches provide more accurate and robust estimations [11,12]. Gray-box models leverage existing process data through machine learning (ML) or artificial intelligence (AI) algorithms, effectively bridging gaps in mechanistic modeling [10].

## CASE STUDY

The presented case study covers the applicability and performance evaluation of gray-box models e.g., hybrid, semi-parametric simulations models, within system simulations of large-scale, modular water electrolysis plants.

## Anion Exchange Membrane Electrolysis

The Anion Exchange Membrane Electrolysis (AEMEL) is a low-temperature technology that combines advantages of PEMEL and AEL: operational flexibility (PEMEL) and low investment and operational costs (AEL) [13]. Currently, three AEMEL stack units, combined into one AEMEL module, exist as a demonstrator within the module pool of the Process-to-Order (P2O) Lab Learning Factory at TU Dresden.

The base level model for the hybrid, semi-parametric AEMEL stack model is a mechanistic AEMEL stack model developed in MATLAB/Simulink, modeled according to generic modular modeling principles [5]. Dimensionality is neglected for the base model since high computational power is required for 1D – 3D models and does not align with the goal of modular system design and automation. Therefore, the model is constructed as a lumped parameter (0D) model. To develop a lumped simulation model of the electrolyzer stacks, each cell side—anode and cathode—is represented as an ideal continuously stirred tank reactor (CSTR), with the separator or membrane serving as a shared interface.

To ensure a generic stack-unit model, first-principles models are prioritized, with the option to extend them using customizable empirical equations [5]. Several submodels, namely the mass accumulation/transfer, thermal, fluidic, electrochemical, and electric models, are each considered. Equations (1) – (6) show the generic mass accumulation/transfer submodel and the generic energy accumulation and thermal submodel as they are the most relevant for the hybrid, semi-parametric modeling part in the next section. Further model equations and assumptions can be found in [5].

The mass accumulation is modeled as dynamic component mass balances for each component $i$ in each cell side $j$, according to (1):

$$\frac{dm_i^j}{dt} = \dot{m}_{in}^j \omega_{in,i} - \dot{m}_{out}^j \omega_i^j + \dot{m}_{R,i}^j \pm \dot{m}_{cross,i} \quad (1)$$

with $\dot{m}_{in}^j$ as the inlet mass flow in each cell side, $\omega_{in,i}$ as the inlet mass fraction of each component, $\dot{m}_{out}^j$ out as the outlet mass flow in each cell side, $\omega_i^j$ as the mass fraction of each component in each cell side, $\dot{m}_{R,i}^j$ as the reaction rate (cf. equation 2) of each component in each cell side and $\dot{m}_{cross,i}$ as the crossover flow through the common interface.

The thermal model determines the temperature within the stack unit, which is crucial for calculating thermo-physical substance properties and cell voltage. Cell temperatures are computed using dynamic energy balances for each cell side, as described in equation (2):

$$\frac{dE^j}{dt} = \dot{m}_{in}^j e_{in} - \dot{m}_{out}^j e^j \pm \dot{m}_{cross} e^j + \dot{Q}_{loss} - \dot{Q}_{amb} - \dot{Q}_{hx} \quad (2)$$

with $\dot{Q}_{loss}$ as the heat generated due to current losses in the reaction, $\dot{Q}_{amb}$ as the heat exchanged with the surrounding environment and $\dot{Q}_{hx}$ as heat exchanged between the cell sides due to temperature difference.

$$\dot{Q}_{loss} = i\, A_{act}(U_{cell} - U_{tn}) \quad (3)$$

$U_{cell}$ is the voltage of the electrolytic cell and $U_{tn}$ the thermoneutral voltage of the water electrolysis reaction described by equation (4) with $\Delta H$ as the reaction enthalpy at operating conditions.

$$U_{tn} = \frac{\Delta H}{n\, F} \quad (4)$$

The heat exchange $\dot{Q}_{amb}$ with the environment is calculated for both cell sides according to (5) [14]:

$$\dot{Q}_{amb} = k_{amb} A_{amb}(T^j - T_{amb}) \quad (5)$$

with $k_{amb}$ as the heat transfer coefficient from the stack unit to the environment, $A_{amb}$ as half the surface area of the stack, due to the heat loss occurring in both cell sides, and $T_{amb}$ as the assumed constant ambient temperature. Similarly, the internal heat exchange between the cell sides is modeled according to (6):

$$\dot{Q}_{hx} = k_{hx} A_{hx}(T^{an} - T^{cat}) \quad (6)$$

with $k_{hx}$ as the heat transfer coefficient between the cell sides, $A_{hx}$ as the heat exchange area inside the stack unit and $T^{an/cat}$ as the respective temperatures inside the anode and cathode channel. The coefficients for $k_{amb}$ and $k_{hx}$ can be determined based on the prevailing flow regime and cell structure, derived empirically for specific stack units, or assumed constant [15]. In case of this generic modeling approach, constant values are assumed.

To enhance flexibility and reusability, the model interfaces are designed to be compatible with advanced mass and energy balance frameworks commonly used in flowsheeting tools. Additionally, the developed models are exported as Functional Mock-Up Units (FMUs), allowing for platform-independent model exchange [5].

## Hybrid AEM Model

The model parameters for the current mechanistic AEMEL model are based on literature estimations [16-18] and do not fully represent the existing lab setup (cf. [5]). The AEMEL was purchased as a pre-configured stack unit by Enapter. It offers a limited number of sensors for process data collection and cannot be retrofitted.

The heat loss within stack, pump, heat exchanger and piping cannot directly be measured and therefore must be approximated through non-parametric estimation from process data. In addition to hydrogen output $\dot{m}_{H_2,out}$, available sensors collect data for the temperature in the lye storage tank $T_{tank}$, the outlet temperature of the stack-unit $T_{out,1}$ and the flow rate into the stack $\dot{m}_{lye,out}$. Using the available data and the mechanistic stack

model, the heat loss $\dot{Q}_{amb}$ to the environment defined by $k_{amb}$ can be estimated.

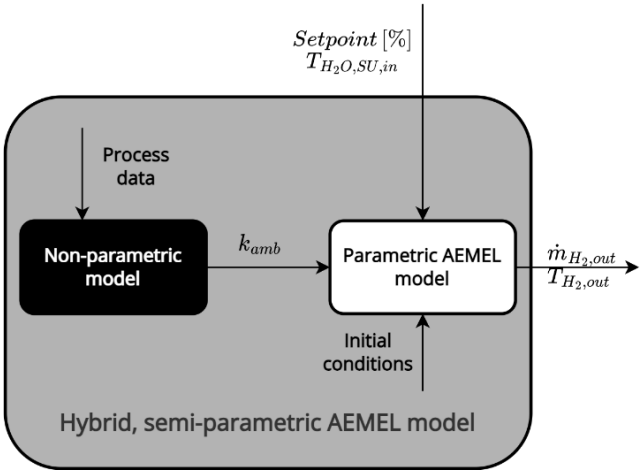



**Figure 2.** Structure overview of the hybrid, semi-parametric AEMEL stack unit model.

The hybrid, semi-parametric model was developed in MATLAB/Simulink as a light gray-box model. The model structure is shown in Figure 2. Currently, the data utilized for the non-parametric estimation within the hybrid model is synthetic process data. The load setpoint of the stack unit and the inlet water temperature $T_{H_2O,SU,in}$ were identified as the control parameters for the AEMEL. To emulate the behavior or real process data collected from the plant, random noise was added to the generated synthetic data from the simulation. The random noise is related to the maximum value of each batch run and simulation output. The Design of Experiments for the data generation is shown in Table 1.

**Table 1:** Design of Experiments (DoE) for the control parameters for synthetic data generation.

| **Control Parameter** | *Load Setpoint* [%] | | | $T_{H_2O,SU,in}$ [°C] | | |
|---|---|---|---|---|---|---|
| **Value** | 33 | 66 | 100 | 5 | 25 | 45 |

## Setup of the System Simulation

The goal of the generic modeling approach for flexible, heterogenous water electrolysis plants is to aid scale-up design and the optimization of plant operation to accommodate price-driven hydrogen production utilizing fluctuating, renewable energy [3]. Therefore, the developed simulation models are tested for their applicability and performance in medium- and large-scale system simulations. The performance of the hybrid, semi-parametric model within the system simulation is compared to the performance of the mechanistic model.

The configuration of the evaluated system simulation is shown in Figure 3. The simulation represents a medium-scale, homogenous electrolysis system which includes 18 AEMEL Stack Units, one Water Supply Unit and Distribution and Mixing Units for the material streams. For the AEMEL, three stack units are aggregated into one module unit, which reflects the laboratory setup for the M16 module in the P2O Lab Learning Factory. The nominal system size is 43.2 kW.

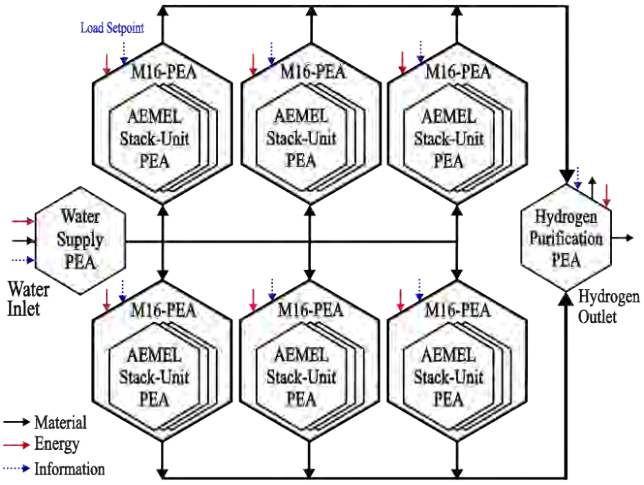



**Figure 3.** Modular plant layout for the presented system simulation with AEMEL.

The system simulation is set up in MATLAB/Simulink as a co-simulation environment shown in Figure 3. To evaluate the applicability of the hybrid, semi-parametric AEMEL model, a load input scenario into the system covering one day of solar power production was selected. The simulation scenario represents the load input for one day of solar power into the electrolysis plant with the input in 5-minute time-steps. The specifications for the simulation scenario can be found in [19]. The simulated system follows the requested load changes of the solar power input profile to emulate real price-driven plant operation.

## Performance Evaluation & Discussion

The performance of the hybrid, semi-parametric AEMEL stack unit model was compared to the previously developed mechanistic AEMEL stack unit model within a system simulation. A comparison of the simulation results for the solar power scenario is shown in Figure 4.

The results show that both the mechanistic and the gray-box system simulation are able to follow the flexible solar power profile with the hydrogen production rate $\dot{m}_{H_2O,plant}$. As shown in Figure 4 (right), the behavior of the hybrid model differs significantly in the temperature profile. The non-parametrically estimated value for $k_{amb}$

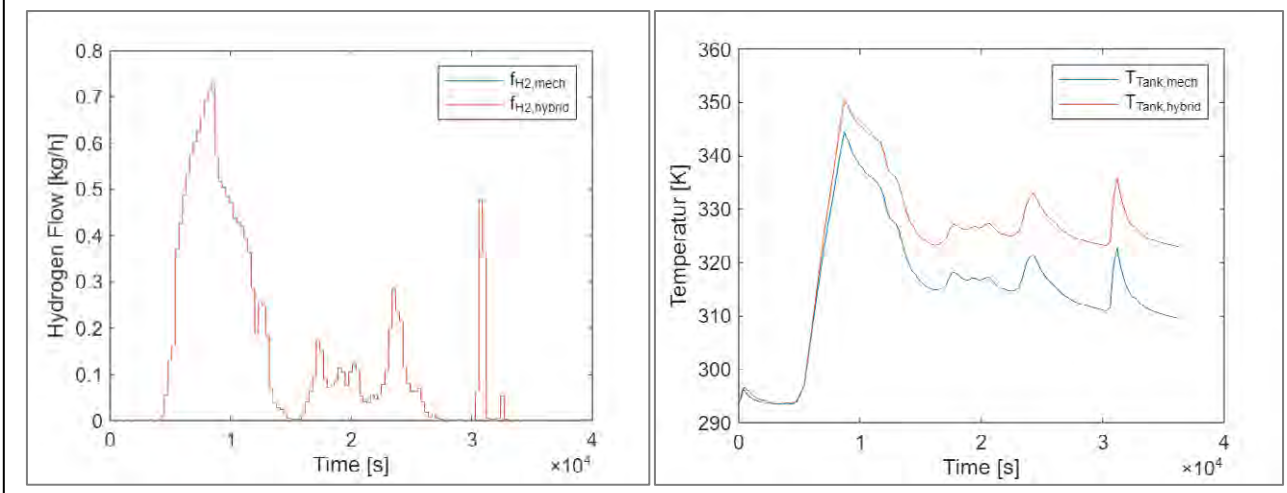



**Figure 4.** Comparison of simulation results for the system simulation: overall hydrogen production rate (left) and stack outlet temperature (right).

is lower than the originally defined value within the mechanistic model. Therefore, the overall heat loss from the system to the environment was overestimated and model reaches a higher temperature in the stack.

Due to the utilization of the synthetic process data for model development, the behavior of the hybrid, semi-parametric AEMEL model resembles the very detailed mechanistic model closely. This problem be amended once real process data can be collected from the demonstrator plant. One approach to leveraging this would be the utilization of more complex physics-informed neural networks (PINNs) [20].

Conceptually, gray-box models, not just hybrid, semi-parametric models, can be utilized in different real-time plant operation scenarios. Especially, in flexible, modular electrolysis plants, which are designed to follow fluctuating power input profiles [7,21], hybrid model structures that utilize online process data allow faster adaption to partial load production and more accurate forecasting of ramp-up and ramp-down cycles.

## CONCLUSION AND OUTLOOK

The presented case study verified the applicability of hybrid models within system simulation of modular water electrolysis systems. Currently, the significance and impact value of the developed hybrid, semi-parametric AEMEL model is limited as the model was developed using only synthetic process data. This represents the first step in the refinement of the generic simulation models for the modular water electrolysis concept. This paper builds the foundation for the concept development of a hybrid, semi-parametric simulation model pool as an addition to the already existing model pool.

A next step in the system simulation for electrolysis scale-up could be the development of faster and less computationally intensive surrogate models from the more accurate hybrid, semi-parametric simulation models. The surrogate models can further be utilized to setup more sophisticated Digital Twins to be used for real-time monitoring and optimization during plant operation.

## DIGITAL SUPPLEMENTARY MATERIAL

The P2O-Lab Learning Factory provides a Github group repository which contains the individual model repositories of the developed simulation models for the generic modular electrolysis plant. It is currently only available upon individual request at https://github.com/orgs/p2o-lab/teams/ap2_external/repositories. The repository includes the mechanistic and hybrid AEMEL stack unit models which are evaluated in this paper. It also provides the models for the balance of plant components and the other electrolysis technologies. The repositories will be openly accessible starting from October 2025.

## ACKNOWLEDGEMENTS

We would like to thank the German Federal Ministry of Education and Research and the project management organization Jülich for their financial support within the framework of the eModule research project (FKZ 03HY116A) of the H2Giga lead platform.

## REFERENCES

1. VDI 2776 Blatt 1, Process engineering plants - Modular plants - Fundamentals and planning modular plants. 2020. Accessed: Apr. 29, 2022. [Online]. Available: https://www.vdi.de/richtlinien/details/vdi-2776-

blatt-1-process-engineering-plants-modular-plants-fundamentals-and-planning-modular-plants
2. Lange, H., Klose, A., Beisswenger, L., Erdmann, D., & Urbas, L. (2024). Modularization approach for large-scale electrolysis systems: a review. Sustainable Energy & Fuels.
3. Mock, M., Viedt, I., Lange, H., & Urbas, L. (2024). Heterogenous electrolysis plants as enabler of efficient and flexible Power-to-X value chains. In Computer Aided Chemical Engineering (Vol. 53, pp. 1885-1890). Elsevier. doi: 10.1016/B978-0-443-28824-1.50315-X.
4. Von Stosch, M., Oliveira, R., Peres, J., & de Azevedo, S. F. (2014). Hybrid semi-parametric modeling in process systems engineering: Past, present and future. Computers & Chemical Engineering, 60, 86-101
5. Große, M., Viedt, I., Lange, H., and Urbas, L., (2024). Electrolysis stack modeling for dynamic system simulation of modular hydrogen plants, International Journal of Hydrogen Energy. (in review)
6. Bruckner, L., Oppelt, M., Urbas, L., & Barth, M. (2020). The current and future use of simulation in discrete and process industries. Siemens AG.
7. Lorenz, J., Klose, A., Lange, H., Kock, T., & Urbas, L. (2023, September). Process control principles for scalable electrolysis systems. In 2023 IEEE 28th International Conference on Emerging Technologies and Factory Automation (ETFA) (pp. 1-4). IEEE.
8. Viedt, I., Gopa, K. R., Mädler, J., & Urbas, L. (2023). Quality assessment of partial models for co-simulation of modular electrolysis plants. In Computer Aided Chemical Engineering (Vol. 52, pp. 1217-1222). Elsevier. https://doi.org/10.1016/B978-0-443-15274-0.50194-3
9. Viedt, I., Lorenz, R., & Urbas, L. (2024). Case study on quality assurance of third-party models for co-simulation using FMI. In Computer Aided Chemical Engineering (Vol. 53, pp. 3403-3408). Elsevier.
10. Glassey, J., & Von Stosch, M. (Eds.). (2018). Hybrid modeling in process industries. CRC Press.
11. Bae, J., Lee, H. J., Jeong, D. H., & Lee, J. M. (2020). Construction of a valid domain for a hybrid model and its application to dynamic optimization with controlled exploration. Industrial & Engineering Chemistry Research, 59(37), 16380-16395.
12. D. Bonvin, C. Georgakis, C. C. Pantelides, M. Barolo, M. A. Grover, D. Rodrigues, ... and D. Dochain, 2016, Linking models and experiments, Ind. Eng. Chem. Res, 55, 25, 6891-6903
13. Vincent, I., & Bessarabov, D. (2018). Low cost hydrogen production by anion exchange membrane electrolysis: A review. Renewable and Sustainable Energy Reviews, 81, 1690-1704.
14. Sinnott, R., & Towler, G. (2019). Chemical engineering design: SI Edition. Butterworth-Heinemann.
15. Sakas, G., Ibáñez-Rioja, A., Ruuskanen, V., Kosonen, A., Ahola, J., & Bergmann, O. (2022). Dynamic energy and mass balance model for an industrial alkaline water electrolyzer plant process. International Journal of Hydrogen Energy, 47(7), 4328-4345.
16. Nafchi, F. M., Afshari, E., & Baniasadi, E. (2024). Anion exchange membrane water electrolysis: Numerical modeling and electrochemical performance analysis. International Journal of Hydrogen Energy, 52, 306-321.
17. An, L., Zhao, T. S., Chai, Z. H., Tan, P., & Zeng, L. (2014). Mathematical modeling of an anion-exchange membrane water electrolyzer for hydrogen production. international journal of hydrogen energy, 39(35), 19869-19876.
18. Vidales, A. G., Millan, N. C., & Bock, C. (2023). Modeling of anion exchange membrane water electrolyzers: The influence of operating parameters. Chemical Engineering Research and Design, 194, 636-648.
19. National Renewable Energy Laboratory. Solar Power Data for Integration Studies 2024. https://www.nrel.gov/grid/solar-power-data.html (accessed November 14, 2024).
20. Zerrougui, I., Li, Z., & Hissel, D. (2025). Physics-Informed Neural Network for modeling and predicting temperature fluctuations in proton exchange membrane electrolysis. Energy and AI, 100474.
21. Lange, H., Klose, A., Lippmann, W., & Urbas, L. (2023). Technical evaluation of the flexibility of water electrolysis systems to increase energy flexibility: A review. International Journal of Hydrogen Energy, 48(42), 15771-15783.

© 2025 by the authors. Licensed to PSEcommunity.org and PSE Press. This is an open access article under the creative commons CC-BY-SA licensing terms. Credit must be given to creator and adaptations must be shared under the same terms. See https://creativecommons.org/licenses/by-sa/4.0/



Systems & Control Transactions

**Research Article - Peer Reviewed Conference Proceeding**
ESCAPE 35 - European Symposium on Computer Aided Process Engineering
Ghent, Belgium. 6-9 July 2025
Jan F.M. Van Impe, Grégoire Léonard, Satyajeet S. Bhonsale,
Monika E. Polańska, Filip Logist (Eds.)

PSE PRESS

# Energy system modelling for studying flexibility on industrial sites

**Jon Vegard Venås[a]*, Lucas Ferreira Bernardino[a], Kasper Emil Thorvaldsen[a], Sigrid Aunsmo[a], Sigmund Eggen Holm[a], Halvor Aarnes Krog[a], Ove Wolfgang[a], and Ingeborg Treu Røe[a]**

[a] SINTEF Energy Research, Trondheim, Norway
* Corresponding Author: jonvegard.venas@sintef.no.

## ABSTRACT

With an increasing share of non-dispatchable renewable energy sources in the European grid, energy flexibility will be key for the industrial sector to support the green transition. The EU-project Flex4Fact aims at finding solutions for energy and process flexibility for industry, using SINTEF's open-source energy system model EnergyModelsX to quantify the potential benefits. This work presents some extensions done in EnergyModelsX, denoted as EnergyModelsFlex, to accommodate energy and industrial flexibility, adding new functionalities to assist with industrial flexibility potential. The extended EnergyModelsX model is described and demonstrated through two case studies in the plastic and polymeric products manufacturing sector to evaluate their potential for increasing renewable generation and flexibility. The first use case, being energy intensive, consumes both natural gas and electricity. This site enables the use of heat recovery and utilization, hydrogen blending, on-site hydrogen production, which can reduce CO2 emissions. The second use case relies solely on electricity consumption, and the considered flexibility is energy shifting by electric batteries and production flexibility. The focus of this case study is on the interplay between energy storage, on-site energy production and process flexibility to increase the degree of self-produced renewable energy in the energy mix. Together, the two case studies demonstrate how the extended EnergyModelsX framework can be used to explore process and energy flexibility in the industry to aid the transition from a fossil-based society to a renewable based society.

**Keywords**: Industrial demand-side flexibility, Energy transition

## INTRODUCTION

To meet the ambitious net zero target of the EU by 2050, it is a top priority to transition from fossil fuels to renewable sources [1]. However, unlike traditional fossil fuel power plants, which can adjust output to match demand, non-dispatchable renewable sources like solar and wind are subject to natural variability and cannot be controlled to meet immediate demands. This is a challenge in the industrial sector where consistent and predictable energy usage is crucial. The EU project Flex4Fact aims to develop solutions to leverage energy and process flexibility in industry to meet a future with high renewable energy penetration [2].

A part of this project seeks to identify optimal investment strategies for enhancing energy flexibility, i.e. the capability of an industry to adapt to variable energy production. The investment strategies arise from energy system modelling, where the key is to understand how different technologies, such as solar power and electric batteries (BESS), complement the industrial site and potential process flexibility. To enable these assessments, SINTEF's open-source energy system model, EnergyModelsX (EMX) [3] has been used and further developed to specifically address flexibility requirements at industrial sites. The considered flexible aspects modelled through Flex4Fact include process flexibility modelled as energy load shifting, allowing multiple energy carriers to cover the demand of single processes, and energy storage technologies. Synergies between these mentioned flexibilities and integrated on-site renewable expansions are focused upon within this work. Sensitivity analyses are conducted to assess the robustness of the investment strategies towards changes in market prices or

scaled production, to capture optimal use of flexibility and investment decisions to the energy system.

This work is structured as follows. We first describe EMX alongside the new flexible functionalities towards industrial flexibility, then present two use cases that is related to the Flex4Fact projects alongside their implementations. Finally, we demonstrate the results regarding the new functionalities on the use cases.

## ENERGY SYSTEM MODELLING

There exist multiple other toolboxes that represent the energy system, but some are more focused on large scale energy systems with details on regional constraints like TIMES [4]. As described in [3], an advantage with EMX compared to other models for the representation and optimization of energy systems at specific sites, such as SpineOpt [5], GenX [6], and the Tulipa Energy Model [7], is the modular structure - by splitting the full model framework into separate, installable packages - with the high focus on extensibility and alternative technology formulations.

### EnergyModelsX

EnergyModelsX (EMX) is an open-source energy system modelling toolbox developed by SINTEF [3]. The toolbox is written in the Julia programming language using the JuMP modelling framework, enabling a fast and modular framework for multiple dispatch models. Emphasis is made on giving modelers a high level of flexibility. Detailed description of the model and its use can be found in [8]. The following will give an overview of the features of EMX relevant for the assessments performed in the presented work.

EMX mirrors real energy systems through generic representations of different technologies. These representations are defined in EnergyModelsBase, and include sink, source, generation and storage technologies, and links between the different technologies. Generic representations can be assigned features specific to the energy system in question such that specifications of that energy system are captured. A source can for instance be assigned emission features to mimic a natural gas source. The technologies are referred to as nodes. Three different fundamental nodes exist; source, sink and network nodes. Interactions between nodes are defined by creating links between them. Source and sink nodes can only give or receive input from the surroundings (i.e. is only linked one way) while network nodes can have two-way interactions.

While links between any nodes can be defined, modelling ease and flexibility are best achieved by defining an Availability node. The Availability node does not have any features assigned to itself but acts as a collector of all links as illustrated as the “av”-node in Figure 1. That way, new nodes can be defined in the framework without changing all the links between the existing nodes.

The modularity of the EMX framework is achieved by Julia’s multiple dispatch functionality when extending the EnergyModelsBase package. Several such extensions have been implemented to ease geographical representation (EnergyModelsGeography) and investments (EnergyModelsInvestments). In the Flex4Fact project a graphical user interface has also been developed for EMX (EnergyModelsGUI). A series of technology specific extensions has also been developed (e.g., for non-dispatchable renewable energy sources like PV power, CO2, Hydrogen and Heat).

Building upon such extensions this work has resulted in a unified extension called EnergyModelsFlex which will be described in the following.

### EnergyModelsFlex

The EnergyModelsFlex extension provides a series of technology node types for EMX enabling energy and process flexibility modeling. The following nodes are described for the present work.

#### StorageEfficiency

The StorageEfficiency node enables storage efficiency control compared to RefStorage. It’s storage resource can be any EMX Resource, and can be used for both the battery technology and the hydrogen storage technology. As for the RefStorage node, investment can be made in both charge/discharge (i.e. the inverter for batteries) and the storage level. Moreover, its generic storage behavior is also inherited from the Base-package but only CyclicStrategic has been considered in the present study. That is, the storage requires cyclic behavior within a strategic period.

### ChargeRateCapacity

The ChargeRateCapacity node is a further development of the StorageEfficiency node where a coupling between the charge rate and capacity has been added. The ChargeRateCapacity node thus mimics a BESS where the charge rate can be limited by the capacity of the battery and ensures that completely decoupled investments into charge rate and battery capacity are avoided. While the node was developed to mimic an electric battery, other types of energy storage, such as thermal storage, is also a enabled.

### PayAsProducedPPA

The PayAsProducedPPA node considers pay-as-produced power purchase agreement (PPA) from off-site solar PV. This non-dispatchable renewable energy source is similar to the node AbstractNonDisRES from the EnergyModelsRenewableProducers extension, but need to dispatch on this type in order to modify the OPEX

constrain to extend to all power produced (including curtailed production).

### LimitedFlexibleInput

The LimitedFlexibleInput node dispatches on the NetworkNode but modifies the flow in constraints by setting upper limits of the input resources. This is needed when hydrogen is to partly replace natural gas but is limited. An upper limit of 20% hydrogen volume (corresponding to a 7.01 % energy fraction) in the H2-NG gas mix is often used as it would not require major alteration in the machinery.

### LoadShifting

The LoadShifting node dispatches on the Sink node where the demand can be altered by load shifting, i.e. the transfer of a predefined quantity of energy (power and duration) from one time to another. This quantity of energy is given as an input to the node, together with the allowed time slots from and to where the load shifting can occur. The load shifting thereby represents a flexible energy demand, but the flexibility is based on (external) constraints rather than a cost benefit or penalty, meaning that the flexibility cannot be optimized from a cost perspective.

## DESCRIPTION OF THE USE CASES

In the Flex4Fact project, a total of five case studies are investigated. We here focus on two that covers much of the goal of investigating both energy and process flexibility. The two use cases are briefly described in the following.

### SPS

Standard Profil Spain (SPS) is a Spanish company specializing in automotive sealing systems for major OEMs (Ford, GM, Renault, etc.). To reduce their carbon footprint, the factory considers onsite renewable energy for hydrogen production via electrolyzers and electricity demands, while gradually replacing natural gas in furnaces with green hydrogen. Hydrogen, process flexibility and BESS storage are also under consideration to maximize energy self-consumption.

Figure 1 illustrates SPS's existing energy system along with potential extensions through investments, as represented in our EMX model implementation. Investment options are marked with dashed lines, and the red text indicates the investments being carried out in the optimization. Energy flows between nodes have a unique colors per energy carrier. The representation of the energy system is based on information provided by SPS to the project and has also been discussed with SPS.

We consider four energy sources: electricity grid, representing electricity purchase under the current contract, PPA, which is an alternative contract for electricity supplied through the grid and produced by PV, on-site PV generation, and natural gas. Four consumption sinks are considered: machinery gas consumption, electricity-specific needs, space heating, and waste heat. Additionally, the model implicitly accounts for curtailed PV and for $CO_2$ emissions.

The energy sources and energy sinks are connected through three node types: energy conversion, energy storage, and energy distribution. However, most of the connections shown in Figure 1 are logical links rather than representing a specific physical distribution system.

The energy conversion nodes are the existing gas oven for space heating, electrolyzers, and heat recovery that convert waste heat into usable space heating. Two heat recovery options are considered: From gas usage in the machinery of the facility, and from the hydrogen production in the electrolyzer. The model also includes two types of energy storage investments: batteries and hydrogen storage. One physical distribution investment is represented: The transport of recycled heat to the space heating site. Finally, there is a conversion node representing the mixing of natural gas and hydrogen to create the energy carrier "gas", which is a blend of natural gas and hydrogen with non-fixed proportions - but with a 20% hydrogen volume cap in the gas mix. For this case study, the dimensioning of each investment option, i.e. MW invested, is a continuous variable with an upper constraint.

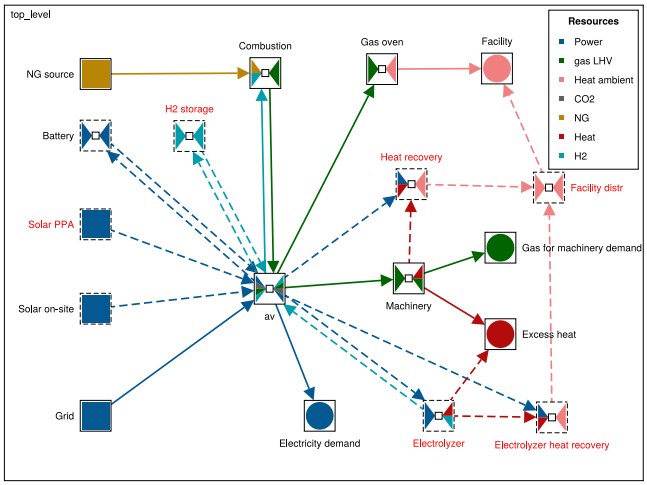



**Figure 1.** Graphical representation of the SPS energy system (current and all investments included) in EMX.

The operation of the energy system is optimized on an hourly basis across the entire year, 8760 sequential hours in total. That annual simulation is conducted for five strategic periods: 2024, 2025 - 2026, 2027 – 2030, 2031 – 2040, and 2041 – 2050. Investments carried out for a strategic period are assumed to be in operation from the start of that strategic period.

## SEAC

SEAC is an Italian producer of diving equipment. The production processes are based on molding, and run solely on electricity, which is therefore the only energy form considered in the energy system analyses. Electricity can be delivered from the power grid or on-site PV panels. The energy demand is divided into process consumption ("Production") and building and factory heating, cooling and lighting ("Base load") as illustrated in Figure 2. In the base case, the Production node is a regular sink. Load shifting-type energy flexibility is enabled by changing the Production node to LoadShifting. Load shifting is constrained to two times per week, with a duration of 8 hours and magnitude of 15 kW. Investment options (PV and BESS) are illustrated with dashed lines in Figure 2. The ChargeRateCapacity node is used to represent the BESS, ensuring that a round-trip efficiency of 0.98 is implemented, and that investments into charge rate follows the investment in charge capacity.

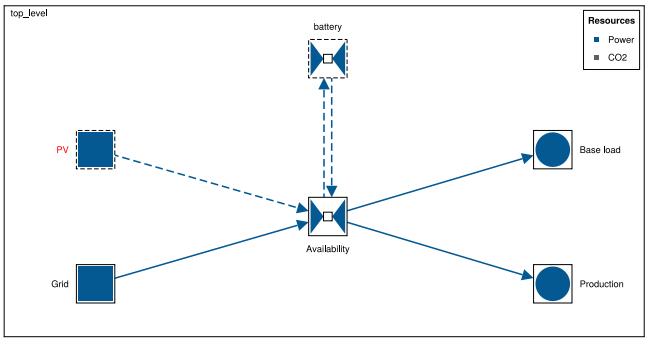



**Figure 2.** Graphical representation of the SEAC energy system (current and all investments included) in EMX.

The operation of the energy system is optimized on an hourly basis across the entire year, 8760 sequential hours in total. That annual simulation is conducted for seven strategic periods: one for each year in the timespan 2024-2030. The CAPEX of the PV and BESS technologies decrease linearly from 1000 €/kWp to 870 €/kWp, and 400 €/kWh to 200 €/kWh, respectively, in the time span 2024 to 2030 [9], [10].

Herein, the SEAC use case illustrates the utilization of load shifting within the EMX framework as a means to enhance renewable energy utilization in industry. Hence the presented results focus on and discuss the load shifting. Other aspects related to the energy system of SEAC, such as which, when and why investments are profitable, will not be discussed although they could be of interest in a different context.

# RESULTS

The following highlights the results from the two use cases that illustrate the features added to the EMX framework throughout the present work. Hence, results related to the energy system of the use cases, but not specifically the added features, are not discussed herein.

## SPS

For SPS the optimal investments are presented in Table 1. The investment in hydrogen is only profitable in the last two periods, where $CO_2$-prices increases significantly (which is not expected to happen before 2030).

**Table 1:** Optimal investments in the base case for SPS.

| Period | Type | Amount |
|---|---|---|
| 2024 | | |
| 2025 - 2026 | PPA contract, solar* | 4778 kWp |
| 2027 - 2030 | | |
| 2031 - 2040 | On-site PV generation | 418 kWp |
| | Electrolyzer | 3 kW |
| | Hydrogen storage | 49 kWh |
| 2041 - 2050 | Electrolyzer | 520 kW |
| | Hydrogen storage | 9790 kWh |

*) Upper constraint for invested amount is binding

For the current analysis we consider a pay-as-produced PPA at 50€/MWh, which is well below the price in the current electricity contract for use of grid electricity. The maximum permitted investment is therefore selected from the start (no investments allowed in 2024). Since this contract is pay-as-produced, and the model does not include a sell back to market option, there is curtailment at the weekends when there is no production in SPS's facility. This can be seen in Figure 3 where 168 hours of data have been extracted from the strategic period of 2025-2026. This thus makes "free" electricity available, but this is not enough to make hydrogen production profitable in that period.

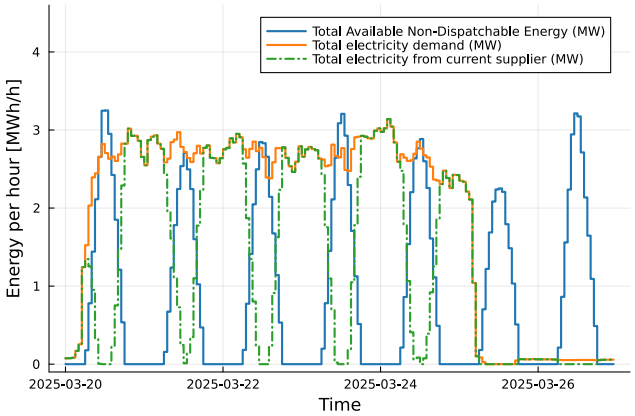



**Figure 3.** Example hours, showing PPA and electricity consumption. The difference is curtailment when PPA is highest and import through grid when electricity consumption is highest.

One of the goals of SPS is to cut $CO_2$ emissions, but with a hard limit of 20% volume of hydrogen in the H2-NG gas mix there is quite limited reduction potential even when the $CO_2$-prices reaches 500€/t$CO_2$eq [11] in the strategic period 2041-2050. This can be illustrated in Figure 3 where the 7.01% energy limit of hydrogen (corresponding to the 20 % volumetric share) is reach with "inf" $CO_2$ prices. The further reduction of $CO_2$ to 11.79% in total is due to investments in excess heat utilization (resulting in lower gas consumption).

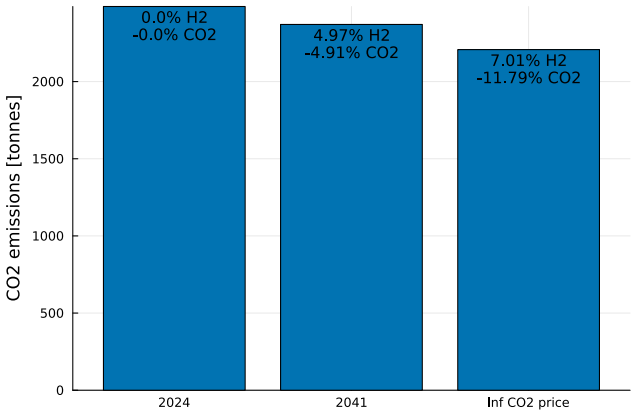



**Figure 4.** Total $CO_2$ emissions annually for the current system (2024), the final period of our analysis (2041-50), and for a case where the $CO_2$ cost is set very high. The share of hydrogen in total gas consumption (natural gas plus hydrogen) and the $CO_2$ reduction relative to the 2024 case is printed on each bar.

## SEAC

In the SEAC use case, energy flexibility modelled through the LoadShifting node is in focus. Figure 5 illustrates the implementation of load shifting, where a quantity of energy ("Energy shifted" in green), corresponding to a production batch in SEAC, may be shifted from of time of the day to another, or even to another day. In the this case, two load shifts are allowed within a working week, and only within the working hours. The figure illustrates that batches are shifted from the afternoon to the morning or midday. This corresponds relatively well with the availability of renewable energy from the PV panels as well as the price of electricity from the power grid.

Table 2 compares the load shifting to product-based rescheduling performed by SEAC. Contrary to the energy-based load shifting, the production-based rescheduling of SEAC accounts for costs, such as man hours, associated with rescheduling of production, and optimizes the production of unique products. One advantage with the production-based rescheduling compared to the load shifting is that production schedules are developed, giving additional information on the operation of the facility. However, complexity increases since detailed information on each product's energy demand and production time is necessary, along with personnel requirements, work hours and salaries. Insignificant differences between the rescheduling and the load shifting in the overall facility performance are found. We notice, however, that the load shifting is sensitive to the input, and that the energy of producing the batch must be predefined. Extensive preprocessing of data may therefore be necessary.

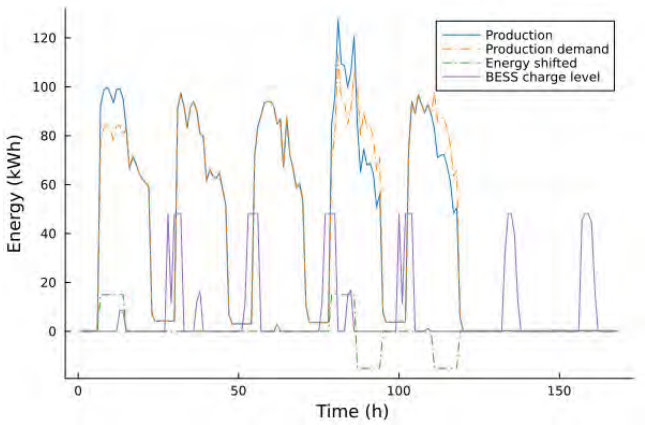



**Figure 5.** Illustration of load shifting over a week in the SEAC use case. The energy shifted (in green dashdotted) represents a production batch. The original production demand (in orange dashdotted) is optimised relative to the energy availability from on-site PV panels and the power grid prices, and results in the production (in blue). The charge of the BESS (in purple) follows the balance between energy availability and demand, and is thus affected by the load shifting.

**Table 2:** Comparison between load shifting and the production-based rescheduling of the production.

| | Cost (€/MWh) | PV consumption (%) | Grid consumption (%) |
|---|---|---|---|
| Base case | 110.4 | 50.2 | 49.8 |
| Production-based rescheduling | 107.7 | 51.7 | 48.3 |
| EMX load shift | 107.7 | 51.5 | 48.3 |

An advantage of EMX's implementation of load shifting is that the impact of flexibility on investments on a longer timescale can be explored. In SEAC, the load shifting was coupled with investments in BESS and PV. Table 3 displays the results for the load shifting-coupled investment model compared to an investment model without the load shifting. Investments in PV and BESS investments increased by 1.7 % and 4.5 %, respectively, with load

shifting compared to without. While the difference between the two models is relatively small due to the limited magnitude of the load shifting in SEAC, the increased BESS investments are interesting. Typically, we expect that the load shifting reduces the investments into BESS systems since the consumption can be shifted according to the availability of the PV power.

**Table 3:** Optimal investments in SEAC in 2030 using energy systems modelling in EMX as set up in Figure 2 with and without load shifting.

| | PV (kWp) | BESS (kWh) | Flexibility (kWh/year) |
|---|---|---|---|
| EMX without load shift | 294.8 | 194.6 | 0 |
| EMX load shift | 299.8 | 203.3 | 12 480 |

The reason for this behavior in SEAC can be that the constraint on the duration and timing of the load shifting inhibits a perfect match between the shifted production and the PV energy generation. Figure 5 illustrates how making use of BESS therefore is necessary to exploit the full potential of the load shifting, and to increase the utilization of the renewable energy from the PV panels.

## CONCLUSIONS

The EnergyModelsX framework provides a high level of flexibility in modelling energy systems. Its primary strength lies in the exploitation of the multiple dispatch feature provided by the Julia programming language. New technologies can be introduced in the model by dispatching on existing implementations resulting in less complex code.

The application of EnergyModelsX to industrial settings has proven to provide the flexibility needed to model the goals of the analysis. The main challenge is to achieve the correct data and the implementation of these into constraints.

The present work has demonstrated that the implementation of load shifting can adequately represent the production flexibility of industrial settings. One of the major advantages with load shifting is the relative incomplexity compared to production-based rescheduling algorithms, which ultimately enable investigations into the impact of process and energy flexibility on a long timescale. In industries where the magnitude of the load shifting is larger than in SEAC, this can have a significant impact. This is, however, given that the load shifting represents the process flexibility of the industry, which may require extensive preprocessing of data and industry information and remains one of the key challenges with the representation of process flexibility through load shifting.

## ACKNOWLEDGEMENTS

This work was funded by FLEX4FACT. FLEX4FACT is receiving funding from the European Union's Horizon Europe research and innovation programme under grant agreement 101058657.

## REFERENCES

1. Directorate-General for Climate Action (European Commission), Going climate-neutral by 2050: a strategic long term vision for a prosperous, modern, competitive and climate neutral EU economy. Publications Office of the European Union, 2019. Accessed: Jan. 28, 2025. [Online]. Available: https://data.europa.eu/doi/10.2834/02074
2. "FLEX4FACT project - Official website of the Horizon Europe project," Flex4fact. Accessed: Jan. 28, 2025. [Online]. Available: https://flex4fact.eu/
3. L. Hellemo, E. F. Bødal, S. E. Holm, D. Pinel, and J. Straus, "EnergyModelsX: Flexible Energy Systems Modelling with Multiple Dispatch," Journal of Open Source Software, vol. 9, no. 97, p. 6619, May 2024, doi: 10.21105/joss.06619.
4. IEA-ETSAP, TIMES Model Generator. (Jan. 25, 2025). Zenodo. doi: 10.5281/zenodo.14740450.
5. M. Ihlemann et al., "SpineOpt: A flexible open-source energy system modelling framework," Energy Strategy Reviews, vol. 43, p. 100902, Sep. 2022, doi: 10.1016/j.esr.2022.100902.
6. L. Bonaldo et al., GenXProject/GenX.jl: v0.4.3. (Jan. 30, 2025). Zenodo. doi: 10.5281/zenodo.14768811.
7. A. Soares Siqueira et al., Tulipa Energy Model. (Jan. 29, 2025). Zenodo. doi: 10.5281/zenodo.14761062.
8. E. F. Bødal et al., "Hydrogen for harvesting the potential of offshore wind: A North Sea case study," Applied Energy, vol. 357, p. 122484, Mar. 2024, doi: 10.1016/j.apenergy.2023.122484.
9. J. Trüby et al., "Hydrogen4EU - Charting pathways to enable net zero," IFP Energies Nouvelles, SINTEF Energi, Deloitte Finance, 2021. Accessed: Oct. 07, 2024. [Online]. Available: https://www.hydrogen4eu.com/_files/ugd/2c85cf_a3c72fe01d0744959ee03e8472fd2b2e.pdf
10. I. Tsiropoulos, D. Tarvydas, and N. Lebedeva, Li-ion batteries for mobility and stationary storage applications: scenarios for costs and market growth. Publications Office of the European Union, 2018. Accessed: Oct. 04, 2024. [Online]. Available: https://data.europa.eu/doi/10.2760/87175
11. Enerdata, "Carbon Price Forecast 2030-2050: Assessing Market Stability & Future Challenges | Enerdata." Accessed: Nov. 21, 2024. [Online]. Available:

https://www.enerdata.net/publications/executive-briefing/carbon-price-projections-eu-ets.html

© 2025 by the authors. Licensed to PSEcommunity.org and PSE Press. This is an open access article under the creative commons CC-BY-SA licensing terms. Credit must be given to creator and adaptations must be shared under the same terms. See https://creativecommons.org/licenses/by-sa/4.0/

Systems & Control Transactions

**Research Article - Peer Reviewed Conference Proceeding**
ESCAPE 35 - European Symposium on Computer Aided Process Engineering
Ghent, Belgium. 6-9 July 2025
Jan F.M. Van Impe, Grégoire Léonard, Satyajeet S. Bhonsale,
Monika E. Polańska, Filip Logist (Eds.)

PSE PRESS

# An MIQCP Reformulation for the Optimal Synthesis of Thermally Coupled Distillation Networks

**Kevin Pfau[a], Arsh Bhatia[a], Carl D. Laird[a]*, George Ostace[b], Goutham Kotamreddy[b]**

[a] Carnegie Mellon University, Department of Chemical Engineering, Pittsburgh, PA, USA
[b] Braskem, 550 Technology Dr., Pittsburgh PA, USA
* Corresponding Author: claird@andrew.cmu.edu

## ABSTRACT

Superstructure based approaches have long been employed for optimal process synthesis problems. Due to the difficulties of using rigorous process models and simultaneous solutions, shortcut calculations have been the preferred means of modeling unit operations within larger process network problems. However, even with the use of shortcut equations to model the behaviour of unit operations, the resulting mixed-integer programs can be challenging to solve. Furthermore, generating the problem superstructure has often been done manually, presenting issues for scaling to larger problems. We demonstrate the use of an algorithmic approach to generate network superstructures for synthesis problems coupled with equation reformulations to yield an MIQCP (Mixed-Integer Quadratically Constrained Program) for networks of thermally coupled distillation columns. The combination of rapid problem generation with the ability to leverage recent advances in the performance of QCP (Quadratically Constrained Program) solvers enables efficient and scalable solutions for these process synthesis applications.

**Keywords**: Optimization, Distillation

## INTRODUCTION

The design of systematic and algorithmic approaches for the synthesis of optimal separation systems is a highly developed research area within process systems [8,9]. While recent research has moved beyond previous heuristic-based approaches, finding global optimum through rigorous models and simultaneous solutions has still remained a difficult task [7].

Process synthesis problems for separation networks face two main challenges: combinatorial complexity and a high degree of nonlinearity. The combinatorial complexity of a separation network synthesis problem results from the need to determine an optimal sequence of separation tasks. As the number of components to be separated increases, the search space of possible separation cuts grows combinatorically, resulting in a large number of binary variables. Furthermore, rigorous modeling of individual separation unit operations is typically done with the MESH equations [5]. The resulting optimization model for the full space formulation of a separation network is a large-scale MINLP that is often intractable using off-the-shelf solvers.

Determining a suitable representation of the process superstructure is the first step in optimization-based process synthesis. State-task networks (STN) provide a formalism to construct the process topology that will define the search space of the optimization problem [12]. For the case of distillation networks, states are defined as mixtures of components and tasks are defined as a separation cuts between components. Figure 1 shows an STN representation for a separation network for a mixture of four components, ordered by decreasing relative volatility. The separation tasks shown do not necessarily have a one-to-one association with actual unit operation equipment.

In many process synthesis problems, the state-task network is generated by hand for the specific use case [2]. Manually writing out a superstructure can be tedious and error-prone. The network size, both the number of nodes and edges, will increase rapidly with the number of components to be separated. Thus, the manual generation of a process superstructure can become prohibitive for problems of even reasonably large size.

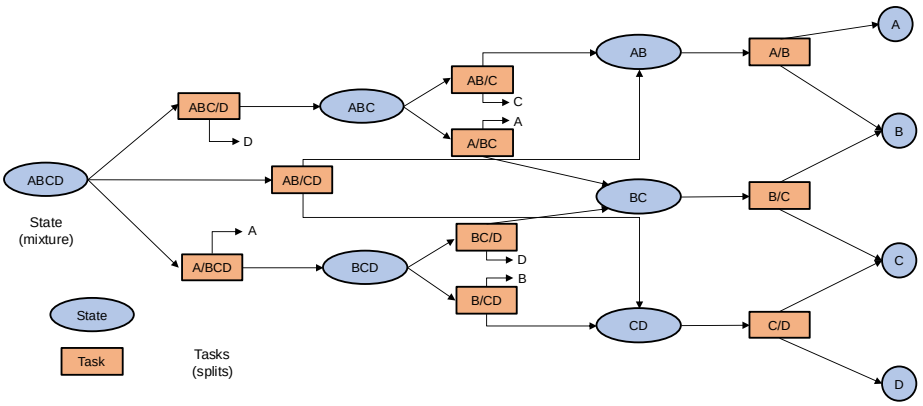



**Figure 1.** A state-task network for the separation of a 4-component mixture into pure components. The mixture components are ordered by decreasing relative volatility. The network uses splits between consecutive key components.

Many separation network synthesis approaches utilize shortcut equations, as opposed to the full set of MESH equations, to model unit operation behavior [9]. The Fenske-Underwood-Gilliland (FUG) equations are some of the most commonly used shortcut equations for modeling multicomponent separations. While the FUG equations are limited in their application based on their modeling assumptions (constant relative volatilities between components, non-azeotropic mixtures, etc.) they can still prove useful in initial system design applications.

Distillation network design places a large emphasis on reducing the utility consumption of a process. Distillation processes are costly to operate due to the high thermal requirements associated with heat exchangers. Thermal coupling of distillation columns can reduce the system operating expense by reducing both the number of heat exchangers needed and the overall heat load on the system [3]. Figure 2 shows an example of thermal coupling in which vapor and liquid streams are exchanged between separation tasks. A single reboiler and condenser provide the heating and cooling for the fully thermally coupled system.

Caballero & Grossmann [4] present a mathematical formulation for the synthesis of thermally coupled columns modeled as a generalized disjunctive program (GDP). Separation tasks are modeled with mass balances and shortcut equations in a set of disjuncts. Heat exchangers, reboiler and condensers associated with a distillation column, are modeled in a separate set of disjuncts. This formulation allows for the selection or absence of heat exchangers. The absence of a heat exchanger between tasks represents a thermal couple, in which separation tasks exchange liquid and vapor flows and the heat duty for a task is provided by a single heat exchanger.

Previous distillation modeling approaches had only used conventional columns, in which each column has an associated reboiler and condenser [1]. The thermally coupled model introduces significantly more complexity in the superstructure of the mathematical program. Solution algorithms not only have to determine the optimal selection of separation tasks, but also the selection of intermediate and final state heat exchangers, that are realized as reboiler and condensers associated with distillation columns. The disjuncts for separation tasks and heat exchangers can be written conceptually as:

$$\begin{bmatrix} Y_t \\ \text{Mass and component balance in each column} \\ \text{Product recovery specification} \\ \text{Shortcut equations (Underwood, Fenske)} \\ \text{Empirical cost and sizing correlations} \end{bmatrix} \vee \begin{bmatrix} \neg Y_t \\ \text{Material flows} = 0 \\ \text{Capital cost} = 0 \end{bmatrix} \quad \forall\, t \in Tasks \tag{1}$$

$$\begin{bmatrix} Z_s \\ \text{Heat duty calculations} \\ \text{Utility costing calculation} \\ \text{Empirical cost and sizing correlations} \end{bmatrix} \vee \begin{bmatrix} \neg Z_s \\ \text{Heat flows} = 0 \\ \text{Capital cost} = 0 \end{bmatrix} \quad \forall\, s \in States \tag{2}$$

The modeling of networks of thermally coupled columns as a GDP allows for a more conceptually understandable problem formulation. Each separation task disjunct can be understood to act as a separation column that is selected or not selected. While the FUG equations are used in this particular formulation, other shortcut equations could be substituted into the disjunctive formulation. Furthermore, Caballero & Grossmann use the Boolean variables associated with the separation task and heat exchanger disjuncts to construct logical relations that enforce the conceptual structure of the problem within the mathematical program. The GDP is

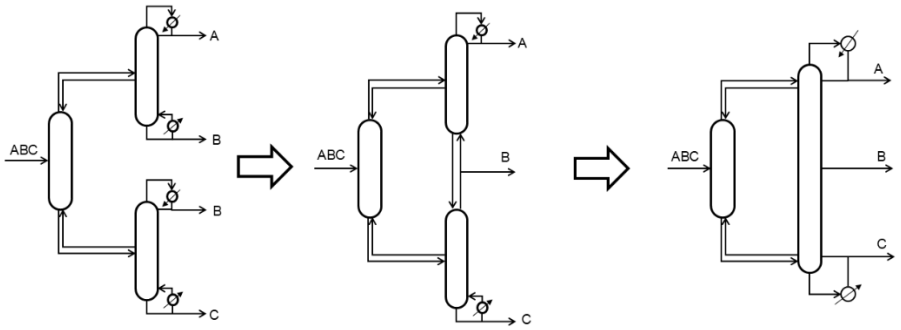



**Figure 2.** Separation of a three-component mixture using varying degrees of thermally coupled columns. The leftmost system uses a prefractionator units with two conventional columns. The right most system represent a fully thermally coupled configuration.

transformed into a mixed-integer nonlinear program and a heuristic decomposition algorithm is used to solve the problem.

In this work, we present a novel superstructure generation algorithm and an MIQCP (Mixed-Integer Quadratically Constrained Program) reformulation of the thermally coupled distillation superstructure optimization model developed by Caballero and Grossmann[4] that shows orders of magnitude improvement in solution times.

## METHODOLOGY

### Superstructure Generation

Generation of process superstructures has often been done manually. For smaller case studies or single problems, a manual approach is not prohibitive. However, for larger synthesis problems generating the superstructure and index sets manually is cumbersome and error prone. An algorithmic approach for automatically generating state-task network superstructures and their corresponding index sets allows for a much faster generation of problems. For the case of state-task networks as the process superstructure we can employ approaches from n-ary tree representations. N-ary trees are a generalization of binary trees that allow parent nodes to have at most *n* child nodes in a tree structure. State-task networks can be generated with recursive n-ary tree approaches using alternating state and task nodes with appropriately specified parent-child relations.

The difficulty that arises in naively applying n-ary data structure approaches to state-task networks is that the STNs are networks, not trees. The STN shown in Figure 1 has multiple parent nodes pointing to the same child node and the layers of the network cannot be easily decomposed into bipartite graphs. A key insight into how to algorithmically generate a problem superstructure is that we do not have to directly generate an STN as depicted in the network graph, shown in Figure 1. Constructing the actual mathematical program does not require a graph structure, only the index sets that arise from the STN.

Our algorithmic approach relies on generating an n-ary tree structure of alternating state and task nodes and then searching through the data structure to build up index sets that define relations between the nodes. Figure 3 shows a tree structure that can be easily constructed for a four-component separation. In the tree data structure, we build two distinct classes of nodes: state nodes and task nodes. State nodes can have an arbitrary number of child nodes, while task nodes are restricted to having exactly two child nodes: a distillate and a bottoms. The data structure is constructed recursively by alternating between these node types until the final state nodes, representing pure components, are produced. Once the tree structure is built, we perform a recursive search through the structure to construct the index sets for the problem, ensuring uniqueness during this search.

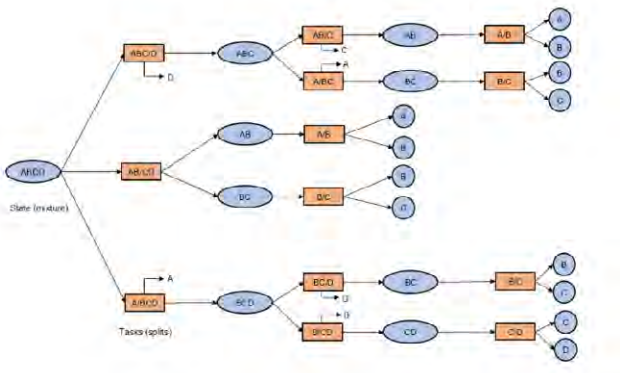


**Figure 3.** Tree representation of superstructure for the separation of a four component mixture. Note that, unlike in the network structre shown in Figure 1, there are duplicate state and task nodes.

For example, the index set for tasks that

can generate a state includes the entry: Tasks_to_statesBC: {A/BC, BC/D}. The process superstructure shown in Figure 1 has only one state node BC. A recursively generated tree, as shown in Figure 3, will have two state nodes BC, with parent task nodes *A/BC* and *BC/D*. In constructing the index sets for the optimization problem we recursively search through the generated tree and return all the tasks that are the parent for a given state node. This approach avoids generating a graph structure that becomes increasingly complex in its connections as the number of components in the system increases.

## MIQCP Reformulation

Using the formulation for thermally coupled columns from Caballero & Grossmann (2004), the separation tasks and heat exchangers for a network of distillation columns are modeled using generalized disjunctive programming. The FUG (Fenske-Underwood-Gilliland) are used to model column behavior. After the transformation of the GDP, commercial solvers can fail to find solutions for the resulting MINLP. In the original work, a heuristic solution approach is used that exploits knowledge about the structure of the problem. Because most of the nonlinearities present in the thermally coupled GDP model are bilinear, we develop a solution methodology that leverages recent advances in MIQCP solver performance to find globally optimal solutions.

Each separation task in the thermally coupled model is represented as a pair of disjunctive relations, as shown below. The left side disjunct is for an active separation task, *t*, and the right side disjunct is for an inactive separation task, in which associated variables are set to zero. The total molar flow mass balances, component summations, and recovery specifications are linear equations in terms of the decision variables of the problem. The Underwood equations are used to model internal vapor flows of each separation task and are the only modeling equations that have general nonlinear terms [11]. When a Big-M transformation is applied to the separation task disjuncts the Underwood equations yield general nonlinear terms in the MINLP.

Eqn. (3) shows one of the Underwood equations, in which $F_{i,t}$, $V_{r,t}$ and $V_{s,t}$ are molar flow rates. The relative volatility of a component *i*, $\alpha_i$, is assumed to be constant, and is thus a parameter. The other decision variable present in the equations is the Underwood root, $\phi_{r,t}$. By introducing an intermediate variable, $Z_{i,r,t}$, in Eqn. (4), we can reformulate the shortcut equations into two constraints, Eqns. (5) and (6) that are bilinear.

$$\sum_{i \in Components} \frac{\alpha_i F_{i,t}}{\alpha_i - \phi_{r,t}} - \left(V_{r,t} - V_{s,t}\right) = 0 \qquad (3)$$

$$z_{i,r,t} = \frac{1}{\alpha_i - \phi_{r,t}} \qquad (4)$$

$$z_{i,r,t}\left(\alpha_i - \phi_{r,t}\right) = 1 \qquad (5)$$

$$\sum_{i \in Components} \alpha_i F_{i,t}\, z_{i,r,t} - \left(V_{r,t} - V_{s,t}\right) = 0 \qquad (6)$$

After reformulating the shortcut equations, Big-M transformation of the GDP will yield a non-convex MIQCP. The transformation from a MINLP to a MIQCP is useful

Mass Balance

$$\begin{bmatrix} Y_t \\ FT_t = DT_t + BT_t \\ DT_t + L_{r,t} = V_{r,t} \\ BT_t + V_{s,t} = L_{s,t} \end{bmatrix}$$

Component Summation

$$FT_t = \sum_{i \in Components} F_{i,t}$$

$$DT_t = \sum_{i \in Components} D_{i,t}$$

Recovery Specification

$$BT_t = \sum_{i \in COMP} B_{i,t}$$

$$D_{i,t} \geq x_i F_{i,t} \quad i \in LK_t$$

$$B_{i,t} \geq x_i F_{i,t} \quad i \in HK_t$$

Underwood Equations

$$\sum_{i \in Components} \frac{\alpha_i F_{i,t}}{\alpha_i - \phi_{r,t}} - \left(V_{r,t} - V_{s,t}\right) = 0$$

$$\sum_{i \in Components} \frac{\alpha_i D_{i,t}}{\alpha_i - \phi_{r,t}} \leq V_{r,t}$$

$$\sum_{i \in Components} \frac{\alpha_i B_{i,t}}{\alpha_i - \phi_{r,t}} \leq -V_{s,t}$$

Tray Number & Empirical Correlations

$$N_{trays,t} = 2 \cdot N_{min\ trays,t}$$

$$Height_t = f(Diameter, N_{trays})$$

$$Area_t = g(\rho_L, \rho_V, V_{r,t}, V_{s,t}, \sigma)$$

$$Cost_t = h(Diameter, N_{trays}, P)$$

$$\vee \begin{bmatrix} \neg Y_t \\ FT_t = DT_t = BT_t = 0 \\ F_{i,t} = D_{i,t} = B_{i,t} = 0 \quad \forall i \in Components \\ V_{r,t} = V_{s,t} = 0 \\ L_{r,t} = L_{s,t} = 0 \\ Area_t = Height_t = N_{trays,t} = 0 \\ Cost_t = 0 \end{bmatrix}$$

$$\forall\, t \in Tasks$$

because of recent advancements in solver performance for MIQCPs. While solving large-scale MINLPs still remains a challenge, Gurobi has seen a 450 times speedup in solving large-scale non-convex MIQCPs between versions 8 and 11 [6]. Note that this reformulation of the shortcut equations is exact, i.e. solving the MIQCP with a global solver will yield a solution to the original MINLP formulation.

## RESULTS

To demonstrate the computational advantages of the problem reformulation we use an example problem for the separation of a mixture of linear hydrocarbons. The model for thermally coupled columns is formulated as a MINLP and a MIQCP. Computational times are shown in Table 1 for an increasing number of components in the feed mixture. The superstructure of each problem instance was generating using the approach described in the Methodology section. We solve the MINLP with BARON and solve the MIQCP with both BARON [10] and Gurobi [6]. We achieve optimal results for increasingly large instances of the MIQCP in short run times. In solving the MINLP, BARON is able to find an incumbent solution, but after several hours of run time fails to make progress at reducing the gap.

The computational results demonstrate that the MIQCP reformulation significantly improves performance, especially for larger problem instances where conventional MINLP approaches struggle. Notably, all problem instances were constructed using automated superstructure generation methods, making the time required to build each instance negligible.

We also present the solution of a case study problem for the separation of a mixture of hydrocarbons. Table 2 shows the system feed specifications and desired recoveries. The problem is built using the automated superstructure approach as an MIQCP and solved with Gurobi. Figure 4 shows an illustration of the separation network that results from the solution. The system includes thermal coupling between some, but not all tasks, and can have the final separation tasks B/C and C/D integrated into the same column shell.

**Table 2.** System feed specifications for the separation of a zeotropic mixture of linear hydrocarbons.

| **Feed** ($F_{T0}$) | | 250 [kmol/hr] |
|---|---|---|
| **Desired Recovery** | | 0.98 |
| **Species** | **Molar Fraction in System Feed** | **Relative Volatility** |
| Hexane (A) | 0.1 | 8.9 |
| Heptane (B) | 0.25 | 5.7 |
| Octane (C) | 0.4 | 3.2 |
| Nonane (D) | 0.25 | 1 |

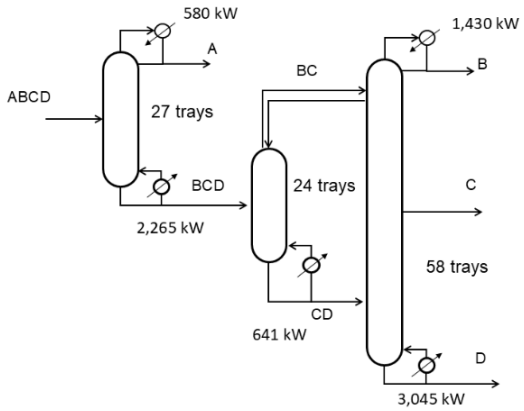



**Figure 4.** Illustration of the solution for the separation of a four component mixture of linear hydrocarbons. The second column, which is thermally coupled with the final column, acts as a prefractionator. The tasks B/C and C/D lack final product heat exchangers for C, so the component is taken off as a side draw.

It is worth noting that there are a variety of reasons for which the exact solution that results from the optimization problem may not be a good one to construct. Specifically, operability and control are some of the largest concerns with complex distillation arrangements. Since thermal couples have to exchange liquid and vapor stream between different separation tasks, maintaining precise control of column pressure is critical. Still, since the problems can be generated and solved quickly the solutions can be used to reduce the

**Table 1.** Computational results for the separation of a mixture of linear hydrocarbons with different formulations of the model for thermally coupled distillation columns.

| Problem Formulation | | MINLP | MIQCP | |
|---|---|---|---|---|
| # of components in feed mixture | # of separation tasks | BARON solve time (secs) | BARON solve time (secs) | Gurobi solve time (sec) |
| 3 | 4 | 171.7 | 899.66 | 0.51 |
| 4 | 10 | 7 hours (no progress) | 7 hours (no progress) | 2.8 |
| 5 | 20 | - | - | 105.96 |
| 6 | 35 | - | - | 1159.67 |

very high dimensional solution space of all column configurations to a few good initial designs as starting points. A modeler could alter the feed conditions or recovery fractions and quickly iterate through different solutions.

The computational speed-up presents an opportunity to solve much larger problems, such as non-sharp separation and divided wall column extensions [13].

## CONCLUSION

Despite decades of research, general process synthesis problems for separations remain challenging to formulate and solve. Traditional optimization approaches have often relied on heuristic algorithms tailored to specific problem instances, which limits their broader applicability and scalability. In this work, we demonstrated how automatic superstructure generation paired with state-of-the-art MIQCP solvers can provide an extensible and robust framework for process design. Our methodology facilitates the rapid design of thermally coupled distillation networks without the need for manual superstructure generation or heuristic decomposition methods. Our approach reduces the complexity of problem formulation and ensures that the solution process scales effectively to larger systems.

The success of this approach in distillation network synthesis highlights its potential to be extended to other process synthesis challenges, such as membrane separation systems. Many other separation systems, such as membrane systems, also involve separating N-pure components and the automated superstructure generation process can be adapted for those systems as well. If governing equations for membrane separations or other separation techniques can be expressed as quadratic constraints, advanced MIQCP solvers could be employed to find optimal solutions. Such extensions hold promise for applications such as a network for critical mineral recovery, where membrane systems are valued for their energy efficiency and selectivity.

## REFERENCES


1. Andrecovich, M. J., & Westerberg, A. W. (1985). An MILP formulation for heat-integrated distillation sequence synthesis. *AIChE Journal*, *31*(9), 1461–1474.
2. Caballero, J. A., & Grossmann, I. E. (2001). Generalized Disjunctive Programming Model for the Optimal Synthesis of Thermally Linked Distillation Columns. *Industrial & Engineering Chemistry Research*, *40*(10), 2260–2274.
3. Caballero, J. A., & Grossmann, I. E. (2003). Thermodynamically equivalent configurations for thermally coupled distillation. *AIChE Journal*, *49*(11), 2864–2884.
4. Caballero, J. A., & Grossmann, I. E. (2004). Design of distillation sequences: From conventional to fully thermally coupled distillation systems. *Computers & Chemical Engineering*, *28*(11), 2307–2329.
5. Gorak, A., & Sorensen, E. (2014). *Distillation: Fundamentals and principles*. Elsevier.
6. Gurobi Optimization, LLC (2024). Gurobi Optimizer Reference Manual 2024.
7. Nallasivam, U., Shah, V. H., Shenvi, A. A., Tawarmalani, M., & Agrawal, R. (2013). Global optimization of multicomponent distillation configurations: 1. Need for a reliable global optimization algorithm. *AIChE Journal*, *59*(3), 971–981.
8. Novak, Z., Kravanja, Z., & Grossmann, I. E. (1996). Simultaneous synthesis of distillation sequences in overall process schemes using an improved minlp approach. *Computers & Chemical Engineering*, 2012, 1425–1440.
9. Ramapriya, G. M., Selvarajah, A., Jimenez Cucaita, L. E., Huff, J., Tawarmalani, M., & Agrawal, R. (2018). Short-Cut Methods versus Rigorous Methods for Performance-Evaluation of Distillation Configurations. *Industrial & Engineering Chemistry Research*, *57*(22), 7726–7731.
10. Tawarmalani M., & Sahinidis N.V. (2005). A polyhedral branch-and-cut approach to global optimization. *Mathematical Programming 103*(2), 225-249.
11. Underwood, A. J. V. *Fractional Distillation of Multicomponent Mixtures | Industrial & Engineering Chemistry*. 1949
12. Yeomans, H., & Grossmann, I. E. (1999). A systematic modeling framework of superstructure optimization in process synthesis. *Computers & Chemical Engineering*, *23*(6), 709–731.
13. Caballero, J. A, & Grossmann, I. E. (2013). Synthesis of complex thermally coupled distillation systems including divided wall columns. *AIChE Journal, 59*(4), 1139 – 1159.



© 2025 by the authors. Licensed to PSEcommunity.org and PSE Press. This is an open access article under the creative commons CC-BY-SA licensing terms. Credit must be given to creator and adaptations must be shared under the same terms. See https://creativecommons.org/licenses/by-sa/4.0/




Systems & Control Transactions

**Research Article - Peer Reviewed Conference Proceeding**
ESCAPE 35 - European Symposium on Computer Aided Process Engineering
Ghent, Belgium. 6-9 July 2025
Jan F.M. Van Impe, Grégoire Léonard, Satyajeet S. Bhonsale,
Monika E. Polańska, Filip Logist (Eds.)

PSE PRESS

# Multi-objective Optimization of Steam Cracking Microgrid for Clean Olefins Production

**Saba Ghasemi Naraghi, Tylee Kareck[a], and Zheyu Jiang[s]***

[a] Oklahoma State University, Department of Chemical Engineering, Stillwater, Oklahoma, USA
* Corresponding Author: zheyu.jiang@okstate.edu.

## ABSTRACT

Olefins are essential precursors in producing a wide range of chemical products, including plastics, detergents, adhesives, rubber, and food packaging. Ethylene and propylene are the most ubiquitous olefin components and are predominantly produced through steam cracking. However, steam cracking is highly energy- and carbon-intensive, making its decarbonization a priority as the energy sector shifts toward clean, renewable electricity. Electrifying the steam cracking process is a promising pathway to reduce carbon emissions. However, this is challenged by the intrinsic conflict between the continuous operational nature of ethylene plants and the intermittent nature of renewable energy sources (e.g., solar and wind) in modern power systems. Massive energy storage systems or full plant reconfigurations to meet the power demand of electrified crackers are shown to be economically and practically infeasible. Thus, a more viable solution is to pursue a gradual electrification pathway and operate an ethylene plant as a microgrid that adopts diverse energy sources. To optimize the operational strategy of such a microgrid considering uncertainties in renewable energy generation and market prices, in this work, we introduce a stochastic multi-objective optimization approach that minimizes operating costs and carbon emissions of steam cracking. Results from a case study not only elucidate the trade-offs between economic and environmental objectives, but also provide insights into the optimal operating scheme in sustainable ethylene production.

**Keywords**: Steam cracking, Ethylene, Multi-objective Optimization, Renewable and Sustainable Energy, Decarbonization

## INTRODUCTION

The U.S. energy landscape is undergoing a fundamental transition as the proportion of clean, renewable electricity in total U.S. electricity generation will double to 44% between now and 2050 [1]. Thus, electrification is a promising pathway to decarbonize various energy-intensive chemical processes, including the steam cracking process for olefins production. Recently, there have been significant advancements in electrified cracking technology [2]. While conventional cracking furnaces transfer only 40-45% of firing energy to process fluids, electrified furnaces achieve efficiencies of at least 95% [2-4]. Most U.S. ethylene plants are large-scale, continuously operating facilities with capacities exceeding 1 million tons annually. Due to the intermittent nature of variable renewable electricity (VRE), energy storage solutions must be in place. However, the intermittent nature and seasonal variation in VAE generation will lead to a 1~2-order increase in battery storage requirements compared to the storage requirement based on the average daily power supply, making energy storage purely using battery an expensive option [5,6]. On the other hand, the use of byproduct hydrogen ($H_2$) as energy storage substantially reduces battery size. The combined use of solar and wind energy can significantly reduce storage requirements [5]. And low but continuing use of fossil fuels and a gradual transition from conventional crackers to electrified ones are feasible intermediate solutions toward long-term complete decarbonization [7].

In **Figure 1**, we propose a novel process scheme for steam cracking decarbonization that incorporate these important aspects. The envisioned process is a microgrid – a localized electric grid capable of independent

operation. Both electrified and conventional crackers are considered in this superstructure. Diverse energy sources, including on-site VRE, battery storage, electrolyzers, $H_2$ fuel cells as well as conventional natural gas and liquid fuel, can be adopted. Operating the cracking plant as a microgrid offers several advantages, including enhanced resilience, efficiency, and flexibility [8]. For example, a microgrid can operate in grid-connected mode to benefit from low electricity prices or in islanded mode to ensure continuous operation during grid outages or price spikes.

This study builds on our previous work [7] and explores the optimization of microgrid scheduling for clean ethylene production based on the superstructure shown in **Figure 1**. A hypothetical ethylene plant located on the Texas Gulf Coast is used as a case study, with ethane selected as the primary feedstock due to its prevalence in U.S. crackers [1]. A deterministic, steady-state, multi-objective MILP model will be developed to determine the optimal electrification level for our hypothetical plant, and uncertainties in VRE generation and market price predictions will be considered as different scenarios.

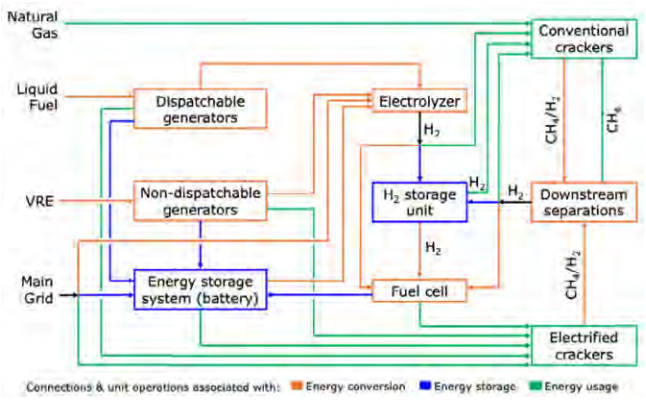



**Figure 1.** Our envisioned framework for using electricity to supply process heat for steam cracking [7]. Based on the context, the connections shown in the superstructure can represent either energy or mass flows.

## MULTI-OBJECTIVE SCENARIO-BASED OPTIMAL SCHEDULING FORMULATION

Before formulating the microgrid scheduling problem, a preliminary calculation [6] demonstrates the importance of incorporating diverse energy sources and energy storage systems for electrified cracking. In the case of a plant with an ethylene production capacity of 1 million tons/year, even if one ignores seasonal variation, since VRE is accessible for only 30% of the day on average, around 70% of the daily energy demand – equivalent to 3,356 MWh – must be stored to ensure uninterrupted operation of electrified crackers. Relying solely on battery would require an excessive amount of battery storage units. For example, if all the electricity is stored using Tesla Megapack, each with 3.9 MWh of energy capacity and 40.7 $m^3$ of storage volume [12], the resulting battery volume would occupy a massive structure of 32.7 m × 32.7 m × 32.7 m. Furthermore, this storage requirement could increase by one to two orders of magnitude due to variations in daily and seasonal weather patterns [5]. These findings highlight the need for a hybrid energy landscape, as illustrated in **Figure 1**, which integrates both dispatchable and non-dispatchable generators. Dispatchable generators, powered by fossil fuel (e.g., diesel) and controlled by microgrid master controllers, are subject to operational constraints such as generation limits, ramping rates, and minimum on/off times [13]. In contrast, non-dispatchable generators are driven solely by the availability and capacity of VRE sources and operate independently. Motivated by these results, we develop a multi-objective scenario-based mixed-integer linear programming (MILP) model to identify the optimal schedule for the microgrid and the optimal degree of electrification for ethane cracking.

### Mathematical Formulation

In this section, we describe MILP model in detail. First, the objective function (1) minimizes the expected daily operating cost, which includes fuel costs ($c^{NG}$), electricity costs from the main grid ($c^G$), local energy generation costs by dispatch units ($c^D$) and fuel cell units ($c^{FC}$), startup ($c^D_{SU}$) and shutdown costs ($c^D_{SD}$), and $H_2$ generation($c^{EL}$) and storage ($c^{HS}$) costs across all scenarios $\omega \in \Omega$. The maximization function in the startup and shutdown costs in the objective function can be easily linearized. Constraint (2) adopts the $\epsilon$-constraint approach for modeling the trade-off between operating costs and environmental impacts by ensuring that the expected total released $CO_2$-equivalent emissions in every hour generated by all cracker units do not exceed a specified level. Note that burning one ton of natural gas in conventional cracker releases approximately 2.95 ($E^{NG}$) tons of $CO_2$-equivalent emissions [14]. Meanwhile, based on current power generation technologies, each MWh of electricity from the power grid is associated with 0.434 ($E^G$) tons of $CO_2$-equivalent emissions [15]. Equations (3) and (4) are energy balance equations with respect to the amount of ethylene produced by conventional crackers (CC) and electrified (EC) ones, respectively. In our previous work [7], we developed a differential-algebraic equation (DAE) numerical model for ethane cracking based on detailed kinetics model [16] and solved the resulting dynamic optimization problem in pyomo.dae [17] to obtain that the minimum energy required to produce one ton of ethylene in a conventional cracker ($P^{CC}$) and electrified cracker ($P^{EC}$) are 4.27 MWh and 1.75 MWh, respectively (due to different thermal efficiencies). The RHS of Equations (3) and (4) uses the lower heating values of natural gas

($LHV^{NG}$) (13.826 MWh/ton) and $H_2$ ($LHV^{H_2}$) (33.320 MWh/ton). Assuming year-round continuous and steady-state operation of CCs and ECs, Equation (5) ensures that the hourly production rate of ethylene ($F^{C_2H_4}$) of all CCs and ECs must be 114.155 ton/h to achieve an annual production target of 1 million tons. After steam cracking, the product stream undergoes a series of downstream processing steps to obtain individual product streams, including $C_2H_4$, $C_3H_6$, $H_2$, and other value-added hydrocarbons. For $CH_4$ produced by ECs and CCs, it will be directly recycled to power the CCs, as shown in Equation (6). For byproduct $H_2$, it can either be stored in $H_2$ storage (HS) units, or be used to power the CCs or produce electricity in fuel cell (FC) units [18], as described in Equation (7). The mole fractions of $CH_4$ ($R^{Mix,CH_4}$) and $H_2$ ($R^{Mix,H_2}$) in the product mixture are 0.469 and 0.531, respectively [7]. Furthermore, we assume $CH_4$ and $H_2$ recovery rates in downstream separation units to be 99.7% ($r^{CH_4}$) and 99% ($r^{H_2}$), respectively [7]. Next, given that the ratio of product flow rates between $H_2$ and $C_2H_4$ ($R^{H_2}$) is 0.149 as determined from the DAE model [7], equations (8-9) indicate that not all $CH_4$ and $H_2$ produced have to be recycled. Equation (10) limits the amount of $H_2$ in a HS unit to its storage capacity ($HSC$) which is 15 tons. Equations (11-12) are hydrogen balances around the HS unit and electrolyzer (EL). The energy balance for the electrolyzer is shown in Equation (13) using the NREL-validated PEM stack efficiency ($\eta^{EL}$) of 73.6% [19] and the theoretical electrolysis energy requirement ($\dot{Q}^{H_2}$) of 40 MWh/ton. Equation (14) indicates the current $H_2$ production capacity ($F_{EL}^{H_2}$) from the electrolyzer (0.6 ton/h). The fuel cell energy balance, generation limit, and power distribution constraints are formulated in Equations (15-17), where we assume a 65% fuel cell efficiency ($\eta^{FC}$) and a power generation capacity ($\bar{P}^{FC}$) of 1 MW. Equations (18-22) show power distribution associated with the local non-dispatchable, dispatchable, energy storage system (both charging and discharging), and main grid. In Equation (23), we set the allowable power withdrawal from the main grid to the microgrid to be at most 50 MW ($\bar{P}^{G}$). Additional constraints related to local dispatchable generation, ramping, up/downtime, energy storage charging/discharging, and power storage are described in [9] and also included in the model [7].

$$\min \sum_{\omega\in\Omega}\sum_{t\in T}\rho_\omega[c^{NG}F_{CC,t,\omega}^{NG}\Delta t+\sum_{g\in G}\big(c^{NG}F_{g,t,\omega}^{D}\Delta t+ c^{D}p_{g,t,\omega}^{D}+ c_{SU}^{D}\max\{0,x_{g,t,\omega}^{D}- x_{g,t-1,\omega}^{D}\}+ c_{SD}^{D}\max\{0,x_{g,t-1,\omega}^{D}- x_{g,t,\omega}^{D}\}\big)+c_{t,\omega}^{G}P_{t,\omega}^{G}+c^{FC}p_{t,\omega}^{FC}+ c^{EL}F_{EL,t,\omega}^{H_2}\Delta t+ c^{HS}M_{HS,t,\omega}^{H_2}\ ],(1)$$

$$\sum_{\omega\in\Omega}\rho_w\Delta t\left[E^{NG}\left(F_{CC,t,\omega}^{NG}+F_{sep,t,\omega}^{NG}+\sum_{g\in G}F_{g,t,\omega}^{D}\right)+E^{G}P_{t,\omega}^{G}\right]\le\epsilon,\forall t\in T,\ (2)$$

$$P^{CC}F_{CC,t,\omega}^{C_2H_4}=LHV^{NG}\big(F_{CC,t,\omega}^{NG}+F_{sep,t,\omega}^{CH_4}\big)+LHV^{H_2}\big(F_{sep,t,\omega}^{H_2}+F_{EL,CC,t,\omega}^{H_2}+F_{HS,CC,t,\omega}^{H_2}\big),\forall t\in T,\omega\in\Omega,(3)$$

$$P^{EC}F_{EC,t,\omega}^{C_2H_4}=\sum_{g\in G}p_{EC,g,t,\omega}^{D}+P_{EC,t,\omega}^{ND}+P_{EC,t,\omega}^{G}+P_{EC,t,\omega}^{ESS}+P_{EC,t,\omega}^{FC},\forall t\in T,\omega\in\Omega,(4)$$

$$F_{CC,t,\omega}^{C_2H_4}+F_{EC,t,\omega}^{C_2H_4}=F^{C_2H_4},\quad\forall t\in T,\omega\in\Omega\ (5)$$

$$F_{sep,CC,t,\omega}^{CH_4}=r^{CH_4}R^{Mix,CH_4}\big(F_{CC,sep,t,\omega}^{C_2H_4,H_2}+F_{EC,sep,t,\omega}^{C_2H_4,H_2}\big),\forall t\in T,\omega\in\Omega,(6)$$

$$F_{sep,CC,t,\omega}^{H_2}+F_{sep,HS,t,\omega}^{H_2}+F_{sep,FC,t,\omega}^{H_2}=r^{H_2}R^{Mix,H_2}\big(F_{CC,sep,t,\omega}^{C_2H_4,H_2}+F_{EC,sep,t,\omega}^{C_2H_4,H_2}\big),\forall t\in T,\omega\in\Omega,(7)$$

$$F_{CC,sep,t,\omega}^{C_2H_4,H_2}\le R^{H_2}F_{CC,t,\omega}^{C_2H_4},\forall t\in T,\omega\in\Omega,(8)$$

$$F_{EC,sep,t,\omega}^{C_2H_4,H_2}\le R^{H_2}F_{EC,t,\omega}^{C_2H_4},\forall t\in T,\omega\in\Omega,(9)$$

$$0\le M_{HS,t,\omega}^{H_2}\le HSC,\forall t\in T,\omega\in\Omega,(10)$$

$$M_{HS,t,\omega}^{H_2}=M_{HS,t-1,\omega}^{H_2}+\Delta t\big(F_{sep,HS,t,\omega}^{H_2}+F_{EL,HS,t,\omega}^{H_2}-F_{HS,FC,t,\omega}^{H_2}-F_{HS,CC,t,\omega}^{H_2}\big),\forall t\in T,\omega\in\Omega,(11)$$

$$F_{EL,t,\omega}^{H_2}=F_{EL,FC,t,\omega}^{H_2}+F_{EL,HS,t,\omega}^{H_2}+F_{EL,CC,t,\omega}^{H_2},\forall t\in T,\omega\in\Omega,(12)$$

$$F_{EL,t,\omega}^{H_2}=\frac{\eta^{EL}}{\dot{Q}^{H_2}}\left(\sum_{g\in G}p_{EL,g,t,\omega}^{D}+P_{EL,t,\omega}^{ND}+P_{EL,t,\omega}^{G}+P_{EL,t,\omega}^{ESS}\right),\forall t\in T,\omega\in\Omega,(13)$$

$$0\le F_{EL,t,\omega}^{H_2}\le F_{EL}^{H_2},\forall t\in T,\omega\in\Omega,(14)$$

$$p_{t,\omega}^{FC}=\eta^{FC}LHV^{H_2}\big(F_{HS,FC,t,\omega}^{H_2}+F_{EL,FC,t,\omega}^{H_2}+F_{sep,FC,t,\omega}^{H_2}\big)\Delta t,\forall t\in T,\omega\in\Omega,(15)$$

$$0\le p_{t,\omega}^{FC}\le\bar{P}^{FC}x_{t,\omega}^{FC},\forall t\in T,\omega\in\Omega,(16)$$

$$p_{t,\omega}^{FC}=p_{EC,t,\omega}^{FC}+p_{ESS,t,\omega}^{FC},\forall t\in T,\omega\in\Omega,(17)$$

$$P_{t,\omega}^{WT}+P_{t,\omega}^{PV}=p_{EC,t,\omega}^{ND}+p_{ESS,t,\omega}^{ND}+p_{EL,t,\omega}^{ND},\forall t\in T,\omega\in\Omega,(18)$$

$$P_{g,t,\omega}^{D}=p_{EC,g,t,\omega}^{D}+p_{ESS,g,t,\omega}^{D}+p_{EL,g,t,\omega}^{D},\forall g\in G,t\in T,\omega\in\Omega,(19)$$

$$P_{C,t,\omega}^{ESS}=\sum_{g\in G}p_{ESS,g,t,\omega}^{D}+p_{ESS,t,\omega}^{G}+p_{ESS,t,\omega}^{ND}+p_{ESS,t,\omega}^{FC},\forall t\in T,\omega\in\Omega,(20)$$

$$P_{DC,t,\omega}^{ESS}=P_{EC,t,\omega}^{ESS}+P_{EL,t,\omega}^{ESS},\forall t\in T,\omega\in\Omega,(21)$$

$$P_{t,\omega}^{G}=p_{EC,t,\omega}^{G}+p_{ESS,t,\omega}^{G}+p_{EL,t,\omega}^{G},\forall t\in T,\omega\in\Omega,(22)$$

$$0\le P_{t,\omega}^{G}\le\bar{P}^{G},\forall t\in T,\omega\in\Omega.(23)$$

## ILLUSTRATIVE CASE STUDY

In this section, we illustrate the proposed multi-objective scenario-based MILP model in a case study of a hypothetical plant designed with an ethylene production capacity of 1 million tons per year. Each cracking furnace in the U.S. typically can produce 100,000 to 250,000 tons of ethylene per year. Based on this, we assume the plant operates with five ethane crackers, each with a production capacity of 200,000 tons of $C_2H_4$ per year. The microgrid is equipped with 20 natural gas-powered local generators with minimum (resp. maximum) capacity of 1 (resp. 5) MW, a minimum up/downtime of 3 hr, a ramp-up/down rate of 2.5 MW/h, and an operating cost of $33.4/MWh. The battery storage units have a total capacity of 20 MWh with 5 hours of minimum charging/discharging time. The minimum and maximum capacities of charging/discharging power are 0.8 and 4 MW, respectively. Our planning horizon is 24 hours.

**Table 1:** Probability of generated scenarios for LMP, wind power, and PV.

| Scenario number used in Table 2 | Probability of uncertain parameter (%) | | |
|---|---|---|---|
| | LMP | WP | PV |
| 1 | 64.50 | 14.48 | 4.86 |
| 2 | 2.92 | 1.52 | 60.31 |
| 3 | 3.26 | 64.91 | 15.81 |
| 4 | 1.29 | 6.18 | 32.96 |
| 5 | 28.03 | 13.91 | 16.06 |

**Table 2:** Probability of generated scenarios (after scenario reduction) for the microgrid problem after scenario reduction.

| Combined scenario | Selected LMP scenario | Selected WP scenario | Selected PV scenario | Probability (%) |
|---|---|---|---|---|
| 1 | 5 | 3 | 2 | 18.21 |
| 2 | 1 | 3 | 4 | 45.56 |
| 3 | 1 | 1 | 3 | 4.54 |
| 4 | 5 | 3 | 3 | 9.50 |
| 5 | 1 | 3 | 5 | 22.19 |

Electricity market prices, along with solar and wind energy generation, are inherently intermittent. To account for these uncertainties in our model, we generate five scenarios for each uncertain parameter using Monte Carlo simulations based on a log-normal distribution, ensuring that no negative parameter values are produced [7]. These scenarios are derived using publicly available data from the Texas grid (ERCOT) for August 2024. For locational marginal pricing (LMP), we select Bus TC-KO arbitrarily as a representative case without loss of generality. **Table 1** summarizes the probabilities of scenarios for each uncertain parameter. Note that the combination of these scenarios results in $5^3 = 125$ possible outcomes. To manage this complexity, we apply a scenario reduction technique to identify 5 representative combinations. This is achieved using a probability distance algorithm based on the Kantorovich distance [9] (see **Table 2**). **Figures 2 through 4** illustrate the mean and average values for electricity market prices, wind power, and solar power across the 5 representative scenarios synthesized.

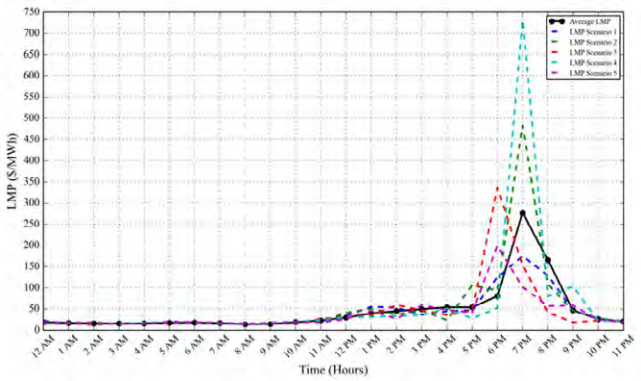



**Figure 2.** The electricity market prices (in $/MWh) of the five scenarios considered.

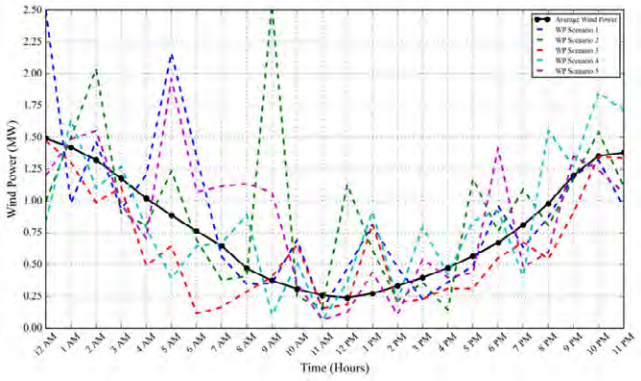



**Figure 3.** The generation output (in MW) of wind turbines of the five scenarios considered.

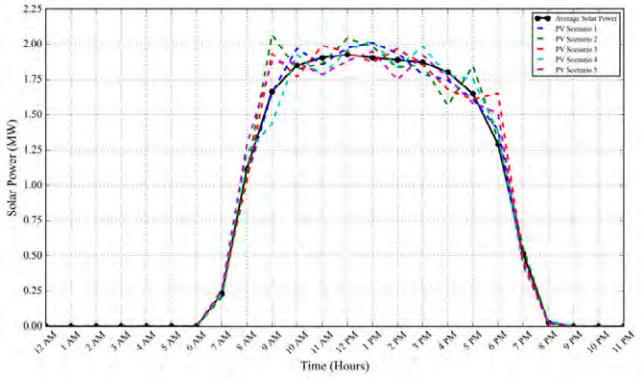



**Figure 4.** The output power (in MW) of solar panels of the five scenarios considered.

First, we solve the problem without incorporating the $\epsilon$ -constraint of Equation (2) to determine the

minimum operating cost and the corresponding degree of electrification (i.e., % of ethylene produced from ECs) required. The minimum expected daily operating cost is calculated to be $11,705.22, with 5.28% of the daily ethylene production coming from electrified crackers. The expected daily $CO_2$-equivalent emissions amounted to 919.42 tons, with the maximum hourly emissions reaching 39.43 tons (the first row in **Table 3**).

Next, we solve the problem for different values of $\epsilon \in [32,39]$ to evaluate the corresponding optimal operating and degree of electrification. It is important to note that the problem becomes infeasible when $\epsilon = 32$, indicating that reducing the hourly $CO_2$-equivalent emissions to less than 33 tons is not feasible with the current technology. The results, summarized in **Table 3**, show that the highest degree of electrification achievable is 19.25%, which corresponds to an operating cost of $33,884.81 – a 189.5% increase compared to the case without the $\epsilon$-constraint (the first row in **Table 3**). On the other hand, the expected daily $CO_2$-equivalent emissions are reduced by 13.86% (almost 130 tons).

**Table 3:** Summary of expected operating costs, degrees of electrification, and $CO_2$-equivalent emissions for different values of $\epsilon$, highlighting the trade-offs between emissions reduction and associated costs.

| # | $\epsilon$ (tons) | Expected $CO_2$-equiv emissions (tons) | Degree of electrification (%) | Expected operating cost ($) |
|---|---|---|---|---|
| 1 | 39 | 918.70 | 5.46 | 11,755.57 |
| 2 | 38 | 910.08 | 7.65 | 12,172.48 |
| 3 | 37 | 887.99 | 12.06 | 14,225.26 |
| 4 | 36 | 863.99 | 14.59 | 17,556.30 |
| 5 | 35 | 840.00 | 16.77 | 21,792.20 |
| 6 | 34 | 815.99 | 18.49 | 27,436.60 |
| 7 | 33 | 792.00 | 19.25 | 33,884.81 |

Here, we discuss some of the key findings and results. First, **Figures 5 and 6** illustrate the Pareto front and the operating cost-degree of the electrification relationship, respectively, providing quantitative insights into the trade-off between the two important measures. Meanwhile, **Figure 7 and 8** illustrate changes in the expected transferred power from the main grid to the microgrid and the charge/discharge status of local energy storage system (batteries). As one would expect, these fluctuations are partly driven by hourly variations in electricity market prices (as shown in **Figure 2**). During peak hours, there will be less power transferred from the main grid to the microgrid, thereby prompting the chemical plant to prioritize local power generation or stored energy to maintain continuous operation. During off-peak hours, the microgrid can rely more on the main grid power to reduce operating costs. Additionally, this figure highlights the environmental considerations affecting grid power usage. As stricter $CO_2$-equivalent emission constraint ($\epsilon$) is enforced, the microgrid reduces its reliance on the main grid and favors cleaner, locally generated energy sources. This is due to the relatively high carbon footprint associated with main grid electricity given the existing energy landscape. Therefore, decarbonization of chemical manufacturing should not be considered in silo. Instead, it must be synergistically coupled with decarbonization in power systems to achieve holistic decarbonization that is economically favorable.

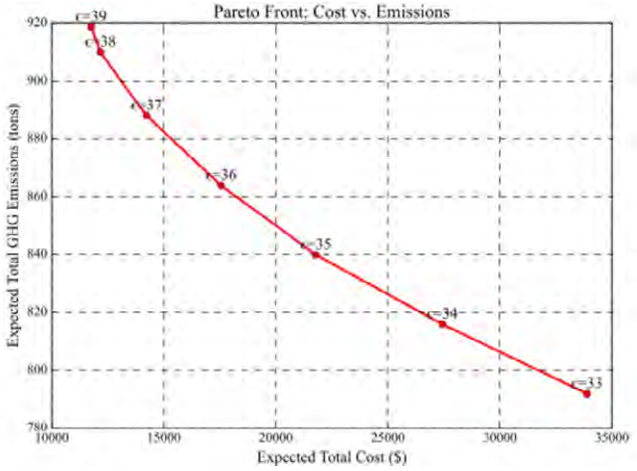



**Figure 5.** Pareto front showing the trade-off between expected daily operating cost and expected daily $CO_2$-equivalent emissions for different values of $\epsilon$. Each point represents an optimal solution for a specific $\epsilon$-value.

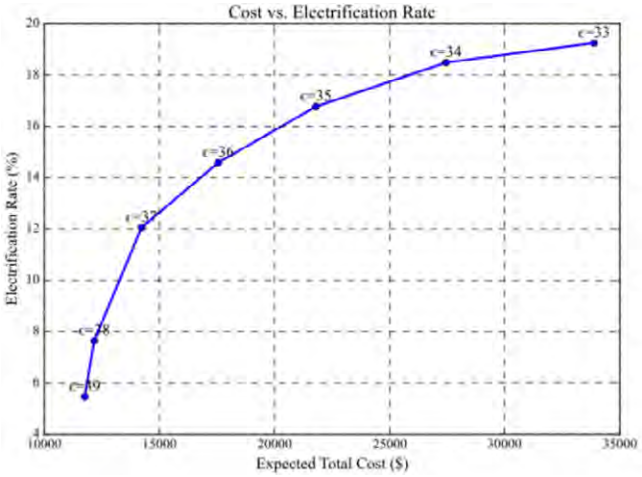



**Figure 6.** A concave relationship between expected operating cost and degree of electrification for different values of $\epsilon$. The plot highlights how the tightness of emission constraint affects of optimal degree of electrification and cost.

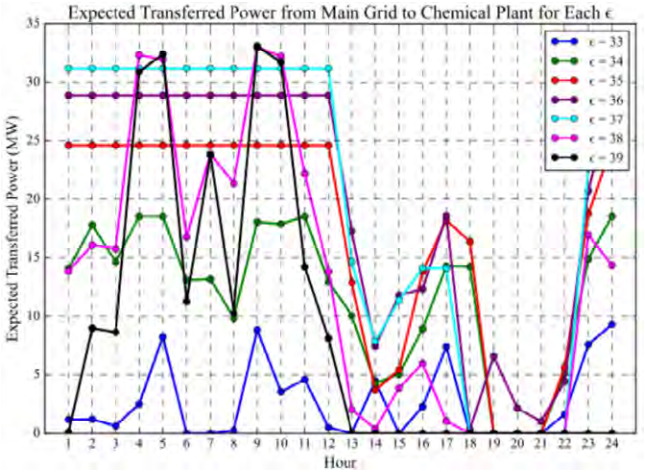



**Figure 7.** Expected transferred power from the main grid to the chemical plant.

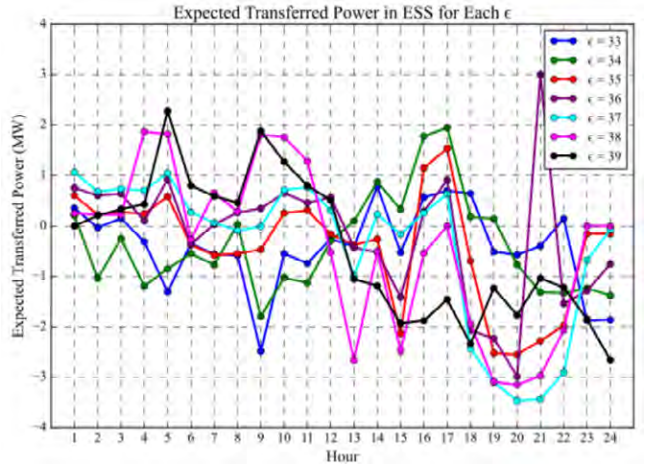



**Figure 8.** Expected charge/discharge power from ESS to ECs.

## CONCLUSION

This work presents an optimization framework for operating the microgrid that integrates electrified and conventional steam crackers along with renewable energy sources and diverse energy sources and storage systems. The proposed multi-objective scenario-based MILP model illustrates the feasibility of reducing CO2-equivalent emissions and the resulting process economics trade-off. The results suggest that, while higher degree of electrification leads to lower emissions, there is a lower limit to which electrification and decarbonization of steam cracking process can reach given 1) the limited capacities of energy storage systems and technology readiness of fuel cells and electrolyzers, and 2) the resulting increase in operating cost. Overall, operating the ethylene plant as a microgrid offers flexibility and resilience as it can better cope with the ongoing industrial decarbonization initiatives and the evolving U.S. energy landscape. Our proposed microgrid superstructure provides a viable solution for energy-intensive steam cracking process to transition toward being sustainable while economically competitive. Looking ahead, further research should explore the integration of emerging energy storage technologies, such as advanced batteries and thermal storage, to enhance the stability of electrified steam cracking. Additionally, policy incentives and carbon pricing mechanisms could play a critical role in making sustainable production pathways more economically viable. Future studies should also investigate the electrification of other key process units, such as distillation systems using heat pumps, and assess the feasibility of fully electrified cracking plant. Addressing these aspects will unlock the full decarbonization potential of clean olefins production while ensuring operational reliability and economic feasibility.

## ACKNOWLEDGEMENTS

This work is supported by the U.S. National Science Foundation under Award 2343072.

## REFERENCES

1. U.S. EIA. Annual Energy Outlook 2022. (2022)
2. T. Sinn, M. Hofstaetter, R. Kemper, and G. Kracker, Powering the Transition to Net Zero with Electric Cracking Technology. Chem. Eng. Prog. 120:42-49. (2024)
3. R. Agrawal, Z. Chen, and P. Oladipupo. Electrically heated dehydrogenation process. U.S. Patent Application: 2021395170-A1 (2021)
4. D. Maporti, F. Galli, P. Mocellin, and G. Pauletto. Flexible ethylene production: Electrified ethane cracking coupled with oxidative dehydrogenation. Eng Conversion and Management, 298:117761. (2023)
5. S. Du, Z. Chen, and R. Agrawal. Assessing large energy storage requirements for chemical plants powered with solar and/or wind electricity. Chem. Eng. J. 505:158863. (2024)
6. R. Agrawal and J. Siirola. Decarbonization of chemical process industries via electrification. (2023)
7. S. Ghasemi Naraghi, T. Kareck, R. Reed, P. Ramanan, and Z. Jiang. Decarbonization of Steam Cracking for Clean Olefins Production: Microgrid Planning and Operation. In: Optimization of Sustainable Process Systems: Multiscale Models and Uncertainties. John Wiley & Sons, Inc. (2025)
8. D. T. Ton and M. A. Smith. The U.S. department of energy's microgrid initiative. The Electricity Journal 25:84–94. (2012)
9. A. Khodaei. Microgrid optimal scheduling with multi-period islanding constraints. IEEE Transactions on Power Systems 29:1383–1392.

(2013)
10. A. G. Tsikalakis and N. D. Hatziargyrio. Centralized control for optimizing microgrids operation. IEEE power and energy society general meeting 1–8. (2011)
11. A. Gholami, T. Shekari, F. Aminifar, and M. Shahidehpour. Microgrid scheduling with uncertainty: The quest for resilience. IEEE Transactions on Smart Grid 7:2849–2858. (2016)
12. Tesla. Industrial lithium-ion battery emergency response guide. (2022)
13. A. Elmouatamid, R. Ouladsine, M. Bakhouya, N. El Kamoun, M. Khaidar, and K. ZineDine. Review of control and energy management approaches in micro-grid systems. Energies 14:168. (2020)
14. U.S EIA. Carbon dioxide emissions coefficients. https://www.eia.gov/environment/emissions/co2_vol_mass.php. (2024)
15. U.S EPA. Greenhouse gas equivalences calculator. https://www.epa.gov/energy/greenhouse-gas-equivalencies-calculator-calculations-and-references. (2022)
16. M.S. Yancheshmeh, S.S. Haghighi, M. Gholipour, O. Dehghani, M. Rahimpour, and S. Raeissi. Modeling of ethane pyrolysis process: A study on effects of steam and carbon dioxide on ethylene and hydrogen productions. Chem. Eng. J. 215:550. (2013)
17. B. Nicholson, J. Siirola, J.-P. Watson, V. Zavala, and L. Biegler. pyomo.dae: a modeling and automatic discretization framework for optimization with differential and algebraic equations. Mathematical Programming Computation, 10:187. (2018)
18. D.-Y. Lee and A. Elgowainy. By-product hydrogen from steam cracking of natural gas liquids (NGLs): Potential for large-scale hydrogen fuel production, life-cycle air emissions reduction, and economic benefit. International Journal of Hydrogen Energy 43:20143–20160. (2018)
19. U.S. DOE. Renewable electrolysis integrated systems development and testing. (2016)

© 2025 by the authors. Licensed to PSEcommunity.org and PSE Press. This is an open access article under the creative commons CC-BY-SA licensing terms. Credit must be given to creator and adaptations must be shared under the same terms. See https://creativecommons.org/licenses/by-sa/4.0/



Systems & Control Transactions

**Research Article - Peer Reviewed Conference Proceeding**
ESCAPE 35 - European Symposium on Computer Aided Process Engineering
Ghent, Belgium. 6-9 July 2025
Jan F.M. Van Impe, Grégoire Léonard, Satyajeet S. Bhonsale,
Monika E. Polańska, Filip Logist (Eds.)

PSE PRESS

# Pareto optimal solutions for decarbonization of oil refineries under different electricity grid decarbonization scenarios

**Keerthana Karthikeyan[a†], Sampriti Chattopadhyay[a†], Rahul Gandhi[b], Ignacio E Grossmann[a], Ana I Torres[a*]**

[a] Department of Chemical Engineering, Carnegie Mellon University, Pittsburgh 15213, PA, USA
[b] Shell Technology Center, Houston, 77082, USA
[†] Contributed equally
[*] Corresponding author: aitorres@cmu.edu

## ABSTRACT

In response to global efforts to reduce carbon emissions, the oil refining sector, a major source of industrial emissions, has set ambitious decarbonization targets. This study analyzes trade-offs between minimizing $CO_2$ emissions and costs through the use of Pareto optimal solutions. A superstructure optimization framework evaluates various technological pathways and timelines, employing a bi-criterion optimization approach using the $\epsilon$-constraint method. Results show that cost-effective, higher-emission solutions often involve natural gas-based technologies with carbon capture, while expensive, low-emission solutions favor electric power-based technologies. The analysis incorporates detailed assumptions about grid carbon intensity of varying degrees and accounts for varying national policies. Comparative case studies across locations highlight how grid carbon profiles influence optimal strategies, providing insights to inform local policies and incentivize technologies.

**Keywords**: Process Design, Optimization, Renewable and Sustainable Energy, Energy Policy, Carbon Capture, Decarbonization, Electrification

## INTRODUCTION

With each successive UN Climate Change Conference, the need for decisive climate action becomes increasingly evident. This year, for the first time, Earth is projected to exceed the 1.5°C of warming above pre-industrial levels, emphasizing the need for immediate action [1]. In response, nations worldwide have implemented stricter carbon pricing mechanisms, and set more ambitious net-zero targets to mitigate the accelerating climate crisis. The industrial sector is a major contributor to these global GHG emissions, with the key contributors in the US being oil refining (15%), cement production (7-8%), steel manufacturing (7-9%), and chemical production (4-6%) [2]. In particular, the oil refining sector faces increasing pressure to align with these climate objectives, while maintaining economic viability.

A conventional refinery processes various types of crude oil with variable compositions to produce various products, including liquified petroleum gas, gasoline, jet fuel, diesel, and paraffin through distillation and conversion units like hydrotreaters, crackers, and reformers. Burning of fossil fuels for heat, the Fluid Catalytic Cracker (FCC), and the Steam Methane Reformer (SMR), are identified as the main primary sources of scope 1 emissions accounting for 94% of total $CO_2$ emissions [4]. Recent studies have explored future refinery configurations and potential decarbonization pathways. Griffith et al. [3] highlight the dual role of refineries as both major contributors to greenhouse gas emissions, and critical actors in transitioning to sustainable energy systems in their critical review of socio-technical systems. They emphasize the importance of tailored strategies, including carbon pricing, stricter emissions controls, renewable technology investments, and subsidies. Bryum et al. [4] advocate for low-carbon hydrogen fuels, electrification, and Carbon Capture and Storage (CCS) as key measures,

proposing two conceptual designs for low-emission refineries. However, both studies offer qualitative insights without quantitative optimization strategies. Complementary analyses, such as those by Nixon et al. [5] evaluate the feasibility of CCS for oil refineries, and emphasize the need for combined approaches involving fuel substitution and emission offsets, while Li et al. [6] assess cost-effective $CO_2$ abatement technologies in China's refineries. These studies perform techno-economic assessments for different decarbonized technologies. Yáñez et al. [7] analyze $CO_2$ mitigation pathways for a Colombian oil refinery, while Sachs et al. [8] emphasize diverse technology mixes to meet climate targets, although their methodologies may not yield optimal solutions. Optimization-based approaches provide a more systematic perspective on refinery decarbonization. De Maigret et al. [9] employ a multiobjective optimization framework to minimize $CO_2$ emissions and costs for an Italian refinery, though their model focuses on short-term cost minimization without a transition timeline. Similarly, a paper by Zhang et al. [10] develops a multiperiod optimization model to obtain biomass-based retrofits, but omits options for scope-1 and scope-2 emission reductions. Beyond the refining sector, Sotiriou et al. [11] have developed a multi-objective optimization framework tailored to the dynamic policy context of EU member states, exploring trade-offs between stronger decarbonization ambitions and associated costs. This study has demonstrated the use of multi-objective optimization in planning problems involving longer time horizons.

Although techno-economic analyses are available for individual decarbonization initiatives, Chattopadhyay et al. [12][13] have highlighted the need for a specialized tool that can find decarbonization pathways for individual refineries based on specific factors such as production capacity, plant structure, and the cost of renewable energy sources. They have developed an optimization tool to address this problem. However, scope 2 emissions (stemming from the indirect consumption of purchased electricity) were not accounted for in their paper. The reality presents a complex landscape where scope 2 emissions significantly influence the economic viability, especially for electrification-based alternatives. This is relevant for multinational corporations whose refineries operate across different regions, each with unique regulatory frameworks and economic conditions. Our study addresses these limits and proposes a multi-objective optimization (MOO)-based framework for analysis. The rest of the paper is organized as follows; the various decarbonization pathways considered in the superstructure are presented, followed by the problem statement considered. A MOO problem modeling the superstructure by minimizing $CO_2$ emissions, and the present value of cost, are presented in the methodology section. Finally, in the results section, we compare the results obtained for Canada and the United States, subject to respective natural gas and electricity prices and carbon emission reduction policies.

The superstructure (Fig.1) consists of several decarbonized and current pathways for hydrogen production and steam generation. Alternatives for hydrogen production include traditional fossil-based processes, blue hydrogen production (involving steam methane reforming (SMR) augmented with post combustion or precombustion-based capture), and green hydrogen production via electrolysis, supported by technologies like proton exchange membrane electrolyzer (PEME) and alkaline electrolyzers (AE). Precombustion carbon capture requires less energy and is more cost-effective in terms of both capital and operational expenses. However, it is compatible only with gasification units that generate flue gas containing higher $CO_2$ concentrations. In contrast, post-combustion $CO_2$ capture, while demanding more energy, is capable of managing flue gas with lower $CO_2$ concentrations. Alkaline electrolyzers (AEs) are less energy efficient and have the drawback related to their shutdown current as they cannot operate at low current densities, but are cheaper than PEMEs. Process heating is achieved using high pressure steam (HPS), which is produced by natural gas boilers with or without carbon capture, or electric boilers. The superstructure also includes a pathway to capture $CO_2$ from flue gas emissions from other units such as FCC or furnaces, using post-combustion carbon capture. The problem involves strategic selection and timely implementation of the best set of initiatives for retrofitting the supply of HPS and hydrogen to the given refinery considering the operating data for a typical crude-based refinery, with a distillation capacity of 220 kbbl crude oil per day to minimize emissions and present value of cost.

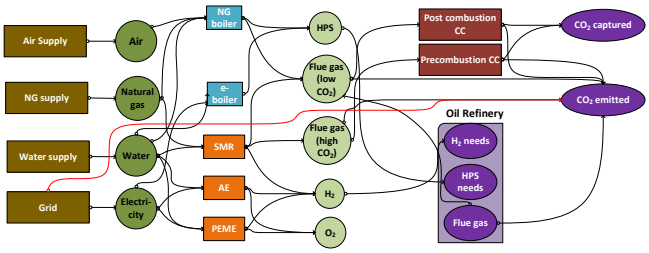



**Figure 1.** Superstructure showing options considered for decarbonization

## METHODOLOGY

The variables used in the model are, $F_{k,j,yr}$, a positive continuous variable representing the amount of component $k$ present in a stream flowing to or from a unit $j$ in year $yr$. $y_{j,yr}$ is a binary variable indicating whether the installation of a specific unit of technology $j$ (e.g. PEME, AE) takes place in the year $yr$. $Q_{j,yr}$; $(QE_{j,yr}/QD_{j,yr})$, a continuous variable indicating the total (expansion

in/decommissioned) capacity of a technology j in a given year $yr$. These constraints apply to all years in the entire time horizon i.e. 2022-2040 unless specified otherwise.

## Mass balance constraints

The proposed formulation requires specifying balances across the task nodes (or the technology units) and the resource nodes (or the components). The task balance involves Eqs. (1) and (2) relating the amount of components present in the inlet and outlet streams to a certain key component through simplified yield-based models. Eq. (1) represents a yield-based model where $\mu_{k,j}$ is the yield coefficient relating the flowrate of reactant $k$ to produce a certain flowrate of key component $k'_j$ in unit $j$. Similarly, in Eq. (2), $-\mu_{k,j}$ denotes the amount of by-product (e.g. $CO_2$) $k$ in the outlet stream of unit $j$, given a certain amount of key component $k'_j$ in the outlet stream. The total hydrogen and HPS produced across all pathways must match the refinery's overall hydrogen and HPS requirements. The $CO_2$ captured and emitted after passing through carbon capture units are proportional, determined by the efficiency of the respective CC equipment. Likewise, the steam generation and losses via the purge stream (blowdown) from boilers are proportional, governed by a constant factor.

$$F_{k,j,yr} = \mu_{k,j} F_{k_j',j,yr} \; if \; k \in \{In(j)\}, \mu_{k,j} \geq 0, \forall yr,$$

$$\forall \, j \in \{\text{AE, PEME, e-boiler, CC units, NG boiler, SMR}\} \quad (1)$$

$$F_{k,j,yr} = -\mu_{k,j} F_{k_j',j,yr} \; if \; k \in \{Out(j)\}, \mu_{k,j} \leq 0, \forall yr,$$

$$\forall \, j \in \{\text{AE, PEME, e-boiler, CC units, NG boiler, SMR}\} \quad (2)$$

Here, the notations $In(j)$ and $Out(j)$ represent the set of resource nodes connected at the inlet and outlet of node $j$ respectively. Additionally, mass balances are imposed across the resource nodes as shown in Eq. (3). Here $k$ denotes a particular component node and $In(k)$ and $Out(k)$ denote the set of task nodes connected at the inlet and outlet of resource node k. K denotes the set of all component nodes.

$$\sum_{l \varepsilon \, In(k)} F_{k,l,yr} = \sum_{j \varepsilon \, Out(k)} F_{k,j,yr} \quad \forall \, k \in \text{K}, \forall \, yr \quad (3)$$

## Energy balance and $CO_2$ intensity constraints

Energy balances for e-boilers, and electrolyzers are given by Eqs. (4) and (5) respectively where $P_{j,yr}$ denotes the power drawn from equipment j in a given year $yr$.

$$P_{\text{e-boiler, } yr} \eta_{\text{e-boiler}} = \Delta H_{vap} F_{H_2O,\text{e-boiler, } yr} \; \forall \; yr \quad (4)$$

$$F_{Hydrogen,j,yr} \Delta H_{electrolysis} = P_{j,yr} \, \eta_j, j \in \{PEME, AE\}, \forall \, yr \quad (5)$$

where $\eta_j$ denotes the energy efficiency of equipment $j$. The emissions from the grid are calculated using the Eq. (6) Here $CI_{yr}$ denotes the $CO_2$intensity of the grid.

$$CI_{yr} \sum_{j \varepsilon \, Out(Grid)} P_{j,yr} = \text{F}_{\text{grid,CO}_2,yr} \quad (6)$$

## Capacity expansion constraints

Eqs. (7) and (8) impose logical constraints on the capacity expansion/decommissioning capacity reduction in any year.

$$LB_j y_{j,yr} \leq QE_{yr} \leq UB_j y_{j,yr}$$

$$\forall \, \text{j} \in \{\text{AE, PEME, e- boiler, CC units}\} \quad (7)$$

$$LB_j y_{j,yr} \leq QD_{yr} \leq UB_j y_{j,yr} \; \forall \, \text{j} \in \{\text{SMR, NG-boiler}\} \quad (8)$$

Eqs. (9) and (10) evaluate the total capacity at the end of any year $yr$. [23, 19].

$$QE_{j,yr} + Q_{j,yr-1} = Q_{j,yr}$$

$$\forall \, \text{j} \in \{\text{AE, PEME, e-boiler, CC units}\} \quad (9)$$

$$-QD_{j,yr} + Q_{j,yr-1} = Q_{j,yr} \; \forall \, \text{j} \in \{\text{SMR, NG boiler}\} \quad (10)$$

Eqs. (11) and (12) state that the operating flow rate or power is less than the installed capacity and greater than a certain fraction (the minimum possible turn down $\chi_j$) of the installed capacities.

$$\chi_j Q_{j,yr} \leq P_{j,yr} \leq Q_{j,yr} \quad \text{j} \in \{\text{e-boiler, PEME, AE}\} \quad (11)$$

$$\chi_j Q_{j,yr} \leq F_{k'_j,yr} \leq Q_{j,yr} \; \text{j} \in \{\text{NG boiler, SMR, CC}\} \quad (12)$$

We assume that the capacity expansion for e-boilers and CC facilities can vary continuously, while the expansion of electrolyzer capacity is restricted to discrete increments corresponding to standard sizes. To handle this, we introduce non-negative integer variables $w_{j,s,yr}$ which denote how many electrolyzers, in year $yr$, of type $j \in \{\text{PEME, AE}\}$ are of size s, where $s \in [1, \text{Num. of available discrete sizes}]$, with $d_{j,s}$ denoting the available sizes for each type of electrolyzer. Eq. (13) adds the size of all installed electrolyzers to calculate the total capacity expansion in any given year [10].

$$\sum_s w_{j,s,yr} d_{j,s} = QE_{j,yr} \quad \text{j} \in \{\text{PEME, AE}\} \quad (13)$$

## Cost constraints and objective function

Eq. (14) expresses the total CAPEX for an expansion as $\alpha + \beta QE$, where $\alpha$ represents the fixed cost and $\beta QE$ represents the variable cost, $dur(j)$ represents the time taken to build a unit of tech. $j$. Eq. (15) enforces an upper limit on the annual capital expenditure (CAPEX) that can be allocated to these decarbonization initiatives.

$$CAPEX_{yr} = \Sigma_j \sum_{h=0}^{dur(j)-1} \frac{\alpha_{j,yr+h} y_{yr+h}}{dur(j)} + \sum_{h=0}^{dur(j)-1} \frac{\beta_{j,yr+h} \; QE_{j,yr+h}}{dur(j)} \quad (14)$$

$$CAPEX_{yr} \leq CAPEX \; CAP \quad (15)$$

The annual OPEX associated with decarbonization efforts, shown in Eq. (16), includes two key components: one arising from the use of natural gas and electricity, and the other, associated with the energy related to capture in CC units. The capture cost is directly proportional to the amount of emissions reduced via carbon capture.

$$OPEX_{yr} = \Big( \sum_{j \epsilon Out(NG)} \$_{\frac{NG}{unit\ mass}} F_{NG,j,yr} + \sum_{j \epsilon Out(Power)} \$_{\frac{electricity}{unit\ energy}} P_{j,yr} + \sum_{j \epsilon CCS\ Units} OPEX_j \, F_{Captured\ CO_2,j,yr} \Big) time \quad (16)$$

Finally, we formulate the objective functions as the present value of the cost of the decarbonization project (17), and the total emissions over the transition period

(18). The amount of $CO_2$ and other gases present in the flue-gas released from the rest of the operations in the refinery are specified additionally.

$$Minimize \sum_{yr=1}^{19}(CAPEX_{yr} + OPEX_{yr})/(1+i)^{yr} \quad (17)$$

$$Minimize \sum_{yr=1}^{19}\sum_{j\,\epsilon In(CO_2\ emission)} F_{CO_2 emission,\,j,yr} \quad (18)$$

The $\epsilon$-constraint method [14] is used to convert the second objective Eq. (18) into a constraint and the Pareto front is generated by plotting the ordered pair of objective values for the non-dominated solutions.

## RESULTS

The retrofit MILP model was implemented in Pyomo 6.6.1 with the Gurobi 10.0.1 solver [15] for a 19-year horizon, involving 1,160 variables (133 discrete, 1,027 continuous) and 1,197 constraints. Results are presented for two case studies, based on energy prices, policies, and grid carbon intensities for Canada and the USA. The Pareto fronts from the bi-criterion optimization highlight the effects of carbon mitigation policies, such as carbon taxes and tax credits, on the cost-emissions trade-off. The analysis also examines the role of scope-2 emissions on the non-dominated solutions. The CAPEX for carbon capture technologies was modeled as a linear function of the processed $CO_2$, with an intercept. Similarly, CAPEX for electrolyzers and e-boilers vary linearly with an intercept installed capacity, reflecting economies of scale. OPEX for carbon capture was tied to the amount of $CO_2$ captured.

### Canada

Electricity and natural gas prices for Canada, sourced from [16] [17] and shown in Figure 2 (a) and (b), were used to estimate the operational costs. While Canada aims for a net-zero electricity grid by 2035 [18], our scenarios project a 100% emissions reduction by 2040 (optimistic), 2043 (baseline), and 2045 (pessimistic), based on predicted greenhouse gas emissions from Annesley et al. [19] and grid mix forecasts from Canada's Energy Future 2021 [20] (shown in Fig. 2 (c)).

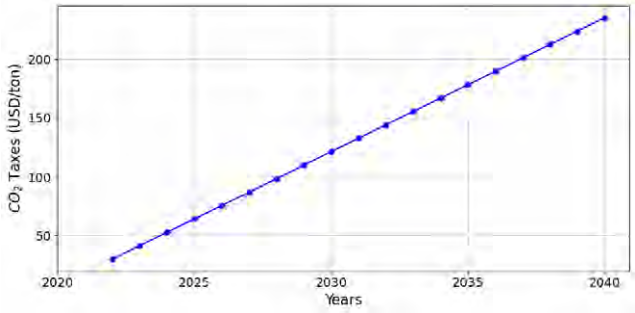



**Figure 3.** $CO_2$ taxes implemented as per Canadian rates

When $CO_2$ taxes are implemented as per the rates shown in Figure 3, we see that the Pareto front compresses towards low emission solutions as compared to the baseline solution (shown in Figure 4). Beyond a certain point, increasing the ε value does not reduce $CO_2$ emissions further, as the ε-constraint becomes inactive. Remaining within the ε limit is financially advantageous due to the penalties for exceeding it. Non-dominated solutions incur higher costs than the baseline due to the imposed penalties. Figure 5 shows that low-cost, non-dominated solutions obtained when $CO_2$ taxes are

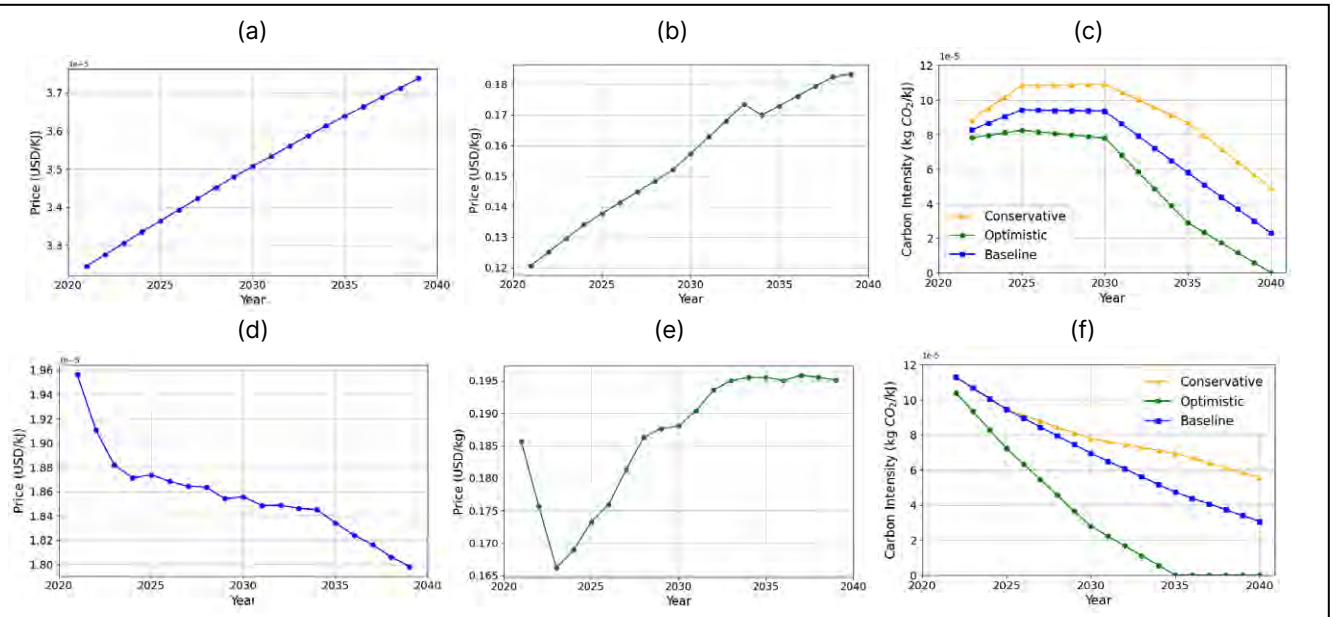



**Figure 2** (a) Canadian electricity price forecasts (b) Canadian natural gas price forecasts (c) Carbon intensity scenario forecasts for Canadian grid (d) US electricity price forecasts (e) US natural gas price forecasts (f) Carbon Intensity Scenarios for US grid

implemented. These favor carbon capture options. For higher cost and lower emission non-dominated solutions earlier, and higher adoption of both pre- and post-combustion carbon capture takes place. Since no cases include e-based options, variations in grid intensity profiles have no significant impact on the Pareto front.

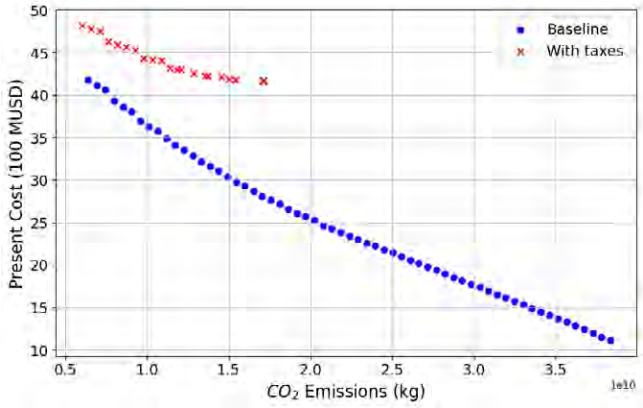



**Figure 4.** Pareto front with $CO_2$ taxes implemented

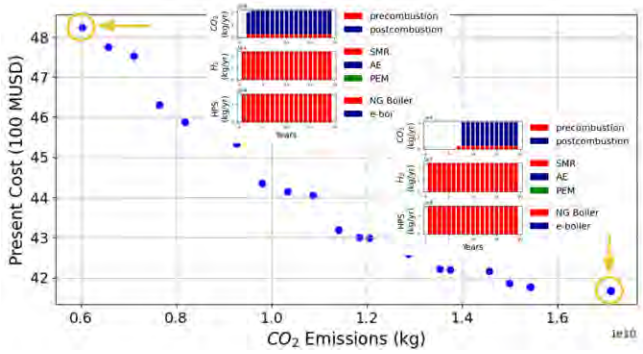



**Figure 5.** Canada with $CO_2$ taxes: Pareto front with the solutions shown for a few points.

## United States

The electricity and natural gas price projections, based on EIA data (Figure 2 (d) and 2 (e)), were used to estimate the operational cost estimates. Carbon intensity scenarios for the electricity grid included 3 cases with the optimistic case, predicting a 100% reduction in emissions by 2035, baseline 95% by 2050, and the pessimistic case 65% by 2050, informed by Leard et al [21]. Evaluating the effect of scope-2 emissions for different carbon intensity profiles of the grid (as shown in Figure 2 (f)) on the non-dominated solutions, we see in Figure 6 that with higher grid $CO_2$ intensities, carbon capture (CC)-based solutions were favored over e-based alternatives. The point on the Pareto-front with the lowest $CO_2$ emissions involve e-based solutions but was feasibly obtained only with the optimistic grid intensity predictions as shown in Figure 6. As per the 45Q tax credit rates under the Inflation Reduction Act USD [22], $ 85 are provided per metric ton of $CO_2$ captured and stored securely underground. It is assumed that the 45 Q credits increase at the same rate as the carbon taxes. Additionally, according to the 45 V tax credits, at least 0.6 USD tax credits are provided per kg of green $H_2$ produced. With the imposition of these incentives, as shown in Figure 7, the Pareto front shifts towards low-emission solutions, though the NPV values are lower than the base case due to the received credits. As shown in Figure 8, the non-dominated solutions resemble those in Figure 3, but the highest-cost, lowest-emission solution includes partial adoption of e-boilers.

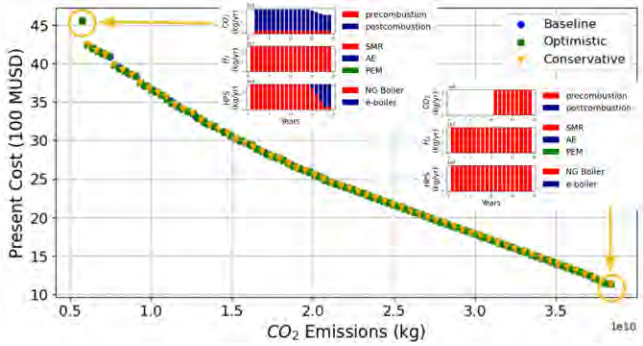



**Figure 6.** US : Pareto front under changing grid intensity profiles.

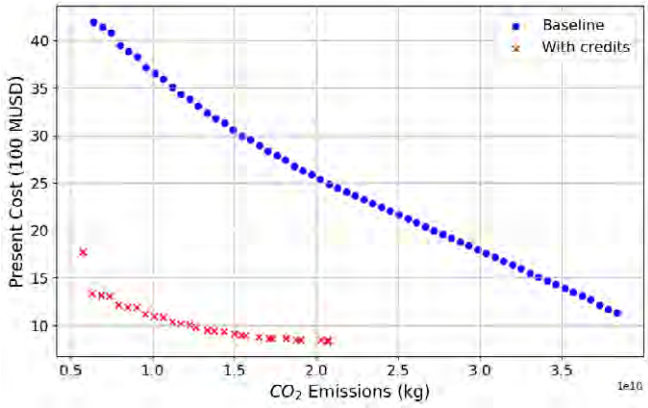



**Figure 7.** Pareto front with $CO_2$ credits implemented

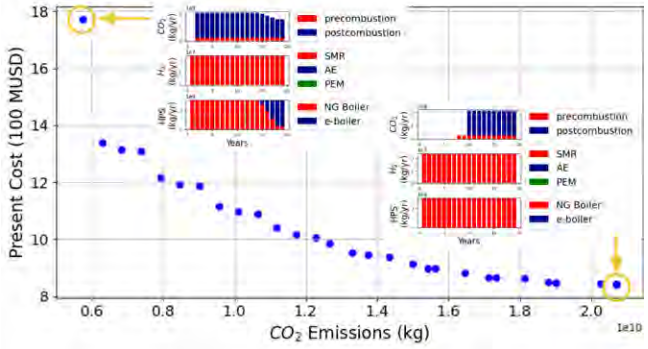



**Figure 8.** US with carbon credits: Pareto front with the solutions shown for a few points

## CONCLUSIONS

The multi-objective optimization framework developed in this paper, minimizes retrofit decarbonization costs and $CO_2$ emissions, providing insights into the trade-offs between cost and emissions under various scenarios. Solutions incorporating carbon capture (CC)

equipment were unaffected by changes in grid intensity, with several non-dominated solutions favoring earlier adoption of CC. E-based technologies are chosen exclusively when $CO_2$ emissions reach their minimum on the Pareto front, assuming the grid's $CO_2$ intensity decreases in line with optimistic projections. Carbon mitigation policies, such as carbon taxes and 45Q/V tax credits. compress the Pareto frontier toward low-emission, high-cost solutions, demonstrating their effectiveness in incentivizing aggressive emission reductions.

## ACKNOWLEDGMENTS

This work was financed [in part] by a grant from the Commonwealth of Pennsylvania, Department of Community and Economic Development. We acknowledge the support and funding from Shell Global and Shell Polymers Monaca.

## REFERENCES

1. Intergovernmental Panel on Climate Change (Climate Change 2022: Mitigation of Climate Change - Chapter 2: Emissions Trends and Drivers. (2022)
2. International Energy Agency. Emissions from Oil & Gas Operations in Net Zero Transitions. IEA (2022).
3. Griffiths, S.; Sovacool, B.; Kim, J.; Bazilian, M.; Uratani, J. Decarbonizing the oil refining industry: A systematic review of sociotechnical systems, technological innovations, Energy Research and Social Science, 89, 102542. (2022)
4. Byrum, Z.; Pilorgé, H.; Wilcox, J. Technological Pathways for Decarbonizing Petroleum Refining, World Resources Institute (2021)
5. Nixon, S.; Andrea, B.; David, D.; Mai, B.; Andres, G.-G.; Benoît, C. A pathway towards net-zero emissions in oil refineries. Frontiers in Chemical Engineering, 4, (2022)
6. Li, Y.; Wang, B.; Xie, Y.; Zhu, L. Cost and potential for CO2 emissions reduction in China's petroleum refining sector—A bottom-up analysis. Energy Reports 6,497–506.
7. Yáñez, C. E.; Meerman, H.; Ramírez, A.; Castillo, E.; Faaij, A. Fully Integrated CO2 Mitigation Strategy for an Existing Refinery: A Case Study in Colombia. Applied Energy, 307, 11877
8. Sachs, J.; Hidayat, S.; Giarola, S.; Hawkes, A. he role of CCS and biomass-based processes in the refinery sector for different carbon scenario Computer Aided Chemical Engineering; Elsevier B.V., Vol. 43; pp 1365–1370 (2018)
9. de Maigret, J.; Viesi, D.; Mahbub, M. S.; Testi, M.; Cuonzo, M.; Thellufsen, J. Z.; Østergaard, P. A.; Lund, H.; Baratieri, M.; Crema, L. A multi-objective optimization approach in defining the decarbonization strategy of a refinery. Smart Energy, 6, 100076. (2022)
10. Zhang, L.; Torres, A.; Bingzhen, C.; Zhihong, Y.; Grossmann, I. Optimal Retrofitting of Conventional Oil Refinery into sustainable Bio-refinery under uncertainty. AIChE Journal. (2023)
11. Sotiriou, C., & Zachariadis, T. A multi-objective optimisation approach to explore decarbonisation pathways in a dynamic policy context. Journal of Cleaner Production, 3sa19, 128623 (2021)
12. Chattopadhyay, S.; Gandhi, R.; Torres, A. I.; Grossmann, I. E. Optimization of Retrofit Decarbonization in Oil Refineries. In Proceedings of Foundations of Computer-Aided Process Design, (2024).
13. Chattopadhyay, S.; Karthikeyan, K.; Gandhi, R.; Grossmann, I.; Torres, A. Optimal retrofit decarbonization in oil refineries, Industrial & Engineering Chemistry Research, (Under Review).
14. Mesquita-Cunha, M.; Figueira, J. R.; Barbosa-Póvoa, A. P. New ϵ-Constraint Methods for Multi-Objective Integer Linear Programming: A Pareto Front Representation Approach, European Journal of Operational Research, 306(1), 286-307. (2023)
15. Gurobi Optimization, LLC, Gurobi Optimizer Reference Manual [Online]. (2023)
16. Canada Energy Regulator. Canada's Energy Future 2016: Energy Supply and Demand Projections to 2040. (2016)
17. Statista. Price of industrial electricity in Canada 2005-2040. https://statista.com/elec-prices-canada
18. Government of Canada. A Clean Electricity Standard in Support of a Net-Zero Electricity Sector: Discussion Paper. Environment and Climate Change Canada, (2022)
19. Public Policy Forum. Net Zero Electricity in Canada: Ensuring Electricity Capacity for a Net Zero Economy. Public Policy Forum,
20. Canada Energy Regulator. www.cer-rec.gc.ca/en/data-analysis/canada-energy-future
21. Leard, B & Greene, D. Coordinating the electric vehicle transition and electricity grid decarbonization in the U.S. is not essential to achieving substantial long-term carbon dioxide emissions reductions. Environmental Research Letters (2023)
22. Internal Revenue Service. https://www.irs.gov/instructions/i8933

© 2025 by the authors. Licensed to PSEcommunity.org and PSE Press. This is an open access article under the creative commons CC-BY-SA licensing terms. Credit must be given to creator and adaptations must be shared under the same terms. See https://creativecommons.org/licenses/by-sa/4.0/



Systems & Control Transactions

**Research Article - Peer Reviewed Conference Proceeding**
ESCAPE 35 - European Symposium on Computer Aided Process Engineering
Ghent, Belgium. 6-9 July 2025
Jan F.M. Van Impe, Grégoire Léonard, Satyajeet S. Bhonsale,
Monika E. Polańska, Filip Logist (Eds.)

PSE PRESS

# Green Hydrogen Transport across the Mediterranean Sea: A Comparative Study of Liquefied Hydrogen and Ammonia as Carriers

**Federica Restelli[a]*, Elvira Spatolisano[a], and Laura A. Pellegrini[a]**

[a] GASP - Group on Advanced Separation Processes & GAS Processing, Dipartimento di Chimica, Materiali e Ingegneria Chimica "G. Natta", Politecnico di Milano, Piazza Leonardo da Vinci 32, 20133 Milano, Italy
* Corresponding Author: federica.restelli@polimi.it.

## ABSTRACT

Green hydrogen is widely recognized as a key player in the decarbonization of the energy system. To transport it efficiently, hydrogen must be converted into a carrier, such as liquefied hydrogen or ammonia, to increase its volumetric density. The supply chain of these carriers includes hydrogen conversion into the carrier, overseas transport, and carrier reconversion back to hydrogen. A case study involving hydrogen transportation across the Mediterranean Sea is used to evaluate the carrier efficiency. The processes involved in the supply chain are simulated in Aspen Plus® V11 to determine material and energy balances, and the "net equivalent hydrogen" method is applied to calculate the equivalent amount of hydrogen needed to supply thermal or electric power. The efficiency, defined as the ratio of net hydrogen delivered (after accounting for consumption and boil-off losses) to the initial hydrogen input, is higher for ammonia than for liquefied hydrogen (73% vs 60%, respectively). This advantage lies in the lower overall hydrogen consumption for ammonia synthesis and cracking compared to liquefaction.

**Keywords**: green hydrogen, green ammonia, liquefied hydrogen, hydrogen carrier, energy efficiency

## INTRODUCTION

Green hydrogen is commonly regarded as a key player in the transition towards a low-carbon future [1]. It can be efficiently produced in regions with abundant renewable resources, which are often remote and distant from major consumption centers. Therefore, the efficient and cost-effective transportation of $H_2$ from production hubs to end users is essential. However, $H_2$ has an extremely low volumetric density at ambient conditions. To overcome this issue, hydrogen carriers, such as liquefied hydrogen ($LH_2$) and ammonia ($NH_3$), are being explored for its transportation on a large-scale [1].

This study assesses the energy consumption involved in the supply chain of these carriers, focusing on the processes of converting hydrogen into the carrier and reconverting it back to hydrogen. For $LH_2$, these processes involve hydrogen liquefaction and regasification, while for $NH_3$, they include ammonia synthesis and cracking. The simulations are conducted using Aspen Plus® V11 [2] to determine the material and energy balances. The analysis adopts the "net equivalent hydrogen" method, which is analogous to the widely used "net equivalent methane" method [3]. This approach assesses the equivalent amount of hydrogen that would need to be burned to power specific equipment. By using this unified energy basis, the method allows for a fair comparison between different processes.

## METHODS

The case study considered is for green hydrogen transportation across the Mediterranean Sea [1]. The feed hydrogen conditions are assigned in terms of temperature ($T_{in}$ = 25 °C), pressure ($P_{in}$ = 20 bar) and flowrate ($F_{in}$ = 1,800 kg/h), which resemble the conditions at the outlet of an alkaline electrolyzer. The $H_2$ is converted into the considered carrier, transported overseas covering a distance of 2,500 km, and finally reconverted to $H_2$ at the utilization site. The conditions of the delivered hydrogen

are selected based on the requirements for industrial application. Therefore, the $H_2$ purity is 99.9 mol% and the pressure is 30 bar.

The energy analysis is based on the "net equivalent hydrogen" (NEH) method, which evaluates the equivalent amount of hydrogen that would need to be burned to power specific equipment. The Net Equivalent Hydrogen Delivered (*NEHD*) is then calculated by subtracting both the Net Equivalent Hydrogen Consumed (*NEHC*) and the hydrogen lost due to the boil-off phenomenon during shipping ($F_{lost}$) from the total hydrogen fed into the plant:

$$NEHD = F_{in} - NEHC - F_{lost} \quad (1)$$

The energy interactions can be categorized in:

- heating below ambient temperature,
- cooling above ambient temperature,
- heating above ambient temperature,
- cooling below ambient temperature,
- supplying of electrical power.

According to the methodology described by Pellegrini et al. [3], heating below ambient temperature (< 25 °C) and cooling above ambient temperature (> 25 °C) do not consume hydrogen since service water can be used to provide or remove heat, respectively. In the studied processes, heating above ambient temperature is achieved, where feasible, by coupling process streams. When this is not possible, heating is supplied by burning the hydrogen carrier (hydrogen, ammonia, and their mixtures) as a fuel with air in a furnace. In this case the Net Equivalent Hydrogen Consumed for heating ($NEHC_{he}$) is related to the hydrogen content of the fuel mixture and is computed as:

$$NEHC_{he} = F_{fuel} \cdot w_{hydrogen} \quad (2)$$

where $F_{fuel}$ is the flowrate of the carrier used as fuel, and $w_{hydrogen}$ is the weight fraction of hydrogen in the fuel. Cooling below ambient temperature is accomplished through heat exchange with fluids flowing in refrigeration cycles. Therefore, the hydrogen consumed is indirectly linked to the electric power required to operate the compressors in these cycles. The Net Equivalent Hydrogen Consumed for supplying electric power ($NEHC_{el}$), used for driving compressors and pumps, is computed assuming hydrogen utilization in fuel cells with an efficiency $\eta_{FC}$ of 60%:

$$NEHC_{el} = \frac{W}{\eta_{FC} \cdot LHV} \quad (3)$$

where *W* is the electric power consumption, and *LHV* is the lower heating value of hydrogen.

The efficiency of the value chain ($\eta$) is then computed as the ratio between the *NEHD* and the hydrogen feed flow rate:

$$\eta = \frac{NEHD}{F_{in}} \quad (4)$$

A schematic of the hydrogen carrier supply chain is depicted in Figure 1.

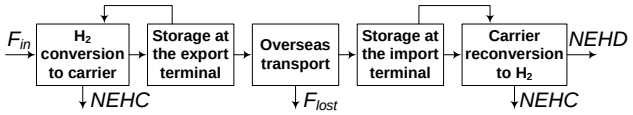



**Figure 1.** Schematic of the hydrogen carrier supply chain.

## PROCESS SIMULATION

The processes involved in the $LH_2$ and $NH_3$ value chains are simulated using Aspen Plus® V11 [2] to obtain material and energy balances, necessary for the NEH assessment. It is supposed that the impurities in the hydrogen feed have been removed before the hydrogen enters the processes. Heat exchangers' pressure drops are neglected. An isentropic efficiency of 0.8 is assumed for pumps, compressors and turbine expanders, unless otherwise stated.

### Liquefied hydrogen supply chain

#### Hydrogen liquefaction process

The hydrogen liquefaction process involves cooling hydrogen gas to extremely low temperatures until it transitions from gas to liquid. This happens at about -250 °C at atmospheric pressure. The process typically includes a precooling section, where nitrogen or other refrigerants are used to remove heat, and a cryogenic section, where further cooling happens using Joule-Thomson expansion or other cryogenic methods until hydrogen reaches its liquefaction point. Various process configurations have been explored in the literature. Among them, the process described by Cardella [4], which employs a mixed refrigerant Joule-Thomson cycle for precooling and a dual-pressure hydrogen Claude cycle for cryogenic cooling, stands out as the most balanced in terms of complexity and specific electricity consumption for the small-capacity plant under consideration [5]. For simulating this process, the Peng-Robinson thermodynamic package, modified as detailed in [6], is used to account for the behavior of equilibrium hydrogen and to model continuous ortho-para hydrogen conversion, which is achieved by packing a suitable catalyst within the tubes carrying the processed hydrogen. The Process Flow Diagram (PFD) is depicted in Figure 2a. The hydrogen stream (H2 in Figure 2a) undergoes precooling to -173 °C in the multi-stream heat exchanger HX-1, where it flows counter-currently to a mixed refrigerant. The composition of this refrigerant, optimized by Cardella [4] to minimize temperature differences between the cold and hot composite curves in HX-1, is 14 mol% nitrogen, 30 mol% methane, 31 mol% ethane and 25 mol% iso-butane. The mixed refrigerant is

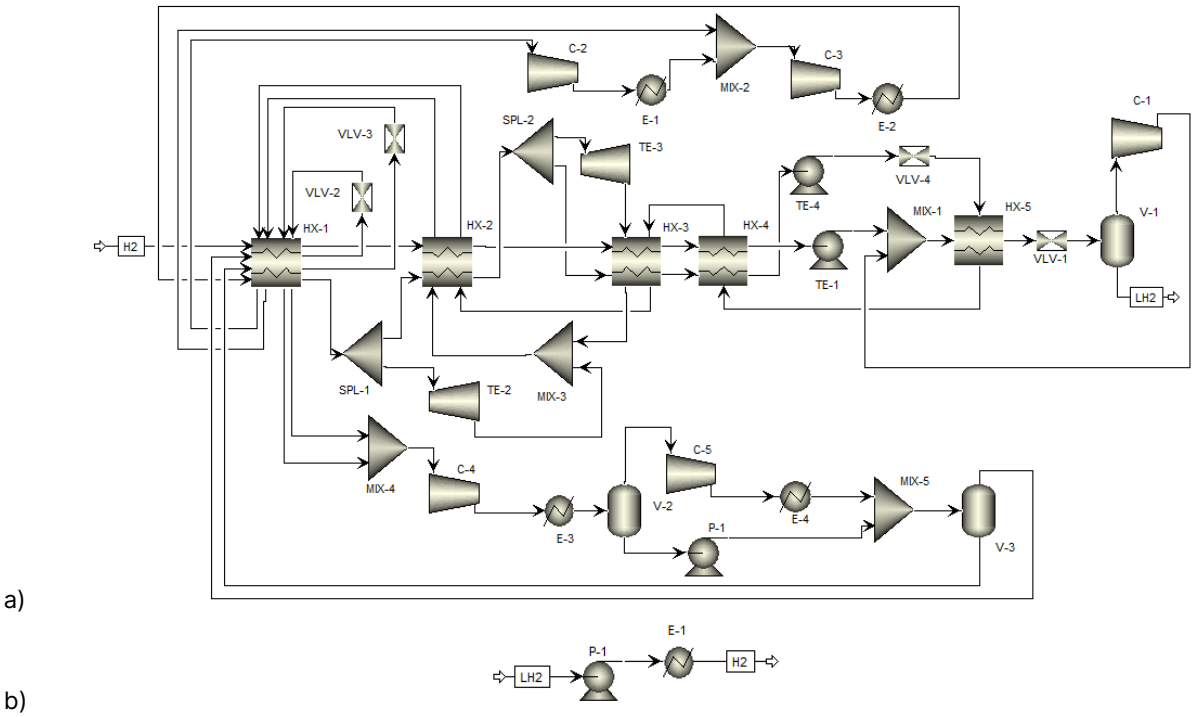



**Figure 2.** PFD of the processes involved in the $LH_2$ supply chain: a) $H_2$ liquefaction and b) $LH_2$ regasification.

compressed to 25 bar in compressor C-4, cooled to 30 °C in heat exchanger E-3 using service water, and separated in flash vessel V-2 to avoid the presence of liquid at the inlet of the second compressor. The separated vapor is compressed to 50 bar in C-5, cooled to 25 °C in E-4, and mixed with the liquid from V-2 after it is pumped to 50 bar in pump P-1. This mixture is separated in V-3, with liquid and vapor streams sent to the hot side of HX-1. The former is precooled to -110 °C and expanded to 2.9 bar through Joule-Thomson valve VLV-2. The latter is precooled to -193 °C and expanded to 2.9 bar through VLV-3. These low-pressure streams are directed to the cold side of HX-1 and are mixed at its outlet in mixer MIX-4. The design of the dual-pressure $H_2$ Claude cycle has been optimized by Cardella [4] to reduce temperature differences in the heat-exchangers HX-2, HX-3, HX-4, and HX-5. The low-pressure $H_2$ refrigerant is compressed to 8.3 bar in C-2, cooled to 30 °C in E-1 using service water, and mixed with the intermediate-pressure $H_2$ refrigerant in MIX-2. The mixture is compressed to 49.9 bar in C-3, and cooled to 25 °C in E-2. The resulting high-pressure $H_2$ refrigerant is precooled to -173°C in HX-1 and then split in splitter SPL-1, directing 38.8 % of the flow to turbine expander TE-2, where it is expanded to an intermediate pressure of 8.3 bar. This stream is mixed with a recycle stream in MIX-3 and routed to the cold side of HX-2. The remaining flow from SPL-1 passes at the hot side of HX-2, reaching an outlet temperature of -213 °C, and is then split in SPL-2. Of this, 73.8 % is directed to TE-3, where it expands to 8.3 bar, then passes at the cold side of HX-3 to cool the processed hydrogen stream. The remaining flow from SPL-2 passes at the hot side of HX-3, reaching -237 °C at the outlet. The processed hydrogen and the high-pressure hydrogen refrigerant are further cooled in HX-4 to -249 °C. At the outlet of HX-4, the processed hydrogen is expanded in TE-1 to 5 bar, then mixed with the vapor from the flash separator V-1 and cooled in HX-5 to -251 °C. The high-pressure refrigerant is expanded to 3 bar in TE-4 and then to 1.4 bar in VLV-4, then passes as cold stream through HX-5, HX-4, HX-3, HX-2, and HX-1. The processed hydrogen is finally throttled to the storage pressure (1.3 bar) in VLV-1. A minimum approach temperature of 3 °C is maintained in all heat exchangers, except for the exchanger where hydrogen undergoes a phase change (HX-5), where the minimum approach temperature is set to 1 °C.

## Liquefied hydrogen storage and transport

The produced liquid hydrogen is stored in properly insulated tanks. The boil-off gas is assumed to be reliquefied at the export terminal and sent to the regasification process at the import terminal. During overseas transport, the boil-off gas is lost with a rate of 0.2 % per day [1]. The total hydrogen loss during transport is calculated based on the travel distance and an average shipping speed of 30 km/h [1].

## Liquefied hydrogen regasification process

Regasification involves converting liquid hydrogen back into its gaseous state. This process is relatively straightforward, involving the pumping of liquefied hydrogen followed by heating it to ambient temperature.

The PFD of the process is depicted in Figure 2b. The discharge pressure of the pump (P-1) is set to 30 bar to meet the pressure requirements for industrial application. The pump is assumed to have an efficiency of 0.6, and service water is used as the heating medium in the vaporizer (E-1).

## Ammonia supply chain

### Ammonia synthesis process

$NH_3$ is synthesized from nitrogen and hydrogen, according to the reaction:

$$3H_2 + N_2 \rightarrow 2NH_3 \quad (5)$$

The simulation utilizes the Redlich-Kwong-Soave equation of state with the alpha function modification proposed by Boston and Mathias (RKS-BM). The PFD of the process is shown in Figure 3a. The nitrogen required for the synthesis is determined by the stoichiometric ratio given in Eq. (5). Nitrogen is produced from air using the process scheme proposed in [7]. Air (AIR in Figure 2a) is compressed to 9.9 bar and then precooled to its dew point in the multi-stream heat exchanger HX-6. The resulting stream is sent to the high-pressure rectification column T-1, which consists of 50 theoretical stages. This column separates the air into two streams: a nitrogen-rich vapor (residual oxygen content of 2 ppm) as the top product and a bottom product comprising an approximately equimolar mixture of oxygen and nitrogen. The bottom stream is expanded to 3.3 bar and fed into the low-pressure stripping column T-2, which separates the feed into a top stream resembling the composition of air and an oxygen-enriched bottom stream. The oxygen-

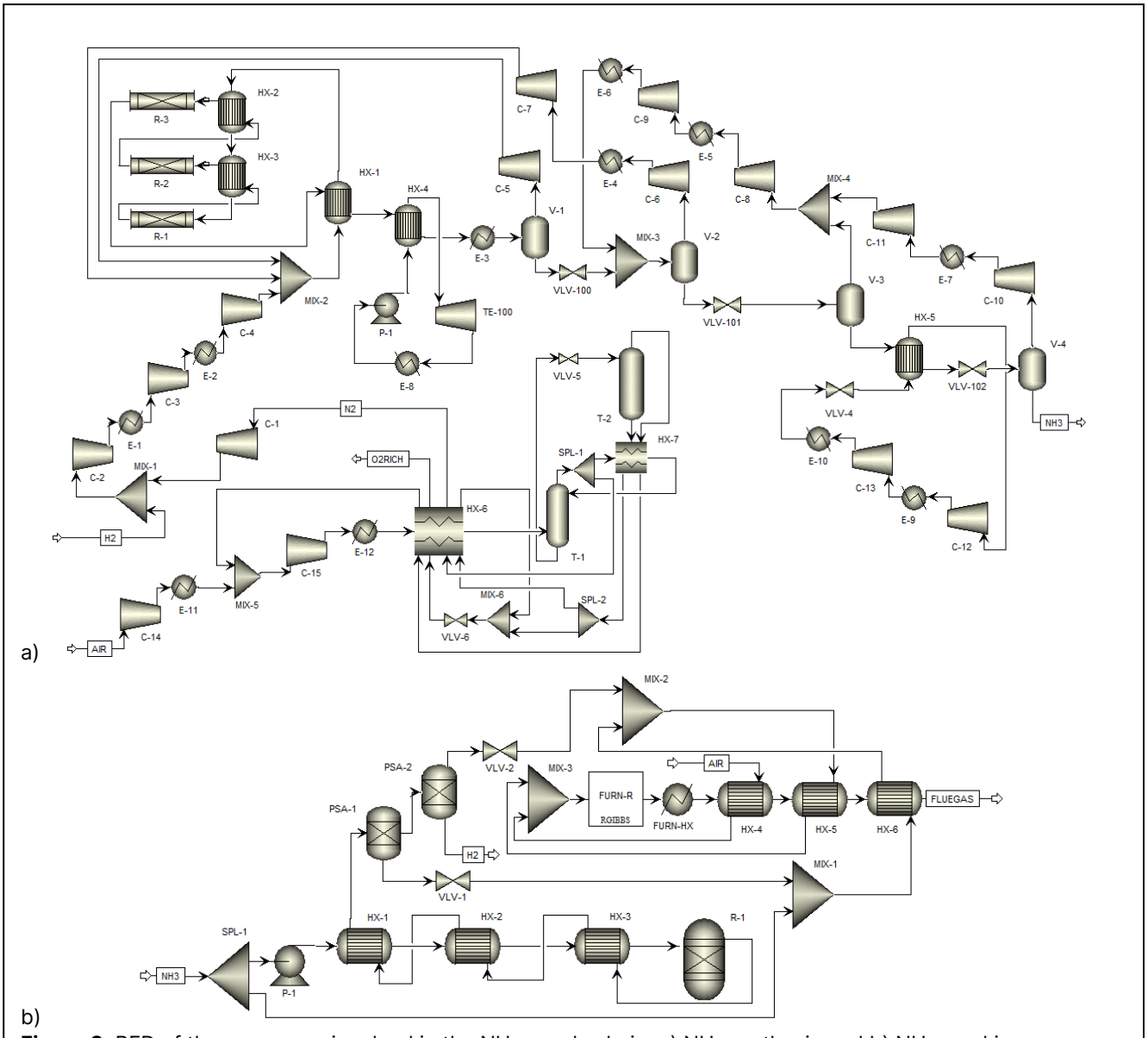



**Figure 3.** PFD of the processes involved in the $NH_3$ supply chain: a) $NH_3$ synthesis and b) $NH_3$ cracking.

enriched stream is routed through process exchangers HX-7 and HX-6 and exits as a product (O2RICH in Figure 3a). The top stream also passes as a cold stream in HX-7 and HX-6 and is then recycled to mixer MIX-5, where it mixes with the incoming air feed. The cooling required to condense part of the nitrogen-rich vapor from the high-pressure column, providing reflux, is achieved by evaporating the bottom product of the low-pressure column. HX-7 operates with an approach temperature difference of 1 °C. The produced nitrogen stream (N2 in Figure 3a) feeds the ammonia synthesis section. The hydrogen stream (H2 in Figure 3a) is mixed with N2, after being compressed to 20 bar, and then compressed to 200 bar in a three-stage compressor with intercooling. The resulting stream is mixed with the recycle streams, the vapors exiting the V-1 and V-2 separators, suitably compressed, and heated to 347 °C using a series of process-process heat exchangers (HX-1, HX-2, HX-3), which recovers heat from the streams exiting the reactor beds, before being sent to the first catalytic stage R-1. The reaction section comprises three adiabatic catalytic beds (R-1, R-2, R-3) with intermediate cooling. Iron-based catalysts are used to enhance the conversion (Haber-Bosch process). The stream exiting the last reactor stage R-3 contains ammonia along with hydrogen and nitrogen. The unconverted reagents must be separated and recycled to the reactor. The goal is to produce liquid ammonia at near-ambient pressure (1.3 bar), with a purity exceeding 99.95%, as defined by legislation [8]. To achieve this, the stream is first cooled to 50 °C in HX-4, transferring heat to a steam Rankine cycle, and further cooled to 30 °C in heat exchanger E-3 using service water. The resulting biphasic stream is separated in the V-1 separator: the vapor phase is recycled to the reaction section, while the liquid phase undergoes further purification through downstream expansion and cooling stages. Specifically, flash vessels V-2, V-3, and V-4 operate at pressures of 40 bar, 7 bar, and 1.3 bar, respectively. Cooling is achieved in HX-5 using an ammonia refrigeration cycle.

### Ammonia storage and transport

Liquefied ammonia storage takes place in properly insulated tanks. The boil-off gas is assumed to be reliquefied at the export terminal and directed to the cracking process at the import terminal. During overseas transport, a boil-off gas loss rate of 0.024 % per day is considered [1].

### Ammonia cracking process

The dissociation of ammonia is a highly endothermic process, described by the following reaction:

$$2NH_3 \rightarrow 3H_2 + N_2 \quad (6)$$

Commercially, small-scale ammonia cracking reactors (capacities ranging from 1 $Nm^3/h$ and 1,000 $Nm^3/h$), operating at temperatures between 800 and 1,000 °C with Ni-based catalysts are available. The endothermic reaction is supported by electricity.

The simulation of the ammonia cracking process assumes the use of the thermocatalytic technology with Ni-based catalysts, as this is the most mature technology. Figure 3b illustrates the PFD of the process. Upon reaching the utilization site, ammonia (NH3 in Figure 3b) is pumped to 30 bar, preheated through a series of heat exchangers (HX-1, HX-2 and HX-3) that recover heat from the reaction products, and fed into the cracking reactor (R-1). The reactor is modeled using Aspen Plus's RGibbs module due to the lack of sufficiently detailed kinetic data. As a result, the ammonia conversion is assumed to follow thermodynamic equilibrium at the reactor's operating conditions of 30 bar and 900 °C. The heat required for the endothermic cracking reaction is supplied by burning a portion of the ammonia, which is mixed with hydrogen-rich waste streams from the purification section. Air (AIR in Figure 3b), used as the oxidizer, is added slightly above the stoichiometric ratio to ensure complete combustion. Following the reaction stage, hydrogen is separated from the unconverted ammonia and nitrogen via pressure swing adsorption units (PSA-1 and PSA-2).

## RESULTS AND DISCUSSION

The Net Equivalent Hydrogen Consumed is calculated from the material end energy balances obtained from process simulations using Eqs. (2)-(3), then the Net Equivalent Hydrogen Delivered is computed using Eq. (1). Figure 4 presents the results through Sankey diagrams, which are particularly effective for visualizing where hydrogen is consumed or lost within the supply chain. Processes characterized by a low efficiency must be the primary targets for future research efforts. The *NEHD* for $LH_2$ is 1,072 kg/h, reflecting an overall efficiency of 60% for the supply chain. Among the processes, hydrogen liquefaction exhibits the highest equivalent hydrogen consumption, with approximately one-third of the hydrogen input being consumed during the process. This highlights the need to focus research on optimizing the process to minimize electricity consumption. One potential solution is the use of refrigerant mixtures in both the precooling and cryogenic cooling stages, with their composition optimized to achieve a close match between the hot and cold composite curves of the heat exchangers, while ensuring that no components precipitate as solid at the operating temperature of the refrigeration cycle. Another approach is to explore energy integration opportunities with processes that require low-temperature heat, such as liquefied natural gas regasification. The *NEHD* for $NH_3$ is 1,323 kg/h, corresponding to an overall $\eta$ of 73% for the supply chain. Ammonia cracking accounts for the highest equivalent hydrogen consumption, utilizing approximately one-fifth of the total hydrogen input during the

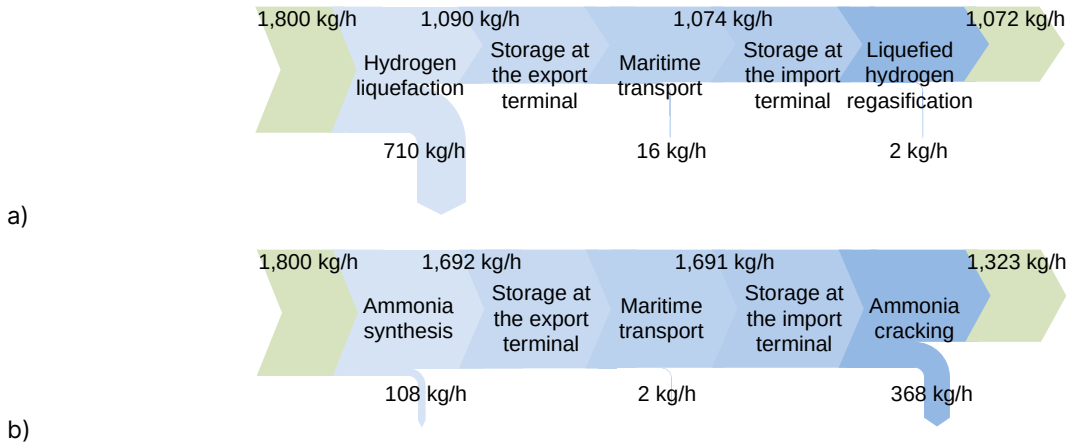



**Figure 4.** NEH assessment for the a) $LH_2$ and b) $NH_3$ supply chains.

process. Therefore, research efforts should focus on improving this process by exploring alternative and sustainable methods for supplying the heat of reaction.

The *NEHD* is higher for $NH_3$ than $LH_2$ because the combined hydrogen consumption for ammonia synthesis and cracking is lower than that required for the liquefaction process. The difference in *NEHD* between the two carriers is 251 kg/h, meaning that hydrogen liquefaction would need to consume 459 kg/h, equivalent to one-fourth of the total hydrogen input, to break even with $NH_3$. In addition, hydrogen losses due to boil-off during maritime transport are smaller for $NH_3$, even if their contribution does not significantly impact the overall results. Therefore, $NH_3$ is the most efficient hydrogen carrier for hydrogen delivery considering the final hydrogen application to the industrial sector.

## CONCLUSIONS

The processes involved in the liquefied hydrogen and ammonia supply chains for hydrogen overseas transportation have been analyzed from an energy consumption perspective. The ammonia supply chain is more efficient than the liquefied hydrogen supply chain, with efficiencies of 73% and 60%, respectively. This is because the combined equivalent hydrogen consumption for ammonia synthesis and cracking is lower than that required for the liquefaction process. Ammonia would become even more attractive if it could be used directly by end consumers, eliminating the inefficiency associated with its reconversion back to hydrogen.

## REFERENCES


1. Pellegrini LA, Spatolisano E, Restelli F, De Guido G, de Angelis AR, Lainati A. Green $H_2$ Transport through $LH_2$, $NH_3$ and LOHC: Opportunities and Challenges. Springer Nature Switzerland (2024)
2. AspenTech. Aspen Plus® V11 (2019)
3. Pellegrini LA, De Guido G, Valentina V. Energy and exergy analysis of acid gas removal processes in the LNG production chain. *J Nat Gas Eng* 61:303-319 (2019) https://doi.org/10.1016/j.jngse.2018.11.016
4. Cardella U. Large-scale hydrogen liquefaction under the aspect of economic viability. PhD Thesis, Technische Universität München (2018)
5. Restelli F, Spatolisano E, Pellegrini LA, Cattaneo S, de Angelis AR, Lainati A, Roccaro E. Liquefied hydrogen value chain: a detailed techno-economic evaluation for its application in the industrial and mobility sectors. *Int J Hydrogen Energy* 52:454-466 (2024) https://doi.org/10.1016/j.ijhydene.2023.10.107
6. Restelli F, Spatolisano E, Pellegrini, LA. Hydrogen Liquefaction: a Systematic Approach to its Thermodynamic Modeling. *Chem Eng Trans* 99:433-438 (2023) https://doi.org/10.3303/CET2399073
7. Agrawal R, Thorogood RM. Production of medium pressure nitrogen by cryogenic air separation. *Gas Sep Purif* 5(4):203-209 (1991) https://doi.org/10.1016/0950-4214(91)80025-Z
8. ECHA. https://echa.europa.eu/registration-dossier/-/registered-dossier/15557



© 2025 by the authors. Licensed to PSEcommunity.org and PSE Press. This is an open access article under the creative commons CC-BY-SA licensing terms. Credit must be given to creator and adaptations must be shared under the same terms. See https://creativecommons.org/licenses/by-sa/4.0/

Systems & Control Transactions

**Research Article - Peer Reviewed Conference Proceeding**
ESCAPE 35 - European Symposium on Computer Aided Process Engineering
Ghent, Belgium. 6-9 July 2025
Jan F.M. Van Impe, Grégoire Léonard, Satyajeet S. Bhonsale,
Monika E. Polańska, Filip Logist (Eds.)

PSE PRESS

# Integrating offshore wind energy into the optimal deployment of a hydrogen supply chain: a case study in Occitanie

**Melissa Cherrouk[a,b], Catherine Azzaro-Pantel[a]*, Florian Dupriez Robin[b], Marie Robert[b]**

[a] Laboratoire de Génie Chimique, Université de Toulouse, CNRS, INPT, UPS, France
[b] France Energies Marines, 525 avenue Alexis de Rochon, 29280, Plouzané, France
* Corresponding Author: Catherine.azzaropantel@toulouse-inp.fr

## ABSTRACT

The urgent need to mitigate climate change and reduce reliance on fossil fuels highlights green hydrogen as a key component of the global energy transition. This study assesses the feasibility of producing hydrogen offshore using wind energy, focusing on economic and environmental aspects. Offshore wind energy offers several advantages: access to water for electrolysis, potentially lower hydrogen export costs compared to electricity, and storage systems that stabilize wind energy output. However, significant challenges remain, including the high costs of storage solutions, capital expenditures (CAPEX), and operational costs (OPEX). A Mixed-Integer Linear Programming (MILP) model optimizes the production units, storage, and distribution processes. A case study in southern France examines hydrogen production from a 150 MW floating wind farm. While hydrogen produced from offshore wind ranks among the most environmentally friendly, its costs remain high, and production volumes fall short of meeting regional demand. The findings emphasize the need to optimize power capacities and explore hybrid renewable systems to better balance economic and environmental trade-offs, enhancing offshore wind's competitiveness in hydrogen production and its role in the global energy transition.

**Keywords**: offshore wind, hydrogen, supply chain, optimization, mixed-integer linear programming

## INTRODUCTION

The urgent need to mitigate climate change and reduce dependence on fossil fuels has led to the exploration of alternative energy solutions, with green hydrogen emerging as a key player in the global energy transition [1].

France's National Hydrogen Strategy aims to achieve 6.5 GW of renewable hydrogen production capacity by 2030 [2]. Leveraging its extensive maritime zone, France is advancing the deployment of floating offshore wind farms and exploring the integration of wind energy into hydrogen production systems. Floating offshore wind farms (OWFs) offer a compelling array of benefits: an access to high-capacity wind resources in deep waters, proximity to water for the electrolysis process, and the elimination of land-use constraints that onshore systems face. Such characteristics position offshore wind energy as a promising enabler of hydrogen production [3]. However, the integration of such systems presents significant challenges such as high capital (CAPEX) and operational (OPEX) costs [4]. Existing literature on supply chain modeling for offshore wind and hydrogen systems identifies two major gaps [[5], [6]]:

1. **Limited integration of offshore wind and electrolyzer constraints**: Most studies lack an explicit consideration of the constraints and challenges associated with coupling offshore wind farms and electrolyzers for hydrogen production. This oversight limits the ability to develop realistic and comprehensive models for supply chain optimization.
2. **Narrow focus on deployment optimization**: Current research tends to prioritize electrical aspects or specific system-level developments rather than addressing the broader optimization of deploying

these sectors. While system design and performance evaluations are valuable, they often neglect the strategic deployment of offshore wind and hydrogen production systems within a supply chain framework.

For instance, studies analyzing the performance and energy output of autonomous wind-hydrogen hybrid systems often focus on technical performance without incorporating optimization considerations [7]. This study addresses these gaps by focusing on systems-level modeling that explicitly incorporates the constraints of coupling offshore wind and hydrogen production while optimizing their deployment at the supply chain level.

The scientific research question is formulated as follows: How can spatial energy planning in maritime areas anticipate and address the challenges and opportunities associated with developing future hydrogen networks?

Therefore, the specific objectives of this study are:

- To assess the potential of floating offshore wind farms as an energy source for hydrogen production in a regional context.
- To optimize the design and operation of hydrogen supply chains, including production units, storage systems and distribution networks.
- To analyze two optimization scenarios: one focusing on cost minimization, and the other on greenhouse gas emissions reduction.

# METHODOLOGICAL FRAMEWORK

## Modeling concepts

This study's model builds upon the foundational work of [8], the main innovation is the integration of floating offshore wind farms as a primary energy source within a previously established framework. The optimization problem is formulated as a multi-period mono-objective model, divided into five-years periods. The problem is formulated as a linear programming problem, and the optimizer used is of Mixed-Integer Linear Programming (MILP) type, the model is implemented using the GAMS® modeling language with the CPLEX 12 solver. More details regarding the parameters, formulas and constraints are documented in [8].

## Assumptions

The assumptions of the model can be summarized by:

- The components of the hydrogen supply chain considered are as follows: primary energy sourcing, production, storage, transport, and refueling stations.
- The territory is divided into cells, each characterized by a specific hydrogen demand.
- Two production methods are evaluated: electrolysis powered by renewable electricity or nuclear energy, and steam methane reforming (SMR). Note that nuclear energy was included to represent an alternative, as it constitutes a major share of the French electricity mix (approximately 65% of the national grid).
- Three electrolyzer sizes are available: small, medium, and large. Production units can only be installed on designated cells.
- The offshore cell is modelled by being directly connected to onshore cell n°2 (the closest) to simplify its representation.
- The offshore components - electrolyzers, desalination, pipeline, floating platform – are incorporated into the model through a cost parameter, as a part of the total CAPEX of the offshore system.
- The produced hydrogen is dedicated to transport applications and distributed via refueling stations.

## Optimization criteria

Two optimization scenarios are analyzed, based on two different criteria. The first aims to minimize the total daily cost (TDC) of the hydrogen network, which is an important criterion to ensure the economic feasibility and deployment of the technology. The second focuses on minimizing the global warming potential (GWP) of the supply chain to progress towards the zero emissions goal.

1. **Total Daily Cost:** The TDC (in $) ensures that both operational and capital expenses are optimized over the project's lifespan. It is defined as follows:

$$TDC = \sum_p Cost(p) \quad (1)$$

Where $Cost(p)$ represents the discounted cost for each period $p$, calculated as:

$$Cost(p) = \frac{CAPEX(p)}{(1+r)^{nn(p)}} + [OPEX(p) + ESC(p)] * \sum_{m=1}^{5} \frac{1}{(1+r)^{YEAR(p,m)}} \quad (2)$$

In this formula, $ESC(p)$ is the primary energy source cost and the sum term accounts for discounted values over time using a discount rate r. The number of years in a period is denoted by $m$ and ranges from 1 to 5 years, and capital costs are discounted over the lifespan of the project $nn(p)$.

2. **Global warming potential:**

$$GWPtot = \sum_p [PGWP(p) + SGWP(p) + TGWP(p)] \quad (3)$$

The total GWP of the hydrogen supply chain represents the combined environmental impact of production $PGWP(p)$, storage $SGWP(p)$ and transport activities $TGWP(p)$, expressed in $CO_2$-equivalent emissions.

## Case study

The Occitanie region in southern France is chosen as a first case study for offshore wind integration into hydrogen production. The imagined floating wind farm is located 30 km from the coast and has a capacity of 150 MW, consisting of 10 floating turbines, each with a capacity of 15 MW. As part of the offshore cell, the setup includes a centralized hydrogen production unit on a dedicated offshore platform directly connected to the wind farm. This fictitious scenario examines the potential impact on the regional hydrogen production mix if 150 MW of offshore wind energy were allocated to hydrogen production.

The region has been discretized into 13 cells, corresponding to its departmental boundaries. In this case study, the offshore cell acts fully as a hydrogen producer, with zero local hydrogen demand. We considered an offshore hydrogen production in this study as it seems to be one of the efficient configurations for offshore wind-to-hydrogen systems, as it allows for a direct coupling with the wind farm while minimizing transmission losses [5]. More configurations will be explored in future works. The produced hydrogen is transported through an undersea pipeline to the connected onshore cell, where it is stored and distributed to meet regional demand. Other energy sources onshore may complement offshore wind energy to meet hydrogen supply demands, either locally or through transport via tanker trucks. A simplified version of the previously explained territorial discretization of the case study is illustrated in **Figure 1**. Cost parameters for the onshore and offshore subsystems of the supply chain were extracted from [6], [9], and [10], as shown in **Table 1**.

**Table 1:** Cost parameters of key subsystems of the hydrogen supply chain

| Subsystem | CAPEX | OPEX (%/yr) |
|---|---|---|
| Onshore Electrolyzer (AEL) [6] | 866 $/kW | 2.2 |
| Offshore Electrolyzer (PEM) [6] | 1 543 $/kW | 4.4 |
| Desalination [9] | 6 687 $/kW | 3.0 |
| Compression/Liquefaction [10] | 3 000 $/kgH2/d | 4.0 |
| Offshore platform [6] | 250 000 $/kgH2/d | 1.0 |
| Pipeline [6] | 4 873 $/kW | 3.0 |

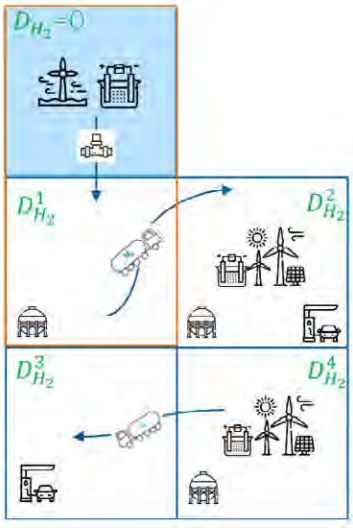



**Figure 1:** Simplified territorial discretization

The region's renewable energy availability – including the contribution from the offshore cell – is represented in **Figure 2** to provide a better visualization on resource allocation and distribution. An important assumption is the inclusion of nuclear energy, available in large volumes across all nodes through the power grid, which allows hydrogen production to benefit from both renewable and nuclear sources. **Figure 3** illustrates the combined energy availability of the interconnected offshore and onshore cell n°2.

The main parameters related to the primary energy sources considered in this study are summarized in **Table 2**: Levelized Cost of Energy (LCOE), Capacity Factor (Cap. Factor), and GWP. The capacity factor of each source is considered in the model through the calculation of energy availability, which reflects the actual amount of energy that can be generated over time based on the source's operational characteristics(Cap. Factor), and GWP. The capacity factor of each source is considered in the model through the calculation of energy availability, which reflects the actual amount of energy that can be generated over time based on the source's operational characteristics.

**Table 2:** Primary energy source parameters

| Energy source | LCOE ($/kWh) | Cap.Factor (%) | GWP ($kgCO_2eq/kgH_2$) |
|---|---|---|---|
| PV | 0.071 | 24 | 1.82 |
| Onshore wind | 0.055 | 38 | 1.08 |
| Offshore wind | 0.078 | 45 | 0.90 |
| Hydro | 0.085 | 51 | 1.68 |
| Nuclear | 0.060 | 85 | 1.24 |
| SMR | 0.160 | - | 10.3 |

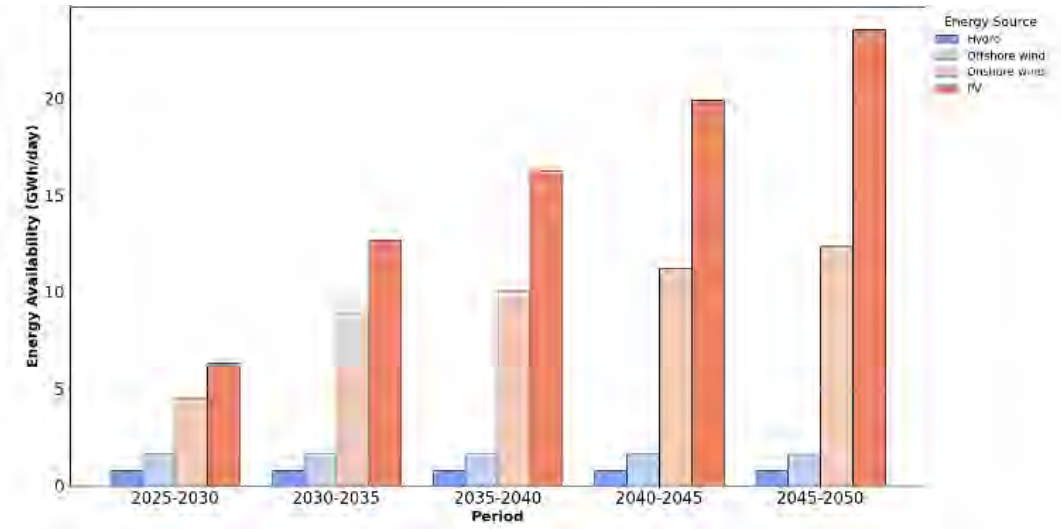



**Figure 2:** Availability of renewable energy sources in Occitanie [11],[12]

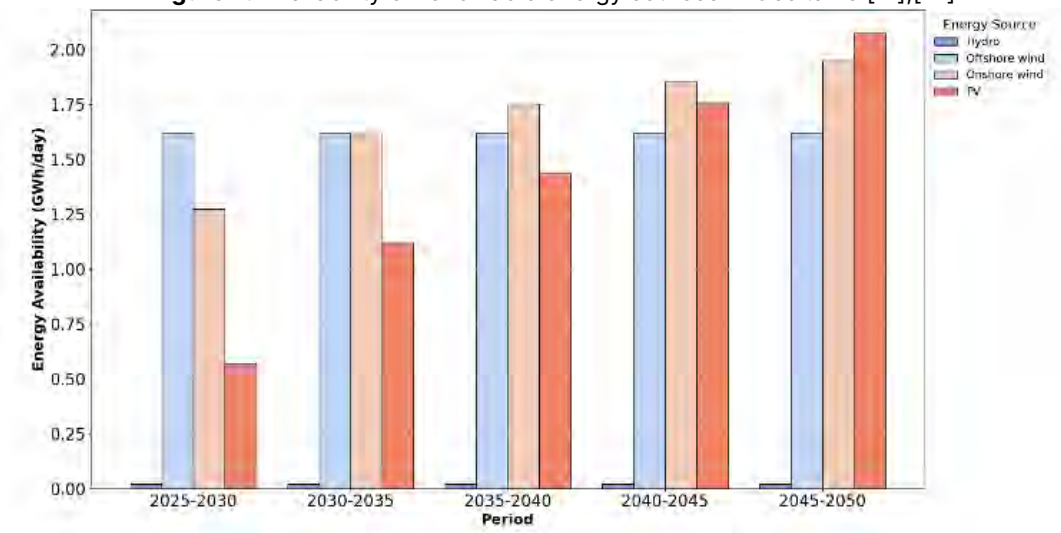



**Figure 3:** Availability of renewable energy sources in cell n°2 [11],[12]

## RESULTS

In this study, two single-objective optimization scenarios – minimizing cost and global warming potential – were evaluated to assess the competitiveness of hydrogen production from offshore wind energy. In a similar manner to the LCOE, a LCOH (Levelized Cost of Hydrogen) is calculated for hydrogen.

Using a multi-period approach, the LCOH is weighted by hydrogen demand across all periods. This method accounts for the varying significance of each period in the total hydrogen demand, as periods with lower demand have less influence on the overall LCOH. The LCOH is calculated as follows:

$$LCOH = \sum_p \frac{DT(p) * LCOH(p)}{\sum_p DT(p)} \quad (4)$$

where $DT(p)$ represents the hydrogen demand in period p.

With TDC minimization, a LCOH of 2.4 \$/kg$H_2$ is obtained. However, this economic optimization results in a trade-off with environmental sustainability, as evidenced by a GWP value of 8.84 kg$CO_2$eq/kg$H_2$. This outcome is directly linked to the resulting energy mix, as illustrated in **Figure 4**. During the initial period, the mix is mainly composed of renewable sources (78% onshore wind and 22% PV), driven by relatively low hydrogen demand, which does not justify the activation of a SMR plant. As demand increases in subsequent periods, SMR is introduced into the energy mix and plays a dominant role in this cost-driven configuration due to its lower capital costs and its ability to meet demand efficiently.

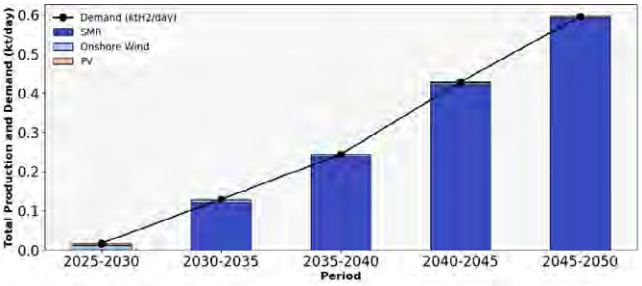



**Figure 4:** Total production and hydrogen demand for the TDC scenario

In contrast, the environmental approach results in a significantly lower GWP value of 1.24 $kgCO_2eq/kgH_2$, which, however, leads to an increase in the LCOH to 8.93 $/kgH_2$, as offshore wind is integrated into the mix with onshore wind and nuclear energy (**Figure 5**), given the higher CAPEX associated with these technologies. Offshore wind, being the least carbon-intensive option, emerges as one of the primary energy sources. As time progresses, offshore capacity is fully utilized, prompting the integration of onshore wind to meet additional hydrogen demand as it increases over time. This shift reflects a progressive reliance on renewable sources.

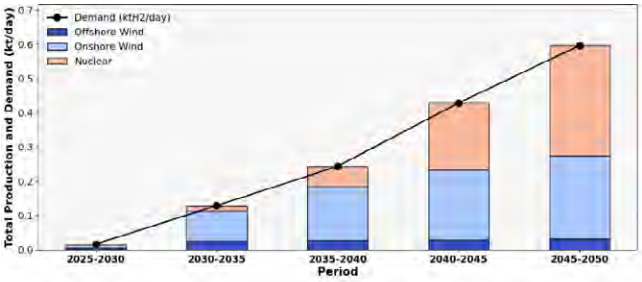



**Figure 5:** Total production and hydrogen demand for the GWP scenario

In this scenario, hydrogen produced offshore is transported via an undersea pipeline to cell n°2, the closest onshore cell. While offshore wind energy is the least carbon-intensive source, one might expect its hydrogen to be prioritized; however, the transport of hydrogen to other cells is constrained. Specifically, offshore hydrogen is primarily routed to cell n°5, due to its proximity to cell n°2, to meet the local hydrogen demand. This configuration is a direct consequence of the scenario's objective to minimize greenhouse gas emissions. Transporting hydrogen over long distances via tanker trucks would increase the carbon footprint. The hydrogen demand in other cells is met using alternative energy sources which are locally available in the cell such as onshore wind and nuclear, which have higher carbon emissions but do not require onshore transport. **Figure 6** illustrates the deployment of the hydrogen supply in the Occitanie region from the first period to the final one, for both optimization scenarios. The different technologies are represented by colored shapes with the numbers inside indicating the quantity of production plants implemented for each source. An important limitation of the current analysis is the assumption that existing electricity sources are fully mobilized for hydrogen production. In practice, only the surplus electricity—available after meeting direct regional demands—would be realistically allocated for hydrogen production. This simplification may overestimate the available energy and influence both cost and environmental outcomes. Future work should refine the model by incorporating detailed regional electricity consumption data, ensuring that only the remaining, truly available electricity is used in the hydrogen production calculations.

Under TDC minimization, electrolysis is the dominant production mode, driven by the low demand during the first period, with a single hydrogen flow from cell n°9. As demand increases, however, the scenario shifts significantly, with SMR becoming the leading technology, resulting in a centralized supply chain and hydrogen transport across cells. In the GWP minimization scenario, electrolysis dominates again, but with a decentralized supply chain. The analysis confirmed the antagonism between the criteria observed in previous studies like [8] and highlights the importance of adopting a multi-objective optimization approach. This is particularly evident when considering the significant disparities between the results of single-objective optimizations. The range obtained for GWP includes the value of 3.38 $kgCO_2eq/kgH_2$, which represents the emission threshold for hydrogen to be considered low-carbon, as defined by European Regulation 2023/1185, further reinforcing the need to balance environmental and economic criteria in the optimization process [13].

## CONCLUSION

The model developed for this study aimed to assess the feasibility and competitiveness of hydrogen production from offshore wind energy. The Occitanie region serves as a case study.

The TDC scenario showed the economic benefits of carbon-intensive methods like SMR, though at significant environmental costs. In contrast, the GWP scenario showcased offshore wind's capacity to lower emissions but required higher economic investment due to offshore infrastructure.

The methodology can be further improved with a multi-objective analysis, which is essential to balance these competing priorities. Future work should explore alternative configurations for integrating offshore wind into hydrogen systems, deepen the understanding of offshore modeling to yield more specific results, and account for wind intermittency to achieve a more refined

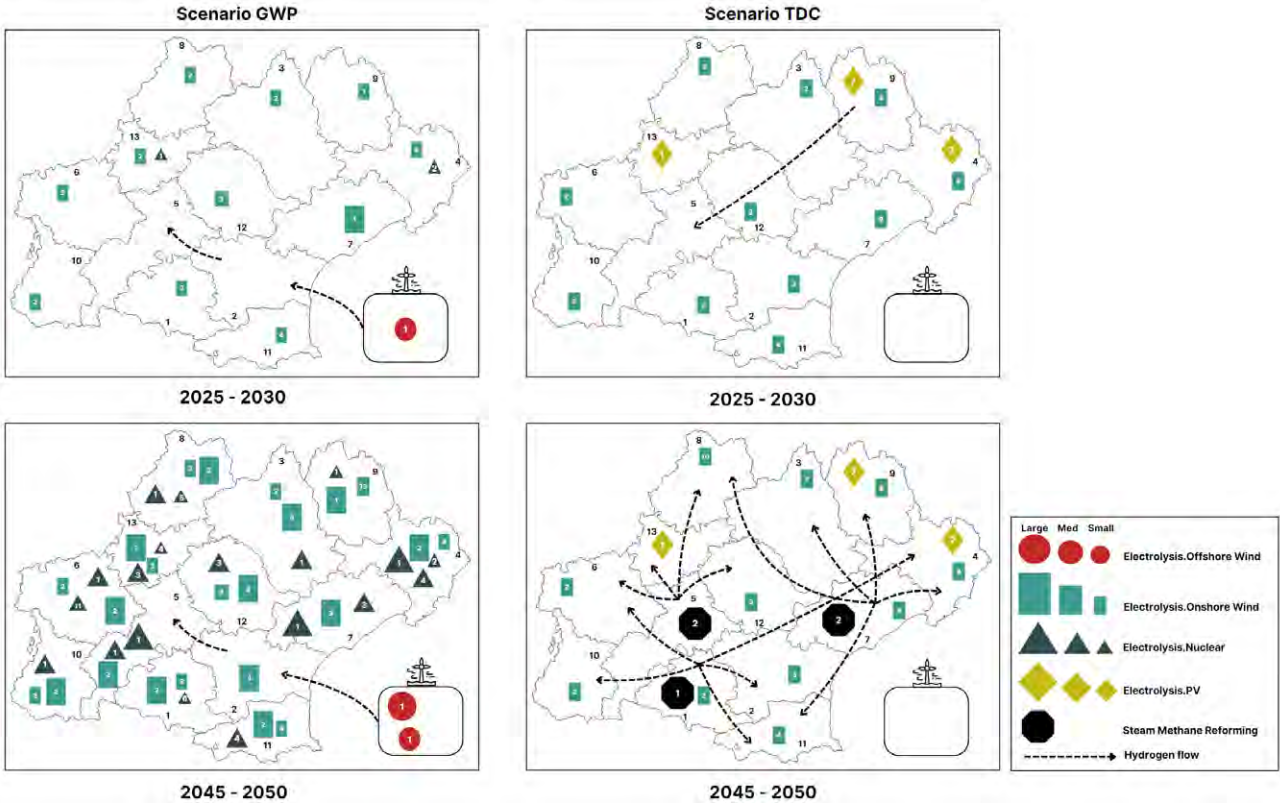



**Figure 6:** Evolution of hydrogen production plants distribution in Occitanie from period 1 to 5

temporal scale. For this study, tanker trucks are selected as the onshore transport option due to their practicality for short-distance distribution and the flexibility they offer in early deployment phases, where hydrogen supply routes remain adaptable. However, to enhance the realism of the model, future work will revisit transport assumptions and consider pipeline-based hydrogen transport at longer time horizons for a more accurate representation. Additionally, it is important to improve the realism of electricity availability for hydrogen production, by considering the remaining electricity after direct regional demands are met, rather than assuming full mobilization of existing sources for hydrogen production.

## ACKNOWLEDGEMENTS

This work is part of the OPHARM2 project led by France Energies Marines, funded by the French National Research Agency (ANR-10-IEED-0006-34) and with partners INP Toulouse, Capénergies, EDF-EIFER, Farwind, GHyGA, Persee, Pôle Mer Méditerranée, Shell, Skyborn, Ekium, Subsea7, Total Energies, Aix Marseille University, Bretagne Occidentale University, Valeco-ENBW.

## REFERENCES

1. "The European Hydrogen Backbone (EHB) initiative | EHB European Hydrogen Backbone." Accessed: Sep. 26, 2024. [Online]. Available: https://www.ehb.eu/
2. "DP - Stratégie nationale pour le développement de l'hydrogène décarboné en France.pdf." Accessed: Jan. 20, 2025. [Online]. Available: DP - Stratégie nationale pour le développement de l'hydrogène décarboné en France.pdf
3. G. Calado and R. Castro, "Hydrogen Production from Offshore Wind Parks: Current Situation and Future Perspectives," Applied Sciences, vol. 11, no. 12, p. 5561, Jun. 2021, doi: 10.3390/app11125561.
4. S. Ramakrishnan, M. Delpisheh, C. Convery, D. Niblett, M. Vinothkannan, and M. Mamlouk, "Offshore green hydrogen production from wind energy: Critical review and perspective," Renewable and Sustainable Energy Reviews, vol. 195, p. 114320, May 2024, doi: 10.1016/j.rser.2024.114320.
5. O. S. Ibrahim, A. Singlitico, R. Proskovics, S. McDonagh, C. Desmond, and J. D. Murphy, "Dedicated large-scale floating offshore wind to hydrogen: Assessing design variables in proposed typologies," Renewable and Sustainable Energy Reviews, vol. 160, p. 112310, May 2022, doi:

10.1016/j.rser.2022.112310.
6. J. Lei et al., “Techno-Economic Assessment of a Full-Chain Hydrogen Production by Offshore Wind Power,” Energies, vol. 17, no. 11, p. 2447, May 2024, doi: 10.3390/en17112447.
7. Z. Luo, X. Wang, H. Wen, and A. Pei, “Hydrogen production from offshore wind power in South China,” International Journal of Hydrogen Energy, vol. 47, no. 58, pp. 24558–24568, Jul. 2022, doi: 10.1016/j.ijhydene.2022.03.162.
8. D. L. Almaraz, “Multi-objective optimisation of a hydrogen supply chain”.
9. A. Rogeau, J. Vieubled, M. De Coatpont, P. Affonso Nobrega, G. Erbs, and R. Girard, “Techno-economic evaluation and resource assessment of hydrogen production through offshore wind farms: A European perspective,” Renewable and Sustainable Energy Reviews, vol. 187, p. 113699, Nov. 2023, doi: 10.1016/j.rser.2023.113699.
10. “19001_hydrogen_liquefaction_costs.pdf.” Accessed: Jan. 16, 2025. [Online]. Available: DOE Hydrogen and Fuel Cells Program Record 19001: Current Status of Hydrogen Liquefaction Costs
11. “chiffres_cles_repos_mai2023.pdf.” Accessed: Jan. 17, 2025. [Online]. Available: chiffres_cles_repos_mai2023.pdf
12. R. O. / Pyrénées-Méditerranée, “Région à Énergie Positive,” Région Occitanie / Pyrénées-Méditerranée. Accessed: Jan. 17, 2025. [Online]. Available: https://www.laregion.fr/-REPOS-
13. “Journal-officiel-de-l'union-européenne.pdf.” Accessed: Jan. 20, 2025. [Online]. Available: Publications Office

© 2025 by the authors. Licensed to PSEcommunity.org and PSE Press. This is an open access article under the creative commons CC-BY-SA licensing terms. Credit must be given to creator and adaptations must be shared under the same terms. See https://creativecommons.org/licenses/by-sa/4.0/



Systems & Control Transactions

**Research Article - Peer Reviewed Conference Proceeding**
ESCAPE 35 - European Symposium on Computer Aided Process Engineering
Ghent, Belgium. 6-9 July 2025
Jan F.M. Van Impe, Grégoire Léonard, Satyajeet S. Bhonsale,
Monika E. Polańska, Filip Logist (Eds.)

PSE PRESS

# Optimisation Under Uncertain Meteorology: Stochastic Modelling of Hydrogen Export Systems

**Cameron Aldren[a,b]*, Nilay Shah[a,b], and Adam Hawkes[a,b]**

[a] Sargent Centre for Process Systems Engineering, Imperial College London, SW7 2AZ
[b] Department of Chemical Engineering, Imperial College London, SW7 2AZ
* Corresponding Author: cameron.aldren19@imperial.ac.uk

## ABSTRACT

Deriving accurate cost projections associated with producing hydrogen within the context of an energy-export paradigm is a challenging feat due to non-deterministic nature of weather systems. Many research efforts employ deterministic models to estimate costs, which could be biased by the innate ability of these models to 'see the future'. To this end we present the findings of a multistage stochastic model of hydrogen production for energy export (using liquid hydrogen or ammonia as energy vectors), the findings of which are compared to that of a deterministic programme. Our modelling found that the deterministic model consistently underestimated the price relative to the non-deterministic approach by \$ 0.08 – 0.10 $kg^{-1}(H_2)$ (when exposed to the exact same amount of weather data) and saw a standard deviation 40% higher when modelling the same time horizon. In addition to comparing modelling paradigms, different grid-operating strategies were explored in their ability to mitigate three critical co-sensitive factors of the production facility: high-cost hydrogen storage, uncertainty in weather forecasting and sluggish production processes. We found that a 'grid-wheeling' strategy substantially reduces the production cost for a solar system (by 16% and 21% for $LH_2$ and $NH_3$, respectively) due to its ability to guarantee the return of energy borrowed overnight during the day, but was not effective for the wind system, due to the non-periodic nature of aeolian weather patterns.

**Keywords**: Hydrogen, Non-Deterministic Programming, Non-Convex Optimisation, Stochastic Modelling.

## INTRODUCTION

The fervent interest in hydrogen's use as a decarbonisation tool has begun to show early signs of stagnation, primarily due to challenges associated with bridging its high production cost to that necessary to support its use in industry. However, in a net zero paradigm, many projections still see the deployment of the hydrogen economy as unavoidable, due to challenges associated with decarbonising specific 'hard-to-abate' sectors such as aviation, heavy industry and ammonia production.

Whilst technological innovations will substantially influence the prospects of the hydrogen economy, there is still a significant opportunity to reduce costs through optimal supply chain planning and design. This has led to hydrogen production within an export paradigm being a very active research area within the field of process systems engineering.

In order to design supply chains which operate at minimal cost, many research efforts employ deterministic optimisation with cost-minimising objectives. These supply chain models are unavoidably complex, due to the need to account for the dynamic nature of weather systems. There are numerous approaches available to account for the influence of weather system dynamics on the design of the hydrogen value chain. Some research efforts elect to use fixed capacity factors [1,2], a strategy which significantly simplifies the computational load, but is known to underpredict the cost of production by approximately 60% [3].

Other research efforts employ time-indexed Mixed-Integer-Programming, taking meteorological data at hourly intervals for a representative years' operation [4,5]. This modelling approach is, naturally, significantly more computationally demanding than employing fixed capacity factors, but in return cost estimates are more

realistic. In order to mitigate this increase in complexity, some of these papers elect to cluster the meteorological time-series [5,6], employing different strategies to ensure time-critical decisions are still made accurately.

Stochastic optimisation allows for decisions to be made in stages, reflecting the influence of uncertainty on the optimal planning and operation of stochastic processes. This methodology offers numerous benefits as it is able to limit the foresight the optimisation model has, but does so with increased computational load. A further benefit of this methodology is that it allows for a better quantification of the cost-benefit yielded by operational strategies which aim to mitigate the cost of uncertainty in weather (such as having a grid connection).

Whilst some studies have used similar methodologies (i.e., those which quantify the influence of uncertainty) on liquid hydrogen or ammonia production systems [7,8,9], they have yet been used in a comparative context and to evaluate the cost-benefit yielded by specific operational strategies. As such, this research aims to do the following:

- Compare the cost estimates of a multistage stochastic model for hydrogen production, against those of a deterministic model.
- Quantify the cost-benefit of different grid operational strategies, such as grid wheeling (a strategy where energy can be 'borrowed' from the grid if it is returned within a fixed time period) and compare this benefit between $LH_2$ and $NH_3$.

# METHODOLOGY

## Model Description

This model is of a hydrogen production facility, for export and thus employs either liquefaction or Haber-Bosch synthesis to convert the hydrogen to a form that is suitable for long distance transportation. For the solar system, the facility is located in the north of Chile and the south of Chile for the wind system. A brief overview of the 'production model' is given, diagrammatically, in the centre of figure 1. The objective of this model was to minimise the levelised cost of hydrogen, the equation for which is shown below in equation 1.

$$\mathrm{LCOH} = \frac{\sum_{t=0}^{T_f}\left[\frac{C_{op}}{(1+r)^n}\right]+C_{cap}}{\sum_{t=0}^{T_f}\left[\frac{8760}{h_f(1+r)^n}\sum_{h=0}^{h_f}\dot{m}_{H_2}(h)\right]} \quad (1)$$

Where $C_{op}$ is the annual operating cost of all equipment, $r$ is the discount factor, $C_{cap}$ is the capital cost of all equipment, $h_f$ is the number of hours modelled (serially), $T_f$ is the lifetime of the plant, $\dot{m}_{H_2}(h)$ is the hourly (mass) production of $H_2$.

The scale factor for this system is the number of parallel trains employed for the Haber-Bosch or Liquefaction process, with 5 and 12 trains used for each respectively. This enabled the hydrogen production to be a free variable, meaning the influence of weather variations manifested in the weekly production quantities of hydrogen.

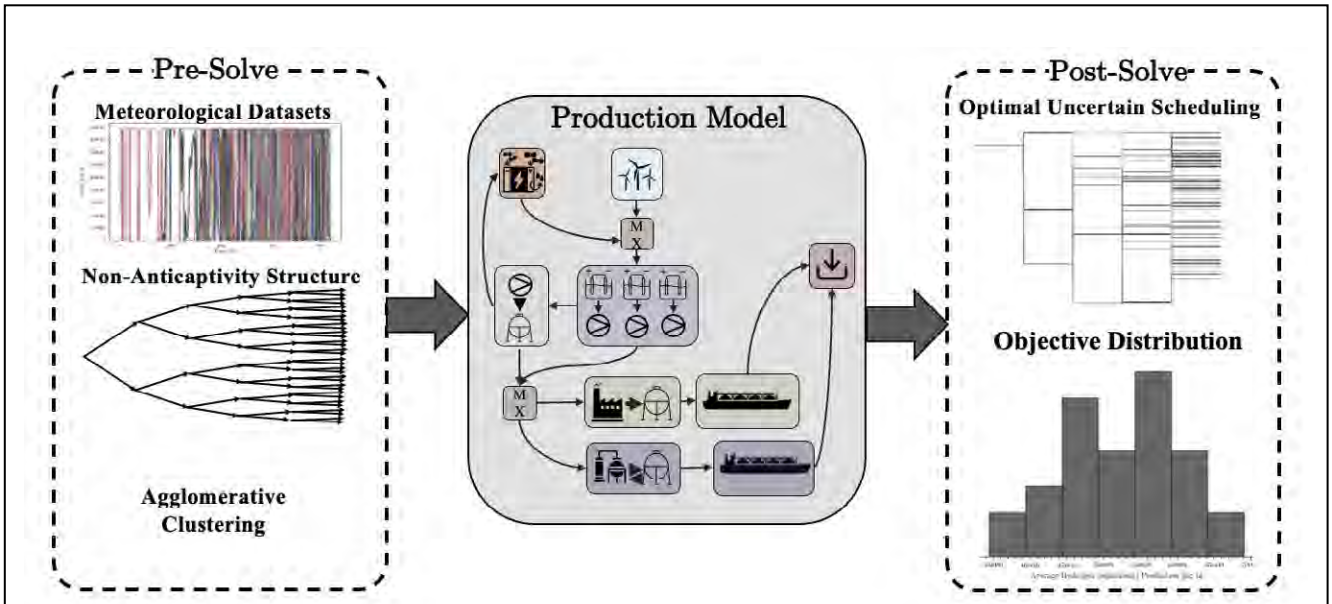



**Figure 1:** Diagram showing the modelling work flow for the stochastic systems modelling. During the pre-solve stages of the modelling, meteorological datasets are sampled and subsequently agglomeratively clustered using Ward's method [10]. Then, a non-anticipativity structure is produced using indexing rules in order to generate a contiguous time-series, which is sampled from the clustered weather dataset.

This, unavoidably so, results in the system being non-linear as both the system Net-Present-Cost (analogous the numerator of the LCOH quotient) and discounted lifetime hydrogen production (the denominator) were endogenous optimisation variables. The strategies involved in simplifying and solving this formulation are discussed in the forthcoming section.

## Mathematical Formulation

The optimisation problem is formulated as a non-convex mixed integer quadratic programme, of structure that is shown below:

$$\min_{x,y} \; f(x,y)\cdot[g(x,y)]^{-1}$$

$$\text{s.t.} \quad B\boldsymbol{x} + C\boldsymbol{y} \le \boldsymbol{a}$$

$$0 \le x \le \boldsymbol{x^u}$$

$$0 \le \boldsymbol{y} \le \boldsymbol{y^U}$$

$$\boldsymbol{x} \in \mathbb{R}^n, y \in \mathbb{Z}^m$$

Where: B $\in \mathbb{R}^{n\times l}$, C $\in \mathbb{R}^{m\times l}$, $\boldsymbol{a} \in \mathbb{R}^l, \boldsymbol{x^u} \in \mathbb{R}^n, \boldsymbol{y^U} \in \mathbb{Z}^m$. This form of model can be solved iteratively using the Dinkelbach algorithm for fractional programming problems [10]. The solution approach involves replacing the objective with a linearised form (equation 2).

$$\lambda g(x,y) - f(x,y) \tag{2}$$

This modified sub-problem is subsequently solved iteratively, updating the value of $\lambda(\tilde{x},\tilde{y})$ in accordance with equation 3 after each iteration.

$$\lambda(\tilde{x},\tilde{y}) = f(\tilde{x},\tilde{y})\cdot\ [g(\tilde{x},\tilde{y})]^{-1} \tag{3}$$

Where $\tilde{x}, \tilde{y}$ correspond to the optimal values from the previous solution. This means, given sufficient iterations, the value of the subproblem's objective will converge to 0 at $\tilde{x} = x^*$.

$$\lim_{(x,y)\to(x,y)^*} [f(x,y) - \lambda^* g(x,y)] \to 0 \tag{4}$$

In this case, this is iterated subject to the convergence condition shown in equation 5 (with $\varepsilon = 0.05$ used in these studies).

$$\lambda g(x^*,y^*) - f(x^*,y^*) \le \varepsilon\,\lambda \tag{5}$$

Casting context to the system model at hand, the linearised equation is the Net-Present-Value (NPV) of the system, where $\lambda$ is the sale price per kg of hydrogen. The LCOH is minimised when the NPV = 0, i.e. the sale price is equal to the unit production cost.

In order to simplify the computational complexity of this programme, as shown in figure 1, the model employs agglomerative clustering for the aeolian time series. This reduces the number of variables and equations in the model by clustering together identical values, thus improving tractability whilst minimising accuracy loss. For this model, Ward's method of agglomerative clustering was employed [11], with hierarchical grids to ensure key time-dependent decisions could still be made.

This clustering is performed as the initial pre-solve stage and influences the indexing of the stochastic programme's formulation. This is all handled by a standalone python module, called PyStochOpt, for which more information is given in the digital supplementary information.

## Multistage Stochastic Programme

The objective of the stochastic programme was to model a months' operation of a hydrogen production facility (for export), using a *multistage* stochastic model in order to manifest the influence of non-deterministic weather forecasting on the optimal planning and operation of the facility. For this model, we take our meteorological system to be a stochastic process, $\{Z_n\}_{n\in N_s}$, defined on the probability space $(\Omega, \mathcal{F}, \mathbb{P})$. Here, for each $n$, $Z_n$ is defined to be a random vector consisting of 168 random variables.

In context of the above problem description, each random vector consists of a weeks' renewable energy production, with the index $h \in (1,2,\dots,168)$ enumerating a contiguous set of data. To reduce model complexity and size, this programme employs an inheritance-based indexing structure, rather than traditional non-anticaptivity constraints.

Specifically, for each $n \in (1,\dots,4)$, let $\mathcal{F}_n := \sigma(Z_1,\dots Z_n)$ denote the $\sigma$-algebra generated by the random variables up until week $n$. Subsequently, the set of time-dependent decision variables: $\{x_t, y_t\}$ are enforced to be $\mathcal{F}_n$-measurable, where $n$ is the current week of operation given hour $t$, and is determined in accordance with equation 6.

$$n := \left\lfloor \frac{t}{168} \right\rfloor \tag{6}$$

This ensures that the model is not able to anticipate the future perfectly and can only make decisions based on the realised values of the stochastic process, up to week $n$. Regarding the equations used to model the system, equations 1-34 and 49-55 were taken from [5] and used in this study.

## Single-Stage Deterministic Programme

For the counterfactual analysis, a deterministic analogue to the abovementioned stochastic programme was developed. In order to give consistency and comparability between the studies, the deterministic model uses the same formulation as the stochastic programme, but with a single stage.

The stochastic programme with three stages and three branches requires 40 distinct weeks weather data (27 + 9 + 3 + 1), in order to model the four weeks' operation. As such, in accordance with the first aim of this research, two deterministic models were developed: one with 4 weeks' data, and one with 40 weeks data.

## Modelling Scenarios

In order to achieve the second and third aim of this research, a series of modelling scenarios in the form of Pareto optimal fronts, were developed. For each front, the analyses were repeated for both liquid-hydrogen and ammonia producing facilities, each employing both Solar and Wind power respectively (i.e., four different scenarios per front). These fronts studied the following operational strategies:

- Variations in hydrogen price. This was employed to study the behaviour of the abovementioned Dinkelbach algorithm. These price variations will also be used to study the behaviour of the deterministic model.
- Cost of employing a grid connection. Here, the grid energy cost, as a fraction of the levelised cost of power (for the wind or solar farm), was varied.
- The period at which the model may 'grid wheel'. As aforementioned, grid wheeling is an operational strategy allowed by some grid operators, such as in South Africa and Egypt.

# RESULTS AND DISCUSSION

## Dinkelbach Algorithm

Figure 2, below, shows the findings of employing the Dinkelbach algorithm for the wind production model. The findings of the solar model showed similar results and as such are not repeated here (but can be found in the digital supplementary information).

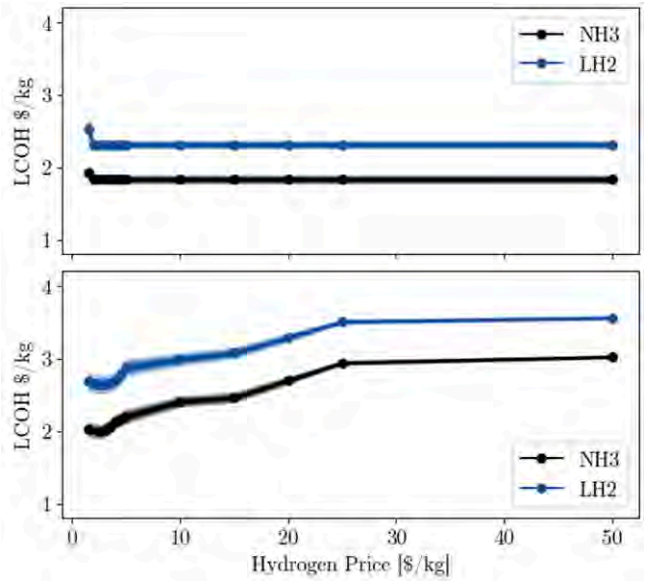



**Figure 2:** Pareto front for the grid connected (top) and islanded (bottom) Dinklebach algorithms. The shaded region represents the spread in LCOH from each of the leaf-nodes of the multistage stochastic model (27 total).

It is clear to see that the presence of the grid connection has a significant influence on the capacity of the production process to 'adapt' to different hydrogen prices. This manifests through varied investments in hydrogen storage. As such, when the hydrogen price is low, the model will elect to curtail excess energy.

In figure 3, below, we see the influence of employing the stochastic programme as opposed to the deterministic. In general, there is more 'noise' in the predictions as opposed to those shown in figure 2, and the deterministic model consistently *underpredicts* the cost of hydrogen production by an average of $ 0.08 $kg^{-1}(H_2)$ for $LH_2$. The case is similar for the $NH_3$ production model, but with a greater average under-prediction of $ 0.10 $kg^{-1}(H_2)$, which is proportionally more significant given the lower average production cost of $NH_3$. It is of note that both models are given the same amount of weather data and, as such, the difference in cost observed is due to the *overoptimised* nature of deterministic models.

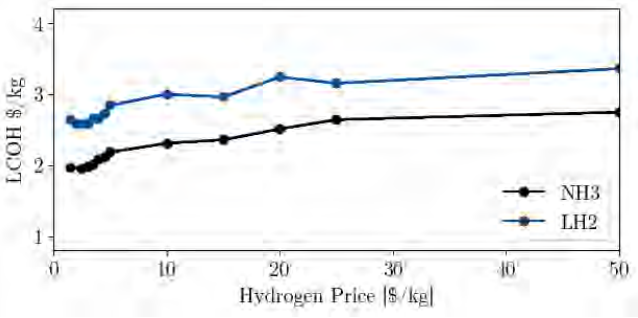



**Figure 3**: Pareto front showing an islanded Dinkelbach algorithm for a wind-powered deterministic model. This is for comparison to the bottom Pareto front of figure 2. This model employs a continuous series of 40 weeks weather data.

To understand the consistency of these models when modelling the same period (4 weeks), the models were solved numerous times whilst varying the random seed used in sampling the meteorological dataset. The deterministic model saw an average cost of $2.80 $kg^{-1}(H_2)$ with a standard deviation of $ 0.25 $kg^{-1}(H_2)$ for $LH_2$ and $2.23 $kg^{-1}(H_2)$ with a standard deviation of $ 0.21 $kg^{-1}(H_2)$ for $NH_3$ (for the islanded, wind powered systems). However, the stochastic model saw average production costs of $2.92 $kg^{-1}(H_2)$ with a lower standard deviation of $ 0.16 $kg^{-1}(H_2)$ for $LH_2$ and $2.26 $kg^{-1}(H_2)$ with a standard deviation of $ 0.16 $kg^{-1}(H_2)$ for $NH_3$. This finding serves to evidence the benefit of including non-determinism in cost estimates when modelling a short time period, as it enables much greater exposure of the model to a variety of weather patterns.

## Grid Energy Cost

Figure 5 shows the influence of varying the cost of

grid energy on the LCOH. An interesting observation is how the grid-energy 'buffers out' any uncertainty in weather energy, when it is available at a low cost. When the cost is high, the model elects to curtail more energy, meaning variations in weather have a more significant influence on the profitability of operation.

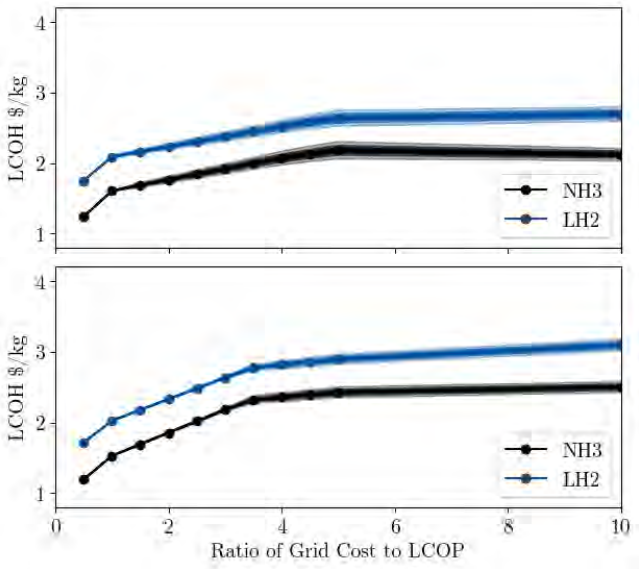



**Figure 5:** Pareto fronts for a grid-connected wind-powered system (top) and a grid-connected solar powered system (bottom). LCOP stands for levelised cost of power, referring to the cost of energy from the wind and solar farm, respectively.

Below a cost ratio of 1, the model will elect to not build a solar or wind farm as it is cheaper to use the grid energy directly. Above this ratio, the solar model uses the grid energy in lieu of storing or curtailing excess energy. The wind model, however, will use some grid energy, but will also begin curtailing energy and investing in storage (evidenced by the increased spread in LCOH values). This is because the capacity factor for the solar farm is lower than that of the wind, meaning the increase in output begotten when using grid energy warrants paying a high price for it, rather than using a curtailment strategy.

When the grid cost becomes excessively high, both models elect to employ storage and curtailment and do not use any grid energy. When not using grid energy the model is less able to 'buffer out' the variations in wind output and, as such, directly influences production quantities of hydrogen.

## Grid Wheeling

The analysis of grid wheeling allowed for unlimited energy to be 'borrowed' within a given period (again, contingent on it being returned within the same period). The pareto fronts demonstrating the results of these analysis are shown in figure 6.

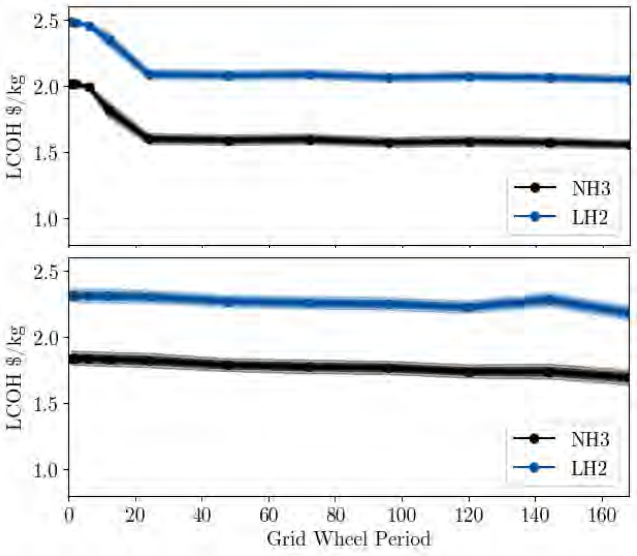



**Figure 6:** Pareto front for variations in the greed wheeling 'period' for the solar (top) and wind (bottom) system.

It is clear to see from figure 6 that enabling the system to grid-wheel offers a substantial benefit for the solar powered system when the wheeling period is above 24 hours, at which the model will wheel up to 42% of the solar farm's capacity. This makes sense given the diurnality of solar production. For the wind system, the benefit is much less significant, which we hypothesise to be due to the more stochastic nature of aeolian weather patterns, meaning it is difficult to guarantee that any 'borrowed energy' can be returned in a singular fixed interval.

## CONCLUSIONS

This research aimed to study the potential benefit yielded by employing a multistage deterministic model for hydrogen export systems and use it to study the cost-benefit yielded by different operational strategies. The stochastic model yielded some benefit over the deterministic system including highlighting the slight underestimation of the cost of hydrogen when compared to the deterministic model and the reduced standard deviation of LCOH prediction when modelling the same time period.

Another key benefit of the stochastic system is in its ability to model a solar system for a short time period. This is important as it is more challenging to cluster a solar time series than an aeolian, due to it being more continuously dynamic in nature. This challenge leads to many researchers using 'representative days' in order to model the solar time series, which assists in reducing computational load. Here, without clustering, the solar model was able to process 27 distinct 4-week weather patterns, giving a large exposure to different weather patterns whilst still solving in a reasonable time-frame.

Although the stochastic model offers slight improvements to the accuracy and repeatability of cost

estimation, it is more computationally intense and scales geometrically with the number of decision-making stages, hence this analysis was limited to studying a months' operation. Whilst a month is a functional period to study in this context, it is insufficient when studying a full value chain which would include shipping between supply and demand regions.

Grid wheeling was found to be very effective in a solar system due to its ability to guarantee the return of energy in a given time period. There is a natural question as to the 'greenness' of wheeled energy, given on balance green energy is contributed to the grid and green energy is removed; but the energy used to produce the hydrogen when 'borrowing' may not be green itself.

Whilst the infrastructural requirements of endorsing a grid-wheeling approach would be significant, the potential economic remuneration associated with cutting hydrogen export costs by up to 20% would serve to stimulate interest in such strategies. As such, it is not untenable given the broad political interest in hydrogen export with certain nations. However, whilst this strategy shows promise, some nations have set limits on the amount of energy that can be wheeled, which could serve to limit the economic benefit of such an approach.

## DIGITAL SUPPLEMENTARY MATERIAL

Digital supplementary material are available for this research and can be found at the following hyperlink: LAPSE:2025.0004.

## ACKNOWLEDGEMENTS

The authors would like to acknowledge funding for this research through the UKRI Engineering and Physical Sciences Research Council via an iCASE studentship in partnership with Shell plc, and through HI-ACT (Hydrogen Integration for Accelerated Energy Transitions) (EP/X038823/2).

## REFERENCES

1. Guerra, C.F., Reyes-Bozo, L., Vyhmeister, E., Caparrós, M.J., Salazar, J.L., and Clemente-Jul, C. Technical-economic analysis for a green ammonia production plant in Chile and its subsequent transport to Japan. Renew Energy 157:404–414 (2020) https://doi.org/10.1016/j.renene.2020.05.041
2. Lee, H., Roh, G., Lee, S., Choung, C., and Kang, H. Comparative economic and environmental analysis of hydrogen supply chains in South Korea: Imported liquid hydrogen, ammonia, and domestic blue hydrogen. *Int J Hydrogen Energy* 78:1224–1239 (2024) https://doi.org/10.1016/j.ijhydene.2024.06.367
3. Nayak-Luke, R.M., and Bañares-Alcántara, R. Techno-economic viability of islanded green ammonia as a carbon-free energy vector and as a substitute for conventional production. *Energy Environ Sci* 13, 2957–2966 (2020) https://doi.org/10.1039/D0EE01707H
4. Egerer, J., Grimm, V., Niazmand, K., and Runge, P. The economics of global green ammonia trade - "Shipping Australian wind and sunshine to Germany". *Appl Energy* 334 (2023) https://doi.org/10.1016/j.apenergy.2023.120662
5. Aldren C., Shah N. and Hawkes A. Quantifying key economic uncertainties in the cost of trading green hydrogen. *Cell Rep Sustain*, 2:100324 (2025). https://doi.org/10.1016/j.crsus.2025.100342
6. Palys, M.J., and Daoutidis, P. Using hydrogen and ammonia for renewable energy storage: A geographically comprehensive techno-economic study. *Comput Chem Eng* 136:106785. (2020). https://doi.org/10.1016/j.compchemeng.2020.106785
7. Verleysen, K. Robust design optimization of a power-to-ammonia process for seasonal hydrogen storage (Doctoral Thesis). Vrije Universiteit Brussel (2023)
8. Kim, S., Park, J., Chung, W., Adams, D., & Lee, J. H. Techno-economic analysis for design and management of international green hydrogen supply chain under uncertainty: An integrated temporal planning approach. *Energy Conversion and Management*, 301:118010 (2024) https://doi.org/10.1016/j.enconman.2023.118010
9. Robles, J. O., Azzaro-Pantel, C., & Aguilar-Lasserre, A. Optimization of a hydrogen supply chain network design under demand uncertainty by multi-objective genetic algorithms. *Computers & Chemical Engineering*, 140:106853 (2020) https://doi.org/10.1016/j.compchemeng.2020.106853
10. Werner Dinkelbach. On Nonlinear Fractional Programming. Management Science 13(7):492-498 (1967) https://doi.org/10.1287/mnsc.13.7.492
11. Ward Jr, J.H. Hierarchical Grouping to Optimize an Objective Function. *J Am Stat Assoc* 58:236–244 1963) https://doi.org/10.1080/01621459.1963.10500845

© 2025 by the authors. Licensed to PSEcommunity.org and PSE Press. This is an open access article under the creative commons CC-BY-SA licensing terms. Credit must be given to creator and adaptations must be shared under the same terms. See https://creativecommons.org/licenses/by-sa/4.0/



Systems & Control Transactions

**Research Article - Peer Reviewed Conference Proceeding**
ESCAPE 35 - European Symposium on Computer Aided Process Engineering
Ghent, Belgium. 6-9 July 2025
Jan F.M. Van Impe, Grégoire Léonard, Satyajeet S. Bhonsale,
Monika E. Polańska, Filip Logist (Eds.)

PSE PRESS

# Process integration and waste valorization for sustainable biodiesel production toward a transportation sector energy transition

**Vibhu Baibhav[a]*, Daniel Florez Orrego[a], Pullah Bhatnagar[s], Francois Maréchal[a]**

[a] Industrial Process and Energy Systems Engineering Laboratory, École Polytechnique Fédérale de Lausanne (EPFL), Valais-Wallis, Sion, Switzerland.
* Corresponding Author: vibhu.baibhav@epfl.ch

## ABSTRACT

Fossil fuel reliance in the transportation sector remains a leading contributor to global greenhouse gas emissions, underscoring the urgent need for renewable alternatives like biodiesel. Derived from renewable feedstocks, biodiesel can reduce emissions, enhance energy independence, and support rural economies. However, its production faces challenges such as low energy efficiency, process optimization barriers, and the limited utilization of byproducts like glycerol, which elevate costs and hinder large-scale adoption. This study addresses these challenges by developing an integrated framework for biodiesel production and byproduct valorization, supporting the long-term decarbonization of biofuel production. Three key feedstocks—refined palm oil, rapeseed oil, and soybean oil—are evaluated for biodiesel yield. The single-step transesterification process is enhanced through a two-stage approach, optimizing fatty acid methyl ester conversion under varying methanol and NaOH catalyst split ratios. Glycerol valorization strategies, including combustion, purification, and anaerobic digestion, are analyzed to improve economic and environmental sustainability. Using mixed-integer linear programming (MILP), the study minimizes total costs by balancing operational and capital expenditures while incorporating process integration constraints. The findings provide actionable insights into cost-effective and sustainable biodiesel production pathways, promoting the broader adoption of biofuels in the transition toward net-zero emissions.

**Keywords**: Process Design, Alternative Fuels, Energy Efficiency, Techno-economic optimization, Mixed Integer Linear Programming (MILP)

## INTRODUCTION

The extensive reliance on fossil fuels as an energy source is a primary contributor to greenhouse gas emissions, driving global warming and environmental degradation. The combustion of fossil fuels disrupts the carbon cycle by releasing carbon that has been long sequestered underground into the atmosphere. In contrast, biomass represents the fourth largest energy source after coal, oil, and natural gas, making it a crucial renewable alternative. Biomass-derived fuels can contribute to a net-zero carbon cycle, as the carbon released during combustion is offset by the carbon absorbed during feedstock growth. Biodiesel has emerged as a promising alternative to fossil-based diesel for use in compression ignition engines due to its significant environmental benefits. It can be produced from a variety of renewable feedstocks, including vegetable oils, animal fats, and waste cooking oils. The production of biodiesel typically involves a transesterification reaction, in which triglycerides react with an alcohol—predominantly methanol—in the presence of an acid or alkali catalyst. Alkali-catalyzed transesterification, commonly using sodium hydroxide (NaOH), is highly efficient but requires feedstocks with a free fatty acid (FFA) content below 1%. Degummed and neutralized vegetable oils are ideal feedstocks, achieving high biodiesel yields (>98%). Figure 1 shows the reaction mechanism where a triglyceride molecule undergoes three reversible steps to form three fatty acid methyl ester (FAME) molecules and one molecule of glycerol.

Excess of methanol is added to shift the reaction to the product side (Le Chatelier's principle of chemical equilibrium) [1]. The fatty acid composition varies among different vegetable oils. For instance, palm oil primarily consists of palmitic acid (C16:0) and oleic acid (C18:1), soybean oil contains more than 50% linoleic acid (C18:2) along with oleic acid, and rapeseed oil is rich in oleic acid (>60%).

The choice of feedstock significantly impacts the energy efficiency and economic feasibility of biodiesel production. This is often assessed using the Net Energy Ratio (NER), which is calculated by dividing the energy content of the produced biodiesel by the total energy consumed throughout its life cycle, including crop cultivation, oil extraction, and biodiesel production. A study in Thailand estimated the NER of palm oil biodiesel at 2.42, with an annual biodiesel energy output of 94.7 GJ per hectare and a total life cycle energy consumption of 39.16 GJ/ha·y [2]. Similarly, rapeseed biodiesel was found to have an NER of 1.69 when accounting for the energy contribution of two by-products—rape meal and glycerol [3]. In comparison, soybean biodiesel had an estimated NER of 1.97 after mass allocation of all by-products [4]. Both rapeseed and soybean biodiesel exhibit lower energy yields than palm oil, with output of 26.7 GJ/ha·y and 17 GJ/ha·y, respectively. Additionally, these studies highlight the substantial fossil energy requirements associated with biodiesel production, particularly the energy consumed in methanol synthesis, which is a crucial component of the transesterification process.

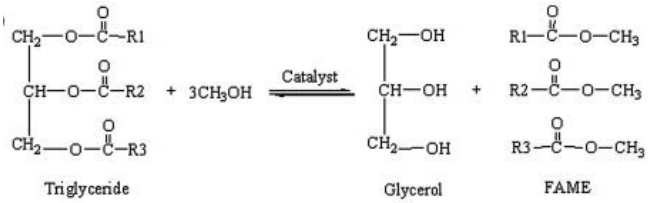



**Figure 1.** Trans-esterification reaction mechanism. R1, R2, and R3 are long chains of fatty acids and vary with the source of Triglyceride (feedstock).

This study focuses on the biodiesel production process from the extracted vegetable oil and aims to model the production process of trans-esterification of Palm, Rapeseed, and Soybean oil along with the further conversion steps to get pure biodiesel. The model is then used to optimize the process design to maximize yield while minimizing reaction time and methanol consumption. The heat and mass streams are characterized, and process integration strategies are explored to improve the economic and environmental performance. In addition, every ton of biodiesel production generates approximately 100 kg of crude glycerol as a by-product. Due to the presence of impurities such as methanol, catalysts, and water, crude glycerol has limited economic value and is classified as a hazardous material, restricting its disposal. To enhance its utilization, this study explores valorization pathways, including purification to pharmaceutical-grade glycerol (>99.5% purity) and anaerobic digestion for energy recovery. Although glycerol has a lower heating value (LHV) of 16.2 MJ/kg, as reported in [5], its high auto-ignition temperature and viscosity at room temperature create challenges for combustion, necessitating specialized burners for co-combustion with other fuels. Due to these technical constraints, crude glycerol combustion has not been considered in this process integration study.

## METHODOLOGY

The biodiesel production process was modeled in ASPEN Plus, using a reference flowsheet from Zhang et al. [6]. The model includes a transesterification reactor, methanol recovery column, water washing, glycerol purification, catalyst removal, and biodiesel purification. The reactor operates with a kinetic reaction model, while catalyst removal is modeled as a fixed conversion neutralization reaction. Water washing is simulated using a liquid-liquid extractor, and methanol recovery, glycerol purification, and biodiesel purification are carried out using RadFrac distillation columns. The composition profile of palm oil was taken from Che Man [7], and the reaction kinetic parameters were based on Narvaez et al. [8]. The reference model was adapted to simulate biodiesel production from rapeseed and soybean oils, with their triglyceride compositions sourced from the literature [9]. The triglyceride composition for rapeseed oil includes 36% OOO, 16% LiLnO, 15% OOLI, 13% POLi, 10% OOLn, 7% LiOLi, and 3% OPO, whereas soybean oil consists of 27% LiLiLi, 25% OLiLi, 19% PLiLi, 15% OOLi, and 13% PliO [10]. Here, "PLiO" represents a triglyceride with one palmitic acid (R1), one linoleic acid (R2), and one oleic acid (R3) chain, while "Ln" denotes linolenic acid. The reaction parameters were modeled similarly to the reference case using palm oil. All relevant components, including diglycerides and monoglycerides as reaction intermediates, were available in the ASPEN APV110 Biodiesel Database.

The model was used to evaluate biodiesel yields for palm, rapeseed, and soybean oils under varying reaction temperatures and residence times. As shown in Fig. 1, triglycerides and FAME molecules share the same chemical constituents, meaning that, theoretically, 1 ton of oil should yield approximately 1 ton of biodiesel. This serves as an indicator of the completeness of the transesterification reaction. The reaction yield was calculated using Eq. 1, and a summary of the feedstock compositions is provided in Table 1.

$$Yield = \frac{Pure\ biodiesel\ produced, FAME\ (\frac{ton}{hr})}{Input\ vegetable\ oil(\frac{ton}{hr})} \quad (1)$$

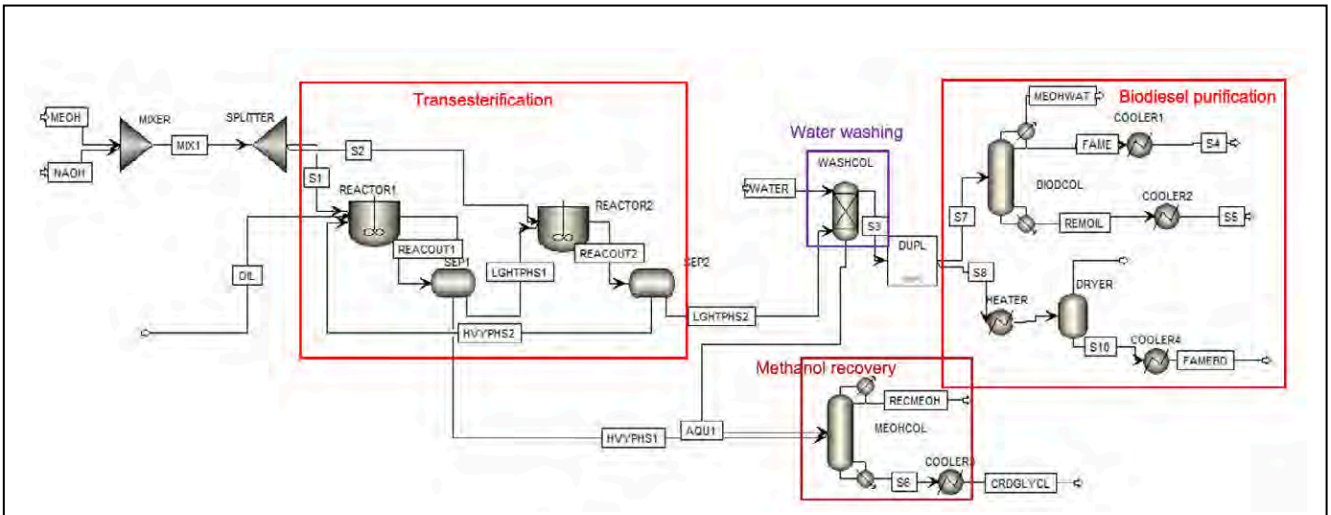



**Figure 2:** ASPEN Plus Model of the Biodiesel production considered. The two-step reaction is introduced to the reference model along with decanters. The heavier phase separated after the second reactor is sent back to the first reactor to reduce the methanol and Alkali catalyst consumption. This is as per the Lurgi process described in [12].

## Two-step Transesterification reaction

To reduce the reaction time for mass production and increase the biodiesel yield, the trans-esterification reaction is modeled in two steps. Previous studies have shown increased conversion yield when doing the reaction in two steps compared to the single-step reactions[11].

**Table 1:** Fatty acid constituents in three vegetable oil feedstocks considered for biodiesel production. They have been calculated based on individual triglyceride constituents in previous studies [7], [9], [10].

| Constituent | Percentage in Input Feedstock (%) | | |
|---|---|---|---|
| | Palm Oil | Soybean Oil | Rapeseed Oil |
| Oleic Acid | 40 | 22 | 67 |
| Linolenic Acid | 10 | 67 | 19 |
| Palmitic Acid | 45 | 11 | 5 |
| Linolenic Acid | - | - | 9 |
| Stearic Acid | 4 | - | - |
| Myristic Acid | 1 | - | - |

Figure 2 shows the ASPEN model with two reactors and gravity-based phase separators. The heavier phase from separator two is recirculated to Reactor 1, following the patented Lurgi process outlined in [12]. This modification reduces methanol and catalyst consumption while enhancing the reaction yield. The heavier phase from separator one, along with the water from biodiesel washing, is directed to the methanol recovery column, where excess unreacted methanol is recovered and returned to the reactors. The impact of varying methanol and catalyst split fractions on the two reaction steps is evaluated by comparing reaction yields for different values. The results are presented both with and without the implementation of the Lurgi process for rapeseed oil.

## Process Integration and Crude Glycerol Valorization

After methanol separation from glycerol, the remaining steam contains water and catalyst (NaOH). The catalyst is separated by adding phosphoric acid, with a neutralization reaction and a filter to precipitate out the salts. The resulting crude glycerol, though suitable for market sale, has a lower value. For pharmaceutical or food applications, high-purity glycerol is required, which is achieved through distillation columns. Given the high-water content (40-60%) in crude glycerol, mechanical vapor recompression (MVR) is employed to recover heat during the separation process. In ASPEN Plus, the mixture is heated to 110°C and expanded under a vacuum pressure of 0.5 bar. The separated vapors are directed to a two-stage compression process to generate steam at 2.5 bar, with an intercooler placed between stages to prevent the vapor temperature from exceeding 210°C, under steam compressor design constraints. The condensed water vapor, now substituting for fossil-based steam, is recycled back into the biodiesel water washing process, offering additional operational cost benefits. The model of these two options is depicted in Figure 3. After water evaporation, the resulting glycerol can also be directed to anaerobic digestion instead of the distillation column. Due to its high chemical oxygen demand (COD) and substantial volatile solids content, it is an ideal substrate for co-digestion, enhancing methane production as demonstrated in previous studies [13]

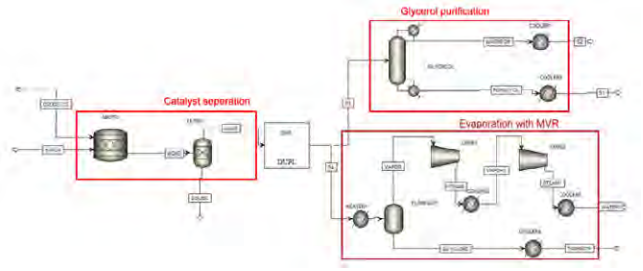



**Figure 3.** The crude glycerol valorization model considered in the process integration study.

All mass and heat streams from ASPEN for the various models are integrated into the OSMOSE software. OSMOSE, developed as a system integration platform for multi-objective optimization at IPESE Lab, EPFL [14], allows for the integration of glycerol valorization routes and utilities into the biodiesel production process. The system is solved as a Mixed-Integer Linear Programming (MILP) problem to minimize total costs. Additionally, carbon emissions resulting from electricity and natural gas use are incorporated, with constraints placed on the total emission value to generate a list of decarbonization solutions for the biodiesel production process. The digestion of crude glycerol is modeled with a total solids content of 1000.8 g/L, and a volatile solids content of 947.8 g/L [13]. The Biomethane Potential (BMP) is 408 $Nm^3$ $CH_4$/kg glycerol, based on the composition of the resulting stream after glycerol-water evaporation, consistent with findings from previous studies [15][16].

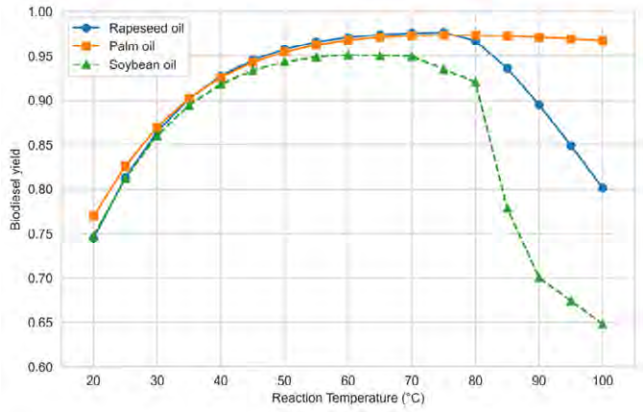
## RESULTS AND DISCUSSION

The biodiesel yield variation for three feedstocks is compared based on a single-step trans-esterification reaction model. Then, the results of the two-step reaction process for Rapeseed oil are shown, followed by the process integration part.

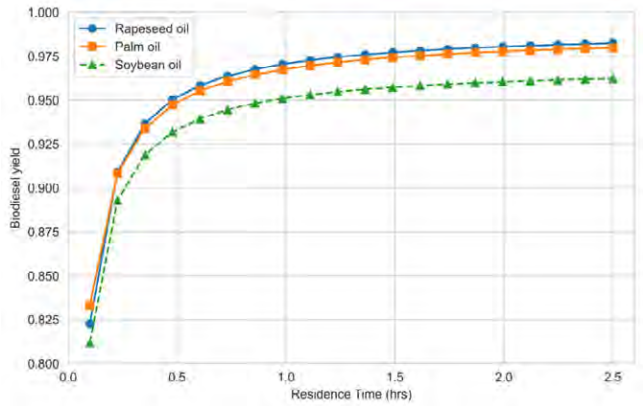
### Influence of Reaction parameters

Figure 4 illustrates the variation in reaction yield for Soybean, Rapeseed, and Palm oils at different operating temperatures and residence times in the reactor. These simulations were conducted using a 6:1 molar ratio of methanol to oil. Palm and Rapeseed oils achieve higher biodiesel conversion yields compared to Soybean oil. The optimal reaction temperatures are 80°C for Palm oil, 75°C for Rapeseed oil, and 60°C for Soybean oil. The yield increases steadily with residence time for all three feedstocks. For a 10-minute residence time at 60°C, more than 80% of the triglyceride content is converted to FAME molecules. The yield continues to increase non-linearly, with Soybean oil requiring over 1 hour to reach a 95% conversion yield.

As shown in Figure 4, even after a reaction time of 2.5 hours, Rapeseed oil achieved the highest yield of 98.2% at an operating temperature of 60°C. However, this is not optimal for mass production, and implementing a multi-step reaction could reduce the residence time while maintaining high yields. Figure 5 illustrates the yield variation in two reactors with different split fractions of methanol and NaOH. Without using the Lurgi process—i.e., sending the heavier phase from both separators back for methanol recovery while maintaining a 6:1 molar ratio—the conversion yields are lower. For a residence time of 12 minutes and a temperature of 60°C in both reactors, the total yield was only 90.8% for the 6:1 methanol-to-oil ratio (as shown in Figure 5a). This yield increased to 98.8% when the ratio was adjusted to 9:1, as shown in Figure 5b. The optimal split ratio was found to be 60% to Reactor 1. However, when the Lurgi process is used, reaction yields are higher and are at lower split ratios. Figure 5c demonstrates that a 99% yield can be achieved at lower operating temperatures and residence times with a 6:1 molar ratio. Recycling the heavier phase back to the first reactor significantly improves yields while reducing methanol consumption.

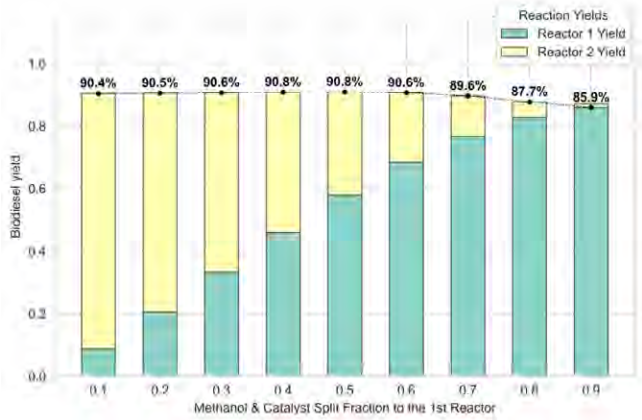



(a) Residence time is 1 hour for all the simulations

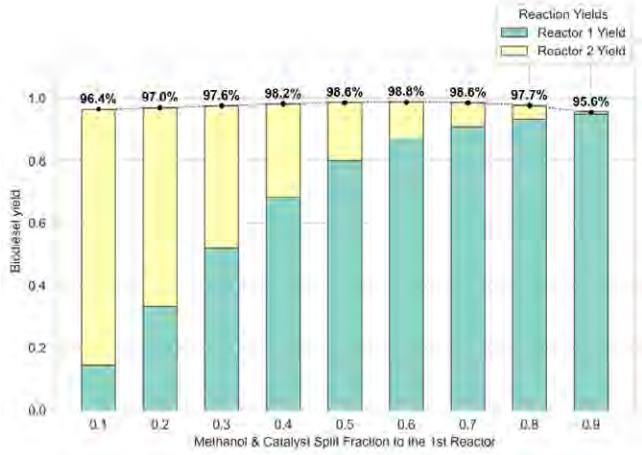



(b) The operating temperature is 60°C for all the simulations.

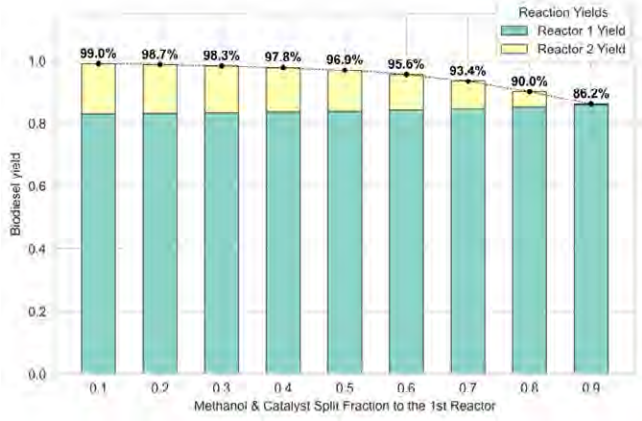
**Figure 4.** Reaction yield variation for different residence times and operating temperatures for three feedstocks. Influence of Two-step trans-esterification reaction




(a) Residence time is 12 min and operating temperature of 60°C for both reactors without the Lurgi process (Methanol ratio 6:1)

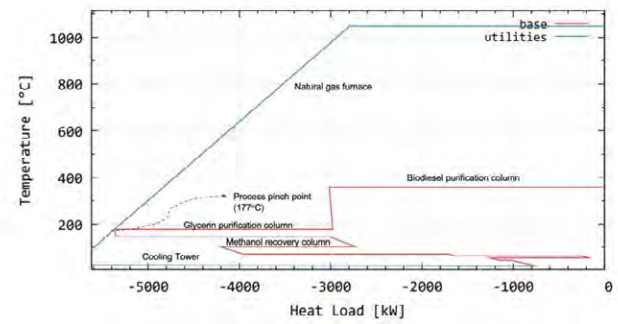



(b) Residence time is 12 min and operating temperature of 60°C for both reactors without the Lurgi process (Methanol ratio 9:1)

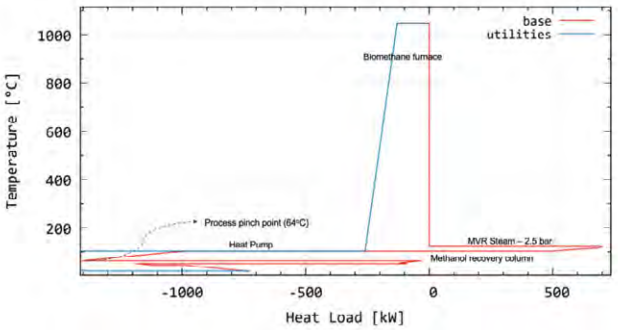



(c) Residence time is 10 min, and the operating temperature of 50°C for both reactors with the Lurgi process (Methanol ratio 6:1)

**Figure 5.** Reaction yield variation for different methanol-catalyst split fractions in the two reactors for Rapeseed oil




(a) With biodiesel and glycerol purification columns and all the heat coming from fossils resulting in minimal total cost.




(b) With biodiesel drying, crude glycerol anaerobic digestion, and MVR cycle with water recycling. A heat pump is also integrated to improve the exergy efficiency.

**Figure 6.** Integrated composite curves for two different configurations of the biodiesel production process.

## Process Integration

The streams from the two-step Lurgi reaction model for Rapeseed oil were integrated with a list of options. The heat cascade incorporates pinch analysis to maximize internal heat recovery, thereby minimizing the heating and cooling requirements of the biodiesel production process. Figure 6a presents the integrated composite curve (ICC) for the minimum total cost configuration, which includes biodiesel and glycerol purification columns, a natural gas furnace, and a cooling tower. This configuration results in the highest carbon emissions and low exergy efficiency. International standards specify a minimum of 96.5% FAME content in biodiesel. If the reaction yield falls below this threshold, the unconverted oil fraction in the stream after water washing must be separated, requiring a distillation column. However, with a yield exceeding 98% using the Lurgi process, the biodiesel drying process is employed instead of the purification column. The stream is heated to 115°C and expanded in a tank at 0.2 bar vacuum pressure. The dry biodiesel is then cooled to ambient temperature to maximize heat recovery. Unlike crude glycerol evaporation, integrating MVR is not cost-effective due to the lower water content (<0.2%). Figure 6b displays the ICC without the biodiesel and glycerol purification columns. The crude glycerol produced after evaporation is sent for anaerobic

digestion, and the methane generated from the purified biogas is partially used to supply process heat. The excess methane is injected into the gas grid, resulting in negative carbon emissions. Additionally, the steam generated from the integrated MVR cycle during glycerol water evaporation is used to supply process heat, reducing the size of the required gas furnace. The process pinch temperature of 64°C makes the methanol recovery distillation column's reflux condenser an ideal source for the heat pump. The heat pump extracts heat from below the pinch and supplies heat above the pinch to the column's reboiler at 100°C. This not only reduces heating requirements but also decreases the load on the cooling tower. In regions with a low-carbon electricity mix, the biodiesel production process can even become carbon-negative, as a result of the biomethane production from crude glycerol.

## CONCLUSION

The biodiesel production process from three feedstocks—palm, rapeseed, and soybean oil—was modeled in Aspen Plus, and reaction yields were compared under different operating temperatures and residence times. Palm and rapeseed oils exhibited similar yield values, while soybean oil had the lowest yield. A two-step transesterification reaction resulted in significantly higher biodiesel conversion (98.9%) at a much lower residence time compared to a single-step process (82.1% yield at 10 min residence time and 50°C). However, the two-step reaction required a higher methanol-to-oil ratio, increasing the energy demand for methanol recovery. The Lurgi process, which recirculates the heavier phase from the second reactor, reduced methanol and catalyst consumption, improving overall process efficiency. The optimal split ratio for the methanol-catalyst mixture was 10% to the first reactor.

Process integration strategies, such as heat recovery, heat pumps in methanol recovery distillation, and mechanical vapor recompression (MVR) for crude glycerol evaporation, improved exergy efficiency and reduced fossil steam consumption. Further sustainability gains can be achieved by valorizing crude glycerol, either through purification to pharmaceutical-grade glycerol or anaerobic digestion for biogas production. The developed methodology can be extended to optimize biodiesel production from second-generation feedstocks, including waste cooking oils and animal fats, enhancing both economic and environmental sustainability. The $CO_2$ generated from biogas purification can also be integrated with solid oxide fuel cells, enabling negative emissions and additional chemical production.

## REFERENCES


1. Van Gerpen, J et al. (July 2004). Biodiesel Production Technology: August 2002–January 2004. en. Tech.rep. NREL/SR-510-36244, 15008801, NREL/SR–510–36244, 15008801. DOI: 10.2172/15008801.
2. Pleanjai, Somporn and Shabbir H. Gheewala (Nov. 2009). “Full chain energy analysis of biodiesel production from palm oil in Thailand”. In: Applied Energy. Bio-fuels in Asia 86, S209–S214. ISSN: 0306-2619. DOI: 10.1016/j.apenergy.2009.05.013
3. Ozturk, H. (Dec. 2014). “Energy Analysis For Biodiesel Production From Rapeseed Oil”. In: Energy Exploration & Exploitation 32. DOI: 10.1260/0144-5987.32.6.1005
4. Rajaeifar, Mohammad Ali et al. (Mar. 2014). “Energy life-cycle assessment and CO2 emissions analysis of soybean-based biodiesel: a case study”. In: Journal of Cleaner Production 66, pp. 233–241. ISSN: 0959-6526.DOI: 10.1016/j.jclepro.2013.10.041
5. Zhang, Jianan et al. (May 2022). “Crude glycerol and glycerol as fuels and fuel additives in combustion applications”. In: Renewable and Sustainable Energy Reviews 159, p. 112206. ISSN: 1364-0321. DOI: 10.1016/j.rser.2022.112206
6. Y. Zhang, M.A. Dube, D.D. McLean, M. Kates, "Biodiesel Production from Waste Cooking Oil: 1. Process Design and Technological Assessment", Bioresource Technology, 89:1-16, 2003
7. Y.B. Che Man, T. Haryati, H.M. Ghazali, B.A. Asbi, "Composition and Thermal Profile of Crude Palm Oil and Its Products", Journal of American Oil Chemical Society, 76:237-242, 1999
8. P.C. Narvaez, S.M. Rincon, F.J. Sanchez, "Kinetics of Palm Oil Methanolysis", Journal of American Oil Chemical Society, 84:971-977, 2007
9. Guan, Mei et al. (June 2016). “A Study on Triacylglycerol Composition and the Structure of High-Oleic Rapeseed Oil”. In: Engineering 2.2, pp. 258–262. ISSN: 2095-8099. DOI: 10.1016/J.ENG.2016.02.004
10. Mello, Marcia de et al. (Feb. 2017). “Biodiesel production by the methylic-alkaline and ethylic-enzymatic routes: Discussion of some environmental aspects”. In: Journal of Cleaner Production 144, pp. 347–357. ISSN: 0959-6526. DOI: 10.1016/j.jclepro.2017.01.032.
11. Luna, D. et al. (Mar. 2014). “Technological challenges for the production of biodiesel in arid lands”.In: Journal of Arid Environments 102, pp. 127–138. ISSN: 0140-1963. DOI: 10.1016/j.jaridenv.2013.11.014
12. Thoai, Dang Nguyen et al. (Mar. 2019). “Review on biodiesel production by two-step catalytic con-

version". In: Biocatalysis and Agricultural Biotechnology 18, p. 101023. ISSN: 1878-8181. DOI: 10.1016/j.bcab.2019.101023
13. Alves, Ingrid R. F. S. et al. (Dec. 2020). "Assessing the use of crude glycerol from biodiesel production as an alternative to boost methane generation by anaerobic co-digestion of sewage sludge". In: Biomass and Bioenergy 143, p. 105831. ISSN: 0961 9534. DOI: 10.1016/j.biombioe.2020.105831.
14. Dardor, Dareen et al. (Sept. 2024). "ROSMOSE: A web-based decision support tool for the design and optimization of industrial and urban energy systems". In: Energy 304, p. 132182. ISSN: 0360 5442.
DOI: 10.1016/j.energy.2024.132182.
15. Viana, M. B. et al. (Nov. 2012). "Anaerobic digestion of crude glycerol: a review". In: Environmental Technology Reviews 1.1. Publisher: Taylor & Franciseprint:,p. 81–92. ISSN: 2162-2515. DOI: 10.1080/09593330.2012.692723
16. Dubrovskis, Vilis and Imants Plume (May 2024). Biogas potential from biodiesel production residues. DOI: 10.22616/ERDev.2024.23.TF104

© 2025 by the authors. Licensed to PSEcommunity.org and PSE Press. This is an open access article under the creative commons CC-BY-SA licensing terms. Credit must be given to creator and adaptations must be shared under the same terms. See https://creativecommons.org/licenses/by-sa/4.0/



Systems & Control Transactions

**Research Article - Peer Reviewed Conference Proceeding**
ESCAPE 35 - European Symposium on Computer Aided Process Engineering
Ghent, Belgium. 6-9 July 2025
Jan F.M. Van Impe, Grégoire Léonard, Satyajeet S. Bhonsale,
Monika E. Polańska, Filip Logist (Eds.)

PSE PRESS

# Optimization-based planning of carbon-neutral strategy: Economic priority between CCU vs CCS

**Siuk Roh, Chanhee You, Woochang Jeong, Donggeun Kang, Dongin Jung, Donghyun Kim, Jiyong Kim***

Sungkyunkwan University(SKKU), Department of Chemical Engineering, Suwon, Republic of Korea
* Corresponding Author: jiyongkim@skku.edu.

## ABSTRACT

This study aims to develop an optimization-based approach to design the carbon capture, utilization, and storage (CCUS) supply chain and analyze the optimal configuration and investment strategies. To achieve this goal, we develop an optimization model that determines the logistic decision-making to maximize the net present value (NPV) and minimize the net $CO_2$ emissions (NCE) of the strategies of the CCUS supply chain under logical and practical constraints. We estimate the technical (production scale and energy consumption), economic (capital and operating expenditure), and carbon-related ($CO_2$ emissions) parameters based on the literature. By adjusting major cost drivers and economic bottlenecks, we determined major decision-making problems in the CCUS framework, such as sequestration vs. utilization. As a real case study, the future CCUS system of South Korea was evaluated, which includes three major $CO_2$ emitting industries in South Korea (power plants, steel, and chemicals), as well as transportation modes and sequestration sites. As a result, we analyzed different design and operation strategies based on various objectives. We provided a strategic solution for national-level planning of the CCUS supply chain. The major finding of this study can support industry stakeholders and government policymakers by providing a practical guideline for investing in the deployment of CCUS.

**Keywords**: Carbon capture, utilization, and storage (CCUS), optimization, South Korea, MILP, supply chain

## 1. INTRODUCTION

Global warming is one of the most important issues for humanity, receiving significant attention from the scientific community. Carbon dioxide ($CO_2$) is one of the major greenhouse gases that can affect global warming. $CO_2$ emissions are mainly generated through three key areas: fuel combustion, industrial processes, and natural gas processing [1]. According to recent estimates, global $CO_2$ emissions from fossil fuel combustion have exceeded 37.1 Gt, marking a notable increase of over 2.7% compared to 2017. [2]. To achieve the 1.5°C target set by the Paris Agreement, substantial reductions in $CO_2$ emissions are required, amounting to 24 Gt of $CO_2$ per year by 2030, 14 Gt of $CO_2$ per year by 2040, and 5 Gt of $CO_2$ per year by 2050 [2, 3]. Achieving these reductions necessitates implementing advanced technological solutions, among which Carbon capture, utilization, and storage (CCUS) has emerged as a promising solution.

In the CCUS process, $CO_2$ is captured from air or industrial sources using carbon capture technology. Captured $CO_2$ is then transported to its destination into two main technological pathways. The first pathway is carbon capture and storage (CCS), where $CO_2$ is delivered to a designated storage site and permanently sequestered in geological formations, such as depleted oil and gas reservoirs or deep saline aquifers. The second pathway is carbon capture and utilization (CCU), which utilizes $CO_2$ as a key carbon feedstock for producing value-added products. CCUS technologies can reduce $CO_2$ effectively. For example, gasoline production can reduce more than 5 kg of $CO_2$ eq per unit of fuel [4]. However, the implementation of associated technologies within the industrial sector is challenging. The limitations are caused by the lack of a supply chain, including CCU and CCS with existing energy and industrial infrastructures.

Recently, a few studies have focused on addressing the CCUS supply chain design. Huang et al. examined the CCUS supply chain utilizing $CO_2$-enhanced coal bed methane ($CO_2$-ECBM) recovery [5]. Leonzio et al.

incorporated methanol (MeOH) production via dry reforming for CCU and developed the CCUS supply chain for Germany [6]. A few studies about the economic optimization of CCS are reported for distinct geographical characteristics: Klokk et al. for Norway, and Zhang et al. for China [7,8]. The preceding studies highlight the necessity of developing region-specific CCUS supply chain optimization models, for unique characteristics and constraints specific to each region. These models emphasize the significance of multi-stage planning in achieving efficient carbon management systems. Nevertheless, the expansion of the scope of research is imperative, integrating approaches that address multi-objective and multi-period scenarios. These approaches are essential for capturing the dynamic nature of $CO_2$ supply and demand, technological advancements, and fluctuating economic and regulatory landscapes.

In this study, we develop an optimization-based framework for the CCUS supply chain to integrate the overall CCUS infrastructure into the supply chain to maximize net present value (NPV). $CO_2$ is captured, compressed, and transported from $CO_2$ emission sources. After transporting captured $CO_2$, we consider the $CO_2$ utilization technologies, which involve the production of MeOH, and the $CO_2$ storage option, which includes the $CO_2$ intermediate storage terminals and offshore storages to sequester $CO_2$. Then, two distinct scenarios with different criteria (social cost of $CO_2$, and $CO_2$ capture rate) are analyzed over a multi-period framework. The proposed model presents strategies that incorporate economic and environmental considerations while addressing future scenarios.

## 2. METHODOLOGY

### 2.1. Problem statement

The main objective of this study is to develop an optimization-based approach to design a supply chain incorporating both CCS and CCU. The proposed CCUS supply chain optimization model comprises the following components: $CO_2$ sources, $CO_2$ capture processes, transportation infrastructure, $CO_2$ storage facilities, and $CO_2$ utilization systems. $CO_2$ storage facilities include intermediate storage terminals and offshore storage sites, while $CO_2$ utilization focuses on the MeOH production process via direct hydrogenation. The system boundary of the model is illustrated in Figure 1.

In the proposed model, carbon-related data ($CO_2$ emission sources, location, and annual emissions), transportation data (loading/unloading times and transportation capacities), and technical data (production scales, and raw material consumption) are utilized as basic elements for decision-making [9]. The model determines the optimal number and location of $CO_2$ storage terminals and MeOH production facilities.

To simplify the model, the following assumptions are made:

- Each $CO_2$ emission source is linked to a single $CO_2$ intermediate storage terminal or MeOH production facility.
- MeOH prices are assumed to increase due to inflationary trends, while hydrogen prices are projected to decrease in a multi-period context, reflecting expected technological advancements and market dynamics [9].

### 2.2. Optimization model

The objective function of the optimization model is to maximize the NPV of the CCUS supply chain. The optimization is formulated using a mixed integer linear programming (MILP) model. The NPV is calculated as the total revenue minus the total cost and is defined as follows:

$$\max NPV = Revenue + TSC - TPC \quad (1)$$

TPC (total production cost) consists of PCC (production capital cost), SCC (storage capital cost), TCC (transportation capital cost), POC (production operating cost), SOC (storage operating cost), and TOC (transportation operating cost).

$$TPC = PCC + SCC + TCC + POC + SOC + TOC \quad (2)$$

PCC & POC quantify the capital expenditures and operating expenditures of MeOH production facilities. TCC &

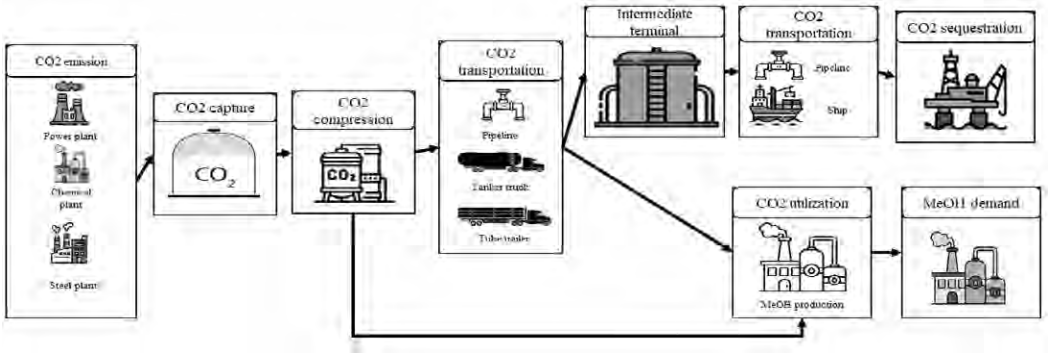



**Figure 1:** System boundary of CCUS supply chain

TOC quantify the capital expenditures and operating expenditures of transporting $CO_2$ from its emission sources to MeOH production facilities/$CO_2$ intermediate storage terminals and from $CO_2$ intermediate storage terminals to offshore storage facilities. SCC & SOC quantify the capital expenditures and operating expenditures of $CO_2$ intermediate storage terminals. Revenue quantifies the profit from MeOH sales in CCU. TSC (total salvage cost) quantifies the total salvage cost of MeOH production facilities and $CO_2$ intermediate storage terminals.

For the mass balance constraints at the $CO_2$ capture and transportation, Eq (3) indicates that the amount of captured $CO_2$ is equal to the total amount of $CO_2$ transported to intermediate terminals of MeOH production facilities.

$$CC_{rt} = \sum_{r'} Q^{T}_{trr'} + \sum_{s} Q^{T}_{trs} + F_{jrt} \quad (3)$$

Where $CC_{rt}$ and $F_{jrt}$ indicate amount of captured $CO_2$ and utilized $CO_2$. $Q^{T}_{trr'}$ and $Q^{T}_{trs}$ denote the amount of $CO_2$ transported to MeOH production facility and $CO_2$ storage terminals.

For $CO_2$ storage, Eq (4) indicates the amount of $CO_2$ transported to storage terminals is equal to the amount of $CO_2$ sequestered.

$$\sum_{s} CT^{T}_{ts} = \sum_{q} S^{T}_{tq} \quad (4)$$

$CT^{T}_{ts}$ and $S^{T}_{tq}$ present the amount of $CO_2$ stored in $CO_2$ intermediate storage terminals and sequestered in offshore storage.

Regarding transportation capacity constraints, Eq (5) the amount of $CO_2$ does not exceed the capacity of the respective transportations.

$$N^{T}_{trr}\vartheta_p \le Q^{T}_{trr'} \le N^{T}_{trr}\theta_p \quad (5)$$

Where $\vartheta_p$ and $\theta_p$ indicate minimum capacity and maximum capacity of $CO_2$ transportation. $N^{T}_{trr'}$ presents the number of transportation unit. $Q^{T}_{trr'}$ indicates the amount of $CO_2$ from $CO_2$ source to MeOH production facility.

## 3. CASE STUDY: APPLICATION TO SOUTH KOREA

To demonstrate the effectiveness of the optimization model, we present a case study on the supply chain in South Korea. With annual $CO_2$ emissions amounting to approximately 600 million tons, representing 1.6% of global emissions, South Korea's major contributors include fossil fuel combustion and industrial activities such as power generation, steel production, and chemical manufacturing. To align with the government's 2050 net-zero target, substantial reductions in industrial sector emissions are projected, aiming to cut up to 80% of current levels through the implementation of CCUS technologies. A comprehensive survey was conducted involving 157 facilities across the country, encompassing 25 power plants, 46 steel facilities, and 86 chemical plants. The annual $CO_2$ emissions of these facilities were assessed, with the data summarized in Table 1.

**Table 1:** Category of $CO_2$ emission sources

| $CO_2$ source | Number of factories | Total $CO_2$ emissions |
|---|---|---|
| Power plant | 25 | 49.96 Mt |
| Steel plant | 46 | 123.53 Mt |
| Chemical plant | 86 | 300.78 Mt |
| Total | 157 | 474.27 Mt |

These facilities were identified as potential MeOH production sites, using captured $CO_2$ as a feedstock. For $CO_2$ sequestration, two depleted gas reservoirs located in the East Sea and West Sea were selected as storage sites. Additionally, $CO_2$ intermediate storage terminals were strategically proposed for each province. Coastal areas favored terminals at ports, while inland areas selected locations in plains over mountainous regions to minimize infrastructure and transport costs. To facilitate offshore sequestration, the transport network links $CO_2$ intermediate storage terminals to the selected ports. To visualize the $CO_2$ flow from emission sources to MeOH production facilities or $CO_2$ intermediate storage terminals, $CO_2$ emissions were evaluated at the provincial level, as depicted in Figure 2.

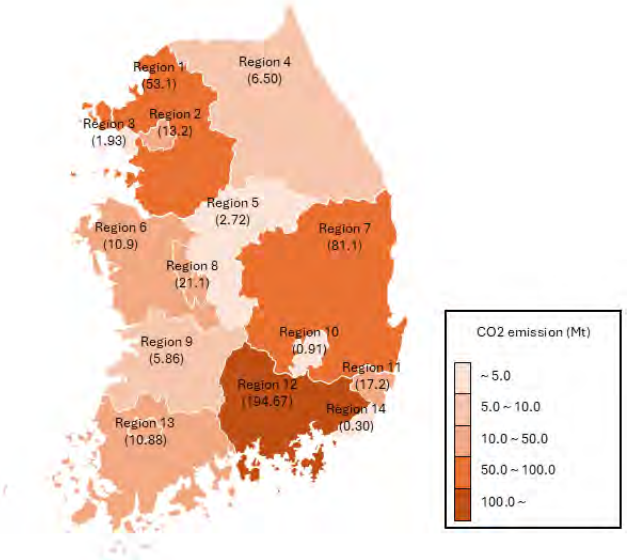



**Figure 2.** $CO_2$ emissions map in Korea in 2030

## 4. RESULTS AND DISCUSSION

This section presents the results of the optimized CCUS supply chain applied to South Korea, demonstrating the efficacy of the developed model. The optimization problem formulated as a MILP model and solved using

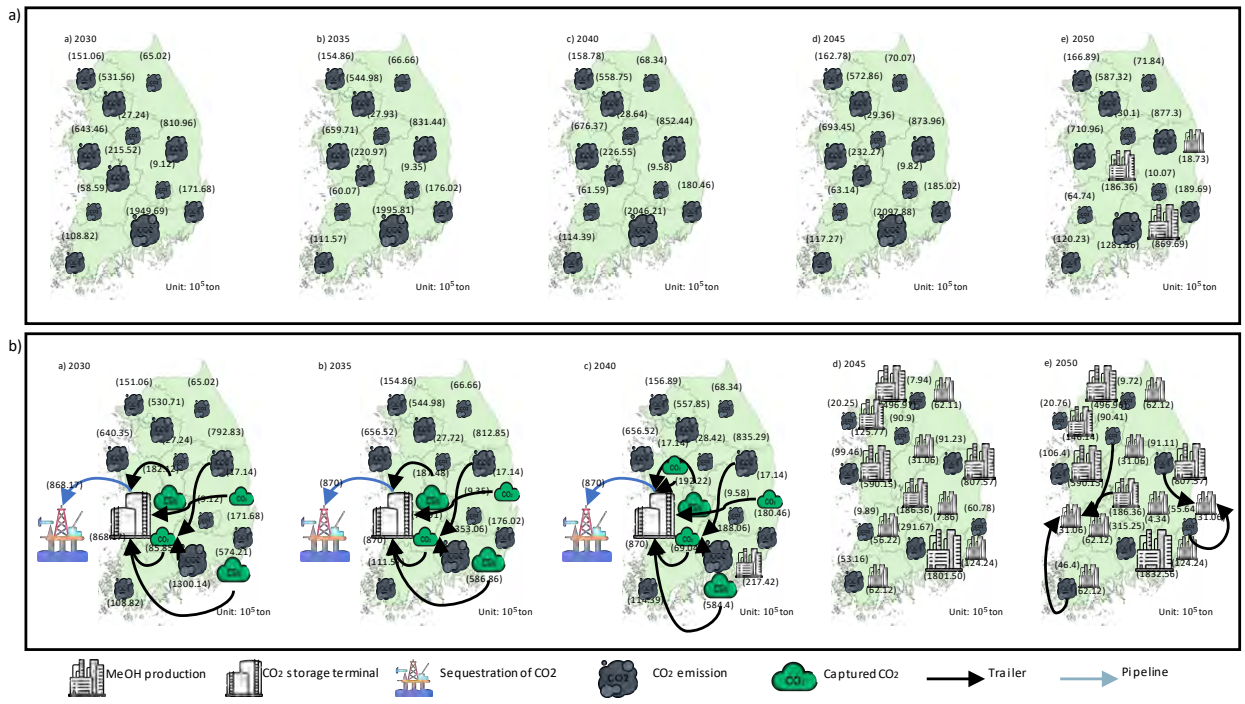



**Figure 3:** Topology of the optimized CCUS supply chain with (a) \$40 and (b) \$170 of social cost in South Korea from 2030 to 2050

CPLEX, aimed to maximize the NPV of the system. The analysis was conducted under two scenarios: (1) incorporating social costs of $CO_2$ emissions which is the monetary value of the environmental damage of each additional ton of $CO_2$ emitted, and 2) varying $CO_2$ capture rates for emission sources [10]. The social cost of $CO_2$ is evaluated from a baseline of \$0 per ton of $CO_2$, representing no economic impact, up to a maximum of \$185 per ton of $CO_2$ reflecting the potential role of the social cost of $CO_2$ emissions as a financial penalty [11]. Additionally, the CO2 capture rates for emission sources are assessed up to maximum efficiency of $CO_2$ capture technology.

## 4.1 Results for CCUS supply chain with social costs

In scenarios with low social costs for $CO_2$ emissions, the optimization results reveal that deploying CCUS facilities is not economically viable. Instead, the atmospheric emission of $CO_2$ continues to be economically favorable. However, as the social cost increased to \$40 per ton, the CCUS supply chain model suggests the deployment of CCU technologies to produce MeOH as a viable strategy by 2050. The graphical topology of this supply chain at \$40 and \$170 of social cost is shown in Figure 3. At this price point, the model suggested that regional $CO_2$ emissions from regions 7, 8, and 12 are captured and utilized directly at local MeOH production sites, eliminating transportation costs. Regions 7, 8, and 12 are primarily associated with steel production facilities, where the relatively low cost of carbon capture serves as a key driver for $CO_2$ capture implementation. When the social cost reaches \$170 per ton, the model predicts the construction of $CO_2$ intermediate storage terminals in selected regions such as region 9, by 2030. This cost level facilitates the sequestration of 86.8 million tons of $CO_2$, reflecting the increased feasibility of CCS under higher social costs.

A multi-period analysis demonstrates that declining hydrogen prices, from \$4.21 per kg in 2030 to \$3.21 per kg in 2040, and rising MeOH prices influenced by inflationary trends enhance the attractiveness of CCU technologies. Consequently, $CO_2$ initially allocated for storage is reallocated for utilization, underscoring the dynamic adaptability of the supply chain to economic fluctuations.

## 4.2 Results for CCUS supply chain with capture rates

This study systematically evaluates the performance of the CCUS supply chain under varying $CO_2$ capture rates, focusing on $CO_2$ allocation, infrastructure development, and the economic and operational performance of the network.

At a capture rate of 10%, all captured $CO_2$ amounting to 47.4 million tons by 2030 is directed to offshore storage. The graphical topology of this supply chain at 10% and 30% of the capture rate is shown in Figure 4. Infrastructure development in this scenario required constructing intermediate storage terminals in region 9 and

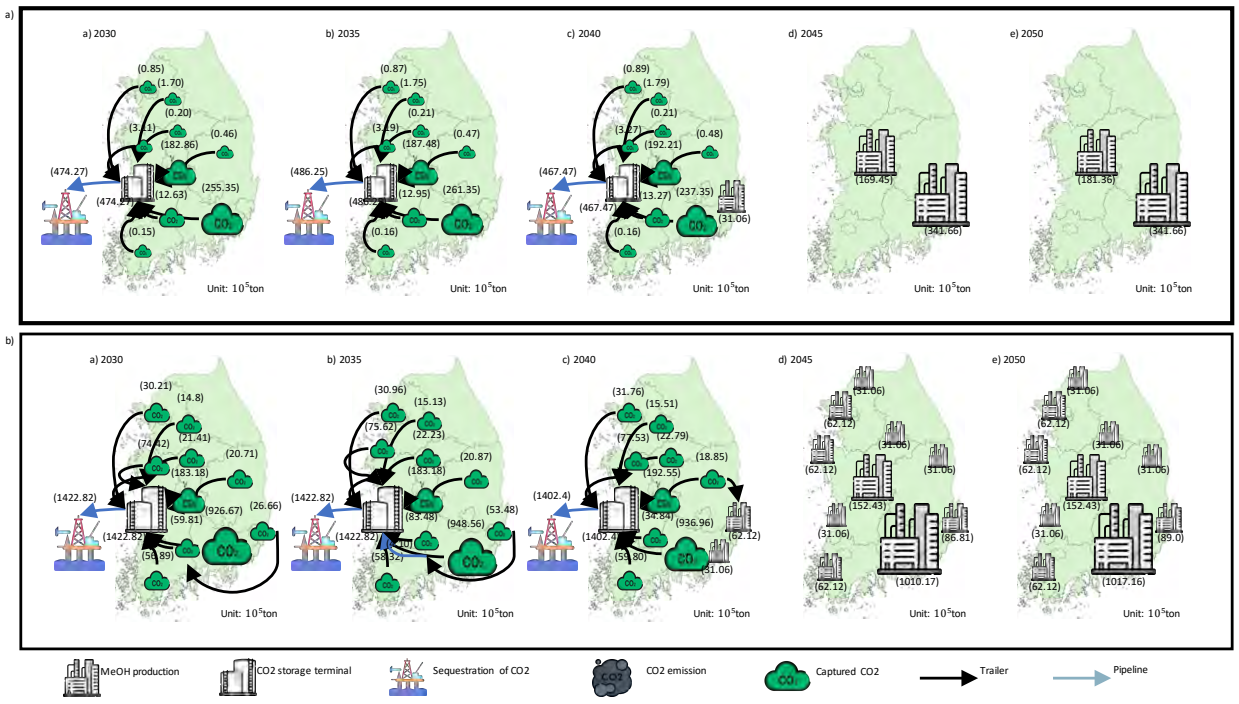



**Figure 4:** Topology of the optimized CCUS supply chain with (a) 10% and (b) 30% of capture rate in South Korea from 2030 to 2050

deploying pipelines to transport $CO_2$ to the West Sea. In a multi-period analysis, CCU facilities emerge in regions 8 and 12, enabling MeOH production from captured $CO_2$ by 2040. Capture rates of 30% or higher facilitate the establishment of additional $CO_2$ intermediate storage terminals and production facilities.

## 5. CONCLUSION

The CCUS supply chain plays a critical role in South Korea's efforts to achieve its carbon neutrality target by 2050. This study presents a CCUS supply chain model incorporating two distinct scenario criteria (the social cost of $CO_2$ and $CO_2$ capture rate) over a multi-period framework. The result demonstrated that 1) $CO_2$ utilization holds an economic priority over $CO_2$ storage due to the significant costs associated with injecting $CO_2$ into offshore storage sites, and 2) higher social costs and capture rates act as drivers for promoting carbon capture. This study confirms the effectiveness of implementing an optimization strategy for multi-objective, multi-period CCUS supply chains to address the uncertainties in strategic planning. By applying a systematic approach that adapts multi-period and multi-objective scenarios, the proposed model facilitates comprehensive planning that incorporates economic and environmental considerations. The proposed model successfully demonstrates the potential to achieve such integration and optimization, providing valuable insights for future CCUS applications. By utilizing the optimization model from this study, stakeholders and policymakers can develop deployment strategies that effectively balance economic and environmental objectives.

## 6. REFERENCES


1. Federico d'Amore, Farbrizio Bezzo. Economic optimisation of European supply chains for $CO_2$ capture, transport and sequestration. *Int. J. Greenh. Gas Control* 65:99-116 (2017) https://doi.org/10.1016/j.ijggc.2017.08.015
2. Hisham Al Baroudi, Adeola Awoyomi, Kumar Patchigolla, Kranthi Jonnalagadda, E.J. Anthony. A review of large-scale $CO_2$ shipping and marine emissions management for carbon capture, utilisation and storage. *Appl.Energy* 287 (2021) https://doi.org/10.1016/j.apenergy.2021.116510
3. Grazia Leonzio, David Bogle, Pier Ugo Foscolo, Edwin Zondervan. Optimization of CCUS supply chains in the UK: A strategic role for emissions reduction. *Chem. Eng. Res. Des.* 155:211-228 (2020) https://doi.org/10.1016/j.cherd.2020.01.002
4. Thai Ngan Do, Chanhee You, Jiyong Kim. A $CO_2$ utilization framework for liquid fuels and chemical production: techno-economic and environmental analysis. *Energy Environ. Sci.* 15:169-184 (2022) https://doi.org/10.1039/D1EE01444G
5. Yuping Huang, Qipeng P. Zheng, Neng Fan, Kashy Aminian. Optimal scheduling for enhanced coal bed methane production through $CO_2$ injection. *Appl.Energy* 113: 1475-1483 (2014)

https://doi.org/10.1016/j.apenergy.2013.08.074
6. Grazia Leonzio, Pier Ugo Foscolo, Edwin Zondervan. An outlook towards 2030: Optimization and design of a CCUS supply chain in Germany. *Comput.Chem.Eng* 125:499-513 (2019) https://doi.org/10.1016/j.compchemeng.2019.04.001
7. Q. Klokk, P.F. Scheriner, A. Pages-Bernaus, A. Tomasgard. Optimizing a $CO_2$ value chain for the Norwegian continental shelf. *Energy Policy* 38:6604-6614(2010) https://doi.org/10.1016/j.enpol.2010.06.031
8. Shuai Zhang, Linlin Liu, Lei Zhang, Yu Zhuang, Jian Du. An optimization model for carbon capture utilization and storage supply chain: A case study in Northeastern China. *Appl.Energy* 231:194-206 (2018) https://doi.org/10.1016/j.apenergy.2018.09.129
9. Chanhee-You, Chanmok-Kim, Hyeon Yang, Jiyong Kim. Optimization-based framework for techno-economic and environmental assessment of $CO_2$ capture, utilization, and storage strategies. *Comput. Aided Chem. Eng.* 53:2173-2178 (2024) https://doi.org/10.1016/B978-0-443-28824-1.50363-X
10. Desy Caesary, Hana Kim, Myung-Jin Nam. Cost effectiveness of carbon capture and storage based on probability estimation of social cost of carbon. *Appl.Energy* 377 (2025) https://doi.org/10.1016/j.apenergy.2024.124542
11. Kevin Rennert, Frank Errickson, Brian C. Prest, Lisa Rennels. Comprehensive evidence implies a higher social cost of $CO_2$. *Nature.* 610: 687-692 (2022) https://doi.org/10.1038/s41558-023-01680-x
12. Korean Ministry of Environment. https://www.2050cnc.go.kr/base/board/read?boardManagementNo=4&boardNo=101&searchCategory=&page=1&searchType=&searchWord=&menuLevel=2&menuNo=15
13. Jee-Hoon Han, Jun-Hyung Ryu, In-Beum Lee. Developing a mathematical modeling framework of carbon dioxide capture, transport, and storage networks. *J.Chem.Eng.Jpn.* 45:504-527 (2012) https://doi.org/10.1252/jcej.11we268
14. Suh-Young Lee, In-Beum Lee, Jee-Hoon Han. Design under uncertainty of carbon capture, utilization and storage infrastructure considering profit, environmental impact, and risk preference. *Appl.Energy* 238:34-44 (2019) https://doi.org/10.1016/j.apenergy.2019.01.058
15. Hyonjeong Noh, Kwangu Kang, Cheol Huh, Seong-gil Kang, Seong-Jong Han, Hyungwoo Kim. Conceptualization of $CO_2$ terminal for offshore CCS using system engineering process. *Energies* 12:22 (2019) https://doi.org/10.3390/en12224350
16. Kevin Reenert, Frank Errickson, Brian C.Prest, Lisa Rennels, Richard G.Newell. Comprehensive evidence implies a higher social cost of $CO_2$. *Nature* 610:687-692 (2022) https://doi.org/10.1038/s41586-022-05224-9

© 2025 by the authors. Licensed to PSEcommunity.org and PSE Press. This is an open access article under the creative commons CC-BY-SA licensing terms. Credit must be given to creator and adaptations must be shared under the same terms. See https://creativecommons.org/licenses/by-sa/4.0/



Systems & Control Transactions

**Research Article - Peer Reviewed Conference Proceeding**
ESCAPE 35 - European Symposium on Computer Aided Process Engineering
Ghent, Belgium. 6-9 July 2025
Jan F.M. Van Impe, Grégoire Léonard, Satyajeet S. Bhonsale,
Monika E. Polańska, Filip Logist (Eds.)

PSE PRESS

# Joint Optimization of Fair Facility Allocation and Robust Inventory Management for Perishable Consumer Products

**Saba Ghasemi Naraghi, and Zheyu Jiang[a]***

[a] Oklahoma State University, Department of Chemical Engineering, Stillwater, Oklahoma, USA
* Corresponding Author: zheyu.jiang@okstate.edu.

## ABSTRACT

Perishable consumer products like food, cosmetics, and household chemicals face challenges in supply chain management due to limited shelf life and uncertainties in demand and transportation. To address some of these issues, this work proposes a robust optimization framework for jointly optimizing facility allocation and inventory management. The framework determines optimal locations for distribution centers and their assigned customers, as well as inventory policies that minimize the total costs related to transportation, distribution, and storage under uncertain demand in a robust setting. Specifically, we develop a two-stage mixed-integer linear programming (MILP) model is that incorporates First-In-First-Out (FIFO) inventory policy to reduce spoilage. The bilinear FIFO constraints are linearized to improve computational efficiency. Social equity is integrated by defining a fairness index and incorporating it in facility allocation. Demand uncertainty is tackled using a robust optimization approach with affine demand functions to handle multiple scenarios. The model is solved using row and column generation techniques for scalability. Overall, this robust optimization framework is expected to enhance supply chain resilience, reduce waste, and improve cost-effectiveness in managing perishable products.

**Keywords**: Optimization, Supply Chain, Facility Allocation, Perishable Products

## INTRODUCTION

The optimization of facility location and inventory management is a critical area in operations research, with applications spanning healthcare, telecommunications, and supply chain logistics. For perishable consumer products like food, cosmetics, and household chemicals, the challenges are further intensified by their limited shelf life and uncertain demand. For instance, every year in the U.S., 38% of all food goes unsold or uneaten, which translates to almost 145 billion meals' worth of food, or roughly 1.8% of U.S. GDP [1]. Overestimating demand can lead to excessive holding costs and spoilage, while underestimating it results in unmet demand, penalties, and delays. These challenges necessitate robust optimization frameworks that account for perishability, uncertainty, and the dynamic nature of supply chain operations [2].

Facility location problems, particularly the Uncapacitated Facility Location (UFL) problem, aim to identify optimal facility placements that minimize allocation costs via optimization approaches [3,4]. Despite significant advancements in areas such as mixed-integer programming (MIP), large-scale problems often require advanced computational techniques like Lagrangian relaxation and decomposition methods such as row and column generation algorithms for efficient solutions [5,6].

Meanwhile, by introducing ethical and social aspects along with efficiency and cost-effectiveness, fairness has emerged as an important consideration in facility allocation. Metrics such as Rawlsian maximin, leximax criteria [7], group parity measures [8], and proportional fairness [9] address equitable resource allocation. In this work, a state-level social fairness is contextualized by prioritizing disadvantaged communities based on poverty and unemployment rates, thereby ensuring equitable access to consumer products being distributed. We remark that, in this work, we define the social fairness index by simply calculating the weighted sum of state-level poverty rate and unemployment rate obtained from the most recent U.S. Census as proof of concept. A more refined definition of social fairness will be developed in future studies.

This study proposes a joint optimization framework that integrates fair facility allocation with robust inventory management for perishable products. Adopting the robust inventory management framework proposed in [10], a linearized FIFO inventory policy is incorporated to minimize spoilage and maintain product shelf life. We also incorporate robust optimization techniques such as affine demand functions to model demand uncertainty and ensure resilience of the optimal solution found. The problem is decomposed and solved using row and column generation technique [5] to ensure scalability and computational efficiency.

## PROBLEM STATEMENT

Perishable goods, such as food, cosmetics, and household chemicals (e.g., detergents and pesticides), represent a significant portion of consumer products, creating stringent requirements for supply chain network design and inventory management. The perishable nature of these products, combined with uncertainties in product transportation and demand, requires us to holistically consider facility allocation and inventory management within a joint optimization framework. In this study, we consider a hypothetical U.S. nation-wide perishable food (including dairy, meat, fruits, and vegetables) supply chain network that needs to be jointly optimized for facility allocation and inventory management subject to demand uncertainty at a state level.

The objective is to identify the optimal locations for food distribution centers, assign customers to these centers, and determine inventory management strategies that effectively meet uncertain demand. The problem is formulated as a two-stage mixed-integer linear programming (MILP) model and is solved using row and column generation technique. The master problem determines the optimal facility locations, customer assignments, and initial inventory decisions for a finite set of demand scenarios, whereas the subproblem iteratively identifies new worst-case demand scenarios that could increase costs. These scenarios are incorporated into the master problem until no further costly scenarios are found, thereby ensuring the solution is robust against demand uncertainty.

## FORMULATION

As mentioned earlier, in the first stage of our proposed two-stage multi-objective robust optimization framework, we determine the optimal locations for food distribution centers, their capacities, customer allocations, and the amount of perishable products to be purchased from the supplier. Then, in the second stage, optimal inventory management is carried out based on the FIFO policy. Note that our inventory management and bilinear FIFO policy extend the original framework of [10] by incorporating linking constraints between facility allocation in the first stage and inventory management in the second stage, which leads to a nonconvex MINLP model in the first place. Nevertheless, by implementing the reformulation strategy introduced in [10], we can reformulate the second-stage problem as a scenario-based linear programming (LP) problem, thus making the joint problem a MILP with significantly improved computational efficiency and tractability.

### First stage: Fair capacitated facility allocation

In the first stage, the here-and-now decisions are made, which include selecting locations/states $i \in I$ for establishing food distribution centers, determining their capacities, and assigning customers. The objective is to minimize the total opening cost, which consists of land acquisition and construction costs ($\$313/\text{ft}^2$), permit costs ($\$2.75/\text{ft}^2$), labor costs ($\$0.3/\text{ft}^2$), energy costs ($\$0.00134$ kWh/$\text{ft}^2$.day), shipping costs ($3.19/mile), and the cost of purchasing products from the supplier (dairy: $0.88/lb, meat: $2.25/lb, fruits: $0.75/lb, and vegetables: $0.75/lb). Equation (1a) represents the objective function of the here-and-now stage. Considering an annual hurdle rate of 12% and a distribution center lifespan of 39 years, the corresponding 15-day discount factor is 0.005. To formulate the trade-off between economic and social fairness objectives, we use the $\epsilon$-constraint in Equation (2a), which ensures that the overall social fairness index does not fall below a specified level. Equations (3a-5a) are standard integer constraints for facility location problems. Equation (6a) ensures that the size of a food distribution center ranges from $50{,}000\ \text{ft}^2 \times 30\ \text{ft}$ to $800{,}000\ \text{ft}^2 \times 30\ \text{ft}$. Generally, at most 85% of the warehouse capacity can be utilized for inventory purposes, while the remaining space is allocated for other functions such as office use. Therefore, Equation (7a) ensures that the amount of products purchased from the supplier does not exceed the effective storage capacity. Furthermore, the average volume per pound ($v_p$) for dairy products, meat, fruits, and vegetables are given by 0.025, 0.025, 0.033, and 0.036 ($\text{ft}^3$/lb), respectively.

$$F^{H\&N} = \min \sum_{i \in I} \left[ 0.005\left(313 + 2.75 + c_i^{land}\right) + \sum_{t \in T} \left(0.3 + 0.00134\, c_t^{energy}\right) \right] \frac{q_i}{30} + \sum_{i \in I} \sum_{t \in T} \sum_{p \in P} c_p^{supply} u_{i,t,p}^{supply}, \quad (1a)$$

$$\sum_{i \in I} r_i^{fairness} y_i \geq \sum_{i \in I} r_i^{fairness} \epsilon, \quad (2a)$$

$$\sum_{i \in I} x_{i,j} = 1, \forall j \in J, \quad (3a)$$

$$x_{i,j} \le y_i, \forall i \in I, j \in J, (4a)$$

$$\sum_{j \in J} x_{i,j} \ge y_i, \forall i \in I, (5a)$$

$$1.5 \times 10^6 y_i \le q_i \le 24 \times 10^6 y_i, \forall i \in I, (6a)$$

$$\sum_{p \in P} v_p u_{i,t,p}^{supply} \le 0.85 q_i, \forall i \in I, t \in T, (7a)$$

## Second stage: Robust inventory management

In the second stage, the wait-and-see (W&S) decisions are made and must reflect the robust inventory management policy. Since our inventory management model is similar to that in [10], we only present its reformulation here. The objective is to minimize holding, backlog, and spoilage costs across all possible scenarios while considering the specified level of conservatism (Γ). Equation (1b) is the objective function associated with the second stage. Equation (2b) ensures that the total cost minimized in (1b) corresponds to the worst-case scenario, which is a standard formulation technique in robust optimization. In Equation (2b), the holding cost is assumed to be 15% of the supply cost, and the backlog cost is equal to the supply cost, and the spoilage cost factor $\beta^{spoil}$ can take difference values and is a user-defined parameter. Constraint (3b) ensures that under every possible scenario, the total amount of stored products in the inventory does not exceed the effective storage capacity ($0.85q_i$). Constraints (4b) and (5b) respectively represent the amount of stored and backlogged products subject to demand uncertainty, which consists of infinite number of scenarios ξ that belong to an uncertainty set Ξ. Equations (6b) and (7b) implements the FIFO policy in calculating spoilage [10].

$$F^{W\&S} = \min z, (1b)$$

$$z \ge \sum_{i \in I} \sum_{t \in T} \sum_{p \in P} \left(0.15 c_p^{supply} u_{i,t,p,\xi}^{inv} + c_p^{supply} u_{i,t,p,\xi}^{backlog} + \beta^{spoil} c_p^{supply} u_{i,t,p,\xi}^{spoil}\right), \forall \xi \in \Xi, (2b)$$

$$\sum_{p \in P} v_p u_{i,t,p,\xi}^{inv} \le 0.85 q_i, \forall \xi \in \Xi, i \in I, t \in T, (3b)$$

$$u_{i,t,p,\xi}^{inv} \ge \sum_{k=1}^{t} \left(u_{i,t,p}^{supply} - \sum_{j \in J} D_{p,j,k}(\xi) x_{i,j} - u_{i,k,p,\xi}^{spoil}\right), \forall \xi \in \Xi, i \in I, t \in T, (4b)$$

$$u_{i,t,p,\xi}^{backlog} \ge \sum_{k=1}^{t} \left(\sum_{j \in J} D_{p,j,k}(\xi) x_{i,j} + u_{i,k,p,\xi}^{spoil} - u_{i,t,p}^{supply}\right), \forall \xi \in \Xi, i \in I, t \in T, (5b)$$

$$u_{i,t,p,\xi}^{spoil} = 0, \forall \xi \in \Xi, i \in I, t \le m, (6b)$$

$$u_{i,t+m,p,\xi}^{spoil} = \max\left\{0, \sum_{k=1}^{t} u_{i,t,p}^{supply} - \sum_{k=1}^{t+m} \sum_{j \in J} D_{p,j,k}(\xi) x_{i,j} - \sum_{k=m+1}^{t+m-1} u_{i,k,p,\xi}^{spoil}\right\}, \forall \xi \in \Xi, i \in I, t \le |T| - m, (7b)$$

## Row and column generation

The proposed problem contains an infinite number of variables and constraints, making it inherently intractable. To address this, we employ an iterative approach that alternates between solving a relaxed master problem and separation problems. While the master problem is still nonlinear (due to Equation (7a)) for now, it can be easily linearized using standard techniques and it is a finite optimization problem, unlike the infinite optimization formulations discussed above. Consider $S \subset \Xi$ be a finite set of scenarios generated by the separation problem. The restricted master problem (RMP) is defined as follows.

$$(RMP): \min F^{H\&N} + F^{W\&S}, (1c)$$

$$(2a) - (7a),$$

$$z \ge \sum_{i \in I} \sum_{t \in T} \sum_{p \in P} \left(0.15 c_p^{supply} u_{i,t,p,\xi}^{inv} + c_p^{supply} u_{i,t,p,\xi}^{backlog} + \beta^{spoil} c_p^{supply} u_{i,t,p,\xi}^{spoil}\right), \forall \xi \in S, (2c)$$

$$\sum_{p \in P} v_p u_{i,t,p,\xi}^{inv} \le 0.85 q_i, \forall \xi \in S, i \in I, t \in T, (3c)$$

$$u_{i,t,p,\xi}^{inv} \ge \sum_{k=1}^{t} \left(u_{i,t,p}^{supply} - \sum_{j \in J} D_{p,j,k}(\xi) x_{i,j} - u_{i,k,p,\xi}^{spoil}\right), \forall \xi \in S, i \in I, t \in T, (4c)$$

$$u_{i,t,p,\xi}^{backlog} \ge \sum_{k=1}^{t} \left(\sum_{j \in J} D_{p,j,k}(\xi) x_{i,j} + u_{i,k,p,\xi}^{spoil} - u_{i,t,p}^{supply}\right), \forall \xi \in S, i \in I, t \in T, (5c)$$

$$u_{i,t,p,\xi}^{spoil} = 0, \forall \xi \in S, i \in I, t \le m, (6c)$$

$$u_{i,t+m,p,\xi}^{spoil} = \max\left\{0, \sum_{k=1}^{t} u_{i,t,p}^{supply} - \sum_{k=1}^{t+m} \sum_{j \in J} D_{p,j,k}(\xi) x_{i,j} - \sum_{k=m+1}^{t+m-1} u_{i,k,p,\xi}^{spoil}\right\}, \forall \xi \in S, i \in I, t \le |T| - m, (7c)$$

After solving the (RMP), the optimal facility locations, their capacities, customer assignments, the amount of products purchased from the supplier, and the worst-case scenario inventory management cost ($z^*$) for the current scenarios can be determined. The separation problem (SP) is proposed to find a new scenario with a higher inventory management cost.

$$(SP): w = \max \sum_{i \in I} \sum_{t \in T} \sum_{p \in P} \left(0.15 c_p^{supply} u_{i,t,p}^{inv} + c_p^{supply} u_{i,t,p}^{backlog} + \beta^{spoil} c_p^{supply} u_{i,t,p}^{spoil}\right), (1d)$$

$$\xi \in \Xi, (2d)$$

$$\sum_{p\in P} v_p u^{inv}_{i,t,p} \le \eta q^*_i,\ \forall i \in I^*,\ t \in T, (3d)$$

$$u^{inv}_{i,t,p} = \max\left\{0, \sum_{k=1}^{t}\left(u^{supply*}_{i,t,p} - \sum_{j\in J^*_i} D_{p,j,k}(\xi) - u^{spoil}_{i,k,p}\right)\right\},\ \forall i \in I^*,\ t \in T, (4d)$$

$$u^{backlog}_{i,t,p} = \max\left\{0, \sum_{k=1}^{t}\left(\sum_{j\in J^*_i} D_{p,j,k}(\xi) + u^{spoil}_{i,k,p} - u^{supply*}_{i,t,p}\right)\right\},\ \forall i \in I^*,\ t \in T, (5d)$$

$$u^{spoil}_{i,t,p} = 0, \forall i \in I^*,\ t \le m, (6d)$$

$$u^{spoil}_{i,t+m,p} = \max\left\{0, \sum_{k=1}^{t} u^{supply*}_{i,t,p} - \sum_{k=1}^{t+m}\sum_{j\in J^*_i} D_{p,j,k}(\xi) - \sum_{k=m+1}^{t+m-1} u^{spoil}_{i,k,p}\right\}, \forall i \in I^*,\ t \le |T| - m, (7d)$$

If there exists a $\xi^*$ such that $w^*(\xi^*) > z^*$, then $\xi^*$ is added to $S$, and the (RMP) is solved again with the updated set of scenarios. This iterative approach continues until no new scenario with a higher inventory management cost is found. By implementing this row and column generation method, the problem can be solved with a finite number of variables and constraints. Note that the linearization technique for (SP) is discussed in [10].

## ILLUSTRATIVE CASE STUDIES

To evaluate the effectiveness of our proposed framework, we conduct a hypothetical case study featuring the national supply chain of perishable food products. This case study illustrates the trade-offs among total cost, fairness, and inventory efficiency for perishable consumer products.

By incorporating the poverty and unemployment rates of all 50 states in 2023 [11], we develop a social fairness index that assigns equal weight to these socioeconomic factors. And the overall social fairness $\sum_{i\in I} r^{fairness}_i \epsilon$ can vary from $\epsilon = 0$ (excluding the fairness) to $\epsilon = 1$ (maximum fairness). **Figure 1** shows the average daily demand (in Mlbs) for these products per state in 2023 [12,13]. In our study, we investigate a planning horizon of 15 days, and the storage duration is $m = \{2,5\}$ days. Furthermore, we consider the spoilage cost factor $\beta^{spoil} \in \{0.5,1,1.5,2\}$ and the uncertainty parameter $\Gamma \in \{1,3,5\}$ Mlbs, where $\Gamma = 1$ represents the least conservative case, and $\Gamma = 5$ represents the most conservative case.

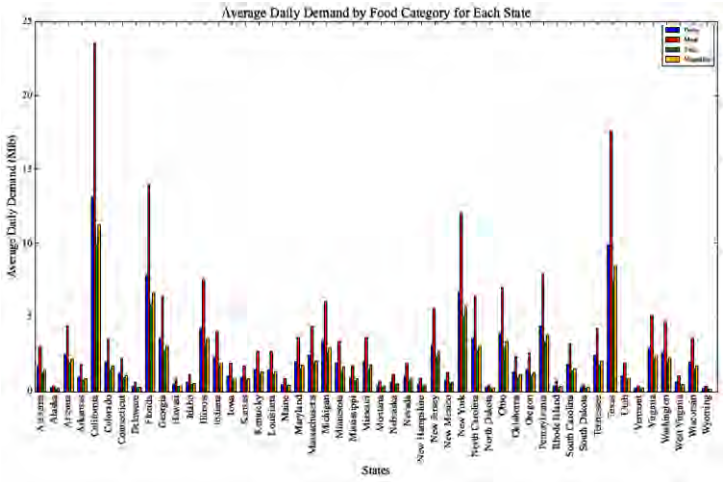



**Figure 1.** Average daily demand of dairy products, meat, fruits, and vegetables per state.

**Figures 2**, **3**, **4**, and **5** illustrate the Pareto front between social fairness and total costs, the percentage of spoilage for all products, the total amount of backlogged products, and the total amount of stored products for various $\epsilon$ levels for the case when $m = 5$, $\Gamma = 3$, and $\beta^{spoil} = 1$. First, as $\epsilon$ increases, the total costs would continuously increase. Additionally, lower $\epsilon$ values, which indicate that fewer facilities will be chosen, are associated with higher spoilage percentage and higher backlogging. However, the trend for the total inventory level behaves exactly the opposite way. This suggests that, when fewer facilities are established, which leads to higher backlogs, the inventory level decreases as if the supply chain system transfers its weight from stored inventory to unmet demand. This opposite trend illustrates the trade-off and delicate interplay between storage and shortages in the supply chain.

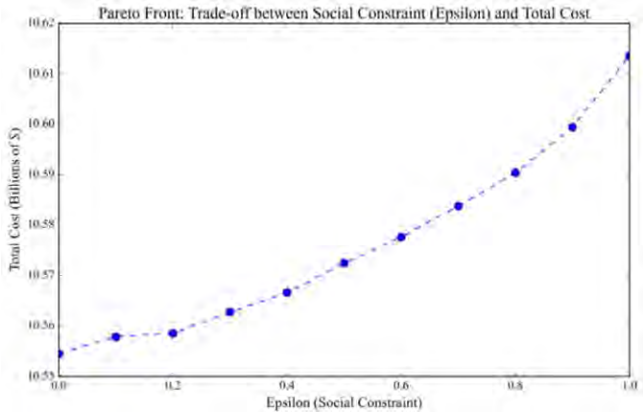



**Figure 2.** Pareto front showing the trade-off between social fairness and the total cost for the case where $m = 5, \Gamma = 3, \beta^{spoil} = 1$.

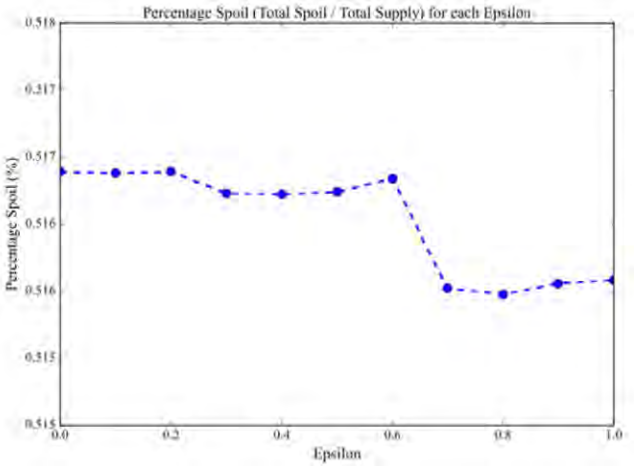



**Figure 3.** The percentage of total spoiled products for different levels of social fairness when $\mathrm{m} = 5, \Gamma = 3, \beta^{\mathrm{spoil}} = 1$.

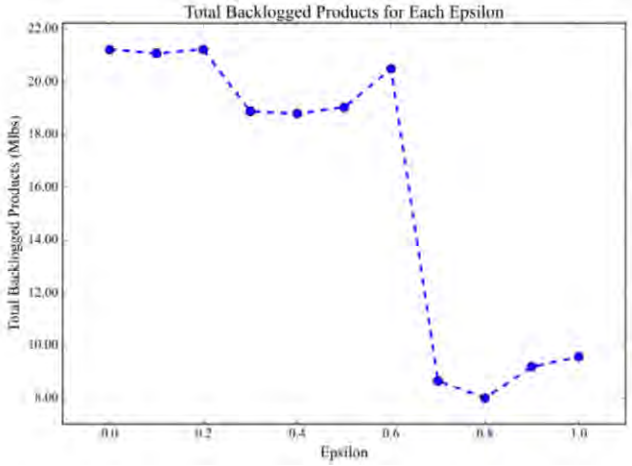



**Figure 4.** The percentage of total backlogged products for different levels of social fairness when $\mathrm{m} = 5$, $\Gamma = 3, \beta^{\mathrm{spoil}} = 1$.

Next, we conduct a sensitivity analysis to understand how spoilage changes under different levels of conservatism and social fairness. **Figures 6** presents the results for the total amount of spoiled products under various scenarios. As the uncertainty level $\Gamma$ increases, in most of the cases, the amount of spoiled products also increases. However, increasing the number of days that products can be stored in inventory and raising the spoilage cost factor help reduce the total amount of spoilage by making spoiled products more expensive. For instance, when the cost of spoiled products is doubled compared to the supply cost, spoilage is completely eliminated across all levels of conservatism.

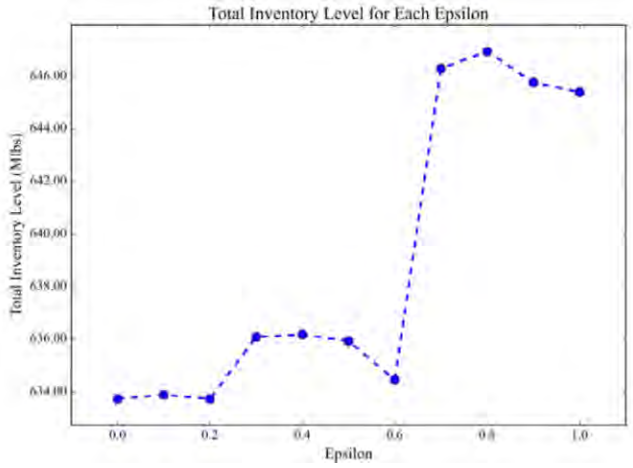



**Figure 5.** The percentage of total stored products for different levels of social fairness by varying $\epsilon$ for $\mathrm{m} = 5$, $\Gamma = 3, \beta^{\mathrm{spoil}} = 1$.

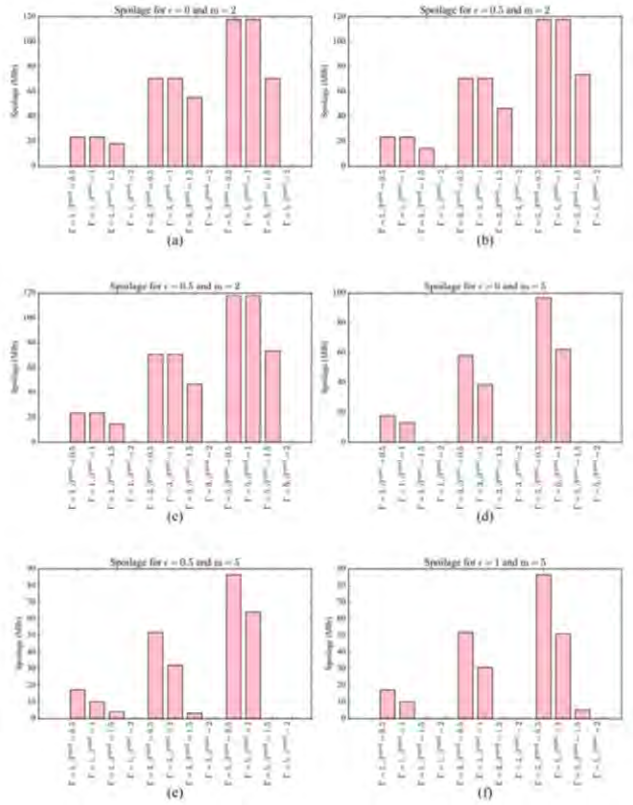



**Figure 6.** Total amount of spoiled products under different levels of fairness level $\epsilon$, uncertainty level, and cost factors. (a-c) correspond to $\mathrm{m} = 2$, while (d-f) represent $\mathrm{m} = 5$.

On the other hand, when the spoilage cost factor is half of the supply cost, the highest amount of waste is generated across all levels of conservatism. For example, when the storage duration $\mathrm{m} = 2$ days, $\Gamma = 5$ Mlbs, and $\beta^{\mathrm{spoil}} = 0.5$, the total amount of waste for all three levels of fairness is almost 120 Mlbs, which represents the

highest recorded spoilage.

## CONCLUSION

In this study, we develop a robust mixed-integer linear programming (MILP) model to jointly optimize facility allocation and inventory management for perishable consumer products. Our approach incorporates a FIFO inventory policy, leveraging prior results for constraint linearization [10], and employs row and column generation techniques to improve scalability. To account for social equity, we introduce a fairness index based on poverty and unemployment rates across U.S. states [11], allowing for trade-off analysis between fairness, cost, and inventory efficiency. Through a national case study, we examine how factors such as demand uncertainty, storage duration, and spoilage cost sensitivity influence supply chain outcomes. Our results reveal that higher levels of conservatism in demand forecasting lead to increased spoilage, while higher fairness levels result in rising total costs. Additionally, storage duration and spoilage cost penalties significantly impact waste levels, with severe penalties eliminating spoilage altogether. These findings underscore the need for systematic optimization approaches to balance supply chain resilience, cost efficiency, and waste mitigation, consistent with our previous research [14,15]. In terms of future research, we will primarily focus on three main aspects: 1) refine social fairness characterization backed by rigorous, comprehensive prior research in game theory and regional economics; 2) investigate novel approaches (e.g., political districting) to model and solve facility allocation while ensuring fairness; and 3) accelerate the computational efficiency by developing more effective decomposition and/or distributed optimization techniques.

## ACKNOWLEDGEMENTS

This work is supported by the start-up fund of the College of Engineering, Architecture, and Technology at Oklahoma State University.

## REFERENCES

1. ReFED.org. https://refed.org/food-waste/the-problem
2. D. Bertsimas, and A. Thiele. A robust optimization approach to inventory theory. Operations Research 54:150-168. (2006)
3. S. Meisel, and D. Mattfeld. Synergies of operations research and data mining. Eur. J. Oper. Res 206:1-10. (2010)
4. S. Olafsson, X. Li, and S. Wu. Operations research and data mining. Eur. J. Oper. Res 187:1429-1448. (2008)
5. A. Agra, M. C. Santos, D. Nace, and M. Poss. A dynamic programming approach for a class of robust optimization problems. SIAM Journal on Optimization 26:1799-1832. (2016)
6. D. Bienstock. Computing robust basestock levels. Discrete Optimization 5:389–414. (2008)
7. W. Ogryczak, H. Luss, M. Pjoro, D. Nace, and A. Tomaszewski. Fair optimization and networks: A survey. Journal of Applied Mathematics 1:612018. (2014)
8. M. De-Arteaga, S. Feurriegel, and M. Saar-Tsechansky. Algorithmic fairness in business analytics: Direction for research and practice. Production and Operations Management 31:3749-3770. (2022)
9. D. Bertsimas, and I. Dunning. Multistage robust mixed-integer optimization with adaptive partitions. Operations Research 64:980-998. (2016)
10. M. C. Santos, A. Agra, and M. Poss. Robust inventory theory with perishable products. Annuals of Operations Research 289:473-494. (2020)
11. U.S Department of Labor (BLS). https://www.bls.gov/news.release/pdf/srgune.pdf. (2024)
12. Statista. https://www.statista.com/
13. U.S. Department of Agriculture. https://www.ers.usda.gov/data-products/dairy-data. (2024)
14. S. Ghasemi Naraghi, Z. Jiang, Stochastic optimization of agrochemical supply chains with risk management. Computer Aided Chemical Engineering 52:3337-3343 (2023). https://doi.org/10.1016/B978-0-443-15274-0.50532-1
15. S. Ghasemi Naraghi, Z. Jiang, Stochastic Optimization of Global Agrochemical Supply Chains with Risk Management: Modeling and Reformulation. Available at arXiv:2401.12348. https://doi.org/10.48550/arXiv.2401.12348

© 2025 by the authors. Licensed to PSEcommunity.org and PSE Press. This is an open access article under the creative commons CC-BY-SA licensing terms. Credit must be given to creator and adaptations must be shared under the same terms. See https://creativecommons.org/licenses/by-sa/4.0/



Systems & Control Transactions

**Research Article - Peer Reviewed Conference Proceeding**
ESCAPE 35 - European Symposium on Computer Aided Process Engineering
Ghent, Belgium. 6-9 July 2025
Jan F.M. Van Impe, Grégoire Léonard, Satyajeet S. Bhonsale,
Monika E. Polańska, Filip Logist (Eds.)

PSE PRESS

# A two-level model to assess the economic feasibility of renewable urea production from agricultural waste

**Diego C. Lopes[a], Moisés Teles dos Santos[a]**

[a] University of São Paulo, Department of Chemical Engineering, São Paulo, SP, Brazil
* Corresponding Author: dclopes@usp.br

## ABSTRACT

This work proposes a two-level model, combining process and supply chain models, and an optimization framework for an integrated biorefinery system to convert agricultural residues into renewable urea via gasification routes. The process model of the gasification, ammonia and urea synthesis was developed in Aspen Plus® to identify key performance indicators such as energy consumption and relative yields for urea for different biomasses and operating conditions; then, these key process data were used in a mixed-integer linear programming (MILP) model, designed to identify the optimal combination of energy source, technological route of urea production and plant location that maximizes the net present value of the system. The model was applied to the whole Brazilian territory, divided into 5569 cities and 558 micro-regions. Each region's agricultural production was evaluated to estimate biomass supply and urea demand. The Assis microregion, in close proximity with sugarcane and soybean crops, was found to be an optimal location for the plant, with an NPV of 110 MMUSD. Urea demand was found to be the main limiting factor, with more than 30 microregions needed to consume the plant's production. The results indicate the feasibility of producing renewable urea from agricultural waste and the importance of considering a two-level approach to assess the economic performance of the entire system.

**Keywords**: fertilizer, renewability, optimization

## INTRODUCTION

Since 1961, worldwide food supply per capita has raised by 30%, in large part because of the increase of use of nitrogen fertilizers to improve agricultural productivity [1]. The importance of fertilizers on agriculture cannot be overstated, with research indicating that half of the world's population is sustained by mineral fertilizers [2]. Fertilizers account for a fifth of the producer's costs on the US [3], while on Brazil, the financial impact on cultures such as soya is between 30% and 40% [4]. The agricultural sector is also responsible for approximately 11% and 15% of all greenhouse gas (GHG) emissions worldwide [5], with fertilizers accounting for 2% to 3% of emissions [6]. Production of mineral fertilizers is dependent on fossil fuels and raw materials, including mineral extraction, transportation, manufacturing, and power supply. In this scenario, decarbonizing the fertilizer sector is equally important to the industry's expansion [7], considering the GHG emissions reduction preconized in the 2015 Paris agreement.

The mineral fertilizers divide themselves into three main categories, each one corresponding to the main macronutrient present in its composition: nitrogen (N), phosphorus (P) and potassium (K). Although none of the macronutrients can be considered more or less important than the other, nitrogen is the one consumed at higher volumes, and also the one with the more energetically intensive manufacturing process and heavily reliant on fossil fuels throughout its manufacturing process, both as energy input and as a direct feedstock [2]. Out of all nitrogen fertilizers, urea is the main commercial product, produced by the synthesis of ammonia with carbon dioxide via the Basarov reaction [8]. Since both ammonia and urea synthesis are energetically intensive, efforts were made throughout the 20th century to improve its energy efficiency, involving equipment changes, process control and residual heat utilization. With these efforts, current

ammonia production is very close to the theoretical minimum energy consumption [2] . Considering the small efficiency improvements still possible, a natural future step is to search for sustainable replacements for the process' feedstocks and energy usages.

In this scenario, biomass is a promising feedstock replacement. Although biomass presents a polymeric structure, divided in cellulose, hemicellulose and lignin as its main polymers, it can be represented in a simplified way as a mixture of carbon (C), hydrogen (H), oxygen (O) and nitrogen (N) [9]. Most of the chemicals produced with oil or natural gas can be produced with biomass, by resorting to either thermochemical routes such as gasification or pyrolysis, or biological routes such as fermentation [10].

Urea production using biomass gasification as a feedstock has also been the object of recent studies [11-13] focused on process modeling and obtaining ideal operational parameters and technological routes. There is an obvious synergy in producing urea with agricultural waste, as the regions with high biomass supplies will necessarily have high urea demand. However, none of these studies consider supply-chain and location specific aspects, which can be critical at the planning stage [14]. This highlights the need to combine both a traditional process modeling approach with a robust optimization framework that takes spatial data, local biomass supply and urea demand into account. The present work proposes such a model to fill this literature gap.

# METHODOLOGY

## Process models

A process model of the full biomass gasification, ammonia and urea synthesis was developed in Aspen Plus v8.8 [13]. A simplified process topology is presented on Figure 1.

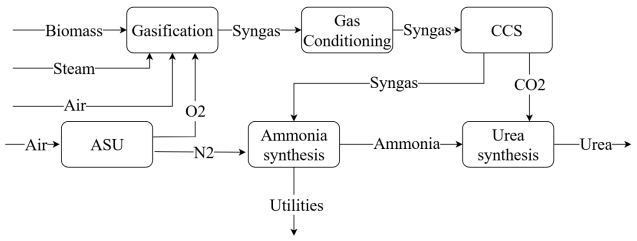



**Figure 1.** Process flow diagram

Biomass is firstly dried to 15% moisture and sent to a gasification unit, modeled with a non-stoichiometric equilibrium approach [15]. A global gasification reaction can be described as:

$$CH_aO_bN_c + wH_2O_l + sH_2O_g + e(O_2 + \rho N_2) + dCO_2 \rightleftharpoons n_{CH_4}CH_4 + n_{CO_2}CO_2 + n_{CO}CO + n_{H_2}H_2 + n_{H_2O}H_2O + n_{O_2}O_2 + n_{N_2} \quad (1)$$

With a, b and c being derived from the biomass composition; w, s, e, $\rho$ and d representing the gasifying agent mixture, and n being the number of moles of each component in the syngas. At equilibrium, the Gibbs energy of the mixture (G) must be at minimum:

$$G = \sum_{i=1}^{M} n_i G_i^0 + \sum_{i=1}^{M} n_i RTln(\frac{n_i}{n_{tot}}) \quad (2)$$

The number of moles of each component, $n_i$, are constrained by the mole balance of each atom C, H, O and N on the biomass. Tar formation is not considered in this model. The minimization of Gibbs energy is obtained on the Gibbs reactor block (RGibbs) in Aspen Plus. Syngas properties were calculated using the Peng-Robinson equation of state, with Boston-Mathias modifications.

The gasification agents are a mixture of air, steam and pure oxygen, produced in an air separation unit (ASU), with an optional $CO_2$ intake. The syngas composition is adjusted to improve $H_2$ concentration in a gas conditioning unit, consisting of two water-gas shift reactors and a methanation unit. The $CO_2$ present is the syngas is captured at a physical solvent carbon capture unit using DEPG (Dimethyl Ether of Polyethylene Glycol) as a solvent [16]. The purified syngas is mixed with nitrogen and sent to an ammonia synthesis unit, modeled with three catalytic beds and intermediate intercooling, based on a state of the art design [17]. The ammonia and captured $CO_2$ are sent to the urea synthesis plant, modeled as a $CO_2$ stripping process based on the commercial Stamicarbon® technology [8]. The final urea is concentrated to 99 wt. % in a double effect evaporator and sent to a granulation or prilling unit. A utility plant was designed to recover heat from the gasification, ammonia and urea synthesis. High pressure steam is generated in the syngas cooling stages and expanded into a multi-stage turbine to be used by the main steam consumers of the plant. The remaining steam generated is condensed at 0.1 bar, generating power. The purpose of the process model was to obtain the conversion of biomass to urea and the utilities consumption for any combination of operational parameters.

## Supply-chain

The whole Brazilian territory was divided into 5569 cities, grouped in 558 micro-regions and 137 macro-regions. The open database PAM [18] from IBGE (Instituto Brasileiro de Geografia e Estatística) was used to obtain the total agricultural production for each location. Based on this, 5 crops were chosen as the most representative of the Brazilian agricultural scenario. Each crop's residue production was estimated using fixed ratios [19] to obtain an individual biomass supply for each location. Individual urea demand was also estimated using published data for mineral fertilizer usage by crop [20] and planted area.

Table 1 summarizes the chosen crops, biomass it produces and urea demand.

**Table 1:** Biomass supply and urea demand per crop

| Crop | Biomass production (kg/ kg crop) | Urea demand (kg N / ha) |
|---|---|---|
| Rice | 0.620 | 83 |
| Coffee | 0.295 | 161 |
| Corn | 0.672 | 68 |
| Soy | 0.690 | 16 |
| Sugarcane | 0.185 | 76 |

Sugarcane residue production is divided between straw and bagasse. Distances and travel times between all locations were obtained from geographical data [21]. Power prices were also individually considered using published tariffs [22].

## Economical model

The capital costs for all subunits of the process were estimated by using the scale factor methodology [23], with an estimation of 368.7 MMUSD for a reference 35 t/h process. The CAPEX for other capacities ranging from 0 to 80 t/h was estimated using piecewise linearization.

Net present value is defined as:

$$NPV = \sum_{t=1}^{n} \frac{F_t}{(1+r)^t} - CAPEX \quad (3)$$

With $F_t$ being the net cash flow at year $t$, $r$ being the discount rate (by default at 10%) and $CAPEX$ being the total capital costs of the plant. Net cash flow is defined as:

$$F_t = -CAPEX_t + R + C_b + C_{tb} + \mathrm{C_{tu}} + C_u \quad (4)$$

With $R$ being urea revenue, $C_b$ being biomass costs, $C_{tb}$ being biomass transport costs, $C_{tu}$ being urea transport costs, and $C_u$ being utility costs.

Table 2 summarizes the main economical assumptions for the model.

**Table 2:** Economical assumptions

| Parameter | Unit | Value |
|---|---|---|
| Urea price | USD/t | 310.0 |
| Biomass price | USD/GJ | 4.50 |
| Transport price | USD/km/t | 0.058 |

Power prices are considered in a city-by-city basis using published tariffs.

## Optimization model

A mixed-integer linear programming (MILP) optimization model was built using the Pyomo open-source software suite, to obtain the ideal location and capacity of a renewable urea plant, based on the process model performance. The model can be divided into 4 layers, best represented in Fig. 2.

The model consists of 3 main sets:

$L$: set of possible locations ($l$)

$B$: set of biomasses ($b$)

$R$: set of technological routes for urea production (e.g.: pure oxygen gasification vs. air mixed gasification).

With:

$CV_{br}$: conversion of biomass $b$ to urea at route $r$, in $t\ urea/t\ biomass$

$D_l$: urea demand at location $l$.

$S_{bl}$: Supply of biomass $b$ at location $l$.

The decision variables of the model are:

$W_l$: binary variable corresponding to the installation of the plant at location $l$

$BS_{bll'}$: biomass $b$ sold from location $l$ to location $l'$

$BU_{brl}$: biomass $b$ used to produce urea via route $r$ at location $l$

$UP_{rl}$: urea produced via route $r$ at location $l$

$US_{ll'}$: urea sold from location $l$ to location $l'$

$C$: capacity of the plant in tons urea/h

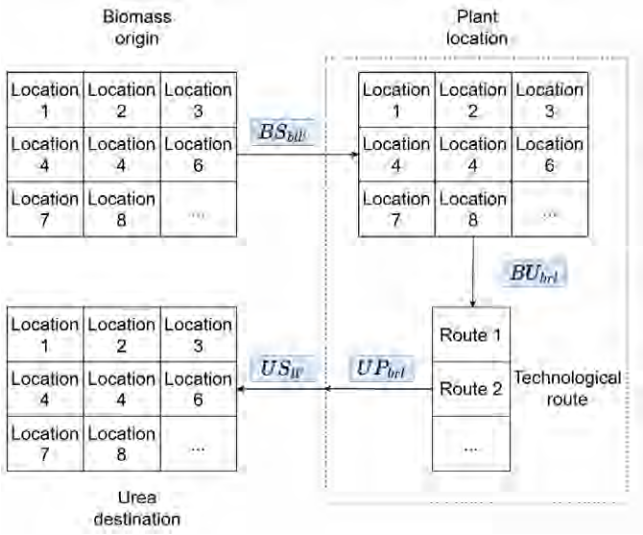



**Figure 2** – Layers of decision

The objective function of the model is to maximize the NPV of the plant. Biomass consumption and utility usage for each technological route is given by the process model. Transport costs are calculated by using the distance from location $l$ to location $l'$. The main constraints of the model, connecting the decision variables, are:

$$\sum_{l \in L} W_l = 1 \quad (5)$$

$$\sum_{b \in B} \sum_{r \in R} \sum_{l \in L} UP_{brl} = \mathrm{C} \cdot 8300 \quad (6)$$

$$\sum_{r \in R} UP_{rl} = \sum_{l' \in L} US_{ll'} \quad \forall\, l \in L \quad (7)$$

$$\sum_{r \in R} UP_{rl} = M \cdot W_l \quad \forall\, l \in L \quad (8)$$

$$UP_{rl} = \sum_{b \in B} BU_{brl} \cdot CV_{br} \quad \forall\, r \in R, l \in L \quad (9)$$

$$\sum_{r \in R} BU_{brl} = \sum_{l' \in L} BS_{bl'l} \quad \forall\, b \in B, l \in L \quad (10)$$

**Table 3** – Process model results - Summary

| Biomass | HHV (MJ/kg) | Moisture (%) | Route 1: O2 gasification | | Route 2: Air mixed gasification | |
|---|---|---|---|---|---|---|
| | | | Conversion (t urea/t bio) | Utility (MWh/t bio) | Conversion (t urea/t bio) | Utility (MWh/t bio) |
| Rice husks | 16.62 | 12 | 0.7015 | 0.3215 | 0.6894 | 0.2710 |
| Coffee husks | 20.92 | 12 | 0.8209 | 0.2716 | 0.7854 | 0.2356 |
| Corn stover | 19.06 | 15 | 0.7783 | 0.2905 | 0.7358 | 0.2487 |
| Soy straw | 18.53 | 15 | 0.7550 | 0.2971 | 0.7241 | 0.2513 |
| Sugarcane straw | 18.72 | 15 | 0.7616 | 0.2944 | 0.7211 | 0.2501 |
| Sugarcane bagasse | 18.16 | 40 | 0.5712 | 0.3261 | 0.5458 | 0.2771 |

**Table 4** – Optimization model results - Summary

| | Unit | Scenarios | | | | | |
|---|---|---|---|---|---|---|---|
| | | Brazil | South | Midwest | North | Northeast | Northeast – Max. |
| Plant capacity | t/h | 80.0 | 80.0 | 80.0 | 2.011 | 2.863 | 80.0 |
| Total revenue | MMUSD | 205.84 | 205.84 | 205.84 | 2.018 | 7.367 | 205.84 |
| Biomass costs | MMSUD | 62.078 | 61.773 | 61.793 | 1.458 | 1.983 | 62.433 |
| Power costs | MMUSD | 25.546 | 24.736 | 25.696 | 0.586 | 0.875 | 20.601 |
| Biomass transport costs | MMUSD | 5.049 | 5.476 | 5.040 | 0.132 | 0.184 | 6.522 |
| Urea transport costs | MMUSD | 9.593 | 10.737 | 11.018 | 0.096 | 0.202 | 36.309 |
| FCF | MMUSD | 103.572 | 103.115 | 102.29 | 2.901 | 4.122 | 79.970 |
| CAPEX | MMUSD | 772.29 | 772.29 | 772.29 | 23.94 | 34.075 | 772.29 |
| NPV | MMUSD | 109.476 | 105.592 | 98.569 | 0.764 | 1.018 | -91.448 |

$$\sum_{l' \in L} BS_{bll'} \leq S_{bl} \qquad \forall\, b \in B, l \in L \qquad (11)$$

$$\sum_{l' \in L} US_{l'l} \leq D_l \qquad \forall\, l \in L \qquad (12)$$

# RESULTS

## Process model

The plant's performance was evaluated using the process model for all 6 types of biomasses and 2 technological routes, totaling 14 runs. Gasification temperature was set to 1200 °C, controlled by the oxygen intake. Two technological routes were chosen for this study: pure oxygen gasification, and air mixed gasification. In pure oxygen gasification, the only gasifying agent used is oxygen, while the nitrogen required by the ammonia synthesis is separated at the air separation unit and directly mixed before the syngas compression stage, controlling the $N_2/H_2$ ratio in the ammonia synthesis at 3.0. Meanwhile, in air mixed gasification, the air intake controls the $N_2/H_2$ ratio and oxygen is complemented to keep the gasification temperature at the desired setpoint. Table 3 summarizes the results. The informed utility consumption already takes into account internal power production; overall, oxygen gasification is more efficient in converting biomass into urea, but power generation is also smaller in comparison. Sugarcane bagasse has high average moisture, which explains the large difference between this biomass and all the others. Also, higher moisture increases steam consumption in the drying stage but reduces the need of steam injection at the gas conditioning phase to adjust the gas composition.

## Optimization model

The commercial solver Gurobi was used to solve the MILP model, taking 19.11 mins on average on a Ryzen 7 CPU at the largest simulation. The database used in the simulations, as well as the full results, are provided in the supplementary material. Table 4 provides the summary of the results.

The optimization model was initially applied to the whole country at the micro-region level (558 locations). In this scenario, it was found that the Assis microregion in the state of São Paulo is the optimal location for the installation of the renewable urea plant. Pure oxygen gasification was the route chosen, and the biomasses used are a 50/50 mix of soybean straw and sugarcane straw, leveraging the large sugarcane crops in the São Paulo state. The plant capacity was constrained to a maximum

of 80 t/h to limit the errors on capital costs estimation. The total urea produced (663,000 tons/year) is enough to supply 50% of the state demand and 9.2% of the national urea demand.

The Assis microregion has enough biomass available to provide 99% of the required biomass of the plant. However, the urea produced needs to be sold 30 different microregions, crossing state borders and navigating more than 250 km. Figure **4** shows the plant location and all optimal markets for the urea product destination.

The model was constrained to other regions of Brazil to evaluate local feasibility. In the south region, the microregion of Cianorte presented the best NPV results, using a mixture of rice husks and sugarcane straw as biomasses. In this case, the local supply of biomass is not enough to satisfy the plant's demands, so biomass needs to be imported from close regions, which raises transport costs. The Midwest region consists of a large agricultural belt in Brazil, and the optimal location in this region was found to be the "Sudoeste de Goiás" microregion. At this scenario the plant uses 100% soybean residues, which forms much of the biomass available in the Midwest. In both scenarios, the urea must also be sold to more than 20locations as the local markets cannot accommodate the total plant production.

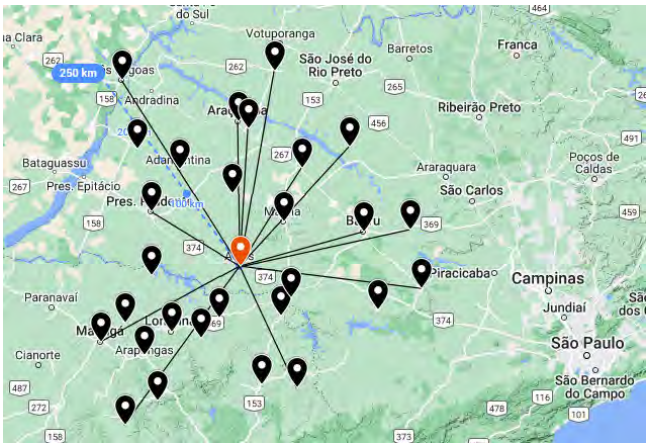



**Figure 4** – Plant location and urea consumers for main scenario.

The model's results for the other two regions of Brazil (North and Northeast) show that a large-scale renewable urea plant is not feasible, with optimal capacities of 2.01 and 2.83 t/h respectively. Despite large biomass supplies in these regions, the distance between urea markets is too large and local urea demand is too small, to the point where the logistical costs of transporting urea become the main limiting factor. To illustrate this, an additional scenario, called "Northeast – Max." was modeled constraining the possible locations to the Northeast region but also fixing the plant's capacity to the maximum (80 t/h). In this scenario, the NPV is -91 MMUSD, with the urea transport costs increasing to 36 MMUSD.

## CONCLUSIONS

A two-level model for the production of renewable urea was developed, combining a traditional process model with a supply-chain and optimization framework. The process model was applied to 6 different biomasses and 2 technological routes, obtaining the key performance indicators (KPIs) for all 14 scenarios. These KPIs were used in the supply-chain model to obtain the optimal combination of plant location, biomass used and technological routes considering local biomass supplies, urea demands and distance between regions. It was found that the optimal location for a renewable plant in Brazil is in the São Paulo state, given the high urea demand and short distances between markets. When constraining the model to different regions, it was found that the logistical costs of urea distribution bottlenecks the feasibility of the plant. This highlights the need for a robust supply chain model coupled with a traditional process modeling approach.

## DIGITAL SUPPLEMENTARY MATERIAL

The database used in the simulations, as well as the full results, are provided in the following link, hosted in the Living Archive for Process Systems Engineering – LAPSE: https://psecommunity.org/LAPSE:2025.0015

## REFERENCES


1. C. Mbow et al., "IPCC Special Report on Land and Climate Change. Chapter 5: Food Security," 2019.
2. IEA, "Ammonia Technology Roadmap: Towards more sustainable nitrogen fertiliser production," Oct. 2021. Accessed: Oct. 31, 2022. [Online]. Available: https://www.oecd-ilibrary.org/energy/ammonia-technology-roadmap_f6daa4a0-en
3. "Impacts and Repercussions of Price Increases on the Global Fertilizer Market," USDA Foreign Agricultural Service. Accessed: Oct. 17, 2022. [Online]. Available: https://www.fas.usda.gov/data/impacts-and-repercussions-price-increases-global-fertilizer-market https://doi.org/10.1234/56789.10
4. "Conab - Boletim da Safra de Grãos." Accessed: Oct. 17, 2022. [Online]. Available: http://www.conab.gov.br/info-agro/safras/graos/boletim-da-safra-de-graos
5. IFA, "Estimating & Reporting Fertilizer-Related Greenhouse Gas Emissions:," Sep. 2016.
6. F. Brentrup, A. Hoxha, and B. Christensen, "Carbon footprint analysis of mineral fertilizer production in Europe and other world regions," Oct. 2016.

7. M. Ouikhalfan, O. Lakbita, A. Delhali, A. H. Assen, and Y. Belmabkhout, “Toward Net-Zero Emission Fertilizers Industry: Greenhouse Gas Emission Analyses and Decarbonization Solutions,” Energy Fuels, vol. 36, no. 8, pp. 4198–4223, Apr. 2022, doi: 10.1021/acs.energyfuels.2c00238.
8. J. Meessen, “Urea synthesis,” Chem. Ing. Tech., vol. 86, no. 12, pp. 2180–2189, 2014, doi: 10.1002/cite.201400064.
9. P. Basu, Biomass gasification and pyrolysis: practical design and theory. Burlington, MA: Academic Press, 2010.
10. T. Werpy and G. Petersen, “Top Value Added Chemicals from Biomass: Volume I -- Results of Screening for Potential Candidates from Sugars and Synthesis Gas,” p. DOE/GO-102004-1992, 15008859, Aug. 2004, doi: 10.2172/15008859.
11. H. Zhang, L. Wang, J. Van herle, F. Maréchal, and U. Desideri, “Techno-economic comparison of 100% renewable urea production processes,” *Appl. Energy*, vol. 284, p. 116401, Feb. 2021, doi: 10.1016/j.apenergy.2020.116401.
12. M. Domingos, D. Flórez-Orrego, S. Sharma, M. Teles, and F. Maréchal, “Integrated production of urea and nitric acid in the pulp industry: techno-economic and environmental analysis of black liquor gasification-based processes,” presented at the 7th International Conference on Contemporary Problems of Thermal Engineering CPOTE, Warsaw, Poland, Sep. 2022.
13. D. Lopes, M. Teles dos Santos, and M. E. G. Domingos, “Comparative study of urea production integrated to lignocellulosic processes,” in *Anais do 24° Congresso Brasileiro de Engenharia Química*, 2023. doi: 10.17648/cobeq-2023.
14. T. Schröder, L.-P. Lauven, and J. Geldermann, “Improving biorefinery planning: Integration of spatial data using exact optimization nested in an evolutionary strategy,” *Eur. J. Oper. Res.*, vol. 264, no. 3, pp. 1005–1019, Feb. 2018, doi: 10.1016/j.ejor.2017.01.016.
15. A. Gambarotta, M. Morini, and A. Zubani, “A non-stoichiometric equilibrium model for the simulation of the biomass gasification process,” *Appl. Energy*, vol. 227, pp. 119–127, Oct. 2018, doi: 10.1016/j.apenergy.2017.07.135.
16. E. Martelli, M. Gatti, F. Maréchal, and S. Consonni, “Multi-objective Optimization of a Selexol® Process for the Selective Removal of CO2 and H2S from Coal-derived Syngas,” in *ECOS 2015 - THE 28TH INTERNATIONAL CONFERENCE ON EFFICIENCY, COST, OPTIMIZATION, SIMULATION AND ENVIRONMENTAL IMPACT OF ENERGY SYSTEMS*, Jul. 2015.
17. D. Flórez-Orrego, “Process synthesis and optimization of syngas and ammonia production in nitrogen fertilizers complexes: Exergy, energy integration and CO2 emissions assessment,” University of São Paulo, São Paulo, 2018.
18. “IBGE - PAM - Produção Agrícola Municipal.” Accessed: Jan. 27, 2025. [Online]. Available: https://www.ibge.gov.br/estatisticas/economicas/agricultura-e-pecuaria/9117-producao-agricola-municipal-culturas-temporarias-e-permanentes.html
19. L. Souza *et al.*, “Theoretical and technical assessment of agroforestry residue potential for electricity generation in Brazil towards 2050,” *Energy Rep.*, vol. 7, pp. 2574–2587, Nov. 2021, doi: 10.1016/j.egyr.2021.04.026.
20. “IFASTAT | Fertilizer Use By Crop.” Accessed: Jan. 28, 2025. [Online]. Available: https://www.ifastat.org/consumption/fertilizer-use-by-crop
21. L. R. de Carvalho, P. V. M. do Amaral, and P. S. Mendes, “Matrizes de distâncias e tempo de deslocamento rodoviário entre os municípios brasileiros : uma atualização metodológica para 2020,” *Textos Para Discussão Cedeplar-UFMG*, Art. no. 630, Mar. 2021, Accessed: Jan. 28, 2025. [Online]. Available: https://ideas.repec.org//p/cdp/texdis/td630.html
22. “ANEEL | Portal Reports Abertos.” Accessed: Jan. 28, 2025. [Online]. Available: https://portalrelatorios.aneel.gov.br/luznatarifa/bastarifas

© 2025 by the authors. Licensed to PSEcommunity.org and PSE Press. This is an open access article under the creative commons CC-BY-SA licensing terms. Credit must be given to creator and adaptations must be shared under the same terms. See https://creativecommons.org/licenses/by-sa/4.0/



Systems & Control Transactions

**Research Article - Peer Reviewed Conference Proceeding**
ESCAPE 35 - European Symposium on Computer Aided Process Engineering
Ghent, Belgium. 6-9 July 2025
Jan F.M. Van Impe, Grégoire Léonard, Satyajeet S. Bhonsale,
Monika E. Polańska, Filip Logist (Eds.)

PSE PRESS

# Evolutionary Algorithm Based Real-time Scheduling via Simulation-Optimization for Multiproduct Batch Plants

**Engelbert Pasieka[a*], Sebastian Engell[b]**

[a] INOSIM Software GmbH, Joseph-von-Fraunhofer-Str. 20, 44227 Dortmund, Germany
[b] TU Dortmund, Department of Biochemical and Chemical Engineering, Emil-Figge-Str. 70, 44221 Dortmund, Germany
* engelbert.pasieka@inosim.com

## ABSTRACT

Production scheduling in the process industry is an area of significant activity in research and of great practical importance for the performance of industrial companies. In the vast majority of research papers, the scheduling problem is formulated as an off-line problem where a number of jobs is scheduled on a number of resources and the efficiency of the formulation and the solution algorithms is discussed. In reality, however, scheduling is a continuous activity that has to react to the arrival of new orders, to variations in processing times, breakdowns, lack of resources etc. This is termed real-time (or online) scheduling. Available commercial solutions usually provide solutions with relatively long update intervals due to the necessary computation times and a delayed flow of information from the manufacturing execution systems where the data on the current state of the production is collected. Thus the computed schedules are outdated quickly, if not already at the point in time when they become available, and new orders and all kinds of variations and disturbances are handled by the operators and plant supervisors. There has been little concern for systematic solutions for real-time scheduling that continuously react to the changing situation in the plant. In this contribution we present a simulation-optimization approach to real-time scheduling where a detailed discrete-event simulation of the plant is coupled with an evolutionary algorithm. The simulation model is continuously updated with the latest plant data, and the optimization algorithm continuously improves the schedule based on the currently available information. We validate our approach using an example of a multiproduct, multistage batch plant in the pharmaceutical industry from the literature, demonstrating that the proposed approach can generate high-quality solutions quickly. We compare the results with those of an ideal (clairvoyant) scheduler, demonstrating that our method effectively manages unforeseen disturbances.

**Keywords**: Modelling and Simulation, Large Scale Desing, Planning/Scheduling.

## INTRODUCTION

Production scheduling is a decision-making process that determines the optimal allocation to resources and sequence of operations in production processes. This improves plant efficiency, reduces operational costs, and improves customer satisfaction by meeting the promised delivery dates. Scheduling in the scientific literature is typically considered in an offline setting where a static problem for a given production environment, given jobs and timing constraints, and a given cost function is solved. In industrial practice, scheduling is usually done periodically with relatively long intervals between the computations or manual generations of updated schedules due to the complexity and required computation time as well as the lack of fast feedback from the shop floor.

Real-world production environments however are subject to frequent unforeseen events such as machine breakdowns, new order arrivals, varying processing times and changes of the availability of resources. Such events may render the available schedules inefficient or even infeasible so that adaptations are needed.

Real-time scheduling systems have the task to generate updates of the production plans based on a continuous exchange of information with the shop floor systems. These plans should be executable by the real plant

because otherwise time-consuming modifications or refinements are necessary. So there are two, contradictory requirements: The computation of the schedules must be fast, where sufficiently fast is defined by the execution times of the production plant. When an operation is finished, the next executable operation must be started with a delay that should not be larger than a small fraction of the average execution time. On the other hand, for a schedule to be executable, the scheduling system should be based on a detailed model of the plant that includes all relevant conditions and constraints for the execution of the production plans. This excludes the use of simplified models which consider only basic constraints as e.g. the sequence of operations within jobs, exclusivity of the use of resources and changeover times. Many existing approaches fall short to deliver timely responses and to generate schedules that are interpretable and executable by plant operators [1]. One possible way of solving the real-time or online scheduling problem is to see the scheduler as a controller that continuously monitors the current state and applies corrective actions to keep the system on track toward the reference trajectory [2]. Then offline scheduling is analogous to providing the reference trajectory or setpoint of a dynamic system. However, while this is a convincing analogy, there are fundamental differences, in particular regarding what "tracking" means for schedules. Our approach here therefore is similar to the "all in one" optimizing control approach [3]. Specifically, we employ simulation-optimization to realize this idea.

In [4], MILP-based methods using state-space formulations were introduced for online scheduling in a feedback loop. However, as noted in [4], these approaches require advanced solution techniques to handle high-complexity and high-fidelity problems to maintain computational feasibility.

Simulation-optimization (SO) is well suited for this task as high-fidelity simulation models that represent the production process in detail can be used and therefore the scheduler will generate production plans that the plant operators can implement without modification. Simulation models can easily be adapted to changes of the structure (e.g. available resources) and the parameters (e.g. predicted execution times) of the production system and to new jobs and re-computed schedules. For scheduling on the basis of detailed complex stimulation models, rigorous scheduling methods usually are not well suited because the transformation of the simulation model into the underlying formalism leads to very complex models and excessive computation times. Therefore in SO generally metaheuristics as e.g. evolutionary algorithms are applied. Such algorithms are less performing than rigorous algorithms for the solution of MILPs or constraint satisfaction problems as long as the solution times of the rigorous algorithms are acceptable, but have the advantage of being more generally applicable and leading to acceptable solutions early in the solution process, however without guarantees for the closeness of the solution to the true optimum. In [5], a successful application of SO with evolutionary algorithms to a complex real-world industrial scheduling problem was reported. It was also shown in [6] for general video game playing (GVGA) that evolutionary algorithms (EA) with simulation models compete well in environments where changes of the decision space are frequent and fast responses are crucial.

Our proposed simulation-optimization approach provides greater flexibility and adaptability for handling complex scheduling problem and the results are easier to interpret, thereby facilitating practical adoption in industrial settings. In [7], we presented the idea of a reactive real-time scheduling approach based on SO. In this paper, we extend our previous work by providing a more detailed explanation of the interaction between the real plant and the scheduling system, by exploring the influence of critical parameters and by discussion a case study of a complex pharmaceutical batch production [8], simulating a typical 8-hour production shift with major disruptions.

## APPROACH

Our online scheduling framework uses simulation-optimization with real-time feedback from the production process that is used to update the simulation model to align with the state of the production. The framework contains two components, the scheduling system and the production system. Figure 1 shows the components and their interactions.

### Scheduling System

The evolutionary algorithm runs continuously and improves the schedules gradually based on the currently available information. The simulation system (a detailed commercial discrete-event simulator) uses heuristics and logic constraints to generate the detailed schedules, i.e. it acts as the schedule builder. The model in the scheduler is updated continuously with the latest information from the plant. The detailed schedule that is passed to the production management system is executable on the shop floor. This is achieved by the execution logic and, if needed repair mechanisms that are implemented in the simulator. E.g., no new operation can be started on a resource which has become unavailable. Transferring schedules that are generated fast after changes in the plant or in the structure of the orders provide an immediate response to disturbances. As this happens after few iterations of the EA, their quality will be lower, but in the following iterations of the EA they are further improved.

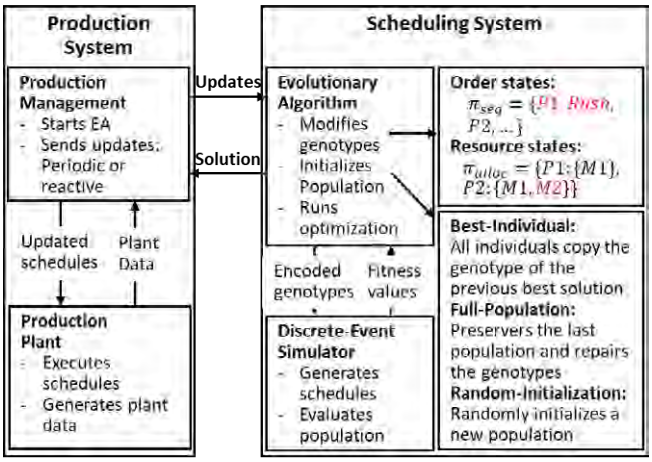



**Figure 1.** The reactive real-time scheduling framework integrates a scheduling system with an evolutionary algorithm and discrete event simulator and a production system with data access to the plant to dynamically adapt to changes and disruptions in the plant. The scheduling system modifies genotypes representing order sequences and resource allocations and uses a discrete-event simulation to evaluate schedules. The evolutionary algorithm iteratively updates and refines schedules for the current model of the production system. The production system provides data from the plant and triggers updates in response to events such as delays, rush orders, and maintenance tasks, ensuring continuous alignment between schedules and the current plant state.

In the case investigated here, the scheduling solutions are encoded as genotypes which contain a global sequence of orders, e.g. $\pi_{seq} = \{P1, P2, P3, \dots\}$, and the allocation of orders to resources, e.g., $\pi_{alloc} = \{P1:\{M1\}, P2:\{M1, M2\}, \dots\}$. In more complex examples, further degrees of freedom can be encoded, e.g. the splitting of customer orders into production jobs (see [4]). The EA explores the space of feasible schedules through selection, recombination, and mutation. The repeated execution of the EA starts with the modification (if needed) and initialization of the genotypes. In each iteration, the algorithm evaluates the fitness of each genome in the population by the execution on the updated simulation model, selects the most promising candidates, and applies recombination and mutation to generate new solutions. A survivor selection process ensures which solutions are carried forward. During the evaluation of the genomes, the simulator builds a detailed schedule that complies with all known constraints. The best available detailed schedule is transferred to the plant when an update is requested.

## Production System

The production system provides real-time information to the scheduling system. It consists of the production management system and the production plant itself. The production management system initiates and parametrizes the evolutionary algorithm and monitors the real-time data from the production plant for deviations that require updates of the scheduling model or of the genotypes and of the genomes of the solutions in the population. Updates are performed either periodically, updating the current state of the execution of the schedule and parameters as e.g. expected execution times, or reactively in response to significant disruptive events, such as rush orders, breakdowns, large delays in the execution of operations or maintenance requirements.

## Information Exchange

Figure 2 illustrates the information exchange between the production system and the scheduling system.

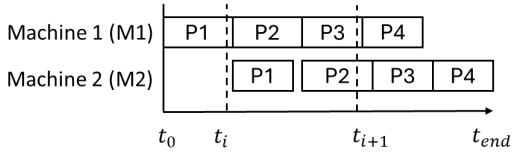



**Figure 2.** Gantt Chart with update events. M1 and M2 process the orders sequentially (first on M1, then on M2).

At each update instance $t_i$, the production system provides the scheduling system with real-time operational data, including the current status of ongoing tasks, estimated remaining processing times, and details of disruptions such as machine breakdowns, maintenance tasks, or urgent new orders. At the same time, the scheduling system sends an updated detailed schedule for the next period starting at $t_{i+1}$.

After the exchange at $t_i$, the scheduling system updates its simulation model and configures the evolutionary algorithm by adjusting decision variables if needed. It then continues optimizing the schedule for the next period (starting at $t_{i+1}$). Operations that are already in progress (e.g., P2 on M1) remain fixed.

Disruptive events, such as maintenance activities or new order arrivals, trigger immediate reactive updates. The scheduling system instantly integrates this new information, modifies the simulation model and reconfigures the evolutionary algorithm. After a predefined interval after such disruptive events, a revised schedule is generated and sent to the production system after which the evolutionary algorithm continues its optimization for the rest of the regular update interval.

## Reinitialization of the population

A key element in designing the scheduling system is how the population is managed between updates, as this can be used to preserve information between updates and to control the balance between exploiting current solutions and exploring new ones. We investigated three options:

**Best-Individual:** The best individual from the previous population (i.e., the best schedule found before $t_i$) is copied into the new population, and only the parts affected by the changed conditions are adjusted randomly.

**Full-Population:** The entire population is carried over to the next generation, and the solutions are only repaired to fit the updated constraints (e.g., new tasks or changed machine availability). The balance of exploration and exploitation largely depends on the diversity of the previous population.

**Random-Initialization:** The entire population is reinitialized randomly, producing a new and diverse population. This enhances the exploration and may help avoid local minima that arise when solutions become too similar.

The three strategies can be mixed, e.g. by updating a fraction of the population with random solutions after a disruptive event. Another option is to modify the strategy parameters of the EA, e.g. the mutation strength, at disruptive events and then including them in the optimization process (Co-evolution, [9]).

## EXPERIMENTS

The case study addressed in this work is taken from Kopanos, et al., [8]. It is a multiproduct batch plant with 17 units (machines) that are organized in 6 stages (Figure 3). The problem, which is a variant of a hybrid flow shop problem, comprises 12 instances that vary in the number of orders, the objectives, and in the storage policy. The features of the problem include limited product-unit flexibility, machine-dependent processing times, sequence-dependent changeover times, and product-specific recipes, meaning that certain jobs are not processed on some of the available stages.

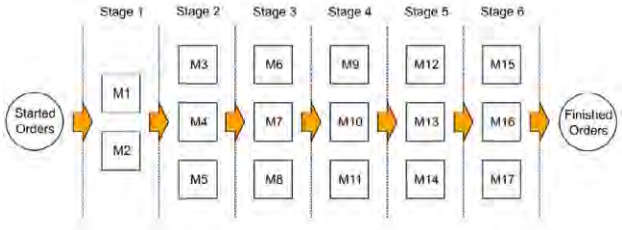



**Figure 3:** Plant layout of the case study.

A series of experiments were executed to evaluate the performance of the proposed real-time scheduling system and to show the effects of the length of the update intervals, the time required to evaluate one generation, and of the initialization strategy. The experiments simulate one production shift in the multiproduct batch plant and include disruptive events. The results are compared to the outcomes from using a clairvoyant scheduler that anticipates all disruptive events. This solution was computed by optimizing the full schedule over the full time horizon with the disruptive events taken into account. The same evolutionary algorithms was used and run over 1000 generations.

In total, 20 combinations of parameters were evaluated, with each case being repeated 20 times to account for the inherent randomness of the evolutionary algorithm. The experiments differ in the length of the update intervals of the production system, the time before the immediate response must be provided, the time to evaluate one generation of the scheduling system, and the initialization strategy after update events.

### Fixed Parameters

The following parameters were used across all experiments to ensure comparability:

**Problem setting:** Initially 30 orders have to be fulfilled within a time horizon of 32 hours. For each order there is a due date. All orders are released at time 0. The prime objective (Equation (1)) is the minimization of the maximum tardiness T. If the tardiness is below 0, the objective shifts to the largest negative earliness. This pushes the completion times $C_i$ of the orders $i$ further away from their due dates $d_i$ if all due dates can be met.

$$F = \max_i \ (C_i - d_i) \tag{1}$$

**Simulation Horizon**: Each simulation run consists of 8 hours (28,800 seconds) of production, representing a typical production shift. Note that this is only a fraction of the execution time of a schedule. The schedules are evaluated over the full execution time, i.e. using the completion times of the orders that finish in the simulation horizon and the predicted (simulated) completion times of the remaining orders.

**Initial Solution:** The simulation was initialized with a high-quality scheduling solution that was computed in a separate run with the same objective and 1000 generations, serving as a reference schedule. The initial solution has an objective value of -1.34 (i.e. all orders finish early). The total time to complete the full production schedule is 30 hours and 23 minutes.

**Disruptive Events:** Table 1 lists the eight disruptive events that were introduced during each simulation to represent real-world disturbances.

**Table 1:** Disruptive events and their arrival times.

| Event | Time (sec) | Info |
|---|---|---|
| Release of P01_Rush | 2400 | Due in 12h |
| Release of P03_Rush | 4200 | Due in 12h |
| Maintenance of M1 | 4800 | 1h duration |
| Maintenance of M3 | 7200 | 1h duration |
| Maintenance of M19 | 12000 | 1h duration |
| Release of P05_Rush | 13800 | Due in 12h |
| Maintenance of M13 | 18000 | 1h duration |
| Maintenance of M16 | 21600 | 0.5h duration |

All maintenance orders were non-preemptive,

meaning they had to be executed after the current operation on the respective machine had completed.

**Population Size:** The population consists of 32 individuals, which are evaluated in parallel using 32 threads on a machine with 16 cores (Intel Core i9-14900K). The offspring size was set to 32, with an elitist size of 16.

**Mutation Operator:** We used a permutation mutation, which selects a subsection of the gene and shuffles it randomly. The mutation rate was set to 1, meaning every individual underwent mutation.

**Crossover Operator:** The cycle crossover operator was applied to preserve as much information as possible about the absolute position of the elements [10]. The crossover rate was set to 1.

**Parent Selection:** Rank-based selection was used to choose parent individuals for the next generation.

**Survivor Selection:** Random survivor selection was employed, with an elitist fraction of 50%. The top 50% of the individuals from the previous generation were retained, while the remaining individuals were selected randomly from the remaining population.

**Decision Variables of the EA:** Only the sequence of orders, e.g., $\pi_{seq} = \{P1, P2, P3, \dots\}$, was encoded in the genomes of the individuals of the EA. The allocation of orders to machines was performed by the simulator using a greedy FIFO rule. Each operation is executed on the machine where it finishes the earliest.

## Variable Parameters

To study their effect on the performance of the scheduling system, the following parameters were varied:

**Update Interval:** The length of the periodic update interval was set to 60 and to 300 seconds.

**Simulation time:** This parameter is a fictitious time for the evaluation of one generation of solutions. It determines the number of generations that are evaluated. Simulations times of 3s and 12s were tested.

**Immediate Response Time:** This is the time when after a disruptive event a new solution is sent to the production system. The minimum time is the time needed to evaluate on generation of solutions. The second value that was tested is 60 seconds.

**Initialization:** The modes *Full-Population*, *Best-Individual* and *Random* were tested.

# RESULTS

Figure 4 shows the distribution of the mean fitness values for the three different initialization modes. The mean fitness values for all experiments at the minimum time needed to evaluate the generation of solutions after each disruptive event in Table 1.

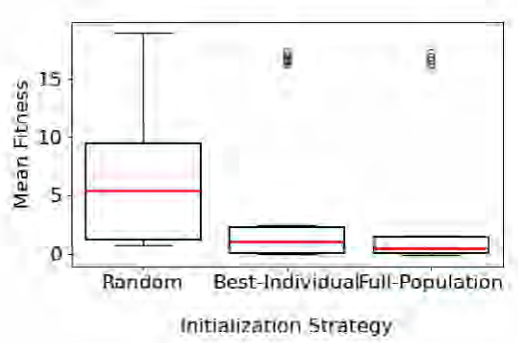



**Figure 4:** Distribution of the schedule quality for different initialization strategies after the disruptive events.

The Random initialization is clearly inferior. There are only small differences between the *Best-Individual* and *Full-Population* strategies. As the latter performs slightly better, only results for this strategy are shown in the sequel.

Figure 5 shows the evolution of the mean fitness over all 20 runs and of the best 25% of the runs at the end of the simulation horizon over the simulated 8 hours of production with the disruptive events listed in Table 1 for different configurations (300 s periodic update interval, 3 and 12 s/gen, immediate response after one generation (0) and after 60 seconds). Additionally, the performance without replanning is indicated by the solid black line.

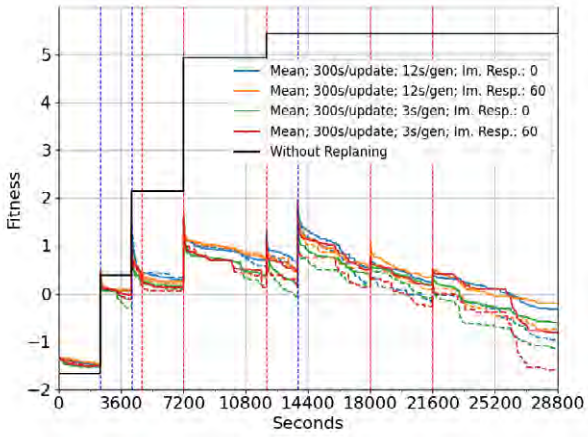



**Figure 5:** Mean (colored solid line) and mean of best 25% (colored dashed line) fitness values of 20 experimental runs for different configurations (300 s/update, 3 and 12 s/gen, im. Resp after one generation and 60 seconds). The disruptive events are marked as dashed vertical lines (blue for maintenances and red for new order arrivals).

Table 2 shows the results for all configurations. The clairvoyant scheduler uses the same algorithm but has the a priori information about all disruptive events. This provides a lower bound that cannot be achieved by a real-time scheduler.

**Table 2:** Best, mean, mean of best 25% of fitness values for the different configurations (formatted as "seconds per update, seconds per generation, immediate response time"), for the clairvoyant scheduler, and for the case without replanning.

| Configurations | Best | Mean | Mean Best 25% |
|---|---|---|---|
| 300, 12, 60 | -1.30 | -0.20 | -0.74 |
| 300, 12, 0 | -1.67 | -0.32 | -0.96 |
| 300, 3, 60 | -1.76 | -0.81 | -1.60 |
| 300, 3, 0 | -2.10 | -0.61 | -1.14 |
| 60, 12, 0 | -1.68 | -0.52 | -1.08 |
| 60, 12, 60 | -1.61 | -0.23 | -0.74 |
| 60, 3, 0 | -2.10 | -0.68 | -1.34 |
| 60, 3, 60 | -1.53 | -0.24 | -0.83 |
| Clairvoyant | -4.37 | | |
| W/o replan | 5.44 | | |

The differences between the configurations are relatively small when the results at the end of the simulation horizon are compared. The best configuration realizes 75 – 80% of the possible improvement. The simulation time has a negative influence but due to the long optimization interval at the end it is not very pronounced. Between disruptive events the shorter simulation time leads to significantly faster improvements. The influence of the immediate response time is small and nonuniform.

For the disruptive events considered here, the deterioration of the performance of the production system with rescheduling is relatively small, pointing to the system not being operated under full load.

## SUMMARY

We proposed an approach to real-time scheduling which is based on simulation-optimization using a detailed discrete-event simulator with schedule building heuristics and an evolutionary algorithm that handles the key decision variables. The main idea is to run the evolutionary algorithm continuously with updates of the simulation model and of the decision vector being performed periodically and in response to disruptive events. Maintaining the previous population except for changes required by changes of the decision parameters is preferable over other possible initializations. The resulting performance is good even for low numbers of generations that are evaluated during the update interval.

We characterized the performance by comparison with the execution of the schedule without changes due to the disruptive events and with the results obtained with a fictitious clairvoyant scheduler which cannot be achieved in a situation where these events are not known before.

We considered the influence of simulation time on the performance. Other cases with demanding simulation times may require additional simplifications or algorithmic optimizations to meet the time constraints. This aspect will be further studied.

In this paper we only reported results for a small number of relatively infrequent disruptive events for lack of space. It will be studied in the future which influence the parameters of the algorithm have in situations where the plant operates at the capacity limit.

## REFERENCES


1. Espinaco F, Henning P. Industrial Rescheduling Approaches: Where Are We and What is Missing? *Production Research–Americas, pp 461–467* (2023).
2. Engell S. Uncertainty, decomposition and feedback in batch production scheduling. *Proc. ESCAPE19, pp 43-62* (2009).
3. Engell S. Feedback control for optimal process operation. *Journal of Process Control, Vol. 17, pp 203-219 (2007).*
4. Gupta D, Maravelias CT. A General State-Space Formulation for Online Scheduling. *Processes, vol. 5, no. 4, pp 69 (2017).*
5. Klanke C, Engell S. Scheduling and batching with evolutionary algorithms in simulation–optimization of an industrial formulation plant. *Computers & Industrial Engineering, Vol. 174 (2022).*
6. Gaina RD, Devlin S, Lucas SM, Perez-Liebana, D. Rolling Horizon Evolutionary Algorithms for General Video Game Playing. *IEEE Conference on Computational Intelligence and Games* (2020).
7. Pasieka E, Engell S. Reactive Real-time Scheduling Using Simulation-Optimization and Evolutionary Algorithms.*10th International Conference on Control, Decision and Information Technologies (CoDIT) (2024).*
8. Kopanos GM, Méndez CA, Puigjaner L. MIP-based decomposition strategies for large-scale scheduling problems in multiproduct multistage batch plants: A benchmark scheduling problem of the pharmaceutical industry. *European Journal of Operational Research, pp 644-655 (2010).*
9. Beyer HG, Schwefel HP. Evolution Strategies A comprehensive introduction. *Natural Computing, Vol. 1, pp 3–52, (2002).*
10. Eiben AE, Smith JE. Introduction to Evolutionary Computing. *Ed: 2, Natural Computing Series, Springer Berlin, Heidelberg (2015).*



© 2025 by the authors. Licensed to PSEcommunity.org and PSE Press. This is an open access article under the creative commons CC-BY-SA licensing terms. Credit must be given to creator and adaptations must be shared under the same terms. See https://creativecommons.org/licenses/by-sa/4.0/




Systems & Control Transactions

**Research Article - Peer Reviewed Conference Proceeding**
ESCAPE 35 - European Symposium on Computer Aided Process Engineering
Ghent, Belgium. 6-9 July 2025
Jan F.M. Van Impe, Grégoire Léonard, Satyajeet S. Bhonsale,
Monika E. Polańska, Filip Logist (Eds.)

PSE PRESS

# Pipeline Network Growth Optimisation for CCUS: A Case Study on the North Sea Port Cluster

**Victoria Brown[a]*, Joseph Hammond[a], Diarmid Roberts[a], and Solomon Brown[a]**

[a] School of Chemical, Materials, and Biological Engineering, University of Sheffield, Sheffield, S1 3JD, England, UK
* Corresponding Author: victoria.brown@sheffield.ac.uk

## ABSTRACT

By 2050 around 12% of cumulative emissions reductions will come from Carbon Capture, Utilisation and Storage (CCUS) making it an essential component in the path towards net zero [1]. Focus will initially be on the retrofitting of fossil fuel power plants, which will shift to hard-to-decarbonise industries such as iron, steel, and concrete [1]. Such industries are often grouped together in industrial clusters. Comprising both large and small point sources concentrated over a defined geographical area, industrial clusters offer an opportunity to maximise the impact of CCUS whilst also improving economic feasibility [2]. The North Sea Port (NSP) cluster an example of this. Within the NSP cluster an initial set of five emitters are to join a capture, conditioning, and transport network by 2030. From there other emitters within the area will be able to join incrementally to 2050 [3]. However, the emitters who join and the timing of their connection will have a significant effect on the evolution the network. The pipeline network design will balance design requirements for initial emitters in a backbone network, with requirements for encouraging and enabling expansion. This study builds on scenarios defined between 2030 and 2050 [3] and applies a multi-period evolutionary-based approach (Steiner tree with Obstacles Genetic Algorithm (StObGA)) to predict pipeline year-on-year network growth in the NSP cluster. This provides a novel approach to the problem. The results are used in an examination of the potential growth of the pipeline network and an investigation of trade-offs necessary in the infrastructure design.

**Keywords**: Carbon Dioxide Capture, Genetic Algorithm, Modelling and Simulations, Energy, Carbon Capture.

## BACKGROUND

Carbon Capture, Utilisation and Storage (CCUS) is a key technology in the pathway to meaningful CO2 abatement. If the application of CCUS is to be successful, the planning of the infrastructure required must be comprehensive and consider several factors. Technical, geographical, political, and social factors all require extensive planning/research if any CCUS infrastructure is to be successfully deployed. If improperly planned and risks/uncertainties are not accounted for there could be serious economic repercussions for emitters, thus dissuading any further uptake [4,5,6].

One way to make CCUS more enticing to emitters is the formation of industrial clusters. Here emitters within a set geographical area are grouped and can share infrastructure, thus increasing the potential for economy of scale and reducing the cost to individual entities [4,5]. However, the cost is influenced by many factors including number and size of emitters, availability of potential transport methods, distance from utilisation/storage sites, upcoming policies and regulations, and social acceptance of CCUS within the area. Subsequently, despite the benefits that industrial clusters offer, the infrastructure must still be properly planned [7].

Figure 1 outlines the major infrastructure elements of the CCUS supply chain. Starting with CO2 sources, the gas is captured and conditioned (usually compressed and purified) then it is transported onward for either utilisation or storage.

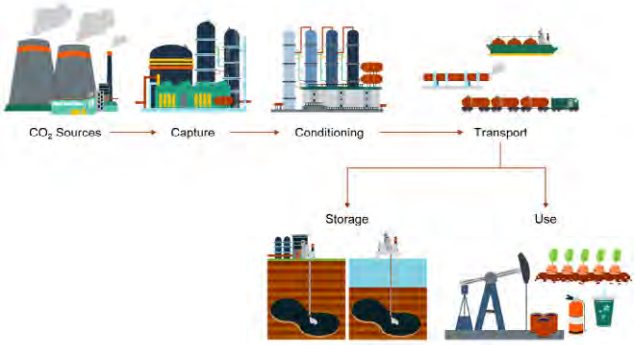



**Figure 1.** Diagram of the key stages in the CCUS supply chain.

In general, capture occurs at the site of large stationary emitters. The vast majority of which are from power plants, and other industries such as concrete, steel and chemical production [8]. Once captured, CO2 must be conditioned to ensure safe and efficient transport. Whilst often sited with capture, it can be considered as a distinct and vital stage in the CCUS supply chain. Conditioning encompasses several processes including dehydration, purification, and compression.

There are several options when considering CO2 transport infrastructure, each with their own advantages and disadvantages.

For smaller, discontinuous volumes of gas, rail and road are valid options. Shipping, however, is a candidate that can be scaled up to meet these demands, and, geography depending, can also be implemented with minimal infrastructure capital expenditure [4,5]. This is particularly evident in locations of well-established industrial clusters along coastlines and canal networks. As CCUS projects become established, shipping is seen as a viable option for the initial timeframe when pipeline infrastructure has yet to be established, and/or fewer emitters have joined the network.

Pipeline transport is anticipated to be the most economically efficient transportation option for large stationary emitters over industrial clusters [9-11] Pipelines also have the advantage of being able to efficiently transport CO2 over large distances and multiple terrains.

Whilst pipelines do have the potential to be an effective mode of transport, they require extensive infrastructure investment. This can be involved, requiring knowledge on pipeline sizing; locations of emitters and storage sites; specifications for transport and storage; network expansion over time [12]. Fortunately, gaseous phase pipeline infrastructure technologies for are well established, so existing standards on sizing and material can be drawn on when designing networks [12, 13]. However liquid phase pipeline transport requires additional considerations [6].

Extra complexity is added when considering network expansion, as geographic information needs to be combined with predictive models to create the most future-proof network.

Generally, pipeline network designs are modelled using graphs with emitters and offtake sites are taken as nodes with the pipelines themselves as arcs between them. To model both the topology and pipeline sizing simultaneously is computationally expensive so the two are generally modelled separately [14].

For length minimisation, Minimum Spanning Tree algorithms, such as Kruskal's are commonly used. This allows for generalised cost minimisation [15].

However, for any simulation to be truly representative, real-world constraints must be considered. In some cases, this can be circumvented, by utilising existing infrastructure such as road, or gas networks to provide predefined routes [16].

However, these methods are inflexible and do not consider novel routes, thus eliminating many possible optimal solutions.

Graph-based methods, such as Steiner points can also be used to enhance design flexibility, however this can also be limiting due to high computational expense, and inability to consider different geographic obstacles [14].

A more recently developed methodology by Rosenberg et al. (2021), displayed the viability of combining the Steiner tree method with a genetic algorithm to design networks that consider such obstacles [17]. This methodology is built on here, by applying it to CCS networks within an industrial cluster.

## Methodology

The methodology used in this work produces an optimised pipeline route for CCUS pipeline networks that connects point sources with offtake locations. Also taken into consideration, is a set of real-world constraints such as urban areas and waterways. These may be regions in which construction cannot occur, or in which a higher cost will be incurred to traverse them, known and solid and soft obstacles respectively. Such obstacles are represented as a graph consisting of polygons, each is assigned a crossing weight representative of the ease of traversal, with those that are un-traversable given an infinite value. An obstacle's crossing weight is multiplied with the length of the pipeline that crosses it.

## Topology

To separate the topology from sizing, the necessary assumption that the shortest route will be the most cost-effective is made. To find the minimum length between emitters and offtake, the Euclidean Steiner tree problem with soft and solid obstacles (ESTPO) is applied. To solve this for a set of given constraints, a genetic algorithm for Steiner trees with obstacles (StObGA) can be used. This was developed by Rosenberg et al. (2021) [17].

The genetic algorithm utilises the following chromosome type structure:

$$\{(x_1, y_1), (x_2, y_2), (x_3, y_3), \dots, (x_s, y_s)\} + \{1|0|1|0|0|0|1|1|0|0\} \quad (1)$$

This is split into two distinct parts, the first being the x-y coordinates of s number of Steiner points of variable length, and the second is a fixed length binary list which determines four obstacle corners to be used in the network.

To connect the terminals, Steiner points and obstacle nodes, weighted edges are created using Kruskal's minimum spanning tree [18]. The weighting depends on edge length and whether is traverses any obstacles.

The nodes and edges found this way are then subject to an optimisation regarding given emission and offtake values, with all edges assumed to be unidirectional.

## Sizing

Pipeline sizing is determined using a mixed integer nonlinear programming (MINLP) optimisation. With constraints being hydraulic, structural, and commercial. The following objective function minimised the total cost in $, C, for a defined set of arcs A:

$$C = (1 + 0.03) \sum_{i|(i,j)\in A} C_{ij}^{C} \quad (2)$$

Where the total cost is the sum of the capital costs ($C^C$ in the equation below) and the operating costs (assumed to be 3% of $C^C$.

The capital cost is a function of pipeline length L, outer diameters $D^{po}$, and considers the material, labour, right-of-way and other miscellaneous costs:

$$C^C = [674(dia)^2 + 11754(dia) + 234085](length) + 405000 \quad (3)$$

Where diameter (*dia*) is in inches, length is in miles, and cost is in dollars.

Additional constraints are material balance, discrete sizing, and erosion velocity as described by Ejeh et al 2023b, and Hammond et al 2025 [19, 20].

An overview of the methodology can be found in Figure 2.

# CASE STUDY

The method described above has been applied to the case study illustrated in Figure 3. Here an industrial cluster spread over the North Sea Port region which spans Belgium and The Netherlands.

The emitters have been selected as a selection of the largest in the region with respect to their 2023 verified emissions data [21]. The planned base route is as described in Ejeh et al 2023a. This is predicated to start working in 2030, and will include Zeeland Refinery, Sloe Centrale, DOW Benelux, Yara Sluiskil B.V., and ArcelorMittal. From there the network can then expand to encompass more and more emitters in the cluster.

This will then expand over successive years to 2050 in increments shown in Table 1.

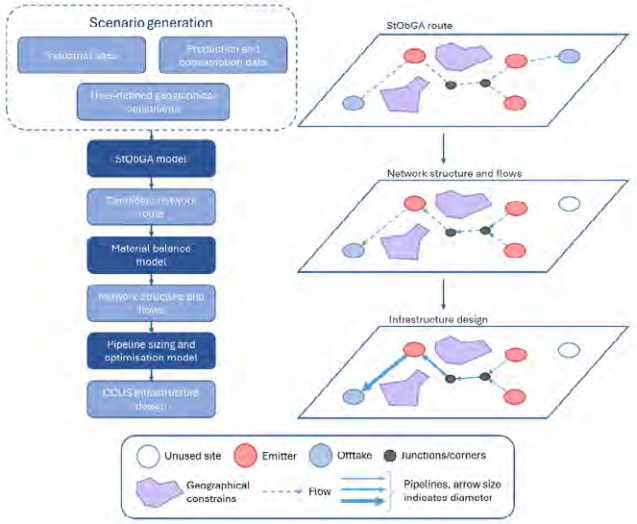



**Figure 2.** The worflow of the model showing consectutive steps and the final output.

**Table 1.** The list of point sources within the NSP cluster with the assumed year that they will join the network.

| Number of emitters | Assumed Addition year |
|---|---|
| 5 | 2030 |
| 11 | 2035 |
| 17 | 2040 |
| 23 | 2045 |
| 29 | 2050 |

A diagram displaying all emitters, obstacles, and the currently planned 2030 route is shown in Figure 3. The route shown in Figure 3 is based work previously conducted by C4U [3].

Compared with previous work [20, 22], the network developed here spans across a much smaller area with a higher density of emitters and industrial/urban areas. Providing a set of scenarios to further refine the network expansion methodology.

The network expansion was divided into Graded increases, with predetermined additions at 5-year intervals. This was further split into two distinct scenarios. The first (Graded Perfect), where the final network was simulated, and the intermediates were then built to match it. The second (Graded), was build piecewise with no knowledge of the final network. This allowed for a comparison of the two levels of implied knowledge.

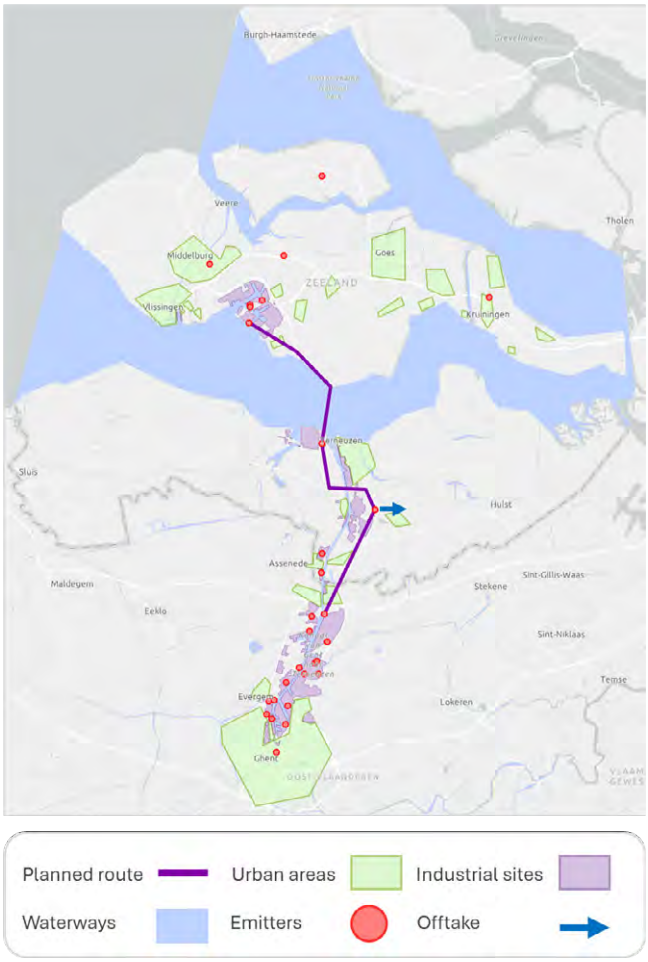



**Figure 3.** The NSP cluster showing the location of all point source emitters, built up areas, and the currently planned pipeline route.

## RESULTS AND DISCUSSION

A numerical summary of the results is shown in Table 2, with topological results presented in Figure 4. It can be seen in Table 2 Graded Perfect is longer than Graded but is cheaper, this indicates that it routed around areas with higher weighting when compared to the Graded system (Table 2 and Figure 4). The difference in length is 0.71% whereas the difference in costs is 7.9%. Indicating the importance of routing around areas with higher cost weightings. Highlighting the advantages of a predetermined final network when considering known, phased additions.

The difference in routing is clearly visible Figure 4, where the Graded Perfect method has deviated from the original set out in Figure 3. Providing an interesting contrast between partially fixed sections of the infrastructure with that of a fully variable one. The difference between the two networks is most likely due to the prioritisation of cost reduction over pipeline length.

The difference also highlights the potential for many possible routes across the same geographical area.

Here, the cost weightings of the urban and industrial areas have dictated the shape of the routes, specifically the Graded Perfect (Figure 4a) where no pre-existing initial route was enforced. This left the algorithm to find the most cost-effective route across the cluster, leading to a different final network to the Graded results (Figure 4b). To fully assess the impact of the cost weightings on the final network may be altered to bring the Graded Perfect network in line with that of the Graded.

This emphasises inherent uncertainties in pipeline network design, as small changes in decision-making can affect the final network. Such changes can have an impact on overall costs due to differing infrastructure requirements needed to counter pressure drops and cross certain obstacles, so require fully assessing before construction can begin.

Further work will be required to understand the effect of predetermined infrastructures fully.

**Table 2.** Summary of simulated pipelines, with calculated costs based on pipeline lengths, diameters, and operating costs

| Scenario | Total Length (km) | Total cost ($million) |
|---|---|---|
| Graded Perfect | 115.04 | 162.20 |
| Graded | 114.23 | 174.94 |
| % Difference | 0.71 | 7.9 |

## CONCLUSIONS

This work has provided an extension to previous work on pipeline network design that considers topological constraints. Here, the decreased length scale and increased density of point source emitters has provided a unique view of this method.

The Authors have successfully demonstrated its applicability in this case, thus increasing the scope of the method to shorter distances and more densely populated areas. The effect of cost weighting on soft obstacles was presented. The Authors also believe that the consideration of known and unknown final infrastructures will facilitate more informed decision making by allowing for consideration of a wide array of possible arrangements.

Future work should focus on further quantifying the impact of the addition of point source emitters over varying time periods. With particular emphasis on prior knowledge of the final infrastructure. The impact of predetermined sections of infrastructure on final outcomes should also be investigated.

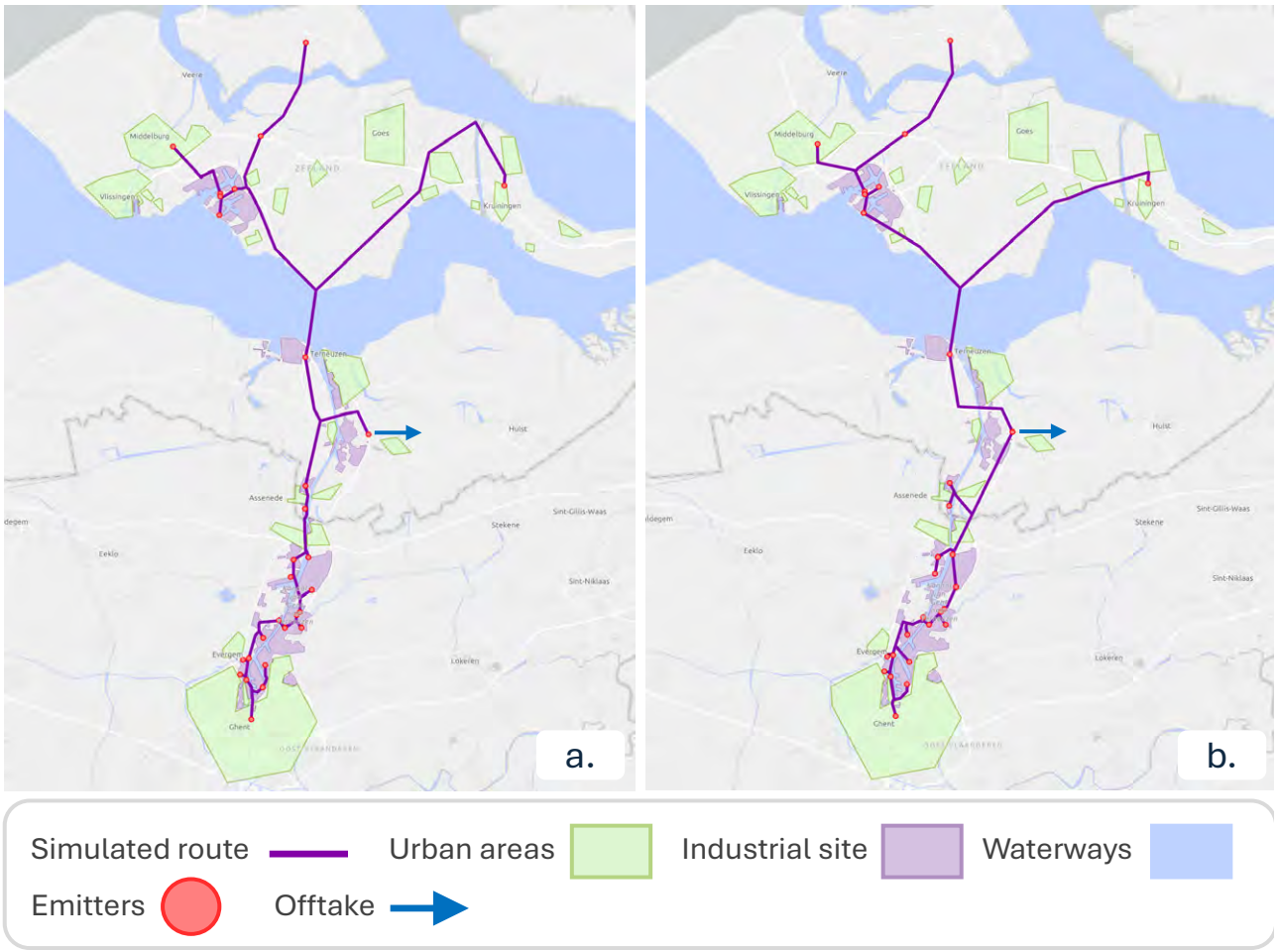



**Figure 4:** The NSP cluster showing the simulated pipeline infracstructure routes with a. Graded Perfect, and b. Graded.

## ACKNOWLEDGEMENTS

This work has received funding from the European Union's Horizon 2020 Research and Innovation program under grant agreements no. 884418 (C4U project).

## REFERENCES

1. The International Energy Agency (IEA). https://www.iea.org/reports/energy-technology-perspectives-2020
2. Realise CCUS. https://realiseccus.eu/ccus-and-refineries/industrial-clusters
3. J. O. Ejeh, S. Brown and D. Roberts. D4.8. Report on Techno-Economic Evaluation of the 2030 North Sea Port cluster. C4U. (2023a)
4. Geske J, Berghout N, van den Broek M. Cost-effective balance between CO2 vessel and pipeline transport - Part 1. Int. J. Greenhouse Gas Control 36:175-188 (2015) https://doi.org/10.1016/j.ijggc.2015.01.026
5. Geske J, Berghout N, van den Broek M. Cost-effective balance between CO2 vessel and pipeline transport - Part 2. Int. J. Greenhouse Gas Control 33:122-134 (2015) https://doi.org/10.1016/j.ijggc.2014.12.005
6. Mechleri E, Brown S, Fennell P, Mac Dowell N. CO2 capture and storage (CCS) cost reduction via infrastructure right sizing. Chemical Engineering Research and Design 119:130-139 https://doi.org/10.1016/j.cherd.2017.01.016
7. D'Amore F, Romano M, Bezzo F, Optimal design of European supply chains for carbon capture and storage from industrial emission sources including pipe and ship transport. Int. J. Greenhouse Gas Control 109, 103372. (2021) https://doi.org/10.1016/j.ijggc.2021.103372
8. Romano M, Anantharaman R, Arasto A, Can Ozcan D, Ahn H, Wilco Dijkstra J, Carbo M, Boavida D. Application of advanced technologies for CO2 capture from industrial sources. Energy Procedia 37: 7176-7185 (2013)

https://doi.org/10.1016/j.egypro.2013.06.655
9. Grant T, Guinan A, Shih C, Lin S, Vikara D, Morgan D, Remson D. Comparative analysis of transport and storage options from a CO2 source perspective. Int. J. Greenhouse Gas Control 72:175–191 (2018) https://doi.org/10.1016/j.ijggc.2018.03.012
10. Knoope M, Ramírez A, Faaij P. A state-of-the-art review of techno-economic models predicting the costs of CO2 pipeline transport. Int. J. Greenhouse Gas Control 16, 241–270 (2013) https://doi.org/10.1016/j.ijggc.2013.01.005
11. Wilkes M, Mukherjee, S, Brown, S. Linking CO2 capture and pipeline transportation: sensitivity analysis and dynamic study of the compression train. Int. J. Greenhouse Gas Control 111: 103449 (2021) https://doi.org/10.1016/j.ijggc.2021.103449
12. BS EN 10208-2 Steel pipes for pipelines for combustible fluids. Technical delivery conditions - Pipes of requirement class B. (2009)
13. ISO 6708:1995(en) Pipework components — Definition and selection of DN (nominal size)
14. Heijnen W, Ligtvoet A, Stikkelman M, Herder M. Maximising the worth of nascent networks. Networks and Spatial Economics: 14, 27-46 (2013) https://doi.org/10.1007/s11067-013-9199-1
15. André J, Auray S, Brac J, Wolf D, Maisonnier G, Ould-Sidi M, Simonnet A. Design and dimensioning of hydrogen transmission pipeline networks: European Journal of Operational Research229, 239-251 (2013) https://doi.org/10.1016/j.ejor.2013.02.036
16. Parolin F, Colbertaldo P, Campanari S. Development of a multi-modality hydrogen delivery infrastructure: An optimization model for design and operation. Energy Conversion and Management: 266 (2022) https://doi.org/10.1016/j.enconman.2022.115650
17. Rosenberg M, French T, Reynolds M, While L. A genetic algorithm approach for the Euclidean Steiner tree problem with soft obstacles. Genetic and Evolutionary Computation Conference 618-626 (2021) https://doi.org/10.1145/3449639.3459397
18. Kruskal J. On the shortest spanning subtree of a graph and the traveling salesman problem. Proceedings of the American Mathematical Society 7:48–50 (1956) https://doi.org/10.2307/2033241
19. Ejeh J, Martynov S, Brown S. An MINLP model for the optimal design of CO2 transportation infrastructure in industrial clusters. Computer Aided Chemical Engineering 52:3085-3090 (2023b) https://doi.org/10.1016/B978-0-443-15274-0.50492-3
20. Hammond J, Rosenburg M, Brown S. Understanding Costs in Hydrogen Infrastructure Networks: A Multi-Stage Approach for Spatially-Aware Pipeline Design. Int. J. Hydrogen Energy 102:430-443 (2025). https://doi.org/10.1016/j.ijhydene.2024.12.273
21. Abrell J. EUETS.INFO
22. Hammond J, Rosenburg M, Brown S. A Genetic Algorithm-Based Design for Hydrogen Pipeline Infrastructure with Real Geographical Constraints. Computer Aided Chemical Engineering 53:631-636 (2024) https://doi.org/10.1016/B978-0-443-28824-1.50106-X

© 2025 by the authors. Licensed to PSEcommunity.org and PSE Press. This is an open access article under the creative commons CC-BY-SA licensing terms. Credit must be given to creator and adaptations must be shared under the same terms. See https://creativecommons.org/licenses/by-sa/4.0/



Systems & Control Transactions

**Research Article - Peer Reviewed Conference Proceeding**
ESCAPE 35 - European Symposium on Computer Aided Process Engineering
Ghent, Belgium. 6-9 July 2025
Jan F.M. Van Impe, Grégoire Léonard, Satyajeet S. Bhonsale,
Monika E. Polańska, Filip Logist (Eds.)

PSE PRESS

# Flow Simulation of Plastic Life Cycle Considering Carbon Renewability and Environmental Impact

**Kota Chida[a], Heng Yi Teah[b], Yuichiro Kanematsu[b], Yasunori Kikuchi[a,b,c]***

[a] Department of Chemical System Engineering, The University of Tokyo, Bunkyo-ku, Tokyo, Japan
[b] Presidential Endowed Chair for "Platinum Society", The University of Tokyo, Bunkyo-ku, Tokyo, Japan
[c] Institute for Future Initiatives, The University of Tokyo, Bunkyo-ku, Tokyo, Japan
* Corresponding Author: ykikuchi@ifi.u-tokyo.ac.jp

## ABSTRACT

Renewable carbon sources, such as biomass and waste, are being explored as alternatives for sustainable plastic production. However, the significant uncertainties surrounding the environmental impact of biomass supply processes raise questions about whether these plastics positively contribute to society. Furthermore, the lack of systematic knowledge about plastics and incomplete understanding among stakeholders pose challenges to conducting comprehensive assessments and designing effective plastic life cycle systems. This study aims to clarify the carbon flow within the life cycle of biomass- and recycled-derived plastics and to design a plastic life cycle that enables the introduction of renewable carbon sources. To this end, the study analyzed the structure of plastics containing renewable carbon and conducted a flow analysis of packaging plastics in Japan. The flow analysis was conducted in the form of an optimization problem. Greenhouse gas (GHG) emissions and the proportion of renewable carbon were selected as assessment indicators and objective functions. Constraints for optimization included the availability of biomass supply, the demand for product resins, and the processing capacity of various End-of-Life (EoL) methods. As a result, it was revealed that the priority of resin types to be produced and recycled shifts in response to changes in constraints such as biomass input and recycling capacity. Furthermore, a trade-off between reducing environmental impact and increasing the renewability of carbon was identified, highlighting the necessity of designing systems that balance these factors. This research provides valuable insights for designing sustainable plastic life cycles in the future.

**Keywords**: Life Cycle Analysis, Flow analysis, Biomass-derived plastic, Recycling, Carbon renewability

## INTRODUCTION

Fossil-based plastics, owing to their convenience, are materials that contribute significantly to modern societal benefits. However, their production and disposal are accompanied by substantial environmental challenges, including GHG emissions [1] and the issue of marine plastic pollution [2], making it clear that urgent countermeasures are required. Plastics derived from biomass or recycled materials utilize sustainable carbon sources and are considered to emit lower GHG levels across their life cycles. As such, their broader adoption is being explored as an alternative to conventional fossil-based plastics. Research on the environmental impacts of these plastics has been vigorous. For instance, case studies employing life cycle assessment (LCA) have assessed the environmental and economic impacts of specific plastics, such as PHBH (Poly(3-hydroxybutyrate-co-3-hydroxyhexanoate)) and Bio-PE, comparing them to traditional fossil-derived plastics [3, 4]. Nevertheless, it remains unclear whether the adoption of these materials will genuinely yield positive environmental and societal outcomes. Variations in environmental assessments arise due to differences in factors such as the type of biomass used as feedstock, resin production processes, and geographic boundaries. Moreover, comprehensive and quantitative assessments of the environmental impacts that arise from introducing multiple resins into existing societal systems remain scarce. A further complication is the incomplete understanding of the carbon flow pathways within the plastic life cycle. This lack of clarity weakens the connections between stakeholders involved

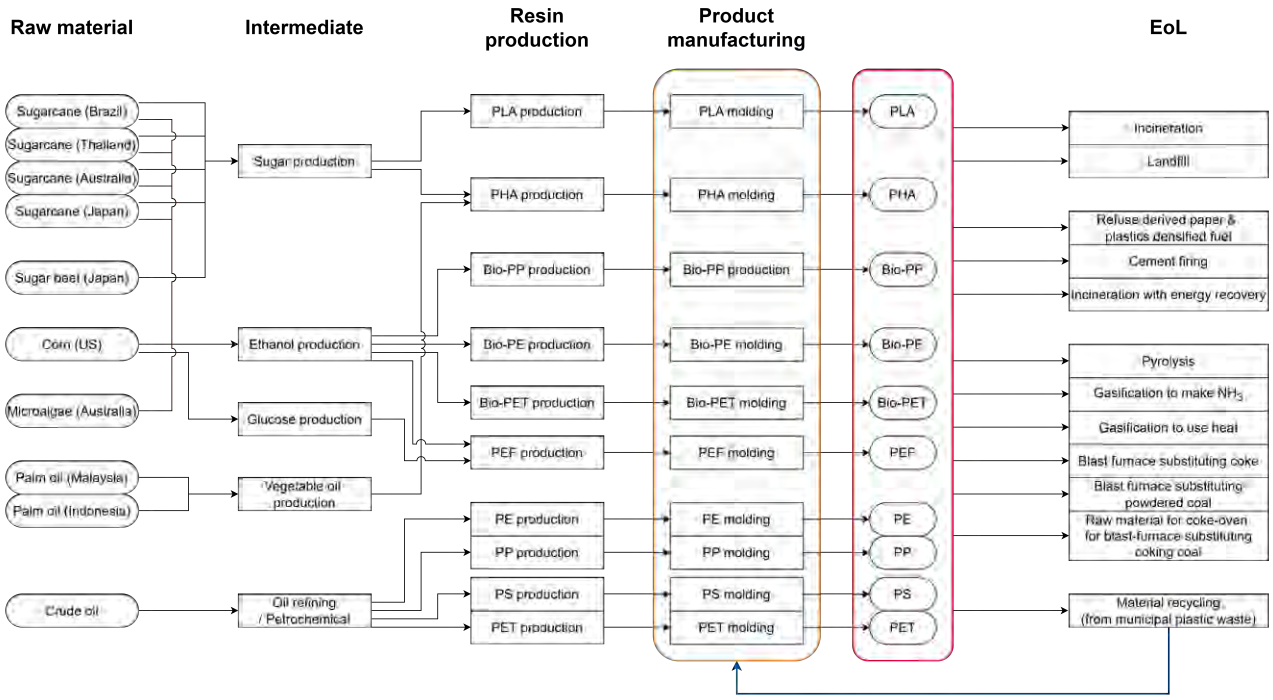



**Figure 1:** The life cycle of plastics considered in the flow analysis.

in various stages of the plastic life cycle, creating challenges in designing flexible, sustainable life cycles aligned with a sustainable society.

This study first aims to elucidate the potential changes in the overall carbon life cycle brought about by the introduction of plastics derived from biomass and recycled carbon sources. Building on this understanding, it aims to conduct a flow analysis from the perspectives of environmental impact and carbon renewability. Ultimately, the study aspires to design more sustainable life cycles that facilitate the adoption of biomass- and recycled-derived plastics.

# METHOD

## Assessment targets / indicators

In this study, a case analysis was conducted, focusing exclusively on plastics used for packaging applications in Japan. The resins selected for assessment included conventional fossil-derived plastics commonly used in packaging (PE, PP, PS, PET) as well as biomass-derived plastics such as Bio-PE, Bio-PP, Bio-PET, PEF (Polyethylene Furanoate), PHA (Polyhydroxyalkanoates), and PLA (Poly-Lactic Acid). PHA, PLA, and PEF were chosen as examples of biomass-derived plastics with either significant current production volumes or well-established manufacturing technologies [5]. Meanwhile, Bio-PE, Bio-PP, and Bio-PET were selected to explore the feasibility of substituting existing fossil-based plastics with biomass-derived counterparts that possess identical physical properties. Additionally, recycled resins produced through material recycling of these plastics were also included in the assessment.

The assessment criteria were established based on challenges identified in the current plastic life cycle. Climate change, measured through GHG emissions, was selected as the key indicator for assessing environmental impacts. To quantify the renewability of carbon within the life cycle, the amount of renewable carbon (sourced from biomass or recycling) within the system was adopted as a supplementary indicator.

## System boundaries

To establish the system boundary, a bibliometric analysis was first conducted to cluster relevant literature, extracting key terms associated with the resins and technologies under assessment. Subsequently, based on these keywords, an extensive review of existing literature on plastics was carried out. Information on raw materials, manufacturing methods, applications, and EoL strategies—including those not yet commercialized—was collected for various plastics. This data facilitated the creation of a superstructure for the plastic lifecycle [6]. The superstructure revealed that the introduction of renewable carbon into the plastic system creates numerous combinations of technologies at both the raw material and EoL stages [7, 8]. The choice of raw material, the resulting resin, and the selection and combination of EoL

strategies significantly influence the environmental impact and carbon renewability across the entire lifecycle. The system boundary for analyzing the flow of plastic packaging materials was constructed based on this superstructure, as illustrated in **Figure 1**. In this study, sugarcane, sugar beet, corn, microalgae, and palm oil were considered as biomass feedstock options. The geographic boundaries for each raw material were also taken into account. The raw materials are processed into plastics via intermediate products such as sugar, bioethanol, starch, and vegetable oils. For waste plastics, the EoL options examined included no-recovery methods like incineration and landfilling, as well as energy recovery, non-closed-loop chemical recycling, and closed-loop material recycling.

## Model construction

A linear programming approach was employed to optimize the flow. The objective functions for environmental impact and carbon renewability were defined as shown in equations (1) and (2), respectively, and calculations were performed for each.

$$\text{Min. } G_{total} = \sum_{mat}^{all}\sum_{tech}^{all}\sum_{resin}^{all} M_{mat,tech,resin}E_{mat,tech,resin} + \sum_{resin}^{all}\sum_{EoL}^{all} M_{resin,EoL}E_{resin,EoL} \quad (1)$$

$$\text{Min. } W_{total} = \sum_{\text{mat}}^{fossil}\sum_{tech}^{all}\sum_{resin}^{all} M_{mat,tech,resin} + w \cdot G_{total} \left(w \cdot G_{total} \ll M_{mat,tech,resin}\right) \quad (2)$$

Here, M [t] represents the mass of product resin in the equation, E [t-$CO_2$ eq/t-product] denotes the GHG emission factor, and w [–] signifies the weighting coefficient in the weighted sum method. The second term in equation (2) is provided to manage the flows at the product's EoL stage, excluding material recycling processes that do not affect carbon renewability. GHG emission factors and inventory data for each process in the equations were primarily sourced from the literature. The details of the data sources are provided in the supplementary information. The constraints considered include technological feasibility, the supply availability of various biomass feedstocks, the demand for product resins, and the processing capacities of each EoL method. Technological feasibility was defined such that M = 0 t for flows deemed infeasible or excluded under specific cases. The upper limits for biomass supply were set based on the current production ratios for each raw material and were assumed to vary proportionally while maintaining these ratios. The demand for product resins was estimated from the current consumption volumes (assumed equal to production volumes) of PE, PP, PS, and PET in packaging applications [9], representing the functional requirements plastics must fulfill in society. It was assumed that these functional requirements would remain unchanged even if replaced with renewable carbon-derived plastics. For substitution with other resin types, calculations were based on prior studies comparing the environmental impacts of bio-based and fossil-based plastics [10-12], assuming resins of the same volume have equivalent functionality. The upper limits for the processing capacities of EoL methods were determined using data on the current processing volumes for each method in Japan.

In this study, three cases, as shown in **Table 1**, were examined to visualize changes in the life cycle due to variations in constraint conditions. Case I and Case II represent cases in which the availability of biomass supply improves, while Case III alters the values of constraint conditions related to both the biomass supply and the capacity for material recycling processing. In Case I, the production of all resins shown in **Figure 1** is considered. In contrast, Case II excludes PHA from the target resins, reflecting the fact that the life cycle of PHA is not yet well established. All other constraint conditions and parameters are set identically.

# RESULTS AND DISCUSSIONS

**Figure 2** presents the results of GHG emission optimization in Case I based on Equation (1). The horizontal

**Table 1:** Cases of Future Changes in Plastic Life Cycles Considered in the Flow Analysis

| | Case I | Case II | Case III |
|---|---|---|---|
| **Assessment targets** | All plastics shown in Figure 1 | Excluding PHA from Case I | All plastics shown in Figure 1 |
| **Biomass Supply Potential** | Variable | Variable | Constant (1% of the production volume of each biomass material is available for use) |
| **Recycling capacity** | Constant (equivalent to current capacity) | Constant (equivalent to current capacity) | Variable |

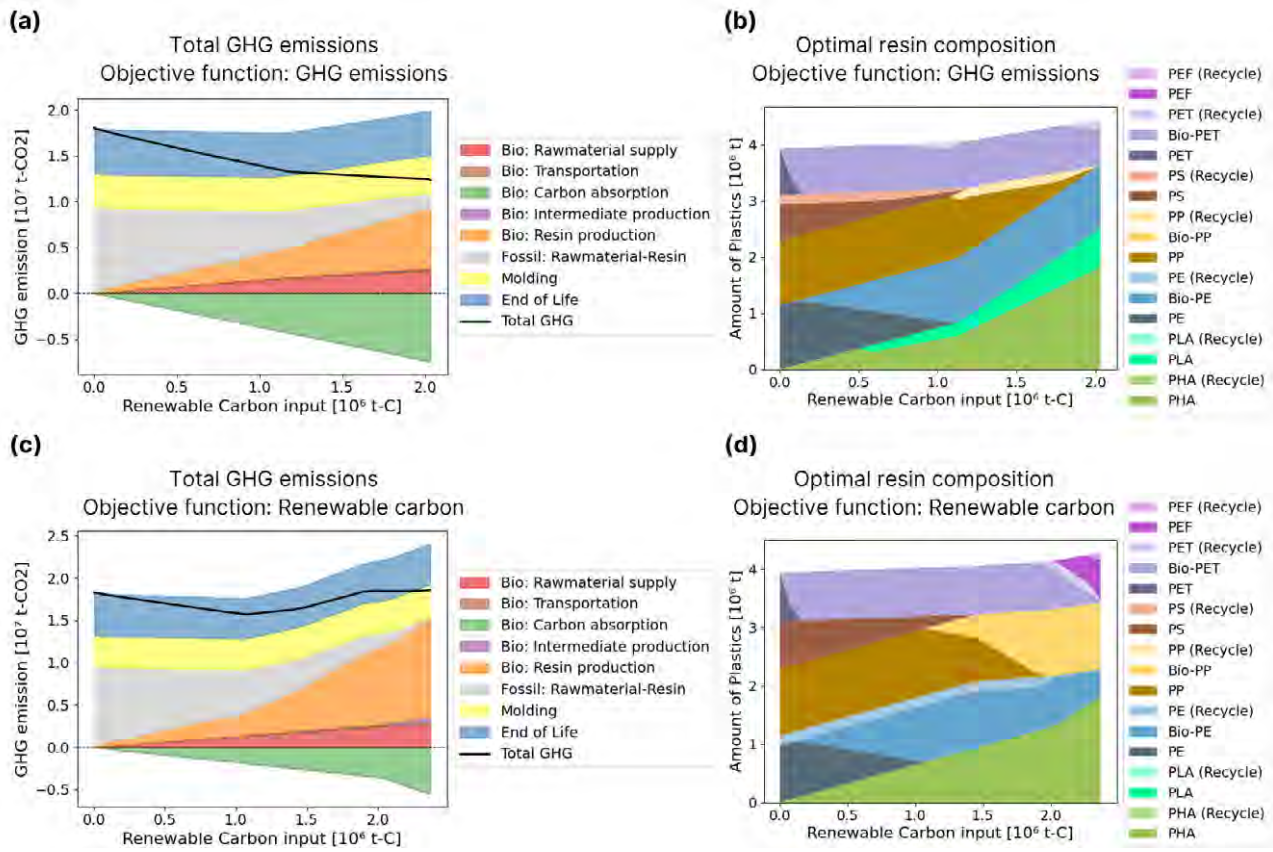



**Figure 2:** Flow analysis results for Case I. (a, c) Objective function: GHG emissions (b, d) Objective function: Renewable carbon within the system. The left-hand diagram shows the changes in the contribution of GHG emissions from each life cycle stage within the system, corresponding to variations in the amount of renewable carbon introduced. The right-hand diagram illustrates the changes in the types of resin products as the amount. of renewable carbon introduced varies.

axis represents the amount of renewable carbon introduced into the system. The points at which the slope of total GHG emissions changes in **Figures 2(a) and 2(c)** correspond to shifts in the types of resins prioritized for production or recycling, as well as transitions in the raw materials used for production, as shown in **Figures 2(b) and 2(d)**. As shown in **Figure 2(a)**, GHG emissions decrease with increasing biomass input, demonstrating the superiority of biomass from the perspective of GHG emission reduction. This reduction is primarily attributed to carbon sequestration during biomass cultivation. Additionally, regardless of the level of biomass input, various life cycle stages—such as raw material supply, carbon absorption by biomass, resin production, and EoL processes—significantly contribute to the total GHG emissions of container and packaging plastics. This highlights the necessity of designing the system across the entire life cycle. **Figure 2(b)** reveals that PET should be replaced with Bio-PET and PS should be substituted with PHA or recycled alternatives as a priority. This indicates that considering the environmental burdens of biomass feedstock and the avoided impacts of recycling, these substitutions achieve significant reductions in GHG emissions. **Figures 2(c) and 2(d)** illustrates the results when minimizing the amount of fossil-derived carbon within the system in Case I. By introducing approximately 2.3 Mt of renewable carbon, defossilization within the system was achieved. Compared to the GHG-optimized result, as seen in **Figure 2(d)**, the types and order of resins prioritized for introduction or recycling differ, with Bio-PP introduction and PE recycling taking precedence. However, as shown in **Figure 2(c)**, a trade-off was observed in which the total net GHG emissions increased with biomass introduction. This suggests that balancing environmental impacts and renewability must be carefully considered when designing a sustainable system reliant on biomass.

In the GHG optimization results for Case II, PLA and PEF were selected as biomass applications instead of PHA, which was prioritized for introduction in Case I but was absent in Case II. However, as PLA and PEF are less advantageous than PHA in terms of environmental impact, the system's total GHG emissions increased by up to 4% during the renewable carbon introduction process.

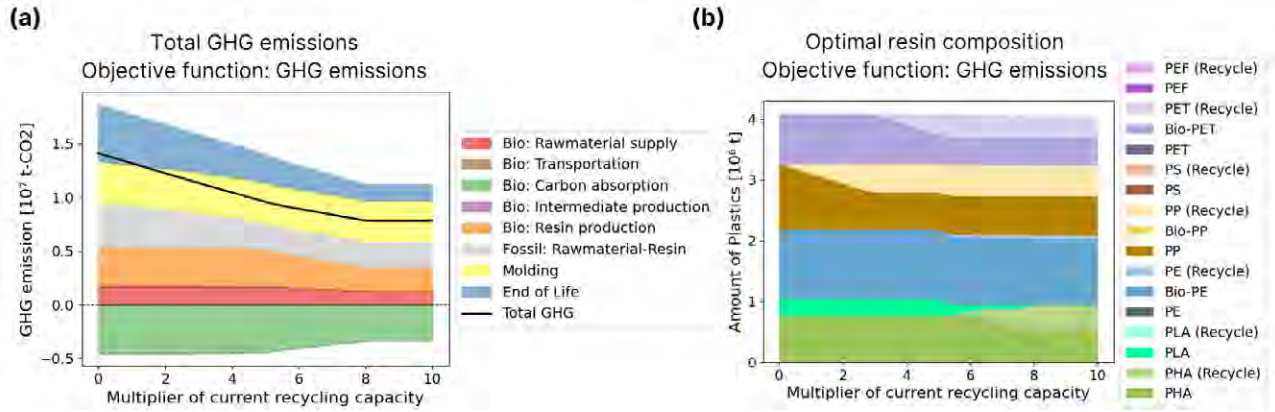



**Figure 3:** Flow analysis results for Case III (Objective function: GHG emissions) Figure 3(a) shows the changes in the contribution of GHG emissions from each life cycle stage within the system, corresponding to variations in the recycling capacity. Figure 3(b) illustrates the changes in the types of resin products resulting from variations in recycling capacity.

**Figure 3** presents the results of GHG emission optimization in Case III, based on Equation (1). The horizontal axis represents the multiplier relative to the current material recycling capacity. From the results in **Figure 3(b)**, it is evident that material recycling is prioritized in the order of PP, PET, and PHA. This prioritization reflects the combined environmental impact of recycling itself and the avoided environmental burden of raw material supply, favoring resins with the greatest reduction potential. As shown in **Figure 3(a)**, an increase in the upper limit of recycling capacity leads to a monotonic decrease in the system's overall GHG emissions, supporting the effectiveness of recycling. However, when the input of biomass feedstock is low, increasing recycling capacity beyond a certain point no longer impacts the objective function value, and complete defossilization remains unachieved. At this stage, the proportion of carbon derived from recycling is approximately 30-40%. This limitation arises from incorporating the substitution rate into the model to account for the degradation in quality of recycled materials. These findings suggest that, while recycling is effective, achieving greater system renewability requires the continued expansion of biomass feedstock introduction. Furthermore, closed-loop chemical recycling methods, such as repolymerization, which were not considered in this study, have the potential to reintegrate plastics into their life cycle while maintaining high quality. Such methods may offer advantages over the currently considered EoL processes in terms of both environmental impact and resource renewability [13, 14]. Therefore, incorporating these advanced recycling methods into flow analysis is essential for designing a more sustainable life cycle.

## CONCLUSIONS

In this study, a flow analysis methodology was developed to assess the plastic life cycle in Japan's packaging sector, focusing on the introduction of biomass-derived and recycled carbon. The assessment was conducted from the perspectives of environmental impact and carbon renewability. The findings revealed the types of resins that should be prioritized for production and recycling under constrained conditions, such as limited biomass supply and recycling capacity, as well as the effects of such prioritization. Furthermore, it was demonstrated that a trade-off may exist between reducing GHG emissions and improving carbon renewability. Achieving a low-GHG, decarbonized system requires the dual advancement of biomass utilization and recycling expansion.

The developed flow analysis framework is adaptable to changes in assessment targets, technologies, and variables. Future expansions of the model should incorporate additional applications, resin types, and processes, including chemical recycling, to enable more comprehensive flow analyses. Moreover, sustainability discussions should assess additional environmental indicators, such as eutrophication—which may be significantly affected by the introduction of biomass—and the potential for introducing biodegradable plastics, taking into account plastic leakage into the environment. Taking these considerations into account, a sustainable life cycle should be carefully designed through scenario analysis that takes into account future system changes.

## DIGITAL SUPPLEMENTARY MATERIAL

For a detailed explanation of the methodology for system boundary construction and the data sources

used for flow analysis model construction, including GHG emission intensities, please refer to the supplementary material available at https://psecommunity.org/LAPSE:2025.0040.

## ACKNOWLEDGEMENTS

This study partially includes outcomes from the NEDO commissioned project (JPNP20012), the JST COI-NEXT program for co-creation support (JPMJPF2003), the Environment Research and Technology Development Fund (Grant Number JPMEERF20243004) of the Environmental Restoration and Conservation Agency of Japan, and the Grants-in-Aid for Scientific Research program (JP23K21780). The University of Tokyo's "Platinum Society" Endowed Chair operates with contributions from Mitsui Fudosan Co., Ltd., Sekisui House, Ltd., East Japan Railway Company, and Toyota Tsusho Corporation.

## REFERENCES

1. Zheng, J., & Suh, S., Strategies to reduce the global carbon footprint of plastics. Nat. Clim. Change., 9(5), 374-378 (2019) https://doi.org/10.1038/s41558-019-0459-z
2. Wu, P., Huang, J., Zheng, Y., Yang, Y., Zhang, Y., He, F., Chen, H., Quan, G., Yan, J., Li, T. & Gao, B. Environmental occurrences, fate, and impacts of microplastics. Ecotoxicol. Environ., 184, 109612 (2019) https://doi.org/10.1016/j.ecoenv.2019.109612
3. Amasawa, E., Yamanishi, T., Nakatani, J., Hirao, M., & Sato, S., Climate change implications of bio-based and marine-biodegradable plastic: evidence from poly (3-hydroxybutyrate-co-3-hydroxyhexanoate). Environ. Sci. Technol., 55(5), 3380-3388 (2021) https://doi.org/10.1021/acs.est.0c06612
4. Gursel, I. V., Moretti, C., Hamelin, L., Jakobsen, L. G., Steingrimsdottir, M. M., Junginger, M., Høibye, L. & Shen, L. Comparative cradle-to-grave life cycle assessment of bio-based and petrochemical PET bottles. Science of The Total Environment, 793, 148642 (2021) https://doi.org/10.1016/j.scitotenv.2021.148642
5. European Bioplastics, Bioplastics market development update 2023 https://www.european-bioplastics.org/bioplastics-market-development-update-2023-2/
6. Hasebe, S., Process synthesis using superstructures (in Japanese). Oukan, 10(1), 38-46 (2016) https://doi.org/10.11487/trafst.10.1_38
7. Verlinden, R. A., Hill, D. J., Kenward, M. A., Williams, C. D., & Radecka, I., Bacterial synthesis of biodegradable polyhydroxyalkanoates. J. Appl. Microbiol., 102(6), 1437-1449 (2007) https://doi.org/10.1111/j.1365-2672.2007.03335.x
8. Li, K., Liu, S., & Liu, X. An overview of algae bioethanol production. Int. J. Energy Res., 38(8), 965-977 (2014) https://doi.org/10.1002/er.3164
9. Plastic Waste Management Institute, An Introduction to Plastic Recycling in Japan 2024 (in Japanese)
10. Choi, B., Yoo, S., & Park, S. I. Carbon footprint of packaging films made from LDPE, PLA, and PLA/PBAT blends in South Korea. Sustainability, 10(7), 2369 (2018) https://doi.org/10.3390/su10072369
11. Suwanmanee, U., Varabuntoonvit, V., Chaiwutthinan, P., Tajan, M., Mungcharoen, T., & Leejarkpai, T. Life cycle assessment of single use thermoform boxes made from polystyrene (PS), polylactic acid,(PLA), and PLA/starch: cradle to consumer gate. Int. J. Life Cycle Assess., 18, 401-417 (2013) https://doi.org/10.1007/s11367-012-0479-7
12. Papong, S., Malakul, P., Trungkavashirakun, R., Wenunun, P., Chom-in, T., Nithitanakul, M., & Sarobol, E. Comparative assessment of the environmental profile of PLA and PET drinking water bottles from a life cycle perspective. J. Cleaner Prod., 65, 539-550 (2014) https://doi.org/10.1016/j.jclepro.2013.09.030
13. Uekert, T., Singh, A., DesVeaux, J. S., Ghosh, T., Bhatt, A., Yadav, G., Afzal, S., Walzberg, J., Knauer, K. M., Nicholson, S. R., Beckham. G. T. & Carpenter, A. C. Technical, economic, and environmental comparison of closed-loop recycling technologies for common plastics. ACS Sustainable Chem. Eng., 11(3), 965-978 (2023) https://doi.org/10.1021/acssuschemeng.2c05497
14. Kara, S., Hauschild, M., Sutherland, J., & McAloone, T. Closed-loop systems to circular economy: A pathway to environmental sustainability? CIRP Ann., 71(2), 505-528 (2022) https://doi.org/10.1016/j.cirp.2022.05.008

© 2025 by the authors. Licensed to PSEcommunity.org and PSE Press. This is an open access article under the creative commons CC-BY-SA licensing terms. Credit must be given to creator and adaptations must be shared under the same terms. See https://creativecommons.org/licenses/by-sa/4.0/



Systems & Control Transactions

**Research Article - Peer Reviewed Conference Proceeding**
ESCAPE 35 - European Symposium on Computer Aided Process Engineering
Ghent, Belgium. 6-9 July 2025
Jan F.M. Van Impe, Grégoire Léonard, Satyajeet S. Bhonsale,
Monika E. Polańska, Filip Logist (Eds.)

PSE PRESS

# A Digital Scheduling Hub for Natural Gas Processing: a Petrobras Case-Study Using Rigorous Process Simulation

**Tayná E. G. Souza[a,b]*, Letícia C. dos Santos[a], Caio R. Soares[c,d]**

[a] Petrobras: Petróleo Brasileiro S.A., Brazil
[b] Federal University of Rio de Janeiro, Chemical Engineering Program/COPPE, Rio de Janeiro, RJ, Brazil
[c] Celiga Electric Maintenance Ltda, Brazil
[d] Federal University of Rio de Janeiro, School of Chemistry, Rio de Janeiro, RJ, Brazil
* Corresponding Author: taynaegs@petrobras.com.br.

## ABSTRACT

To address the dynamic operational demands of the gas processing sector, which is continuously evolving due to gas market opening, increase in natural gas production, and the growing challenge of upstream-midstream integration in a competitive environment, this work presents the Integrated-Gas-Scheduling-System, IntegraGAS. The proposed methodology innovates by using first principles rigorous process simulation coupled with a scheduling tool for short/medium/long-term, enabling gas plants to swiftly adapt to varying operational conditions and meet the requirements of this new market. IntegraGAS was implemented in Petrobras and has significantly enhanced scheduling efficiency, reducing execution time by up to 99.2% and avoiding approx. US$ 2.3 million in annual labor costs, optimizing resource utilization. By integrating Excel for the frontend, Aspen HYSYS for process simulation, VBA for automation, and Microsoft PowerBI for real-time data visualization, IntegraGAS improves decision-making, regulatory compliance, and operational agility. Its key functionalities include alerts for operational limit violations, automated mass and energy balance calculations, optimized gas allocation, integration with maintenance shutdown plans and KPI monitoring. With an intuitive interface and a robust architecture driven by digital transformation, IntegraGAS eliminates manual inefficiencies, ensures seamless coordination among stakeholders, and enables rapid responses to market dynamics.

**Keywords**: Scheduling, Modelling and Simulations, Natural Gas, Planning, Planning & Scheduling, additional keywords separated by commas

## INTRODUCTION AND OBJECTIVES

Natural gas processing plays a pivotal role in the oil and gas production chain, being responsible for treating the raw gas and separating impurities that can impair product quality [1]. This process not only ensures that gas meets the standards for end-use, but also maximizes production efficiency and resource value. Furthermore, in the context of global energy transition, natural gas is gaining increasing relevance due to its ability to function as an intermediary energy source — cleaner than oil and coal, yet still essential to meet global energy demand while renewable alternatives are not fully viable [1, 2].

In Brazil, the importance of natural gas processing has been further accentuated by the development of pre-salt reserves, where the high gas-oil ratio is a challenge, creating a need for advanced infrastructure for its processing and commercialization. This gas must be separated and appropriately treated before being transported or utilized. Therefore, the increase in natural gas production demands efficient and innovative solutions, both to optimize industrial operations and to ensure competitiveness in the global energy market.

The opening of the gas market in Brazil, driven by recent regulatory reforms, has marked a significant change in the country's energy sector [3]. With the approval of Law 11.909/2009, all companies gained access to gas transportation and processing infrastructure, previously restricted to the owner of the processing facility. This move aims to increase competitiveness, reduce gas

costs, stimulate investments in new infrastructure and contribute to the diversification of supply sources, which is essential for national energy security [3, 4]. This new framework thus yielded a more dynamic, fast-paced and complex multi-party environment.

Gas market opening has introduced new operational and logistic challenges, particularly regarding management and scheduling of gas processing and its products. Previously centralized within a single player, scheduling now involves a multitude of stakeholders with varying demands and priorities. The complexity has increased as each economic actor requires dynamic and efficient management to handle its products, ensure contract compliance, transport optimization, cost management and adherence to regulatory standards [3, 4].

In this context, scheduling of natural gas processing plants has become a critical process, as production planning needs to be frequently adjusted to meet variable demand while simultaneously optimizing resources. The need to perform detailed and accurate simulations to manage multiple scenarios, involving variables such as gas flowrates, processing capacity and contractual requirements, calls for more elaborated tools [3, 4].

Whereas traditional works on chemical production scheduling rely on simplified models (linearized versions of highly nonlinear systems and/or recovery factors) [7] and do not consider key process variables such as flows, compositions and temperatures [7], this is no longer sufficient to address the complexity of this new context. This work intends to fill this gap by proposing an innovative integrated first principles scheduling methodology and applying it into a digital-based tool for industrial application. Throughout this article, the details of IntegraGAS implementation at Petrobras, observed benefits, and its contributions to the digital transformation of the natural gas sector will be explored.

## METHODOLOGY

To reach the objective of this work, a practical case study was chosen for proof of concept and industrial application: Petrobras integrated natural gas processing assets. IntegraGAS was developed, tested and applied at each gas asset for: plant modeling, automation, integration and management of the scheduling processes. The next subsections will cover details on the case-study system, plant modeling and computational aspects that yielded IntegraGAS.

### System Description

The system in study consists of four industrial gas processing assets: UTGC, UTGCA, UTGCAB and UTGITB. They are part of Petrobras natural gas processing area, which is illustrated in Figure 1. In each of those midstream assets, three main scheduling processes are carried out; they vary in time-horizon, level of detail required from planning and frequency, as detailed in Table 1.




**Figure 1.** Illustration of Petrobras integrated natural gas processing system, showing the connections between upstream and midstream (UTGC, UTGCA, UTGCAB, UTGITB) facilities along Brazil coast.

**Table 1:** The three scheduling processes that are considered in this work. Details include the number of simulation scenarios, time basis and frequency of each of them.

| Time horizon | Simulation scenarios | Time basis | Frequency |
|---|---|---|---|
| Short | 30 | days | daily |
| | 92 | days | monthly |
| Medium | 15 | months | monthly |
| Long | 12 | months | annually |
| | 15 | years | annually |

### Plant Modeling

Unlike most scheduling tools [7], this work chose a first principles rigorous approach for plant modeling. This decision was based on business evaluation, considering that the requirements of this new dynamic market scenario are not anymore satisfied by classic simplified approaches, such as recovery factors and linear models.

Aspen HYSYS was the commercial simulator chosen for all plant modeling, due to its widespread usage and peer-recognition for natural gas processing simulation. Every asset had its specific first-principles process model, as illustrated in Figure 2. Each model was developed in the light of the current official plant Process Flow Diagrams (PFDs), allowing for rigorous and accurate representation of the industrial asset as well as for easy verification and third-party auditing of the model and its results. Proper model validation was then carried out along with the plant Operations team, by comparing product flowrate outputs, per model, against actual data.

The simulations were specifically tailored for scheduling application, ensuring appropriate compromise between model fit, execution time and open-market transparency requirements. Also, an extensive engineering work was carried out on mapping key process plant variables, i.e. the ones to which production scheduling was

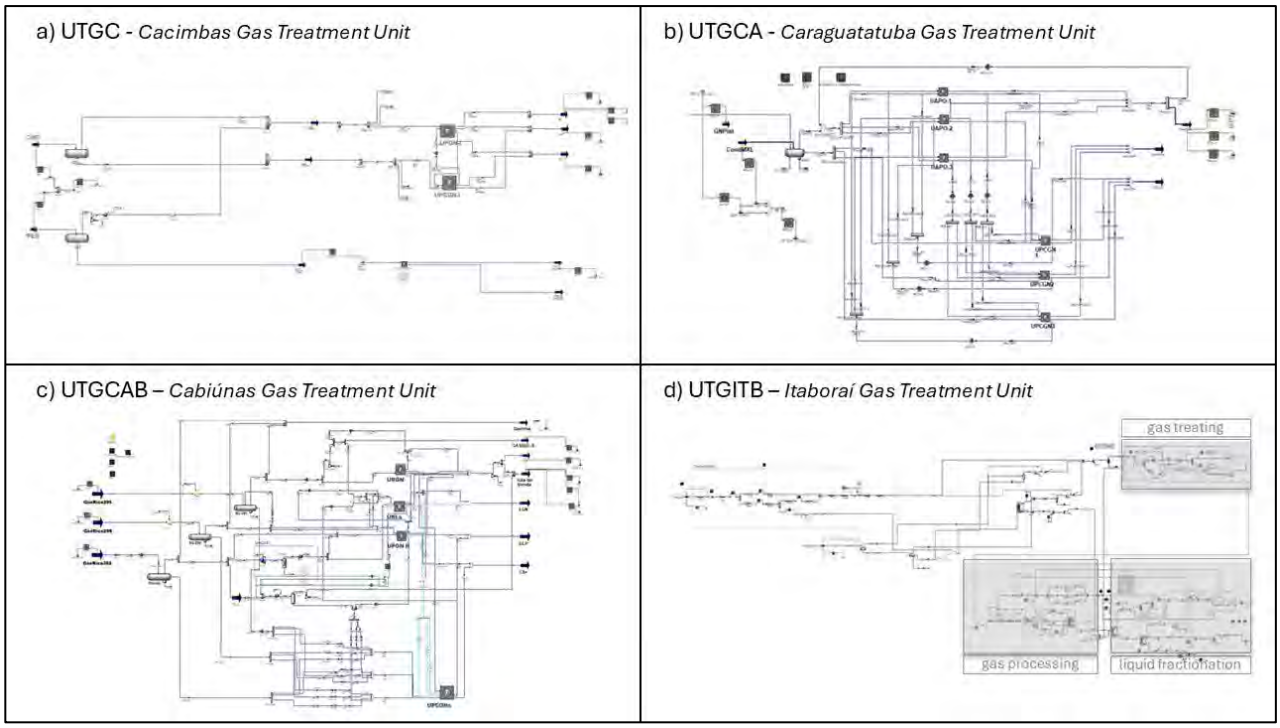



**Figure 2.** Representation of the main flowsheet from Aspen HYSYS simulation model of UTGC (a), UTGCA (b), UTGCAB (c) and UTGITB (d).

the most sensitive and adding them as frontend user inputs (manipulated variables at IntegraGAS) in two levels: a) main and b) specific.

## Computational aspects

### Architecture

IntegraGAS architecture was conceived based on the following business goals: (1) plant modeling should be rigorous and executed on recognized commercial process simulator; (2) interface and usability should be user-friendly and easy for Process Engineers to adapt, thus increasing software adoption; (3) software maintainability and improvement should be easy and fast to implement, in accordance with business dynamics.

Based on these criteria, IntegraGAS architecture used Microsoft Excel for the frontend, VBA (Visual Basic for Applications) for engine calculations and an OLE connection between VBA and Aspen HYSYS to enable automated rigorous process simulation, as seen in Figure 3.

From Figure 3, it is important to emphasize that IntegraGAS connection with plant modeling was such that HYSYS simulation files stay totally transparent to the end user, who interacts only with the application frontend (Excel). Thus, while IntegraGAS robustly guarantees accurate and rigorous process simulation results, it is not necessary for the end user to be familiar with HYSYS, keeping the access to IntegraGAS simple and easy to use throughout a wide range of users from the gas plants. This is especially important for this application, since the short-time scheduling process is required by contract to be executed every day, even on weekends; this means that different shifts will be working to meet this process.




**Figure 3.** IntegraGAS architecture made in this work.

### Features

IntegraGAS is organized into three main sections, designed to address the scheduling processes detailed in Table 1. Each section incorporates functionalities that enhance user efficiency and ensure seamless integration with operational workflows:

1. **Data input:** streamlines the collection and consolidation of raw gas data by integrating information from various processes, systems, and departments through standardized Excel spreadsheets. This feature reduces manual data handling errors and ensures consistency across dataflow.
2. **Simulation environment:** offers an intuitive and dynamic workspace to: a) configure multiple scenarios by adjusting key manipulated variables, enabling flexible *what-if* analyses; b) execute rigorous process simulations with speed and accuracy; c) analyze detailed results and turn them into actionable

insights for business planning and decision-making.

3. **Scheduling export**: automates the generation and export of production planning results tailored to short-, medium-, and long-term needs, facilitating seamless interaction between teams and systems.

### User Interface and Engine

IntegraGAS frontend uses Microsoft Excel due to its familiarity among process engineers, enabling smooth adoption and seamless integration into daily workflows. Excel's intuitive interface simplifies data input, scenario configuration and result analysis without requiring additional training or specialized software expertise.

The engine, built in VBA, connects directly to Aspen HYSYS simulations, offering:

1. **Flexibility:** Custom functionalities tailored to plant-specific needs.
2. **Dynamic Updates:** Easy fit to plant modifications, business demands, and new scheduling methods.
3. **Automation:** Streamlined calculations and integration with first-principles HYSYS models, ensuring accuracy with minimal manual effort.

The interface is designed for simplicity and efficiency, featuring well-structured Excel worksheets with drop-down menus, conditional formatting, and automated alerts. This reduces cognitive load and allows engineers to focus on optimizing production plans and evaluating scenarios.

### Information Security

In all sections of IntegraGAS the appropriate information security measures are applied. This means that the user does not manipulate the input/output data at any time nor has editing privileges to alter any of these numbers after the input/output procedure is complete, since the tool is password protected and only the development team has admin privileges. This guarantees a secure and reliable dataflow, a primary requirement for this application in case of auditing or questioning by third parties.

## Operation aspects

To further enhance usability and reliability, IntegraGAS included a suite of advanced features focusing on operation performance:

1. **Automatic Alerts:** Notifications for operational limit violations and convergence status, ensuring compliance with safety and performance standards.
2. **Data Consistency Checks:** Built-in validation mechanisms to identify and correct inconsistencies in input data before simulation.
3. **Mass and Energy Balance Calculations:** Automated balances ensure all simulations maintain physical accuracy and adhere to process constraints.
4. **Integration with Shutdown Plans:** Synchronizes scheduling with planned maintenance activities to minimize downtime and operational disruptions.
5. **Automated Gas Allocation:** Streamlines the distribution of processed gas, including calculations for flaring and fuel gas, to optimize resource utilization.
6. **KPIs:** Calculation and graphical display of the main business key performance indicators of each asset.

Moreover, by combining advanced modeling capabilities with a user-friendly interface, IntegraGAS not only simplifies complex scheduling tasks but also empowers process engineers to focus on strategic decision-making. The robust architecture and automation reduce manual effort, enhance operational accuracy and support plants in achieving optimal performance with minimal downtime.

# RESULTS AND DISCUSSION

## Plant Modeling

Plant simulations were carried out in Aspen HYSYS v11/v14. Each model was validated against actual plant history data and showed good fit, with deviations under 10 % – the validation results and methodology followed previous literature works from the same research group [5, 6], where further details can be found on the model.

## Computational aspects

### Features: development and gains

The main features that were created specifically for IntegraGAS are shown in Figure 4, which gather multiple screenshots from the tool Main Dashboard (a) and Simulation Environment (b). This structure aimed to fulfill the requirements mapped in Table 1 besides making the scheduling process easy to be conducted. They are reflected in the three sections of the Main Dashboard (Figure 4.a): short-term (a.1), medium-term (a.2) and long-term (a.3). For each, the main features are:

1. **Data input:** Represented by the yellow buttons in Figure 4a. Collects data via VBA code. Data refers to the plant inlet gas stream, per entry point, at 20 °C and 1 atm, mole composition, temperature and pressure. IntegraGAS collects information from those files, manipulates them and presents to the user in a friendly and easy-to-interpret layout (shown in Figure 4b.2).
2. **Simulation environment (Figure 4b):** The process engineering core of IntegraGAS. It is the main hub from where user defines the main manipulated variables (Figure 4b.3), configures and executes simulations (Figure 4b.1), and analyzes input/output data (Figure 4b.1/b.4). Allows for automatized multi-case execution of simulation scenarios (Figure 4b.1) and performs input data checking (Figure 4b.1).
3. **Scheduling export:** Represented by the yellow buttons in Figure 4a. Generates structured planning output, fitted to the scheduling process under execution. Exports the results as an Excel file and saves

it in a user-selected folder.

Those implemented features yielded several gains. The main were, per feature: (1) secure and seamless data flow; information integrity and consistency between gas plants, (2) centralized information from different sources in one environment, reducing manual data handling; easy manipulation of plant simulation from Excel frontend, even for users without HYSYS experience; multi-case execution of simulations in one go; easy data checking and error identification, (3) automatic file generation in standard layout, reducing labor expense and human errors.

## Execution time

By automatizing the process, one of the major gains was on the reduction of total execution time to generate planning results. The manual approach required several data handling, manipulation and one-by-one input in the HYSYS simulation files. This process was extremely laborious and inefficient – IntegraGAS approach was up to 125 times faster, as seen in the numbers from Table 2.

## Performance Gains: Business aspects

The expressive reduction in execution time, discussed in the previous section, yielded a direct gain for business: lower labour cost and resource optimization. With this time saving, plant Process Engineers can focus on more specialized tasks, such as results analysis, process investigation and plant optimization.

For instance, considering only the short-term scheduling, a total of 992 process simulations are executed per month, per gas asset – or 11'904 per year. Considering the reduction in execution time (Table 2) and a reference labour cost of US$ 53.9 per working hour (Bureau of Labor Statistics), IntegraGAS is returning a total savings of US$ 2.3 million per year for Petrobras natural gas processing sector. Still adds to this number the potential gains for medium- and long-term scheduling.

## Petrobras Natural Gas Strategic Plan

IntegraGAS did also cover the main scheduling process in Petrobras: Annual Strategic Plan. This process is key for being highly strategic for long-term business decisions – and consequently demands a high level of interaction and flow of information with other systems and business departments, such as: Strategy, Performance, Logistics, Marketing, Commercialization and Upstream/Midstream Operations.

IntegraGAS was successfully used in Petrobras Natural Gas Strategic Planning 2025-2029, conveying a

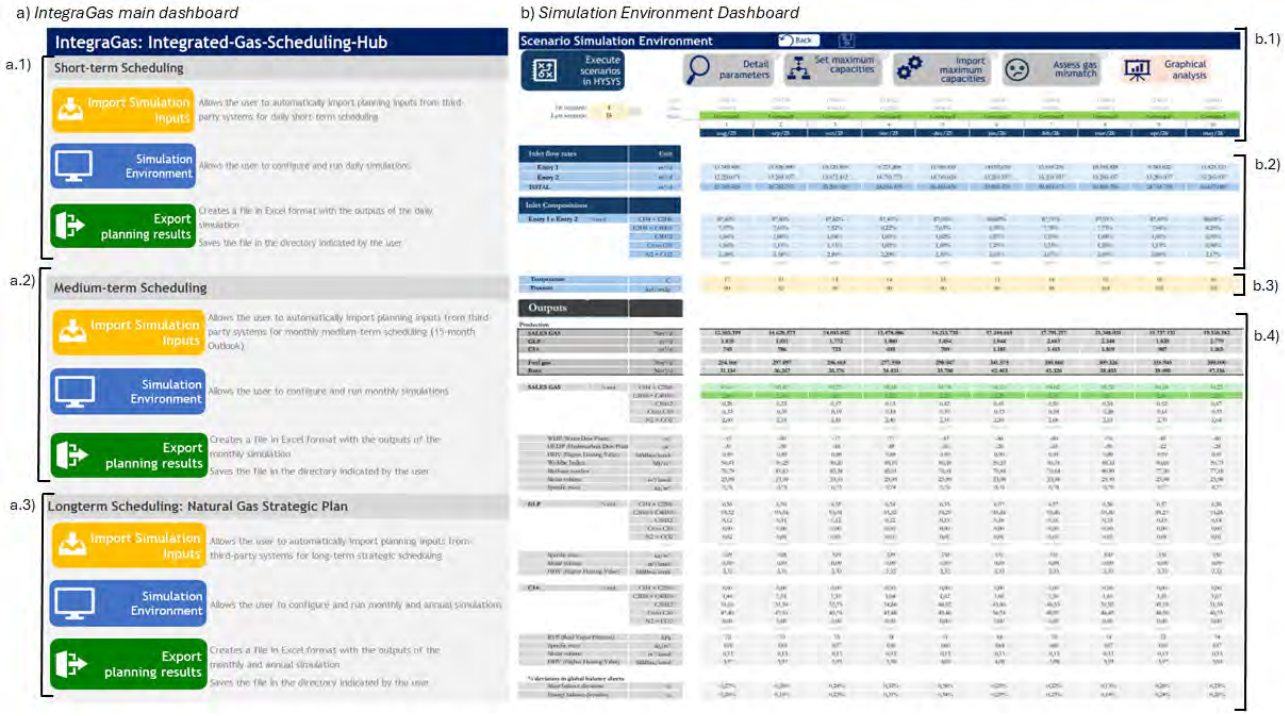



**Figure 4. a)** Main dashboard in Excel, where desired planning is chosen: **a.1)** short-, **a.2**) medium-, or **a.3)** long-term. Each has three features (buttons): input data import (yellow), access to the Simulation Environment Dashboard (blue) and export of simulated results (green). **b)** Simulation Environment Dashboard, where users can analyze and simulate data: **b.1)** Dedicated buttons to additional functionalities. Displays simulation times and convergence status. **b.2)** Input data such as flowrates and compositions, marked in blue. **b.3)** User-manipulated variables, marked in yellow. **b.4**) Simulation results, marked in gray, including mass and energy balances.

seamless functionality that integrated all this scattered information and yielded consistent and reliable results for proper decision-making on investment analysis and strategic planning. Also, by providing structured input and output results, IntegraGAS enabled the development of a Business Intelligence (BI) layer for data visualization, making strategic data readily available online across departments, thus reducing time spent on data handling and information sharing, as well as ensuring proper information security, access control and data levelling.

**Table 2:** Comparison between planning execution time with manual and IntegraGAS approaches, by gas asset.

| Asset | Execution time (min) | |
|---|---|---|
| | manual | IntegraGAS |
| UTGC | 50 | 0.8 |
| UTGCA | 50 | 0.4 |
| UTGCAB | 50 | 2 |
| UTGITB | 50 | 1 |

### Visual Identity

A logo (Figure 5) was created to strengthen IntegraGAS identity and symbolize departmental integration for optimizing gas processing.




**Figure 5.** IntegraGAS logo created by this work.

## CONCLUSIONS AND FUTURE WORKS

This work intended to propose a novel approach for production scheduling, utilizing the implementation of a digital-based tool (IntegraGAS) in four assets of Petrobras natural gas processing sector as case study. IntegraGAS architecture used Excel for frontend, VBA for engine and direct OLE communication between VBA and Aspen HYSYS – this facilitated software retention by end users, who are familiar with Excel applications. The most distinguishing and innovative feature of this approach is the transparent use of first principles rigorous simulation for plant modeling, what guarantees consistent, verifiable and reliable simulation results – key requirements of the multi-party open gas market scenario – while being transparent to the end user. The implementation of IntegraGAS was successful and it has been in use in the industry since 2022, with hundreds of thousands of simulations successfully executed so far, considering short-, medium-, and long-term planning.

This work contributed to the literature by successfully developing, implementing and testing a novel first-principles integrated scheduling tool, with industrial application, that delivered rigorously accurate yet fast, auditable and reliable automated results. For future works, the suggestion is to develop a higher-level decision layer, by integrating upstream and midstream planning as a single system (Figure 1), thus opening the path for unified planning and optimization studies.

## ACKNOWLEDGEMENTS

Financial support from Petróleo Brasileiro S.A. (PETROBRAS) is gratefully acknowledged.

## REFERENCES

1. S. Faramawy, T. Zaki, A.A.-E. Sakr, Natural gas origin, composition, and processing: A review, Journal of Natural Gas Science and Engineering, Volume 34, Pages 34-54, (2016). https://doi.org/10.1016/j.jngse.2016.06.030
2. Mokhatab, S., Poe, W. A., & Mak, J. Y., Handbook of natural gas transmission and processing: principles and practices. Gulf professional publishing, (2018).
3. dos Santos, E. M., Peyerl, D., & Netto, A. L. A., Opportunities and Challenges of Natural Gas and Liquefied Natural Gas, Ed. Letra Capital, ISBN: 978-65-87594-44-6, (2020).
4. Ferraro, M. C, Hallack, M., The development of the natural gas transportation network in Brazil: Recent changes to the gas law and its role in co-ordinating new investments, Energy Policy, Volume 50, Pages 601-612, ISSN 0301-4215, (2012). https://doi.org/10.1016/j.enpol.2012.07.063.
5. Souza, T.E.G. et al. Modeling and economic optimization of an industrial site for natural gas processing: a nonlinear optimization approach. Digital Chemical Engineering, 6, 100070. (2023). https://doi.org/10.1016/j.dche.2022.100070
6. Souza, T.E.G. et al. Modeling and economic optimization of an industrial site for natural gas processing: an MINLP approach. Computer Aided Chemical Engineering, 53, 3307-3312. (2024). https://doi.org/10.1016/B978-0-443-28824-1.50552-4
7. Harjunkoski, I. et al. Scope for industrial applications of production scheduling models and solution methods. Computers and Chemical Engineering, 62, 161-193. (2014).

© 2025 by the authors. Licensed to PSEcommunity.org and PSE Press. This is an open access article under the creative commons CC-BY-SA licensing terms. Credit must be given to creator and adaptations must be shared under the same terms. See https://creativecommons.org/licenses/by-sa/4.0/

Systems & Control Transactions

**Research Article - Peer Reviewed Conference Proceeding**
ESCAPE 35 - European Symposium on Computer Aided Process Engineering
Ghent, Belgium. 6-9 July 2025
Jan F.M. Van Impe, Grégoire Léonard, Satyajeet S. Bhonsale,
Monika E. Polańska, Filip Logist (Eds.)

PSE PRESS

# Temporal Decomposition Scheme for Designing Large-Scale $CO_2$ Supply Chains Using a Neural Network-Based Model for Forecasting $CO_2$ Emissions

**José A. Álvarez-Menchero*, Rubén Ruiz-Femenia, Raquel Salcedo-Diaz, Isabela Fons Moreno-Palancas, and José A. Caballero**

University of Alicante, Department of Chemical Engineering, Alicante, Spain
* Corresponding Author: joseantonio.alvarez@ua.es .

## ABSTRACT

The battle against climate change and the search for innovative solutions to mitigate its effects have become the focus of the researchers' attention. One potential approach to reduce the impacts of the global warming could be the design of a Carbon Capture and Storage Supply Chain (CCS SC). However, the high complexity of the model requires exploring alternative ways to optimise it. In this work, a CCS multi-period supply chain for Europe is designed. Data on $CO_2$ emissions have been sourced from the EDGAR database, which includes information spanning the last 50 years. Since this problem involves optimising the cost and operation decisions over a 10-year time horizon, it would be advisable to forecast carbon dioxide emissions to enhance the reliability of the data used. For this purpose, a neural network-based model is implemented for forecasting N-Beats. Furthermore, a temporal decomposition scheme is used to address the intractability issues of the model. The selected method is Lagrangean decomposition, which has been employed in other high complexity works, demonstrating strong performance and significant computational savings.

**Keywords**: Mathematical Programming, Generalized Disjunctive Programming, Supply chain, Mixed Integer Linear Programming, Lagrangean Decomposition, Time Series Forecasting, Deep learning.

## 1. INTRODUCTION

Over the last decades, climate change has become one of the main challenges that society must address. Consequently, many recent breakthroughs have focused on this issue. This is the case with $CO_2$ capture and storage supply chains, which have emerged as one of the most promising possible options to decarbonize the industrial sector. D'Amore, for example, proposes a European Carbon Capture and Storage Supply Chain (CCS SC) [1,2]. To achieve this, a Mixed Integer Linear Program (MILP) is implemented. As a result, the problem becomes computationally intractable for $CO_2$ reduction targets exceeding 70% due to its high complexity. A possible solution to overcome this difficulty might be the use of decomposition methods, such as the Lagrangean Decomposition [3]. Similarly, Jackson and Grossmann propose a temporal decomposition scheme based on this Lagrangean approach to solve a multiperiod nonlinear programming optimization model, obtaining satisfactory results [4]. Additionally, designing a supply chain over a time horizon involves inherent uncertainties, such as future $CO_2$ emissions. Therefore, it is crucial to explore methods to enhance data reliability.

Altogether, this paper implements a temporal decomposition technique based on Lagrangean Decomposition to design a CCS SC in the Iberian Peninsula. The model is optimized over a 10-year time horizon. As a result, the suitability of applying this resolution method to solve such complex problems is analyzed. Furthermore, a neural network-based model (N-BEATS) is implemented to forecast $CO_2$ emissions over the same 10-year time horizon [5].

## 2. PROBLEM STATEMENT

As mentioned earlier, this paper proposes a temporal decomposition technique based on Lagrangean decomposition to optimize a CCS SC within the Spanish and Portuguese territory over a 10-year time horizon.

The model is formulated as a grid-based, spatially explicit Mixed Integer Linear Program (MILP). Consequently, the territory is divided into smaller regions *g*. The $CO_2$ emissions for each region are sourced from the Emissions Database for Global Atmospheric Research (EDGAR) [6], which is a global database of anthropogenic emissions of greenhouse gases and air pollution on Earth. Additionally, potential $CO_2$ storage sites are obtained from the $CO_2$Stop Project database [7], which provides information on the locations and capacities of underground geological formations in Europe that could be suitable to store $CO_2$.

It is now necessary to define how the $CO_2$ is captured and transported. On the one hand, three different possible technologies *k* are considered regarding the $CO_2$ capture: post-combustion, pre-combustion and oxy-fuel combustion. On the other hand, they can be transported by onshore or offshore pipelines *L* depending on the region's location.

## 3. NOMENCLATURE

### Sets

| | |
|---|---|
| $g$ | regions |
| $k$ | capture technology {post$^{comb}$, pre$^{comb}$, oxy$^{fuel}$} |
| $l$ | pipelines {onshore, offshore} |
| $t$ | time period {1,2,…,10} |
| $CR_{g,g'}$ | It is possible to connect *g* to *g'* by a pipeline |

### Parameters

| | |
|---|---|
| $\alpha$ | $CO_2$ reduction target |
| $E_{g,t}$ | Region g $CO_2$ emissions at time period t [$10^7$ tons] |
| $S_g$ | Storage capacity in region g [$10^9$ tons] |
| $UC_k$ | Capture technology k unitary cost [€/ton] |
| $FC_{g,g'}$ | Pipeline between g and g' construction cost [€] |
| $OC_{g,g'}$ | Pipeline between g and g' operational cost [€/year] |
| $D_{g,g'}$ | Distance between g and g' [km] |
| $C^{IR}$ | Intra-regional transport cost [€/(ton·km)] |
| $SIZE_g$ | Region g size [km] |
| $\eta_k$ | Capture technology k efficiency |
| $\gamma_{g,k}$ | Technology k feasibility in region g according to fuels contribution to emission |
| $Q^{MAX}$ | Transport capacity of the pipelines [$10^7$ tons/year] |
| $C^{MAX}$ | Upper limit for the construction rate of pipelines [km/year] |
| $CAP^{INJ}$ | Maximum injection well capacity [tons/year] |
| $depth_g$ | Injection depth in region [km] |
| $CCR$ | Capital cost rate for injection well |
| $OM$ | Mainteneance rate for injection well |

### Continuous Variables

| | |
|---|---|
| $p_{k,g,t}$ | Processed $CO_2$ through technology k in region g at time period t [$10^7$ tons] |
| $c_{k,g,t}$ | Captured $CO_2$ through technology k in region g at time period t [$10^7$ tons] |
| $q_{g,g',t}$ | $CO_2$ transported from g to g' at time period t [$10^7$ tons] |
| $s_{g,t}$ | $CO_2$ sequestred in region g at time period t [$10^9$ tons] |

### Binary Variables

| | |
|---|---|
| $y_{g,g',t}$ | Takes a value of 1 if a pipeline from g to g' is built |
| $\widehat{y_{g,g',t}}$ | Duplicate of binary variable $y_{g,g',t}$ |

### Integer Variables

| | |
|---|---|
| $n_{g,t}^{wells}$ | Number of injections well constructed in region g at time period t |

In this model It is possible to identify three different problems:

- Capture Problem.
- Transport Problem.
- Sequestration Problem.

The capture problem is modeled using Eqs. (1-4). First, Eq. (1) defines that the total processed $CO_2$ in region g at time t cannot exceed its emissions $E_{g,t}$. Next, Eq. (2) sets the maximum $CO_2$ that can be processed by each technology k. Then, Eq. (3) specifies the minimum total $CO_2$ that must be processed across all regions g over the 10-year time horizon. Finally, Eq. (4) establishes the relationship between $c_{k,g,t}$ and $p_{k,g,t}$.

$$\sum_k p_{k,g,t} \leq E_{g,t}, \quad \forall g, \forall t \tag{1}$$

$$p_{k,g,t} \leq \gamma_{g,k} E_{g,t}, \quad \forall k, \forall g, \forall t \tag{2}$$

$$\sum_{k,g,t} \eta_k \, p_{k,g,t} \geq \alpha \sum_{g,t} E_{g,t} \tag{3}$$

$$c_{k,g,t} = \eta_k p_{k,g,t}, \quad \forall k, \forall g, \forall t \tag{4}$$

Regarding the transport problem, the mass balance is established in Eq. (5).

$$\sum_c c_{c,g,t} + \sum_{g' \in SR_{g,g'}} q_{g',g,t} = 100 s_{c,g,t} + \sum_{g' \in SR_{g,g'}} q_{g,g',t} \quad \forall g, \forall t \tag{5}$$

Additionally, as $CO_2$ transport from region g to

region g' at time t depends on if the pipelines that connects both regions is built at that time, the Boolean variable $Y_{g,g',t}$ is defined. This Boolean variable is true if the pipeline to transport $CO_2$ from region g to region g' is built at time t.

The disjunctive model is formulated as follows:

$$\underset{(g,g'\in CR_{g,g'})}{\vee} \begin{bmatrix} Y_{g,g',t} \\ q_{g,g',t} \le Q^{MAX} \end{bmatrix}, \quad t \in T \tag{6}$$

It is now necessary to establish that if a pipeline between a region g and a region g' is built at time t-1, then the pipeline will remain there at time t. The logical relationship which defines it is shown in Eq. (7).

$$Y_{g,g',t-1} \Rightarrow Y_{g,g',t}, \ \forall g \in CR_{g,g'}, \forall g' \in CR_{g,g'}, \forall t \tag{7}$$

Eqs. (6) and (7) reformulated in terms of binary variables are shown below in Eqs. (8) and (9).

$$q_{g,g',t} \le Q^{MAX} y_{g,g',t}, \ \forall g, g' \in CR_{g,g'}, \forall t \tag{8}$$

$$y_{g,g',t} - y_{g,g',t-1} \ge 0, \ \forall g, g' \in CR_{g,g'}, \forall t \tag{9}$$

Furthermore, Eqs.(10) and (11) establish an upper limit to the total length of pipelines built throughout a year.

$$\sum_{g,g'} D_{g,g'} \left(y_{g,g',t} - y_{g,g',t-1}\right) \le C^{\text{MAX}}, \quad \forall t > 1 \tag{10}$$

$$\sum_{g,g'} D_{g,g'} y_{g,g',t} \le C^{MAX}, \quad t = 1 \tag{11}$$

Next, the sequestration problem is defined below:

$$\sum_t s_{g,t} = S_g, \quad \forall g \tag{12}$$

$$n_{g,t}^{wells} = \frac{s_{g,t}}{CAP^{INJ}}, \quad \forall g, \forall t \tag{13}$$

Eq. (12) sets the maximum $CO_2$ which can be store at each region as its storage capacity, and Eq. (13) defines the number of wells built at region g at time t.

Lastly, the objective function shown in Eq. 14 minimizes the total cost of the supply chain given by the cost of capturing the $CO_2$ plus the pipeline's construction and operational cost, the shipping cost and the storage cost.

$$\begin{aligned} min\ \Phi = {} & 10^{-1} \sum_{k,g,t} UC_k \eta_k p_{k,g,t} + \\ & 10^{-8} \sum_{g,g' \in SR_{g,g'}} FC_{g,g'} y_{g,g',T} + \\ & 10^{-8} \sum_{g,g',t \in SR_{g,g'}} OC_{g,g'} y_{g,g',t} + \\ & 10^{-1} \sum_{g,g',t \in SR_{g,g'}} \mathrm{D}_{g,g'} \mathrm{q}_{g,g',t} + \\ & 10^{-1} C^{IR} \sum_{\mathrm{k},g,t} \mathrm{SIZE}_g \gamma_k p_{k,g,t} + \\ & 10^{-8} \sum_{g,t} (CCR + OM)\left(m_1 depth_g + m2\right) n_{g,t}^{wells} \end{aligned} \tag{14}$$

Notice that the model has been scaled in order to improve the numerical stability and efficiency of the solver.

## 4. SOLUTION STRATEGY

The Mixed Integer Linear Programming (MILP) described by Eqs. (1)-(14) can easily become an intractable problem as the number of regions g, the reduction target, or the time horizon increase. Therefore, given the model's structure, a decomposition method could be suitable to overcome these issues. The decomposition algorithm, outlined in Figure 1, follows the approach by Jackson and Grossmann [4].

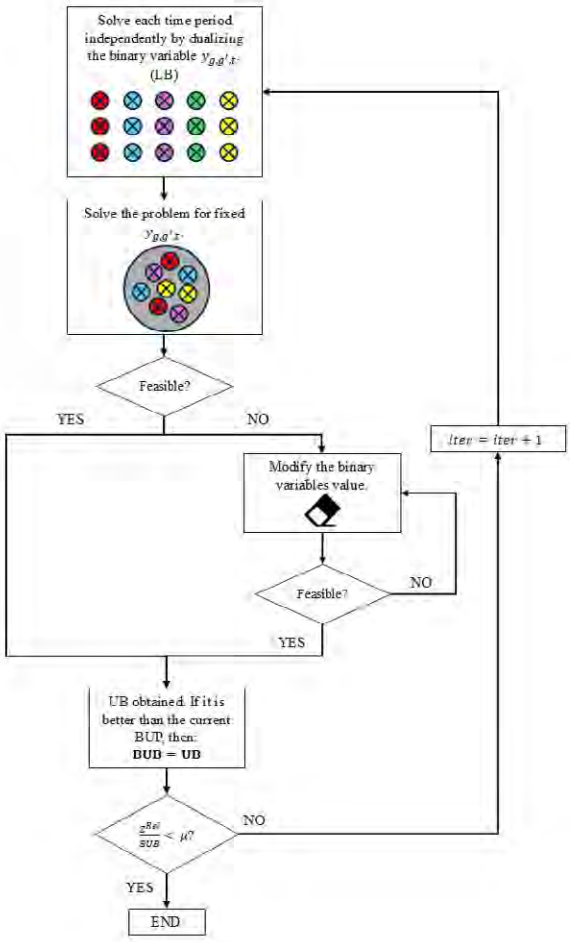



**Figure 1.** Decomposition algorithm steps.

We adopt a temporal decomposition scheme. To implement it, we first identify the constraints which couple the time periods. In this case, these constraints are Eqs. (9) and (10). Thus, the binary variables $y_{g,g',t}$ must be duplicated, as formulated in Eq. (15).

$$y_{g,g',t} = \widehat{y_{g,g',t}}, \quad \forall g \in CR_{g,g'}, \forall g' \in CR_{g,g'}, \forall t \tag{15}$$

Now, Eqs. (16) and (17) are obtained after rewriting the affected equations.

$$y_{g,g',t} - \widehat{y_{g,g',t-1}} \ge 0, \quad \forall g, \forall g', \forall t > 1 \tag{16}$$

$$\sum_{g,g'} \left[D_{g,g'} \left(y_{g,g',t} - \widehat{y_{g,g',t-1}}\right)\right] \le C^{\text{MAX}} \tag{17}$$

Eq. (15), which is called interconnection constraint, is dualized so that the Lagrangean Decomposition is applied. After dualizing, Eq. (15) transforms into Eq. (18).

$$min\ \Phi_{\mathrm{LR}} = \Phi + \sum_{g,g',t\in SR} \lambda_{g,g',t}\left(y_{g,g',t} - \widehat{y_{g,g',t}}\right) \quad (18)$$

As indicated in Figure 1, a lower bound is obtained once each subproblem is optimized. Then, the binary variables are fixed to the values given by the decomposed model and the original problem, comprising Eqs. (1)-(14) is solved. If the problem is infeasible, which is more likely due to the high number of variables, a strategy must be designed to modify the binary variables. The following algorithm is proposed to guarantee that a solution is achieved:

$If \quad \sum_t y^k_{g,g',t} \geq 2,$

Being $Y$ the first time period $t$ with $y^k_{g,g',t} = 1$, for all $t > Y$:

$$y^k_{g,g',t} = 1, \quad \forall t > Y$$

Else

$$y^k_{g,g',t} = 0, \quad \forall t$$

**Figure 2.** Binary variables modification algorithm

Lastly, Eqs. (19) and (20) update the Lagrange multipliers $\lambda_{g,g',t}$, ensuring convergence across iterations.

$$step^k = 0.5\frac{LB_k - UB}{\sum_{g,g',t}\left(y^k_{g,g',t} - \widehat{y^k_{g,g',t}}\right)^2} \quad (19)$$

$$y^{k+1}_{g,g',t} = y^k_{g,g',t} - step^k\left(y^k_{g,g',t} - \widehat{y^k_{g,g',t}}\right) \quad (20)$$

# 5. $CO_2$ EMISSIONS FORECAST

As mentioned earlier, N-BEATS is the neural network-based model selected for forecasting $CO_2$ emissions. This section explains the methodology implemented to select the most suitable model.

## 5.1 Exploratory Data Analysis

Given a dataset containing multiple series, Exploratory Data Analysis is conducted to identify potential correlation between the series and exploit this knowledge to enhance the training process.

In this regard, cross-correlation is a widespread tool to assess the degree of correlation between two time series. We compare series pairwise by computing its Pearson correlation coefficient and visualize the results with the aid of heatmaps. The Pearson correlation coefficient is shown in Eq. (21).

$$\rho_{x,y} = \frac{cov(X,Y)}{\sigma_x \sigma_y} \quad (21)$$

Where X and Y represent two different time series.

As this metric might be affected by the autocorrelation among preceding lags, this within-series dependence must be first removed. This is achieved by recursively differencing each series until the ADF test proofs its stationarity.

## 5.2 Data preprocessing

Before training forecasting models, historical data was normalized for convenience using min-max normalization

$$x_{scaled} = \frac{x - x_{min}}{x_{max} - x_{min}} \quad (22)$$

Then, data was also split into train (80%), validation (10%) and test (10%) sets.

## 5.2 Model Selection

The model architectures studied are shown in Figure 3.

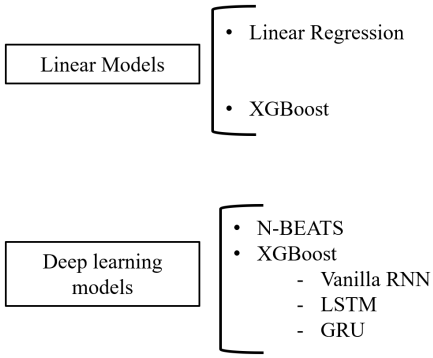



**Figure 3.** Model architectures studied.

Their performance was benchmarked against a baseline model, namely, the moving average of the last two preceding values.

For each model type, the best hyperparameter configuration (BHC) was search inside a predefined search space. While a grid search approach was preferred for regression models, the tuning process of deep learning models was carried out using the open-source library Optuna [5]. The BHC was found by training different models varying the hyperparameter values, evaluating its mean absolute percentage error (MAPE) on the validation set and using the minimum MAPE as selection criteria.

For neural network-based models, the learning rate of the model with the BHC was further refined given the impact of this hyperparameter on model performance. This was achieved by running the training process again, this time increasing the learning rate after each batch is processed. The evolution of the loss function is logged, and loss vs. learning rate plots are used as guidance for choosing a good value of this hyperparameter.

Next, the model with the BHC found so far was retrained on the whole training set (concatenation of test and validation sets), and its performance was evaluated on the test set.

Finally, the model reporting the lowest MAPE in the test set will be the one selected to generate future forecasts.

### 5.3 Results

The heatmap in Figure 4 represents the cross-correlation between the $CO_2$ emissions in the regions considered for this case study. It evidences strong correlations among the $CO_2$ emissions in regions, as is the case of regions 26 and 14.

The results of the model selection process are shown in Table 1. For comparison purposes, all models were trained for 200 epochs, using a batch size of 32, and the forecasts are obtained one year at a time.

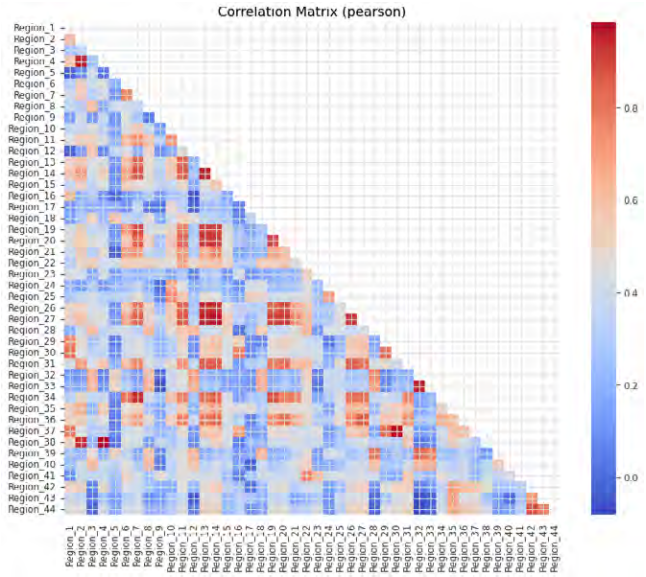



**Figure 4.** Heatmap of Pearson correlation coefficient.

**Table 1**: Results of tuning process and performance on the test set.

| | $MAPE_{test}$ | BHC |
|---|---|---|
| **Moving average** | 14.31% | window size = 2 |
| **Linear Regression** | 14.63% | lags = 4 |
| **XGB** | 14.96% | lags = 2 |
| **N-BEATS** | 14.16% | input_chunk 3<br>num_blocks = 2<br>num_layers = 4<br>num_stacks = 2<br>layer_width = 256<br>batch_size = 32<br>learning_rate = $10^{-4}$ |
| **RNNs** | 15.13% | Model type: LSTM<br>num_layers = 4<br>input_chunk = 4<br>batch_size = 32<br>learning_rate=$2{\cdot}10^{-3}$<br>optimizer = ADAM |

In light of the results shown in Table 1, N-BEATS model was selected to forecast $CO_2$ emissions for a 10-year time horizon.

## 6. RESULTS AND DISCUSSION

The model was implemented in GAMS 46.5.0 and solved using Gurobi 11.0.1 solver. All code was executed on an Intel® Core™ i7-4790 CPU (3.60 GHz) with 8.00 GB RAM. The results are presented in Table 2.

**Table 2**. Optimization results.

| | No. of iterations | Solution time (s) | Solution obtained | Gap (%) |
|---|---|---|---|---|
| Full-Space | - | 8’26 | 1180.74 | - |
| Lag. Dec. | 47 | 13’ 44” | 1257.13 | 6.47 |

As observed, the Lagrangean decomposition algorithm provides a good solution to this problem. However, it requires a significant amount of computational time to close the gap between the lower and upper bounds. Since this method is intended to be applied to problems of higher complexity, the proposed algorithm shown in Figures 1 and 2 needs to be improved. The supply chain obtained at the end of the 10-year time horizon is displayed in Figure 5.

## 7. CONCLUSION

The decomposition algorithm has demonstrated its effectiveness. However, further research is needed to improve the algorithm shown in Figure 2 and enhance the proposed resolution method, as it requires many iterations to close the gap.

Regarding the time series forecast, although N-BEATS proved to be the best model (Table 1), it performed only slightly better than a simple linear regression when applied to this case. This is due to the small size of the dataset used for forecasting. If a larger dataset had been used, the difference between the two methods would have been considerably greater.

## ACKNOWLEDGEMENTS

The authors gratefully acknowledge financial support of the Spanish “Ministerio de Ciencia, Innovación y Universidades” under project PID2021-124139NB-C21. They would also like to thank “Generalitat Valenciana: Conselleria d’Educació, Cultura, Universitats i Ocupació” and the European Social Fund Plus (ESF+) for the PhD grant (CIACIF/2023/117).

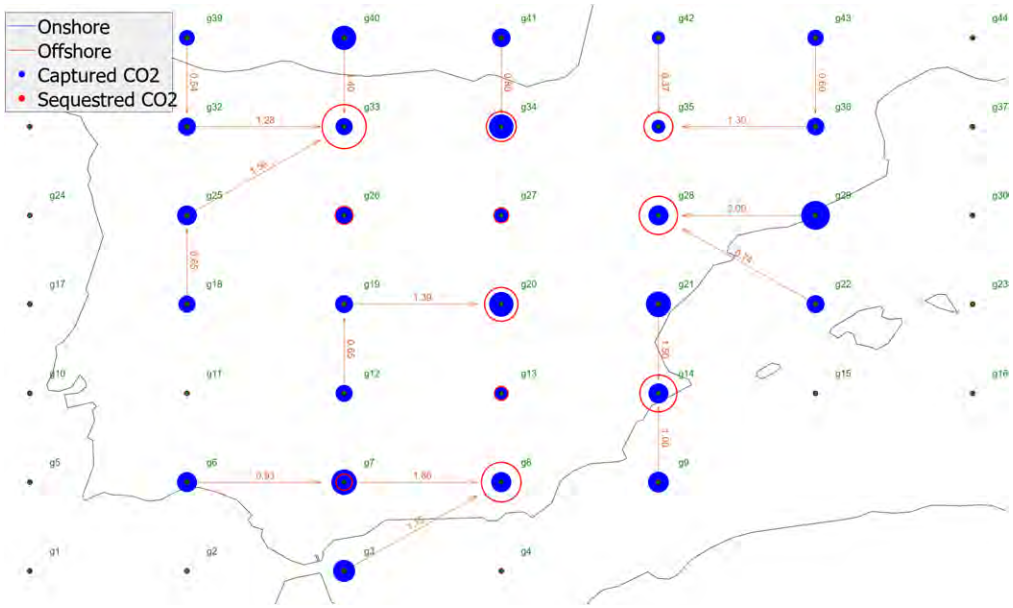



**Figure 5:** Carbon Capture and Storage Supply Chain obtained.

## REFERENCES


1. D'Amore, F, Bezzo, F. Economic optimisation of European supply chains for $CO_2$ capture, transport and sequestration. *Int J Greenh Gas Control* 65:99-116 (2017) https://doi.org/10.1016/j.ijggc.2017.08.015
2. D'Amore, F, Romano, MC, Bezzo, F. Economic optimisation of European supply chains for $CO_2$ capture, transport and sequestration. *J Clean Prod* 290 (2021) https://doi.org/10.1016/j.jclepro.2020.125202
3. Guignard, M, S. Kim. Lagrangean Decomposition: A model yielding Stronger Lagrangean Bounds. *Math Program* 39:215-228 (1987) https://doi.org/10.1051/ro/1987210403071
4. Jackson JR, Grossmann IE. Temporal decomposition scheme for nonlinear multisite production planning and distribution models. Ind Eng Chem Res 42:3046–3054 (2003) http://dx.doi.org/10.1021/ie030070p
5. Akiba, T, Sano, S, Yanase, T, Ohta, T, Koyama, M. Optuna: A Next-generation Hyperparameter Optimization Framework. *Proc 25th ACM SIGKDD Int Conf Knowl Discovery Data Mining* 2623-2631 (2019) https://doi.org/10.48550/arXiv.1907.10902
6. Joint Research Centre. Emission Database for Global Atmospheric Research (EDGAR). https://edgar.jrc.ec.europa.eu/index.php
7. Joint Research Centre. $CO_2$ Storage Potential in Europe (2020) https://setis.ec.europa.eu/european-co2-storage-database_en


© 2025 by the authors. Licensed to PSEcommunity.org and PSE Press. This is an open access article under the creative commons CC-BY-SA licensing terms. Credit must be given to creator and adaptations must be shared under the same terms. See https://creativecommons.org/licenses/by-sa/4.0/

Systems & Control Transactions

**Research Article - Peer Reviewed Conference Proceeding**
ESCAPE 35 - European Symposium on Computer Aided Process Engineering
Ghent, Belgium. 6-9 July 2025
Jan F.M. Van Impe, Grégoire Léonard, Satyajeet S. Bhonsale,
Monika E. Polańska, Filip Logist (Eds.)

PSE PRESS

# Agent-Based Simulation of Integrated Process and Energy Supply Chains: A Case Study on Biofuel Production

**Farshid Babaei[a]*, David B. Robins[a], Robert Milton[a], and Solomon F. Brown[a]**

[a] School of Chemical, Materials, and Biological Engineering, University of Sheffield, United Kingdom
* Corresponding Author: f.babaei@sheffield.ac.uk.

## ABSTRACT

Despite the potential benefits of decision-level integration for process and energy supply chains (SCs), these systems are traditionally assessed and optimised by incorporating simplified unit operation models within a spatially distributed network. The desired organisational-level integration cannot be achieved without leveraging complex computational tools and concepts. This work proposes a multi-scale agent-based model to facilitate the transition from traditional practices to coordinated SCs. The proposed multi-agent system framework incorporates different enterprise dimensions of the process and energy SCs, including raw material suppliers, rigorous processing plants, and consumers. The behaviour of each agent type and its interactions are implemented, and their impact on the overall system is investigated. This approach allows for the simultaneous assessment and optimisation of process and SC decisions. By integrating each decision level into the operation, the devised framework goes beyond existing studies in which the impacts of lower decision levels are neglected. A biofuel SC example comprising farmers, biorefineries, and end-users is presented to demonstrate the application of the proposed multi-agent system. The involved actors seek to increase their payoffs given their interdependencies, intra-organisational variables, and the underlying dynamics of the network. The aggregated payoff of the supply network is optimised under different scenarios, and fractions of capacity allocated to biofuel production and consumption are obtained. The results indicate that integrated decision-making significantly influences SC performance. The proposed research expounds a more realistic view of multi-scale coordination schemes in process and energy SCs.

**Keywords**: Process and energy systems, Decision level integration, Agent-based models, Biofuel supply chains, Payoff optimisation

## INTRODUCTION

Effective coordination between supply chain (SC) levels from operational to strategic areas is an essential tool for improving the comprehensiveness of process and energy system models [1]. Such a decision-level integration notion is true for models encompassing changing policy decisions and technological innovations, such as those in biofuel SCs [1]. Biofuels can provide an essential alternative to fossil fuels as they utilise renewable feedstocks whilst allowing for lower net carbon dioxide emissions [2]. Although the further adoption of biofuels has been touted as a possible key contributor to meeting the climate objectives, the complex interactions between stakeholders, such as raw material suppliers, processing plants, and consumers, and the impact of government policies, such as subsidies, result in unclear or oversimplified outcomes from conventional biofuel SC models.

Several studies have explored the optimisation of biofuel SCs to meet sustainability objectives [3-5]. Whilst some explore the impact of technology options on SCs, none were found to investigate the effects of biorefinery process details on biofuel adoption. In this context, computational approaches such as agent-based modelling have been used to handle the complexities and uncertainties associated with biofuel SCs, specifically the feedback relationships between agents [1]. The most rigorous studies [1, 6], proposed agent-based models to simulate the adoption of biofuels by stakeholders in response to government policies such as differing subsidy

levels and products' social and environmental impacts. The current investigation utilises a multi-scale agent-based model to capture the organisational structure of integrated SCs. Such multi-faceted features allow for simultaneous assessment and optimisation problems, particularly exploring the optimal adoption in biofuel-driven processes and energy systems. The framework extends decision-making beyond that from prior studies by including decisions at the firm level, through adjustments to intra-organisational planning options, as well as at lower levels, through the incorporation of biorefinery process variables.

# METHODOLOGY

## Biofuel Adoption Problem Formulation

In this work, a biofuel SC is modelled as an interrelated system of computational ecosystems featuring distributed and asynchronous decision-making, and incomplete information.The conceptual structure of the system is shown in Figure 1.

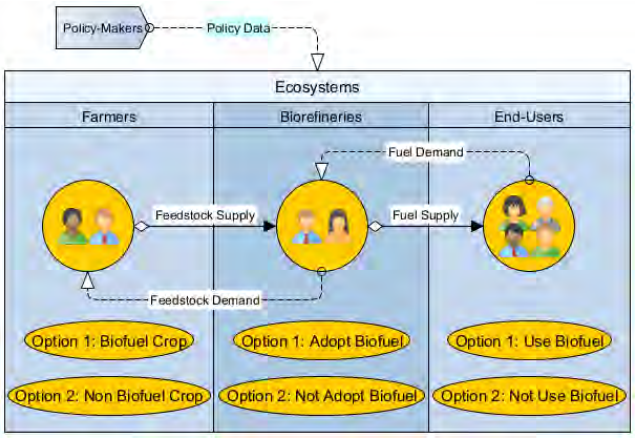



**Figure 1.** Conceptual model of the biofuel SC [1].

The system comprises multiple actors, including farmers, biorefinery facilities, and end-users, each with binary options regarding biofuel adoption. The biofuel adoption problem is formulated as follows.

$$max_{P,O}\ \mathcal{U}_T = \sum_{e\in SCE}\sum_{t_m\in T_m}\mathcal{U}_t(P,O) \tag{1a}$$

$$s.t.\ P \in \Theta_P, O \in \Theta_O \tag{1b}$$

Where $\mathcal{U}_T$ is the total utility of all involved ecosystems ($SCE$) in all sample periods ($T_m$), which is calculated by the individual payoff functions ($\mathcal{U}_t(P,O)$). The planning decision variables ($P$) include re-evaluation frequencies, while the operational-level decisions ($O$) entail adjusting biorefining facility process parameters. Additionally, the feasible regions of both levels confined by equality, inequality, and implicit constraints are denoted by sets $\Theta_P$ and $\Theta_O$.

## Supply Chain Dynamic Behaviour

The SC behaviour at the aggregate level is driven by actors alternating between adopting or not adopting biofuels and changing the ecosystem's payoff. The following constraints determine the rate at which actors choose the former at the ecosystem level [1].

$$\frac{df_e}{dt} = \alpha_e\left(\rho_e\left(f_i(t-\tau_e)\right) - f_e(t)\right), \forall e,i \in SCE \tag{2}$$

$$\rho_e = \frac{1}{2}\left(1+\text{erf}\left(\frac{G_{e1}(f_i)-G_{e2}(f_i)}{2\sigma_e}\right)\right), \forall e,i \in SCE \tag{3}$$

$$\alpha_e \in (\alpha_{e,min}, \alpha_{e,max}) \tag{4}$$

Where $f_e$ is the fraction of actors in an ecosystem adopting biofuels and $\alpha_e$ $[\frac{1}{month}]$ is the re-evaluation frequency for each ecosystem, bounded by minimum and maximum values ($\alpha_{e,min}, \alpha_{e,max}$). The preference probability of biofuel adoption ($\rho_e$) depends on the payoff of selecting said option. As a result, two utility functions, represented as $G_{e1}$ and $G_{e2}$ are defined for adopting or not adopting biofuels, respectively, influenced by same-tier and neighbouring ecosystem adoption fractions. $\tau_e$ denotes the delay parameter and accounts for the asynchronous information flows between ecosystems and the inherent inertia to respond to external changes. Finally, the uncertainties are introduced through measurement errors of utility functions, characterised by $\sigma_e$ [1].

## Biorefinery Model

The production process behaviour is reflected via a nonlinear model of a biodiesel plant described elsewhere [7]. The closed form of the process model is described below.

$$\mathcal{F}(\mathcal{X}) = 0 \tag{5}$$

$$x \in (x_{min}, x_{max}), \forall x \in \mathcal{X} \tag{6}$$

Where $\mathcal{X}$ refers to the process variables and parameters, including feed and solvent flow rates and temperatures along with water mass flow and the boiler pressure. The set $\mathcal{F}$ relates the final product flow rate, purity, temperature, and heat duty requirement to the input parameters [7].

The plant's overall profit is calculated based on the following equation.

$$Profit = Sale_{Biodiesel} - TAC \tag{7}$$

Where $Sale_{Biodiesel}$ represents the final product sale, and $TAC$ refers to the total annual costs, which include the operational and annualised capital costs discounted by a given factor.

## Multi-Scale Agent-Based Model

A multi-agent system encompasses various actors carrying out numerous tasks. These agents can select from multiple resources to complete their assignments.

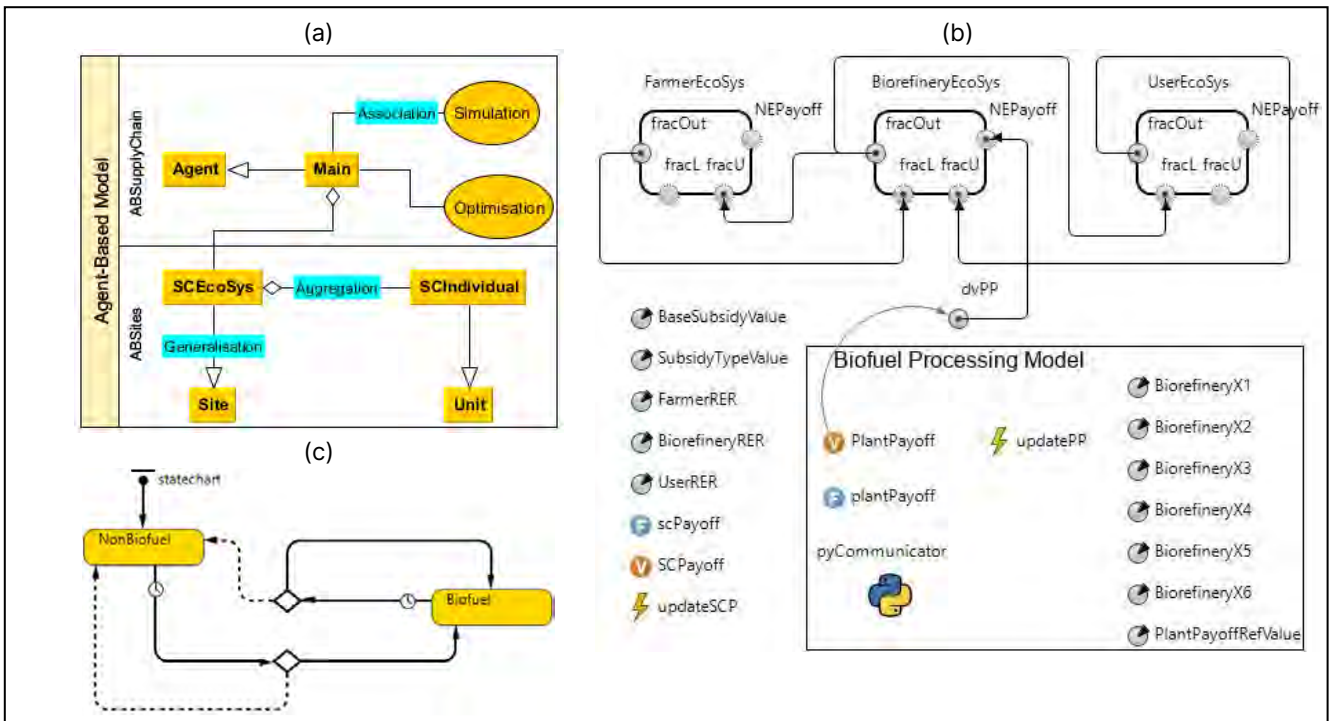



**Figure 2:** Schematic representation of the agent-based model employed. (a) shows the higher abstraction levels, (b) gives a representation of the biofuel SC at the planning level, and (c) illustrates an entity behaviour at the individual level.

Their choices are based on the perceived benefits of each resource. While these decisions are rational, they may not always result in the best overall performance for the system. Due to these similarities, the agent-based modelling approach is selected to reflect the complex process and energy systems. The framework materialises a two-level hierarchy by conceptualising and abstracting specific supply networks [1, 8]. For implementation purposes, the AnyLogic software (ver. 8.7.9) [9] is employed due to its ease of use in incorporating different intricacy levels.

## Supply Chain Domain Model

Figure 2(a) shows the domain model, in which connections of two broad modules are established. The supply chain module offers the main functionality to represent the overall structure of supply networks. At the same time, the site module involves elements comprising Unit and Site to capture the details of an individual or ecosystem in a network.

## Application-Level Model

The specialised model, as illustrated in Figure 2(b), supports the high-abstraction model for the biofuel adoption problem and encompasses three interconnected agents to represent partners of the SC. The framework reflects the two-option behaviour of each component in the system, as demonstrated in Figure 2(c). A linear realisation of coupled payoff functions is used, similar to the case discussed in the previous investigation [1]. The process model is deployed in Python using Pyomo (ver. 6.8.0 ) [10] and connected to the main platform via the Pypeline interface.

## Solution Strategy

The solution strategy is depicted in Figure 3.

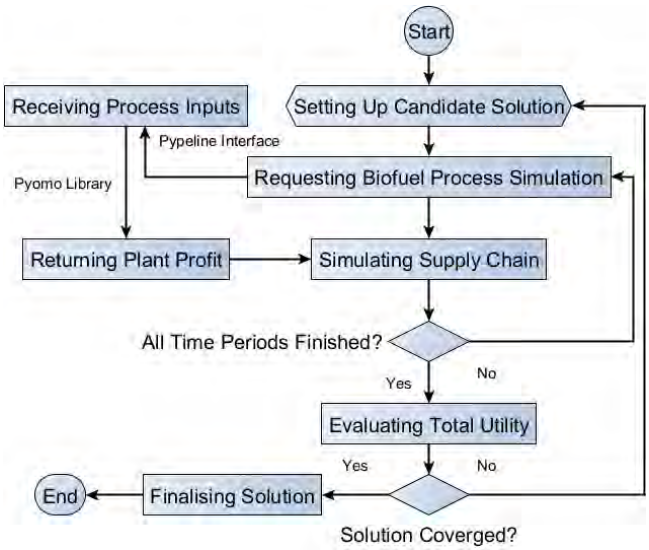



**Figure 3.** The solution workflow.

As seen in the figure, the optimisation engine creates a candidate solution comprising the re-evaluation

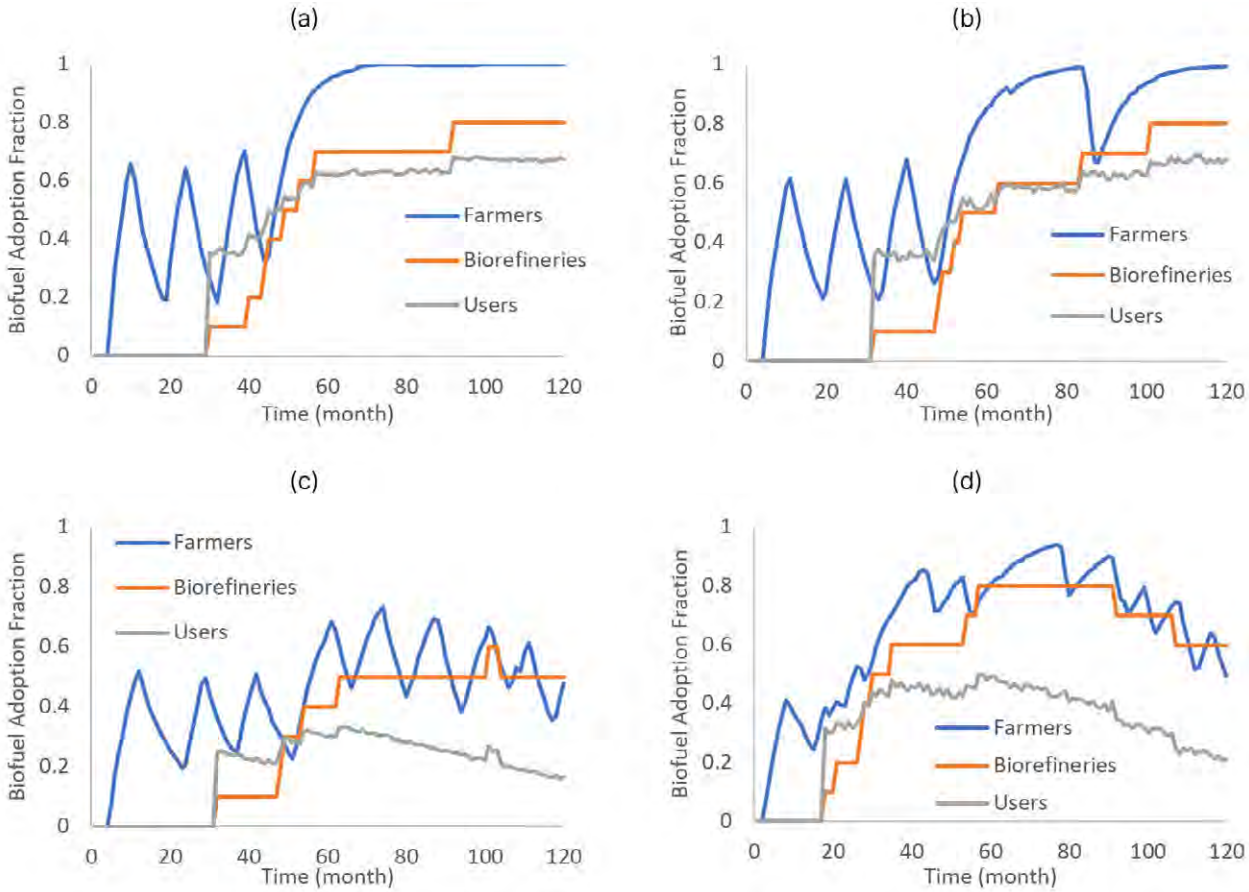



**Figure 4:** The variation of adoption fraction over time for (a) Scenario 1, (b) Scenario 2, (c) Scenario 3, and (d) Scenario 4.

rates and biofuel process variables and sends it to the corresponding ecosystems. Each ecosystem computes its contribution to the total utility and sends the information to the main agent. For the biorefinery optimisation, process variables are sent to the external Python model, and the obtained profit value is used to scale the respective ecosystem payoff. In this context, the process model is an implicit constraint of the optimal adoption problem. The aggregated utilities are then calculated, and if required, a new candidate solution is generated to be utilised for the next iteration. Notably, without the biorefinery's implicit constraints and under specific conditions with no delays and uncertainties, the optimisation and agent interactions may lead to an equilibrium point (See [1]).

## CASE STUDY

A biofuel SC case study is adopted from the prior study [1]. The specific model and parameters for biofuel plants [7] are also incorporated into the optimisation problem. Four scenarios are considered, details of which are summarised in Table 1. As seen in the table, the considered cases are characterised by different subsidy levels or delay parameters (scaled against default values), and the inclusion or absence of the biorefinery considerations (Equations 5-7). Notably, two subsidy types, constant and phased-out policies, are considered. The subsidy values positively affect the payoff of adopting biofuels in each ecosystem. While both types have a similar base value, the latter is in full effect at the start and linearly decreases to zero at the final period [1].

**Table 1:** Implemented scenarios.

| No. | Process Constraints | Subsidy (Base Value) | Delay Scale Factor |
|---|---|---|---|
| 1 | No | Constant (5) | 1 |
| 2 | Yes | Constant (5) | 1 |
| 3 | Yes | Phased-Out (5) | 1 |
| 4 | Yes | Phased-Out (5) | 1/2 |

The dynamic adoption problem (Equations 1-7), implemented in the AnyLogic environment, is optimised using OptQuest solver across 10 years with monthly sample periods. Ecosystem populations of farmers, biorefineries,

and users are 1000, 10, and 30000, respectively. A maximum of 1000 generations is used as the convergence measure to improve performance, compared to the default criteria. Other considerations, such as raw material and biodiesel prices and bounds for the ecosystem parameters, remain the same as in the prior works [1, 7]. Notably, the existence of delay and uncertain parameters and process constraints pose a serious challenge in reaching and identifying equilibria in discussed scenarios. The implemented scenarios intend to evidence the impacts of decision-level integrations and intricate considerations (delays and uncertainties) on the SC's overall performance. All experiments are performed on an Intel(R) Xeon(R) CPU E5-2620 processor and 128GB RAM.

## RESULTS AND DISCUSSION

Figure 4 presents the predicted adoption fraction over time for the different scenarios. In addition, the supply chain decision variables and utility function values are listed in Table 2. In the following sections, the study results are discussed.

**Table 2:** Scenario results.

| No. | $\alpha_{Farmers}$ | $\alpha_{Biorefineries}$ | $\alpha_{Users}$ | $u_T$ |
|---|---|---|---|---|
| 1 | 0.165 | 0.009 | 12.68 | 540.31 |
| 2 | 0.13 | 0.008 | 26.81 | 536.15 |
| 3 | 0.089 | 0.008 | 7.33 | 823.24 |
| 4 | 0.083 | 0.014 | 18.11 | 731.63 |

### Influences of The Biofuel Process Model

As seen in Figures 4(a) and 4(b), there is a significant difference in the adoption fraction of actors in the system, particularly in the later time horizons. This comparison indicates the impacts of the biofuel process on SC behaviour. While biorefineries attain similar adoption fractions in both cases, a late accelerated adoption and a subsequent drop (particularly for farmers) can be seen in the second scenario. This observation can be attributed to the fact that processing plant integration enhances the whole environment's visibility, slightly downgrading the actors' participation. In addition, the second scenario features the coupling of raw material supply from farmers and biofuel demand from users. At later planning stages, the increased potential supply of feedstocks creates local competition among farmers, adversely influencing their adoption. The resulting drop has cascading effects on downstream actors, as shown in Figure 4(b).

The same conclusion can be drawn by comparing the objective function values in Table 2, in which incorporating plant constraints leads to a more accurate estimation of the total utility. Here, the changes in SC decision variables are more noticeable, particularly the re-evaluation rates of users. Based on Table 2, due to the introduction of process constraints, users re-evaluate their decisions more frequently. At the same time, other ecosystems assess their decisions less regularly, so emergent and asymmetrical effects on farmers and users can be observed.

### Subsidy and Delay Effects

Figures 4(b) and 4(c) show that a constant subsidy leads to higher overall adoption fractions, indicating its effectiveness in promoting consistent adoption. However, the declining subsidy leads to a higher total utility value, owing to the regular changes in the adoption patterns. Therefore, a trade-off between subsidy types and values exists, potentially guaranteeing a less oscillating adoption and higher payoffs.

Scenario 4 has a reduced delay factor compared to Scenario 3. Figures 4(c) and 4(d) reveal that a smaller delay factor results in faster adoption rates, highlighting the importance of information flow and responsiveness in the SC. The reduced information delay also translates to higher adoption fractions across all parties. In contrast, increased information flows lead to a lower utility and a less stable adoption pattern, specifically for biorefineries and end-users.

Overall, Figure 4 and Table 2 provide evidence supporting the argument that biofuel SC models should consider process details, policy types, and information delays to represent system behaviour accurately. These factors directly impact the adoption patterns of different actors, ultimately influencing the success of policy implementation.

## CONCLUSION

This work proposes an agent-based framework to explore the multi-scale integration of process plant constraints and the dynamic interactions of multiple actors in the context of process and energy SCs. The developed model implements a bilevel structure to reflect the general and specialised cases such as biofuel SCs. The agent technology effectively captures the interdependencies and feedback relationships among different actors. By accounting for these actors' individual decisions and behaviours, the model provides a more comprehensive representation of the SC dynamics and reveals the potential for emergent system-level behaviours that may not be apparent in simpler models and conventional research works.

The capability of the framework is evidenced via a biofuel SC case study. The SC actors, namely farmers, biorefineries, and end-users, interact in a dynamic network. The case study aims to find an optimal collective adoption pattern based on a two-option strategy at individual levels. Multiple optimisation scenarios featuring

different parameter values and subsidy types are implemented to evaluate the SC aggregated payoff and adoption behaviours. The results show that integrated decision-making leads to a more realistic and insightful biofuel SC model. Integrating process constraints results in a more accurate estimation of the total utility function compared to models that rely on simplified unit operation representations. The findings also underscore the importance of moving beyond the traditional assumption that biorefineries are the sole decision-makers in the SC.

The advantages that arise from this framework extend beyond those mentioned in this study. In this regard, future research should include a better representation of individual payoff functions to capture the intricacies and interactions in biofuel SCs. Furthermore, policy efforts should focus on implementing more complex subsidy types and environmental sustainability measures. By embracing a more holistic and dynamic modelling approach, researchers and decision-makers can better understand the biofuel SC and develop more effective strategies to address the challenges and opportunities associated with this emerging industry.

## ACKNOWLEDGEMENTS

This research is funded by the Department of Health and Social Care using UK Aid funding and is managed by the EPSRC. The views expressed in this publication are those of the authors and not necessarily those of the Department of Health and Social Care.

## REFERENCES

1. D. Agusdinata, S. Lee, F. Zhao, W. Thissen. Simulation modeling framework for uncovering system behaviors in the biofuels supply chain network. *SIMULATION* 90 (2014):1103–1116 https://doi.org/10.1177/0037549714544081
2. D. Kumari, R. Singh. Pretreatment of lignocellulosic wastes for biofuel production: a critical review. *Renewable and Sustainable Energy Reviews* 90 (2018):877-891 https://doi.org/10.1016/j.rser.2018.03.111
3. S. Shirazaki, M. S. Pishvaee, M. A. Sobati. Integrated supply chain network design and superstructure optimization problem: a case study of microalgae biofuel supply chain. *Computers & Chemical Engineering* 180 (2024): 108468 https://doi.org/10.1016/j.compchemeng.2023.108468
4. M. Umar, M. Tayyab, H. R. Chaudhry, C.-W. Su, N. Navigating epistemic uncertainty in third-generation biodiesel supply chain management through robust optimization for economic and environmental performance. *Annals of Operations Research* (2023): 1-40 https://doi.org/10.1007/s10479-023-05574-1
5. S. Bairamzadeh, M. Saidi-Mehrabad, M. S. Pishvaee. Modelling different types of uncertainty in biofuel supply network design and planning: A robust optimization approach. *Renewable energy* 116 (2018): 500-517 https://doi.org/10.1016/j.renene.2017.09.020
6. P. Yang, X. Cai, X. Hu, Q. Zhao, Y. Lee, M. Khanna, Y.R. Cortés-Peña, J.S. Guest, J. Kent, T.W. Hudiburg, E. Du. An agent-based modeling tool supporting bioenergy and bio-product community communication regarding cellulosic bioeconomy development. *Renewable and Sustainable Energy Reviews* 167 (2022): 112745 https://doi.org/10.1016/j.rser.2022.112745
7. L. Zhou, M. Pan, J.J. Sikorski, S. Garud, L.K. Aditya, M.J. Kleinelanghorst, I.A. Karimi, M. Kraft. Towards an ontological infrastructure for chemical process simulation and optimization in the context of eco-industrial parks. *Applied Energy* 204 (2017): 1284-1298 https://doi.org/10.1016/j.apenergy.2017.05.002
8. R. Milton, P. Jagroop, S. F. Brown. Technoeconomic process modelling of waste remediation within a supply chain network. *Computer Aided Chemical Engineering*. 52 (2023) 2649-2654 https://doi.org/10.1016/B978-0-443-15274-0.50421-2
9. A. Borshchev. Multi-method modelling: AnyLogic. (2014): 248-279 In: Discrete-Event Simulation and System Dynamics for Management Decision Making. Ed: S. Brailsford, L. Churilov, B. Dangerfield John Wiley & Sons, Ltd (2014) https://doi.org/10.1002/9781118762745.ch12
10. William E. Hart, Jean-Paul Watson, David L. Woodruff. Pyomo: modeling and solving mathematical programs in Python. *Mathematical Programming Computation* 3(3) (2011): 219-260 https://doi.org/10.1007/s12532-011-0026-8

© 2025 by the authors. Licensed to PSEcommunity.org and PSE Press. This is an open access article under the creative commons CC-BY-SA licensing terms. Credit must be given to creator and adaptations must be shared under the same terms. See https://creativecommons.org/licenses/by-sa/4.0/



Systems & Control Transactions

**Research Article - Peer Reviewed Conference Proceeding**
ESCAPE 35 - European Symposium on Computer Aided Process Engineering
Ghent, Belgium. 6-9 July 2025
Jan F.M. Van Impe, Grégoire Léonard, Satyajeet S. Bhonsale,
Monika E. Polańska, Filip Logist (Eds.)

PSE PRESS

# Comparison of optimization methods for studying the energy mix of infrastructures. Application to an infrastructure in Oise, France

**Julien JEAN VICTOR[a], Zakaria A. SOULEYMANE[b], Augustin MPANDA[b], Philippe TRUBERT[c], Laurent FONTANELLI[a], Sébastien POTEL[a], Arnaud DUJANY[a]***

[a] Institut Polytechnique UniLaSalle, GeNumEr, URR 7511, 60000 Beauvais, France
[b] Institut Polytechnique UniLaSalle, GeNumEr, URR 7511, 80080 Amiens, France
[c] Syndicat mixte de l'aéroport de Beauvais-Tillé (SMABT), 1 rue du Pont de Paris - 60000 Beauvais
* Corresponding Author: arnaud.dujany@unilasalle.fr

## ABSTRACT

In the last decades, the growing awareness of climate change and the high political sensitivity of critical resources such as energy have emphasized a need for local, renewable and optimized energy mixes at various scales. Several studies have therefore aimed to optimize renewable energy technologies and plant locations to develop more renewable and efficient Energy Mixes. Following this trend, this paper applies and compares Goal Programming, Branch-and-Cut and NSGA-II to a multi-objective combinatorial optimization problem focused on the energy mix of Oise, France. Results show more optimality for Goal Programming and Branch-and-Cut, accompanied by a high sensitivity to constraints, while NSGA-II provides more technological diversity in the computed solutions.

**Keywords**: Energy Systems, Optimization, Genetic Algorithm, Stochastic Optimization, Goal Programming, Branch-and-Cut, Energy Mix

## 1. INTRODUCTION

The global rise of climate change awareness and its urgency has prompted governmental and intergovernmental organisations to update their policies in several areas. Environmental considerations have become paramount in the design of energy mixes, and renewable energy sources are now widely preferred to fossil fuels. The latter have also become highly sensitive to geopolitical issues and conflicts, making energy a critical resource more than ever. These environmental and economic incentives have led economic regions at different scales to improve their energy mixes and achieve energy independence [1]. The development of optimized, renewable and local energy mixes is therefore strongly supported by both environmental and economic situations globally [2].

The optimization of renewable energy technologies, plant locations and energy mixes has been the objective of several studies in the last decades, aiming to develop more renewable and efficient energy mixes [3]. Most of these optimization problems are solved using Mixed-Integer Linear Programming (MILP), Mixed-Integer Non-Linear Programming (MINLP) or heuristic algorithms [3].

This study aims to compare three optimization methods in their application to the optimization of the energy mix of Oise, France, focused on the Paris-Beauvais Airport, from environmental and economic perspectives.

The focus is put on annual production potential at a regional scale and therefore does not consider decomposition optimization methods, better suited to problems involving temporal variation or multiple time periods. For this study, Goal Programming, Branch-and-Cut and Non-dominated Sorting Genetic Algorithm II (NSGA-II) were selected for their wide use and coverage of problem formulations The first two can easily handle MILP and MINLP problems but require the problem to be expressed as a single objective function. On the other hand, NSGA-II can handle both objectives separately [4,5].

After census of energy resources already present in the target area, the available energy mix undergoes a

carbon footprint evaluation that serves as the environmental component of the problem [6]. The economic component is based on the Levelized Cost of Energy (LCOE), an aggregation of operating, maintenance and installation costs. These two components constitute the objectives of the problem, either treated separately or weighted in a single objective function depending on the optimization method. The three selected methods are applied to the problem, and the results provided by each are gathered and assessed based on criteria such as optimality of solutions, sensitivity to constraints and parameters, execution time and diversity of solutions. The evaluated methods are then compared against these criteria, to identify their strengths and weaknesses of each method regarding the studied problem.

The aim of the study is to assess not only optimality but also diversity of solutions and to identify acceptable trade-offs between the two. This could lead to the development of a hybrid method ideally fitted to this energy mix optimization problem.

# 2. METHODS

## 2.1 Choice of optimization methods

The methods compared in this study are Goal Programming, Branch-and-Cut and NSGA-II. They approach problems very differently but are all recognized and widely used for multi-objective combinatorial optimization problems. Each of these methods has its own strengths and weaknesses, but all three are suitable for the energy mix optimization problem studied and described later in this paper [7,8].

### 2.1.1 Goal Programming

Goal Programming is known for being ideal in multi-criteria decision-making problems, especially with conflicting objectives. Computationally, it is the simplest method of the three, essentially defining an ideal solution from given objectives and calculating deviations between possible solutions and the ideal one. In this way, it can handle multiple conflicting objectives, allowing the decision-makers to prioritize one objective over others, addressing trade-offs explicitly. In the case of energy-related problems, it has been applied to several energy-planning issues, especially to handle the conflict between financial costs and greenhouse gases emissions [7,9]. Its simplicity and its ease in dealing with conflicting objectives make Goal Programming fitted to the energy mix optimization problem later described in this paper.

### 2.1.2 Branch-and-Cut

The Branch-and-Cut optimization method combines Branch-and-Bound and Cutting-Planes, two algorithmic approaches, to solve mixed-integer linear programming (MILP) problems. Branch-and-Cut explores the space of feasible solutions by creating branches of decision variables, then refines the solution space with cutting planes to remove identified non-optimal solutions. While it can find guaranteed global optima for MILP problems, its computation times can rise quickly depending on problem size. However, Branch-and-Cut is well suited to problems involving discrete variables, which is often the case with Energy-related scenarios [10]. Despite it being a combinatorial optimization problem, the studied optimization problem is rather small and can be optimized using the Branch-and-Cut method.

### 2.1.3 Non-dominated Sorting Genetic Algorithm (NSGA-II)

Unlike previous methods, NSGA-II uses a stochastic approach to solve more complex, non-linear problems. It is widely used for multi-objective optimization problems, including energy mix optimization problems. It generates successive populations of candidate solutions before ranking them according to Pareto dominance. Although it is computationally intensive, it provides flexibility in handling non-linear, non-convex problems, making it a widely used method in a variety of fields, including energy problems for energy development and greenhouse gases (GHG) emission reduction [8,11]. In the case of the studied energy mix optimization problem, the key asset it provides is the Pareto-front solutions which, while not guaranteeing global optimality, allows to test trade-offs without having to implement weights. A comparison of optimality between NSGA-II solutions and deterministic algorithms will allow to assess the acceptability of solutions regarding optimality, while still exploring technological diversity in the computed energy mix optimizations.

## 2.2 Studied optimization problem

The case study for this work is a combinatorial optimization problem for the energy mix of Oise, France. The problem consists in the selection of energy sources from a given dataset [12–15], presenting as a list of potential installations. The optimization algorithms then combine multiple of these installations to build an energy mix. To do so, the objective function is based on two criteria, an environmental criterion and a economic criterion. The first is derived from the energy mix evaluation method proposed in [6]. It consists of three emission components, expressed in tons of expressed in tons of CO2eq per year. The first component is a product of energy production and an energy source emission factor, the second represents emissions due to urbanization, and the third translate the emissions depending on the distance between the energy source and the consuming infrastructure.

The economic criterion is based on the Levelized Cost Of Energy (LCOE) data from [16]. It also depends on

the annual production and is expressed in euros per year. The problem is therefore expressed in Equations (1), (2) and (3).

$$minf_{env}(P) = \sum_{i=1}^{n}(P_i * EES_i + CFU_i + CFD_i) \quad (1)$$

$$minf_{eco}(P) = \sum_{i=1}^{n}(P_i * LCOE_i) \quad (2)$$

$$\sum_{i=1}^{n}(P_i) \geq PMin \quad (3)$$

With EES the GHG emission factor assigned to production, CFU the emissions of urbanization and CFD the emissions assigned to distance [6,12,13]. PMin is the target annual production to reach and varies between 0 and the total annual production for the dataset.

## 2.3 Python Implementation

The optimization of the problem with Goal Programming, Branch-and-Cut and NSGA-II was implemented using the Python programming language, chosen for its versatility and wide number of libraries. Moreover, Python offers accessibility and is ideal for open-source applications.

### 2.3.1 Goal Programming

The solving of the optimization problem by Goal Programming was implemented using PuIP, an open-source Python library. To guide the algorithm in decisions between the conflicting objectives, weights $\alpha$ and $\beta$ were introduced, summing to 1 and weighting the environmental and economic criteria respectively. Both components were then added up in a single objective function and therefore needed to be comparable. The LCOE value, expressed in €/y, was converted to $tCO_{2eq}$/y using the Social Cost of Carbon (SCC) as the average of calculations in the literature from 2018 to 2022 [17]. The final objective function for Goal Programming application is expressed in Equation (4).

$$minf_{env}(P) = \alpha \sum_{i=1}^{n}(P_i * EES_i + CFU_i + CFD_i) + \beta \sum_{i=1}^{n}(P_i * LCOE_i * SCC) \quad (4)$$

Using the PuIP library, a Linear Programming problem was specified. The decision variable for each item was defined as a binary value: each item is either included or not included in the final solution. Deviations were defined from zero for objectives to minimize, and from PMin for the target production constraint.

### 2.3.2 Branch-and-Cut

The solving of the optimization problem with Branch-and-Cut was also implemented using PuIP. The weights implemented in the Goal Programming method were retained to allow comparison between the two approaches. Similarly, both objectives were combined into a single objective function, and the LCOE value was also converted to $tCO_{2eq}$/y using the SCC. The PuIP library-implementation also uses the *LpProblem* function and a binary decision variable. The cutting plane methods used for this optimization were Gomory cuts, Knapsack cuts, suitable for combinatorial problems, and Probing cuts, which are suited to problems with binary variables.

### 2.3.3 Non-dominated Sorting Genetic Algorithm (NSGA-II)

The solving of the optimization problem with NSGA-II was implemented using the DEAP Python library. Unlike previous methods, both objectives can be evaluated together without having to sum them or implement weights. The algorithm was initially run with a population of 100 at generation 0, a crossover probability of 75% and a mutation probability of 20%, for a duration of 300 generations. To ensure that the production constraint is met, an infinite penalty is applied to both minimization objectives for all individuals that do not reach the production objective.

# 3. RESULTS

## 3.1 Goal Programming

Goal Programming was applied to the problem with a weight of 0.65 for the $\alpha$ parameter and 0.35 for $\beta$, while the minimum energy production (PMin) was set at 1422 GWh/y, representing 60% of the maximum possible production. Results showed a significant dominance of wind energy, with 53 out of the 66 selected installations being wind turbines, accounting for approximately 81% of the total production (**Table 1**).

**Table 1:** Summed results for the Goal Programming optimization, with PMin=1422, $\alpha$=0.65, $\beta$ =0.35. P_Tot is the total production, in GWh/y. T_Env is the environmental component of the objective function and T_Eco the economic component of the objective function, both in $tCO_{2eq}$/y.

| Energy | Count | P_Tot | T_Env | T_Eco |
|---|---|---|---|---|
| Wind | 53 | 1153.2 | 25112 | 20373 |
| Solar | 2 | 0.1 | 5 | 4 |
| Biomethane | 11 | 268.7 | 6290 | 8508 |
| Total | 66 | 1422.0 | 31408 | 28885 |

Further computations were performed with weight values varying between 0.05 and 0.95, and target production varying between 40% and 60% of total production. PMin is the most influential parameter on results,

and the algorithm is less sensitive to weighting when PMin is lower, resulting in fewer optimal solutions and more convergence (**Figure 1**).

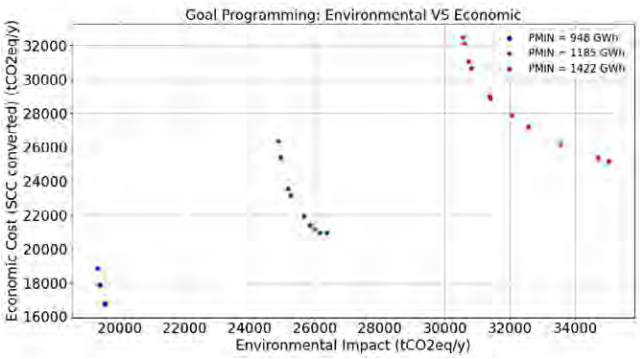



**Figure 1:** Compared results of the optimization with the Goal Programming approach, with varying PMin, $\alpha$ and $\beta$

## 3.2 Branch-and-Cut

The Branch-and-Cut method was applied to the optimization problem, with the same values of PMin, $\alpha$, and $\beta$, and with the same variations as with Goal Programming. The results obtained were identical: the total values were the same, as the exact same elements were selected by both approaches. The trends observed based on the variables therefore remain consistent for Branch-and-Cut. The only difference observed between the methods is a variation in execution time, with Branch-and-Cut being 8% faster than Goal Programming.

## 3.3 NSGA-II

Unlike previous methods, no weights were applied in the NSGA-II optimization. As a stochastic approach, the algorithm was run multiple times with the same PMin value and could inherently explore different trade-offs. Different iterations with identical parameters therefore resulted in slightly different Pareto-fronts. The computed results differ significantly from those produced by Goal Programming and Branch-and-Cut (**Figure 2**).

NSGA-II computed results are globally less optimal for both criteria, and tend to exceed the production constraint more than necessary, often by more than 1 GWh/y. They also tend to return higher values for the environmental objective and favour minimizing the economic component of the problem. Computation times for the NSGA-II optimizations were about 15 times faster than Goal Programming or Branch-and-Cut and rarely lasting more than a dozen seconds. The initial population size was therefore increased to 2000 and 5000, which showed a positive impact and partially resolves the optimality problem, with results much closer to Goal Programming and Branch-and-Cut, although still less optimal. However, computation times were raised significantly (circa 500 times longer for a population of 5000).

The population size increase mitigated the excess production in solutions, although solutions provided still exceed the threshold production constraint. On the other hand, NSGA-II solutions appear to provide more diversity in the technologies used to reach that threshold (**Table**

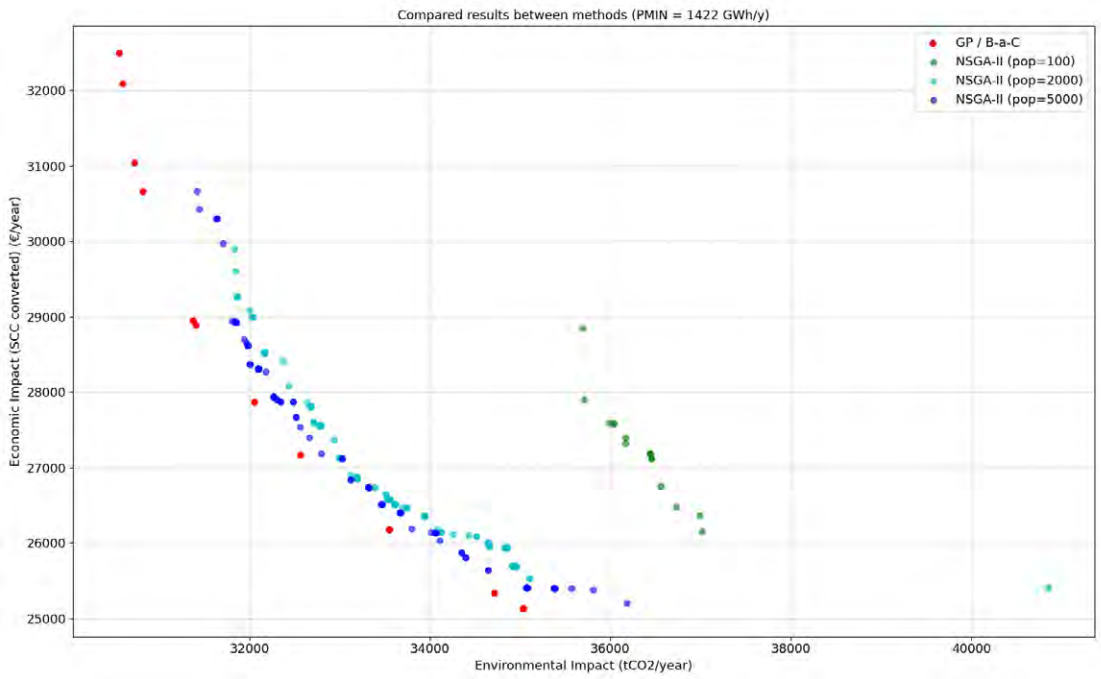



**Figure 2:** Comparison of optimization results for three NSGA-II runs with results for Goal Programming / Branch-and-Cut. Production target value is fixed to 1422 GWh/y.

**2**), using more solar plants than Goal Programming or Branch-and-Cut methods. Upscaling tests were performed, and results suggest that the optimality difference between NSGA-II and deterministic methods increases with the number of selectable items, as well as the computation times, while maintaining technological diversity.

**Table 2:** Mean results for NSGA-II optimization computation with PMin=1422. P_Tot is the reached production, in GWh/y.

| Energy | Count | P_Tot |
|---|---|---|
| Wind | 54.79 | 1231.59 |
| Solar | 111.22 | 10.58 |
| Biomethane | 8.88 | 181.03 |
| Bioenergy | 0.32 | 0.53 |
| Total | 175.22 | 1423.74 |

## 4. DISCUSSION

The Goal Programming results show an over-representation of wind energy installations compared to the original dataset. This can be explained by the evaluation methods, which both favor wind power installation. Moreover, wind turbines are individually some of the most productive installations, so the reward for incorporating them in the mix is high. This bias could be controlled and limited by adding a third objective, possibly regarding the flexibility or controllability of the production, or social acceptance of the project.

The high similarity between Goal Programming and Branch-and-Cut results confirms the optimality of found solutions. These two computational approaches, both deterministic, are therefore computationally closer to each other than to NSGA-II, thus explaining the observed disparities with the latter's results. Though they provide optimality in this study, further work may introduce additional objectives and constraints that may be too complex for deterministic approaches and require an evolution of the method. In addition, the algorithms require weights to explore the solution space, which induces a high dependency between the results and the $\alpha$ and $\beta$ parameters, especially with high PMin values. This could mean that a small number of items in the dataset are significantly better than others in regard to both criteria and would therefore be systematically preferred in cases with low PMin, resulting in a weight dependence increasing with target production. On the other hand, NSGA-II can explore different regions of the solution space and find trade-offs without these weights.

Concern is raised regarding NSGA-II, since the pareto fronts produced were not as optimal as the results of previous methods. The efficiency of the method on this problem can be doubted, although some explanation can also be provided by the strong penalties implemented in the computation. The algorithm is so strongly encouraged to reach the production constraint, that it seems reluctant to slightly reduce production to find more optimal solutions in terms of the environmental and economic objectives. Although increasing the population size partially solved this issue, upscaling the problem could prove difficult, with a larger dataset implying even longer computation times. However, the technological diversity provided by NSGA-II is significantly better than that of deterministic approaches, which supports interest in pursuing the research of trade-offs between optimality and technological diversity, as long as computational times remain acceptable. To pursue this goal, a hybrid approach could be considered, incorporating portions of the deterministic approaches to reduce the solution space and thus guide the NSGA-II towards more optimized results.

## 5. CONCLUSION

The comparative analysis of Goal Programming, Branch-and-Cut, and NSGA-II for a combinatorial energy mix optimization problem in Oise, France, shows nuanced insights. Goal Programming and Branch-and-Cut produced remarkably similar results, demonstrating good solution optimality and computational efficiency with a strong dependence to the input dataset, translating to a distinct preference for wind energy installations. This underlines an interesting development opportunity for introducing additional objectives like production flexibility or social acceptance to create more fitted optimization approaches.

NSGA-II provided less optimal solutions than deterministic methods across both environmental and economic criteria, which correlates with existing literature. However, the optimality difference reduces with the population size used for NSGA-II computation, with an increase in computational time. The method's performance was constrained by strict production penalties, which may have limited its ability to find optimal solutions and explore more nuanced trade-offs. However, its overperformance regarding the production threshold criteria and the greater technological diversity it provides in its solutions suggest that an acceptable trade-off between optimality, computation time and technological diversity can be found.

Future research should focus on refining penalty mechanisms, implementing additional objectives and constraints to progress towards better suited optimization algorithms, both in terms of computational methodology and parameter definition. Opportunities for hybrid methods should not be ignored and will be considered in future works.

## ACKNOWLEDGEMENTS

The authors gratefully thank the SMABT and the SAGEB, the research chair "GéoAgroÉnergies et Environnement" and the Hauts-de-France region (N° PAS ALRC2.0-000701) for the support provided for this work and the financing of the thesis of Julien JEAN-VICTOR and Zakaria A. SOULEYMANE.

## REFERENCES

1. International Renewable Energy Agency (IRENA). Renewable power generation costs in 2022. Abu Dhabi: IRENA; 2023.
2. Østergaard PA, Sperling K. Towards Sustainable Energy Planning and Management. Int J Sustain Energy Plan Manag. 2014; 1:1–5.
3. Ilbahar E, Cebi S, Kahraman C. A state-of-the-art review on multi-attribute renewable energy decision making. Energy Strategy Rev. 2019 Aug 1; 25:18–33.
4. Jaber A, Younes R, Lafon P, Khoder J. A Review on Multi-Objective Mixed-Integer Non-Linear Optimization Programming Methods. Eng. 2024; 5(3) p. 1961–79.
5. Moret S, Bierlaire M, Maréchal F. Strategic Energy Planning under Uncertainty: A Mixed-Integer Linear Programming Modeling Framework for Large-Scale Energy Systems. In: Kravanja Z, Bogataj M, editors. Computer Aided Chemical Engineering. Elsevier; 2016. p. 1899–904. (26 European Symposium on Computer Aided Process Engineering; vol. 38). doi: 10.1016/B978-0-444-63428-3.50321-0
6. Jean Victor J, Labauge C, Trubert P, Mpanda A, Fontanelli L, Potel S, et al. Development of an energy mix evaluation method of an infrastructure based on a multi-layered territorial approach. In: Manenti F, Reklaitis GV, editors. Computer Aided Chemical Engineering; Elsevier; 2024 p. 3391–6. (34 European Symposium on Computer Aided Process Engineering / 15 International Symposium on Process Systems Engineering; vol. 53). doi: 10.1016/B978-0-443-28824-1.50566-4
7. Chang CT. Multi-choice goal programming model for the optimal location of renewable energy facilities. Renew Sustain Energy Rev. 2015; 41:379–89. doi: 10.1016/j.rser.2014.08.055
8. Verma S, Pant M, Snasel V. A Comprehensive Review on NSGA-II for Multi-Objective Combinatorial Optimization Problems. IEEE Access. 2021; 9. doi: 10.1109/ACCESS.2021.3070634
9. San Cristóbal JR. A goal programming model for the optimal mix and location of renewable energy plants in the north of Spain. Renew Sustain Energy Rev. 2012; 16(7): 4461–4. doi: 10.1016/j.rser.2012.04.039
10. Marcovecchio MG, Novais AQ, Grossmann IE. Deterministic optimization of the thermal Unit Commitment problem: A Branch and Cut search. Comput Chem Eng. 2014; 67:53–68. doi: 10.1016/j.compchemeng.2014.03.009
11. Koroneos C, Michailidis M, Moussiopoulos N. Multi-objective optimization in energy systems: the case study of Lesvos Island, Greece. Renew Sustain Energy Rev. 2004; 8(1): 91–100. doi: 10.1016/j.rser.2003.08.001
12. European Environment Agency [Online]. [cited 30/11/2024]. Carbon stocks and sequestration in terrestrial and marine ecosystems: a lever for nature restoration? Available from: https://www.eea.europa.eu/publications/carbon-stocks-and-sequestration-rates/carbon-stocks-and-sequestration-in
13. Documentation des jeux de données monocritères issus de la Base Carbone® | Base Empreinte® [Online]. [cited 30/11/2024]. Available from: https://base-empreinte.ademe.fr/documentation/base-carbone
14. Points d'injection de Biométhane en France en service [Online]. [cited 30/11/2024]. Available from: https://odre.opendatasoft.com/explore/dataset/points-dinjection-de-biomethane-en-france/information/
15. Registre national des installations de production et de stockage d'électricité [Online]. [cited 30/11/2024] Available from: https://odre.opendatasoft.com/explore/dataset/registre-national-installation-production-stockage-electricite-agrege/information/
16. Arnaud B, Parrouffe JM, Louillat S, Haeusler L, Toe S, Elmoujarrade C. Coûts des énergies renouvelables et de récupération - données 2022 [Online]. Angers: ADEME; 2022. Report No.: 011599. ISBN: 979-10-297-1862-5. Available from: https://librairie.ademe.fr/societe-et-politiques-publiques/5460-couts-des-energies-renouvelables-et-de-recuperation-en-france.html
17. Tol RSJ. Social cost of carbon estimates have increased over time. Nat Clim Change. 2023 Jun;13(6):532–6. doi: 10.1038/s41558-023-01680-x

© 2025 by the authors. Licensed to PSEcommunity.org and PSE Press. This is an open access article under the creative commons CC-BY-SA licensing terms. Credit must be given to creator and adaptations must be shared under the same terms. See https://creativecommons.org/licenses/by-sa/4.0/



Systems & Control Transactions

**Research Article - Peer Reviewed Conference Proceeding**
ESCAPE 35 - European Symposium on Computer Aided Process Engineering
Ghent, Belgium. 6-9 July 2025
Jan F.M. Van Impe, Grégoire Léonard, Satyajeet S. Bhonsale,
Monika E. Polańska, Filip Logist (Eds.)

PSE PRESS

# Integration of MILP and Discrete-Event Simulation for Flowshop Scheduling Using Benders Decomposition

**Roderich Wallrath[a,b], Edwin Zondervan[b], and Meik B. Franke[a]***

[a] University of Twente, Faculty of Science and Technology, Enschede, The Netherlands
[b] Bayer AG, Kaiser-Wilhelm Allee 1, Leverkusen, Germany
* Corresponding Author: m.b.franke@utwente.nl.

## ABSTRACT

Real-world flowshop problems which are very common in the chemical industry are often difficult to solve in a reasonable time with allocation, sequencing, and lot-sizing decisions. Although great progress has been made in the last 20 years regarding MILP model formulations and solution algorithms, realistically-sized flowshop problems with resource and buffer constraints are still difficult to solve. On the other hand, discrete-event simulation (DES) allows for very detailed modelling of process plants, but lacking of optimization capabilities. Simulation Optimization (SO) combines the high-detail DES with mathematical optimization. We show that is possible to integrate MILP and DES using Benders decomposition. We explain the Benders-DES (BDES) approach with a small motivation example with makespan minimization objective and apply it to a real-world case study of a formulation plant with seven formulation and filling lines with sequencing, allocation, and lot-sizing decisions. We show that the BDES approach performs comparably to the original monolithic-sequential MILP-DES approach. However, the key advantage of this method is the ability to leverage MILP optimization power without requiring a detailed model description.

**Keywords**: Planning & Scheduling, Optimization, Algorithms, Process Operations, Batch Process, Benders Decomposition

## INTRODUCTION

### General Motivation

In the chemical process industry, optimization-based scheduling is a critical advantage in today's fast-paced and interconnected world. However, the complexity when optimizing chemical processes is high: A chemical process that requires personnel and processing equipment, consumes raw materials and utilities, and is linked to a complex supply chain, is naturally subject to many constraints and objectives [1]. Discrete Event Simulation (DES) models can describe complex real-world processes to a great level of detail, have relatively short computation times, and allow to include uncertain parameters. However, since DES models have limited optimization capabilities, the solutions of DES models may be far away from the optimum. While MILP models enable global optimization, they quickly grow to intractable size, when trying to include all relevant constraints. In addition, MILP models can be difficult to set up, validate, and maintain for real-world applications.

### Simulation Optimization

Simulation Optimization (SO) combines the high-detail DES with mathematical optimization. SO has repeatedly shown success in solving process design and operations problems [2]. The interested reader is referred to the review [3] on DES-based optimization methods for industrial engineering problems.

However, SO approaches struggle with complex real-world models that contain many discrete and continuous decision variables and constraints. For example, in [2] the same hybrid flowshop as in this paper is solved with a genetic algorithm (GA). The authors use a detailed DES model of the plant and include lot-sizing decisions. The GA requires 200 generations with a population size of 20, which leads to several hours of solution time on large computer resources.

In [4], a simulation-optimization approach for adaptive manufacturing capacity planning in small and medium-sized enterprises is developed. An artificial neural

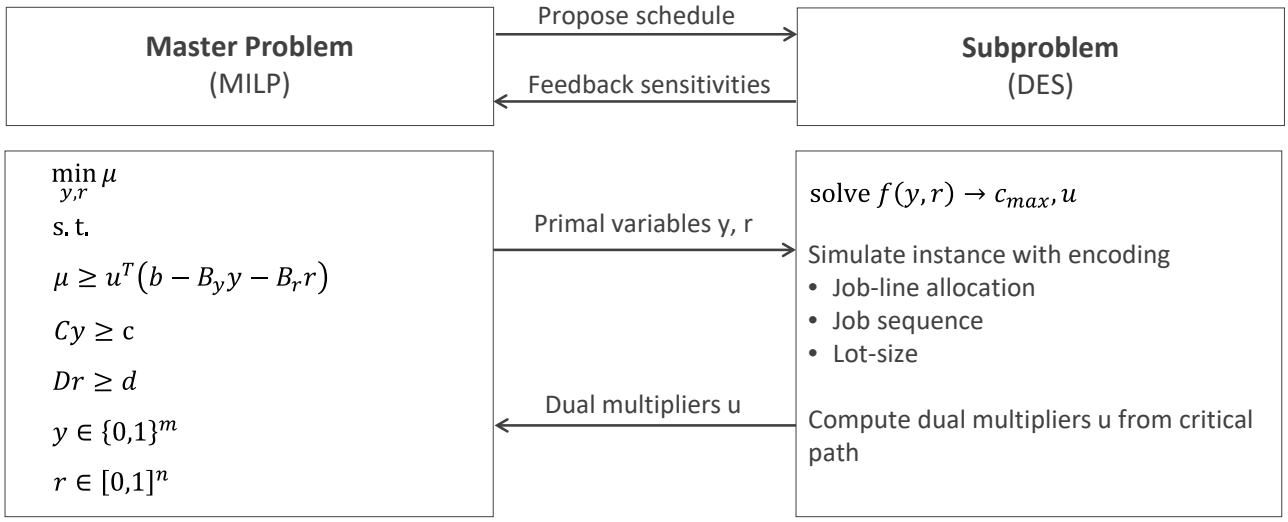



**Figure 1:** Benders-DES algorithm for hybrid flowshops. $y$ represents the discrete allocation and sequence decision variables; $r$ the continuous lot-sizing variables as split factors, which indicate what percentage of the job is covered by the lot. The objective is to minimize the makespan $c_{max}$.

network (ANN) is trained on production data of an industrial case study of pastry production and a GA is used to optimize the ANN. While this is a practical solution approach for complex problems it is concluded that the GA can be a limiting factor when exact solutions with guaranteed optimality are required.

In [5], a Digital Twin-driven dynamic scheduling approach is presented featuring a MILP model and a 3D shop floor simulation model to address a hybrid flow shop problem in perfume manufacturing. While the approach is effective and practical, it requires a "human-in-the-loop" to assess the results of the simulation model. Similarly to [6], there is no automatic feedback from the simulation to the optimization model which is a disadvantage compared to the aforementioned SO approaches.

### Contribution of this Work

This work presents a novel SO approach that integrates DES and Benders Decomposition. Sequencing, allocation, and lot-sizing are included in the Benders master problem, while important real-world constraints such as sequence-dependent changeover times, limited personnel resources, and limited intermediate buffer capacities are considered in the Benders subproblem. It is shown that the BDES can be applied to a real-world hybrid flowshop as presented in [6] and that good schedules in a reasonable amount of time can be obtained.

## METHODOLGY

### Benders Decomposition Framework

The Benders decomposition framework is shown in Figure 1. This master MILP problem proposes a new schedule (job sequence) as well as job-line allocation and lot-sizing decisions if required. Based on this information, the DES subproblem calculates the resulting schedule and returns an upper bound of the makespan and sensitivities (dual multipliers) using the concept of critical path mapping, which is explained in the next section. The dual multipliers are used to set up the Benders cuts. For every DES schedule, one Benders cut is added to the MILP master problem leading a new lower bound for the makespan. If the lower bound reaches the upper bound or the upper bound is not improving any more, the algorithm will stop. Further details can be found in [7].

### Motivating Example

The BDES approach is explained with a small flowshop problem with no intermediate storage, processing only 3 jobs (see Figure 2). The objective is to find the job sequence which minimizes the makespan. For the sake of simplicity, allocation and lot-sizing decisions play no role here. It can be shown by enumeration that *Schedule 2* of Figure 2 is the optimal one with a makespan of 6 h.

For the above mentioned flowshop, a MILP problem (1) – (6) is set up. The model formulation is based on precedence variables. The precedence variable $y_{ij}$ is one, if a job $i \in I = \{1,2,3\}$ is processed before job $j \in I = \{1,2,3\}$. $s_{il}$ is the start time variable of a job $i$ on stage $l \in L = \{1,2\}$. $p_{il}$ are the processing time parameters which can be read from Figure 2. $T$ is the Big-M constant. A valid (but weak) estimate for this value can be the summation of all processing times.

The objective (1) is to minimize the makespan $c_{max}$. Constraint (2) is the makespan constraint. Constraint (3) ensures that a job on a stage only starts after the processing of the previous stage concluded. The constraint

(4) ensures that only one job is processed at a given time on a given stage. (5) is a logical constraint.

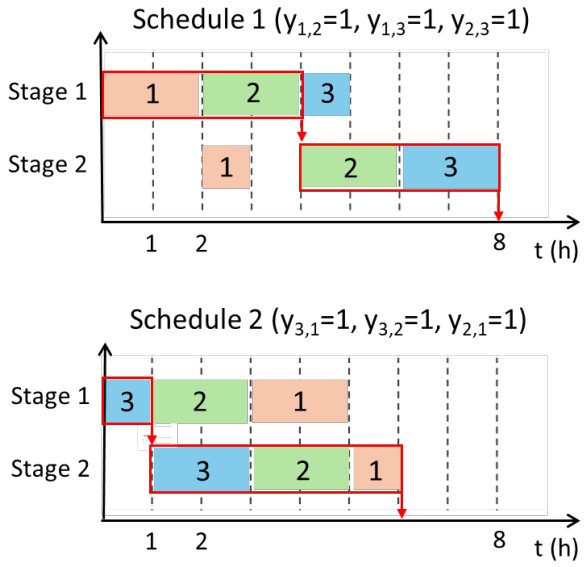



**Figure 2.** Small flowshop problem with 3 jobs and no intermediate storage (numbers in the Gantt bars indicate the job number, not the processing time). The critical paths are are indicated by the red boxes.

$$\min c_{max} \tag{1}$$

$$\text{s.t.} \quad c_{max} \geq s_{i2} + p_{i2} \; \forall \, i \in I \tag{2}$$

$$s_{il} + p_{il} - s_{il+1} \leq 0 \; \forall \, i \in I, l \in L \backslash \{2\} \tag{3}$$

$$s_{jl} + p_{jl} - T y_{ij} - s_{il} \leq 0 \; \forall \, l \in L, i, j \in I : i \neq j \tag{4}$$

$$y_{ij} + y_{ji} = 1 \quad \forall \, i, j \in I : i \neq j \tag{5}$$

When fixing the precedence variables $y_{ij}$, the MILP reduces to a LP. Defining $y_{ij}$ as complicated variables, the LP becomes the Benders subproblem in the classical Benders decomposition approach [8]. In the BDES approach, the subproblem corresponds to one DES simulation.

The LP solution returns the information of the binding constraints. For example, for *Schedule 1* in Figure 2, the following sequencing constraints are active:

$$s_{32} + p_{32} - c_{max} \leq 0 \tag{6}$$

$$s_{21} + p_{21} - s_{22} \leq 0 \tag{7}$$

$$s_{11} + p_{11} - T y_{21} - s_{21} \leq 0 \tag{8}$$

$$s_{22} + p_{22} - T y_{32} - s_{32} \leq 0 \tag{9}$$

All active constraints are associated with a non-zero dual multiplier $u$ which is -1 in case of makespan minimization, and the Benders cut can then be set up accordingly:

$$\mu \geq -u \cdot (p_{32} + p_{21} + p_{11} - T y_{21} + p_{22} - T y_{32}) \tag{10}$$

This dual information can also be obtained from the critical path of the Gantt diagram of the DES simulation (see Figure 2). The makespan is obtained by summing over all lot processing times on the critical path. For *Schedule 1* ($y_{21} = 0$ and $y_{32} = 0$), the makespan can be derived from the Benders cut (11): $p_{11} + p_{21} + p_{22} + p_{32} = 8$. For every DES simulation, a new Benders cut is generated and added to the MILP, as shown in Figure 1.

## CASE STUDY

As a case study, a hybrid flowshop problem of a agrochemical formulation plant as presented in [6] is considered. The process is a two-stage formulation and filling process that takes place in a multi-product batch plant, as shown in Figure 3. In the formulation stage, raw materials are milled, mixed, and brought to reaction. In the filling stage, the intermediate products are filled into final containers of different sizes. The plant has seven parallel production lines (machines) per stage, each with different run rates per product and sequence-dependent changeover times. There are seven optional buffer tanks to decouple formulation and filling between the two stages. In addition, shift personnel is limited and organized into two different schedules. The process is exposed to 50 raw materials on the input side and a highly fragmented demand for 83 finished products on the output side. The goal is to process various products (jobs) in the shortest possible makespan, which results in a complex flowshop optimization problem.

## PROBLEM FORMULATION

### MILP Core Problem

The core problem of the presented case study is a hybrid flowshop MILP problem. The model formulation is based on assignment and precedence variables as suggested in [8]. Binary assignment variables $a_{biml}$ indicate whether lot $b \in \{1, \ldots, B\}$ of job $i \in \{1, \ldots, N\}$ is processed on machine $m \in \{1, \ldots, M\}$ in process stage $l \in \{1, \ldots, L\}$. Binary indicator variables $h_{bb'ijml}$ indicate whether lot $b \in \{1, \ldots, B\}$ of job $i \in \{1, \ldots, N\}$ and lot $b' \in \{1, \ldots, B\}$ of job $j \in \{1, \ldots, N\}$ are both processed on the same machine $m \in \{1, \ldots, M\}$ in process stage $l \in \{1, \ldots, L\}$. Binary precedence variables $y_{bb'ijml}$ indicate whether lot $b$ of job $i$ is processed before lot $b'$ of job $j$ on machine $m$ in process stage $l$. Continuous lot-sizing variables $r_{bi} \in [0,1]$ represent the split factors, which indicate what percentage of job $i$ is covered by lot $b$. Start time variables $s_{biml}$, completion time variables $c_{biml}$, and processing time parameters $t_{iml}$ define the resulting schedule. $T$ is the Big-M constant.

The objective (11) is to minimize the makespan $c_{max}$.

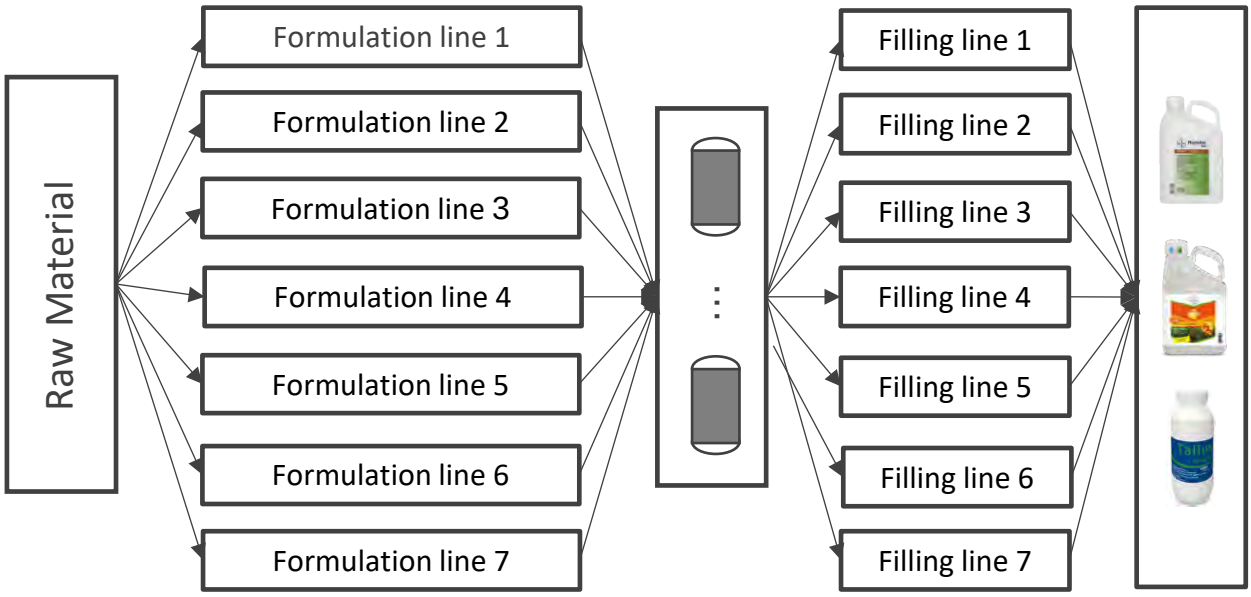



**Figure 3:** Equipment layout of the agrochemical formation plant treated in the case study. The case study is a two-stage flexible flowshop problem with seven formulation lines (stage 1) and seven filling lines (stage 2). The intermediated (formulated) product can be stored in seven buffer tanks before being processed in the filling lines.

(12) is the makespan constraint. Constraint (13) sets the start and completion times according to the processing times, (14) enforces the lot sequence on each machine, (15) ensures valid start times of lots when switching from one stage to the next, (16) forces each lot to be processed on exactly one machine in each stage, and (17) defines for each machine the precedence relation between lots which are assigned to that machine. Constraints (18) to (20) build the binary indicator variables $h_{bb'ijml}$ and (21) enforces valid lot sizes.

$$\min c_{max} \tag{11}$$

$$\text{s.t.} \quad c_{max} \geq c_{bimL} \; \forall \, b \in B, i \in N, m \in M \tag{12}$$

$$s_{biml} + r_{bi} t_{iml} \leq c_{biml} + T(1 - a_{biml}) \; \forall \, b \in B, i \in N, m \in M, \mathrm{l} \in L \tag{13}$$

$$c_{biml} + r_{b'j} t_{jml} \leq c_{b'jml} + T\left(1 - y_{bb'ijml}\right) \; \forall \, b, b' \in B, i, j \in N : i \neq j, m \in M, l \in L \tag{14}$$

$$T(a_{biml} - 1) + s_{biml} + r_{bi} t_{iml} \leq s_{binl+1} + T(1 - a_{binl+1}) \; \forall \, b \in B, i \in N, m, n \in M, l \in L \backslash \{Lmax\} \tag{15}$$

$$\sum_{m=1}^{M} a_{biml} = 1 \; \forall \, b \in B, i \in N, l \in L \backslash \{Lmax\} \tag{16}$$

$$y_{bb'ijml} + y_{b'bjiml} = h_{bb'ijml} \; \forall \, b, b' \in B, i, j \in N : i \neq j, m \in M, l \in L \tag{17}$$

$$h_{bb'ijml} \leq a_{biml} \; \forall \, b, b' \in B, i, j \in N : i \neq j, m \in M, l \in L \tag{18}$$

$$h_{bb'ijml} \leq a_{b'jml} \; \forall \, b, b' \in B, i, j \in N : i \neq j, m \in M, l \in L \tag{19}$$

$$h_{bb'ijml} \geq a_{biml} + a_{b'jml} - 1 \; \forall \, b, b' \in B, i, j \in N : i \neq j, m \in M, l \in L \tag{20}$$

$$\sum_{b=1}^{B} r_{bi} = 1 \quad \forall \, i \in N \tag{21}$$

## Benders Master Problem

From the MILP core problem, the Benders master problem (22) to (29) is derived. The Benders cuts in (23) are based on the dual variables $u_{biml}$ which assume a value of -1 if lot $b$ of job $i$ on machine $m$ in stage $l$ is on the critical path, and 0 otherwise. Constraints (24) to (27) ensure valid lot-machine assignments and lot sequencing. Constraint (29) enforce valid lot sizes.

$$\min \mu \tag{22}$$

$$s.t. \quad \mu \geq \sum_{b=1}^{B} \sum_{b'=1}^{B} \sum_{i=1}^{N} \sum_{j=1}^{N} \sum_{m=1}^{M} \sum_{l=1}^{L} -u_{biml} \left( r_{bi} t_{iml} - T\left(1 - y_{bb'ijml}\right)\right) \tag{23}$$

$$\sum_{m=1}^{M} a_{biml} = 1 \; \forall \, b \in B, i \in N, l \in L \tag{24}$$

$$y_{bb'ijml} + y_{b'bjiml} = h_{bb'ijml} \; \forall \, b, b' \in B, i, j \in N : i \neq j, m \in M, l \in L \tag{25}$$

$$h_{bb'ijml} \leq a_{biml} \; \forall \, b, b' \in B, i, j \in N : i \neq j, m \in M, l \in L \tag{26}$$

$$h_{bb'ijml} \leq a_{b'jml} \; \forall \, b, b' \in B, i, j \in N : i \neq j, m \in M, l \in L \tag{27}$$

$$h_{bb'ijml} \geq a_{biml} + a_{b'jml} - 1 \; \forall \, b, b' \in B, i, j \in N : i \neq j, m \in M, l \in L \tag{28}$$

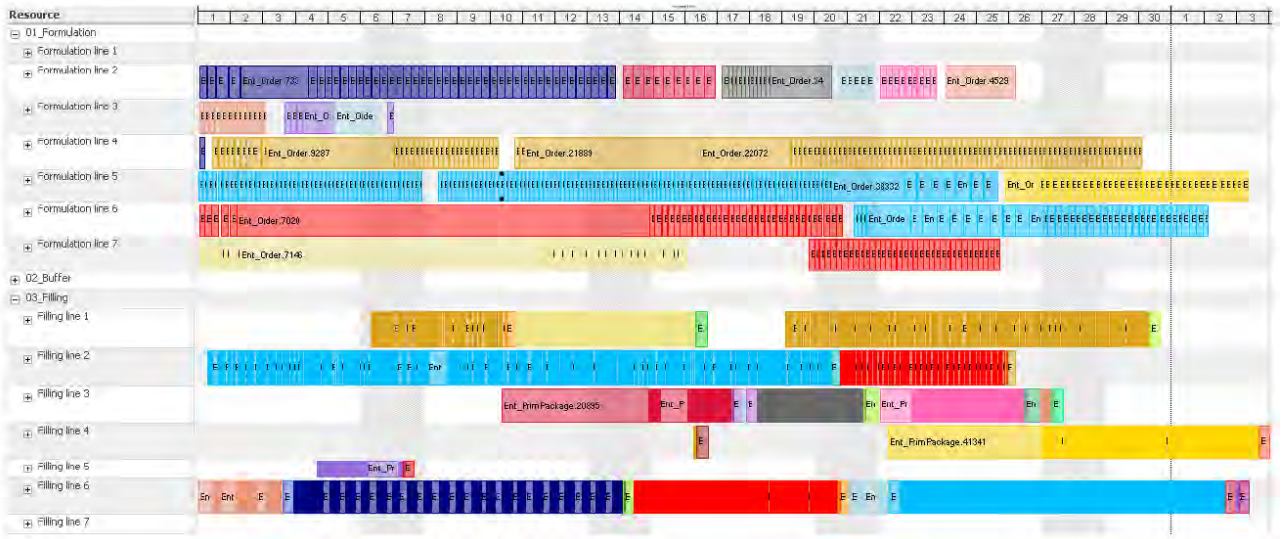



**Figure 4:** Gantt chart of best solution after solving one-month production dataset with BDES for 360 seconds.

$$\sum_{b=1}^{B} r_{bi} = 1 \quad \forall\, i \in N \tag{29}$$

Note that the cuts (23) only include the processing times as contributors to the critical path because they were derived from the core flow shop problem. If these cuts are applied to the detailed DES model of the case study, they remain valid inequalities as discussed in [7], but omit certain features of the problem such as secondary resources and changeover times. In this case, the cuts represent valid underestimators to the DES makespan with a gap $\delta \geq c_{max} - \mu^* \geq 0$.

## Benders Subproblem

For the Benders subproblem, a DES model of the case study flow shop is assumed. In contrast to the MILP, the DES does not suffer from the curse of dimensionality, and computation times do not increase exponentially with problem size. This makes it possible to accurately model, simulate, and analyze complex systems. The DES model is considered as a black box function $f: y_{bb'ijml}, a_{biml}, r_{bi} \rightarrow s_{biml}, c_{biml}, c_{max}$ that computes a solution for the non-complicating variables and dual multipliers, given an input solution of the complicating variables. In the case study, the input contains the lot sequences, lot-line assignments, and lot sizes. The output includes the starting and completion times of all lots. In addition, the dual multipliers are calculated from the critical path.

# RESULTS

BDES is applied to the one-month production dataset 2 of the case study in [6, Table 4]. As DES Python-based SimPy 4.1.1 is used, and for MILP gurobipy 11.0.1 with Gurobi 9.5.2. Similar to the monolithic-sequential MILP-DES approach of [6], BDES can compute an optimized one-month production schedule for the formulation and filling plant. This schedule is found after approximately one minute of solution time, which is faster than the monolithic MILP model, which required approximately ten minutes for the first optimization step to schedule the production within the month without backlog. However, a shortcut DES model was used, and the makespan in the same full-space DES model as used in [6] is 33 days (see Figure 4). This result is comparable to the manually generated DES schedule and implies that some backlog quantities occur.

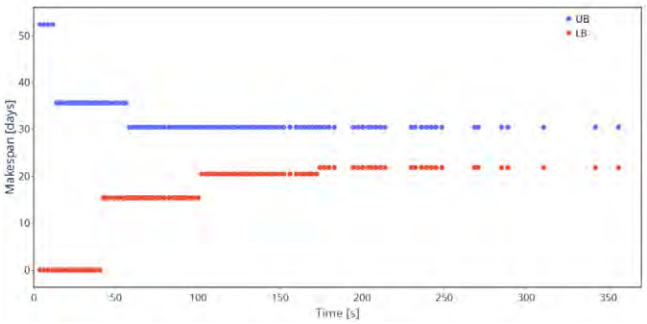



**Figure 5.** Makespan bounds progression when solving a one-month production dataset with BDES for 360 seconds.

Figure 5 shows that the lower bounds on the makespan increase after a solution with a makespan of 30.5 days has already been found. This information can be helpful in practice to terminate the search process prematurely, as it can be assured that no better solutions than with a makespan of 20 days can be found. Meaningful lower bounds can be computed for the one-month case study dataset because eligibility constraints are

added to the master problem. These constraints rule out many lot-line assignments, reducing the search space a priori.

Lot-sizing is an important degree of freedom that enables efficient scheduling with minimal makespan. However, BDES only exploits splitting for some products. For example, the first products on formulation lines 5 and 6 exploited the split factor of two (see Figure 4). Therefore, a split factor of two already supports a high utilization of formulation and filling lines. An unlimited split factor as implemented in [6] may lead to further makespan improvements but also increases the model complexity. In this work, experiments with higher split factors indicated that the complexity can be prohibitive for BDES because the search space for the Benders master problem grows exponentially.

Furthermore, Figure 4 shows that fewer changeovers in the filling stage occur compared to the result in [6]. This is because the objective function in this work is not to minimize changeover costs but the makespan. In [6], many changeovers occurred due to favorable changeover cycles in the filling stage that minimized the overall changeover costs.

The application of BDES to the one-month production dataset shows that the performance of BDES is generally comparable to the manual-DES approach in [6] for real-world scheduling tasks. Furthermore, BDES requires similar solution times as the MILP-DES approach in [6] but yields slightly worse results. However, building the complex, monolithic MILP model and manually reconciling the MILP results with the DES model is not necessary. Instead, a Benders master model of a generic, hybrid flowshop (see Section "Problem Formulation") is used to guide the search process in the DES subproblem.

## CONCLUSIONS

This work presents a novel BDES algorithm to minimize the makespan of hybrid flowshop with allocation, sequencing, and lot-sizing decisions as well as secondary resource constraints. BDES performs similarly to the sequential monolithic MILP-DES approach of [6]. Although BDES yields slightly worse results compared to the approach of [6], the setup of BDES is less complex compared to a monolithic MILP approach.

The main advantage of BDES is that it can apply MILP in the form of simple Benders cuts to highly detailed DES models. It is not necessary to build a complex MILP model, but a MILP Benders master model of a generic hybrid flowshop with precedence variables is used while the real-world constraints being moved to the DES subproblem. This work shows that combining the strengths of rigorous optimization and detailed modeling can be attractive from a practical perspective since it allows for fast model development and implementation.

Future research will focus on the investigation of the generality of the approach, i.e., the influence of different problem instances on the solution quality as well as strengthening the Benders cuts and generation of robust schedules.

## ACKNOWLEDGEMENTS

We thank the Bayer AG, Leverkusen, Germany for providing the case study.

## REFERENCES

1. Harjunkoski I, et al. Scope for industrial applications of production scheduling models and solution methods. *Comput. Chem. Eng.* 62:161 (2014)
2. Klanke C, Engell S. Scheduling and batching with evolutionary algorithms in simulation–optimization of an industrial formulation plant. *Comput. Ind. Eng.* 174 (2022)
3. de Sousa Junior WT, et al. Discrete simulation-based optimization methods for industrial engineering problems: A systematic literature review. *Comput. Ind. Eng.* 128:526-540 (2019)
4. Teerasoponpong S, Sopadang S. A simulation-optimization approach for adaptive manufacturing capacity planning in small and medium-sized enterprises. *Expert Syst. Appl.* 168 (2021)
5. Tliba K, et al. Digital twin-driven dynamic scheduling of a hybrid flow shop. *J. Intell. Manuf.* 34:2281–2306 (2023)
6. Wallrath R, et al. A time-bucket MILP formulation for optimal lot-sizing and scheduling of real-world chemical batch plants. *Comput. Chem. Eng.* 177 (2023)
7. Wallrath R, Franke MB. Integration of MILP and discrete-event simulation for flow shop scheduling using Benders cuts. *Comput. Chem. Eng.* 189 (2024)
8. Rahmaniani R, et al. The Benders decomposition algorithm: A literature review. *Eur. J. Oper. Res.* 259:801–817 (2017)
9. Demir Y, Kürsat Isleyen, S. Evaluation of mathematical models for flexible job-shop scheduling problems. *Appl. Math. Model.* 37:977–988 (2013)

© 2025 by the authors. Licensed to PSEcommunity.org and PSE Press. This is an open access article under the creative commons CC-BY-SA licensing terms. Credit must be given to creator and adaptations must be shared under the same terms. See https://creativecommons.org/licenses/by-sa/4.0/



Systems & Control Transactions

**Research Article - Peer Reviewed Conference Proceeding**
ESCAPE 35 - European Symposium on Computer Aided Process Engineering
Ghent, Belgium. 6-9 July 2025
Jan F.M. Van Impe, Grégoire Léonard, Satyajeet S. Bhonsale,
Monika E. Polańska, Filip Logist (Eds.)

PSE PRESS

# A Blockchain-Supported Framework for Transparent Resource Trading and Emission Management in Eco-Industrial Parks (EIPs)

**Manar Y. Oqbi[a*], Dhabia M. Al-Mohannadi[b]**

[a]Artie McFerrin Department of Chemical Engineering, Texas A&M University, College Station, TX, 77843, USA
[b]Department of Chemical Engineering, Texas A&M University at Qatar, P.O Box 23874, Education City, Doha, Qatar
* Corresponding Author: manar.oqbi@tamu.edu.

## ABSTRACT

Sustainable industrial development depends on optimizing resource and energy integration within Eco-industrial parks (EIPs), combined with stringent carbon emissions reduction policies. The main challenge is ensuring transparency, accountability, and data privacy while optimizing the conversion of raw materials and energy into valuable products and controlling emissions within EIPs. This research introduces an innovative framework to design optimized EIPs and deploy a blockchain-enabled trading platform for resources and emissions management, tackling these key issues. The proposed framework integrates EIPs with emission control policies, supported by two distinct smart contracts: one dedicated to blockchain-based resource trading and another handling financial transactions related to emission control policies, including other regulations such as income tax. The resource trading platform fosters transparency, enabling accurate tracking of material and energy flows. Furthermore, the framework integrates an off-chain Mixed-Integer linear Programming model (MILP) to optimize EIP design and operations, which is seamlessly integrated with smart contracts on the Ethereum blockchain (BC) to ensure data privacy and traceability among processes to meet environmental targets. The model also determines emission reductions and investments in carbon capture technology, promoting operational efficiency. By incorporating identity verification and external entities for compliance, the framework ensures secure and regulated operations. Offering a powerful tool to decision-makers and authorities, this framework enhances comprehension of resource and emissions tracking, paving the way for the development of innovative policies and fostering regulatory compliance. This development promotes sustainable industrial activities and supports environmental goals.

**Keywords**: Optimization, Sustainable Industry Practices, Transparency, Resource Trading, Emission Reduction Systems, Digital Transformation in Industry, Blockchain Technology

## INTRODUCTION

The global push for sustainable development, spearheaded by the United Nations' Sustainable Development Goals (SDGs), highlights the importance of integrated resource management to balance environmental and economic sustainability. While progress has been made in SDG monitoring, critical data gaps remain, hindering comprehensive assessments and the formulation of effective policies [1]. The efficient and transparent management of material and energy resources is essential for mitigating environmental impacts and promoting the long-term sustainability and adaptability of industrial ecosystems [2]. However, assessments of EIPs have revealed persistent challenges, such as low compliance in resource management and environmental performance, underscoring the urgent need for technological solutions [3]. Addressing these challenges requires innovative strategies that integrate transparent resource management, strict adherence to sustainability standards, and robust compliance with regulatory frameworks.

Significant research has focused on optimizing resource integration to enhance sustainability in industrial systems. A two-step MILP approach was developed to

design cost-effective carbon dioxide ($CO_2$) reduction networks, integrating renewable energy to reduce mitigation costs [4]. Multi-objective frameworks for $CO_2$ Capture, Utilization, and Storage (CCUS) supply chains have been proposed, balancing economic, environmental, and safety objectives through Pareto optimization [5]. $CO_2$ and heat integration approaches have also been explored to minimize net energy demand and emissions, leveraging synergies such as process heat recovery to reduce $CO_2$ capture costs [6]. Additionally, a MILP-based optimization for CCUS supply chains in the UK demonstrated the economic viability of emissions reduction strategies under $CO_2$ tax policies, highlighting the role of site selection in minimizing costs and maximizing net present value [7].

For water and energy integration, an extended pinch analysis was used to design water recycling networks [8], while seasonal variations in water-energy systems were addressed using a mixed-integer non-linear optimization framework (MINLP) to ensure robust designs under peak demand [9]. Multi-objective optimization has also been applied to minimize $CO_2$ and water footprints while maximizing economic returns in industrial clusters [10]. Lastly, integrating renewable energy with $CO_2$ capture and utilization has been shown to enable net-zero emissions in energy systems through dynamic optimization [11].

While previous research has advanced resource integration strategies in EIPs, a critical challenge remains - the lack of transparency in resource management, emissions tracking, and regulatory compliance. Studies indicate that industrial parks often struggle with inadequate transparency in environmental practices, leading to inefficient resource utilization and unchecked pollution emissions [12]. Additionally, the absence of reliable data-sharing mechanisms hinders effective industrial symbiosis, as firms face barriers such as data inaccessibility, lack of trust, and inconsistent byproduct supply [13]. Policy inconsistencies further exacerbate these challenges, as gaps in the adherence to EIP guidelines and misinterpretations of sustainability principles reduce the effectiveness of implementation strategies [14]. These transparency-related inefficiencies not only limit the potential for industrial collaboration but also weaken the environmental and economic benefits that EIPs aim to achieve.

To address these transparency gaps, emerging technologies such as BC have been proposed to enhance data integrity, traceability, and regulatory enforcement in industrial ecosystems. Permissioned BC frameworks have been explored for $CO_2$ emission trading, aiming to reduce fraud, improve monitoring, and facilitate secure, automated transactions [15]. In the context of CCUS supply chains, BC-based smart contracts have been shown to enhance tracking, compliance, and cost efficiency by reducing reliance on third-party verifiers [16]. Beyond emissions management, BC is increasingly recognized as a solution for data governance in EIPs, offering decentralized platforms that enable peer-to-peer resource exchange, transparent record-keeping, and enhanced industrial collaboration [17] [18]. These developments highlight the potential of integrating optimization models with BC-based smart contracts to create a secure, transparent, and efficient framework for managing resource flows and emissions within EIPs.

Despite advancements in resource integration and the application of BC for transparency, existing frameworks still exhibit significant limitations. Most models focus either on optimization-based resource integration or BC-enabled trading mechanisms but rarely synthesize both in a way that ensures simultaneous economic, environmental, and operational efficiency. Additionally, while BC applications have been explored for $CO_2$ markets and CCUS supply chains, they often lack comprehensive integration with broader EIP resource flows, including water, energy, and materials. Furthermore, transparency challenges persist in data tracking, regulatory compliance, and secure material, energy, and financial resource exchanges, as many frameworks do not incorporate accurate monitoring of industrial symbiosis. This research addresses these gaps by introducing a hybrid optimization-BC framework that integrates a MILP model for EIP design with smart contract-based resource exchange. By leveraging BC's architecture, the proposed framework ensures secure, transparent, and efficient management of resource flows, emissions, and financial transactions. This approach not only enhances trust and compliance within EIPs but also establishes a scalable and adaptable solution for industrial ecosystems aiming to meet sustainability targets while maintaining operational resilience.

## FUNDAMENTALS OF BLOCKCHAIN AND SMART CONTRACTS

BC is a decentralized digital ledger that enables secure, transparent, and tamper-proof transactions across various industries, including finance, healthcare, supply chains, and energy systems [19]. Unlike centralized databases, it eliminates intermediaries, reducing fraud and enhancing security through cryptographic hashing and consensus mechanisms such as Proof of Work (PoW) and Proof of Stake (PoS) [20]. Transactions, once validated, are stored in linked blocks, ensuring immutability and trust, making BC ideal for applications requiring secure financial transactions, identity verification, and supply chain tracking [21].

Key BC features include decentralization, which prevents system failures and reduces fraud [20]; immutability, ensuring a tamper-proof and auditable record of transactions [19]; and transparency, allowing participants

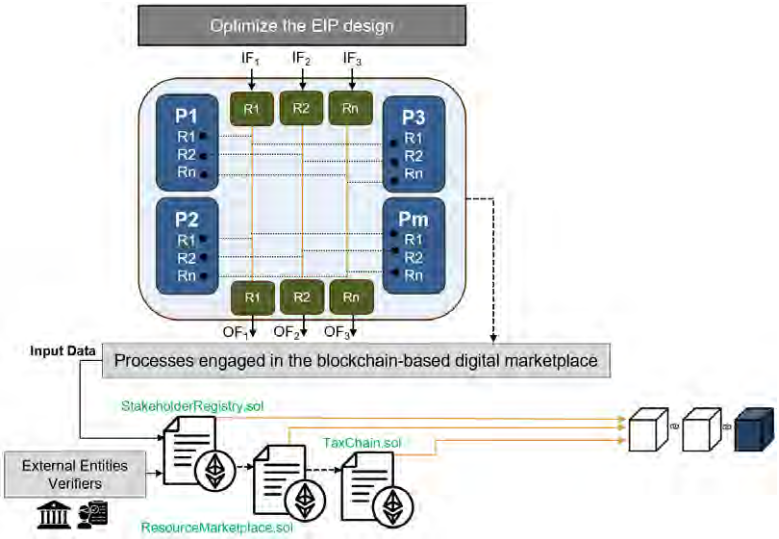



**Figure 1:** Proposed Blockchain-Integrated Framework for EIP Optimization and Operation.

to access synchronized data, promoting accountability [21]. Security is reinforced through cryptographic encryption, protecting data from cyber threats [22], while smart contracts automate transactions, streamlining operations and reducing the need for intermediaries [23].

These features drive BC adoption across multiple sectors. In healthcare, it ensures secure patient data management and prevents counterfeit pharmaceuticals [24]. Supply chain management benefits from BC's immutable records, enhancing product traceability and fraud prevention [25]. In energy systems, BC facilitates peer-to-peer energy trading, reducing dependency on centralized grids and supporting renewable energy adoption [26]. It also enhances electoral security in government systems [23], and secures machine-to-machine transactions in smart manufacturing [27]. Furthermore, BC optimizes financial transactions by supporting cryptocurrencies, decentralized finance and automated smart contracts [28]. With its secure and transparent architecture, BC transforms industries by enhancing data security, fraud prevention, and operational efficiency, driving digital innovation and sustainable development.

## PROPOSED FRAMEWORK AND METHODOLOGY

This study presents a multi-stage optimization and BC-based framework to enhance resource integration, transparency, and emissions management within an EIP. The methodology comprises two primary components: (1) Optimization of the EIP design using
an extended MILP model which was initially proposed by [10], and (2) BC-enabled smart contracts for transparent resource trading and financial transactions. Figure 1 illustrates the architecture of the proposed system.

### 1. Optimization of the EIP Design

The first stage of the methodology involves optimizing the selection and capacity of industrial processes within the EIP. A MILP model is employed to identify the optimal set of processes, ensuring maximum economic profitability while adhering to environmental constraints, including $CO_2$ emissions cap and zero untreated wastewater discharge. The objective function is defined as:

$$\text{Max Profit} = \text{TR} - (\text{CC} + \text{OC} - \text{Taxes}) \quad (1)$$

where TR, CC, and OC represent the total revenue, capital cost, and operating cost, respectively. Total Revenue is generated from resource exchanges, and Capital/Operating Costs are associated with process operation. Taxes include $CO_2$ tax for excess $CO_2$ emissions and income tax, incentivizing industries that collaborate within the EIP. The mass balances for resource exchanges among processes is defined using:

$$\text{IF} - \text{RE} - \text{OF} = 0 \quad (2)$$

where IF, RE, and OF represents the input flow of the resource, resource exchange, and outlet flow respectively. For each process, mass balance constraints ensure:

$$\text{REP} - (\text{FP} \times \text{PC}) = 0 \quad (3)$$

where REP, FP, and PC represent the resource exchange with processes, flow parameter, and process capacity, respectively. Process capacities and resource imports/exports are bounded by upper and lower limits, ensuring realistic operational feasibility. Additionally, a constraint is imposed to eliminate untreated wastewater discharge, forcing all generated wastewater to be treated before release. $CO_2$ emissions are constrained based on a predefined $CO_2$ cap. If the emissions exceed the limit, a $CO_2$ tax is applied to the excess amount:

$$\mathrm{CE} - (\mathrm{CCA} + \mathrm{TCA}) \leq \mathrm{CAcap} \quad (4)$$

where CE, CCA, TCA, and CAcap represent the $CO_2$ emissions, captured $CO_2$ emissions, taxed $CO_2$ emissions, and the predefined $CO_2$ cap, respectively. The model dynamically adjusts process operations to optimize the costs of $CO_2$ taxation and $CO_2$ capture units.

## 2. Blockchain-Based Resource Exchange and Taxation

Once the optimal EIP configuration is determined, the activated processes participate in a BC-based digital marketplace for secure and transparent resource transactions. Ethereum is chosen as the BC platform due to its robust smart contract functionality and wide adoption.

### 2.2 Blockchain Transaction Process

The BC-based resource exchange mechanism follows a structured process to ensure secure and transparent transactions within the EIP. Initially, processes register through the StakeholderRegistry.sol smart contract, which verifies and maintains the identity of each participant. Once registered, industries list their available resources on the ResourceMarketplace.sol contract, specifying key attributes such as flow rate, quality, pressure, temperature, and price. When a process initiates a trade, the smart contract verifies resource availability, compliance with EIP constraints, and pricing conditions. Upon successful validation, the trade is executed, and the transaction is recorded on the BC, ensuring an immutable record of resource exchanges. Additionally, financial transactions, such as $CO_2$ tax and income tax payments, are automated through TaxChain.sol, which deducts applicable taxes from the EIP and transfers the payment to the regulatory authority. This decentralized mechanism eliminates manual oversight, reducing delays and ensuring compliance with environmental and financial regulations. By integrating BC into resource exchange and taxation, the system fosters trust, efficiency, and automated enforcement of sustainability policies within the EIP.

### 2.3 Advantages, Considerations, and Challenges

Ensuring trust, traceability, and regulatory compliance in industrial symbiosis is a major challenge. The proposed BC-enabled system enhances transparency by maintaining immutable records, minimizing fraud and data manipulation. Smart contracts automate verification, ensuring only registered processes participate in trades while meeting environmental and economic criteria. By requiring complete resource data before execution, the system prevents omissions, duplicates, and unauthorized transactions. The decentralized ledger allows external audits without intermediaries, while automated compliance checks enforce emission limits, wastewater treatment, and taxation policies, reducing administrative burdens. This framework ensures regulatory adherence and incentivizes industries to adopt sustainable practices.

The proposed MILP-BC framework enhances EIP efficiency by integrating process optimization with smart contract-based resource trading, ensuring optimal resource allocation, cost reduction, and emissions control. Automated $CO_2$ and income tax enforcement simplifies compliance, while BC's immutable ledger strengthens data security, transparency, and fraud prevention. Additionally, decentralization fosters accountability, promoting sustainable industrial practices while improving financial performance. However, several challenges must be addressed. Balancing data privacy and transparency is critical, as BC's immutability could expose sensitive information. The high computational cost of smart contracts and the lack of clear regulatory frameworks pose further obstacles. Additionally, industry adoption may be hindered by technical complexity and resistance to change. Overcoming these barriers requires scalability improvements, privacy-preserving techniques, and regulatory collaboration to ensure effective deployment and widespread adoption of the framework.

## ILLUSTRATIVE EXAMPLE

To evaluate the proposed system, a case study was conducted on an EIP integrating both product-based processes and emissions mitigation strategies. The industrial processes include Air Separation Unit (ASU), Ammonia Plant (AP), Cement Plant (CP), Methanol Plant (MP), Natural Gas Power Plant (NGPP), Seawater Reverse Osmosis (SWRO), Steam Methane Reforming Unit (SMR), Urea Plant (UP), and Wastewater Treatment Unit (WWTU). Emissions mitigation strategies incorporate $CO_2$ capture technologies (CC), utilization pathways (methanol, urea), enhanced oil recovery (EOR), direct air capture (DAC), and sequestration. The EIP aims to maximize net profit by optimizing resource exchanges and $CO_2$ capture, while adhering to a $CO_2$ cap of 250,000 tons $CO_2$/year, a $CO_2$ tax of \$40/ton $CO_2$, and an income tax of 15%. Process data for DAC, sequestration, EOR, NGPP, and its capture unit were sourced from [11], while data for other processes were obtained from [10]. The project lifespan is 20 years, with required inputs including capital and operating costs, as well as resource flow parameters expressed in tons per ton of the main product (t/t Ref).

Capacity limits were defined for each unit, with ASU, AP, MP, SMR, UP, and EOR capped at 200,000 t/y, CP and CP CC at 1,000,000 t/y and 500,000 t/y, respectively, NGPP at 600,000 MWh/y, and NGPP CC, SMR CC, and DAC at 1,500,000 t/y. SWRO and WWTU capacities were set at 8,000,000 t/y and 300,000 t/y, respectively, while sequestration was limited to 500,000 t/y. The $CO_2$ composition in emissions varies across processes, with

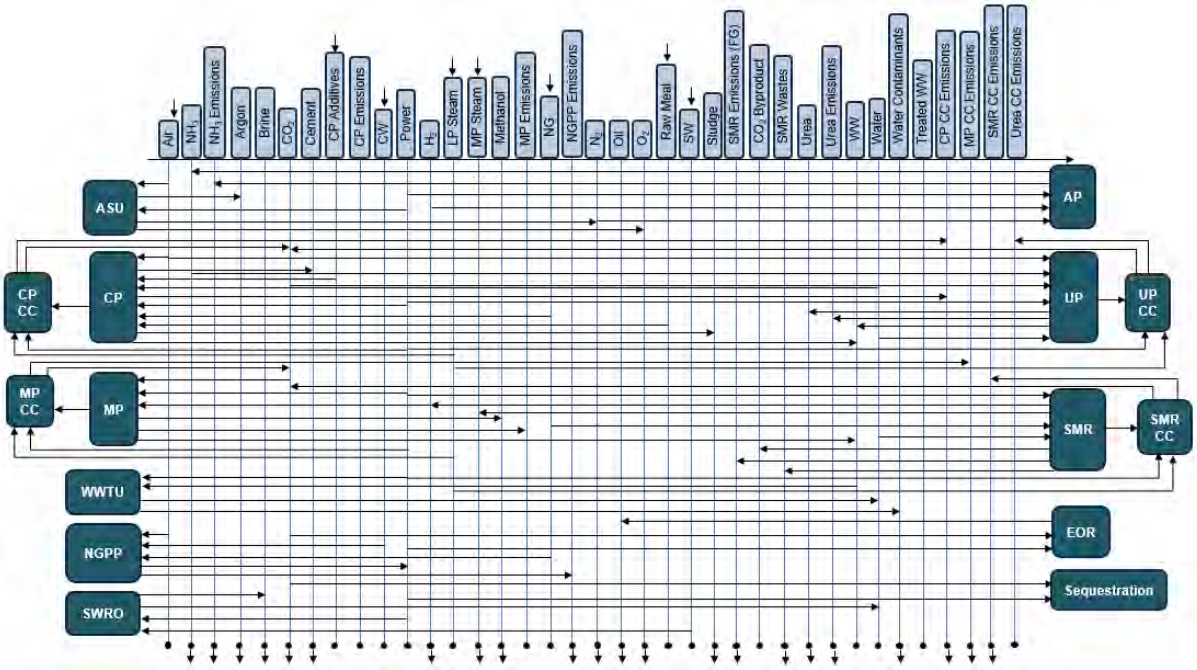



**Figure 2:** Resource Flow Network in the Optimized EIP.

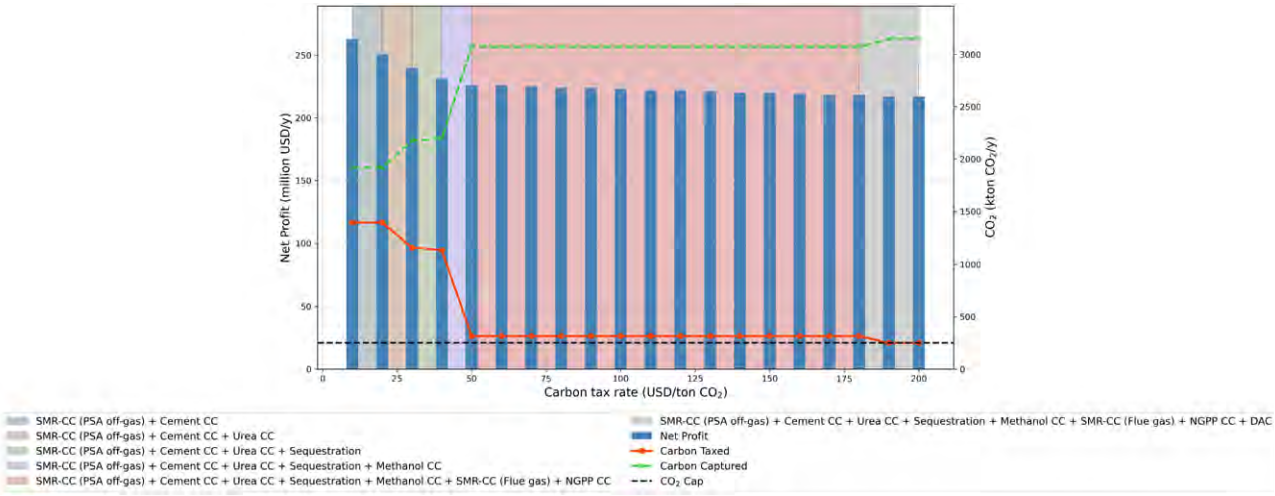



**Figure 3:** Impact of Carbon Tax Rate on Net Profit and $CO_2$ Emissions.

values ranging from 0.7% to 82%, depending on the emission source. This case study demonstrates the feasibility of resource optimization and emissions control within an EIP under regulatory and economic constraints.

The results show that the activated product-based processes include ASU, AP, CP, MP, SMR, UP, WWTU, and EOR, with NGPP and SWRO serving as utility plants. Emissions control strategies incorporate $CO_2$ capture from SMR-PSA off-gas, cement, and urea production, alongside sequestration and $CO_2$ taxation. The system successfully captured 1,945,930 tons of $CO_2$ per year, while 882,628 tons were taxed, demonstrating effective $CO_2$ management and regulatory compliance. Figure 2 presents the optimized EIP configuration, highlighting resource flows, activated processes, and emissions control measures.

The sensitivity analysis on the $CO_2$ tax rate, shown in Figure 3, explores its impact on net profit, $CO_2$ taxed, and $CO_2$ captured across a range of 10 to 200 \$/ton $CO_2$ with a step size of 10. The activated processes include ASU, AP, CP, MP, NGPP, SWRO, SMR, UP, WWTU, and EOR. The $CO_2$ cap was set at 250 kton $CO_2$/year, requiring any excess $CO_2$ to be either captured or taxed. As the $CO_2$ tax rate rises, the system shifts toward greater $CO_2$ capture and lower $CO_2$ taxation to minimize costs. The net profit decreases as $CO_2$ mitigation strategies become

more expensive, with higher tax rates making sequestration and capture more viable than direct taxation. The analysis identifies six regions of $CO_2$ mitigation progression: (1) at 10-20 \$/ton $CO_2$, capture is limited to SMR-PSA off-gas and cement, with the highest taxed $CO_2$; (2) from 20-30 \$/ton $CO_2$, urea capture begins; (3) from 30-40 \$/ton $CO_2$, sequestration is activated; (4) from 40-50 \$/ton $CO_2$, methanol capture is added; (5) from 50-180 \$/ton $CO_2$, capture extends to SMR flue gas and NGPP; and (6) at 180-200 \$/ton $CO_2$, DAC is introduced, reducing taxed $CO_2$ to zero at 190 \$/ton $CO_2$. This transition demonstrates how a rising $CO_2$ tax incentivizes a shift toward more extensive $CO_2$ capture, ultimately reducing emissions but at the cost of declining net profit.

The integration of BC in this EIP framework enhances transparency, efficiency, and regulatory compliance, particularly by automating the transition from MILP-optimized process capacities to real-world applications. Smart contracts ensure seamless execution of resource exchanges, taxation, and emissions management, maintaining adherence to optimized parameters while recording immutable, auditable transactions. This approach bridges the gap between theoretical optimization models and practical implementation, providing industries and policymakers with insights into resource utilization and emissions tracking. By ensuring accurate $CO_2$ taxation and automated compliance verification, BC fosters sustainable industrial operations and could enable incentive mechanisms, such as tax benefits or tradable environmental credits. The secure, transparent nature of BC further supports the development of standardized $CO_2$ credit trading, promoting a circular economy and data-based policies. This approach is adaptable to other energy-intensive industries such as steel production, chemical manufacturing, and renewable energy systems. In these sectors, the ability to optimize resource use, reduce emissions, and enhance operational transparency is crucial. Digitalization plays a pivotal role by enabling real-time data access, improving decision-making, and ensuring compliance with environmental standards. Thus, our methodology is well-suited to address similar challenges across various industrial contexts, promoting sustainable and efficient practices and supporting broader sustainability goals.

## CONCLUSIONS

This study presents a BC-integrated framework for optimizing EIP operations, combining MILP-based optimization with smart contract automation to enhance resource management, transparency, and regulatory compliance. By seamlessly linking optimized resource flows to smart contracts, the system ensures efficient trading, automated taxation, and emissions tracking, reducing $CO_2$ emissions while maintaining economic viability. The immutable ledger enables secure, auditable transactions, supporting policy enforcement and sustainability monitoring. This approach improves industrial efficiency and provides a scalable model for broader applications in decarbonization and circular economy initiatives. The integration of BC into EIP management paves the way for data-driven policymaking and enhanced environmental governance, fostering sustainable industrial development.

## ACKNOWLEDGEMENTS

The researchers extend their sincere appreciation to Qatar Foundation (QF) for their financial support to conduct this study.

## REFERENCES

1. ns, “The Sustainable Development Goals (SDGS),” 2024. https://unstats.un.org/sdgs/report/2024/ (accessed Nov. 28, 2024).
2. A. Bruel and R. Godina, “A Smart Contract Architecture Framework for Successful Industrial Symbiosis Applications Using Blockchain Technology,” Sustain., vol. 15, no. 7, 2023, doi: 10.3390/su15075884.
3. D. van Beers, K. Tyrkko, A. Flammini, C. Barahona, and C. Susan, “Results and lessons learned from assessing 50 industrial parks in eight countries against the international framework for eco-industrial parks,” Sustain., vol. 12, no. 24, pp. 1–33, 2020, doi: 10.3390/su122410611.
4. D. M. Al-Mohannadi, G. Kwak, and P. Linke, “Identification of optimal transitions towards climate footprint reduction targets using a linear multi-period carbon integration approach,” Comput. Chem. Eng., vol. 140, 2020, doi: 10.1016/2020.106907.
5. M. Oqbi, L. Véchot, and D. M. Al-Mohannadi, “Safety-driven design of carbon capture utilization and storage (CCUS) supply chains: A multi-objective optimization approach,” Comput. Chem. Eng., vol. 192, no. July 2024, 2025, doi: 10.1016/j.compchemeng.2024.108863.
6. R. J. Hassiba, D. M. Al-mohannadi, and P. Linke, “Carbon dioxide and heat integration of industrial parks,” J. Clean. Prod., vol. 155, pp. 47–56, 2017, doi: 10.1016/j.jclepro.2016.09.094.
7. G. Leonzio, D. Bogle, P. U. Foscolo, and E. Zondervan, “Optimization of CCUS supply chains in the UK: A strategic role for emissions reduction,” Chem. Eng. Res. Des., vol. 155, pp. 211–228, 2020, doi: 10.1016/j.cherd.2020.01.002.
8. H. H. Chin, P. Y. Liew, P. S. Varbanov, and J. J. Klemeš, “Extension of pinch analysis to targeting

and synthesis of water recycling networks with multiple contaminants," Chem. Eng. Sci., vol. 248, 2022, doi: 10.1016/j.ces.2021.117223.
9. M. Oqbi, P. Linke, D. Al-Mohannadi, and S. Bishnu, "Synthesis of Water-Energy Network Considering Seasonality," Chem. Eng. Trans., vol. 94, no. April, pp. 1045–1050, 2022, doi: 10.3303/CET2294174.
10. R. O. Ahmed, D. M. Al-Mohannadi, and P. Linke, "Multi-objective resource integration for sustainable industrial clusters," J. Clean. Prod., vol. 316, no. December 2020, p. 128237, 2021, doi: 10.1016/j.jclepro.2021.128237.
11. M. Lameh, P. Linke, and D. M. Al-Mohannadi, "Carbon neutral energy systems: Optimal integration of energy systems with CO2 abatement pathways," AIChE J., no. July, 2024, doi: 10.1002/aic.18568.
12. Y. Geng and R. Côté, "Environmental management systems at the industrial park level in China," Environ. Manage., vol. 31, no. 6, pp. 784–794, 2003, doi: 10.1007/s00267-002-2854-9.
13. X. Song, Y. Geng, H. Dong, and W. Chen, "Social network analysis on industrial symbiosis: A case of Gujiao eco-industrial park," J. Clean. Prod., vol. 193, pp. 414–423, 2018, doi: 10.1016/j.jclepro.2018.05.058.
14. H. Hong and A. Gasparatos, "Eco-industrial parks in China: Key institutional aspects, sustainability impacts, and implementation challenges," J. Clean. Prod., vol. 274, 2020, doi: 10.1016/j.jclepro.2020.122853.
15. A. Muzumdar, C. Modi, and C. Vyjayanthi, "A permissioned blockchain enabled trustworthy and incentivized emission trading system," J. Clean. Prod., vol. 349, no. July 2021, 2022, doi: 10.1016/2022.131274.
16. M. Y. Oqbi and D. M. Al-Mohannadi, "Deciphering the Policy-Technology Nexus: Enabling Effective and Transparent Carbon Capture Utilization and Storage Supply Chains," Proc. 10th Int. Conf. Found. Comput. Process Des. FOCAPD 2024, vol. 3, no. Focapd, pp. 844–852, 2024, doi: 10.69997/sct.185903.
17. S. N. Ahmad Termizi, S. R. Wan Alwi, Z. A. Manan, and P. S. Varbanov, "Potential Application of Blockchain Technology in Eco-Industrial Park Development," Sustainability, vol. 15, 2023, doi: 10.3390/su15010052.
18. M. Y. Oqbi and D. M. Al-Mohannadi, "Towards Sustainable Development: Synthesizing Optimal Integrated Peer-to-Peer Eco-Industrial Parks (EIPs) with Blockchain Technology," Chem. Eng. Trans. , vol. 114, no. May, pp. 313–318, 2024, doi: 10.3303/CET24114053.
19. R. Beck, M. Avital, M. Rossi, and J. B. Thatcher, "Blockchain Technology in Business and Information Systems Research," Bus. Inf. Syst. Eng., vol. 59, no. 6, pp. 381–384, 2017, doi: 10.1007/s12599-017-0505-1.
20. A. A. Monrat, O. Schelén, and K. Andersson, "A survey of blockchain from the perspectives of applications, challenges, and opportunities," IEEE Access, vol. 7, pp. 117134–117151, 2019, doi: 10.1109/ACCESS.2019.2936094.
21. J. Al-Jaroodi and N. Mohamed, "Blockchain in Industries: A Survey," IEEE Access, vol. 7, pp. 36500–36515, 2019, doi: 10.1109/ACCESS.2019.2903554.
22. L. Guo, H. Xie, and Y. Li, "Data encryption based blockchain and privacy preserving mechanisms towards big data," J. Vis. Commun. Image Represent., vol. 70, 2020, doi: 10.1016/j.jvcir.2019.102741.
23. C. Vanmathi, A. Farouk, S. M. Alhammad, R. Mangayarkarasi, S. Bhattacharya, and M. S. B. Kasyapa, "The Role of Blockchain in Transforming Industries Beyond Finance," IEEE Access, no. September, pp. 148845–148867, 2024, doi: 10.1109/2024.3468611.
24. T. McGhin, K. K. R. Choo, C. Z. Liu, and D. He, "Blockchain in healthcare applications: Research challenges and opportunities," J. Netw. Comput. Appl., vol. 135, no. January, pp. 62–75, 2019, doi: 10.1016/2019.02.027.
25. P. Gonczol, P. Katsikouli, L. Herskind, and N. Dragoni, "Blockchain Implementations and Use Cases for Supply Chains-A Survey," IEEE Access, vol. 8, pp. 11856–11871, 2020, doi: 10.1109/2020.2964880.
26. O. Juszczyk and K. Shahzad, "Blockchain Technology for Renewable Energy: Principles, Applications and Prospects," Energies, vol. 15, no. 13, 2022, doi: 10.3390/en15134603.
27. T. Alladi, V. Chamola, R. M. Parizi, and K. K. R. Choo, "Blockchain Applications for Industry 4.0 and Industrial IoT: A Review," IEEE Access, vol. 7, pp. 176935–176951, 2019, doi: 10.1109/ACCESS.2019.2956748.
28. Y. Guo and C. Liang, "Blockchain application and outlook in the banking industry," Financ. Innov., vol. 2, no. 1, 2016, doi: 10.1186/s40854-016-0034-9.

© 2025 by the authors. Licensed to PSEcommunity.org and PSE Press. This is an open access article under the creative commons CC-BY-SA licensing terms. Credit must be given to creator and adaptations must be shared under the same terms. See https://creativecommons.org/licenses/by-sa/4.0/



# Section 4

## Model Based Optimisation and Advanced Control

Systems & Control Transactions

**Research Article - Peer Reviewed Conference Proceeding**
ESCAPE 35 - European Symposium on Computer Aided Process Engineering
Ghent, Belgium. 6-9 July 2025
Jan F.M. Van Impe, Grégoire Léonard, Satyajeet S. Bhonsale,
Monika E. Polańska, Filip Logist (Eds.)

PSE PRESS

# Implementation and assessment of fractional controllers for an extractive distillation system

**Luis R. Flores-Gómez [a], Fernando I. Gómez-Castro [a]*, Francisco López-Villarreal [b], and Vicente Rico-Ramírez [c]**

[a] Universidad de Guanajuato, Campus Guanajuato, División de Ciencias Naturales y Exactas, Departamento de Ingeniería Química, Guanajuato, Guanajuato, México
[b] Instituto Tecnológico de Villahermosa, Departamento de Ingeniería Química, Bioquímica y Ambiental, Villahermosa, Tabasco, México
[c] Tecnológico Nacional de México en Celaya, Departamento de Ingeniería Química, Celaya, Guanajuato, México
* Corresponding Author: fgomez@ugto.mx.

## ABSTRACT

This work presents an approach to implement and assess fractional controllers in an extractive distillation system. The experimental dynamic data for an extractive distillation column is used as a case study. A strategy is developed to fit the operation data to fractional-order transfer functions. Then, the fractional controllers are designed in the Simulink environment in Matlab, tuning the controllers through a hybrid optimization approach. First, the approach uses a genetic algorithm to find an initial point, and then the solution is improved through the fmincon algorithm. According to the results of the design of fractional controllers, the sum of the square of errors is below $2.9 \times 10^{-6}$ for perturbations in heat duty, and $1.2 \times 10^{-5}$ for perturbations in the reflux ratio. Moreover, after controller tuning, a minimal value for ISE of 1,278.12 is obtained, which is approximately 8% lower than the value obtained for an integer-order controller.

**Keywords**: Fractional calculus, fractional controllers, extractive distillation

## INTRODUCTION

Process intensification is a strategy applied to chemical engineering which is devoted to the development of technologies that enhance the performance of the operations in a chemical process. The philosophy of process intensification can be summarized through its four principles: (i) maximizing the effectiveness of intra and intermolecular events, (ii) giving each molecule the same processing experience, (iii) optimizing the driving forces at every scale, and (iv) maximizing the synergistic effects from partial processes [1]. This is achieved through the implementation of modified equipment and/or multi-tasking equipment, among other approaches. Among the common operations in chemical processes, distillation is a candidate for intensification, since it is a separation process with high energy requirements and, consequently, high operational costs and high environmental impact. Diverse approaches have been proposed to intensify distillation structures, such as thermally coupled distillation schemes, where modified configurations are used to make a proper use of the heat of the internal streams and the composition profiles to reduce the energy requirements (e.g. [2]); or reactive distillation, where the operations of reaction and distillation are performed in a single unit [3]. Extractive distillation is another example of an intensified distillation operation, where an entrainer is employed to allow the separation of azeotropic mixtures [4]. Further enhancements can be obtained by using advanced entrainers [5] or with the implementation of thermal couplings to the extractive distillation system [6].

Various studies have demonstrated that the dynamic properties of intensified systems can be, for some cases, better than those of conventional configurations (e.g. [7]). In the case of extractive distillation, there are various aspects that may affect the performance of the control structure, such as the kind of solvent employed [8], the solvent flow rate [9], and the pressure [10]. In a study presented by Yi and Chien [11], a modification of the steady-state design is proposed to enhance the performance of the control system. This indicates that the

development of better control structures is still necessary [12]. The use of fractional controllers can be an alternative to achieve this target.

Fractional PID controllers (or $PI^{\lambda}D^{\mu}$ controllers) take advantage of the concepts of fractional calculus, increasing the flexibility and robustness of the controller by allowing fractional orders for the derivative and the integral actions. These characteristics make fractional controllers adequate to be implemented in systems with complex dynamics, which may be difficult to control with classical PID controllers [13]. However, the additional flexibility implies a higher complexity to perform the tuning of the controller, since additional parameters must be included in the analysis. Fractional order controls have been widely implemented to process units like reactors [14,15]. Only few works have reported the implementation of fractional controllers for distillation systems. Mishra et al. [16] assessed the performance of a fractional order fuzzy PID controller for a binary distillation column, reporting a superior performance when compared to a fuzzy PID controller. Haji Haji and Monje [17] used a dynamic version of the metaheuristic bat algorithm to perform the tuning of a fractional-order PID controller in a distillation column. Marques de Almeida et al. [18] reported the implementation of a decentralized fractional-order PI controller on a TITO distillation column, reporting a superior performance of the fractional system in comparison with integer-order controllers and model predictive control structures. In the case of intensified distillation systems, to the authors knowledge, the only antecedent is given by the work of Edet [19], who reported the implementation of a fractional PI controller to a reactive distillation system. However, the implementation of $PI^{\lambda}D^{\mu}$ controllers for intensified distillation systems has not been reported. Thus, in this work a fractional-order model, based on transfer functions, is developed for an extractive distillation system. The model is obtained through experimental data to ensure that the proposed fractional approach properly represents actual operational data. A fractional controller is implemented in the model, developing a tuning strategy based on rigorous optimization. The performance of the fractional controller is compared with that of an integer order controller.

## METHODOLOGY

The experimental dynamic data reported by Kumar et al. [20] for an extractive distillation column has been used as a case study. The column is used to separate the mixture acetone-methanol, employing water as solvent. In this study, changes in the measured variables reported for perturbations in the reflux rate and the steam pressure on the reboiler are used to perform the analysis. Since the experimental data had been reported in graphical form, the tool *WebPlotDigitalizer4.6* has been used to extract the numerical data.

The experimental data has been fitted to fractional order functions. The general form of the transfer function is given by Equation (1).

$$G(s) = \frac{Ke^{-\theta s}}{As^{\alpha}+Bs^{\beta}} \quad (1)$$

Where $0 < \alpha < 1$ for a pseudo-first order model, and $1 < \alpha < 2$ for a pseudo-second order model. The numerical fitting has been performed in the *FOMCON* toolbox of Matlab, using the Grünwald-Letnikov definition of the fractional derivative [21]. The parameters of the model are adjusted, aiming to minimize the deviation of the predictions of the model in comparison to the experimental data. The effect of the step size *h* over the fitting is also analyzed.

The implementation of the fractional controllers is performed in the Simulink environment of Matlab. The response of the fractional controller, $u(t)$, is given by Equation (2).

$$u(t) = K_p e(t) + K_i D^{-\lambda} e(t) + K_d D^{\mu} e(t) \quad (2)$$

Where $K_p$, $K_i$ and $K_d$ are the gains for the proportional, integral and derivative actions, respectively. On the other hand, $\lambda$ and $\mu$ are the orders for the fractional integral and derivative operators.

An LV configuration is employed, using the reflux rate and the steam pressure in the reboiler as the manipulated variables. The measured variables are the compositions on the distillate and the bottoms. Decoupling elements are added to the control structure to reduce the interactions among the input and output variables of the control loops. The implementation of the fractional elements is performed through the interaction between Simulink and *FOMCON*. The controllers are tuned using a hybrid optimization approach. First, a genetic algorithm is used to find an initial guess. Then, the solution is refined with the *fmincon* algorithm. The objective in the optimization procedure is to minimize the total value for the integral square error (ISE). A penalization term *F* is incorporated to avoid solutions with high overshooting. Thus, the objective function *f* is given by Equation (3).

$$f = F \sum_{i=1}^{n} ISE_i \quad (3)$$

Where *i* represents the number of the corresponding product stream. For the distillate, $i = 1$. On the other hand, for the bottoms, $i = 2$.

## RESULTS

For fitting the experimental data to a fractional order function, a strong dependence of the fitting over the step size *h* has been observed. Figure 1.a shows that, based on the experimental data available, the fitting is adequate only for a relatively large step size. As the step size is reduced, the predictions of the model have a higher

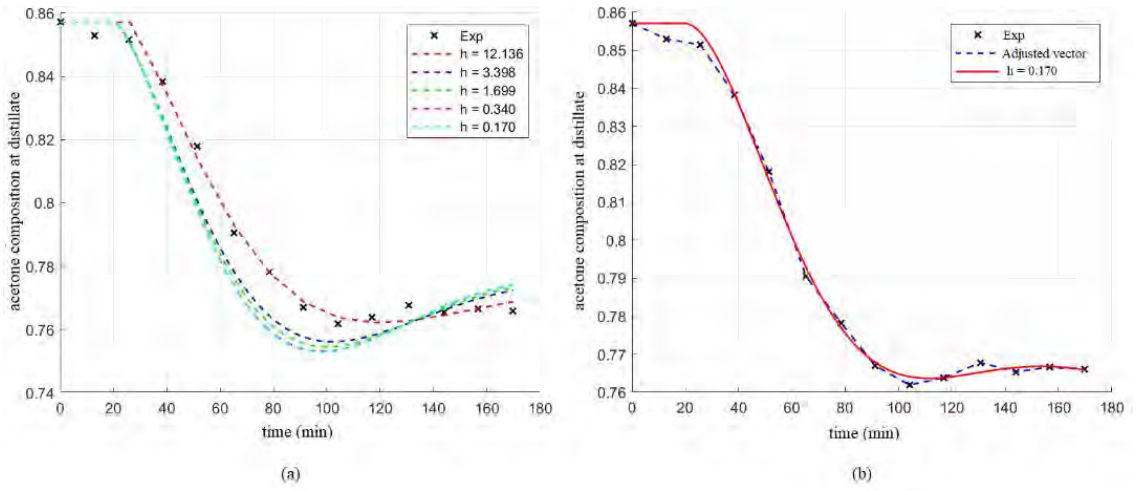



**Figure 1:** Effect of the step size in the adjustment of experimental data to fractional order transfer functions, (a) adjustment with the original data, (b) adjustment with the interpolation of data.

deviation from the experimental data. For *h* = 12.136, an acceptable fit is obtained, but there are still experimental points out of the trend. To further enhance the prediction, 1000 additional points have been generated by interpolating the experimental data. Using this approach, the prediction produced with low step sizes is considerably enhanced, as shown in Figure 1.b.

Tables 1 and 2 show the parameters obtained for the fractional transfer functions and the deviation for each fitting, where θ is given in minutes. It is important to notice that the delay time considers the period before the first experimental response is reported, which causes apparently large values for this parameter.

In general terms, low deviations are obtained through the fitting to fractional order transfer functions. It is also observed that, for all the cases, the values of α indicate pseudo-second order models. However, the values of that parameter for most cases are far from being integer. A similar trend is observed for the values of β. Thus, the relaxation of the order for the denominator in the transfer function allows flexibility in the data fitting. Although small deviations are obtained, it is important to mention that the error obtained when using integer-order transfer functions is similar to that obtained with the fractional functions. Thus, the studied system does not show a significant fractional response.

Table 3 shows the parameters of the fractional controllers after the optimization of the objective function given by Equation (2). It is observed that the integral and derivative actions are both relevant for the controller of the acetone composition in the distillate, with orders relatively close to unity. However, for the control of methanol composition in the bottoms, the derivative action has a low order, relatively close to zero. The controller in the distillate has a higher proportional gain, showing an oscillatory response.

**Table 1:** Results for the fitting of experimental data to fractional-order transfer functions when a perturbation in reflux rate occurs.

| | **Acetone composition at distillate** | **Methanol composition at bottoms** |
|---|---|---|
| K | 0.00080453 | 0.00014573 |
| A | 267.27 | 43.855 |
| B | 1 | 1 |
| θ | 415.444 | 434.55 |
| α | 1.7388 | 1.5568 |
| β | 0.11565 | 0.29164 |
| Deviation | $3.2015 \times 10^{-5}$ | $1.2120 \times 10^{-5}$ |

**Table 2:** Results for the fitting of experimental data to fractional-order transfer functions when a perturbation in steam pressure occurs.

| | **Acetone composition at distillate** | **Methanol composition at bottoms** |
|---|---|---|
| K | -0.0074095 | -0.00069622 |
| A | 121.14 | 23.576 |
| B | 1 | 1 |
| θ | 206.69 | 196.69 |
| α | 1.8119 | 1.6776 |
| β | 0.2643 | 0.41674 |
| Deviation | $5.2494 \times 10^{-5}$ | $2.9317 \times 10^{-6}$ |

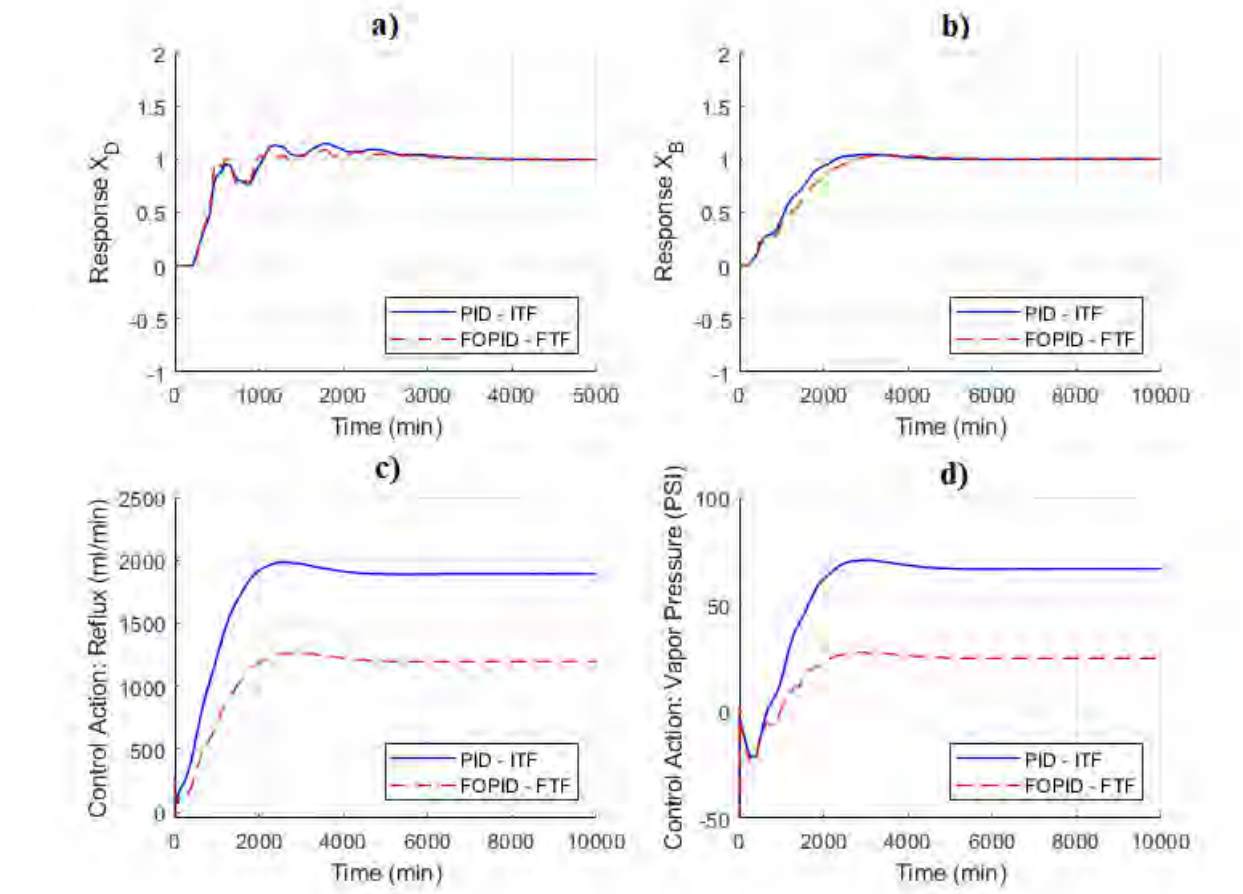



**Figure 2:** Responses and control actions for the PI$^{\lambda}$D$^{\mu}$ controller, compared with a PID controller, (a) response for the composition of acetone in the distillate, (b) response for the composition of methanol in the bottoms, (c) control action over the reflux rate, (d) control action over the steam pressure on the reboiler.

**Table 3:** Optimized parameters for the fractional controllers.

| Parameter | Distillate controller | Bottoms controller |
|---|---|---|
| $K_p$ | -128.0115 | 18.6006 |
| $K_i$ | -3.2562 | 0.2160 |
| $K_d$ | -0.7867 | -9.2389 |
| $\lambda$ | 0.8587 | 0.8229 |
| $\mu$ | 0.7091 | 0.1674 |

With the objective function used in the analysis, an overshooting percentage of 9.622 and 0% for the controllers in the distillate and the bottoms has been obtained, respectively. This is a lower percentage compared to that obtained if an integer-order controller is used, where the optimized parameters lead to overshooting values of 14.593 and 4.502% for the distillate and the bottoms, respectively. The objective function for the fractional controller has a value of 1278.12, which is approximately 8% lower than the value obtained for an integer-order controller.

Figure 2 presents the responses of the compositions when the fractional-order controller is used. The responses are compared with those obtained with an integer-order PID controller, where an integer-order transfer function is used to represent the dynamic performance of the column. Both cases use the optimized parameters of each controller. The optimized parameters for the integer-order controllers are presented in Table 4. Figure 2 also shows the corresponding control action.

**Table 4:** Optimized parameters for integer-order controllers.

| Parameter | Distillate controller | Bottoms controller |
|---|---|---|
| $K_p$ | -120.1442 | 12.9061 |
| $K_i$ | -1.8031 | 0.1253 |
| $K_d$ | -2.3642 | -6.3010 |

A similar performance is observed for the responses

of the measured variables for both kinds of controllers. The time required to reach a new steady state is similar for both kinds of controllers, with approximately 3,000 minutes needed for the stabilization of the response for both, the acetone and the methanol compositions. However, a higher over-shooting is observed for the integer-order controller, which is consistent with the over-shooting percentages described in the previous lines. The reduction on the over-shoot is highly desirable for the control of a chemical process [22,23]. Additionally, the fractional controllers allow reaching the new steady state with a lower increase in the control variables, as can be observed in Figures 2.c and 2.d. Whereas the integer controller requires increasing the reflux to a maximum value of 2,000 ml/min, the fractional controller only requires increasing the variable to approximately 1,300 ml/min. Similarly, the steam pressure in the reboiler changes to a maximum of approximately 30 psi with the fractional controller, whereas the integer controller requires increasing the manipulated variable to a value of approximately 70 psi. However, it is important to notice that this may be associated with multiplicity, which is a common situation in distillation systems [24]. Thus, the comparison in terms of the control action must be carefully verified.

## CONCLUSIONS

In this work, the use of fractional controllers in an intensified distillation system has been proposed. The studied system is an extractive distillation column. Experimental data has been used to ensure that the model fits actual operating trends. The data is successfully fitted to fractional-order transfer functions, obtaining low deviations after the fitting of parameters. However, to obtain a better fitting, it is necessary to generate additional data points. Although the fitting is adequate, the improvement achieved with fractional control is not significant when compared to that resulting from the use of an integer-order transfer function; such result indicates that the dynamic response may not have significant memory effects. In fact, for the controllers, the dynamic responses are not considerably different between the integer and the fractional-order controllers. On the other hand, the fractional controllers have been successfully designed, showing that the use of such controllers allows reducing the overshooting while obtaining responses with a lower change in the control variables. Moreover, the changes performed by the controller over the control variables to achieve the new steady-state have lower magnitudes than those required when the integer-order controller is used.

## ACKNOWLEDGEMENTS

The authors acknowledge the financial support of the Universidad de Guanajuato, and the scholarship granted to Luis Refugio Flores-Gómez by the Consejo Nacional de Humanidades, Ciencia y Tecnología (CONAHCyT, now SECIHTI), Mexico.

## REFERENCES

1. Ramírez Corona N, Palacios Rosas A, Generalities about process intensification. In: Process Intensification – Design Methodologies. Ed: Gómez-Castro FI, Segovia-Hernández JG. De Gruyter (2019).
2. Calzon-McConville CJ, Rosales-Zamora MB, Segovia-Hernández JG, Hernández S, Rico-Ramírez V, Design and optimization of thermally coupled distillation schemes for the separation of multicomponent mixtures. *Ind Eng Chem Res* 45:724-732 (2006) https://doi.org/10.1021/ie050961s
3. Malone MF, Doherty MF, Reactive distillation. *Ind Eng Chem Res* 39:3953-3957 (2000) https://doi.org/10.1021/ie000633m
4. Aquilon AF, Cargullo DM, Onayan J, Sarno J, Molino VM, Lopez ECR, Recent advances in extractive distillation. *Eng Proc* 56:11 (2023) https://doi.org/10.3390/ASEC2023-15261
5. Han J, Lei Z, Dong Y, Dai C, Chen B, Process intensification on the separation of benzene and thiophene by extractive distillation. *AIChE J* 61:4470-4480 (2015) https://doi.org/10.1002/aic.15009
6. Pan C, Qiu X, Guo J, Liu Y, Feng B, Li G, Gai H, Song H, Xiao M, Huang T, Zhu Q, Efficient purification of n-butanol by thermally coupled extractive distillation with mixed entrainer. *Sep Purif Technol* 336:126365 (2024) https://doi.org/10.1016/j.seppur.2024.126365
7. Segovia-Hernández JG, Hernández S, Rico-Ramírez V, Jiménez A, A comparison of the feedback control behavior between thermally coupled and conventional distillation schemes. *Comput Chem Eng* 28:811-819 (2004) https://doi.org/10.1016/j.compchemeng.2004.02.019
8. Luyben WL, Effect of solvent on controllability in extractive distillation. *Ind Eng Chem Res* 47:4425-4439 (2008) https://doi.org/10.1021/ie701757d
9. Wang Y, Shisheng L, Bu G, Liu W, Zhang Z, Zhu Z, Effect of solvent flow rates on controllability of extractive distillation for separating binary azeotropic mixture. *Ind Eng Chem Res* 54:12908-12919 (2015) https://doi.org/10.1021/acs.iecr.5b03666
10. Zhu Z, Yu M, Zhang W, Liu Y, Cui P, Yang J, Wang

Y, Gao J, Exploration of the effects of pressure on the controllability of extractive distillation for separating pressure-sensitive azeotropes. *Sep Purif Technol* 227:115681 (2019) https://doi.org/10.1016/j.seppur.2019.115681
11. Yi C-C, Chien I-L, Control study to enhance the controllability of heterogeneous extractive distillation: cyclohexane/cyclohexene separation. *Ind Eng Chem Res* 58:3211-3224 (2019) https://doi.org/10.1021/acs.iecr.9b00341
12. Wang C, Wang C, Cui Y, Guang C, Zhang Z, Economics and controllability of conventional and intensified extractive distillation configurations for acetonitrile/ethanol/benzene mixtures. *Ind Eng Chem Res* 57:10551-10563 (2018) https://doi.org/10.1021/acs.iecr.8b01875
13. Patnaik S, Hollkamp JP, Semperlotti F, Applications of variable-order fractional operators: a review. *Proc R Soc A: Math Phys Eng Sci* 476:20190498 (2020) https://doi.org/10.1098/rspa.2019.0498
14. Gupta D, Goyal V, Kumar J, Design of fractional-order NPID controller for the NPK model of advanced nuclear reactor. *Prog Nucl Energy* 150:104319 (2022) https://doi.org/10.1016/j.pnucene.2022.104319
15. Mukherjee D, Lloyds Raja G, Kundu P, Ghosh A, Improved fractional augmented control strategies for continuously stirred tank reactors. *Asian J Control* 25:2165-2182 (2023) https://doi.org/10.1002/asjc.2887
16. Mishra P, Kumar V, Rana KPS, A fractional order fuzzy PID controller for binary distillation column control. *Expert Syst Appl* 42:8533-8549 (2015) https://doi.org/10.1016/j.eswa.2015.07.008
17. Haji Haji V, Monje CA, Fractional-order PID control of a MIMO distillation column process using improved bat algorithm. *Soft Comput* 23:8887-8906 (2019) https://doi.org/10.1007/s00500-018-3488-z
18. Marques de Almeida A, Kaminski Lenzi M, Kaminski Lenzi E, Decentralized fractional-order PIλ control applied to a TITO distillation column: a comparative study with PID and MPC. *Cuadernos de Educación y Desarrollo* 16:e6021 (2024) https://doi.org/10.55905/cuadv16n10-131
19. Edet E, On fractional order predictive PI controller design for a MIMO reactive distillation process. *IFAC-PapersOnLine* 53:3644-3649 (2020) https://doi.org/10.1007/s00500-018-3488-z
20. Kumar S, Wright JD, Taylor PA, Modelling and dynamics of an extractive distillation column. *Can J Chem Eng* 62:185-192 (1984) https://doi.org/10.1002/cjce.5450620608
21. Vinagre BM, Monje CA, Calderón AJ, Suárez JI, Fractional PID controllers for industrial application. A brief introduction. *J Vib Control* 13:1419-1429 (2007) https://doi.org/10.1177/1077546307077498
22. Khare YB, Singh Y, PID control of heat exchanger system. *Int J Comput Appl* 8:22-28 (2010) https://doi.org/10.5120/1213-1742
23. Tsavnin A, Efimov S, Zamyatin S, Overshoot elimination for control systems with parametric uncertainty via a PID controller. *Symmetry* 12:1092 (2020) https://doi.org/10.3390/sym12071092
24. Sánchez-Correa CA, Arturo-Calvache JE, Gil-Chaves ID, Rodríguez-Niño G, Multiplicities in ethanol dehydration by extractive distillation processes with ethyleneglycol. *Chem Eng Process* 174:108886 (2022) https://doi.org/10.3390/sym12071092

© 2025 by the authors. Licensed to PSEcommunity.org and PSE Press. This is an open access article under the creative commons CC-BY-SA licensing terms. Credit must be given to creator and adaptations must be shared under the same terms. See https://creativecommons.org/licenses/by-sa/4.0/



Systems & Control Transactions

**Research Article - Peer Reviewed Conference Proceeding**
ESCAPE 35 - European Symposium on Computer Aided Process Engineering
Ghent, Belgium. 6-9 July 2025
Jan F.M. Van Impe, Grégoire Léonard, Satyajeet S. Bhonsale,
Monika E. Polańska, Filip Logist (Eds.)

PSE PRESS

# Refinery Optimal Transitions by Iterative Linear Programming

**Michael Mulholland***

University of KwaZulu-Natal, Department of Chemical Engineering, Durban, KwaZulu-Natal, South Africa
* Corresponding Author: mulholland@ukzn.ac.za

## ABSTRACT

This paper focuses on the control and dynamics of an oil refinery process on an intermediate level - the flows, masses and compositions of and between units within the refining operation. It aims to elucidate optimal strategies for the routing of streams during upset events imposed on the process. A general flowsheet simulation technique including tunable controllers for flows, compositions, levels and reaction extents is incorporated in a Linear Programming model. A standard node represents a mixed receiving tank, with exit streams which can be split, converted and separated. These nodes can be inter-connected arbitrarily in the flowsheet. The method is demonstrated for the case of a planned 3-day shutdown of the catalytic cracker.

**Keywords**: flowsheet, control, horizon, profit, maximisation, constrained

## 1. INTRODUCTION

A number of authors report work on the optimization of the journey of “parcels” of crude oil through a refinery complex. Examples of this type of MILP/MINLP production planning (or “inventory planning”) are presented in the work of [1-4]. In [5], tank levels are tracked throughout, from crude supply to customer dispatch, allowing for service disruptions. In the work of [6], model predictive control is used up to a moving horizon, taking cognisance of the present status of crude parcel storage and processing, and anticipated deliveries. The approach in [7] was to use a genetic algorithm to optimize crude oil movements, allowing for uncertainty of tank availability.

The present work focuses instead on the actual control dynamics of the refining process, within and between the flowsheet units. Intermediate storages may be provided to ease startups and upsets, so the optimization becomes a type of supply-chain problem. The authors in [8] considered how the locations and sizes of intermediate storage could be economically optimized taking into account capital costs, operating costs and product specifications and values. Their refinery representation was based on data from [9] and [10]. The present work uses the same data to construct a linear programming model of the refinery, with the purpose of examining the sequence of dynamic changes and flow re-routings required to maximise profitability during planned and unplanned upsets.

## 2. MODEL

With the aim of representing a range of process flowsheets, a systematic method of creating the linear programming equations was sought. This was based on a multi-purpose “node” consisting of a mixed storage tank which received inflows, with optional configurable reactors, separators and splitters on its outflows (Fig. 1). Here stream flows $\boldsymbol{f}$, stream compositions $\boldsymbol{x}$, tank compositions $\boldsymbol{X}$, component masses $\boldsymbol{m}$ and tank masses $\boldsymbol{M}$ are used to define the mass balances. Such nodes could be interconnected arbitrarily, even allowing recycles.

In the basic mass balance, the compositions of the streams leaving the storage are expected to equate to the composition of the tank inventory, resulting in non-linear terms $f_j\boldsymbol{m}_k/M_k$ in the mass balance. In the present work, this problem was dealt with using estimates of the tank compositions $\boldsymbol{X}_k=\boldsymbol{m}_k/M_k$ based on the previous solution of the linear program, and updating on each iteration until convergence. The inclusion of conversion, separation and stream splitting for multiple streams leaving a “tank” meant that final departing stream compositions $\boldsymbol{x}_j$ were ultimately fixed on the basis of the tank composition $\boldsymbol{X}_k$, determined in the preceding LP solution.

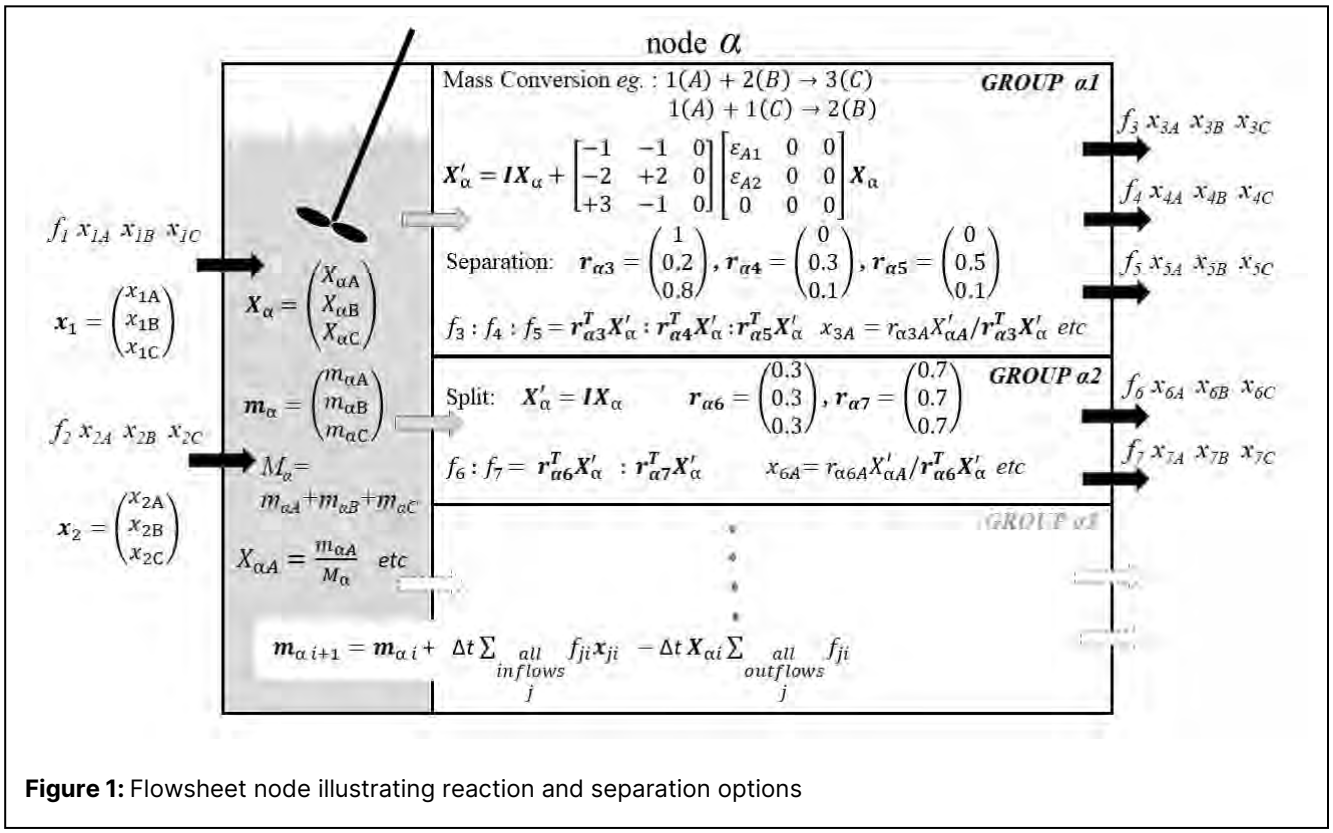



**Figure 1:** Flowsheet node illustrating reaction and separation options

Fig. 1 shows how conversion of an exit stream is handled according to the mass-stoichiometry and set reaction extents. Set-points for the extents ($\varepsilon_{A1}$, $\varepsilon_{A2}$, $\varepsilon_{B3}$, etc) are specified for each such reactor, and secondary linear programming solutions are performed for each reactor on each iteration in order to get as close as possible to these extents by minimizing the sum of weighted absolute deviations. After conversion, components may be split according to the ratios $\boldsymbol{r}_{\alpha k}$, resulting in different stream sizes as shown.

Tank levels (masses), tank compositions, reaction extents, and stream flow rates may all be controlled to specified setpoints. In linear programming, this is done by equating setpoint deviations as $\Delta=\delta_P-\delta_M$ where $\delta_P$ and $\delta_M$ are specified as non-negative, and minimising the weighted sum of these $\delta$'s. as part of the objective function.

Features of the optimisation of the time-varying flowsheet over the specified time-horizon include:

- Setpoint control of flows, storage masses & compositions, and reaction extents
- High and Low constraints for flows, storage masses & compositions
- All setpoints and setpoint weights, as well as constraints, can vary in time
- A weight (marginal value) can be set on the total mass in a tank for the objective function
- Move suppression for steady control, by penalty weights on absolute flow changes in the objective function
- Rate-of-change (ramp) limits for flows
- Exit streams from a tank can undergo reaction, fractional component separation, or total flow splitting
- A small storage volume simulates a pipe junction

## 3. FLOWSHEET REPRESENTATION AND OPERATING CONDITIONS

The simplified oil refinery flow diagram in Fig. 2 is adequate to represent the main features of transition dynamics that are investigated. This diagram and the operating conditions are based on the data of [8] shown in Tables A2 and A3 with constraints as in Table 1. In Fig. 1, AD is the atmospheric crude distiller, CC the catalytic cracker and RF the catalytic reformer. Four main Straight Run crude fraction streams: gas, naphtha, diesel and fuel oil (3-SRG, 4-SRN, 5-SRDS, 6-SRFO) move from left to right on the diagram, partially passing through the two main reaction units (RF and CC).

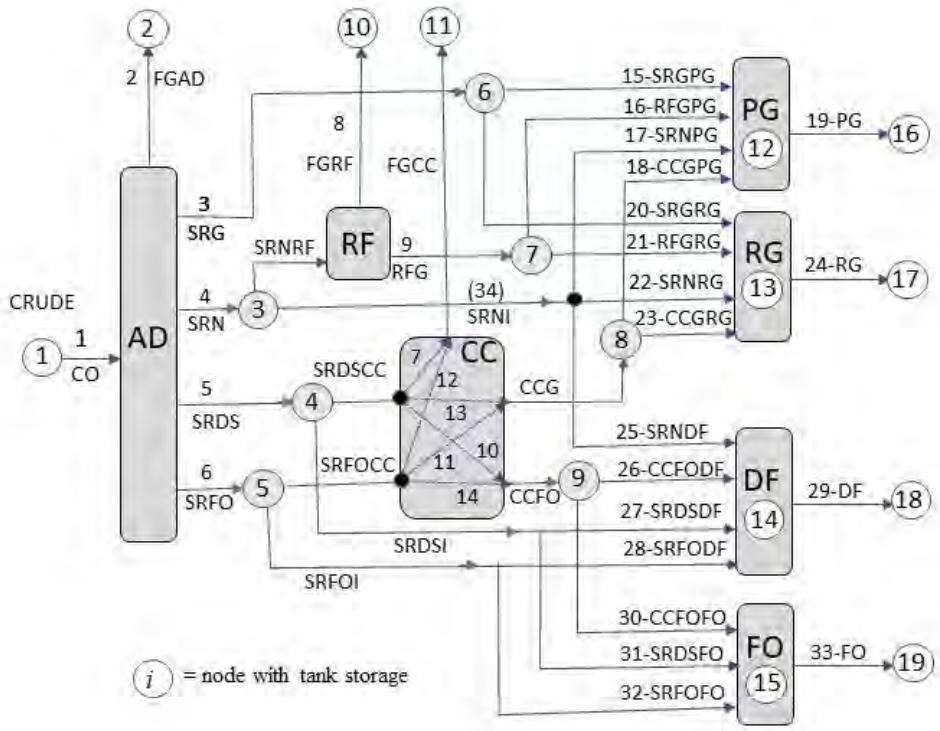



**Figure 2:** Simplified oil refinery flow diagram following [8]

**Table 1:** Economically optimal steady-state daily rates accounting for crude oil and product marginal values and associated processing costs, but excluding depreciation.

| **Stream** [bbl/day] | **Constraint** | **Optimal SS** |
|---|---|---|
| 1-COCrude Oil | ≤ 100000 | (max) 100000 |
| 19-PG Premium Gasol. | ≥ 23557 | 52645 |
| 24-RG Regular Gasol. | ≥ 11260 | 21942 |
| 29-DF Diesel Fuel | ≥ 8419 | 14058 |
| 33-FO Fuel Oil | ≥ 2826 | (min) 2826 |
| (8,9) SRN to Reformer | | (all) 23700 |
| (7,10,13) 5-SRDS to CC | | 0 |
| (12,11,14) 6-SRFO to CC | | (all) 37200 |
| (2,7,8,12) Total off-gas | | 8528 |
| OCT-PG 19-PG octane | ≥ 93 | (min) 93.0 |
| OCT-RG 24-RG octane | ≥ 87 | (min) 87.0 |
| VP-PG 19-PG vap pres | ≤ 12.7 | 8.88 mmHg |
| VP-RG 24-RG vap pres | ≤ 12.7 | 11.97 mmHg |
| DENS-DF 29-DF density | ≤ 306 | 293.3 lb/bbl |
| DENS-FO FO density | ≤ 352 | 293.4 lb/bbl |
| SULPH-DF 29-DF sulphr | ≤ 0.5 | 0.430 lb/bbl |
| SULPH-FO 33-FO sulphr | ≤ 3.0 | 0.726 lb/bbl |

**Net profit / day** (after material & operating costs, excluding capital depreciation) **$1.918\times10^6$ $/day**

**Return on USED crude oil value** **32.92%**

These create additional streams which, together with direct streams from the crude distiller, are combined in various ways to achieve the requirements of four main product streams: Premium Gasoline, Regular Gasoline, Diesel Fuel and Fuel Oil (19-PG, 24-RG, 29-DF, 33-FO) which are drawn from the finished product tanks marked PG, RG, DF and FO. The PG and RG are required to exceed minimum octane levels, and to be below a maximum vapour pressure level. The DF and FO must be below maximum density and sulphur levels (Table 1).

Around the outside of the diagram are nodes 1,2,10,11 and 16-19 – which are accumulators representing a supplier (crude oil) and customers (off-gas, premium & regular gasoline, diesel, fuel oil) for accounting purposes. "Off-gas" here refers to the byproduct gas discarded from the distillation, reforming and catalytic cracking. The objective in a 20-day case study was to maximise the value of the total inventory of the plant – including the accumulators. The marginal values and processing costs are given in tables A1 and A4. The internal nodes in the process have level setpoints of 67%, representing 2 days of operation at optimal conditions. These will reveal which storage best contributes in the event of an upset. Level setpoint weights are sufficient to prevent internal inventory emptying out to more valuable product.

## 4. STEADY-STATE OPTIMAL OPERATION

- Table 1 and Fig. 4a: Operation is stretched between minimizing octane for PG and RG at the top end (to spread available octane as far as possible), and minimizing FO production at the bottom end (which is a loss against the crude oil value – see Table A1)
- Straight Run Diesel (SRDS) bypasses the Catalytic Cracker to make up the entire Fuel Oil output (FO), and part of the Diesel Fuel (DF), where the sulphur is diluted using cracked Fuel Oil
- Cracked Fuel Oil, with its moderate octane, also becomes a major contributor to PG and RG where it helps to lower vapour pressure.
- All Straight Run Naphtha is reformed to 104 octane and sent to PG

## 5. PLANNED 3-DAY SHUTDOWN OF THE CATALYTIC CRACKER

The plant is initially running at its steady-state economic optimum. With all setpoints satisfied, only the economic terms (marginal values Table A1 and processing costs Table A4) influence the objective function. A planned 3-day shutdown of the catalytic cracker starts on day 6, so some evasive actions start in the first 5 days of the simulation. These include pre-shutdown surges of CCG to the PG product (Fig. 3a), and of CCFO to the DF product, followed by similar brief recovery surges just after the shutdown. There are surges of the SRFO to both the DF (Fig. 3b) and FO (Fig. 3c) products near the end of the shutdown, with the FO product struggling to maintain is minimum flow by draining both its storage vessel 15 (Fig. 3d) and SRFO storage 5 (Fig. 3e). The surge in SRFO to the DF product causes the DF product to reach its maximum sulphur content briefly (Fig. 3f). Extra SRG re-routed from PG to the RG product (Fig. 3g) during the shutdown causes RG to briefly reach its maximum vapour pressure (Fig. 3h). Although the crude feed rate manages to remain steady at is maximum, production rates of PG (Fig. 3i) and DF (Fig. 3j) fluctuate, reaching their minima.

In Fig. 4a a visual impression is given of the sequence of events at times before and during the shutdown. In Fig. 4b storage of SRFO is being drained whilst catalytically cracked fractions are rapidly dispatched to PG in advance of the shutdown.

The average net profit per day (over the 20 days) decreases marginally from 1.918 to 1.914 × $10^6$ $/day, as a result of the shutdown. Likewise there is a slight decrease in the profit per barrel of crude oil used, from 32.92 to 32.84%. This remarkably small impact during a major upset is largely due to the use of the Straight Run Fuel Oil storage at node 5 during the transition (Fig. 3e). The case of an *unplanned* shutdown (not presented here) is simulated with a shutdown start at steady-state on day 1, and shows similar but more radical recovery actions thereafter.

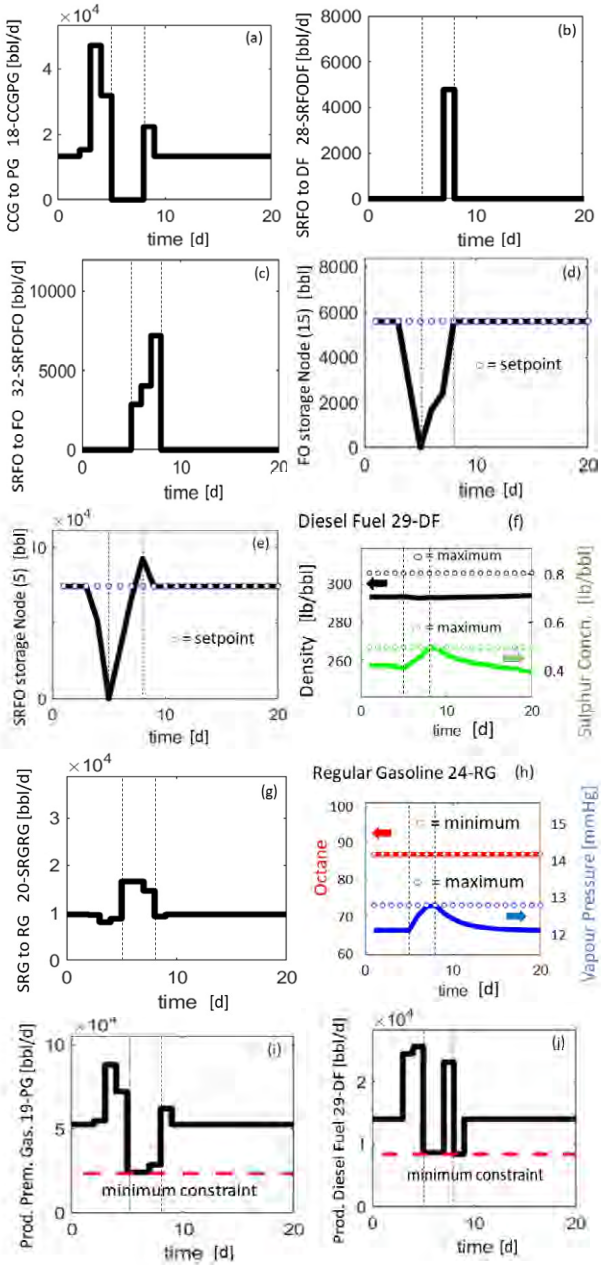



**Figure 3.** Planned 3-day shutdown of the catalytic cracker.

## 6. CONCLUSION

In this work a method is presented for dynamic optimisation of a process flowsheet, accounting for storage responses where necessary, and synchronizing transfers between units. The iteration of the LP solver provides an opportunity to update stream compositions, facilitating conversions, separations and stream splits.

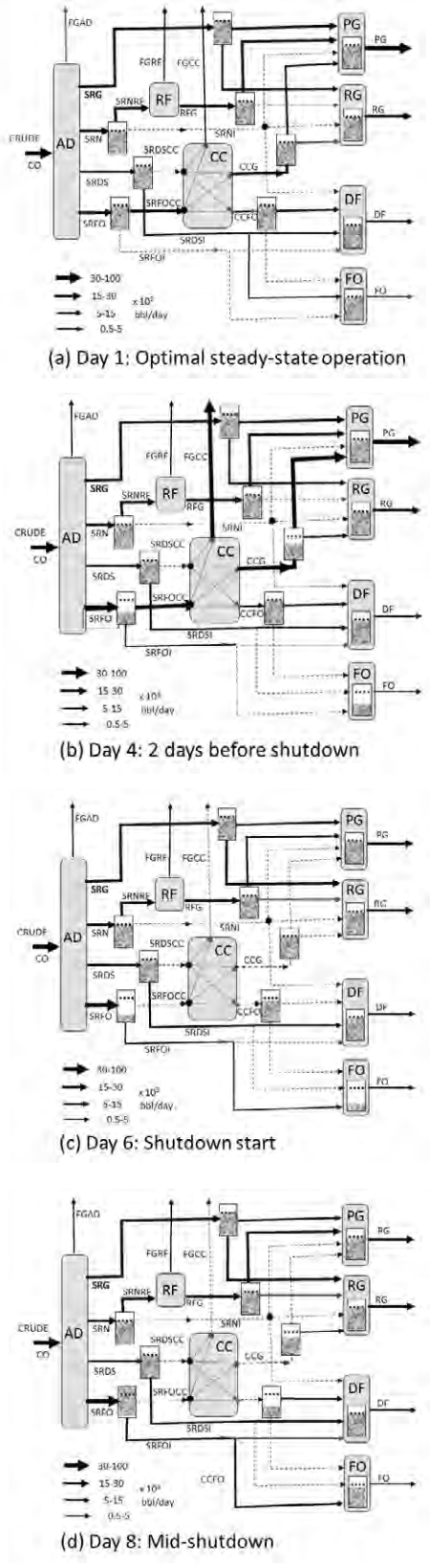



**Figure 4.** Stream flows and storage during a 3-day planned shutdown of the catalytic cracker

The method is effective for dealing with the inherent non-linearity of the mass-balance, allowing use of the robust features of linear programming. Between LP solutions, stream compositions are calculated on the basis of the recent solution, and then frozen as fixed variables for the next LP solution. At convergence, the original non-linear mass balances are all satisfied. Instability is avoided by smoothing the composition update.

A feature of the work which eased the loading of the LP variables and equations was the idea of the standard node which could provide mixing, splitting, conversion and component separation based on specified fractions and desired reaction extents. Configured to represent the operating conditions of [8], as shown in Tables A2 and A3, the steady-state economic optimum operating point was found, and subjected to upsets such as a crude change, reformer shutdown, and catalytic cracker shutdown. As seen in the latter case presented here, the process is rapidly returned to its steady-state economic optimuml operating point. The generous provisions of inter-unit storage served to reveal those storages which particularly helped minimize loss.

In this refinery simulation, the key free variables were obviously the flows $\boldsymbol{f}$. Like all other free variables these were subject to range inequality constraints as noted in Table 1. Additionally, flows were subject to flow ratio equality constraints as detailed in Fig. 1, as well as rate-of-change ramp constraints. Other free variables were tank total masses $\boldsymbol{M}$, compositions $\boldsymbol{X}$ and conversion extents $\boldsymbol{\varepsilon}$. These variables could all be controlled to setpoints (though flow setpoints and composition setpoints were unweighted in this solution). So that requires two more free variables in each case – non-negative plus and minus deviations $\boldsymbol{\delta_P}$, $\boldsymbol{\delta_M}$ from setpoint. The objective function penalised these deviations, rewarded tank inventory values, and penalised a similar absolute value of flow steps for move suppression.

In the present study all utilised setpoints were achievable at steady-state – therefore the steady-state yielded the economic optimum. One notes that the "optimality" of a transition requires prior knowledge of the future – eg. the length of a shutdown. Future work will consider placing the solution in an updated ("best guess") predictive control loop.

With the above variables individually represented at each time over the simulation horizon (20 steps), the total number of free variables amounted to 7700. These were constrained by 2120 inequality equations and 5180 equality equations. All solutions converged within 9 iterations taking a maximum of 50 seconds. Programming was done in MATLAB under Windows 10 E with a PC specification: Core 17-10510U @ 1.80 GHz with 4 cores, 8 Logical Processors and 16 GB RAM.

## APPENDIX

**Table A1:** Product and intermediate marginal values [8,10].

| Node | US$/bbl |
|---|---|
| 1 (CRUDE) | 58.38 |
| 2 (FGAD)* | 20.83 |
| 10 (FGRF)* | 20.83 |
| 11 (FGCC)* | 20.83 |
| 13 & 17 (RG) | 76.47 |
| 14 & 18 (DF) | 78.36 |
| 15 & 19 (FO) | 55.92 |
| 3-9# | 58.38 |

* Off-gas marginal values estimated from available data
# Nominal value of inventory

**Table A2:** Profiles of streams arriving at blenders [8,9].

| Stream | Octane | Vapour Press. [mmHg] | Density [lb/bbl] | Sulphur [lb/bbl] |
|---|---|---|---|---|
| 15-SRGPG | 78.5 | 18.40 | | |
| 16-RFGPG | 104.0 | 2.57 | | |
| 17-SRNPG | 65.0 | 6.54 | | |
| 18-CCGPG | 93.7 | 6.90 | | |
| 20-SRGRG | 78.5 | 18.40 | | |
| 21-RFGRG | 104.0 | 2.57 | | |
| 22-SRNRG | 65.0 | 6.54 | | |
| 23-CCGRG | 93.7 | 6.90 | | |
| 25-SRNDF | | | 272.0 | 0.283 |
| 26-CCFODF | | | 294.4 | 0.353 |
| 27-SRDSDF | | | 292.0 | 0.526 |
| 28-SRFODF | | | 295.0 | 0.980 |
| 30-CCFOFO | | | 294.4 | 0.353 |
| 31-SRDSFO | | | 292.0 | 0.526 |
| 32-SRFOFO | | | 295.0 | 0.980 |

**Table A3:** Reactor fractional product contributions [8,9].

| | In-streams | | |
|---|---|---|---|
| Out-streams | 4-SRN(RF) | 5-SRDS(CC) | 5-SRFO(CC) |
| 8-FGRF | 0.072 | | |
| 9-RFG | 0.928 | | |
| 7-FGCC | | 0.192 | |
| 12-FGCC | | | 0.092 |
| 13-CCG | | 0.619 | |
| 11-CCG | | | 0.688 |
| 10-CCFO | | 0.189 | |
| 14-CCFO | | | 0.220 |

**Table A4:** Estimated processing costs [8,10].

| Unit | Capacity [bbl/day] | Operating Cost [$/bbl] |
|---|---|---|
| Crude Distillation AD | 100000 | 1.00 |
| Catalytic Reformer RF | 25000 | 2.50 |

## REFERENCES


1. Pinto JM, Joly M, Moro LF. Planning and scheduling models for refinery operations. *Comput Chem Eng* 24(9):2259–2276 (2000)
2. Joly M, Moro LF, Pinto JM. Planning and scheduling for petroleum refineries using mathematical programming. *Braz J Chem Eng* 19(2):207–228 (2002)
3. Gao X, Jiang Y, Chen T, Huang D. Optimizing scheduling of refinery operations based on piecewise linear models. *Comput Chem Eng* 75:105-119 (2015)
4. Xu J, Zhang S, Zhang J, Wang S, Xu Q. Simultaneous scheduling of front-end crude transfer and refinery processing. *Comput Chem Eng* 96:212-236 (2017)
5. Pitty SS, Li W, Adhitya A, Srinivasan R, Karimi IA. Decision support for integrated refinery supply chains Part 1 - Dynamic simulation. *Comput Chem Eng* 32:2767–2786 (2008)
6. Yuzgec U, Palazoglu A, Romagnoli JA. Refinery scheduling of crude oil unloading, storage and processing using a model predictive control strategy. *Comput Chem Eng* 34:1671–1686 (2010)
7. Panda D, Bayu F, Ramteke M. Discrete time reactive scheduling of gasoline blending and product delivery in presence of demand and component uncertainties using graphical genetic algorithm. *Comput Chem Eng* 143:107100 (2020)
8. Boucheikhchoukh A, Berger V, Swartz CLE, Deza A, Nguyen A, Jaffer S. Multiperiod refinery optimization for mitigating the impact of process unit shutdowns. *Comput Chem Eng* 164:107873 (2022)
9. Pike RW. Optimization for Engineering Systems. Van Nostrand Reinhold (1986)
10. US Energy Information Administration. November 2019 Monthly Energy Review Technical Report (2019)



© 2025 by the authors. Licensed to PSEcommunity.org and PSE Press. This is an open access article under the creative commons CC-BY-SA licensing terms. Credit must be given to creator and adaptations must be shared under the same terms. See https://creativecommons.org/licenses/by-sa/4.0/




Systems & Control Transactions

**Research Article - Peer Reviewed Conference Proceeding**
ESCAPE 35 - European Symposium on Computer Aided Process Engineering
Ghent, Belgium. 6-9 July 2025
Jan F.M. Van Impe, Grégoire Léonard, Satyajeet S. Bhonsale,
Monika E. Polańska, Filip Logist (Eds.)

PSE PRESS

# Optimization Of Heat Exchangers Through an Enhanced Metaheuristic Strategy: The Success-Based Optimization Algorithm

**Oscar D. Lara-Montaño[a], Fernando I. Gómez-Castro[b*], Claudia Gutiérrez-Antonio[a], and Elena N. Dragoi[c]**

[a] Facultad de Ingeniería, Universidad Autónoma de Querétaro, Cerro de las Campanas S/N, Querétaro, Querétaro, Mexico 76010
[b] Departamento de Ingeniería Química, División de Ciencias Naturales y Exactas, Campus Guanajuato, Universidad de Guanajuato, Noria Alta S/N Col. Noria Alta, Guanajuato, Guanajuato, Mexico 36050.
[c] Cristofor Simionescu Faculty of Automatic Control and Computer Engineering, Gheorghe Asachi Technical University of Iasi, Str. Prof. Dr. Doc. Dimitrie Mangeron, nr. 27, Iai, Romania 700050
* Corresponding Author:fgomez@ugto.mx

## ABSTRACT

The optimization of shell-and-tube heat exchangers (STHEs) is critical for improving energy efficiency, reducing operational costs, and mitigating environmental impacts in industrial applications. This study evaluates the performance of the Success-Based Optimization Algorithm (SBOA), a novel metaheuristic strategy inspired by behavioral patterns in success perception, against seven established algorithms—Cuckoo Search, Differential Evolution (DE), Grey Wolf Optimization (GWO), Jaya Algorithm, Particle Swarm Optimization, Teaching-Learning Based Optimization, and Whale Optimization Algorithm—for minimizing the total annual cost (TAC) of STHE designs. Using the Bell-Delaware method, the optimization framework incorporates eleven decision variables, including geometric and operational parameters, subject to thermo-hydraulic constraints. A penalty function method enforces feasibility by dynamically adjusting constraint weights. Statistical analysis of 30 independent runs reveals that DE achieves the lowest mean TAC (6,090 USD/year) with minimal variability (SD = 22.57), while GWO attains the best median TAC (6,076 USD/year). Although SBOA identifies competitive solutions (minimum TAC = 6,074 USD/year), its high standard deviation (270.66) underscores inconsistency in convergence.

**Keywords:** metaheuristic optimization, Success-Based Optimization algorithm, shell-and-tube heat exchangers, Bell-Delaware method.

## INTRODUCTION

The optimization of shell-and-tube heat exchangers (STHEs) plays a significant role in enhancing energy efficiency, reducing operational costs, and minimizing environmental impacts across various industries, including petrochemicals, power generation, and HVAC systems. STHEs are favored for handling high pressures and temperatures while maintaining an effective balance between heat transfer area and spatial footprint. However, designing an optimal STHE involves managing a set of thermo-hydraulic equations and multiple decision variables, such as tube diameter, baffle spacing, deflector configuration, and the number of tube passes [1, 2].

Traditional deterministic optimization methods, including MINLP and algorithms like BARON and DICOPT, have been widely employed to address these design challenges. These methods rely on mathematical programming and gradient-based techniques to provide precise solutions with rapid convergence for convex problems. Despite their effectiveness, deterministic approaches encounter limitations when applied to real-world scenarios characterized by non-linearity, multiple local optima, and mixed discrete-continuous variables. Additionally, the dependency on explicit mathematical models difficult their applicability when utilizing commercial simulators like Aspen Plus® or HYSYS®, which do not always offer direct mathematical formulations of the

design problems.

Although this study employs an explicit model based on established thermo-hydraulic equations (e.g., Bell–Delaware method, pressure-drop correlations), the complexity arises from (a) mixed discrete-continuous decision variables and (b) non-convex behavior that can lead to multiple local optima. While deterministic solvers, in principle, handle nonlinear mixed-integer problems, preliminary attempts indicated considerable computational effort and occasional convergence to suboptimal solutions, depending on initial guesses.

Metaheuristic optimization algorithms present an alternative approach capable of handling the inherent complexities of STHE design. Algorithms such as Genetic Algorithms (GAs), Particle Swarm Optimization (PSO), Grey Wolf Optimization (GWO), and Differential Evolution (DE) have been applied to optimize STHE configurations by balancing exploration and exploitation within complex, high-dimensional search spaces [3]. These algorithms effectively avoid local optima and adapt to various problem landscapes without the need for gradient information, making them suitable for practical optimization tasks where traditional methods fall short.

The wide variety of metaheuristic algorithms introduces opportunities and challenges in selecting the most appropriate method for specific STHE optimization problems. The NFL Theorem's [4] implications extend to practical engineering challenges, where algorithm performance hinges on problem-specific features such as dimensionality, constraint types, and the balance between discrete and continuous variables. Recent advances in metaheuristics have introduced hybrid and adaptive strategies to address these challenges, yet a systematic comparison of their efficacy in STHE optimization remains underexplored. This study bridges this gap by rigorously testing SBOA, a behaviorally inspired algorithm, against seven benchmark methods. By integrating dynamic sub-populations and probabilistic exploration-exploitation mechanisms, SBOA aims to balance global search capabilities with local refinement—a critical requirement for complex STHE design problems.

This study focuses on applying and comparing the performance of the Success-Based Optimization Algorithm (SBOA) with several established metaheuristic algorithms—Cuckoo Search (CS), Differential Evolution (DE), Grey Wolf Optimization (GWO), Jaya Algorithm (JAYA), Particle Swarm Optimization (PSO), Teaching-Learning Based Optimization (TLBO), and Whale Optimization Algorithm (WOA)—in the optimization of STHE designs. The research aims to identify effective strategies for minimizing the total annual cost (TAC) while adhering to operative and geometrical constraints. The comparative analysis seeks to provide insights into the strengths and limitations of each algorithm, thereby assisting practitioners in selecting the most suitable optimization tool for their specific heat exchanger design needs.

# METODOLOGY

## The Success-Based Optimization Algorithm

The SBOA was developed with initial inspiration drawn from psychological studies on human perceptions of success and failure [5]. According to Frieze and Weiner [6], an individual's success in performing an activity is influenced by personal ability, applied effort, task difficulty, and luck. Building on these insights, SBOA integrates behavioral patterns that prioritize successful solutions while maintaining diversity within the population to prevent premature convergence.

SBOA begins by generating an initial population of candidate solutions. Each candidate solution $x_{i,j}$ is represented within a matrix $\mathrm{X}$ of size $\mathrm{n} \times \mathrm{m}$, where $\mathrm{n}$ is the number of candidate solutions and $\mathrm{m}$ is the number of decision variables. The initial candidate solutions are generated randomly within the defined lower (lb) and upper (ub) bounds for each decision variable using the equation 1.

$$x_{i,j} = lb_j + \mathrm{rand}(0,1) \cdot (ub_j - lb_j), \quad i = 1, \ldots, n; \quad j = 1, \ldots, m \tag{1}$$

Each candidate solution is evaluated using the objective function $f_{obj}$, resulting in a fitness vector $F$, shown in equation 2.

$$\mathrm{F} = \left[f_{\mathrm{obj}}(X_1), f_{\mathrm{obj}}(X_2), \ldots, f_{\mathrm{obj}}(X_n)\right] \tag{2}$$

The SBOA utilizes two sub-populations of influence, spA and spB, to guide the search process.

- Sub-population *spA***:** This sub-population consists of the top three candidate solutions based on fitness, shown in equation 3.

$$spA = \begin{bmatrix} x_{spA1,1}, & \cdots & x_{spA1,j}, & \cdots & x_{spA1,m} \\ x_{spA2,1}, & \cdots & x_{spA2,j}, & \cdots & x_{spA2,m} \\ x_{spA3,1}, & \cdots & x_{spA3,j}, & \cdots & x_{spA3,m} \end{bmatrix} \tag{3}$$

- Sub-population *spB*: The composition of *spB* varies dynamically. Initially, it includes candidates ranked between the best solution and those near the population mean. As the algorithm progresses and diversity decreases, a fixed number of individuals are assigned to *spB* to maintain exploration capabilities.

A probability criterion $r \leq C_{p1}$ determines whether new candidate solutions are influenced by *spA* or *spB*, where r is a random number between 0 and 1.

When $r \leq 1C_{p1}$, new candidate solutions are

generated using *spA* as in equation 4:

$$G_j = spA_{1,j} + D_1 \cdot (2r2_j - 1) \cdot \left|(2r3_j - j) \cdot (spA_{\text{rand},j} - X_{i,j})\right| \quad (4)$$

Here, $D_1$ decreases linearly from 1 to 0 over the iterations, facilitating the transition from exploration to exploitation. The new candidate solution GG replaces the current solution $X_i$ only if $f_{obj}(G) \leq f_{obj}(X_i)$.

When $r > 1C_{p1}$, the updating process leverages *spB* to enhance exploration. Two strategies are employed based on another probability criterion $r \leq 1C_{p2}$, if it is satisfied equation 5 is used, otherwise equation 6 is employed.

$$X_{i,j}^{t+1} = X_{i,j}^{t} + D_2 \cdot (2r4_j - 1) \cdot (2r5_j) \cdot (spB_{\text{rand},j} - X_{i,j}^{t}) \quad (5)$$

$$X_{i,j}^{t+1} = X_{i,j}^{t} + D_2 \cdot (2r4_j - 1) \cdot (2r5_j) \cdot (spB_{\text{avg},j} - X_{i,j}^{t}) \quad (6)$$

In both cases, $D_2$ decreases linearly from 1 to 0, promoting finer search as iterations proceed.

## Application to STHE Optimization

The SBOA was applied to optimize the design of shell-and-tube heat exchangers using the Bell-Delaware method. The optimization problem involves eleven decision variables:

### Continuous Variables:

- Shell Internal Diameter ($D_s$).
- Outer Tube Diameter ($d_o$).
- Central Baffle Spacing ($L_{b,c}$).
- Inlet and Outlet Baffle Spacing ($L_{b,i}$, $L_{b,i}$).
- Diametral Gap between Shell and Baffles ($\delta_{sb}$).
- Diametral Gap between Tubes and Baffles ($\delta_{tb}$).
- Outer Diameter of Tube Bundle ($D_{otl}$).

### Discrete Variables:

- Tube Pitch ($P_t$):
- Tube Layout Angle (TL)
- Baffle Cut Percentage ($B_c$)
- Number of Tube Passes ($N_p$)

The objective is to minimize the Total Annual Cost (TAC), which comprises the annualized fixed cost ($C_{fix}$) and the operating cost ($C_{op}$), as shown in equation 7.

$$TAC = C_{\text{fix}} + C_{\text{op}} \quad (7)$$

The optimization problem is subject to constraints ensuring operational and geometrical feasibility, including limits on pressure drops, fluid velocities, and tube length, as described in equations 8-13.

$$\min_x \quad \text{TAC}(x) \quad (8)$$

subject to:

$$\Delta P_t \leq \Delta P_{\text{max},t} \quad (9)$$

$$\Delta P_s \leq \Delta P_{\text{max},s} \quad (10)$$

$$v_{\text{min},t} \leq v_t \leq v_{\text{max},t} \quad (11)$$

$$\frac{L}{D_s} \leq 15 \quad (12)$$

$$lb_i \leq x_i \leq ub_i \quad (13)$$

Where $\Delta P_t$ and $\Delta P_s$ are the pressure drops on the tube and shell sides, $v_t$ is the fluid velocity in the tubes, $L$ is the tube length, $D_s$ is the shell diameter, $lb_i$ and $ub_i$ are the lower and upper bounds for the decision variables, and $x$ is the vector containing the eleven decision variables shown in Tables 1 and 2, where their limits and allowed values are displayed.

**Table 1.** Limits for continuous design variables.

| Design Variable | Symbol | Lower Limit | Upper Limit |
|---|---|---|---|
| Shell Internal Diameter | $D_s$ | 300 mm | 1,500 mm |
| Outer Tube Diameter | $d_o$ | 6.35 mm | 50.8 mm |
| Central Baffle Spacing | $L_{b,c}$ | $0.2D_s$ | $0.55D_s$ |
| Inlet and Outlet Baffle Spacing | $L_{b,i}$, $L_{b,o}$ | $L_{b,c}$ | $1.6L_{b,c}$ |
| Diametral Gap between Shell and Baffles | $\delta_{sb}$ | $0.01D_s$ | $0.1D_s$ |
| Diametral Gap between Tubes and Baffles | $\delta_{tb}$ | $0.01d_o$ | $0.1d_o$ |
| Outer Diameter of Tube Bundle | $D_{otl}$ | $0.8(D_s - \delta_{sb})$ | $0.95(D_s - \delta_{sb})$ |

**Table 2.** Allowed values for discrete design variables.

| Design Variable | Symbol | Allowed Values |
|---|---|---|
| Tube Pitch | $P_t$ | $1.25d_o, 1.5d_o$ |
| Tube Layout Angle | $TL$ | $30°, 45°, 90°$ |
| Baffle Cut Percentage | $B_c$ | 25%, 30%, 40%, 45% |
| Number of Tube Passes | $N_p$ | 1, 2, 4 |

To manage constraints during the optimization process, a penalty function method is applied. This approach incorporates penalty terms into the objective function to account for any constraint violations. The modified objective function is expressed as equation 14.

$$\begin{aligned} min \quad & \text{TAC}(x) + \lambda_1 \, max\left(0, \Delta P_t - \Delta P_{\max,t}\right) \\ & + \lambda_2 \, max\left(0, \Delta P_s - \Delta P_{\max,s}\right) \\ & + \lambda_3 \, max\left(0, v_t - v_{\max,t}\right) \\ & + \lambda_3 \, max\left(0, v_{\min,t} - v_t\right) \\ & + \lambda_4 \, max\left(0, \frac{L}{D_s} - 15\right) \end{aligned} \tag{14}$$

To handle the constraints (Eqs. 9–13), it was implemented a dynamic penalty approach. The penalty coefficients ($\lambda$) initially take moderate values and increase linearly up to 50,000 over the course of the iterations. This strategy allows exploration in the early stages, while ensuring that near the final steps all constraints are strictly enforced. Although penalty methods may cause steep cost surfaces, we mitigated potential numerical issues by careful parameter tuning and by gradually escalating the penalty values until the stablished value.

**Table 3.** Parameter setting for optimization algorithms.

| CS | DE | GWO | JAYA |
|---|---|---|---|
| Yang and Deb [7[ | Storn [8] | Mirjalili et al. [9] | Rao [10] |
| n = 50 | n = 50 | n = 50 | n = 50 |
| $\alpha = 1$ | $C_r = 0.7$ | | |
| $p_a = 0.25$ | $F = 0.6$ | | |
| **PSO** | **TLBO** | **WOA** | |
| Kennedy and Eberhart [11] | Rao et al. [12] | Mirjalili and Lewis [13] | |
| n = 50 | n = 50 | n = 50 | |
| w - linearly decreasing from 0.9 to 0.2 | | | |
| $v_{max} = 6$ | | | |
| $c_1 = 2$ | | | |
| $c_2 = 2$ | | | |

Several optimization algorithms were included in this comparison to evaluate their effectiveness in solving the presented problem. The participating algorithms are Cuckoo Search (CS), Differential Evolution (DE), Grey Wolf Optimization (GWO), Jaya Algorithm (JAYA), Particle Swarm Optimization (PSO), Teaching-Learning Based Optimization (TLBO), and Whale Optimization Algorithm (WOA). For each algorithm, 30 independent experiments were conducted, each comprising 100 iterations with 50 candidate solutions per iteration. This rigorous experimental framework ensures the statistical validity and reliability of the comparative results. The parameters used for the different employed optimization algorithms are reported in Table 3.

## Case studies

The case study involves distilled water located on the shell side with a mass flow rate of 22.07 kg/s. The inlet and outlet temperatures for the distilled water are 33.9°C and 29.4°C, respectively. The cold fluid is hard water situated on the tube side, exhibiting a mass flow rate of 35.31 kg/s with inlet and outlet temperatures of 23.9°C and 26.7°C, respectively.

Carbon steel is utilized as the construction material for both the shell and the tubes. The correction factors applied for calculating the installation cost are Cm=1.7, Ct=1.0, and Cp=1.0.

# RESULTS

Table 4 displays the statistical outcomes for the third case study's TAC. GW achieves a consistently small standard deviation (SD) across multiple experiments, indicating uniform solutions. Although DE only manages to reduce its SD after iteration 35, it ultimately attains a stable convergence with the lowest mean TAC and smallest SD overall. The SBOA finds the best solution in at least one experiment, but the final SD remains high. This outcome suggests a lack of consistency among the solutions generated by SBOA, similar to the performance observed in PSO and TLBO. GWO's median TAC is slightly lower than DE's, whereas SBO's median is 6,154 USD/year, indicating that at least half of SBO's solutions deviate considerably from its best result.

**Table 4.** Statistical Results for Case Study

| | CS | DE | GWO | JA |
|---|---|---|---|---|
| Median | 6213.14 | 6079.54 | 6076.45 | 6392.31 |
| Mean | 6214.27 | 6090.73 | 6115.13 | 6385.67 |
| SD | 97.25 | 22.57 | 109.93 | 194.52 |
| Minimum | 6080.67 | 6074.89 | 6075.18 | 6107.79 |
| | **PSO** | **SBOA** | **TLBO** | **WOA** |
| Median | 6225.49 | 6154.87 | 6284.85 | 6859.73 |
| Mean | 6246.88 | 6273.03 | 6343.07 | 6871.36 |
| SD | 165.56 | 270.66 | 193.23 | 467.50 |
| Minimum | 6077.77 | 6074.83 | 6153.98 | 6228.60 |

Comparisons indicate that GWO records the lowest median TAC, while DE provides the smallest average TAC and standard deviation. SBOA's single best solution is on par with the top-performing algorithms, but its overall variability is notable.

The SBOA-derived design (Table 5) features a

compact shell diameter (0.30 m) and high tube count (900), achieving a heat transfer area of 42 m². The 90° tube arrangement and single-pass configuration minimize pressure drops (14,100 Pa tube-side, 5,180 Pa shell-side), aligning with efficiency goals. However, the 18 baffles and narrow central spacing (0.113 m) may pose maintenance challenges, underscoring the trade-offs between cost minimization and practicality.

**Table 5.** Values for the different variables for the best STHE design found.

| Variable | Value |
|---|---|
| Shell diameter (m) | 0.3000 |
| Outer tube diameter (mm) | 6.3500 |
| Number of tubes | 900 |
| Heat transfer area (m²) | 42.0000 |
| Tube length (m) | 2.3400 |
| Tube pitch (mm) | 7.9400 |
| Tube arrangement angle (°) | 90 |
| Number of tube passes | 1 |
| Central baffle spacing (m) | 0.1130 |
| End baffle spacing (m) | 0.1810 |
| Baffle cut (%) | 45 |
| Baffle-tube diametrical gap (mm) | 0.0635 |
| Baffle-shell diametrical gap (mm) | 3.0000 |
| Bundle outer diameter (m) | 0.2750 |
| Number of baffles | 18 |
| Tube velocity (m/s) | 1.8300 |
| L/D ratio | 7.8000 |
| Tube-side pressure drop (Pa) | 14100.0 |
| Shell-side pressure drop (Pa) | 5180.0 |
| Shell mass flow rate (kg/s) | 22.1000 |
| Tube mass flow rate (kg/s) | 35.5000 |

The dynamic penalty coefficients effectively enforced constraints, with final designs satisfying all pressure drop and velocity limits. However, the aggressive penalty escalation (to 50,000) risks overshadowing the primary objective in early iterations, potentially discarding promising infeasible solutions. Future work could explore adaptive penalty strategies that weigh constraint violations relative to TAC reductions.

A one-way ANOVA (Table 6) was done to compare the mean cost across eight different optimization algorithms. The results indicate a statistically significant difference among these means, as shown by the relatively large F-value (29.8160) and the very small p-value ($7.010874 \times 10^{-33}$). In other words, the variation in cost between the algorithm groups is unlikely to be due to chance alone, and we can reject the null hypothesis that all algorithms have the same mean cost. This finding suggests that at least one of the algorithms demonstrates a different average performance compared to the others.

Table 6. One-way ANOVA analysis.

| | Sum of Squares | df | F-value | p-value |
|---|---|---|---|---|
| Algorithm | $4.4402X10^{+6}$ | 8.0 | 29.81 | $7.0108 X10^{-3}$ |
| Residual | $4.8585 X10^{+6}$ | 261.0 | - | - |

Table 7 shows the average runtime for each algorithm per experiment. DE requires only 0.2987 seconds on average, while GWO and JAYA follow closely, also maintaining sub-second times. SBOA takes slightly longer. The runtime differences may be attributed to the simpler operator structure of DE, which involves fewer internal loops and parameters compared to algorithms like SBO (which employs dual sub-populations). All tested methods remain computationally feasible in practical engineering contexts according to the computational time.

**Table 7.** Computational time per experiment.

| | CS | DE | GWO | JA |
|---|---|---|---|---|
| Time (s) | 0.7795 | 0.2987 | 0.3423 | 0.3044 |
| | **PSO** | **SBOA** | **TLBO** | **WOA** |
| Time (s) | 0.3261 | 0.5205 | 0.7926 | 0.4523 |

## CONCLUSION

This study underscores the effectiveness of metaheuristic algorithms in optimizing STHE, with DE and GWO as particularly robust options for minimizing total annual cost under operational constraints. DE is distinguished by its consistency and computational efficiency, making it well-suited for routine optimization tasks, while GWO excels in searching in complex, non-linear search spaces due to its hierarchical search mechanism. The SBOA also demonstrates significant potential, achieving competitive solutions in terms of cost minimization. However, its performance exhibits higher variability across independent runs compared to DE and GWO, which may require additional refinement for applications demanding strict reproducibility.

The selection of an appropriate algorithm remains a critical consideration, as highlighted by the No-Free-Lunch Theorem, which asserts that no single method outperforms others across all problem types. DE's strength lies in its ability to handle mixed-variable problems through a balanced mutation-recombination process, while GWO's structured approach effectively avoids local optima. SBOA, inspired by behavioral patterns in success perception, introduces a unique dual-subpopulation strategy that balances exploration and exploitation. Although this approach yields highly

competitive solutions in certain runs, its variability suggests that further tuning or hybridization with deterministic methods could enhance its consistency.

In terms of constraint management, the dynamic penalty functions employed in this study effectively enforce feasibility by progressively increasing penalty weights. This approach ensures that final solutions adhere to operational and geometric constraints, though the aggressive scaling of penalties in early iterations may occasionally hinder the exploration of promising regions in the search space. Future work could explore adaptive penalty strategies that more flexibly balance constraint satisfaction and objective optimization.

From a practical perspective, the optimal designs generated by SBOA, such as its compact shell diameter and high tube count, demonstrate its ability to identify cost-effective configurations. However, certain design features, like the narrow baffle spacing, may pose maintenance challenges, underscoring the need to balance cost savings with operational practicality.

## REFERENCES


1. Sinnott RK. Coulson and Richardson's Chemical Engineering Series - Chemical Engineering Design. Pergamon (2005)
2. Shah RK, Sekulic DP. Fundamentals of Heat Exchanger Design. John Wiley & Sons (2003)
3. Lara-Montaño OD, Gómez-Castro FI, Gutiérrez Antonio C. Comparison of the performance of different metaheuristic methods for the optimization of shell-and-tube heat exchangers. Comput Chem Eng 152: 107403. https://doi.org/10.1016/j.compchemeng.2021.107403
4. Wolpert DH, Macready WG. No free lunch theorems for optimization. IEEE Trans Evol Comput 1: 67–82. https://doi.org/10.1109/4235.585893
5. Lara-Montaño OD, Gómez-Castro FI, Gutiérrez-Antonio C, Dragoi EN. Success-Based Optimization Algorithm (SBOA): Development and enhancement of a metaheuristic optimizer. Comput Chem Eng 194:108987. https://doi.org/10.1016/j.compchemeng.2024.108987
6. Frieze I, Weiner B. Cue utilization and attributional judgments for success and failure. J Pers 39: 591–605. https://doi.org/10.1111/j.1467-6494.1971.tb00065.x
7. Yang X-S, Deb S. Cuckoo Search via Lévy Flights, In: Proceedings of the 2009 World Congress on Nature & Biologically Inspired Computing. IEEE (2009).
8. Storn R. On the usage of differential evolution for function optimization. In Proceedings of North American Fuzzy Information Processing. IEEE (1996).
9. Mirjalili S, Mirjalili SM, Lewis A. Grey Wolf Optimizer. Adv Eng Softw 69:46–61 (2014). https://doi.org/10.1016/j.advengsoft.2013.12.007
10. Rao RV. Jaya: A simple and new optimization algorithm for solving constrained and unconstrained optimization problems. Int J Ind Eng Comput, 7:19–34 (2016). https://doi.org/10.5267/j.ijiec.2015.8.004.
11. Kennedy J, Eberhart R. Particle swarm optimization. In: Proceedings of ICNN'95 - International Conference on Neural Networks. IEEE (1995).
12. Rao RV, Savsani VJ, Vakharia DP. Teaching–learning-based optimization: A novel method for constrained mechanical design optimization problems. Comput Aided Des 43:303–315 (2011). https://doi.org/10.1016/j.cad.2010.12.015
13. Mirjalili S, Lewis A. The Whale Optimization Algorithm. Adv Eng Softw 95:51–67 (2016). https://doi.org/10.1016/j.advengsoft.2016.01.008



© 2025 by the authors. Licensed to PSEcommunity.org and PSE Press. This is an open access article under the creative commons CC-BY-SA licensing terms. Credit must be given to creator and adaptations must be shared under the same terms. See https://creativecommons.org/licenses/by-sa/4.0/




Systems & Control Transactions

**Research Article - Peer Reviewed Conference Proceeding**
ESCAPE 35 - European Symposium on Computer Aided Process Engineering
Ghent, Belgium. 6-9 July 2025
Jan F.M. Van Impe, Grégoire Léonard, Satyajeet S. Bhonsale,
Monika E. Polańska, Filip Logist (Eds.)

PSE PRESS

# Production scheduling based on Real-time Optimization and Zone Control Nonlinear Model Predictive Controller

**José Matias[a*], and Alvaro Acevedo[b]**

[a] KU Leuven, Department of Chemical Engineering, Sint-Katelijne-Waver, Belgium
[b] YPFB Refinación S.A., Service Management, Cochabamba, Bolívia
* Corresponding Author: jose.matias@kuleuven.be.

## ABSTRACT

The motivation of this work is an application of a production scheduling based on Real-Time Optimization and Zone Control Nonlinear Model Predictive Controller on a liquid recovery unit of an LPG production plant. In this unit, the scheduling-relevant disturbances occur on a time scale relevant to the system dynamics; thus, we propose a novel combination of a well-known control strategies leading to a hierarchical two-layered strategy, where the lower layer employs a zone control nonlinear model predictive controller (NMPC) to define inventory setpoints while the upper layer uses real-time optimization (RTO) to determine optimal plant-wide flow rates from an economic perspective. Unlike a traditional RTO, the proposed upper-layer problem is parameterized by product demands, with a distinct optimization problem formulated for each demand scenario. Our novel approach allows for proactive mitigation of potential inventory issues by dynamically recalculating the distribution of plant products. This approach addresses the challenges of storage bottlenecks and inventory fluctuations, and it is more effective than the typical operator decisions from an economic perspective in the system of interest.

**Keywords**: Process Operations, Planning & Scheduling, Model Predictive Control, Zone Control, Real-time Optimization

## INTRODUCTION

Chemical industry has a high demand for process optimization methods and tools that enhance profitability while operating near the nominal capacity. The implementation of such methods can lead to significant productivity gains, particularly when the used strategy adopts a holistic perspective considering inventory [1,2].

Products inventory, both in-process and end-of-process, serve as buffers to mitigate fluctuations in operation and demand while maintaining consistent and predictable production. Efficient product inventory management is crucial for the profitable operation of chemical plants. To ensure optimal operation, various strategies have been proposed that consider in-process storage and aim to satisfy mass balances while avoiding bottlenecks [3].

When final product demand is highly oscillatory with unexpected stoppages, end-of-process inventories must be carefully controlled within minimum and maximum bounds. This prevents plant shutdowns and ensures compliance with legal product supply requirements. In both cases, a plant-wide perspective should be considered when making in- and end-of-process product inventory level decisions to improve overall profitability [4].

To address this problem, we propose a holistic hierarchical two-layered strategy. The upper layer uses real-time optimization (RTO) to determine optimal plantwide flow rates from an economic perspective. The lower layer employs a zone control nonlinear model predictive controller (NMPC) to define inventory setpoints. The idea is that RTO defines setpoints for flow rates that manipulate plant throughput, while NMPC maintains inventory levels within desired bounds while keeping flow rates as close as possible to the RTO-defined setpoints.

Despite the fact that the individual strategies used here have been widely studied, the use of this two-layered holistic approach is novel for this specific problem and our main contribution; however, a secondary contribution is the introduction of an ensemble of optimization problems at the RTO level. Each RTO problem is associ-

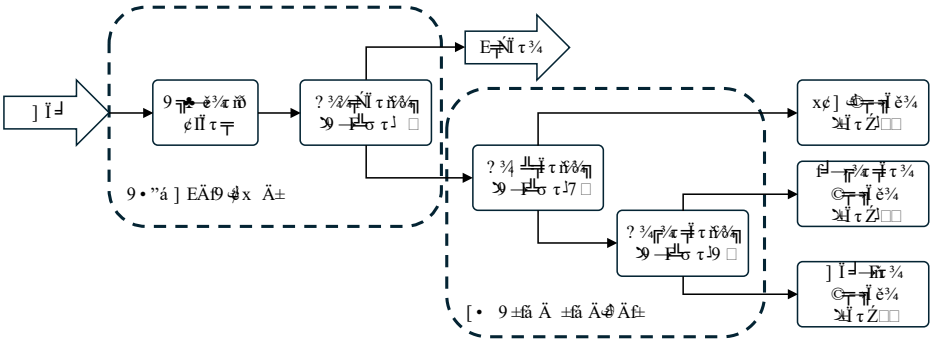


**Figure 1.** Liquid recovery unit block diagram. Only columns A, B and C will be considered in the optimization model.

ated with a different product demand scenario, which enables us to recompute optimal throughput plant manipulator setpoints using a steady-state method whereas inventory disturbances are inherently dynamic. In addition to the numerical results, we carried out a qualitative comparison between the decisions of the proposed strategy and typical actions taken by plant operators.

## LIQUID RECOVERY UNIT

The motivating case study for the development of our strategy is a three-stage distillation column system that separates a mixture of four products, inspired by a LPG production plant with recycle split vapor invented by Ortloff Ltd [5], which is illustrated in Figure 1.

The Liquid Recovery Unit contains a cryogenic plant with an improved overhead recycle (IOR) scheme. The cryogenic plant consists of two columns, an Absorber (7 theoretical stages) and a Demethanizer (Column A) of 32 theoretical stages. The top product from the Demethanizer is cooled and partially condensed, with the resulting liquids providing reflux for both columns. The cooling required to partially condense the upper vapor of the Demethanizer is provided by the top product of the Absorber. The two columns normally operate at approximately the same pressure, with pumps providing the energy necessary to transfer the liquids between the columns [6]. Subsequently, the bottom product is sent to the fractionation unit, which separates liquefied petroleum gas (LPG) from gasoline. The fractionation unit consists of 2 columns. A 27-stage debutanizer column produces LPG as its overhead product, and a 12-stage depentanizer column that separates stabilized gasoline at the top and a bottom product enriched in iso-pentanes.

While the lightest and cheapest product (ethane) is directly sent to a pipeline, the other three more valuable products are stored in tanks. Demand for these three products fluctuates significantly. In some cases, the fluctuations can be forecasted in advance, allowing for proactive measures. In other cases, when the changes cannot be predicted, a quick and effective response is necessary. This presents a significant challenge for operators, given the system's complexity and the limited time available to decide on the best countermeasures. If the latter scenario (with unpredicted changes) is relatively frequent during the operation, our proposed strategy becomes an interesting tool for improving the plant economic performance.

## INTEGRATING DECISION LAYERS

Traditionally, scheduling, production economic optimization, and control problems are considered individually and solved in a sequential way, each one representing a different decision layer. Scheduling problems usually set production targets to address the timing of actions for different manufacturing facilities. For example, avoiding storage overflow or shortage, timing production operating mode changes, etc. Scheduling decisions can be translated to targets, such as production sequences, that are sent to the production optimization layer. In this layer, real-time optimization (RTO) provides ideal economic setpoints for the control layer, which is responsible to implement these setpoints while handling plant disturbances [7]. Such sequential strategies result in upper-level decisions made with little knowledge of the production constraints at the lower levels of the decision-making hierarchy. The decisions are usually assumed to be inflexible, and lower-levels decision makers either achieve the targets at higher costs, or fail to achieve those targets [1].

Similar to the integration of continuous production optimization strategies and advanced control (e.g., economic model predictive control [8]), the scheduling layer and the continuous optimization layer can be integrated in cases where scheduling-relevant disturbances occur on a time scale relevant to the system dynamics [9]. The goal in this case is to improve overall performance by simultaneously optimizing all major continuous and discrete degrees of freedom that are influential at control and scheduling time scales. Apart from the time-scale overlap, there are other reasons for such an integration of advanced process control and scheduling: planning

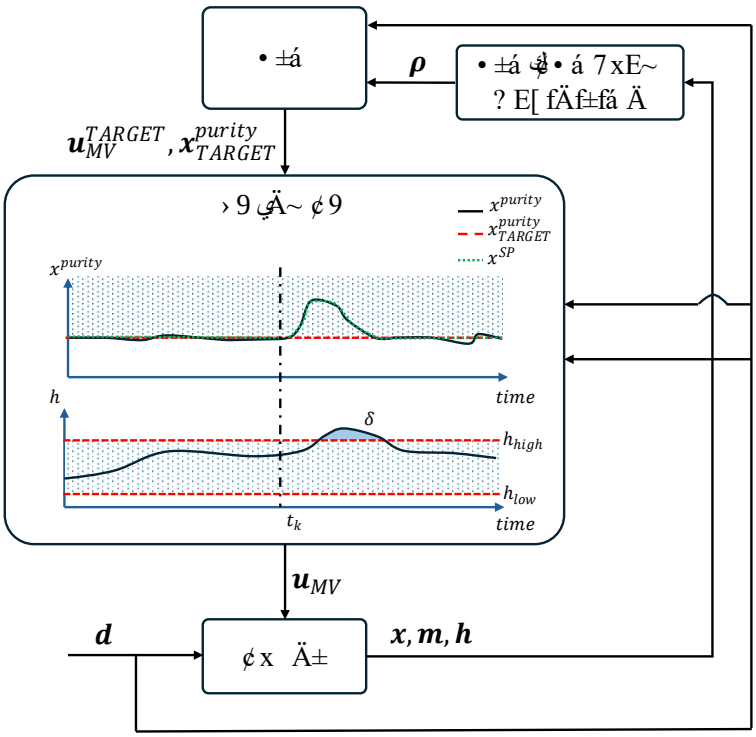



**Figure 2:** Block diagram of the proposed method. The variables that are sent between different blocks are indicated. The definition of the variables can be found in the Mathematical Formulation section. Inside the ZC-NMPC block, we illustrate an operating scenario and the action taken by the controller.

sequences that avoid costly set-ups and changeovers, reducing the duration and the lost product during transitions, avoiding schedules that lead to operational problems, using more precise and timely information in scheduling, etc. [1].

## Traditional Formulation

A range of problem formulations is used for solving scheduling problems. Typically, a mixed-integer linear program is formulated to determine when and how the operating conditions should be modified, taking into account the timing of actions as well their feasibility [1].

In contrast, RTO optimizes an economic objective function subject to a detailed first principle steady-state model that describes the plant behavior. At each RTO sampling time, key parameters of the steady state model are updated to reduce the plant-model mismatch, using plant measurements [10]. Then, the setpoint values, obtained by the economic model optimization, are fed to the control layer below, typically a model predictive controller (MPC) [7].

MPC predicts future system behavior and calculates a sequence of control actions that minimize the deviation from the setpoints defined at the RTO level. The literature is rich in diverse MPC formulations. Here, we use zone control (ZC) MPC. This strategy is interesting when maintaining outputs within defined zones is more important than achieving precise set point tracking. Therefore, while the outputs are within the pre-determined zone, the controller "gains" additional degrees of freedom that can be used to track other targets, such as input targets, giving the controller some flexibility [11].

## Proposed Strategy

Figure 2 depicts the proposed strategy and illustrates how it works. Within the controller block (ZC-NMPC), we show a specific operating condition and the corresponding controller actions. The top plot displays the purity trajectory of one of the column's products, while the bottom plot shows the level of the associated tank. The dotted pattern in both plots indicates the desired operating zone for the controller: the product purity should be larger than the target value, and the tank level must remain within the defined low-high level limits.

In this illustrative scenario, we assume a sudden unexpected decrease in product demand at time $t_k$. Consequently, the tank level $h$ begins to rise. The operator would typically respond by reducing the plant's overall feed rate to prevent tank overflow. While this action resolves the immediate issue, it can significantly impact plant profitability due to a decrease in the production of other products.

In contrast, when the proposed strategy is implemented, the controller takes two simultaneous actions.

Firstly, it increases the purity of the affected product. This higher purity typically leads to a reduced product flow rate, helping to stabilize the tank level. Secondly, the controller adjusts the operating conditions of the other columns within the plant based on the setpoints determined by the RTO level. This coordinated adjustment ensures that the tank level remains within safe operating limits while minimizing disruptions to the overall production process and maximizing plant profitability.

## MATHEMATICAL FORMULATION

Before presenting the mathematical formulation of the RTO and ZC-NMPC layers, we introduce some useful simplifications used to model the liquid recovery unit.

First, we consider only 4 generic components in the system $C_1$, $C_2$, $C_3$, and $C_4$ and assume constant relative volatility. The model keeps track of the fraction of the three lightest components in each tray of columns $A$, $B$, and $C$ (i.e., from tray 1 to $N_T$). The fractions are represented by $\boldsymbol{x}$. Note that the fraction of the heaviest component ($C_4$) can be easily obtained from the other three.

The system inputs are divided into freely manipulated variables (column's reflux and boil-up rates) $\boldsymbol{u}_{MV}$ and the remaining input variables (distillate and bottoms flow rates) $\boldsymbol{u}_{DV}$. We also defined the process measured disturbances $\boldsymbol{d}$ (feed flow rate and composition, as well as product demands)**.** We represent the system steady-state model as $\boldsymbol{f}$, which consists of mass balances and component mass balances, and the state and inputs feasible region as $\mathcal{X}$ and $\mathcal{U}$, respectively. Additionally, we define the operating constraints

$$\boldsymbol{g}(\boldsymbol{x}) = \begin{bmatrix} x_1^{purity} \\ x_2^{purity} \\ x_3^{purity} \\ x_4^{purity} \end{bmatrix} = \begin{bmatrix} x_{B,C1,N_T} - 0.07 \\ x_{B,C3,N_T} - 0.07 \\ \left(1 - \sum_{j=\{C1,C2,C3\}} x_{B,j,N_T}\right) - 0.002 \\ 0.95 - \left(1 - \sum_{j=\{C1,C2,C3\}} x_{C,j,1}\right) \end{bmatrix}, \quad (1)$$

where the first three algebraic equations from top to bottom represent the impurity constraints on the top product (tray $N_T$) of column $B$ whereas the remaining algebraic equations represents a constraint on the purity of the bottom product of the third column $C$. The calculation "$1 - \sum x$" is made in order to obtain the fraction of the lightest component $C_4$.

For the dynamic model, we need to define the holdup of all trays of the three columns, $\boldsymbol{m}$, as well as the levels in the tanks 1, 2, and 3, $\boldsymbol{h}$. The dynamic model $\boldsymbol{F}$ consists of (i) dynamic mass and component balances as well as, for each column, P-controllers relating the reboiler (stage 1) and condenser (stage $N_T$) with the respective variables in $\boldsymbol{u}_{DV}$; and (ii) dynamic mass balances of the tanks. The steady-state and dynamic models were based on [12].

### Real-time Optimization (RTO) Layer

The RTO problem is posed as follows:

$$\begin{aligned} \max_{\boldsymbol{x},\boldsymbol{u}_{MV},\boldsymbol{u}_{DV}} \quad & \varphi \\ s.t. \quad & \boldsymbol{f}(\boldsymbol{x},\boldsymbol{u}_{MV},\boldsymbol{u}_{DV};\boldsymbol{d}) = \boldsymbol{0} \\ & \boldsymbol{g}(\boldsymbol{x}) \le \boldsymbol{0} \\ & \boldsymbol{x} \in \mathcal{X} \\ & \boldsymbol{u}_{MV},\boldsymbol{u}_{DV} \in \mathcal{U} \end{aligned} \quad (2)$$

All variables have been previously defined, with the exception of the economic objective function

$$\varphi = (\rho_1 D_A + \rho_2 D_B + \rho_3 D_C + \rho_4 B_C) - \rho_5 \sum_{i=\{A,B,C\}} V_i, \quad (3)$$

where $D_i$ and $V_i$ are the distillate and boil-up rates of column $i$, which are contained in $\boldsymbol{u}_{DV}$ and $\boldsymbol{u}_{MV}$, respectively. The weight vector $\boldsymbol{\rho} := [\rho_1, \rho_2, \rho_3, \rho_4, \rho_5]$ is determined based on the operating condition:

$$\boldsymbol{\rho} := \begin{cases} if \quad h_{low} \le \boldsymbol{h} \le h_{high} & [0 \ +1 \ 0 \ 0 \ 0.01] \\ if \quad h_1 \ge h_{high} & [0 \ -1 \ 0 \ 0 \ 0.01] \\ if \quad h_2 \ge h_{high} & [0 \ 0 \ -1 \ 0 \ 0.01] \end{cases} \quad (4)$$

Each of these rules represent one desired operating scenario. The second rule, for example, indicates that in the case that the level of the tank storing the product of the second column reaches a high level condition, we want to minimize the second column distillate flow rate. Note that $\boldsymbol{\rho}$ is determined prior to the RTO execution based on the tank levels. Note also that the set of rules presented here is used only to illustrate how one can choose $\boldsymbol{\rho}$ based on the operating conditions. This set can be easily extended in order to encompass different operating scenarios depending on the practitioner needs.

### Zone Nonlinear Model Predictive Control Layer

After solving Equation (2), the RTO solution is sent to the ZC-NMPC layer as purity targets $\boldsymbol{x}_{TARGET}^{purity}$, calculated using the relations in Equation (1), and manipulated variables targets $\boldsymbol{u}_{MV}^{TARGET}$. The control problem is:

$$\begin{aligned} \min_{\boldsymbol{u}_{MV},\boldsymbol{x}_{i,k}^{SP}} \quad & \sum_{k=1}^{P_H} \Big( \sum_{i=1}^{4} \big(x_{i,k}^{purity} - x_{i,k}^{SP}\big)^2 \\ & + \gamma_1 \sum_{j=1}^{6} \big(u_{MV,j,k} - u_{MV,j}^{TARGET}\big)^2 \Big) \\ & + \gamma_2 \sum_{l=1}^{3} \delta_l{}^2 \\ s.t. \quad & \begin{bmatrix} \boldsymbol{x}_{k+1} \\ \boldsymbol{m}_{k+1} \\ \boldsymbol{h}_{k+1} \end{bmatrix} = \boldsymbol{F}\big(\boldsymbol{x}_k, \boldsymbol{m}_k, \boldsymbol{h}_k \boldsymbol{u}_{MV,k}, \boldsymbol{u}_{DV,k}; \boldsymbol{d}\big) \\ & \big|\boldsymbol{u}_{MV,k} - \boldsymbol{u}_{MV,k-1}\big| \le \Delta u_{max} \\ & h_{low} \le h_{l,\boldsymbol{k}} + \delta_l \le h_{high}, \quad l \in \{1,2,3\} \\ & 0 \le x_{1,k}^{SP} \le x_{1,TARGET}^{purity} \\ & 0 \le x_{2,k}^{SP} \le x_{2,TARGET}^{purity} \\ & 0 \le x_{3,k}^{SP} \le x_{3,TARGET}^{purity} \\ & x_{4,TARGET}^{purity} \le x_{4,k}^{SP} \le 1 \\ & \boldsymbol{x_k} \in \mathcal{X} \quad \boldsymbol{u}_{MV,k}, \boldsymbol{u}_{DV,k} \in \mathcal{U} \end{aligned} \quad (5)$$

where the subscript $k$ indicates time. The variables in Equation (5) have been already defined except: $x^{SP}$ that represents the setpoint of the purity targets that, due to zone control formulation, become variables in the problem. This means that $x^{SP}$can be freely changed by the controller given that the setpoints remain in the admissible zone purity; $\delta_{1,2,3}$ are slack variables for the tank level constraints. The plots ins Figure 2 visually demonstrate the effect of slack variables. The high-level constraint on the tank level is briefly violated (indicated by the blue area in the plot). However, this violation incurs a penalty within the objective function. As a result, the controller actively seeks to decrease the tank level as quickly as possible to minimize this penalty and return to within the acceptable operating range.

In addition to the variables above, the control formulation has the parameters $P_H$ that represents the controller prediction horizon, $\gamma_1$ and $\gamma_2$ that are weights of different terms in the objective function, and $\Delta u_{max}$ that represents the maximum allowable input change.

Plant profitability is significantly enhanced by the target tracking term in the objective function of Equation (5). Since the RTO layer determined these target values to maximize overall plant profitability (i.e., maximize $\varphi$), the controller prioritizes keeping the manipulated variables as close as possible to these targets due to the inclusion of this term. This ensures that controller actions not only address immediate operational issues, such as the tank level violation, but also contribute to maintaining optimal economic performance across the entire plant.

## CASE STUDY DESCRIPTION & RESULTS

As the case study, we chose a representative operation scenario where the demand of one of the tanks is suddenly interrupted at a given point in time as shown in Figure 3. The simulations start at a suboptimal point both from a steady-state economic perspective as well as from a product quality perspective, where the top product of the distillation column does not meet the purity constraint ($x_{B,C1,N_T} \leq 0.07$).

If the controller was not in place, the operator would first try to change the column operation to keep the product within the quality targets. After achieving the targets, they would handle the tank level problem. In the case of the demand decrease in Tank 2, they would monitor the level, and once it reaches a given threshold, they would decrease the unit load, significantly affecting the plant's profitability.

On the other hand, the controller reacts to both simultaneously. As the simulation begins, it immediately brings the fraction of $C_1$ at the top of column $B$ within the admissible bounds (Figure 4 - middle plot). However, since the level is decreasing rapidly before the demand change at $t = 100$ min, the controller decisions lead to purer distillate stream. The goal is to decrease the product flow rate. After the demand disturbance, we observe a short period where the top stream impurity increases, affecting the product quality.

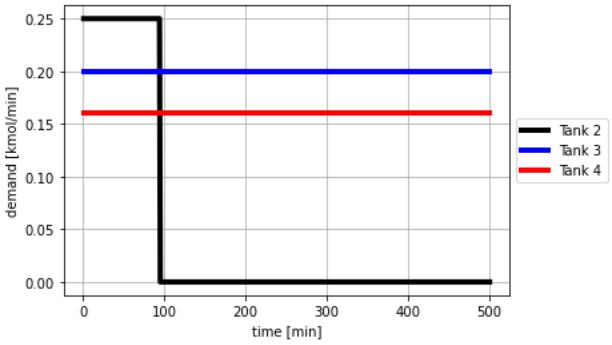



**Figure 3.** Change in the demand of Tank 2 at 99 minutes. Demands are in kmol/min

The proposed strategy then starts counteracting this effect immediately by increasing the reflux (Figure 4 - bottom plot). Next, the reflux rate is adjusted such that level constraint on Tank 2 is not violated. This effect can be seen in the slope change of the tank level trajectory (Figure 4 - top plot). Note that at time 500 minutes, the tank reaches the high-level threshold and the plant load will have to be decreased. However, this happens much later in comparison to the operator-based strategy, which can also give more time to the plant planning team to resolve the issue causing the demand problem.

## CONCLUSIONS

This work demonstrates the application of a hierarchical two-tier control strategy combining Real-Time Optimization (RTO) and Zone Control Nonlinear Model Predictive Control (ZC-NMPC) to a liquid recovery unit of an LPG production plant. Results indicate that this approach has the potential to effectively address production scheduling challenges, and significantly reduce excessive inventory fluctuations. By dynamically adjusting plant flow rates based on real-time economic objectives and uncertain demand scenarios, the proposed strategy significantly outperforms traditional operator-based decisions in terms of economic performance.

Future work will be divided in two stages. First, the proposed method will be compared to a single layer economic ZC-MPC as well as to the typical operator decisions. Both strategies will serve as a baseline for the performance proposed method. Second, we will further develop the method envisioning a practical implementation. For example, the RTO layer will be replaced by a look-up table and, since the optimal purity targets typically lie on the constraints to avoid product give-away, the possibility of replacing the nonlinear control structure by a linear

control one will also be studied. Furthermore, the controller performance will be analyzed in face of different operating scenarios to evaluate its robustness and potential economic benefits.

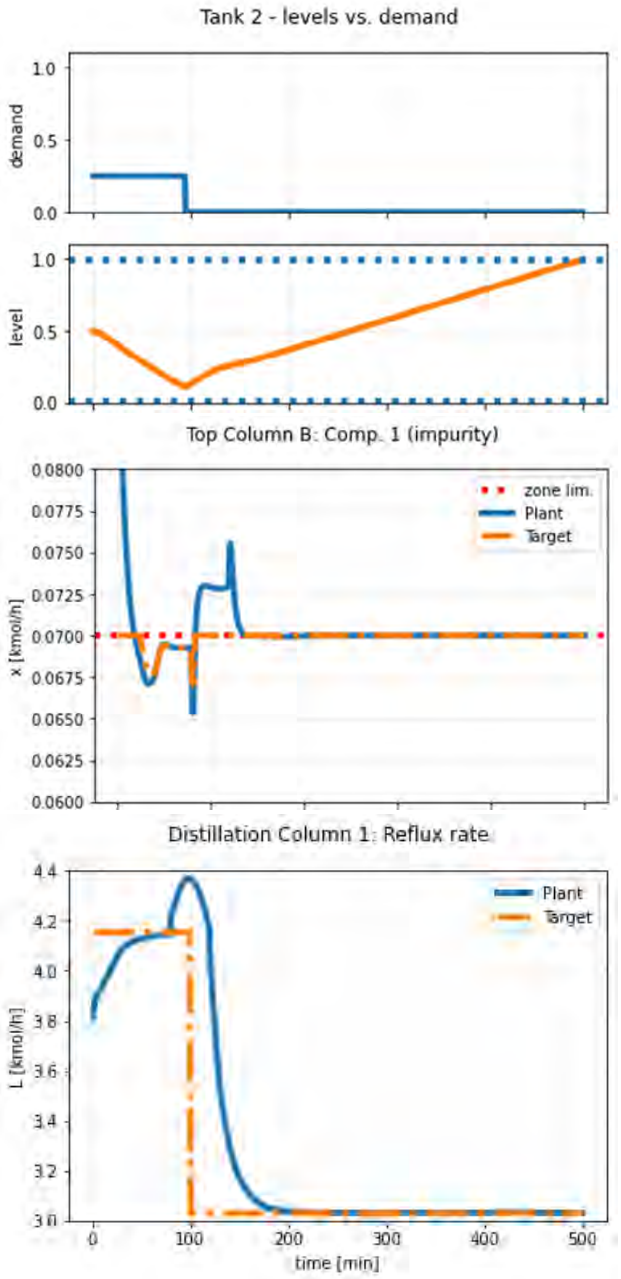



**Figure 4.** Case Study Results.

## REFERENCES


1. Engell, S., Harjunkoski, I.. Optimal operation: Scheduling, advanced control and their integration. Computers & Chemical Engineering, 47, 121-133 (2012).
2. Pinto, J. M., Joly, M., Moro, L. F. L.. Planning and scheduling models for refinery operations. Computers & Chemical Engineering, 24(9-10), 2259-2276 (2000).
3. S. Skogestad, "Control structure design for complete chemical plants", Computers and Chem. Eng., 28 (1-2), 219-234 (2004).
4. Downs, J. J., Skogestad, S.. An industrial and academic perspective on plantwide control. Annual Reviews in Control, 35(1), 99-110 (2011).
5. Zhang S. et al. Comprehensive Comparison of Enhanced Recycle Split Vapour Processes for Ethane Recovery, Energy Reports, 6, pp.1819–1837 (2020).
6. Elhefnawy, W., Gad, F., Elsayed, N., Shehata, W.. Simulation and Optimization Analysis of Natural Gas Liquid (NLG) Recovery Process from Natural Gas. Journal of Petroleum and Mining Engineering, (2017).
7. Darby, M.L., Nikolaou, M., Jones, J. Nicholson D.. RTO: an overview and assessment of current practice, J. Process Contr. 21 (6), 874–884 (2011).
8. Ellis, M., Durand, H., Christofides, P.. A tutorial review of economic model predictive control methods. J. Process Contr. 24 (8), 1156-1178 (2014).
9. Dering, D., Swartz, C. L. E.. Integrated scheduling and control with closed-loop prediction. IFAC-PapersOnLine 58(14), 640-645 (2024).
10. Miletic, I.P., Marlin, T.E.. On-line statistical results analysis in real-time operations optimization, Ind. Eng. Chem. Res. 37 (9), 3670–3684 (1998).
11. Graciano, J. E. A., Jäschke, J., Le Roux, G. A., Biegler, L. T. Integrating self-optimizing control and real-time optimization using zone control MPC. Journal of Process Control, 34, 35-48 (2015).
12. Skogestad, S., Postlethwaite, I., Multivariable Feedback Control: Analysis and Design. John Wiley & Sons (2005).



© 2025 by the authors. Licensed to PSEcommunity.org and PSE Press. This is an open access article under the creative commons CC-BY-SA licensing terms. Credit must be given to creator and adaptations must be shared under the same terms. See https://creativecommons.org/licenses/by-sa/4.0/

Systems & Control Transactions

**Research Article - Peer Reviewed Conference Proceeding**
ESCAPE 35 - European Symposium on Computer Aided Process Engineering
Ghent, Belgium. 6-9 July 2025
Jan F.M. Van Impe, Grégoire Léonard, Satyajeet S. Bhonsale,
Monika E. Polańska, Filip Logist (Eds.)

PSE PRESS

# A simple model for control and optimisation of a produced water re-injection facility

**Rafael D. De Oliveira[a], Edmary Altamiranda[b], Gjermund Mathisen[c], Johannes Jäschke[a]***

[a] Department of Chemical Engineering, Norwegian University of Science and Technology (NTNU), Trondheim, Norway.
[b] Technology Department, Aker BP ASA, Stavanger, Norway.
[c] Subsea Operations, Aker BP ASA, Stavanger, Norway.
* Corresponding Author johannes.jachke@ntnu.no.

## ABSTRACT

Model-based control and optimisation strategies can play a key role in improving energy efficiency and reducing emissions into produced water re-injection facilities. However, building a model that adequately describes the plant is challenging and can also be used in online decision-making procedures. This work proposes a simple model based on a real water re-injection facility operating on the Norwegian continental shelf. The results demonstrate the model's flexibility, which could be fitted to different plant operating points while being fast to solve when embedded in optimisation problems. The developed model is expected to aid the implementation of strategies like self-optimising control and real-time optimisation on produced water re-injection facilities.

**Keywords**: Modelling, Water Injection, Subsea, Control, Optimisation.

## INTRODUCTION

Water injection (or water flooding) is an enhanced oil recovery technique that injects water into the reservoir to maintain pressure. The injected water can come either from the sea or the water separated from the oil and gas production (produced water). The reservoir engineers typically decide the amount of injected water in each well, and many methodologies have been proposed so far in the literature where reservoir models are usually applied [1]. Once the injection targets have been defined, the water injection network system can be optimised.

A relevant optimisation problem in this context may consist of the optimal operation of the pump system topside while ensuring the integrity of the subsea water injection system by maximising the lifetime of the equipment. Usually, the works in that phase are modelling the system at a macro-level where each unit is represented as a node in a network [2-3].

The use of simple and lower-level models where the manipulated variables and measured variables can be directly connected proved to be useful in the design of new control strategies [5-6] as well as in real-time optimisation formulations where the model parameters can be updated in real-time [4].

Several requirements should be fulfilled when a model-based control and optimisation strategy is developed: 1) The formulated model should adequately describe the target plant behaviour [5]; 2) The model should be able to be fitted to the plant available measurements considering the intrinsic uncertainty [7]; 3) A optimisation problem embedding the model should be able to be reliably solvable in the required time [4].

This work proposes a simplified mechanistic model of a produced water re-injection facility that aims to meet all those requirements. The model is shown to be capable of matching real industrial data. Furthermore, this work provides original insights into the challenge of training models with real operation data.

## BACKGROUND

### Oil and gas offshore production

Offshore oil and gas production has been used for over a century and is expected to still play a role in the next decades years. A typical offshore oil and gas production facility consists of a reservoir containing oil, gas and water. The reservoir's high pressure is the driving force to make the mixture flow through the production wells. A manifold connects all the wells through a riser that will transport the mixture to a separator that is

usually located topside, but subsea separators may also be applied [5]. A three-phase separator is used to separate the oil, which is then transported to the shore through the production lines or ships. The same is done with the produced gas.

After years of operation, the reservoir starts to decrease in natural pressure, resulting in production reduction. Production can be kept at a plateau using enhanced recovery (EOR) techniques. The gas-lift technique is one of the most common methods and consists of recirculating part of the produced gas using compressors and re-injecting it into the bottom of the well [7]. This reduces the hydrostatic pressure of the mixture in the well, and a higher production. Another technique commonly applied in addition to gas-lift, is to inject the water into the reservoir in separate injection wells. This keeps the reservoir pressure high, such that a high production can be maintained.

### Produced water (PW) re-injection facility

The outflow of water from the separator is called the produced water (PW). The destination of the PW has been the topic of many government regulations [8]. The simple solution would be to discharge the PW into the sea. However, since the separator is not 100 % efficient, drops of oil are carried into the PW. Therefore, the PW needs to be submitted to treatment before discharge, in a way that complies with the regulations [2,8].

Another possible destiny for the PW is to re-inject it into the reservoir. This strategy also has the advantage of being an enhanced oil recovery technique and can increase the revenues from the asset. However, the amount of water injected into each well must be carefully chosen. If too much water is injected into a well, the water cut (ratio of produced water compared to other liquids) will increase, potentially making oil production infeasible [9]. On the other hand, if insufficient water is injected, the reservoir pressure will decrease, lowering production [9]. As a complement, seawater can also be used for water injection.

### Produced water model-based optimal control and optimisation

Many tools were developed for subsea operations, multi-phase flow control [5], gas-lift optimal injection [7], electric submersible pump operation [10] and separator control [6]. Sometimes, the models were used to develop simple feedback solutions [10]. In other cases, the model was used to generate predictions in a Model Predictive Control structure [7].

The decision-making process in PW management is made on different layers [2,11]. On higher layers, decisions are made over the long horizon of many years, where the equipment's health condition should be considered, such as pump and valve degradation. A health-aware control strategy can be applied if a degradation model is available [12]. The injection targets are typically updated over months.

On a faster time scale, the production optimisation decisions are taken. Here the optimal flow rates and pump speeds are decided [2]. Those flow rates are typically sent to the lowest layer, the control and automation layer, where feedback loops and simple controllers are used to track the setpoints coming from the layer above.

## RELATED WORK

Many studies have been conducted to control and optimize PW facilities. Most use reservoir models to obtain the optimal injection flow rates based on reservoir dynamics [1,9]. Another set of works assumed that the injection targets were given and worked only on the production optimisation layer. The main goals of those works were to efficiently operate the pumping system and consider the seawater discharger regulation. The system is treated as a network, where the nodes can be pumping stations, tanks, valves or wells.

[9] proposed a mixed integer linear programming method to solve the PW system operating optimization problem. [2] proposed an economic model predictive control formulation for optimizing daily injection, with a strong focus on compliance with environmental regulation of PW sea discharging. As far as we are concerned, no work on lower-level layers of control and automation was developed.

### Motivation and contribution of the paper

We have two main motivatiors for building a new model for the PW re-injection facility: i) Obtaining a model that can be used on real-time control and optimization strategies; ii) To address the challenges of obtaining a model that can be easily fitted to real facility data. To address those goals, a static model for the PW was developed in this work.

The model is designed to be applied to operation and production strategies that are not fully explored and adapted yet in the industry. For example real-time optimisation Here, the optimal valve openings, pump speeds, and flows can be computed to minimize energy consumption while operating within the pump envelopes and reducing the risk of cavitation on the injection valves. The model is also suitable for obtaining insights on how a simple optimizing control structure may be implemented (e.g. self-optimizing control [14]).

## MATHEMATICAL MODEL

### System description

The system to be modelled is presented in Figure 1. It is based on a real reinjection facility operated on the

Norwegian continental shelf. The system in consideration has nine boundaries: three inflows and six outflows. The outflows consist of the reservoir injection wells placed in distinct locations. The inflows consist of a seawater return, and two produced water streams. Since the goal is to obtain a simple model, the focus was to include only the primary operations that can contribute to achieving the water injection targets or the energy efficient optimisation. Therefore, the PW treatment and the separators were excluded from the model development. The interested reader is referred to [6].

The overall water injection system is divided into two parts: the topside part (on a platform or a ship) and the subsea part. A topside tank is used to store the seawater inflow, which is mainly used to complement the PW streams. The tank guarantees a steadier flow and are connected to a fixed-speed pump C. Two variable-speed pumps A and B are used to pump water to the different injection wells of the reservoirs. The second part of the model is the subsea injection system, which uses flow modules and choke valves on top of the well to precisely control each well's injection flow rate.

## Main assumptions

The main assumption made was that a steady-state model can well describe the system. This decision was based on analysing past process data and the system's relative fast dynamics. Besides, it was discussed previously that static models suffice in most cases of daily production optimisation [11]. Model accuracy was another reason for building a steady-state model, as calibrating dynamic models can be challenging in real facilities [7] and requires state estimators. Besides, steady-state models can be more easily applied in real-time optimisation (RTO) approaches [4].

Another important assumption made is the description of the reservoir behaviour, which is considered to behave linearly based on the pressure gradient between the bottom hole pressure and the reservoir pressure. That assumption is commonly used since reservoir dynamics are much slower than pumping system dynamics, and the injection parameter can be obtained experimentally by operators through injectivity tests [2].

## Topside equations

The first part of the equations describes the topside of the water injection facility. The inlet flow on the tank is controlled by a valve. Since the goal was to obtain a steady-state model, we assumed a perfect control of the tank level ($h_{tank}$). Therefore, the ordinary differential equation originating from the mass balance in the tank was not included explicitly in the model.

The pump located downstream of the tank has a fixed speed (Pump C) and the outlet flow ($F_s$) can be computed using the pump equations, where the pressure in the bottom of the tank ($P_{out}^{tank}$) is computed using a static pressure equation. Another control valve is used for manipulating the flow ($P_{out}^{c}$) downstream Pump C. The Pump C head ($H_c$) is provided by the pump curve equation.

$$F_s = CV_s z_s \sqrt{P_{out}^{c} - P_{out}^{valve}} \tag{1}$$

$$P_{out}^{tank} = P_{tank} + \rho g h_{tank} \tag{2}$$

$$P_{out}^{c} = P_{out}^{tank} + \rho g H_1 \tag{3}$$

$$H_c = a_{10} + a_{11} F_s + a_{12} F_s^2 \tag{4}$$

Downstream the pump, the flow is split into two separate lines that will connect with the two PW streams. The

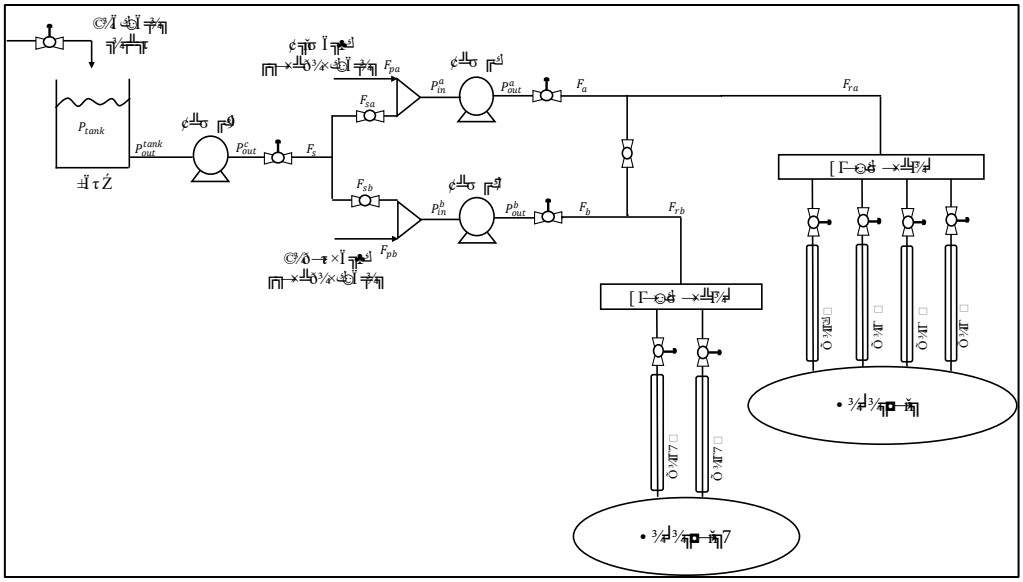



**Figure 1** – Illustration of the modelled produced water facility.

mass balances on those nodes are described as follows:

$$F_s = F_{sa} + F_{sb} \quad (5)$$

$$F_a = F_{sa} + F_{pa} \quad (6)$$

$$F_b = F_{sb} + F_{pb} \quad (7)$$

The two variable speed injection pumps are described using the pump equations, as well as the respective control valves.

$$H_a = a_{20}\omega_a^2 + a_{21}\omega_a F_a + a_{22}F_a^2 \quad (8)$$

$$H_b = a_{30}\omega_b^2 + a_{31}\omega_b F_b + a_{32}F_b^2 \quad (9)$$

$$F_a = CV_a z_a \sqrt{P_{out}^a - P_n^a} \quad (10)$$

$$F_b = CV_b z_b \sqrt{P_{out}^b - P_n^b} \quad (11)$$

$$P_a^{out} = P_a^{In} + \rho g H_1 \quad (12)$$

$$P_b^{out} = P_b^{In} + \rho g H_2 \quad (13)$$

## Subsea system equations

The second set of equations describes the flow modules, wells and reservoirs. The pressure on the flow modules as well as the mass balance are described as follow:

$$P_m^a = P_i^a + \rho g h_{riser}^a \quad (14)$$

$$F_{ra} = F_a + F_{an} \quad (15)$$

$$P_m^b = P_i^b + \rho g h_{riser}^b \quad (16)$$

$$F_{rb} = F_b + F_{bn} \quad (17)$$

Each well (i = B1, B2, A1, A2, A3 and A4) is described by the pressure in the top of the well ($P_{top}^i$) computed using the static valve equation, the bottom hole pressure ($P_{bhp}^i$) and the linear water injection on the reservoir's equation:

$$F_i^{valve} = CV_i z_i \sqrt{P_m^i - P_{top}^i} \quad (18)$$

$$P_{bhp}^i = P_{top}^i + \rho g h_i \quad (19)$$

$$F_i^{res} = (P_{bhp}^i - P_{res}^i) J_i \quad (20)$$

$$F_i^{res} = F_i^{valve} \quad (21)$$

## DATA GATHERING AND PARAMETER ESTIMATION

The industrial data was gathered from a PW facility operated on the Norwegian continental shelf. The available measurements were pressures, volumetric flow rates and pump and valve operating data. Outliers were removed, and all the data set was normalized. Figure 2 shows the water flow rate for pumps A and B during the collected period. Since the model to be fitted is static, five different steady-state operating points were selected to evaluate the model's capability of describing different scenarios.

The model comprises of 44 algebraic variables and nonlinear equations, 14 inputs and 31 parameters. Model parameters related to equipment dimensions and the valve's flow coefficient were fixed as in the real industrial system. The remaining 15 parameters were estimated using least squares regression from the field data ($P_{tank}$, $P_a^{In}$, $P_b^{In}$, $P_{res}^i$ and $J_i$).

A nonlinear weighted least-square problem was solved, where the weight used was the inverse of the variance of each measurement. Pump envelops and valve operation ranges were used to constrain the optimisation problem. The problem was implemented in MATLAB using the CasADi tool with automatic differentiation and the NLP solver IPOPT.

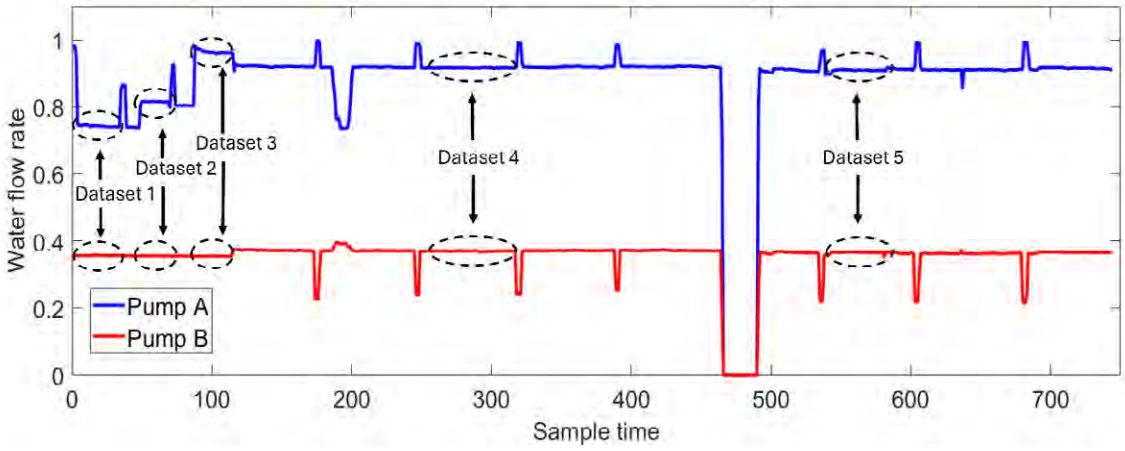



**Figure 2** – Five datasets used for parameter estimation.

## RESULTS

The fitted pump curves for pumps A and B are visualised in Figure 3, as well as the pumps operation envelopes that were used to constrain the problem feasible region. This is a crucial part of the model for future applications, because many optimal operation strategies try to optimise the pump performance [2].

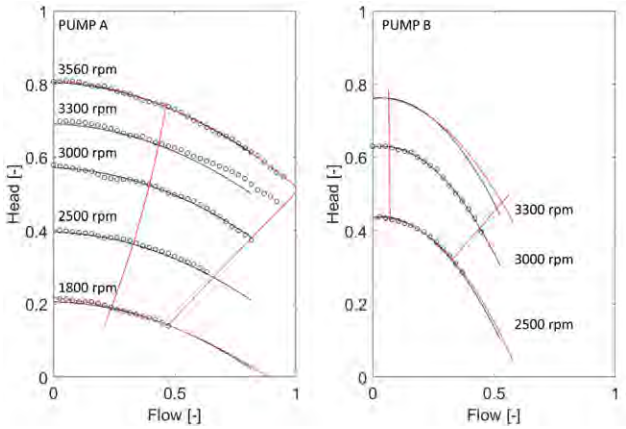



**Figure 3** –Normalized pump curves: Pump curves datapoints (circles), model predictions (black line) and operation envelopes (red line).

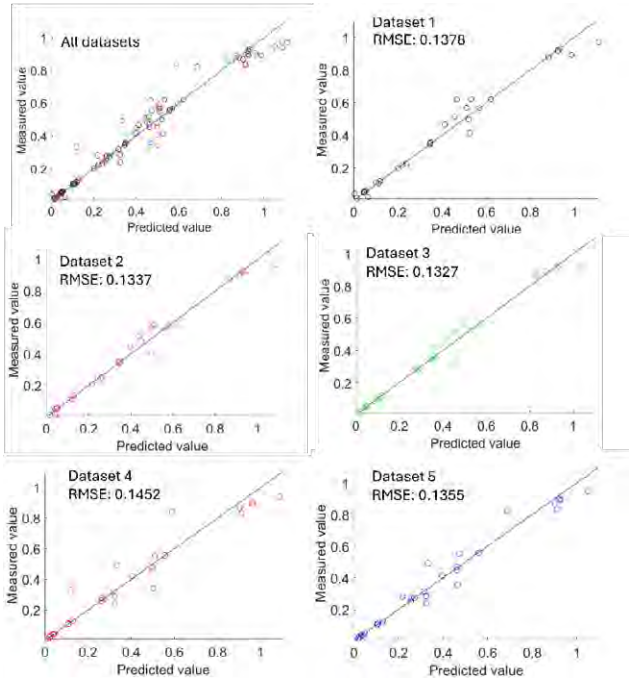



**Figure 4** – Scatter plot of the predicted and measured values for the five datasets.

A scatter plot comparing the model predictions and measurements for the five different steady state datasets can be visualized in Figure 4. All the five operating points could be described by the model with a relative equal root-mean square error (RMSE), with a slightly difference for dataset four.

The water injection rates for the different wells are the most relevant variables for optimizing water injection, since the rates should be driven to their respective targets provided by upper layers decision makers. Therefore, in Figure 5 a closer look on the predicted and measured water injection rates are shown.

Overall, the model could describe the injection rates satisfactorily, with a few exceptions. Operating points 1 and 2 have a distinct feature since either well A1 or A2 were shut down. However, the model predicted a low remnant injection rate on those wells. Furthermore, the model underpredicted wells B1 and B2 rates in almost all cases.

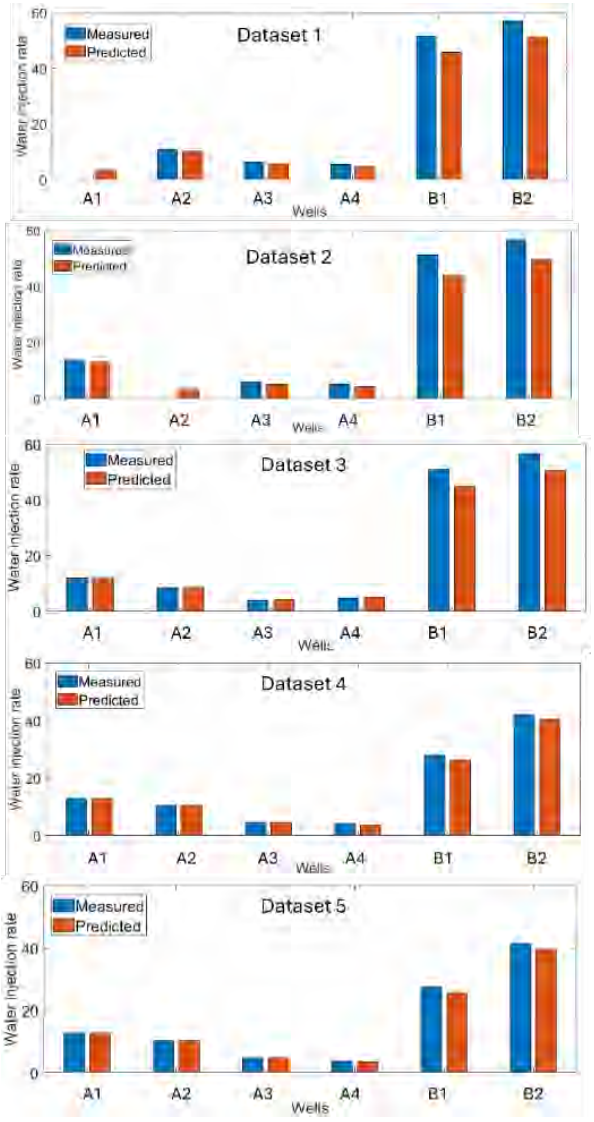



**Figure 5 –** Measured and predicted water injection rate of all the wells on the five different data-sets.

## CONCLUSIONS

A simple steady-state model could be fitted to

datasets from a real produced water re-injection facility. Overall, the model was flexible enough to fit different operating points with relatively small prediction errors.

Future work will focus on applying the developed model to applications such as real-time optimisation [4] and health-aware control by adding equipment degradation models [12]. Furthermore, an Economic Model Predictive Control strategy can also be explored. For that purpose, a dynamic model of the facility can be built based on the developed steady-state model.

## ACKNOWLEDGEMENTS

The authors acknowledge the support of the Norwegian Research Council through the AutoPRO project.

## REFERENCES

1. Grema, A. S., and Yi Cao. "Optimal Feedback Control of Oil Reservoir Waterflooding Processes." Int. J. Autom. Comput. 13 (1): 73–80.(2016) https://doi.org/10.1007/s11633-015-0909-7
2. Ivo OF, and Lars SI. "Framework for Produced Water Discharge Management with Flow-Weighted Mean Concentration Based Economic Model Predictive Control." Comput. Chem. Eng. 157 (January):107604.(2022) https://doi.org/10.1016/j.compchemeng.2021.107604
3. Ivo OF, and Lars SI. "Analysis of Optimal Control Strategies for Efficient Operation of a Produced Water Reinjection Facility for Mature Fields." IFAC-PapersOnLine,54,(3):115–21.(2021) https://doi.org/10.1016/j.ifacol.2021.08.228
4. Matias J, Oliveira JPC, Le Roux GAC, and Jäschke J. "Steady-State Real-Time Optimization Using Transient Measurements on an Experimental Rig." J. Process Control. 115(July):181–96.(2022) https://doi.org/10.1016/j.jprocont.2022.04.015
5. Sivertsen H, John-Morten G, Faanes A, and Skogestad S. "CONTROL SOLUTIONS FOR SUBSEA PROCESSING AND MULTIPHASE TRANSPORT." IFAC Proceedings Volumes, 39 (2):1069–74.(2006) https://doi.org/10.3182/20060402-4-BR-2902.01069
6. Das T., and Jäschke J. "Simplified First-Principles Model of a Compact Flotation Unit for Use in Optimization and Control." Ind. Eng. Chem. Res. 58 (3):1273–85.(2019) https://doi.org/10.1021/acs.iecr.8b04018
7. Diehl FC, Machado TO, Anzai TK, Almeida CS, Moreira CA, Nery Jr. GA, Campos MM, Farenzena M, Trierweiler JO. "10% Increase in Oil Production through a Field Applied APC in a Petrobras Ultra-Deepwater Well." *Control Eng. Pract.* 91 (October):104108.(2019) https://doi.org/10.1016/j.conengprac.2019.104108.
8. Beyer J, Goksøyr A, Hjermann DØ, and Klungsøyr J. "Environmental Effects of Offshore Produced Water Discharges: A Review Focused on the Norwegian Continental Shelf." *Mar. Environ. Res.* 162 (December):105155.(2020) https://doi.org/10.1016/j.marenvres.2020.105155
9. Zhou X, Liang Y, Xin S, Di P, Yan Y, Zhang H. "A MINLP Model for the Optimal Waterflooding Strategy and Operation Control of Surface Waterflooding Pipeline Network Considering Reservoir Characteristics." Comput. Chem. Eng. 129 (October):106512.(2019) https://doi.org/10.1016/j.compchemeng.2019.106512
10. Krishnamoorthy D, Fjalestad K, and Skogestad S. "Optimal Operation of Oil and Gas Production Using Simple Feedback Control Structures." *Control Eng. Pract.* 91 (October):104107.(2019) https://doi.org/10.1016/j.conengprac.2019.104107.
11. Foss B, Knudsen BR, and Grimstad B. "Petroleum Production Optimization – A Static or Dynamic Problem?" *Comput. Chem. Eng.*, 2017, 114 (June):245–53.(2018) https://doi.org/10.1016/j.compchemeng.2017.10.009.
12. De Oliveira, RD, and Jäschke J. "Integration of Time Scales in Health-Aware Control." *IFAC-PapersOnLine*, 58 (14): 222–27.(2024) https://doi.org/10.1016/j.ifacol.2024.08.340.
13. Zhang H, Liang Y, Zhou X, Yan X, Qian C, and Liao Q. "Sensitivity Analysis and Optimal Operation Control for Large-Scale Waterflooding Pipeline Network of Oilfield." *J. Pet. Sci. Eng.* 154 (June):38–48.(2017) https://doi.org/10.1016/j.petrol.2017.04.019.
14. Skogestad S. "Plantwide Control: The Search for the Self-Optimizing Control Structure." *J. of Process Control* 10 (5): 487–507. (2000) https://doi.org/10.1016/S0959-1524(00)00023-8.

© 2025 by the authors. Licensed to PSEcommunity.org and PSE Press. This is an open access article under the creative commons CC-BY-SA licensing terms. Credit must be given to creator and adaptations must be shared under the same terms. See https://creativecommons.org/licenses/by-sa/4.0/



Systems & Control Transactions

**Research Article - Peer Reviewed Conference Proceeding**
ESCAPE 35 - European Symposium on Computer Aided Process Engineering
Ghent, Belgium. 6-9 July 2025
Jan F.M. Van Impe, Grégoire Léonard, Satyajeet S. Bhonsale,
Monika E. Polańska, Filip Logist (Eds.)

PSE PRESS

# Design of Process Systems for Flexibility and Resilience Using Multi-Parametric Programming

**Natasha J. Chrisandina[a,b,c], Eleftherios Iakovou[b,d,e], Efstratios N. Pistikopoulos[a,b], Mahmoud M. El-Halwagi[a,b,c]***

[a] Artie McFerrin Department of Chemical Engineering, Texas A&M University, College Station, TX, USA
[b] Texas A&M Energy Institute, Texas A&M University, College Station, TX, USA
[c] Gas and Fuels Research Center, Texas A&M Engineering Experiment Station, College Station, TX, USA
[d] Department of Multidisciplinary Engineering, Texas A&M University, College Station, TX, USA
[e] Department of Engineering Technology and Industrial Distribution, Texas A&M University, College Station, TX, USA
* Corresponding Author: el-halwagi@tamu.edu.

## ABSTRACT

Process systems are negatively impacted by manufacturing uncertainties, and increasingly by unknown-unknown disruptive events. To this effect, systems need to be designed with the inherent flexibility and resilience to overcome the impacts of uncertainties and disruptions respectively as it is more challenging to retrofit existing systems with such capabilities. To this end, we propose a methodology based on flexibility analysis to systematically explore the feasibility of design alternatives under parameter uncertainty and discrete disruption scenarios simultaneously. Multi-parametric programming is utilized to generate explicit relationships between design decisions and the resulting system's ability to maintain feasible operations under uncertainty and disruptive events. We capture this ability by introducing the Combined Flexibility-Resilience Index (CFRI), which describes the likelihood that the system is feasible under the relevant uncertainty and disruption sets. With explicit functions for the CFRI, the flexibility and resilience objectives can be incorporated into a general superstructure design optimization problem alongside other objectives, allowing for the exploration of trade-offs among flexibility, cost and resilience. Our methodology provides the foundation of a holistic approach for design optimization for both flexibility and resilience. A case study involving a process plant with multiple sources of uncertainties and disruptive events is used to illustrate the application of the proposed methodology.

**Keywords**: Design Under Uncertainty, Multiscale Modelling, Optimization, Resilience, Flexibility

## INTRODUCTION

An important goal for process synthesis and design is hedging against future uncertainties. A realized design decision determines the range of operational strategies that can be deployed to respond to disruptions and uncertainties, which means that an overly restrictive or rigid design could be detrimental long-term even if it meets short-term objectives such as minimized investment cost. However, it is impossible to predict every fluctuation from nominal operating conditions and every disruption event with absolute certainty. Stress-testing with a set of highly probable scenarios is a commonly used method to assess the resilience of various design alternatives, but this may result in designs that are not adaptable to previously unseen disasters [1,2]. Methods that systematically evaluate process behavior within the entire range of possible realizations, such as the flexibility analysis framework, could bring additional insights into the expected performance of a particular design alternative under uncertainty. Furthermore, flexibility analysis can serve as a unifying framework for simultaneously considering resilience against specific disruption scenarios, reliability and availability of process equipment, and design under uncertainty.

Flexibility analysis in general, as initially formulated by Swaney and Grossmann [3], describes the range of uncertainty where a particular design configuration remains feasible. Variations of the flexibility analysis have introduced more complexities in the representation of

uncertainty, such as the stochastic flexibility analysis which considers the specific probability distribution of the uncertainty [4], flexibility-availability analysis which adds information about the likelihood that a specific design state will occur [5], and considerations of measured and unmeasured uncertainties [6]. This formulation has been used to generate designs for process systems as well as supply chains with a specific level of performance against uncertain parameters [7-9].

In this work, we showcase the use of an adapted stochastic flexibility analysis for optimizing the design of a process system under uncertainty and disruption scenarios. Specifically, the stochastic flexibility analysis is used to represent uncertain parameters and their probability distributions as well as discrete disruption scenarios. The combined flexibility-resilience index (CFRI) represents the probability that a particular design configuration will remain feasible under the given uncertainty and disruption scenarios. The CFRI can be expressed in terms of design variables, either through an analytical approach or numerical approximation. This function can then be incorporated into a superstructure optimization programming problem to assess trade-offs between prioritizing flexibility and resilience and other objectives such as cost minimization. The proposed methodology is demonstrated through a case study for retrofitting a process plant.

# METHODOLOGY

## Framework summary

In this work, a stochastic flexibility-based approach is used to represent how uncertainties and discrete disruption scenarios simultaneously affect the feasibility of a given design, which is taken as the representation of whether the design would be resilient under these disruption scenarios. From this approach, a Combined Flexibility-Resilience Index (CFRI) is generated which describes the likelihood that a design configuration is feasible under the set of uncertainties and disruption scenarios. This section describes the derivation of the CFRI as well as how it is utilized to explore trade-offs between resilience and other objectives in the design stage.

## Combined Flexibility-Resilience Index (CFRI) derivation

To derive the CFRI, a superstructure for the system at hand is first generated. At this initial stage, it is important to determine the allowable range for design variables and the desired performance goal (e.g. must meet 100% of demand). Additionally, the uncertainty set and discrete disruption scenario set are generated. These sets describe the full extent of uncertainties and disruptions that the optimal design should be feasible under.

## Calculating CFRI for one design realization

The stochastic flexibility index $SF$ represents the probability that a design configuration is feasible under the specific probability distribution for $\theta$ [4]. Mathematically, this is expressed as:

$$SF = \Pr(\psi \leq 0) \tag{1a}$$
$$s.t.\ \psi(d,\theta) = \max u \tag{1b}$$
$$s.t.\ f_j(d,\theta) \leq u \quad \forall j \in J \tag{1c}$$
$$h_m(d,\theta) = 0 \quad \forall m \in M \tag{1d}$$
$$\theta : P_d(\theta) \tag{1e}$$

For a given design configuration, the stochastic flexibility is expressed by the integral of the joint distribution function of $\theta$, $P_d(\theta)$ over the feasible region:

$$SF = \int_{\theta:\psi(d,\theta)\leq 0} P_D(\theta)\, d\theta \tag{2}$$

For cases where $\theta$ is normally distributed and $\psi(\theta)$ is linear, an exact value for the stochastic flexibility can be derived. For cases where $\theta$ has a non-standard distribution, numerical approaches such as the use of Gaussian quadratures or a sample average approximation approach can be used as an approximation [9, 10].

An assumption that is still implicit in the stochastic flexibility formulation is that the process constraints $f_j, h_m$ are fixed. However, discrete disruption scenarios realize as a modification on these constraints (e.g. loss of equipment capacity changes a constraint that caps the amount that can be produced). A change in process constraints means that the feasible region has changed, which would in turn change the value of the stochastic flexibility index for each scenario (see Figure 1). The Combined Flexibility-Resilience Index (CFRI), therefore, is the weighted sum of the stochastic flexibility index for all discrete scenarios given the probability of each scenario:

$$CFRI = \mathbb{E}(SF) \tag{3}$$

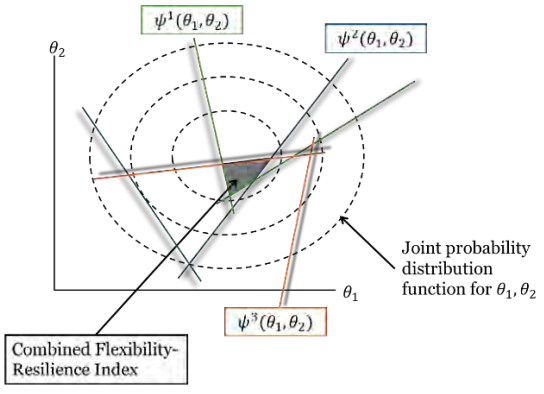



**Figure 1.** Graphical illustration of the CFRI for three potential discrete disruption scenarios and two independent, normally-distributed uncertain parameters

To efficiently calculate the CFRI for one design realization and a given set of uncertainties and disruption scenarios, the following steps can be performed:

1. Generate reduced subproblems based on each disruption scenario
2. For each subproblem, formulate the feasibility test problem
3. Solve the feasibility test problem via multi-parametric programming to yield explicit equations for $\psi(\theta)$
4. Use the $\psi(\theta)$ expression to calculate the stochastic flexibility for the given probability distribution of the uncertainty
5. Calculate the CFRI as the weighted sum of the stochastic flexibility for each disruption scenario (Equation 2)

### CFRI as a function of design variables

With the CFRI calculated for different design realizations, a correlation between the CFRI and design variables can then be derived. This correlation can then be used to express a flexibility-resilience goal in a design optimization problem. Numerical approximations such as using Gaussian quadratures and sample average approximation methods have been proposed for relating flexibility with design variables [7, 9, 10]. In this work, a sample average approximation approach is utilized to approximate CFRI as a function of design variables.

## Superstructure optimization to yield optimal design

For a problem where the objective is to minimize design and nominal operating costs, the design optimization problem can be constructed as follows:

$$\min CAPEX(d) + OPEX(d, \theta^{NOM}) \quad (4a)$$
$$s.t.\, f_j(d, \theta) \leq 0 \quad \forall j \in J \quad (4b)$$
$$h_m(d, \theta) = 0 \quad \forall m \in M \quad (4c)$$
$$CFRI(d) \geq CFRI^{target} \quad (4d)$$

Where Equations 4b, 4c describe the process constraints and Equation 4d describes the minimum desirable CFRI as a function of design variables. To obtain a Pareto front that describes trade-off between cost and CFRI, the simplest method is to solve Equation 4 repeatedly for different values of $CFRI^{target}$. If $CFRI(d)$ is a non-linear function, the optimization problem is a non-linear program (NLP) which might also be non-convex. This increases the difficulty in obtaining a continuous Pareto front parametrically, as the problem would then need to be reformulated as an mp-NLP (multi-parametric NLP). Several algorithms have been proposed in literature [11-14] to obtain either global solutions or approximations for mp-NLP problems which can be used to obtain explicit functions that describe trade-offs between objectives.

# CASE STUDY

## Setup

To demonstrate how the CFRI can be used as part of a design optimization problem, a case study is constructed based on the co-generation plant first described in Al-Fadhli, et al. [15]. The plant, pictured in Figure 2, consists of a steam power plant and a PV system for electricity generation as well as a reverse osmosis plant and a thermal desalination plant (based on multi-stage flash units) for water generation.

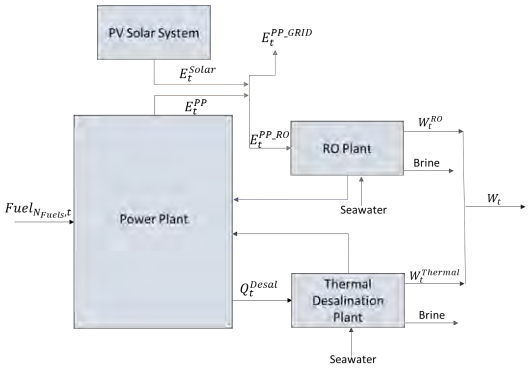



**Figure 2.** Simple process flowsheet for the co-generation plant case study. Adapted from Al-Fadhli, et al. [15].

The process constraints are given as follows:

$$E^{PP} = 0.13F_1 + 0.15F_2 + 0.82F_3 + 0.50F_4 - 0.43Q^{Desal} \quad (5a)$$
$$E^{PPGrid} = 0.85(E^{PP} + E^{Solar}) - E^{RO} \quad (5b)$$
$$W^{Thermal} = 9.95Q^{Desal} \quad (5c)$$
$$W^{RO} = 192E^{RO} \quad (5d)$$
$$W^{Thermal} + W^{RO} \geq W^{Demand} \quad (5e)$$
$$E^{PP} + E^{Solar} \geq E^{Demand} \quad (5f)$$
$$W^{Thermal} \leq cap_{MSF} d_{MSF} \quad (5g)$$
$$W^{RO} \leq cap_{RO} d_{RO} \quad (5h)$$
$$E^{Solar} \leq cap_{PV} d_{PV} \quad (5i)$$

Demand for both water and electricity are assumed to be normally distributed, as shown in Figure 3.

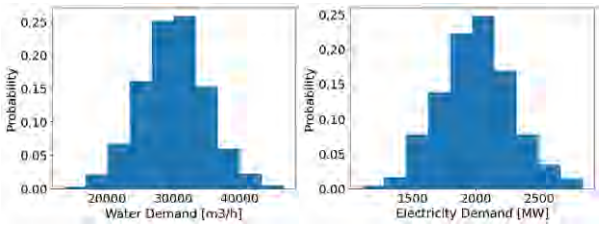


**Figure 3.** Probability distribution for water ($W^{Demand}$, left) and electricity ($E^{Demand}$, right) demand

Equipment failure scenarios are also generated for the PV, RO, and MSF units ($cap_{PV}, cap_{RO}, cap_{MSF}$ respectively), which includes both partial (25%, 50%, 75% capacity loss) and full (100% capacity loss) failures as represented in Figure 4. In total, 125 mutually exclusive scenarios are generated with different discrete probabilities. The goal of this case study is to retrofit the existing plant through expansion of the PV, RO, and MSF plants up to 2X their current capacities to maximize its resilience against uncertain demand and failure scenarios simultaneously while minimizing retrofit cost.

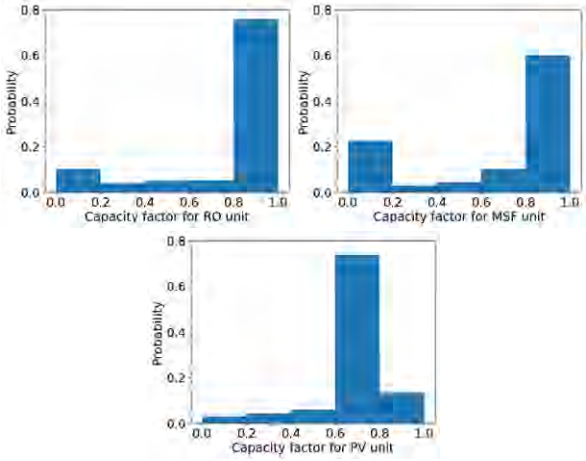



**Figure 4.** Discrete probability distribution for capacity loss disruption scenarios for RO (left), MSF (right), and PV (bottom) plants

With $W^{Demand}, E^{Demand}$ as the uncertain parameters and $d_{MSF}, d_{RO}, d_{PV}$ as the design variables, a multi-parametric reformulation can be constructed to derive the feasibility function $\psi(\theta, d)$ which is then used to derive the CFRI.

## Results and discussion

For the set of process constraints in Equation 4 and nominal design values of $d_{MSF} = 20836\frac{m^3}{h}, d_{RO} = 11364\frac{m^3}{h}, d_{PV} = 1000\ MW$, the feasibility regions that each represent a different expression for $\psi(\theta)$ are shown in Figure 5 below. This figure represents the feasibility region map, which provides information about how to evaluate the design feasibility depending on the realized water and electricity demand values. The stochastic flexibility for the nominal design values given the demand distributions is calculated to be $SF = 1$. To incorporate equipment failure scenarios, reduced subproblems are generated based on the discrete failure probabilities presented in Figure 4. Finally, the CFRI can be calculated as a weighted average of the stochastic flexibility across scenarios. For the nominal design values, $CFRI = 0.26$. Appendix A describes the derivation of the CFRI value in more detail.

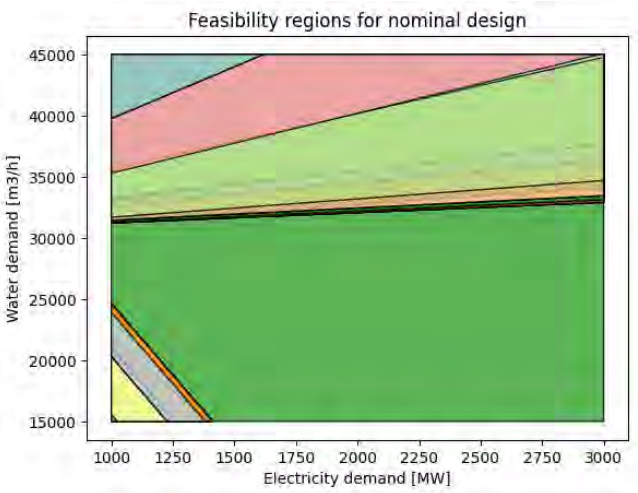



**Figure 5.** Feasible region map, where one color represents one feasibility region (a distinct $\psi(\theta)$ function), for the nominal design variables of $d_{MSF} = 20836\frac{m^3}{h}, d_{RO} = 11364\frac{m^3}{h}, d_{PV} = 1000\ MW$, under the scenario of 0% capacity loss. This figure was generated via PPOPT (Python Parametric Optimization Toolbox), a Python-based multi-parametric program solver [16].

To derive a function that describes how the three design variables affect system resilience under uncertainty and disruptions $CFRI(d_{RO}, d_{MSF}, d_{PV})$, a sample average approximation method is used. The CFRI value is calculated for 1000 random samples of design realizations that fall within the desired design variable range ($20836 \le d_{MSF} \le 41672\frac{m^3}{h}, 11364 \le d_{RO} \le 22728\frac{m^3}{h}, 1000 \le d_{PV} \le 2000\ MW$). The function is then fitted to a polynomial form in terms of normalized design capacity to yield the following expression:

$$\begin{aligned} CFRI = -1.93 &+ 1.37\widehat{d_{RO}} + 1.19\widehat{d_{MSF}} + 1.00\widehat{d_{PV}} - 0.17\widehat{d_{RO}}^2 \\ &- 0.62\widehat{d_{RO}}\widehat{d_{MSF}} - 0.39\widehat{d_{RO}}\widehat{d_{PV}} - 0.54\widehat{d_{MSF}}^2 \\ &+ 0.71\widehat{d_{MSF}}\widehat{d_{PV}} - 0.60\widehat{d_{PV}}^2 + 0.002\widehat{d_{RO}}^3 \\ &+ 0.05\widehat{d_{RO}}^2\widehat{d_{MSF}} + 0.02\widehat{d_{RO}}^2\widehat{d_{PV}} \\ &+ 0.16\widehat{d_{RO}}\widehat{d_{MSF}}^2 - 0.09\widehat{d_{RO}}\widehat{d_{MSF}}\widehat{d_{PV}} \\ &+ 0.12\widehat{d_{RO}}\widehat{d_{PV}}^2 + 0.05\widehat{d_{MSF}}^3 \\ &- 0.07\widehat{d_{MSF}}^2\widehat{d_{PV}} - 0.09\widehat{d_{MSF}}\widehat{d_{PV}}^2 \\ &+ 0.09\widehat{d_{PV}}^3 \end{aligned} \quad (5)$$

The general design optimization problem (Equation 3) is then constructed where Equation 4 describes the process constraints and Equation 5 describes the minimum desirable CFRI value based on how CFRI correlates with design variables. The optimization problem is then

solved with different $CFRI^{target}$ values to demonstrate the relationship between retrofit costs and achievable resilience and flexibility performance.

**Table 1**: Design retrofit alternatives with different CFRI values

| CFRI | Retrofit cost [$MM] | $d_{RO}[m^3/h]$ | $d_{MSF}[m^3/h]$ | $d_{PV}\ [MW]$ |
|---|---|---|---|---|
| 0.26 | 0 | 11,364 | 20,836 | 1,000 |
| 0.53 | 225 | 22.728 | 20,836 | 1,000 |
| 0.59 | 1,000 | 22,728 | 20,836 | 2,000 |
| 0.63 | 1,200 | 22,728 | 27,086 | 2,000 |

Table 1 shows the achievable gains in flexibility and resilience with retrofit of the RO, MSF, and PV units. Expanding the RO capacity is paramount to increasing the flexibility and resilience of the co-generation, leading to the conclusion that water production is the bottleneck which prevents the system from being more adaptable to the expected set of disruptions. It can also be observed that a large financial cost is required to invest in additional PV and MSF capacity, but the resulting flexibility and resilience gains are not as significant. This may represent a point where capacity expansion no longer serves as a cost-effective resilience measure, and strategies such as energy and/or water storage may be introduced.

## CONCLUSION

To design process systems that can adequately respond to a variety of disruptions and uncertainties, resilience needs to be an integral part of the conceptual design process alongside other critical objectives such as economic feasibility. By extending the stochastic flexibility analysis framework to also consider discrete disruption scenarios, we have formulated a Combined Flexibility-Resilience Index which accounts for the ability of a particular design alternative to handle uncertainties and disruptions simultaneously. Furthermore, we have demonstrated how the CFRI can be used within a superstructure optimization problem to uncover trade-offs between investment cost and flexibility-resilience goals. This provides a method for assessing the performance of a design alternative, as well as a method for synthesizing new alternatives that may uncover cost-competitive resilient design alternatives. Data from flowsheet simulations can be harnessed to construct the range of uncertainties that needs to be designed for. To apply this method for more complex systems, decomposition algorithms may be needed to reduce the computational burden involved in simulating a large number of disruption scenarios.


## ACKNOWLEDGEMENTS

The authors acknowledge support from Texas A&M University and Texas A&M Energy Institute.


## NOMENCLATURE

| Symbol | Description |
|---|---|
| $SF$ | Stochastic flexibility index |
| $\psi(d,\theta)$ | Feasibility function as a function of design variables $d$, uncertain parameters $\theta$ |
| $\psi(\theta)$ | Feasibility function as a function of uncertain parameters $\theta$, for a specific design configuration |
| $u$ | Auxiliary variable for flexibility problem |
| $f_j(d,\theta)$ | Inequality process constraint as a function of design variables $d$, uncertain parameters $\theta$ |
| $h_m(d,\theta)$ | Equality process constraint as a function of design variables $d$, uncertain parameters $\theta$ |
| $P_d(\theta)$ | Probability distribution function for uncertain parameters $\theta$ |
| $CFRI$ | Combined Flexibility-Resilience Index |
| $E^{PP}$ | Amount of electricity produced by power plant [MW] |
| $F_i$ | Amount of fuel type $i$ used |
| $Q^{Desal}$ | Amount of steam sent from power plant to thermal desalination unit $\left[\frac{m^3}{h}\right]$ |
| $E^{Solar}$ | Amount of solar power generated by PV unit [MW] |
| $E^{RO}$ | Amount of electricity needed by RO unit [MW] |
| $E^{PPGrid}$ | Amount of electricity sent to power grid [MW] |
| $W^{Thermal}$ | Amount of water produced by thermal desalination unit $\left[\frac{m^3}{h}\right]$ |
| $W^{RO}$ | Amount of water produced by RO unit $\left[\frac{m^3}{h}\right]$ |
| $W^{Demand}$ | Amount of water demanded $\left[\frac{m^3}{h}\right]$ |
| $E^{Demand}$ | Amount of electricity demanded [MW] |

## APPENDIX A: CASE STUDY – DETAILED CFRI DERIVATION

The feasibility function problem for the case study presented is given as follows:

$$\psi = \min u \tag{A1}$$

$$s.t.\ E^{PP} = 0.13F_1 + 0.15F_2 + 0.82F_3 + 0.50F_4 - 0.43Q^{Desal} \tag{A2}$$

$$E^{PPGrid} = 0.85(E^{PP} + E^{Solar}) - E^{RO} \tag{A3}$$

$$W^{Thermal} = 9.95Q^{Desal} \tag{A4}$$

$$W^{RO} = 192E^{RO} \tag{A5}$$

$$W^{Demand} - (W^{Thermal} + W^{RO}) \le u \tag{A6}$$

$$E^{Demand} - (E^{PP} + E^{Solar}) \le u \tag{A7}$$

$$W^{Thermal} - cap_{MSF}d_{MSF} \le u \tag{A8}$$

$$W^{RO} - cap_{RO}d_{RO} \le u \tag{A9}$$

$$E^{Solar} - cap_{PV}d_{PV} \le u \tag{A10}$$

$$E_{LB}^{Demand} \leq E^{Demand} \leq E_{UB}^{Demand} \quad \text{(A11)}$$

$$W_{LB}^{Demand} \leq W^{Demand} \leq W_{UB}^{Demand} \quad \text{(A12)}$$

Where $W^{Demand}, E^{Demand}$ are uncertain parameters and $d_{RO}, d_{MSF}, d_{PV}$ are design variables. To derive the CFRI for one $d_{RO}, d_{MSF}, d_{PV}$ realization, the next steps are:

1. Reduced subproblems based on the disruption scenarios are generated. The disruption scenarios are represented as capacity factors $cap_{RO}, cap_{MSF}, cap_{PV}$ that represent a reduction of production capacity of the RO, MSF, and PV units (see Figure 4).
2. For each reduced subproblem, the actual production limit quantity can be substituted into Equations $A8, A9, A10$ to simplify those equations. The feasibility function problem is then be solved parametrically to obtain expressions for $\psi(W^{Demand}, E^{Demand})$.
3. Because the uncertain parameters are normally distributed and $\psi(W^{Demand}, E^{Demand})$ is a linear function, the stochastic flexibility for each reduced subproblem can be calculated analytically [4].
4. The CFRI for the $d_{RO}, d_{MSF}, d_{PV}$ realization is a weighted average of the stochastic flexibility index for all reduced subproblems (Equation 2).

## REFERENCES


1. Gong, J. and You, F., 2018. Resilient design and operations of process systems: Nonlinear adaptive robust optimization model and algorithm for resilience analysis and enhancement. Computers & Chemical Engineering, 116, pp.231-252.
2. Sun, H., Wang, H., Yang, M. and Reniers, G., 2022. A STAMP-based approach to quantitative resilience assessment of chemical process systems. Reliability Engineering & System Safety, 222, p.108397.
3. Swaney, R.E. and Grossmann, I.E., 1985. An index for operational flexibility in chemical process design. Part I: Formulation and theory. AIChE Journal, 31(4), pp.621-630.
4. Pistikopoulos, E.N. and Mazzuchi, T.A., 1990. A novel flexibility analysis approach for processes with stochastic parameters. Computers & Chemical Engineering, 14(9), pp.991-1000.
5. Thomaidis, T.V. and Pistikopoulos, E.N., 1994. Integration of flexibility, reliability and maintenance in process synthesis and design. Computers & chemical engineering, 18, pp.S259-S263.
6. Ochoa, M.P. and Grossmann, I.E., 2020. Novel MINLP formulations for flexibility analysis for measured and unmeasured uncertain parameters. Computers & Chemical Engineering, 135, p.106727.
7. Straub, D.A. and Grossmann, I.E., 1993. Design optimization of stochastic flexibility. Computers & Chemical Engineering, 17(4), pp.339-354.
8. Wang, H., Mastragostino, R. and Swartz, C.L., 2016. Flexibility analysis of process supply chain networks. Computers & Chemical Engineering, 84, pp.409-421.
9. Luo, Y. and Ierapetritou, M., 2023. Multifeedstock and Multiproduct Process Design Using Neural Network Surrogate Flexibility Constraints. Industrial & Engineering Chemistry Research, 62(5), pp.2067-2079.
10. Bansal, V., Perkins, J.D. and Pistikopoulos, E.N., 2000. Flexibility analysis and design of linear systems by parametric programming. AIChE Journal, 46(2), pp.335-354.
11. Pappas, I., Kenefake, D., Burnak, B., Avraamidou, S., Ganesh, H.S., Katz, J., Diangelakis, N.A. and Pistikopoulos, E.N., 2021. Multiparametric programming in process systems engineering: Recent developments and path forward. Frontiers in Chemical Engineering, 2, p.620168.
12. Pappas, I., Diangelakis, N.A., Kenefake, D., Avraamidou, S., Oberdieck, R. and Pistikopoulos, E.N., 2023. Multi-parametric Nonlinear Programming. In *Encyclopedia of Optimization* (pp. 1-8). Cham: Springer International Publishing.
13. Pistikopoulos, E.N., Diangelakis, N.A. and Oberdieck, R., 2020. *Multi-parametric optimization and control*. John Wiley & Sons.
14. Dua, V., Papalexandri, K.P. and Pistikopoulos, E.N., 1999. A parametric mixed-integer global optimization framework for the solution of process engineering problems under uncertainty. *Computers & Chemical Engineering*, *23*, pp.S19-S22.
15. Al-Fadhli, F.M., Alhajeri, N., Ettouney, H., Sengupta, D., Holtzapple, M. and El-Halwagi, M.M., 2022. Simultaneous optimization of power generation and desalination systems: a general approach with applications to Kuwait. Clean Technologies and Environmental Policy, 24(7), pp.2129-2141.
16. Kenefake, D., and Pistikopoulos, E.N., 2022. PPOPT – Multiparametric solver for explicit MPC. Computer Aided Chemical Engineering, 51, pp.1273-1278.



© 2025 by the authors. Licensed to PSEcommunity.org and PSE Press. This is an open access article under the creative commons CC-BY-SA licensing terms. Credit must be given to creator and adaptations must be shared under the same terms. See https://creativecommons.org/licenses/by-sa/4.0/




Systems & Control Transactions

**Research Article - Peer Reviewed Conference Proceeding**
ESCAPE 35 - European Symposium on Computer Aided Process Engineering
Ghent, Belgium. 6-9 July 2025
Jan F.M. Van Impe, Grégoire Léonard, Satyajeet S. Bhonsale,
Monika E. Polańska, Filip Logist (Eds.)

PSE PRESS

# Learning-based Control Approach for Nanobody-scorpion Antivenom Optimization

**Juan Camilo Acosta-Pavas[a], David Camilo Corrales[a], Susana María Alonso Villela[a], Balkiss Bouhaouala-Zahar[b], Georgios Georgakilas[c], Konstantinos Mexis[d], Stefanos Xenios[d], Theodore Dalamagas[c], Antonis Kokossis[d], Michael O'donohue[a], Luc Fillaudeau[a], César Arturo Aceves-Lara[a]***

[a] TBI, Université de Toulouse, CNRS UMR5504, INRAE UMR792, INSA, Toulouse, France

[b] Laboratoire des Biomolécules, Venins et Applications Théranostiques (LBVAT), Institut Pasteur de Tunis, 13 Place Pasteur, BP-74, 1002 Le Belvédère, Tunis, Tunisia

[c] Athena Research Center, Marousi, Greece

[d] School of Chemical Engineering, National Technical University of Athens, Iroon Polytechneiou 9, Zografou, 15780 Athens, Greece
* Corresponding author: aceves@insa-toulouse.fr

## ABSTRACT

One market scope of bioindustries is the production of recombinant proteins for its application in serotherapy. However, its process's monitoring and optimization present limitations. There are different approaches to optimize bioprocess performance; one is using model-based control strategies such as Model Predictive Control (MPC). Another strategy is learning-based control, such as Reinforcement Learning (RL). In this work, an RL approach was applied to maximize the production of recombinant proteins in *E. coli* at the induction phase using as a control variable the substrate feed flow rate ($F_{in}$). The RL model was trained using the actor-critic Twin-Delayed Deep Deterministic (TD3) Policy Gradient agent. The reward corresponded to the maximum value of protein productivity. The environment was represented with a dynamic hybrid model. The optimization was evaluated by stages of two hours to check the protein productivity performance. Afterwards, the results were compared with an MPC approach. Finally, the control approaches were trained considering temperature disturbances. The results elucidate that the RL approach could be implemented as a control strategy, reaching values from 0.014 mg/h to 0.079 mg/h through all the optimization stages previously demonstrated to be the optimal ones. Despite exhibiting temperature disturbances, the RL approach demonstrated its robustness by adapting the control action to maintain similar protein productivity values.

**Keywords**: Model predictive control, Reinforcement Learning, TD3, Protein production, *E.Coli*

## INTRODUCTION

Scorpion sting envenoming (scorpionism) is a severe public health issue in developing countries in North Africa, the Middle East, and Central and South America [1,2]. The symptoms associated with scorpion stings are intense local pain, sweating, tachypnea, tachycardia, agitation, pancreatitis, pulmonary edema, hemolysis, necrosis, and, in severe cases, leads to death. The use of antivenom is the only effective treatment against scorpion stings where different types of molecules can neutralize the venom. Those antivenom molecules were commonly obtained from animal origin [1,2].

Advances in serotherapy allowed for the production of recombinant proteins using species such as *E. coli*, becoming one of the critical market scopes of bioindustries [3,4]. Nevertheless, its process's monitoring, control, and optimization are challenging. Different approaches to optimize bioprocess performance exist: model-based control strategies, such as Model Predictive Control (MPC), and learning-based control, like Reinforcement Learning (RL). Dubencovs *et al.* [5] used an MPC to optimize the growth of *E. coli* BL21 (DE3) and the production of two different recombinant proteins, nerve growth factor (NGF) and coat protein of bacteriophage Qβ (Qβ-CP). In their paper, three experiments were conducted: the first focused on finding the optimal "Golden batch" states without any induction, the second considered induction for NGF protein production, and the third

considered induction of the bacteriophage Qβ coat protein (Qβ-CP). It was concluded that MPC demonstrates rapid adaptability to various systems, where a meticulous estimation of model parameters could significantly reduce the number of experiments required to optimize the model. The proposed methodology allowed satisfactory control of biomass growth, with deviations between 6-12% compared to the values calculated as the Golden batch. Bonanni *et al*. [6] proposed a deep-learning approach to optimize recombinant protein production using *E. coli*. The authors proposed ML approaches based on a recurrent Neural Network (NN) to predict the optical density (DO) from several process variables such as pH, dissolved oxygen, temperature, etc.

Although the results are prominent, the optimizations were focused on improving cell growth rather than directly maximizing protein production. Additionally, the MPC requires highly detailed knowledge of the process, which must be represented in the model; learning techniques require a large quantity of data [7]. RL appears to be an innovative approach to optimize and control biological processes.

RL refers to mapping situations to actions by maximizing a numerical reward signal. The goal of the RL agent is not to indicate which actions to take; it must discover which actions yield the most reward by associating them with the outcomes they produce [8]. In other words, the goal is to find the best sequence of control actions that generate the optimal outcome by interacting with its environment [9]. In RL, the agent interacts with the environment and learns which actions to take by trial and error. Each interaction implies executing an action over the environment. The agent receives a reward for its actions. In this manner, the agent learns the best control policy that maximizes the total accumulated reward [7,9]. The majority of the RL learners are based on policy gradient methods. This method directly obtains a policy by maximizing a desired performance index [10]. Petsagkourakis *et al*. [10] applied RL over three computational case studies. The first study is a "real" photo-production system; however, the exact model is unknown, and a simplified deterministic model is assumed. In the second case, however, it was assumed that the simplified model is supposed to follow a Wiener stochastic process. The last case was a photoproduction of phycocyanin synthesized by *cyanobacterium Arthrospira platensis*. The results highlight the possibility of obtaining a near-optimal policy for a stochastic system when true dynamics are unknown. However, RL has no applications for recombinant protein production in *E. coli*.

In this work, an actor-critic agent was selected due to the continuous actions space property. For a determinate observation action, the critic returns an approximation of the policy value. For a determinate observation, the actor returns the action that maximizes the policy value. Overall, the actor learns the best action to take using the feedback from the critic.

This work proposes a learning-based RL approach to optimize the glucose feed flow rate at the induction phase to maximize protein productivity. The contributions of this work are summarized as follows:

- A learning-based RL approach was designed to maximize protein productivity by manipulating the feed flow rate at the induction phase
- An actor-critic Twin-Delayed Deep Deterministic (TD3) policy gradient Agent was used for the first time over a protein production process using *E.coli*
- The impact of temperature disturbances was considered in the training of the TD3 agent
- The results demonstrated that the RL approach produced superior outcomes in comparison to the MPC approach

# MATERIALS AND METHODS

## Optimization problem statement

The process variables correspond to Glucose $(S)$, Biomass $(X)$, Protein $(P)$, and Volume $(V)$ of the liquid phase in the bioreactor; The Manipulated variables refers to the glucose feed flow rate $(F_{in})$. The aim is to maximize protein productivity $(Pprod = P \cdot V/t)$ through process simulation by finding the optimal $F_{in}$ profile at induction phase $(t \geq 8h)$. The optimization strategy was divided into six different control intervals "stages" from the beginning of the induction phase $(t \geq 8h)$ until the end of the process $(t = 20h)$, as shown in Figure 1.

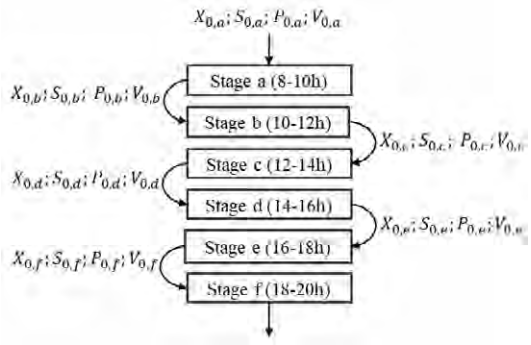



**Figure 1.** Stages of the optimization strategy. Protein production using *E. coli* CH10-12 with an induction temperature of 28°C.

The in-Silico experiment was conducted for protein production using *E. coli* CH10-12 with an induction temperature of 28°C. In this work, It was considered one of the specific conditions reported in Alonso Villela *et al*. [11]; The simulated conditions were conducted in batch phase at $2L$ and 37°C with an initial glucose concentration of $10g_{glucose}/L$ $(pO_2 > 15\%, pH = 6.8)$ for $3.4h$. Then,

in the fed-batch phase at 37°C the glucose feed was $300 g_{glucose}/L$ with a flowrate $1.0 \times 10^{-3} L/h$ for $8.0h$. Afterwards, the inductor ($1mM$ of isopropyl- thiogalactopyranoside IPTG) was added to start protein production, and temperature was lowered to 28°C.

It is assumed that the optimization stage "a" started at $8h$, considering as inputs the last point of the feed batch process, and successively the output of each optimization stage corresponds to the input of the next stage. This guarantees to check the $Pprod$ performance every two hours until the final process time ($t = 20h$).

## Dynamic hybrid model

Since the optimization will be conducted through process simulation, it is used the dynamic hybrid model (DHM) for the nanobody-based antivenom (protein) production process proposed by Corrales *et al.* [12]. The model is referred to as dynamic because the estates are represented by differential equations based on the first principles mass balances Eq. (1)-(4), and hybrid due to the integration of machine learning algorithms to estimate kinetics that are not easier to establish, such as the specific productivity of the protein production Eq. (5)-(4).

$$\frac{dX}{dt} = r_X - X\frac{F_{in}}{V} \quad (1)$$

$$\frac{dS}{dt} = \frac{F_{in}}{V}S_{in} - r_S - S\frac{F_{in}}{V} \quad (2)$$

$$\frac{dP}{dt} = r_P \quad (3)$$

$$\frac{dV}{dt} = F_{in} \quad (4)$$

with $X$ and $S$ in $g/L$; $P$ in $mg/L$; $V$ in $L$; $F_{in}$ $(L/h)$ is the glucose feed flow rate, with $S_{in}(g/L)$ as the concentration of glucose; $r_X$ $(g/L/h)$; and $r_S$ $(g/L/h)$ the production rate of biomass and glucose, respectively.

The production rate of proteins $r_P(mg/L/h)$ is defined as Eq. (5).

$$r_P = \begin{cases} 0 & if\ there\ is\ not\ induction \\ q_P X & if\ there\ is\ an\ induction \end{cases} \quad (5)$$

$q_P$ $\left(mg_{protein}/g_{CDW}/h\right)$ intended for the specific productivity of the protein production, which was modeled using a Radial Basis Function (RBF) Support Vector Machine (SVM) learner. The SVM was trained with experimental data provided by in Alonso Villela *et al.* [11] as Eq. (6).

$$q_P = SVM_{Model}(\mu, T) \quad (6)$$

with $\mu\,(1/h)$ and $T(°C)$ as the specific growth rate and process temperature. The algorithm was trained using a 5-fold cross-validation using the optimized hyperparameters: $C = 0.4165$, $\varepsilon = 0.0329$, and $\sigma = 0.0825$.

# RL DEVELOPMENT

## Reinforcement learning training

Figure 2 shows the structure of the learning-based RL training. The actor and critic networks are initialized with random parameters to obtain an initial value of $F_{in}$. Similarly, the dynamic model is initialized using the final conditions of the fed-batch process ($X_0, S_0, P_0, V_0$).

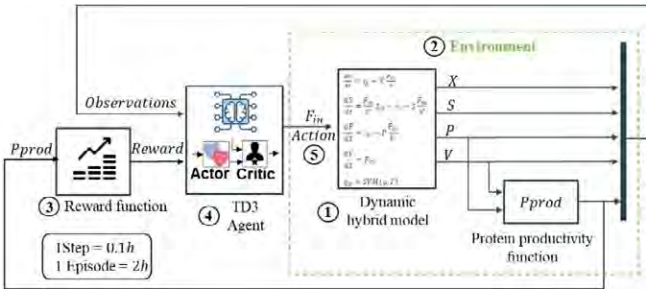



**Figure 2.** RL structure for protein productivity optimization. Numbers 1-5 in the Figure corresponds to the diagram workflow.

For each episode, *i.e.*, for the subsequent two hours of induction, the environment simulates a single fixed step (0.1h), the observations $(X, S, P, V + Pprod)$ are sent to the TD3 agent, and it is calculated the reward ($Reward$). Finally, the agent policy (actor-critic interaction) is updated and the new action (optimal $F_{in}$), subject to $0.001 \leq F_{in} \leq 0.020\ L/h$ and $1.5 \leq V \leq 5.0\ L$, is computed and sent back to the environment. This process is repeated until the maximum number of episodes is reached (max number of episodes=1000). An additionally restriction is imposed to the agent in case of achieve a physical constraint $1.5 \leq V \leq 5.0\ L$.

The workflow is summarized as follows [7]:

1. Initialize the environment $(X_0, S_0, P_0, V_0)$

**While** stop criterion not satisfied (max number of episodes):

  **for** each step in an episode:

2. Simulate the environment for a single step (0.1h)
3. Provide the observations $(X, S, P, V + Pprod)$ to the TD3 agent and calculate the reward ($Reward$)
4. Perform the policy iteration (actor-critic interaction)
5. Provide action to the environment ($F_{in}$)

  **end for**

**end while**

## Environment

In learning-based control, the DHM and the computation of $Pprod$ are considered the environment (representation of the process).

## Agent

The actor-critic Twin-Delayed Deep Deterministic (TD3) Policy Gradient Agent was used due to the continuous action-space property of the environment, and NN's were used as function approximators for the actor and

critic. The critic NN presented an Observation/Action path comprising three layers with 64/32/32 nodes per layer and 2 ReLU activation functions. The actor NN presented an Observation patch consisting of one layer with 32 nodes and a Tanh activation function. The training options are reported in Table 1.

**Table 1:** Training options for the TD3 RL agent.

| | |
|---|---|
| Optimizer | Adam |
| Max Episode Number | 1000 |
| Simulation time ($h$) | 2 |
| Agent sample time (h) | 0.1 |
| Episode Steps | 20 |
| Total Agent Steps | 20000 |
| Experience Buffer Length | $1\times10^{6}$ |
| Mini batch size | 100 |
| Standard deviation | 0.3 |
| Standard deviation decay rate | $1\times10^{-5}$ |
| TargetSmoothFactor | $1\times10^{-3}$ |
| DiscountFactor | 0.9 |
| LearnRate | Critic= $1\times10^{-3}$; Actor= $1\times10^{-4}$ |
| GradientThreshold | Critic= Actor= 1.0 |
| Total Agent Steps | 20000 |

## Reward Function

The TD3 RL agent learns the optimal policies by maximizing the reward function. In this case it corresponds to the final value of $Pprod$, which is calculated as in Eq (7)

## Model Predictive Control

The results of the learning-based control approach were compared with a model-based control approach in terms of an MPC; the open loop optimization problem is represented in Eq. (7).

$$\max_{\{F_{in}\}} (Pprod = P \cdot V/t) \tag{7}$$

$$Subject\ to \begin{cases} Equations\ 1-4 \\ 0.001 \le F_{in} \le 0.020\ L/h \\ 1.5 \le V \le 5.0\ L \end{cases} \tag{8}$$

To maintain conditions similar to the RL approach, in the MPC, the goal was to optimize the $Pprod$ every $2\ h$ with a prediction horizon of $2\ h$ as a manipulated variable the $F_{in}$ and subject to the constraints of Eq. (8). In this work, the time step (solver step) of the DHM was fixed at $0.1h$ to allow the comparison between the two approaches.

# RESULTS AND DISCUSSION

All simulations were run using a 13th Gen Intel® Core(TM) i7-13800H 2.50 GHz, 32 GB RAM computer. The *fmincon* function from MATLAB® was used to obtain optimal feed flow rate performance to develop the MPC control. The TD3 RL agent from the reinforcement learning toolbox from MATLAB® was used to develop the RF.

## RL training results

Figure 3 shows the results of the training using the TD3 RL agent. In the optimization stage "a" (Figure 3a), the episode reward ($Ep\ rew$) and the average reward ($Av\ rew$) started at approximately 0.13 until episode 280, where it converged to 0.14. In the following stages, the $Ep\ rew$ and $Av\ rew$ increased to 0.45 (stage b), 0.78 (stage c), 1.10 (stage d), 1.36 (stage e), and 1.57 (stage f). This is expected since $Pprod$ depends on protein concentration and process time, increasing $Av\ rew$. The average rewards showing the highest variability occurred in stage "a", while the other stages stabilized during the first episodes. This is due to the learning limitation given by the nature of the optimization; each starting point depends on the previous output conditions. A statistical evaluation ($Ev\ Stat$) was performed with a frequency of 100 episodes considering a number of 50 episodes. In all optimization stages, the $Ev\ Stat$ (red squares in Figure 3) fits with the average reward, indicating that the agent's training is appropriately done.

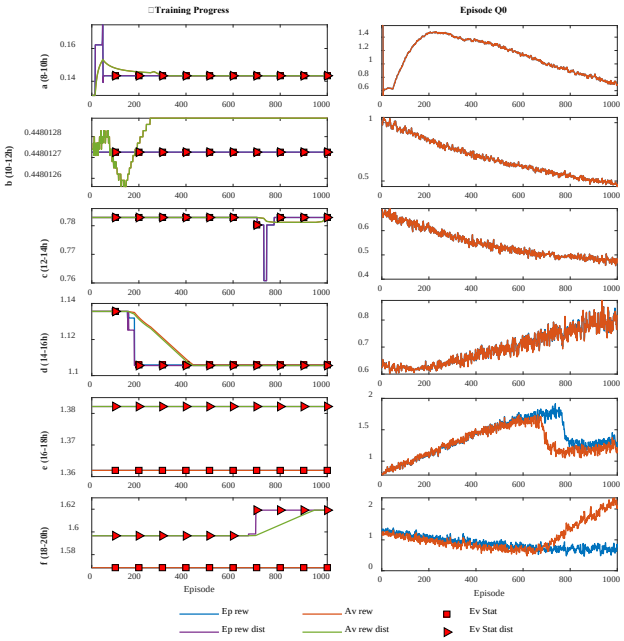



**Figure 3**. RL training progresses every 2 hours at the induction stage. The episode reward (Ep rew), Average reward (Av rew), and Statistical evaluation (Ev Stat). The variables with temperature disturbances are indicated as dist.

## RL and MPC test

Figure 4 displays the results of evaluating the MPC and RL optimizations. It is observed how the dynamics of variables $S$, $X$, and $V$ changes over the bath, fed-batch, and induction phases. Additionally, it is displayed the

optimized $F_{in}$ and the $Pprop$ respond to these actions. Temperature disturbance at induction phase is presented to relate it with the pair $F_{in}$ action – $Pprod$ response.

The dynamic variables $S$, $X$, $V$, and $P$ presents different behaviors with both approaches. Table 2 summarizes the main results. The RL approach suggests maintaining a $F_{in} = 0.02\ L/h$ in the optimization stages "a"-"c" and then changing to $F_{in} = 0.001$ L/h in optimization stages "d"-"f". In contrast, the MPC approach suggests maintaining a $F_{in} = 0.02\ L/h$ in stages "a", "d"- "f", and reducing to $F_{in} = 0.0014$ L/h and $F_{in} = 0.019\ L/h$ in stages "b" and "c", respectively. Those changes represent a $Pprod$ difference between the MPC and RL of $0.016 mg/h$, $0.009 mg/h$, $0.006 mg/h$, $0.009 mg/h$, and $0.012 mg/h$ thought stages "b", "c", "d", "e", and "f" (see Table 2).

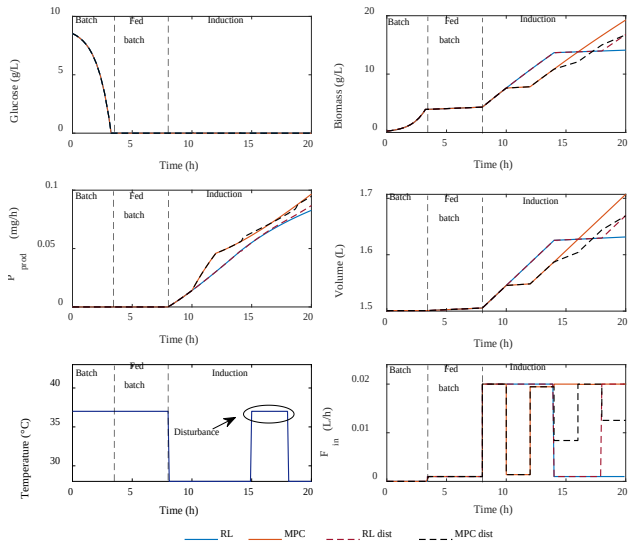



**Figure 4.** Dynamic behavior results with the MPC and TD3 RL at induction temperatures of 28°C. States: Glucose $(S)$, Biomass $(X)$, Protein $(P)$, and Volume $(V)$; Manipulated variable: glucose feed flow rate $(F_{in})$; Optimized variable: protein productivity $(Pprod)$.

Given the variability in the results obtained from both approaches, the protein yield $(Pyield)$ was calculated at the end of each optimization stage, Eq. (9). The $Pyield$ accounts for the relation between the protein produced and the quantity of substrate added in each optimization step.

$$Pyield = \frac{P \cdot V - P_0 \cdot V_0}{Glu_0 \cdot V_0 + Glu_{in} \cdot F_{in} \cdot t_{induction}} \quad (9)$$

$P_0$, $Glu_0$, and $V_0$ refers to the protein and glucose concentrations, and volume at the beginning of each optimization stage. $t_{induction}$ is the duration of the optimization stage.

The RL shows the highest $Pyield$ increase from stage "c" to "f" (Table 2), which indicates that the $F_{in}$ profile exhibited with the RL approach could be a better alternative to optimize the protein production, *i.e.*, the optimal control policy the training of the TD3 agent and the use of the DHM as environment permits to find the optimal $F_{in}$ actions to maximize the $Pprod$. In summary, it can be concluded that although MPC achieves higher $Pprod$ than RL, it requires significantly more $F_{in}$. RL can achieve competitive $Pprod$ with MPC while using less $F_{in}$.

**Table 2:** Optimization results with MPC and RL approaches.

| Stage | $Fin$ $(L/h)$ | $Pprod$ $(mg/h)$ | $Pyield$ $(mg/g)$ | Average optimization time (s)* |
|---|---|---|---|---|
| | | **MPC** | | |
| a | 0.020 | 0.014 | $1.173\times10^{-2}$ | 0.2490<br>0.2821 |
| b | 0.001 | 0.046 | $4.890\times10^{-1}$ | 0.4084<br>0.5051 |
| c | 0.019 | 0.056 | $1.929\times10^{-2}$ | 0.7140<br>0.8661 |
| d | 0.020 | 0.068 | $2.541\times10^{-2}$ | 0.1021<br>0.3133 |
| e | 0.020 | 0.082 | $3.227\times10^{-2}$ | 0.2684<br>0.3115 |
| f | 0.020 | 0.091 | $3.880\times10^{-2}$ | 0.2046<br>0.5431 |
| | | **RL** | | |
| a | 0.020 | 0.014 | $1.173\times10^{-2}$ | 0.8534<br>3.8471 |
| b | 0.020 | 0.030 | $1.843\times10^{-2}$ | 0.1512<br>0.5540 |
| c | 0.020 | 0.047 | $2.579\times10^{-2}$ | 0.1884<br>0.4821 |
| d | 0.001 | 0.062 | $5.437\times10^{-1}$ | 0.1968<br>0.5925 |
| e | 0.001 | 0.073 | $5.506\times10^{-1}$ | 0.6449<br>0.3126 |
| f | 0.001 | 0.079 | $5.576\times10^{-1}$ | 0.3794<br>0.4553 |
| $Pprod$ difference⁺ | Stage a= 0.000; Stage b= 0.000; Stage c= 0.016; Stage d= 0.009; Stage e= 0.006; Stage f= 0.009 | | | |

*Without (first line) and with (second line) temperature disturbance. ⁺It corresponds to the difference MPC $Pprod$-RL $Pprod$.

## Temperature Disturbance analysis

A temperature disturbance is simulated between 15 and $18h$, *i.e.*, the temperature increased from 28 to 37°C between the optimization stages "d" and "e" (see temperature in Figure 4). Figure 3 displays the training results for optimization stages "a" to "d". The $Ep\ rew$ and $Av\ rew$ were the same as the process without disturbances. In the optimization stages "e"-"f", the $Ep\ rew$ and $Av\ rew$ differ, which is related to the citric episode $Q0$. This means the critic expected different cumulative $Q0$ values for

each step episode with and without temperature disturbance. Figure 4 presents the behavior of dynamic variables considering the temperature disturbances. Until $14h$, both control approaches followed the same behavior, with and without disturbance.

The RL follows the same behavior with and without temperature disturbance. In the subsequent optimization stages, both approaches optimized $F_{in}$ to maintain the $Pprod$ differences $< 0.016mg/h$, *e.g.*, the RL approach suggest to change $F_{in}$ from $0.001L/h$ to $0.02L/h$ in the last optimization stage "f" to maintain similar productivities with and without temperature disturbances. This implies that the optimal control policy can adapt the control actions (optimal $F_{in}$), including temperature disturbances. Although the MPC approach presented the lowest average optimization time (see Table 2) concerning the RL approach, the latest is preferred due to its performance.

## CONCLUSIONS

Model Predictive Control and Reinforcement Learning approaches were explored to optimize protein production in *E. coli*. The optimization was evaluated by stages of two hours to check the protein productivity performance at the induction phase. Protein productivity values of $0.091mg/h$ and $0.079mg/h$ were reached with the MPC and RL approaches after $20h$ of process. Nevertheless, the latest exhibited the highest $Pyield$ increase through the optimization stages "c" to "f", indicating that this approach produces a higher quantity of protein per hour by applying a lower $F_{in}$ concerning the MPC approach. The results suggest that the RL approach yields an optimal control policy by interacting with the environment (dynamic hybrid model) and can adapt the control action during the optimization process, accounting for temperature disturbances. In future work, rewards that include protein productivity and yield can be studied, enabling a better understanding of the process. Additionally, the integration of two Critic NNs in the training of the TD3 agent can be applied, allowing for enhanced process optimization through the learning-based strategy.

## ACKNOWLEDGEMENTS

This work was funded (or co-funded) by the European Union under the Horizon Europe project Bioindustry 4.0, grant n. 101094287

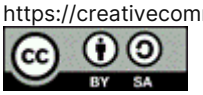
## REFERENCES

1. Ben Abderrazek R, Ksouri A, Idoudi F, Dhaouadi S, Hamdi E, Vincke C, et al. Neutralizing Dromedary-Derived Nanobodies Against BotI-Like Toxin From the Most Hazardous Scorpion Venom in the Middle East and North Africa Region. Front Immunol. 13:863012 (2022) https://doi.org/10.3389/fimmu.2022.863012
2. Olivares-Hernández R, Riaño-Umbarila L, Becerril B, Alagón A, Vázquez-López H. Pharmacokinetic evaluation of a single chain antibody fragment against scorpion toxins in sheep. Toxicon 242:107691 (2024) https://doi.org/10.1016/j.toxicon.2024.107691
3. Alonso Villela SM, Kraïem-Ghezal H, Bouhaouala-Zahar B, Bideaux C, Aceves Lara CA, Fillaudeau L. Production of recombinant scorpion antivenoms in E. coli: current state and perspectives. Appl Microbiol Biotechnol 107:4133–52 (2023) https://doi.org/10.1007/s00253-023-12578-1
4. Romero-Moreno JA, Serrano-Posada H, Olamendi-Portugal T, Possani LD, Becerril B, Riaño-Umbarila L. Development of a human antibody fragment cross-neutralizing scorpion toxins. Mol Immunol 155:165–74 (2023) https://doi.org/10.1016/j.molimm.2023.02.006
5. Dubencovs K, Suleiko A, Sile E, Petrovskis I, Akopjana I, Suleiko A, et al. The Application of Adaptive Model Predictive Control for Fed-Batch Escherichia coli BL21 (DE3) Cultivation and Biosynthesis of Recombinant Proteins. Fermentation 9:1015 (2023) https://doi.org/10.3390/fermentation9121015
6. Bonanni D, Litrico M, Ahmed W, Morerio P, Cazzorla T, Spaccapaniccia E, et al. A Deep Learning Approach to Optimize Recombinant Protein Production in Escherichia coli Fermentations. Fermentation 9:503 (2023) https://doi.org/10.3390/fermentation9060503
7. Monteiro M, Kontoravdi C. Bioprocess Control: A Shift in Methodology Towards Reinforcement Learning. Comput. Aided Chem. Eng 53:2851–6 (2024) https://doi.org/10.1016/B978-0-443-28824-1.50476-2
8. Sutton RS, Barto AG. Reinforcement learning: an introduction. Second edition. Cambridge, Massachusetts: The MIT Press (2018).
9. Grondman I, Busoniu L, Lopes GAD, Babuska R. A Survey of Actor-Critic Reinforcement Learning: Standard and Natural Policy Gradients. IEEE Trans Syst Man Cybern Part C Appl Rev 42:1291–307 (2012) https://doi.org/10.1109/TSMCC.2012.2218595
10. Petsagkourakis P, Sandoval IO, Bradford E, Zhang D, Del Rio-Chanona EA. Reinforcement learning for batch bioprocess optimization. Comput Chem Eng 133:106649 (2020) https://doi.org/10.1016/j.compchemeng.2019.106649
11. Alonso Villela SM, Ghezal-Kraïem H, Bouhaouala-Zahar B, Bideaux C, Aceves Lara CA, Fillaudeau L. Effect of temperature on the production of a

recombinant antivenom in fed-batch mode. Appl Microbiol Biotechnol 105:1017–30 (2021) https://doi.org/10.1007/s00253-021-11093-5

12. Corrales DC, Villela SMA, Cescut J, Daboussi F, Fillaudeau L, Aceves-Lara CA. Dynamic Hybrid Model for Nanobody-based Antivenom Production (scorpion antivenom) with E. coli CH10-12 and E. coli NbF12-10. Comput. Aided Chem. Eng 53:145-50 (2024) https://doi.org/10.1016/B978-0-443-28824-1.50025-9

© 2025 by the authors. Licensed to PSEcommunity.org and PSE Press. This is an open access article under the creative commons CC-BY-SA licensing terms. Credit must be given to creator and adaptations must be shared under the same terms. See https://creativecommons.org/licenses/by-sa/4.0/



Systems & Control Transactions

**Research Article - Peer Reviewed Conference Proceeding**
ESCAPE 35 - European Symposium on Computer Aided Process Engineering
Ghent, Belgium. 6-9 July 2025
Jan F.M. Van Impe, Grégoire Léonard, Satyajeet S. Bhonsale,
Monika E. Polańska, Filip Logist (Eds.)

PSE PRESS

# Safe Bayesian Optimization in Process System Engineering

**Donggyu Lee[a], Ehecatl Antonio del Rio Chanona*[a]**

[a] Sargent Centre for Process Systems Engineering, Department of Chemical Engineering, Imperial College London, London, SW7 2AZ, United Kingdom
* Corresponding Author: a.del-rio-chanona@imperial.ac.uk

## ABSTRACT

Safe Bayesian Optimization (Safe BO) has demonstrated significant promise in enhancing data-driven optimization strategies in safety-critical settings, where model discrepancies, noisy measurements, and unknown safety constraints are prevalent. Despite these advancements, there still remains a limited understanding on the effectiveness and applicability of these Safe BO methods, particularly within process system engineering. Specifically, this study adapts and examines Safe Exploration for Optimization with Gaussian Processes (**SafeOpt**), Goal-oriented Safe Exploration (**GoOSE**), Gaussian Processes with Trust Region (**GPs-TR**) and Adversarially Robust Gaussian Processes (**StableOpt**). Methods such as **SafeOpt** and **GoOSE** face challenges in managing continuous systems due to their reliance on system discretization and together with **StableOpt**, lack the capability to manage multiple safety constraints. Thus, this work presents a comprehensive evaluation of state-of-the-art safe BO methods, with our own addition and enhancements, focusing on their performance in process system engineering. The performances of methods are assessed using a case study on the William Otto Reactor, focusing on convergence speed, unknown constraints mitigations, practicality, and robustness against adversarial perturbations. Overall, this study underscores the unique strengths and limitations of safe BO methods in process system engineering, advancing the field on data-driven approaches in safety-critical processes while also identifies areas where further improvements are necessary.

**Keywords**: Safe Bayesian Optimization, Data-Driven Optimization, Model Uncertainty

## INTRODUCTION

In the realm of Process Systems Engineering (PSE), performing optimization under safety-critical settings is paramount for enhancing process operational safety and efficiency [1]. Conventional optimization methods typically rely on detailed mathematical models of the system and the availability of derivative information for both objective function and constraints. However, developing precise models are frequently hindered by complexity of the process and computational burdens which leads to inherent model discrepancies. These challenges often result in treating objective and constraint functions as black-box functions without available derivative information.

To address these challenges, data-driven and derivative-free optimization methods have emerged as viable alternatives for handling black-box functions [2]. These methods include both direct and model-based methods, with model-based methods showing promise in presence of safe-critical constraints.

Among these, Bayesian Optimization (BO) has emerged as a powerful model-based approach for optimizing expensive black-box functions, particularly in presence of uncertainty and unknown safe constraints [3-6]. BO generally employs Gaussian Process (GP) as a probabilistic surrogate model to guide acquisition function and balance exploration and exploitation. Despite the successes of classical BO, ensuring safe exploration in the presence of unknown constraints remain a significant challenge. Consequently, various approaches have been proposed as safe BO methods, specifically designed to address the challenges inherent in safety-critical applications [7-10].

However, the current literature reveals a substantial gap in our understanding of how safe BO methods perform in complex process systems. Many existing approaches rely on system discretization and incapability to manage multiple safety constraints. These restrictions hinder the practical applicability in PSE.

Thus, in this paper, we bridge these gaps by providing an integrated review of the state-of-the-art safe BO methods alongside our own enhancements. Specifically, we introduce modifications to **SafeOpt**, **GoOSE**, and **StableOpt** to overcome discretization issues and improve their capability to manage multiple constraints, in addition to evaluating the algorithms including **GPs-TR**. Through a case study on the William Otto Reactor, we compare these methods in terms of conversion speed, unknown constraints management, practicality, and robustness against adversarial perturbations.

By combining a critical literature review with methodology advancements, our work aims to advance data-driven approaches in safety-critical process systems while highlighting areas for future improvements.

# PRELIMINARIES

## Problem Setup

Consider the constrained optimization problem defined by an unknown but measurable objective function $f : \mathcal{D} \subseteq \mathbb{R}^p \to \mathbb{R}$ and a set of unknown but measurable constraint functions $g_i : \mathcal{D} \subseteq \mathbb{R}^p \to \mathbb{R},$, where the goal is to:

$$\min_{\boldsymbol{x}\in\mathcal{D}} f(\boldsymbol{x}) \quad s.t.\, g_i(\boldsymbol{x}) \geq 0, \forall i \in \mathcal{I}_g \tag{1}$$

At iteration $t$, we query $f$ at a single input $\boldsymbol{x}_t \in \mathcal{D}$ and observe noisy samples $y_{f,t} = f(\boldsymbol{x}_t) + \epsilon_t$ and $y_{i,t} = g_i(\boldsymbol{x}_t) + \epsilon_{t,i}, \forall i \in \mathcal{I}_g$, where $\epsilon_t \sim \mathcal{N}(0, \sigma_\epsilon^2)$. **SafeOpt**, **GoOSE**, and **GPs-TR**, follow this problem setup, but **StableOpt**, on the other hand, extends the formulation by incorporating perturbation variable, which will be elaborated in Section 3.4.

## Introduction to Gaussian Processes

Gaussian Processes (GPs) are widely used in non-parametric Bayesian regression to model distributions over functions. GP is parameterized by a prior mean function $m_t(x)$ and a covariance function $k(\boldsymbol{x}, \boldsymbol{x}')$ as

$$f(\boldsymbol{x}) \sim \mathcal{GP}(\mathrm{m}(\boldsymbol{x}), \mathrm{k}(\boldsymbol{x}, \boldsymbol{x}')) \tag{2}$$

If we have $t$ previous observations of the objective $y_t = [y_1, \ldots, y_t]^T$ at inputs $\boldsymbol{X}_t = [x_1, \ldots, x_t]$ with the measurements being noisy as $y_t = f(\boldsymbol{x}_t) + \epsilon_t$ where $\epsilon_t \sim \mathcal{N}(0, \sigma_\epsilon^2)$, the posterior distributions are given by the mean $\mu_t$ and variance $\sigma_t^2$

$$\mu_t(\boldsymbol{x}) = \mathbf{k}_t^T(\boldsymbol{x})(\mathbf{K}_t + \sigma_\epsilon^2 \mathbf{I})^{-1}\mathbf{y}_t \tag{3}$$

$$\sigma_t^2(\boldsymbol{x}) = k(\boldsymbol{x}, \boldsymbol{x}') - \mathbf{k}_t^T(\boldsymbol{x})(\mathbf{K}_t + \sigma_\epsilon^2 \mathbf{I})^{-1}\mathbf{k}_t(\boldsymbol{x}') \tag{4}$$

where $\mathbf{k}_t(\boldsymbol{x}) = \left(k(\boldsymbol{x}_1, \boldsymbol{x}), \ldots, k(\boldsymbol{x}_t, \boldsymbol{x})\right)^T$ is a vector of covariances between input $\boldsymbol{x}$ and observed points $\boldsymbol{X}_t$, $\mathbf{K}_t$ is the positive definite kernel matrix $[\boldsymbol{K}_t]_{ij} = k(x_i, x_j)$ for all $i, j \in \{1, \ldots, t\}$, and $\mathbf{I} \in \mathbb{R}^{t\times t}$ denotes the identity matrix. In Bayesian Optimization, GP serve as a surrogate model for the objective and constraint functions, enabling the construction of acquisition functions $\mathcal{A}(\boldsymbol{x})$. A common choices for an acquisition function are Lower Confidence Bound (LCB), $l_t(\boldsymbol{x}) = \mu_{t-1}(\boldsymbol{x}) - \beta_t \sigma_{t-1}(\boldsymbol{x})$, and Expected Improvement, $EI(\boldsymbol{x}) = E[\max(0, f_{best} - f(\boldsymbol{x}))]$. $\beta_t$ represents a confidence level that balances the trade-off between exploration and exploitation when selecting the next query point using acquisition function. In this work, we primarily employ LCB as the acquisition function as shown in Equations (6), (7), (9), (12), (13) etc. Nonetheless, other acquisition functions are compatible to be used. Also, LCB is used to adopt a conservative approach on safety constraint predictions in this study for safe explorations as:

$$S = \{\boldsymbol{x} \in \mathcal{D} \,|\forall i \in \mathcal{I}_g : l_{i,t}(\boldsymbol{x}) \geq 0\} \tag{5}$$

# METHODOLOGY

## Safe Exploration for Optimization with Gaussian Processes (SafeOpt)

**SafeOpt**, first introduced by Sui et al. (2015) [7], is a Bayesian optimization algorithm tailored for safe exploration in constrained optimization problems. In each iteration, **SafeOpt** partitions the safe set $S_t$ into two subsets: a minimizer set within safe region that are likely to be minimal and an expander set that are likely to expand the safe set when observed, based on Lipschitz continuity. For each iteration, **SafeOpt** queries the most uncertain point of the objective function within the two subsets, where uncertainty is quantified as $w_t(x) = u_{f,t}(\boldsymbol{x}) - l_{f,t}(\boldsymbol{x})$. By querying the most uncertain point in minimizer, we gain a more accurate understanding of the minimal point within the safe set; by querying the most uncertain point in the expander, we expand the safe set and thus better characterizes its safe boundaries. The original **SafeOpt** algorithm relied on domain discretization, which is computationally prohibitive for large or high-dimensional domains. We address this limitation by modifying the algorithms to operate in continuous domain.

For each iteration, **SafeOpt** queries minimal points for each subset. The most uncertain point in the minimizer set is selected as:

$$\boldsymbol{x}_{M,t+1}^* \in \operatorname*{argmax}_{\boldsymbol{x}\in S_t} w_t(\boldsymbol{x}) \quad s.t\ l_{f,t}(\boldsymbol{x}) \leq \min_{\boldsymbol{z}\in S_t} u_{f,t}(\boldsymbol{z}) \tag{6}$$

The expander set focuses on expanding the boundaries of the safe region by leveraging Lipschitz continuity. This is achieved by identifying pairs of points $x$ (in the

safe set) and $z$ (in the unsafe set) such that Lipschitz $u_i(\boldsymbol{x}) - L_i \cdot d(\boldsymbol{x}, \boldsymbol{z}) \geq 0,\ \forall i \in \mathcal{I}_g$ is satisfied where $L_i$ is the Lipchitz constant for the $i$-th constraint, and $d$ represents distance function. Thus, the most uncertain point in the expander set is selected as:

$$\boldsymbol{x}^*_{G,t+1} \in \underset{\boldsymbol{x}\in S_t,\ \boldsymbol{z}\in D\setminus S_t}{\operatorname{argmax}}\ w_t(\boldsymbol{x}) \tag{7}$$

$$s.t\ u_{i,t}(\boldsymbol{x}) - \max \left|\left|\nabla\mu_{i,t}\right|\right|_\infty \cdot d(\boldsymbol{x}, \boldsymbol{z}) \geq 0, \qquad \exists i \in \mathcal{I}_g$$

Here, Lipchitz constant $L_i$ is replaced with $L_i \approx \max \left|\left|\nabla\mu_{i,t}\right|\right|_\infty$ as $L_i$ is assumed to be unknown.

**SafeOpt** selects the next query point $x^*_{t+1}$ by choosing the most uncertain point from both the minimizer and the expander sets as:

$$\boldsymbol{x}^*_{t+1} \in \arg\max(w_t(\boldsymbol{x}^*_{M,t+1}), w_t(\boldsymbol{x}^*_{G,t+1})) \tag{8}$$

This process ensures an efficient trade-off between refining the objective function in known safe regions and expanding the safe for further explorations.

## Goal Oriented Safe Exploration (GoOSE)

**GoOSE**, introduced by Turchetta et al. (2019) [8], enhances the safe exploration capabilities using an oracle during safe set expansion. **GoOSE** partitions the safe set into two subsets: pessimistic safe set and optimistic safe set. The pessimistic safe set corresponds to conventionally defined safe set in equation (2), while the optimistic safe set comprises points outside of the safe region, but that are likely to become safe based on Lipchitz continuity. During exploration, the objective function is set as LCB which encourages more exploration in finding the minimal point. The original **GoOSE** algorithm was formulated for discretized domains and single constraints. Our modifications extend **GoOSE** to operate over continuous domains and handle multiple constraints, analogous to our enhancements to **SafeOpt**.

For each iteration, **GoOSE** queries minimal points from each subset. The minimal point in pessimistic safe set is selected as:

$$\boldsymbol{x}^*_{P,t+1} \in \underset{\boldsymbol{x}\in S_t}{\operatorname{argmin}}\ \mathcal{A}_{f,t}(\boldsymbol{x}) \tag{9}$$

At optimistic set, **GoOSE** focuses on finding minimal point (oracle) by leveraging Lipschitz continuity similarly to **SafeOpt**. This involves identifying pairs of points $x$ (in the safe set) and $z$ (in the unsafe set) but focuses on finding the minimal point of $z$ rather than the most uncertain point in $x$, as **SafeOpt** does. Hence, the minimal point in in optimistic safe set is selected as:

$$\boldsymbol{z}^*_{O,t+1} \in \underset{\boldsymbol{z}\in D\setminus S_t,\ \boldsymbol{x}\in S_t}{\operatorname{argmin}}\ \mathcal{A}_{f,t}(\boldsymbol{z}) \tag{10}$$

$$s.t\ \mathrm{u}_{i,t}(\boldsymbol{x}) - max \left|\left|\nabla\mu_{i,t}\right|\right|_\infty \cdot d(\boldsymbol{x}, \boldsymbol{z}) \geq 0\ \exists i \in \mathcal{I}_g$$

Once the optimal points from both sets are determined, **GoOSE** compares them. If $\boldsymbol{x}^*_{P,t+1}$ has lower $l_{f,t}$, it is directly queried for exploration. If the point from the optimistic safe set ($\boldsymbol{z}^*_{O,t+1}$) is more promising, **GoOSE** queries the nearest points in the pessimistic safe set:

$$\boldsymbol{x}^*_{t+1} \in \underset{\boldsymbol{x}\in S_t}{\operatorname{argmin}}\ d\left(\boldsymbol{x}, \boldsymbol{z}^*_{O,t+1}\right) \tag{11}$$

## Gaussian Processes with Trust Region (GPs-TR)

**GPs-TR**, introduced by del Rio Chanona et al. (2019) [9], is a derivative-free optimization method designed to ensure robust and efficient exploration. As its core, **GPs-TR** restricts the search domain at each iteration to a trust region, where the prediction of the objective function and the constraints are considered to be reliable. The step $d_{t+1}$ is determined as follows:

$$\boldsymbol{d}_{t+1} \in \underset{\boldsymbol{d}\in\mathbb{R}^{\mathrm{p}}}{\arg\min}\ \mathcal{A}_{f,t}(\boldsymbol{x} + \boldsymbol{d}) \tag{12}$$

$$s.t\ ||\boldsymbol{d}|| \leq \Delta_{\mathrm{t}},\ \ \boldsymbol{x} + \boldsymbol{d} \in S_t \tag{13}$$

where $\Delta^t$ denotes the trust-region radius. The size and center of the trust region are adaptively updated based on the accuracy ratio $\rho_{t+1}$, which evaluates the improvement of GPs predictions relative to the observed improvement.

$$\rho_{t+1} := \frac{y_{f,t+1} - y_{f,t}}{\mu_{f,t+1}(\boldsymbol{x}_t + \boldsymbol{d}_{t+1}) - \mu_{f,t}(\boldsymbol{x}_t)} \tag{14}$$

The update rules for the trust region are governed by predefined trust region parameters $(\eta_1, \eta_2, \gamma_{\mathrm{inc}}, \gamma_{\mathrm{red}}, \Delta_{max}, \Delta_{min})$. If $\rho_{t+1} > \eta_2$ and constraints are satisfied at point $(\boldsymbol{x}_t + \boldsymbol{d}_{t+1})$, then trust region radius is expanded $\Delta_{t+1} = \gamma_{\mathrm{inc}}\Delta_{\mathrm{t}}$ and the center is updated to $\boldsymbol{x}_t = \boldsymbol{x}_t + \boldsymbol{d}_{t+1}$. If $\rho_{t+1} < \eta_1$ or constraints are violated, then trust region radius is contracted $\Delta_{t+1} = \gamma_{\mathrm{red}}\Delta_{\mathrm{t}}$ and trust region center remains unchanged. If $\eta_1 < \rho_{t+1} < \eta_2$, then both the radius and the center remain unchanged. To prevent trust region radius being excessively enlarged or diminished, maximal and minimal trust-region radius $\Delta_{max}, \Delta_{min}$ are imposed.

## Adversarially Robust Gaussian Processes (StableOpt)

**StableOpt**, proposed by Bogunovic et al. (2019) [10], addresses the challenge of optimizing functions under adversarial perturbations. **StableOpt** ensures robustness in GP-based optimization by explicitly accounting for worst-case scenarios of objective function in the presence of input perturbations. **StableOpt** operates with a robust optimization problem within an input domain $\mathcal{D} \subseteq \mathbb{R}^{p_x}$, subject to perturbations $\delta \in \mathcal{U} \subseteq \mathbb{R}^{p_\delta}$, where $\mathcal{U} = \{\delta \mid d(\delta) \leq \Gamma\}$. Here, $d$ represents a distance function, and $\Gamma$ represents a predefined maximum allowable perturbation magnitude, determined based on prior knowledge.

The original **StableOpt** algorithm did not support

handling single or multiple constraints. To addres this limitation, we have enhanced the algorithm so it can manage multiple constraints under adversarial perturbations, factoring in worst-case scenarios for both the objective functions and the constraints.

Thus, **StableOpt** finds the minimal point by solving the following robust optimization problem.

$$\boldsymbol{x}^*_{t+1} \in \arg\min_{\boldsymbol{x}\in\mathcal{D}} \max_{\boldsymbol{\delta}\in\mathcal{U}} \mathcal{A}_{f,t}(\boldsymbol{x}+\boldsymbol{\delta}) \quad (15)$$

$$\text{s.t} \min_{\boldsymbol{\delta}\in\mathcal{U}} l_{i,t}\,(\boldsymbol{x}+\boldsymbol{\delta}) \geq 0,\ \forall i \in \mathcal{I}_g$$

The worst-case scenario for the objective function corresponds to the maximum value within $\mathcal{U}$, as the goal is to minimize the objective function. Conversely, the worst-case scenario for the constraints corresponds to the minimum value within $\mathcal{U}$, as the objective is to ensure the constraints remain satisfied, i.e., above zero. To achieve robustness, **StableOpt** iteratively identifies the optimal point ($\boldsymbol{x}^*_{t+1}$) and the corresponding worst-case perturbation $\boldsymbol{\delta}_{t+1}$ selected as:

$$\boldsymbol{\delta}_{t+1} \in \arg\max_{\boldsymbol{\delta}\in\mathcal{U}} \mathcal{A}_{f,t}(\boldsymbol{x}^*_{t+1}+\delta) \quad (16)$$

The point $\boldsymbol{x}^*_{t+1}$ is then queried with the perturbation $\delta_{t+1}$, ensuring that the robustness of the solution under the maximum adversarial perturbation.

## Prior Mean of Constraints

Typically, a prior means of Gaussian Processes (GPs) are set to zero. This approach, however, permits exploration of unknown regions that may potentially violate the constraints as the prior means being zero allow the GPs to satisfy constraints where $g \geq 0$. To mitigate this, the prior means of the GPs for constraints can be set to a negative value. The degree of conservatism one applies in setting an unexplored area as unsafe depends on the magnitude of the negative value. Overall, the negative prior means were set in all the algorithms except **StableOpt** in this work. If the prior means for the constraints are set below zero for **StableOpt**, the algorithm may interpret the negative prior mean as part of the worst-case scenario, potentially leading to the entire search space being considered unsafe and preventing any explorations.

# RESULTS AND DISCUSSION

The performance of the algorithms was tested on a

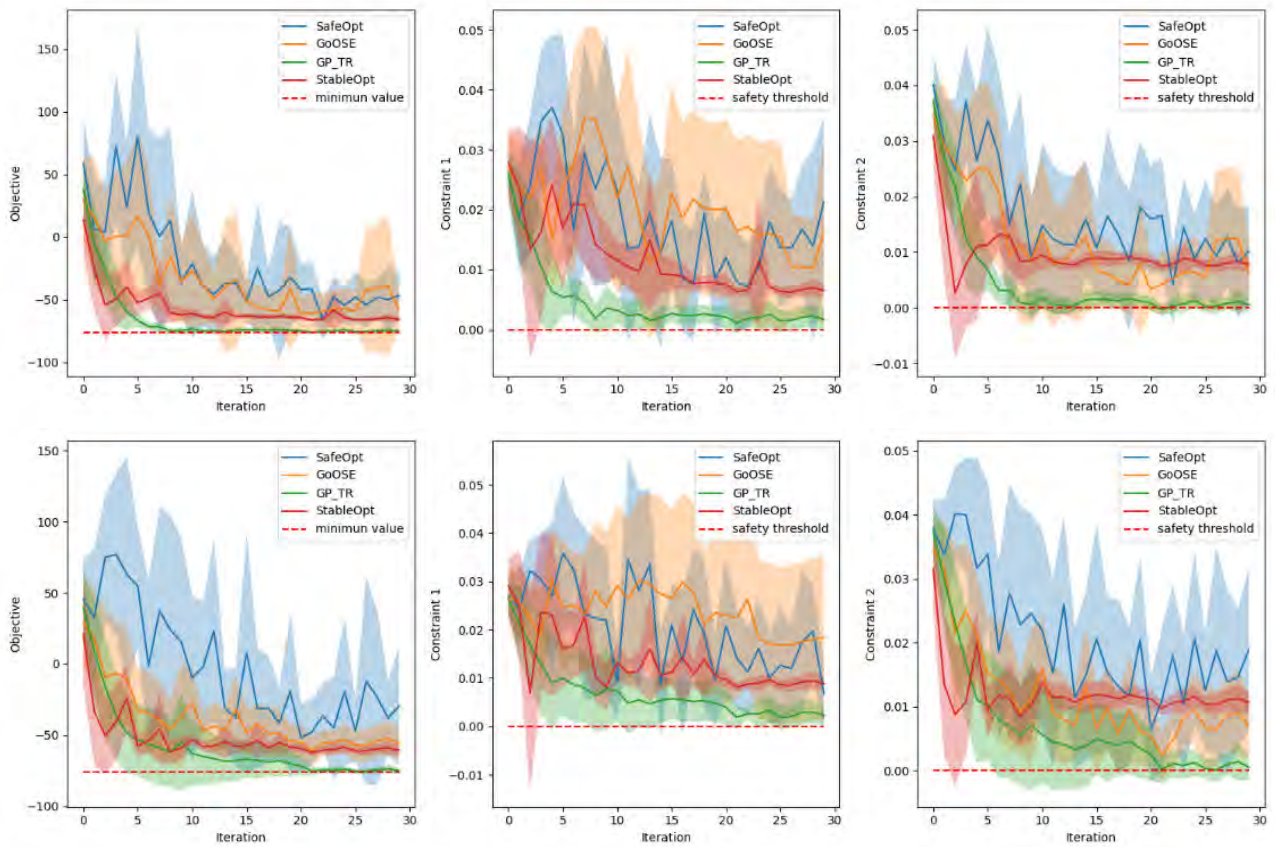



**Figure 1:** Average objective and two constraints under noise variance of inlet flowrate ($\sigma^2_{F_A}$) at (a) 0.005 and (b) 0.01

Williams Otto CSTR, which is frequently used to benchmark algorithms on process optimization. The objective is to minimize the economic cost by manipulating feed flowrate of component B, $F_B$, and the reactor temperature, $T_R$, with mass fraction of component $A$, $X_A$, and G, $X_G$, to be below 0.08 and 0.12. In this study we set two different scenarios where each has a Gaussian noise with variances $\sigma_{F_A}^2 = 0.005, 0.01$ exist as a perturbation in the feed flowrate of component A, $F_A$. In this case study, trust region parameters are set as $\eta_1 = 0.2, \eta_2 = 0.8, \gamma_{\text{inc}} = 1.2, \gamma_{\text{red}} = 0.8, \Delta_{max} = 1.5, \Delta_{min} = 0.1$. Confidence level is set as $\beta = 2$ for all algorithms. Also, differential evolution [11], a population-based stochastic optimization algorithm, has been used on all four algorithms while Sequential Least Squares Programming (SLSQP) [12] has been additionally used in **StableOpt** to find maximum and minimum value of objective function and constraints within $\delta \in \mathcal{U}$ to find the worst-case scenario. The objective (cost) of William Otto Reactor consistently declined towards minimal value across all algorithms.

**StableOpt** demonstrates a rapid and safe progress, approaching to an adversarially robust optimum value while not violating both constraints except during the early stages. Furthermore, its performance remains unaffected by varying levels of noise variance, which indicates a robustness to mitigate the effect of adversarial perturbations. This aligns with the findings of Paulson, Makrygiorgos, and Mesbah[13] where they demonstrated that ARBO(StableOpt) can significantly reduce constraint violations in a bioprocess while maintaining high product yields**.** Notable constraint violations at the early stages are attributed to the prior mean not being initialized below zero, allowing **StableOpt** to explore unsafe regions at the early phase.

**GPs-TR** emerges as the algorithm with fastest progress at smaller noise ($\sigma_{F_A}^2 = 0.005$) with slight violations on the constraints. However, the performance of the algorithm gets worse at the higher noise level ($\sigma_{F_A}^2 = 0.01$) where it exhibits significant variations and big violations of the constraints. These findings underscore the strengths and limitations of the trust region approach. While it enables accurate predictions within a reliable region and facilitates an efficient path toward optimal solutions, its vulnerability to noise is evident. Noise can introduce misleading values, causing the algorithm to temporarily stagnate in suboptimal regions due to restrictions imposed by the trust region. Additionally, the performance of **GPs-TR** is highly sensitive to the tuning of trust-region parameters, suggesting that optimized parameter settings could enhance its performance under higher noise conditions.

**SafeOpt** and **GoOSE** exhibit similar characteristics in the performances. They make slower progress with high fluctuations and variance on objective function and constraints. For **SafeOpt**, this variability arises from frequent alternations between selecting points between minimizer and expander. In contrast, **GoOSE** primarily selects points in the pessimistic safe set that are closest to the oracle within the optimistic safe set, but the oracles and the closest points are often varied for each simulation due to the noise in the system. Between the two, **GoOSE** typically converges faster by querying the points to minimize the objective function wheras SafeOpt selects the most uncertain point for its next query. This behaviour aligns with the findings of Turchetta et al.[8].

## CONCLUSION

This study introduces four Safe Bayesian Optimization algorithms, specifically tailored for applications in Process Systems Engineering. Our proposed modifications have successfully enabled these algorithms to handle multiple constraints and perform optimization within continuous systems. Their performance was demonstrated through the optimization of the William Otto Reactor, subject to perturbations in one of the flow rates. Among the algorithms, **StableOpt** exhibited notable robustness and rapid convergence, albeit with initial constraint violations attributed to its prior settings. **GPs-TR** outperformed others under low-noise conditions but showed vulnerability to higher noise levels. **SafeOpt** and **GoOSE** provided viable alternatives, though their persistent fluctuations and sensitivity to noise constrained their effectiveness. Given the significant dependence of algorithmic performance on problem characteristics, further studies are recommended across diverse applications in Process System Engineering. Additionally, future research should prioritize enhancements to **StableOpt**, focusing on mitigating early-stage constraint violations to improve its robustness in handling multiple constraints.

## REFERENCES


1. Chen, Y., Yuan, Z. and Chen, B. (2018). “Process optimization with consideration of uncertainties—An overview.” Chinese Journal of Chemical Engineering, 26(8), pp.1700–1706.
2. Larson, J., Menickelly, M. and Wild, S.M. (2019). “Derivative-free optimization methods.” Acta Numerica, 28, pp.287–404.
3. van de Berg, D., Savage, T., Petsagkourakis, P., Zhang, D., Shah, N. and del Rio-Chanona, E.A. (2022). “Data-driven optimization for process systems engineering applications.” Chemical Engineering Science, 248, pp.117135.
4. Gramacy, R.B. and Lee, H.K. (2011). “Optimization Under Unknown Constraints.” Oxford University Press eBooks, pp.229–256.
5. Gelbart, M.A., Snoek, J. and Adams, R.P. (2014). “Bayesian optimization with unknown constraints.”

Uncertainty in Artificial Intelligence, pp.250–259.
6. Gardner, J., Kusner, M., Zhixiang, Weinberger, K. and Cunningham, J. (2014). “Bayesian Optimization with Inequality Constraints.” International Conference on Machine Learning, pp.937–945.
7. Sui, Y., Gotovos, A., Burdick, J., and Krause, A. (2015). “Safe Exploration for Optimization with Gaussian Processes.” In Proceedings of the 32nd international conference on machine learning, pp.997–1005.
8. Turchetta, M., Berkenkamp, F., and Krause, A. (2019). “Safe Exploration for Interactive Machine Learning.” In Proceedings of the 32nd International Conference on Machine Learning, pp. 2891–2901.
9. del Rio Chanona, E.A., Alves Graciano, J.E., Bradford, E., and Chachuat, B. (2019). Modifier-Adaptation Schemes Employing Gaussian Processes and Trust Regions for Real-Time Optimization. IFAC-PapersOnLine, 52(1), pp.52–57.
10. Bogunovic, I., Scarlett, J., Jegelka, S., and Cevher., V. (2018). “Adversarially Robust Optimization with Gaussian Processes.” In Advances in Neural Information Processing Systems, pp. 5760–5770.
11. Storn, R., & Price, K. (1997). “Differential Evolution – A Simple and Efficient Heuristic for Global Optimization over Continuous Spaces.” Journal of Global Optimization, 11(4), 341–359.
12. Kraft, D. (1988). “A Software Package for Sequential Quadratic Programming.” DFVLR-Forschungsbericht 88-28. Institut für Dynamik der Flugsysteme, Oberpfaffenhofen, Germany.
13. Paulson, J.A., Makrygiorgos, G., and Mesbah, A. (2021). “Adversarially robust Bayesian optimization for efficient auto-tuning of generic control structures under uncertainty.” AIChE Journal, e17591.

© 2025 by the authors. Licensed to PSEcommunity.org and PSE Press. This is an open access article under the creative commons CC-BY-SA licensing terms. Credit must be given to creator and adaptations must be shared under the same terms. See https://creativecommons.org/licenses/by-sa/4.0/



Systems & Control Transactions

**Research Article - Peer Reviewed Conference Proceeding**
ESCAPE 35 - European Symposium on Computer Aided Process Engineering
Ghent, Belgium. 6-9 July 2025
Jan F.M. Van Impe, Grégoire Léonard, Satyajeet S. Bhonsale,
Monika E. Polańska, Filip Logist (Eds.)

PSE PRESS

# Multi-Model Predictive Control of a Distillation Column

**Mehmet Arıcı[a,c]*, Wachira Daosud[b], Jozef Vargan[a,d] and Miroslav Fikar[a]**

[a] Faculty of Chemical and Food Technology, Slovak University of Technology in Bratislava, Bratislava 81237, Slovakia
[b] Faculty of Engineering, Burapha University, Chonburi 20131, Thailand
[c] Faculty of Engineering and Natural Sciences, Gaziantep Islam Science and Technology University, 27010, Gaziantep, Turkey
[d] Universite de Lorraine, CNRS, LRGP, F-54000, Nancy, France
* Corresponding Author: mehmet.arici@gibtu.edu.tr

## ABSTRACT

Successful implementation of optimization-driven control techniques, such as model predictive control (MPC), is highly dependent on an accurate and detailed model of the process. As complexity in the system increases, linear approximation used in MPC may result in poor performance since a critical operating point is valid in only a small neighborhood of operation. To address this problem, this paper proposes a collaborative approach that combines linear and data-based models to predict state variables individually. The outputs of these models, along with constraints, are then incorporated into the MPC algorithm. For data-based process model, a multi-layered feedforward network is used. Additionally, the offset-free technique is applied to eliminate steady-state errors resulting from model-process mismatch. To demonstrate the results, a binary distillation column process which is multivariable and inherently nonlinear is chosen as testbed. We compare the performance of the proposed method to MPC using the full nonlinear model and also to single-model MPC methods for both the linear model and neural network model. We show that the proposed method is only slightly suboptimal with respect to the best available performance and greatly improves over individual methods. In addition, the computational load is reduced when compared to the full nonlinear MPC.

**Keywords**: Distillation column, Multiple Models, Model Predictive Control, Data-based Modeling

## INTRODUCTION

Distillation column process constitutes a reasonably proper benchmark for a designer aiming superior control which finds solution to strongly coupled nonlinear multi-input multi-output (MIMO) system that is prone to input disturbances [1,2]. MPC is among the leading methods that provide control solutions for the plants with aforementioned challenges [3-6]. Due to the increasing demand for performance and rising complexity of systems, classical model predictive control (MPC) techniques are often inadequate and new applications often requires some modifications in predictive control mechanism [7-9]. The modifications frequently include reformulation of optimal control in order to cope with system uncertainties, external perturbations and adverse effect of rapid changes in operating points [10]. As complexity in the system increases, successful implementation of this optimization-driven control technique is highly dependent on an accurate and detailed model of the process. However, the linear approximation at a critical point used in MPC may result in poor performance and remains valid in only a small neighborhood of operation. In such a case, nonlinear system model can be used for optimal control signal calculation but lack of reliable dynamic process model and high computational burden are major drawbacks in real time implementation of MPC schemes [11]. A multi model predictive controller (Multi-MPC) based on integration of linear system models may provide efficient control of nonlinear process with reduced computational complexity along with covering a large space of operating regions [12-15]. Alternatively, considering uncertainties in real-time operations, data-based models may complement linear approximation models for the prediction of MPC and enlarge the operational region of controller.

In this paper, we propose to employ multiple models that can describe the same process dynamics to a certain degree. In addition to the linear model, multi-layered feedforward network is used for data-based modeling

and constitutes an additional process model. A cost function formulation is proposed to enable both models to collaborate in predicting state variables individually, with their outputs and constraints incorporated into the MPC algorithm. The aim is to enhance efficiency and robustness in process control by compensating for the limitations of each individual model. Additionally, the offset-free technique is applied to eliminate steady-state errors resulting from model-process mismatch. To demonstrate the potential challenges addressed above, a binary distillation column process is chosen as testbed. The process is multivariable, inherently nonlinear and extremely sensitive to input uncertainty especially when LV configuration is selected [16]. We compare the performance of the proposed method to MPC using the full nonlinear model and also to single-model MPC methods for both the linear model and neural network model.

## PROCESS MODELING

A methanol-water binary distillation process schematic is depicted in Figure 1. Before giving the mathematical description of the system, the following assumptions are made:

- Heat losses are zero and temperature changes along the column are small.
- Constant liquid flow along the column.
- Liquid on every tray is well mixed.
- Each plate, which contains liquid and vapor leaving, is in equilibrium.
- There is no vapor holdup on trays.
- There is a constant liquid holdup on trays, reboiler, and condenser.
- The column operates at a constant pressure of 1 atm.
- Real liquid phase molar fraction equals the ideal liquid phase molar fraction, $x = x^*$.

Efficiency and vapor molar fractions are correlated with the following equation:

$$\eta_i = \frac{y_i - y_{i+1}}{y_i^* - y_{i+1}} \tag{1}$$

where $y_i$ is real concentration of vapor phase on $i$-th tray and $y^*$ is ideal concentration of vapor phase on $i$-th tray. The theoretical vapor and liquid molar fractions are correlated with the following empirical relation which is obtained by using a laboratory scale distillation column data:

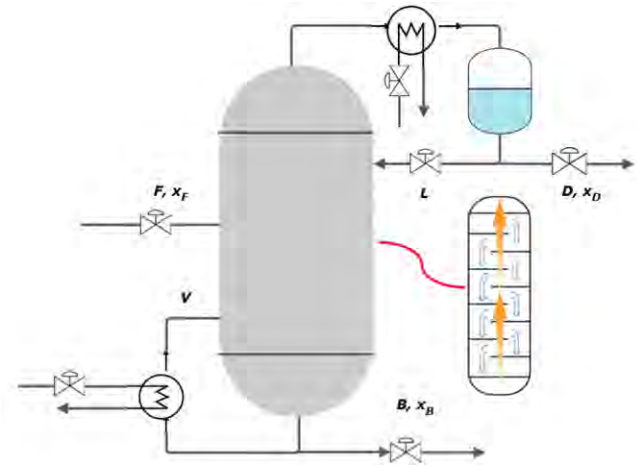



**Figure 1.** Distillation column schematic diagram.

$$y^* = -23.805x^6 + 82.142x^5 - 112.570x^4 + 78.529x^3 - 29.821x^2 + 6.524x + 0.003 \tag{2}$$

We consider 10 trays for the column, treating the condenser and reboiler as individual trays. Tray numbering starts from the top (tray 1) to the bottom (tray 10). The liquid mixture enters the column at tray 6. Considering mass balance for the entire column, the nonlinear state-space model is given by the following equations [17]:

$$\frac{dx_1}{dt} = -\frac{(D+L)}{N_1}x_1(t) + \frac{V}{N_1}y_2(t) \tag{3}$$

$$\frac{dx_i}{dt} = -\frac{L}{N_1}x_i(t) + \frac{L}{N_1}x_{i-1}(t) + \frac{V}{N_i}y_{i+1}(t) - \frac{V}{N_i}y_i(t), \quad i = 2,\dots,5 \tag{4}$$

$$\frac{dx_6}{dt} = -\frac{L+F}{N_6}x_6(t) + \frac{L}{N_6}x_5(t) + \frac{F}{N_6}x_F(t) + \frac{V}{N_6}y_7(t) - \frac{V}{N_6}y_6(t) \tag{5}$$

$$\frac{dx_i}{dt} = -\frac{L+F}{N_i}x_i(t) + \frac{L+F}{N_i}x_{i-1}(t) + \frac{V}{N_i}y_{i+1}(t) - \frac{V}{N_i}y_i(t), \quad i = 7,\dots,9 \tag{6}$$

$$\frac{dx_{10}}{dt} = -\frac{B}{N_{10}}x_{10}(t) + \frac{L+F}{N_{10}}x_9(t) - \frac{V}{N_{10}}y_{10}(t) \tag{7}$$

where $N_i$ is holdup in $i$-th tray, $x_F$ is the molar fraction of volatile component in feed, $F$ is the molar flow of feed, $D$ is the molar flow of distillate, $V$ is the molar flow of vapor, $L$ is the molar flow of reflux, $B$ is the molar flow of bottom, $x_i$ is the molar fraction of methanol in $i$-th tray in liquid phase, $x_i^*$ is the ideal molar fraction of methanol in $i$-th tray in liquid phase, $y_i$ is the molar fraction of methanol in $i$-th tray in vapor phase and $y_i^*$ is the ideal molar fraction of methanol in $i$-th tray in vapor phase. Table 1 shows the process parameters.

The above equations including theoretical vapor and liquid molar fractions correlation imply that high purity distillation process has strong nonlinearity and any realistic study should take this into account. It is important to start control design with properly selected manipulated variables for the system of concern due to the system

complexity. There are various control variable pairings in practice such as LV, LB, DV, and LD where LV configuration is the most commonly used in industrial practice and chooses liquid and vapor flows as manipulated variables. In this study we select LV configuration for the optimal control application.

**Table 1:** Distillation column operating parameters.

| Description | Variable | Unit | Value |
|---|---|---|---|
| Feed molar flow | $F$ | $\mathrm{kmolh}^{-1}$ | 0.300 |
| Vapor molar flow | $V$ | $\mathrm{kmolh}^{-1}$ | 0.264 |
| Reflux molar flow | $L$ | $\mathrm{kmolh}^{-1}$ | 0.104 |
| Distillate molar flow | $D$ | $\mathrm{kmolh}^{-1}$ | 0.160 |
| Feed molar fraction | $x_{\mathrm{F}}$ | - | 0.650 |
| Distillate molar fraction | $x_{\mathrm{D}}$ | - | 0.904 |
| Bottom molar fraction | $x_{\mathrm{B}}$ | - | 0.164 |
| Reboiler holdup | $N_{10}$ | kmol | 1 |
| Tray/condenser holdup | $N_i$ | kmol | 0.2 |
| Tray efficiency | $\eta_t$ | - | 0.8 |
| Reboiler efficiency | $\eta_b$ | - | 1 |

## Linear System Model

A linear state-space model is used as the first approximation of the distillation process. System state variables represent concentrations in liquid phase for each tray, $\boldsymbol{x} = (x_1, x_2, \dots, x_{10})^{\mathrm{T}}$, with initial conditions $x_i(0) = x_{i0}$ for $i = 1,2,\dots,10$. The concentrations of interest are distillate fraction $x_{\mathrm{D}} = x_1(t)$ and bottom product $x_{\mathrm{B}} = x_{10}(t)$ which are considered as outputs of the process to be controlled by manipulated variables reflux $L$ and boilup $V$. We assume that the process is in steady-state at $t = 0$ where we start the system from operating point such that $\boldsymbol{x}_{\mathrm{op}} = (x_1(0), x_2(0), \dots, x_{10}(0))^{\mathrm{T}}$ and $\boldsymbol{u}_{\mathrm{op}} = (u_1(0), u_2(0))^{\mathrm{T}} = (L(0), V(0))^{\mathrm{T}}$. Then, the process is linearized in the steady-state with the assumption of small the deviation from operating point in the form of $\boldsymbol{x}_{ss} = \boldsymbol{x}(t) - \boldsymbol{x}_{\mathrm{op}}$, $\boldsymbol{u}_{ss} = \boldsymbol{u}(t) - \boldsymbol{u}_{\mathrm{op}}$. The resulting multi-input multi-output (MIMO) state-space model in discrete time can be represented as follows:

$$\boldsymbol{x}_{ss}(k+1) = \boldsymbol{A}\boldsymbol{x}_{\mathrm{ss}}(k) + \boldsymbol{B}\boldsymbol{u}_{\mathrm{ss}}(k), \tag{8a}$$

$$\boldsymbol{y}_{ss}(k) = \boldsymbol{C}\boldsymbol{x}_{\mathrm{ss}}(k) + \boldsymbol{D}\boldsymbol{u}_{\mathrm{ss}}(k) \tag{8b}$$

## Neural Network Model

The second process model is created by acquiring system dynamics directly from data without using first principle models. A multi-layered feedforward neural network is used due to its effectiveness in process modeling and control. To construct data-driven model, datasets for training, testing, and validation are derived from a nonlinear simulation of a distillation process. Excitation signals are carefully designed to ensure the data encapsulates the system dynamic behavior across a wide range of operating conditions. Specifically, multilevel pseudorandom step (MLPRS) signals are applied to the manipulated variables with a sampling interval of 0.5 s. These signals feature varying frequencies and amplitudes, constrained within the operational limits of the manipulated variables (e.g., reflux flow L and vapor molar flow V), to excite the nonlinear dynamics sufficiently for accurate prediction and control. Since all system input/output variables change in range of (0, 1) preprocessing of raw data does not require scaling. The neural network (NN) model accepts current and previous values of system outputs plus current and previous values of manipulated variables as inputs and predicts two system outputs $\mathrm{x_D}$ and $\mathrm{x_B}$. The model has 8 inputs and gives one-step ahead prediction of 2 outputs. We can write the discrete input-output model of NN in the following form

$$\boldsymbol{y}(k+1) = \boldsymbol{f}_{\mathrm{nn}}(\boldsymbol{y}(k), \boldsymbol{y}(k+1), \boldsymbol{u}(k), \boldsymbol{u}(k-1)) \tag{9}$$

where $\boldsymbol{y}(k) = (x_{\mathrm{D}}(k), x_{\mathrm{B}}(k))^{\mathrm{T}}$ and $\boldsymbol{u}(k) = (L(k), V(k))^{\mathrm{T}}$. In the NN design we use tanh activation function for nodes in the hidden layer and a linear activation in output layer. The defined NN is trained by using Levenberg-Marquardt algorithm for error convergence between predicted and actual target values. The dataset is split into training (70%), validation (15%), and testing (15%) subsets, ensuring no overlap in operating conditions between splits. The final architecture (16-8-16-8) is selected based on the lowest validation mean squared error (MSE) and satisfactory performance on the test set, achieving MSE = $4.0 \times 10^{-7}$ for both outputs.

# MULTI-MODEL PREDICTIVE CONTROL

The control goal is to utilize linear system model and NN model to predict future states and maintain the system covering a broader space of operating points. Since the scenario is to use linear model in (8) and data-based model in (9) as MPC predictors, plant-model mismatch is likely to occur when a large deviation from operating point is started. In order to overcome this problem, the value of the state disturbance is estimated using the measurement of current process states and linear system states as follows [18]

$$\boldsymbol{d}_{\mathrm{ss}}(k) = \big(\boldsymbol{x}(k) - \boldsymbol{x}_{\mathrm{op}}\big) - (\boldsymbol{A}\boldsymbol{x}_{\mathrm{ss}}(k-1) + \boldsymbol{B}\boldsymbol{u}_{\mathrm{ss}}(k-1)) \tag{10}$$

Then the state and output predictions for linear MPC are calculated with the help of (10) and can be rewritten as

$$\boldsymbol{x}_{\mathrm{ss}}(k+i|k) = \boldsymbol{A}\boldsymbol{x}_{\boldsymbol{ss}}(k+i-1|k) + \boldsymbol{B}\boldsymbol{u}_{\mathrm{ss}}(k+i-1|k) + \boldsymbol{d}_{\mathrm{ss}}(k), \quad i = 1, \dots, p, \tag{11a}$$

$$\boldsymbol{y}_{\mathrm{ss}}(k+i|k) = (x_{\mathrm{ss,D}}(k+i|k), x_{\mathrm{ss,B}}(k+i|k))^{\mathrm{T}}, \quad i = 1, \dots, p. \tag{11b}$$

where $p$ is the length of the prediction horizon and the notation $\boldsymbol{x}_{\mathrm{ss}}(k+i|k)$ denotes variable x predicted for a

future sample $k+i$, but calculated at the current sample time $k$. The same mechanism for output disturbance estimation can be applied to the NN model. Off-set values between NN model outputs and actual process outputs are estimated with the following formulation

$$\boldsymbol{d}_{\mathrm{nn}}(k) = \boldsymbol{y}(k) - \boldsymbol{f}_{\mathrm{nn}}(\boldsymbol{y}(k-1), \boldsymbol{y}(k-2), \boldsymbol{u}(k-1), \boldsymbol{u}(k-2)) \quad (12)$$

Considering (12), the output predictions are then be calculated as follows

$$\boldsymbol{y}_{\mathrm{nn}}(k+i|k) = \boldsymbol{f}_{\mathrm{nn}}(\boldsymbol{y}_{\mathrm{nn}}(k+i-1|k), \boldsymbol{y}_{\mathrm{nn}}(k+i-2|k), \boldsymbol{u}\big((k+i-1|k)\big), \boldsymbol{u}\big((k+i-2|k)\big) + \boldsymbol{d}_{\mathrm{nn}}(k), \quad i = 1, \dots, p. \quad (13)$$

## Predictive Control Formulation

Control design aims to combine precision of each model over prediction horizon of MPC to obtain process outputs $\boldsymbol{y}(k+i|k) = (x_{\mathrm{D}}(k+i|k), x_{\mathrm{B}}(k+i|k))^{\mathrm{T}}$ using the calculated present and future control $\boldsymbol{u}(k+m-1|k) = L(k|k), \dots, L(k+m-1|k), V(k|k), \dots, V(k+m-1|k)^{\mathrm{T}}$ where $m$ is the control horizon. Subsequently, optimization problem for reference tracking with partial costs can be represented as

$$J_{\mathrm{ss}}(k) = \sum_{i=1}^{p} \boldsymbol{e}_{\mathrm{ss}}(k+i|k)^{\mathrm{T}} \boldsymbol{Q}_y \boldsymbol{e}_{\mathrm{ss}}(k+i|k) + \sum_{i=0}^{m-1} \boldsymbol{\Delta u}(k+i|k)^{\mathrm{T}} \boldsymbol{Q}_u \boldsymbol{\Delta u}(k+i|k) \quad (14a)$$

$$J_{\mathrm{nn}}(k) = \sum_{i=1}^{p} \boldsymbol{e}_{\mathrm{nn}}(k+i|k)^{\mathrm{T}} \boldsymbol{Q}_y \boldsymbol{e}_{\mathrm{nn}}(k+i|k) + \sum_{i=0}^{m-1} \boldsymbol{\Delta u}(k+i|k)^{\mathrm{T}} \boldsymbol{Q}_u \boldsymbol{\Delta u}(k+i|k) \quad (14b)$$

$$\text{s.t.} \quad \boldsymbol{e}_{\mathrm{ss}}(k+i|k) = \boldsymbol{y}_{\mathrm{ref}}(k+i|k) - \boldsymbol{y}_{\mathrm{ss}}(k+i|k) \quad (14c)$$

$$\boldsymbol{e}_{\mathrm{nn}}(k+i|k) = \boldsymbol{y}_{\mathrm{ref}}(k+i|k) - \boldsymbol{y}_{\mathrm{nn}}(k+i|k) \quad (14d)$$

$$\boldsymbol{y}_{\min} \le \boldsymbol{y}_{\mathrm{ss}}(k+i|k) \le \boldsymbol{y}_{\max}, \quad (14e)$$

$$\boldsymbol{y}_{\min} \le \boldsymbol{y}_{\mathrm{nn}}(k+i|k) \le \boldsymbol{y}_{\max}, \quad (14f)$$

$$\boldsymbol{u}_{\min} \le \boldsymbol{u}(k-1+i|k) \le \boldsymbol{u}_{\max}, \quad (14g)$$

$$i = 1, \dots . p,$$

where $\boldsymbol{y}_{\mathrm{ref}}(k+i|k)$ denotes the future reference, $\boldsymbol{Q}_y$ and $\boldsymbol{Q}_u$, are the penalizations on outputs and control increments, respectively. There are lower/upper constraints on the manipulated variables ($\boldsymbol{u}_{min}, \boldsymbol{u}_{max}$) and outputs ($\boldsymbol{y}_{min}, \boldsymbol{y}_{max}$). The state and output disturbance, $\boldsymbol{d}_{\mathrm{ss}}$ and $\boldsymbol{d}_{\mathrm{nn}}$, for each model plays a crucial role in multi-model MPC and the proposed control configuration uses weighted costs for optimization problem which is defined as:

$$\min_{\boldsymbol{u}(k)} \{\omega(k) J_{\mathrm{ss}}(k) + (1-\omega(k)) J_{\mathrm{nn}}(k)\}, \text{ s.t. (14)} \quad (15)$$

where $\omega(k)$ represents weighting parameter of performance functions at each sampling instant $k$, which depends on the values of modeling errors. Using the Euclidean norm for vectors of estimated off-set values of models, it can be calculated as follows:

$$\omega(k) = 1 - \frac{\|\boldsymbol{d}_{\mathrm{ss}}(k)\|}{\|\boldsymbol{d}_{\mathrm{ss}}(k)\| + \|\boldsymbol{d}_{\mathrm{ss}}(k)\|} \quad (16)$$

## RESULTS AND DISCUSSION

Nonlinear system simulations are conducted on a workstation equipped with an i7 10750H Intel 6-core CPU (base clock speed of 2.60 Ghz up to 4.8 GHz) and 16 GB of RAM. The simulations are performed in the MATLAB environment by utilizing ode15s solver with a relative tolerance of $1\,x\,10^{-6}$ and simulation step size of 0.5 s. The calculation of optimal control inputs for predictive control is performed using the `fmincon` function.

For MPC setup, all controllers run with $\boldsymbol{Q}_y = \mathrm{diag}(1,1)$ and $\boldsymbol{Q}_u = \mathrm{diag}(0.05,0.05)$, the prediction horizon and control horizon are set to $p = 10, m = 3$. The control inputs of the plant, $\boldsymbol{u}(k) = (L(k), V(k))^{\mathrm{T}}$ i.e, reflux liquid flow rate and vapor flow rate are constrained such that distillate flow rate must be kept in the interval of $0.01 < D < 0.200$ kmol/h as well as having the physical constraints. The controlled outputs $\boldsymbol{y}(k) = (x_{\mathrm{D}}(k), x_{\mathrm{B}}(k))^{\mathrm{T}}$ are constrained as well

$$\begin{bmatrix}0.01\\0.01\end{bmatrix} \le \boldsymbol{u}(k) \le \begin{bmatrix}0.3874\\0.5874\end{bmatrix}, \quad \begin{bmatrix}0.8973\\0.0600\end{bmatrix} \le \boldsymbol{y}(k) \le \begin{bmatrix}0.9663\\0.2261\end{bmatrix} \quad (17)$$

We also consider slack variables of outputs at constraints for SSMPC and NNMPC so as to ensure feasibility of the optimization problem in a case of unknown disturbances such that

$$\boldsymbol{y}_{\min} - \boldsymbol{\varepsilon}(i) \le \boldsymbol{y}_{\mathrm{ss}}(k+i|k) \le \boldsymbol{y}_{\max} + \boldsymbol{\varepsilon}(i) \quad (18a)$$

$$\boldsymbol{y}_{\min} - \boldsymbol{\varepsilon}(i) \le \boldsymbol{y}_{\mathrm{nn}}(k+i|k) \le \boldsymbol{y}_{\max} + \boldsymbol{\varepsilon}(i) \quad (18b)$$

where slack variable $\boldsymbol{\varepsilon}(i)$ is subject to the constraint $\boldsymbol{\varepsilon}(i) \ge 0$. Consequently, cost of optimization problem given in (14a) and (14b) is updated with slack variable as

$$J(k) = \sum_{i=1}^{p} \left[\boldsymbol{e}(k+i|k)^{\mathrm{T}} \boldsymbol{Q}_y \boldsymbol{e}(k+i|k) + \boldsymbol{\varepsilon}(i)^{\mathrm{T}} \boldsymbol{Q}_{\varepsilon} \boldsymbol{\varepsilon}(i)\right] + \sum_{i=0}^{m-1} \boldsymbol{\Delta u}(k+i|k)^{\mathrm{T}} \boldsymbol{Q}_u \boldsymbol{\Delta u}(k+i|k) \quad (19)$$

The penalization of new variable is set to $\boldsymbol{Q}_{\varepsilon} = \mathrm{diag}(0.5,0.5)$ for both NN-MPC and SS-MPC. The parameters listed in Table 1 are used to derive linear process model of distillation column. The operating point, for this steady state data, corresponds to a lower purity of compositions $x_{\mathrm{D}}$ and $x_{\mathrm{B}}$. Here, it is desired to drive the system to another operating point with high purity of top product, which implies that large perturbations from steady state are expected. Therefore, a linear state-space model may not be adequate to give sufficiently accurate predictions for MPC mechanism. It should be noted that the nonlinear process accepts $x_{\mathrm{F}}$ and $F$ as disturbance inputs in addition to manipulated variables $L$ and $V$ in the selected control setup, and they are assumed to be constant for all simulation scenarios. Simulations are started with an initial condition selected in the vicinity of steady-state data

which is used to linearize nonlinear column model. To evaluate the reference tracking performance of all controllers, the following four distinct step changes in the setpoints are applied to both outputs

$$\boldsymbol{y}_{\text{ref},1} = \begin{bmatrix} 0.928 \\ 0.190 \end{bmatrix}, \boldsymbol{y}_{\text{ref},2} = \begin{bmatrix} 0.897 \\ 0.226 \end{bmatrix}, \boldsymbol{y}_{\text{ref},3} = \begin{bmatrix} 0.941 \\ 0.126 \end{bmatrix}, \boldsymbol{y}_{\text{ref},4} = \begin{bmatrix} 0.966 \\ 0.060 \end{bmatrix}$$

A predictive control employing exact nonlinear process model, which is referred to as Nonlinear-MPC in this context, is selected as benchmark for time response performance evaluation. The optimization problem in (19) subject to the constraints given in (17) and (18) is also valid for Nonlinear-MPC case. Single-model approaches, including Nonlinear-MPC, NN-MPC, and SSMPC, are compared with Multi-MPC. Their reference tracking capabilities are demonstrated in Figure 2. It can be seen from the figure that both SS-MPC and NN-MPC approaches are prone to exhibit large overshoots especially when the plant is forced to run in a high purity point coinciding with output constraints. NN-MPC approach has slightly better time response whereas it generates more aggressive control inputs. On the other hand, controlled process using Multi-MPC formulations exhibits better reference tracking performance along with reduced control effort. Nonlinear-MPC, which is base control for simulations, exhibits the best performance among the controllers.

**Table 2:** Performance indicators of MPC methods

| Controller | $J$ (%) | Average CPU Time (sec) |
|---|---|---|
| NN-MPC | 107 | 4.802 |
| SS-MPC | 107 | 3.378 |
| Multi-MPC | 102 | 4.157 |
| Nonlinear-MPC | 100 | 5.106 |

For the purpose of better understanding of results, the performance of controllers are also evaluated by using closed-loop objective function with the following formulation

$$J = \sum_{i=1}^{N} \boldsymbol{e}(i)^{\mathrm{T}} \boldsymbol{Q}_x \boldsymbol{e}(i) + \Delta \boldsymbol{u}(i)^{\mathrm{T}} \boldsymbol{Q}_u \Delta \boldsymbol{u}(i) \qquad (20)$$

where $N$ is the number of sampling instants within the total simulation time. The closed-loop performance costs in Table 2 are normalized with respect to the benchmark Nonlinear-MPC. In the case of using approximate models as predictors, Multi-MPC achieves superior reference tracking for both process outputs while generating less aggressive control signals. It also performs better compared with SS-MPC and NN-MPC in terms of the performance cost. Multi-MPC requires slightly less computational effort compared to Nonlinear-MPC, as indicated by the average CPU time. Note that CPU time for SS-MPC was found using the default NLP solver and it would be significantly reduced using a QP solver.

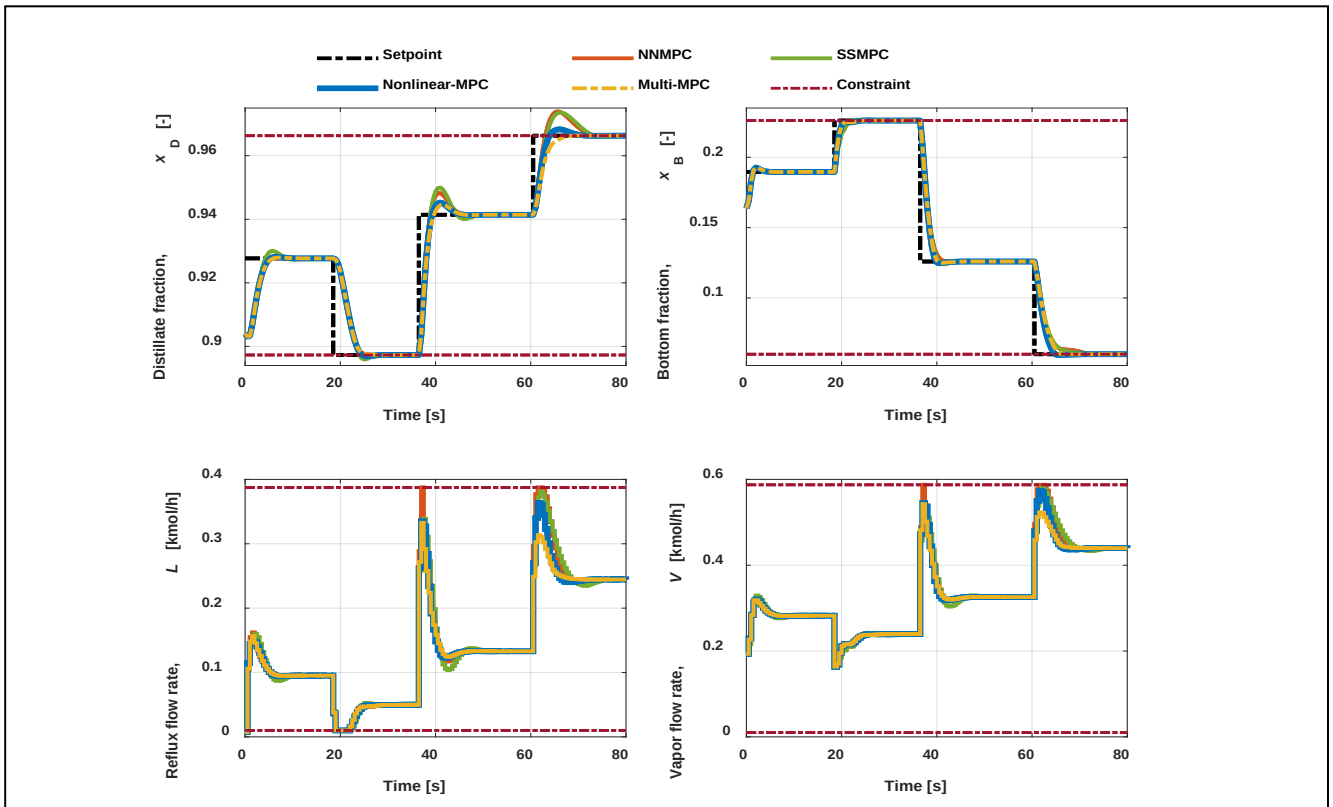



**Figure 2:** Setpoint tracking results of controlled system outputs (top two plots) and manipulated variables

## CONCLUSION

This study represents an implementation of multi-model predictive control to a distillation column process which constitutes a notably proper benchmark for multi-input interacting nonlinear MIMO systems. Time responses of both single-model and multi-model MPC formulations are demonstrated via computer simulations under various control scenarios including operational limits as well as input and output constraints. Running the system in a large space operating regions allows us to observe that multi-model MPC outperforms linear and data-based single model approaches. The results are validated with closed-loop performance cost values of all controllers. In addition, time response and performance indicators show that offset-free technique successfully eliminates steady state errors resulting from model-process mismatch for all control methods. The proposed multi-model MPC formulation demonstrates that collaboration of linear and data-based models might be an acceptable candidate instead of full nonlinear MPC with less computational time.

## ACKNOWLEDGEMENTS

This research is funded by the Slovak Research and Development Agency (APVV-21-0019), by the European Commission (FrontSeat, 101079342), and by EU RePower project VAIA (FS-Match, 09I01-03-V04-00024). Mehmet Arıcı acknowledges support from The Scientific and Technological Research Council of Turkey TUBITAK no. 1059B192300919.

## REFERENCES

1. Shen Z, Qu Q, Chen M, Lyu H, Sun J. Advancements in methanol distillation system: A comprehensive overview. *Chem Eng Res Des* 199:130-151 (2023).
2. Abraham A, Vyas P. Generalized predictive control design of benchmark distillation columns: A case study for multi-input multi-output system. *Springer Nature Switzerland* (2023).
3. Mayne D. Robust and stochastic model predictive control: Are we going in the right direction?. *Annu Rev Control* 41:184-192 (2016).
4. Ellis M, Liu J, Christofides PD. Economic Model Predictive Control. Springer (2017).
5. Gouta H, Saïd SH, Barhoumi N, M'Sahli F. Generalized predictive control for a coupled four tank MIMO system using a continuous-discrete time observer. *ISA Trans* 67:280-292 (2017).
6. Banerjee S, Khan O, El Mistiri M, Nandola NN, Rivera DE. Data-driven control of highly interactive systems using 3DoF model-on-demand MPC: Application to a MIMO CSTR. *IFAC-PapersOnLine* 58(15):420-425 (2024).
7. Mayne DQ. Model predictive control: Recent developments and future promise. *Automatica* 50(12):2967-2986 (2014).
8. Kvasnica M, Herceg M, Čirka Ľ, Fikar M. Model predictive control of a CSTR: A hybrid modeling approach. *Chem Pap* 64:301-309 (2010).
9. Liu J, Muñoz De La Peña D, Christofides PD. Distributed model predictive control of nonlinear process systems. *AIChE J* 55:1171-1184 (2009).
10. Magni L, Raimondo DM, Allgöwer F. Nonlinear Model Predictive Control: Towards New Challenging Applications. Springer (2008).
11. Dyrska R, Horváthová M, Bakaráč P, Mönnigmann M, Oravec J. Heat exchanger control using model predictive control with constraint removal. *Appl Therm Eng* 227:120366 (2023).
12. Rastegarpour S, Feyzmahdavian HR, Isaksson AJ. Enhancing reinforcement learning robustness via integrated multiple-model adaptive control. *IFAC-PapersOnLine* 58(14): 360-366 (2024).
13. Du J, Johansen TA. Integrated multilinear model predictive control of nonlinear systems based on gap metric. *Ind Eng Chem Res* 54(22):6002-6011 (2015).
14. Aufderheide B, Bequette BW. Extension of dynamic matrix control to multiple models. *Comput Chem Eng.* 27:1079-1096 (2003).
15. Kumar KK, Patwardhan SC. Nonlinear predictive control of systems exhibiting input multiplicities using the multimodel approach. *Ind Eng Chem Res* 41(13):3186-3198 (2002).
16. Skogestad S, Morari M. Control of ill-conditioned plants: High-purity distillation. *Chem Eng* 206:41 (1986).
17. Mikleš J, Fikar M. Process Modelling, Identification, and Control. Springer (2007).
18. Tatjewski P. Offset-free nonlinear model predictive control with state-space process models. *Arch Control Sci* 27(4) (2017).

© 2025 by the authors. Licensed to PSEcommunity.org and PSE Press. This is an open access article under the creative commons CC-BY-SA licensing terms. Credit must be given to creator and adaptations must be shared under the same terms. See https://creativecommons.org/licenses/by-sa/4.0/



Systems & Control Transactions

**Research Article - Peer Reviewed Conference Proceeding**
ESCAPE 35 - European Symposium on Computer Aided Process Engineering
Ghent, Belgium. 6-9 July 2025
Jan F.M. Van Impe, Grégoire Léonard, Satyajeet S. Bhonsale,
Monika E. Polańska, Filip Logist (Eds.)

PSE PRESS

# Optimal Design of Extraction-Distillation Hybrid Processes by Combining Equilibrium and Rate-Based Modeling

**Kai F. Kruber[a], Anjali Kabra[a], Lukas Polte[b], Andreas Jupke[b], and Mirko Skiborowski[a]***

[a] Hamburg University of Technology, Institute of Process Systems Engineering, Hamburg, Germany
[b] RWTH Aachen University, Chair of Fluid Process Engineering, Aachen, Germany
* Corresponding Author: mirko.skiborowski@tuhh.de.

## ABSTRACT

Liquid-liquid extraction (LLX) is an essential technique for separating heat-sensitive, highly diluted, or azeotropic mixtures. However, the design and optimization of LLX processes can be challenging due to mass transfer limitations and complex fluid dynamics. While distillation can often be modeled using equilibrium-based (EQ-based) approaches with (constant) height equivalent to theoretical stage (HETS) values, these kinetic effects can limit the applicability of EQ-based LLX models for conceptual design. Non-equilibrium (NEQ) or rate-based modeling can account for detailed mass transfer and fluid dynamics but further increases the nonlinearity and complexity of the respective optimization problems, which should account for closed-loop solvent recovery. To successfully address these complexities, we propose an integrated methodology combining NEQ-based simulation with EQ-based superstructure optimization to design a hybrid extraction-distillation process. An NEQ model is first used to derive operation-dependent HETS correlations, which are then incorporated into an EQ-based superstructure model for techno-economic optimization targeting total annualized cost. This approach balances model fidelity and computational efficiency, providing more reliable solutions by capturing the solvent-specific mass transfer behavior. We illustrate the methodology for a dilute acetone-water system with different solvents.

**Keywords**: Hybrid Processes, Process Design, Superstructure Optimization

## INTRODUCTION

Liquid-liquid extraction (LLX) is a critical technique for separating mixtures that are sensitive to high temperatures, highly diluted, or exhibit azeotropic behavior [1]. The technique relies on the distribution of target components between two immiscible liquid phases, making it particularly effective when conventional distillation alone becomes impractical or even impossible. Despite its usefulness, LLX requires subsequent solvent recovery, which can be accomplished by distillation in many cases. As a result, hybrid extraction-distillation processes have emerged as a standard combination in the chemical and biochemical industries, integrating the strengths of both unit operations and offering potentially lower energy consumption and improved selectivity for challenging separations [2].

Despite its widespread industrial application, the design and optimization of LLX processes remain challenging, mainly due to the necessity of selecting a suitable solvent. In contrast to distillation, where equilibrium-based (EQ-based) models with constant values for the height equivalent to a theoretical stage (HETS) are mostly considered sufficient to yield accurate results, LLX is significantly affected by kinetic phenomena, e.g., fluid dynamics, due to the much lower density difference between the phases compared to vapor-liquid equilibria in distillation, and mass transfer limitations [3]. Therefore, it has been reported that an EQ model with constant stage efficiencies [4] or a constant HETS [5] can introduce considerable inaccuracies when designing LLX processes.

Non-equilibrium (NEQ) models, which incorporate a dedicated description of mass transport and fluid dynamics, offer a superior representation but are

associated with a substantial increase in model complexity [3,6], as well as additional requirements of system-specific transport property data and equipment-specific hydrodynamics and mass transfer kinetics. Additionally, the necessary consideration of solvent recovery in a closed-loop process further increases the challenges for an optimization-based design. This complexity represents a significant obstacle to the frequent use of NEQ models in process optimization, particularly in large-scale industrial applications [7].

In a previous study, Kampwerth et al. [3] employed a rate-based NEQ dispersion model of a counter-current LLX column based on population balance equations accounting for complex and interconnected kinetic phenomena. For the considered hybrid process, the rate-based LLX model is complemented by a shortcut model (Fenske-Underwood-Gilliland) for the distillation column for solvent recovery and product purification. By neglecting the mutual solubility of the carrier and the solvent and assuming a sharp split in the solvent recovery column, the process recycle comprises a pure solvent. Therefore, the recycle stream is not explicitly considered, which simplifies the model notably. Based on this model, Kampwerth et al. [3] perform a solvent selection by manually determining the optimal solvent-to-feed ratio based on a sensitivity analysis considering the total annualized costs (TAC) as their objective. Using the Kremser method [8] to estimate the minimum number of EQ stages in the LLX column, Kampwerth et al. [3] determined solvent-specific HETS values based on their optimal process conditions, reporting a broad range for the HETS values ranging from 0.26 m to 1.10 m. In a following study, Kampwerth et al. [6] extend their model by considering mutual solubility of the carrier and the solvent in the two-phase liquid system to include solvent loss in the raffinate and evaluate the impact of different alternatives for raffinate purification. Based on the results of the study, the authors highlight the importance of fluid dynamics and mass transfer phenomena when selecting solvents and designing LLX columns.

In order to expand the scope of the study to an increased solvent search space, Polte et al. [9] combined the developed NEQ model and the design procedure with a computer-aided molecular and process design method (CAMPD) introduced by Scheffczyk et al. [10]. The combination allows for generating new solvent candidates using a genetic algorithm. The NEQ model framework provides the TAC concerning the optimal solvent-to-feed ratio as a fitness function for the genetic algorithm. The approach successfully demonstrates the automatic evaluation and design of solvent candidates based on a rigorous rate-based LLX model with an enlarged solvent design space. However, the hybrid process was still evaluated based on a shortcut representation of the distillation column, assuming a perfect separation of the product and solvent recycle stream. Moreover, besides the solvent selection, all studies consider a single design degree of freedom (DDoF), namely the solvent-to-feed ratio, due to their chosen model types and assumptions.

In contrast to the latter approach that focuses on the detailed modeling of the LLX column, Kruber et al. [11] proposed an EQ-based superstructure model to optimize the closed-loop hybrid extraction-distillation process in the context of solvent screening. The resulting problem is effectively solved as a successively relaxed mixed-integer nonlinear programming (SR-MINLP) problem [12]. The polylithic solution strategy allows for an efficient optimization of multiple operational DDoF, e.g., the solvent-to-feed ratio as well as the reboiler and condenser duty in the distillation column, and structural DDoF, e.g., the column heights and diameters. Nonetheless, the model relies on pre-specified constant HETS values for the LLX and distillation column. The study did consider these fixed for all investigated solvents and operating conditions.

To overcome the limitations of the individual approaches, an integrated approach that combines the NEQ modeling by Kampwerth et al. [3,6] with an EQ-based superstructure optimization for a hybrid extraction-distillation process [11] is presented in this work. The objective is to develop a reliable method for process optimization that captures the essential features of mass transfer and fluid dynamics in the LLX column without the computational burden of full rate-based representation throughout the entire design process. In the initial phase, the NEQ representation of an LLX column is employed to calculate HETS values specific to the selected solvent and contingent on the operational conditions [6]. Based on the generated data, solvent-specific HETS correlations are generated and incorporated into an EQ-based extraction-distillation superstructure model [11], thereby enabling accurate incorporation of mass transport phenomena in combination with a rigorous closed-loop process optimization. The efficacy of the proposed design approach is illustrated through its application to the separation of a diluted acetone-water mixture. The cost-optimal process designs for a range of solvents are evaluated, with a particular focus on the specific HETS values. Furthermore, the results are compared to those derived for constant HETS values across all solvents and operating conditions. Finally, a conclusion and an outlook for future research opportunities are given.

## METHODOLOGY

By combining a rigorous superstructure optimization based on the assumption of EQ conditions with a detailed NEQ-based approach to determine solvent-specific

HETS values, the developed methodology partly preserves the accuracy of the rate-based approach while being computationally efficient for superstructure optimization. A schematic depiction of the methodology is shown in Figure 2. First, a database of HETS values for the LLX column is generated based on calculations for each selected solvent using the NEQ-based simulation at different ratios of continuous and dispersed phases. A polynomial regression is performed to generate solvent-specific surrogate models for the HETS values. Subsequently, an economic superstructure optimization is carried out, incorporating the gained correlation for the HETS value. The following subsections briefly explain the main parts of the procedure.

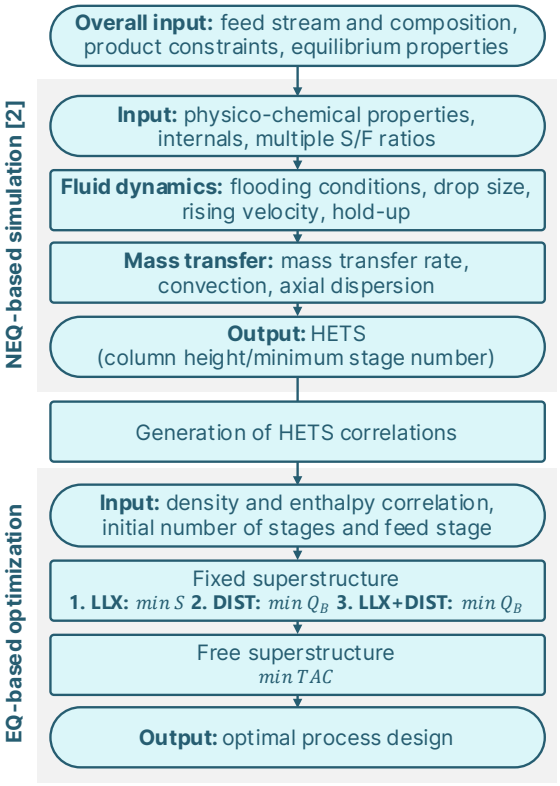



**Figure 1.** Conceptual framework for integrating HETS correlations derived by NEQ-based simulations into an EQ-based superstructure optimization.

## NEQ-based prediction of HETS values

A one-dimensional, rate-based dispersion model is employed to capture mass transfer effects in the extraction column. The primary output of interest is the column height, which reflects the extent of mass transfer required under specified conditions (e.g., temperature, phase ratio, column load). Physical property-based correlations (densities, viscosities, interfacial tension) are used to estimate key fluid dynamic parameters such as drop size distribution, sedimentation velocity, holdup, and dispersion coefficients. These parameters determine interfacial area and residence time available for mass transfer, eventually defining the necessary column height. Once the column height is determined for the required separation and operating condition, the method by Kremser [8] is applied to calculate the minimum number of EQ stages, thus enabling the estimation of HETS. Details on the underlying correlations and boundary conditions regarding the rate-based modeling approach can be found in Kampwerth et al. [3].

To achieve simple HETS-correlations, quadratic, cubic, and quartic polynomial models are investigated based on their corrected Akaike information criterion (AICc) [13]. The AICc enables a comparison of different models by considering the model's accuracy and simplicity, balancing the risks of under- and overfitting. It is generally recommended to use the corrected version of the AIC, which accounts for small sample sizes. Based on the insights gained, a cubic polynomial of the ratio of continuous and dispersed phases results in a sufficiently accurate and simple representation of the solvent-specific HETS values.

## EQ-based superstructure optimization

The superstructure model for the hybrid extraction-distillation process is illustrated in Figure 2. The process feed (F) and the lean solvent enter the column at the top and bottom, respectively, to form the countercurrent flow. While the depleted raffinate stream (R) leaves at the bottom, the enriched extract stream (E) is heated to boiling conditions before entering a distillation column. Depending on the mixture topology, the product (P) is either obtained as distillate or bottom product. Prior to the LLX column, the recycle stream is cooled to the operating condition of the extraction and fed to a decanter. The solvent-rich phase leaving the decanter and a solvent make-up stream (S) are recycled to the the LLX column. The solvent-lean phase from the decanter is mixed with the raffinate stream, leaving the process.

The overall structure of the process is predefined, while the height of each unit is introduced as a DDoF by a superstructure formulation with variable feed, reflux, and boil-up positions [11,14]. The superstructure model comprises continuous and discontinuous variables resulting in a mixed-integer nonlinear programming (MINLP) problem, which is efficiently solved as a series of successively penalized MINLP problems [12]. The solution strategy follows a polylithic approach to ensure a robust model and a high-quality local optimal solution based on profound starting values [11]. The second half of Figure 1 captures the core steps of the polylithic solution approach.

The robustness of the model is further increased by using external equations to calculate the equilibrium conditions and the necessary enthalpies. Using external equations notably reduces the number of variables and

equations in the process model. Furthermore, dedicated solution strategies can be employed inside the external equations to calculate the different phase equilibria efficiently, further improving robustness and reliability.

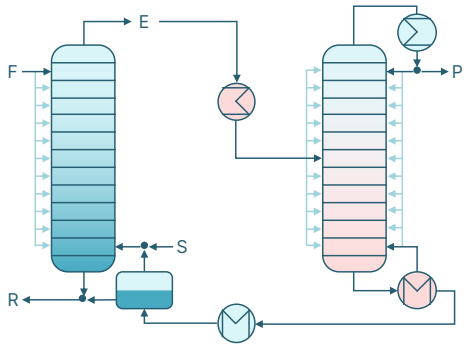



**Figure 2.** Extraction-distillation superstructure model.

## RESULTS

The separation of a diluted acetone-water mixture demonstrates the application of the developed approach. The acetone-water system forms a tangent pinch at high acetone compositions, resulting in high reflux ratios and low energy efficiency for conventional distillation [15]. Previous studies have already suggested the separation by LLX and highlighted the impact of fluid dynamics and mass transport [3,9]. In accordance with these studies, we use the same feed conditions of 76 mol·s$^{-1}$ (5 m$^3$·h$^{-1}$) with an acetone content of 2 mol% (5.5 wt%), representing a highly aqueous feed stream. The solvent make-up stream consists of pure solvent. A minimum product purity of 94 mol% acetone and a maximum impurity of 0.01 mol% acetone in the raffinate stream are set as inequality constraints. The necessary physico-chemical property data is taken from the DIPPR database. The non-random two-liquid model (NRTL) represents the EQ behavior, which is fitted to predicted activity coefficients using COSMO-RS [9].

Kampwerth et al. [3] investigated 14 frequently used solvent candidates, out of which five that provide a balanced distribution of the published HETS values are considered in the current study. Therefore, the two solvents with the lowest and highest HETS values are selected, n-butanol (BUT) and methyl isobutyl ketone (MIBK) (low HETS), as well as tetralin (TET) and cyclohexanol (CYC) (high HETS). Toluene (TOL) is also selected as a solvent with an intermediate HETS value close to the reference value of 0.5 m.

The LLX column and the decanter are operated at ambient conditions (25 °C, 1 atm), with a maximum of 15 stages in the LLX column and 50 stages in the distillation column (EQ model). The superstructure models are implemented in GAMS 34.3, and the local SQP solver SNOPT is employed. TAC are determined via the bare module method by Woods [14], using a CEPCI value of 567.5 (2017), a depreciation time of ten years, an interest rate of 6%, and an exchange rate of 0.87 €·$^{-1}$ [3]. The costs for fresh solvent make-up are initially considered with 1000 €·t$^{-1}$ for all investigated solvents.

### Correlation of HETS data

The calculation of solvent-specific HETS values is described in detail by Kampwerth et al. [3]. HETS data are generated for a range of volume ratios using the rate-based simulation model, to fit a cubic polynomial in MATLAB using the built-in “polyfit” function. TOL serves as the benchmark solvent and generally shows an increase in HETS with a rising volume ratio, reflecting changes in solvent flow rate. All solvents follow a similar trend except TET, for which an inversion in phase densities leads to distinct droplet behavior and deviations in the HETS values. The cubic correlations result in a sufficient representation of the data for all five solvents with a minimum $R^2$ of 0.90 and an average of 0.96.

### Superstructure optimization

Figure 3 illustrates the distribution of the capital expenditures (CAPEX) for the optimized flowsheets of all considered solvents for a constant HETS of 0.5 m (left bar) and the correlated HETS (right bar). As expected, TET and CYC exhibit the highest CAPEX, driven primarily by their large HETS values of, on average, 1.2 m and 1.5 m, respectively. The CAPEX of the LLX column for TET and CYC is approximately 50% higher compared to the other solvents. In contrast, TOL shows more moderate CAPEX due to a much lower overall HETS value close to the reference of 0.5 m. Although MIBK and BUT exhibit similar phase diagrams with acetone and water compared to CYC, considering the size of the miscibility gap and the slope of the tie lines, the CAPEX for the LLX column differ strongly.

Interestingly, when comparing the CAPEX based on a constant HETS of 0.5 m, CYC initially appears more cost-effective, but the investment costs increase substantially once volume-ratio-dependent HETS values are incorporated, making it less attractive than MIBK and BUT. Comparing the overall CAPEX, there are differences between the constant and correlated HETS of up to 29%, stressing the importance of considering mass transfer and fluid dynamics, even in a simplified form.

Figure 4 depicts the operating expenditures (OPEX), revealing the dominant influence of solvent make-up flow rates and associated utility requirements. For MIBK, CYC, and BUT, pronounced solvent losses into the raffinate inflate their solvent make-up and drive OPEX substantially above TOL and TET. Losses in the product stream can be tolerated since they account for less than 0.15% of the overall losses for MIBK, CYC, and BUT only.

TET not only shows high investment costs in the extraction column but also suffers elevated utility expenses for distillation due to its large heat of vaporization. As a result, despite differences in the LLX column size and design, the overall TAC across the various solvents primarily depend on the OPEX for the considered economic parameters.

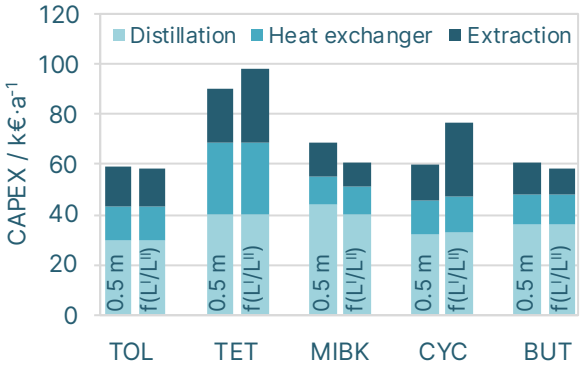



**Figure 3.** Capital expenditures (CAPEX) of the optimal process design for the solvents toluene (TOL), tetralin (TET), methyl isobutyl ketone (MIBK), cyclohexanol (CYC), and butanol (BUT) with constant and correlated HETS values.

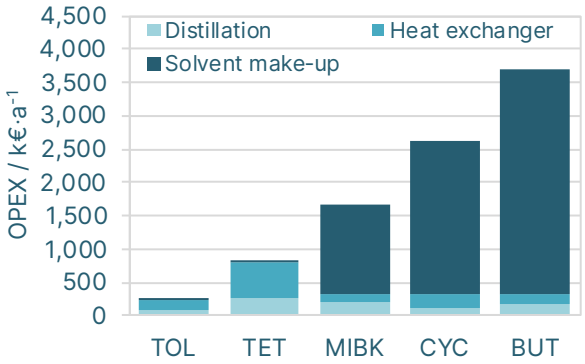



**Figure 4.** Operational expenditures (OPEX) of the optimized process design for the solvents toluene (TOL), tetralin (TET), methyl isobutyl ketone (MIBK), cyclohexanol (CYC), and butanol (BUT) with correlated HETS values.

The impact of the CAPEX on the TAC is comparably small, especially for those solvents that require large make-up streams, rendering the impact of the fluid-dynamics-related costs negligible. In order to evaluate the impact of the specific solvent costs, the cost for solvent recovery by raffinate treatment are evaluated based on the optimization of a heteroazeotropic distillation (HAD) superstructure model [17] for the solvents MIBK, CYC, and BUT, as these require large make-up streams. Based on the small acetone impurities, the solvent recovery from the raffinate is evaluated as a binary separation problem with a purity constraint of 99.99 mol% of water in the waste stream and a saturated solvent recycle, resulting in an average solvent recovery of 99%. Adjusting the assumed solvent make-up costs on the basis of these calculations, the TAC of the overall process can be reduced by approximately 80% on average. As this model is evaluated separately from the extraction–distillation framework, these corrections should be verified in a closed-loop process model.

In addition to solvent recovery, a straightforward estimation of potential savings through energy integration reveals further cost reduction possibilities. Since the preheater and cooler operate at comparable heat loads for all five solvents, heat integration by means of a heat pump is very attractive. The favorable temperature difference also supports direct integration for a large portion of the heat, saving the investment for a heat pump setup. As illustrated in Figure 5, these measures could yield overall savings of up to 92% of the TAC for the three solvents, making them competitive with TET. Besides improving economic viability, such strategies also shift the balance between capital and operating costs, making the LLX column design a more critical element in the overall process configuration.

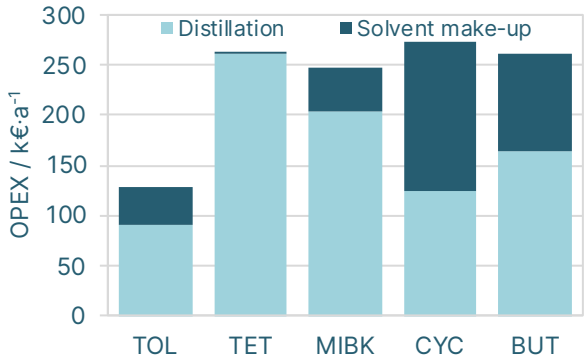



**Figure 5.** Adjusted operational expenditures (OPEX) with improved solvent recovery for the solvents methyl isobutyl ketone (MIBK), cyclohexanol (CYC), and butanol (BUT) and heat integration for all five solvents.

## CONCLUSION AND OUTLOOK

The current work introduces a novel approach that combines NEQ modeling with EQ-based superstructure optimization to design and evaluate LLX processes with integrated solvent recovery. The approach is successfully applied to the separation of a diluted acetone-water mixture, illustrating that solvent-specific HETS are of decisive importance for the accurate design of extraction columns and associated investment costs. If the investment costs are comparably small in respect to the operating costs, as is the case in the current study,

solvent recovery including losses in the raffinate, and proper heat integration are decisive for the choice of the best solvent. These results stress the importance of a holistic process design approach, in particular, the consideration of processes with closed recycle streams and heat integration.

Therefore, future research should expand the balance envelope for these processes and investigate a broader range of solvents and separation tasks. Regarding the incorporation of kinetic phenomena, the correlated HETS values should be expanded, e.g., towards a temperature dependency. This opens the opportunity to add the temperature as a DDoF rather than a predefined parameter. However, special care needs to be taken to ensure correct thermodynamic behavior with respect to the liquid-liquid equilibrium. Such extensions will require further refinement of the model formulation as well as improved initialization strategies to account for an increase in process complexity.

## REFERENCES


1. Sattler K. Thermische Trennverfahren. Wiley (2012)
2. Blahušiak M, Kiss AA, Babic K, Kersten SR, Bargeman G, Schuur B. Insights into the selection and design of fluid separation processes. Sep Purif Technol 194:301–318 (2008) https://doi.org/10.1016/j.seppur.2017.10.026
3. Kampwerth J, Weber B, Rußkamp J, Kaminski S, Jupke A. Towards a holistic solvent screening: On the importance of fluid dynamics in a rate-based extraction model. Chem Eng Sci 227:115905 (2020) https://doi.org/10.1016/j.ces.2020.115905
4. Sanpui D, Singh MK, Khanna A. Mass transfer studies on ternary systems in a bench-scale liquid-liquid extraction (LLX) column and a comparison with simulations. Korean J Chem Eng 21(2):511–520 (2004) https://doi.org/10.1007/BF02705442
5. Weber B, Meyer C, Jupke A. Performance Map for the Design of Liquid-Liquid Extraction Columns. Chem Ing Tech 91(11):1674–1680 (2019) https://doi.org/10.1002/CITE.201900057
6. Kampwerth J, Roth D, Polte L, Jupke A. Model-based simultaneous solvent screening and column design based on a holistic consideration of extraction and solvent recovery. Ind Eng Chem Res 61(9)3374-3382 (2022) https://doi.org/10.1021/acs.iecr.1c03312
7. Waltermann T, Schlueter S, Benfer R, Knoesche C, Górak A, Skiborowski M. Model Discrimination for Multicomponent Distillation – A Geometrical Approach for Total Reflux. Chem Ing Tech 92(7):890–906 (2020) https://doi.org/10.1002/cite.202000026.
8. Kremser A. Theoretical analysis of absorption process. Natl Petrol News 22:43-49 (1930)
9. Polte L, Raßpe-Lange L, Latz F, Jupke A, Leonhard K. COSMO-CAMPED – Solvent Design for an Extraction Distillation Considering Molecular, Process, Equipment, and Economic Optimization. Chem Ing Tech 95(3):416–426 (2023) https://doi.org/10.1002/cite.202200144
10. Scheffczyk J, Schäfer P, Fleitmann L, Thien J, Redepenning C, Leonhard K, Marquardt W, Bardow A. COSMO-CAMPD: a framework for integrated design of molecules and processes based on COSMO-RS. Mol Syst Des Eng 3(4):645–657 (2018) https://doi.org/10.1039/c7me00125h
11. Kruber KF, Scheffczyk J, Leonhard K, Bardow A. A hierarchical approach for solvent selection based on successive model refinement. Comput Aided Chem Eng 43:325-330 (2018) https://doi.org/10.1016/B978-0-444-64235-6.50060-7
12. Kossack S, Kraemer K, Marquardt W. Efficient Optimization-Based Design of Distillation Columns for Homogenous Azeotropic Mixtures. Ind Eng Chem Res 45(25):8492-8502 (2006) https://doi.org/10.1021/ie060117h
13. Burnham KP, Anderson DR. Model Selection and Multimodel Inference. Springer New York (2004)
14. Scharzec B, Kruber KF, Skiborowski M. Model-based evaluation of a membrane-assisted hybrid extraction-distillation process for energy and cost-efficient purification of diluted aqueous streams. Chem Eng Sci 240:116650 (2021) https://doi.org/10.1016/j.ces.2021.116650
15. Skiborowski M, Kruber KF. Exergy-based optimization for the synthesis of heat pump assisted distillation columns. Comput Aided Chem Eng 53:1351-1356 (2024) https://doi.org/10.1016/B978-0-443-28824-1.50226-X
16. Woods DR. Rules of Thumb in Engineering Practice. Wiley (2007)
17. Kruber KF, Skiborowski M. Topology-Based Initialization for the Optimization-Based Design of Heteroazeotropic Distillation Processes. Processes 10(8):1482 (2022) https://doi.org/10.3390/pr10081482



© 2025 by the authors. Licensed to PSEcommunity.org and PSE Press. This is an open access article under the creative commons CC-BY-SA licensing terms. Credit must be given to creator and adaptations must be shared under the same terms. See https://creativecommons.org/licenses/by-sa/4.0/




Systems & Control Transactions

**Research Article - Peer Reviewed Conference Proceeding**
ESCAPE 35 - European Symposium on Computer Aided Process Engineering
Ghent, Belgium. 6-9 July 2025
Jan F.M. Van Impe, Grégoire Léonard, Satyajeet S. Bhonsale,
Monika E. Polańska, Filip Logist (Eds.)

PSE PRESS

# Advanced Regulatory Control Structure for Proton Exchange Membrane Water Electrolysis Systems

**Marius Fredriksen[a] and Johannes Jäschke[a]***

[a] Norwegian University of Science and Technology, Department of Chemical Engineering, Trondheim, Norway
* Corresponding Author: johannes.jaschke@ntnu.no.

## ABSTRACT

Due to the intermittent nature of most renewable energy sources, developing good and flexible control structures for green electrolysis systems is crucial for maintaining efficient and safe plant operation. This work uses the "top-down" section of Skogestad's plantwide control procedure to propose a suitable control architecture for PEM electrolysis systems based on advanced regulatory control. Advanced regulatory control structures, such as active constraint control, may offer several advantages over MPC and AI-based control methods as they are computationally less expensive, less affected by model accuracy, easier to scale, and offer fast disturbance rejection. In our approach, we first mapped the constraint regions for the system. Then, we reduce the complexity by reformulating the optimization problem slightly, to remove some constraint regions to obtain a simpler solution structure that gives a negligible loss. Finally, we propose an active constraint control architecture using PI controllers and a selector for switching between the active constraint regions. We found that the system's fully constrained solution is close to the optimal solution, implying that our active constraint control approach may be used with little loss in efficiency. The proposed control structure was shown to perform well in dynamic simulations.

**Keywords**: PEM electrolysis, Modelling, Advanced Regulatory Control, Active Constraint Control

## INTRODUCTION

Global warming and climate change necessitate a transition from carbon-based energy sources to Renewable Energy Sources (RES) such as wind and solar power. Two significant challenges in this transition are the intermittent nature of these energy sources and their reliance on geographical factors. Carbon-free energy carriers like hydrogen can help address these challenges by facilitating efficient energy storage and transportation. Hydrogen is a promising candidate as it is already widely used in chemical industries, such as ammonia production, and can replace fossil fuels in processes that are difficult to electrify. However, successfully integrating hydrogen into the future energy economy depends on developing sustainable, efficient, and safe production methods. Currently, about 95% of the world's hydrogen is produced from fossil fuels, primarily grey hydrogen, through steam methane reforming [6].

A well-established method for producing green hydrogen is water electrolysis, in which an electric current separates water into hydrogen and oxygen gases. The two most prominent types of water electrolyzers used in industry are alkaline and Proton Exchange Membrane (PEM) electrolyzers. While alkaline electrolyzers are more mature and well-established, PEM electrolyzers are gaining popularity due to their greater flexibility, compact design, less corrosive electrolyte, and higher hydrogen purity compared to alkaline systems [6]. However, to fully take advantage of the benefits offered by PEM technology, it is essential to develop suitable control structures.

Most control architectures for PEM electrolysis systems primarily consist of relatively simple control structures of Proportional-Integral-Derivative (PID) and on-off controllers. Some works investigate more advanced control structures, such as model predictive control (MPC) and AI-based control methods [9]. However, few studies have been conducted on the viability of using Advanced Regulatory Control (ARC) structures [11], such as active constraint control and constraint switching strategies, for PEM systems. These control architectures offer several advantages: Being part of the regulatory control layer,

they provide fast local disturbance rejection, are easier to scale, less affected by model accuracy, and less computationally intensive than methods like MPC, while remaining relatively simple [2]. The main contribution of this paper is the application of ARC [11] to a PEM water electrolysis system. To the author's best knowledge, this type of control structure (with selectors for constraint switching) has not been reported for PEM systems before.

## METHODOLOGY

This section provides a brief overview of the PEM model and the development and implementation of our control structure. The model focuses on the system's electrochemical and gas crossover phenomena and is based on the PEM models developed by Afsari et al. [1] and Crespi et al. [3].

### Case study

We consider a 60 kW PEM electrolysis system, as presented in Figure 1. Deionized water is stored in a buffer tank and cooled by a heat exchanger before being fed to the electrolyzer stack. In the stack, an electric current splits the water into hydrogen and oxygen gases. The gases are separated from the water in separators, and the water is recycled back to the deionized water tank. The hydrogen gas is compressed to 30 barg for storage, while the oxygen is vented.

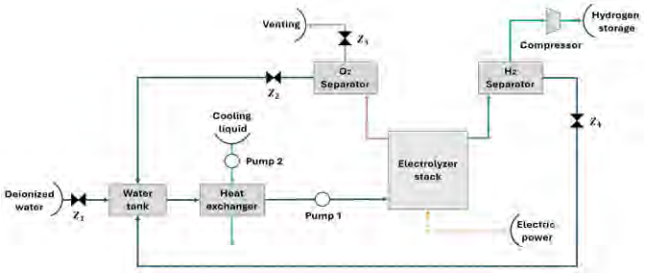



**Figure 1.** PEM water electrolysis system layout.

### PEM stack model

The PEM electrolyzer stack consists of multiple cells that are electrically connected in series. The PEM membrane, which acts as the electrolyte, divides each cell into an anode and cathode compartment. Water is fed to the anode, where it is oxidized to oxygen gas. The protons then cross the membrane to the cathode, where they are reduced to hydrogen gas.

### Electrochemical submodel

The voltage of each cell ($V_{cell}$) is the sum of the reversible cell voltage ($V_{rev}$), the ohmic overpotential ($V_{ohm}$), the activation overpotential ($V_{act}$), and the concentration overpotential ($V_{con}$):

$$V_{cell} = V_{rev} + V_{ohm} + V_{act} + V_{con} \quad (1)$$

The reversible cell voltage is the minimal theoretical voltage necessary to drive the reaction. It is estimated using the reaction's Gibbs free energy ($\Delta G_0(T)$) and the Nernst equation to account for pressure variations [3],

$$V_{rev} = \frac{\Delta G_0(T)}{zF} + \frac{RT}{zF} ln\left(\frac{P_{H_2} P_{O_2}^{0.5}}{P_0^{1.5}}\right). \quad (2)$$

Here, $z$ is the number of electrons participating in the reaction, $F$ is Faraday's constant, $R$ is the universal gas constant, $T$ is the stack temperature, $P_i$ is the partial pressure of species $i$, and $P_0$ is the reference pressure (1 bar).

The ohmic overpotential accounts for the electric and ionic resistance in the cells. It is found using an analytical expression for the membrane conductivity of the Nafion 117 membrane [3].

$$V_{ohm} = \left(\frac{\delta_{mem}}{(0.5139\lambda - 0.326)\, exp\left(1268\left(\frac{1}{303} - \frac{1}{T}\right)\right)} + R_{el}\right) i_{el} \quad (3)$$

$\delta_{mem}$ is the thickness of the membrane, $\lambda$ is the humidity factor, $R_{el}$ is the electric resistance of the electrodes, and $i_{el}$ is the current density.

The activation overpotential represents the energy required to initiate the reaction. It is approximated using Tafel kinetics [8],

$$V_{act} = \frac{RT}{\alpha_{an} zF} \ln\left(\frac{i_{el}}{i_{0,an}}\right) + \frac{RT}{\alpha_{cat} zF} \ln\left(\frac{i_{el}}{i_{0,cat}}\right), \quad (4)$$

where $\alpha_{an}$ and $\alpha_{cat}$ are the charge transfer coefficients and $i_{0,an}$ and $i_{0,cat}$ are the exchange current densities at the anode and cathode.

We also use Tafel kinetics to describe the concentration overpotential, which represents the resistance to mass transfer within the cells [10],

$$V_{con} = \frac{RT}{zF} \ln\left(\frac{C_{O_2}^{mem}}{C_{O_2}^{0}}\right) + \frac{RT}{zF} \ln\left(\frac{C_{H_2}^{mem}}{C_{H_2}^{0}}\right). \quad (5)$$

$C_{H_2}^{mem}$ and $C_{O_2}^{mem}$ are the concentration of hydrogen and oxygen at the membrane surface, which was found by applying Fick's law [1], and $C_{H_2}^{0}$ and $C_{O_2}^{0}$ are the concentration of hydrogen and oxygen in the flow channels.

### Thermal submodel

Due to the overpotentials in the stack, the stack produces heat, warming up the system. To calculate the temperature changes, we use the following reformulation of the general energy balance [8]:

$$\frac{dT}{dt} = \frac{1}{nC_p}\left(\sum \dot{n}_{in,i} C_{p,i} (T_{in} - T) + \left(V_{stack} - \frac{\Delta_r H}{zF}\right) i_{el} + Q\right) \quad (6)$$

Where $V_{stack}$ is the stack voltage, $\Delta_r H$ the heat of reaction, $T_{in}$ the feedwater temperature, $C_{p,i}$ the heat capacity of species $i$, $\dot{n}_{in,i}$ the molar inflow of species $i$, and $n$ the total amount of moles inside the stack. The heat transfer ($Q$) between the stack and the environment is given by,

$$Q = -\frac{1}{R_{th}} (T - T_{env}). \quad (7)$$

Where $R_{th}$ is the thermal resistance and $T_{env}$ is the temperature of the environment [8].

## Mass transport submodel

The inventories of the cathode and anode flow channels are lumped together, representing the stack as a large cell divided into one anode and one cathode compartment. The change in the molar inventories of hydrogen, oxygen, and water in each compartment is given by

$$\frac{dn_i}{dt} = \dot{n}_{in,i} - \dot{n}_{out,i} + \dot{n}_{gen,i} + \dot{n}_i^{cross}. \quad (8)$$

Here $\dot{n}_{in,i}$ is the molar inlet flow, $\dot{n}_{out,i}$ is the molar outlet flow, $\dot{n}_{gen,i}$ is the number of moles consumed or generated, and $\dot{n}_i^{cross}$ is the number of moles crossing the membrane of species $i$.

The crossover through the membrane is driven by diffusion ($\dot{n}_i^{diff}$), pressure gradients ($\dot{n}_i^{dp}$), and the electroosmotic drag ($\dot{n}_i^{eod}$),

$$\dot{n}_i^{cross} = \dot{n}_i^{diff} + \dot{n}_i^{dp} + \dot{n}_i^{eod}. \quad (9)$$

The diffusion is approximated by Fick's law [1],

$$\dot{n}_i^{diff} = D_{i,mem}^{diff} H_i \frac{P_{i,cat}^{mem} - P_{i,an}^{mem}}{\delta_{mem}} A_{stack}, \quad (10)$$

where $H_i$ is Henrys constant and $D_{i,mem}^{diff}$ is the diffusion coefficient of species $i$, and $A_{stack}$ is the surface area of the membrane. The subscripts $an$ and $cat$ is used to represent the anode and cathode section, respectively.

To reduce the oxygen contamination in the hydrogen, we usually have a higher cathode pressure than anode pressure, resulting in hydrogen being pushed from the cathode to the anode,

$$\dot{n}_i^{dp} = \epsilon_i^{dp} \frac{P_{i,cat} - P_{i,an}}{\delta_{mem}} A_{stack}. \quad (11)$$

$\epsilon_i^{dp}$ is the diffusion constant of $i$ due to pressure difference. The oxygen crossover due to the pressure gradient is neglected as it is very small [1].

As the protons cross the membrane, they drag with them water and gasses. The electroosmotic drag moves the hydrogen and oxygen from the anode to the cathode, thus working against the pressure and diffusion-driven hydrogen crossover [1],

$$\dot{n}_i^{eod} = \pm \frac{i_{el}}{F} \zeta \frac{P_i H_i}{C(H_2O)} A_{stack}, \quad (12)$$

where $\zeta$ is the drag coefficient, and $C(H_2O)$ is the concentration of water in the membrane.

## Separator models

The hydrogen and oxygen separators separate the gases from the liquid water using gravity. We assume that the holdup time in the separators is sufficiently large to separate all the gas bubbles from the water. However, some hydrogen and oxygen will remain dissolved in the water. This amount is approximated using Henry's law.

$$n_{i_{dissolved}} = H_i \left(\frac{n_{g,i}}{n_g}\right) \frac{n_{H_2O} M_{H_2O}}{\rho_{H_2O}} P. \quad (13)$$

Where $M_{H_2O}$ is the molar mass and $\rho_{H_2O}$ is the density of water and $n_g$ is the moles of gas in the system. Furthermore, we assume that the heat loss from the separators is negligible.

## Water tank model

The deionized water buffer tank is modeled as a simple adiabatic mixing tank. It collects the water recycled from the separators and new deionized water that is added to replace the water consumed in the reaction.

## Heat exchanger model

The heat exchanger is divided into three sections: a hot flow section, a cold flow section, and a dividing wall section. The sections are further divided into segments following the hot stream flow direction. This gives us temperature gradients inside the heat exchanger, which we use to calculate the heat transfer from the hot to the cold liquid [7].

## Compressor and pump work

The compressor and pumps consume some of the power supplied to the system, establishing a minimum power requirement to start hydrogen production. We can reduce the compressor work by raising the pressure in the cathode section of the electrolyzer stack; however, this will also decrease the stack's overall efficiency. We assume the compression happens in multiple stages with cooling, thus representing the compression as isothermal. The compression work ($W_c$) is given by,

$$W_c \, \eta_c = \dot{n}_{H_2} \cdot R \cdot T_{separator} \cdot \ln\left(\frac{P_{storage}}{P_{separator}}\right). \quad (14)$$

The pump work ($W_p$) is given by,

$$W_p \, \eta_p = \left(P_{final} - P_{initial}\right) \frac{\dot{n} M}{\rho}. \quad (15)$$

Where $\eta_p$ (75%) and $\eta_c$ (80%) are the efficiency factors of the pumps and compressor, respectively.

## Development of control structure

The control structure is developed inspired by the "top-down" section of Skogestad's plantwide control procedure [12]:

1. Identify constraints and a cost function that characterizes optimal operation.
2. Identify the degrees of freedom.
3. Analyze the optimal solution for various disturbances to find the primary control variables.
4. Determine where to place the production rate.

## Step 1: Cost function and constraints

Our objective is to maximize the plant's hydrogen production while minimizing the hydrogen loss due to crossover using the system's manipulated variables (MVs). The cost function is to maximize the hydrogen output from the cathode separator ($\dot{n}_{H_2}$).

$$\begin{aligned} \min_{\text{MVs}} \quad & -\dot{n}_{H_2} \\ s.t. \quad & \textit{Process model equations} \\ & \textit{Operational constraints} \end{aligned} \tag{16}$$

Maintaining the stack pressure, temperature, and hydrogen-to-oxygen ratio (HTO) within a specified operating range is essential to prevent damage to the PEM membrane and other system components. To establish the upper temperature and pressure bounds, we refer to the operating conditions provided by Crespi et al. [3]. The absolute upper bound of the HTO is given by the lower explosion limit of 4 vol% $H_2$. However, to incorporate a safety margin, we lower the upper bound of the HTO in the anode separator to 2 vol% [2, 4]. We do not limit the oxygen content in the cathode separator, as these values are neglectable and far from the explosion limit. The resulting operating constraints are presented in Table 1.

**Table 1.** Operational constraints for the system.

| Condition: | Upper bound: | Lower bound: |
|---|---|---|
| Anode pressure | 2.7 barg | 0.2 barg |
| Cathode pressure | 30 barg | 0.2 barg |
| Temperature | 60 °C | 10 °C |
| HTO | 2 vol% | 0 vol% |
| Cooling liquid | ~0.9 L/h | 0 L/h |

## Step 2: Degrees of freedom

The second step in the procedure is to identify the degrees of freedom. Our system consists of four valves, two pumps, and one compressor. However, we have three liquid inventories requiring control: the liquid level in the water tank and the anode and cathode separators. Additionally, we need to keep the amount of water fed to the electrolyzer stack constant. This results in three degrees of freedom that we use to optimize the operation.

## Step 3: Optimal solution

The input power is assumed to be our primary disturbance. This leads to an optimization problem in which power is distributed to the stack, pumps, and compressor to maximize hydrogen production. The resulting steady-state optimization problem, as expressed in Equation 16, was solved 120 times for power inputs ranging from 0 kW to 60 kW in Julia using JuMP with the interior point solver IPOPT and the linear solver Ma57 from HSL [5, 13]. IPOPT is a local solver; thus, it does not guarantee optimal global solutions. However, the solution is consistent with the behavior reported for PEM electrolysis systems [1, 8, 13].

Figure 2 presents the active constraint regions for the optimal solution as a function of the power input. Each region is defined by the constraints that are currently active. A constraint is active when it either reaches its upper ($g/g_{max} = 1$) or lower limit ($g/g_{max} = 0$). The system has five active constraint regions. In Region 1, both pressure constraints are active; in Region 2, only the anode pressure constraint is active; in Region 3, the cooling liquid constraint and anode pressure constraint are active; in Region 4, the anode pressure and stack temperature constraint are active, and in Region 5, only the stack temperature constraint is active. Thus, the system has one or two active constraints in each region.

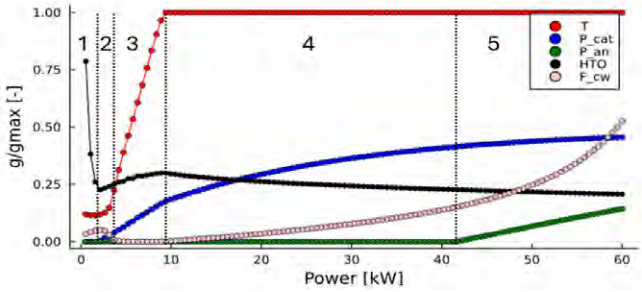



**Figure 2.** Constraint regions for optimal PEM operation.

## Altered solution:

Implementing the solution in Figure 2 is quite complicated. Thus, we propose slightly altering the optimization problem to achieve a different solution with fewer active constraint regions by adding terms to maximize the cathode and minimize the anode pressure to our cost function.

$$\min_{\text{MVs}} \quad -\dot{n}_{H_2} - 10^{-3}(P_{cat} - P_{an}). \tag{17}$$

The pressures were adjusted as they have a small impact on the overall stack efficiency and are not active constraints in several of the constraint regions in Figure 2.

The resulting fully constrained system presented in Figure 3 has three active constraint regions, which share several similarities with those found for alkaline systems by Cammann and Jäschke [2]. In Region 1, the system is heating up as the power increases, and the HTO is at its upper bound, limiting the rise of the cathode pressure.

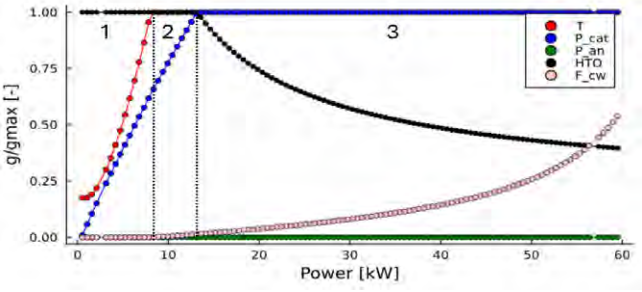



**Figure 3.** Constraint regions for fully constrained system.

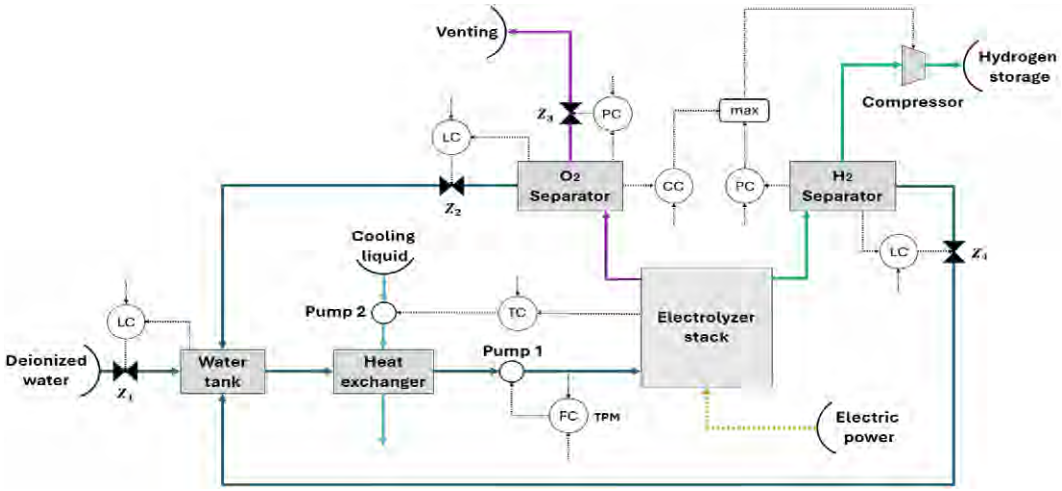



**Figure 4.** Block diagram of suggested control structure for PEM electrolysis system using active constraint control.

In Region 2, the system reaches its maximum temperature and starts using cooling liquid. When we cross from Region 2 to Region 3, the HTO constraint stops being active, and the cathode pressure reaches its upper bound. The four safety constraints - HTO, temperature, and anode and cathode pressures - are our control variables (CVs).

### Step 4: Production rate and control structure

We use decentralized control with single-loop PI controllers to design the control structure. We pair the CVs and MVs in the system using the "pair close" and "input saturation" pairing rules [11]. First, we pair the stack feedwater flow rate with the feedwater pump (Pump 1). Second, we close the inventory loops. That is, we pair the liquid inventories with the valves $z_1$, $z_2$, and $z_4$. The last valve $z_3$ is paired with the anode pressure, which is kept at its lower bound during the entire operational range.

We propose a simple MV-CV switch between active constraint Region 1 and 2. From Figure 3 we see that the temperature control can be given up when the cooling liquid saturates, we pair the stack temperature to the cooling liquid pump (Pump 2) and add anti-windup to the temperature controller [11].

Switching from Region 2 to 3, we have a CV-CV switch, as we stop controlling the anode separator HTO in favor of the cathode pressure. We introduce a maximum selector since both constraints can be satisfied by increasing the compressor work [11]. Thus, both the HTO and the cathode pressure are paired to the compressor through the selector. Figure 4 presents the resulting control structure.

## RESULTS AND DISCUSSION

By altering our cost function from Equation 16 to Equation 17, we have moved away from the original optimal point of operation. As a result, there is a slight loss in hydrogen production. The loss is a function of the power input and is highest at low power loads, see Figure 5. This will not make a big difference in practice, as we prefer to operate at high power because the stack is more efficient at high power loads. The loss is ca. 0.1 % of the total hydrogen production above 40 kW. The maximum loss is slightly above 0.5 % as we approach zero power input (no production).

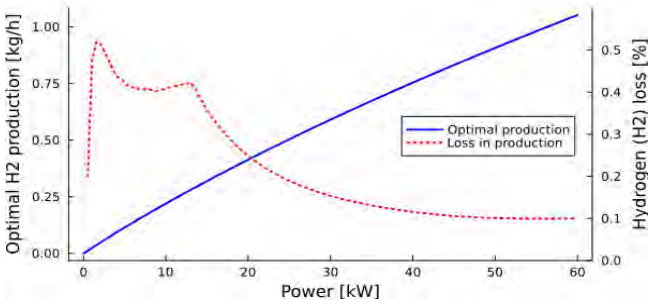



**Figure 5.** Loss in hydrogen output of the cathode separator by altering our objective function.

We conducted a dynamic simulation to test our control structure, focusing on the anode separator HTO and the cathode pressure, the CVs linked to the selector. After 2 minutes, we exposed the system to a power drop, decreasing the power input from 56 kW to 10 kW with a two-second ramp response. We then simulated the system for 30 minutes before increasing the power back to 56 kW and ran the simulation for another 20 minutes.

Figure 6 shows that the cathode pressure is reduced to counteract the rapid increase in the HTO within the anode separator. This occurs when the ratio controller takes over control of the compressor as the HTO rises. After approximately 20 minutes, the HTO stabilizes at the setpoint without significant overshoot or oscillations. As

power increases, the HTO decreases, and the pressure controller regains control of the compressor. The pressure in the cathode separator then returns to its setpoint. Overall, the controllers and the selector perform well.

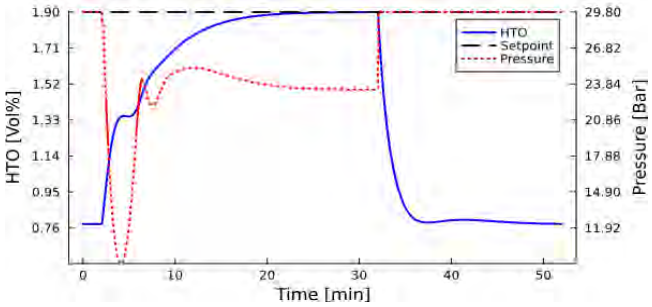



**Figure 6.** Control of HTO and cathode pressure.

## CONCLUSION AND FUTURE WORK

We have found that the optimal solution of the PEM electrolysis system is close to the fully constrained solution in all operating regions. This implies that active constraint control structures may be used to control the system with relatively little loss in hydrogen production. We implemented the active constraint control structure in our dynamic PEM electrolysis model using PI controllers and a selector. When exposed to power changes, the system controlled the HTO and cathode pressure well.

To simplify the model, we assumed that Henry's constant and the diffusion coefficients for hydrogen and oxygen are not temperature dependent. Introducing temperature dependencies might shift the active constraint regions somewhat, but we do not expect it to change the solution structure significantly. As such, we believe that the control structure will continue to work well.

For future work, the active constraint control structure should be compared to the performance of an MPC or AI-based control method.

## ACKNOWLEDGEMENTS

This work is supported by the HYDROGENi Research Centre (hydrogeni.no) under the Norwegian research program FMETEKN. The authors acknowledge the industry partners in HYDROGENi for their contributions and the Research Council of Norway (333118).

## REFERENCES

1. Afshari, E., Khodabakhsh, S., Jahantigh, N., & Toghyani, S. Performance assessment of gas crossover phenomenon and water transport mechanism in high pressure PEM electrolyzer. International Journal of Hydrogen Energy, 46(19), 11029-11040.(2021)
2. Crespi, E., Guandalini, G., Mastropasqua, L., Campanari, S., & Brouwer, J. Experimental and theoretical evaluation of a 60 kW PEM electrolysis system for flexible dynamic operation. Energy conversion and management, 277, 116622. (2023)
3. Cammann, L., & Jäschke, J. A simple constraint-switching control structure for flexible operation of an alkaline water electrolyzer. IFAC-PapersOnLine, 58(14), 706-711. (2024)
4. Haug, P., Koj, M., & Turek, T. Influence of process conditions on gas purity in alkaline water electrolysis. *International Journal of Hydrogen Energy*, *42* (15), 9406-9418. (2017)
5. HSL. A collection of Fortran codes for large scale scientific computation. http://www.hsl.rl.ac.uk/
6. Kumar, S. S., & Lim, H. An overview of water electrolysis technologies for green hydrogen production. Energy reports, 8, 13793-13813. (2022)
7. Leruth, A. *Heat exchanger network self-optimising control: Application to the crude unit at Mongstad refinery* (Master's thesis, NTNU). (2012)
8. Majumdar, A., Haas, M., Elliot, I., & Nazari, S. Control and control-oriented modeling of PEM water electrolyzers: A review. *International Journal of Hydrogen Energy*, *48*(79), 30621-30641. (2023)
9. Mao, J., Li, Z., Xuan, J., Du, X., Ni, M., & Xing, L. A review of control strategies for proton exchange membrane (PEM) fuel cells and water electrolyser: from automation to autonomy. Energy and AI, 100406. (2024)
10. Ojong, E. T., Kwan, J. T. H., Nouri-Khorasani, A., Bonakdarpour, A., Wilkinson, D. P., & Smolinka, T. Development of an experimentally validated semi-empirical fully-coupled performance model of a PEM electrolysis cell with a 3-D structured porous transport layer. International journal of hydrogen energy, 42(41), 25831-25847. (2017)
11. Skogestad, S. Advanced control using decomposition and simple elements. Annual Reviews in Control, 56, 100903. (2023)
12. Skogestad, S., & Postlethwaite, I. Multivariable feedback control: analysis and design. john Wiley & sons. (2005)
13. Wächter, A., & Biegler, L. T. On the implementation of an interior-point filter line-search algorithm for large-scale nonlinear programming. *Mathematical programming*, *106*, 25-57. (2006)

© 2025 by the authors. Licensed to PSEcommunity.org and PSE Press. This is an open access article under the creative commons CC-BY-SA licensing terms. Credit must be given to creator and adaptations must be shared under the same terms. See https://creativecommons.org/licenses/by-sa/4.0/

Systems & Control Transactions

**Research Article - Peer Reviewed Conference Proceeding**
ESCAPE 35 - European Symposium on Computer Aided Process Engineering
Ghent, Belgium. 6-9 July 2025
Jan F.M. Van Impe, Grégoire Léonard, Satyajeet S. Bhonsale,
Monika E. Polańska, Filip Logist (Eds.)

PSE PRESS

# Design of Microfluidic Mixers using Bayesian Shape Optimization

**Rui Fonseca* and Fernando Bernardo**

CERES, University of Coimbra, Department of Chemical Engineering, Coimbra, Portugal
* Corresponding Author: ruifo@sapo.pt.

## ABSTRACT

Microfluidic mixing has gained popularity in the Pharmaceutical Industry due to its application in the field of Nano-based Drug Delivery Systems (DDS). The flow conditions in Microfluidic mixers enable very efficient mixing conditions, which are crucial for the production of Nanoparticles by Flash Nanoprecipitation (FNP), as it enables reproducible production of particles with low-size variability. Mixer geometry is one of the most determinant factors, as it largely determines the flow patterns and the degree of contact between the two mixing streams. In this paper, a shape optimization methodology using Computational Fluid Dynamics (CFD) and Bayesian optimization is applied to the toroidal micromixer design, considering three different operating conditions. It consists of first defining a geometry solution space and then using Multi-Objective Bayesian optimization to explore the different designs. Mixer performance is evaluated with CFD simulations and two objective functions are considered: mixing time and pressure drop. Approximations of the Pareto front for each case study are obtained and the analysis of the best geometries enabled to derive some general geometric features of optimal mixer designs.

**Keywords**: Micromixing, Geometry Optimization, Multi-objective Optimization, Computational Fluid Dynamics.

## INTRODUCTION

Mixing and mass transfer are fundamental aspects of many chemical and biological processes. Microfluidic mixing has recently gained much traction as an advantageous technology in the field of Nano-based Drug Delivery Systems in the Pharmaceutical Industry [1]. Several Drug products, such as peptides and nucleic acids, must rely on specialized nanostructures to protect the Active Drug Ingredient (API), and are therefore able to achieve the desired Drug Pharmacokinetic and Pharmacodynamic properties [2]. These systems, usually Nanoparticles, are synthesized by Flash Nanoprecipitation (FNP), which consists in the rapid dilution of a solution containing amphipatic molecules with an anti-solvent. This sudden change of solubility results in the rearrangement of the solute molecules and consequent formation of Nanoparticles [3].

The reduced channel size of Microfluidic mixers entails a high mass-transfer area/ volume ratio, which enables the very fast mixing of the two solutions. This reduces the mass transfer resistance during the FNP process, allowing the formation of particles of controlled size and low polydispersity, both critical quality attributes (CQA) of these products. Consequently, Microfluidic mixing is generally a more fit process to reproducibly comply with the tight quality demands of the product, when compared with the traditional alternatives [4].

Conceptually, Microfluidic mixing is merely the passive mixing of two solutions. Process optimization is therefore limited to the tuning of two operating parameters (Total Flow Rate (TFR) and Flow Rate Ratio (FRR) of the two inlet streams) and of the mixer's geometry. Optimizing the flow rates for a given geometry can be done experimentally with general Quality by Design (QbD) procedures. In contrast, mixer geometry optimization presents some challenges. The limitless degrees of freedom in mixer design ensue a very large number of experiments to realistically cover the broad solution space. Furthermore, the experimental evaluation of each design is in itself a cumbersome and expensive task, as it would involve the iterative design, fabrication and testing of each device.

In this paper, we present a systematic approach for

the geometry optimization of the toroidal micromixer. The adopted methodology begins with the comprehensive parametrization of the mixer geometry solution space, using continuous and discrete geometric parameters with established bounds. Mixer performance evaluation is achieved through the simulation of the Villermaux-Dushman reaction system [5-6] inside the mixer, using Computational Fluid Dynamics (CFD). Two metrics, pressure drop and mixing time, are then considered in the multi-objective optimization problem. The solution space is subsequently navigated employing a Bayesian optimization framework, by iteratively selecting the solution point most likely to improve the Hypervolume indicator. Three case-studies are presented considering different operating conditions.

## METHODOLOGY

### Toroidal micromixer

The toroidal micromixer [7] has become a widely used system for the synthesis of nanoparticles, with applications mainly in the development of drug delivery systems. As shown in Figure 1, it consists of a Y-mixer with additional toroidal mixing elements. The curved geometry of the mixer's channels prompts the formation of Dean flows, which effectively increases the area of contact between the two mixing fluids. As also depicted in Figure 1, the mixer's geometry can be described by the following parameters: channel width and height, number of toroids and their radii, neck angle and length, and Y-mixer entry angle. An additional parameter was considered regarding the smoothness of the geometry's corners ("Corner Length").

### Problem formulation

This mixer shape optimization problem aims to maximize the mixing performance for three operating conditions. The TFR value is 10 ml/min for all cases and the FRR values are 1, 2 and 4. The goal is to find the optimal micromixer design for each operating condition and investigate the differences between the obtained geometries. To achieve this, two objectives were considered: minimizing pressure drop, with the goal of minimizing energy consumption but more importantly reducing the risk of device breakage; and minimizing mixing time, which is defined as the characteristic time constant of mixing described as a process of exponential decay of system heterogeneity. Mixing time is used to describe the rate in which the solutions are homogenized, inferring mass-transfer resistance. The mixing time can be estimated from the selectivity analysis of the Villermaux-Dushman competing reactions[5-6].

The evaluations of the two objective functions require the simulation of the system using CFD. This implies the automation of the non-trivial steps of geometry and mesh generation in the CFD simulation workflow. This was done using in-house Python™ code to describe the channel geometries as sets of hexahedral blocks, which were subsequently discretized, using the `blockMesh` utility of OpenFOAM®, to produce the system's mesh.

The complex and expensive nature of the objective functions evaluation calls for the use of efficient optimization algorithms able to locate great performing geometries with minimal number of function evaluations. This is achieved using a Bayesian optimization methodology, as illustrated in Figure 2. In this case, the first 30 system evaluation points were defined using SOBOL sampling. The subsequent 170 points were chosen in a sequential matter by fitting the previously attained data into a Gaussian Process and subsequently maximizing the Expected Hypervolume Improvement function (qEHVI method) [8], totaling 200 function evaluations. The optimization loop was carried out using the Adaptive Experimentation Platform package (Ax-platform) for Python™ [9].

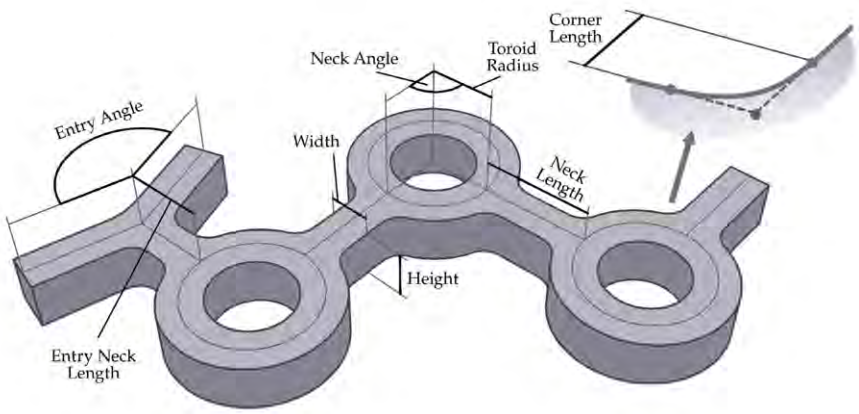



**Figure 1.** Geometry of the toroidal micromixer and respective parametrization.

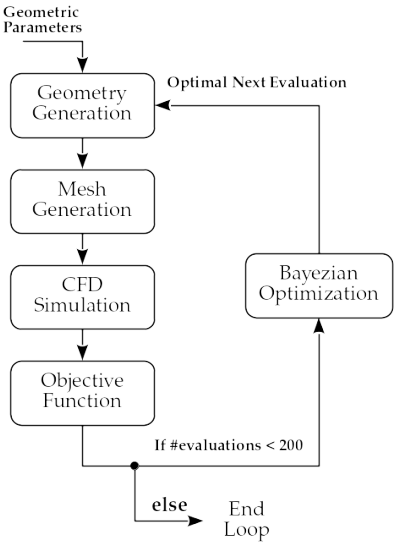



**Figure 2.** Illustration of the shape optimization loop.

The geometric domain was defined using the aforementioned geometry parametrization of the toroidal mixer and assigning bounds for each parameter, as presented in Table 1. Additional constraints were also implemented in order to avoid the generation of invalid geometries.

**Table 1.** List of the geometry parameters and additional constraints.

| Parameter | Value Range | Units |
|---|---|---|
| Entry Angle | [45, 180] | ° |
| Entry Neck Length | [200, 500] | μm |
| Width | [100, 400] | μm |
| Height | [0.1, 0.3] | μm |
| Neck Angle | [90, 270] | ° |
| Neck Length | [200, 700] | μm |
| Toroid Radius | [100, 600] | μm |
| # Toroids | [1, 5] | - |
| Corner Length | [10, 150] | μm |
| **Constraints** | | |
| 1.5 Width ≤ Toroid Radius | | |
| 1.5 Width ≤ Neck Length | | |
| 2.2 Corner Length + Width ≤ Neck Length | | |
| 2.2 Corner Length + Width ≤ Entry Neck Length | | |

## CFD simulation

In order to evaluate mixer performance, CFD simulations were carried out for each mixer design, considering single-phase, incompressible steady-state flow. Considering the mentioned geometry space, the Reynolds number ($Re$) range is ≈ [476, 1666], which approaches the upper limit of laminar flow in internal flows. Moreover, the toroidal mixer's geometry is conducive to flow separation and the formation of eddies. A RANS modelling approach was therefore applied using the SST k-ω turbulence model, which is appropriate for lower-Reynolds flows. For boundary conditions, fixed values for velocity and all scalar fields (except pressure) were considered at the inlets. No backflow was allowed at the outlet, and no-slip conditions were considered at the walls. The remaining boundary conditions were modeled as zero gradient conditions. The Villermaux-Dushman reaction is modeled by considering both reactants and reaction products as passive scalars and including the reaction terms in the corresponding transport equations. The reaction kinetics are taken from the literature [6].

The simulations were carried out using OpenFOAM® v2312 and post-processing was done in Python™ using the PyVista package [10].

## Villermaux-Dushman Reaction and IEM model

The Villermaux-Dushman competing reaction (Figure 3) consists of a quasi-instantaneous neutralization reaction (R1) and a fast redox reaction (R2) competing for hydrogen ions. The rate of R1 is highly dependent on the mass transfer process and, as such, some hydrogen ions are left to be consumed by the slower reaction (R2). As a result, the selectivity of the Villermaux-Dushman reaction is directly related to mass transfer resistance.

The concept of mixing time ($t_m$) arises from the Interaction by Exchange with the Mean (IEM) micromixing model, in which mixing time appears as a measure of mass transfer resistance. The model considers two separate volumes of fluid which exchange mass with each other. The mass transfer rate is proportional to the difference in concentration between each volume and the weighted average of both, as written in Equation 1:

$$\begin{cases} \frac{dC_{k,1}}{dt} = \frac{\overline{C_k} - C_{k,1}}{t_m} + R_{k,1} \\ \frac{dC_{k,2}}{dt} = \frac{\overline{C_k} - C_{k,2}}{t_m} + R_{k,2} \\ \overline{C_k} = \alpha C_{k,1} - (1-\alpha) C_{k,2} \end{cases} \quad (1)$$

where $C_{k,1}$, $C_{k,2}$, and $\overline{C_k}$ are the concentrations of species $k$ in volume 1, volume 2, and the weighted average of both, respectively. $R_{k,1}$ and $R_{k,2}$ are the source/sink terms for each species k in volume 1 and 2. Lastly, $\alpha$ and $(1-\alpha)$ correspond to the fractions of volumes 1 and 2 with respect to the total volume.

A calibration curve between mixing time and concentration of the R2 reaction product ($I_2$) in equilibrium can be obtained by solving the IEM model for a range of mixing time values. Since the relationship between both values is linear, a simple linear regression model can be used. This method is extensively used in literature to experimentally characterize the performance of micromixers [5]. This methodology is implemented here to relate the CFD-simulated $I_2$ concentration data, at the outlet, with a mixing time value.

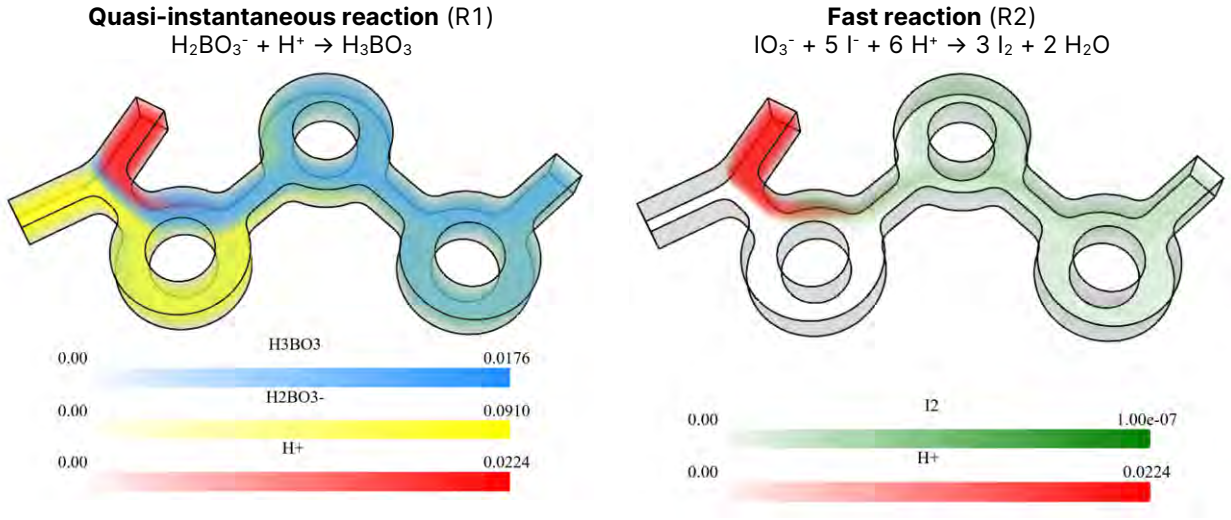



**Figure 3.** Representation of the CFD simulation of Villermaux-Dushman reaction system. Concentrations of the reactants and product of both reactions are presented in mol.dm$^{-3}$, using volume rendering of the CFD data of one of the simulations.

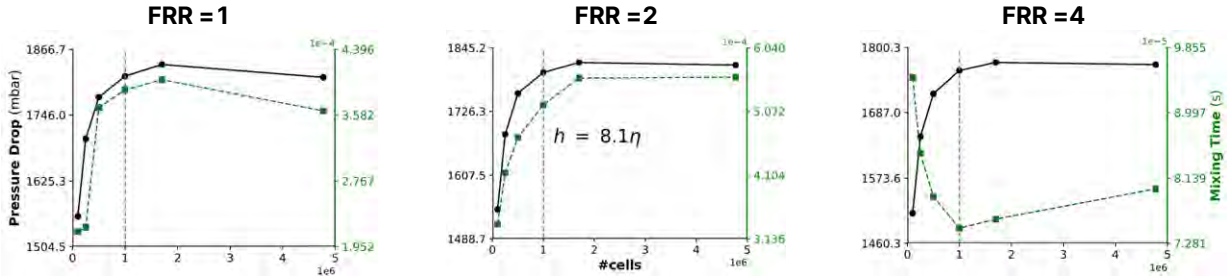



**Figure 4.** Results of the mesh convergence test. Plot of both objective functions (pressure drop in black and mixing time in green) as a function of the mesh number of cells. The vertical dotted line corresponds to the mesh parameter used in the optimization loop.

## Mesh Convergence

The choice of an appropriate mesh is a crucial factor for building faithful CFD models. A grid convergence test was therefore carried out for each operating condition, considering the geometry of the commercially available NanoAssemblr™ Ignite™ cartridge. In Figure 4, both objective functions (ΔP and $t_m$) are plotted against the number of cells of the respective mesh. Unlike for pressure drop, mixing time convergence was not fully reached. The relation between mixing time and grid size ($h$) was also not monotonic, likely due to the highly non-linear reaction terms of the Villermaux-Dushman system.

Establishing an appropriate mesh size criteria for all the geometries generated by the optimization algorithm is a non trivial task. It must be robust enough to provide accurate simulations throughout the whole solution space, without producing any type of numerical bias towards any kind of solutions. The criteria should also not be overly conservative to avoid the inefficient use of computational resources in prohibitively expensive meshes. In this case, the Kolmogorov turbulent length scale ($\eta$) was used as a reference to determine the appropriate mesh size. From the mesh convergence test, a mesh size of 5.78 µm was chosen as good compromise between model accuracy and computational cost. This corresponded to a grid size 8.1 times larger than the turbulent length scale. This factor was kept constant for the mesh generation throughout the optimization cycles. The turbulent length scale could be estimated prior to mesh generation using Equation 2 [11]:

$$\eta \approx D_h Re^{-3/4} \quad (2)$$

which considers the channel's hydraulic diameter ($D_h$), calculated with the geometry's height and width values, and the Reynolds number ($Re$), estimated with the TFR.

## RESULTS AND DISCUSSION

The optimization cycle for each value of FRR produces a set of geometry solutions and respective objective function values. These results are illustrated in Figure

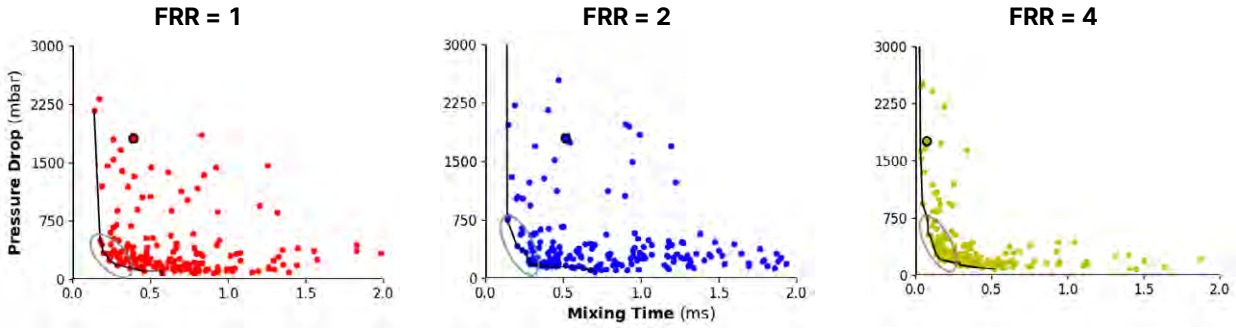



**Figure 5.** Scatter plot of each solution's objective functions, for each considered FRR. The Pareto front approximation is plotted as black line. The knee fraction of the Pareto front is circled in gray. The point circled in black represents the simulated performance of the reference geometry.

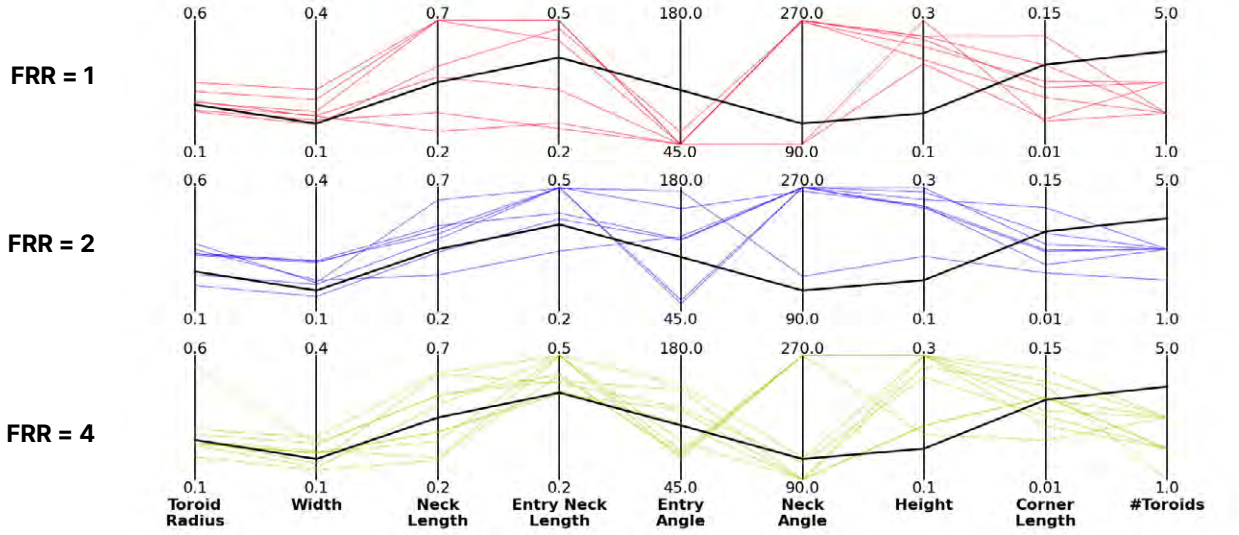



**Figure 6.** Geometric parameters of the nondominated solutions inside the knee fraction area, for each FRR. The reference geometry parameters are plotted in black.

5, in which the values of the solution's objective functions are compared to the NanoAssemblr™ Ignite™ geometry as a reference. Generally, this reference geometry performed suboptimally when compared to the respective obtained approximation of the Pareto front, in particular for low values of FRR. The main shortcoming being the elevated values of pressure drop.

In Figure 5, the knee fraction of each Pareto front is highlighted within a gray circle. The geometric parameters of the nondominated points of these subsets are presented and compared with the benchmark geometry in Figure 6 for each case study. From these results, it is clear that there is some solution redundancy, as considerably different mixers have similar performance values. This is not surprising, as many engineering problems present the same problem. For this reason, it is difficult to pinpoint how and which geometric parameters are affected by the change in FRR. The clearest exception is the "Entry Angle" parameter which is clearly minimized when FRR = 1 to reduce pressure drop. This is not the case with larger values of FRRs, where the lower flow rate stream is enveloped by the largest one at the inlet junction. This engulfment phenomenon contributes to faster mixing times and is likely enhanced with a wider angle of entry.

Moreover, when comparing the best obtained geometries with the benchmark, the biggest differentiating factor is the increased "Height" of the channels. This has two main effects: first, the cross-sectional area of the channel is increased, reducing pressure drop; second, since the inlets meet laterally, the increase in channel height results in a larger contact area between the flows, promoting mixing. Other significant differences include the reduced number of toroids and the maximization of the "Neck Angle" (90° and 270° produce symmetrical geometries).

Figure 7 illustrates the geometry of good solutions for each FRR value and the reference mixer. Values of the

respective objective function values are also presented. The methodology was able produce improved geometries with a ≈75% reduction of pressure drop in the mixer and a ≈50% reduction in mixing time (except for FRR=4).

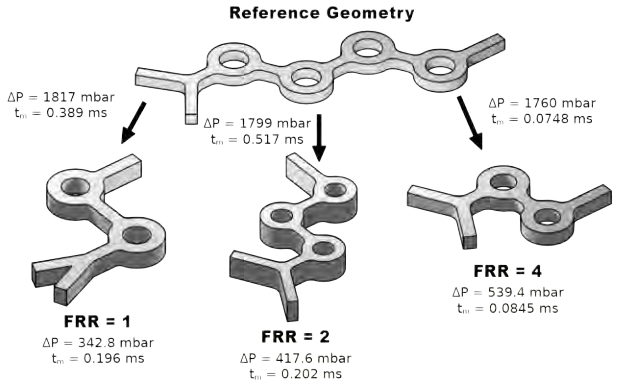



**Figure 7.** Illustration of the reference geometry and selected solutions for each FRR, and respective objective function values.

## CONCLUSION AND PERSPECTIVES

In this work, a shape optimization methodology, using Multi-Objective Bayezian Optimization, was presented and applied to the micromixer design problem. A set of improved geometries were presented and compared to a commercially available reference geometry for three different operating conditions. The most significant geometrical features to mixing performance were identified by analysing the geometrical parameters of the best-found solutions.

The results indicate some discrepancies in the ideal geometry for each operating condition. Thus, future work will consider the formulation of a robust Bayesian optimization framework to optimize the micromixer geometry design for a given range of operating conditions.

## ACKNOWLEDGEMENTS

The authors thank financial support from Project “CiNTech - Technological Hub for Innovation, Translation and Industrialization of Complex Injectable Drugs” (reference: 7131), in the scope of PRR - Recovery and Resilience Plan and by the Next Generation EU European Funds, following NOTICE No. 02/C05-i01/2022, Component 5 - Capitalization and Business Innovation - Mobilizing Agendas for Business Innovation.

## REFERENCES

1. Alavi SE, Alharthi S, Alavi SF, Alavi SZ, Zahra GE, Raza A, and Shahmabadi HE. Microfluidics for personalized drug delivery. *Drug Discovery Today* 29:103936 (2024).
2. Chen C, Chen C, Li Y, Gu R, and Yan X. Characterization of lipid-based nanomedicines at the single-particle level. *Fundamental Research* 3:488–504 (2023).
3. Pustulka KM, Wohl AR, Lee HS, Michel AR, Han J, Hoye TR, McCormick AV, Panyam J, and Macosko CW. Flash nanoprecipitation: Particle structure and stability. *Molecular Pharmaceutics* 10:4367–4377 (2013).
4. Webb C, Forbes N, Roces CB, Anderluzzi G, Lou G, Abraham S, Ingalls L, Marshall K, Leaver TJ, Watts JA, Aylott JW, Perrie Y. Using microfluidics for scalable manufacturing of nanomedicines from bench to gmp: A case study using protein-loaded liposomes. *International Journal of Pharmaceutics* 582:119266 (2020).
5. Panić S, Loebbecke S, Tuercke T, Antes J, Bošković D. Experimental approaches to a better understanding of mixing performance of microfluidic devices. *Chemical Engineering Journal* 101:409–419 (2004).
6. Commenge JM, Falk L. Villermaux–dushman protocol for experimental characterization of micromixers. *Chemical Engineering and Processing: Process Intensification* 50:979–990 (2011).
7. Wild A, Leaver T, Taylor RJ. Bifurcating mixers and methods of their use and manufacture. US10076730B2 (2016).
8. Daulton S, Balandat M, Bakshy E. Differentiable expected hypervolume improvement for parallel multi-objective bayesian optimization. (2020).
9. Bakshy E, Dworkin L, Karrer B, Kashin K, Letham B, Murthy A, Singh S. AE: A domain-agnostic platform for adaptive experimentation. (2018).
10. Sullivan C, Kaszynski A. Pyvista: 3d plotting and mesh analysis through a streamlined interface for the visualization toolkit (vtk). *Journal of Open Source Software* 4:1450 (2019).
11. Tiselj I, Stalio E, Angeli D, Oder J. Direct numerical simulations for liquid metal applications. In: Thermal Hydraulics Aspects of Liquid Metal Cooled Nuclear Reactors. Ed: Roelofs F. Woodhead Publishing (2019)

© 2025 by the authors. Licensed to PSEcommunity.org and PSE Press. This is an open access article under the creative commons CC-BY-SA licensing terms. Credit must be given to creator and adaptations must be shared under the same terms. See https://creativecommons.org/licenses/by-sa/4.0/

Systems & Control Transactions

**Research Article - Peer Reviewed Conference Proceeding**
ESCAPE 35 - European Symposium on Computer Aided Process Engineering
Ghent, Belgium. 6-9 July 2025
Jan F.M. Van Impe, Grégoire Léonard, Satyajeet S. Bhonsale,
Monika E. Polańska, Filip Logist (Eds.)

PSE PRESS

# Probabilistic Model Predictive Control for Mineral Flotation using Gaussian Processes

**Victor Dehon[a], Paulina Quintanilla[b], Antonio Del Rio Chanona[a]**

[a] Department of Chemical Engineering, Imperial College London, South Kensington Campus, London SW7 2AZ, United Kingdom
[b] Department of Chemical Engineering, Brunel University of London, Uxbridge, UB8 3PH, United Kingdom
Corresponding Authors: paulina.quintanilla@brunel.ac.uk; a.del-rio-chanona@imperial.ac.uk

## ABSTRACT

Recent advancements in machine learning and time series analysis have opened new avenues for improving predictive control in complex systems such as mineral flotation. Techniques leveraging multivariate predictive control in mineral flotation have seen significant progress in recent years. However, challenges in developing an accurate dynamic model that encapsulates both the pulp and froth phases have hindered further advancements. Now, with a readily available model containing equations that describe the physics of flotation froths, an opportunity for novel control strategies presents itself. In this study, a Gaussian Process (GP) Model Predictive Control (MPC) strategy is proposed to integrate uncertainty quantification directly into the control framework. By leveraging the probabilistic nature of GP models, this approach captures process variability and adapts dynamically to new data, ensuring continuous refinement of the GP model within the MPC strategy. Unlike previous implementations where model parameters remained static, this methodology updates the GP model in real time, allowing for improved decision-making in the face of process uncertainty. The GP model was trained, optimized with JAX, evaluated using relevant metrics, and implemented as a surrogate within the MPC framework. The results demonstrate the capability of the GP model to accurately represent process dynamics while minimising prediction errors. Moreover, incorporating uncertainty reduction through standard deviation minimisation in the objective function enhances both control performance and system robustness. This paper sets the basis for the potential of using GP-MPC to enhance both the accuracy and robustness of mineral froth flotation control.

**Keywords**: Mineral Flotation, Model Predictive Control, Gaussian Processes, Machine Learning

## INTRODUCTION

Machine learning has rapidly become one of the most exciting and revolutionary tools in modern industrial processes [1]. Leveraging data-driven models, such as Gaussian Processes (GPs), offers sophisticated methods to tackle the inherent complexity and nonlinearity of chemical processes. Mineral flotation is recognised as a critical separation technique in the mining industry, playing a vital role in extracting value from low-grade and complex ore bodies [2]. This process utilises differences in surface properties to selectively separate valuable minerals from the gangue. The process can be fine-tuned by adjusting various parameters such as air flow rate, chemical dosages, and pulp level to optimise recovery and grade (purity) of the desired minerals. However, the introduction of non-linear dynamics, complex interactions, and instability arising from multi-phase operation introduce challenges to achieving effective control [3]. GPs are particularly valuable in these contexts because they provide a flexible, probabilistic approach to modelling complex systems, allowing for both accurate predictions and uncertainty quantification. This makes them well-suited for optimising and controlling industrial processes where uncertainty and variability are significant challenges. Optimal control and optimisation in mineral froth flotation processes have made significant progress in recent times [5,6]. In mineral froth flotation, key control variables, such as air flow rate and pulp level, play a crucial role in maintaining process stability and optimising

performance. These parameters directly influence the dynamics of both the pulp and froth phases, affecting the efficiency of the separation process. The process is of particular interest to researchers due to marginal improvements in efficacy yielding substantial economic benefits as well as helping with global efforts of meeting increasing demand effectively.

### Problem Description

A common control strategy in flotation is Model Predictive Control (MPC), widely recognised as one of the most efficient for multi-variable processes. Its development for mineral flotation was previously limited by the lack of a dynamic model accurately representing the complex froth flotation interactions [3]. Earlier MPC implementations relied on empirical models capturing only the pulp phase, neglecting the froth phase, which significantly impacts flotation performance [5]. However, due to the contributions made by Quintanilla et al. [5,6], a physics-based model has been proposed, developed, and calibrated. This opens the possibility of applying state-of-the-art probabilistic modelling to a control strategy for this mineral flotation process. Building on the success of using this process model to implement an economic-model predictive controller [4], this paper aims to design a novel GP-MPC control strategy for the optimal operation of a mineral froth flotation process. By integrating GPs into the MPC framework, this strategy aims to achieve higher recovery rates and better product quality, ultimately contributing to more sustainable and economically viable mineral processing practices.

## BACKGROUND

### Gaussian Processes

Gaussian Processes (GPs) have become a powerful tool in various fields, including process control [16]. A key advantage is their ability to capture residual uncertainty from plant-model mismatches, useful in control systems where understanding the confidence of predictions is crucial. Unlike traditional mathematical optimisation, which assumes exact function evaluations, GPs model observations as stochastic, providing a probabilistic system representation. Although GPs in control for a mineral flotation process are not well documented, the use of GP as a surrogate model are present in the control community. GPs alongside MPC first started appearing in the early 2000's with Murray Smith et al [7]. The inclusion of information about the trust in the model depending on the region, enabled a more nuanced exploration of the control space. Overall, this departure from the traditional deterministic view creates a novel opportunity for optimal control by leveraging uncertainty to refine dynamic models, improving robustness. Given the process's inherent nonlinearities [6], GP-based probabilistic modeling holds strong potential for mineral flotation.

### Model Predictive Control for Mineral Flotation

Flotation is a key recovery process in the mineral industry. Studying this process is crucial due to its versatility and efficiency in processing large ore volumes, where even small improvements can yield significant economic benefits [3]. Attempts to introduce a robust and effective control strategy for the mineral flotation process have been made [8,9]. However, in previous work, modelling for control purposes was challenging. Most models have only focused on the pulp phase rather than the froth phase [5]. A comprehensive phenomenological model has been created by Quintanilla et al [5,6]. The model involves several innovative features, encompassing not only the representation of the pulp phase but also the inclusion of variables pertinent to the froth phase, such as froth stability, bursting rate, and air recovery. The equations in the model facilitate the estimation of critical variables associated with the key performance indicators: grade (product purity) and recovery. Such variables could then be seamlessly integrated into a dynamic optimisation objective function formulation for an MPC strategy. The availability of this dynamic model enables novel control strategies to be attempted. While success in stochastic data-driven MPC using GPs and froth flotation MPC is documented, applying GPs and MPC to mineral flotation will be, to the best of the authors' knowledge, the first of its kind.

## METHODOLOGY

### Gaussian Process Training and Implementation

As previously outlined, GP's offer a flexible and nonparametric approach to modelling processes. In the context of MPC, this GP will serve as a surrogate model that predicts the future states of the process given current and past inputs. The structure of the GP model is designed to handle the multi-input, multi-output nature of the froth flotation process with multiple training datasets provided by the synthetic flotation model. This training data consisted of 9 state variables and 2 control variables. Before training the GP model, all input data were standardised to have zero mean and unit variance. This preprocessing step prevents any one input feature from dominating the prediction due to scale differences. A negative-log-likelihood (NLL) objective function was deployed in the training process to optimise the hyperparameters of the GP model. The negative log likelihood is given by:

$$NLL(\boldsymbol{\theta}) = -\log P\left(\boldsymbol{Y} \mid \boldsymbol{\theta}\right) \quad (1)$$

NLL is a standard objective function employed in hyper-parameter optimisation for GP's due to its versatility and being directly related to the model's predictive performance. In this GP formulation, a radial basis function (RBF) kernel was selected with respective hyper-parameters acquired through the maximisation of the marginal likelihood for each parameter (or equivalently, the minimisation of the negative log likelihood). With an 11-dimensional input space, a multi-start strategy improved exploration. These samples were passed to a stochastic gradient-based optimisation algorithm, specifically the Adam algorithm, to generate optimal hyperparameters, as seen in Algorithm 1. The selection of this solver was due to its computational efficiency as well as its capabilities in handling noisy and large volumes of data. An area of concern for this iterative process was the length of time taken to arrive at a suitable solution due to the computational complexity, nonconvexity, and taxing matrix operations conducted in the GP formulation procedure. To speed up this hyper-parameter optimisation procedure, the JAX python library was deployed. Notable advantages such as vectorised mapping, just-in-time compilation through XLA [10] and automatic differentiation allows for efficient computation of gradients in regard to the GP log-likelihood objective function. Due to the repeated nature of complicated matrix operations such as the inversion of the optimal covariance matrix, JAX's GPU acceleration capabilities can dramatically speed up the central matrix calculations in the GP computations.

**Algorithm 1.** JAX GP – Creation & Inference

1. **Input**: Xdat, Ydat, Kernel, multi_hyper, var_out
2. **Initialise**: Normalise Xdat and Ydat
3. Set bounds for optmisation procedure
4. Generate initial points using Sobol sequences
5. **For** i in initial points & GP output:
    a. **Define:** $-\log p(X \mid \theta)$ ***where*** $\boldsymbol{\theta} = \{\boldsymbol{\iota_{opt}}, \boldsymbol{\sigma^2_{f,opt}}, \boldsymbol{\sigma^2_{n,opt}}\}$
    b. Compute $\nabla_\theta NLL(\theta \mid X)$
    c. Update parameters using SGD: $\theta_{t+1} = \theta_t - \eta \nabla_\theta Loss(\theta_t)$
    d. **If** Max iterations or convergence criteria met **Then:**
        i. Select optimal solution $\theta_i^*$ with smallest $-\log p(X_i^* \mid \theta^*_i)$ value **end if**
    e. **End for**
6. Computer optimal coveriance matrix: $cov_{ij} = \sigma_f^2(-\frac{1}{2} dist_{ij})$
7. Computer inverse of covariance matrix: $K^{-1}$
8. Computer covariance between the test and training points: $k$
9. Computer predicted mean: $\mu_* = k^T K^{-1} Y$
10. Compute predicted variance: $\sigma_*^2 = max(0, \sigma_f^2 - k^T K^{-1} Y)$
11. **Output:** $\theta_{opt} = \{\boldsymbol{\iota_{opt}}, \boldsymbol{\sigma^2_{f,opt}}, \boldsymbol{\sigma^2_{n,opt}}\}$, $\mu_*$, : $\sigma_*^2$

## Gaussian Process Model Predictive Control

The objective function contains 3 objectives. The first is related to the concentration of valuable materials lost in the tailings (Equation 2) due to the primary goal of flotation being to optimise the separation of valuable minerals. Secondly, the control effort (Equation 3) explicitly incorporates the cost of actuator movements, which is important due to controls such as pulp height ($h_p$) being controlled via a valve. Finally, the standard deviation penalty is introduced to discourage the MPC from making decisions on uncertain estimates and rather to guide it towards more reliable and robust control strategies (Equation 4).

$$J_{loss} = \sum_{k=0}^{N-1} Loss_k \tag{2}$$

$$J_{control} = \sum_{k=1}^{N-1} (u_k - u_{k-1})^2 \tag{3}$$

$$J_{std} = \sum_{k=0}^{N-1} \sigma^2_{GP_k} \tag{4}$$

The three equations are then put altogether with weighting constant values of 50,1 and 10 respectively to form a multi-objective function to be minimised by an SLSQP method.

The GP-MPC approach leverages the predictive capabilities of GP models to enhance the performance of MPC by providing more accurate and probabilistic forecasts of the system's behaviour. The combination of both should enable better adaptation to dynamic conditions and improve overall system robustness. The use of a surrogate model involves the creation of simplified models that approximate the behaviour of complex systems. This approach reduces the computational burden typically associated with solving the optimisation problem at each MPC iteration, as it allows for faster evaluations of the system's future states without sacrificing accuracy. This efficiency is crucial in this mineral froth flotation application where computational resources and time are limited. In the context of this mineral froth flotation process MPC framework, the trained GP model will be employed at each time step to predict the future states of the system for the entire prediction horizon, allowing the MPC to evaluate the impact of different control actions over this horizon. These GP-generated predictions, which include

both mean estimates and associated uncertainties, are fed into the MPC's objective function. The MPC then optimises the control inputs based on these predictions to achieve desired future outcomes while considering uncertainties. The GP can be updated online as new data becomes available. As the system evolves, the updated models are then used to predict the next set of future states, ensuring that the control strategy remains relevant and effective as the system dynamics change. The overall process of training the GP, simulating the surrogate within the MPC framework, calculating the optimal control and finally updating with the relevant process model states as depicted in Figure 1.

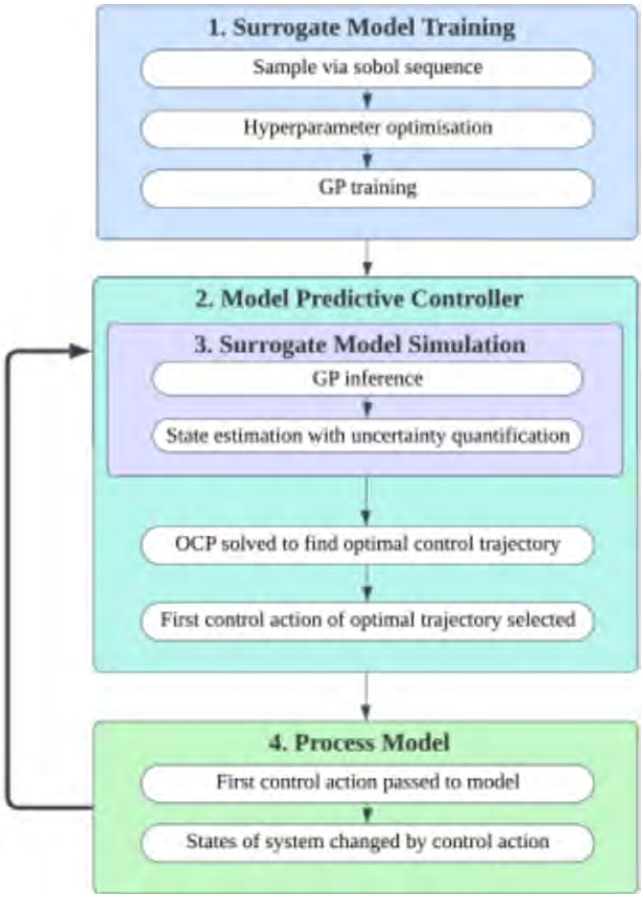



**Figure 1** - GP-MPC Flow Diagram

## RESULTS AND DISCUSSIONS

### GP Training and Validation

Evaluating the effectiveness of the GP surrogate implementation was done with a training and validation dataset. It is important to note that this is a state-space GP model, where the states are: mineral ($M_{min}$), gangue masses ($M_{gangue}$), gas holdup classes ($\varepsilon_1 - \varepsilon_5$), pulp level ($h_p$) and tailings flow rate ($Q_{tails}$). Both datasets were generated using the physics-based process model from [5,6]. Various statistical measures were used to evaluate the performance of the GP surrogate model, including negative log predictive density (NLPD), mean absolute percentage (MAPE), and root mean squared percentage error (RMSPE). Before the calculations of these statistical parameters, the states were normalised to avoid problems due to differences in the order of magnitude of the different states. Figure 2 displays the GP predictions closely following the underlying system data. It was observed that the testing results show slightly higher error rates than the training data, which is expected. The $\epsilon$'s are slightly less accurate and confident, with the GP predictions deviating slightly from the real data and a wider confidence region. Confidence regions remain consistent from training to testing, with estimations related to Qtails, $h_p$, $M_{gangue}$ and $M_{min}$ showing the highest confidence in estimations due to a tighter standard deviation. Overall, from graphical interpretation, the model seems to fit the training data well, with predictions closely following the experimental data points. Tables 1 and 2 reflect a similar conclusion drawn from the graphs, with a low RMSPE and MAPE.

**Table 1:** GP Without JAX Testing Metric Results

| Experiment No. | RMSPE | NLPD | MAPE |
|---|---|---|---|
| Experiment 1 | 0.15% | -5.47 | 0.09% |
| Experiment 2 | 0.24% | -5.29 | 0.14% |
| Experiment 3 | 0.36% | -4.91 | 0.20% |

A low NLPD is also seen, portraying good probabilistic predictions and uncertainty quantification. The metrics show consistent performance across all three testing experiments, with little variation, suggesting robustness in the GP model. Results from the JAX-enhanced GP formation are seen in Figure 2 which also illustrates similar prediction patterns and confidence intervals across the training and testing dataset. Quantitatively, the performance metrics for the JAX-GP in Table 2 demonstrates comparability with the non-JAX GP. Some differences can be observed from the JAX-GP and non-JAX GP, such as estimation of the states $M_{min}$ and $Q_{tails}$ in the testing data, which are slightly less accurate in the JAX-GP, with a smoother mean being estimated. The estimations of states $M_{min}$, $h_p$ and $\epsilon$'s are confident with an observable tight standard deviation. The most notable improvement was observed in compilation time, with a reduction of 33% when run on an Apple M2 chip running on macOS 14.4.1. This speedup in compilation, coupled with the preservation of model accuracy, underscores the potential of JAX to enhance the efficiency of GP implementations.

**Table 2:** GP with JAX testing metric results

| Experiment No. | RMSPE | NLPD | MAPE |
|---|---|---|---|
| Experiment 4 | 0.40% | -4.78 | 0.26% |
| Experiment 5 | 0.40% | -4.79 | 0.28% |
| Experiment 6 | 0.63% | -4.17 | 0.44% |

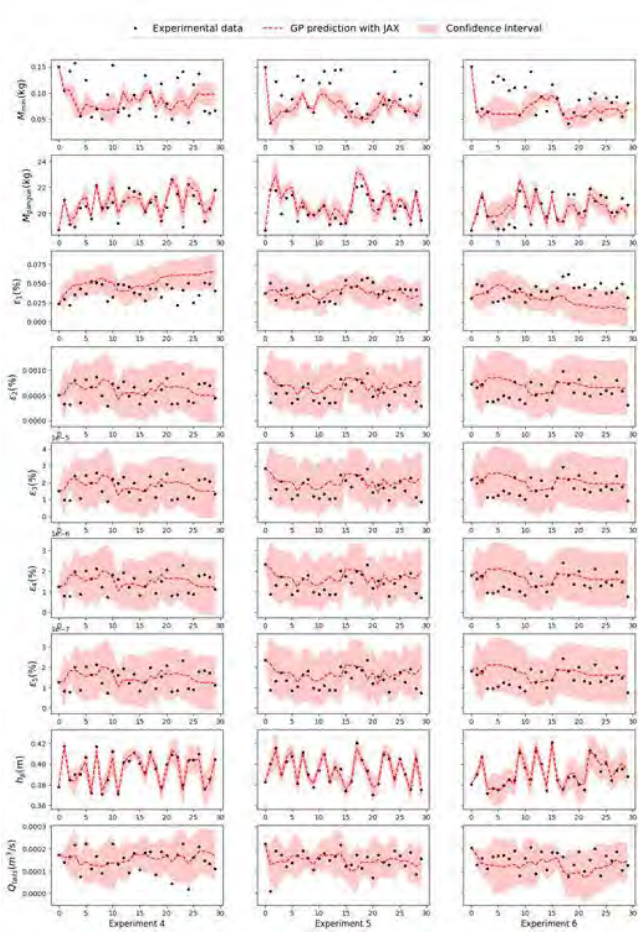



**Figure 2** – GP with JAX results illustrating the evolution of system states and predictions. The black dots represent the experimental data from the process, the red lines indicate the GP predictions, and the red shadows depict two standard deviations from the GP model. These states are assumed to be observable within the MPC framework.

## GP-MPC Control Performance

The effectiveness of the overall control strategy was assessed using MAE, RMSE, and ISE metrics, comparing the desired setpoint with the actual control actions. Table 3 depicts these metrics, showing that the control mechanism appears to be effective in maintaining the desired levels for both $h_p$ and $Q_{air}$. Additionally, the evaluation considered the average concentration of valuable material lost in the tails. The dataset fed was unseen by the GP and MPC. Figure 3 demonstrates the GP estimates for the $h_p$ (pulp height) state evolution with associated confidence intervals as well as the resulting optimal control action for $h_p$ control. The GP predictions follow closely the process, with tight uncertainty region suggesting a well-calibrated surrogate model for the process. Moreover, Figure 4 visualises the air flow rate ($Q_{air}$) control strategy derived by the MPC strategy with an overall trend of increasing air flow over time, which typically promotes increased bubble production and mineral recovery in froth flotation.

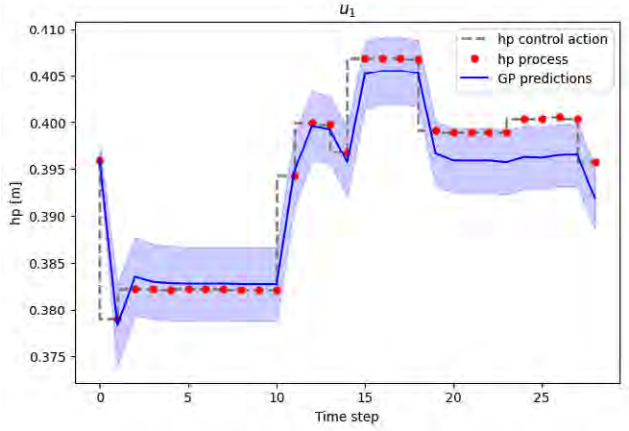



**Figure 3 –** Pulp height ($h_p$) control output from GP-MPC

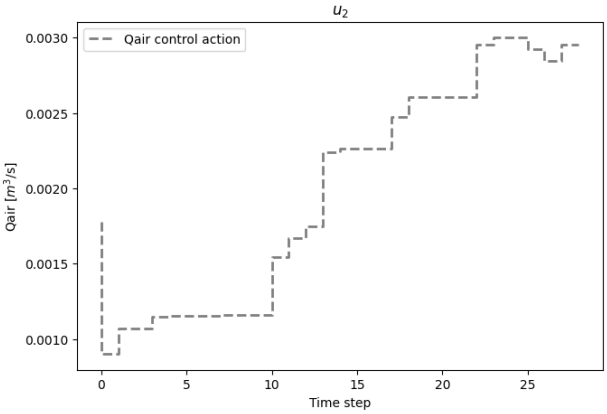



**Figure 4** - $Q_{air}$ control output from GP-MPC

**Table 3:** Non-JAX GP with MPC metric values

| Metric | $h_p$ [m] | $Q_{air}$ [$m^3/s$] |
|---|---|---|
| MAE | 0.012431 | 0.000758 |
| RMSE | 0.015232 | 0.000957 |
| ISE | 0.006728 | 0.000027 |
| Mean Loss in Tails ($kg/m^3$) | 0.630612 | |

Overall, the control strategy balances stability and responsiveness, initially maintaining constant action (time steps 2-10) and introducing significant adjustments around steps 12 and 20 to manage the trade-off between metallurgical recovery and grade. Lower pulp heights, which yield higher grades but reduce recovery, are dynamically adjusted alongside air flowrate $Q_{air}$ to optimise flotation performance. This aligns with findings on peak air recovery and froth stability from prior studies [5], highlighting the importance of $Q_{air}$ in achieving optimal recovery. Furthermore, Figure 4 demonstrates a stepped approach rather than continuous increase, suggesting the controller is allowing the flotation system to stabilise at each air flow level before making further adjustments. The strategy demonstrated efficiency, with low mean material loss in tailings (0.630612 kg/m³). Control metrics, including low MAE, RMSE, and ISE values, confirm precise and robust system performance, validating the effectiveness of the GP-MPC approach.

## CONCLUSION

MPC strategies have proven effective in mineral froth flotation, improving recovery and grade. However, many models focus on the pulp phase and struggle with the froth phase. With a more accurate process model for both phases now available, an opportunity arises for GPs to be applied, leveraging confident decisions. MPC with GPs for mineral froth flotation has not been widely explored. The findings from the implemented models demonstrated that the surrogate model generates accurate and certain inferences on unseen datasets with low amounts of associated error. Moreover, the possibility of accelerating the surrogate model creation was outlined with the implementation of JAX. The MPC strategy utilised the GP surrogate to generate an optimal control trajectory. Most notably, the mean loss in tails was measured at a low 0.630612 kg/m³. The performance is further evidenced by examining the control accuracy, with both $h_p$ and $Q_{air}$ parameters exhibiting low MAE and RMSE values, indicating precise control overall. These findings reinforce the benefits of leveraging the uncertainty quantification and probabilistic attributes of the GP model alongside an MPC control strategy. Being the first of its kind to apply GP-MPC to a mineral froth flotation process, this work drives forward the objective of multivariate predictive control of flotation processes, providing an alternative probabilistic approach to enhancing mineral recovery and grade. In addition, the improvements noted in this study related to reduced compilation outline the possibility for an accurate and fast control strategy.

## REFERENCES


1. McCoy JT, Auret L. Machine learning applications in minerals processing: A review. Minerals Engineering. 2019;132:95–109.
2. Wang B, Peng Y. The effect of saline water on mineral flotation--A critical review. Minerals Engineering. 2014;66:13–24.
3. Quintanilla P, Neethling SJ, Brito-Parada PR. Modelling for froth flotation control: A review. Minerals Engineering. 2021;162:106718.
4. Quintanilla P, Navia D, Neethling S, Brito-Parada P. Experimental implementation of an economic model predictive control for froth flotation. In: Computer Aided Chemical Engineering. Elsevier; 2024. p. 1759–64.
5. Quintanilla P, Neethling SJ, Navia D, Brito-Parada PR. A dynamic flotation model for predictive control incorporating froth physics. Part I: Model development. Miner Eng 173:107192 (2021).
6. Quintanilla P, Neethling SJ, Mesa D, Navia D, Brito-Parada PR. A dynamic flotation model for predictive control incorporating froth physics. Part II: Model calibration and validation. Minerals Engineering. 2021;173:107190.
7. Girard A, Rasmussen CE, Quinonero Candela J, Murray-Smith R. Gaussian process priors with uncertain inputs & application to multiple-step ahead time series forecasting. In: Advances in Neural Information Processing Systems (NIPS) 15. MIT Press (2003).
8. Wan K, Xu D, Cai Y. Data-driven-based model predictive control of reagents addition for tungsten flotation process. In: Proceedings of the 2021 China Automation Congress (CAC), IEEE, pp. 1629-1634 (2021).
9. Cubillos FA, Lima EL. Identification and optimizing control of a rougher flotation circuit using an adaptable hybrid-neural model. Miner Eng (1997).
10. Google. JAX quickstart guide. Accessed: 2024-08-24. Available at: https://jax.readthedocs.io/en/latest/quickstart.html (2023).



© 2025 by the authors. Licensed to PSEcommunity.org and PSE Press. This is an open access article under the creative commons CC-BY-SA licensing terms. Credit must be given to creator and adaptations must be shared under the same terms. See https://creativecommons.org/licenses/by-sa/4.0/




Systems & Control Transactions

**Research Article - Peer Reviewed Conference Proceeding**
ESCAPE 35 - European Symposium on Computer Aided Process Engineering
Ghent, Belgium. 6-9 July 2025
Jan F.M. Van Impe, Grégoire Léonard, Satyajeet S. Bhonsale,
Monika E. Polańska, Filip Logist (Eds.)

PSE PRESS

# A Bayesian optimization approach for data-driven Petlyuk distillation column

**Alexander Panales-Pérez[a], Antonio Flores-Tlacuahuac[b]*, Luis Fabián Fuentes-Cortés[c], Miguel Angel Gutierrez-Limon[d] and Mauricio Sales-Cruz[e]**

[a] Tecnológico Nacional de México, Instituto Tecnológico de Celaya, Departamento de Ingeniería Química, Celaya, Guanajuato, Mexico, 38010.
[b] Escuela de Ingeniería y Ciencias, Tecnológico de Monterrey, Campus Monterrey Ave. Eugenio Garza Sada 2501, Monterrey, N.L, 64849, México.
[c] Department of Energy Systems and Environment, IMT Atlantique, GEPEA, rue Alfred Kastler, Nantes, 44000, France.
[e] Departamento de Energía, Universidad Autónoma Metropolitana-Azcapotzalco, Av. San Pablo 180. C.P. 02200, Ciudad de México, México.
[d] Departamento de Procesos y Tecnología, Universidad Autónoma Metropolitana-Cuajimalpa, Av. Vasco de Quiroga 4871. C.P. 05348, Ciudad de México, México.
* Corresponding Author: antonio.flores.t@tec.mx

## ABSTRACT

Recently, the focus on increasing process efficiency to reduce energy consumption has driven the adoption of alternative systems, such as Petlyuk distillation columns. It has been proven that, when compared to conventional distillation columns, these systems offer significant energy and cost savings. From an economic standpoint, achieving high-purity products alone does not ensure the feasibility of a process. Instead, balancing the trade-off between product purity and cost necessitates multi-objective optimization. While conventional optimization methods are effective, novel strategies like Bayesian optimization offer distinct advantages for handling complex systems. Bayesian optimization requires no explicit mathematical model and can efficiently optimize even when starting from a single initial point. However, as a black-box method, it demands a detailed analysis of hyperparameters, such as the acquisition function and the number of initial points, to ensure optimal performance. This work presents a case study of a Petlyuk distillation column, focusing on the influence of key hyperparameters in Bayesian optimization. Additionally, the role of uncertainty in the optimization process is explored, as it is a critical factor in real-world applications. By simulating uncertainty, this study provides insights into its impact on the optimization process.

**Keywords**: Process Design, Distillation, Artificial Intelligence, Aspen Plus.

## INTRODUCTION

In chemical engineering, complex systems such as Petlyuk distillation columns have been analyzed to achieve considerable energy savings compared to traditional distillation columns, due to its configuration, a Petlyuk column consists of a prefractionator and a main column, where vapor and liquid streams are thermally coupled, thus, unlike conventional sidestream columns, it uses a single reboiler and a single condenser. Therefore, various methodologies have been employed for the operation and design of Petlyuk columns, including nonlinear programming (NLP) [5] and mixed-integer nonlinear programming (MINLP) [10]. Traditional solvers for NLP and MINLP problems frequently face convergence challenges. In practice, these solvers often fail to identify the global optimum due to the non-convex nature of the problem. Alternative solution approaches, such as genetic algorithms, have been explored. However, their performance improvements over the past two decades have been limited [9], highlight the need to explore alternative methods, such as data-driven optimization. In this manner, Bayesian optimization (BO), a black-box method, does not require an explicit mathematical model

of the problem suited to this problem. The core of this method is the construction of a surrogate probabilistic model, most commonly a Gaussian process (GP), which efficiently guides the sequential acquisition of new data through an acquisition function. Whose role is to balance the trade-off between exploration and exploitation. In practical terms, exploration targets points where the surrogate model variance is high, while exploitation focuses on points with a high surrogate model mean. This balance allows BO to intelligently select evaluation points for the objective function, thereby guiding the search toward the optimal value effectively. Moreover, the optimal solution is reached either after a specified number of iterations or when a stopping condition based on the objective function is achieved. This method is especially suited for handling expensive objective functions, where “expensive” refers to high computational or experimental costs. Additionally, the objective function can be expressed as a multi-objective function [4]. The problem to be addressed can be formally stated as follows: "Given an initial set of potentially noisy process measurements of system outputs, determine the optimal operational policy that maximizes a defined operational target. In this context, the process outputs may include stream compositions, such as mole fractions, or other composition metrics. Achieving the specified operational target requires selecting a set of input variables to enforce optimal operation. As evident from this definition, the problem falls within the domain of dynamic optimization. However, it is important to note that dynamic process calculations are not involved. Instead, it is assumed that the application of input variables drives the system to a new steady state, where calculations are repeated iteratively until the target conditions are satisfied. BO emerges as a robust alternative to the reinforcement learning methodologies commonly utilized in modern artificial intelligence systems, offering a structured and efficient approach to address such optimization challenges. This work proposes a data-driven optimization strategy tailored for complex process systems, such as the Petlyuk column, where traditional optimization methods are computationally expensive. The approach utilizes a multi-objective function that aims to minimize cost while maximizing the desirable component purities in each output stream of the Petlyuk column. Furthermore, the impact of random noise on the BO process is investigated to assess the feasibility of the proposed strategy in real-world applications

## METHODOLOGY

The use of BO that can be used to evaluate expensive objective functions, as mentioned before the term “expensive” can be used for both economic or computational cost to evaluate a process or an experiment. In the absence of a Petlyuk column to realize the experiments, the commercial simulator Aspen plus was used to mimic the behavior to obtain the results of the expensive objective function. Moreover, in the figure 1 explains the Bayesian optimization process, where the core are two steps [2]: First, the estimation of the black-box function from data through a probabilistic surrogate model, the most common a GP and secondly, maximizing an acquisition function that trade off the parameters of exploration and exploitation. Therefore, the criteria of the convergence test can be in different ways as a stop criterion for a condition in the objective function or a defined number of iterations, the last one was selected for a more balanced comparative of the hyperparameters; by stop the optimization process after 50 iterations in all cases.

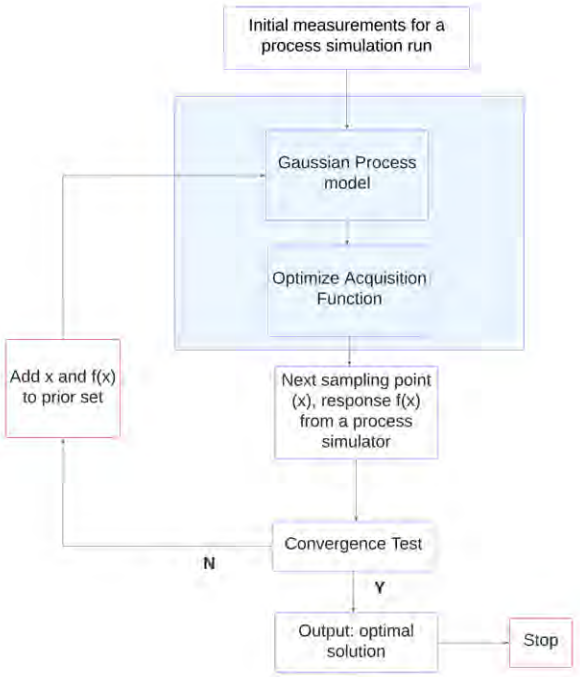



**Figure 1.** Flow chart for the BO process. Key steps, such as GP and the acquisition function, are denoted in blue. The optimization loop begins with the IP obtained from the simulation and adapted to the GP, and then the next sample is determined by the Acquisition Function. Furthermore, the loop terminates when the user objective function criteria are met for the convergence test.

To analyses the Petlyuk column, the involve mixture consists of feed flow (F=800 kmol/h) of benzene(A), toluene(B), and xylene(C) (figure 2) also known as a BTX mixture [3]. Therefore, the selected manipulated variables are the Distillate flow rate of the main column(D), reflux ratio (R), liquid flow rate (LR) and vapor flow rate(VR) to the pre-fractionator column, the interval of the manipulated variables in the same order are: $D \in [5–100]$ kmol/h, $R \in [2–35]$, $LR \in [20–150]$ kmol/h and $VR \in [20–150]$ kmol/h. The BO process is computing using the

Scikit-Optimize library [6], in Python and establish a connection with the ASPEN Plus simulator through Windows Component Object Model (COM) access. Additionally, all manipulable variables are normalized in the GP and denormalized for use in the Aspen Plus simulator.

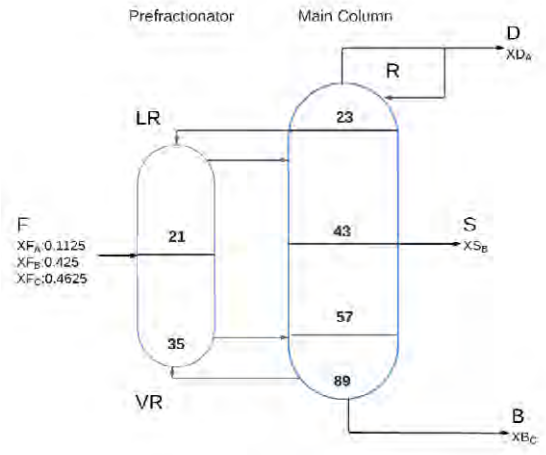



**Figure 2.** Flowsheet of a Petlyuk column system, consisting of a main column and a prefractionator, the locations of streams and stages are illustrated.

The multi-objective function, defined in Equation 1, is formulated as a minimization function, where we aim to maximize the desired composition of the component of interest in each stream: the distillate ($XD_A$), the lateral side ($XS_B$), and the bottoms ($XB_C$). In this case study, the function also seeks to improve economic performance by maximizing the desirable components in each stream while minimizing the total operational cost (TOC), which is calculated based on the costs of cooling water and steam incorporated into the ASPEN simulation. Moreover, the composition variables obtained from the Aspen Plus simulation are already normalized to values between 0 and 1. However, in the case of TOC, two preliminary BO runs are conducted, using default values Matern for the kernel and LCB for the acquisition function. These runs define the upper (UB) and lower (LB) bounds of TOC values by minimizing and maximizing TOC as an objective function. The resulting bounds are then used to perform a min-max normalization, as defined in Equation 2 [8]. This normalization ensures that the multi-objective function maintains an equitable trade-off among all decision variables.

$$\Omega_i = \left(XD_{B,i} + XD_{C,i} - XD_{A,i}\right) + \left(XS_{A,i} - XS_{C,i} - XS_{B,i}\right) + \left(XB_{A,i} + XB_{B,i} - XB_{C,i}\right) + \phi_{TOC,i} \quad (1)$$

$$\phi_{cost,i} = \frac{cost_i - LB_{cost}}{UB_{cost} - LB_{cost}} \quad (2)$$

Some aspects are analyzed: First, the number of initial points is varied. Instead of providing random information, these initial points are designed to generate insights into the possible optimal zone using an initial BO run with default values. This initial run starts with a single point at the center of the search space for all manipulated variables. The optimal result obtained from this run is then used to generate initial points (IPs) by varying the optimal manipulated variables within a random range of ±5%, creating new initial points. This approach aims to provide high-quality information to the Gaussian Process (GP) rather than relying on arbitrary random points in a non-optimal region. Second, this process is executed using different acquisition functions, including Expected Improvement (EI), Lower Confidence Bound (LCB), and Probability of Improvement (PI). Additionally, uncertainty is analyzed by incorporating noise into the results. This is done by introducing cumulative noise (ε) into the objective function value (Ω), adding random variations at a level of ±5% of the value of Ω, as shown in Equation 3.

$$\Gamma_i = \Omega_i + \varepsilon \quad (3)$$

## RESULTS

As is denoted in tables (1-6), each of the different acquisition functions with the variation of the initial points was computed, with the iteration at which the optimal value is reached also counting the initial points added. First, in the case of EI (tables 1-2), there is no notable difference in the objective value of the optimal solution achieved with an increase in the number of initial points. Even with 30 initial points, the objective value does not show a significant increase compared to using 20 initial points; instead, it decreases to the level observed with 5 initial points. Moreover, this minimal change in the objective function indicates that when the purity product fractions are analyzed across all optimal solutions, there is no sharp difference. The purities achieved are 0.99, 0.96, and 0.96 for $XD_A$, $XS_B$, and $XB_C$, respectively, for all cases. On the other hand, only the flow of VR is the manipulable variable that shows a notable change from 150 kmol/h (1 initial point) to 110.02 kmol/h (5 initial points). Therefore, regarding the economic aspect, the solutions related to the R value fall within the same interval, which is directly related to operational costs. In this manner, the trend of no notable difference continues.

Secondly, for the LCB acquisition function (tables 3-4), there is a slight increase in the optimal value of the objective function. This results in a slight improvement in the achieved purity of the products, allowing the purity of the intermediate component $X_{SB}$ to reach up to 0.96 and the bottom component $X_{BC}$ to reach 0.98. However, in the trade-off with TOC, there is an increase of more than 0.47x $10^6$ USD/year, and this occurs only when using more than 10 initial points. Only the case with 30 initial points can achieve a trade-off with similar economic performance to EI, while also achieving better purity values for the components ($XS_B$ = 0.964; $XB_C$ = 0.986).

**Table 1:** Manipulable variables Petlyuk column EI.

| IP | Manipulable variables | | | |
|---|---|---|---|---|
| | D | R | VR | LR |
| 1 | 79.55 | 16.75 | 150.00 | 150.00 |
| 5 | 79.0 | 16.26 | 110.02 | 148.91 |
| 10 | 78.59 | 16.53 | 115.76 | 150.00 |
| 20 | 78.59 | 16.30 | 121.28 | 150.00 |
| 30 | 78.66 | 16.30 | 132.32 | 150.00 |

**Table 2:** Results BO EI.

| IP | Description | | | TOC | Ω | Iter. |
|---|---|---|---|---|---|---|
| | $XD_A$ | $XS_B$ | $XB_C$ | x $10^6$ | | |
| 1 | 0.999 | 0.961 | 0.967 | 5.11 | -2.480 | 48 |
| 5 | 0.999 | 0.963 | 0.962 | 4.95 | -2.487 | 39 |
| 10 | 0.999 | 0.964 | 0.965 | 5.00 | -2.491 | 51 |
| 20 | 0.999 | 0.962 | 0.965 | 4.93 | -2.494 | 48 |
| 30 | 0.999 | 0.960 | 0.965 | 4.93 | -2.488 | 44 |

**Table 3:** Manipulable variables Petlyuk column LCB.

| IP | Manipulable variables | | | |
|---|---|---|---|---|
| | D | R | VR | LR |
| 1 | 77.18 | 16.74 | 126.07 | 150.00 |
| 5 | 79.37 | 16.47 | 131.18 | 150.00 |
| 10 | 80.95 | 17.64 | 136.92 | 150.00 |
| 20 | 80.95 | 17.64 | 123.92 | 129.88 |
| 30 | 78.64 | 16.82 | 132.23 | 150.00 |

**Table 4:** Results BO LCB.

| IP | Description | | | TOC | Ω | Iter. |
|---|---|---|---|---|---|---|
| | $XD_A$ | $XS_B$ | $XB_C$ | x $10^6$ | | |
| 1 | 0.999 | 0.957 | 0.962 | 4.96 | -2.475 | 48 |
| 5 | 0.999 | 0.965 | 0.970 | 5.03 | -2.500 | 45 |
| 10 | 0.999 | 0.968 | 0.987 | 5.47 | -2.509 | 8 |
| 20 | 0.999 | 0.968 | 0.987 | 5.47 | -2.509 | 8 |
| 30 | 0.999 | 0.964 | 0.986 | 5.06 | -2.520 | 78 |

**Table 5:** Manipulable variables Petlyuk column PI.

| IP | Manipulable variables | | | |
|---|---|---|---|---|
| | D | R | VR | LR |
| 1 | 78.82 | 17.38 | 126.00 | 150.00 |
| 5 | 79.65 | 16.52 | 131.18 | 150.00 |
| 10 | 78.04 | 17.59 | 136.92 | 150.00 |
| 20 | 77.45 | 17.03 | 123.92 | 129.88 |
| 30 | 78.78 | 16.27 | 132.33 | 150.00 |

**Table 6:** Results BO PI.

| IP | Description | | | TOC | Ω | Iter. |
|---|---|---|---|---|---|---|
| | $XD_A$ | $XS_B$ | $XB_C$ | x $10^6$ | | |
| 1 | 0.999 | 0.964 | 0.968 | 5.26 | -2.479 | 42 |
| 5 | 0.999 | 0.964 | 0.968 | 5.06 | -2.493 | 36 |
| 10 | 0.999 | 0.965 | 0.980 | 5.26 | -2.505 | 52 |
| 20 | 0.999 | 0.962 | 0.962 | 5.06 | -2.476 | 42 |
| 30 | 0.999 | 0.961 | 0.965 | 4.93 | -2.489 | 45 |

Finally, in the case of PI (tables 5-6), the performance shows the trend of EI, with achieved purities of 0.99 ($XD_A$), 0.96 ($XS_B$), and 0.96 ($XB_C$). The results are very similar, with the difference in the objective function between the cases of 1 and 10 initial points being just 0.001. In this manner, the economic aspect also shows only slight differences. Additionally, when comparing the different acquisition functions, the differences are minimal.

Similarly to the previous results, when noise is added to the objective function, as shown in Tables 7–12, the trend of achieving a high-purity distillate product ($XD_A$ = 0.999) continues, except for an outlier in the LCB acquisition function with 30 IPs. Additionally, both $XS_B$ and $XB_C$ maintain purities of ≥0.95, showing no significant difference compared to the noise-free case.

On the economic side, TOC results remain in the range of 4.63 to 6.85 × $10^6$ USD, with an exception for an outlier in the EI acquisition function with 1 IP. Thus, no improvements are observed in relation to any acquisition function, and increasing the number of IPs does not lead to better performance in the objective functions. It is important to highlight, as in the previous case, that adding noise does not negatively impact the BO process, and good results can still be achieved even with just one IP. Moreover, when comparing the different acquisition functions with and without uncertainty, the differences between the results are minimal. Therefore, the number of IPs providing quality information is not necessarily associated with better objective function performance, regardless of the acquisition function. Additionally, the multi-objective function ensures that the trade-off between purities and TOC remains balanced. However, as mentioned before, although TOC stays within a narrow range, its scale ($10^6$ USD) means that even a slight change, especially in the reflux ratio (R), can significantly impact TOC, either increasing or decreasing it by a considerable amount.

**Table 7:** Manipulable variables with noise Petlyuk column EI.

| IP | Manipulable variables | | | |
|---|---|---|---|---|
| | D | R | VR | LR |
| 1 | 80.74 | 22.32 | 150.00 | 150.00 |
| 5 | 77.65 | 19.63 | 150.00 | 150.00 |
| 10 | 75.79 | 19.83 | 110.25 | 115.46 |
| 20 | 79.40 | 18.28 | 150.00 | 150.00 |
| 30 | 79.62 | 18.63 | 150.00 | 150.00 |

**Table 8:** Results BO EI with noise.

| IP | Description | | | TOC x $10^6$ | Γ | iteration |
|---|---|---|---|---|---|---|
| | $XD_A$ | $XS_B$ | $XB_C$ | | | |
| 1 | 0.999 | 0.972 | 0.975 | 6.85 | -2.503 | 34 |
| 5 | 0.999 | 0.962 | 0.966 | 5.82 | -2.521 | 51 |
| 10 | 0.999 | 0.957 | 0.962 | 5.73 | -2.519 | 21 |
| 20 | 0.999 | 0.966 | 0.970 | 5.56 | -2.583 | 59 |
| 30 | 0.999 | 0.967 | 0.971 | 5.68 | -2.550 | 73 |

**Table 9:** Manipulable variables with noise Petlyuk column LCB.

| IP | Manipulable variables | | | |
|---|---|---|---|---|
| | D | R | VR | LR |
| 1 | 81.75 | 18.75 | 150.00 | 150.00 |
| 5 | 77.29 | 19.61 | 150.00 | 150.00 |
| 10 | 79.12 | 16.51 | 114.92 | 150.00 |
| 20 | 73.25 | 21.17 | 90.45 | 20.00 |
| 30 | 79.99 | 16.28 | 118.43 | 150.00 |

**Table 10:** Results BO LCB with noise.

| IP | Description | | | TOC x $10^6$ | Γ | Iter. |
|---|---|---|---|---|---|---|
| | $XD_A$ | $XS_B$ | $XB_C$ | | | |
| 1 | 0.999 | 0.969 | 0.976 | 5.90 | -2.570 | 34 |
| 5 | 0.999 | 0.961 | 0.965 | 5.78 | -2.535 | 50 |
| 10 | 0.999 | 0.965 | 0.964 | 5.03 | -2.612 | 46 |
| 20 | 0.999 | 0.949 | 0.955 | 5.90 | -2.490 | 20 |
| 30 | 0.999 | 0.964 | 0.969 | 5.02 | -2.579 | 51 |

**Table 11:** Manipulable variables with noise Petlyuk column PI.

| IP | Manipulable variables | | | |
|---|---|---|---|---|
| | D | R | VR | LR |
| 1 | 79.41 | 19.41 | 150.00 | 150.00 |
| 5 | 76.25 | 16.41 | 149.13 | 150.00 |
| 10 | 76.83 | 18.07 | 150.00 | 150.00 |
| 20 | 76.70 | 15.67 | 130.34 | 150.00 |
| 30 | 77.82 | 17.27 | 132.73 | 150.00 |

**Table 12:** Results BO PI with noise.

| IP | Description | | | TOC x $10^6$ | Γ | Iter. |
|---|---|---|---|---|---|---|
| | $XD_A$ | $XS_B$ | $XB_C$ | | | |
| 1 | 0.999 | 0.967 | 0.971 | 5.89 | -2.550 | 9 |
| 5 | 0.999 | 0.946 | 0.952 | 4.81 | -2.534 | 17 |
| 10 | 0.999 | 0.958 | 0.963 | 5.32 | -2.550 | 21 |
| 20 | 0.999 | 0.945 | 0.951 | 4.63 | -2.570 | 51 |
| 30 | 0.999 | 0.965 | 0.963 | 5.16 | -2.572 | 51 |

## CONCLUSIONS

In this work, we present a practical methodology for solving multi-objective problems. The results obtained demonstrate a favorable trade-off between objectives for the Petlyuk distillation column, which serves as an energy-saving alternative to traditional sequences. This approach allows for analyzing the feasibility of the process without specifying a particular conversion fraction, as is typically required in distillation optimization problems. The solutions indicate that the achieved trade-off demonstrates the possibility of equilibrium between cost and product purity, with all cases achieving high purity fractions (≥0.96). Furthermore, as mentioned earlier, in low-dimensional Bayesian optimization problems like the one presented, there is no significant difference in performance based on the number of initial points or the acquisition function used. Additionally, despite variations in the number of initial points (IPs), the acquisition function, and the influence of noise in the process, no notable differences were observed, and all results remained within the same range of manipulable variable settings. However, even a slight change in the normalized cost represents a relatively significant change in the total operational cost (TOC) due to its magnitude ($10^6$ USD/year). While these differences are noticeable, increasing the number of initial points does not necessarily lead to better performance in the objective function. This work highlights the potential of Bayesian Optimization (BO) for process simulation, demonstrating that, when combined with modern computing power, it can achieve an optimal design in just a few fast iterations unlike traditional techniques that rely on explicit mathematical models, which often require simplifications. Thus, regardless of the number of initial points or the acquisition function selected, in cases with a low number of manipulated variables and system uncertainties, a multi-objective function can still provide a good trade-off for the Petlyuk column. Moreover, the procedure is easily extendable to other problems, not only those that are complex due to model structure but also large-scale or stochastic problems where computational costs are significant. These types of approaches will be explored in future work.

## REFERENCES


1. Gutiérrez-Antonio C, Briones-Ramírez A. Pareto front of ideal Petlyuk sequences using a multiobjective genetic algorithm with constraints. *Computers & Chemical Engineering* 33(2):454–464 (2009). https://doi.org/10.1016/j.compchemeng.2008.11.004
2. Moriconi R, Deisenroth MP, Sesh Kumar K. High-dimensional Bayesian optimization using low-dimensional feature spaces. *Machine Learning* 109:1925–1943 (2020).
3. Premkumar R, Rangaiah G. Retrofitting conventional column systems to dividing-wall columns. *Chemical Engineering Research and Design* 87(1):47–60 (2009). https://doi.org/10.1016/j.cherd.2008.06.013
4. Pérez-Ones O, Flores-Tlacuahuac A. A stochastic data-driven Bayesian optimization approach for intensified ethanol–water separation systems. *Chemical Engineering and Processing - Process Intensification* 197:109708 (2024). https://doi.org/10.1016/j.cep.2024.109708
5. Ramirez-Corona N, Jiménez-Gutiérrez A, Castro-Agüero A, Rico-Ramírez V. Optimum design of Petlyuk and divided-wall distillation systems using a shortcut model. *Chemical Engineering Research and Design* 88(10):1405–1418 (2010).
6. Scikit-optimize. Sequential model-based optimization. scikit-optimize/scikit-optimize. https://github.com/scikit-optimize/scikit-optimize (2020).
7. Siivola E, Paleyes A, Gonzalez J, Vehtari A. Good practices for Bayesian optimization of high-dimensional structured spaces. *Applied AI Letters* (2021). https://doi.org/10.1002/ail2.24
8. Singh D, Singh B. Investigating the impact of data normalization on classification performance. *Applied Soft Computing* 97:105524 (2020). https://doi.org/10.1016/j.asoc.2019.105524
9. Velasco L, Guerrero H, Hospitaler A. A literature review and critical analysis of metaheuristics recently developed. *Archives of Computational Methods in Engineering* 31(1):125–146 (2024).
10. Ye H, Gao W, Guang Dong H, Bi M. An inherently safer development approach for thermally coupled distillation sequences: Application in hazardous chemical separation. *Process Safety and Environmental Protection* 160:786–802 (2022). https://doi.org/10.1016/j.psep.2022.02.044



© 2025 by the authors. Licensed to PSEcommunity.org and PSE Press. This is an open access article under the creative commons CC-BY-SA licensing terms. Credit must be given to creator and adaptations must be shared under the same terms. See https://creativecommons.org/licenses/by-sa/4.0/




Systems & Control Transactions

**Research Article - Peer Reviewed Conference Proceeding**
ESCAPE 35 - European Symposium on Computer Aided Process Engineering
Ghent, Belgium. 6-9 July 2025
Jan F.M. Van Impe, Grégoire Léonard, Satyajeet S. Bhonsale,
Monika E. Polańska, Filip Logist (Eds.)

PSE PRESS

# Accelerating Solvent Design Optimisation with Group-Contribution Machine Learning Surrogate Classifiers

**Lifeng Zhang[a], Benoît Chachuat[a], and Claire S. Adjiman[a]***

[a] Department of Chemical Engineering, The Sargent Centre for Process Systems Engineering, Imperial College London, London SW7 2AZ, United Kingdom
* Corresponding Author: c.adjiman@imperial.ac.uk.

## ABSTRACT

Asserting the phase stability of multi-component mixtures is an important task in computer-aided mixture/blend design (CAM$^b$D), but it is often hindered by the lack of reliable and tractable models. In this paper, we propose a group-contribution machine-learning (GC-ML) method to predict phase coexistence for a large set of ternary mixtures consisting of two solvents and one (fixed) solute. Each solvent is represented by a vector of functional group numbers, encoded by integer values. The solvent vectors are combined with mixture composition and temperature to form the input features to a GC-ML surrogate classifier, which distinguishes between four types of stable phase configurations as possible outputs: liquid (L), solid-liquid (SL), liquid-liquid (LL) or solid-liquid-liquid (SLL). To explore the performance of the trained GC-ML multi-classifier, it is embedded as a surrogate phase-stability constraint in the optimisation of an ibuprofen crystallisation process. A two-step solution strategy is proposed, iterating between a surrogate-based subproblem and a rigorous UNIFAC-based subproblem, to design binary solvent mixtures that improve the yield of ibuprofen. A high classification accuracy score of over 0.96 is achieved in identifying the correct phase configurations with the surrogate model, making it possible to accurately predict whole phase diagrams for numerous mixtures. Moreover, reliable solutions to the crystallisation design problem are generated with the two-step strategy, yielding objective function values close to those with the UNIFAC-based model at a lower computational cost. These results reveal the value of the proposed surrogate model in guiding the search for better solvent mixtures in CAM$^b$D applications.

**Keywords**: Solvent design, Machine learning, Group contribution, Optimisation, Phase stability

## INTRODUCTION

Identifying optimal multicomponent mixtures is critical in process design, e.g., extraction, absorption and crystallisation [1]. In the past few decades, the computer-aided mixture/blend design (CAM$^b$D) formalism has been widely used to guide the design of solvent mixtures as part of process optimisation efforts. The CAM$^b$D problem is often formulated as a mixed-integer nonlinear programming (MINLP) model, which includes process constraints and property prediction constraints [2]. In addition, ensuring the phase stability of the designed blends is important to avoid undesirable demixing behaviour of the mixture during operation. Given a mixture at a specific temperature, pressure, and composition, phase stability is achieved at the global minimum of the Gibbs free energy of the mixture. It can be enforced by ensuring the sign of the minimum tangent plane distance (TPD) is non-negative [3]. However, the need to use nonlinear thermodynamic models to model complex mixtures makes TPD minimisation a nonconvex optimisation problem. Embedding this nonconvex problem within the CAM$^b$D results in a bilevel problem that is highly challenging and expensive to solve within reasonable runtime in practice. Although tailored optimisation strategies and algorithms have been developed to address the phase stability problem [4,5] or to embed heuristic phase stability checks within CAM$^b$D [6], this remains a hurdle to designing stable mixtures.

Recently, the idea of replacing the lower-level phase stability constraint in the CAM$^b$D problem with a data-




**Figure 1:** Overview of the main steps, namely data generation, model training and optimisation in proposed framework to develop a surrogate ANN multi classifier and implement it in the solvent design optimisation problem.

driven machine learning model has been gaining attention. The use of artificial neural networks (ANNs) as surrogate models has been investigated due to their ability to achieve high accuracy and the potential to embed them as linear constraints, which are preferable in optimisation [7]. In principle, this approach provides a way to simplify nonconvex problems and to reduce computational cost. ANNs [8,9] and support vector machines (SVMs) [10] have previously been trained to predict the phase stability of a specific mixture and have been found to reduce computational cost. However, these mixture-specific models have limited potential for use in CAM$^b$D when many mixture candidates are considered in the design space. To address this, Karia et al. [11] trained an ANN classifier to predict the phase stability of all binary mixtures for a set of predefined solvent candidates, using parameters that describe the solvent identities along with composition and temperature as inputs. The classifier model was used to replace the phase stability criterion and was found to lead to improvements in optimisation efficiency and solution quality. This work was extended by considering SVM classifiers and introducing an additional surrogate model to replace the phase equilibrium (solubility) constraints [12], demonstrating further the potential of data-driven models in CAM$^b$D.

Although these studies revealed that training surrogate models for phase stability prediction can lower computational cost, the exploration of solvent mixtures beyond the dataset is restricted as the solvent identities are linked to a subset of the UNIFAC parameters [13], namely surface and volume. Furthermore, the need to train different surrogate models for solubility and phase stability prediction increases model complexity. To overcome these limitations, a group-contribution machine learning (GC-ML) ANN is developed in this work to predict the phase behaviour of ternary mixtures. In GC-ML, the number and identity of functional groups in a molecule are used as inputs to an ML model to predict a target property. It has been used for pure component properties [14,15], but, to the best of our knowledge, not for mixture properties. Here, each solvent is represented by a vector of functional groups, resulting in a more general surrogate model than that in [11,12]. In addition, a multi-class classifier is developed to determine phase coexistence, instead of relying on a binary classifier for phase stability; this gives the ability to generate entire phase diagrams. The framework for constructing the GC-ML model is described in detail in the next section. The design of a binary solvent mixture for ibuprofen crystallisation is next presented as a case study. Conclusions are developed in the final section.

## METHODOLOGY

The model construction is described in the context of a binary solvent mixture and a solute at conditions where the solute may crystallise and/or the ternary mixture may exhibit one or more liquid phases. It is assumed that the pressure $p$ is fixed but the temperature $T$ is variable. The approach can be extended to other mixtures or phase equilibria. Figure 1 illustrates the steps required to construct the surrogate model, including data generation and model training, and to use it in optimisation.

### Data generation

A set of $N_S$ common solvent candidates is collected from [16]. Each solvent is decomposed into $N_G$ groups by GCIdentifier.jl [17] in Julia. The groups can either be UNIFAC functional groups [13] or SAFT-$\gamma$ Mie [18] functional groups. The input features for the GC-ML model are two $N_G$ -dimensional vectors of group numbers describing each solvent, a 2-dimensional mole fraction vector and the temperature. To obtain a diverse dataset that includes all the solvent candidates, each component is paired with $N_p$ other solvents to create $N_s \times N_p$ solvent mixtures. Notice that not all possible mixtures within the design space are selected. A dataset with $N$ points is generated by adding the solute (e.g., ibuprofen) to each solvent pair and sampling the space of compositions via a Sobol' sequence [19] and the space of temperatures at

regular intervals. A $pT$ flash calculation is executed for each sample with the rigorous model (phasepy [20] with UNIFAC), to identify the stable phase configuration. There are four possible outcomes or categories: liquid ($L$), solid-liquid ($SL$), liquid-liquid ($LL$) or solid-liquid-liquid ($SLL$). The resulting dataset is split into a training dataset (80%$N$) and a test dataset (20%$N$). The sampled mixtures are distributed across both datasets to ensure that the model effectively learns from each functional group.

## Model training

The ANN classifier is developed in Pytorch [21]. The classifier structure, including the number of layers, the number of neurons per layer and the activation function, is defined before training. For the $i^{th}$ input, the ANN yields four real output values, $z_{i,k}$, where $k \in K = \{L, SL, LL, SLL\}$ represents the category. These outputs are normalised into the likelihood $\hat{y}_{i,k}$ via a softmax function:

$$\hat{y}_{i,k} = \frac{\exp(-z_{i,k})}{\sum_{kk \in K} \exp(-z_{i,kk})} \quad \forall k \in K, i = 1, \dots, N \tag{1}$$

The binary label $y_{i,k}$ is then set to 1 for $k = \underset{k \in K}{\operatorname{argmax}}\, \hat{y}_{i,k}$ and to 0 for other values of $k$ and the cross-entropy loss function $L$ is given by:

$$L = -\frac{1}{N} \sum_{i=1}^{N} \sum_{k \in K} y_{i,k} \log(\hat{y}_{i,k}) \tag{2}$$

Once the loss function has been minimized, the chosen architecture is assessed. Given that the dataset is extremely imbalanced since data points in categories LL and SLL are rare, the Matthews Correlation Coefficient (MCC) [22] is applied as a metric to evaluate model performance instead of the more usual accuracy metrics. The MCC score is defined as follows:

$$MCC = \frac{\sum_k \sum_l \sum_m C_{kk} C_{lm} - C_{kl} C_{mk}}{\sqrt{(\sum_k \sum_l C_{kl})(\sum_k \sum_l C_{lk})(\sum_k \sum_m C_{km})(\sum_l \sum_m C_{lm})}} \tag{3}$$

Here $C_{lm}$ refers to the number of samples in the confusion matrix which are predicted as belonging to category $m$ while the true category is $l$. The MCC score takes into account all the prediction results and varies from -1 (a totally wrong prediction) to 1 (a perfect prediction). The MCC score for the test dataset is compared to a threshold $MCC_{min}$ and the model architecture is modified by either adding hidden layers or increasing the number of neurons until the threshold is reached.

## Optimisation strategy

To use the surrogate within an optimisation problem, it is converted into a set of algebraic constraints via the OMLT [23] and embedded into the solvent design optimisation problem in Pyomo [24]. To solve the overall design problem, a two-step approach is implemented. First, the surrogate-based model is formulated by replacing all equations related to phase equilibrium or stability calculations, including the thermodynamic model, with the trained ANN classifier. The surrogate-based model involves binary and continuous variables and may be linear or nonlinear depending on the activation function. Additionally, process constraints may also be nonlinear. With the surrogate model, the phase stability and phase equilibria are replaced by constraints based on the predicted probability values $\hat{y}_k, k \in K,$. To ensure a stable liquid phase, the following constraints are used to ensure $k = L$ has the highest probability:

$$\hat{y}_L \geq \hat{y}_k \quad \forall k \in \{SLL, SL, LL\} \tag{4}$$

To approximate the phase equilibrium constraint, such as SL equilibrium (solubility), the difference between the likelihoods of the two relevant categories, $\hat{y}_{SL}$ and $\hat{y}_L$, should be within a predefined error $\varepsilon$:

$$|\hat{y}_L - \hat{y}_{SL}| \leq \varepsilon \tag{5}$$

The resulting surrogate-based MILP or MINLP is then solved to obtain optimal solvent identities, compositions, and process conditions. Only the optimal solvent identities are retained for the second step. The second optimisation subproblem is an NLP (fixed solvent identities) which includes the rigorous phase equilibrium constraints and a surrogate phase stability check, formulated as the following constraint [11]:

$$\hat{y}_L + \hat{y}_{SL} \geq \hat{y}_{LL} + \hat{y}_{SLL} \tag{6}$$

This constraint ensures that the probability of having one stable liquid phase is larger than that of having two stable liquid phases. If desired, the process of generating candidate solvent mixtures can be repeated by adding integer cuts to eliminate previous solutions.

# CASE STUDY

## Problem description

The proposed framework is demonstrated on an ibuprofen crystallisation process [25]. At the initial state, the ibuprofen is dissolved in a binary solvent mixture consisting of solvents $s_1$ and $s_2$ at temperature $T_0$. There are no crystals in this state. During the crystallisation, more solvent $s_2$ can be added to the mixture as an antisolvent and the mixture can be cooled to temperature $T$. In the present case study, the ranges of $T_0$ and $T$ are taken to be $[293.15\,K,\ 313.15\,K]$ and $N_S = 48$ solvent candidates are considered. The goal of the optimisation is to select the binary solvent mixture from the $N_s$ solvent candidates (2,256 possible mixtures), as well as the mixture composition and temperature, that maximise the yield of ibuprofen. The solvents combine any of $N_G = 33$ UNIFAC functional groups and the predicted mixture properties are compared against UNIFAC [13] as the rigorous thermodynamic model. More details on this case study can be found in [11,25].

All models are trained and optimised on Windows11 using Intel(R) Xeon(R) Gold 6226R CPU @ 2.90GHz with 64GB RAM and NVIDIA RTX A4000 GPU with 16GB RAM.

## Performance of multi-class classifier

A parametric study is carried out for the given number of solvent candidates and temperature ranges to

determine the appropriate size of the dataset for training. As a result, $N_p$=30 is applied, leading to $N_s \times N_p$=1,440 randomly generated solvent mixtures. The temperature range is sampled every 2 K, leading to 11 temperature values. For each solvent mixture at each temperature, 400 mole fraction vectors are sampled, leading to a large set of inputs that consists of 6,336,000 data points. The phasepy calculations are conducted in parallel and require nearly 3 hours of wall time. An overview of the dataset is presented in Table 1.

**Table 1:** Overview of the dataset.

| Category | # input vectors | % category |
|---|---|---|
| LLS | 371,350 | 5.86% |
| LL | 183,962 | 2.90% |
| LS | 3,428,021 | 54.10% |
| L | 2,333,993 | 36.84% |
| E | 18,674 | 0.30% |
| # inputs | 6,336,000 | 100.00% |
| # valid inputs | 6,317,326 | 99.70% |

Category E refers to input vectors for which phasepy does not converge. This small subset is discarded. As expected, the LS and L categories are most abundant in the dataset, making up 90% of the data.

Since 33 functional groups are used to define one solvent, the input vector has 69 elements consisting of the two solvents, the temperature as well the mole fraction of each solvent. As shown in Table 2, the final ANN includes a first hidden layer of 80 neurons and a second layer with 30 neurons. The number of epochs is set to 30, and the batch size is set to 2,056 with a learning rate of 0.005. The tanh activation function is used based on previous experience to avoid introducing redundant binary variables that can slow down convergence [12]. The training time is mostly determined by the large dataset.

**Table 2:** Training statistics for the final ANN model.

| Parameters | Values |
|---|---|
| Activation function | tanh |
| Model complexity | [69,80,30,4] |
| Epochs | 30 |
| Batch size | 2,056 |
| Learning rate | 0.005 |
| Training time /s | 14,032 |
| MCC for training dataset | 0.9771 |
| MCC for test dataset | 0.9698 |

Encouragingly, for a value of $MCC_{min} = 0.96$, a surrogate model that achieves a high MCC score for both the training dataset (0.9771) and the test dataset (0.9698) is obtained. This indicates that the surrogate model captures the nature of the phase coexistence at different temperatures and for different mixtures. To investigate the performance of the trained ANN multi-class classifier, the model is used to generate phase diagrams for four combinations of solvent 1/solvent 2/temperature that do not appear in the dataset: chloroform-tetrachloromethane (CCl4) at T=300.15 K, water-chloroform at T=300.15 K, water-toluene at T=308.15 K and ethylene glycol-anisole at T=308.15 K. These are shown in Fig. 2, where the predictions from the classifier are marked with different colours. The true phase boundaries are also obtained with the rigorous UNIFAC model and are denoted by black solid curves. The yellow dashed curves represent metastable solid-liquid equilibrium points in a region of solid-liquid-liquid equilibrium. The predicted phase boundaries are in good agreement between the two models. For example, the chloroform-$CCl_4$ mixture (Fig. 2a) only displays SL and L, indicating that no liquid-liquid demixing occurs. The solubility of ibuprofen, denoted by the black solid line, is described well by the classifier. For the remaining mixtures, which all exhibit two liquid phases, SLL and LL regions are indeed identified. For water-chloroform and water-toluene (Figs. 2b-c), misclassification occurs when the composition is close to pure $s_1$, predicting SL instead of the true LL and SLL regions. This probably arises from the presence of other mixtures in the dataset that exhibit this behaviour. For ethylene glycol-anisole (Fig. 2d), the surrogate model does not capture the extent of the SLL region very well. There are 254,808 data points that involve anisole, only 4.69% of which are labelled as SLL. The model tends to predict ethylene glycol-anisole mixtures forming a single liquid (SL or L), leading to an underestimation of the SLL region but accurate identification of a tiny L region of pure $s1$ between L and LS, which is most important in solvent design for crystallisation. Overall, the data-driven model captures the phase coexistence of multi-component mixtures well. Finally, parts of the solid-liquid equilibrium boundary that correspond to a metastable equilibrium are shown with yellow curves in Fig. 2. If the phase stability constraint were not included in the solvent design, solutions that fall on these undesirable parts of the curve would likely be identified.

## Optimisation performance

The problem is solved with the proposed two-step approach. Details on the process can be found in [11]. Here a summary of the surrogate-based model is given:

$$\max \text{ yield of ibuprofen} \tag{7}$$

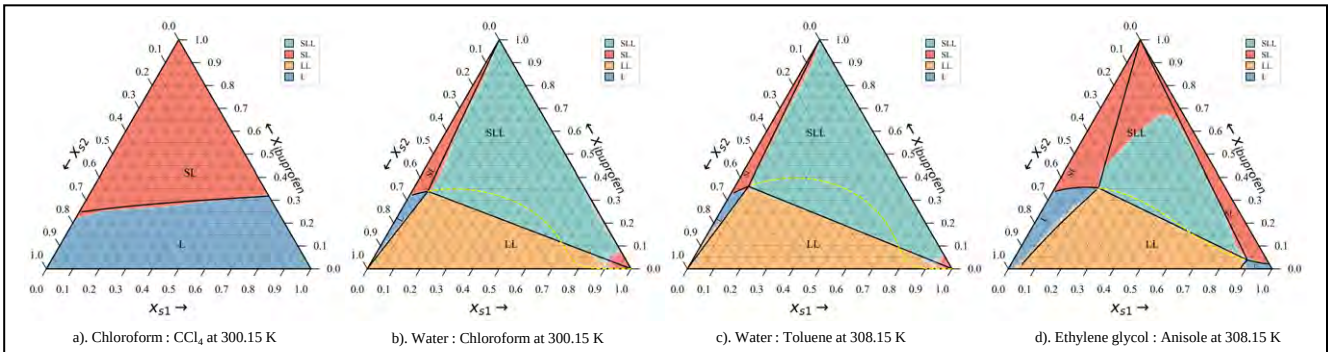
$$\text{s. t. process constraints} \tag{8}$$

$$\text{mixture formulation constraints} \tag{9}$$

$$\hat{y}_{k,st} = f_{ANN}(x_{in,st}) \; \forall k \in K, st \in \{\text{initial, final}\} \tag{10}$$

$$\left|\hat{y}_{L,st} - \hat{y}_{LS,st}\right| \leq \varepsilon \; \forall st \in \{\text{initial, final}\} \tag{11}$$

$$\hat{y}_{L,st} \geq \hat{y}_{k,st} \; \forall k \in K \backslash \{L\}, st \in \{\text{initial}\} \tag{12}$$




a). Chloroform : $CCl_4$ at 300.15 K b). Water : Chloroform at 300.15 K c). Water : Toluene at 308.15 K d). Ethylene glycol : Anisole at 308.15 K

**Figure 2:** Phase diagrams generated by the surrogate model and the rigorous model for four solvent mixtures at 300.15 K or 308.15 K. The mixture is shown as $s_1{:}\,s_2$ in each figure caption. The colours denote the prediction from the surrogate model. The solid curves are the phase boundaries generated by $pT$ flash calculations with UNIFAC. The yellow curves denote parts of the solid-liquid equilibrium boundaries that are metastable, as computed with UNIFAC. The regions are labelled L, LL, SL and SLL based on the results of the rigorous model.

$$\hat{y}_{SL,st} \geq \hat{y}_{k,st}\ \forall k \in K\backslash\{SL\}, st \in \{\text{final}\} \quad (13)$$

Equation (10) represents the ANN with $x_{in,st}$ referring to the input vector at state $st \in \{\text{initial}, \text{final}\}$. A value of $\varepsilon = 0.1$ is used in Equation (11). Equation (12) ensures the mixture at the initial state is in region L. It is not necessary to impose that the mixture be saturated at the initial temperature, although it is desirable as it leads to lower solvent consumption. Equation (13) ensures the final mixtures is in the SL region after crystallisation, while Equation (11) ensures it is close to equilibrium solubility.

Neither of the models can be solved within 3 hours with global solvers. Instead, sBB [26] is used to solve the surrogate-based MINLP and CONOPT [27] is used for the UNIFAC-based NLP. Five solutions are listed in Table 3, including the runtime needed to generate each solution, the yield of ibuprofen from each step, and the outcome of the phase stability check in phasepy. All the solutions have the same optimal temperature range, from 313.15 K to 293.15 K, except for the first solution whose final temperature is 302.06 K. Every subproblem can be solved within 3 minutes. This small runtime makes a more extensive search of the design space possible. Ibuprofen yields of around 0.77 are obtained from all instances of step 1. In all cases apart from iteration 3, good agreement between the yields from the two subproblems is found. In iteration 3, a deviation of 0.051 is observed, arising from misclassifications for the benzene-p-cymene mixture. All the solvent mixtures designed only present one liquid phase at both the initial and final states, which satisfies the stability check. This is in contrast to approaches in which this constraint is only enforced *a posteriori* [25]. Applying data-driven surrogates of phase stability to assist solvent design in CAM$^b$D results not only in lower computational cost but, more importantly, in more reliable solutions.

## CONCLUSIONS AND FUTURE WORK

We proposed a multi-class classifier for predicting phase coexistence and stability. The group contribution concept was adopted to represent solvent candidates with a vector of functional groups, leading to a GC-ML ANN that can predict a whole phase diagram. This framework was tested on a crystallisation optimisation problem with ibuprofen as the target compound. The results showed that the trained classifier can generate phase diagrams for unseen mixtures with sufficient accuracy for use in CAM$^b$D. A two-stage strategy was proposed to obtain solutions to the crystallisation process optimisation problem. High-quality designs were obtained, exhibiting a homogeneous liquid phase as desired. The proposed classifier surrogate offers a promising alternative for the formulation of CAM$^b$D problems. However, misclassifications arising from the data-driven model can occasionally misdirect the search to a suboptimal or infeasible solution. Future work will thus focus on developing strategies such as active learning to improve model accuracy.

**Table 3:** Optimal binary solvent mixtures for the ibuprofen crystallisation process via the optimisation.

| Iter. | Runtime /s | Solvent A: Solvent B | **Yield** (Step 1) | **Yield** (Step 2) | Phase stability (initial: final) |
|---|---|---|---|---|---|
| 1 | 137.20 | DMSO: Formic acid | 0.784 | 0.799 | L: L |
| 2 | 74.14 | Formic acid: Anisole | 0.779 | 0.770 | L: L |
| 3 | 112.72 | Benzene: p-Cymene | 0.779 | 0.728 | L: L |
| 4 | 145.23 | Anisole: Formic acid | 0.766 | 0.770 | L: L |
| 5 | 124.84 | Chloroform: Hexane | 0.764 | 0.752 | L: L |

## ACKNOWLEDGEMENTS

The authors gratefully acknowledge funding from the UK Engineering and Physical Sciences Research Council (EPSRC) under grant EP/W003317/1.

## REFERENCES

1. Jonuzaj, S. *et al*. The formulation of optimal mixtures with generalized disjunctive programming: A solvent design case study. *AIChE J.* **62**, 1616–1633 (2016).
2. Gani, R. Computer-Aided Methods and Tools for Chemical Product Design. *Chem. Eng. Res. Des.* **82**, 1494–1504 (2004).
3. Baker, L. E., Pierce, A. C. & Luks, K. D. Gibbs Energy Analysis of Phase Equilibria. *Soc. Pet. Eng. J.* **22**, 731–742 (1982).
4. Mitsos, A. & Barton, P. I. A dual extremum principle in thermodynamics. *AIChE J.* **53**, 2131–2147 (2007).
5. McDonald, C. M. & Floudas, C. A. Global optimization for the phase stability problem. *AIChE J.* **41**, 1798–1814 (1995).
6. Karunanithi, A. T., Achenie, L. E. K. & Gani, R. A computer-aided molecular design framework for crystallization solvent design. *Chem. Eng. Sci.* **61**, 1247–1260 (2006).
7. Schweidtmann, A. M. & Mitsos, A. Deterministic Global Optimization with Artificial Neural Networks Embedded. *J. Optim. Theory Appl.* **180**, 925–948 (2019).
8. Schmitz, J. E., Zemp, R. J. & Mendes, M. J. Artificial neural networks for the solution of the phase stability problem. *Fluid Phase Equilibria* **245**, 83–87 (2006).
9. Lopez-Ramirez, E. *et al*. Artificial Neural Networks (ANNs) for Vapour-Liquid-Liquid Equilibrium (VLLE) Predictions in N-Octane/Water Blends. *Processes* **11**, 2026 (2023).
10. Gaganis, V. & Varotsis, N. Non-iterative phase stability calculations for process simulation using discriminating functions. *Fluid Phase Equilibria* **314**, 69–77 (2012).
11. Karia, T. *et al*. Classifier surrogates to ensure phase stability in optimisation-based design of solvent mixtures. *Digit. Chem. Eng.* 100200 (2024).
12. Zhang, L. *et al.* Comparative study of classifier models to assert phase stability in multicomponent mixtures. in *Computer Aided Chemical Engineering* (eds. Manenti, F. & Reklaitis, G. V.) vol. 53 1465–1470 (Elsevier, 2024).
13. Published Parameters UNIFAC - DDBST GmbH. https://www.ddbst.com/published-parameters-unifac.html.
14. Mann, V., Gani, R. & Venkatasubramanian, V. Group contribution-based property modeling for chemical product design: A perspective in the AI era. *Fluid Phase Equilibria* **568**, 113734 (2023).
15. Paduszyński, K. & Domańska, U. Viscosity of Ionic Liquids: An Extensive Database and a New Group Contribution Model Based on a Feed-Forward Artificial Neural Network. *J. Chem. Inf. Model.* **54**, 1311–1324 (2014).
16. Prat, D. *et al.* CHEM21 selection guide of classical- and less classical-solvents. *Green Chem.* **18**, 288–296 (2016).
17. Walker, P. J., Riedemann, A. & Wang, Z.-G. GCIdentifier.jl: A Julia package for identifyingmolecular fragments from SMILES. *J. Open Source Softw.* **9**, 6453 (2024).
18. Haslam, A. J. *et al.* Expanding the Applications of the SAFT-γ Mie Group-Contribution Equation of State: Prediction of Thermodynamic Properties and Phase Behavior of Mixtures. *J. Chem. Eng. Data* **65**, 5862–5890 (2020).
19. Sobol', I. M. On the distribution of points in a cube and the approximate evaluation of integrals. *USSR Comput. Math. Math. Phys.* **7**, 86–112 (1967).
20. Chaparro, G. & Mejía, A. Phasepy: A Python based framework for fluid phase equilibria and interfacial properties computation. *J. Comput. Chem.* **41**, 2504–2526 (2020).
21. Paszke, A. *et al.* PyTorch: An Imperative Style, High-Performance Deep Learning Library. Preprint at http://arxiv.org/abs/1912.01703 (2019).
22. Chicco, D. & Jurman, G. The advantages of the Matthews correlation coefficient (MCC) over F1 score and accuracy in binary classification evaluation. *BMC Genomics* **21**, 6 (2020).
23. Ceccon, F. *et al.* OMLT: Optimization & Machine Learning Toolkit.
24. Bynum, M. L. *et al. Pyomo — Optimization Modeling in Python*. vol. 67 (Springer International Publishing, Cham, 2021).
25. Watson, O. L. *et al.* Computer Aided Design of Solvent Blends for Hybrid Cooling and Antisolvent Crystallization of Active Pharmaceutical Ingredients. *Org. Process Res. Dev.* **25**, 1123–1142 (2021).
26. SBB. https://www.gams.com.html.
27. Drud, A. CONOPT: A GRG code for large sparse dynamic nonlinear optimization problems. *Math. Program.* **31**, 153–191 (1985).

© 2025 by the authors. Licensed to PSEcommunity.org and PSE Press. This is an open access article under the creative commons CC-BY-SA licensing terms. Credit must be given to creator and adaptations must be shared under the same terms. See https://creativecommons.org/licenses/by-sa/4.0/

Systems & Control Transactions

**Research Article - Peer Reviewed Conference Proceeding**
ESCAPE 35 - European Symposium on Computer Aided Process Engineering
Ghent, Belgium. 6-9 July 2025
Jan F.M. Van Impe, Grégoire Léonard, Satyajeet S. Bhonsale,
Monika E. Polańska, Filip Logist (Eds.)

PSE PRESS

# Machine Learning-Aided Robust Optimisation for Identifying Optimal Operational Spaces under Uncertainty

**Sam Kay[a], Mengjia Zhu[a], Amanda Lane[b], Jane Shaw[b], Philip Martin[a], and Dongda Zhang[a]***

[a] Department of Chemical Engineering, University of Manchester, Manchester, M13 9PL, UK.
[b] Unilever R&D Port Sunlight, Bromborough Road, Bebington, Wirral, CH63 3JW, UK.
* Corresponding Author: dongda.zhang@manchester.ac.uk.

## ABSTRACT

Process optimisation and quality control are crucial in process industries for minimising product waste and improving plant economics. Identifying robust operational regions that ensure both product quality and performance is particularly valued in industries. However, this task is complicated by operational uncertainties, which can lead to violations of product quality constraints and significant batch discards. We propose a novel robust optimisation strategy that integrates advanced machine learning and process systems engineering to systematically identify optimal operational regions under uncertainty. Our approach begins by using a process model to screen a broad operational space across various uncertainty scenarios, pinpointing promising control trajectories to satisfy process constraints and product quality. Machine learning is then employed to cluster these trajectories into sub-regions. Finally, a two-layer dynamic optimisation framework is employed to determine the optimal control trajectory and corresponding operable space within each promising sub-region. To demonstrate the efficiency of our approach, we used a case study focusing on the quality control of a dynamic batch process for formulation product manufacturing. The resulting operational regions were shown to meet product quality demands and offer a significant improvement in optimality over the current operation, highlighting the advantage and industrial potential of our strategy.

**Keywords**: Operational regions, Machine learning, Optimisation under uncertainty, Process control, Dynamic optimisation

## INTRODUCTION

Product quality control is a critical concern in industries such as pharmaceuticals, speciality chemicals, and formulation processes, where strict regulatory standards are enforced to ensure safety, efficacy, and economic viability [1]. As a result, manufacturers face growing pressure to minimise product waste, a challenge particularly pronounced in pharmaceutical production, where batch rejections due to variability and quality deviations can result in significant economic and environmental consequences. To maintain a competitive edge while adhering to sustainability goals, there is a strong need for process optimisation strategies that enhance efficiency, reduce waste, and improve operational flexibility. Traditionally, process control has relied on rigid set-point strategies, where specific operating conditions are predetermined and maintained through fixed state profiles [2]. While effective in ensuring stable operations, such approaches lack adaptability in the face of uncertainty, making them prone to inefficiencies. Furthermore, the rigid nature of set-point control often results in excessive energy consumption, as significant resources are required to maintain precise operational conditions [3]. Even in cases where real-time closed loop feedback control is implemented to account for variability, the reliance on extensive sensor networks and rapid data processing can introduce prohibitive costs and practical limitations. Furthermore, unaccounted uncertainties can lead to deviations in key performance indicators (KPIs), increasing the likelihood of batch failures and product inconsistencies.

To address these challenges, robust optimisation techniques have been widely explored in the literature. One commonly employed approach is stochastic optimisation, which leverages probability distributions to model uncertainties and has been successfully applied in

complex, non-linear systems [4]. A particularly effective subset of stochastic optimisation is scenario tree optimisation, which transforms probabilistic problems into a structured deterministic framework by propagating uncertainty across different realisations of a process [5].

An emerging alternative to traditional set-point-based control is operational space control, which shifts the focus from maintaining rigid state profiles to defining feasible operational spaces within which a process can be adjusted [6]. This approach has found use in the chemical and pharmaceutical sectors, where it is often referred to as design space identification. For instance, [6] demonstrated the effectiveness of operational space methodologies in the temperature control of a fed-batch bioreactor under uncertainty, ensuring ethanol production constraints were met despite process variability. Such methodologies provide greater flexibility and adaptability than conventional set-point control, making them well-suited for processes characterised by uncertainty and dynamic variability [7].

Despite its advantages, current operational space methodologies still face notable challenges. Existing approaches often limit the consideration of uncertainty to parameter variations alone, overlook optimality in favour of robustness, and rely on computationally expensive sampling techniques. Moreover, there has been little research into the systematic identification of multiple feasible operational spaces for a given process, despite the potential benefits of having multiple viable operating regions. Notably, operational space control has yet to be applied in formulation industries, where the need for flexible quality control and real-time process monitoring is particularly pronounced.

In this paper, we address these gaps by proposing a novel scenario tree optimisation framework that integrates flexible operational spaces with dynamic optimisation. This framework not only enables the identification of multiple optimal and flexible operational regions but also enhances product quality control in a manner that is useful to real-world manufacturing constraints. Additionally, we present the first case study applying operational space methodologies to formulation processes, demonstrating the practical benefits of this approach in an industrial setting.

## METHODOLOGY

Operational spaces can generally be categorised into three key classifications. The feasible space represents the multidimensional range of operating conditions that satisfy all process constraints. Within this, the flexible space forms a subset that is not only feasible but also resilient to uncertainties. Lastly, the optimal space is another subset of the feasible space where operating conditions are selected to maximise performance according to a predefined objective. In this study, we introduce a novel methodology to systematically identify the intersection of the flexible and optimal spaces, ensuring that the resulting solution space consists exclusively of operating conditions that are both robust to uncertainty and optimal in performance.

Additionally, as multiple distinct optimal operating conditions may exist, we seek to distinguish and characterise separate optimal regions within the identified design space. Each region is defined by a unique optimal state profile—or a set of profiles if multiple state variables are involved—along with its corresponding operational boundaries. In this work, we utilise an interval-based representation, where operating spaces are defined by upper and lower limits on the identified optimal state profiles. The overall methodology can be summarised into 4 steps, which are shown in Figure 1.

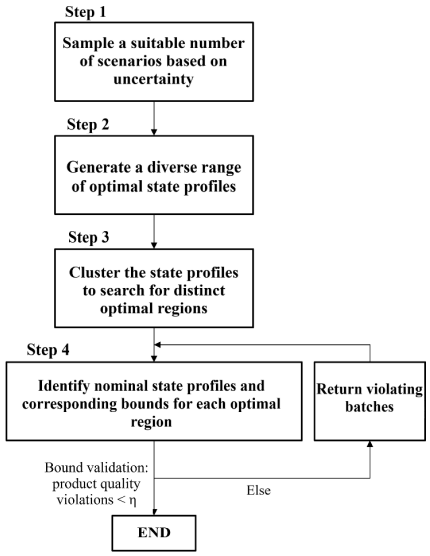



**Figure 1.** Schematic showing the general framework proposed in this study.

### General Problem Formulation

We consider a mathematical model that captures the dynamics of the process, where state variables are categorised into two distinct groups: (i) Flexible state variables, denoted as $\dot{\boldsymbol{x}}_{flexible}(t_j) \in \mathbb{R}^{n_{flexible}}$, represent variables that can be directly adjusted through control inputs. Here, $t_j$ indicates a specific time point within the operational time horizon. (ii) Dependent state variables, represented as $\dot{\boldsymbol{x}}_{dept}(t_j) \in \mathbb{R}^{n_{dept}}$, are those influenced by both control inputs and flexible state variables but cannot be directly regulated. The process dynamics are described by the following system of differential equations:

$$\dot{\boldsymbol{x}}_{flexible}(t) = \boldsymbol{F}_{flexible}(t, \boldsymbol{x}_{flexible}(t), \boldsymbol{\theta}, \boldsymbol{\xi}, \boldsymbol{u}(t)) \quad (1a)$$

$$\dot{\boldsymbol{x}}_{dept}(t) = \boldsymbol{F}_{dept}(t, \boldsymbol{x}_{dept}(t), \boldsymbol{x}_{flexible}(t), \boldsymbol{\theta}, \boldsymbol{\xi}) \quad (1b)$$

Where $\boldsymbol{u}(t_j) \in \mathbb{R}^m$ represents the vector of control inputs, $\boldsymbol{\theta} \in \mathbb{R}^p$ is the vector of fixed parameters, and $\boldsymbol{\xi} \in \mathbb{R}^r$ denotes the vector of uncertain parameters. Each source of uncertainty, $\xi_i$ for $i = 1 \cdots r$, is modelled as a Gaussian-distributed random variable, with its mean set to the nominal parameter value, and its variance reflecting expected variability. Both parameters are assumed to be known.

The goal of this study is to determine a flexible, optimal, and practical operational space for $\boldsymbol{x}_{flexible}(t_j)$ ensuring that key performance indicators (KPIs), such as product quality, are consistently met while maximising process efficiency despite the presence of uncertainties. Herein, the term operational space will be used to refer specifically to the identified flexible state space of $\boldsymbol{x}_{flexible}(t_j)$.

## Step 1: Sampling Uncertainty

We utilise scenario tree analysis, as discussed in Section 1, to capture the potential range of uncertainties encountered during processing. The full scenario tree is constructed by sampling each uncertainty source from its respective distribution, with a detailed description available in [8]. It is crucial to ensure that uncertainty is well-represented to develop a robust control strategy. Therefore, selecting a sufficient number of uncertainty samples is needed. However, this must be balanced against the increased computational cost associated with expanding the scenario tree. Once the scenario tree is established, all optimisation strategies are executed across the entire tree, ensuring that any imposed constraints are met under all considered uncertainty scenarios. An important note to consider is the computational expense of the methodology, which is largely dependent on the system under study. For high dimensional and complex systems, it should be encouraged to explore parallelisation, high performance computing alongside scenario reduction methods.

## Step 2: Filling out the Optimal Region

Since multiple optimal state profiles of $\boldsymbol{x}_{flexible}(t)$ can satisfy process constraints while ensuring KPIs remain within specification, Step 2 (illustrated in Figure 1) focuses on refining the broad process design space. The goal is to identify promising operational regions that likely contain the majority of optimal state profiles of $\boldsymbol{x}_{flexible}(t)$. When successfully designed, these optimal operational regions should consist primarily—if not entirely—of state trajectories that adhere to a predefined standard of process efficiency while respecting constraints under all uncertainties represented in the scenario tree. Specifically, for each set of optimal state profiles, the objective is to minimise a process cost $C_{avg}$, which is computed as the average cost across all scenarios in the scenario tree, while ensuring that the calculated KPI remains within the specified range and close to its target value as defined in the PFD.

The operational time horizon is discretised into $N$ intervals. To simplify control efforts, we assume that $\boldsymbol{x}_{flexible}(t)$ remains constant within each interval, meaning it follows a piecewise constant representation ($\boldsymbol{x}_{flexible}(t) = \boldsymbol{x}_k^{flexible}$, for $t \in [t_k, t_{k+1})$ and $k = 0 \cdots N-1$), where $t_k = k\Delta t$ and $\Delta t = {}^{t_f}/_{N}$. Furthermore, due to physical constraints on control actions $\boldsymbol{u}(t)$, the flexible state variables are also bounded within a predefined range, $[\underline{\boldsymbol{x}}_k^{flexible}, \overline{\boldsymbol{x}}_k^{flexible}]$ for $k = 0 \cdots N-1$. The process is also subject to constraints, $\boldsymbol{g}(\boldsymbol{x}_{k,s}^{dept}, \boldsymbol{x}_k^{flexible})$ for $s = 1 \cdots S$, where $S$ represents the number of uncertain scenarios in the scenario tree. Additionally, it is assumed that the initial state $\boldsymbol{x}_0^{dept}$ is known. With these considerations, the optimisation problem is defined to determine the optimal state trajectories of $\boldsymbol{x}_{flexible}$.

$$min_{x_k^{flexible}, k=0,\dots,N-1} \lambda_1 \cdot obj_1 + \lambda_2 \cdot C_{avg} \quad (2)$$

$$s.t.$$

$$for\ k = 0, \dots, N-1, s = 1, \dots, S,$$

$$obj_1 = (1/S) \sum_{s=1}^{S} \left(y_{KPI,s} - y_{KPI,T}\right)^2$$

$$C_{avg} = (1/S) \sum_{s=1}^{S} C_s$$

$$y_{KPI,s} = h\left(\boldsymbol{x}_{k,s}^{dept}, \boldsymbol{x}_k^{flexible}\right)$$

$$\boldsymbol{x}_{k+1,s}^{dept} = \boldsymbol{f}_{dept}\left(\Delta t, \boldsymbol{x}_k^{dept,s}, \boldsymbol{x}_k^{flexible}, \boldsymbol{\theta}, \boldsymbol{\xi}_s\right)$$

$$\boldsymbol{g}\left(\boldsymbol{x}_k^{dept,s}, \boldsymbol{x}_k^{flexible}\right) \leq 0$$

$$\boldsymbol{x}_0^{dept} = \boldsymbol{x}^{dept}(0)$$

$$\underline{\boldsymbol{x}}_k^{flexible} \leq \boldsymbol{x}_k^{flexible} \leq \overline{\boldsymbol{x}}_k^{flexible}, \underline{y}_{KPI} \leq y_{KPI,s} \leq \overline{y}_{KPI}$$

Here, $\lambda_1$ and $\lambda_2$ are weighting parameters assigned to each objective. $obj_1$ represents the average sum-of-squared deviations from the target KPIs across all scenarios, while $C_s$ denotes the process cost for each scenario. The function $h(\cdot)$ describes the transformation between process states and their corresponding KPIs, where $y_{KPI,s}$ and $y_{KPI,T}$ represent the KPI value for Scenario $s$ and the target KPI value, respectively. The term $\boldsymbol{f}_{dept}(\cdot)$ accounts for the numerical integration of the dependent state variables. $\boldsymbol{g}(\cdot)$ is the process inequality constraints.

To obtain a diverse set of optimal state trajectories and explore a broader operational space, the optimisation of Problem 2 is initially performed. Once this is complete, additional optimal state profiles can be identified by re-optimising the problem with an additional penalty function, $p$, introduced into the objective function. The penalty used may be:

$$p = \lambda_3 \cdot \sum_{d=1}^{D_{curr}} \sum_{j=1}^{n_{flexible}} \sum_{k=0}^{N-1} \left( \frac{\left(x_{flexible,j,k} - x^*_{flexible,j,k,d}\right)}{\Delta \bar{x}_{flexible,j,k}} \right) \quad (3)$$

Here, $\boldsymbol{\lambda_3}$ serves as the weighting parameter that regulates the strength of the penalty function. Higher values encourage greater variation among solutions, thereby facilitating the identification of more distinct optimal regions. The term $D_{curr}$ denotes the number of previous optimisation iterations, which increases as the number of iterations does. Within this framework, $x^*_{flexible,j,k,d}$ represents the discretised optimal state value from an already identified trajectory, whereas $x_{flexible,j,k}$ corresponds to the state value in the current optimisation. To ensure comparability across variables with different scales, the term $\Delta\bar{x}_{flexible,j,k}$ represents the maximum range of $x_{flexible,j,k}$ across previously identified trajectories. By applying this iterative approach, and with a sufficiently large number of iterations $D_{max}$ , one can systematically explore the entire design space to uncover a broad set of high-quality optimal state profiles that remain feasible under uncertainty.

## Step 3: Clustering Optimal Regions

After completing Step 2, multiple operational spaces may emerge. To systematically identify and characterise these spaces, clustering algorithms are employed. Given that clustering is an unsupervised learning approach, it is crucial to validate the results by applying different clustering methods and analysing the resulting cluster characteristics. This ensures a clear distinction between solutions and assists to assess variations in their behaviours. In this work, several algorithms were used and compared in order to ensure consistent results for the recommended number of clusters. These are k-means, DBSCAN, and spectral clustering [9].

## Step 4: Nominal State and Bound Estimation Strategy

In Steps 2 and 3 (as shown in Figure 1), estimations for a set of distinct optimal operational regions are made. The next step involves refining these regions by determining the nominal state profiles for each region, as well as the upper and lower bounds for each flexible state variable. An optimal operational region for a particular flexible state variable is characterised by its nominal profile and associated bounds, where staying within these bounds provides feasibility under the given uncertainties.

The nominal profiles, which represent the optimised state variable set-points at various stages of the process, are identified through a dynamic optimisation approach, as described in Problem 2. At this point, the search space is limited to the clustered region defined in Step 3. This ensures the solution remains within the appropriate cluster. Consequently, the bounds in Problem 2, $\underline{\boldsymbol{x}}_k^{flexible}$ and $\overline{\boldsymbol{x}}_{\mathrm{k}}^{flexible}$, are adjusted to reflect the specific characteristics of the cluster. Once the nominal profiles are determined, a two-step algorithm is proposed to independently find the upper and lower bounds, maximising the distance between them while still adhering to process constraints. The optimisation strategy for determining the lower bound is shown in Equation 4.

$$\max_{\substack{x_k^{flexible,lb} \\ k=0\cdots N-1}} \min_{j=1}^{(n_{flexible})} \min_{k=1}^{(N-1)} \underline{w}_{j,k} \cdot \left(x_{j,k}^{flexible,nominal} - x_{j,k}^{flexible,lb}\right)$$

$$s.t. \tag{4}$$

$$\underline{w}_{j,k} = \frac{1}{x_{j,k}^{flexible,nominal} - \underline{x}_{j,k}^{flexible}}$$

$$y_{KPI,s} = h\left(\boldsymbol{x}_{k,s}^{dept}, \boldsymbol{x}_k^{flexible}\right)$$

$$\boldsymbol{x}_{k+1,s}^{dept} = \boldsymbol{f}_{dept}\left(\Delta t, \boldsymbol{x}_{k,s}^{dept}, \boldsymbol{x}_k^{flexible,lb}, \boldsymbol{\theta}, \boldsymbol{\xi}_s\right)$$

$$\boldsymbol{g}\left(\boldsymbol{x}_{k,s}^{dept}, \boldsymbol{x}_k^{flexible,lb}\right) \leq 0$$

$$\boldsymbol{x}_0^{dept} = \boldsymbol{x}^{dept}(0)$$

$$\underline{\boldsymbol{x}}_k^{flexible} \leq \boldsymbol{x}_k^{flexible,lb} \leq \boldsymbol{x}_k^{flexible,nominal}, \underline{y}_{KPI} \leq y_{KPI,s} \leq \overline{y}_{KPI}$$

Problem 4 is designed to maximise the minimum distance between the nominal flexible state, $x_{j,k}^{flexible,nominal}$, and the lower bound of the flexible state, $x_{j,k}^{flexible,lb}$, across all flexible state variables and time steps. The normalisation parameter, $\underline{w}_{j,k}$, is used to standardise the influence of different flexible states on the objective function. By formulating the objective this way, the goal is to spread the bounds as evenly as possible across the entire trajectory for each flexible state variable. This reduces the need for highly precise set-point control at any given time step.

This optimisation strategy can be repeated for the upper bound to provide the full operational region where control of the design variables can be relaxed but achieve good process performance and required specifications. As the two-step algorithm determines the upper and lower bounds independently, each bound is ensured to meet the constraints on its own. However, this does not guarantee that all state profiles sampled within these bounds will adhere to the constraints. Therefore, it is crucial to validate these bounds by randomly sampling state profiles within them and identifying instances where constraints are violated. Once these violating samples are recorded, they are reintroduced into the framework by incorporating a penalty function into the objective functions of Equations (4) and (5). This penalty function serves to narrow the bounds, ensuring that future state profiles do not violate the constraints. The penalty function may take many forms dependant on the study, but one must consider its practicality against its conservativeness.

# CASE STUDY

To illustrate the effectiveness of the proposed framework, an in-silico case study has been developed using a dynamic model designed to simulate a real-world industrial formulation process. A simplified schematic of the primary mixing unit is presented in Figure 2. This case study focuses on the production of a multiphase, non-Newtonian liquid formulation via a batch mixing process where the process flow diagram (PFD) is characterised by a sequence of ingredient additions, alongside key processing such as temperature and shear rate. Due to the complex nature of multiphase mixing mechanisms, the product KPI is inherently challenging to control and cannot be measured in real-time. As a result, defining a robust operational space that ensures both process flexibility and consistent product quality is essential. Furthermore, it is desired to reduce operational expense and improve the sustainability of the process through reducing the batch cycle time (i.e., the process cost).

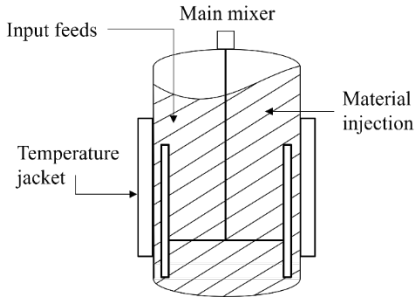



**Figure 2.** Diagram of the batch mixing unit for which the case study is based on.

Within this study, both the sequence of ingredient additions and the final ingredient ratio and mass are predefined by established protocols. As a result, the selection of flexible state variables is limited to standard processing parameters such as shear rate, pressure, temperature, and flowrate. For this investigation, two process parameters are chosen, along with an additional variable representing the timing of ingredient additions, leading to a total of three distinct types of flexible state variables. A mechanistic model exists to describe the dynamic mixing process with high accuracy, a full description of which can be found in [10]. In this model, there exists a set of 5 key ingredient concentrations (dependent states), determined dynamically through 3 material transformation equations, which influence the product quality. Furthermore, there are 3 flexible state variables used to control the process, and in total, there are 14 model parameters which were parameterised. The 3 flexible state variables were each discretised into 5 decision variables for the purpose of solving the optimal control problem (i.e., a total of 15 decision variables). The 3 flexible state variables will henceforth be referred to as Process Parameters 1, 2 and 3.

The primary challenges in this case study stems from the difficulty in achieving the desired end-product quality, which is influenced by various process uncertainties typically encountered in standard operations. These uncertainties were categorised into three sources. The first being variations in the input feed composition, which are reflected in the estimated model parameters. The second source is human error, primarily introduced through inconsistencies in precisely following the scheduled timing for ingredient additions. The third source is system control error, which involves deviations in state variables from their set-point values. The uncertainty levels for these variables were assumed to be 10%, 20%, and 5%, respectively. Additionally, 100 uncertain scenarios were considered in the assembly of the scenario tree.

## RESULTS AND DISCUSSION

The methodology outlined in Section 2 was fully implemented, resulting in the identification of 40 optimal set-points during step 2. In Step 3, the analysis revealed the presence of two distinct clusters, each associated with separate state profiles which were both carried forth for Step 4. From application of Step 4, the initial nominal state profiles and corresponding bounds for Process Parameters 1 and 2 in each cluster were determined as shown in Figures 3 (initial bounds) and 4 (refined bounds).

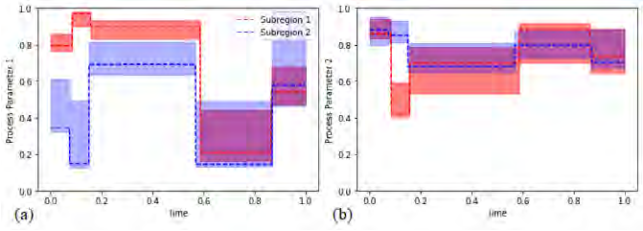



**Figure 3.** Normalised state profiles and operational region for Process Parameters 1(a) and 2(b) for each of the clusters identified before bound refinement

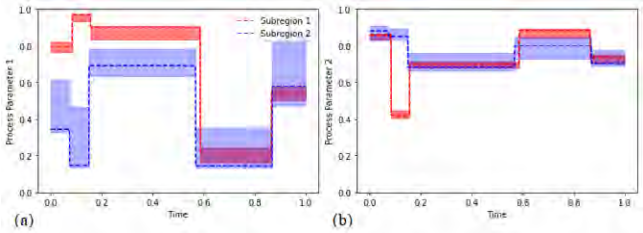



**Figure 4.** Normalised state profiles and operational region for Process Parameters 1(a) and 2(b) for each of the clusters identified after bound refinement.

To validate the initial bounds for both clusters, 1000 state trajectories were randomly sampled from within the optimal operational regions, across 100 unseen uncertain scenarios (i.e., $10^5$ tests). To compare the performance, the batch failure rate is defined: this is the fraction of the

test batches that encounter a product quality violation. After validation of the initial bounds (Figure 3), the results showed that Cluster 1 and 2 had a batch failure rate of 0.9% and 0.1%, respectively, suggesting that the initial bounds are reasonably robust to uncertainties.

When the bounds were refined (Figure 4), the batch failure rates dropped significantly to 0% and 0.009% for Clusters 1 and 2, respectively. However, it is immediately noticed that the refined operational area of Cluster 2 is much greater than that of Cluster 1. Specifically, Cluster 1's refined operational areas are 67.1% and 59.2% smaller for Process Parameters 1 and 2, respectively. Using these results, we can conclude that although it may be possible to achieve a 0% batch failure rate, it may be more practical to permit a small batch failure rate in order to largely improve flexibility in the operational area.

Overall, this case study demonstrates the framework's capacity to identify multiple distinct optimal regions, each offering operational areas that are practically resilient to uncertainties. Additionally, both identified regions led to a significant reduction in batch time compared to the existing set-point control approach used for the system, achieving a 38.6% decrease in both cases. After a thorough evaluation of each operational region's performance, it is likely that Region 2 would be recommended for execution, given its greater operational flexibility to Region 1.

## CONCLUSION

In conclusion, operational space design provides an innovative approach for integrating uncertainties into the development of robust control strategies, ensuring that key process constraints are reliably met. By combining flexibility with optimality, this approach enables the creation of control strategies that are both reliable and high-performing. A significant advantage over traditional set-point control is the increased operability, which allows processes to operate within broader ranges instead of being constrained to strict set-point conditions. Additionally, the systematic identification of various operating regions within the entire optimal space offers a major benefit over traditional set-point control, which may overlook the existence of such regions. This methodology not only aids in designing robust controls but also provides valuable insights into how processes can be operated, helping operators identify areas where the process may be more stable and easier to control.

## REFERENCES


1. A. Hicks *et al.*, "A two-step multivariate statistical learning approach for batch process soft sensing," *Digital Chemical Engineering*, vol. 1, p. 100003, Dec. 2021.
2. H. Efheij, A. Albagul, and N. A. Albraiki, "Comparison of Model Predictive Control and PID Controller in Real Time Process Control System," *19th International Conference on Sciences and Techniques of Automatic Control and Computer Engineering, STA 2019*, pp. 64–69, May 2019.
3. H. S. Asad, R. K. K. Yuen, and G. Huang, "Multiplexed real-time optimization of HVAC systems with enhanced control stability," *Appl Energy*, vol. 187, pp. 640–651, Feb. 2017.
4. Q. P. Zheng, J. Wang, and A. L. Liu, "Stochastic Optimization for Unit Commitment - A Review," *IEEE Transactions on Power Systems*, vol. 30, no. 4, pp. 1913–1924, Jul. 2015.
5. J. Silvente, L. G. Papageorgiou, and V. Dua, "Scenario tree reduction for optimisation under uncertainty using sensitivity analysis," *Comput Chem Eng*, vol. 125, pp. 449–459, Jun. 2019.
6. T. Forster, D. Vázquez, I. F. Moreno-Palancas, and G. Guillén-Gosálbez, "Algebraic surrogate-based flexibility analysis of process units with complicating process constraints," *Comput Chem Eng*, vol. 184, p. 108630, May 2024.
7. J. Djuris and Z. Djuric, "Modeling in the quality by design environment: Regulatory requirements and recommendations for design space and control strategy appointment," *Int J Pharm*, vol. 533, no. 2, pp. 346–356, Nov. 2017.
8. T. Homem-de-Mello and G. Bayraksan, "Monte Carlo sampling-based methods for stochastic optimization," *Surveys in Operations Research and Management Science*, vol. 19, no. 1, pp. 56–85, Jan. 2014.
9. N. Murugesan, I. Cho, and C. Tortora, "Benchmarking in Cluster Analysis: A Study on Spectral Clustering, DBSCAN, and K-Means," *Studies in Classification, Data Analysis, and Knowledge Organization*, vol. 5, pp. 175–185, 2021.
10. A. W. Rogers *et al.*, "Integrating knowledge-guided symbolic regression and model-based design of experiments to automate process flow diagram development," May 2024.



© 2025 by the authors. Licensed to PSEcommunity.org and PSE Press. This is an open access article under the creative commons CC-BY-SA licensing terms. Credit must be given to creator and adaptations must be shared under the same terms. See https://creativecommons.org/licenses/by-sa/4.0/




Systems & Control Transactions

**Research Article - Peer Reviewed Conference Proceeding**
ESCAPE 35 - European Symposium on Computer Aided Process Engineering
Ghent, Belgium. 6-9 July 2025
Jan F.M. Van Impe, Grégoire Léonard, Satyajeet S. Bhonsale,
Monika E. Polańska, Filip Logist (Eds.)

PSE PRESS

# Enhancing Energy Efficiency of Industrial Brackish Water Reverse Osmosis Desalination Process using Waste Heat

**Alanood A. Alsarayreh[a], Mudhar A. Al-Obaidi[b], Iqbal M. Mujtaba[c]***

[a] Chemical Engineering Department, Faculty of Engineering. Mu'tah University, Al Karak, Jordan
[b] Technical Instructor Training Institute, Middle Technical University, Baghdad, Iraq
[c] School of Engineering, University of Bradford, Bradford, West Yorkshire, BD7 1DP, UK
* Corresponding Author: I.M.Mujtaba@bradford.ac.uk

## ABSTRACT

The Reverse Osmosis (RO) system has the potential as a vibrant technology to generate high-quality water from brackish water sources. Nevertheless, the progressive growth in water and electricity demands necessitates the development of a sustainable desalination technology. This can be achieved by reducing the specific energy consumption of the process, which would also reduce the environmental footprint. This study proposes the concept of reducing the overall energy consumption of a multistage multi-pass RO system of Arab Potash Company (APC) in Jordan via heating the feed brackish water. The utilisation of waste heat generated from different units of production plant of APC such as steam condensate supplied to a heat exchanger is a feasible technique to heat brackish water entering the RO system. To systematically assess the contribution of water temperature on the performance metrics including specific energy use, a generic model of RO system is developed. Model based simulation is used to evaluate the effect of water temperature. The results indicate a clear enhancement of specific energy consumption while using water temperatures close to the maximum recommended temperature of the manufacture. It has been noticed that an increase in water temperature from 25 ºC to 40 ºC can result an overall energy saving of more than 27%.

**Keywords**: Brackish water desalination, Reverse Osmosis process, Arab Potash Company, Simulation, Specific energy consumption.

## 1. INTRODUCTION

Due to limited sources of freshwater and progressive increase of global population, there is a rapid engineering pace to produce freshwater from seawater and brackish water. This would interpret the global capacity of water production, which exceeds 100 million $m^3$ per day (Jones et al., 2019). In this regard, the utilisation of Reverse Osmosis desalination process is remarkably increased beyond the thermo-driven distillation. Zotalis et al. (2014) ascertained that the RO technology is dominated the global water desalination technologies by more than 70%. This can be ascribed to the simplicity and compact design of RO process with consuming less energy if compared to thermal ones. Wang et al. (2020) elaborated that the conventional thermal desalination plants requires 3 kWh/$m^3$ of specific energy consumption compared to 0.8 kWh/$m^3$ of RO process. Also, the RO process can be easily scaled up or down to meet variable water demands (Al-Obaidi et al., 2022). Interestingly, the freshwater production cost of RO process based seawater and brackish water ranges between 0.5 to 1.5 USD$/$m^3$ compared to 0.7 to 2.0 USD$/$m^3$ for thermal distillation units (Al-Hotmani et al., 2020). Furthermore, the continuous improvement in RO membrane technology and pre-treatment approaches has upgraded the effectiveness of RO systems, making them more attractive than conventional thermal processes.

Despite the fact that the RO process generally offers lower freshwater production cost and reduced specific energy consumption compared to thermal distillation methods, there is still a vital need for further minimising the energy requirements of RO process. Thus, several researchers are clearly focused on exploring advanced practices to ensuring sustainable and low specific energy consumption of cost-effective process.

A number of studies were conducted to examine the effect of water temperature on the performance indicators of RO process. For instance, Koutsou et al. (2020) analysed the impacts of feed-water temperature on the specific energy consumption in RO desalination processes, concentrating on both seawater and brackish treatment. The researchers systematically examined the itemized contributions to specific energy consumption, bearing in mind both positive belongings from increased permeate flux and mitigated viscosity, and negative belonging of reduced salt rejection. For brackish water, an increase in water temperature generally causes a significant reduction in specific energy consumption. However, these advantages were diminished for seawater beyond 25 °C as a result to elevated osmotic pressure. This research has ascertained the need for careful water temperature management in RO system design and operation.

The current research attempts to alleviate the overall energy consumption of the multistage multi pass medium-sized spiral wound brackish water RO desalination plant of Arab Potash Company (APC) located in Jordan with a capacity 1200 m³/day. Specifically, the pre-heating of feed water of RO process is the main objective of this research while investigating its impact on the overall specific energy consumption. To conduct this aim, the concept of waste heat recovery is utilised here via exploiting the generated heat of the potash production process or other nearby industrial operations. More specifically, this can be achieved through using heat exchangers that transfer heat from exhaust gases or hot fluids to the feed water. The simulation of the RO process is achieved using a developed model of the multistage RO process of APC while considering the effect of a selected range of water temperature on the specific energy consumption at a fixed set of feed salinity of brackish water, feed flowrate and pump pressure of RO process. Expectedly, this research would therefore aid to introduce a practicable solution to enhance the overall economic feasibility of RO process desalination of Arab Potash Company. This in turn would be in line of meeting the growing demand for a high-quality (low-salinity) water, which is delivered to ion exchangers and then used in the boilers of APC. Also, this research would address environmental concerns associated with energy use in brackish water desalination.

## 2. BRACKISH WATER RO DESALINATION SYSTEM OF APC

The BWRO desalination plant of APC was designed with a nominal low-salinity water capacity of 1200 m³/day with a product salinity of around 2 ppm. The brackish water is fed into the treatment plant at 100 ppm and (pH = 7.45-7.59) to a set of treatment stages including pre-treatment of three multi-media filters and three cartridge filters, two high-pressure pumps and one standby pump, two passes of 20 pressure vessels with 120 RO membrane modules, post treatment to re-mineralize product water. Two parallel stages of six pressure vessels with arrangement (4:2) constitute the 1st pass while the 2nd pass comprises four pressure vessels with arrangement (2:1:1). Figure 1 depicts a schematic diagram of two passes multi-stage RO process. Six series polyamide thin-film composite spiral wound membranes of 37.2 m² (TMG20D-400, Toray Membrane USA Inc.) are included in each pressure vessel.

The membrane features are provided in Table 3.

## 3. MODELLING OF RO SYSTEM AND VALIDATION

A comprehensive model was established by Al-Obaidi et al. (2018) to predict the performance indicators of the APC. The model consists of a number of algebraic equations. Some of these equations are presented in Table 1. The model was validated against experimental data of the first pass of APC and showed a good consistency as depicted in Table 2 with insignificant errors.

**Table 1:** Model equations (Al-Obaidi et al., 2018).

| **Model Equations** |
|---|
| 1 - $Q_p = A_{w(T)}\, NDP_{fb}\, A_m$ |
| 2 - $A_{w(T)} = A_{w(25\,C)}\, TCF_p\, F_f$ |
| 3- $TCF_p = \exp[0.0307\,(T-25)]$ |
| 4 - $NDP_{fb} = P_{fb} - P_p - \pi_b + \pi_p$ |
| 5 - $P_{fb} = P_f - \frac{\Delta P_{drop,E}}{2}$; $\Delta P_{drop,E} = \frac{9.8692x10^{-6}\, A^*\, \rho_b\, {U_b}^2\, L}{2 d_h\, Re_b^n}$ |
| 6 - $U_b = \frac{Q_b}{W\, t_f\, \epsilon}$; $Q_b = \frac{Q_f + Q_r}{2}$ |
| 7 - $\pi_b = 0.7994\, C_b\, [1 + 0.003\,(T-25)]$ |
| 8 - $C_p = \frac{C_f}{Rec}\,[1-(1-Rec)]^{(1-Rej)}$ |
| 9 - $\rho_b = 498.4\, m_f + \sqrt{[248400\, m_f^2 + 752.4\, m_f\, C_b]}$; $m_f = 1.0069 - 2.757x10^{-4}\, T$ |
| 10 - $D_b = 6.72510^{-6}\, exp\left\{0.154610^{-3}\, C_b - \frac{2513}{T+273.15}\right\}$ |
| 11 - $\mu_b = 1.234x10^{-6}\, exp\left\{0.0212\, C_b + \frac{1965}{T+273.15}\right\}$ |
| 12 - $k = 0.664\, k_{dc}\, Re_b^{0.5}\, Sc^{0.33}\, \left(\frac{D_b}{d_h}\right)\left(\frac{2d_h}{L_f}\right)^{0.5}$ |
| 13 - $Re_b = \frac{\rho_b\, d_h\, Q_b}{t_f\, W\, \mu_b}$ |
| 14 - $Rec = \frac{Q_p}{Q_f}\, x100$ |
| 15 - $Sc = \frac{\mu_b}{\rho_b\, D_b}$ |
| 16 - $Rej = \frac{C_f - C_p}{C_f}\, x100$ |
| 17 - $SEC = \frac{\left(P_f\, x101325)\, Q_f\right)}{\frac{Q_p\, \epsilon_{pump}}{36x10^5}}$ |

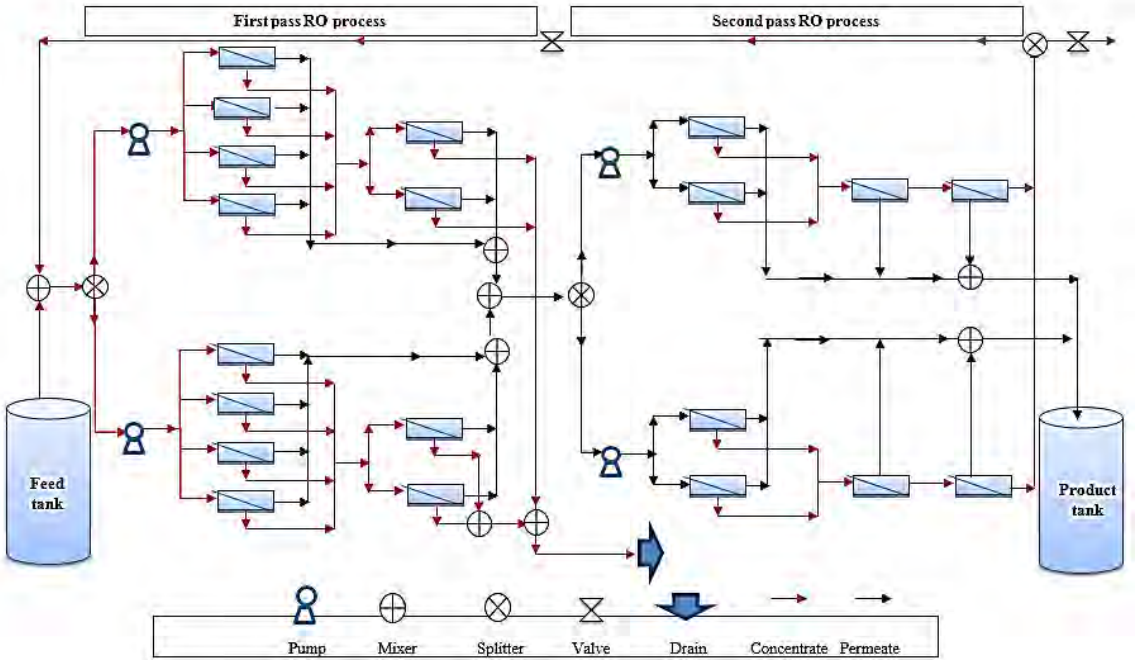



**Figure 1.** A representation of BWRO desalination plant of APC (Adapted from Al-Obaidi et al., 2018).

**Table 2:** Comparison of experimental data and model predictions (Adapted from Al-Obaidi et al., 2018).

| Parameters and units | Experimental data | Model predictions | %Error |
|---|---|---|---|
| Feed flow rate ($Q_f$) | 12.57 | 12.576 | -0.05 |
| Retentate flow rate ($Q_r$) | 8.38 | 8.44 | -0.72 |
| Permeate flow rate ($Q_p$) | 29.23 | 29.42 | -0.65 |
| Recovery rate ($Rec$) | 95.46 | 95.46 | 0.00 |
| Solute rejection ($Rej$) | 58.46 | 58.84 | -0.65 |

**Table 3:** Membrane characteristics (Al-Obaidi et al., 2018).

| Parameter | Value |
|---|---|
| Membrane type | TMG20D-400, Ultra low pressure BWRO |
| Spacer type | NALTEX-129 |
| Spacer thickness of feed and permeate channels (m) | $8.6\times10^{-4}$ and $5.5\times10^{-4}$ |
| Hydraulic diameter of the feed spacer channel $d_h$ (m) | $8.126\times10^{-4}$ |
| Membrane length and width (m) | 1 and 37.2 |
| $A_{w\,(T_o)}$(m/ atm s) | $9.6203\times10^{-7}$ at 25 °C |
| $B_{s(T_o)}$ (m/s) | $1.61277\times10^{-7}$ at 25 °C |
| length of filament $L_f$ (m) | $2.77\times10^{-3}$ |
| $A^{'}$ (-) | 7.38 |
| n (-) | 0.34 |
| $\varepsilon$ (-) | 0.9058 |
| $k_{dc}$ (-) | 1.501 |

## 4. PERFORMANCE ANALYSIS OF SPECIFIC ENERGY CONSUMPTION. IMPACT OF WATER TEMPERATURE

SEC is specifically representing the required energy to generate a unit volume of fresh water. Determining the specific energy consumption of RO process is vital to optimise the overall performance and associated water production cost. In other words, analysing SEC can help to elevate water productivity, and product water quality besides improving the RO membrane configurations. Indeed, lessening SEC can therefore enhance the sustainability of the entire desalination process by reducing the carbon footprint associated with energy use. Utilising heat waste of APC, this section emphasis on demonstrating the simulation results of variable water temperatures' effect on the specific energy consumption of RO process of APC. In this aspect, the water temperature varies between 25 °C to 45 °C. The maximum value of 45 °C is taken based on the maximum allowed temperature recommended by the membrane's supplier (Toray Membrane USA Inc.). It is also important to declare that the present simulation is carried out using the following operating conditions of 1098.62 ppm of brackish water salinity, 74 $m^3/h$ of feed flowrate, 9.22 atm of pump pressure.

Figure 2 introduces the consequence of increasing water temperature from 25 °C to 45 °C on the specific energy consumption considering a fixed inlet conditions. Clearly, a decrease of specific energy consumption can be seen as a response to increasing water temperature. Statistically, the reduction of 27% can be accomplished as a response to this action. This behaviour can be ascribed to a number of plausible reasons. First of all, an increase of water temperature can decrease water density and viscosity of water. This in turn can facilitate easier flow through the feed channel of RO module. Also, the decrease of viscosity property can result in lower resistance to flow, permitting for greater water flux through the membrane pores. second, using an elevated temperature can improve the water diffusion rate, which is related to improving the driving force of water from the feed channel to the permeate channel as a result to limiting the concentration polarization and osmotic pressure and therefore improving the pressure gradient across the membrane. Third, warmer water can make changes on membrane structure with increasing pore size, which would exhibit a greater water permeability constant and enhanced water flux.

Eq. 2 of Table 1 specifies the increase of water permeability constant as a result to increasing water temperature. Referring to the above mentioned reasons, it can be said that water permeation is improved due to increasing water temperature, which finally shows an increase of water productivity. Eqs. 9 and 11 introduce the fact that both water density and viscosity can be decreased with increasing water temperature. This would positively affect the mobility of water molecules to pass through the membrane pores. Eq. 17 of Table 1 introduces the fact of reduced specific energy consumption with increasing permeate flowrate. Furthermore, it has been ascertained that the increase of water temperature from 25 °C to 45 °C has resulted in a growth in water productivity from 1.99 ppm to 25 ppm, respectively. This behavior can be attributed to increasing membrane pore size, which allows for more solute to pass through the membrane texture. This has resulted in an increase of product water salinity. Although this rise in product water salinity, it is crucial to mention that the resulted water remains within tolerable limits for high-quality water standards.

On top of this, the overall advantage of having higher water productivity at elevated temperatures and reduced specific energy consumption would outweigh the concern of increased product water salinity to 25 ppm at 45 °C, as long as water quality keeps within an acceptable range.

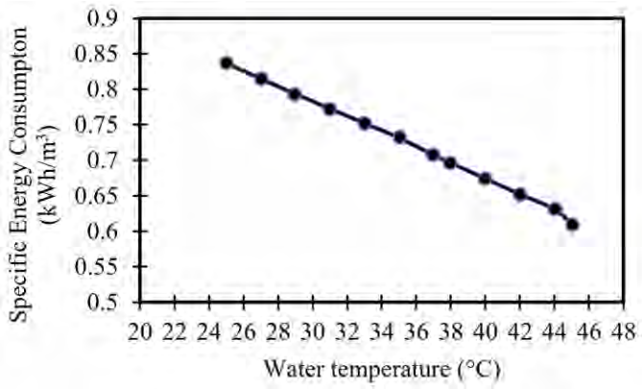



**Figure 2:** Influence of water temperature on specific energy consumption.

The above results come to an agreement with the findings of Yagnambhatt et al. (2024) who appraised the potential of thermally enhanced RO seawater desalination on the overall energy consumption and water permeation. The researchers looked for discussing the trade-off between pump energy savings and the thermal energy input required to heat the seawater. The associated results indicated that an increase of feed water from 20 °C to 50 °C can result in reductions of specific energy consumption of 24% and 33% for seawater and brackish water, respectively. Also, Ghourejili et al. (2022) examined the impacts of water temperature and pH on the specific energy consumption, and outlet water quality of different configurations of RO systems, including simple single-stage, single-stage hybrid, simple two-stage, and two-stage hybrid designs. The researchers specified that a higher water temperature can reduce the energy consumption. In this regard, the configuration of two-stage

hybrid system has shown the lowest specific energy consumption in a comparison to other configurations.

## 5. CONCEPTUAL IDEAS TO RAISE FEED WATER TEMPERATURE OF RO SYSTEM

Section four elucidates the prosperity of elevated brackish water temperature on the specific energy consumption of RO process of APC. This section defines conceptual approaches to increase the water temperature as represented below;

- Waste heat can be provided from a heat exchanger from a nearby industrial process or power generation facility. Successfully, the heat exchanger can transfer thermal energy to the brackish water before entering the RO system, which would increase the temperature and improving performance.
- The integration of heat and power systems which produce both electricity and heat can be exploited to preheat water temperature of the brackish water via the excess heat generated.
- Utilising a solar thermal collector is another possible option to harness solar energy and heating brackish water. Indeed, this option can meaningfully increase water temperature especially in sunny regions besides reducing the dependence on conventional energy sources.
- Heat pumps is another feasible option to preheat brackish water. The heat pump can extract heat from the environment and easily transfer it to the brackish water.

## 6. CONCLUSIONS

The current research intended to evaluate the utilisation of waste heat to increase brackish water temperature and consequently assessing its impact on the specific energy consumption of multi-stage RO process of APC. The simulation results were conducted using a developed validated model. The simulation results introduced a reduction of 27% in specific energy consumption due to increasing water temperature from 25 °C to 45 °C (within the maximum water temperature). This improvement was ascribed to the possible changes of the membrane structure, water transport parameter in addition to physical properties. A number of possible techniques to exploit waste heat from nearby industrial processes and preheating brackish water were illustrated at the end.

## NOMENCLATURE

$Q_p$ : Permeate flow rate (m³/s)

$A_{w(T)}$ : Water permeability constant (m/atm s)

$A_m$ : Effective membrane area (m²)

$B_{s(T)}$ : Solute permeability constant (m/s)

$C_b$ : Bulk solute concentration (ppm)

$k$ : Mass transfer coefficient (m/s)

$T$ : Brackish water temperature (°C)

$L$ : The membrane length (m)

$d_h$ : The hydraulic diameter (m)

$SEC$: Specific energy consumption (kWh/m³)

$Rec$: Recovery rate (-)

$k_{dc}$ : Constant (-)

$D_b$ : Solute diffusion coefficient (m²/s)

$Ff$: Fouling factor (1/s)

$\mathrm{P_{fb}}$ : Bulk pressure (atm)

$P_p$ : Permeate pressure (atm)

$P_r$ : Retentate pressure (atm)

$\pi_b$ : Bulk osmotic pressure at the feed channel (atm)

$\pi_p$ : Permeate osmotic pressure (atm)

$Q_f$ : Feed flowrate (m³/s)

$Q_b$ : Bulk flowrate (m³/s)

$Q_r$ : Retentate flowrate (m³/s)

$Q_s$ : Solute flux (kg/m² s)

$C_w$ : Solute concentration on the membrane wall (ppm)

$C_p$ : Permeate solute concentration (ppm)

$Re_b$ : Reynolds number (-)

$Sc$ : Schmidt number (-)

$\rho_b$ : Density (kg/m³)

## REFERENCES


1. Al-Hotmani OMA, Al-Obaidi MA, Filippini G, Manenti F, Patel R, Mujtaba IM. Optimisation of multi effect distillation based desalination system for minimum production cost for freshwater via repetitive simulation. *Comput. Chem. Eng.*, 135:106710 (2020). https://doi.org/10.1016/j.compchemeng.2019.106710
2. Al-Obaidi MA, Alsarayreh AA, Al-Hroub AM, Alsadaie S, Mujtaba IM. Performance analysis of a medium-sized industrial reverse osmosis brackish water desalination plant. *Desalination*, 443:272-284 (2018). https://doi.org/10.1016/j.desal.2018.06.010
3. Al-Obaidi MA, Rasn KH, Aladwani SH, Kadhom M,

Mujtaba IM. Flexible design and operation of multi-stage reverse osmosis desalination process for producing different grades of water with maintenance and cleaning opportunity. *Chem. Eng. Res. Des.* 182:525-543 (2022). https://doi.org/10.1016/j.cherd.2022.04.028
4. Ghourejili S, Vahidfard V, Mousavi Y, Babapoor A, Faraji M. Effect of temperature on energy consumption and recovery rate of the reverse osmosis brackish systems in a different arrangement. *Scientia Iranica*, 29(6):3167-3178 (2022). https://doi.org/10.24200/sci.2022.57816.5432
5. Jones E, Qadir M, van Vliet MT, Smakhtin V Kang SM. The state of desalination and brine production: A global outlook. *Sci. Total Environ*. 657:1343-1356 (2019). https://doi.org/10.1016/j.scitotenv.2018.12.076
6. Koutsou CP, Kritikos EM, Karabelas AJ, Kostoglou M. Analysis of temperature effects on the specific energy consumption in reverse osmosis desalination processes. *Desalination* 476:114213 (2020). https://doi.org/10.1016/j.desal.2019.114213
7. Wang L, Violet C, DuChanois RM, Elimelech M. Derivation of the theoretical minimum energy of separation of desalination processes. *J. Chem. Educ*. 97(12):4361-4369 (2020). https://pubs.acs.org/doi/10.1021/acs.jchemed.0c01194?goto=supporting-info&articleRef=control
8. Yagnambhatt S, Khanmohammadi S, Maisonneuve J. Reducing the specific energy use of seawater desalination with thermally enhanced reverse osmosis. *Desalination* 573:117163 (2024). https://doi.org/10.1016/j.desal.2023.117163
Zotalis K, Dialynas EG, Mamassis N, Angelakis AN. Desalination technologies: Hellenic experience. *Water*, 6(5):1134-1150 (2014). https://doi.org/10.3390/w6051134

© 2025 by the authors. Licensed to PSEcommunity.org and PSE Press. This is an open access article under the creative commons CC-BY-SA licensing terms. Credit must be given to creator and adaptations must be shared under the same terms. See https://creativecommons.org/licenses/by-sa/4.0/



Systems & Control Transactions

**Research Article - Peer Reviewed Conference Proceeding**
ESCAPE 35 - European Symposium on Computer Aided Process Engineering
Ghent, Belgium. 6-9 July 2025
Jan F.M. Van Impe, Grégoire Léonard, Satyajeet S. Bhonsale,
Monika E. Polańska, Filip Logist (Eds.)

PSE PRESS

# Optimization of Heat Transfer Area for Multiple Effects Desalination (MED) Process

**Salih M. Alsadaie[a], Sana I. Abukanisha[a], Amhamed A. Omar[b], and Iqbal M. Mujtaba[c]***

[a] Sirte University, Department of Chemical Engineering, Sirte, Libya
[b] Sirte Oil Company, National Oil Corporation, Libya
[c] Bradford University, Department of Chemical Engineering, Bradford BD7 1DP, UK
* Corresponding Author: I.M.Mujtaba@bradford.ac.uk.

## ABSTRACT

Seawater desalination is considered as the only available solution that can cope with the increasing demand for freshwater around the world. Improving the desalination techniques may help to cut off the cost and increase sustainability. In this paper, a mathematical model describing the MED process is developed within gPROMs software. The model includes all the necessary mass and energy balance equations together with thermodynamic and physical properties equations. The model predictions are validated against the actual plant data before using the model for optimizing the process to achieve minimum heat transfer area. For two different operating conditions (summer and winter) and a fixed production demand, the heat transfer area is minimised while optimising different parameters of the MED process. The results showed that a 10.4% reduction in the heat transfer area can be achieved under summer operating conditions and around 26% decrease in the heat transfer area can be met under winter operating conditions.

**Keywords**: gProms, Modelling and Simulations, Optimization, MED Desalination, Heat Transfer Area

## INTRODUCTION

The improvement in the living standard and increasing abstraction of available freshwater put more stress on the desalination industries to cope with the increasing demand for freshwater. Unfortunately, seawater desalination is the last and maybe the only available option to produce freshwater by removing the salt from the seawater. However, with the increasing world population and improved standard of living, freshwater production processes face the challenge of producing freshwater at higher quality and lower cost. The most known techniques for water desalination are thermal techniques such as Multistage Flash desalination (MSF) and Multiple Effect desalination (MED) and membrane techniques such as Reverse Osmosis (RO). Although the installed capacity of (RO) remarkably surpasses the MSF and MED [1], the MED process, operating considerably at a much lower temperature, is more preferred option for new construction plants in different locations around the world where waste heat is available [2]. However, the MED desalination technology is highly energy intensive (ranging from 5.5 to 20 kW h/m3) [3]. In addition, the product cost of freshwater from the MED process may vary between 0.27 and 1.49 USD/m3 [4]. It is still quite expensive and hence, it is believed that more work is required to cut off the costs and increase the profitability by operating the plant at minimal energy consumption. Some previous studies in the literature have been carried out to reduce the cost of freshwater by hybrid MED process with other desalination techniques. Al-hotmani et al. [5] integrated the MED process with the RO process to find more room for improvement. With a slight reduction of the consumed energy, the results showed that 9% increase in production rate and a 5% reduction in the brine flow rate. Others attempt to reduce the cost by powering the MED process with renewable sources of energy such as wind and solar energy. Kaabinejadian et al. [6] investigated the advantages of integration of MED with a humidification-dehumidification (HDH) unit powered by solar energy. The optimised total cost is found to be 0.548 $/s. Moreover, integrating the HDH unit with the MED process resulted in an increase in the freshwater production and the cost by 0.5% and 0.1%, respectively. However, the main drawbacks of renewable energies are their dependencies on climate conditions (available sunshine, wind power). The

optimization of a single MED process can be classified into two categories; finding the optimal operating conditions that result in minimum energy consumption and maximum production rate and/or finding the optimum design configuration that results in minimum fixed cost of the plant. Al-Mutaz and Wazeer [7] optimized the number of effects that result in minimum capital cost and steam cost. The results showed that increasing the number of effects from 11 to 15 would result in a reduction of water cost by 0.029 $/m3. With the aid of solar energy as supplied heat, Talebbeydokhti, et al. [8] carried out a performance analysis to investigate the feasibility of finding the optimum operating conditions at different numbers of effects and different heat sources. Processes with different number of effects (7, 9 and 11 effects) were investigated and obtained optimum operating conditions for each case. Sadri et al. [9] conducted multi-objective optimization to increase the gain output ratio (GOR) and minimise the heat transfer area. For the fixed mass flow rate of the seawater, the results showed an increase of 11.32 % in the GOR and a 17.29 % reduction in the heat transfer area. Harandi et al. [10] performed multi-objective optimization for the MED process integrated with a gas power plant using nondominated sorting genetic algorithm II. Considering GOR and annual cost as objective functions, it was found that higher GOR can be obtained for 9 effects MED and lower annual cost can be obtained for 4 effects MED. Rivera et al. [11] carried out multi-objective optimization for two different-sized MED plants one with 9 effects and the second with 12 effects. The objective of the study was to find optimum operating conditions that minimise the thermal energy and the cost of produced water and maximize the production rate. The authors claimed that different optimal solutions can be found depending on the objectives of the optimization.

Most of the previous studies consider the MED process in one single mode (Summer/Winter) and a typical MED configuration. In this paper, a mathematical model for MED is developed and solved using gPROMs software. For a fixed production rate, several operating parameters are optimized to minimise the heat transfer area of the MED process. Unlike most of the previous works, the optimization procedure is conducted for two different seasons (summer and winter). Further, the MED plant under investigation interestingly has a different design configuration with two large effects and two small effects combined together in a single MED process which makes it unique to other types of MED plants around the world.

## MED PROCESS DESCRIPTION

The MED process, as presented in Figure 1, consists of two large effects, two small effects and a condenser. The heating steam coming from the ejector flows inside the tubes of the first effect while a portion of the feed seawater is sprayed around the outside surface of the tubes of the first effect. The other seawater portion is divided over the rest of the effect based on the size of each effect. The release of the latent heat of the steam causes an increase in the temperature of the seawater resulting in the evaporation of some water. The evaporated water then flows through the channel into the tubes of the second effect and the process is repeated until the fourth effect. In most configurations of the MED, part of the low-pressure entrained vapour is taken from the last effect and introduced to high-pressure motive steam through the ejector. However, in the MED process considered here, the part of the low-pressure-entrained vapour is taken from the second effect leading to a smaller amount of vapour entering the third and fourth effects. As a result, the installed third and the fourth effects have a smaller area. More details of the process can be found in the literature.

## MATHEMATICAL MODEL OF MED PROCESS

A steady-state mathematical model is developed to simulate the MED process. The model is built based on mass and energy balance equations, and it is supported with physical and thermodynamic properties correlations. The developed model is divided into three parts: evaporators, a steam ejector and a down condenser. The two plate heat exchangers are also modelled as a simple heat exchanger, but their model equations are not included here. More details of the model equations and physical properties correlations can be obtained from Al-Mutaz and Wazeer [12]. For the sake of simplicity and to obtain reasonable results from the model, the following assumptions are made:

1. The distillate product is salt-free.
2. There are no heat losses to the surroundings as the equipment is well insulated.
3. The release of non-condensable gases is neglected.
4. The heat of mixing is neglected.

The following are the governing equations of the process including the physical properties correlations.

### Evaporator

$$\Delta T = \left[T_{b_out(1)} - T_{b_out(n)}\right]/[n-1] \quad (1)$$

$$T_{b_out(1)} = T_s - \Delta T \quad (2)$$

$$T_{b_out} = T_{b_in} - \Delta T \quad (3)$$

$$T_{v_out(1)} = T_{b_out(1)} - BPE \quad (4)$$

$$F + B_{in} = V_{vapour} + V_{brine} + V_{dist} + B_{out} \quad (5)$$

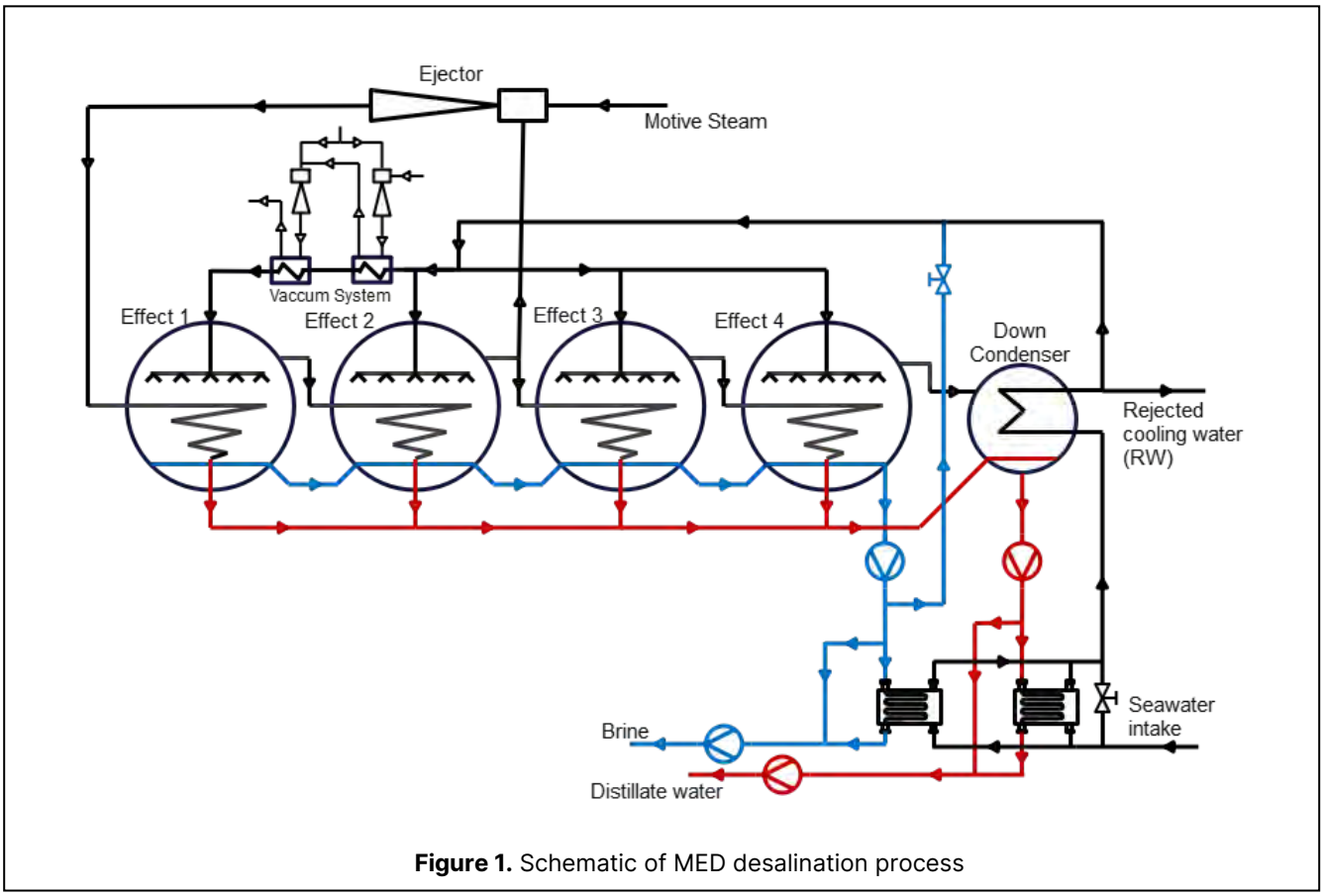



**Figure 1.** Schematic of MED desalination process

$$X_F\,F + X_{b_in}B_{in} = X_{b_out}B_{out} \quad (6)$$

$$V_{_in}\lambda_{in} = F\,Cp_w\left(T_{b_out} - T_f\right) + V_{vapour}\lambda_{out} \quad (7)$$

$$V_{_in}\,\lambda_{in} = A_e\,U\,(T_{v-in} - T_{v-out}) \quad (8)$$

$$V_{brine} = \left[B_{in}Cp_{brine}(T_{b_{in}} - T^{'})\right]/[\lambda_{in}] \quad (9)$$

$$T^{'} = T_{b_out} - NEA \quad (10)$$

$$NEA = \left[33\left(T_{b_{in}} - T_{b_{_out}}\right)^{0.55}\right]/\left[T_{v_out}\right] \quad (11)$$

$$V_{dist} = \left[D_{in}Cp_{dist}\,(T_{cond} - T^{'})\right]/[\lambda_{out}] \quad (12)$$

$$T^{"} = T_{v_out} + NEA' \quad (13)$$

$$NEA' = \left[33\left(T_{C_{in}} - T_{v_{_out}}\right)^{0.55}\right]/\left[T_{v_out}\right] \quad (14)$$

$$T_{cond} = T_{v-in} - \Delta T_{loses} \quad (15)$$

$$V_{out} = V_{vapor} + V_{brine} + V_{dist} \quad (16)$$

## Down Condenser

$$V_{out(n)}\lambda_{out(n)} = F\,Cp_{cw}\,(T_F - T_{cw}) \quad (17)$$

$$V_{out(n)}\lambda_{out(n)} = A_cU_cLMTD_C \quad (18)$$

$$LMTD_C = \left[(T_f - T_{cw})\right]/\left[\ln\left(\frac{T_{v-out} - T_{cw}}{T_{v-out} - T_f}\right)\right] \quad (19)$$

## Steam Injector

$$M_s = M_{ev} + M_u \quad (20)$$

$$R_a = 0.296\,\frac{{P_S}^{1.19}}{{P_{ev}}^{1.04}}\left(\frac{P_m}{P_{ev}}\right)^{0.015}\left(\frac{PCF}{TCF}\right) \quad (21)$$

$$PCF = 3\times10^{-7}\left({P_m}^2\right) - 0.0009\,P_m + 1.6101 \quad (22)$$

$$TCF = 2\times10^{-8}({T_{ev}}^2) - 0.0009\,T_{ev} + 1.0047 \quad (23)$$

$$CR = P_s/P_{ev} \quad (24)$$

$$P_s = 1000\times\exp\left(\frac{-3892.7}{T_s+273.15-42.6776} + 9.5\right) \quad (25)$$

$$P_{ev} = 1000\times\exp\left(\frac{-3892.7}{T_{ev}+273.15-42.6776} + 9.5\right) \quad (26)$$

$$GOR = D_{total}/M_S \quad (27)$$

## Physical properties correlations

### Specific Heat Capacity (Cp)

$$\mathrm{Cp} = (\mathrm{a} + \mathrm{bT} + \mathrm{cT}^2 + \mathrm{dT}^3)\times10^{-3}$$

Where:

$$\mathrm{a} = 4206.8 - 6.6197\,\mathrm{S} + 1.2288\times10^{-2}\mathrm{S}^2$$

$$\mathrm{b} = -1.1262 + 5.4178\times10^{-2}\,\mathrm{S} - 2.2719\times10^{-4}\mathrm{S}^2$$

$$\mathrm{c} = 1.2026\times10^{-2} - 5.3566\times10^{-4}\,\mathrm{S} - 1.8906\times10^{-6}\mathrm{S}^2$$

$$\mathrm{d} = 6.877\times10^{-7} + 10517\times10^{-6}\,\mathrm{S} - 404268\times10^{-9}\mathrm{S}^2$$

## Boiling Point Elevation

$$BPE = Xb \times ((A + B \times Xb) + (C \times Xb^2))$$

$$A = 8.325 \times 10^{-2} + 1.883 \times 10^{-4} T_{b-out} + 4.02 \times 10^{-6} T_{b-out}^{\ 2}$$

$$B = -7.625 \times 10^{-4} + 9.02 \times 10^{-5} T_{b-out} - 5.02 \times 10^{-7} T_{b-out}^{\ 2}$$

$$C = 1.522 \times 10^{-4} - 3 \times 10^{-6} T_{b-out} - 3 \times 10^{-8} (T_{b-out})^2$$

## Boiling Point Elevation

$$\lambda_{in} = 2499.5689 - 2.20486\, T_s - 0.00176\, T_s^{\ 2}$$

$$\lambda_{out} = 2499.5689 - 2.20486\, T_{v-out} - 0.00176\, T_{v-out}^{\ 2}$$

In the above two equations, the temperature is in °C, and latent heat is in kJ/kg.

## Simulation and Validation

The MED plant under this investigation is located in Sirte, Libya. It was installed in 2010 and got into actual operation after 2016. Table 1 presents input operating parameters for two different modes: summer mode and winter mode. The accuracy of the model predictions is very important in any simulation. Hence, the model is validated against actual data for the summer mode. The actual plant data and the simulation results are shown in Table 2. As can be seen, good agreement against actual data has been obtained. Normally in winter mode, the plant operates in different conditions. However, due to the lack of full actual winter operating data from the plant, the validation is carried out only against summer operating data.

**Table 1:** Input parameters of 4 effects MED process for summer and winter modes

| Parameters | Summer mode | Winter mode |
|---|---|---|
| Motive steam pressure (bar) | 11.4 | 11.4 |
| Motive steam flowrate (kg/s) | 5.85 | 5.85 |
| Inlet steam temperature to the first effect (°C) | 68.5 | 68.5 |
| Mass flow of the seawater to the effects (kg/s) | 144.444 | 144.444 |
| Intake seawater temperature (°C) | 27 | 14 |
| Recycle brine flowrate (kg/s) | 0.0 | 60.444 |
| Last stage brine outlet temperature (°C) | 52 | 50 |

## Optimization Problem

To obtain the optimal operating conditions that result in a minimum heat transfer area, an optimization approach is carried out to minimize the heat transfer area at a fixed demand of freshwater. Motive steam flowrate, entrained vapour to the ejector, last effect's brine temperature, feed flowrate and intake seawater flowrate are optimized to achieve the objective. For winter mode, the recycle brine flow rate is also optimized. To maintain the feasible operating conditions, the optimised parameters are controlled by introducing equality and inequality constraints including lower and upper desalination plant limits.

**Table 2:** Validation of the simulation results against actual operating parameters.

| Parameters | Values | | |
|---|---|---|---|
| | Actual | Model | Error |
| Top Boiling Temp. (°C) | 64 | 64.38 | 0.6% |
| Distillate flowrate (kg/s) | 47.91 | 45.89 | -4.2% |
| Distillate water temp. (°C) | 52 | 51.45 | -1% |
| The feed seawater temp. (°C) | 46.41 | 46.72 | 0.7% |
| **Heat transfer area, Ae ($m^2$)** | | | |
| First effect | 3760 | 3674.2 | -2.3% |
| Second effect | 3760 | 3673.2 | -2.3% |
| Third effect | 810 | 775.8 | -4.2% |
| Fourth effect | 810 | 779.6 | -3.7% |
| Gain Output Ratio (GOR) | 8.19 | 7.82 | -4.5% |

The optimization problem can be described as follows:

Optimization Problem

| Minimize | Optimize |
|---|---|
| Ae | Mev, Mu, Tb(n), F, seawater intake and brine recycle for winter mode only |

Subject to:

Equality constraints: the fixed demand for freshwater ($D_{TOTAL}$ = 45.89 kg/s)

Inequality constraints: the lower and upper limits of some constraints are different between summer and winter.

**Table 2**

| Summer conditions | | | | Winter conditions | | | |
|---|---|---|---|---|---|---|---|
| Lower | | Parameter | upper | Lower | | Parameter | upper |
| 0.0 | < | RW (kg/s) | < 50 | 0.0 | < | RW (kg/s) | < 50 |
| 1.0 | < | CR | < 3.0 | 1.0 | < | CR | < 3.0 |
| 44 | < | Tf (°C) | < 50 | 40 | < | Tf (°C) | < 50 |
| 35 | < | Td* (°C) | < 45 | 25 | < | Td* (°C) | < 35 |
| 35 | < | Tb** (°C) | < 45 | 25 | < | Tb** (°C) | < 35 |

* Temperature of the distillate leaving the distillate plate heat exchanger

** Temperature of the brine leaving the brine plate heat exchanger

Table 3 shows the new values of the optimized parameters for summer and winter conditions. The flow rate of the main source of energy which is the motive steam slightly decreased by 1.5 % in summer and increased by 3.6 % in winter. In addition, table 4 depicts the results of the optimization process. As can be seen, the values of the constraints in the optimization problem did not violate the constraints' limits. Table 5 shows the results of the optimization process. Interestingly, the total heat transfer area for the 4 effects has been reduced by 10.4% in summer and by 26% in winter. Hence, the new design of the MED process should be based on summer conditions which require more available area. If the MED process is designed based on winter conditions, the available area can not meet the demand for freshwater in the summer season. Other parameters are in the feasible values and the MED process can operate at the new conditions comfortably.

**Table 3:** Optimized parameters and the optimization results for the two seasons

| **Optimized parameters** | | |
|---|---|---|
| Parameters | Summer | Winter |
| Motive steam flowrate, (kg/s) | 5.76 | 6.06 |
| Entrained vapour flowrate, kg/s | 13.68 | 10.97 |
| Last effect temperature $^{o}$C | 49.67 | 43.0 |
| Feed flowrate, kg/s | 150.95 | 170 |
| Seawater intake flowrate, kg/s | 170 | 135 |
| Brine recycle flowrate, kg/s | - | 40.32 |

**Table 4:** optimization results for the two seasons.

| **Optimization results** | | |
|---|---|---|
| Parameters | Summer | Winter |
| Rejected water (RW) (kg/s) | 19.04 | 6.01 |
| CR | 1.569 | 1.83 |
| Tf ($^{o}$C) | 44.75 | 46.67 |
| Td* ($^{o}$C) | 35.2 | 25.14 |
| Tb** ($^{o}$C) | 36.1 | 26.09 |

**Table 5:** Objective function of the optimization process.

| Summer | Winter |
|---|---|
| 1$^{st}$ effect = 3426.2 m$^2$ | 1$^{st}$ effect = 2338.1 m$^2$ |
| 2$^{nd}$ effect = 3343.7 m$^2$ | 2$^{nd}$ effect = 2230.1 m$^2$ |
| 3$^{rd}$ effect = 589.10 m$^2$ | 3$^{rd}$ effect = 638.60 m$^2$ |
| 4$^{th}$ effect = 620.20 m$^2$ | 4$^{th}$ effect = 732.10 m$^2$ |
| Total area = 7979.2 m$^2$ | Total area = 5938.9 m$^2$ |

Total area reduction is 10.4% in summer mode and 26% in winter mode.

## CONCLUSIONS

The optimization problem to minimize the heat transfer area has been solved and the minimum required heat transfer area has been achieved. To accomplish this goal, a detailed mathematical model for the MED process was developed and validated against actual plant data. For a fixed freshwater demand, the results showed the possibility of designing the MED process with less heat transfer area. Moreover, the results depicted that the MED process should be designed based on the summer conditions due to a higher available area and lower motive steam. Moreover, the demand for the freshwater is higher in the summer than in the winter.

## NOMENCLATURE

Ac Heat transfer area of the condenser (m$^2$)
Ae Heat transfer area of the effect (m$^2$)
Bin Brine flow rate entering the effect (kg/s)
Bout Brine flow rate leaving the effect (kg/s)
BPE Boiling Point Elevation ($^{O}$C)
Cpbrine Heat capacity of the brine (kJ/kg.$^{0}$C)
Cpdist Heat capacity of the distillate (kJ/kg.$^{0}$C)
Cpw Heat capacity of seawater (kJ/kg.$^{0}$C)
CR Pressure ratio of compressed steam and entrained steam.
Din Distillate flow rate entering the flash box (kg/s)
DTotal Total product flowrate (kg/s)
F Seawater feed flow rate to the effect (kg/s)
GOR gain output ratio (kg distillate/kg stem)
LMTD Logarithmic mean temperature difference
Mev Mass flow rate of the entrained steam (kg/s)
Ms Mass flow rate of the compressed steam (kg/s)
Mu Motive steam (kg/s)
n Number of effects
NEA Non-Equilibrium Allowance.
PCF The motive steam pressure correction factor
Pev Pressures of the entrained steam (kPa)
Pm Pressures of the motive steam (kPa)
Ps Pressures of the compressed steam (kPa)
Ra Mass ratio of motive steam to entrained steam
RW Rejected cooling water flow rate (kg/s).
T' Temperature to which the brine cools down as it enters the next effect ($^{O}$C).
T" Temperature of the condensing vapour as it enters the flash box ($^{O}$C)
Tb_in Brine inlet temperature ($^{O}$C)
Tb_out Outlet temperature of brine ($^{O}$C)
Tc_in Inlet temperature of the distillate entering the effect ($^{O}$C)
TCF The motive steam temperature correction factor
Tcond The temperature of the distillate vapour ($^{O}$C)
Tcw Temperature of intake seawater ($^{O}$C)
Tf Temperature of feed seawater ($^{O}$C)
Ts Inlet steam temperature ($^{O}$C)
Tv_in Inlet temperature of the vapour ($^{O}$C)
Tv_out The outlet temperature of the vapour ($^{O}$C)

U The overall heat transfer coefficient (Kw/m$^2$.$^o$C)
Uc The overall heat transfer coefficient of the condenser (Kw/m$^2$.$^o$C)
Vbrine Flow rate of the released vapour from the brine pool (kg/s)
V_in Input vapour flow rate (kg/s)
Vout Outlet vapour flow rate (kg/s)
$V_{vapour}$ Vapour evaporated over the surface of the tubes (kg/s)
Xb Salinity (ppm)
Xb_in Inlet brine salinity (ppm)
Xb_out Outlet brine salinity (ppm)
Vbrine Flow rate of the released vapour from the brine pool (kg/s)
Vdist Flow rate of the released vapour from the distillate pool (kg/s)
Xf Feed salinity (ppm)

### Greek letters

$\lambda in$ Latent heat of the entering vapour at the inlet vapour temperature (kJ/kg.$^0$C)
$\lambda out$ Latent heat of the released vapour at the outlet vapour temperature (kJ/kg.$^0$C)
Δt Temperature difference ($^O$C)

## REFERENCES


1. Mayor, B., "Growth patterns in mature desalination technologies and analogies with the energy field," Desalination, vol. 457, pp. 75-84, 2019.
2. Prajapati, M., Shah, M., and Soni, B., "A comprehensive review of the geothermal integrated multi-effect distillation (MED) desalination and its advancements," Groundwater for Sustainable Development, vol. 19, p. 100808, 2022.
3. Ren, J., Zhao, H., Wang, M., Miao, C., Wu, Y., and Li, Q., "Design and Investigation of a Dynamic Auto-Adjusting Ejector for the MED-TVC Desalination System Driven by Solar Energy," Entropy, vol. 24, p. 1815, 2022.
4. Shahouni, R., Abbasi, M., Kord, M., and Akrami, M., "Modelling and optimising of MED-TVC seawater desalination plants assisted with electric heaters," Water Resources and Industry, vol. 32, p. 100262, 2024.
5. Al-hotmani, O. M. A., Al-Obaidi, M. A. A., John, Y. M., Patel, R., and Mujtaba, I. M., "An innovative design of an integrated MED-TVC and reverse osmosis system for seawater desalination: process explanation and performance evaluation," Processes, vol. 8, p. 607, 2020.
6. Kaabinejadian, A., Moghimi, M., and Fakhari, I., "Design, modeling, and thermo-economic optimization of an innovative continuous solar-powered hybrid desalination plant integrated with latent heat thermal energy storage," Applied Thermal Engineering, vol. 219, p. 119576, 2023.
7. Al-Mutaz, I. S. and Wazeer, I., "Economic optimization of the number of effects for the multieffect desalination plant," Desalination and Water Treatment, vol. 56, pp. 2269-2275, 2015.
8. Talebbeydokhti, P., Cinocca, A., Cipollone, R., and Morico, B., "Analysis and optimization of LT-MED system powered by an innovative CSP plant," Desalination, vol. 413, pp. 223-233, 2017.
9. Sadri, S., Ameri, M., and Khoshkhoo, R. H., "Multi-objective optimization of MED-TVC-RO hybrid desalination system based on the irreversibility concept," Desalination, vol. 402, pp. 97-108, 2017.
10. Harandi, H. B., Asadi, A., Rahnama, M., Shen, Z.-G., and Sui, P.-C., "Modeling and multi-objective optimization of integrated MED–TVC desalination system and gas power plant for waste heat harvesting," Computers & Chemical Engineering, vol. 149, p. 107294, 2021.
11. Rivera, C., Cuevas, C., and Farías, Ó., "Multi-objective optimization with multiple Pareto frontiers applied to a MED desalination system," Energy Conversion and Management, vol. 287, p. 117076, 2023.
12. Al-Mutaz, I. S. and Wazeer, I., "Development of a steady-state mathematical model for MEE-TVC desalination plants," Desalination, vol. 351, pp. 9-18, 2014.



© 2025 by the authors. Licensed to PSEcommunity.org and PSE Press. This is an open access article under the creative commons CC-BY-SA licensing terms. Credit must be given to creator and adaptations must be shared under the same terms. See https://creativecommons.org/licenses/by-sa/4.0/




Systems & Control Transactions

**Research Article - Peer Reviewed Conference Proceeding**
ESCAPE 35 - European Symposium on Computer Aided Process Engineering
Ghent, Belgium. 6-9 July 2025
Jan F.M. Van Impe, Grégoire Léonard, Satyajeet S. Bhonsale,
Monika E. Polańska, Filip Logist (Eds.)

PSE PRESS

# Physics-based and data-driven hybrid modelling and dynamic adaptive multi-objective optimization of chemical reactors for $CO_2$ capture via enhanced weathering

**Yalun Zhao, Jin Xuan, and Lei Xing ***

University of Surrey, School of Chemistry and Chemical Engineering, Guildford, UK
* Corresponding Author: l.xing@surrey.ac.uk.

## ABSTRACT

Enhanced weathering (EW) of alkaline minerals in chemical reactors with a controlled environment is recognized as a promising approach for gigaton-level carbon dioxide removal. However, reactor configuration and operating conditions must be optimized to balance the interfacial areas between gas, liquid and solid phases prior to industrial application. We developed a physics-based and data-driven hybrid modelling approach, coupled with multi-objective optimization, to study and compare three typical chemical reactors, i.e., trickle bed, packed bubbling columns, and stirred slurry reactors, and the optimal design to improve $CO_2$ capture rate and reduce energy and water consumptions. Then an adaptive optimization is proposed to dynamically adjust the operating of the reactors in response to intermittent $CO_2$ emission and renewable energy supply. Results indicated that forced stirring enhances $CO_2$ capture rates by accelerating mass transport but increases energy consumption. Trickle bed reactor achieves the highest capture rate and lowest energy and water consumption. The AI-enabled, multi-objective, and adaptive optimization developed in response to intermittent $CO_2$ and energy supplies shows considerable potential for industrial applications, advancing progress towards achieving SDG #13.

**Keywords**: $CO_2$ capture, Enhanced weathering, Chemical reactors, Data-driven, Optimization

## 1. INTRODUCTION

Enhanced weathering (EW) of minerals is considered as a promising method for large-scale sequestering atmospheric $CO_2$, with the potential to absorb approximately a billion tonnes annually [1]. This process primarily occurs in specific natural environments where $CO_2$ interacts with water and minerals and converts to bicarbonate [2]. Despite its potential, the inherently slow rate of natural weathering raises critical questions about its capacity to scale up effectively to meet the ambitious goal of limiting global warming to 1.5°C by the end of the century [3]. Recent studies have shown that deploying crushed minerals in controlled engineering reactors rather than natural settings can significantly enhance $CO_2$ capture efficiencies [4]. EW has undergone validation through various scales of testing, including laboratory experiments, small-scale field trials, and idealized land ecosystem simulations [5]. However, the transition to larger operational scales presents substantial challenges, primarily due to the significant resources and energy consumption involved. This includes substantial quantities of water, energy for crushing minerals, and the transport and circulation of liquid and gas reactants during EW-based $CO_2$ capture reactions.

Trickle bed reactors (TBR), packed bubble columns (PBC), and stirred slurry reactors (SSR) are three common types of multi-phase reactors utilized in the chemical industry. To investigate their potential in EW-based $CO_2$ capture, we developed detailed mechanistic models that describe the unique mass transport characteristics of each reactor type. These models were rigorously validated using experimental data. Following validation, we developed data-driven models employing machine learning algorithms, which were further enhanced with multivariable and multi-objective optimization approaches. This methodology allows for the identification of trade-off solutions between $CO_2$ capture rate, and water and

energy consumption. Ultimately, these reactors were integrated into renewable energy systems with intermittent energy and $CO_2$ supplies. Dynamic adaptive optimization was conducted, enabling the autonomy of the system to respond effectively to fluctuations in energy and $CO_2$ availability. This integration facilitates the effective model predictive control of $CO_2$ capture systems and offers significant performance enhancement, cost reduction and environmental benefits.

## 2. PHYSICS-BASED MODELLING AND MODEL VALIDATION

Physics-based mechanistic models for the three reactor types were developed by integrating reaction kinetics with mass transport processes. For $CO_{2(g)}$, the following equation is used to describe the mass balance:

$$\varepsilon_G \frac{\partial}{\partial t} c_{CO_2(g)} + \nabla \cdot (u_G c_{CO_2(g)}) = -r_{G-L} \quad (1)$$

The mass balance for aqueous species *i* is described by:

$$\varepsilon_L \frac{\partial}{\partial t} c_i - \varepsilon_L E_L \nabla^2 c_i + u_L \nabla \cdot c_i = r_i \quad (2)$$

where $\varepsilon_G$ and $\varepsilon_L$ are the gas holdup, $r_{G-L}$ and $r_i$ are the source terms for gas and aqueous species, $u_G$ and $u_L$ are the gas and liquid superficial velocities, $c$ is the concentration, $E_L$ is the dispersion coefficient.

More details for model development can be found elsewhere [4,6-9]. The following assumptions are used:

- Mineral particles are loaded at the start of the operation without further replenishment.
- Isothermal operations at 20 °C without considering the reaction heat.
- Radial gradients of concentration or velocity are omitted.
- An average particle-shrinking rate was applied to all calcite particles, independent of the location inside the packed bed.
- No gas impurities influencing reaction kinetics.

In each model, a counter-current flow of gas and liquid is applied, allowing the rising $CO_2$-rich gas to make thorough contact with the mineral particles and the liquid phase within the reactor. At the gas-liquid interface, $CO_2$ dissolves into the aqueous environment, and at the solid-liquid interface, chemical reactions occur as mineral particles dissolve. Consequently, $CO_2$ in the gas phase is converted and sequestered as bicarbonates and carbonates in the liquid phase, enabling long-term storage. As shown in Figure 1, the solid particles in the TBR are only partially wetted by the liquid, necessitating a packed bed of several meters to ensure sufficiently long residence times for the reactants to reach equilibrium [4]. The PBC contactor provides the three-phase environment necessary for EW-based $CO_2$ capture, benefiting from the stagnant packed bed and controllable volume ratios between solid, liquid, and gas, which are expected to reduce energy consumption. However, due to the lack of agitation, the random kinetics of bubble coalescence and breakup could lead to the formation of large bubbles. These larger bubbles have a lower surface area-to-volume ratio, subsequently reducing the gas-liquid interfacial area essential for effective $CO_2$ dissolution into the liquid [6]. The SSR also facilitates a three-phase solid-liquid-gas environment essential for EW reaction. The SSR benefits from stirring, which permits the use of smaller packing particle sizes and generates smaller bubbles, thereby increasing the solid-liquid contact area and enhancing mass transfer through improved gas-liquid interfacial area. However, the agitation required in this setup consumes more energy [10].

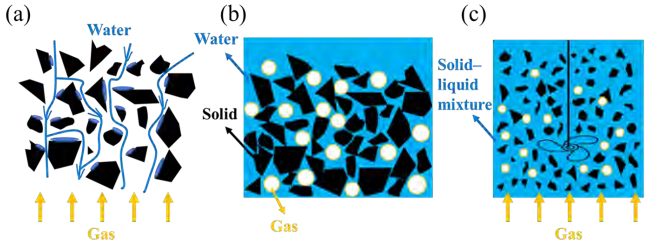



**Figure 1.** Sketch of (a) TBR, (b) PBC, (c) SSR.

In summary, there are notable differences in component representation across three reactor types. In the TBR, the gas phase is continuous, eliminating the need to consider bubbles. The liquid forms a thin, discontinuous film on the solid particles, resulting in partial wetting and a relatively high gas-liquid interface area, with mass transfer occurring across this liquid film. In contrast, the PBC and SSR feature solid particles fully immersed in the liquid phase, with bubbles forming the discontinuous phase. The interfacial area in these reactors depends on the sizes of the bubbles and particles. Additionally, the TBR experiences a lower pressure drop due to less liquid filling the void spaces, unlike the PBC and SSR. In the PBC, where the volume of liquid typically exceeds that of the solid, a two-layer bed usually forms, in which one layer at the bottom is a three-phase packed bed, while the other layer at the top consists only of gas and liquid without solid. Conversely, in the SSR, agitation creates a well-mixed three-phase mixture.

Although the chemical reactions remain consistent across the models, the governing equations for mass transport vary slightly to accommodate differences in fluid dynamics and mass transfer behaviors among the different reactors. These variations include the interfacial areas of gas-liquid and solid-liquid as well as the mass transport coefficients. The specific expressions used for calculating these areas and coefficients are summarized in Table 1. Other expressions could be found elsewhere

**Table 1:** Specific expressions for the areas and coefficients of different reactors.

| Reactors | Gas-liquid mass transfer interface area, $a_{G-L}$ ($m^{-1}$) | Reference |
|---|---|---|
| TBR | $a_{G-L} = [6(1-\varepsilon)/d_p]\left\{1 - exp\left[-1.45\left(\frac{\sigma_C}{\sigma_L}\right)^{0.75} Re_L^{0.1}\, F\, r_L^{-0.05} We_L^{0.2}\right]\right\}$ | [11, 12] |
| PBC | $a_{G-L} = 6\varepsilon_G/d_b$ | Calculated |
| SSR | $a_{G-L} = 6\varepsilon_G/d_b$ | Calculated |
| | **Solid-liquid mass transfer interface area, $a_{S-L}$ ($m^{-1}$)** | |
| TBR | $a_{S-L} = [6(1-\varepsilon)/d_p]\{1 - exp[-1.986 Fr_L^{0.139} Mo_L^{0.0195} \varepsilon_M^{-1.55}]\}$ | [13] |
| PBC | $a_{S-L} = 6(1-\varepsilon)/d_p$ | [14] |
| SSR | $a_{S-L} = 6(1-\varepsilon)/d_p$ | [14] |
| | **Mass-transfer coefficients on the liquid side, $k_L$ (m $s^{-1}$)** | |
| TBR | $k_L = 0.0051(\frac{\rho_L u_L}{a_{G-L}\mu_L})^{2/3}(\frac{\mu_L}{\rho_L D_{Lm}})^{-0.5}(a_t d_p)^{0.4}\left(\frac{\rho_L}{\mu_L g}\right)^{-1/3}$ | [12] |
| PBC | $k_L = \sqrt{D_L u_S/d_b}$ | [15] |
| SSR | $k_L = 0.5 g^{5/8}(d_b E_L)^{1/2}(\sigma/\rho_c)^{-3/8}$ | [16] |
| | **Bubble diameter, $d_b$ (m)** | |
| TBR | - | - |
| PBC | $d_b = 26 d_R Bo_L^{-0.50} Ga_L^{-0.12} Fr_G^{-0.12}$ | [16] |
| SSR | $d_b = 0.72(\mu_B/\rho_B)^{0.22} U_g^{0.33}$ | [17] |

[4, 6-9].

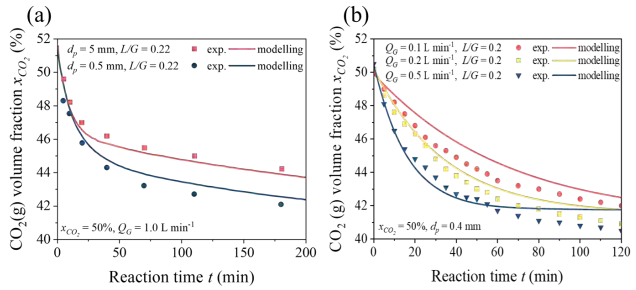



**Figure 2.** Results of model validation (a) PBC (b) SSR.

We developed laboratory-scale setups specifically designed to meet the unique requirements of various reactor types, e.g., a volume of 18 L and an internal diameter of 12 cm. $CO_2$ concentrations ranging from 4% to 20% were applied to simulate typical flue gas emissions from power plants. We conducted experiments under a range of conditions including varying $CO_2$ concentrations, gas and liquid flow rates, liquid-to-gas volume ratios, particle sizes, and temperatures. Figure 2 illustrates the progression of $CO_2$ pressure above the liquid phase within the PBC and SSR over time. This pattern indicates that equilibrium was reached when the reaction time was sufficiently long. In most cases, the predicted results closely aligned with the experimental data, demonstrating the acceptable accuracy of the developed mechanistic models. The discrepancies between the experimental and modeling results are likely attributable to imperfect sealing of the reactor. It is worth noting that no experiments were conducted on the TBR because all the governing equations are from well-validated previous work [18, 19]. However, we developed a set of equations to determine the maximum allowable operating superficial gas and liquid flow rates as functions of particle size, which are designed to prevent flooding when gas flows counter currently upward from the bottom.

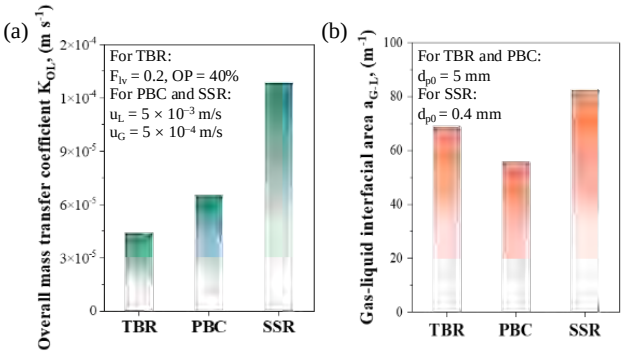



**Figure 3.** Gas-liquid mass transfer coefficient (a) and interfacial area (b) in reactors. $x_{CO2}$ = 10%, $H_{bed0}$ = 5 m.

The mass transfer coefficients and gas-liquid interfacial areas were compared between TBC, PBC and SSR. As illustrated in Figure 3, the SSR achieves the highest mass transfer coefficient, attributed to its smaller particle size and the enhanced agitation effect. Additionally, the TBR maintains a slightly higher gas-liquid contact area than PBC due to continuous airflow. Under agitation conditions, the SSR produces smaller gas bubbles, resulting in a greater gas-liquid contact area compared to both PBC and TBR. Our research further reveals that in both the PBC and SSR systems, $CO_2$ capture rates can be

significantly enhanced by increasing the $CO_2$ concentration in the feed air. Even modest enrichment of $CO_2$ in the inlet air can lead to substantial enhancement of capture rate and savings in energy and water.

## 3. DATA-DRIVEN SURROGATE MODELLING AND MULTI-VARIABLE OPTIMIZATION

After validating our models on a laboratory scale, we scaled them up to explore the impact of design variables on key performance indicators, including $CO_2$ capture rate (CR), operational energy consumption (EC), and water consumption (WC). Identifying optimal solutions through exhaustive enumeration and search is often cumbersome. While complex Multiphysics simulations can reduce time and resource demands, more efficient methods are still required for analyzing the Pareto fronts across different reactor types for optimization purposes. To address this, leveraging physics-based simulation data to develop data-driven surrogate models presents a viable approach for tackling multivariable optimization challenges effectively. In our work, machine learning algorithms, e.g., RSM, RBF, SVR and E-AHF, and optimization approaches, e.g., GA and NSGA-II, were employed [11]. The established data-driven surrogate models significantly reduce simulation computation time and enable rapid prediction of reactor performance metrics. The R2 values for RSM and E-AHF predictions of CR and WC exceed 0.84. Notably, for the TBR, the calculated R2 value surpasses 0.96. Using the RSM model to predict SSR performance yields $R^2$ values for WC and CR above 0.99, while the $R^2$ for EC is 0.87, exceeding the prediction accuracy for EC in both TBR and PBC systems (approximately 0.79). Further improvements in prediction accuracy are observed when outliers are excluded or the E-AHF model is applied, with $R^2$ increasing to 0.89. Figure 4 presents the optimal outcomes of the three reactors under different objectives. In terms of energy consumption, SSR requires higher energy due to continuous stirring. However, when aiming for minimal water consumption (WC) or maximal carbon capture rate (CR), SSR exhibits comparable or even lower energy usage. Notably, PBC achieves substantial energy savings while minimizing water consumption.

Figure 4 shows the optimal performance of three different reactors under various objectives. SSR requires higher energy for continuous stirring, yet it shows comparable or lower energy consumption when optimizing for minimal WC or maximum CR. Notably, PBC achieves significant energy savings, particularly when reducing WC is prioritized. Meanwhile, TBR excels in scenarios that focus on water reduction due to its discrete liquid flow. SSR, operating in batch mode, utilizes the least water overall. Optimization with surrogate models significantly enhanced performance metrics for continuous systems: CR increased by 37.8% for TBR and 13.1% for the PBC. EC decreased by 37.4% in TBR and 23.8% in PBC, while WC dropped by 12.5% and 40.7%, respectively. Comparatively, SSR reduced water requirements to 0.9045 $m^3$, which is about 60% of that required by TBR (1.4928 $m^3$) and PBC (1.4966 $m^3$), achieving a CR of 1.11 kg $h^{-1}$, comparable to TBR's 0.73 kg $h^{-1}$ and lower than PBC's 1.91 kg $h^{-1}$. The CR of SSR reached 2.93 kg $h^{-1}$, surpassing PBC's 2.01 kg $h^{-1}$. Although SSR's EC (1.2567 MJ) and WC (3.6675 $m^3$) per kg of $CO_2$ captured were lower than PBC's (1.7331 MJ and 14.142 $m^3$), they were slightly higher than that of TBR due to increased energy for stirring and higher material processing energy from the smaller packing material. Despite the higher energy input, SSR's efficient mixing and the buoyant forces from upward flow reduced operational energy, leading to a CR of 2.44 kg $h^{-1}$ with an EC of 0.9853 MJ and a WC of 2.9167 $m^3$ per kg $CO_2$ captured.

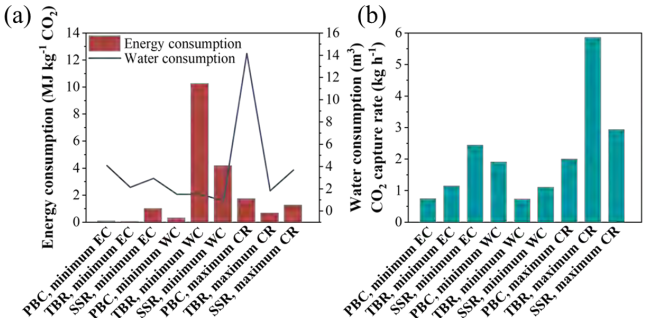



**Figure 4.** Comparison of optimization results for EC, WC and CR across different systems with minimum energy consumption, water consumption (a) and maximum $CO_2$ capture rate (b).

## 4. RESPONSIVE $CO_2$ CAPTURE FOR MANAGING VARIABLE FLUE GAS

Due to the intermittent nature of $CO_2$ emissions and renewable energy sources such as wind and solar, the availability of $CO_2$ and energy dynamically changes over time. To enhance the efficiency of EW-based $CO_2$ capture systems, developing an adaptive optimization strategy is crucial. This strategy could predict the availability of $CO_2$ and energy for the upcoming hour, enabling the determination of optimal operating conditions. Adaptive multi-objective optimization integrates process modeling with optimization algorithms to enable dynamic system optimization [20]. By leveraging adaptive optimization, optimal solutions can be forecasted before optimization actions are executed. By developing machine learning surrogate models from existing physics-based models, we can achieve more accurate chemical system modeling. This approach is particularly effective for handling time-dependent data and evolving patterns, enabling the

model to learn from historical process data, adapt to real-time changes, and predict reactor behavior. Such advancements will significantly enhance the flexibility and robustness of the EW-based $CO_2$ capture systems in response to fluctuations in external environments.

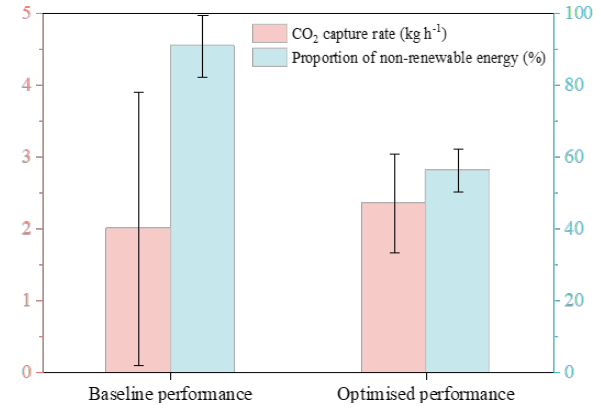



**Figure 5.** Improvement of EW-based $CO_2$ capture system after adaptive optimization.

In our study, we initially developed two deep learning models, a two-stage multilayer perceptron (2-stage MLP), and a long short-term memory (LSTM) network, for the prediction of the dynamic performance of the reactor and $CO_2$ emissions and wind energy forecasts. We then trained these models using data on $CO_2$ emissions from a coal-based power plant in China and wind energy data from the UK, collected over a period of 500 hours. We assessed the predictive accuracy of our data-driven surrogate models by comparing their predictions with those from mechanistic models. The surrogate models demonstrated superior accuracy over traditional LSTM techniques, achieving $R^2$ values of 0.99 for $CO_2$ capture rate and 0.98 for energy consumption predictions, compared to 0.99 and 0.92, respectively, for the LSTM models. Additionally, the adaptive optimization framework, enhanced by these machine learning models, aids in predicting external system variables, thereby improving system performance. The LSTM-based model for the prediction of wind energy and $CO_2$ concentration achieved $R^2$ values of 0.908 and 0.981, respectively. By using the NSGA-II algorithm to adaptively optimize the reactor in response to fluctuations in $CO_2$ concentrations and wind energy, and by equally weighting both objectives, we achieved a 16.7% increase in the capture rate and a 36.3% reduction in non-renewable energy consumption over a month of continuous operation, as shown in Fig. 5.

## 5. CONCLUSION

EW-based $CO_2$ capture accelerates natural processes to potentially achieve Gt atmospheric carbon sequestration in ocean. To reveal the potential of various chemical reactors for EW-based $CO_2$ capture, we developed physics-based mechanistic models of these reactors by coupling reaction kinetics and mass transport processes. The models were experimentally validated under laboratory conditions before scaling up to industrial scales. Then data-driven surrogate modeling and multivariable optimization were employed to significantly save computational resources, enabling efficient identification of optimal operating conditions with respect to various scenarios. Our finding revealed the importance of gas-to-liquid mass transport that could be considered as the main rate-limiting process in most cases. Operated at 4%-20% $CO_2$, after optimization, the EC, WC and CR are: SSR-0.9853 MJ per kg $CO_2$, 0.9045 $m^3$, and a $CO_2$ capture rate of 2.93 kg $CO_2$ $h^{-1}$, TBR-0.04368 MJ per kg $CO_2$, 1.4928 $m^3$, and 5.8568 kg $CO_2$ $h^{-1}$, PBC-0.07115 MJ per kg $CO_2$, 1.4966 $m^3$, and 2.0013 kg $CO_2$ $h^{-1}$.

The minimum WC is about 1.5 $m^3$ per $CO_2$ captured for all reactors. Compared to packed bubble column (PBC), the stirred slurry reactor (SSR) improves the capture rate, but at the cost of a significant increase in energy consumption. Additionally, under batch operation conditions, the water consumption of the SSR is nearly half that of the PBC. In summary, TBR holds the greatest potential for EW-based $CO_2$ capture.

Our findings also underscore the importance of enhancing $CO_2$ capture efficiency while reducing energy and water consumption. This can be achieved by using $CO_2$-rich feedstocks, such as flue gas from power plants (which is more effective than atmospheric capture), and by generating smaller bubbles to further accelerate gas-to-liquid mass transfer. Leveraging the advancements in AI and model predictive control, the adaptive optimization of the EW-based $CO_2$ capture system could be further optimized to mitigate the fluctuation of intermittent $CO_2$ supply and renewable energy. The models and methodologies developed in our work are poised to contribute to the broader adoption of EW-based $CO_2$ capture technology across the industry, serving as a reference for sustainable and large-scale $CO_2$ capture at an industrial level.

## ACKNOWLEDGEMENTS

The authors would like to acknowledge EPSRC with project codes of EP/V042432/1 and EP/V011863/1.

## REFERENCES

1. D.J. Beerling, E.P. Kantzas, M.R. Lomas, P. Wade, R.M. Eufrasio, P. Renforth, B. Sarkar, M.G. Andrews, R.H. James, C.R. Pearce, J.F. Mercure, H. Pollitt, P.B. Holden, N.R. Edwards, M. Khanna, L. Koh, S. Quegan, N.F. Pidgeon, I.A. Janssens, J. Hansen, S.A. Banwart, Potential for large-scale $CO_2$ removal via enhanced rock weathering with croplands,

*Nature* 583(7815) (2020) 242-248. https://doi.org/10.1038/s41586-020-2448-9
2. P. Renforth, The negative emission potential of alkaline materials, *Nat. Commun.* 10 (2019) 8. https://doi.org/10.1038/s41467-019-09475-5
3. T. Terlouw, C. Bauer, L. Rosa, M. Mazzotti, Life cycle assessment of carbon dioxide removal technologies: a critical review, *Energy Environ. Sci.* 14(4) (2021) 1701-1721. https://doi.org/10.1039/d0ee03757e
4. L. Xing, R.C. Darton, A.D. Yang, Enhanced weathering to capture atmospheric carbon dioxide: Modeling of a trickle-bed reactor, *AIChE J.* 67(5) (2021) 18. https://doi.org/10.1002/aic.17202
5. J. Fuhrman, C. Bergero, M. Weber, S. Monteith, F.M. Wang, A.F. Clarens, S.C. Doney, W. Shobe, H. McJeon, Diverse carbon dioxide removal approaches could reduce impacts on the energy-water-land system, *Nat. Clim. Chang.* 13(4) (2023) 341. https://doi.org/10.1038/s41558-023-01604-9
6. L. Xing, H. Pullin, L. Bullock, P. Renforth, R.C. Darton, A.D. Yang, Potential of enhanced weathering of calcite in packed bubble columns with seawater for carbon dioxide removal, *Chemical Engineering Journal* 431 (2022) 12. https://doi.org/10.1016/j.cej.2021.134096
7. L. Xing, H. Jiang, S. Wang, V.J. Pinfield, J. Xuan, Data-driven surrogate modelling and multi-variable optimization of trickle bed and packed bubble column reactors for $CO_2$ capture via enhanced weathering, *Chemical Engineering Journal* 454 (2023) 19. https://doi.org/10.1016/j.cej.2022.139997
8. J.Y. Zhang, A.D. Yang, R. Darton, L. Xing, A. Vaughan, Surrogate modelling-assisted comparison of reactor schemes for carbon dioxide removal by enhanced weathering of minerals using seawater, *Chemical Engineering Journal* 461 (2023) 9. https://doi.org/10.1016/j.cej.2023.141804
9. H. Jiang, S. Wang, L. Xing, V.J. Pinfield, J. Xuan, Machine learning based techno-economic process optimisation for $CO_2$ capture via enhanced weathering, *Energy AI* 12 (2023) 15. https://doi.org/10.1016/j.egyai.2023.100234
10. A.K. Bin, Mass transfer to the free interface in stirred vessels, *Chem. Eng. Commun.* 31(1-6) (1984) 155-183. https://doi.org/10.1080/00986448408911148
11. K. Onda, H. Takeuchi, Y. Okumoto, Mass transfer coefficients between gas and liquid phases in packed columns, *J.chem.eng.japan* 1(1) (1968) 56-62.
12. B.I. Dvorak, D.F. Lawler, J.R. Fair, N.E. Handler, Evaluation of the Onda correlations for mass transfer with large random packings, *Environ. Sci. Technol.* 30(3) (1996) 945-953. https://doi.org/10.1021/es950408+
13. C. Julcour-Lebigue, F. Augier, H. Maffre, A.M. Wilhelm, H. Delmas, Measurements and Modeling of Wetting Efficiency in Trickle-Bed Reactors: Liquid Viscosity and Bed Packing Effects, *Industrial & Engineering Chemistry Research* 48(14) (2009) 6811-6819. https://doi.org/10.1021/ie9002443
14. F. Benyahia, K.E. O'Neill, Enhanced voidage correlations for packed beds of various particle shapes and sizes, *Part. Sci. Technol.* 23(2) (2005) 169-177. https://doi.org/10.1080/02726350590922242
15. P.V. Danckwerts, Significance of Liquid-Film Coefficients in Gas Absorption, *Industrial & Engineering Chemistry Research* 43(6) (1981) 1460-1467.
16. K. Akita, F. Yoshida, Gas Holdup and Volumetric Mass Transfer Coefficient in Bubble Columns. Effects of Liquid Properties, *Industrial & Engineering Chemistry Research* 12(1) (1973) 76-80. https://doi.org/10.1021/i260045a015
17. R. Darton, D. Harrison, Some Properties of Gas Bubbles in Three-Phase Fluidized Beds, 1974.
18. R. Billet, M. Schultes, Fluid dynamics and mass transfer in the total capacity range of packed columns up to the flood point, *Chem. Eng. Technol.* 18(6) (1995) 371-379. https://doi.org/10.1002/ceat.270180602
19. R. Billet, M. Schultes, Prediction of mass transfer columns with dumped and arranged packings - Updated summary of the calculation method of Billet and Schultes, *Chem. Eng. Res. Des.* 77(A6) (1999) 498-504. https://doi.org/10.1205/026387699526520
20. O.J. Fisher, L. Xing, X. Tian, X.Y. Tai, J. Xuan, Responsive $CO_2$ capture: predictive multi-objective optimisation for managing intermittent flue gas and renewable energy supply, *Reaction Chemistry & Engineering* 9(2) (2024) 235-250. https://doi.org/10.1039/d3re00544e

© 2025 by the authors. Licensed to PSEcommunity.org and PSE Press. This is an open access article under the creative commons CC-BY-SA licensing terms. Credit must be given to creator and adaptations must be shared under the same terms. See https://creativecommons.org/licenses/by-sa/4.0/

Systems & Control Transactions

**Research Article - Peer Reviewed Conference Proceeding**
ESCAPE 35 - European Symposium on Computer Aided Process Engineering
Ghent, Belgium. 6-9 July 2025
Jan F.M. Van Impe, Grégoire Léonard, Satyajeet S. Bhonsale,
Monika E. Polańska, Filip Logist (Eds.)

PSE PRESS

# Integrating Dynamic Risk Assessment with Explicit Model Predictive Control via Chance-Constrained Programming

**Sahithi Srijana Akundi[a,b,c], Yuanxing Liu[a,b,c], Austin Braniff[d], Beatriz Dantas[d], Shayan S Niknezhad[a], Faisal Khan[b,c], Yuhe Tian[d], Efstratios N Pistikopoulos[a,c]***

[a] Texas A&M Energy Institute, Texas A&M University, College Station, TX, USA
[b] Mary Kay O'Connor Process Safety Center (MKOPSC), Texas A&M University, College Station, TX, USA
[c] Artie McFerrin Department of Chemical Engineering, Texas A&M University, College Station, TX, USA
[d] Department of Chemical and Biomedical Engineering, West Virginia University, Morgantown, WV, USA
* Corresponding Author: stratos@tamu.edu.

## ABSTRACT

Maintaining operational efficiency while ensuring safety is a longstanding challenge in industrial process control, particularly in high-risk environments. This paper presents a novel Dynamic Risk-Informed Explicit Model Predictive Control (R-eMPC) framework that integrates safety and operational objectives using probabilistic constraints and real-time risk assessments. Unlike traditional approaches, this framework dynamically adjusts safety thresholds based on Bayesian updates, ensuring a balanced trade-off between reliability and efficiency. The validation of this approach is illustrated through a case study on tank level control, a safety-critical process where maintaining the liquid level within predefined safety limits is paramount. The results demonstrate the framework's capability to optimize performance while maintaining robust safety margins. By emphasizing adaptability and computational efficiency, this research provides a scalable solution for integrating safety into real-time control strategies for similar process systems.

**Keywords**: Model predictive control, Bayesian risk analysis, Dynamic risk assessment, Safety-aware control, Multi-parametric programming, Chance-constrained programming

## INTRODUCTION

Industrial operations, particularly in chemical plants, carry an inherent risk of catastrophic incidents, posing threats to both human safety and the environment [1]. These risks have driven extensive research and the development of systematic methods to enhance process functional safety [2]. While traditional safety measures, such as Hazards and Operability analysis and fault tree analysis [3], have significantly contributed to accident prevention, the increasing complexity of industrial processes necessitates advanced optimization, control, and machine learning techniques capable of integrating safety and performance objectives seamlessly [4,5].

Traditional Model Predictive Control (MPC) frameworks, though widely adopted, rely on rigid constraints to enforce safety, often leading to overly conservative operations [6]. Recent efforts have explored merging safety principles with MPC through adaptive, learning-based [7], and probabilistic approaches [8,9]. However, these methods often fall short in dynamically quantifying and updating risk parameters in real time, limiting their applicability in highly dynamic and uncertain environments [10].

This paper addresses these gaps by introducing the Dynamic Risk-Informed Model Predictive Control (R-eMPC) framework. Inspired by dynamic risk-based design and optimization principles [11], R-eMPC incorporates Bayesian updates and chance-constrained programming to dynamically adjust safety thresholds along a receding horizon [12]. This integration ensures a robust balance between safety and operational efficiency while responding to real-time process variations. The proposed framework is systematically applied to a tank-level control case study, demonstrating its potential for scalable and adaptive safety-critical applications.

The remainder of this paper is organized as follows: Section 2 introduces the case study, providing the context and system dynamics for evaluating the proposed framework. Section 3 details the R-eMPC methodology

and demonstrates its sole application to the case study of tank level control. Section 4 present results and discusses the implications of the framework, while Section 5 concludes with key findings and outlines potential future research directions.

## TANK-LEVEL CONTROL CASE STUDY

The tank level control system serves as a representative case study to evaluate the proposed R-eMPC framework (Figure 1). In industrial operations, precise regulation of the liquid level within a storage tank is crucial to prevent safety-critical incidents. Overflow scenarios may result in hazardous spills with severe environmental and operational consequences, while underflow conditions can disrupt downstream processes, leading to inefficiencies and potential system failures. The inherent dynamics and uncertainty associated with this system make it an ideal testbed for assessing the efficacy of the proposed methodology.

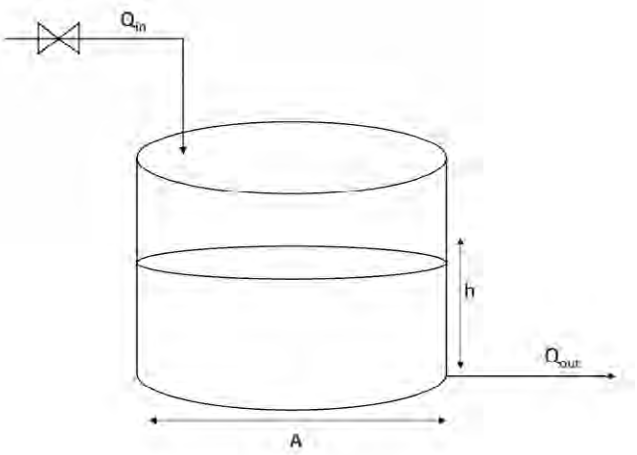



**Figure 1.** The schematic of the tank-filling system

The control system is designed to manage the liquid level by regulating the inflow, while the outflow is governed by the tank's current level and outlet characteristics. The system dynamics are mathematically described as:

$$\frac{dh(t)}{dt} = \frac{Q_{in}(t) - Q_{out}(t)}{A} + \frac{w(t)}{A} \quad (1)$$

where
$h(t)$ represents the liquid level
$Q_{in}(t)$ represents the inflow
$Q_{out}(t)$ represents the outflow
$A$ represents the cross-sectional area of the tank

$w(t)$ captures external disturbances that influence the system. The primary control objective is to maintain $h(t)$ within predefined safety limits while optimizing operational performance, even in the presence of uncertainties and dynamic variations.

The choice of the tank level control system as a case study is motivated by its direct relevance to the challenges of managing safety-critical processes under dynamic and uncertain conditions. This system exemplifies the interplay between operational constraints and safety requirements, where deviations in liquid levels can result in hazardous overflows or disruptive underflows. Traditional control strategies, which often rely on static constraints, struggle to accommodate real-time disturbances, leading to conservative or infeasible operations. By applying the R-eMPC framework, this study aims to bridge this gap by integrating dynamic risk assessment and probabilistic constraints into the control process. The framework's ability to adaptively balance safety and efficiency under varying conditions underscores its potential for broader applications in safety-critical process control.

## RISK- INFORMED EXPLICIT MPC FRAMEWORK

In this section, we introduce a stochastic control framework as an extension to 'Dynamic Risk-based Design and Control Optimization framework' developed in [11]. This framework serves as a comprehensive approach for the seamless integration of safety and control elements, achieved through the dynamic inclusion of risk factors within a controller optimization framework. This unique approach facilitates real-time monitoring of risk levels and the implementation of adaptive control strategies. The ensuing section provides a step-by-step elucidation of the procedural aspects of this framework.

The R-eMPC framework under discussion represents a nuanced and adaptive approach to address the complexities inherent in managing uncertain systems. This innovative paradigm seamlessly blends several pivotal elements. Firstly, it employs a Receding Horizon MPC strategy, continuously optimizing control inputs while considering the dynamics of the evolving system. Secondly, it introduces a dynamic probabilistic constraint, strategically integrating real-time risk management into the control framework to maintain system operation within predefined risk thresholds. Complementing this, a Bayesian update mechanism is seamlessly incorporated, allowing for the dynamic adaptation of these risk thresholds based on live system observations. This integrated approach represents a comprehensive strategy that not only prioritizes safety but also enables the system to adaptively optimize its performance within the realm of uncertainties—a pragmatic and adaptable solution for contemporary engineering challenges. The implementation of the framework is given below:
R-eMPC:

$$min_u\ J = x_N^T P x_N + \sum_{k=1}^{OH-1} \Big( (y_k - y_k^R)^T Q R_k (y_k - y_k^R) \Big) \quad (2a)$$

$$+ \sum_{k=0}^{CH-1} (\Delta u_k - \Delta u_k^R)^T R_k (\Delta u_k - \Delta u_k^R) + f(x_k)$$

s.t. $$x_{k+1} = Ax_k + Bu_k + C[d_k, De] \quad (2b)$$

$$y_k = Dx_k \quad (2c)$$

$$P[Event|x(t)] \le \epsilon_t \quad (2d)$$

$$\bar{x} \le x \le \underline{x} \qquad \bar{u} \le u \le \underline{u} \qquad \bar{y} \le y \le \underline{y} \quad (2e)$$

Bayesian update (time step t out of prediction horizon k)

$$P[Event|x(t+1)] = L(x(t)) * P[Event|x(t)] \quad (2f)$$

where $P$ is terminal weight, $QR$ and $R$ are controller weights, $OH$ and $CH$ are output and control horizons, $N$ represents the terminal step of the prediction horizon, superscript $R$ is setpoint, $t$ represents the time step for the entire operation of the controller, where at each step, the Bayesian update is applied to refine risk estimates dynamically. The function $f(x_k)$ represents the loss function for safety, which penalizes unsafe behaviors and is formulated based on the specific system under consideration. The details of its selection and impact are discussed in the subsequent section [17] (in (7a)). $L$ is the likelihood function (detailed by [18]). $x$, $y$, $u$ represent the state, output and input vectors respectively. Here, $x_k$ corresponds to the system state at prediction horizon $k$, while $x(t)$ denotes the state at each time step $t$ within the receding horizon framework. The index $k$ represents the prediction step within the optimization window of the receding horizon MPC. At each time step $t$, the controller solves an optimization problem over the prediction horizon, updating the control inputs accordingly.

$Event$ represents the occurrence of a failure scenario or an undesirable event within the system. It can be defined using mathematical expressions or conditions that capture the event of concern. For instance, in engineering, the event might relate to a variable exceeding a certain threshold. $\epsilon_t$ is the threshold value denotes the acceptable level of risk associated with the event. It quantifies the maximum probability at which the event can occur without exceeding acceptable risk levels. The choice of $\epsilon_t$ reflects the trade-off between safety and system performance, with lower values indicating a lower tolerance for risk. The probability constraint is handled via chance-constrained programming by obtaining its deterministic approximation [14] (more description in Eqs (5) and (6)).

## TANK-LEVEL CONTROL: IMPLEMENTATION, RESULTS & DISCUSSIONS

The proposed R-eMPC framework was applied to the tank-level control system to validate its efficacy in maintaining safety-critical constraints while optimizing performance.

### Step 1: High Fidelity Dynamic Modeling

The system dynamics were modeled using mass balance equations, where the liquid level $h(t)$ was regulated by controlling the inlet flow rate $Q_{in}(t)$. The outlet flow rate $Q_{out}(t)$ was assumed proportional to the current liquid level, modeled as $Q_{out}(t) = k\ h(t)$, with $k$ as the proportionality constant. External disturbances $w(t) \sim \mathcal{N}(0,0.5)$, were introduced to simulate uncertainties, making the control problem more realistic. The resulting high-fidelity model from Eq. (1) is expressed as follows:

$$\frac{dh(t)}{dt} = \frac{-kh(t)}{A} + \frac{Q_{in}(t)}{A} + \frac{w(t)}{A} \quad (3)$$

### Step 2: Model Reduction

To facilitate the design of an optimal control strategy, the high-fidelity dynamic model was simplified into a linear state-space representation. This reduction is typically performed using system identification tools for nonlinear systems to derive an approximate representation that facilitates control design. However, since our system is inherently linear, we can directly express the linear state-space model as:

$$h(i+1) = \left(1 - \frac{k}{A}\right) h(i) + \frac{1}{A} Q_{in}(i) + \frac{1}{A} w(i) \quad (4)$$

### Step 3: Risk Modeling via Safety Constraints

Risk modeling was incorporated via probabilistic constraint.

$$P[h(t) > h_{max}] \le \epsilon_t \quad (5)$$

The probabilistic constraint ensured that the liquid level remained below the maximum allowable height ($h_{max} = 8\ m$) with a predefined risk tolerance ($\epsilon_t$). To ensure computational feasibility, the probabilistic constraint was converted to a deterministic equivalent using chance-constrained programming. Assuming $h(t)$ follows a normal distribution with mean $\mu_t$ and standard deviation $\sigma_t$, the reformulation yielded:

$$h(t) \leq h_{max} + (z_t \sigma_t) \quad (6)$$

where $z_t = \varphi^{-1}(\epsilon_t)$ represents the z-score corresponding to the risk tolerance, and $\varphi^{-1}$ is the inverse cumulative distribution function of the standard normal distribution. This deterministic form simplifies the inclusion of the constraint in the optimization problem [14].

## Step 4: Risk Informed Explicit Model Predictive Controller

The control objective was to minimize deviations from the setpoint $h_{sp} = 6.4\ m$ while penalizing safety violations using an inverted normal loss function (INLF) [17]. The optimization problem was expressed as:

$$min_u\ J = \sum_{i=1}^{OH-1} \left( \left( (h_i - h_{sp})^2 \right) + INLF(h_i, h_{sp}) \right) \quad (7a)$$

s.t.

$$h(i+1) = \left(1 - \frac{k}{A}\right) h(i) + \left(\frac{1}{A}\right) Q_{in}(i) + \left(\frac{1}{A}\right) w(i) \quad (7b)$$

$$0 \leq h(i) \leq h_{max} \quad (7c)$$

$$P(\Delta h > 0|t) \leq \epsilon_t \quad (7d)$$

Bayesian Update:

$$P[\Delta h > 0|t+1] = L(h(t)) * P[\Delta h > 0|t] \quad (7e)$$

Bayesian update is calculated out of the optimization problem before rolling into the next time step in the horizon. The likelihood function being used in Bayesian update is of the functional form that supports the probabilities in the direction of minimal difference between the instantaneous state and the set-point.

$$L(h(t)) = \frac{1}{\sqrt{2\pi}\sigma} \exp\left( -\frac{(h(t) - h_{sp})^2}{2\sigma^2} \right) \quad (7f)$$

The deterministic reformulation of the risk-informed problem is solved using multi-parametric programming, with the initial state $h_0$ and the parameter $(z_t \sigma_t)$ varying within the range of -3 to +3. This approach enables the explicit computation of control laws as functions of the varying parameters, facilitating efficient real-time implementation while ensuring robust performance under the prescribed risk tolerance. The resulting explicit control map (Figure 2) provide a precomputed map, which can be efficiently used to calculate the optimal solutions for the entire parameter space, ensuring real-time applicability and robust performance under the prescribed risk tolerance [15,16].

The results obtained from the proposed framework provide valuable insights into the behavior and limitations of the control strategies under varying scenarios. Initially, the system was tested with a standard hard-constrained MPC, enforcing the liquid level to strictly adhere to $h(t) \leq h_{max}$. For the first seven-time steps $t = 7$, the controller maintained the liquid level within the permissible range, effectively keeping the system stable. However, as shown in Figure 2, the strict nature of the constraint led to infeasibility at $t = 7$, causing the MPC to fail. Upon failure, the system reverted to an open-loop response, resulting in uncontrolled deviations where the liquid level rapidly exceeded $h_{max}$. This behavior illustrates the rigidity of hard constraints, which, while effective in maintaining safety under ideal conditions, lack the robustness to handle uncertainty and disturbances effectively.

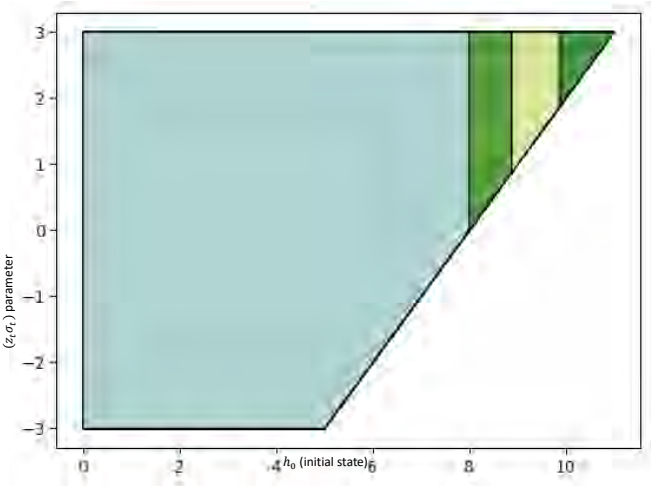



**Figure 2**. Explicit Control law map of Tank level control

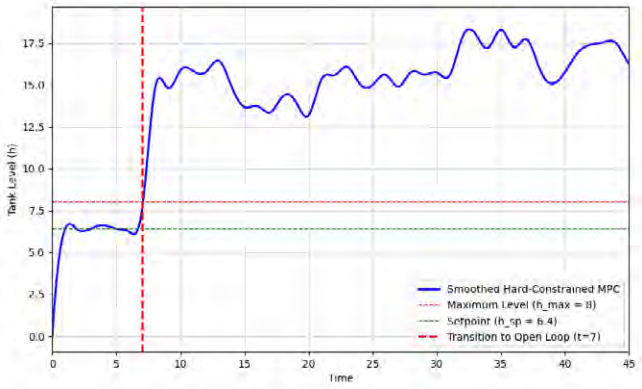



**Figure 3.** Liquid level evolution under hard-constrained MPC

Recognizing the limitations of a hard-constrained approach, the framework was extended to include probabilistic constraints. By introducing a predefined risk tolerance ($\epsilon_t$), the system gained the ability to handle uncertainties more flexibly. Probabilistic constraints allowed for occasional controlled violations of $h_{max}$ within the acceptable bounds of risk. As depicted in Figure 3, this approach alleviated the infeasibility issues observed with hard constraints, enabling the controller to operate continuously. However, while the liquid level was better

regulated, noticeable excursions beyond $h_{max}$ occurred. These excursions highlight the trade-off inherent in probabilistic constraints: a reduction in controller infeasibility at the expense of occasional deviations beyond safety limits. This raised the need for further refinements to address these excursions effectively.

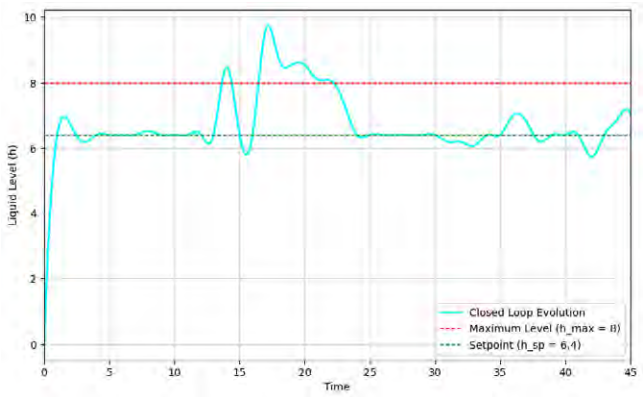



**Figure 4.** Liquid level evolution under probabilistic constraints

To mitigate the deviations observed in the probabilistic MPC, Bayesian updates and safety-aware objectives were incorporated into the control strategy. Bayesian updates dynamically adapted the risk tolerance ($\epsilon_t$) based on real-time deviations from the setpoint $h_{sp} = 6.4\ m$. The likelihood of deviations was quantified using a functional form that penalized large deviations while favoring adherence to the setpoint. Simultaneously, safety losses were added to the objective function to ensure a direct penalty for violations of $h_{max}$, effectively steering the system toward safer operation.

The effectiveness of this enhanced framework is evident in Figure 4, where the liquid level remained closer to $h_{sp}$, with significant reductions in excursions beyond $h_{max}$. Notably, when deviations beyond $h_{max}$ did occur, the system rapidly adapted its behavior, a capability driven by the dynamic nature of the Bayesian updates. This is further supported by the risk tolerance evolution shown in Figure 5, where $\epsilon_t$ sharply decreased during periods of significant deviations, indicating increased caution, and subsequently recovered as the system stabilized. This adaptive response underscores the robustness of the framework in balancing performance and safety under uncertainty.

The comparison of the control strategies highlights the progressive improvement offered by each enhancement. The transition from hard-constrained MPC to probabilistic constraints reduced infeasibility but introduced the challenge of controlling safety violations. The integration of Bayesian updates and safety-aware objectives addressed these challenges by dynamically adapting risk tolerance and penalizing safety violations, ensuring compliance with safety requirements while optimizing system performance. Together, these results demonstrate the proposed R-eMPC framework's ability to provide a robust, adaptive, and computationally efficient solution for managing safety-critical systems under uncertain environments.

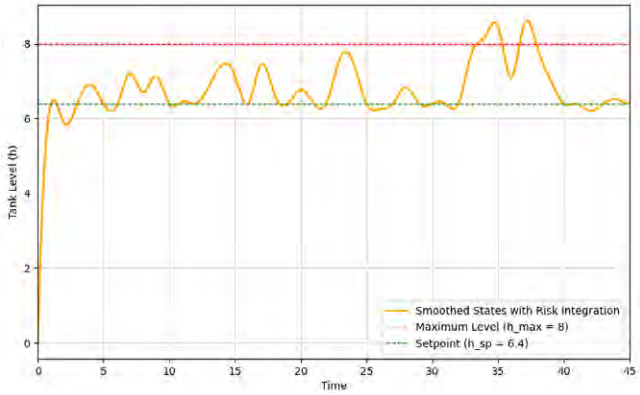



**Figure 5.** Liquid level evolution with Bayesian updates and safety losses

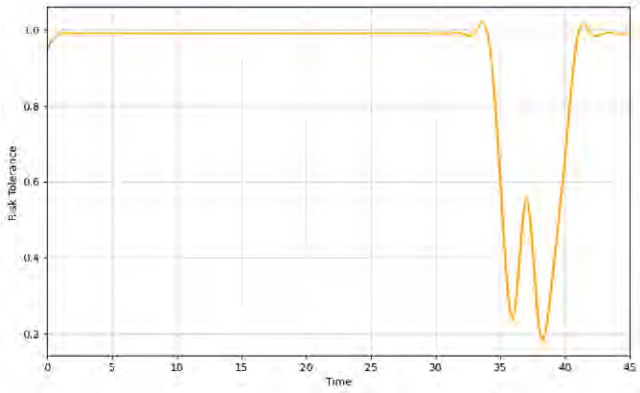



**Figure 6.** Risk tolerance evolution under Bayesian updates

## CONCLUDING REMARKS

In conclusion, the proposed R-eMPC framework demonstrated its efficacy in addressing the critical challenges associated with balancing safety and performance in a safety-critical system under uncertainty. Through a structured progression of enhancements, starting with a conventional hard-constrained MPC, we identified its inherent limitations in handling disturbances and uncertainties, which resulted in system infeasibility and subsequent failure.

By introducing probabilistic constraints, the framework gained flexibility, allowing for controlled risk while maintaining continuous operation. However, the excursions beyond the safety limit highlighted the need for further refinement. The incorporation of Bayesian updates and safety-aware objectives marked a significant step forward, dynamically adapting risk tolerance in real time and penalizing safety violations directly in the objective function. This adaptive capability resulted in substantial

improvements, as the system successfully managed uncertainties while keeping safety-critical constraints in check.

The results underline the importance of incorporating probabilistic considerations and adaptive mechanisms in modern control frameworks. The R-eMPC approach not only mitigated infeasibility but also demonstrated robustness and resilience in handling uncertain conditions, ultimately maintaining safety and improving operational efficiency. These findings highlight the potential of the proposed framework as a powerful tool for safety-critical applications, paving the way for future advancements in adaptive and uncertainty-aware control methodologies.

## ACKNOWLEDGEMENTS

The authors acknowledge financial support from NSF RETRO Project CBET-2312457 Texas A&M Energy Institute, Mary O'Connor Process Safety Center and Energy Institute at Texas A&M University and Department of Chemical and Biomedical Engineering at West Virginia University.

## REFERENCES

1. Crowl, D. A., & Louvar, J. F. (2001). Chemical process safety: fundamentals with applications. Pearson Education.
2. Kadri, S., Peters, G., VanOmmeren, J., Fegley, K., Dennehy, M., & Mateo, A. (2014). So we all have been implementing process safety metrics—what next?. Process Safety Progress, 33(2), 172-178.
3. Khan, F. I., & Abbasi, S. A. (2000). Towards automation of HAZOP with a new tool EXPERTOP. Environmental Modelling & Software, 15(1), 67-77.
4. Venkatasubramanian, V. (2011). Systemic failures: challenges and opportunities in risk management in complex systems. AIChE Journal, 57(1), 2-9.
5. Pistikopoulos, E. N., Akundi, S. S., Kenefake, D., & Diangelakis, N. A. (2024). The quest towards the integration of process control, process operations, and process operability–Industrial need or academic curiosity?. *Computers & Chemical Engineering*, *180*, 108470.
6. Mayne, D. Q., Rawlings, J. B., Rao, C. V., & Scokaert, P. O. (2000). Constrained model predictive control: Stability and optimality. Automatica, 36(6), 789-814.
7. Aswani, A., Gonzalez, H., Sastry, S. S., & Tomlin, C. (2013). Provably safe and robust learning-based model predictive control. Automatica, 49(5), 1216-1226
8. Akundi, S. S., Braniff, A., Dantas, B., Liu, Y., Tian, Y., Niknezhad, S. S., ... & Pistikopoulos, E. N. (2024). Advanced system control strategies for enhanced safety and efficiency of energy systems. In *Methods in Chemical Process Safety* (Vol. 8, pp. 243-260). Elsevier.
9. Albalawi, F., Durand, H., Alanqar, A., & Christofides, P. D. (2018). Achieving operational process safety via model predictive control. Journal of Loss Prevention in the Process Industries, 53, 74-88.
10. Rivotti, P., Lambert, R. S., & Pistikopoulos, E. N. (2012). Combined model approximation techniques and multiparametric programming for explicit nonlinear model predictive control. Computers & Chemical Engineering, 42, 277-287.
11. Ali, M., Cai, X., Khan, F. I., Pistikopoulos, E. N., & Tian, Y. (2023). Dynamic risk-based process design and operational optimization via multi-parametric programming. Digital Chemical Engineering, 7, 100096.
12. Kalantarnia, M., Khan, F., & Hawboldt, K. (2009). Dynamic risk assessment using failure assessment and Bayesian theory. Journal of Loss Prevention in the Process Industries, 22(5), 600-606.
13. Pistikopoulos, E. N., Diangelakis, N. A., & Oberdieck, R. (2020). Multi-parametric optimization and control. John Wiley & Sons.
14. Ismail, M., El-Hefnawy, A., & Saad, A. E. N. (2018). New deterministic solution to a chance constrained linear programming model with Weibull random coefficients. Future Business Journal, 4(1), 109-120.
15. Pistikopoulos, E. N., Diangelakis, N. A., & Oberdieck, R. (2020). *Multi-parametric optimization and control*. John Wiley & Sons.
16. Kenefake, D., Akundi, S. S., & Pistikopoulos, E. N. A Partial Multiparametric Programming method for Model Predictive Control.
17. Hashemi, S. J., Ahmed, S., & Khan, F. (2014). Loss functions and their applications in process safety assessment. *Process Safety Progress*, *33*(3), 285-291.
18. Amin, M. T., Khan, F., & Imtiaz, S. (2019). Fault detection and pathway analysis using a dynamic Bayesian network. *Chemical Engineering Science*, *195*, 777-790.

© 2025 by the authors. Licensed to PSEcommunity.org and PSE Press. This is an open access article under the creative commons CC-BY-SA licensing terms. Credit must be given to creator and adaptations must be shared under the same terms. See https://creativecommons.org/licenses/by-sa/4.0/



Systems & Control Transactions

**Research Article - Peer Reviewed Conference Proceeding**
ESCAPE 35 - European Symposium on Computer Aided Process Engineering
Ghent, Belgium. 6-9 July 2025
Jan F.M. Van Impe, Grégoire Léonard, Satyajeet S. Bhonsale,
Monika E. Polańska, Filip Logist (Eds.)

PSE PRESS

# Analysis of Control Properties as a Sustainability Indicator in Intensified Processes for Levulinic Acid Purification

**Tadeo E. Velázquez-Sámano[a], Heriberto Alcocer-García[b]*, Eduardo Sánchez-Ramírez[a], Carlos R. Caceres-Barrera[a], and Juan G. Segovia-Hernández[a]**

[a] Guanajuato University, Chemical Engineering Department, Guanajuato, Guanajuato, México
[b] Guanajuato University, Civil and Ambiental Engineering Department, Guanajuato, Guanajuato, México
* Corresponding Author: h.alcocer@ugto.mx.

## ABSTRACT

The evaluation of control properties in industrial processes is essential to achieve sustainability, a very relevant topic today. This study emphasizes the importance of control studies to ensure that processes are efficient, operable and safe. While strategies such as process intensification can reduce the size, cost, and consumption of energy, it can present challenges in control and operability. This work focuses on the evaluation of the control properties of schemes with different degrees of intensification for the purification of levulinic acid, with the aim of identifying designs with the best control properties and the best economic and environmental indicators. The schemes were designed under a systematic synthesis strategy and optimized using the hybrid method of differential evolution with a tabu list, considering the total annual cost and Eco-indicator 99. An open-loop study analyzed the relationship between manipulable variables and output variables using total condition number, sensitivity index, and relative gain matrix analysis. The dynamic behavior in a closed loop was subsequently analyzed using the minimization of the absolute error integral as a criterion. The results showed that the design, which includes a liquid-liquid extraction column, three distillation columns, and thermal coupling, presented the best dynamic performance. This design had a low total condition number, a below-average sensitivity index, a stable control structure, and low values of the absolute error integral. In addition, it stood out for its excellent cost and environmental impact indicators, which makes it the most favorable option among the proposed designs.

**Keywords**: Stochastic optimization, Control, Distillation, Bioproducts.

## INTRODUCTION

The obtaining of bioproducts from lignocellulosic biomass as a sustainable alternative has gained strength in recent years. However, the processes for obtaining these bioproducts generate very dilute product streams, which represents a challenge due to the high energy consumption that their purification entails [1].

An alternative to guarantee the viability of obtaining bioproducts is the use of Process Intensification (PI). PI is an ideology that is born from the need to increase the efficiency of processes, saving energy, and maximizing production and profits, while at the same time reducing emissions of $CO_2$ and other by-products or polluting wastes [2]. The PI has been implemented in distillation, obtaining hybrid schemes, such as reactive distillation that combines reaction and separation, as well as HiGee columns that have external assistance [3]. Furthermore, if non-reactive hybrid separation PI is considered, there are schemes such as dividing wall columns (DWC), Petlyuk columns and thermally coupled columns present significant energy savings, obtaining savings of more than 25%.

PI is a powerful strategy for creating more efficient, economical, safe, and environmentally friendly processes. However, the industrial operability of these intensified processes can be challenging due to their complexity and the need for sophisticated control structures [4]. Some studies show that intensified designs may have better control properties, while others suggest that

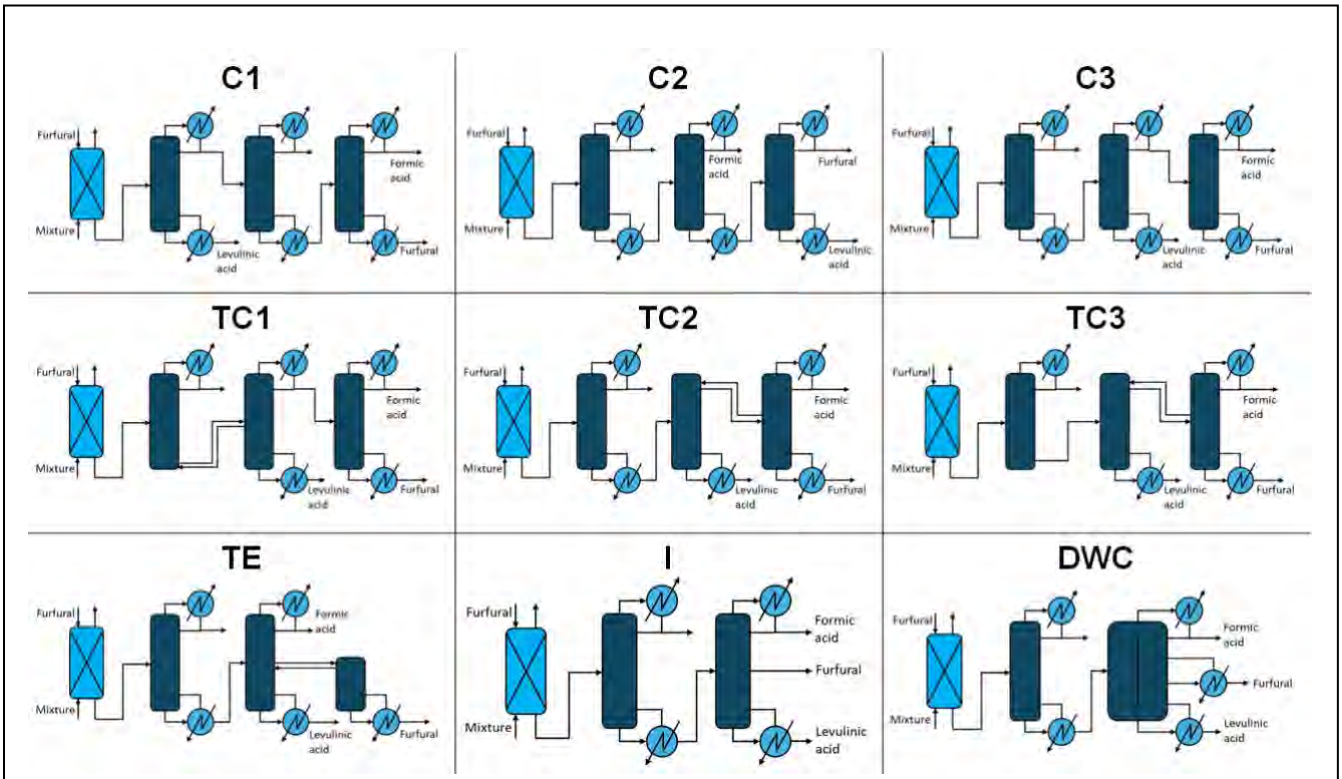



**Figure 1:** Schemes analyzed in the study, proposed by Alcocer-García et al. [12]

increased complexity does not always improve control. An in-depth analysis of control properties is essential to develop effective strategies and contribute to more sustainable and efficient processes. Specific challenges include modeling and parameter tuning, complex dynamic behavior, and reduced degrees of freedom. Addressing these challenges allows progress toward the Sustainable Development Goals (SDGs) and the transition to Industry 4.0, promoting more precise and sustainable production.

Incorporating process operability indices during design allows for the development of efficient, economically viable, and dynamically stable chemical processes. To analyze the control of distillation systems and other industrial systems, techniques and indices have been developed that help to understand their dynamic behavior. Molina-Guerrero et al. [5] performed an open-loop control analysis of an extractive distillation system, while Li et al. [6] focused on minimizing the IAE for systems with thermally coupled columns. Pushkala et al. [7] studied the optimal control structure for a reactive distillation column using the RGA. Alcocer-García et al. [8] found that schemes with greater intensification do not always have the best control properties. Therefore, dynamic analyses are essential to understand the behavior of processes and build effective control strategies.

On the other hand, levulinic acid (LA), considered one of the twelve main bioproducts through biomass, presents a bottleneck in its separation process. This is because the current resulting from thermal pretreatment and acid hydrolysis generates a very dilute current, causing the formation of azeotropes and increasing the cost of their separation, and consequently the production cost [9]. Recently, Alcocer et al. [10] developed schemes with varying degrees of intensification for the purification of levulinic acid, demonstrating significant economic and environmental savings. However, these schemes lack a comprehensive analysis of control properties. Consequently, this study undertakes an in-depth analysis of the control properties for the systems proposed by Alcocer et al. [10], thereby contributing to the understanding and enhancement of operability in intensified systems and to obtain safer and more sustainable designs.

The schemes studied consist of conventional sequences (C1, C2, C3), thermally coupled (TA1, TA2, TA3), thermally equivalent (TE), intensified with n-1 columns (I) and with dividing wall (DWC) were obtained, all with a previous liquid-liquid extraction process, shown in Figure 1. These schemes were optimized using the hybrid method of differential evolution with a tabu list, taking as a multi-objective function the total annual cost (TAC) Eco-Indicator 99 (EI99). The analysis of the control properties was carried out using two approaches: open loop and closed loop. In the open-loop analysis, the indices of total condition number, RGA and power sensitivity were incorporated as indicators, as well as a closed-loop analysis seeking to minimize the IAE by tuning the gain and integral time of the controllers. The objective is to determine the dynamic properties of the schemes to predict

and resolve control problems. The collected information on TAC, environmental impact using the EI99, and control properties provides a comprehensive understanding of the schemes and their industrial viability.

## METODOLOGY

An open-loop analysis was performed using three indicators: γ, which measures directionality in multiple-input, multiple-output (MIMO) systems; the RGA, which evaluates the interactions between the output variables and the manipulable variables; and the SI, which assesses the sensitivity of the system to disturbances in feeding. The schemas were simulated in Aspen Plus and exported to Aspen Dynamics to obtain dynamic responses to disturbances, using the NRTL-HO thermodynamic model. The NRTL-HOC thermodynamic model, suitable for highly non-ideal chemical systems, was employed to calculate liquid-vapor equilibrium and the thermodynamic properties of the vapor phase of organic acids.

For the open loop, 0.5% perturbations were applied to the manipulable variables to calculate the following indices: Total Condition Number (TCN), Relative Gain Matrix (RGA), and Sensitivity Index (SI). The responses obtained were fitted to a transfer function in MATLAB and transformed into the frequency domain to calculate γ and RGA. The open loop methodology is shown in Figure 2.

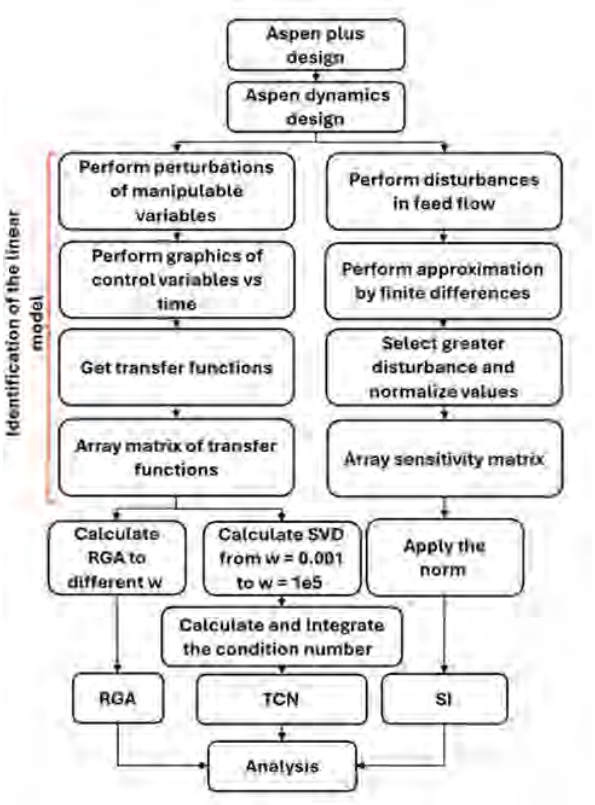



**Figure 2.** Open-loop methodology.

TCN will allow us to identify the input-output control relationship of the system. This will be calculated using the method of Santaella et al. [11], where the integral of the crow generated by the condition number γ and the frequency ω is calculated.

$$TCN = \int_{\omega_1}^{\omega_2} \gamma d\omega \quad (1)$$

A high γ suggests that the system is sensitive to input uncertainties, but it does not always imply greater sensitivity in practice. Systems with a lower γ are expected to have better dynamic performance and be easier to control, as they are less sensitive to disturbances. This facilitates the implementation of simple and straightforward control strategies, such as Proportional-Integral-Derivative control.

The RGA analysis shows how the manipulable variables affect the system's outputs. In distillation columns, the most used control structure is the LV configuration, which controls the distillate composition with the reflux ratio (RR) and the bottom composition with the reboiler heat duty (RHD). However, in intensified schemes, different structures can be identified at LV (DLV), where a different manipulable variable than the one established in the LV configuration has a greater influence on the output variable. In addition, it is possible that some configurations at different frequencies have a changing control structure (CCS) entre la LV y DLV. The RGA on the other hand will allow us to find the best control pairing, calculated as follows:

$$\mathrm{RGA(G)} = \Lambda(G) \triangleq G \otimes (G^{-1})^T \quad (2)$$

In this study evaluated the consistency of the control structure by calculating the RGA at three frequencies: steady state (0 rad/h), near steady state (0.001 rad/h), and high frequency (1e5 rad/h). The variation in the control structure at different frequencies indicates frequency dependence, suggesting nonlinearity and variations in interactions between process variables, which can affect control effectiveness and require adaptive or robust control strategies.

The SI allows us to observe the sensitivity of the output variables according to the input perturbations, which was calculated using the method of Prado-Rubio et al. [12] through finite differences:

$$SI(t) \approx \frac{X[F_{in}(t)+\Delta F_{in}(t)]-X(F_{in})}{\Delta F_{in}} \frac{F_{in}(0)}{X(0)} \quad (3)$$

A high SI value suggests that the system is very sensitive to disturbances in the feed, which requires the implementation of robust control strategies. This can include predictive control to anticipate and correct disturbances, as well as adaptive control to adjust parameters in real-time and maintain process stability and efficiency.

For the closed loop, perturbations were performed at the output of the LA at 5% and 30%, varying and tuning

the gain (Kc) and the integral time (τi) to find the minimum IAE using PI proportional-integral composition controllers. This with the objective of exploring dynamic behavior to a small disturbance and another of greater magnitude.

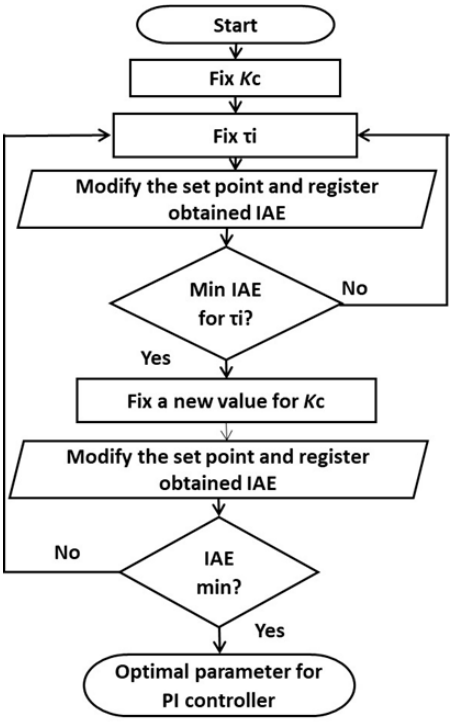



**Figure 3**. Process diagram for tuning PIC.

## RESULTS

The open-loop analysis, shown in Table 1, revealed that the C2, TA1 and TA2 designs have an LV configuration at all frequencies, which translates into systems that can be controlled with direct and less complex strategies, reducing the need for advanced and expensive control systems. In particular, the TA2 design is distinguished by the lower TAC and IAE values, making it the most economical option with the lowest environmental impact. Therefore, considering that it presents a stable control structure, it is positioned as one of the best alternatives of the schemes studied.

On the other hand, the C3, TE, and DWC designs have a DLV configuration, which is stable, but may need more specific control. In these cases, a more specific control refers to the need to adjust and tune the manipulable variables more precisely to maintain the desired performance of the system. This could include the use of advanced control techniques such as predictive control, which anticipates future changes and adjusts control variables accordingly, or adaptive control, which adjusts controller parameters in real-time to respond to variations in process behavior. Although the TAC and EI99 values are slightly higher, they are still good alternatives. However, the C1, TA3 and TE designs, with CCS structure, are unstable and require advanced control strategies. Advanced control strategies are necessary for these designs because of the added complexity and nonlinear interaction between process variables. These strategies can include the use of nonlinear control, which handles the complex, nonlinear relationships between variables, and robust control, which is designed to maintain system performance under a wide range of uncertainty and disturbance conditions. It may also be necessary to implement multivariable control systems, which coordinate multiple inputs and outputs simultaneously to optimize the overall performance of the system.

Due to the increase in interconnection flows in the generated recycles, the TA3 design, which has two thermal couplings, has a greater sensitivity to disturbances in the power supply, generating an increase in SI. And also negatively impacting the TAC and HAI, being the design with the worst values in these indicators and presenting an unstable control structure, which positions it as the worst alternative of those studied.

Design factors such as column diameter and location of thermal couplings significantly impact TCN, with smaller diameter columns facilitating more effective control and reduced operating costs. In summary, systems with low TCN and SI values are more stable and less sensitive to disturbances, while systems with high values require more sophisticated and costly control strategies.

**Table 1:** Open-loop results analisis

| Design | TAC | EI99 | TCN | SI | RGA |
|---|---|---|---|---|---|
| C1 | 1.85E+07 | 5.35E+09 | 5.87E+09 | 13.37 | CCS |
| C2 | 1.56E+07 | 4.70E+09 | 1.04E+07 | 6.68 | LV |
| C3 | 1.49E+07 | 4.60E+09 | 1.95E+08 | 12.37 | DLV |
| TA1 | 1.64E+07 | 4.56E+09 | 4.68E+09 | 0.50 | LV |
| TA2 | 1.39E+07 | 4.21E+09 | 6.44E+06 | 11.28 | LV |
| TA3 | 1.90E+07 | 5.16E+09 | 1.78E+07 | 33.15 | CCS |
| TE | 1.43E+07 | 4.35E+09 | 1.18E+07 | 11.50 | DLV |
| I | 1.77E+07 | 5.22E+09 | 6.30E+07 | 7.56 | CCS |
| DWC | 1.43E+07 | 4.34E+09 | 1.23E+07 | 11.49 | DLV |

The results of the closed-loop analysis are shown in Figure 4. Design TA1 presented the lowest IAE values in all perturbations due to the recycling between the first two distillation columns, which helps dampen disturbances. Additionally, this design shows the smallest Kc values, which improves stability and reduces oscillations. On the other hand, design C1 has the highest IAE values because it recovers levulinic acid in the first distillation column, complicating thermodynamic stability. Designs C2, C3, TA2, TA3, TE, I, and DWC stand out for having similar IAE values in all perturbations, revealing homogeneous dynamic behavior. This suggests that despite differences in configurations, their response to disturbances is uniformly balanced, facilitating a more

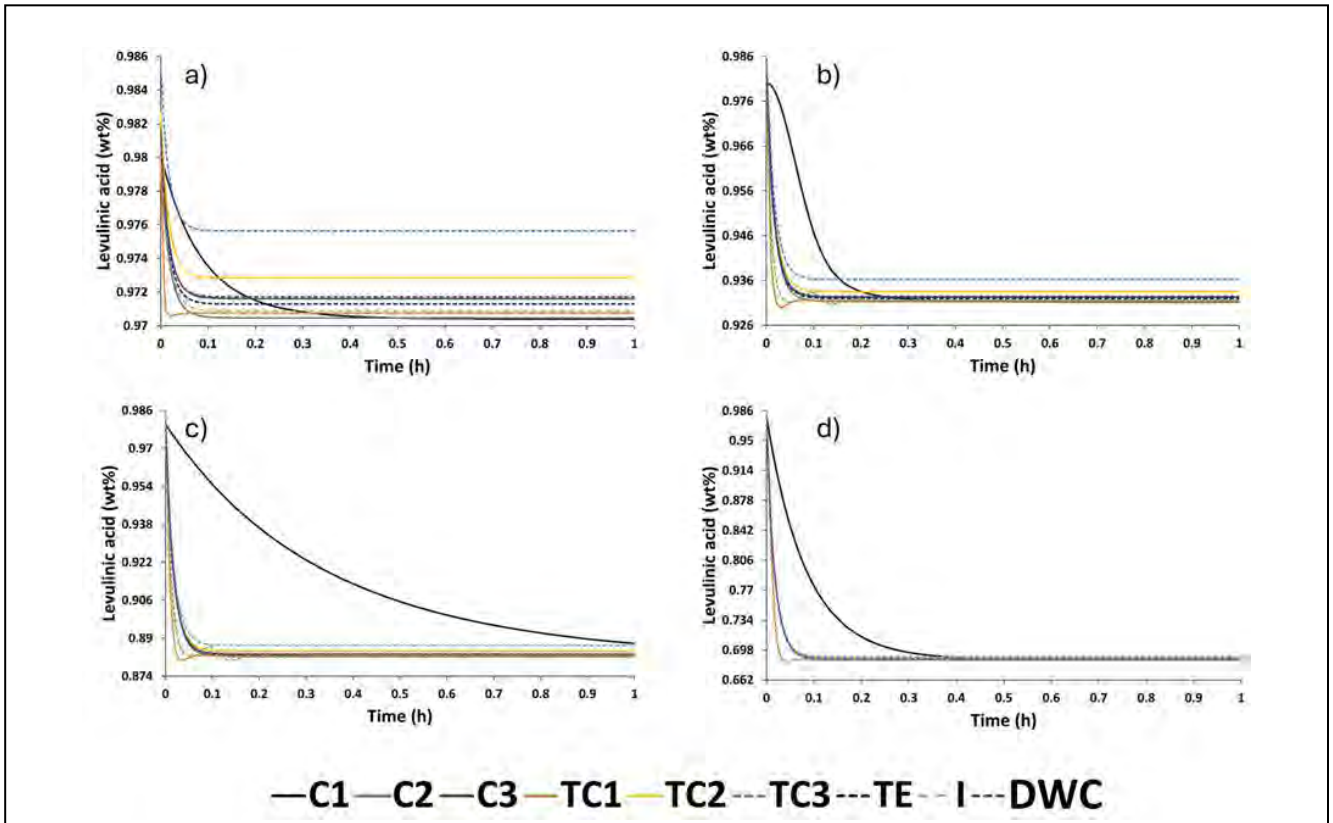



**Figure 4:** Closed-loop responses 1% (a), 5%(b), 10%(c) and 30%(d).

predictable implementation of control strategies.

These findings not only contribute to the understanding of operability in intensified systems but also highlight the importance of selecting appropriate configurations and optimizing specific factors to achieve effective control. The incorporation of additional thermal couplings, as in the TA3 design, improves the distribution of disturbances and the stability of the System in the face of disturbances in the manipulable variables, but makes it unstable in the face of disturbances in the feed.

In addition, sensitivity analysis and interactions between manipulable and output variables underscores the need for robust and adaptive control strategies, especially in designs with higher TCN and SI values. Finally, the economic and environmental benefits derived from the optimization and control of these systems underscore the relevance of these approaches to move towards a more sustainable and efficient industry. In particular, the TA2 design is positioned as the most balanced choice in terms of stability, control efficiency, and costs, which is crucial for the successful implementation of intensified processes in industrial practice. Design TA2 is low TAC and EI99 not only reflect its economic efficiency, but also its lower environmental footprint, standing out as a model for future sustainable designs in the industry.

## CONCLUSIONS

The analyses conducted on open and closed loops revealed significant differences in the dynamic performance and control requirements of the various designs evaluated. Notably, the C2, TA1, and TA2 designs, which exhibit LV configurations at all frequencies, stand out for their superior dynamic performance and stability, obtaining the best values in RGA and IAE analyses and showing a homogeneous response to disturbances.

In contrast, designs such as C3, TE, and DWC, while stable in DLV configurations, may require more specific control techniques like predictive or adaptive control to maintain desired performance. Although the TAC and EI99 values are slightly higher, they remain good alternatives. However, C1, TA3, and TE designs with CCS structures proved unstable and necessitate advanced control strategies like nonlinear and robust control to handle complex interactions.

Factors such as column diameter and the location of thermal couplings significantly impact TCN, with smaller diameter columns facilitating more effective control and reduced operating costs. The TA2 design is particularly noteworthy, presenting the best TAC and EI99 values, making it the most economical option with the least environmental impact. The results underscore that systems with low TCN and SI values are more stable and less

sensitive to disturbances, allowing for more predictable and efficient control, while systems with high values require sophisticated control strategies.

The economic and sustainability benefits from optimizing and controlling these systems highlight their relevance to a more sustainable and efficient industry. The TA2 design stands out as the most balanced option in terms of stability, control efficiency, and costs, with its LV RGA configuration ensuring a stable and predictable control structure. These findings emphasize the importance of selecting suitable configurations and optimizing specific factors like column diameters and thermal couplings to achieve effective control, lower environmental impact, and reduced operational costs. This study provides a clear path toward optimizing the stability and efficiency of control systems in distillation column design.

## REFERENCES


1. Ukawa-Sato R, Hirano N, Fushimi C. Design and techno–economic analysis of levulinic acid production process from biomass by using co-product formic acid as a catalyst with minimal waste generation. *Chem. Eng. Res. Des* 192:389–401 (2023) https://doi.org/10.1016/J.CHERD.2023.02.046
2. Olujić Ž, Jödecke M, Shilkin A, Kaibel, B. Equipment improvement trends in distillation. *Chem. Eng. Process.: Process Intensif* 48:1089–1104 (2009) https://doi.org/10.1016/J.CEP.2009.03.004
3. Tian Y, Demirel SE, Hasan MMF, Pistikopoulos EN. An overview of process systems engineering approaches for process intensification: State of the art. *Chem. Eng. Process.: Process Intensif* 133:160–210 (2018) https://doi.org/10.1016/J.CEP.2018.07.014
4. Villegas-Uribe CA, Medina-Herrera N, Hernández-Magallanes JA, Tututi-Avila S. Optimal design and control of three simplified sargent four-product dividing-wall columns. *Chem. Eng. Process.: Process Intensif* 174:108860 (2022) https://doi.org/10.1016/J.CEP.2022.108860
5. Arenas-Grimaldo C, Avendaño-Guerrero JG, Molina-Guerrero CE, Segovia-Hernández JG. Design and control of a distillation sequence for the purification of bioethanol obtained from sotol bagasse (Dasylirium sp.). *Chem. Eng. Res. Des* 203:11–17 (2024) https://doi.org/10.1016/J.CHERD.2023.12.039
6. Li M, Peng J, Cheng Y, Zhu X, Ma Y, Zhang Z, Gao J. Dynamic control of an energy-saving process with two extractive dividing-wall columns for separation of acetone/methanol/butanone/tert-butyl alcohol mixtures. *Chem. Eng. Res. Des* 200:281–291 (2023) https://doi.org/10.1016/J.CHERD.2023.10.045
7. Pushkala SP, Panda RC. Design and analysis of reactive distillation for the production of isopropyl myristate. *Clean. Chem. Eng* 5:100090 (2023) https://doi.org/https://doi.org/10.1016/j.clce.2022.100090
8. Alcocer-García H, Segovia-Hernández JG, Prado-Rubio OA, Sánchez-Ramírez E, Quiroz-Ramírez JJ. Multi-objective optimization of intensified processes for the purification of levulinic acid involving economic and environmental objectives. Part II: A comparative study of dynamic properties. *Chem. Eng. Process.: Process Intensif* 147:107745 (2020) https://doi.org/10.1016/j.cep.2019.107745
9. Schmidt LM, Mthembu LD, Reddy P, Deenadayalu N, Kaltschmitt M, Smirnova I. Levulinic acid production integrated into a sugarcane bagasse based biorefinery using thermal-enzymatic pretreatment. *Ind Crops Prod* 99:172–178 (2017) https://doi.org/10.1016/J.INDCROP.2017.02.010
10. Alcocer-García H, Segovia-Hernández JG, Sánchez-Ramírez E, Caceres-Barrera CR, Hernández S. Sequential Synthesis Methodology in the Design and Optimization of Sustainable Distillation Sequences for Levulinic Acid Purification. *Bioenergy Res* 1-15 (2024) https://doi.org/10.1007/s12155-024-10765-0
11. Santaella MA, Jiménez LE, Orjuela A, Segovia-Hernández JG. Design of thermally coupled reactive distillation schemes for triethyl citrate production using economic and controllability criteria. *Chem. Eng. J* 328:368–381 (2017) https://doi.org/10.1016/J.CEJ.2017.07.015
12. Prado-Rubio OA, Jørgensen SB, Jonsson G. Control System Development for Integrated Bioreactor and Membrane Separation Process. *Comput. Aided Chem. Eng* 28:289–294 (2010) https://doi.org/10.1016/S1570-7946(10)28049-5



© 2025 by the authors. Licensed to PSEcommunity.org and PSE Press. This is an open access article under the creative commons CC-BY-SA licensing terms. Credit must be given to creator and adaptations must be shared under the same terms. See https://creativecommons.org/licenses/by-sa/4.0/




Systems & Control Transactions

**Research Article - Peer Reviewed Conference Proceeding**
ESCAPE 35 - European Symposium on Computer Aided Process Engineering
Ghent, Belgium. 6-9 July 2025
Jan F.M. Van Impe, Grégoire Léonard, Satyajeet S. Bhonsale,
Monika E. Polańska, Filip Logist (Eds.)

PSE PRESS

# Systematic design of structured packings based on shape optimization

**Alina Dobschall*, Elvis Michaelis, and Mirko Skiborowski**

Hamburg University of Technology, Institute of Process Systems Engineering, Hamburg, Germany
* Corresponding Author: alina.dobschall@tuhh.de.

## ABSTRACT

Distillation is not only a widely-used but also an energy-intensive separation process, in which internals such as structured packings play an important role. Increasing mass transfer efficiency by designing improved structured packings in order to provide a large interfacial area while enabling low pressure drop is one promising approach to quickly reduce the energy requirements of vacuum distillation where low pressure drop is important for separation efficiency and thermal stability of the processed media. The current work presents an innovative method to optimize structured packings by means of constrained shape optimization on the basis of computational fluid dynamics simulations to minimize the pressure drop while maintaining a constant specific surface area. To solve the fluid dynamic optimization problem, a gradient-based local optimization algorithm in a continuous adjoint formulation is utilized. The shape optimization is applied for a commonly used Rombobak packing, and tested as a refinement method for an initial structure derived by topology optimization. The results demonstrate a successful reduction of the pressure drop in both cases, which can be attributed to several factors, including the refinement of the edges and the mending of the dead zones.

**Keywords**: structured packings, CFD simulation, optimization-based design

## INTRODUCTION

The design of structured packings for thermal separation columns has been the subject of extensive research for 60 years [1]. Despite the profound expertise and considerable advances that have already been gained in this field, it remains a challenging but promising task. This is due to the fact that the packing performance depends on a variety of fluid dynamic and mass transfer-related parameters, which exert a mutual and not necessarily beneficial influence on one another. The systematic development of improved packings by means of computational fluid dynamics (CFD) simulations is a promising approach to yield improved designs that can be manufactured on the basis of the derived computer aided design (CAD) models.

Various research groups conducted parameter variations of specific structured packings based on CFD simulations to systematically generate new improved designs [2,3]. However, only a limited number of studies have employed mathematical optimization for this purpose. While Lange and Fieg [4] focused on the optimization of novel structures by means of topology optimization based on CFD simulations, Blauth et al. [5] performed shape optimization of a specific structured packing that was initially derived from the Rombopak 9M packing [6]. In the topology optimization approach [4], the material distribution is varied in a predefined grid structure making use of an evolutionary algorithm. While this approach provides high potential for innovation, it can only produce rough design drafts for tractable grid sizes. In contrast, shape optimization modifies a given structure gradually based on gradient information of the objective function, as obtained through adjoint simulations [7]. This approach does not allow for the generation of new structures, but can be beneficial as a refinement tool for further improvement of existing packing designs or initial course structures. As demonstrated and experimentally validated by Blauth et al. [5], the shape optimization has been proven to be successful, resulting in an increased separation efficiency of 20%.

In this contribution, shape optimization coupled with

single-phase CFD simulations of the gas phase is used to improve two initial packing structures. By starting from a topology-optimized packing structure, the sequential integration of both optimization methods is evaluated, while the shape optimization approach is further tested for an established structured packings on the basis of an initial Rombopak packing.

## METHODOLOGY

The initial structures of the two different packing elements are depicted in Figure 1, showing the topology-optimized packing [4] and the Rombopak packing. The individual structural elements of the topology-optimized packing (left) consist of cubes. Due to the sharp edges, they exert a detrimental impact on the overall flow such that vortex formation can occur here, which are associated with increased pressure drop. The Rombopak packing (right) consists of thin, x-shaped structural elements, which are already significantly more conducive to the flow. The size of the packings to be optimized is a single packing element at laboratory scale with a diameter of 54 mm diameter and a height of 100 mm selected based on the dimensions of an available experimental setup to measure the fluid dynamics.

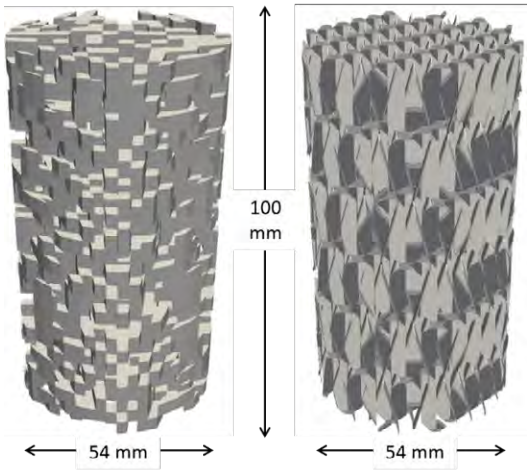



**Figure 1.** Initial packings for shape optimization: topology-optimized packing (left) and Rombopak packing (right).

### CFD simulations

To evaluate the pressure drop of the different packings generated during shape optimization, CFD simulations are performed using the software OpenFOAM. The fluid flow through the packings is modelled based on the continuity equation and the Navier Stokes equations. Whereas the primary focus of this study is on the fluid dynamics, the specific surface area serves as a simplified metric for the potential interfacial area for mass transfer, assuming a completely wetted packing surface. While this assumption is certainly optimistic it allows to use simple single-phase simulations instead of a complex multiphase model, which is important for the complex optimization task. The air flow is entered at the bottom of the packing with a velocity of 0.2 m/s, corresponding to an F-factor of 0.22 $Pa^{0.5}$. At these conditions, the flow can be assumed as incompressible. Further assumptions for the CFD simulations include steady state and laminar flow. Newtonian fluid behavior is be assumed and the flow is modeled at ambient pressure and temperature. The domain includes the packing element surrounded by a hollow cylinder representing the column wall. For convergence reasons, the cylinder is enlarged to a diameter of 63.5 mm. Furthermore, the length of the cylinder exceeds that of the packing on both sides to effectively simulate the inlet and outlet areas of the fluid. To solve the CFD simulations, the SIMPLE algorithm is used. The pressure drop is evaluated over the inlet and outlet of the computational domain. Furthermore, post-processing tools are employed to calculate the specific surface area of the structured packing, which is defined as the ratio of the surface area to the volume. To execute shape optimization, an additional solver is used, which is described in the following section.

### Adjoint-based shape optimization

The shape optimization problem can be stated as

$$\min J(\boldsymbol{u}, p, \boldsymbol{\beta}) \; s.t. \, \boldsymbol{h}(\boldsymbol{u}, p, \boldsymbol{\beta}) = 0 \wedge g(\boldsymbol{\beta}) = 0 \qquad (1)$$

with the objective function J describing the pressure drop Δp, $\boldsymbol{h}$ corresponding to the mathematical model of the fluid dynamics problem, consisting of the continuity and the Navier Stokes equations, as well as a geometric constraint $g$, which keeps the specific surface area a constant. The design variables $\boldsymbol{\beta}$ of the optimization algorithm are defined as the surface points of the packing, which form the faces and thereby the shape of the packing. The surface points can be moved along the surface normal during the optimization in order to deform the packing in a targeted manner for minimizing the objective function.

A gradient-based local optimization algorithm in a continuous adjoint formulation is used to solve the fluid dynamic optimization problem [7]. An overview of the iterative process of shape optimization is depicted in Figure 2. The initial geometry is provided in the form of a $stl$ file and is meshed before the optimization of the current iteration starts.

To obtain information about the extent for shifting the surface points, the gradients are necessary, which are also referred to as sensitivities in this context. An effective method for calculating the sensitivities with a large number of design variables, as in this case, is the adjoint method. In addition to the conventional system of equations based on the continuity equation and the

Navier Stokes equations, referred to as primal equation system, a similarly structured adjoint equation system is set up. This second system is a purely mathematical construct. To solve the constrained optimization problem of equation 1, the Lagrange method is applied. The resulting Lagrange function is shown in equation 2, where $\Omega$ corresponds to the solution domain of the fluid dynamic problem and the Lagrange multipliers are represented by the adjoint velocity $\boldsymbol{u_a}$ and the adjoint pressure $p_a$.

$$L = J + \int (\boldsymbol{u_a}, p_a) \boldsymbol{h} d\Omega \tag{2}$$

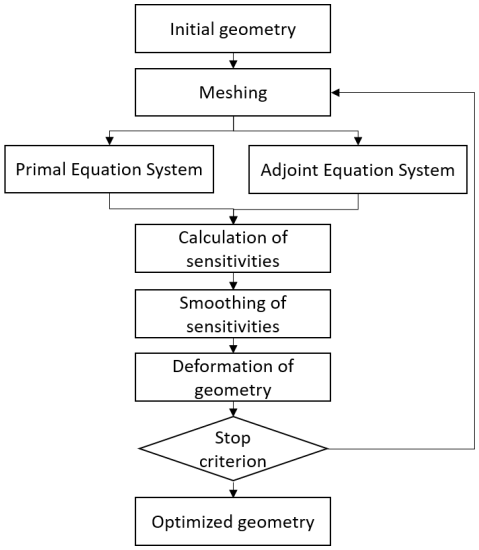



**Figure 2.** Schematic visualization of the iterative process of shape optimization.

The sensitivity field with respect to the design variables can then be calculated from the scalar product of the wall-normal gradients of the primary and adjoint velocities:

$$\frac{\partial L}{\partial \boldsymbol{\beta}} = -\nu (\boldsymbol{n} \cdot \nabla) \boldsymbol{u_a} \cdot (\boldsymbol{n} \cdot \nabla) \boldsymbol{u} \tag{3}$$

The geometrical constraint of a constant specific surface area is implemented using a penalty method whereby a penalty term weighted with a penalty parameter γ is added to the sensitivity values as illustrated in equation 4. The specific surface area of the initial packing is denoted by $a_0$ and the lower limit for the specific surface area $a_{min}$ is defined as $a_0$ subtracted by a tolerance value of 1.5 m²/m³ for both packing types. In order to prevent uncontrolled expansion of the structural elements, which leads to a decrease in the free cross-sectional area and thus to an increase in pressure drop, all negative sensitivities are set to zero once the geometric constraint is violated. Consequently, the correction of the sensitivity field is constrained to positive sensitivities.

$$\frac{\partial L}{\partial \boldsymbol{\beta}_{corrected}} = \frac{\partial L}{\partial \boldsymbol{\beta}_{>0}} + \gamma \frac{a_{min} - a}{a_0} \tag{4}$$

Subsequent to the calculation of the sensitivity values, a smoothing equation with a specified number of iterations can be used in order to reduce the scatter of the sensitivity field. Depending on the specific application, the magnitude of the sensitivity field varies, which can result in complications, such as overlapping faces when using the deformation tool. To address this, the sensitivities are normalized to the largest value. For the deformation of the surface points, the method of steepest descent with a specified step size α is applied. As indicated by equation 5, the surface normal displacement of the packings' surface points is obtained by multiplying the step size by the negative gradient of the surface sensitivities, which indicates the search direction.

$$\boldsymbol{\beta}^{i+1} = \boldsymbol{\beta}^{i} + \alpha \left( -\frac{\partial L}{\partial \boldsymbol{\beta}}^{i} \right) \tag{5}$$

The iterative shape optimization continues as the deformed geometry is used as a new initial packing in the next iteration step. The process continues until a specified stop criterion is reached.

In order to ensure that the cylindrical shape of the structured packing is retained and that it can be stacked in height without gaps, a maximum volume is introduced and sensitivities on the outer surfaces of the packing in this volume are set to zero. This approach also provides a constant cylindrical reference volume for the calculation of the specific surface area, thereby ensuring the comparability of the packings across different iterations of shape optimization.

The success of shape optimization is subject to the selection of the previously outlined hyperparameters, for which the values selected on the basis of preceding preliminary studies are shown in Table 1. For both structured packings, a step size of $10^{-4}$ is used whereas a higher penalty parameter and no smoothing iterations are used for the Rombopak packing compared to the topology-optimized packing for ensuring the specific surface area to remain above the prescribed lower limit.

**Table 1**. Selected parameters for the shape optimization algorithm

| Parameter | Topology-optimized packing | Rombopak packing |
|---|---|---|
| Step size | $10^{-4}$ | $10^{-4}$ |
| Penalty parameter | 10,000 | 100,000 |
| Smoothing iterations | 10 | 0 |

## RESULTS

The shape optimization results are first discussed for the topology-optimized packing and subsequently for the Rombopak packing, analyzing the development of the pressure drop and specific surface area, as well as the deformation of the packings induced by shape

optimization and the respective velocity plots and streamlines.

## Topology-optimized packing

Figure 3 shows the progression of shape optimization regarding pressure drop and specific surface area over the course of the iterations. For the initial packing, the pressure drop is 0.063 mbar/m and the specific surface area of the packing is 375.3 $m^2/m^3$. It should be noted that the pressure drop is relatively low, which is a consequence of the low F-factor. As the number of iterations increases, the pressure drop decreases continuously. In the first 20 iterations, the decline is precipitous, followed by a more modest decrease that is almost stagnating in the last 10 iterations. The specific surface area is characterized by a fluctuating course over the iterations. It decreases until the defined lower limit of 373.8 $m^2/m^3$, is attained, at which point the geometric constraint becomes effective. After the 136th iteration, the minimum limit for the specific surface area is permanently undercut, so that the optimum is found at this point. The pressure drop of this packing is 0.053 mbar/m and the specific surface area 374.0 $m^2/m^3$. Overall, the pressure drop is reduced by 16% during the process of shape optimization while the specific surface area is kept constant with minor deviations of 0.3%

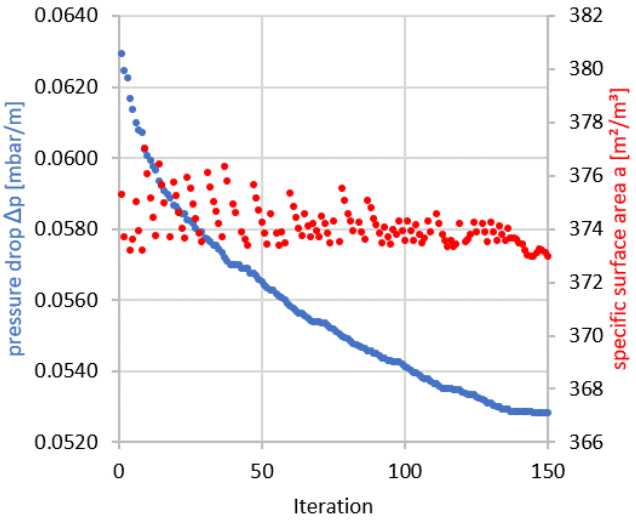



**Figure 3.** Shape optimization results of the pressure drop and specific surface area for the topology-optimized packing.

In order to conduct a more thorough examination of the effect of shape optimization, a comparison is made between the initial packing and the optimized packing shown in Figure 4. It becomes evident that the initially cubic structural elements are rounded, as expected, and extended in the direction of the flow. This results in a reduction in pressure drop, attributable to the gentler deflection of the fluid flow. Moreover, a reduction in horizontal surfaces is evident subsequent to shape optimization. In a distillation column, this phenomenon is anticipated to result in diminished stagnant liquid and a more frequent renewal of the liquid film, thereby enhancing mass transfer. A more detailed analysis of the two zoomed-in sections in Figure 4 offers additional insights. The section is situated at the bottom of the packing, with the cube in the center representing a dead zone since it is only open at the bottom. The figure demonstrates that this zone is filled with material during shape optimization, a factor that exerts a positive influence on both the pressure drop and the distribution of the fluid.

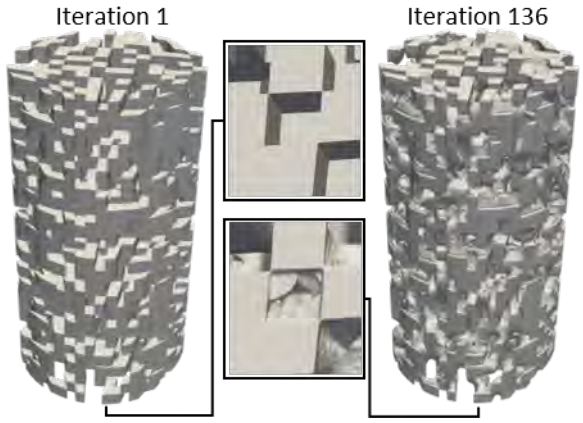



**Figure 4.** Packing element of the initial topology-optimized packing and after 136 shape optimization iteration steps including zoomed-in sections at the bottom of the packing.

To analyze the effects of the deformations on the fluid dynamics, sections of the velocity plots and the streamlines in Figure 5 are considered, where the initial packing and the optimized packing of iteration 100 are compared. For both cases, it is evident that subsequent to entering the packing from the bottom at 0.2 m/s, substantial variations in velocity occur, with velocities reaching up to 0.7 m/s in the constricted segments. These velocity differences contribute substantially to the formation of vortex structures, which are particularly evident in the outlet area, on top of the packing section. However, the flow stabilizes further downstream, which is not depicted in the section shown. Smaller vortices can also be observed within the packing. Furthermore, a considerable part of the fluid flows past the exterior of the packing between the packing and the cylindrical wall. The augmentation of the cylinder diameter, which is imperative for convergence reasons of the adjoint equation system, exerts a substantial influence on the flow behavior. However, it is noteworthy that the optimization process remains effective. Despite the general resemblance of the structure and velocity fields, it is evident that initial regions exhibiting minimal velocity are being replenished

with material (see black ellipsoid) fostering a more homogeneous fluid distribution in the cross-section. Furthermore, a discernible weakening of the vortex structures is apparent following the shape optimization, accompanied by a reduction in dissipation and, consequently, a decrease in pressure drop. This phenomenon is primarily attributable to the rounding of the structural elements, which deflects the fluid flow more gently. Yet it needs to be noted that the obvious bypassing close to the wall is merely affected by the improvements.

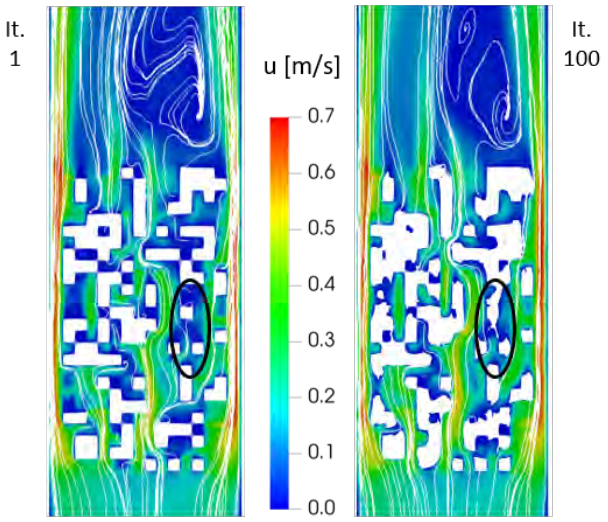



**Figure 5.** Section of velocity profiles of the initial topology-optimized packing (left) and after 100 shape optimization iterations (right) in central 2D section with streamlines; sections of the cylinder above and below the packing have been removed.

## Rombopak packing

The result of the shape optimization of the Rombopak packing is depicted in Figure 5. The development of the pressure drop and the specific surface area over the course of the iterations exhibits a resemblance to the previously studied packing. The specific surface area shows less fluctuation since the geometric constraint is undercut more frequently for this packing. At iteration 49, the specific surface area ceased to exceed the minimum defined value of 499.4 $m^2/m^3$ and therefore marks the optimum for this packing. The initial pressure drop of 0.036 mbar/m is reduced by 3% whereas the specific surface area remains constant with a negligible deviation of 0.3%.

The initial Rombopak packing and the resulting deformation after 49 shape optimization iterations, depicted in Figure 6, appear rather identical. However, a more thorough examination of the zoomed-in section reveals the deformations of shape optimization. It can be observed that the introduction of new material, particularly in the middle of the structural element and at the joints between different structural elements has been incorporated. Furthermore, as with the topology-optimized packing, the presence of rounded edges is evident. These rounded edges serve to prevent an abrupt change in the direction of fluid flow, thereby preventing flow separation and reducing pressure drop.

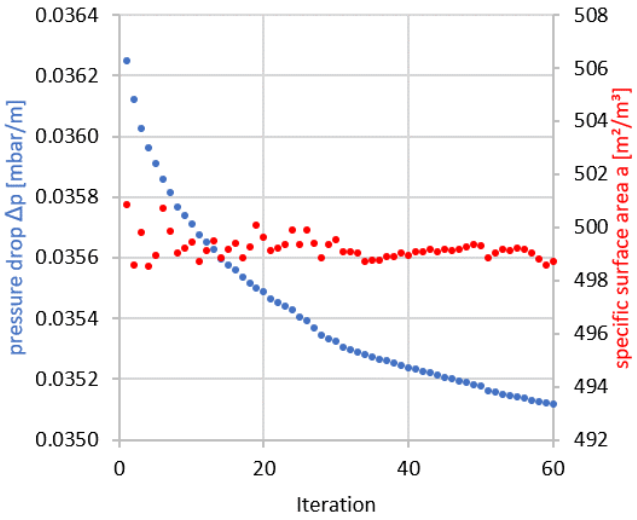



**Figure 6.** Shape optimization results of the pressure drop and specific surface area for the Rombopak packing.

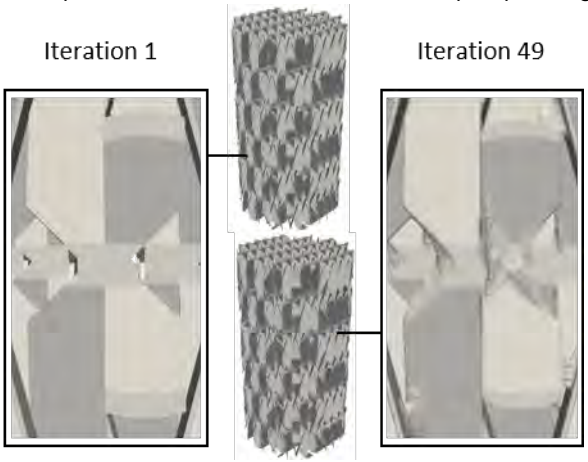



**Figure 7.** Packing element of the initial Rombopak packing and after 49 shape optimization iteration steps including zoomed-in sections.

An analysis of the velocity profiles and streamlines of the Rombopak packing before and after shape optimization, as shown in Figure 7, reveals more linear streamlines and a more uniform fluid distribution along the cross section compared to the topology-optimized packings, which has a positive effect on the pressure drop. While shape optimization does not significantly affect the velocity plots and streamlines in this case, zoomed-in sections highlight the deformations of the packings. As illustrated in Figure 6, the bottom right ellipse indicates the process of material addition at the joints of structural elements. Furthermore, the top left ellipse demonstrates

that there is an extension of the structural elements in the direction of the flow. An examination of the overall longitudinal section yields the finding that the deformations occur primarily on the outer elements.

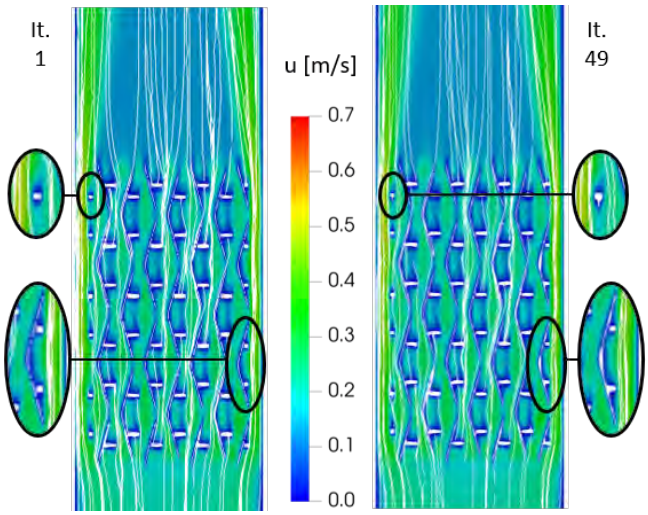



**Figure 7.** Section of velocity profiles of the initial Rombopak packing (left) and after 49 shape optimization iterations (right) in central 2D section with streamlines with zoomed-in sections; sections of the cylinder above and below the packing have been removed.

## CONCLUSION & OUTLOOK

The two optimization studies indicate the successful application of the shape optimization with reduced pressure drop at constant specific surface area. The initial pressure drop of the coarse topology-optimized packing is effectively reduced by 16%, while the pressure drop of the Rombopak packing is reduced only slightly by 3%, and the optimal result was attained after 49 iterations. These differences are however expected due to the coarser structure of the topology-optimized packing, which provides significantly larger potential for improvement. Overall, it can be concluded that shape optimization provides an effective tool for the refinement of existing packing structures.

To further improve the optimization, it is essential to systematically vary the parameterization of the optimization algorithm for every packing considered. A particular emphasis should be placed on the tolerance value for the lower limit of the geometric constraint, as an increase in this value may contribute to a higher freedom for deformation. In order to ascertain the impact of shape deformation on the separation efficiency, experiments of the optimized packings in a distillation column are imperative.

## ACKNOWLEDGEMENTS

Funded by the Deutsche Forschungsgemeinschaft (DFG, German Research Foundation) – 544956881.

## REFERENCES

1. L. Spiegel, W. Meier. Distillation columns with structured packings in the next decade. *Chem. Eng. Res. Des.* 81:39-47 (2003) https://doi.org/10.1205/026387603321158177
2. J. Neukäufer, F. Hanusch, M. Kutscherauer, S. Rehfeldt, H. Klein, T. Grützner. Methodology for the development of additively manufactured packings in thermal separation. *Chem. Eng. Technol.* 42:1970-1977 (2019) https://doi.org/10.1002/ceat.201900220
3. D. Zawadzki, M. Blazkiewicz, M. Jaskulski, M. Piątkowski, J. Koop, R. Loll, A. Górak. Design and Optimisation of Structural Packings for Rotating Bed Absorbers Using Computational Fluid Dynamics Simulation. *Chem. Eng. Res. Des.* 195:508-525 (2023) https://doi.org/10.2139/ssrn.4222640
4. A. Lange, G. Fieg. Designing novel structured packings by topology optimization and additive manufacturing. *Comp. Aided Chem. Eng.* 49:1291-1296 (2020) https://doi.org/10.1016/B978-0-323-85159-6.50215-3
5. S. Blauth, D. Stucke, M. A. Ashour, J. Schnebele, T. Grützner, C. Leithäuser. CFD-based shape optimization of structured packings for enhancing separation efficiency in distillation. *Chem. Eng. Sci.* 302:120803 (2025) https://doi.org/10.1016/j.ces.2024.120803
6. J. Neukäufer, M. A. Ashour, N. Sarajlic, H. Klein, S. Rehfeldt, H. Hallmann, S. Meinicke, J. Paschold, C. Knösche, T. Grützner. Development of enhanced three-dimensional printed packings for scale-up of distillation columns: a successful case study. *AIChE J.* 69:e17902 (2022) https://doi.org/10.1002/aic.17902
7. C. Othmer. A continuous adjoint formulation for the computation of topological and surface sensitivities of ducted flows. *Int. J. Numer. Meth. Fluids* 58:861-877 (2008) https://doi.org/10.1002/fld.1770

© 2025 by the authors. Licensed to PSEcommunity.org and PSE Press. This is an open access article under the creative commons CC-BY-SA licensing terms. Credit must be given to creator and adaptations must be shared under the same terms. See https://creativecommons.org/licenses/by-sa/4.0/

Systems & Control Transactions

**Research Article - Peer Reviewed Conference Proceeding**
ESCAPE 35 - European Symposium on Computer Aided Process Engineering
Ghent, Belgium. 6-9 July 2025
Jan F.M. Van Impe, Grégoire Léonard, Satyajeet S. Bhonsale,
Monika E. Polańska, Filip Logist (Eds.)

PSE PRESS

# Enhancing Consumer Engagement in Plastic Waste Reduction: A Stackelberg Game

**Chunyan Si[a,b] , Yee Van Fan[a,c], Monika Dokl[b], Lidija Čuček[b,*], Zdravko Kravanja[b], and Petar Sabev Varbanov[d]**

[a] Sustainable Process Integration Laboratory – SPIL, NETME Centre, Faculty of Mechanical Engineering, Brno University of Technology - VUT Brno, Technická 2896/2, 616 69 Brno, Czech Republic
[b] University of Maribor, Faculty of Chemistry and Chemical Engineering, Maribor, Slovenia
[c] Environmental Change Institute (ECI), University of Oxford, Oxford OX1 3QY, United Kingdom
[d] Széchenyi István University, Vehicle Industry Research Center, H-9026 Győr, Hungary
* Corresponding Author: lidija.cucek@um.si

## ABSTRACT

Circular economy is recognized as one of the most effective strategies for promoting plastic sustainability. However, its implementation requires to enhance consumer engagement, which remains a primary target of regulatory initiatives designed to promote plastic circular economy. To ensure sustained consumer participation, it is essential to evaluate and optimize various incentives, including regulatory policies, voluntary programs, and market-related mechanisms. This study applies Stackelberg Game Approach to quantitatively capture the strategic interactions between the authorities (as the leader) and consumers (as followers). The model incorporates key consumer behaviors, i.e., "use less," "use longer," and "recycling", to reflect their role in advancing plastic circular economy goals. By integrating factors such as governmental utility (gains of benefits), consumer utility (welfare), and plastic waste reduction, the model identifies the optimal intensities of various public initiatives, which represent the quantitative levels of policy intervention necessary to maximize desired outcomes. A case study based on EU-27 data demonstrates the model's applicability, revealing optimal intensities of 0.91, 0.41 and 0.8 for regulatory, voluntary, and market-related initiatives. At these optimal intensities, regulatory measures achieve the highest governmental utility (benefits) and plastic waste reduction, while market-related mechanisms yield more favorable outcomes for consumer welfare. The findings highlight the need for a balanced policy mix that effectively aligns government objectives with consumer incentives.

**Keywords**: Circular Economy, Plastic Waste Reduction, Government initiatives Consumer behavior, Stackelberg Game

## INTRODUCTION

The conventional plastic consumption model, characterized by a linear "use-and-dispose" pattern, is gradually being replaced by a more sustainable approach known as the plastic circular economy [1]. This model emphasizes behaviors such as "use less", "use longer", and "recycling", which collectively aim to minimize plastic waste and maximize resource efficiency [2]. Howe-er, the transition to a circular economy presents significant challenges, particularly in influencing and sustaining changes in consumer behavior.

Governments play a pivotal role in this transition by implementing a range of initiatives designed to either incentivize or regulate consumer behavior. These measures include regulatory policies, voluntary programs, and market-related mechanisms such as taxes or subsidies [3]. While these initiatives are essential, their effectiveness largely depends on how consumers respond [4], making the dynamic interaction between government interventions and consumer behaviors a key issue.

Previous research has extensively explored this relationship, primarily through qualitative methods, such as consumer surveys and behavioral assessments [5]. Although these studies provided valuable insights into

consumer preferences and policy acceptance, they often lack quantitative evaluation of how different policy intensities affect consumer behavior and plastic waste reduction. Most existing literature tends to focus on broad initiative evaluations, such as the overall impact of policies on waste reduction, rather than exploring the strategic interactions between policymakers and consumers in a structured, decision-theoretic manner [5].

To address this gap, this study employs a Stackelberg game model, a well-established framework for analyzing hierarchical decision-making processes where one player (the leader) makes decisions anticipating the responses of another player (the follower) [6]. In the context of the plastic circular economy, the government acts as the leader, setting initiatives to influence consumer behaviors, while consumers act as followers, adjusting their actions to maximize their utility in response to these initiatives. This approach allows for the quantitative evaluation of interactions between the government and consumers, providing insights into how different measure intensities affect not only plastic waste reduction but also the benefits of both parties.

The contributions of this work are outlined as follows,

1) The establishment of a Stackelberg Game model to quantitatively capture the interaction between the government and consumers, addressing the lack of quantitative focus in the existing literature.

2) Assessment of the interactions between government initiatives, i.e., regulatory, voluntary, and market-related, and consumer behaviors such as "use less," "use longer," and "recycling," providing a quantitative evaluation of how these factors influence the plastic circular economy.

3) Optimization of the intensities of various government initiatives, considering the balance between government utility, consumer welfare, and plastic waste reduction, providing a decision- making framework for government initiatives.

The remainder of this work is organized as follows: Section 2 proposes the developed Stackelberg game model for capturing the interactions between government and consumer. Section 3 introduces a numerical case study based on the EU-27. The numerical results are presented and discussed in Section 4. This work is concluded in Section 5. All symbols used in this work are illustrated in Table 1.

**Table 1:** Symbols.

| | |
|---|---|
| **Sets** | |
| $I$ | Types of government initiatives and/or policies implemented to promote a circular economy in plastics |
| $J$ | Types of consumer behaviors relevant to fostering a circular economy for plastics |
| **Indices** | |
| $i$ | Index for initiatives aimed at promoting the circular use of plastics, $i$ = {Regulatory measure, Voluntary measure, Market-based measure} |
| $j$ | Index for consumer behavior supporting the adoption of a circular economy for plastics, $j$ = {Reduce plastic use (Use less), Extend plastic product lifespan (Use longer), Recycling plastics} |
| **Parameters** | |
| $\alpha_i$ | Consumer sensitivity or resistance to $i$-th government initiative. ($\alpha_i \leq 0$) |
| $B$ | The total budget for voluntary measures, measured in € |
| $C_c$ | The cost of carbon price for consumer (€/kg) |
| $C_d$ | The charges of consumer plastic disposal, i.e., landfill (€/kg) |
| $C_e$ | The cost of government education investment (€/kg) |
| $C_r$ | The cost of consumer plastic recycling (€/kg) |
| $C_v$ | The cost of plastic virgin raw material consumption (€/kg) |
| $C_w$ | The cost of plastic waste management (€/kg) |
| $F_r$ | The consumer refundable fees of plastic recycling (€/kg) |
| $P_p$ | The price of plastics (€/kg) |
| $P_s$ | The prices of plastic substitutes (€/kg) |
| $T_c$ | The tax paid by consumer on plastic consumption (€/kg) |
| $W_0$ | The total amount of plastic waste generated (kg) |
| **Decision Variables** | |
| $\delta_{ij}$ | The impact of the $i$-th government initiative on the $j$-th consumer behaviour, where a value of 0 indicates no impact and a value of 1 indicates full impact. |
| $S_i$ | Government measure intensity, where $S_i \in [0,1]$. |
| **Functions** | |
| $R(S_i)$ | The response rate of the consumer behavior under the $i$-th government initiative and/or policy |
| $U_{ci}$ | Consumer utility under the $i$-th government initiative (€) |
| $U_{gi}$ | Government utility under the $i$-th government initiative (€) |
| $W_{di}$ | Reduction in plastic waste achieved under the $i$-th government initiative (kg) |

## STACKELBERG GAME MODEL

The Stackelberg Model is a framework designed to

describe strategic decision-making processes between hierarchical players under conditions of incomplete information [7]. In this work, the two-stage framework of government and consumer is illustrated in Figure 1. In the first stage, the government acts as the leader, selecting a measure from set $I$ and anticipates the corresponding consumer response. In the second stage, consumers, as followers, adjust their behaviors by choosing a strategy from set $J$ based on the selected government measure $i$ to maximise their benefits in response to these initiatives, primarily through actions such as using less, extending plastic product lifespan (use longer), and promoting plastic recycling.

Note that stage 2 captures the aggregated response of a heterogeneous consumer population, considering variations in overall consumer behavior under different government interventions. $\delta_{ij}$ is introduced to represent the impact of various government initiatives on corresponding consumer behaviours, while it equals 0 if there is no impact on consumer behaviours, as shown in Table 2. For instance, if the government adopts a regulatory measure, the consumer's strategy set includes only "Use less", while there is no impact on "Use longer" and "Recycling".

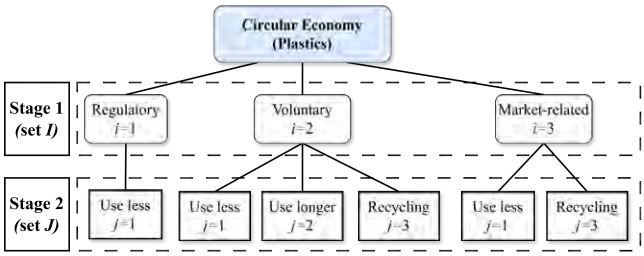



**Figure 1.** Two-stage Stackelberg Game model for plastic circular economy.

**Table 2:** The impact of government initiatives on consumer behaviors.

| | Regulatory | Voluntary | Market-based |
|---|---|---|---|
| Use less | $\delta_{11}=1$ | $\delta_{21}=1/3$ | $\delta_{31}=2/3$ |
| Use longer | $\delta_{12}=0$ | $\delta_{22}=1/3$ | $\delta_{32}=0$ |
| Recycling | $\delta_{13}=0$ | $\delta_{23}=1/3$ | $\delta_{33}=1/3$ |

Building upon the two-stage Stackelberg framework, the mathematical models are elaborated. As followers, consumers adjust their behaviors in response to the government's initiatives based on the intensity of initiative implementation, denoted by $S_i$. These intensities correspond to specific policy measures, such as the extent of regulatory enforcement, financial support for voluntary programs, and subsidies or market-based instruments promoting recycling. While consumers generally exhibit certain responsiveness (i.e., $R(S_i)$ ) to different government measures, new initiatives often trigger resistance [8]. This resistance constrains the sensitivity of consumer responses, causing the reaction function to exhibit saturation effects rather than continuous linear growth as the intensity of the government's measures increases. The parameter $\alpha_i$ is introduced to represent the resistance constrains, as shown in Eq. (1).

$$R(S_i)=\frac{\alpha_i {S_i}^3}{1+\alpha_i(S_i+{S_i}^2)} \quad (1)$$

The total reduction in plastic waste under the $i$-th government initiative, i.e., $W_{di}$, is determined by the combined effects of consumer responses to the employed government initiative. Specifically, it is the weighted sum of the impacts of each consumer behaviours, multiplied by the initial amount of plastic waste $W_0$. This relationship is expressed in Eq. (2) as follows:

$$W_{di}=\sum_{j=1}^{3}\delta_{ij}R(S_i)W_0 \quad (2)$$

The $i$-th government's utility function, $U_{gi}$, as shown in Eq. (3), consists of two main components: (1) the benefits derived from the implementation of measures, such as the reduction in waste disposal costs and the avoidance of raw material consumption due to waste reduction, tax revenue generated by market-related measures, and charges collected from the disposed plastic waste; and (2) the costs associated with the implementation of these measures, including the costs from the introduction of substitutes, the costs of voluntary measures, and the recycling deposits to be refunded to consumers. It is noted that only under market-related measures does the 'use less' behavior of consumers get influenced by the tax, $T_c$.

$$U_{gi}=(C_w+C_v)W_{di}-\left(P_p-P_s\right)\delta_{i1}R(S_i)W_0-\delta_{i2}S_iC_eW_0-F_r\delta_{i3}R(S_i)W_0+T_c\delta_{31}R(S_3)W_0+(W_0-W_{di})C_d \quad (3)$$

The function of consumer welfare under the $i$-th government initiative, $U_{ci}$, as shown in Eq. (4), also consists of two components: (1) the benefit component, which includes the reduction in carbon costs due to decreased plastic waste and the net benefit from plastic recycling (recycling revenue minus recycling costs); and (2) the cost component, which includes the additional expenses required for using plastic substitutes and the charges incurred for disposing of plastic waste.

$$U_{ci}=C_cW_{di}-(P_s-P_p)\delta_{i1}R(S_i)W_0+(F_r-C_r)\delta_{i3}R(S_i)W_0-(W_0-W_{di})C_d \quad (4)$$

The model's constraints are shown in Eqs. (5)–(8). The intensity of government measures ($S_i$) and the range of the consumer response function $R(S_i)$ are both within [0,1] (see Eqs. (5) and (6) ). The reduction in waste $W_{di}$ under the $i$-th government initiative should not exceed the total amount of waste $W_0$ (see Eq. (7) ). Voluntary measures, such as education, are primarily aimed at all

plastic waste, and their total cost should equal the total budget allocated for voluntary measures, as shown in Eq. (8).

$$0 \le S_i \le 1, \forall i \in \{1,2,3\} \quad (5)$$

$$0 \le R(S_i) \le 1, \forall i \in \{1,2,3\} \quad (6)$$

$$W_{di} \le W_0 \quad (7)$$

$$C_e \times W_0 = B \quad (8)$$

## CASE STUDY

A case study based on the EU-27 is conducted using the proposed Stackelberg model to quantitatively assess the interactions between government initiatives and consumer behaviors, aiming to promote a circular economy for plastic sectors. The case study utilizes data from official EU reports, industry surveys, and relevant literature data to numerical analyze the effects of varying intensities of regulatory, voluntary, and market-based interventions on consumer responses. This allows for an assessment of how various measure intensities and consumer reactions influence both government and consumer welfare, as well as the effectiveness of the strategies for plastic circular economy. All relevant parameters, including their descriptions, numerical values and data sources, are presented in Table 3.

**Table 3:** Collected data for proposed Stackelberg Game model in the EU-27.

| Parameters | Description | Values | Ref. |
|---|---|---|---|
| $\alpha_1$ | Consumer sensitivity to regulatory initiative. | -1.125 | [9] [10] [11] |
| $\alpha_2$ | Consumer sensitivity to voluntary initiative. | -3 | |
| $\alpha_3$ | Consumer sensitivity to market-related initiative. | -1.33 | |
| $B$ | The total budget for voluntary measures. | 13,850,000 € | [12] |
| $C_c$ | The cost of carbon price for consumer. | 0.16 €/kg | [13] |
| $C_d$ | The charges of consumer plastic disposal. | 0.8 €/kg | [14] |
| $C_e$ | The cost of government education investment. | 0.0021 €/kg | [15] |
| $C_r$ | The cost of consumer plastic recycling. | 0.73 €/kg | [16] |
| $C_v$ | The cost of plastic virgin raw material consumption. | 2.7€/kg | [17] |
| $C_w$ | The cost of plastic waste management. | 0.116 €/kg | [18] |
| $F_r$ | The consumer refundable fees of plastic recycling. | 1.2 €/kg | [19] |
| $P_p$ | The price of plastics. | 1.154 €/kg | [20] |
| $P_s$ | The prices of plastic substitutes. | 1.546 €/kg | [21] |
| $T_c$ | The tax paid by consumer on plastic consumption. | 0.8035 €/kg | [22] |
| $W_0$ | The total amount of plastic waste generated | 32·109 kg | [23] |

The collected numerical values are substituted into Eqs. (1)-(4) and calculated using backward induction. The specific steps are as follows:

**(1)** Under the given government $i$-th strategy, the objective of consumer is to maximize their benefits:

$$\max U_{ci} \quad (9)$$

This involves determining the optimal consumer response that yields the highest benefits based on the given government initiative.

**(2)** Take the first derivative of $U_{ci}$ with respect to $S_i$ and set it equal to zero to identify the optimal policy intensity that maximizes consumer's benefits:

$$\frac{dU_{ci}}{dS_i} = 0 \quad (10)$$

This condition helps determine the critical points where consumer utility reaches its maximum under the given government initiative.

**(3)** Substitute the optimal $S_i$, constrained by Eq. (5) within the range [0,1], into the government utility function $U_{gi}$ (Eq. (3)), the consumer utility function $U_{ci}$ (Eq. (4)), and the plastic waste reduction equation $W_{di}$ (Eq. (2)). This allows for the calculation of maximum benefits for government and consumer, and the plastic waste reduction under the optimal policy intensity $S_i$.

## RESULTS AND DISSCUSSION

The case study is conducted using the proposed Stackelberg Game model, calculated in Mathematica 14.0 software [24]. Figure 2 presents the optimal benefits for both the government and consumer, and plastic waste reduction under the optimal government strategy intensity.

As shown in Figure 2, the government initiative intensities are as follows: regulatory measure: 0.91, voluntary measure: 0.41, and market-related measures: 0.8, For each optimal strategy intensity, the government utility (represented by the blue bars in Figure 2) and waste reduction (represented by the green bars in Figure 2) resulting from the regulatory measure outperform those of the voluntary and market-related measures. This suggests that, within the context of the given case study, regulatory measures are the most effective in maximizing

government utility and reducing plastic waste, provided that the intensity reaches 0.91. These findings underscore the importance of carefully calibrating the strength of government interventions when formulating policies aimed at advancing a circular economy in the plastic sector [25].




**Figure 2.** The results under different initiative intensities for government utility ($U_{gi}$), consumer utility ($U_{ci}$), and plastic waste reduction ($W_{di}$): S1: Regulatory intensity; S2: Voluntary intensity; S3: Market-related intensity.

With the optimal intensities for government interventions, all consumer utilities are negative (represented by the orange bars in Figure. 2), whereas market-related measures, at an intensity of 0.8, exhibit the highest consumer utility. This suggests that while regulatory measures may achieve significant government utility and plastic waste reduction, they come at the expense of consumer welfare. On the other hand, market-related measures seem to strike a better balance, offering more favorable outcomes for consumers [3]. This indicates that when designing effective policies, it is crucial to consider not only the environmental and economic goals of the government but also the potential impacts on consumer behavior and utility. Striking this balance can help ensure more sustainable and effective strategies for promoting a circular economy in the plastic sector.

## CONCLUSION

This study develops a Stackelberg game model to quantitatively capture the interactions between the government (as the leader) and consumers (as the followers) in promoting the circular economy of plastics. By considering both the benefits and costs of the government and consumer within the plastic circular economy, a case study of the EU-27 is implemented. The optimal intensities of various government initiatives are captured: regulatory measures at 0.91, voluntary measures at 0.41, and recycling measures at 0.8.

The proposed Stackelberg Game model provides valuable insights into the strategic decision-making process between government interventions and consumer behaviour. By utilising this framework, policymakers can better assess the potential outcomes of different intervention strategies and determine the most effective measure intensities to promote sustainability in the plastic sector. The model highlights the trade-offs between government utility, consumer welfare, and environmental goals, offering a more comprehensive approach to policy design in the context of a circular economy in plastic sector.

The limitation of this study lies in not considering the combined effects of the various government initiatives, as well as the detailed consumer responses to each measure. Future research will address this by incorporating the synergistic impacts of the three initiatives and refining the model to capture more nuanced consumer behavior in response to government initiatives.

## ACKNOWLEDGEMENTS

The research was supported by Slovenian Research Agency for core research funding No. P2-0421 and project No. N2-0361.

## REFERENCES

1. Shi, X., Chen, Z., Wei, W., & Ni, B. J.. Perspectives on sustainable plastic treatment: a shift from linear to circular economy. TrAC Trends in Analytical Chemistry, 117631 (2024) https://doi.org/10.1016/j.trac.2024.117631
2. Reike, D., Vermeulen, W. J., & Witjes, S.. The circular economy: new or refurbished as CE 3.0?—exploring controversies in the conceptualization of the circular economy through a focus on history and resource value retention options. Resources, conservation and recycling, 135, 246-264 (2018) https://doi.org/10.1016/j.resconrec.2017.08.027
3. Uehara, T., Asari, M., Sakurai, R., Cordier, M., & Kalyanasundaram, M.. Behavioral barrier-based framework for selecting intervention measures toward sustainable plastic use and disposal. Journal of Cleaner Production, 384, 135609 (2023) https://doi.org/10.1016/j.jclepro.2022.135609
4. Heidbreder, L. M., Bablok, I., Drews, S., & Menzel, C.. Tackling the plastic problem: A review on perceptions, behaviors, and interventions. Science of the total environment, 668, 1077-1093 (2019) https://doi.org/10.1016/j.scitotenv.2019.02.437
5. Jacobsen, L. F., Pedersen, S., & Thøgersen, J.. Drivers of and barriers to consumers' plastic packaging waste avoidance and recycling–A systematic literature review. Waste Management, 141, 63-78 (2022)

https://doi.org/10.1016/j.wasman.2022.01.021
6. Tang, M., Liao, H., & Wu, X.. A Stackelberg game model for large-scale group decision making based on cooperative incentives. Information Fusion, 96, 103-116 (2023) https://doi.org/10.1016/j.inffus.2023.03.013
7. Yao, J., Yi, W., Wang, H., Zhen, L., & Liu, Y.. Stackelberg game model for construction waste disposal network design. Automation in Construction, 144, 104573 (2022) https://doi.org/10.1016/j.autcon.2022.104573
8. Gonzalez-Arcos, C., Joubert, A. M., Scaraboto, D., Guesalaga, R., & Sandberg, J. "How do I carry all this now?" Understanding consumer resistance to sustainability interventions. Journal of Marketing, 85(3), 44-61 (2021) https://doi.org/10.1177/0022242921992052
9. Nikiema, J., Asiedu, Z. A review of the cost and effectiveness of solutions to address plastic pollution. Environ Sci Pollut Res 29, 24547–24573 (2022) https://doi.org/10.1007/s11356-021-18038-5
10. fundsforNGOs. https://www.fundsforngos.org/proposals/global-strategies-to-eliminate-plastic-waste-a-circular-economy-approach/
11. Surfrider Foundation. https://www.surfrider.eu/learn/news/the-deposit-return-scheme-for-the-reuse-of-packaging-and-the-reduction-of-plastic-pollution/
12. European Commission. https://single-market-economy.ec.europa.eu/industry/strategy/hydrogen/funding-guide/eu-programmes-funds/life-programme_en
13. Edgar Meza. https://www.cleanenergywire.org/news/consumers-not-sufficiently-prepared-cost-increases-eu-carbon-price-env-agency
14. Weronika Ż., Inés B. de T.. https://wts.com/global/publishing-article/20240508-plastic-taxation-europe-update-2024~publishing-article
15. European Parliament. https://www.europarl.europa.eu/pdfs/news/expert/2018/12/story/20181212STO21610/20181212STO21610_en.pdf
16. Trading Economics. https://zh.tradingeconomics.com/country-list/wages?continent=europe&utm_source=chatgpt.com
17. European Environment Agency. https://www.eea.europa.eu/en/circularity/thematic-metrics/materialsandwaste/resource-productivity
18. Van Camp, N., Lase, I. S., De Meester, S., Hoozée, S., & Ragaert, K.. Exposing the pitfalls of plastics mechanical recycling through cost calculation. Waste Management, 189, 300-313 (2024) https://doi.org/10.1016/j.wasman.2024.08.017
19. Wts global. https://wts.com/wts.com/publications/climate-protection-green-tax-energy/2024/wts-global-plastic-taxation-2024-updated.pdf#page=6
20. Mintec by Expana. https://www.mintecglobal.com/top-stories/european-plastics-prices-rise-on-higher-production-costs-and-shipping-disruptions?utm_source=chatgpt.com
21. Nuojua, S., Pahl, S., & Thompson, R. C.. Plastic alternatives and substitutes in the packaging sector–A UK consumer perspective. Sustainable Production and Consumption, 46, 68-81 (2024) https://doi.org/10.1016/j.spc.2024.02.019
22. PRO European. https://www.pro-e.org/files/PRO-Europe-Participation-Costs-Overview-2022.pdf
23. European Commission. https://environment.ec.europa.eu/topics/plastics_en
24. Mathematica. https://www.wolfram.com/mathematica/
25. Knoblauch, D., & Mederake, L.. Government policies combatting plastic pollution. Current opinion in toxicology, 28, 87-96 (2021) https://doi.org/10.1016/j.cotox.2021.10.003

© 2025 by the authors. Licensed to PSEcommunity.org and PSE Press. This is an open access article under the creative commons CC-BY-SA licensing terms. Credit must be given to creator and adaptations must be shared under the same terms. See https://creativecommons.org/licenses/by-sa/4.0/



Systems & Control Transactions

**Research Article - Peer Reviewed Conference Proceeding**
ESCAPE 35 - European Symposium on Computer Aided Process Engineering
Ghent, Belgium. 6-9 July 2025
Jan F.M. Van Impe, Grégoire Léonard, Satyajeet S. Bhonsale,
Monika E. Polańska, Filip Logist (Eds.)

PSE PRESS

# Utilizing ML Surrogates in CAPD: Case Study of an Amine-based Carbon-Capture Process

**Florian Baakes, Gustavo Chaparro, Thomas Bernet, George Jackson, Amparo Galindo, Claire S. Adjiman***

Department of Chemical Engineering, Sargent Centre for Process Systems Engineering, Imperial College London, South Kensington Campus, SW7 2AZ, London, UK
* Corresponding Author: c.adjiman@imperial.ac.uk.

## ABSTRACT

Anthropogenic carbon-dioxide emissions, exceeding 51 billion tons annually, are a major driver of global climate impacts. Aqueous amine scrubbing offers an effective carbon-capture solution, but the energy-intensive thermal regeneration step of the process significantly increases costs, limiting large-scale adoption. To address these challenges, computational optimization of process and molecular design is promising but often too resource-intensive, emphasizing the need for efficient surrogate models. Specifically, we develop a surrogate model based on an artificial neural network (ANN) that is employed to replace rigorous phase-equilibrium computations performed with the SAFT-γ Mie group contribution method within a steady-state aqueous amine carbon-capture process model. Our ANN is trained on 32,768 vapour–liquid equilibrium data points of a quaternary mixture of water, monoethanolamine, carbon dioxide, and nitrogen over industrially relevant temperature, pressure, and composition ranges, achieving mean-relative errors below 2% for most variables. The ANN is integrated into a computer aided process design (CAPD) framework and evaluated via mathematical optimization, with the total annualized cost (TAC) as the objective function. Compared to the rigorous process model, the model with the ANN surrogate exhibits reduced computational times of up to 81% while converging to near-identical optima within 1% of the TAC. With a robustness analysis across the lean-loading and desorber-pressure design space we show that the ANN effectively captures 90% of the investigated design space, vs. 77% for the rigorous model. In a multi-start optimization ensuring global optimality, the surrogate converges to the same point as the rigorous model, taking 10 h less. This demonstrates that carefully trained surrogate models can significantly accelerate process optimization and enable larger-scale applications, paving the way for future solvent and process co-design efforts.

**Keywords**: Carbon Capture, Machine Learning, Phase equilibria, Process Design, gPROMS

## INTRODUCTION

Annual anthropogenic carbon dioxide ($CO_2$) equivalent emissions total approximately 51 billion tons, contributing to measurable climate change, manifested as droughts, storms, and floods [1]. Carbon capture is widely recognized as a key technology to reduce or even reverse these emissions by separating $CO_2$ from exhaust gases in power, cement, and steel plants for storage or utilization. A commonly considered approach is amine scrubbing, in which $CO_2$ is absorbed in an aqueous amine solution via the equilibrium formation of bicarbonate and carbamate species and subsequently released through a thermally driven process. This second step requires considerable energy, increasing costs and diminishing incentives for large-scale implementation [2].

Mathematical optimization can address cost and efficiency challenges by identifying optimal process designs [3]. The solvent choice presents a significant optimization problem, greatly increasing complexity and computational cost. In a recent study, Lee *et al.* [4] introduced an algorithm to solve the integrated solvent and process design problem reliably. However, the associated computational costs remain prohibitively high,

necessitating significant model simplifications, such as employing equilibrium-stage models instead of more detailed rate-based models. Surrogate models have historically been used to mitigate the burden of high computational costs [5], and the emergence of accessible machine-learning (ML) packages has further enhanced their utility, enabling tractable solutions to problems previously limited by rigorous thermodynamic models [6].

A notable example is the study by Zhang *et al.* [7], in which an ANN surrogate was employed to compute the solubility of $CO_2$ in ionic liquids in a carbon-capture process. The use of the surrogate made the global optimization of the integrated solvent and process design possible. In recent studies, Karia *et al.* [8] and Zhang *et al.* [9] evaluated various surrogate models for predicting the phase stability of liquid mixtures in a solvent design problem, showing that the integration of surrogates within optimization could be used to achieve much greater tractability. Nentwich *et al.* [10] tested several surrogate models – ANNs, Gaussian Processes (GPs), and Support Vector Machines (SVMs) – to calculate the distribution coefficient for the hydroformylation of 1-dodecane, replacing a rigorous PC-SAFT thermodynamic model. Using these ML surrogates successfully transformed an intractable rigorous model into a tractable one. In another study by Forster *et al.* [11], symbolic regression surrogates were investigated for use in optimization. These authors concluded that, with the currently available training methods, the surrogates were too inaccurate and required excessive training time to be practical. There is yet no consensus on when it is possible to achieve a satisfactory balance between accuracy and computational cost with surrogate models, and model development for a new application usually requires extensive trial and error. The most promising areas appear to be the use of surrogate models to replace models with no closed algebraic form (e.g., phase stability [8, 9]) or to replace expensive components of the model to facilitate solutions with local or global solvers.

Phase-equilibrium calculations, due to their expense and nonlinearity-induced numerical issues, are ideal for surrogate substitution. We aim to eliminate these costly computations in aqueous amine carbon-capture design by replacing the SAFT-$\gamma$ Mie GC equation of state calculations [12, 13] with an ANN model. We consider a quaternary mixture of water ($H_2O$), monoethanolamine (MEA), $CO_2$, and nitrogen ($N_2$). MEA is chosen as the solvent as it is widely utilized, making it an ideal benchmark for evaluation.

In this article, we first introduce the process model and detail the ANN architecture and training. Next, we incorporate the ANN surrogate into our process design and optimization framework, focusing on lean loading and desorber pressure as decision variables, and compare its performance against the rigorous thermodynamic model, evaluating computational efficiency, robustness, and convergence to thoroughly assess accuracy and reliability.

# METHODS

## Process Model

The process model used in our study (see Figure 1) is a steady-state, two-column aqueous amine capture system implemented in the process simulation software gPROMS Process 2023.1.0. It comprises an absorber, heat exchanger, desorber, condenser, reboiler, and mixer, with equipment dimensions calculated from stream properties and process requirements (e.g., capture rate). The model is derived from our previous work [14, 15], considering a 400 MWe combined-cycle gas-turbine plant [14], but where a rate-based model [15] replaces the equilibrium-stage absorber model in [14]. All thermodynamic properties are computed with the SAFT-$\gamma$ Mie GC method [12]. The total annualized cost (TAC) is obtained as given by Lee *et al.* [14] assuming a lifespan of 25 years and fixing the capture rate to 90%.

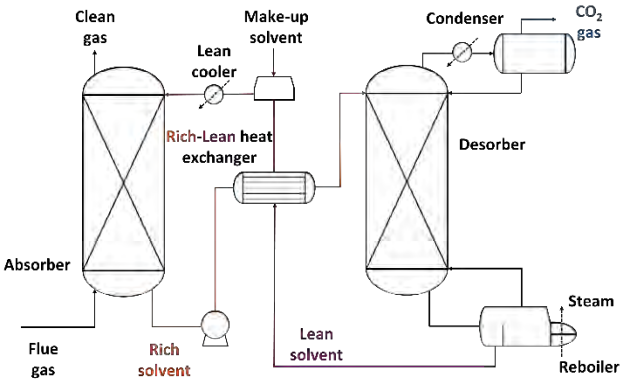



**Figure 1.** Flowsheet representation of the modelled aqueous amine carbon-capture process in our current work adapted from [14] licensed under CC BY 4.0.

## Artificial Neural Network (ANN) – Architecture, Training and Results

The ANN features are the inputs of a standard $Tp$-flash algorithm, namely temperature $T$, pressure $p$, and the global composition vector $\boldsymbol{z}$. After performing a hyperparameter study using OPTUNA [16], we found that two hidden layers with 50 nodes each adequately reproduce the fluid-phase behaviour, as more layers or nodes yielded diminishing returns. The hidden layers employ the ELU activation function, chosen for its smoothness and suitability in gradient-based optimization. The output of the ANN passes through a sigmoid function, bounded between 0 and 1. The elementwise multiplication of the resulting output vector $\boldsymbol{w}$, and the global composition vector $\boldsymbol{z}$, are used to obtain the liquid-phase mole amounts,

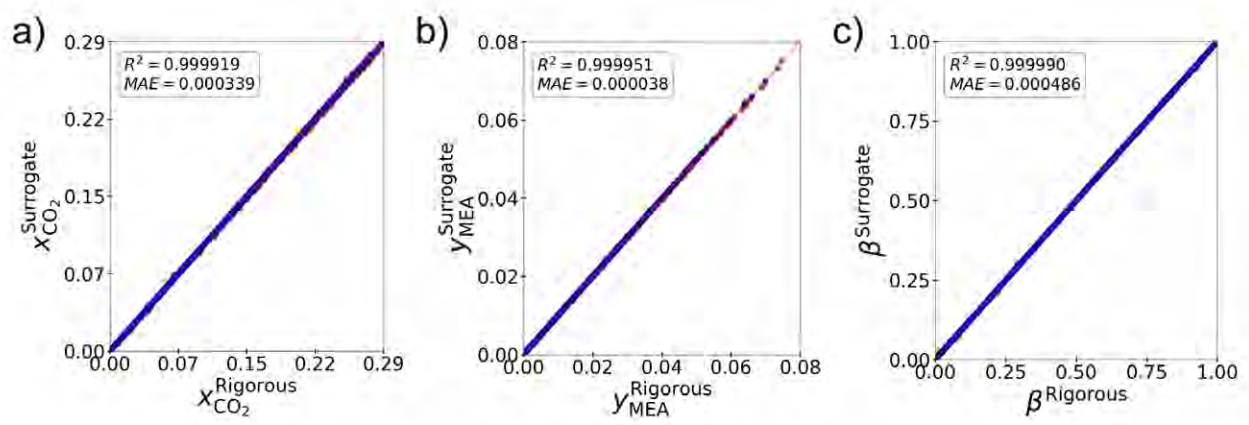



**Figure 2:** Parity plots comparing the description of the phase equilibria with rigorous thermodynamic model and phase-equilibria calculations against predictions of the the trained surrogate for all points in the test set for a) the liquid molar fraction of $CO_2$, b) the vapour molar fraction of MEA, and c) the vapour phase fraction.

vector $\boldsymbol{n_x}$:

$$n_{x,i} = z_i w_i, i \in \mathcal{C} = \{H_2O, MEA, CO_2, N_2\}. \quad (1)$$

The vector $\boldsymbol{n_y}$ of vapour-phase amounts is computed by

$$\boldsymbol{n_y} = \boldsymbol{z} - \boldsymbol{n_x}, \quad (2)$$

the vectors of mole fractions in the liquid and vapour phases, $\boldsymbol{x}$ and $\boldsymbol{y}$, respectively, follow as

$$\boldsymbol{x} = \boldsymbol{n_x}\left(\sum_{i\in\mathcal{C}} n_{x,i}\right)^{-1}, \ \boldsymbol{y} = \boldsymbol{n_y}\left(\sum_{i\in\mathcal{C}} n_{y,i}\right)^{-1}, \quad (3)$$

and the vapour-phase fraction β is given by

$$\beta = \left(\sum_{i\in\mathcal{C}} z_i - \sum_{i\in\mathcal{C}} n_{x,i}\right)\left(\sum_{i\in\mathcal{C}} z_i\right)^{-1} \quad (4)$$

In training the ANN, we used 32,768 vapour-liquid equilibrium (VLE) data points for the chosen $H_2O$-MEA-$CO_2$-$N_2$ mixture within the input domains of $T = [298.15, 420]$ K, $p = [0.1, 0.25]$ MPa, $z_{H_2O} = [0.43,\ 0.984]$, $z_{MEA} = [0.001,\ 0.15]$, $z_{CO_2} = [0.015,\ 0.25]$, and $z_{N_2} = [0,\ 0.4]$, based on typical process ranges established from previous work [15]. The data points are sampled using a Sobol sequence and generated using the gSAFT $Tp$-flash algorithm with the SAFT-γ Mie equation of state [12] and the relevant model parameters [13]. The data are split into training, validation, and test sets using an 8:1:1 split. Both labels and features are normalized using a mean-variance standardization. A learning rate $\alpha = 0.001$ is identified as suitable with the OPTUNA framework. The model is trained for 3000 epochs, tracking training and validation losses saving all parameter sets that achieved a lower validation loss than the lowest loss recorded so far. Twelve parallel pieces of training are performed with different seeds to mitigate initialization bias, and the best-performing model parameter set is implemented in the process model. The setup and training of the ANN are performed using the Pytorch 2.21 and CUDA 11.8 framework in Python 3.8. Data sampling and training takes 7 h on a Z8 HP workstation with 32 GB working memory, an Intel Xeon 5416S processor, and an NVIDIA T1000 graphics card.

### ANN Implementation and Process Optimization

The ANN is incorporated into gPROMS via its ForeignObject (FO) framework. The ANN code is first translated into C++ using the Libtorch library and then compiled into a custom FO file. This setup provides direct access to all custom functions and their analytical derivatives, computed through backpropagation, facilitating efficient gradient-based optimization.

Process optimization is executed using a Control Vector Parameterization Single Shooting algorithm. The objective function is the TAC. The primary decision variables are lean loading $\theta_{CO_2}$ and desorber pressure $p_{des}$. Optimization runs employ either the rigorous phase-equilibrium model or the ANN surrogate. Subsequently, the results of these two models are compared in terms of speed, robustness, and consistency in finding optima from different initial conditions.

## RESULTS AND DISCUSSION

### ANN Training Results

Our ANN is found to be highly accurate. For the given quaternary mixture of $H_2O$-MEA-$CO_2$-$N_2$, the ANN allows the successful prediction of the molar amounts in both phases and the phase fractions. Due to space constraints, presenting all 17 parity plots is beyond the scope of this publication. Instead, we include the parity plots of

the liquid molar fraction of $CO_2$, the vapour molar fraction of MEA, and the vapour phase fraction as representative results of the test set between the rigorous and the surrogate model shown in Figure 2 a), b), and c), respectively. Excellent agreement is apparent from these plots, with most points lying on the 45-degree line and the few deviations remaining very close. The maximum mean-relative error is 2% for the vapour mole amount of the MEA, whereas the minimum mean-relative error of 0.15% is reported for the liquid fraction of MEA. Following these promising results, we integrate the ANN into the process model and conduct optimizations.

## Process Design and Trajectories Comparison

We conduct a process design optimization, evaluating both the rigorous and surrogate models. Starting at two distinct initial points, one closer to the best known optimal solution (Initial point 1, IP1: desorber pressure of $p_{\mathrm{des}} = 0.181$ MPa and lean loading of $\theta_{\mathrm{CO_2}} = 0.250$), and one further away (Initial point 2, IP2: desorber pressure $p_{\mathrm{des}} = 0.181$ MPa, lean loading $\theta_{\mathrm{CO_2}} = 0.030$). The results of these runs are reported in Table 1. For IP1, both models are in good agreement on the TAC (36.02 M$/year for the rigorous model vs. 36.51 M$/year for the surrogate model), while for IP2, there is a more significant deviation (99.51 M$/year for the rigorous model and 132.21 M$/year for the surrogate). This is caused by minor inaccuracies in the predicted phase compositions that influence properties such as heat and flow, which in turn lead to a higher TAC, indicating the high degree of sensitivity of the model near IP2.

As shown in Table 1, for IP1, the solutions obtained following optimization are in good agreement, with a 1% deviation in TAC and less than 2% deviation in the design variables. Regarding computational efficiency, the total optimization time is reduced by 71% using the surrogate model, requiring 52 s compared to 182 s. The surrogate took 32 iterations to converge, whereas the rigorous model took 41. Model evaluation times are, similarly, reduced by 63%.

For IP2, despite the initial difference in TAC, the optimizer converges to very similar values. The surrogate model deviates slightly from the previous optimal point with respect to the optimal pressure. This, however, can be explained by the fact that the value of the objective function is relatively insensitive to the desorber pressure in this region of the design space, see Figure 3 b). Regarding the computational efficiency, the total optimization time is reduced by 82% when using the surrogate model. The surrogate took 89 iterations to converge, whereas the rigorous model took 104. Model evaluation times are, reduced to a lesser extent (38%). Using the surrogate model within optimization brings additional benefits by increasing the speed of gradient evaluations and reducing the number of iterations needed for convergence. The surrogate maintains an accuracy within 1% for the objective function and less than 5% deviation in the design space.

Finally, a comparison between the optimization trajectories taken by both models is performed and presented using the contours of the TAC of the rigorous and surrogate model as a background, see Figure 3 a) and b), respectively. When comparing the trajectories taken for IP1, it is evident that both models follow the same path, and the speed advantage of the ML model stems purely from the faster evaluation of the model and gradients at each iteration. However, when comparing the trajectories for IP2, the rigorous model requires more iterations, resulting in the 82% speedup compared to the 71% speedup achieved for the optimization performed starting from the closer initial point. These results exemplify the possible benefits of using an ML surrogate in optimization. One can observe slow progress near the final point, as the line search does not lead to improved points. Successful convergence is achieved after reinitialization at the optimal solution for both models, suggesting that the optimization tolerance is most likely not met due to corruption of the Hessian caused by quasi-Newton updates, indicating there is scope for further acceleration.

## Robustness and Multi-start Optimization

To compare the robustness of both models, a sampling of the design space within the bounds of $p_{\mathrm{des}} = [0.1, 0.35]$ MPa and $\theta_{\mathrm{CO_2}} = [0.02, 0.5]$ is conducted. The results are summarized in Figures 3 a) and b), where the coverages for both models are shown as a contour plot showing the TAC values. The surrogate model covers approximately 90% of the sampled space, whereas the rigorous model covers 77%.

When analyzing the relative deviation between the

**Table 1:** Comparison of optimization results starting from two different initial points for the rigorous and the surrogate models, in terms of speed and accuracy.

| | Initial point 1 | Rigorous | Surrogate | Initial point 2 | Rigorous | Surrogate |
|---|---|---|---|---|---|---|
| $\theta_{lean}$ / - | 0.250 | 0.314 | 0.315 | 0.030 | 0.317 | 0.314 |
| $p_{des}$ / MPa | 0.181 | 0.206 | 0.199 | 0.181 | 0.203 | 0.194 |
| TAC / (M$/year) | 36.08/36.52 | 32.09 | 32.33 | 99.05/132.13 | 32.09 | 32.34 |
| Time / s | - | 182 | 52 | - | 454 | 80 |
| Time per model eval. / s | - | 0.082 | 0.031 | - | 0.042 | 0.026 |

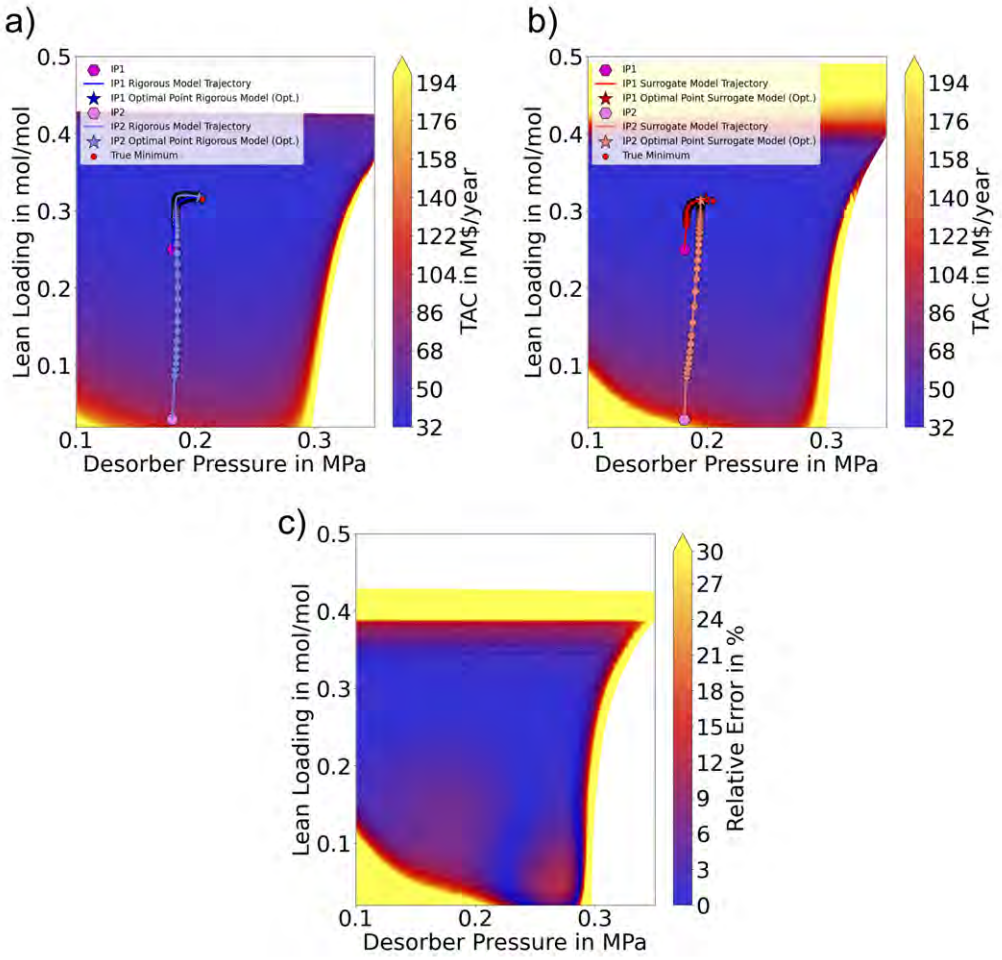



**Figure 3:** Feasible region of a) the rigorous model and b) the surrogate model with the objective function as a contour plot, including the trajectories for both optimizations performed from initials points IP1 and IP2. In c) the relative error between both models is shown as a contour plot. The contour plots are clipped at a TAC of 200 M$/year and 30% relative deviation, respectively.

values of the objective function in the overlapping areas, as presented in Figure 3 c), the deviation is below 10% in most of the space and close to 0% in proximity to the optimal region. However, at the edges, the deviation rises to a maximum of several million percentage points.

Lastly, we perform a global search based on multi-start optimization. We initialize the optimization at 128 points within the given design space using a Sobol' sequence. In the case of the surrogate, the ten best solutions are re-optimized with the rigorous model to improve accuracy. The average time to converge to the optimal point is 672 s for the rigorous model, whereas the surrogate requires just 175 s, a time reduction of 74%. This amounts to a total time of 23.91 h for the rigorous model compared to 6.8 h for the surrogate, including the re-optimization, which in turn equates to a ~10 h total time advantage for the surrogate model, considering the 7 h sampling and training time. The ten best solutions for the surrogate after re-optimization converge to the point $p_{\mathrm{des}} = 0.202995 \pm 0.000242$ MPa, $\theta_{\mathrm{CO_2}} = 0.317342 \pm 0.000058$ with a $\mathrm{TAC} = 32.0914 \pm 0.000082$ M$/year. The values for the rigorous model are $p_{\mathrm{des}} = 0.203184 \pm 0.000783$ MPa, $\theta_{\mathrm{CO_2}} = 0.317355 \pm 0.000003$ with a $\mathrm{TAC} = 32.09132 \pm 0.000092$ M$/year. It is apparent that using this approach, both methods effectively converge to the same optimal solution.

## CONCLUSIONS

We have demonstrated how integrating an ANN into the model of an aqueous amine carbon-capture plant, to replace rigorous phase-equilibrium calculations, can reduce the optimization time by up to 82%. We have also conducted a detailed analysis comparing the ANN to the rigorous model, which makes use of the SAFT-γ Mie GC approach in terms of optimization paths and robustness

across the design space as well as in a multi-start optimization. We show that a well-trained surrogate can converge to the solution with a time reduction between 70% and 80% compared to the rigorous model. The ANN surrogate successfully represents 90% of the investigated design space compared with 77% for the rigorous model. Additionally, the surrogate model successfully converged to the same point in a multi-start optimization taking 74% less time than the rigorous model

Our work demonstrates that ANN-based surrogates for phase-equilibrium calculations can be significantly faster and more robust than rigorous thermodynamic models, making them ideal for complex optimization tasks with a high number of decision variables or dynamic conditions. A transfer learning approach could further mitigate lengthy sampling and training challenges. In future work, we plan to extend this framework to tackle coupled process and molecular design problems.

## ACKNOWLEDGEMENTS

We acknowledge the UK Research and Innovation grant for funding the ECO-AI project under the AI4Net-Zero program (EP/Y006143/1, EP/Y005732/1).

## REFERENCES

1. H., Ritchie; P., Rosado and M. Roser. https://ourworldindata.org/co2-and-greenhouse-gas-emissions visited on: 28.01.2025
2. M., Bui *et al*. Carbon capture and storage (CCS): the way forward, *Energy Environ. Sci.* 11: 5 (2018) https://doi.org/10.1039/C7EE02342A
3. A. M., Schweidtmann *et al*. A review and perspective on hybrid modelling methodologies. *Dig. Chem. Eng.* 10:100136 (2023) https://doi.org/10.1016/j.dche.2023.100136
4. L., Lee *et al*. Enabling the direct solution of challenging computer-aided molecular and process design problems: Chemical absorption of carbon dioxide. *Comp. Chem. Eng.* 174*:* 108204 (2023) https://doi.org/10.1016/j.compchemeng.2023.108204
5. K., McBride and K., Sundmacher. Overview of Surrogate Modeling in Chemical Process Engineering. *Chem. Ing. Tech.* 91:228-239 (2019) https://doi.org/10.1002/cite.201800091
6. R., Misener and L., Biegler. Formulating data-driven surrogate models for process optimization. *Comp. Chem. Eng.* 179:108411 (2023) https://doi.org/10.1016/j.compchemeng.2023.108411
7. X., Zhang *et al*. Integrated ionic liquid and rate-based absorption process design for gas separation: Global optimization using hybrid models. *AIChE J.* 67:e17340(2021) https://doi.org/10.1002/aic.17340
8. T., Karia *et al.* Classifier Surrogates to ensure phase stability in optimization-based design of solvent mixtures. *Dig. Chem. Eng.* 100200 (2024) https://doi.org/10.1016/j.dche.2024.100200
9. L., Zhang *et al.* Comparative study of classifier models to assert phase stability in multicomponent mixtures. *CAPE J.*. 53:1465-1470(2024) https://doi.org/10.1016/B978-0-443-28824-1.50245-3
10. C., Nentwich *et al*. Optimization of chemical processes applying surrogate models for phase equilibrium calculations. *IJCNN:* 1-8 (2019) https://doi.org/10.1109/IJCNN.2019.8851816
11. T., Forster *et al*. Algebraic surrogate-based process optimization using Bayesian symbolic learning. *AIChE J.* 69*:* e18110 (2023) https://doi.org/10.1002/aic.18110
12. V., Papaioannou *et al*. Group contribution methodology based on the statistical associating fluid theory for heteronuclear molecules formed from Mie segments. *J. Chem. Phys.* 140*:* 054107 (2014) https://doi.org/10.1063/1.4851455
13. F., Perdomo *et al*. A predictive group-contribution framework for the thermodynamic modelling of $CO_2$ absorption in cyclic amines, alkyl polyamines, alkanolamines and phase-change amines: New data and SAFT-γ Mie parameters. *Fluid Ph. Equilib.* 566*:* 113635 (2023) https://doi.org/10.1016/j.fluid.2022.113635
14. L., Lee *et al*. A predictive model for the techno-economic assessment of $CO_2$ chemisorption processes applicable to a large number of amine solvents. *Chem. Eng. R&D.* 200*:* 615-636 (2023) https://doi.org/10.1016/j.cherd.2023.11.007
15. C. V., Brand *et al*. On the use of molecular-based thermodynamic models to assess the performance of solvents for $CO_2$ capture processes: monoethanolamine solutions. *Faraday Discuss.* 192*:* 337-390 (2016) https://doi.org/10.1039/C6FD00041J
16. T., Akiba *et al*. Optuna: A Next-generation Hyperparameter Optimization Framework. *Proc. ACM SIGKDD Int. Conf. Knowl. Discov. Data Min.* 19*:* 2623-2631 (2019) https://doi.org/10.1145/3292500.3330701

© 2025 by the authors. Licensed to PSEcommunity.org and PSE Press. This is an open access article under the creative commons CC-BY-SA licensing terms. Credit must be given to creator and adaptations must be shared under the same terms. See https://creativecommons.org/licenses/by-sa/4.0/



Systems & Control Transactions

**Research Article - Peer Reviewed Conference Proceeding**
ESCAPE 35 - European Symposium on Computer Aided Process Engineering
Ghent, Belgium. 6-9 July 2025
Jan F.M. Van Impe, Grégoire Léonard, Satyajeet S. Bhonsale,
Monika E. Polańska, Filip Logist (Eds.)

PSE PRESS

# Evaluation of the Controllability of Distillation with Multiple Reactive Stages

**Josué J. Herrera Velázquez[a,c], J. Rafael Alcántara Avila[b], Salvador Hernández[a], and Julián Cabrera Ruiz[a]***

[a] Universidad de Guanajuato, Departamento de Ingeniería Química, Guanajuato, 36050, Mexico
[b] Pontificia Universidad Católica del Perú, Departamento de Ingeniería, Lima, 15074, Peru
[c] Instituto Tecnológico Superior de Guanajuato, Departamento de Ingeniería en Industrias Alimentarias, Guanajuato, 36262, Mexico
* Corresponding Author: j.cabreraruiz@ugto.mx.

## ABSTRACT

Intensified schemes, such as reactive distillation, have been proposed to produce silane ($SiH_4$). Several studies have been carried out around this intensified scheme focusing directly on its improvement in energy or economic criteria. However, these mentioned criteria do not ensure that the scheme is also optimal from the control point of view. There is a direct compromise between the economic criterion and the control criterion. Thus, the best controllable scheme is not necessarily the most economical and vice versa. Analyses have been proposed to evaluate the controllability of steady-state processes using open-loop with Singular Value Decomposition (SVD) under quantitative a criterion such as $A_\gamma + \gamma_{sm}$ with simplified first-order transfer functions. This work considers four feasible designs with multiple reactive zones and evaluates their controllability from their open-loop dynamic responses obtained from Aspen Dynamics® by calculating the condition number for different frequency ranges analyzing qualitative aspects and the $A_\gamma + \gamma_{sm}$ criterion evaluating the controllability of each scheme and the conditions of the simplification of their dynamic responses. For this, simplifications of first and second order transfer function models are compared with the models that robustly predict their behavior. The results of this study show that first order functions, despite their simplicity, can predict well the complex model of these distillation schemes. However, for low frequencies (i.e. $\omega < 10$ rad/h) second order functions are better options because they capture the overshooting (damping) effect. The proposed methodology can be applied in global optimization with controllability as an additional criterion in the objective function.

**Keywords**: Silane, Reactive Distillation, Singular Value Decomposition, Process Control, Dynamic Behaviour

## INTRODUCTION

Various energy alternatives to fossil fuels have been proposed; one option for generating electricity in homes and industries is silicon-based solar photovoltaics (PV). Huang et al., [1] proposed the production of silane ($SiH_4$) from the disproportionation process of trichlorosilane in a reactive distillation column ($RD$). The studies of Zang et al., [2] for this $RD$, based on parametric studies, found that partitioning the reactive zone into three reactive zones improves the energy consumption being lower than the energy consumption used in the scheme proposed in the previous reference. Alcántara-Maciel et al., [3] took the three reactive zone scheme and optimized this problem through the Total Annual Cost ($TAC$) minimization using dynamic boundaries allowing to analyze in a single optimization the three cases for reactive zones finding that the optimal scheme tends to be a single reactive zone.

The best solution evaluated under an economic criterion does not ensure that it is the best design in terms of controllability. In a study carried out on a $RD$ for silane production [4] the trade-off between economic and controllability criteria was observed. Generally, the review of the process control is carried out after the optimization [5].

Aspen Dynamics solves the MESH equation system in a dynamic state to provide responses to perturbations that occur on the system. They are represented in a transfer function matrix after an adjustment of known transfer functions to model their behavior. Eq. 1 shows the case of a binary distillation column where the reflux ratio and reboiler load are perturbed for two components.

$$G(s) = \begin{bmatrix} g_{C1,RR}(s) & g_{C1,Q_H}(s) \\ g_{C2,RR}(s) & g_{C2,Q_H}(s) \end{bmatrix} \quad (1)$$

Where $C_1$ and $C_2$ refer to component 1 and 2 respectively, $RR$ to the reflux ratio perturbation and $Q_H$ to the reboiler duty perturbation. A small perturbation was performed ($\approx \pm 0.5\%$). The SVD technique has been used to evaluate the dynamic controllability of industrial processes [6,7] and particularly for distillation columns [8]. The systems controllability can be known by calculating their maximum ($\sigma^*$) and minimum ($\sigma_*$) singular values.

The calculation of the SVD is carried out with Eq. 2, where $\mathbb{A} \in \mathbb{R}_r^{m \times n}$ is the matrix finding singular values, in this case $G(s)$ in the frequency domain (i.e., $s = \omega j$), $\mathbb{U} \in \mathbb{R}_r^{m \times n}$ and $\mathbb{V} \in \mathbb{R}_r^{m \times n}$ are orthogonal matrices and $\Sigma$ is a matrix where the diagonal have the singular values [7].

$$\begin{aligned} &\mathbb{A} = \mathbb{U}\Sigma\mathbb{V}^T \\ &\Sigma = \mathrm{diag}(\sigma^*, \cdots, \sigma_*) \end{aligned} \quad (2)$$

A large value of the $\sigma^*$ suggests good invertibility of the system, while a small value of the $\sigma_*$ suggests bad invertibility of the system [6,9]. For a distillation column, the $\sigma^*$ corresponds to the change in the composition or temperature of the products depending on the setting of a vapor or liquid valve; a large value of $\sigma^*$ implies that the composition or temperature of products can be controlled with a change in that liquid or vapor flow. If $\sigma_*$ is small, it is related to a change in the vapor or liquid valve, it means that a small change in that flow does not have a large effect on the compositions or temperatures of the products. A measure that relates the $\sigma^*$ and $\sigma_*$ is the condition number ($\gamma^*$) shown in Eq. 3

$$\gamma^* = \sigma^*/\sigma_* \quad (3)$$

$\gamma^*$ indicate the sensitivity of the system to small changes or perturbations in its inputs and gives information of the system from four aspects [10]:

- **Sensitivity:** A large $\gamma^*$ indicates that the system is sensitive to small perturbations in the inputs. It will be impractical or impossible to satisfy the entire set of control objectives (regardless of the control strategy used).
- **Controllability:** If $\gamma^*$ is low (close to 1), the system is well conditioned, and the inputs uniformly affect the outputs. A high $\gamma^*$ indicates that the system is poorly conditioned (some variables are easily controlled, others cannot even be influenced).
- **Stability:** A large $\gamma^*$ can be related to the instability of the system and an unpredictable behavior. A low $\gamma^*$ indicates that the system is stable and predictable to variations in the inputs.
- **Dimensions and optimal control:** If $\gamma^*$ is large it may be an indication that the system is considering variables that do not significantly affect the system. A small $\gamma^*$ allows for simpler controllers to be designed [11].

Evaluating the $\gamma^*$ over a range of frequencies allows identifying critical ranges where the system may become more unstable or where a more robust control needs to be designed to handle certain input frequencies. It is recommended to do this type of analysis for frequency ranges of $0 < \omega \leq 100\ rad/h$, larger ranges are physically meaningless [12].

The criterion to determine if a scheme is better or worse in terms of controllability with the described technique has been defined qualitatively by comparing the $\gamma^*$ vs frequency graphs resulting from applying the SVD technique [5,8,13]. Cabrera Ruiz et al. [14] propose the following: *"it can be inferred that the best solution will have the minimum area below $\gamma^*$ in the frequency domain. That area of the condition number can be used as the controllability index $A_\gamma$"*. However, $\gamma^*$ values sometimes show sharp peaks in some frequency ranges, such a rapid change of these values is not suitable from the control and stability point of view (model singularities). Cabrera Ruiz et al. [15] complements the criterion $A_\gamma$ adding the term $\gamma_{sm}$ that allows to quantify the presence of such peaks in the area under the curve of $\gamma^*$evaluated in the frequency range.

$\gamma_{sm}$ acts as a "punishment" factor, since the presence of peaks in the curve will increase the total value of the area. The complete criterion $A_\gamma + \gamma_{sm}$ that qualitatively evaluates the controllability of an open-loop analysis via the SVD technique is the Eq. 4

$$\begin{aligned} A_\gamma + \gamma_{sm} &= \frac{\int_{\log a}^{\log b} \log(\gamma^*)\, d(\log \omega)}{\log b - \log a} \\ &+ \int_{\log a}^{\log b} \Delta log(\omega)\, |\gamma'_{i+1} - \gamma'_i|\, d(\log \omega) \end{aligned} \quad (4)$$

Where:

$$\gamma'_{i+1} - \gamma'_i = \frac{log[\gamma^*(\omega_{i+1})] - log[\gamma^*(\omega_i)]}{log(\omega_{i+1}) - log(\omega_i)} - \frac{log[\gamma^*(\omega_i)] - log[\gamma^*(\omega_{i-1})]}{log(\omega_i) - log(\omega_{i-1})}$$

where the logarithm of the $\gamma^*$ values for the frequency $\omega$

is taken by numerically integrating the data resulting from the SVD analysis to calculate the area. $b$ is the upper limit and $a$ is the lower limit of the evaluated frequency range.

Eq. 4 has been used to evaluate the controllability of an open-loop system in steady state via multi-objective optimization by approximating first-order transfer functions [4,15,16]. It has been shown that for some intensified schemes this approximation works well for frequencies lower than $100\ rad/h$ [14,15]. However, this has not been tested for reactive distillation schemes with multiple reactive zones.

In this work, three designs are taken of a previous multi-objective optimization where the objective functions are the $TAC$ and the $Q_H$, and the solution of Zang et al. [2] is also taken considering three reactive zones. These designs were evaluated with the criterion $A_\gamma + \gamma_{sm}$ of Eq. 4 for the adjustment of transfer function matrices $G(s)$ in four ways: best possible fit using the most suitable transfer function for each scheme (i.e., Robust fit), approximation using only first order transfer functions (FO), using only second order transfer functions with dumpling (SO), using only second order transfer functions without dumpling (SOL). The robust fit (RF) was done by adjusting dynamic responses to not only first or second order functions, but to other functions such as first and second order in competence, death time, etc. prioritizing that overshoot and damping effects are depicted by the functions while minimizing the error in Eq. 5. The Robust fit adjustment considered first order with and without deadtime $\theta$ ($\theta > 0$ and $\theta = 0$, respectively), second order with $0 < \zeta < 1$ with and without dead time and second order with $\zeta = 1$ with and without deadtime.

## METHODOLOGY

### Case Study

The processes described in Figure 1 were simulated using Aspen Plus V12® software and the Peng-Robinson

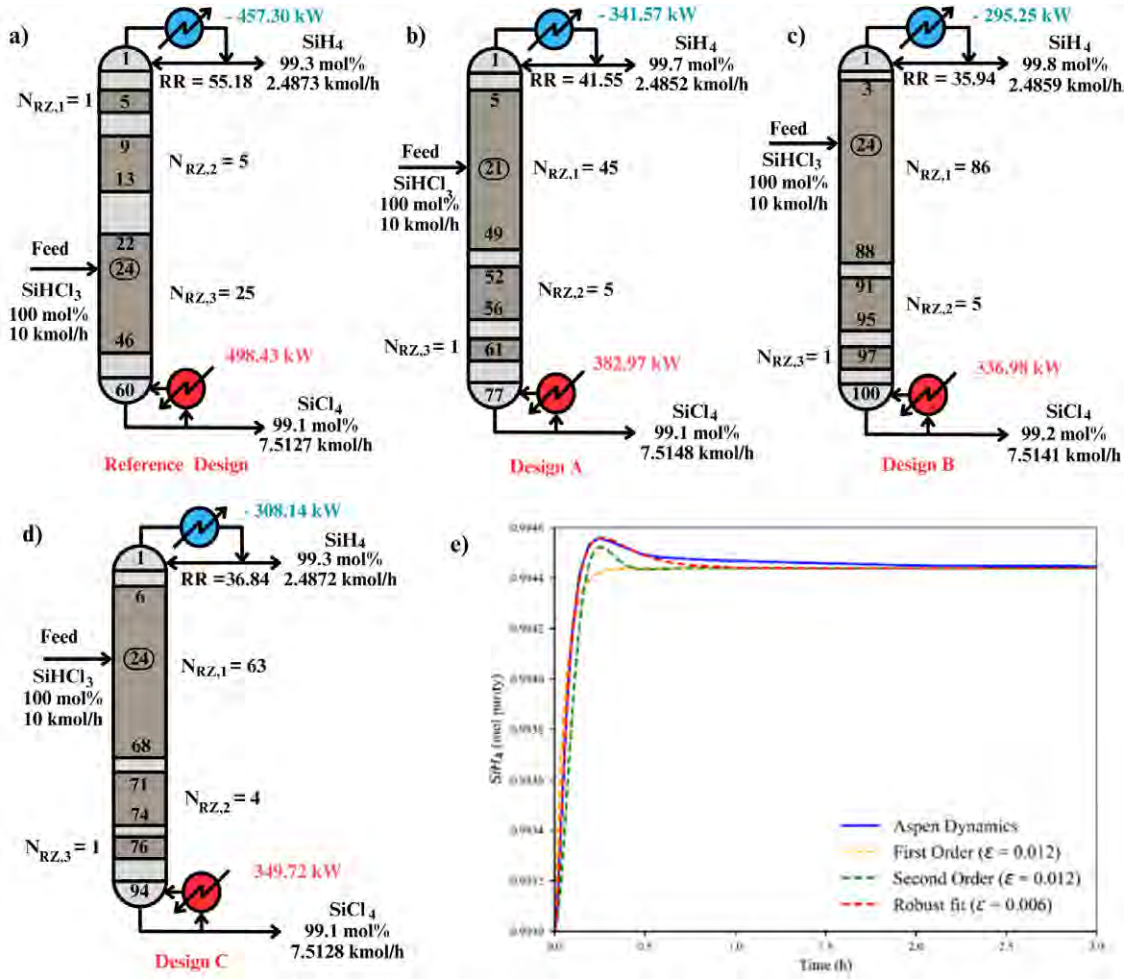



**Figure 1:** a) Reference design, b) Design with minimum $TAC$, c) Design with minimum $Q_H$, d) Design with 50/50 balance for $TAC$ and $Q_H$ and e) Positive perturbation response of $SiH_4$ of Design A for $RR$ considering different fit.

thermodynamic model was used. Figure 1a corresponds to the design proposed by Zang et al. [2] (Reference Design), Figure 1b is the design with the minimum $TAC$ (Design A), Figure 1c is the design with the minimum $Q_H$ (Design B) and Figure 1d is the design that has a 50/50 balance between $TAC$ and $Q_H$ [17]. Figure 1e, shows a dynamic response using Aspen Dynamics V12® with a $+0.5\%$ disturbance in the reflux flow. The solid blue line represents the response obtained from Aspen dynamics, the FO adjustment corresponds to the yellow dotted line, the SO adjustment corresponds to the green dotted line, and the Robust fit adjustment corresponds to the red dotted line.

## Dynamic Responses: Model Adjustment

For the FO, SO, and SOL adjustments, all the transfer functions in the matrix $G(s)$ are the same type, while for the Robust fit adjustment, the transfer functions of the matrix $G(s)$ can be of different type.

To fit all the models, a minimization of the error $\varepsilon$ between the Aspen Dynamics responses $X_i$ (simulation data) in the time domain and $Y_i$ (adjusted response) as shown in Eq. 5.

$$\min \varepsilon = \min \sum_i |X_i - Y_i| \qquad s.t. \quad \theta \geq 0, \ \ \tau > 0, \ \ 0 < \zeta \leq 1 \tag{5}$$

It is worth mentioning that minimizing Eq. 5 can fail to reach the damping/overshooting values, which can be misleading in the sense of having a low error value but not completely representing the trajectory of the disturbance response. The transfer functions shown in Figure 1e are presented below: Eq. 6, 7 and 8 for first order, second order and robust fit respectively.

$$g_{SiH_4,RR}(s) = \frac{0.5748}{1 + 0.0564\, s} \tag{6}$$

$$g_{SiH_4,RR}(s) = \frac{0.5748}{3.6000x10^{-3}\, s^2 + 0.0804\, s + 1} \tag{7}$$

$$g_{SiH_4,RR}(s) = -\frac{0.2045}{1 + 0.1715\, s} + \frac{0.7793}{(1 + 0.0771\, s)(1 + 0.0144\, s)} \tag{8}$$

Figure 1e shows that the first and second orders have the same error $(\varepsilon = 0.012)$ but the second order transfer function fits better the real trajectory of the dynamic response. It is imperative to review various types of simplified adjustments to determine their final impact on the application of the SVD and verify which is the best option.

## RESULTS AND DISCUSSION

Tables 1, 2, 3 and 4 present the results of $A_\gamma + \gamma_{sm}$ for each case. The area that comes closest to the robust fit is highlighted in bold. In addition, number 1 refers to the design with $\theta = 0$ and 2 to $\theta > 0$.

Figure 2 shows the $\gamma^*$ for the robust fit and its transfer function matrix (shaded area), as well as the estimates by the proposed models for each of the designs. Table 5 shows a summary of results.

**Table 1:** Values of $A_\gamma + \gamma_{sm}$ for different frequencies $(rad/h)$ for the reference design (Figure 1a).

| Model | | $10^0$ | $10^1$ | $10^2$ | $10^3$ | $10^4$ |
|---|---|---|---|---|---|---|
| $FO$ | 1 | 3.0985 | 3.6609 | 4.2235 | 4.7860 | 5.3541 |
| | 2 | 2.8495 | 3.2017 | 3.3613 | 3.6444 | 4.3278 |
| $SO$ | 1 | 2.8043 | 3.3140 | 3.8811 | 4.4513 | 5.0272 |
| | 2 | 2.8093 | 3.1051 | 3.2042 | 3.7988 | 4.5034 |
| $SOL$ | 1 | 2.9436 | 3.4682 | 4.0029 | 4.5380 | 5.0783 |
| | 2 | 2.8379 | 3.1608 | 3.2522 | 3.7538 | 4.5625 |
| $RF$ | - | 1.3986 | 1.5409 | 1.7998 | 2.0649 | 2.3328 |

**Table 2:** Values of $A_\gamma + \gamma_{sm}$ for different frequencies $(rad/h)$ for the Design A (Figure 1b).

| Model | | $10^0$ | $10^1$ | $10^2$ | $10^3$ | $10^4$ |
|---|---|---|---|---|---|---|
| $FO$ | 1 | 0.6430 | 0.7371 | 0.7779 | 0.8150 | 0.8524 |
| | 2 | 0.6440 | 0.7396 | 0.7641 | 0.7876 | 0.8111 |
| $SO$ | 1 | 0.6451 | 0.7207 | 0.7714 | 0.8288 | 0.8868 |
| | 2 | 0.6451 | 0.7209 | 0.8167 | 1.3179 | 1.9950 |
| $SOL$ | 1 | 0.6451 | 0.7218 | 0.7834 | 0.8633 | 0.9442 |
| | 2 | 0.6451 | 0.7212 | 0.8073 | 0.9223 | 1.0398 |
| $RF$ | - | 0.6663 | 0.7883 | 0.8270 | 0.9174 | 1.0118 |

**Table 3:** Values of $A_\gamma + \gamma_{sm}$ for different frequencies $(rad/h)$ for the Design B (Figure 1c).

| Model | | $10^0$ | $10^1$ | $10^2$ | $10^3$ | $10^4$ |
|---|---|---|---|---|---|---|
| $FO$ | 1 | 0.6331 | 0.7215 | 0.7974 | 0.8733 | 0.9499 |
| | 2 | 0.6334 | 0.7128 | 0.7645 | 0.8158 | 0.8790 |
| $SO$ | 1 | 0.6366 | 0.7390 | 0.9304 | 1.2300 | 1.5933 |
| | 2 | 0.6366 | 0.7343 | 0.8503 | 1.0202 | 1.2331 |
| $SOL$ | 1 | 0.6367 | 0.7405 | 0.9230 | 1.1576 | 1.3992 |
| | 2 | 0.6341 | 0.7096 | 0.8330 | 0.958 | 1.0844 |
| $RF$ | - | 0.5910 | 0.6799 | 0.7465 | 0.7617 | 0.7732 |

**Table 4:** Values of $A_\gamma + \gamma_{sm}$ for different frequencies $(rad/h)$ for the Design C (Figure 1d).

| Model | | $10^0$ | $10^1$ | $10^2$ | $10^3$ | $10^4$ |
|---|---|---|---|---|---|---|
| $FO$ | 1 | 0.2237 | 0.3178 | 0.4815 | 0.6533 | 0.8270 |
| | 2 | 0.2237 | 0.3186 | 0.4895 | 0.6705 | 0.8480 |
| $SO$ | 1 | 0.2242 | 0.3484 | 0.6503 | 0.9915 | 1.3370 |
| | 2 | 0.2243 | 0.3499 | 0.7194 | 1.4372 | 2.2121 |
| $SOL$ | 1 | 0.2242 | 0.3484 | 0.6503 | 0.9915 | 1.3370 |
| | 2 | 0.2242 | 0.3484 | 0.6504 | 0.9918 | 1.3348 |
| $RF$ | - | 0.2314 | 0.2985 | 0.4414 | 0.5951 | 0.7475 |

**Table 5:** Summary of the frequency of occurrence of the best fit according to $A_\gamma + \gamma_{sm}$ of all designs and all models at different frequencies

| Model | | $10^0$ | $10^1$ | $10^2$ | $10^3$ | $10^4$ | Total |
|---|---|---|---|---|---|---|---|
| $FO$ | $\theta = 0$ | 1 | 1 | 1 | 1 | 1 | 5 |
| | $\theta > 0$ | 0 | 1 | 1 | 2 | 2 | 6 |
| $SO$ | $\theta = 0$ | 3 | 0 | 0 | 0 | 0 | 3 |
| | $\theta > 0$ | 0 | 1 | 2 | 0 | 0 | 3 |
| $SOL$ | $\theta = 0$ | 0 | 0 | 0 | 0 | 0 | 0 |
| | $\theta > 0$ | 0 | 1 | 0 | 1 | 1 | 3 |

By comparing the results for RF at $100\ rad/h$, the controllability improves in the following order: Reference design < Design A< Design B < Design C. In addition, Design A and Design B have similar values. For FO-1 the order is: Reference design < Design B < Design A < Design C. However, Design A and Design B are very similar. FO-2 has the same order as RF. For the second order adjustments (i.e., SO-1, SO-2, SOL-1, SOL-2): Reference design < Design B < Design A < Design C. However, the difference between Design A and Design B is higher than that for FO-1

## CONCLUSIONS

For $100\ rad/h$, the FO-2 adjustments showed the same order as in RF in terms of controllability. Therefore, first-order transfer functions can reliably be used as approximations to dynamic responses in stochastic optimization to assess design and controllability simultaneously. By increasing the complexity in adjustments by using second-order transfer functions, the order of controllability improvement differs from that in RF. Moreover, the controllability index difference

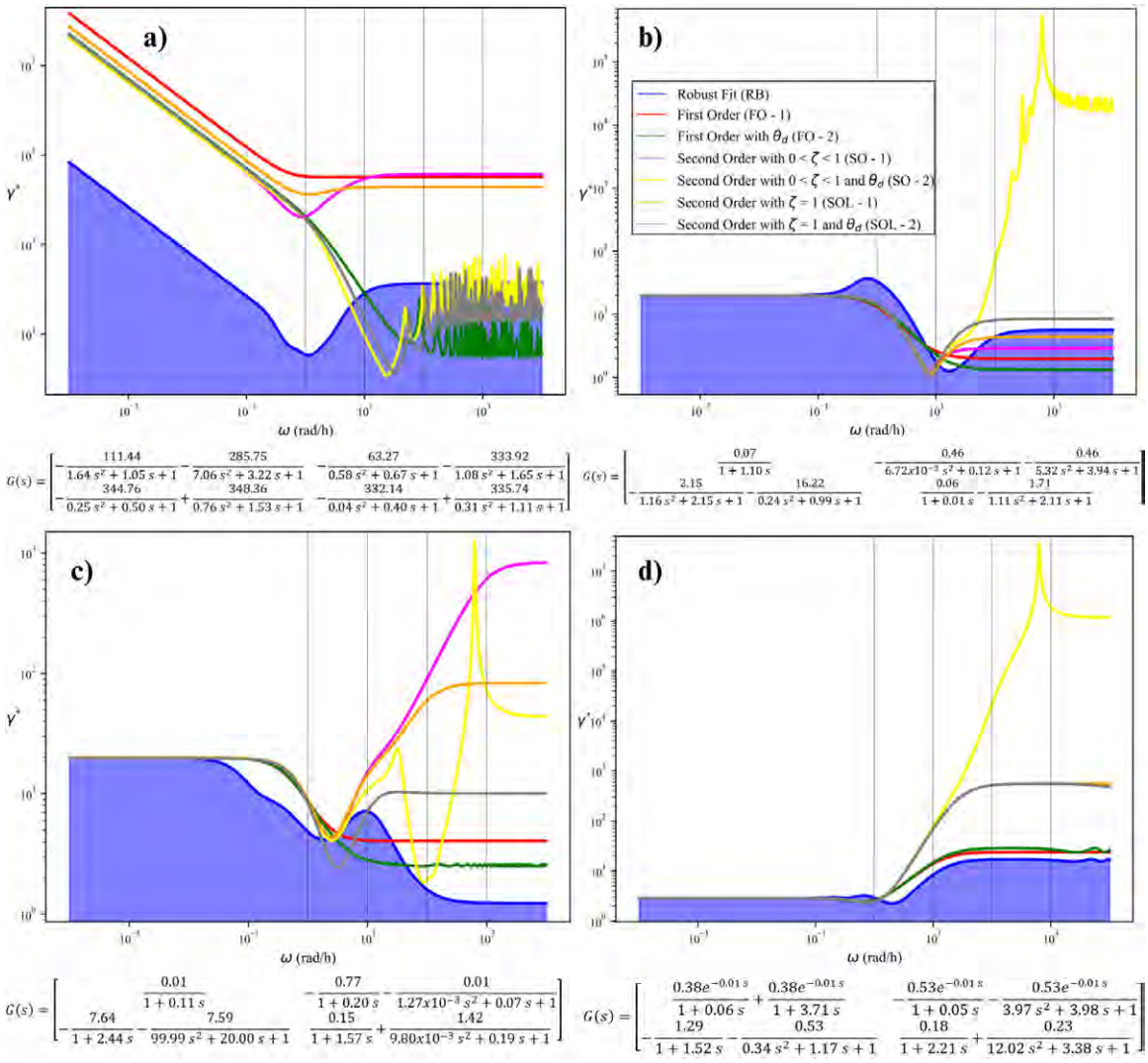



**Figure 2:** Condition number ($\gamma^*$) for different frequencies and models for the response of a positive disturbance ($\pm 0.05$) for a) Reference design, b) Design A, c) Design B and d) Design C.

between Design A and Design B was little (0.02) for FO-1, but one order of magnitude for SO-1 (0.15), and SOL-1 (0.2). Therefore, using more complex transfer functions can be counterproductive in assessing controllability properties.

## REFERENCES


1. Huang X, Ding W, Yan J, Xiao W. Reactive distillation column for disproportionation of trichlorosilane to silane: reducing refrigeration load with intermediate condensers. *Ind Eng Chem Res* 52:6211-6220 (2013) https://doi.org/10.1021/ie3032636
2. Zang X, Huang K, Yuan Y, Chen H, Zhang L, Wang S, Wang K. Reactive distillation columns with multiple reactive sections: a case study on the disproportionation of trichlorosilane to silane. *Ind Eng Chem Res* 56(3):717-727 (2017) https://doi.org/10.1021/acs.iecr.6b03715
3. Alcántara Maciel FD, Casillas Céspedes VE, López García JA, Cabrera Ruiz J, Ramírez Márquez C, Alcántara Avila JR. Economic optimization of a reactive distillation column with multiple reactive sections for silane production. *Comp Aided Chem Eng* 51:475-480 (2022) https://doi.org/10.1016/B978-0-323-95879-0.50080-1
4. Alcántara Avila JR, Cabrera Ruiz J, Lee H. Open-loop analysis for the stability of reactive distillation columns with intermediate condenser for the production of silane. *IFAC-Papers Online* 55(7):632-637 (2022) https://doi.org/10.1016/j.ifacol.2022.07.514
5. Acosta Solórzano ADA, Guerrero Farfán O, Ramírez Márquez C, Gómez Castro FI, Segovia Hernández JG, Hernández S, Gutiérrez Antonio C, Briones Ramírez A. Controllability analysis of distillation sequences for the separation of biojet fuel and green diesel fractions. *Chem Eng Tech* 39:273-2283 https://doi.org/10.1002/ceat.201600095
6. Moore C. Application of singular value decomposition to the design, analysis, and control of industrial processes. *Ame Ctrl Conf*:643-650 (1986) https://doi.org/10.23919/ACC.1986.4789019
7. Klema VC, Laub AJ. The singular value decomposition: its computation and some applications. *IEEE Trans Auto Ctrl* 25(2):164-176 (1980) https://doi.org/10.1109/TAC.1980.1102314
8. Segovia Hernández JG, Alcántara Avila JR, Cabrera Ruiz J, Hernández S, Guang Rong B. Design and control analysis of thermally coupled configurations for quaternary distillations. *Comp Aided Chem Eng* 24:871-876 (2007) https://doi.org/10.1016/S1570-7946(07)80168-4
9. Smith CA, Corripio AB. Process Control: Theory and Practice. Ed: 1st. John Wiley & Sons (1991).
10. Skogestad S, Postlethwaite I. Introduction to multivariable control. In Multivariable feedback control: analysis and design. Ed: 2nd. John Wiley & Sons (2005).
11. Morari M, Grimm W, Oglesby MJ, Prosser ID. Design of resilient processing plants - VII. Design of energy management systems for unstable reactors – new insights. *Chem Eng Sci* 40(2):187-198 (1985) https://doi.org/10.1016/0009-2509(85)80058-0
12. Morari M, Zafiriou E. Robust Stability and performance. In Robust process control. Ed: 1st. Prentices Hall (1989).
13. Tamayo Galván VE, Segovia Hernández JG, Hernández S, Cabrera Ruiz J, Alcántara Ávila JR. Controllability analysis of alternate schemes to complex column arrangements with thermal coupling for the separation of ternary mixtures. Comp Chem Eng 32(12):3057-3066 (2008) https://doi.org/10.1016/j.compchemeng.2008.04.007
14. Cabrera Ruiz J, Santaella MA, Alcántara Ávila JR, Segovia Hernández JG, Hernández S. Open-loop based controllability criterion applied to stochastic global optimization for intensified distillation sequences. *Chem Eng Res Des* 123:165-179 (2017) https://doi.org/10.1016/j.cherd.2017.05.006
15. Cabrera Ruiz J, Ramírez Márquez C, Hasebe S, Hernández S, Alcántara Ávila JR. Outlook of the Dynamic behavior of closed-loop control through open-loop analysis for intensified separation processes. *Ind Eng Chem Res* 57(49):16795-16808 (2018) https://doi.org/10.1021/acs.iecr.8b04164
16. Arreola Nájera LG, Ramírez Márquez C, Cabrera Ruiz J, Segovia Hernández JG. Towards sustainability assessment through a flexibility index as the condition number. *Chem Eng Process Process Intensif* 182:109184 (2022) https://doi.org/10.1016/j.cep.2022.109184
17. Herrera Velazquez JJ. Implementación de Nuevas Estrategias de Optimización Estocástica Global Multiobjetivo Aplicadas a Diseños de Procesos Intensificados. Master Thesis, Universidad de Guanajuato (2024)



© 2025 by the authors. Licensed to PSEcommunity.org and PSE Press. This is an open access article under the creative commons CC-BY-SA licensing terms. Credit must be given to creator and adaptations must be shared under the same terms. See https://creativecommons.org/licenses/by-sa/4.0/




Systems & Control Transactions

**Research Article - Peer Reviewed Conference Proceeding**
ESCAPE 35 - European Symposium on Computer Aided Process Engineering
Ghent, Belgium. 6-9 July 2025
Jan F.M. Van Impe, Grégoire Léonard, Satyajeet S. Bhonsale,
Monika E. Polańska, Filip Logist (Eds.)

PSE PRESS

# Revenue Optimization for Dynamic Operation of a Hybrid Solar Thermal Power Plant

**Dibyajyoti Baidya, Mani Bhushan*, and Sharad Bhartiya**

Indian Institute of Technology Bombay, Department of Chemical Engineering, Powai, Maharashtra, India
* Corresponding Author: mbhushan@iitb.ac.in

## ABSTRACT

Solar Thermal Power Plants (STPPs) use solar energy for large-scale electricity production but face significant operational challenges. These include variations in solar radiation, cloud cover, electricity demand fluctuations, and the need for frequent shutdowns if energy storage is inadequate. Deciding an optimal STPP operating conditions is challenging due to these factors. While revenue maximization has been used as an objective in existing literature, current models are often static and fail to capture the dynamic nature of STPPs. In contrast, this work proposes a dynamic model-based revenue optimization approach that accounts for plant dynamics and operational constraints, such as solar radiation variability and changing electricity demand. The objective function is designed to maximize revenue while considering power generation and fluctuating electricity prices. A simulation model of 1 MWe hybrid solar thermal power plant in Gurgaon, India, featuring two solar fields—Parabolic Trough Collector (PTC) and Linear Fresnel Reflector (LFR), is chosen as a case study. The optimization focuses on the oil mass flow rate through the PTC, which influences steam production. The mass flow rate of oil side is optimized at discrete time intervals, forming the decision variables in a nonlinear programming problem (NLP). The results demonstrate the effectiveness of this approach in significantly enhancing the STPP's revenue.

**Keywords**: Optimization, Dynamic Modelling, Parabolic Trough Collector, Linear Fresnel Reflector

## INTRODUCTION

In recent years, there has been a global push to commercialize renewable energy sources as an alternative to fossil fuels. Among these alternatives, solar energy has gained considerable attention due to its abundance, widespread availability, and minimal carbon emissions. Solar energy is a key source for generating electricity, harnessed through photovoltaic (PV) systems and solar thermal power plants (STPPs). PV Systems convert sunlight directly into electricity, while STPP use mirrors or lenses to concentrate sunlight, generating heat that drives turbines to produce power [1]. Specifically, STPP captures the direct normal irradiation (DNI) of the sun, concentrates it onto a receiving surface, converts the absorbed heat into mechanical work, and subsequently produces electricity, typically through advanced thermodynamic power cycles. STPP is an environmentally friendly technology that offers significant potential for energy conservation and environmental protection [2].

To unlock the full potential of an STPP, several studies have focused on optimizing the operation of STPP from various perspectives. Simon et al. [3] explored the techno-economic optimization of low-temperature solar thermal plants ($< 100^\circ C$). Alix et al. [4] introduced dynamic real-time optimization (DRTO) with an emphasis on improving storage management and reducing operating costs and excess energy delivery. Antonio et al. [5] proposed solutions to boost sales revenue by optimizing turbine inlet temperature and prioritizing energy production during high sales price hours, particularly in low solar radiation months. Luigi et al. [6] focused on maximizing revenue in solar thermal plants with limited storage capacity through optimal control. Sun [7] developed a self operation and low-carbon scheduling optimization model, demonstrating that thermal storage improves power generation capacity and revenue. However, no previous work has specifically addressed revenue optimization based on electricity cost fluctuations in an STPP while incorporating dynamic nature of plantwide operations.

This paper presents a revenue optimization strategy for a dynamic plantwide solar thermal plant, focusing on electricity production in response to time varying electricity demand and solar radiation variability. Thus, unlike traditional methods that focus solely on performance optimization, this approach considers both supply-side factors (solar energy availability) and demand-side factors (market prices) to determine the optimal electricity production levels. Since the operation of STPP is highly complex and nonlinear, finding an optimal operating strategy in presence of the different kind of variations in these factors can be challenging. Therefore, in the current work, an optimization approach is proposed for the same.

In this study, we focus on a 1 MWe (or 5 MW thermal) Hybrid STPP (HSTPP) located at the National Institute of Solar Energy (NISE), affiliated with the Ministry of New and Renewable Energy (MNRE), Government of India (GoI), situated in Gwalpahari, Gurgaon (28°25′N, 77°09′E), India [7, 8, 9]. The HSTPP system employs parabolic trough collectors (PTC) and linear Fresnel reflectors (LFR) as its main energy concentrators, contributing to its hybrid nature. No previous reports on an optimization study exist for this system. However, dynamic models of various components of this HSTPP are available in literature [10], and hence we have selected this plant for our study.

The rest of the paper is organized as follows: PLANT OVERVIEW section provides a description of the various components of the (HSTPP). METHODOLOGY outlines the approach and techniques used to address the problem formulation. RESULTS AND DISCUSSIONS presents the outcomes from the case study, followed by CONCLUSIONS AND FUTURE SCOPE.

## PLANT OVERVIEW

### Plant components

Figure 1 illustrates the schematic of the Gurgaon HSTPP [9, 11]. This plant has five primary components. These components along with the corresponding dynamic model as available in literature [10] are briefly discussed below:

- Concentrator: Parabolic Trough Collectors (PTCs) are efficient and reliable collectors in STPP systems, utilizing an absorber tube with heat transfer fluid (HTF) flowing through it. The absorber tube is enclosed by a glass envelope to minimize heat losses, while solar radiation is focused by a parabolic reflector [9, 11, 12]. In contrast, Linear Fresnel Reflectors (LFRs) use fixed ground-based mirrors and a water-steam mixture, lowering costs and simplifying maintenance [13]. The PTC model includes three partial differential equations (PDEs) for temperature profiles, whereas the LFR model involves five PDEs for mass, momentum, and energy balances [13].
- Energy storage: Thermal energy storage is crucial for STPPs, enabling power generation during cloudy periods or nighttime by storing heat in fluids such as molten salts or thermal oil [15, 16]. The HSTPP in Gurgaon uses two relatively low-capacity oil storage units namely high temperature (HT) and low temperature (LT) tanks to enable plant operation for 10-15 minutes during low solar availability [9]. Both the tanks are modeled by two ordinary differential equations (ODEs) each.
- Heat Exchanger: The heat exchanger in an STPP transfers thermal energy between fluids, enabling steam generation for turbine and electricity production [17]. The HSTPP at Gurgaon uses multiple heat exchangers such as pre-heater (PH), steam generator (SG) and super-heater (SH), with the PH and SH modeled by two ODEs each for fluid outlet temperatures and the SG described by five ODEs considering various system variables [9].
- Steam Drum: The steam drum (SD) separates the two-phase flow from LFR tubes into liquid water and vapor, with the liquid recirculated and reheated in the LFR receiver, while the steam is pressurized and sent to the SH for turbine operation [7, 9]. The drum dynamics are modeled using five ODEs [9].
- Turbine & Generator: The turbine generates power by utilizing the pressure difference between high-pressure steam from the SG and the low-pressure condenser, driving the turbine blades and generating electricity through the connected generator [8]. The power output is calculated using Willan's line equation, as described in the literature [7, 9].

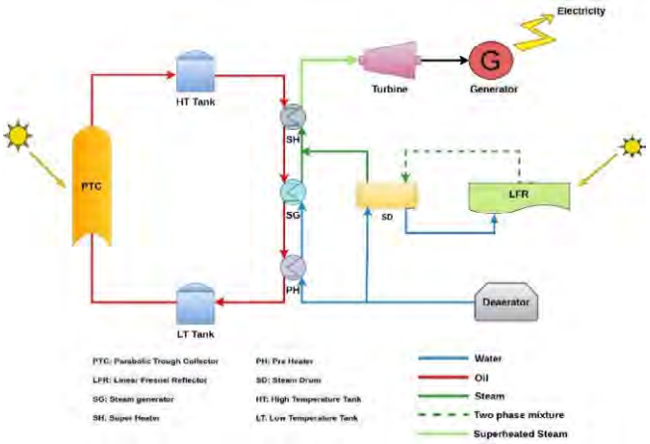



**Figure 1.** HSTPP block diagram.

The overall HSTPP model is comprised of a total of 58 ODEs (without LFR and SD) after conversion of PDEs to ODEs via spatial discretization. The LFR side (LFR+SD) is modeled by a total of 1,20,005 ODEs but is decoupled from the PTC loop. The dynamic model has been preliminarily validated using field data [10] and is considered in the current work.

### HSTPP standard operating procedure

Apart from the differential equations representing the dynamic behaviour, the HSTPP operations also involves discrete decisions corresponding to connections between various components. These are necessitated due to the daily startup and shutdown requirement of the plant. For example, at startup, when the PTC oil outlet temperature is lower than the HT oil temperature, the HT is bypassed, and the oil flow path follows LT-PTC-LT. However, when the PTC oil outlet temperature reaches or exceeds the HT oil temperature, the HT is integrated into the loop, and the flow path shifts to LT-PTC-HT-LT. Similarly, the various heat exchangers (SG, SH, PH) are brought inline when appropriate conditions are met [10].

## METHODOLOGY

### Proposed approach

The electricity price fluctuates throughout the day based on various factors, particularly market demand, thereby opening up the possibility of increasing revenue by intelligently varying the plant operation. In this context, the oil flow rate through the PTC in an HSTPP emerges as a critical decision variable since it ultimately affects revenue generation as shown in Figure 2.

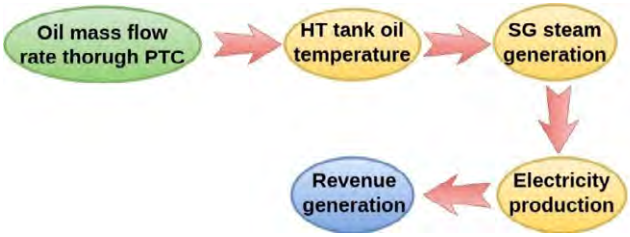



**Figure 2.** HSTPP block diagram.

This work focuses on developing a strategy to maximize revenue by dynamically adjusting the oil flow rate in response to market price fluctuations and solar radiation variations. For the current study, plant operation in a 10-hour window (8 AM - 6 PM) is considered. The corresponding electricity price is assumed to be proportional to the reported electricity demand [16] on a typical day, and is depicted in Figure 3(a). It is seen that the price varies across 15 minute intervals. Also, the real-time solar insolation data has been taken from a typical summer day at the plant site in Gurgaon, India, specifically from May 14th, 2014 [12] for our simulation as shown in Figure 3(b).

### Proposed formulation

The objective in our work is to determine the optimal oil mass flow rate through the PTC loop during daytime operation of HSTPP, so to ensure maximum revenue from electricity generation while adhering to the operational constraints of the HSTPP. This revenue optimization

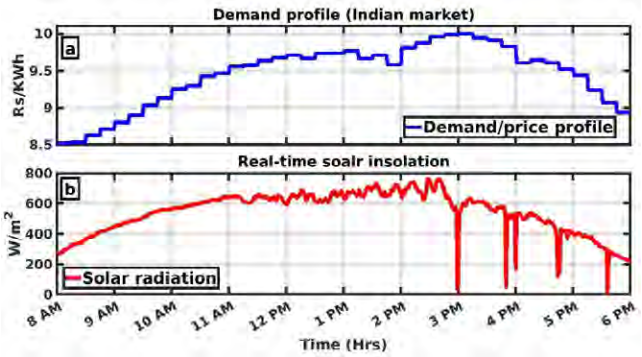



**Figure 3. (a)** Realtime electricity demand profile [16]. **(b)** Realtime solar insolation profile [10].

problem is defined as Formulation 1:

**Formulation 1:**

$$\max_{u(t),\ t_0 \le t < t_f} \int_{t_0}^{t_f} W_{PB}(t) P(t)\ d(t) \tag{1a}$$

$$\text{s.t.} \quad \dot{\tilde{x}} = \tilde{f}\big(\tilde{x}(t), u(t), s(t)\big) \tag{1b}$$

$$u_L \le u(t) \le u_U, \quad \forall\ t_0 \le t < t_f \tag{1c}$$

where the objective function (Equation (1a)) represents revenue generated by HSTPP in a day, and Equation (1b) represents the dynamic model of the HSTPP. Further, $W_{PB}$: Power generation from turbine (MW), $P$: Price per unit of electricity generation (Rs/MWh), $\tilde{x}$: State variables of HSTPP, $u$: Decision variables (manipulated inputs), namely PTC oil flow rate ($\dot{m}_{oil,PTC}$) that can be adjusted to influence the states in the optimization problem with upper and lower bound $u_L$ and $u_U$, $s$: Solar radiation profile, and $t_0$ and $t_f$ correspond to the period over which optimization is performed. Since $u(t)$ is a continuous variable, this is an infinite dimensional optimization problem. Further, the plant model involves a large number of nonlinear differential equations coupled with discrete connection operations. This makes Formulation 1 computationally tough to solve. Thus, we make the following simplifications to make the problem tractable:

- **Control Vector Parametrization:** We approximate the decision variable (DV) profile $u(t)$ by discretizing it over time, such that: $\mathrm{u}(t) = u(t_p)$, for $t_p \le t < t_{p+1}, p = 0,1,..,P-1$, where $P$ is the number of discretization intervals. Thus, the manipulated variable trajectory is approximated as a piecewise constant function over each time

interval.

- **Decoupling of LFR+SD Loop:** The LFR+SD operation is not affected by the PTC oil flowrate. Hence, we precompute the profile of steam ($r\ (t)$) generated by LFR+SD loop for the given solar insolation profile (Figure 3(b)). The dynamic equations corresponding to LFR+SD are then excluded from the model and instead $r(t)$ profile is used. The resulting dynamic model thus comprises of 58 ODEs with states represented as vector $x$.
- **Numerical Integration of Model Equations:** The dynamic model equations cannot be solved analytically. Hence, they are integrated numerically within the optimization formulation.

With these simplifications, Formulation 1 is reformulated as follows:

**Formulation 2:**

$$\max_{u(t_p),\ p=0,1,..,P-1} \sum_{j=1}^{N} W_{PB}(t_j)P(t_j)\Delta t \qquad (2a)$$

$$\text{s.t.} \quad x(t_{j+1}) = \int_{t_j}^{t_{j+1}} f(x(t), u(t_j), s(t_j), r(t_j))\ dt + x(t_j) \qquad (2b)$$

$$u(t_j) = u(t_p), \quad for \quad (p-1)M \le t_j < pM \qquad (2c)$$

$$u_L \le u(t_p) \le u_U, \quad p = 0,1,\dots,P-1 \qquad (2d)$$

Equations (2b,2c) are written for $j = 0,1,\dots,N-1$. Equation (2b) corresponds to numerical integration of the HSTPP model other than the LFR+SD component, with step size $\Delta t = 1$ minute. Model-equation integration and objective function evaluation is done at 1 minute interval to capture the significant dynamic variations in the plant. However, if the DV $u$ were to be determined at each 1 minute of time interval, the dimensionality of the problem would increase significantly, making it computationally very complex to solve. To mitigate this issue, the DV $u$ is held constant using zero-order hold over a time period $M = \frac{t_f - t_0}{P}$. Specifically, for each interval of $M$ minutes, $u(t_j)$ remains the same. This approach reduces the dimensionality of the problem while still capturing the dynamic variation of the system over the given simulation period.

## Solution strategy

Formulation 2 is a nonlinear programming (NLP) optimization problem. Further, the constraints are not explicit due to the need for numerical integration of model equations within the optimizer. The model equations are nonlinear, and non-differentiable at finite time instants, due to presence of discrete variables within model equations. Genetic Algorithm (GA), a popular meta-heuristic approach, are suited for solving such problems and are used in the current work.

# RESULT AND DISCUSSION

## Case Study

We consider three cases, each focusing on the revenue optimization problem but with varying number of DVs. These cases aim to explore the impact of adjusting key operational parameter, namely PTC oil mass flow rate ($\dot{m}_{oil,PTC}$) on the overall revenue generation in presence of varying electricity prices (Figure 3(a)) and solar radiation (Figure 3(b)). The study aims to identify optimal strategies for maximizing the HSTPP plant revenue under different levels of operational complexity.

The HSTPP stops electricity generation if the HT tank oil temperature drops below $300^{\circ}C$ for 5 minutes which leads to plant shutdown [9]. As solar radiation decreases at the end of the day, the temperature of the HT tank begins to fall. Consequently, the total plant runtime will vary for different oil mass flow rates.

The GA relevant parameters are listed in Table 1.

**Table 1:** GA-relevant parameters for case study.

| Parameter | Value |
|---|---|
| Population size | 100 |
| Number of generations | 50 |
| Elite count | 2 |
| Lower ($u_L$) and upper ($u_U$) bound | 2,5 kg/sec |

## Case-1 ($P = 1$):

In this optimization problem, a single DV is used, i.e., representing a simplified scenario for analysis. Throughout the 10-hours simulation period, the oil mass flow rate through the PTC loop is kept constant, regardless of the varying electricity demand. The optimizer determines the optimal mass flow rate as $\dot{m}_{oil,PTC} = 2.7\ kg/sec$, with corresponding revenue being $Rs.25{,}636$ for the $8.8\ hrs$ of plant run. In contrast, the designed oil mass flow rate $\dot{m}_{oil,PTC} = 3\ kg/sec$ as reported in literature [9], would correspond to revenue of $Rs.24{,}462.5$ for $7.2\ hrs$ of plant run (results not shown here). This revenue value is taken as the base case for comparison.

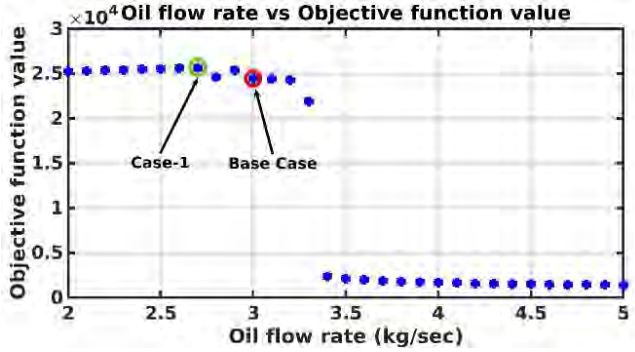



**Figure 4.** The validation of optimal value for Case-1

### Validation of Case-1:

To validate the optimizer results, we computed revenue for 30 different constant mass flow rate values in the range $2-5\ kg/sec$ (Figure 4). The Figure demonstrates the optimality of the GA obtained solution, despite the highly nonlinear and non-differentiable nature of the model equations.

### Case-2 ($P = 10$):

This case considers 10 DVs, offering more degrees of freedom. Here, while the mass flow rate is held constant for each hour starting from 8 AM to 6 PM for the 10 hrs of simulation, the flow rates across different hours can be different. The optimizer generated mass flow rate profile for this case is shown in Figure 5. The corresponding generated one-day revenue amounts to $Rs.25730.2$ for the daytime plant run of $8.76\ hrs$.

### Comparison of Case-1 and Case-2:

The power generated for these cases are depicted in Figure 6(a). It is seen that power generation profile for Case-2 is marginally higher (see Figure 6(a) inset) during the day. However, it is significantly higher during the beginning (9-9.30 AM) which leads to larger revenue. To understand this difference, consider Figures 6(b), 6(c).

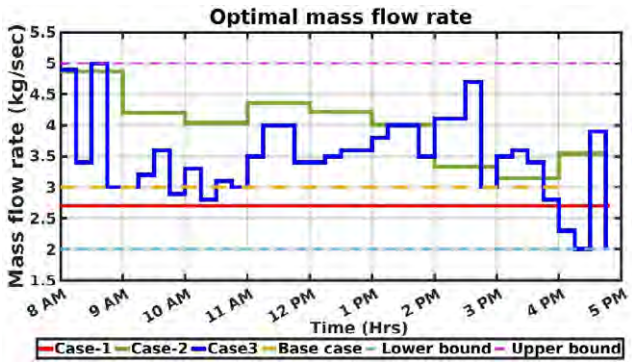



**Figure 5.** Optimal mass flow rate of oil for the three cases

The plant operation for both cases corresponds to warm startup where the plant has been operating for several days prior to the simulation. The corresponding starting temperatures are: HT tank: $306^{\circ}C$, LT tank: $240^{\circ}C$, and the PTC oil temperature: $30^{\circ}C$. During the initial start-up phase, only the PTC and LT tanks are connected since PTC oil outlet temperature is lower than HT tank oil temperature. In Case-1, the mass flow rate of the oil is $2.7\ kg/sec$ while it is $4.9\ kg/sec$ for Case-2 in the initial period. This leads to faster rise of PTC oil temperature in Case-2 due to injection of higher flowrate from the LT tank which is at higher temperature than the PTC oil temperature. This way of operation, namely injecting higher flowrate in the beginning, is non-intuitive but has been discovered by the optimizer to result in higher revenue generation. Further examination of Figure 6(b) and Figure 6(c) reveals that Case-2 maintains a lower HT oil outlet temperature ($T_{(o,o,HT)}$) throughout the 10-hours simulation but exhibits a higher oil mass flow rate (Figure 5) compared to Case-1. This increased flow rate results in a higher steam flow rate from the SH to the turbine in Case-2 compared to Case-1 leading to higher power generation. This demonstrates that optimizing the DVs can enhance the performance of HSTPP.

### Case-3 ($P = 40$):

We also considered a case with 40 DVs where oil flow rate change is allowed every 15 minutes. This led to revenue of $Rs.25895.7$ ($8.75$ hrs of plant operation) which is higher than that obtained in Case-1 and Case-2. Thus, an increase in the number of DVs offers greater opportunity to increase revenue generation. However, optimizing this case is considerably more complex. For the sake of brevity, detailed results for Case-3 are not presented here.

For our problem we also tried the gradient-based method 'fmincon' (MATLAB inbuilt function). However, the results were inferior to those obtained by GA.

## Performance metrics

Various performance metrics for the three cases are listed in Table 2. From this Table, it is seen that Case-3, with larger number of DVs, demonstrates the best performance in terms of both energy output and economic benefit. Specifically, considering a single, 10, and 40 DVs optimization strategy yields a revenue increase of $4.80\%, 5.18\%,$ and $5.86\%$ compared to the base case. These findings highlight the critical role of optimizing key operational variables to enhance the revenue generation of STPPs. Also, the significant computation times for the three cases indicate that the problem is computationally intensive to solve.

**Table 2:** Performance metrics for case study.

| Parameters | Base Case | Case-1 | Case-2 | Case-3 |
|---|---|---|---|---|
| Steam generation from SG (kg) | 9548.5 | 9989.4 | 10134 | 10488 |
| Steam Generation from LFR (kg) | 17535 | 18660 | 18645 | 18632 |
| Total steam produced (kg) | 27083 | 28649 | 28778 | 29120 |
| Electric energy produced (MWe) | 2.54 | 2.66 | 2.68 | 2.69 |
| Duration of power generation (hrs) | 7.2 | 8.8 | 8.76 | 8.75 |
| Revenue (Rs.) | 24462 | 25636 | 25730 | 25895 |
| % revenue increase (over base case) | - | 4.80 | 5.18 | 5.86 |
| Computation time (days) | - | 6 | 6.5 | 7 |

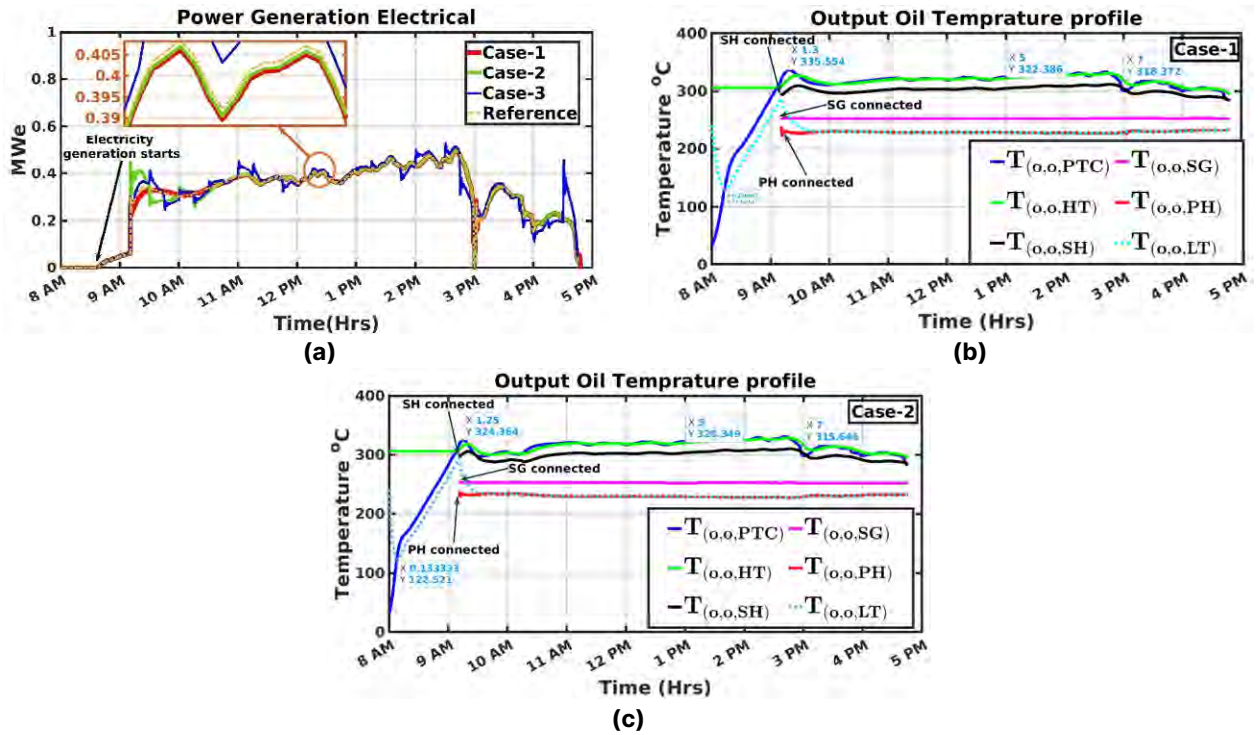



**Figure 6.** (a) Electricity generation profile for various cases, (b) Case-1 HSTPP oil profile, (c) Case-2 HSTPP oil profile. Here $T_{(o,o,K)}$ is represent the oil outlet temperature (°C) of component K, K ∈ {PTC,HT,SH,SG,PH,LT}.

## CONCLUSION AND FUTURE SCOPE

This paper presents an NLP revenue optimization approach that accounts for plant complexities such as solar radiation variability, fluctuating electricity demand, and process dynamics. The results demonstrate that increasing the number of decision variables (PTC oil flowrate variations) offers greater flexibility in plant operation, which in turn enhances performance and revenue for the HSTPP. The results underscore the importance of integrating dynamic models and optimization techniques to increase profitability of HSTPP by improved operation without any capital investment. In future, other operating variables such as mass flow rates from the HT tank and SD, can also be optimized to further increase revenue generation. Further, the current optimization approach servers as proof-of-concept and can be scaled up by applying it to STPPs with much larger production ratings.

## REFERENCES


1. Camacho, E. F., & Berenguel, M. (2012). Control of solar energy systems. *IFAC Proceedings Volumes,* 45(15), 848–855.
2. Muller-Steinhagen, H., & Trieb, F. (2004). Concentrating solar power - a review of the technology. *Ingenia,* 18(1), 43–50.
3. Scolan, S., Serra, S., Sochard, S., Delmas, P., & Reneaume, J. M. (2020). Dynamic optimization of the operation of a solar thermal plant. *Solar Energy,* 198(3), 643–657.
4. Untrau, A., Sochard, S., Marias, F., Reneaume, J. M., Roux, G. A. L., & Serra, S. (2023). Dynamic real-time optimization of a solar thermal plant during daytime. *Computers and Chemical Engineering,* 172.
5. Subires, A. J., & Rovira, A. (2023). Economic optimization of a thermal solar power plant that operates with a HRB cycle by improving the operation schedule. *SolarPACES Conference Proceedings,* 1(12).
6. Cirocco, L. R., Belusko, M., Bruno, F., Boland, J., & Pudney, P. (2016). Maximising revenue via optimal control of a concentrating solar thermal power plant with limited storage capacity. *IET Renewable Power Generation,* 10(5), 729–734.
7. Sun, J. (2024). Self-operation and low-carbon scheduling optimization of solar thermal power plants with thermal storage systems. *Energy Informatics,* 7(12).
8. Desai, N., Bandyopadhyay, S., Nayak, J., Banerjee, R., & Kedare, S. (2014). Simulation of 1MWe solar thermal power plant. *Energy Procedia,* 57, 507–516. 2013 ISES Solar World Congress.
9. Bhutka, J., Gajjar, J., & Harinarayana, T. (2016). Modelling of solar thermal power plant using parabolic

trough collector. *Journal of Power and Energy Engineering,* 4(8), 9.
10. S. Kannaiyan, S. Bhartiya, and M. Bhushan, "Dynamic modeling and simulation of a hybrid solar thermal power plant," *Industrial & Engineering Chemistry Research*, vol. 58, no. 18, pp. 7531–7550, 2019.
11. Kannaiyan, S., Bhartiya, S., & Bhushan, M. (2021). Plant-wide decentralized controller design for hybrid solar thermal power plant. *Frontiers in Control Engineering.*
12. Djenane, M. S., Hadji, S., Touhami, O., & Zitouni, A. H. (2024). A novel design of parabolic trough solar collector's absorber tube. *Journal of Solar Energy Engineering, Transactions of the ASME,* 146(6).
13. Baidya, D., Kannaiyan, S., & Bokde, N. D. (2024). Study of parabolic trough collector with crucial analysis on controller and estimator with variable mirror efficiency. *Journal of Process Control,* 143, 103317.
14. Desai, N. B., & Bandyopadhyay, S. (2015). Integration of parabolic trough and linear Fresnel collectors for optimum design of concentrating solar thermal power plant. *Clean Technologies and Environmental Policy,* 17(2), 1945–1961.
15. Seitz, M., Cetin, P., & Eck, M. (2014). Thermal storage concept for solar thermal power plants with direct steam generation. *Energy Procedia,* 49, 993–1002.
16. Rahman, A., Fumo, N., & Smith, D. (2015). Simplified modeling of thermal storage tank for distributed energy heat recovery applications. *Energy Sustainability Series*.
17. Baidya, D., Kannaiyan, S., Bhushan, M., & Bhartiya, S. (2025). Plantwide operation of hybrid solar thermal power plant with salt storage tank. Available at SSRN: https://ssrn.com/abstract=5117946
18. G. controller of INDIA limited, "Grid-india." https://posoco.in/en/, 2025.

© 2025 by the authors. Licensed to PSEcommunity.org and PSE Press. This is an open access article under the creative commons CC-BY-SA licensing terms. Credit must be given to creator and adaptations must be shared under the same terms. See https://creativecommons.org/licenses/by-sa/4.0/



Systems & Control Transactions

**Research Article - Peer Reviewed Conference Proceeding**
ESCAPE 35 - European Symposium on Computer Aided Process Engineering
Ghent, Belgium. 6-9 July 2025
Jan F.M. Van Impe, Grégoire Léonard, Satyajeet S. Bhonsale,
Monika E. Polańska, Filip Logist (Eds.)

PSE PRESS

# Control of the WWTP Water Line Using Traditional and Model Predictive Approaches

**Gheorghe A. Bodescu[a], Romina G. Dărăban[a], Norbert B. Mihály[a], Castelia E. Cristea[a], Elisabeta C. Timiș[a], Anton A. Kiss[b], Vasile M. Cristea[a]***

[a] Babeş-Bolyai University, Department of Chemical Engineering, Cluj-Napoca, Cluj, Romania
[b] Delft University of Technology, van der Maasweg 9, 2629 HZ Delft, Netherlands
* Corresponding Author: mircea.cristea@ubbcluj.ro.

## ABSTRACT

Wastewater treatment and resources recovery from large wastewater flowrates of the municipalities and circular bio-based economy ask for efficient control solutions. The paper presents solutions for operating the wastewater treatment plant, based on advanced process control methods aimed to merge the benefits of the cooperation between the lower-level regulatory control loops and the upper-level model predictive control strategy. The lower-level is designed to regulate the nitrification in the aerated bioreactors by controlling the Dissolved Oxygen or the ammonia concentration and to control the denitrification in the anoxic reactor by controlling the nitrates concentration. The model predictive controller either sets the setpoints of the regulatory layer or directly manipulates the air and nitrate recycle flow rates. The plant performance results obtained using the regulatory Proportional and Integral control are compared to the direct or the supervisory model predictive control outcomes. Both feedback and feedforward control configurations were considered, with the influent ammonia concentration as a representative disturbance. The WWTP control results were assessed using the Pumping and Aeration Energy, Effluent Quality, and Green House Gases emissions performance indices. They showed the advantage of the two-level control system for ammonia and nitrates concentration control with setpoints driven by the constrained model predictive controller, in association with the feedforward control.

**Keywords**: Wastewater, Model Predictive Control, Supervisory Control, Energy, Effluent Quality, and Green House Gas Emissions.

## INTRODUCTION

Driven by increasing urbanization and industrialization, the demand for clean water has firmly become one of humanity's top problems. The restoration of wastewater quality and recovery of wastewater resources have emerged as topics of high interest for researchers and practitioners of the wastewater industry. As the typical drinking water and wastewater treatment plants (WWTP) account for 30% to 40% of the total urban energy consumption and greenhouse gas (GHG) of the WWTP sector account for 1% to 2 % of the global GHG emissions, the importance of economic and sustainable operation of the WWTP constantly increases. The recovery of resources from the wastewater adds tempting opportunities and raises challenges. As biomass is a carbon-neutral resource and biowaste enzymatic transformations use water as a solvent, they became a high-potential resource to obtain bio-based valuable products, such as 5-hydroxymethylfurfural (HMF) [1]. Emerged wastewater has to be processed for water quality and resource recovery, and the WWTP has the main responsibility for performing these tasks. Modelling and process control have the remarkable potential to support the tough energy and GHG emissions restrictions and cope with continuously stricter regulations for clean water quality.

Modelling the complex biochemical processes specific to this technology has been greatly achieved by the family of the Activated Sludge Models no. 1, 2, 2d and 3 [2], in association with the Benchmark Simulation Models 1 and 2 [3]. Their benefits have emerged as invaluable

support for improving the wastewater treatment plant operation via traditional and advanced solutions [4,5].

The rapidly growing perspective and need for resource recovery from wastewater is asking for complex control solutions [6]. The present work contributes to this challenge by investigating new WWTP control system configurations. The novelty also consists in finding the control structure to satisfy the comprehensive assessment of plant performance by the triplet of the effluent quality, spent energy, and GHG emissions indices. Model Predictive Control (MPC) was used in either a single control layer or at the top of a supervisory control configuration with PI control loops at the regulatory layer. Investigations were carried out to find the most favourable combination of controlled variables for the nitrification and denitrification processes, to improve the performance indices. Candidates considered as potential controlled variables were the ammonia concentration ($S_{NH}$) and Dissolved Oxygen (DO) in the aerated bioreactor, and nitrates and nitrites ($S_{NO}$) concentration in the anoxic reactor. MPC with feedback and feedforward control configurations were studied. The results assessed the way MPC supervisory control with the regulatory PI loops for the $S_{NH}$ and $S_{NO}$, augmented with feedforward control, enhanced the WWTP performance indices.

# METHODS

## WWTP description

This study considered the WWTP with an Anaerobic-Anoxic-Oxic configuration, as shown in Figure 1.

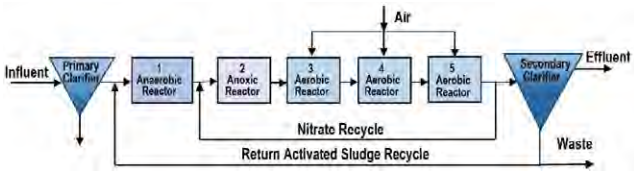



**Figure 1.** Layout of the A$^2$O WWTP.

**Table 1:** Main WWTP equipment parameters.

| WWTP Unit | Parameter | Value | Unit |
|---|---|---|---|
| Primary settler | Area | 2,125 | $m^2$ |
| | Height | 3.5 | m |
| Anaerobic bioreactor | Volume | 9,015 | $m^3$ |
| Anoxic bioreactor | Volume | 12,678 | $m^3$ |
| Aerobic bioreactors | Volume | 33,066 | $m^3$ |
| | Area | 6,012 | $m^2$ |
| Secondary settler | Area | 11,304 | $m^2$ |
| | Height | 3.0 | m |

The main design parameters of the Cluj-Napoca municipal WWTP, used as a case study, are presented in Table 1.

The software simulator of the plant was built using the mathematical models of the primary settler, the five ASM1 biological reactors [1] and the secondary settler. The simulator of the WWTP was calibrated with process data from the Cluj-Napoca municipal WWTP, designed for 420,000 PE and a typical wastewater influent flowrate of 120,000 $m^3$/day.

The calibrated simulator for the municipal WWTP was implemented in Simulink™ software environment. S-functions in the dynamic simulator were written as C-files and compiled into executable forms to reduce the simulation time.

## Control structures

The continuously changing influent variables of the WWTP (flowrate, concentration of pollutants, temperature), with values ranging in a ratio of up to four times, represent the main challenge for the control system.

Model Predictive Control was used as main control approach, in either direct control layer or at the top of a supervisory control configuration with PI control loops at the regulatory layer. It is aimed to cope with the challenges and bring expected new control solutions. The investigated control system configurations are PI control, presented in Figure 2; Direct MPC control, shown in Figure 3; Supervisory MPC Control, displayed in Figure 4.

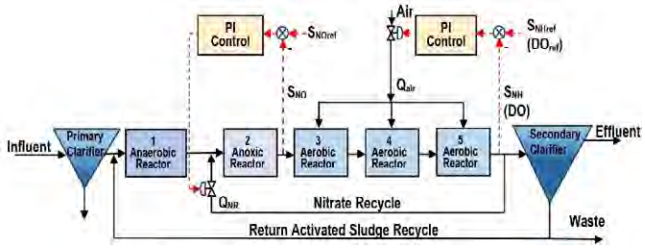



**Figure 2.** PI control structure.

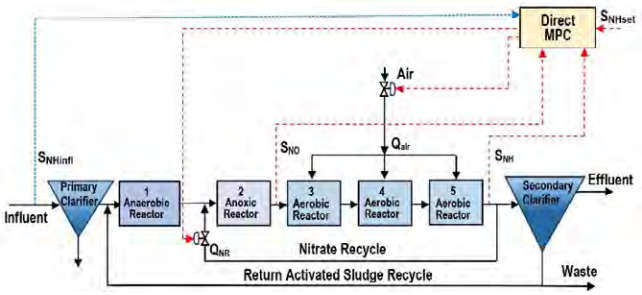



**Figure 3.** Direct MPC control structure.

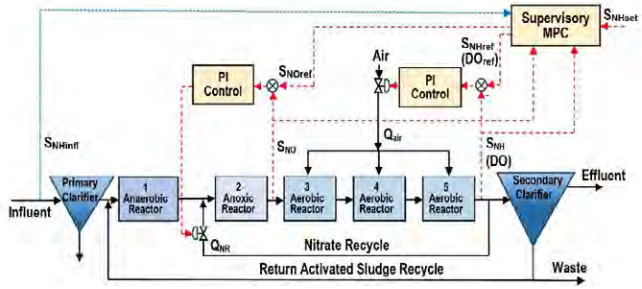



**Figure 4.** Supervisory MPC control structure.

## Controlled variables

To ensure the efficiency of the nitrification process two candidates were considered as controlled variables. They were DO (measured by the LDO sc sensor), and $S_{NH}$ in the effluent of the aerated bioreactors (measured by the Amtax sc sensor). The $S_{NO}$ in the anoxic reactor (measured by the Nitratax clear sc sensor) was the controlled variable, aiming to keep the denitrification process at a suitable rate. However, considering the importance of the nitrification process on the energy, effluent quality and GHG emissions, the control was mostly directed to the $S_{NH}$ control, as a more straightforward solution when compared to the DO control. The $S_{NO}$ control was used to assist this main control target.

## Manipulated variables

The manipulated variables for the PI control structures and for the Direct MPC control structures were the air flowrate ($Q_{air}$) entering the aerobic reactors, alone or together with the Nitrate Recycle ($Q_{NR}$) flowrate. The manipulated variables for the Supervisory MPC control structures consist in the setpoints to the regulatory layer of the PI control loops, with either the $DO_{ref}$ and $S_{NOref}$ pair or the $S_{NHref}$ and $S_{NOref}$ pair. The regulatory control loops use $Q_{air}$ and $Q_{NR}$ flowrates as manipulated variables. They are the most effective manipulated variables acting on the controlled ones and are typically available in WWTPs.

The study also included feedforward control, together with the feedback one, by considering as representative disturbance the influent concentration of ammonia ($S_{NHinfl}$).

The control cases and their associated control structure are presented in Table 2.

**Table 2:** Investigated control structures

| No. | Control Structure | Controlled variables | Manipulated variables | Feed-forwd. |
|---|---|---|---|---|
| 1 | PI | DO<br>$S_{NO}$ | $Q_{air}$<br>$Q_{NR}$ | - |
| 2 | PI | $S_{NH}$<br>$S_{NO}$ | $Q_{air}$<br>$Q_{NR}$ | - |
| 3 | PI | $S_{NH}$ | $Q_{air}$ | - |
| 4 | Direct MPC | $S_{NH}$ | $Q_{air}$<br>$Q_{NR}$ | - |
| 5 | Direct MPC | $S_{NH}$ | $Q_{air}$<br>$Q_{NR}$ | + |
| 6 | Supervisory MPC | $S_{NH}$ | $DO_{ref}$<br>$S_{NOref}$ | - |
| 7 | Supervisory MPC | $S_{NH}$ | $DO_{ref}$<br>$S_{NOref}$ | + |
| 8 | Supervisory MPC | $S_{NH}$ | $S_{NHref}$<br>$S_{NOref}$ | - |
| 9 | Supervisory MPC | $S_{NH}$ | $S_{NHref}$<br>$S_{NOref}$ | + |

## Design and tuning the controllers

Due to its straightforwardness and lower requirements for computing resources, linear MPC was used in this study. The transfer function models employed by the MPC controllers for making predictions were developed using a specific model identification methodology. It first consisted of finding the plant's nominal steady-state operating point, followed by simulating the plant's response to an appropriate sequence of model input changes. The acquired input and plant response time series were subsequently used to identify the model's form and parameters that best fit the time series data. The regulatory control loops were chosen to have a Proportional Integral (PI) form.

Tuning the MPC controllers was achieved using the following parameters, mentioned in the order of their importance: weighting factors for the control (manipulated) variable moves and for the controlled (output) variables, prediction horizon, control horizon, constraints on the controlled and manipulated variables (for the feasibility of preserving the last ones to positive values). The tuning parameters were set by a two-step procedure. The MPC controller was first tuned against the control of the linearized model of the plant and then tuning was refined by simulations implying the nonlinear WWTP behaviour.

The regulatory PI controllers were tuned based on balancing the open-loop crossover frequency and targeting a phase margin of 60°. Again, simulations with control of the nonlinear plant were used to refine the PI tuning.

Simulations and controllers' tuning were performed in Matlab and Simulink® software in association with the System Identification™, MPC and Control System Toolboxes.

## Controlled WWTP performance assessment

The performance of the different control structures, presented as cases in Table 2, was primarily evaluated by the conventional offset from the setpoint value and by the overshoot. Additionally, the operation benefits brought by control to the WWTP were evaluated according to the following four performance indices.

Aeration Energy (AE):

$$AE = \frac{SO_{sat}}{T \cdot 1.8 \cdot 1000} \cdot \int_0^T (\sum_3^5 Bioreact_i \cdot Vol_i \cdot K_L a_i(t))dt \quad (1)$$

Pumping Energy (PE):

$$PE = \frac{1}{T} \cdot \int_0^T [0.004 \cdot Q_{NR}(t) + 0.08 \cdot Q_{RAS}(t) + 0.05 \cdot Q_{waste}(t)]dt \quad (2)$$

Effluent Quality (EQ):

$$EQ = \frac{1}{T \cdot 1000} \cdot \int_0^T [PU_{TSS}(t) + PU_{COD}(t) + PU_{BOD}(t) + PU_{TKN}(t) + PU_{NO}(t)] \cdot Q_{effluent}(t)d \quad (3)$$

Detailed descriptions of the notations and values of

the parameters of equations (1) to (3) can be found in [3].

The GHG emissions index includes the sum of the on-site and off-site emissions of the $CO_2$ and $N_2O$ gases, computed according to the following relationships [7].

Onsite $CO_2$ gas emissions:

$$P_{CO_2,on-site} = Q_{influent} \cdot 0.99 \cdot (1 - Y_H) \cdot \eta_{ASP} \cdot bCOD + Q_{influent} \cdot 1.03 \cdot Y_H \cdot \eta_{ASP} \cdot bCOD \cdot \frac{k_{d,H} \cdot MCRT}{1 + k_{d,H} \cdot MCRT} \quad (4)$$

Offsite $CO_2$ gas emissions:

$$P_{CO_2,off-site} = k_{PG} \cdot e_D \quad (5)$$

Onsite $N_2O$ gas emissions:

$$P_{N_2O,on-site} = Q_{influent} \cdot (TN_{in} - TN_{out}) \cdot r_{N_2O} \quad (6)$$

Offsite $N_2O$ gas emissions:

$$P_{N_2O,off-site} = N_{effluent} \cdot EF_{effluent} \quad (7)$$

Reaching reduced values of the key performance indices Total Energy (Pumping and Aeration), Effluent Quality and GHG emissions were targeted by the control system.

## RESULTS AND DISCUSSION

The investigated control structures were proposed with the assumption that effluent ammonia concentration is the most important variable to be targeted by the aeration control. Besides direct MPC, the supervisory MPC control structure was considered for its potential to combine incentives of centralized control with the regulatory layer and for the capability of systematically handling constraints. Simulations were performed for 22 days. The PI controllers worked on a continuous-time basis, while the MPC was implemented in a discrete-time framework, using a sample time of 10 min. Due to its minimal form, Case 3 was considered the reference case to the other control structure cases. Best case is highlighted in red.

Aeration energy index results are shown in Figure 5.

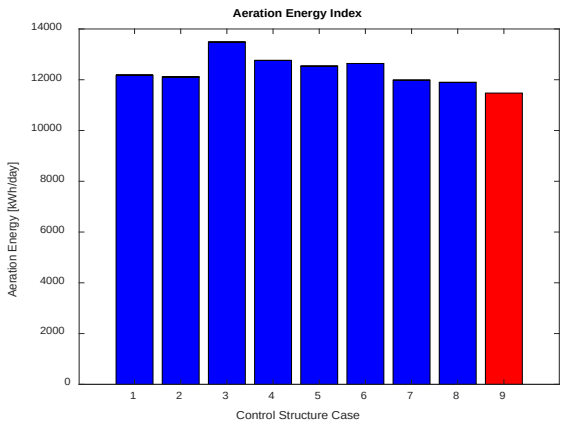



**Figure 5.** Aeration Energy Performance Index.

They reveal the advantages of the feedforward Supervisory MPC control structure of Case 9. Compared to the reference case, the reduction of AE is about 15%. Figure 5 shows the advantages of the Supervisory MPC over the Direct MPC. Additionally, the superiority of the $S_{NHref}$ manipulated variable over the $DO_{ref}$ one is confirmed.

Figure 6 presents the control results of the Pumping Energy index.

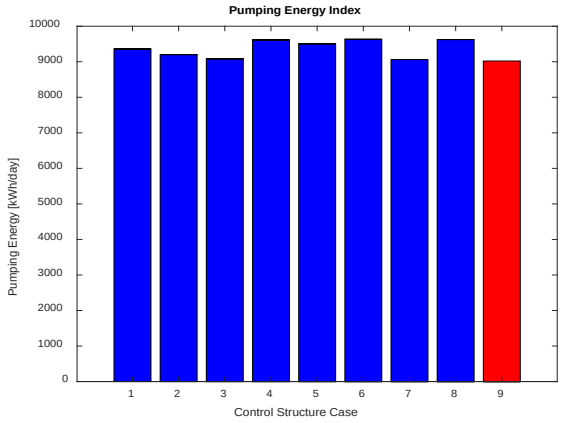



**Figure 6.** Pumping Energy Performance Index.

The pumping energy spent by WWTP for the investigated control structure cases shows again that feedforward Supervisory MPC control structure of Case 9 is the best, with the PE index value very close to those of Cases 7 and 3. When compared to Case 3, a slightly lower value of 0.7% was reported. However, the sum of the AE and PE energy indices consolidates the Total Energy advantage of the Case 9 control design by the diminished value of about 9% with respect to the reference case.

Figure 7 shows the results obtained for the Effluent Quality Index.

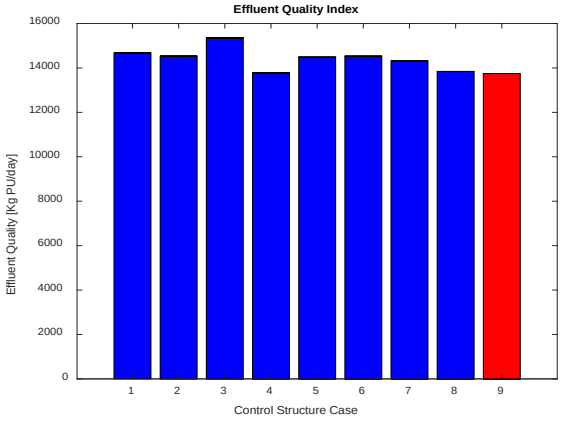



**Figure 7.** Effluent Quality Performance Index.

Evaluated by a weighted sum of discharged effluent pollutants mass flowrates, the WWTP effluent quality indices computed for the considered cases confirm the

control superiority of the feedforward Supervisory MPC Case 9. The reduction of the EQ index value is 10% with reference to Case 3. It may be noted that Direct MPC Case 4 showed marginally lower performance than Case 9.

Figure 8 presents the GHG emissions results.

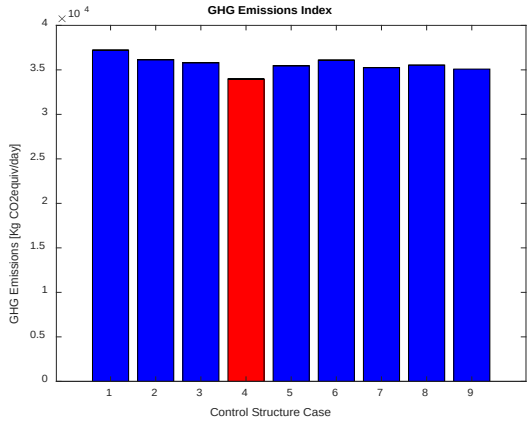



**Figure 8.** GHG Emissions Performance Index.

The best performance was demonstrated by the Direct MPC control of Case 4, followed by the feedforward Supervisory MPC of Case 9. The latter case showed lower performance than Case 4 by about 3%. When compared to the reference case, the improvement of Case 9 was evaluated at around 2%. All values reported for the performance Indices were computed as daily mean values over the considered period.

A set of results emerged from the detailed examination of each of the effluent pollutant mean concentration values, over the simulated period.

The effluent Total COD mean values showed reduced differences between the investigated cases. Cases 3 to 9, which present the lowest values of the effluent Total COD, differ by less than 1% when they are referred to the typical value of 21 g COD/$m^3$.

Figure 9. presents effluent ammonia concentration.

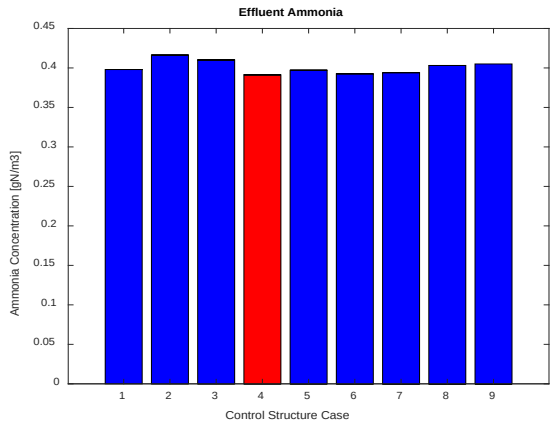



**Figure 9.** WWTP effluent $S_{NH}$ mean concentration.

For the majority of the cases, the mean value of the effluent ammonia concentration shows a higher value when compared to the $S_{NH}$ setpoint value of 0.39 gN/$m^3$. The largest difference from setpoint was +6%, for Case 2, and the lowest difference was -0.002%, for Case 4. Case 9 $S_{NH}$ mean value differs from setpoint by +3%.

The WWTP effluent mean concentration of nitrates and nitrites presents large differences among the control cases. These results are presented in Figure 10.

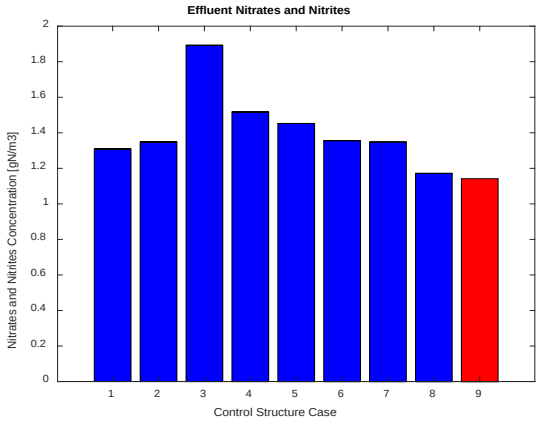



**Figure 10.** WWTP effluent $S_{NO}$ mean concentration.

The lowest $S_{NO}$ value was obtained for the feedforward Supervisory MPC control structure of Case 9. It reveals a considerable reduction of the concentration by roughly 65% when it is compared to the reference Case 3.

The WWTP effluent mean Total Nitrogen concentration, presented in Figure 11, reveals the superiority of Cases 8 and 9, i.e. the Supervisory MPC structure. This is partially induced by their lower $S_{NO}$ concentration values.




**Figure 11.** WWTP Total Nitrogen mean concentration.

When the comparison is made to the reference Case 3, the Total Nitrogen reduction was 17.5% for Case 8 and 17% for Case 9.

Given the high amplitude changes of the WWTP

influent variables, the overshoot of the $S_{NH}$ controlled variable of Case 9 was also considered to be good. Figure 12 shows the comparative control results between Cases 3 and 9, for the period between the 15th and the 20th day of controlled operation.

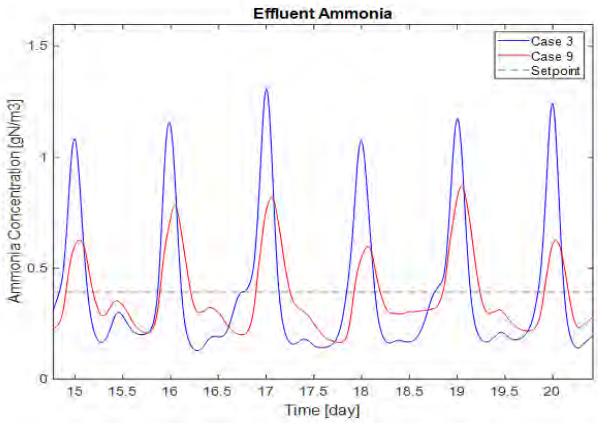



**Figure 12.** $S_{NH}$ control results for Case 3 and Case 9, as detailed plot for the period between days 15 and 20.

Figure 12 shows that overshoot is considerably smaller in Case 9 than in the reference Case 3. Further reduction of the overshoot may be obtained to the detriment of robustness and leads to the deterioration of the WWTP performance indices.

In comparison with literature results, the best-proposed control structure is based on a more comprehensive GHG-based approach and shows improvements (the effluent quality was improved, for e.g. by 17% for the effluent total nitrogen, versus 8.1 % reported in [4]).

## CONCLUSIONS

The four performance indices and WWTP effluent concentrations were analysed to find which of the investigated control structure candidates globally demonstrates the dominant incentives. The study concluded that feedforward Supervisory MPC with $S_{NH}$ and $S_{NO}$ manipulated variables is the first-ranked candidate, as it prevails in being best for most of the performance indices. Additionally, it succeeds in keeping effluent total nitrogen at the lowest values, without significantly increasing the effluent total COD. Compared to the reference case of the $S_{NH}$ PI control, this control structure improves the performance indices of Total Energy, EQ and GHG emissions, assessed to range between 2 and 10%.

The study also revealed that MPC performs better in the supervisory than in the direct control structure. For the Supervisory MPC the combination of $S_{NH}$ and $S_{NO}$ manipulated variables showed better results than the DO and $S_{NO}$ pair.

## ACKNOWLEDGEMENTS

Authors acknowledge the support from the project "Advanced (multi)-enzymatic synthesis and purification processes for bio-based furan derivatives – ASPIRE" (CF 25/14.11.2022).

## REFERENCES

1. Janković T, Straathof AJJ, Kiss AA. Turning waste into value: eco-efficient recovery of by-products from biomass pretreatment in lignocellulosic biorefineries. *Biofuel Bioprod Bior* 17:1654-1667, (2023) https://doi.org/10.1002/bbb.2532
2. Henze M, Gujer W, Mino T, van Loosedrecht M. Activated Sludge Models ASM1, ASM2, ASM2d and ASM3. IWA Publishing (2000).
3. Alex J, Benedetti L, Copp J, Gernaey KV, Jeppsson U, Nopens I, Pons MN, Rieger L, Rosen C, Steyer JP, Vanrolleghem PA, Winkler S. Benchmark Simulation Model No. 1. IWA Publishing (2008).
4. Bernardelli A, Marsili-Libelli S, Manzini A, Stancari S, Tardini G, Montanari D, Anceschi G, Gelli P, Venier S. Real-time model predictive control of a wastewater treatment plant based on machine learning. *Water Sci Technol* 81:2391-2400, (2020) https://doi.org/10.2166/wst.2020.298
5. Mihály NB, Luca AV, Simon-Várhelyi M, Cristea VM. Improvement of air flowrate distribution in the nitrification reactor of the waste water treatment plant by effluent quality, energy and greenhouse gas emissions optimization via artificial neural networks models, *J Environ Manage* 54:103935 (2023) https://doi.org/10.1016/j.jwpe.2023.103935
6. Vaidyanathan V, Saikia K, Kumar PS, Rathankumar AK, Rangasamy G, Dattatraya GS. Advances in enzymatic conversion of biomass derived furfural and 5-hydroxymethylfurfural to value-added chemicals and solvents. *Bioresour Technol* 378:128975 (2023) https://doi.org/10.1016/j.biortech.2023.128975
7. Luca AV, Simon-Várhelyi M, Mihály NB, Cristea VM. Fault detection and diagnosis of the wastewater nitrate and nitrite sensors using PCA and FDA combined with assessment of the economic and environmental impact of the faults. *Environ Monit Assess* 197:121 (2025) https://doi.org/10.1007/s10661-024-13593-z

© 2025 by the authors. Licensed to PSEcommunity.org and PSE Press. This is an open access article under the creative commons CC-BY-SA licensing terms. Credit must be given to creator and adaptations must be shared under the same terms. See https://creativecommons.org/licenses/by-sa/4.0/

Systems & Control Transactions

**Research Article - Peer Reviewed Conference Proceeding**
ESCAPE 35 - European Symposium on Computer Aided Process Engineering
Ghent, Belgium. 6-9 July 2025
Jan F.M. Van Impe, Grégoire Léonard, Satyajeet S. Bhonsale,
Monika E. Polańska, Filip Logist (Eds.)

PSE PRESS

# Optimization of the Power Conversion System for a Pulsed Fusion Power Plant with Multiple Heat Sources using a Dynamic Process Model

**Oliver M. G. Ward[a], Federico Galvanin[a], Nelia Jurado[b], Daniel Blackburn[c], Robert J. Warren[c] and Eric S. Fraga[a]***

[a] Department of Chemical Engineering, University College London, Torrington Place, London, WC1E 7JE, UK
[b] Department of Mechanical Engineering, University College London, Torrington Place, London, WC1E 7JE, UK
[c] United Kingdom Atomic Energy Authority, Culham Science Centre, Abingdon, OX14 3DB, UK
* Corresponding Author: e.fraga@ucl.ac.uk.

## ABSTRACT

The optimization of the power conversion system, responsible for thermal-to-electrical energy conversion, for a pulsed fusion power plant is presented. A spherical tokamak is modelled as three heat sources, all pulsed, with different stream temperatures and available amounts of heat. A thermal energy storage system is considered in the design to compensate for the lack of thermal power during a dwell. Thermal storage enables continued power generation during a dwell and can avoid thermal transients in sensitive components like turbomachines. Multiple lower grade heat sources are integrated into the process through parallel preheating trains. The evaluation of a dynamic model of the power conversion system is used to define an objective function with multiple criteria. A bi-objective optimization problem is defined to investigate the trade-off between the size of the thermal energy storage system and the variability in turbine power output during a dwell. The set of non-dominated designs demonstrates the trade-off, with designs covering the range from steady state turbine power output to a design that reduces the turbine power output by 46.3% during a dwell. The dynamics of three non-dominated designs demonstrate the power conversion system can maintain relatively stable conditions at the turbine inlet under different operating conditions, but molten salt temperature control is an issue.

**Keywords**: Optimization, Dynamic Modelling, Energy Conversion, Energy Storage, Fusion Power, Modelica

## INTRODUCTION

The United Kingdom Atomic Energy Authority (UKAEA) is leading the Spherical Tokamak for Energy Production (STEP) programme to design and build a fusion power plant that demonstrates net electricity generation [1,9]. Fusion is an appealing prospect for clean and abundant energy but faces several engineering challenges. Two of these challenges are addressed here:

- Pulsed tokamak operation - the steady state nature of early fusion power demonstrators, notably tokamaks, will be challenging due to operational uncertainty and, as for conventional tokamaks, pulsed operation may be required. Rapid dynamics of the plasma compound this issue
- Multiple heat sources - generated thermal power is distributed to multiple tokamak components, and will be extracted via multiple coolant streams at different temperatures and flow rates

A power conversion system design for a pulsed fusion tokamak is presented, featuring a thermal energy storage system, using molten salts as is common in solar thermal power plants, and two parallel feed water trains to integrate multiple lower grade heat sources.

The pulsed heat generation requires the use of dynamic models to evaluate the performance of the power conversion system. The dynamic models are used within an optimization framework such that each objective

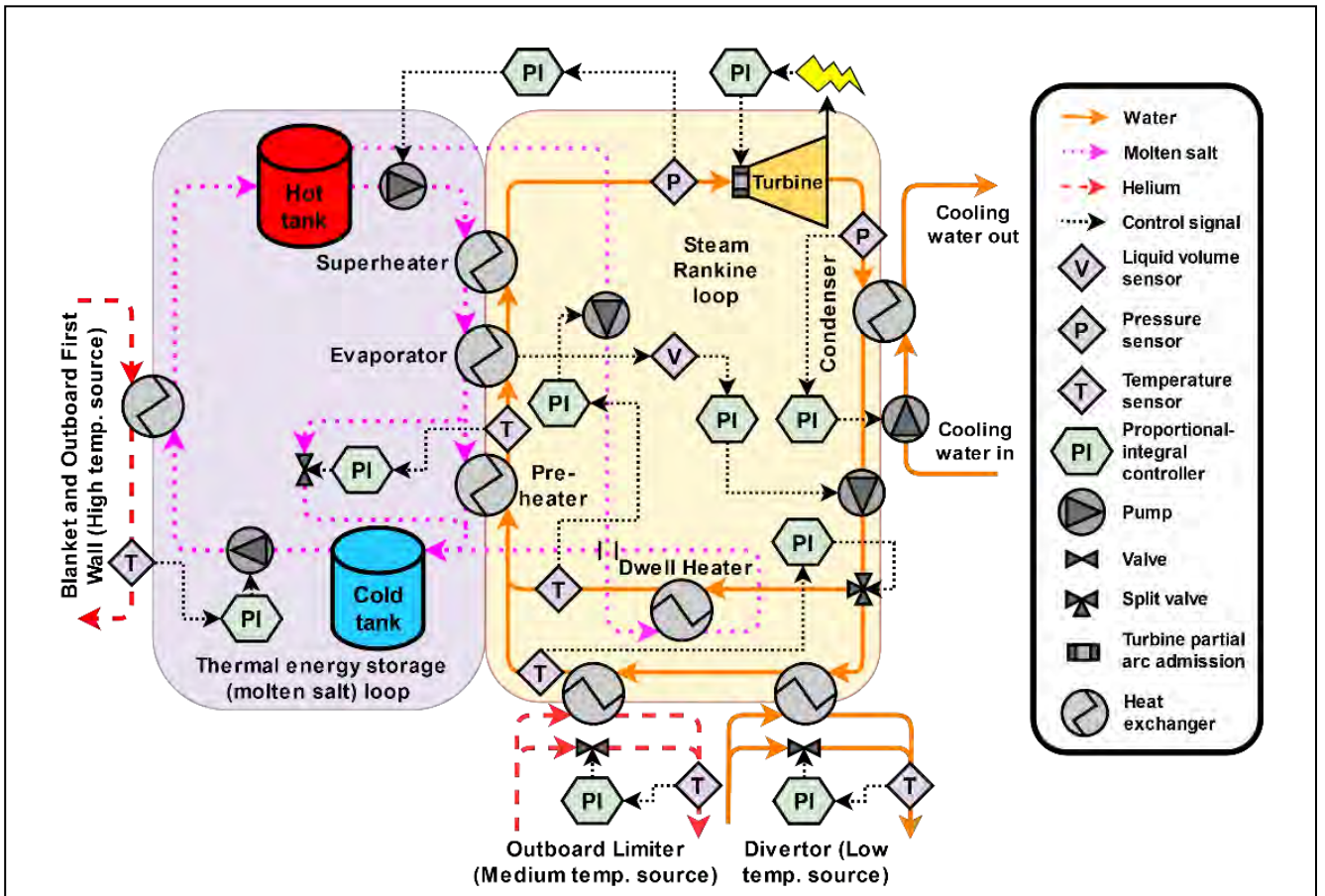



**Figure 1:** Power conversion system layout for a fusion tokamak with three pulsed sources. The high temperature source is used to heat and store molten salt for use during a dwell. The other two sources are used to heat feed water during a pulse. Their heat duty is replaced by a dwell heater, fed by molten salt, during a dwell. Note that all heat exchangers are counter current.

function evaluation involves a dynamic simulation of the designs identified by the optimization procedure.

## DYNAMIC POWER CONVERSION SYSTEM MODEL

Figure 1 shows the proposed power conversion system layout. There are three heat sources available from the fusion tokamak, with pulse and dwell values summarized in Table 1. While the tokamak outlet temperatures are fixed as the model boundary conditions, the temperature of the coolant returning to the tokamak is not fixed. Each source follows a $C^1$-continuous pulsed profile with an initial 2 h pulse period, a 5 min ramp down, a 15 min dwell period followed by a 5 min ramp up back to pulse.

The high temperature source exchanges heat with the molten salt in the thermal energy storage loop (left side of the process diagram in Figure 1) via the high temperature heat exchanger. The hot molten salt is stored in an insulated tank, at a target temperature of 550°C, where it can be pumped on demand to provide heat to the steam Rankine cycle (the right side of the process diagram in Figure 1). The cooled molten salt is stored in another insulated tank, at a target temperature of 350°C, for pumping and reheating by the high temperature heat source.

**Table 1:** Parameters of the available heat sources from the tokamak during a pulse, with values during a dwell given in brackets. These are early estimate values.

| Source grade | Coolant | Outlet temperature (°C) | Target return temperature (°C) | Thermal power (MWth) |
|---|---|---|---|---|
| High | Helium | 600 (450) | 450 (450) | 1,350 (0) |
| Medium | Helium | 450 (225) | 225 (225) | 215 (0) |
| Low | Water | 300 (275) | 275 (275) | 270 (0) |

A steam Rankine cycle is used to generate electrical power. Feed water is pumped through two parallel heating trains: the low and medium temperature heat exchangers that heat the feed water from their respective

heat sources during a pulse; and a dwell heater that heats the feed water using molten salt from the hot tank. The feed water then passes through a preheater, an evaporator and a superheater, with heat provided by the hot molten salt in counter current exchanges. The water exits as superheated steam. The steam then drives a turbine to generate electrical power before being condensed back to the liquid phase by the condenser, exchanging heat with cooling water, closing the loop for the steam cycle.

There are ten proportional-integral controllers in Figure 1. Two controllers regulate the feed water temperature at the outlet of the parallel heating trains by controlling the flow rate of molten salt to the dwell heater and the split fraction of feed water between the two trains. This allows the plant control to switch between the two heating modes when the tokamak switches between pulse and dwell.

The condenser pressure is regulated by a controller manipulating the flow of cooling water. A controller manipulates the mass flow rate of feed water in the Rankine cycle to ensure the evaporator doesn't flood or dry out due to a lack or excess of evaporation respectively. The turbine power output and inlet pressure are regulated by two controllers manipulating the turbine's partial arc admission and the mass flow rate of hot molten salt to the superheater respectively.

There is a bypass for the molten salt around the preheater, where the bypass valve opening is manipulated by a controller regulating the temperature of feed water leaving the preheater. This is to avoid the feed water boiling before the evaporator. Each of the heat sources has a controller regulating the temperature of coolant returning to the tokamak.

For the high temperature source, the mass flow rate of cold molten salt is manipulated. For the other two sources, the openings of bypass valves for the coolants are manipulated. The controllers are all hand tuned by repeated simulations here to reduce the dimension of the optimization problem. Previous work has looked at the controller parameters as decision variables [10].

The model has been implemented in the Modelica language [6] and solved numerically using OpenModelica [8]. Full descriptions of the dynamic models will be published in a future paper that is currently under review.

## OPTIMIZATION OF THE POWER CONVERSION SYSTEM FOR REDUCED DWELL POWER

Based on industry experience with thermal energy storage for solar thermal power plants, thermal energy storage systems are a significant fraction of total investment. For a 50MWel concentrating solar power plant, a cost of 33M€ was predicted [7]. With STEP expected to be generating ~500MWel (before parasitic loads like the tokamak itself), significant thermal storage would be required to generate a steady amount of power for fusion tokamaks [1]. The size of the storage system could be reduced by reducing the power generation during a dwell; stopping power generation entirely is infeasible due to the thermal stresses this would place on the components.

To investigate this, we propose an optimization problem to find the trade-off between the size of the thermal storage system, quantified as the volume of each tank $V_{tank}$ and the dwell power fraction $\varphi$, the fraction by which the turbine power setpoint is reduced during dwell relative to pulse. The bi-objective optimization problem is stated as:

$$\begin{aligned} &\min_{\boldsymbol{x}} \begin{bmatrix} V_{tank} \\ -\varphi \end{bmatrix} \\ &s.t.\ \boldsymbol{g}(\boldsymbol{x}) \leq \boldsymbol{0} \\ &\boldsymbol{h}(\boldsymbol{x}) = \boldsymbol{0} \end{aligned} \tag{1}$$

where the decision vector $\boldsymbol{x} = [V_{tank}, \varphi, P_{pulse}]^T$ includes the turbine power setpoint during a pulse $P_{pulse}$. This is necessary as designs that reduce the power generated during a dwell will necessarily generate more power during the pulse to satisfy energy balances in the overall process over time. Between a pulse and dwell periods, the setpoint smoothly transitions between $P_{pulse}$ and $\varphi P_{pulse}$ by following a sinusoidal curve. The equality constraints $\boldsymbol{h}(\boldsymbol{x})$ represent the dynamic model. The inequality constraints $\boldsymbol{g}(\boldsymbol{x})$ include requirements for long term operability of the plant. For a simulation to be completed, the volume of molten salt in either tank $V_{MS}$ must stay in the range $0.05 \leq V_{MS}/V_{tank} \leq 0.95$ for the $T_{sim} = 15900s$ of simulated time. The simulated time covers an initial pulse period $T_{pulse} = 7200s$, a dwell period $T_{dwell} = 900s$ and another pulse period, with a ramp down and ramp up between them of $T_{ramp} = 300s$. These are estimated from the DEMO pre-concept design [2]. The simulation covers the period of interest, namely the ramp-dwell-ramp dynamics. The bounds on the decision variables are $2000m^3 \leq V_{tank} \leq 8000m^3$, $0.25 \leq \varphi \leq 1$ and $500MW \leq P_{pulse} \leq 750MW$.

To evaluate the inequality constraints, a simulation must be performed using the dynamic model of the power conversion system presented in section 2. A multi-objective plant propagation optimization algorithm, as implemented by the Fresa.jl package [5], is used to solve the optimization problem. Fresa is a black-box optimization algorithm that does not require gradients which would be computationally costly to estimate using finite differences. Fresa is also population-based, allowing for many simulations to be run in parallel, making effective use of multi-core desktop computers. The OMJulia.jl

**Table 2:** Parameters used for the *solve* function of Fresa. For more detailed explanations, please refer to the documentation at ucl.ac.uk/~ucecesf/fresa.html.

| Description | Parameter | Value |
|---|---|---|
| Number of objective evaluations before stopping | $nfmax$ | $100$ |
| Number of solutions to propagate each generation | $np$ | $(20,40)$ |
| Parameter for similarity function | $\epsilon$ | $0.01$ |
| Multi-objective solutions ranked based on [2] | $fitnesstype$ | $:nondominated$ |
| Solutions are compared based on their values of $\boldsymbol{x}$ | $issimilar$ | $Fresa.similarx$ |
| The non-dominated solutions are automatically included in the next generation | $elite$ | $true$ |
| Any pruned non-dominated solutions are added back to the population at the end of the run | $archiveelite$ | $true$ |

**Table 3:** Infeasibility $g$ of different simulation outcomes, favoring designs that are expected to be closer to being feasible. $t_{failure}$ is the internal simulation time at the failure. $\Delta V_{MS}$ is the change in stored hot molten salt at the end of the simulation relative to one full cycle earlier in the simulation.

| Simulation Outcome | Reasoning | $g$ |
|---|---|---|
| Simulation takes longer than $1{,}800s$ | Undesirable behaviour, like oscillations, are slowing the simulation | $1e6$ |
| Simulation fails before initialization | Unknown error | $1e3$ |
| Simulation fails after initialization | Molten salt is being greatly over/under-utilized in the design, so $P_{pulse}$ needs to be adjusted | $1+(1-\frac{t_{failure}}{T_{sim}})$ |
| Simulation completes successfully | Designs that underutilize molten salt will be feasible but outcompeted by propagated designs that balance molten salt better and have smaller tanks – useful to keep in the population | $-\frac{\Delta V_{MS}}{V_{tank}}-0.01$ |

package is used to run the Modelica model within Julia. The Fresa parameters used are presented in Table 2. With these parameters, 126 calls of Fresa.solve are made, each one being initialized with the final population of the previous run. This is necessary to clear simulation processes from memory periodically.

The simulation based objective function assigns an infeasibility value, g, to every design. Designs with g≤0 are considered feasible and other values indicate infeasible designs. This indication of feasible and infeasible is used by Fresa in the selection of solutions to propagate during the search. To help the algorithm search, different simulation outcomes are identified for calculating g, shown in Table 3.

## NON-DOMINATED DESIGNS OF THE POWER CONVERSION SYSTEM

The set of non-dominated designs found by the optimization algorithm is presented in Figure 2. The flexibility in turbine operation during a dwell can allow for the volume of the molten salt tanks to be reduced by up to 40.5% at the cost of a 46.3% reduction in the dwell turbine power output relative to pulse values.

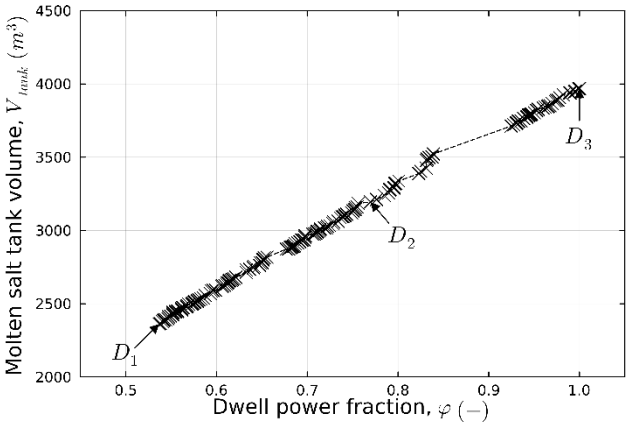



**Figure 2:** Non-dominated designs showing the trade-off between the size of the thermal energy storage and the fraction of pulse turbine power produced during dwells. Three designs $D_1$, $D_2$, $D_3$ are selected for later discussion.

To investigate the effectiveness of the power conversion system designs, three designs are selected evenly across the range of φ to show their different dynamics. These are shown in Figure 2, and their decision variables are given in Table 4. The dynamics at the turbine are presented in Figure 3, as it is identified as being one of the most sensitive components to large transients.

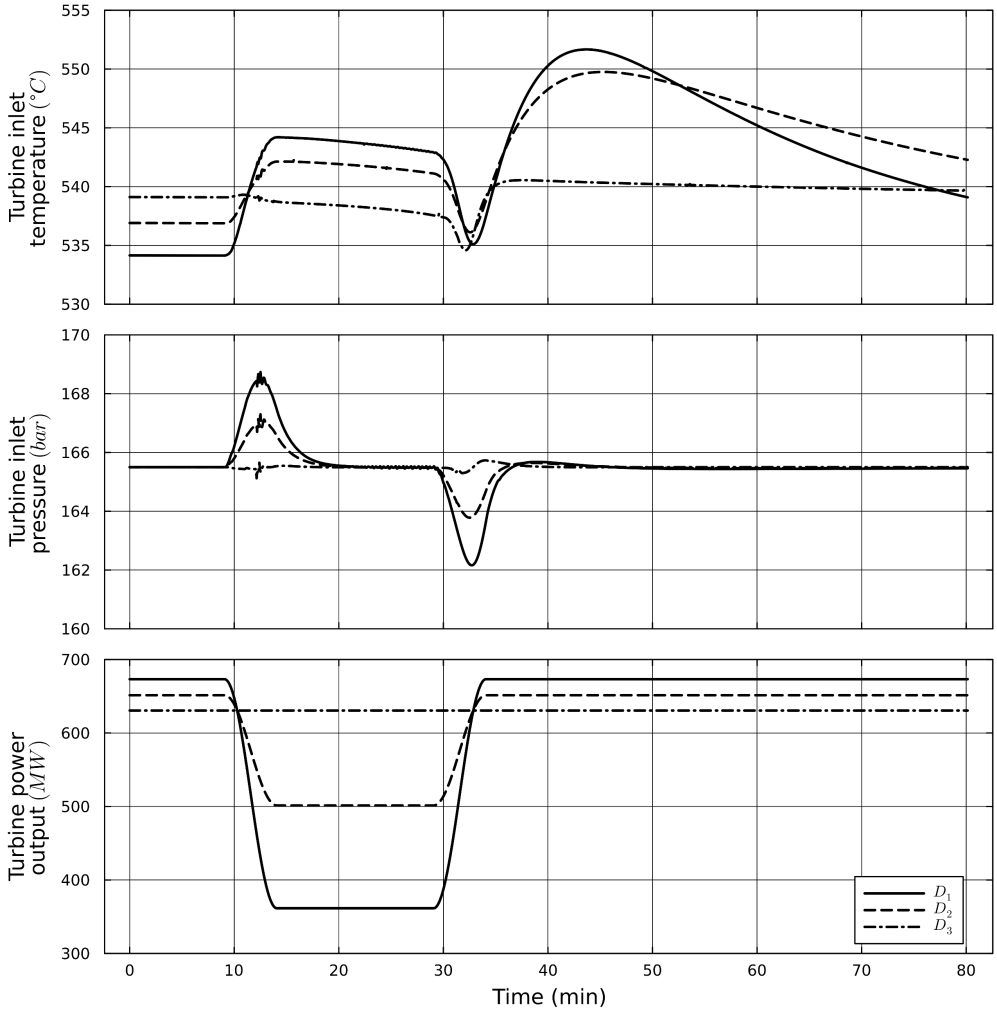



**Figure 3:** Dynamics of the turbine inlet temperature, inlet pressure and power output of three non-dominated designs from the final population. The time covers a dwell period and part of a subsequent pulse period, when process transients are most significant. Note that the turbine inlet temperature is not directly controlled by a proportional-integral controller, unlike the other two variables.

**Table 4:** Decision variables of the three highlighted designs in Figure 2.

| | $V_{tank}$ (m$^3$) | $\varphi$ (-) | $P_{pulse}$ (MW) |
|---|---|---|---|
| $D_1$ | 2,363 | 0.5369 | 673.2 |
| $D_2$ | 3,195 | 0.7697 | 651.4 |
| $D_3$ | 3,969 | 1 | 630.6 |

Turbine inlet temperature is not directly controlled by any of the controllers and is largely driven by the temperature of molten salt in the hot tank and the flow rate of hot molten salt and steam through the superheater. Design $D_3$ shows the smallest fluctuation in turbine inlet temperature, which is due to the steam mass flow rate being approximately constant to maintain a constant power output in that design. Designs $D_1$, $D_2$ show larger fluctuations due to the decreasing mass flow rate of steam during a dwell. The slower decay of the temperature in design $D_2$ relative to $D_1$ is attributed to the increased thermal inertia of molten salt in the hot tank due to the larger tank size, and hence larger mass of 'residual' molten salt that will always be present in valid designs due to the constraints on tank levels discussed in section 3. For all three designs, the temperature change is small enough, and over long enough time periods, that thermal stresses should be acceptable [3].

The turbine inlet pressure is controlled by manipulating the mass flow rate of hot molten salt to the superheater, and the ramp periods can be seen to cause a pressure fluctuation in all the designs. As with the inlet temperature, the magnitude of the changes is larger for designs with larger changes in dwell power, with design

$D_3$ showing the smallest changes. During the ramp down, all three designs show a small period of small, higher frequency oscillations. This could be due to feedback between multiple controllers or poorly tuned controllers. This could be solved by using more advanced control methods, such as model predictive control, or by including key controller parameters as decision variables.

The turbine power output is well controlled by the controller manipulating the partial arc admission of steam to the turbine, with all designs following the set points well. As expected, designs that produce less power during the dwell produce more power during the pulse, as the total energy input to the system is the same for all designs and hence the total energy output will be the same too, neglecting small differences in efficiency.

Molten salt temperatures below freezing point occur at the preheater and dwell heater outlets for lower values of φ. For every design, heat exchangers are currently sized the same. Resizing the dwell heater for each design, based on its dwell power set point, or adjusting the control system to better regulate molten salt temperatures, such as via electric heaters, could address this.

## CONCLUSION

The use of a dynamic process model of a power conversion system for a pulsed fusion power plant in an optimization-based design procedure is presented. The process features the integration of multiple pulsed heat sources of different grades into a single power cycle. Simulations demonstrate this configuration is capable of effectively utilizing the lower grade heat, while maintaining stable operation of the steam Rankine cycle. The dynamic model is developed to minimize simulation time and support automated simulations, allowing for its use within an objective function of an optimization problem.

By using the dynamic model in an optimization framework, the flexibility of the power conversion system design to different dwell operating conditions was investigated. A set of non-dominated designs showed that the size of the molten salt tanks could be reduced by 40.5% by reducing the turbine power output during a dwell by 46.3% relative to during pulse. The dynamics of three non-dominated designs are presented, showing good control of the turbine inlet conditions in all three designs, even for designs with large changes in turbine power output. The control system caused small pressure oscillations in all three designs. Future work could be to include control system parameters as decision variables alongside the process variables considered here and to improve molten salt temperature control. Another interesting direction is to consider plant design for load following.

The optimization methodology can easily be extended to any process model developed in OpenModelica, which is a multi-domain simulation environment. Integration with Julia allows complex analysis to be performed with the design simulation results, giving great flexibility in the objective functions.

## ACKNOWLEDGEMENTS

This work is partially funded by, and in collaboration with, the UKAEA.

## REFERENCES

1. J. Acres, I. Antoniou, F. Christie, D. Blackburn, S. Knight. Staying positive: producing net power. Phil. Trans. R. Soc. A. 382:20230404. (2024) https://doi.org/10.1098/rsta.2023.0404
2. L. Barucca, W. Hering, S. Perez Martin, E. Bubelis, A. Del Nevo, M. Di Prinzio, M. Caramello, et al. Maturation of critical technologies for the DEMO balance of plant systems. Fusion Eng. Des. 179:113096 (2022) https://doi.org/10.1016/j.fusengdes.2022.113096
3. F. Casella, F. Pretolani. Fast start-up of a combined-cycle power plant: a simulation study with Modelica fast start-up of a combined-cycle power plant: a simulation study with Modelica. The Modelica Association (2006)
4. K. Deb. An efficient constraint handling method for genetic algorithms. Comput. Methods Appl. Mech. Eng. 186:311-338 (2000) https://doi.org/10.1016/S0045-7825(99)00389-8
5. E. S. Fraga. Fresa: a plant propagation algorithm for black-box single and multiple objective optimization. Int. J. on Eng. Technol. Inf. 2:110-111 (2021) https://doi.org/10.51626/ijeti.2021.02.00022
6. Modelica Association. https://modelica.org/
7. G. Morin. Techno-economic design optimization of solar thermal power plants. Fraunhofer Verlag (2011) https://doi.org/10.24406/publica-fhg-278914
8. Open Source Modelica Consortium. https://openmodelica.org/
9. UKAEA. https://step.ukaea.uk/
10. O. M. G. Ward, F. Galvanin, N. Jurado, C. Clements, M. Abdallah, D. Blackburn, E. S. Fraga. Optimization of a PID controller within a dynamic model of a steam rankine cycle with coupled energy storage. Chem. Eng. Trans. 99:583–588 (2023) https://doi.org/10.3303/CET2399098

© 2025 by the authors. Licensed to PSEcommunity.org and PSE Press. This is an open access article under the creative commons CC-BY-SA licensing terms. Credit must be given to creator and adaptations must be shared under the same terms. See https://creativecommons.org/licenses/by-sa/4.0/



Systems & Control Transactions

**Research Article - Peer Reviewed Conference Proceeding**
ESCAPE 35 - European Symposium on Computer Aided Process Engineering
Ghent, Belgium. 6-9 July 2025
Jan F.M. Van Impe, Grégoire Léonard, Satyajeet S. Bhonsale,
Monika E. Polańska, Filip Logist (Eds.)

PSE PRESS

# Optimization of steam power systems in industrial parks considering the distributed heat supply and auxiliary steam turbines

**Lingwei Zhang[a], Yufei Wang[a]***

[a] China University of Petroleum (Beijing), School of Chemical Engineering and Environment, Changping, Beijing, China
* wangyufei@cup.edu.cn

## ABSTRACT

In the steam power system for the centralized heat supply in an industrial park, heat demands of all consumers are satisfied by the energy station, leading to the high steam delivery costs caused by the several distant enterprises. Additionally, the number of steam levels is limited due to the trade-off between distance-related costs and heat cascaded utilization, thus some consumers are supplied with heat at higher temperature than that of required, resulting in the low energy efficiency. To deal with the above problems, this work proposes an optimization model for steam power systems (SPSs) in industrial parks, which incorporates the distributed heat supply and auxiliary steam turbines (ASTs). Field erected boilers (FEBs) can independently supply heat to consumers, thereby avoiding the excessive pipeline costs. ASTs are used for the re-depressurization of steam received by consumers, which can increase the electricity generation capacity and improve the temperature matching of heat supply and demand. A mathematical model is established for the problem, in which the influence of different numbers of steam levels is considered, and the SPSs are optimized by the objective function of minimizing the total annual cost (*TAC*). A case study illustrates that the optimal number of steam levels, and the selective installation of FEBs and ASTs for consumers, can effectively reduce the cost of pipeline network, increase the income of electricity generation, and minimize the *TAC* of the system.

**Keywords**: Steam power systems, Steam turbines, Distributed heat supply

## 1. INTRODUCTION

The optimization of steam power systems (SPSs) has been extensively studied since the 1980s. In previous studies, SPSs of individual plants were optimized mainly in terms of the equipment structure and operating conditions for the minimum total costs. Papoulias and Grossmann [1] were the first to adopt mathematical programming method to optimize stream flowrates and sizes of units in SPSs. The equipment efficiency and the steam physical properties were given as parameters in their work. Bruno et al. [2] used second order polynomial correlations to calculate steam physical properties, and added the constraints related to steam physical properties in the model. Aguilar et al. [3] developed the equipment models, so that the variations in equipment efficiency were described. Sun et al. [4] noted the unsaturated steam conditions and obtained more realistic energy targets. Recently, Jiménez-Romero et al. [5] were the first to consider the effects of different numbers of steam levels in SPSs. However, in their study, the spatial scale of the SPSs was still limited to a single plant, thus the distance-related costs were neglected. At the spatial scale of industrial parks, there is a trade-off between energy cascaded utilization and distance-related costs in SPSs. As a remedy, we previously proposed a distributed steam turbine system model for optimizing the SPSs in industrial parks [6], aiming to balance the energy cascaded utilization and distance-related costs. Nevertheless, in Ref. [6], all consumers were supplied by a centralized energy station, leading to the high steam delivery costs caused by the several distant enterprises. Therefore, based on our previous research, this work provides consumers with the option of distributed heat

supply in an effort to further reduce the distance-related costs and the total cost of the system.

## 2. PROBLEM STATEMENT

In an industrial park, enterprises and the energy station have been built at fixed locations. Enterprises are the heat consumers with different required temperatures and heat loads, and are denoted as $i$, $i \in I$, $I = \{I_1, I_2, \ldots, I_m\}$. The energy station supplies heat to enterprises using steam as the medium. In the energy station, very high pressure steam (VHPS) is produced in a large package boiler (LPB) with fuel consumed, and then is depressurized through main steam turbines (MSTs) into lower-pressure steam for heat supply, while electricity is generated, so that energy is utilized in cascade. Steam levels are denoted as $s$, $s \in S$, $S = \{S_1, S_2, \ldots, S_n\}$. Nonetheless, extremely high cost of the pipeline network is incurred when each required temperature is corresponded with a level of steam. Therefore, the number of steam levels is limited, and some consumers are supplied with heat at higher temperature than that is required. In this situation, auxiliary steam turbines (ASTs) are selectively installed for consumers, by which the received steam is re-depressurized, thereby increasing the electricity generation capacity. In addition, each consumer can choose to install a field erected boiler (FEB) for the distributed heat supply, so that the cost of steam pipeline network (SPN) is reduced. In the SPS, the costs include the capital cost of LPB ($C^{LPB,cap}$), the cost of fuel consumed by LPB ($C^{LPB,fuel}$), the cost of FEBs ($C^{FEB}$), the cost of steam turbines ($C^{turb}$), and the cost of SPN ($C^{pipe}$), while the income from electricity generation ($I^{elec}$) is obtained. In this study, the mathematical model is established and solved to determine the optimal number of steam levels, the operating conditions (such as saturation temperature and mass flow rate) and supply scheme of each steam level, and the configuration of FEBs and ASTs, aiming to design the SPS with the minimum total annual cost (*TAC*). The objective function is expressed by Eq. (1). The superstructure for the SPSs is expressed in Figure 1.

$$min\{TAC = C^{LPB,cap} + C^{LPB,fuel} + C^{FEB} + C^{turb} + C^{pipe} - I^{elec}\} \quad (1)$$

## 3. MODEL FORMULATION

### 3.1. Centralized steam production model

The pressure and temperature of VHPS are set as 4.5 MPa and 400 °C, respectively. The corresponding saturation temperature ($T^{VHPS,sat}$) and specific enthalpy ($h^{VHPS}$) are 257.4 °C and 3207 kJ.kg$^{-1}$, respectively. The physical properties of steam levels are calculated by fitting formulas Eqs. (2)-(5), with saturation temperature of steam levels $T_s^{MST,sat}$ as the independent variable.

$$h_s^{l,MST,sat} = 4.431 \cdot T_s^{MST,sat} - 29.89 \quad (2)$$

$$\Delta h_s^{is,MST} = -4.876 \cdot T_s^{MST,sat} + 1251 \quad (3)$$

$$\rho_s^v = 0.0005078 \cdot \left(T_s^{MST,sat}\right)^2 - 0.1053 \cdot T_s^{MST,sat} + 6.148 \quad (4)$$

$$\rho_s^l = -1.053 \cdot T_s^{MST,sat} + 1071 \quad (5)$$

where $h_s^{v,MST,sat}$ and $h_s^{l,MST,sat}$ are the specific enthalpies of saturated vapor and liquid of steam level $s$, respectively. $\Delta h_s^{is,MST}$ is the specific isentropic enthalpy difference of steam across the MST. $\rho_s^v$ and $\rho_s^l$ are the densities of vapor and condensate of steam level $s$.

The performance of MSTs is formulated by the

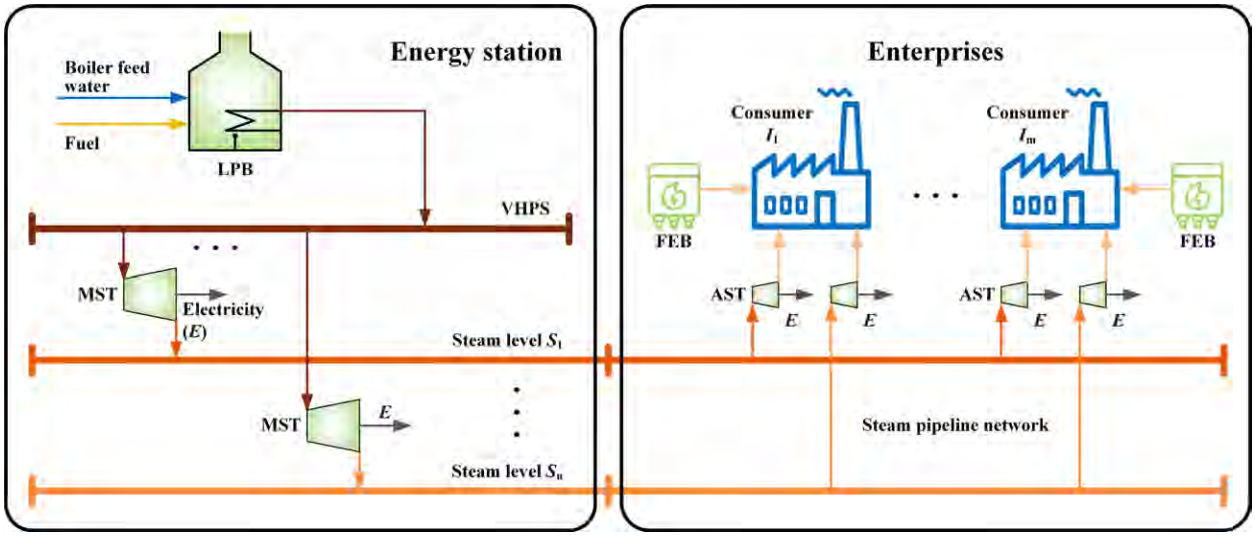



**Figure 1:** Superstructure of SPSs in industrial parks with FEBs and ASTs

model developed by Aguilar et al. [3], as expressed by Eqs. (6)-(8).

$$W_s^{MST} = \frac{m_s^{level} \cdot \Delta h_s^{is,MST} - [a_0 + a_1 \cdot (T^{VHPS} - T_s^{MST,sat})]}{a_2 + a_3 \cdot (T^{VHPS} - T_s^{MST,sat})} \quad (6)$$

$$h_s^{v,MST,out} = \frac{m_s^{level} \cdot h^{VHPS} - W_s^{MST}}{m_s^{level}} \quad (7)$$

$$h_s^{HV,MST} = h_s^{v,MST,out} - h_s^{l,MST,sat} \quad (8)$$

where $W_s^{MST}$ is the shaft work of the MST for steam level $s$. $a_0$, $a_1$, $a_2$ and $a_3$ are the parameters. $h_s^{v,MST,out}$ and $h_s^{HV,MST}$ are the specific enthalpy and specific heat value of steam out from the MST, respectively.

The mass balance of steam levels is represented by Eq. (9).

$$m^{VHPS} = \sum_s m_s^{level} \quad (9)$$

## 3.2. Centralized steam supply model

In this work, the steam pipeline network is simply formulated. Consumers are divided into four directions, and are connected to the energy station by main and branch pipelines. Directions are denoted as $d$, $d \in D$, $D$ = {East, West, North, South}. Consumers in each direction are denoted as $j$, $j \in J$, $J = \{J_1, J_2, \ldots, J_k\}$. The lengths of main pipeline segments $L_{d,j}^{main,seg}$ is calculated by Eq. (10) and Eq. (11), and the lengths of branch pipeline segments $L_{d,j}^{bran}$ is calculated by Eq. (12).

$$L_{d,j}^{main} = \begin{cases} X_i, & d = \text{East}(\,|X_i| \geq |Y_i|, X_i > 0) \\ |X_i|, & d = \text{West}(\,|X_i| \geq |Y_i|, X_i < 0) \\ Y_i, & d = \text{North}(\,|X_i| < |Y_i|, Y_i > 0) \\ |Y_i|, & d = \text{South}(\,|X_i| < |Y_i|, Y_i < 0) \end{cases} \quad (10)$$

$$L_{d,j}^{main,seg} = \begin{cases} L_{d,j}^{main} & (j = J_1) \\ L_{d,j}^{main} - L_{d,j-1}^{main} & (j \neq J_1) \end{cases} \quad (11)$$

$$L_{d,j}^{bran} = \begin{cases} |Y_i|, & d = \text{East} \\ |Y_i|, & d = \text{West} \\ |X_i|, & d = \text{North} \\ |X_i|, & d = \text{South} \end{cases} \quad (12)$$

where $L_{d,j}^{main}$ is the distance of consumer $j$ in direction $d$ from the energy station in the main direction. $X_i$, $Y_i$ are the coordinates of consumer $i$ while the location of the energy station is set as the original coordinate.

The binary variable $y_{s,d,j}^{sup}$ is used to determine the supply scheme of steam levels, as expressed by the Big-M constraint Eq. (13).

$$m_{s,d,j}^{sup} \leq y_{s,d,j}^{sup} \cdot M^{sup,max} \quad (13)$$

where $m_{s,d,j}^{sup}$ is the mass flow rate of steam level $s$ supplied to consumer $j$ in direction $d$. Parameter $M^{sup,max}$ is the upper bound of $m_{s,d,j}^{sup}$.

The temperature constraint of steam supply is represented by Eq. (14).

$$T_s^{MST,sat} \geq y_{s,d,j}^{sup} \cdot T_{d,j}^{need} \quad (14)$$

where $T_{d,j}^{need}$ is the required temperature of each heat consumer.

The mass balance of steam in the pipeline network is formulated by Eqs. (15)-(17).

$$m_s^{level} = \sum_d m_{s,d}^{dire} \quad (15)$$

$$m_{s,d}^{dire} = \sum_j m_{s,d,j}^{sup} \quad (16)$$

$$m_{s,d,j}^{main,seg} = \begin{cases} m_{s,d}^{dire} & (j = J_1) \\ m_{s,d,j-1}^{main,seg} - m_{s,d,j-1}^{sup} & (j \neq J_1) \end{cases} \quad (17)$$

where $m_{s,d,j}^{sup}$ is the mass flow rate of steam level $s$ supplied to direction $d$. $m_{s,d,j}^{main,seg}$ is the mass flow rate of steam in each main pipeline segment.

The inner diameters of steam main and branch pipeline segments ($D_{s,d,j}^{in,v,main,seg}$ and $D_{s,d,j}^{in,v,bran}$) are calculated by Eq. (18) and Eq. (19), respectively. The inner diameters of condensate main and branch pipeline segments ($D_{s,d,j}^{in,l,main,seg}$ and $D_{s,d,j}^{in,l,bran}$) are calculated by Eq. (20) and Eq. (21), respectively. The above inner diameters of pipelines are used to calculate the capital cost of the pipeline network $C^{pipe}$.

$$D_{s,d,j}^{in,v,main,seg} = \sqrt{\frac{4 \cdot m_{s,d,j}^{main,seg}}{\pi \cdot u^v \cdot \rho_s^v}} \quad (18)$$

$$D_{s,d,j}^{in,v,bran} = \sqrt{\frac{4 \cdot m_{s,d,j}^{sup}}{\pi \cdot u^v \cdot \rho_s^v}} \quad (19)$$

$$D_{s,d,j}^{in,l,main,seg} = \sqrt{\frac{4 \cdot m_{s,d,j}^{main,seg}}{\pi \cdot u^l \cdot \rho_s^l}} \quad (20)$$

$$D_{s,d,j}^{in,l,bran} = \sqrt{\frac{4 \cdot m_{s,d,j}^{sup}}{\pi \cdot u^l \cdot \rho_s^l}} \quad (21)$$

## 3.3. Consumer side model

The conditions of steam received by each consumer, including the saturation temperature $T_{d,j}^{rece}$, the mass flow rate $m_{d,j}^{rece}$, the specific enthalpy $h_{d,j}^{v,rece}$, the specific heat value $h_{d,j}^{HV,rece}$, are calculated by Eqs. (22)-(25).

$$T_{d,j}^{rece} = \sum_s \left( y_{s,d,j}^{sup} \cdot T_s^{MST,sat} \right) \quad (22)$$

$$m_{d,j}^{rece} = \sum_s \left( y_{s,d,j}^{sup} \cdot m_{s,d,j}^{sup} \right) \quad (23)$$

$$h_{d,j}^{v,rece} = \sum_s \left( y_{s,d,j}^{sup} \cdot h_s^{v,MST,out} \right) \quad (24)$$

$$h_{d,j}^{HV,rece} = \sum_s \left( y_{s,d,j}^{sup} \cdot h_s^{HV,MST} \right) \quad (25)$$

The existence of AST for each consumer is determined by the binary variable $z_{d,j}^{AST}$, and it is related to the

saturation temperature drop $\Delta T_{d,j}^{sat,AST}$, as expressed by Eq. (26).

$$\Delta T_{d,j}^{sat,AST} \le z_{d,j}^{AST} \cdot \Delta T^{sat,AST,max} \quad (26)$$

where parameter $\Delta T^{sat,AST,max}$ is the upper bound of $\Delta T_{d,j}^{sat,AST}$.

The performance of ASTs is formulated by Eqs. (27)-(31).

$$\Delta h_{d,j}^{is,AST} = \frac{\Delta T_{d,j}^{sat,AST}}{1854-1931 \cdot h_{d,j}^{HV,rece}} \quad (27)$$

$$W_{d,j}^{AST} = \frac{m_{d,j}^{rece} \cdot \Delta h_{d,j}^{is,AST} - \left(z_{d,j}^{AST} \cdot a_0 + a_1 \cdot \Delta T_{d,j}^{sat,AST}\right)}{a_2 + a_3 \cdot \Delta T_{d,j}^{sat,AST}} \quad (28)$$

$$h_{d,j}^{v,AST,out} = \frac{m_{d,j}^{rece} \cdot h_{d,j}^{v,rece} - W_{d,j}^{AST}}{m_{d,j}^{rece}} \quad (29)$$

$$h_{d,j}^{l,AST,sat} = 4.431 \cdot \left(T_{d,j}^{rece} - \Delta T_{d,j}^{sat,AST}\right) - 29.89 \quad (30)$$

$$h_{d,j}^{HV,AST} = h_{d,j}^{v,AST,out} - h_{d,j}^{l,AST,sat} \quad (31)$$

where $\Delta h_{d,j}^{is,AST}$ is the specific isentropic enthalpy difference of steam across the AST, and it is calculated by Singh's model [7]. $W_{d,j}^{AST}$ is the shaft work of the AST. $h_{d,j}^{v,AST,out}$ and $h_{d,j}^{HV,AST}$ are the specific enthalpy and specific heat value of steam out from the AST, respectively. $h_{d,j}^{l,AST,sat}$ is the specific enthalpy of saturated liquid of steam out from the AST.

The existence of FEB for each consumer is determined by the binary variable $z_{d,j}^{FEB}$. The relations among the centralized steam supply, AST, and FEB for each consumer are represented by Eq. (32) and Eq. (33).

In this work, it is assumed that the FEBs produce saturated steam at the required temperature of consumers, thus no electricity is generated at the same time. The saturation temperature of steam and the heat load actually used by each consumer ($T_{d,j}^{use}$ and $Q_{d,j}^{use}$) are expressed by Eq. (34) and Eq. (35), respectively. The former is constrained by Eq. (36), and the latter satisfies the energy balance, as expressed by Eq. (37).

$$\sum_s y_{s,d,j}^{sup} + z_{d,j}^{FEB} = 1 \quad (32)$$

$$z_{d,j}^{AST} \le \sum_s y_{s,d,j}^{sup} \quad (33)$$

$$T_{d,j}^{use} = \left(T_{d,j}^{rece} - \Delta T_{d,j}^{sat,AST}\right) + z_{d,j}^{FEB} \cdot T_{d,j}^{need} \quad (34)$$

$$Q_{d,j}^{use} = m_{d,j}^{rece} \cdot h_{d,j}^{HV,AST} + z_{d,j}^{FEB} \cdot Q_{d,j}^{need} \quad (35)$$

$$T_{d,j}^{use} \ge T_{d,j}^{need} \quad (36)$$

$$Q_{d,j}^{use} = Q_{d,j}^{need} \quad (37)$$

where $Q_{d,j}^{need}$ is the required heat load of each heat consumer.

## 3.4. Objective function calculation

The economic terms $C^{LPB,cap}$, $C^{LPB,fuel}$, $C^{FEB}$, and $C^{turb}$ in Eq. (1) are calculated by the formulas presented by Bruno et al. [2]. $C^{pipe}$ and $I^{elec}$ are calculated according to the methods in Ref. [8] and Ref. [9], respectively. The above calculations are not shown in detail here.

In this mathematical programming model, there are non-linear constraints for the steam physical properties, the equipment performance, and the energy balance. Furthermore, binary variables are used for the steam supply selectivity and the existence of equipment. Therefore, the model is formulated as a mixed-integer nonlinear programming (MINLP) model.

# 4. CASE STUDY

## 4.1. Data

As shown in Table 1, this case includes fourteen consumers. Different numbers of steam levels (*n*) are considered, ranging from one to five.

## 4.2. Model solution and results

The model is solved by a two-layer algorithm to deal with the solution difficulty, as shown in Figure 2. In the outer layer, the particle swarm optimization (PSO) algorithm transforms the variable $T_s^{MST,sat}$ into a parameter, and assigns it to the inner MINLP model. Once the saturation temperature of each steam level is determined, the supply selectivity of some consumers is eliminated due to the temperature constraint Eq. (14). Therefore, the feasible region is reduced and the inner model is much easier to be solved. In this work, the inner MINLP model is solved using Gurobi 11.0.1 as the solver.

**Table 1:** Data of consumers.

| i | $X_i$ (m) | $Y_i$ (m) | $T_i^{need}$ (°C) | $Q_i^{need}$ (MW) |
|---|---|---|---|---|
| $I_1$ | 850 | 250 | 180 | 4.3 |
| $I_2$ | 1450 | 400 | 125 | 4.8 |
| $I_3$ | 1700 | -650 | 135 | 3.1 |
| $I_4$ | 1900 | 550 | 200 | 5.2 |
| $I_5$ | -600 | 500 | 160 | 3.4 |
| $I_6$ | -900 | -150 | 175 | 2.9 |
| $I_7$ | -1500 | 300 | 190 | 4.0 |
| $I_8$ | -1800 | -800 | 200 | 6.0 |
| $I_9$ | -250 | 700 | 175 | 4.2 |
| $I_{10}$ | 650 | 1200 | 140 | 5.6 |
| $I_{11}$ | 650 | 1200 | 225 | 2.3 |
| $I_{12}$ | -500 | 1700 | 240 | 5.7 |
| $I_{13}$ | 950 | -1300 | 210 | 4.1 |
| $I_{14}$ | -550 | -1650 | 150 | 6.5 |

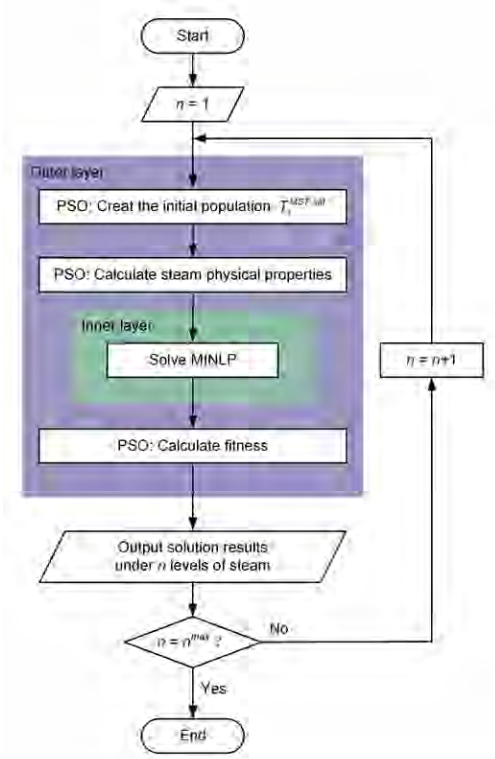



**Figure 2. Solution algorithm.**

The economic performance of the SPS under different numbers of steam levels is shown in Figure 3. It is indicated that the *TAC* of the SPS is minimized when the number of steam levels is two. The corresponding optimal scheme is presented in Figure 4.

## 4.3. Discussion

Figure 3 illustrates that among the different numbers of steam levels, the scheme with two steam levels has the second-lowest $C^{LPB,fuel}$, the second-lowest $C^{pipe}$, and the third-highest $I^{elec}$. The economic items of the system are well balanced, thus the lowest *TAC* is achieved. In this case, three consumers (J3, J4 in the North direction, and J1 in the South direction) require heat at temperatures higher than the saturation temperature of the two steam levels. Their required temperatures are 225 °C, 240 °C, and 210 °C, respectively. Therefore, FEBs are needed by them for distributed heat supply. As a consequence, the total length of the SPN decreases, thus $C^{pipe}$ is reduced. On the other hand, the configuration of FEBs for the three consumers with high required temperature also allows the lower outlet saturation temperature of MSTs in the energy station, leading to the rise of the isentropic enthalpy change of MSTs. Therefore, a substantial electricity generation capacity is obtained, despite the reduction in the mass flow of VHPS. Besides, the combined electricity generation capacity of the three ASTs accounts for 8.5% of the total electricity generation capacity, also contributing to the reduction of *TAC*.

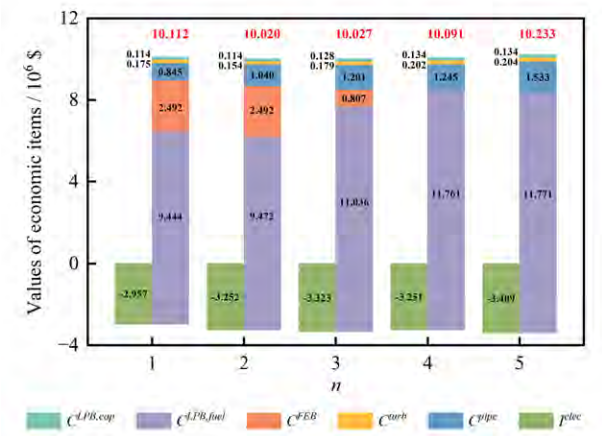



**Figure 3.** Economic results of the SPS.

## 5. CONCLUSIONS

An optimization model including the distributed heat supply and ASTs has been established for the SPSs in industrial parks. A case study demonstrates that the economic items of the SPSs vary with the number of steam levels. In this case, the optimal number of steam levels is two. With the arrangement of three FEBs and three ASTs, $C^{pipe}$ decreases and $I^{elec}$ increases, ultimately leading to the optimal design of the SPS with the minimum *TAC*.


## ACKNOWLEDGEMENTS

Financial support from the National Natural Science Foundation of China under Grant (No. 22393954) is gratefully acknowledged.

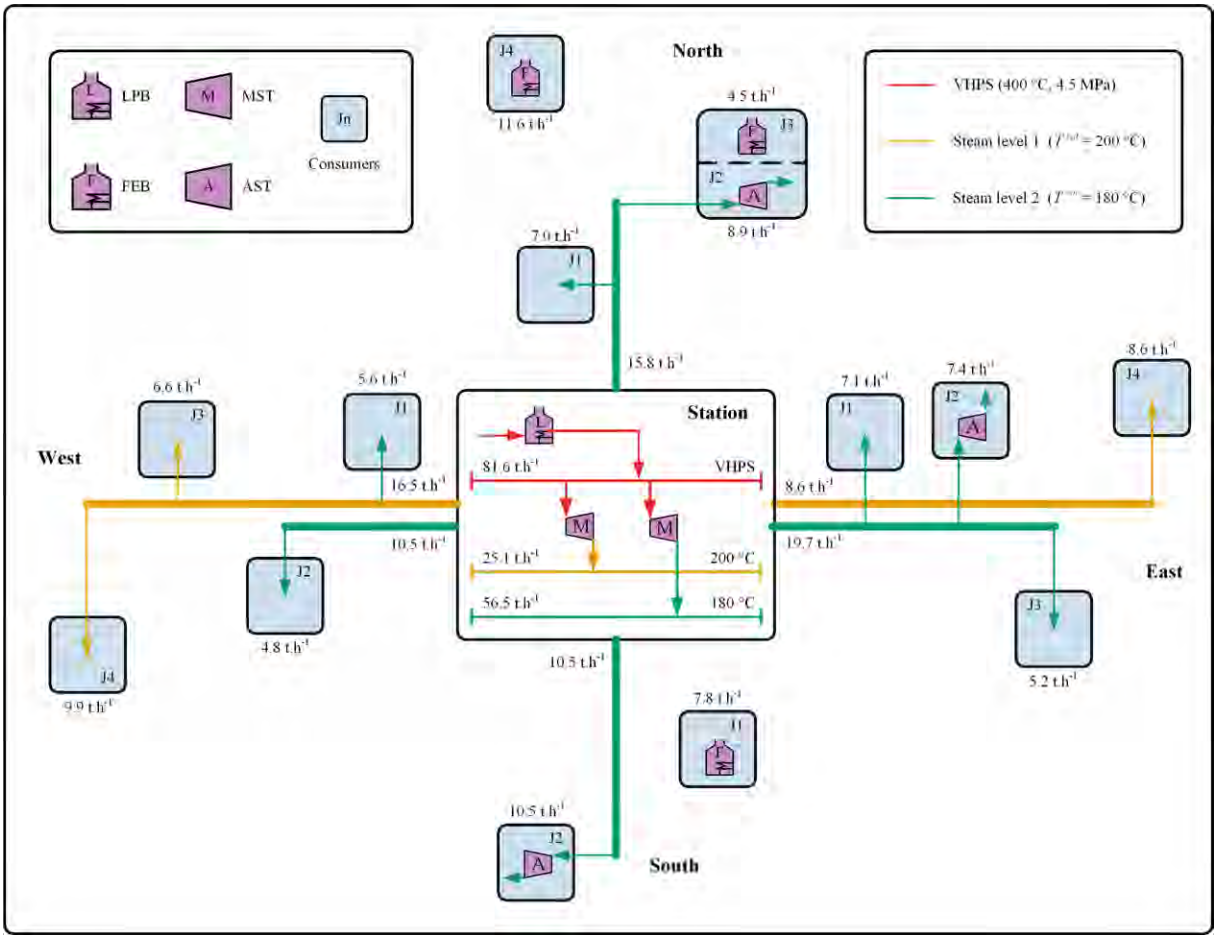



**Figure 4:** The optimal scheme.

## REFERENCES


1. Papoulias SA, Grossmann IE. A structural optimization approach in process synthesis—I: Utility systems. *Comput Chem Eng* 7:695-706 (1983).
2. Bruno JC, Fernandez F, Castells F, Grossmann IE. A rigorous MINLP model for the optimal synthesis and operation of utility plants. *Chem Eng Res Des* 76:246-258 (1998).
3. Aguilar O, Perry SJ, Kim JK, Smith R. Design and optimization of flexible utility systems subject to variable conditions: Part 1: Modelling framework. *Chem Eng Res Des* 85:1136-1148 (2007).
4. Sun L, Doyle S, Smith R. Heat recovery and power targeting in utility systems. *Energy* 84:196-206 (2015).
5. Jiménez-Romero J, Azapagic A, Smith R. Style: A new optimization model for Synthesis of uTility sYstems with steam LEvel placement. *Comput Chem Eng* 170:108060 (2023).
6. Zhang L, Cui Z, Wang Y. Design and optimization of steam power systems in industrial parks based on the distributed steam turbine system. *Chin J Chem Eng* 77:259-272 (2025).
7. Singh H. Minimisation of Flue Gas Emissions for Chemical Process Industries. UMIST (1997).
8. Stijepovic MZ, Linke P. Optimal waste heat recovery and reuse in industrial zones. *Energy* 36:4019-4031 (2011).
9. Chen C, Lin C. Design of entire energy system for chemical plants. *Ind Eng Chem Res* 51:9980-9996 (2012).



© 2025 by the authors. Licensed to PSEcommunity.org and PSE Press. This is an open access article under the creative commons CC-BY-SA licensing terms. Credit must be given to creator and adaptations must be shared under the same terms. See https://creativecommons.org/licenses/by-sa/4.0/

Systems & Control Transactions

**Research Article - Peer Reviewed Conference Proceeding**
ESCAPE 35 - European Symposium on Computer Aided Process Engineering
Ghent, Belgium. 6-9 July 2025
Jan F.M. Van Impe, Grégoire Léonard, Satyajeet S. Bhonsale,
Monika E. Polańska, Filip Logist (Eds.)

PSE PRESS

# Optimisation of a Haber-Bosch Synthesis Loop for PtA

**Joachim W. Rosbo[a], Anker D. Jensen[a], John B. Jørgensen[b], Sigurd Skogestad[c] and Jakob. K. Huusom[a]***

[a] Technical University of Denmark, Department of Chemical Engineering, Kgs. Lyngby, Denmark
[b] Technical University of Denmark, Applied Mathematics and Computer Science, Kgs. Lyngby, Denmark
[c] Norwegian University of Science and Technology, Department of Chemical Engineering, Trondheim, Norway
* Corresponding Author: jhk@kt.dtu.dk.

## ABSTRACT

This work presents a plantwide model of a Haber-Bosch ammonia synthesis loop (HB-loop) in a PtA plant, consisting of heat exchangers, compressors, steam turbines, flash separators and catalytic reactor beds. The total electrical power utility of the HB-loop is a combination of compressor power, refrigeration power, and steam turbine power. We optimise the HB-loop operating parameters, subject to constraints for maximum reactor temperatures, compressor choke and stall, minimum steam temperature, and maximum loop pressure. The loop features six degrees of freedom (DOFs) for the optimisation: three reactor temperatures, reactor $N_2/H_2$-ratio, separator temperature, and loop pressure. The optimisation minimises the total loop power utility for a given hydrogen make-up feed flow, with the PtA load varied by ranging the hydrogen make-up feed flow from 10 % to 120 % of the nominal. Across this load range, different constraints become active, with the compressor surge limit being particularly critical at low loads, significantly increasing HB-loop power consumption. To address this, we investigate configurations with two, three, and four compressor trains operating in parallel. Reductions in total power of 55%, 74%, and 84% are achieved at reduced plant loads, with two, three, and four parallel trains, respectively. In terms of total compressor capital and operating cost, we demonstrated savings of 8.06%, 8.29%, and 7.11% in total cost after ten years of operation with two, three, and four parallel compressor trains compared to a single train configuration.

**Keywords**: Power-to-Ammonia, Synthesis loop model, Optimisation, Parallel compressors.

## 1 INTRODUCTION

Power-to-X (PtX) is one of the most promising solutions for long-term storage of renewable energy such as wind and solar power [1]. Among the various PtX technologies, Power-to-Ammonia (PtA) receives significant attention due to its ability to store and recover energy without carbon dioxide emissions. PtA employs the traditional Haber-Bosch synthesis loop but with hydrogen produced via electrolysis rather than steam-methane reforming and nitrogen from air separation. The hydrogen production consumes around 90 % of the total plant electricity and hence highly depends on the available renewable energy. Due to the intermittent nature of renewable power sources, the synthesis loop is required to operate across a broad operating envelope from 10 % to 120 % of the nominal synthesis feed flow [2]. In [3], we developed dynamic models for three general ammonia reactor types: adiabatic quench-cooled (AQCR), adiabatic indirect-cooled (AICR), and internal direct-cooled reactors (IDCR). These reactors were optimised across a wide range of feed flow rates and evaluated for flexibility and robustness in a PtA plant, with the AICR and IDCR identified as the most suitable options.

In this work, we expand the scope by introducing a model for the entire HB synthesis loop, including an AICR reactor. The study focuses on optimising the HB-loop across the operating range from 10 % to 120 % of the nominal hydrogen make-up feed flow. We evaluate different loop designs with multiple parallel compressors to identify the most economical configuration.

## 2 SYNTHESIS LOOP MODEL AND OPTIMISATION

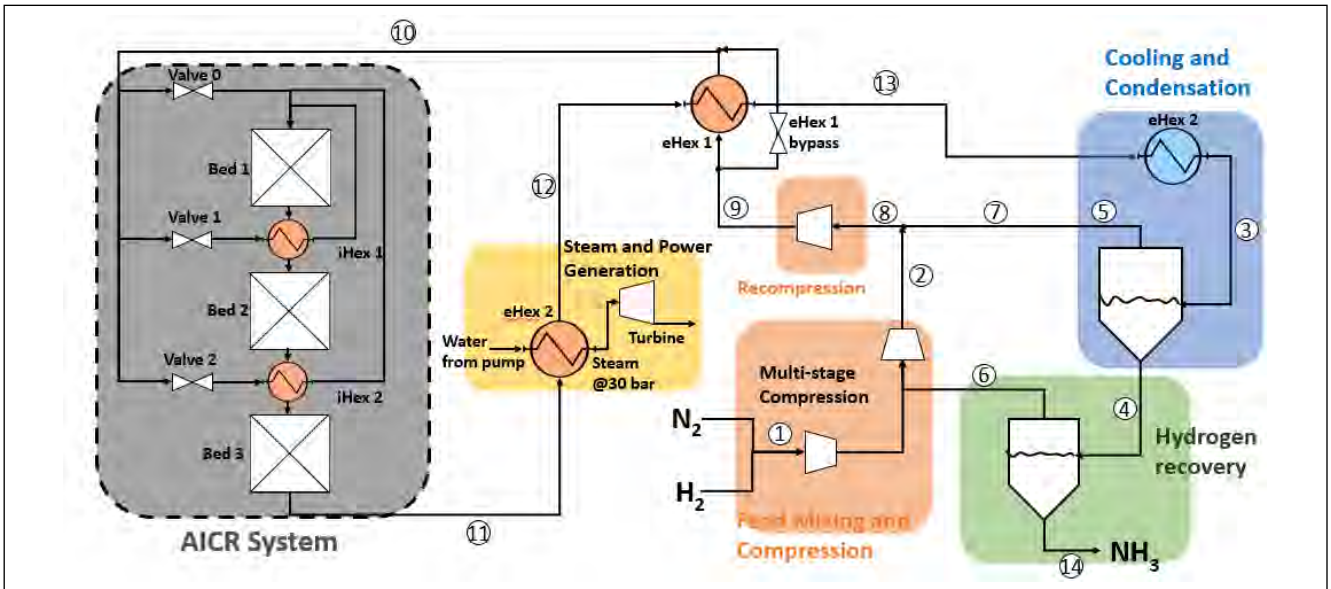



**Figure 1:** Schematic illustration of the Haber Bosch synthesis loop with an adiabatic indirect cooled reactor (AICR). Streams connecting the operating units are numbered as indicated in the diagram.

Figure 1 shows the Haber-Bosch ammonia synthesis loop. The make-up gas of hydrogen and nitrogen is compressed to the high synthesis loop pressure (>80 bar) and preheated before entering the reactor. The nitrogen feed, produced via air separation, contains 0.1% argon, significantly lower than the 1.2% found in conventional ammonia plants, where the nitrogen is supplied directly from combustion air. This eliminates the need for a purge stream in the synthesis loop as the solubility in the liquid ammonia product stream balances the argon build-up.

## 2.1 Reactor and heat exchanger model

The AICR consists of a combination of catalytic fixed beds and counter-current heat exchanges. The catalytic beds are assumed to be adiabatic and modelled in one dimension along the axial direction. Furthermore, we assume no transport limitations within the catalytic particles, which implies isothermal catalytic particle phase and gas phase. The reactor model is extensively described in [3]. The pressure drop across the catalytic bed is determined using Ergun's equation,

$$\frac{\mathrm{d}P}{\mathrm{d}l} = \frac{180\mu^g}{d_p^2}\frac{(1-\epsilon)^2}{\epsilon^3}v_s + \frac{1.75\rho^g}{d_p}\frac{(1-\epsilon)}{\epsilon^3}v_s^2, \qquad (1)$$

in which $P$ is the pressure, $\mu^g$ is the gas viscosity, $\rho^g$ is the gas density, $d_p$ is the hydraulic diameter of the catalyst particles and $v_s$ is the superficial gas velocity.

## 2.2 Compressor model

Centrifugal compressors are employed in the ammonia synthesis loop to compress the make-up feed gas and re-compress the recycle stream. The compressors are modelled based on isentropic compression from inlet pressure, $P_1$, to outlet pressure $P_2$,

$$S(T_1, P_1, F_{comp.}) = S(T_s, P_2, F_{comp.}), \qquad (2a)$$

$$W_{s,\ comp.} = H(P_{out}, T_s, N) - H(P_{in}, T_{in}, N), \qquad (2b)$$

with $W_{s,\ comp.}$ being the work of the isentropic compression. The real outlet temperature, $T_2$, and work, $W_{comp.}$, are found by solving,

$$\eta_s W_{comp.} = W_{s,\ comp.}, \qquad (2c)$$

$$W_{comp.} = H(T_2, P_2, F_{comp.}) - H(T_1, P_1, F_{comp.}), \qquad (2d)$$

where $\eta_s$ is the isentropic efficiency. The compressor efficiency is assumed to follow a polynomial expression as a function of the corrected flow, $F_{cor.}$,

$$\eta_s(F_{cor.}) = -0.44\left(\frac{F_{cor.}}{F_{n,\ comp.}}\right)^2 + 0.85\left(\frac{F_{cor.}}{F_{n,\ comp.}}\right) + 0.35, \qquad (2e)$$

where $F_{n,\ comp.}$ is the nominal compressor flow. The corrected flow is given by, $F_{cor} = F_{comp.}\frac{P_1}{P_{1n}}$, with $P_1$ being the compressor inlet pressure and $P_{1n}$ the inlet pressure at the design point. The coefficients of the polynomial ($a = -0.44, b = 0.85, c = 0.35$) are determined from a qualitative fit of a compressor map generated with Concept NREC® design software for the relevant [$N_2$,$H_2$,Ar,$NH_3$] gas mixture [4]. Furthermore, to prevent compressor surge and choke, the operating range of the compressors is restricted between 65 % and 130 % of the nominal compressor flow. Below 65 % corrected compressor flow, anti-surge recycle control is activated. The feed gas compression is performed using multistage compressors with a maximum compression ratio of 3.5 per stage.

## 2.3 Separator model

Due to the large difference in boiling points between ammonia and the synthesis gas, the product separation

**Table 1:** Optimal operating parameters and power distribution at nominal load.

| Optimal parameters | | Power distribution | |
|---|---|---|---|
| Bed inlet temperatures [K] | [724, 704, 694] | Feed compression | 5.50 MW |
| Reactor inlet pressure | 206.8 bar | Recycle compression | 0.18 MW |
| Separator temperature | 25 °C | Steam generator | 3.60 MW |
| Reactor $H_2/N_2$-ratio | 2.71 | Refrigeration power | 0 MW |
| | | **HB-loop power** | **2.11 MW** |

is achieved via a flash tank. The material balance over the flash tank is,

$$0 = F^{l}_{sep.} + F^{g}_{sep.} - F_{f,\ sep.}, \tag{3a}$$

where $F_{f,\ sep.}$ is the separator inlet flow, and $F^{l}_{sep.}$ and $F^{g}_{sep.}$ are respectively the liquid and gas flow exiting the separator. At vapour-liquid equilibrium the component chemical potentials of the phases are identical,

$$0 = \mu^{g}_{i}\left(T_{sep.}, P_{sep.}, x^{g}\right) - \mu^{l}_{i}\left(T_{sep.}, P_{sep.}, \mathrm{x}^{l}\right), \tag{3}$$

in which the chemical potential, $\mu_i$, of component $i$ is a function of the separator temperature, $T_{sep}$, pressure, $P_{sep}$, and composition, $x_{sep}$. The chemical potential of the gas and liquid mixtures are calculated with the thermodynamic tool `Thermolib` [5].

## 2.4 Cooling and Refrigeration

Cooling is performed before the separator and between stages for make-up feed compression. We assume cooling water is available at 15 °C and the heat exchangers are designed based on a 10 °C minimum temperature approach. Therefore, cooling below 25 °C requires a refrigeration cycle. Assuming a coefficient of performance of three ($COP = 3$), typical for refrigeration around 0 °C [6], the refrigeration power for cooling before the flash tank is,

$$W_{refrigiation} = \frac{\left(\dot{H}(25.0\ ^{\circ}\mathrm{C}, P_{sep.}, F_{sep.}) - \dot{H}(T_{sep.}, P_{sep.}, F_{sep.})\right)}{COP} \tag{4}$$

in which $\dot{H}$ is the enthalpy flow of the stream at the temperature, $T$, pressure, $P$, and flow $F$. The enthalpy flows in Eq. 4 are for two-phase flows.

## 2.5 Rankine cycle

The hot outlet stream from the reactor is around 750-820 K. This temperature facilitates the generation of superheated steam at 30 bar ($T^{@30\mathrm{bar}}_{sat} = 507.0\ ^{\circ}\mathrm{C}$), driving a turbine in a Rankine cycle. We assume a heat-to-electric power efficiency of, $\eta_{rankine} = 40\ \%$, representing a high-efficiency cycle with superheated steam [6]. Thus, the generated electrical power is given by,

$$W_{rankine} = \eta_{rankine}\begin{pmatrix}\dot{H}(T^{out}_{reac.}, P^{out}_{reac.}, F^{out}_{reac.}) \\ -\dot{H}(T_{S12}, P^{out}_{reac.}, F^{out}_{reac.})\end{pmatrix} \tag{5}$$

where $\dot{H}$ is the enthalpy flow of the stream at the temperature, $T$, pressure, $P$, and flow, $F$. $T_{S12}$ is the temperature of stream 12 (see Figure 1) given by $T_{S12} = T_{S10} + 10\ ^{\circ}\mathrm{C}$, where $T_{S10}$ is reactor feed temperature. The addition of $10\ ^{\circ}\mathrm{C}$ ensures sufficient temperature driving force in the pre-reactor external heat exchanger (Figure 1: eHex 1).

## 2.6 Optimisation problem

The electrical power consumption of the Harber-Bosch process consists of compressor and refrigeration power, while the steam turbine generates electricity. The total external electrical utility of the HB-loop, $W_{HB}$, is,

$$W_{HB} = W^{feed}_{comp} + W^{recycle}_{comp} + W_{refrigiation} - W_{rankine}. \tag{6}$$

We assume cooling water is a negligible operational cost. Hence, the total electrical power utility, $W_{HB}$, represents the cost function for the synthesis loop. As no purge stream figures in the PtA synthesis loop (see Figure 1), all hydrogen and nitrogen leave the synthesis loop by conversion to ammonia. This entails that hydrogen and nitrogen are fed at the stoichiometric ratio. Thus, for a given hydrogen make-up feed flow, minimising $W_{HB}$ represent the optimal solution. The optimisation involves six degrees of freedom (DOF): three reactor temperatures, $N_2/H_2$-ratio, separator temperature, and loop pressure. We define the DOFs in a vector, $\nu$,

$$\nu = \left[T^{in,1}_{reac.},\ T^{in,2}_{reac.},\ T^{in,3}_{reac.}, P^{in}_{reac.}, T_{sep.}, S_{\mathrm{H_2/N_2}}\right] \tag{7}$$

The optimal solution is found minimising the objective function across the six DOFs,

$$\min_{\nu} \quad W_{HB}, \tag{8a}$$

$$\text{s.t.} \quad f\left(x, y, F_{S1,\mathrm{H_2}}\right) = 0,\ g(x, y) = 0, \tag{8b}$$

$$0.65 \leq \frac{F_{cor.}}{F_{n,\ comp.}} \leq 1.3 \tag{8c}$$

where Eq. 8b represents the steady-state solution for a given hydrogen make-up flow, $F_{S1,\mathrm{H_2}}$, with $f$ and $g$ denoting the rate function and the algebraic equations as described in [3]. The optimisation problem is solved using the Matlab minimisation function `fmincon`. We define the specific HB-power cost for producing ammonia as,

$$E_{\mathrm{NH_3}} = \frac{W_{HB}}{\dot{m}_{\mathrm{NH_3}}}, \tag{9}$$

Where $\dot{m}_{\mathrm{NH_3}}$ is the mass flow of produced ammonia from the separator.

# 3 RESULTS

## 3.1 Optimisation at nominal load

The nominal load of the HB-loop is defined relative to a hydrogen make-up flow of 1.98 ton/h, corresponding to the 100 MW PtA plant presented in [7]. Table 1 summarises the optimal operating parameters and the corresponding power distribution when solving the optimisation in Eq. 8 at nominal load. The feed compression consumes most of the electrical utility with 5.50 MW, while the recycle compression only constitutes 0.18 MW. The optimal separator temperature of 25 °C is at the lower bound for water cooling, avoiding refrigeration power. A relatively big fraction of the electrical utility for compression is regained through the Rankine cycle delivering 3.6 MW. This sums to a total of 2.11 MW of external electrical utility required to power the HB-loop.

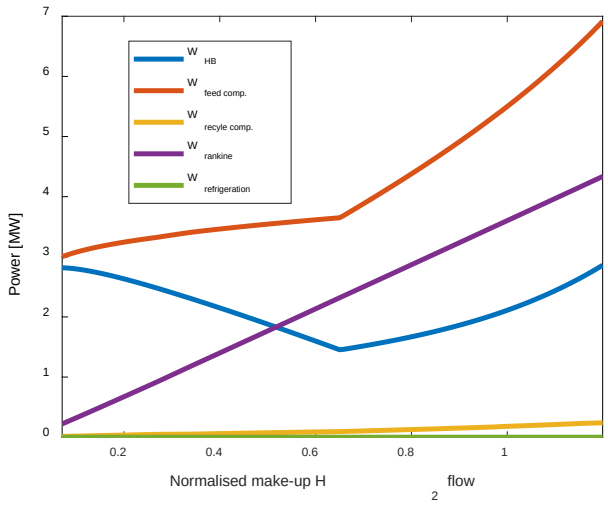



**Figure 2.** Distribution of power in the HB-loop across the operating envelope.

## 3.1 Optimisation across the operating window

We define the hydrogen load, $HL$, as the normalised make-up feed flow relative to the nominal flow,

$$HL = \frac{F_{S1,\mathrm{H_2}}}{F_{S1n,\mathrm{H_2}}}, \tag{10}$$

The optimisation problem in Eq. 8 is solved across the hydrogen load range from 10 % to 120 % of nominal flow. Figure 2 shows the optimal solution for the power utilities of the operating units across the operating window. The feed compressor power naturally decreases with the hydrogen load as less make-up feed gas is supplied. However, at 65 % of nominal hydrogen feed, the reduction in compressor power with hydrogen load is significantly restricted. This can be explained from Figure 3, showing the normalised corrected make-up feed and recycle flow along with the compressor surge limit across the operating envelope. The corrected feed flow intersects the surge line corresponding with the discontinuity in the feed compressor power in Figure 2. Reaching the surge line initiates the anti-surge recycling, limiting the decrease in compressor power. Figure 3 reveals that the recycle compressor reaches the surge line at a significantly lower load than the feed flow; however, its relatively smaller contribution to the total compressor power (see Figure 2) makes this effect negligible.

From Figure 2 we observe that the total HB-power, somewhat counterintuitively, increases with decreasing load when compressor anti-surge recycle is activated. This occurs because the power generated by the steam turbine decreases linearly with the hydrogen load, while the compressor power experiences only a slight reduction. Figure 4 illustrates that this dramatically impacts the specific ammonia production cost shown on the left y-axis. At reduced loads, the specific ammonia cost is up to twenty times higher relative to the nominal load. Additionally, Figure 4 displays the optimal reactor pressure across the operating envelope on the right y-axis. The optimal pressure decreases at reduced loads, explaining the slight decrease in feed compressor power seen in Figure 2 after reaching the surge limit.

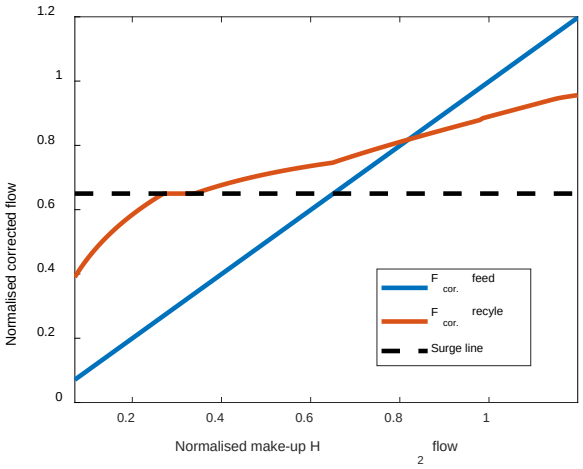



**Figure 3.** Normalised corrected flow for the feed and recycle compressors across the operating envelope.

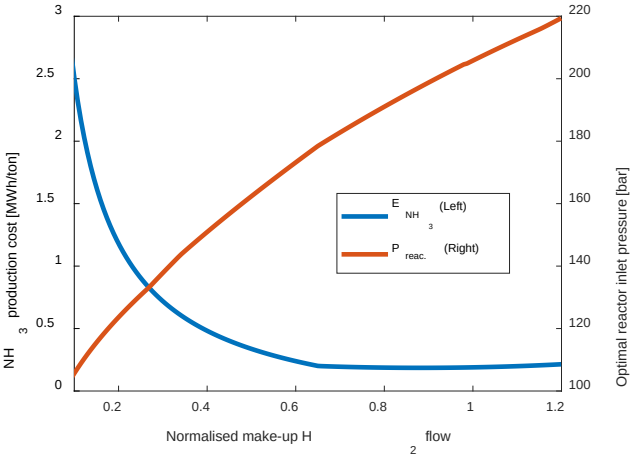



**Figure 4.** Left y-axis: Specific ammonia production cost.

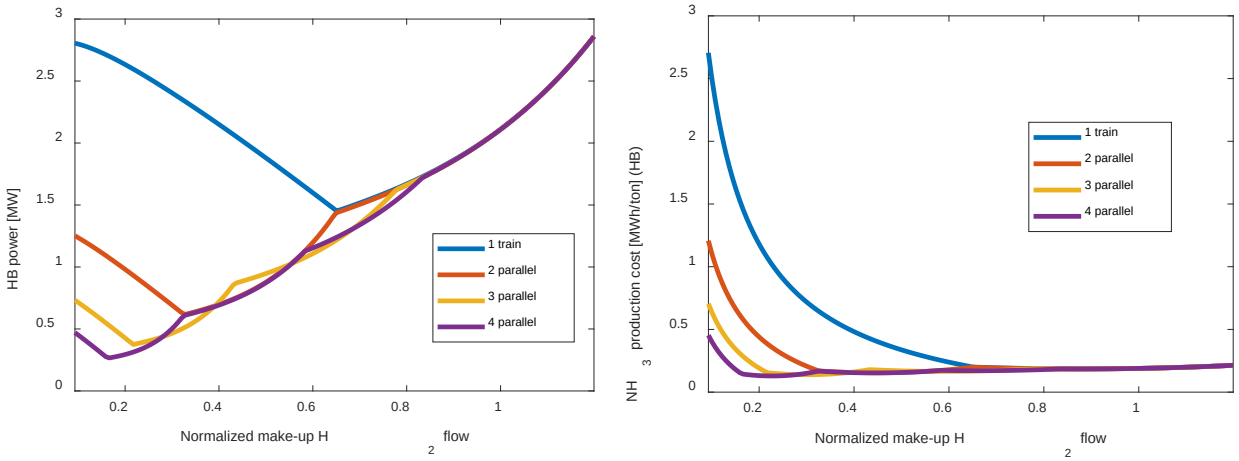



**Figure 4:** a) HB-power requirement and b) Specific ammonia production cost across the operating envelope with one, two, three and four parallel compressor trains.

Right y-axis: Optimal reactor pressure across the operating window.

## 3.1 Compressors in parallel

Figure 4 illustrates the drastic increase in ammonia production cost at low loads, caused by compressor anti-surge recycling. To reduce this loss, we investigate operating with multiple compressor trains in parallel. Parallel compressor trains extend the combined operational range of the compressors as one train can be stopped when the surge limit is reached. Additionally, multiple parallel compressors can facilitate higher compressor efficiency as the compressor flow can be distributed closer to the optimal operating flow. We solve the optimisation problem in Eq. 8 across the operating window with two, three, and four parallel compressor trains. Figure 5a displays the optimal HB-loop power for different compressor configurations, showcasing a significant reduction in HB-power by operating with multiple parallel compressor trains. At around 80 % hydrogen feed load, the configurations with 3 and 4 parallel compressor trains reduce the HB-power due to improved compressor efficiency achieved by pausing one compressor. However, the substantial reduction in HB-power occurs below the compressor surge limit, as the anti-surge recycling is shifted to 32.5 %, 21.7 % and 16.3 % of nominal hydrogen load for two, three and four parallel compressor trains, respectively.

Figure 5b shows the specific ammonia production cost across the operating envelope. Clearly, multiple parallel compressors significantly decrease production costs. At 10 % load, the ammonia production cost is reduced by 55 %, 74 % and 84 % for two, three and four parallel compressor trains, respectively.

# 5 ECONOMIC COMPARISON

Figures 4a and 4b illustrate that operating with multiple parallel compressor trains significantly reduces the HB-loop power during part-load operation. However, to evaluate the economic benefits, it is essential to consider the distribution of operating hours across the hydrogen loads. This is an extensive optimisation problem depending on factors such as the local wind and solar power distribution, the relative size of renewable power to the electrolyser and synthesis loop capacity, hydrogen storage size and electricity price. Performing this optimisation is not the scope of this paper, but was assessed by [2] and [8] . They concluded that wind and solar-powered PtA plants optimally operate mainly at minimum load, during periods of limited renewable power, or nominal load and above, during periods of surplus renewable energy. Complete reactor shutdown should be avoided as start-up times are extensive and frequent shutdowns damage the reactor catalyst [2,8]. Based on this, we assume an HB-loop capacity factor of 70 % with the hydrogen load distribution in Figure 5. The mean power consumption of the HB-loop is found from the probability density function, $p$, via,

$$\overline{W_{HB}} = \int_{0.1}^{1.2} W_{HB}(HL)p(HL)\,\mathrm{d}HL \tag{11}$$

Note $p$ is a piecewise function from the distribution in Figure 5. Table 2 summarises the mean HB-loop power for the four parallel compressor configurations. Approximately 25 % reduction in mean HB-power is achieved by operating with two parallel compressors, while further power savings are less significant for three and four parallel compressors.

**Table 2:** Mean HB-power with one, two, three or four compressor trains in parallel.

| **Par. compressors** | **1** | **2** | **3** | **4** |
|---|---|---|---|---|
| Mean HB-power [MW] | 2.14 | 1.60 | 1.45 | 1.37 |

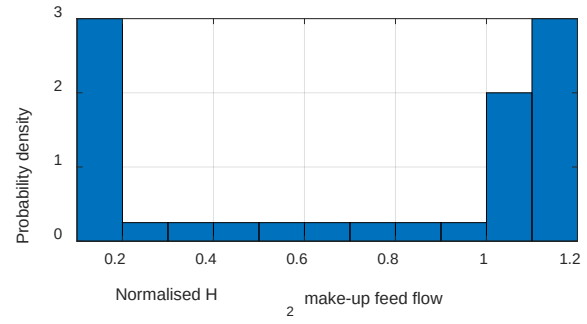



**Figure 5.** Probability density distribution of the synthesis loop load.

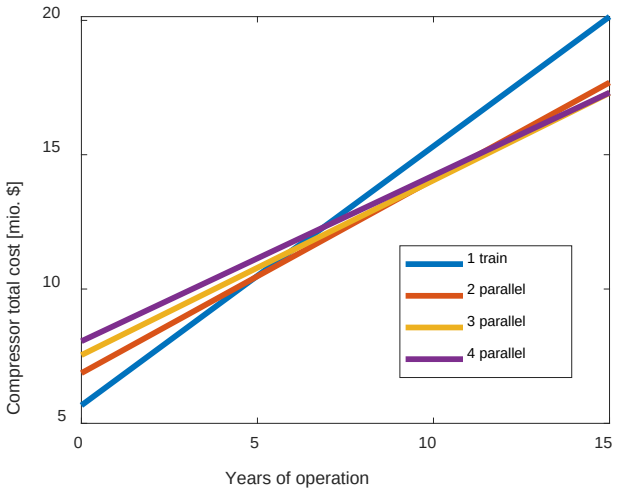



**Figure 6.** Total compressor cost (CAPEX + OPEX) for 15 years of operation with one, two, three or four compressor trains in parallel.

The compressor capital costs are assessed using the bare module cost (BMC) method described in [9]. Electricity is the only operational cost differentiating the parallel compressor configurations. We assume a relatively conservative electricity price of 0.045 $/kWh. Figure 7 displays the compressor systems' total cost (CAPEX + OPEX) as a function of years of operation. Naturally, the initial capital cost increases with the number of parallel compressors. However, the reduced electrical utility cost relatively quickly outweighs the additional capital costs. After ten years, operating with two, three, and four parallel compressor trains saves 8.06%, 8.29% and 7.11% of total costs, compared to a single train configuration. Additionally, from the redundancy principle, the reliability of the synthesis loop is significantly enhanced with more parallel compressors. Specifically, with three parallel trains, near full-load operation can be maintained using the remaining two compressor trains if one is out of function. Therefore, considering economic and reliability factors, we recommend the configurations with two or three parallel compressors for operation in a PtA plant.

## 5 CONCLUSION

In this work, we have introduced a static model of an ammonia synthesis loop to evaluate the total synthesis loop power. The power function was minimised to identify the optimal operating parameters for reactor bed inlet temperatures, reactor inlet pressure, separator temperature and reactor $N_2/H_2$-ratio. The optimisation was performed across the operating window from 10 % to 120% of nominal make-up feed hydrogen flow. This demonstrated that the compressor anti-surge limit strongly impacted the synthesis loop power at reduced loads. The surge boundary constrained the reduction in compressor power, resulting in an increase in total HB-loop power at low loads. To mitigate losses from anti-surge recycling, we evaluated configurations with multiple compressors operating in parallel. Optimisation results showed substantial reductions in HB-loop power at reduced loads: 55%, 74%, and 84% for two, three, and four compressor trains, respectively. This corresponded to total cost savings of 8.06%, 8.29% and 7.11%, respectively, compared to a single train configuration. Additionally, considering the enhanced reliability of configurations with parallel compressors, we recommended the configurations with two or three parallel compressor trains.

## REFERENCES


1. S. Miehling, S. Fendt, and H. Spliethoff, “Optimal integration of Power-to-X plants in a future European energy system and the resulting dynamic requirements,” Energy Convers Manag, vol. 251, 2021.
2. J. Armijo and C. Philibert, “Flexible production of green hydrogen and ammonia from variable solar and wind energy: Case study of Chile and Argentina,” Int J Hydrogen Energy, vol. 45, 2020.
3. J. W. Rosbo, A. D. Jensen, J. B. Jørgensen, and J. K. Huusom, “Comparison, operation and cooling design of three general reactor types for Power-to-Ammonia processes,” Chemical Engineering Journal, vol. 496, p. 153660, 2024.
4. Concepts NREC. https://www.conceptsnrec.com/design-software-solutions
5. T. K. S. Ritschel, J. Gaspar, A. Capolei, and J. B. Jørgensen, “An open-source thermodynamic software library ”. DTU Compute-Technical Report-

2016 No. 12, 2016.
6. R. T. Balmer, “Modern Engineering Thermodymacis”. Boston: Academic Press, 2011.
7. J. W. Rosbo, T. K. S. Ritschel, S. Hørsholt, J. K. Huusom, and J. B. Jørgensen, “Flexible operation, optimisation and stabilising control of a quench cooled ammonia reactor for power-to-ammonia,” Comput Chem Eng, vol. 176, p. 108316, 2023.
8. S. Schulte Beerbühl, M. Fröhling, and F. Schultmann, “Combined scheduling and capacity planning of electricity-based ammonia production to integrate renewable energies,” Eur J Oper Res, vol. 241, pp. 851–862, 2015.
9. K. M. Guthrie, “Process plant estimating evaluation and control”, Craftsman Book Co. (U.S.A.), 1974.

© 2025 by the authors. Licensed to PSEcommunity.org and PSE Press. This is an open access article under the creative commons CC-BY-SA licensing terms. Credit must be given to creator and adaptations must be shared under the same terms. See https://creativecommons.org/licenses/by-sa/4.0/



Systems & Control Transactions

**Research Article - Peer Reviewed Conference Proceeding**
ESCAPE 35 - European Symposium on Computer Aided Process Engineering
Ghent, Belgium. 6-9 July 2025
Jan F.M. Van Impe, Grégoire Léonard, Satyajeet S. Bhonsale,
Monika E. Polańska, Filip Logist (Eds.)

PSE PRESS

# Data-Driven Reinforcement Learning for Greenhouse Temperature Control

**Farhat Mahmood, Sarah Namany, Rajesh Govindan, *Tareq Al-Ansari**

College of Science and Engineering, Hamad Bin Khalifa University, Qatar Foundation, Doha, Qatar

* Corresponding Author: talansari@hbku.edu.qa

## ABSTRACT

Efficient temperature control in greenhouses is essential for optimal plant growth, especially in arid regions where the harsh environment poses significant challenges to maintaining a stable microclimate. Maintaining the optimum temperature range directly influences healthy plant development and overall agricultural productivity, impacting crop yields and financial outcomes. However, the greenhouse in the present case study fails to maintain the optimum temperature as it operates based on predefined settings, limiting its ability to adapt to dynamic climate conditions. To maintain an ideal temperature range within the greenhouse while dynamically adapting to fluctuating external conditions, this study introduces a control framework using Deep Deterministic Policy Gradient, a model-free deep reinforcement learning algorithm, to optimize temperature control in the closed greenhouse. A deep neural network is trained using historical data collected from the greenhouse to accurately represent the nonlinear behavior of the greenhouse system under varying conditions. The deep deterministic policy gradient algorithm learns optimal control policy by interacting with a simulated greenhouse environment, continuously adapting without needing an explicit system dynamics model. Results from the study demonstrated that, over a five-day simulation period, the deep deterministic policy gradient control system outperformed the existing greenhouse climate system in temperature regulation. It achieved a mean squared error of 0.01°C and a mean absolute error of 0.13°C. Additionally, the deep deterministic policy gradient algorithm demonstrated a significant improvement in energy efficiency, reducing total energy consumption by 6.80% compared to the current system.

**Keywords**: Reinforcement learning, Greenhouse temperature control, Closed environment agriculture

## INTRODUCTION

By 2050, the global population is projected to rise to about 9.7 billion, significantly increasing the need for water, energy, and food. To satisfy this growing food demand, agricultural production must be increased by nearly 70% from current levels. However, the persistent effects of climate change create significant challenges for increasing crop yields via conventional open-field farming (1). More frequent extreme weather events, higher temperatures, and changing rainfall patterns compromise these traditional methods. These environmental challenges make traditional farming methods more vulnerable. Therefore, it's essential to develop innovative, high-efficiency agricultural practices that preserve land and resources while providing greater yields (2).

Controlled Environment Agriculture (CEA) represents a viable solution, as it offers a regulated environment that mitigates climate-related risks (3). Among the various CEA technologies, greenhouses effectively optimize crop production by regulating environmental variables such as temperature, humidity, and $CO_2$ levels. However, efficiently managing greenhouse microclimates still poses challenges, necessitating a careful balance of various factors to promote plant growth while minimizing energy and water consumption. To address these challenges, various control strategies have been developed to regulate greenhouse environments, ranging from traditional rule-based methods to advanced model-based approaches. However, the complexity and variability of greenhouse conditions require more adaptive and data-driven solutions.

Reinforcement learning (RL) is a data-driven method that can optimize greenhouse climate control without depending on explicit system models (4). Unlike traditional controllers, RL dynamically adjusts to changing conditions, making it well-suited for complex and uncertain greenhouse environments. Deep reinforcement learning (DRL) methods, such as deep deterministic policy gradient (DDPG) and proximal policy optimization (PPO), have demonstrated significant potential in managing greenhouse operations. These methods use neural networks to learn optimal control policies from data, allowing for real-time adaptation to disturbances such as solar radiation fluctuations and external temperature changes.

Several studies have explored RL-based greenhouse control strategies, demonstrating promising results in improving energy efficiency and climate stability. For instance, a DRL-based controller integrated with robust optimization reduced energy consumption by up to 57% while maintaining stable temperature regulation (5). Multi-agent reinforcement learning approaches have also been applied to coordinate multiple greenhouse subsystems—such as heating, ventilation, and cooling—leading to improved operational efficiency (6). While RL-based strategies have demonstrated significant potential, their implementation still encounters significant challenges.

Despite the advancements, multiple challenges persist in RL-based greenhouse control systems. Training RL agents requires a considerable volume of high-quality data, and inadequate exploration strategies may result in unstable learning behaviors. Furthermore, ensuring safety constraints and interpretability in RL-based controllers continues to represent a significant research area. Additionally, a significant obstacle in RL deployment is the reliance on precise greenhouse models for training and evaluation.

Many researchers use physics-based models to simulate greenhouse dynamics; however, these models often include simplifying assumptions that may not accurately reflect real-world conditions. For instance, they often oversimplify thermal behaviors and may overlook difficult-to-measure factors, such as air leakage through greenhouse walls, heat exchange with the ground, or variations in moisture levels. Such omissions can lead to less accurate predictions about temperature variations and energy consumption, limiting the effectiveness of control strategies. Furthermore, greenhouses present unique challenges compared to traditional structures because of their specific design requirements. They are designed to maximize sunlight for plant growth while also maintaining a stable internal environment. This dual objective complicates thermal and energy management, making traditional control methods less effective when environmental conditions change rapidly. Given these limitations, a data-driven approach can offer a more precise representation of greenhouse dynamics, allowing RL agents to make better-informed decisions.

To address the challenges associated with greenhouse management, this study introduces a deep deterministic policy gradient approach based on data-driven modeling. Operational data has been collected from an actual greenhouse to train a deep neural network (DNN) surrogate model, which captures the intricate relationships among various environmental variables. Utilizing the developed DNN, a DRL agent using the DDPG algorithm was developed to maintain optimal temperature levels within the greenhouse while simultaneously minimizing energy consumption. The performance of the DDPG controller was evaluated in comparison to the existing greenhouse control system under deterministic conditions.

## METHODOLOGY

This study introduces a DRL approach that utilizes the DDPG algorithm to optimize greenhouse temperature control while minimizing energy consumption. The framework integrates two essential components: a DNN surrogate model and a DRL-DDPG architecture. The DNN model, trained using real-world greenhouse data, captures the dynamics of the greenhouse system, including weather conditions, internal temperature, fan operation, HVAC temperature (HT) settings, and energy usage. This surrogate model was integrated into a DRL environment to simulate greenhouse behavior, allowing the DDPG agent to learn an optimal control policy.

### Greenhouse system

The greenhouse, located in Qatar, utilizes glass as its covering material to enhance the penetration of photosynthetically active radiation into the plant canopy, ensuring optimal light for crop growth. To regulate cooling, the facility is equipped with an HVAC system alongside a hydroponic setup that efficiently supplies water, nutrients, and fertilizers to the plants. Figure 1 demonstrates the closed greenhouse.

The greenhouse operates as a closed-loop system that captures hot, humid air from the plant canopy. Instead of releasing this air into the atmosphere, it is redirected to an air-to-water chiller, where its temperature is reduced below the dew point (12-13°C). This cooling mechanism enhances the condensation of water vapor present in the air, enabling the collection of the resulting water for reuse in irrigation, significantly reducing water loss. The cooled air is subsequently reheated to an optimal temperature by the HVAC system prior to its recirculation back into the greenhouse. To meet irrigation requirements, additional water is supplemented from groundwater sources and treated through a reverse osmosis process. The climate control system is calibrated to maintain optimal growth temperatures for crops,

sustaining 18°C during the night and 23°C throughout the day.



**Figure 1:** Closed greenhouse located in Qatar.

## Data collection

Data was collected every 5 min over a one-year period, from September 2023 to September 2024, utilizing a network of sensors installed at the greenhouse. These sensors continuously monitored environmental variables, with solar irradiance and external temperature recorded by devices mounted on the greenhouse roof. The internal temperature within the greenhouse was measured through a sensor box located inside the unit. During the summer months, solar irradiance reached a peak value of 1060 W.m$^{-2}$, and external temperatures to as high as 45.2 °C. A summary of the ranges for all measured variables is detailed in Table 1.

**Table 1:** Range of measured variables.

| Parameter | Value and unit |
|---|---|
| Solar radiation | 0 – 1060 W.m$^{-2}$ |
| Outside temperature | 7.5 – 45.2 °C |
| Fan speed | 25 – 100 % |
| HVAC control | 17 – 22 °C |
| Greenhouse temperature | 12.1 – 25.2 °C |

## Deep reinforcement learning

The DDPG algorithm is a model-free, off-policy actor-critic approach in DRL. It builds upon the deterministic policy gradient method and is appropriate for dynamic environments with large, continuous action spaces (7). DDPG learns an optimal policy through the interaction of two primary components: the actor and critic networks.

The actor network, denoted as $\mu(s \mid \theta^{\mu})$, maps states to deterministic actions. Its goal is to identify the best possible action for a given state by selecting actions that maximize the Q-value predicted by the critic network. The critic network, represented as $Q(s,a \mid \theta^{Q})$, evaluates the quality of actions by estimating the expected cumulative future rewards for each state-action pair. The actor network is trained to improve its policy by maximizing the Q-value, while the critic network is updated using temporal difference learning to refine its predictions based on immediate rewards and estimated future values.

The DDPG algorithm incorporates several techniques to enhance learning stability and efficiency. A replay buffer stores past experiences, which include the current state, the action taken, the resulting reward, the next state, and whether the episode has terminated. By sampling and learning from these experiences, the agent breaks the temporal correlation between consecutive samples, improving the quality and efficiency of the training process.

Separate target networks are used for both the actor and critic. These networks provide stable reference values during training, especially when calculating the temporal difference error. To further enhance stability, DDPG employs a soft update strategy, where the target networks' parameters are gradually updated, preventing abrupt changes that could destabilize the learning process. The weight updates for the actor and critic networks are guided by mathematical equations. The actor's weights are updated to maximize the Q-value of the policy's actions(8):

$$\Delta\theta = \eta_\theta \nabla_\theta \left( \frac{1}{N} \sum_{k \in \mathcal{B}} Q\big(s(k), \pi(s(k) \mid \theta_\pi) \mid \phi_Q\big) \right) \quad (1)$$

Here, $\Delta\theta$ represents the change in the actor's parameters, $\eta_\theta$is the learning rate, $\nabla_\theta$ is a minibatch sampled from the replay buffer, and $N$ is the number of samples in the minibatch. The critic's weights are updated to minimize the difference between the predicted Q-value and the target Q-value (8):

$$\Delta\phi = \eta_\phi \nabla_\phi \left( \frac{1}{N} \sum_{k \in \mathcal{B}} \Big( Q\big(s(k), u(k) \mid \phi_Q\big) - v(k) \Big) \right) \quad (2)$$

Here, $\Delta\phi$ is the change in the critic's parameters, $u(k)$ is the action at time step $k$. Target Q-value is calculated as:

$$v(k) = r(k) + \gamma Q'\big(s(k+1), \pi'(s(k+1) \mid \theta_{\pi'}) \mid \phi_{Q'}\big) \quad (3)$$

where $r(k)$ is the immediate reward, $\gamma$ is the discount factor, $Q'$ is the target critic network, and $\pi'$ is the target policy network. By iteratively refining the actor and critic networks, DDPG efficiently learns optimal control policies without requiring an explicit model of the environment, making it highly suitable for control tasks in complex, continuous systems.

## System model

The surrogate model's accuracy in predicting future states is critical for an effective control strategy.

Traditional analytical models for greenhouses often rely on estimated parameters, introducing errors that compromise predictive reliability. To overcome this, a DNN was developed using PyTorch (9) to accurately represent the greenhouse system, capturing the nonlinear relationships among variables like solar irradiance, ambient temperature, HT, and fan speed.

The architecture of the DNN includes an input layer that processes 12 input features as illustrated in **Figure 2**. The model is trained using the Adam optimizer, which efficiently handles parameter updates, and the MSE loss function, which quantifies the prediction error. Training is conducted over 50 epochs to ensure the model converges to a solution that accurately captures the system's dynamics. By using this DNN-based surrogate model, the greenhouse system's behavior can be predicted with greater precision, providing a robust foundation for the control strategy.

**Figure 2:** DNN model for the greenhouse system.

### Reward function

The reward function for the DDPG agent is designed to achieve two main goals: minimizing the difference between the greenhouse temperature and the desired set point and reducing energy consumption. By penalizing both temperature deviations and energy usage, the reward function ensures the agent prioritizes maintaining optimal conditions while being energy efficient. The function assigns specific weights to each component, allowing for flexibility in emphasizing either precise temperature control or energy savings, depending on the desired objectives. The reward function is expressed as:

$$R(k) = -\left(\alpha \cdot |T(k) - T_{\text{set}}(k)| + \beta \cdot E(k)\right) \quad (4)$$

### Training

The critic network in the DDPG framework processes both state and action inputs through two fully connected layers, each containing 256 neurons. These layers use ReLU activation functions and include batch normalization to stabilize and improve the learning process. The network outputs a single Q-value, representing the expected cumulative reward for the given state-action pair. Similarly, the actor network processes the state inputs through two fully connected layers with 256 neurons each. These layers also use ReLU activation functions, along with batch normalization, to ensure stable and efficient learning. The network concludes with a Tanh activation function, which outputs the control actions within the required range. The training phase for the DRL agent spaned 500 epochs, with each epoch representing one day of operation, divided into 288 steps corresponding to 5-minute intervals. This high-resolution sampling enabled the agent to respond effectively to rapid changes in the greenhouse environment, which was crucial for maintaining optimal growing conditions.

The training process used a learning rate of $1\times10^{-4}$ to ensure steady weight updates. A soft update coefficient $\tau$ of 0.005 was employed for gradual updates to the target networks, enhancing stability during learning. The discount factor $\gamma$ was set to 0.99, balancing the importance of immediate rewards with long-term gains.

## RESULTS AND DISCUSSION

### Model performance

The DNN model, developed using historical data, was evaluated for its ability to predict greenhouse temperatures over a five day period from March 27th to April 1st, 2024. The model was trained on a dataset of 24,480 samples, with predictions generated at 5 min intervals. It demonstrated high accuracy, achieving an $R^2$ score of 0.94 and an MSE of 0.676 °C, as illustrated in Figure 3. While the model slightly underestimated greenhouse temperatures during peak solar irradiance hours on the last two days, it successfully captured the overall diurnal trend.

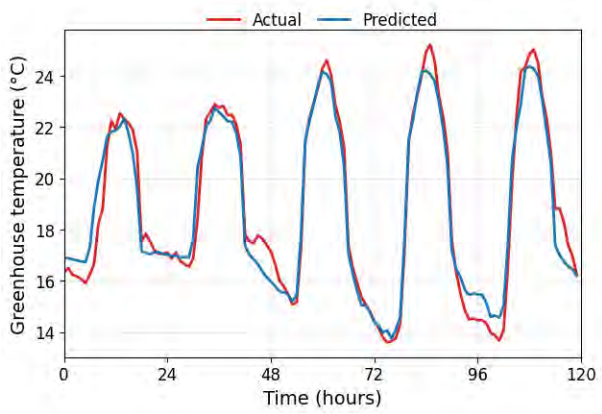



**Figure 3:** DNN greenhouse temperature prediction performance.

### Deep deterministic policy gradient performance

The performance of the DDPG controller in regulating greenhouse temperatures was assessed over a five-

day simulation, comparing its performance to the existing greenhouse control system for fixed setpoints of 23°C during the daytime and 18 °C at night. As illustrated in Figure 4, the DDPG controller outperformed the GCS in achieving temperature control. The DDPG controller (represented by the blue line) maintained temperatures within ±0.1°C of the setpoints (green line), ensuring smooth adjustments with minimal overshooting or undershooting. In contrast, the GCS experienced significant temperature variability, with actual temperatures (red line) often significantly deviating from the setpoints, reaching peaks of 24.3°C during the day and dropping to lows of 13.8°C at night. The GCS resulted in an MSE of 3.89 °C and an RMSE of 1.97 °C, while the DDPG controller achieved a lower MSE of 0.01 °C and an RMSE of 0.13 °C, demonstrating its superior performance in temperature regulation.

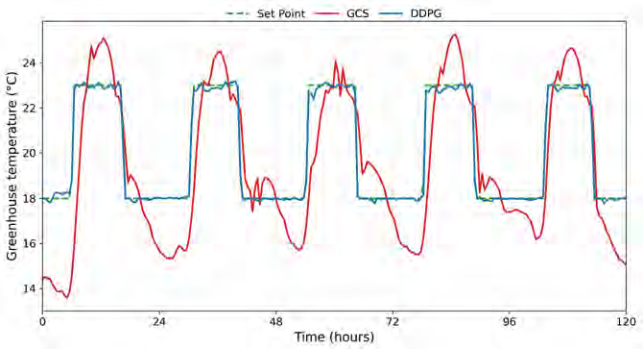



**Figure 4:** Temperature control performance comparison between GCS and DDPG.

The control actions of the DDPG controller were compared to the actual control actions implemented by the GCS, as demonstrated in Figure 5. The DDPG controller operated the fan at relatively lower speeds than the GCS, ensuring smoother transitions in operation. Additionally, the fan speed was always operated above 25%, maintaining consistent $CO_2$ circulation within the greenhouse. For HVAC control, the GCS operated on fixed temperature setpoints of 17°C at night and 22°C during the day. In contrast, the DDPG controller adopted a more dynamic approach, adjusting the temperature in response to changing environmental conditions. This adaptive behavior resulted in improved temperature regulation and overall greenhouse climate control.

Figure 6 illustrates the energy consumption over five days, demonstrating that the DDPG controller consistently resulted in lower energy consumption compared to the GCS. The DDPG controller accounted for a total energy usage of 7,789 kWh, while the GCS utilized 8,357 kWh. This led to an overall reduction of 6.80% in energy consumption with the DDPG compared to the GCS.

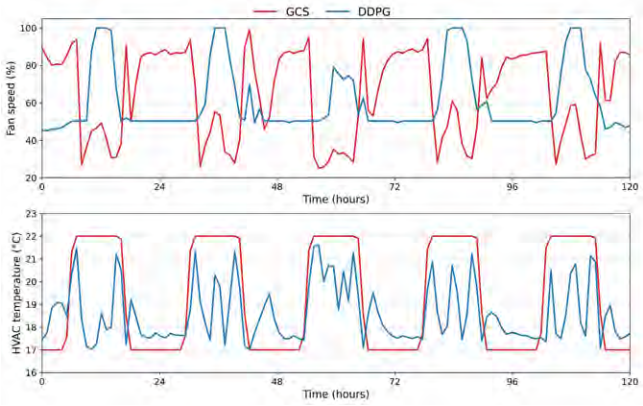



**Figure 5:** Control action comparison of GCS and DDPG.

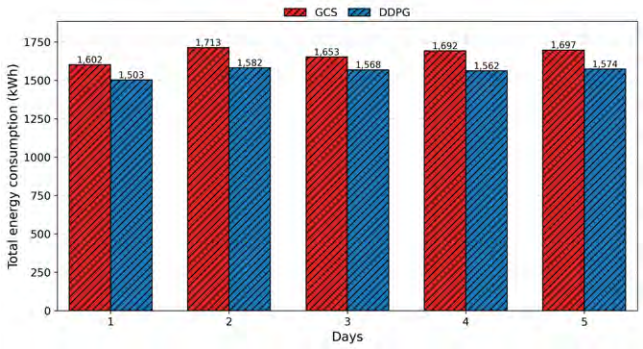



**Figure 6:** Energy utilization comparison of GCS and DDPG.

## CONCLUSION

This study demonstrated the effectiveness of a deep reinforcement learning approach using DDPG for greenhouse temperature control. The developed control system significantly outperformed the existing greenhouse control system, achieving superior temperature regulation with a mean squared error of 0.01°C and root mean squared error of 0.13°C, compared to 3.89°C and 1.97°C respectively, for the existing greenhouse system. The DDPG controller maintained temperatures within ±0.1°C of the setpoints while implementing smoother control actions, particularly in fan speed transitions. Furthermore, the controller achieved a 6.80% reduction in energy consumption, utilizing 7,789 kWh compared to the existing greenhouse system's 8,357 kWh over the five-day testing period.

## ACKNOWLEDGEMENTS

The authors acknowledge the support provided by Hamad bin Khalifa University, Education, City Doha, Qatar, a member of the Qatar Foundation.

## REFERENCES

1. Mahmood F, Govindan R, Yang D, Bermak A, Al-

Ansari T. Forecasting cooling load and water demand of a semi-closed greenhouse using a hybrid modelling approach. International Journal of Ambient Energy. 2022 Dec 31;43(1):8046–66.
2. Sajid MU, Mahmood F, Bicer Y, Al-Ansari T. Cost analysis of agricultural greenhouse yield production using spectrum selective fluids. Solar Energy. 2024 Jun;275:112607.
3. Mahmood F, Ghiat I, Hazrat B, Luqman M, Al-Ansari T. A framework based on an input-yield model for greenhouse optimisation for varying environmental conditions. Energy Conversion and Management: X. 2024 Apr;22:100555.
4. Goldenits G, Mallinger K, Raubitzek S, Neubauer T. Current applications and potential future directions of reinforcement learning-based Digital Twins in agriculture. Smart Agricultural Technology. 2024 Aug;8:100512.
5. Ajagekar A, Mattson NS, You F. Energy-efficient AI-based Control of Semi-closed Greenhouses Leveraging Robust Optimization in Deep Reinforcement Learning. Advances in Applied Energy. 2023 Feb;9:100119.
6. Ajagekar A, Decardi-Nelson B, You F. Energy management for demand response in networked greenhouses with multi-agent deep reinforcement learning. Appl Energy. 2024 Feb;355:122349.
7. Tan H. Reinforcement Learning with Deep Deterministic Policy Gradient. In: 2021 International Conference on Artificial Intelligence, Big Data and Algorithms (CAIBDA). IEEE; 2021. p. 82–5.
8. Morcego B, Yin W, Boersma S, van Henten E, Puig V, Sun C. Reinforcement Learning versus Model Predictive Control on greenhouse climate control. Comput Electron Agric. 2023 Dec;215:108372.
9. Imambi S, Prakash KB, Kanagachidambaresan GR. PyTorch. In 2021. p. 87–104.

© 2025 by the authors. Licensed to PSEcommunity.org and PSE Press. This is an open access article under the Creative Commons CC-BY-SA licensing terms. Credit must be given to creator and adaptations must be shared under the same terms. See https://creativecommons.org/licenses/by-sa/4.0/



Systems & Control Transactions

**Research Article - Peer Reviewed Conference Proceeding**
ESCAPE 35 - European Symposium on Computer Aided Process Engineering
Ghent, Belgium. 6-9 July 2025
Jan F.M. Van Impe, Grégoire Léonard, Satyajeet S. Bhonsale,
Monika E. Polańska, Filip Logist (Eds.)

PSE PRESS

# Aotearoa-New Zealand's Energy Future: A Model for Industrial Electrification through Renewable Integration

**Daniel J S Chong[a*], Timothy G Walmsley[a], Martin J Atkins[a], Botond Bertok[b], Michael RW Walmsley[a]**

[a] Ahuora – Centre for Smart Energy Systems, School of Engineering, The University of Waikato, Waikato, New Zealand
[b] Szechenyi István University, Gyor, Egyetem tér 1, Hungary
* Corresponding Author: daniel.chong@waikato.ac.nz.

## ABSTRACT

This work explores Aotearoa-New Zealand's potential to fully electrify and source industrial process heat demands from renewable energy for 286 industrial sites while exploring the feasibility of green methanol production using excess electricity. Most energy models rely on spatially aggregated supply and demand, which limits the accurate representation of energy value chains. To address this limitation, the model incorporates industrial sites with varied temperature profiles, enabling the use of diverse heating technologies such as heat pumps, electrode boilers, bubbling fluidised bed reactors and biomass boilers. The proposed Mixed-Integer Linear Programming energy model uses the Accelerated Branch-and-Bound (ABB) algorithm, which is implemented within the P-graph framework to optimise the system. The model considers different energy transportation modes, including road transport for biomass and grid infrastructure for electricity. The multi-period design determines optimal heating technology capacities for each unique industrial site while accounting for renewable energy variability, spot electricity prices, and sectoral energy demand fluctuations. The optimisation results reveal the most effective configurations of heat technologies for industrial sites and projected 1.03 Mt/y of green methanol production in New Zealand when the selling price exceeds NZD1050 /ton (EUR 569 /ton). The findings demonstrate a 41.3% reduction in total process energy supply from 25.9 TWh/year to 18.8 TWh/year, driven by the higher coefficients of performance (COP) and efficiencies of electrification.

**Keywords**: Energy Systems, Optimization, Energy Management, Hydrogen, Modelling and Simulations

## INTRODUCTION

Aotearoa-New Zealand is transitioning toward a net zero, climate resilient future where total energy supply is generated by renewable resources. The government has set aims to eliminate greenhouse gas emissions before the year 2050, with the exception of biogenic methane from agriculture and waste. The Climate Change Commission's demonstration pathway envisions a large-scale transition away from coal and fossil fuels. Under the current plans, the use of coal will be phased out by 2037 and similarly fossil gasses by 2050 [1].

In terms of direct renewable energy use in New Zealand, only 30% of primary energy consumption is supplied by renewables [2]. The hard to abate sectors namely industrial processes are primarily reliant on fossil fuels such as natural gas and coal. Industries such as dairy, meat, chemical, pulp, wood and paper sectors require larger amounts of high temperature heating where it might be prohibitively expensive or infrastructure lacking to be supplied by electrification.

Electricity consumption in New Zealand's industrial sector holds a significant share of the country's total usage. In 2022, New Zealand's industrial sector accounted for approximately 13.7 TWh or 34% of the nation's total electricity consumption. Industrial process heat which encompasses systems such as hot water, direct heat, process steam is responsible for 8.3 Mt of carbon dioxide equivalent emissions annually, where 35% of the nation's total energy use is consumed for process heat [3]. Energy efficiency and switching to low-carbon fuels help reduce the energy needed to provide useful heating. This, in turn, lowers the carbon footprint associated with meeting the heating demand.

A utility system delivers the heating, cooling, and power essential for industrial processes. Renewable energy resources have the potential for the generation of process heat namely direct combustion (e.g. bioenergy) and indirect heating via electrification. Wood energy industrial symbiosis is particularly important to create a circular economy in the forestry and wood processing sector and potentially solving energy problems in industries. Wood processing regions have substantial forestry resources which could potentially alleviate the infrastructure cost of full electrification reducing the need for capacity upgrades and grid reliance [4].

Optimisation models have been generally accepted as the most applied methodology for energy system analysis since 2010 [5]. It is also a robust method due to the inclusion of techno-economic structure and the capability to simulate numerous scenario-based projections which would inherently be important for policy makers to undergo decision making processes. These energy system optimization models (ESOMs) determine the cost-optimal mix of fuels and conversion technologies required to meet energy demand efficiently. Among them, the most prominent ESOMs frameworks are Long-range Energy Alternatives Planning (LEAP), MARKet and Allocation (MARKAL), The Integrated MARKAL-EFOM System (TIMES), Model for Energy Supply Strategy Alternatives and their General Environmental Impact (MESSAGEix) [5].

Geographic information system (GIS) has been partially addressed in studies to deal with spatial-related difficulties [6]. Spatial tools are often used to conduct analysis and geographic data processing. GIS is combined with energy system modelling tools such as The Integrated MARKAL-EFOM System [7]. The integration effort demands a variety of parameters and datasets, and increased analytical effort which amplifies the model's complexity, resulting in longer computational run-time.

An alternative approach is to build an energy systems model from a generic modelling framework, such as P-graph connected with ArcPy. The P-graph framework is introduced along with the systematic creation of defined mathematical optimisation models for process synthesis [8]. P-graph has been employed as an energy modelling tool. For example, Aviso et al. have extended the scope of P-graph into macroscale energy systems modelling [9]. Xu et al. investigated the technoeconomic feasibility of converting electricity generated from renewable sources into hydrogen using P-graph [10]. P-graph framework has been popularised in solving large models with low computational power which leads to many hybrid uses of P-graph being carried out. The efficiency of P-graph solvers has encouraged the development of an open-sourced Python library which allows P-graph models to be scaled more seamlessly to build and solve large scale problems more efficiently [11].

The implementation of ArcPy automates the analysis for one or a series of spatial tools for each row of the dataset [12]. For example, Wang has applied ArcPy within the Python environment to process qualitative and quantitative descriptions in the urban building energy model [13]. ArcPy is also used to assess solar generation output for the electrification of transportation [14]. The benefit of ArcPy lies in its extensive range of spatial tools. As such, ArcPy is used to estimate distances across various levels or layers in each successive step. Additionally, ArcPy is used to identify the points of connection assigned to specific generation and factory sites by defining electricity transmission and distribution lines as barrier boundaries.

As noted, existing energy models tend to aggregate industrial heat loads without distinguishing temperature demand profiles resulting in poor resolution and the selection of non-optimal solutions (e.g. boilers instead of heat pumps) [15]. Separating temperature profiles by sector would provide better resolution for evaluating different heating technologies or implementing heat cascading in energy models [16]. However, this also elicits the need to build a new model using a generic framework and packages.

The aim of this research is to develop a national energy transition model, applying the P-graph approach, to assess Aotearoa-New Zealand's potential to achieve net zero in the industrial sector in the future. This includes exploring opportunities to produce high-value, hydrogen-rich compounds, all within the country's resource constraints.

The content of the paper is structured as follows. The context and the scope of the model introduce the extent of the research. In the methods section, it outlines the software implementation and model structure which introduce the application of modelling tools and the approaches which are used to design the structure. The results section presents the configurations of heat technologies in the optimisation model while the conclusions summarise the key findings.

## SCOPE OF THE MODEL

The purpose of this model is to identify the most suitable heating technologies which run on renewables resources for every industrial site nationwide using more than 1 GWh/y. These include various classes of industrial heat pumps (HPs) designed for specific thermal profiles, electrode boilers for high-temperature applications, and biomass boilers for using biomass fuels.

Given the research aim involves heat cascading across different plants in Aotearoa-New Zealand, a high level of detail in spatial resolution is essential. Temporal dynamics of industry energy demand is accessed in a monthly time series. The time period is important to take account the intermittent renewable generation which

affects the capacity factor of electricity output, monthly average electricity spot price for each point of connection, heat and power demand profiles for industrial, residential and commercial consumption. The analysis covers one year to capture seasonal changes in heating capacity and green methanol production capacity.

# METHODS

## Software Implementation and Tools

The national energy transition model (NET-Mod) is implemented as Python. Python is a high-level programming language equipped with an extensive range of libraries which is suitable for data analysis and mathematical optimisation. The Python-based model utilised the following libraries: Pgraph, ArcPy and RenewablesNinja.

## P-graph Optimisation Model

P-graph is a directed bi-partite graph which consists of two types of vertices: operating units, ($O$) and material nodes ($M^*$). The P-graph superstructural model, $S$ comprises three main sets, expressed as $S = (P, R, O)$ where $P$ and $R$ are the subset of set of materials $M^*$, representing the products and raw materials respectively [8]. Additionally, operating units ($O$) generate subgraphs $(M^*, O)$ and $(O, M^*)$ to represent the interconnections between two material nodes, incorporating transformation coefficients that define the flow conversion between the connected nodes [9]. The sets and indices in the model are stated in **Table 1**.

**Table 1.** Sets and indices in the model.

| | |
|---|---|
| $i, u \in I$: Point of Connections | $t \in T$: Monthly Periods |
| $j \in J$: Electricity Generation Sites | $(i, u) \in V$: Edges between POCs |
| $k \in K$: Biomass Supply Sites | $n \in N$: Heating Technologies |
| $q \in Q$: Temperature Profiles | $l \in L$: Factory Sites |
| $p \in P$: Electricity Generation Technologies | |

In the model, the "raw material" nodes represent the resources supplied to the energy system. These include the electricity generated using technology $p$ at site $j$ at time $t$, denoted as $E_{j,p,t}$ and biomass resource available at site $k$ at time $t$, represented by $B_{k,t}$. The "product" nodes define the targets for the energy model, which must be fulfilled for a feasible process network synthesis problem (PNS) solution. The product set includes the temperature profile demand $q$ at site $l$ at time $t$ ($D^{in}_{l,q,t}$), green methanol production at site $j$ ($G_j$), residential and commercial demand at POC $i$ at time $t$ ($D^{re}_{i,t}$) and electricity curtailment at site $j$ at time $t$ ($H_{j,t}$). The "operating unit" nodes are critical components of the model, influencing costs as well as endogenous and exogenous flows within the system. The elements include electricity generation capacity using technology $p$ at site $j$ ($Cap^{e}_{j,p}$), methanol plant capacity at site $j$ ($Cap^{g}_{j}$), and heat technology capacity $n$ at industrial site $l$ ($Cap^{ht}_{l,n}$). Additionally, transmission and distribution charges in POC $i$ at time $t$ ,($T^{e}_{i,t}$), biomass transport costs from site $k$ to industrial site $l$ at time $t$($T^{b}_{k,l,t}$) and biomass transport costs from site $k$ to electricity generation site $j$ at time $t$, ($T^{b}_{k,j,t}$) are included within the set of "operating unit" nodes. The equations defining the sets are:

$$R = \{E_{j,p,t}, B_{k,t}\} \quad (1)$$

$$P = \{D^{in}_{l,q,t}, G_{j,t}, D^{re}_{i,t}, H_{j,t}\} \quad (2)$$

$$O = \{Cap^{e}_{j,p}, Cap^{g}_{j}, Cap^{ht}_{l,n}, T^{e}_{i,t}, T^{b}_{k,l,t}, T^{b}_{k,j,t}\} \cup O' \quad (3)$$

In this work, time step is a crucial factor in the optimisation model, as it determines the sizing of operations.
The optimisation model is formulated in **Equation 4**:

$$\min CC_R + CC_O - CC_P \quad (4)$$

where the total annualised cost is the sum of resource costs ($CC_R$) and operating units costs ($CC_O$), subtracting the total revenue or product costs ($CC_P$).
The detailed cost formulation for $CC_R$, $CC_O$ and $CC_P$ are outlined in **Equation 5-7**. The symbol $C$ represents a cost function, where the respective subscript and superscript specify costs for different components.
The resource cost is formulated as:

$$CC_R = \sum_{j\in J}\sum_{t\in T}\sum_{p\in P} C^{e}_{j,p,t} \cdot E_{j,p,t} + \sum_{t\in T}\sum_{k\in K} C^{b}_{k} \cdot B_{k,t} \quad (5)$$

The operating cost is outlined as:

$$CC_O = \sum_{j\in J}\sum_{p\in P} C^{cap^e}_{j,p}\, Cap^{e}_{j,p} + \sum_{j\in J} C^{cap^g}_{j}\, Cap^{g}_{j} + \sum_{l\in L}\sum_{n\in N} C^{ht}_{n}\, Cap^{ht}_{l,n} + \sum_{t\in T}\sum_{i\in I} C^{e}\, T^{e}_{i,t} + \sum_{t\in T}\sum_{k\in K}\sum_{l\in L} C^{b}\, T^{b}_{k,l,t} + \sum_{t\in T}\sum_{k\in K}\sum_{j\in J} C^{b}\, T^{b}_{k,j,t} \quad (6)$$

The product cost is given by:

$$CC_P = \sum_{t\in T}\sum_{l\in L}\sum_{q\in Q} C^{in}_{q} D^{in}_{l,q,t} + \sum_{t\in T}\sum_{j\in J} C^{g} G_{j,t} + \sum_{t\in T}\sum_{i\in I} C^{re} D^{re}_{i,t} + \sum_{t\in T}\sum_{j\in J} C^{H} H_{j,t} \quad (7)$$

## Model Structure

The model comprises five parts: utility generation, transmission, local generation, biomass resources, factory sites, and green methanol plants. **Figure 1** provides a simplified model structure, showing utility-scale generation and green methanol production for a single time step. For local generation, the structure is similar, but the electricity node bypasses transmission and connects directly after distribution charges.

Electricity is generated either at the utility scale or local scale, with the capacity and utilisation factor (or capacity factor) specified. Electricity generated from utility power stations can be delivered to the National Grid by injecting it into the designated points of connection.

Additionally, both utility-scale and local-scale electricity have the option to convert excess electricity into green hydrogen, which serves as a raw ingredient to produce green methanol.

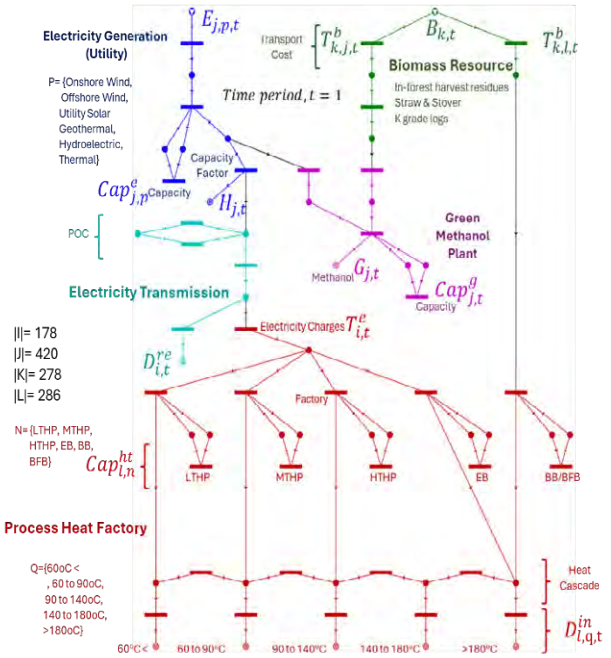



**Figure 1**. Example of the P-graph structure for the energy model for a single time period, t=1, for one generic industrial site, existing electricity demand at the POC, and one new green methanol plant, all supplied by renewable electricity generation and/or biomass.

Note. POC=point of connection, LTHP=low temperature heat pump, MTHP=medium temperature heat pump, HTHP=high temperature heat pump, EB=electrode boiler, BFB=bubbling fluidised bed reactor, BB=biomass boiler.

The National Grid is interconnected through a network of transmission infrastructure, primarily a series of points of connection. Electricity can flow in two directions but only one direction at a time, necessitating the application of mutual exclusion for each connection. The electricity is then supplied to meet the residual demand of industrial, commercial, and residential consumers. The aggregate electricity demand includes the current industrial electricity demand behind POC nodes, which distinguishes electricity demand from energy demand met by non-renewable fuels. Subsequently, the electrical flow is directed to the respective factories and distributed among four operating units, each representing a different heating technology tailored to specific temperature profiles. Consequently, there will be multiple configurations for each factory across New Zealand.

On the biomass side, three different biomass types are specified, none of which exhibit intermittent characteristics or serve as intermediate commodities for further processing. The biomass resources used in this study are k-grade log wood, in-forest harvest residues as well as straw and stover. Biomass can be directly supplied to factories for high-temperature heating or delivered to prospective green methanol plants as a source of carbon and hydrogen. Since biomass is transported by trailers, there is a direct relationship between transport distance and associated transportation costs. The transport cost is estimated at 0.3 NZD per ton-km.

The NET-Mod comprises 420 electricity generation power stations, which include commissioned, consented, proposed, or under appeal facilities (342 utility-scale and 78 local-scale); 286 industrial sites with an annual process heat demand exceeding 1 GWh; 178 points of connection; 278 biomass sites; 14,956 connections between factories and biomass sites; and 18,980 connections between biomass sites and generation facilities. In total, there are 202031 variables (117021 material nodes and 85010 operating units) and 104210 equations.

**Table 2** presents the efficiencies or coefficient of performance (COP) of each heating technology and its respective specifications. It is particularly important for the introduction of heat pumps in industries as it has a higher COP and efficiency when operating in lower temperature, meaning useful energy is supplied to fulfil the load demand in the processes.

**Table 2.** Specifications of proposed industrial heating technologies.

| Tech | Fuel | Temperature (°C) | COP | Cost (NZD /MW·y) |
|---|---|---|---|---|
| **LTHP** | Electricity | 60< | 4.57 | 342,933 |
| **MTHP** | Electricity | 60-90 | 2.69 | 201,399 |
| **HTHP** | Electricity | 90-140 | 1.73 | 129,983 |
| **EB** | Electricity | >180 | 0.99 | 7,920 |
| **BB** | K-log wood, In-forest residue | >140 | 0.80 | 83,333 |
| **BFB** | Straw and Stover | >140 | 0.70 | 53,333 |

## RESULTS

The Accelerated Branch and Bound (ABB) solver was executed on an Intel CPU 2.30 GHz i7-12700H processor with 32 GB of RAM. The solver required 60 mins to find the optimal solution. In the solution, 15.9% of process heat energy is sourced from biomass, as indicated by the energy model. This significant share highlights the diverse dependence on various energy sources. The reliance on biomass varies significantly across regions, reflecting disparities in energy resource availability and industrial demand (**Figure 2**). For example, industrial sites in the central and southern part of the South Island

heavily rely on bioenergy for process heat, with 55% of the process heat met locally by abundant biomass resources. **Figure 2** illustrates that the Central North Island regions such as Waikato and the Bay of Plenty region also benefit from biomass resource due to their high concentrations of forest plantation-based pulp and paper mills. In contrast, regions such as Northland, Auckland, Taranaki and Wellington region face limited biomass mass availability, resulting in a high dependence on electricity for industrial heat demands, exceeding 95%.

In process heat sectors, **Figure 3** illustrates the heat technologies used in different types of industrial sectors. High-temperature heating technologies not only supply heat to their intended temperature profiles but cascade residual heat to lower-temperature processes, maximising energy utilisation. Although highly efficient heat pumps offer notable benefits, the economic feasibility of biomass boilers, especially in regions with abundant biomass resources, makes them a more practical choice for industrial heating. For instance, the high utilisation of electrode boilers in the Taranaki Region is largely attributed to Methanex, a grey methanol plant. According to the model, a proposed scenario for its future operation involves replacing all heating with electricity while retaining natural gas as a raw material for chemical processes.

**Table 3.** The energy requirements for industrial process heat by proposed heating technologies.

| Heating Technologies | Energy required (TWh/y) |
|---|---|
| **Electricity Total** | **15.85** |
| **- LTHP** | 0.36 |
| **- MTHP** | 1.12 |
| **- HTHP** | 3.29 |
| **- EB** | 11.01 |
| **Biomass Total** | **2.99** |
| **- BB** | 2.97 |
| **- BFB** | 0.02 |

**Table 4.** Projected green methanol production by region and power generation type (at NZD 1050/tonne).

| Zone | Region | Type | Production (kt/y) |
|---|---|---|---|
| **UNI** | Northland | Geothermal, Wind | 839.29 |
| **CNI** | Waikato | Geothermal, Wind | 36.34 |
| **LNI** | Manawatu-Wanganui | Wind | 6.66 |
| **CSI** | Canterbury | Hydroelectric | 152.09 |
| **Total Production** | | | **1034.37** |

The shift towards combined electrification and increased biomass utilisation has reduced the total process heat demand across industrial sites in New Zealand. Advanced energy technologies, such as heat pumps and electrode boilers, have significantly enhanced energy efficiency. These technologies operate with much higher efficiency, requiring lower input power to deliver the same amount of process heating compared to conventional systems. **Table 3** illustrates the end-user demand fulfilled by each heating technologies. The transition has contributed to a 41.3% reduction in total end-use heating demand, from 25.9 TWh/year to 18.8 TWh/year.

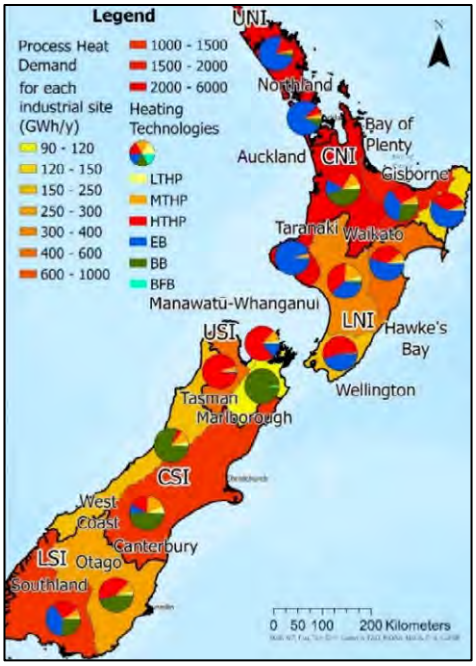



**Figure 2.** Process heat demand and its respective heating technologies across New Zealand.

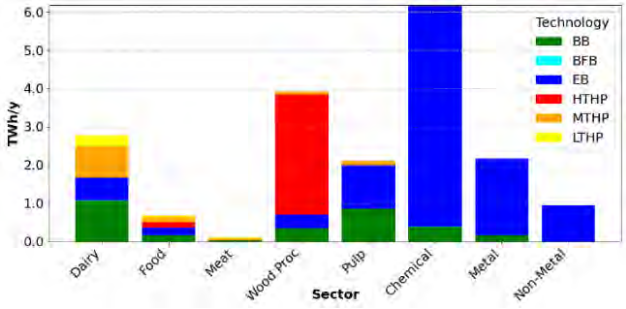



**Figure 3.** The amount of energy required from heating technologies across industrial sections in New Zealand.

As the model incorporates a new green methanol industry to showcase the potential for sustainable industrial practices in New Zealand, the economic feasibility of this production is influenced by the total capital and fixed operating cost of 180 NZD/tonne whereas the variable operating cost such as electricity and biomass are based on their respective distances and locations [17]. According to the modelling simulation, green methanol becomes profitable when the selling price exceeds NZD 1050/ton. **Table 4** outlines the potential off-grid production of green methanol and its respective power generation

type. To produce one tonne of green methanol, the process requires 3.44 MWh of electricity for electrolysis and 4.38 MWh of biomass as carbon and hydrogen sources.

Given the promising path of power-to-fuel technologies, it is vital to access other green hydrogen-based chemical compounds, such as ammonia, urea and sustainable aviation fuel, to meet New Zealand goals to achieve net-zero carbon emissions by 2050.

## CONCLUSIONS

The nationwide modelling approach offers an outlook on decarbonising industrial process heat demand with a good firming capacity from biomass and electricity supply. The results indicate a reduction in industrial energy supply from 25.9 TWh/year to 18.8 TWh/year within national resource constraints. Additionally, a green methanol economy is feasible in specific regions of New Zealand where surplus electricity and biomass resources are available, provided the selling price exceeds NZD1050/tonne. The utilisation of the open-source P-graph framework enables users to conduct custom analysis on site specific modelling studies by modifying and customising key parameters.

## ACKNOWLEDGEMENTS

This research has been supported by the program "Ahuora: Delivering sustainable industry through smart process heat decarbonisation", an Advanced Energy Technology Platform, funded by the Aotearoa New Zealand Ministry of Business, Innovation and Employment.

## REFERENCES

1. Climate Change Commission. https://www.climatecommission.govt.nz/public/Inaia-tonu-nei-a-low-emissions-future-for-Aotearoa/Inaia-tonu-nei-a-low-emissions-future-for-Aotearoa.pdf
2. MBIE. https://www.mbie.govt.nz/assets/energy-in-new-zealand-2023.pdf
3. EECA. https://www.eeca.govt.nz/
4. P. Hall. Wood Energy Industrial Symbiosis. (2021)
5. S. Pfenninger, A. Hawkes, and J. Keirstead. Energy systems modeling for twenty-first century energy challenges *Renew. Sustain. Energy Rev.*, 33:74–86, (2014) https://doi.org/10.1016/j.rser.2014.02.003
6. F. A. Plazas-Niño, N. R. Ortiz-Pimiento, and E. G. Montes-Páez. National energy system optimization modelling for decarbonization pathways analysis: A systematic literature review. *Renew. Sustain. Energy Rev.*, 162:112406, (2022) https://doi.org/10.1016/j.rser.2022.112406
7. N. Chagnon-Lessard and L. Gosselin. Heat cascade and heuristics to optimize ORC and identify the best internal configuration. *Appl. Therm. Eng.*, 233:121071, (2023) https://doi.org/10.1016/j.applthermaleng.2023.121071
8. A. Bartos and B. Bertok. Parameter tuning for a cooperative parallel implementation of process-network synthesis algorithms. *Cent. Eur. J. Oper. Res.,* 27:551–572, https://doi.org/10.1007/s10100-018-0576-1 (2019)
9. K. B. Aviso, J.-Y. Lee, J. C. Dulatre, V. R. Madria, J. Okusa, and R. R. Tan. A P-graph model for multi-period optimization of sustainable energy systems. *J. Clean. Prod.*, 161:1338–1351, (2017) https://doi.org/10.1016/j.jclepro.2017.06.044
10. Y. Xu *et al.* Optimal renewable energy export strategies of islands: Hydrogen or electricity? *Energy*, 269:126750, (2023), https://doi.org/10.1016/j.energy.2023.126750
11. S. Y. Teng, Á. Orosz, B. S. How, J. Pimentel, F. Friedler, and J. J. Jansen. Framework to embed machine learning algorithms in P-graph: Communication from the chemical process perspectives. *Chem. Eng. Res. Des.*, 188:265–270 (2022), https://doi.org/10.1016/j.cherd.2022.09.043
12. B. Resch *et al.* GIS-Based Planning and Modeling for Renewable Energy: Challenges and Future Research Avenues. *ISPRS Int. J. Geo-Inf.*, 3:662–692 (2014) https://doi.org/10.3390/ijgi3020662
13. M. Biberacher. GIS-based modeling approach for energy systems. *Int. J. Energy Sect. Manag.*, 2:3,368–384 (2008) https://doi.org/10.1108/17506220810892937
14. S. Toms. ArcPy and ArcGIS – Geospatial Analysis with Python. Packt Pub Ltd (2015)
15. M. Wang *et al.*, Unlock city-scale energy saving and peak load shaving potential of green roofs by GIS-informed urban building energy modelling. *Appl. Energy*, 366:123315, (2024) https://doi.org/10.1016/j.apenergy.2024.123315
16. A. M. Moore, Meeting Off-Grid Transportation Energy Needs: A Resource Evaluation Model for a Solar Vortex Power Generation System. Georgia Institute of Technology (2016)
17. S. Pratschner, F. Radosits, A. Ajanovic, and F. Winter. Techno-economic assessment of a power-to-green methanol plant. *J. CO2 Util.*, 75:102563 (2023) https://doi.org/10.1016/j.jcou.2023.102563

© 2025 by the authors. Licensed to PSEcommunity.org and PSE Press. This is an open access article under the creative commons CC-BY-SA licensing terms. Credit must be given to creator and adaptations must be shared under the same terms. See https://creativecommons.org/licenses/by-sa/4.0/



Systems & Control Transactions

**Research Article - Peer Reviewed Conference Proceeding**
ESCAPE 35 - European Symposium on Computer Aided Process Engineering
Ghent, Belgium. 6-9 July 2025
Jan F.M. Van Impe, Grégoire Léonard, Satyajeet S. Bhonsale,
Monika E. Polańska, Filip Logist (Eds.)

PSE PRESS

# Non-Linear Model Predictive Control for Oil Production in Wells Using Electric Submersible Pumps

**Carine Menezes Rebello[a,*], Erbet Almeida Costa[a], Marcos Pellegrini Ribeiro[b], Marcio Fontana[c], Leizer Schnitman[d], Idelfonso Bessa dos Reis Nogueira[a]**

[a] Department of Chemical Engineering, Norwegian University of Science and Technology, Gløshaugen, Trondheim, 7034, Norway
[b] CENPES, Petrobras R&D Center, Av. Horacio ´ Macedo 950, Cid. Universitaria, ´ Ilha do Fundao, ˜ Rio de Janeiro, RJ, Brazil
[c] Department of Electrical and Computer Engineering, Federal University of Bahia, Polytechnic School, R. Prof. Aristídes Novis, 2 - Federação, Salvador, 40210-630, Brazil
[d] Department of Chemical Engineering, Federal University of Bahia, Polytechnic School, R. Prof. Aristídes Novis, 2 - Federação, Salvador, 40210-630, Brazil
* Corresponding Author: carine.m.rebello@ntnu.no

## ABSTRACT

The oil production in wells using electric submersible pumps (ESPs) demands precise control of parameters within safety and efficiency constraints to minimise failures, extend equipment lifespan, and reduce costs. This study proposes a non-linear model predictive control (NMPC) system designed for ESP-lifted wells, leveraging pump frequency and choke valve adjustments to maximise production while adhering to operational limits. Tested on a simulated pilot plant using a first-principles model to predict key variables like flow and liquid column height, the NMPC demonstrated offset-free performance, effective disturbance rejection, and ensured stable, safe, and optimised operations, addressing challenges in nonlinear, constraint-intensive environments.

**Keywords:** Nonlinear Predictive Control, ESP, Oil Wells, Operating envelope

## INTRODUCTION

Oil production using electric submersible pumps (ESPs) is common in artificial lift systems due to their versatility, high flow capacity, and efficiency under demanding conditions [1,2,3]. ESPs adapt to vertical, deviated, and horizontal wells and handle diverse fluid compositions like high water-cut, viscous, or low-gravity crude oil [4,5]. Their compact design suits space-limited wells, while advances in materials and sealing technology improve reliability in high-temperature and high-pressure environments [6].

On the other hand, stable and safe operation is important, as it minimises equipment failures, prolongs the lifespan of components, and significantly reduces costs associated with repairs, maintenance, and production downtime [7]. Additionally, ensuring operational stability helps mitigate revenue losses caused by unexpected equipment failures or suboptimal production processes [8].

In this sense, the effectiveness of these systems depends heavily on the precise control of operational parameters while strictly adhering to safety and efficiency constraints. Indeed, advanced process control has emerged as a tool for reducing constraint violations and optimising production [9,10,11]. By maintaining operations within a well-defined operational envelope, control strategies help avoid common issues such as excessive vibrations, which can lead to premature wear and tear of the pump.

The growing demand for advanced control techniques for nonlinear systems, such as oil wells assisted by ESPs, has driven extensive research into applying nonlinear model predictive control (NMPC) strategies.

While PI/PID controllers are common in industrial applications, they face limitations in managing multivariable systems with strong interactions and operational constraints. NMPC offers a key advantage by predicting future behaviour, coordinating multiple variables, and incorporating constraints directly into the control strategy. Studies such as Sharma & Glemmestad (2013) [12] and Mejía et al. (2018) [13] demonstrate that NMPC outperforms PI/PID in ESP systems, particularly in disturbance rejection and constraint handling

Recently, Mirzaie Harsini et al. (2022) [14] introduced an NMPC designed explicitly for oil wells with ESPs, emphasising its effectiveness in tracking setpoints and managing the complex dynamic interactions between the pump and the reservoir while adhering to the system's operational constraints. This work highlights the importance of robust modelling for optimisation and efficient control.

In earlier studies, Sharma and Glemmestad (2013) [15] explored the optimisation and control of ESP-lifted systems using nonlinear techniques to maximise production and ensure operational stability. Subsequently, the authors expanded this work (Sharma and Glemmestad, 2014 [16]) by applying NMPC to the optimal operation of oil fields with ESPs, demonstrating significant improvements in system performance through detailed simulations.

Mejía et al. (2018) [17] advanced the development of control strategies for ESP-assisted wells by implementing model-based NMPC techniques. Their work underscored the NMPC's ability to handle the complex dynamics of wells and meet the operational demands under strict safety and efficiency constraints.

More recently, Santana et al. (2023) [18] investigated embedded MPC strategies for ESP-lifted wells, evaluating the performance of nonlinear techniques through hardware-in-the-loop (HIL) analyses. This study provided valuable insights into the practical implementation of NMPC strategies, highlighting their feasibility in industrial systems.

This work aims to develop an NMPC system specifically designed for a well-equipped ESP. This NMPC framework integrates the pump's operational constraints while efficiently leveraging the available degrees of freedom to optimise performance. Its primary goal is to maximise oil production while ensuring strict compliance with physical and safety-related system constraints. Compared to traditional PID-based control methods, this approach offers a more advanced and structured solution, making it particularly effective in managing the nonlinear dynamics and constraint-intensive nature of oil well operations.

# METHODOLOGY

## ESP pilot plant

This study involves a pilot plant located at the Industrial Automation Technological Training Center (CTAI) at the Federal University of Bahia (UFBA). The system features a vertical oil well with a 32-meter column and a multistage electric submersible pump (ESP) at 22.8 meters. The pump, a 15-stage model driven by an 18-horsepower motor, circulates mineral-based lubricating oil (API gravity 10) through a closed-loop system with a storage tank (T-101).

The setup includes sensors for pressure, flow rate, motor speed, and auxiliary components such as compressors and chokes.

Figure 1 illustrates the pilot plant's instrumentation and layout, providing an overview of the key components and their arrangement.

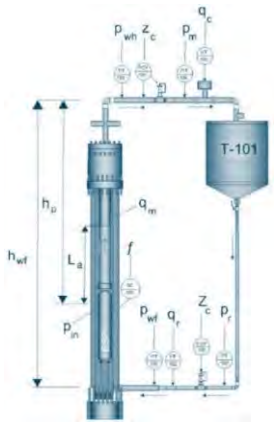



**Figure 1.** Schematic representation of the ESP pilot plant with key variables and components.

In Figure 1, the system inputs are the ESP motor frequency ($f$) and choke valve opening ($Z_c$), with the liquid level in the well ring ($L_a$) as the pump intake reference. Key pressures include reservoir ($p_r$), bottom-hole ($p_{bh}$), intake ($p_{in}$), choke ($p_c$), and manifold ($p_m$). Distances are measured from the choke valve reference ($h_c = 0\,;\, m$), with $h_p$ as the distance to the pump inlet and $h_{bh}$ to the well bottom. Flow rates include reservoir inflow ($q_r$), average well flow ($q_m$), and production flow ($q_c$).

## ESP model

The experimental pilot plant is represented by a virtual plant (Table 1) based on the validated model proposed by Costa et al. (2021) [19].

The phenomenological model of the ESP system is based on the principles of mass and momentum conservation, assuming an isothermal system with incompressible and monophasic fluid, and constant physical and thermal properties. The key variables describing the system include the ESP intake pressure $(p_{in})$, choke pressure $(p_c)$, and the average flow rate in the column $(q_m)$.

Table 2 summarises the parameters employed in the model, encompassing geometric configurations, fluid attributes, and key pump specifications.

**Table 1:** Mathematical representation of ESP system dynamics and flow characteristics.

| Description | Equation |
|---|---|
| Dynamics of intake pressure ($\boldsymbol{p_{in}}$) | $\frac{dp_{in}}{dt} = \left(\frac{g}{A}\right)(q_r - q_m)$ |
| Dynamics of choke pressure ($\boldsymbol{p_c}$) | $\frac{dp_c}{dt} = \left(\frac{1}{V}\right)(q_m - q_c)$ |
| Momentum balance for flow ($\boldsymbol{q_m}$) | $\frac{dq_m}{dt} = \left(\frac{1}{l}\right)(p_{wf} - p_c - \Delta P_p - \Delta P_h - \Delta P_f)$ |
| Hydrostatic pressure loss ($\boldsymbol{\Delta P_h}$) | $\Delta P_h = \Delta P_{h1} + \Delta P_{h2}$, $\Delta P_{h1} = \rho g\,(h_{wf} - h_p)$, $\Delta P_{h2} = \rho g(h_p - h_c)$ |
| Average pressure ($\boldsymbol{\rho_{bar}}$) | $\rho_{bar} = \frac{(\rho_1 V_1 + \rho_2 V_2)}{(V_1 + V_2)}$ |
| Pressure increment by ESP ($\boldsymbol{\Delta P_p}$) | $\Delta P_p = H(f, q_b)\, g, H(f, q_b) = H_0(q_b, f_0)\,(f/f_0)\text{^}2$ |
| Pump polynomial for freshwater ($\boldsymbol{H_0}$) | $H_0 = x_2\, q_m^2 + x_1\, q_m + x_0$ |
| Frictional pressure loss ($\boldsymbol{\Delta P_f}$) | $\Delta P_f = F_1 + F_2$, $F_i = f_i\left(\rho\, L_i\, \frac{D_i}{4}\right)\left(\frac{q_i}{A_i}\right)^2$ |
| Average system length ($\boldsymbol{l_{bar}}$) | $l_{bar} = \frac{(l_1 + l_2)}{2}$ |
| Flow rates through valves ($\boldsymbol{q_r, q_c}$) | $q_r = K_r\, Z_r \sqrt{(p_r - p_{wf})}$, $q_c = K_c\, Z_c \sqrt{(p_c - p_{wf})}$ |

**Table 2:** Parameters and physical properties of the ESP pilot plant system.

| Parameter | Value |
|---|---|
| Gravity constant, g (m/s²) | 9.81 |
| Fluid density, ρ (kg/m³) | 855 |
| Fluid viscosity, μ (Pa·s) | 0.00889 |
| Bulk modulus, $\beta_e$ (Pa) | $1.8\times10^9$ |
| Cross-section area of the annulus, A (m²) | 0.033059 |
| Average cross-section area, Â (m²) | 0.0108 |
| Pipe radius below ESP, $r_1$ (m) | 0.110 |
| Pipe radius above ESP, $r_2$ (m) | 0.0375 |
| Length from the pump intake to choke, $l_2$ (m) | 22.7 |
| Length from the reservoir to choke, $l_1$ (m) | 9.3 |
| Average length, l (m) | 16 |
| Pipe volume below ESP, $V_1$ (m³) | 0.3286 |
| Pipe volume above ESP, $V_2$ (m³) | 0.103 |
| Head's polynomial coefficient, $x_2$ (s²/m³) | -75.397 |
| Head's polynomial coefficient, $x_1$ (s/m³) | 7.8962 |
| Head's polynomial coefficient, $x_0$ (m) | 180.7986 |
| Reservoir valve constant, $K_a$ (m³/s·Pa) | 0.7221 |
| Choke valve constant, $K_e$ (m³/s·Pa$^{0.5}$) | 0.2283 |
| Minimum flow rate, $q_{min}$ (m³/s) | $1\times10^{-3}$ |
| Maximum flow rate, $q_{max}$ (m³/s) | 0.1 |
| ESP characteristic ref freq, $f_0$ (Hz) | 60 |
| Height from the pump intake to choke, $h_p$ (m) | 22.7 |
| Height from the reservoir to choke, $h_{\beta h}$ (m) | 32 |

## Nonlinear MPC

The NMPC is formulated to optimise the system performance by minimising a cost function $J_k$, which consists of three terms: the tracking error term, the error correction term, and the movement suppression term. This approach ensures that the controlled system achieves its desired objectives while maintaining adherence to operational and safety constraints. The cost function is expressed as:

$$J_k = \sum_{j=1}^{H_p} \left\| y_{k+j|k} - y_{sp} + e_{k|k} \right\|_Q^2 + \sum_{j=0}^{H_c-1} \left\| \Delta \mathrm{u}_{\mathrm{k+j|k}} \right\|_R^2 \quad (1)$$

subject to:

$$-\Delta u_{max} \le \Delta \mathrm{u}_{\mathrm{k+j|k}} \le \Delta u_{max}$$

$$u_{min} \le \mathrm{u}_{\mathrm{k+j|k}} \le u_{max}$$

$$j = 0, \ldots, m-1, \Delta u_{k+j|k} = 0, \forall j \ge m$$

$$y_{min} \le y_{k+j|k} \le y_{max}$$

$$\Delta \mathrm{u}_{\mathrm{k+j|k}} = \mathrm{u}_{\mathrm{k+j|k}} - \mathrm{u}_{\mathrm{k+j-1|k}}$$

where $H_p$ is the prediction horizon, $H_c$ is the control horizon, and $Q$ and $R$ are tuning parameters that adjust the weights of the respective terms.

The first term, the tracking error term, represents the deviation between the predicted outputs $y_{k+j|k}$ and the reference setpoints $y_{sp}$, ensuring that the system tracks the desired trajectory effectively over the prediction horizon. The second term, the error correction term, accounts for the initial deviation $e_{k|k}$ at the start of the horizon, enhancing the system's ability to address pre-existing errors. The third term, the movement suppression term, penalises excessive changes in the manipulated variables $\Delta \mathrm{u}_{\mathrm{k+j|k}}$, promoting smoother control actions that minimise wear and energy consumption.

To maintain operational feasibility, the NMPC framework incorporates constraints such as limits on the rate of change of the manipulated variables ($-\Delta u_{max} \le \Delta \mathrm{u}_{\mathrm{k+j|k}} \le \Delta u_{max}$) control input bounds ($u_{min} \le \mathrm{u}_{\mathrm{k+j|k}} \le u_{max}$), and output constraints ($y_{min} \le y_{k+j|k} \le y_{max}$). Additionally, adjustments to the control inputs are limited to the control horizon , ($\Delta u_{k+j|k} = 0, \forall j \ge m$ ).

In this formulation, the controlled variables are the liquid column height (head) and the production flow, while the manipulated variables are the ESP motor frequency and the choke valve opening. The NMPC balances accurate tracking, operational stability, and smooth control actions, providing an advanced solution for managing nonlinear systems with dynamic and constraint-intensive behaviour.

The NMPC's nonlinear optimization problem was solved using FMINCON, MATLAB's optimization toolbox, providing a reliable benchmark for simulations.

## RESULTS

The NMPC performance was evaluated in two distinct scenarios: a servo case focused on setpoint tracking and a regulatory case involving two situations with unmeasured disturbances, one with noise and the other without noise, as is shown in Figure 2 and 3. The results highlight the controller's ability to manage monitoring and regulatory tasks while respecting operational constraints effectively. The NMPC was configured with a prediction horizon of 10 and a control horizon of 6. The tuning parameters were set as Q = [1000, 100] and R = [1, 1], ensuring a balance between accurate tracking and smooth control actions.

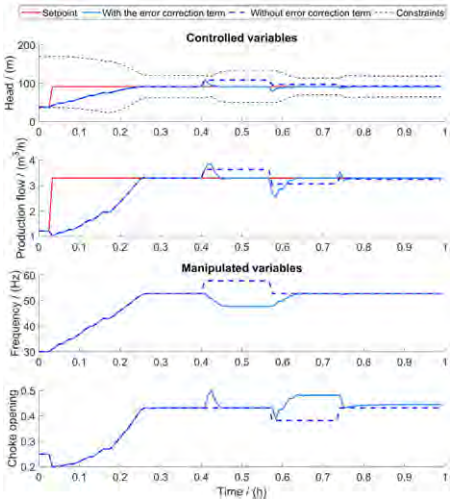



**Figure 2.** NMPC performance in servo and regulatory scenarios with noise disturbance.

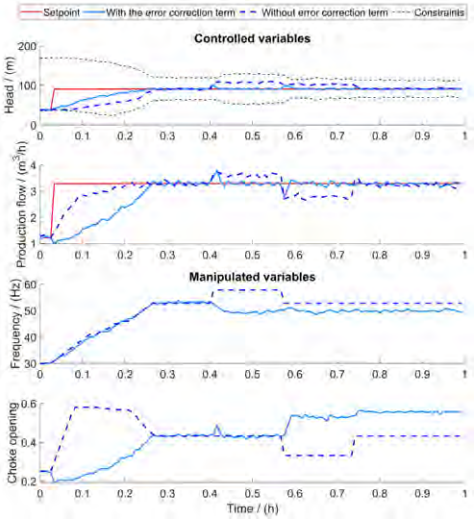



**Figure 3.** NMPC performance in servo and regulatory scenarios without noise disturbance.

In the servo case, the NMPC precisely tracked the reference setpoints for the controlled variables, namely head and production flow. The inclusion of the error correction significantly improved the tracking performance, resulting in smoother transitions and reduced oscillations, particularly in the production flow. The manipulated variables, represented by the ESP motor frequency and choke opening, gradually adjusted to achieve the desired setpoints without causing abrupt changes. This smooth behaviour underscores the controller's ability to optimise performance while avoiding unnecessary stress on the system.

The regulatory case demonstrated the NMPC in rejecting unmeasured disturbances. Without noise, the controller effectively maintained the controlled variables within their constraints and close to their setpoints. The manipulated variables responded predictably, adapting smoothly to compensate for disturbances. When noise was introduced, the NMPC continued to perform well, with only minor fluctuations observed in the controlled variables due to the noise. The error correction term's presence further mitigated the noise's impact, ensuring stable operation and minimising deviations from the setpoints. The manipulated variables remained within acceptable operational ranges, highlighting the controller's ability to handle noisy environments.

Comparing the scenarios with and without the error correction term revealed its significant impact on system performance. The error correction term reduced tracking errors during setpoint transitions and enhanced disturbance rejection capabilities. It also contributed to smoother adjustments of the manipulated variables, promoting stable and efficient operation. Across all scenarios, the NMPC maintained the controlled variables within predefined constraints, demonstrating its ability to manage nonlinear dynamics and constraint-intensive processes effectively.

Figure 4 illustrates the convergence of the objective function during the optimisation process in the regulatory and servo scenarios without noise. The curve shows a sharp initial decrease, indicating rapid minimisation of the objective function in the early iterations. This behaviour reflects the NMPC's ability to quickly adjust the manipulated variables to align the controlled variables with the desired setpoints. After approximately 20 iterations, the objective function stabilises, demonstrating the controller's efficiency in achieving a steady-state solution with minimal computational effort without noise.

Figure 5 depicts the convergence of the objective function in the presence of noise for both regulatory and servo scenarios. Similar to the noise-free case, the objective function exhibits a rapid initial decrease, signifying effective adjustments by the NMPC. However, the curve is less smooth compared to the noise-free case, with slight fluctuations observed during the optimisation process. These fluctuations are attributable to the noise disturbance, which introduces variability in the system's

responses. Despite this, the objective function stabilises after approximately 25 iterations, highlighting the effectiveness of the NMPC in handling noisy environments and maintaining convergence toward an optimal solution.

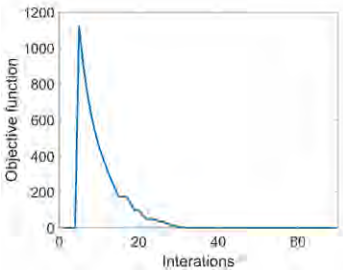



**Figure 4.** Convergence of the objective function in the regulatory and servo scenarios without noise disturbance.

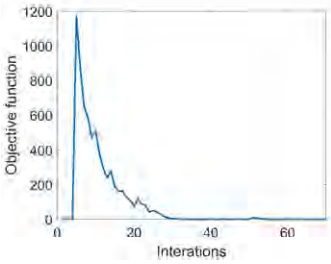



**Figure 5.** Convergence of the objective function in the regulatory and servo scenarios with noise disturbance.

The results validate the NMPC's effectiveness in both servo and regulatory cases. The controller achieved accurate setpoint tracking, disturbance rejection, and stable operation, even under the influence of noise.

To assess the NMPC's robustness, a new simulation was conducted with plant-model mismatch and measurement noise. A 5% uncertainty in the pump's maximum head simulated performance variations, while stochastic noise modelled sensor inaccuracies. Figure 6 shows that the NMPC adapts well, maintaining constraints and stability. The error correction term improves setpoint tracking by mitigating steady-state offsets. Despite minor fluctuations in the manipulated variables due to noise, the controller ensures smooth adjustments, demonstrating its feasibility for real-world ESP applications. Figure 7 presents the convergence of the objective function under noise disturbances in regulatory and servo scenarios.

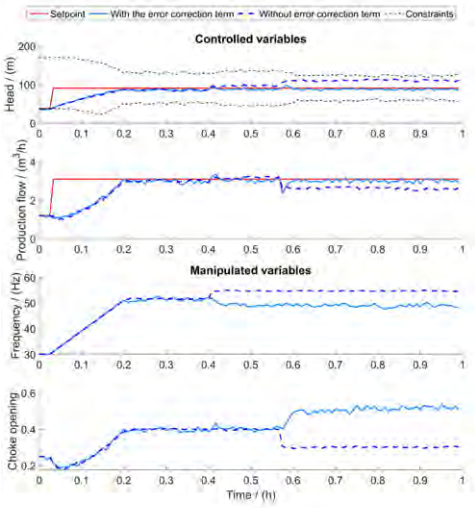



**Figure 6.** NMPC performance under plant-model mismatch and measurement noise: comparison with and without the error correction term.

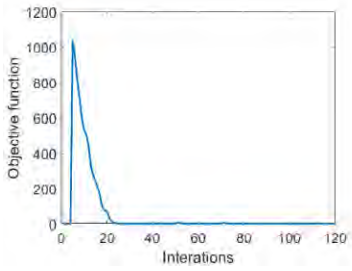



**Figure 7.** Convergence of the objective function in the regulatory and servo scenarios with plant-model mismatch and measurement noise.

## CONCLUSIONS

The results demonstrate that the NMPC effectively handles ESP-lifted oil wells' nonlinear dynamics and constraints, ensuring stable operation and improved setpoint tracking. The controller adapts well to plant-model mismatch and noise, highlighting its capability for real-world applications. In future work, the NMPC will be implemented in the pilot plant to validate its experimental performance and compare it with conventional PI/PID controllers under real operating conditions.

## ACKNOWLEDGEMENTS

This work was carried out as a part of SUBPRO, a Research-based Innovation Centre within Subsea Production and Processing. The authors gratefully acknowledge the project support from SUBPRO (grant number 237893), which is financed by the Research Council of Norway, major industry partners and NTNU.

## REFERENCES

1. FAKHER, Sherif; KHLAIFAT, Abdelaziz; NAMEER, Hashim. Improving electric submersible pumps efficiency and mean time between failure using permanent magnet motor. Upstream Oil and Gas Technology, v. 9, p. 100074, 2022.
2. ZHU, Jianjun; ZHANG, Hong-Quan. CFD simulation of ESP performance and bubble size estimation under gassy conditions. In: SPE Annual Technical Conference and Exhibition?. SPE, 2014. p. SPE-170727-MS.
3. ZHU, Jianjun et al. A numerical study on flow patterns inside an electrical submersible pump (ESP) and comparison with visualization experiments. Journal of Petroleum Science and Engineering, v. 173, p. 339-350, 2019.
4. KOLAWOLE, Oladoyin; GAMADI, Talal; BULLARD, Denny. Comprehensive review of artificial lift system applications in tight formations. In: SPE Eastern Regional Meeting. SPE, 2019. p. D021S002R008.
5. CARPENTER, D. E.; MCCREA, A. A. Beta field history: submersible pumps in heavy crude. In: SPE Oklahoma City Oil and Gas Symposium/Production and Operations Symposium. SPE, 1995. p. SPE-29508-MS.
6. SHARMA, R. & GLEMMESTAD, B. Optimal control strategies with nonlinear optimization for an Electric Submersible Pump lifted oil field. Modeling, Identification and Control 2013;34(2):55-67 http://dx.doi.org/10.4173/mic.2013.2.2.
7. AL-BALLAM, Shaikha; KARAMI, Hamidreza; DEVEGOWDA, Deepak. A Data-Based Reliability Analysis of ESP Failures in Oil Production Wells. Journal of Energy and Power Technology, v. 4, n. 4, p. 1-29, 2022.
8. CARIDAD, Jose; SHANG, Song. Advancing High-Temperature ESP Technology for SAGD Applications. In: SPE Gulf Coast Section Electric Submersible Pumps Symposium?. SPE, 2019. p. D031S006R001. https://doi.org/10.2118/194387-MS
9. YUSUPBEKOV, Nodirbek et al. Application of advanced process control technologies for optimization of polymers production processes. In: International Conference on Theory and Application of Soft Computing, Computing with Words and Perceptions. Cham: Springer International Publishing, 2019. p. 345-351.
10. NOGUEIRA, Idelfonso BR et al. Dynamics of a true moving bed separation process: Linear model identification and advanced process control. Journal of Chromatography A, v. 1504, p. 112-123, 2017.
11. NOGUEIRA, Idelfonso BR et al. A robustly model predictive control strategy applied in the control of a simulated industrial polyethylene polymerization process. Computers & Chemical Engineering, v. 133, p. 106664, 2020.
12. SHARMA, Roshan; GLEMMESTAD, Bjørn. Nonlinear optimization and control of an electric submersible pump lifted oil field. In: 2013 5th International Conference on Modelling, Identification and Control (ICMIC). IEEE, 2013. p. 26-31. DOI: 10.2316/P.2014.809-042.
13. MEJÍA, Jorge Andrés Prada; SILVA, Luis Angel; FLÓREZ, Julián Andrés Peña. Control strategy for oil production wells with electrical submersible pumping based on the nonlinear model-based predictive control technique. In: 2018 IEEE ANDESCON. IEEE, 2018. p. 1-6.
14. MIRZAIE HARSINI, Farid Aldin; NAZARISARAM, Mahdi; HOSSEINIAN, Armin Hosseinian. Nonlinear model predictive controller for electrical submersible pump lifted wells. Journal of Petroleum Research, v. 32, n. 1401-4, p. 145-161, 2022. 10.22078/pr.2022.4734.3124
15. SHARMA, Roshan; GLEMMESTAD, Bjørn. Nonlinear optimization and control of an electric submersible pump lifted oil field. In: 2013 5th International Conference on Modelling, Identification and Control (ICMIC). IEEE, 2013. p. 26-31. 10.2316/P.2014.809-042
16. SHARMA, Roshan; GLEMMESTAD, Bjørn. Nonlinear model predictive control for optimal operation of electric submersible pump lifted oil field. In: Proceedings of the IASTED International Conference on Modelling, Identification and Control. 2014. p. 229-236.
17. MEJÍA, Jorge Andrés Prada; SILVA, Luis Angel; FLÓREZ, Julián Andrés Peña. Control strategy for oil production wells with electrical submersible pumping based on the nonlinear model-based predictive control technique. In: 2018 IEEE ANDESCON. IEEE, 2018. p. 1-6.
18. SANTANA, Bruno A. et al. Embedded MPC Strategies for ESP-Lifted Oil Wells: Hardware-in-the-Loop Performance Analysis of Nonlinear and Robust Techniques. Processes, v. 11, n. 5, p. 1354, 2023.
19. COSTA, E. A. et al. A Bayesian approach to the dynamic modeling of ESP-lifted oil well systems: An experimental validation on an ESP prototype. Journal of Petroleum Science and Engineering, v. 205, p. 108880, 2021.

© 2025 by the authors. Licensed to PSEcommunity.org and PSE Press. This is an open access article under the creative commons CC-BY-SA licensing terms. Credit must be given to creator and adaptations must be shared under the same terms. See https://creativecommons.org/licenses/by-sa/4.0/



Systems & Control Transactions

**Research Article - Peer Reviewed Conference Proceeding**
ESCAPE 35 - European Symposium on Computer Aided Process Engineering
Ghent, Belgium. 6-9 July 2025
Jan F.M. Van Impe, Grégoire Léonard, Satyajeet S. Bhonsale,
Monika E. Polańska, Filip Logist (Eds.)

PSE PRESS

# MORL4PC: Multi-Objective Reinforcement Learning for Process Control

**Niki Kotecha[a], Max Bloor[a], Calvin Tsay[b], and Antonio del Rio Chanona[a]***

[a] Department of Chemical Engineering, Sargent Centre for Process Systems Engineering, Imperial College London, SW7 2AZ, United Kingdom
[b] Department of Computing, Imperial College London, SW7 2AZ, United Kingdom
* Corresponding Author: a.del-rio-chanona@imperial.ac.uk.

## ABSTRACT

In chemical process control, decision-making often involves balancing multiple conflicting objectives, such as maximizing production, minimizing energy consumption, and ensuring process safety. Traditional approaches for multi-objective optimization, such as linear programming and evolutionary algorithms, have proven effective but struggle to adapt in real-time to the dynamic and nonlinear nature of chemical processes. In this paper, we propose a framework that combines Reinforcement Learning (RL) with Multi-Objective Evolutionary Algorithms (MOEAs) to address these challenges. Specifically, we utilize MOEAs, such as NSGA-II, to optimize the parameter space of policy neural networks, resulting in a Pareto front of policies. This Pareto front provides a diverse set of policies that enable operators to dynamically switch control strategies based on real-time system conditions and prioritized objectives. Our proposed methodology is applied to a Controlled Stirred Tank Reactor (CSTR) case study, focusing on balancing the objectives of minimizing set point error and operational costs. The case studies highlight the adaptability of the method in dynamic environments, including scenarios involving fouling, showcasing its resilience and flexibility in complex, nonlinear systems. This work demonstrates the potential of combining RL and MOEAs to advance decision-making in chemical process control, providing a robust and adaptable framework for navigating environments with changing objectives. The methodology can also be extended to other industrial applications with similarly challenging multi-objective requirements.

**Keywords**: Process Control, Machine Learning, Industry 4.0, Reinforcement Learning

## INTRODUCTION

In recent years, the field of Process Systems Engineering (PSE) has experienced a significant shift towards advanced optimization techniques that can handle the inherent complexities of modern systems, whether in process control, sustainable supply chains, or other industrial operations. A key challenge in these systems is optimizing multiple, often conflicting objectives —such as minimizing operational costs, ensuring process safety, improving product quality, and reducing environmental impact. This challenge has been amplified by a growing emphasis on sustainability and efficiency in industrial operations which highlights the need to develop decision-making frameworks that can handle dynamic environments with shifting priorities.

In industrial process control, balancing multiple objectives, such as optimizing productivity, reducing energy consumption, minimizing environmental impact, whilst maintaining safety is crucial. However, traditional control methods struggle to handle these competing goals, especially when unexpected disruptions occur, leading to emergency shutdowns and costly downtime.

Traditionally, industrial control problems have been addressed using model-based techniques, such as proportional-integral-derivative (PID) controllers, model predictive control (MPC), and multi-objective optimization (MOO) methods. These methods rely on mathematical models of system dynamics and predefined performance criteria to achieve optimal control. While effective in many industrial settings, they often struggle to manage the complexities of nonlinear, high-dimensional, and

dynamically changing environments.

For instance, PID controllers are limited in their ability to handle multi-variable interactions and time-varying dynamics. MPC, although more robust, can become computationally expensive and less effective when confronted with nonlinear stochastic systems or unexpected disturbances. Similarly, traditional MOO techniques rely on explicit trade-offs between objectives and are often static. These approaches can be inflexible, failing to adapt to evolving priorities in real-world decision-making where conflicting or shifting objectives are common.

Reinforcement Learning (RL) has emerged as a promising alternative to overcome these limitations. As a data-driven, model-free approach, RL enables agents to learn optimal control policies by interacting with the environment, making it well-suited for dynamic and nonlinear stochastic systems [1]. By framing control tasks as sequential decision-making problems, RL offers a natural framework for optimizing processes over time. This adaptability makes it particularly effective for applications such as chemical reactors, power grids, and supply chains, where system behavior can be complex and difficult to model explicitly.

Despite its advantages, standard RL algorithms are typically designed to optimize a single objective, which limits their effectiveness in scenarios requiring trade-offs among multiple competing goals. This limitation has driven the development of multi-objective reinforcement learning (MORL), an extension of RL tailored to handle multiple objectives simultaneously.

MORL methods can be broadly categorized into scalarization-based, Pareto-based, and decomposition-based approaches. Scalarization converts multiple objectives into a single reward function, often requiring prior knowledge of preference weights [2]. Pareto-based methods, such as Pareto Q-learning [3], maintain a set of non-dominated solutions, by learning a set of Pareto-optimal policies, enabling agents to explore multiple trade-offs without explicit weighting. Decomposition-based approaches, including MORL/D [4], break multi-objective problems into smaller subproblems and leverage reinforcement learning to solve them iteratively. Recent advances, such as deep reinforcement learning for multi-objective optimization (DRL-MOA) have further improved the scalability and generalization of MORL methods.

Multi-Objective Evolutionary Algorithms (MOEAs), for instance, offer a robust way to search across a broad solution space without requiring differentiable objective functions. Their ability to maintain a population of solutions, each addressing different trade-offs between objectives, makes them a natural fit for tackling multi-objective problems in dynamic environments. In this paper, we combine the adaptive decision-making capabilities of RL with MOEAs' ability to balance diversity and proximity to the Pareto front. Specifically, we use MOEAs to search the parameter space of neural network policies, resulting in a Pareto front of policies. This equips the decision-maker with a swarm of policies, allowing for dynamic switching between policies based on the current system objectives and dynamics. This strategy ensures flexibility in real-time decision-making under uncertainty, allowing the system to adapt quickly to changing conditions without the need to evolve policies continuously.

The rest of the paper is organized as follows: the preliminaries section provides the background on reinforcement learning and evolutionary strategies, the methodology section describes the proposed multi-objective evolutionary algorithm-based reinforcement learning framework in more detail. The case study section discusses the simulation and experimental results and finally, we summarize the paper and provide an outlook for future work.

## PRELIMINARIES

### Introduction to Reinforcement Learning

In single agent reinforcement learning, the agent aims to learn an optimal policy by interacting with the environment and learning through trial-and-error. In RL, the agent observes the current state $x_t \in X \subseteq \mathbb{R}^{n_x}$, chooses an action $u \in U \subseteq \mathbb{R}^{n_u}$ with probability given by the policy $\pi(u|x)$ and transitions into the next state, $x_{t+1} \in X \subseteq R^{n_x}$ with probability given by the state transition probability function $P(x_{t+1}|x_t,u_t)$ and receives a reward $r_{t+1} = \mathcal{R}(x_t,u_t,x_{t+1}) \in \mathbb{R}$. The agent finds an optimal policy $\pi^*$ by maximizing the expected sum of rewards over a time horizon defined as:

$$J(\pi) = \mathbb{E}_{(x_t,u_t)\sim\pi}\left[\sum_{t=0}^{T-1}\gamma^t r_{t+1}(x_t,\, u_t = \pi(x_t))|\right]$$

$$\pi^* \in \arg\max_{\pi} J(\pi)$$

Where $\gamma \in [0,1]$. In practice, the policy is parameterized such that $\pi^* \approx \pi^*(u|x;\theta)$, where $\theta \in \Theta \subseteq \mathbb{R}^{n_\theta}$ represents the weights of the neural network and $\Theta$ is the parameter space. The aim is to optimize parameters $\theta$ to maximize the cumulative rewards, learning an effective mapping from states $x$ to actions $u$.

To achieve this, policy-gradient methods optimize parameters $\theta$ by estimating gradients of the expected reward with respect to parameters $\theta$. This approach contrasts to value-based methods, as they directly update the policy, making it suitable for continuous action spaces and high dimensions. Algorithms like REINFORCE, Proximal Policy Optimization (PPO), and Trust Region Policy Optimization (TRPO) are popular choices here, as they leverage policy gradients and surrogate objectives to improve stability and performance [5,6]. However, policy gradient methods rely on sampling rollouts to

estimate gradients. These samples can exhibit large variance due to the stochastic nature of the environment and policy, leading to noisy gradient estimates.

An alternative approach is using Evolutionary Strategies (ES). ES methods optimize parameters $\theta$ by exploring the parameter space $\Theta$ through simulating an evolutionary process. Rather than relying on gradient-based updates, ES methods employ population-based search techniques to evolve policies. In each iteration, a population of candidate policies is evaluated based on a reward metric, with the most successful candidates selected to "reproduce" via mutation and recombination, guiding the search toward high-performing areas of the parameter space.

Evolutionary strategies for reinforcement learning (ES-RL) have shown promising results in optimizing policy parameters due to their lack of need for backpropagation. Instead of relying on gradient information, ES-RL evaluate policy performance by sampling multiple trajectories and directly update the parameters towards those that lead to higher performance. This method enhances scalability in distributed settings as its easier to parallelize. There's also fewer hyperparameters to tune compared to gradient-based methods and they are less likely to get stuck in local optima as they are population-based methods so search "globally" rather than relying on stochastic estimates of gradients to optimize the parameters. Although ES-RL has demonstrated competitive performance, as highlighted in OpenAI's work [7], where it showed comparable results to other policy gradient methods on environments like MuJoCo and Atari, it is important to note that ES-RL does not universally outperform policy gradient methods. Rather, ES-RL is particularly advantageous in specific contexts, especially when extended to multi-objective evolutionary reinforcement learning (MOEA-RL). The population-based search techniques of ES-RL can be leveraged to handle multiple, conflicting objectives in complex, dynamic environments providing a framework for optimization problems where traditional RL methods may face limitations.

## METHODOLOGY

This section presents the proposed multi-objective reinforcement learning framework which integrates traditional reinforcement learning with multi-objective evolutionary strategies.

### MORSE - Multi-Objective Reinforcement learning via Strategy Evolution

Due to the aforementioned benefits of evolutionary strategies, the proposed methodology leverages multi-objective evolutionary strategies (MOEA) for multi-objective reinforcement learning (MORL). In this work, we leverage NSGAA-II [8] to directly optimize the parameter space of the policies, building a Pareto set of policies rather than a Pareto set of solutions, as is common in traditional multi-objective optimization methods. This approach provides the decision maker with a diverse set of adaptable and dynamic policies, facilitating rapid decision-making in complex environments. The proposed methodology is shown in Algorithm 1 and Figure 1.

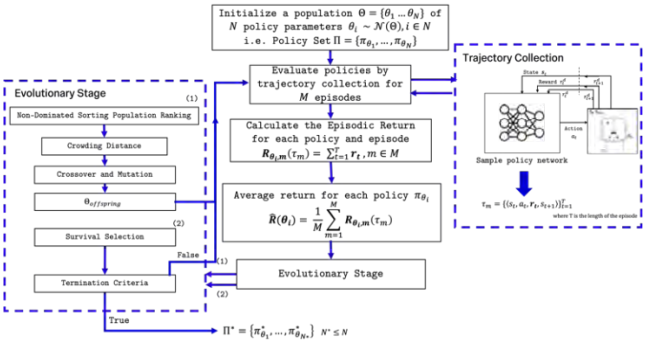



**Figure 1.** Schematic overview of our MORSE framework.

This results in a Pareto front of policies rather than a single policy. This allows decision-makers to have the flexibility to switch between policies and choose one that gives the best trade-off according to the needs in real-time. This is valuable in dynamic environments where priorities may shift due to external disruptions to the system [3,5,9].

### Multi-Objective Markov Decision Process

The sequential decision-making problem is formulated as a Multi-Objective Markov Decision Process, which can be defined as a tuple $\langle X, U, \mathcal{T}, \gamma, \mu, \mathbf{R} \rangle$ where $X$ is the state space, $U$ is the action space, $\mathcal{T}$ is the probability transition function where $\mathcal{T} : X \times U \times X \to [0,1]$, $\mu : X \to [0,1]$ is a probability distribution over initial states and $R : X \times U \times X \to R^d$ is a vector valued reward function where $d \geq 2$ is the number of objectives. The vector-valued reward function $R$ is one of the differences between single-objective RL and multi-objective RL. Finally, a policy $\pi : X \to U \in \Pi$, maps states to actions where $\Pi$ is a set of all the possible policies. Another notable difference between multi-objective and single-objective MDPs is the vector valued value function, $V^\pi \in R^d$ which is conditioned on the number of objectives and is defined as $V^\pi(x) = \mathbb{E}_\pi \sum_{t=0}^{T-1} \gamma^t r_{t+1}$ where $r_{t+1} = R(x_t, u_t, x_{t+1})$.

A note that due to the multi-objective nature of the definition, it is possible to encounter a situation where for objectives $j$ and $k$ where $j, k \in \{1, 2, \dots, d\}$ and policies $\pi$ and $\pi'$ where $\pi, \pi' \in$, both of the following inequalities can hold true:

$$V_j^\pi(x) > V_j^{\pi'}(x) \text{ Policy } \pi \text{ is better for objective } j$$

$$V_k^\pi(x) < V_k^{\pi'}(x) \text{ Policy } \pi' \text{ is better for objective } k$$

This indicates that while policy $\pi$ outperforms policy $\pi'$ in

objective $j$, it underperforms in terms of objective $k$. This illustrates the concept of trade-offs in multi-objective reinforcement learning, where optimizing for one objective can lead to suboptimal performance in another. Therefore, the agent must make decisions based on the relative importance of each objective.

## Computational Case Study

The modelled system is a Controlled Stirred Tank Reactor (CSTR), a complex and nonlinear dynamical system which can be modelled using two ordinary differential equations. A schematic is also shown in Figure 2.

$$\frac{\mathrm{d}C_A}{\mathrm{d}t} = \frac{q}{V}\left(C_{A_f} - C_A\right) - kC_A e^{\frac{-E_A}{RT}}$$

$$\frac{\mathrm{d}T}{\mathrm{d}t} = \frac{q}{V}\left(T_f - T\right) - \frac{\Delta H_R}{\rho C_p} kC_A e^{\frac{-E_A}{RT}} + \frac{UA}{\rho C_p V}\left(T_c - T\right)$$

The equations above describe a CSTR where an irreversible chemical reaction occurs which converts species A to B with cooling provided by water flowing through a coiled tube

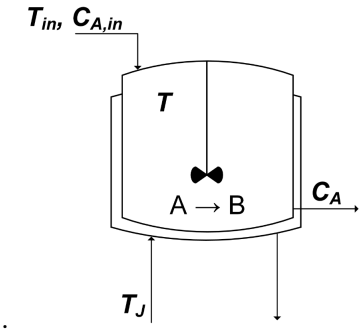



**Figure 2.** Schematic overview of Controlled Stirred Tank Reactor (CSTR)

The state variables are the concentration of species A, $C_A$ and the reactor temperature T, which constitute the state representation in our RL framework. At any given time step, the state can be expressed as a vector $x_t = [C_A, T]$, which provides the agent with the necessary information about the system's current conditions. The state variables evolve dynamically according to the system's governing equations.

Our system features one input control variable, the cooling water temperature $T_c$, modelled as a continuous variable.

Due to the non-linear dynamics, evident in the exponential term which includes the reactor temperature $T$, strong coupling between state variables, and potential for instability, the control of the CSTR presents significant challenges [10]. These difficulties are further exacerbated in systems with multiple conflicting objectives and when objectives change over time depending on the dynamics of the system. For instance, optimizing reactor performance might involve simultaneously maintaining a desired product concentration, minimizing energy consumption, and ensuring safe operating conditions, which often conflict with one another.

**Algorithm 1** MORSE

**Input:** Number of policies $N$, Maximum generations $G$, Evaluation episodes $E$
**Output:** Pareto front set of policies $\mathcal{F}_{\text{Pareto}}$

**Step 1: Initialization**
Generate a population of policies $\Pi = \{\pi_1, \pi_2, \ldots, \pi_N\}$, where each policy $\pi_i$ is parameterized by $\theta_i$
**Step 2: Policy Evaluation**
**for** each policy $\pi_i \in \Pi$ **do**
  **for** each episode $e = 1, 2, \ldots, E$ **do**
    Initialize state $s_0$ from the environment
    **for** each time step $t = 0, 1, \ldots, T$ **do**
      Select action $a_t \sim \pi_{\theta_i}(s_t)$ based on the policy
      Execute action $a_t$, observe reward $r_t$, next state $s_{t+1}$
      Accumulate discounted reward for each objective
    **end for**
  **end for**
  Compute average objective values over $E$ episodes
**end for**
**Step 3: Non-dominated Sorting**
Sort policies into fronts based on dominance relationships: $\mathcal{F}_1, \mathcal{F}_2, \ldots$
**Step 4: Crowding Distance Calculation**
**for** each front $\mathcal{F}_j$ **do**
  Compute crowding distance $d(\pi_i)$ for each policy $\pi_i$
**end for**
**Step 5: Selection and Reproduction**
Binary tournament selection, then crossover & mutation:
$\theta_{\text{offspring}} = \text{Crossover}(\theta_i, \theta_j) + \text{Mutation}(\theta_k)$
**Step 6: Survival Selection**
Combine parent population $\mathcal{P}$ and offspring $\mathcal{P}_{\text{offspring}}$. Select top $N$ policies based on non-domination rank and crowding distance:
$\mathcal{P}' = \text{Top-}N(\mathcal{P} \cup \mathcal{P}_{\text{offspring}})$
**Step 7: Termination Criteria**
**if** Termination criteria met **then**
  **break**
**end if**
**Step 8: Pareto Front Identification**
Identify non-dominated solutions in the final population:
**return** Pareto front set $\mathcal{F}_{\text{Pareto}}$ ; $\Pi = \{\pi_1^*, \pi_2^*, \ldots, \pi_{n*}^*\}$

In this study, our CSTR model integrates two cumulative objective functions throughout the time horizon: Minimize the set point error and minimize the costs (composed of heat costs and emergency shutdown costs). The reward function therefore is a vector-valued function at each time step:

$$\boldsymbol{R}_t = \left[\left(C_A(t) - C_A^*(t)\right)^2, \alpha\left(T_c - T(t)\right)^2 + \beta\mathbb{I}(shutdown)\right]$$

The first term represents the squared error between the actual concentration of species A and the desired set point concentration, $C_A^*(t)$. The second term captures the heat costs related to the deviation between the cooling temperature $T_c$ and reactor temperature $T(t)$ where $\alpha$ is a constant; the term $\beta\mathbb{I}(shutdown)$ accounts for emergency shutdown costs where $\mathbb{I}(shutdown)$ is an indicator function that takes value 1 if an emergency shutdown takes place and 0 otherwise. The cost coefficient $\beta$ reflects the severity of this event.

The goal is to ascertain the optimal control action during each time period $t$ spanning over a total of $T$ time periods within a discrete-time setup. The environment is implemented by adapting PC-Gym [10].

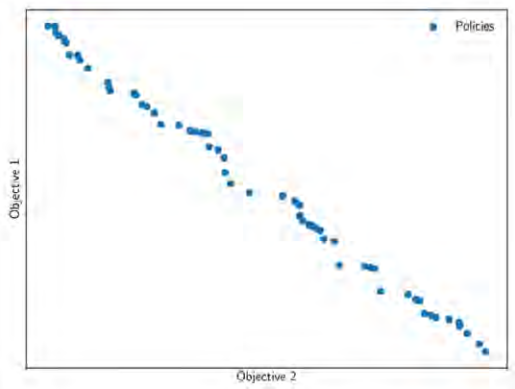



Figure 3. The resulting Pareto front showing the set of non-dominated policies, illustrating the trade-off between two competing objectives.

## SCENARIOS

In this section, we examine the adaptability of our methodology through several case studies. Using our approach, we derive a Pareto set of policies, as shown in Figure 3, that optimally balance competing objectives. When a disruption affects the system, this Pareto set allows for swift policy switching, enabling us to select a policy that best meets the real-time needs and constraints. By dynamically adjusting to changing conditions, we demonstrate how our method offers resilience and flexibility in complex environments.

### Scenario 1: Fouling

Fouling is a common issue in chemical processes, particularly in CSTRs, where unwanted material accumulates on the reactor walls or heat exchanger surfaces. This buildup can significantly reduce heat transfer efficiency, alter reaction rates, and increase operating costs due to the need for additional energy to maintain the desired temperature.

In this case study, we simulate fouling by introducing a time-dependent reduction in the heat transfer coefficient. As fouling progresses, maintaining optimal product concentrations and minimizing energy costs become increasingly challenging. Using our methodology, we analyze how the Pareto set of policies adapts to these conditions. For instance:

- Policies that prioritize minimizing set-point error may involve increasing the heat input to compensate for the reduced heat transfer efficiency.
- Policies that that prioritize cost minimization may tolerate larger deviations from the desired set-point to avoid excessive energy consumption.

The results shown in Figure 4 demonstrate that the proposed approach can dynamically adjust control actions to balance competing objectives under fouling conditions, ensuring safe and efficient reactor operation. The dynamic policy significantly outperforms the constant policy in minimizing set point error (Objective 1), showcasing its ability to respond quickly to disturbances and maintain the system closer to the desired operating range. However, the difference in costs (Objective 2) between the dynamic and constant policies is relatively small, indicating that both approaches manage costs effectively under normal fouling conditions.

This small difference in costs suggests that cost optimization may not be as sensitive to dynamic control under routine disruptions. However, costs could become a much more prominent factor in scenarios where fouling leads to severe disruptions, such as an emergency shutdown or significant system failure.

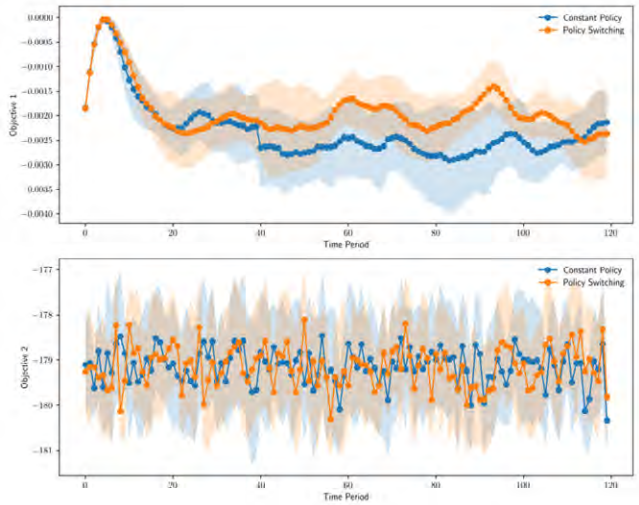



**Figure 4.** Execution profiles of the fouling case study, showing objective 1 (set point error) and objective 2 (costs) with shaded variance.

## CONCLUSIONS AND FUTURE WORK

In conclusion, we have proposed a methodology which leverages reinforcement learning (RL) and multi-objective evolutionary algorithms (MOEAs) to address the challenges of controlling a CSTR with competing objectives. By leveraging a Pareto-based approach, by using MOEAs to search the parameter space of the neural network policies, we successfully derive a set of non-dominated policies that balance objectives such as minimizing set-point error and operational costs. The case studies highlight the adaptability of the method in dynamic environments, including scenarios involving fouling showcasing its resilience and flexibility in complex

systems.

Future work will focus on improving the efficiency of the evolutionary search process by integrating domain-specific knowledge and operator expertise. Additionally, we will investigate collaborative decision-making strategies across interconnected processes by extending this work to multi-unit reactor systems. We also plan to adapt our method to handle partially observable environments, which are often encountered in industrial settings with incomplete measurements. Finally, the incorporation of additional objectives such as emissions control, stability and long-term maintenance costs, will further enhance its relevance to real-world applications. Source code for this study is available on GitHub.

## REFERENCES


1. Bloor, M.; Ahmed, A.; Kotecha, N.; Tsay, C.; Mercangöz, M.; Del Rio-Chanona, A. Hierarchical Reinforcement Learning for Plantwide Control. In Computer Aided Chemical Engineering; Elsevier, 2024; Vol. 53, pp 1639–1644. https://doi.org/10.1016/B978-0-443-28824-1.50274-X
2. Van Moffaert, K.; Drugan, M. M.; Nowe, A. Scalarized Multi-Objective Reinforcement Learning: Novel Design Techniques. In 2013 IEEE Symposium on Adaptive Dynamic Programming and Reinforcement Learning (ADPRL); IEEE: Singapore, Singapore, 2013; pp 191–199. https://doi.org/10.1109/ADPRL.2013.6615007
3. Van Moffaert, K.; Nowé, A. Multi-Objective Reinforcement Learning Using Sets of Pareto Dominating Policies. J. Mach. Learn. Res. 2014, 14 (1), 3483–3512.
4. Felten, F.; Talbi, E.-G.; Danoy, G. Multi-Objective Reinforcement Learning Based on Decomposition: A Taxonomy and Framework. J. Artif. Intell. Res. 2024, 79, 679–723. https://doi.org/10.1613/jair.1.15702
5. Hayes, C. F.; Radulescu, R.; Bargiacchi, E.; Källström, J.; Macfarlane, M.; Reymond, M.; Verstraeten, T.; Zintgraf, L. M.; Dazeley, R.; Heintz, F.; Howley, E.; Irissappane, A. A.; Mannion, P.; Nowé, A.; Ramos, G.; Restelli, M.; Vamplew, P.; Roijers, D. M. A Practical Guide to Multi-Objective Reinforcement Learning and Planning. Auton. Agents Multi-Agent Syst. 2022, 36 (1), 26. https://doi.org/10.1007/s10458-022-09552-y
6. Kotecha, N.; Chanona, A. del R. Leveraging Graph Neural Networks and Multi-Agent Reinforcement Learning for Inventory Control in Supply Chains. arXiv October 24, 2024. https://doi.org/10.48550/arXiv.2410.18631
7. Salimans, T.; Ho, J.; Chen, X.; Sidor, S.; Sutskever, I. Evolution Strategies as a Scalable Alternative to Reinforcement Learning. arXiv September 7, 2017. https://doi.org/10.48550/arXiv.1703.03864
8. Deb, K.; Pratap, A.; Agarwal, S.; Meyarivan, T. A Fast and Elitist Multiobjective Genetic Algorithm: NSGA-II. IEEE Trans. Evol. Comput. 2002, 6 (2), 182–197. https://doi.org/10.1109/4235.996017
9. Qiu, Y.; Kotecha, N.; Del Rio Chanona, A. Leveraging Reinforcement Learning and Evolutionary Strategies for Dynamic Multi Objective Decision Making in Supply Chain Management. IFAC-Pap. 2024, 58 (14), 598–603. https://doi.org/10.1016/j.ifacol.2024.08.402
10. Bloor, M.; Torraca, J.; Sandoval, I. O.; Ahmed, A.; White, M.; Mercangöz, M.; Tsay, C.; Chanona, E. A. D. R.; Mowbray, M. PC-Gym: Benchmark Environments For Process Control Problems. arXiv December 5, 2024. https://doi.org/10.48550/arXiv.2410.22093



© 2025 by the authors. Licensed to PSEcommunity.org and PSE Press. This is an open access article under the creative commons CC-BY-SA licensing terms. Credit must be given to creator and adaptations must be shared under the same terms. See https://creativecommons.org/licenses/by-sa/4.0/




Systems & Control Transactions

**Research Article - Peer Reviewed Conference Proceeding**
ESCAPE 35 - European Symposium on Computer Aided Process Engineering
Ghent, Belgium. 6-9 July 2025
Jan F.M. Van Impe, Grégoire Léonard, Satyajeet S. Bhonsale,
Monika E. Polańska, Filip Logist (Eds.)

PSE PRESS

# Extremum seeking control applied to operation of dividing wall column – DWC

**Ivar J. Halvorsen[a,c*], Leontine I.M. Aarnoudse[b], Mark A.M. Haring[a], Sigurd Skogestad[c]**

[a] SINTEF Digital, Department of Mathematics and Cybernetics, Trondheim, Norway
[b] Norwegian University of Science and Technology, Department of Geoscience, Trondheim, Norway
[c] Norwegian University of Science and Technology, Department of Chemical Engineering, Trondheim, Norway
* Corresponding Author: ivar.j.halvorsen@sintef.no

## ABSTRACT

The dividing wall column (DWC) has significant energy saving potential compared to conventional column sequences. However, to reach these savings in practice, it is essential that the control structures can track the optimal operation point despite inevitable changes in feed properties, performance characteristics and other uncertainties. Otherwise, the energy consumption may rise significantly or, more commonly, the DWC becomes unable to produce pure products even at its maximum reboiler duty. Extremum seeking control (ESC) is a model-free optimisation technique that may mitigate off-optimal operation in this environment. By active perturbation of selected manipulative variables, the algorithm infers gradient properties of the measured cost function and, by that, enables tracking of a moving optimum. Extremum seeking control can be used also in combination with other approaches, e.g. self-optimising control. Applied to the DWC, the presented perturb-and-observe algorithm, which can be classified as ESC, appears to be able to track changes in the optimal values of the manipulated variables and setpoints.

**Keywords**: Distillation, Energy Efficiency, Process Control, Optimization, Machine Learning, Perturb and Observe, Dividing Wall Column

## INTRODUCTION

The dividing wall column (DWC) is an attractive integrated distillation arrangement, since there are significant saving potentials in energy and capital cost compared to conventional column sequences [1, 2]. Despite that challenges in operation and design have been listed in the literature as a key obstacle, there are developments in this area that can enable more widespread industrial usage [3]. In a conventional column sequence, e.g., the direct split configuration, controlling the purities of each column to their specifications implicitly gives the lowest overall energy consumption [4]. In DWC operation, there are some pitfalls that may lead to either higher energy consumption and/or failure to produce the designed product purities [5]. Thus, it is of great interest to develop operating strategies that can handle real-world uncertainties and enable the DWC to operate such that it always maintains its designed capabilities in low energy consumption and simultaneous high product purity.

The characteristics of optimal operation have been described in detail for ideal mixtures and infinite number of stages [6] and also for finite stages [7], but the practical challenge is to use these insights to devise a control structure that can implement the optimal moves of the key manipulative variables as unmeasured disturbances affect the optimum process characteristics. This kind of on-line optimisation is needed in addition to the regulatory control that is required for maintaining the products inside the given purity specifications.

Herein, the focus is on perturbation-based optimisation of the available manipulators. Perturbation-based optimization methods such as extremum seeking control (ESC) are capable of optimizing many types of processes, even when these processes vary in time and model knowledge is limited [8–10]. In this paper, we consider the application of perturb-and-observe, a type of ESC, to approach optimal operation points for the dividing wall column. The main idea of this method is to iteratively perturb the available manipulative variables, observe the outcome and move in the direction of improvement. This leads to fast convergence to the optimal

operation point, as well as fast tracking if the optimal operation point changes over time.

## PERTURB AND OBSERVE

In this section, the perturb-and-observe method for model-free adaptive optimization is introduced. Consider the problem of minimizing an unknown, time-varying function $f(k,u(k))$ with input $u(k)$, where $k = 1,2,\ldots$ denotes the time index. We make the following assumptions:

1. The function $f$ is unknown at any time $k$, but we can obtain noisy measurements of the form
2. $$y(k) = f\big(k,u(k)\big) + \varepsilon(k). \quad (1)$$
3. The magnitude of the measurement disturbance $\varepsilon(k)$ is small compared to the range of possible function values.
4. At any time $k$, function $f$ has a unique minimum.
5. The rate of change of $f$ is small compared to the sampling frequency.
6. The function $f\big(k,u(k)\big)$ is static. If the underlying process contains dynamics, $f\big(k,u(k)\big)$ represents the steady-state behavior.

Function $f\big(k,u(k)\big)$ can represent many different processes. In the context of the dividing wall distillation column considered in this paper, a typical choice is the energy consumption $V$ of the reboiler as a function of the liquid split $R_l$ , i.e., $f\big(k,u(k)\big) = V\big(k,R_l(k)\big)$ with $u(k) = R_l(k)$. The corresponding measurement $y(k)$ could be a direct, noisy measurement of the reboiler energy consumption, or an estimate based on, e.g., temperature measurements.

The aim is to find the input $u(k)$ that minimizes $f\big(k,u(k)\big)$ and tracks this minimum while it changes over time. To this end, a perturb-and-observe method is employed. The main idea is to perturb the input variable $u$ and determine the direction of improvement from the corresponding measurements $y$. Consider an initial input $u(1)$, for which output $y(1)$ is measured. The next input is chosen as

$$u(2) = u(1) + \Delta_u, \quad (2)$$

for some step size $\Delta_u$. For $k = 2,3,\ldots$, the corresponding measurement $y(k)$ is compared to the previous measurement $y(k-1)$ to obtain the direction of improvement $g(k+1) \in \{-1,1\}$ as follows:

$$g(k+1) = \begin{cases} g(k), & if\ \ y(k) \le y(k-1), \\ -g(k), & if\ \ y(k) > y(k-1). \end{cases} \quad (3)$$

Next, the direction of improvement is used to determine the next input by taking

$$u(k+1) = u(k) + g(k+1)\Delta_u. \quad (4)$$

Thus, if input $u(k)$ leads to a smaller measured output $y(k)$ compared to the previous input $u(k-1)$, we are moving towards the minimum and the direction of movement remains unchanged. If $y(k) > y(k-1)$, we are moving away from the minimum and need to reverse the direction of movement. The iterative method is summarized in the flowchart in Figure 1.

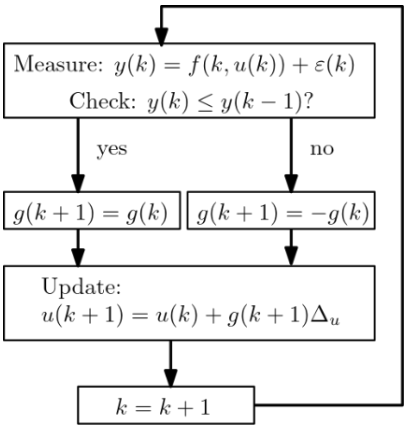



**Figure 1.** Flowchart for perturb and observe.

### Implementation of perturb and observe

The implementation of the perturb-and-observe method described here is straightforward, as it consists only of updating an input parameter and observing the resulting outcome. Still, there are some implementation aspects that need to be considered. First, it is noted that the method can be applied to maximization instead of minimization of a function by changing the update rule for the direction of improvement to

$$g(k+1) = \begin{cases} g(k), & if\ \ y(k) \ge y(k-1), \\ -g(k), & if\ \ y(k) < y(k-1). \end{cases} \quad (5)$$

In this case, $y(k)$ being smaller than $y(k-1)$ leads to a change in direction.

A second consideration when implementing perturb and observe is that this method continues perturbing the input after the minimum has been found. In case of time-varying processes, this behavior is desired as it enables tracking of the time-varying optimal operating point. However, if the optimal operating point can be assumed to be time-invariant, it is in general preferred to reduce the step size $\Delta_u$ over time to limit the amount of unnecessary perturbation. Possible extensions also include resetting the automatic reduction of $\Delta_u$ once a change in the process is detected through additional sensors, see, e.g., [10] for ideas in this direction.

Third, the influence of the measurement disturbances $\varepsilon(k)$ needs to be considered. If $\varepsilon(k)$ is stochastic in nature and its magnitude is similar to the absolute difference between $y(k)$ and $y(k-1)$, one measurement might

not be sufficient to determine the direction of improvement. In this case, it is recommended to keep the input $u(k)$ constant for several time steps and average the resulting measurements to obtain more accurate estimates of $f(k,u(k))$.

## DWC CASE DESCRIPTION

We consider the "standard" ternary dividing wall column (DWC) as illustrated in Figure 2. It is operated at constant pressure. The feed (F) enters the prefractionator sections (1,2) at the left side of the wall and is described by its molar fractions (z) of pure components (A,B,C) and its liquid fraction (q). There are three product specifications, given by the main component purities in each product stream (D,S,B). There are five manipulated variables (MVs): 1) boilup vapor rate (V), 2) reflux rate (L), 3) side product draw rate (S), 4) the liquid split ratio ($R_l$) above the wall and 5) the vapor split ratio ($R_v$) below the dividing wall.

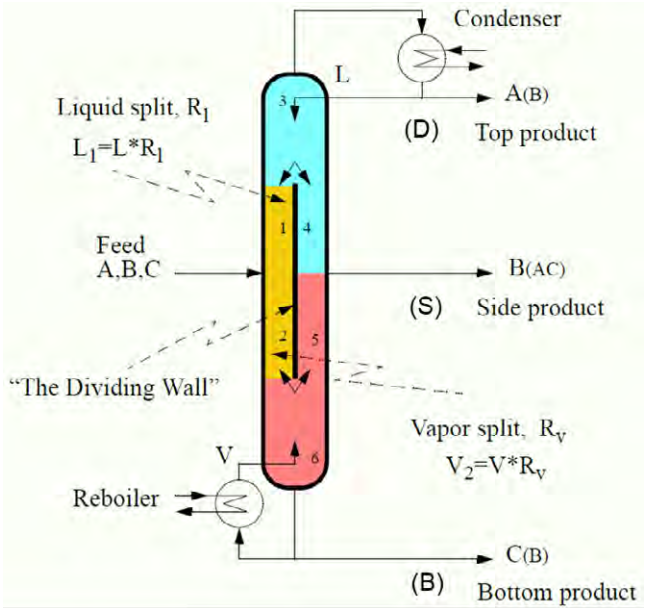



**Figure 2.** The ternary Dividing Wall Column (DWC). Section 1,2 is the prefractionator and 3,4,5,6 is denoted main column.

For the virtual infinite stage case and ideal feed mixture components, the minimum energy condition is precisely described by the Vmin-diagram [6]. Figure 3 shows this for the ideal case with equimolar feed, liquid fraction q=0.5 and relative volatilities $\alpha = [4,2,1]$ referred to the heavy component (C). The two peaks represent minimum vapor (in the top) for the sharp A/BC and AB/C splits. Point P is the so-called preferred split, which is minimum vapor for the AB/BC split. In a DWC, the highest peak sets the overall minimum reboiler vapor requirement. However, this minimum is only reachable when the prefractionator is operated at a point exactly on the (bold) line from the preferred split (P) on the boundary line to a balance point (B) (where all sections in the main column are at their minimum vapor simultaneously).

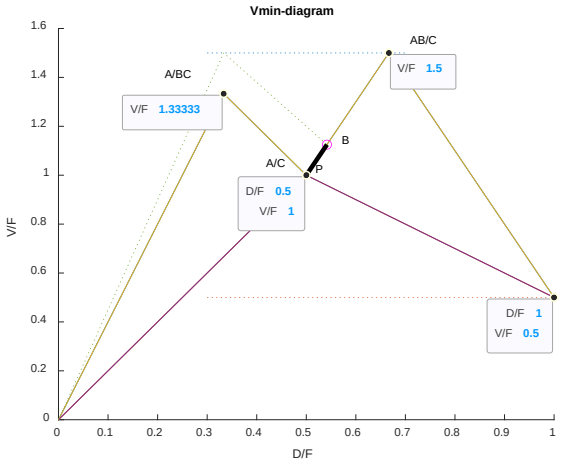



**Figure 3.** Vmin-diagram for the equimolar feed showing the optimality region for prefractinator operation at (bold) line from the so-called preferred split to the balance point (P to B).

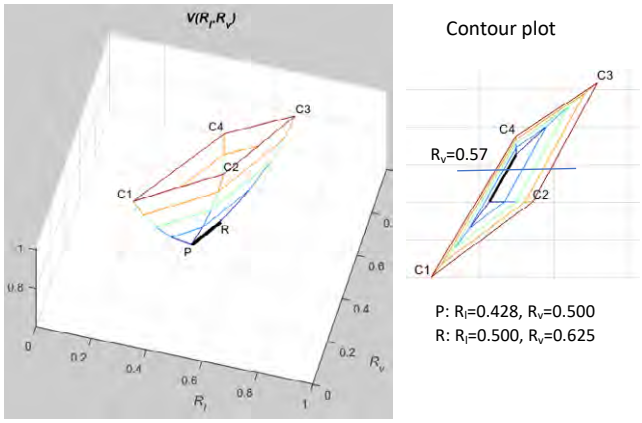



**Figure 4.** Perspective and contour view of the reboiler vapor solution surface V($R_l$,$R_v$ ) for a sharp product split and an infinite number of stages. The optimality region PR maps directly from the Vmin-diagram to the $R_l$,$R_v$ space. Each contour represents a 10% increase in V. The maximum reboiler saving for this case is as high as 39% (compared to conventional "direct split" and 30% in the condenser).

Most industrial DWC-implementations set the vapor split by design of the wall placement and tray/packing pressure drop characteristics. It is crucial that the obtained vapor split is properly checked to cover the expected feed property variation range, since the Vmin-diagram and solution surface will move whenever feed properties change. A constant, properly designed $R_v$=0.57 is illustrated in the contour plot in Figure 4 as a line that hits approximately the middle of the PR-line.

Then, it will usually be sufficient to adjust only the liquid split $R_l$ to track the optimum on a moving solution surface.

In the simulation case considered here, the number of stages has been set to 16 in each of the 6 sub-sections. This leads to the real minimum boilup being about 6-7% above Vmin. In practice, this corresponds to about 2.3 times the minimum stage number for a product purity of 99%. A rigorous stage design should evaluate the pareto curve that balances capital and operational costs [3], but this level of detail is not required for this study.

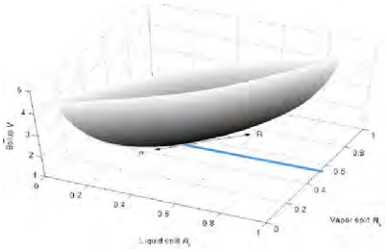


**Figure 5.** Finite stage solution surface, cf. Figure 4.

The impact to the finite stage solution surface, see Figure 5, is that it will be more rounded and not have the sharp edges shown in Figure 4. The optimality region will not be completely flat like the PR-line, but clearly much steeper perpendicular to the PR direction than along PR.

## Temperature profiles

For each disturbance, a set of grid points $V(R_l)$ have been calculated as illustrated below in Figure 6.

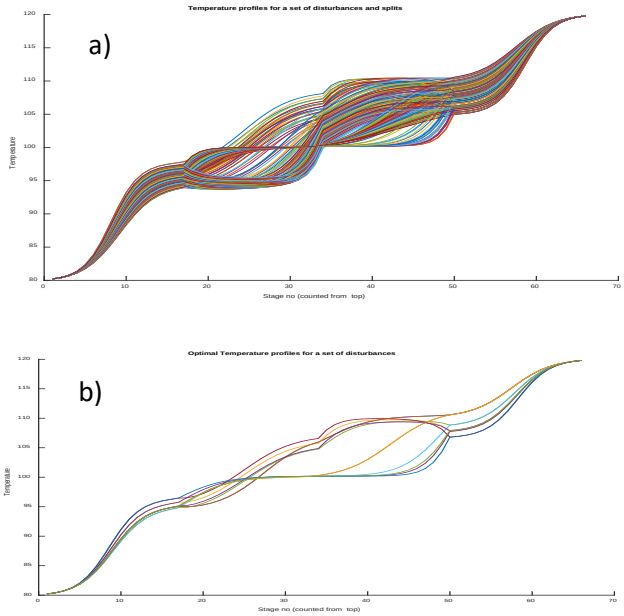



**Figure 6.** a) Temperature profiles for a set of disturbances and liquid split values, while the product composition is controlled, and b) The profiles where liquid split is optimised for each disturbance.

Figure 6 shows the all the executed runs in the upper plot but only the optimal profiles for each disturbance in the lower plot. The profiles may look a bit crowded, but a certain symmetry in the optimised plots can be observed, and that symmetry changes in different ways depending on which side of the optimum the DWC is operated. This gave rise to propose the so-called "Difference Temperature Symmetry" (DTS) described in more detail in [7], which is the sum of differences across the wall in the middle of sections 1,2,4,5 (see Figure 2): DTS=(T1-T4)-(T2-T5).

## Self optimising control of the DWC

In self optimising control (SOC), the idea is to find a variable that contains some gradient-like information for a given cost function such that when this controlled variable (CV) is regulated to a setpoint by applying the available MV for optimisation as a regulatory controller MV, the deviation from the optimum upon disturbances is reduced compared to keeping the MV constant.

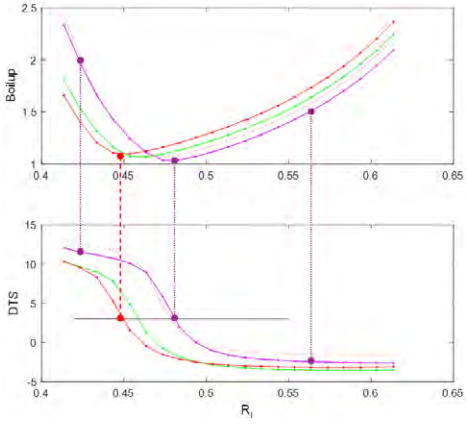



**Figure 7.** The relation between the SOC CV=DTS, the primary manipulated variable $R_l$ and the boilup $V(R_l)$

Figure 7 indicates qualitatively that the DTS as a self optimising controlled variable has close to ideal properties; namely, that for low values the operation is at one side of the optimum and for high values on the other side. And by controlling to the setpoint, e.g. DTS=3, as for the nominal optimum, this value ensures close to optimum operation for the considered disturbances too.

But still, the optimal setpoint value for any given case cannot be assumed to be known, and this calls for a smart procedure for adjusting the setpoint. And here is where the perturb-and-observe algorithm is handy.

# SIMULATION RESULTS

The relations between the MVs and the column state have been obtained by simulating the DWC with the products controlled to meet specifications by use of simple PI controllers for a range of grid-points for the

optimisation MV around the calculated optimum for each disturbance scenario. The perturb-and-observe algorithm has no information about the active disturbance acting on a system and is just given a suitable (feasible) initial value for the MV. The perturb-and-observe algorithm considers basically the structure illustrated in Figure 8.

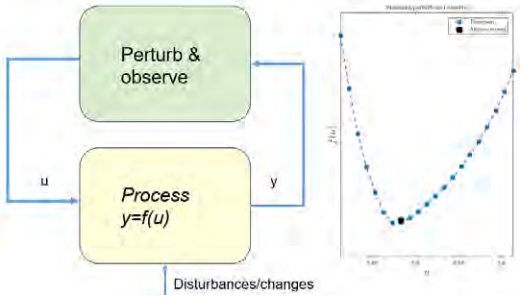



**Figure 8.** The general structure for the perturb-and-observe algorithm during extremum search.

## Manipulating liquid split ratio

The first scenario is a case where some changes are applied to the feed composition and liquid fraction. The vapor split is set constant (as in most industrial cases).

Applied to the DWC, the structure of y=f(u) is illustrated in Figure 9 where u is the liquid split ($R_l$) and y is the reboiler vapor (V) which in this case is used as energy measure. It is an "output" in this context since its value is manipulated by the product purity controls to maintain the CVs at specification setpoints. The challenge is that the cost function is influenced by unknown disturbances and the actual optimum needs to be tracked by the perturb-and-observe algorithm.

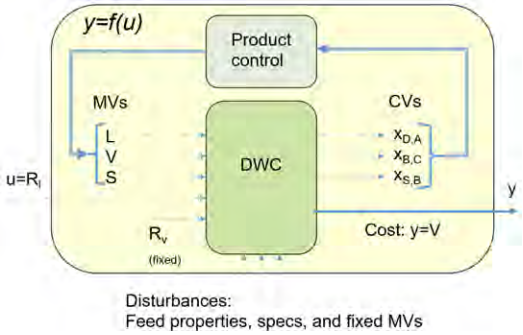



**Figure 9.** The cost function y=f(u) for the DWC is on top the basic regulatory product purity control. The optimisation MV is the liquid split u=$R_l$.

Figure 10 illustrates the minimisation search when the set of disturbances are applied. For each disturbance the cost function is moved as illustrated in the left graph. Noise is added to the measurement (y) and it can be observed in the upper right graph that the applied manipulated (perturbed) u-value (green) very soon after a change tracks the current optimal value (black) which is of course unknown to the algorithm. The feed composition and liquid fraction are changed at k=30,60,90,120. Note that white noise is added to the measurements to simulate measurement noise.

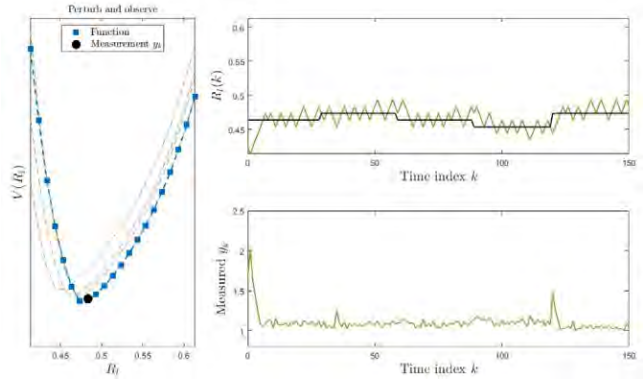



**Figure 10.** The resulting tracking of the optimal liquid split obtained by the perturb-and-observe algorithm.

## Manipulating SOC setpoint

The structure of the basic regulatory control, including a self optimising control loop is shown in Figure 11. The perturb-and-observe algorithm will work with the SOC setpoint as its manipulative variable "u".

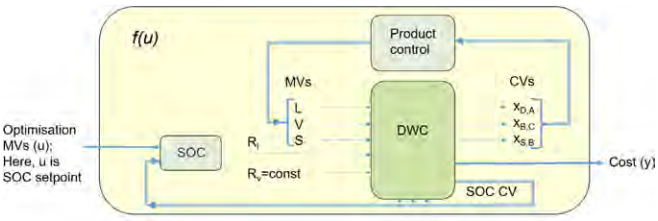



**Figure 11.** The cost y=f(u) when the perturb-and-observe is manipulating the SOC setpoint.

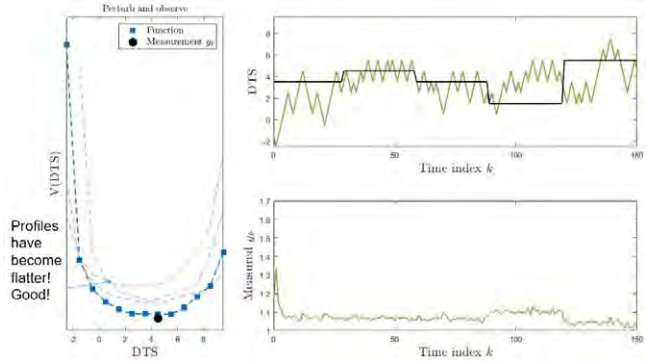



**Figure 12.** The tracking of y=f(u=DTS) for the same disturbance scenario as in Figure 7. Observe that the solution surface is "flattened" cf. Figure 7, thus being more robust for the exact setpoint.

A key advantage with use of the SOC is that it will

reject fast disturbances in the regulatory layer. A disturbance may have some impact to the optimal setpoint, and then the perturb-and-observe algorithm can do the search for the best setpoint on the slower time scale. This configuration ensures less off-optimal operation time in the case with frequent variations in the disturbances.

## DISCUSSION

The first question to be raised is how the perturb-and-observe method will perform in a true dynamic plant environment. The presented procedure is basically a steady-state method intended to be used on a process that is stabilised by its regulatory control system, and such that changes in the optimisation MVs do not interfere and degrade process transient performance and stability properties. This can typically be done by time-scale separation, e.g. by using a sample period in the ballpark of the typical closed-loop settling time for the regulatory control level. It is not required to have complete steady-state conditions (which in practice never occur perfectly in a plant) since the algorithm is robust against somewhat noisy measurements.

In distillation in general, including for the DWC, inferential product composition control is usually based on temperature measurements, and often on-line measurements of compositions are not available. Temperature based product purity control has been simulated too. The corresponding results are similar to the results for perturb-and-observe as shown in this work.

For products that are being quality controlled in a lab, it is possible to update the correlation between temperature setpoints and product composition. For temperature points in the profiles in the prefractionator, these kinds of correlations are not available, so some kind of tweaking of the setpoints will always be required. For this case, the perturb-and-observe algorithm fits perfectly since there is no alternative to pre-calculate the optimal setpoints exactly based on product data. Another desirable function for industrial practice is to gracefully handle a scenario where the optimal solution becomes constrained and to include some kind of safety supervision to prevent malfunction.

## CONCLUSION

The simulation study indicates that extremum seeking control by the perturb-and-observe algorithm can track the moving optimum value of the available manipulated optimisation variable when the DWC is exposed to some unknown disturbances that alter the optimal operating point. The algorithm can also be used in combination with self optimising control on the regulatory layer by using that controller's setpoint as the manipulative optimisation variable.


## ACKNOWLEDGEMENTS

Funded by The Research Council of Norway, Project No.: 345272: Data-driven optimization of industrial processes in time-varying environments.


## REFERENCES


1. Kaibel G (1987) Distillation columns with vertical partitions. Chem Eng Technol 10:92–98. https://doi.org/10.1002/ceat.270100112
2. Dejanovic I, Matijaševic Lj, Olujic Ž (2010) Dividing wall column—A breakthrough towards sustainable distilling. Chem Eng Process Process Intensif 49:559–580. https://doi.org/10.1016/j.cep.2010.04.001
3. Asprion N, Kaibel G (2010) Dividing wall columns: Fundamentals and recent advances. Chem Eng Process Process Intensif 49:139–146. https://doi.org/10.1016/j.cep.2010.01.013
4. Gordon LM (1986) Simple optimization for dual composition control. Hydrocarb Process U S 65:6:
5. Ränger L-M, Halvorsen IJ, Grützner T, Skogestad S (2025) What can go wrong in a dividing wall column and how to detect it. Sep Purif Technol 354:. https://doi.org/10.1016/j.seppur.2024.129151
6. Halvorsen IJ, Skogestad S (2003) Minimum Energy Consumption in Multicomponent Distillation. 2. Three-Product Petlyuk Arrangements. Ind Eng Chem Res 42:605–615. https://doi.org/10.1021/ie0108649
7. Halvorsen IJ, Skogestad S (1999) Optimal operation of Petlyuk distillation: Steady-state behavior. J Process Control 9:407–424. https://doi.org/10.1016/S0959-1524(99)00009-8
8. Tan Y, Moase W, Manzie C, et al (2010) Extremum seeking from 1922 to 2010. Proc 29th Chin Control Conf
9. Scheinker A (2024) 100 years of extremum seeking: A survey. Automatica 161:111481. https://doi.org/10.1016/j.automatica.2023.111481
10. Femia N, Petrone G, Spagnuolo G, Vitelli M (2005) Optimization of perturb and observe maximum power point tracking method. IEEE Trans Power Electron 20:963–973. https://doi.org/10.1109/TPEL.2005.850975



© 2025 by the authors. Licensed to PSEcommunity.org and PSE Press. This is an open access article under the creative commons CC-BY-SA licensing terms. Credit must be given to creator and adaptations must be shared under the same terms. See https://creativecommons.org/licenses/by-sa/4.0/




Systems & Control Transactions

**Research Article - Peer Reviewed Conference Proceeding**
ESCAPE 35 - European Symposium on Computer Aided Process Engineering
Ghent, Belgium. 6-9 July 2025
Jan F.M. Van Impe, Grégoire Léonard, Satyajeet S. Bhonsale,
Monika E. Polańska, Filip Logist (Eds.)

PSE PRESS

# Modeling, Simulation and Optimization of a Carbon Capture Process Through a TSA Column

**Eduardo S. Funcia[a], Yuri S. Beleli[a], Enrique V. Garcia[b], Marcelo M. Seckler[a], José L. Paiva[a] and Galo A. C. Le Roux[a]***

[a] University of Sao Paulo, Polytechnic School, Department of Chemical Engineering, Sao Paulo, Sao Paulo, Brazil
[b] Federal University of Ceara, Department of Chemical Engineering, Fortaleza, Ceara, Brazil
* Corresponding Author: galoroux@usp.br.

## ABSTRACT

By capturing carbon dioxide from biomass flue gases, energy processes with negative carbon footprint are achieved. Among carbon capture methods, the fluidized temperature swing adsorption (TSA) column is a promising low-pressure alternative, but it has been developed on small scales. This work aims to model, simulate and optimize a fluidized TSA multi-stage equilibrium system to obtain a cost estimate and a conceptual design for future process scale up. A mathematical model described adsorption in multiple stages, each with a heat exchanger, coupled to the desorption operation. The model was based on elementary macroscopic molar and energy balances, coupled to pressure drops in a fluidized bed designed to operate close to the minimum fluidization velocity, and coupled to thermodynamics of adsorption equilibrium of a mixture of carbon dioxide and nitrogen in solid sorbents (the Toth equilibrium isotherm was used). The complete fluidized TSA process has been optimized to minimize costs, considering equilibrium in each stage. The optimal configuration for heat exchangers was determined and a unit cost for carbon dioxide capture was estimated. It was found that a small number of stages is required to meet captured carbon specification at 95% molar purity, while process cost per metric ton of $CO_2$ was within range of other capture technologies. These findings show that the methodology developed here is useful for guiding the conceptual design of fluidized TSA process for carbon capture.

**Keywords**: Technoeconomic Analysis, Carbon Dioxide Capture, Adsorption, GAMS, Optimization, Modelling and Simulations.

## INTRODUCTION

### Motivation

The Paris Agreement is a legally binding international treaty adopted in 2015 by 196 countries. Its goal is to limit global warming to below 1.5°C, by reducing greenhouse gas emissions [1]. In the context of global decarbonization efforts, carbon capture and storage (CCS) technologies are often emphasized as a necessary pathway to limit global warming [2]. Bioenergy CCS (BECCS) is particularly promising due to its potential for achieving negative emissions, as it captures and permanently stores $CO_2$ that was originally removed from the atmosphere during biomass growth.

However, most optimization studies to date on the BECCS field focus on linear spatial and temporal analysis of networks of plants, farms and transportations, instead of diving into operational details and process variables in each site [3,4]. Process simulations and optimizations could provide key insights into relatively new $CO_2$ capture technologies in order to scale up processes and make them more mature.

Among recently developed $CO_2$ capture technologies that could benefit from such insights is the fluidized temperature swing adsorption (TSA) column, where a solid adsorbent flows countercurrent to an upward $CO_2$-rich gas [5,6]. Some works in the literature have already explored packed-beds TSA simulations [7,8], but fluidized TSA process optimization works remain scarce and limited to small scales [9,10]. This process is a suitable $CO_2$ capture method due to its high selectivity, reusability of solid adsorbents, and lower energy consumption

compared to conventional absorption-based methods. Adsorption-based methods using solid sorbents, such as zeolite 13X binder free, offer higher $CO_2$ selectivity and lower regeneration energy requirements [6].

## Objective

The study aims an optimization-based design of fluidized TSA systems for large scale $CO_2$ capture from biomass-derived flue gases. This simulation study integrates process modeling and optimization techniques to improve fluidized TSA performance under realistic operating conditions, to develop basic guidelines to process scale up, in order to enhance process efficiency and minimize operational costs. This objective aligns with the need (highlighted in a previous study) to obtain a cost estimate for $CO_2$ capture through fluidized TSA process [5]. It also aligns with the Sustainable Development Goals set by the United Nations for 2030, including 7: Affordable and Clean Energy; 9: Industry, Innovation and Infrastructure; and 13: Climate Action [11].

# MATERIALS AND METHODS

## Hypothesis and parameters

The fluidized TSA system consists of two fluidized columns—one for adsorption and another for desorption—with continuous adsorbent recirculation. Each column has a heat exchanger at the gas inlet in the bottom, and each bed in each column also has a heat exchanger to optimize temperature. The recirculating solid adsorbent also passes through a heat exchanger between the columns. The number of adsorption stages should be optimized based on $CO_2$ purity targets and energy efficiency considerations. Our initial simplified simulations indicated that a small number of adsorption stages (as low as 3-5) suffices to obtain $CO_2$ at over 90%v/v purity [12]. Table 1 presents the hypothesis for the process modeling, while Table 2 presents the values and units for several parameters assumed for the optimization.

**Table 1:** Fluidized TSA modeling hypothesis.

| |
|---|
| No chemical reactions |
| No flue gas contaminants, only $N_2$ and $CO_2$ |
| Ideal gases |
| No phase changes |
| Part of solid adsorbent replaced monthly |
| Equilibrium reached within each stage |
| No gradients within each stage |
| Spheric solid adsorbent particles |
| Air viscosity independent with respect to pressure |
| Startup cost is 10% of fixed capital investment [13] |
| Pressure drop due to stage heat exchangers neglected |
| Steady state |

**Table 2:** Parameter values used in the GAMS code for modeling the fluidized TSA column.

| Parameter description | Value |
|---|---|
| Flue gas molar flow | 413 $mol.s^{-1}$ |
| Flue gas molar composition | 15%v/v $CO_2$ and 85%v/v $N_2$ |
| Flue gas temperature | 328 K |
| Flue gas pressure | 1 bar |
| $CO_2$ max concentration after adsorption | 0.5%v/v |
| Stage height *H* | 1 m |
| Captured $CO_2$ min concentration | 95%v/v |
| Zeolite 13XBF specific heat | 880 $J.kg^{-1}.K^{-1}$ [14] |
| Zeolite 13XBF bulk density | 1287 $kg.m^{-3}$ [6] |
| Zeolite 13XBF spheric particle diameter $D_p$ | $5.10^{-4}$ m [6] |
| Compressor efficiency | 72% [15] |
| Overall heat transfer coefficient in each heat exchanger | 170 $W.K^{-1}.m^{-2}$ [15] |
| Marshall & Swift index for late 2024 | 2500 [16] |
| Work hours per year | 8000 $h.yr^{-1}$ |
| Plant lifetime *t* | 20 yr |
| Interest rate *i* | 10%p.a. |
| Cost of land | 0 USD |
| Cost of cold water | 0.492 $USD.GJ^{-1}$ [17,18] |
| Cost of high-pressure steam | 24.6 $USD.GJ^{-1}$ [17,18] |
| Cost of zeolite 13X BF | 2 $USD.kg^{-1}$ |
| Adsorbent monthly losses | 10% |

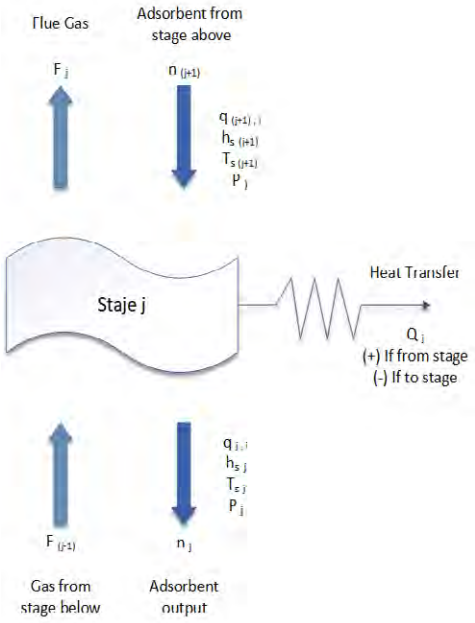



**Figure 1.** Modelling scheme of a generic equilibrium stage in the fluidized TSA column [6].

## Modeling

A multistage fluidized bed receives an adsorbent stream from the upper side (solid phase inlet) and a biomass post-combustion flue gas stream at atmospheric pressure (1.01325 bar) from the lower side (flue gas inlet). The bed interior is subdivided into various stages; each stage receives the adsorbent and the flue gas from the neighboring stages. As each stage depends on the solution of other stages, an iterative solution is required. Figure 1 presents a sketch for a generic stage. A compressor is used at the bottom of the adsorption column to increase the flue gas pressure so it flows upwards.

The model is based on molar and energy balances of each gas component in each stage and in each external heat exchanger, coupled with thermodynamics of adsorption heat, according to previous studies where further details can be found [5,6] The Toth equation describes adsorption equilibrium within each stage, with model parameters from previous empirical results. For this study, based on our previous experimental results [6], we consider the heterogeneity parameter for $N_2$ to equal unity and not change with temperature.

Since particles in the present simulation are of Geldart group B and the system fluidizes readily (since minimum fluidization velocity and minimum bubbling velocity are similar) [19], air velocity was limited to twice the minimum fluidization velocity, which was calculated according to Equation 1 [20] where $U_{mf}$ is the minimum fluidization velocity; $g$ is gravity (9.80665 m.s$^{-2}$); $\mu$ is air viscosity; and $\rho_g$ and $\rho_p$ are respectively the gas and particle densities. The void fraction was calculated according to the semi empirical Ergun equation, which covers the entire range of flow rates as shown in Equation 2 [21], where $\Delta P$ is stage pressure drop; $U$ is superficial air velocity; and $\varepsilon$ is the bed void fraction. The pressure drop in each stage at the point of incipient fluidization was calculated according to the traditional Equation 3 [21], where $\varepsilon_{mf}$ is the minimum fluidization void fraction.

$$U_{mf} = 0.0008g(\rho_p - \rho_g)D_p^2/\mu \quad (1)$$

$$\frac{\Delta P}{H} = \frac{150U\mu(1-\varepsilon)^2}{D_p^2\varepsilon^3} + \frac{1.75U^2\rho_g(1-\varepsilon)}{\varepsilon^3 D_p} \quad (2)$$

$$\Delta \mathrm{P} = gH(\rho_p - \rho_g)(1 - \varepsilon_{mf}) \quad (3)$$

The fixed capital investment (FCI) for the plant consisted in equipment, freight and installation cost for columns, heat exchangers and compressors. Correlations taken from the literature were generally in the form of Equation 4 [22], where $K$ is an equipment constant; $C$ is equipment capacity; $n \leq 1$ is a dimensionless scale factor; and $F$ is a shape and material factor. The FCI was then annualized and then added to the yearly cost of utilities and startup cost according to Equation 5 [15]. The Marshall & Swift (*M&S*) index in Equation 4, which adjusts prices for inflation, was estimated as 2500 for late 2024 from values reported in the literature [16]. The utilities costs (cold water and high-pressure steam) were obtained from the literature for 2012 [17] and corrected for inflation [18] as shown in Table 2. Labor costs, taxes, depreciation, storage and transport costs, and revenues were not considered in this study, neither were carbon credits or other forms of subsidy.

$$FCI = \sum_{eqpts.} \frac{M\&S}{280} K(C)^n(F + 2.2) \quad (4)$$

$$\text{annualized cost} = \text{utilities yearly cost} + (FCI + \text{startup cost} + \text{cost of land}) \times \frac{i}{1-(1+i)^{-t}} \quad (5)$$

The balance, thermodynamic and Toth equations, along with equations for pressure drops, velocity, void fraction and costs (constraints), were implemented and solved in an environment within GAMS software (GAMS Software GmbH), release 48.2.0, using the non-linear programming solver CONOPT4 [23]. The model has 320 constraints (including inequalities) and 305 variables, with 95 definitional constraints. The objective function was to minimize the annualized cost defined in Equation 5 divided by yearly $CO_2$ capture (in mass units).

## RESULTS AND DISCUSSION

As expected for a non-linear formulation, the problem convergence was heavily dependent on initial guesses and variable bounds. Pressure, temperature and Toth equilibrium parameters were therefore bound at the maximum and minimum theoretical values, and strictly positive initial guesses were applied to variables that would have cause undefinition errors if set to zero.

Low particle Reynolds numbers in each stage in adsorption and desorption, between 4 and 7, indicate the system readily fluidizes. It also indicates that viscous and kinetic energy losses during air flow past the particles are of similar order of magnitude, thus the use of both terms of the Ergun equation in Equation 2 is justified [21]. Calculated minimum fluidization porosity by the Ergun semi-empirical equation was about 0.42, similar to the 0.43 value reported in a previous study [6] and within the usual 0.40-0.45 range for spherical particles [21]. Stage pressure at the adsorption column was initially fixed at 1.8 bar in preliminary simulations, then set as a variable. Optimized results set the pressure between 1.42 bar (bottom stage) and 1.17 bar (top stage). It is worth mentioning that the simulated bed height had a conservative estimate (1 m, as shown in Table 2).

An initial assessment of the influence of stage numbers in adsorption and desorption columns resulted in a small number of stages reaching the specified project constraints on separation and purity of Table 2. In fact, only 5 adsorption stages and a single desorption stage were enough to extract $CO_2$ from a 15%v/v composition

flue gas into a 0.5%v/v composition stream, while $CO_2$ captured and recovered was 95%v/v. This supports claims that capturing $CO_2$ at purities greater than 90% is physically as well as economically feasible [12]. This also confirms previous results from the authors [5,6], indicating that fluidized TSA column size is probably not an impediment for scaling up this $CO_2$ capture technology. Additionally, increasing the flue gas molar flow from 1.556 $mol.s^{-1}$ [5,6] to 413 $mol.s^{-1}$ showed economies of scale effects on the $CO_2$ capture cost per mass unit.

Figure 2 shows the optimized setup with five adsorption stages, indicating temperatures and process streams. It was also possible to confirm that not all stages in the columns needed heat exchangers, with some heat loads being set at zero during the optimization [5]. Figure 3 shows the heat load per heat exchanger for the entire process, and the heat exchanger between columns removes most of the heat applied in the desorption column.

Utilities are the main cost drivers, as shown in Figure 4, which highlights the importance of adequate energy efficiency management. Future studies might simulate a fluidized TSA process with a heat pump between the adsorption and desorption columns, which could render the heat exchanger for the recirculating solid obsolete. Figure 4 also shows that, from all equipment costs comprising the FCI, the compressor at the bottom of the adsorption column is the most expensive. In most conventional setups, flue gas is delivered at atmospheric pressure because its thermal and kinetic energy is largely expended during upstream processes. However, if these processes are optimized or even omitted, the inherent pressure drop in the system preceding the column can be minimized. Consequently, the flue gas could maintain a higher pressure from the combustion process to the TSA column. This elevated pressure at the column inlet would reduce or eliminate the necessity for a compressor, decreasing costs.

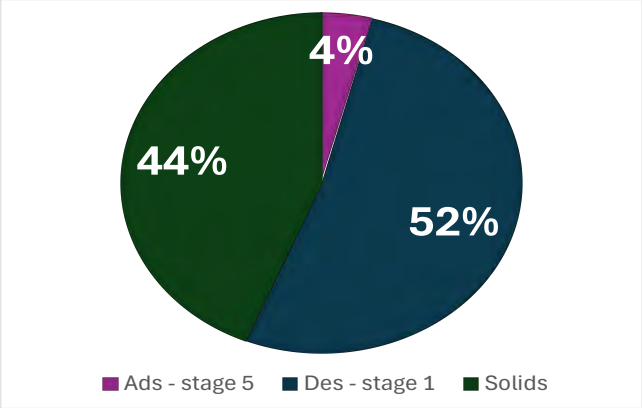



**Figure 3.** Heat loads per heat exchanger in an optimized fluidized TSA process.

The objective function value, the $CO_2$ capture cost per mass unit, was optimized at 84.6 $USD.t^{-1}$. This value falls within ranges reported in the literature for some technologies, and is significantly smaller than costs for direct air capture [2,30], as shown in Table 3. It is still, however, larger than amine-based absorption technologies [31], which are more mature despite their shortcomings. However, there is still room for fluidized TSA processes improvement before scale-up, such as development of new adsorbents as well as even greater economies of scale. For reference, the estimated market price of $CO_2$ at 96%v/v in Brazil is about 100 $USD.t^{-1}$, and

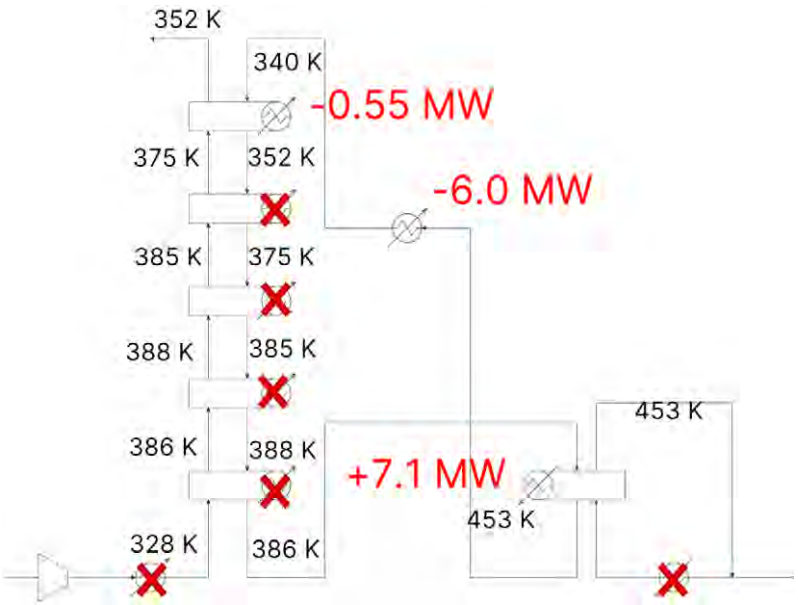



**Figure 2:** Fluidized TSA process schematics.

carbon credits for compliant industries sell as high as 50 USD.t$^{-1}$ in some countries.

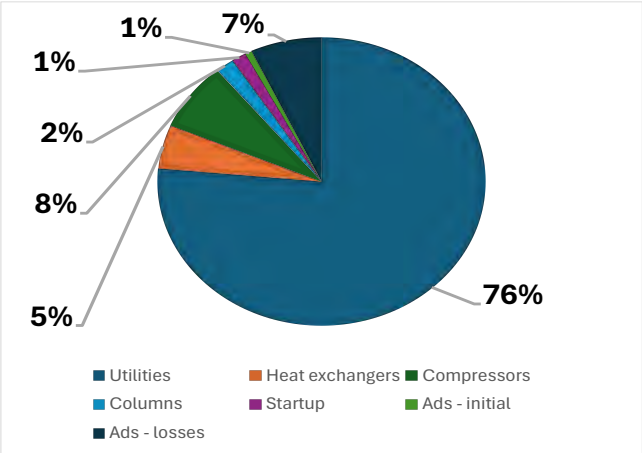



**Figure 4.** Main annualized cost drivers in an optimized fluidized TSA process.

**Table 3:** $CO_2$ capture costs reported in the literature.

| Reference | $CO_2$ capture cost (USD.t$^{-1}$) | $CO_2$ source |
|---|---|---|
| [2] | 40-120 | Industrial processes with diluted $CO_2$ streams |
| [2] | 134-342 | Direct air capture |
| [24] | 25-190 | BECCS |
| [25] | 20-290 | Several industrial processes |
| [26] | 36-107 | Industrial processes with diluted $CO_2$ streams |
| [27] | 84-129 | 5-20%v/v $CO_2$ |
| [28] | 104-147 | Wet flue gas, 15%v/v $CO_2$ |
| [29] | 88-288 | BECCS |
| [30] | 177-399 | Direct air capture |
| [31] | 31-45 | Blast furnace gas |

## CONCLUSION

These findings show that the methodology developed here is useful for guiding the conceptual design of fluidized TSA processes for carbon capture. This study draws key conclusions based on modeling and optimization of a fluidized TSA process to capture $CO_2$ from biomass flue gases. Process-wide optimization is crucial for balancing $CO_2$ capture efficiency and energy consumption, particularly in large-scale implementations. The study identifies key design parameters, such as heat exchanger placements, that significantly impact process efficiency. The research establishes guidelines for scaling up TSA systems, emphasizing computational tools for process design refinement. This study thus contributes to the development of fluidized TSA systems for biomass-based $CO_2$ capture, supporting the bioenergy sector and global decarbonization efforts. Multi-scale integrated modeling approaches should be integrated into future process optimization studies to further assess residence time distribution, assist in temperature control, and improve energy efficiency.

## ACKNOWLEDGEMENTS

This study was financed by Brazil's National Council for Scientific and Technological Development – CNPq, scholarship 153526/2024-6, through the INCT project CAPICUA 406710/2022-8. This study was also financed in part by the Coordenação de Aperfeiçoamento de Pessoal de Nível Superior – Brasil (CAPES) – Finance Code 001. We gratefully acknowledge support of the RCGI – Research Centre for Greenhouse Gas Innovation, hosted by the University of São Paulo (USP) and sponsored by FAPESP – São Paulo Research Foundation (2014/50279-4 and 2020/15230-5) and by Shell Brasil. We also thank the strategic and important support given by ANP (Brazil's National Oil, Natural Gas and Biofuels Agency) through the R&D levy regulation. The authors appreciate the reviewers' comments which have improved this work.

## REFERENCES

1. United Nations Framework Convention on Climate Change secretariat. https://unfccc.int/process-and-meetings/the-paris-agreement
2. International Energy Agency. https://www.iea.org/commentaries/is-carbon-capture-too-expensive
3. Patange OS, Garg A, Jayaswal S. An integrated bottom-up optimization to investigate the role of BECCS in transitioning towards a net-zero energy system: A case study from Gujarat, India. *Energy* 255:124508 (2022). https://doi.org/10.1016/j.energy.2022.124508
4. Sadr M, Aliabadi DE, Jordan M, Thrän D. A bottom–up regional potential assessment of bioenergy with carbon capture and storage in Germany. *Environ Res Lett* 19:114047 (2024). https://doi.org/10.1088/1748-9326/ad7edd
5. Beleli YS, Paiva JL, Seckler MM, Le Roux GAC. Optimization of a continuous multi-stage fluidized bed system for $CO_2$ capture utilizing temperature swing adsorption. *Comp Aided Chem Eng* 52:3233:3238 (2023). https://doi.org/10.1016/B978-0-443-15274-0.50515-1
6. Prado DS, Garcia EV, Sampronha E, Beleli YS, Moreira FS, Paiva JL, Le Roux GAC, Bastos-Neto M, Azevedo DCS, Silva ECN, Seckler MM. Multiple approaches for large-scale $CO_2$ capture by adsorption with 13X zeolite in multi-stage fluidized

beds assessment. *Adsorption* 30:429–455 (2024) https://doi.org/10.1007/s10450-023-00422-x
7. Peh SB, Farooq S, Zhao D. Techno-economic analysis of MOF-based adsorption cycles for postcombustion $CO_2$ capture from wet flue gas. *Chem Eng Sci* 268:118390 (2023). https://doi.org/10.1016/j.ces.2022.118390
8. Peh SB, Farooq S, Zhao D. A metal-organic framework (MOF)-based temperature swing adsorption cycle for postcombustion $CO_2$ capture from wet flue gas. *Chem Eng Sci* 250:117399 (2022). https://doi.org/10.1016/j.ces.2021.117399
9. Amiri M, Shahhosseini S. Optimization of $CO_2$ Capture from Simulated Flue Gas Using $K_2CO_3/Al_2O_3$ in a Micro Fluidized Bed Reactor. *Energy Fuels* 32(7): 7978-7990 (2018). https://doi.org/10.1021/acs.energyfuels.8b00789
10. Nazari NS, Afshari F, Mahmoudkani M, Ghaemi A. Optimization of carbon dioxide adsorption from industrial flue gas using zeolite 13X: A simulation study with Aspen Adsorption and response surface methodology. *Results Eng* 24:103206 (2024). https://doi.org/10.1016/j.rineng.2024.103206
11. United Nations. https://sdgs.un.org/goals
12. Brandl P, Bui M, Hallett JP, Dowell NM. Beyond 90% capture: Possible, but at what cost? *Int J Greenh Gas Control* 105:103239 (2021) https://doi.org/10.1016/j.ijggc.2020.103239
13. Peters MS, Timmerhaus KD. Plant Design and Economics for Chemical Engineers. McGraw Hill (1991).
14. Mette B, Kerskes H, Drück, H, Müller-Steinhagen H. Experimental and numerical investigations on the water vapor adsorption isotherms and kinetics of binderless zeolite 13X. *Int J Heat Mass Transf* 71:555-561 (2014). http://dx.doi.org/10.1016/j.ijheatmasstransfer.2013.12.061
15. Biegler LT, Grossmann IE, Westerberg AW. Systematic Methods of Chemical Process Design . Prentice Hall (1997).
16. Medina YC, Escalona AAS, Mediaceja YR, Morales OFG. Use of air cooled condenser in biomass power plants: a case study in Cuba. *Int J Heat Tech* 38:425-431 (2020). https://doi.org/10.18280/ijht.380218
17. Turton R, Bailie RC, Whiting WB, Shaeiwitz JA, Bhattacharyya D. Analysis, Synthesis, and Design of Chemical Processes. Prentice Hall (2012).
18. Bureau of Labor Statistics, USA government. https://data.bls.gov/cgi-bin/cpicalc.pl
19. Couper JR, Penney WR, Fair JR, Walas SM. Chemical Process Equipment: Selection and Design. Elsevier (2005).
20. Cheremisinoff NP, Cheremisinoff PN. Hydrodynamics of Gas-Solids Fluidization. Gulf Pub Co (1984).
21. McCabe WL, Smith JC, Harriott P. Unit Operations of Chemical Engineering. McGraw Hill (2005).
22. Douglas JM. Conceptual Design of Chemical Processes. McGraw Hill (1988).
23. GAMS Software GmbH. https://www.gams.com/46/docs/S_CONOPT4.html
24. Hochman G, Appasamy V. The case for carbon capture and storage technologies. *Environments* 11:52 (2024). https://doi.org/10.3390/environments11030052
25. Skobelev DO, Cherepovitsyna AA, Guseva TV. Carbon capture and storage: net zero contribution and cost estimation approaches. *J Min Inst* 259:125-140 (2023). https://doi.org/10.31897/PMI.2023.10
26. Cameron L, Carter A, Sievert K. https://www.iisd.org/articles/deep-dive/why-carbon-capture-storage-cost-remains-high
27. Costa A, Henrotin A, Heymans N, Dubois L, Thomas D, De Weireld G. Multi-objective optimization of a hybrid carbon capture plant combining a vacuum pressure swing adsorption (VPSA) process with a carbon purification unit (CPU). *Chem Eng J* 493:152345 (2024). https://doi.org/10.1016/j.cej.2024.152345
28. Peh SB, Farooq S, Zhao D. Techno-economic analysis of MOF-based adsorption cycles for postcombustion $CO_2$ capture from wet flue gas. *Chem Eng Sci* 268:118390 (2023). https://doi.org/10.1016/j.ces.2022.118390
29. Wiesberg IL, Medeiros JL, Mello RVP, Maia JGSS, Bastos JBV, Araújo OQF. Bioenergy production from sugarcane bagasse with carbon capture and storage: Surrogate models for techno-economic decisions. *Renew Sustain Energy Rev* 150:111486 (2021). https://doi.org/10.1016/j.rser.2021.111486
30. Shi WK, Zhang XJ, Liu X, Wei S, Shi X, Wu C, Jiang L. Temperature-vacuum swing adsorption for direct air capture by using low-grade heat. J Clean Prod 414:137731 (2023). https://doi.org/10.1016/j.jclepro.2023.137731
31. Ding X, Chen H, Li J, Zhou T. Comparative techno-economic analysis of $CO_2$ capture processes using blended amines. *Carbon Capture Sci Tech* 9:100136 (2023). https://doi.org/10.1016/j.ccst.2023.100136

© 2025 by the authors. Licensed to PSEcommunity.org and PSE Press. This is an open access article under the creative commons CC-BY-SA licensing terms. Credit must be given to creator and adaptations must be shared under the same terms. See https://creativecommons.org/licenses/by-sa/4.0/



Systems & Control Transactions

**Research Article - Peer Reviewed Conference Proceeding**
ESCAPE 35 - European Symposium on Computer Aided Process Engineering
Ghent, Belgium. 6-9 July 2025
Jan F.M. Van Impe, Grégoire Léonard, Satyajeet S. Bhonsale,
Monika E. Polańska, Filip Logist (Eds.)

PSE PRESS

# Safe Reinforcement Learning with Lyapunov-Based Constraints for Control of an Unstable Reactor

**José R. Torraca Neto[a*], Bruno D. O. Capron[a], Argimiro R. Secchi[a,b] and Antonio d.R. Chanona[c]**

[a] Universidade Federal do Rio de Janeiro, Chemical and Biochemical Process Engineering – EQ, Rio de Janeiro, RJ, Brazil
[b] Universidade Federal do Rio de Janeiro, Chemical Engineering Program – COPPE, Rio de Janeiro, RJ, Brazil
[c] Imperial College London, Sargent Centre for Process Systems Engineering, London, United Kingdom
* Corresponding Author: joseneto@eq.ufrj.br.

## ABSTRACT

This work presents a Lyapunov-based framework for safe reinforcement learning (RL) applied to the control of an unstable reactor. The proposed method imposes stability constraints on the value and Q-functions through a Lyapunov candidate function defined as the negative of these functions, $L(s)=-V(s)$ and $L(s,a)=-Q(s,a)$. Constraints enforce positivity of the Lyapunov candidate function and non-positive time derivatives, promoting monotonic behavior aligned with Lyapunov stability conditions. The framework was tested on both on-policy (PPO) and off-policy (SAC, TD3, and DDPG) RL algorithms, with performance evaluated against their baseline versions and a nonlinear Model Predictive Controller (NMPC). Results showed that stability constraints significantly improved control performance across all tested algorithms, yielding consistently higher cumulative rewards, reduced overshoot, and decreased variability. Derivative-based constraints successfully mitigated abrupt changes and oscillatory behavior in the Q and value functions, especially evident in PPO, DDPG, and TD3. This work demonstrates that Lyapunov-based constraints are an effective tool for improving the safety and stability of RL algorithms in safety-critical applications. The proposed approach avoids the complexity of auxiliary optimization and offers a computationally efficient solution for enhancing the safety and stability of RL algorithms in safety-critical control applications.

**Keywords**: Lyapunov functions, process control, safety-critical systems, unstable dynamics

## INTRODUCTION

Reinforcement Learning (RL) has shown great potential for solving complex control tasks. However, its application in safety-critical systems, such as unstable reactors, remains limited due to the absence of closed-loop stability guarantees and inherent mechanisms for enforcing hard constraints, unlike traditional Model Predictive Control (MPC) formulations [1]. These limitations pose significant challenges in process control, where stability and constraint satisfaction are of prime importance.

Safe RL aims to address these challenges by incorporating mechanisms that enforce stability and safety constraints during both training and deployment. Unlike conventional control methods, which explicitly encode these properties, RL optimizes policies directly from data, often without structured guarantees of stability, particularly in model-free RL approaches. To overcome these challenges, this work introduces a Lyapunov-based framework to enforce closed-loop stability by directly constraining the value function, without relying on explicit system models.

It is important to distinguish between safety constraint enforcement, which ensures the system operates within predefined safety bounds, and closed-loop stability guarantees, which ensure that the system converges to a stable/stabilized operating point over time. While both aspects are critical for safe control, our approach focuses on the latter by leveraging Lyapunov functions to directly enforce stability during policy learning.

Lyapunov functions provide a mathematical framework for enforcing stability by ensuring that the system's "energy" decreases over time. However, designing such functions for RL controllers is challenging and often requires detailed system-specific knowledge [2]. For instance, Brunke et al. [3] emphasized the importance of

developing RL algorithms that maintain safety during training and deployment, especially in uncertain environments where modelling errors or disturbances can compromise stability. Moreover, Gu et al. [4] highlighted that constructing Lyapunov constraints that remain valid across varying conditions remains an open challenge, particularly in high-dimensional and stochastic settings.

Recent advancements in safe RL have highlighted the potential of integrating stability guarantees directly into the learning process. For example, methods leveraging Lyapunov functions [5] define invariant state domains that ensure stability under neural network control policies. This approach provides a framework for guaranteeing system convergence to an equilibrium point while managing nonlinearities and disturbances. Similarly, Osinenko et al. [6] proposed an RL framework incorporating Lyapunov-like constraints, which utilize a control Lyapunov function (CLF) as a basis to establish semi-global stability guarantees through an online sample-and-hold optimization scheme, demonstrating its efficacy in maintaining closed-loop stability during learning. Another notable advancement involves using control invariant sets (CIS) [7], which streamline training by embedding stability guarantees into the learning process through invariant set constraints.

Despite these advancements, significant gaps remain. Lyapunov-based methods often require identifying suitable Lyapunov functions or barrier functions, which can be computationally expensive and challenging for highly nonlinear systems. Furthermore, these approaches frequently rely on predefined invariant domains or approximations that may lack generalization across diverse operational conditions. CIS-based methods, while efficient in improving sample efficiency and providing robust stability guarantees, require precise state reset mechanisms and careful integration of invariant constraints into both offline and online phases, which may not always translate effectively to complex control environments.

Building on these foundations, this work introduces a Lyapunov-based framework that simplifies the enforcement of closed-loop stability by directly constraining the value function. Unlike existing methods that rely on auxiliary cost objectives, this approach integrates stability constraints into the reinforcement learning process, reducing computational overhead and improving scalability.

Conventional RL implementations typically fall into two main categories: on-policy and off-policy algorithms. On-policy methods, such as Proximal Policy Optimization (PPO), update the policy using data sampled sequentially from the current policy, allowing for consistent tracking of changes in the value function over time. This sequential sampling simplifies the computation of time derivatives, making on-policy algorithms more stable under policy updates. However, these methods require significant amounts of data due to the need for fresh samples in each update cycle. Conversely, off-policy methods, such as Soft Actor-Critic (SAC), Twin Delayed Deep Deterministic Policy Gradient (TD3), and Deep Deterministic Policy Gradient (DDPG), use experience replay buffers that enable random sampling of past experiences. This improves sample efficiency but complicates the estimation of time derivatives due to the lack of temporal ordering in the samples, making the learning process more prone to instability.

This work proposes to enforce closed-loop stability across on-policy and off-policy RL algorithms using Lyapunov-based constraints. Specifically, the Lyapunov candidate functions were defined explicitly as the negatives of the value (on-policy) and Q-functions (off-policy), $L(s) = -V(s)$ and $L(s,a) = -Q(s,a)$. Stability is enforced by penalizing positive values of the original functions, thus ensuring $V(s), Q(s,a) < 0$. Additionally, penalties on time derivatives encourage monotonic increases in these original functions, which translates directly to monotonic decreases in the Lyapunov functions, satisfying the Lyapunov stability condition ($dL/dt \leq 0$). These constraints promote that the resulting learned policies consistently meet stability requirements. The main contributions of this work are as follows:

- A unified Lyapunov-based stability constraint framework applicable to both on-policy and off-policy RL algorithms.
- A comparative analysis of time derivative-based and positivity constraints and their impact on training stability.
- An evaluation of the proposed approach to control an unstable reactor, demonstrating improved safety and performance compared to baseline methods.

The remainder of this paper is structured as follows: Section 2 presents the framework and implementation details. Section 3 provides experimental results and discussion. Section 4 concludes with a summary and future research directions.

## METHODOLOGY

### Framework and Environment Design

This work utilizes PC-Gym [8], an open-source framework for developing RL environments in chemical process control systems, for implementing the environment. PC-Gym provides robust tools for simulating process control problems, including customizable constraints, disturbance generation, and reward function design. It offers compatibility with RL algorithms like PPO, SAC, DDPG, and TD3, enabling standardized

benchmarking for process systems engineering problems.

The environment was constructed to simulate the dynamics of a Continuous Stirred Tank Reactor (CSTR), a nonlinear system often used as a benchmark in process systems engineering due to its complex dynamics and control challenges. The CSTR involves an irreversible reaction that converts species A into species B, with cooling provided by water circulating through a coiled tube. Two coupled nonlinear ordinary differential equations govern the dynamics:

$$\frac{dC_A}{dt} = \frac{q}{V}(C_{A,f} - C_A) - kC_A e^{\frac{-E_A}{RT}} \quad (1)$$

$$\frac{dT}{dt} = \frac{q}{V}(T_f - T) - \frac{\Delta H_R}{\rho C_p} kC_A e^{\frac{-E_A}{RT}} + \frac{UA}{\rho C_p V}(T_c - T) \quad (2)$$

Here, $C_A$ and T represent the concentration of reactant A and reactor temperature, respectively, while $T_c$ is the cooling water temperature, serving as the control input. Additional model parameters include feed concentration ($C_{A,f}$), feed temperature ($T_f$), volumetric flow rate (q), reactor volume (V), reaction rate constant (k), activation energy ($E_A$), universal gas constant (R), reaction enthalpy ($\Delta H_R$), fluid density (ρ), heat capacity ($C_p$), and heat transfer coefficient-area product (UA). The nonlinearities, particularly the exponential dependence of reaction rate on temperature, pose significant control challenges, including potential instability and multiple steady states. Simulation parameters and constraints were designed to realistically represent process control challenges:

**Action Space:** The manipulated variable $T_c$ was defined as a continuous range between 250 K and 350 K, normalized to [0, 1] during training.

**Observation Space:** The state variables $C_A$, T, and setpoint temperature $T_{SP}$ were normalized to [0,1] based on their physical bounds ([0.0, 200 K, 300 K] to [1.0, 600 K, 400 K]). Additionally, Gaussian measurement noise proportional to 0.1% of each observed state value was introduced during training.

**Reward Function:** Negative squared error between normalized T and $T_{SP}$.

**Dynamic Setpoint Strategy:** The setpoint dynamically transitioned midway through the episode to evaluate the RL algorithms' adaptability.

**Disturbance Generation:** Time-indexed disturbances in feed concentration ($C_{A,f}$) and inlet temperature ($T_f$) were dynamically generated to emulate real-world variability. These disturbances were sampled from predefined bounds and applied over multiple episodes to test robustness.

The implementation includes a steady-state solver to initialize the system state variables, ensuring valid initial conditions under varying disturbances. The reward function was designed so that the difference between the normalized reactor temperature and the setpoint temperature was squared and scaled, ensuring that the reward signal directly incentivized accurate tracking of the setpoint while maintaining interpretability.

The setpoint strategy was implemented dynamically, splitting the episode into two phases. During the first half of each episode, the setpoint was initialized to the steady-state temperature derived from the system's initial conditions. In the second half, the setpoint transitioned to a fixed value (e.g., 340 K). This approach tests the RL agent's ability to adapt to changing operational goals while maintaining system stability.

## Safe RL Implementation

The proposed stability enforcement mechanism is inspired by Lyapunov principles, focusing explicitly on the positive definiteness and monotonic decrease conditions required for stability. Given our reward function defined as the negative squared difference between the current state and desired setpoint, we define Lyapunov candidate functions as L(s) = −V(s) and L(s,a) = −Q(s,a) to maintain a consistent formulation where L > 0 and dL/dt ≤ 0 indicate stable behavior. The stability constraints, consistently applied across PPO, SAC, DDPG, and TD3 algorithms, are:

**Positive Definiteness Constraint:** Penalizing positive values of the original value/Q-functions (V, Q) to promote them remains negative, thereby enforcing L > 0.

**Time Derivative Constraint:** Penalizing decreases in the original value/Q-functions between consecutive time steps, ensuring their monotonic increase. This promotes a non-positive time derivative (dL/dt ≤ 0), satisfying the Lyapunov stability criteria.

These constraints were applied dynamically during training, with penalties weighted by hyperparameters $\lambda_{pos}$ (positive definiteness) and $\lambda_{der}$ (time derivative constraint) —additionally, the algorithms logged mean values and time derivatives of value/Q functions for interpretability and transparency.

### Safe RL Algorithm Implementations

#### 1. DDPG and TD3:

These off-policy methods relied on replay buffers for experience sampling. The critic loss incorporated stability constraints as follows:

$$\text{critic_loss} = \text{MSE_loss}(\text{curr_Q}, \text{target_Q}) + \lambda_{pos} \cdot \max(0, \text{curr_Q}) + \lambda_{der} \cdot \max(0, \text{prev_Q} - \text{curr_Q}) \quad (3)$$

where $\lambda_{pos}$ and $\lambda_{der}$ are penalty weights. Here:

$\text{curr_Q}$: The instantaneous Q-values estimated by the critic for the current batch of samples.

$\text{prev_Q}$: The Q-values for the same batch are computed during the previous gradient step in the current training iteration.

TD3 further used twin critics and applied constraints

to the minimum of the critics' Q-values for robustness. Noise models for exploration were algorithm-specific:

**DDPG:** Ornstein-Uhlenbeck noise was used, introducing temporal correlations in action exploration.

**TD3:** Normal noise was employed along with target policy noise and noise clipping for stable updates.

### 2. SAC:

The entropy-regularized objective was preserved in the SAC implementation to balance exploration and exploitation while incorporating stability constraints into the Q-function updates. The critic loss was computed as:

$$\text{critic_loss} = 0.5 \sum_i \text{MSE_loss}(\text{curr_Q}_i, \text{target_Q}) + \lambda_{pos} \cdot \max(0, \text{curr_Q}) + \lambda_{der} \cdot \max(0, \text{prev_Q} - \text{curr_Q}) \quad (4)$$

where $i$ indexes over multiple critics.

The actor loss was computed using the minimum Q-value across critics and included the entropy regularization term:

$$\text{actor_loss} = \mathbb{E}[\alpha \ \log \pi(a|s) - \text{minQ(s, a)}] \quad (5)$$

where $\alpha$ is the entropy coefficient, and $\pi(a|s)$) is the stochastic policy. This promotes safe exploration while optimizing the policy.

### 3. PPO:

PPO, an on-policy method, inherently stabilizes training using a clipped surrogate objective. Additional constraints on the value function $V(s)$ were introduced:

$$\text{loss} = \text{policy_loss} + \beta_{vf} \cdot \text{value_loss} + \lambda_{ent} \cdot \text{entropy_loss} + \lambda_{pos} \cdot \max(0, -\text{V(s)}) + \lambda_{der} \cdot \max(0, \text{V(s)} - \text{prev_V}) \quad (6)$$

where $\beta_{vf}$ and $\lambda_{ent}$ are coefficients for the value and entropy losses. Value functions were dynamically monitored for compliance with these constraints.

## Hyperparameter Optimization

This work employed Optuna [9], a hyperparameter optimization framework, to tune both common and algorithm-specific hyperparameters across all reinforcement learning (RL) algorithms. Optuna utilizes the Tree-structured Parzen Estimator (TPE) as its default optimization algorithm, enabling efficient exploration of the hyperparameter space.

A unified approach was used for tuning common hyperparameters across all algorithms, including:

- Learning rate ($\alpha$),
- Discount factor ($\gamma$),
- Replay buffer size (off-policy only),
- Batch size,
- Start step for training,
- Target network update factor ($\tau$).

Algorithm-specific optimizations included:

**DDPG:** Ornstein-Uhlenbeck action noise parameters ($\mu, \sigma, \theta, dt$).

**TD3:** Target policy noise parameters ($\sigma$, noise clip).

**PPO:** Epoch count, Generalized Advantage Estimation (GAE) parameters ($\lambda$), clip range, and entropy coefficient.

**SAC:** Entropy coefficient and seed for reproducibility.

For all Safe RL implementations, additional stability-specific hyperparameters were tuned:

- $\lambda_{pos}$: Weight for the positive definiteness penalty.
- $\lambda_{der}$: Weight for the time derivative penalty.

## Evaluation

To establish a performance benchmark, the baseline RL cases and a nonlinear Model Predictive Controller (NMPC) were implemented [8]. This controller leveraged full knowledge of the system dynamics and perfect state estimation to solve the optimal control problem at each time step. The NMPC formulation incorporated features absent in the RL-based controllers, such as state tracking and normalized control effort terms for consistent scaling across variables. Additionally, the system dynamics were discretized using orthogonal collocation to achieve high accuracy. This oracle served as the performance ceiling, representing near-optimal control strategies under perfect conditions, allowing us to quantitatively assess the efficacy of the RL algorithms.

Each RL policy (PPO, SAC, DDPG, and TD3) was evaluated across 20 episodes, each initialized with identical initial conditions and setpoint profiles that differed from those encountered during training. The primary variation among these episodes was introduced through progressively increasing levels of state measurement noise, linearly scaled from 0.0% to 0.5%. Performance metrics, including cumulative rewards and control effort, were collected to assess each policy's robustness to measurement noise. The collected data were aggregated to compute median cumulative rewards and mean value/Q functions. Since the reward was defined as the negative squared difference between the controlled states and setpoints, it offers a meaningful comparison to the NMPC oracle. Additionally, the evaluation tracked the evolution of the value/Q functions and their time derivatives for each policy. Reward distributions were visualized using histograms computed from cumulative rewards across evaluation episodes.

# RESULTS AND DISCUSSION

Figures 1 and 2 present the median performance of RL algorithms (SAC, PPO, DDPG, and TD3) compared to the NMPC oracle across 20 unseen evaluation episodes.

Figure 1 corresponds to the algorithms without stability constraints, while Figure 2 shows their performance under stability constraints.

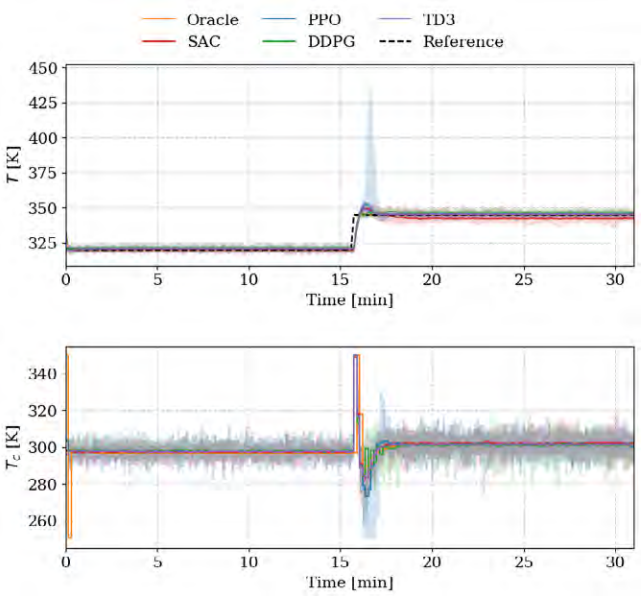



**Figure 1.** Performance of RL algorithms without stability constraints compared to the NMPC oracle (shaded areas: min-max, solid lines: median). Plots show (top) reactor temperature (T) and (bottom) control input $T_c$.

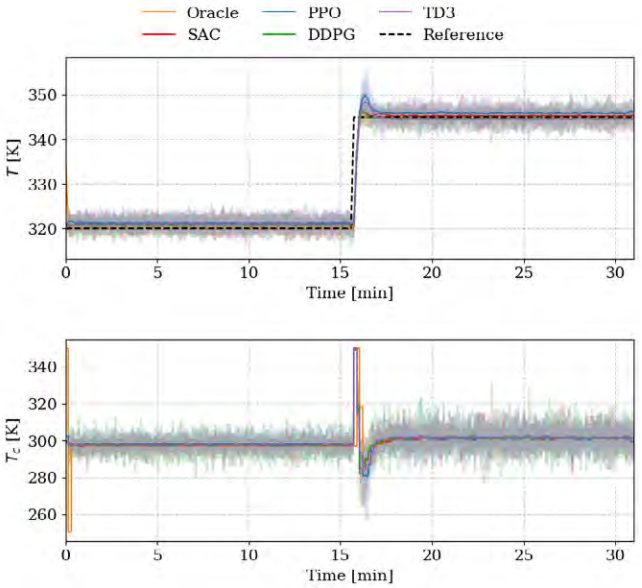



**Figure 2.** Performance of RL algorithms with stability constraints compared to the NMPC oracle (shaded areas: min-max, solid lines: median). Plots show (top) reactor temperature (T) and (bottom) control input $T_c$.

Under the baseline scenario (Figure 1), PPO and SAC exhibit significant overshoot and oscillations in reactor temperature following the setpoint change at 15 min, with PPO showing the largest transient deviation, indicating less stability. Coolant temperature ($T_c$) shows significant fluctuations, particularly for PPO.

In contrast, the safe RL scenario (Figure 2) demonstrates improved stability across all RL algorithms tested. Overshoot and variability are significantly reduced, while manipulated variable responses ($T_c$) also present smaller transient fluctuations, especially PPO.

The reward distribution (Figure 3) highlights the performance differences between safe and baseline RL algorithms. The safe RL strategies (SAC, PPO, and DDPG) generally achieve cumulative rewards that are more concentrated and shifted towards higher values compared to their baseline counterparts. Baseline methods such as SAC and DDPG display wider distributions with lower reward values, indicating greater variability and less consistent performance.

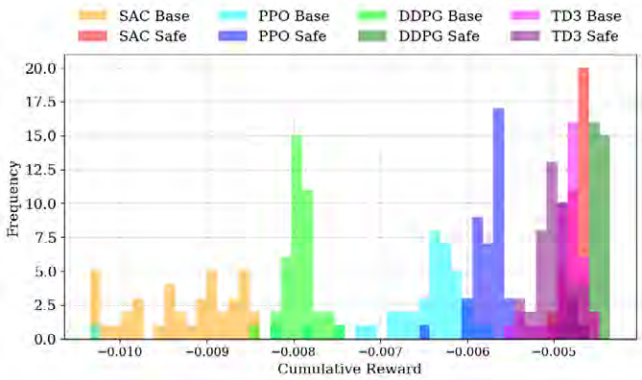



**Figure 3.** Distribution of cumulative rewards comparing baseline and safe RL strategies (SAC, PPO, DDPG, and TD3).

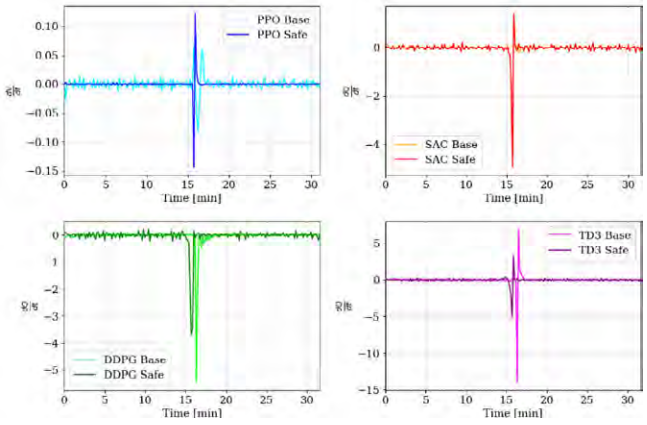



**Figure 4.** Comparison of time derivatives of Q-function (SAC, DDPG, TD3) or value function (PPO) for baseline and safe RL implementations.

Figure 4 shows the time derivatives of the Q/value functions for SAC, TD3, DDPG, and PPO, comparing baseline and safe implementations. Standard deviations are omitted for clarity. Safe PPO exhibits the most significant reduction in fluctuations, with near-zero oscillations. Safe implementations for DDPG and TD3 demonstrate reduced spikes, indicating improved stability.

However, safe PPO and SAC display larger transition spikes, likely due to value/Q function penalization on the setpoint change.

The spikes during setpoint transitions could be softened by "freezing" or temporarily relaxing constraint penalties during these events. Increasing training episodes or fine-tuning constraints may also further enhance stability across all algorithms.

## CONCLUSION

This work introduced a Lyapunov-based framework for stabilizing RL algorithms by directly constraining value and Q-functions. The proposed approach significantly improved the control performance of an unstable reactor when compared to baseline methods. Results demonstrated consistently higher cumulative rewards across all tested algorithms, indicating a reduction in setpoint tracking errors. Furthermore, safe RL substantially reduced overshoot and control variability, especially in SAC, PPO, and DDPG.

Time derivative-based penalties were critical for achieving monotonic decreases in the defined Lyapunov functions (L=−V and L=−Q), thereby promoting Lyapunov stability criteria. This improvement was particularly evident in DDPG and TD3, with reduced transient spikes. In contrast, PPO showed the lowest overall oscillations but still displayed higher transient spikes, which could be due to the value function penalization on the setpoint change.

The results demonstrate that the proposed Lyapunov-based framework effectively enhances stability in RL-based control of unstable systems. Future work should explore dynamic penalty tuning, mechanisms to reduce transient spikes during disturbances (e.g., freezing penalties), and application to more complex environments to broaden its applicability.

## ACKNOWLEDGEMENTS

Jose Rodrigues Torraca Neto reports financial support provided by Coordination for the Improvement of Higher Education Personnel (CAPES), Finance Code 001. Argimiro R. Secchi reports a relationship with CNPq that includes funding grants (303587/2020-2). Other authors declare that they have no known competing financial interests or personal relationships that could have appeared to influence the work reported in this paper.

## REFERENCES

1. Badgwell TA, Lee JH, Liu KH. Reinforcement learning – overview of recent progress and implications for process control. In: 13th International Symposium on Process Systems Engineering (PSE 2018). Eds: Eden MR, Ierapetritou MG, Towler GP. Vol 44, pp 71–85. Elsevier (2018) https://doi.org/10.1016/B978-0-444-64241-7.50008-2
2. Annaswamy AM. Adaptive control and intersections with reinforcement learning. Annu Rev Control Robot Autom Syst 6:65–93 (2023) https://doi.org/10.1146/annurev-control-062922-090153
3. Brunke L, Greeff M, Hall AW, Yuan Z, Zhou S, Panerati J, Schoellig AP. Safe learning in robotics: from learning-based control to safe reinforcement learning. Annu Rev Control Robot Autom Syst 5:411–444 (2022) https://doi.org/10.1146/annurev-control-042920-020211
4. Gu S, Yang L, Du Y, Chen G, Walter F, Wang J, Knoll A. A review of safe reinforcement learning: methods, theories, and applications. IEEE Trans Pattern Anal Mach Intell 46:11216-11235 (2024) https://doi.org/10.1109/TPAMI.2024.3457538
5. Gu S, Kumar R. Robust optimal safe and stability guaranteeing reinforcement learning control for quadcopter. arXiv (2024) https://arxiv.org/abs/2412.14003
6. Osinenko P, Beckenbach L, Göhrt T, Streif S. A reinforcement learning method with closed-loop stability guarantee. IFAC-PapersOnLine 53(2):8043–8048 (2020) https://doi.org/10.1016/j.ifacol.2020.12.2237
7. Bo S, Agyeman BT, Yin X, Liu J. Control invariant set enhanced safe reinforcement learning: improved sampling efficiency, guaranteed stability and robustness. arXiv (2023) https://arxiv.org/abs/2305.15602
8. Bloor M, Torraca J, Sandoval IO, Ahmed A, White M, Mercangöz M, Tsay C, Del Rio Chanona EA, Mowbray M. PC-Gym: benchmark environments for process control problems. arXiv (2024) https://arxiv.org/abs/2410.22093
9. Akiba T, Sano S, Yanase T, Ohta T, Koyama M. Optuna: a next-generation hyperparameter optimization framework. arXiv (2019) https://arxiv.org/abs/1907.10902

© 2025 by the authors. Licensed to PSEcommunity.org and PSE Press. This is an open access article under the creative commons CC-BY-SA licensing terms. Credit must be given to creator and adaptations must be shared under the same terms. See https://creativecommons.org/licenses/by-sa/4.0/



Systems & Control Transactions

**Research Article - Peer Reviewed Conference Proceeding**
ESCAPE 35 - European Symposium on Computer Aided Process Engineering
Ghent, Belgium. 6-9 July 2025
Jan F.M. Van Impe, Grégoire Léonard, Satyajeet S. Bhonsale,
Monika E. Polańska, Filip Logist (Eds.)

PSE PRESS

# Cost-effective Process Design and Optimization for Decarbonized Utility Systems Integrated with Renewable Energy and Carbon Capture Systems

**Haryn Park[a], Joohwa Lee[a], Bogdan Dorneanu[b], Harvey Arellano-Garcia[b]*, and Jin-Kuk Kim[a]***

[a] Hanyang University, Department of Chemical Engineering, Seoul, Republic of Korea
[b] Brandenburg University of Technology Cottbus - Senftenberg, Process and Plant Technology, Cottbus, Germany
* Corresponding Authors: arellano@b-tu.de, jinkukkim@hanyang.ac.kr

## ABSTRACT

Industrial decarbonization is considered one of the key objectives in mitigating global climate change. To achieve a net-zero industry requires actively transitioning from fossil fuel-based energy sources to renewable alternatives. However, the intermittent nature of renewable energy sources poses challenges to a reliable and robust supply of energy for industrial sites. Therefore, the integration of renewable energy systems with existing industrial processes, subject to energy storage solutions and main grid interconnections, is essential to enhance operational reliability and overall energy resilience. This study proposes a novel framework for the design and optimization of industrial utility systems integrated with renewable energy sources. A monthly-based analysis is adopted to consider variable demand and non-constant availability in renewable energy supply. Moreover, carbon capture is considered in this work as a viable decarbonization measure, which can be strategically combined with renewable-based electrification. The proposed optimization model evaluates the economic trade-offs of integrating carbon capture, renewable energy, and energy storage. By applying this approach, systematic design guidelines are developed for the transition of a conventional steady-state utility system toward renewable energy integration, ensuring economically viable and sustainable energy management in process industries.

**Keywords**: Renewable energy, CO2 capture, Industrial utility operation, Cost optimization, Process integration

## INTRODUCTION

The International Energy Agency (IEA) estimates that the industrial sector, including power generation, accounts for a major portion of overall $CO_2$ emission [1]. Therefore, the 2030 targets for industrial energy consumption focus on increasing the share of electricity while reducing reliance on fossil fuels. In particular, electricity generated from renewable sources is identified as a key solution to achieve environmental improvements in the industrial sector.

In South Korea, where most energy supply systems rely on fossil fuel-based facilities, the integration of renewable energy systems with existing infrastructure for process utility enhances system operational stability by addressing the intermittency of renewable energy sources. Additionally, carbon capture technology, as the additional solution of industrial decarbonization, can complement existing fossil fuel-based utilities by reducing environmental burdens [2], while helping to resolve potential challenges that may occur during the transitional period to complete process integration. However, previous studies on the optimization of integrated energy supply systems often fail to fully account for the flexibility and/or constraints associated with renewable energy production. In many cases, the power demand of the utility systems is met through electricity imported from external plants for renewable electricity, rather than reflecting the complexity of direct integration [3]. Furthermore, the impact of $CO_2$ emitted from fossil fuels in the integrated process is often oversimplified as a carbon tax without considering the potential role and benefits of incorporating carbon capture processes.

This study proposes integrating conventional utility

systems with $CO_2$ capture processes and renewable energy systems, including electricity storage, as a practical approach for industrial decarbonization. A cost-based optimization framework is developed as a monthly-based analysis to evaluate strategies for the economically efficient operation of the integrated process. Monthly minimum costs are determined using weather data specific to South Korea, allowing for more accurate cost predictions in renewable electricity generation and enhancing the reliability of the optimization model.

## METHODOLOGY

To achieve an environmentally upgraded utility system, the integration of renewable energy and carbon capture processes is optimized with the objective function, as given in Eq. (1), of minimizing overall system costs while meeting practical energy demands as outlined in **Table 1**.

$$f_{Total,Min} = f_{Utility,Min} + f_{Renewable,Min} \quad (1)$$

Steam demand is supplied exclusively by fossil fuel-based systems, with the low-pressure (LP) steam demand allowed to vary during process optimization, while steam requirements for other pressure levels remain fixed at constant values. Electricity demand can be met either through the integrated system or by purchasing it from external sources, depending on the specific scenario evaluated. The process flow diagram illustrating the overall system in this study is described in **Figure 1**.

**Table 1:** Energy demand of a Total site.

| Energy | Unit | Values |
|---|---|---|
| Electricity | $MW_e$ | Min. 68.0 |
| VHP steam | t/h | 20.0 |
| HP steam | t/h | 54.5 |
| MP steam | t/h | 55.9 |
| LP steam | t/h | 128.0+$\alpha$* |

The costing parameters used to calculate the annualized cost of each system are based on previous studies [3, 5]. For renewable facilities, the cost references were adjusted by scaling down costs according to the GDP ratio to account for the differences in economic contexts between South Korea and the UK, from which the original data was derived. The cost-related values applied in this study are summarized in **Table 2**.

### Utility Process

The fossil fuel-based utility system uses a traditional configuration with boilers and gas turbines (GT) paired with heat recovery steam generators (HRSG), followed by electricity generation via steam turbines (ST). In line with current industrial trends, coal and natural gas are selected as the primary fuel sources for steam and electricity production. The system meets four different steam demands at varying pressure levels, as outlined in **Table 1**. Residual steam is used to generate electricity via back-pressure steam turbines. For simplicity, the fossil fuel-based facility is represented using a streamlined model developed in UniSim®, as referenced previously in [3].

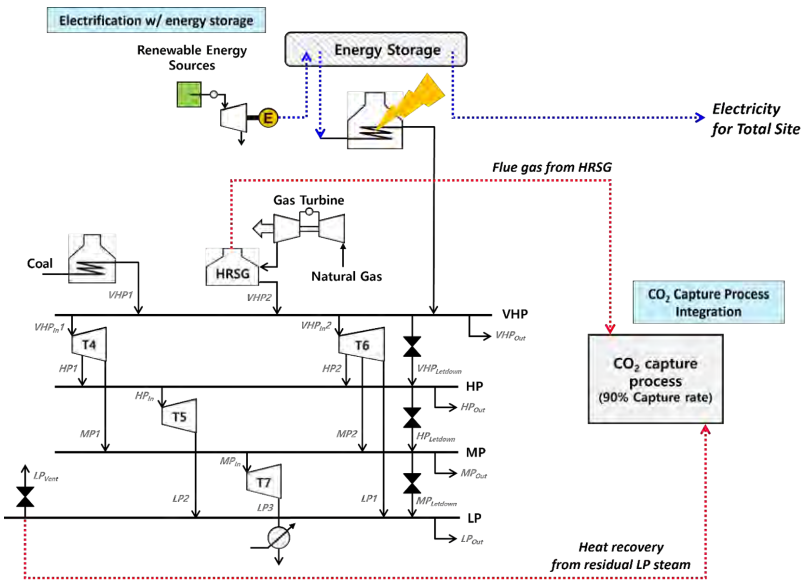



**Figure 1:** Simplified process flow diagram of the utility system integrated with renewable energy supply and carbon capture.

**Table 2:** Costing parameters considering the site location for the integrated utility process.

| Parameters | Unit | Description | Values |
|---|---|---|---|
| $C_{coal}$ | \$/t | Coal price | 65 |
| $C_{NG}$ | \$/t | Natural gas price | 220 |
| $NHV_{coal}$ | kJ/kg | Net heating value of coal | 28,000 |
| $NHV_{NG}$ | kJ/kg | Net heating value of Natural gas | 47,206 |
| $C_{elec,ex}$ | \$/kWh | Electricity price (Export) | 0.067 |
| $C_{elec,im}$ | \$/kWh | Electricity price (Import) | 0.081 |
| $C_{water}$ | \$/t | Water price | 0.005 |
| $CP_{PV}$ | \$/kW | PV capital cost | 781.3 |
| $OP_{variable,PV}$ | \$/kWh | PV variable O&M cost | 0.004 |
| $OP_{fixed,PV}$ | \$/kW/yr | PV fixed O&M cost | 9.8 |
| $CP_{WT}$ | \$/kW | WT capital cost | 3156.4 |
| $OP_{variable,WT}$ | \$/kWh | WT variable O&M cost | 0.5 |
| $OP_{fixed,WT}$ | \$/kW/yr | WT fixed O&M cost | 23.4 |
| $CP_{EST}$ | \$/kW | EST capital cost | 421.9 |
| $OP_{variable,EST}$ | \$/kWh | EST variable O&M cost | 0.004 |
| $n$ | yr | Plant lifetime | 30 |
| $r$ | % | Interest rate | 12 |
| $CR$ | kg$CO_2$/kWh | $CO_2$ emission from renewable system | 0.254 |
| $CT$ | \$/t$CO_2$ | Carbon tax | 20 |

The optimization framework of the utility steady-state operation is formulated with the objective function of minimizing system costs. This includes the operating costs from fuel consumptions, capital costs for conventional equipment, and carbon tax, and is described by:

$$f_{Utility,Min} = f_{OP,Utility} + f_{CP,Utility} + f_{CT,Utility} \quad (2)$$

$$f_{OP,Utility} = C_{coal} f_{coal}(m_{coal}) + C_{NG} f_{NG}(m_{NG}) + C_{water} Q_{condensor\ for\ BFW} \quad (3)$$

$$f_{CP,Utility} = f_{Boiler} + f_{GT} + f_{HRSG} + f_{ST} \quad (4)$$

$$f_{CT,Utility} = CT f_{coal}(m_{coal}) NHV_{coal} + 10^{-3} CT f_{NG}(m_{NG}) NHV_{NG} \quad (5)$$

Each term in the objective function is determined based on the optimized fuel consumption which can be calculated as a function of VHP steam mass flowrate ($m_{coal}$, $m_{NG}$) generated from each fuel. Specifically, the capital cost function is calculated using the capacity of each piece of equipment, which also reflects fuel consumption. As a result, major variables for minimizing fossil fuel-based processes are the quantities of coal and natural gas consumed. This optimization is carried out using the UniSim® optimization tool, incorporating the parameters, constraints, and boundaries outlined in [3].

For the flue gas emitted from the HRSG by natural gas, a conventional Monoethanolamine (MEA)-based $CO_2$ capture process, commonly used for post-combustion capture, is considered as referenced for capturing $CO_2$ from the NGCC plant [5]. A percentage of 90% of $CO_2$ is captured, with the remaining $CO_2$, including the flue gas from a coal-fired boiler, subject to a carbon tax penalty.

The primary optimization variable for the capture process is the thermal energy consumed by the stripper reboiler, typically supplied as LP steam generated by the utility. The LP steam demand for the capture process varies depending on the optimization of natural gas consumption. Therefore, the fluctuation in LP steam demand by the capture process is also considered in the optimization of the integrated utility as $\alpha$* in **Table 1**, although the operating and capital costs of the capture process are not reflected. The thermal energy demands of each month for the capture process are optimized in UniSim®.

## Renewable Process

Renewable electricity is generated using weather data of South Korea, solar irradiation ($I_{solar}$) for the photovoltaic (PV) system and wind speed ($v_{WT}$) for the wind turbine (WT) system. Monthly generated power is calculated from the accumulated observational data and system operating time ($T_{PV}$, $T_{WT}$), followed by calculating the system costs, including the carbon tax. Cost minimization of renewable energy is carried out by optimizing the capacity of each system. For PV and WT systems, the plant area ($A_{PV}$, $A_{WT}$) is considered for the optimization to determine the cost-based electricity production.

To address the irregular nature of renewable energy sources, an electricity storage (EST) system is introduced to supply power as needed. Hence, storage utilization for the overall site demand depends on the renewable energy available each month. The maximum storage capacity is limited to 5 $MW_e$ to reduce uncertainty during the optimization process, helping to identify the most cost-efficient operating conditions. When electricity exceeds this capacity, the surplus can be sold to the main grid connected to the site, generating additional revenue. Based on the costing parameters outlined in **Table 2**, the objective function considers all the costing elements of the renewable system from Eq. (6) to (11). In Eq. (9) and (10), $i$ which can be PV, WT, and EST is used to simplify the costing equations.

$$f_{Renewable,Min} = f_{OP,Ren} + f_{CP,Ren} + f_{CT,Ren} \quad (6)$$

$$P_{PV} = \frac{\sum_t 0.5\eta_{PV}A_{PV}I_{solar}(1-COS(34.5))}{T_{PV}} \quad (7)$$

$$P_{WT} = \frac{\sum_t 0.5\eta_{WT}A_{WT}v_{WT}^3}{T_{WT}} \quad (8)$$

$$f_{OP,Ren} = \sum_i (P_i OP_{fixed,i}/8760 + P_i OP_{variable,i}) - \begin{cases} C_{elec,im}P_{Grid}, & P_{Grid} < 0 \\ C_{elec,ex}P_{Grid}, & P_{Grid} > 0 \end{cases} \quad (9)$$

$$f_{CP,Ren} = \sum_i P_i CP_i \frac{r(1+r)^n}{(1+r)^n - 1} \quad (10)$$

$$f_{CT,Ren} = 10^{-3} CRCT(P_{PV} + P_{WT}) \quad (11)$$

The modeling and optimization of the renewable process are conducted using MATLAB® due to the data-driven nature of the process, which is more challenging to visualize compared to the fossil fuel-based process. A mathematical approach facilitates system cost optimization, providing valuable support for comprehensive strategic decision-making, particularly in complex, interdependent processes. This approach also has the advantage of being easily integrated with existing simulation software.

The optimization methodology for the integrated utility system is illustrated in **Figure 2**, which explains the overall applicable scenarios, including electricity generation, storage, and selling beyond the site through the main grid linked with the processes. This utility management can be explained by Eq. (12) and (13), which represents the key energy balance, including electricity storage, by adjusting the equations in previous studies [3, 4]. Moreover, inequality constraints required for the cost minimization are shown in **Table 3**. Especially, the boundaries of PV and WT system capacity serve to ensure that each system is optimized within an industrially feasible range based on the weather conditions.

$$P_{Utility} + P_{Renewable} - P_{Grid} - 68 = 0 \quad (12)$$

$$P_{Renewable} - (P_{PV} + P_{WT} - P_{EST}) = 0 \quad (13)$$

**Table 3:** Inequality constraints for the Integrated utility process optimization.

| Variable | Unit | Low bound | Upper bound |
|---|---|---|---|
| HP1 | t/h | 15 | - |
| MP2 | t/h | 30 | - |
| LP2 | t/h | 0 | - |
| $LP_{out}$ | t/h | 128+$\alpha$ | - |
| Steam letdown | t/h | 0 | - |
| PV system capacity ($A_{PV}$) | $m^2$ | 0 | 100,000 |
| WT system capacity ($A_{WT}$) | $m^2$ | 0 | 100,000 |
| Renewable electricity to Total site ($P_{Renewable}$) | $MW_e$ | 0 | 68 |
| Grid electricity ($P_{Grid}$) | $MW_e$ | - | 68 |
| EST capacity ($P_{EST}$) | $MW_e$ | 0 | 5 |

## RESULTS AND DISCUSSION

The variations in renewable resources is analyzed from weather data to ensure that only available renewable energy applicable within the operating range allowed is utilized. Therefore, PV system considers its operating time to be limited to daylight hours, and WT system considers cut-in and cut-out speed for the feasible system operation according to the reference [4]. Considering these constraints, **Figure 3** presents the monthly cumulative solar irradiation and wind speed, along with the operating hours of each system.

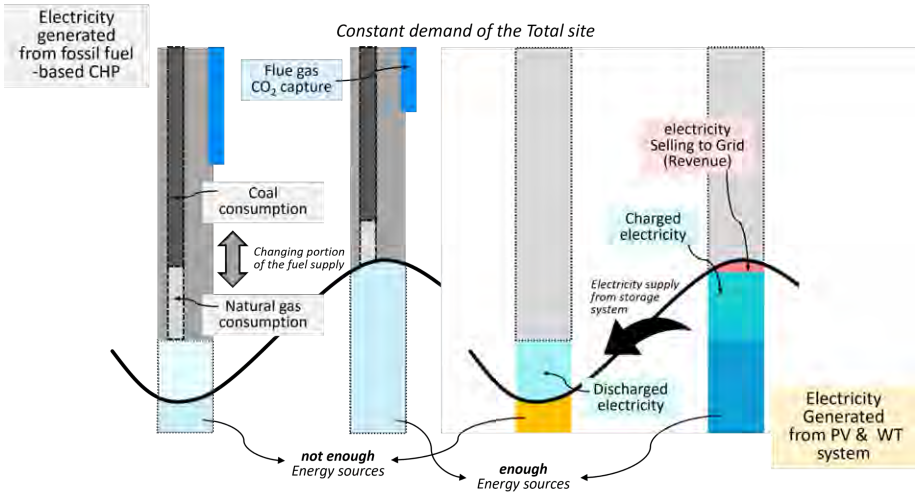



**Figure 2:** Research methodology for modeling and optimization of the integrated processes with a monthly basis.

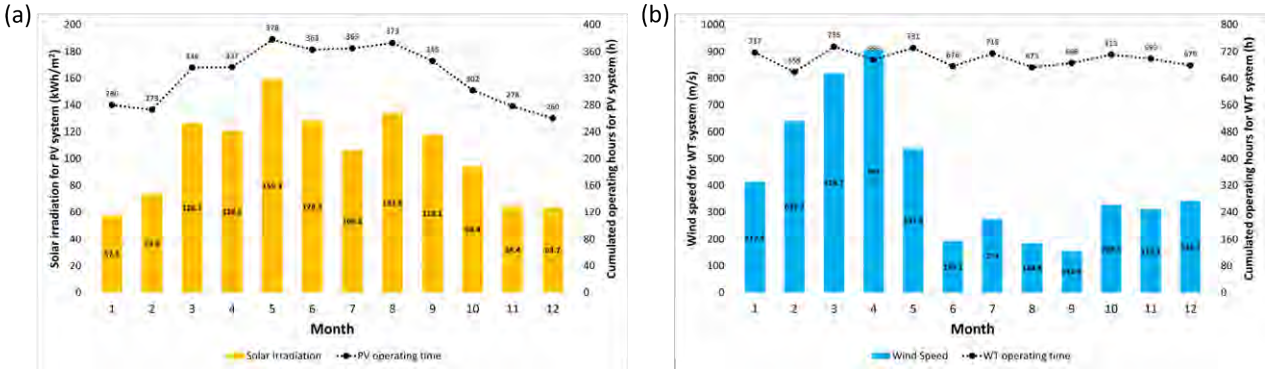



**Figure 3:** Monthly weather data for the analysis of (a) Solar irradiation and operating hours for PV system and (b) Wind speed and operating hours for WT system.

**Figure 4** illustrates the monthly optimized results of the integrated process under \$20/t$CO_2$ of carbon tax. Each month fully meets the Total site electricity demand of 68 MW, with fossil fuel-based systems contributing a significantly larger share than renewable systems. This is due to the lower costs associated with fuels and equipment in fossil fuel-based systems compared to the costs of renewable systems. In particular, during March and April, the higher electricity generation from the WT system leads to a substantial increase in the overall cost of the integrated utility. Therefore, it is observed that the fossil fuel-based system is chosen as the only operating system. Compared to the WT system, the PV system generates less electricity for the same plant area. Consequently, the contribution of the PV system to the site demand remains relatively small.

Although renewable electricity does not make up a large portion of the total power supply, the results in **Figure 4** (a) highlight the contribution of the integrated processes optimization. Renewable electricity can replace between 4.78% and 34.32% of the total site electricity demand each month, confirming the effective validation of the preliminary stage of the integrated utility process design and supporting the goal of establishing renewable energy-based electrification. This variation trend directly influences the system cost, as shown in **Figure 4** (b). The annualized cost of the utility process serves as the base case for comparison with the monthly optimized results. The cost reduction is primarily attributed to the WT system within the renewable energy system, which plays a dominant role in the optimization. The annualized cost in May shows the largest decrease of 5.53%, driven by peak renewable electricity generation, compared to the base case. The optimization also contributes to a 2.67% reduction in the annual cost of the integrated overall processes, with the price portion of the fossil fuel-based system decreasing by 6.15%.

The $CO_2$ emissions from fossil fuels account for the majority of the carbon tax, as shown in **Figure 4** (b). This is because the smaller emission per unit of electricity generated by renewables, along with the lower energy output from the renewable systems, leads to different optimization results concerning the ratio of renewable energy to fossil fuel-based systems. **Figure 5** shows the impact of carbon tax on integrated process optimization through sensitivity analysis. As carbon tax increases, the

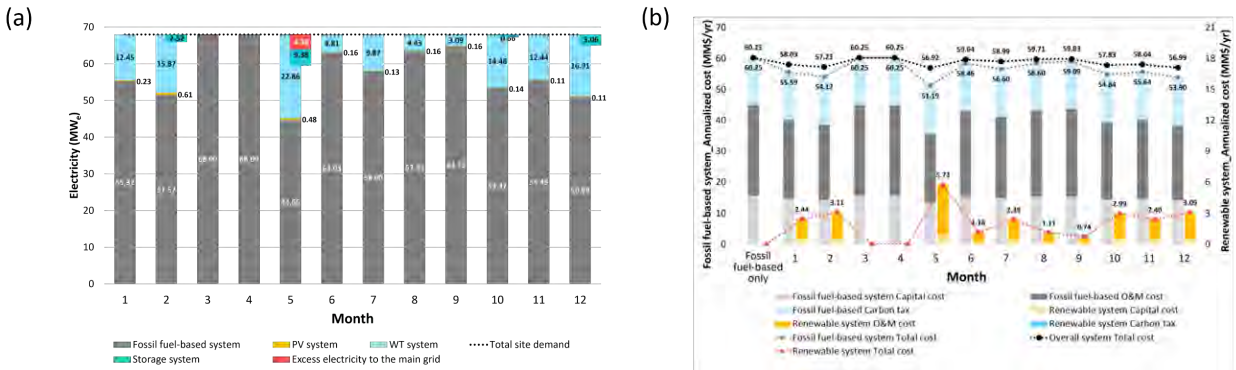



**Figure 4:** Monthly optimized results of integrated utility processes under \$20/t$CO_2$ of carbon tax. (a) Electricity generated from each system (b) Annualized cost breakdown.

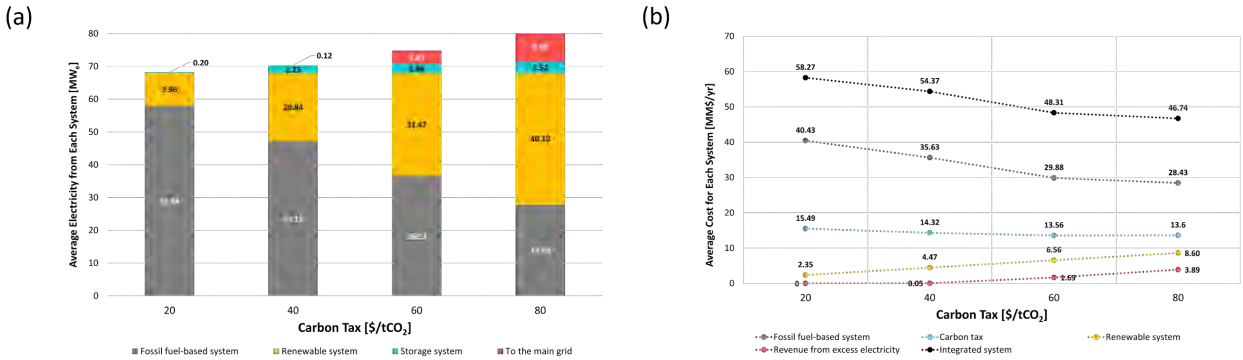



**Figure 5:** Average optimization results for the sensitivity analysis in carbon tax. (a) Electricity breakdown for each system and (b) Average annualized cost for each system.

portion of renewable electricity in the overall system grows due to the increased penalty for fossil fuel consumption. Accordingly, the cost of each system also changes in the same trend with electricity breakdown, and the cost of integrated processes ultimately decreases, as shown in **Figure 5** (b). At a 4 times increase in carbon tax, average overall system cost is reduced about 19.7%, highly affected by about 29.7% decrease of fossil fuel-based system.

## CONCLUSION

This study demonstrates the successful integration of renewable and $CO_2$ capture processes with conventional utility processes as an industrial decarbonization strategy. The optimization framework effectively addresses efficient management in process industries, providing a practical method for balancing economic sustainability with environmental improvement during the transition toward a fully renewable-based system.

If renewable systems with improved cost competitiveness are considered in the future, their increased contribution to the system's power demand could reduce fossil fuel consumption and the additional energy required for the carbon capture process, leading to lower $CO_2$ emissions across the overall processes. Furthermore, this approach mitigates the vulnerability to price fluctuations of fossil fuels on the international market, enhancing the cost stability of process operation through renewable energy integration.

Future work will focus on expanding the current framework to incorporate other renewable technologies. In particular, introducing the CSP system from the perspective of heat integration could add complexity, making it challenging to optimize steam demand across renewable energy with thermal energy storage and existing utilities. Moreover, sensitivity analysis on various costing parameters would provide valuable insights for planning decarbonized industries.

## ACKNOWLEDGEMENTS

This work was supported by the National Foundation of Korea under the framework of international cooperation program (No. 1711200829, FY2023), grant funded by the Korea government(MIST) (RS-2025-00515836), and the German Research Foundation (DFG) under the OPTIMGRID project (AE707 5-1).

## REFERENCES

1. International Energy Agency. $CO_2$ Emissions in 2022, IEA (2023) https://www.iea.org/reports/co2-emissions-in-2022
2. Metz B, Davidson O, Coninck Hd, Loos M, Meyer L. Carbon Dioxide Capture and Storage. Intergovernmental Panel on Climate Change (2005)
3. Park H, Kim J-K, Yi SC. Optimization of site utility systems for renewable energy integration. *Energy* 269:126799 (2023) https://doi.org/10.1016/j.energy.2023.126799
4. Sidnell T, Clarke F, Dorneanu B, Mechleri E, Arellano-Garcia H. Optimal design and operation of distributed energy resources systems for residential neighbourhoods. *Smart Energy* 4:100049 (2021) https://doi.org/10.1016/j.segy.2021.100049
5. Schemitt T, Leptinsky S, Turner M, Zoelle A, Woods M, Shults T, James R. Fossil energy baseline revision 4a. National Energy Technology Laboratory (2022) https://doi.org/10.2172/1893822

© 2025 by the authors. Licensed to PSEcommunity.org and PSE Press. This is an open access article under the creative commons CC-BY-SA licensing terms. Credit must be given to creator and adaptations must be shared under the same terms. See https://creativecommons.org/licenses/by-sa/4.0/

Systems & Control Transactions

**Research Article - Peer Reviewed Conference Proceeding**
ESCAPE 35 - European Symposium on Computer Aided Process Engineering
Ghent, Belgium. 6-9 July 2025
Jan F.M. Van Impe, Grégoire Léonard, Satyajeet S. Bhonsale,
Monika E. Polańska, Filip Logist (Eds.)

PSE PRESS

# A Subset Selection Strategy for Gaussian Process Q-Learning of Process Optimization and Control

**Maximilian Bloor[a], Tom Savage[a], Calvin Tsay[b]*, Ehecatl Antonio Del Rio Chanona[a]* and Max Mowbray[a]***

[a] Imperial College London, Department of Chemical Engineering, United Kingdom
[b] Imperial College London, Department of Computing, United Kingdom
* Corresponding Authors: m.mowbray@imperial.ac.uk, a.del-rio-chanona@imperial.ac.uk, c.tsay@imperial.ac.uk

## ABSTRACT

This work addresses a practical challenge in batch process optimization: the need for sample efficient learning methods due to the high cost and time-intensive nature of running physical batch processes. While reinforcement learning (RL) offers a promising framework for optimizing batch processes, traditional approaches require numerous experimental runs to converge to optimal policies. A novel sample efficient RL method that leverages Gaussian Processes (GPs) to accelerate learning from limited batch data is proposed. However, the direct application of GPs becomes computationally intractable as data accumulates batch-to-batch, and their performance degrades when training distributions shift during policy improvement. To address these challenges, an integrated framework that combines Q-learning with GPs was developed and a strategic subset selection mechanism using determinantal point processes is introduced to maintain computational efficiency while preserving diverse, high-performing samples. The method exploits problem structure and backward induction to further maximize sample efficiency and incorporates both aleatoric and epistemic uncertainty for robust policy improvements. The approach is demonstrated on a non-isothermal semi-batch reactor case study, showing significantly improved learning efficiency compared to exact GP strategies while maintaining computational tractability. The results highlight the method's practical applicability to industrial batch process optimization where experimental data is limited and costly to obtain.

**Keywords**: Reinforcement Learning, Gaussian Processes, Batch Process Control

## INTRODUCTION

Fed-batch process control and online optimization is an area of focus within the process systems engineering community. This is a problem well described by finite horizon stochastic optimal control; however, identification of optimal policies is inherently challenging. This is in part due to the difficulty in identifying systems models and their uncertainty and then propagating that uncertainty over the decision horizon. This latter element is a primary focus within the stochastic model predictive control (sMPC) community [1], [2]. This has led to interest in the development of batch-to-batch learning schemes.

For example, [3] demonstrated the use of policy gradients and transfer learning to improve an initial parametric policy function approximation directly from batch process data. Similar ideas were exploited in [4] and [5] using Gaussian process (GP) models that were iteratively updated with new batch process data and then exploited to improve the operational strategy.

All the works detailed above exploit methods common to Reinforcement Learning and bandit strategies. State-action value learning is a subset of Reinforcement Learning algorithms that aim to solve Markov decision process formulations of the online batch process optimization problem, through concepts broadly termed approximate dynamic programing (ADP). ADP aims to identify an optimal state-value function approximation through function approximation, and sampling-based policy evaluation and policy improvement steps to approximate the workings of exact dynamic programming (DP) solvers. It is worth noting that DP is not applicable in

this problem setting due to computational intractability. From this optimal function approximation, one can derive the optimal policy by acting greedily with respect to it in each state.

In chemical engineering applications, the high cost and time-intensive nature of running physical batch processes makes it crucial to develop sample efficient methods for reinforcement learning. Traditional RL approaches often require numerous iterations to converge to optimal policies, which becomes prohibitively expensive when each episode represents a complete batch process. This motivates our focus on combining Gaussian Process (GP) models with Bayesian Optimization (BO) principles to create more sample efficient RL methods that can learn effective control policies with significantly fewer experimental runs. This approach is particularly valuable in chemical engineering contexts where each experiment may involve substantial material costs, energy usage, and time investment.

State-action value learning algorithms typically exploit function approximations to provide point estimates of the expected state-action value function, rather than modelling it explicitly a conditional random variable. This has led to uncertainty aware approaches to state-action value learning. Perhaps the most common approach to integrating uncertainty within policy learning is GP approximations to process dynamics. This then enables identification of the state-action value function through formulation of a nonlinear program. However, this requires that the process be well described by a GP model [6].

An alternative means is to use the GP for approximating the state-action value function directly. For example, the GP Temporal Difference (GPTD) framework aims to identify a value function approximation under a given control policy and leverages the SARSA algorithm for approximate policy improvement steps [7]. Bayesian neural network approaches have also been explored for approximating the state-action value function, which enabled the use of Thompson sampling rollout policies – effectively balancing exploration and exploitation of the decision space [8].

In this work, a sample efficient reinforcement learning strategy for process control based on Gaussian processes and Bayesian optimization principles is proposed. To address the poor scaling of Gaussian processes with data, and the well-known distributional shift challenge in reinforcement learning a subset selection strategy is introduced. Finally, it is shown how the exploitation of problem structure and backward induction can maximize sample efficiency in this context.

This paper is structured as follows. The methodology section presents the foundations of Q-learning and Gaussian Process function approximation, followed by our approaches to Thompson sampling policies and uncertainty-aware Q-learning. The method for maintaining computational tractability with GPs is introduced and then the complete algorithmic implementation is detailed. A computational case study of a non-isothermal semi-batch reactor demonstrates the practical application of our approach. Finally, results are presented that compare our GP-based Q-learning method to an exact GP strategy, followed by conclusions.

# METHODOLOGY

## Q-Learning

Reinforcement learning (RL) describes a set of sampling-based algorithms for solving Markov decision process (MDP). Finite MDP formulations of batch process optimization may be defined as a six tuple $< \mathcal{X}, \mathcal{U}, p, \phi, \gamma, T >$; with $\boldsymbol{x} \in \mathcal{X}$ denoting a state space, $\boldsymbol{u} \in \boldsymbol{\mathcal{U}}$ a set of controls, $X_{t+1} \sim p(\boldsymbol{x}_{t+1} \mid \boldsymbol{x}_t, \boldsymbol{u}_t)$ a state transition probability density function, $\phi: \mathcal{X} \times \mathcal{U} \rightarrow \mathbb{R}$ a cost function, $\gamma \in [0,1]$ a discount factor, and $T$ the finite time horizon over which the MDP evolves, after which the process terminates. In finite horizon MDPs, the aim is to identify a state feedback policy, $\boldsymbol{u}_t = \pi(\boldsymbol{x}_t)$, to minimize the expected sum of costs over a discrete time horizon of length $T$ from any given state. This quantity is otherwise known as the state-action value function, $Q(\mathbf{x}_t, \mathbf{u}_t)$. Dynamic programming (via backward induction) is known to find optimal solutions to MDPs; however, its use becomes intractable in large discrete or continuous state and control spaces.

Q-Learning is a model-free reinforcement learning algorithm that estimates the optimal state-action value function, $Q^*(\mathbf{x}, \mathbf{u})$, which may be defined recursively as:

$$Q^*(\mathbf{x}_t, \mathbf{u}_t) = \mathbb{E}_{\pi^*}\left[\phi(\mathbf{x}_t, \mathbf{u}_t) + Q\left(\boldsymbol{x}_{t+1}, \pi^*(\boldsymbol{x}_{t+1})\right)\right] \quad (1)$$

subject to,

$$\pi^*(\mathbf{x}_{t+1}) = \underset{\mathbf{u}_{t+1}}{\operatorname{argmin}} Q^*(\mathbf{x}_{t+1}, \mathbf{u}_{t+1}). \quad (2)$$

In practice, one does not have access to the actual Q-function and must estimate and learn it from interactions with the samples of the underlying MDP. Q-learning may be thought as an approximate dynamic programming (DP) strategy, which is constituted by iterative application of an approximate policy evaluation step, and a policy improvement step. The policy evaluation step used by Q-learning is inspired by stochastic approximation,

$$Q(\mathbf{x}_t, \mathbf{u}_t) \leftarrow Q(\mathbf{x}_t, \mathbf{u}_t) + \alpha_k \delta_t, \quad (3)$$

where $\alpha_k$ is the learning rate at update step $k$ and $\delta_t$ is the TD error,

$$\delta_t = \phi(\boldsymbol{x}_t, \boldsymbol{u}_t) + \gamma \min_{\mathbf{u}_{t+1}} Q(\mathbf{x}_{t+1}, \mathbf{u}_{t+1}) - Q(\mathbf{x}_t, \mathbf{u}_t). \quad (4)$$

The TD error is a bootstrapped estimate of the error in the state-action value approximation of the optimal policy, and under some conditions the update ensures convergence to the optimal policy. One condition is that there must be sufficient coverage of the state-control space through learning iterations. This is enabled by a rollout policy which balances exploration and exploitation. Such a rollout policy is usually defined through the application of a bandit strategy with respect to the state-action value function, such as the $\epsilon$-greedy strategy.

In continuous state and control, one becomes interested in constructing an approximation to the state-action value function, typically through a parametric function. These approaches tend to be sample inefficient. In this work, the utility of constructing Gaussian process approximations is explored, which are a class of Bayesian non-parametric models.

## Gaussian Process Function Approximation

A Gaussian process (GP) is a probability model defined on a collection of random variables, such that every finite subset is described by a multivariate Gaussian distribution. Specifically, it is assumed that given some dataset, $\mathcal{D}_t = \{\boldsymbol{v}_{t,i}, Q_{t,i}\}_{i=1:N}$ with $\boldsymbol{v}_t = [\boldsymbol{x}_t, \boldsymbol{u}_t]^T$, and a test point $\boldsymbol{v}_{t,*}$, the joint multivariate prior distribution may be defined,

$$\begin{bmatrix} Q_{t,1} \\ \vdots \\ Q_{t,N} \\ Q_{t,*} \end{bmatrix} \sim \mathcal{N}\left( \begin{bmatrix} m(\boldsymbol{v}_{t,1}) \\ \vdots \\ m(\boldsymbol{v}_{t,N}) \\ m(\boldsymbol{v}_{t,*}) \end{bmatrix}, \begin{bmatrix} K(V_t, V_t) & k(\boldsymbol{v}_{t,*}, V_t)^T \\ k(\boldsymbol{v}_{t,*}, V_t) & k(\boldsymbol{v}_{t,*}, \boldsymbol{v}_{t,*}) \end{bmatrix} \right), \quad (5)$$

where $k(\cdot,\cdot)$ is the kernel function that evaluates the covariance of the random variables, $K(V_t, V_t)$ is the gram matrix which evaluates covariance of the data $V_t = [\boldsymbol{v}_{t,1}, \ldots, \boldsymbol{v}_{t,N}]^T$, and $m(\cdot)$ is a prior mean function. Since the joint prior distribution is a multivariate Gaussian one can obtain conditional and marginal distributions as Gaussian distributions also. This enables one to exploit Bayes' rule to make predictions about a test point, given data via a Gaussian posterior distribution,

$$Q_{t,*} \mid \boldsymbol{v}_{t,*}, \mathcal{D}_t \sim \mathcal{N}\left(m(\boldsymbol{v}_{t,*} \mid \boldsymbol{\mathcal{D}}_t), \sigma^2(\boldsymbol{v}_{t,*} \mid \boldsymbol{\mathcal{D}}_t)\right), \quad (6)$$

with $m(\boldsymbol{v}_{t,*} \mid \boldsymbol{\mathcal{D}}_t)$ and $\sigma^2(\boldsymbol{v}_{t,*} \mid \boldsymbol{\mathcal{D}}_t)$ provided in closed form through the conditioning equations. The posterior prediction provides means to estimate the state-action value of a new state and control pair $\boldsymbol{v}_{t,*}$ given access to a discrete dataset.

## Thompson Sampling Policies

In this work, it is assumed that such a dataset is built iteratively in a batch-to-batch fashion by rolling out a policy that leverages the GP state-action value function approximation and its uncertainty. Specifically, the method takes advantage of the explicit uncertainty quantification of GPs to define a Thompson Sampling (TS) rollout policy. This policy makes use of an approximated sample $\tilde{Q}_t$ of the posterior distribution using a decoupled sampling method, described by [9], which is minimized to select the next control input:

$$\tilde{Q}_t \sim Q_t \mid \mathcal{D}_t \quad (7)$$

$$\pi_{TS}(x_t) = \arg\min_{u_t} \tilde{Q}_t(x_t, u_t) \quad (8)$$

This behavioral policy naturally balances exploration and exploitation - areas of high uncertainty can be targeted for exploration, while areas of low uncertainty and high predicted value can be exploited. Furthermore, the minimization of the Q-function follows the standard Q-learning paradigm.

## Uncertainty Aware Q-Learning

Our approach implements an adaptive learning rate mechanism that automatically adjusts based on the model's predictive uncertainty. While traditional Q-learning employs a fixed learning rate $\alpha_k$ in the update equation ((9). Instead, the method uses the analytical uncertainty estimates from the GPs to adapt to this learning rate as follows:

$$Q_t(\mathbf{x}_t, \mathbf{u}_t) \leftarrow \alpha_k * Q_t(\mathbf{x}_t, \mathbf{u}_t) + \cdots (1 - \alpha_k) * (r_t + \gamma \arg\min_{u'} Q_{t+1}(\mathbf{x}_{t+1}, \mathbf{u}_{t+1})), \quad (9)$$

$$\text{where } \alpha_k = \frac{1}{1+\sigma_t^2}. \quad (10)$$

Here, $\sigma_t^2$ represents the GP for timestep $t$ predictive normalized variance at the current state-action pair. When the model exhibits high uncertainty in its Q-value predictions, $\alpha_k$ approaches zero, causing the update to rely more heavily on the observed returns. Conversely, when the model is confident in its predictions (low variance), $\alpha_k$ approaches unity, giving more weight to the current Q-value estimates. This mechanism (Equation 10) ensures that the learning process naturally adapts to the model's confidence, leading to more conservative updates in regions of high uncertainty while maintaining efficient learning in well-understood parts of the state-action space.

### Subset Selection Strategy

To handle the computational expense of GPs with large datasets while maintaining accurate modeling of promising regions, a reparametrized determinantal point processes (DPPs) was employed, which can be sampled to give diverse and high performing subsets of our original datasets [10].

These subsets are constructed of points, $\boldsymbol{v} \in V$, which are sampled with the probability proportional to the determinant of the gram matrix of the DPP $|K_V|$ and the quality function $q: \mathcal{X} \times \mathcal{U} \rightarrow \mathbb{R}$:

$$\mathbb{P}(V) \propto |K_V| \star \prod_{v \in V} q(v)^2, \tag{11}$$

where the quality function is larger for higher performing subsets. This formulation is particularly valuable for Q-learning as it allows us to naturally forget poor-performing historical data while maintaining a diverse set of high-value state-action pairs, effectively focusing our modeling capacity on regions of the Q-function that are most relevant for policy improvement.

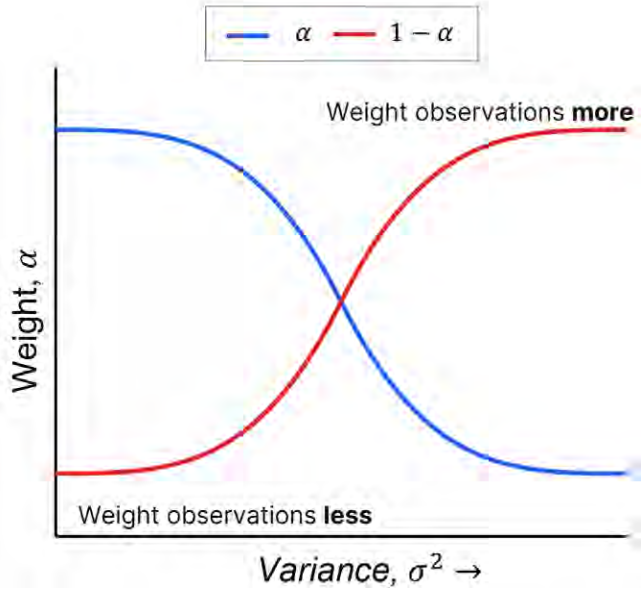



**Figure 1.** Uncertainty-aware learning rate

## Algorithmic Implementation

Our GP-Based Q-learning algorithm combines GP function approximation with temporal difference learning. The outer loop iterates over batches, where each batch collects new trajectories through policy rollouts in the process. It is assumed that the process dynamics do not change between batches. The inner loop is over timesteps in reverse order, from $T-1$ to 0, to allow information from the end of the episode to flow to the initial state-action pairs for correct credit assignment. All Q-values in the dataset for the current timestep are updated with the current model estimate via. a TD update as an approximate policy iteration step. A subset selection strategy preserves a subset of data points for training using the method described in the previous section. An overview of the Q-learning algorithm is described below.

**Algorithm 1:** GP-Based Q-learning

**Data:** Initial Data, $\mathcal{D}_{0,j,t} = \{(\mathbf{x}_t, \mathbf{u}_t, q_t)_i\}_{i=1:N}$

**Inputs:** Total number of batch runs $B$, Batch process operation $\mathcal{P}(\cdot)$, Subset selection strategy $\mathcal{M}(\cdot)$, Data collection strategy $\pi(\cdot)$, Q-learning algorithm, $\mathcal{Q}(\cdot)$.

**Outputs:** GP models, $\mathcal{F}_*(\mathcal{D}_*) = \{f_{*,t}(\cdot; \mathcal{D}_{*,t})\}_{\{t=0:T-1\}}$

Initialize GP models $\mathcal{F}_0(\mathcal{D}_0)$

**For Each** $b \in \{0, \dots, B-1\}$ **do**

  Rollout policy in process, $\{\mathcal{D}_{new,t}\}_t = \mathcal{P}(\pi(\mathcal{F}_b))$

  Append $\mathcal{D}_{b+1,t} = \mathcal{D}_{b,t} \cup \mathcal{D}_{new,t} \quad \forall\, t$

  **For Each** $t \in \{T-1 \dots 0\}$ **do**

    Update data $\mathcal{D}_{b+1,t} = \mathcal{Q}\left(\mathcal{D}_{b+1,t}, f_{b,t:t+1}(\cdot)\right)$

    Select data for training, $\mathcal{D}^{\mathcal{T}}_{b+1} = \mathcal{M}\left(\mathcal{D}_{b+1,t}, f_{b,t}(\cdot)\right)$

    Train GP model independently, $f_{b+1,t}(\cdot, \mathcal{D}^{\mathcal{T}}_{b+1,t})$

**Return** $\mathcal{F}_*(\mathcal{D}_*) = \mathcal{F}_B(\mathcal{D}_*)$

## COMPUTATIONAL CASE STUDY

The case study used to demonstrate the control algorithm described in previous sections is a non-isothermal semi-batch reactor [11]. The aim of the case study is to assess how the proposed algorithm performs again other GP-based methods and whether it approaches the optimum. The reactor carries out the following reactions:

$$\mathrm{A} \longrightarrow B \longrightarrow 3\mathrm{C} \tag{12}$$

Where both reactions are catalysed and are first-order reactions. The first step is exothermic and the second is endothermic which are both characterised by rate constants $k_{1A}(T)$ and $k_{2B}(T)$ that are functions of temperature. A cooling jacket is used to manipulate the reactor temperature. The state of the system $\mathbf{x}$ contains the concentration of all three species, the temperature, and volume of the reactor:

$$\mathbf{x} = [C_A, C_B, C_C, T, V].$$

The two control inputs are the temperature of the cooling jacket and the feed flow rate of A:

$$\mathbf{u} = [T_a, F].$$

The dynamics of the reactor are defined as follows:

$$\frac{\mathrm{d}C_A}{\mathrm{d}t} = -k_{1A}C_A + (C_{A0} - C_A)\frac{F}{V} \tag{13}$$

$$\frac{\mathrm{d}C_B}{dt} = \frac{1}{2}k_{1A}C_A - k_{2B}C_B - C_B\frac{F}{V} \tag{14}$$

$$\frac{\mathrm{d}C_C}{\mathrm{d}t} = 3k_2C_B - C_C\frac{F}{V} \tag{15}$$

$$\frac{\mathrm{d}V}{\mathrm{d}t} = F \tag{16}$$

$$\frac{\mathrm{d}T}{\mathrm{d}t} = \frac{\mathrm{UA}(\mathrm{T_a} - T) - F_{A0}C_{P_A}(T - T_0) + \cdots}{[C_AC_{P_A} + C_BC_{P_B} + C_CC_{P_C}]V + N_{H_2SO_4}C_{P_{H_2SO_4}}} \\ \frac{[(\Delta H_{R1A})(-k_{1A}C_A) + (\Delta \mathrm{H_{R2B}})(-k_{2B}C_B)]V}{[C_AC_{P_A} + C_BC_{P_B} + C_CC_{P_C}]V + N_{H_2SO_4}C_{P_{H_2SO_4}}}. \tag{17}$$

The case study is implemented using the PC-Gym Python package [12]. The episode length is defined as four hours

with timesteps of 24 minutes where control inputs are applied. The objective is to maximize the final amount of the desired product (species C) this results in the following reward function of:

$$\phi_t = \begin{cases} C_C V \; if \; t = \; T-1 \\ 0 \; otherwise \end{cases} \tag{18}$$

## RESULTS

The GP-based Q-learning algorithm presented in Algorithm 1 was trained with an initial dataset $\mathcal{D}_0$ size of 10, 20 and 30 trajectories then trained for a further 25 batches of training. This training was repeated 5 times to ensure repeatability of the algorithm. The resulting policy is rolled out for 20 repetitions to measure the final objective value. When rolling out the policy in testing the actions are selected by maximizing over the mean function of the resulting GPs from training. This algorithm is compared to work by Savage et. al (2021) [13] which differs mainly by using expected-improvement as its behavioural policy, follows the Monte-Carlo learning scheme and having no subset selection scheme The algorithms are also compared to an oracle which is a Nonlinear Model Predictive Controller (NMPC) with a perfect model as implemented by the PC-Gym [12] which acts as a ceiling to performance on this case study.

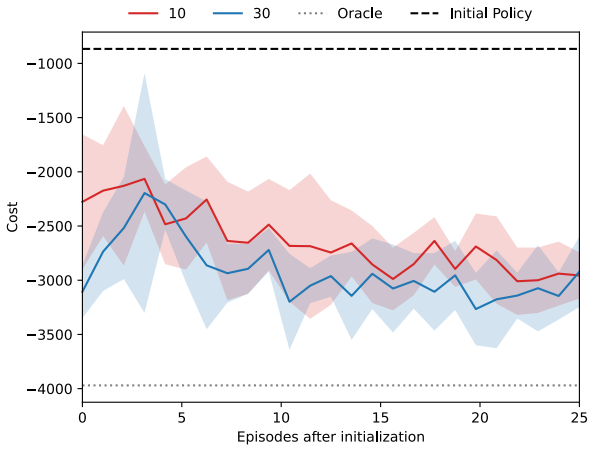



**Figure 2.** Learning Curve of GP-based Q-learning for initial dataset size of 10 and 30 compared to the average initial policy (dashed) and oracle (dotted).

Figure 2 shows the learning curve of our algorithm when using an initial dataset size of 10 and 30 trajectories. The oracle is shown with a dotted line, and the average performance of the initial dataset is shown as a dashed line. The initial performance is higher when using 30 trajectories compared to 10 trajectories, as the larger dataset provides more information for constructing the models of the Q-function. Over the first 5 training episodes, a decrease in performance for both dataset sizes is observed due to the exploration behavior induced by the Thompson sampling rollout policy.

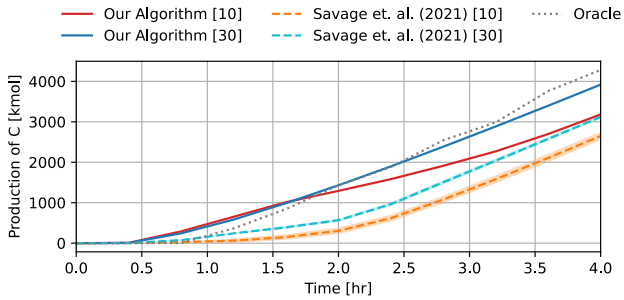



**Figure 3.** Objective value over the test episode for different sized intial datasets compared to the oracle and Savage et.. al. (2021) [13].

The mean objective value for over the test episode is shown in Figure 3. Higher performance is obtained with our algorithm for both initial dataset sizes compared to Savage et. al. (2021)'s [13] algorithm, and with the 30-trajectory dataset our algorithm approaches the oracle's performance. The variance in performance across repetitions is larger for Savage et. al.'s [13] algorithm, as indicated by the wider shaded areas.

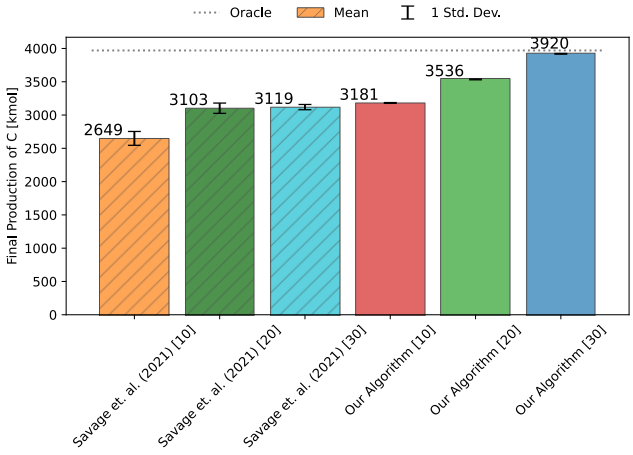



**Figure 4**. Comparison of final objective values for different initial dataset sizes.

A comparison of final objective values for all initial dataset sizes is presented in Figure 4. Our algorithm's performance approaches the oracle's as the dataset size increases. A significant portion of this performance difference can be attributed to our use of TD learning updates, enabling the method to learn about the optimal greedy policy when following a non-greedy rollout policy.

## CONCLUSION

This work compared a Gaussian Process Q-learning

approach with subset selection against prior methods on a non-isothermal semi-batch reactor. With 30 initial trajectories, our approach nearly matched the performance of an oracle NMPC controller demonstrating the effectiveness of our TD learning updates over Monte Carlo for learning optimal policies from non-greedy rollouts.

## ACKNOWLEDGEMENTS

Maximilian Bloor would like to acknowledge funding provided by the Engineering & Physical Sciences Research Council, United Kingdom through grant code EP/W524323/1. Calvin Tsay acknowledges support from a BASF/Royal Academy of Engineering Senior Research Fellowship.

## REFERENCES

1. A. Mesbah, 'Stochastic Model Predictive Control: An Overview and Perspectives for Future Research', IEEE Control Syst., vol. 36, no. 6, pp. 30–44, Dec. 2016, doi: 10.1109/mcs.2016.2602087.
2. E. Bradford, L. Imsland, D. Zhang, and E. A. Del Rio Chanona, 'Stochastic data-driven model predictive control using gaussian processes', Comput. Chem. Eng., vol. 139, p. 106844, Aug. 2020, doi: 10.1016/j.compchemeng.2020.106844.
3. P. Petsagkourakis, I. O. Sandoval, E. Bradford, F. Galvanin, D. Zhang, and E. A. D. Rio-Chanona, 'Chance constrained policy optimization for process control and optimization', J. Process Control, vol. 111, pp. 35–45, Mar. 2022, doi: 10.1016/j.jprocont.2022.01.003.
4. M. Mowbray, P. Petsagkourakis, E. A. Del Rio-Chanona, and D. Zhang, 'Safe chance constrained reinforcement learning for batch process control', Comput. Chem. Eng., vol. 157, p. 107630, Jan. 2022, doi: 10.1016/j.compchemeng.2021.107630.
5. H.-E. Byun, B. Kim, and J. H. Lee, 'Multi-step lookahead Bayesian optimization with active learning using reinforcement learning and its application to data-driven batch-to-batch optimization', Comput. Chem. Eng., vol. 167, p. 107987, Nov. 2022, doi: 10.1016/j.compchemeng.2022.107987.
6. J. Kocijan, R. Murray-Smith, C. E. Rasmussen, and A. Girard, 'Gaussian process model based predictive control', in Proceedings of the 2004 American Control Conference, Boston, MA, USA: IEEE, 2004. doi: 10.23919/acc.2004.1383790.
7. Y. Engel, S. Mannor, and R. Meir, 'Reinforcement learning with Gaussian processes', in Proceedings of the 22nd international conference on Machine learning - ICML '05, Bonn, Germany: ACM Press, 2005, pp. 201–208. doi: 10.1145/1102351.1102377.
8. K. Azizzadenesheli and A. Anandkumar, 'Efficient Exploration through Bayesian Deep Q-Networks', Sep. 06, 2019, arXiv: arXiv:1802.04412. doi: 10.48550/arXiv.1802.04412.
9. J. T. Wilson, V. Borovitskiy, A. Terenin, P. Mostowsky, and M. P. Deisenroth, 'Efficiently Sampling Functions from Gaussian Process Posteriors', Aug. 16, 2020, arXiv: arXiv:2002.09309. doi: 10.48550/arXiv.2002.09309.
10. A. Kulesza and B. Taskar, 'Determinantal point processes for machine learning', Found. Trends® Mach. Learn., vol. 5, no. 2–3, pp. 123–286, 2012, doi: 10.1561/2200000044.
11. E. Bradford and L. Imsland, 'Economic Stochastic Model Predictive Control Using the Unscented Kalman Filter', IFAC-Pap., vol. 51, no. 18, pp. 417–422, 2018, doi: 10.1016/j.ifacol.2018.09.336.
12. M. Bloor et al., 'PC-Gym: Benchmark Environments For Process Control Problems', Dec. 05, 2024, arXiv: arXiv:2410.22093. doi: 10.48550/arXiv.2410.22093.
13. T. Savage, D. Zhang, M. Mowbray, and E. A. D. Río Chanona, 'Model-free safe reinforcement learning for chemical processes using Gaussian processes', IFAC-Pap., vol. 54, no. 3, pp. 504–509, 2021, doi: 10.1016/j.ifacol.2021.08.292.

© 2025 by the authors. Licensed to PSEcommunity.org and PSE Press. This is an open access article under the creative commons CC-BY-SA licensing terms. Credit must be given to creator and adaptations must be shared under the same terms. See https://creativecommons.org/licenses/by-sa/4.0/



Systems & Control Transactions

**Research Article - Peer Reviewed Conference Proceeding**
ESCAPE 35 - European Symposium on Computer Aided Process Engineering
Ghent, Belgium. 6-9 July 2025
Jan F.M. Van Impe, Grégoire Léonard, Satyajeet S. Bhonsale,
Monika E. Polańska, Filip Logist (Eds.)

PSE PRESS

# Optimal Operation of Middle Vessel Batch Distillation using Model Predictive Control

**Surendra Beniwal[a], Sujit S. Jogwar[a]***

[a] Indian Institute of Technology Bombay, Department of Chemical Engineering, Mumbai, Maharashtra, India
* Corresponding Author: jogwar@iitb.ac.in

## ABSTRACT

Middle vessel batch distillation (MVBD) is an alternative configuration of the conventional batch distillation with improved sustainability index. This article presents a comparison of model-based control approaches for MVBD column. Specifically, two control approaches - sequential (open-loop optimization followed by closed-loop control) and simultaneous (closed-loop optimization and control) are pursued. These two approaches are compared in terms of their effectiveness, overall performance, and robustness to plant-model mismatch. The effectiveness of these control strategies is illustrated using a simulation case study of a ternary mixture separation consisting of benzene, toluene and o-xylene.

**Keywords**: Batch distillation, model-based control, economic model predictive control

## INTRODUCTION

Batch distillation is a preferred separation process for small-scale production, multi-product and high-purity separations because of its operational flexibility and cost-effectiveness. However, it also encounters challenges like long batch time and low thermodynamic efficiency. Multi-vessel (also known as multi-effect) batch distillation is an alternative configuration of the conventional batch distillation with reduced energy consumption for multicomponent separation. Middle vessel batch distillation (MVBD), as shown in Figure 1, is a special case of multi-effect distillation with a single intermediate vessel. It allows for simultaneous separation of a ternary mixture wherein relatively pure products are collected in the three holdup vessels.

Several studies have focused on optimization and control of the MVBD configuration. Hasebe et al. (1995) used vessel holdups as manipulated variables to control composition of the products in multi-effect batch distillation [1]. Wittgens et al. (1996) proposed a temperature-based feedback control structure for multi vessel column. The temperature at a particular location in each column section is controlled using reflux flows which allows for indirect adjustment of the vessel holdup [2-3]. Further, this control strategy was examined by Furlonge et al. (1999) using dynamic optimization to determine the controller gains and set points. They demonstrated existence of a trade-off between quality of temperature control and minimum energy consumption for the separation [4]. Zhu et al. (2016) investigated composition and temperature control structures for MVBD. It was found that composition control structure was unable to control the process stably [5]. Krishna et al. (2021) showed that a cascade control structure provided more effective control than a single layer feedback control for the MVBD column [6].

The MVBD is a highly interactive system with nonlinear dynamics and requires coordinated manipulation of heat input and reflux flows to achieve desired separation. The studies mentioned above underline challenges associated with implementation of traditional linear feedback controllers. For energy integrated batch distillation, Vibhute et al. (2020) demonstrated performance improvement with model-based feedback control strategies [7]. Along similar lines, model-based control configurations can be employed to MVBD to achieve desired separation and address stability and optimality of the operation.

In this paper, two types of model-based control approaches are explored for efficient operation of a MVBD column. Firstly, in a sequential approach, optimal set-point trajectory generated with offline optimization is

tracked using a model predictive control (MPC). Alternatively, in the simultaneous approach, performance optimization and control are integrated using an economic MPC.

The rest of the paper is organized as follows. A brief overview of the MVBD configuration and operating principles is presented in the next section. The following section presents design of model-based control strategies for a MVBD column. Comparison of closed-loop performance of the MVBD column with these control strategies is presented using a simulation case study of benzene, toluene and o-xylene separation.

## MIDDLE VESSEL BATCH DISTILLATION

As shown in Figure 1, middle vessel batch distillation consists of two column sections separated by a vessel for the separation of a ternary mixture. It works on the principle of multi-effect operation wherein vapour from one column section is used to drive the subsequent effects, thus reducing the overall energy consumption. The entire system is operated under total reflux and at the end of the batch, the three products are accumulated in the three vessels (distillate, middle and bottom vessels).

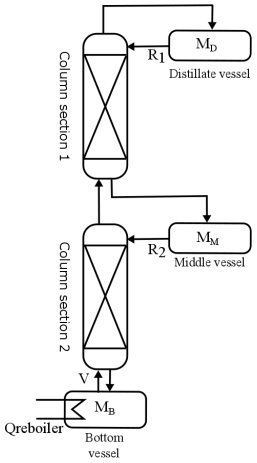



Figure 1. Middle vessel batch distillation configuration.

The mathematical model to capture the dynamics of MVBD configuration, with the assumptions of constant molar overflow and constant tray holdup, is given in Eq. (1).

### Distillate vessel:

$$\frac{dM_D}{dt} = V - R_1, \qquad \frac{d(M_D x_{D,j})}{dt} = V y_{1,j} - R_1 x_{D,j}$$

### Column section 1:

$$\frac{d(M_t x_{i,j})}{dt} = R_1\left(x_{(i-1),j} - x_{i,j}\right) + V\left(y_{(i+1),j} - y_{i,j}\right)$$

Middle vessel:

$$\frac{dM_M}{dt} = R_1 - R_2, \qquad \frac{d(M_M x_{M,j})}{dt} = R_1 x_{N_{T1},j} - R_2 x_{M,j}$$

### Column section 2:

$$\frac{d(M_t x_{i,j})}{dt} = R_2\left(x_{(i-1),j} - x_{i,j}\right) + V\left(y_{(i+1),j} - y_{i,j}\right)$$

### Bottom vessel:

$$\frac{dM_B}{dt} = R_2 - V, \qquad \frac{d(M_B x_{B,j})}{dt} = R_2 x_{N_{T2},j} - V y_{B,j} \qquad (1)$$

Here $M$, $x$, and $y$ represent molar holdup, liquid phase mol fraction, and vapor phase mol fraction, respectively. V, $R_1$, and $R_2$ represent the vapor flow rate and reflux flow rates from the distillate and middle vessel, respectively. Subscripts $D$, $M$, and $B$ refer to the distillate vessel, middle vessel, and bottom vessel, respectively. Subscripts $t$, $i$, and $j$ denote tray, stage number (from the top of the column), and component j, respectively. Subscripts $N_{T1}$ and $N_{T2}$ refer to the last stage of column section 1 and 2, respectively.

### Performance quantification

In MVBD, a ternary mixture is separated into valuable products using thermal energy. Therefore, the performance of MVBD can be effectively evaluated with the inclusion of separation and energy efficiency. Motivated by this, overall performance index (OPI) was previously defined to incorporate both production and energy consumption [9]. The OPI is defined as the ratio of the value of products obtained to the cost of energy supplied to distillation. It can be computed using the following expression:

$$OPI = \frac{\sum_{i=1}^{3}(C_i * M_i(t_{batch}))}{\int_0^{t_{batch}}[C_Q * Q_{reboiler}]dt} \qquad (2)$$

Here $M_i$, $C_Q$, and $t_{batch}$ represent $i^{th}$ vessel holdup, cost of the reboiler duty, and batch processing time, respectively.

## MODEL BASED CONTROL STRATEGIES

In previous work, the OPI was maximized to generate optimal operation policy (initial feed distribution, vessel holdup profile, and input variable profile) for the MVBD by redistributing holdup in the three vessels [9]. Specifically, it was shown that material holdup in the column can be dynamically redistributed among the three vessels to maximize OPI for the entire batch. This optimal operation policy obtained with open-loop optimization can be directly implemented in the MVBD column. However, in the presence of external disturbances and plant-model mismatch (primarily due to simplifying modeling assumptions and vapor liquid equilibrium), a feedback

control is required to maintain product purity and operational optimality.

To this end, model-based feedback control strategies can be formulated using two different approaches. In a sequential approach, offline optimization is used to derive dynamic trajectory for key process variables (vessel holdup, product purity, material and energy flows) to maximize OPI for the entire batch. Subsequently, a feedback controller is used to track this trajectory in an online manner. In the case of MVBD operation, as shown in Figure 2, this can be achieved by tracking optimal vessel holdup or product composition profiles by manipulating the reflux and vapor flows. Alternatively, in the simultaneous approach, optimization is combined with feedback control into a single step, similar to the framework of an economic model predictive control. Specifically, the typical regulatory control objective is replaced by OPI maximization and the corresponding optimal input trajectory is sent to the column in a receding horizon manner. For the MVBD operation, as shown in Figure 3, the MPC uses OPI maximization over the prediction horizon ($N_p$) to estimate vapor and reflux flow profile over the control horizon.

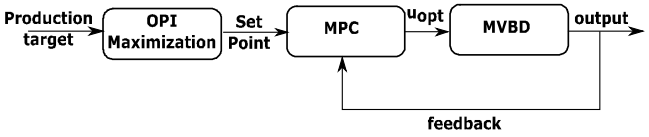



**Figure 2.** Sequential approach.

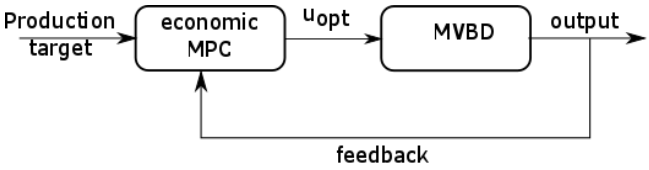



**Figure 3.** Simultaneous approach.

Under normal operating scenario, the sequential approach results in optimal performance. However, it meets challenges in achieving the desired product purity and/or maintain optimality in presence of significant disturbances and plant-model mismatch, since the optimal trajectory is obtained in the absence these factors. On the other hand, the simultaneous approach can effectively handle disturbances and plant-model mismatch due to active feedback. However, it can result in comparatively lower OPI since it considers a smaller prediction horizon ($N_p \ll t_{batch}$) for optimization than the sequential approach. Both these approaches are explored for MVBD column.

Let us now set up the corresponding controller formulations. At every instant, the MPC solve the following optimization problem.

$$\min_{u(t)} \quad J$$

Subject to:

Dynamic model for MVBD (Eq. (1))

Input bounds: $u_{min} \leq u(t) \leq u_{max}$

Input move constraints: $\Delta u_{min} \leq \Delta u(t) \leq \Delta u_{max}$

Vessel holdup constraints: $M_{min} \leq M(t) \leq M_{max}$

Feasible composition constraints:

$$0 \leq x(t) \leq 1,\ 0 \leq y(t) \leq 1 \qquad (3)$$

The sequential and simultaneous approaches differ only in terms of their objective function.

## Sequential approach

Here, optimal set-point trajectory generated with offline optimization (OPI maximization) is tracked using a model predictive control (MPC). The dynamics of the MVBD column, as shown in Eq. (1), is nonlinear; therefore a nonlinear model predictive controller (NMPC) is designed. The key variable to be tracked are composition of the products or holdup of the vessels. The corresponding objective functions are given in Eq. (4) and Eq. (5).

Vessel holdup tracking:

$$J = \sum_{i=1}^{N_p} (M_{set}(i) - M(i)) Q1 (M_{set}(i) - M(i))^T \qquad (4)$$

Product composition tacking:

$$J = \sum_{i=1}^{N_p} (x_{set}(i) - x(i)) Q2 (x_{set}(i) - x(i))^T \qquad (5)$$

Here the subscript $set$ refers to the optimal offline trajectory, Q1 and Q2 are positive definite weighting matrices and $N_P$ is the prediction horizon. Tracking holdup trajectory has the benefits of faster response and low sensor cost requirement but it relies on indirect control of product composition. On the other hand, tracking composition profile ensures product quality but suffers from slower response due to measurement delays and increased sensing cost (costly composition sensor or need for state estimator).

## Simultaneous approach

The primary objective of the controller is to maximize OPI. However, due to the absence of any penalty term on product purity, the controller would rarely achieve the desired purity at the end of the batch. Therefore, the controller objective consists of two parts, maximization of OPI for the time window of prediction horizon and minimization of difference between desired product purity and product composition in the vessels, as shown in Eq. (6).

$$J = -w_1 * OPI(N_p) + w_2 \left(x_{D1,desired} - x_{D1}(N_p)\right) + w_3 \left(x_{M2,desired} - x_{M2}(N_p)\right) + w_4 (x_{B3,desired} - x_{B3}(N_p)) \qquad (6)$$

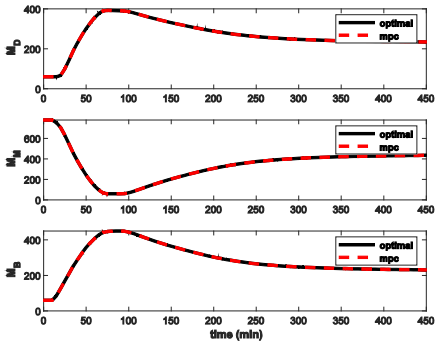
Here, the OPI is computed for the prediction horizon by replacing $t_{batch}$ in Eq. (2) by $N_p$. This formulation is similar to the economic MPC as the prediction horizon for this controller is much smaller than the batch time. The tuning parameters $w_1, w_2, w_3$ and $w_4$ are adjusted to attain desired product purity with optimal performance. They also provide a trade off between quality (achieving product purity) and efficiency (optimal operation).

## SIMULATION CASE STUDY

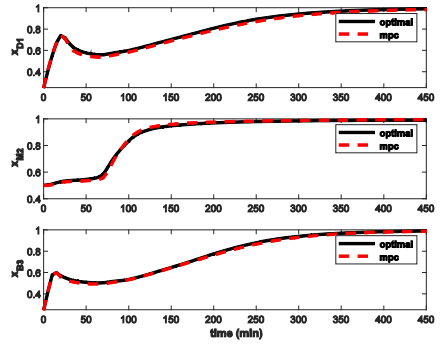
Let us now evaluate and compare the performance of these proposed control approaches with a case study of benzene, toluene, and o-xylene separation in MVBD column. The MVBD column consists of total 65 trays ($N_{T1} = 36$, $N_{T2} = 29$) to process 1000 kmol fresh feed ($F$) with a composition of (0.25, 0.5, 0.25). The modified Raoult's law is used to capture the vapor liquid equilibrium relationship. The activity coefficients and vapor pressure are computed using the NRTL model and Antoine equation, respectively [9]. Implicit Euler scheme with a time step of 5 min is used for the discretization of MVBD dynamics. The optimization problem is solved using the CasADi framework in MATLAB version R2022a [8]. The maximum and minimum value for each input variable is taken as 10 kmol/min and 2 kmol/min, respectively. Their rate of change across the time steps is bounded to ±0.5 kmol/min. The vessel holdups are constrained between 60 kmol and 900 kmol, respectively. Lastly, cost of each product and hot utility are taken as 15 rcu/mol and 2.3 rcu/MJ, respectively (rcu refers to relative cost unit). The OPI value of base case operation without optimization is 12.88.

In our previous work [9], we had generated optimal operation policy for the separation of above ternary mixture in MVBD column, by solving open loop optimization problem for OPI maximization. It was determined that feeding the system through the middle vessel results in optimal performance. The corresponding optimal OPI value and batch time are 26.8 and 450 minutes, respectively.

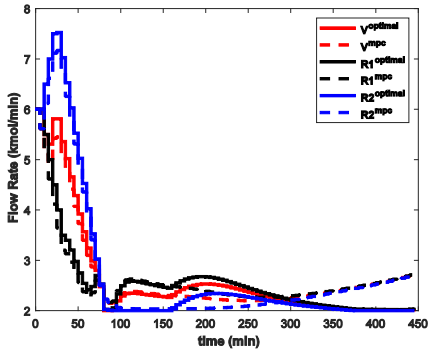
Let us first consider the sequential approach to track this optimal profile in the absence of any disturbances. Figure 4(a) shows the tracking of vessel holdup trajectory using Eq. (3) and (4). It can be observed that the nonlinear MPC is able to track the optimal trajectory of vessel holdup and desired product purity (Figure 4(b)) is achieved as well. Since the controller objective does not incorporate OPI, the optimal trajectory of vessel holdup can be achieved with various combinations of input variables. The vapour flow rate, shown in Figure 4(c), is comparatively higher than the optimal trajectory. Consequently, the OPI value with the holdup controller is 25.6, a drop of 4.5% from the openloop optimal value.




(a) Vessel holdup (M)



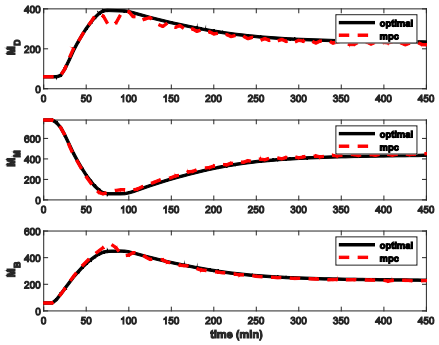

(b) Product composition



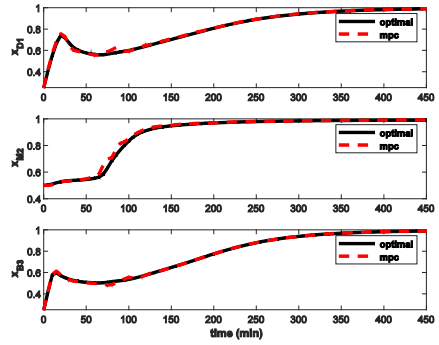

(c) Input variables

**Figure 4.** Dynamic response for the sequential approach with vessel holdup tracking in the absence of disturbance

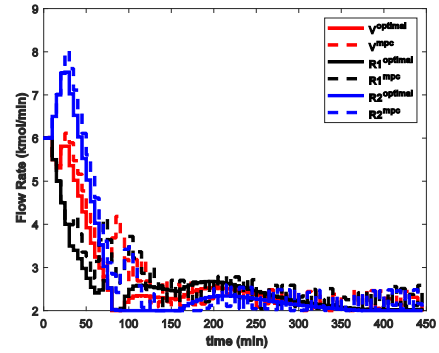
Similarly, product composition tracking using Eq. (3) and (5) is shown in Figure 5. In this case as well, the controller is able to track the optimal trajectory and reach the desired product purity. The corresponding OPI value is 24.40, a drop of 9% as compared to the openloop optimal value, due to higher vapour flow rate.




(a) Vessel holdup (M)



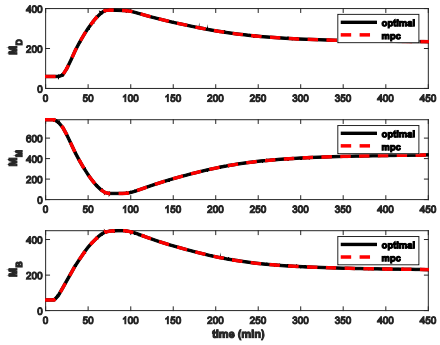

(b) Product composition



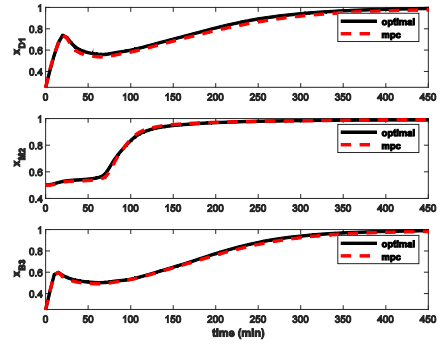

(c) Input variables

**Figure 5.** Dynamic response for the sequential approach with composition tracking in the absence of disturbance

Let us now consider a disturbance scenario (plant-model mismatch) in implementation of the sequential approach. It is considered that after 50 min of operation, tray efficiency for all the trays in the MVBD column is dropped by 10% due to an undetected fault. As the openloop optimization does not incorporate this disturbance, the MPC set point trajectory remains the same. In the case of vessel holdup tracking, even though the holdup tracking is done effectively, it fails to meet desired purity. The corresponding dynamic responses are as shown in Figure 6. On the other hand, in the case of product composition tracking, continuous feedback from plant ensures that at the end of the operation, desired product purity of all the components is attained. However, as the original composition trajectory is not longer optimal in this disturbance scenario, the OPI value decreases from 24.4 to 22.4, reduction of 8.2% due to presence of plant-model mismatch. The corresponding dynamic responses are depicted in Figure 7.




(a) Vessel holdup (M)

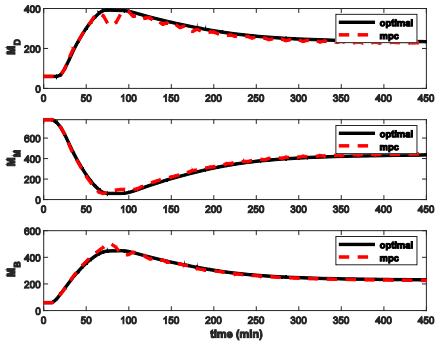



(b) Product composition

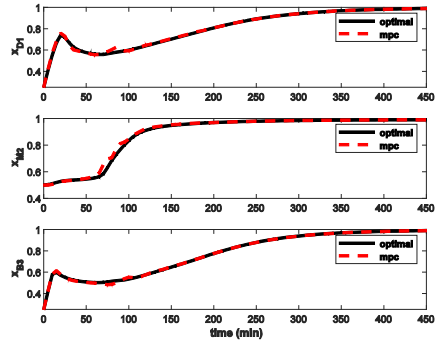
**Figure 6.** Dynamic response for the sequential approach with vessel holdup tracking in the presence of disturbance

Let us now assess the performance of the simultaneous approach. A nonlinear MPC is implemented using Eq. (3) and (6). Tuning parameter values are selected as $w_1 = 9 * 10^{-4}$, $w_2 = 44 * 10^{-4}$, $w_3 = 7.55$, $w_4 = 13.2$ to achieve good balance between purity attainment and performance optimization. The dynamic response of the controller in the absence of any disturbance is shown in Figure 8. Similar to the sequential approach, this controller is also able to achieve the desired product purity at the end of the batch. However, it can be observed from Figure 8(a) that the simultaneous approach is not able to capture the holdup distribution profiles obtained with open loop optimization. Previously [9], it was shown that OPI maximization requires two phases of vessel holdup redistribution for the optimal performance. During the first phase (up to 90 min), the material from the middle vessel is redistributed between the top and bottom vessel such that the composition of the heaviest component in the top vessel and lightest component in the bottom

vessel is negligible. This requires top and bottom compositions to drop during the first phase (see Figure 4(b)). These purities are subsequently recovered during the second phase. As the simultaneous approach has a smaller prediction (and thus optimization) window, it cannot exploit this vessel holdup redistribution effectively, resulting in a smaller OPI value of 17.92.

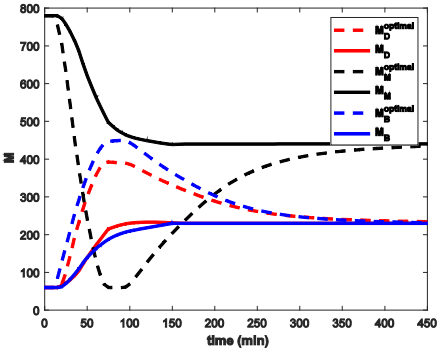



(a) Vessel holdup (M)

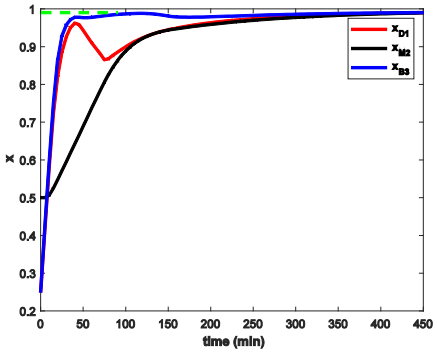



(b) Product composition

**Figure 7.** Dynamic response for the sequential approach with composition tracking in the presence of disturbance



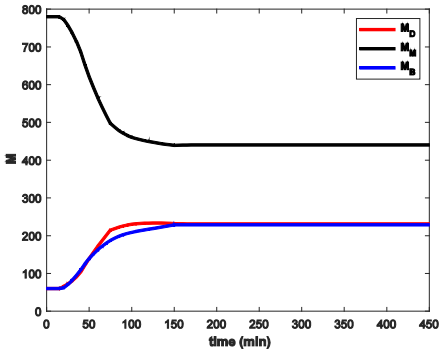

(a) Vessel holdup (M)



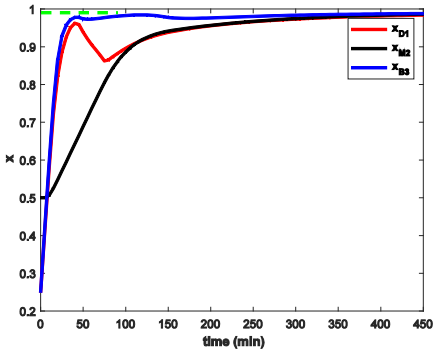

(b) Product composition

**Figure 8.** Dynamic response for the simultaneous approach in the absence of disturbance

In the next simulation, the performance of simultaneous approach is analysed for plant-model mismatch. The same disturbance scenario of 10% drop in the tray efficiency after 50 min of operation is considered. Figure 9 shows the corresponding vessel holdup and product composition profiles. It can be seen that the controller is still able to achieve the desired product purity at the end of the batch. Furthermore, the OPI value in this case is again 17.92. Due to runtime optimization of OPI, this controller is robust to plant-model mismatch.




(a) Vessel holdup (M)




(b) Product composition

**Figure 9.** Dynamic response for the simultaneous approach in the presence of disturbance

Overall, it can be concluded that, in the absence of any plant-model mismatch, all the controllers are able to meet the desired product purity. The sequential approach exhibits better performance (OPI) than the simultaneous approach due to its longer optimization horizon. However, in the presence of significant plant-model mismatch, it shows substantial decline in performance. Furthermore, the holdup tracking approach can also fail to achieve the desired end of the batch purity. On the other hand, the simultaneous approach cannot match the openloop optimal performance in terms of OPI due to its shorter optimization window. However, it is quite robust in terms of maintaining this performance and product purity even in the presence of significant plant-model mismatch.

## CONCLUSION

In this paper, a comparison of two model-based control strategies, sequential (two-step) approach and simultaneous (one-step) approach, is presented for middle vessel batch distillation. The objective of optimal control is to produce products at the desired purity with optimal performance. An economic performance index (OPI) is used to evaluate the performance of MVBD column. For the case study of benzene, toluene and o-xylene separation, the proposed approaches are compared in terms of the effectiveness, overall performance and robustness to plant-model mismatch. In the absence of any disturbance, both the approaches effectively track the optimal trajectory. However, in presence of significant plant-model mismatch, the sequential approach results in substantial performance deterioration. The simultaneous approach shows robustness to plant-model mismatch, but at the cost of sub-optimal performance. Thus a trade-off between performance and robustness is observed through the sequential and simultaneous approaches.

## REFERENCES


1. Hasebe S, Kurooka T, Hashimoto I. Comparison of the separation performances of a multi-effect batch distillation system and a continuous distillation System. *IFAC Proceedings Volumes* 28(9), 249–254 (1995)
2. Wittgens B, Litto R, Sørensen E, Skogestad S. Total reflux operation of multivessel batch distillation. *Computers and Chemical Engineering* 20(SUPPL.2), 1041–1046 (1996).
3. Skogestad S, Wittgens B, Litto R, Sørensen E. Multivessel batch distillation. *AIChE Journal* 43(4):971-8 (1997)
4. Furlonge HI, Pantelides CC, Sørensen E. Optimal operation of multivessel batch distillation columns. *AIChE Journal* 45(4):781-801 (1999).
5. Zhu Z, Li X, Cao Y, Liu X, Wang Y. Design and control of a middle vessel batch distillation process for separating the methyl formate/methanol/water ternary system. *Industrial & Engineering Chemistry Research* 16;55(10):2760-8 (2016).
6. Krishna P, Desikan B, Rao C. Control and dynamic optimization of middle vessel batch distillation column for the separation of ethanol/propanol/butanol mixture. *Chemical Engineering Research and Design* 176, 267–278 (2021)
7. Vibhute M, Jogwar SS. Model-based control of vapor-recompressed batch distillation column. *IFAC-PapersOnLine* 51(18), 554–559 (2018)
8. Andersson J, Gillis J, Horn G, Rawlings JB, Diehl M. CasADi: a software framework for nonlinear optimization and optimal control. *Math. Program. Comput*. 11(1):1–36 (2019)
9. Beniwal S, Jogwar SS. Batch distillation performance improvement through vessel holdup redistribution—Insights from two case studies. *Digital Chemical Engineering* 13, 100187 (2024)



© 2025 by the authors. Licensed to PSEcommunity.org and PSE Press. This is an open access article under the creative commons CC-BY-SA licensing terms. Credit must be given to creator and adaptations must be shared under the same terms. See https://creativecommons.org/licenses/by-sa/4.0/




Systems & Control Transactions

**Research Article - Peer Reviewed Conference Proceeding**
ESCAPE 35 - European Symposium on Computer Aided Process Engineering
Ghent, Belgium. 6-9 July 2025
Jan F.M. Van Impe, Grégoire Léonard, Satyajeet S. Bhonsale,
Monika E. Polańska, Filip Logist (Eds.)

PSE PRESS

# Perturbation Methods for Modifier Adaptation with Quadratic Approximation

**Mohamed Aboelnour[a]*, and Sebastian Engell[b]**

[a] BASF SE, Advanced Process Control, Ludwigshafen, Germany
[b] Technical University Dortmund, Biochemical and Chemical Engineering Department, Dortmund, Germany
* Corresponding Author: mohamed.aboelnour@basf.com.

## ABSTRACT

Real-time optimization (RTO) is a model-based technique that drives plants to optimal operating conditions. Modifier Adaptation (MA) is a class of methods that adjusts the optimization problem using gradient information. This enables the plant to reach the optimum operating point or batch trajectory without the need of a precise model which reduces the necessary modeling efforts. However, computing the gradients of the cost function or of the plant outputs with respect to the inputs online is a challenging task. Modifier Adaptation with Quadratic Approximation (MAWQA) integrates MA with Quadratic Approximation (QA), which helps mitigate the challenges of estimating gradients from noisy measurements by utilizing historical operating data. However, the distribution of these past operating points significantly affects the effectiveness of the MAWQA strategy. To address this issue in this contribution, new methods to compute probing points which lead to fast convergence to the optimum are proposed. The effectiveness of these methods is validated using the Williams-Otto reactor benchmark.

**Keywords**: Modifier Adaptation, Real-time Optimization, Derivative Free Optimization, Probing.

## INTRODUCTION

In recent years, the field of real-time optimization (RTO) has gained significant attention. This is due to the increasing pressure to operate processing plants optimally from both economic and emissions perspectives. A key challenge in RTO is ensuring that plant models are accurate enough to determine feasible and optimal operating inputs or batch trajectories. While re-estimating model parameters online can enhance the performance when the plant model is structurally correct, Modifier Adaptation (MA) addresses both parametric and structural plant-model mismatch without updating the model [1, 2]. This iterative method adjusts the gradients of the cost function and the constraints based on measurement information, so that the first-order optimality conditions are satisfied upon convergence.

In this contribution, we investigate Modifier Adaptation with Quadratic Approximation (MAWQA). This algorithm combines MA with a Quadratic Approximation (QA) approach that was adapted from derivative-free optimization, thereby alleviating the problem of estimating the gradients from noisy measurements [3]. However, the distribution of the points that are used for the approximation significantly influences the QA. If the prior operating data points are not well-distributed, the optimization process may become trapped in a region away from the true optimum. In such cases, additional trials are necessary. For gradients computed via finite differences, it was proposed in [1] to solve an optimization problem to determine a trial input that improves the geometry of the set of past data points. While this strategy is effective for simplex gradients, it is less suited for QA.

In this paper, we discuss different methods to compute additional probing points, which improve the quality of the fitted quadratic surrogate model. The first method extends the approach introduced in [3] in which the input is computed by averaging with distant points. The second method uses the perturbation method from [1] to improve the distribution by solving an optimization problem. This method is then modified such that it is better suited for QA. By solving an optimization problem, it is ensured that the data matrix used in the QA is invertible and well-conditioned. This is based on optimizing the condition

number, which is a computationally expensive problem. This motivates the next approach, which simplifies the computations by using LU decomposition of the data matrix and transforming the polynomial basis such that the additional input can be computed by solving a scalar quadratic optimization problem [4]. Finally, we extend this approach to a completely model-free optimization by introducing well distributed trial points to compute an initial QA, followed by the application of the MAWQA algorithm. We compare these methods using the Williams-Otto reactor benchmark.

## MODIFIER ADAPTATION

We consider a real process with the objective function $J_p(\boldsymbol{u})$, where $\boldsymbol{u}$ is a vector of $n_u$ inputs of the stationary or periodic operation of the plant. The operation is subject to $n_c$ constraints $G_p(\boldsymbol{u})$. The optimal set of inputs $\boldsymbol{u}_p^*$ is defined by (1).

$$\boldsymbol{u}_p^* = \operatorname{argmin}_u J_p(\boldsymbol{u}) \quad \text{s.t. } G_p(\boldsymbol{u}) \leq 0. \tag{1}$$

However, in practice, the mappings $J_p(\boldsymbol{u})$ and $G_p(\boldsymbol{u})$ are not exactly known. We assume that an approximation of these mapping is available, and we denote these models by $J_m(\boldsymbol{u})$ and $G_m(\boldsymbol{u})$. The optimum of the optimization model $\boldsymbol{u}_m^*$ due to plant-model mismatch is not equal to the actual optimum $\boldsymbol{u}_p^*$. In MA, the optimization problem is adapted with modifiers to ensure that the KKT conditions of the plant are satisfied upon convergence [1, 2]. The inputs $\boldsymbol{u}_{ad|\,k}$ in the $k^{th}$ iteration that result from the adapted model are computed from (2), where $\boldsymbol{u}_k$ is the input applied at iteration $k$.

$$\boldsymbol{u}_{ad|\,k} := \operatorname{argmin}_{\boldsymbol{u}} \left( J_m(\boldsymbol{u}) + \epsilon_k^J + \left(\psi_k^J\right)^T (\boldsymbol{u} - \boldsymbol{u}_k) \right), \tag{2a}$$

$$\text{s.t. } G_m(\boldsymbol{u}) + \epsilon_k^G + \left(\psi_k^G\right)^T (\boldsymbol{u} - \boldsymbol{u}_k) \leq 0. \tag{2b}$$

$\epsilon_k^J$, $\epsilon_k^G$, $\psi_k^J$, and $\psi_k^G$ represent the cost function and constraints modifiers. The modifiers can be computed using at least $n_l := n_u + 1$ measurements. To reduce the impact of the estimation errors in the gradients of the actual plant, the inputs can be filtered by

$$\boldsymbol{u}_{ad|k+1}^* = K \cdot \boldsymbol{u}_{ad|\,k+1} + (I - K) \cdot \boldsymbol{u}_k^*, \tag{3}$$

where $K$ is a gain matrix [2]. The computation of the gradients in the MA algorithm is based on finite difference approximations using the past data points [1]. The decision to apply additional perturbations is based on the value of the condition number of past data points. Should the condition number drop below a certain threshold, a probing input is computed from (4).

$$\boldsymbol{u}_\tau = \operatorname{argmax}_{\boldsymbol{u}} \operatorname{cond}(\mathcal{S}_k^{-1}), \tag{4a}$$

$$\text{s.t. } G_m(\boldsymbol{u}) + \epsilon_k^G + \left(\psi_k^G\right)^T (\boldsymbol{u} - \boldsymbol{u}_k) \leq 0, \tag{4b}$$

$$\mathcal{S}_k = \left[\boldsymbol{u}_k - \boldsymbol{u}, \ldots, \boldsymbol{u}_k - \boldsymbol{u}_{k-n_u}\right]^T. \tag{4c}$$

## Modifier adaptation with quadratic approximation (MAWQA)

MAWQA combines MA with elements from derivative-free optimization (DFO) [4]. In the MAWQA framework, when enough data points are available, the modifiers in equation (2) are calculated by analytically differentiating the fitted quadratic functions corresponding to the measurements of $J_p$ and $G_p$ and evaluating them at $\boldsymbol{u}_k$. This works well if the regression set is well-poised. Poisedness refers to the quality of the regression set in terms of its ability to accurately represent the underlying function [4]. To achieve a well-poised regression set, a screening algorithm is employed. The regression set $\boldsymbol{\mathcal{U}}_k$ should include well-distributed distant data points $\boldsymbol{\mathcal{U}}_k^{dist}$, which serve as anchors, alongside neighboring points $\boldsymbol{\mathcal{U}}_k^{nb}$ near the current best iterate $\boldsymbol{u}_k^*$ within a radius of $\Delta$, which reduces the effects of the measurement noise [3]. The regression set contains $n_m$ data points, each data point is an $n_u$ input vector $\boldsymbol{u}$; $\boldsymbol{\mathcal{U}}_k = \{\boldsymbol{u}_k^*, \boldsymbol{\mathcal{U}}_k^{dist}, \boldsymbol{\mathcal{U}}_k^{nb}\}$. The quadratic polynomial used for this fit is defined by

$$\mathcal{P}(\boldsymbol{u}, \boldsymbol{\beta}) = c + \sum_{i=1}^{n_u} \left(b_i u(i)\right) + \sum_{i=1}^{n_u} \sum_{j=1}^{i} \left(a_{i,j} u(i) u(j)\right), \tag{5}$$

where $\boldsymbol{\beta} = \left[c,\ b_1, \ldots, b_{n_u}, a_{1,1}, \ldots, a_{n_u,n_u}\right]^T$ and $u(i)$ denotes the $i^{th}$ element in the vector $\boldsymbol{u}$. The polynomial basis, which correspond to the polynomials in (5), is defined by

$$\begin{aligned} \boldsymbol{\Gamma}(\boldsymbol{u}) = \{&1, u(1), \cdots, u(n_u), u(1)^2, u(1)\,u(2), \cdots, \\ &u(n_u - 1) u(n_u), u(n_u)^2\}. \end{aligned} \tag{6}$$

To fit the cost function $J_p(\boldsymbol{u})$, at least $n_Q := |\boldsymbol{\beta}| = (n_u + 1)(n_u + 2)/2$ observations of the function must be available, which are in stored in $\boldsymbol{\mathcal{U}}_k$ in the MAWQA algorithm. To determine the values of $\boldsymbol{\beta}$, the linear system of equations (7) is solved if $n_m = n_Q$ and in least squares sense if $n_m > n_Q$ .

$$\begin{bmatrix} \Gamma_1(\mathcal{U}_{1|k}) & \Gamma_2(\mathcal{U}_{1|k}) & \cdots & \Gamma_{n_q}(\mathcal{U}_{1|k}) \\ \Gamma_1(\mathcal{U}_{2|k}) & \Gamma_2(\mathcal{U}_{2|k}) & \cdots & \Gamma_{n_q}(\mathcal{U}_{2|k}) \\ \vdots & \vdots & \vdots & \vdots \\ \Gamma_1(\mathcal{U}_{n_m|k}) & \Gamma_2(\mathcal{U}_{n_m|k}) & \cdots & \Gamma_{n_q}(\mathcal{U}_{n_m|k}) \end{bmatrix} \begin{bmatrix} \beta_1 \\ \beta_2 \\ \vdots \\ \beta_{n_q} \end{bmatrix} = \begin{bmatrix} J_p(\mathcal{U}_{1|k}) \\ J_p(\mathcal{U}_{2|k}) \\ \vdots \\ J_p(\mathcal{U}_{n_m|k}) \end{bmatrix}$$

$$\mathcal{M}(\boldsymbol{\Gamma}(\boldsymbol{u}), \boldsymbol{\mathcal{U}}_k)\beta = J_p(\boldsymbol{\mathcal{U}}_k) \tag{7}$$

The notation $\mathcal{U}_{j|k}$ means the data point with index $j$ in the regression set $\boldsymbol{\mathcal{U}}$ in the $k^{th}$ iteration. The constraints are also fitted in the same way as the cost function. To ensure the adequacy of the fitted model, the method proposed in [5] can be employed when fitting the parameters $\boldsymbol{\beta}$. This involves employing the General Quadratic Convex Under-estimator (GQCU) to ensure that the fitted surrogate model remains convex by enforcing the Hessian matrix to be positive semi-definite. Since the fitted model is only a local approximation of the original function around $\boldsymbol{u}_k^*$, a trust region is employed while searching

for $\boldsymbol{u}_{k+1}$. In the MAWQA algorithm, the trust region depends on the regression set $\mathcal{U}_k$.

$$\boldsymbol{u}^*_{\phi|k+1} := \operatorname{argmin}_{\boldsymbol{u}} J_\phi(\boldsymbol{u}), \tag{8a}$$
$$\text{s.t. } G_\phi(\boldsymbol{u}) \leq 0, \tag{8b}$$
$$(\boldsymbol{u}-\boldsymbol{u}_k)^T \operatorname{cov}(\mathcal{U}_k)\,(\boldsymbol{u}-\boldsymbol{u}_k) \leq \gamma^2, \tag{8c}$$

where $J_\phi$ and $G_\phi$ are the fitted quadratic functions of $J_p$ and $G_p$. A tuning factor, denoted by $\gamma$, is used to scale the trust-region. The quality of the surrogate model is compared to that of the adapted process model. MAWQA solves either $(2a, b)$ with $(8c)$ or $(8a-c)$ depending on which model predicts the last $J_p$ and $G_p$ better [3].

**Algorithm** 1. MAWQA

**Step 1.** Collect $n_l$ measurements by applying feasible and well distributed data points.

**Step 2.** Apply MA until $n_Q$ measurements are collected. **If** $\operatorname{cond}(\mathcal{S}_k^{-1}) < \epsilon$, compute $\boldsymbol{u}_{k+1}$ from $(4)$.

**Step 3.** Construct the regression set $\mathcal{U}_k$ and compute $u_{k+1}$ from $(2)$ or $(8)$.

**Step 4.** If $\boldsymbol{u}_{k+1}$ lies near $\boldsymbol{u}^*_k$; $\|\boldsymbol{u}_{k+1}-\boldsymbol{u}^*_k\| < \Delta$, where $\Delta$ is a tuning parameter, then apply an explorative input $\boldsymbol{u}_{k+1} = \boldsymbol{u}_\alpha$, to improve the quadratic models.

**Step 5.** Apply $\boldsymbol{u}_{k+1}$ to the plant and check the improvement in the cost function.

**Step 6.** Successful iteration: **If** $J_p(\boldsymbol{u}_{k+1}) < J_p(\boldsymbol{u}^*_k)$, and $G_p(\boldsymbol{u}_{k+1}) \leq 0$ **then** set $\boldsymbol{u}^*_{k+1} = \boldsymbol{u}_{k+1}$, and increase $k$ by one then return to **Step 3**.

**Step 7.** **Otherwise** Add $\boldsymbol{u}_{k+1}$ to the regression set $\mathcal{U}_k$ and return to **Step 3**.

In [3], it is suggested to compute $\boldsymbol{u}_\alpha$ by applying two steps. First a data point is chosen from the distant points that are included in the regression set.

$$\boldsymbol{u}_i \in \mathcal{U}_k, \|\boldsymbol{u}_i - \boldsymbol{u}^*_k\| \geq 2\Delta, \tag{9a}$$
$$\boldsymbol{u}_\alpha = (\boldsymbol{u}_i + \boldsymbol{u}^*_k)/2. \tag{9b}$$

This approach has the same goal as the criticality step of the derivative free algorithm introduced in [4], which is a model improvement step. Experience however shows that this step often is inefficient in this form. In addition, MAWQA also relies on the explorative nature of the algorithm, that leads to improving the poisedness [6].

## PERTURBATION METHODS FOR MAWQA

In this section, we investigate four different options to improve the poisedness of the data points that are visited by the MAWQA algorithm. This improves the quality of the locally fitted quadratic models.

### Method I: Averaging with Distant Points

Here the original approach is adjusted to ensure that $u_\alpha$ adheres to the estimated process constraints. The initial input $u_i$ for starting Algorithm 2 can be chosen based on various criteria, such as prioritizing the best cost, or selecting the furthest point from $\boldsymbol{u}^*_k$ first, or ensuring a good geometric distribution.

**Algorithm** 2. Averaging with distant points

**Select** $\boldsymbol{u}_i$ and **compute** $\boldsymbol{u}_\alpha$ from $(9)$.
**If** $G_\phi(\boldsymbol{u}_\alpha) \leq 0$ **then** $\boldsymbol{u}_{k+1} = \boldsymbol{u}_\alpha$ **otherwise** choose a different $\boldsymbol{u}_i$.

### Method II: Simplex Gradients

The second method is the same as the perturbation method used in [1]. This means solving $(10)$ and replacing $\boldsymbol{u}_\alpha$ by $\boldsymbol{u}_\varepsilon$.

$$\boldsymbol{u}_\varepsilon = \operatorname{argmax}_{\boldsymbol{u}\in B} \operatorname{cond}(\mathcal{S}_k^{-1}), \tag{10a}$$
$$\text{s.t. } G_{\phi|k}(\boldsymbol{u}) \leq 0, \tag{10b}$$

where $B$ is a sphere with radius $r$.

### Method III: QA Matrix Conditioning

In the context of the MAWQA, it is crucial for the matrix $\mathcal{M}$ from $(7)$ to be well conditioned to avoid numerical instability and unreliable results. It is established in [4] that well-poisedness is related to the condition number of the matrix $\mathcal{M}(\boldsymbol{\Gamma}(\boldsymbol{u}), \widehat{\boldsymbol{\mathcal{U}}}_k)$, where $\widehat{\boldsymbol{\mathcal{U}}}_k := \boldsymbol{\mathcal{U}}_k - \boldsymbol{u}^*_k$ is a shifted version of $\boldsymbol{\mathcal{U}}_k$ with respect to $\boldsymbol{u}^*_k$. In Method III, the condition number of $\mathcal{M}(\boldsymbol{\Gamma}(\boldsymbol{u}), \widehat{\boldsymbol{\mathcal{U}}}_k)$ is optimized for the given set $\widehat{\boldsymbol{\mathcal{U}}}_k$ augmented with $\boldsymbol{u}_\omega$, the additional perturbation input.

$$\boldsymbol{u}_\omega = \operatorname{argmin}_{\boldsymbol{u}\in B} \operatorname{cond}\left(\mathcal{M}(\boldsymbol{\Gamma}(\boldsymbol{u}), \{\widehat{\boldsymbol{\mathcal{U}}}_k, (\boldsymbol{u}-\boldsymbol{u}^*_k)\})\right),$$
$$\text{s.t. } G_{\phi|k}(\boldsymbol{u}) \leq 0, \tag{11}$$

where $B$ is a sphere with radius $r$. The optimization problem computes a probing input $\boldsymbol{u}_\omega$ that improves the poisedness of $\widehat{\boldsymbol{\mathcal{U}}}_k$ and the surrogate quadratic model quality.

### Method IV: Pivot Polynomials

This method simplifies the computations by avoiding the need to solve the complex optimization problem $(11)$. It is a variant of the algorithms introduced in [4, Chapter 6]. The algorithm performs an LU decomposition of $\mathcal{M}(\boldsymbol{\Gamma}(\boldsymbol{u}), \widehat{\boldsymbol{\mathcal{U}}}_k)$ through Gaussian elimination. The matrix $\mathcal{M}(\boldsymbol{\Gamma}(\boldsymbol{u}), \widehat{\boldsymbol{\mathcal{U}}}_k)$ is factored into a lower triangular matrix $L$ and an upper triangular matrix $U$; $\mathcal{M}(\boldsymbol{\Gamma}(\boldsymbol{u}), \widehat{\boldsymbol{\mathcal{U}}}_k) = L \cdot U$. To enhance the numerical stability during this decomposition, pivoting is employed. Pivoting involves the selection of pivot elements prior to executing the Gaussian elimination process, thereby mitigating risks associated with division by small numbers and minimizing numerical inaccuracies. The algorithm decomposes $\mathcal{M}(\boldsymbol{\Gamma}(\boldsymbol{u}), \widehat{\boldsymbol{\mathcal{U}}}_k)$ into $L$ and $U$ such that $L$ contains ones along its diagonal, while $U$ contains pivot values along the diagonal. The symbolic functions yielding these pivot values are the output of the algorithm, these functions are referred to as the pivot polynomials $\boldsymbol{\Phi}(\boldsymbol{u})$. By this operation we obtain symbolic

functions in the diagonal of the computed upper triangular matrix. The condition number of the upper triangular matrix is improved by maximizing $|\Phi_i(\boldsymbol{u})|$, the $i^{th}$ polynomial in the set $\boldsymbol{\Phi}(\boldsymbol{u})$. The condition number of the matrix $\mathcal{M}(\boldsymbol{\Gamma}(\boldsymbol{u}), \widehat{\boldsymbol{\mathcal{U}}}_k)$ is improved indirectly by optimizing the pivots of the matrix $U$. In Algorithm 3 presented below, we differentiate between $\Phi_i(\hat{\mathcal{U}}_{j|k})$, which is a numerical scalar value that is computed from the $j^{th}$ data point in $\widehat{\boldsymbol{\mathcal{U}}}_k$, and $\Phi_i(\boldsymbol{u})$ which is a symbolic function of $\boldsymbol{u}$ (see **Steps e-f**). The algorithm starts under the assumption that $\widehat{\boldsymbol{\mathcal{U}}}_k$ is initiated with $\boldsymbol{u}_k^*$ as its first element; $\hat{\mathcal{U}}_{1|k} = \boldsymbol{u}_k^*$. In the $i^{th}$ iteration, the data point $\hat{\mathcal{U}}_{j|k}$ that maximizes the pivot polynomial $\Phi_i$ is identified in **Step b**. The data points $\hat{\mathcal{U}}_{j|k}$ and $\hat{\mathcal{U}}_{i|k}$ are then swapped in $\widehat{\boldsymbol{\mathcal{U}}}_k$ in **Step c**. Afterwards Gaussian elimination is applied to all subsequent rows to update the pivot polynomials as shown in the loop **Steps e-f**. The algorithm starts with the basis $\boldsymbol{\Phi}(\boldsymbol{u}) = \boldsymbol{\Gamma}(\boldsymbol{u})$ and progressively updates its entries using the row operations derived from Gaussian elimination.

**Algorithm** 3. Perturbation using pivot polynomials

**Require:** $\widehat{\boldsymbol{\mathcal{U}}}_k$; $|\widehat{\boldsymbol{\mathcal{U}}}_k| := n_m \geq 1$, $\boldsymbol{u}_k^*, \nu > 0$ a tuning factor.
**Initialization:** set $\boldsymbol{\Phi}(\boldsymbol{u}) = \boldsymbol{\Gamma}(\boldsymbol{u})$.
**LU decomposition using Gaussian elimination:**
**Step a**. **For** $i = 1, \dots, \min(m, n_Q)$
**Step b**. find $j = \underset{i \leq j \leq p}{\mathbf{argmax}} |\Phi_i(\hat{\mathcal{U}}_{j|k})|$
**Step c**. **If** $|\Phi_i(\hat{\mathcal{U}}_{j|k})| > \nu$ **then** swap the data points $\hat{\mathcal{U}}_{i|k}$ and $\hat{\mathcal{U}}_{j|k}$ in the regression set $\widehat{\boldsymbol{\mathcal{U}}}_k$
**Step d**. **Else** compute the $\boldsymbol{u}_{k+1}$ using (12) and terminate.
**Step e**. **For** $l = i + 1, \dots, n_Q$
**Step f**. $$\Phi_l(\boldsymbol{u}) \longleftarrow \Phi_l(\boldsymbol{u}) - \frac{\Phi_l(\hat{\mathcal{U}}_{i|k})}{\Phi_i(\hat{\mathcal{U}}_{i|k})} \Phi_i(\boldsymbol{u}).$$

$$\boldsymbol{u}_\xi = \operatorname{argmax}_{\boldsymbol{u} \in B} |\Phi_i(\boldsymbol{u})|, \tag{12a}$$
$$\text{s.t. } G_\phi(\boldsymbol{u}) \leq 0, \tag{12b}$$

where $B$ is a sphere with radius $r$.

In scenarios where $p < n_Q$, the regression set $\widehat{\boldsymbol{\mathcal{U}}}_k$ is completed by solving (12). To ensure numerical stability, a threshold $\nu$ is selected to mitigate the risk of division by small numbers in **Step f**. In instances where a data point cannot be identified such that $|\Phi_i(\hat{\mathcal{U}}_{j|k})| > \nu$, the algorithm computes a new input using (12). The algorithm continues until it computes the final pivot polynomial, then (12) is solved, to compute $\boldsymbol{u}_\xi$. The algorithm can be started with just one data point or less than $n_Q$ data points, however the constraint (12b) must be replaced by (2b) or (4b) depending on availability of data points.

As in the case of Method III, we apply Algorithm 3 in **Steps 2** and **4** of the MAWQA algorithm. The optimization problem (12) is significantly less computationally demanding than solving (10) or (11) because it solely involves optimizing a second-order polynomial.

## Model-Free Optimization (MFO)

As Algorithm 3 does not require $n_Q$ initial points, it can be used to formulate a completely model-free iterative optimization algorithm. First $n_Q$ data points are generated using Algorithm 3 and then iterative quadratic optimization is applied.

**Algorithm** 4. Model-free optimization

**Require:** $\boldsymbol{u}_0^*$, $\Delta$, $\nu$ and $\gamma$.
**Step i.** Apply Algorithm 3. until $n_Q$ points are available. Select the admissible point with the best objective value $\boldsymbol{u}_k^*$ as the first entry of $\boldsymbol{\mathcal{U}}_k$.
**Step ii.** Once $n_Q$ points are available, the optimization problem (8) is solved to compute the $u_{k+1}$.
**Step iii.** If $\boldsymbol{u}_{k+1}$ lies near $\boldsymbol{u}_k^*$; $\|\boldsymbol{u}_{k+1} - \boldsymbol{u}_k^*\| < \Delta$, then apply Algorithm 3.
**Step iv.** Apply $\boldsymbol{u}_{k+1}$ to the plant.
**Step v.** **If** $J_p(\boldsymbol{u}_{k+1}) < J_p(\boldsymbol{u}_k^*)$, $G_p(\boldsymbol{u}_{k+1}) \leq 0$,
Successful iteration: **then** set $\boldsymbol{u}_{k+1}^* = \boldsymbol{u}_{k+1}$, and increase $k$ by one then return to **Step ii**.
Unsuccessful iteration: **Otherwise** add $\boldsymbol{u}_{k+1}$ to the regression set $\boldsymbol{\mathcal{U}}_k$ and return to **Step ii**.

At each iteration, the first element of $\boldsymbol{\mathcal{U}}_k$ can change, which updates the center in Algorithm 3, resulting in exploration of the surrounding of current best iterate $\boldsymbol{u}_k^*$.

# RESULTS

In this section, we perform a comparative numerical study of the proposed methods for the generation of probing points. For this purpose, we have selected the Williams-Otto plant, which serves as a benchmark problem for evaluating RTO schemes [3, 7]. The variable definitions and parameter values originate from [7]. The core is a CSTR with chemical reactions:

$$A + B \xrightarrow{k_1} C, \qquad k_1 = 1.66 \times 10^6 e^{\frac{-6666.7}{(\theta + 273.15)}}$$
$$C + B \xrightarrow{k_2} P + E, \qquad k_2 = 7.212 \times 10^8 e^{\frac{-8333.3}{(\theta + 273.15)}}$$
$$P + C \xrightarrow{k_3} G, \qquad k_3 = 2.675 \times 10^{12} e^{\frac{-11111}{(\theta + 273.15)}}$$

where $k_1, k_2$ and $k_3$ are the reaction constants of the plant. Reactants $A$ and $B$ are continuously added to the reactor with mass flow rates denoted as $F_A$ and $F_B$. The primary objective is to synthesize the desired products $P$ and $E$, while $C$ serves as an intermediate product and $G$ is considered an undesired byproduct. The reactor operates under isothermal, maintaining a constant temperature $\theta$, with a constant mass holdup of $2105\text{kg}$. $F_A$ is kept at a constant value of $1.8275\ \text{kg/s}$, while $F_B$ and the reactor temperature are treated as decision variables; $\boldsymbol{u} = [F_B\ \ \theta]^T$. These decision variables are normalized by their operating intervals ($F_B$: 3 – 6 kg/s, $\theta$: 70 – 100 C°). The main goal of this operational setup is to maximize the profit,

which results from calculating the differences in price between the products and the consumed reactants.

$$\mathcal{V}(F_B,\theta) = 1143.38(F_A + F_B)\,X_P + 25.92\,X_E - 76.23\,F_A - 114.34\,F_B,$$

where $X_P$ and $X_E$ signify the mass fraction of products $P$ and $E$. $\mathcal{V}(F_B,\theta)$ is corrupted with noise, which follows a Gaussian distribution with a standard deviation $\sigma$. It is assumed that the process is not well understood. The optimization model contains only two reactions:

$$A + 2B \xrightarrow{\hat{k}_1} P + E, \qquad \hat{k}_1 = 2.189 \times 10^8 e^{\frac{-8077.6}{(\theta+273.15)}},$$
$$A + B + P \xrightarrow{\hat{k}_2} G + E, \; \hat{k}_2 = 4.31 \times 10^{13} e^{\frac{-12438}{(\theta+273.15)}},$$

where $\hat{k}_1$ and $\hat{k}_2$ denote the reaction constants of the optimization model. The tuning parameters for the MAWQA algorithm are set to $\Delta = r = 0.1$ and $\gamma = 3$. We used the furthest admissible point from $\boldsymbol{u}_k^*$ as $\boldsymbol{u}_i$ in (9). As for the matrix $\mathcal{S}_k$ in (10), we used the most recent $n_u$ data points chosen by the screening algorithm to construct $\boldsymbol{\mathcal{U}}_k$. In Algorithm 3, the tuning parameter is chosen to be $\nu = 0.25$, which is also used in the model-free optimization. Figures 1-5 demonstrate the results of applying the methods.

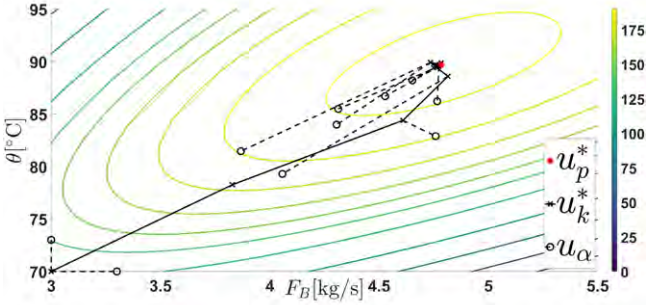



**Figure 1.** Results of applying the MAWQA Algorithm with Method I to the Williams-Otto reactor for $\sigma = 0.5$.

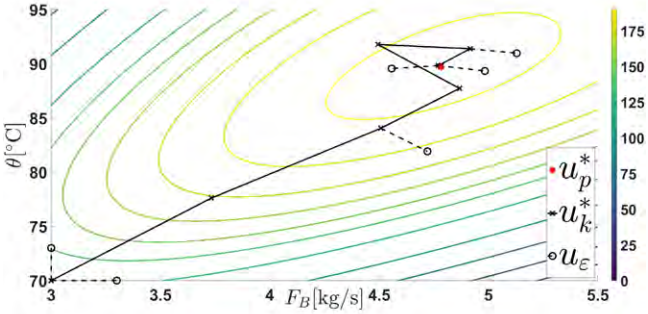



**Figure 2.** Results of applying the MAWQA Algorithm with Method II to the Williams-Otto reactor for $\sigma = 0.5$.

All the methods succeeded in finding $\boldsymbol{u}_p^*$ in a few iterations with good accuracy. From the results, Method I exhibits limitations in achieving good distribution of data points near the optimum. This is mainly due to its reliance on previously visited data points when calculating explorative moves, leading to a concentration of points on one side of the optimum. As for the remaining methods, well poisedness is reached at $\boldsymbol{u}_k^*$.

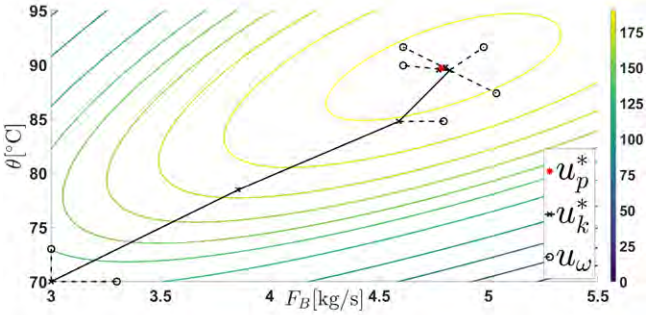



**Figure 3.** Results of applying the MAWQA Algorithm with Method III to the Williams-Otto reactor for $\sigma = 0.5$.

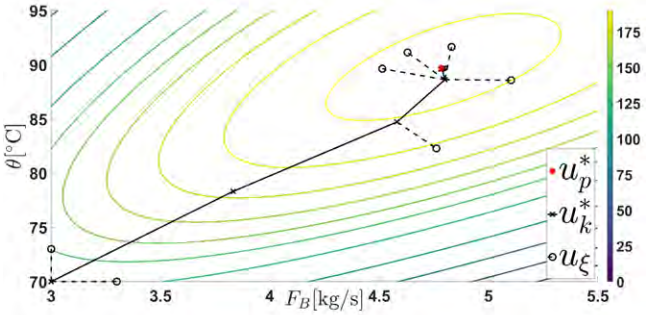



**Figure 4.** Results of applying the MAWQA Algorithm with Method IV to the Williams-Otto reactor for $\sigma = 0.5$.

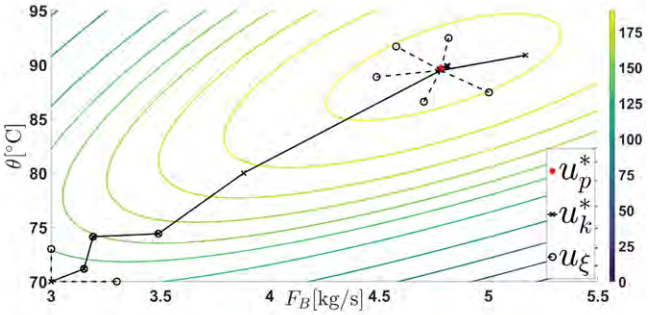



**Figure 5.** Results of applying model-free optimization (Algorithm 4) to the Williams-Otto reactor for $\sigma = 0.5$.

The proposed methods are compared against the performance of the original MA without QA [1] for 3 different levels of noise. As there are no constraints in this case study, Method I is the same as the method introduced in [3]. Each method was tested with 200 simulation runs. To avoid excessive probing, inputs that are at least $\Delta/2$ away from already visited data points are probed. Three key performance indicators (KPIs) were calculated.

1. **Optimum Proximity KPI**: This KPI assesses the distance between the $\boldsymbol{u}_k^*$ after 30 iterations and $\boldsymbol{u}_p^*$.
2. **Average steps KPI**: This indicator provides the average number of iterations needed to reach

the vicinity of the plant optimum, defined as $\left\|\boldsymbol{u}_p^* - \boldsymbol{u}_k^*\right\| \leq 0.05$.

3. **Poisedness KPI**: This KPI reflects the value of the $\Lambda$- Poisedness after 30 iterations, following the definition from [4]. $\Lambda \geq \max_{0\leq i\leq n_Q} \max_{\boldsymbol{u}} |\ell_i(\boldsymbol{u})|$ ,

where $\ell_i(\boldsymbol{u})$ are the Lagrange polynomials associated with $\mathcal{U}_k$. A lower value indicates a more favorable distribution. The best achievable $\Lambda$-poisedness is 1.

**Table 1:** Results of the 200 simulation runs for $\sigma = 0.5$.

| Method | Opt. Proximity | Av. steps | Poisedness |
|---|---|---|---|
| MA [1] | $0.0786 \pm 0.060$ | $16.1 \pm 4.0$ | 3.51 |
| I | $0.0164 \pm 0.010$ | $10.0 \pm 1.6$ | 5.07 |
| II | $0.0201 \pm 0.013$ | $9.3 \pm 1.6$ | 3.2 |
| III | $0.0130 \pm 0.010$ | $9.1 \pm 1.5$ | 2.02 |
| IV | $0.0107 \pm 0.009$ | $9.8 \pm 1.6$ | 1.75 |
| MFO | $0.0106 \pm 0.009$ | $11.9 \pm 2.1$ | 1.82 |

**Table 2:** Results of the 200 simulation runs for $\sigma = 1$.

| Method | Opt. Proximity | Av. steps | Poisedness |
|---|---|---|---|
| MA [1] | $0.0891 \pm 0.059$ | $17.2 \pm 4.4$ | 3.25 |
| I | $0.0264 \pm 0.017$ | $10.9 \pm 2.8$ | 5.31 |
| II | $0.0260 \pm 0.016$ | $10.5 \pm 3.6$ | 2.95 |
| III | $0.0203 \pm 0.016$ | $10.3 \pm 2.4$ | 1.98 |
| IV | $0.0187 \pm 0.013$ | $10.0 \pm 2.0$ | 1.66 |
| MFO | $0.0193 \pm 0.014$ | $12.3 \pm 2.4$ | 1.75 |

**Table 3:** Results of the 200 simulation runs for $\sigma = 2$.

| Method | Opt. Proximity | Av. steps | Poisedness |
|---|---|---|---|
| MA [1] | $0.1033 \pm 0.066$ | $19.0 \pm 6.1$ | 2.81 |
| I | $0.0380 \pm 0.025$ | $11.9 \pm 4.4$ | 5.16 |
| II | $0.0388 \pm 0.026$ | $12.7 \pm 6.0$ | 2.90 |
| III | $0.0330 \pm 0.024$ | $11.9 \pm 4.4$ | 1.99 |
| IV | $0.0337 \pm 0.021$ | $11.4 \pm 3.7$ | 1.81 |
| MFO | $0.0325 \pm 0.023$ | $13.5 \pm 3.5$ | 1.84 |

As the level of noise increases, both the accuracy and speed of convergence of all methods to the optimum decreases. The MA approach from [1] demonstrated the lowest accuracy and the slowest convergence across all levels of noise. This reduced accuracy can be attributed to the noise interference, which causes the MA to oscillate around $\boldsymbol{u}_p^*$. However, this continuous oscillation contributes to a good poisedness. Method I exhibited poor poisedness in the three noise levels, followed by MA without QA and Method II. This outcome aligns with our expectations, as these methods do not adequately address the poisedness required for QA. In contrast, Methods III and IV demonstrated robust and similar poisedness across varying noise levels, with Method IV consistently achieving slightly better results. Maintaining good poisedness improves the accuracy of the gradient estimation, which is crucial for tackling more complex problems. MFO achieved a level of accuracy comparable to Method IV, however with slightly more test points (20% more) than the model-based methods. On the other hand, the method does not need any plant model and is purely based on data collected at the plant. Moreover, the optimization problems (10) and (11) are significantly more computationally demanding than the other methods. The average computation time for (10) was recorded at 1.38s, while the average for (11) was 1.87s. Conversely, the optimization problem (12) has an average computation time of 7ms, which is ~200 times faster than solving (10), (11).

## CONCLUSION

In this paper, we investigated improvements of the MAWQA algorithm, with focus on the criticality step. Our proposed methods improve the distribution of the data points, which is vital for finding true plant optimum fast and reliably. We demonstrated their potential using the Williams-Otto reactor benchmark. The results show that these methods significantly improve the poisedness of the regression set, resulting in more reliable and accurate gradient estimations, as well as increased robustness against noise. Moreover, we presented an effective model-free optimization strategy that converges to the true plant optimum but requires more probing steps in the initial phase. Future work will address cases with higher dimensions of the input vector and complex constraints.

## REFERENCES


1. Gao, W. and Engell, S. Iterative set-point optimization of batch chromatography. *Computers & Chemical Engineering*, 29: 1401–1409 (2005).
2. Marchetti, A., Chachuat, B., and Bonvin, D. Modifier-adaptation methodology for real-time optimization. *Industrial & Engineering Chemistry Research*, 48:6022–6033 (2009).
3. Gao, W., Wenzel, S., and Engell, S. A reliable modifier-adaptation strategy for real-time optimization. *Computers & Chemical Engineering*, 91:318–328 (2016).
4. Conn, A. R., Scheinberg, K., and Vicente, L. N. Introduction to Derivative-Free Optimization. Society for Industrial and Applied Mathematics, (2009).
5. Gottu Mukkula, A.R. and Engell, S. Guaranteed model adequacy for modifier adaptation with quadratic approximation. *European Control Conference (ECC):* 1037–1042 (2020).
6. Gao, W., Hernández, R., and Engell, S. A study of explorative moves during modifier adaptation with

quadratic approximation. *Processes*, 4 (2016).
7. Marchetti, A., Chachuat, B., and Bonvin, D. A dual modifier-adaptation approach for real-time optimization. *Journal of Process Control*, 20: 1027–1037 (2010).

© 2025 by the authors. Licensed to PSEcommunity.org and PSE Press. This is an open access article under the creative commons CC-BY-SA licensing terms. Credit must be given to creator and adaptations must be shared under the same terms. See https://creativecommons.org/licenses/by-sa/4.0/



Systems & Control Transactions

**Research Article - Peer Reviewed Conference Proceeding**
ESCAPE 35 - European Symposium on Computer Aided Process Engineering
Ghent, Belgium. 6-9 July 2025
Jan F.M. Van Impe, Grégoire Léonard, Satyajeet S. Bhonsale,
Monika E. Polańska, Filip Logist (Eds.)

PSE PRESS

# Optimal Energy Scheduling for Battery and Hydrogen Storage Systems Using Reinforcement Learning

**Moritz Zebenholzer[a]*, Lukas Kasper[a], Alexander Schirrer[b] and René Hofmann[a]**

[a] TU Wien, Institute of Energy Systems and Thermodynamics, Vienna, Austria
[b] TU Wien, Institute of Mechanics and Mechatronics, Vienna, Austria
* Corresponding Author: moritz.zebenholzer@tuwien.ac.at

## ABSTRACT

Optimal energy scheduling for sector-coupled multi-energy systems is becoming increasingly important as renewable energies such as wind and photovoltaics continue to expand. They are very volatile and difficult to predict. This creates a deviation between generation and demand that can be compensated for by energy storage technologies. For these, rule-based control is well established in industry, and mixed-integer model predictive control (MPC) is an area of research that promises the best results, usually regarding minimal costs. Drawbacks of MPC include the need for an adequate system model, often associated with high modeling effort, high computational effort for larger prediction horizons, and complications with stochastic variables. In this work, Reinforcement Learning is used in an attempt to overcome these difficulties without applying elaborate mixed-integer linear programming. The self-learning algorithm, which requires no explicit knowledge of the system behavior, can learn a control policy and uncertainties of the variables just by interaction with the (simulated) system model. It is demonstrated that Reinforcement Learning (exchange factor = 36.8 %) can learn complex system behavior with comparable quality to model predictive control (ex. = 32.4 %) and outperforms rule-based control (ex. = 41.8 %). This is done in a case study with the goal of minimizing the exchange of energy with the grid, with a battery and hydrogen system providing storage flexibility. These results were achieved in the context that the Reinforcement Learning agent only has instantaneous rather than predictive information, i.e., a very limited state of information compared to the MPC. The trained policy is then deployed while significantly decreasing the computational effort.

**Keywords**: Optimal Energy Scheduling, Reinforcement Learning (RL), Model-Predictive-Control (MPC)

## INTRODUCTION

Due to the energy transition, the share of renewable sources of energy, such as wind and photovoltaic, is steadily increasing [1-3]. These are highly volatile, resulting in a discrepancy between generation and demand, which must be balanced by storage at any time but which is difficult to predict [2]. To accomplish this balancing efficiently and reliably, sector-coupled multi-energy systems (MES) combined with battery and hydrogen storage systems are deployed. These include batteries for daily fluctuations and electrolyzers, fuel cells and hydrogen storage systems for weekly volatility, for example. [1,2] As wind energy and photovoltaics, in particular, are decentralized and distributed, the electricity grid can be strained by uneven feed-in. More flexibility is therefore required at the place of power supply, whereby the energy exchange between production and load and the grid should be minimized. [1]

The optimal and safe operation of such MES requires operational planning, typically done by rule-based controllers (RBC) in industry [3]. In contrast, more elaborate model predictive control (MPC) strategies are the subject of current research. This form of optimal control is generally seen as delivering the best possible performance, usually aiming for minimum operating costs in compliance with the system-relevant constraints. [2,3]

However, the main obstacle to realizing MPC is that the optimization depends on an adequate model of the system dynamics. In addition, the uncertain prediction of

stochastic fluctuating quantities such as renewable energy generation, demand, and electricity prices significantly affect the control performance. Moreover, in scenarios that require long prediction horizons and detailed models, the arising mixed-integer optimization problems may require excessive computational effort. [2]

For these reasons, a control system that delivers optimal online performance without major computing effort is required. This can, for example, be achieved through Reinforcement Learning (RL), a form of machine learning that requires no explicit prior knowledge of the system dynamics. It can learn a control policy and the uncertainties of the input variables on the system only through repetitive interaction with the system model. RL has achieved excellent results in various disciplines, such as robotics and operational planning in industrial energy systems. [4]

Key contributions of this work are a consistent comparison between RBC, MPC and RL and an RL-based controller with comparable performance to MPC. It is demonstrated that this is possible with limited, instantaneous state information.

## THEORETICAL BACKGROUND

The basic control methods of MPC [5] and RL [4], as well as their corresponding advantages and disadvantages with regard to industrial energy systems, are described below.

### Model Predictive Control

In model predictive control, a mathematical model of the system dynamics called the design model hereafter is used to predict the system's future behavior based on the current state and a sequence of future control input values. The controlled system's response is optimized over a specific prediction horizon $\Delta T_{\text{pred}}$. The schematic control loop is shown in Figure 1.

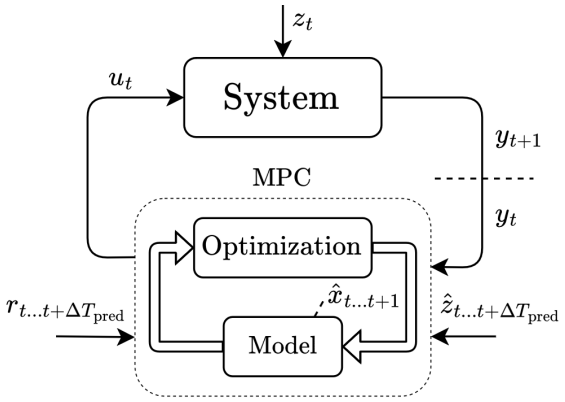



**Figure 1.** Model predictive control loop with control variables $u_t$, system state prediction $\hat{x}_{t\ldots t+T_{\text{pred}}}$ output $y_t$, disturbance $z_t$ and reference $r_t$ for timestep $t$ and prediction horizon $\Delta T_{\text{pred}}$ adapted from [5].

For simplicity of time discrete notation, index $t$ refers to the current sample, $t+1$ to the next, and $t+\Delta T_{\text{pred}}$ to the last sample in the current prediction horizon where the full trajectory $o_{t\ldots t+\Delta T_{\text{pred}}}$ is denoted hereafter with only the basis $o$. The sequence of the control variables $u$, is determined so that a predefined objective $J$, a cost function, is minimized, see Equation 1. These can be, for example, minimal costs, minimal deviations from a reference trajectory $r$ or minimal energy consumption. Constraints are imposed on the system's input variables $u$ and design model state estimates $\hat{x}$ via equality $(h(\cdot)=0)$ and inequality $(g(\cdot)\leq 0)$ constraints to ensure safe and physically feasible operation. The set $\mathrm{X}$ contains both real and integer-valued variables.

$$\begin{aligned} &\underset{u}{\operatorname{argmin}} \;\; J(\hat{x},u,\hat{z},r) \\ &\text{s.t.} \quad h(x,u)=0 \\ &g(x,u)\leq 0 \\ &x\in X, u\in U \end{aligned} \tag{1}$$

Only the control variables $u_t$ of the first-time step $t$ are applied to the system; all others are discarded. At the next time step, $t+1$, this iterative optimization process is repeated, using new predictions and measured values of the output $y_{t+1}$ and associated, updated system state estimate $\hat{x}_{t+1}$, also known as *receding horizon control*. It is particularly suitable for multivariable systems that contain complex relationships, relevant constraints and well-predictable inputs.

When both continuous and discrete variables are involved, as is often the case with energy systems, the optimal control problem (1) is usually formulated as a mixed-integer linear program (MILP) and solved using branch and bound algorithms [12]. Since the variables are typically linked across several time steps and constraints, it is difficult to decompose the problem. Binary variable formulations lead to combinatorial complexity, which becomes intractable as problem size increases. However, for practical applications, a large prediction horizon is often required, increasing the number of decision variables with each discrete time step and, therefore, the computational effort significantly. Although the MILP problem can be solved, it may be too complex for the necessary sampling time step size.

### Reinforcement Learning

In Reinforcement Learning, an entity called *agent* interacts with its environment with the purpose of learning to make sequential decisions. It receives a state observation $s_t$ and prior reward $r_t$ signal and performs an action $a_t$ that influences the environment, which evolves according to the internal system dynamics. The successor state $s_{t+1}$ and reward $r_{t+1}$ are the result. This process is sketched in Figure 2 and is understood in a stochastic sense as a Markov Decision Process (MDP).

Here, the agent learns by trial and error, guided by a reward function. Its goal is to maximize the discounted, cumulative reward over the considered period (episode)

$$\max \sum_{t=1}^{T} r(s_t, a_t, s_{t+1}) \cdot \gamma^{t-1}, \qquad (2)$$

with discount factor $\gamma$. While deriving a control law $a_t = \pi(s_t)$, which maps states to actions. Striking a good balance between exploration, i.e., visiting new state-action combinations, and exploitation, i.e., taking the actions with the highest cumulative reward expectation, is essential to the training process.

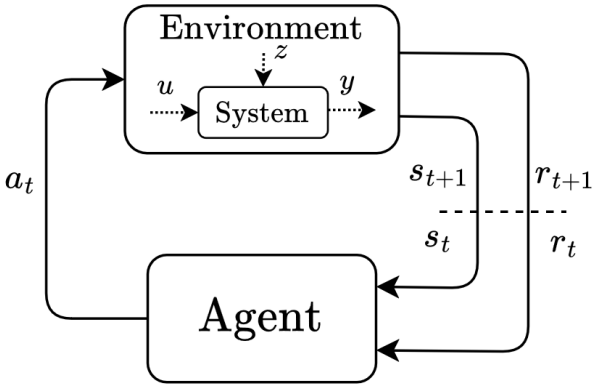



**Figure 2.** Reinforcement Learning control loop with control variables $u$, output $y$ and disturbance $z$, as well as, state observation $s_t$, action $a_t$ and reward $r_t$ for timestep $t$ adapted from [4].

In deep RL, the internal relationships in the agent are represented by deep neural networks (NN), which endows it with the ability to model any non-linear, high-dimensional function. Another advantage is that RL does not depend on modeling using first principles but learns from direct experience, allowing it to adapt to changing system dynamics even after the training process. This allows the performance to improve over time and can help reduce the prediction's uncertainty.

However, this method has difficulties with performance and stability guarantees, as it is challenging to provide for neural networks. In addition, the learning process is very sample-inefficient and a convergent learning process is not guaranteed in general. These topics are highly active fields of research. [6]

## METHODS

This chapter first outlines the use case and the underlying modeling adapted from [3]. It then links to the control methods and discusses the parameterization and implementation.

### Use Case

RL's potential is demonstrated through a representative use case, a MES providing storage flexibility. It consists of a battery (BSS) and a hydrogen storage system (HSS) comprising an electrolyzer, a fuel cell and a hydrogen storage unit. This MES, shown in Figure 3, is influenced, on the one hand, by generation $p_{\text{gen}}$ and consumption $p_{\text{de}}$ and, on the other hand, by the energy exchange not compensated for by the storage systems with the grid ($p_{\text{gr}}^{\text{in}}$,$p_{\text{gr}}^{\text{out}}$). All quantities are non-negative.

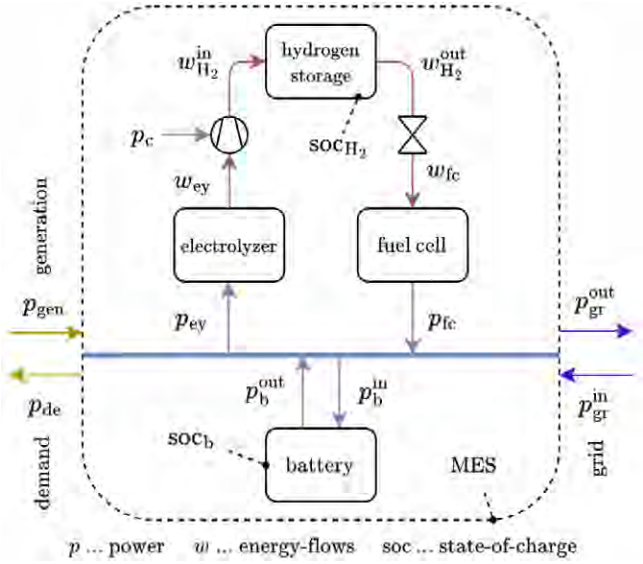



**Figure 3.** Multi-energy system (MES) with battery (b) and hydrogen storage systems, comprising electrolyzer (ey), storage ($H_2$) and fuel cell (fc).

The components can be modeled using the following relationships for the battery

$$\text{soc}_{\text{b,t+1}} = \text{soc}_{\text{b,t}} + \frac{\Delta t_{\text{sim}}}{C_{\text{b}}} \begin{cases} p_{\text{b},t}^{\text{in}} \cdot \eta_{\text{b}}, \text{ charge} \\ -p_{\text{b},t}^{\text{out}} / \eta_{\text{b}}, \text{ discharge} \end{cases} \qquad (3)$$

where $\text{soc}_{\text{b}}$ is the state-of-charge, $\eta$ the efficiency and $C_{\text{b}}$ the battery's capacity. The battery can either be charged by $p_{\text{b}}^{\text{in}}$ or discharged by $p_{\text{b}}^{\text{out}}$. The hydrogen storage is modeled using

$$\text{soc}_{\text{H}_2,\text{t+1}} = \text{soc}_{\text{H}_2,\text{t}} + \frac{\Delta t_{\text{sim}} \cdot \eta_{\text{H}_2}}{C_{\text{H}_2}} \left( w_{\text{H}_2,t}^{\text{in}} - w_{\text{H}_2,t}^{out} \right), \qquad (4)$$

and analogously $\text{soc}_{\text{H}_2}$ is the state-of-charge and $C_{\text{H}_2}$ is the capacity of the hydrogen storage. The energy level is increased when hydrogen is fed in ($w_{\text{H}_2}^{in}$) and decreased by $w_{\text{H}_2}^{\text{out}}$. The electrolyzer and the fuel cell are modeled using non-linear equations $w_{\text{ey}} = f_{\text{ey}}(p_{\text{ey}})$ and $w_{\text{fc}} = f_{\text{fc}}(p_{\text{fc}})$, respectively. An isentropic compressor, used to increase the pressure $pr$, using power $p_{\text{c}} = f_{\text{c}}(w_{\text{ey}}, pr)$, is located upstream of the storage tank, whereby the following applies, $w_{\text{H}_2}^{in} = w_{\text{ey}}$. Downstream of the hydrogen storage there is a valve for which $w_{\text{H}_2}^{\text{out}} = w_{\text{fc}}$ applies. For the MPC

design model all non-linear equations are piecewise linearized.

The energy equation

$$p_{\text{gen}} - p_{\text{de}} + p_{\text{fc}} - p_{\text{ey}} + p_{\text{b}}^{\text{out}} - p_{\text{b}}^{\text{in}} - p_{\text{c}} + p_{\text{gr}}^{\text{in}} - p_{\text{gr}}^{\text{out}} = 0 \quad (5)$$

links the various components' powers. The performance indicator, the exchange factor $\epsilon_t$, is defined as the ratio between the energy exchange with the grid and the difference of generation and demand sampled with $\Delta t_{sim}$

$$\epsilon_t = \frac{\sum_{\tau=0}^{\tau=t} p_{\text{gr},\tau}^{\text{in}} + p_{\text{gr},\tau}^{\text{out}}}{\sum_{\tau=0}^{\tau=t} |p_{\text{gen},\tau} - p_{\text{de},\tau}|}. \quad (6)$$

Here, $\epsilon_t = 0$ means that storage flexibility can compensate for any difference between generation and consumption. If $\epsilon_t = 1$, the entire difference is passed through to the grid.

## Control Engineering

In the control engineering sense, the process variables for the MPC can be divided up as follows. The control variable $u_t$ consists of the power flows into and out of the battery, the electrolyzer and the fuel cell

$$u_t = \left[p_{\text{b}}^{\text{in}} \quad p_{\text{b}}^{\text{out}} \quad p_{\text{ey}} \quad p_{\text{fc}}\right]_t^T. \quad (7)$$

The system's output $y_t$ comprises the state-of-charge for battery and hydrogen storage and the power exchange with the grid:

$$y_t = \left[\text{soc}_{\text{b}} \quad \text{soc}_{\text{H}_2} \quad p_{\text{gr}}^{\text{in}} \quad p_{\text{gr}}^{\text{out}}\right]_t^T. \quad (8)$$

The disturbance forecast $\hat{z}$, sampled with $\Delta t_{\text{opt}}$, consists of the generation and demand prediction from timestep $t$ to the prognosis horizon $t + \Delta T_{\text{pred}}$ acting on the system

$$\hat{z} = \begin{bmatrix} p_{\text{gen},t} & p_{\text{de},t} \\ \vdots & \vdots \\ p_{\text{gen},t+\Delta T_{\text{pred}}} & p_{\text{de},t+\Delta T_{\text{pred}}} \end{bmatrix}^T. \quad (9)$$

The objective of the MPC is to minimize the exchange of energy with the grid, i.e., the area under the absolute value of the power curve using a sampling time of $\Delta t_{\text{opt}}$,

$$\underset{u}{\text{argmin}} \sum_t^{t+\Delta T_{\text{pred}}} \left(p_{\text{gr},t}^{\text{in}} + p_{\text{gr},t}^{\text{out}}\right) \cdot \Delta t_{\text{opt}}. \quad (10)$$

The action $a_t$ of the RL agent is equivalent to the control variable $u_t$. The observation state $s_t$ consists in part of the system output $y_t$ and the disturbance $\hat{z}_t$ and can be written as

$$s_t = \left[\text{soc}_{\text{b}} \quad \text{soc}_{\text{H}_2} \quad p_{\text{gen}} \quad p_{\text{de}}\right]_t^T \quad (11)$$

and reward information comprises

$$r_t = \left[p_{\text{gr}}^{\text{in}} \quad p_{\text{gr}}^{\text{out}}\right]_t^T. \quad (12)$$

The reward function of the RL agent, sampled with $\Delta t_{\text{opt}}$, and chosen discount factor as $\gamma = 0.99$ can be written as

$$\max \sum_t^{t+\Delta T_{\text{pred}}} -\left(p_{\text{gr},t}^{\text{in}} + p_{\text{gr},t}^{\text{out}}\right) \cdot \Delta t_{\text{opt}} \cdot \gamma^{t-1}, \quad (13)$$

and a sampling time of $\Delta t_{\text{opt}}$ is used. All system-specific constraints are represented in the design model for the MPC and inherently in the simulation model for RL training and for the method comparison.

## Parameters & Data

Generation and demand data for Austria for 2023 were used as the data basis [7]. Five representative weeks according to their distribution were calculated, and one exemplary week (Figure 4, 19.6 - 26.6.2023) was used to test the use case. Energy production comprises 75 % photovoltaics and 25 % wind power. The data was normalized and scaled so that, on average, the demand is $\overline{P_{\text{de}}} = 250\,kW$ and generation $\overline{P_{\text{gen}}} = 300\,kW$, respectively. The data was subjected to white noise, whereby the signal-to-noise ratio is a factor of 20. The non-noisy data is used for the prediction of the MPC and for training the RL agent, while the noisy curves are declared as ground truth in the simulation.

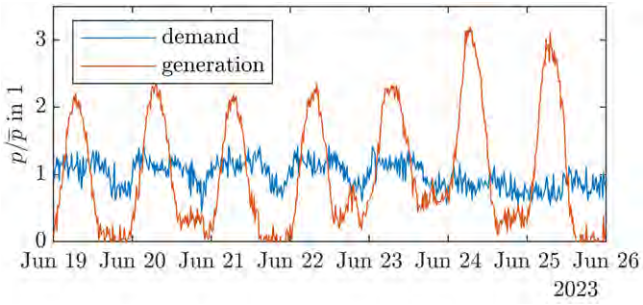



**Figure 4.** Demand and generation for a representative summer week of Austria, 2023 [7].

The MES components' parameters are listed in Table 1, and the simulation data in Table 2.

**Table 1.** MES Properties

| Battery System | | Hydrogen System | | |
|---|---|---|---|---|
| Property | Value | Property | Value | Unit |
| $C_{\text{b}}$ | 500 | $C_{\text{H}_2}$ | 3000 | kWh |
| $p_{\text{b}}^{max}$ | 100 | $p_{ey}^{max}$ | 400 | kW |
| | | $p_{fc}^{max}$ | 100 | kW |
| $\text{soc}_{\text{b}}^{min}$ | 0.2 | $\text{soc}_{\text{H}_2}^{min}$ | 0.1 | - |
| $\text{soc}_{\text{b}}^{max}$ | 0.8 | $\text{soc}_{\text{H}_2}^{max}$ | 0.9 | - |
| $\eta_{\text{b}}$ | 0.9 | $\eta_{\text{H}_2}$ | 1 | - |

## Simulation & Training

In the simulation environment, the system equations are solved with a time step size of $\Delta t_{\text{sim}}$. After $\Delta t_{\text{opt}}$, either the optimization for the MPC is solved or the trained neural network for RL is evaluated. For the MPC, the

prediction horizon $\Delta T_{\text{pred}}$ is divided into 96 time-steps with size $\Delta t_{\text{opt}}$. The RL agent is trained with a sampling time of $\Delta t_{\text{opt}}$. Proximal Policy Optimization (PPO) [8] is used as the RL algorithm, where it is trained for ~$10^4$ episodes.

**Table 2.** Simulation Properties

| Property | Value | Unit |
|---|---|---|
| $\Delta t_{\text{sim}}$ | 1 | min |
| $\Delta t_{\text{opt}}$ | 15 | min |
| $\Delta T_{\text{pred}}$ | 24 | h |
| $\Delta T_{\text{sim}}$ | 168 | h |

The neural network architecture used for the value-function critic is a fully connected, feedforward NN with ~1200 degrees of freedom. A stochastic Gaussian actor is implemented with ~3500 degrees of freedom.

## Implementation

The simulation environment was programmed in MatLab [9], whereby the optimization problem (MPC) was set up with YALMIP [10] and solved with Gurobi [11]. The PPO agent was trained with the MatLab Reinforcement Learning Toolbox [12] and 64 parallel workers. These were simulated on a system with 128 cores and 256 GB RAM (AMD EPYC 7702P).

## RESULTS & DISCUSSION

The results of the simulation are the process variables of the use case, whereby the control variables resulting from the optimization (MPC, NN-RL) and the state-of-charges are shown in Figure 6. Two tiles are used for the MPC (top) and two for the RL (bottom). These, in turn, are divided into hydrogen-related variables of the electrolyzer $p_{\text{ey}}$, the fuel cell $p_{\text{fc}}$ and the storage tank $p_{\text{H}_2}$ as well as battery-related variables charge $p_{\text{b}}^{\text{in}}$, discharge $p_{\text{b}}^{\text{out}}$ and state of charge $\text{soc}_{\text{b}}$. The powers are normalized, i.e. divided by the maximum power, because of $p_{\text{min}} = 0$. Without loss of relevant information aspects, three days were chosen from the test week and

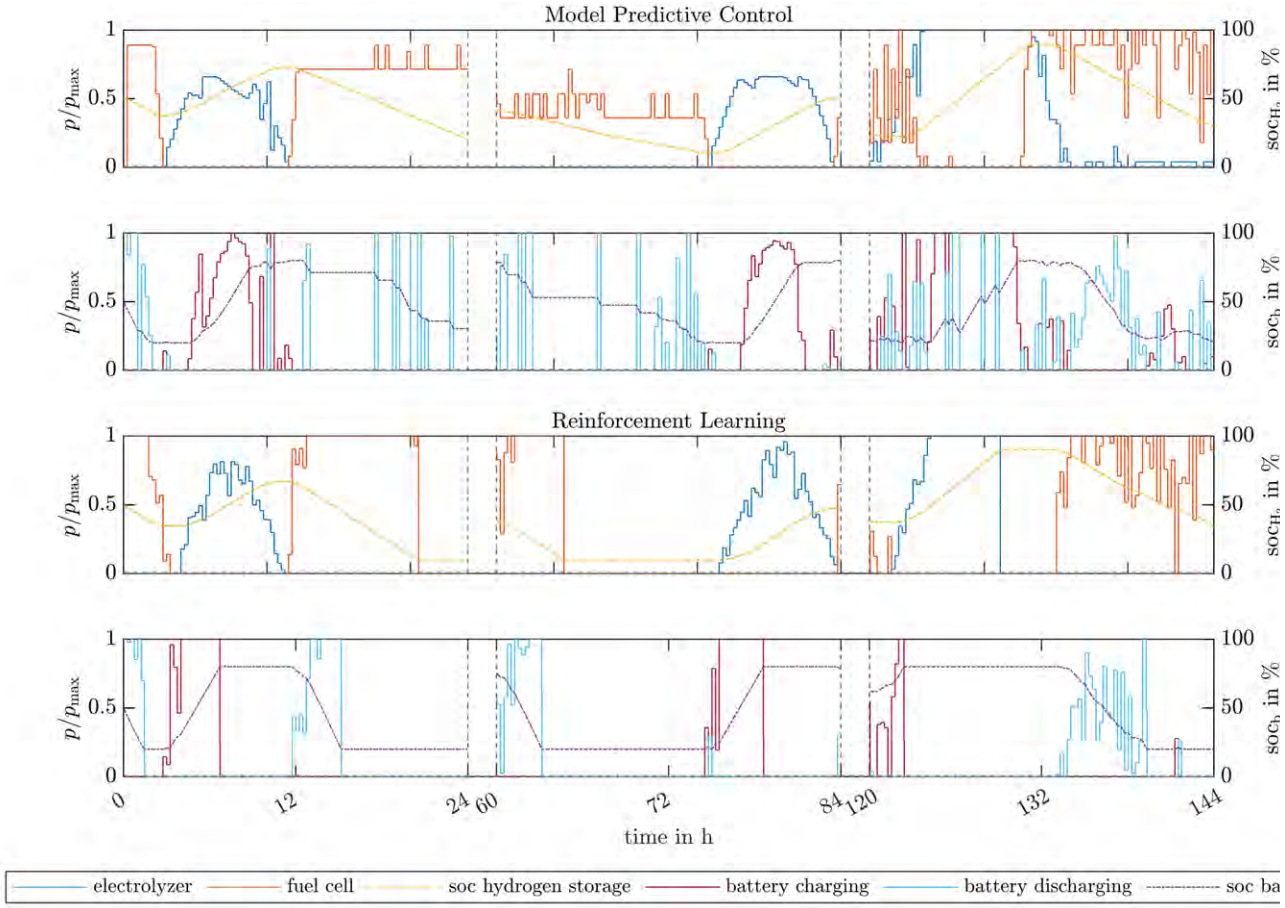



**Figure 5.** Setpoints electrolyzer power $p_{\text{ey}}$, fuel cell power $p_{\text{fc}}$ and fill level of storage tank $\text{soc}_{\text{H}_2}$ as well as battery-related variables charging power $p_{\text{b}}^{\text{in}}$, discharging power $p_{\text{b}}^{\text{out}}$and state-of-charge $\text{soc}_{\text{b}}$ for multi-energy system use case for model predictive control and Reinforcement Learning.

displayed for better visualization. In principle, as can be seen in Figure 5, two different operating modes can be identified: If more energy is generated than consumed, battery charging and electrolyzer are activated, and if there is a negative residual load, the battery is discharged, and the fuel cell is used. This only works as long as the storage units are not at their limits. Therefore, Predictive information is required on how the externally imposed energy flows will adjust to provide optimal flexibility. However, only the MPC has access to the inherent forecast information $\hat{z}_{t\ldots t+\Delta T_{\text{pred}}}$. The RL agent, which only has access to instantaneous observations, can only learn an implicit average prediction for future states through the sequence of observed states (trajectory). However, this assumes a similarity between the trained and tested generation and demand curves, which has been fulfilled in the tested scenario. Figure 6 shows the exchange factor $\varepsilon_t$ for MPC and RL, whereby the first 24 h can be regarded as a run-in effect, as the MPC has a forecast horizon of 1 day. The performance is comparable in the first 5 days; a difference can only be seen when a lot of renewable energy is produced and little is consumed.

In these situations, it is optimal to use a discontinuous switching behavior of the storage. It can be concluded that the lack of predictive information hinders the RL agent from performing better. After a one-week test phase, there is a difference in exchange factor of approx. 4 %.

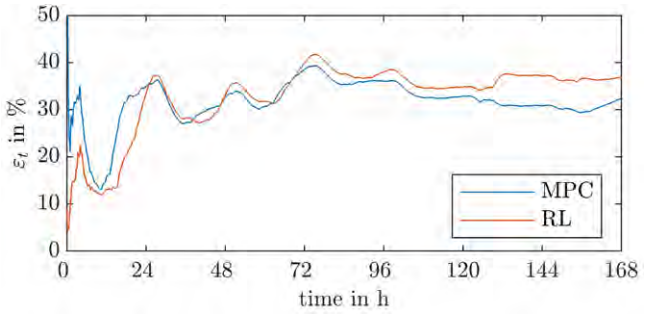



**Figure 6.** Energy exchange factor $\varepsilon_t$ with grid for 1 week.

## CONCLUSION & OUTLOOK

In this study, the performance of a Reinforcement Learning-based control strategy for sector-coupled multi-energy systems providing storage flexibility was evaluated. With Reinforcement Learning, a performance comparable to that of model predictive control can be achieved, which can be regarded as the upper limit in the nominal case. The Reinforcement Learning agent can outperform the industry standard rule-based control. With only instantaneous observations and without complex mixed-integer linear program modeling, the system can be controlled by a self-learning algorithm. The following questions are to be answered in a further study:

Can the Reinforcement Learning agent achieve better control quality if the same predictive information is provided for complete comparability? Can the self-learning system accomplish the same performance as model predictive control if unpredictable errors can be learned better than represented by a deterministic MPC?

## ACKNOWLEDGEMENTS

The authors want to acknowledge the support provided by the doctoral school *Smart Industrial Concept* (https://www.tuwien.at/doc/sic) and the TU Wien Bibliothek for financial support through its Open Access Funding Programme.

## REFERENCES

1. Le, T. S., et al. (2023). Optimal sizing of renewable energy storage: A techno-economic analysis of hydrogen, battery and hybrid systems considering degradation and seasonal storage. Applied Energy, 336, 120817. https://doi.org/10.1016/j.apenergy.2023.120817
2. Van, L. P., et al. (2023). Review of hydrogen technologies based microgrid: Energy management systems, challenges and future recommendations. International Journal of Hydrogen Energy, 48(38), 14127–14148. https://doi.org/10.1016/j.ijhydene.2022.12.345
3. Holtwerth, A., et al. (2024). Closed-loop model predictive control of a hybrid battery-hydrogen energy storage system using mixed-integer linear programming. Energy Conversion and Management: X, 22, 100561. https://doi.org/10.1016/j.ecmx.2024.100561
4. Perera, A. T. D., & Kamalaruban, P. (2021). Applications of reinforcement learning in energy systems. Renewable and Sustainable Energy Reviews, 137, 110618. https://doi.org/10.1016/j.rser.2020.110618
5. Schwenzer, M., et al. (2021). Review on model predictive control: An engineering perspective. The International Journal of Advanced Manufacturing Technology, 117(5–6), 1327–1349. https://doi.org/10.1007/s00170-021-07682-3
6. Jin, M., & Lavaei, J. (2020). Stability-Certified Reinforcement Learning: A Control-Theoretic Perspective. IEEE Access, 8, 229086–229100. https://doi.org/10.1109/ACCESS.2020.3045114
7. ENTSO-E Transparency Platform. (n.d.). Retrieved January 14, 2025, from https://transparency.entsoe.eu
8. Schulman, J., et al. (2017). Proximal Policy Optimization Algorithms (arXiv:1707.06347). arXiv. https://doi.org/10.48550/arXiv.1707.06347

9. The MathWorks Inc. (2024). MATLAB version: 23.2 (R2023b), Natick, Massachusetts: The MathWorks Inc. https://www.mathworks.com.
10. Löfberg, Johan. “A toolbox for modeling and optimization in MATLAB.” Proceedings of the CACSD Conference (2004), https://www.mathworks.com.
11. The MathWorks Inc. (2024). Reinforcement Learning Toolbox version: 23.2 (R2023b), Natick, Massachusetts: The MathWorks Inc. https://www.mathworks.com.
12. Gurobi Optimization, LLC. “Gurobi Optimizer Reference Manual.” (2024). https://www.gurobi.com.

© 2025 by the authors. Licensed to PSEcommunity.org and PSE Press. This is an open access article under the creative commons CC-BY-SA licensing terms. Credit must be given to creator and adaptations must be shared under the same terms. See https://creativecommons.org/licenses/by-sa/4.0/



Systems & Control Transactions

**Research Article - Peer Reviewed Conference Proceeding**
ESCAPE 35 - European Symposium on Computer Aided Process Engineering
Ghent, Belgium. 6-9 July 2025
Jan F.M. Van Impe, Grégoire Léonard, Satyajeet S. Bhonsale,
Monika E. Polańska, Filip Logist (Eds.)

PSE PRESS

# Recurrent Deep Learning Models for Multi-step Ahead Prediction: Comparison and Evaluation for Real Electrical Submersible Pump (ESP) System.

**Vinicius V. Santana*[a], Carine M. Rebello[a], Erbet A. Costa[a], Odilon S. L. Abreu[b], Galdir Reges[b], Téofilo P. G. Mendes[b], Leizer Schnitman[b], Marcos P. Ribeiro[c], Márcio Fontana[b], Idelfonso Nogueira[a]*.**

[a] Norwegian University of Science and Technology, Department of Chemical Engineering, Trondheim, Norway
[b] Federal University of Bahia, CTAI, Salvador, Bahia, Brazil
[c] CENPES, Petrobras R&D Center, Brazil
* Corresponding Author: idelfonso.b.d.r.nogueira@ntnu.no, vinicius.santana@ntnu.no

## ABSTRACT

Predicting processes' future behavior based on past data is vital for automatic control and dynamic optimization in engineering. Recent advances in deep learning, particularly Artificial Neural Networks, have improved predictions in various engineering fields. Recurrent Neural Networks (RNNs) are well-suited for time series data, as they naturally evolve through dynamic systems with recurrent updates. Despite their high predictive power, RNNs may underperform if their training ignores the model's future application. In Model Predictive Control, for example, the model evolves over time using only current information, relying on its own predictions at later steps. A model trained for one-step-ahead predictions may fail when tasked with multi-step-ahead forecasting in autoregressive mode. This study explores deep recurrent neural network models for predicting critical operational time series of a large-scale Electric Submersible Pump system. We present an innovative training approach, framing the task as a multi-step-ahead prediction problem. Results show that aligning model training with its future use is crucial to ensure real-time performance.

**Keywords**: Deep Learning, System Identification, Electric Submersible Pumps, Artificial Neural Networks

## INTRODUCTION

Models play an important role in chemical and industrial engineering practice. First-principles models describe the energy and mass transport in unit operations through continuous conservation laws, rate, and equilibrium expressions. They are usually capable of providing reliable predictions in a broad range of conditions and have parameters with physical meaning. On the other hand, dynamic high-fidelity models can be tricky to frame correctly and identify, especially for highly nonlinear systems with few observable states [1].

Black-box or data-driven models are often used to circumvent such a problem. In this sense, Artificial Neural Networks (ANNs) are essential for identifying nonlinear dynamic systems in chemical engineering. ANNs have been widely used since the 1980s for nonlinear dynamic system identification, mainly as the nonlinear function for systems identification in the Nonlinear AutoRegressive with Exogenous inputs (NARX) formulation [2], [3]. It is well-known that the NARX formulation is suitable for prediction tasks (short-term horizons) but may perform poorly recursively for long-term predictions (simulation mode).

In contrast, the Nonlinear Output Error (NOE) representation is more appropriate for engineering systems and long-term predictions (simulation) as noise is assumed to be an output additive, i.e., there is a deterministic dynamic of states, and noise is placed only at observables [2], [4]. When the NOE nonlinearity is framed with a neural network, its resemblance with recurrent neural networks (RNNs) is evident [5]. NOE is one of the most important representations for simulation in engineering systems, but it is often misused and comprehended in practice.

In real-time applications requiring multi-step-ahead

predictions and sensor feedback, such as predictive control, choosing the appropriate formulation for a data-driven model plays an essential role in the final predictive capacity and it can be a significant source of confusion. To address these questions, this study assesses the performance of a multi-step ahead predictor designed explicitly for model predictive control (MPC) applications. The predictor employs deep recurrent neural networks (RNNs) and is evaluated using real operating data from an Electrical Submersible Pump (ESP) system deployed in an offshore oil field.

Electric Submersible Pumps (ESPs) are a vital technology in the oil and gas industry, enabling the efficient lifting of fluids from subsea reservoirs to the surface. Their effective operation and control require a comprehensive understanding of the complex interactions between the reservoir, pump, and surface conditions. While models are instrumental for understanding these dynamics, first-principles modeling is particularly challenging due to the complexity of the governing equations. This makes data-driven approaches an appealing alternative for modeling ESP system dynamics.

Several studies have investigated data-driven methods for modeling ESP behavior. For example, Jordanou et al. (2022) developed an Echo State Network (ESN) as a surrogate nonlinear dynamic model using training data from a rigorous mechanistic model [6]. Similarly, Abreu et al. (2024) applied ESNs for zone-based Nonlinear Model Predictive Control (NMPC) of an ESP-lifted oil well to maximize oil production using data from a mechanistic model [7]. In another study, Costa et al. (2024) proposed a deep neural network for system identification and uncertainty quantification, leveraging mechanistic model data [8].

However, to our knowledge, no prior work has demonstrated the predictive capabilities of deep-learning-based, data-driven models using real operational data from ESP systems. The remainder of this text is organized as follows:

The Methodology details the model representation, data collection, model training and hyperparameter tuning strategies. In the Results, the test set performance is evaluated. The conclusions summarize the main findings and points to future research directions.

# METHODOLOGY

## Recurrent Neural Networks

A recurrent neural network (RNN) is an artificial neural network designed to process sequential information, such as time series data. It has a deterministic $h$ state, and an evolution rule defines how the state changes based on its computed values and input data. This rule is typically a parameterized function $\mathcal{F}(\mathcal{W}_u, \mathcal{W}_x, b_u)$, such as a multilayer perceptron in a standard RNN or a more sophisticated structure in long-short-term memory (LSTM) architectures [9].

Training an RNN involves evolving the states according to the update rule and the current parameters. These states are mapped to outputs matching the dimensions of the observed data through a readout layer ($\mathcal{G}$). The prediction error is computed and used to adjust the parameters, often through gradient descent. This process is illustrated in Figure 1.

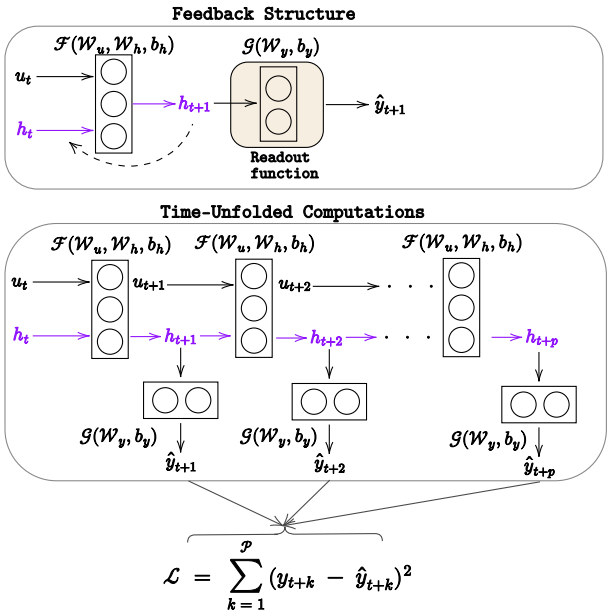



**Figure 1.** Diagrammatic representation of RNNs computations

However, practical implementations raise several questions: How many times should the states evolve? How many state observations should be used to calculate the error? There is no definitive answer to these questions. The training approach should align with the model's intended application [10]. In this work, we frame the model training as the closest to match a potential final application of model predictive control, as in [10].

## Data collection and processing

Identifying nonlinear dynamic models from real process data presents significant challenges. Industrial processes typically operate at fixed set points, and shifting these points to gather dynamic data involves safety and financial risks. Consequently, many studies develop and validate mechanistic models to be later used as a data source instead - a strategy called simulation-assisted identification [10]. However, identifying mechanistic models for industrial-scale ESP systems is particularly challenging.

In this work, real operational data was used to train the models. Only a small subset of the total operational

data - usually during startup and shutdown - proves useful for dynamic model identification. The Figure 2 and the the Figure 3 highlight these regions for the two normalized target variables – TV1, TV2 and the two manipulated variables – MV1, MV2. The variables and time have been normalized to avoid disclosing sensitive information about the data source. The two variables have different levels of noise in the process and were selected to evaluate how robust to noise is the used methodology.

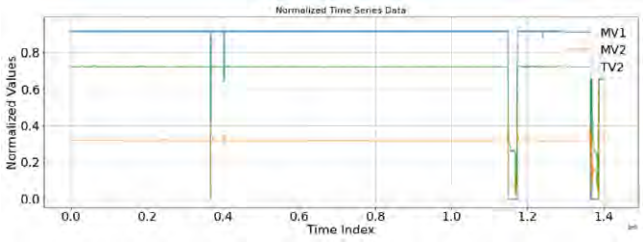



**Figure 2.** ESP real operational data history for MV1, MV2 and TV2.

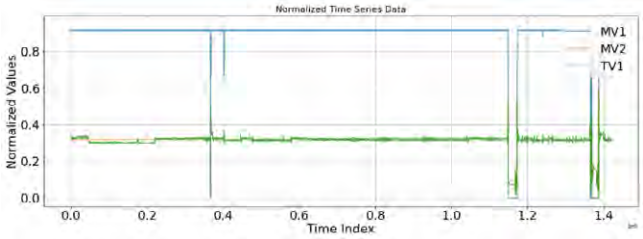



**Figure 3.** ESP real operational data history for MV1, MV2 and TV1.

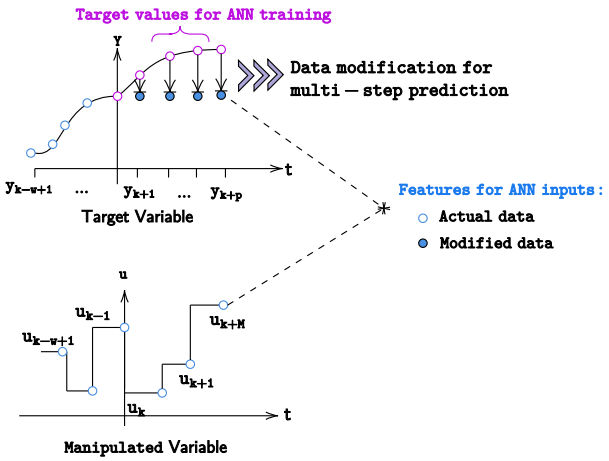



**Figure 4.** Illustration of the data preprocessing and organization for RNN training targeted at an MPC application. Adpated from [10].

The process data needs to be prepared differently to accommodate the particularities of each representation (NARX, NOE) and the final application for parameter identification (training) and inference. For this work, we are adopting a multi-step ahead prediction strategy that requires a unique data organization and follows the structure proposed in [10] and is depicted in **Figure 4**. The proposed data organization aligns well with the computations required in predictive control strategies, which should favor the model's predictive accuracy when handling this task. In contrast, **Figure 5** illustrates the traditional approach for preparing the data for single-step-ahead predictions. In this setting, the target output is a one-dimensional sequence of points. Multi-step-ahead predictions at inference time require a set of input distributions the model was not trained for.

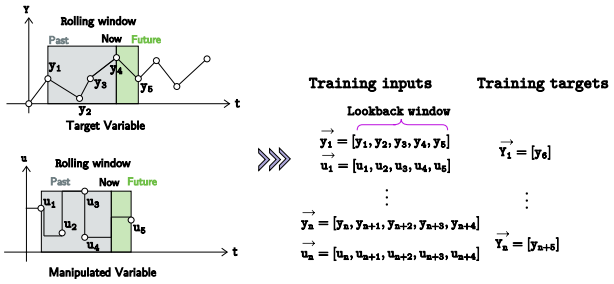



**Figure 5.** Illustration of the traditional data processing for single-step ahead prediction for training an RNN.

The dataset was split into training, validation, and test sets, ensuring no time overlap. Time series data was processed using a sliding window with a stride of 1, moving forward in time. The total window size was 12-time steps, including features and labels.

For the target variable to be used as features (predictors), 8 of the 12-time steps were actual past observations (white circles with blue contours). At the same time, the remaining 4 were repeated from the last valid observation (filled blue circles). For the manipulated variables (MV1 and MV2), all 12 points were actual observations (white circles with blue contours on the manipulated variable). The target consisted of 4 future actual observations (white circles with pink contours), as illustrated in the **Figure 4**.

This process resulted in a 3-dimensional feature tensor $X \in \mathbb{R}^{n_b \times 12 \times 3}$ where $n_b$ is the number of sequences of size 12 and 3 corresponding to the two MVs and the target variable being predicted. The target is also a 3D tensor $Y \in \mathbb{R}^{n_b \times 4 \times 1}$.

## Model Training and Hyperparameter Tunning

The estimation of the predictor's parameters constitutes the model training. One model was trained for each target variable (TVs), forming two multiple-input single-output (MISO) models. The mean squared error is the most common cost function for continuous numerical variables such as those used here.

For the proposed predictor, the cost function to be minimized is here proposed to be written as:

$$J(W,b) = \frac{1}{2m}\sum_{i=1}^{m}\sum_{k=1}^{4}\left(\hat{y}_{i,k},(W,b) - y_{i,k}\right)^2 \qquad (1)$$

$i$ varies from 1 to the number of training sequences $m$. $k$ varies from 1 to the number of time-steps 4. W and $b$ are the trainable weights and biases. Typically, the number of sequences is chucked into smaller data sets, forming batch sequences for updating the parameters.

In RNN parameter identification, layer-wise gradients are typically computed using Backpropagation Through Time (BPTT) to solve the optimization problem. However, this method often leads to convergence problems in recurrent neural networks due to vanishing or exploding gradients. Over the years, various RNN variants have been proposed to address these issues. Among them, the Long Short-Term Memory (LSTM) variant has been widely adopted to extract long-range patterns in time series data [9]. Therefore, this architecture was used in this work.

Model selection entails defining its architecture before parameter estimation, including the number of layers, neurons, activation functions, and optimizer parameters such as learning rate, momentum (for momentum-based optimizers), decay, epochs, and mini-batch size. The hyperparameter space comprises a set of discrete and continuous variables, making their selection a complex task. One recent approach to select them efficiently is wrapping another learning algorithm (hyper-learner) around the original learning problem to select hyperparameters by monitoring a cost function from a separated dataset (validation data set). The hyper-learner may also have more parameters, but it is simpler to choose than the hyperparameters.

Machine learning practitioners often employ exploratory random and grid search for hyperparameter tuning [11]. However, they are very time-consuming as they allocate the same resources for all sampled hyperparameters. Most recently, it has been possible to find a method called HYPERBAND [12], which has the advantage of being up to 30 times faster in search speed than random grid search. HYPERBAND formulates hyperparameter optimization as a pure-exploration problem where a predefined resource is allocated to randomly sampled configurations.

The neural network's initialization, the training process, and the hyperparameter tuning were implemented using TensorFlow 2.10.1 [13] and Keras [14] tuner version 1.4.7, respectively.

## Inference and state initialization

RNNs have a deterministic state variable that evolves according to the update rule (parameterized function $\mathcal{F}(\mathcal{W}_u, \mathcal{W}_x, b_u)$) in **Figure 6**. The initialization of this variable defaults to the null vector in many deep learning frameworks, including TensorFlow. During training with gradient descent, the default policy is that the states are restarted to zero for each batch. It has been shown that this is an effective way of learning the patterns in time series. However, this policy must be modified during real-time inference in a predictive control environment to accommodate the incoming data stream. In this sense, we propose the following state update policy for inference:

**Algorithm 1** Neural Network Inference Policy

**Input:** Time-series data $\mathbf{X} \in \mathbb{R}^{T \times F}$, LSTM model $M$, warm-up steps $W$, step size $S$.
**Output:** Predictions $\hat{\mathbf{Y}}$, True Values $\mathbf{Y}_{\text{true}}$.
**Step 1: Preprocessing**
Normalize each feature $f$:

$$\mathbf{X}_f = \frac{\mathbf{X}_f - \min(\mathbf{X}_f)}{\max(\mathbf{X}_f) - \min(\mathbf{X}_f)}.$$

Reshape data to 3D:

$$\mathbf{X}_{3D} \in \mathbb{R}^{1 \times T \times F}.$$

**Step 2: Warm-up**
Extract the first $W$ time steps:

$$\mathbf{X}_W = \mathbf{X}_{3D}[:, : W, :].$$

Reset the LSTM model's $M$ state.
Pass $\mathbf{X}_W$ through $M$ to initialize the state:

$$M(\mathbf{X}_W).$$

Save the updated state $\mathbf{S}_W$.
**Step 3: Forecasting Loop**
Initialize empty sets $\hat{\mathbf{Y}}, \mathbf{Y}_{\text{true}}$.
**for** $i = 0$ to $\lfloor \frac{T-W}{S} \rfloor - 1$ **do**
  Define start and end indices:

$$\text{start} = W + i \cdot S, \quad \text{end} = W + (i+1) \cdot S.$$

  Extract future data:

$$\mathbf{X}_S = \mathbf{X}_{3D}[:, \text{start} : \text{end}, :].$$

  Apply zero-order hold (ZOH) to the Target Variable with index 3:

$$\mathbf{X}_S[:, t, 2] = \mathbf{X}_{3D}[:, \text{start} + t - 1, 2], \quad \forall t \in \{1, \ldots, S\}.$$

  Predict outputs:

$$\hat{\mathbf{Y}} = M(\mathbf{X}_S).$$

  Save predictions $\hat{\mathbf{Y}}$ and true values:

$$\mathbf{Y}_{\text{true}} = \mathbf{X}_{3D}[:, \text{start} : \text{end}, 3].$$

  Restore the state $\mathbf{S}_W$:

$$\text{set_lstm_states}(M, \mathbf{S}_W).$$

  Perform one additional step to update the state:

$$\mathbf{X}_1 = \mathbf{X}_{3D}[:, \text{end} : \text{end} + 1, :].$$

  **if** $\mathbf{X}_1 \neq \emptyset$ **then**
    Use $M(\mathbf{X}_1)$ to update the state $\mathbf{S}_W$.
  **end if**
**end for**
**Output:** Predictions $\hat{\mathbf{Y}}$, True Values $\mathbf{Y}_{\text{true}}$.

**Figure 6.** Algorithm for inference and state initialization.

The algorithm operates in two alternating phases to emulate real-time application behavior. The first phase updates the internal states of the LSTM model using the most recent incoming data, ensuring that the model updates its states based on the latest observation. The second phase performs a 4-time-step-ahead prediction based on the updated state. These two phases are executed alternately across the test set, simulating a real-time scenario where the model continuously processes

new data while concurrently making multi-step future predictions based on the last observation and MV's actual inputs.

## Results and Discussion

The hyperparameter search space was limited to the numbers of neurons in the LSTM layer between 60 and 160 and step of 20, the activation function between hyperbolic tangent and rectified linear unit and minibatch size between 16 and 256 with step of 32. The ADAptive Moment estimation (ADAM) optimizer was used with a fixed learning rate of 0.001. The validation data set error was used to determine the best architecture during the search. The hyperband was parametrized with a factor of maximum allocated epochs of 100 and 1 iteration. The best configurations for TV1 and TV2 are displayed in the tables.

**Table 1.** Hyperparameters for TV1 and TV2 RNNs.

| Neurons | Activation | Batch size | Variable |
|---|---|---|---|
| 60 | tanh | 16 | TV1 |
| 160 | tanh | 16 | TV2 |

After finding the best hyperparameters, the model was retrained with the selected architecture for 1000 epochs, with early stopping and 100-step patience, by monitoring the validation set to avoid overfitting.

By applying the algorithm in **Figure 6**, a test set mean absolute error of $1.22 \times 10^{-3}$ for TV1 and $2.3 \times 10^{-3}$ for TV2.

The **Figure 7** and **Figure 8** show the parity plot and history for TV1. In the parity plot, predictions and actual values seem to be randomly distributed along the diagonal line in Figure. Still, there is a considerable variance due to the noise in the data. In **Figure 8**, it is possible to observe that the predictions follow the observations satisfactorily.

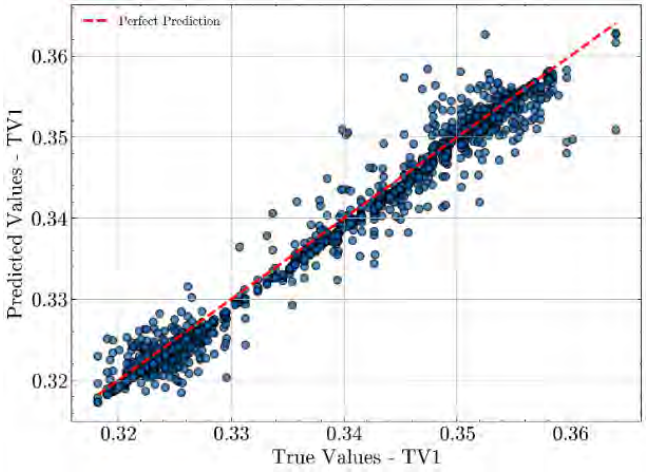



**Figure 7.** Parity plot for TV1.

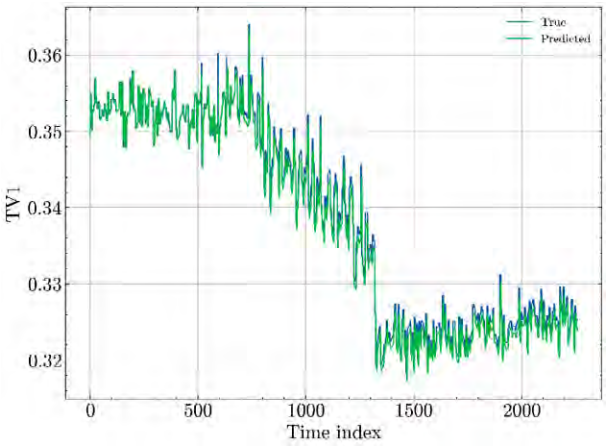



**Figure 8.** History of actual values and predictions for TV1.

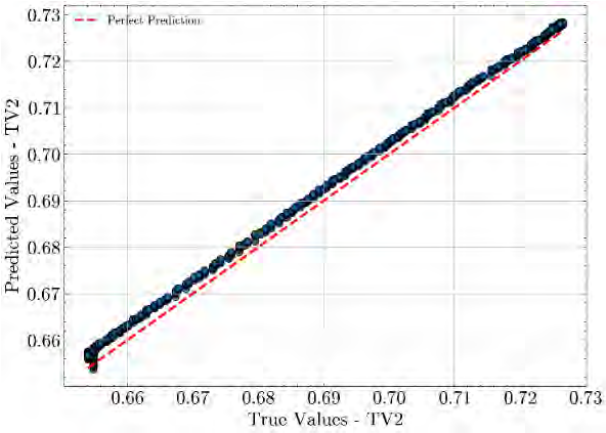



**Figure 9.** Parity plot for TV2.

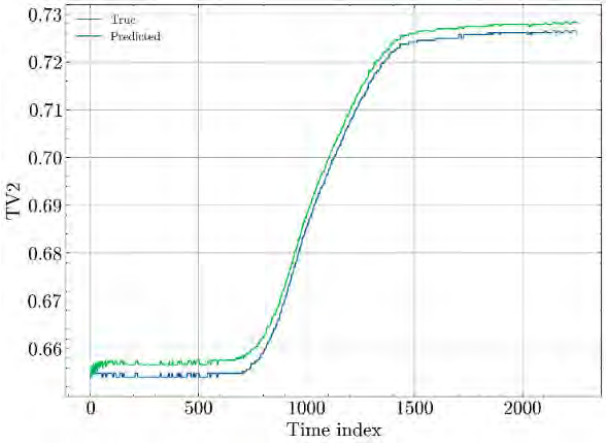



**Figure 10.** History of actual values and predictions for TV2.

The **Figure 9** and **Figure 10** show the parity plot and history for TV2 for the test set data set. They show that the predictions' dynamic behavior is close to that of the actual values. However, a slight bias prevents a better prediction. The prediction bias is more evident in **Figure 10** where the target variable 2 is displayed over time. However, for a real-time model-based application such as MPC, this mismatch would fit into the minimum requirements, and the additional modeling efforts and data

requirements would be beneficial, but the improvement in control performance may become marginal [15].

## CONCLUSIONS

This works investigates the formulation of dynamic system identification for an industrial size electrical submersible pump system using a multi-step ahead predictor targeted at model predictive control. The data processing considers how information is processed in real-time and formulate the model architecture and parameter identification accordingly. It has been shown the strategy provides a satisfactory predictive capacity and further attempts of improving may become marginal in a possible control strategy implementation. Future works might explore the use of new deep learning architectures for processing sequenced information such as Transformers and the introduction of physics constraints of the observed variables for enhanced extrapolation power.

## ACKNOWLEDGEMENTS

This work was carried out as a part of SUBPRO-Zero, a Research Centre at the Norwegian University of Science and Technology (project code 100589 and CristinID 2720670). The authors gratefully acknowledge the project support from SUBPRO-Zero, which is financed by major industry partners and NTNU. This publication has been produced with support from the HYDROGENi Research Centre (hydrogeni.no), performed under the Norwegian research program FMETEKN. The authors acknowledge the industry partners in HYDROGENi for their contributions and the Research Council of Norway (333118).

## REFERENCES

1. O. Levenspiel, “Modeling in chemical engineering,” 2002. [Online]. Available: www.elsevier.com/locate/ces
2. Q. Zhang, “Nonlinear system identification with output error model through stabilized simulation,” IFAC Proc. Vol., vol. 37, no. 13, pp. 501–506, 2004, doi: 10.1016/S1474-6670(17)31273-9.
3. A. U. Levin and K. S. Narendra, “Recursive identification using feedforward neural networks,” Int. J. Control, 1995, doi: 10.1080/00207179508921916.
4. H. Koivisto, “A Practical Approach to Model Based Neural Network Control Hannu Koivisto,” Tampere University of Technology, Tampere, 1995. [Online]. Available: https://citeseerx.ist.psu.edu/viewdoc/summary?doi=10.1.1.113.6407
5. D. M. Himmelblau, “Applications of artificial neural networks in chemical engineering,” Korean J. Chem. Eng., vol. 17, no. 4, pp. 373–392, Jul. 2000, doi: 10.1007/BF02706848.
6. J. P. Jordanou, I. Osnes, S. B. Hernes, E. Camponogara, E. A. Antonelo, and L. Imsland, “Nonlinear Model Predictive Control of Electrical Submersible Pumps based on Echo State Networks,” Adv. Eng. Informatics, vol. 52, no. December 2021, p. 101553, 2022, doi: 10.1016/j.aei.2022.101553.
7. O. S. L. de Abreu, M. P. Ribeiro, B. P. Foresti, L. Schnitman, and M. A. F. Martins, “An implementable zone-based NMPC with Echo State Networks applied to an ESP-lifted oil well for maximum oil production,” 34th Eur. Symp. Comput. Aided Process Eng. / 15th Int. Symp. Process Syst. Eng., vol. 53, pp. 1717–1722, 2024, doi: https://doi.org/10.1016/B978-0-443-28824-1.50287-8.
8. E. Almeida Costa et al., “An uncertainty approach for Electric Submersible Pump modeling through Deep Neural Network,” Heliyon, vol. 10, no. 2, Jan. 2024, doi: 10.1016/j.heliyon.2024.e24047.
9. S. Hochreiter and J. Schmidhuber, “Long Short-Term Memory,” Neural Comput., 1997, doi: 10.1162/neco.1997.9.8.1735.
10. J. Park, “Hybrid Machine Learning and Physics-Based Modeling Approaches for Process Control and Optimization,” Brigham Young University, USA, 2022.
11. J. Bergstra and Y. Bengio, “Random search for hyper-parameter optimization,” J. Mach. Learn. Res., 2012.
12. L. Li, K. Jamieson, G. DeSalvo, A. Rostamizadeh, and A. Talwalkar, “Hyperband: A novel bandit-based approach to hyperparameter optimization,” J. Mach. Learn. Res., vol. 18, pp. 1–52, 2018.
13. M. Abadi et al., “TensorFlow: A system for large-scale machine learning,” in Proceedings of the 12th USENIX Symposium on Operating Systems Design and Implementation, OSDI 2016, 2016.
14. F. Chollet, “Keras: The Python Deep Learning library,” Keras.Io, 2015.
15. S. Zhan and A. Chong, “Data requirements and performance evaluation of model predictive control in buildings: A modeling perspective,” Renew. Sustain. Energy Rev., vol. 142, no. February, p. 110835, 2021, doi: 10.1016/j.rser.2021.110835.

© 2025 by the authors. Licensed to PSEcommunity.org and PSE Press. This is an open access article under the creative commons CC-BY-SA licensing terms. Credit must be given to creator and adaptations must be shared under the same terms. See https://creativecommons.org/licenses/by-sa/4.0/



Systems & Control Transactions

**Research Article - Peer Reviewed Conference Proceeding**
ESCAPE 35 - European Symposium on Computer Aided Process Engineering
Ghent, Belgium. 6-9 July 2025
Jan F.M. Van Impe, Grégoire Léonard, Satyajeet S. Bhonsale,
Monika E. Polańska, Filip Logist (Eds.)

PSE PRESS

# Enhanced Computational Approach for Simulation and Optimisation of Vacuum (Pressure) Swing Adsorption

**Yangyanbing Liao, Andrew Wright, and Jie Li***

The University of Manchester, Centre for Process Integration, Department of Chemical Engineering, Manchester, UK
* Corresponding Author: jie.li-2@manchester.ac.uk.

## ABSTRACT

Vacuum (pressure) swing adsorption (V(P)SA) has received considerable attention in the past decades. Existing studies typically estimate vacuum pump energy consumption using an approximate constant energy efficiency or an empirical energy efficiency correlation, leading to inaccurate representation of realistic vacuum pump performance. In this paper an enhanced computational approach is proposed for simulation and optimisation of V(P)SA through simultaneous integration of realistic vacuum pump data and adsorption bed fluidisation limits. The computational results show that the developed prediction models accurately represent the actual performance curves of the vacuum pump. Incorporation of the vacuum pump prediction models and fluidisation constraints in V(P)SA optimisation leads to significantly different optimal solutions compared to when these factors are not considered.

**Keywords**: Pressure swing adsorption, Process simulation, Optimization, Vacuum pump modelling, bed fluidization

## INTRODUCTION

Vacuum (pressure) swing adsorption (V(P)SA) has received considerable attention for gas separation and purification in the past decades [1]. Mathematical modelling of V(P)SA involves description of the spatial and temporal evolution of mass, momentum and energy, resulting in coupled stiff hyperbolic/parabolic partial differential equations (PDEs). Auxiliary nonlinear equations including gas adsorption isotherms and pressure drop correlations are also included to complement process dynamics [2].

In most existing V(P)SA models, a time-dependent pressure profile or a fixed flow rate is used in the boundary conditions (BCs) at the vacuum pump end of the adsorption bed to estimate the performance of a real vacuum pump. With these predefined BCs, the total energy consumption of the vacuum pump is then determined by dividing the isentropic gas compression work by an estimated energy efficiency. It is reported that the vacuum pump can contribute at least 60% to the overall energy consumption in a VSA cycle for $CO_2$ capture [3]. Hence, accurate estimation of the vacuum pump efficiency and quantification of its energy consumption are crucial for the economic analysis of the V(P)SA processes.

Most existing computational studies on V(P)SA have assumed constant vacuum pump efficiency ranging from 60% to 100% where the vacuum pump efficiency of 72% was most used [4]. However, 72% is a typical efficiency value for compressors, instead of vacuum pumps [5]. A low efficiency of 30% was reported [5]. All these have indicated that the energy consumption of the vacuum pump could have been underestimated by at least a factor of two in many existing computational studies.

Instead of assuming a constant vacuum pump efficiency, an efficiency correlation has been developed to more accurately evaluate the vacuum pump performance. It has been observed that the efficiency tends to remain constant around 80% when the inlet pressure of the vacuum pump approaches 1 atm, whilst decreasing sharply to a very low value (e.g., below 20%) at lower pressures [6]. An empirical correlation was thus derived to relate the vacuum pump efficiency to the inlet pressure. However, their correlation fails to conform to the trend suggested by the data points at higher pressures due to significant deviations between data points and model predictions at high pressures.

The adsorption bed fluidisation is another key factor that must be accounted for in designing and operating

the V(P)SA process. This is because bed fluidisation incurs rapid adsorbent attrition and eventually results in a substantial decrease in the separation performance [7]. Nevertheless, only a few have considered the impact of bed fluidisation. They considered the effects of bed fluidisation at specific stages in PSA simulation. However, bed fluidisation can occur at any point along the bed during any step [8]. In other words, fluidisation may be experienced at certain points along the bed during certain steps in the above studies.

To address the above research gaps, in this work we first employ the data-driven modelling approach [9,10] to develop prediction models for the pumping speed and power of the vacuum pump based on real performance curves. This approach enables accurate predictions of the vacuum pump's flow rate and energy consumption. We then develop a new, comprehensive V(P)SA mathematical formulation with incorporation of the proposed vacuum pump performance models. This allows for an accurate evaluation of the V(P)SA process performance without relying on estimated vacuum pump energy efficiency or pressure/flow rate BCs at the vacuum pump end of the adsorption bed. To determine the optimal operating conditions and prevent bed fluidisation, we then construct a new optimisation problem that simultaneously incorporates the proposed V(P)SA model and the bed fluidisation constraints. To the best of our knowledge, this is the first work that considers simultaneously real vacuum pump performance data and bed fluidisation in V(P)SA optimisation. The capability of the developed V(P)SA model is illustrated through a case study.

## PROBLEM STATEMENT

A PSA process operates cyclically with three fundamental steps, including pressurisation, high-pressure adsorption, low-pressure regeneration. Some complementary steps such as pressure equalisation, rinse and purge are included to enhance process performance. An example of the 4-step PSA cycle is illustrated in Figure 1. This cycle involves adsorption, blowdown, evacuation and feed pressurisation. The problem can be stated below:

Given:

1. The number of adsorption bed, and bed configuration.
2. Feed conditions such as flow rate, composition, temperature, and pressure.
3. Adsorbent layers, physical properties of the adsorbent and the corresponding adsorption isotherms.
4. Product purity and recovery requirements.

Determine:

1. The time for each step.
2. Operating conditions, such as operating pressures and feed flow velocity.

For the illustrative example of the 4-step PSA cycle, the decision variables would be the time required for pressurisation, high-pressure adsorption, blowdown, and evaluation, the high adsorption pressure, the intermediate pressure, and the low pressure and the interstitial feed velocity. The degree of freedom is 8.

Assumptions:

- Gas phase follows ideal gas law.
- Non-isothermal adsorption process.
- The bulk flow pattern follows a plug flow model.
- The adsorption equilibrium is described by a dual-site Langmuir model with pure component isotherms dependent on gas phase concentration.
- The mass transfer is described by a linear driving force (LDF) model where the mass transfer resistance is controlled by the molecular diffusion in the macropores.
- The heat of adsorption of each gas component is constant.
- Instantaneous heat transfer between bulk fluid and adsorbent.
- Uniform bed with constant bed void fraction, particle porosity and particle size.
- No radial gradients in concentration, temperature, or pressure.

The objective is to minimise the energy penalty or cost. Other objectives such as minimize total annualised cost can also be employed.

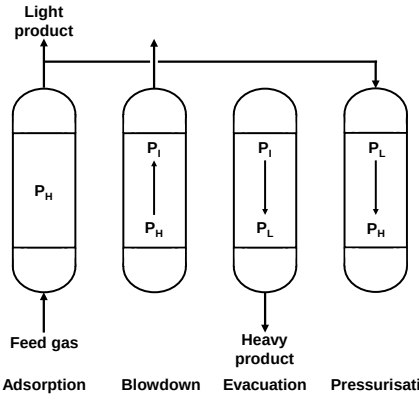



**Figure 1.** Example of a 4-step V(P)SA cycle.

## MATHEMATICAL FORMULATION FOR V(P)SA SIMULATION AND OPTIMISATION

## Rigorous PSA model

The dimensionless model equations for a general PSA process are provided as follows,

$$\frac{\partial y_i}{\partial \tau} = -\frac{\bar{T}}{\bar{P}}\frac{\partial}{\partial Z}\left(\frac{y_i \bar{P}}{\bar{T}}\bar{v}\right) - \psi\frac{\bar{T}}{\bar{P}}\frac{\partial x_i}{\partial \tau} - \frac{y_i}{\bar{P}}\frac{\partial \bar{P}}{\partial \tau} + \frac{y_i}{\bar{T}}\frac{\partial \bar{T}}{\partial \tau} \quad (1)$$

$$\frac{\partial \bar{P}}{\partial \tau} = -\bar{T}\frac{\partial}{\partial Z}\left(\frac{\bar{P}}{\bar{T}}\bar{v}\right) - \psi\bar{T}\sum_i^{n_{comp}}\frac{\partial x_i}{\partial \tau} + \frac{\bar{P}}{\bar{T}}\frac{\partial \bar{T}}{\partial \tau} \quad (2)$$

$$\frac{\partial \bar{T}}{\partial \tau} = -\Omega_1\frac{\partial}{\partial Z}(\bar{v}\bar{P}) - \Omega_2\bar{T}\sum_i^{n_{comp}}\frac{\partial x_i}{\partial \tau} + \sum_i^{n_{comp}}\left(\sigma_i\frac{\partial x_i}{\partial \tau}\right) - \Omega_3(\bar{T} - \bar{T}_w) - \Omega_1\frac{\partial \bar{P}}{\partial \tau} \quad (3)$$

$$\frac{\partial x_i}{\partial \tau} = \alpha_i(x_i^* - x_i) \quad (4)$$

$$q_i^* = \frac{q_{sb,i}b_i c_i}{1+\sum_{i=1}^{n_{comp}} b_i c_i} + \frac{q_{sd,i}d_i c_i}{1+\sum_{i=1}^{n_{comp}} d_i c_i} \quad (5)$$

$$-\frac{\partial \bar{P}}{\partial Z} = \frac{150}{4}\frac{1}{r_p^2}\left(\frac{1-\varepsilon}{\varepsilon}\right)^2\frac{v_0 z_0}{P_0}\mu\bar{v} + \frac{1.75}{2}\frac{1}{r_p}\left(\frac{1-\varepsilon}{\varepsilon}\right)\rho_g|\bar{v}|\bar{v} \quad (6)$$

Equation (1) is mass balance for each component. (2) is momentum balance equation. (3) is bed energy balance equation. (4) is linear driving force. (5) is adsorption isotherm equation. (6) is the Ergun equation for pressure drop. The boundary conditions for each cycle will be referred to [4].

We assume that the adsorption bed is connected directly to the vacuum pump with no pressure drop between them (see Figure 2). Given the same temperature, the outlet volumetric flow rate and pressure of the adsorption bed are equal to the inlet volumetric flow rate and pressure of the vacuum pump, respectively, as specified by Eqs. (7) and (8). In Figure 4, $Z = 0$ represents the vacuum pump end of the adsorption bed, $P_{out,B}$ and $V_{out,B}$ are the outlet pressure and volumetric flow rate of the bed, $P_{in,VP}$ and $V_{in,VP}$ are the inlet pressure and volumetric flow rate of the vacuum pump, and $P_{dis}$ is the discharge pressure of the vacuum pump, which is assumed to be equal to the atmospheric pressure, $P_{atm} = 1$ bar.

$$P_{out,B} = P_{in,VP} \quad (7)$$

$$V_{out,B} = V_{in,VP} \quad (8)$$

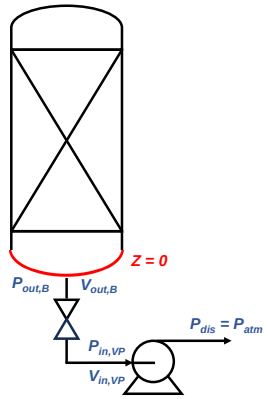



**Figure 2.** Direct connection between the adsorption bed and a vacuum pump

The inlet volumetric flow rate of the vacuum pump ($V_{in,VP}$) must satisfy the vacuum pump pumping speed prediction model, as shown by Eq. (10), where $f_1(P_{in,VP})$ represents the best model developed.

$$V_{in,VP} = f_1(P_{in,VP}) \quad (9)$$

At the vacuum pump end, the outlet flow rate of the bed needs to satisfy the pressure drop correlation $f_2(P_{out,B})$, as shown by Eq. (9), which is usually the Ergun equation [Eq. (6)] or Darcy's law.

$$V_{out,B} = f_2(P_{out,B}) \quad (10)$$

$V_{out,B}$ and $P_{in,VP}$ can be computed by combining Eqs. (7)-(10). It should be noted that the pumping speed curves are normally measured at 298.15 K and 1 atm. Therefore, the volumetric flow rate must be converted to match the corresponding operating conditions.

Given $V_{out,B}$, the outlet interstitial velocity of the adsorption bed $V_{out,B}$ can be computed:

$$v_{out,\,B} = \frac{V_{out,B}}{\varepsilon A} \quad (11)$$

where $\varepsilon$ is the adsorption bed void fraction, and A is the cross-section area of the column.

We define $PW_{tot,VP}$ as the total power required by the vacuum pump, which can be evaluated by the power prediction model, $f_3(P_{in,VP})$, as shown by Eq. (12).

$$PW_{tot,VP} = f_3(P_{in,VP}) \quad (12)$$

The instantaneous isentropic gas compression power ($PW_{isen,VP}$) can be evaluated using Eq. (13).

$$PW_{isen,VP} = \frac{\kappa}{\kappa-1}P_{in,VP}\cdot\varepsilon\cdot\pi\cdot r_{in}^2\cdot v_{out,B}\left[\left(\frac{P_{dis}}{P_{in,VP}}\right)^{\frac{\kappa-1}{\kappa}} - 1\right] \quad (13)$$

where $\kappa$ represents the gas isentropic constant, and $r_{in}$ is the inner radius of the column.

The instantaneous vacuum pump efficiency, $\eta_{VP}$, is therefore defined as the ratio of the isentropic gas compression power to the total vacuum pump power.

$$\eta_{VP}(\%) = \frac{PW_{isen,VP}}{PW_{tot,VP}} \times 100\% \quad (14)$$

Based on the instantaneous values from Eqs. (13) and (14), Eqs. (15) and (16) are used to compute the total energy consumption and the time-averaged efficiency of the vacuum pump:

$$E_{tot,VP} = \int_{t_{ini}}^{t_f} PW_{tot,VP}\,dt \quad (15)$$

$$\eta_{ave,VP}(\%) = \frac{1}{t_f - t_{ini}}\int_{t_{ini}}^{t_f}\eta_{VP}\,dt \quad (16)$$

where $t_{ini}$ and $t_f$ represent the initial and final time points between which the vacuum pump operates, $E_{tot,VP}$ is the total vacuum pump energy consumption, and $\eta_{ave,VP}$ is

the time-averaged efficiency of the vacuum pump over the period between $t_{ini}$ and $t_f$, respectively.

## Adsorption Bed Fluidisation

The adsorption bed fluidisation is characterised by the approach to fluidisation (ATF):

$$ATF = \frac{\frac{\partial P}{\partial Z}\big|_{local}}{\frac{\partial P}{\partial Z}\big|_{min.fluid}} \tag{17}$$

where $\frac{\partial P}{\partial Z}\big|_{local}$ denotes the pressure gradient at a specific location in the bed, and $\frac{\partial P}{\partial Z}\big|_{min.fluid}$ is the minimum fluidisation pressure gradient in the upflow direction.

$$-\frac{\partial P}{\partial Z}\big|_{min.fluid} = (\rho_g - \rho_s) \cdot (1 - \varepsilon) \cdot g \tag{18}$$

where $\rho_g$ and $\rho_s$are the density of gas and adsorbent, respectively; $\varepsilon$ is the bed void fraction; $g$ is the gravitational constant. Eq. (18) essentially states that bed fluidisation occurs when the upward force exerted on a section of the bed offsets its gravity due to the pressure drop.

To prevent the onset of fluidisation, the ATF value should be limited within some values in the upflow and downflow operations, respectively.

$$ATF_{up} \leq \theta_{up} \tag{19}$$

$$ATF_{down} \leq \theta_{down} \tag{20}$$

where $ATF_{up}$ and $ATF_{down}$ represent the ATF value in the upflow and downflow directions, respectively.

## Additional constraints

The following constraints are imposed in addition to the V(P)SA model. First, the required product purity and recovery must be satisfied.

$$Purity \geq Purity_{req}^{tar} \tag{21}$$

$$Recovery \geq Recovery_{req}^{tar} \tag{22}$$

$$Purity = \frac{Moles\ of\ target\ gas\ in\ product}{Total\ moles\ of\ product} = \frac{\frac{\varepsilon A}{R}\int_0^{t_p} \frac{v_{out} \cdot y_{out,i} \cdot P_{out}}{T_{out}} dt}{\frac{\varepsilon A}{R}\int_0^{t_p} \frac{v_{out} \cdot P_{out}}{T_{out}} dt} \tag{23}$$

$$Recovery = \frac{Moles\ of\ target\ gas\ in\ product}{Total\ moles\ of\ target\ gas\ fed} = \frac{\frac{\varepsilon A}{R}\int_0^{t_p} \frac{v_{out} \cdot y_i \cdot P_{out}}{T_{out}} dt}{\frac{\varepsilon A}{R}\sum_{j=1}^{n_{step}} \int_0^{t_f} \frac{v_f^j \cdot y_{f,i}^j \cdot P_f^j}{T_f^j} dt} \tag{24}$$

where $Purity^{tar}$ and $Recovery^{tar}$ are are the purity and recovery of the target gas, and $Purity_{req}^{tar}$ and $Recovery_{req}^{tar}$ denote the required purity and recovery.

We also constrain the bed length-to-diameter ratio ($L/D$) to either a fixed value or within specified bounds.

The lower and upper bounds are imposed for all decision variables, generally represented by a vector $\mathbf{x}$.

$$\mathbf{x}^{lb} \leq \mathbf{x} \leq \mathbf{x}^{ub} \tag{25}$$

where $\mathbf{x}$ is a vector of all decision variables, $\mathbf{x}^{lb}$ and $\mathbf{x}^{ub}$ are the lower and upper bounds. The V(P)SA optimisation problem (denoted as **P**) is defined as follows:

$$\begin{aligned} &min \quad obj \\ &s.t. \quad \text{PSA model equations } 1-6 \\ &\quad\quad \text{Eqs. } 7-11, \text{or estimated vacuum pump efficiency} \\ &\quad\quad \text{Equations } 12-24 \\ &\quad\quad L/D = R_{fixed} \text{ or } R^{lb} \leq L/D \leq R^{ub} \\ &\quad\quad \text{Boundary conditions in [4]} \\ &\quad\quad \mathbf{x}^{lb} \leq \mathbf{x} \leq \mathbf{x}^{ub} \end{aligned}$$

where $obj$ is the objective function, which usually denotes the total cost. Genetic algorithm (GA) in MATLAB is used to solve the optimisation problem **P** with a population size of 24 times of the number of decision variables and a maximum generation of 50 [3].

It should be noted that the V(P)SA model **P** enables computation of the instantaneous outlet gas velocity and pressure of the adsorption bed on the vacuum pump end. As a result, an estimated boundary condition, such as a constant flow rate or a predefined pressure profile, is not required. It enables accurate evaluation of the vacuum pump pumping speed and energy consumption, from which the vacuum pump efficiency is determined post-simulation. This contrasts with the common approaches where predefined estimations of the necessary BCs and vacuum pump efficiency are required in previous studies.

# RESULTS AND DISCUSSION

## Performance Prediction Models of Vacuum Pumps

After reviewing a large number of vacuum pump vendor manuals, ten vacuum pump performance curves are identified, which account for a broad range of the pumping speed. The ten vacuum pumps are given below,

- Leybold DRYVAC DV 800 screw vacuum pump
- Leybold LEYVAC LV 140 screw vacuum pump (50 Hz)
- Leybold LEYVAC LV 140 screw vacuum pump (60 Hz)
- Zhaohan 2BE1 202 liquid ring pump (790 RPM)
- Zhaohan 2BE1 202 liquid ring pump (880 RPM)
- Edwards EDS 300 dry screw vacuum pump
- Edwards EDS 480 dry screw vacuum pump

- Edwards nXDS20i dry scroll vacuum pump
- Edwards nXDS15i dry scroll vacuum pump
- Edwards nXDS10i dry scroll vacuum pump

Data points are extracted from each performance curve using WebPlotDigitizer to establish the prediction models of vacuum pump pumping speed and power (i.e., eqs. 10 and 12) using the data-driven approach [9,10]. The training and test results for pumping speed are provided in Table 1. It is quantitatively shown that each performance model demonstrates close agreement with the data, as indicated by the low RMSE values and coefficient of determination ($R^2$) values near 1.

**Table 1.** Training and test results

| Pump | Pumping speed | | | |
|---|---|---|---|---|
| | Training | | Test | |
| | $R^2$ | RMSE | $R^2$ | RMSE |
| **DV 800** | 0.9998 | 3.18 | 0.9985 | 9.0900 |
| **50 Hz** | 1.0000 | 0.14 | 0.9998 | 0.4866 |
| **60Hz** | 1.0000 | 0.09 | 1.0000 | 0.2588 |
| **790 RPM** | 0.9997 | 4.1074 | 0.9965 | 4.1737 |
| **880 RPM** | 0.9992 | 1.5844 | 0.9992 | 1.7538 |
| **EDS 300** | 0.9999 | 0.5709 | 0.9996 | 1.5020 |
| **EDS 480** | 0.9999 | 1.0752 | 0.9995 | 2.7210 |
| **nXDS20i** | 0.9998 | 0.0774 | 0.9995 | 0.1294 |
| **nXDS15i** | 0.9999 | 0.0414 | 0.9998 | 0.0658 |
| **nXDS10i** | 0.9999 | 0.0348 | 0.9997 | 0.0550 |

## VPSA Optimization Results

We take the VSA cycle from [3] to illustrate the process optimisation results by simultaneously considering the vacuum pump performance prediction models and the fluidisation constraints. The VSA cycle is illustrated in Figure 1. The feed gas mixture, consisting of 20% $CO_2$ and 80% $N_2$, enters the bed at 313.15 K. Parameters such as the adsorbent physical properties, adsorption isotherms, column configuration are adapted from [3]. The objective function is $CO_2$ capture cost from [3].

We compare the optimisation results by using a constant efficiency of 72%, the efficiency correlation from [6], and the developed V(P)SA model involving vacuum pump performance models, respectively. The constant efficiency of 72% is used in case 1, whilst the correlation from [6] is used in case 2. The developed V(P)SA model is used in case 3. The objective is to minimise the $CO_2$ capture cost [3]. The purity and recovery of product $CO_2$ are required to be at least 0.95 and 0.90, respectively. The length-to-diameter ratio is fixed at 3 [3].

**Table 2.** Optimisation results for cases 1-4 with fluidisation constraints

| Case | 1 | 2 | 3 | 4 |
|---|---|---|---|---|
| Vacuum pump efficiency | 72% | – | – | 36% |
| Operating conditions | | | | |
| Fixed variables | | | | |
| Length-to-diameter ratio (–) | 3 | 3 | 3 | 3 |
| Decision variables | | | | |
| Adsorption time (s) | 351 | 349 | 357 | 364 |
| Pressurisation time (s) | 58 | 54 | 58 | 64 |
| Blowdown outlet velocity (m $s^{-1}$) | 0.94 | 0.94 | – | 0.77 |
| Evacuation outlet velocity (m $s^{-1}$) | 1.49 | 1.40 | – | 1.23 |
| Intermediate pressure (bar) | 0.05 | 0.06 | 0.11 | 0.07 |
| Low pressure (bar) | 0.02 | 0.02 | 0.03 | 0.02 |
| Feed velocity (m $s^{-1}$) | 0.48 | 0.50 | 0.50 | 0.50 |
| Column length (m) | 6.73 | 6.01 | 3.97 | 5.51 |
| Dependent variables | | | | |
| Maximum feed pressure (bar) | 1.16 | 1.15 | 1.11 | 1.17 |
| Blowdown time (s) | 225 | 188 | 212 | 190 |
| Evacuation time (s) | 560 | 588 | 1406 | 665 |
| Blowdown outlet velocity (m $s^{-1}$) | – | – | 0.39 | – |
| Evacuation outlet velocity (m $s^{-1}$) | – | – | 0.41 | – |
| Train configuration | | | | |
| No. of columns per train (–) | 4 | 4 | 6 | 4 |
| No. of parallel trains (–) | 188 | 231 | 543 | 274 |
| Total adsorbent volume ($m^3$) | 12602 | 11028 | 11208 | 10080 |
| Process performance | | | | |
| Purity (%) | 95.01 | 95.03 | 95.01 | 95.01 |
| Recovery (%) | 90.08 | 90.02 | 90.04 | 90.01 |
| Productivity (mol $m^{-3}$ $s^{-1}$) | 0.09 | 0.11 | 0.11 | 0.12 |
| Overall power consumption ($MW_e$) | 36.43 | 57.56 | 43.84 | 58.67 |
| Overall time-averaged efficiency (%) | – | 42.12 | 36.14 | – |
| Approach to fluidisation (ATF) | | | | |
| Upflow | | | | |
| Maximum adsorption ATF | 0.35 | 0.44 | 0.60 | 0.56 |
| Maximum blowdown ATF | 0.73 | 0.74 | 0.35 | 0.55 |
| Downflow | | | | |
| Maximum evacuation ATF | 0.86 | 0.80 | 0.20 | 0.69 |
| Maximum pressurisation ATF | 1.48 | 1.51 | 1.31 | 1.35 |
| $CO_2$ capture cost (€/$t_{CO2,\ avoided}$) | 60.93 | 69.56 | 131.23 | 74.86 |

The optimisation results for cases 1-3 are provided in Table 2. When the constant efficiency of 72% and the efficiency correlation from [6] are used (i.e., cases 1-2),

the resulting vacuum pressure $P_L$ is 0.02 bar and the evacuation time is significantly longer than the blowdown time. These results correspond to the fact that deep vacuum and long evacuation are necessary to satisfy purity and recovery requirements. the lowest $CO_2$ capture cost of 60.93 €/t$CO_2$, avoided is achieved in case 1 with the constant efficiency of 72%. The cost in case 2 is 69.56 €/t$CO_2$, avoided, which is 14% higher than that in case 1. The $CO_2$ capture cost in case 3 is 131.23 €/t$CO_2$, avoided, which is the highest cost among these three cases. This is primarily due to the low outlet interstitial velocity in the blowdown and evacuation steps when using the DV 800 vacuum pump. The low flow rate eventually leads to longer blowdown and evacuation, which greatly increases the number of columns required to process the same amount of feed gas, resulting in a higher column cost and fixed operating cost.

We use the time-averaged efficiency of 36% obtained from case 3 as a constant efficiency to further illustrate the importance and effectiveness of incorporating the proposed vacuum pump performance models. The illustration is created as case 4. The optimisation results for case 4 are also provided in Table 2. The $CO_2$ capture cost is 74.86 €/t$CO_2$, avoided in case 4, which is 43% lower than 131.23 €/t$CO_2$, avoided in case 3. This indicates that the $CO_2$ capture cost can be significantly underestimated even when a well-estimated efficiency value is used. From Table 2, it is shown that the maximal ATF values in all cases have been constrained within the critical thresholds (i.e., 0.8 in the upflow and 1.8 in the downflow) at the final optimal solutions. The maximal ATF values in the pressurisation step remain the highest, as a sufficiently low $P_L$ is essential for satisfying both purity and recovery requirements.

We also compare the optimisation results without consideration of adsorption bed fluidisation, which are presented in Table 3. By comparing results in Tables 2 and 3, the duration of each step has been significantly extended to achieve lower ATF values. Notably, the adsorption time is 350, 348, 356 and 364 s for cases 1-4, respectively, which has been increased by 130% for case 3, and at least 160% for cases 1-2 and 4. The pressurisation time, which is an additional decision variable, increases less significantly from a fixed value of 30 s in Table 3 to ~60 s in Table 2, due to a slightly larger difference between $P_I$ and $P_L$. To maintain a small pressure drop across the bed and reduce the fluidisation level during the adsorption step, the feed velocity in Table 2 becomes almost half of that in Table 3 (i.e., 0.48 vs. 1.08 m $s^{-1}$ for case 1, 0.50 vs. 1.04 m $s^{-1}$ for case 2, 0.50 vs. 1.05 m $s^{-1}$ for case 3 and 0.50 vs. 0.99 m $s^{-1}$ for case 4), which in turn increases the number of parallel trains and the amount of the adsorbent required, leading to higher column and adsorbent costs. As a result, the optimal CO2 capture costs for cases 1-4 are increased by at least 16% compared those in Table 3. These results show that incorporating fluidisation constraints into PSA optimisation leads to substantial differences in the optimal solution, indicating a significant impact on PSA design.

**Table 3.** Optimisation results for cases 1-4 without fluidisation constraints

| **Case** | **1** | **2** | **3** | **4** |
|---|---|---|---|---|
| Vacuum pump efficiency | 72% | – | – | 36% |
| Operating conditions | | | | |
| Fixed variables | | | | |
| Length-to-diameter ratio (–) | 3 | 3 | 3 | 3 |
| Decision variables | | | | |
| Adsorption time (s) | 127 | 133 | 156 | 134 |
| Blowdown outlet velocity (m $s^{-1}$) | 1.71 | 1.47 | – | 1.49 |
| Evacuation outlet velocity (m $s^{-1}$) | 1.29 | 1.20 | – | 0.77 |
| Intermediate pressure (bar) | 0.05 | 0.05 | 0.12 | 0.05 |
| Low pressure (bar) | 0.03 | 0.03 | 0.03 | 0.04 |
| Feed velocity (m $s^{-1}$) | 1.08 | 1.04 | 1.05 | 0.99 |
| Column length (m) | 5.84 | 5.81 | 3.73 | 5.55 |
| Dependent variables | | | | |
| Maximum feed pressure (bar) | 1.46 | 1.43 | 1.27 | 1.36 |
| Blowdown time (s) | 119 | 130 | 167 | 126 |
| Evacuation time (s) | 486 | 512 | 1237 | 653 |
| Blowdown outlet velocity (m $s^{-1}$) | – | – | 0.44 | – |
| Evacuation outlet velocity (m $s^{-1}$) | – | – | 0.47 | – |
| Train configuration | | | | |
| Number of columns per train (–) | 7 | 7 | 11 | 8 |
| Number of parallel trains (–) | 94 | 101 | 259 | 119 |
| Total adsorbent volume ($m^3$) | 6368 | 7605 | 8116 | 8947 |
| Process performance | | | | |
| Purity (%) | 95.02 | 95.00 | 95.00 | 95.00 |
| Recovery (%) | 90.01 | 90.00 | 90.00 | 90.01 |
| Productivity (mol $m^{-3}$ $s^{-1}$) | 0.16 | 0.15 | 0.15 | 0.13 |
| Overall power consumption ($MW_e$) | 30.75 | 43.68 | 44.52 | 51.62 |
| Overall time-averaged efficiency (%) | – | 44.67 | 36.22 | – |
| Approach to fluidisation (ATF) | | | | |
| Upflow | | | | |
| Maximum adsorption ATF | 1.21 | 1.12 | 1.35 | 1.00 |
| Maximum blowdown ATF | 1.66 | 1.34 | 1.09 | 1.44 |
| Downflow | | | | |
| Maximum evacuation ATF | 0.58 | 0.54 | 0.23 | 0.41 |
| Maximum pressurisation ATF | 2.29 | 2.29 | 2.08 | 2.29 |
| VSA capture cost (€/$t_{CO2,\ avoided}$) | 46.53 | 52.69 | 113.97 | 65.25 |

## CONCLUSION

In this work, we developed an enhanced computational approach for simulation and optimisation of the vacuum (pressure) swing adsorption (V(P)SA) by incorporating both the realistic vacuum pump performance prediction models and adsorption bed fluidisation constraints. The computational results demonstrated that the predictions from the developed performance prediction models closely matched the vacuum pump data. The

developed V(P)SA model did not assume an estimated energy efficiency or predefined pressure/flow rate boundary conditions for the vacuum pump. The vacuum pump efficiency typically falls in the range of 20% to 40%. This is consistent with the efficiency of 30% reported in a pilot study. When an estimated vacuum pump efficiency was applied, the optimal $CO_2$ capture cost was underestimated by at least 42%. It was found that bed fluidisation occurs when using a large rate of change in the pressure boundary conditions, or a vacuum pump with an excessively high pumping speed. Incorporating the vacuum pump performance prediction models and accounting for bed fluidisation constraints have a significant impact on V(P)SA optimisation outcomes, with the optimal solution varying considerably under different conditions. Future research will integrate vacuum pump performance prediction models into industrial-scale V(P)SA simulations to further evaluate the effectiveness of the proposed computational approach.

## ACKNOWLEDGEMENTS

Jie Li would like to appreciate the financial support from UKRI Impact Acceleration Account (IAA 424).

## REFERENCES

1. Beck J, Friedrich D, Brandani S, Guillas S, Fraga ES. Surrogate based optimisation for design of pressure swing adsorption systems. Comput. Aided Chem. Eng. xx:1217-1221 (2012) https://doi.org/10.1234/56789.10
2. Ruthven DM. PRINCIPLES OF ADSORPTION AND ADSORPTION PROCESSES. John Wiley & Sons (1984).
3. Subraveti SG, Roussanaly S, Anantharaman R, Riboldi L, Rajendran A. Techno-economic assessment of optimised vacuum swing adsorption for post-combustion CO2 capture from steam-methane reformer flue gas. Separation and Purification Technology **256**:117832 (2021).
4. Haghpanah R, Majumder A, Nilam R, et al. Multiobjective optimization of a four-step adsorption process for postcombustion CO2 capture via finite volume simulation. Ind. Eng. Chem. Res. **52**(11):4249-65 (2013).
5. Krishnamurthy S, Rao VR, Guntuka S, et al. CO2 capture from dry flue gas by vacuum swing adsorption: a pilot plant study. AIChE Journal **60**(5):1830-42 (2014).
6. Maruyama RT, Pai KN, Subraveti SG, Rajendran A. Improving the performance of vacuum swing adsorption based CO2 capture under reduced recovery requirements. International Journal of Greenhouse Gas Control **93**:102902 (2020).
7. Liu Y, Zheng X, Dai R. Numerical study of flow maldistribution and depressurization strategies in a small-scale axial adsorber. Adsorption **20**:757-68 (2014).
8. Marcinek A, Bárcia P, Guderian J. Scale-up analysis of a twin-bed PSA pilot plant. Adsorption **29**(3):125-39 (2023).
9. Li J, Xiao X, Boukouvala F, et al. Data - driven mathematical modeling and global optimization framework for entire petrochemical planning operations. AIChE Journal **62**(9):3020-40 (2016).
10. Wang W, Ma Y, Maroufmashat A, Zhang N, Li J, Xiao X. Optimal design of large-scale solar-aided hydrogen production process via machine learning based optimisation framework. Applied Energy **305**:117751 (2022).

© 2025 by the authors. Licensed to PSEcommunity.org and PSE Press. This is an open access article under the creative commons CC-BY-SA licensing terms. Credit must be given to creator and adaptations must be shared under the same terms. See https://creativecommons.org/licenses/by-sa/4.0/



Systems & Control Transactions

**Research Article - Peer Reviewed Conference Proceeding**
ESCAPE 35 - European Symposium on Computer Aided Process Engineering
Ghent, Belgium. 6-9 July 2025
Jan F.M. Van Impe, Grégoire Léonard, Satyajeet S. Bhonsale,
Monika E. Polańska, Filip Logist (Eds.)

PSE PRESS

# NLP Deterministic Optimization of Shell and Tube Heat Exchangers with Twisted Tape Turbulence Promoters

**Jamel Eduardo Rumbo-Arias [a], Fabián Pino [b], Martin Picón-Nuñez [a*], Fernando Israel Gómez-Castro [a], and Jorge Luis García-Castillo [a]**

[a] University of Guanajuato, Department of Chemical Engineering, Guanajuato, Guanajuato, Mexico
[b] Universitat Jaume I (UJI), Institute of Advanced Materials (INAM), Castelló de la Plana, Castellón, Spain
* Corresponding Author: picon@ugto.mx

## ABSTRACT

This study presents a deterministic optimization methodology for the design of shell-and-tube heat exchangers with twisted tape turbulence promoters, focusing on minimizing the total annualized cost (TAC) while balancing thermal performance and energy consumption. A sensitivity analysis was carried out as Case I (Methanol-Water), it reveals that increasing the twist ratio (TR) reduces flow turbulence, resulting in lower fluid velocity, pressure drop ($\Delta P_i$), and overall heat transfer coefficient (U). Among the turbulence promoters evaluated, twisted tapes with V-cuts achieved a 21.1% increase in U with a 52.27% increase in pressure drop, demonstrating an optimal balance between thermal enhancement and energy cost. In contrast, promoters with circular rings and multiple perforations showed the highest U improvements (26.7% and 25.8%, respectively) but incurred significant pressure drops (93.5% and 97.9%). The optimization problem has been stated as a nonlinear programming (NLP) problem and solved with the CONOPT solver. Results from two case studies emphasize the importance of operating with similar mass flows, directing the smaller flow through the tubes to maximize promoter effectiveness and achieve balanced heat transfer and pressure drop. For Case II (Residue-Water), the TAC was estimated at 11,467 USD/year, with the equipment cost as the major contributor. Case III (Water-Water) demonstrated improved balance in convective coefficients due to lower thermal effectiveness and similar mass flow rates, highlighting the positive impact of turbulence promoters on performance. This work demonstrates the potential of turbulence promoters for enhancing heat exchangers while emphasizing the importance of careful design to optimize performance and cost.

**Keywords** Deterministic optimization, NLP, thermo-hydraulic design, turbulence promoter, retrofit.

## INTRODUCTION

Techniques for enhancing heat transfer in existing designs are frequently utilized in heat recovery systems. One of the most common methods is the incorporation of twisted tape turbulence promoters, which increase thermal efficiency but simultaneously induce flow disturbances that result in higher pressure drops [1]. When designing shell-and-tube (SH&T) heat exchangers with twisted tape turbulence promoters, the design varies depending on the type of promoter used, and it is determined by several geometric variables, including the internal diameter [2]. Among the types of twisted tape inserts, plain twisted tape, perforated tape, tape with circular rings, tape with three centered perforations, and V-cut tape, can be mentioned [3,4,5,6]. The use of these promoters has been reported to enhance the thermo-hydraulic performance of the equipment from 6.3% to 360%, compared to smooth-tube exchangers [7].

Detailed methodologies for designing SH&T heat exchangers are widely available in the literature [8, 9], making their design straightforward. However, when designing with twisted tape turbulence promoter inserts, the calculation of the free-flow cross-sectional area remains an underexplored area, Figure 1 [1].

This study presents a retrofit case (***CASE I:***

***Methanol-Water***) where a sensitivity analysis is conducted to observe the behavior of heat exchanger design variables as the twist ratio (TR) varies, the twist ratio (TR) is a key geometric parameter in the design of heat exchangers with twisted tapes. It is defined as the ratio between the twist pitch length and the tube diameter. A high TR implies less twisting per unit length, reducing flow turbulence and pressure drop, while a low TR generates higher turbulence, enhancing heat transfer but increasing flow resistance. In heat exchanger design, finding a balance between thermal transfer and pressure drop is crucial for system efficiency. A retrofit case refers to the improvement of an existing design.

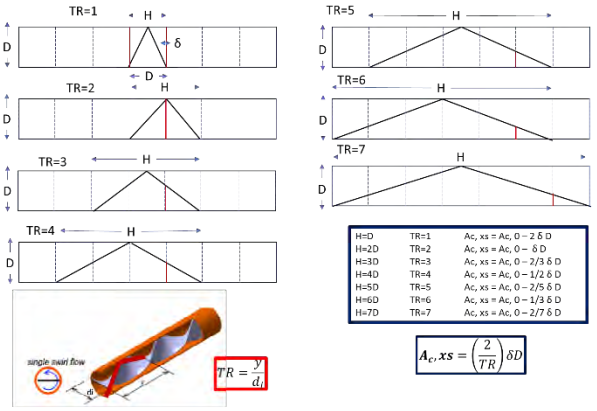



**Figure 1.** Calculation of the free-flow cross-sectional area with the turbulence promoters.

Additionally, a comparative study among different types of promoters is carried out, evaluating the increase in the overall heat transfer coefficient (U) and the pressure drop within the tubes.

Identifying the best alternative for design and process intensification involves selecting the optimal combination of geometric variables. In literature, optimization techniques have generally been employed to evaluate factors or performance correlations that do not involve costs or a complete equipment design [10, 11].

The primary objective in designing these systems is to minimize total cost, which entails enhancing heat transfer while reducing pumping power. Therefore, determining the optimal combination of parameters for calculating flow velocities, overall heat transfer coefficient (U), and pressure drops within the tubes becomes critical [12].

This work develops a deterministic optimization methodology for solving a nonlinear programming (NLP) problem, where the objective function is to minimize the total annualized cost (TAC) of the equipment and identify the optimal design variables, hence, two cases are studied, ***CASE II: Residue - Water*** and ***CASE III: Water-Water*** [13]. The variables of each case are presented in Table 1.

## METHODOLOGY

To carry out the optimization process of the design of heat exchanger with twisted tape inserts, the design methodology followed is shown in Figure 2.

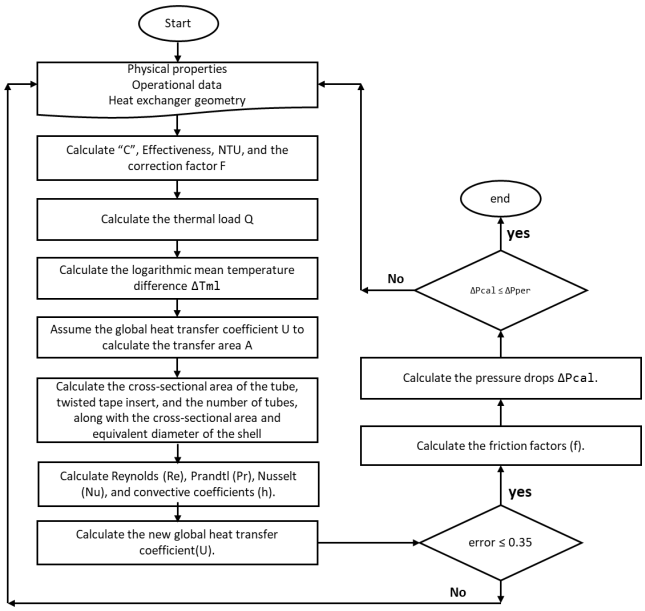



**Figure 2.** Methodology of design for a T&Sh heat exchanger.

According to Kern's methodology, we assume a starting value for the overall heat transfer coefficient of the system, then, this value is compared with the calculated overall heat transfer coefficient, until the difference between them is within the accepted error range (<35%). Once the condition is reached, the pressure drop is calculated in both sections of the system (tube and shell) [8, 9].

In the diagram of Figure 2, the expressions to estimate the total heat transfer area are calculated from the thermal load (Q), overall heat transfer coefficient (U), correction factor (F), and logarithmic mean temperature difference ($\Delta T_{ml}$).

$$A = \frac{Q}{U * F * \Delta Tml} \quad (1)$$

$$Q = m * C_p * \Delta T \quad (2)$$

Where, $m$ is mass flow, $C_p$, is the heat capacity and $\Delta T$ is the temperature difference. $\Delta T_{ml}$ and the correction factor F are given as:

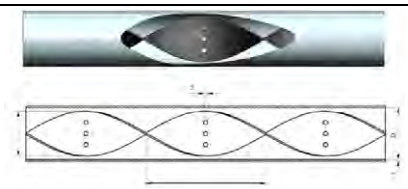
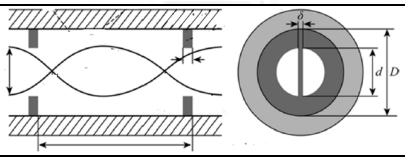
$$\Delta T_{ml} = \frac{\Delta T_1 - \Delta T_2}{Ln\left(\frac{\Delta T_1}{\Delta T_2}\right)} \quad (3)$$

$$\mathrm{F} = \frac{Q}{NTU * \Delta T_{ml} * C_{min}} \quad (4)$$

**Table 1:** Case studies for optimization applications

| Case I: Sensibility and Retrofit Analysis | | | |
|---|---|---|---|
| Variable | | Methanol (Shell – hot) | Water (Tube-cold) |
| **Mass Flow** | $\left[\frac{Kg}{s}\right]$ | 27.7 | 68.9 |
| **Inlet temperature** | $[^{o}C]$ | 95 | 25 |
| **Outlet temperature** | $[^{o}C]$ | 40 | 40 |
| **Effectiveness** | $[-]$ | 0.78 | |
| **Case II: Optimization Methodology Application** | | | |
| Variable | | Residue (Shell – hot) | Water (Tube-cold) |
| **Mass Flow** | $\left[\frac{Kg}{s}\right]$ | 47 | 75 |
| **Inlet temperature** | $[^{o}C]$ | 131 | 66 |
| **Outlet temperature** | $[^{o}C]$ | 79 | 79 |
| **Effectiveness** | $[-]$ | 0.8 | |
| **Case III: Optimization Methodology Application** | | | |
| Variable | | Water (Shell – hot) | Water (Tube-cold) |
| **Mass Flow** | $\left[\frac{Kg}{s}\right]$ | 3 | 3 |
| **Inlet temperature** | $[^{o}C]$ | 70 | 9.99 |
| **Outlet temperature** | $[^{o}C]$ | 40 | 39.9 |
| **Effectiveness** | $[-]$ | 0.49 | |

**Table 2:** Thermal-hydraulic correlations for different Twisted Tape promoters

| Promotor | Desing | Correlations |
|---|---|---|
| **Smooth twisted tape** [7] |  | $Nui = 0.224 * Re_i^{0.66} * Pr^{0.4} * TR^{-0.6}$<br>$f = 65.4 * Re_i^{-0.52} * TR^{-1.31}$ |
| **Smooth twisted tape several perforations** [3] |  | $Nu = a * Re^{b}$<br>$f = c * Re_i^{d}$<br>$a = 0.0002 * R_p^3 - 0.004 * R_p^2 + 0.033 * R_p + 0.6569$<br>$b = 0.00005 * R_p^3 - 0.0013 * R_p^2 + 0.0073 * R_p + 0.5501$<br>$c = -0.0027 * R_p^3 + 0.0583 * R_p^2 + 0.0455 * R_p + 24.536$<br>$d = 0.00009 * R_p^3 - 0.0013 * R_p^2 + 0.0073 * R_p - 0.6006$ |
| **Smooth twisted tape V-cut** [14] |  | $Nu = 0.0296 * Re^{0.853} * Pr^{0.33} * TR^{-0.222} * \left(1 + \frac{d_e}{W}\right)^{1.148} * \left(1 + \frac{w}{W}\right)^{-0.751}$<br>$fi = 8.632 * Re^{-0.615} * TR^{-0.269} * \left(1 + \frac{d_e}{W}\right)^{2.477} * \left(1 + \frac{w}{W}\right)^{-1.914}$ |
| **Smooth twisted tape with three center perforation** [5] |  | $Nu = 0.3528 * Re^{0.62} * Pr^{0.4} * TR^{-0.638} * \left(\frac{l}{di}\right)^{-0.00973}$<br>$fi = 6.2565 * Re^{-0.404} * TR^{-0.5828} * \left(\frac{d}{di}\right)^{-0.0113}$ |
| **Smooth twisted tape with circular ring** [4] |  | $Nu = 0.326 * Re^{0.724} * Pr^{0.4} * TR^{-0.406} * \left(\frac{l}{di}\right)^{-0.475}$<br>$fi = 13.99 * Re^{0.202} * TR^{-0.619} * \left(\frac{l}{di}\right)^{-0.927}$ |

NTU is the number of heat transfer units and $C_{min}$ is lower mass flow-heat capacity between the two streams.

To calculate the overall heat transfer coefficient (U) the thermal-hydraulic correlations for Nusselt number and friction factor presented in Table 2 were employed.

$$U = \frac{1}{\frac{1}{h_i} + \frac{1}{h_s}} \quad (5)$$

The pressure drop in the tube is calculated by equation 6.

$$DPi = N * \left[8 * fi * \frac{L}{di} * \left(\frac{\mu}{\mu_w}\right)^{-0.14} + 2.5\right] * \frac{\rho * v_i^2}{2} \quad (6)$$

The expression for pressure drop in the shell side is:

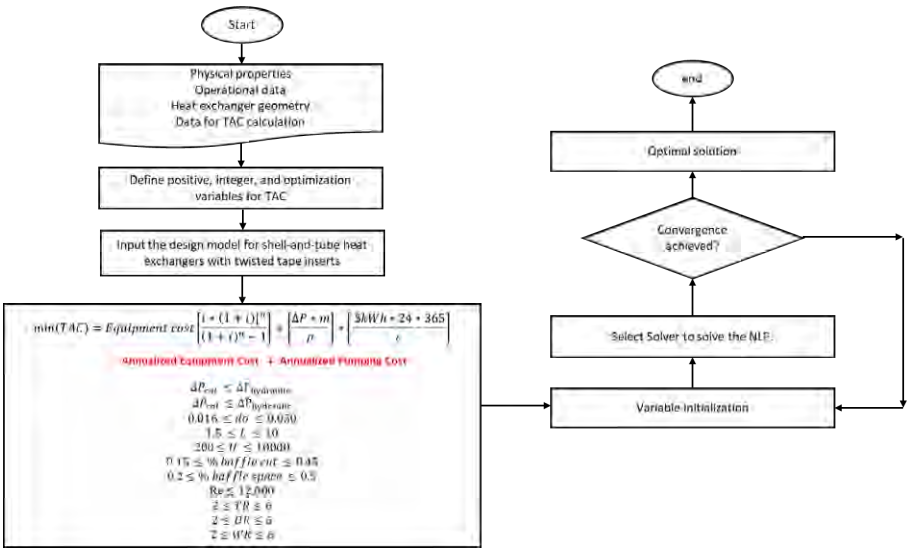
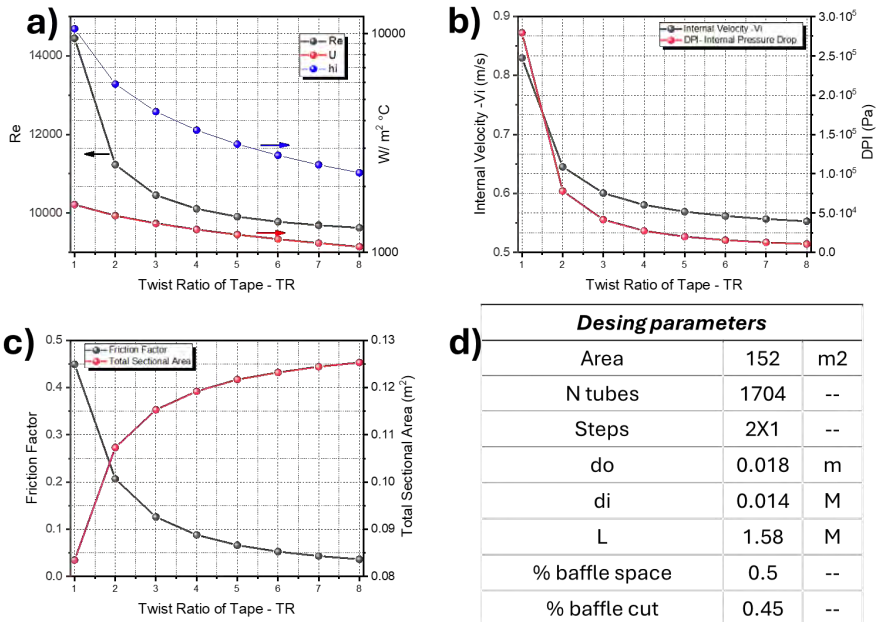



**Figure 3.** Methodology of optimization with twisted tape




d)

| *Desing parameters* | | |
|---|---|---|
| Area | 152 | m2 |
| N tubes | 1704 | -- |
| Steps | 2X1 | -- |
| do | 0.018 | m |
| di | 0.014 | M |
| L | 1.58 | M |
| % baffle space | 0.5 | -- |
| % baffle cut | 0.45 | -- |

**Figure 4.** Sensibility analysis of design of SH&T varying the twisted tape. a) Re, U and h vs TR; b) Internal velocity and pressure drop vs TR; c) Friction factor and total sectional area vs TR, and d) design parameters.

$$DPs = 8 * fs * \left(\frac{D_s}{d_e}\right) * \left(\frac{L}{l_B}\right) * \frac{\rho * v_s^2}{2} * \left(\frac{\mu}{\mu_w}\right)^{-0.14} \quad (7)$$

The mathematical model was implemented in GAMS software, as a Non-Linear Programming Model (NLP), and it was solved using the CONOPT solver. The optimization methodology to solve the SH&T heat exchanger with twisted tape inserts is based on reducing cost (TAC), which is in function on the equipment cost and the annualized energy consuming due to pumping. Figure 3 shows the design constraints.

## RESULTS AND DISCUSSION

From Figure 4, (a) and (b), it is evident that increasing the twist ratio (TR) of the twisted tape results in wider and less frequent twists, reducing the intensity of flow mixing and turbulence within the tube.

This leads to a decrease in fluid velocity (Vi), as it encounters less resistance, which in turn reduces the pressure drop (DPi) and the overall heat transfer coefficient (U). Higher TR values produce a smoother flow that

**Table 3:** Thermal-hydraulic comparative performance using different turbulence promoters for case I: Retrofit Methanol-Water.

| Type of twisted tape | U $\left[\frac{W}{m^2\,ºC}\right]$ | [%] | Dpi $[Pa]$ | [%] |
|---|---|---|---|---|
| **Smooth tube** | 959 | 0 | 9445 | 0 |
| **Smooth twisted tape** | 1127 | 14.8 | 66160 | 85.7 |
| **Smooth twisted tape with three center perforation** | 1149 | 16.5 | 33058 | 71.4 |
| **Smooth twisted tape with circular ring** | 1309 | 26.7 | 460044 | 97.9 |
| **Smooth twisted tape several perforations** | 1292 | 25.8 | 146286 | 93.5 |
| **Smooth twisted tape V-cut** | 1216 | 21.1 | 19791 | 52.27 |

**Table 4:** Results of the optimization process for a SH&T heat exchanger with inserts Case II: Residue-Water.

| Design varible | Units | Data | Design varible | Units | Data | Design varible | Units | Data |
|---|---|---|---|---|---|---|---|---|
| **di** | [m] | 0.0127 | **Ds** | [m] | 1.498 | **Space** | [%] | 0.48 |
| **do** | [m] | 0.0167 | **As** | $[m^2]$ | 0.1462 | **Q** | [W] | 4086 |
| **L** | [m] | 1.5 | **LB** | [m] | 0.7308 | **U** | $\left[\frac{W}{m^2\,ºC}\right]$ | 430 |
| **#-Tubes** | [ - ] | 4445 | **Vs** | $\left[\frac{m}{s}\right]$ | 0.3680 | **A** | $[m^2]$ | 350 |
| **Ac** | $[m^2]$ | 0.2033 | **Res** | $[m^2]$ | 174 | **TR** | [ - ] | 6 |
| **Vi** | $\left[\frac{m}{s}\right]$ | 0.3689 | **hs** | $\left[\frac{W}{m^2\,ºC}\right]$ | 475 | **Equipment cost** | $\left[\frac{USD}{Año}\right]$ | 9368 |
| **Ri** | [ - ] | 11980 | **fs** | [ - ] | 0.0664 | **Dpi Cost** | $\left[\frac{USD}{Año}\right]$ | 1460 |
| **hi** | $\left[\frac{W}{m^2\,ºC}\right]$ | 4502 | **Cut** | [%] | 0.45 | **DPs Cost** | $\left[\frac{USD}{Año}\right]$ | 637 |
| **fi** | [ - ] | 0.0172 | **de** | [m] | 0.0119 | **DP Total cost** | $\left[\frac{USD}{Año}\right]$ | 2098 |
| **DPi** | [Pa] | 2545 | **Dps** | [Pa] | 8136 | **Cost (TAC)** | $\left[\frac{USD}{Año}\right]$ | 11467 |

**Table 5.** Results of the optimization process for a SH&T heat exchanger with promoters Case III: Water-Water.

| Design variable | Units | Data | Design variable | Units | Data | Design variable | Units | Data |
|---|---|---|---|---|---|---|---|---|
| **di** | [m] | 0.0189 | **Ds** | [m] | 0.3734 | **Space** | [%] | 0.2 |
| **do** | [m] | 0.0229 | **As** | $[m^2]$ | 0.0149 | **Q** | [W] | 375.5 |
| **L** | [m] | 1.5 | **LB** | [m] | 0.0747 | **U** | $\left[\frac{W}{m^2\,ºC}\right]$ | 1438 |
| **#-Tubes** | [ - ] | 84 | **Vs** | $\left[\frac{m}{s}\right]$ | 0.2017 | **A** | $[m^2]$ | 9.07 |
| **Ac** | $[m^2]$ | 0.0094 | **Res** | $[m^2]$ | 3638 | **TR** | [ - ] | 2.6 |
| **Vi** | $\left[\frac{m}{s}\right]$ | 0.3252 | **hs** | $\left[\frac{W}{m^2\,ºC}\right]$ | 2129 | **Equipment cost** | $\left[\frac{USD}{Año}\right]$ | 1369 |
| **Ri** | [ - ] | 12000 | **fs** | [ - ] | 0.040 | **Dpi Cost** | $\left[\frac{USD}{Año}\right]$ | 22.01 |
| **hi** | $\left[\frac{W}{m^2\,ºC}\right]$ | 4434 | **Cut** | [%] | 0.45 | **DPs Cost** | $\left[\frac{USD}{Año}\right]$ | 30.08 |
| **fi** | [ - ] | 0.0287 | **de** | [m] | 0.0162 | **DP Total cost** | $\left[\frac{USD}{Año}\right]$ | 52.10 |
| **DPi** | [Pa] | 2163 | **Dps** | [Pa] | 2991 | **Cost (TAC)** | $\left[\frac{USD}{Año}\right]$ | 1420.6 |

is less efficient in heat transfer, as the ability to effectively induce turbulence is diminished.

Figure 4(c) shows that the friction factor decreases as TR increases. The tape causes less obstruction, which reduces the fluid velocity and consequently lowers the pressure drop. Additionally, with higher TR, the tape occupies less space in the cross-section tube, increasing the available free cross-sectional area and allowing the fluid to flow more easily.

According to the results shown in Table 3, smooth

twisted tape turbulence promoters with circular rings and multiple perforations provide the highest percentage increase in the heat transfer coefficient (U), achieving improvements of 26.7% and 25.8% compared to a smooth tube. However, these results also exhibit the highest pressure drop increase ($DP_i$) of 97.9% and 93.5%, indicating a significant energy cost. In contrast, twisted tapes with V-cuts achieve a 21.1% increase in U while maintaining a lower pressure drop of 52.27%, positioning them as a more balanced option.

From case II (Table 4), TAC was estimated at 11,467 USD/year, where the largest contribution comes from the equipment cost (9,368 USD/year), while the pumping costs are 2,098 USD/year. This analysis shows that the convective heat transfer coefficient of the shell side ($h_s$) is significantly lower compared to that of the tubes ($h_i$), indicating that the heat transfer is controlled by the fluid flowing through the shell. This situation causes the improvement in heat transfer coefficient on the tube side, not being significant in the overall heat transfer coefficient. This prevents the inserts from achieving the intended operational performance. In this case, a better design configuration is to send the fluid with the lowest mass flow rate through the tubes. Yet, another operating feature that affects the magnitude in which a promoter enhances heat transfer is thermal effectiveness. Higher effectiveness heat exchangers tend to dampen the increment in heat load.

The results of the optimization methodology applied to Case III are presented in Table 5. It can be observed that the convective heat transfer coefficients, $h_i$ (4,434 W/m²°C) and $h_s$ (2,129 W/m²°C), are slightly more balanced compared to Case II. In this configuration, the mass flow rates are equal, which does not constrain the increase in the overall heat transfer coefficient. This is because heat transfer is more evenly distributed, attributed to the heat exchanger exhibiting a balanced thermal effectiveness and *C* relation average.

## CONCLUSIONS

Based on the sensitivity analysis results, it can be concluded that an increase in the twist ratio (TR) of the twisted tape promoter causes the twists to become wider. This reduces flow turbulence, which inversely affects fluid velocity, decreasing speed (Vi), pressure drop ($\Delta P_i$), and the overall heat transfer coefficient (U). The twisted tape with V-cuts shows a 21.1% increase in the overall heat transfer coefficient (U) and a 52.27% increase in the pressure drop (ΔPi) compared to the smooth tube without promoters, making it the best option to maximize heat transfer with minimal impact on energy consumption.

An optimization methodology was developed for the design of shell and tube heat exchangers with turbulence promoters. The results indicate two key issues that determine the magnitude of performance improvement achievable with turbulence promoters: (1) a larger overall performance increase is observed when the lower mass flow rate fluid passes through the tube, and (2) higher increases in heat load are achieved when turbulence promoters are used in units with low thermal effectiveness.

## ACKNOWLEDGEMENTS

Authors wish to express their gratitude to the Mexican Council of Science, Humanities and Technology (CONAHCyT) for the grant provided to Jamel Eduardo Rumbo-Arias during this research.

## REFERENCES

1. Crespo-Quintanilla, J.A., García-Castillo, J.L., I. Minchaca-Mojica, J., Picón-Núñez, M.: Enhancing heat exchanger performance with combined twisted tubes and twisted Tapes: Design and retrofit strategies. Therm. Sci. Eng. Prog. 54, 102817 (2024). https://doi.org/10.1016/j.tsep.2024.102817
2. Picón-Núñez, M., Minchaca-Mojica, J.I., Durán-Plazas, L.P.: Selection of turbulence promoters for retrofit applications through thermohydraulic performance mapping. Therm. Sci. Eng. Prog. 42, 101876 (2023). https://doi.org/10.1016/j.tsep.2023.101876
3. Bhuiya, M.M.K., Chowdhury, M.S.U., Saha, M., Islam, M.T.: Heat transfer and friction factor characteristics in turbulent flow through a tube fitted with perforated twisted tape inserts. Int. Commun. Heat Mass Transf. 46, 49–57 (2013). https://doi.org/10.1016/j.icheatmasstransfer.2013.05.012
4. Eiamsa-ard, S., Kongkaitpaiboon, V., Nanan, K.: Thermohydraulics of Turbulent Flow Through Heat Exchanger Tubes Fitted with Circular-rings and Twisted Tapes. Chin. J. Chem. Eng. 21, 585–593 (2013). https://doi.org/10.1016/S1004-9541(13)60504-2
5. Gunes, S., Karakaya, E.: Thermal Characteristics in a Tube With Loose-Fit Perforated Twisted Tapes. Heat Transf. Eng. 36, 1504–1517 (2015). https://doi.org/10.1080/01457632.2015.1024985
6. Eiamsa-ard, S., Promvonge, P.: Thermal characteristics in round tube fitted with serrated twisted tape. Appl. Therm. Eng. 30, 1673–1682 (2010). https://doi.org/10.1016/j.applthermaleng.2010.03.026
7. Eiamsa-ard, S., Thianpong, C., Eiamsa-ard, P.: Turbulent heat transfer enhancement by

counter/co-swirling flow in a tube fitted with twin twisted tapes. Exp. Therm. Fluid Sci. 34, 53–62 (2010). https://doi.org/10.1016/j.expthermflusci.2009.09.002
8. Sadik, K.: Heat Exchanger. CRC Press, 6000 Broken Sound Parkway NW, Suite 300 Boca Raton, FL 33487-2742 (2012)
9. Sinnott, R.: Chemical Engineering Design: Chemical Engineering Volume 6. Elsevier Science & Technology, Jordan Hill (2005)
10. Keklikcioglu, O., Günes, S., Senyigit, E., Akcadirci, E., Ozceyhan, V.: The optimization of the thermal and hydraulic characteristics of a tube with twisted tapes using Taguchi-based-AHP-TOPSIS approach. J. Therm. Anal. Calorim. 147, 13711–13723 (2022). https://doi.org/10.1007/s10973-022-11518-x
11. Kola, P.V.K.V., Pisipaty, S.K., Mendu, S.S., Ghosh, R.: Optimization of performance parameters of a double pipe heat exchanger with cut twisted tapes using CFD and RSM. Chem. Eng. Process. - Process Intensif. 163, 108362 (2021). https://doi.org/10.1016/j.cep.2021.108362
12. Picón-Núñez, M., Rumbo-Arias, J.E.: Improving thermal energy recovery systems using welded plate heat exchangers. Energy. 235, 121373 (2021). https://doi.org/10.1016/j.energy.2021.121373
13. Sebastian anak Sidi, Feasibility study on the replacement of tradisional heat exchanger by alfa laval compabloc, 2009

© 2025 by the authors. Licensed to PSEcommunity.org and PSE Press. This is an open access article under the creative commons CC-BY-SA licensing terms. Credit must be given to creator and adaptations must be shared under the same terms. See https://creativecommons.org/licenses/by-sa/4.0/



Systems & Control Transactions

**Research Article - Peer Reviewed Conference Proceeding**
ESCAPE 35 - European Symposium on Computer Aided Process Engineering
Ghent, Belgium. 6-9 July 2025
Jan F.M. Van Impe, Grégoire Léonard, Satyajeet S. Bhonsale,
Monika E. Polańska, Filip Logist (Eds.)

PSE PRESS

# Optimizing Methane Conversion in a Flow Reactor System Using Bayesian Optimization and Model-Based Design of Experiments Approaches: A Comparative Study

**Michael Aku, Solomon Gajere Bawa, Arun Pankajakshan, Lauren Ye Seol Lee, Federico Galvanin***

Department of Chemical Engineering, University College London (UCL), Torrington Place, WC1E 7JE London, United Kingdom
* Corresponding Author: f.galvanin@ucl.ac.uk

## ABSTRACT

Reaction processes require optimization to enhance key performance indicators (KPIs) such as yield, conversion, and selectivity. Techniques like Bayesian Optimization (BO), Model-Based Design of Experiments (MBDoE), and Goal-Oriented Optimal Experimental Design (GOOED) play pivotal roles in achieving these objectives. BO efficiently explores the design space to identify optimal conditions, while MBDoE maximizes the information gain by reducing kinetic model uncertainty. In contrast, GOOED focuses solely on maximizing the KPIs without considering the system uncertainty, identifying reactor conditions in the design space guaranteeing optimal performance. This study compares BO, MBDoE, and GOOED in optimizing methane oxidation in an automated flow reactor. Performance is assessed based on optimal methane conversion, reduced system uncertainty and minimal experimental efforts to achieve maximum conversion. BO quickly identifies high-conversion conditions, MBDoE minimizes experimental runs while providing insights into parameter sensitivities, and GOOED prioritizes conversion efficiency. The findings highlight trade-offs between convergence speed, robustness, and information gain, providing valuable insights for designing data-driven, physics-informed experiments..

**Keywords**: Bayesian Optimization, Model-Based Design of Experiments, Methane Conversion

## 1 INTRODUCTION

Reaction processes play a significant role in scientific and industrial applications in the production of chemicals, energy, and materials [1]. These processes are driven by interconnected factors such as reaction kinetics, thermodynamics, and transport phenomena [2], and their optimal performance in terms of key performance indicators (KPIs) such as yield, conversion, and selectivity depend on the precise control and fine-tuning of process parameters. Addressing these challenges requires advanced optimization techniques capable of navigating this intricate landscape.

Traditional methods like trial-and-error experimentation and design of experiments (DoE) [3] have proven effective in several applications. These techniques have been instrumental in refining reaction conditions, balancing exploration and exploitation of the design space, and offering insights into reactor behaviour. However, their limitations, particularly in high-dimensional, dynamic, or noisy systems, have spurred the development of novel approaches.

Emerging techniques such as Bayesian Optimization (BO) [4], Model-Based Design of Experiments (MBDOE) [5], and Goal-Oriented Optimal Experimental Design (GOOED) [6] provide more efficient strategies for optimizing reaction processes.

BO excels at identifying optimal conditions with a minimal number of experiments by balancing exploration and exploitation in black-box systems [7]. MBDOE emphasizes the maximization of information gain to improve parameter estimation and reduce uncertainty in physics-based model predictions. The MBDoE approach can also be applied to design experimental design campaigns online [8].

In contrast, GOOED focuses solely on achieving target KPIs, such as maximizing conversion, without prioritizing information gain or uncertainty reduction, making it

highly effective for applications where achieving maximum performance is the primary objective.

The goal of the study is to evaluate the relative merit of the different experimental design approaches and establish which among the three techniques (BO, MBDoE, and GOOED) represents the optimal experimental design scenario by examining the reaction for methane total oxidation in an automated flow reactor as a case study.

A comparative analysis of the three techniques as experimental design scenarios is carried out to quantify their relative performance in terms of (i) conversion of methane; (ii) uncertainty in the evaluation of the optimal conversion; (iii) confidence level of parameter estimates, and (iv) number of experiments required for the maximum KPI to be achieved. The analysis demonstrates how the three techniques can distinctly balance convergence speed and experimental robustness ultimately guiding the choice of more effective experimental design campaigns.

# 2 METHODOLOGY

## 2.1 Generic Model and System Description

The system under consideration is represented by a set of differential and algebraic equations (DAEs), where the measured variables $\mathbf{y}$ can be sampled at discrete time points:

$$\mathbf{f}(\dot{\mathbf{x}}, \mathbf{x}, \mathbf{u}, \boldsymbol{\theta}, t) = 0 \qquad \mathbf{y} = g(\mathbf{x}, \mathbf{u}, \mathbf{v}) \quad (1,2)$$

where **f** is a set of model equations, **x,** $\dot{\mathbf{x}}$ and are $N_x$ -dimensional vectors of state variables and their first derivatives respectively, **u** is a $N_u$ -dimensional vector of control variables, $t$ is time, **θ** is a $N_\theta$-dimensional vector of model parameters, **y** is a $N_y$-dimensional vector of response variables that are measurable.

Eq. (1), and (2) establish the fundamental structure upon which the specific methane oxidation reactor model is developed in Section 2.2

## 2.2 Methane Oxidation: System & Reactor Model

Building on the general modeling framework from Section 2.1, this section details a specific application to methane oxidation in flow reactor system as presented by Bawa et al. [12]. In their research, they presented a reactor model characterized by the following set of ordinary differential algebraic equations:

$$\begin{aligned}
\frac{dx_1}{dw} &= \frac{R.u_1}{u_2 P_{avg}} . (-r) \quad x_1(0) = u_4 \\
\frac{dx_2}{dw} &= \frac{R.u_1}{u_2 P_{avg}} . (-2r) \quad x_2(0) = u_3.u_4 \\
\frac{dx_3}{dw} &= \frac{R.u_1}{u_2 P_{avg}} . (r) \\
\frac{dx_4}{dw} &= \frac{R.u_1}{u_2 P_{avg}} . (2r) .
\end{aligned} \qquad (3)$$

For the methane oxidation system, the control variables (**u**) is defined in Eq. 4, while **y** represents the response variables for $CH_4$, $CO_2$, $O_2$ measured at the reactor outlet. The state variables **x,** control variables **u** and model parameters **θ** are defined for the reactor model as follows:

$$\begin{aligned}
\mathbf{x} &= [x_1, x_2, x_3, x_4] \\
\mathbf{u} &= [u_1, u_2, u_3, u_4] \\
\boldsymbol{\theta} &= [\theta_1, \theta_2, \theta_3, \theta_4, \theta_5, \theta_6]
\end{aligned} \qquad (4)$$

where $x_1$ $x_2$ $x_3$ $x_4$ are mole fraction of methane, oxygen, carbon dioxide and water, respectively, and $u_1, u_2, u_3, u_4$ represent temperature [℃], flow rate of the feed $[Nml\ min^{-1}]$, oxygen-to-methane mole fraction $R_{O_{2/CH_4}}$ $[mol\ mol^{-1}]$, and inlet methane mole fraction $[mol\ mol^{-1}]$ respectively. These controls form the design vector $\boldsymbol{\varphi}$ which is bounded within the experimental design domain as shown in Table 1. In the model $R$ $[J\ mol^{-1}\ K^{-1}]$ is the universal gas constant, $r$ $[mol\ g^{-1}\ min^{-1}]$ the reaction rate according to the kinetic model, and $w$ $[g]$ is the catalyst mass along the reactor. The experimental design examined the effects of key control variables on methane oxidation by varying them within defined ranges (Table 1).

**Table 1**. Experiment control variables

| Control Variables | Range | Units |
|---|---|---|
| Temperature | 250-350 | ℃ |
| Mass flow rate | 20-30 | $Nml\ min^{-1}$ |
| Oxygen to methane mole ratio | 2-4 | $mol\ mol^{-1}$ |
| Methane mole fraction | 0.005-0.025 | $mol\ mol^{-1}$ |

The Mars Van Krevelen (MVK) model reaction rate expression (Eq. 5) was adopted as the true model in this study as a representation of the system under consideration:

$$r_{ch4} = \frac{k_1 k_2 P_{CH_4} P_{O_2}}{k_1 P_{O_2} + 2\, k_2 P_{CH_4} + \frac{k_1 k_2}{k_3} (P_{O_2} P_{CH_4})} \qquad (5)$$

Eq. 5 was identified and validated in [11], where the authors calibrated the MVK model from flow reactor data. The authors also stressed that the oxidation of methane involved three steps: 1. Surface oxidation 2. Surface Reduction. 3. Desorption of product. Kinetic model parameters of the MVK model (i.e. rate constants $k$, and activation energies $E_a$) were identified and formulated with respect to these steps thus giving rise to six parameters, $k_1$ , $k_2$ , $k_3$, $E_{a_1}$, $E_{a_2}$, $E_{a_3}$. Furthermore, these parameters were reparameterised to the vector form **θ** and estimated as **θ** = [5.77, 6.72, 5.87, 9.51, 10.17, 7.98]. These parameter values are used as the true parameter vector in this work.

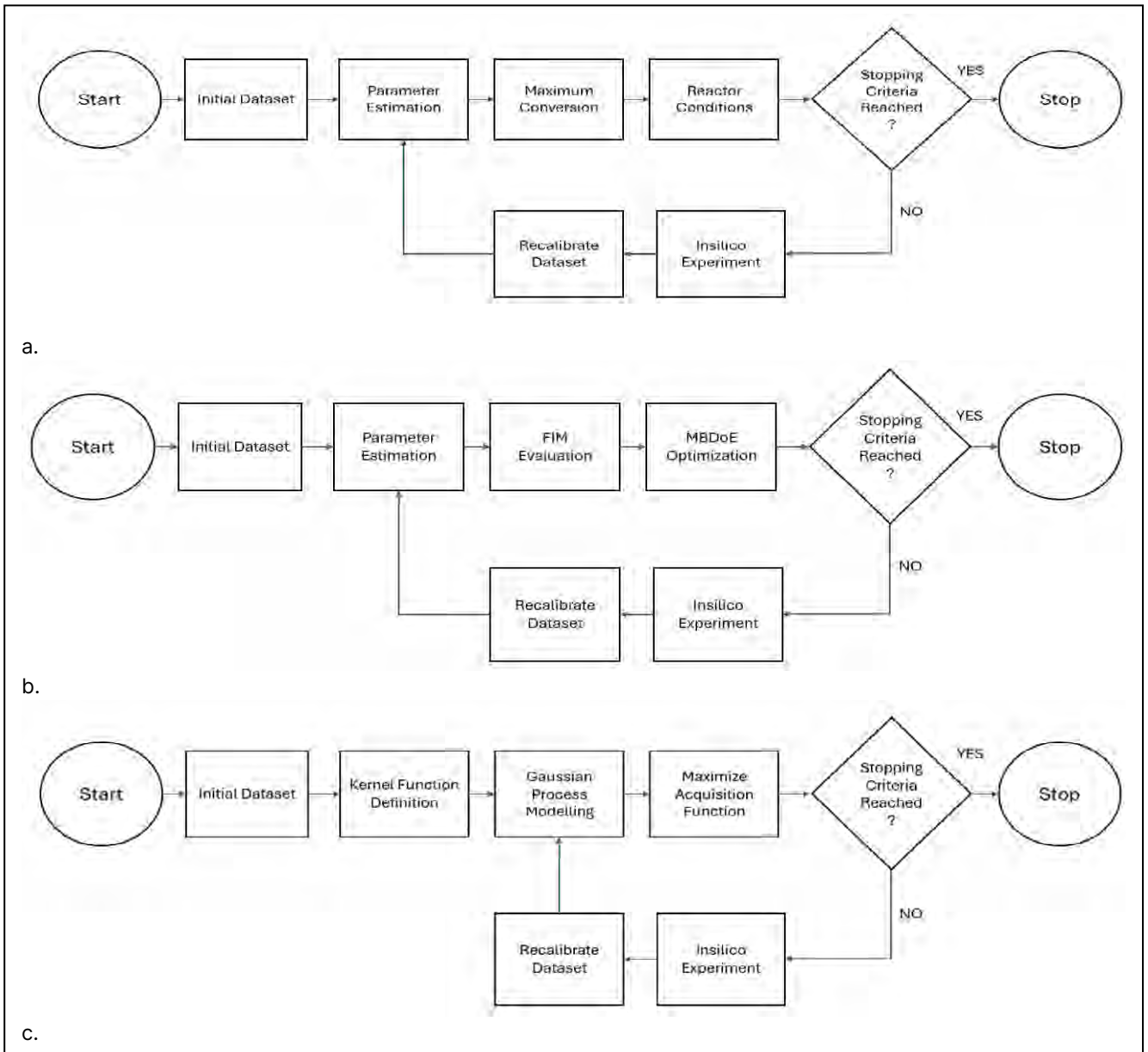



**Figure 1.** Procedural Framework showing workflow procedures for (a) GOOED (b) MBDoE and (c) BO scenarios.

## 2.3 Procedural Approach for GOOED, MBDOE, and BO

The procedural approach for the three experimental design scenarios is tailored to their distinct objectives as shown in Figure 1. GOOED (a) and MBDoE (b) are both exploitative approaches. While they have distinct objectives, they both focus on identifying the optimal point, albeit with different goals in mind. The objective of (a) is to maximise a specific KPI, whereas (b) focuses on the improvement of model predictions by minimising uncertainty in parameter estimation and (c) BO balances exploration and exploitation through adaptive learning to optimize system performance without using mechanistic modelling insights on the system. The stopping criteria used to terminate the procedures for any of the scenarios can be one of the following: a. experimental budget termination b. satisfied $t$ −test on model parameters.

The objective function that describes maximizing methane conversion and used by both GOOED and BO is shown in Eq. 6 below.

$$\mathbf{u}^* = argmin_{\mathbf{u}\in U} - h\,(\mathbf{u}) \tag{6}$$

where $h\,(\mathbf{u})$ is the predicted conversion at any experimental condition $\mathbf{u}$, The algorithms mostly perform minimization, so we minimize $-h\,(\mathbf{u})$, which is the same as maximizing $h\,(\mathbf{u})$, $\mathbf{u}^*$ is the optimal condition at maximum conversion. The design space, $U$, is the boundary

conditions of the control variables shown in Table 1.

### 2.3.1 GOOED

In the GOOED approach the objective is to maximize the conversion of methane. The objective function Eq. 7 which is a slight modification of Eq. 6 is shown below.

$$\mathbf{u}^{*}_{\boldsymbol{GOOED}} = argmin_{\mathbf{u}\in U} - h\,(\mathbf{u}) \tag{7}$$

The steps defining the GOOED procedure are illustrated in Figure 1a and summarised below.

1. *Initial Dataset*: An initial dataset from 12 preliminary experimental runs, created using statistical design of experiments (DoE) methodology as described in [11], serves as the starting point for the procedure.
2. *Parameter Estimation*: Using computational methods and Eq. 6, the observations are utilized to estimate model parameters and estimates are evaluated for statistical significance.
3. *Maximize Methane Conversion.* The optimization of methane conversion is guided by the experimental conditions defined in Table 1; the objective function is represented in Eq. 7. The system undergoes an optimization routine to identify the maximum achievable conversion of methane.
4. *Optimal Reactor Conditions.* During this process, the corresponding operating conditions that yield the maximum conversion are also determined.
5. *In Silico Experiment*: Simulations are run to forecast how the reaction will behave under the determined optimal conditions.
6. *Iterate Until Stopping Criterion*: The procedure continues, updating the dataset and improving predictions of the optimal conversion based on feedback from each experimental run.
7. *Procedure termination*: The process stops when the stopping criterion is met, i.e. the maximum experimental budget is exhausted, or the *t*-test results are statistically significant – both of which are the stopping criteria.

### 2.3.2 MBDoE

In the MBDoE approach, the objective function is designed to maximize the determinant of the Fisher Information Matrix (FIM), $H_{\hat{\theta}}$ this function is defined in Eq. 8 which represents dynamic systems.

$$\mathbf{H}_{\hat{\boldsymbol{\theta}}}(\hat{\boldsymbol{\theta}}, \boldsymbol{\varphi}) = [\mathbf{V}^{0}_{\hat{\theta}}]^{-1} + \sum_{i=1}^{n_{sp}} \left(\frac{d\hat{\mathbf{y}}}{d\hat{\boldsymbol{\theta}}}\right)_i^{T} \sum_{y}^{-1} \left(\frac{d\hat{\mathbf{y}}}{d\hat{\boldsymbol{\theta}}}\right)_i \tag{8}$$

where $\mathbf{V}^{0}_{\hat{\theta}}$is the $N_\theta\ x\ N_\theta$ prior variance-covariance matrix of model parameters, while $(\frac{d\hat{y}}{d\hat{\theta}})$is the $N_y\ x\ N_\theta$ matrix with first-order derivatives of model responses with respect to the parameters at time point *i*. The parameter estimates are obtained from Eq. 11, which provides the initial values for MBDoE based on the model and available data. To assess the quality of these estimates, Eq. 8 computes the Fisher Information Matrix (FIM) which allows to predict the expected precision of parameter estimates. The *t*-values are calculated as metric of parameter precision (see Section 2.4.1), and statistical conditions are checked to ensure the validity of the estimates.

The procedural approach for MBDoE (Fig 1b) is the following

1. *Initial Dataset*: Same as in GOOED
2. *Parameter Estimation:* Same as in GOOED
3. *FIM Evaluation:* The evaluation of the expected FIM was computed at the current value of the parameter estimates.
4. *Optimal Design of Experiment:* Based on the estimated parameters and uncertainties, new experimental conditions are determined by maximizing the determinant of the expected FIM [8].
5. *In Silico Experiment:* The new experimental conditions are applied, the experiment is simulated generating new data in silico, and the experimental dataset is updated.
6. *Iterative Process:* The process continues iteratively until the t-test results are statistically significant, or the experimental budget is terminated both of which are the stopping criteria.

### 2.3.3 Bayesian Optimization (BO)

In the third scenario, we adopted the BO technique due to its ability to effectively find the optimized value of the objective function. The objective function which is a modification of Eq. 6 is defined below in Eq. 9

$$\mathbf{u}^{*}_{\boldsymbol{BO}} = argmin_{\mathbf{u}\in U} - h\,(\mathbf{u}) \tag{9}$$

The choice of a composite kernel function Eq. 10 combining constant kernel *C*, and RBF kernel to effectively capture both global scaling and local variability in the relationship between experimental conditions $\mathbf{u}$ and the conversion of methane (Eq. 14). This combination helps the GP to represent system behaviour and optimize control variables for maximum conversion efficiency.

$$k(\mathbf{u}, \mathbf{u}') = C.RBF\ (\mathbf{u}, \mathbf{u}') \tag{10}$$

where $\mathbf{u}, \mathbf{u}'$ are two different sets of experimental conditions.

The procedural approach for the BO (Fig 1c) is outlined below:

1. *Initial Dataset*: Same as in GOOED
2. *Define the Kernel and Gaussian Process (GP) Model*: We defined the GP with a composite kernel function Eq. 10 where $C$ is a constant kernel with an initial value of 1.0 (bounded between $10^{-3}$ and $10^{3}$), and $RBF$ (Radial Basis Function) has a length scale initialized at 1.0 with bounds between $10^{-2}$ and $10^{2}$). The hyperparameters of the kernel are optimized during model training by maximizing the log marginal likelihood using gradient-based optimization technique [13].
3. *Train the GP Model*: The GP model is trained using an initial dataset to learn the relationship between the input conditions and the corresponding system response variables [14]. To account for noise in the data, the GP model incorporates the noise and variance from the preliminary dataset.
4. *Cross-Validation*: To ensure the GP model generalizes well, 5-fold cross-validation is performed on the initial datasets. The data is split into 5 subsets, where the model is trained on 4 subsets and tested on the remaining one [15], repeating the process 5 times. The average performance metric (e.g., RMSE) is used to assess model robustness and prevent overfitting.
5. *Define the Acquisition Function (AF)*: An AF is chosen to guide the search for optimal experimental conditions in our case we chose the Expected Improvement (EI).
6. *Optimize the AF*: The chosen acquisition function is then optimized this leads to selection of the next experimental condition $\mathbf{u}_{\text{new}}$ to test.
7. *In Silico Experiment*: At this new experimental condition $\mathbf{u}_{\text{new}}$, the experiment is simulated generating new data in silico, and the experimental dataset is updated.
8. *Procedure termination*: The process stops when the stopping criterion – the experimental budget is exhausted.
9. The next experiment is conducted at the selected reactor conditions, $\mathbf{u}_{\text{new}}$ The process continues iteratively until the experimental budget of 20 runs is reached, at which point the process stops.

## 2.4 Parameter Estimation

Parameter estimates (indicated as $\theta$) from the experimental data were computed by minimizing the difference between measured responses ($y$) and predicted responses ($\hat{y}$) through the negative log-likelihood function [6].

$$L(\hat{\boldsymbol{\theta}}) = \frac{N}{2}\log(2\pi) + \frac{n_{sp}}{2}\log\left(det|\boldsymbol{\Sigma}_{\boldsymbol{y}}\right) + \frac{1}{2}\sum_{i=1}^{n_{sp}}[\boldsymbol{y_i} - \hat{\boldsymbol{y}}_{\boldsymbol{i}}\,(\hat{\boldsymbol{\theta}})]^T\ \boldsymbol{\Sigma_y}^{-1}[\boldsymbol{y_i} - \hat{\boldsymbol{y}}_{\boldsymbol{i}}(\hat{\boldsymbol{\theta}})] \quad (11)$$

$n_{sp}$ is the number of sampling points considering all the Ne performed experiments, namely $n_{sp} = \sum_{i=1}^{N_e} N_{sp_i}$ is the number of sampling points in the $i_{th}$ experiment), $N$ is the total number of experimental measurements calculated as $N$. In GOOED and MBDoE the $\hat{y}_i$ is computed from the mechanistic model. In BO $\hat{y}_i$ is computed from GP predictions.

### 2.4.1 Uncertainty in Parameter Estimates

Parameter precision is quantified using the $N_\theta\ x\ N_\theta$-dimensional covariance matrix ($V_\theta$), approximated by the inverse of the observed Fisher Information Matrix ($H_\theta$) (Eq. 8). From the covariance matrix, the 95% confidence interval for the $ith$ parameter is calculated using Eq. 12 as the square root of the variance element $v_{\theta,ii}$, multiplied by the *t*-value at the 95% confidence level:

$$95\%\ \text{CI} = \sqrt{\boldsymbol{v_{\theta,ii}}} \times \text{t}\ (95\%, \text{DoF})\ \text{for i} = 1, \ldots, N_\theta \quad (12)$$

$$t_i = \frac{\hat{\boldsymbol{\theta}}_{\boldsymbol{i}}}{95\%\ Confidence\ Interval_i} \quad (13)$$

The *t*-value for each parameter was calculated by dividing the parameter estimate by the 95% confidence interval, as shown in Eq. 13. A high *t*-value indicates a reliable parameter estimate, while a low *t*-value suggests that the confidence interval may include zero, implying the parameter might not be statistically significant and could be excluded from the model, and the corresponding uncertainty is then computed for each parameter estimates.

## 2.5 Conversion of Methane

The conversion of methane is the KPI used in this study, and it is defined in Eq. 14 as the ratio

$$\alpha = \frac{Y_{CH_4} - y}{Y_{CH_4}}, \quad (14)$$

where $Y_{CH_4}$ and $y$ are the inlet and outlet concentration of methane respectively [12]. To account for uncertainties in methane conversion, error propagation of the uncertainties associated with the conversion was performed using statistical methods [16].

## 2.6 Preliminary Dataset

The preliminary dataset used in this study was derived from a series of experiments designed using DoE as reported in [11], aimed at investigating the kinetics of complete methane oxidation over the $Pd/Al_2O_3$ catalyst.

## 2.7 Performance Metrics for the Design Scenarios

Results are compared in terms of (a) conversion and

associated uncertainty; (b) operating conditions in the design space; (c) parameter estimation significance after the stopping criteria are reached; (d) number of experiments required to satisfy stopping criteria. Simulations for the three different scenarios were all implemented in Python including SciPy library functions, *scalar* and *minimize* functions while a custom class called Gaussian Regressor was specifically developed to solve the BO scenario.

## 3 RESULTS & DISCUSSION

This section compares the three (3) different scenarios using the performance metrics from 2.7.

### 3.1 Methane Conversion and Associated Uncertainty

Table 2 illustrates the conversion percentages and associated uncertainties for GOOED, MBDoE, and BO under the evaluated scenarios. Key observations are the following:

**GOOED:** Exhibited the highest conversion with values as high as 97 – 99%, but with high uncertainty, highlighting variability in the results.

**MBDoE**: Delivered a moderate conversion values hovering at 45% with low uncertainty values ensuring reliability and consistency.

**BO**: Achieved an optimal conversion (~87%) with moderate uncertainty, obtaining a balance between performance and reliability. Table 2 compares the scenarios, showing how GOOED maximizes conversion, MBDOE minimizes uncertainty, and BO essentially balances both objectives.

**Table 2:** Methane Conversion and Corresponding Uncertainty for GOOED, MBDOE, and BO Scenarios

| Exp | GOOED Scenario | MBDOE Scenario | BO Scenario |
|---|---|---|---|
| 13 | 99.00±94.00 | 42.90 ±0.57 | 43.9 ±9.81 |
| 14 | 99.04±64.00 | 88.90 ±0.37 | 87.45 ±5.78 |
| 15 | 97.70 ± 4.00 | 40.30 ±0.18 | 88.01 ±5.08 |
| 16 | 97.93 ± 4.26 | 37.00 ±0.16 | 87.71 ±4.98 |
| 17 | 97.95 ± 4.26 | 46.40 ±0.13 | 87.72 ±4.85 |
| 18 | 98.07 ± 4.28 | 79.20 ±0.08 | 87.72 ±4.78 |
| 19 | 98.07 ± 4.04 | 48.40 ±0.06 | 87.72 ±4.65 |
| 20 | 98.06 ± 4.13 | 44.80 ±0.05 | 88.01 ±4.08 |

### 3.2 Operating Conditions in the Design Space

Figures 2a, 2b, and 2c illustrates the distribution of the reactor conditions in the experimental design space for GOOED, MBDOE, and BO campaigns. Key observations include:

**GOOED:** The reactor conditions identified reflects a strong exploitation of known high-performing conditions, with no emphasis on uncertainty reduction**.**

**MBDoE:** The reactor conditions for this scenario show transition from exploration to exploitation ensures improved system understanding while maintaining reliability in predictions**.**

**BO:** The reactor conditions selected by BO demonstrate a balance between exploration and exploitation by achieving average conversion rates while exploring under-characterized areas for further improvement. The oxygen-to-methane ratio for the simulated reactor condition for the three scenarios is reported in Table 3.

**Table 3.** Simulated Oxygen to Methane Mole Ratio in (mol/mol)

| Exp | GOOED | MBDOE | BO |
|---|---|---|---|
| 13 | 3.8 | 3.9 | 3.5 |
| 14 | 4 | 4 | 3.9 |
| 15 | 4 | 4 | 3.9 |
| 16 | 4 | 4 | 4 |
| 17 | 3.7 | 4 | 3.9 |
| 18 | 4 | 2 | 3.9 |
| 19 | 3.9 | 2.1 | 4 |
| 20 | 3.8 | 2.1 | 3.9 |

### 3.3 Parameter Estimation Statistics

For the evaluation metrics based on significance of parameter estimates, we focused on only two of the scenarios: GOOED, and MBDOE. This is because BO is a data-driven process and has no kinetic model parameter representation.

**GOOED:** At the end of the twenty (20) experiments, the t-test value for the 4th parameter failed the test as its value were less than the reference *t*-value as shown in Table 4.

**MBDoE:** For this scenario, the parameter estimates all passed the t-test evaluation successfully as shown in Table 4, this occurred at the 17th experiment making it one of the most efficient scenarios based on minimum number of experiments, and uncertainty. Table 4 shows that *t*-values obtained from MBDoE were statistically significant, including the critical parameter $\boldsymbol{\theta_4}$, at the end of the 17$^{th}$ experiment as their values were all greater than the reference.

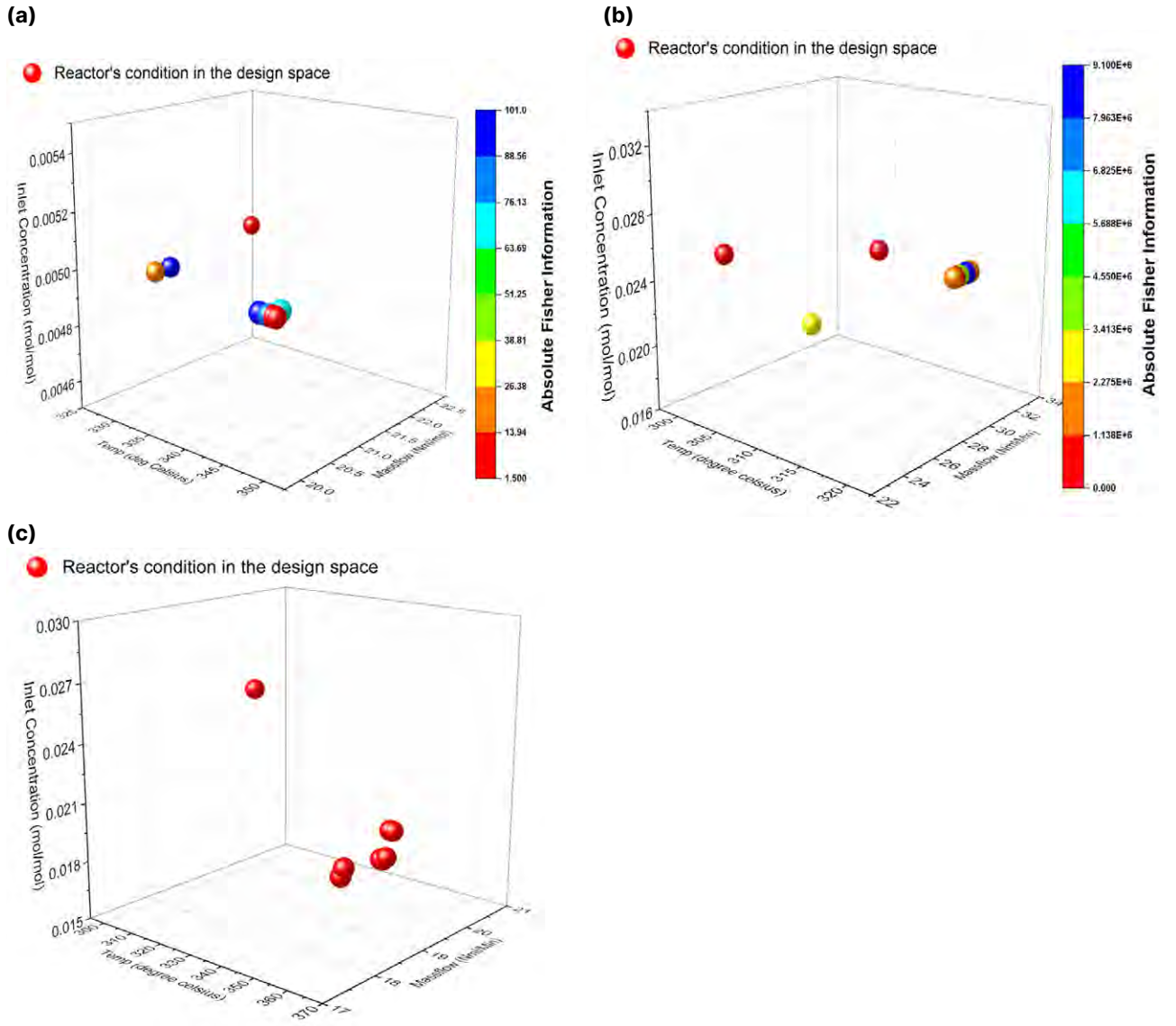



**Figure 2.** Plot of reactor conditions within the design space for the three scenarios: (a) GOOED, (b) MBDOE, (c) BO, respectively. The subplot (c) shows no Fisher information as they are not computed for the BO scenario

**Table 4.** Parameter estimation results for GOOED & MBDoE after stopping criteria successfully terminated (the reference *t*-value is $t^{ref}$ = 1.67, the parameter failing the t-test is indicated in boldface).

| S/N | Parameters | GOOED Estimates | *t*-value | MBDoE Estimates | *t*-value |
|---|---|---|---|---|---|
| 1 | $\boldsymbol{\theta_1}$ | 6.08 | 13.02 | 5.92 | 17.48 |
| 2 | $\boldsymbol{\theta_2}$ | 7.43 | 1.91 | 6.86 | 2.24 |
| 3 | $\boldsymbol{\theta_3}$ | 5.54 | 6.41 | 4.06 | 3.77 |
| 4 | $\boldsymbol{\theta_4}$ | 7.52 | 0.94 | 9.84 | 1.74 |
| 5 | $\boldsymbol{\theta_5}$ | 9.84 | 11.69 | 10.52 | 111.17 |
| 6 | $\boldsymbol{\theta_6}$ | 7.70 | 1.715 | 6.96 | 6.23 |

## 3.4 Number of Experiments

The minimum number of experiments (see Table 5) required to achieve optimal conditions were based on the pre-defined stopping criteria. The MBDOE achieved the lowest number of experimental runs as the parameters were successfully estimated at the 17th experiment.

**Table 5**. Minimum no. of experiments required

| **Scenarios** | GOOED | MBDOE | BO |
|---|---|---|---|
| **No of Experiment** | 20 | 17 | 20 |

## 3.5 Optimizing Conversion with Reduced uncertainty

In this study, the MBDOE demonstrated reduced

uncertainty, and required the fewest experiments. At the 17th experiment, it satisfied the stopping criteria. To validate the strength and performance of this scenario (MBDOE), we optimized the system to achieve maximum conversion at the 17th experiment for this scenario and the method achieved a predicted conversion of 95% which is a good conversion value for the system.

### 3.6 Best Scenario performance

The best scenario included the scenario providing the highest conversion value of methane, lowest value of conversion uncertainty and minimum number of experiments. Table 6 shows that MBDOE performed better than the other scenarios, as it had maximum predicted conversion with reduced uncertainty and satisfactory *t*-values with only 17 runs.

**Table 6**. Scenarios and Performance Metrics

| Scenarios | Conversion (%) | Uncertainty (%) | No. of Experiment | *t*-value Results |
|---|---|---|---|---|
| GOOED | 98 | ± 22.87 | 20 | Failed |
| MBDOE | 95 | ± 0.2 | 17 | Passed |
| BO | 87 | ± 5.5 | 20 | N/A |

## 4 CONCLUSION

In comparing GOOED, MBDoE, and BO, distinct differences emerge across conversion, parametric uncertainty, reactor conditions and experimental efficiency. GOOED achieves the highest conversions (98%) but the prediction of the KPI is affected by a significant uncertainty. MBDoE balances exploration and exploitation, delivering a high conversion (~95%) with the lowest uncertainty, requiring only 17 experiments to meet the parameter precision termination criterion. BO, while needing 20 experiments like GOOED, provides a moderate conversion (~87%) associated with a higher uncertainty, because of balancing exploration and exploitation in the design space. Overall, MBDoE proves to be the most efficient method as it shows minimum variance, reduced uncertainty across experiments, maximum conversion of methane and minimum number of experiments required to achieve maximum conversion.

## ACKNOWLEDGEMENTS

The authors are grateful to the Department of Chemical Engineering at University College London (UCL), the Petroleum Technology Development Fund (PTDF) and the Galvanin System Identification Group (GSIG) for their support in this research.

## REFERENCES

1. Kumar, R., & Gupta, R. B. (2000). Fundamentals of Reaction Engineering. Chemical Engineering Journal, 80(1), 1-12.
2. Taylor, C. J., Pomberger, A., Felton, K. C., Grainger, R., Barecka, M., Chamberlain, T. W., ... & Lapkin, A. A. (2023). A brief introduction to chemical reaction optimization. Chemical Reviews, 123(6), 3089-3126.
3. Montgomery, D. C. (2017). Design and Analysis of Experiments (9th Edition). Wiley.
4. Shahriari, B., Swersky, K., Wang, Z., Adams, R. P., & De Freitas, N. (2016). Taking the Human Out of the Loop: A Review of Bayesian Optimization. Proceedings of the IEEE, 104(1), 148-175.
5. Huang, C., Cattani, F., & Galvanin, F. (2023). An optimal experimental design strategy for improving parameter estimation in stochastic models. Computers & Chemical Engineering, 170, 108133.
6. Attia, A., Alexanderian, A., & Saibaba, A. K. (2018). Goal-oriented optimal design of experiments for large-scale Bayesian linear inverse problems. Inverse Problems, 34(9), 095009.
7. Zhu, M., Mroz, A., Gui, L., Jelfs, K. E., Bemporad, A., del Río Chanona, E. A., & Lee, Y. S. (2024). Discrete and mixed-variable experimental design with surrogate-based approach. Digital Discovery.
8. Friso, A., & Galvanin, F. (2024). An optimization-free Fisher information driven approach for online design of experiments. Computers & Chemical Engineering, 187, 108724.
9. Cenci, Francesca, Arun Pankajakshan, Pierantonio Facco, and Federico Galvanin (2023). An exploratory model-based design of experiments approach to aid parameters identification and reduce model prediction uncertainty. Computers & Chemical Engineering 177 (2023): 108353.
10. Feres, R., Cloninger, A., Yablonsky, G. S., & Gleaves, J. T. (2009). A general formula for reactant conversion over a single catalyst particle in TAP pulse experiments. Chemical Engineering Science, 64(21), 4358–4364.
11. Pankajakshan, A., Bawa, S. G., Gavriilidis, A., & Galvanin, F. (2023). Autonomous kinetic model identification using optimal experimental design and retrospective data analysis: methane complete oxidation as a case study. Reaction Chemistry & Engineering, 8(12), 3000-3017.
12. Bawa, S. G., Pankajakshan, A., Waldron, C., Cao, E., Galvanin, F., & Gavriilidis, A. (2023). Rapid Screening of Kinetic Models for Methane Total Oxidation using an Automated Gas Phase Catalytic Microreactor Platform. Chemistry-Methods, 3(1),

e202200049.
13. Gustafsson, O., Villani, M., & Stockhammar, P. (2023). Bayesian optimization of hyperparameters from noisy marginal likelihood estimates. Journal of Applied Econometrics, 38(4), 577-595.
14. Cicirello, A., & Giunta, F. (2022). Machine learning based optimization for interval uncertainty propagation. Mechanical Systems and Signal Processing, 170, 108619.
15. Bergmeir, C., & Benítez, J. M. (2012). On the use of cross-validation for time series predictor evaluation. Information Sciences, 191, 192-213.
16. Tellinghuisen, J. (2001). Statistical error propagation. The Journal of Physical Chemistry A, 105(15), 3917-3921.

© 2025 by the authors. Licensed to PSEcommunity.org and PSE Press. This is an open access article under the creative commons CC-BY-SA licensing terms. Credit must be given to creator and adaptations must be shared under the same terms. See https://creativecommons.org/licenses/by-sa/4.0/



Systems & Control Transactions

**Research Article - Peer Reviewed Conference Proceeding**
ESCAPE 35 - European Symposium on Computer Aided Process Engineering
Ghent, Belgium. 6-9 July 2025
Jan F.M. Van Impe, Grégoire Léonard, Satyajeet S. Bhonsale,
Monika E. Polańska, Filip Logist (Eds.)

PSE PRESS

# A Decomposition Approach to Feasibility for Decentralized Operation of Multi-stage Processes

**Ekundayo Olorunshe[a], Nilay Shah[a], Benoît Chachuat[a] and Max Mowbray[a]***

[a] The Sargent Centre for Process Systems Engineering, Imperial College London, London, United Kingdom
* Corresponding Author: m.mowbray@imperial.ac.uk

## ABSTRACT

The definition of strategies for operation of process networks is a key research focus in process systems engineering. This challenge is commonly formulated as a numerical constraint satisfaction problem, where most practical algorithms are limited to identifying inner approximations to the feasible operational envelope. Sampling-based approaches so far have only been developed for formulations that required coordinated operation of the units within the network. We propose a decomposition approach that enables decentralized operation for acyclic muti-unit processes by sampling. Our methodology leverages problem structure to decompose unit-wise and deploys surrogate models to couple the resultant subproblems. We demonstrate it on a serial, batch chemical reactor network. In future research, we will extend this framework to consider the presence of uncertain unit parameters robustly.

**Keywords**: Process Operations, Machine Learning, Numerical Methods, Algorithms, Simulation

## INTRODUCTION

### Constraint Satisfaction and Process Operation

Significant interest within the process systems engineering community has been directed towards the numerical solution of constraint satisfaction problems (CSP) to define process operational strategies. This is underpinned by decision problems such as the feasibility and flexibility index, introduced in the early 1980s [1]. In pharmaceutical manufacturing, recent research has focused on design space characterization [2], as the multidimensional combination and interaction of input variables (e.g., material attributes) and process parameters that have been demonstrated to provide assurance of quality. The design space can be understood as the feasible space (FS) of operational parameters that ensure the process' defining constraints are satisfied.

Most research to date has focused on characterizing the FS within single-unit systems, with comparatively less attention to multi-unit systems [3]. However, manufacturing processes are inherently integrated, making it essential to investigate the interactions between unit operations. Typical approaches to identifying multi-unit FS are underpinned by mathematical programming and sampling [1,3]. The former approach is computationally efficient but has limitations in its application. For example, the problem formulation aims to identify a convex inner approximation to the FS – itself generally nonconvex - and defines a multilevel program. Therefore, identifying global optima is a challenge and significantly conservative solutions can be returned. Instead sampling approaches may aim to build a discrete set of operational parameter values that provide an inner approximation to the FS. Given they rely only on model evaluations they are an approach particularly suited to characterizing nonconvex FS [2].

In the context of multi-unit systems, there are two strategies: centralized (CO) and decentralized (DO) operation. These paradigms govern how decisions are made and how constraints are managed across interconnected units within a network. Effective management of such systems requires careful consideration of these strategies, as each offers distinct advantages and trade-offs. CO treats the system monolithically, with decisions made by a single entity that has complete visibility of the entire network. This approach enables the best coordination across units. For example, a CO can adjust upstream and downstream parameters jointly to meet constraints, ensuring that the system operates cohesively. However, it often requires complex communication

systems and can face bottlenecks when dealing with high-dimensional problems [5]. DO divides the system into smaller, autonomous units that make decisions locally. Each unit operates within its defined FS, independently of upstream or downstream units. This implies the decentralized FS is a subset of the centralized one. This approach reduces the need for communication and enables robust operations, particularly in distributed systems where central coordination is impractical. This autonomy enhances fault tolerance and scalability [5]. However, DO requires local FS to account for all possible interactions between adjacent units, which may lead to significantly reduced flexibility.

## Contributions

Two major challenges exist in the identification of decentralized multi-unit FS through sampling. The first is the system dimensionality. Applying the logic of the curse of dimensionality, as the size of the process network grows, the volume of the search space increases exponentially, which can imply a dramatic increase in computational expense. In this research, a decomposition strategy is proposed that formulates a series of unit-wise problems, solved incrementally via sampling. In doing so, the approach exploits network structure, retaining the advantages of sampling solutions and mitigating the curse of dimensionality. The second challenge is ensuring that the solution returned provides an FS of maximum volume. In the discussion below, we outline a methodology that leverages this network structure to enhance sampling efficiency for identification of a solution set of maximum volume. The key contributions include:

1. Developing a class of CSPs built upon a directed acyclic graph (DAG) structure representative of the process network to define a DO strategy.
2. Introducing constraint propagation methods that work relative to a precedence order defined by the DAG structure of the CSP.
3. Applying sampling-based solvers for constraint propagation to identify decentralized FS for multi-unit systems.
4. Formulation of a log marginal likelihood maximisation to optimize the volume of FS solution returned.

The paper is organised as follows. Section 2 introduces the methodology, then Section 3 provides details of case study and results, and conclusions are provided in Section 4. Note that details of sampling approaches to solve relevant CSP are omitted for conciseness. For discussion the reader is directed to [2].

# METHODOLOGY

## Problem Statement

The problem setup assumes a network of interconnected unit operations. This can be represented on a DAG, $\mathcal{G} \coloneqq (\mathcal{N}, \mathcal{E})$, where $\mathcal{N}$ is the set of units, denoted as $\mathcal{N} \coloneqq \{1, \dots, N\}$, and $\mathcal{E}$ represents the edges, which denote the order of connection between units, with $(i, j) \in \mathcal{E}$ indicating a connection from unit $i$ to unit $j$. The connectivity of the graph may also be expressed using an asymmetric adjacency matrix $A \in \{0,1\}^{N \times N}$, where $A_{i,j} = 1$ indicates a directed flow between unit $i$ and unit $j$. The following data and restrictions are assumed for simplicity of presentation:

- A set of upstream units, $\mathcal{N}_i^{in} \subset \mathcal{N}$, with $card(\mathcal{N}_i^{in}) \leq 1$, which provide feed streams to unit $i \in \mathcal{N}$ .
- A set of downstream units, $\mathcal{N}_i^{out} \subset \mathcal{N}$, with $card(\mathcal{N}_i^{out}) \leq 1$, which receive product streams from unit $i \in \mathcal{N}$.
- The attributes, $\boldsymbol{u}_i^j \in \mathbb{R}^{n_{u_{ij}}}$, of any feed stream connected to unit $i$ from upstream unit $j \in \mathcal{N}_i^{in}$.
- The attributes, $\boldsymbol{y}_i^k \in \mathbb{R}^{n_{y_{ik}}}$, of any product stream from unit $i$ connected to downstream unit $k \in \mathcal{N}_i^{out}$.
- The properties of the product streams of unit $i$ defined as,

$$\boldsymbol{y}_i^k = \boldsymbol{F}_i^k\,(\boldsymbol{v}_i, \boldsymbol{u}_i), \tag{1}$$

where $\boldsymbol{v}_i \in \mathbb{R}^{n_{v_i}}$ are process parameters local to unit $i$, and $\boldsymbol{u}_i \coloneqq \left(\boldsymbol{u}_i^j\right)_{j \in \mathcal{N}_i^{in}} \in \mathbb{R}^{n_{u_i}}$ denotes the concatenation of all inlet stream properties to unit $i$.

- The connection between the stream properties at the outlet of unit $i$ and those at the inlet of the downstream unit $k \in \mathcal{N}_i^{out}$, related by,

$$\boldsymbol{u}_k^i = \mathbf{C}_k^i(\boldsymbol{y}_k^i)\,. \tag{2}$$

- The inequality constraint functions imposed on each unit in the process train, expressed,

$$\mathbf{G}_i(\boldsymbol{v}_i, \boldsymbol{u}_i) \coloneqq \boldsymbol{g}_i(\boldsymbol{v}_i, \boldsymbol{u}_i, \boldsymbol{y}_i) \preccurlyeq \mathbf{0}. \tag{3}$$

Using the data associated with the setup, the centralized problem formulation is defined [3],

$$\mathbb{V}_{\mathrm{CO}} \coloneqq \left\{ \boldsymbol{v} \in \mathcal{K}_v \;\middle|\; \begin{array}{c} \forall i \in \mathcal{N}, \exists\, (\boldsymbol{u}_i, \boldsymbol{y}_i) \in \mathbb{R}^{n_{u_i}} \times \mathbb{R}^{n_{y_i}} : \\ \mathbf{0} \succcurlyeq \mathbf{G}_i(\boldsymbol{v}_i, \boldsymbol{u}_i) \\ \boldsymbol{y}_i^k = \mathbf{F}_i^k(\boldsymbol{v}_i, \boldsymbol{u}_i), \forall k \in \mathcal{N}_i^{out} \\ \boldsymbol{u}_k^i = \mathbf{C}_k^i(\boldsymbol{y}_k^i), \forall k \in \mathcal{N}_i^{out} \end{array} \right\}, \tag{4}$$

with $\mathcal{K}_v \coloneqq \prod_{\mathrm{i} \in \mathcal{N}} \mathcal{K}_{v_i} \subset \mathbb{R}^{n_v}$ denoting a compact set defined through prior knowledge. In [3], a solution approach is provided by approximately solving unit-wise subproblems,

$$\mathbb{VU}_{i,CO} := \left\{ (\boldsymbol{v}_i, \boldsymbol{u}_i) \in \mathcal{K}_{vu_i} \;\middle|\; \begin{array}{c} \mathbf{0} \succcurlyeq \mathbf{G}_i(\boldsymbol{v}_i, \boldsymbol{u}_i) \\ \forall k \in \mathcal{N}_i^{out}, \exists (\boldsymbol{v}_k, \boldsymbol{u}_k) \in \mathbb{VU}_{k,CO}: \\ \boldsymbol{u}_k^i = \mathbf{C}_k^i \left( \mathbf{F}_i^k (\boldsymbol{v}_i, \boldsymbol{u}_i) \right) \\ \forall j \in \mathcal{N}_i^{in}, \exists (\boldsymbol{v}_j, \boldsymbol{u}_j) \in \mathbb{VU}_{j,CO}: \\ \boldsymbol{u}_i^j = \mathbf{C}_i^j \left( \mathbf{F}_j^i (\boldsymbol{v}_j, \boldsymbol{u}_j) \right) \end{array} \right\}. \quad (5)$$

An exact solution to these subproblems ensures that the unit-wise parameters, $(\boldsymbol{v}_i, \boldsymbol{u}_i)$, i) satisfy constraints defined on the unit, ii) produce output stream properties that in turn provide feasible input stream properties to downstream units $k \in \mathcal{N}_i^{out}$, and iii) all input variables $\boldsymbol{u}_i$ are produced as a result of feasible operation of upstream units $j \in \mathcal{N}_i^{in}$.

The decentralized FS is a subset, $\mathbb{V}_{DO} \subseteq \mathbb{V}_{CO}$, of the centralized. A decentralized unit-wise subproblem may also be defined,

$$\mathbb{VU}_{i,DO} := \left\{ (\boldsymbol{v}_i, \boldsymbol{u}_i) \in \mathcal{K}_{vu_i} \;\middle|\; \begin{array}{c} \mathbf{0} \succcurlyeq \mathbf{G}_i(\boldsymbol{v}_i, \boldsymbol{u}_i) \\ \forall k \in \mathcal{N}_i^{out}, \exists (\boldsymbol{v}_k, \boldsymbol{u}_k) \in \mathbb{VU}_{k,DO}: \\ \boldsymbol{u}_k^i = \mathbf{C}_k^i \left( \mathbf{F}_i^k (\boldsymbol{v}_i, \boldsymbol{u}_i) \right) \\ \forall j \in \mathcal{N}_i^{in}, \forall (\boldsymbol{v}_j, \boldsymbol{u}_j) \in \mathbb{VU}_{j,DO}: \\ \boldsymbol{u}_i^j = \mathbf{C}_i^j \left( \mathbf{F}_j^i (\boldsymbol{v}_j, \boldsymbol{u}_j) \right) \end{array} \right\}. \quad (6)$$

This subproblem (6) differs subtly from (5) and ensures that the unit-wise parameter values $\boldsymbol{v}_i$, i) satisfy constraints defined on the unit, and ii) produce output stream properties that in turn provide feasible input stream properties to downstream units $k \in \mathcal{N}_i^{out}$ for all input variables values $\boldsymbol{u}_i$ produced as a result of feasible operation of upstream units $j \in \mathcal{N}_i^{in}$. Solving these unit-wise subproblems and taking the Cartesian product, $\mathbb{V}_{DO} := \prod_{i \in \mathcal{N}} \mathbb{V}_{i,DO}$ of the projection of the sets, $\mathbb{VU}_{i,DO}$ onto the subspace of unit-wise process parameters, $\mathbb{V}_{i,DO}$, yields the decentralized FS.

In practice, solving (6) is challenged as solution to any given unit requires knowledge of the solution to all other unit subproblems, i.e. one must already know a solution $\mathbb{V}_{DO}$. In the following, a sampling-based graph decomposition methodology is proposed that aims to identify a solution that maximizes a measure of the volume of $\mathbb{V}_{DO}$ with a minimum number of model evaluations.

## A Decomposition Approach

In this section, a sampling-based solution algorithm that acts with respect to a precedence ordering defined on the graph, $\mathcal{G}$, is presented. The algorithm provides incremental solution of unit-wise subproblems $i \in \mathcal{N}$, which provide approximations to,

$$\mathbb{V}_{i,DO} := \left\{ \boldsymbol{v}_i \in \boldsymbol{\mathcal{K}}_{v_i} \;\middle|\; \forall k \in \mathcal{N} \backslash \{i\}, \exists \boldsymbol{v}_k \in \mathcal{K}_{v_k}: (\boldsymbol{v}_j)_{j \in \mathcal{N}} \in \mathbb{V}_{DO} \right\},$$

where $\mathbb{V}_{DO} := \prod_{i \in \mathcal{N}} \mathbb{V}_{i,DO}$. Our main hypothesis is that a) solving this sequence of subproblems is more sample efficient than solving the problem directly, b) that doing so enables tuning of the solution set identified, and c) the solution yielded may be less conservative than other approaches by inheriting the advantages of sampling.

## Subproblem relaxations and propagations

In the following, two subproblem relaxations are presented that represent two separate steps of the methodology. The first is referred to as the backward propagation; and the second, the forward propagation. They are applied sequentially to approximate (6).

The backward propagation has previously been presented in [3], and so its presentation is brief. The subproblem relaxation deletes constraints enforcing feasible operation upstream,

$$\mathbb{VU}_{i,DO}^{(\mathrm{b})} := \left\{ (\boldsymbol{v}_i, \boldsymbol{u}_i) \in \mathcal{K}_{vu_i}^{(\mathrm{b})} \;\middle|\; \begin{array}{c} \mathbf{0} \succcurlyeq \mathbf{G}_i(\boldsymbol{v}_i, \boldsymbol{u}_i) \\ \forall k \in \mathcal{N}_i^{out}, \exists (\boldsymbol{v}_k, \boldsymbol{u}_k) \in \mathbb{VU}_{k,DO}^{(\mathrm{b})}: \\ \boldsymbol{u}_k^i = \mathbf{C}_k^i \left( \mathbf{F}_i^k (\boldsymbol{v}_i, \boldsymbol{u}_i) \right) \end{array} \right\} \quad (7)$$

with constraints only considering operational viability of the unit and those downstream. The search space $\mathcal{K}_{vu_i}^{(\mathrm{b})} := \mathcal{K}_{v_i} \times \mathcal{K}_{u_i}^{(b)}$ is estimated via an initialization procedure presented later in this paper. As discussed in [3], the relaxation admits an initial leaf unit problem that may be solved, given $\mathcal{N}_i^{out} = \emptyset$. As a result, the solution is according to the reverse of the precedence ordering. In principle the cartesian product set, $\mathbb{V}_{DO}^{(b)} = \prod_{i \in \mathcal{N}} \mathbb{V}_{i,DO}^{(b)}$ could be used as a search space reduction for identification of (4) as discussed in [3].

Utilizing the intermediate results in estimation of $\mathbb{VU}_{i,DO}^{(b)}$, the forward propagation is defined,

$$\mathbb{VU}_{i,DO}^{(\mathrm{f})} := \left\{ (\boldsymbol{v}_i, \boldsymbol{u}_i) \in \mathbb{VU}_{i,DO}^{(\mathrm{b})} \;\middle|\; \begin{array}{c} \mathbf{0} \succcurlyeq \mathbf{G}_i(\boldsymbol{v}_i, \boldsymbol{u}_i) \\ \forall k \in \mathcal{N}_i^{out}, \exists (\boldsymbol{v}_k, \boldsymbol{u}_k) \in \mathbb{VU}_{k,DO}^{(\mathrm{b})}: \\ \boldsymbol{u}_k^i = \mathbf{C}_k^i \left( \mathbf{F}_i^k (\boldsymbol{v}_i, \boldsymbol{u}_i) \right) \\ \forall j \in \mathcal{N}_i^{in}, \forall (\boldsymbol{v}_j, \boldsymbol{u}_j) \in \mathbb{VU}_{j,DO}^{(\mathrm{f})}: \\ \boldsymbol{u}_i^j = \mathbf{C}_i^j \left( \mathbf{F}_j^i (\boldsymbol{v}_j, \boldsymbol{u}_j) \right) \end{array} \right\}. \quad (8)$$

In addition to the properties of (7), (8) enforces that the selection of $\boldsymbol{v}_i$ be feasible given any unit input stream property from feasible upstream operation $j \in \mathcal{N}_i^{in}$. In contrast to (7), however, these subproblems are solved according to the precedence ordering of $\mathcal{G}$ proceeding from the root node forward. A solution may then be identified as $\mathbb{V}_{DO} = \prod_{i \in \mathcal{N}} \mathbb{V}_{i,DO}^{(\mathrm{f})}$.

## Approximate solutions for general problems

Due to the general assumptions made in problem definition, identifying closed forms for these approximations is highly challenging. Instead, as in [3], adaptive sampling schemes are deployed to gain a discrete inner-approximation $\overline{\mathbb{VU}}_{i,DO}^{(d)} \subset \mathbb{VU}_{i,DO}^{(d)} \quad \forall\, d \in \{b, f\}$.

Parameterizations may then be identified to tackle (7) and (8).

## Parameterizing the extended feasible space

As in [3] binary classifiers, $\overline{\mathbf{G}}_i: \mathbb{R}^{n_{v_i}} \times \mathbb{R}^{n_{u_i}} \to \mathbb{R}$ are learned to parameterize $\mathbb{VU}_{i,DO}^{(d)}$, as follows,

$$\mathbb{VU}_{i,DO}^{(\mathrm{d})} \approx \left\{(\boldsymbol{v}_i, \boldsymbol{u}_i) \in \mathcal{K}_{vu_i}^{(\mathrm{d})} \middle| 0 \geq \overline{\mathbf{G}}_i^{(\mathrm{d})}(\boldsymbol{v}_i, \boldsymbol{u}_i)\right\},$$

using training data generated in sampling the solution, $\overline{\mathbb{VU}}_{i,DO}^{(d)}$. Having detailed means to approximate the relaxations, discussion moves to outline a three-step solution methodology based on defining subproblems amenable to sampling solutions.

## Step 0: Initialization of the unit-wise search spaces

First, estimate of $\mathcal{K}_{u_i}^{(b)}\ \forall i \in \mathcal{N}$ is gained through a box-outer approximation to data generated from a sampling-based initialization procedure. The data is generated by forward simulation of the process network under parameter values, $\boldsymbol{v}$, sampled from $\mathcal{K}_v$ according to a Latin hypercube design.

## Step 1: Backward Propagation

Then, as in [3], approximation is made to (7). The existence conditions in (7) are recast as auxiliary optimization problems,

$$\mathbb{VU}_{i,DO}^{(\mathrm{b})} \approx \left\{(\boldsymbol{v}_i, \boldsymbol{u}_i) \in \mathcal{K}_{vu_i}^{(\mathrm{b})} \middle| \begin{array}{c} \mathbf{0} \succcurlyeq \mathbf{G}_i(\boldsymbol{v}_i, \boldsymbol{u}_i) \\ \forall k \in \mathcal{N}_i^{out}:\ 0 \geq \min\limits_{\boldsymbol{v}_k, \boldsymbol{u}_k} \overline{\mathbf{G}}_k^{(\mathrm{b})}(\boldsymbol{v}_k, \boldsymbol{u}_k) \\ s.t.\ \boldsymbol{u}_i^i = \mathbf{C}_k^i\left(\mathbf{F}_i^k(\boldsymbol{v}_i, \boldsymbol{u}_i)\right) \end{array}\right\}.$$

The solution set is sampled, $\overline{\mathbb{VU}}_{i,DO}^{(b)} \subset \mathbb{VU}_{i,DO}^{(b)}$, through evaluation of the process model and constraints $\mathbf{G}_i(\cdot)$ and solution of a box-constrained nonlinear program (NLP). It is worth noting that the equality constraint is reduced into the objective, as $\boldsymbol{u}_k^i$ is provided through evaluation of the process model; additionally, the surrogate constraints $\overline{\mathbf{G}}_k^{(\mathrm{b})}(\cdot)$ are available from the solution of units $k \in \mathcal{N}_i^{out}$.

## Step 2: Forward Propagation

With the approximation to (7) completed, approximation to (8) is then made. The robustness conditions in (8) are recast as auxiliary optimization problems. Conveniently evaluation of the existence conditions and constraints in (8) is avoided via the approximation. This removes the requirement for further process model evaluations, and instead only relies on the solution to general NLP defined on surrogates,

$$\mathbb{VU}_{i,DO}^{(\mathrm{f})} \approx \left\{(\boldsymbol{v}_i, \boldsymbol{u}_i) \in \mathbb{VU}_{i,DO}^{(\mathrm{b})} \middle| \begin{array}{c} \left.\begin{array}{c} 0 \geq \max\limits_{(\boldsymbol{v}_j, \boldsymbol{u}_j) \in \mathbb{VU}_{j,DO}^{(\mathrm{f})}} \overline{\mathbf{G}}_i^{(\mathrm{b})}(\boldsymbol{v}_i, \boldsymbol{u}_i) \\ s.t.\ \boldsymbol{u}_i^j = \overline{\boldsymbol{F}}_{j\to i}\left(\boldsymbol{v}_j, \boldsymbol{u}_j\right), \forall j \in \mathcal{N}_i^{in} \end{array}\right\}(i) \\ \left.\begin{array}{c} \forall j \in \mathcal{N}_i^{in}: \quad 0 \geq \min\limits_{(\boldsymbol{v}_j, \boldsymbol{u}_j) \in \mathbb{VU}_{j,DO}^{(\mathrm{b})}} \overline{\mathbf{G}}_j^{(\mathrm{b})}\left(\boldsymbol{v}_j, \boldsymbol{u}_j\right) \\ s.t.\ \boldsymbol{u}_i^j = \overline{\boldsymbol{F}}_{j\to i}\left(\boldsymbol{v}_j, \boldsymbol{u}_j\right) \end{array}\right\}(ii) \end{array}\right\}$$

where $\overline{\boldsymbol{F}}_{j\to i}(\cdot) \approx \boldsymbol{C}_i^j\left(\mathbf{F}_j^i(\cdot)\right)$ is an ML regressor identified in the backward propagation. Within the formulation above, (i) enforces conditions on $\boldsymbol{v}_i \in \mathbb{V}_{i,DO}^{(\mathrm{f})}$ with (ii) enforcing restrictions on $\boldsymbol{u}_i \in \mathbb{U}_{i,DO}^{(\mathrm{f})}$, such that $\mathbb{VU}_{i,DO}^{(\mathrm{f})} = \mathbb{V}_{i,DO}^{(\mathrm{f})} \times \mathbb{U}_{i,DO}^{(\mathrm{f})}$. Specifically, (i) ensures that the selection of $\boldsymbol{v}_i$ satsfies constraints defined on the unit, and that outlet stream properties ensure feasibility downstream, no matter the operation of units upstream; whereas (ii) enables identification of the set of unit input stream properties arising from feasible operation upstream, identification of which is required for the purpose of decomposition. It is worth noting that the root node problems have no upstream units and so are only constituted by a modified variant of (i),

$$\mathbb{VU}_{i,DO}^{(\mathrm{f})} \approx \left\{(\boldsymbol{v}_i, \boldsymbol{u}_i) \in \mathbb{VU}_{i,DO}^{(\mathrm{b})} \middle| 0 \geq \overline{\mathbf{G}}_i^{(\mathrm{b})}(\boldsymbol{v}_i, \boldsymbol{u}_i)\ \right\} \quad \forall i \in \mathcal{N}^r$$

with $\mathcal{N}^r = \left\{ i \in \mathcal{N} \mid \mathcal{N}_i^{in} = \emptyset \right\}$. As before solution sets are sampled $\overline{\mathbb{VU}}_{i,DO}^{(f)} \subset \mathbb{VU}_{i,DO}^{(f)}$, and a solution returned as $\mathbb{V}_{DO} \approx \prod_{i\in\mathcal{N}} \overline{\mathbb{V}}_{i,DO}^{(f)}$.

## Tuning step 2: A classifier backoff strategy

In most cases, multiple solution sets, $\mathbb{V}_{DO}$, exist, corresponding to different allocations of operational flexibility to each unit. Solving step 2 as defined provides greater operational flexibility to upstream units. To balance operational flexibility, we introduce tuning parameters, $\boldsymbol{\epsilon} \in \mathbb{R}_+^N$, in the forward propagation – one for each unit,

$$\mathbb{VU}_{i,DO}^{(\mathrm{f})}(\boldsymbol{\epsilon}) \approx \left\{(\boldsymbol{v}_i, \boldsymbol{u}_i) \in \mathbb{VU}_{i,DO}^{(\mathrm{b})} \middle| \begin{array}{c} 0 \geq \max\limits_{(\boldsymbol{v}_j, \boldsymbol{u}_j) \in \mathbb{VU}_{j,DO}^{(\mathrm{f})}(\boldsymbol{\epsilon})} \overline{\mathbf{G}}_i^{(\mathrm{b})}(\boldsymbol{v}_i, \boldsymbol{u}_i) + \epsilon_i \\ s.t.\ \boldsymbol{u}_i^j = \overline{\boldsymbol{F}}_{j\to i}\left(\boldsymbol{v}_j, \boldsymbol{u}_j\right), \forall j \in \mathcal{N}_i^{in} \\ \forall j \in \mathcal{N}_i^{in}: \quad 0 \geq \min\limits_{(\boldsymbol{v}_j, \boldsymbol{u}_j) \in \mathbb{VU}_{j,DO}^{(\mathrm{b})}} \overline{\mathbf{G}}_j^{(\mathrm{b})}\left(\boldsymbol{v}_j, \boldsymbol{u}_j\right) + \epsilon_j \\ s.t.\ \boldsymbol{u}_i^j = \overline{\boldsymbol{F}}_{j\to i}\left(\boldsymbol{v}_j, \boldsymbol{u}_j\right) \end{array}\right\},$$

with root node unit problems adjusted appropriately. This implies the solution set is dependent on the parameters, $\mathbb{V}_{DO}(\boldsymbol{\epsilon})$. In the following, we utilize an adaptive sampling scheme, namely nested sampling as in [2] to provide a discrete inner approximation $\overline{\mathbb{VU}}_{i,DO}^{(\mathrm{f})}(\boldsymbol{\epsilon}) \subset \mathbb{VU}_{i,DO}^{(\mathrm{f})}(\boldsymbol{\epsilon})$. Nested sampling was initially proposed to estimate the marginal likelihood in Bayesian estimation problems. In the context of feasibility, the marginal likelihood has an interpretation as a measure of the volume of a set. Here,

we exploit this as means of defining an objective for tuning the backoffs,

$$\min_{\boldsymbol{\epsilon}} -\sum_{i\in\mathcal{N}} \log Z_i(\boldsymbol{\epsilon}) \tag{9}$$

where $Z_i(\boldsymbol{\epsilon}) = \int_{(\boldsymbol{v},\boldsymbol{u})\in K_{vu_i}} l_i\,(\boldsymbol{v}_i,\boldsymbol{u}_i,\boldsymbol{\epsilon}) p(\boldsymbol{v}_i,\boldsymbol{u}_i) d(\boldsymbol{v}_i,\boldsymbol{u}_i)$ is the marginal likelihood associated with the solution to the unit $i$ subproblem, $\mathbb{VU}_{i,DO}^{(\mathrm{f})}(\boldsymbol{\epsilon})$. In implementation, $l_i\colon \mathcal{K}_{vu_i} \times \mathbb{R}_+^{\mathrm{N}} \to \mathbb{R}$ is a continuous, non-negative monotonic approximation to the indicator function which assesses set-membership. Here $l_i(\boldsymbol{v}_i,\boldsymbol{u}_i,\boldsymbol{\epsilon}) = \prod_{l\in\{i\}\cup\mathcal{N}_i^{in}} l_{i,l}\,(\boldsymbol{v}_i,\boldsymbol{u}_i,\epsilon_l)$,

$$l_{i,l}(\boldsymbol{v}_i,\boldsymbol{u}_i,\epsilon_l) = \begin{cases} sigmoid(0) & \boldsymbol{if}\ z_{i,l}^*(\boldsymbol{v}_i,\boldsymbol{u}_i,\epsilon_l) \le 0 \\ sigmoid\left(-z_{i,l}^*(\boldsymbol{v}_i,\boldsymbol{u}_i,\epsilon_l)\right) & \boldsymbol{otherwise} \end{cases}$$

with $sigmoid(\cdot)$ indicating the univariate, scalar sigmoid function, and $z_{i,l}^*(\boldsymbol{v}_i,\boldsymbol{u}_i,\epsilon_l)$ indicating the optimal objective value of the $l^{th}$ auxiliary optimization problem, or the tightened constraint value in the case of the root-node, in the approximate forward propagation, $\mathbb{VU}_{i,DO}^{(\mathrm{f})}(\boldsymbol{\epsilon})$. Given the use of $l_i(\cdot)$ and assessment of the unit-wise subproblems, $\mathbb{VU}_{i,DO}^{(f)}(\boldsymbol{\epsilon})$, rather than the indicator function itself and the unit-wise projections, $\mathbb{V}_{i,DO}^{(f)}(\boldsymbol{\epsilon})$, this yields an approximation to a measure of the FS.

# CASE STUDY

## Problem formulation

We demonstrate the decomposition approach on a batch chemical reactor network that consists of two batch reactors connected in series. The reaction mechanism characterizing the reactors is the same, and is that described in [3],

$$2A \to^{k_1} B \to^{k_2} C$$

where component B is the desired product. The reactor dynamics are ODEs that describe the evolution of component molar concentrations in continuous time. The system adheres to Arrhenius kinetics, with $k_r(T)$, indicating the temperature $(T)$ dependent rate constant of reaction step $r \in \{1,2\}$. For the definition of these Arrhenius kinetics please refer to the Digital Supplementary. The volume of both reactors is assumed $V = 1$ m$^3$. Each ODE system is given by,

$$\begin{aligned} \dot{c}_{A,j}(t) &= -2k_1(T_j)c_{A,j}(t)^2 \\ \dot{c}_{B,j}(t) &= \mathrm{k_1(T_j)c_{A,j}(t)^2} - \mathrm{k_2(T_j)c_{B,j}(t)} \\ \dot{c}_{C,j}(t) &= \mathrm{k_2(T_j)c_{B,j}(t)} \end{aligned}$$

where $c_{i,j}(t)$ $(kmol\,m^{-3})$ describes the molar concentration of component $i$ in reactor $j$; and $T_j$, the temperature in reactor $j$. Each reactor is operated over a time horizon, $t \in [0,\ \tau_j\ ]$, where $\tau_j$ is the batch time. The initial concentration of the first reactor is fixed, whereas the initial concentration of the second reactor is the first reactor's composition at the end of operation, subject to separation of C, as presented in [3]. This separation is considered perfect and, therefore, is excluded from the FS identification. The critical operational parameters in the characterization are the temperature and batch time of both reactors, such that $\boldsymbol{v_j} = [T_j, \tau_j]^T$. Inequality constraints are imposed to ensure the molar impurity of component C at the end of the first operation and on that of component B at the end of operating the second batch reactor:

$$\frac{c_{C,1}(\tau_2)}{c_{A,1}(\tau_2) + c_{B,1}(\tau_2) + c_{C,1}(\tau_2)} \le b_1$$

$$\frac{c_{B,2}(\tau_2)}{c_{A,2}(\tau_2) + c_{B,2}(\tau_2) + c_{C,2}(\tau_2)} \ge b_2$$

with $b_1 = 0.15$ and $b_2 = 0.74$. The search spaces $\mathcal{K}_{v_1}$ and $\mathcal{K}_{v_2}$ are defined such that $\tau_j \in [250,800]$ (min) and $T_j \in [250,1000]$ (K).

## Implementation Details

Full implementation details together with a description of the algorithm are available within Digital Supplementary. The Nested Sampling algorithm was utilised to solve each unit level problem using the DEUS package [2]. Each unit level problem was considered solved when $card\left(\overline{\mathbb{VU}}_i^{(d)}\right) = 2000$. Due to the nature of sampling algorithms a high degree of parallelisation was leveraged.

Initialization and then backward propagation steps were first applied, and neural network SoftMax binary classifiers and regressors with tanh activations were trained to high validation accuracy in solution to the unit level problems using the FLAX python package. Solution to the box-constrained NLP was provided by the L-BFGS-B implementation in OPTAX. The tuning problem (9) was then solved using a Bayesian optimization strategy. This consists of iteratively solving forward propagations using different values of $\boldsymbol{\epsilon}$. The decision bounds, $\boldsymbol{\epsilon} \in [0,0.5]^2$, were identified from knowledge of the range of the SoftMax binary classifier. An initial dataset was identified through a Latin hypercube space filling design on $\boldsymbol{\epsilon} \in [0,0.5]^2$ for 3 backoff values. In the forward propagations, the general NLP problems that couple the units were solved using IPOPT and formulated in CasADI. The ML surrogates were embedded using the CasADI callback feature, allowing JAX automatic differentiation routines to pass necessary Jacobian information. A Gaussian process model was built, exploited, and retrained to optimize (8) using the expected improvement acquisition function and a budget of 7 additional samples to the initial dataset.

## Results and Discussion

The results of the Bayesian optimization strategy to approximately solve (9) is shown in Fig. 1. Specifically, Fig. 1 shows the improvement in objective per evaluation

of the forward propagation. The figure shows that in general the objective is improved in each iteration highlighting the approach's utility in expanding the flexibility or volume of the decentralized FS.

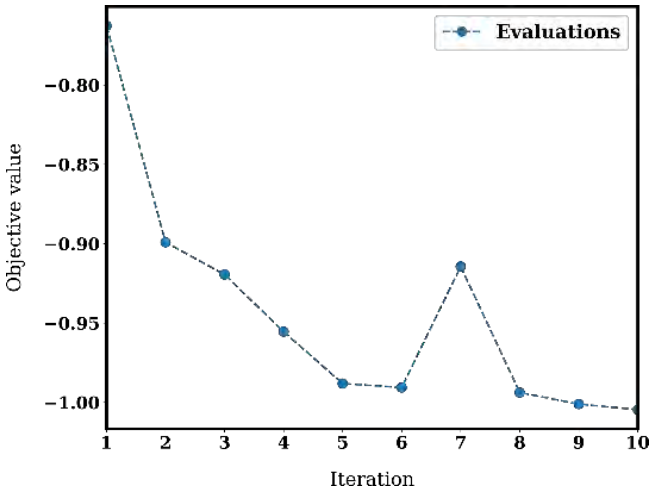



**Figure 1:** Tuning progress of the decentralized FS through Bayesian optimization.

The decentralized FS with largest volume from the optimization was identified during the 10th sample. The unit-wise projections of the discrete set to approximate (8) are plotted in Fig. 2 in red scatter. Also plotted in Fig. 2 are samples used to initialize the search spaces for the backward propagation (grey) and the centralized FS (blue). The latter was identified using the direct sampling method discussed in [3]. What is notable is that the decentralized FS is a proper subset of the centralized – yielding reduced flexibility. However, this is traded for a more robust operational strategy with lower capital overhead for implementation of control. The quality of the decentralized FS was verified by performing 10000 forward process network evaluations using operational parameters sampled from the approximation to $\mathbb{V}_{DO}$ – all of which yielded feasible operation. It should be emphasised that the approximation was identified using just 18092 evaluations of the unit models in total. Given the identified decentralized FS, $\overline{\mathbb{V}}_{DO} \subset \mathbb{V}_{DO}$, is constituted by $4 \times 10^6$ parameter settings this is a significant sample efficiency.

## CONCLUSION

In this research, a decomposition strategy has been presented to sample decentralized feasible spaces for multi-unit process networks. The methodology leverages DAG formulations of process networks, adaptive sampling and machine learning surrogates to define constraint propagation methods that return inner-approximations to the feasible space efficiently. The methodology was applied to a serial batch reactor network and demonstrated to be effective in identifying a subset of the centralized FS to enable decentralized operation. Future work will consider robust formulations to account for uncertain model parameters.

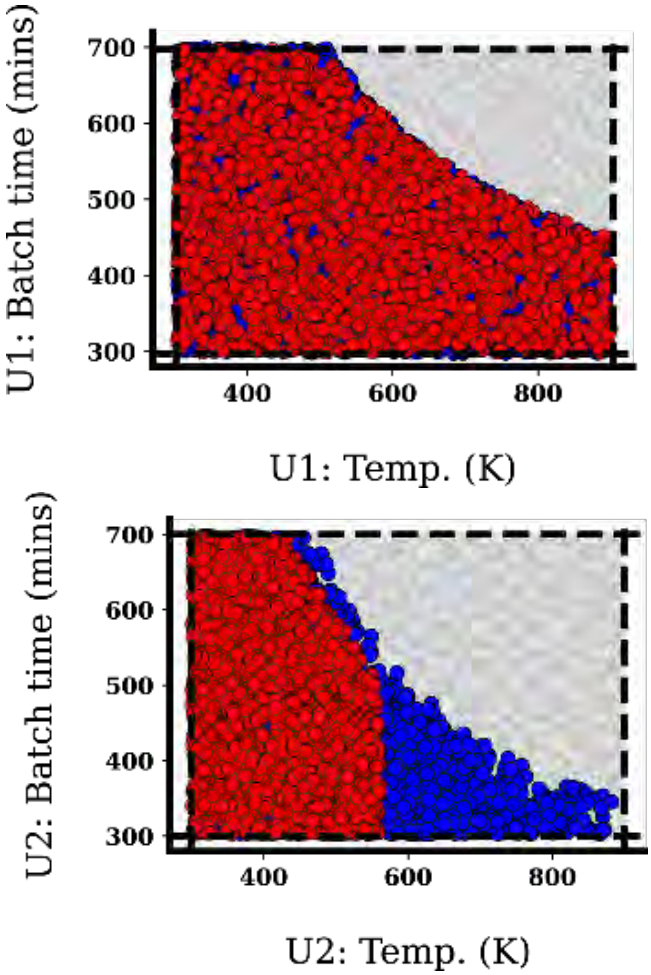



**Figure 2:** The optimized decentralized FS (red scatter), centralized FS projections (blue scatter), and samples used to initialise the search space (grey scatter).

## DIGITAL SUPPLEMENTARY MATERIAL

Digital supplementary is provided by a Python software package, **μF**, available at: https://github.com/maw-bray/mu.F. The DEUS package for solving numerical constraint satisfaction problems through Nested Sampling is available at https://github.com/omega-icl/deus.


## ACKNOWLEDGEMENTS

This work is co-funded by Eli Lilly & Company through the Pharmaceutical Systems Engineering Lab (PharmaSEL) and by the Engineering and Physical Sciences Research Council (EPSRC) as part of its Prosperity Partnership Programme under grant EP/T518207/1. EO would like to acknowledge the support of Petroleum Technology Development Fund (PTDF) under grant number PTDF/ED/OSS/MSC/EMO/5672.

## REFERENCES


1. Halemane, K. P. & Grossmann, I. E. (1983) Optimal process design under uncertainty. AIChE Journal. 29 (3), 425–433.
2. Kusumo, K. P., Gomoescu, L., Paulen, R., García Muñoz, S., Pantelides, C. C., Shah, N. & Chachuat, B. (2019) Bayesian approach to probabilistic design space characterization: A nested sampling strategy. Industrial & Engineering Chemistry Research. 59 (6), 2396–2408.
3. Mowbray, M., Kontoravdi, C., Shah, N., & Chachuat, B. (2024). A Decomposition Approach to Characterizing Feasibility in Acyclic Multi-Unit Processes. IFAC-PapersOnLine, 58(14), 216-221.
4. Harwood, S. M. & Barton, P. I. (2017) How to solve a design centering problem. *Mathematical Methods of Operations Research.* 86 215–254.
5. Samyudia, Y., Lee, P. L., Cameron, I. T., & Green, M. (1995). A new approach to decentralized control design. *Chemical Engineering Science*, *50*(11), 1695-1706.



© 2025 by the authors. Licensed to PSEcommunity.org and PSE Press. This is an open access article under the creative commons CC-BY-SA licensing terms. Credit must be given to creator and adaptations must be shared under the same terms. See https://creativecommons.org/licenses/by-sa/4.0/




Systems & Control Transactions

**Research Article - Peer Reviewed Conference Proceeding**
ESCAPE 35 - European Symposium on Computer Aided Process Engineering
Ghent, Belgium. 6-9 July 2025
Jan F.M. Van Impe, Grégoire Léonard, Satyajeet S. Bhonsale,
Monika E. Polańska, Filip Logist (Eds.)

PSE PRESS

# Simulation and Optimisation of Cryogenic Distillation and Isotopic Equilibrator Cascades for Hydrogen Isotope Separation Processes in the Fusion Fuel Cycle

**Emma A. Barrow[a], Iryna Bennett[b], Franjo Cecelja[a], Eduardo Garciadiego-Ortega[b], Megan Thompson[b], and Dimitrios Tsaoulidis[a*]**

[a] School of Chemistry and Chemical Engineering, University of Surrey, Guildford, Surrey, United Kingdom
[b] United Kingdom Atomic Energy Authority, Culham Science Centre, Abingdon, Oxfordshire, United Kingdom
* Corresponding Author: d.tsaoulidis@surrey.ac.uk

## ABSTRACT

Hydrogen isotope separation is a critical component of the fusion fuel cycle, particularly for achieving the desired purity levels of deuterium and tritium while minimising tritium inventory. This study investigates the cryogenic distillation of hydrogen isotopes, with a focus on the effects of isotopic equilibrium reactions at reduced temperatures and different system configurations. A one-column architecture was analysed to evaluate the impact of feed and side stream equilibrator temperatures and flowrates on separation performance and tritium inventory. Additionally, a two-column architecture was studied, incorporating multiple isotopic equilibrators in interconnecting streams, to further reduce unwanted heteronuclear isotopologues and improve system efficiency. Comparative analysis of the proposed configurations highlights significant operational advantages of optimising equilibrator temperatures, including reduced tritium contamination and inventory. Results indicate that reducing equilibrator temperatures to 77.4 K not only improves separation efficiency but also enables reductions in the number of theoretical stages required, minimising tritium inventory. A case study of the ITER Isotope Separation System demonstrates that reducing equilibrator temperatures achieves comparable performance with fewer stages in key columns, validating the benefits of optimised equilibrator operation for practical application. These findings contribute to the development of more efficient, cost-effective designs for fusion fuel cycle isotope separation systems.

**Keywords**: Aspen Plus, Modelling and Simulations, Optimization, Process Design, Nuclear, Fusion Fuel Cycle, Tritium Inventory Minimisation

## INTRODUCTION

Global distribution of deuterium-tritium (DT) fusion power has the potential to provide a limitless supply of low-carbon energy and be revolutionary towards tackling today's climate crisis. One of the key challenges in realising DT fusion power plant development lies in designing a fuel cycle capable of achieving "tritium self-sufficiency" [1]. This condition is met when the fuel cycle can continuously supply tritium to sustain the fusion reaction while producing a surplus for the start-up of subsequent power plants. Achieving this is crucial, given the extremely limited global supply of tritium [2].

A pivotal factor in ensuring tritium "self-sufficiency" is minimising tritium losses throughout the fuel cycle. This involves two key strategies, i.e., enhancing separation performance to reduce losses to the environment and minimising the tritium inventory to limit decay-related losses [1]. Among the various systems within a given fuel cycle architecture, the cryogenic distillation processes for hydrogen isotope separation have been identified as a major contributor to high tritium inventories [3]. Therefore, optimising these processes to reduce tritium inventory without compromising on its separation performance is a priority for the fusion community.

### Hydrogen Isotope Separation System

The hydrogen isotope separation system (ISS) within a fusion fuel cycle is tasked with separating a mixture of hydrogen isotopes into at least two distinct product streams; a tritium-rich stream and a protium-rich stream (examples shown in figures 1 and 2). The tritium-rich product typically comprises a 50/50 mixture of tritium and deuterium, with minimal protium impurities, and is recycled to fuel the fusion reaction. Meanwhile, the protium-rich stream is discharged from the fuel cycle, either directly or through additional detritiation processes. The protium-rich product must adhere to stringent tritium emission limits to ensure the plant's compliance with environmental safety regulations [2, 4].

### Cryogenic Distillation Column Cascades

Cryogenic distillation is a well-established process for hydrogen isotope separation, leveraging the slight differences in boiling points of the hydrogen isotopologues ($H_2$ = 20.39 K, HD = 22.13 K, HT = 22.92 K, $D_2$ = 23.67 K, DT = 24.38 K, and $T_2$ = 25.04 K) [5]. Unfortunately, the presence of the heteronuclear isotopologues - arising from the isotope equilibrium reactions (given in equations (1) to (3)) catalysed by metals, light, or beta particle from tritium decay – adds significant complexity to the design of the cryogenic distillation systems [6]. For instance, the isotopologue HT is more volatile than $D_2$, making it challenging to remove excess $D_2$ in the distillate without contaminating the protium-rich product with HT.

$$H_2 + D_2 \rightleftarrows 2HD \quad (1)$$

$$H_2 + T_2 \rightleftarrows 2HT \quad (2)$$

$$D_2 + T_2 \rightleftarrows 2DT \quad (3)$$

### Isotopic Equilibrator Reactors

To address the issue of tritium contamination within HT in the protium-rich top product, isotopic equilibrator reactors are commonly integrated into the cryogenic distillation column cascades to remove the undesired heteronuclear isotopes from the system. The literature suggests various placements for isotopic equilibrators, including feed streams, column interconnections, and/or side streams [2, 4, 7]. However, there is very limited information on their optimal integration and operation.

An initial experimental study on a $H_2$-HD-$D_2$ cryogenic distillation separation system demonstrated that side stream location and flowrate are critical for effective removal of the undesired isotopologue (HD). The side stream must be positioned where HD concentration exceeds equilibrium composition, with a flow rate that matches the rate of HD entering the column [8]. Subsequent operational insights, such as those from the DTE1 campaign at JET, suggested that equilibrators should target locations with excess deuterium to facilitate the removal of unwanted HT [9].

In terms of modelling attempts of the isotopic equilibrium reactions, across the literature these reactions are assumed to take place instantaneously under room temperature conditions [10, 11]. There is limited experimental data and no rate-based models for isotope equilibrium reactions.

Uda et al. [12] measured first-order reaction rates for HD, HT, and DT formation of $7.0 \times 10^{-2}$ $h^{-1}$, $5.4 \times 10^{-2}$ $h^{-1}$, and $4.6 \times 10^{-2}$ $h^{-1}$, respectively (catalysed by the beta decay of 30.5 kPa tritium). McConville et al. [13] reported significantly higher rates of DT formation in a 304 stainless steel mixing chamber, with $k \approx 0.03$ $min^{-1}$ (1.8 $h^{-1}$) at 295 K (30% $T_2$ at 0.4 bara). Increased rates were likely observed due to differing tritium concentrations or metal impurities catalysing the reaction. They found that reaction rates peaked around 195 K ($k \approx 0.6$ $min^{-1}$) and suggested reaction kinetics for temperatures as low as 150 K are comparable, if not improved, to the kinetics observed at 298 K.

Sherman et al. [14] experimentally demonstrated that side stream equilibrators effectively remove the heteronuclear isotopologues (HD) for improved product purity. Iraola et al. [10] replicated the setup of Sherman et al. [14] in Aspen HYSYS, validating the thermodynamic package developed by Noh et al. [11] and demonstrating that the equilibrators achieving equilibrium at 298 K across a precious metal catalyst is an appropriate assumption.

Despite these insights, limited data exists on reaction rates under varied conditions or in the presence of different catalysts, highlighting a critical gap in understanding the kinetics of isotopic equilibrium reactions. Furthermore, while early studies emphasized the importance of isotopic equilibrator positioning and flowrates, recent research and optimisation efforts in hydrogen isotope separation have largely neglected the importance of these reactors within the system [2, 5, 15, 16]. Their placement within cryogenic distillation column cascades is often mentioned with minimal justification, leaving significant room for improvement in system optimization.

This work aims to address these gaps by exploring the impact of equilibrator operating temperature on separation performance, and comparing equilibrators integrated into side streams with those positioned at column interconnections to determine the optimal operational strategy. Additionally, this study underscores the need for experimental investigations into isotopic equilibrator reaction kinetics to validate and refine the proposed designs. Ultimately, the goal is to enhance hydrogen isotope separation performance while minimising tritium inventory.

## METHODOLOGY

### Simulation of the Isotope Separation System

Commercially available simulation software is a useful tool for the design and optimisation of industrial processes. In the literature, Aspen Plus has been used to study the cryogenic distillation processes used for hydrogen isotope separation. Several studies have provided guidance on the thermodynamic packages and hydrogen isotope property parameters required for accurate system simulation [5, 6, 10, 11].

## Thermodynamics and Physical Property Data

The isotope separation process was modelled in Aspen Plus using a thermodynamic package adapted from the work of Noh et al. [11]. This package modifies the Peng-Robinson equation of state with the Twu alpha function (Equation 4) to address inaccuracies in vapour pressure predictions at cryogenic temperatures. The Twu alpha function redefines the standard alpha function by incorporating regression analysis of pure component vapour pressure data from Souers [6] to obtain the coefficients, *L*, *M*, and *N* (values given in Table 1).

$$\alpha(T) = {T_r}^{N(M-1)} \exp\left[L\left(1 - {T_r}^{NM}\right)\right] \quad (4)$$

To accommodate gaps within the Aspen Plus physical property database for heteronuclear and tritium containing isotopologues (HD, HT, DT, and $T_2$), a complete set of physical property data and Antoine coefficients for all isotopologues were redefined from the physical property inputs reported by Wang et al. [5].

**Table 1:** Coefficients L, M, and N of the Twu alpha function of the modified Peng-Robinson equation of state regressed from the vapour pressure data of Souers [6].

| | $H_2$ | HD | HT | $D_2$ | DT | $T_2$ |
|---|---|---|---|---|---|---|
| **L** | 1.715 | 2.103 | 1.956 | 1.704 | 1.930 | 2.339 |
| **M** | -1.031 | -0.613 | -0.593 | -0.692 | -0.517 | -0.389 |
| **N** | 0.3266 | 0.3563 | 0.2914 | 0.3003 | 0.3581 | 0.4741 |

## Process Flow and Design Parameters

The ISS was modelled using the RadFrac distillation column in Aspen Plus. This study investigates the impact of isotopic equilibrator temperature on the separation performance of one- and two-column configurations. Three equilibrator configurations were evaluated:

1. **Feed Stream Integration**: Equilibrators placed in the feed streams of the distillation columns (equilibrator 1 in figures 1 and 2).
2. **Side Stream Integration**: Equilibrators integrated into column side streams (equilibrator 2 in figure 1).
3. **Interconnection Integration**: Equilibrators positioned between two distillation columns (equilibrators 2 and 3 in figure 2).

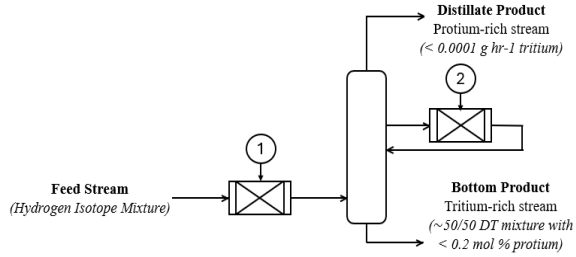



**Figure 1:** One-column configuration of a hydrogen ISS.

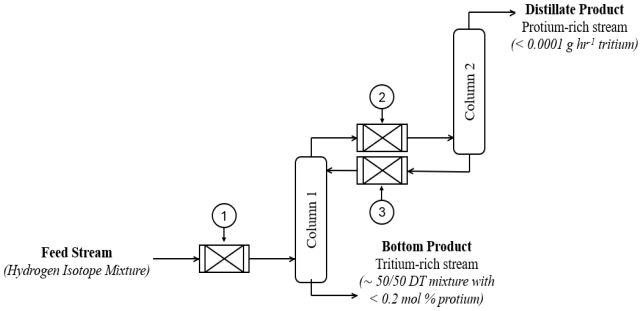



**Figure 2:** Two-column configuration of a hydrogen ISS.

The feed composition was maintained at 100 mol $h^{-1}$ with a molar ratio of H-D-T as 0.05:0.55:0.40. Design parameters for the one- and two-column configurations are summarised in tables 2 and 3, respectively. Feed location was adjusted proportional to changes in the number of stages within the column. Stage number is given by a top-to-bottom numbering scheme.

**Table 2:** Initial design parameters for the one-column configuration displayed in figure 1.

| Design Parameter | Value |
|---|---|
| Number of Stages | 50 |
| Feed Stage | 40 |
| HETP | 0.0667 m |
| Reflux Ratio | 35 |
| Boil-up Ratio | 11 |
| Column Diameter | 0.044 m |

**Table 3:** Initial design parameters for the two-column configuration displayed in figure 2.

| Design Parameter | Column 1 | Column 2 |
|---|---|---|
| Number of Stages | 45 | 45 |
| Feed Stage | 36 | 36 |
| HETP | 0.0667 m | 0.0667 m |
| Reflux Ratio | 1 | 20 |
| Boil-up Ratio | 15 | 1 |
| Column Diameter | 0.046 m | 0.042 m |

## Equilibrator Temperature Optimisation

Equilibrator temperatures ranging from 50 K to 298 K were investigated to assess their impact on separation performance and tritium inventory. The following cases were studied:

- **298 K (Base Case)**: Represents typical operational conditions.
- **150 K and 200 K**: Selected based on experimental data suggesting comparable or improved reaction kinetics relative to 298 K.
- **77.4 K**: Corresponds to liquid nitrogen temperature, offering a practical cooling source.
- **50 K**: Explores performance improvements at ultra-low temperatures.

For side-stream equilibrators, side stream flow rates up to 100 mol $h^{-1}$ were evaluated to determine optimal operating conditions.

### Modelling the Isotopic Equilibrator Reactions

The equilibrium constants for isotopic reactions, determined experimentally by Souers [6], are summarised in table 4. As observed, lower equilibrator temperatures favor the backward reaction, promoting homonuclear isotopologue formation while reducing unwanted heteronuclear species, such as HT. This behaviour is crucial for minimising contamination in the product stream. Regression analysis was performed to fit the constants A, B, C, and D in equation 5 (Table 5), enabling the calculation of the isotope equilibrium constants (Table 4) within ± 5 % accuracy across the 50-300 K temperature range.

$$\ln(K_{eq}) = A + \frac{B}{T} + C\ln(T) + DT \quad (5)$$

### Tritium Inventory Calculation

The tritium inventory calculation followed the methodology outlined by Wang et al. [5]. The temperature and hydrogen isotope composition data inputs were extracted from the Aspen Plus simulations and calculations performed using Excel.

Due to limited experimental data on the kinetics of the isotopic equilibrium reactions, the tritium inventory calculation cannot include the inventory contained within the reactors due to limited data availability for equipment sizing calculations. Hence, in this work the calculation method only accounts for tritium within the columns.

**Table 4:** Equilibrium constants ($K_{eq}$) for equations 1 to 3 [6].

| **Temperature *[K]*** | $H_2 + D_2 \rightleftarrows 2HD$ | $H_2 + T_2 \rightleftarrows 2HT$ | $D_2 + T_2 \rightleftarrows 2DT$ |
|---|---|---|---|
| 0 | 0 | 0 | 0 |
| 50 | 1.41 | 0.33 | 2.57 |
| 77.4 | 1.94 | 0.64 | 3.06 |
| 150* | 2.70 | 1.57 | 3.54 |
| 200 | 2.98 | 1.94 | 3.69 |
| 298* | 3.25 | 2.56 | 3.82 |

**Values obtained through interpolation.*

**Table 5:** Regressed constants for modelling the isotopic equilibrium reactions using equation (5).

| | $H_2 + D_2 \rightleftarrows 2HD$ | $H_2 + T_2 \rightleftarrows 2HT$ | $D_2 + T_2 \rightleftarrows 2DT$ |
|---|---|---|---|
| **A** | 4.761 | 7.049 | -0.3239 |
| **B** | -95.11 | -196.0 | -3.139 |
| **C** | -0.6997 | -1.186 | 0.3534 |
| **D** | 0.002431 | 0.004393 | -0.001136 |

## RESULTS AND DISCUSSION

### One-Column Architecture

#### Effect of Feed Equilibrator Temperature on Inventory

Table 6 shows that when no heteronuclear isotopes are present (feed equilibrator temperature at 0 K), the system achieves the desired separation performance (displayed in Figure 1), producing a protium-rich distillate free of HT contamination. As feed equilibrator temperature rises, the formation of heteronuclear isotopologues (particularly HT) becomes significant, reducing separation efficiency and distillate purity. Achieving desired separation under these conditions without further design modifications becomes challenging. Additionally, increased feed equilibration temperature increases tritium inventory within the column due to enhanced HT formation. Formation of HT in the feed stream is directed up through the enriching section of the column, increasing the overall tritium inventory.

#### Effect of Side Stream Isotopic Equilibrator Temperature and Flow Rate

A potential solution to reduce HT contamination involves incorporating an isotopic equilibrator in a side stream of the cryogenic distillation column. The side stream is taken from the top tray, where HT concentration is highest, and returned to the second tray after passing through the equilibrator. Table 7 shows the system performance for a one-column configuration with a side stream flow rate of 100 mol $h^{-1}$. Compared to results without a side stream (Table 6), the separation performance (lower tritium content in the distillate) has improved for all equilibrator temperatures. However, this improvement comes at the cost of increased tritium inventory within the column.

Figure 3 illustrates the trade-off between separation performance and inventory. Higher side stream flow rates reduce tritium content in the distillate but increase overall tritium inventory. Notably, reducing the equilibration temperature simultaneously lowers both tritium content in the distillate and tritium inventory, making it a key factor in optimizing system performance.

**Table 6:** Separation performance and tritium inventory of the one-column configuration (as shown in figure 1 with design parameters given in table 2) with no side stream flow.

| Equilibrator 1 Temperature *[K]* | Tritium in Distillate *[g hr$^{-1}$]* | Tritium Inventory *[g]* |
|---|---|---|
| 0 K | 5.423 x 10$^{-5}$ | 3.076 |
| 50 K | 6.427 | 4.550 |
| 77.4 K | 8.302 | 4.642 |
| 150 K | 9.879 | 4.748 |
| 200 K | 10.33 | 4.779 |
| 298 K | 10.94 | 4.803 |

**Table 7:** Separation performance and tritium inventory of the one-column configuration (as shown in figure 1) with a side stream flow rate of 100 mol hr$^{-1}$.

| Equilibrator 1 and 2 Temperature *[K]* | Tritium in Distillate *[g h$^{-1}$]* | Tritium Inventory *[g]* |
|---|---|---|
| 0 K | 5.423 x 10$^{-5}$ | 3.076 |
| 50 K | 1.908 | 4.706 |
| 77.4 K | 2.497 | 4.860 |
| 150 K | 3.015 | 5.029 |
| 200 K | 3.166 | 5.079 |
| 298 K | 3.377 | 5.125 |

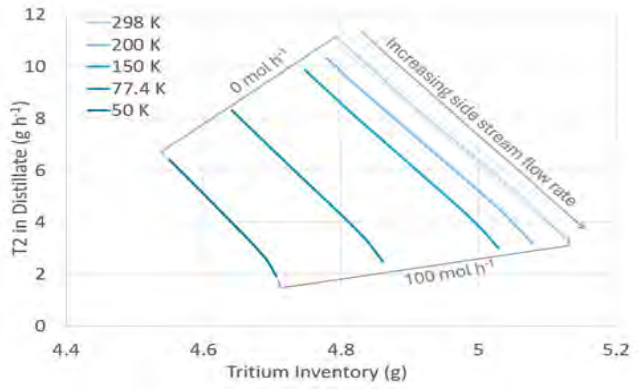



**Figure 3:** Separation performance vs tritium inventory at varying equilibrator temperatures for the one-column configuration with side stream flowrates from 0 to 100 mol hr$^{-1}$.

## Two-Column Architecture

### Effect of Column Interconnection Isotopic Equilibrators

Introducing a second column with isotopic equilibrators provides another method for reducing HT contamination in the distillate. Twelve case studies are presented in tables 8 and 9 evaluating the impact of operating isotopic equilibrators 1, 2, and 3 (see figure 2) at reduced temperatures (from 298 K to 77.4 K).

**Table 8:** Two-column configuration (as displayed in figure 2 with the initial design parameters displayed in table 3) with modified equilibrator temperatures.

| Case Study | Equilibrator Temperature *[K]* | | | T in distillate *[g hr$^{-1}$]* | Tritium Inventory *[g]* |
|---|---|---|---|---|---|
| | **1** | **2** | **3** | | |
| 1 | 298 | 298 | 298 | 0.1504 | 29.32 |
| 2 | 77.4 | 298 | 298 | 0.1148 | 27.67 |
| 3 | 298 | 77.4 | 298 | 0.1148 | 29.32 |
| 4 | 298 | 298 | 77.4 | 0.1495 | 29.30 |
| 5 | 77.4 | 77.4 | 298 | 0.08771 | 27.66 |
| 6 | 77.4 | 77.4 | 77.4 | 0.08726 | 27.65 |

**Table 9:** Two-column configuration (as shown in figure 2) with number of stages in column 1 is manipulated to keep tritium flow rate in the distillate constant (approximately 0.150 g h$^{-1}$).

| Case Study | Equilibrator Temperature *[K]* | | | Number of column 1 stages | Tritium Inventory *[g]* |
|---|---|---|---|---|---|
| | **1** | **2** | **3** | | |
| 7 | 77.4 | 298 | 298 | 38 | 26.78 |
| 8 | 298 | 77.4 | 298 | 38 | 28.33 |
| 9 | 77.4 | 77.4 | 298 | 34 | 26.21 |
| 10 | 77.4 | 77.4 | 77.4 | 34 | 26.19 |
| 11 | 298 | 298 | n/a | 45 | 29.32 |
| 12 | 77.4 | 77.4 | n/a | 34 | 26.19 |

Case studies 1–6 demonstrate improved separation performance and reduced inventory with lower equilibrator temperatures. Case studies 7–10 explore manipulating the number of stages in column 1 to maintain a top product tritium content of ~0.150 g h$^{-1}$ under reduced equilibrator temperatures. Results show that reduced equilibrator temperatures achieve comparable separation with fewer stages, lowering the tritium inventory. These findings align with prior studies (e.g., Urm et al. [16]), which report a trade-off between improved separation performance and increased tritium inventory for an increased number of stages. Key findings for individual equilibrators include:

- **Equilibrator 1** temperature reductions effectively reduce HT contamination within the system, reducing both tritium contamination in the distillate and inventory within the columns.
- **Equilibrator 2** temperature reductions effectively reduce HT flow to the distillate, though its impact on system inventory is minimal due to the small tritium inventory within column 2 relative to column 1.

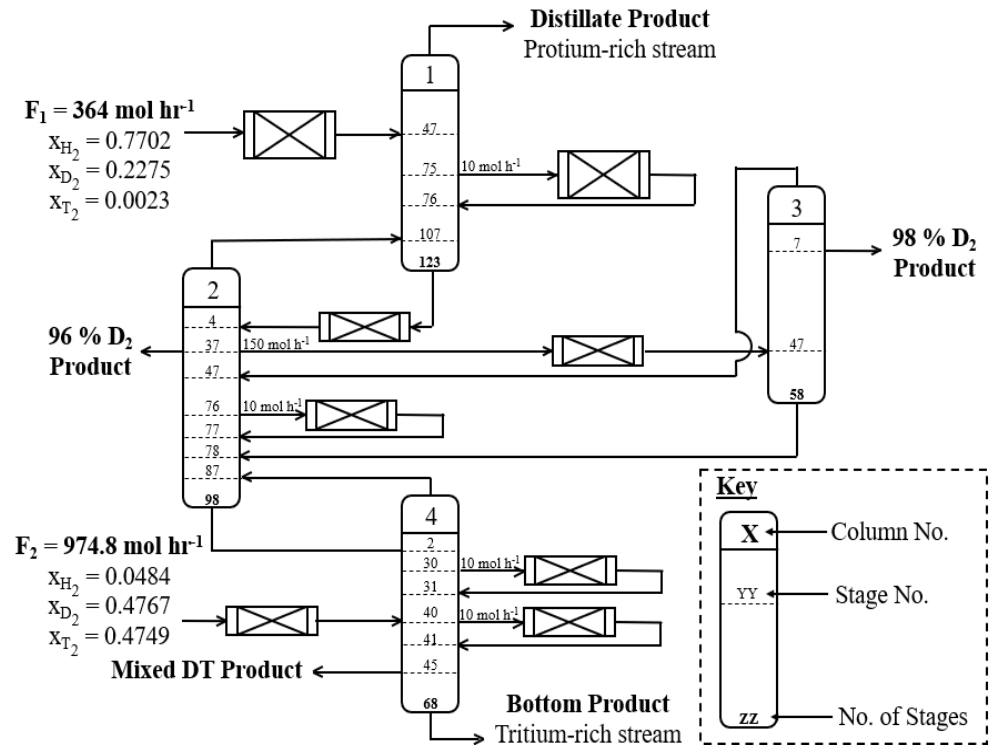



**Figure 8:** ISS configuration proposed for ITER.

- Case studies 11 and 12 (relative to case studies 1 and 10, respectively) indicate redundancy of **equilibrator 3** due to its proximity with equilibrator 2. This suggests that the internal inventory of this equilibrator will likely outweigh any marginal benefits to separation performance it provides.

The best configuration for minimizing tritium inventory within the two-column architecture is shown in case study 12, where equilibrators 1 and 2 operate at 77.4 K and equilibrator 3 is omitted. This configuration achieves a 10% reduction in tritium inventory compared to the baseline design (case study 1), demonstrating the importance of optimising equilibrator temperature.

## ITER Isotope Separation System

To assess the potential improvement for reduced equilibrator temperatures, the ISS configuration for ITER, as described in the work of Noh et al. [11], was analysed for comparison. The overall system configuration and design parameters, including feed flows and H/D/T ratios, were the same as in Noh et al. [11], however, the current work extends the analysis by investigating the effects of reducing temperature of the isotopic equilibrators from 298 to 77.4 K. Additionally, specific side stream flow rates (illustrated in Figure 8) were introduced in this study, as these were not reported in the original work.

Table 10 presents the results of this comparison. The DT flow rate in the tritium-rich bottom product was used as the key metric for separation performance. At 298 K, significant DT contamination was observed in the bottom product, but reducing the equilibrator temperatures to 77.4 K evidently decreased the DT contamination. Noh et al. [11] proposed that achieving the desired tritium purity in the bottom product requires 68 stages in column 4. The results of this work show that by reducing the equilibrator temperatures, a comparable separation performance can be achieved with only 60 stages in column 4. This reduction in stages—specifically, by removing 8 stages between the mixed DT product and the bottom theoretical tray—demonstrates a 10% reduction in tritium inventory, underscoring the dual benefit of improved separation and inventory reduction. These findings validate the hypothesis that reduced equilibrator temperatures enhance the system's overall performance and provide a compelling case for incorporating such modifications in future ISS designs.

**Table 10:** ITER ISS DT contamination in the tritium-rich bottom product and system tritium inventory for varying isotopic equilibrator temperatures.

| Equilibrator Temperature *[K]* | Number of column 4 stages | DT in bottom product *[mol hr$^{-1}$]* | Tritium Inventory *[g]* |
|---|---|---|---|
| 298 | 68 | 22.19 | 140.7 |
| 77.4 | 68 | 19.03 | 141.6 |
| 77.4 | 60 | 21.56 | 126.1 |

## CONCLUSION

This study presents a detailed investigation of hydrogen isotope separation via cryogenic distillation, with a focus on optimising isotopic equilibrator temperatures to enhance separation performance and minimize tritium inventory. Investigating a one-column configuration with an isotopic equilibrator within a side stream effectively reduced HT contamination in the distillate product. The two-column system demonstrated that reducing temperature of equilibrators significantly improved separation performance and allowed a reduction in the number of theoretical stages, thereby lowering inventory. Eliminating equilibrator 3 was shown to have negligible impact, suggesting opportunities for design simplifications.

A comparison with the ITER ISS validated these findings. Reduced equilibrator temperatures to 77.4 K achieved comparable performance with fewer stages in column 4, resulting in a 10% reduction in tritium inventory. Extrapolating these results to the DEMO, where 600 g of tritium is expected in the ISS, this reduction would equate to a 3.4% decrease in overall plant inventory, offering a meaningful improvement in operational safety and efficiency.

These findings underscore the importance of temperature optimisation in isotopic equilibrators and provide actionable insights for designing cost-effective, energy-efficient isotope separation systems critical to future fusion power applications.

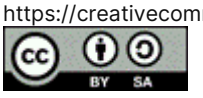
## ACKNOWLEDGEMENTS

The authors gratefully acknowledge the UK Atomic Energy Authority (UKAEA) and the University of Surrey for their financial support of this research.

## REFERENCES

1. Abdou, M., et al., Physics and technology considerations for the deuterium–tritium fuel cycle and conditions for tritium fuel self sufficiency. Nuclear fusion, 2020. 61(1): p. 013001.
2. Day, C., et al., The pre-concept design of the DEMO tritium, matter injection and vacuum systems. Fusion Engineering and Design, 2022. 179: p. 113139.
3. Schwenzer, J., et al., Operational tritium inventories in the EU-DEMO fuel cycle. Fusion Science and Technology, 2022. 78(8): p. 664-675.
4. Glugla, M., et al., The ITER tritium systems. Fusion Engineering and Design, 2007. 82(5-14): p. 472-487.
5. Wang, X., et al., Hydrogen isotope inventory evaluation of hydrogen isotopes separation system of CFETR using Aspen Plus simulator. Fusion Engineering and Design, 2022. 177: p. 113078.
6. Souers, P.C., Hydrogen properties for fusion energy. 1986: Univ of California Press.
7. Sherman, R.H., et al., The role of sidestream recycle in hydrogen isotope separation and column cascade design. Fusion engineering and design, 1995. 28: p. 392-396.
8. Yamanishi, T., M. Enoeda, and K. Okuno, Experimental study for characteristics of cryogenic distillation column having feedback stream with HDT system. Journal of Nuclear Science and Technology, 1994. 31(9): p. 937-947.
9. Bainbridge, N., et al., Operational experience with the JET AGHS cryodistillation system during and after DTE1. Fusion engineering and design, 1999. 47(2-3): p. 321-332.
10. Iraola, E., et al., Dynamic simulation tools for isotopic separation system modeling and design. Fusion Engineering and Design, 2021. 169: p. 112452.
11. Noh, J., et al., Estimation of thermodynamic properties of hydrogen isotopes and modeling of hydrogen isotope systems using Aspen Plus simulator. Journal of Industrial and Engineering Chemistry, 2017. 46: p. 1-8.
12. Lda, T., K. Okuno, and Y. Naruse, Hydrogen isotope exchange reaction rates in tritium, hydrogen and deuterium mixed gases. Radiochimica Acta, 1992. 56(4): p. 209-214.
13. McConville, G., D. Menke, and R. Ellefson, Reaction rates for the formation of deuterium tritide from deuterium and tritium. Fusion Technology, 1985. 8(2P2): p. 2245-2256.
14. Sherman, R., et al. Application of sidestream recycle to the separation of hydrogen isotopes by cryogenic distillation. in 15th IEEE/NPSS Symposium. Fusion Engineering. 1993. IEEE.
15. Urm, J.J., et al., Dynamic Optimization Study for Cryogenic Distillation in Hydrogen Isotope Separation System. IFAC-PapersOnLine, 2022. 55(7): p. 168-173.
16. Park, D., et al., Dynamic optimization of cryogenic distillation operation for hydrogen isotope separation in fusion power plant. International Journal of Hydrogen Energy, 2021. 46(47): p. 24135-24148.

© 2025 by the authors. Licensed to PSEcommunity.org and PSE Press. This is an open access article under the creative commons CC-BY-SA licensing terms. Credit must be given to creator and adaptations must be shared under the same terms. See https://creativecommons.org/licenses/by-sa/4.0/



Systems & Control Transactions

**Research Article - Peer Reviewed Conference Proceeding**
ESCAPE 35 - European Symposium on Computer Aided Process Engineering
Ghent, Belgium. 6-9 July 2025
Jan F.M. Van Impe, Grégoire Léonard, Satyajeet S. Bhonsale,
Monika E. Polańska, Filip Logist (Eds.)

PSE PRESS

# Efficient approximation of the Koopman operator for large-scale nonlinear systems

**Gajanand Verma[a], William Heath[b], and Constantinos Theodoropoulos[a]***

[a] Department Chemical Engineering, The University of Manchester, Manchester, M13 9PL, UK
[b] School of Computer Science and Engineering, Bangor University, Bangor, LL57 1UT, UK
* Corresponding Author: k.theodoropoulos@manchester.ac.uk

## ABSTRACT

Implementing Model Predictive Control (MPC) for large-scale nonlinear systems is often computationally challenging due to the intensive online optimization required. To address this, various reduced-order linearization techniques have been developed. The Koopman operator linearizes a nonlinear system by mapping it into an infinite-dimensional space of observables, enabling the application of linear control strategies. While Artificial Neural Networks (ANNs) can approximate the Koopman operator in a data-driven manner, training these networks becomes computationally intensive for high-dimensional systems as the lifting into a higher-dimensional observable space significantly increases data size and complexity. In this work, we propose a technique, combining Proper Orthogonal Decomposition (POD) with an efficient ANN structure to reduce the training time of ANN for large order systems. By first applying POD, we obtain a low order projection of the system. Subsequently, we train the ANN with an efficient structure to approximate the Koopman operator, significantly decreasing training time without sacrificing accuracy.

**Keywords**: Koopman operator, efficient training of NN, large-scale systems, nonlinear systems, model predictive control, MPC, nonlinear control

## 1 INTRODUCTION

Model predictive control (MPC) is a well-known strategy for control of dynamical systems, offering key advantages such as handling constraints and optimizing the control input trajectory [1,2]. MPC of large order systems is challenging as the computational efforts required for online optimization is significant. Model order reduction (MOR) methodologies such as Proper Orthogonal Decomposition (POD), are generally exploited in such cases to project the original system onto a lower dimensional subspace, thereby reducing the computational burden of MPC [3–7].

For large order non-linear systems, only MOR, may still be insufficient, as the resulting nonlinear models remain challenging for optimization and stability analysis. An alternative is to linearize the system in a suitably reduced space [8] . In recent years, the Koopman operator framework has gained significant attention as a potential route to enable linear MPC for otherwise nonlinear systems [9–13]. According to Koopman theory, a nonlinear dynamical system can be represented as a linear system in an infinite-dimensional space of observables (i.e., functions of the state) [14]. In practice, a finite approximation of Koopman operator is necessary for its application in MPC [9,15,16].

A commonly used data-driven method to approximate the Koopman operator is Extended Dynamic Mode Decomposition (EDMD) [9]. In EDMD, the nonlinear state is augmented with a set of manually chosen state functions (observables). However, choosing the observables manually may limit the accuracy of approximation [15]. To address this, Artificial Neural Networks (ANNs) have been explored as a means of automatically learning suitable observables from data, thus improving approximation [15–17]. To train the ANN, usually large data set is required. Nevertheless, for large order systems the training of ANNs takes significant time.

While [15,17] use ANNs for Koopman approximation to automate the selection of lifting functions, these approaches do not address the challenges associated with training ANNs for high-dimensional systems. Recently, [18] proposed a POD-based Koopman approximation technique; however, their method does not incorporate

ANNs for Koopman approximation. In this work, we propose combining POD with ANN (PANN) for Koopman operator approximation. First, we apply POD to snapshot data to derive a low-dimensional state space in a purely data-driven manner. Subsequently, we employ ANNs to "lift" this low-dimensional state into a higher-dimensional space of observables, where the dynamics can be represented in a linear form. This approach significantly reduces the training time compared to directly learning the full-state observables, without sacrificing the accuracy of the Koopman operator approximation.

## 2 PRELIMINARIES

### 2.1 Koopman operator

Koopman operator theory was proposed by Bernard O. Koopman in 1931 [14]. The core idea is to embed the non-linear dynamics into an infinite-dimensional space of observables where the observables evolve linearly along the trajectories of the original nonlinear dynamics.

Consider a discrete nonlinear system represented by:

$$\boldsymbol{x}_{k+1} = f(\boldsymbol{x}_k) \tag{1}$$

where $\boldsymbol{x}_k \in \mathbb{R}^n$ is the state vector at the k$^{th}$ time step. Let the system be lifted to the space of observables using a transformation $\phi: \mathbb{R}^n \rightarrow \mathbb{R}^N$ where N>>n. The Koopman operator $\mathcal{K}$ acts on the on the lifted state $\boldsymbol{\psi}$ ($\boldsymbol{\psi}_k = \boldsymbol{\varphi}(\boldsymbol{x}_k)$) such that:

$$\phi(\boldsymbol{x}_{k+1}) = \mathcal{K}\ \phi(\boldsymbol{x}_k) \tag{2}$$

$$\boldsymbol{\psi}_{k+1} = \mathcal{K}\ \boldsymbol{\psi}_k \tag{3}$$

This framework can be applied to design a linear MPC for a nonlinear dynamical system. Consider a controlled dynamical system represented by:

$$\boldsymbol{x}_{k+1} = f(\boldsymbol{x}_k, \boldsymbol{u}_k) \tag{4}$$

where $\boldsymbol{u}_k \in \mathbb{R}^m$. Exploiting the Koopman theory a linear representation of the above system can be obtained as:

$$\boldsymbol{\psi}_{k+1} = \mathrm{A}\boldsymbol{\psi}_k + B\boldsymbol{u}_k \tag{5}$$

where $A \in \mathbb{R}^{N\ x\ \mathrm{N}}$ and $B \in \mathbb{R}^{N\ x\ \mathrm{m}}$. The original state can be reconstructed as:

$$\hat{\boldsymbol{x}}_k = C\boldsymbol{\psi}_k \tag{6}$$

where $C \in \mathbb{R}^{n\ \mathrm{x}\ \mathrm{N}}$. Notably since $\boldsymbol{u}_k$ has not been lifted and $\hat{\boldsymbol{x}}_k$ is assumed to be linear combination of $\boldsymbol{\psi}_k$, linear constraints can be applied on both, facilitating linear MPC of underlying nonlinear system.

Koopman matrices *A* and *B* can be obtained in a data-driven manner using EDMD. Despite being a data driven method, EDMD requires manual selection of observables which require prior understanding of the system for good approximation accuracy [8]. Randomly chosen observables may limit the accuracy of approximation. Alternatively, ANNs can be used to approximate the matrices *A* and *B*, eliminating the need for manual selection of observables. Nevertheless, for large-scale nonlinear systems, training ANNs is computationally intensive. Additionally, lifting such systems to a higher-dimensional space of observables further increases the computational burden associated with ANN training. To reduce the computational burden of ANN training we first reduce the dimensionality of the large-scale nonlinear system using POD. Subsequently, the reduced-order variables are lifted into a higher-dimensional observable space.

### 2.2 Proper Orthogonal Decomposition (POD)

Proper Orthogonal Decomposition (POD) is an effective technique for systematically reducing the dimensionality of large-scale systems, leveraging principles from spectral theory. The key idea behind POD is the decomposition of the solution space into a maximal invariant subspace corresponding to dominant modes (i.e., large eigenvalues), and its orthogonal complement containing less significant mode [4,19–21]. These dominant modes capture most of the system's energy or variance and thus characterize the essential dynamics.

Formally, POD decomposes the state variables into spatial and temporal components, where the spatial variation is captured by eigenfunctions, and the temporal variation is encapsulated by time-dependent coefficients [4]. Notably, POD does not require an explicit analytical form of the governing equations; it can be performed solely on snapshot data arising from simulations or experiments, making it a completely data driven method for MOR.

## 3. METHODOLOGY

Figure 1 shows an overview of the proposed POD and ANNs (PANN) framework for reduced order Koopman operator approximation. The detailed steps are as follows:

### 3.1 Snapshots collection

A high-fidelity simulation or experimental state data for the nonlinear system across discrete time steps is collected for appropriate range of parameters to form the snapshot matrix *S*, where each column represents a state vector $\boldsymbol{x}_k$.

$$S = \{\boldsymbol{x}_1, \dots\dots\dots\dots, \boldsymbol{x}_M\} \tag{7}$$

$S \in \mathbb{R}^{n\ x\ \mathrm{M}}$, where M is the total number of snapshots.

### 3.2 POD based dimensionality reduction

POD provides basis function for dimensionality reduction. After obtaining POD modes, only dominant modes are retained, yielding reduced order state $\boldsymbol{z}_k \in \mathbb{R}^{\mathrm{r}}$

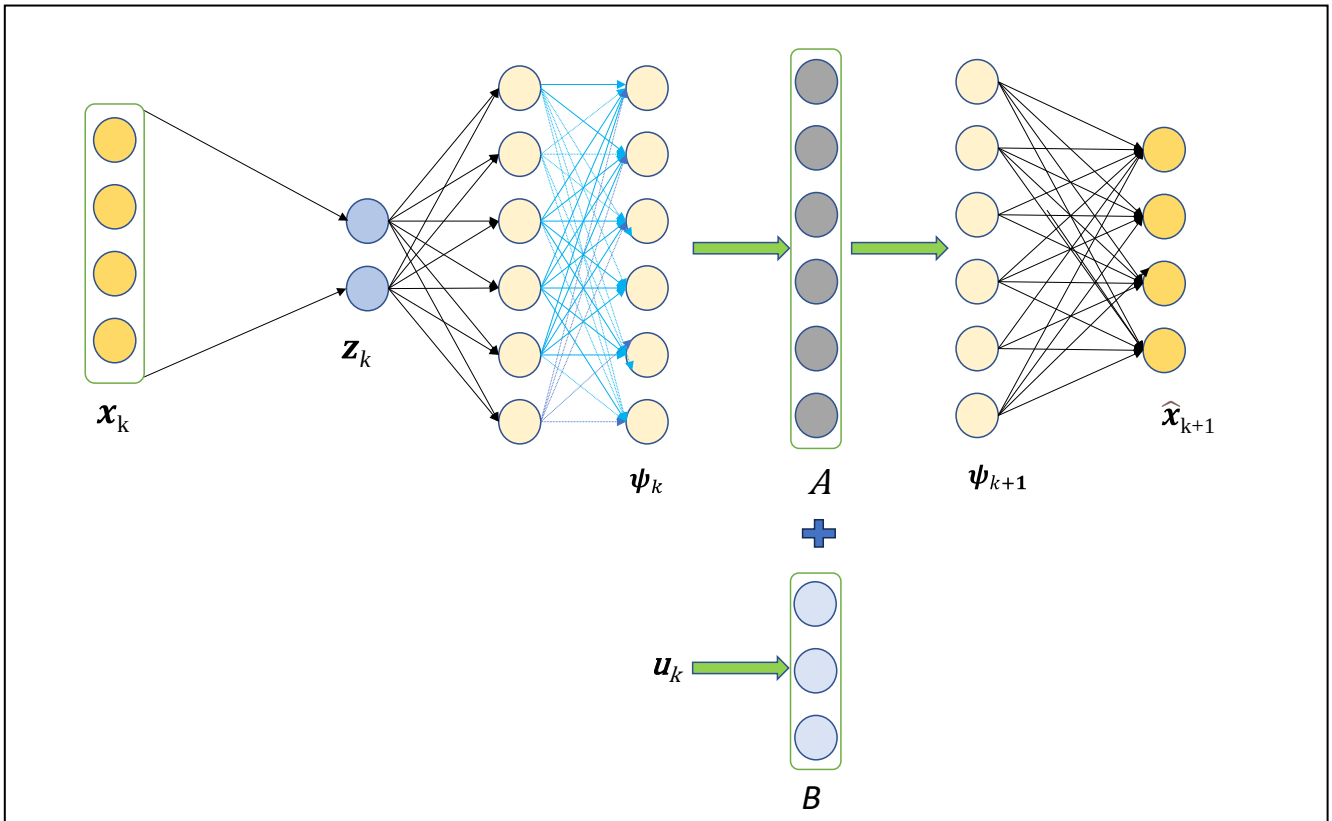



**Figure 1:** PANN framework for efficient approximation of Koopman operator for large-scale nonlinear systems.

(r<<n). Following are the steps:

1. After creating the snapshot matrix *S*, center the data by subtracting the mean state $\bar{x}$, creating matrix *S′*.

$$\bar{x} = \frac{1}{M}\sum_{k=1}^{M} x_k \tag{8}$$

2. Construct a correlation matrix $D \in \mathbb{R}^{M\,x\,M}$

$$D = \frac{1}{M} S'^{T} S' \tag{9}$$

3. Eigenvalue decomposition is performed on correlation matrix D

$$D v_i = \lambda_i v_i \tag{10}$$

where $\lambda_i$ are the eigenvalues, ordered in descending magnitude and $v_i$ are the corresponding eigenvectors.

4. POD modes ($\varphi \in \mathbb{R}^n$) are derived by projecting the centered snapshot data onto the eigenvectors $v_i$.

$$\varphi_i = \frac{1}{\sqrt{\lambda_i}} S' v_i \tag{11}$$

5. The number of retained modes r is determined based on the cumulative energy criterion:

$$\sum_{i=1}^{r} \lambda_i \geq \alpha \sum_{i=1}^{M} \lambda_i \tag{12}$$

$\alpha$ is chosen such that the retained modes capture most of the system's dynamics.

### 3.3 ANN based Koopman operator approximation

The ANN architecture (Figure 1) is designed to efficiently map the reduced-order state $z_k \in \mathbb{R}^r$ into a higher-dimensional observable space $\psi_k \in \mathbb{R}^N$, where N≫r. The architecture divided into 4 main sections:

1. **Section 1**: The role of this section is to lift the reduced-order state $z_k$ to $\psi_k$. It consists of an input layer (with r neurons), multiple hidden layers with ReLU activations, and an output layer (with N neurons).
2. **Section 2**: This section captures Koopman matrix A as described in equation 5. This NN layer is a shallow linear layer with bias=0.
3. **Section 3:** This section captures Koopman matrix B. This layer too is a linear layer with bias =0.
4. **Section 4:** This section reconstructs the original high dimensional nonlinear state $x_k$ from the lifted state $\psi_k$.

The ANN is trained to minimize the error between

the predicted and actual next-step observables, ensuring that the lifted dynamics approximate the Koopman operator.

## 4. IMPLEMENTATION

We applied the PANN method to a nonlinear tubular reactor system. The schematic of the tubular reactor [22] is given in figure 2. There is an exothermic reaction(A→B) going inside the reactor. To control the exit temperature of the product (B), the wall of the reactor is divided into three sections. The temperature of each section can be controlled independently. The temperature and concentration profile of the reactor exhibits a Hopf bifurcation (sustained oscillations) at a recycle ratio $r_c$ = 0.5.

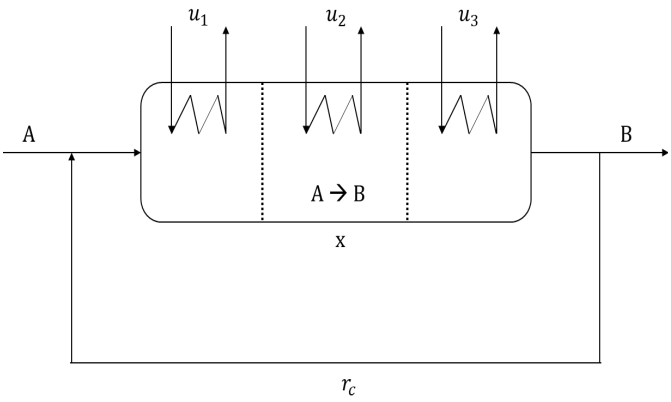



**Figure 2.** Schematic of the tubular reactor.

The system is governed by the set of following PDEs in terms of dimensionless variables:

$$\frac{\partial \mathbf{c}}{\partial t} = \frac{1}{P_m}\frac{\partial^2 \mathbf{c}}{\partial x^2} - \frac{\partial \mathbf{c}}{\partial x} - Da(1+\mathbf{c})\exp\left(\frac{\alpha_a \mathbf{T}}{1+\mathbf{T}}\right) \quad (13)$$

$$\frac{\partial \mathbf{T}}{\partial t} = \frac{1}{P_h}\frac{\partial^2 T}{\partial x^2} - \frac{\partial \mathbf{T}}{\partial x} + c_1 Da(1+\mathbf{c})\exp\left(\frac{\alpha \mathbf{T}}{1+\mathbf{T}}\right) + \beta(\mathbf{u_W} - \mathbf{T}) \quad (14)$$

The boundary conditions are given as:

$$\frac{\partial \mathbf{c}}{\partial x} = -P_m[(1-r_c)\mathbf{c}_0 + r_c\,\mathbf{c}|_{x=1} - \mathbf{c}\,|_{x=0}] \quad (15)$$

$$\frac{\partial \mathbf{T}}{\partial x} = -P_h[(1-r_c)\mathbf{T}_0 + r_c\,\mathbf{T}|_{x=1} - \mathbf{T}\,|_{x=0}] \quad (16)$$

$$\frac{\partial \mathbf{T}}{\partial x} = \frac{\partial \mathbf{c}}{\partial x} = 0 \qquad \text{at } x = 1 \quad (17)$$

Here c is the dimensionless concentration, T the dimensionless temperature, and $\mathbf{u_w}$ the dimensionless wall temperature. The model parameters were as follows:

**Table 1:** Parameter values for the tubular reactor system.

| Parameter | Value |
|---|---|
| Peclet number for mass transfer ($P_m$) | 7 |
| Peclet number for heat transfer ($P_h$) | 7 |
| Damköhler number (Da) | 0.1 |
| Activation energy ($\alpha_a$) | 10 |
| Adiabatic temperature rise ($c_1$) | 2.5 |
| Heat transfer coefficient (β) | 2 |
| Recycle ratio ($r_c$) | 0.5 |

The system was discretized into 15 nodes along the length of the reactor resulting into total 30 state variables with 3 manipulated variables. We generated 1000 trajectories each with 300 time steps. The snapshots were generated using randomized control inputs between 0.1 and 2. In the time interval between timesteps 10 and 150 we forced the control inputs to increase and between timesteps 150 to 300 to decrease, using randomised values, to ensure a wide representation of system states. For all the trajectories we used $r_c$ = 0.5.

A snapshot matrix *S*, of the system was obtained and POD was performed to extract the reduced order basis as described in section 2. The reduced order state $\boldsymbol{z_k}$ was obtained.

$\boldsymbol{z_k}$ was lifted to $\boldsymbol{\psi_k}$ using ANNs as depicted in figure 1. n=30 while N was chosen twice of input to the ANNs. The dataset was split into training and validation (80%, 20%) to prevent overfitting. The number of hidden layers in section 1 was 1. We employed the Adam optimizer for ANN training, a widely used adaptive optimization algorithm for faster and efficient ANN training. Unlike traditional stochastic gradient descent (SGD), which uses a fixed learning rate throughout training, Adam dynamically adjusts the learning rate.

## 5. RESULTS AND DISCUSSION

The spectrum of matrix D is depicted in Figure 3. Only two eigenvalues corresponding to two eigenmodes are significant. The rapid decay of singular values in the POD process indicates a clear separation of scales within the system, enabling the most significant modes to capture the primary dynamics.

**Table 2:** ANN vs PANN based Koopman operator approximation

| Method | MSE | Training time |
|---|---|---|
| ANN | $1.5 \times 10^{-8}$ | 4 hrs |
| PANN | $1.2 \times 10^{-8}$ | 12 min |

Figure 4 depicts the energy ($\alpha$) captured by the retained modes (r). More than ninety-nine percent of the energy is captured by retaining only two modes corresponding to the two highest eigenvalues as depicted in

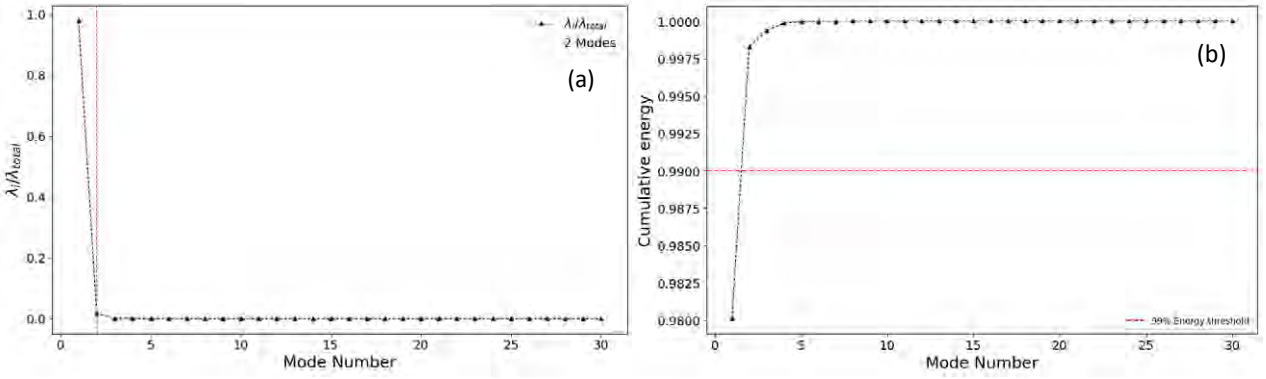



**Figure 3: (a)** POD modes **(b)** Cumulative energy captured by r number of modes

Figure 4.

Koopman operator was first approximated using standard ANNs with full nonlinear state ( $\boldsymbol{x}_k \in \mathbb{R}^n, n = 30$ ) as input and lifted dimension as 2n. The PANN framework was then applied with number of retained POD modes r =2 and the lifted dimension as 2r.

Table 2 provides the comparison of performance of both the methods. A significant speedup of the training time was noted in PANN framework.

## 6. CONCLUSIONS AND FUTURE DIRECTION

In this study, we proposed a hybrid framework, termed PANN, that integrates POD with ANNs to efficiently approximate the Koopman operator for large scale nonlinear systems. The incorporation of model reduction capabilities of POD significantly decreased the ANN training time while improving the accuracy of the approximation. We successfully demonstrated this framework on a non-linear tubular reactor system. The standard ANN for Koopman approximation took four hours to converge with the full-dimensional system, whereas PANN required only twelve minutes to train, owing to the pre-model order reduction. In future work, we aim to further reduce the training time by exploring different ANN architectures and training methods.

## ACKNOWLEDGMENTS

The financial contribution of the Ministry of Social Justice & Empowerment, Government of India is gratefully acknowledged.

## REFERENCES

1. Mayne D. Nonlinear model predictive control: Challenges and opportunities. Nonlinear model predictive control. 2000;23–44.
2. Rawlings JB, Mayne DQ, Diehl M, others. Model predictive control: theory, computation, and design. Vol. 2. Nob Hill Publishing Madison, WI; 2017.
3. Theodoropoulos C. Optimisation and linear control of large scale nonlinear systems: A review and a suite of model reduction-based techniques. Coping with complexity: Model reduction and data analysis. 2010;37–61.
4. Xie W, Bonis I, Theodoropoulos C. Data-driven model reduction-based nonlinear MPC for large-scale distributed parameter systems. Journal of Process Control. 2015;35:959–1524.
5. Peter B, GRIVET TALOCIA S, Alfio Q, Gianluigi R, Wil S, Silveira LM, et al. Model Order Reduction. Volume 1: System-and Data-Driven Methods and Algorithms. 2021;
6. Adel A, Salah K. Model order reduction using genetic algorithm. In: 2016 IEEE 7th Annual Ubiquitous Computing, Electronics & Mobile Communication Conference (UEMCON). IEEE; 2016. p. 1–6.
7. San O, Maulik R, Ahmed M. An artificial neural network framework for reduced order modeling of transient flows. Communications in Nonlinear Science and Numerical Simulation. 2019;77:271–87.
8. Bonis I, Xie W, Theodoropoulos C. A linear model predictive control algorithm for nonlinear large-scale distributed parameter systems. AIChE Journal. 2012;58(3):801–11.
9. Korda M, Mezic I. Linear predictors for nonlinear dynamical systems: Koopman operator meets model predictive control. Automatica. 2018 Jul;93:149–60.
10. Mamakoukas G, Di Cairano S, Vinod AP. Robust Model Predictive Control with Data-Driven Koopman Operators. In: 2022 American Control Conference (ACC). 2022. p. 3885–92.
11. Narasingam A, Son SH, Kwon JSI. Data-driven

feedback stabilisation of nonlinear systems: Koopman-based model predictive control. International Journal of Control. 2023;96(3):770–81.
12. Otto SE, Rowley CW. Koopman operators for estimation and control of dynamical systems. Annual Review of Control, Robotics, and Autonomous Systems. 2021;4(1):59–87.
13. Williams MO, Kevrekidis IG, Rowley CW. A data–driven approximation of the koopman operator: Extending dynamic mode decomposition. Journal of Nonlinear Science. 2015;25:1307–46.
14. Koopman BO. Hamiltonian systems and transformation in Hilbert space. Proceedings of the National Academy of Sciences. 1931;17(5):315–8.
15. Wang M, Lou X, Wu W, Cui B. Koopman-based MPC with learned dynamics: Hierarchical neural network approach. IEEE Transactions on Neural Networks and Learning Systems. 2022;
16. Xiao Y, Zhang X, Xu X, Liu X, Liu J. Deep Neural Networks With Koopman Operators for Modeling and Control of Autonomous Vehicles. IEEE Transactions on Intelligent Vehicles. 2023;8(1):135–46.
17. Verma G, Heath W, Theodoropoulos C. Robust stability analysis of Koopman based MPC system. In: Computer Aided Chemical Engineering. Elsevier; 2024. p. 1927–32.
18. Zhang X, Han M, Yin X. Reduced-order Koopman modeling and predictive control of nonlinear processes. Computers & Chemical Engineering. 2023;179:108440.
19. Taira K, Brunton S, Dawson S, Rowley C, Colonius T, McKeon B, et al. Modal analysis of fluid flows: An overview. AIAA journal. 2017;55(12):4013–41.
20. Nguyen VB, Tran SBQ, Khan SA, Rong J, Lou J. POD-DEIM model order reduction technique for model predictive control in continuous chemical processing. Computers & Chemical Engineering. 2020;133:106638.
21. Rizzo C, de Barros F, Perotto S, Oldani L, Guadagnini A. Adaptive POD model reduction for solute transport in heterogeneous porous media. Computational Geosciences. 2018;22:297–308.
22. Jensen KF, Ray WH. The bifurcation behavior of tubular reactors. Computers and Chemical Engineering. 1982;37:199–222.

© 2025 by the authors. Licensed to PSEcommunity.org and PSE Press. This is an open access article under the creative commons CC-BY-SA licensing terms. Credit must be given to creator and adaptations must be shared under the same terms. See https://creativecommons.org/licenses/by-sa/4.0/



Systems & Control Transactions

**Research Article - Peer Reviewed Conference Proceeding**
ESCAPE 35 - European Symposium on Computer Aided Process Engineering
Ghent, Belgium. 6-9 July 2025
Jan F.M. Van Impe, Grégoire Léonard, Satyajeet S. Bhonsale,
Monika E. Polańska, Filip Logist (Eds.)

PSE PRESS

# Optimal Control of PSA Units Based on Extremum Seeking

**Beatriz C. da Silva[ab]*, Ana M. Ribeiro[ab], Alexandre F.P. Ferreira[ab], Diogo Rodrigues[ab] and Idelfonso B.R. Nogueira[c]**

[a] LSRE-LCM – Laboratory of Separation and Reaction Engineering - Laboratory of Catalysis and Materials, Faculty of Engineering, University of Porto, Rua Dr. Roberto Frias, 4200-465 Porto, Portugal
[b] ALiCE – Associate Laboratory in Chemical Engineering, Faculty of Engineering, University of Porto, Rua Dr. Roberto Frias, 4200-465 Porto, Portugal
[c] Chemical Engineering Department, Norwegian University of Science and Technology, Sem Sælandsvei 4, Kjemiblokk 5, Trondheim 7491, Norway
* Corresponding Author: up201707213@fe.up.pt .

## ABSTRACT

The application of Real-time Optimization (RTO) to dynamic operations is challenging due to the complexity of the nonlinear problems involved, making it difficult to achieve robust solutions. The literature on RTO in Pressure Swing Adsorption (PSA) units relies on Model Predictive Control (MPC) and Economic Model Predictive Control (EMPC), which rely heavily on an accurate model representation of the industrial plant. Given the importance of PSA systems on multiple separation operations, establishing alternatives for control and optimization in real-time is in order. With that in mind, this work aimed to explore alternative model-free RTO techniques that depend on simple control elements, as is the case of Extremum Seeking Control (ESC).The chosen case study was Syngas Upgrading. Extremum Seeking Control successfully optimized the $CO_2$ productivity in PSA units for syngas upgrading/$H_2$ purification. The results demonstrate that ESC can be a valuable tool in optimizing and controlling PSA processes and does not require the unit to reach a Cyclic Steady State to adjust the operation.

**Keywords**: Extremum Seeking Control, Pressure Swing Adsorption, Real-time Optimization, Simple Control Strategies

## INTRODUCTION

The optimization of industrial plant operations is known for its complex nature. More often than not, the models employed in simple optimization are not representative of the plant to be optimized, leading to inaccurate optimization procedures. In the last 30 years, Real-time Optimization (RTO) has emerged to overcome some of optimization's weak points when applied to the industry by ensuring a better representation of the plant and continuous optimization to improve process performance autonomously [1, 2].

The fact that some operations have an inherent Dynamic nature still poses a challenge in a robust RTO application for most cases, although some alternatives have emerged [3]. Nevertheless, cyclic adsorption processes such as Pressure Swing Adsorption (PSA) and Temperature Swing Adsorption (TSA) never reach a traditional steady state; only a cyclic steady state (CSS) where identical dynamic behavior is obtained for consecutive cycles [4]. Control of the process in real time is essential to maintain or increase productivity. Disturbances can be critical if they prompt a CSS alteration, leading to extended periods of suboptimal operation. Furthermore, since the productivity of these processes is deeply intertwined with external conditions subject to frequent fluctuations, updating the process to fit those changes is crucial to ensure maximum profit [5].

There are very few works in the literature that contemplate the exploration of this field. In the case of PSA, the most common technique is Model Predictive Control (MPC). In the literature, it is possible to find MPC applications for PSA units for hydrogen recovery [6, 7] or syngas production [8-10], amongst others. These applications usually manipulate the durations of cycle steps to optimize the purity, recovery and/or the productivity obtained for the desired products within the different cases.

Nevertheless, the real-time optimization of PSA

units remains an underdeveloped subject in the literature with a notorious absence of alternative strategies to MPC and EMPC.

In other processes, several other RTO techniques have been employed [11]. A method that stands out when one wants to have some independence from the need to model the process is Extremum Seeking Control (ESC).

ESC is a method based on the constant perturbation of the system's input that analyses the response of the plant to determine the input that leads to the optimum of a given objective function and ensures the control of the plant. First proposed by Leblanc in 1922, ESC's essence has also been applied under different names such as extremum seeking regulator, optimizing control system, and hill-climbing systems [12, 13]. However, the ESC lacked a design analysis and stability proofs that were more recently developed by Luxat and Lees [14] and Krstić and Wang [15].

ESC has been applied to different contexts. Probably the most popular example of an ESC application is the Anti-lock Braking System (ABS). It was first approached by Drakunov et al. [16], in which the maximal value of the tire friction force is to be reached during emergency braking without prior knowledge of the optimal slip.

Looking more specifically at the chemical engineering field, the range of applications is broad, such as jet mixing technologies to maximize the decay rate and the mixing performance [17] or redox wastewater treatments to guarantee that the discharged water meets the specifications of Chemical Oxygen Demand [18].

Nevertheless, to the best of the authors' knowledge, using ESC in Cyclic Adsorption Processes remains an unexplored field in literature. Therefore, this work's primary goal is to explore the applicability of Extremum Seeking Control as a possible methodology for the real-time optimization and control of PSA units.

# METHODS

This work implemented ESC in a virtual syngas purification PSA unit. Syngas purification was chosen by its relevance in providing syngas to Fischer-Tropsch processes, known for representing an alternative path to fuel production [19]. Besides that, the same infrastructure can be adapted to provide $H_2$ for ammonia production and diminish the resulting $CO_2$ emission [20].

## PSA Model

The phenomenological model used in the simulations, together with descriptions of the experimental installation and mode of operation of the PSA unit can be found in the work of Regufe et al. [21].

In this case study, the goal was to maximize the $CO_2$ productivity (Equation 1). The integral limits are here defined by the beginning ($t_i$) and ending ($t_f$) of the cycle steps where $CO_2$ is be obtained (blowdown and purge) and consumed (rinse). This objective function also takes into consideration the cross-section area of the bed ($A_{bed}$), the mass of dry adsorbent ($m_{dry\ ads}$), the total duration of the PSA cycle ($t_{cycle}$), the superficial gas velocity ($u_0$) and the $CO_2$ concentration ($C_{CO_2}$). The manipulated variable was the duration of the feed step ($t_{feed}$) that impacts $t_{cycle}$ and the amount of $CO_2$ fed in the stream to be purified.

$$CO_2\ Productivity\ (mol_{CO_2} kg^{-1} h^{-1}) = \frac{A_{bed}}{t_{cycle} m_{dry\ ads}} \left( \int_{t_{i_{blow}}}^{t_{f_{blow}}} C_{CO_2} u_0|_{z=0}\ dt + \int_{t_{i_{purge}}}^{t_{f_{purge}}} C_{CO_2} u_0|_{z=0}\ dt - \int_{t_{i_{rinse}}}^{t_{f_{rinse}}} C_{CO_2} u_0|_{z=0}\ dt \right) \quad (1)$$

The motive for choosing this objective function was its capability of reaching a well-defined optimal value without the need to impose constraints to the process, as would be necessary for other objective functions.

## Extremum seeking control

The basic diagram for ESC is presented in Figure 1.

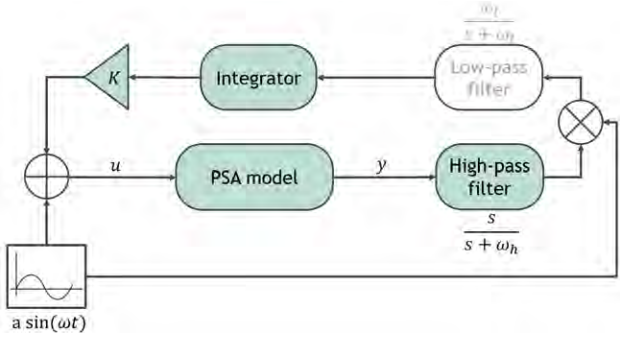



**Figure 1:** Extremum Seeking Control block diagram for Single-Input Single-Output problems.

In the diagram, the previously presented model will represent the plant and will be used to calculate the objective function value $y$ that one aims to optimize and control. A High-pass Filter (HF) and a Low-pass Filter (LF) clear the signal from the DC component and high-frequency noise, respectively, to get a clearer response to the changes affecting the system.

The signal of the input variable $u$ is constantly perturbed by a sinusoidal wave that assists in evaluating the evolution of the objective function by putting the system in constant disruption. By multiplying the filtered value of $y$ by the sinusoidal wave in a demodulation process, the true effect of the sinusoidal change in the manipulated variable $u$ on the response signal can be retrieved. Later, the demodulated and filtered signal will be integrated, providing the signal shift necessary to impose on the manipulated variable so that the objective function gets closer to the optimum, often affected by a gain $K$ to accelerate the convergency.

The low-pass filter was not included in the work here presented since the model output was considered noise-free, hence its washed-out color in Figure 1.

Three different case studies were used to test the ESC applicability in PSA operations, as displayed in Table 1. In case 1, the $t_{feed}$ only changes after 10 cycles of operation, the estimated amount for the process to reach the CSS. In cases 2 and 3, that update is made after each PSA cycle when the plant is in a transient state.

To ensure a similar starting point, a head start of 9 cycles was given before the first iteration in case 2, so that the optimization of both case 1 and case 2 was started after 10 PSA cycles. This ensures that the initialization of the unit does not lead to misguided results since the productivity is naturally lower in the first few cycles of operation. To verify the importance of these initiation cycles, case 3 was performed using the same ESC parameters as case 2 but with the optimization starting in cycle number 1.

**Table 1:** Tuning parameters and initialization procedure for three simulations of ESC of the $CO_2$ productivity with the manipulation of $t_{feed}$.

| Parameter | Case 1 | Case 2 | Case 3 |
|---|---|---|---|
| $a$ | 1 | 1 | 1 |
| $\omega$ | 20 | 20 | 20 |
| $K$ | 25 000 | 25 000 | 25 000 |
| $\omega_h$ | 15 | 15 | 15 |
| Number of PSA cycles per sample | **10** | 1 | 1 |
| Initial $t_{feed}$ (s) | 300 | 300 | 300 |
| Initialization | - | **Yes** | **No** |

## Computational resources

The phenomenological model was implemented in gPROMS Model Builder 7.0.7. Due to the communication protocols established between gPROMS and MATLAB, Simulink was the software chosen to run the optimization and control simulations. The MATLAB version used in the simulation results presented in this article was R2023b (23.2.02365128) 64-bit for Windows.

The solver used was a fixed-step method automatically chosen by Simulink, with a step size of 0.04 s (considered the sampling time) for an overall simulation time of 10 s. This means that Simulink operates for 250 samples. In each sample, an ESC cycle like the one in Figure 1 is executed. In the PSA model block, the simulation continues until the number of cycles assigned for each case in Table 1 is performed in that sample. It is also important to notice that the simulation time is inherent to the Simulink simulation and does not correlate to any real time measure in this case.

The option of a variable-step method was set aside because the perturbation imposed on the system was regular and cyclic. Furthermore, each sampling corresponds with one gPROMS communication after a given number of cycles. If one chose a variable-step method, the system would be out-of-phase since the number of cycles sampled would remain the same, independently of the time-step being 0.01 s or 1 s.

For the simulations presented in this work, the ode3 solver was chosen by the software.

As for hardware resources, the simulations were run on a computer with 128 GB of RAM and an AMD Ryzen 9 5950X 16-Core @ 3.40 GHz processor.

# RESULTS

Figures 2, 3, and 4 display the change in feed time obtained and its effect on $CO_2$ productivity as a function of the simulation time for cases 1, 2 and 3, respectively.

The objective function was considered stabilized in the optimum after 6 s of simulation time for cases 1 and 2 (corresponding to 150 samples). From 6 s to the end of simulation, $t_{feed}$ only increases 2 seconds with no visible alteration in the productivity of $CO_2$ for both cases.

Three different metrics were used to evaluate the different strategies studied. Their values are presented in Table 2.

**Table 2.** Evaluation metrics for the three case studies. (*= before the crash)

| | Case 1 | Case 2 | Case 3 |
|---|---|---|---|
| CPU time /s | 7 857 | 816 | 113 |
| Number of PSA cycles until optimal operation | 1510 | 160 | 18* |
| Time until the optimal operation /h | 4473.4 | 33.2 | 4.6* |

The CPU time relates to the computational effort required for the entire run in Simulink in each case. This metric accounts for the time spent in the PSA unit simulation in gPROMS and the effort to determine the new $t_{feed}$ in each ESC iteration. T

The number of PSA cycles until optimal operation aims to compare the number of PSA cycles required to reach stability in each case. In case 2, this value also considers the cycles used during the initialization procedure.

The time until optimal operation is the cumulative sum of the cycle's duration until stability is reached. It is calculated by Equation 2.

$$\text{Time until the optimal operation } (h) = \sum_{i=1}^{150}\left[\text{Number of PSA cycles per sample } \left(t_{feed,i} + t_{rinse} + t_{blow} + t_{purge}\right)\right] \quad (2)$$

where $t_{rinse}$, $t_{blow}$, and $t_{purge}$ are the duration of the rinse, blowdown and purge steps, respectively, and $t_{feed,i}$ is the input value for $t_{feed}$ for sample $i$.

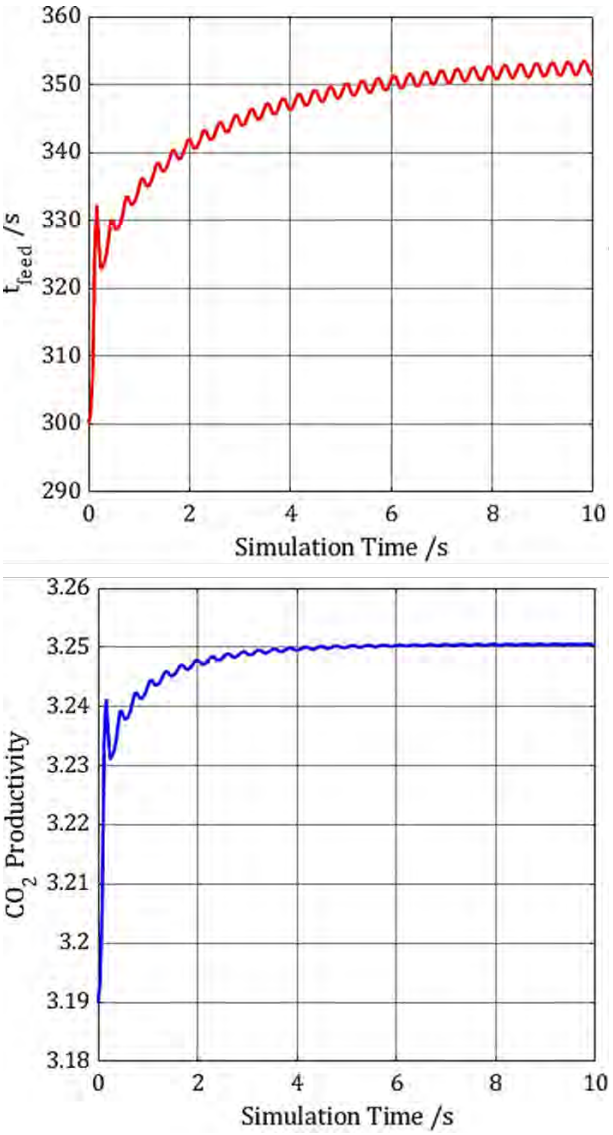



**Figure 2.** ESC action on time of feed value and effect on the productivity of $CO_2$ for case 1.

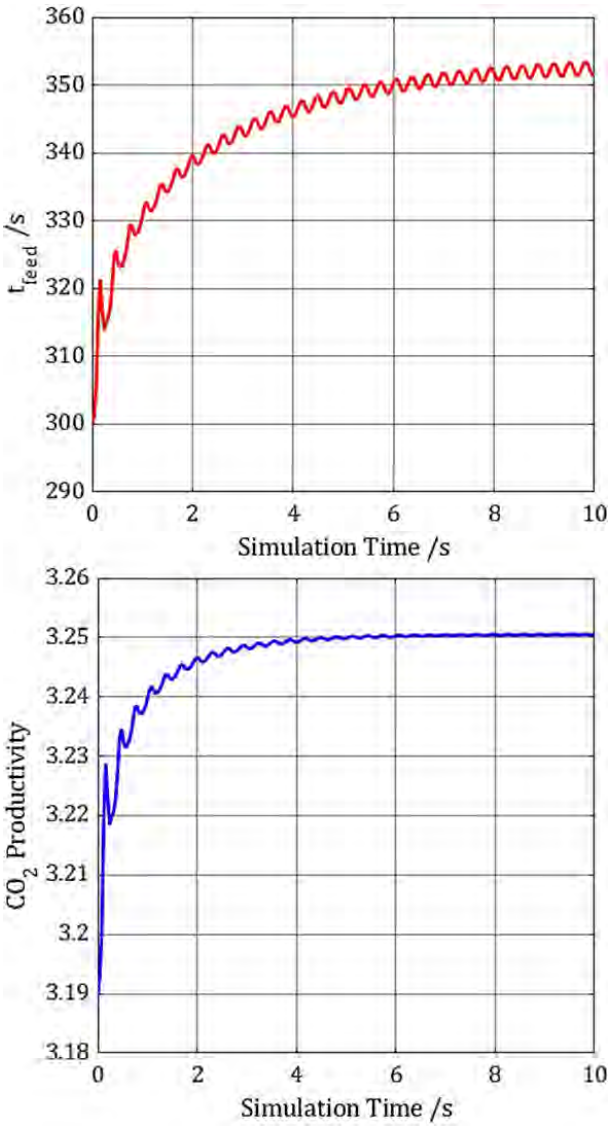



**Figure 3.** ESC action on time of feed value and effect on the productivity of CO2 for case 2.

As can be seen by the comparison between case 1 and case 2, there was no downside in operating the optimization in a transient state and not waiting for the plant to stabilize in a CSS operation before collecting data on the current value of the productivity. However, case 3 clearly demonstrates the relevance of letting the unit run a few cycles before initiating the ESC optimization.

Furthermore, it can also be observed that waiting for the CSS occurrence only delays convergence to the optimum because, although the first iterations achieve higher productivity faster in case 1, the stabilization occurs nearly at the same simulation time for cases 1 and 2, with equal productivity and $t_{feed}$ values achieved.

Therefore, considering the number of PSA cycles and the time until optimal operation, the transient application with initialization is far more advantageous than a cyclic steady-state one. One can even say that the time frame for case 1 is unrealistic since it approaches the 6 months operation for a single objective optimization. The dynamic evaluation reduces that time to a little over a day.

Regarding computational time, it is important to mention that a considerable amount of time is dedicated to the model simulation mechanisms between gPROMS and MATLAB. Despite that, case 2 presented a running time of 13.6 minutes that is not prohibitive.

As can also be perceived from Figures 2 and 3, ESC allows for smooth alteration of the manipulated variables, which can be considered an advantage of this technique, and can be employed in PSA units with encouraging

results. However, this is only the case if the unit has been properly initialized before the ESC application or if one waits for the CSS to update the parameters, otherwise the system tends to the instability, as shown in Figure 4.

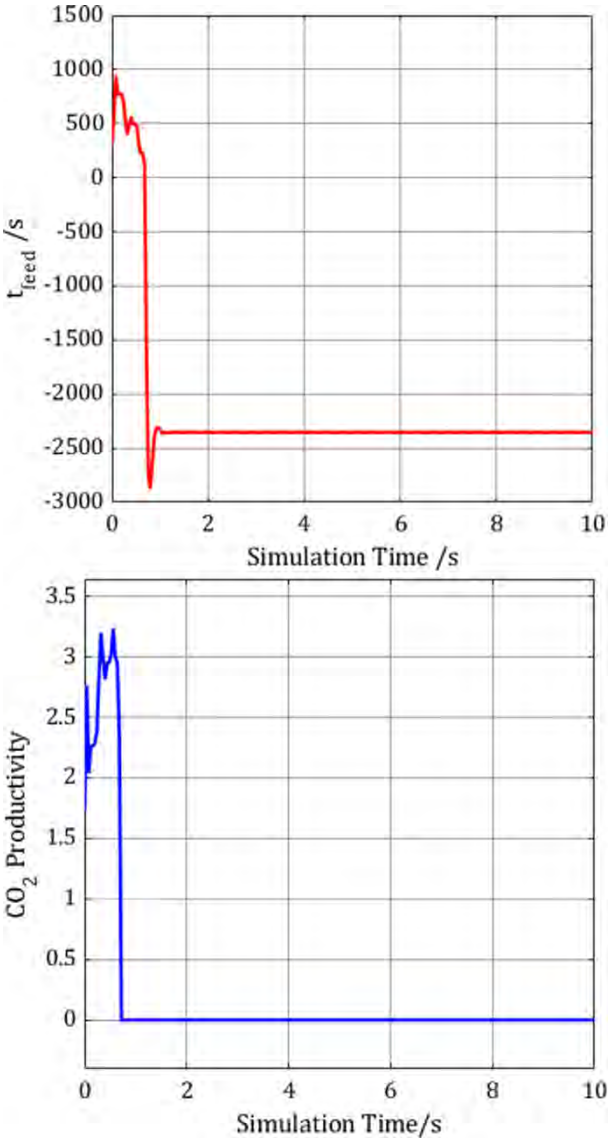



**Figure 4.** ESC action on time of feed value and effect on the productivity of CO2 for case 3.

## CONCLUSIONS

The main objective of analyzing ESC as an alternative to the mainstream methodologies in this understudied topic of RTO applied in PSA systems was fulfilled.

ESC has proven itself as a model-free viable technique for simultaneous control and optimization of PSA units. It has also been demonstrated that there is no need to wait for the unit to reach the CSS after each alteration of the $t_{feed}$ value if an initialization methodology is adopted (in this case, the occurrence of a certain number of PSA cycles before the ESC was activated).

Following this first approach on the ESC implementation in PSA units, some key aspects must be considered in the future work to be developed.

First, this work did not take into consideration the noise present in measurements that a real PSA unit would be subjected to. Despite ESC usually having a proper filter with the goal of filtering such noise (the low pass filter that was not implemented in this work), its capacity to actuate in the system in such circumstances must be evaluated.

In addition, the response to the external disturbances that can affect the process has not been studied in the scope of this work and remains a key aspect to be analyzed to further cement the ESC as an alternative to MPC.

Lastly, for this methodology to reach its full potential, the coordinated optimization of multiple objectives and multiple inputs is crucial. Some works in the literature already cover this topic [22]. However, no references for its application in cyclic adsorption processes could be found at this point, reinforcing the importance of the exploration of such topic.

## ACKNOWLEDGEMENTS

This work was supported by national funds through FCT/MCTES (PIDDAC): LSRE-LCM, UIDB/50020/2020 (DOI: 10.54499/UIDB/50020/2020) and UIDP/50020/2020 (DOI: 10.54499/UIDP/50020/2020); and ALiCE, LA/P/0045/2020 (DOI: 10.54499/LA/ P/0045/2020). Beatriz Silva acknowledges her Ph.D. scholarship 2023.00674.BD (DOI: 10.54499/2023.00674.BD) funded by FEDER funds through NORTE 2020 and by national funds through FCT/MCTES.

## REFERENCES

1. Bonvin, D., Special Issue “Real-Time Optimization” of Processes. Processes, 2017. 5(2). https://doi.org/10.3390/pr5020027.
2. Pfaff, G., J. Fraser Forbes, and P. James McLellan, Generating information for real-time optimization. Asia-Pacific Journal of Chemical Engineering, 2006. 1(1-2): p. 32-43. https://doi.org/10.1002/apj.5.
3. Kameswaran, S. and L.T. Biegler, Simultaneous dynamic optimization strategies: Recent advances and challenges. Computers & Chemical Engineering, 2006. 30(10): p. 1560-1575. https://doi.org/10.1016/j.compchemeng.2006.05.034.
4. Cruz, P., et al., Cyclic adsorption separation processes: analysis strategy and optimization procedure. Chemical Engineering Science, 2003. 58(14): p. 3143-3158.

https://doi.org/10.1016/S0009-2509(03)00189-1.
5. Zhang, R., et al., A Review of Numerical Research on the Pressure Swing Adsorption Process. Processes, 2022. 10(5). https://doi.org/10.3390/pr10050812.
6. Khajuria, H. and E.N. Pistikopoulos, An Explicit/Multi-Parametric Controller Design for Pressure Swing Adsorption System. IFAC Proceedings Volumes, 2010. 43(5): p. 206-211. https://doi.org/10.3182/20100705-3-BE-2011.00034.
7. Khajuria, H. and E.N. Pistikopoulos, Optimization and Control of Pressure Swing Adsorption Processes Under Uncertainty. AIChE Journal, 2013. 59(1): p. 120-131. https://doi.org/10.1002/aic.13783.
8. Martins, M.A.F., et al., Artificial Intelligence-oriented economic non-linear model predictive control applied to a pressure swing adsorption unit: Syngas purification as a case study. Separation and Purification Technology, 2021. 276: p. 119333-119333. https://doi.org/10.1016/j.seppur.2021.119333.
9. Martins, M.A.F., et al., Handling model uncertainty in control of a pressure swing adsorption unit for syngas purification: A multi-model zone control scheme-based robust model predictive control strategy. Separation and Purification Technology, 2023. 306: p. 122668-122668. https://doi.org/10.1016/j.seppur.2022.122668.
10. Oliveira, P.H.M., et al., A Robust Model Predictive Controller applied to a Pressure Swing Adsorption Process: An Analysis Based on a Linear Model Mismatch. IFAC-PapersOnLine, 2021. 54(3): p. 219-224. https://doi.org/10.1016/j.ifacol.2021.08.245.
11. Skogestad, S., J. Jäschke, and D. Krishnamoorthy. Overview and Classification of online process optimization approaches. 2019 [Access 22/01/2024]; Available from: https://folk.ntnu.no/skoge/presentation/dycops2019-workshop-rto/DYCOPS_workshop_final0.pdf.
12. Scheinker, A., 100 years of extremum seeking: A survey. Automatica, 2024. 161: p. 111481-111481. https://doi.org/10.1016/j.automatica.2023.111481.
13. Tan, Y., et al. Extremum seeking from 1922 to 2010. in Proceedings of the 29th Chinese Control Conference. 2010.
14. Luxat, J.C. and L.H. Lees, Stability of Peak-Holding Control Systems. IEEE Transactions on Industrial Electronics and Control Instrumentation, 1971. IECI-18(1): p. 11-15. https://doi.org/10.1109/TIECI.1971.230455.
15. Krstic, M. and H.-H. Wang, Stability of extremum seeking feedback for general nonlinear dynamic systems. Automatica, 2000. 36(4): p. 595-601. https://doi.org/10.1016/S0005-1098(99)00183-1.
16. Drakunov, S., et al., ABS control using optimum search via sliding modes. IEEE Transactions on Control Systems Technology, 1995. 3(1): p. 79-85. https://doi.org/10.1109/87.370698.
17. Wu, Z., et al., Closed-loop enhancement of jet mixing with extremum-seeking and physics-based strategies. Experiments in Fluids, 2016. 57(6): p. 107-107. https://doi.org/10.1007/s00348-016-2194-9.
18. Martínez, E., Extremum-seeking control of redox processes in wastewater chemical treatment plants, in Computer Aided Chemical Engineering, V. Plesu and P.S. Agachi, Editors. 2007, Elsevier. p. 865-870. https://doi.org/10.1016/S1570-7946(07)80167-2.
19. de Klerk, A., Fischer–Tropsch Process, in Kirk-Othmer Encyclopedia of Chemical Technology. p. 1-20. https://doi.org/https://doi.org/10.1002/0471238961.fiscdekl.a01.
20. Khosravani, H., et al., Chapter 1 - Introduction to syngas products and applications, in Advances in Synthesis Gas : Methods, Technologies and Applications, M.R. Rahimpour, M.A. Makarem, and M. Meshksar, Editors. 2023, Elsevier. p. 3-25. https://doi.org/10.1016/B978-0-323-91878-7.00014-9.
21. Regufe, M.J., et al., Syngas Purification by Porous Amino-Functionalized Titanium Terephthalate MIL-125. Energy & Fuels, 2015. 29(7): p. 4654-4664. https://doi.org/10.1021/acs.energyfuels.5b00975.
22. Kumar, S. and N. Gans. Extremum Seeking Control for multi-objective optimization problems. in 2016 IEEE 55th Conference on Decision and Control (CDC). 2016. https://doi.org/10.1109/CDC.2016.7798416.

© 2025 by the authors. Licensed to PSEcommunity.org and PSE Press. This is an open access article under the creative commons CC-BY-SA licensing terms. Credit must be given to creator and adaptations must be shared under the same terms. See https://creativecommons.org/licenses/by-sa/4.0/



Systems & Control Transactions

**Research Article - Peer Reviewed Conference Proceeding**
ESCAPE 35 - European Symposium on Computer Aided Process Engineering
Ghent, Belgium. 6-9 July 2025
Jan F.M. Van Impe, Grégoire Léonard, Satyajeet S. Bhonsale,
Monika E. Polańska, Filip Logist (Eds.)

PSE PRESS

# Machine Learning-Based Soft Sensor for Hydrogen Sulfide Monitoring in the Gas Treatment Section of an Industrial-Scale Oil Regeneration Plant

**Luis F. Sánchez[a], Eva C. Coelho[b], Francesco Negri[ac], Francesco Gallo[c], Mattia Vallerio[a], Henrique A. Matos[b], Flavio Manenti[a]***

[a] CMIC Department "Giulio Natta", Politecnico di Milano, Piazza Leonardo da Vinci 32, Milano, 20133, Italy
[b] Departamento de Engenharia Química, Instituto Superior Técnico, Avenida Rovisco Pais 1, Lisboa, 1049-001, Portugal
[c] Itelyum Regeneration S.p.A., Via Tavernelle, 19, Pieve Fissiraga, 26854, Italy
* Corresponding Author: flavio.manenti@polimi.it

## ABSTRACT

Monitoring chemical composition is key in several industrial-scale chemical processes. However, traditional composition sensors usually convey drawbacks, including high costs, short lifetimes, and frequent calibration requirements. As an alternative, software (soft) sensors have gained attention in recent years due to their accuracy, ease of training, and potential of integrating widely known machine learning techniques. This study presents the methodology followed to train a soft sensor for hydrogen sulfide monitoring in the gas treatment section of an industrial facility in Italy. In particular, this methodology includes a novel approach for steady-state determination from historical plant data in the presence of several steady states and noise. Unfortunately, only four steady states were found in the plant data, which was insufficient for accurate soft sensor training. As an alternative, these steady states were used to develop and validate a rigorous Aspen HYSYS process simulation. The relative error of the simulation compared to the steady states found was around 1%. This simulation was used to extract additional steady state data, which was sufficient for soft sensor training. The soft sensor, trained following a Kriging Gaussian Process regression, showed a relative error with respect to the rigorous simulation of around 0.7%. The high accuracy of the sensor suggests it is a quick, low-cost, and accurate alternative to estimate the hydrogen sulfide composition and identify potential operating conditions that may lead to off-specification conditions. Future work will focus on field implementation and evaluation of the trained sensor.

**Keywords**: Process Control, Soft sensor, Simulation, Steady-State

## INTRODUCTION

Control systems are key in the operation of chemical processes to maintain their stability, meet production targets, and fulfill safety, quality, and environmental constraints. Nowadays, most industrial-scale processes depend on conventional or classical control systems, based on closed loops of sensors, controllers, and final control elements [1]. Despite all these components playing an important role, sensors are particularly critical since the performance of the control loop depends on the quality of the data they provide [2].

Conventional sensors measure physical quantities to monitor key process variables like temperatures, pressures, levels, and flow rates. However, tracking variables such as compositions is complex, and the sensors required for this task are equally sophisticated. Moreover, these sensors usually convey several drawbacks, including high capital and operating costs, long measurement delays, short lifetimes, sensitivity to harsh environments, or frequent calibration requirements [2].

A widely spread alternative for composition evaluation is its indirect measurement. A classic example is evaluating the composition inside a distillation column using equilibrium calculations and the temperature measured at a determined stage. This method is particularly

efficient for binary or pseudo-binary mixtures [3]. However, composition inference increases in complexity in multi-component systems or when the mathematical correlation between variables is uncertain [4].

Novel methodologies for indirect composition measurement have benefitted from the growing interest in Machine Learning. In particular, inferential models built from process data called software sensors (or soft sensors) have gained attention in recent years [4]. They have been successfully implemented to assess the composition of complex mixtures present in processes such as polymeric isomerization [5] and fermentation [6].

Data quality significantly impacts the final model accuracy, as in any data-based approach. Therefore, it is essential not only to gather enough process data but also to preprocess it effectively to maximize the available information. In the literature, soft sensors are typically trained using datasets that require preprocessing steps, such as noise removal [7] or steady-state identification [8]. However, these studies often address only one of these tasks.

In the absence of a generalized methodology for steady-state detection in the literature, this work presents an innovative approach used in the steady-state detection of the gas treatment section of an oil regeneration plant in Italy. This methodology will support the development of a rigorous simulation of the process and posterior training of a hydrogen sulfide soft sensor.

## PROBLEM STATEMENT

The case study considered in this work is the gas treatment section of an industrial-scale plant located in Pieve Fissiraga, Italy. This plant, property of Itelyum S.p.A., produces high-quality lubricants from wasted oils, following the Revivoil™ process [9]. Combined with a second plant in Ceccano, Italy, Itelyum currently achieves a wasted oil treatment capacity of around 200 kt/y. Figure 1 presents the Block Flow Diagram (BFD) including the main unit operations of the Revivoil™ process.

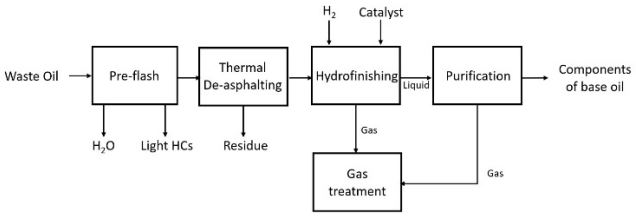



**Figure 1.** BFD of the Revivoil™ waste oil regeneration process.

The gas treatment section aims to remove acid gases such as hydrogen sulfide and carbon dioxide from gaseous products obtained in the hydro-finishing section of the plant. This is done via absorption in Diethanolamine (DEA) and its subsequent regeneration. Figure 2 presents a simplified scheme of the gas treatment section, highlighting the key process streams.

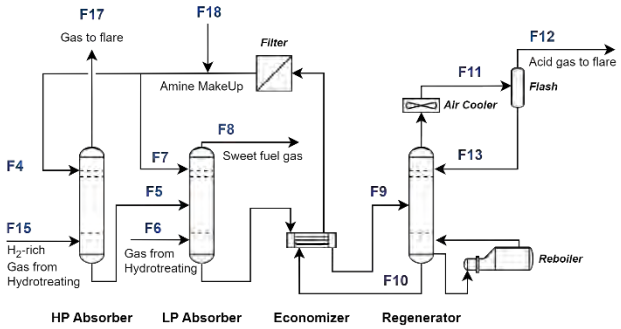



**Figure 2.** Simplified Process Flow Diagram of the gas treatment section showing key streams for the soft-sensor training.

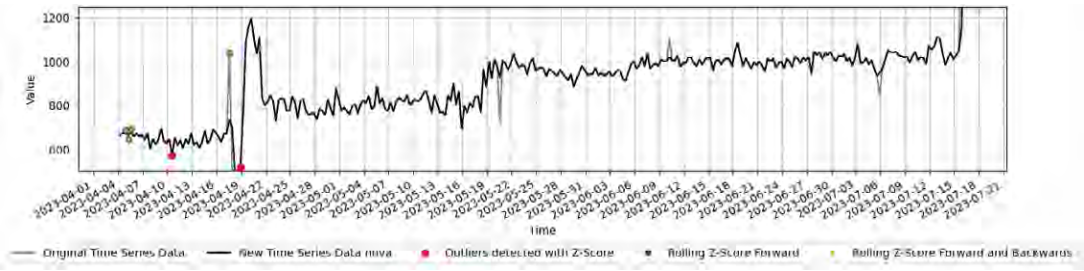
Hydrogen sulfide is a toxic gas that contributes to acid rain formation. Consequently, its emissions are strictly controlled, especially in the European Union [10]. Hydrogen sulfide composition in the facility considered in this work is measured in a laboratory via gas sample analysis by a gas chromatographer. This procedure has demonstrated delays of up to eight hours in the determination of hydrogen sulfide composition, which could potentially lead to long off-specification operation periods. Considering these complexities, a soft sensor of the gas treatment section would be a low-cost immediate solution to provide a quick and accurate estimate of hydrogen sulfide composition in order to identify operating conditions with the potential to lead the process off-specifications.

## PROCESS DATA AND PRE-PROCESSING

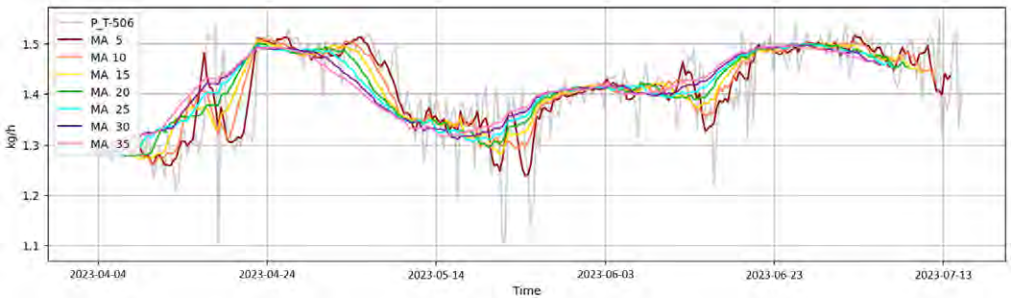
**Table 1:** Variables with a potential influence on the $H_2S$ concentration of the sweet fuel gas stream.

| Stream / Unit | Variables | Description |
|---|---|---|
| F15 | F, T | Gas stream entering HP absorber from hydrotreatment. |
| F6 | F, T | Gas stream entering LP absorber from hydrotreatment. |
| F18 | F, T | DEA makeup stream. |
| LP Abs. | P | Pressure in LP absorber. |
| HP Abs. | P | Pressure in HP absorber. |
| Regen. | P | Pressure in the regenerator. |

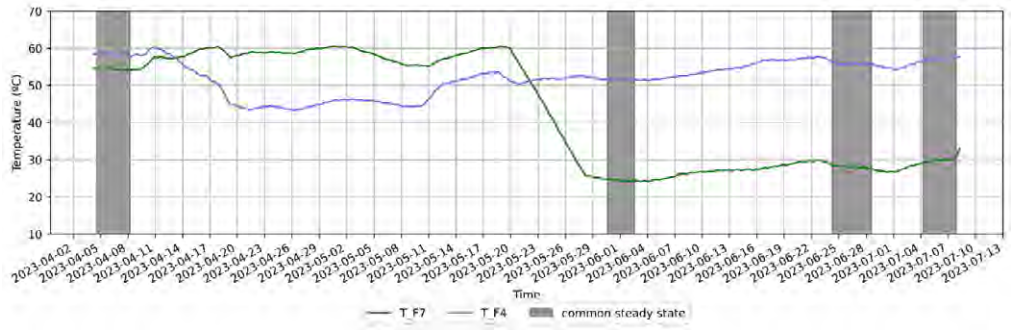
Historical data from variables expected to influence $H_2S$ composition in streams F8, F12, and F17 was obtained from the plant records (see Table 1). However, data pre-processing was required to extract the most




**a)** Outlier detection for the flow rate of stream F9. Outliers found with the forward z-scores method are highlighted in green, with the backward in red, and with both in gray.




**b)** Sensitivity analysis of the number of points in the rolling window for the noise reduction using the moving average approach using the pressure in the LP absorber.




**c)** Steady-state detection results showing the temperature profiles of F4 (purple), F7 (green), and the common steady states for all the analyzed variables as the zones shaded in grey.

**Figure 3:** Data preprocessing results for the historical data of the gas treatment section.

information from these records. Typical pre-processing activities include data normalization, outlier detection, missing data insertion, noise reduction, and data reconciliation. These methodologies were applied using the NumPy, SciPy, and Scikit Learn Python packages.

## Outlier detection

Outliers are data points that deviate from the dataset trend and could bias an eventual model, reducing its accuracy [11]. z-score methodology (Equation 1) is commonly used for outlier detection and removal.

$$Z_{score} = \frac{x-\bar{x}}{\sigma} \quad (1)$$

Where $x$ is the data point, $\bar{x}$ is the mean, and $\sigma$ the variance of the considered dataset. Nonetheless, this methodology may be unsuccessful if multiple steady states are present in the dataset. As an alternative, a rolling z-scores methodology was used. The methodology was applied to the dataset rolling it forward and backward. The number of points considered in each window was 10, which was visually verified to remove actual outliers while avoiding deleting points that may provide useful information. Figure 3.a presents the outlier detection for the flow rate of stream F9.

## Data reconciliation

Every sensor measurement involves errors, which may be systematic or random. The reliability of these measurements may increase by evaluating whether mass and energy balances using the measurements are respected or not by following a data reconciliation.

From a mathematical point of view, data reconciliation is an optimization problem, where mass balance errors are minimized. The mass balances for the gas treatment section are shown in Equations 2 to 6. The optimization constraints, which aim to keep the stability and physical meaning of the simulation are shown in Equations 7 and 8.

### Mass balances

$$\textbf{LP Absorber}: \ 0 = F4 + F15 - F17 - F5 \quad (2)$$

$$\textbf{HP Absorber}: 0 = F5 + F7 + F6 - F8 - F9 \quad (3)$$

$$\textbf{Regenerator}: \ 0 = F9 + F13 - F11 - F10 \quad (4)$$

$$\textbf{Condenser}: \quad 0 = F11 - F12 - F13 \quad (5)$$

$$\textbf{DEA balance}: \ 0 = F4 + F7 - F10 - F18 \quad (6)$$

### Optimization constraints

$$\textbf{HP Absorber}: \ F15 > F17 \quad (7)$$

$$\textbf{LP Absorber}: \ F6 > F8 \quad (8)$$

## Noise reduction

A standard methodology for noise reduction is the moving average. In this study, the moving average window size was studied for the specific problem. As an example, Figure 3.b presents the sensitivity analysis of the window parameter observed in the pressure of the LP absorber. A window size of 15 points was used so as not to lose relevant information from the dataset while reducing its noise.

## Steady-state identification

The estimation of the gas treatment section dead times was not possible due to limitations in the experimentation in the industrial-scale process. This impeded the direct training of a dynamic soft sensor of the system, such as in the approach of Herceg et al. for a 2,3-dimethylbutane dynamic soft sensor in an isomerization process [5]. As an alternative, a steady-state soft sensor was proposed. This is expected to provide information to identify operating conditions that could potentially lead the process out of specifications.

In the absence of a generalized methodology for steady-state estimation in noisy datasets with multiple possible steady state values, a novel approach was proposed. This methodology was based on the rolling window for outlier detection. In this case, the number of points contained in the sliding window was kept at 10. Inside each window, a linear regression model was fit. Then, the slope of the regression was compared to a threshold value, set at 0.6, to classify it as a steady state. This procedure was followed with all the involved variables to determine the presence of common steady states for all of them.

The results of the steady state determination are shown in Figure 3.c. Four steady states-common for all the analyzed variables of Table 1- were found. These states had between 3 and 5 days of stable operating conditions. The number of points in the rolling window and the slope threshold were graphically validated to confirm the presence of reasonable steady states.

# PROCESS SIMULATION

The small number of steady-states found in the historical data impeded the direct training of the data-based soft sensor. As an alternative, these steady states supported the development and validation of a rigorous process simulation in Aspen HYSYS, which was later used to simulate additional steady states.

The rigorous simulation considered DEA, water, hydrogen, hydrogen sulfide, carbon monoxide, carbon dioxide, nitrogen, methane, ethane, propane, butane, pentane, and a heavy mix of hydrocarbons as components. The thermodynamic package used was *Acid Gas and Chemical Solvents*, ideal for gas sweetening operations. The simulation was validated with process and laboratory data, and the results are shown in Table 2.

**Table 2:** Process simulation accuracy for flow rate [kg/h] compared to the steady-states found in historical data.

| Stream | Preprocessed | Simulation | Rel. Error |
|---|---|---|---|
| F4 | 829.0 | 828.0 | 0.1% |
| F15 | 170.4 | 163.4 | 4.1% |
| F17 | 147.9 | 146.3 | 1.1% |
| F5 | 851.5 | 845.1 | 0.8% |
| F7 | 156.1 | 154.5 | 1.0% |
| F6 | 150.2 | 153.0 | 1.9% |
| F8 | 116.5 | 115.7 | 0.7% |
| F9 | 1041.0 | 1037.0 | 0.4% |
| F13 | 279.4 | 279.2 | 0.1% |
| F11 | 334.6 | 334.5 | 0.0% |
| F10 | 986.2 | 981.6 | 0.5% |
| F12 | 55.2 | 55.7 | 0.9% |
| **Average** | | | **0.9%** |

The rigorous simulation demonstrated a high fidelity with the plant's historical data. However, its complexity and long computational times motivated its splitting into two sections: The first section included the high and low-pressure absorbers (Figure 4), and the second considered the DEA regeneration (Figure 5). The splitting increased the number of required variables, due to the presence of streams interacting in both simulations.

These streams are shown in Table 3. The pre-processing activities were repeated to consider the effect of the new variables.

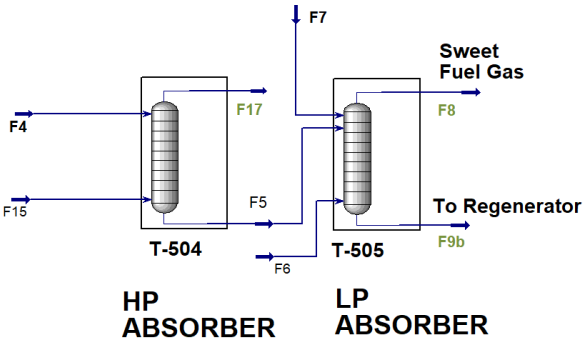



**Figure 4.** Simulation of the absorbers of the gas treatment section using Aspen HYSYS.

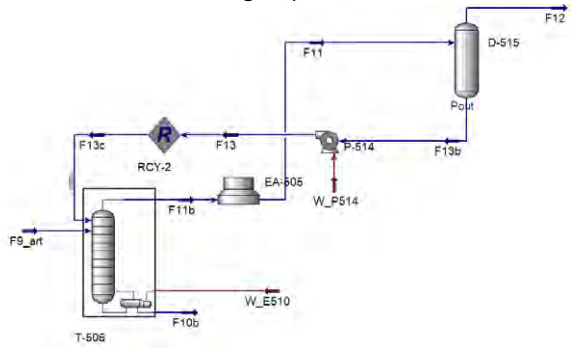



**Figure 5.** Simulation of the DEA regenerator of the gas treatment section in Aspen HYSYS.

**Table 3:** Additional variables with a potential influence on the $H_2S$ concentration of the sweet fuel gas stream due to simulation split.

| Streams | Variable | Description |
|---|---|---|
| F4 | F, T | DEA stream entering HP Absorber. |
| F7 | F, T | DEA stream entering LP Absorber. |
| F9 | F, T | DEA stream entering regenerator from absorbers. |

## SOFT-SENSOR TRAINING

The data-driven soft-sensor model was trained extracting steady-state data from the rigorous simulation. For this purpose, several different combinations of the simulation input values were evaluated via Design of Experiments (DoE). In total, the absorption section had 10 input variables from streams F4, F15, F7, and F6, and units LP Abs. and HP Abs., while the regeneration section had 5 input variables from streams F9 and F13, and the Regenerator unit (See Tables 2 and 3).

The algorithm chosen for DoE was the maximin-optimized Latin Hypercube method, one of the most widely implemented methodologies to guarantee the even spatial distribution of points [12]. A total of 150 combinations of input values for the absorbers section and 75 for the regeneration were tested in the rigorous simulation. These numbers correspond to 15 times the number of input variables, slightly higher than the 10 usually recommended as a minimum for effective computer experiments [13]. This number was selected to consider possible non-convergent simulations. In the end, 118 and 64 simulations for the absorption and regeneration sections reached convergence, respectively.

The generated data was divided into 80/20 partitions, where 80% of the data was used for model training and validation, and 20% for model testing. The training set was subsequently divided into 80/20 partitions used for model training and validation, respectively. The model chosen was the Kriging Gaussian Process with different common kernels such as Radial Basis Function (RBF), Linear, Polynomial, and Rational Quadratic (RQ). The most accurate kernel to model the hydrogen sulfide composition in streams F8, F17, and F12 was chosen via 5-fold cross-validation using the training and validation sets. The results for the accuracy of the soft sensor model evaluated in the test set are presented in Table 4.

**Table 4:** Soft sensor test set error for the output variables ($H_2S$ composition) of the gas treatment section.

| Stream | Variable | Best kernel | Rel. Error |
|---|---|---|---|
| F17 | $x_{H2S}$ | RBF | 0.05% |
| F8 | $x_{H2S}$ | RQ | 1.00% |
| F12 | $x_{H2S}$ | Linear | 0.93% |
| **Average** | | | **0.66%** |

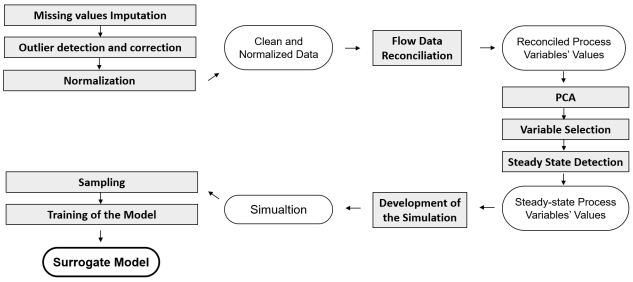



**Figure 6.** Final soft-sensor training methodology implemented for the soft-sensor training.

Table 4 shows the high accuracy of the trained soft sensor compared to simulation data, showing errors below 1%. In addition, the high accuracy of the rigorous process simulation suggests that the soft-sensor may be a practical alternative for hydrogen sulfide concentration estimation, in particular for the identification and prevention of potential off-specification operating conditions in

the gas treatment section of the plant. The methodology followed in this work, including the novel methodology for steady state identification for the soft-sensor training, is summarized in Figure 6.

## CONCLUSIONS

In this work, process data from the gas treatment section of an industrial-scale facility was pre-processed with literature standard methodologies, plus a novel steady-state detection methodology. This methodology considered the combination of a sliding window and a linear regression to assess the dataset which presented noise and multiple steady states. In the end, the steady state data was graphically validated, and used to train a rigorous process simulation of the process. This simulation supported the training of an accurate Kriging-based soft sensor with different kernel functions.

The relative error of the simulation compared to the real process was around 1%, while the relative error of the soft sensor model compared to the rigorous simulation was around 0.7%. The high accuracy of the soft sensor suggests that it is a quick, low-cost, and accurate alternative to estimate the exit composition of hydrogen sulfide and to identify potential operating conditions that may lead to off-specification conditions in the plant. Future work will focus on the implementation of the soft sensor in field operations.

## ACKNOWLEDGEMENTS

The present work is within the MUSA – Multilayered Urban Sustainability Action – project, funded by the European Union – NextGenerationEU, under the National Recovery and Resilience Plan (NRRP) Mission 4 Component 2 Investment Line 1.5: Strengthening of research structures and creation of R&D "innovation ecosystems", set up of "territorial leaders in R&D".

## REFERENCES

1. H. L. Wade, Basic and Advanced Regulatory Control: System Design and Application, 3° edizione. ISA, 2017.
2. A. W. Koch, Measurement and Sensor Systems: A Comprehensive Guide to Principles, Practical Issues and Applications, 1st ed. 2023 edition. Cham: Springer, 2024.
3. M. Kano, K. Miyazaki, S. Hasebe, and I. Hashimoto, 'Inferential control system of distillation compositions using dynamic partial least squares regression', Journal of Process Control, vol. 10, no. 2, pp. 157–166, Apr. 2000, doi: 10.1016/S0959-1524(99)00027-X.
4. Y. Liu and M. Xie, 'Rebooting data-driven soft-sensors in process industries: A review of kernel methods', Journal of Process Control, vol. 89, pp. 58–73, May 2020, doi: 10.1016/j.jprocont.2020.03.012.
5. S. Herceg, Ž. Ujevic Andrijic, and N. Bolf, 'Support Vector Machine-based Soft Sensors in the Isomerisation Process', Chem. biochem. eng. q. (Online), vol. 34, no. 4, pp. 243–255, 2021, doi: 10.15255/CABEQ.2020.1825.
6. P. Yan, M. Gai, Y. Wang, and X. Gao, 'Review of Soft Sensors in Anaerobic Digestion Process', Processes, vol. 9, no. 8, Art. no. 8, Aug. 2021, doi: 10.3390/pr9081434.
7. Y. Wang et al., 'Blank sample denoising algorithm (BSDA): An effective spectral noise reduction in water sample LIBS detection', Talanta, vol. 275, p. 126086, Aug. 2024, doi: 10.1016/j.talanta.2024.126086.
8. H. Ji, Y. Liu, R. Zhang, Z. Yuan, and F. Meng, 'Detection and recognition of toluene and butanone in mixture based on SnO2 sensor via dynamic transient and steady-state response analysis in jump heating voltage mode', Sensors and Actuators B: Chemical, vol. 376, p. 132969, Feb. 2023, doi: 10.1016/j.snb.2022.132969.
9. 'TMView'. Accessed: Jan. 20, 2025. [Online]. Available: https://www.tmdn.org/tmview/#/tmview/detail/EM500000008525222
10. 'Directive - 2016/2284 - EN - EUR-Lex'. Accessed: Jan. 21, 2025. [Online]. Available: https://eur-lex.europa.eu/eli/dir/2016/2284/oj/eng
11. L. Salano, E. Moioli, M. Vallerio, and F. Manenti, 'Biogas Reforming: Data Reconciliation and Model Validation with Industrial Data', Dec. 03, 2024, Social Science Research Network, Rochester, NY: 5042990. doi: 10.2139/ssrn.5042990.
12. K. McBride and K. Sundmacher, 'Overview of Surrogate Modeling in Chemical Process Engineering', Chemie Ingenieur Technik, vol. 91, no. 3, pp. 228–239, 2019, doi: 10.1002/cite.201800091.
13. J. L. Loeppky, J. Sacks, and W. J. Welch, 'Choosing the Sample Size of a Computer Experiment: A Practical Guide', Technometrics, vol. 51, no. 4, pp. 366–376, Nov. 2009, doi: 10.1198/TECH.2009.08040.

© 2025 by the authors. Licensed to PSEcommunity.org and PSE Press. This is an open access article under the creative commons CC-BY-SA licensing terms. Credit must be given to creator and adaptations must be shared under the same terms. See https://creativecommons.org/licenses/by-sa/4.0/



Systems & Control Transactions

**Research Article - Peer Reviewed Conference Proceeding**
ESCAPE 35 - European Symposium on Computer Aided Process Engineering
Ghent, Belgium. 6-9 July 2025
Jan F.M. Van Impe, Grégoire Léonard, Satyajeet S. Bhonsale,
Monika E. Polańska, Filip Logist (Eds.)

PSE PRESS

# Principles and Applications of Model-free Extremum Seeking – A Tutorial Review

**Laurent Dewasme and Alain Vande Wouwer**

Systems, Estimation, Control and Optimization (SECO), University of Mons, 7000 Mons, Belgium [laurent.dewasme; alain.vande-wouwer@umons.ac.be]

## ABSTRACT

This article aims to tutorial a few important extremum seeking control approaches that can be used for the model-free optimization of industrial processes in various fields. The application of several methods is illustrated with a simple case study related to the production of algal biomass in photobioreactors. Other methods and applications are briefly reviewed.

**Keywords**: Process Control, Optimization, Biosystems

## INTRODUCTION

Extremum seeking (ES) has become a large family of perturbation-based methods whose origins can be traced back to the work of the French Engineer Leblanc in 1922, who sought to transmit electrical power to a train car contactlessly [1]. Since then, extremum seeking has gained significant attention, especially in the past three decades, notably thanks to the seminal work of Krstic and his co-workers, who provided conditions for convergence and stability analysis [2]. ES is a practical approach aimed at achieving optimal performance of a system by continuously seeking the extremum of an online-measured cost function. The method finds various applications in different fields, provided that the required measurement information is available, and an optimality principle can be formulated. While many simulation studies have confirmed the effectiveness of extremum seeking, relatively few experimental studies have been conducted to validate its real-world applications. This gap between theory and practice is a common challenge in real-time optimization and control.

This article will provide a tutorial introduction to the foundational principles and applications of extremum seeking control (ESC), using a simple case study of micro-algal growth in a photo-bioreactor (PBR) whose productivity can be adjusted by manipulating the dilution rate. More practical applications are briefly cited and available in previous review papers [3-5].

## TUTORIAL EXAMPLE

A dynamic Droop model describes the growth of micro-algae by the following differential equations:

$$\dot{X} = \mu(Q,I)X - D\,X \tag{1a}$$

$$\dot{S} = -\rho(S,Q)X - D\,(S - S_{in}) \tag{1b}$$

$$\dot{Q} = \rho(S,Q) - \mu(Q,I)\,Q \tag{1c}$$

where *X*, *S* and *Q* respectively stand for the biomass, nitrogen substrate source, and internal nitrogen quota, *I* is the light irradiance, $S_{in}$ the substrate concentration in the feed, $D = F_{in}/V$ the dilution rate (assumed to be the sole input). In this latter expression, $F_{in}$ is the feed flow rate, and *V* is the photobioreactor volume. $\mu$ and $\rho$ are the growth and substrate uptake rates, respectively, which are nonlinear functions of the states and light. $\mu$ is modeled by Droop kinetics:

$$\mu(Q,I) = \mu_{max}\frac{I}{K_{I,s}+I+\frac{I^2}{K_{I,i}}}\left(1-\frac{Q_{min}}{Q}\right) \tag{2}$$

and $\rho(S)$ by Monod kinetics:

$$\rho(S,Q) = \rho_{max}\frac{S}{S+K_S}\left(1-\frac{Q}{Q_{max}}\right) \tag{3}$$

where $\mu_{max}$ and $\rho_{max}$ are the maximum rate constants, $Q_{min}$ and $Q_{max}$ the minimum and maximum internal quota capacities, $K_{I,s}$ and $K_S$ the half-saturation constants, and $K_{I,i}$ is the rate inhibition constant. Parameter values relative to the strain Isochrysis galbana are reported in [6]. A bifurcation analysis is also achieved in this study, providing stability conditions on the input steady-state value $D_e$ as follows:

$$D_e < \mu_{max} \quad (4a)$$

$$D_e < \frac{\mu_{max}\,\rho_{max}}{\rho_{max} + \mu_{max}\,Q_{min}} \quad (4b)$$

Defining biomass productivity $y = D\,X$ as the cost function to optimize, a steady-state convex objective function can be obtained:

$$y(D_e) = \frac{D_e S_{in}(\mu_{max} - D_e)}{\mu_{max}\,Q_{min}} \quad (5)$$

and the corresponding optimal operating conditions:

$$D_e^* = \frac{1}{2}\mu_{max} \quad (6a)$$

$$y_e^* = \frac{S_{in}\,\mu_{max}}{4\,Q_{min}} \quad (6b)$$

The process model and optimal operating conditions are unknown in the following, but productivity can be measured online at a fast rate (every minute), and the objective of extremum seeking is to determine the optimal operating conditions quickly and reliably.

## PRINCIPLES OF ESC

### Modulation-Demodulation

The nowadays standard ES approach [2] consists of injecting a periodic perturbation signal (also called dither signal) in the system to extract information using a modulation-demodulation procedure, as represented in Figure 1. The perturbation can be a simple periodic signal, such as a sinusoid with adjustable amplitude and pulsation if only one parameter $\theta$ has to be estimated, or a combination of several periodic signals with different frequencies if several parameters have to be extracted. These parameters refer to a measurable static map

$$y = g(\theta) \quad (7)$$

of a dynamic system

$$\begin{aligned} \dot{x} &= f(x, y) \\ y &= h(x) \\ u &= q(x, \theta) \end{aligned} \quad (8)$$

If the perturbation signal changes slowly with respect to the system dynamics, the latter can be assumed in pseudo-steady state (the process output is then noted $y_{ss}$) and the following relations can be established for the modulated signal $y_{mod}(t)$, the high-pass filtered signal $y_{HP}(t)$, the demodulated signal $y_{demod}(t)$, and the low-pass filtered signal $y_{LP}(t)$

$$\begin{aligned} y_{mod}(t) &\approx y_{ss} + g' a \sin(\omega t) \\ y_{HP}(t) &\approx |G_{HP}(\omega)| g' a \sin(\omega t + \varphi_{HP}) \\ y_{demod}(t) &\approx |G_{HP}(\omega)| g' \frac{a^2}{2}(\cos(\varphi_{HP}) - \cos(2\omega t + \varphi_{HP})) \\ y_{LP}(t) &\approx |G_{LP}(\omega)||G_{HP}(\omega)| g' \frac{a^2}{2}\cos(\varphi_{HP}) \end{aligned} \quad (9)$$

If the cutoff pulsations of the filters $\omega_{HP}$ and $\omega_{LP}$ are well-chosen (they must be smaller than the pulsation of the perturbation signal), then

$$y_{LP}(t) \approx g' \frac{a^2}{2} \qquad if \quad \omega > \omega_{HP}, \omega_{LP} \quad (10)$$

and the low-pass filtered signal contains information about the gradient of the static map g(θ). Modulation-demodulation thus provides a way to estimate the gradient of the cost function to optimize, and the integrator, which follows the low-pass filter in the block diagram of Figure 1, will act as a simple controller pushing to zero this gradient, i.e., seeking for an extremum of the static map.

The application of BOF-ESC (for bank of filters as the modulation-demodulation approach uses several filters) to the microalgal PBR is shown in Figures 2-3.

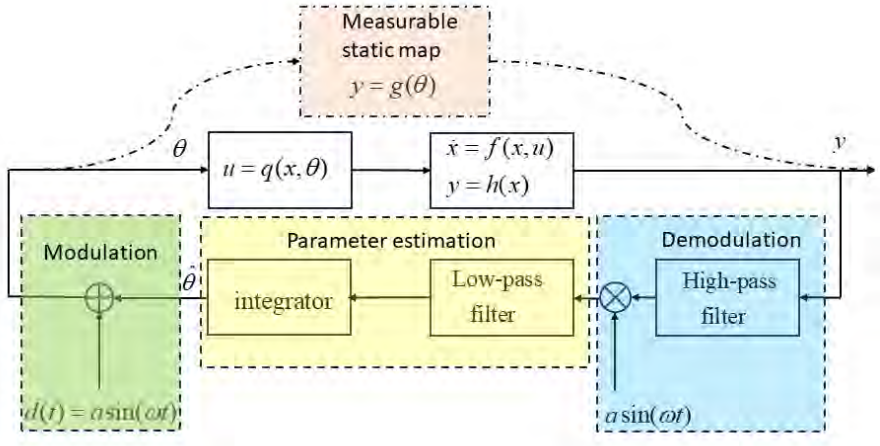



**Figure 1:** Extremum seeking control based on modulation with a dither signal, and demodulation and parameter estimation using demodulation and a bank of filters – BOF (high pass, low pass filters) + integrator.

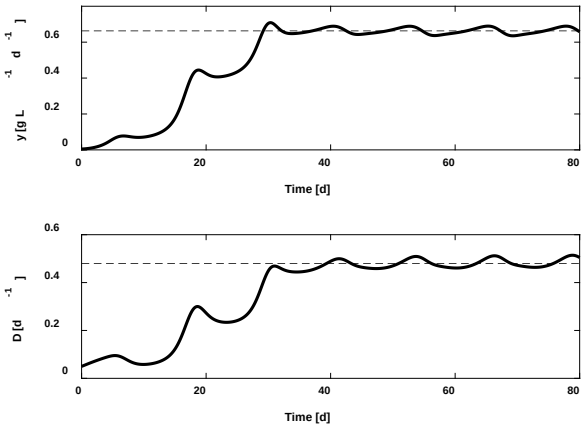



**Figure 2.** Productivity *y* and dilution *D* trajectories over time.

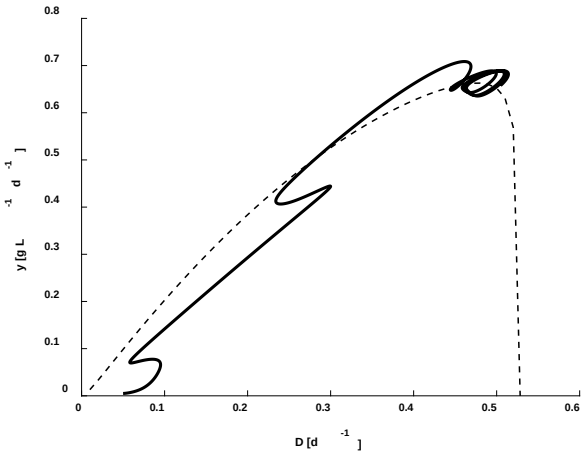



**Figure 3.** Productivity *y* vs dilution *D* diagram.

The perturbation signal is $d(t) = 0.02\,sin(\,0.5t)$, the high-pass filter pulsation $\omega_{HP} = 0.45$ rad/day, and the integrator gains 70. There is no low-pass filter in this design, as the integrator already plays an attenuation role. Figure 3 shows in the dashed line the static map and in the solid line the trajectory of the ESC, with sustained oscillation around the optimum due to the perturbation signal. Convergence is achieved in about 40 days, a pretty long time interval! This highlights the challenges of applying ESC to slow processes (such as those encountered in biotechnology) facing the limitation of the three-time scale separation:

- The process is considered as the fast dynamics;
- The perturbation signal is slow compared to the process dynamics but fast compared to the filter bandwidths;
- Parameter estimation is, therefore, the slowest.

BOF-ESC is a popular approach that has been applied in various fields (see the review paper [3] for a panel of applications) and has been successfully implemented for fast processes such as wind turbines or solar panels (see, for instance, [7] for an application to solar panels). For slower processes, it is critical to accelerate convergence, and various ways are explored in the following.

## PI Extremum seeking

One intuitive way to speed up convergence is to use a PI controller instead of a plain integrator, as initially proposed and analyzed in [8]. The results of applying this strategy to our PBR example by including a proportional action with a gain of 0.5 (see Table 1 for a summary of the parameter values) are shown in Figures 4-6. Convergence is twice as fast (i.e., about 20 hours).

## Block-Oriented Models and ESC

An alternative is to eliminate the filters and replace the modulation-demodulation approach with an estimator, e.g., recursive least-squares, as originally introduced in [9], or Kalman filters, as proposed in [10] where it is applied to the control of thermoacoustic instabilities (another fast system).

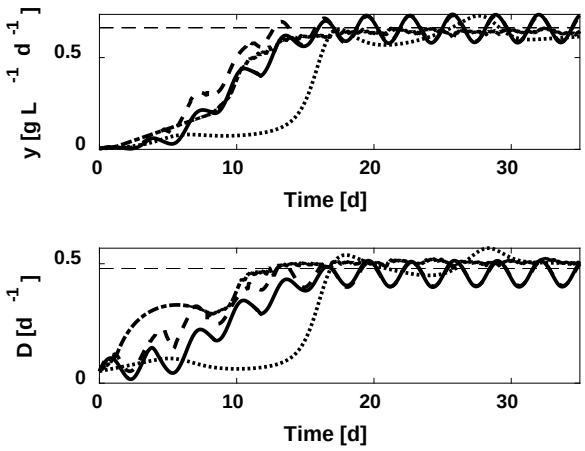



**Figure 4.** Productivity *y* and dilution *D* trajectories over time. Dotted line: PI-ESC; Continuous line: BOM-ESC; Dashed line: NB-ESC; Dashed-dotted line: STAB-ESC.

The structure of this ESC approach is displayed in Figure 7, where the controller can be a simple I control, a PI controller as in the previous subsection, or even a pole placement controller as in [11]. If we consider a recursive least square estimator it is also possible to describe the process in a slightly more detailed way to distinguish the static map from the dominant dynamics, as in Figure 8. The model of choice is a Hammerstein model, which combines a static block with a linear dynamic block (this type of model belongs to the family of block-oriented models – BOM in the following). The consideration of the process dynamics can improve parameter estimation and alleviate biased estimation. In our example, a quadratic map

**Table 1.** Parameter tuning of the reviewed extremum-seeking methods

| Parameter | PI-ESC | BOM-ESC | NB-ESC | STAB-ESC |
|---|---|---|---|---|
| $\omega_1$ (rad/d) | 0.5 | 2 | 2 | 100 |
| $\omega_2$ (rad/d) | / | 1 | 1 | / |
| $a_1$ ($d^{-1}$) | 0.02 | 0.05 | 0.05 | / |
| $a_2$ ($d^{-1}$) | / | 0.025 | 0.025 | / |
| $k_i$ | 70 | 6 | 6 | / |
| $k_p$ | 0.5 | 0 | 0 | / |
| g | / | 3 | 3 | / |
| $\lambda$ | / | 0.99 | 0.99 | / |
| $\omega_{HP}$ (rad/d) | 0.45 | / | / | / |
| $\alpha$ | / | / | / | 0.0002 |
| k | / | / | / | 4000 |

with two parameters, $M_1$ and $M_2$, is considered in combination with a first-order transfer function. The estimation of 4 parameters requires a sufficiently rich excitation signal and here $d(t) = a_1 \sin\omega_1 t + a_2 \sin\omega_2 t$. The quadratic map is a local approximation of the local convex optimum. The selected parameters are given in Table 1 and the results displayed in Figures 4-6.

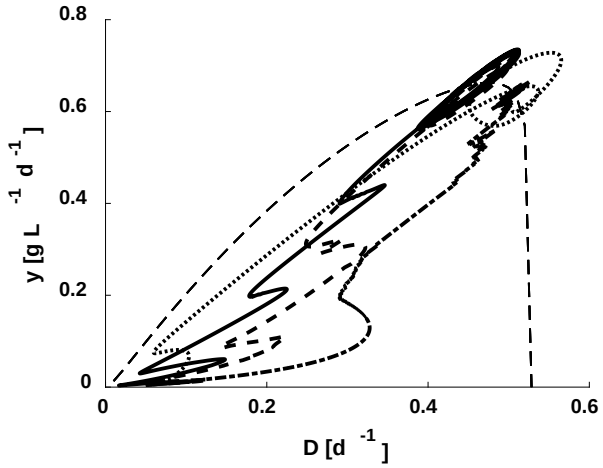



**Figure 5.** Productivity *y* vs dilution *D* diagram trajectories. Dotted line: PI-ESC; Continuous line: BOM-ESC; Dashed line: NB-ESC; Dashed-dotted line: STAB-ESC.

$$
\begin{aligned}
e &= y - \Phi^T \hat{\xi} \\
\dot{\hat{\xi}} &= K R^{-1} \Phi^T e \\
\dot{R} &= K(\Phi^T \Phi - \lambda R) \\
\dot{\hat{\theta}} &= k_i \, \hat{\xi} \\
\theta &= \hat{\theta} + d,
\end{aligned} \tag{11}
$$

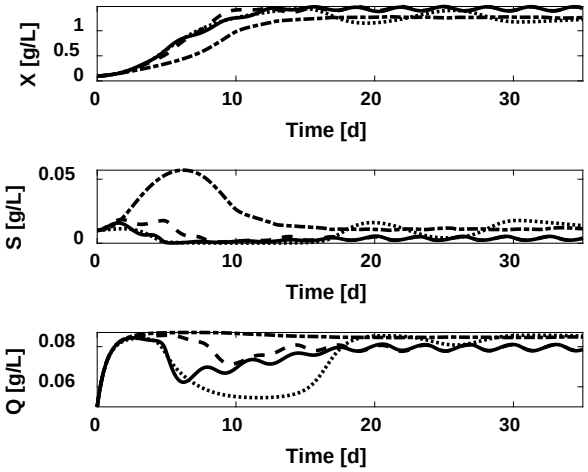



**Figure 6.** State trajectories over time. Dotted line: PI-ESC; Continuous line: BOM-ESC; Dashed line: NB-ESC; Dashed-dotted line: STAB-ESC.

## Newton seeking

It is also possible to improve ESC's line search by considering second-order information in addition to the gradient information. This allows scaling the gradient by the Hessian, as in the classical Gauss-Newton optimization algorithm. This approach was originally introduced in [12]. The application of this technique to our tutorial example is illustrated in Table 1 and Figures 4-6 (NB-ESC). When used in combination with a Hammerstein model, the Hessian is readily available in parameter $M_1$, which makes the application of the method particularly straightforward. Newton seeking is, however, mostly useful in multiple input problems with different relative gains, where the Hessian scaling will be particularly beneficial.

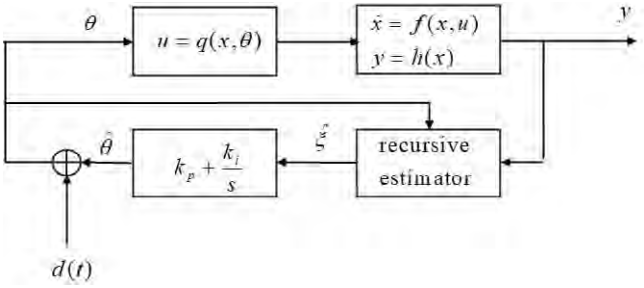



**Figure 7.** ESC using a parameter estimator (recursive least-squares or Kalman filtering) and a PI controller.

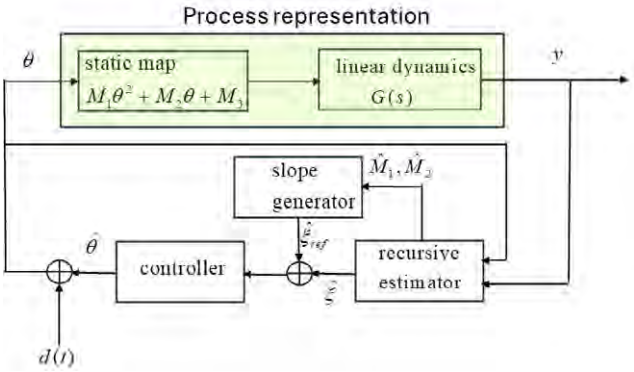



**Figure 8.** ESC using a parameter estimator (recursive least-squares or Kalman filtering), a block-oriented model (BOM) of the process, a slope generator and a generic controller.

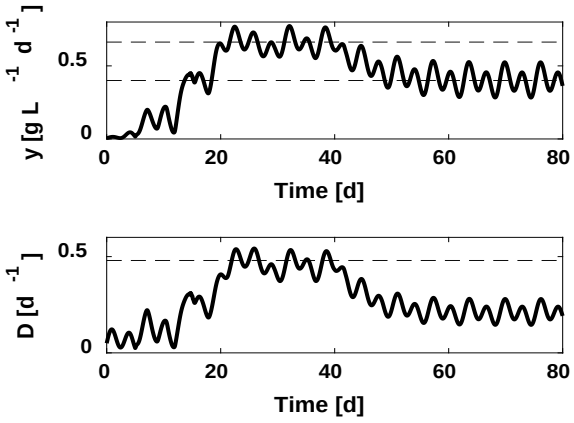



**Figure 9.** Productivity *y* and dilution *D* trajectories over time with BOM-ESC until 40 days ($y_{ref} = y^*$), followed by slope seeking ($y_{ref} = 0.4\ g\ L^{-1}\ d^{-1}$) until 80 days.

## Slope seeking

As illustrated in Figure 8, using ESC to achieve suboptimal operating points corresponding to non-zero gradients is also possible. Indeed, the controller can achieve any gradient setpoint. This can be used to alleviate the problem posed by a flat optimum, as might be the case in active flow control [13]. This can also be used in conjunction with a slope generator to achieve the desired level of productivity as suggested by [14].

Figure 9 shows a scenario where the extremum seeking is switched after 40 days to a specific slope set-point, corresponding to a productivity reference $y_{ref} = 0.4\ g\ L^{-1}\ d^{-1}$.

## Stabilizing Extremum seeking

In the search for more robustness, particularly to measurement noise, a new ESC framework was proposed in [15].

The cost function J, assumed to be a cost Lyapunov function (CLF), is included in the argument of a bounded periodic signal

$$\dot{\theta} = \sqrt{\alpha\omega}\cos(\omega t - kJ) \tag{12}$$

as shown in Figure 9.

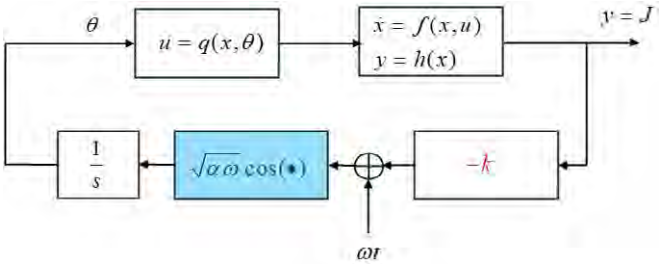



**Figure 10.** ESC using a parameter estimator (recursive least-squares or Kalman filtering) and a PI controller

As for the original proofs of convergence provided in [2], averaging techniques are required, with in addition, the concept of weak limits. This elaborate mathematical framework is detailed in [15] with the end result that

$$\dot{\hat{\theta}} = \frac{k\alpha}{2}\nabla J \tag{13}$$

The application of this technique is also shown in Table 1 and Figures 4-6.

# CONCLUSIONS

Extremum-seeking control is a multifaceted, versatile approach that allows optimizing process operation without the need for the tedious development of a dynamic model. It usually yields very satisfactory results in fast applications (MPPT in solar or wind systems, flow control, etc), but is more delicate to design and tune in slower processes, as illustrated in our tutorial application. Fundamental multi-input aspects can be found in [18]. The interested reader can also find experimental applications of ESC to micro-algae systems in [14, 16] and an application of the recent stabilizing ESC approach [15] to bioprocesses in [17].

## REFERENCES


1. Leblanc, M. Sur l'électrification des chemins de fer au moyen de courants alternatifs de fréquence élevée. *Revue Générale De L'Électricité*, *12*, 275–277 (1922).
2. Ariyur, K.B., Krstic, M. Real-Time Optimization by Extremum-Seeking Control. John Wiley & Sons, Inc.: Hoboken, NJ, USA, (2003).
3. Tan, Y., Moase, W., Manzie, C., Nesic, D., Mareels, I. Extremum Seeking from 1922 to 2010. In Proceedings of the 29th Chinese Control Conference, 14–26 (2010).
4. Dewasme, L., Vande Wouwer A. Model-free extremum seeking control of bioprocesses: A review with a worked example. *Processes* 8.10 (2020).
5. Scheinker, A. 100 years of extremum seeking: A survey. *Automatica* 161 (2024).
6. Dewasme, L., Letchindjio, C. G. F., Zuniga, I. T., Vande Wouwer, A. Micro-algae productivity optimization using extremum-seeking control. In 2017 25th Mediterranean Conference on Control and Automation (MED, IEEE), 672-677 (2017).
7. Leyva, R., Olalla, C., Zazo, H., Cabal, C., Cid-Pastor, A., Queinnec, I., Alonso, C. MPPT based on sinusoidal extremum-seeking control in PV generation. *International Journal of Photoenergy* (2012).
8. Guay, M. A Perturbation-Based Proportional Integral Extremum-Seeking Control Approach. *IEEE Trans. Autom. Control*, 61, 3370–3381 (2016).
9. Dewasme, L., Srinivasan, B., Perrier, M., Vande Wouwer, A. Extremum-seeking algorithm design for fed-batch cultures of microorganisms with overflow metabolism. *J. Process Control*, 21, 1092–1104 (2011).
10. Gelbert, G., Moeck, J. P., Paschereit, C. O., King, R. Advanced algorithms for gradient estimation in one-and two-parameter extremum seeking controllers. *Journal of Process Control*, 22(4), 700-709 (2012).
11. Feudjio Letchindjio, C.G., Dewasme, L., Deschênes, J.S., Vande Wouwer, A. An Extremum Seeking Strategy Based on Block-Oriented Models: Application to Biomass Productivity Maximization in Microalgae Cultures. *Ind. Eng. Chem. Res.*, 58, 13481–13494 (2019).
12. W. H. Moase, C. Manzie, and M. J. Brear, Newton-like extremum seeking for the control of thermoacoustic instability, *IEEE Trans. Automat. Contr.*, vol. 55, pp. 2094–2105, (2010).
13. L. Henning, R. Becker, G. Feuerbach, R. Muminovic, R. King, A. Brunn, W. Nitsche, Extensions of adaptive slope-seeking for active flow control, Proceedings of the Institution of Mechanical Engineers, *Part I: Journal of Systems and Control Engineering* 222 (5) 309–322 (2008).
14. Feudjio Letchindjio, C. G., Dewasme, L., Vande Wouwer, A. An experimental application of extremum seeking control to cultures of the microalgae Scenedesmus obliquus in a continuous photobioreactor. *International Journal of Adaptive Control and Signal Processing*, *35*(7), 1285-1297 (2021).
15. Scheinker, A., Krstić, M. Model-free stabilization by extremum seeking. Cham, Switzerland: Springer International Publishing (2017).
16. Feudjio Letchindjio, C., Zamudio Lara, J., Dewasme, L., Hernández Escoto, H., Vande Wouwer, A. Dual-Input Slope Seeking Control of Continuous Micro-Algae Cultures with Experimental Validation. *Applied Sciences*, *11*(16), 7451 (2021).
17. Dewasme, L., Vande Wouwer, A. Stabilizing extremum seeking control applied to model-free bioprocess productivity optimization. *IFAC-PapersOnLine*, *58*(14), 712-717 (2024).
18. Ghaffari, A., Krstić, M., & Nešić, D. (2012). Multivariable Newton-based extremum seeking. Automatica, 48(8), 1759-1767.



© 2025 by the authors. Licensed to PSEcommunity.org and PSE Press. This is an open access article under the creative commons CC-BY-SA licensing terms. Credit must be given to creator and adaptations must be shared under the same terms. See https://creativecommons.org/licenses/by-sa/4.0/




Systems & Control Transactions

**Research Article - Peer Reviewed Conference Proceeding**
ESCAPE 35 - European Symposium on Computer Aided Process Engineering
Ghent, Belgium. 6-9 July 2025
Jan F.M. Van Impe, Grégoire Léonard, Satyajeet S. Bhonsale,
Monika E. Polańska, Filip Logist (Eds.)

PSE PRESS

# Updated-Absolute Expected Value Solution Approach for multistage stochastic programming problems

**Yasuhiro Shoji and Selen Cremaschi***

Department of Chemical Engineering, Auburn University, Auburn, AL 36849, USA
* Corresponding Author: szc0113@auburn.edu.

## ABSTRACT

This paper introduces the Updated Absolute Expected Value Solution, U-AEEV, a heuristic for solving multi-stage stochastic programming (MSSP) problems with type 2 endogenous uncertainty. U-AEEV is an evolution of the Absolute Expected Value Solution, AEEV [1]. This paper aims to show how U-AEEV overcomes the drawbacks of AEEV and performs better than AEEV. To demonstrate the performance of U-AEEV, we solve 6 MSSP problems with type 2 endogenous uncertainty and compare the solutions and computational resource requirements.

**Keywords**: Stochastic Optimization, endogenous uncertainty, heuristics

## 1. INTRODUCTION

Multi-stage stochastic programming (MSSP) is a common mathematical framework used to solve decision-making problems, such as planning and process design problems, under uncertainty often encountered in the process industry [2-3]. In MSSP problems, the outcomes of uncertain events materialize over a given time horizon, and the realized outcomes distinguish given scenarios, allowing the decision-maker to take corrective action in distinguished scenarios. Taxonomically [4], there are two categories of uncertainty in stochastic programming: decision-independent, also known as exogenous uncertainty, and decision-dependent, also known as endogenous uncertainty. The endogenous uncertainty can be further categorized into three sub-classes: type 1, where the probability distribution is decision-dependent; type 2, where the information structure is decision-dependent; and type 3, where both probability distribution and the information structure are decision-dependent. As for type 2 endogenous uncertainty, which U-AEEV mainly deals with, decisions affect the resolution of uncertainty, i.e., information structure (the shape of a scenario tree) is decision-dependent. The non-anticipativity constraints (NACs) used to ensure the indistinguishability among scenarios before knowing the outcomes of future events cause significant complexities and computational intractability in solving real-life-sized problems. This challenge has motivated researchers to develop various heuristic and decomposition-based solution approaches, such as the sample average approximation algorithm [5], and Benders decomposition [6], to obtain solutions.

A heuristic, Absolute Expected Value Solution (AEEV), which our group developed [1], yields feasible solutions to MSSP problems with type 2 endogenous uncertainty. AEEV circumvents the computational intractability by decomposing scenarios of an original MSSP problem into multiple deterministic sub-problems with expected uncertain parameter values. In each period from the initial to the end of the time horizon, AEEV iterates to solve a sub-problem, fixes the here-and-now decision variable values, judges uncertainty realization, updates the expected uncertain parameter values based on the realized uncertainty, solves deterministic recourse sub-problems to determine corrective action, and fixes wait-and-see decision variable values. A drawback of AEEV is that it may fail to generate a feasible solution if the original MSSP problem does not have complete recourse. More precisely, the expected uncertain parameter for a recourse sub-problem does not always ensure feasible corrective action following uncertainty realization; accordingly, the sub-problem may be infeasible if the original MSSP problem lacks complete recourse.

In this paper, we introduce the Updated Absolute Expected Value Solution (U-AEEV), which expands the applicability of the AEEV to MSSP problems without complete recourse by eliminating the potential infeasibility is-

sues. The U-AEEV iteratively solves scenario-decomposed deterministic sub-problems using the outcomes of each scenario instead of the expected values of the uncertain parameters, evaluates the solutions to the sub-problems in terms of infeasibility and quality, and selects one. The U-AEEV yields tight feasible solutions without significant growth in computational time.

## 2. THE FRAMEWORK OF MSSP WITH TYPE 2 ENDOGENOUS UNCERTAINTY

MSSP problems with type 2 endogenous uncertainty consider multiple scenarios and a discretized time horizon, where scenarios gradually become distinguishable over the time horizon. Equations (1)-(15) represent a common formulation of MSSP with type 2 endogenous uncertainty (this is an extended formulation from [1]).

$$\min z = \sum_{s\in\mathcal{S}} p_s \sum_{i\in\mathcal{I},t\in\mathcal{T}} G_{i,t,s}\left(V_{i,t},\theta_{i,s},b_{i,t,s},x_{i,t,s},y_{i,t,s},w_{i,t,s}\right) \quad (1)$$

subject to

$$g\left(V_{i,t},\theta_{i,s},b_{i,t,s},x_{i,t,s},y_{i,t,s},w_{i,t,s}\right)\le 0 \quad \forall i\in\mathcal{I},\quad \forall t\in\mathcal{T},\quad \forall s\in\mathcal{S} \quad (2)$$

$$h\left(V_{i,t},\theta_{i,s},b_{i,t,s},x_{i,t,s},y_{i,t,s},w_{i,t,s}\right)= 0 \quad \forall i\in\mathcal{I},\quad \forall t\in\mathcal{T},\quad \forall s\in\mathcal{S} \quad (3)$$

$$b_{i,1,s}=b_{i,1,s'} \quad \forall i\in\mathcal{I},\quad \forall s,s'\in\mathcal{S} \quad (4)$$

$$x_{i,1,s}=x_{i,1,s'} \quad \forall i\in\mathcal{I},\quad \forall s,s'\in\mathcal{S} \quad (5)$$

$$b^{\mathrm{dif}}_{i,t,s}=b_{i,t,s}\Leftrightarrow Z_{t,s,s'}=H\left(b_{i,t,s}\right) \quad \forall i\in\mathcal{D}(s,s'),\quad \forall t\in\mathcal{T},\quad \forall s,s'\in\mathcal{S} \quad (6)$$

$$w^{\mathrm{dif}}_{i,t,s}=w_{i,t,s}\Leftrightarrow Z_{t,s,s'}=H\left(w_{i,t,s}\right) \quad \forall i\in\mathcal{D}(s,s'),\quad \forall t\in\mathcal{T},\quad \forall s,s'\in\mathcal{S} \quad (7)$$

$$Z_{t,s,s'}=H\left(b^{\mathrm{dif}}_{i,t,s},w^{\mathrm{dif}}_{i,t,s}\right) \quad \forall i\in\mathcal{D}(s,s'),\quad \forall t\in\mathcal{T},\quad \forall s,s'\in\mathcal{S} \quad (8)$$

$$\begin{bmatrix} Z_{t,s,s'} \\ b_{i,t+1,s}=b_{i,t+1,s'} \\ x_{i,t+1,s}=x_{i,t+1,s'}\end{bmatrix}\vee\left[\neg Z_{t,s,s'}\right] \quad \forall i\in\mathcal{I},\quad \forall t\in\mathcal{T}|t\le T-1,\quad \forall s,s'\in\mathcal{S} \quad (9)$$

$$\begin{bmatrix} Z_{t,s,s'} \\ y_{i,t,s}=y_{i,t,s'}\end{bmatrix}\vee\left[\neg Z_{t,s,s'}\right] \quad \forall i\in\mathcal{I},\quad \forall t\in\mathcal{T},\quad \forall s,s'\in\mathcal{S} \quad (10)$$

$$b_{i,t,s}\in\{0,1\} \quad \forall i\in\mathcal{I},\quad \forall t\in\mathcal{T},\quad \forall s\in\mathcal{S} \quad (11)$$

$$x_{i,t,s}\ge 0 \quad \forall i\in\mathcal{I},\quad \forall t\in\mathcal{T},\quad \forall s\in\mathcal{S} \quad (12)$$

$$y_{i,t,s}\ge 0 \quad \forall i\in\mathcal{I},\quad \forall t\in\mathcal{T},\quad \forall s\in\mathcal{S} \quad (13)$$

$$w_{i,t,s}\ge 0 \quad \forall i\in\mathcal{I},\quad \forall t\in\mathcal{T},\quad \forall s\in\mathcal{S} \quad (14)$$

$$Z_{t,s,s'}\in\{0,1\} \quad \forall t\in\mathcal{T},\quad \forall s,s'\in\mathcal{S} \quad (15)$$

The formulation includes two types of decision variables: here-and-now decision variables corresponding to $b_{i,t,s}$ (binary) and/or $x_{i,t,s}$ (continuous or integer), and wait-and-see decision variables corresponding to $y_{i,t,s}$ (continuous or integer), with the problem-specific index $i\in\mathcal{I}=\{1,2,\dots,I\}$, time index $t\in\mathcal{T}=\{1,2,\dots,T\}$, and scenario index $s\in\mathcal{S}=\{1,2,\dots,S\}$. Variable $w_{i,t,s}$ notates non-decision variables that are entirely dependent on here-and-now and wait-and-see decision variables. If a scenario pair $s$ and $s'$ becomes distinguishable due to uncertainty realization at time $t$, here-and-now decision variables can take different values at $t+1$ and after, as conditional NACs (9) imply. In other words, here-and-now decision variables must take the same values at $t$ because the decisions are made before realization at $t$. Since conditional NACs (9) do not ensure the scenario indistinguishability at $t=1$, here-and-now decision variables need initial NACs by separate equations (4)-(5). In contrast to here-and-now decision variables, wait-and-see decision variables can take different values at $t$ when scenario realization occurs to determine the corrective action after realization, as conditional NACs (10) imply. Equation (10) includes initial NACs for wait-and-see decision variables, i.e., wait-and-see decision variables can omit separate equations for the initial NACs. The binary variable $Z_{t,s,s'}$ in conditional NACs (9)-(10) is called the indicator variable, which is 1 if a scenario pair $s$ and $s'$ is indistinguishable at the end of time $t$ and 0 otherwise. The value of the indicator variable switches based on the values of particular binary decision variables or non-decision variables. We define the particular variables as differentiator variables, $b^{\mathrm{dif}}_{i,t,s}$ and $w^{\mathrm{dif}}_{i,t,s}$, in (6) and (7), i.e., a binary decision variable or a non-decision variable is a differentiator variable if the indicator variable is bounded using these variables. The differentiator variables switch the value of the indicator variable through the expression $H\left(b^{\mathrm{dif}}_{i,t,s},w^{\mathrm{dif}}_{i,t,s}\right)$ in (8). $\mathcal{D}(s,s')$ in (6)-(8) is a differentiator set, a set of $i$ that has different outcomes in an uncertain parameter pair $\theta_{i,s}$ and $\theta_{i,s'}$. The objective function (1) provides the optimum of expression $z$ based on the probability, $p_s$, of scenario $s$ and the contribution of the scenario, $G_{i,t,s}\left(V_{i,t},\theta_{i,s},b_{i,t,s},x_{i,t,s},y_{i,t,s},w_{i,t,s}\right)$. The two given parameters, $V_{i,t}$ and $\theta_{i,s}$, are deterministic and uncertain parameters, respectively. Equations (2)-(3) express scenario-specific inequality and equality constraints, such as demand constraints, capacity constraints, and material balances.

## 3. UPDATED ABSOLUTE EXPECTED VALUE SOLUTION APPROACH (U-AEEV)

The U-AEEV, similar to AEEV, is a scenario-decomposition approach to mitigating the computational intractability of an MSSP problem with type 2 endogenous uncertainty. The U-AEEV solves deterministic sub-problems using each scenario outcome for the uncertain parameters and enumerates multiple 'decision candidates' in a stage-wise (in the sense of MSSP) manner. It evaluates the 'decision candidates' and adopts a feasible and promising candidate for the current stage. After finding the end of the stage by detecting uncertainty realization,

U-AEEV stores the stage's decision variable values to ensure the indistinguishability of scenarios by fixing them when it solves sub-problems in subsequent stages.

**Figure 1** is an example (a process network synthesis problem [2]) to illustrate how U-AEEV works. Raw materials C and D are used to produce intermediate B through new Process 1 and Process 2, and intermediate B is used to produce product A through existing Process 3. The decision maker can purchase B and must satisfy the demand for product A by production or purchase while maximizing the expected net present value.

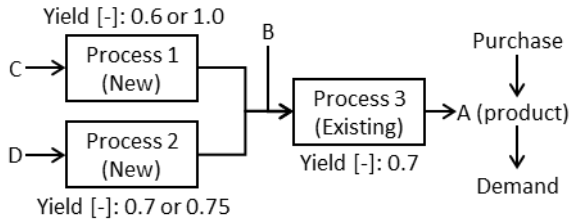



**Figure 1.** An example problem [2] to illustrate U-AEEV.

The here-and-now decisions of the example are the installation and capacity of each process, as well as the flow rates of raw materials and purchased intermediate B. The wait-and-see decision is the purchase rate of Product A. The source of endogenous uncertainty is the yield of Process 1 and Process 2, which materializes by installing and operating the process. The decision maker determines here-and-now decisions, such as installation, capacity, and flow rates, at the start of a time, waits until the yield of processes becomes clear, and then determines the rate of A purchased. **Table 1** lists scenarios and the yield and probability of each scenario.

**Table 1:** Scenarios, yields, and probabilities of the example problem in Figure 1.

| Scenario | Yield [-] | | Probability |
|---|---|---|---|
| | Process 1 | Process 2 | |
| $s1$ | 0.6 | 0.7 | 0.4 |
| $s2$ | 0.6 | 0.75 | 0.3 |
| $s3$ | 1.0 | 0.7 | 0.2 |
| $s4$ | 1.0 | 0.75 | 0.1 |
| Expected | 0.72 | 0.72 | - |

The U-AEEV starts by solving four deterministic sub-problems with each scenario outcome and enumerates the decision candidates suggested by each scenario, as shown in **Figure 2**. In the case of this example, Scenario 1 ($s_1$) suggests Candidate 1, in which neither Process 1 nor 2 is installed, Scenario 2 ($s_2$) suggests installing Process 2 at Time 1 ($t_1$) in Candidate 2, and Scenario 3 ($s_3$) and 4 ($s_4$) suggest installing Process 1 at Time 1 ($t_1$) in Candidate 3. Note that the time horizon of the example has three time periods.

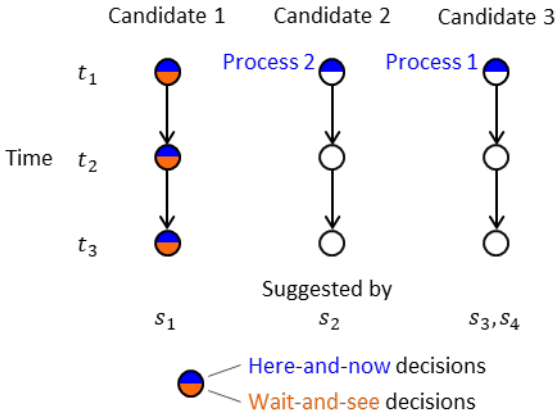



**Figure 2.** Decision candidates of the first stage (up to the first realization)

Since U-AEEV solves deterministic sub-problems stage-wise, decision candidates at this step refer to the decisions of the first stage (up to the first realization). In other words, the decision candidates of Candidate 1 are the here-and-now and wait-and-see decisions from Time 1 ($t_1$) to Time 3 ($t_3$) because Candidate 1 sees no uncertainty realization throughout the time horizon. Similarly, the decision candidates of Candidate 2 and 3 are the here-and-now decisions at Time 1 ($t_1$) because uncertainty partially materializes by installing and operating Process 2 or 1. For example, Scenarios 1 and 3 or Scenarios 2 and 4 become distinguishable through operating Process 2 in Candidate 2.

The U-AEEV picks up candidates to be evaluated based on the total probability of a candidate, $p^{\mathrm{c}}$, in (16) and weighted objective value, $\mathrm{obj}^{\mathrm{c}}$, in (17), where $p_s$ is the probability of the scenario $s$, $\mathrm{obj}_s$ is the objective value of the sub-problem solved with the outcome of scenario $s$, and $S^{\mathrm{c}}$ is a set of scenarios that suggest candidate $\mathrm{c}$.

$$p^{\mathrm{c}} = \sum_{s \in S^{\mathrm{c}}} p_s \tag{16}$$

$$\mathrm{obj}^{\mathrm{c}} = \frac{\sum_{s \in S^{\mathrm{c}}} p_s \, \mathrm{obj}_s}{\sum_{s \in S^{\mathrm{c}}} p_s} \tag{17}$$

The U-AEEV only evaluates the candidates on the Pareto front of the $p^{\mathrm{c}}$-$\mathrm{obj}^{\mathrm{c}}$ plane (**Figure 3**), i.e., the candidates with high probabilities and high objective values (in a maximization problem) are evaluated. In a minimization problem, the Pareto front is formed based on high probabilities and low objective values. The selection using a Pareto front helps to reduce computational time by focusing only on promising candidates. Since the example is a maximization problem, Candidates 1 and 3 on the Pareto front in Figure 3 are evaluated.

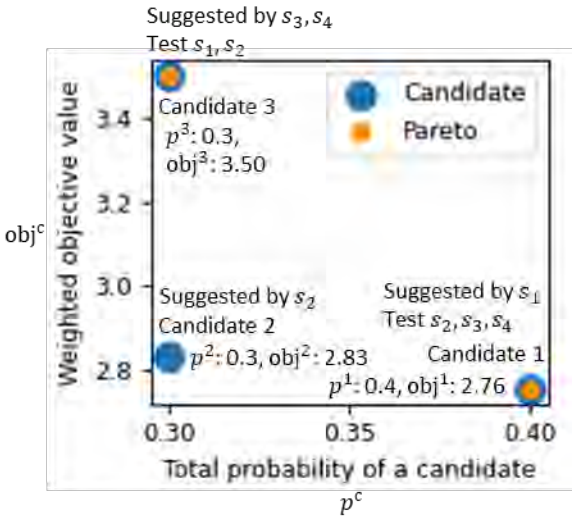



**Figure 3.** The total probability of a candidate ($p^c$) and weighted objective value ($\text{obj}^c$) plane for the evaluation of decision candidates

The U-AEEV checks feasibility and compares the expected objective values of candidates, $\underset{s\in S^{\text{InD}}}{\text{E}}[\text{obj}_s]$, in (18) on the Pareto front by testing each candidate with all other scenario outcomes that did not suggest the candidate. In the example, the U-AEEV solves sub-problems with Scenario 2 ($s_2$), 3 ($s_3$), and 4 ($s_4$) outcomes for Candidate 1, and Scenario 1 ($s_1$) and 2 ($s_2$) outcomes for Candidate 3, and adopts the best candidate regarding the expected objective value calculated with (18). $S^{\text{InD}}$ is a set of indistinguishable scenarios associated with the sub-problems, i.e., Scenarios 1, 2, 3, and 4 in the example, since none of the scenarios are distinguishable at the first stage.

$$\underset{s\in S^{\text{InD}}}{\text{E}}[\text{obj}_s] = \sum_{s\in S^{\text{InD}}} p_s \,\text{obj}_s \tag{18}$$

The candidate with the largest expected objective value is adopted in a maximization problem, and the candidate with the smallest expected objective value is adopted in a minimization problem. If a candidate turns out to be infeasible when solving sub-problems due to a lack of complete recourse, the U-AEEV excludes the candidate from the evaluation process. Then, it forms a new Pareto front and evaluates candidates located on the updated Pareto front. For example, the U-AEEV removes Candidate 3 from the evaluation process and evaluates Candidate 2, located on the updated Pareto front, if Candidate 3 is infeasible.

Finally, the U-AEEV finds the end of the stage, i.e., the time uncertainty realization occurs and distinguishable scenarios at the time, and stores the decision variable values of the stage. The stored decision variable values are used to fix the decision variables of the stage to ensure scenario indistinguishability when the U-AEEV repeats the same procedure in the following stage. The U-AEEV continues the procedure until the final stage, i.e., until no uncertainty realization is found.

Equations (19)-(27) are the formulation of sub-problems solved in U-AEEV.

$$\min z^{\text{UAEEV}} = \sum_{i\in\mathcal{I},t\in\mathcal{T}} G_{i,t}\left(V_{i,t},\theta_i^n,b_{i,t},x_{i,t},y_{i,t},w_{i,t}\right) \tag{19}$$

subject to

$$g\left(V_{i,t},\theta_i^n,b_{i,t},x_{i,t},y_{i,t},w_{i,t}\right) \le 0 \quad \forall i\in\mathcal{I}, \quad \forall t\in\mathcal{T} \tag{20}$$

$$h\left(V_{i,t},\theta_i^n,b_{i,t},x_{i,t},y_{i,t},w_{i,t}\right) = 0 \quad \forall i\in\mathcal{I}, \quad \forall t\in\mathcal{T} \tag{21}$$

$$\begin{bmatrix} b_{i,t} = b_{i,t}^{\text{str},n} \\ x_{i,t} = x_{i,t}^{\text{str},n} \\ w_{i,t}^{\text{dif}} = w_{i,t}^{\text{difstr},n} \end{bmatrix} \quad \forall i\in\mathcal{I}, \quad \forall t\in\mathcal{T}|t\le t^{\text{PRend},n} \tag{22}$$

$$y_{i,t} = y_{i,t}^{\text{str},n} \quad \forall i\in\mathcal{I}, \quad \forall t\in\mathcal{T}|t< t^{\text{PRend},n} \tag{23}$$

$$b_{i,t}\in\{0,1\} \quad \forall i\in\mathcal{I}, \quad \forall t\in\mathcal{T} \tag{24}$$

$$x_{i,t}\ge 0 \quad \forall i\in\mathcal{I}, \quad \forall t\in\mathcal{T} \tag{25}$$

$$y_{i,t}\ge 0 \quad \forall i\in\mathcal{I}, \quad \forall t\in\mathcal{T} \tag{26}$$

$$w_{i,t}\ge 0 \quad \forall i\in\mathcal{I}, \quad \forall t\in\mathcal{T} \tag{27}$$

Equations (19), (20), and (21) are the scenario-decomposed objective function and scenario-specific constraints corresponding to (1), (2), and (3). The uncertain parameter $\theta_{i,s}$ in (1), (2), and (3) is replaced with a scenario outcome $\theta_i^n$ in (19), (20), and (21), where $n$ denotes a sub-problem. Since the U-AEEV decomposes scenarios, it does not include NACs and indicator variable $Z_{t,s,s'}$ in its formulation. Instead, Equation (22) fixes all here-and-now decision variables and differentiator variables at and until the end time of the previous stage, $t^{\text{PRend},n}$, to ensure scenario indistinguishability using stored variables $b_{i,t}^{\text{str},n}$, $x_{i,t}^{\text{str},n}$, and $w_{i,t}^{\text{difstr},n}$. Similarly, Equation (23) fixes all wait-and-see decision variables using stored variable $y_{i,t}^{\text{str},n}$ until the previous time of the previous stage's end time.

The U-AEEV never fails to generate a solution even if a problem lacks complete recourse, as long as one of the decision candidates assumes the extremist (most pessimistic, optimistic, best, or worst) scenario. Also, it may locate tighter feasible solutions and yield smaller optimality gaps compared to the AEEV because the U-AEEV evaluates decision candidates suggested by all scenario outcomes and selects a good one, whereas decisions are offered only by the expected scenario outcomes (for example, the expected yields of Process 1 and 2 shown in Table 1 is 0.72) in AEEV. On the other hand, the U-AEEV may increase the computational time compared to the AEEV because it solves sub-problems with all scenario outcomes instead of solving sub-problems using only expected scenario outcomes. The U-AEEV offsets the increase in computational time by solving sub-problems stage-wise instead of AEEV's time-wise approach.

## 4. COMPUTATIONAL PERFORMANCE

We examine the U-AEEV performance using 6 published MSSP problems with type 2 endogenous uncertainty. **Table 2** lists the problem name, programming type (MILP or MINLP), the presence of complete recourse, the MSSP instance size, and the relative termination tolerance in solving the instances. The instance sizes are large, and the MSSP models cannot be solved to optimality within 48 hours. We implemented U-AEEV with Python 3.9.13, built optimization models using Pyomo 6.4.0, and solved all instances with CPLEX 20.10 for MILP or BARON 17.4.1 for MINLP problems, employing 48 processors (Intel(R) Xeon(R) Gold 6248R) and 380 GB of RAM on a node from Auburn University Easley Cluster. **Table 3** compares the computational performance of MSSP, U-AEEV, and AEEV. The second column from the left represents the optimality gaps reached at 48 hours for the MSSP models. The definition of the optimality gap, $\text{gap}^{\text{MSSP}}$, is the relative error between the feasible (upper/lower) and infeasible (lower/upper) bounds, $FB^{\text{MSSP}}$ and $IB^{\text{MSSP}}$, as defined in (28). The third and fourth columns from the left are the relative error, $\text{gap}^{\text{heu}}$, between the feasible bounds obtained as the MSSP solution and our heuristics ($FB^{\text{heu}}$), as defined in (29) and (30) for minimization and maximization problems, respectively. Negative gaps indicate that the feasible bounds yielded by our heuristics are better than those by the MSSP models. 'No sol.' in the AEEV column indicates that AEEV fails to generate a feasible solution because of a lack of complete recourse. The fifth and sixth columns from the left are the orders of magnitude, MAG, in computational speed defined in (31), where $t^{\text{MSSP}}$ and $t^{\text{heu}}$ are the computational time of MSSP and heuristic models, respectively. Equation (31) implies the computational speed is 10, 100, 1,000, and 10,000 times faster if the orders of magnitude are 1, 2, 3, and 4, respectively. Note that $t^{\text{MSSP}}$ is 48 hours in all instances.

$$\text{gap}^{\text{MSSP}} = \frac{\left|FB^{\text{MSSP}} - IB^{\text{MSSP}}\right|}{FB^{\text{MSSP}}} 100 \tag{28}$$

$$\text{gap}^{\text{heu}} = \frac{FB^{\text{heu}} - FB^{\text{MSSP}}}{FB^{\text{MSSP}}} 100 \tag{29}$$

$$\text{gap}^{\text{heu}} = \frac{FB^{\text{MSSP}} - FB^{\text{heu}}}{FB^{\text{MSSP}}} 100 \tag{30}$$

$$\text{MAG} = \log_{10}\left(\frac{t^{\text{MSSP}}}{t^{\text{heu}}}\right) \tag{31}$$

The U-AEEV yielded feasible solutions for all problem instances. However, the gaps in U-AEEV are large depending on the instance, as the gap of the demand-side response scheme planning problem shows 12.3 %. For this instance, we observed that only the candidate suggested by the worst scenario successfully generated a solution, while all other candidates failed due to the lack of complete recourse. This result implies the decision candidates suggested by scenario outcomes may not always include a good one. All failed candidates are infeasible in their corrective actions, which is caused by solving scenario-decomposed sub-problems without considering the information of other scenarios, unlike MSSP. Utilizing outcomes of other scenarios when solving sub-problems remains a topic for future work.

The gaps among comparable instances between U-AEEV and AEEV are smaller by 5.7 % in U-AEEV on average. However, U-AEEV yielded larger gaps than AEEV for some problems, as the gap of the offshore oilfield infrastructure planning problem is 2.43 % for U-AEEV, while 1.78 % for AEEV. We observed that only one extreme decision candidate was evaluated and selected in the evaluation process, which caused a larger gap in U-AEEV. The problem has many combinations of decisions based on three binary, one integer, and six continuous decision variables. Accordingly, each scenario outcome generates a different candidate. Since the probability of candidates is equal and the problem is a maximization problem, only one extreme candidate with the largest objective value forms the Pareto front in the evaluation process and is selected. This result implies the decision candidate suggested by the extremist (most pessimistic, optimistic, best, or worst) scenario is not always a better decision than a moderate decision suggested by an expected scenario outcome in AEEV. When an extreme candidate is selected, i.e., when the number of candidates and the number of scenarios suggesting candidates are the same and only one candidate is evaluated on the Pareto front, a moderate candidate suggested by the expected uncertain parameter may result in a tighter optimality gap. In other words, incorporating the idea of AEEV into U-AEEV

**Table 2:** MSSP problems with type 2 endogenous uncertainty to examine U-AEEV performance.

| Problem name | Programming type | Complete recourse | MSSP size | | Relative termination tolerance |
|---|---|---|---|---|---|
| | | | Variables | Constraints | |
| Clinical trial planning [7] | MILP | Yes | 556,033 | 1,806,849 | 0.01 % |
| Process network synthesis [2] | MILP | No | 8,577 | 57,489 | 0.01 % |
| R&D project portfolio management [5] | MILP | Yes | 20,097 | 298,881 | 0.01 % |
| Offshore oilfield infrastructure planning [3] | MINLP | Yes | 31,154 | 66,178 | 0.1 % |
| Vehicle routing [8] | MILP | No | 20,711 | 59,778 | 0.01 % |
| Demand-side response scheme planning [6] | MILP | No | 2,939,317 | 15,682,701 | 0.01 % |

**Table 3:** Computational performance of MSSP, U-AEEV, and AEEV.

| Problem name | Optimality gap [%] | Gap from MSSP feasible bound [%] | | Orders of magnitude in computational speed [-] | |
|---|---|---|---|---|---|
| | MSSP | U-AEEV | AEEV | U-AEEV | AEEV |
| Clinical trial planning | 4.86 | -1.33 | 8.96 | 1.4 | 4.5 |
| Process network synthesis | 16.0 | 3.69 | No sol. | 2.9 | - |
| R&D project portfolio management | 6.29 | -1.53 | 5.93 | 2.7 | 4.0 |
| Offshore oilfield infrastructure planning | 10.6 | 2.43 | 1.78 | 0.8 | 1.3 |
| Vehicle routing | 6.99 | 0.50 | No sol. | 3.7 | - |
| Demand-side response scheme planning | 27.3 | 12.3 | No sol. | 1.7 | - |

may be a promising idea for future work.

The computational speed of U-AEEV is 0.8 to 3.7 orders faster than MSSP, while it is 1.6 orders slower than AEEV. The difference in computational speed between U-AEEV and AEEV mainly depends on the number of scenarios, stages, and time periods. The U-AEEV needs to solve more sub-problems as the number of scenarios and stages is larger because it tests each scenario outcome stage-wise. On the other hand, the AEEV needs to solve more sub-problems as the number of time periods is larger because it solves sub-problems time-wise. For example, the number of maximum stages of the clinical trial planning problem (1024 scenarios and 12 time periods) is 10 in U-AEEV and 1 in AEEV, and U-AEEV solved 16789 sub-problems, while AEEV solved only 12 sub-problems. Note that the number of stages is not constant in MSSP problems with type 2 endogenous uncertainty because the shape of a scenario tree is decision-dependent.

## 5. CONCLUSIONS AND FUTURE DIRECTIONS

We introduced the Updated Absolute Expected Value Solution, U-AEEV, a heuristic for solving MSSP problems with type 2 endogenous uncertainty. We examined 6 MSSP problems involving Type 2 endogenous uncertainty with U-AEEV. The results showed that the U-AEEV generates a tight feasible solution even if the problem lacks complete recourse. The gap from the MSSP feasible bound was smaller by 5.7 % for U-AEEV than AEEV on average. The computational speed of U-AEEV is 0.8 to 3.7 orders faster than MSSP, while 1.6 orders slower than AEEV. Future studies will focus on publishing a Python package of U-AEEV. The package will automate the procedure of U-AEEV following converting the MSSP model into the U-AEEV sub-problem model utilizing input information, such as the model, here-and-now and wait-and-see decision variables, differentiator variables, uncertain parameters, and NACs of the original MSSP problem.

## REFERENCES


1. Zeng, Z. & Cremaschi, S. A general primal bounding framework for large-scale multistage stochastic programs under endogenous uncertainties. *Chem. Eng. Res. Des*. 141, 464-480 (2019).
2. Tarhan, B. & Grossmann, I. E. A multistage stochastic programming approach with strategies for uncertainty reduction in the synthesis of process networks with uncertain yields. *Comput. & Chem. Eng.* 32(4-5), 766-788 (2008).
3. Gupta, V. & Grossmann, I. E. Multistage stochastic programming approach for offshore oilfield infrastructure planning under production sharing agreements and endogenous uncertainties. *J. Pet. Sci. Eng.* 124, 180-197 (2014).
4. Hellemo, L., Barton, P. I., & Tomasgard, A. Decision-dependent probabilities in stochastic programs with recourse. *Comput. Manag. Sci.* 15, 369-395 (2018).
5. Solak, S., Clarke, J. P. B., Johnson, E. L., & Barnes, E. R. Optimization of R&D project portfolios under endogenous uncertainty. *Eur. J. Oper. Res.* 207(1), 420-433 (2010).
6. Giannelos, S., Konstantelos, I., & Strbac, G. Option Value of Demand-Side Response Schemes Under Decision-Dependent Uncertainty. *IEEE Trans.*, 33(5), 5103-5113 (2018).
7. Colvin, M. & Maravelias, C. T. A stochastic programming approach for clinical trial planning in new drug development. *Comput. & Chem. Eng.* 32, 2626-2642 (2008).
8. Khaligh, F. H. & MirHassani, S. A. A mathematical model for vehicle routing problem under endogenous uncertainty. *Int. J. Prod. Res.* 54:2, 579-590 (2016).



© 2025 by the authors. Licensed to PSEcommunity.org and PSE Press. This is an open access article under the creative commons CC-BY-SA licensing terms. Credit must be given to creator and adaptations must be shared under the same terms. See https://creativecommons.org/licenses/by-sa/4.0/




# Section 5

## Concepts, Methods and Tools

Systems & Control Transactions

**Research Article - Peer Reviewed Conference Proceeding**
ESCAPE 35 - European Symposium on Computer Aided Process Engineering
Ghent, Belgium. 6-9 July 2025
Jan F.M. Van Impe, Grégoire Léonard, Satyajeet S. Bhonsale,
Monika E. Polańska, Filip Logist (Eds.)

PSE PRESS

# A Python/Numpy-based package to support model discrimination and identification

**Seyed Zuhair Bolourchian Tabrizi[a,b], Elena Barbera[a], Wilson Ricardo Leal da Silva[b], and Fabrizio Bezzo[a]***

[a] Department of Industrial Engineering, University of Padova, via Marzolo 9, 35131 Padova PD, Italy
[b] FLSmidth Cement, Green Innovation, Denmark
* Corresponding Author: fabrizio.bezzo@unipd.it.

## ABSTRACT

Addressing challenges in process design and optimisation, especially with complex models and data uncertainties, requires effective tools for model development, selection, and identification. Techniques such as Model-based Design of Experiments (MBDoE) help support this task by screening and discriminating between models and, eventually, calibrating them. Open-source and user-friendly Python packages have implemented some model identification techniques. However, the need for a tool that can couple with various model simulators and account for the steps of model identification as well as physical constraints of systems in design of experiments remains unmet. In that light, we present the python package MIDDOE (Model-(based) Identification, Discrimination, and Design of Experiments) to address this gap. It integrates rival models screening, parameter estimation, uncertainty analysis, and MBDoE techniques, while adapting to various process constraints. These functionalities are demonstrated via an in-silico study for a semi-batch fermentation reactor model identification.

**Keywords**: model identification, model-based design of experiments, model discrimination, model calibration, open-source software

## INTRODUCTION

Process design and optimisation often requires the precise determination of underlying phenomena and identification of accurate models to describe them. This process becomes complex when multiple rival models and high uncertainty exist, and is further complicated by the costly data required for model discrimination and calibration. To address these challenges, numerical techniques have been introduced to streamline the pre-discrimination stage by screening models and narrowing the pool of candidates without additional experimental effort. Building on these techniques, MBDoE methods have been developed to design new experiments that maximize information, enabling easier discrimination between rival models (MBDoE-MD) [1]. Additionally, they reduce the confidence ellipsoid volume of estimated parameters by enriching the information matrix (MBDoE-PP) via optimal experiment design [1].

Open-source Python packages, most notably PYOMO [2], are essential tools for digital modeling frameworks. PYOMO facilitates parameter estimation using Parmest [3] and supports MBDoE-PP through DOE [4]. Despite many advantages in integrating with the PYOMO ecosystem, these tools have some limitations. They are effective when screening, reparametrizing, and discriminating between models are not required. Additionally, they rely on PYOMO's array and model structure, which makes them incompatible with other types of simulators. This dependency limits their flexibility in handling diverse model structures, solvers, and constraints related to design decisions. Another significant limitation is the lack of coherence in problem definitions across the entire workflow. This arises from the need to use different packages for tasks such as screening, identifying, designing experiments, validating, and illustrating results. Additionally, some of these tools are not readily available, further complicating the workflow.

These gaps are here addressed by proposing the Python package MIDDOE

(https://pypi.org/project/middoe), which wraps dynamic lumped models using standard Python/NumPy arrays and integrates seamlessly with simulators. MIDDOE provides tools not only for calibrating models, but also for screening, discriminating, and validating models. It provides flexibility to perform these tasks using local methods (single start or multi-core, multi-start) as well as global or joint methods (multi-core) ensuring high computational efficiency.

The package offers MBDoE techniques tailored for both discrimination and calibration, specifically adapted to the physical constraints of experimental campaigns and apparatus. Key features include options for enforcing constraints on design decisions and cost functions, with the flexibility to structure MBDoE optimization problems to accommodate these limitations. This functionality significantly aids experimenters in designing feasible and optimal experiments.

Finally, MIDDOE emphasizes user-friendliness by clearly distinguishing model components and enabling one-time definitions for all techniques, eliminating additional programming. Designed as a numerical wrapper, it can integrate with external simulators or internal Python/NumPy functions, enabling non-expert users to avoid specific programming syntaxes. Data import is simplified by allowing experimental data to be added as Excel files, organized into batches using separate sheets. It supports various data input types and automates the generation and restoration of results, data, and figures. By representing its structure, we demonstrate a part of its novel capabilities through an in-silico experimental campaign for identifying a generic model.

## PACKAGE ARCHITECTURE

MIDDOE is a Python library designed to provide a modular structure (see Figure 1) for performing essential model identification steps. These steps include: 1) setting up models and configuring control variables and constraints; 2), 3) screening models with sensitivity and estimability analyses; 4), 5) parameter estimation and uncertainty analysis; 6), 7) designing experiments for model discrimination and parameter precision; and 8) model validation. The package organizes these steps into a user-friendly syntax, beginning with the first step, which involves importing the model(s) for the identification problem and defining structured dictionaries to symbolically decode and classify model components. Models are imported as Differential-Algebraic Equations (DAEs) and solved using a method that efficiently handles both stiff and non-stiff problems simultaneously. Variables are categorized as time-variant or time-invariant inputs and outputs, while parameters are addressed separately. The design space, along with its associated physical constraints, is also defined, followed by specifying the solver properties. Furthermore, each module requires and received its own specific properties to ensure flexibility and adaptability.

For screening methods, the software includes two advanced techniques: Global Sensitivity Analysis (GSA) using the Sobol method [5] and Estimability Analysis (EA) using the orthogonalization method [6] corresponding to steps 2 and 3, respectively. EA, a key feature of the package, helps restructure parametrically complex models by ranking parameters from higher to lower significance. This analysis introduces a methodology for calculating corrected critical ratios and selecting an optimal subset of parameters for estimating, prioritizing those with the lowest corrected critical ratios. This selection ensures that the model structure avoids over-parameterization and biases.

Once the set of rival models is defined, parameter estimation and uncertainty analysis are employed to assess the precision of estimations and the predictability of the identified model, corresponding to steps 4 and 5. These steps are carried out with the flexibility to choose

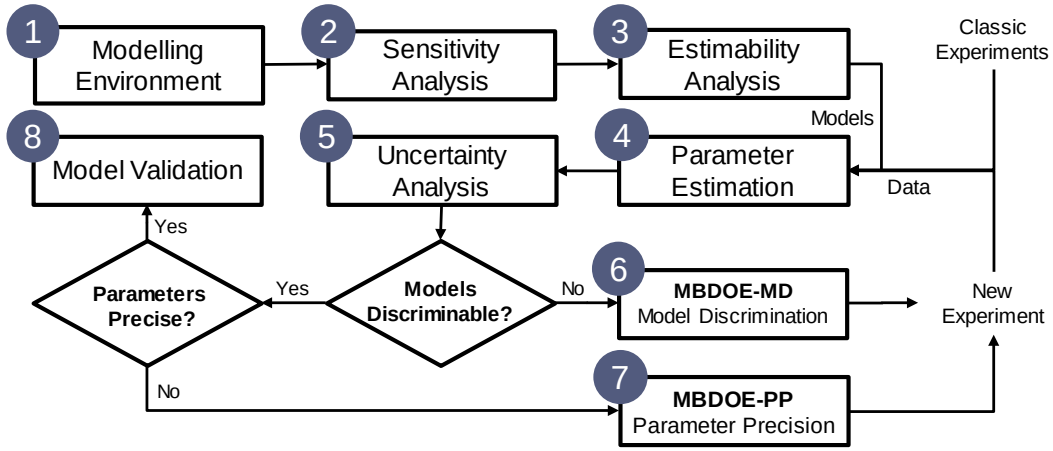



**Figure 1:** Model identification logic and modules provided in the package.

**Table 1:** True parametric values for in-silico experiments and their definitions in Monod model.

| Parameter | Units | Value | Definition |
|---|---|---|---|
| $\theta_1$ | $[\mathrm{h}^{-1}]$ | 0.31 | Maximum specific growth rate |
| $\theta_2$ | $[\mathrm{g.L}^{-1}]$ | 0.11 | Michaelis constant |
| $\theta_3$ | $[-]$ | 0.65 | Yield coefficient |
| $\theta_4$ | $[\mathrm{h}^{-1}]$ | 0.25 | Biomass loss rate due to non-modeled factors |
| $\theta_5$ | $[\mathrm{g.L}^{-1}]$ | 5.00 | Substrate inhibition constant |

**Table 2:** Design space for time-invariant and -variant process controls in Monod model.

| Variable | Units | Range | Approximation Profile | Definition |
|---|---|---|---|---|
| $y_{1,0}$ | $[\mathrm{g.L}^{-1}]$ | $1-10$ | – | Biomass initial concentrations |
| $y_{2,0}$ | $[\mathrm{g\cdot L}^{-1}]$ | $1-10$ | – | Substrate initial concentrations |
| $\mathbf{u_1}$ | $[\mathrm{h}^{-1}]$ | $0.05-0.2$ | Constant Piecewise-relaxed | Time-variant dilution rate |
| $\mathbf{u_2}$ | $[\mathrm{g\cdot L}^{-1}]$ | $5-35$ | Constant Piecewise-decreasing | Time-variant feed substrate concentration |

between global, gradient-free methods or local, gradient-based methods, supported by an internal Finite Difference Method (FDM) auto-differentiator. A key practical feature of the package addresses scenarios where the experimental campaign fails to effectively discriminate between rival models. In such cases, MBDoE-MD [7] is proposed as step 6. Similarly, MBDoE-PP is utilized in step 7 to design experiments that improve parameter precision in the selected model. Both modules offer flexibility in cost function selection, addressing discrimination and precision goals while incorporating physical constraints into the MBDoE framework.

Finally, an identified model can undergo iterative validation tests against experimental batches in step 8 to assess its robustness. Our proposed package also includes additional visualization tools to support the conclusions of the modeling campaign, such as:

- model fitting with calibration and validation data,
- visualization of inter-parametric confidence ellipsoid areas and hyper-ellipsoid volume shrinkage,
- parameter precision evaluation via t-values and confidence interval changes across batches, and
- p-value comparisons across models.

# CASE STUDY AND RESULTS

## Model structure and design space

As a matter of example, the software applies estimability analysis (step 3) and MBDoE-PP (step 7). However, executing steps 1, 4, and 5 is necessary to support these tasks. Simplified in silico simulated experiments with a normally distributed noise of 5% on both of the responses are considered using a generic Monod model [8]. This model predicts the concentrations of biomass ($\mathbf{y_1}$ $[\mathrm{g.L}^{-1}]$) and substrate ($\mathbf{y_2}$ $[\mathrm{g.L}^{-1}]$) in a semi-batch fermentation reactor with continuous feed. Table 1 presents the process model parameters for Eqs. (1) to (3), while Table 2 presents the design space for input variables. The experimental campaign begins with 2 experiments at the center, and maximum of design space boundaries, followed by up to five MBDoE-designed experiments. Each experiment has a budget of 6 sampling points and spans a duration of 10 hours. The use of E-optimality criterion ensures parameter precision exceeds the t-value threshold for all parameter estimations.

$$\frac{\partial y_1(t)}{\partial t} = (r - u_1(t) - \theta_4) \cdot y_1(t) \tag{1}$$

$$\frac{\partial y_2(t)}{\partial t} = -\frac{r \cdot y_1(t)}{\theta_3} \cdot u_1(t)(u_2 - y_2) \tag{2}$$

$$r = \left(\frac{\theta_1 \cdot x_2}{\theta_2 + x_2}\right) \cdot exp\left(-\frac{x_2}{\theta_5}\right) \tag{3}$$

## Estimability analysis

After providing the necessary information and specifications as domain knowledge (step 1) to the software and simulating the initial experiments, the initial observation matrix is formed. Then, this matrix is used for estimation of parameters (steps 4, and 5), providing enough information to return to Step 3: Estimability Analysis. This step evaluates the significance ranking of parameters and derives the optimal subset for estimation. The ranking of parameters based on their significance, from highest to lowest, is $\theta_4$, $\theta_3$, $\theta_1$, $\theta_5$, and $\theta_2$ for the first experiment observations, and $\theta_1$, $\theta_4$, $\theta_3$, $\theta_5$, and $\theta_2$ for the combined observations from the first and second experiments.

Based on this ranking, the estimability analysis calculates the corrected critical ratios for the estimated

subset of parameters as illustrated in Figure 2. With a limited observation matrix, it suggests retaining $\theta_4$ and $\theta_3$ and with an extended one it suggests retaining $\theta_1$, $\theta_4$, and $\theta_3$, as these correspond to the subset with the lowest critical ratio. For both cases, $\theta_2$ and $\theta_5$ are evaluated as insignificant and suggested to be dropped out in the identification procedure by fixing them to their rough estimation. This approach aligns with the t-values (a precision metric based on the 95% confidence intervals of parameters after estimation) obtained at the end of the identification campaign, viz. Figure 3 that indicates greater uncertainty in the estimation of $\theta_2$ with a t-value of 0.006.

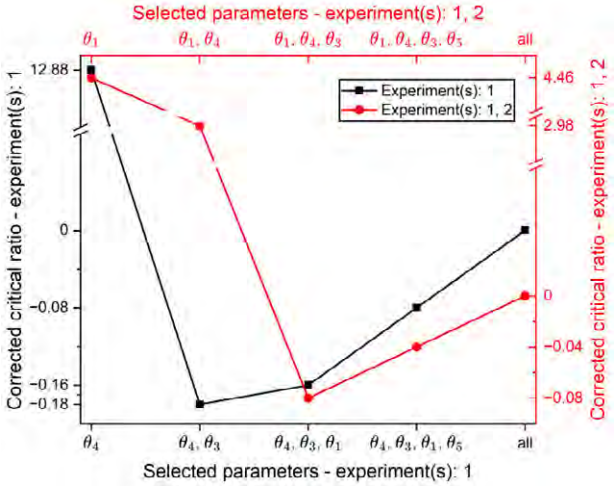



**Figure 2:** Corrected critical ratios across parameter subsets.

Assuming no additional experimental budget is available and avoiding further experimentation, $\theta_2$ and $\theta_5$ are fixed, resulting in a reduced model with only three parameters to estimate. This reduced model is subsequently employed for parameter estimation (Steps 4 and 5). It achieves a slight improvement in accuracy for all parameters by shifting the Probability Density Function (PDF) of estimates closer to the true values. Additionally, it significantly enhances precision, as indicated by the narrower distribution and more reliable estimates, although the t-values of $\theta_1$, and $\theta_3$ remain below the reference threshold of 2.08.

This module is particularly effective in scenarios with limited experimental budgets, where accurate predictions and precise estimation of key parameters are critical. However, to avoid structural simplifications and achieve higher precision in estimating the original model, we revert to its full form and design new experiments. In Step 7 (Figure 1), MBDoE-PP is employed to design new experiments, enhance the information content of the observation matrix, and estimate all parameters with acceptable precision.

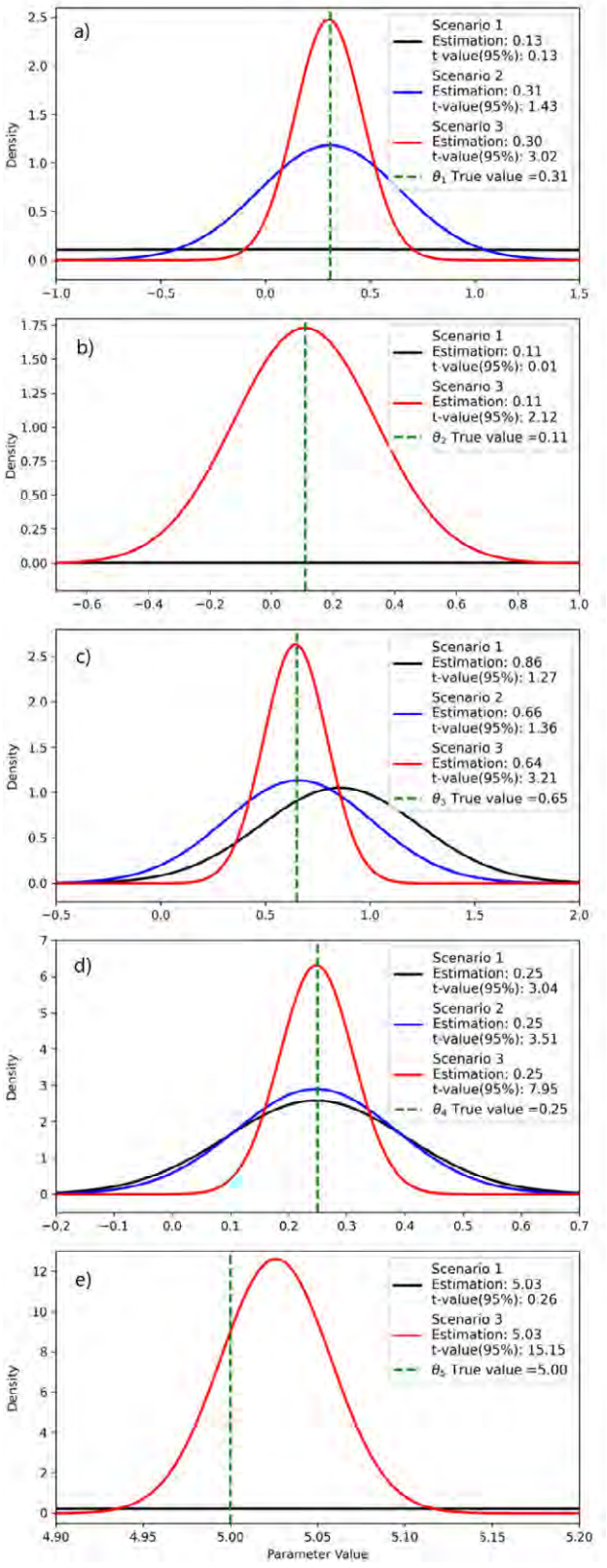



**Figure 3:** Estimation PDFs, mean and 95% t-values for a) $\theta_1$, b) $\theta_2$, c) $\theta_3$, d) $\theta_4$, and e) $\theta_5$, for the initial experiments (Scenario 1), reduced model (Scenario 2), and MBDoE-assisted campaign (Scenario 3).

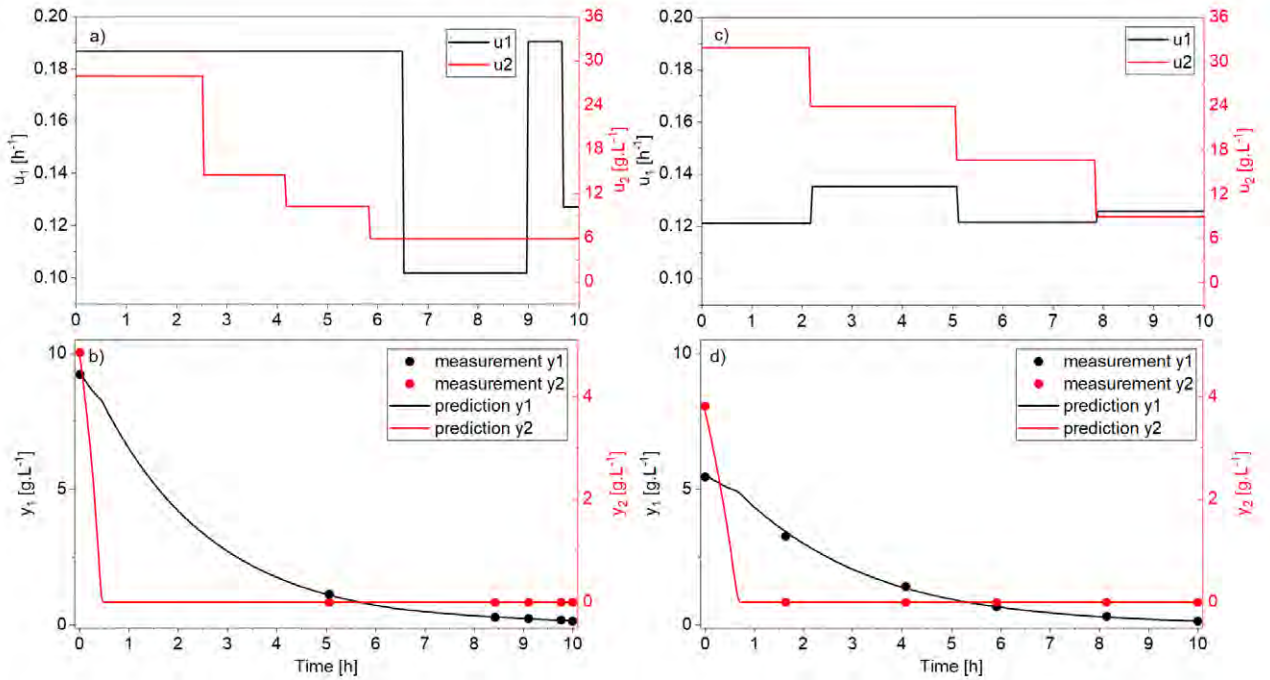



**Figure 4:** Control vectors $\mathbf{u_1}$ and $\mathbf{u_2}$ for a) 1st, and c) 2nd MBDoE designed experiments and experimental data and corresponding model responses $\mathbf{y_1}$ and $\mathbf{y_2}$ for b) 1st, and d) 2nd MBDoE designed experiments

## Model-based design of experiments

The MBDoE-related designs incorporate constraints detailed in Table 2 and additional physical constraints to demonstrate the capabilities of the code. These constraints include three switching times for time-variant controls, with a minimum signal variation of $\mathbf{u_1}$ and $\mathbf{u_2}$ set at 0.015 $[\mathrm{h}^{-1}]$ and 3.0 $[\mathrm{g \cdot L}^{-1}]$, respectively. Switching and sampling times are required to have a minimum interval of 15 minutes, and additional sampling is prohibited during the first and last 15 minutes of the experimental campaign. Not only the signal levels of controls but also the switching times and sampling times are part of the design decisions in the MBDoE-PP optimization problem.

The design decisions for the MBDoE problem are obtained using a global-local joint optimisation algorithm that employs Differential Evolution for the initial exploration of the design space, followed by Sequential Quadratic Programming (SQP) with a trust-region method for refinement. These results are illustrated in Figures 4a and 4c, showing that all obtained results comply with the previously enforced physical constraints of the system.

By simulating the experiments and complementing the observations matrix, steps 4 and 5 are repeated. The model is successfully identified using only two MBDoE-designed experiments when the t-value for all parameters exceeds the reference threshold of 2.02, while predictivity remains high with $R^2$=0.98. Figures 4b and 4d illustrate the model's behaviour in comparison with the experimental data, and Figure 3 summarizes the accuracy and precision achieved with this approach after the identification procedure.

The MBDoE-assisted experimental campaign improves the likelihood of identifying parameters previously considered insignificant or difficult to estimate with acceptable precision. These estimations are not only precise but also accurate, closely aligning with the true parameter values. However, in cases of limited experimental budgets or when restructuring the system or reproducing samples is infeasible, estimability analysis can help identify a predictive model that remains acceptably precise.

## CONCLUSION

We present a new Python library (MIDDoE) designed to perform essential model identification steps, including rival model screening, parameter estimation, uncertainty analysis, and model-based design of experiments (MBDoE). MIDDoE offers a modular and flexible workflow that accounts for process constraints and solver flexibilities, making it suitable for various physical systems and computational platforms. Part of these capabilities, aimed at improving the precision and accuracy of estimations, along with the application of estimability analysis and model-based design of new experiments, are demonstrated using an in-silico case study.

## ACKNOWLEDGEMENTS

This work is part of the CO2Valorize project that has received funding from the European Union's Horizon Europe research and innovation programme under the Marie Skłodowska-Curie Grant Agreement No. 101073547.

## REFERENCES

1. Franceschini G., Macchietto S. Model-based design of experiments for parameter precision: state of the art. Chem Eng Sci 63:4846–4872 (2008). https://doi.org/10.1016/j.ces.2007.11.034
2. Hart W. E., Watson J. P., Woodruff D. L. Pyomo: modeling and solving mathematical programs in Python. Math Program Comput 3:219–260 (2011). https://doi.org/10.1007/s12532-011-0026-8
3. Klise K. A., Nicholson B. L., Staid A., Woodruff D. L. Parmest: parameter estimation via Pyomo. Muñoz SG, Laird CD, Realff MJ, Eds. Proceedings of the 9th International Conference on Foundations of Computer-Aided Process Design 47:41–46 (2019). https://doi.org/10.1016/B978-0-12-818597-1.50007-2
4. Wang J., Dowling A. W. Pyomo.DOE: an open-source package for model-based design of experiments in Python. AIChE J 68:e17813 (2022). https://doi.org/10.1002/aic.17813
5. Saltelli A., Ratto M., Tarantola S., Campolongo F. Sensitivity analysis for chemical models. Chem Rev 105:2811–2827 (2005). https://doi.org/10.1021/cr040659d
6. Wu S., McLean K. A. P., Harris T. J., McAuley K. B. Selection of optimal parameter set using estimability analysis and MSE-based model-selection criterion. Int J Adv Mechatron Syst 3:188–197 (2011). https://doi.org/10.1504/IJAMECHS.2011.042615
7. Chen B. H., Asprey S. P. On the design of optimally informative dynamic experiments for model discrimination in multiresponse nonlinear situations. Ind Eng Chem Res 42:1379–1390 (2003). https://doi.org/10.1021/ie0203025
8. Espie D., Macchietto S. The optimal design of dynamic experiments. AIChE J 35:223–229 (1989). https://doi.org/10.1002/aic.690350206

© 2025 by the authors. Licensed to PSEcommunity.org and PSE Press. This is an open access article under the creative commons CC-BY-SA licensing terms. Credit must be given to creator and adaptations must be shared under the same terms. See https://creativecommons.org/licenses/by-sa/4.0/



Systems & Control Transactions

**Research Article - Peer Reviewed Conference Proceeding**
ESCAPE 35 - European Symposium on Computer Aided Process Engineering
Ghent, Belgium. 6-9 July 2025
Jan F.M. Van Impe, Grégoire Léonard, Satyajeet S. Bhonsale,
Monika E. Polańska, Filip Logist (Eds.)

PSE PRESS

# The Paradigm of Water and Energy Integration Systems (WEIS): Methodology and Performance Indicators

**Miguel Castro Oliveira[a,b]*, Rita Castro Oliveira[c], Pedro M. Castro[b] and Henrique A. Matos[b]**

[a] Research, Develoment and Innovation, Instituto de Soldadura e Qualidade, 2740-120 Porto Salvo, Portugal
[b] Centro de Recursos Naturais e Ambiente (CERENA), Department of Chemical Engineering, Instituto Superior Técnico, Avenida Rovisco Pais 1, 1049-001 Lisboa, Portugal
[c] Department of Computer Science and Engineering, Instituto Superior Técnico, Avenida Rovisco Pais 1, 1049-001 Lisboa, Portugal
* Corresponding Author: dmoliveira@isq.pt, miguelmcoliveira@tecnico.ulisboa.pt

## ABSTRACT

This work approaches a detailed characterization of the aspects inherent to the innovative paradigm of Water and Energy Integration Systems (WEIS). These consists in conceptual physical systems which consider all potential energy-using and water-using processes in a site, all potential recirculation of material and energy streams between these and the integration of several categories of state-of-the-art technologies. The WEIS have the ultimate aim to promote the sustainability character associated to existing installations (through the reduction of energy and water input and contaminants output). The specific characteristics of WEIS are compared to existing similar process integration methodologies and a set of performance indicators are determined, having as a basis two previous case-studies approached for the Engineering project of WEIS. The performed analysis in this work revealed that the innovative paradigm is able to constitute Engineering projects with associated sustainability promotion potential, with the possibility to be modelled with existing computational tools and not being associated to impediments in terms of the maturity and availability of constituting technologies.

**Keywords**: Water and energy integration systems, water-energy nexus, energy recovery, sustainability, performance indicators

## 1. INTRODUCTION

The water-energy nexus has been introduced on the scope of the most relevant sustainability policies of each region of the world. This concept deals with all potential interdependencies between water and energy, and the full understanding of the inherent aspects is fundamental for the promotion of simultaneous water and energy use-related benefits [1–3].

The paradigm of Water and Energy Integration Systems (WEIS) was recently developed by a working group of researchers from both ISQ – Instituto de Soldadura e Qualidade and CERENA – Centro de Recursos Naturais e Ambiente [4]. It consists of physical systems encompassing a set of water and energy-using units in a site, and the water and energy recirculation between these units, with the goal of achieving economic and environmental benefits. In parallel to the development of this innovative paradigm, a digital twin-based computational tool has been developed by the authors for the virtual implementation of WEIS in the context of end-use sector case-studies, designated as ThermWatt [4–6].

The innovative WEIS paradigm was developed to expand the Total Site Integration (TSI) and Combined Water-Energy Integration (CWEI) concepts, and to attend to their limitations. The WEIS paradigm focus on energy-using and water-using processes as a whole (in opposition to a standalone focus on each process category), adapting conceptual elements from both TSI and CWEI and introducing new ones. These include technologies for energy recovery from water/ wastewater units (such as electrolysis) and the supply of thermal energy (direct waste heat) or electric energy (indirectly produced in thermodynamic cycles) to fulfill already existing energy requirements (hot utilities, in this case) and additional ones (wastewater treatment units).

In this work, it is performed a detailed description of the methodology inherent to the innovative paradigm of Water and Energy Integration Systems, subsisting on the

definition of most generic superstructures which may be furtherly adapted to each end-use sector case-study in specific. The specific characteristics associated to the WEIS methodology is compared to the existing methodology and a set of performance indicators are determined to assess the viability of these systems in terms of the integration of these on real-life Engineering projects.

## 2. METHODOLOGY

In general, the conceptualization of Water and Energy Integration Systems (WEIS) passes by the simultaneous application of the principles of water recirculation and heat recovery. In this prospect, two different configurations have been primarily conceptualized:

- **Configuration 1**: Standard Configuration (combustion-based process in continuous operation);
- **Configuration 2**: Dynamic Configuration (combustion-based process in continuous and batch operation and implementing thermal energy storage).

The general description points associated to all superstructures may be extensively defined as follows:

- The WEIS encompasses M combustion-based processes and N water-using processes;
- Each combustion-based process encompasses the feeding of a fuel stream (primary energy source) and combustion air stream;
- Each combustion-based process encompasses a set of waste heat streams, which jointly constitute a potentially recirculated heat stream (to the same process or other processes);
- The set of all combustion-based processes and its inlet and outlet streams constitutes the designated thermal process system;
- The set of a combustion-based process and recirculated heat streams that are transported from the outlet to the inlet of processes constitute a thermal process sub-system;
- In the context of the superstructures furtherly represented, the recirculated heat stream directed to a combustion-based process's inlet may (direct heat recovery) or may not (indirect heat recovery) be mixed with the inlet ambient air stream (it depends whether the recirculated heat stream is air or an exhaust gas, as commonly verified and implemented);
- The recirculated heat stream at the outlet of a combustion-based process may be recirculated to the same combustion-based process or the other M – 1 combustion-based processes;
- In Configuration 2, another recirculated heat stream is transported to an energy storage system (TES) to heat up a heat sink stream, which is then split to be fed to each combustion-based processes;
- For each water-using process is installed a WWT unit for the treatment of the wastewater stream at the outlet of the water-using process, in addition to a heater and a cooler;
- The set of all water-using processes, WWT units, heater, cooler and inlet, outlet and recirculated streams constitutes the water system;
- The set of a water-using process, associated WWT unit, heater, cooler and respective inlet, outlet and recirculated streams (which do not recirculate to other N – 1 water-using processes) constitute a water subsystem;
- Each water sub-system is fed by a freshwater stream and a discharged water stream results as an outlet stream;
- At the outlet of the water-using process, WWT unit, heater and cooler results several recirculated streams (recycled, reused and by-passed):
    - From the water-using process to the WWT unit inlet, heater inlet, cooler inlet, the WS outlet, other N – 1 heaters and other N – 1 coolers;
    - From the WWT unit to WP inlet, heater inlet, cooler inlet, the WS outlet, other N – 1 heaters and other N – 1 coolers;
    - From the heater to WP inlet, WWT unit inlet and WS outlet;
    - From the cooler to WP inlet, WWT unit inlet and WS outlet;
    - For each WWT unit, a sludge stream is generated and then directed to the inlet of a wastewater-to-energy module (mixed with the discharged water stream);
    - The generated energy (in the form of fuel) in the wastewater-to-energy is directed to the inlet of each combustion-based process sub-system and a combustion chamber which is (by hypothesis) installed within the thermodynamic cycle;
    - In the context of the configuration furtherly represented, the additional fuel stream may be (directly) mixed with the primary fuel stream or be (indirectly) transported to each combustion chamber.
- In addition to the recirculation within the thermal process system, the recirculated heat may be directed to the water system (the stream is divided for each water sub-system, and in its turn for each heater and WWT unit), a thermodynamic cycle (for the production of additional electric energy) and the WtE unit (according to the specific energy input in this process). The generated electricity is directed to each WWT unit and the WtE unit.

The most generic superstructure-based formulation of both WEIS configurations is presented in the sequence of Figure 1 (presented for Configuration 2, Configuration 1 is only different in the aspect that does not consider the Thermal Energy Storage unit).

Systems & Control Transactions

**Research Article - Peer Reviewed Conference Proceeding**
ESCAPE 35 - European Symposium on Computer Aided Process Engineering
Ghent, Belgium. 6-9 July 2025
Jan F.M. Van Impe, Grégoire Léonard, Satyajeet S. Bhonsale,
Monika E. Polańska, Filip Logist (Eds.)

PSE PRESS

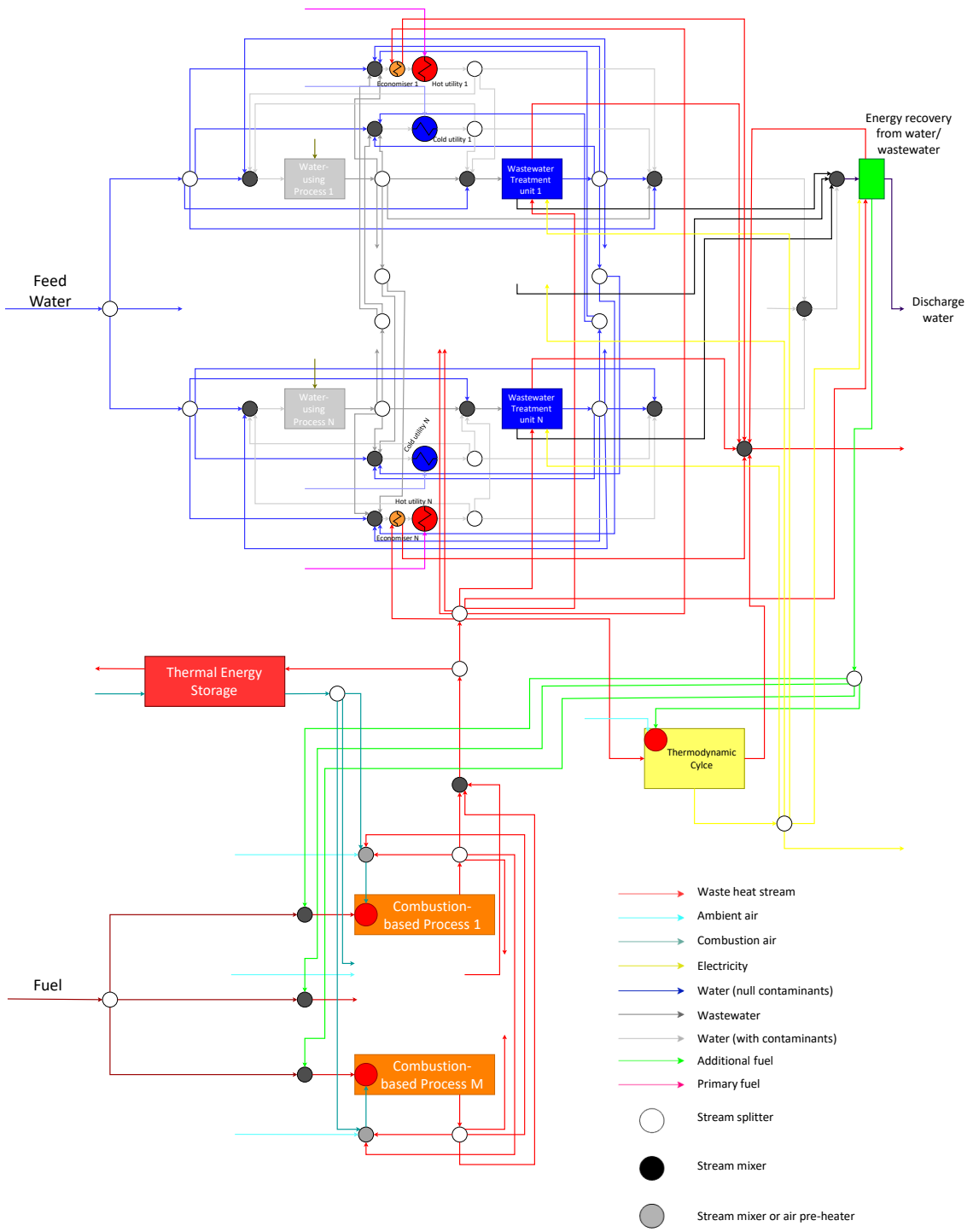



**Figure 1:** Generalized superstructure for WEIS Configuration 2 (Dynamic, transient state-based)

**Table 1:** Comparison between Methodologies

| Existing Methodologies | Water and Energy Integration Systems (WEIS) |
|---|---|
| **Combined Water and Energy Integration (CWEI)** [7] | • The object of study is a set of water-using and combustion-based thermal pro-cesses within a plant;<br>• It is based on the assessment of all potential recirculation points, in which waste heat streams may be recirculated to all pro-cesses with thermal energy requirements (combustion-based processes and water system hot utilities), as well as for the purpose of electricity generation, and discharge water streams may be recirculated from one unit operation of one water-using line to the inlet of the others within the same line and to the inlet of all the processes within the other water-using lines;<br>• The practical method is based on the valorisation of output streams, rather than on the rationalization of input streams;<br>• In terms of technological integration, it over-all encompasses the same technologies as CWEI and TSI and in addition units for the energy recovery from water/ wastewater. |
| • The object of study is a water network constituted by a set of water-using processes and wastewater treatment units;<br>• It is based on the application of steady state-based optimisation methodologies for the assessment of the most favourable levels of water stream recirculation in several points of the water network;<br>• Being based on the use of a resource as both an additional water and heat source, it only considers water streams for re-circulation. | |
| **Total Site Integration (TSI)** [8] | |
| • The object of study is a set of energy-using processes connected by a common utility system;<br>• It is based on the analysis of heat recovery between several processes through consumption and generation of utilities, in each the heating and cooling needs of each process are identified for the purpose of utility targeting;<br>• The supply of utilities with the aim to improve energy use may be performed through several measures (utility replacement, recirculated heat streams and renewable energy resources);<br>• For variable energy demand and supplies, it may involve the use of thermal energy storage units;<br>• It is itself an extension of the simpler heat integration methodologies (such as pinch analysis). | |

As may be evidenced by the analysis of Table 1:

- The innovative methodology may be considered a simultaneous expansion and combination of the CWEI and TSHI methodologies in conceptual terms. Such is attributed to it overall considering categories of processes that are not considered in CWEI (only approaching water-using processes and associated consumption of material and energy-related utilities) and TSI (only approaching energy-using processes and related utility system);
- While TSI does not only consider energy efficiency improvement but also on the adaptation/ substitution of energy inputs, the general concept of WEIS considers system-level improvements only through discharge stream recirculation (which would otherwise be classified as several types of wastes). The WEIS paradigm does not completely disregard the consideration of other energy inputs (such as renewable resources and alternative hot and cold utilities), it only focuses on waste stream valorisation.

## 3. PERFORMANCE INDICATORS

The overall assessment of the viability of the WEIS paradigm for practical implementation depends on the several aspects which may be analysed according to the determination of several performance indicators. In Table 2, it is presented the determination of several indicators according to each category of interest. The presented aspectual and numeric values have been gathered from the results associated to previous works by the authors, namely two cases (Cases 1 and 2) within a Portuguese ceramic industry plant [4–6]. The operation of the mentioned plant is associated to a 375.26 TJ/year energy consumption and a 10.77 $dam^3$/year water consumption. The WEIS Engineering projects include Organic Rankine cycle (ORC) units, multi-effect distillations (MED) units and a phase change material (PCM)-based heat exchanger unit (Case 2 only). The sustainability assessment has been performed considering the benchmark values of 2 – 3 year payback period and 0.722 kton $CO_{2,eq}$/year emissions reduction. An extensive description in respect to the characterization of the case-studies, developed simulation models (and final configurations), optimisation models and post-processing assessments is presented in the digital supplementary material (with information adapted from [4]).

In relation to the determined performance indicators presented in Table 2:

- The set of implemented simulation and optimisation modelling methodologies revealed to be suitable for the development of digital twins of set-to-be-implemented WEIS;
- The balanced combination of all capabilities associated to the Modelica and Python languages revealed to be effective for the development of a customised digital tool for WEIS;
- It is furtherly necessary to exploit the potential for the interface between Modelica-based simulation models and dynamic programming models, for a reason of achieving the highest possible integration associated to the digital tool;
- The determined sustainability assessment-based indicators revealed the sustainability promotion potential associated to WEIS-based case-studies;

Furthermore, in respect to the considered technology assessment-related indicators, it is possible to observe that the technologies considered for implementation in the context of the two approached WEIS with lowest technological maturity are in general associated to

the lowest technology readiness (TRL) level of TRL5. Such is significant that the considered technologies have been at least validated in a relevant operational environment. In this prospect, it may be affirmed that overall technological maturity is not a particularly relevant factor which affects the potential implementation of WEIS in real-life taking as a basis the conditions associated to the two approached case-studies, since the considered technologies have been at least validated for similar operational conditions. Moreover, it further proves the technological development potential associated to the WEIS paradigm, in which the requirement for the Engineering projects of these types of systems and their further real-life implementation (itself caused by significant needs for water and energy efficiency improvement in end-use sectors) necessarily creates the necessity for the implementation of the referred technologies in a real-life perspective (and thus the increase of the maturity of these from a development phase to a deployment phase).

**Table 2:** Determination of performance indicators

| Indicator | Case 1 | Case 2 |
|---|---|---|
| **Computational Model-based** | | |
| Simulation Model (OpenModelica) | Completed | Completed |
| Steady state-based Optimisation Model (Python GEKKO package) | Completed | Completed (Water System) |
| Dynamic Optimisation Model (OpenModelica) | Not applicable | Completed (Combustion-based Processes System) |
| Application of OpenModelica Python (OMPython) API | Completed | Semi-completed (Not between simulation model and DP optimisation model) |
| **Sustainability Assessment-based** | | |
| Energy Savings | 8.57% | 6.88% |
| Water Savings | 23.71% | 38.57% |
| Eco-efficiency promotion | 6.46% | 4.00% |
| Payback period | 1 year and 10 months | 2 years and 10 months |
| Emission reductions | 2.42 kton $CO_{2,eq}$/year | 1.76 kton $CO_{2,eq}$/year |
| **Technology assessment-based** | | |
| Technology readiness level (associated to the considered technology with the less maturity) | TRL5 (Heat-driven water/ waster treatment technologies with less maturity [9]) | TRL5 (Heat-driven water/ waster treatment technologies with less maturity [9]) TRL5-7 (Phase change material-based thermal energy storage [10]) |

## 4. CONCLUSIONS

This work approaches the fundamental aspects of the paradigm of Water and Energy Integration (WEIS) which has been created and approached in previous works by the authors, and which consists of an innovative methodology that compensates for conceptual gaps associated to similar methodologies. In this prospect, the innovative methodology (subsisting in two most generic superstructures for these types of physical systems), the comparison of this one with existing methodologies and a set of performance indicators have been presented and analysed.

In terms of the developed methodological framework and the determined performance indicators, the following affirmations may be performed:

- The WEIS methodology had already successfully expanded and complemented existing process integration methodologies;
- The WEIS methodology has still to be furtherly updated to include all potential categories of energy-using processes, in addition to combustion-based ones.
- The set of implemented modelling methodologies revealed to be suitable for the development of WEIS digital twins and the sustainability assessment procedure for two approached case-studies revealed the economic and environmental viability associated to the implementation of WEIS in real-life end-use sector sites (industrial plants);
- The implementation of WEIS in real-life is not substantially compromised by technological maturity of involved technologies, and it even has a potential to boost the TRL of less mature technologies;
- It is furtherly necessary to exploit the potential for a more automatic integration (co-simulation) of

simulation models and dynamic programming models.

Taking into account the aforementioned aspects, it is possible to affirm that the developed paradigm of Water and Energy Integration Systems is a relevant opportunity for end-use sectors, being able to constitute Engineering projects with associated sustainability promotion potential, possibility to be modelled with existing computational tools and not being associated to impediments in terms of the maturity and availability of constituting technologies.

## DIGITAL SUPPLEMENTARY MATERIAL

Digital supplementary material is available at https://psecommunity.org/LAPSE:2025.0035.

## ACKNOWLEDGEMENTS

This work was funded through the base funding component of the Center for Technology and Innovation—ISQ, under the terms defined in AAC nº 03/C05-i02/2022, and CERENA, under grant UIDB/04028/2020_UIDP/04028/2020.

## DEDICATION

The authors would like to dedicate this contribution to the memory of Professor Pedro Castro, who passed away during the review process. His guidance, knowledge and friendship will be greatly missed.

## REFERENCES

1. Walsh B.P., Murray S.N., O'Sullivan D.T.J. The water energy nexus, an ISO50001 water case study and the need for a water value system. *Water Resour. Ind.* 10: 15–28 (2015) https://doi.org/10.1016/j.wri.2015.02.001
2. Gabbar H.A., Abdelsalam A.A. Energy—water nexus: Integration, monitoring, KPIS tools and research vision. *Energies* 13: 24 (2020) https://doi.org/10.3390/en13246697
3. Souza R.G., Barbosa A., Meirelles G. The Water–Energy Nexus of Leakages in Water Distribution Systems. *Water* 1: 22 (2023) https://doi.org/10.3390/w15223950
4. Castro Oliveira M. Simulation and Optimisation of Water and Energy Integration Systems (WEIS): An Innovative Approach for Process Industries. *PhD Thesis, IST* (2023) https://shorturl.at/knqzS
5. Castro Oliveira M., Iten M., Matos H.A. Simultaneous optimisation of energy recovery and water recirculation in a ceramic plant. *Comput. Aided Chem. Eng.* 52: 2785–2790 (2023) https://doi.org/10.1016/B978-0-443-15274-0.50443-1
6. Castro Oliveira M., Castro Oliveira R., Matos H.A. Dynamic simulation and optimisation of water and energy consumption in a ceramic plant: Application of the customised ThermWatt computational tool. *Comput. Aided Chem. Eng.* 53: 2377–2382 (2024) https://doi.org/10.1016/B978-0-443-28824-1.50397-5
7. Savulescu L.E., Alva-Argaez A. Process Integration Concepts for Combined Energy and Water Integration. *Handb. Process Integr. Minimisation Energy Water Use, Waste Emiss.* 461–483 (2013) https://doi.org/10.1533/9780857097255.4.461
8. Perry S., Varbanov P.S. Total Site Methodology. *Handbook of Process Integration*. 201–261 (2013)
9. Lienhard V J.H., Thiel G.P., Warsinger D.M., Banchik L.D. Low Carbon Desalination: Status and Research, Development, and Demonstration Needs. Report of a workshop conducted at the Massachusetts Institute of Technology in association with the Global Clean Water Desalination Alliance. *MIT Abdul Latif Jameel World Water Food Secur Lab* (2016): 1–127.
10. European Commission. Competitiveness of clean energy technology - Novel thermal energy storage technologies (2023).

© 2025 by the authors. Licensed to PSEcommunity.org and PSE Press. This is an open access article under the creative commons CC-BY-SA licensing terms. Credit must be given to creator and adaptations must be shared under the same terms. See https://creativecommons.org/licenses/by-sa/4.0/



Systems & Control Transactions

**Research Article - Peer Reviewed Conference Proceeding**
ESCAPE 35 - European Symposium on Computer Aided Process Engineering
Ghent, Belgium. 6-9 July 2025
Jan F.M. Van Impe, Grégoire Léonard, Satyajeet S. Bhonsale,
Monika E. Polańska, Filip Logist (Eds.)

PSE PRESS

# Comparison of Multi-Fidelity Modelling Methods for Bayesian Optimization

**Stefan Tönnis[a], Luise F. Kaven[a], Eike Cramer[a,*]**

[a] Process Systems Engineering (AVT.SVT), RWTH Aachen University, 52074 Aachen, Germany
* Corresponding Author: eike.cramer@avt.rwth-aachen.de

## ABSTRACT

In process systems engineering (PSE), obtaining accurate process models for optimization can be expensive and time-consuming. Black-box Bayesian Optimization (BO) with Gaussian process (GP) surrogates offers a promising approach. However, full black-box optimization neglects valuable prior knowledge, which could otherwise improve the optimization process. This work explores methods of integrating prior knowledge in the form of low-fidelity data into BO by evaluating these methods on synthetic multi-fidelity test functions. Our results highlight possibilities for improved convergence of the BO optimization. However, our work further highlights potential pitfalls of these multi-fidelity models, such as bias, convergence to local optima, and overfitting on low-fidelity data. Hence, leveraging low-fidelity data in multi-fidelity models can improve BO convergence, but there are instances where the algorithms are more susceptible to failure.

**Keywords**: Process Design, Optimization, Machine Learning, Numerical Methods

## INTRODUCTION

Process models are not always available and can be prohibitively expensive to obtain for model-based optimization. Hence, the process systems engineering (PSE) community has gained an interest in Bayesian Optimization (BO). BO uses Gaussian process (GP) surrogate models as a probabilistic approximation of objective functions. The BO algorithm iteratively queries the black-box objective with experimental conditions obtained from optimizing over the so-called acquisition function [1]. Although BO is generally known as sample-efficient, treating chemical engineering design problems as fully black-box problems can still be prohibitively expensive, particularly for high-cost technical-scale experiments with many degrees of freedom (DoF). At the same time, the past 150 years of chemical engineering research provide extensive knowledge, modeling, and databases that are neglected by black-box algorithms such as BO. Hence, we investigate different possibilities of including such prior knowledge in the BO algorithm.

Other works from the PSE community investigate options to combine BO with known model equations, e.g., in compositions of GPs with mechanistic equations [2, 3]. In this work, however, we consider the case of available data, e.g., from low-cost simulations, approximate models, or similar processes.

One widely known option to include such prior knowledge in BO is prior mean modeling [4], where the user complements the BO algorithm with an initial guess, i.e., a prior mean. Such prior means may be derived from a scientist's intuition or fitted to available lower-fidelity data. A similar yet structurally different alternative are multi-fidelity GPs designed to handle lower-fidelity data [5]. These multi-fidelity models enhance the model's predictive capabilities by transferring knowledge from low-fidelity observations to the high-fidelity regime. Prominent methods are multi-task and multi-fidelity GPs utilizing special kernels to model the relations between different fidelities or the recursive GP model introduced by Kennedy and O'Hagen [6, 7].

In this work, we compare the usage of different multi-fidelity and prior mean modeling techniques for BO design problems. We focus on improving BO convergence in the high-fidelity regime, utilizing low-fidelity data as a supplementary source of information. Our analysis shows that utilizing lower-fidelity data in BO can generally improve the convergence of the BO optimization. However, our analysis also highlights some potential pitfalls and causes for failure, such as convergence to

local optima, overfitting, and model training errors. For this conference proceeding, we restrict our analysis to established multi-fidelity test functions, e.g., Forrester, Rosenbrock, and Rastrigin test functions.

## BAYESIAN OPTIMIZATION

Black-box optimization refers to optimization problems where the objective function $f(\mathbf{x})$ lacks an analytical expression or is expensive to evaluate. The general form of a black-box optimization problem is:

$$\min_{\mathbf{x}\in\mathcal{X}} f(\mathbf{x}) \tag{1}$$

Here, $\mathbf{x}$ is the vector of DoF from a feasible domain $\mathcal{X} \subseteq \mathbb{R}^{\mathrm{d}}$, and $f(\mathbf{x})$ is the objective function to be minimized. BO is a widely adopted approach for solving such problems, leveraging probabilistic surrogate models to approximate the objective function, enabling efficient exploration and exploitation of the search space while keeping the number of evaluations low.

GPs are a popular choice for the probabilistic surrogate model for BO due to their data efficiency and inherent uncertainty quantification. GPs are an extension of a multivariate normal distribution to infinite dimensions, i.e., continuous functions, with the prior distribution $p(f)$ of the objective function $f$ defined as:

$$p(f) = \mathcal{N}\left(f; \mu(\mathbf{x}), k(\mathbf{x},\mathbf{x}') = \mathcal{GP}\big(\mu(\mathbf{x})\big), k(\mathbf{x},\mathbf{x}')\right) \tag{2}$$

Here, $\mu(\mathbf{x})$ is the mean function representing the expected value of the objective function $f$, and $k(\mathbf{x},\mathbf{x}')$ is the covariance function describing the relation between two arbitrary vectors $\mathbf{x}$ and $\mathbf{x}'$. The joint distribution of the prior belief $f$ and exact observations $\mathbf{y}$ is Gaussian:

$$p(f,\mathbf{y}) = \mathcal{GP}\left(\begin{bmatrix}\mu(\mathbf{x})\\ \mathbf{m}\end{bmatrix}, \begin{bmatrix}k(\mathbf{x},\mathbf{x}') & k(\mathbf{x},\mathbf{X})^{\mathrm{T}}\\ k(\mathbf{X},\mathbf{x}) & \mathbf{K}(\mathbf{X},\mathbf{X})\end{bmatrix}\right), \tag{3}$$

The vector of means of the observations, $\mathbf{m}$, is typically set directly to the observations. For the case of exact observations, this simplifies to $\mathbf{y} = \{f(\mathbf{x}_i)\}_{i=1}^{N}$, where $N$ denotes the number of observations. The matrix $\mathbf{X} = \{\mathbf{x}_i\}_{i=1}^{N}$ represents the corresponding set of data points in the input dimension and $\mathbf{K}(\mathbf{X},\mathbf{X})$ corresponds to the covariance matrix evaluated at these data points, using a kernel function $k(\cdot,\cdot)$. Conditioning the GP prior $p(f)$ on the noise-free observation data $\mathcal{D} = \{\mathbf{x}_i, f(\mathbf{x}_i)\}_{i=1}^{N}$ yields the posterior $p(f|\mathcal{D})$, which is also Gaussian:

$$p(f|\mathcal{D}) = \mathcal{GP}(f; \mu_{\mathcal{D}}(\mathbf{x}), k_{\mathcal{D}}(\mathbf{x},\mathbf{x}')) \tag{4}$$

The posterior mean and covariance functions read:

$$\mu_{\mathcal{D}}(\mathbf{x}) = \mu(\mathbf{x}) + K(\mathbf{x},\mathbf{X})K(\mathbf{X},\mathbf{X})^{-1}\big(\mathbf{m} - \mu(\mathbf{X})\big) \tag{5}$$

$$k_{\mathcal{D}}(\mathbf{x},\mathbf{x}') = k(\mathbf{x},\mathbf{x}') - k(\mathbf{x},\mathbf{X})K(\mathbf{X},\mathbf{X})^{-1}k(\mathbf{X},\mathbf{x}) \tag{6}$$

Since the surrogate model is probabilistic, it allows the user to formulate an expression of a preference over the uncertain outcomes, also known as an acquisition function $\alpha : \mathcal{X} \to \mathbb{R}$. Thus, the inference of the next observation location $\hat{\mathbf{x}}$ boils down to maximizing the acquisition function:

$$\hat{\mathbf{x}} \in \underset{\mathbf{x}\in\mathcal{X}}{\operatorname{argmax}}\, \alpha(\mathbf{x},\mathcal{D}) \tag{7}$$

One of the most common acquisition functions is the expected improvement acquisition function, which is defined as:

$$\mathrm{EI}_{y^*}(\mathbf{x}) = \mathbb{E}_{f(\mathbf{x})}[\max(0, f(\mathbf{x}) - y^*)]\,, \tag{8}$$

where the incumbent $y^* = \max \mathbf{y}$ is the best function value observed so far [8].

### Bayesian optimization with available lower-fidelity data

In many chemical engineering problems, data often comes from simulations or experiments that can be performed at varying levels of detail, precision, or cost. These levels of detail are commonly referred to as fidelities. Each level of fidelity can be represented by a different function $f_t(\mathbf{x})$, where $t = 1, \ldots, T$ indicates the fidelity level, with $t = T$ representing the highest fidelity. Each fidelity level provides a set of data points, $\mathcal{D}_t = \{(\mathbf{x}_i, f_t(\mathbf{x}_i))\}_{i=1}^{N_t}$ where $\mathbf{x}_i$ represents DoF and $f_t(\mathbf{x}_i)$ the corresponding function evaluations, with $N_t$ denoting the number of observations in the $t$-th fidelity.

The goal of multi-fidelity optimization is to efficiently determine the optimal choice of the DoF $\mathbf{x}^*$ that minimizes the highest-fidelity function $f_T(x)$. This is achieved by leveraging data from the lower-fidelity levels $\{\mathcal{D}_t\}_{t=1}^{T-1}$, which are typically less expensive to compute, to inform and reduce the need for evaluations of $f_T(\mathbf{x})$. The challenge lies in effectively combining information from these fidelities to balance accuracy and computational efficiency.

While multi-fidelity optimization often incorporates a cost-aware perspective, assigning evaluation costs to fidelities and using a joint acquisition function to minimize expected cost, this work focuses solely on the highest-fidelity function. Here, lower-fidelity data is used to enhance the predictive model of $f_T(\mathbf{x})$, improving accuracy and reducing the number of high-cost evaluations required.

### Prior mean modeling

The prior mean function $\mu(\mathbf{x})$ of a GP is typically assumed to be either zero or a constant value in order to avoid any unwanted bias on our decisions caused by spurious structure in the prior process [1, 9]. By specifying the prior mean function $\mu(\mathbf{x})$ of the prior belief of the objective function $p(f)$, high-level information about the objective function can incorporated into the BO process. The GP posterior of the objective function $p(f|\mathcal{D})$ is then updated by the available data but still inherits the

previously encoded knowledge.

A practical approach to integrating low-fidelity data into the prior mean of a Gaussian process involves training a regression model on the low-fidelity dataset. The resulting model is then utilized as the prior mean function for the Gaussian process. In this study, we consider a fifth-order polynomial regression with L2 regularization and a neural network. For the polynomial regression model, the prior mean of the GP is defined as:

$$\mu(\mathbf{x}) = \Phi(\mathbf{x})\mathbf{w} \tag{9}$$

Here $\Phi(\mathbf{x})$ represents the feature matrix, and $\mathbf{w}$ the respective weights of the polynomial regression model. The prior mean of the neural network is defined as:

$$\mu(\mathbf{x}) = \mathrm{NN}(\mathbf{x}) \tag{10}$$

Here, $\mathrm{NN}(\boldsymbol{x})$ represents the neural network.

## Recursive co-kriging model

The recursive co-kriging model, commonly referred to as the auto-regressive (AR1) model, was first introduced by Kennedy and O'Hagen [6] and further elaborated upon by Gartiet [7]. This model is widely used for multi-fidelity modeling and leverages an auto-regressive structure to represent dependencies across fidelity levels. It assumes a Markov property, wherein each fidelity level is dependent only on the immediately preceding level. The general formulation of the AR1 model for $T$ fidelity levels can be expressed as:

$$f_t(\mathbf{x}) = \rho_{t-1} f_{t-1}(\mathbf{x}) + \delta_t(\mathbf{x}), \qquad t = 2, \dots, T \tag{11}$$

Here, $f_t(\mathbf{x})$ represents the GP associated with the $t$-th fidelity level, while $f_{t-1}(\mathbf{x})$ is the GP conditioned on the data from the preceding fidelity level. The parameter $\rho_{t-1}$ serves as a scaling factor that quantifies the influence of the $(m-1)$-th fidelity level on the current fidelity level. The term $\delta_t(\mathbf{x})$ is a GP that models the residual errors between the high-fidelity data at the $t$-th level and the predictions provided by $f_{t-1}(\mathbf{x})$.

Due to the AR1 model's Markov property, the data points at a given fidelity level only influence the predictions of that level and all subsequent fidelity levels, but not the preceding fidelity levels. Consequently, the model is well-suited for datasets with such a hierarchical structure.

## Multi-Fidelity Modeling

Unlike the recursive co-kriging model, which leverages an auto-regressive structure to model the fidelity relation sequentially, other multi-fidelity approaches adopt a joint modeling framework. A key challenge in such models lies in accurately defining and learning the cross-covariance structure between tasks or fidelities, which is critical for effective knowledge transfer.

Two notable examples of such an approach are the multi-task GP model formulation proposed by [10] and the multi-fidelity GP model formulation proposed by [11]. The multi-task model captures these relationships using a learnable inter-task covariance matrix. In contrast, the multi-fidelity model by [11] represents fidelity as a continuous parameter and employs a covariance function to describe inter-task dependencies. Both approaches rely on decomposing the covariance between outputs into components that reflect task/fidelity dependencies and input space similarities. This can be formally expressed as:

$$k_{multi}\big((\mathbf{x}, t), (\mathbf{x}', t')\big) = k_t(t, t') \cdot k_{\mathbf{x}}(\mathbf{x}, \mathbf{x}') \tag{12}$$

or equivalently in tensor form:

$$k_{multi}\big((\mathbf{x}, t), (\mathbf{x}', t')\big) = \mathbf{K}_t \otimes k_{\mathbf{x}}(\mathbf{x}, \mathbf{x}') \tag{13}$$

Here, $t$ and $t'$ denote task or fidelity indices, $k_t$ represents the covariance of tasks or fidelities, and $k_x$ encodes input space similarity. The choice of representation depends on whether tasks are treated as discrete entities, e.g., in multi-task GPs, or part of a continuous fidelity spectrum, e.g., in multi-fidelity GPs.

# RESULTS AND DISCUSSION

The different multi-fidelity BO methods are evaluated on optimization test problems, specifically on multi-fidelity versions of the Forrester, the Rosenbrock, shifted and rotated Rastrigin, and the Heterogeneous test functions. Both the shifted and rotated Rastrigin and the Heterogeneous function are multi-modal functions, i.e., these functions exhibit multiple local optima. The key characteristics are summarized in Table 1. For a detailed explanation of the test function, the reader is referred to the original source [12]. The different methods are compared to a baseline, i.e., a standard GP conditioned only on high-fidelity data. All evaluated methods are summarized in Table 2.

**Table 1:** Evaluated multi-fidelity test functions [12].

| # | Function | # Dimensions | # Fidelities |
|---|---|---|---|
| 1 | Forrester | 1 | 4 |
| 2 | Rosenbrock | 2 | 3 |
| 3 | Rastrigin | 2 | 3 |
| 4 | Heterogeneous | 1 | 2 |

The performance of the different methods is evaluated on the success rate of optimization runs. We evaluate the success of an optimization run using a convergence score. The convergence score is defined as:

$$\phi_i = \frac{f_{max} - y_i^*}{f_{max} - f_{min}} \tag{14}$$

Here, $f_{min}$ and $f_{max}$ are the minimum (optimum) and maximum function values in the search domain, respectively.

Here, $y_i^*$ is the incumbent from the methods in the i-th optimization step. The convergence score is then compared to a required convergence score $\phi \leq \phi_{req}$. If the required convergence score is reached, the optimization run will be deemed successful. Note that we can define the convergence score as we consider test functions with known optima.

**Table 2:** Evaluated multi-fidelity modeling methods.

| # | Methods | Description |
|---|---|---|
| 1 | Baseline | GP conditioned on high-fidelity data |
| 2 | Prior Mean Polynomial | GP conditioned on high-fidelity data and using a polynomial regression model trained on low-fidelity data. |
| 3 | Prior Mean NN | GP conditioned on high-fidelity data and using a neural network regression model trained on low-fidelity data. |
| 4 | Multi-Fidelity GP | Multi-fidelity GP model as described in [11], conditioned on multi-fidelity data. |
| 5 | Multi-Task GP | Multi-task GP model as described in [10], conditioned on multi-fidelity data. |
| 6 | Recursive Co-Kriging | Recursive Co-Kringing model as described in [6], conditioned on multi-fidelity data. |

All methods are run for a total number of 100 optimization runs, with varying initial data and with a maximum budget of 100 optimization steps. We use 10 initial data points per dimension for each low-fidelity function. Additionally, one data point per dimension in the target fidelity was considered as initial data. A small observation noise covariance prevents numerical instability, assuming exact observations otherwise. The logarithmic expected improvement is used as an acquisition function. The logarithm of the expected improvement is maximized to account for vanishing gradients in low-value regimes [8].

Figure 1 shows the evaluation results for the convergence score. Each subplot (1-4) corresponds to one optimization problem from Table 1, with the x-axis in logarithmic scale representing the number of iterations and the y-axis depicting the success rate, ranging from 0 to 100%. The success rate measures the proportion of the total optimization runs that successfully reached the desired performance threshold in each iteration step. The markers indicate failed optimization runs.

The Baseline achieves 100% success after 15, 31, 33, and 79 iterations for problems 1–4, respectively. For the Heterogeneous problem, 90% of runs converge by iteration 32, with a few requiring up to 79 iterations.

The Prior Mean Polynomial method slightly outperforms the Baseline for the Forrester problem, converging 1.5 iterations faster on average. It performs significantly better in the Rosenbrock problem during the first 15 iterations, achieving a 3.2 iteration faster average convergence while matching the Baseline for full convergence. Performance on the Rastrigin problem mirrors the Baseline, but for the Heterogeneous optimization problem, it falls short, with 32 runs failing to converge, achieving only a final success rate of 68%.

The Prior Mean Neural Network underperforms across all problems, with slower average convergence of 0.3, 2.9, 11.2, and 5.1 iterations, respectively, only considering successful runs. It fails to converge on three out of four optimization problems, with two failed runs for the Forrester problem, nine for the Rastrigin problem, and 34 for the Heterogeneous problem.

The Multi-Fidelity GP method encounters issues in the Forrester problem, with 23 runs failing due to model fitting errors (77% success rate). For successful runs, convergence is slower by 2.4 iterations. Meanwhile, the Multi-fidelity GP generally achieves faster convergence for problems 2–4, with average improvements of 4.6, 2.8, and 7.8 iterations, respectively. Nevertheless, one optimization trial in the Heterogeneous problem does not converge within the given iteration limit.

The Multi-Task GP excels in the Forrester problem, achieving 99% convergence within six iterations and full convergence in 11, outperforming the Baseline by 6.5 iterations on average. In the Rosenbrock problem, despite five model fitting errors lowering the success rate to 95%, successful runs converge 13.8 iterations faster. For the Rastrigin problem, 60% of runs converge within 21 iterations, averaging 3.5 iterations faster, but failed runs result in an overall slowdown of 2.1 iterations. In the Heterogeneous problem, the method achieves 75% success with an average speedup of 3.0 iterations, though eight runs fail to converge.

The Recursive Co-Kriging model demonstrates significantly faster convergence compared to the Baseline for the Forrester, Rosenbrock, and Heterogeneous problems, with average improvements of 5.8, 10.1, and 8.6 iterations. In the Rastrigin problem, 70% of runs converge 4.7 iterations faster, but the remainder either match or lag behind the Baseline, resulting in a marginal 0.3 iteration faster average overall.

The Prior Mean Polynomial regression model demonstrates that prior mean information can enhance convergence to the optimal solution, particularly for the Forrester and Rosenbrock optimization problems, where it outperforms the baseline. However, as seen in the Heterogeneous problem, the prior mean can also mislead the optimization. When convergence failed, excessive sampling at domain boundaries occurred, likely due to

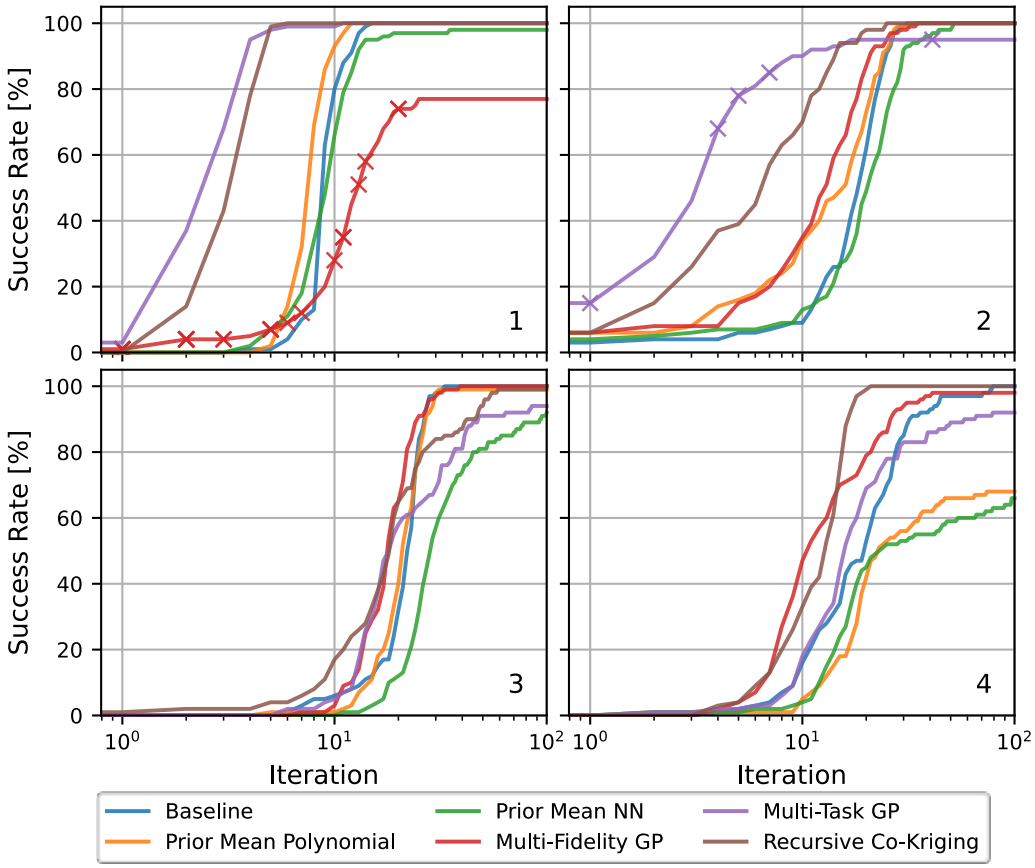



**Figure 1:** Success rate of the different multi-fidelity methods evaluated on the Forrester, Rosenbrock, Rastrigin and Heterogeneous multi-fidelity test problems (1-4). The success rate is plotted against the number of iterations for each method. The methods compared are: Baseline, Prior Mean Polynomial, Prior Mean NN, Multi-Task GP, Multi-Fidelity GP, and Recursive Co-Kriging. Markers indicate failed optimization runs.

unfavorable prior mean predictions leading to large lengthscale parameters, reduced predictive variance, and repeated boundary selections. In these instances, a near-linear structure of the polynomial regression prior biases the first BO step toward the domain boundary. A visualization of one of these instances can be seen in Figure 2. High regularization penalties further reinforce this tendency.

The cause of failure for the Neural Network regression model on the Heterogeneous test problem is similar to that of the Polynomial regression model. For the Rosenbrock test function, overfitting to the different fidelity observations contributes to the method's poor performance. For the Rastrigin test problem, the lower-fidelity functions penalize the region around the optimum, leading to repeated observations in areas of local optima.

Similar behavior is observed in the Multi-Task GP and Recursive Co-Kriging methods, for which the Multi-Task GP seems to generally struggle with the multi-modal test problems 3-4. The Multi-Fidelity GP method, on the other hand, outperforms the Baseline on test problems 2-4. Both the Multi-Task GP and the Multi-Fidelity GP tend to fail to converge during model training. This is likely due to their higher number of hyperparameters which complicates model training. Additionally, the Multi-Fidelity GP method assumes an ordering of the fidelity functions as the model assumes that the fidelity of the function is monotonic in the parameter [11]. If such a structure is not given, the model can fail during training due to an ill-conditioned covariance matrix. In summary, all multi-fidelity methods are prone to biases from poorly distributed initial low-fidelity samples, with the Multi-Fidelity GP being the most resilient. Among the considered methods, the Recursive Co-Kriging model is the most promising, consistently outperforming the Baseline on average across all optimization problems.

## CONCLUSION

This paper evaluates several common multi-fidelity modeling methods using multi-fidelity test functions and

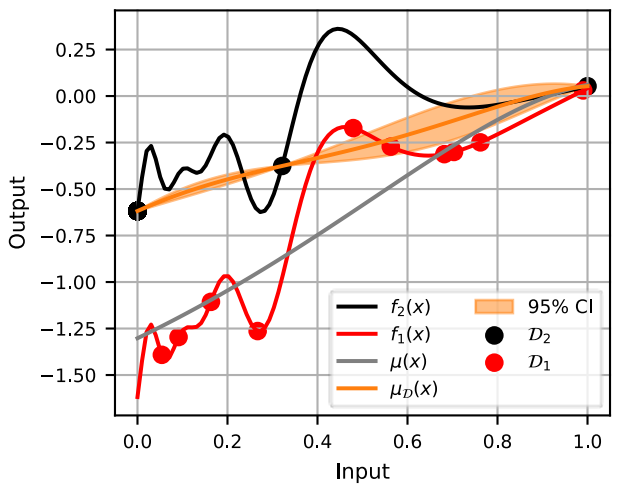



**Figure 2.** Failed optimization run of the Prior Mean method on the Heterogeneous test function showing the posterior GP prediction, conditioned on data points $\mathcal{D}_2$, using low-fidelity data $\mathcal{D}_1$ to train the polynomial regression mean $\mu(\mathrm{x})$, with the 95% confidence interval of the posterior GP indicated as CI.

identifies key pitfalls associated with these approaches. A fundamental limitation of all evaluated methods is their purely data-driven nature, making their performance highly dependent on data quality. If the available low-fidelity data is unfavorably distributed or biased, the optimization process may get misguided. This is especially evident for the prior mean modeling method, which, while being an easy-to-implement and potentially effective strategy, showed poor performance when using a Neural Network prior mean. The Neural Network severely overfitted the available data, encoding misleading information that negatively impacted optimization performance. Therefore, careful consideration is necessary when selecting and designing a prior mean model.

The more advanced multi-fidelity modeling methods may offer enhanced capability but are not exempt from the issue of misleading prior information, especially in the case of multi-modal objective functions. Among the evaluated methods, the Recursive Co-Kriging model demonstrated the most consistent performance, outperforming the baseline across all test problems, while the Multi-Fidelity GP proved the most resilient to the issue of misleading biases. To fully leverage the potential of multi-fidelity modeling, robust model fitting algorithms should be employed to improve reliability.

Finally, this study focuses on low-dimensional test functions. While the presented methods can be applied to high-dimensional problems, appropriate data scaling becomes crucial as dimensionality increases. Bayesian optimization often struggles in higher dimensions, but techniques like TURBO have been shown to improve performance [13].

## REFERENCES


1. Garnett R. *Bayesian optimization*. Cambridge University Press, Cambridge, United Kingdom (2023).
2. Astudillo R, Frazier PI. Bayesian Optimization of Composite Functions doi:10.48550/arXiv.1906.01537 (2019) (Epub ahead of print) .
3. González LD, Zavala VM. BOIS: Bayesian Optimization of Interconnected Systems. *IFAC-PapersOnLine* 58(14), 446–451 (2024).
4. Chitre A, Cheng J, Ahamed S *et al.* pHbot: Self-Driven Robot for pH Adjustment of Viscous Formulations via Physics-informed-ML**. *Chemistry Methods* 4(2) (2024).
5. Wu J, Frazier PI. Continuous-Fidelity Bayesian Optimization with Knowledge Gradient (2017).
6. Kennedy M. Predicting the output from a complex computer code when fast approximations are available. *Biometrika* 87(1), 1–13 (2000).
7. Le Gratiet L, Garnier J (2012). *Recursive Co-Kriging Model for Design of Computer Experiments with multiple Levles of Fidelity*.
8. Ament S, Daulton S, Eriksson D, Balandat M, Bakshy E (2023). *Unexpected Improvements to Expected Improvement for Bayesian Optimization*.
9. Ath G de, Fieldsend JE, Everson RM. What do you mean? *Proceedings of the 2020 Genetic and Evolutionary Computation Conference Companion*. Presented at: *GECCO '20: Genetic and Evolutionary Computation Conference*. Cancún Mexico, 08 07 2020 12 07 2020.
10. Bonilla EV, Chai, Kian Ming A., Williams CKI. Multi-task Gaussian Process Prediction (2007).
11. Wu J, Toscano-Palmerin S, Frazier PI, Wilson AG. Practical Multi-fidelity Bayesian Optimization for Hyperparameter Tuning. *Proceedings of The 35th Uncertainty in Artificial Intelligence Conference*.
12. Mainini L, Serani A, Rumpfkeil MP *et al.* (2022). *Analytical Benchmark Problems for Multifidelity Optimization Methods*.
13. Eriksson D, Pearce M, Gardner JR, Turner R, Poloczek M. Scalable Global Optimization via Local Bayesian Optimization doi:10.48550/arXiv.1910.01739 (2019) (Epub ahead of print).



© 2025 by the authors. Licensed to PSEcommunity.org and PSE Press. This is an open access article under the creative commons CC-BY-SA licensing terms. Credit must be given to creator and adaptations must be shared under the same terms. See https://creativecommons.org/licenses/by-sa/4.0/

Systems & Control Transactions

**Research Article - Peer Reviewed Conference Proceeding**
ESCAPE 35 - European Symposium on Computer Aided Process Engineering
Ghent, Belgium. 6-9 July 2025
Jan F.M. Van Impe, Grégoire Léonard, Satyajeet S. Bhonsale,
Monika E. Polańska, Filip Logist (Eds.)

PSE PRESS

# AutoJSA: A Knowledge-Enhanced Large Language Model Framework for Improving Job Safety Analysis

**Shuo Xu[a], Jinsong Zhao[a]***

[a] Tsinghua University, Department of Chemical Engineering, Beijing, China
* Corresponding Author: jinsongzhao@tsinghua.edu.cn.

## ABSTRACT

Job Safety Analysis (JSA) is critical for proactively identifying workplace hazards, assessing their potential consequences, and implementing effective control measures. However, traditional JSA methods can be inefficient and prone to errors, particularly in complex industrial environments. This paper introduces AutoJSA, a knowledge-enhanced framework that leverages large language models (LLMs) to automate and optimize the JSA process. We collected 73 high-quality JSA reports from a chemical engineering company and divided the JSA workflow into three key tasks: hazard identification, consequence identification, and control measure generation. Two approaches — fine-tuning and retrieval-augmented generation (RAG) — were employed on a base LLM (GLM-4-9B-Chat) to adapt it for these domain-specific tasks. Experimental results demonstrate that both fine-tuning and RAG significantly improve task performance relative to the unmodified model, with fine-tuning generally providing larger gains. While RAG offers the advantages of dynamic knowledge retrieval and simpler implementation, it yields more modest improvements compared to fine-tuning. Moreover, a direct combination of fine-tuning and RAG did not show additional benefits under the current approach. Overall, AutoJSA effectively addresses the limitations of traditional JSA by increasing the accuracy and efficiency of safety analysis, laying the groundwork for fully automated JSA report generation. The findings underscore the potential of advanced artificial intelligence and natural language processing techniques to enhance workplace safety management in complex and rapidly evolving industrial settings.

**Keywords**: Artificial Intelligence, Job Safety Analysis, Large Language Model

## 1. INTRODUCTION

In the chemical process industry, tasks such as calibrating temperature control systems, replacing seals on reactors, and conducting maintenance on pumps and compressors are essential for maintaining safe and efficient operations. However, these activities can expose workers to hazards like electrical shock, high-temperature burns, or poisoning. Job Safety Analysis (JSA) is crucial for mitigating these risks by systematically examining each task, identifying potential hazards, and implementing effective control measures [1].

Heinrich is considered the first scholar to introduce the term Job Safety Analysis [2]. Since then, JSA has been widely applied in industries such as process engineering, construction, and healthcare [3], with various guidelines available for conducting JSA [4,5]. A comprehensive JSA typically includes four key components: Job Description, Hazard Identification, Consequence Identification, and Control Measures Generation. JSA improves workplace safety by identifying and addressing potential risks before work begins, helping to reduce accidents and injuries [6,7], and identifying potential human errors to ensure quality performance [8].

However, traditional JSA faces several challenges: it may fail to identify all potential risks, especially those arising from unforeseen circumstances or complex scenarios [9]. Additionally, it is time-consuming, particularly in dynamic environments [10], and there can be significant variations in hazard identification quality, as different individuals may have different expertise levels [11].

To address these challenges, researchers have explored AI methods to automate JSA. For example, one study integrated JSA with a modified Petri net for non-

routine operations, which helped identify sequential anomalies. However, its static and semi-quantitative nature limits dynamic risk simulation and the ability to account for complex interactions [12]. Another study developed a knowledge graph for automatic JSA using GRAKN.AI, which provided solid risk assessments, but it relied on pre-existing JSA documents and lacked real-time data or natural language support [13]. Similarly, a third proposed an ontology-based framework combined with Building Information Modeling for automated JSA. However, it overlooks dynamic factors, such as site layout changes, and requires manual rule adjustments [14]. While these approaches are sophisticated, they often suffer from limited accuracy and adaptability due to their reliance on expert rules, structured data, and static models, which can miss subtle or emerging risks and restrict cross-domain applicability.

Large language models (LLMs), like ChatGPT and GPT-4 [15], present a solution by handling unstructured text, detecting new risks, and adapting across domains—making them ideal for automating hazard identification and safety reporting. Although some studies have explored the application of LLMs for similar tasks [16-18], systematic evaluation of LLMs for the entire JSA process remains limited.

This paper introduces AutoJSA, a knowledge-enhanced LLM framework using fine-tuning and retrieval-augmented generation (RAG) techniques to improve JSA accuracy, efficiency, and adaptability in complex industrial environments.

## 2. METHODOLOGY

### 2.1 Framework Overview of AutoJSA

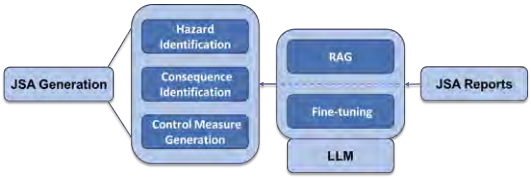



**Figure 1.** Framework overview of AutoJSA.

**Figure 1** illustrates the framework of this study, which aims to generate JSA reports using LLMs. The dataset consists of high-quality JSA reports for training, validation, and testing.

The JSA report generation is divided into three subtasks: hazard identification, consequence identification, and control measure generation. Each task has corresponding JSA reports split into training, validation, and test sets.

Fine-tuning and RAG are applied to each sub-task. Fine-tuning optimizes the base model for task-specific data, while RAG enhances information retrieval and output generation using a structured knowledge base. Both methods are evaluated through a predefined framework to assess performance under different parameters.

The best-performing parameters, selected from validation results, are tested on the test set to compare the fine-tuned model, RAG-enhanced model, and base model. The evaluation will determine the effectiveness of fine-tuning and RAG in improving JSA report generation.

### 2.2 Data Description

The data used in this study consists of 73 high-quality JSA reports obtained from a chemical engineering company. These reports cover various jobs and provide a detailed safety analysis for each step of the job. Each JSA report is composed of two main sections: JobInfo and JSA. A detailed description of the data structure can be found in **Figure 2**.

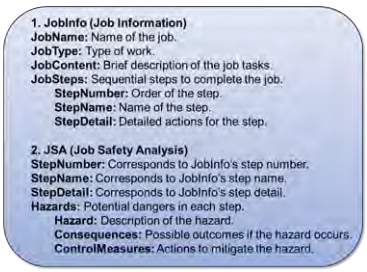



**Figure 2.** Detailed description of JSA report.

These reports are divided into three parts: 58 for training, 8 for validation, and 7 for testing.

### 2.3 Task Breakdown of JSA

AutoJSA subdivides the JSA process into three key tasks: Hazard Identification, Consequence identification, and Control Measure Generation. This division reflects the actual workflow followed during safety analysis, where each task builds upon the previous one to comprehensively assess and mitigate risks associated with a job.

Task 1 — Hazard Identification: This task identifies potential hazards for each job step. The inputs include the job name, job content, job step name, and step details. The output is a list of hazards associated with the specific step.

Task 2 — Consequence Identification: This task assesses the potential consequences of each identified hazard. The inputs include the same information as in Hazard Identification, plus the specific hazard. The output is a list of possible consequences.

Task 3 — Control Measure Generation: This task generates control measures to mitigate the identified hazards. The inputs include the job name, job content, job step details, hazard, and consequence. The output is a set of control measures.

**Table 1** shows the number of samples in the training

set, validation set, and test set for each task.

**Table 1:** Distribution of samples across training, validation, and test sets for each task.

| Task | Sample Size | | |
|---|---|---|---|
| | Train | Validation | Test |
| Task 1 | 241 | 38 | 30 |
| Task 2 | 759 | 117 | 92 |
| Task 3 | 759 | 117 | 92 |

## 2.4 Application of LLM

LLMs are advanced AI systems trained on extensive textual data to generate human-like text and perform tasks like text generation, translation, and question answering. In this study, LLMs automate and improve the JSA process, aiding in hazard identification, consequence identification, and control measure generation. Fine-tuning and RAG techniques are used to optimize the model for better accuracy and relevance in the JSA domain.

Considering the task's complexity and resource requirements, we use GLM-4-9B-Chat [19] as the base model. GLM-4-9B-Chat is a large language model with approximately 9 billion parameters, developed as part of the GLM-4 series by Zhipu AI. By fine-tuning and applying RAG, we adapt the model for JSA report generation, improving its ability to identify hazards, assess consequences, and suggest control measures.

### 2.4.1 Fine-tuning




**Figure 3:** A sample from the dataset used in Task 1. The data used in this study is in Chinese. For the convenience of reading, all related content here and in subsequent sections has been translated into English.

Fine-tuning involves adapting a pre-trained LLM to a specific task or domain by continuing its training on a smaller, domain-specific dataset [20]. While pre-trained models like LLMs are trained on large, diverse datasets to capture general linguistic patterns, fine-tuning helps the model specialize in a particular domain—in this case, JSA. This approach improves the model's ability to identify hazards, assess consequences, and generate control measures, ensuring that the outputs are relevant and accurate for the specific task.

Fine-tuning works by initializing the pre-trained model with knowledge from its original training, followed by further training on task-specific data. In addition to task-specific inputs (as described in Section 2.3), prompt engineering [21] is also employed to guide the model during training. **Figure 3** illustrates an example dataset used for Task 1, and similar datasets were created for Tasks 2 and 3. The corresponding datasets can be found in the supplementary materials. Fine-tuning is performed by adjusting parameters based on the loss values from the training and validation sets, and the model with the lowest validation loss is selected for testing.

### 2.4.2 RAG

RAG enhances LLMs by incorporating external retrieval mechanisms to provide domain-specific, up-to-date information [22]. Unlike traditional models that rely solely on pre-trained knowledge, RAG retrieves relevant external data to improve accuracy. In the RAG framework, the model retrieves documents based on the input query, enhancing generation for more contextually appropriate responses, which is crucial for tasks like JSA.

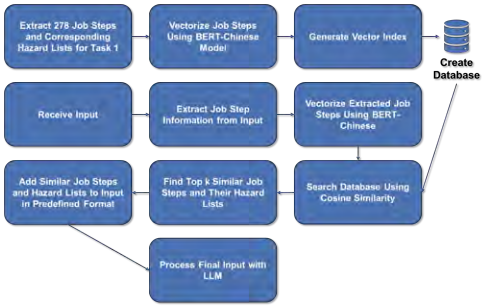



**Figure 4.** RAG framework uesd in this study.

For this study, we augmented the model's inputs with content retrieved via knowledge retrieval, as shown in **Figures 3** and **4**. For Task 1, a knowledge database was created by extracting 278 job steps and hazard lists. Using the BERT-base-Chinese model [23], we vectorized the job steps and indexed them. The model retrieves the **k** most similar job steps based on cosine similarity and incorporates the corresponding hazard lists into the input for the LLM. Similar processes were applied to Tasks 2 and 3, with variations in the search fields and content retrieved, and the RAG database used in this study is

available in the supplementary materials.

We evaluated different values of **k** to determine the optimal performance for each task, selecting the value that performed best on the validation set.

### 2.4.3 Evaluation Criteria

Model performance was assessed by measuring semantic similarity between model outputs and ground truth. Our similarity evaluation employs a BERT-based semantic encoding scheme: texts are first encoded using the BERT-base-Chinese model (768-dimensional hidden states), where the **[CLS]** token's hidden state serves as sentence embeddings. After L2-normalization, we compute cosine similarity through $\mathbf{sim}(a,b)=a^{\top}b$ to quantify semantic similarity.

## 3. RESULTS AND DISCUSSION

### 3.1 Fine-tuning

We adjusted the fine-tuning parameters based on the model's loss performance on the validation set. After multiple rounds of experimentation, we identified a set of reasonable parameters that resulted in a lower validation loss. The specific parameters used can be found in the supplementary materials. **Figure 5** illustrates the training and validation loss curves for the three tasks under these parameters during model training.

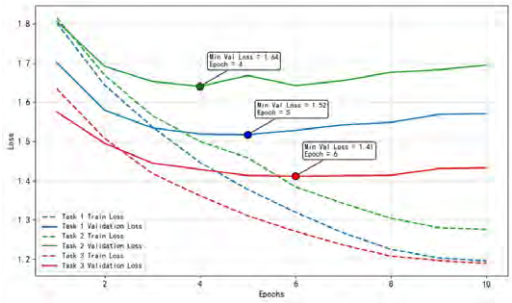



**Figure 5.** Training and validation loss for three tasks.

From the data trends, under the parameter settings used in this study, the training and validation losses for all three tasks showed a decreasing trend as the number of training epochs increased. This indicates that fine-tuning was effective for all three tasks. However, after a certain number of epochs, the validation loss for each task started to increase, suggesting overfitting. Based on these experimental results, we selected the models corresponding to the epochs with the lowest validation loss — 5, 4, and 6 epochs for Tasks 1, 2, and 3, respectively — to be tested on the test set.

### 3.2 RAG

In the construction of the RAG framework, we optimized the value of **k** for each task based on the validation set scores. **Figure 6** shows the model's scores on the validation set for the three tasks with different values of **k**, along with the time consumption per output generation.

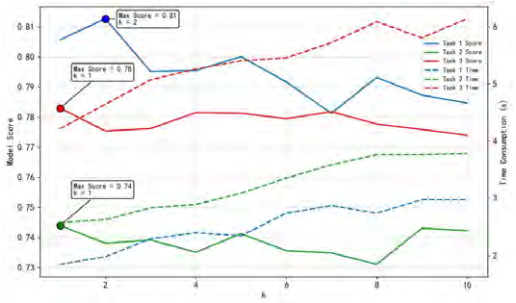



**Figure 6.** Model scores and time consumption vs. **k**.

During the RAG framework construction, the model's performance did not exhibit a significant trend with varying **k** values. However, when looking at all three tasks, smaller values of **k** already yielded good results. This suggests that the LLM places more importance on the most similar inputs, and it is more effective at leveraging the most relevant knowledge to solve the problem. As the value of **k** increases, more knowledge did not result in improved model performance. This could be due to the inclusion of more low-similarity knowledge, which may have interfered with the model's reasoning. Additionally, as **k** increases, the input text becomes longer, leading to longer inference times. Based on these observations, we selected **k**=2, **k**=1, and **k**=1 for Tasks 1, 2, and 3, respectively, for testing on the test set.

### 3.3 Test Results

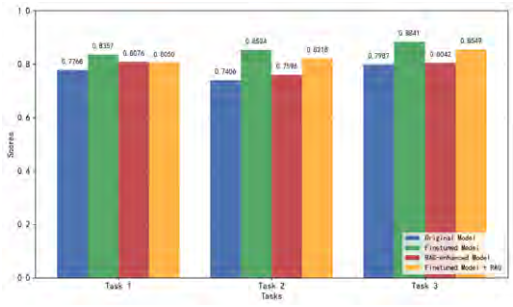



**Figure 7.** Different model scores on the test set.

**Figure 7** shows the performance scores of the original model, the fine-tuned model, and the RAG-enhanced model on the test set for the three tasks. It also includes the results of the fine-tuned model when further augmented with RAG.

The test results show that both the fine-tuned and RAG-enhanced models outperform the original model. However, RAG provides modest improvements, while fine-tuning offers more substantial gains. Fine-tuning requires more computational resources and a complex

| Model | Output | Score |
|---|---|---|
| **Original model** | Hot work causing fire or explosion, electrical equipment causing electric shock, lack of warning signs leading to unauthorized personnel entering hazardous areas, insufficient preparation of protective equipment leading to injuries. | **0.7135** |
| **Fine-tuned model** | Hot work risk, temporary electricity risk, inadequate equipment preparation, insufficient protective equipment. | **0.8477** |
| **RAG-enhanced model** | Improper handling of hot work and temporary electrical work permits, incorrect placement of warning signs, inadequate equipment preparation, insufficient preparation of gas detectors and protective equipment, insufficient personnel training. | **0.7725** |
| **Expected** | Fire or explosion caused by hot work, electric shock due to electrical equipment usage, failure to set up warning signs leading to unauthorized entry into hazardous areas, inadequate preparation of protective equipment resulting in injuries. | **-** |

**Table 2:** Comparison of output results.

implementation, while RAG is simpler and allows dynamic updates to the knowledge base, offering flexibility.

When we combined the fine-tuned model with RAG, no performance improvement was observed over fine-tuning alone. This suggests that a more advanced integration approach, such as using a separate model to combine the outputs of both, may be needed to fully leverage the strengths of both techniques for optimizing JSA report generation.

### 3.4 Case Study

**Table 2** shows the results of the original, fine-tuned, and RAG-enhanced models for hazard identification, as described in **Figure 3**. The original model provides a broad list of potential hazards in wastewater plant piping welding, covering a wide range of risks such as gas leaks, fire hazards, and equipment malfunctions. While comprehensive, this list can be overwhelming and less relevant to the task, requiring users to filter key risks.

The fine-tuned model provides a more focused output, listing four primary hazards: hot work operations, temporary electrical risks, inadequate equipment preparation, and insufficient protective equipment. This approach improves clarity and helps users quickly identify critical hazards, although it may overlook secondary risks. The RAG-enhanced model incorporates external databases, identifying five specific hazards, including non-compliance with safety permits and improper equipment placement. This model offers a detailed and practical identification of risks, but its effectiveness depends on the quality of the external data used.

In summary, the original model offers broad coverage but may lead to information overload. The fine-tuned model provides precise and efficient results, ideal for quick hazard identification. The RAG-enhanced model ensures comprehensive hazard identification with external knowledge. A better approach may involve strategically combining fine-tuning and RAG to enhance accuracy and detail.

## 4. CONCLUSION

The results demonstrate that the AutoJSA framework enhances the accuracy and efficiency of Job Safety Analysis by leveraging fine-tuning and RAG with LLMs. Both methods outperform the base model in hazard identification, consequence assessment, and control measure generation, with fine-tuning generally providing more significant improvements. The fine-tuned model produces more concise outputs, while the RAG-enhanced model generates more comprehensive results.

However, the study has limitations. The current framework does not explicitly incorporate traditional risk assessment factors such as hazard severity and probability of occurrence. The dataset of 73 Chinese JSA reports, while sufficient for proof of concept, may not fully represent the diversity of tasks in broader industrial settings or different linguistic contexts. Fine-tuning, though effective, involves high computational cost, and combining it with RAG did not yield additional benefits, suggesting potential inefficiencies in their integration. Additionally, the BERT-based similarity metric used may not capture all qualitative aspects of JSA effectiveness.

Future research directions could address current limitations by integrating risk assessment metrics into the framework, expanding the dataset to encompass diverse industrial scenarios across different linguistic and cultural contexts, exploring integration strategies for RAG and fine-tuning to enhance complementary benefits, and developing hybrid evaluation metrics that combine BERT-based similarity with qualitative safety performance indicators.

AutoJSA demonstrates AI's transformative potential in workplace safety management by enhancing hazard

identification, consequence Identification, and control measure generation. The framework paves the way toward fully automating JSA reports and ensuring safer operational practices in complex industries.

## DIGITAL SUPPLEMENTARY MATERIAL

The datasets, fine-tuning parameters, and all experimental results in this study can be accessed via the following link:
https://cloud.tsinghua.edu.cn/d/f80c1ca00d694f7ea7f9/

## ACKNOWLEDGEMENTS

This work was supported by the National Key R&D Program of China under Grant 2024YFC3013600.

## REFERENCES

1. Analysis JH, Lebowitz J. Essentials of job hazard analysis. Chem Eng Prog 114:52-6 (2018).
2. Albrechtsen E, Solberg I, Svensli E. The application and benefits of job safety analysis. Saf Sci 113:425-37 (2019).
3. Ghasemi F, Doosti-Irani A, Aghaei H. Applications, shortcomings, and new advances of job safety analysis (JSA): findings from a systematic review. Saf Health Work 14(2):153-62 (2023).
4. Swartz G. Job hazard analysis: A guide to identifying risks in the workplace. Government Institutes (2001).
5. Geronsin R. Job hazard assessment: a comprehensive approach. Prof Saf 46(12):23 (2001).
6. Yoon IK, Seo JM, Jang N, Oh SK, Shin D, Yoon ES. A practical framework for mandatory job safety analysis embedded in the permit-to-work system and application to the gas industry. J Chem Eng Jpn 44(12):976-88 (2011).
7. Palega M. Application of the job safety analysis (JSA) method to assess occupational risk at the workplace of the laser cutter operator. Manag Prod Eng Rev 12(3) (2021).
8. Roughton J, Crutchfield N. Job Hazard Analysis: A Guide for Voluntary Compliance and Beyond. Butterworth-Heinemann (2015).
9. Zheng W, Shuai J, Shan K. The energy source-based job safety analysis and application in the project. Saf Sci 93:9-15 (2017).
10. Chi NW, Lin KY, Hsieh SH. Using ontology-based text classification to assist job hazard analysis. Adv Eng Informatics 28(4):381-94 (2014).
11. Namian M. Factors Affecting Construction Hazard Recognition and Safety Risk Perception. North Carolina State University (2017).
12. Li W, Cao Q, He M, Sun Y. Industrial non-routine operation process risk assessment using job safety analysis (JSA) and a revised Petri net. Process Saf Environ Prot 117:533-8 (2018).
13. Pandithawatta S, Ahn S, Rameezdeen R, Chow CW, Gorjian N, Kim TW. Development of a knowledge graph for automatic job hazard analysis: The schema. Sensors 23(8):3893 (2023).
14. Zhang S, Boukamp F, Teizer J. Ontology-based semantic modeling of construction safety knowledge: towards automated safety planning for job hazard analysis (JHA). Autom Constr 52:29-41 (2015).
15. Achiam J, Adler S, Agarwal S, Ahmad L, Akkaya I, Aleman FL, ... McGrew B. GPT-4 technical report. arXiv preprint arXiv:2303.08774 (2023).
16. Bernardi ML, Cimitile M, Pecori R. Automatic job safety report generation using RAG-based LLMs. In: 2024 International Joint Conference on Neural Networks (IJCNN). Ed: IEEE (2024) p. 1-8.
17. Uddin SJ, Albert A, Ovid A, Alsharef A. Leveraging ChatGPT to aid construction hazard recognition and support safety education and training. Sustainability 15(9):7121 (2023).
18. Kvale DK. Deep Learning in Construction Safety: Quality Assessment, Hazard Identification, and Preventive Measure Proposals in Job Safety Analysis. NTNU (2023).
19. GLM T, Zeng A, Xu B, Wang B, Zhang C, Yin D, ... Wang Z. ChatGLM: a family of large language models from GLM-130B to GLM-4 all tools. arXiv preprint arXiv:2406.12793 (2024).
20. Dodge J, Ilharco G, Schwartz R, Farhadi A, Hajishirzi H, Smith N. Fine-tuning pretrained language models: weight initializations, data orders, and early stopping. arXiv preprint arXiv:2002.06305 (2020).
21. White J, Fu Q, Hays S, Sandborn M, Olea C, Gilbert H, ... Schmidt DC. A prompt pattern catalog to enhance prompt engineering with ChatGPT. arXiv preprint arXiv:2302.11382 (2023).
22. Lewis P, Perez E, Piktus A, Petroni F, Karpukhin V, Goyal N, ... Kiela D. Retrieval-augmented generation for knowledge-intensive NLP tasks. Adv Neural Inf Process Syst 33:9459-74 (2020).
23. Devlin J. BERT: pre-training of deep bidirectional transformers for language understanding. arXiv preprint arXiv:1810.04805 (2018).

© 2025 by the authors. Licensed to PSEcommunity.org and PSE Press. This is an open access article under the creative commons CC-BY-SA licensing terms. Credit must be given to creator and adaptations must be shared under the same terms. See https://creativecommons.org/licenses/by-sa/4.0/



Systems & Control Transactions

**Research Article - Peer Reviewed Conference Proceeding**
ESCAPE 35 - European Symposium on Computer Aided Process Engineering
Ghent, Belgium. 6-9 July 2025
Jan F.M. Van Impe, Grégoire Léonard, Satyajeet S. Bhonsale,
Monika E. Polańska, Filip Logist (Eds.)

PSE PRESS

# Refrigerant Selection and Cycle Design for Industrial Heat Pump Applications exemplified for Distillation Processes

**Jonas Schnurr[a], Momme Adami[a], and Mirko Skiborowski[a]***

[a] Hamburg University of Technology, Institute of Process Systems Engineering, Am Schwarzenberg-Campus 4, 21073 Hamburg, Germany
* Corresponding Author: mirko.skiborowski@tuhh.de.

## ABSTRACT

Mechanical compression heat pumps are indispensable to facilitate the transition from thermally driven processes to renewable energy by electrification, upgrading low-temperature waste heat to recycle it at a higher temperature level. However, the implementation of such heat pumps up to date encounters limitations, due to equipment limitations and a lack of tools for the design of process concepts for the application of high-temperature heat pumps. The optimal design of heat pumps relies heavily on the selection of an appropriate refrigerant, as the thermodynamic properties significantly affect the heat pump cycle design and performance. While existing methods are capable of identifying thermodynamically beneficial refrigerants, they do not directly account for practical constraints such as limitations on the compressor discharge temperature, compression ratio, and vacuum operation. The current study proposes a fast-screening approach for arbitrary heat pump applications, considering a large set of established refrigerants. The method automatically assesses the performance of the refrigerants for a specified set of heat sink and source, adjusting the heat pump design with an optional internal heat exchanger in case of necessary superheating prior to compression. The approach is illustrated for the evaluation of heat pump-assisted distillation processes.

**Keywords**: Heat pump, Refrigerant, Screening tool, Energy integration, Distillation

## INTRODUCTION

In the context of global warming and increasing costs of $CO_2$ emissions, the transition to renewable energy sources and the improvement of energy efficiency are essential objectives for the chemical industry. One potential approach to achieve both of these goals in a single step is the implementation of heat pumps, which recover low-temperature waste heat that would otherwise be lost to the environment through cooling water and elevate the heat to a higher temperature level at which it can be reused or recycled within the process [1]. Heat pumps present a distinctive and transformative opportunity for the electrification of industrial processes, which can immediately improve the sustainability through an expanded share of renewable electricity generation. Furthermore, the integration of heat pumps may not even require significant modifications to the existing equipment, thereby rendering them a versatile solution for both new processes and retrofitting of existing processes. This allows for significant energy savings in existing plants without the need for extensive modifications [1]. While a variety of heat pump concepts can be used to upgrade the available heat, compression heat pumps are used in most applications [2].

The left-hand Clausius-Rankine cycle, which is employed to describe the thermodynamic process associated with a closed-cycle compression heat pump, is illustrated in **Figure 1 (a-c)**. The initial step of this cycle involves an irreversible pressure increase within the vapor phase, which is subsequently followed by an isobaric energy exchange in the form of heat as the refrigerant undergoes condensation. The condensed refrigerant is expanded during the isenthalpic pressure reduction, and subsequently, heat is exchanged during the evaporation of the refrigerant.

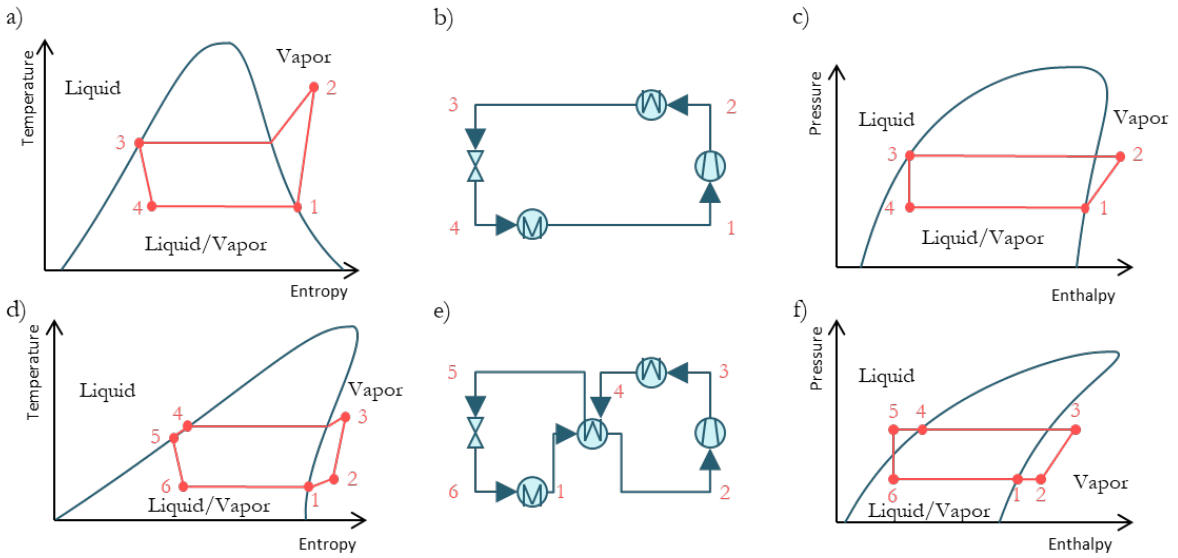



**Figure 1:** T-s diagram without a) and with d) superheating, heat pump cycle without b) and with e) superheating and p-h diagram without c) and with f) superheating

In the event that the refrigerant exhibits a hanging two-phase envelope the vapor needs to be superheated before entering the compressor to ensure that no liquid droplets form during compression which can cause damage to the compressor. For superheating the vapor, an additional heat exchanger and heat source are required. The additional heat exchanger can be implemented in the form of an internal heat exchanger (IHX), as shown in **Figure 1 (d-f)**. This configuration ensures the superheating through subcooling the refrigerant at higher pressure prior to expansion, thereby eliminating the need for external heating. However, this approach results in more complex behavior during start-up and limited operational flexibility for different temperature levels [3].

Today the implementation of heat pumps in industry is still limited due to a limited availability and experience on the use of high-temperature heat pumps, as well as the large investment costs, required for the expensive compressor [4]. In addition to these economic challenges, there are also persistent technical limitations to the application of compressors for industrial applications. Post-compression temperatures exceeding 160 °C and temperature lifts beyond 95 °C are still regarded as technically limitations [5], while exceeding these limits to yield sink temperatures up to 200 °C is expected to enable a huge range of applications [6]. Another important limitation dependent on the compressor type is the compression ratio, which is typically in the range of 2-4 with a practical limit of approximately 8 for the majority of compressor types [1]. However, some reciprocating compressors are reportedly capable of compression ratios as high as 12 at low flow rates [1]. High compression ratios can better be achieved by means of multistage compression cycles [7], or multiple cascade heat pumps with individual working fluid cycles, but these solutions are more complex and require significant investment costs, rendering them practically uneconomic [1].

The performance of external heat pumps depends largely on the specific refrigerant, which due to its thermal properties mandates the design of the compression cycle and the required work. The selection of an appropriate refrigerant for a given process depends on a number of criteria, including thermodynamic suitability, environmental compatibility, safety, efficiency and cost-effectiveness [4]. As no single refrigerant dominates all of these criteria, a trade-off must be made.

Various methods have been proposed to identify an appropriate refrigerant for a given process. Some methods focus on the thermodynamic properties and safety aspects of a range of different refrigerants, such as the work of Mateu-Royo et al. [8] and Koundinya and Seshadri [9], who evaluate refrigerants and cycle configurations quantitatively based on energy and exergy requirements, environmental impact, and economic considerations. Other authors, such as Kiss et al. [10] and Jiang et al. [11], propose general heuristics for the selection and assessment of heat pumps and refrigerants. The most general and recent methods investigate the sensitivity of refrigerants and heat pump configurations across a wide range of operating conditions [12] or solve the inverse problem, seeking an optimal refrigerant for a given application and cycle configuration based on continuous molecular targeting [13]. All these methods provide valuable tools for the identification of suitable refrigerants and

heat pump designs, given that the specific application has been fixed. However, none of these methods was integrated in conceptual process design studies.

The present study proposes a computationally efficient methodology for the rapid screening and identification of a suitable refrigerant and heat pump cycle design that can be integrated in process design studies. The method considers a wide range of established pure refrigerants to provide practical solutions, automatically evaluating heat pumps with adaptive use of IHX, required in case of superheating of the refrigerant prior to compression. The case study illustrates the application for a combined refrigerant selection and conceptual design of heat pump-assisted distillation processes, based on the shortcut screening approach proposed by Skiborowski [14].

## CALCULATION PROCEDURE OF A HEAT PUMP CYCLE

The calculations for the external heat pumps are based on the cycle designs and state diagrams illustrated in **Figure 1**. The computations only require the specification of the refrigerant's property parameters, as well as the temperature levels and heat duties of the source and sink. First, the lower pressure level of the heat pump is determined such that the saturated vapor temperature of the refrigerant has a pre-defined approach temperature to the minimum temperature of the heat source. Subsequently, the pressure after the compression is determined on the basis of flash calculations, ensuring that the refrigerant's saturated liquid temperature has the same approach temperature to the maximum temperature of the heat sink. In case the resulting pressure exceeds the critical pressure of the refrigerant, it is deemed thermodynamically unsuitable for this particular application, as it would create a trans- or supercritical heat pump process.

In case isentropic compression results in partial condensation, superheating prior to compression is facilitated by an IHX, which mitigates the need for an external heat source while simultaneously enhancing the specific enthalpy difference during the evaporation of the refrigerant. The degree of superheating is set such that the temperature of the refrigerant subsequent to isentropic compression must be at least equal to its saturated vapor temperature at the higher pressure level.

In this scenario, the specific enthalpy of the refrigerant on the higher pressure level after the IHX and prior to the throttle $h_5(T_5, p_{high})$ is determined based on the enthalpy balance of the IHX that is reduced to

$$h_5 = h_4 - (h_2 - h_1) \tag{1}$$

based on the specific enthalpy after the condensation in the heat exchanger with the external sink $h_4(T_{p_{high}}^{saturated\ liquid}, p_{high})$, and the difference between the specific enthalpy of the refrigerant at the low pressure level after the IHX and prior to the compressor $h_2(T_2, p_{low})$ and after the evaporation due to heat exchange with the source prior to the IHX $h_1(T_{p_{low}}^{saturated\ vapor}, p_{low})$. The specific enthalpy at the compressor inlet $h_2(T_2, p_{low})$ is calculated based on the temperature after superheating, which exceeds the saturated vapor temperature at the lower pressure by the degree of superheating. The specific enthalpy after compression

$$h_3(T_3, p_{high}) = \frac{h_{isentropic} - h_2}{\eta_{isentropic}} + h_2 \tag{2}$$

is calculated on the basis for the specific enthalpy for an isentropic compression $h_{isentropic}(T_{isentropic}, p_{high})$ and the isentropic efficiency $\eta_{isentropic}$, which results in an additional temperature increase due to the inefficiencies. Subsequently, the required refrigerant flow rate

$$\dot{n}_{Ref,sink} = \frac{\dot{Q}_{original,sink}}{|h_4 - h_3|} \tag{3}$$

for complete integration of the heat duty of the sink $\dot{Q}_{original,sink}$, and the refrigerant flow rate

$$\dot{n}_{Ref,source} = \frac{|\dot{Q}_{original,source}|}{h_1 - h_6} \tag{4}$$

for complete integration of the heat duty of the source $\dot{Q}_{original,source}$ are calculated. Note that the absolute value is considered, since heat duties for the sink are defined as negative values. The smaller of the two flow rates is then selected as the refrigerant flow rate $\dot{n}_{Ref}$, in order to guarantee complete integration of the smaller evaporation or condensation duty.

Adiabatic expansion results in the specific enthalpy of the refrigerant prior to evaporation at the lower pressure $h_6(T_6, p_{low})$ being equivalent to the specific enthalpy at the IHX outlet at the higher pressure $h_5(T_5, p_{high})$. In the absence of superheating, the specific enthalpy at the compressor inlet $h_2(T_2, p_{low})$ is equivalent to the saturated vapor enthalpy at lower pressure $h_1(T_{p_{low}}^{saturated\ vapor}, p_{low})$. Additionally, $h_5(T_5, p_{high})$ is equal to the saturated liquid enthalpy at the higher pressure $h_4(T_{p_{high}}^{saturated\ liquid}, p_{high})$.

In the following step, the remaining heat that is not covered by the heat pump is determined. In case the heat pump does not provide the full heat duty required by the heat sink

$$\dot{Q}_{sink} = \dot{Q}_{original,sink} - \dot{n}_{Ref} \cdot |(h_4 - h_3)| \tag{5}$$

must be provided by an external heat source, while an additional external cooling source with

$$\dot{Q}_{source} = \dot{Q}_{original,source} + \dot{n}_{Ref} \cdot |(h_1 - h_6)| \tag{6}$$

is required in case the heat pump cannot use all of the

heat from the heat source. Finally, the electrical compressor duty is determined as,

$$\dot{W}_{el} = \frac{h_3 - h_2}{\eta_{mechanical}} \quad (7)$$

taking into account a mechanical efficiency, $\eta_{mechanical}$.

## SHORTCUT-BASED SCREENING OF ALTERNATIVE PROCESS CONFIGURATIONS

The proposed method for the design of external heat pumps can directly be linked with a shortcut-based screening method for distillation-based processes, as presented by Skiborowski [14]. This shortcut method screens various distillation column configurations, including direct, indirect, and intermediate split configurations, as well as their thermally coupled versions on the basis of minimum energy demand calculations, building on the Rectification Body Method [15]. This provides the minimum energy demand and temperature levels of the condensers and reboilers of each configuration for a specified separation task. The proposed screening tool for external heat pumps can further evaluate the design of external heat pumps for any combination of heat source or sink from the respective process configurations, if not already utilized for another type of heat integration.

## CASE STUDY

The case study investigates the combination of the external heat pump evaluation and the shortcut-based screening for distillation-based process, for the separation of a zeotropic mixture of hexanol, octanol, and decanol. The mixture is fed with equimolar composition and a flow rate of 10 mol/s in the column, assuming saturation conditions at the operating pressure of the column, where it is separated into pure products under isobaric and adiabatic conditions at 80 mbar. The further discussion focuses exemplarily on the comparison of the two simple sequences, the direct split (DS) and indirect split (IS), and a thermally coupled dividing-wall column (DWC). For the purpose of this study, an isentropic efficiency of 85 % and a mechanical efficiency of 95 % are assumed for the compressor of the heat pumps. All computations are based on the extended Antoine equation in combination with the UNIQUAC model for the nonideality of the liquid and the Redlich-Kwong equation of state for the nonideality of the vapor phase. Additionally, DIPPR correlations are employed for the specific heat capacity and heat of vaporization. The respective property parameters are extracted from the AspenPlus PURE39 and NIST-TRC databases.

The temperatures in the heat exchangers and the energy demand of the different sequences without heat pumps are presented in **Table 1**. The dividing wall column has the lowest energy demand, 22 %/ 35 % lower than the DS/ IS sequence, since the thermal coupling reduces the internal mixing losses.

**Table 1:** Temperature in heat exchangers and energy demand of the different sequences without heat pumps.

| | DS | IS | DWC |
|---|---|---|---|
| $T_{Top}$ [°C] | | | |
| - Column 1 | 92.26 | 103.32 | 92.26 |
| - Column 2 | 122.78 | 92.26 | |
| $T_{Bottom}$ [°C] | | | |
| - Column 1 | 132.84 | 151.70 | 151.70 |
| - Column 2 | 151.70 | 122.78 | |
| Energy demand [kW] | | | |
| - Column 1 | 368.64 | 597.89 | 592.80 |
| - Column 2 | 386.62 | 322.03 | |
| - Net total | 755.26 | 919.91 | 592.80 |

For each of the possible heat sources and sinks possible implementations of external heat pumps are evaluated. The refrigerant screening is exemplary discussed for the DWC column. This configuration has the largest temperature difference between the reboiler and condenser of 59.44 K. Considering an approach temperature of 5 K requires the refrigerant condensation temperatures in the heat pump of 156.7 °C and the heat pump to perform a temperature lift of 69.44 K.

Half of the initial set of 38 refrigerants are discarded as the required high-level pressure exceeds their critical pressure. The individual heat pump design for the remaining 19 refrigerants and the respective minimum energy demands are listed together with the respective pressure levels and compressor discharge temperature in **Figure 2**. For all refrigerants, complete electrification of the DWC column is feasible, requiring only external cooling. The net energy demand can be reduced with a heat pump by 54 % with R1233zd and even 76 % with water (R718). Yet, water as refrigerant is practically infeasible in a single-stage heat pump due to the sub-atmospheric operation, and a compressor discharge temperature of 377 °C, which would mandate multi-stage compression with interstage cooling. Practical limitations of ambient pressure (dotted line) and 170 °C (dashed line) are indicated in **Figure 2**, in order to identify unpractical refrigerants.

The selection of the preferred refrigerant, among the practical suitable ones, focuses solely on the lowest net energy demand, which identifies acetone as the preferred choice, despite the additional heat exchanger required for superheating. While R1130 has a comparable energy demand without this additional heat exchanger, there are concerns about its toxicity and ozone depletion potential, underscoring important safety and environmental factors that were not considered in the current selection process and should be addressed in future

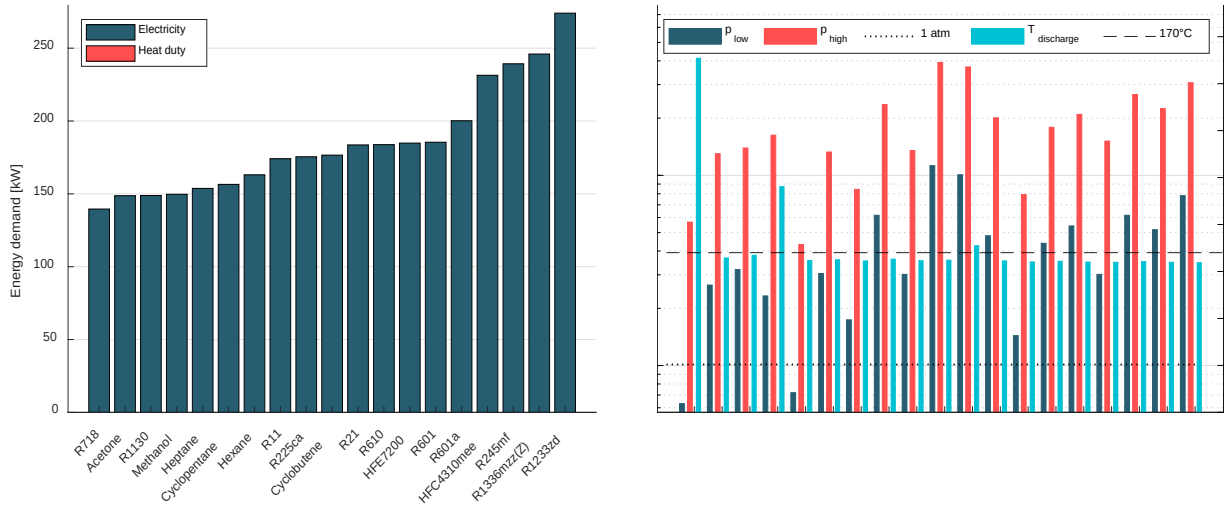



**Figure 2:** Energy demand (left) of DWC with heat pump and pressure levels (right) for thermodynamically feasible refrigerants.

evaluations.

As acetone is also among the preferred refrigerants in terms of total energy demand for DS and IS, it is utilized as a representative refrigerant for further performance comparison of the different sequences with heat pumps. Due to the fact that DS and IS possess two columns, four different configurations with a single heat pump, as well as two configurations with two heat pumps are possible, resulting in 16 different (heat pump-assisted) process variants for this separation task. The energy demand of the process variants and the potential energy saving of the best heat pump configuration compared to their process without heat pump are summarized in **Figure 3**.

With 83 % net energy savings the heat pump-assisted DS with two heat pumps does not only provide the largest saving potential but also shows the lowest net energy requirement overall. The study does not only highlight the potential of the integrated approach, but also illustrates that the heat pump-assisted simple sequence may require less energy that the heat pump-assisted DWC, which however requires only a single column shell and a single compressor and may be cost-beneficial.

The heat pump-assisted IS variants 11 and 14 in **Figure 3** employ a heat pump to utilize the heat from the condenser of column 2 to provide the necessary heat for the reboiler of column 1. These variants require additional

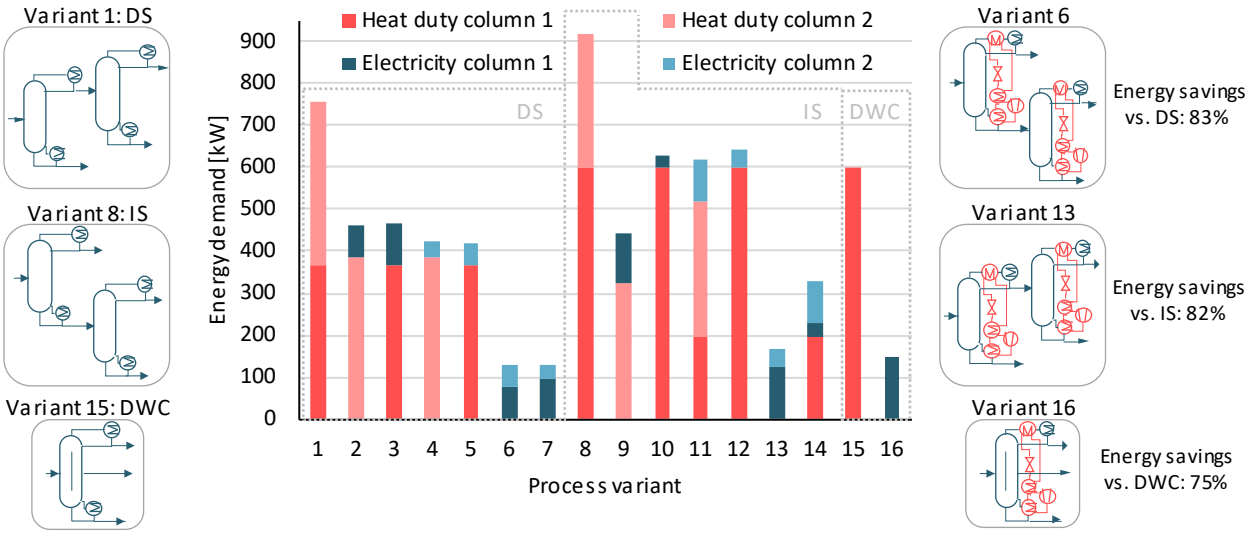



**Figure 3:** Energy demand for a selection of process alternatives and energy saving potential of intenfication with compression heat pumps with acetone as refrigerant.

heating for column 1, as the discrepancy in energy demand between the two columns (see **Table 1**) leads to the upgraded heat being insufficient to fully integrate the required energy demand of the reboiler. Consequently, the full electrification of process variant 14 is not feasible.

## CONCLUSION

The present study introduces a novel methodology for the efficient screening of heat pump cycles and refrigerants based on knowledge of the heat sink and source of the specific application, thereby facilitating its applicability to a wide range of industrial processes. The current implementation of the method assesses the heat pump design, energy demand, as well as thermodynamic and practical constraints of 38 pure refrigerants for a given application which is further showcased for the evaluation of heat pump-assisted distillation processes. As illustrated by the case study, the integration of heat pumps in distillation processes can be complemented by other energy integration methods, thus further reducing the energy demand, whereas possible combinations should be explored quantitatively on a case-specific basis. The scope of the study will be extended in further work to consider other energy-integrated distillation processes and additional heat sources and sinks.

## REFERENCE


1. Kiss AA, Infante Ferreira CA. Heat Pumps in Chemical Process Industry. CRC Press (2016)
2. Kiss AA, Smith R. Rethinking energy use in distillation processes for a more sustainable chemical industry. Energy 203:117788 (2020) https://doi.org/10.1016/j.energy.2020.117788
3. Fernández-Moreno A, Mota-Babilono A, Giménez-Prades P, Navarro-Esbrí J. Optimal refrigerant mixture in single-stage high-temperature heat pumps based on a multiparameter evaluation. Sustain Energy Technol Assess 52:101989 (2022) https://doi.org/10.1016/j.seta2022.101989
4. Arpagaus C, Bless F, Uhlmann M, Schiffmann J, Bertsch SS. High temperature heat pumps: Market overview, state of the art, research status, refrigerants, and application potentials. Energy 152:985-1010 (2018) https://doi.org/10.1016/j.energy.2018.03.166
5. Schlosser F, Jesper M, Vogelsang J, Walmsley TG, Arpagaus C, Hesselbach J. Large-scale heat pumps: Applications, performance, economic feasibility and industrial integration. Renew Sustain Energy Rev 133:110219 (2020) https://doi.org/10.1016/j.rser.2020.110219
6. Marina A, Spoelstra S, Zondag HA, Wemmers AK.
7. An estimation of the European industrial heat pump market potential. Renew Sustain Energy Rev 139:110545 (2021) https://doi.org/10.1016/j.rser.2020.110545
8. Luyben WL. Compressor heuristics for conceptual process design. Ind Eng Chem Res 50:13984-13989 (2011) https://doi.org/10.1021/ie202027h
9. Mateu-Royo C, Arpagaus C, Mota-Babiloni A, Navarro-Esbrí J, Bertsch SS. Advanced high temperature heat pump configurations using low GWP refrigerants for industrial waste heat recovery: A comprehensive study. Energy Convers Manag 229:113752(2021) https://doi.org/10.1016/j.enconman.2020.113752
10. Koundinya S, Seshadri S. Energy, exergy, environmental, and economic (4E) analysis and selection of best refrigerant using TOPSIS method for industrial heat pumps. Therm Sci Eng Prog 36:101491 (2022) https://doi.org/10.1016/j.tsep.2022.101491
11. Kiss AA, Flores Landaeta SJ, Infante Ferreira CA. Towards energy efficient distillation technologies - Making the right choice. Energy 47:531-542 (2012) https://doi.org/10.1016/j.energy.2012.09.038
12. Jiang J, Hu B, Ge T, Wang RZ. Comprehensive selection and assessment methodology of compression heat pump system. Energy 241:122831 (2022) https://doi.org/10.1016/j.seta.2022.101989
13. Andresen MP, Zühlsdorf B, Markussen WB, Jensen JK, Elmegaard B. Selection of working fluids and heat pump cycles at high temperatures: Creating a concise technology portfolio. Appl Energy 376:124312 (2024) https://doi.org/10.1016/j.apenergy.2024.124312
14. Mairhofer J, Stavrou M. A multi-criteria study of optimal working fluids for high temperature heat pumps. Chem Ingenieur Technik 95:458-466 (2023) https://doi.org/10.1002/cite.202200106
15. Skiborowski M. Fast screening of energy and cost efficient intensified distillation processes. Chem Eng Trans 69:199-204 (2018) https://doi.org/10.3303/CET1869034
16. Bausa J, Watzdorf Rv, Marquardt W. Shortcut methods for nonideal multicomponent distillation: I. Simple columns. AIChE J 44:2181-2198(1998) https://doi.org/10.1002/aic.690441008



© 2025 by the authors. Licensed to PSEcommunity.org and PSE Press. This is an open access article under the creative commons CC-BY-SA licensing terms. Credit must be given to creator and adaptations must be shared under the same terms. See https://creativecommons.org/licenses/by-sa/4.0/




Systems & Control Transactions

**Research Article - Peer Reviewed Conference Proceeding**
ESCAPE 35 - European Symposium on Computer Aided Process Engineering
Ghent, Belgium. 6-9 July 2025
Jan F.M. Van Impe, Grégoire Léonard, Satyajeet S. Bhonsale,
Monika E. Polańska, Filip Logist (Eds.)

PSE PRESS

# Companies' Operation and Trading Strategies under the Triple Trading and Gaming of Electricity, Carbon Quota and Commodities: A Game Theory Optimization Modeling

**Chenxi Li[a], Nilay Shah[b], Zheng Li[a] and Pei Liu[a]***

[a] State Key Lab of Power System Operation and Control, Department of Energy and Power Engineering, Tsinghua-BP Clean Energy Centre, Tsinghua University, Beijing, 100084, China
[b] Department of Chemical Engineering, Imperial College London, SW7 2AZ, United Kingdom
* Corresponding Author: liu_pei@tsinghua.edu.cn.

## ABSTRACT

Electricity and carbon trading towards carbon reduction are highly coupled. The research on joint trading is essential for helping companies identify optimal strategies and enabling policymakers to detect potential policy loopholes. This study presents a novel game theory optimization model involving both power generation companies (GenCos) and factories to explore optimal operation strategies under electricity-carbon joint trading. By fully capturing the operational characteristics of power generation units and the technical energy consumption of electricity-consuming enterprises, it describes the relationship between renewable energy, fossil fuels, electricity, and carbon emissions detailedly. Considering the correlation between production volume and price of the same product, the case actually encompasses three trading systems: electricity, carbon, and commodities. Transforming this nonlinear model into a mixed-integer linear form through piecewise linearization and discretization, this study examines, through a virtual case with three GenCos and four factories, the impact of various emission reduction targets, comparisons of different carbon allocation mechanisms, and the influence of allowing zero-emission companies into carbon trading. Results reveal that since consumers may cut production rather than implement low-carbon technologies to lower emissions, driving up product prices to maintain profits, high electricity, and carbon prices become unsustainable for GenCos due to reduced electricity demand. Moreover, while intensity mechanisms can incentivize production, overall system profits decrease, which is undesirable for policymakers. Lastly, under strict carbon reduction targets, zero-emission companies may transform the carbon market into a seller's market by purchasing carbon to raise carbon prices, thereby reducing electricity prices and lowering their operating costs.

**Keywords**: electricity-carbon joint trading, game theory optimization, Nash equilibrium, decarbonization strategy, electricity-consuming factories

## INTRODUCTION

It is a consensus that trading is the most effective way to achieve carbon emission reductions [1]. Currently, in most parts of the world, both electricity and carbon trading exist, which are both capable of decreasing carbon emissions. The high overlap in the range of trading participants and the high correlation of traded items make electricity and carbon trading deeply coupled [2]. The transaction behavior and equilibrium of joint trading must be emphasized. Corporations can acknowledge their reasonable and optimal decisions for higher profits in advance and policymakers can both verify the validity and detect potential policy loopholes.

Previous studies about the electricity-carbon joint transaction mostly focus on power generation companies (GenCos) [3, 4], while a large number of electricity consumers directly emitting $CO_2$, such as steel producers, participate in carbon trading. Although a few studies included electricity consumers before, their descriptions were quite simplified. Studies provided relatively detailed descriptions of end-users only primarily relied on the

inverse function relationship between electricity price and demand [5], load curves and utility functions [6, 7]. The relationship between the consumption of electricity and fossil fuels in electricity consumption companies is seldom depicted. Thus, the transaction behavior of this class of firms participating in the electricity-carbon coupled market is always simplified. In addition, the competitive market for products between similar firms is naturally present and indispensable. Due to its prevalence and importance, the product market is one of the most vital factors for companies to make decisions [8], while it is hardly taken into consideration in previous electricity-carbon joint trading studies.

Therefore, this study proposes a novel game theory-based optimization model that includes both GenCos and electricity-consuming factories. Considering both the electricity-carbon joint trading and the competitive trading for substitution of similar products, this model detailedly depicts the correlations between the consumption of fossil energy, renewable energy, generation and consumption of electricity, as well as carbon emissions, through technologies and infrastructure, thereby obtain the Nash equilibrium for triple trading that is closer to the real trading situation. Moreover, this model is implemented on a virtual case with 3 GenCos and 4 electricity-consuming companies to discuss three problems: the enterprises' operational strategies under varying emission reduction requirements, the pros and cons of cap and intensity carbon quota allocation mechanisms, and the impact of integrating zero-emission enterprises into carbon trading.

# METHODOLOGY

## Modeling of power generation companies

The total power supply of each GenCo in each time slice $s$ in one day can be written as Eq.(1), where $\eta$ denotes the efficiency of batteries and the duration of each time slice is one hour, indicating that it is the sum of all kinds of generation $gi$ and the net discharge of battery. This day is assumed to be the only representative day in a year. The power generation of each technology, $pg_{GenCo,s,gi}$, is restricted by its installed capacity and maximum operation hours. Additionally, for simplicity, the fuel consumption and carbon emissions of GenCos are directly proportional to the corresponding fossil fuel power generation. The longest continuous charging and discharging time is limited to 2 hours.

$$pg.sum_{GenCo,s} = \sum_{gi} pg_{GenCo,s,gi} + pw.discharge_{GenCo,s} * \eta - pw.charge_{GenCo,s}/\eta \quad (1)$$

The operational goal of power generation companies is to maximize their positive profit, which can be expressed as Eq.(2), where the income equals the product of power supply and electricity price, $fix.cost_{GenCo}$ denotes the average annual investment and operating costs of generation units, $pg.grid.cost_{GenCo}$ is considered as the electricity grid connection cost that enterprises need to undertake, $ramp.cost_{GenCo}$ refers to the additional costs caused by changes in the output of fossil energy units.

$$pg.profit_{GenCo} = \sum_s pg.sum_{GenCo,s} * ep_s * 365 - fix.cost_{GenCo} - grid.cost_{GenCo} - fuel.cost_{GenCo} - ramp.cost_{GenCo} - \sum_s pg.tradecarbon_{GenCo,s} * cp_s * 365 \quad (2)$$

Obviously, due to the product of two variables, both from electricity and carbon trading, our model becomes nonlinear, as summarized in Eq.(3). To linearize it, we discretize the variable $y$ to $\{Y_i\}$ and introduce binary variables $b_i$, transforming the problem into Eq.(4), where $M$ is a positive big number. In our model, the price is discretized.

$$z = xy, x \text{ and } y \text{ are all constant variables} \quad (3)$$

$$\begin{cases} z = \sum_i \gamma_i Y_i \\ y = \sum_i b_i Y_i, \ \sum_i b_i = 1 \\ \gamma_i \le x, \ \gamma_i \ge x - M(1-b_i), \ \gamma_i \le M b_i, \ \gamma_i \ge -M b_i \end{cases} \quad (4)$$

## Modeling of electricity-consuming companies

In our case study, there are four factories A~D and only their direct carbon emissions are recognized to avoid duplicate accounting. Factory A and Factory B are both equipped with the same two technologies, but in different proportions, producing identical products P. Factory C does not emit $CO_2$, and only meets known electricity needs through purchased electricity and self-provided energy storage batteries. Factory D needs to complete the signed orders through two technologies. The operational goal of the four factories is the maximization of their positive profit. The revenue of Factory A and B is the product of their output and commodity prices, while the revenue and output of Factory C and Factory D have been determined through contracts. In order to describe the competition market for similar products P, we use the Cournor model to describe the negative correlation between production and price, as shown in Eq.(5), where $fac \in \{A, B\}$, $pi$ stands for two production technologies and a, b are given parameters. This relationship is linearized by Eq.(6), where $K$ is given.

$$P.price = a - b * \sum_{fac,pi,s} P.produce_{fac,pi,s} \quad (5)$$

$$P.price = a - \frac{Kb(i-1)}{n}, \frac{K(i-1)}{n} \le x < \frac{Ki}{n}, i = 1,2,\dots,n \quad (6)$$

The costs of all four factories consist of fixed costs, production costs, fuel costs, electricity purchase costs, and carbon trading costs. Production costs are positively proportional to production volume, which is strictly limited by installed infrastructure. In addition, for Factories

A, B and D, due to the different demands for fuels and electricity required by various technologies, and the consumption of fossil fuels often accompanied by carbon emissions, this model can reflect the negative correlation between the average electricity demand and direct carbon emissions per unit production of factories.

## Modeling of electricity-carbon joint trading and calculation of Nash equilibrium

Not considering the transaction center, our model assumes equal buying and selling prices for electricity and carbon, with prices stable throughout the day. Electricity trading should be in real-time and meet supply and demand balance. Carbon trading also needs to meet the supply and demand balance requirement. Unlike electricity trading, carbon trading only requires companies to fulfill their emission obligations at the final moment.

This model directly uses the results of Nash equilibrium to solve the equilibrium in the joint transactions, as shown in Eq.(7a), which equals Eq.(7b). Obviously, this introduces significant nonlinearity to the model. Therefore, special ordered sets of type 2 (SOS2) variables, $\lambda_i$, are introduced to make our model linear, as shown in Eq.(8).

$$\max obj = \prod_{GenCo} profit_{GenCo} \prod_{factory_i} profit_{factory_i} \quad (7a)$$

$$\max obj = \sum_{GenCo} LN(profit_{GenCo}) + \sum_{factory_i} LN\left(profit_{factory_i}\right) \quad (7b)$$

$$\begin{cases} profit = \sum_i \lambda_i * i \\ LN(profit) = \sum_i \lambda_i * LN(i) \\ \sum_i \lambda_i = 1 \end{cases} \quad (8)$$

In conclusion, this research set up a nonlinear problem(NLP) and transform it into a mixed-integer linear programming(MILP) problem through methods including discretization and piecewise linearization to describe the triple trading of electricity, carbon, and commodities involving both power generation and consumption companies.

## CASE STUDY

A diagram of our case study, including fundamental settings, is illustrated in Figure 1. Battery charging and discharging efficiencies are set at 90%, and the price for discharging photovoltaic and energy storage batteries into the grid is 0.1 yuan/kWh. The costs of coal-fired and gas-fired power due to changes in output are 0.05 yuan/kWh and 0.01 yuan/kWh, respectively. Electricity prices range from 0.5 to 1.5 yuan/kWh, while carbon prices range from 0.2 to 4.5 yuan/kg.

Factory A and Factory B both produce product P using two technologies, PT1 and PT2, with details provided in Table 1. The parameters in Eq.(5), a and b, are set as

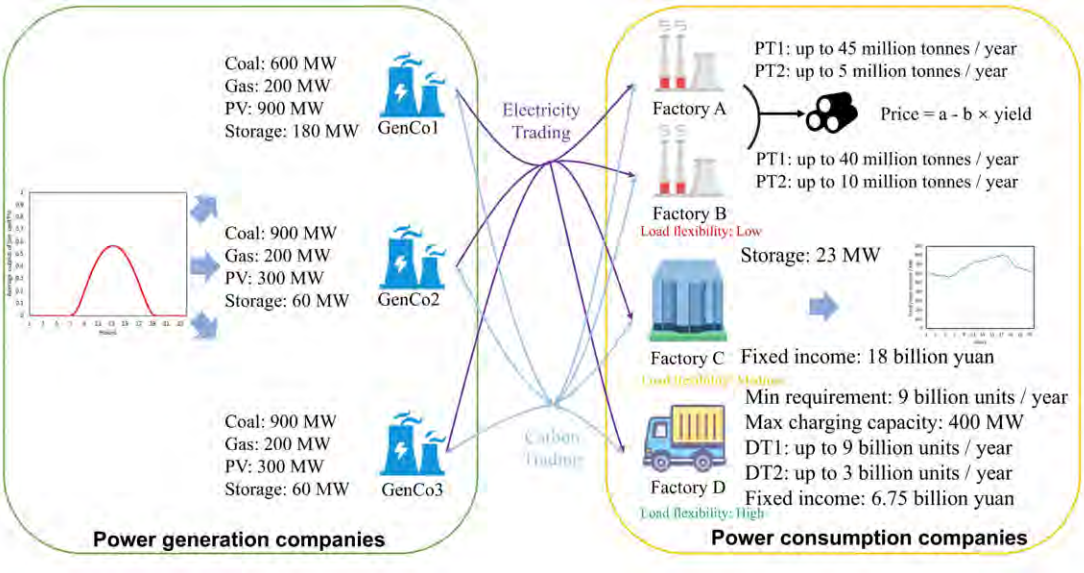



**Figure 1:** The diagram of the case study

**Table 1:** Detailed information of PT1 and PT2

| Name | Fixed price (¥ / tonne) | Produce price (¥ / tonne ) | Electricity demand (kWh / tonne) | $CO_2$ (kg / kg) | Ramp price (¥ / tonne) |
|---|---|---|---|---|---|
| PT1 | 160 | 3300 | 200 | 2.42 | 400 |
| PT2 | 160 | 3800 | 600 | 1.9 | 200 |

**Table 2:** Detailed information of DT1 and DT2

| Name | Fixed price (¥ / unit) | Fuel demand (kg or kWh / unit) | Fuel price (¥ / kg) | $CO_2$ (kg / unit) |
|---|---|---|---|---|
| DT1 | 0.012 | Fossil fuel: 0.0245 kg | 9.3 | 0.07791 |
| DT2 | 0.08 | Electricity: 0.66 kWh | Variable | 0 |

45 and 10. For Factory D, the specifics of its two technologies, DT1 and DT2, are given in Table 2.

## RESULTS AND DISCUSSION

### Enterprises' operational strategies under varying emission reduction requirements

Eight scenarios are established to analyze operational strategies and identify patterns. In the Base and the EM only scenario, carbon trading is not allowed, and the electricity price is designated as 0.75 yuan/kWh in the Base scenario. For the scenarios JM0.9 to JM0.4, both carbon trading and electricity trading are allowed, with prices negotiated among participants. Initial carbon quotas are set based on emissions from the EM only scenario; for instance, JM0.9 provides 90% of that carbon quota. Factory C is restricted from participating in carbon trading. Significant results are summarized in Table 3.

Different from previous studies which found that more stringent carbon reduction targets drive up both carbon and electricity prices simultaneously [9], our findings show that when emission reduction targets are exceptionally strict, carbon prices increase while electricity prices decrease. This phenomenon needs to be explained by combining the competition of similar products P and the carbon trading willingness of each enterprise shown in Figure 2(a-f).

**Table 3**: Trading prices, yield and generation structure under different reduction targets (MT is the abbreviation of million tonnes)

| Scenario | Electricity price (¥ / kWh) | Carbon price (¥ / kg) | Total yield of P (MT) | Price of P (¥ / tonne) |
|---|---|---|---|---|
| Base | 0.75 | / | 65 | 3900 |
| EM only | 1.1 | / | 60 | 3950 |
| JM0.9 | 1.2 | 0.2(min) | 50 | 4050 |
| JM0.8 | 1.25 | 0.2(min) | 45 | 4100 |
| JM0.7 | 1.25 | 0.2(min) | 40 | 4150 |
| JM0.6 | 1.25 | 0.8 | 35 | 4200 |
| JM0.5 | 1.2 | 2.0 | 30 | 4250 |
| JM0.4 | 1.0 | 3.75 | 24 | 4300 |

GenCos generally act as carbon sellers, profiting from both electricity and carbon sales, while factories tend to be buyers in both markets. GenCos can only sell electricity and carbon when consumers continue production, as reduced production means decreased demand for both electricity and carbon allowances. If both prices rise incredibly, consumers will choose to cut production to maintain their profit through raising unit prices, which can be seen from Table 3, then GenCos cannot sell so much. Therefore, electricity prices and carbon prices cannot both increase much. In addition, electricity price contributes more to electricity consumers' total costs

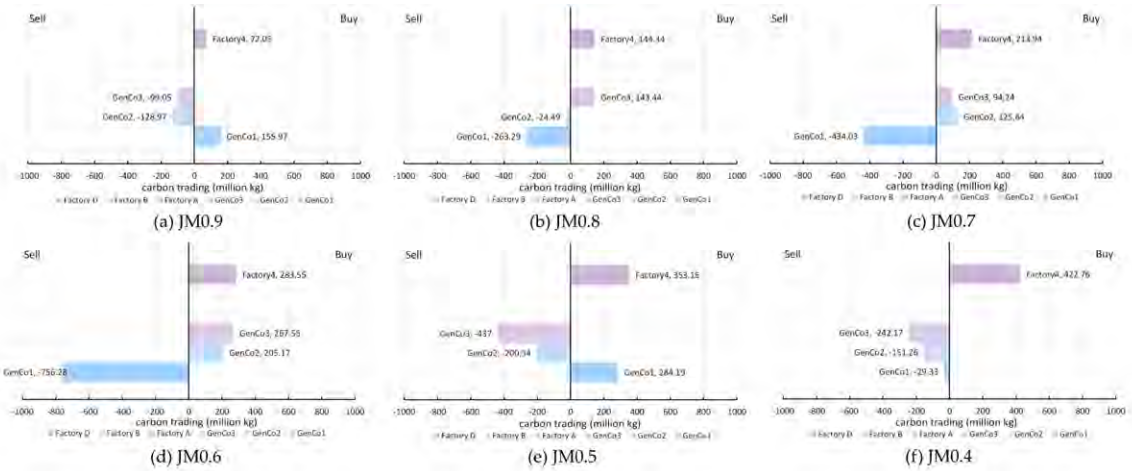



**Figure 2:** Carbon trading results under different reduction target

**Table 4:** Trading prices, yield and profit under different quota allocation mechanisms

| Scenario | Electricity price (¥ / kWh) | Carbon price (¥ / kg) | Total yield of P (MT) | Profit of each enterprise (Billion yuan) (GenCo1~3; factory A~D) |
|---|---|---|---|---|
| JM0.9 | 1.2 | 0.2(min) | 50 | 5.10, 5.16, 5.10; 4.80, 4.70, 5.87, 4.30 |
| JM0.8 | 1.25 | 0.2(min) | 45 | 5.00, 4.92, 5.00; 4.40, 4.35, 5.61, 4.31 |
| Int-JM0.9 | 0.9 | 0.8 | 55 | 3.87, 4.30, 4.60; 3.70, 3.77, 7.44, 3.90 |
| Int-JM0.8 | 0.8 | 0.8 | 45 | 1.97, 3.04, 4.34; 2.39, 2.40, 8.27, 4.21 |

compared with carbon cost; therefore, only when the electricity price is lower would they like to maintain a relatively high production volume. Previous studies were unable to reach these results because they often overlooked the probability of factories' reducing production and price yield relationship in commodity trading. The difference in conclusions also proves the necessity of considering the behavior of electricity-consuming factories more carefully in the electricity-carbon joint trading.

Although there is currently no empirical evidence to support the idea that electricity prices will drop as carbon prices rise due to end-use firms drastically reducing production to meet stricter emission targets, prior studies have observed similar patterns. When the cost of reducing carbon emissions becomes prohibitively high, end-use companies may opt to cut production and increase prices [10]. We speculate that this has not led to a reduction in electricity prices, possibly because these firms are not major electricity consumers within their regions, limiting their tariff negotiation power. However, this hypothesis requires further validation.

In addition, the results also state that factories are not willing to either use any expensive low-carbon technologies to reduce their emissions or purchase costly carbon quotas. This means that if there are no restrictions, the emission reduction of the system will mainly be achieved through the decarbonization of the power system and the reduction of factory production. However, the reduction of yield and the soaring of the price might not align with the goals of market regulators. Therefore, regulators must strictly limit the factories participating in the electricity-carbon joint market to prevent them from maliciously reducing production to maintain profits under the carbon target.

## Pros and cons of cap and intensity carbon quota management mechanisms

In order to quantitatively acknowledge the pros and cons of the cap and intensity quota management mechanisms, the two most widely implemented in carbon trading in reality, this study proposes two additional scenarios: Int–JM0.9 and Int-JM0.8. In the two intensity scenarios, the sum of each enterprise's carbon emissions and carbon trading volume does not exceed the fixed percentage of the product of its production and emission intensity under the EM only scenario. Key findings are shown in Table 4.

Results show that under the intensity mechanism, factories' production enthusiasm can be improved, which is consistent with official cognition, confirming the reliability of our study. The electricity price decreases and the carbon price rises, which seems to be beneficial to both the production and carbon reduction. However, the profits of enterprises involved in carbon trading are all vulnerable under the intensity mechanism, making the total market profit decline violently. Although all the firms in the system are 'selfish' and want to maximize their own profit, the governor of the system always wishes that the total profit would be as high as possible from an economic development perspective. From this point of view, the cap mechanism is much better.

## The impact of integrating zero-emission enterprises into carbon trading

Although some enterprises, such as Factory C in our case study, do not emit $CO_2$ directly, we still try to let them participate in carbon trading, exploring the impact of integrating zero-emission enterprises into carbon trading. Because that they do not own the initial carbon quota, leading to their non-negative net carbon purchases, thereby further promoting the system's carbon mitigation. The difference of involving Factory C into carbon trading is exhibited in Table 5.

**Table 5**: Trading prices, yield and profit under different quota allocation mechanisms

| Scenario | Electricity price (¥ / kWh) | Carbon price (¥ / kg) | Total yield of P (MT) |
|---|---|---|---|
| JM0.5-exclude | 1.2 | 2.0 | 30 |
| JM0.4-exclude | 1.0 | 3.75 | 24 |
| JM0.5-include | 1.0 | 4.5(max) | 30 |
| JM0.4-include | 0.95 | 4.5(max) | 24 |

First and foremost, the yield is not likely to be influenced. It can be also found that the inclusion of carbon-free enterprises in carbon trading will lead to a drop in electricity prices and an increase in carbon prices. These enterprises attempt to increase the scarcity of tradable quotas by increasing carbon trading volume, thereby raising carbon prices. Due to the fact that the electricity

and carbon price cannot increase violently simutanesouly, thus they can pay a smaller cost in exchange for a drop in electricity prices, thereby minimizing their total costs.

## CONCLUSION

This study proposes a non-linear program to describe the triple gaming and trading of electricity, carbon and commodity between both power generation and consumption companies. Transforming it into a MILP problem and using a case with 3 GenCos and 4 factories in 3 types, this study discusses the optimal operation mode of enterprises under coupled transactions. Results state that power consumers are more likely to achieve reduction targets through reducing yield instead of implementing low-carbon technologies or trading quotas, which also leads to the inability of electricity and carbon prices in the electricity-carbon joint trading to be high at the same time. Meanwhile, if zero-emitting enterprises participate in the carbon market, they can increase the scarcity of carbon in the market by purchasing carbon, thereby reducing electricity prices and ensuring their own profits. This study also provides ideas for market managers. It is necessary to strictly control the output of electricity consuming enterprises and prioritize the use of Cap carbon management mechanisms when considering the total profit of the system.

However, our study has certain limitations. Future research should incorporate more detailed considerations, such as real-time electricity prices, policy analyses based on our proposed model, and discussions on parameter sensitivity, to better support the ongoing development of the electricity-carbon joint market.

## ACKNOWLEDGEMENTS

The authors gratefully acknowledge the support by the the Phase IV Collaboration between BP and Tsinghua University and the Ph.D. Short-term Visiting Scholar Fund of Tsinghua University.

## REFERENCES

1. Haitao Xu, Xiongfeng Pan, Jinming Li, Shenghan Feng, Shucen Guo. Comparing the impacts of carbon tax and carbon emission trading, which regulation is more effective? *J. Environ. Manage.* 330:117156 (2023) https://doi.org/10.1016/j.jenvman.2022.117156
2. Yan Li, Tian-tian Feng, Li-li Liu, Meng-xi Zhang. How do the electricity market and carbon market interact and achieve integrated development?--A bibliometric-based review. *Energy* 265:126308 (2023) https://doi.org/10.1016/j.energy.2022.126308
3. Zijun Yuan, Heng Zhang, Xiaohu Zhang, Xueqin Tian, Zaozhong Cheng. Joint clearing model of electricity-carbon coupling market based on unified bidding trading pattern. *2024 9th Asia Conference on Power and Electrical Engineering (ACPEE)* 311-316 (2024) https://doi.org/10.1109/ACPEE60788.2024.10532286
4. Wangdry Rodriguew Faria, Gregorio Muñoz-Delgado, Javier Contreras, Benvindo Rodrigues Pereira Junior. Distribution and transmission coordinated dispatch under joint electricity and carbon day-ahead markets. *Sustainable Energy, Grids and Networks* 38:101393 (2024) https://doi.org/10.1016/j.segan.2024.101393
5. Ming Meng, Lan Jiang. Optimal production decision of hybrid power generation enterprises in complex trading conditions. *Energy Reports* 9:4195-4204 (2023) https://doi.org/10.1016/j.egyr.2023.03.063
6. Yuyan Yang, Xiao Xu, Li Pan, Junyong Liu, Jichun Liu, Weihao Hu. Distributed prosumer trading in the electricity and carbon markets considering user utility. *Renewable Energy* 228:120669 (2024) https://doi.org/10.1016/j.renene.2024.120669
7. Wang Xu, Feilong Lin, Riheng Jia, Changbing Tang, Zhonglong Zheng, Minglu Li. Game-Based Pricing for Joint Carbon and Electricity Trading in Microgrids. *IEEE Internet of Things Journal* 11(16):27732-27743 (2024) https://doi.org/10.1109/JIOT.2024.3400392
8. Dejan Trifunović, Nikola Stojadinović, Bojan Ristić, Predrag Jovanović. Investigating the market share convergence and welfare potentials of asymmetric train access charges for the commercial passenger rail services. *Research in Transportation Economics* 107:101465 (2024) https://doi.org/10.1016/j.retrec.2024.101465
9. Fatemeh Nazifi, Stefan Trück, Liangxu Zhu. Carbon pass-through rates on spot electricity prices in Australia. *Energy Economics* 96:105178 (2021) https://doi.org/10.1016/j.eneco.2021.105178
10. Xuhui Wang, Haonan Xi. Carbon mitigation policy and international tourism. Does the European Union Emissions Trading System hit international tourism from member states? *Annals of Tourism Research* 103:103684 (2023) https://doi.org/10.1016/j.annals.2023.103684

© 2025 by the authors. Licensed to PSEcommunity.org and PSE Press. This is an open access article under the creative commons CC-BY-SA licensing terms. Credit must be given to creator and adaptations must be shared under the same terms. See https://creativecommons.org/licenses/by-sa/4.0/



Systems & Control Transactions

**Research Article - Peer Reviewed Conference Proceeding**
ESCAPE 35 - European Symposium on Computer Aided Process Engineering
Ghent, Belgium. 6-9 July 2025
Jan F.M. Van Impe, Grégoire Léonard, Satyajeet S. Bhonsale,
Monika E. Polańska, Filip Logist (Eds.)

PSE PRESS

# Design of Experiments Algorithm for Comprehensive Exploration and Rapid Optimization in Chemical Space

**Kazuhiro Takeda[a]*, Masaru Kondo[b], Muthu Karuppasamy[c,d], Mohamed S. H. Salem[c,e], and Shinobu Takizawa[c]**

[a] Shizuoka University, Department of Applied Chemistry and Biochemical Engineering, Hamamatsu, Shizuoka, Japan
[b] University of Shizuoka, Yada, Shizuoka, Japan
[c] SANKEN, Osaka University, Ibaraki, Osaka 5670047, Japan
[d] Graduate School of Pharmaceutical Sciences, Osaka University, 1-6 Yamada-oka, Suita, Osaka 565-0871, Japan
[e] Suez Canal University, Pharmaceutical Organic Chemistry Department, Faculty of Pharmacy, Ismailia 41522, Egypt
* Corresponding Author: takeda.kazuhiro@shizuoka.ac.jp.

## ABSTRACT

Bayesian optimization is known to be able to search for the optimal conditions based on a small number of experiments. However, these experiments are insufficient to understand the experimental condition space. In contrast, we report the development of an algorithm that combines a low-confounding definitive screening design with Bayesian optimization, allowing for rapid optimization and ensuring sufficient experiments to understand the experimental condition space with a low confounding.

**Keywords**: Optimization, Algorithms, Bayesian optimization, Definitive screening design.

## INTRODUCTION

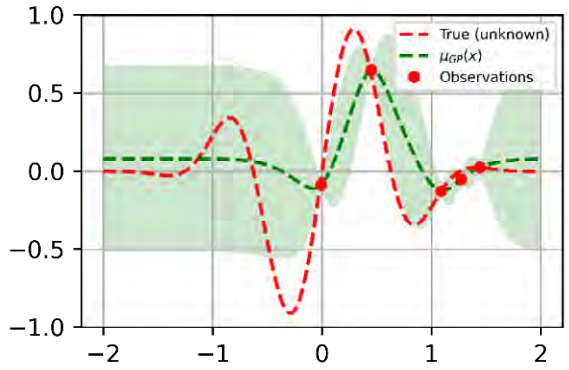
It has been established that Bayesian optimization (BO) [1,2] is capable of searching for the optimal conditions based on a limited number of experiments. Accordingly, prior to implementing the BO, preliminary experiments are conducted in accordance with the principles of the design of experiments. Many methods for the designs of experiment have been proposed, including the factorial design[3], the Plackett Burman design [4], the Box Behnken design [5], the central composite design[6], the Latin hypercube design [7], and the definitive screening design (DSD) [8]. The results of experiments designed by the DSD may contribute to an understanding of the chemical space with minimal confounding factors and a limited number of steps. Subsequently, preliminary experiments are conducted based on the design of experiment, utilizing the design of experiment methods, and a search for the optimal conditions is then undertaken by the BO. This enables the experimental space to be optimized following a comprehensive investigation and to gain insight into the surrounding conditions of the optimal parameters. However, as the design of experiment is conducted independent of the BO, it contributes no more than the preliminary experiments to the optimization process. As a result of comparing the Box Behnken design and response surface methodology with adaptive Bayesian optimization, the BO should be combined with the design of experiments, since the BO could not investigate the experimental space [9]. Therefore, in this study, the design of experiment was evaluated by the acquisition function from within the DSD, and the design of experiment is accordingly modified. The results of running the modified design of experiment are suitable for optimization by the BO, thus allowing the subsequent BO to rapidly search for the optimum conditions.

This paper presents the development of an algorithm that combines a small confounding of the DSD with the BO, thus allowing for rapid optimization and ensuring sufficient experiments to understand the experimental condition space with a small confounding.

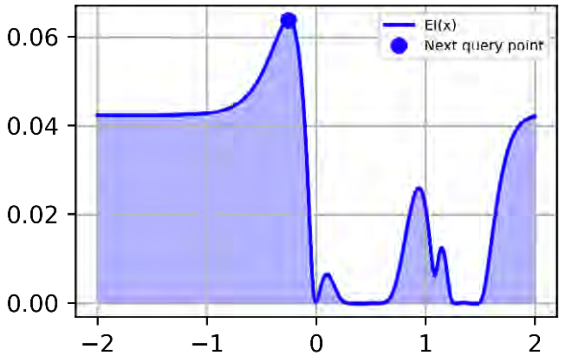
## BAYESIAN OPTIMIZATION

The BO is a method that is known to converge towards the optimum value based on a limited number of experiments. A schematic representation of the process by which the subsequent trial point is formulated is provided in Figure 1. A regression is performed on the observed values with the base estimator frequently being a

Gaussian process regression. An acquisition function is calculated based on the regression model, and the point with the maximum acquisition function value is the next trial point. The acquisition functions most commonly employed are LCB (lower confidence bound), EI (negative expected improvement), PI (negative probability of improvement) and gp_hedge, which probabilistically combines them.




(a) Gaussian process regression from observations.




(b) Next query point by acquisition function.

**Figure 1.** Schematics of Bayesian optimization.

## DEFINITIVE SCREENING DESIGN

The DSD [1,2] is one of the famous design methods of experiments. The DSD is characterised by the following attributes:

- Low confounding between factors.
- A relatively limited number of experiments.

$$N = 2n + 1 + 4f \quad (1)$$

where $N$ is the number of experiments, $n$ is the number of factors, and $f$ is the number of fake factors.

- Three levels for each factor.

The fake factor allows the error to be estimated independently of model selection. The design of experiment with the DSD utilizing a 3 variables model without a fake factor is presented in Table 1. There are 7 $(= 2 \cdot 3 + 1 + 4 \cdot 0)$ entries for 3 variables and no fake factor.

**Table 1:** Designed experiments by the DSD with 3 variables and no fake factor.

| Entry | A | B | C |
|---|---|---|---|
| 1 | 0 | 1 | 1 |
| 2 | 0 | -1 | -1 |
| 3 | 1 | 0 | -1 |
| 4 | -1 | 0 | 1 |
| 5 | 1 | -1 | 0 |
| 6 | -1 | 1 | 0 |
| 7 | 0 | 0 | 0 |

## INTEGRATION OF DEFINITIVE SCREENING DESIGN AND BAYESIAN OPTIMIZATION

The algorithm proposed in this study is presented in the following section. The initial stage of the study comprises preliminary experiments, which are conducted in accordance with the design of experiment formulated by the DSD (Step 1). However, the design of experiment is modified with the objective of incorporating the experimental data into the subsequent BO process. Specifically, in order to calculate the acquisition function for each factor, a preliminary experiment is conducted in accordance with the planned methodology until each variable value is no longer unique (Step 2). Subsequently, the acquisition function is calculated for the remaining experiments, and the experiment with the highest acquisition function value is selected for experimentation (Steps 3, 4, and 5). This process is repeated for Steps 3, 4, and 5 until no further designed experiments remain (Step 6). Once all the designed experiments have been conducted, the optimal conditions can be identified through Bayesian optimization (Steps 7, 8, and 9). By prioritizing the condition with the largest acquisition function value in Steps 3, 4, and 5, the experimental values that are most suitable for the Bayesian optimization performed after Step 7 can be acquired. Furthermore, the planned experimental conditions based on the DSD satisfy the DSD characteristics of a small confounding and a small number of experiments to understand the experimental space.

Example) The proposed algorithm is applied to the designed experiment in Table 1. Step 1 is to formulate Table 1. Step 2 is to execute the experiment up to Entry 3 as designed. Step 3 is to calculate the acquisition function values from Entry 4 onwards. In step 3, the acquisition function values for entry 4 and subsequent entries are calculated. In order to preserve the sign, the

acquisition function values are calculated in the range 0 to 1 for the condition value 1, in the range 0 to -1 for the condition value -1, and in the range 0 for the condition value 0. In Step 6, Steps 3 to 5 are executed until no further entries remain. In Step 7, the condition with the maximum acquisition function over the entire range is identified based on the experimental results up to Step 6, and experiments are conducted using Step 8. In Step 9, Steps 7 and 8 are repeated until convergence is confirmed.

### Proposed Algorithm

Step 1: Design experiment by the DSD.

Step 2: Experiment until all elements are not unique under the DSD definition, in which + and – are the maximum and minimum between the chemical space, respectively.

Step 3: Determine all the remaining experimental conditions for the maximum acquisition function value within the same sign region.

Step 4: Select the experimental condition with the maximum acquisition function value between those of the remaining designed experiments.

Step 5: Perform an experiment with the determined conditions.

Step 6: Go to the next step if all the experiments are executed, else return to Step 3.

Step 7: Search the optimum condition for the maximum acquisition function value.

Step 8: Perform an experiment with the condition.

Step 9: Finish if the convergence conditions are satisfied, else go to Step 7.

## NUMERICAL SIMULATION

In order to ascertain the efficacy of the algorithm proposed in this study, a numerical comparison was conducted. In the present study, the design of experiment was formulated by the DSD and compared with nine different designs of experiment using PyDOE2 [10]. These included a factorial design, a Plackett Burman design, a Box Behnken design, and the DSD. The DSD had three types of designs of experiment (0, 2, and 4) depending on the number of fake factors. Furthermore, a comparison was conducted between the proposed algorithm and Bayesian optimization with randomly generated initial values and no design of experiment. In order to examine the differences between the design of experiment and Bayesian optimization in terms of how they are combined, the following cases were considered: In the case of 'Sequential BO', the BO was performed subsequent to the design of the experiment. In the case of 'In BO', the experimental conditions were set to the condition with the maximum acquisition function value based on the results of Step 3. In the case of 'In Remain BO', the experimental conditions were set to the condition with the maximum acquisition function value based on the acquisition function value and the order of the design with the latter being switched based on the acquisition function values, as determined by Step 4.

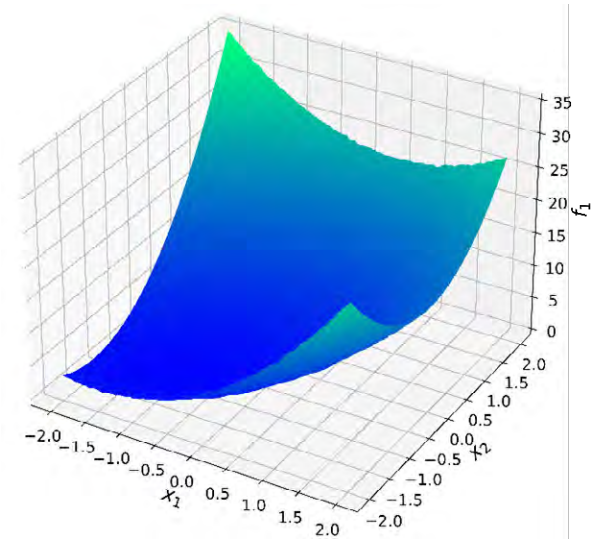



**Figure 2.** Quadratic objective function with one peak.

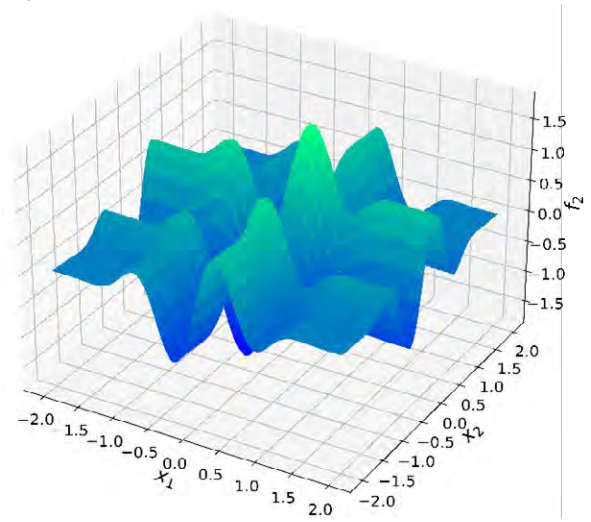



**Figure 3.** Tanh objective function with many peaks.

The objective functions were two distinct types: unimodal and multimodal. The former is illustrated in Eq. (2) (Figure 2), while the latter is shown in Eq. (3) (Figure 3). In Figure 3, $x_3 = 0$ for illustration.

$$f_1(x_1, x_2) = 3 + 2x_1 + 4x_2 - 2x_1^2 - 2x_1x_2 + 3x_2^2 \quad (2)$$

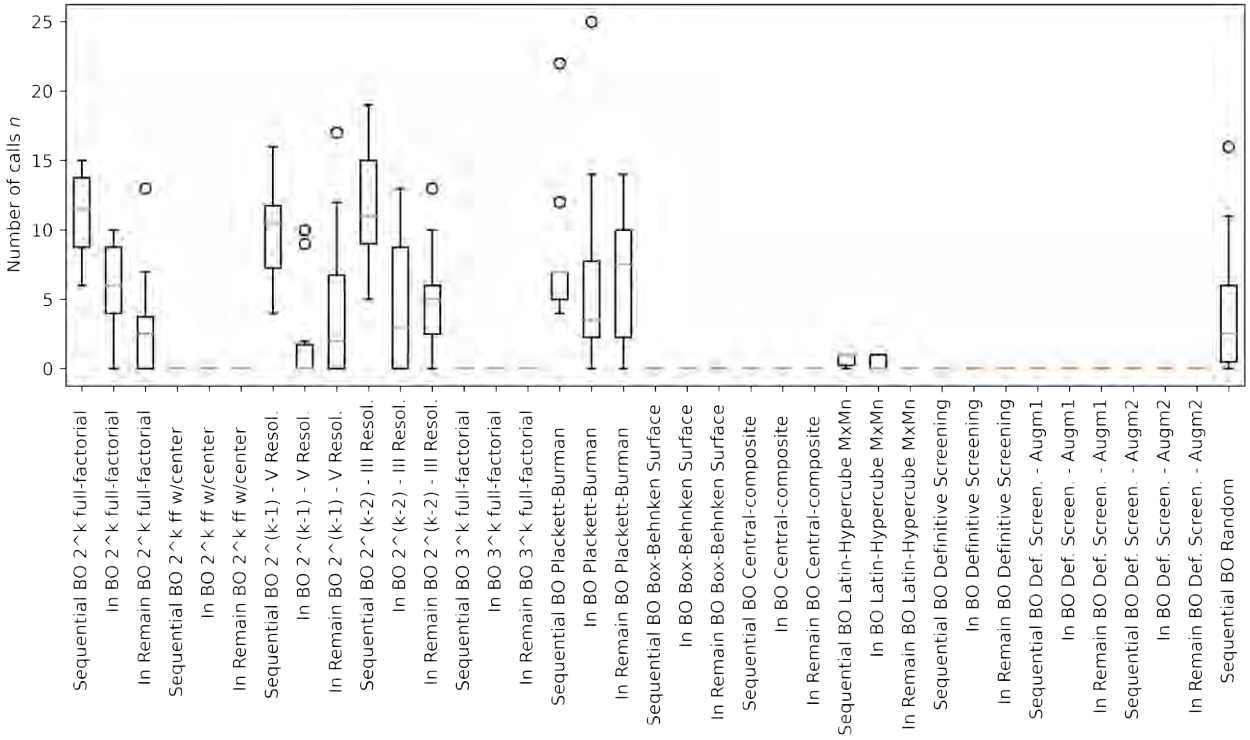



**Figure 4:** Box plots for number of iterations for quadratic function using each algorithm. Orange line represents 50%tile, box represents from 25%tile to 75%tile, whiskers represent minimum and maximum values, and circle represents outliers. For 'Sequential BO', the BO was executed after DoE. For 'In BO', DoE was affected by acquisition function. For 'In Remain BO', DoE was affected and rearranged by acquisition function. '2^k full-factorial' is 2 level general full factorial, '2^k ff w/center' is 2 level general full factorial with zero matrix, '2^(k-1) - V Resol.' Is V resolution 2 level fractional factorial, '2^(k-2) - III Resol.' Is III resolution 2 level fractional factorial, '3^k full-factorial' is 3 level general full factorial, 'Plackett-Burman' is Plackett Burman, 'Box-Behnken Surface' is Box Behnken, 'Central-composite' is central composite, 'Latin-Hypercube MxMn' is Latin hypercube, 'Definitive Screening' is the DSD, 'Def. Screen. - Augm1' is the DSD with 2 fake factors, and 'Def. Screen. - Augm2' is the DSD with 4 fake factors. 'Random' is random initial conditions.

$$f_2(x_1, x_2, x_3) = \sin(5x_1) \cdot (1 - \tanh(x_1^2)) + \sin(5x_2) \cdot (1 - \tanh(x_2^2)) + \sin(5x_3) \cdot (1 - \tanh(x_3^2)) \quad (3)$$

The functions were constrained as follows.

$$-2.0 \leq x_1 \leq 3.0, -3.0 \leq x_2 \leq 4.0, -2.0 \leq x_3 \leq 3.0 \quad (4)$$

A total of 10 trials were conducted for each case in the simulation.

## RESULTS AND DISCUSSION

### Case 1: unimodal objective function

Figure 4 illustrates the distribution of experiments conducted to optimize the unimodal objective function. The number of experiments designed by each method was quite different, the Plackett Burman required only 4 experiments but the 3 level general full factorial required 27 experiments. As the total number of experiments including the designed experiments was not suitable for evaluating the performance of Bayesian optimization after designed experiments, the number of calls after each designed experiment was counted. As the number of convergences of the BO varied between experiments, ten experiments were conducted until a neighbourhood of the optimum value of 3.0 was reached at 5.0. As the optimum value of the unimodal objective function is readily discernible, in numerous instances the experimental conditions proximate to the optimum value were attained during the preliminary experimental phase. The results demonstrated that convergence was achieved in a significantly reduced number of experiments compared to those conducted using the 'Sequential BO Random' method, in which the initial values were randomly generated.

In the case of the 2-level general full factorial, designated as a '2^k full-factorial', and the III resolution 2-

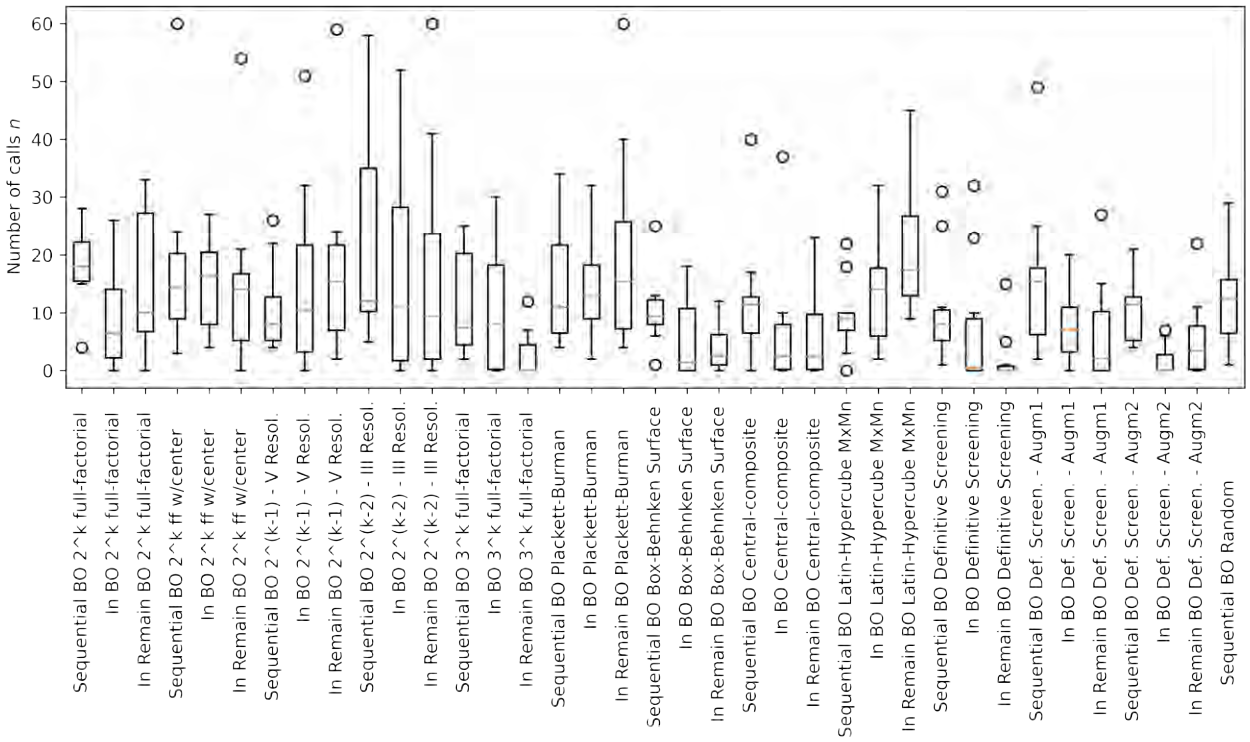



**Figure 5:** Box plots for number of iterations for quadratic function using each algorithm. Orange line represents 50%tile, box represents from 25%tile to 75%tile, whiskers represent minimum and maximum values, and circle represents outliers. For 'Sequential BO', the BO was executed after DoE. For 'In BO', DoE was affected by acquisition function. For 'In Remain BO', DoE was affected and rearranged by acquisition function. '2^k full-factorial' is 2 level general full factorial, '2^k ff w/center' is 2 level general full factorial with zero matrix, '2^(k-1) - V Resol.' Is V resolution 2 level fractional factorial, '2^(k-2) - III Resol.' Is III resolution 2 level fractional factorial, '3^k full-factorial' is 3 level general full factorial, 'Plackett-Burman' is Plackett Burman, 'Box-Behnken Surface' is Box Behnken, 'Central-composite' is central composite, 'Latin-Hypercube MxMn' is Latin hypercube, 'Definitive Screening' is the DSD, 'Def. Screen. - Augm1' is the DSD with 2 fake factors, and 'Def. Screen. - Augm2' is the DSD with 4 fake factors. 'Random' is random initial conditions.

level fractional factorial, designated as '2^(k-2) - III Resol.', it is evident that the case of 'In BO' converged. This occurred less frequently than in the cases of the 'Sequential BO' and 'In Remain BO'. The fact that the case of 'In BO' converged less often than the case of 'Sequential BO' demonstrates the value of optimizing the experimental conditions through the acquisition function during the preliminary experiment based on the design of experiment. This demonstrated the value of optimizing the experimental conditions with the acquisition function during the preliminary experiment based on the design of experiment. The case of the 'In Remain BO' converged fewer times than the case of 'In BO', indicating the benefit of utilizing the acquisition function to alter the design order during the preliminary experiment based on the design of experiment.

## Case 2: multimodal objective function

Figure 5 illustrates the distribution of experiments conducted for the purpose of optimizing the multimodal objective function. Similarly, for the unimodal function, to evaluate the performance of Bayesian optimization after designed experiments, the number of calls after each designed experiment was counted. Ten experiments were conducted for the multimodal objective function with the number of experiments continuing until a neighborhood of the optimum value of -2.8 was reached at -1.0. In comparison to the unimodal objective function, the search for the optimal value of the multimodal objective function was more challenging and necessitated the execution of several tens of experiments.

In a considerable number of designs of experiment, the case of 'In BO' converged less often than the case of 'Sequential BO', and the case of 'Sequential BO' converged less often than the case of 'In Remain BO'

In comparison to the 'Sequential BO Random' method, which employed randomly generated initial values, i.e., the Box-Behnken 'Box-Behnken Surface' and the

central Composite 'Central-composite' methods, the DSD 'Definitive Screening', and the 'Def. The following abbreviations were used: 'Screen', 'Augm1' and 'Def'. Furthermore, the 'Def. Augm1' and 'Def. Augm2' methods were also considered. The 'Screen. - Augm2' method demonstrated a high degree of convergence in a relatively small number of cycles. Notably, in the case of employing the proposed algorithm within the DSD framework, it exhibited a markedly superior convergence rate compared to the 'Sequential BO Random' method.

In both cases, the proposed algorithm, in which the DSD designed experiments were influenced and rearranged by the acquisition function, could converge faster than the 'Sequential BO Random' method. These findings highlight the value of optimizing the experimental conditions through the acquisition function, and of modifying the design of experiment order through the acquisition function during the preliminary experiment, independent of the objective function. Since faster convergence for BO means that the exploration of the experimental condition space was more useful. Therefore, in the proposed algorithm, the BO was able to perform on sufficient experiments designed by the DSD to understand the experimental condition space.

## CONCLUSIONS

We put forth a novel algorithm that integrates the DSD and the BO to address confounding factors and optimize the experimental conditions. Optimizing the magnitude and orders of the designed experiments of the DSD based on the BO contributed to effectively accelerate the convergence rate. Our proposed algorithm exhibits the potential for a faster convergence than existing algorithms in numerical experiments. Furthermore, we have demonstrated the value of rearranging the order of experiments in achieving more efficient outcomes. Furthermore, in the proposed algorithm, the BO was able to perform on sufficient experiments designed by the DSD to understand the experimental condition space.

In future work, we will investigate wet experiments to verify the efficacy of our proposed algorithm.

## ACKNOWLEDGEMENTS

This study was financially supported by a Grant-in-Aid for Transformative Research Areas (A) (Grant Number 21H05207, 21H05222, and 21H05217) for Digitalization-driven Transformative Organic Synthesis (Digi-TOS) from the Ministry of Education, Culture, Sports, Science, and Technology (MEXT), Japan.

## REFERENCES

1. Snoek J., Larochelle H., Adams R. P., Practical Bayesian Optimization of Machine Learning Algorithms, *arXiv*:1206.2944:1-9 (2012) https://doi.org/10.48550/arXiv.1206.2944
2. Kondo M., Wathsala H. D. P., Ishikawa K., Yamashita D., Miyazaki T., Ohno Y., Sasai H., Washio T., Takizawa S., Bayesian optimization-assisted screening to identify improved reaction conditions for Spiro-Dithiolane synthesis, *Molecules*, 28, 13, 5180 (2023) https://doi.org/10.3390/molecules28135180
3. Fisher, R. A., The arrangement of field experiments. *Journal of the Ministry of Agriculture*. 33:503-515 (1926) https://doi.org/10.23637/rothamsted.8v61q
4. Plackett, R. L., Burman, J. P., The Design of Optimum Multifactorial Experiments. *Biometrika*, 33(4):305–325 (1946) https://doi.org/10.2307/2332195
5. Box, G. E. P., Behnken, D. W., Some New Three Level Designs for the Study of Quantitative Variables. *Technometrics*, 2(4):455–475 (1960) https://doi.org/10.1080/00401706.1960.10489912
6. Box,G.E.P., Wilson,K.B., On the Experimental Attainment of Optimum Conditions, *Journal of Royal Statistical Society Series B*, 13:1-45 (1951) https://doi.org/10.1111/j.2517-6161.1951.tb00067.x
7. Mckay, M. D., Beckman, R. J., Conover, W. J., A Comparison of Three Methods for Selecting Values of Input Variables in the Analysis of Output from a Computer Code. *Technometrics*, 42(1):55–61 (2000) https://doi.org/10.1080/00401706.2000.10485979
8. Jones, B., Nachtsheim, C. J., A Class of Three-Level Designs for Definitive Screening in the Presence of Second-Order Effects. *Journal of Quality Technology*, 43(1):1–15 (2011) https://doi.org/10.1080/00224065.2011.11917841
9. Rummukainen H., Horhammer H., Kuusela P., Kilpi J., Sirvio J., Makela M., Traditional or adaptive design of experiments? A pilot-scale comparison on wood delignification. *Heliyon*, 10:e24484 (2024) https://doi.org/10.1016/j.heliyon.2024.e24484
10. Sjogren R., Svensson D., https://github.com/clicumu/pyDOE2

© 2025 by the authors. Licensed to PSEcommunity.org and PSE Press. This is an open access article under the creative commons CC-BY-SA licensing terms. Credit must be given to creator and adaptations must be shared under the same terms. See https://creativecommons.org/licenses/by-sa/4.0/



Systems & Control Transactions

**Research Article - Peer Reviewed Conference Proceeding**
ESCAPE 35 - European Symposium on Computer Aided Process Engineering
Ghent, Belgium. 6-9 July 2025
Jan F.M. Van Impe, Grégoire Léonard, Satyajeet S. Bhonsale,
Monika E. Polańska, Filip Logist (Eds.)

PSE PRESS

# Multi-Objective Optimization and Analytical Hierarchical Process for Sustainable Power Generation Alternatives in the High Mountain Region of Santurbán: case of Pamplona, Colombia

**Nicolas Cabrera[a], A.M Rosso-Cerón[b], and Viatcheslav Kafarov[a]***

[a] Universidad Industrial de Santander, Department of Chemical Engineering, Bucaramanga, Santander, Colombia
[b] Universidad de Pamplona, Department of Chemical Engineering, Pamplona, Norte de Santander, Colombia
* Corresponding Author: kafarov@uis.edu.co

## ABSTRACT

This study presents an integrated approach combining the Analytic Hierarchy Process (AHP) with a Mixed-Integer Multi-Objective Linear Programming (MOMILP) model to evaluate sustainable power generation alternatives for Pamplona, Colombia. The MOMILP model includes solar, wind, biomass, and diesel technologies, aiming to minimize costs (net present value) and $CO_2$ emissions while considering design, operational, and budget constraints. The AHP method evaluates multiple criteria such as social acceptance, job creation, technological maturity, and environmental impact. The results show that solar panels are prioritized, with small diesel plants added due to resource limitations. The most sustainable option is a hybrid system with 49% solar, 29% wind, 14% biomass and 8% diesel, generating a net present value of 121,360 USD and 94,720 kg of $CO_2$ emissions. The proposed methodology can be applied to assess and select the most feasible alternative within a wide range of new projects for the integration of renewable energy systems for the extension of existing power grids.

**Keywords**: Analytical Hierarchical Process, Multi-objective optimization, Numerical Methods, Renewable and Sustainable Energy, Technoeconomic Analysis.

## INTRODUCTION

Energy systems are fundamental for economic and social development; however, around 66% of global energy supply still relies on fossil fuels, contributing to 75% of GHG emissions [1]. Given the continuous population growth and rising energy demand, these percentages are likely to increase in the future [2]. To address this issue, many countries have prioritized the integration of RES into their power distribution systems as a strategy to reduce GHG emissions and mitigate climate change [3]. Colombia, for instance, generates approximately 70% of its electricity from hydropower, significantly decreasing its reliance on fossil fuels [4].

Despite this progress, heavy dependence on hydropower poses a risk, as water resources are highly affected by climate variability [5]. Recognizing the need to diversify its energy mix, Colombia introduced Law 1715 in 2014 to regulate the integration of RES into the SIN. The law includes various incentives, such as income tax deductions, VAT exemptions, import duty exemptions, and accelerated asset depreciation, to promote the adoption of RES [6].

To effectively integrate RES into power grids, several studies have utilized MCDM methods. For example, Arikan et al. (2024) applied AHP and VIKOR to identify the most suitable non-conventional technology for a hotel's power supply, considering technical, economic, and environmental aspects [7]. Similarly, Xu et al. (2023) evaluated a hybrid RES using an optimization model combined with AHP, focusing on technical, economic, and environmental criteria [8]. However, these studies often overlook social factors, which are crucial for the successful design and implementation of hybrid energy systems. Ali et al. (2020) addressed this gap by incorporating social criteria, such as social acceptance and policy impacts, in their

assessment of RES options for a refugee camp in Bangladesh using the AHP method [9]. Despite the extensive body of research on RES integration, there is still a need for more comprehensive studies that consider social criteria and involve direct input from experts. Additionally, existing studies frequently fail to account for specific geographical characteristics of the case study area.

Addressing these gaps, this research employs a MOMILP model and the AHP to evaluate the integration of PV panels, biomass gasifiers, wind turbines, and diesel generators into the SIN to meet the energy demand of Pamplona, Colombia. The MOMILP model is designed with a 16-year planning horizon starting in 2024. It aims to minimize both costs and $CO_2$ emissions, considering design, operational, and budget constraints. The model also explores the potential for selling surplus electricity, which could contribute to local economic growth and enhance energy independence. To select the most sustainable alternative from the Pareto front, the AHP method is employed, using a comprehensive set of criteria: economic, technical, environmental, and social. It includes sub-criteria reflecting specific geographical aspects and social factors such as social acceptance and job creation. The weighting of these criteria and sub-criteria is determined through expert input, using the Delphi method and Saaty's scale. This integrated approach allows for a more holistic evaluation of RES integration strategies, ensuring that both technical and socio-economic factors are considered in the decision-making process.

## MATHEMATICAL FORMULATION

In this section, the objective functions and constraints of the MOMILP model are presented.

### Objective functions:

The objective functions aim to minimize the total generation system cost (NPV, which is the result of subtracting the energy costs — CAPEX, OPEX, and energy sales to the grid) (Eq. 1) and $CO_2$ emissions (Eq. 2):

$$NPV=\sum_t \frac{1}{(1+TD)^t}\cdot[\sum_p \widehat{InvCo}_{p,t}\cdot CaA_{p,t} + \sum_p \widehat{FixCo}_{p,t}\cdot CaT_{p,t} + \sum_p \widehat{VarCo}_{p,t}\cdot EnG_{p,t} + \sum_p \widehat{FuCo}_{p,t}\cdot FuR_{p,t} - \sum_p \widehat{SellCo}_{p,t}\cdot EnVe_{p,t}] \quad (1)$$

$$CO_2=\sum_t [\sum_p \widehat{Em}_p \cdot EnG_{p,t}] \quad (2)$$

### Operational constraints:

The operational constraints are included to meet the electricity and power demand of the community, as well as to account for energy and power surpluses for sale, ensuring system reliability.

**Energy balance:** The generated energy must meet the electrical demand, with 5% of the demand allocated for surplus energy sales

$$\sum_p EnG_{p,t} = \widehat{DE}_t + \sum_p EnVe_{p,t} \quad (3)$$

**Reserve margin:** To ensure system reliability, a reserve margin of 6% is set over the maximum power demand.

$$\sum_p PoG_{p,t} \geq (1+\rho)\cdot \widehat{DP}_t \quad (4)$$

**Availability factor:** The fraction of time during which generation plants operate without forced outages, maintenance, repairs, or climatic variations must be considered.

$$EnG_{p,t} = A_p \cdot DB_t \cdot PoG_{p,t} \quad (5)$$

**Capacity factor:** The ratio between the average power generated by the plant and the power that would be generated under ideal conditions.

$$PoG_{p,t} \leq F_p \cdot CaT_{p,t} \quad (6)$$

### Design constraints:

These constraints ensure that the system is not oversized by considering the capacity limits to be added, the construction time, and the specific consumption of available resources.

**Available installed capacity:** Existing capacity plus the newly added capacity of the generation plant.

$$CaT_{p,t} = ICa_{p,t}\cdot Op_{p,t} + \sum_{v \leq t-T_p} CaA_{p,t} \quad (7)$$

**Added capacity limits:** Limits are set on the added capacity to prevent oversizing and ensure that the capacities added during the planning horizon do not exceed the established maximum capacity.

$$\widehat{Camin}_p \cdot In_{p,t} \leq CaA_{p,t} \leq \widehat{Camax}_p \cdot In_{p,t} \quad (8)$$

$$\sum_t CaA_{p,t} \leq \widehat{Camax}_p \quad (9)$$

**Installed capacities per period:** The amount of plant constructions is limited during specific period

$$\sum_p In_{p,t} \leq 2 \quad (10)$$

**Limits on the specific consumption of available resources:** The primary resources used for energy generation must not exceed the available primary resources in the area.

$$\widehat{Rw}_{r,p} \cdot EnG_{p,t} \leq PriT_{r,t} \quad (9)$$

**Specific fossil fuel consumption (diesel plants):** The primary resource used in diesel plants is the amount of fossil fuel consumed.

$$\widehat{Rw}_{r,p} \cdot EnG_{p,t} = FuR_{r,t} \quad (10)$$

### Budgetary constraint:

The investment to add new capacities is limited by the budget allocated to the region of interest, as established by the Financial Support Fund for the

Electrification of Interconnected Rural Areas

$$\sum_t \frac{1}{(1+r)^t} \cdot [\sum_p \widehat{InvCo_{p,t}} \cdot CaA_{p,t}] \leq \widehat{BugCo} \quad (11)$$

The MOMILP model is built in Python using the Pyomo package and solved using the ε-constraint method with the 'GLPK' solver (SIMPLEX method), yielding 10 alternatives in the Pareto chart.

## Technical and financial parameters:

The parameters used to solve the MOMILP model are presented in Table 1. In addition, as the model considers later years, the financial parameters were projected with consumer price index (IPC) (Eq. 12):

$$C_n = C_0 * \left(\frac{IPC_n}{IPC_0}\right) \quad (12)$$

Where $C_n$ is the cost in the year to be projected, $C_0$ is the base year cost, $IPC_n$ is the IPC of the year to be projected and $IPC_0$ the IPC of the base year [10].

# MULTI-CRITERIA DECISION-MAKING METHOD (AHP)

## AHP approach:

**Hierarchy Structure:** The problem is decomposed into a hierarchical structure consisting of 4 criteria (C1. Economic, C2. Technical, C3. Environmental, C4. Social), 10 sub-criteria (C2.1 Efficiency, C2.2 Technological Maturity, C2.3 Reliability, C2.4 Access Routes, C3.1 Pollutant Waste, C3.2 Land Requirement, C3.3 Habitat Impact, C3.4 CO2 Emissions, C4.1 Job Creation, C4.2 Social Acceptance), and 10 alternatives (A1:A10) (Figure 1)

**Information Collection**: The individual weights of the criteria and sub-criteria are obtained through expert opinion collection using the Delphi method and a scale from 1-9 (Saaty scale).

**Pairwise Comparison between Criteria and Sub-Criteria:** This matrix comparison determines the relative importance of each criterion and sub-criterion compared to the others.

**Consistency Ratio (C.R.):** Consistency between the comparisons is verified through the consistency ratio (C.R.). If C.R. is less than 0.1, the comparisons are consistent.

**Evaluation of Alternatives:** The priority of each alternative is determined through pairwise comparisons, considering the relative importance (weights) of each criterion and sub-criterion.

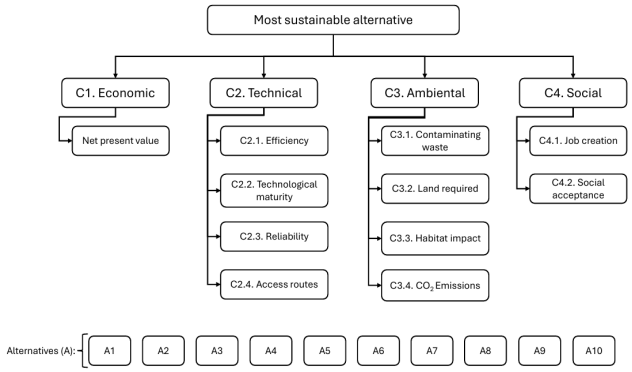



**Figure 1.** Hierarchical levels of the AHP method.

## Case study description

The MOMILP model was applied to the municipality of Pamplona, Colombia, due to its proximity to the high mountain region of the Santurbán páramo, which supplies water to around 2.5 million people and supports rich biodiversity. This municipality is connected to the National Interconnected System (SIN) and has an approximate population of 56,894 people [12] with an electricity demand of 699 MWh [13].

# RESULTS AND ANALYSIS

The 10 alternatives obtained on the Pareto front for the objective functions of net present value (NPV) and $CO_2$ emissions are shown in Table 2. The values of the NPV refer to the net gains up to the year 2040 resulting from the sale of excess electricity generated (5% of the electrical demand). The objective functions have a direct relationship, meaning that if the gains increase, $CO_2$ emissions also rise, and vice versa. Therefore, alternative A1 achieves the greatest profits, with a value of 159,470 USD, and the highest CO2 emissions, reaching 245.88 tons. Conversely, alternative A10 yields the smallest profits, amounting to 121,360 USD, and the lowest CO2

| Parameters | PV panel | Wind turbine | Biomass gasifier | Diesel plants |
|---|---|---|---|---|
| Availability factor | 0.21 | 0.74 | 0.58 | 0.98 |
| Capacity factor | 0.25 | 0.25 | 0.8 | 0.5 |
| Emissions factor ($kgCO_2/kWh$) | 0.0 | 0.0 | 0.68 | 0.79 |
| Construction time (years) | 1.0 | 2.0 | 3.0 | 2.0 |
| Investment cost (USD/kW) | 758.00 | 1,160.00 | 1,800.00 | 448.00 |
| Unit fixed O&M costs (USD/kW) | 0.02 | 0.01 | 0.09 | 4.74 |
| Unit variable O&M costs (USD/kW) | 0.0 | 0.0 | 0.0001 | 0.004 |
| Fuel cost (USD/unit fuel) | 0.0 | 0.0 | 0.0 | 1.91 |

**Table 1:** Technical and financial parameters of renewable energies [11].

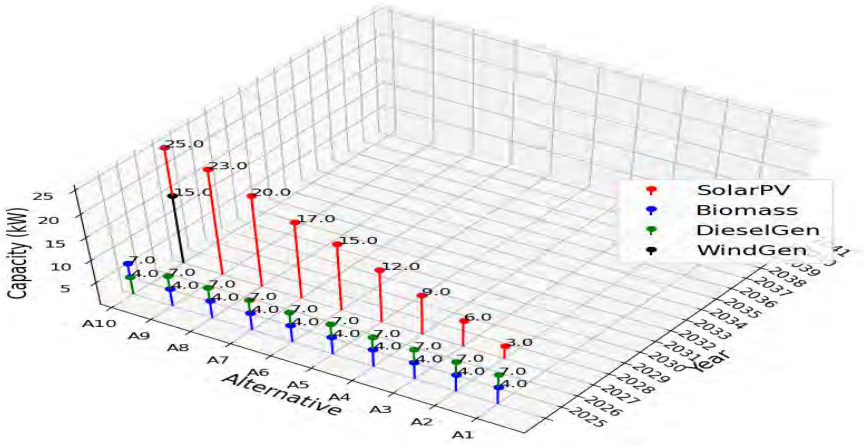



**Figure 2:** Added capacities in each alternative.

emissions, producing 94.72 tons.

**Table 2:** Pareto front alternatives.

| Alternative | NPV (USD) | $CO_2$ emissions (Ton) |
|---|---|---|
| A1 | 159,470 | 245.88 |
| A2 | 158,670 | 227.57 |
| A3 | 157,330 | 209.70 |
| A4 | 155,990 | 191.84 |
| A5 | 154,640 | 173.98 |
| A6 | 153,290 | 156.13 |
| A7 | 152,390 | 144.22 |
| A8 | 151,050 | 126.36 |
| A9 | 149,700 | 108.51 |
| A10 | 121,360 | 94.72 |

Each alternative considers adding different generation plant capacities (Figure 2). The obtained alternatives favour the addition of solar plants, biomass gasifiers, and diesel plants. Although diesel plants produce the highest $CO_2$ emissions, the available resources in the area lead to their inclusion to meet the electricity demand. Alternative A1 generates the highest profits but does not consider $CO_2$ emissions reduction. This alternative considers including only diesel plants and biomass gasifiers with proportions of 64% and 36%, respectively.

In contrast, alternative A10, while generating the lowest profits, seeks to minimize $CO_2$ emissions as much as possible, promoting the construction of solar plants, wind turbines, biomass gasifiers and diesel generators with proportions of 49%, 29%, 14% and 8%, respectively. This last alternative is the only one that includes wind generation, as the area's wind speeds are not strong enough to install plants with capacities greater than 1 kW.

The energies generated by the added capacities are shown in Table 3. Biomass gasifiers predominate as the main technology up to alternative A8, since they guarantee energy supply and produce less $CO_2$ emissions compared to diesel plants. From alternative A9 onwards, photovoltaic panels stand out as the main source of electricity generation. It should be noted that, in alternative A10, wind energy contributes a small proportion of the total electricity generation, which contributes to this alternative having the lowest emissions. Furthermore, due to the high $CO_2$ emissions produced by diesel plants, these are used only as backup sources to ensure a continuous and reliable electricity supply.

Applying the AHP method to the expert opinions

| Total energy generated by installed plants (kWh) (percentage) | | | | |
|---|---|---|---|---|
| **Alternative** | **Photovoltaic** | **Eolic** | **Biomass** | **Diesel** |
| A1 | 0 (0 %) | 0 (0 %) | 324,480.81 (91.16 %) | 31,482.24 (8.84 %) |
| A2 | 26,214.3 (7.36 %) | 0 (0 %) | 302,465.45 (84.97 %) | 27,283.31 (7.66 %) |
| A3 | 52,428.6 (14.73 %) | 0 (0 %) | 276,363.69 (77.64 %) | 27,170.77 (7.63 %) |
| A4 | 78,642.9 (22.09 %) | 0 (0 %) | 250,149.39 (70.27 %) | 27,170.77 (7.63 %) |
| A5 | 104,857.2 (29.46 %) | 0 (0 %) | 223,935.09 (62.91 %) | 27,170.77 (7.63 %) |
| A6 | 131,071.5 (36.82 %) | 0 (0 %) | 197,720.79 (55.55 %) | 27,170.77 (7.63 %) |
| A7 | 148,547.7 (41.73 %) | 0 (0 %) | 180,244.59 (50.64 %) | 27,170.77 (7.63 %) |
| A8 | 174,762.0 (49.10 %) | 0 (0 %) | 154,030.29 (43.27 %) | 27,170.77 (7.63 %) |
| A9 | 200,976.3 (56.46 %) | 0 (0 %) | 127,815.99 (35.91 %) | 27,170.77 (7.63 %) |
| A10 | 218,452.5 (61.37 %) | 839.45 (0.24 %) | 121,694.26 (34.19 %) | 14,976.85 (4.21 %) |

**Table 3:** Total energy generated by installed plants.

| Power plant | C1 | C2.1 | C2.2 | C2.3 | C2.4 | C3.1 | C3.2 | C3.3 | C3.4 | C4.1 | C4.2 | Total |
|---|---|---|---|---|---|---|---|---|---|---|---|---|
| Solar | 0.086 | 0.02 | 0.005 | 0.004 | 0.002 | 0.056 | 0.015 | 0.008 | 0.042 | 0.006 | 0.074 | 0.302 |
| Biomass | 0.014 | 0.008 | 0.004 | 0.008 | 0.002 | 0.011 | 0.004 | 0.017 | 0.020 | 0.053 | 0.027 | 0.167 |
| Diesel | 0.183 | 0.010 | 0.018 | 0.017 | 0.002 | 0.005 | 0.002 | 0.053 | 0.004 | 0.025 | 0.012 | 0.331 |
| Wind | 0.026 | 0.008 | 0.012 | 0.002 | 0.002 | 0.056 | 0.015 | 0.005 | 0.009 | 0.019 | 0.045 | 0.200 |
| Total | 0.308 | 0.029 | 0.039 | 0.030 | 0.010 | 0.128 | 0.037 | 0.082 | 0.076 | 0.103 | 0.158 | 1.000 |

**Table 4:** Weights of the criteria, subcriteria, and power plants.

collected through the Delphi method, the prioritization scores for the criteria, subcriteria, and generation plants are shown in Table 4. The most important criterion is environmental, followed by economic, social, and technical. Social acceptance (C4.2) is considered by the experts as the second most important criterion for evaluating the alternatives, as it ensures that the beneficiary region or community makes the most of these sustainable technologies and contributes to their care. In addition, the job creation sub-criterion (C4.1) has a high weight due to its relevance for the socio-economic development of the region. As a result, in the AHP evaluation, conventional technologies can be given more weight in the prioritisation of alternatives. Although the diesel power plant produces the highest $CO_2$ emissions, it has the lowest habitat impact, the lowest investment cost, and the best technological aspects. These characteristics make the diesel plant the highest prioritized. Furthermore, since the alternatives obtained through MOMILP consider a mix of generation plants, the best alternative was selected based on the individual criterion and the percentage of energy generated by each plant throughout the planning horizon (Table 5).

**Table 5:** Percentage of alternatives prioritization.

| Alternative | Prioritization weight | Ranking |
|---|---|---|
| A1 | 0.1848 | 10 |
| A2 | 0.1930 | 9 |
| A3 | 0.2028 | 8 |
| A4 | 0.2126 | 7 |
| A5 | 0.2224 | 6 |
| A6 | 0.2322 | 5 |
| A7 | 0.2388 | 4 |
| A8 | 0.2486 | 3 |
| A9 | 0.2584 | 2 |
| A10 | 0.2601 | 1 |

Since electricity generation from diesel plants is similar across all alternatives, the prioritization is influenced by the installation of photovoltaic panels. Consequently, Alternative A10, with a score of 0.1848, turns out to be the least favourable option, as it does not include the implementation of any PV capacity. Similarly, the alternative A10, with a score of 0.268, is the preferred option to meet Pamplona's energy demand while simultaneously reducing $CO_2$ emissions.

## CONCLUSIONS

A Mixed-Integer Linear Multi-Objective Optimization model was implemented to evaluate the Pareto front alternatives that integrate solar, wind, biomass, and diesel power plants into the National Interconnected System, in order to meet the electricity demand of the municipality of Pamplona, Colombia. The alternatives promoted the construction of solar plants, aiming to minimize $CO_2$ emissions. Additionally, due to the limitation of available resources, diesel plants were required to generate energy to meet demand and sell to energy distributors. The most sustainable alternative was determined by collecting expert opinions using the Delphi method and the AHP method, which considered economic, technical, environmental, and social criteria, and included 10 subcriteria. The most important criterion was environmental, followed by economic, social, and technical. Among the power plants, the diesel plant is preferred due to its higher efficiency and lower impact on habitats. The evaluation of the alternatives determined that alternative A10 is the highest priority, which consists of implementing solar plants, wind turbines, biomass gasifiers and diesel generators with proportions of 49%, 29%, 14% and 8%, respectively. The proposed methodology can be applied to assess and select the most feasible alternative within a wide range of new projects for the integration of renewable energy systems for the extension of existing power grids.

## NOMENCLATURE

### Model parameters

*TD*: Discount rate
$\widehat{InvCo_{p,t}}$ : Unit investment costs (USD/kW)
$\widehat{FixCo_{p,t}}$: Unit fixed costs (USD/kW)
$\widehat{VarCo_{p,t}}$ : Unit variable costs (USD/kW)
$\widehat{FuCo_{p,t}}$ : Unit cost of fossil fuel (USD/fossil fuel unit)
$\widehat{SellCo_{p,t}}$: Unit Price of electricity (USD/kW)
$\widehat{Em_p}$ : CO2 emission factor (kgCO2/kWh)
$\widehat{DE_t}$ : Energy demand (kWh)
$\rho$ : Reserve margin (kW)
$\widehat{DP_t}$ : Peak demand (kW)
$A_p$ : Availability factor

$DB_t$ : Block duration
$F_p$ : Capacity factor
$\widehat{Camin}_p$ : Minimum capacity (kW)
$\widehat{Camax}_p$ : Maximum capacity (kW)
$\widehat{Rw}_{r,p}$ : Consumption factor of primary resources (primary resource units/kWh)
$\widehat{BugCo}$ : Total budget (USD)

## Sets

p: Power generation plants
r: Primary resources
t,v : Time period (2024-2040)
Tp: Construction time

## Decision variables

$CaA_{p,t}$ : Capacity to be added (kW)
$CaT_{p,t}$ : Total available capacity (kW)
$EnG_{p,t}$ : Energy generated (kWh)
$FuR_{r,t}$ : Fossil fuel unit
$EnVe_{p,t}$ : Surplus energy sold (kWh)
$PoG_{p,t}$ : Power generated (kW)

## Decision binary variables

$Op_{p,t}$ : If the installed capacity is operational
$In_{p,t}$ : If new capacity is to be installed

## Abbreviations

*RES* : Renewable Energy System
*SIN* : National Interconnected System
*IPC* : Consumer price index

## ACKNOWLEDGEMENTS

The authors would like to acknowledge the financial support from the Ministry of Science, Technology, and Innovation of Colombia for the project "Development of a computational tool and renewable energy technologies for energy transition in high mountain areas post-pandemic," CD 82605 CT ICETEX 2022-0644.

## REFERENCES

1. José Luis Torres-Madroñero, César Nieto-Londoño, Erika Arenas-Castiblanco, Zulamita Zapata-Benabithe, Hussam Jouhara. Multi-objective optimisation of hybrid renewable energy systems for Colombian non-interconnected zones, *Therm. Sci. Eng. Prog*. 55 (2024) https://doi.org/10.1016/j.tsep.2024.102927.
2. International Energy Agency – IEA. Climate change: Energy and climate are inextricably linked (2023). https://www.iea.org/topics/climate-change
3. United Nations, The Sustainable Development Goals Report 2023: Special edition. https://unstats.un.org/sdgs/report/2023/The-Sustainable-Development-Goals-Report-2023.pdf
4. Climate Transparency. The Country Profile of Colombia (2020). https://www.climate-transparency.org/wp-content/uploads/2021/01/Colombia-CT-2020.pdf
5. Oscar Pupo-Roncallo, Javier Campillo, Derek Ingham, Kevin Hughes, Mohammed Pourkashanian. Large scale integration of renewable energy sources (RES) in the future Colombian energy system, *Energy* 186 (2019) https://doi.org/10.1016/j.energy.2019.07.135.
6. Congress of Colombia, Law 1715 of 2014, Whereby the integration of non-conventional renewable energies to the National Energy System is regulated (In Spanish).
7. Arıkan Kargı, Vesile Sinem, and Fatma Cesur. Renewable Energy Technology Selection for Hotel Buildings: A Systematic Approach Based on AHP and VIKOR Methods. *Buildings* 14, 9: 2662 (2024) https://doi.org/10.3390/buildings14092662
8. Xiangguo Xu, Zhe Zhang, Jiawei Yuan, Junqiang Shao. Design and multi-objective comprehensive evaluation analysis of PV-WT-BG-Battery hybrid renewable energy systems in urban communities, *Energy Convers. Manag.: X* 18 (2023) https://doi.org/10.1016/j.ecmx.2023.100357.
9. Tausif Ali, Ahmed Jaudat Nahian, Hongzhong Ma. A hybrid multi-criteria decision-making approach to solve renewable energy technology selection problem for Rohingya refugees in Bangladesh, *J. Clean. Prod.*, 273 (2020)
10. Comisión de Regulación de Energía y Gas – CREG. Definition of the electricity tariff formula for the next tariff period (In Spanish) (2005)
11. International Renewable Energy Agency – IRENA. Renewable Power Generation Costos in 2023, Abu Dhabi (2023)
12. DANE. Population projections and retroprojections for the period 1985-2017(In Spanish) (2020) https://www.dane.gov.co/index.php/estadisticas-por-tema/demografia
13. Ortiz-Flórez D.A. Estimation of the Demand for Electricity and Heat with Projection to the Year 2040 for Two Case Studies of the Páramo of Santurbán, (In Spanish), Bachelor Thesis, Universidad de Pamplona, Colombia (2022)

© 2025 by the authors. Licensed to PSEcommunity.org and PSE Press. This is an open access article under the creative commons CC-BY-SA licensing terms. Credit must be given to creator and adaptations must be shared under the same terms. See https://creativecommons.org/licenses/by-sa/4.0/



Systems & Control Transactions

**Research Article - Peer Reviewed Conference Proceeding**
ESCAPE 35 - European Symposium on Computer Aided Process Engineering
Ghent, Belgium. 6-9 July 2025
Jan F.M. Van Impe, Grégoire Léonard, Satyajeet S. Bhonsale,
Monika E. Polańska, Filip Logist (Eds.)

PSE PRESS

# A Comparison of Robust Modeling Approaches to Cope with Uncertainty in Independent Terms, considering the Forest Supply Chain Case Study

**Frank Piedra-Jimenez[a], Ana Inés Torres[b], and Maria Analia Rodriguez[a]***

[a] Universidad Nacional de Córdoba, CONICET, Instituto de Investigación y Desarrollo en Ingeniería de Procesos y Química Aplicada, Córdoba, Córdoba, Argentina
[b] Carnegie Mellon University, Department of Chemical Engineering, Pittsburgh, Pennsylvania, United States
* Corresponding Author: analia.rodriguez@unc.edu.ar.

## ABSTRACT

Uncertainty plays a crucial role in strategic supply chain design. In this study, we explore robust approaches to model uncertainty when the non-deterministic parameters are placed in the independent term, on the right-hand side (RHS) of the constraints. We consider the "disjunctive adjustable column-wise robust optimization" (DACWRO), a disjunctive formulation introduced previously in our group, and compare it with the adjustable column-wise robust optimization (ACWRO) formulation, a specific technique for solving robust optimization problems when the original robust optimization approach may assume too-conservative results. Given that the proposed method is based on the generalized disjunctive programming (GDP) technique, it is a higher lever modelling approach that represents the discrete nature of the decision process. In addition, it provides alternative MILP representations that can be further tested and compared. The analysis assesses the computational performance and reformulation tightness of both approaches in the context of the forest supply chain design problem.

**Keywords**: Design Under Uncertainty, Modelling, Optimization, Supply Chain, Biomass

## INTRODUCTION

The need to consider uncertainty in the decision-making process is widely acknowledged in the PSE community, which distinguishes three main modeling paradigms for optimization under uncertainty, namely robust optimization (RO), stochastic programming (SP), and chance-constrained programming (CCP). The last two paradigms are challenging due to the need for complete distributional knowledge or the involvement of non-linearities [1]. Instead, RO does not require the probabilistic behavior of uncertain parameters and strikes a good balance between solution quality and computational tractability [2].

One widely used method for RO is the static robust optimization one initially proposed by Bertsimas and Sim [3]. They proposed the budgeted uncertainty set, which allows flexible handling of the level of conservatism of robust solutions in terms of probabilistic limits of constraint violations. It defines for each uncertain parameter a deviation bound from its nominal value and a budget parameter to determine the number of uncertain parameters that are allowed to take their worst value in each equation. In the case that there is only one uncertain parameter in the independent term, on the RHS of the equations, this method may adopt a too-conservative perspective, considering the worst-case scenario for each constraint.

To address this concern, an extension of this method is proposed in [4] and applied to the water distribution system design problem. This method is recognized to better handle uncertainty in this context, such as in [5,6]. The method is called “adjustable column-wise robust optimization” (ACWRO) because it defines the number of uncertain realizations that the decision-maker is willing to satisfy. Initially presented as a nonlinear model, it is later reformulated to achieve a linear formulation.

Motivated by the disjunctive nature of the decision process of this case, the present paper proposes an alternative method applying a linear disjunctive

formulation, called "disjunctive adjustable column-wise robust optimization" (DACWRO). One of the contributions of this article is that it extends the use of Generalized Disjunctive Programming (GDP) to a new application domain. Additionally, taking advantage of the high-level representation capability of GDP, Big-M and Hull MILP reformulations are derived from the proposed formulation. Here, the proposed method is applied to the forest supply chain design problem and it is compared with the ACWRO approach for a large number of instances showing the tightness of each reformulation and computational performance.

## DISJUNCTIVE ADJUSTABLE COLUMN-WISE ROBUST OPTIMIZATION APPROACH

In this section, we develop the DACWRO approach to deal with uncertainty when there is only one uncertain parameter in the constraint and it is on the right-hand side (RHS) of the equation. The novel approach is an alternative robust reformulation of the ACWRO. For details of this approach, the reader is referred to this reference [4]. Let us examine the following linear optimization model:

$$Min\ Z = \sum_j c_j \cdot x_j \tag{1}$$

$$\sum_j A_{i,j} \cdot x_j \geq \tilde{b}_i \quad \forall i \tag{2}$$

$$L \leq x_j \leq U \quad \forall i \tag{3}$$

where $\tilde{b}_i$ are the uncertain parameters. Here, the uncertain realization of each $\tilde{b}_i$ is handled by a box uncertainty set $U_{box} = \{(\boldsymbol{b}|b_i^L \leq \tilde{b}_i \leq b_i^U, \forall i)\}$. This defines the range of each uncertain parameter in the vector of uncertain parameters $\boldsymbol{b}$. That is, $b_i^L$ and $b_i^U$ represent the lower and the upper bounds of each uncertain parameter, respectively. Assuming a symmetric variation of the uncertain parameter, Eqs. (4) and (5) are presented:

$$b_i - \hat{b}_i = b_i^L \quad \forall i \tag{4}$$

$$b_i + \hat{b}_i = b_i^U \quad \forall i \tag{5}$$

where $b_i$ is the nominal value and $\hat{b}_i$ represents the maximal absolute variation that the uncertain parameter is subject to change. In the robust approach, each uncertain parameter $\tilde{b}_i$ is transformed into a decision variable that represents the value of the uncertain parameter the decision maker is willing to satisfy. Given Eqs. (4) and (5), this variable can be expressed by a new variable $\eta_i = (\tilde{b}_i - b_i)/\hat{b}_i$ that takes values in the interval $[-1,1]$. Additionally, a new redundant constraint is introduced, i.e., Eq. (2) is summed for all *i* and the RHS is rewritten in terms of parameters $b_i$, $\hat{b}_i$ and variable $\eta_i$, in Eq. (6).

$$\sum_i \sum_j A_{i,j} \cdot x_j \geq \sum_i b_i + \sum_i \eta_i \cdot \hat{b}_i \tag{6}$$

Eq. (6) is now rewritten as (7) introducing a protection function, where larger values of $\sum_i \eta_i \cdot \hat{b}_i$ result in higher protection against uncertainty. Thus, Eq. (6) is replaced by Eq. (7) and the variable $\eta_i$ takes values in the interval $[0,1]$. Note that $I$ is a set of uncertain parameters, $S_i$ is the subset of $I$ that takes their worst-case values. The number of elements of $S_i$ is given by the budget parameter $\Gamma$, that indicates the level of conservatism of the system. Conceptually, the protection function is a fundamental goal of robust optimization: finding a solution that not only maximizes the objective function *Z* but also assures that *Z* remains optimal with high probability given some error in predicting $\tilde{b}_i$ values [3]. This inner problem is reformulated by Eqs. (8) - (10).

$$\sum_i \sum_j A_{i,j} \cdot x_j \geq \sum_i b_i + \max_{\{S_i | S_i \subseteq I, |S_i| = \Gamma\}} \{\sum_i \eta_i \cdot \hat{b}_i\} \tag{7}$$

$$Max \sum_i \eta_i \cdot \hat{b}_i \tag{8}$$

$$0 \leq \eta_i \leq 1 \quad \forall i \tag{9}$$

$$\sum_i \eta_i \leq \Gamma \tag{10}$$

Given that problem in Eqs. (8)–(10) is feasible and bounded by $\Gamma$, its dual pair is also feasible and bounded with the identical objective value according to the strong duality property. The problem in Eqs. (1)–(3), (7)–(10) is reformulated as Eqs. (1), (3), (11)–(13).

$$\sum_i \sum_j A_{i,j} \cdot x_j \geq \sum_i b_i + \Phi \cdot \Gamma + \sum_i \Omega_i \tag{11}$$

$$\Phi + \Omega_i \geq \hat{b}_i \quad \forall i \tag{12}$$

$$\sum_j A_{i,j} \cdot x_j \geq b_i + \hat{b}_i \quad \forall i \tag{13}$$

Note that Eq. (11) is equivalent to Eq. (7) where $\Phi$ and $\Omega_i$ are dual variables. Variable $\Phi$ represents the common variation for all $b_i$ elements, i.e., $\Phi$ remains constant for each uncertain constraint $i \in I$, but the value of $\Omega_i$ differs according to the corresponding value of $\hat{b}_i$. Equation (12) determines to the sum of the dual variables corresponding to each equation from the primal model (Eq. (8) – (10)), while Eq. (13) replaces Eq. (2) assuming the Bertsimas and Sim approach [3]. That is, the worst-case scenario is assumed for each constraint subject to this type of uncertainty.

As mentioned, the aim of the proposed approach, as in [4], is to define the degree of uncertainty the decision maker is willing to cover. For this purpose, a disjunctive formulation is introduced to control the degree of conservatism $\Gamma$. Equation (13) is replaced by Eqs. (14) – (17). Note that Eqs. (14) and (15) ensure that for all $i \in I$, the uncertain parameter will remain between its nominal value and its worst-case value. The disjunction is introduced in Eq. (16) where $\Psi_i$ is a Boolean variable. In the positive case, the uncertain parameter of constraint $i \in S_i$ must take its worst value, which is determined by the auxiliary variable $\Lambda_i$ that is equal to the sum of the dual variables ($\Phi$ and $\Omega_i$) generated from the robust

reformulation. In the negative case ($\neg\Psi_i$), the uncertain parameter remains at its nominal value. Therefore, auxiliary variable $\Lambda_i$ and the specific variation of element $b_i$ determined by dual variable $\Omega_i$ are zero. Finally, the number of uncertain parameters that take their worst-case value is controlled by the $\Gamma$ parameter, as shown in Eq. (17). Note that the degree of conservatism ($\Gamma$) must necessarily be an integer parameter that takes values in the range $[0, |S_i|]$. Finally, DAWRO formulation is given by Eqs. (1), (3), (11)–(12), (14)–(17).

$$\sum_j A_{i,j} \cdot x_j \leq b_i + \hat{b}_i \qquad \forall i \qquad (14)$$

$$\sum_j A_{i,j} \cdot x_j \geq b_i + \Lambda_i \qquad \forall i \qquad (15)$$

$$\begin{bmatrix} \Psi_i \\ \Lambda_i = \Phi + \Omega_i \\ \psi_i = 1 \end{bmatrix} \vee \begin{bmatrix} \neg\Psi_i \\ \Lambda_i = 0 \\ \Omega_i = 0 \\ \psi_i = 0 \end{bmatrix} \qquad \forall i \qquad (16)$$

$$\sum_i \psi_i \geq \Gamma \qquad (17)$$

## FOREST SUPPLY CHAIN RE-DESIGN AND PLANNING PROBLEM

In this section the case study is briefly described. The problem consists of the optimal design and planning of the forest supply chain in the Argentinean context. There are feedstock nodes that produce pine and eucalyptus logs, forest residues, and sawmill residues; the processing facilities convert biomass into paper pulp, fuels, and intermediates; and the consumer nodes are biodiesel plants or petroleum refineries. There are some fixed facilities and some potential locations for new stand-alone and integrated facilities. The model decides in each time period the location of forest nodes, harvesting decisions, technologies and capacity levels in the industrial locations, product mix, production levels and compounds' flows along all transportations links to meet specific demand levels and minimize present costs. The complete model formulation and case study data is presented in [7]. Let introduce the uncertain constraint from this formulation given by Eq. (18), which means that the amount of product *o* delivered to each demand node *l* in each period *t* must satisfy the demand level given by uncertain parameter $\widetilde{\chi_{o,l,t}}$.

$$\sum_{\substack{m,k \\ m \in M_O}} F3_{o,k,m,l,t} \geq \widetilde{\chi_{o,l,t}} \qquad \forall\, (o,l) \in O_L, t \qquad (18)$$

Applying the proposed robust reformulation, the following set of constraints is introduced, as shown in Eqs. (19) – (24).

$$\sum_{\substack{o,k,m,l,t \\ m \in M_O \\ (l,o) \in O_L}} F3_{o,k,m,l,t} \geq \sum_{\substack{o,l,t \\ (l,o) \in O_L}} \left(\chi_{o,l,t} + \Omega_{o,l,t}\right) + \Phi^{de} \cdot \Gamma^{de} \qquad (19)$$

$$\Phi^{de} + \Omega_{o,l,t} \geq \hat{\chi}_{o,l,t} \qquad \forall\, (o,l) \in O_L, t \qquad (20)$$

$$\sum_{\substack{m,k \\ m \in M_O}} F3_{o,k,m,l,t} \leq \chi_{o,l,t} + \hat{\chi}_{o,l,t} \quad \forall\, (o,l) \in O_L, t \qquad (21)$$

$$\sum_{\substack{m,k \\ m \in M_O}} F3_{o,k,m,l,t} \geq \chi_{o,l,t} + \Lambda_{o,l,t} \quad \forall\, (o,l) \in O_L, t \qquad (22)$$

$$\begin{bmatrix} \Psi^{de}_{o,l,t} \\ \Lambda_{o,l,t} = \Phi^{de} + \Omega_{o,l,t} \\ \psi^{de}_{o,l,t} = 1 \end{bmatrix} \veebar \begin{bmatrix} \neg\Psi^{de}_{o,l,t} \\ \Lambda_{o,l,t} = 0 \\ \Omega_{o,l,t} = 0 \\ \psi^{de}_{o,l,t} = 0 \end{bmatrix} \quad \forall\, (o,l) \in O_L, t \qquad (23)$$

$$\sum_{\substack{o,l,t \\ (l,o,t) \in O_L}} \psi^{de}_{o,l,t} \geq \Gamma^{de} \qquad (24)$$

This formulation can be reformulated by applying Big-M and Hull reformulations, which are called DACWRO-BM and DACWRO-H, respectively.

## RESULTS AND DISCUSSION

The key features and dimensions of the sample runs are outlined in Table 1. Four supply chain structures are set corresponding to each example. For each example, a set of instances is determined by varying the budget parameter (third column). The number of instances for each example is presented in the fourth column. Model sizes are displayed in the last three columns. The supply chain structure in Example 1 has 10 supply sources, 3 kraft pulp mills, 13 potential biorefinery locations, and 10 demand nodes. In subsequent examples, the number of nodes gradually increased to 25 supply nodes and 23 demand nodes. Different levels of deviation in uncertain demand parameters are also considered.

Figure 1 shows that all approaches present very similar performance in terms of the mean value of the CPU time. As expected, as the size of the examples are increased, the execution time is also greater. In examples 1 to 3, all instances tested present an execution time near the mean value. However, heterogenous results are obtained among instances of example 4, that is, large dispersion is observed in the execution time, showing data dependency when the size of the model is increased. Figure 2 presents the ratio of the relaxed solution in the root node with respect to the final optimal solution for each method. It is noteworthy that the three methods present very tight results and they are homogeneous among the examples and approaches. Note that all mean values of this ratio are the same for each method what may explain the similar performance in terms of CPU time (Fig. 1). DACWRO is as good as the ACWRO in terms of computational performance, but it represents the disjunctive nature of level of uncertainty selection process in a more

straightforward way.

**Table 1**. Features of executed examples and their size

| Example | Reformulation | Budget parameter | Number of instances executed | Number of equations | Number of continuous variables | Number of binary variables |
|---|---|---|---|---|---|---|
| 1 | ACWRO | 20 to 70 | 6 | 27721 | 30531 | 2700 |
| 1 | DACWRO-BM | 20 to 70 | 6 | 27721 | 30531 | 2700 |
| 1 | DACWRO-H | 20 to 70 | 6 | 27791 | 30671 | 2700 |
| 2 | ACWRO | 30 to 100 | 24 | 29911 | 48261 | 2730 |
| 2 | DACWRO-BM | 30 to 100 | 24 | 29911 | 48261 | 2730 |
| 2 | DACWRO-H | 30 to 100 | 24 | 30011 | 48461 | 2730 |
| 3 | ACWRO | 10 to 150 | 30 | 30261 | 49311 | 2780 |
| 3 | DACWRO-BM | 10 to 150 | 30 | 30261 | 49311 | 2780 |
| 3 | DAWRO-H | 10 to 150 | 30 | 30811 | 50761 | 2780 |
| 4 | ACWRO | 10 to 200 | 30 | 45291 | 75461 | 3890 |
| 4 | DACWRO-BM | 10 to 200 | 30 | 45291 | 75461 | 3890 |
| 4 | DACWRO-H | 10 to 200 | 30 | 45591 | 76061 | 3890 |

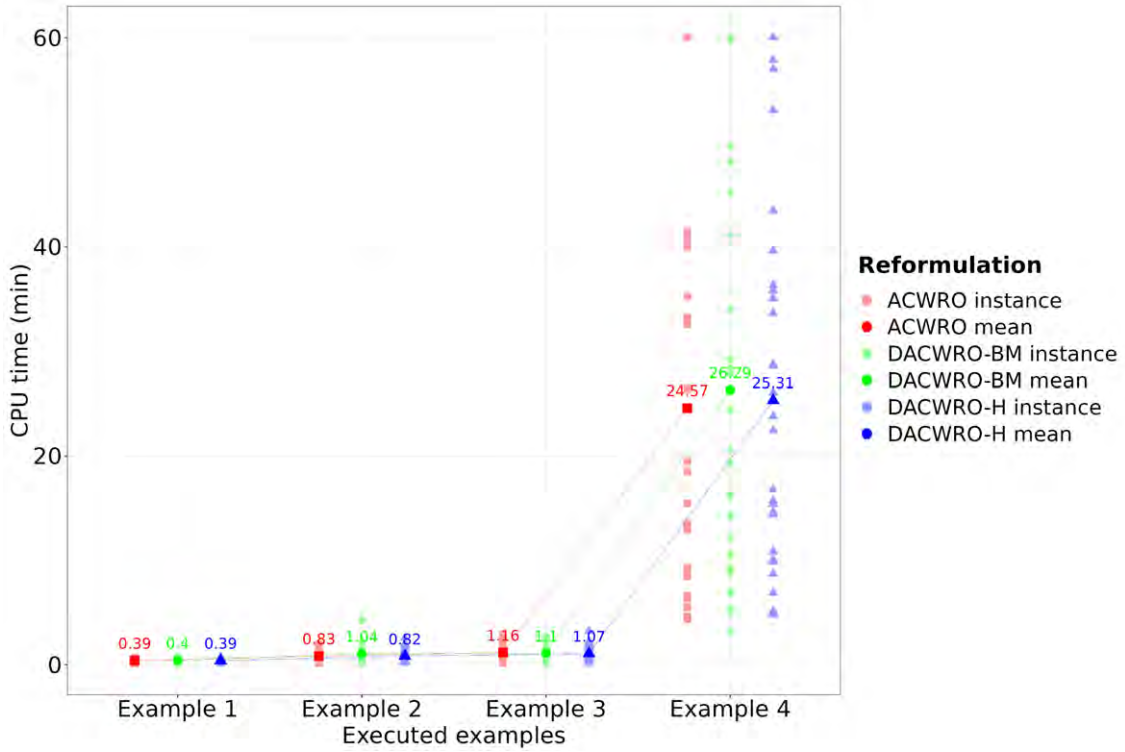



**Figure 1**. Execution time (min).

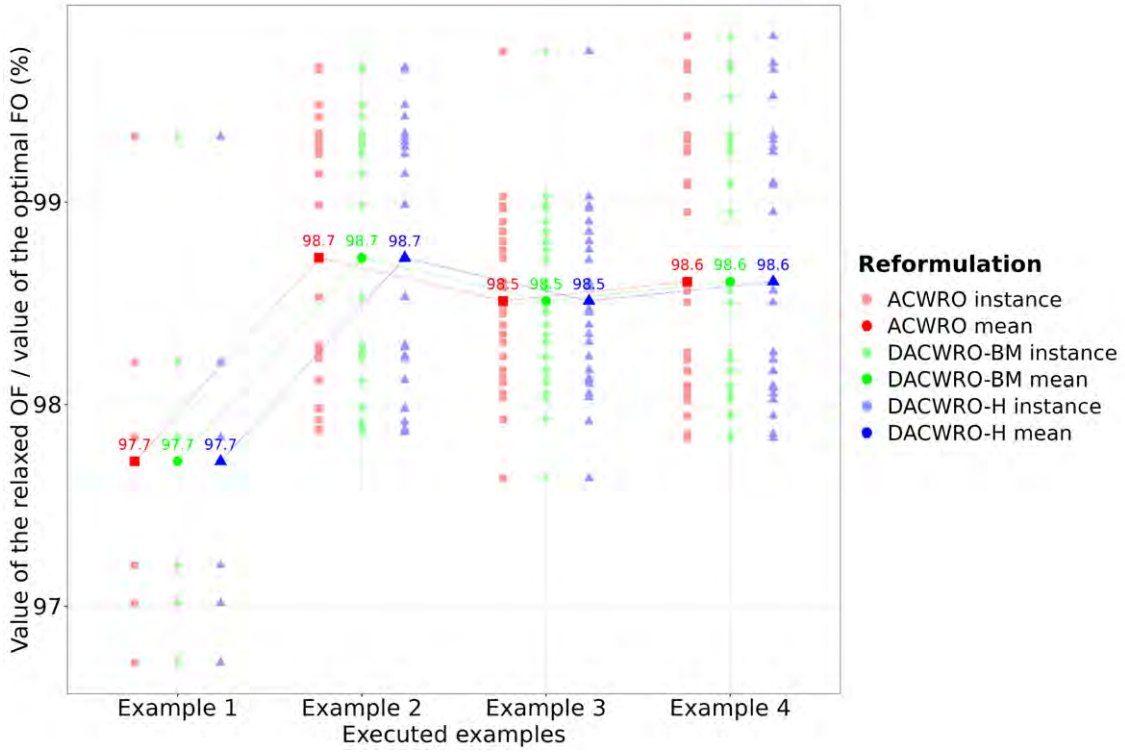



**Figure 2**. Initial relaxed solution vs. optimal solution.

## CONCLUSIONS

In this article a new method, named DACWRO, is proposed to model uncertainty that is compared to ACWRO [4]. These methods present the advantage that the decision maker can select the level of conservatism is willing to assume. These approaches are particularly interesting in the case the uncertain parameters are part of the independent term of the equations. The proposed method is based on a disjunctive formulation that is reformulated applying Big-M and Hull relaxations to obtain the equivalent mixed integer linear models.

To compare the approaches, the formulations were applied to the forest supply chain design problem assuming uncertainty in the demand constraints. A set of 270 instances were executed. From the instances tested, due to a tight reformulation, efficient and homogeneous results are obtained in all cases. The proposed method extends the use of GDP to a novel application domain. Additionally, it capitalizes on the high-level representational power of GDP to develop Big-M and Hull MILP reformulations based on the proposed formulation. Future work includes analyzing larger instances to evaluate the behaviour of the approaches for more challenging cases as well as expanding the scope of the present approach to other types of uncertainties. Also, new problem domains and case studies will be considered to check differences between methods in other contexts.

## ACKNOWLEDGEMENTS

The authors would like to acknowledge ANPCyT, through project PICT 2019-4162, for funding this contribution.

## REFERENCES

1. Chen Y, Yuan Z, Chen B. Process optimization with consideration of uncertainties—An overview. *Chinese J. Chem. Eng.* 26:1700–1706 (2018) https://doi.org/10.1016/j.cjche.2017.09.010
2. Ning C, You F. Optimization under uncertainty in the era of big data and deep learning: When machine learning meets mathematical programming. *Comput. Chem. Eng.* 125:434–448 (2019) https://doi.org/10.1016/j.compchemeng.2019.03.034
3. Bertsimas D, Sim M. The Price of Robustness. *Oper. Res.* 52:35–53 (2004) https://doi.org/10.1287/opre.1030.0065
4. Ghelichi Z, Tajik J, Pishvaee MS. A novel robust

optimization approach for an integrated municipal water distribution system design under uncertainty: A case study of Mashhad. *Comput. Chem. Eng.* 110: 13–34 (2018) https://doi.org/10.1016/j.compchemeng.2017.11.017
5. Razm S, Dolgui A, Hammami R, Brahimi N, Nickel S, Sahebi H. A two-phase sequential approach to design bioenergy supply chains under uncertainty and social concerns, *Comput. Chem. Eng.* 145:107131 (2021) https://doi.org/10.1016/j.compchemeng.2020.107131
6. Razm S, Brahimi N , Hammami R, Dolgui A. Row and column-wise robust optimization model for biorefineries storing perishable biomass under weather uncertainty: Boosted by machine learning, *Comp. & Ind. Eng.*, 200:110823 (2025) https://doi.org/10.1016/j.cie.2024.110823
7. Piedra-Jimenez F, Torres AI, Rodriguez MA. "A robust disjunctive formulation for the redesign of forest biomass-based fuels supply chain under multiple factors of uncertainty". *Comput. Chem. Eng.* 181:108540 (2024) https://doi.org/10.1016/j.compchemeng.2023.108540

© 2025 by the authors. Licensed to PSEcommunity.org and PSE Press. This is an open access article under the creative commons CC-BY-SA licensing terms. Credit must be given to creator and adaptations must be shared under the same terms. See https://creativecommons.org/licenses/by-sa/4.0/



Systems & Control Transactions

**Research Article - Peer Reviewed Conference Proceeding**
ESCAPE 35 - European Symposium on Computer Aided Process Engineering
Ghent, Belgium. 6-9 July 2025
Jan F.M. Van Impe, Grégoire Léonard, Satyajeet S. Bhonsale,
Monika E. Polańska, Filip Logist (Eds.)

PSE PRESS

# Introducing Competition in a Multi-Agent System for Hybrid Optimization

**Veerawat Udomvorakulchai[a*], Miguel Pineda[a], and Eric S. Fraga[a]**

[a] Sargent Centre for Process Systems Engineering, University College London (UCL), Gower Street, London WC1E 7JE, United Kingdom
* Corresponding Author: veerawat.udomvorakulchai.22@ucl.ac.uk.

## ABSTRACT

Process systems engineering optimization problems may be challenging. These problems often exhibit nonlinearity, non-convexity, discontinuity, and uncertainty, and often only the values of objective and constraint functions are accessible. Additionally, some problems may be computationally expensive. In such scenarios, black-box optimization methods may be appropriate to tackle such problems. A general-purpose multi-agent framework for optimization has been developed to automate the configuration and use of hybrid optimization, allowing for multiple optimization solvers, including different instances of the same solver. Solvers can share solutions, leading to better outcomes with the same computational effort. Alongside cooperation, competition is introduced by dynamically allocating more computational resource to solvers best suited to the problem. Each solver is assigned a priority that adapts to the evolution of the search. The scheduler is priority-based and uses similar algorithms to those in multi-tasking operating systems. The impact on the number of priority levels is investigated. The framework allows for the use of both metaheuristic and direct search methods. Metaheuristics explore the full search space while direct search methods are good at exploiting solutions. The framework has been implemented in Julia, making full use of multiprocessing. A multiobjective case study on the design of a micro-analytic system is presented. The case study demonstrates the benefits of a multi-solver hybrid optimization approach with both cooperation and competition. The framework adapts to the evolving requirements of the search. Often, a metaheuristic method is allocated more computational resource at the beginning of the search while direct search methods are prioritized later.

**Keywords**: multi-agent systems, hybrid solution methods, computational resource allocation, multiobjective optimization

## INTRODUCTION

Solving optimization problems in process systems engineering is often a challenging endeavor. These problems may exhibit nonlinearity, non-convexity, discontinuity, and uncertainty, which render derivative information unavailable or difficult to obtain. As a result, gradient-based optimization methods may not be appropriate. Instead, black-box optimization methods may be more convenient for tackling such problems as they require only the values of objective functions.

For some optimization problems in process systems engineering there may be another challenge: the computational expense required to evaluate the models may be large, such as when the models are based on differential equations. For problems that have high computational requirements, the number of times the objective function and the constraints may be evaluated will be limited. In these cases, the efficient use of multiple cooperating optimization methods may be necessary. Prior experience suggests that hybrid approaches can lead to better outcomes compared with using a single optimization method, with the same computational effort [1,2]. However, the effectiveness of each method depends on the problem and may actually vary throughout the search, posing difficulties for decision-makers in selecting the appropriate optimization methods. To address this, this paper introduces competition among optimization methods in the multi-agent system to dynamically allocate a finite computational resource. The aim is to have the

most effective methods given access to the resource at the right time during the evolution of the search.

## MULTI-AGENT FRAMEWORK

A multi-agent system consists of multiple autonomous computing elements, referred to as *agents*, that interact with one another by sending and receiving *messages* [3]. Such an environment can be used to facilitate the hybridization of optimization methods by assigning optimization methods to agents, with the agents working together to solve the same problem [4]. This concept has been exemplified in works such as [5] and [6].

A general-purpose multi-agent framework for solving optimization problems has recently been developed [1] to automate the configuration and use of hybrid optimization. This framework enables the use of multiple solvers to solve a given optimization problem, whether it is an NLP or MINLP. The solvers may be different optimization methods or variations of the same method with different parameter settings, a concept also used in [7]. Since the parameters associated with an optimization method affect its behavior, and identifying appropriate values often requires significant experimentation, incorporating variations of the same method may be beneficial.

A key distinction of this implementation is the decoupling of solvers from the model evaluation process. In this setup, the solvers do not have direct access to the model, which enables the implementation of a *scheduler* agent that allocates the computational resource to different solvers more efficiently.

The framework is implemented in the Julia programming language, which provides easy access to CPU threads and enables the full use of multiprocessing.

The multi-agent system includes the following agents:

- Multiple instances of a **solver agent** where each instance is a particular optimization method with specific parameter values;
- One or more instances of a **model agent**; this agent evaluates the model when given a point in the search space;
- A **scheduler agent** whose duty is to allocate points requested by the solvers to available model agents, based on the information provided by the analysis agent;
- The **analysis agent** which analyzes all evaluated points and provides the scheduler with information about the search domain, aiding in managing competition among solvers.

One feature of this framework is *cooperation*, where solvers share information at the scheduler agent level with support from the analysis agent. The purpose is to guide the search toward the most promising regions in the search space by distributing useful information about the search domain.

## INTRODUCING COMPETITION

The concept of competition is to reward the more effective solvers and penalize those that are not as effective. The reward consists of allowing more evaluations of points in the search requested by the solver agents. It is hoped that this will ensure the best use of the typically limited computational resource available. It is expected that the effectiveness of different solvers will vary during the evolution of the search. Therefore, the reward mechanism needs to be adaptive and based on the actual performance as the search progresses.

Competition among solvers is implemented by the scheduler agent. This agent manages two queues (shown in Figure 1):

- **Availability queue**, a single queue for messages from the model agents indicating their availability to accept a point for model evaluation;
- **Request queue**, consisting of $n_l$ levels of first-in-first-out (FIFO) queues for requests from solver agents for evaluation of a point in the search domain, where $n_l$ represents the highest priority level set by the user.

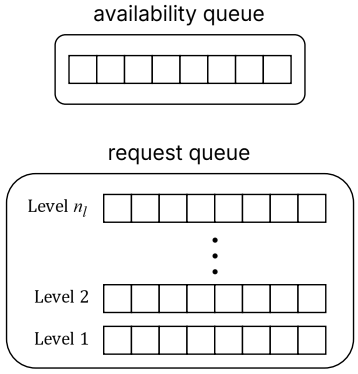



**Figure 1.** Data structures of the queues managed by the scheduler.

Each solver is assigned a priority [8], ranging from 1 to $n_l$. The value of $n_l$ is a configuration parameter for the agent system. The impact of the value of this parameter on the performance of the system is discussed below. The priority determines the placement of each request in the request queue and implicitly determines the solver's access to a model agent, with requests at the highest priority level gaining access first. These priorities are dynamic and subject to being adjusted throughout the search based on each solver's performance, also

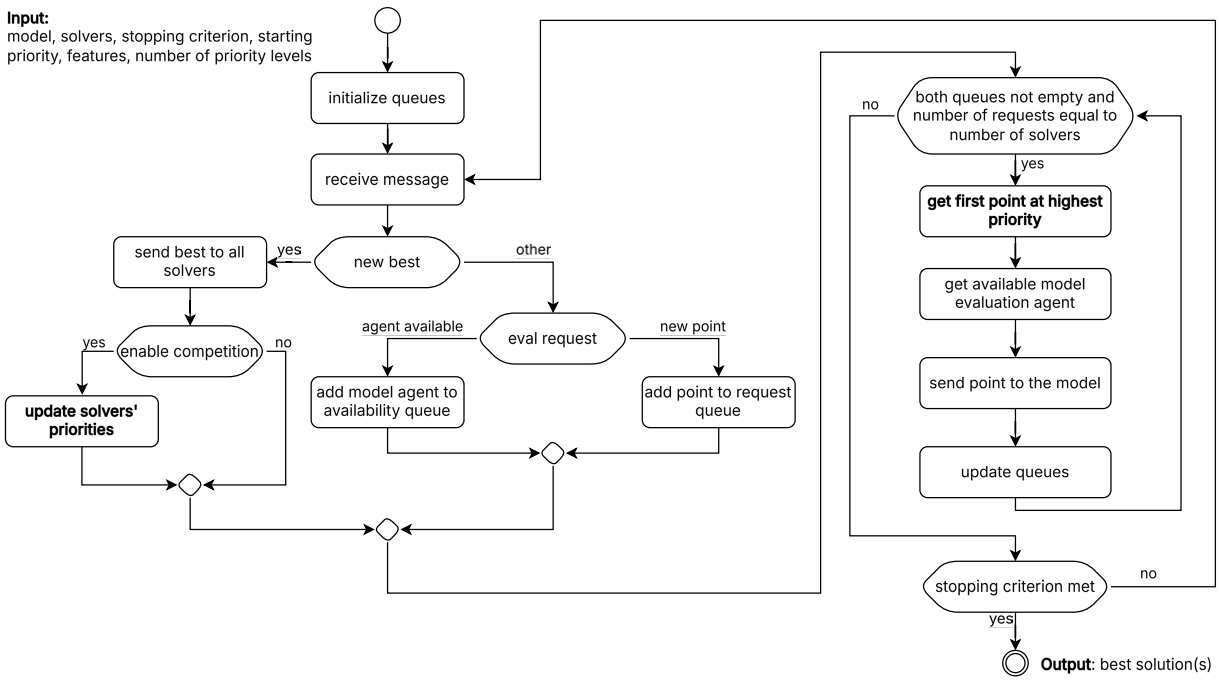



**Figure 2:** Flowchart illustrating the scheduler agent's process for allocating requests to model agents and managing competition when a new best message is received.

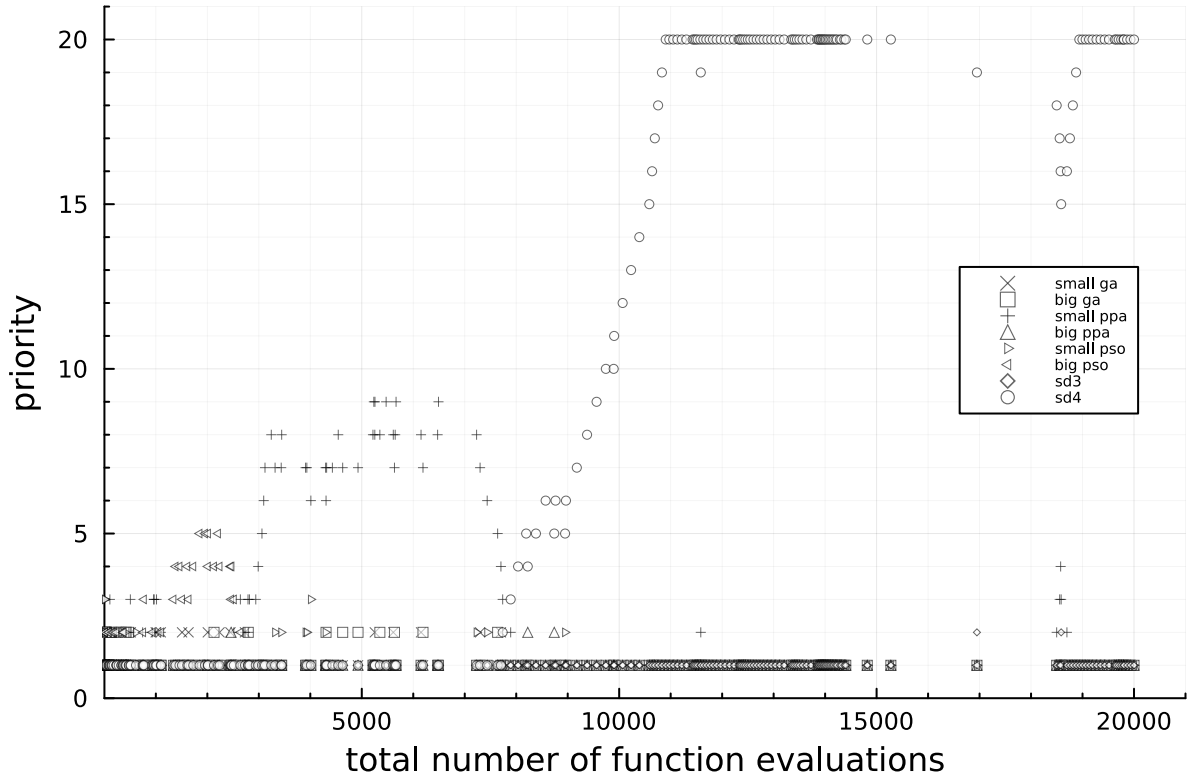



**Figure 3:** Priority profile of solvers when incorporating both cooperation and competition with 20 priority levels.

described below.

The flowchart in Figure 2 illustrates the main loop of the scheduler in the multi-agent system. Within this loop, the scheduler waits for incoming messages. The element

of competition comes into play when the scheduler receives a new *best* message from the analysis agent, indicating an improvement in the currently best known solution (or the introduction of a new point into the set of non-dominated points). This message contains information about the solution and the solver responsible for it. A solver that is responsible for the improvement is *rewarded* with an increase in its priority, while the priorities of other solvers may be *decreased*, provided they are not already at the lowest level.

Other messages the scheduler may receive can come from a solver agent or a model agent. Based on the type of message, each message is then processed and added to its corresponding queue, either the request queue or the availability queue. For requests from solver agents, this particular message (point) is placed at a specific level of the request queue according to the priority of the solver at the time the request is sent.

The scheduling of the queues occurs when both queues are not empty, and the number of requests is equal to the number of solvers. This assumes that all solvers will continue to submit points for evaluation, which may not be the case for direct search methods in general, as there may be cases where the direct search methods run out of points. For the problems we have considered, the issue has not arisen, but we will, in the future, generalize this condition to ensure that deadlock does not occur. The first point at the highest priority level in the request queue is dispatched to an available model agent. The request queue is then updated: the first entry in each FIFO queue is moved to the end of the next higher priority level if not already at the highest level. This scheduling approach resembles that used in the implementation of multitasking in operating systems [9], ensuring that all solvers are eventually allocated some computational resource.

There are different approaches to adjusting the priority levels and several such approaches have been investigated. One approach involves introducing a decay function for priorities as a function of the number of function evaluations. This decay function, however, introduces an additional configuration parameter. It may be difficult to identify *a priori* an appropriate value of this parameter for any given problem. Another approach considers adjusting the priority increment proportionally to the improvement in the objective function value when a solver finds a new best solution. However, this method is difficult to implement for multi-objective problems as it is difficult to define a metric which quantifies the quality of non-dominated solutions. The approach used in the results presented below is the simplest: reward the solver responsible for the improvement in the best known solution by increasing its priority by one and reducing the priorities of all the other solvers by the same magnitude.

## CASE STUDY: A DESIGN OF A MICROFLUIDIC ANALYSIS SYSTEM

An optimization-based design of a micro total analytic system ($\mu$TAS) for on-line detection of radionuclides [10] is presented to examine the impact of incorporating the element of competition into the framework. The goal of the design is to detect and identify the presence of two different radionuclides. The identification of designs is a problem of design under *uncertainty*, formulated as a set of differential equations with continuous design variables. This problem involves two objective functions: the first minimizes the system's limit of detection ($\phi$), and the second combines the number of false negatives ($n_f$) and false positives ($n_p$), with greater emphasis placed on the number of false negatives due to safety reasons.

This problem serves as a good test case for the proposed framework, as the problem is computationally expensive, and the search space is likely multi-modal [10]. Prior experience has demonstrated the benefits of information sharing; however, introducing competition may offer the potential for further improvement in outcomes more quickly.

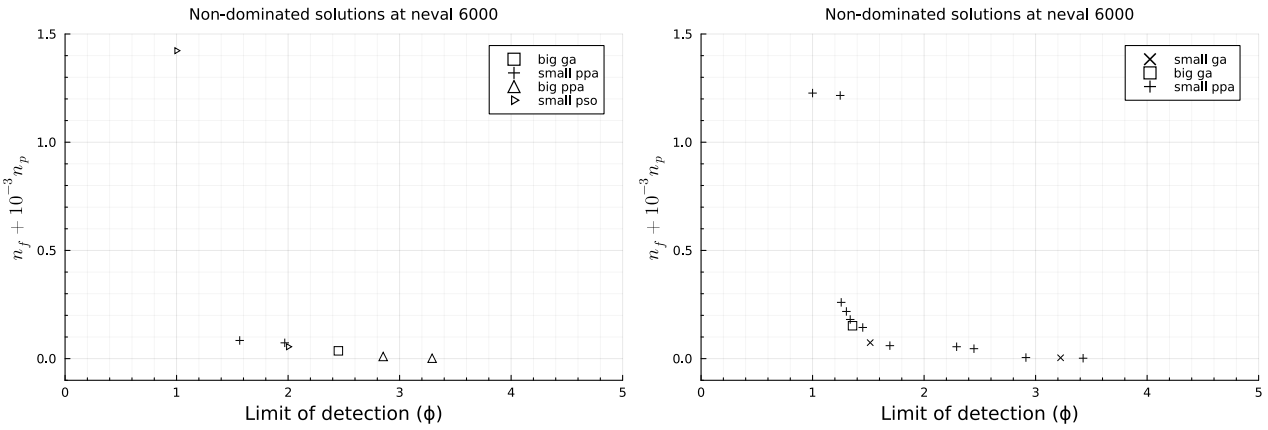
This study employs two types of solvers: nature-inspired metaheuristic methods [11] and direct search methods [12]. The solvers used are as follows:

- Genetic Algorithm (GA)
- Plant Propagation Algorithm (PPA)
- Particle Swarm Optimization (PSO)
- Steepest Descent (SD)
- Coordinate Search (CS)

The key parameter for the GA and the PSO methods is the population size; for the PPA, it is the number of solutions considered for propagation. Multiple instances of the solvers are explored using different parameter values, defined as a function of the base population size, $n_s$ (set to 20 in this case study). For the GA, the population sizes are $2 \times n_s$(small) and $5 \times n_s$ (big). For the PPA, the number of solutions to propagate is $n_s/2$ (small) and $2 \times n_s$ (big). For the PSO, the sizes are $n_s$ (small) and $5\times n_s$ (big).

The instances of direct search methods, on the other hand, are explored by assigning different weighting factors, $\omega$, used in the weighted sum method to aggregate multiple objectives into a single objective function value. Four weighting factors are applied: 0.2, 0.4, 0.6, and 0.8. Direct search solvers treat the base initial population of size $n_s$ as a multi-start, initiating a search from each member of the population sequentially.

None of the implementations here could be considered the *best in class*, but we intend to assess the performance of the collection of algorithms to investigate




(a) Cooperating (b) Cooperating and competing ($n_l$=20)

**Figure 4:** Non-dominated solution sets at 6,000 function evaluations with different configuration settings. *Neval* represents the total number of function evaluations, with each solution labeled by the responsible solver. $n_f$ and $n_p$ denote the number of false negatives and false positives, respectively.

the impact of cooperation and competition. The stopping criterion is set to 20,000 total function evaluations by all the solvers.

## Impact of competition

To investigate the impact of competition, a set of 10 runs has been conducted incorporating both cooperation and competition, with the number of priority levels, $n_l$=20. Figure 3 illustrates the priority profiles of each solver during the search, with output printed whenever a new non-dominated solution is identified. Solver instances for the direct search methods are distinguished by the suffixes 1, 2, 3, and 4 corresponding to the weighting factors of 0.2, 0.4, 0.6, and 0.8, respectively.

Two phases of the search can be observed from Figure 3. Initially, the search focuses on exploration, during which metaheuristic solvers, particularly the small PPA, frequently find new non-dominated solutions, as reflected in their increasing priority. This is followed by the exploitation phase, where the SD4 solver (a direct search method) identifies improved solutions, although typically minor improvements. Toward the end of the search, the small PPA identifies some new non-dominated solutions, which are promptly refined by one of the direct search solvers through information sharing, similar to the findings from the previous study [1]. The CS solvers are omitted from the figures as they do not ever find a non-dominated solution.

## Sensitivity to the number of priority levels

The number of priority levels, $n_l$, is a configuration parameter that may influence the performance of the system. Comparing sets of runs with different values of $n_l$,: 5, 10, and 20, two observations are found. First, a higher number of priority levels results in greater difference between computational resource allocated to the most effective solver and to the others, with the largest difference observed when $n_l$=20. This occurs because solvers require more iterations to transition from the lowest to the highest priority level. Second, the distinction between the exploration and exploitation phases of the search becomes more apparent with higher $n_l$ values. For example, when $n_l$=20, the exploration phase lasts shorter compared with $n_l$=10, whereas for $n_l$=5, this distinction is blurred. Therefore, it can be concluded that the number of priority levels determines the degree of competition among solvers. A higher number of priority levels closely resembles the individual use of the most effective solver, while lower values result in minimal competition.

Given the motivation of this paper–to make efficient use of a limited resources–we compare sets of non-dominated solutions at 6,000 total function evaluation (Figure 4), where the advantages of incorporating competition are evident. Under computational time constraints, the combined use of both cooperation and competition with 20 priority levels leads to the best outcomes, being able to explore the search space most effectively, with many points covering the objective space.

Although the solution sets in Figure 4 differ, quantifying which is better can be challenging, particularly as the true Pareto front is unknown in this case study. Nevertheless, the results show that incorporating competition alongside cooperation is likely to enhance the exploration process, with almost the same computational effort, and the degree of improvement depends on the number of priority levels. This is particularly beneficial when acceptable solutions are required with limited computational resource. Although the methods are stochastic and repeated attempts will lead to different outcomes, the results presented here are representative.

## CONCLUSION

A generic multi-agent framework for hybrid optimization has been developed to automate the configuration and integration of metaheuristic and direct search optimization methods. While information sharing among solvers has been shown to improve outcomes [1], equal allocation of computational resource to all solvers may not be ideal as optimization problems often have evolving requirements at different stages of the search. This motivates the use of competition alongside cooperation in the framework, enabling solvers to be dynamically prioritized based on performance. The framework is able to dynamically allocate computational resource as the search progresses, for instance, prioritizing metaheuristic methods to explore the search space at the start of the search and later shifting emphasis to direct search methods to refine the solutions. The overall outcome is more effective use of limited computational resource. The degree of competition is defined by the total number of priority levels, a key configuration parameter of the system.

Future work will explore more sophisticated scheduling algorithms within the scheduler agent and examine the potential benefits when the scheduler has the knowledge about the properties of the methods and the objective space.

## ACKNOWLEDGEMENTS

Mr. Veerawat is grateful for the support provided by the Royal Thai Government Scholarship, which covers his tuition fees and living stipends throughout the duration of his studies at University College London (UCL). The authors also gratefully acknowledge the funding received from UK Research & Innovation through the grant EP/R019223/1 which supported the development of the case study used in this paper.

## REFERENCES

1. Fraga ES, Udomvorakulchai V, Papageorgiou LG. A multi-agent system for hybrid optimization. In: 34th European Symposium on Computer Aided Process Engineering / 15th International Symposium on Process Systems Engineering. *Computer Aided Chemical Engineering* 53:3331-3336 (2024). https://doi.org/10.1016/B978-0-443-28824-1.50556-1
2. Fraga ES. Hybrid methods for optimisation. In: Computer Aided Methods in Optimal Design and Operations. Ed: Zilinskas J, Bogle IDL. World Scientific Connect (2006). https://doi.org/10.1142/9789812772954_0001
3. Wooldridge MJ. An Introduction to Multiagent Systems. 2nd Edition. Wiley (2009).
4. Silva MAL, De Souza SR, Souza MJF, et al. Hybrid metaheuristics and multi-agent systems for solving optimization problems: A review of frameworks and a comparative analysis. *Applied Soft Computing* 71:433-459 (2018).
5. Silva MAL, De Souza SR, Souza MJF, et al. A multi-agent metaheuristic optimization framework with cooperation. In: 2015 Brazilian Conference on Intelligent Systems (BRACIS). 104-109 (2015).
6. Ajmi F, Zgaya H, Othman SB, et al. Generic agent-based optimization framework to solve combinatorial problems. In: 2020 IEEE International Conference on Systems, Man, and Cybernetics (SMC). 950-956 (2020).
7. Gebreslassie BH, Diwekar UM. Homogenous multi-agent optimization for process systems engineering problems with a case study of computer aided molecular design. *Chemical Engineering Science* 159:194-206 (2017). https://doi.org/10.1016/j.ces.2016.05.026
8. Peterson JL, Silberschatz A. Operating System Concepts. Addison-Wesley Longman Publishing Co., Inc. (1983). ISBN 0201060973.
9. Madnick SE, Donovan JJ. Operating Systems. McGraw-Hill (1974). ISBN 0070394555.
10. Pineda M, Tsaoulidis D, Filho PIO, et al. Design optimization of microfluidic-based solvent extraction systems for radionuclides detection. *Nuclear Engineering and Design* 383:111432 (2021). https://doi.org/10.1016/j.nucengdes.2021.111432
11. Fraga ES, Nature inspired methods for optimization: A Julia primer for Process Engineering (2022). https://doi.org/10.5281/zenodo.7016482
12. Kelly CT. Iterative Methods for Optimization. SIAM (1999).

© 2025 by the authors. Licensed to PSEcommunity.org and PSE Press. This is an open access article under the creative commons CC-BY-SA licensing terms. Credit must be given to creator and adaptations must be shared under the same terms. See https://creativecommons.org/licenses/by-sa/4.0/



Systems & Control Transactions

**Research Article - Peer Reviewed Conference Proceeding**
ESCAPE 35 - European Symposium on Computer Aided Process Engineering
Ghent, Belgium. 6-9 July 2025
Jan F.M. Van Impe, Grégoire Léonard, Satyajeet S. Bhonsale,
Monika E. Polańska, Filip Logist (Eds.)

PSE PRESS

# A Component Property Modeling Framework Utilizing Molecular Similarity for Accurate Predictions and Uncertainty Quantification

**Youquan Xu[a], Zhijiang Shao[a], Anjan K. Tula[a,*]**

[a] State Key Laboratory of Industrial Control Technology, College of Control Science and Engineering, Zhejiang University, Hangzhou 310027, China
* Corresponding Author: anjantula@zju.edu.cn.

## ABSTRACT

A key step in developing high-performance industrial products lies in the design of their constituent molecules. Computer-aided molecular design (CAMD) has garnered significant attention for its potential to accelerate and improve the design process. The mainstream method involves using property prediction models to predict the properties of potential molecules and selecting the best candidates based on these predictions. However, prediction errors are inevitable, introducing unreliability into the design. To address this issue, this paper proposes a novel component property modeling framework based on a molecular similarity coefficient. By calculating the similarity between a target molecule and those in an existing database, the framework selects the most similar molecules to form a tailored training dataset. The similarity coefficient also quantifies the reliability of the property predictions. In tests across various properties, this framework not only provides a quantifiable evaluation of prediction reliability but also improves the prediction accuracy of molecules with high reliability, which has the potential to enhance the integrity of molecular design.

**Keywords**: Property prediction, Molecular design, Similarity coefficient

## 1. INTRODUCTION

Developing chemical products used as working media in industrial settings is a crucial aspect of the industrial process. One of the most important elements in this development is the design of molecular structures for these products. Traditional design methods, which rely on expert experience, are often time-consuming, labor-intensive, and prone to overlooking potentially excellent molecules. As a result, computer-aided molecular design (CAMD) is gaining increasing attention. This approach utilizes molecular property data in conjunction with efficient optimization algorithms to identify product molecules that exhibit optimal performance.

When designing a new product molecule, it is essential to predict the properties of unknown molecules based on existing molecular property data. This process is referred to as the property prediction model. The property prediction model primarily utilizes molecular structure information along with known data about molecular structures and their properties. It employs data fitting methods to establish the mapping relationship between molecular structures and their properties. Among the most classical molecular property prediction models are the Group Contribution (GC) method[1], Quantitative Structure-Property Relationship (QSPR) modeling[2], and ab initio quantum-mechanics-based methods[3]. With advancements in artificial intelligence, many new property prediction models and variations of classical models have been developed[4]. For instance, Zhang et al.[5] developed an accurate and interpretable QSPR molecular property prediction model based on deep neural networks. Alshehri et al.[6] introduced a new generation of molecular property prediction models based on Gaussian processes, which achieved higher accuracy compared to simpler GC-based models.

However, these models are not strictly mechanistic relationships between molecular structure and property,

so prediction errors are inevitable. In the process of molecular design using the property prediction model, the basis of molecular selection is the predicted value of molecular properties. Therefore, the prediction error of the property prediction model will directly affect the process of molecular screening, and easily lead to a serious mismatch between the properties of the designed molecules and the values of the experimentally verified properties. In other words, the reliability of the property prediction largely determines the reliability of the molecular design. At present, there is no quantitative method for the reliability of property prediction.

To solve this problem, this paper innovatively proposes a property prediction modeling framework based on molecular similarity. Firstly, this framework customizes a training set for the target molecules according to molecular similarity. The properties of target molecules are predicted using this training set, and the similarities between the molecules in the training set and the target molecules are used to provide a quantitative index of prediction reliability for target molecules.

## 2. MOLECULAR SIMILARITY COEFFICIENT

If the reliability of predicted property values can be assessed prior to experimental validation, the only information that can be utilized is that derived from the training molecules used in modeling these properties. Specifically, the adequacy of the information that training molecules provide for the target molecules is crucial. The greater the similarity between two molecules, the stronger the correlation in their properties. This similarity allows us to leverage the relationship between training and target molecules to gauge how adequately the training molecules can inform predictions about the target molecules. Consequently, it becomes possible to quantitatively measure the reliability of property predictions for the target molecules. Therefore, this paper introduces a novel method for calculating the molecular similarity coefficient.

Here, the group contribution method is used to describe the structure of a molecule. For molecules $M_1$ and $M_2$, their structures can be described as follows,

$$M_1: [n_{1\,1}, n_{1\,2}, n_{1\,3}, n_{1\,4}, \cdots, n_{1\,i}, \cdots, n_{1\,424}]$$

$$M_2: [n_{2\,1}, n_{2\,2}, n_{2\,3}, n_{2\,4}, \cdots, n_{2\,i}, \cdots, n_{2\,424}]$$

The 424 dimensions represent 424 groups which are used to form molecules [7,8]. $n_{1\,i}$ and $n_{2\,i}$ represent the number of the $i^{th}$ group inside the molecules. If a molecule doesn't have this group, then the value is just 0.

First, a classical mathematical method is introduced, that is, Jaccard similarity coefficient. It is an efficient tool to calculate the similarity between two sets. Its overall logic is to calculate the ratio of the number of elements in the intersection and union of two sets, and the general formula is as follows:

$$JSC(A,B) = \frac{|A \cap B|}{|A \cup B|} = \frac{|A \cap B|}{|A| + |B| - |A \cap B|}$$

Jaccard similarity coefficient ranges in [0,1]. Specially, when A is identical to B, then $JSC(A,B) = 1$. If two sets have no common elements, then $JSC(A,B) = 0$. If Jaccard similarity coefficient is directly applied to calculate the similarity between $M_1$ and $M_2$, the result is as follows.

$$\mathrm{JSC}(M_1, M_2) = \frac{\sum_1^{424} Minimum(n_{1\,i}, n_{2\,i})}{\sum_1^{424} Maximum(n_{1\,i}, n_{2\,i})}$$

However, this result only considers a molecule as a mathematical set containing the groups forming the molecule. In other words, it never considers the chemical features of a molecule, mainly the type of compound and the size of molecule here. As for the type of compound, the similarity of two molecules belonging to the same type of compound should be higher than that belonging to two different types of compounds. For example, based on the Jaccard similarity coefficient, the similarity of $CH_3(CH_2)_6SO_2CH_3$ and $CH_3(CH_2)_6CH_3$ is 0.89 while the similarity of $CH_3(CH_2)_6SO_2CH_3$ and $CH_3(CH_2)_4SO_2CH_3$ is 0.78. However, chemically speaking, the first set of molecules belong to two types of compounds and the second set of molecules belong to the same type of compound. Therefore, this leads to a phenomenon that the similarity of two molecules belonging to different types is higher than that belonging to the same type, which is unacceptable. As for the size of molecule, the difference of two molecules is determined by the absolute difference of the structure not the relative difference of the structure. For example, for molecules described by $[1,1,0,0,\cdots]$ and $[1,1,1,0,\cdots]$, their similarity is 0.67 while the similarity of molecules $[1,1,1,1,1,1,1,1,0,0,\cdots]$ and $[1,1,1,1,1,1,1,1,1,0,\cdots]$ is 0.89. The structure differences in these two sets of molecules are both one group, but their difference of similarity is so large. This is because of the difference of the molecular size. For small size of molecules, the effect of one different group is more significant than large size of molecules. However, the information one molecules can provide for another molecule in the first set is also relatively valuable like the second set of molecules. So, the difference on the similarity due to the molecular size is too large and needs to be reduced. Additionally, if it is not reduced, only large molecules can find similar molecules and small molecules are hard to find similar molecules which is unacceptable as well.

Based on the above analysis, this paper proposed a molecular similarity coefficient calculation method which considers the molecule as a chemical concept. First, consider the type of compound. The type of compound is determined by the type of group inside its molecule. If there

are some groups whose number is 0 in one molecule but not 0 in another molecule, then these molecules belong to two different types. If two molecules are composed of the same types of groups but only the number is different, then these molecules belong to the same type and their similarity increases as the number becomes closer. Therefore, a warping function here is used to transform the molecular group vector, as follows,

$$y = \log(x + 1)$$

The warping function needs to satisfy that the derivative is maximum when the input is near 0, and gradually becomes smaller as the input becomes larger, which conforms to the above analysis of molecular type discrimination. Then molecules $M_1$ and $M_2$ are transformed as follows,

$$M_1^{warping}: [\log(n_{1\,1}+1), \cdots, \log(n_{1\,i}+1), \cdots, \log(n_{1\,424}+1)]$$

$$M_2^{warping}: [\log(n_{2\,1}+1), \cdots, \log(n_{2\,i}+1), \cdots, \log(n_{2\,424}+1)]$$

Their intersection and union are:

$$Intersection^{warping}: [a_1, a_2, \cdots, a_i, \cdots, a_{424}], a_i = min(log(n_{1\,i}+1), log(n_{2\,i}+1))$$

$$Union^{warping}: [b_1, b_2, \cdots, b_i, \cdots, b_{424}], b_i = max(log(n_{1\,i}+1), log(n_{2\,i}+1))$$

Then, consider the molecular size. Since the ratio of the elements number of the intersection and the union is a relative comparison but the difference of the elements number is the absolute comparison, the division operation of the intersection and union elements needs to be converted into a subtraction operation. Therefore, for $M_1$ and $M_2$ after warping transformation, the following method is used to calculate their similarity,

$$\mathrm{MSC}_\alpha(M_1, M_2) = \frac{\alpha^{\sum_1^{424} a_i}}{\alpha^{\sum_1^{424} b_i}} = \alpha^{\sum_1^{424} a_i - \sum_1^{424} b_i}$$

where $\alpha$ is a parameter greater than 1. The number of intersection and union elements in the formula appear in the exponents in the numerator and denominator respectively, so the division is converted to subtraction. Finally, in order to convert the value range of the molecular similarity coefficient to [0,1], it is necessary to normalize it, as shown below.

$$\mathrm{MSC}_\alpha(M_1, M_2) = \frac{\alpha^{\sum_1^{424} a_i} - \alpha^{\min(\sum_1^{424} a_i)}}{\alpha^{\sum_1^{424} b_i} - \alpha^{\min(\sum_1^{424} a_i)}} = \frac{\alpha^{\sum_1^{424} a_i} - 1}{\alpha^{\sum_1^{424} b_i} - 1}$$

Here, $\alpha^{\min(\sum_1^{424} a_i)}$ is a normalized item, which is 1 obviously when the intersection elements are all 0.

## 3. MODELING FRAMEWORK BASED ON MOLECULAR SIMILARITY

When the formula of molecular similarity is proposed, a modeling framework based on it can be further proposed. The dataflow is shown in Figure 1. For a target molecule and a known database containing $m$ molecules, the similarity between the target molecule and all the molecules in the dataset should be calculated one by one to obtain $m$ similarities, namely, $\mathrm{MSC}_1$, $\mathrm{MSC}_2$, $\cdots$, $\mathrm{MSC}_\mathrm{m}$. Then, the $n$ molecules having the highest similarities will be selected to form a subset, which contains the molecules which can provide the most valuable information for the property prediction of the target molecule. Then this subset is used as the training dataset to train the model and use the target molecule as the input to get the predicted value of its property. Simultaneously, the similarities of the customized training molecules to the target molecule can be used to form a quantitative index that reflects the prediction reliability of the target molecule. In this paper, the maximum similarity of all the training molecules is employed as the reliability index defined by R. Consequently, the prediction result using this modeling framework is composed of two parts, that is, the predicted property and the reliability index R, which are used together to guide the molecular design. Additionally, the customized training set can provide much more pertinent and valuable information for the target molecule to improve the prediction accuracy of the target molecules with high reliability R.

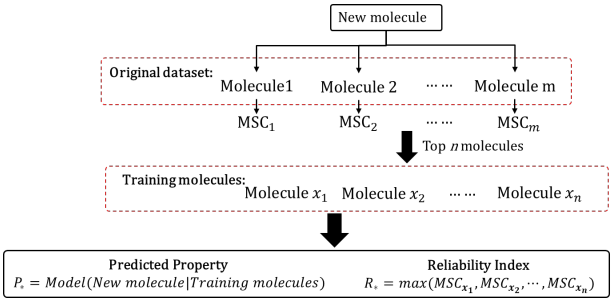



**Figure 1.** The dataflow of the modeling framework.

## 4. TEST AND DISCUSSION

### 4.1 Test method

To verify whether the property prediction framework proposed in this paper possesses the characteristics outlined, a series of tests were conducted. The modeling framework does not limit the types of models used, so three property prediction models were employed for the tests: a simple Group Contribution (GC) model[9], a Support Vector Regression (SVR) model[6], and an improved Gaussian Process Regression (GPR) model[10].

For each model, a test group utilized the proposed modeling framework, while a control group did not, allowing for a comparison to assess the framework's effectiveness. To ensure the test results are objective and reliable, nine different properties were selected for testing, as shown in Table 1. The data for each property was

divided into a candidate training set and a testing set, using an 80:20 ratio. Customized training molecules were chosen from the candidate training set.

**Table 1:** The information of 9 testing properties

| | Property | Symbol | Data volume |
|---|---|---|---|
| **1** | Critical volume (mL/mol) | Vc | 636 |
| **2** | Critical pressure (bar) | Pc | 651 |
| **3** | Auto ignition temperature (K) | Ait | 477 |
| **4** | Gibbs energy of formation at 298 K (kJ/mol) | Gf | 616 |
| **5** | Standard enthalpy of formulation (kJ/mol) | Hf | 787 |
| **6** | Hildebrandt solubility parameter at 298 K ($MPa^{1/2}$) | Hsolp | 1102 |
| **7** | Enthalpy of formation at 298 K (kJ/mol) | Hv | 326 |
| **8** | Liquid molar volume at 298 K (mL/mol) | Lmv | 855 |
| **9** | Critical temperature (K) | Tc | 706 |

To determine the optimal number of molecules to achieve the best prediction accuracy, the test group was further separated into two subgroups: using 10 molecules and 50 molecules for training. In contrast, the control group used all the molecules from the candidate training dataset for training. Finally, the predicted values and reliability indices for the molecules in the testing set were recorded.

## 4.2 Result analysis

### 4.2.1 Verify the quantification of the prediction reliability

In order to verify that the reliability index R can really be used as a quantitatively measure for the prediction reliability, two cases are displayed first in Figure 2.

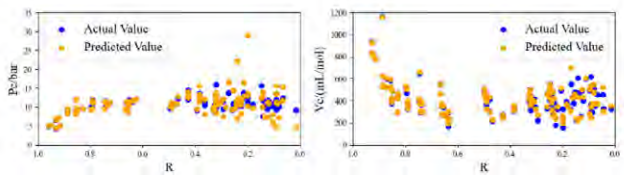



**Figure 2.** The results of Pc and Vc.

It can be seen that as R decreases from 1 to 0, the gap becomes much larger gradually. Further, the test results of all properties using the proposed modeling framework are displayed in Figure 3. Here, to eliminate the interference of some outlier data points, the following formula is used to calculate the Average Prediction Error (APE) of test molecules with reliability greater than u,

$$APE(R \geq u) = \frac{\sum_{R_i \geq u} error_i}{\sum_{R_i \geq u} 1}$$

All the test results are displayed with reliability R as the horizontal coordinate and APE as the vertical coordinate. From these results, as R decreases, APE always has an increasing tendency. Besides, when fewer molecules are used for training, APE increases more rapidly. From the result analysis above, the reliability index R based on the proposed molecular similarity coefficient can be used as a quantitative index for the reliability of property prediction without model limitation.

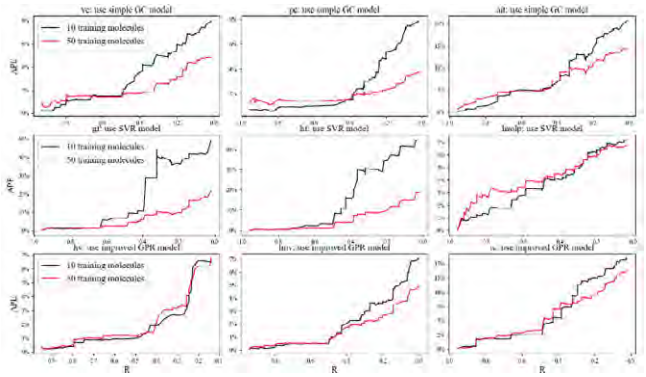



**Figure 3.** The results of 9 properties (list 3 properties for each model: Vc, Pc and Ait use simple GC model; Gf, Hf and Hsolp use SVR model; Hv, Lmv and Tc use improved GPR model).

### 4.2.2 Verify the improvement of the prediction accuracy

Then, in order to verify the prediction accuracy improvement of the proposed modeling framework, the results of all the properties are summarized according to different number of training molecules, namely, 10 training molecules, 50 training molecules and all the candidate training molecules. The average prediction error under different level of reliabilities is shown for different number of training molecules. The results using simple GC model, SVR model and improved GPR model are listed in Table 2, Table 3 and Table 4.

For each line representing the same level of reliability, we compare the prediction errors among three columns that utilize different numbers of training molecules. The green color scale indicates the case with the lowest prediction error, followed by a light green scale, and finally, the white scale, which represents the highest prediction error. From these tables, it is evident that regardless of the model used, when dealing with molecules that have high reliability (R), applying a subset of molecules from the candidate training dataset—specifically, the proposed modeling framework—results in significantly better prediction accuracy compared to the routine method that uses all candidate training molecules. Only when the reliability (R) is at a low level does the prediction accuracy of using all candidate training molecules surpass that of the proposed modeling framework.

The primary reason for this result is that when molecules with high similarity to the target molecules are identified, using a subset of these molecules can provide significantly more relevant information for predicting the properties of the target molecules. In contrast, molecules

**Table 2:** The result of simple GC model

| Reliability level | 10 training molecules | 50 training molecules | All candidate training molecules |
|---|---|---|---|
| R≥0.9 | 0.67% | 1.22% | 2.70% |
| R≥0.85 | 0.81% | 1.56% | 3.00% |
| R≥0.8 | 0.89% | 1.72% | 3.09% |
| R≥0.7 | 1.30% | 1.96% | 3.26% |
| R≥0.6 | 1.93% | 2.14% | 3.43% |
| R≥0.5 | 2.05% | 2.29% | 3.47% |
| R≥0.4 | 4.70% | 3.45% | 4.48% |
| R≥0.3 | 9.62% | 5.87% | 7.00% |
| R≥0.2 | 11.04% | 6.82% | 7.40% |
| R≥0.1 | 13.77% | 8.94% | 8.48% |
| R≥0 | 15.56% | 10.17% | 9.61% |

**Table 3:** The result of SVR model

| Reliability level | 10 training molecules | 50 training molecules | All candidate training molecules |
|---|---|---|---|
| R≥0.9 | 0.63% | 1.19% | 2.74% |
| R≥0.85 | 0.81% | 1.78% | 2.89% |
| R≥0.8 | 1.29% | 1.73% | 2.86% |
| R≥0.7 | 2.22% | 2.62% | 3.06% |
| R≥0.6 | 3.77% | 3.48% | 3.38% |
| R≥0.5 | 4.10% | 3.57% | 3.48% |
| R≥0.4 | 7.09% | 4.91% | 4.34% |
| R≥0.3 | 13.19% | 6.68% | 6.11% |
| R≥0.2 | 14.06% | 7.26% | 6.58% |
| R≥0.1 | 16.13% | 9.30% | 7.82% |
| R≥0 | 17.83% | 10.92% | 8.92% |

**Table 4:** The result of improved GPR model

| Reliability level | 10 training molecules | 50 training molecules | All candidate training molecules |
|---|---|---|---|
| R≥0.9 | 0.59% | 0.80% | 1.01% |
| R≥0.85 | 0.69% | 0.88% | 1.08% |
| R≥0.8 | 0.76% | 0.92% | 1.21% |
| R≥0.7 | 1.18% | 1.48% | 1.72% |
| R≥0.6 | 1.80% | 1.93% | 2.09% |
| R≥0.5 | 1.92% | 2.05% | 2.20% |
| R≥0.4 | 5.37% | 4.22% | 4.07% |
| R≥0.3 | 10.92% | 5.95% | 5.68% |
| R≥0.2 | 12.48% | 7.32% | 6.62% |
| R≥0.1 | 14.86% | 9.60% | 8.08% |
| R≥0 | 16.00% | 11.44% | 9.50% |

that are too dissimilar from the target molecules tend to offer little valuable information and may even lead to misleading conclusions; therefore, they have been excluded. This process enhances prediction accuracy. As the similarity among molecules in the training set decreases, the value and relevance of the information also diminish. If a small number of training molecules are still used, the prediction accuracy will decline due to insufficient data. Consequently, it is essential to increase the amount of data. When the reliability (R) approaches 0, it becomes challenging to find similar molecules for the target molecules within the candidate training dataset. At this point, maximizing the amount of data is crucial—using all available candidate training molecules is necessary to achieve the best prediction accuracy. However, even when all data is utilized, the informational value of these molecules regarding the target molecules remains minimal, resulting in significant prediction errors and low reliability, as demonstrated in the tables.

## 5. DATA CONSISTENCY TEST

Based on the molecular similarity coefficient, a methodology for data consistency testing can be established. If molecules with high MSC serve as the training dataset but the predicted property value of the target molecule deviates significantly from the actual value, it suggests that errors may exist in the property data of the training molecules or the target molecule itself.

For instance, in a property database of Tc, the prediction error for $CH_3(CH_2)_{16}COOH$ reached 10.55% while its prediction reliability was 0.9437. Table 5 details the 10 training molecules for further analysis.

**Table 5:** The training data before correction

| No | MSC | Tc (real)/K | $CH_3$ | $CH_2$ | COOH |
|---|---|---|---|---|---|
| Target molecule | 1 | 799 | 1 | 16 | 1 |
| Molecule 1 | 0.943662 | 474.2 | 1 | 17 | 1 |
| Molecule 2 | 0.940299 | 590 | 1 | 15 | 1 |
| Molecule 3 | 0.893333 | 809 | 1 | 18 | 1 |
| Molecule 4 | 0.880597 | 785 | 1 | 14 | 1 |
| Molecule 5 | 0.820896 | 693 | 1 | 13 | 1 |
| Molecule 6 | 0.761194 | 568 | 1 | 12 | 1 |
| Molecule 7 | 0.701493 | 591.15 | 1 | 11 | 1 |
| Molecule 8 | 0.641791 | 618 | 1 | 10 | 1 |
| Molecule 9 | 0.58209 | 654 | 1 | 9 | 1 |
| Molecule 10 | 0.522388 | 456.86 | 1 | 8 | 1 |

It can be noted that these molecules are of the same compound type, with the primary difference being the number of $CH_2$ groups. According to physicochemical principles, the property Tc of these molecules generally varies consistently with the number of carbon atoms (C). Consequently, the relationship between Tc and the number of carbon atoms before correction has been plotted in Figure 4. The Tc values of these molecules do not exhibit a consistent relationship with the number of carbon atoms (C). This observation suggests a significant possibility of errors in the Tc data for either the training molecules or the target molecule. To address this, we verified the actual Tc values of these molecules by ICAS[8] and discovered mistakes in the training data. The corrected data is shown in Table 6.

**Table 6:** The training data after correction

| No | MSC | Tc (real)/K | $CH_3$ | $CH_2$ | COOH |
|---|---|---|---|---|---|
| Target molecule | 1 | 799 | 1 | 16 | 1 |
| Molecule 1 | 0.943662 | 812[a] | 1 | 17 | 1 |
| Molecule 2 | 0.940299 | 793[a] | 1 | 15 | 1 |
| Molecule 3 | 0.893333 | 821[a] | 1 | 18 | 1 |
| Molecule 4 | 0.880597 | 785 | 1 | 14 | 1 |
| Molecule 5 | 0.820896 | 775[a] | 1 | 13 | 1 |
| Molecule 6 | 0.761194 | 765[a] | 1 | 12 | 1 |
| Molecule 7 | 0.701493 | 754[a] | 1 | 11 | 1 |
| Molecule 8 | 0.641791 | 734[a] | 1 | 10 | 1 |
| Molecule 9 | 0.58209 | 732[a] | 1 | 9 | 1 |
| Molecule 10 | 0.522388 | 722.1[a] | 1 | 8 | 1 |

a: checked in ICAS (Integrated Computer Aided System).

Similarly, the Tc values and the number of C after correction are plotted in Figure 4. It illustrates that after correction, the Tc values and the number of C atoms

exhibit a consistently increasing trend. This suggests that the dataset has likely been corrected at this stage. The corrected dataset is then utilized to predict Tc of the target molecule, revealing a prediction error of only 0.42%. This result further confirms that the errors in the original dataset have been addressed.

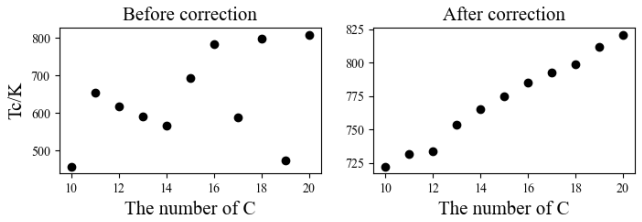



**Figure 4.** The data of Tc with the number of C.

## 6. CONCLUSION

This paper introduces a modeling framework based on the molecular similarity coefficient. This framework utilizes the similarity between molecules in a candidate training dataset and target molecules to create a customized training dataset specifically for the target molecules. Testing was conducted on nine properties. The results confirm that this modeling framework provides a quantitative measure of prediction reliability and significantly enhances the prediction accuracy for molecules with a high reliability index. For molecular design, the framework proposed in this paper offers a novel two-fold evaluation system. It emphasizes that the molecular design process should assess not only the predicted properties but also the reliability of those predictions. However, the analysis presented in this paper indicates that the prediction performance of the proposed framework is somewhat sensitive to data errors because using a smaller amount of data for model training amplifies the impact of mistakes in the training dataset. Therefore, the data consistency testing method proposed in this study should be further developed, and the modeling framework should be implemented alongside this testing method to achieve more reliable, accurate, and stable prediction performance.

## ACKNOWLEDGMENTS

Financial support from the Natural Science Foundation of China (No. 22150410338) is gratefully acknowledged.

## REFERENCE

1. Gani R. Group contribution-based property estimation methods: advances and perspectives. Curr Opin Chem Eng 2019;23:184–96. https://doi.org/10.1016/j.coche.2019.04.007.
2. Le T, Epa VC, Burden FR, Winkler DA. Quantitative structure-property relationship modeling of diverse materials properties. Chem Rev 2012;112:2889–919. https://doi.org/10.1021/cr200066h.
3. Wen S, Nanda K, Huang Y, Beran GJO. Practical quantum mechanics-based fragment methods for predicting molecular crystal properties. Physical Chemistry Chemical Physics 2012;14:7578–90. https://doi.org/10.1039/c2cp23949c.
4. Jirasek F, Hasse H. Machine Learning of Thermophysical Properties. Fluid Phase Equilib 2021;549. https://doi.org/10.1016/j.fluid.2021.113206.
5. Zhang J, Wang Q, Su Y, Jin S, Ren J, Eden M, et al. An accurate and interpretable deep learning model for environmental properties prediction using hybrid molecular representations. AIChE Journal 2022;68. https://doi.org/10.1002/aic.17634.
6. Alshehri AS, Tula AK, You F, Gani R. Next generation pure component property estimation models: With and without machine learning techniques. AIChE Journal 2022;68. https://doi.org/10.1002/aic.17469.
7. Joback KG, Reid RC. Estimation of Pure-Component Properties from Group-Contributions. Chem Eng Commun 1987;57:233–43. https://doi.org/10.1080/00986448708960487.
8. Gani R, Hytoft G, Jaksland C, Jensen AK. An integrated computer aided system for integrated design of chemical processes. Comput Chem Eng 1997;21:1135–1146. https://doi.org/10.1016/S0098-1354(96)00324-9.
9. Hukkerikar AS, Sarup B, Ten Kate A, Abildskov J, Sin G, Gani R. Group-contribution + (GC +) based estimation of properties of pure components: Improved property estimation and uncertainty analysis. Fluid Phase Equilib 2012;321:25–43. https://doi.org/10.1016/j.fluid.2012.02.010.
10. Cao X, Gong M, Tula A, Chen X, Gani R, Venkatasubramanian V. An Improved Machine Learning Model for Pure Component Property Estimation. Engineering 2024;39:61–73. https://doi.org/10.1016/j.eng.2023.08.024

© 2025 by the authors. Licensed to PSEcommunity.org and PSE Press. This is an open access article under the creative commons CC-BY-SA licensing terms. Credit must be given to creator and adaptations must be shared under the same terms. See https://creativecommons.org/licenses/by-sa/4.0/

Systems & Control Transactions

**Research Article - Peer Reviewed Conference Proceeding**
ESCAPE 35 - European Symposium on Computer Aided Process Engineering
Ghent, Belgium. 6-9 July 2025
Jan F.M. Van Impe, Grégoire Léonard, Satyajeet S. Bhonsale,
Monika E. Polańska, Filip Logist (Eds.)

PSE PRESS

# Phenomena-Based Graph Representations and Applications to Chemical Process Simulation

**Yoel R. Cortés-Peña[a] and Victor M. Zavala[a]**

[a] University of Wisconsin Madison, Department of Chemical and Biological Engineering, Madison, Wisconsin, United States
* Corresponding Author: zavalatejeda@wisc.edu.

## ABSTRACT

Rapid and robust simulation of chemical production processes is critical to address core scientific questions related to process design, optimization, and sustainability. Efficiently solving a chemical process, however, remains a challenge due to their highly coupled and nonlinear nature. Graph abstractions of the underlying physical phenomena within unit operations may help identify potential avenues to systematically reformulate the network of equations and enable more robust convergence of flowsheets. To this end, we further refined a flowsheet graph-theoretic abstraction that consists of a mesh of interconnected variable nodes and equation nodes. The new network of equations is formulated at the phenomenological level—agnostic to the thermodynamic property package—by extending equation formulations widely used to solve multistage equilibrium columns. Decomposition of the graph by phenomena linearizes material and energy balances across the flowsheet by decoupling phenomenological nonlinearities (e.g., phase equilibrium, chemical reactions). Additionally, we further improved a preliminary simulation algorithm which employs this phenomena-based decomposition and demonstrated that it can perform more rapid and robust simulation of large, highly-coupled systems than sequential modular simulation.

**Keywords**: Process Simulation, Graph-Theory, Flowsheet Convergence, Distillation, Liquid Extraction

## INTRODUCTION

Critical to the design and development of sustainable production processes, chemical process simulation seeks to model the flow rate of material and energy between unit operations and their internal components. Physical phenomena (e.g., phase equilibrium, chemical reactions, adsorption, and heat exchange) which drive a production process also introduce nonlinearities to the material and energy balances. This nonlinear coupling between unit operations is the core difficulty in solving for the steady-state solution of a production process in any algorithmic paradigm (e.g., sequential modular simulation, equation-oriented simulation, pseudo-transient modeling). Large, highly coupled systems lead to substantially longer computation time and lower rates of successful convergence than small, sparse systems [1]. This inability to scale the simulation of complex systems limits researchers' ability to optimize the sustainability of emerging production processes.

In sequential-modular simulation, each unit operation is treated as a black-box model with only material streams as inputs and outputs [2]. All mass, energy, and thermodynamic equations are formulated and solved independently within each unit operation. While specialized convergence strategies are employed to converge individual units, the convergence of recycle systems can be challenging due to nonlinear coupling between unit operations. Equation-based modeling leverages the full set of equations and employs algebraic differentiation to aid numerical methods in finding the steady state solution [3]. Equation-based modeling may be faster than the sequential modular approach particularly when the initial guess is close to the steady state solution. However, highly-coupled networks of equations introduce instabilities that lead to convergence failures.

If a process flowsheet could become aware of the connectivity of the governing phenomenological equations, robust solution strategies could be formulated that aggregate linear relationships and decouple nonlinearities. With the wealth of decomposition algorithms and computing architectures that enable the solution of

complex and large-scale problems, it may be feasible to screen for alternative problem formulations of a production process that result in more rapid and robust convergence. The problem formulation and the selection of a suitable solution method, however, is not a simple task. Graph-theoretic abstractions of the equations within unit operations may provide an avenue to systematically reformulate the network of equations and enable advanced, equation-based convergence of flowsheets.

In classical representations of a chemical process, units are represented as nodes and streams as edges. Fundamentally, each unit encapsulates a set of equations with internal variables and each stream carries a set of variables with a unique connection. At the phenomenological level, however, each variable may relate multiple equations and may not have a unique connection. For example, temperature may play multiple roles in thermodynamic phase equilibrium, energy balances, and reaction rates. Graphical abstractions of process phenomena may unfold the sets of equations and variables present in unit operations to capture how mass, energy, equilibrium, reaction, and transport equations are related through shared variables. Distillation column models are a classic example where equations are decoupled by phenomena. For example, the Wang-Henke bubble point method converges all stages by iteratively solving mass, equilibrium, summation, and enthalpy (MESH) equations [4].

In our previous work, we introduced a flowsheet graph abstraction which represents all the equations and variables as a bipartite graph of equation nodes and variable nodes [5]. Additionally, it was shown that decomposing the network of equations by phenomena improved the convergence speed of an extractive distillation process flowsheet. However, because of the redundancy between variables and how highly coupled the equations are, the abstraction was too complex to provide any key topological insights. The graph abstraction needs to be further refined by eliminating variable redundancy and strategically aggregating intermediary equations not relevant to the decomposition. Harmonizing the graph with respect to the decomposition is the next step towards gaining mathematical insight into how the decomposition improves convergence.

The goal of this study was to further refine and improve the graph abstraction and phenomena-based decomposition introduced in our last study for the broader goal of improving the convergence of large and highly coupled systems. To this end, we completed the following objectives: (i) refined the phenomena-based graph abstraction of chemical process flowsheets, (ii) generalized the graph-based decomposition scheme to any set of unit operations, and (iii) benchmarked a convergence algorithm leveraging this decomposition scheme. We implemented the phenomena-oriented simulation algorithm in BioSTEAM—an open-source process simulation platform implemented in Python [6]—and benchmarked its convergence against sequential modular simulation for an industrial process for the dewatering of acetic acid using ethyl acetate solvent.

## MATERIALS & METHODS

### Phenomenological Graph Framework

The graph abstractions in this study represent variables as grey ring nodes and equations as solid nodes. The color of equation nodes depends on what subset of equations they pertain to within the phenomena decomposition. Edges connect variables to equations and define shared variables among equations. It is also possible to obtain different graph representations by reformulating the equations. For example, variable nodes can be eliminated via substitution of equations and new edges may be formed to reflect changes in the equation formulation. Nodes that were not relevant to the phenomena decomposition scheme were eliminated to minimize the complexity. By aggregating equations in this manner, the various decomposition schemes are represented at a phenomenological level that is agnostic to the specific thermodynamic property package (e.g., the selection between ideal gas or mixture equations of state has no impact on the equations). Input variables that are held constant within a subgraph are not displayed to avoid creating edges between equation nodes that are decoupled. This reduces connectivity between equations and highlights how the decomposition scheme reduces complexity. PhenomeNode [5], an open-source Python library for phenomena-based graph representations, was used to automate the generation of graphical abstractions.

### Phenomenological decomposition

Key material and energy variables are represented by “$x$” while variables related to coefficients for the material and energy balances are denoted by “$y$”. Aggregated models (e.g., shortcut columns) are effectively stages with respect to the resolution of the flowsheet. To generalize the equations to an arbitrary reference stage, we introduce subscripts “$i$” and “$o$” that describe the unique connectivity of an inlet or outlet to its source or sink, respectively. If a variable does not have an “$i$” or “$o$” subscript, it means that the variable pertains to the reference stage. An “$s$” subscript is used to denote a variable specific to the source stage of a stream (e.g., temperature, phase ratio). In special cases, an additional subscript “$j$” may be used to reference outlet streams other than the arbitrary “$o$”. Function definitions are abstracted at the level that is relevant to the decomposition; detailed equations to compute phenomenological variables (e.g., enthalpy) are not described as they depend on the specific property package. Subscript, function, and constant definitions are detailed in Tables 1-3, respectively.

Central equations are presented in the same color as their respective nodes in the graph representations (e.g., material balances are purple). Equations to compute coefficients to the material and energy balances are not considered central equations. Within the graph abstraction, we strategically aggregate these equations to their respective central equations for simplicity. In this study, pressures are assumed to be constants (controlled by valves and pumps) and do not appear as a variable in the graphs nor equations.

**Table 1.** Subscript definitions.

| | Definition | | Definition |
|---|---|---|---|
| i | arbitrary inlet | j | arbitrary outlet |
| o | arbitrary outlet | F | flow rate |
| s | arbitrary stage | T | temperature |
| c | arbitrary component | Φ | phase ratio |
| γ | activity coefficient | S | separation factor |
| VLE | VLE-specific | R | reaction rate |
| LLE | LLE-specific | M | molar fraction |
| E | key energy variable | A | light phase |
| K | partition coefficient | B | heavy phase |

**Table 2.** Function outputs.

| Function | Definition |
|---|---|
| H | enthalpy flow rate |
| h | specific enthalpy |
| N | total flow rate |
| C | heat capacity flow rate |
| R | reaction rate |
| P | phase equilibrium variables |
| M | molar composition |
| S | separation factor |
| Φ | phase ratio (by Rashford-Rice equation) |
| γ | activity coefficient |

Table 3. Constants.

| Constant | Definition | Constant | Definition |
|---|---|---|---|
| Q | duty | t, b | split |

The material balance equations are used to solve for all flow rates, $x_{F,c}$, given the separation factors, $y_{S,c}$, and the generation (or consumption) of chemicals, $y_{R,c}$. The conservation of mass, material separation, and splitting equations are generalized for any stage as follows:

$$\Sigma_o x_{F,c,o} - \Sigma_i x_{F,c,i} = y_{R,c} \quad (1)$$

$$y_{S,c}\Sigma_{o \in B} x_{F,c,o} - \Sigma_{o \in A} x_{F,c,o} = 0 \quad (2)$$

$$x_{F,c,o \in A} - t_o \Sigma_{j \in A} x_{F,c,j} = 0 \quad (3)$$

$$x_{F,c,o \in B} - b_o \Sigma_{j \in B} x_{F,c,j} = 0 \quad (4)$$

$$y_{R,c} = R_c(x_{F,c,o}, x_T) \quad (5)$$

$$y_{S,c} = y_{K,c} x_\Phi \quad (6a)$$

$$y_{S,c} = S(x_{F,c,o}, x_T) \quad (6b)$$

Eq 6a is only relevant for an equilibrium stage while eq 6b is applicable to any module. The function $S$ will depend on the module. For shortcut columns, $S$ is an iteration of the Fenske Underwood Gilliland method, without bubble and dew point temperature calculations.

At steady state, the enthalpy balance equation at the reference stage and can be generalized as follows:

$$0 = \Sigma_o H_o(x_{F,c,o}, x_T) - \Sigma_i H_i(x_{F,c,i}, x_{T,i}) - Q \quad (7a)$$

Assuming $Q$ is constant, we can reformulate equation 7a in terms of a key energy variable (denoted by "E") by a 1st degree Taylor expansion:

$$\Sigma_{i,s} \Delta x_{E,s} \frac{\partial H_i(x_{F,c,i}, x_T)}{\partial x_{E,s}} - \Delta x_E \Sigma_o \frac{\partial H_o(x_{F,c,o}, x_T)}{\partial x_E} = \Sigma_o H_o(x_{F,c,o}, x_T) - \Sigma_i H_i(x_{F,c,i}, x_{T,i}) - Q \quad (7b)$$

We can reformulate eq 7b as a linear equation by isolating the nonlinear terms and separating variables:

$$\Sigma_{i,s} x_{E,s} y_{E,i} - x_E \Sigma_o y_{E,o} = y_{H,s} \quad (7c)$$

This equation may solve for a range of parameters that depend on the type of phenomena exhibited by the stage and its specifications. For example, VLE is most sensitive to the boil-up ratio, $x_\Phi$, (i.e., the ratio of vapor to liquid flow rate) while that LLE is more sensitive to the temperature, $x_T$, than the ratio of extract to raffinate. Assuming a constant liquid flow rate, the local sensitivity of $\Phi$ on the enthalpy of a stream leaving a stage in VLE is given by:

$$y_{E,o \in A} = \frac{\partial H_{o \in A}}{\partial x_{\Phi,s \in VLE}} = t_o h_{gas}(x_{F,c,o}, x_T) N(x_{F,c,j \in B}) \quad (8)$$

$$y_{E,o \in B} = \frac{\partial H_{o \in B}}{\partial x_{\Phi,s \in VLE}} = 0 \quad (9)$$

When a stream leaving a stage is not in VLE (i.e., superheated or subcooled), the key energy variable is assumed to be the temperature:

$$y_{E,o} = \frac{\partial H_o}{\partial x_T} = C(x_{F,c,o}, x_T) \quad (10)$$

Given these definitions, the term on the right-hand side of eq 7c becomes:

$$y_{H,s} = \Sigma_o H_o(x_{F,c,o}, x_T) - \Sigma_i H_i(x_{F,c,i}, x_{T,i}) - Q - \Sigma_{i,s} x_{E,s} y_{E,i} + x_E \Sigma_o y_{E,o} \quad (11)$$

The enthalpy balance is only relevant for stages where the duty, $Q$, is specified (e.g., adiabatic stages). Otherwise, when either temperature or vapor fraction is user-specified, the duty can be computed at the end of simulation, after all variables have converged.

Equations related to the VLE criteria depend on user specifications. The variables $y_K$ and $x_T$ for a VLE stage can be evaluated by a bubble point routine (within a

thermodynamic property package; eq 12a). If the temperature of a stage is specified, then $y_K$ and $x_\Phi$ are computed through a pressure and temperature flash routine (eq 12b). For other unit operations which include outlet streams in VLE (e.g., shortcut columns), the outlet temperature of each stream can be computed by bubble and dew point routines (eq 12c):

$$y_K, x_T = P_{VLE,c}(x_{F,c,o \in B}) \quad (12a)$$

$$y_K, x_\Phi = P_{VLE,c}(x_{F,c,o}) \quad (12b)$$

$$x_{T,o} = P_{VLE,c}(x_{F,c,o}) \quad (12c)$$

The partition coefficient, $y_K$, and the phase ratio, $x_\Phi$, for a LLE stage are evaluated using the pseudo-equilibrium approach and the Rashford-Rice equation, respectively:

$$y_{M,c} = M_c(x_{F,c,B}, T, y_{\gamma,c,A}) \quad (13)$$

$$y_{\gamma,c,A} = \gamma_c(y_{M,c}, T) \quad (14)$$

$$y_{K,c} = P_{LLE,c}(x_{F,c,B}, T, y_{\gamma,c,A}) \quad (15)$$

$$x_\Phi = \Phi(y_{K,c}, x_{F,c,o}) \quad (16)$$

## Phenomena-based simulation algorithm

The new simulation algorithm iteratively solves the complete flowsheet by sequential substitution. The phenomenological nonlinearities are solved first, then material and energy balances solved as systems of linear equations. To prevent the algorithm from failing due to poor conditioning of the initial guess (i.e., material and energy variables of all streams), we integrate sequential modular simulation for more robust convergence. All together, we propose the following algorithm as a preliminary architecture for phenomena-based simulation:

1. In the absence of an initial guess for $x_{F,c,o}$ and $x_E$, for each stage, run each unit operation sequentially and use the result as the initial guess.
2. For each unit operation:
   - 2.1 Simulate the unit operation and update all variables associated to the unit.
   - 2.2 Using the linear material balance equations (eqs 1–6), solve $x_{F,c,o}$ for all stages.
   - 2.3 Using the linear energy balance equations (eqs 7c–11), solve $x_{E,s}$ for all stages.
3. Using the VLE criteria (eq 12a-c), solve for $y_K$ and $x_T$ at each stage and/or stream.
4. Solve $y_{K,c}$ and $x_{F,c,o}$ for all LLE stages iteratively until they converge within a specified tolerance:
   - 4.1 Using the pseudo-equilibrium concept (eqs 13-15), solve $y_{K,c}$ for each stage.
   - 4.2 Using the material balance equations (eqs 1–6), solve $x_{F,c,o}$ for all LLE stages as a system of linear equations.
   - 4.3 If $y_{K,c}$ and $x_{F,c,o}$ have not converged, repeat steps 4.1 and 4.2
5. Using the Rashford-Rice equation (eq 16), solve $x_\Phi$ for all LLE stages.
6. Solve material and energy balances for the complete flowsheet (steps 2.2 and 2.3).
7. If any variables have not converged under a specified tolerance, repeat steps 2–5.

## Acetic Acid Purification Benchmark

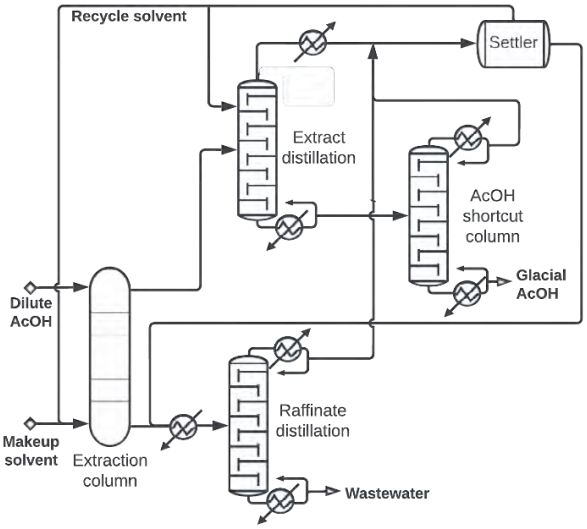



**Figure 1.** Process flowsheet for acetic acid dewatering.

The industrial separation of acetic acid from water (Figure 1) was chosen as a representative case to benchmark the new convergence algorithm against sequential modular simulation. The system includes highly coupled vapor-liquid equilibrium (VLE) and liquid-liquid equilibrium (LLE) stages and recycle loops that connect the end of the process with the start. In this process, ethyl acetate (EtOAc) is used to extract acetic acid from a dilute aqueous mixture [7]. The extract is distilled to recycle the solvent and recover glacial acetic acid. The raffinate is also distilled to recover EtOAc from the wastewater. Both distillates are sent to a decanter to separate the aqueous phase that forms after condensation. Only results pertinent to flowsheet convergence were considered, including duties and material flows across unit operations and stages. Sizing and costing of unit operations were not considered as they do not impact mass and energy balances and are therefore irrelevant to benchmarking.

The "true" solution of the process was considered to be the best solution (i.e. the solution with the minimum error) out of the two simulation strategies at the final iteration. The simulation error is defined as the sum of the

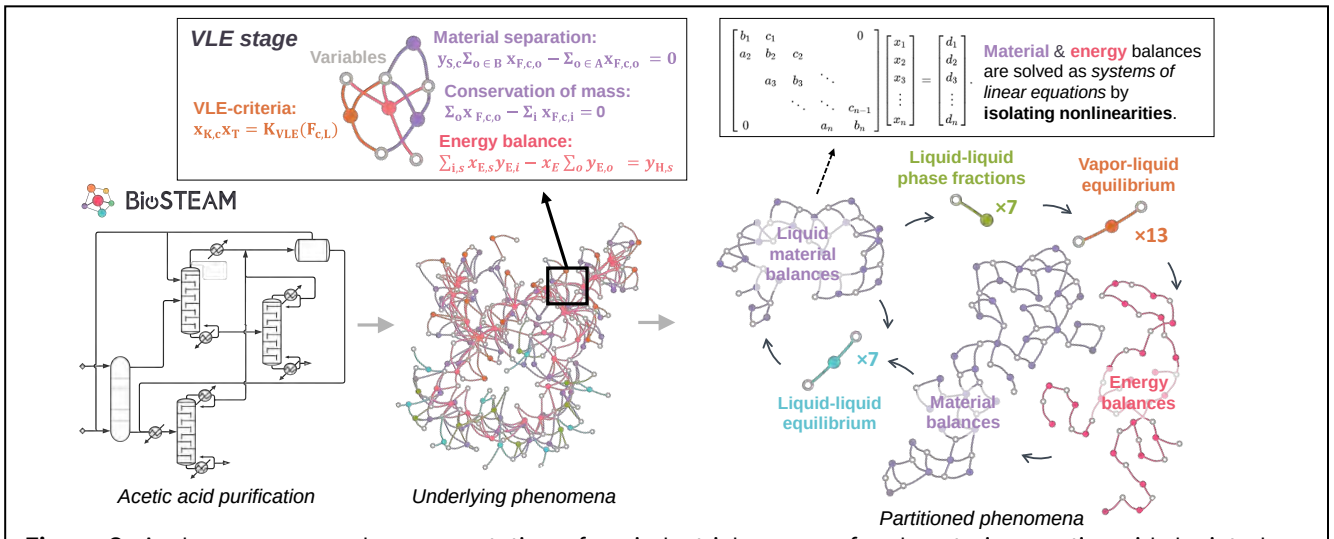



**Figure 2.** A phenomena graph representation of an industrial process for dewatering acetic acid depicts how decoupling phenomenological equations may result in a more maganeable formulation for complex systems.

change in component flow rates and temperatures of each stream after the simulation of each stage in parallel:

$$\text{Error} = \sum_{s}\sum_{o}\left(\left|x^{n}_{T,s,o} - x^{n-1}_{T,s,o}\right| + \sum_{c}\left|x^{n}_{F,c,s,o} - x^{n-1}_{F,c,s,o}\right|\right)$$

## RESULTS & DISCUSSION

The graph representation of the flowsheet for the purification of acetic acid, representing a complex system with 3 recycles and 48 stages, depicts how the phenomenological equations have an underlying structure (Figure 2). While there can be many effective ways to decompose the flowsheet (e.g, sequential or parallel modular), the phenomena-based decomposition has the advantage of linearizing the material and enthalpy balances across all unit operations and their stages by decoupling phenomenological nonlinearities. This decomposition can be considered a generalization of MESH formulations commonly used to solve multistage unit operations. For the special case of multistage vapor-liquid equilibrium columns, these equations reduce to the equations in Wang-Henke's bubble point method [4], which iteratively solves for the bubble point partition coefficients and temperature, then the boil-up ratios of all stages using the linear energy balance equations, and finally the material flow rates using the linear mass balance equations. Additionally, for the special case of multistage liquid-liquid equilibrium, these equations reduce to the decomposition in the Tsuboka method [8], which employs an inner loop using the pseudo equilibrium concept to iteratively solve partition coefficients and the material balance, phase fractions are solved by the Rashford-Rice equation, and, lastly, stage temperatures are solved using the linear energy balances. Although the decomposition of equations is specialized for the type of phenomena (e.g., vapor-liquid equilibrium vs. liquid-liquid equilibrium), these methods have an underlying structure that enables material flows and key energy variables to be solved as systems of linear equations. Through the phenomena-based graph abstraction and the generalization of the mass and energy balances, we can unfold the underlying equations in unit operations in manner that is consistent with classical decomposition approaches for multistage unit operations and leverage existing solution strategies at the unit level to develop a phenomena-oriented flowsheet simulation algorithm.

The new simulation algorithm is a fusion of the sequential modular approach with sequential substitution of the phenomena decomposition. In step 2, the material and energy balances are solved after each unit operation is simulated, enabling new information gathered from a single unit simulation to spread through the flowsheet while consolidating mass and energy balances. Phenomenological nonlinearities are then solved in steps 3-5 and the material and energy balances are solved in step 6, which follows common solution strategies for multistage equilibrium columns. Together, steps 3-6 may help accelerate convergence by treating the entire flowsheet as if it were a single unit operation.

In the benchmark flowsheet for the dewatering of acetic acid, the preliminary phenomena-based simulation algorithm converged in 75% less time than the sequential modular approach (Figure 3 A, B). The phenomena-based algorithm was also able to achieve greater numerical accuracy in simulations than the sequential modular approach. While the phenomena-based approach treats the flowsheet as a single unit, sequential modular accumulates numerical error as it simulates each unit

Ultimately, these results suggest that the phenomena-based approach may enable faster and more robust convergence for large, highly-coupled systems. It is important to note, however, that this approach was only

benchmarked against sequential modular simulation and equation-oriented simulation may converge faster. Additionally, this separation process is limited to only phase-based separations. Future work will focus on benchmarking systems with reactions and mass and energy transfer-based unit operations that are common in a production process against both the sequential modular and the equation-oriented approaches. It is possible that different decompositions may be more effective for different sets of physical phenomena and the decoupling strategies presented here may need to further refinement. We envision a family of phenomena-based simulation architectures that are optimized for different problems based on the relevant phenomena of the system, level of connectivity between unit operations, and chemical interactions that drive coupling between phenomenological equations. Ultimately, the phenomena graph representations introduced in this study may aid in the development of unified decoupling and linearization strategies that can allow for more rapid and robust flowsheet convergence.

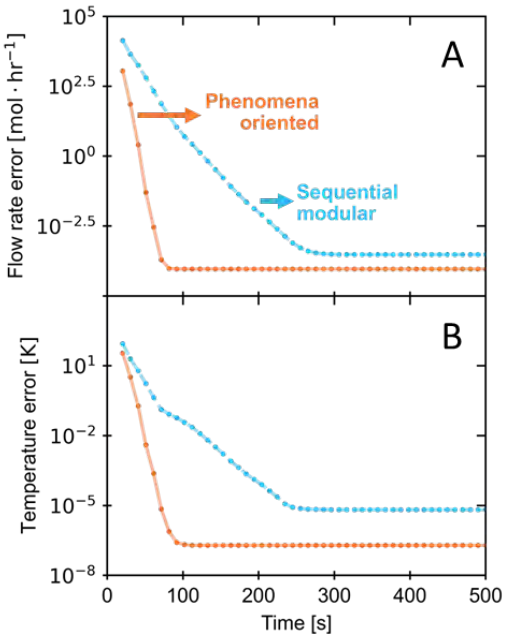



**Figure 3.** The total error of the flow rate (A) and temperature (B) across all streams is plotted over simulation time of the benchmark case for the phenomena-based (orange) and sequential modular (blue) approaches.

## CONCLUSION

Efficiently solving a flowsheet remains a challenge due to the tightly coupled, non-linear nature of chemical processes. The graph representations developed in this study helped identify how decoupling equations by phenomena can be used to formulate a strategy to converge the complete flowsheet. While the proposed algorithm showed promising advantages in convergence speed compared to sequential modular, further analysis is needed to fully characterize the speed, robustness, and applicability to a broader set of chemical processes.

## ACKNOWLEDGEMENTS

This material is based upon work supported by the U.S. Department of Energy, Office of Energy Efficiency and Renewable Energy, Bioenergy Technologies Office under Award Number DE-EE0009285.

## REFERENCES

1. Mah RSH. Chemical Process Structures and Information Flows. Butterworths; 1990.
2. Motard RL, Shacham M, Rosen EM. Steady state chemical process simulation. AIChE J. 1975;21(3):417-436. doi:10.1002/aic.690210302
3. Bogle IDL, Perkins JD. Sparse newton-like methods in equation oriented flowsheeting. Computers & Chemical Engineering. 1988;12(8):791-805. doi:10.1016/0098-1354(88)80018-8
4. Monroy-Loperena R. Simulation of Multicomponent Multistage Vapor–Liquid Separations. An Improved Algorithm Using the Wang–Henke Tridiagonal Matrix Method. Ind Eng Chem Res. 2003;42(1):175-182. doi:10.1021/ie0108898
5. Cortes-Pena YR, Zavala VM. Graph-Based Representations and Applications to Process Simulation. LAPSE; 2024:129-136. doi:10.69997/sct.184650
6. Cortes-Peña Y, Kumar D, Singh V, Guest JS. BioSTEAM: A Fast and Flexible Platform for the Design, Simulation, and Techno-Economic Analysis of Biorefineries under Uncertainty. ACS Sustainable Chem Eng. 2020;8(8):3302-3310. doi:10.1021/acssuschemeng.9b07040
7. Seader JD, Henley EJ, Roper DK. Separation Process Principles: Chemical and Biochemical Operations. 3rd ed. Wiley; 2011.
8. Tsuboka T, Katamaya T. General design algorithm based on pseudo-equilibrium concept for multistage multi-component liquid-liquid separation processes. Journal of Chemical Engineering of Japan. 1976;9(1):40-45.

© 2025 by the authors. Licensed to PSEcommunity.org and PSE Press. This is an open access article under the creative commons CC-BY-SA licensing terms. Credit must be given to creator and adaptations must be shared under the same terms. See https://creativecommons.org/licenses/by-sa/4.0/

Systems & Control Transactions

**Research Article - Peer Reviewed Conference Proceeding**
ESCAPE 35 - European Symposium on Computer Aided Process Engineering
Ghent, Belgium. 6-9 July 2025
Jan F.M. Van Impe, Grégoire Léonard, Satyajeet S. Bhonsale,
Monika E. Polańska, Filip Logist (Eds.)

PSE PRESS

# A Benchmark Simulation Model of Ammonia Production: Enabling Safe Innovation in the Emerging Renewable Hydrogen Economy

**Niklas Groll[a], Gürkan Sin[a]***

[a] Process and System Engineering Center (PROSYS), Department of Chemical and Biochemical Engineering, Technical University of Denmark (DTU), 2800 Kgs. Lyngby, Denmark
* Corresponding Author: gsi@kt.dtu.dk.

## ABSTRACT

The green transition accelerates innovations and developments targeting the integration of green hydrogen in the chemical industry. However, all new hydrogen pathways and process designs must be tested on operability and safety. A big challenge is the typical fluctuating characteristic of green hydrogen supply that contrasts the steady-state operation of most conventional chemical processes. Therefore, to adequately assess control and monitoring techniques, a benchmark model tailored to the relevant aspects of the hydrogen economy is required. We introduce a benchmark model based on the production of green ammonia using the Haber-Bosch process that remains operable when coupled to a fluctuating hydrogen supply from water electrolysis. The main section of the process model is an adiabatic indirect cooled reactor system that provides realistic modeling of industrial applications. Like the ammonia reactor, all process units and the underlying control structure are precisely dimensioned to ensure feasible operation across various hydrogen supply rates. Eventually, the flexible operating ammonia benchmark model can serve as a new benchmark for analyzing process safety and control aspects.

**Keywords**: Simulation Benchmark Model, Renewable Ammonia Production, Process Safety

## INTRODUCTION

The relevance of green hydrogen is rapidly increasing because of its vital part in the transition to a more sustainable industry. Hydrogen can serve as both a sustainable feedstock and an energy carrier in heating and transport applications [1]. Accordingly, a great interest emerged in designing new process routes based on green hydrogen produced from water electrolysis. However, many challenges are still related to integrating green hydrogen into established chemical processes, like hydrogen storage, transportation, and safety [1,2]. In particular, coupling a fluctuating hydrogen supply, due to its production from renewable electricity, based on constantly changing weather conditions, with a conventional chemical process formally established for steady-state operation challenges all three areas.

One of the most prominent products of the chemical industry, stemming directly from hydrogen, is ammonia. Ammonia is the second most produced chemical globally, mainly because of its use in the fertilizer industry [2]. However, it also serves several more applications, *e.g.*, as a platform chemical [3] or as an energy carrier [4], and its global demand is predicted to increase further [4]. Traditionally, ammonia is produced using the Haber-Bosch (HB) process, which has seen only minor modifications since its inception in the early 20th century [5]. During the HB process, hydrogen reacts with nitrogen to form ammonia. The process requires a metal catalyst and high pressure and temperature conditions. Common HB plants use steam gas reforming for hydrogen production and, thus, generate high carbon emissions. Following the decarbonization trend, green hydrogen as feedstock drastically reduces ammonia's carbon footprint [6]. Eventually, the green hydrogen pathway to green ammonia will be applied on big industrial scales [3].

All green hydrogen pathways, including ammonia production, require thorough safety testing and

validation, and the variable nature of hydrogen production coupled with a chemical downstream process poses explicit challenges. Commonly, benchmark models are used to test and develop new process control and monitoring techniques. One of the most popular is the Tennessee-Eastman model, which mimics a standard fossil-based chemical process [7]. Many more benchmark models specialized for different niches developed over time, like the fed-batch fermentation model of penicillin production for biochemical applications [8] or the fluid catalytic cracking model for refinery processes [9]. Nevertheless, despite many recent developments, the hydrogen economy lacks an appropriately tailored benchmark model.

In the following, we aim to take the first step in providing a benchmark model that comprises the coupling of a fluctuating green hydrogen supply with a former steady-state chemical process, the HB process. This contribution focuses on designing and dimensioning of process units and control structures using steady-state simulations. We aim to design the HB process to be operable in a wide ammonia production rate range to promote its operation in combination with a variable supply of green hydrogen.

## PROCESS MODELING

We establish a process model for converting green hydrogen from water electrolysis and nitrogen from an air separation unit (ASU) to green ammonia. For realistic process modeling and dimensioning, we use AVEVA Process Simulation software and simulate all process streams based on pressure gradients between unit operations using steady-state simulations. The nominal production capacity of ammonia is defined as 500,000 t/y, but we consider variable product loads ranging from 30 to 130 % of its nominal value. The minimal purity of the produced ammonia is set to be 99.9 mol-%. We include a measurement and control structure in our process model comparable to real industrial systems to ensure feasible operation under different loads.

Figure 1 illustrates the process flowsheet and its separation into three sections: The feed stream compression, the ammonia reactor, and the ammonia purification. In the first section, multi-stage compression adjusts the feed streams to the favorable reactor operating conditions. In the ammonia reactor, the feed gases are converted to ammonia. Here, we model an industrial reactor system with advanced heat integration to recover the heat of the reaction. After the reactor, unreacted hydrogen and nitrogen are separated and recycled. Subsequently, the ammonia is purified to match the fixed purity constraint. In the following subsections, we explain the modeling of each part in detail and explicitly focus on the implemented control structure. Thereafter, we briefly describe the challenges posed by dimensioning the process units under variable loads.

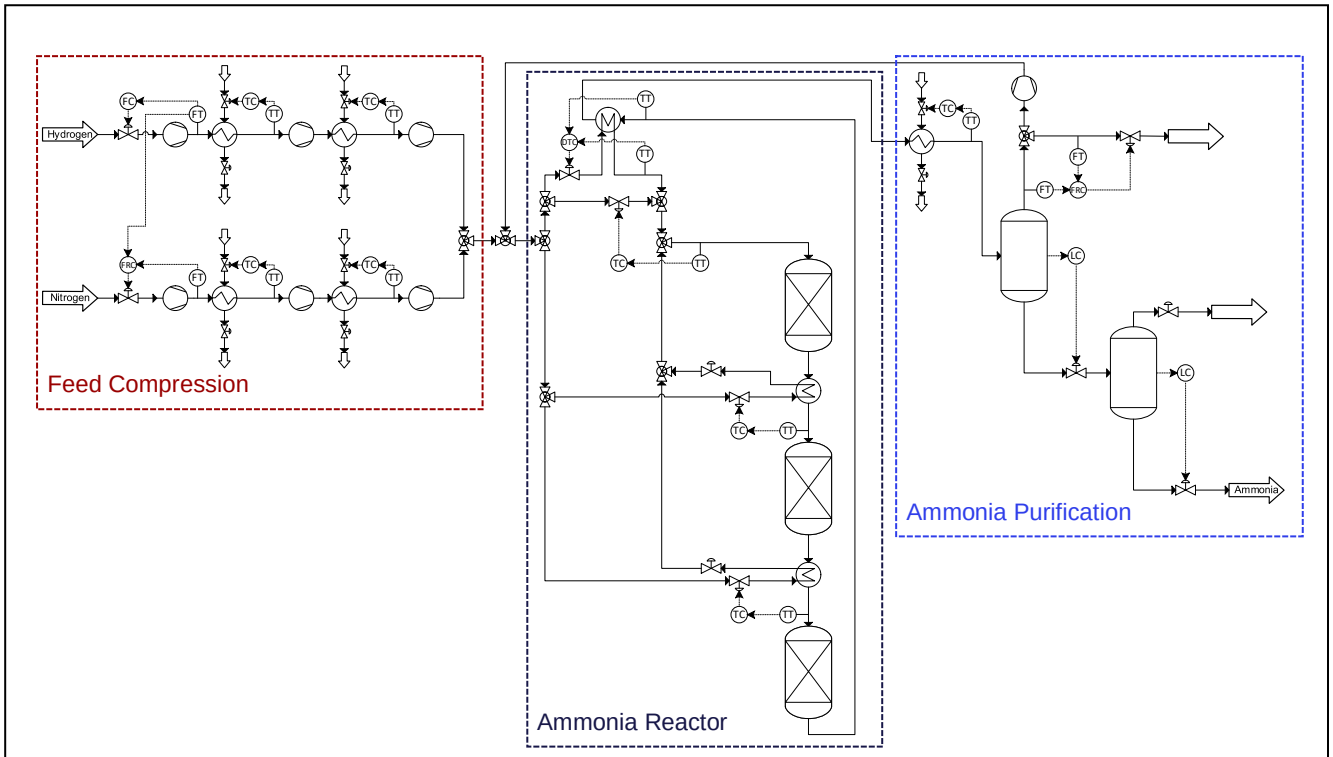



**Figure 1:** Process flowsheet of the Haber-Bosch process for green ammonia production separated into three sections: Feed compression, ammonia reactor, and ammonia purification

## Section 1: Feed Compression

For the feed streams, we consider pure hydrogen from a proton exchange membrane (PEM) electrolysis at 10 bar and 80 °C and nitrogen from an ASU at 10 bar and 25 °C with a small argon impurity (0.5 mol-%). We use the Soave-Redlich-Kwong equation of state model to capture nonidealities of the thermodynamic properties in the vapor phase. The feed streams are compressed by various compressors to reach the favored reactor pressure range from 100 to 250 bar. Each compressor is modeled with an adjusted adiabatic gas head curve, an isentropic efficiency of 75 %, and polytropic correction factors from Sandberg and Colby [10]. Between the three compressor stages, the gas streams are cooled to 50 °C to improve the compression efficiency. A flow controller adjusts the hydrogen inflow to simulate varying hydrogen supply. Last, to realize a nearly stoichiometric mixture of the reactants in front of the ammonia reactor, the nitrogen inflow is adjusted by a mass flow ratio controller.

## Section 2: Ammonia Reactor

Different types of ammonia reactors are operated in industry. All consist of multiple beds and different kinds of heat integration [11,12]. The adiabatic quench-cooled reactor (AQCR) is the most common in former fossil-based plants because of its comparatively easy control. However, because of higher conversion rates, the internal direct-cooled reactor (IDCR) and the adiabatic indirect-cooled reactor (AICR) are favored in new ammonia plants [11]. Our model focuses on the AICR type with three beds and interbed cooling using the feed stream. The bed inlet temperatures are controlled by adjusting the stream to the reactor feed effluent heat exchanger (FEHE) and the interbed heat exchangers. For a similar reactor setup, Rosbo *et al.* (2024) [11] showed that stable operation under varying loads can be obtained.

The control ability for the AICR is achieved by splitting the reactor feed inlet into four substreams. The first substream recovers heat from the reactor outlet in the FEHE. To operate the FEHE at a constant capacity, its tube mass flow is adjusted by a flow controller so that the minimal temperature difference between the shell inlet and tube outlet remains steady at 8 °C. Flow controllers also adjust the two substreams used for cooling in the interbed heat exchangers. Accordingly, the bed inlet temperatures of the second and third reactor beds can be constantly controlled to 650 K. The fourth substream is a bypass that is mixed with the three preheated substreams to adjust the temperature of the first reactor bed to 650 K. The split of the reactor feed stream enables controlling the bed inlet temperatures while efficiently integrating heat produced by the exothermic reaction

$$3\,\mathrm{H_2} + \mathrm{N_2} \rightarrow 2\,\mathrm{NH_3} \text{ with } \Delta \mathrm{H}_R = -92\ \mathrm{kJ/mol}. \qquad (1)$$

The reaction in the reactor beds is implemented with the Temkin-Pyzhev kinetic using kinetic and catalytic parameters from Mordu and Skogestad (1998) [13]. A separate plug flow reactor models each reactor bed, and the beds' dimensions increase to counteract the lower reaction rates at higher product fractions (see Table 1). The reactor operating pressure varies with the load; at nominal load, the pressure in front of the first reactor bed is about 210 bar. The occurring pressure drop over the reactor beds is calculated with the Ergun equation assuming a void fraction of 0.33 and an average particle diameter of 8 mm. Overall, the performance of the three-bed AICR can be calculated by the single-pass hydrogen conversion

$$X_{\mathrm{Single}Pass\ \mathrm{H_2}} = 1 - \dot{n}_{\mathrm{AICR\ Out\ H_2}} / \dot{n}_{\mathrm{AICR\ In\ H_2}}. \qquad (2)$$

**Table 1:** AICR beds' and flash drums' dimensions

| | Diameter D | Length L | Volume V |
|---|---|---|---|
| **AICR** | | | |
| Bed 1 | 2 m | 6 m | 18.84 $m^3$ |
| Bed 2 | 2.5 m | 7.5 m | 36.80 $m^3$ |
| Bed 3 | 3 m | 9 m | 63.59 $m^3$ |
| **Flash 1** | 1.2 m | 2.4 m | 3.17 $m^3$ |
| **Flash 2** | 1.2 m | 2.4 m | 3.17 $m^3$ |

## Section 3: Ammonia Purification

The reactor effluent contains about 25 mol-% ammonia, unreacted hydrogen and nitrogen, as well as the inert gas argon. In the first step, the unreacted reactants are recovered using a flash separator at reactor pressure and 20 °C. Subsequently, we recycle the flash's top stream and merge it with the incoming feed streams before the reactor. However, 1 % of the recycle stream must be purged to prevent the accumulation of the inert gas argon. We stabilize the purge rate with a mass flow ratio controller that adjusts the opening of the purge valve. Eventually, the bottom stream of the first flash drum contains 98 mol-% ammonia and is purified further in a second unit at 16.8 bar. Table 1 shows the dimensions of both flash drums. The liquid levels in both separators are controlled by level controllers adjusting the respective liquid outflows. After the two-step flash separation, we obtain 99.9 mol-% pure ammonia.

## Dimensioning of Process Units

All process units are sized to be operatable for the above-mentioned ammonia load range. In particular, the valves and heat exchangers must be dimensioned precisely so that the control structure properly functions in the pressure-controlled fluid flow simulations. Accordingly, the valve flow coefficients $C_V$ are adjusted to be applicable for varying mass flows, and the areas of the heat exchangers are defined so that the minimal temperature differences can be calculated to about 10 °C. Hereby, we assume the overall heat transfer coefficients

U for internal heat integration to be 500 kW/kmol/K and for cooling 400 kW/kmol/K. The cooling medium is water at 15 °C and 1.5 bar, and flow controllers regulate the cooling flows to achieve the set process temperatures. With the precise sizing of each process unit, we ensure feasible process operation within a wide operating range from 30 to 130 % with respect to the nominal ammonia production rate.

## SIMULATION RESULTS

In our simulation study, we vary the ammonia production rate from 30 to 130 % of its nominal value. With the implemented control structure, the process model can adapt autonomously to the changing load conditions and adjust the feed flow rates, cooling water flow rates, and rector feed split rates. Further, the respective controllers keep the liquid levels in the flash drums and the purge ratio constant. Detailed results supporting the above-mentioned claims are shown and discussed below.

Figure 2 illustrates the linear increase of the feed mass flows of hydrogen and nitrogen for a rising ammonia rate. At the nominal ammonia load of 1370 t/d, the molar ratio of hydrogen and nitrogen in the reactor feed stream matches the stochiometric mixture of the reactants in Equation 2. At different ammonia loads, the recycle stream composition is altered because of varying reaction rates, which also affects the composition of the reactor inlet stream. However, by controlling the nitrogen feed rate according to Equation 1, we stabilize the reactor inlet stream composition for all ammonia demands, and the molar ratio of hydrogen and nitrogen only diverges slightly from its nominal value of three.

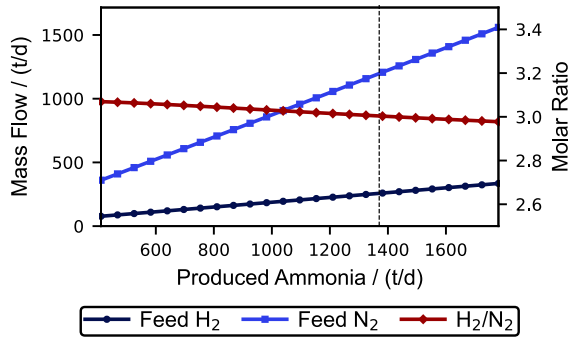



**Figure 2.** Feed streams mass flows and reactants ratio in front of the ammonia reactor for varying ammonia production rates

Since the reactor feed composition remains almost constant, changes in the reaction rate mainly depend on the AICR bed inlet temperatures and operating pressure. The reactor operating pressure is freely adjusted as described by Fahr *et al.* (2023) [14] in detail and enables effective usage of the hydrogen supply. This operation results in a constant high total hydrogen conversion of about 94.5 mol-% while meeting the ammonia purity constraint (refer to Figure 3). The changes in the reactor pressure result in bounding the single pass conversion to relatively little variations (23.7 to 36.1 mol-%) compared to its nominal value of 34 mol-% and, thus, stabilize the AICR's performance for varying ammonia loads. Our results align with those of Rosbo *et al.* (2024) [11], who found very similar conversion rates for their AICR model.

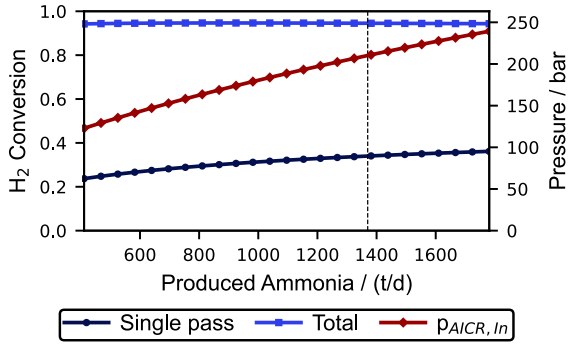



**Figure 3.** Molar hydrogen conversion and AICR inlet pressure for varying ammonia production rates

Contrasting the automatically adjusting reactor pressure, we set the AICR beds' inlet temperatures to 650 K. The temperatures are controlled with four mass flow controllers adapting the mass flows to the reactor FEHE, bypass, and interbed heat exchangers by opening and closing the respective valves. Figure 4 displays the interactions of the pre-reactor valves' opening positions and mass flows for different ammonia production rates. For low ammonia loads and thus a small total mass flow, the mass flow to the reactor FEHE is increased to ensure sufficient heat integration. Accordingly, the FEHE always works at the desired capacity independently of the stream conditions in the AICR outlet. For high ammonia production rates, more interbed cooling is necessary to stabilize the beds' inlet temperatures. Thus, the mass flow rates to the interbed heat exchanger are comparatively high for increased ammonia loads. Accordingly, at low ammonia loads, when relatively more heat is integrated, the split mass ratio of the bypass substream is reduced.

The adjusted opening positions of the corresponding valves mostly follow similar relations compared to their respective mass flows. However, the varying total mass flow and the reactor operating pressure also affect the valves' positions. This influence is exemplified by looking at the valve regulating the substream to the FEHE. Here, the split mass flow ratio decreases for higher ammonia rates, though the valve position is controlled to open more. That illustrates the complexity of controlling the mass flows before the AICR beds. Nevertheless, our

dimensioning of valves and heat exchangers resulted in a control structure that fulfills all defined process and product constraints and ensures feasible steady-state operations for the whole ammonia load range.

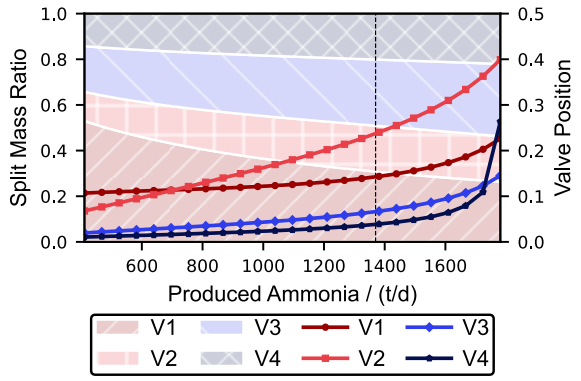



**Figure 4.** Split mass ratios (areas) of the AICR inlet substream to the FEHE (V1), the bypass (V2), the cooling heat exchanger before bed 2 (V3), and the cooling heat exchanger before bed 3 (V4), as well as the corresponding valve positions (lines) for varying ammonia production rates

One objective of flexibly operating green ammonia production is to reduce expensive hydrogen storage. The following exemplary power calculations assume a direct coupling of the PEM electrolyzer and the ASU with the HB plant. The total power demand for the production of ammonia comprises the power to produce hydrogen $P_{\mathrm{PEM}}$ and nitrogen $P_{\mathrm{ASU}}$ as well as the power demand of the HB process $P_{\mathrm{HB}}$, including the power for compressions and neglecting the power for cooling water pumping.

For the hydrogen production via PEM electrolysis, we assume a constant electrolyzer efficiency $\eta_{\mathrm{PEM}}$ of 85 % for all loads compared to the higher heating value [15]

$$P_{\mathrm{PEM}} = \frac{\dot{m}_{\mathrm{Feed\,H_2}} * \Delta \mathrm{H}^0}{\mathrm{M}_{\mathrm{H_2}} * \eta_{\mathrm{PEM}}} \text{ with } \Delta \mathrm{H}^0 = 285.9\ \mathrm{kJ/mol}. \quad (3)$$

In an ASU, gaseous nitrogen is produced as a by-product. Therefore, we do not include the total operational power of an ASU; instead, we only consider the fraction related to the production of pure nitrogen. We assume a linear relation between the ASU's power demand and production rate, according to Anele *et al.* (2015) [16]

$$P_{\mathrm{ASU}}/\dot{m}_{\mathrm{N_2}} = 0.421\ \mathrm{kWh/kg}\,. \quad (4)$$

Figure 5 illustrates that the total power demand is mainly influenced by the power required to produce hydrogen via PEM electrolysis. The power used to produce nitrogen and to operate the HB plant is comparatively low. Therefore, the total power range matches the investigated ammonia load range, stretching from 30 to 130 % with respect to the power demand at nominal conditions. Overall, the variable operation of the investigated system results in a high variability of the total power demand.

From the system's total power, the specific energy demand to produce green ammonia can be calculated by

$$e_{\mathrm{NH_3}} = P_{\mathrm{Total}}/\dot{m}_{\mathrm{NH_3}}\,. \quad (5)$$

Despite varying ammonia loads, the specific energy demand for our process setup varies little and amounts to about 9.6 MWh/t (refer to Figure 5), which is in the range of literature values for renewable ammonia production [4, 6].

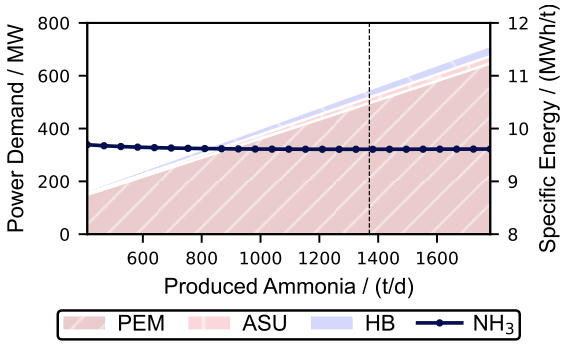



**Figure 5.** Power demand (areas) for hydrogen production via PEM electrolysis (PEM), nitrogen production via air separation (ASU), and the HB plant (HB), as well as the specific energy demand (line) of the ammonia production ($NH_3$) for varying ammonia production rates

Overall, the simulation results depict that the designed ammonia process can efficiently produce green ammonia for a wide range of varying rates. With the implemented control structure, the streams to the ammonia reactor are automatically adjusted, promoting efficient operation. This results in a constant specific energy demand at all production rates due to the primary influence of the PEM electrolyzer.

## CONCLUSION

We presented a new benchmark process model to produce renewable ammonia from green hydrogen through PEM electrolysis and nitrogen from an ASU with an advanced AICR system. The increased attention to flexible ammonia production from variable green hydrogen supply challenges the design of HB plants. In particular, the dimensioning of process units and control structures must be performed carefully. We showed that our precisely dimensioned process model can simulate production for a wide range of green ammonia rates at steady-state. Pivotal for this is the implemented control structure that autonomously controls the AICR operation for high process efficiency.

While the community traditionally relied on the Tennessee Eastman plant for benchmarking studies, this

reference becomes less relevant when studying the dynamics and operational challenges of the renewable hydrogen industry. Therefore, this new benchmarking approach is particularly valuable as it directly addresses the fluctuating nature of renewable hydrogen supply central to renewable ammonia production. In future works, the steady-state ammonia process model can be upgraded to feature transient simulations of dynamic interactions during the process operation, *e.g.*, failures and abnormalities. The obtained dynamic data could be valuable for developing new process safety and monitoring techniques and supporting ongoing innovations in the green hydrogen economy as a novel safety benchmark model.

## ACKNOWLEDGEMENTS

This research was funded by the European Union Horizon Europe 2022 Research and Innovation Programme under the Marie Sklodowska-Curie Grant Agreement No. 101119358 (PROSAFE).

## REFERENCES

1. Dawood F, Anda M, Shafiullah GM. Hydrogen production for energy: An overview. *Int J Hydrogen* Energy. 457:3847-69 (2020) doi.org/10.1016/j.ijhydene.2019.12.059
2. Olabi AG, Abdelkareem MA, Al-Murisi M, et al. Recent progress in Green Ammonia: Production, applications, assessment; barriers, and its role in achieving the sustainable development goals. *Energy Convers Manag* 277 (2023) doi.org/10.1016/j.enconman.2022.116594
3. Ishaq H, Crawford C. Review of ammonia production and utilization: Enabling clean energy transition and net-zero climate targets. *Energy Convers Manag* 300:117869 (2024) doi.org/10.1016/J.ENCONMAN.2023.117869
4. MacFarlane DR, Cherepanov P V., Choi J, et al. A Roadmap to the Ammonia Economy. *Joule* 46:1186-205 (2020) doi.org/10.1016/J.JOULE.2020.04.004
5. Smith C, Hill AK, Torrente-Murciano L. Current and future role of Haber–Bosch ammonia in a carbon-free energy landscape. *Energy Environ Sci* 132:331-44 (2020) doi.org/10.1039/C9EE02873K
6. Bicer Y, Dincer I, Zamfirescu C, Vezina G, Raso F. Comparative life cycle assessment of various ammonia production methods. *J Clean Prod* 135:1379-95 (2016) doi.org/10.1016/J.JCLEPRO.2016.07.023
7. Downs JJ, Vogel EF. A plant-wide industrial process control problem. *Comput Chem Eng* 173:245-55 (1993) doi.org/10.1016/0098-1354(93)80018-I
8. Birol G, Ündey C, Çinar A. A modular simulation package for fed-batch fermentation: penicillin production. *Comput Chem Eng* 2611:1553-65 (2002) doi.org/10.1016/S0098-1354(02)00127-8
9. Santander O, Kuppuraj V, Harrison CA, Baldea M. An open source fluid catalytic cracker - fractionator model to support the development and benchmarking of process control, machine learning and operation strategies. *Comput Chem Eng* 164:107900 (2022) doi.org/10.1016/j.compchemeng.2022.107900
10. Sandberg ME, Colby GM. Limitations of ASME PTC 10 in Accurately Evaluation Centrifugal Compressor Thermodynamic Performance. In: Proceedings of the 42nd Turbomachinery Symposium. Turbomachinery Laboratory, Department of Mechanical Engineering, Texas A&M University (2013) doi.org/10.21423/R1505Q
11. Rosbo JW, Jensen AD, Jørgensen JB, Huusom JK. Comparison, operation and cooling design of three general reactor types for Power-to-Ammonia processes. *Chem Eng J* 496:153660 (2024) doi.org/10.1016/j.cej.2024.153660
12. Khademi MH, Sabbaghi RS. Comparison between three types of ammonia synthesis reactor configurations in terms of cooling methods. *Chem Eng Res Des* 128:306-17 (2017) doi.org/10.1016/J.CHERD.2017.10.021
13. Morud JC, Skogestad S. Analysis of instability in an industrial ammonia reactor. *AIChE J* 444:888-95 (1998) doi.org/10.1002/AIC.690440414
14. Fahr S, Schiedeck M, Schwarzhuber J, Rehfeldt S, Peschel A, Klein H. Design and thermodynamic analysis of a large-scale ammonia reactor for increased load flexibility. *Chem Eng J*. 471:144612 (2023) doi.org/10.1016/J.CEJ.2023.144612
15. Shiva Kumar S, Himabindu V. Hydrogen production by PEM water electrolysis – A review. *Mater Sci Energy Technol* 23:442-54 (2019) doi.org/10.1016/j.mset.2019.03.002
16. Aneke M, Wang M. Potential for improving the energy efficiency of cryogenic air separation unit (ASU) using binary heat recovery cycles. *Appl Therm Eng* 81:223-31 (2015) doi.org/10.1016/j.applthermaleng.2015.02.034

© 2025 by the authors. Licensed to PSEcommunity.org and PSE Press. This is an open access article under the creative commons CC-BY-SA licensing terms. Credit must be given to creator and adaptations must be shared under the same terms. See https://creativecommons.org/licenses/by-sa/4.0/



Systems & Control Transactions

**Research Article - Peer Reviewed Conference Proceeding**
ESCAPE 35 - European Symposium on Computer Aided Process Engineering
Ghent, Belgium. 6-9 July 2025
Jan F.M. Van Impe, Grégoire Léonard, Satyajeet S. Bhonsale,
Monika E. Polańska, Filip Logist (Eds.)

PSE PRESS

# Bayesian uncertainty quantification of graph neural networks using stochastic gradient Hamiltonian Monte Carlo

**Qinghe Gao[a], Daniel C. Miedema[a], Yidong Zhao[b], Jana M. Weber[c], Qian Tao[b], and Artur M. Schweidtmann[a]***

[a] Process Intelligence Research Team, Department of Chemical Engineering, Delft University of Technology, Van der Maasweg 9, Delft 2629 HZ, The Netherlands
[b] Department of Imaging Physics, Delft University of Technology, Delft, the Netherlands
[c] Pattern Recognition and Bioinformatics, Department of Intelligent Systems, Delft University of Technology, Van Mourik Broekmanweg 6, 2628 XE Delft, The Netherlands
* Corresponding Author: a.schweidtmann@tudelft.nl.

## ABSTRACT

Graph neural networks (GNNs) have proven state-of-the-art performance in molecular property prediction tasks. However, a significant challenge with GNNs is the reliability of their predictions, particularly in critical domains where quantifying model confidence is essential. Therefore, assessing uncertainty in GNN predictions is crucial to improving their robustness. Existing uncertainty quantification methods, such as Deep ensembles and Monte Carlo Dropout, have been applied to GNNs with some success, but these methods are limited to approximate the full posterior distribution. In this work, we propose a novel approach for scalable uncertainty quantification in molecular property prediction using Stochastic Gradient Hamiltonian Monte Carlo (SGHMC). Additionally, we utilize a cyclical learning rate to facilitate sampling from multiple posterior modes which improves posterior exploration within a single training round. Moreover, we compare the proposed methods with Monte Carlo Dropout and Deep ensembles, focusing on error analysis, calibration, and sharpness, considering both epistemic and aleatoric uncertainties. Our experimental results demonstrate that the proposed parallel-SGHMC approach significantly outperforms Monte Carlo Dropout and Deep ensembles in terms of calibration and sharpness. Specifically, parallel-SGHMC reduces the sum of squared errors by 99.4% and 75%, respectively, when compared to Monte Carlo Dropout and Deep Ensembles. These findings suggest that parallel-SGHMC is a promising method for uncertainty quantification in GNN-based molecular property prediction.

**Keywords**: Uncertainty quantification, graph neural networks, property prediction

## INTRODUCTION

Graph neural networks (GNNs) have demonstrated promising potential in accelerating the computational estimation of molecular properties [1-3]. However, their reliability remains a significant challenge, e.g., in safety-critical applications where understanding model confidence is crucial. Accurately assessing the uncertainty of GNN predictions is essential for enhancing their robustness, particularly when predicting complex molecular behaviors.

Uncertainty in machine learning can generally be divided into two types: aleatoric and epistemic uncertainty [4]. Aleatoric uncertainty arises from inherent noise in the data generation process, such as experimental measurement errors or environmental variations, and is considered irreducible. In contrast, epistemic uncertainty stems from the lack of knowledge of a model, often due to limited data or an incomplete understanding of the process, and can be reduced through additional data collection or improved model design. For instance, in modeling complex chemical reactions, using a more advanced model architecture—such as incorporating reaction kinetics and thermodynamic principles—can reduce

epistemic uncertainty by capturing the process dynamics more accurately. Estimating both types of uncertainty is critical in domains like molecular property prediction, where errors can have substantial consequences.

Two popular methods for jointly uncertainty quantification of machine learning models are Deep ensembles and Monte Carlo Dropout (MC-dropout). MC-dropout [5] applies dropout during both training and inference, generating multiple stochastic forward passes to approximate the posterior distribution of the model. Deep ensembles [6] involves training multiple independent models and averaging their predictions, with the variance among them reflecting the model uncertainty. Although both methods have been widely adopted for scalable uncertainty estimation in molecular property prediction [7], they have some limitations. Deep ensembles primarily focus on the maximum a posteriori (MAP) estimate, neglecting broader regions of the posterior distribution. Conversely, MC-dropout samples from a single mode, overlooking the possibility of multiple modes in the posterior.

We propose a novel approach using Stochastic Gradient Hamiltonian Monte Carlo (SGHMC) [8] to quantify the uncertainty of GNNs for molecular property prediction task. Specifically, we incorporate a cyclical learning rate, which combines the strengths of both sampling strategies and has been successfully utilized in medical imaging domain [9]. We benchmark the proposed SGHMC method against Deep ensembles and MC-dropout on molecular property prediction tasks. Specifically, we evaluate the models with three different metrics: Error analysis, calibration, and sharpness.

# METHODS

## Preliminary

To quantify the uncertainty of GNNs in molecular property prediction tasks, the aim is to transform a single prediction (aleatoric uncertainty) and a deterministic weight (epistemic uncertainty) into a distribution, respectively [10]. For aleatoric uncertainty, the mean-variance estimation is often considered as the most practical approach. The mean-variance approach is simply splitting the last layers of neural networks to predict both mean $\mu(x)$ and variance $\sigma^2(x)$ of Gaussian distribution $N(y;\mu(x),\sigma^2(x))$. Therefore, during the inference time, the test case $y_i = \mu(x_i) + \epsilon(x_i)$ where $\epsilon \sim N\left(0,\sigma^2(x_i)\right)$. Additionally, the corresponding objective function (Eq. 1) becomes minimizing the Gaussian negative log-likelihood (NLL) loss function:

$$NLL(w) = \frac{1}{N}\sum_{i=1}^{N}\frac{1}{2}\left[\frac{1}{\sigma_w^2}(x_i)\left(y_i - \mu_w(x_i)\right)^2 + \log\left(2\pi\sigma_w^2(x_i)\right)\right] \quad (1)$$

Moreover, the Bayesian approach is used to get the epistemic uncertainty, which essentially approximates the prior distribution $p(w|D) \propto p(w)p(D|w)$. Therefore, during the inference time on a test case: $x_i$ :

$$p(y_i|x_i, D) = \int_w p(w|D)p(y_i|x_i, w)\, dw \quad (2)$$

However, in reality, the prior distribution and the integral are intractable. Therefore, they are commonly approximated with MC integration over samples $w_i$ drawn from an approximate posterior distribution $q(w)$:

$$p(y_i|x_i, D) = \frac{1}{M}\sum_{j=1}^{M} p(y_i|x_i, w_j),\ w_j \sim q(w) \quad (3)$$

## SGHMC

The proposed SGHMC [9] algorithm samples from the posterior distribution based on the Hamiltonian equation of motion. The Hamiltonian function is given by:

$$H(q,r) = U(q) + K(r) \quad (4)$$

where an object moves on a potential energy surface $U(q)$ with kinetic energy $K(r)$ where $q$ represents the positions and $r$ represents the momenta. Using the canonical distribution (probability of the states based on the energy), the joint probability distribution over positions and momenta can be defined as:

$$p(q,r) \propto e^{-H(q,r)} = e^{-U(q)}\, e^{-K(r)} \quad (5)$$

When the potential energy $U(q)$ is expressed as the NLL of the model combined with a prior, the canonical distribution with respect to $U(q)$ corresponds to posterior distribution of the model parameters $w$. Minimizing $U(w)$ is equivalent to finding the mode of the posterior distribution:

$$U(w) = -\log[p(w|D)] = NLL(w) + \lambda\left|\left|w\right|\right|^2 \quad (6)$$

The choice of distribution over momenta $r$ can be arbitrary. Here, we chose a quadratic form for the kinetic energy:

$$K(r) = \frac{1}{2}r^T M^{-1} r \quad (7)$$

resulting in Gaussian distribution over $r$. The mass matrix $M$, typically set to the identity matrix for simplification [11].

Therefore, the dynamics in the end are governed by equations:

$$dw = M^{-1} r\, dt \quad (8)$$

$$dr = -\nabla U(w)\, dt \quad (9)$$

Additionally, to address the computational challenge of evaluating the full gradient $\nabla U(w)$ in large datasets, SGHMC uses a noisy gradient estimate $\nabla\widetilde{U}(w)$ based on mini-batches. The introduced noise can be mitigated by a friction term A in the momentum update:

$$r_i = r_{i-1} - \nabla\widetilde{U}(w_{i+1})h - Ar_{i-1}h + \sqrt{2AhT}N(0, I) \quad (10)$$

This formulation is similar to SGD with momentum but includes an additional Gaussian noise term, controlled by temperature $T$. The temperature modulates the sensitivity of the posterior distribution to the potential energy: $T = 1$ yields the standard Bayesian posterior, $T < 1$ (cold posterior) increases sensitivity to low-loss regions, while $T > 1$ broadens exploration at potential cost of accuracy.

## Evaluation metric

The quality of uncertainty estimates in predictive models can be assessed using three key metrics: error analysis, calibration, and sharpness. For the metric error analysis, we utilize the root mean square error (RMSE) and the coefficient of determination (R2). Calibration methods assess how well predicted uncertainties align with observed errors. Here, we utilize two metrics: NLL and sum of squared errors (SSE). Rather than only using the NLL as a loss function during training, it is also used as a quantitative measure to assess the quality of the predictive distribution after training. SSE measures the total squared error between the predicted quantiles and the observed empirical quantiles. If the SSE is small, it means that the predictions of the models are well-calibrated with respect to the observed data. Sharpness measures the informativeness of uncertainty estimates with root mean predicted variance (RMV) and coefficient of variation $C_v$. Specifically, RMV is denoted as:

$$RMV = \sqrt{\frac{1}{n}\sum_{i=1}^{n} \widehat{\sigma_i^2}} \tag{11}$$

where $\widehat{\sigma_i^2}$ is predicted variance or uncertainty. A low RMV indicates the model on average predicts low uncertainty and thus low expected error. Additionally, $C_v$ is denoted as:

$$C_v = \frac{\sqrt{\frac{1}{N}\sum_{i=1}^{N}(\hat{\sigma}_i - \sigma_*)}}{\sigma_*} \tag{12}$$

where $\hat{\sigma}_i$ is the predicted standard deviation (uncertainty) of instance $i$ and $\sigma_*$ is the mean predicted standard deviation. A high $C_v$ suggests significant dispersion (heteroscedasticity), indicating that uncertainty estimates are highly dependent on the input. In contrast, a $C_v$ of zero indicates constant (homoscedastic) uncertainty, meaning the estimates are uninformative and do not vary with the input [10].

## Experiment design

The dataset used is the QM9 benchmark [12], consisting of 132,481 small organic molecules (CHONF) with 13 target properties, evaluated at the B3LYP/6-31G(2df,p) level. An 80:10:10 train/validation/test split was applied, using heat capacity at 298.15 K as the target property. The Directed Message Passing Neural Network (D-MPNN) is used as a base model implemented in Chemprop [13], with a mean-variance output and heteroscedastic noise model. The models contain three message passing layers and two feed-forward layers, each with a hidden size of 300.

All uncertainty methods were optimized using the Gaussian NLL loss function with a regularization parameter of $\lambda$ = 0.0001. The initial learning rate was set to 0.01, with an exponential decay (γ = 0.95) and a batch size of 50. MC-Dropout models are trained for 216 epochs with the SGD optimizer and a dropout rate of $p$ = 0.1, and 24 predictions are collected for the ensemble with different dropouts. Deep Ensemble models are trained for 650 epochs with the SGD optimizer (momentum $m$ = 0.9), with three ensemble predictions from different models. Parallel-SGHMC models are trained for 650 epochs with SGHMC (momentum $m$ = 0.9), with noise injected at $T$ = 0.01 after 60% of training. Posterior samples were collected every ten epochs after noise injection. 24 ensemble predictions are collected from posterior samples. To explore multiple local modes of the posterior, we additionally propose Cyclical-SGHMC model. It uses four cycles within a 650-epoch budget, with a reset learning rate of 0.00025 after the first cycle. Noise was injected with $T$ = 0.01 after 60% of each cycle. Similarly, 24 ensemble predictions are collected from posterior samples. All simulations ran on a Windows server with a 3.5 GHz 24-core Intel(R) Xeon(R) W-2265 CPU, an NVIDIA GeForce RTX 3090 GPU, and 64 GB of memory.

Figure 1 provides a conceptual representation of various posterior sampling strategies employed during a single training process. The x-axis represents the model parameter space www, while the y-axis shows the posterior probability distribution $P(w|D)$ given the data $D$. The black curve represents the posterior distribution with multiple modes. Deep Ensembles typically sample from a single local mode within a training cycle, limiting their ability to explore the broader posterior distribution. In contrast, both MC-Dropout and parallel-SGHMC exhibit similar sampling behaviours, generating multiple samples from the local regions surrounding the current mode. Notably, cyclical-SGHMC offers a more robust exploration of the posterior by sampling from multiple regions across different modes, facilitated by its cyclical learning rate, which enables escape from local minima and exploration of diverse posterior landscapes.

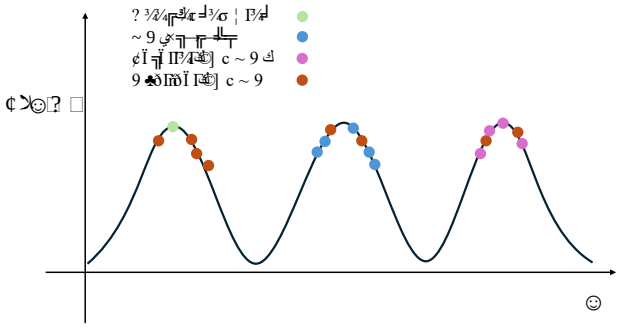


**Figure 1.** Conceptual representation of the different

**Table 1:** Uncertainty quantification results from four different models. RMSE stands for the root mean square error, R2 for coefficient of determination, SSE for the sum of squared errors, NLL for the negative log likelihood, RMV for the root mean predicted variance, and CV for coefficient of variation.

| Models | Error | | Calibration | | Sharpness | |
|---|---|---|---|---|---|---|
| | RMSE↓ | $R^2$↑ | SSE↓ | NLL↓ | RMV↓ | $C_V$↑ |
| Parallel-SGHMC | 0.6650 | 0.9735 | 0.0003 | -0.4921 | 0.5137 | 2.0178 |
| Cyclical-SGHMC | 0.6156 | 0.9773 | 0.0405 | -0.3522 | 0.6393 | 1.6555 |
| MC-dropout | 0.7227 | 0.9687 | 0.0500 | 0.4678 | 0.9167 | 0.9897 |
| Deep ensemble | 0.7399 | 0.9672 | 0.0012 | 0.4357 | 0.7905 | 1.0112 |

posterior sampling strategies for one training process employed by Deep ensembles, MC-dropout, parallel-SGHMC, and cyclical-SGHMC.

## RESULTS AND DISCUSSION

Table 1 presents the performance of four uncertainty quantification models - parallel-SGHMC, cyclical-SGHMC, MC-Dropout, and Deep ensemble - on key evaluation metrics, including error, calibration, and sharpness.

In terms of error analysis, SGHMC-based models demonstrate superior performance with respect to predictive error. Specifically, cyclical-SGHMC achieves the lowest RMSE (0.6156) and the highest $R^2$ (0.9773), indicating that it provides the most accurate predictions. The potential reason is that cyclical-SGHMC samples a richer posterior, capturing parameter uncertainty more effectively than methods like MC-Dropout.

For the calibration category, parallel-SGHMC outperforms the other models with the lowest SSE of 0.0003 and the lowest NLL score of -0.4921. This indicates that its predicted uncertainties are highly aligned with the actual errors, suggesting that this model provides the most reliable uncertainty estimates. Cyclical-SGHMC, with an SSE of 0.0405 and an NLL of -0.3522, also performs well, although its uncertainty estimates are slightly less aligned with the observed errors compared to parallel-SGHMC. By contrast, MC-Dropout and Deep ensemble exhibit poorer calibration performance. Their SSE values of 0.0500 and 0.0012, respectively, and their higher NLL values (0.4678 and 0.4357) suggest that these models tend to overestimate uncertainty. This misalignment between predicted uncertainties and actual errors could lead to less reliable uncertainty estimates in practice, making these models less desirable for applications where accurate uncertainty quantification is important.

In terms of sharpness, parallel-SGHMC performs better than the other models, achieving the lowest RMV of 0.5137 and the highest $C_V$ of 2.0178. This suggests that its uncertainty intervals are narrow and focused, indicating high confidence in its predictions. Cyclical-SGHMC is the next best model with an RMV of 0.6393 and a $C_V$ of 1.6555, providing moderately sharp uncertainty intervals, which reflect a balance between confidence and calibration. On the other hand, MC-Dropout and Deep ensemble exhibit significantly less sharp uncertainty estimates, with RMV values of 0.9167 and 0.7905, respectively. Their lower $C_V$ values (0.9897 for MC-Dropout and 1.0112 for Deep Ensemble) further indicate that these models generate broader uncertainty intervals, reflecting lower confidence in their predictions. While broader intervals can be beneficial in risk-averse or highly uncertain environments, they are less desirable in scenarios where tight confidence bounds are required.

In summary, the parallel-SGHMC model is recommended for tasks requiring accurate predictions, well-calibrated uncertainties, and narrow confidence intervals. Cyclical-SGHMC provides a balanced alternative, while MC-Dropout and Deep ensemble may be more appropriate for scenarios where broader, conservative uncertainty estimates are desired.

## CONCLUSIONS

We proposed a novel approach to perform scalable uncertainty quantification for molecular property prediction with GNNs. Specifically, SGHMC with cyclical learning rate was researched for scalable uncertainty quantification in molecular property prediction with the D-MPNN architecture with mean variance. A comparative study was performed among SGHMC, Deep Ensemble and MC-dropout with the QM9 dataset with the heat capacity target property. Our results indicate that the proposed parallel-SGHMC approach outperforms MC-dropout and Deep ensembles in terms of calibration and sharpness. Specifically, parallel-SGHMC reduces the sum of squared errors (SSE) by 99.4% and 75%, respectively. These findings suggest that parallel-SGHMC is particularly suited for applications requiring narrow confidence intervals, where high precision in uncertainty quantification is essential, such as in safety-critical predictions or regulatory settings in pharmaceutical applications. While Deep ensemble and MC-dropout may offer advantages in scenarios where broader uncertainty bounds are required, such as in early-stage exploratory research.

## REFERENCES


1. Schweidtmann AM, Rittig JG, Konig A, Grohe M, Mitsos A, Dahmen M. Graph neural networks for prediction of fuel ignition quality. Energy & Fuels 34:11395-11407 (2020) https://doi.org/10.1021/acs.energyfuels.0c01533
2. Wieder O, Kohlbacher S, Kuenemann M, Garon A, Ducrot P, Seidel T, Langer T. A compact review of molecular property prediction with graph neural networks. Drug Discov Today: Technol 37:1-12 (2020) https://doi.org/10.1016/j.ddtec.2020.11.009
3. Rittig JG, Mitsos A. Thermodynamics-consistent graph neural networks. Chem Sci 15(44):18504-18512 (2024) https://doi.org/10.1039/D4SC04554H
4. Abdar M, Pourpanah F, Hussain S, Rezazadegan D, Liu L, Ghavamzadeh M, et al. A review of uncertainty quantification in deep learning: techniques, applications and challenges. Inf Fusion 76:243-297 (2021) https://doi.org/10.1016/j.inffus.2021.05.008
5. Gal Y, Ghahramani Z. Dropout as a Bayesian approximation: representing model uncertainty in deep learning. Int Conf Mach Learn 1050-1059 (2016) https://doi.org/10.48550/arXiv.1506.02142
6. Lakshminarayanan B, Pritzel A, Blundell C. Simple and scalable predictive uncertainty estimation using deep ensembles. Adv Neural Inf Process Syst 30 (2017) https://doi.org/10.48550/arXiv.1612.01474
7. Wang F, Liu Y, Liu K, Wang Y, Medya S, Yu PS. Uncertainty in graph neural networks: a survey. arXiv preprint (2024) https://doi.org/10.48550/arXiv.2403.07185
8. Chen T, Fox E, Guestrin C. Stochastic gradient Hamiltonian Monte Carlo. Proc 31st Int Conf Mach Learn, PMLR 32(2):1683-1691 (2014) https://doi.org/10.48550/arXiv.1402.4102
9. Zhao Y, Yang C, Schweidtmann A, Tao Q. Efficient Bayesian uncertainty estimation for nnU-Net. Int Conf Med Image Comput Comput Assist Interv 535-544 (2022) https://doi.org/10.1007/978-3-031-16452-1_51
10. Busk J, Jørgensen PB, Bhowmik A, Schmidt MN, Winther O, Vegge T. Calibrated uncertainty for molecular property prediction using ensembles of message passing neural networks. Mach Learn Sci Technol 3(1):015012 (2021) https://doi.org/10.1088/2632-2153/ac3eb3
11. Neal RM. MCMC using Hamiltonian dynamics. In: Handbook of Markov Chain Monte Carlo. Chapman and Hall/CRC 113-162 (2011) https://doi.org/10.1201/b10905
12. Ramakrishnan R, Dral PO, Rupp M, von Lilienfeld OA. Quantum chemistry structures and properties of 134 kilo molecules. Sci Data 1:1-7 (2014) https://doi.org/10.1038/sdata.2014.22
13. Heid E, Greenman KP, Chung Y, Li SC, Graff DE, Vermeire FH, et al. Chemprop: a machine learning package for chemical property prediction. J Chem Inf Model 64:9-17 (2023) https://doi.org/10.1021/acs.jcim.3c01250



© 2025 by the authors. Licensed to PSEcommunity.org and PSE Press. This is an open access article under the creative commons CC-BY-SA licensing terms. Credit must be given to creator and adaptations must be shared under the same terms. See https://creativecommons.org/licenses/by-sa/4.0/




Systems & Control Transactions

**Research Article - Peer Reviewed Conference Proceeding**
ESCAPE 35 - European Symposium on Computer Aided Process Engineering
Ghent, Belgium. 6-9 July 2025
Jan F.M. Van Impe, Grégoire Léonard, Satyajeet S. Bhonsale,
Monika E. Polańska, Filip Logist (Eds.)

PSE PRESS

# pyDEXPI: A Python framework for piping and instrumentation diagrams (P&IDs) using the DEXPI information model

**Dominik P. Goldstein[a], Lukas Schulze Balhorn[a], Achmad Anggawirya Alimin[a], and Artur M. Schweidtmann[a]***

[a] Process Intelligence Research Group, Department of Chemical Engineering, Delft University of Technology, Van der Maasweg 9, Delft 2629 HZ, The Netherlands
* Corresponding Author: a.schweidtmann@tudelft.nl.

## ABSTRACT

Developing piping and instrumentation diagrams (P&IDs) is a fundamental task in process engineering. For designing complex installations, such as petroleum plants, multiple departments across several companies are involved in refining and updating these diagrams, creating significant challenges in data exchange between different software platforms from various vendors. The primary challenge in this context is interoperability, which refers to the seamless exchange and interpretation of information to collectively pursue shared objectives. To enhance the P&ID creation process, a unified, machine-readable data format for P&ID data is essential. A promising candidate is the Data Exchange in the Process Industry (DEXPI) standard. We present pyDEXPI, an open-source implementation of the DEXPI format for P&IDs in Python. pyDEXPI makes P&ID data more efficient to handle, more flexible, and more interoperable. We envision that, with further development, pyDEXPI will act as a central scientific computing library for the domain of digital process engineering, facilitating interoperability and the application of data analytics and generative artificial intelligence on P&IDs. We provide the pyDEXPI package with the documentation on GitHub at https://github.com/process-intelligence-research/pyDEXPI.

**Keywords**: Piping and instrumentation diagram, DEXPI, FAIR data, Data model, Software toolbox, Open-source

## 1. INTRODUCTION

Piping and instrumentation diagrams (P&IDs) are chemical engineering diagrams that depict the process equipment, piping, pumps, instruments, valves, and further fittings of a chemical plant [1]. They act as a central, interdisciplinary reference document throughout the plant's life cycle including construction, start-up, and operation [2]. For large-scale plants, such as petrochemical processes, P&IDs may span over 1000 pages, containing a vast amount of engineering data.

For such complex projects, many different departments from several companies and parties need to work together to plan, construct, and operate the process plant. The parties involved in this include engineering, procurement, and construction companies, owner-operators, vendors, site services, and authorities. A seamless exchange of P&ID data between contributors is crucial. In reality, however, this seamless exchange is obstructed by the lack of interoperability between different Computer-Aided Engineering (CAE) software systems and other systems used by the participating stakeholders. The software systems use different underlying data representations of the P&IDs, and it is difficult to extract information from these data representations to use in different software.

Missing interoperability of P&ID data representations not only hinders effective engineering workflows but also disrupts the adoption of novel digital process engineering tools, including data analytics or generative artificial intelligence (GenAI) [3]. Recent research works have demonstrated the potential rooted in GenAI to

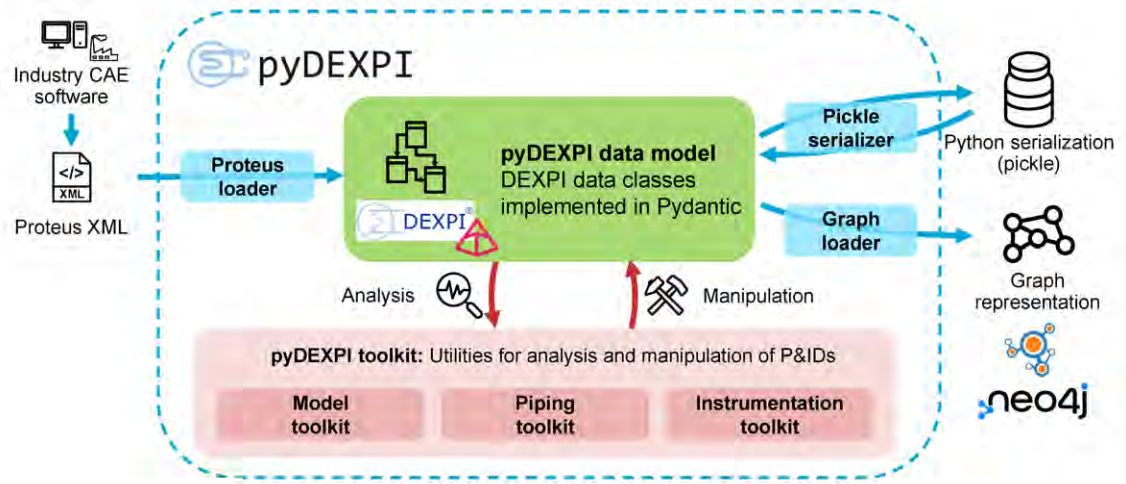



**Figure 1:** Overview of the pyDEXPI functionality. The Python implementation of the DEXPI data classes lies at the heart of the package (green). The package includes import and export of data (blue), and toolkit functionality for analysis and manipulation (red).

assist, automate, and improve the engineering process [4-9]. However, missing interoperability causes a lack of machine-readable data and hinders the integration of solutions into existing systems. To enable seamless exchange of P&ID data and facilitate integration of novel digital process engineering tools, a unified, machine-readable data format for P&ID data is necessary.

An emerging exchange format for P&ID data is the Data Exchange in the Process Industry (DEXPI) data format [10]. It defines a data model for P&IDs intended to facilitate the handover of data across CAE software. The DEXPI format was developed by the DEXPI initiative, which is supported by several industrial software vendors and chemical engineering companies. However, there is no open-source implementation of the DEXPI class framework. This makes it difficult to use this framework for interoperable data exchange in practice, and the application in digital process engineering.

To address the need for an open-source implementation of the industry-compatible DEXPI framework, we have created pyDEXPI, which implements the DEXPI information model for Python (Figure 1). P&ID data can be imported to pyDEXPI from DEXPI-conform Proteus XML files, saved in Python pickle files, and exported to NetworkX graphs. Within pyDEXPI, a model toolkit allows the analysis and manipulation of P&ID data, e.g., by retrieving certain objects with attributes of interest or reconnecting piping connections. With pyDEXPI, we aim to provide an interoperable and accessible informatics package for P&ID data.

## 2. DEXPI: DATA EXCHANGE FOR THE PROCESS INDUSTRY

The DEXPI initiative has defined the DEXPI information model with support from industrial software vendors, chemical companies, and academic partners. The objective of the information model is the definition of a system-independent, uniform data model for P&ID data that can be exported and imported by participating CAE software vendors [10]. The established version of DEXPI is Version 1.3, although the newest Version 1.4 was recently published in December 2024. The DEXPI data model defines a set of data classes and their relationships. DEXPI P&IDs are exchanged in the Proteus XML schema [11], therefore, the DEXPI specification also outlines how the data model is mapped into this XML schema.

The DEXPI 1.3 specification defines 473 data classes, data types, and enumerations organized into 11 packages. The packages are *DexpiModel*, *MetaData*, *PlantStructure*, *Equipment*, *Piping*, *Instrumentation*, *Customization*, *Enumerations*, *PhysicalQuantities*, *Graphics*, and *DataTypes*. The classes have five properties that define the class relationships and the stored information. First, a DEXPI class can have a set of supertypes, from which it inherits all properties. Second, a class can have subtypes, to which it passes on its properties. This is the inverse of the supertype relationship. Third, a class has a set of compositional attributes, which are lower-level DEXPI classes that the class conceptually consists of. Fourth, a class has reference attributes, which can be all other references to DEXPI classes that do not constitute a composition, such as the target of a pipe. Finally, a DEXPI class can have a set of data attributes, which store the class information in the form of basic data types or enumerations. The data types and enumerations are also defined within the DEXPI framework. For more details on

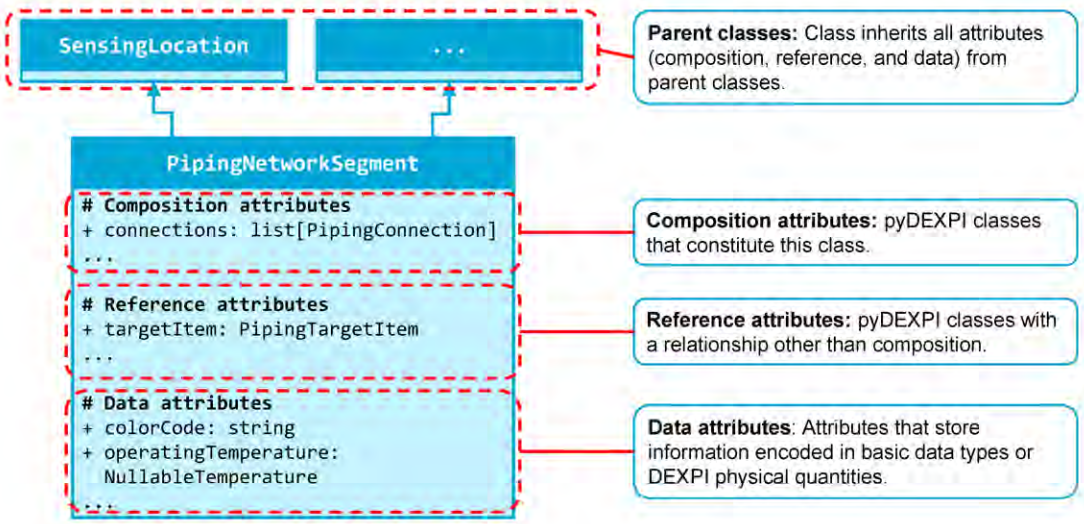



**Figure 2:** The partial UML diagram of the pyDEXPI class *PipingNetworkSegment* with an example parent class and example attributes.

the DEXPI information model, we refer the reader to the specification of the DEXPI information model [10].

While the DEXPI framework is a promising format for interoperable P&ID data, there was no open-source implementation available. The main, openly available tool for examining data in a DEXPI format is the P&ID Verificator [12]. This application has a comprehensive user interface to visualize a P&ID, investigate the underlying data model, and display verification messages. However, it is not open-source and has no interfaces for other software, which prevents it from being used for further applications beyond DEXPI data verification. Typically, DEXPI data is only exchanged via the Proteus XML schema. However, this is difficult to apply in practice due to the inconsistent design of Proteus XML and DEXPI [10]. Since no prior open-source implementation exists, the value of DEXPI for interoperability and its applicability for GenAI is limited.

## 3. THE PYDEXPI PYTHON PACKAGE

The pyDEXPI package provides an implementation of the DEXPI class framework in Python. Data can be imported and exported in several formats. To make the data more accessible to users, pyDEXPI also includes functionality to analyze and manipulate P&ID data. An overview of the functionality of pyDEXPI is depicted in Figure 1.

### 3.1. Implementation of the DEXPI information model as Python data classes

At the heart of pyDEXPI lie the data classes of the DEXPI information model. They are implemented as data classes of the Pydantic Python package [12], which specializes in data modeling and validation. The classes are organized into Python packages corresponding to the DEXPI framework's packages. All pyDEXPI classes inherit from a common base class called *DexpiBaseModel*, which defines some common behavior to use them effectively in Python programming. This includes defining a UUID for each class instance and assigning a new UUID if an object is copied. The data types of DEXPI are also implemented as Pydantic classes but inherit from a different common base class *DexpiDataTypeBaseModel*. This is because data types require different behavior than normal data classes. For example, a data class does not require an ID, but an evaluation of equality. The DEXPI classes representing basic data types, such as strings and integers, are omitted and replaced with the corresponding inbuilt data types of Python. The enumerations of DEXPI are implemented as Python enumerations.

The pyDEXPI classes implement the characteristics of the DEXPI classes with Python programming concepts. The class supertype relationship is implemented using regular class inheritance. Each class has the pyDEXPI classes corresponding to its supertypes as parent classes. This also covers the inverse, subtype relationship of DEXPI. Furthermore, each pyDEXPI class defines a set of attribute fields. The attribute fields have type annotations with the required data type defined in DEXPI, and the type annotations are enforced by Pydantic data validation. To distinguish between composition, reference, and data attributes, the pyDEXPI attribute fields are annotated with an additional indicator using the Pydantic field annotations functionality. The indicator *attribute_category* takes the values *composition*, *reference*, or *data*.

To illustrate the structure of a typical pyDEXPI class, Figure 2 depicts the partial UML diagram of the pyDEXPI

class *PipingNetworkSegment*. A *PipingNetworkSegment* is a child of *SensingLocation*, among others, and inherits all its attributes. A *PipingNetworkSegment* consists, among others, of *PipingConnections* which compose the segment as compositional attributes. In contrast, a *PipingNetworkSegment* references a *PipingTargetItem* as its target. The target item, which may be an equipment nozzle, for example, is in the compositional hierarchy of a different class. Finally, a *PipingNetworkSegment* contains a set of data attributes, which are stored in basic data types or pyDEXPI physical quantities.

### 3.2. Importing and exporting data with pyDEXPI

While the pyDEXPI class model established the structural foundation of the package, pyDEPXI also includes functional components to enable practical application for data import, export, and manipulation. These are essential for the effective utilization of pyDEXPI in data science applications. Most importantly, this includes importing and exporting of P&ID data in different formats.

pyDEXPI includes several possibilities for importing, exporting, loading, and saving data. The most notable import functionality is the import of P&ID data from DEXPI-conform Proteus XML files. This interface enables importing data extracts from DEXPI-compliant CAE tools, which unlocks access to a vast repository of P&ID data. Further, pyDEXPI supports saving and loading data quickly and easily in a Python pickle format.

Although pyDEXPI proposes a unified framework for the handling of P&ID data, downstream data analytics tasks require P&ID data in different formats and granularities to fit the needs of the method applied [3]. pyDEXPI supports exporting data as a graph, in the form of a NetworkX graph object. A P&ID is expressed as a graph intuitively since P&IDs depict the piping and signal connections between process equipment. Furthermore, a graph representation facilitates the application of novel graph machine-learning techniques for advanced P&ID tasks [3]. While the graph export is a very powerful export format, we envision a plethora of additional export formats, such as sequences like the SFILES 2.0 format [14], tables, etc. to accommodate more data representation requirements.

### 3.3. The pyDEXPI toolkit: Analyzing and manipulating P&ID data

Next to importing and exporting P&ID data, pyDEXPI offers some functionality to analyze and manipulate the data. The DEXPI framework of over 400 classes is extensive and includes complex class relationships and implicit rules. Therefore, it is difficult to find and retrieve data of interest from a model. The pyDEXPI toolkit offers methods to maneuver the class framework, e.g., by retrieving all objects in a model of a certain type or with certain attribute values. Further, the toolkits help assist in the modification of pyDEXPI P&IDs by automatically handling the design rules of the DEXPI framework.

The functions are organized in modules with respect to their scope. Model-level functions are grouped into the *model_toolkit*, functions about piping are in the *piping_toolkit*, and functions for instrumentation are found in the *instrumentation_toolkit*.

## 4. OUTLOOK: PYDEXPI IN PRACTICE

We envision pyDEXPI as a central computing library for P&IDs, accommodating expert usability, system interoperability, and data analytics and AI applications. Our vision is illustrated in Figure 3.

pyDEXPI already offers several utilities for P&ID data interoperability. On the one hand, integration with existing systems is available via the import of DEXPI-conform Proteus XML files. On the other, the pyDEXPI toolkit acts as a programming interface that makes P&ID data more accessible to users. We anticipate an expansion of the current functionality, e.g., by exporting data back into the interoperable Proteus XML format or by including a graphical interface for direct user interaction with P&ID data. Furthermore, we expect an expansion of pyDEXPI's capabilities for importing and exporting P&ID data in formats suitable for data analytics and AI tasks.

In some of our current work, we already demonstrate the value of pyDEXPI for data analytics and generative AI projects [3]. We envision that computer vision algorithms [15] with digitize image-/paper-based P&IDs and represent them as pyDEXPI P&IDs in the future. This makes them available to further, downstream GenAI applications. Schulze Balhorn et al. [16] propose autocorrection of P&ID based on a graph representation that is generated automatically from pyDEXPI. The algorithm detects errors in P&IDs through rule- and AI-based methods and replaces these with a corrected version. Alimin et al. [17] use P&ID graphs from pyDEXPI as inputs to large language models (LLM). This approach enables the LLM to retrieve information from the P&ID during text generation. Engineers interacting with such LLMs can easily access P&ID information through conversational queries, eliminating the need for manual lookup. This can assist with many time-intensive engineering tasks, such as hazard and operability studies (HAZOPs). In a notable contrast to previous work on AI on P&IDs, these case studies can leverage the interoperability of the pyDEXPI framework to interact with other tools and services, and potentially be integrated as plugins or services in different, existing CAE software with limited effort. They will also profit directly from future improvements to the framework.

We expect many more applications of pyDEXPI-based data representations in the future. For the existing

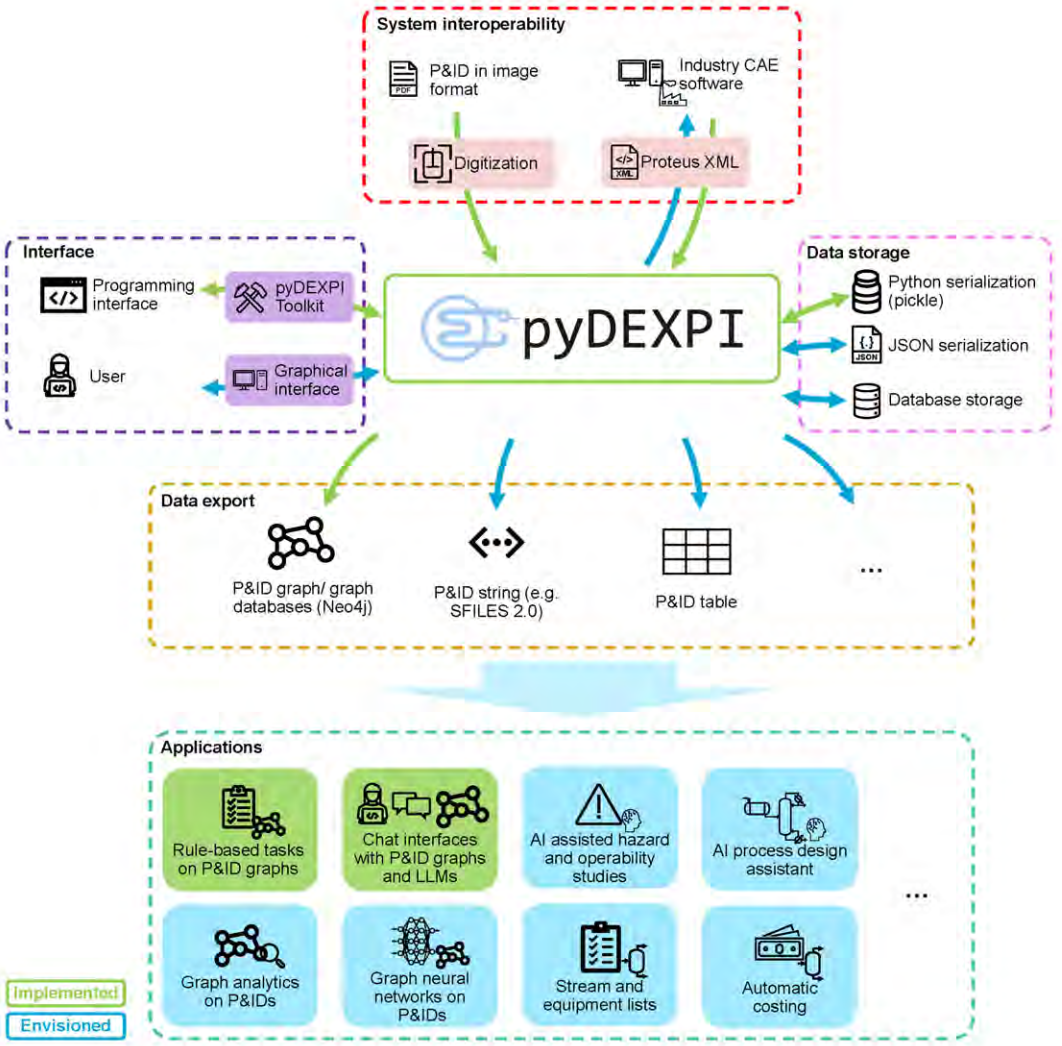



**Figure 3:** Our vision for pyDEXPI: A powerful P&ID informatics package that enables (1) interoperable data exchange between industry systems and import of digitized P&ID images (2) interfacing with users and other systems for P&ID analysis and manipulation (3) Saving and loading P&ID data in a variety of formats, depending on the requirements (4) Exporting P&ID data to a multitude of machine-readable data formats suitable for downstream data analytics, AI, and GenAI applications.

export of graph representations, future applications can include the use of graph analytics methods or graph neural networks on P&IDs. Additionally, we expect additional data export formats to become available in the future, such as sequences, strings, or tables. This will allow researchers and industry to select the most suitable data representation for their use cases and easily exchange their output with further tools or existing CAE software.

## 5. CONCLUSION

Addressing the need for interoperability for P&ID data, we present pyDEXPI, an open-source Python implementation of the DEXPI specification. pyDEXPI implements the data classes outlined by the DEXPI information model, which is widely supported by industry and research. pyDEXPI can import DEXPI data from the Proteus XML format, save and load it from a Python pickle file, and export it to a graph format suitable for graph data analytics and graph machine learning tasks. We anticipate a substantial expansion of pyDEXPIs data import, export, analysis, and manipulation capabilities, and envision pyDEXPI to become a central data analytics package for P&ID data. Finally, we foresee that pyDEXPI will be an enabling software for future development and adoption of GenAI technologies for the process industry [3].

## 6. ACKNOWLEDGEMENTS

We gratefully acknowledge the support provided by Linde GmbH, Linde Engineering and Siemens Aktiengesellschaft (DPG), Fluor© and the Dutch government via the Top Sector Alliance for Knowledge and Innovation (TKI) (CHEMIE.PGT.2023.033) (LSB), as well as the Indonesia Endowment Fund for Education Agency LPDP (AAA).

## 7. REFERENCES

1. Towler GP, Sinnott RK. Chemical Engineering Design. Elsevier/Butterworth-Heinemann (2008).
2. Toghraei M. Piping and Instrumentation Diagram Development, First Edition. John Wiley & Sons, Inc. (2019).
3. Schweidtmann AM. Generative artificial intelligence in chemical engineering. *Nature Chemical Engineering* 1:193–193 (2024) https://doi.org/10.1038/s44286-024-00041-5
4. Oeing J, Welscher W, Krink N, Jansen L, Henke F, Kockmann N. Using artificial intelligence to support the drawing of piping and instrumentation diagrams using DEXPI standard. *Digital Chemical Engineering* 4:100038 (2022) https://doi.org/10.1016/j.dche.2022.100038
5. Nabil T, Le Moullec Y, Le Coz A. Machine learning based design of a supercritical CO2 concentrating solar power plant. In: Conference Proceedings of the European sCO2 Conference 3rd European Conference on Supercritical CO2 (sCO2) Power Systems 2019: 19th–20th September 2019. 148-157 (2019) https://doi.org/10.17185/DUEPUBLICO/48885
6. Gowaikar S, Iyengar S, Segal S, Kalyanaraman S. An agentic approach to automatic creation of P&ID diagrams from natural language descriptions. *arXiv preprint* (2024) https://doi.org/10.48550/ARXIV.2412.12898
7. Schulze Balhorn L, Caballero M, Schweidtmann AM. Toward autocorrection of chemical process flowsheets using large language models. In 34th European Symposium on Computer Aided Process Engineering / 15th International Symposium on Process Systems Engineering. 3109-3114 (2025)
8. Vogel G, Schulze Balhorn L, Schweidtmann AM. Learning from flowsheets: a generative transformer model for autocompletion of flowsheets. *Computers & Chemical Engineering* 171:108162 (2023) https://doi.org/10.1016/j.compchemeng.2023.108162
9. Hirtreiter E, Schulze Balhorn L, Schweidtmann AM. Toward automatic generation of control structures for process flow diagrams with large language models. *AIChE Journal* 70(1) (2023) https://doi.org/10.1002/aic.18259
10. Theißen M, Wiedau M. DEXPI P&ID Specification. DEXPI Initiative (2021).
11. Proteus XML. Proteus schema for P&ID exchange. https://github.com/ProteusXML/proteusxml
12. pnb plants & bytes GmbH. PID Verificator 1.0.1 for DEXPI 1.3. Software (2025) https://www.plants-and-bytes.de/en/p-id-and-dexpi
13. Colvin S. Pydantic. https://github.com/pydantic/pydantic
14. Vogel G, Hirtreiter E, Schulze Balhorn L, Schweidtmann AM. SFILES 2.0: an extended text-based flowsheet representation. *Optimization and Engineering* 24:2911–2933 (2023) https://doi.org/10.1007/s11081-023-09798-9
15. Theisen MF, Flores KN, Schulze Balhorn L, Schweidtmann AM. Digitization of chemical process flow diagrams using deep convolutional neural networks. *Digital Chemical Engineering* 6:100072 (2023) https://doi.org/10.1016/j.dche.2022.100072
16. Alimin AA, Goldstein DP, Schulze Balhorn L, Schweidtmann AM. ChatP&ID: talking to P&IDs through large language models and knowledge graphs. In: ESCAPE35 - Proceedings of the 35th European Symposium on Computer Aided Process Engineering, Ghent, Belgium. (2025)
17. Schulze Balhorn L, Seijsener N, Dao K, Kim M, Goldstein DP, Driessen GHM, Schweidtmann AM. Rule-based autocorrection of piping and instrumentation diagrams (P&IDs) on graphs. In: ESCAPE35 - Proceedings of the 35th European Symposium on Computer Aided Process Engineering, Ghent, Belgium. (2025)

© 2025 by the authors. Licensed to PSEcommunity.org and PSE Press. This is an open access article under the creative commons CC-BY-SA licensing terms. Credit must be given to creator and adaptations must be shared under the same terms. See https://creativecommons.org/licenses/by-sa/4.0/



Systems & Control Transactions

**Research Article - Peer Reviewed Conference Proceeding**
ESCAPE 35 - European Symposium on Computer Aided Process Engineering
Ghent, Belgium. 6-9 July 2025
Jan F.M. Van Impe, Grégoire Léonard, Satyajeet S. Bhonsale,
Monika E. Polańska, Filip Logist (Eds.)

PSE PRESS

# Kolmogorov Arnold Networks (KANs) as surrogate models for global process optimization

**Tanuj Karia[a], Giacomo Lastrucci[a], and Artur M. Schweidtmann[a]***

[a] Process Intelligence Research Group, Department of Chemical Engineering, Delft University of Technology, Van der Maasweg 9, 2629 HZ, Delft, The Netherlands
* Corresponding Author: a.schweidtmann@tudelft.nl.

## ABSTRACT

Surrogate models are widely used to improve the tractability of process optimization. Some commonly used surrogate models are obtained via machine learning such as multi-layer perceptrons (MLPs), Gaussian processes, and decision trees. Recently, a new class of machine learning models named Kolmogorov Arnold Networks (KANs) have been proposed. Broadly, KANs are similar to MLPs, yet they are based on the Kolmogorov representation theorem instead of the universal approximation theorem for the MLPs. Compared to MLPs, it was reported that KANs require significantly fewer parameters to approximate a given input/output relationship. One of the bottlenecks preventing the embedding of MLPs into optimization formulations is that MLPs with a high number of parameters (larger width or depth) are more challenging to globally optimize. We investigate whether the parameter efficiency of KANs relative to MLPs can be translated to computational benefits when embedding them into optimization problems and solving them to global optimality. We propose a Mixed-Integer Nonlinear Programming (MINLP) formulation of a KAN and test its effectiveness using a case study on the optimization of an auto-thermal reforming process. We observe that KANs are a promising alternative as surrogate models particularly for cases with low number of inputs or outputs. For surrogate models with higher inputs or outputs, stronger formulations must be developed to improve global optimization of models with KANs embedded.

**Keywords**: Surrogate modeling, Kolmogorov Arnold Networks, Deterministic Global Optimization, Mixed-Integer Nonlinear Programming

## INTRODUCTION

Recent advances in machine learning have paved the way for increased use of surrogate models for mathematical optimization of chemical processes [1]. A large plethora of machine learning models are used for surrogate modeling and optimization, namely Gaussian processes [2], support vector machines [3], decision trees [4], and multi-layer perceptrons [5,6]. Among these models, the use of multi-layer perceptrons is widespread due to their ability to universally approximate any input/output relationship given a nonlinear activation function and a sufficiently high number of neurons in the hidden layer [7].

The most commonly used activation functions for multi-layer perceptrons are Rectified Linear Units (ReLU) and hyperbolic tangent (tanh) functions. Schweidtmann and Mitsos [8] conducted an extensive evaluation of the impact of varying architectures of multi-layer perceptrons embedded into optimization formulations on the computational effort required for deterministic global optimization. They reported that for multi-layer perceptrons with tanh activation function, increasing the size of the MLP makes them more challenging to solve to global optimality [8]. More recently, in a similar study conducted for MLPs with ReLU activation function solved using GUROBI [9], it was reported that GUROBI (v10) struggles to solve modestly deep MLPs containing six hidden layers with 500 neurons each [9].

Recently, a new class of machine learning models called Kolmogorov Arnold Networks (KANs) have been proposed [10]. KANs are based on the Kolmogorov representation theorem, which states that for a given vector $\boldsymbol{x_0}$ of $n_0$ variables, a continuous function $f(\boldsymbol{x_0})$ in a

bounded domain $\mathcal{X} \in \mathbb{R}^{n_0}$ such that $f: \mathcal{X} \to \mathbb{R}$ can be expressed with $2n_0 + 1$ additions of function $\Phi$, which is a finite composition of $n_0$ univariate functions $\phi$ [11]. Hence, a network based on the Kolmogorov representation theorem comprises an input layer, a single hidden layer with $2n_0 + 1$ neurons and an output layer. However, these networks are unlearnable in practice since the 1D functions $\phi$ may be non-smooth or fractal [10]. To overcome this issue, Kolmogorov Arnold networks were proposed, which is a generalization of the Kolmogorov representation theorem to consider networks of arbitrary depths and widths [10].

One of the advantages that KANs offer over MLPs is that they require fewer parameters to approximate a given input/output relationship relative to MLPs [10]. Hence, in this study, we aim to investigate whether this parametric efficiency offered by KANs can be translated into computational efficiency for deterministic global optimization of models with surrogate models embedded. We propose a Mixed-Integer Nonlinear Programming (MINLP) formulation of a KAN. We test the effectiveness of the formulation by considering the case study on optimization of the auto thermal reforming process [12]. Additionally, we also compare the performance of KANs with ReLU networks of varying architectures with deterministic global MINLP solver SCIP (v9.2) [13].

## BACKGROUND

For a Kolmogorov Arnold Network with $L + 1$ layers, including the input and output layers, the number of neurons in each layer is defined by the vector $\boldsymbol{N} := [n_0, n_1, \ldots, n_l, \ldots, n_L]$. Here, $n_0$ is the number of inputs, $n_l$ is the number of neurons in the $l^{th}$ layer of the KAN and $n_L$ is the number of neurons in the final layer $L$ equivalent to the number of outputs from the KAN, as shown in the directed acyclic graph in Figure 1.

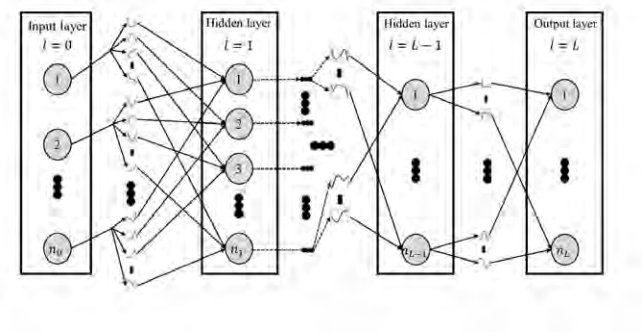



**Figure 1.** Directed acyclic graph of a Kolmogorov Arnold Network.

For a KAN, as opposed to an MLP, the activation lies on the edge connecting two neurons rather than on the neuron itself [10]. Denoting a neuron in the $l^{th}$ layer as $(l, i)$, where $i$ represents the index of the neuron in the layer $l$ and it can take values ranging from 1 to $n_l$. The activation ($\phi_{l,j,i}$) connecting the neuron $i$ in layer $l$ to neuron $j$ in layer $l + 1$ is a univariate function,

$$\phi_{l,j,i}(x_{l,i}),\ l = 0, \ldots, L-1, i = 1, \ldots, n_l, j = 1, \ldots,\ n_{l+1}. \tag{1}$$

Here, $x_{l,i}$ represents the pre-activation value of the neuron $i$ in layer $l$. For the input layer, this corresponds to the inputs to the network. Hence, the input to a neuron in the layer $l + 1$ is given by [10],

$$x_{l+1,j} = \sum_{i=1}^{n_l} \phi_{l,j,i}(x_{l,i}),\ j = 1, \ldots, n_{l+1} \tag{2}$$

Equation (2) can be equivalently represented as matrices,

$$\begin{pmatrix} x_{l+1,1} \\ \vdots \\ x_{l+1,n_{l+1}} \end{pmatrix} = \begin{pmatrix} \phi_{l,1,1}(\cdot) & \cdots & \phi_{l,1,n_l}(\cdot) \\ \vdots & \ddots & \vdots \\ \phi_{l,n_{l+1},1}(\cdot) & \cdots & \phi_{l,n_{l+1},n_l}(\cdot) \end{pmatrix} \begin{pmatrix} x_{l,1} \\ \vdots \\ x_{l,n_l} \end{pmatrix} \tag{3}$$

Compactly, Equation (3) can be expressed as,

$$\boldsymbol{x_{l+1}} = \boldsymbol{\Phi_l}(\boldsymbol{x_l}) \tag{4}$$

where, $\boldsymbol{\Phi}$ is the composition of univariate functions $\phi$. Hence, the overall network can be represented as:

$$\boldsymbol{x_L} = \mathbf{KAN}(\boldsymbol{x_0}) := \boldsymbol{\Phi_{L-1}}(\boldsymbol{x_{L-1}}(\ldots(\boldsymbol{\Phi_1}(\boldsymbol{x_1}(\boldsymbol{\Phi_0}(\boldsymbol{x_0})))))) \tag{5}$$

For a KAN, the activation functions ($\phi$) are weighted sums of a base activation function ($b$) and a spline function ($s$) expressed as [10],

$$\phi_{l,j,i}(x_{l,i}) = w^b_{l,j,i}\, b_{l,j,i}(x_{l,i}) + w^s_{l,j,i}\, s_{l,j,i}(x_{l,i}) \tag{6}$$

where $w^b_{l,j,i}$ and $w^s_{l,j,i}$ are the weights of each activation, and they are trainable parameters. This ensures that the overall KAN activation ($\phi$) is trainable, further distinguishing it from an MLP, where the activation is fixed. Typically, the Sigmoid Linear Unit (SiLU) function is used as the base activation function ($b$) in KANs [10],

$$b_{l,j,i}(x_{l,i}) := \mathrm{silu}(x_{l,i}) = \frac{x_{l,i}}{1 + e^{-x_{l,i}}} \tag{7}$$

Finally, the spline activation function can be defined as [10],

$$s_{l,j,i}(x_{l,i}) = \sum_{g=0}^{G+k-1} c_{l,j,i,g}\, B_{l,j,i,g,k}(x_{l,i}) \tag{8}$$

Here, $G$ represents the number of grid points used to characterise the spline basis functions $B$ of degree $k$. $c_{l,j,i,g}$ is the coefficient for each spline basis function $B_{l,j,i,g,k}$. $c_{l,j,i,g}$ is also a trainable parameter. For further information on KANs, the reader is referred to [10].

## METHODOLOGY

In this section, we propose a Mixed-Integer Nonlinear Programming (MINLP) formulation to optimize over a

trained KAN, provide details about the implementation of the formulation, and the case study used to test the MINLP formulation of a KAN.

## Formulation

The presence of a spline function in the activation makes each activation distinct. The spline basis functions are determined as

$$B_{l,j,i,g,0}(x_{l,i};\ \mathbf{t}) = \begin{cases} 1, & t_{l,j,i,g} \le x_{l,i} < t_{l,j,i,g+1} \\ 0, & \text{otherwise} \end{cases} \tag{9}$$

$$B_{l,j,i,g,d}(x_{l,i};\ \mathbf{t}) = \frac{x_{l,i} - t_{l,j,i,g}}{t_{l,j,i,g+d} - t_{l,j,i,g}} B_{l,j,i,g,d-1}(x_{l,i};\ \mathbf{t}) + \frac{t_{l,j,i,g+d+1} - x_{l,i}}{t_{l,j,i,g+d+1} - t_{l,j,i,g+1}} B_{l,j,i,g+1,d-1}(x_{l,i};\ \mathbf{t}), d = 1, \ldots, k \tag{10}$$

Here, $\mathbf{t}$ is a vector of $G + 1$ uniformly-spaced non-decreasing points in the range $[x_{l,i}^L, x_{l,i}^U]$, $B_{l,j,i,g,0}$ are zeroth-order spline basis functions and $B_{l,j,i,g,d}$ are higher-order spline basis functions defined up to the degree $k$ of the spline.

A Mixed-Integer Quadratically Constrained Programming (MIQCP) formulation has been proposed to model spline functions described in Equations (7) – (9) by Grimstad [14]. Herein, we adopt the proposed MIQCP formulation in [14] in our formulation for KAN. We represent the zeroth-order basis functions $B_{l,j,i,g,0}$ as binary variables. To ensure they are only activated for the case as described in Equation (8), we introduce the following linear constraints (Equations (10) and (11)) into the formulation:

$$(t_{l,j,i,g} - t_{l,j,i,0}) B_{l,j,i,g,0} + t_{l,j,i,0} \le x_{l,i}, g = 0, .., G + 2k - 1 \tag{11}$$

$$(t_{l,j,i,g+1} - t_{l,j,i,G+2k}) B_{l,j,i,g,0} + t_{l,j,i,0} \ge x_{l,i}, g = 0, .., G + 2k - 1 \tag{12}$$

To determine the higher-order spline basis functions ($B_{l,j,i,g,d}$) for $d = 1, \ldots, k$, we include the quadratic Equation (9) for all $g = 0, .., G + 2k - 1 - d$. Finally, we also include the partition of unity cuts [14] in our formulation as,

$$\sum_{g=0}^{G+2k-1-d} B_{l,j,i,g,d} = 1, d = 0, \ldots, k \tag{13}$$

Equations (10) – (13) allow for the calculation of $k^{\text{th}}$-order spline basis functions required to characterise the spline function ($s$) in Equation (8), which is also included in the formulation. The base activation function ($b$) is formulated as described in Equation (7). Finally, the overall activation is formulated as described in Equation (5). To model the connections in the network as shown in Figure 1, Equation (14) is added to the formulation.

$$x_{l+1,j} = \left(\sum_{i=1}^{n_l} \phi_{l,j,i}(x_{l,i})\right) + a_{l,j}, i = 1, \ldots, n_l, j = 1, \ldots, n_{l+1}, \text{and } l = 0, \ldots, L - 1 \tag{14}$$

The presence of the term $a_{l,j}$ distinguishes Equation (14) from Equation (1). While not necessary for a KAN, bias term $a_{l,j}$ is included in the implementation for sparsity regularization and improved training performance [10].

Therefore, the MINLP formulation of a KAN presented here consists of Equations (6) – (8), (10) – (14). For a trained KAN embedded into an optimization formulation $w_{l,j,i}^b$, $w_{l,j,i}^s$, $c_{l,j,i,g}$, and $a_{l,j}$ are fixed parameters. Hereafter, the overall formulation is denoted as **TKAN.** We would like to remind readers that all equations in the formulation are linear or quadratic except for Equation (7). Using the `SiLU` function as the base activation introduces the nonlinearity into the formulation.

## Case Study

We consider the case study of optimizing an autothermal reforming process used in the documentation of OMLT [15] and in a recent review article on optimization formulations for trained machine learning models [12]. The dataset comprises two inputs: Bypass fraction ($\alpha$) and natural gas steam ratio ($SR$). The bounds for $\alpha$ and $SR$ are [0.1, 0.8] and [0.8, 1.2] respectively. There are 12 outputs in the dataset: the steam flowrate, the reformer duty, and the composition of the outlet stream. Outlet stream comprises 10 components. The reader is referred to [15] for additional details about the case study. For the optimization problem formulation, only two outputs are of interest: the concentration of hydrogen in the outlet stream ($c_H$) and the concentration of nitrogen in the outlet stream ($c_N$). The objective of the problem is to maximize $c_H$ while constraining $c_N$ to be lower than 0.34. Hence, the optimization problem with KAN embedded is as follows:

$$\begin{aligned} \max_{\alpha, SR} \quad & c_H \\ s.t. \quad & \mathbf{TKAN}(\alpha, SR) = 0 \\ & c_N \le 0.34 \end{aligned} \tag{15}$$

Similarly, the optimization problem with MLP embedded is:

$$\begin{aligned} \max_{\alpha, SR} \quad & c_H \\ s.t. \quad & \mathbf{MLP}(\alpha, SR) = 0 \\ & c_N \le 0.34 \end{aligned} \tag{16}$$

Two different network architectures are considered: one considering the two outputs present in the optimization formulation as the two outputs from the network and another with all twelve outputs in the dataset as the outputs from the network.

## Implementation

The proposed MINLP formulation has been implemented using the Pyomo optimization framework [16]. Object-oriented programming framework is leveraged to create separate classes for an activation and a layer, enabling a simple definition of a KAN using a Pyomo block. For importing all the necessary parameters: $w_{l,j,i}^b$, $w_{l,j,i}^s$, $c_{l,j,i,g}$, $t_{l,j,i,g}$, and $a_{l,j}$, a method is written to export all these parameters to a JSON file on reading a trained KAN

model object. All KANs are trained using the pykan repository (v0.0.2) [10]. For comparing the effectiveness of a KAN with MLPs, MLPs with ReLU activation are trained using Tensorflow (v2.17.0) and imported into Pyomo using OMLT (v1.2.1) [15]. We consider MLPs with one, two and three layers, each with 20 neurons for comparison. We only consider the BigM formulation of ReLU MLPs for investigation. For all instances, a time limit of 300 seconds is imposed. Relative termination tolerance of $1.0E-4$ is used for all instances. All the instances are solved via Pyomo/GAMS (v48.6) using SCIP (v9.2) on a Dell Latitude 7440 laptop with 13th generation Intel Core i7-1365U processor @1.80 GHz with 16 GB of RAM running Windows 10.

## RESULTS AND DISCUSSION

This section presents the results related to training different networks and solving the optimization models with the trained network embedded.

### Training results

All networks are trained by splitting the dataset into training and testing subsets in the proportion of 0.75 : 0.25 (train : test). Detailed discussions in relation to training times of different networks are not provided because KANs require significantly more computational effort to train relative to MLPs [10]. A similar observation is also made in this study.

Both KANs are trained with one hidden layer comprising two neurons with six grid points ($G = 6$) using 125 training steps. For MLPs, the number of hidden layers ranging from one to three, each with 20 neurons, is considered. Hundred epochs with default learning rate and batch size are used to train all MLPs. Mean squared error (MSE) on the training and test sets and the number of parameters in the network are reported in Table 1.

In Table 1 for both cases of two and twelve outputs, we observe the parameter efficiency of KANs over MLPs. The KAN with 12 outputs (KAN12) has a training MSE of 5.11E-5, which is approximately half of the deepest ReLU MLP. Similarly, for the case with two outputs, KAN2 exhibits orders of magnitude lower train MSE than any of the ReLU MLPs trained. While we observe that the MSE on the test set is comparable for all the networks trained, the lower MSE on training sets indicates that KANs are more accurate than MLPs though inconclusive. Finally, it is important to point out that KANs have approximately the same number of parameters as MLPs with one hidden layer for both the cases of two and twelve outputs; they exhibit significantly lower MSE values on the training set than for any MLPs.

Table 1. Details of training for different networks. The network name is defined using the type of network (KAN or MLP) followed by the number of outputs (2 or 12) from the network. For MLPs, the number of hidden layers is shown in parentheses. For example, the network with the name 'ReLU12(2)' corresponds to a ReLU MLP with twelve outputs and two hidden layers.

| Network | Train MSE | Test MSE | # of param. |
|---|---|---|---|
| ReLU12(1) | 3.10E-4 | 4.30E-3 | 312 |
| ReLU12(2) | 1.08E-4 | 4.10E-3 | 732 |
| ReLU12(3) | 1.32E-4 | 3.80E-3 | 1152 |
| KAN12 | 5.11E-5 | 4.21E-3 | 311 |
| ReLU2(1) | 1.25E-4 | 4.90E-3 | 102 |
| ReLU2(2) | 1.41E-4 | 4.60E-3 | 522 |
| ReLU2(3) | 5.05E-4 | 4.30E-3 | 942 |
| KAN2 | 4.20E-8 | 4.73E-3 | 91 |

### Optimization results

All trained networks are solved to global optimality at the specified tolerance. For all the networks, the value of the objective, i.e., the concentration of hydrogen in the outlet stream ($c_H$) is found to be approximately $\approx 0.33$. The actual value of the global maximum is not known or reported. Hence, the ability of a network to accurately describe the global solution cannot be further evaluated. We repeat the global optimization of all networks using SCIP five times. The average wall time elapsed to achieve convergence to global optimality over the five runs is reported in **Figure 2**. Repeated runs are carried out to ensure higher confidence in the results since the wall time needed to achieve global optimality is low ( < 10 seconds for most cases).

On comparing the results between the two cases of twelve outputs and two outputs in **Figure 2**, we observe that reducing the number of outputs for MLPs has a minor effect on the computational effort to prove global optimality. For ReLU(2) and ReLU(3), there is a slight reduction in the average time taken to achieve convergence. Whereas, for ReLU(1), this increases slightly by reducing the number of outputs, albeit for both cases, the runtime is still less than 1 second. On the other hand, for the KAN, the runtime reduces by an order of magnitude. This observation can be explained by considering the nature of a KAN. For a KAN, the activation lies on the edge connecting two neurons in the network. On reducing the number of outputs from 12 to 2, the total number of activations in the network reduces from 28 to 8. Moreover, considering each activation comprises the spline function, which introduces $G + 2k$ binary variables (c.f. Equations (11) and (12)), reducing the number of activations in the networks significantly reduces the computational effort required to optimize the trained KAN to global optimality. We do not see the same for MLPs because, for an MLP, the activation lies in the neuron itself.

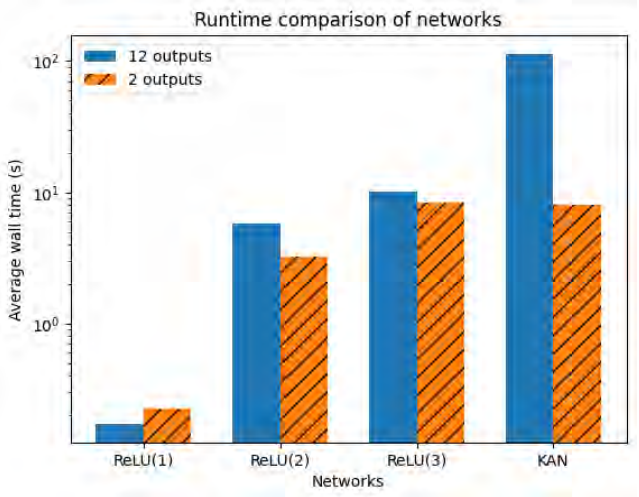



**Figure 2.** Comparison of runtimes among different networks. The networks compared are 'ReLU(1)', 'ReLU(2)', 'ReLU(3)', and 'KAN' corresponding to MLPs with one, two, and three hidden layers and a Kolmogorov Arnold Network, respectively. Two different cases of two and twelve outputs are considered shown by shaded orange bars and solid blue bars respectively.

Comparing KANs and MLPs, we observe that for the case of 12 outputs, KAN requires an order of magnitude higher computational effort to be solved to global optimality using SCIP relative to MLPs. Hence, it is not competitive with MLPs. However, when reducing the number of outputs, the computational effort required for KAN is comparable to that of MLPs with three hidden layers. However, it requires more computational effort than MLPs with one or two hidden layers. This behavior is explained by the fact that for a KAN, we solve an MINLP, but for a `ReLU` modeled using the BigM formulation, a Mixed-Integer Linear Programming (MILP) formulation is solved. MILPs are relatively easier to solve than MINLPs. Additionally, the algorithms to solve MILPs are more advanced than MINLPs.

For the case study considered, the MSE on the test set are comparable for both MLPs and KANs. However, KANs are expected to offer better generalization capabilities compared to MLPs [10]. Considering that the computational effort required to optimize KANs is comparable to MLPs with three layers, a comprehensive evaluation should be conducted with multiple other case studies to thoroughly evaluate the potential of KANs as surrogate models.

## CONCLUSIONS

In this study, we presented a Mixed-Integer Nonlinear Programming formulation for embedding Kolmogorov Arnold Networks into optimization formulations. Using an autothermal process optimization case study, we investigated the potential of using Kolmogorov Arnold Networks as surrogate models for process optimization. We observed that they are a promising alternative as surrogate models, particularly when a low number of inputs or outputs are involved.

For applications requiring a high number of inputs or outputs, stronger formulations for KAN need to be developed to improve their computational tractability for deterministic global optimization. Alternatively, activation functions such as `ReLU` should be investigated as base activation functions instead of `SiLU`. Doing so would potentially avoid the solution of an MINLP and a more tractable MIQCP would be solved instead. Finally, more extensive testing of the formulation with different case studies to comprehensively evaluate the effectiveness of KANs.

## ACKNOWLEDGEMENTS

Financial support from Shell Global Solutions International B.V. is gratefully acknowledged.

## REFERENCES

1. Misener R, Biegler L. Formulating data-driven surrogate models for process optimization. Comput Chem Eng. 2023 Nov 1;179:108411.
2. Schweidtmann AM, Bongartz D, Grothe D, Kerkenhoff T, Lin X, Najman J, et al. Deterministic global optimization with Gaussian processes embedded. Math Program Comput [Internet]. 2021 Sep 1 [cited 2025 Jan 29];13(3):553–81. Available from: https://link.springer.com/article/10.1007/s12532-021-00204-y
3. Schweidtmann AM, Weber JM, Wende C, Netze L, Mitsos A. Obey validity limits of data-driven models through topological data analysis and one-class classification. Optimization and Engineering [Internet]. 2022 Jun 1 [cited 2025 Jan 29];23(2):855–76. Available from: https://link.springer.com/article/10.1007/s11081-021-09608-0
4. Thebelt A, Kronqvist J, Mistry M, Lee RM, Sudermann-Merx N, Misener R. ENTMOOT: A framework for optimization over ensemble tree models. Comput Chem Eng. 2021 Aug 1;151:107343.
5. Schweidtmann AM, Bongartz D, Mitsos A. Optimization with Trained Machine Learning Models Embedded. Encyclopedia of Optimization [Internet]. 2023 [cited 2025 Jan 24];1–8. Available from: https://link.springer.com/referenceworkentry/10.1007/978-3-030-54621-2_735-1

6. Schweidtmann AM, Esche E, Fischer A, Kloft M, Repke JU, Sager S, et al. Machine Learning in Chemical Engineering: A Perspective. Chemie Ingenieur Technik [Internet]. 2021 Dec 1 [cited 2025 Jan 29];93(12):2029–39. Available from: https://onlinelibrary.wiley.com/doi/full/10.1002/cite.202100083
7. Hornik K, Stinchcombe M, White H. Multilayer feedforward networks are universal approximators. Neural Networks. 1989 Jan 1;2(5):359–66.
8. Schweidtmann AM, Mitsos A. Deterministic Global Optimization with Artificial Neural Networks Embedded. J Optim Theory Appl [Internet]. 2019 Mar 15 [cited 2025 Jan 24];180(3):925–48. Available from: https://link.springer.com/article/10.1007/s10957-018-1396-0
9. Webinar: Using Trained Machine Learning Predictors in Gurobi - YouTube [Internet]. [cited 2025 Jan 24]. Available from: https://www.youtube.com/watch?v=jaux5Oo4qHU
10. Liu Z, Wang Y, Vaidya S, Ruehle F, Halverson J, Soljaci´c MS, et al. KAN: Kolmogorov-Arnold Networks. 2024 Apr 30 [cited 2025 Jan 24]; Available from: https://arxiv.org/abs/2404.19756v4
11. Arnold VI. On the representation of functions of several variables as a superposition of functions of a smaller number of variables. Collected Works [Internet]. 2009 [cited 2025 Jan 24];25–46. Available from: https://link.springer.com/chapter/10.1007/978-3-642-01742-1_5
12. López-Flores FJ, Ramírez-Márquez C, Ponce-Ortega JM. Process Systems Engineering Tools for Optimization of Trained Machine Learning Models: Comparative and Perspective. Ind Eng Chem Res [Internet]. 2024 Aug 14 [cited 2025 Jan 24];63(32):13966–79. Available from: https://pubs.acs.org/doi/full/10.1021/acs.iecr.4c00632
13. Bolusani S, Besançon M, Bestuzheva K, Chmiela A, Dionísio J, Donkiewicz T, et al. The SCIP Optimization Suite 9.0. 2024 Feb 27 [cited 2025 Jan 24]; Available from: https://arxiv.org/abs/2402.17702v2
14. Grimstad B. A MIQCP formulation for B-spline constraints. Optim Lett [Internet]. 2018;12(4):713–25. Available from: https://doi.org/10.1007/s11590-017-1190-1
15. Ceccon F, Jalving J, Haddad J, Thebelt A, Tsay C, Laird CD, et al. OMLT: Optimization & Machine Learning Toolkit. Journal of Machine Learning Research [Internet]. 2022 [cited 2025 Jan 27];23(349):1–8. Available from: http://jmlr.org/papers/v23/22-0277.html
16. Bynum ML, Hackebeil GA, Hart WE, Laird CD, Nicholson BL, Siirola JD, et al. Pyomo — Optimization Modeling in Python. 2021 [cited 2025 Jan 27];67. Available from: http://link.springer.com/10.1007/978-3-030-68928-5

© 2025 by the authors. Licensed to PSEcommunity.org and PSE Press. This is an open access article under the creative commons CC-BY-SA licensing terms. Credit must be given to creator and adaptations must be shared under the same terms. See https://creativecommons.org/licenses/by-sa/4.0/



Systems & Control Transactions

**Research Article - Peer Reviewed Conference Proceeding**
ESCAPE 35 - European Symposium on Computer Aided Process Engineering
Ghent, Belgium. 6-9 July 2025
Jan F.M. Van Impe, Grégoire Léonard, Satyajeet S. Bhonsale,
Monika E. Polańska, Filip Logist (Eds.)

PSE PRESS

# Redefining Stage Efficiency in Liquid-Liquid Extraction: Development and Application of a Modified Murphree Efficiency

**Mahdi Mousavi[a]*, and Ville Alopaeus[a]**

[a] Aalto University, School of Chemical Engineering, Department of Chemical and Metallurgical Engineering, Espoo, Uusimaa, Finland
* Corresponding Author: mahdi.mousavi@aalto.fi

## ABSTRACT

Liquid-liquid extraction stages often deviate from equilibrium due to factors like insufficient mixing, making accurate efficiency modeling essential for process simulation. This study addresses the limitations of Aspen Plus (AP), which distorts equilibrium calculations by directly multiplying efficiency with the distribution coefficient. A modified Murphree efficiency definition, more suitable for liquid-liquid systems but absent in AP's Extraction Column module, was implemented using Aspen Custom Modeler (ACM). The custom multi-stage extraction column model replaces mole fractions with mole flows to better represent mass transfer and phase interactions, enhancing simulation accuracy when imported into AP. Two test cases validated the custom model's effectiveness. Test Case I, utilizing the UNIQ-RK thermodynamic model, compared the ACM model to AP's built-in module, revealing that the ACM model provides a more realistic representation of extraction processes under varying stage efficiencies. It captured gradual efficiency changes and aligned with expected mass transfer behavior, while the built-in module showed reduced sensitivity and accuracy. Test Case II, using the UNIF-LL thermodynamic model, demonstrated the model's robustness across different thermodynamic frameworks. It highlighted how varying Murphree efficiency from 0 to 1 directly affects separation performance, with higher efficiencies leading to better separation and increased extract phase composition. These findings confirm that the modified Murphree efficiency is a reliable and effective approach, enabling engineers to optimize liquid-liquid extraction processes with greater accuracy and efficiency.

**Keywords**: Liquid-liquid extraction, Murphree efficiency, Aspen Custom Modeler, Extraction column, Process simulation

## INTRODUCTION

Liquid-liquid extraction (LLX) is a widely used separation process in chemical engineering, particularly for systems where the components to be separated are not suitable for conventional distillation due to factors such as thermal sensitivity or low relative volatility [1]. In LLX, components are distributed between two immiscible liquid phases—typically an aqueous phase and an organic solvent phase—based on their relative solubility or affinity for each phase. This process is employed in diverse industries, including petrochemicals, pharmaceuticals, hydrometallurgy, and wastewater treatment [2].

Despite its broad applicability, LLX processes are often plagued by inefficiencies that result in deviations from ideal equilibrium. These inefficiencies arise from factors such as insufficient mixing, poor phase dispersion, non-ideal phase interactions, and mass transfer limitations [3, 4]. Insufficient mixing reduces the interfacial area available for mass transfer, leading to incomplete component transfer between phases. Similarly, operational factors such as stage design, solvent-to-feed ratios, and flow patterns can further exacerbate these inefficiencies, resulting in lower extraction performance. Experimental studies have shown that deviations from ideal mixing and equilibrium are significant, particularly in multi-stage extraction columns where the cumulative effect of inefficiencies can drastically reduce overall

separation performance [5].

Traditional approaches for modeling stage efficiency in liquid-liquid extraction (LLX) often oversimplify these complex behaviors. For example, simulation tools like Aspen Plus (AP) apply a concept sometimes referred to as "vaporization efficiency," which originates from its use in systems such as steam distillation. This method defines stage efficiency by scaling the component distribution coefficient ($Ki$) with an efficiency term ($Ei$), as represented in Equation 1:

$$E_i = \frac{x_i^{L2}}{K_i x_i^{L1}} \quad (1)$$

Here, $x_i$ represents the mole fractions of a component in stage $i$ in the liquid phases $L_1$ and $L_2$, respectively. While this formulation simplifies equilibrium calculations, it introduces significant limitations when applied to LLX systems. The concept of vaporization efficiency, as detailed in references such as Wankat's Equilibrium Staged Separations, is more relevant to steam distillation, where it is directly defined using vapor pressures [6]. This basis is not applicable to LL systems, where equilibrium is governed by distribution coefficients rather than vapor pressures. In LLX systems, directly scaling the equilibrium coefficient inherently distorts the mass transfer behavior, especially in non-ideal conditions where deviations from equilibrium are pronounced [7]. This limitation is particularly critical in systems with low efficiencies, where stage performance depends strongly on factors such as mixing quality, interfacial mass transfer rates, and phase equilibrium dynamics. Such discrepancies underscore the need for approaches better tailored to the specific complexities of LLX processes.

To address these challenges, this work introduces a modified Murphree efficiency definition tailored for LLX processes. The Murphree efficiency, traditionally applied in vapor-liquid systems, compares the actual performance of a stage to its ideal counterpart, effectively capturing deviations from equilibrium. For LLX systems, however, the use of mole fractions in the traditional Murphree definition fails to account for the continuous nature of mass transfer and phase interactions. Instead, this study proposes a modification wherein mole flows replace mole fractions, ensuring a more consistent and physically accurate representation of stage performance. The modified efficiency better reflects real-world process behavior by incorporating both the composition and the flow dynamics of the system.

The importance of accurately modeling stage efficiency cannot be overstated. Experimental studies have shown that small inefficiencies at individual stages can propagate through multi-stage columns, significantly reducing overall extraction efficiency and leading to suboptimal solvent utilization [8]. Furthermore, non-idealities such as solvent entrainment, phase back-mixing, and viscosity effects can further complicate the extraction process [9]. Addressing these inefficiencies requires models that not only account for equilibrium deviations but also reflect the dynamic interactions between feed and solvent phases. The modified Murphree efficiency presented here provides a step toward bridging the gap between idealized models and real-world LLX systems.

The proposed efficiency model was implemented in a multi-stage extraction column using Aspen Custom Modeler (ACM) and imported into AP for verification. It is important to emphasize that the tools used in this study, namely ACM and AP, serve merely as implementation platforms. The modified Murphree efficiency can be applied in any appropriate modeling environment capable of supporting custom efficiency definitions. This flexibility broadens the applicability of the approach, making it suitable for a wide range of LLX systems and scenarios.

In summary, this work presents a modified efficiency definition that addresses the limitations of existing models for LLX processes. By accounting for mass transfer dynamics and phase interactions more rigorously, the proposed approach provides a robust framework for simulating and optimizing LLX systems in a realistic way. The findings have implications for the design and operation of extraction columns, particularly in processes where deviations from equilibrium play an important role in determining overall performance.

## METHODOLOGY

The accurate modeling of stage efficiency in LLX processes requires an approach that accounts for both mass transfer and deviations from equilibrium. The proposed methodology addresses these challenges by redefining the Murphree efficiency for liquid-liquid systems, making it more applicable and realistic in representing stage performance.

The Murphree efficiency is traditionally defined for vapor-liquid equilibrium systems, evaluating the performance of a stage based on the deviation of the actual composition change from the ideal change. The original definition for vapor-liquid is expressed as:

$$E_i^M = \frac{x_i^V - x_{i-1}^V}{K_i x_i^L - x_{i-1}^V} \quad (2)$$

Here, $E^M$ represents the Murphree efficiency of stage $i$. $\mathrm{V}$ and $\mathrm{L}$ are stand for vapor and liquid phases, respectively. This definition is well-suited for vapor-liquid processes.

In liquid-liquid systems, the traditional Murphree efficiency is less effective because equilibrium is rarely achieved at each stage due to slower mass transfer rates and insufficient mixing. Additionally, it is worth noting that in liquid-liquid systems, the distinction between the two phases, analogous to vapor and liquid in vapor-liquid systems, is less clear. LL systems exhibit a more symmetric behavior in this regard, making it ambiguous which

phase should correspond to "V" or "L." Trials with both interpretations showed similar results, further supporting this symmetry. Furthermore, traditional mole fraction-based efficiencies for LL systems were also tested but presented challenges, particularly in cases where total molar flows varied. In such scenarios, linking mole fractions at the inlet and outlet becomes less logical, leading to somewhat inconsistent results. This issue is effectively addressed in the present formulation by using mole flows, which inherently account for variations in total molar flow and ensure consistency in the efficiency calculation. mixing. Moreover, mole fractions alone are insufficient to capture the phase interactions and mass transfer dynamics that are essential to understanding the performance of LLX stages. Instead, the mass transfer behavior in such systems is better represented by mole flows, which consider both the amount of material transferred and the phase equilibrium composition. To address these challenges, the Murphree efficiency was modified by substituting mole flows for mole fractions in the traditional definition. The modified efficiency for components is expressed as:

$$E^M = \frac{x_i^{L2}\,\dot{n}_i^{L2} - x_{i-1}^{L2}\,\dot{n}_{i-1}^{L2}}{K_i x_i^{L1} \varphi^{*,L1}\left(\dot{n}_i^{L1}+\dot{n}_i^{L2}\right) - x_{i-1}^{L2}\,\dot{n}_{i-1}^{L2}} \tag{3}$$

Here, $\dot{n}$ represent the molar flow rate, $\varphi*$ denotes the equilibrium phase fraction. This modification ensures that the efficiency definition aligns with the physical principles of mass transfer and captures the continuous nature of phase interactions in liquid-liquid systems. To incorporate this modified efficiency into the modeling framework, component and overall mole balances were established for the system. The component mole balance for the second liquid phase can be calculated from the overall mole balance of each component:

$$x_i^{L1}\,\dot{n}_i^{L1} + x_i^{L2}\,\dot{n}_i^{L2} = x_{i-1}^{L1}\,\dot{n}_{i-1}^{L1} + x_{i-1}^{L2}\,\dot{n}_{i-1}^{L2} \tag{4}$$

The overall mole balance for the system becomes:

$$\dot{n}_i^{L1} + \dot{n}_i^{L2} = \dot{n}_{i-1}^{L1} + \dot{n}_{i-1}^{L2} \tag{5}$$

These equations relate the modified Murphree efficiency to the principles of mass transfer and phase equilibrium, offering a framework for accurately representing stage performance. By incorporating the interplay between stage efficiency, composition and flow rates, the approach captures the dynamics of LLX systems.

To apply the modified efficiency, a multi-stage LLX column model was implemented. The model accounts for gradual changes in efficiency and composition across stages, reflecting the interactions between feed and solvent phases in a counter-current setup as represented in Figure 1.

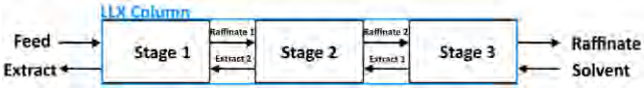



**Figure 1.** Counter-current LLX scheme with 3 stages.

The model was implemented using ACM, where the modified Murphree efficiency and mass balance equations were defined. It was then imported into AP for comparison with the built-in extraction modules. While ACM and AP were used for this study, the methodology itself is flexible and can be applied in other simulation environments capable of supporting custom efficiency definitions.

## RESULTS AND DISCUSSION

The performance of the modified Murphree efficiency in LLX was evaluated through two test cases that assessed its implementation in a custom ACM model imported into AP. These cases demonstrate the model's capacity to simulate stage efficiencies and its superiority over the built-in AP extraction module for realistic system behavior and accuracy. The system configuration for the LLX process is shown in Figure 2, where the feed and solvent streams enter the extraction column (LLX Column), and the resulting extract and raffinate streams exit the column. This setup highlights the counter-current interaction of the phases, which drives the separation process.

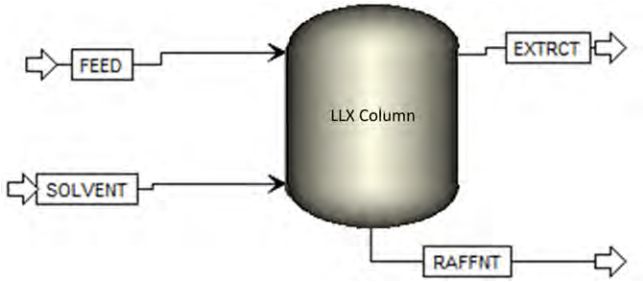



**Figure 2.** Schematic representation of a LLX column showing the flow of feed, solvent, extract, and raffinate streams.

### Test Case I: Comparison Between ACM and AP Built-In Models

The performance of the modified Murphree efficiency implemented in the ACM model was evaluated in comparison to AP's built-in extraction module. Test Case II focused on a LLX system involving three components: acetic acid (HAC), water, and n-hexane, operating over 3 to 7 stages with varying stage efficiencies. To model the phase behavior and distribution of components between the aqueous and organic phases, the UNIQ-RK thermodynamic model was employed.

Table 1 provides an overview of the feed and solvent

components along with their respective flow rates. The analysis emphasized column efficiency, component distributions, and overall extraction performance.

**Table 1:** Test case I feed and solvent components with flow rates.

| Stream | Description | Flow |
|---|---|---|
| Feed | Water | 8 kmol/hr |
| | HAC | 2 kmol/hr |
| Solvent | N-hexane | 30 kmol/hr |

The results from the ACM model, illustrated in Figure 3, showed a clear and consistent increase in column efficiency as the number of stages increased. The behavior aligns with expected mass transfer dynamics, where increasing the number of stages and improving efficiency enhances the separation performance. As illustrated in the Figure 3, constant Murphree efficiencies of 0.25, 0.5, and 1 demonstrated progressively higher column efficiencies. At an efficiency of 1, the column approaches equilibrium, achieving the maximum possible separation. Conversely, when the efficiency was set to 0, no separation occurred, and the extract and raffinate compositions mirrored the feed and solvent, confirming the physical expectation of no phase interaction.

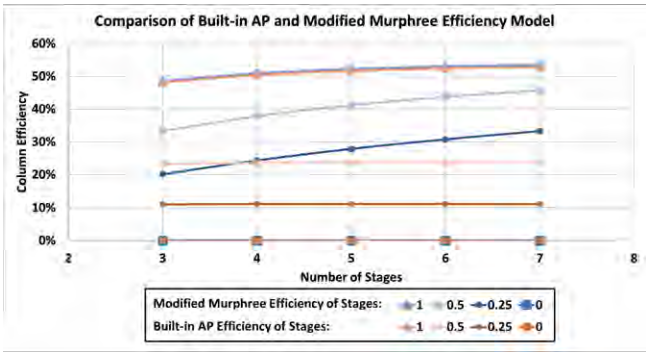



**Figure 3.** Comparison of column efficiency for built-in AP and modified Murphree models at varying efficiencies.

In contrast, the built-in AP model fails to capture the gradual and realistic changes in column performance, particularly at lower efficiencies. The results exhibit a discontinuous and overly simplistic response to variations in efficiency, where changes in stage performance are not reflected accurately. This lack of sensitivity is problematic for systems that require precise predictions of mass transfer behavior and separation performance across multiple stages. The inaccuracies become especially apparent when the efficiency is set to zero. Under this condition, the AP model produces physically unrealistic results, redistributing all of the solvent into the raffinate phase, as shown in Figure 4. This outcome violates fundamental mass balance principles and misrepresents the behavior of the system, where, in reality, no separation should occur, leaving the extract and raffinate phases identical to the feed and solvent compositions.

The results confirm that incorporating the modified Murphree efficiency into a custom ACM model provides a more realistic representation of liquid-liquid extraction. While the ACM model occasionally encountered convergence issues during integration with AP, its flexibility and ability to realistically simulate stage efficiencies offer significant benefits for process optimization. By addressing real-world inefficiencies, such as non-ideal mixing and deviations from equilibrium, the modified Murphree efficiency model provides a framework to evaluate extraction performance in multi-stage systems.

## Test Case II: Effect of Stage Efficiency on Column Performance

In the second test case, a system consisting of acetone and water as the feed and 3-methylhexane as the solvent was simulated in a multi-stage LLX column. The thermodynamic model used in this case was UNIF-LL, a liquid-liquid activity coefficient model tailored for systems with significant non-ideal behavior. This test case was specifically designed to demonstrate the robustness and versatility of the implemented modified Murphree efficiency model in handling different thermodynamic frameworks.

The feed and solvent components and their flow rates are summarized in Table 2. The model simulated constant Murphree efficiencies of 0, 0.25, 0.5, and 1 across 3 to 7 stages. Column efficiency, defined as:

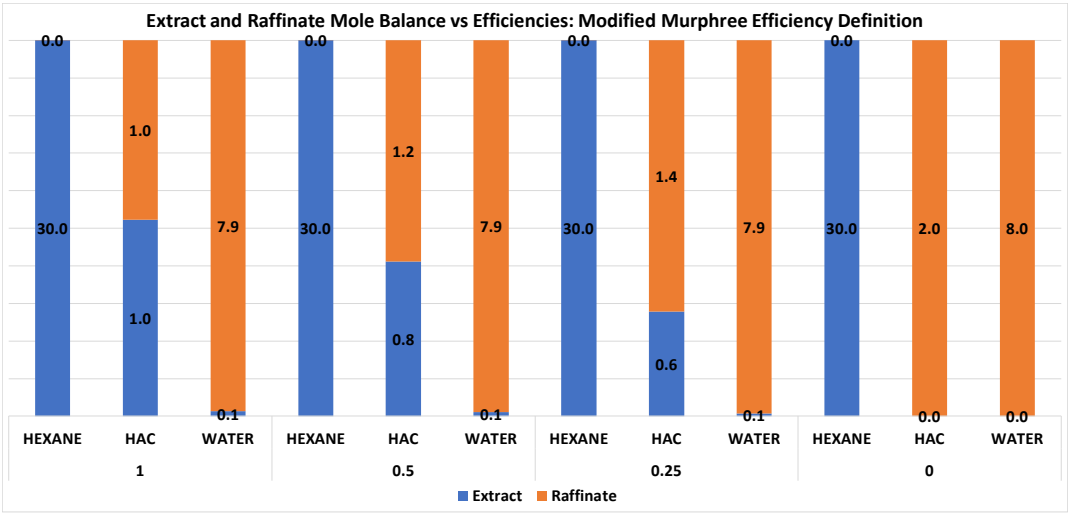
$$Column\ Efficiency\ = \frac{n_E^{Feed} - n_E^{Raffinate}}{n_E^{Feed}} \qquad (6)$$

where $\dot{n}_E$ represents the molar flow rate of the extracted component $E$ (in this case, acetone) in the feed and raffinate phases.

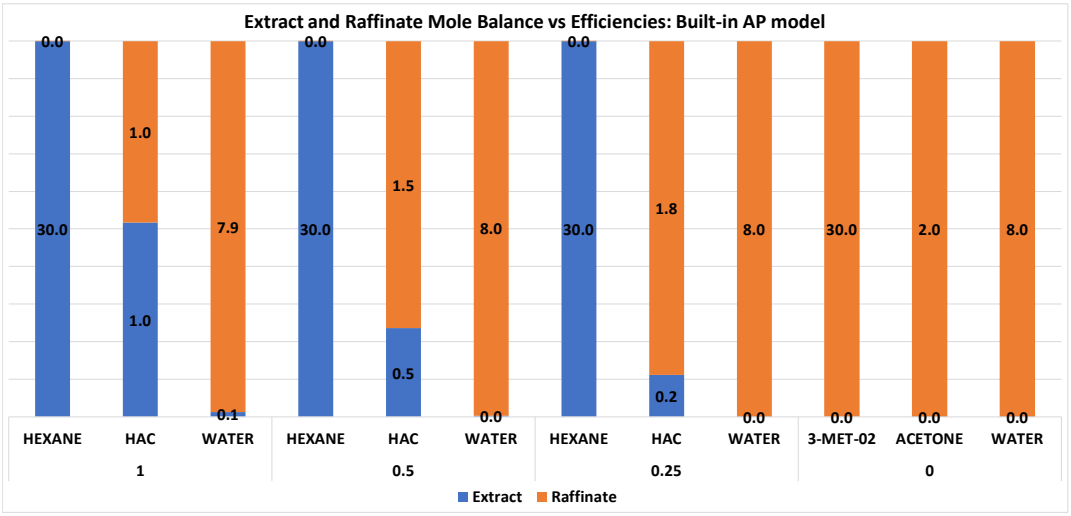
**Table 2:** Test case II feed and solvent components with flow rates.

| Stream | Description | Flow |
|---|---|---|
| Feed | Water | 8 kmol/hr |
| | Acetone | 2 kmol/hr |
| Solvent | 3-methylhexane | 10 kmol/hr |

The results, illustrated in Figure 5, show a clear relationship between Murphree efficiency and column performance. When Murphree efficiency was set to zero, no separation occurred, and column efficiency remained at 0%, as indicated by the flat blue line. This scenario reflects a system with no mass transfer, where the composition of the extract and raffinate phases is identical to the feed and solvent. As Murphree efficiency increased to 0.25 and 0.5, column efficiency improved steadily with the number of stages. This trend highlights the effect of additional stages in enhancing separation performance




(a)




(b)

**Figure 4.** Extract and raffinate mole balances at varying stage efficiencies for (a) the modified Murphree efficiency model developed using ACM and (b) the built-in AP model. The modified Murphree efficiency model shows a gradual and realistic distribution of components, while the built-in AP model demonstrates less sensitivity and unrealistic behavior at lower efficiencies.

under moderate efficiencies. At a Murphree efficiency of 1, the system achieved equilibrium conditions, resulting in the maximum column efficiency, as shown by the yellow line approaching 100%. Under these conditions, the separation was optimal, and the extract phase contained the highest amount of acetone.

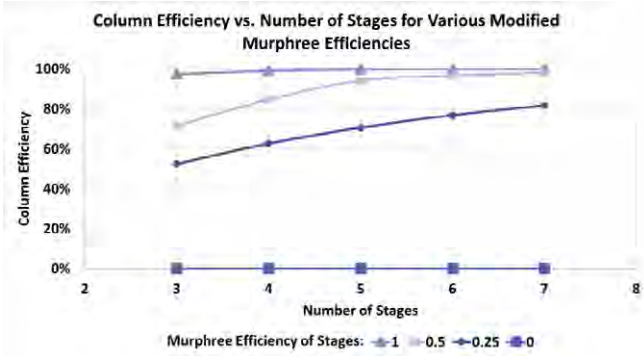



**Figure 5.** Effect of Murphree efficiency on column efficiency as a function of the number of stages. Lower efficiencies show limited separation performance.

The results highlight the significant influence of Murphree efficiency on extraction performance. Higher efficiencies lead to improved separation, whereas deviations from ideal conditions result in a notable decline in column performance. This emphasizes the importance of accurately modeling stage efficiency to better represent the behavior of LLX systems in practice.

## CONCLUSION

This work introduced a modified Murphree efficiency definition to address challenges in modeling stage efficiencies in LLX processes. By using mole flows instead of mole fractions, the approach provides a framework that better reflects the mass transfer and phase interactions in systems where deviations from equilibrium occur.

The implementation of this approach in a custom ACM model and its integration into AP were used to evaluate its applicability. Through test cases, the model demonstrated its capacity to capture the relationship between stage efficiency and separation performance under varying conditions. The observations showed how stage efficiencies influence the distribution of components between extract and raffinate phases and highlighted the limitations of existing built-in simulation modules.

The methodology is not restricted to the tools used in this study. It can be implemented in other simulation platforms capable of supporting custom efficiency definitions. This general applicability allows the approach to be used for further studies and practical applications in different extraction systems. By addressing the relationship between stage performance, efficiency, and mass transfer, the modified Murphree efficiency provides a foundation for understanding and improving LLX processes.

## DIGITAL SUPPLEMENTARY MATERIAL

Digital supplementary material, including data sheets, simulation files, models, and source code, is available upon request.

## ACKNOWLEDGEMENTS

The authors gratefully acknowledge the financial support provided by Neste, Finland for this project.

## REFERENCES

1. Treybal RE. Mass-Transfer Operations. McGraw-Hill (1980).
2. Lo TC, Baird MH, Hanson C. Handbook of Solvent Extraction. Wiley (1983).
3. King CJ. Separation Processes. McGraw-Hill (1971).
4. Nanda AK, Sharma MM. Effective interfacial area in liquid–liquid extraction. Chem Eng Sci 21:707-713 (1966) https://doi.org/10.1016/0009-2509(66)80022-2
5. Seader JD, Henley EJ, Roper DK. Separation Process Principles: With Applications Using Process Simulators. Wiley (2016).
6. Wankat PC. Equilibrium-Staged Separations: Separations in Chemical Engineering. Prentice Hall (1988).
7. Thornton JD. Science and Practice of Liquid-Liquid Extraction. Oxford University Press (1996).
8. Luyben WL. Distillation Design and Control Using Aspen Simulation. John Wiley & Sons (2013).
9. Dimian AC, Bildea CS, Kiss AA. Integrated Design and Simulation of Chemical Processes. Elsevier (2014).

© 2025 by the authors. Licensed to PSEcommunity.org and PSE Press. This is an open access article under the creative commons CC-BY-SA licensing terms. Credit must be given to creator and adaptations must be shared under the same terms. See https://creativecommons.org/licenses/by-sa/4.0/



Systems & Control Transactions

**Research Article - Peer Reviewed Conference Proceeding**
ESCAPE 35 - European Symposium on Computer Aided Process Engineering
Ghent, Belgium. 6-9 July 2025
Jan F.M. Van Impe, Grégoire Léonard, Satyajeet S. Bhonsale,
Monika E. Polańska, Filip Logist (Eds.)

PSE PRESS

# A Stochastic Techno-Economic Assessment of Emerging Artificial Photosynthetic Bio-Electrochemical Systems for $CO_2$ Conversion

**Haris Saeed[a]*, Aidong Yang[a], and Wei Huang[a]**

[a] University of Oxford, Department of Engineering Science, Oxford, United Kingdom
* Corresponding Author: haris.saeed@eng.ox.ac.uk.

## ABSTRACT

Artificial Photosynthetic Bio-Electrochemical Systems (AP-BES) offer a promising approach for converting $CO_2$ to valuable bioproducts, addressing carbon mitigation and sustainable production. This study employs a stochastic techno-economic assessment (TEA) to estimate the viability of rhodopsin driven AP-BES, from carbon capture to product purification. Unlike traditional deterministic TEAs, this approach uses Monte Carlo simulations to model uncertainties in key technoeconomic parameters, including energy consumption, $CO_2$ conversion efficiency, and bioproduct market prices. The analysis generates probability distributions for economic metrics such as Operational Expenditure (OPEX), Capital Expenditure (CAPEX), and profit. Enhancements in light-harvesting efficiency and advancements in reactor materials were predicted to reduce the payback period to just one year, thereby making large-scale deployment a feasible option.

**Keywords**: Artificial Photosynthesis, Techno Economic Assessment, Carbon Conversion, Synthetic Biology.

## INTRODUCTION

Global warming has driven the need for sustainable energy generation and manufacturing, a 3°C rise in global temperatures could halve GDP growth by 2050 and dramatically increase species extinction rates and flood risks [1], [2]. Staying below this limit requires significant reductions in greenhouse gas emissions, particularly $CO_2$ [1], [2]. Carbon Capture and Utilization (CCU) presents itself as a solution, offering the benefit of mitigating climate change while enabling sustainable manufacturing.

Biologically mediated CCU shows promise due to its ability to operate under ambient conditions, potentially lowering operating costs. Artificial Photosynthetic Bio-electrochemical Systems (AP-BES) are a novel class of these technologies, integrating biological and electrochemical processes to mimic natural photosynthesis. Yet, despite their potential, the adoption of AP-BES is hindered by major challenges such as system inefficiencies, and economic uncertainties. Thus, we propose a comprehensive evaluation framework that addresses the inherent variability and uncertainties in both technical and economic factors through a Monte Carlo approach.

## SYSTEM PRINCIPLES

### The Rhodopsin Driven AP-BES Reactor

At the heart of the system lies a bio-electrochemical reactor utilizing rhodopsin, a light-sensitive protein, to drive $CO_2$ fixation [3], [4], as illustrated in Figure 1. When exposed to light, primarily at wavelengths around 530 nm, rhodopsin undergoes conformational changes that result in transmembrane proton pumping [5]. At the same time, an engineered electron transfer pathway, using the MtrCAB complex found in electroactive bacteria, facilitates extracellular electron uptake [3].This combination of light-driven proton pumping and engineered electron transfer enables the efficient regeneration of ATP and reducing equivalents within the system, accelerating $CO_2$ conversion as shown in Figure 1. The host bacteria used, *Ralstonia eutropha,* has been used to produce a range of bioproducts, from commodities such as biomass, to hydrocarbons and even to pharmaceuticals such as α-humulene (C15), a potential drug to treat cancer[6]. When utilized in an AP-BES, *R. eutropha* has been shown to produce, riboflavin and PHB [3], [4], [5]. Thus, we opted

to focus on these two, in addition to biomass (cells) as representative, high value, medium value and low value products respectively.

This integration of a rhodopsin-based light harvesting with the engineered electron transfer pathways has been demonstrated to result in a system with an estimated electron transfer efficiency of ~20%, significantly surpassing the typical efficiency of natural photosynthesis in most crops (~5%) [3], [4], [5], [7].

## System Integration and Efficiency

Evaluating the viability of our AP-BES reactor requires examining it in the context of a complete carbon capture and utilization (CCU) system. This consists of three subsystems: carbon capture, carbon conversion (the AP-BES reactor), and separation, as illustrated in Figure 1 (system boundaries fully defined in S2.1.). The carbon capture subsystem is designed to remove $CO_2$ from either flue gas (14% $CO_2$) [8] or directly from the atmosphere (480 ppm $CO_2$) [9]. After $CO_2$ conversion in the AP-BES reactor, the separation subsystem refines and purifies the resulting organic products, ensuring they meet the purity standards required for downstream applications. Both the carbon capture and separation systems are analyzed using a black-box approach, relying on first-order cost estimates (see S2.3.).

# METHODOLOGY

The stochastic approach in techno-economic analysis (TEA) estimates uncertainty in performance by combining a deterministic base model with probabilistic hyperparameter sampling. This uncovers behaviours often overlooked by deterministic models. Sensitivity analyses identify parameters that significantly affect system economics and performance, with the varied parameter treated as deterministic.

## Deterministic Basis

Our techno-economic assessment (TEA) of Artificial of the rhodopsin driven Photosynthetic Bio electrochemical System (AP-BES) focussed on the three subsystems: carbon capture, carbon conversion, and separation, with system boundaries (fully defined in S2.1.). We estimated operational expenditure (OPEX) primarily considering energy and maintenance costs (further discussed in S2.2.). Energy requirements for separation processes were calculated with thermodynamic efficiencies from literature (S2.2.). Yearly maintenance costs were estimated as 10% of capital expenditure (CAPEX) [10], while labour costs were estimated as 20% of base OPEX (excluding maintenance) [10]. For CAPEX estimates, we employed three model types: energy-based models using the Lange equation[11], literature-based results using the 6/10ths rule, and equipment-based models in order of increasing

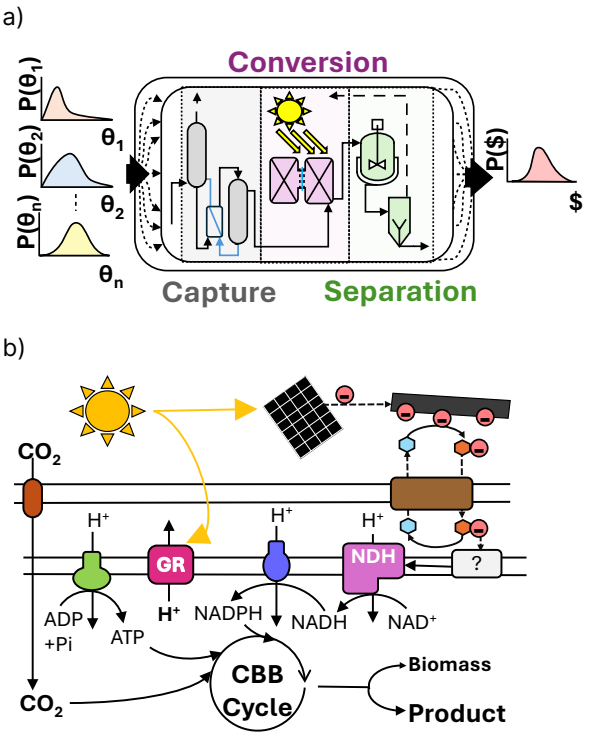



**Figure 1: (a)** Reference plant schematic (see S2.1) with stochastic TEA, model hyperparameters (e.g. separation efficiency) are modelled as random variables, from this an ensemble of predictions allows estimation of uncertainty. **(b)** Reference schematic at the cellular level for the reactor subsystem, through the inclusion of rhodopsin, ATP regeneration can be enhanced, thereby resulting in 'artificial' photosynthesis in this subsystem.

accuracy (further discussed in S2.3). In the reactor subsystem (the focus of this paper), equipment-based design and the 6/10ths rule were applied[10] for CAPEX estimates. To enhance accuracy, we applied correction factors such as Lang factors and the Chemical Engineering Plant Cost Index (CEPCI) to adjust for project complexities and inflation effects [10] (further discussed in S2.4) [16]. Total Annualised Cost (TAC) was calculated assuming a 10% interest rate and 10-year plant lifespan.

## Monte Carlo Sampling

To generate ensemble estimates of costs, we employed a Monte Carlo approach. Key parameters were modelled probabilistically using appropriate distributions based on their characteristics and available data (S2.6.). We performed 5,000 iterations for each operating condition assessed each time randomly sampling from the defined distributions. This approach aimed to capture inherent uncertainties and variabilities in the system, providing a more realistic representation of potential outcomes. Key parameters modelled stochastically included: Material Costs, efficiencies and Bioproduct market prices (see further in S2.6.). Statistical tests are outlined in S2.5.

## RESULTS & DISCUSSION

### Carbon Capture Subsystem

The techno-economic analysis of the carbon capture subsystem considered two scenarios: direct air capture (DAC) of $CO_2$ from ambient air at 440 ppm, and flue gas capture from an effluent stream containing 14 wt.% $CO_2$. For a complete system that converts 1 kilotonne of $CO_2$ a year (kt $yr^{-1}$), CAPEX for DAC ranged from £1.7M to £2.6M, compared to £0.9M to £1.2M for flue gas capture when considered at the reference condition (90% capture efficiency, 20% 2nd Law efficiency and a required purity of 95%, further defined in S.2.6.). Base OPEX (excluding maintenance), remained below £0.3M $yr^{-1}$ for both. Sensitivity analyses, shown in Figure 2, demonstrate how predicted OPEX shows strong dependency on both required effluent purity and second-law efficiency. Predicted OPEX was minimized when effluent purity was reduced to 10–20% and second-law efficiency approached 100% (further shown in Figure S1.1). Second-law efficiency, typically around 20% for systems of this type, emerged as the most significant driver of CAPEX variability. Constraining efficiency to 20% resulted in raw CAPEX (£) one order of magnitude greater than base OPEX (£/yr, excluding maintenance costs).

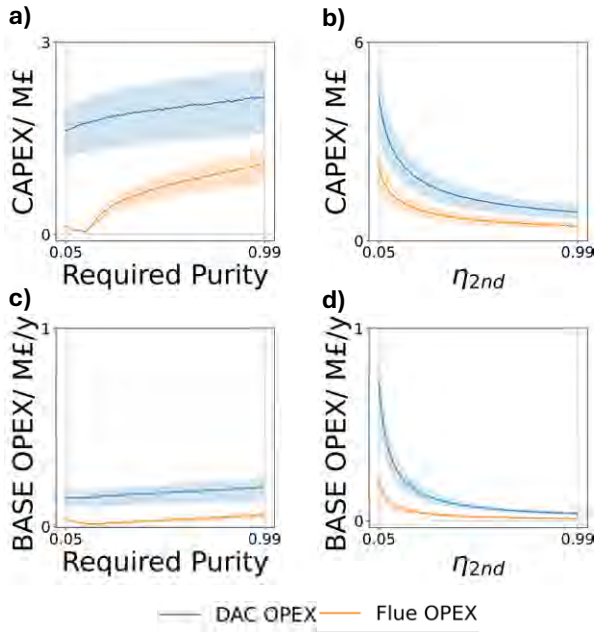



**Figure 2: ,** Plots of CAPEX (**a,b**) and Base OPEX **(c,d)** at a range of plant conditions for DAC (blue) and Flue (Orange). A reference condition of a 1 kilotonne scale, 90% capture efficiency, 20% 2nd Law efficiency and a required purity of 95% were used, all properties and parameters have an error of 50%. Plots **(a)** & **(c)**, examine the impact of required purity at the reference condition. Plots **(c)** & **(d)**, examine the impact of 2nd law efficiency at the operating point.

### Carbon Conversion Subsystem

The carbon conversion subsystem, the AP-BES reactor, enables the bio-electrochemical conversion of $CO_2$ into valuable bioproducts. To assess its economic performance, we analyzed the impact of light-harnessing efficiency, electrode materials, and membrane materials.

#### Impact of Electrode and Membrane Configurations

We assessed two electrode materials: carbon felt (CF), a low-cost, lower-performance option, and reticulated vitreous carbon (RVC), a higher-cost material with superior performance [12]. We also evaluated three membranes: Nafion (high-cost, high-performance)[13], BioChar (low-cost, low-performance), and earthenware (low-cost, low-performance)[14].

At the 1 kilotonne per year (kT $yr^{-1}$) scale, systems using RVC electrodes paired with low-cost membranes were predicted to be the optimal configuration, minimizing both expected OPEX and CAPEX as seen in Figure 3 (see table S1.1 for numerical results). Switching from CF to RVC significantly reduced expected OPEX (CF systems: 5.49-5.79 M£/yr; RVC systems: 4.26-4.60 M£/yr), with a p-value of less than 0.1% across all comparisons. For a given membrane, moving from CF to RVC reduced OPEX costs in 84.8% of cases, and when disregarding membrane choice (i.e. choosing a suboptimal membrane), this reduction occurred in at least 78.42% of cases. While Nafion was the best membrane for minimizing OPEX ($p<1\%$ within same electrode category), it only outperformed EarthWare in at most 61% of cases, confirming electrode material choice dominates OPEX considerations.

For CAPEX, electrode choice remained key, CF systems showed higher expected CAPEX (11.07-11.99 M£) than RVC systems (6.73-7.75 M£) with $p<0.001$. The probability of any RVC configuration providing lower CAPEX than any CF configuration was at least 69.04%, with RVC systems also exhibiting significantly lower uncertainty. Unlike OPEX, the optimal membrane choice for CAPEX favoured BioChar and EarthWare, which performed similarly (6.73-6.76 M£), while Nafion showed the highest costs (7.75 M£ for RVC+Nafion, $p<0.001$). BioChar outperformed Nafion with RVC electrodes in 82.64% of cases, with a significant expected difference of 1.02 M£ ($p<0.001$). The most economical configuration overall was RVC+BioChar or RVC+EarthWare, balancing expected OPEX (4.46-4.60 M£/yr) and expected CAPEX (6.73-6.76 M£).

#### Sensitivity to Light-Harnessing Efficiency

Sensitivity analysis of required light intensity (photosynthetic photon flux density: PPFD), shown in Figure 3, revealed predicted OPEX as highly dependent on PPFD

in all configurations. This is due to the direct coupling between required PPFD and energy. In contrast, reductions in required PPFD had minimal effects on CAPEX. Thus, research targeting enhanced light capture and utilization are critical for reducing OPEX of large-scale systems.

## Cost Distributions and Key Drivers

When evaluating impact of plant scale, CF-based systems had higher CAPEX with significant uncertainty due to increased specific volume requirements. In contrast, RVC-based systems exhibited tighter cost distributions, indicating greater predictability and lower financial risk. A similar trend was observed in OPEX, though cost distributions remained comparable across configurations. Despite the uncertainty in CF system cost estimates, RVC consistently lowered both CAPEX and OPEX across all tested configurations, reducing costs in at least 75% of cases when comparing systems at the same scale with the same membrane, highlighting RVC's cost advantage in developed models

Thus, we identified three primary cost drivers:

- **Electrode performance**: High-efficiency materials like RVC reduce OPEX & CAPEX by improving efficiency, particularly at larger scales.
- **Membrane selection**: Low-cost membranes provide substantial CAPEX reductions with minimal OPEX increases.
- **PPFD requirements:** Reducing light requirements directly impacts energy consumption, offering substantial OPEX reductions across all systems.).

These findings highlight the need for continued research into advanced reactor designs that balance performance and cost. By optimizing material choices and light utilization, the carbon conversion subsystem can achieve significantly reduced costs, supporting the commercialization of AP-BES technology.

## Separation Subsystem

The separation subsystem plays a crucial role in isolating the desired products from the reactor effluent, and its costs are primarily influenced by the product form and yield. We focused on three key products: riboflavin, polyhydroxybutyrate (PHB), and raw biomass, representing high (£60,000/T [15]), medium (£500/T [16], and low (£300/T [17]) added value products respectively. Figure 4 illustrates the impact of different process configurations on the capital expenditure (CAPEX) and operational expenditure (OPEX) at the 1 kilotonne scale. Costs are minimised when raw biomass is the sole product, but increase with additional products, peaking at zero biomass.

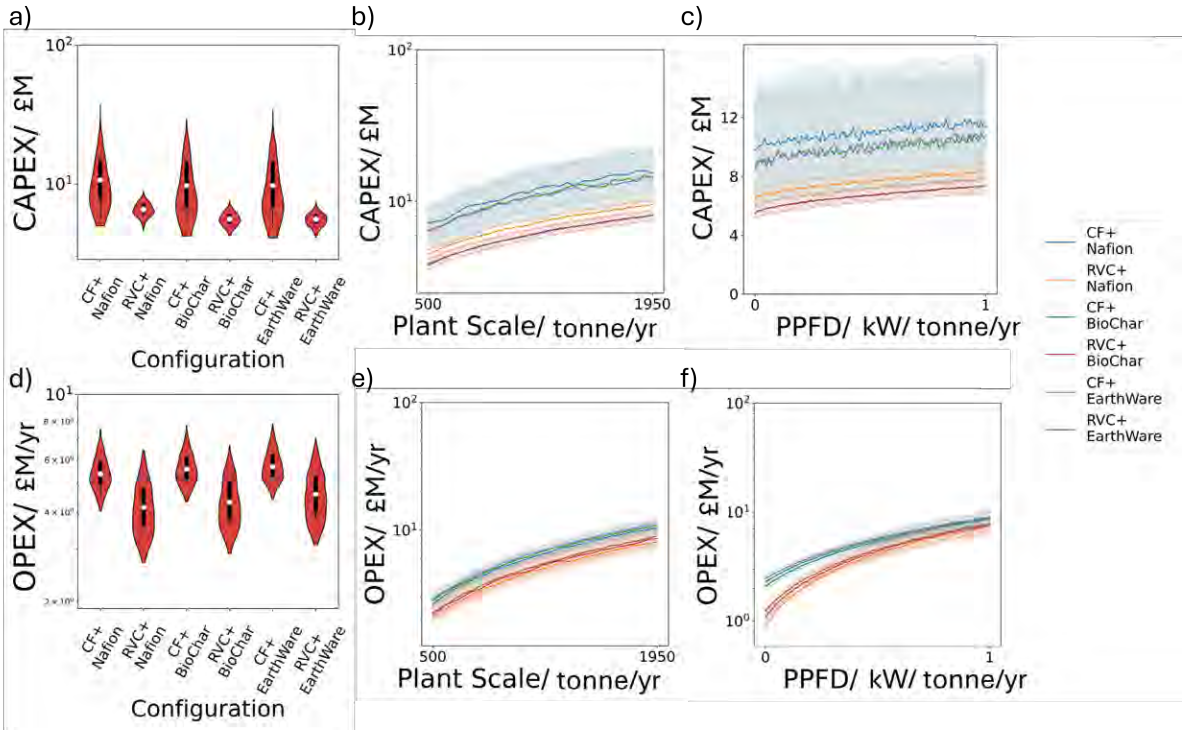



**Figure 3:** Plots of Estimated plant CAPEX **(a,b,c)** and OPEX **(d,e,f)** for each of the 6 key configurations. Electrodes of CF (Carbon Felt) and RVC (Reticulated Vitreous carbon), and membranes of Nafion, BioChar and Earthenware based materials are assessed. Plots **(a)** & **(c)**, examine the distribution of costs at the 1 kilotonne scale. Plots **(b)** & **(e)**, examine the impact of plant scale at the operating point. Plots **(c)** & **(f)**, examine the impact of required illumination on costs. All non-varied properties are fixed at the specified operating point defined in S2.6.

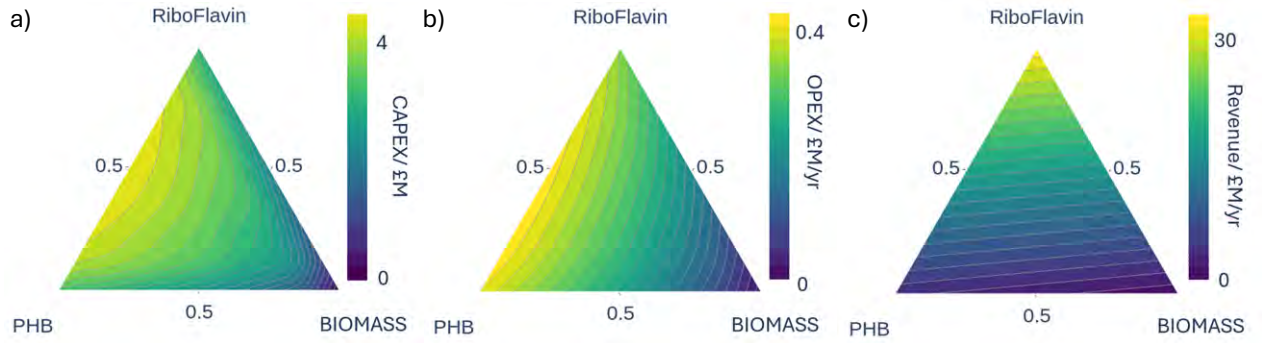



**Figure 4:** Plots of separation subsystem predicted CAPEX **(a),** OPEX **(b),** and Revenue **(c)** at the 1 kilotonne scale as a function of of product split between low (biomass), medium (PHB), and high (riboflavin) value added products.

Owing to its high value, separation subsystem revenue is predicted to be predominantly influenced by riboflavin yield, demonstrating the impact of high value end products. For a 1 kilotonne per year (kt $yr^{-1}$) plant, with riboflavin yields in the range of 10-20%, expected revenue is between £5 million and £15 million per year, with subsystem OPEX under £0.5 million per year and CAPEX ranging from £0.5 million to £5 million.

## Overall System Analysis

At the kilotonne scale both total CAPEX is estimated to be £12M and OPEX is estimated to be £8M/yr resulting in a TAC (total annualized cost) of approximately £10M, assuming Flue gas Carbon capture. Thus, at this scale riboflavin production is key to viability. To increase profit we identified 4 potential measures: (1) Reducing costs of the carbon capture subsystem, (2) Increasing bioreactor volumetric efficiency, (3) Reducing required illumination by engineering rhodopsin, (4) Using low-cost reactor materials.

Figure 5 shows the impact of each of these measures on estimated OPEX, CAPEX and profit at the 1 kilotonne scale with a 20% yield of Riboflavin when employing flue gas as a carbon source. With the current technology, the system can be considered unprofitable owing to the large volume of the reactor and the high energy and capital costs incurred. Cases 2 and 3 overcome this challenge in two different ways. Case 2 employs an RVC electrode, reducing required volume, simultaneously reducing required illumination and capital. Case 3 employs an engineered protein halving lighting requirement, significantly reducing OPEX. Thus, while OPEX reductions from using both novel reactor materials and engineered proteins is significant, a combination of these two approaches is required to have a reliably profitable system.

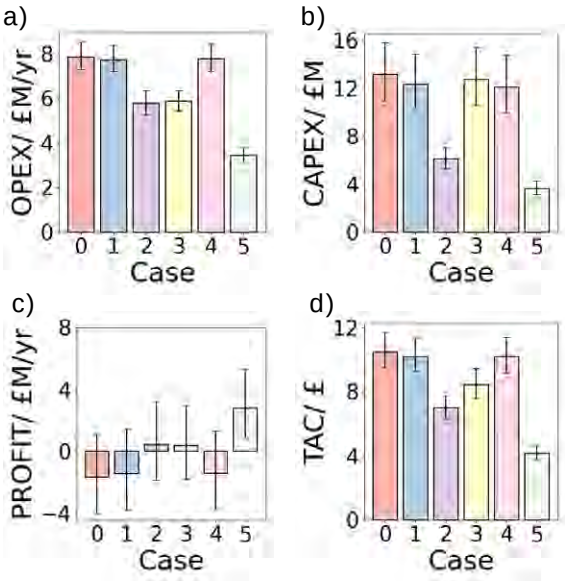



**Figure 5:** Plots of predicted CAPEX **(a)**, OPEX **(b)**, Profit **(c),** and TAC **(d)** at the 1 kilotonne scale assuming a 20% yield of Riboflavin. Case 0 represents the base case(a system with an unmodified carbon felt electrode with a Nafion membrane, the published state of technology[3], [4]) , Case 1 reduces required $CO_2$ purity to 20%, Case 2 implements an RVC electrode reducing required volume, Case 3 reduces required PPFD by 50%, Case 4 reduces Membrane cost to 0, Case 5 is the cumulative effect of all perturbations.

## SUMMARY

Our study reveals both challenges and opportunities for rhodopsin-driven BIO-ELECTROCHEMICAL synthesis in carbon capture and utilization (CCU). While the current configuration is not yet economically feasible at the 1 kilotonne scale, improvements in light-harvesting efficiency and reactor materials are predicted to achieve a one-year payback time, making large-scale deployment realistic. Our stochastic techno-economic analysis (sTEA) approach helps navigate technological uncertainties by considering parameter variability, providing crucial insights for optimization. This study thus serves as both an assessment of rhodopsin-driven Artificial Photosynthetic Bio-electrochemical Systems for CCU and a broader framework for evaluating emerging

technologies.

## DIGITAL SUPPLEMENTARY MATERIAL

Supplementary info hosted at:
https://github.com/hs280/TEA/tree/main
And consists of:

S1: Supplementary Results
S2: Supplementary Methods
S3: Code repository

## ACKNOWLEDGEMENTS

We acknowledge the support from BBSRC UK-Japan Engineering Biology project (APP38606), and DTP grant EP/W524311/1.

## REFERENCES

1. H.O. Portner, D. Roberts, C. Trisos, and N. Simpson, 'Summary for Policymakers: Climate Change 2022: Impacts, Adaptation, and Vulnerability. Contribution of Working Group II to the Sixth Assessment Report of the Intergovernmental Panel on Climate Change', Nov. 2022, doi: 10.1017/9781009325844.001.
2. J. Rising, M. Tedesco, F. Piontek, and D. A. Stainforth, 'The missing risks of climate change', Nature 2022 610:7933, vol. 610, no. 7933, pp. 643–651, Oct. 2022, doi: 10.1038/s41586-022-05243-6.
3. W. Tu, J. Xu, I. P. Thompson, and W. E. Huang, 'Engineering artificial photosynthesis based on rhodopsin for CO2 fixation', Nature Communications 2023 14:1, vol. 14, no. 1, pp. 1–12, Dec. 2023, doi: 10.1038/s41467-023-43524-4.
4. P. A. Davison et al., 'Engineering a Rhodopsin-Based Photo-Electrosynthetic System in Bacteria for CO2Fixation', ACS Synth Biol, vol. 11, no. 11, pp. 3805–3816, Nov. 2022, doi: 10.1021/ACSSYNBIO.2C00397/ASSET/IMAGES/LARGE/SB2C00397_0007.JPEG.
5. W. Tu, H. Saeed, and W. E. Huang, 'Rhodopsin-based light-harvesting system for sustainable synthetic biology', Microb Biotechnol, vol. 17, no. 7, p. e14521, Jul. 2024, doi: 10.1111/1751-7915.14521.
6. L. Santolin, S. L. Riedel, and C. J. Brigham, 'Synthetic biology toolkit of Ralstonia eutropha (Cupriavidus necator)', Applied Microbiology and Biotechnology 2024 108:1, vol. 108, no. 1, pp. 1–18, Aug. 2024, doi: 10.1007/S00253-024-13284-2.
7. R. E. Blankenship et al., 'Comparing photosynthetic and photovoltaic efficiencies and recognizing the potential for improvement', Science, vol. 332, no. 6031, pp. 805–809, May 2011, doi: 10.1126/SCIENCE.1200165.
8. C. Song et al., 'Trireforming of Methane over Ni Catalysts for CO2 Conversion to Syngas With Desired H2/CO Ratios Using Flue Gas of Power Plants Without CO2 Separation', 2004, pp. 315–322. doi: 10.1016/S0167-2991(04)80270-2.
9. N. McQueen, K. V. Gomes, C. McCormick, K. Blumanthal, M. Pisciotta, and J. Wilcox, 'A review of direct air capture (DAC): scaling up commercial technologies and innovating for the future', Progress in Energy, vol. 3, no. 3, p. 032001, Apr. 2021, doi: 10.1088/2516-1083/ABF1CE.
10. G. Towler and R. Sinnott, Chemical Engineering Design. Elsevier, 2022. doi: 10.1016/C2019-0-02025-0.
11. M. Tsagkari, J. L. Couturier, A. Kokossis, and J. L. Dubois, 'Early Stage Capital Cost Estimation of Biorefinery Processes: A Comparative Study of Heuristic Techniques', ChemSusChem, vol. 9, no. 17, pp. 2284–2297, Sep. 2016, doi: 10.1002/CSSC.201600309.
12. V. M. Vasconcelos, G. O. S. Santos, K. I. B. Eguiluz, G. R. Salazar-Banda, and I. de Fatima Gimenez, 'Recent advances on modified reticulated vitreous carbon for water and wastewater treatment – A minireview', Chemosphere, vol. 286, p. 131573, Jan. 2022, doi: 10.1016/J.CHEMOSPHERE.2021.131573.
13. S. Zhao et al., 'Application of biochar in microbial fuel cells: Characteristic performances, electron-transfer mechanism, and environmental and economic assessments', Ecotoxicol Environ Saf, vol. 267, p. 115643, Nov. 2023, doi: 10.1016/J.ECOENV.2023.115643.
14. J. Winfield, I. Gajda, J. Greenman, and I. Ieropoulos, 'A review into the use of ceramics in microbial fuel cells', Bioresour Technol, vol. 215, pp. 296–303, Sep. 2016, doi: 10.1016/J.BIORTECH.2016.03.135.
15. 'Riboflavin Price, 2024 Riboflavin Price Manufacturers & Suppliers | Made-in-China.com'. Accessed: Mar. 29, 2024. [Online]. Available: https://www.made-in-china.com/products-search/hot-china-products/Riboflavin_Price.html
16. B. Alvarez Chavez, V. Raghavan, and B. Tartakovsky, 'A comparative analysis of biopolymer production by microbial and bioelectrochemical technologies', RSC Adv, vol. 12, no. 25, p. 16105, May 2022, doi: 10.1039/D1RA08796G.
17. 'Animal feed prices - GOV.UK'. Accessed: Mar. 29, 2024. [Online]. Available: https://www.gov.uk/government/statistical-data-sets/animal-feed-prices

© 2025 by the authors. Licensed to PSEcommunity.org and PSE Press. This is an open access article under the creative commons CC-BY-SA licensing terms. Credit must be given to creator and adaptations must be shared under the same terms. See https://creativecommons.org/licenses/by-sa/4.0/



Systems & Control Transactions

**Research Article - Peer Reviewed Conference Proceeding**
ESCAPE 35 - European Symposium on Computer Aided Process Engineering
Ghent, Belgium. 6-9 July 2025
Jan F.M. Van Impe, Grégoire Léonard, Satyajeet S. Bhonsale,
Monika E. Polańska, Filip Logist (Eds.)

PSE PRESS

# Soft-Sensor-Enhanced Monitoring of an Alkylation Unit via Multi-Fidelity Model Correction

**Rastislav Fáber[a]*, Marco Vaccari[b], Riccardo Bacci di Capaci[b], Karol Ľubušký[c], Gabriele Pannocchia[b], and Radoslav Paulen[a]**

[a] Faculty of Chemical and Food Technology, Slovak University of Technology in Bratislava, 812 37 Bratislava, Slovakia
[b] Department of Civil and Industrial Engineering, University of Pisa, 561 22 Pisa, Italy
[c] Slovnaft, a.s., 824 12 Bratislava, Slovakia
* Corresponding Author: rastislav.faber@stuba.sk.

## ABSTRACT

Industrial process monitoring can benefit from utilizing historical data, providing insights for decision-making and operational efficiency. This study develops a soft-sensor-based approach leveraging multi-fidelity modeling to correct discrepancies between online sensors and laboratory analyses. A Gaussian process-based strategy is used to predict deviations between high-frequency low-fidelity sensor data and less frequent high-fidelity laboratory measurements. By exploring static and dynamic modeling frameworks, we assess their suitability for capturing process dynamics and addressing time-dependent variability. The multi-fidelity soft sensor noticeably improves predictive accuracy, outperforming high-fidelity and low-fidelity methods. This approach demonstrates applicability across various industrial settings where integrating diverse data sources enhances real-time process control and monitoring, reducing reliance on costly laboratory sampling.

**Keywords**: Machine Learning, Process Monitoring, Modelling, Information Management, Industry 4.0

## INTRODUCTION

Industrial processes rely on effective monitoring and control to ensure efficiency, safety, and optimal performance. Accurate process data, acquired through sensors and analyzers, form the foundation for decision-making and optimization [1]. Laboratory measurements provide precise, high-fidelity (HF) data but are often infrequent due to cost or logistical constraints. In contrast, online sensors generate low-fidelity (LF) data at high frequencies but can vary in reliability and accuracy [2]. Differences in the quality and frequency of these data sources have motivated the development of advanced modeling approaches to improve process monitoring [3].

Soft sensors (SS) [4] have emerged as a key tool for improving process monitoring by using predictive models to estimate process variables based on online measurements. These models typically rely on periodic calibration with HF data to address sensor drift and inaccuracies. However, traditional calibration processes often use HF data solely for single-point corrections, leaving the potential of historical HF data to improve predictive accuracy over time. Multi-fidelity (MF) modeling [5] addresses this limitation by combining LF and HF data, enhancing predictive accuracy and improving the reliability of process monitoring systems.

MF modeling utilizes historical datasets to develop predictive models that mitigate the discrepancies between LF and HF data. Both static and dynamic models offer viable approaches for capturing the underlying behavior of the system. Static models [6] are well-suited for representing systems in relatively stable states but lack the ability to incorporate time-dependent behaviors, making them less appropriate for processes with significant temporal variability. In contrast, dynamic models [7] explicitly account for temporal dependencies, offering a more comprehensive representation of process variability at the cost of increased structural complexity.

Techniques, such as the Kalman filter [8], can be applied to both static and dynamic models to improve predictive accuracy. By estimating and compensating for potential unmeasured errors or biases in real time, these tools enhance the reliability of predictions, particularly in noisy, high-frequency datasets. While dynamic models

commonly integrate these methods to manage process variability, traditional approaches like bias correction have long been employed in static models to address long-term drifts or measurement inaccuracies.

Gaussian Process Regression (GPR) has demonstrated effectiveness in both single-fidelity and multi-fidelity modeling contexts, providing accurate predictions and quantifying uncertainties in high-dimensional industrial datasets [9]. Within this study, GPR serves as a key tool for fusing LF and HF data, correcting LF signals by predicting deviations and applying these corrections to approximate HF data in real time.

In this context, we aim to develop a MF modeling framework that enhances industrial process monitoring by integrating LF online sensor data with HF laboratory measurements. This approach addresses challenges such as sensor faults and measurement anomalies by utilizing a soft sensor (SS) that estimates true values, reducing reliance on frequent and costly laboratory sampling. By combining static and dynamic methods within a MF modeling framework, this work demonstrates how soft-sensor-based correction can improve predictive performance and reliability in process monitoring applications.

## PROBLEM DEFINITION

This study considers two types of historical datasets: LF data obtained from online sensors, and HF data derived from laboratory measurements. LF data are collected continuously at a high sampling rate, offering detailed temporal information. In contrast, HF data are gathered less frequently and serve as reference points for calibrating and validating the LF sensors.

The time instances for LF measurements are represented as $\mathcal{T}_{LF} = \{t_1, t_2, \ldots, t_{n_{LF}}\}$, and for HF samples as $\mathcal{T}_{HF} = \{\tau_1, \tau_2, \ldots, \tau_{n_{HF}}\}$, with $\mathcal{T}_{HF} \subset \mathcal{T}_{LF}$. Typically, HF data are collected far less frequently than LF data, making $n_{HF} \ll n_{LF}$. The corresponding index sets for HF and LF data are denoted as $\mathrm{I}_{HF} \subset \mathrm{I}_{LF}$, respectively.

The objective is to create a predictive model that maps process variables $\boldsymbol{x} \in R^{n_x}$ to a target output $y \in R$. A linear model at the $i$-th time instant is expressed as:

$$\hat{y}_i = \boldsymbol{\theta}^T \boldsymbol{\varphi}_i + \epsilon_i, \tag{1}$$

where $\hat{y}_i$ is the predicted output, $\boldsymbol{\varphi}_i$ represents a vector of regressors, $\boldsymbol{\theta}$ is the parameter vector, and $\epsilon_i$ accounts for errors or unmodeled variability. Alternatively, a nonlinear model can be defined as:

$$\hat{y}_i = f(\boldsymbol{\theta}, \boldsymbol{\varphi}_i) + \epsilon_i, \tag{2}$$

where $f$ is a nonlinear function parameterized by $\boldsymbol{\theta}$. The structure of the regressor vector $\boldsymbol{\varphi}_i$ depends on the chosen modeling approach:

a) Static model: $\boldsymbol{\varphi}_i = \boldsymbol{x}_i$, this approach relies solely on current input values.

b) Dynamic model: $\boldsymbol{\varphi}_i = (\boldsymbol{x}_{i-1}, \ldots, \boldsymbol{x}_{i-j}, y_{i-1}, \ldots, y_{i-k})$, this approach incorporates lagged inputs and outputs to account for temporal dependencies.

Here, $j$ and $k$ denote the number of lagged values included for the input variables $\boldsymbol{x}$ and output $y$, respectively.




**Figure 1:** Soft sensor development flowchart.

## METHODOLOGY

This section outlines the methodology used to develop and compare static and dynamic modeling approaches (see Figure 1).

### Preprocessing

Raw data, denoted as $\boldsymbol{X}_{raw}$ for input features and $\boldsymbol{y}_{raw}$ for the dependent variable, often contain noise, outliers, and missing values due to plant disturbances. Preprocessing addresses these issues to ensure robust model development [10]. Outliers are detected and replaced while preserving temporal dependencies in the dynamic model, as discussed in [11].

### Feature Selection

Feature selection (FS) aims to identify a subset of relevant process variables, $\boldsymbol{\phi}$, enhancing model interpretability and reducing overfitting. Several methods guide feature selection, balancing statistical rigor with practical relevance informed by process knowledge. As detailed in [11], the following approaches were employed for both static and dynamic models:

a) Principal Component Analysis (PCA) reduces dimensionality by transforming the original variables into uncorrelated principal components (PCs) that maximize variance.

b) Partial Least Squares (PLS) Regression identifies latent variables that maximize covariance between the independent variables and the dependent variable.

c) LASSO Regression introduces an $\ell_1$-norm penalty to enforce sparsity and enhance interpretability.

d) Stepwise Regression (SR) iteratively selects variables based on statistical significance, guided by metrics such as Akaike Information Criterion (AIC), Corrected Akaike Information Criterion (AICc), and the Bayesian Information Criterion (BIC).

Beyond statistical selection, domain knowledge is incorporated to refine the feature set. Process experts review the ranked variables and identify unsuitable candidates that could introduce misleading correlations. The next-best ranked alternative from the best-performing FS method is substituted. This approach ensures the model captures the most relevant process features while maintaining transferability to similar environments with minor adjustments based on site-specific expertise. These methods enhance model interpretability, streamline computational efficiency, and minimize the risk of overfitting [12].

## Soft Sensor Training

The parameters of the model defined in Equation 1 are estimated by solving the following optimization problem:

$$\min_{\boldsymbol{\theta}} \frac{1}{2}||\boldsymbol{y}_l - \hat{\boldsymbol{y}}_l||_2^2 \equiv \min_{\boldsymbol{\theta}} \frac{1}{2}\Sigma_{i=1}^{n_l}(y_{l,i} - \hat{y}_{l,i})^2, \quad (7)$$

where $l \in \{LF, HF\}$ denotes whether the model corresponds to LF or HF data, and $n_l$ is the number of samples in the respective dataset.

## Multi Fidelity Soft Sensor Development

The MF SS integrates trained LF and HF models into a unified MF modeling approach. The predictor matrix $\boldsymbol{\phi}_{MF}$ is constructed as follows:

$$\boldsymbol{\varphi}_{MF,i} = (\boldsymbol{\varphi}_{LF,i}^T, \boldsymbol{\varphi}_{HF,i}^T, \boldsymbol{y}_{LF}^T, \hat{\boldsymbol{y}}_{LF}^T)^T. \quad (8)$$

This matrix combines features and predictions from both fidelity levels. An additional feature selection step can be conducted to further refine the input space.

Subsequently, the MF SS is trained by using a Gaussian Process (GP), which is defined as:

$$\hat{\boldsymbol{y}}_{MF} \sim \mathcal{GP}(m(\boldsymbol{\kappa}), k(\boldsymbol{\kappa}, \boldsymbol{\kappa}')), \quad (9)$$

where $\boldsymbol{\kappa}$ represents selected predictors derived from $\boldsymbol{\phi}_{MF}$. The mean function $m(\boldsymbol{\kappa})$ captures the expected output, while the covariance function, also referred to as the kernel $k(\boldsymbol{\kappa}, \boldsymbol{\kappa}')$, describes dependencies between data points.

In this model, the kernel is defined as:

$$k(\boldsymbol{\kappa}, \boldsymbol{\kappa}') = C.e^{-M} + e^{\frac{2sin^2 M}{\ell^2}} + \sigma^2.\delta_{\kappa,\kappa'}, \quad (10)$$

where $M = 1/2\,||\boldsymbol{\kappa} - \boldsymbol{\kappa}'||^2$ . The kernel comprises four components (from left to right): a constant term $C$, a radial basis function (RBF) kernel to capture smooth variations, a periodic kernel to model sinusoidal behaviors, and a white noise kernel accounting for measurement noise through $\delta_{\kappa,\kappa'}$. The parameters include $\ell$ (length scale), determining the range of influence, and $\sigma^2$, representing noise variance

# CASE STUDY

The alkylation process plays a pivotal role in refineries, producing high-octane branched isoparaffins, known as alkylate, which are crucial components of clean gasoline. This process involves the reaction of $C_3$–$C_4$ olefins with isobutane (i-$C_4$) under the influence of an acid catalyst. The reaction mechanism begins with the protonation of olefins, forming carbonium cations that subsequently react to generate $C_8$ isomers [13, 14].

Efficient alkylate production relies on maintaining an optimal reactant ratio. To ensure this, online analyzers are strategically deployed throughout the plant (Figure 2) to provide real-time measurements of key feed and recycle stream components. This enables precise process control. Over a six-month period, a comprehensive

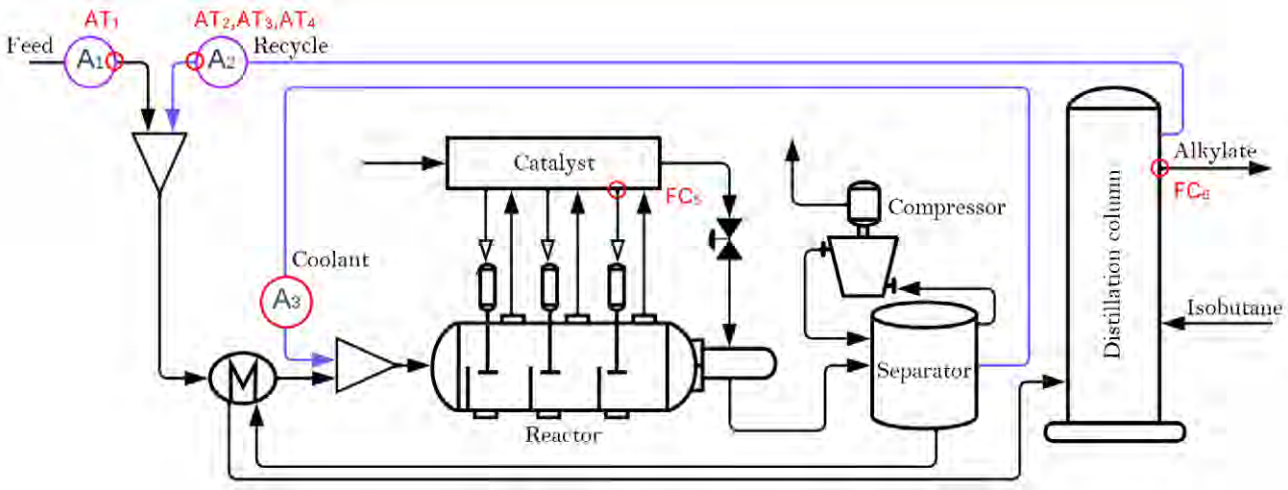



**Figure 2:** Simplified schematic of the alkylation unit, highlighting Analyzer $A_3$ (red) as well as the six selected variables used in soft sensor training.

dataset, $\boldsymbol{X}_{raw}$, was gathered, comprising more than 1085 process variables from online sensors, analyzers, resulting in $N \times 1085$ data points, while the laboratory samples correspond to a subset of these timestamps.

The study focuses on Analyzer $A_3$ and its corresponding laboratory reference data, $\boldsymbol{y}_{LF}$ and $\boldsymbol{y}_{HF}$. Analyzer $A_3$ monitors the i-$C_4$ concentration in the recycle stream but has demonstrated inconsistent performance. These inconsistencies often lead to an over-recycling of i-$C_4$, imposing additional downstream processing burdens, such as increased heating and treatment requirements. Therefore, improving the prediction of analyzer measurements is vital for optimizing production efficiency and minimizing by-products.

## IMPLEMENTATION

We preprocess the raw input data $\boldsymbol{X}_{raw}$ and corresponding raw output data $\boldsymbol{y}_{raw}$ (see Figure 1). The resulting preprocessed data, $\boldsymbol{X}_{proc}$ and $\boldsymbol{y}_{proc}$, are then split into training and testing sets in a 60% to 40% ratio. The training period spans four months, while the testing period covers two months. This selection is particularly relevant as seasonal variations during this timeframe can significantly influence process dynamics, including changes in the characteristics of the feedstream. Given the limited availability of HF data, chronological ordering was maintained to preserve time dependencies.

From the preprocessed dataset $\boldsymbol{X}_{proc}$, we identify the most relevant variables ($\boldsymbol{\phi}_i$) using the best-performing FS method outlined in the Feature Selection subsection. To address the limited HF data, we rely on the LF dataset during FS, as the sparsity of HF data may fail to capture key interactions and trends where the output variable is influenced by time-dependent changes across multiple inputs. By leveraging the more frequent LF measurements, we ensure that the selected features ($\boldsymbol{\phi}_{LF}$) reflect these dynamics more effectively, reducing the risk of missing correlations present in the data that would not be evident in $\boldsymbol{\phi}_{HF}$.

Both static HF and LF SSs ($\hat{\boldsymbol{y}}_{HF}$ and $\hat{\boldsymbol{y}}_{LF}$) are trained using the same set of features $\boldsymbol{\phi}_{LF}$, as described in Equation 1. These features are further refined with insider knowledge to enhance their operational relevance and consistency across both SSs. For the dynamic LF SS, we extend the feature set ($\boldsymbol{\phi}_{LF}$) by incorporating time-shifted versions determined by the model order to capture time-dependent system dynamics. We formulate the SS as a linear state-space model, and system identification is performed using the SIPPY (Systems Identification Package for Python) [15] library, employing the PARSIM-K robust identification method [16]. This approach, aimed for closed-loop data identification, ensures accurate representation of system dynamics with minimal number of parameters. The SS performance is further enhanced using information criteria such as AIC, AICc, and BIC for optimal model order selection. Additionally, a Kalman filter option of the PARSIM-K method is explored to refine the dynamic SS predictive accuracy.

We extend the LF models into MF framework by incorporating a GP model. This approach corrects deviations between LF and HF measurements, leveraging the strengths of both datasets for more accurate real-time monitoring of process variables (as illustrated in Figure 3). The MF SS effectively mitigates signal drift and compensates for the limited availability of HF samples.

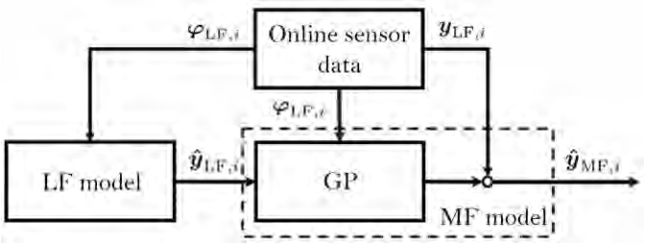



**Figure 3:** Workflow of the MF SS correction of the online analyzer $A_3$.

**Table 1:** RMSE comparison of the online analyzer against the static and dynamic LF prediction models.

| Method | Training RMSE | | Testing RMSE | |
|---|---|---|---|---|
| $\boldsymbol{y}_{LF}$ to $\hat{\boldsymbol{y}}_{LF,s}$ | 0.21 | | 0.37 | |
| $\boldsymbol{y}_{LF}$ to $\hat{\boldsymbol{y}}_{LF,d}$ | w KF | w/o KF | w KF | w/o KF |
| | 0.03 | 0.29 | 0.02 | 0.42 |

**Table 2:** RMSE comparison of the laboratory samples against the applied predictive approaches.

| Comparison | Training RMSE | Testing RMSE |
|---|---|---|
| $\boldsymbol{y}_{HF}$ to $\boldsymbol{y}_{LF}$ | 0.63 | 0.80 |
| $\boldsymbol{y}_{HF}$ to $\hat{\boldsymbol{y}}_{HF}$ | 0.18 | 0.91 |
| $\boldsymbol{y}_{HF}$ to $\hat{\boldsymbol{y}}_{MF,s}$ | 0.22 | 0.46 |
| $\boldsymbol{y}_{HF}$ to $\hat{\boldsymbol{y}}_{MF,d}$ | 0.31 | 0.38 |
| $\boldsymbol{y}_{HF}$ to $\hat{\boldsymbol{y}}_{MF,d_{KF}}$ | 0.21 | 0.46 |

## RESULTS

We standardize the dataset to ensure consistent variable scaling across all analyses. During FS, we prioritize the LF data, as it better captures the time-dependent relationships between input ($\boldsymbol{X}_{proc}$) and output ($\boldsymbol{y}_{proc}$). The sparse nature of $\boldsymbol{y}_{HF}$ can overlook these dynamic interactions, as it fails to capture the nuances of how $\boldsymbol{y}_{LF}$ responds to changes in $\boldsymbol{x}$ over time. We select SR as the most suitable feature selection method based on the results from [11]. Additionally, we refine these features with domain knowledge, improving their relevance and ensuring consistency across both static and dynamic models. The final feature set includes six critical variables, highlighted in Figure 2: four concentrations ($AT_1$ to $AT_4$) and

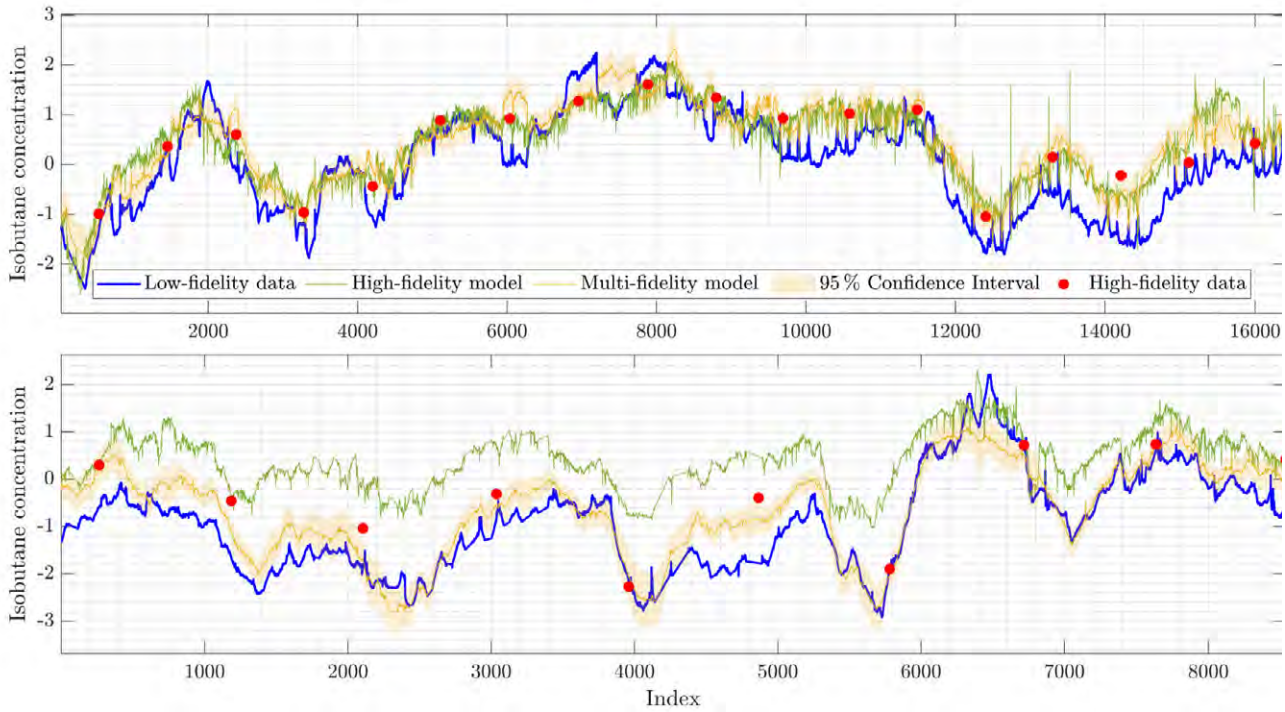



**Figure 4:** Predicted normalized i-$C_4$ concentration for the training set (top) and testing set (bottom) as time series.

two flow rates ($FC_5$ and $FC_6$).

We aim to predict the measurements from the online analyzer $A_3$. We train a static LF SS $\hat{\boldsymbol{y}}_{LF,s}$ with the six previously selected inputs. This approach achieves RMSE values of 0.21 during training and 0.37 during testing (Table 1). However, the alkylation unit operates with multiple recycles, where process streams re-enter the system at different stages, causing data variations. These recycles introduce complexities that static models cannot address. We develop a dynamic LF model $\hat{\boldsymbol{y}}_{LF,d}$ to address the temporal dependencies in the data. We optimize the SS complexity through system identification and select a 4th-order model to balance accuracy and computational efficiency based on AIC, AICc, and BIC criteria. We achieve a RMSE value of 0.29 for training and 0.42 for testing. To improve predictive accuracy, we integrate a Kalman filter into the $\hat{\boldsymbol{y}}_{LF,d}$, defined as $\hat{\boldsymbol{y}}_{LF,d_{KF}}$, significantly reducing RMSE values to 0.03 for training and 0.02 for testing. The Kalman filter proves instrumental in mitigating disturbances and improving reliability.

The performance metrics for all predictive approaches are summarized in Table 2, with laboratory data ($\boldsymbol{y}_{HF}$) compared against all SSs. The current online analyzer $A_3$ ($\boldsymbol{y}_{LF}$) exhibits RMSE values of 0.63 for training and 0.80 for testing, resulting in inaccurately capturing the real process trends.

The HF SS $\hat{\boldsymbol{y}}_{HF}$ (green line in Figure 4) achieves an RMSE of 0.18 on the training set, which increases to 0.91 on the testing set. This increased RMSE value highlights that both, the features selected, and the limited amount of HF data available likely hamper the SS ability to capture the full variability within the HF dataset; as further visual analysis suggests that the HF SS effectively captures the trends in the HF data.

To obtain the MF SS output, we train a GP to predict deviations of the LF analyzer data from the HF laboratory measurements, defined as $\boldsymbol{\Delta}_{HF,i} = \mathbf{y}_{HF,i} - \mathbf{y}_{LF,i}, \forall i \in \mathfrak{I}_{HF}$. This approach enables operators to monitor $\boldsymbol{\Delta}_{HF}$ and its dispersion, offering a practical means to assess the calibration of the online analyzer and identify potential deviations in its accuracy. The GP model can incorporate either the static LF model ($\hat{\boldsymbol{y}}_{LF,s}$) or the dynamic LF model ($\hat{\boldsymbol{y}}_{LF,d}$) as an additional input, with the latter having two variations: with ($\hat{\boldsymbol{y}}_{LF,d_{KF}}$) and without Kalman filtering. PCA is applied to reduce the dimensionality of the input variables, consisting of the original six process variables and the selected LF model, into four principal components (PCs). Depending on the chosen input, the MF SS predictions are denoted as $\hat{\boldsymbol{y}}_{MF,s}$, $\hat{\boldsymbol{y}}_{MF,d}$, or $\hat{\boldsymbol{y}}_{MF,d_{KF}}$.

The static MF SS ($\hat{\boldsymbol{y}}_{MF,s}$) achieved an RMSE of 0.22 during training and 0.46 during testing. Although this approach provides promising results during training, its higher testing RMSE indicates similar limitations in addressing the aforementioned system dynamics.

When selecting the most suitable additional input within the dynamic MF SS ($\hat{\boldsymbol{y}}_{MF,d}$), $\hat{\boldsymbol{y}}_{LF,s}$ achieves a lower RMSE when compared to $\boldsymbol{y}_{LF}$ (0.37 compared to 0.42 for testing, as shown in Table 1), it exhibits significant deviations from $\boldsymbol{y}_{HF}$. In contrast, $\hat{\boldsymbol{y}}_{LF,d}$ better aligns with the trends in $\boldsymbol{y}_{HF}$, as evidenced by smaller maximum and

minimum errors relative to $\boldsymbol{y}_{HF}$. This suggests that the dynamic SS, despite a higher RMSE against $\boldsymbol{y}_{LF}$, provides a more reliable representation of process dynamics.

The Kalman-filtered dynamic MF SS ($\hat{\boldsymbol{y}}_{MF,d_{KF}}$) amplifies certain LF anomalies, propagating biases that reduce the GPs ability to make unbiased predictions (RMSE = 0.46). Consequently, the non-Kalman dynamic MF SS ($\hat{\boldsymbol{y}}_{MF,d}$) enhances predictive accuracy while mitigating the influence of LF anomalies (RMSE = 0.38). As shown in Figure 4, the blue solid line represents the original LF data ($\boldsymbol{y}_{LF}$), the orange line denotes the MF SS predictions ($\hat{\boldsymbol{y}}_{MF,d}$), and the red markers indicate the HF laboratory data. The orange shaded region illustrates the 95% confidence interval of the GP model.

Ultimately, the most accurate MF SS ($\hat{\boldsymbol{y}}_{MF,d}$) accounts for LF discrepancies with GP-predicted corrections, achieving RMSE values of 0.31 for training and 0.38 for testing. These findings highlight the importance of time-dependent behavior, enabling us to capture system dynamics and adapt to temporal variations, which leads to improved performance over static soft sensors.

## CONCLUSION

In this work, we compare static and dynamic modeling approaches within a multi-fidelity framework to improve the accuracy of online measurements. The static models ($\hat{\boldsymbol{y}}_{LF,s}$) fail to capture temporal dependencies, which limits their applicability in complex systems with time-varying dynamics. Dynamic models ($\hat{\boldsymbol{y}}_{LF,d}$), especially those incorporating Kalman filtering, effectively address these challenges, achieving an improvement in capturing the underlying process behavior. However, incorporating the Kalman filter into the MF SS increases the RMSE, negatively impacting performance in the MF framework. The most viable SS ($\hat{\boldsymbol{y}}_{MF,d}$) demonstrates a 52.50% enhancement in accuracy over the currently implemented online analyzer, significantly improving the alignment between online LF measurements and laboratory HF values.

Future work will focus on refining dynamic modeling techniques by addressing process non-linearities and further optimizing GP implementations to enhance accuracy and robustness.

## ACKNOWLEDGEMENTS

This work is funded by the Slovak Research and Development Agency under the project APVV-21-0019, by the Scientific Grant Agency of the Slovak Republic under the grant 1/0263/25, and by the European Commission under the grant 101079342 (Fostering Opportunities Towards Slovak Excellence in Advanced Control for Smart Industries). RP acknowledges the financial support by the European Commission under the grant scheme NextGenerationEU project no. 09I03-03-V04-00530.

## REFERENCES

1. Mondal PP, Galodha A, Verma VK, Singh V, Show PL, Awasthi MK, Lall B, Anees S, Pollmann K, Jain R, Review on machine learning-based bioprocess optimization, monitoring, and control systems. Bioresource Technology, 370, 128523. (2023)
2. Peherstorfer B, Willcox K, Gunzburger M, Survey of multifidelity methods in uncertainty propagation, inference, and optimization SIAM Rev., 60 (3), pp. 550-591. (2018)
3. Zhu J, Ge Z, Song Z, Gao F, Review and big data perspectives on robust data mining approaches for industrial process modeling with outliers and missing data. Ann. Rev. Control, 46, 107-133. (2018)
4. Sun YN, Qin W, Hu JH, Xu HW, Sun PZH, A causal model-inspired automatic feature-selection method for developing data-driven soft sensors in complex industrial processes. Engineering, 22, 82–93. (2023)
5. Giselle Fernández-Godino M, Review of multifidelity models. Advances in Computational Science and Engineering, 1(4), 351–400. (2023)
6. Zou KH, Tuncali K, Silverman SG, Correlation and simple linear regression. Radiology. 227(3). (2003)
7. Nelles,O, Nonlinear Dynamic System Identification. In: Springer, Cham. (2020)
8. Kalman RE, A new approach to linear filtering and prediction problems. J Basic Eng 82(1):35–45 (1960)
9. Rasmussen CE, Gaussian Processes in Machine Learning, 63–71. Springer Berlin Heidelberg. (2004)
10. Fáber R, Mojto M, Ľubušký K, Paulen R, From data to alarms: Data-driven anomaly detection techniques in industrial settings. In ESCAPE34 - PSE24. (2024)
11. Fáber R, Vaccari M, Bacci di Capaci R, Ľubušký K, Pannocchia G, Paulen R, Improving process monitoring via dynamic multi-fidelity modeling. 14th IFAC Symposium on Dynamics and Control of Process Systems, including Biosystems. (2025)
12. Li J, Cheng K, Wang S, Morstatter F, Trevino RP, Tang J, Liu H, Feature selection: A data perspective. ACM Comput. Surv., 50(6). (2017)
13. Pall Refineries: Application focus $H_2SO_4$ alkylation process description. Tech. report, Pall Corp. (2018)
14. Speight JG, The refinery of the future. Gulf Professional Publishing, Elsevier. (2020)
15. Armenise G, Vaccari M, Bacci di Capaci R, Pannocchia G, An open-source system identification package for multivariable processes. In UKACC 12th International Conference on Control,

152–157. (2018)
16. Pannocchia G, Calosi M, A predictor form parsimonious algorithm for closed-loop subspace identification. Journal of Process Control, 20(4), 517–524. (2010)

© 2025 by the authors. Licensed to PSEcommunity.org and PSE Press. This is an open access article under the creative commons CC-BY-SA licensing terms. Credit must be given to creator and adaptations must be shared under the same terms. See https://creativecommons.org/licenses/by-sa/4.0/



Systems & Control Transactions

**Research Article - Peer Reviewed Conference Proceeding**
ESCAPE 35 - European Symposium on Computer Aided Process Engineering
Ghent, Belgium. 6-9 July 2025
Jan F.M. Van Impe, Grégoire Léonard, Satyajeet S. Bhonsale,
Monika E. Polańska, Filip Logist (Eds.)

PSE PRESS

# Differentiation between Process and Equipment Drifts in Chemical Plants

**Linda Eydam[a]*, Lukas Furtner[a], Julius Lorenz[b] and Leon Urbas[ab]***

[a] TU Dresden, Process-to-Order Group, Process Systems Engineering Group, Dresden, 01069, Germany
[b] TU Dresden, Process-to-Order Group, Chair of Process Control Systems, Dresden, 01069, Germany
* Corresponding Author: linda.eydam@tu-dresden.de

## ABSTRACT

The performance of chemical plants is inevitably related to knowledge about the current state of the system. However, both process and equipment drifts may distort state information. Deviations of process values caused by equipment malfunction may be misinterpreted as process drifts and vice versa. Determining the cause of the drift is further complicated by the fact that equipment drifts typically occur in combination with process drifts. This paper presents a method that uses available additional equipment data to reliably detect and decouple combined equipment and process drifts in chemical plants by combining statistical methods with model-based approaches. The utility of additional equipment information is assessed based on its effect on the decoupling of process and equipment drifts. First results demonstrate the feasibility of the approach in a real plant.

**Keywords**: Fault Detection, Modelling, Process Monitoring, Coupled Drifts, Namur Open Architecture

## 1 MOTIVATION

In the chemical industry a combination of high plant availability and desired product quality is required to operate economically. This is achieved if the desired operating point is maintained, which requires accurate information about the state of both the process and the equipment. If inaccurate process information is used, the plant cannot be operated with sufficient accuracy. The result is loss of quality and, in the worst case, plant shutdowns and a reduction in plant availability. Equipment drifts, such as fouling or wear in sensors or actuators, can lead to inaccurate process information. Measurement deviations that are caused by equipment malfunction or insufficient calibration can be misinterpreted as process drifts and vice versa. When this happens, the operating point is updated even though the process has not changed. As a result, the quality of the product is reduced.

Such equipment drifts typically occur in combination with process drifts. Very often, the data collected in the process control systems and historians is not sufficient to clearly determine the causes of the drifts. However, additional equipment information, such as device health information, is typically collected in modern devices. It has the potential to enable the differentiation and decoupling of coupled drifts. For this reason, a method is developed that uses this additional information to detect and decouple combined process and equipment drifts.

This paper is organized as follows: first, fundamentals of drift types and their detection methods are presented. Then, the developed methodology is explained by describing its assumptions, requirements and workflow for detecting and decoupling of coupled drifts. Furthermore, the evaluation of additional equipment information is explained. A case study in a real plant demonstrates the applicability and feasibility of the approach. Finally, the method is critically evaluated.

## 2 BACKGROUND

### 2.1 Definition of Drifts

In the literature various definitions of process drift and equipment drift can be found. According to Kadlec et al. [1], process drifts affect the measured data and the state of the process. Sensor drifts only affect the measured data. Actuator drifts are not mentioned. In contrast, the NAMUR Recommendation 107 on Self-Monitoring and

Diagnosis of Field Devices [2] describes status signals for the diagnosis of appliances and field devices. Diagnostic bits are used to differentiate between possible error sources. However, only equipment failures are considered. In addition, the International Electrotechnical Commission defines a drift as a "change in the indication of a measuring instrument, generally slow, continuous, not necessarily in the same direction and not related to a change in the measurand" [3]. This definition corresponds to equipment drift.

Each of these definitions is missing some type of drift, and if both process and equipment drift were defined, the definitions would no longer work. Therefore, the information on process drifts affecting the state of the process is taken from Kadlec et al. [1]. In addition, NAMUR Recommendation 107 [2] and the International Electrotechnical Commission [3] provide necessary information on equipment drifts.

Based on this information and in the context of this research, process drift and equipment drift are defined as occurrences with the following results:

**Process drift:**

> unacceptable, unforeseen variation of predefined critical process parameters from their desired operating point for an unacceptable period of time

**Equipment drift:**

> unacceptable, unforeseen variation in the operating principle of measuring or control devices for an unacceptable period of time

## 2.2 Drift Detection Approaches

In the literature, various approaches have been found to detect drifts, some of which also diagnose the cause of the drifts. According to Venkatasubramanian et al. [4], methods of detection are divided into model-based and data-based.

Common model-based approaches are observers and redundancy-based methods. Observers are models that continuously update and improve an estimate of the system state [5]. Redundancy-based methods generate optimal reference values for measured sensor data [6]. Residuals, the differences between the estimated and measured states or the redundant values, are calculated and compared to drift detection thresholds [5], [6]. As model-based approaches describe the system using equipment and process knowledge the modeling effort increases significantly with the complexity of the system. For applications in large chemical plants, it can be concluded that high system complexity can lead to a disproportionate modeling effort [4].

Common data-based approaches are statistical methods and machine learning. Statistical methods are utilized to reduce the dimensions of the data. For instance, cluster analysis is used to divide the data into clusters of normal and abnormal variation. A cluster is an area with specific characteristics, such as an area with a certain drift or an area without any drift. Drifts are detected by analyzing if data points belong to the cluster with normal or abnormal variation [7], [8], [9]. The difficulty with statistical methods is that enough data must be available from the time a drift occurs. Machine learning trains and tweaks models such as neural networks to classify the data. The outputs are different categories such as no drift or drift [10]. However, to build a data-based model, classified data is needed for training, which is very often not available for chemical plants. The reason for this is that it is not known when a drift occurs and what kind of drift it is.

None of these approaches addresses combined drifts and their decoupling. In recent years, the amount of available data has increased greatly due to digitalization. This is not considered in the proposed approaches of the relevant literature. Modern devices record a range of additional information complementing the primary measurement value. If these additional information streams can be accessed, e.g. via the process control system or a side-channel such as the NAMUR open architecture, and utilized, they can help to differentiate between process and equipment drifts and their coupling.

# 3 METHODOLOGY

Due to the large amount of data available in chemical plants nowadays, it is reasonable to use data-based methods such as statistical methods. These methods divide the data into clusters. But there is a problem - after such a cluster analysis it is not possible to assign which cluster belongs to which drift. The solution is to combine statistical methods with model-based approaches. Possible drifts are modeled and compared with the clusters to assign them to the drifts. The idea of decoupling is to reconstruct the individual drifts and span drift vectors to characterize them. Data points that are drift couplings are then also represented as vectors. Drift decomposition splits these data point vectors into individual drifts and decoupling is complete.

However, the combination of these approaches and the decoupling of combined drifts is only possible if process data and additional equipment information are available and can be used.

## 3.1 Assumptions and Requirements

First, assumptions are made about the method being developed. They also address the process and equipment for which the method can be used.

1. Data from the equipment under consideration is accessible. This includes primary measurement

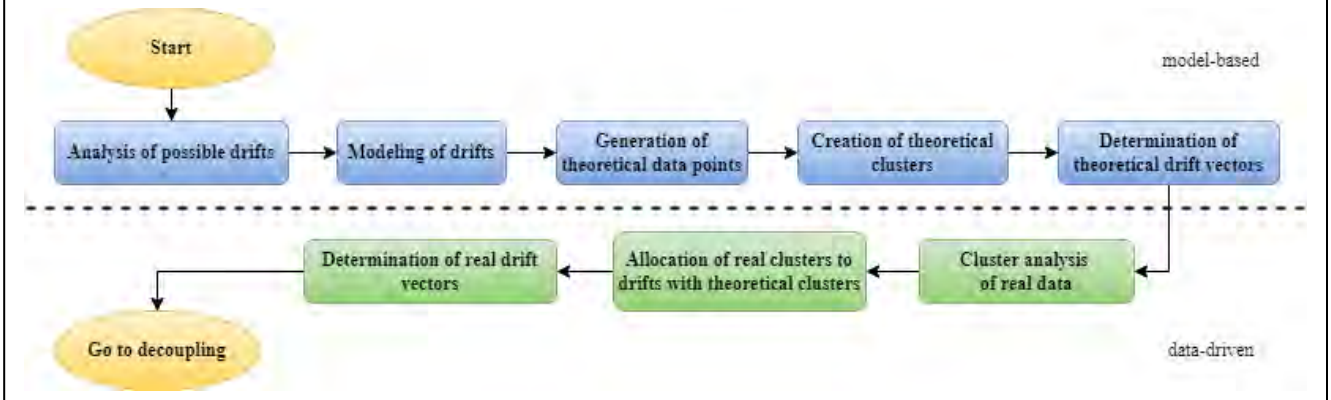



**Figure 1:** Workflow for the identification of drift areas. These steps are necessary to decouple coupled drifts. Yellow is the start and end of the workflow, blue is the model-based part, and green is the data-driven part.

values as well as additional equipment information.

2. Devices without additional equipment information can also be used with this method. Primary measurement values and the information streams of other devices in the chemical plant help to compensate for the lack of additional equipment information.
3. It is known what drifts can occur on the equipment under consideration and their approximate impact on the data streams.
4. The drifts are considered to be independent.
5. The available data can be separated by cluster analysis.
6. The process must be continuous with a steady state setpoint and low dynamics. The method cannot be used for processes with varying process conditions, changing target states or high dynamics.

Requirements related to the goal are:

1. Drift detection.
2. Distinguishing between process and equipment drifts.
3. Determining the cause of the drift.
4. Detecting and unambiguous decoupling of combinations of known drifts.
5. Evaluation of what additional equipment information is needed to decouple the drift combinations.

## 3.2 Drift Areas Identification/Characterization

At the beginning, it is necessary to identify and characterize the areas of the drifts to perform the developed method. The workflow for this is shown in Figure 1. The first step is to analyze possible drifts in the equipment and plant under consideration. These drifts are then modeled mechanistically, allowing the creation of theoretical data points. These theoretical data points are used to build theoretical clusters as a reference for specific clusters. When modeling, it is important to ensure that the theoretical clusters do not overlap. If they overlap during the modeling process, increase the modeling dimension with the help of additional equipment information until they no longer overlap. After that, the centers of the theoretical clusters are formed, e.g. if the theoretical data points are uniformly distributed, as the geometric center of their theoretical data points. To characterize the theoretical drift clusters, vectors are drawn from the center of the cluster without drift to the centers of the drift clusters. These theoretical drift vectors are determined by their direction and their length is positive.

Next, real data is used to perform a cluster analysis. The real clusters are assigned to the drifts by comparison with the theoretical clusters. Then, their centers are calculated, e.g. as the geometric center of their real data points. To characterize the real drift clusters, vectors are drawn from the center of the cluster without drift to the centers of the drift clusters. These real drift vectors are determined by their direction and their length is positive.

## 3.3 Decoupling of Coupled Drifts

When the drift areas are identified and characterized, new data points can be categorized. The first step is to check if the data point belongs to a real cluster. If so, the new data point is assigned to that cluster and the associated drift. Drift detection is complete.

However, if the data point does not belong to a real cluster, there is a high probability of a coupled drift, because only a combination of at least two drifts leads to this area. Vector decomposition and vector addition are

used to determine the individual drifts that are combined. First, a vector is drawn from the center of the cluster without drift to the data point to be categorized. This vector is called the data point vector $\boldsymbol{v}_{\mathrm{DP}}$. Then $\boldsymbol{v}_{\mathrm{DP}}$ is decomposed into individual drifts. This is shown schematically in Figure 2. To decompose $\boldsymbol{v}_{\mathrm{DP}}$, it is compared with the existing real drift vectors $\boldsymbol{v}_{\mathrm{r}}$. The real drift vector that is most parallel to $\boldsymbol{v}_{\mathrm{DP}}$ is selected. In Figure 2 $\boldsymbol{v}_{\mathrm{r1}}$ is more parallel to $\boldsymbol{v}_{\mathrm{DP}}$ than $\boldsymbol{v}_{\mathrm{r2}}$. Therefore, $\boldsymbol{v}_{\mathrm{r1}}$ is chosen. The selected vector is then weighted by projecting $\boldsymbol{v}_{\mathrm{DP}}$ onto it. The resulting vector $\boldsymbol{v}_{\mathrm{rG}}$ corresponds to the first decomposition vector or factor $\boldsymbol{v}_{\mathrm{F1}}$.

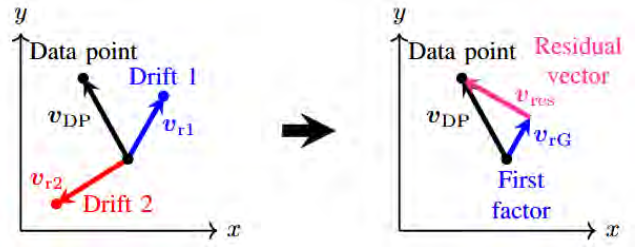



**Figure 2:** Schematic of the decomposition of a data point vector $\boldsymbol{v}_{\mathrm{DP}}$ into individual drift vectors $\boldsymbol{v}_{\mathrm{r}}$. The first factor of the decomposition $\boldsymbol{v}_{\mathrm{rG}}$ and the remaining residual vector $\boldsymbol{v}_{\mathrm{res}}$ are calculated.

Then, it is determined whether this resulting first factor $\boldsymbol{v}_{\mathrm{F1}}$ points to a point within a specified boundary around the data point. For this purpose, the residual vector $\boldsymbol{v}_{\mathrm{res}}$ is spanned from the superposition of the previously determined factors to the new data point. If the square sum of the length of $\boldsymbol{v}_{\mathrm{res}}$ is less than a specified threshold, it is inside the boundary and the decomposition is complete. However, if the computed square sum is greater than a specified threshold, it is outside the boundary. In this case, $\boldsymbol{v}_{\mathrm{res}}$ is used to perform the steps like $\boldsymbol{v}_{\mathrm{DP}}$, from comparing $\boldsymbol{v}_{\mathrm{res}}$ with the existing real drift vectors $\boldsymbol{v}_{\mathrm{r}}$ up to calculating more decomposition factors $\boldsymbol{v}_{F2}, \ldots, \boldsymbol{v}_{Fn}$. At the end of each determination of a new factor, it is checked whether the superposition of the decomposition factors points to a point within the specified boundary around the data point. If this is the case, the decomposition is complete. The calculated factors are the individual drifts that together form the drift coupling:

$$\boldsymbol{v}_{\mathrm{DP}} = \boldsymbol{v}_{\mathrm{F1}} + \cdots + \boldsymbol{v}_{\mathrm{Fn}}. \tag{1}$$

## 3.4 Derivation and Evaluation of Additional Equipment Information

The space with its dimension and axis in which the drifts are modeled and the cluster analysis and decoupling will be performed, is defined with the help of additional equipment information. This can include signal-to-noise ratio, a measurement gain, position feedback, a control value or energy data about the device.

In an ideal world, the combined drifts should be uniquely decoupled. This is the case when the coupled drifts can be unambiguously decomposed into any combination of individual drifts. To achieve this, the drift vectors of the possible individual drifts must be linearly independent. Thus, n drift vectors must span a n-dimensional space. If for example only two drifts occur, a 2-dimensional space is needed. In this space, combinations of the two occurring drifts can be unambiguously decomposed as shown in Figure 3. The vector $\boldsymbol{v}_{\mathrm{DP}}$ of the coupled drift is a combination of the drift vectors $\boldsymbol{v}_{\mathrm{D1}}$and $\boldsymbol{v}_{\mathrm{D2}}$:

$$\boldsymbol{v}_{\mathrm{DP}} = \mathrm{a}\boldsymbol{v}_{D1} + \mathrm{b}\boldsymbol{v}_{D2}. \tag{2}$$

The drift vectors are linearly independent when

$$\mathbf{0} = \lambda_1 \boldsymbol{v}_{D1} + \lambda_2 \boldsymbol{v}_{D2} \tag{3}$$

and the only solution of the system of equations is $\lambda_1 = \lambda_2 = 0$. So $\boldsymbol{v}_{\mathrm{D1}}$and $\boldsymbol{v}_{\mathrm{D2}}$ span the 2-dimensional space. They are defined by their direction and their length is positive. This means that every data point lies in the positive range of both drift vectors.

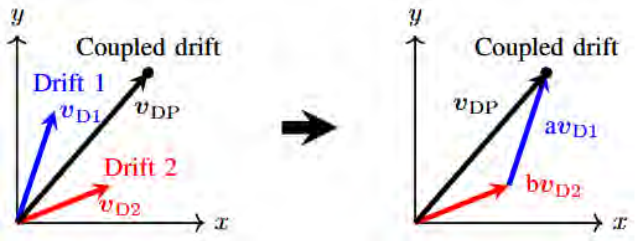



**Figure 3:** Schematic decomposition of a coupled drift vector $\boldsymbol{v}_{\mathrm{DP}}$ in two individual drifts $\boldsymbol{v}_{\mathrm{D1}}$ and $\boldsymbol{v}_{\mathrm{D2}}$.

When the number of occurring drifts become larger than the dimension of the space, the decomposition becomes ambiguous. The drift vectors get linearly dependent. To get from such an ambiguous to an unambiguous decomposition, more additional equipment information is needed. The dimension of the space must be increased to the number of occurring drifts. To derive the necessary information that increases this dimension, available additional information of the equipment under consideration is analyzed. Using assumed connections in the real data, an estimate of the most useful additional information is made. The data used for cluster analysis is extended with the selected information, cluster analysis is performed, and the drift vectors are calculated. The independence of the drift vectors is checked. If they are still linearly dependent, other additional information must be examined until they are linearly independent or no more information is available.

The value of the additional equipment information is judged by its contribution to spanning the n-dimensional space. If the information provides a dimension, it can be used immediately. If not, it is examined to see if it can contribute in combination with other information.

## 4 CASE STUDY

A case study on a real-world brownfield chemical plant is performed to demonstrate the applicability and feasibility of the method. Consider a control valve in a chemical plant through which a fluid flows. Due to the presence of solids, an abrasive mixture is formed. Gas bubbles may also be present. Under the assumption that the control valve is recently installed, four independent drifts may occur in the valve:

- Equipmentdrift 1: Increased amounts of gas bubbles that cause inaccuracy in measuring the flow through the valve.
- Equipmentdrift 2: Increased amounts of solids that cause inaccuracy in measuring the flow through the valve.
- Processdrift 1: Reduced density of the fluid.
- Processdrift 2: Increased density of the fluid.

These four drifts are modelled, and theoretical clusters and drift vectors are determined, as Figure 4 shows. The white areas outside the clusters are where unclassified and unknown drifts or couplings of drifts can occur.

The modeling space is defined with the help of additional equipment information. In particular, the measurement gain and the signal-to-noise ratio of the valve are used along with the main measurements of density and temperature of the mixture. The reason for this is that this additional information adds dimensions to the space so that the theoretical clusters and drift vectors can be well distinguished. The emerging four theoretical drift vectors are linearly independent and span a 4-dimensional space.

The cluster analysis of the real data from the control valve is performed in the 4-dimensional space of the theoretical drift vectors. In this context, the statistical part benefits from the modeling part of the method. The result of the cluster analysis shows only three clusters and outliers. Together with the modelled drifts, these real clusters can be assigned to the drifts. One of the real clusters is the cluster without drift, the other two are drift clusters. Only Equipmentdrift 1, the gas bubbles, and Processdrift 1, a reduced density, occur in the data. These results are shown in the 2-dimensional space of density and measurement gain in Figure 5.

The outliers from the cluster analysis are passed to the method as possible drift combinations. However, if some drifts are not represented in the data, a combination of real and theoretical drift vectors is required. Otherwise, some drift coupling may not be detected and decoupled. This is because drift coupling can only be diagnosed if the drift vectors of the individual drifts that are combined are present. Thus, a 4-dimensional space is created from the real drift vectors of Equipmentdrift 1 and Processdrift 1 and the theoretical drift vectors of Equipmentdrift 2 and Processdrift 2. When the outliers are categorized by the method in this 4-dimensional space, different combinations of drifts are detected and diagnosed. For example, there are couplings of individually occurring drifts, such as the drift coupling data point in Figure 5. This data point is a combination of Equipmentdrift 1 and Processdrift 1. Thus, the vector of the data point $\boldsymbol{v}_{\mathrm{DP}}$ is a linear combination of the vectors of Equipmentdrift 1 $\boldsymbol{v}_{\mathrm{Eq1}}$ and Processdrift 1 $\boldsymbol{v}_{\mathrm{Pd1}}$:

$$\boldsymbol{v}_{\mathrm{DP}} = a\boldsymbol{v}_{\mathrm{Eq1}} + b\boldsymbol{v}_{\mathrm{Pd1}}. \tag{4}$$

This linear equation system is solved, and the parameters a and b are uniquely determined. There are also other combinations of drifts, such as Equipmentdrift 1 and Processdrift 2.

Finally, this use case demonstrates that drift couplings can be detected with the help of additional equipment information. The cause of these drift couplings can also be diagnosed with a high degree of certainty.

## 5 DISCUSSION AND OUTLOOK

In this paper, a method is developed to detect and decouple combined process and equipment drifts. To achieve this goal, statistical methods are combined with model-based approaches. Cluster analysis is performed, and the real clusters are assigned to the drifts using previously modeled clusters. To characterize these theoretical and real clusters, drift vectors are spanned. Drift combinations are then diagnosed using vector decomposition. The key to getting the right data space for the unambiguously decoupling of drift couples is the use of additional equipment information. The n drift vectors of the n possible drifts must span an n-dimensional space. For this purpose, a combination of theoretical and real drift vectors is used. Additional equipment information helps to obtain the required n-dimensional space.

The application of the method on a control valve in a brownfield chemical plant demonstrated that the detection and diagnosis of simultaneously appearing process and equipment drifts is successful. Thus, the feasibility of the approach is shown.

The critical evaluation shows that the developed approach is successful in plants with a continuous process, a steady state setpoint and low dynamics. However, most chemical plants do not meet these requirements. Often there are varied process conditions and changes in the target state. In addition, existing drifts change, and new drifts occur. If the drifts are dependent on each other, this is not considered.

Future directions of research are the development of new strategies to deal with changing process conditions and high dynamics as well as the detection and handling of dependent drifts. Furthermore, the development

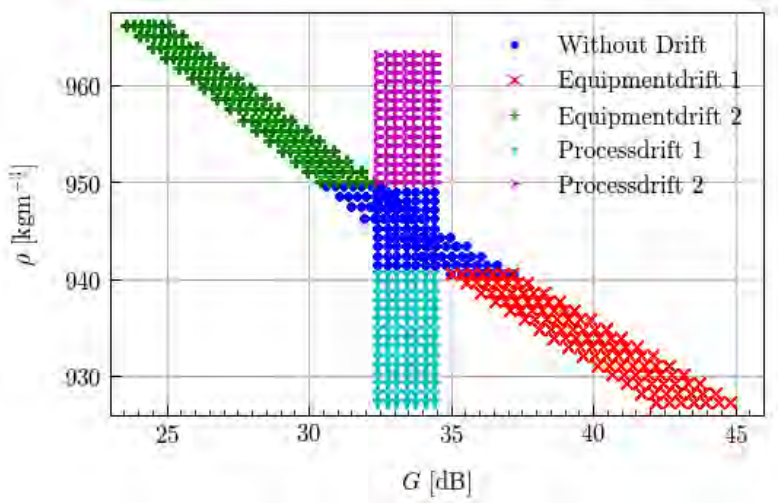



**Figure 4:** Modeled clusters – one cluster with no drift and four with different drifts. The process parameter $\rho$, the density, is the main measured value. The variable G, the measurement gain, is a typical additional information from the same equipment.

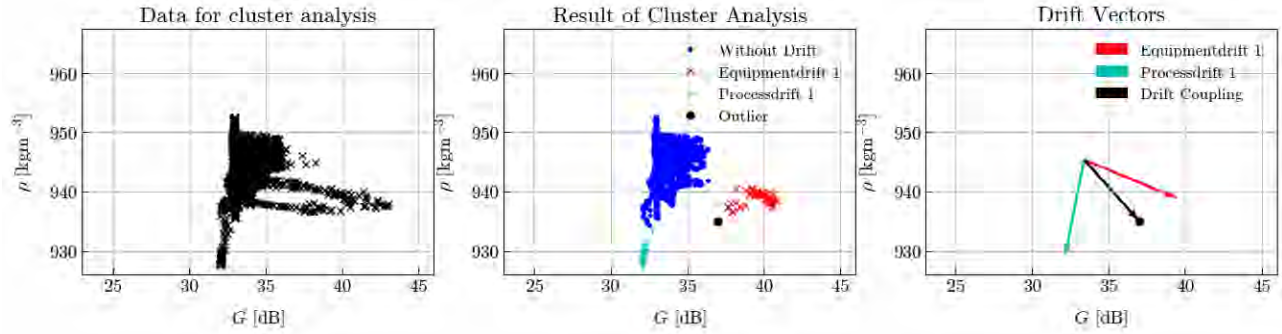



**Figure 5:** Data and results of the case study. Two drifts with their drift vectors and outliers as drift couplings were detected. The process parameter $\rho$ , the density, is the main measured value of the equipment. The variable G, the measurement gain, is a typical additional information from the same equipment.

of a unified equipment data standard deserves to be a topic of future research.

## ACKNOWLEDGEMENTS

The authors thank the partners of the industrial project RUBENS: LANXESS Deutschland GmbH, SAMSON AG, KROHNE Messtechnik GmbH and FOCUS-ON VoF for the collaboration and discussion.

## REFERENCES

1. P. Kadlec, B. Gabrys, and S. Strandt, “Data-driven Soft Sensors in the process industry,” Computers & Chemical Engineering, vol. 33, no. 4, Art. no. 4, Apr. 2009, doi: 10.1016/j.compchemeng.2008.12.012.
2. “NAMUR NE 107 - Self-Monitoring and Diagnosis of Field Devices.” NAMUR – Interessengemeinschaft Automatisierungstechnik der Prozessindustrie e.V., Oct. 04, 2017.
3. IEC, “IEC 60050 - International Electrotechnical Vocabulary - Details for IEV number 311-06-13: ‘drift.’” Accessed: Jan. 06, 2025. [Online]. Available: https://electropedia.org/iev/iev.nsf/display?openform&ievref=311-06-13
4. V. Venkatasubramanian, R. Rengaswamy, S. N. Kavuri, and K. Yin, “A review of process fault detection and diagnosis: Part I: Quantitative model-based methods,” Computers & Chemical Engineering, vol. 27, no. 3, Art. no. 3, Mar. 2003, doi: 10.1016/S0098-1354(02)00160-6.
5. M. Du, J. Scott, and P. Mhaskar, “Actuator and sensor fault isolation of nonlinear process systems,” Chemical Engineering Science, vol. 104, pp. 294–303, Dec. 2013, doi: 10.1016/j.ces.2013.08.009.

6. M. Taiebat and F. Sassani, “Distinguishing sensor faults from system faults by utilizing minimum sensor redundancy,” Trans. Can. Soc. Mech. Eng., vol. 41, no. 3, Art. no. 3, Sep. 2017, doi: 10.1139/tcsme-2017-1033.
7. R. Dunia and S. Joe Qin, “Joint diagnosis of process and sensor faults using principal component analysis,” Control Engineering Practice, vol. 6, no. 4, Art. no. 4, Apr. 1998, doi: 10.1016/S0967-0661(98)00027-6.
8. R. Dunia and S. Joe Qin, “A unified geometric approach to process and sensor fault identification and reconstruction: the unidimensional fault case,” Computers & Chemical Engineering, vol. 22, no. 7, Art. no. 7, Jul. 1998, doi: 10.1016/S0098-1354(97)00277-9.
9. N. M. Nor, C. R. C. Hassan, and M. A. Hussain, “A review of data-driven fault detection and diagnosis methods: applications in chemical process systems,” Reviews in Chemical Engineering, vol. 36, no. 4, Art. no. 4, May 2020, doi: 10.1515/revce-2017-0069.
10. S. Heo and J. H. Lee, “Fault detection and classification using artificial neural networks,” IFAC-PapersOnLine, vol. 51, no. 18, Art. no. 18, Jan. 2018, doi: 10.1016/j.ifacol.2018.09.380.

© 2025 by the authors. Licensed to PSEcommunity.org and PSE Press. This is an open access article under the creative commons CC-BY-SA licensing terms. Credit must be given to creator and adaptations must be shared under the same terms. See https://creativecommons.org/licenses/by-sa/4.0/



Systems & Control Transactions

**Research Article - Peer Reviewed Conference Proceeding**
ESCAPE 35 - European Symposium on Computer Aided Process Engineering
Ghent, Belgium. 6-9 July 2025
Jan F.M. Van Impe, Grégoire Léonard, Satyajeet S. Bhonsale,
Monika E. Polańska, Filip Logist (Eds.)

PSE PRESS

# Enhanced Reinforcement Learning-driven Process Design via Quantum Machine Learning

**Austin Braniff[a], Fengqi You[b], and Yuhe Tian[a]***

[a] Department of Chemical and Biomedical Engineering, West Virginia University, Morgantown, WV, United States
[b] Smith School of Chemical and Biomolecular Engineering, Cornell University, Ithaca, NY, United States
* Corresponding Author: yuhe.tian@mail.wvu.edu.

## ABSTRACT

In this work, we introduce a quantum-enhanced reinforcement learning (RL) framework for process design synthesis. RL-driven methods for generating process designs have gained momentum due to their ability to intelligently identify optimal configurations without requiring pre-defined superstructures or flowsheet configurations. This eliminates reliance on prior expert knowledge, offering a comprehensive and robust design strategy. However, navigating the vast combinatorial design space poses computational challenges. To address this, a novel approach integrating RL with quantum machine learning (QML) is proposed. QML leverages theoretical advantages over classical methods to accelerate searches in large spaces. Built upon our prior work, the approach begins with a maximum set of available unit operations, represented in a flowsheet structure using an input-output stream matrix as RL observations. A Deep Q-Network (DQN) algorithm trains a parameterized quantum circuit (PQC) in place of a classical neural network (NN). The design structures generated by the RL agent are optimized using the IDAES Process Systems Engineering Framework, with the optimization objectives used as rewards to RL (e.g., cost, productivity). This quantum-enhanced algorithm is performed on a hydrodealkylation process case study, showcasing its efficiency and improved performance in navigating complex design spaces.

**Keywords**: Process Design, Process Synthesis, Quantum Computing, Reinforcement Learning

## 1. INTRODUCTION

In the modern era of digitalization, industries are undergoing rapid transformation, driven by advancements in artificial intelligence (AI) and machine learning (ML). These technologies have fundamentally reshaped how chemical and energy processes are designed and optimized, enabling greater efficiency, adaptability, and innovation. Among the many applications of ML, reinforcement learning (RL) has emerged as a particularly promising approach in process systems engineering (PSE) [1-2].

RL-driven process synthesis offers a systematic methodology to identify optimal process configurations without relying on predefined superstructures or flowsheet configurations. By allowing an agent to automatically and intelligently explore and evaluate design decisions, RL minimizes the influence of prior assumptions and heuristics. Despite the potential, RL-driven process synthesis faces significant challenges including the vast combinatorial design space, which often renders the search computationally expensive or even intractable.

Quantum computing presents an exciting opportunity to overcome these limitations by harnessing quantum machine learning (QML) [3-4]. QML algorithms have demonstrated the potential for computational speedups in solving problems that are traditionally constrained by the limitations of classical computation [5]. Leveraging advances in quantum hardware and algorithms, QML can accelerate the search process and address bottlenecks in RL-driven process synthesis. Building on our prior research, this work proposes a novel integration of QML with RL to enhance the efficiency, robustness, and performance of process design frameworks.

This paper introduces the principles, methodologies, and innovations underpinning our quantum-enhanced RL framework for process flowsheet synthesis (Fig. 1). Section 2 reviews the methodology for classical RL-driven process design, touching on key features of

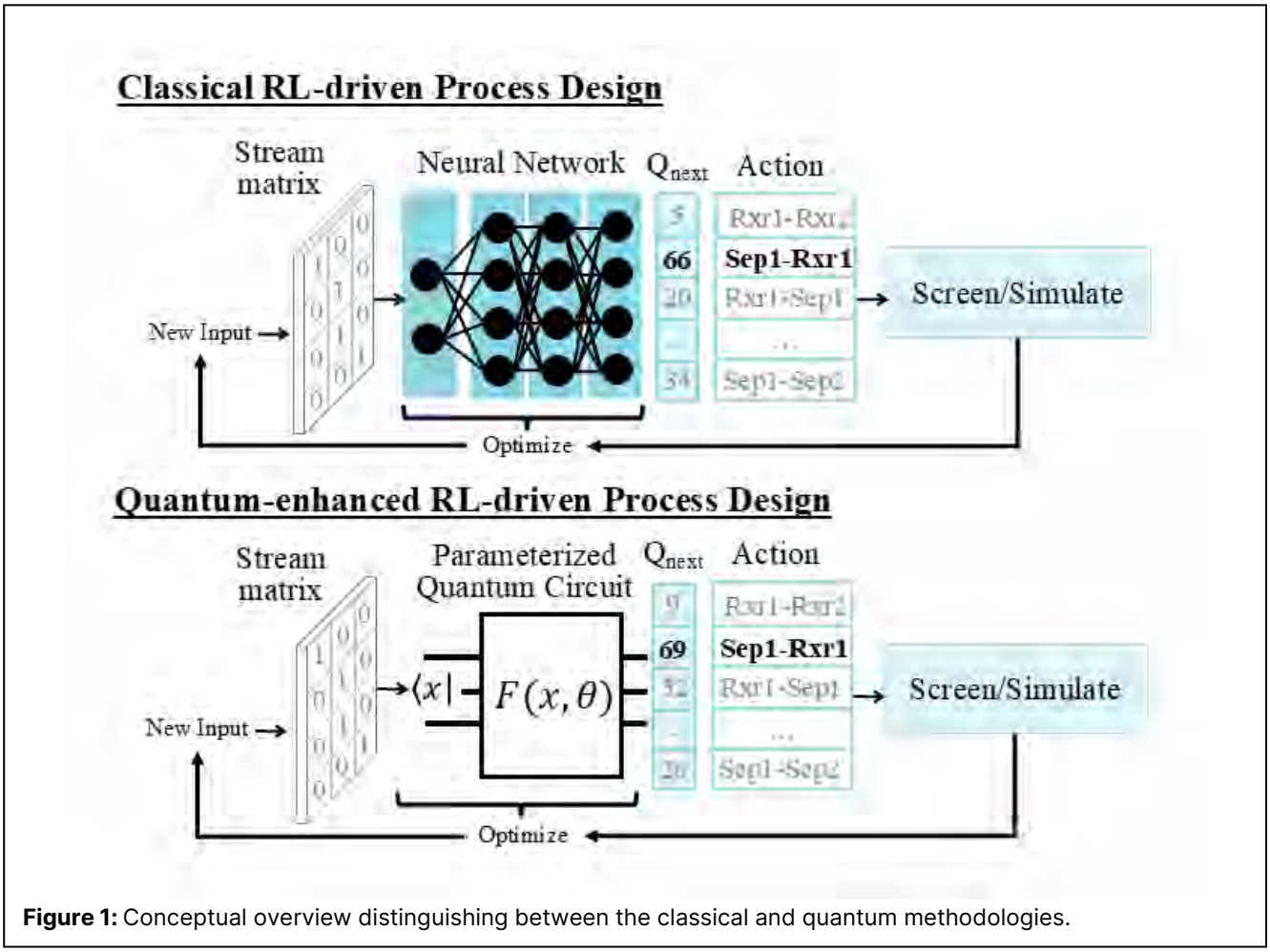



**Figure 1:** Conceptual overview distinguishing between the classical and quantum methodologies.

the algorithm. Section 3 introduces the topic of quantum machine learning and presents our integrated quantum-enhanced framework. Section 4 applies the framework to a representative case study on hydrodealkylation process design, highlighting the methodological advantages over conventional RL approaches. Section 5 concludes with a discussion of ongoing work.

## 2. RL-DRIVEN PROCESS SYNTHESIS

In this section, we briefly review the fundamentals of Deep Q-Network (DQN) algorithm and the prior work [2,7] on RL-driven process synthesis which set up the foundation for the current work.

### 2.1 Deep Q-Network

The DQN algorithm is a form of Q-Learning and is essential to model-free RL. It is designed to address the challenges of high-dimensional state-action spaces using neural networks (NNs). The traditional Q-Learning algorithm approximates the optimal action-value function $Q^*(s,a)$, which represents the maximum cumulative reward achievable from a given state $s$ when taking action $a$ and following the optimal policy thereafter. However, as the state space becomes more complex, approximating the Q-function $Q(s,a)$ becomes computationally intensive. DQN overcomes this limitation by employing an NN as a function approximator to estimate the Q-function instead as $Q(s,a,\theta)$ where $\theta$ denotes the network parameters. The NN serves as a computationally friendly alternative over other methods such as tabular Q-Learning.

Central to this algorithm is the Bellman equation, expressed in Eq. 1 where $s$ and $a$ are the current state action pair, $s'$ and $a'$ are future state-actions, $r$ is the instantaneous reward, and $\gamma$ is a discount factor for future rewards. This equation recursively relates present state-action values to the rewards of future values enabling optimal decision making that considers all future paths.

$$Q(s,a) = r + \gamma \max_{a'} Q\,(s',a') \tag{1}$$

In DQN, the Q-functions on the right and left of Eq. 1 are approximated by NNs. The right being the target network which is periodically updated and the left being the evaluation network which is updated at each transition step. This update is performed by minimizing the mean squared error (MSE) between the current Q-value estimate and the target value, as seen in Eq. 2 where $\mathcal{L}$ is the loss function (in this case MSE), $\theta$ is the vector of

tunable parameters in the evaluation network, and $\theta^-$ is the vector of tunable parameters in the target network.

$$\min_{\theta} \mathcal{L}(\theta) = E\left[\left(r + \gamma \max_{a'} Q(s', a'; \theta^-) - Q(s, a; \theta)\right)^2\right] \quad (2)$$

When the target network is updated, it becomes a copy of the evaluation network at that time (i.e., $\theta^- = \theta$). This approach helps to achieve stability and mitigate bias in the algorithm. In the landmark paper for DQN [6], the authors have established a few other key techniques that help make this algorithm efficient and successful such as experience replay and an epsilon-greedy approach to action selection. The experience replay allows the expectation to be taken over a randomly sampled batch of stared state-action-reward transitions which reduces both recency bias and correlations between consecutive transitions. The epsilon-greedy policy is utilized as a method to balance the tradeoffs between exploration and exploitation. In the early stages of learning random actions are taken more often to explore the state-space while later, once the Q-function is better approximated, the predicted optimal actions are taken more frequently.

## 2.2 Classical RL-Driven Process Synthesis Framework

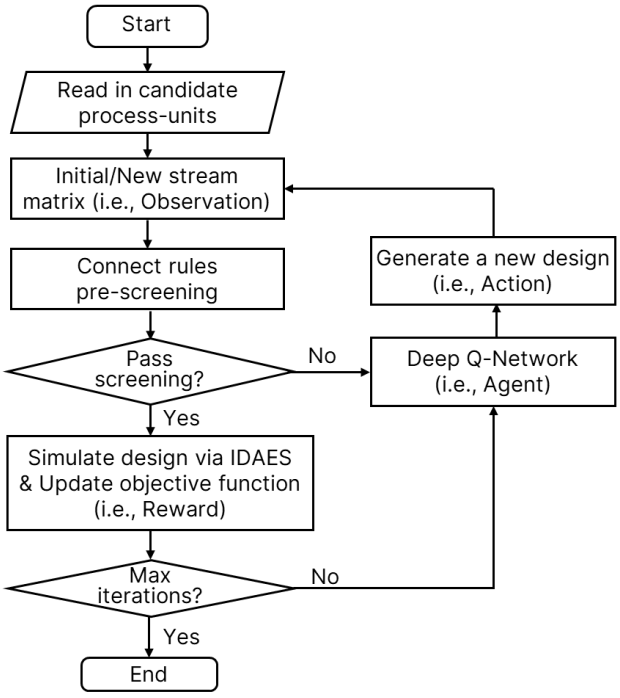



**Figure 2.** RL-driven process synthesis.

Wang et al. [2] developed a RL-driven process synthesis method as summarized in Fig. 2, based on which our previous work [7] enhanced the method with subspace search to more effectively address the combinatorial design space. For a brief review of this classical approach, RL is integrated with the IDAES platform [8] leveraging its extensive process modeling and simulation capabilities to enhance the design and optimization process. This approach begins with the definition of a pool of candidate process units, including reactors, heaters, and flash drums, with user-specified limits on the maximum number of units available. Unlike classic superstructure-based process synthesis approaches, RL-driven process synthesis eliminates the need for prior pre-postulations regarding flowsheet connectivity, allowing for a more thorough exploration of design spaces.

A critical step in this approach is the representation of process flowsheets as stream matrices, where binary variables encode the inlet and outlet relationships between unit operations. These matrices provide compact and efficient representations for the RL agent, enabling it to analyze and manipulate flowsheet structures. The update of these input-output stream matrices, as determined by the RL agent, synthesizes the new flowsheet structure. To ensure feasibility, generated flowsheets are pre-screened against connectivity rules, such as avoiding self-loops and ensuring proper sequencing of unit operations (e.g. a cooler does not directly connect to a heater).

The framework utilizes a DQN algorithm (as summarized in Section 2.1) to train an RL agent in generating optimal process designs. The agent takes stream matrices as inputs to NNs that are used to predict Q-values that correspond to actions such as adding, removing, or reconfiguring unit operations. The new flowsheet is then simulated and optimized using the IDAES platform, which determines the optimal operating variables using nonlinear optimization. The resulting rewards are used to update the parameters of the evaluation network, enabling continuous improvement over successive iterations.

# 3. QUANTUM RL-DRIVEN PROCESS SYNTHESIS

In this section, we introduce quantum machine learning, summarize the key techniques that are pertinent to this work, and present our novel methodology that leverages these for RL-driven process synthesis.

## 3.1 Quantum Machine Learning

QML is an exciting research field that explores the intersection of quantum computing and classical machine learning by implementing classical, quantum, or hybrid algorithms on quantum hardware which performs operations on qubits. The core of QML revolves around parameterized quantum circuits (PQCs), which are regarded as the quantum counterpart of NNs [9]. PQCs (Fig 3.) are quantum circuits that encode data as quantum states, have tunable parameters (e.g., rotation angles within quantum gates), and provide outputs through their observables. These are analogous to input features,

weights and biases, and outputs in NNs where the tunable parameters are optimized with respect to a loss function (e.g., backpropagation). The observables of a circuit are representations of measurements taken from each qubit at the end of the circuit. Common expressions for these relate the Pauli sums or Pauli products of qubits in their final measured states.

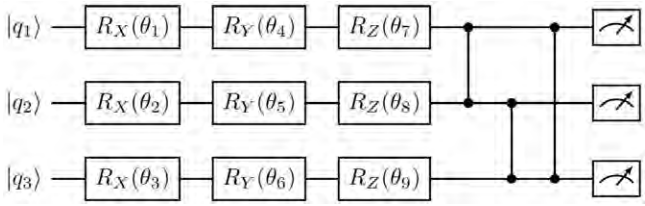



**Figure 3.** Parameterized quantum circuit.

Fig. 3 depicts a three qubit PQC with each being operated on by $R_X$, $R_Y$, and $R_Z$ rotation gates followed by a daisy chaining of CZ gates. The rotation gates perform a manipulation in their respective x, y, or z axis by an angle of rotation specified by $\theta_i$. CZ gates flip the phase of a qubit depending on the state of another qubit thereby imparting entanglement. PQCs similarly serve as universal function approximators and can approximate more efficiently and accurately than their classical counterparts [5]. A common way to increase the expressiveness or efficiency of these circuits is to re-encode data throughout the circuit. This idea is quite similar to the use of skip connections in residual NNs (ResNets) except instead of directly injecting the data into a layer along with that layer's inputs, the data is used in a single qubit gate and can feature its own tunable multiplier (Fig. 4) behavior more like a weight. These circuits are referred to as re-uploading PQCs.

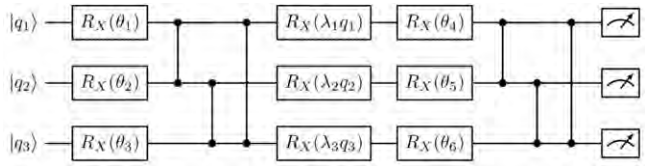



**Figure 4.** Re-uploading parameterized quantum circuit.

Fig. 4 illustrates a re-uploading PQC with three qubits. Each with an $R_X$ gate and then a series of CZ gate operations before reaching another set of $R_X$ gates where the angles are instead a function of the input data rather than a tunable parameter. Here, the angle of rotation is specified by $\lambda_i q_j$ where $\lambda_i$ is a tunable multiplier and $q_j$ is the input data encoded into the $j^{th}$ qubit. In addition to data re-uploading, tunable output weights can be used to increase performance and may be required if the PQC output range cannot sufficiently represent the desired output range (e.g. unconstrained continuous spaces).

## 3.3 Quantum-Enhanced Process Synthesis

Consistent with existing research efforts in quantum reinforcement learning [10], we remove the NNs in our method and incorporate PQCs in their place. This is highlighted in Fig. 1 where the transition is conceptualized. The same underpinning concepts of DQN algorithm are employed with the only distinction being that PQCs are used for the Q-function approximators instead of NNs.

The optimization problem (Eq. 2) is still performed but the vector $\theta$ corresponds to all tunable parameters for the evaluation circuit. In general, this adjustment to the algorithm requires special attention to data encoding and Q-value mapping. For data encoding, it is critical that input data be transformed or scaled in a way that it can be represented by a quantum state. In the context of flowsheet matrices, the binary values can easily be mapped to a quantum state. The observables (circuit outputs) must correspond to an action in the action space which greatly relies on the current problem. In our algorithm, we formulate a unique mapping from one observable to a corresponding action.

Our quantum-enhanced framework broadly follows Fig. 2 by integrating QML into RL-driven process design, replacing classical NNs with PQCs within the DQN architecture. The RL agent similarly uses input-output stream matrices to observe flowsheet structures, and PQCs are trained to approximate Q-functions that implicitly relate to optimal flowsheet designs. The quantum-enhanced DQN retains algorithmic principles to prevent model divergence and biases. This approach is implemented using the IDAES-PSE software for flowsheet simulation and optimization, where operational cost and productivity serve as performance rewards for the RL agent. This approach takes advantage of the novel and promising abilities of quantum computing to outpace classical methods in machine learning and optimization while also utilizing the established principles of RL algorithms.

# 4. HYDRODEALKYLATION CASE STUDY

In this section, we demonstrate the effectiveness and potential advantages of our quantum-enhanced RL-driven process design framework through a hydrodealkylation process benchmarked by the classical RL-driven approach.

## 4.1 Process Description

In line with the prior work [2,7], this study aims to design a hydrodealkylation (HDA) process which uses hydrogen ($H_2$) and toluene ($C_6H_5CH_3$) to form benzene ($C_6H_6$) as shown in Eq. 3. This reaction occurs in the vapor phase and is assumed to occur without any side reactions for the simplification of this analysis.

$$H_2 + C_6H_5CH_3 \rightarrow H_2 + C_6H_6, \Delta H = -1.08 \times 10^5 \frac{\text{J}}{\text{mol}} \quad (3)$$

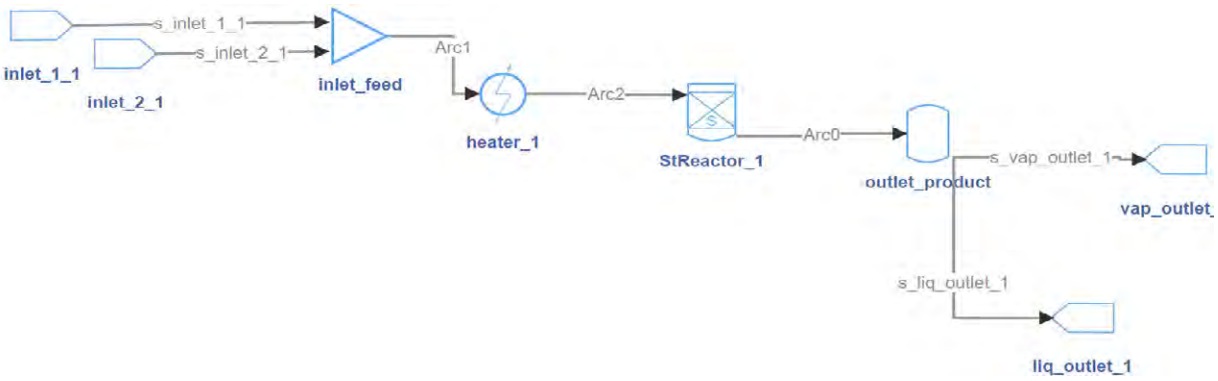



**Figure 5:** Optimal flow sheet design.

The feed streams, detailed in Table 1, include a vapor stream composed of hydrogen and methane, along with a liquid stream of toluene. The available process units are as follows: feed (combined with a mixer), product (integrated with flash operation), heater, cooler, stoichiometric reactor, mixer, flash, splitter, and compressor. The operating constraints of each unit are specified, such as maintaining an outlet temperature between 500–600 K. The product specification requires achieving a vapor product with a benzene purity exceeding 0.55. Mixture separations are assumed to follow ideal vapor-liquid equilibrium behavior. The design objective is to identify processes that optimize the vapor product's flowrate.

Table 1: Feed conditions for inlet process streams.

| | Liquid Feed | Vapor Feed |
|---|---|---|
| Temperature (K) | 303.2 | 303.2 |
| Pressure (kPa) | 350 | 350 |
| Flowrate (mol/s) | | |
| Hydrogen | 0.30 | 0.00 |
| Toluene | 0.00 | 0.30 |
| Methane | 0.02 | 0.00 |
| Benzene | 0.00 | 0.00 |

For this study, the available unit ops to be selected are a heater and a reactor. This provides the minimum necessary conditions to reach the optimal flowsheet design. The selection of more units leads the quantum algorithm to become computationally intractable when being simulated on a classical machine. It is of ongoing work to investigate more capable simulators or move to real-world quantum hardware to provide additional studies.

## 4.2 Performance Comparison

Both the classical and the quantum-enhanced method were able to converge to the optimal flow sheet design in very few iterations. As given in Fig. 5, this flowsheet consists of a heater with an outlet temperature of 536.9 K, followed by a reactor with an outlet temperature of 897.8 K and a flash unit that generates process effluent at 705.7 K and approximately 1 atm. The operational variables of interest are a benzene purity of 0.75, a benzene flowrate of 0.225 mol/s, and an annual revenue of $\$7.65\times10^5$ with the cost data provided by the IDAES simulation platform. This solution is generated on the 63$^{rd}$ epoch for both methods.

Plots of instantaneous reward for each epoch are shown in Figs. 6-7 for the classical and quantum approaches respectively. A large reward (~1500) implies that a suitable stream matrix has been found. This occurs 9 times for the classical approach whereas the quantum-enhanced algorithm discovers 13. The reward plots are nearly identical for around the first 800 epochs and then they start to diverge. This can be attributed to the epsilon-greedy policy from the DQN algorithm prioritizing random exploration in the initial stages. Both methods are performed using the same random generator seeds, so they explore the same scenarios at the same rate.

Not only is the PQC able to provide more solutions over the given amount of training steps, but it does so with less parameters. The PQC has a total of 88 trainable parameters whereas the NN has 1,092. The simulation time for the classical and quantum techniques were 0.58 and 9.06 minutes respectively. These results are summarized in Table 2. The calculation time for the quantum-enhanced approach has the potential to be greatly reduced when moving to real quantum machines and it is important to note that there is little correlation between simulated and true quantum hardware time. Regardless of current computational limitations, the quantum-enhanced framework shows promise in more efficiently searching the design space as compared the prior classical approach.

**Table 2:** Algorithm and model performance indicators.

| | Classical | Quantum |
|---|---|---|
| Max Reward Solutions | 9 | 13 |
| Tunable Parameters | 1,092 | 88 |
| Computational Time (min) | 0.58 | 9.06 |

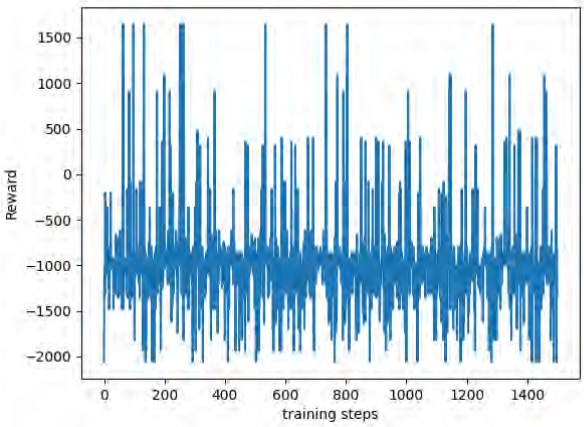



**Figure 6.** Classical RL agent reward for each episode.

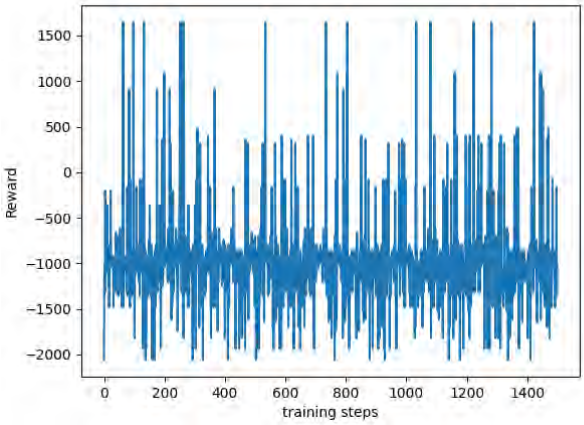



**Figure 7.** Quantum RL agent reward for each episode.

## 5. CONCLUDING REMARKS

This work presents a novel quantum-enhanced RL-driven process design framework, addressing challenges of large combinatorial design spaces. We demonstrate significant potential for improving efficiency and performance for RL algorithms in process synthesis by integrating QML techniques. Ongoing research focuses on expanding the range and scale of applications and scenarios by investigating better quantum simulators and exploring quantum hardware capabilities. Additionally, more efforts will be put into investigating how the hyperparameters of both PQCs and NNs affect the performance of these RL agents.

## ACKNOWLEDGEMENTS

The authors gratefully acknowledge the financial support from NSF GRFP DGE-1102689, NSF EPSCoR RII Track-4 OIA-2327303, and West Virginia University.

## REFERENCES

1. Stops, L., Leenhouts, R., Gao, Q., & Schweidtmann, A. M. (2023). Flowsheet generation through hierarchical reinforcement learning and graph neural networks. AIChE Journal, 69(1), e17938.
2. Wang, D., Bao, J., Zamarripa-Perez, M. A., Paul, B., Chen, Y., Gao, P., ... & Xu, Z. (2023). A coupled reinforcement learning and IDAES process modeling framework for automated conceptual design of energy and chemical systems. Energy Advances, 2(10), 1735-1751.
3. Bernal, D. E., Ajagekar, A., Harwood, S. M., Stober, S. T., Trenev, D., & You, F. (2022). Perspectives of quantum computing for chemical engineering. AIChE Journal, 68(6), e17651.
4. Ajagekar, A., & You, F. (2022). New frontiers of quantum computing in chemical engineering. Korean Journal of Chemical Engineering, 39(4), 811–820.
5. Yu, Z., Chen, Q., Jiao, Y., Li, Y., Lu, X., Wang, X., & Yang, J. Z. (2024). *Non-asymptotic Approximation Error Bounds of Parameterized Quantum Circuits* (arXiv:2310.07528).
6. Mnih, V., Kavukcuoglu, K., Silver, D., Rusu, A. A., Veness, J., Bellemare, M. G., Graves, A., Riedmiller, M., Fidjeland, A. K., Ostrovski, G., Petersen, S., Beattie, C., Sadik, A., Antonoglou, ... & Hassabis, D. (2015). Human-level control through deep reinforcement learning. *Nature*, *518*(7540), 529–533.
7. Tian, Y., Akintola, A., Jiang, Y., Wang, D., Bao, J., Zamarripa, M. A., Paul, B., Chen, Y., Gao, P., Noring, A., Iyengar, A., Liu, A., Marina, O., Koeppel, B., & Xu, Z. (2024). Reinforcement Learning-Driven Process Design: A Hydrodealkylation Example. 387–393.
8. Lee, A., Ghouse, J. H., Eslick, J. C., Laird, C. D., Siirola, J. D., Zamarripa, M. A., ... & Miller, D. C. (2021). The IDAES process modeling framework and model library - Flexibility for process simulation and optimization. Journal of advanced manufacturing and processing, 3(3), e10095
9. Jerbi, S., Gyurik, C., Marshall, S. C., Briegel, H. J., & Dunjko, V. (2021). Parametrized quantum policies for reinforcement learning (arXiv:2103.05577).
10. Skolik, A., Jerbi, S., & Dunjko, V. (2022). Quantum agents in the Gym: A variational quantum algorithm for deep Q-learning. Quantum, 6, 720.

© 2025 by the authors. Licensed to PSEcommunity.org and PSE Press. This is an open access article under the creative commons CC-BY-SA licensing terms. Credit must be given to creator and adaptations must be shared under the same terms. See https://creativecommons.org/licenses/by-sa/4.0/

Systems & Control Transactions

**Research Article - Peer Reviewed Conference Proceeding**
ESCAPE 35 - European Symposium on Computer Aided Process Engineering
Ghent, Belgium. 6-9 July 2025
Jan F.M. Van Impe, Grégoire Léonard, Satyajeet S. Bhonsale,
Monika E. Polańska, Filip Logist (Eds.)

PSE PRESS

# Comparative and Statistical Study on Aspen Plus Interfaces Used for Stochastic Optimization

**Josué J. Herrera Velázquez[a,c], Erik L. Piñón Hernández[a], Luis A. Vega Vega[a], Dana E. Carrillo Espinoza[a], J. Rafael Alcántara Avila[b], and Julián Cabrera Ruiz[a]***

[a] Universidad de Guanajuato, Departamento de Ingeniería Química, Guanajuato, 36050, Mexico
[b] Pontificia Universidad Católica del Perú, Departamento de Ingeniería, Lima, 15074, Peru
[c] Instituto Tecnológico Superior de Guanajuato, Departamento de Ingeniería en Industrias Alimentarias, Guanajuato, 36262, Mexico
* Corresponding Author: j.cabreraruiz@ugto.mx.

## ABSTRACT

New research on complex intensified distillation schemes has popularized the use of several commercial process simulation software. The interfaces between process simulation and optimization-oriented software have allowed the use of rigorous and robust models. This type of optimization is mentioned in the literature as "*Black Box Optimization*", since successive evaluations exploits the information from the simulator without altering the model that represents the given process. Among process simulation software, Aspen Plus® has become popular due to their rigorous calculations, model customization, and results reliability. This work proposes a comparative study for Aspen Plus software and Microsoft Excel VBA®, Python® and MATLAB® interfaces. Five distillation schemes were analyzed: conventional column, reactive column, extractive column, column with side rectifier and a Petlyuk column. The optimization of the $TAC$ (Total Annual Cost) was carried out by a modified Simulated Annealing Algorithm (m-SAA). The evaluation criteria are the time per iteration $(TI)$ and $TAC$ values. The results indicate that the best option to carry out the optimization was by using the VBA interface, however the one carried out with Python did not differ radically (12%).

**Keywords**: Aspen Plus, Stochastic Optimization, Process Optimization, Python, MATLAB, Visual Basic

## INTRODUCTION

The optimization of complex processes is challenging because optimization problems tend to be nonconvex, discontinuous and nonlinear, and consequently, there is not certainty to the global optimum solution [1]. The absence of precise derivatives in their models and the convergence failures that can generate discontinuities in the optimization "surfaces" of the functions make the task of finding the global optimum very difficult.

The optimization of processes using stochastic algorithms has become very relevant because they can be implemented in a relatively simple way by making an interface with commercial process simulators that are responsible for solving mathematical problems by modeling the involved units in the process [2]. Commercial process simulators act as a powerful calculator for highly nonlinear mathematical models without losing model rigorously. This type of software is also known as black box modeling software [3] because the user typically does not come into direct contact with the model equations that describe the process it simulates.

Optimization algorithms began to be developed to directly use the interface between Aspen Plus-VBA using Excel as an IDE [4-5]. MATLAB developed its direct interface with Aspen Plus becoming one of the most popular options to solve chemical process optimization problems [6]. Most recently, the Aspen Plus–Python connection has been studied showing good results in its implementation [7] making use of stochastic optimization libraries developed by the scientific community [8]. The literature is extensive for all the cases and has been applied for single and multi-objective optimization.

There are studies comparing interface methodologies for Aspen Hysys® software [9], but not for Aspen Plus. Ponce-Rocha et al. [10] compare the computing

time between iterations and the best solution between the Aspen Plus-MATLAB and Aspen Plus-Python interfaces for a case study of a bottom distillation train, finding that the interface with Python has the shortest time and the best solution compared to the one made with MATLAB.

## METHODOLOGY

### Optimization framework

In the black box optimization, the writing/reading results are from the contribution of 1) Process simulation software, 2) Middleware protocol, 3) Wrapper protocol and the 4) Platform with the optimization algorithm [11]. The middleware protocol allows the automation of the process simulator and the transfer of information in both directions, for Windows it is ActiveX automation. The Wrapper protocol works to interpret the information transferred by the previous protocol and make it useful for both parties. Accordingly, to Muñoz López et al. [11] interface can be divided into four other parts:

- **Simulation:** The simulation is carried out with the desired characteristics, for a set of variables where its convergence is ensured. The necessary techniques are applied to ensure that the simulation is not corrupted when beginning the optimization process. Aspen Plus V12 software was used.
- **Control interface:** ActiveX (COM) framework is used to build this interface. It allows you to have the API (Application Programming Interface) to manipulate applications that run on Windows.
- **Information interface:** Transfer the required data. The middleware is a set of ASCII type files that contain variable information (name, value, scale factor, specification, units, etc.) and is generated only when the simulation converges. This information makes the Aspen Plus–Optimizer routine possible. Middleware is considered the bottleneck of computational performance.
- **Optimization:** The optimization is carried out according to the optimization algorithm. For Python, Spyder IDE 5.4.1 was used. In the case of MATLAB, R2022a was used. For VBA, Excel Microsoft® 365 2022 version was used.

This overall process is shown in Figure 1. Table 1 presents some general commands to perform any activity that requires connection with any of the programming languages discussed. Step (1) refers to the line of code to open the Aspen Plus document.

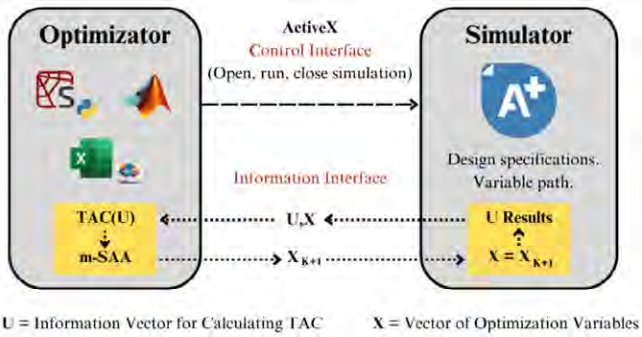



**Figure 1.** Overview of the interface implemented between Aspen Plus and MATLAB/Excel (VBA)/Spyder (Python).

It is possible to work with the *.bkp* or *.apw* extension file. In this work the *.apw* extension file was used. This form of programming is designed so that both, the code file and the simulation are at the same address, so that simply entering the name of the simulation is enough. In the case of MATLAB, it is necessary to define the version of Aspen Plus that will be used. In the case of VBA, the "On Error Resume Next" code is used, and this is to close the pop-up screens that are typical of the language each time a step is carried out. For Python, the "import os" library is used to identify the location address where the code file is saved, while the “import win32com.client” library is the one that allows the Aspen Plus software to operate.

Step (2) and (3) are commands for filling information in Aspen Plus and calling simulation results respectively (In the case of Python it is necessary to place double \ to avoid errors in communication). y is a number, and X is a variable that will be used for subsequent operations. Step (4) is the command to restart the simulation. This command is not recommended if working with complex simulations difficult to converge. In the cases of MATLAB and VBA the use of this command affects the time per iteration to almost double it. Step (5) is the command to run the simulation and step (6) is to close it.

It must be considered that in an optimization process steps (1) and (6) are only performed once per optimization, that is, the simulation is opened, the optimization process is executed for $n$ iterations and once this finished, the simulation is closed. This is because opening and closing the simulation as an environment takes a long time and this could affect the demand for RAM memory resources of the computer equipment. In the case of Python, the iterative process of this type of optimization causes RAM to accumulate, so it is necessary to reset the connection every certain number of iterations to avoid exponential growth in the time per iteration. This work recommends resetting the connection every 125 iterations.

**Table 1:** Starting and execution of the Aspen Plus application from each platform and its main commands for filling and reading information.

| Platform | Step | Code |
|---|---|---|
| MATLAB | (1) | `Aspen = actxserver('Apwn.Document.38.0');`<br>`[stat,mess]=fileattrib;`<br>`Aspen.invoke('InitFromArchive2',[mess.Name '\Simulation_Name.apw']);` |
| | (2) | `Aspen.Application.Tree.FindNode("Simulation\Variable\Path").Value = y;` |
| | (3) | `X = Aspen.Application.Tree.FindNode("Simulation\Variable\Path").Value;` |
| | (4) | `Aspen.Reinit;` |
| | (5) | `Aspen.Engine.Run2();` |
| | (6) | `Aspen.Close;` |
| Excel VBA | (1) | `Set Aspen = GetObject(ThisWorkbook.Path & "\Simulation_Name.apw")`<br>`On Error Resume Next` |
| | (2) | `Aspen.Tree.FindNode("Simulation\Variable\Path").Value = y` |
| | (3) | `X = Aspen.Tree.FindNode("Simulation\Variable\Path").Value` |
| | (4) | `Aspen.Reinit` |
| | (5) | `Aspen.Engine.Run` |
| | (6) | `Aspen.Close` |
| Python | (1) | `import os`<br>`import win32com.client as win32`<br>`Aspen = win32.Dispatch('Apwn.Document')`<br>`Aspen.InitFromArchive2(os.path.abspath('Simulation_Name.apw'))` |
| | (2) | `Aspen.Tree.FindNode("Simulation\\Variable\\Path").Value = y` |
| | (3) | `X = Aspen.Tree.FindNode("Simulation\\Variable\\Path").Value` |
| | (4) | `Aspen.Reinit()` |
| | (5) | `Aspen.Engine.Run2()` |
| | (6) | `Aspen.close()` |

An error called "ExceptionDump" may occur, which appears when the call is fast enough to prevent the completion of the protocols described above and corrupt the optimization process. This error displays the legend:

**"An unexpected error has occurred. An error log has been generated in: C:*file\location*\aspenplus_ExceptionDump_*date*.dmp"**.

The authors recommend using a delay time between 0.05 and 0.1 seconds that gives the platforms time to finish the calling protocols. These are shown in Table 2. `delay` is a number that refers to the delay time that will be carried out between each iteration. The line of code must be written before line (5) mentioned in Table 1.

In the case of the Python platform, it is necessary to call "from time import sleep" to be able to execute the action. In VBA it is not necessary to place a delay as it is rare to see this error in your process.

**Table 2:** Recommended lines of code to avoid the connection error between the platform and Aspen Plus.

| Platform | Code |
|---|---|
| MATLAB | `pause(delay);` |
| Python | `From time import sleep`<br>`sleep(delay)` |

The optimization was performed using the m-SAA algorithm proposed by Cabrera Ruiz et al. [2] which makes use of dynamic bounds and normalization of variables to improve the search for the optimum and find it faster. This algorithm was programmed in the same way for all platforms without the reinit function (line (4) in Table 1), the only difference between programming languages are their own random number functions. Additional parameters of the optimization algorithm are presented in Herrera Velázquez et al. [12]. The normalization of the variables is done as shown in Eq. 1.

$$VN_i = \left(B_{upper} - V_i\right)/\left(B_{upper} - B_{lower}\right) \quad (1)$$

where $VN_i$ is the value of the normalized variable $V_i$, $B_{upper}$ and $B_{lower}$ are the upper and the lower bound of variable $i$ respectively. The stopping criterion was defined the same way for all schemes and platforms: 6 reannealing's of 350 iterations each, giving a total of 2,100 iterations, ensuring a study of at least 200 iterations for each variable. The computer used for all optimizations has an Intel(R) Xeon(R) W-3235 CPU at 3.30 GHz with 48 GB of RAM with the Windows 10 operating system (which is the most stable version for all platforms).

## Case Studies

The five case studies are shown in Figure 2. $N_T$

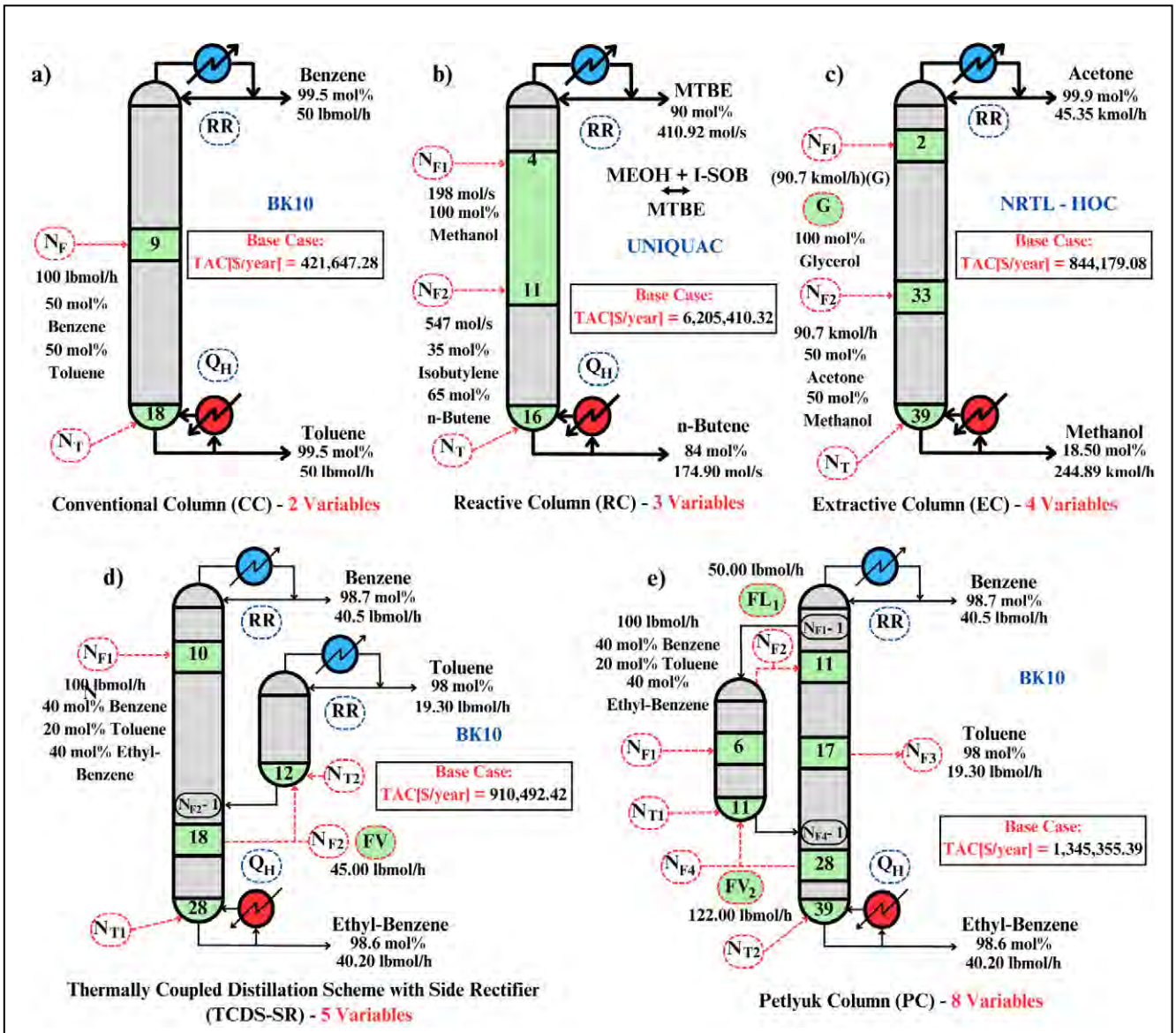



**Figure 2:** Representation of the proposed schemes to carry out the tests and their proposed optimization variables and their thermodynamic model used: a) Conventional Column, b) Reactive Column [13] and c) Extractive Column [14], d) Thermally Coupled Distillation Scheme with Side Rectifier and e) Petlyuk Column.

refers to the total number of stages, $N_F$ is the feed stage, $G$ is the ratio of entrainer to feed, $FV$ is the vapor flow and $FL$ is the liquid flow, both in kmol/h. For the $CC$, $RC$ and $PC$ schemes (Figure 2a, 2b and 2e) the purity and recovery constraints are satisfied by adjusting the reflux ratio ($RR$) and the reboiler load ($Q_H$) through internal design specifications in the simulator. For the $PC$ scheme it is done on the largest column. In the case of the $EC$ and $TCDS-SR$ schemes (Figure 2c and 2d), the constraints are adjusted with the $RR$ on the respective domes, and the $Q_H$ for the $TCDS-SR$ scheme. The optimization limits for each scheme are presented in Table 3.

**Table 3:** Optimization bounds [lower, upper].

| | Variables |
|---|---|
| $CC$ | $N_T = [10, 30]; N_F = [2,\ N_{T1} - 1]$ |
| $RC$ | $N_{T1} = [10, 30]; N_{F1} = [2,\ N_{T1} - 2];$ $N_{F2} = [N_{F1} + 1,\ N_{T1} - 1]$ |
| $EC$ | $N_{T1} = [35, 45]; N_{F1} = [2,\ N_{T1} - 2];$ $N_{F2} = [3,\ N_{T1} - 1]; G = [1, 2.5]$ |
| $TCDS - SR$ | $N_{T1} = [20, 40]; N_{T2} = [5, 15];\ N_{F1} = [2,\ N_{T1} - 2];$ $N_{F2} = [3,\ N_{T1} - 1]; FV = [40, 100]$ |
| $PC$ | $N_{T1} = [5, 15]; N_{T2} = [25, 45];$ $N_{F1} = [2,\ N_{T1} - 2]; N_{F2} = [3,\ N_{T1} - 1];$ $N_{F3} = [N_{F2} + 1,\ N_{T2} - 3]; N_{F4} = [N_{F3} + 2,\ N_{T2} - 1];$ $FL_1 = [20, 110]; FV_2 = [20, 150]$ |

## Mathematical Treatment

The $TAC$ is calculated as show in Eq. 2.

$$TAC\left[\frac{\$}{Year}\right] = C_{Vapor} + C_{Cooling} + \frac{\left(\frac{CEPCI_{2022}}{CEPCI_{2001}}\right)(C_{Shell} + C_{Plates} + C_{Reboiler} + C_{Condenser})}{Recovery\ time\ (Years)} \quad (2)$$

$$s.t. \quad Conv = 0$$

The $TAC$ equation is calculated using the Guthrie method [15] where $C$ is the cost of each module. 5 years of recovery time was used. $Conv$ is a convergence constraint, $Conv = 1$ when the simulation does not converge in Aspen Plus, in this case, the objective functions have a penalty value that is 3 times the value of each function evaluated for the base design, these values are given in Figure 3. $Conv = 0$ if the simulation converges and the functions are calculated with the described model. $TI$ is taken from the time of the complete optimization process (without considering the (1) and (6) steps of Table 1, and in Python considering the time of the restarts every 125 iterations) divided by the total number of iterations.

The optimization was repeated 10 times for each case study. To find anomalous data, hypothesis testing (Grubbs Test) was used [16], which is denoted by Eq. 3 for this work. The test was applied to the $TAC$ and $TI$. The test was done to achieve 90% confidence (i.e., 2.29).

$$H_O: \left[\frac{|TAC_i - \overline{TAC}|}{S_{TAC}} \leq 2.29, \frac{|TI_i - \overline{TI}|}{S_{TI}} \leq 2.29\right]$$
$$H_A: \left[\frac{|TAC_i - \overline{TAC}|}{S_{TAC}} > 2.29, \frac{|TI_i - \overline{TI}|}{S_{TI}} > 2.29\right] \quad (3)$$

where $TAC_i$ is the $TAC$ of optimization $i$, $\overline{TAC}$ and $S_{TAC}$ are the average and standard deviation. The same procedure was followed for $TI$. If $H_O$ is true for both, the $TAC$ and $TI$ are accepted and if $H_A$ is true these results are rejected.

# RESULTS

A delay of 0.05 second is considered to avoid communication errors, this time is considered in the results shown. Table 4 summarizes the results of 10 independent optimizations for each of the platforms and for each of the proposed schemes, totaling 150 total optimizations (30 for each scheme). The results show the average value and standard deviation calculated after applying the Grubbs test. Figure 3 shows the frequency of appearance of each platform as the best solution in each of the evaluated aspects (shown in bold in Table 4).

Of 130 optimizations performed, 6 were eliminated via Grubbs test (4.61%), of which 4 are from the MATLAB platform (3 by $TI$ and 1 by $TAC$), 1 from the Python platform and 1 from VBA (both by $TAC$).

**Table 4:** Summary of results for each scheme and each platform. (M = MATLAB, V = VBA, P = Python).

| CASE | | $TAC$ [$/Year] | $TI$ [$s$] |
|---|---|---|---|
| CC | M | 284,384 ± 1,181 | 0.8783 ± 0.0066 |
| | V | 290,131 ± 1,181 | **0.7445 ± 0.0246** |
| | P | **283,154 ± 204** | 0.8678 ± 0.0085 |
| RC | M | 4,425,792 ± 143,638 | 0.7678 ± 0.0246 |
| | V | 4,323,736 ± 72,576 | **0.6545 ± 0.0455** |
| | P | **4,267,495 ± 48,562** | 0.8433 ± 0.0438 |
| EC | M | 519,843 ± 14,398 | 0.9600 ± 0.0078 |
| | V | **478,751 ± 7,185** | **0.8251 ± 0.0199** |
| | P | 498,593 ± 28,551 | 0.9419 ± 0.0053 |
| TCDS-SR | M | 436,695 ± 10,651 | 1.9364 ± 0.1753 |
| | V | 470,608 ± 1,515 | **1.2959 ± 0.0611** |
| | P | **430,604 ± 5,634** | 1.6973 ± 0.0306 |
| PC | M | 605,647 ± 91,986 | 3.3907 ± 0.8229 |
| | V | **604,607 ± 74,327** | 2.3790 ± 0.0971 |
| | P | 615,599 ± 75,098 | **2.2708 ± 0.1907** |

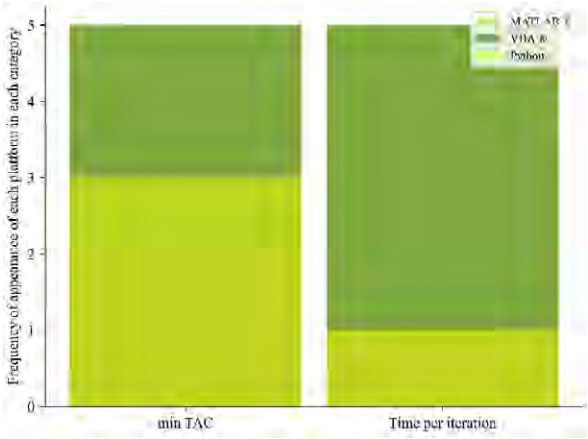



**Figure 3.** Frequency of appearance of platforms in each category.

# CONCLUSIONS

The results indicate that Python is the platform that shows the best numerical results from the $TAC$, especially in simple and complex schemes. The platform that shows the best $TI$ is VBA, although in complex schemes it shows a slight disadvantage compared to Python. Although the $TAC$ results show a certain deviation between platforms, the $TI$ vary a little (12%) between them. This study does not seek to define which platform is better or worse than another, it only seeks to find the areas of opportunity and improvement between them, as well as to define which is the best for the researcher who uses it. According to the results, VBA is the best option; however, MATLAB and

Python may be better options for numerical results (due to the way random numbers are generated on each platform). If a more customizable and open-source environment is needed, Python is the best option, and if more specialized mathematical tools are needed, MATLAB may be the best option.

## REFERENCES


1. Javaloyes Antón J, Kronqvist J, Caballero JA. Simulation-based optimization of distillation processes using an extended cutting plane algorithm. *Comp Chem Eng* 159:107655 (2022) https://doi.org/https://doi.org/10.1016/j.compchemeng.2021.107655
2. Cabrera Ruiz J, Hasebe S, Alcántara Avila JR. Improvement of the Optimal Design Procedure Using Randomized Algorithm and Process Simulators. *MATEC Web Conf* 333:06004 (2021) https://doi.org/10.1051/matecconf/202133306004
3. Penteado AT, Esche E, Weigert J, Repke JU. A framework for stochastic and surrogate-assisted optimization using sequential modular process simulators. *Comp Aid Chem Eng* 48:1903-1908 (2020) https://doi.org/https://doi.org/10.1016/B978-0-12-823377-1.50318-9
4. Sharma S, Rangaiah GP, Cheah KS. Multi-objective optimization using MS Excel with an application to design of a falling-film evaporator system. *Food Bioprod Process* 90:123-134 (2012) https://doi.org/https://doi.org/10.1016/j.fbp.2011.02.005
5. Sánchez Ramírez E, Huerta Rosas B, Quiroz Ramírez JJ, Suárez Toriello VA, Contreras Zarazua G, Segovia Hernández JG. Optimization-based framework for modeling and kinetic parameter estimation. *Chem Eng Res Des* 184:647-660 (2022) https://doi.org/https://doi.org/10.1016/j.cherd.2022.08.040
6. Zheng Y, Wang Z, Pan H, Ling H. Initial design and multi-objeective optimization of four-product dividing wall column. *Sep Purif Technol* 309:122961 (2023) https://doi.org/https://doi.org/10.1016/j.seppur.2022.122961
7. Sánchez Gómez JA, Cabrera Ruiz J, Hernández S. Design and optimization of an intensified process to produce acrylic acid as added product value from glycerol generated in the biodiesel production. *Chem Eng Res Des* 184:543-553 (2022) https://doi.org/https://doi.org/10.1016/j.cherd.2022.08.040
8. Blank J, Deb K. Pymoo: Multi-objective optimization in Python. *IEEE Access* 8:89497-89509 (2020) https://doi.org/10.1109/ACCESS.2020.2990567
9. Santos Bartolome P, Van-Gerven. A comparative study on Aspen Hysys interconnection methodologies. *Comp Chem Eng* 162:107785 (2022) https://doi.org/10.1016/j.compchemeng.2022.107785
10. Ponce Rocha JD, Ramírez Márquez C, Morales Rodríguez R. Performance analysis of virtual platforms focused on multi-objective process optimization. *Comp Aid Chem Eng* 52:843-848 https://doi.org/10.1016/B978-0-443-15274-0.50135-9
11. Muñoz López CA, Telen D, Nimmegeers P, Cabianca L, Logist F, Van-Impe J. A process simulator interface for multiobjective optimization of chemical processes. *Comp Chem Eng* 109:119-137 (2017) https://doi.org/10.1016/j.compchemeng.2017.09.014
12. Herrera Velázquez JJ, Zavala Durán FM, Chávez Díaz LA, Cabrera Ruiz J, Alcántara Avila JR. Hybrid two-step optimization of internally heat-integrated distillation columns. *J Taiwan Inst Chem Eng* 130:103967 (2022) https://doi.org/10.1016/j.jtice.2021.06.061
13. Huang K, Nakaiwa M, Wang SJ, Tsutsumi A. Reactive distillation design with considerations of heats of reaction. *AIChE J* 52:2518-2534 (2006) https://doi.org/https://doi.org/10.1002/aic.10885
14. Sazonova AY, Raeva VM, Frolkova AK. Design of extractive distillation process with mixed entrainer. *Chem Papers* 70:594-601 (2015) https://doi.org/10.1515/chempap-2015-0247
15. Turton R, Bailie RC, Whiting WB, Shaeiwitz JA, Bhattacharyya D. Appendix A: Cost equations and curves for the CAPCOST program. In: Analysis, synthesis, and design of chemical processes. Ed: 4th. Prentice Hall (2012).
16. Grubbs, F. E. (1969). Procedures for Detecting Outlying Observations in Samples. Technometrics, 11(1), 1–21. https://doi.org/10.1080/00401706.1969.10490657



© 2025 by the authors. Licensed to PSEcommunity.org and PSE Press. This is an open access article under the creative commons CC-BY-SA licensing terms. Credit must be given to creator and adaptations must be shared under the same terms. See https://creativecommons.org/licenses/by-sa/4.0/




Systems & Control Transactions

**Research Article - Peer Reviewed Conference Proceeding**
ESCAPE 35 - European Symposium on Computer Aided Process Engineering
Ghent, Belgium. 6-9 July 2025
Jan F.M. Van Impe, Grégoire Léonard, Satyajeet S. Bhonsale,
Monika E. Polańska, Filip Logist (Eds.)

PSE PRESS

# Handling discrete decisions in bilevel optimization via neural network embeddings

**Isabela Fons Moreno-Palancas*, Raquel Salcedo Díaz, Rubén Ruiz Femenia and José A. Caballero**

University of Alicante, Department of Chemical Engineering, San Vicente del Raspeig, Alicante, Spain
* Corresponding Author: isabela.fons@ua.es.

## ABSTRACT

Bilevel optimization is an active area of research within the operations research community due to its ability to capture the interdependencies between two levels of decisions. This study introduces a metamodeling approach for addressing mixed-integer bilevel optimization problems, exploiting the approximation capabilities of neural networks. The proposed methodology employs neural network embeddings to approximate the optimal follower's response, bypassing the inner optimization problem by parametrizing it with continuous leader's decisions. The use of Rectified Linear Unit (ReLU) activations allows the forward pass of the neural network to be represented as a set of mixed-integer linear constraints. Thereby, the bilevel structure is simplified into a single-level optimization model. A case study based on a two-echelon supply chain demonstrates the effectiveness of the approach, with solutions comparable to traditional bilevel optimization methods. The results suggest that neural network embeddings offer a promising alternative for tackling complex bilevel problems even when discrete decisions are involved and unveil the trade-off between prediction accuracy and computational demands. This methodology provides a versatile and efficient framework for solving mixed-integer bilevel optimization problems across diverse domains.

**Keywords**: Bilevel Optimization, Neural Network Embeddings, Supply Chain Planning, Surrogate Modelling, MILP reformulation

## INTRODUCTION

Many problems relevant to process engineering involve multiple stakeholders with conflicting interests and whose individual decisions are affected by each other's actions. Such hierarchical decision-making processes can be effectively modelled as bilevel optimization problems, where upper-level problems are constrained by inner optimization problems.

The nested structure of these models makes bilevel optimization one of the most complex branches of mathematical programming. Specifically, the development of solution algorithms is particularly difficult as it depends on the nature of the inner optimization problem and the interaction between both levels. This complexity is further amplified when the problems involve mixed-integer variables, leading to mixed-integer bilevel problems (MIBPs).

From Moore and Bard's foundational studies on mixed-integer bilevel problems [1], significant progress has been made under the assumption of linearity. In general, the methods to solve mixed integer linear bilevel problems (MILBPs) typically begin with a high-point relaxation—optimizing the upper-level objective while considering both levels' constraints—and systematically explore the feasible region to identify optimal solutions. Strategies such as branch-and-bound, branch-and-cut, Benders decomposition, parametric integer programming, or their combinations have been effectively applied [2]. While these methods often converge to exact solutions for MILBP, solving mixed-integer nonlinear bilevel problems (MINLBPs) remains more challenging, with most algorithms achieving only ε-optimal solutions.

Given the inherent difficulties of MIBPs, data-driven alternatives have gained considerable attention over the recent years. Despite the evident advantages of sophisticated methods such as reinforcement learning (RL), which has demonstrated considerable potential and in

the field of game theory [3,4], neural network embeddings remain a powerful and flexible alternative to conventional methods [5,6,7].

Our proposed approach builds on the idea of using fully connected deep neural networks to approximate the follower's optimal response. When the network induces non-linearity via piecewise linear activation functions, it can be formulated as mixed-integer linear constraints and embedded into the leader's optimization problem. We illustrate the capabilities of the methodology in the optimization of a simplified supply chain, which highlights the potential advantages of this approach and reveals its remaining challenges.

## MATHEMATICAL FRAMEWORK

In this study, we focus on mixed-integer bilevel due to its countless applications in process engineering in areas such as supply chain management and energy systems. The leader's problem, defined in Eq. 1, aims to optimize the function $F(x^L, y^L, x^F, y^F)$ subject to constraints $G(x^L, y^L, x^F, y^F)$. Here, $x^L \in \mathbb{R}^{q^L}$ and $y^L \in \mathbb{Z}^{p^L}$ represent the leader's continuous and integer decision variables, while $x^F \in \mathbb{R}^{q^F}$ and $y^F \in \mathbb{Z}^{p^F}$ denote the follower's continuous and integer decision variables, respectively.

$$\begin{aligned} \min \quad & F(x^L, y^L, x^F, y^F) \\ s.t., \quad & G(x^L, y^L, x^F, y^F) \leq 0 \\ & (x^F, y^F) \in \psi(x^L, y^L) \\ & x^L \in \mathbb{R}^{q^L} \\ & y^L \in \mathbb{Z}^{p^L} \end{aligned} \tag{1}$$

The function $\psi(x^L, y^L)$ corresponds to the parametric solution of the follower's optimization problem, which is presented in Eq. 2. This hierarchical structure introduces significant computational challenges, as the leader must anticipate the follower's optimal response while solving their own problem. Analogously, the leader's decisions influence the follower's objective $f(x^L, y^L, x^F, y^F)$ and feasible set, defined by constraints $g(x^L, y^L, x^F, y^F)$.

$$\begin{aligned} \psi(x^L, y^L) = \quad & \operatorname{argmin} \quad f(x^F, y^F, x^L, y^L) \\ & s.t., \quad g(x^F, y^F, x^L, y^L) \leq 0 \\ & x^F \in \mathbb{R}^{q^F} \\ & y^F \in \mathbb{Z}^{p^F} \end{aligned} \tag{2}$$

## METHODOLOGY

Our approach is grounded in the work developed by Dumouchelle et al. (2022) [8], which utilized neural network embeddings to tackle two-stage stochastic programming problems. The proposed workflow, outlined in **Figure 1**, involves the following steps.

### 1. Identification of the linking variables

As starting point, the bilevel model must be formulated and its structure must be carefully analysed to understand the interaction between both levels. This inspection is essential to identify linking variables that connect the upper and lower levels and contain the information exchanged between the players.

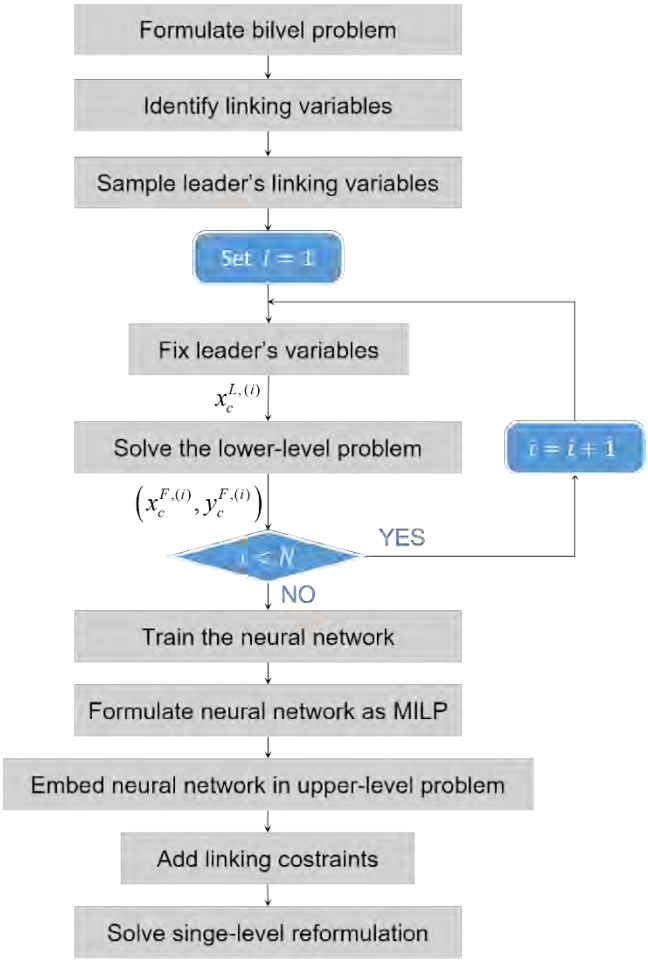



**Figure 1:** Overview of the proposed methodology

Linking variables play a key role in this work, since they constitute the inputs and outputs of the neural network used to approximate the optimal response of the follower. Notably, not all of the leader's variables necessarily influence the follower's decisions, and vice-versa. Identifying this subset helps reducing the dimensionality of the input and output spaces, simplifying the network architecture. Therefore, the linking variables will be a subset of the leader's decision variables $(x_c^L, y_c^L) \subseteq (x^L, y^L)$.

Although in general both leader's continuous and discrete decisions impact the follower's solution, we exclusively contemplate lower-level problems parametrized by continuous leader's decisions (i.e., $\psi(x_c^L)$), since training neural networks with endogenous integer variables is out of the scope of this study.

## 2. Generation of training data

The neural network is trained in a supervised manner. Thus, a set of input-output pairs is required so that it learns the mapping $\psi$ from $x_c^L \mapsto (x^F, y^F)$. Such dataset is generated through an iterative procedure.

First, a set of feasible solutions of the upper-level problem is randomly sampled using strategies such as Latin Hypercube Sampling. Both the sampling method and the number of data points must ensure a representative coverage of the feasible region in problem 1. Then, for each sampled leader's solution, the corresponding label is computed by solving the lower-level problem in Eq. 2, where the leader's variables function as parameters.

## 3. Training of the neural network

A fully connected neural network $(x_F, y_F) = \mathcal{N}(x_L; \theta)$ is trained to predict the optimal follower's decisions as a function of the leader's decisions. Here, coefficients $\theta$ represent the weights and biases of the network that must be optimized during training. Rectified Linear Unit (ReLU) activations introduce non-linearity to the outputs of each neuron in hidden layers, whereas linear transformations are applied in the output layer.

The prepared dataset is divided into training (70%), validation (20%) and test (10%) subsets. The training set is used to fit model weights, the validation set for architecture selection and hyperparameter tuning, and the test set to evaluate model performance.

## 4. Neural network as MILP

Mathematically, the output of a ReLU-activated neuron $j$ in layer $m$ can be written as

$$h_j^m = \max\left(0, \sum_{i=1}^{n_{m-1}} w_{ij}^{m-1} h_i^{m-1} + b_j^{m-1}\right) \tag{3}$$

where $w_{ij}^m$ is the element of matrix $W^m$ at the $i$-th row and $j$-th column and $b_j^m$ is the $j$-th element of vector $b^m$, being $W^m$ and $b^m$ the weights and biases associated with layer $m$, respectively.

Since the expression in Eq. 3 merely describes a piecewise linear function, the forward propagation step of a neural network with ReLU activations can be modelled as a set of linear constraints. Though different reformulation alternatives have been proposed in the literature, they all involve the introduction of binary variables to indicate which region of the ReLU function is active [9]. Following the extended Big-M reformulation proposed by Serra et al. (2017) [10], a representation of an $l$-layered feed-forward neural network is shown in Eq. 4, where $n_m$ identifies the number of neurons in a given layer $m$.

$$\begin{aligned}
&\textstyle\sum_{i=1}^{n_0} w_{ij}^0 x^L + b_j^0 = \hat{h}_j^1 - \check{h}_j^1 && \forall\, j \in \{1, \dots, n_0\} \\
&\textstyle\sum_{i=1}^{n_{m-1}} w_{ij}^{m-1} \hat{h}_j^{m-1} + b_j^{m-1} = \hat{h}_j^m - \check{h}_j^m && \forall\, j \in \{1, \dots, n_m\},\ m \in \{2, \dots, l-1\} \\
&\textstyle\sum_{i=1}^{n_l} w_{ij}^l \hat{h}_j^l + b_j^l = \beta_j && \forall\, j \in \{1, \dots, n_l\} \\
&\hat{h}_j^m \le M^{+m}_j z_j^m && \forall\, j \in \{1, \dots, n_m\},\ m \in \{1, \dots, l-1\} \\
&\check{h}_j^m \le M^{-m}_j \left(1 - z_j^m\right) && \forall\, j \in \{1, \dots, n_m\},\ m \in \{1, \dots, l-1\} \\
&\hat{h}_j^m, \check{h}_j^m \ge 0 && \forall\, j \in \{1, \dots, n_m\},\ m \in \{1, \dots, l-1\} \\
&z_j^m \in \{0,1\} && \forall\, j \in \{1, \dots, n_m\},\ m \in \{1, \dots, l-1\}
\end{aligned} \tag{4}$$

Note that the pair $(\hat{h}_j^m, \check{h}_j^m)$ is complementary, meaning that only one can be non-zero, and only the non-negative counterpart $\hat{h}_j^m$ of the weighted sum is propagated through the network. This exclusive disjunction is enforced by binary variables $z_j^m$. The outputs of the neural network are denoted as $\beta_j$.

In addition, Big-M coefficients $M^+$ and $M^-$ must be carefully chosen to ensure tight linear programming (LP) relaxations. For this purpose, we adopt the propagation rule introduced by Serra et al. [10].

## 5. Single-level reformulation

Replacing the inner optimization problem by the MILP representation of the surrogate model of $\psi(x^L)$ transforms the original bilevel problem in Eq. 1 into a single-level model, which can be directly handled by state-of-the art optimization solvers. The proposed single-level reformulation is presented in Eq. 5.

$$\begin{aligned}
\min \quad & F(x^L, y^L, x^F, y^F) \\
s.t., \quad & G(x^L, y^L, x^F, y^F) \le 0 \\
& \text{Equations in 4} \\
& \text{Linking block} \\
& x^L \in \mathbb{R}^{q^L} \\
& y^L \in \mathbb{Z}^{p^L}
\end{aligned} \tag{5}$$

The Linking block refers to the set of constraints that map $\beta \mapsto (x^F, y^F)$, being therefore case-dependent.

# RESULTS AND DISCUSSION

To illustrate the application of the proposed methodology, we consider the simplified two-echelon supply chain in **Figure 2**, adapted from Yue and You (2017) [11].

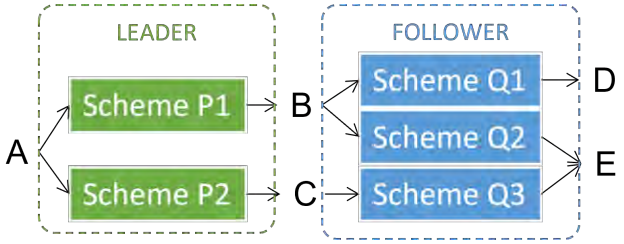



**Figure 2:** Supply chain superstructure

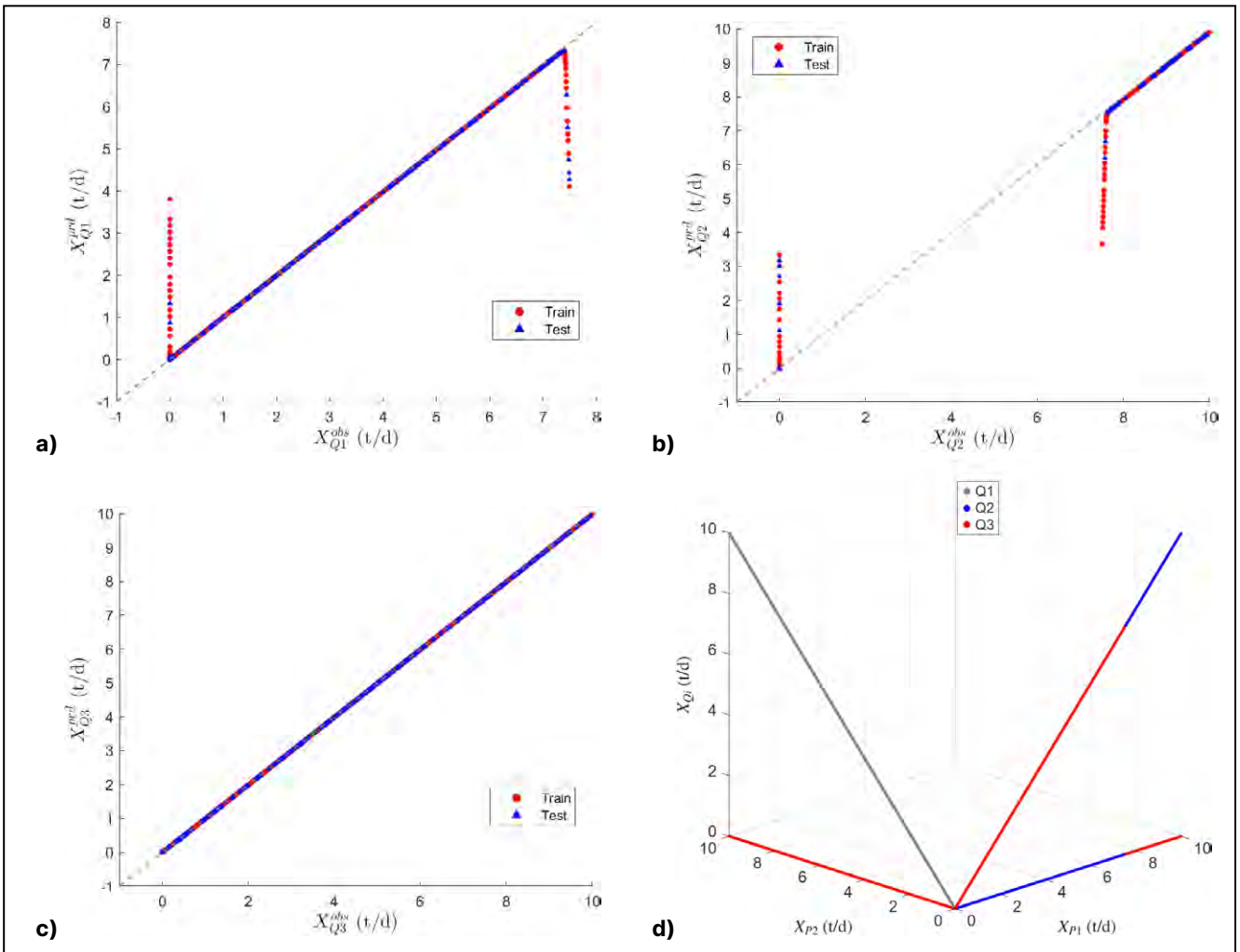



**Figure 3:** Observations versus predictions for the network outputs across training and testing datasets. Subplots (a), (b), and (c) show the predicted versus observed values for $X_{Q1}$, $X_{Q2}$ and $X_{Q3}$, respectively, with the dashed line representing the ideal $y = x$ relationship. Subplot (d) provides a 3D visualization of the network outputs ($X_{Q1}$, $X_{Q2}$ and $X_{Q3}$) as a function of the inputs ($X_{P1}$ and $X_{P2}$).

In this Stackelberg game with a single leader and a single follower, both participants aim at maximizing their own profits. The optimization problems for the upper and lower levels are formulated below.

- Upper-Level Problem (Leader):

$$
\begin{aligned}
\max\ & \text{sales}^L - \text{costs}^L && && (6)\\
s.t.\ & \text{sales}^L = p_B^L X_{P1} + p_C^L X_{P2} + p_E^L (X_{Q1} + X_{Q2}) && \\
& \text{costs}^L = \textstyle\sum_{i \in I^L} (p_A^L + v_i) X_i + f_i Y_i && \\
& \textstyle\sum_{i \in I^L} X_i \le C^L && \\
& \textstyle\sum_{i \in I^L} Y_i \le 1_i && \\
& X_i \ge C^L Y_i && \forall\, i \in I^L \\
& X_i \in \mathbb{R}^+, Y_i \in \{0,1\} && \forall\, i \in I^L \\
& I^L = \{P1, P2\} && \\
& (X_{Q1}, X_{Q2}, X_{Q3}, Y_{Q1}, Y_{Q2}, Y_{Q3}) = \psi(X_{P1}, X_{P2}) &&
\end{aligned}
$$

- Lower-Level Problem (Follower):

$$
\begin{aligned}
& \psi(X_{P1}, X_{P2}) = && && \\
& \max\ \ \text{sales}^F - \text{costs}^F && && \\
& s.t.\ \ \text{sales}^F = p_D^F X_{Q1} + p_E^R (X_{Q2} + X_{Q3}) && && \\
& \quad \text{costs}^F = p_B^F X_{P1} + p_C^F X_{P2} + \textstyle\sum_{i \in I^F} v_i X_i + f_i Y_i && && \\
& \quad \textstyle\sum_{i \in I^F} X_i \le C^F && && (7)\\
& \quad \textstyle\sum_{i \in I^F} Y_i \le 1_i && && \\
& \quad X_i \ge C^F Y_i && \forall\, i \in I^F && \\
& \quad X_i \in \mathbb{R}^+, Y_i \in \{0,1\} && \forall\, i \in I^F && \\
& \quad I^F = \{Q1, Q2, Q3\} && && 
\end{aligned}
$$

To approximate the solution of problem 7, a neural network was trained to predict the follower's optimal real-valued decisions $X_{i \in I^F}$, while binary variables $Y_{i \in I^F}$ are subsequently inferred from the network's predictions. In the above formulations, the parameters $C^L$ and $C^F$ represent the productive capacity of the leader and the follower, respectively. Similarly, $p_s^L$ and $p_s^F$ refer to the selling or purchase price of species $s$, depending on the player.

A dataset containing $5000$ points was generated by solving problem 7 for different combinations of $(X_{P1}, X_{P2})$. CPLEX was used as optimization algorithm and the data generation time rose to $964$ s.

Different network architectures (e.g., varying the number of layers and neurons per layer) were considered. First, we employed Hyperband search to explore the predefined hyperparameter space and select the best architecture. The learning rate was further optimized using the learning rate range test [12]. The network with the optimal hyperparameter configuration was finally trained for $200$ epochs on a combined training and validation set using Adam optimizer. Its performance was then assessed both on the train and test sets, reporting the corresponding mean absolute error (MAE) in **Table 1**. All models were implemented and trained using TensorFlow 2.16.1.

The results, as shown in **Table 1**, indicate low MAE scores, proving the suitability of the neural network as an accurate surrogate for the optimal lower-level solution. The accuracy of the network outputs, as indicated by the low MAE scores, is further validated by the observation-versus-prediction plots in **Figure 3**. Subplots **a**–**c** illustrate that the predictions closely align with the labels across both training and testing datasets, as the points cluster tightly around the diagonal line. Minor deviations are observed only in regions where the original function exhibits discontinuities, consistent with the patterns seen in the 3D representation in **Figure 3d**. Such sharp transitions are inherently challenging for neural networks—or most regression models—to predict, since they are well-suited for capturing differentiable patterns. In this case, these mispredictions are localized and do not compromise the method's overall effectiveness, as the model properly captures the underlying system's behaviour.

Nevertheless, its performance could be improved by either exposing the network to more data during training or adopting more complex network architectures, which, however, are more prone to overfitting. The former approach would increase the data generation time, which is already the bottleneck of the process. In contrast, the latter would negatively impact the convergence rate of the single-level model due to the expansion in size of the neural network embedding. Hence, there is a clear trade-off between prediction accuracy and computational demand.

**Table 1:** Neural network configuration and performance

| | |
|---|---|
| Neurons per layer | $[16,16,16]$ |
| Learning rate | $2 \cdot 10^{-3}$ |
| Batch size | $32$ |
| Optimizer | Adam |
| MAE | $0.052$ (train); $0.054$ (test) |
| Training time (s) | $43.4$ |

**Table 2:** Results comparison

| | NN solution | KKT solution |
|---|---|---|
| Profit Leader (MU/h) | 350 | 350 |
| Profit Follower (MU/h) | 150 | 150 |
| $X_{P1}$ (ton/d) | 0 | 0 |
| $X_{P2}$ (ton/d) | 10 | 10 |
| $X_{Q1}$ (ton/d) | 0 | 0 |
| $X_{Q2}$ (ton/d) | 10 | 10 |
| $X_{Q3}$ (ton/d) | 0 | 0 |
| Solving time (s) | 0.79 | 0.53 |

The single-level reformulation of the original problem, based on the neural surrogate, is given in Eq. 8.

$$
\begin{aligned}
\max\ & \text{sales}^L - \text{costs}^L && (8)\\
s.t.\ & \text{sales}^L = p_B^L X_{P1} + p_C^L X_{P2} + p_E^L\left(X_{Q1} + X_{Q2}\right)\\
& \text{costs}^L = \textstyle\sum_{i\in I^L}(p_A^L + v_i)X_i + f_i Y_i\\
& \textstyle\sum_{i\in I^L} X_i \le C^L\\
& \textstyle\sum_{i\in I^L} Y_i \le 1_i\\
& \textstyle\sum_{i\in I^L} w_{ij}^0 \mathrm{X_i} + b_j^0 = \hat{h}_j^1 - \check{h}_j^1 \quad \forall\, j \in \{1,\dots,16\}\\
& \textstyle\sum_{i=1}^{16} w_{ij}^1 \hat{h}_j^1 + b_j^1 = \hat{h}_j^2 - \check{h}_j^2 \quad \forall\, j \in \{1,\dots,16\}\\
& \textstyle\sum_{i=1}^{16} w_{ij}^2 \hat{h}_j^2 + b_j^2 = \hat{h}_j^3 - \check{h}_j^3 \quad \forall\, j \in \{1,\dots,16\}\\
& \textstyle\sum_{i=1}^{16} w_{ij}^3 \hat{h}_j^3 + b_j^3 = \beta_j \quad \forall\, j \in \{1,2,3\}\\
& \hat{h}_j^m \le M^{+m}_j z_j^m \quad \forall\, j \in \{1,\dots,n_m\}, m \in \{1,2,3\}\\
& \check{h}_j^m \le M^{-m}_j\left(1 - z_j^m\right) \quad \forall j \in \{1,\dots,n_m\}, m \in \{1,2,3\}\\
& \hat{h}_j^m, \check{h}_j^m \ge 0 \quad \forall\, j \in \{1,\dots,n_m\}, m \in \{1,2,3\}\\
& z_j^m \in \{0,1\} \quad \forall\, j \in \{1,\dots,n_m\}, m \in \{1,2,3\}\\
& \begin{bmatrix} \boldsymbol{Y_{Qi}} \\ \beta_i \ge \varepsilon \\ \beta_i - \varepsilon \le X_{Qi} \le \beta_i + \varepsilon \\ 0 \le X_{Qi} \le C^L \end{bmatrix} \veebar \begin{bmatrix} \neg \boldsymbol{Y_{Qi}} \\ \beta_i \le \varepsilon \\ X_{Qi} = 0 \end{bmatrix} \quad i = \{1,2,3\}\\
& X_i \ge C^L Y_i \qquad \forall\, i \in I^L\\
& X_i \in \mathbb{R}^+, Y_i \in \{0,1\} \quad \forall\, i \in I^L\\
& I^L = \{P1, P2\}
\end{aligned}
$$

The Big-M reformulation applied to the disjunction in Eq. 8 results in a set of linear constraints that constitute the so-called $\text{Linking block}$ in Eq. 5. These equations are designed to mitigate the neural network approximation error and ensures that non-selected production schemes of the follower have a production rate of exactly 0. In this context, the parameter $\varepsilon$ acts as a tolerance threshold that accounts for the prediction error of the neural network. Specifically, it limits an allowable margin around the predicted values that guarantees consistency between the network's outputs and the logical conditions of the optimization problem.

For comparison purposes, the original model is solved by applying a direct reformulation using Karush-Kuhn-Tucker (KKT) conditions for all feasible combinations of binary variables. Both models were implemented in Pyomo 6.8.2, using CPLEX 22.1.1.0 as MILP solver and reach identical results, as **Table 2** summarizes, due to the effect of linking constraints.

Since the objective of this work was to demonstrate

the effectiveness and reliability of the proposed methodology in solving mixed-integer bilevel instances, the selected case study was not complex enough to evaluate the potential advantages of the methodology in terms of solution speed compared to traditional approaches. Consequently, future research will focus on exploring the benefits of neural network embeddings in large-scale models.

## CONCLUSION

This contribution presents a metamodeling approach to mixed integer bilevel optimization, where the inner-level problem is parametrized by continuous decisions of the leader. In this study, the lower level is bypassed using a neural network that approximates the optimal follower's response to the leader's decisions. By employing Rectified Linear Unit activations, the neural network can be reformulated as a set of mixed integer linear constraints that are integrated into the leader's problem as a single-level reformulation. Additional constraints are introduced to map the network outputs to the corresponding follower decision variables and to infer their discrete behaviour where needed.

The approach was showcased on a two-echelon supply chain case study, achieving solutions whose quality is comparable to traditional bilevel optimization methods. These results suggest that further effort to improve the use neural network embeddings in mixed-integer bilevel optimization tasks could lead to significant advantages, especially when applied to larger-scale instances. Future research should primarily focus on ensuring prediction accuracy, which remains a critical challenge of the proposed methodology, while carefully balancing model complexity, computational resources and reliability to enhance its competitiveness in terms of computational efficiency.

## ACKNOWLEDGEMENTS

The authors gratefully acknowledge financial support from the Spanish Ministry of Science, Innovation, and Universities via the doctoral grant for training university teachers FPU22/01276 and the R&D and Innovation Project PID2021-124139NB-C21.

## REFERENCES

1. Moore, J. T. and J. F. Bard (1990). The mixed integer linear bilevel programming problem. *Oper. Res.* 38(5):911–921 https://doi.org/10.1287/opre.38.5.911
2. Kleinert T, Labbé M, Ljubić I, Schmidt M. A Survey on Mixed-Integer Programming Techniques in Bilevel Optimization. *EURO J. Comput. Optim.* 9: 100007 (2021) https://doi.org/10.1016/j.ejco.2021.100007
3. Qiang Z, Yefei Y, Fangfang M. A Stackelberg-based deep reinforcement learning approach for dynamic cooperative advertising in a two-echelon supply chain. *Comp. Chem. Eng.* 196:109048 (2025) https://doi.org/10.1016/j.compchemeng.2025.109048
4. Moti M, Uddin RS, Hai MA, Saleh TB, Alam MGR, Hassan MM, Hassan MR, Blockchain Based Smart-Grid Stackelberg Model for Electricity Trading and Price Forecasting Using Reinforcement Learning. *Appl. Sci.* 12(10):5144 (2022) https://doi.org/10.3390/app12105144
5. Jiménez RX. Bilevel optimisation with embedded neural networks: Application to scheduling and control integration. *arXiv* (2023) https://doi.org/10.48550/arXiv.2304.11244
6. Vlah D, Sepetanc K, Pandzic H. Solving bilevel optimal bidding problems using deep convolutional neural networks. IEEE Syst. J. 17(2): 2767-2778 (2023) https://doi.org/10.1109/JSYST.2022.3232942
7. Dumouchelle J, Julien E, Kurtz J, Khalil E. Neur2BiLO: Neural Bilevel Optimization. *arXiv* (2024) https://doi.org/10.48550/arXiv.2402.02552
8. Dumouchelle J, Patel R, Khalil EB, Bodur M. Neur2SP: Neural Two-Stage Stochastic Programming. *arXiv* (2022) https://doi.org/10.48550/arXiv.2205.12006
9. Aftabi N, Moradi N, Mahroo F. Feed-forward neural networks as mixed-integer program. *arXiv* (2024) https://doi.org/10.48550/arXiv.2402.06697
10. Serra T, Tjandraatmadja C, Ramalingam S. Bounding and counting linear regions of deep neural networks. *arXiv* (2017) https://doi.org/10.48550/arXiv.1711.02114
11. Yue D, You F. Stackelberg-game-based modeling and optimization for supply chain design and operations: A mixed integer bilevel programming framework. *Comput. Chem. Eng*. 102:81-95 (2017) https://doi.org/10.1016/j.compchemeng.2016.07.026
12. Smith LN. Cyclical Learning Rates for Training Neural Networks. *IEEE Winter Conference on Applications of Computer Vision (WACV)*, Santa Rosa, CA, USA. 464-472 (2017) https://doi.org/10.1109/WACV.2017.58

© 2025 by the authors. Licensed to PSEcommunity.org and PSE Press. This is an open access article under the creative commons CC-BY-SA licensing terms. Credit must be given to creator and adaptations must be shared under the same terms. See https://creativecommons.org/licenses/by-sa/4.0/



Systems & Control Transactions

**Research Article - Peer Reviewed Conference Proceeding**
ESCAPE 35 - European Symposium on Computer Aided Process Engineering
Ghent, Belgium. 6-9 July 2025
Jan F.M. Van Impe, Grégoire Léonard, Satyajeet S. Bhonsale,
Monika E. Polańska, Filip Logist (Eds.)

PSE PRESS

# Linear and non-linear convolutional approaches and XAI for spectral data: classification of waste lubricant oils

**Ruben Gariso[a], João P. L. Coutinho[a], Tiago J. Rato[a], Marco S. Reis[a,*]**

[a] CERES, Department of Chemical Engineering, University of Coimbra, Portugal
* Corresponding Author: marco@eq.uc.pt.

## ABSTRACT

Waste lubricant oil (WLO) is a hazardous residual that requires proper management, being WLO regeneration the preferred approach. However, regeneration is only viable if the WLO does not coagulate in the equipment. Otherwise, the process needs to be shut down for cleaning and maintenance. To mitigate this risk, a laboratory test is currently used to assess the WLO coagulation potential before it enters the process. This laboratory test is, however, time-consuming, presents several safety risks, and is subjective. To expedite decision-making, process analytics technology (PAT) and machine learning were used to develop a model to classify WLOs according to their coagulation potential. Three approaches were followed, spanning linear and non-linear models. The first approach (benchmark) uses partial least squares for discriminant analysis (PLS-DA) and interval PLS combined with standard chemometric preprocessing techniques (27 model variants). The second approach uses wavelet transforms to decompose the spectra and PLS-DA for feature selection (10 model variants). Finally, the third approach uses convolutional neural networks (CNN) to estimate the optimal filter for feature extraction (1 model variant). These models were trained on real industrial data. The results show that the three modelling approaches can attain high accuracy, with an average of 91%. The spectral filtering using wavelet transforms proved to be a viable option to reduce the number of models to explore compared to the benchmark approach. The CNN was also able to streamline the preprocessing selection by implicitly estimating the optimal filter. The models also provided physical insight into the WLO coagulation phenomenon.

**Keywords**: Waste lubricating oil, Multiblock analysis, PLS, CNN, Classification.

## INTRODUCTION

Waste lubricant oil (WLO) is a hazardous material with the potential to cause severe environmental harm if not properly managed. Within the European Union's waste management hierarchy, regeneration is identified as the preferred method for addressing this type of residual. In Portugal, the entire WLO regeneration supply chain is managed by Sogilub, with the primary objective of recovering base oil – the main component of lubricant oil – from WLO. However, WLO regeneration is only viable if the WLO does not coagulate during processing. Otherwise, the process must be stopped for cleaning and maintenance, and subsequent disposal of the entire production batch. To mitigate this risk, the coagulation potential of WLO is currently assessed using a laboratory test involving an alkaline treatment with potassium hydroxide (KOH) [1]. While effective, this test is time-intensive, poses safety concerns, due to the formation of foams and use of high temperatures, and relies on a subjective visual interpretation by the analyst. As an alternative, the implementation of a process analytical technology (PAT)-based classification system offers a promising solution to accelerate WLO processing, improve safety, and enhance the analytical capacity of laboratories.

This study aims to evaluate and compare the performance of traditional linear models and modern non-linear models in leveraging mid-infrared (MIR) spectroscopy to classify WLO before regeneration. Three methodologies were considered: (i) partial least squares (PLS) [2] and interval partial least squares (iPLS) [3] combined with chemometric preprocessing techniques; (ii) iPLS

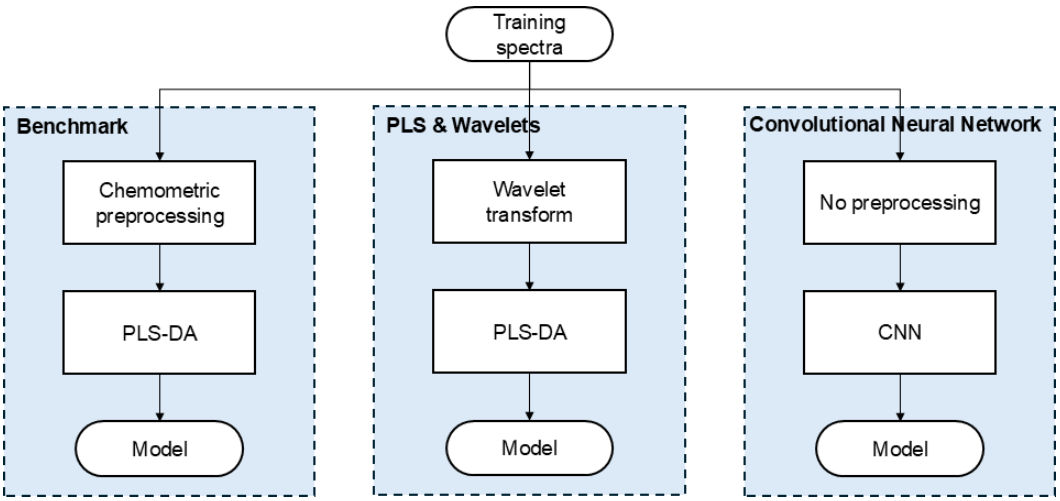



**Figure 1** Overview of the models under comparison using combinations of preprocessing and modeling approaches.

combined with wavelet transforms [4]; and (iii) convolutional neural networks (CNNs) [5].

The remainder of this article is structured as follows. The Methodology section encompasses the preprocessing techniques and modeling methodologies employed. In the Results section, an analysis of the results obtained in this study is made. Finally, the Conclusion section offers a concise summary of the conclusions drawn from the findings.

## METHODOLOGY

This study aims to develop a suitable data-driven model to predict the coagulation potential of WLO using PAT techniques. To achieve this end, three modeling approaches were considered and systematically compared using the SS-DAC framework [6].

In the following subsections, an overview of the preprocessing techniques and modelling methodologies used for model development are described. A simplified diagram of the models under comparison is presented in Figure 1.

### Spectral Preprocessing

Preprocessing of the spectral data is often used to mitigate potential artifacts that may arise due to unintended interactions between light and the sample under examination. Two main classes of preprocessing techniques were considered: (i) classical chemometric approaches; and (ii) wavelet transforms.

### Chemometric Preprocessing

From the class of classical preprocessing techniques typically found in the literature (e.g. [7]), the following were considered:

- Standard Normal Variate (SNV) [8];
- Multiplicative Scatter Correction (MSC) [9];
- Savitzky-Golay differentiation (SGD) [10].

Different combinations of these preprocessing techniques, as well as different parameterizations of SGD (identified as SGD-{derivative order}-{window size}) were examined, leading to nine distinct preprocessing variations (see Table 1).

### Wavelet Transforms

As an alternative to the classical chemometric preprocessing, wavelet transforms were used to decompose the spectra into multiple frequency components by convolution with (fixed) linear filters. The obtained wavelet coefficients were then fed to the modeling methodologies for variable selection.

The discrete wavelet transform (DWT) can be efficiently performed using the recursive algorithm proposed in [4]. Several wavelet filter can be found in the literature [11–13], being the Haar, Daubechies and Symlets wavelets the most common and those used in this study (see Table 1).

### Modeling Methodologies

Two main classes of modeling methodologies were considered in this study: (i) linear; and (ii) non-linear.

From the linear class, partial least squares (PLS) for discriminant analysis (PLS-DA) [14] using the full spectra and two interval-based extensions of PLS, namely forward interval PLS (FiPLS) and backward interval PLS (BiPLS) were used. These models were combined with classical chemometric preprocessing approaches and represent the benchmark. Additionally, wavelet

transforms were used to decompose the spectra by convolution with fixed filters and their wavelet coefficients were then used as features by FiPLS and BiPLS.

From the non-linear class, convolutional neural networks (CNNs) were used. CNNs have recently been considered as a potential alternative to classic chemometric methods for modeling of spectroscopic data [5,15]. The main benefit of CNN models lies in their ability to perform automatic feature extraction of the raw spectra, tailored for each specific dataset and target variables. For better interpretability, we consider only a single convolutional layer with a single filter. After the convolutional layer, the extracted features are passed through a non-linear activation function and multiple hidden layers. Since the problem is a binary classification problem, the output layer has a logistic activation function, and the Binary Cross Entropy loss function is used to estimate the CNN model parameters using the Adam optimizer. We further consider $L_2$ regularization of the loss function to prevent model overfitting.

## Feature Importance

For MIR data, different spectral bands can be associated with specific functional groups. Thus, the analysis of feature importance can provide insights on the critical chemical compounds related with the coagulation phenomenon. For the PLS-based approaches, feature importance was assessed using the Variable Importance in Projection (VIP) method [16,17]. In turn for the CNN model, the feature importance was determined using the Integrated Gradients (IG) method [18]. Whereas the VIP values are calculated based on the entire training dataset, IG values are calculated for each individual spectral sample. In addition, due to the stochastic weight initialization, the IG feature importance was repeated 30 times and the results averaged.

# RESULTS

WLO samples were provided by Sogilub, a non-profit organization responsible for the management of WLO in Portugal. A total of 109 WLO samples were collected for analysis. The coagulation potential of each sample was assessed using a coagulation test involving an alkaline treatment with potassium hydroxide (KOH). Based on the outcomes of this test, the laboratory analyst labeled the samples into two categories: "coagulates" (43 samples) or "does-not-coagulate" (66 samples). Additionally, MIR spectra comprising 1814 wavenumbers in the range of 4000 to 500 $cm^{-1}$ with a resolution of 2 $cm^{-1}$ were obtained for each sample in triplicate.

A total of 38 models, encompassing both linear and non-linear models, were compared using the SS-DAC framework. The first class of models, serving as the benchmark, employed PLS-DA, FiPLS and BiPLS, combined with standard chemometric preprocessing techniques, yielding 27 model variants. The second approach used wavelet transforms to decompose the spectral data into multiple frequency components through convolution with linear filters, followed by feature selection using FiPLS and BiPLS, resulting in 10 model variants. Finally, the third approach used CNN (without preprocessing) for non-linear feature extraction and modeling (1 model variant).

For the BiPLS and FiPLS methodologies using the chemometric preprocessing approaches, the MIR spectra were split into 30 equal intervals. For FiPLS and BiPLS using wavelet transforms the spectra were divided in intervals with a dyadic length of 64 $cm^{-1}$ (leading to into 29 intervals).

In the first stage of the SS-DAC framework, the raw dataset was randomly divided into two datasets: a

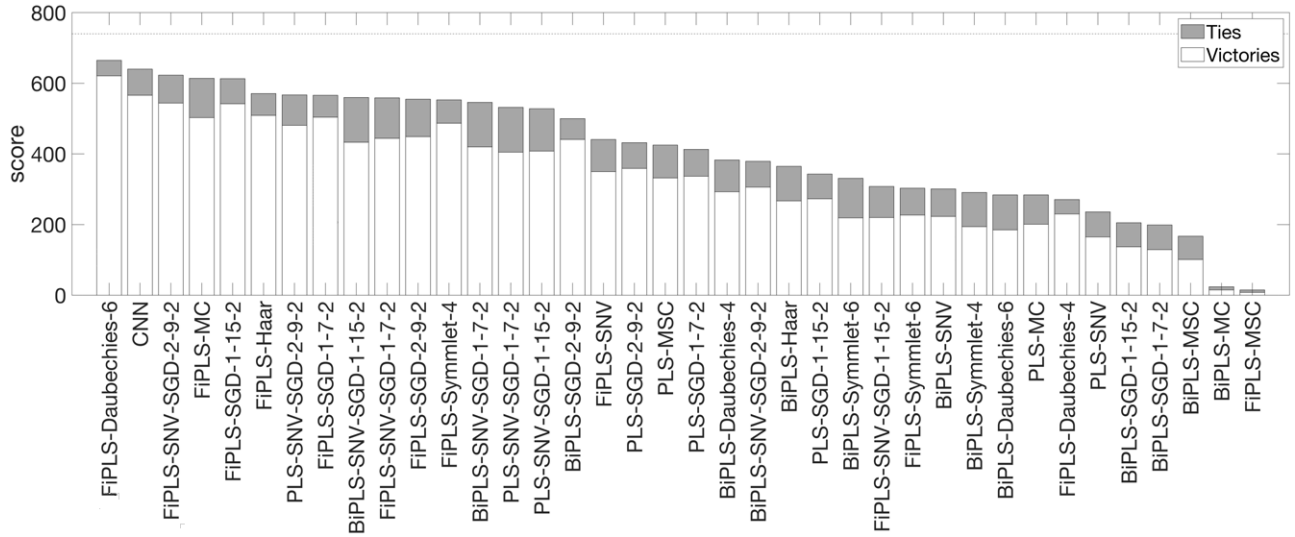



**Figure 2** Score of the models' under comparison using the SS-DAC fremework.

**Table 1** Mean accuracy for each model. The models with the highest rank in each class are highlighted in bold.

| Class | Preprocessing Techniques | Modeling Methodology | | | |
|---|---|---|---|---|---|
| | | PLS | FiPLS | BiPLS | CNN |
| PLS & Chemometric (benchmark) | Mean centering (MC) | 0.82 | 0.88 | 0.69 | - |
| | Standard normal variate (SNV) | 0.84 | 0.64 | 0.77 | - |
| | Multiplicative scatter correction (MSC) | 0.78 | 0.85 | 0.79 | - |
| | Savitzky-Golay differentiation (SGD-{1-7}) * | 0.84 | 0.90 | 0.78 | - |
| | Savitzky-Golay differentiation (SGD-{1-15}) * | 0.84 | 0.89 | 0.78 | - |
| | Savitzky-Golay differentiation (SGD-{2-9}) * | 0.86 | 0.88 | 0.88 | - |
| | SNV & SGD (SNV-SGD-{1-7}) * | 0.87 | 0.88 | 0.88 | - |
| | SNV & SGD (SNV-SGD-{1-15}) * | 0.88 | 0.82 | 0.88 | - |
| | SNV & SGD (SNV-SGD-{2-9}) * | 0.89 | **0.90** | 0.85 | - |
| PLS & Wavelet transform | Haar | - | 0.90 | 0.84 | - |
| | Daubechies 4 | - | 0.80 | 0.85 | - |
| | Daubechies 6 | - | **0.93** | 0.83 | - |
| | Symmlet 4 | - | 0.89 | 0.83 | - |
| | Symmlet 6 | - | 0.84 | 0.83 | - |
| CNN | None | - | - | - | **0.90** |

* The short name of the Savitzky-Golay differentiation preprocessing is coded as SGD-{D,W}, where D is the devative order and W is the window size.

training dataset comprising 80% of the samples and a test dataset containing the remaining 20% of the samples, ensuring balanced distributions across both datasets. Additionally, the replicates of the same sample were assigned to the same dataset to maintain consistency. The hyperparameters of the PLS-based models (number of latent variables and intervals kept in the model) were selected using the training dataset and Monte Carlo Cross-Validation (MCCV). In turn, the hyperparameters of the CNN (learning rate, regularization weights, kernel size, number and size of hidden layers, activation function and type of pooling), were selected by Bayesian Optimization (BO) [19] based on stratified 10-fold cross validation. All models were trained by maximization of the accuracy (ACC) given by:

$$ACC = \frac{TP+TN}{n} \quad (1)$$

where, $TP$ is the number of true positives, $TN$ is the number of true negatives, and $n$ is the total number of samples.

Subsequently, in the second stage of SS-DAC, the models' performance was evaluated on the test dataset using the accuracy as the key performance indicator (KPI).

In the third stage of the SS-DAC, the models were compared using bootstrap to obtain multiple realizations of the KPI in test conditions, and the Wilcoxon signed-rank test [20] to statistically assess the significance of the differences in accuracy of every pair of models. For each pairwise comparison, if a model had a statistically significant higher KPI, it was awarded a "victory", while the competing model received a "defeat". In cases where the accuracy of both models was deemed not statistically different, the comparison outcome was recorded as a "tie". A performance score was then calculated for each model by summing up the number of victories and ties. Models achieving higher scores, characterized by a larger number of victories and ties, were considered to exhibit consistently superior accuracy. The model's score, ranked from highest to lowest score are presented in Figure 2. Table 1 provides the mean accuracy obtained by each model.

The results obtained show that PLS with wavelet transforms, namely the FiPLS-Daubechies-6 model, achieved the best performance (highest score; first place), with a mean ACC of 0.93 and a standard deviation of 0.07. The CNN attained the second place, with a mean ACC of 0.92 with a standard deviation of 0.11. In the benchmark approach (PLS & Chemometric preprocessing), the best model was FiPLS-SNV-SGD-{2-9}, which ranked third place with a mean ACC of 0.90 and a standard deviation of 0.09. Thus, all model classes were able to attain high accuracy levels.

To achieve a high accuracy level using PLS and chemometric preprocessing it was however necessary to screen over several models, being that 26% of them have a mean accuracy lower then 0.80. The full-spectrum PLS models exhibited low performance since they rely on the entire spectral range, which makes them more susceptible to spectral noise. Similarly, the BiPLS-based models also showed low performance since they retained many intervals, leading to a less focused feature selection.

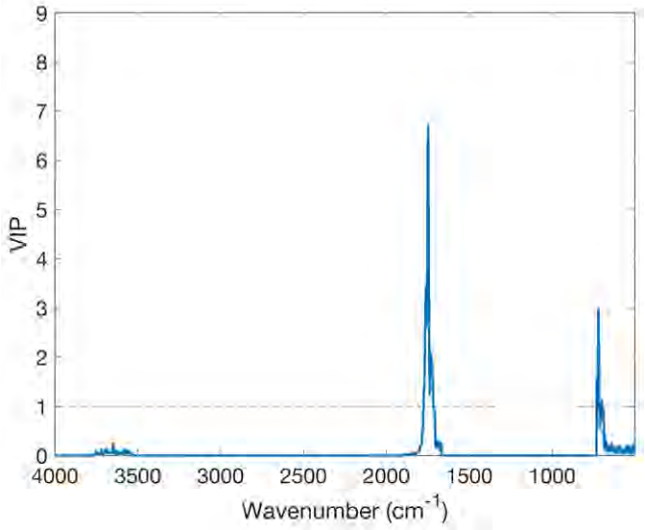



**Figure 3** Feature importance for FiPLS-SNV-SGD-{2-9}.

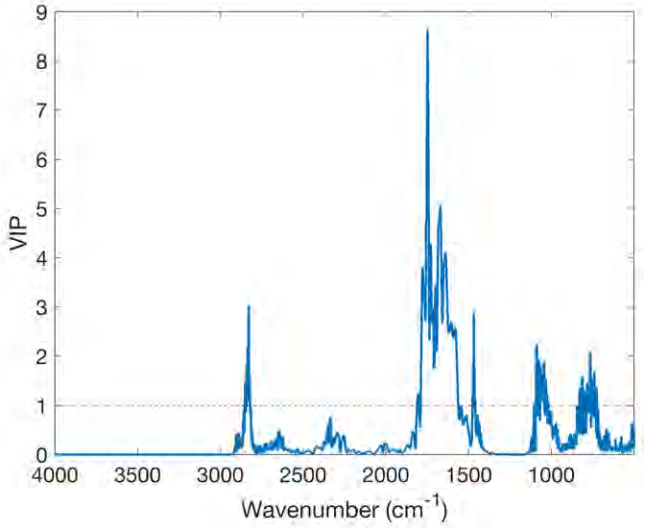



**Figure 4** Feature importance for FiPLS-Daubechies-6.

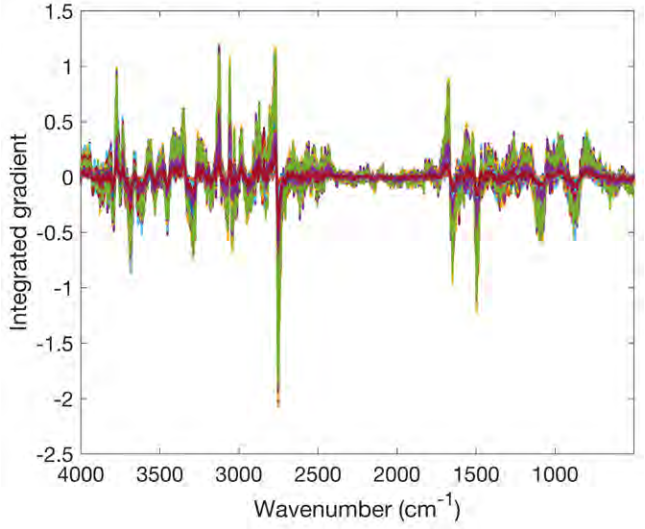



**Figure 5** Feature importance for CNN, calculated for each spectral sample. Refer to the online version for color.

In turn, all models based on PLS with wavelet transforms and CNN have a mean accuracy greater than 0.80. Thus, they are deemed as better modelling alternatives. The CNN model shows good performance even without any preliminary preprocessing of the spectra, which highlights their ability to perform automatic feature extraction. The BO of the CNN hyperparameters resulted in a large kernel, with a size of 184 and a larger structure, with 3 hidden layers with 82 units each. This high number of parameters can justify the slightly larger standard deviation of the CNN model compared to the more parsimonious PLS models.

In terms of feature importance, the FiPLS-SNV-SGD-{2-9} model distinctly identified the spectral band between 1775 and 1700 $cm^{-1}$ as the most critical for classification (Figure 3). Similarly, the FiPLS-Daubechies-6 model highlighted a broader region, identifying the 1790–1574 $cm^{-1}$ band as relevant (Figure 4). In contrast, other FiPLS models, whether using chemometric or wavelet preprocessing, included additional bands beyond this range, which negatively impacted their performance. Unlike the interval PLS models, the identification of the relevant features is less clear for the CNN model, due to the lack of explicit feature selection. Contrary to the other models, the band around 2700 $cm^{-1}$ is identified as the most important, which is related to the C-O stretch, possibly indicating a non-linear relationship with this band and the coagulation class.

Among the spectral bands consistently selected by most models, the 1750–1735 $cm^{-1}$ band stands out. This region is associated with the ester functional group [21]. Based on this, it is conjectured that esters may have a significant effect on the WLO coagulation phenomenon.

As the reference laboratory test is inherently subjective, there is some uncertainty in the WLO labels. Nevertheless, as the large majority of the samples are well discriminated, we believe this label uncertainty does not have a significant impact on the models' overall performance.

## CONCLUSION

The modeling methodologies employed in this study produced models with high predictive accuracy, with a mean ACC ranging from 0.90 to 0.93. The performance of PLS-based models was significantly affected by the choice of preprocessing techniques, emphasizing the importance of evaluating multiple preprocessing strategies during model development.

The use of wavelet transforms to preprocess the spectrum proved to be competitive against the traditional chemometric preprocessing approaches and can reduce the search space during preprocessing selection. The CNN exhibited good performance even without preprocessing. This advantage can reduce the effort typically required by exhaustive preprocessing selection by trial

and error. However, the CNNs requires the optimization of hyperparameters, for which BO is a compelling approach within the realm of automated machine learning.

The top-performing models allowed for the identification of esters as a potential factor in WLO coagulation, offering critical insights into the underlying mechanisms of the coagulation phenomenon.

## ACKNOWLEDGEMENTS

The authors gratefully acknowledge the financial support of SOGILUB – Sociedade de Gestão Integrada de Óleos Lubrificantes Usados, Lda. The authors also acknowledge the support from the Chemical Engineering and Renewable Resources for Sustainability (CERES), which is financed by national funds from FCT/MCTES (with references DOI:10.54499/UIDB/00102/2020 and DOI:10.54499/UIDP/00102/2020).

## REFERENCES

1. Pinheiro CT, Ascensão VR, Reis MS, Quina MJ, Gando-Ferreira LM. A data-driven approach for the study of coagulation phenomena in waste lubricant oils and its relevance in alkaline regeneration treatments. Sci Total Environ 599–600:2054–2064 (2017).
2. Wold S, Sjöström M, Eriksson L. PLS-Regression: A Basic Tool of Chemometrics. Chemom Intell Lab Syst 58:109–130 (2001).
3. Nørgaard L, Saudland A, Wagner J, Nielsen JP, Munck L, Engelsen SB. Interval Partial Least-Squares Regression (iPLS): A Comparative Chemometric Study with an Example from Near-Infrared Spectroscopy. Appl Spectrosc 54:413–419 (2000).
4. Mallat SG. A theory for multiresolution signal decomposition: the wavelet representation. IEEE Trans Pattern Anal Mach Intell 11:674–693 (1989).
5. Yang J, Xu J, Zhang X, Wu C, Lin T, Ying Y. Deep learning for vibrational spectral analysis: Recent progress and a practical guide. Anal Chim Acta 1081:6–17 (2019).
6. Rato TJ, Reis MS. SS-DAC: A systematic framework for selecting the best modeling approach and preprocessing for spectroscopic data. Comput Chem Eng 128:437–449 (2019).
7. Naes T, Isaksson T, Fearn T, Davies T. A User-Friendly Guide to Multivariate Calibration and Classification. NIR Publications (2002).
8. Barnes RJ, Dhanoa MS, Lister SJ. Standard Normal Variate Transformation and De-trending of Near-Infrared Diffuse Reflectance Spectra. Appl Spectrosc 43:772–777 (1989).
9. Geladi P, MacDougall D, Martens H. Linearization and Scatter-Correction for Near-Infrared Reflectance Spectra of Meat. Appl Spectrosc 39:491–500 (1985).
10. Savitzky A, Golay MJE. Smoothing and Differentiation of Data by Simplified Least Squares Procedures. Anal Chem 36:1627–1639 (1964).
11. Mallat S. A Wavelet Tour of Signal Processing. Academic Press (2009).
12. Daubechies I. Orthonormal bases of compactly supported wavelets. Commun Pur Appl Math 41:909–996 (1988).
13. Press WH, Teukolsky SA, Vetterling WT, Flannery BP. Numerical Recipes: The Art of Scientific Computing. Cambridge University Press (2007).
14. Hastie T, Tibshirani R, Friedman J. The Elements of Statistical Learning: Data Mining, Inference, and Prediction. Springer (2009).
15. Cui C, Fearn T. Modern practical convolutional neural networks for multivariate regression: Applications to NIR calibration. Chemom Intell Lab Syst 182:9–20 (2018).
16. Wold S, Johansson E, Cocchi M. PLS: Partial Least Squares Projections to Latent Structures. In: 3D QSAR in Drug Design: Theory, Methods and Applications. Ed. Kubinyi K. 523–550 ESCOM Science Publisher (1993).
17. Eriksson L, Johansson E, Kettaneh-Wold N, Trygg J, Wikström C, Wold S. Multi- and Megavariate Data Analysis: Parte I - Basic Principles and Applications. Umetrics Academy (2006).
18. Sundararajan M, Taly A, Yan Q. Axiomatic attribution for deep networks. In: Proceedings of the 34th international conference on machine learning. Eds. Doina P, Yee Whye T. 70:3319–3328 PMLR (2017).
19. Shahriari B, Swersky K, Wang Z, Adams RP, de Freitas N. Taking the Human Out of the Loop: A Review of Bayesian Optimization. Proc IEEE 104:148–175 (2016).
20. Wilcoxon F. Individual Comparisons by Ranking Methods. Biometrics Bull 1:80–83 (1945).
21. Larkin P. Infrared and Raman Spectroscopy: Principles and Spectral Interpretation. Elsevier (2017).

© 2025 by the authors. Licensed to PSEcommunity.org and PSE Press. This is an open access article under the creative commons CC-BY-SA licensing terms. Credit must be given to creator and adaptations must be shared under the same terms. See https://creativecommons.org/licenses/by-sa/4.0/



Systems & Control Transactions

**Research Article - Peer Reviewed Conference Proceeding**
ESCAPE 35 - European Symposium on Computer Aided Process Engineering
Ghent, Belgium. 6-9 July 2025
Jan F.M. Van Impe, Grégoire Léonard, Satyajeet S. Bhonsale,
Monika E. Polańska, Filip Logist (Eds.)

PSE PRESS

# Unveiling Probability Histograms from Random Signals using a Variable-Order Quadrature Method of Moments

**Menwer Attarakih[a,*], Mark W. Hlawitschka[b], Linda Al-Hmoud[a],and Hans-Jörg Bart[c]**

[a] The University of Jordan, Department of Chemical Engineering, Amman, Jordan
[b] Institute of Process Engineering, Johannes Kepler University (JKU), Linz, Austria
[c] Mechanical & Process Engineering, RPTU Kaiserslautern, Kaiserslautern, Germany
* Corresponding Author: m.attarakihl@ju.edu.jo.

## ABSTRACT

Random signals are crucial in chemical and process engineering, where industrial plants generate big data that can be used for process understanding and decision-making. This makes it necessary to unveil the underlying probability histograms from these signals with a finite number of bins. However, the search for the optimal number of bins is still based on empirical optimisation and general rules of thumb. In this work, we introduce an alternative and general method to unveil probability histograms. Our method employs a novel variable-order QMOM, which adapts automatically based on the relevance of the information contained in the random data. The number of bins used to recover the underlying histogram is found to be proportional to the information entropy, where a search algorithm is developed that generates bins and assigns probabilities to them. The algorithm terminates when no more significant information is available for assignment to the newly created nodes, up to a user-defined threshold. In conclusion, our method is a universal histogram reconstruction technique that only requires enough numbers of moments to work. The method has been validated intensively using synthetic random signals and real-life problems.

**Keywords**: Probability histogram, Modelling, Simulation, Random signals, VOQMOM, Population Balances.

## INTRODUCTION

Random signals are vital in chemical and process engineering, data science, and machine learning. Industrial plants collect and analyze large volumes of data for process understanding, data compression, and decision-making, modelling industry 4.0 and 5.0 transformation and equipment or even process digital twins [1, 2, 3]. However, this data is not free of instrumental errors, where signal processing corrects it, enhances data accuracy and reliability. Despite advanced techniques that have been available, basic methods are commonly used due to resources' limitations which still depend on basic statistical representation methods [1]. In the sense of data compression, probability histograms are widely used as non-parametric density estimators, essential for visualizing data and deriving summary quantities like entropy from the underlying density, determining mechanical and physiochemical properties of particles from industrial systems and for real time online monitoring and control purposes [1]. However, the accuracy of these quantities is influenced by the number of bins selected for the histogram, which, in turn, determines the bin width based on the data range. Moreover, the empirical assumption of using uniform bin width has no solid theoretical support, where in most cases it is used for the simplicity of mathematical treatment [4, 5]. Unfortunately, finding the optimal number of bins is still based on empirical optimization and general rules of thumb. These methods are based on empirical formulas for the uniform optimal bin width by minimizing the integrated mean squared error of the histogram model H(x) as compared to the true and unknown underlying density f(x). Two popular formulas after Freedman and Diaconis [5] and that of Scott [6] were commonly used in which the bin width is inversely proportional to the cubic root of the number of data points in the set, while the proportionality constants are different but depend on the variance and the interquartile range of the data. On the other hand, one of the recent approaches is centered around a data-based method to estimate the optimal uniform bin-width of histograms using an optimization algorithm but not an

explicit empirical formula [4]. The disadvantages include the potentially large number of bins, the uniform bin distribution regardless of weights, and the inconsistency of the histogram with the low-order moments of the true distribution.

In this contribution we took a different approach that is free of the two main drawbacks in the previous work: The histogram's bin width and number of bins. We relaxed the assumption of uniform bin width and the number of the bins are evolved based on the available feasible information in the data set according to Shannon information entropy: $S = -\sum[p_i \ln(p_i)]$ with the constraints that $m_0 = \sum[p_i] = 1$ where $m_0$ is the normalized zeroth moment of the data set and $p_i$ is the $i^{th}$ probability associated with the $i^{th}$ bin of the histogram. Our simple search algorithm for N (Number of data points in the data set) is constrained by the feasible range of the data $R = [x_{min}, x_{max}]$ and the relevance of the probabilities $p_0$ and $p_{N-1}$ of the data in the first and last histogram bins.

## THE VARIABLE ORDER QMOM

As a data compression method, the Quadrature Method Of Moments (QMOM) works based on the calculated moments of the unknown probability density function. In its original formulation, the QMOM algorithm provides closed integrals (and hence moments as special case) of the unknown pdf based on the availability of its low-order moments. It is mainly used to close integrals when the weight function is not known explicitly. Since its introduction by McGraw [7], the QMOM has been the subject of considerable theoretical and applied research during the last two decades. These applications cover wide areas which include aerosols microphysics, nanoparticle formation, turbulent mixing, dispersed phase flows, crystal morphology, cell growth and differentiation and uncertainty propagation through dynamical systems, to name but a few [8]. As an ill-conditioned inverse moment problem, there is no simple and general inversion algorithm to reconstruct the unknown probability histogram from which the moments are calculated or measured. Because of this, the QMOM is rarely used or thought of as a method that can recover the underlying histogram from the available information in the nodes and weights provided by the method itself.

### The QMOM

The QMOM can be mathematically presented as an adaptive data compression method where information about the random signal is converted into a finite set of low-order moments irrespective of the size of the data set. Therefore, given a set of low-order moments $m_r, \mathrm{r} = 0, 1, \ldots 2N_q - 1$ as calculated from a pdf, the QMOM algorithm calculates a set of $N_q$ nodes and weights ($\zeta$, w) with the same principle as that of the Gauss-Legendre quadrature. The domain of the node set $\zeta \in (0,\infty)$ or $\zeta \in [x_{min}, x_{max}]$ depending on the bounds of the random data from which the set $m_r$ is calculated. The QMOM algorithm used in this work is chosen based on the efficient derivation of Upadhyay [9] using the Chebyshev orthogonal polynomials. This can handle large number of nodes that are not necessarily positive when compared to the classical product-difference algorithm (PDA) that was presented by [7]. Actually, Upadhyay [9] showed that the Chebyshev-QMOM (ChebQMOM) is superior to the PDA and is found to be more robust and can be used for a wider class of problems when high number of nodes is required as in our present work.

### The Variable-Order QMOM Algorithm

To proceed in the derivation of the Variable-Order QMOM (VOQMOM), we have to show that the weights ($w_i$, i = 0, 2, ..$N_q$-1) as calculated by the ChebQMOM are nothing more than probabilities of the function f(x;:) that are placed at the corresponding nodal points ($\zeta_i$, i = 1,2, ..$N_q$-1).

$$w_i = \int_{\zeta_{i-1/2}}^{\zeta_{i+1/2}} \mathrm{f(x;:)}dx \tag{1}$$

where ($\zeta_{i-1/2}$, $\zeta_{i+1/2}$) are unknown grid boundaries, which will be referred to as histogram bins. The bins boundaries should satisfy the inequality ($\zeta_{i-1/2} < \zeta_I < \zeta_{i+1/2}$) and the bins are not necessarily equal in width. The estimation of these grid boundaries is given by: $\zeta_{i+1/2} = \frac{1}{2}(\zeta_{i-1} + \zeta_i)$ which are functions only of the low-order moments of the given random signal. To reconstruct the probability histogram $H(\zeta_i)$ with probability ($w_i$) which is placed at ($\zeta_I$), we make use of the integral of the square of errors as defined by [4]:

$$E(H,f) = \int_0^\infty [H(x) - f(x)]^2 dx \tag{2}$$

Since the nodal points ($\zeta_I$) are roots of orthogonal polynomials by definition of ChebQMOM, we can close the integral of Eq.(2) as follows:

$$E(H,f) = \sum_{j=0}^{N_q} \left( w_j f(\zeta_j) - w_j H(\zeta_j) \right) \tag{3}$$

In Eq.(3), we have forced the histogram probability $H(x)$ to have low-order moments that are equal to those of $f(x)$, which is an enough assumption to deem the consistency of the reconstructed histogram w.r.t. the underlying density from which the moments are calculated. Now, for the error in Eq.(3) to vanish at the collocation points ($\zeta_I$), it is sufficient to have:

$$H(\zeta_i) = f(\zeta_i) = \frac{1}{\Delta\zeta_i} \frac{w_i}{\sum w_i} \tag{4}$$

where $\Delta\zeta_i = \zeta_{i+1/2} - \zeta_{i-1/2} = \frac{1}{2}(\zeta_{i+1} - \zeta_{i-1})$.

It is not difficult to show that the order of approximation of $H(\zeta_i)$ in Eq.(4) is $O(\Delta\zeta_i^2)$ because the approximation in Eq.(4) is equivalent to using the midpoint rule to

approximate the integral in Eq,(1). Note that Eq.(4) provides a complete theoretical inversion of the unknown probability density function f($\zeta_i$,:). The order of convergence is proportional to the square of the distance between the (i-
1) and (i+1) bin centers divided by 4.

The question now is how many bins (or quadrature nodes) that are sufficient to resolve the histogram probability $H(x)$ given a set of low-order moments that are computed from the random signal? The answer is nontrivial as it is related to the Shannon information entropy based on the available probabilities ($w_i$):

$$S = -\sum_i w_i \ln(w_i) \quad (5)$$

From Eq.(5), it is evident that as the number of bins used to recover the underlying histogram increases, so does the information entropy, until no more information is required. This implies that adding extra bins will not contribute any relevant information to the histogram, as indicated by very low probability values, signifying the irrelevance of newly added nodes. In the hypothetical limit where the data has zero information entropy (Dirac delta function), the number of bins is reduced to one. In the variable order QMOM realm, the number of bins is determined through a simple search algorithm that optimally assigns nodes through sampling the unknown function or process from which the random data is generated. The algorithm terminates when no more significant information is available for assignment to the newly created nodes, up to a user-defined threshold. If the data originates from a dynamic source with varying mean and variance, the number of bins and its boundaries will adjust itself to reflect the nature of the dynamic data. The complete detailed algorithm is shown in Figure 1. Note that the "while loop" implements the simple search and variable order of the ChebQMOM algorithm where the order is determined if the last computed weight (probability) "$W_{N-1}$" is less than very small, specified tolerance (Tol) and if the maximum and minimum computed nodes are outside their physical range. The algorithm is initiated by providing a vector of computed low-order moments "MOM", initial order "N = 2", Tol, $x_{min}$ and $x_{max}$. The output is a set of computed nodes and weights (ζb, wb). These conditions are found in all simulated cases to correspond to the maximum entropy, as given by Eq.(5). After reaching this point, the entropy "S" begins to decrease because the weights at least on one end of the distribution fall to zero. In Figure 4, the VOQMOM process is illustrated with a real-life sample showing the workflow and the significance of the random signal identification with 22 low-order moments associated with the reconstructed histogram. Also, the plateau of the information entropy is clear near the maximum number of bins. Note that the ChebQMOM is implemented in an efficient way to reduce the numerical round-off errors using MATLAB.

## RESULTS AND DISCUSSION

In this section we will present sample of results using synthetic random signals and real-life case studies. Also, in addition to the static sampling, we present a dynamic case study by solving the simultaneous particle aggregation and growth in a closed batch process.

```
" Input MOM vector of low-order moments, Tol = small "
" ζmin = minimum random variable size "
" ζmax = maximum random variable size "
N ← 2
M_max ← max(MOM)
for r ∈ 0..2·N − 1
  M_r ← MOM_r
(ζ  W) ← ChebQMOM(M,N)
while (M_max·W_0 ∧ M_max·W_N−1) ≥ Tol ∧ N < N_max ∧ (ζ_0 ≥ 0 ∧ ζ_N−1 ≤ ζmax)
  N ← N + 1
  for r ∈ 0..2·N − 1
    M_r ← MOM_r
  (ζt  Wt) ← ChebQMOM(M,N)
N ← N − 1  if  ζ_0 < ζmin ∨ ζ_N−1 ≥ ζmax
for r ∈ 0..2·N − 1
  Mp_r ← MOM_r
(ζb  Wb) ← WNODES(Mp,N)
```

**Figure 1.** Variable-order ChebQMOM algorithm.

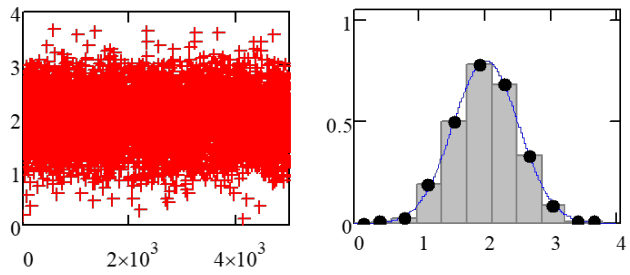



**Figure 2.** Unveiling random signal produced from normal distribution (mean = 2, std = 0.5) using 5000 samples. On the right-hand side is the recoverd probability histogram using 11 bins with 22 low-order moments.

This case study demonstrates how the VOQMOM identifies the data that is coming from a dynamic source with varying mean and variance where the boundaries of the bins move in a dynamic way. In addition to this, similar case studies were conducted on particle breakage in closed and open systems, particle breakage and coagulation, an industrial scale mixer where a light liquid phase is dispersed in water as the continuous phase.

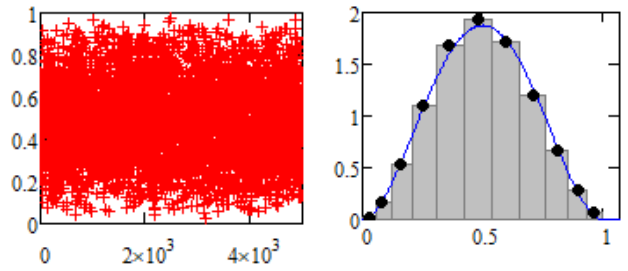


**Figure 3.** Unveiling random signal genrated from a beta distribution (parameters a = 3 and b = 3) using 5000 samples. On the right-hand side is the recovered probability histogram using 11 bins based on 22 low-order moments.

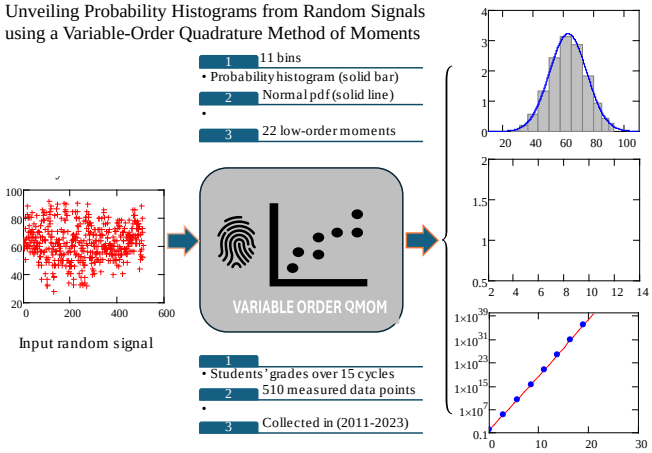



**Figure 4.** Moment-consistent histogram unveiled from students' grades using the Variable-Order QMOM (VOQMOM). To the left is the random signal of students' grades during 15 cycles. In the center is the VOQMOM process, and on the top right is the unveiled density histogram (with 11 bins) compared to the normal pdf with the same mean and variance as the data set. On the right (middle) is the information entropy of the data set as function of number of bins, while on the right bottom is the predicted (filled circles) and original set of moments (solid line).

## Unveiling probability histograms from Synthetic random signals

A sample of three case studies that were synthesized to prove the concept of the VOQMOM using random sampling from normal, beta and lognormal probability density functions (pdf). The random variable "x" is normalized using the relation: $u = \frac{x - x_{max}}{x_{max} - x_{min}}$ and the moments of the sampled data were calculated using the relation $m_r = \frac{1}{N}\sum_{j=0}^{NoSamles} u_j^r \ , r = 0, 1, \ldots \ NoSamples$. This moment transformation results in a moment space that is decreasing exponentially showcasing the irrelevant information contained in the high-order moments which are usually address the information content in the tail of the pdf. Figure 2 (Left) shows the 5000 random samples that are drawn from a normal probability density function with mean = 2, and std = 0.5. The VOQMOM algorithm identified this random signal using the algorithm of Figure 1 which discovered an 11-bin probability density histogram as compared to the original normal pdf showen in Figure 2 (Right). In addition to this, the histogram is consistent w.r.t. 22 low-order moments of the original data. Similarly, Figure 3 shows the results of identifying 5000 random samples drawn from the beta probability density function by the VOQMOM ending with an 11-bin histogram. In Figure 5, the VOQMOM is challenged by 5000 random samples that are drwan from the unsymmetrical log pdf (mean = 1.349 and std = 0.419). Again, with 11 discovered bins, the unveailed probability density histogram is very close to the orignal pdf.

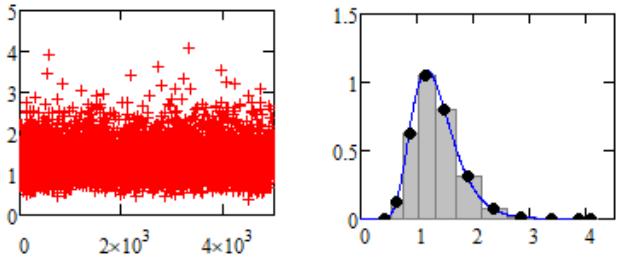


**Figure 5.** Unveiling random signal genrated from a lognormal probability density function (mean = 1.349 and std = 0.419) using 5000 samples. On the right-hand side is the recovered probability histogram using 11 bins based on 22 low-order moments.

**Table 1:** Unveiled probability histograms using the VOQMOM based on different real-life random data.

| Case | Description | No of bins |
|---|---|---|
| 1 | mean maximum air to surface temperature in Amman | 13 |
| 2 | adult diastolic blood pressure | 11 |
| 3 | abalone total weight data | 12 |
| 4 | students' grades for 15 cycles. | 11 |
| 5 | mean wind speed data | 12 |
| 6 | droplet size distribution data | 11 |

From these results, it is evident that the VOQMOM discovers incrementally new nodes and decides to stop when the individual probability carried by the terminal nodes (first & last nodes) becomes less than a user specified tolerance (Tol = 10-12). Also, the physical bounds placed on the terminal nodes is checked accordinglly where the probabilities of the terminal nodes approach zero when the physical bounds are exceeded.

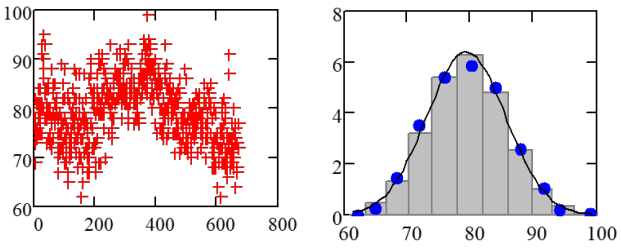



**Figure 6.** Unveiling random signal based on measured diastolic blood pressure of a male adult (age 50-56) using 671 samples. On the right-hand side is the recoverd probability histogram using 11 bins based on 22 low-order moments as compared to the normal pdf.

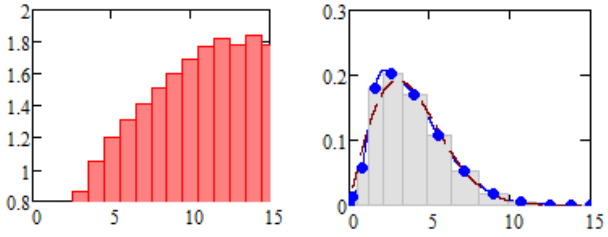



**Figure 7.** Unveiling random signal based on measured mean wind speed [10] using ~35000 samples. On the left-hand side is the information entropy as function of bins number and on the right-hand side is the recoverd probability histogram using 12 bins based on 24 low-order moments., The dashed line is the Weibull pdf with shape and scaling parameters calculated based on the correlations from [10].

## Unveiling probability histograms from real-life random signals

Having validated the concept of the simple search algorithm of the VOQMOM using random signals from a reference pdf, we demonstrate the validity of the method using real-life data sets. Figure 6 (Left) shows 671 random measurements of diastolic blood pressure for an adult male (50-56 years old) during a time span of 6 years. The search algorithm of the VOQMOM identified an 11-bin probability histogram behind these random data set as shown in Figure 6 (Right). The histogram is consistent w.r.t. 22 low order moments. Comparing this unveiled histogram to the normal pdf, it is clear that the data is well presented by this pdf with mean and standard deviation as those of the original data. In the second real case study, a random measured data set of size ~ 35000 which represents mean wind speed data [10] as shown in Figure 7. On the left-hand side of this figure is the information entropy as function of bins number. It is clear when new node or bin is added, the information entropy increases until a point where the probabiltiy of the added node approaches zero. At this point we observed that the entropy drops slightly in all the investigated case studies signifiying the termination of the algorithm at the maximum possible node number. On the right-hand side of Figure 7 is the recoverd probability histogram using 12 bins based on 24 low-order moments. Also, the results are compared to the Weibull pdf (dashed line) with shape and scaling parameters calculated based on the correlations derived by Shu and Jesson [10] using mean wind speed data. It is clear that this data set is well represented by the Weibull pdf. The last case study consists of a data set of abalone total weights in mg that is measured from 4177 individuals [12]. Figure 8 (Left) shows the increase in the information entropy until a flat plateau is reached near the best number of bins (12). The unveiled histogram from these random data is shown in Figure 8 (Right) and is compared to the Weibull distribution with shape and scaling factors that are calculated by correlations from [10]. It is noteworthy to mention here that the optimal number of uniform bins obtained from this data set was found to be 14 using an optimization algorithm of Knuth [4]. Furthermore, Table 1 shows many cases studies which are based on real-life experience with main observation that the number of bins predicted by the VOQMOM ranges from 11 to 14.

## Unveiling probability histograms by solving the population balance equation

In this case study we tested the VOQMOM for the dynamic evolution of simultaneous particle growth and coagulation under constant coagulation rate and growth velocity given by $G(x) = G_0 x/3$ . From the initial condition $f(x) = 3x^2 \exp(-x^3)$, the number of bins is found to be 11. After 10 seconds of simulation time using Heun's method with a time step of 0.025 seconds and $\Lambda$ = 0.75 (ratio of coagulation to growth rate), the number of bins discovered by the VOQMOM is 13. Figure 9 shows the normalized histogram (w.r.t. zeroth moment) at t = 0 (Left) and at t = 10 seconds (Right). All the 22 low-order moments were calculated with high accuracy when compared to the analytical solution of Gelbard and Seinfeld [11]. In spite of the growth of the particle size around 20 times of its initial value, the solution at t = 10 s is free of numerical diffusion due to the integral representation of the growth term thanks to the QMOM. Note that the integral source term in the population balance equation is integrated with a variable order QMOM at each instant of time. The CPU time using Heun's method for this case is in the order of 5 seconds using a state of the art msi-laptop (Intel(R) Core(TM) i7, CPU at 2.6 GHz & 8 GB RAM). The dominance of coagulation over particle growth is manifested by the increase of information entropy from 1.68 to 1.77 that is reflected by the increase of nodes from 11 to 13.

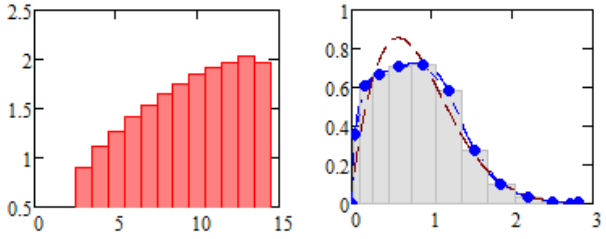



**Figure 8.** Unveiling random signal based on measured abolane total weight in mg using 4177 samples. On the left-hand side is the information entropy as function of bins' number and on the right-hand side is the recoverd probability histogram using 12 bins based on 24 low-order moments as compared to Weibull pdf (dashed line) with shape and scaling parameters calculated based on the correlations of Shu and Jesson [10].

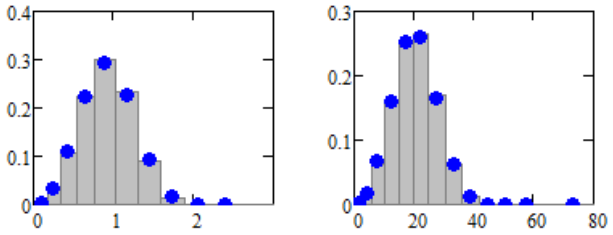



**Figure 9.** Particle growth & coagulation with $\Lambda$ = 0.75 in a simplified batch crystallizer. Left: Normalized histogram at t = 0 with 11 bins. Right: Normalized histogram as compared to the exact ones (filled circles) with number of moving bin centres = 13 at t = 10 s.

## SUMMARY AND CONCLUSIONS

The VOQMOM is a non-parametric method that can be used to identify general probability histograms by processing big random data which is drawn from real-life problems. It works through compressing a given set of random data into low-order moments, which are then processed to encode the underlying pdf from which the data is generated. It uses a simple linear search algorithm coupled with ChebQMOM and needs only a sufficient number of nodes and weights to work with negligible computational cost. Using different analytical and practical case studies, it is found that 10 to 14 bins were sufficient to reconstruct the pdf with a local accuracy of $O(\Delta\zeta_i 2)$. The algorithm terminates when no more informaiton is available to assign to the terminal nodes.

## REFERENCES

1. Thibault, E., Chioua, M., McKay, M., Korbel, M., Patience, G. S. and Stuart, P. R. Experimental methods in chemical engineering: Data processing and data usage in decision-making. Can. J. Chem. Eng. 101: 6055-6078 (2023).
2. Sarramaigna, P., Besbes, M., Zolghadri, M. and Sadoul, P. O. Modelling Industry 4.0 transformation: A comparative approach between academic literature and French companies' transformation cases. Procedia CIRP 120:786-791 (2023).
3. Peterson, L., Gosea, I. V., Benner, P. and Sundmacher, K. . Digital twins in process engineering: An overview on computational and numerical methods. Computers & Chemical Engineering 193:108917 (2025).
4. Knuth, K. H. Optimal data-based binning for histograms and histogram-based probability density models. Digital Signal Processing, 95: 102581 (2019).
5. Freedman, D. and Diaconis, P. On the Histogram as a Density Estimator: L 2 Theory Zeitschrift für Wahrscheinlichkeitstheorie und Verwandte Gebiete 57: 453–476 (1981).
6. Scott, D. W. Sturges' rule. Wires Computational Statistics 1: 303–306 (2009).
7. McGraw, R. (1997). Description of aerosol dynamics by the quadrature method of moments. Aerosol Sci. & Tech. 27:255-265.
8. Attarakih, M., Bart, H.-J. and Abu-Khader, M. On the solution of the population balance equation: From global to local constrained maximum entropy method. Chem. Eng. Sci. 209:115168 (2019).
9. Upadhyay, R. R. Evaluation of the use of the Chebyshev algorithm with the quadrature method of moments for simulating aerosol dynamics. Journal of Aerosol Science 44:11-23 (2012).
10. Shu, Z. R. and Jesson, M. Estimation of Weibull parameters for wind energy analysis across the UK. J. Renewable & Sustainable Energy 13: 023303 (2021).
11. Gelbard, F. and Seinfeld, J. H. Numerical solution of the dynamic equation for particulate systems. J. Comp. Phys. 28:357-375 (1978).
12. Newman, S. Hettich, C.L. Blake, C.J. Merz, UCI repository of machine learning databases, http://www.ics .uci.edu /~mlearn /MLRepository.html (1998).

© 2025 by the authors. Licensed to PSEcommunity.org and PSE Press. This is an open access article under the creative commons CC-BY-SA licensing terms. Credit must be given to creator and adaptations must be shared under the same terms. See https://creativecommons.org/licenses/by-sa/4.0/

Systems & Control Transactions

**Research Article - Peer Reviewed Conference Proceeding**
ESCAPE 35 - European Symposium on Computer Aided Process Engineering
Ghent, Belgium. 6-9 July 2025
Jan F.M. Van Impe, Grégoire Léonard, Satyajeet S. Bhonsale,
Monika E. Polańska, Filip Logist (Eds.)

PSE PRESS

# Sensitivity Analysis of Key Parameters in LES-DEM Simulations of Fluidized Bed Systems Using Generalized Polynomial Chaos

**Radouan Boukharfane[a]*, Nabil El Moçayd[b]**

[a] Mohammed VI Polytechnic University (UM6P), College of Computing, Benguerir, Morocco
[b] Mohammed VI Polytechnic University (UM6P), College of Agriculture and Environmental Sciences, Benguerir, Morocco
* Corresponding Author: radouan.boukharfane@um6p.ma

## ABSTRACT

In applications involving fine powders and small particles, the accuracy of numerical simulations, particularly those employing the Discrete Element Method (DEM) to predict granular material behavior, can be significantly affected by uncertainties in critical parameters. These uncertainties include the coefficients of restitution for particle-particle and particle-wall collisions, viscous damping coefficients, and other related factors. In this study, we use stochastic expansions based on point-collocation non-intrusive polynomial chaos to perform a sensitivity analysis of a fluidized bed system. We treat four key parameters as random variables; each assigned a specific probability distribution over a designated range. This uncertainty is propagated through high-fidelity Large Eddy Simulation (LES)-DEM simulations to statistically quantify its impact on the results. To effectively explore the four-dimensional parameter space, we analyze a comprehensive database comprising over 1,200 simulations. Notably, our findings reveal that variations in the particle and wall Coulomb friction coefficients have a more pronounced influence on streamwise particle velocity than variations in the particle and wall normal restitution coefficients.

**Keywords**: CFD-DEM, gas-solid fluidization, global sensitivity, gPC, linear spring-dashpot model, spring stiffness.

## INTRODUCTION

Gas-solid fluidized bed reactors are widely used in energy and chemical conversion processes due to their high heat and mass transfer rates, thermal homogeneity, and operational flexibility. Despite these advantages, designing and optimizing such reactors remains challenging due to complex multiphase interactions and limited diagnostic capabilities under extreme conditions.

Computational Fluid Dynamics coupled with the Discrete Element Method (CFD-DEM) has emerged as a powerful tool for studying these systems, offering detailed particle-scale resolution but at a high computational cost. CFD-DEM simulations rely on model parameters such as spring stiffness, restitution, and friction coefficients, which significantly impact flow behavior. However, these parameters are often uncertain due to experimental limitations and material variability. While previous studies have analyzed their influence, they typically consider only one or two parameters at a time, limiting the broader understanding of parametric interactions. Given the nonlinear and highly coupled nature of fluidized bed hydrodynamics, a systematic global sensitivity analysis is essential. This study aims to identify critical CFD-DEM model parameters affecting fluidized bed hydrodynamics. Using a statistically designed set of CFD-DEM simulations, we explore parameter sensitivities through uncertainty quantification techniques. The analysis is based on a lab-scale rectangular fluidized bed containing approximately 9,240 particles. A total of 1,200 simulations are conducted using high-performance computing resources, making this one of the most extensive sensitivity analyses of dense-phase particulate flows. The results provide insights into the dominant parameters governing bubble dynamics and particle interactions, contributing to improved predictive capabilities of CFD-DEM models.

Stochastic approaches have been increasingly used

in recent years for uncertainty quantification and sensitivity analysis in numerical flow simulations [3,4]. In this framework, three CFD-DEM input parameters-spring stiffness, normal damping, and friction coefficient-are treated as random variables with prescribed probability distributions. The uncertainty is then propagated through the computational model to statistically quantify their effect on the results. To reduce computational costs, a surrogate model is employed to construct a continuous response surface in the parameter space. A widely adopted non-intrusive approach is the generalized polynomial chaos (gPC) expansion, which represents the quantities of interest as spectral expansions in terms of orthonormal polynomial bases associated with the random parameters. While gPC has been extensively applied to turbulent flow simulations, it has been rarely used in gas-solid fluidized bed simulations. To the best of our knowledge, this study is among the first to employ this approach in such a context, providing new insights into uncertainty quantification in multiphase flow systems.

## STOCHASTIC MODELING AND METHODS

Instead of resorting to Monte Carlo simulations for uncertainty quantification, stochastic expansions based on point-collocation non-intrusive polynomial chaos are used to mitigate computational expenses. The point-collocation strategy involves constructing a surrogate model, employing a least squares approach (i.e., polynomial response surface), by using CFD-DEM output obtained at several Latin Hypercube sample points for uncertainty propagation. In most practical applications, the stochastic response function $M(\xi)$ of, for example, the time-averaged quantity like bed height, pressure loss, distribution of voidage at a specified height in the flow field, which are referred to as the Quantity of Interest (QoI), are function of $m$ independent stochastic variables $\xi_i$ that form the vector $\xi = [\xi_1, \cdots, \xi_m]$. Each random variable $\xi_i$ is characterized by a probability density function (PDF), $w_i(\xi_i)$ in the domain $E_i$. The main idea in this work is to estimate the effect of $\xi$ on the statistics of $M(\xi)$. To do this, a complete probability space $P = (\Omega, \Sigma, dP)$ is defined, where $\Omega$ refers to the set of random events and the probability measure $dP$ is characterized by the $\sigma$-algebra $\Sigma$. The vector $\xi$ follows the probability density function $W = \prod_{i=1}^{m} w_i(\xi_i)$, defined in the domain $E = \prod_{i=1}^{m} E_i$. This stochastic space is spanned by a polynomial basis $\Psi = \{\Psi_0, \Psi_1, \dots\}$ which is orthogonal to $W$ with respect to the inner product $\langle \Psi_j, \Psi_k \rangle = \int_E \Psi_j \Psi_k W d\xi = \delta_{jk} \langle \Psi_j, \Psi_j \rangle$.

The polynomial basis is normalized so that $\langle \Psi_j, \Psi_j \rangle = 1$. When $m > 1, \Psi$ is defined by the tensor product of the unitary polynomials $\psi^{(i)}$, as in $\Psi = \otimes_{i=1}^{m} \psi^{(i)} = \{\Psi_0, \Psi_1, \dots\}$. The base is truncated to a finite number of polynomials by limiting the order of $\Psi_j$ to $p$. In that case, the Quantity of Interest $M$ is written in spectral form as

$$\mathcal{M}(\xi) = \sum_{i=0}^{P} c_{(i)} \Psi_i(\xi)$$

In theory, this series is infinite, but for practical implementation of the polynomial chaos expansions, it is truncated and discretely summed over several output modes, $(P+1)$.

Two parameters determine the number of samples required to generate the response surface: the number of uncertain variables, $n$ and the order of the response surface polynomial, $p$. The total number of samples$N_s$ is then expressed as $N_s = (P+1) = (n+p)!/n!\,p!$.

The Point-Collocation method commences by replacing a stochastic response or random function with its polynomial chaos expansion. Subsequently $N_s$ vectors are selected in random space, and the deterministic code (the CFD flow solver in this case) is evaluated at these points. Finally, a linear system of $N_s$ equations is formulated and solved for the spectral modes of the random variables. Due to the bounded nature of epistemic input uncertainties, Legendre polynomials were used in this study as the basis functions. Additional insights into polynomial chaos theory are provided by Ghanem and Spanos (2003). Sobol indices (global nonlinear sensitivity indices) were utilized to rank the relative contributions of each closure coefficient to the total uncertainty in the output quantities of interest. Sobol indices can be derived via Sobol Decomposition, a variance-based global sensitivity analysis method. This derivation utilizes the polynomial chaos expansion coefficients. First, the total variance, D, can be expressed in terms of the PCE as $D = \sum_{j=1}^{P} c_{(j)}^2 \langle \Psi_j^2(\xi) \rangle$. Then, as demonstrated in [2], the total variance can be decomposed as

$$\mathrm{D} = \sum_{i=1}^{n} \mathrm{D}_i + \sum_{1 \le i < j \le n}^{n-1} \mathrm{D}_{i,j} + \sum_{1 \le i < j < k \le n}^{n-2} \mathrm{D}_{i,j,k} + \cdots + \mathrm{D}_{1,2,\dots,n}$$

where the partial variances $(D_{i_1,\dots,i_s})$ are given by:

$$\mathrm{D}_{i_1,\dots,i_s} = \sum_{\beta \in \{i_1,\dots,i_s\}} c_{(\beta)}^2 \left\langle \Psi_\beta^2(\xi) \right\rangle, \quad 1 \le i_1 < \dots < i_s \le n$$

Then the Sobol indices $(S_{i_1 \cdots i_s})$ are defined as

$,S_{i_1 \cdots i_s} = \frac{D_{i_1,\dots,i_s}}{D}$, which satisfy the following equation:

$$\sum_{i=1}^{n} \mathrm{S}_i + \sum_{1 \le i < j \le n}^{n-1} \mathrm{S}_{i,j} + \sum_{1 \le i < j < k \le n}^{n-2} \mathrm{S}_{i,j,k} + \cdots + \mathrm{S}_{1,2,\dots,n} = 1$$

The Sobol indices provide a sensitivity measure due to the individual contribution from each input uncertain variable $(S_i)$, as well as the mixed contributions $(\{S_{i,j}\}, \{S_{i,j,k}\}, \cdots)$. As demonstrated by [5], the total (combined) effect $(S_{T_i})$ of an input parameter $i$ is defined as the summation of the partial Sobol indices that include the particular parameter $S_{T_i} = \frac{L_i}{D_{i_1,\dots,i_s}} D$, where$L_i = \{(i_1, \cdots, i_s) : \exists k, 1 \le k \le s, i_k = i\}$. From these formulations, it is evident that the Sobol indices can be utilized to

provide a relative ranking of each input uncertainty to the overall variation in the output, considering nonlinear correlations between input variables and output quantities of interest.

## MODELING PARTICLE DYNAMICS IN THE CFD-DEM FRAMEWORK

In the Computational Fluid Dynamics-Discrete Element Method (CFD-DEM) framework, the motion of individual particles is described by Newton's second law, which is expressed as follows:

$$m\frac{du_p}{dt} = \mathbf{f}^{\text{col}} + \mathbf{f}^{f\to p} + mg,\; I\frac{d\psi}{dt} = \mathbf{T}^{\text{col}} + \mathbf{T}^{f\to p}$$

where $u_p$ denotes the particle velocity, $t$ represents time, $m$ is the particle mass, $f^{\text{col}}$ represents contact forces resulting from particle-particle or particle-wall collisions, $f^{f\to p}$ indicates fluid-particle interaction forces (e.g., drag and lift forces), and $g$ denotes the gravitational force. Similarly, $I$ and $\psi$ represent the moment of inertia and angular velocity of the particle, respectively, while $T^{\text{col}}$ and $T^{f\to p}$ denote the torques due to contact forces and fluid-particle interactions, respectively.

The particles are modeled as soft spheres with inter-particle contacts represented by an elastic spring and a viscous dashpot to compute collision forces and torques. In this framework, the collision force $f^{\text{col}}$ acting on particle $i$ is computed as the sum of all pairwise forces $f_{j\to i}^{\text{col}}$ exerted by the $N_p$ particles and $N_w$ walls in contact. As particles and walls are treated similarly during collisions, the index $j$ refers to both; thus, $f^{\text{col}} = \sum_{b=1}^{N_p+N_w} f_{j\to i}^{\text{col}}$, with $f_{j\to i}^{\text{col}} = f_{n,j\to i}^{\text{col}} + f_{t,j\to i}^{\text{col}}$. The normal and tangential contact forces $f_{n,j\to i}^{\text{col}}$ and $f_{t,j\to i}^{\text{col}}$ are determined as follows:

$$f_{n,j\to i}^{\text{col}} = \begin{cases} -\kappa_n \delta_{ij} n_{ij} - 2\gamma_n m_{ij} u_{n,ij}, & \text{if } \delta_{ij} > 0 \\ 0, & \text{otherwise} \end{cases}$$

where $n_{ij} = (x_j - x_i)/\|x_j - x_i\|$ is the unit normal vector from particle $i$ towards particle $j, \delta_{ij} = r_i + r_j - (x_i - x_j)\cdot n_{ij}$ represents the overlap between particles $i$ and $j, m_{ij}$ is the effective mass, $u_{n,ij} = \left((u_{p,i} - u_{p,j})\cdot n_{ij}\right) n_{ij}$ is the normal component of relative velocity, $u_{t,ij} = u_{ij} - u_{n,ij}$ is the tangential component of relative velocity, and $t_{ij} = u_{t,ij}/\|u_{t,ij}\|$ is the unit tangential vector. In the case of a particle-wall collision, the wall is considered as a particle with infinite mass and null radius. This model requires three user-defined parameters: $\kappa_n, \gamma_n$, and $\mu_{\text{friction}}$, representing the spring stiffness, normal vidamping, and friction coefficient of the $i-j$ binary system, respectively. The viscous damping coefficients are computed as

$$\gamma_n = \frac{2\sqrt{m_p k_n} ln\ e_n}{\sqrt{\pi^2 + ln^2\ e_n}}$$

where $e_n$ is the normal restitution coefficient. The other terms involved in the computation of DEM can be found in [1], as the focus of this work is to study the uncertainties of the soft sphere model.

## DATABASE

**Table 1**: Parameters of DEM-LES simulations

| | |
|---|---|
| Fluid phase | |
| Fluid density $\rho_f$ [kg/m$^3$] | 1.2 |
| Fluid viscosity $\mu$ [Pa·s] | $1.8 \times 10^{-5}$ |
| Superficial gas velocity $u_\infty$ [m/s] | 0.6 – 0.9 |
| Solid phase | |
| Number of particle | 9240 |
| Particle diameter $d_p$ [mm] | 1.20 |
| Particle density $\rho_p$ [kg/m$^3$] | 1000 |
| Inter-particle restitution coefficient $\epsilon_{\text{dry}}$ | [0.0,1.0) |
| Particle-wall restitution coefficient $\epsilon_{\text{dry}}$ | [0.0,1.0] |
| Inter-particle restitution coefficient $\mu_c$ | [0.0,1.0] |
| Particle-wall friction coefficient $\mu_c$ | [0.0,1.0] |
| Geometry and Mesh | |
| Bed $L_x \times L_y \times L_z$ [mm$^3$] | $44 \times 288 \times 10$ |
| Grid number $\mathcal{N}_x \times \mathcal{N}_y \times \mathcal{N}_z$ | $16 \times 120 \times 4$ |
| Non-dimensional parameters | |
| Particle Reynolds number $\mathcal{R}\epsilon_p$ | 48, 72 |
| Stokes number $\mathcal{S}t$ | 2.66 – 4 |
| Archimedes number $\mathcal{A}r$ | $6.27 \times 10^4$ |
| Galileo number $\mathcal{G}a$ | 250.41 |

Simulations of a fluidized bed have been performed, and the parameters considered in this study are reported in **Table 1**.

Since the inter-particle restitution coefficient, particle-wall restitution coefficient, and particle-wall friction coefficient are assumed to represent either uncontrolled variations in experiments or unknown perturbations in the DEM model, there is no a priori knowledge of their probability density function. For this reason, the simplest and most general PDF is chosen to describe the distribution of the investigated parameters. Specifically, the PDFs are assumed to be uniform. Given this choice, the Legendre polynomial family is employed for the spectral projection.

The solver used to perform these simulations has been extensively described and validated in previous studies. The reader is referred to [1] for further details.

## RESULTS AND DISCUSSION

In the present simulations of fluidized bed systems, achieving consistency with experimental measurements can be challenging, as illustrated in **Figure 1.** Arbitrary variations in input parameter values may result in significant discrepancies. To address this, we propose an

improved calibration approach by analyzing the sensitivity of the simulations to uncertainties associated with different input parameter values.

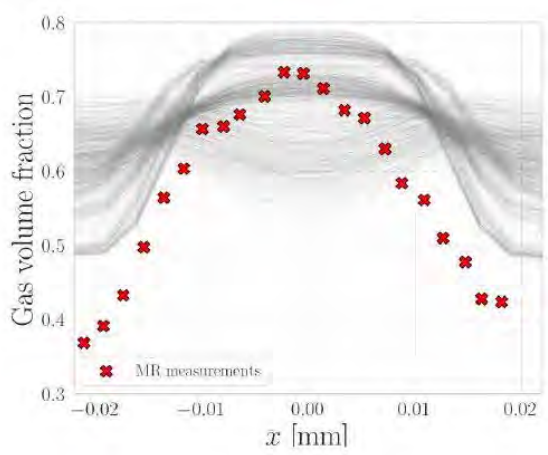



**Figure 1:** Comparison between different set of simulation of fluidized bed and measurements of [8]. Each simulations use different set of values for the input parameters.

We now present the results of the surrogate models alongside the sensitivity analysis in **Figure 2-5**.

As previously outlined, the model aims to simulate four key variables, which are considered our target variables and are believed to carry the uncertainty. Initially, the polynomial degree for the Polynomial Chaos Expansion (PCE) is set to 5. This choice is motivated by the relatively low computational requirements, in terms of the number of simulations to be performed, while still delivering good performance for the surrogate model. One of the main advantages of PCE is its ability to estimate the leave-one-out error analytically.

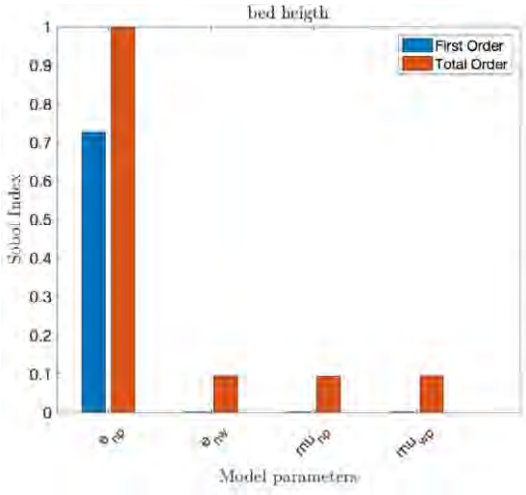



**Figure 2**: Sobol' indices (First order in blue and Total Order in orange) for the four quantities of interest in the model: mean bed height

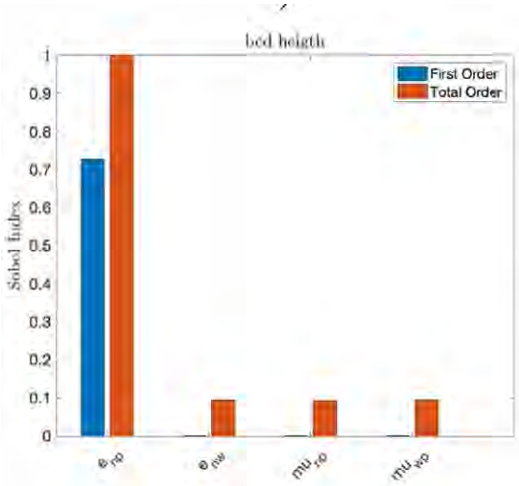



**Figure 3**: Sobol' indices (First order in blue and Total Order in orange) for the four quantities of interest in the model: standard deviation of bed height

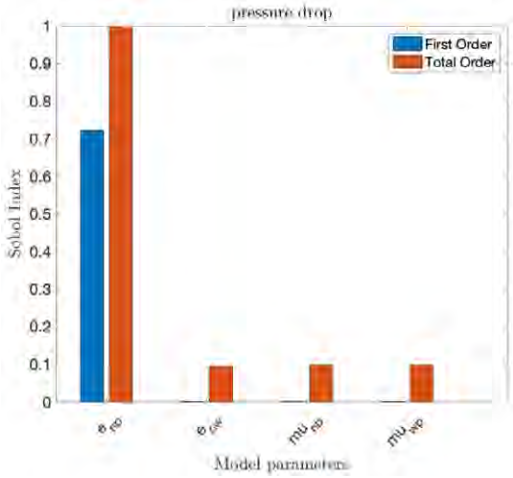



**Figure 4**: Sobol' indices (First order in blue and Total Order in orange) for the four quantities of interest in the model: mean pressure drop.

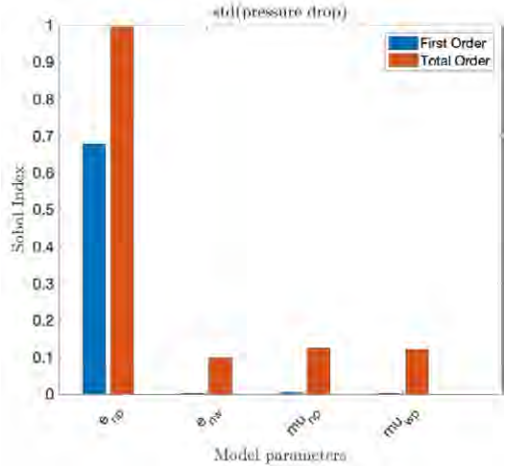



**Figure 5**: Sobol' indices (First order in blue and Total Order in orange) for the four quantities of interest in the model: standard deviation of pressure drop.

In our case, the error value is on the order of $10^{-5}$. This indicates that the error introduced by the polynomial truncation, as well as that arising from the coefficient estimation, is acceptable, thereby enabling a careful sensitivity analysis of the model parameters. Subsequently, using the developed PCE, a sensitivity analysis is carried out following the expansion methodology outlined in the previous section. The results are presented in Figure 2. For each of the quantities of interest, the Sobol' indices for each model parameter are estimated, with both first order and total order indices considered. Our results show that the sensitivity indices exhibit a similar shape across all quantities of interest. Notably, the variable $e_{np}$ is primarily responsible for driving the uncertainty. However, total-order Sobol' indices indicate that uncertainty can also be attributed to the interactions between the four variables. While most of the uncertainty is explained by $e_{np,}$ interactions with the other variables can account for up to 40% of the total uncertainty. These findings highlight the challenges encountered in previous studies when attempting to accurately calibrate such models to experimental data.

## ACKNOWLEDGEMENTS

Please acknowledge your funders in this section, with grant or funding numbers as appropriate. Note that most funding agencies require this.

## REFERENCES

1. F. E.-Z. El Hamra, R. Boukharfane, 2023. Development and assessment of algorithms for DEM-LES simulations of fluidized bed. Particuology 83, 241–257.
2. Sudret, B. (2008). Global sensitivity analysis using polynomial chaos expansions. Reliability engineering & system safety, 93(7), 964-979.
3. M. Elkarii, R. Boukharfane, S. Benjelloun, C. Bouallou, N. El Moçayd 2023a. Global sensitivity analysis for phosphate slurry flow in pipelines using generalized polynomial chaos. Physics of Fluids 35 (6).
4. M. Elkarii, R. Boukharfane, S. Benjelloun, C. Bouallou, N. El Moçayd, 2023b. A gpc-based global sensitivity analysis for phosphate slurry flow in pipelines. In: Computer Aided Chemical Engineering. Vol. 52. Elsevier, pp. 367–373. S.
5. Ghaffari, T. Magin, G. Iaccarino, 2010. Uncertainty quantification of radiative heat flux modeling for titan atmospheric entry. In: 48th AIAA aerospace sciences meeting including the new horizons forum and aerospace exposition. p. 239.
6. R. G. Ghanem, P. D. Spanos, 2003. Stochastic finite elements: a spectral approach. Courier Corporation.
7. C. R. Muller, D. J. Holland, A. J. Sederman, S. A. Scott, J. S. Dennis, L. F. Gladden, 2008. Granular temperature: ¨ comparison of magnetic resonance measurements with discrete element model simulations. Powder Technology 184 (2), 241–253.
8. Müller, C. R., Holland, D. J., Sederman, A. J., Scott, S. A., Dennis, J. S., & Gladden, L. F. (2008). Granular temperature: comparison of magnetic resonance measurements with discrete element model simulations. Powder Technology, 184(2), 241-253.

© 2025 by the authors. Licensed to PSEcommunity.org and PSE Press. This is an open access article under the creative commons CC-BY-SA licensing terms. Credit must be given to creator and adaptations must be shared under the same terms. See https://creativecommons.org/licenses/by-sa/4.0/



Systems & Control Transactions

**Research Article - Peer Reviewed Conference Proceeding**
ESCAPE 35 - European Symposium on Computer Aided Process Engineering
Ghent, Belgium. 6-9 July 2025
Jan F.M. Van Impe, Grégoire Léonard, Satyajeet S. Bhonsale,
Monika E. Polańska, Filip Logist (Eds.)

PSE PRESS

# An Efficient Convex Training Algorithm for Artificial Neural Networks by Utilizing Piecewise Linear Approximations and Semi-Continuous Formulations

**Ece S. Köksal[a,b], Erdal Aydın[a], and Metin Türkay[c,d,*]**

[a] Koc University, Department of Chemical and Biological Engineering, Istanbul, Sariyer, Turkey
[b] Turkish Petroleum Refineries Corporation, Kocaeli, Korfez, Turkey
[c] Koc University, Department of Industrial Engineering, Istanbul, Sariyer, Turkey
[d] SmartOpt, Istanbul, Turkey
* Corresponding Author: mturkay@ku.edu.tr.

## ABSTRACT

Artificial neural networks are widely used as data-driven models for capturing complex, nonlinear systems. However, suboptimal training remains a significant challenge due to the nonlinearity of activation functions and the reliance on local solvers, which makes achieving global solutions difficult. One solution involves reformulating activation functions as piecewise linear approximations to convexify the problem, though this approach often requires substantial CPU time. This study demonstrates that a tailored branch-and-bound algorithm can effectively address these challenges by efficiently navigating the solution space using linear relaxations. The proposed method achieves minimal training error, offering a robust solution to the training bottleneck. Unlike traditional mixed-integer programming approaches, which often struggle to converge within reasonable CPU times, the SOSX algorithm shows superior scalability, with computational demand growing almost linearly rather than exponentially as problem size increases. Experiments on datasets with the same dimensionality confirm that the algorithm's efficiency is not specific to a particular dataset, as it demonstrates consistent CPU time trends across multiple datasets.

**Keywords**: artificial neural networks, piecewise linear functions, convex formulation, mixed-integer linear programming, computational complexity.

## INTRODUCTION

A mechanistic process model relies on physical laws governing the system, but developing such models is in general time-consuming and challenging. In contrast, data-driven models offer a straightforward alternative, especially for representing nonlinear and complex systems. Artificial neural networks (ANNs), inspired by human brain neurons, are a popular type of data-driven models. Among them, feedforward neural networks (FNNs) are simpler, with data flowing in one direction from the input to the output layer, comprising an input layer, output layer, and user-defined hidden layers connected via activation functions.

Common activation functions include Rectified Linear Unit (ReLU), hyperbolic tangent ($tanh$), and sigmoid. ReLU is piecewise linear, while tanh and sigmoid are nonlinear and symmetric. These functions introduce nonlinearities, making ANN training a non-convex optimization problem classified under nonlinear programming (NLP). This can result in issues like underfitting, overfitting, or suboptimal solutions [1]. A major challenge is the reliance on local solvers, as global solvers often struggle to converge or require excessive CPU time due to nonlinearities in the activation function [2].

One way to address the non-convexity of neural network training is by using the piecewise linear (PWL) representation of nonlinear activation functions. Various methods for PWL formulations have been explored such as defining binary variables [3] or special ordered set variables [4]. This transforms the problem from an NLP formulation to a mixed-integer linear programming (MILP) formulation. In addition to these methods, Keha et al. proposed “SOSX variables,” which eliminate the need for

binary variables and enable PWL functions to be modelled with linear programming (LP) subproblems by modifying branching algorithms, yielding equivalent solutions to special ordered set type II (SOS2)-based MILP formulations [5].

Many studies have focused on optimizing ReLU-based neural networks, utilizing their naturally piecewise linear structure. Research on PWL ReLU-trained neural networks has primarily aimed at reducing computational time [6-8]. Beyond ReLU-based formulations, several studies have explored MILP formulations incorporating hyperbolic tangent activation functions in ANNs [9-10]. Similarly, Sildir and Aydin utilized the PWL representation of the hyperbolic tangent function during training with feature selection, effectively reducing the risk of suboptimal training and enhancing test accuracy [11]. However, a key limitation of this approach lies in the MILP formulation. As the number of features, neurons, and hidden layers in the NN increases, the number of binary variables grows exponentially, significantly increasing CPU time. This challenge underscores the need for more efficient MILP formulations to reduce computational demands while maintaining performance. Notably, studies addressing MILP-based neural network training remain relatively limited in the literature.

This work employs PWL approximations for the hyperbolic tangent activation function in a single-layer FNN [10-11] at the training phase. To address computational complexity, the approach by Keha et al. [5] is used to transform the MILP training problem into sequential LP problems by modifying the branching scheme, offering significant computational benefits. The novelty of this research lies in formulating the FNN training problem entirely as specially tailored LP subproblems.

## METHODOLOGY

A feed-forward, fully connected artificial neural network with an identity function as the output layer can be expressed as:

$$\hat{y} = w_2 f(w_1 u + b_1) + b_2 \quad (1)$$

where $\hat{y}$ is the predicted output, $u$ is the input, $w_1$, $w_2$, $b_1$ and $b_2$ are the weights and biases for the hidden and output layers, respectively. Typically, during training, mean squared error (MSE) is minimized. The objective function is given by:

$$\min_{w_1,w_2,b_1,b_2} MSE = \frac{1}{N}\sum_{i=1}^{N}(w_2 f(w_1 u_i + b_1) + b_2 - y_i)^2 \quad (2)$$

where $N$ is the number of training data points and $y_i$ is the actual $i^{th}$ output value. To simplify the optimization and avoid the nonlinearity introduced by the square term, the mean absolute error (MAE) can be minimized instead. The objective function then becomes:

$$\min_{w_1,w_2,b_1,b_2} MAE = \frac{1}{N}\sum_{i=1}^{N}|w_2 f(w_1 u_i + b_1) + b_2 - y_i| \quad (3)$$

However, the absolute value introduces challenges for gradient-based optimization methods due to non-smoothness and non-differentiability at certain points. To address this, a linearized form of the absolute value can be used:

$$\min_{w_1,w_2,b_1,b_2} |\emptyset'| = \frac{1}{N}\sum_{i=1}^{N}|w_2 f(w_1 u_i + b_1) + b_2 - y_i| \quad (4a)$$

$$\emptyset' \le |\emptyset'| \quad (4b)$$

$$-|\emptyset'| \le \emptyset' \quad (4c)$$

Here, $|\emptyset'|$ is the modified objective function. For simplicity, the weight matrix of the output layer, $w_2$, can be extracted during regular training as $w_2^*$ which is an extreme machine learning procedure [11-12].

Hyperbolic tangent (tanh) is a commonly used activation function in neural network training. To mitigate issues caused by its nonlinearity, several studies employ PWL approximations [9-11]. For 3-piece approximation, breakpoints can be defined as [-4,-1,+1,+4]. The 3-piece approximation of $tanh$ function can be defined as [3,10,11]:

$$tanh\,(x)_{3-piece} \approx \begin{cases} 0.08x - 0.68, & -4 \le x \le -1 \\ 0.76x, & -1 \le x \le +1 \\ 0.08x + 0.68, & +1 \le x \le +4 \end{cases} \quad (5)$$

Using a piecewise linear approximation of tanh, the training problem can be reformulated as a MILP problem:

$$\min_{w_1,w_2,b_1,b_2} |\emptyset'| = \frac{1}{N}\sum_{i=1}^{N}|w_2^* f(w_1 u_i + b_1) + b_2 - y_i| \quad (6a)$$

s.t.

$$x = w_1 u_i + b_1 \quad (6b)$$

$$p_0 \le w_1, b_1, b_2 \le p_P \quad (6c)$$

$$\Delta_k = p_k - p_{k-1} \quad (6d)$$

$$g_k = f'(p_k) - f'(p_{k-1}) \quad (6e)$$

$$\forall\, k \in \{1, \dots, P\} \quad (6f)$$

$$p_0 \le x \le p_P \quad (6g)$$

$$x = p_0 + \sum_{k=1}^{P} y_k \quad (6h)$$

$$f'(x) = f(p_0) + \sum_{k=1}^{P} \frac{g_k}{\Delta_k} y_k \quad (6i)$$

$$\lambda_0 \le z_0 \quad (6j)$$

$$\lambda_m \le z_{m-1} + z_m\,, \forall m \in \{1, \dots, P-1\} \quad (6k)$$

$$\lambda_m \le z_{m-1} \quad (6l)$$

$$\sum_{m=0}^{P-1} z_m = 1 \quad (6m)$$

$$z_m \in \{0,1\} \quad (6n)$$

where $x$ is the input to the piecewise linear function, $p_k$ denotes the $k^{th}$ breakpoint, $\Delta_k$ represents the difference between consecutive breakpoints, and $g_k$ is the difference in the function's value between these breakpoints. The parameter $P$ specifies the number of pieces in the approximation. The variables $y_k$ capture the differences used to define the input to the piecewise linear function, $\lambda_m$ are nonnegative auxiliary variables, and $z_m$ are binary variables that aid in formulating the problem as a MILP.

To simplify the problem and allow for formulation as a linear program (LP) before modifying the branching scheme, the following constraints can be used instead of (6j–6n) [13]:

$$\Delta_m s_{m+1} \le \Delta_{m+1} s_m \; \forall m \in \{1, \dots, P-1\} \quad (7a)$$

$$y_1 \le \Delta_1 \quad (7b)$$

$$y_P \geq 0 \quad (7c)$$

Finally, after obtaining the current solution $\tilde{y}$ with with $\tilde{y}_k < u_k$ and $\tilde{y}_{l+k} > 0$ for some $k \in \{1, \ldots, P-l\}$, the following branching options exist [13]:

$$Branch\ 1: y_k = \Delta_k, Branch\ 2: y_{k+1} = \cdots = y_P \quad (8)$$

Since formulations without binary variables provide the same LP bound as those that include them, maintain local ideality, and are more compact, they serve as superior models for PLFs compared to MIP models [5]. The algorithm can be summarized as follows where M denotes the number of neurons:

```
for i=1 to N do:
   for j=1 to M do:
      for k=1 to P do:
         Solve the model:
            Minimize Eq. 6a
            Subject to Eq. 6b-6i,Eq. 7a-7j
            If ỹ_k<u_k and ỹ_{l+k}>0 then
               Branch 1: y_k=△_k
               Branch 2: y_{k+1}=…=y_P
```

Implementing the SOSX algorithm in feedforward neural network training ensures reproducibility of results due to the convexity of the problem formulation. This property guarantees that the same training performance is achieved in every run, whereas regular training may converge to different solutions, potentially leading to suboptimal outcomes.

## RESULTS AND DISCUSSION

We illustrate our proposed method on a case study that examines 253 snapshots of a distillation column, each described by 27 features, including variables such as temperatures, pressures, and flow rates, with the vapor pressure measured in a laboratory as the target variable [14]. The dataset is normalized between -1 and +1. Three training algorithms were applied to this dataset using a 70% training ratio. The first method, NLP training, employing the Adam optimizer [15] in TensorFlow's Keras [16] framework for 100 epochs. The second, MIP training, introducing binary variables to the problem structure, following previously established formulations in Eq.6. The third, SOSX training, using a convex branch-and-bound approach to train the neural network, recording CPU times. All methods used a single-hidden-layer FNN architecture with neurons ranging from 5 to 30, and for SOSX and MIP, piecewise linear approximation of the tanh activation function with 3 segments were implemented. Figure 1 shows the trend for SOSX training CPU times at different number of neurons. Table 1 summarizes the MSE results for both training and test performances. Figures 2 to 7 depict the corresponding trends for training and test performance across different piecewise approximations at varying number of neurons. In these visualizations, "$n$" denotes the number of neurons, while "$p$" represents the number of pieces used in the approximation. The training and test data are divided by a dashed black vertical line called the "train-test split."

The study initially sought to compare the CPU training times of the SOSX and MIP algorithms. However, under default solver settings, including cuts and optimality gap, MIP training failed to converge. As a result, MIP training was terminated once its CPU time equaled that of SOSX training. Consequently, the training and test results for the MIP algorithm are based on these aborted solutions.

A key finding pertains to CPU time. In MIP formulations, CPU time typically grows exponentially with an increase in the number of binary variables. In contrast, the SOSX algorithm, which replaces binary variables, demonstrates a non-exponential increase in CPU time, as represented in Figure 1.

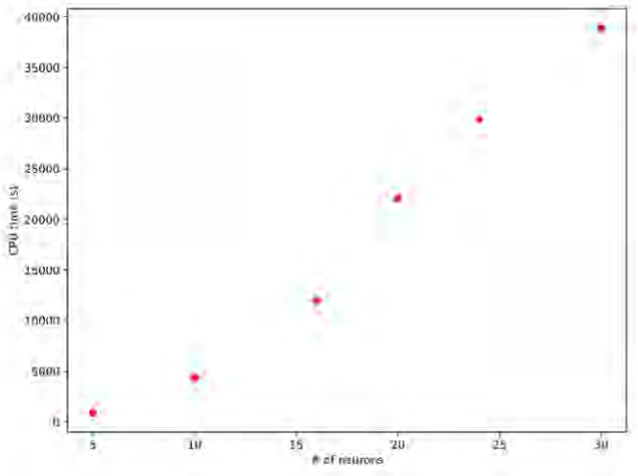



**Figure 1.** CPU times for SOSX training.

Another notable finding from the results is that the SOSX algorithm achieves nearly zero training error without signs of overfitting. The zero-training error is evident in the train split parts of Figures 2-7 as the actual and predicted values overlap. Additionally, in the test splits, SOSX predictions closely follow the actual test value trends, indicating no signs of overfitting. This success is attributed to its specially tailored branching mechanism, which strategically places PWL approximations of the nonlinear activation function. At each iteration, a linear relaxation is solved, and branching progresses based on the location within the PWL function. This approach not only ensures effective network training but also offers a substantial advantage in CPU efficiency.

Figures 2–7 depict the MIP training and test results using green dashed lines. In Figures 2 and 3, which correspond to cases with fewer neurons -specifically, 5-neuron-3-piece (*5n3p*) and 10-neuron-3-piece (*10n3p*)-, MIP training and test results closely follow the actual values compared to cases with a higher number of neurons, although SOSX still outperforms MIP. However, in Figure 4, which represents the 16-neuron-3-piece (*16n3p*) case, no MIP trend is observed, and Table 1 does not contain a corresponding value. This omission occurs because MIP training failed to converge to a feasible solution within the CPU time required by SOSX. In Figure 5, which illustrates the 20-neuron-3-piece (*20n3p*) case, a solution was found, but the MIP training and test results significantly deviate from the actual values. This divergence becomes even more pronounced in Figure 6 for the 24-neuron-3-piece (*24n3p*) case, where MIP training and test results fail to capture the trend altogether. Finally, in Figure 7, representing the 30-neuron-3-piece (*30n3p*) case, no MIP trend is present, mirroring the issue observed in the *16n3p* case. These findings highlight the robustness of the SOSX algorithm, which consistently finds a solution within a timeframe where MIP fails to yield a feasible result. Moreover, SOSX's effectiveness becomes even more evident in cases with a higher number of neurons, indicating its capability to handle more complex scenarios.

An important observation is the difference in test performance between the regular training (NLP) and SOSX algorithms. While SOSX may sometimes underperform due to its reliance on approximations, it still surpasses NLP in 4 out of 6 runs across different number of neurons. The lowest MSE test error was observed in the *24n3p* case, marking a particularly encouraging result. In the test splits of Figures 2–7, this pattern is clearly evident in the trends. Additionally, the actual data exhibit two peaks between data points 200 and 250. For the first peak, NLP predictions overshoot in the *5n3p*, *10n3p*, *16n3p*, and *30n3p* cases, as seen in Figures 2, 3, 4, and 7. Similarly, for the second peak, NLP predictions fall significantly below the actual value in the *24n3p* case, as shown in Figure 6, whereas SOSX predictions closely match the actual values. Overall, SOSX trends remain more aligned with the actual values compared to NLP test performance. These findings indicate that the SOSX algorithm effectively mitigates suboptimal training outcomes by leveraging its convex formulation and robust representation capabilities. Moreover, the benefits of the SOSX algorithm become even more evident in cases with a higher number of neurons.

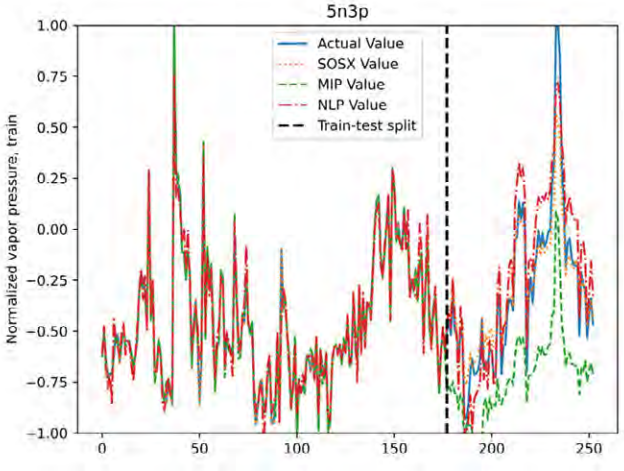



**Figure 2.** Training and test performances for 5 neurons.

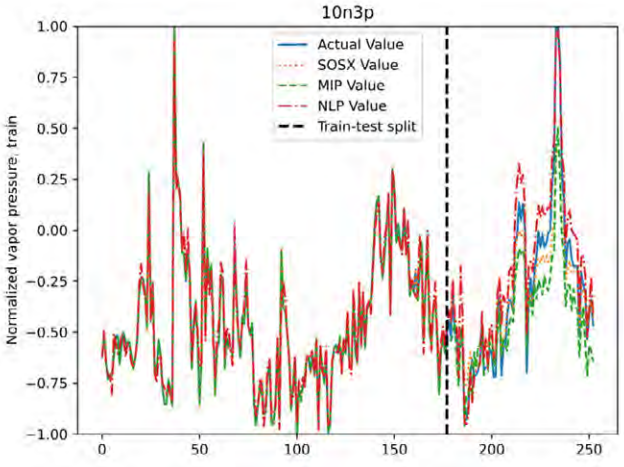



**Figure 3.** Training and test performances for 10 neurons.

| #neuron | CPU time (s) | NLP training | MIP training | SOSX training | NLP testing | MIP testing | SOSX testing |
|---|---|---|---|---|---|---|---|
| 5 | 890 | 0.0048 | 0.0022 | 0 | 0.0238 | 0.2237 | 0.0145 |
| 10 | 4388 | 0.0033 | 0.0002 | 0 | 0.0162 | 0.0393 | 0.0218 |
| 16 | 12011 | 0.0029 | - | 0 | 0.0291 | - | 0.0298 |
| 20 | 22052 | 0.0026 | 0.0823 | 0 | 0.0090 | 0.1981 | 0.0042 |
| 24 | 29856 | 0.0023 | 0.0853 | 0 | 0.0159 | 0.5641 | 0.0024 |
| 30 | 38897 | 0.0034 | - | 0 | 0.0233 | - | 0.0078 |

**Table 1: Training CPU times, training and testing MSE value**

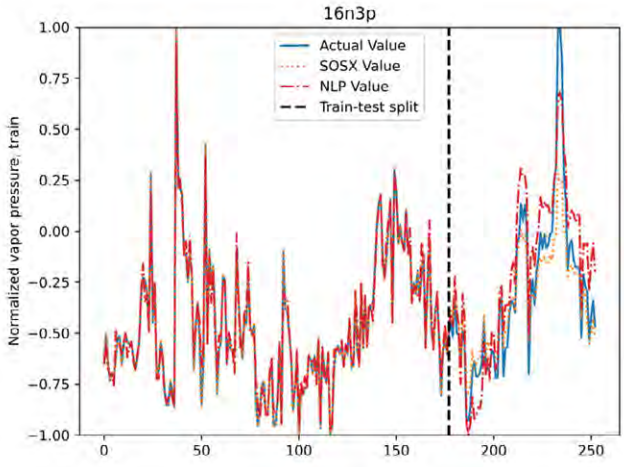



**Figure 4.** Training and test performances for 16 neurons.

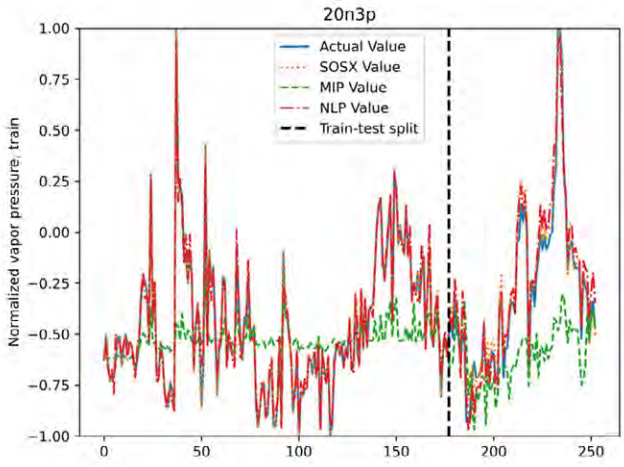



**Figure 5.** Training and test performances for 20 neurons.

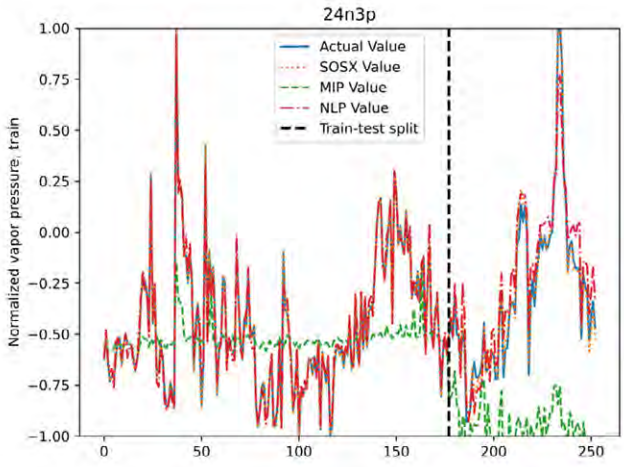



**Figure 6.** Training and test performances for 24 neurons.

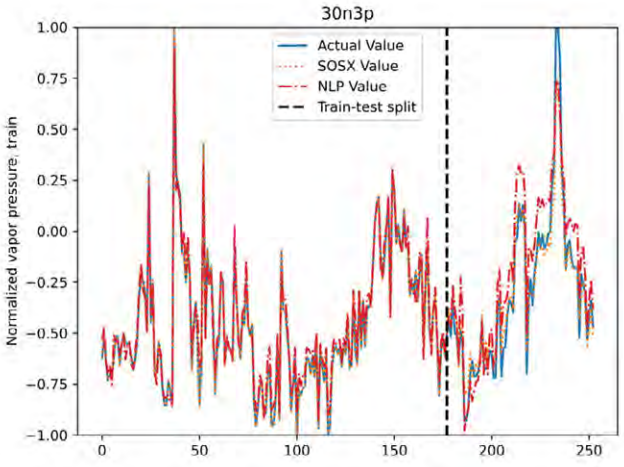



**Figure 7.** Training and test performances for 30 neurons.

The analysis of SOSX CPU times previously focused on how they vary with the number of neurons and piecewise approximations. However, an important question remains: Do these CPU times only apply to the distillation column dataset, or are they statistically significant for datasets with similar dimensionality? To explore this, four datasets are modified to match in dimensionality, ensuring consistency in both dataset size and number of features.

The first dataset is the previously examined distillation column data [14]. The second dataset consists of open simulation data from a wastewater treatment plant, where the target variable represents dissolved oxygen concentration in an activated sludge system [17]. The third dataset comes from a U.S.-based regression study predicting the average annual cancer diagnosis rate based on socioeconomic and demographic factors such as income, population size, age, and race [18]. The fourth dataset is the Boston housing prices dataset, which estimates property values using economic and real estate-related variables [19]. To ensure comparability, all datasets are reduced to eight features using F-value statistics, selecting the variables most strongly correlated with the output. Additionally, the training dataset sizes are standardized to 177 samples across all cases.

Figure 8 presents variations in the logarithm of CPU times across different number of neurons and segmentations in piecewise linear approximations for the four datasets. The plots include 95% confidence intervals, allowing for statistical comparisons between datasets. Since the dataset sizes are adjusted for consistency, their training and test performances should not be directly compared to original benchmarks. Instead, the focus is on determining whether the observed CPU times are statistically significant.

As shown in Figure 8, most data points fall within the 95% confidence interval. Any points outside this range are still close to the boundary and do not qualify as outliers. This suggests that for datasets with the same dimensionality, CPU times remain consistent. Therefore, the CPU times observed in the original analysis are not unique to the distillation column dataset.

## CONCLUSION

This study highlights the efficacy and robustness of the "SOSX" algorithm for convex training of neural networks using PWL approximations. SOSX consistently achieves zero training error while balancing computational efficiency and model accuracy through modifications to the branch-and-bound algorithm. Unlike MIP training, which struggles with convergence for larger problems, SOSX offers superior performance with significantly reduced CPU times.

A comparative analysis reveals key findings. While regular (NLP) training provides reasonable test performance, SOSX outperforms NLP in many cases, such as the *24n3p* configuration, which achieved the lowest MSE test error. Additionally, MIP training struggles with convergence for larger networks, failing to provide feasible solutions within the time frame needed for SOSX.

CPU time analysis shows that SOSX demonstrates greater scalability. Unlike MIP, which exhibits exponential CPU time growth, SOSX displays a more manageable polynomial increase, making it a practical choice for larger-scale problems. In addition, experiments on four different datasets with the same dimensionality show that the CPU times are not dataset specific.

In summary, SOSX offers a robust, efficient framework for training neural networks with piecewise linear approximations. Its ability to achieve zero training error, coupled with its scalability, makes it a promising

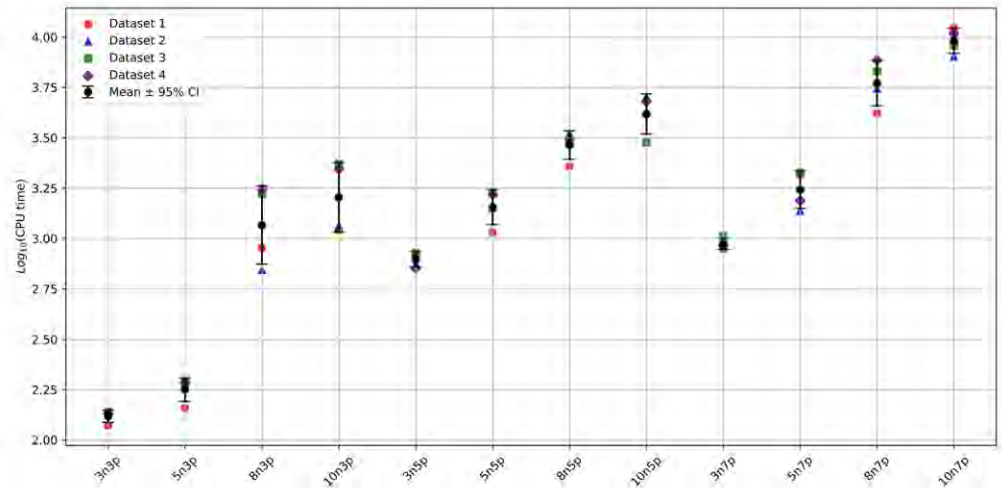



**Figure 8.** CPU times for different datasets.

alternative to methods like NLP and MIP, with strong potential for broader machine learning and optimization applications.

## REFERENCES


1. A. Thebelt, J. Wiebe, J. Kronqvist, C. Tsay, and R. Misener, "Maximizing information from chemical engineering data sets: Applications to machine learning," *Chem Eng Sci*, vol. 252, Apr. 2022, doi: 10.1016/j.ces.2022.117469.
2. M. Bianchini and M. Gori, "Optimal learning in artificial neural networks: A review of theoretical results," 1996.
3. J. P. Vielma, "Mixed integer linear programming formulation techniques," *SIAM Review*, vol. 57, no. 1, pp. 3–57, 2015, doi: 10.1137/130915303.
4. E. M. L. Beale and J. A. Tomlin, "Special facilities in a general mathematical programming system for nonconvex problems using ordered sets of variables," *Operational Research*, vol. 69, pp. 447–454, 1970, [Online]. Available: https://www.researchgate.net/publication/313166553.
5. A. B. Keha, I. R. De Farias, and G. L. Nemhauser, "Models for representing piecewise linear cost functions," *Operations Research Letters*, vol. 32, no. 1, pp. 44–48, Jan. 2004, doi: 10.1016/S0167-6377(03)00059-2.
6. C. Tsay, J. Kronqvist, A. Thebelt, and R. Misener, "Partition-based formulations for mixed-integer optimization of trained ReLU neural networks," Feb. 2021, [Online]. Available: http://arxiv.org/abs/2102.04373
7. J. Katz, I. Pappas, S. Avraamidou, and E. N. Pistikopoulos, "Integrating deep learning models and multiparametric programming," *Comput Chem Eng*, vol. 136, May 2020, doi: 10.1016/j.compchemeng.2020.106801.
8. B. Grimstad and H. Andersson, "ReLU networks as surrogate models in mixed-integer linear programs," *Comput Chem Eng*, vol. 131, Dec. 2019, doi: 10.1016/j.compchemeng.2019.106580.
9. A. M. Schweidtmann and A. Mitsos, "Deterministic Global Optimization with Artificial Neural Networks Embedded," *J Optim Theory Appl*, vol. 180, no. 3, pp. 925–948, Mar. 2019, doi: 10.1007/s10957-018-1396-0.
10. E. S. Koksal and E. Aydin, "Physics Informed Piecewise Linear Neural Networks for Process Optimization," *Comput Chem Eng*, vol. 174, Jun. 2023, doi: 10.1016/j.compchemeng.2023.108244.
11. H. Sildir and E. Aydin, "A Mixed-Integer linear programming based training and feature selection method for artificial neural networks using piece-wise linear approximations," *Chem Eng Sci*, vol. 249, Feb. 2022, doi: 10.1016/j.ces.2021.117273.
12. S. Ding, H. Zhao, Y. Zhang, X. Xu, and R. Nie, "Extreme learning machine: algorithm, theory and applications," *Artif Intell Rev*, vol. 44, no. 1, pp. 103–115, Jun. 2015, doi: 10.1007/s10462-013-9405-z.
13. A. B. Keha, I. R. De Farias, and G. L. Nemhauser, "Models for representing piecewise linear cost functions," *Operations Research Letters*, vol. 32, no. 1, pp. 44–48, Jan. 2004, doi: 10.1016/S0167-6377(03)00059-2.
14. K. Dunn, "Distillation tower [Dataset]," OpenMV.
15. D. P. Kingma and J. Ba, "Adam: A Method for Stochastic Optimization," Dec. 2014, [Online]. Available: http://arxiv.org/abs/1412.6980
16. F. Chollet and et al, "Keras." [Online]. Available: https://keras.io
17. Vanhooren, H., Nguyen, K., Vanrolleghem, P., & Spanjers, H. (1996). *Development of a simulation protocol for evaluation of respirometry-based control strategies*.
18. Otto, M., & Fong, A. (2013). Cancer data of United States of America [Dataset]. *Kaggle. Released under MIT Licence*. https://www.kaggle.com/datasets/varunraskar/cancer-regression/code
19. Harrison, D., & Rubinfeld, D. L. (1978). Hedonic Housing Prices and the Demand for Clean Air. *Journal of Environmental Economics and Management*, *5*, 81–102.



© 2025 by the authors. Licensed to PSEcommunity.org and PSE Press. This is an open access article under the creative commons CC-BY-SA licensing terms. Credit must be given to creator and adaptations must be shared under the same terms. See https://creativecommons.org/licenses/by-sa/4.0/




Systems & Control Transactions

**Research Article - Peer Reviewed Conference Proceeding**
ESCAPE 35 - European Symposium on Computer Aided Process Engineering
Ghent, Belgium. 6-9 July 2025
Jan F.M. Van Impe, Grégoire Léonard, Satyajeet S. Bhonsale,
Monika E. Polańska, Filip Logist (Eds.)

PSE PRESS

# A combined approach to optimization of soft sensor architecture and physical sensor configuration

**Lukas Furtner[a,c]*, Isabell Viedt[a,c], Leon Urbas[a,b,c]**

[a] TUD Dresden University of Technology, Process-to-Order Group, Process Systems Engineering Group
[b] TUD Dresden University of Technology, Process-to-Order Group, Chair of Process Control Systems
[c] TUD Dresden University of Technology, Process-to-Order Group, Process-to-Order (P2O) Lab Learning Factory
* Corresponding Author: lukas.furtner@tu-dresden.de.

## ABSTRACT

In the chemical industry, soft sensors are deployed to reduce equipment cost or allow for a continuous measurement of process variables. Soft sensors monitor parameters not via physical sensors but infer them from other process variables. On the one hand, the precision of a soft sensors is affected by its architecture, the choice of parametric equations like balances and thermodynamic or kinetic dependencies in the soft sensor model. On the other hand, uncertainty that is inherent to the input variable values propagates through the soft sensor model and impacts the output uncertainty. The latter is affected by the configuration of physical sensors in the chemical process. This paper proposes an approach for the combined optimization of soft sensor architecture and physical sensor configuration. For this purpose, the method combines an automatic extraction of all possible soft sensor architectures from a set of system equations with an uncertainty-based evaluation of sensor configurations. Applied to an in-situ Continuous Stirred Tank Reactor (CSTR), the method is capable of automatically identifying the optimal combination of soft sensor model and physical sensor configuration. It is further discussed, how the explainability of the results can be improved via variance-based uncertainty decomposition, by contributing soft sensor prediction uncertainty to individual inputs or operations along the calculation path.

**Keywords**: Soft Sensor, Sensor Configuration, Uncertainty Analysis, Digraph

## INTRODUCTION

Precise monitoring of variables in chemical processes is essential for ensuring safe and efficient operation, whereby critical process variables can serve as key indicators. Traditionally, these parameters have been measured using physical sensors. However high equipment costs or the inherent difficulty to directly measure certain process variables can necessitate the deployment of soft sensors. These monitor parameters not via physical sensors but model them based on other process variables, often by means of parametric equations like balances and thermodynamic or kinetic dependencies.

A large body of literature is devoted to soft sensor modeling. This includes the preprocessing of available data, selection of suitable features, model choice and training, validation and maintenance of these models. However, available process information provided by a combination of physical sensor configuration and a process model can be insufficient to develop an adequate soft sensor to monitor critical process variables with the required quality. This concern is particularly notable in complex systems such as large-scale brownfield chemical plants, with sparse availability of process information. Suitable process information to create the required soft sensor can be obtained via two approaches: Firstly, adjusting the sensor configuration in a greenfield project or retrofitting additional sensors in a brownfield chemical plant. Secondly, optimizing the process model utilized by the soft sensor. In fact, here the case is made that soft sensor modeling and sensor configuration adjustment should be viewed as one interconnected step, rather than separate tasks.

Altering the sensor configuration of a chemical process requires an estimation of the improvement for the soft sensor prior to the physical sensor deployment. Existing approaches to identify the optimal sensor configuration in a process often convert a determined system of

linearly independent state equations that describe the process in the form of a matrix such as the observability covariance matrix [1], sensitivity matrix [2] measurement error covariance matrix [3] or Fischer information matrix [4]. Based on these matrices, a scalar value is derived, serving as a metric for the useful process information. However, these approaches are mainly concerned with the state of the system rather than individual state variables. Defining an adequate equation system for brownfield chemical plants can be challenging due to information gaps. When focusing on a specific process variable, an equation system describing the state of a process or a sub system of this process is likely unnecessary. Moreover, if enough process knowledge is available to describe relationships between process parameters with equations that result in an overdetermined or locally overdetermined equation system, a determined subset of the equations system must be extracted resulting in process information loss.

Representing process variables as nodes and their relationships as edges in a graph allows to incorporate all available system equations. Sign Directed Graphs (SDG) represent process variables as nodes and their relationships as arcs between these nodes. Arc notations can contain information whether a change in one process variable results in a positive or negative change of another. Mobed et al. [5] utilize SDG to identify the optimal sensor configuration of a CSTR-System. However, due to the qualitative information of the connection between the process variables, the approach is limited to fault diagnosis and does not allow for a continuous modeling of a process variable's values. Bond graphs are a graph representation of the relationships between process variables that include mechanistic knowledge from system equations. In fact, bond graphs can be used for rigorous simulation of a single CSTR [6] or a chemical process [7], but are a less common simulation technique in the field of chemical engineering.

This paper presents an approach that combines an automatic extraction of all possible soft sensor architectures from a set of system equations with an uncertainty-based evaluation of sensor configurations [8]. This allows for the coupled optimization of soft sensor architecture and physical sensor configuration.

## METHOD

A system is given via $m$ state equations $E = \{e_1, \dots, e_m\}$ that describe the relationship between a set of $n$ state variables $v = \{v_1, \dots, v_n\}$. In a determined system, $k = n - m$ state variables are known with $v_{init} = \{v_1, \dots, v_k\}$. For $k > n - m$ the system is overdetermined; for $k < n - m$ the system is undetermined. To infer a target variable $v_t$, multiple calculations paths $M_i$ can be possible relying on different subsets of state variables and state equations. The deviation of state variables from a nominal operation point is given through $d = \{d_1, \dots, d_n\}$, with $d_i$ as a probability density function of $v_i$. Each $v_i$ is observed with uncertainty, which is characterized by a set of probability density functions $f = \{f_1, \dots, f_n\}$. The subset of state variables that are directly measured via physical sensors constitutes the sensor configuration $S_i$, whereby $s = \{s_p, \dots, s_q\}$ with $p, q \in \{1 \dots n\}$.

The goal is to identify the optimal combination of the soft sensor architecture $M_i$ and the physical sensor configuration $S_i$ to monitor $v_t$. Due to the limited number of soft sensor architectures and sensor configurations considered in the use case of this paper, a grid search algorithm is applied scattering $S_i$ against all $M_i$.

### Soft sensor architecture

With a recursive call of the function `comp_tree`, all possible soft sensor architectures $M_i$ to monitor a target variable $v_t$ can be identified:

```
comp_tree(v_r, E, d):
  if eqs is empty or d == 0:
    return branch
  for each e in E:
    if e can be solved for v_r:
      for each variable v_b in solution:
        new_branch=comp_tree(v_b, E\{e},d-1)
        Add new branch to tree
```

The function assesses which equations in a list of equations can be solved for a root variable ($v_r$), constituting a new branch with which the root variable can be inferred. Every branch variable $v_b$ in equations $E$ that can be used to infer $v_r$ becomes a new target variable in the recursive call of the function. To prevent loops, the current equation $e$ must be excluded from the list of potential equations to infer $v_b$. The recursive function call breaks if no usable equations are left or a specified number of recursive functions calls $d$ is reached. Initially, `comp_tree` is called with the target variable as root variable and all $\{e_1, \dots, e_m\}$ as an equation system. The result is stored in the form of a dictionary, as depicted in Figure 1. Whenever a target variable can be inferred via multiple equations, one calculation path is formed for every equation, to convert the calculation paths into executable computational graphs.

### Physical sensor configuration

To evaluate the monitoring capability of a given sensor configuration an uncertainty-based approach for sensor selection is adapted from [8], where an in depths explanation of the deployed algorithm can be found. The precision with which the target variable value can be estimated serves as metric for the monitoring quality.

The uncertainty of leave variables in $M_i$ is dependent on $S_i$. If a leave variable is measured directly via a

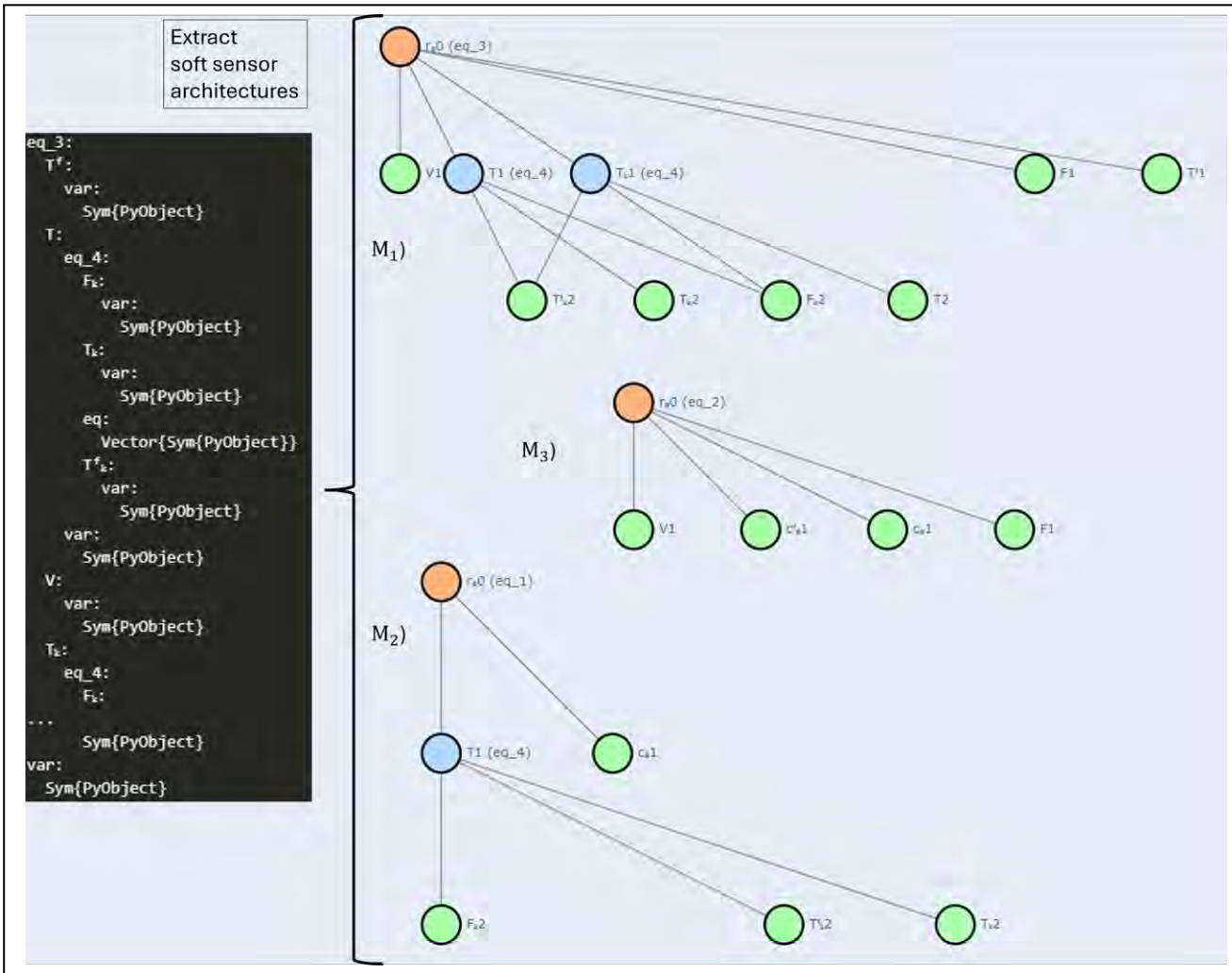



**Figure 1:** Schematic depiction of the automatic extraction of possible soft senor architectures ($M_1$, $M_2$ and $M_3$) given system equations and a targe variable ($r_A$). The recursive call of function `comp_tree` returns a dictionary containing all possible calculation paths that are extracted to form individual models for every soft sensor architecture. The calculation paths are depicted as digraphs. The node colors green, blue and orange indicate a leave, branch or target node, respetively

physical sensor, its uncertainty given through probability density function $f_i$ is expressed via Gaussian sensor error around the nominal operation point. If a leave variable is not measured directly, its uncertainty is expressed via the state variables disturbance $f_i = d_i$ as a best available guess. In a Monte Carlo simulation, all $f_i$ of leave variables are sampled and their uncertainty propagated along the calculation path of $M_i$ yielding an approximation of the ground truth uncertainty of $v_t$.

This sampling-based approach has the advantage of being insusceptible against dependent, non-Gaussian uncertainties. Additionally, the approach promises to incorporate hybrid semi-parametric soft sensors [9], modeling poorly understood effects and dependencies within the process system with data-driven, non-parametric parts.

## USE-CASE STUDY

The proposed algorithm is deployed to an in-situ CSTR, adapted from [3] as can be seen in Figure 2. The reactor feed with substance A has a flow $F$, temperature $T_f$ and concentration $c_A^f$. Within the reactor the concentration $c_A$ of substance A is homogeneous.

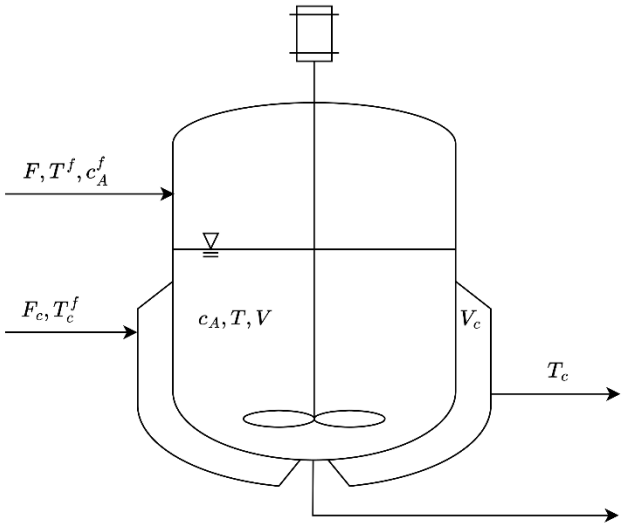



**Figure 2.** Shematic depiction of the in-situ CSTR [8].

The reactor has a volume of $V$ with a homogeneous temperature $T$. The reaction within the CSTR can be described via a first order reaction $A \rightarrow B$ with the reaction enthalpy $\Delta H$, the reaction rate $r_A$, and reaction rate constant $k$. The cooling jacket of the reactor has a volume of $V_c$ containing a coolant flow $F_c$ with coolant inlet temperature $T_c^f$ and coolant outlet temperature $T_c$. For the feed, the fluid density and specific heat capacity are given as $\rho$ and $c_p$ and for the cooling fluid as $\rho_c$ and $c_{p,c}$. Furthermore, the heat transfer area between the reactor and cooling jacket is described by $A$ with a corresponding heat transfer coefficient $h$. The steady-state reactor can be described via the following equations (1)-(4):

$$r_A = k \cdot e^{-\frac{E}{RT}} \cdot c_A \tag{1}$$

$$\dot{c}_A = 0 = \frac{F}{V} \cdot \left(c_A^f - c_A\right) - r_A \tag{2}$$

$$\dot{T} = 0 = \frac{F}{V} \cdot \left(T^f - T\right) + \frac{\Delta H}{\rho \cdot c_p} \cdot r_A - \frac{hA}{\rho \cdot c_p \cdot V} \cdot (T - T_c) \tag{3}$$

$$\dot{T}_c = 0 = \frac{F_C}{V_C} \cdot \left(T_c^f - T_c\right) + \frac{hA}{\rho_c \cdot c_{p,c} \cdot V_c} \cdot (T - T_c) \tag{4}$$

Hereby, the disturbed state variables are $v = \{F, F_c, T^f, T_c^f, V, c_A^f, T, T_c, c_A, r_A\}$ with $v_{init} = \{F, F_c, T^f, T_c^f, V, c_A^f\}$ for the considered sensors. Sensor noise and disturbances are assumed to be independent and normally distributed. The Nominal operation values for the state variables and parameters, the variance of the disturbances, the variance of the sensor noise can be found in [3].

## RESULTS AND DISCUSSION

For the analysis of soft sensor architectures and physical sensor configurations, the reaction rate $r_A$ is considered as target variable. As can be seen in Figure 1, three soft sensor architectures ($M_{1-3}$) can be extracted from the CSTR-equations. Because of the complexity of $M_1$, it is ruled out as soft sensor architecture of choice and $M_2$ and $M_3$ are object of further considerations.

**Table 1:** Sensor configurations $S_{1-3}$.

| **Sensor config** $S_i$ | **Sensor combinations** $s_i$ |
|---|---|
| $S_1$ | $s_1 = \{F, F_c, T^f, T_c^f, V, c_A^f\}$ |
| $S_2$ | $s_2 = \{F, T^f, T_c^f, V\}$ |
| $S_3$ | $s_3 = \{T^f, T_c^f, V\}$ |

The results demonstrate that the choice of sensor configuration significantly influences the monitoring precision of $r_A$. Configuration $S_1$ which deploys all considered sensors $\{F, F_c, T^f, T_c^f, V, c_A^f\}$, provides the lowest uncertainty across both soft sensor models. While being the most expensive, it offers the highest precision in monitoring $r_A$. Configurations $S_2$ and $S_3$ represent reduced sensor setups, with $S_3$ being the most minimalistic, using only $\{T^f, T_c^f, V\}$. The impact of these reduced configurations varies between the two soft sensor models. For $M_2$ , the influence of the sensor configuration is small. On the other hand, $M_3$ shows a significant influence of the sensor configuration changes. Especially reducing the sensor config by the flow sensor for process variable $F$ ($S_2 \rightarrow S_3$) decreases the monitoring precision significantly. As can be seen in Figure 1, the measurement value of $F$ is used as a multiplication factor in the second equation of the equation system which can arguably explain its significance. Nonetheless, the contribution of individual branch nodes or leave node variables to the target variable uncertainty is unknown. The Monte Carlo simulation obtains the uncertainties of all nodes in the calculation path of a soft sensor but yields no information in terms of uncertainty decomposition.

The optimal combination for monitoring $r_A$ is found to be soft sensor architecture $M_3$ with physical sensor configuration $S_1$ under single constraint of target variable value monitoring precision. Additional, constraints like the equipment cost of sensors can be considered [3].

**Table 2:** Soft sensor monitoring precision for $r_A$ in mol/m³/h with combinations of soft sensor architectures $M_{1-2}$ and physical sensor configuration $S_{1-3}$. The optimal combination of soft sensor architecture $M_i$ and physical sensor configuration $S_i$ to monitor $r_A$ is underlined.

| | $M_2$ | $M_3$ |
|---|---|---|
| $S_1$ | 101.1 | <u>26.1</u> |
| $S_2$ | 104.8 | 28.1 |
| $S_3$ | 101.3 | 53.4 |

The choice of soft sensor architecture shows a substantial impact on monitoring precision: $M_3$ consistently outperforms $M_2$ across all sensor configurations. Additionally, the soft sensor architecture has a significant effect on the impact of changes in the sensor configuration. For example, while the change from $S_2 \rightarrow S_3$ results in an insignificant change for $M_2$, the standard deviation of the monitoring precision for $M_3$ almost doubles. This demonstrates the need for a combined examination of changes to the soft sensor architecture $M_i$ and physical sensor configuration $S_i$ in the presented use case.

## CONCLUSION

This paper proposes a combined optimization of changes to the soft sensor architecture and physical sensor configuration. For this purpose, an approach is introduced to automatically extract all possible soft sensors for a critical process variable. It is combined with an uncertainty analysis based approach to sensor configuration adjustments [8]. In an application example, the optimal combination of soft sensor architecture and physical sensor configuration is identified. However, the explainability of the results suffers from the fact that the resulting uncertainty of the critical variable cannot be contributed to individual leave node uncertainties and their interactions. Further work should aim to decompose the uncertainty of target and branch variables within the computational path. Potentially, variance-based uncertainty decomposition can be adapted for this purpose. A key challenge is the likely dependent variable uncertainties along a calculation path which may be accounted for using Shapely effects [10].

## ACKNOWLEDGEMENTS

The authors thank the partners of the industrial project RUBENS, LANXESS Deutschland GmbH, SAMSON AG und KROHNE Messtechnik GmbH for their collaboration and discussion.

## REFERENCES

1. C. Sumana and Ch. Venkateswarlu, “Optimal selection of sensors for state estimation in a reactive distillation process,” Journal of Process Control, vol. 19, no. 6, pp. 1024–1035, Jun. 2009, doi: 10.1016/j.jprocont.2009.01.003.
2. S. Liu, X. Yin, Z. Pan, and J. Liu, “A sensitivity-based approach to optimal sensor selection for complex processes,” Chemical Engineering Science, vol. 278, p. 118901, Aug. 2023, doi: 10.1016/j.ces.2023.118901.
3. K. R. Muske, Christos Georgakis, and C. Georgakis, “Optimal measurement system design for chemical processes,” Aiche Journal, vol. 49, no. 6, pp. 1488–1494, Jun. 2003, doi: 10.1002/aic.690490612.
4. A. J. Lee and U. M. Diwekar, “Optimal sensor placement in integrated gasification combined cycle power systems,” Applied Energy, vol. 99, pp. 255–264, Nov. 2012, doi: 10.1016/j.apenergy.2012.04.027.
5. P. Mobed, J. Maddala, P. Pednekar, D. Bhattacharyya, and R. Rengaswamy, “Optimal Sensor Placement for Fault Diagnosis Using Magnitude Ratio,” Ind. Eng. Chem. Res., vol. 54, no. 38, pp. 9369–9381, Sep. 2015, doi: 10.1021/acs.iecr.5b00482.
6. C. Heny, D. Simanca, and M. Delgado, “Pseudo-bond graph model and simulation of a continuous stirred tank reactor,” Journal of the Franklin Institute, vol. 337, no. 1, pp. 21–42, Jan. 2000, doi: 10.1016/S0016-0032(99)00043-5.
7. K. Tidriri, N. Chatti, S. Verron, and T. Tiplica, “A bond graph modeling for health monitoring and diagnosis of the Tennessee Eastman process,” in 2017 4th International Conference on Control, Decision and Information Technologies (CoDIT), Barcelona: IEEE, Apr. 2017, pp. 0155–0160. doi: 10.1109/CoDIT.2017.8102583.
8. L. Furtner, J. Mädler, and L. Urbas, “An Uncertainty Analysis Based Approach to Sensor Selection in Chemical Processes,” in 2024 IEEE 29th International Conference on Emerging Technologies and Factory Automation (ETFA), Padova, Italy: IEEE, Sep. 2024, pp. 1–4. doi: 10.1109/ETFA61755.2024.10710989.
9. J. Sansana et al., “Recent trends on hybrid modeling for Industry 4.0,” Computers & Chemical Engineering, vol. 151, p. 107365, Aug. 2021, doi: 10.1016/j.compchemeng.2021.107365.
10. N. Benoumechiara and K. Elie-Dit-Cosaque, “Shapley effects for sensitivity analysis with dependent inputs: bootstrap and kriging-based algorithms,” ESAIM: ProcS, vol. 65, pp. 266–293, 2019, doi: 10.1051/proc/201965266.

© 2025 by the authors. Licensed to PSEcommunity.org and PSE Press. This is an open access article under the creative commons CC-BY-SA licensing terms. Credit must be given to creator and adaptations must be shared under the same terms. See https://creativecommons.org/licenses/by-sa/4.0/



Systems & Control Transactions

**Research Article - Peer Reviewed Conference Proceeding**
ESCAPE 35 - European Symposium on Computer Aided Process Engineering
Ghent, Belgium. 6-9 July 2025
Jan F.M. Van Impe, Grégoire Léonard, Satyajeet S. Bhonsale,
Monika E. Polańska, Filip Logist (Eds.)

PSE PRESS

# Flexibility Assessment via Affine Bounds Evaluation

**Diogo A. C. Narciso[a]*, Steven Sachio[b,c], and Maria M. Papathanasiou[b,c]**

[a] Centro de Recursos Naturais e Ambiente, Department of Chemical Engineering, Instituto Superior Técnico, University of Lisbon, 1049-001 Lisboa, Portugal
[b] The Sargent Centre for Process Systems Engineering, Imperial College London, London SW7 2AZ, UK
[c] Department of Chemical Engineering, Imperial College London, London SW7 2AZ, UK
* Corresponding Author: diogo.narciso@tecnico.ulisboa.pt.

## ABSTRACT

Process design deals with the problem of finding the best process set-up, subject to a set of constraints defining the design space (DSp). This selection is guided primarily by economic considerations. Flexibility may also play an important factor in process design, since it embodies "how far" from the design space's bounds are the candidate optimal designs, which in some cases may lead to off-spec products. This work proposes a novel approach for flexibility assessment. In design problems where the design space is constrained by a set of affine bounds, flexibility may be expressed either as the minimum or the maximum distance with respect to the feasible (design) space bounds. For any point in the DSp, the minimum distance provides a good indicator on the minimum flexibility, as the direction that represents the highest risk of violating the constraints. An analogous conclusion can be drawn between the maximum distance and maximum flexibility. These distances can be computed exactly via geometrical approaches, enabling the calculation of a minimum-based and maximum-based flexibility metrics for all points in the DSp. This class of problems are in fact multiparametric programming problems as the goal is to obtain comprehensive flexibility maps, rather than investigating unique points in the DSp. In the case of minimum flexibility, their solutions comprise: (i) a set of critical regions defining a convex hull within the DSp (each associated with a unique nearest bound of the feasible space), (ii) the corresponding optimizer functions (projection at nearest bound), and (iii) objective functions (minimum distance). A novel framework is under development for this class of problems. It enables a new paradigm for flexibility assessment, which can be applied to design problems of any dimension. Complexity is significantly reduced in comparison with the classic multiparametric programming approaches, since only a limited number of active sets need to be considered during solution calculation.

**Keywords**: Process Design, Flexibility, Multiparametric Programming

## INTRODUCTION

Process design is inherently complex, often requiring the need for balancing conflicting objectives across different operational levels. Engineers must navigate physical constraints and specifications which delineate the feasible space within which design decisions can be made [1]. Within this context, process feasibility can be defined as the adherence to a set of predefined constraints during operation. To ensure processes designed are capable of adhering to the constraints, a quantitative measure for process flexibility is required. Swaney and Grossmann (1985) [2] initially addressed this by defining the flexibility index problem, which quantifies the ability of a process to operate within the feasible region under uncertainty. The flexibility index problem aims to identify the size of the largest hyperrectangle that can be inscribed within the feasible space. This concept serves as a crucial metric for determining how robust a process design is against variability in operational parameters and external conditions.

Numerous works have built upon the flexibility index problem to solve complex design and operational challenges. For example, Pistikopoulos and Mazzuchi (1990) [3] introduced a stochastic framework for the flexibility index to quantify the impact of multivariate uncertainty distribution on process flexibility. Kabatek and Swaney (1992) [4] proposed an improved branch-and-bound

algorithm to identify how control actions can compensate for the worst-case scenario problems. In recent years, more work has focused on identifying the full feasible space directly – known as design space identification (DSI). Banerjee and Ierapetritou (2005) [5] proposed to use geometrical envelopes (alpha shapes) for DSI based on the feasibility function. Sachio et al (2023) [6] developed three strategies for constructing alpha shapes, integrating process knowledge and data-driven interpolation to reduce computational effort.

To reduce the computational demand from model simulation, several works have proposed to use data-driven approaches to directly approximate the feasibility function. In this way, the design space is represented by the binary classifier function which indicates the feasibility of an input combination. For this, kriging-based surrogate modelling [7], adaptive sampling techniques [8], and artificial neural networks [9] have been proposed to approximate the classifier function. Such approaches are applicable to high dimensions; however, they do not provide a quantitative measure of process flexibility.

This work builds upon existing foundations in design space identification and feasibility analysis. Specifically, we highlight two key aspects: the process-specific nature of flexibility boundaries, which may not align with box-like assumptions, and the need for flexibility metrics that quantify not just the distance to boundaries but also the variation of process flexibility with this distance. To address these challenges, we propose a novel methodology that leverages multiparametric programming (mp) to integrate design space identification with flexibility analysis. To our knowledge, this is the first application of a mp formulation for this combined problem. Additionally, we introduce two types of flexibility metrics to assess constraint sensitivity and the dependency of average process flexibility on boundary proximity.

## METHODOLOGY

In this work, we consider design spaces defined via a set of affine inequality constraints:

$$Ax \leq b \tag{1}$$

where x is the vector of design variables of size n, and where A and b are a constant matrix and vector, respectively, defining the m bounds of the feasible space. It is assumed that Equation 1 defines a closed convex hull. We denote any design x satisfying Equation 1 as θ, and the full set of θ as the design space Θ.

The goal of this work consists of computing the minimum and maximum distances between all θ in Θ and the corresponding points at the bounds of Θ. Each of these distances are directly related to the minimum and maximum flexibilities: the former/latter concerns the nearest/furthest point at the bounds of the design space with respect to a given θ, and represents, in principle, the highest/lowest risk of violating its bounds.

For design spaces formulated as a set of linear bounds as in Equation 1, the nearest point to a given θ is found when a single bound is active; conversely, the furthest point is found at a corner of the design space. A geometrical motivation is depicted in Figure 1.

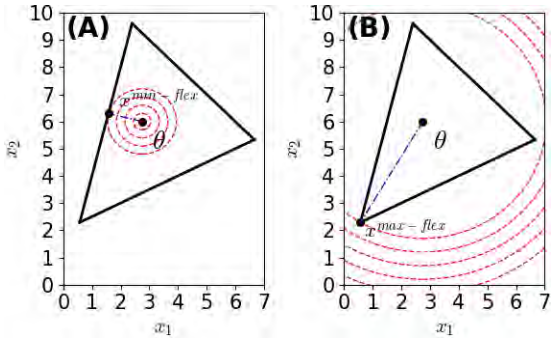



**Figure 1:** 2D illustration of minimum (A) and maximum (B) distances between a given design θ and the bounds of the feasible space as flexibility indicators.

The nearest point to θ (Figure 1A) is obtained by defining the smallest hypersphere centered on θ, such that it includes a unique point - $x^{min-flex}$ – at a single bound of the design space. At $x^{min-flex}$, the hypersphere is tangent to the single active bound, or, in other words, the normal vector connecting θ to $x^{min-flex}$ captures the minimum distance to the bounds. Any combination of the single active bound with one or more bounds of Θ defines a more constrained subspace and cannot contain any point nearer to θ. As a result, the nearest point to any θ at the design space's bounds must conform to this scenario.

The furthest point is obtained by defining the largest hypersphere with center in θ, such that n bounds of Θ are simultaneously active at $x^{max-flex}$ (Figure 1B). By relaxing this condition to include a smaller number of bounds, a less constrained subspace is obtained which necessarily includes points nearer to θ. As a result, the furthest point to any θ must conform to this scenario.

These two extreme scenarios concerning flexibility and a mathematical framework for their calculation are discussed in sequence.

## MINIMUM FLEXIBILITY

Minimum flexibility is defined in this work as the minimum distance between a given θ and the bounds of Θ. The route for its calculation relies on the calculation of all minimum distance functions to each of the m bounds of the feasible space individually. These are defined as the partial minimum flexibilities.

### Partial minimum flexibilities

For design spaces bounded consistently with

Equation 1, the partial minimum flexibilities are computed using simple geometric arguments. Given a design θ and the $j^{th}$ bound of the design space – denoted as $A_j x \leq b_j$ – the nearest point to θ at the $j^{th}$ bound is found via projection:

$$x^{proj,j} - A_j' l^j = \theta \tag{2}$$

$$A_j x^{proj,j} = b_j \tag{3}$$

where $A_j$ is the $j^{th}$ row vector of A and $A_j'$ is the transpose of $A_j$ (column vector), $x^{proj,j}$ is the point at the $j^{th}$ bound of Θ projected from θ along a normal vector to this bound. $l^j$ is a multiplicative factor in Equation 2 defining the depth of the projection. Equation 3, enforces that $x^{proj,j}$ is at the $j^{th}$ bound to obtain the unique nearest point.

Equations 2 and 3 may be written equivalently in a matrix form (Equation 4), and an explicit solution for $x^{proj,j}$ and $l^j$ (Equation 5) is obtained as follows:

$$\begin{bmatrix} I & -A_j' \\ A_j & 0 \end{bmatrix} \begin{bmatrix} x^{proj,j} \\ l^j \end{bmatrix} = \begin{bmatrix} \theta \\ b_j \end{bmatrix} \tag{4}$$

$$\begin{bmatrix} x^{proj,j} \\ l^j \end{bmatrix} = \begin{bmatrix} I & -A_j' \\ -A_j & 0 \end{bmatrix}^{-1} \begin{bmatrix} \theta \\ -b_j \end{bmatrix} \tag{5}$$

The inverse of the symmetric matrix in Equation 5 may be computed numerically or analytically. In this work we focus on the calculation of $l^j$ since it enables a path for minimum distance calculation. For brevity, only the last row of this inverse matrix (at row n+1) is shown:

$$\left[ \begin{matrix} I & -A_j' \\ -A_j & 0 \end{matrix} \right]^{-1} \Bigg|_{n+1} = \frac{[-A_{j,1} \quad \dots \quad -A_{j,n} \quad -1]}{\|A_j\|^2} \tag{6}$$

Since $l^j$ is defined as a multiplicative factor along the direction of the normal vector, it follows that the minimum distance between θ and the $j^{th}$ bound of the design space – $d^{min}_j$ - is obtained from the product of $l^j$ and the norm of $A_j$. Combining Equations 5 and 6:

$$d_j^{min}(\theta) = \frac{[-A_{j,1} \quad \dots \quad -A_{j,n} \quad b_j]}{\|A_j\|} \begin{bmatrix} \theta \\ 1 \end{bmatrix}, j = 1, \dots, m \tag{7}$$

## Computation of minimum flexibility

For any given θ, and consistently with the analysis above, the minimum flexibility - $d^{min}$ - is in fact the minimum of all partial minimum flexibilities. Mathematically:

$$d^{min}(\theta) = \min\{d_1^{min}(\theta), \dots, d_m^{min}(\theta)\} \tag{8}$$

In this work, a solution of this problem for all θ in Θ is required. This is achieved by enforcing the space of parameters via Equation 9 on Equation 8 to deliver a new problem statement. Together, they define a mp problem.

$$A\theta \leq b \tag{9}$$

This formulation is non-conventional in the context of mp, since m candidate optimal objective functions (per each of the m bounds of Θ) are enumerated a priori in Equation 8, instead of a single objective function. This formulation is enabled by the analysis presented earlier, which narrows the optimal candidate active sets for minimum distance calculation to the m single constraint active sets and the corresponding distance functions via Equation 7. The authors are not aware of any algorithm for this class of problems, and the development of a more formal framework will be the subject of future work.

Yet, this problem formulation implicitly suggests a solution strategy as described in sequence. Firstly, we note that explicit expressions for the optimizer functions per optimal active set are not strictly required, though they can be obtained directly from Equation 5. All candidate optimal objective functions of the mp problem are calculated explicitly via Equation 7. To deliver the full solution of this problem it suffices to obtain the critical regions for all m single-constraint active sets. This is achieved via a set of optimality conditions and a set of feasibility conditions. The first kind of conditions results directly from Equation 7: by comparing all partial minimum flexibilities this can be achieved as follows:

$$d_{j1}^{min}(\theta) \leq d_{j2}^{min}(\theta), j_2 = 1, \dots, m, j_2 \neq j_1 \tag{10}$$

where $d^{min}_{j1}$ corresponds to the minimum distance to the $j1^{th}$ bound, which must be lower than or equal to the minimum distances to the remaining bounds. This ensures that the subset of all θ in Θ via Equation 10 yield the minimum distance to this bound. Feasibility conditions must also be defined for critical region construction, which in this case match the bounds of Θ.

# MAXIMUM FLEXIBILITY

Maximum flexibility is defined in this work as the maximum distance to the bounds of the design space for any given θ. The individual distances to all corners of Θ are the relevant candidates for the maximum flexibility, which are defined as the partial maximum flexibilities.

## Partial maximum flexibilities

Given a design θ and the $k^{th}$ corner of the design space – denoted as $\theta^{c,k}$ – the distance between them is computed trivially using the Euclidean norm:

$$d_k^{max}(\theta) = \|\theta - \theta^{c,k}\|, k = 1, \dots, t \tag{11}$$

where t denotes the total number of corners of Θ, which must be computed beforehand. For convenience the square of the partial maximum flexibilities is also presented below, where θ′ denotes the transpose of θ:

$$\left(d_k^{max}(\theta)\right)^2 = \theta'\theta - 2\theta'\theta^{c,k} + (\theta^{c,k})'\theta^{c,k}, \quad k = 1, \dots, t \tag{12}$$

## Computation of maximum flexibility

For any θ, the maximum flexibility - $d^{max}$ - is the

maximum of all partial maximum flexibilities:

$$d^{max}(\theta) = \max\{d_1^{max}(\theta), \dots, d_t^{max}(\theta)\} \quad (13)$$

By combining Equations 9 and 13 a mp problem is defined: it must deliver the maximum distance to the bounds of Θ for all θ in Θ. Similarly to the case of minimum flexibility, the candidate optimal objective functions for each of the t corners are enumerated explicitly in Equation 13. To solve this problem, it suffices to compute the corresponding critical regions. The feasibility constraints are the bounds of Θ (Equation 9), and the optimality constraints are defined conceptually as follows:

$$d_{k1}^{max}(\theta) \geq d_{k2}^{min}(\theta), k_2 = 1, \dots, t, k_2 \neq k_1 \quad (14)$$

where $d^{min}_{k1}$ corresponds to the maximum distance between θ and the $k1^{th}$ corner, which must be greater than the distance to all remaining corners of Θ. This would define a non-linear analytical statement for critical regions construction consistently with Equation 11; to restore linear dependence on the definition of critical regions, it suffices to use the square of the distance functions, enabling a fully equivalent, and more convenient condition (square terms θ'θ cancel each other):

$$\theta'\theta - 2\theta'\theta^{c,k1} + (\theta^{c,k1})'\theta^{c,k1} \geq \theta'\theta - 2\theta'\theta^{c,k2} + (\theta^{c,k2})'\theta^{c,k2},$$
$$k_2 = 1, \dots, t, k_2 \neq k_1 \quad (15)$$

# RESULTS

To illustrate the calculation of the minimum and maximum flexibility maps, two 2D design spaces are presented next. Some notes on high-dimensional problems are presented at the end of this Section.

## Square

We consider the following square design space:

$$\begin{bmatrix} -1 & 0 \\ 1 & 0 \\ 0 & -1 \\ 0 & 1 \end{bmatrix} \begin{bmatrix} x_1 \\ x_2 \end{bmatrix} \leq \begin{bmatrix} 0 \\ 1 \\ 0 \\ 1 \end{bmatrix} \quad (16)$$

### Minimum flexibility map

Firstly, the partly minimum flexibilities are calculated for each of the four bounds of the design space:

$$\begin{bmatrix} d_1^{min} \\ d_2^{min} \\ d_3^{min} \\ d_4^{min} \end{bmatrix} = \begin{bmatrix} 1.000 & 0.000 & 0.000 \\ -1.000 & 0.000 & 1.000 \\ 0.000 & 1.000 & 0.000 \\ 0.000 & -1.000 & 1.000 \end{bmatrix} \begin{bmatrix} \theta_1 \\ \theta_2 \\ 1 \end{bmatrix} \quad (17)$$

Secondly, by comparing each of these distance functions (optimality conditions) and incorporating the bounds of the design space (feasibility conditions), the maps of critical regions for this problem are obtained.

**Table 1:** Critical regions for minimum flexibility in first example ($CR^A\theta \leq CR^b$).

| Critical region | Active bound | $[CR^A \mid -CR^b]$ |
|---|---|---|
| 1 | $\theta_1 = 0$ | $\left[\begin{array}{cc\|c} -1.000 & 0.000 & 0.000 \\ 1.000 & -1.000 & 0.000 \\ 1.000 & 1.000 & -1.000 \end{array}\right]$ |
| 2 | $\theta_1 = 1$ | $\left[\begin{array}{cc\|c} 1.000 & 1.000 & -1.000 \\ -1.000 & -1.000 & 1.000 \\ -1.000 & 1.000 & 0.000 \end{array}\right]$ |
| 3 | $\theta_2 = 0$ | $\left[\begin{array}{cc\|c} -1.000 & 1.000 & 0.000 \\ 1.000 & 1.000 & -1.000 \\ 0.000 & -1.000 & 0.000 \end{array}\right]$ |
| 4 | $\theta_2 = 1$ | $\left[\begin{array}{cc\|c} -1.000 & -1.000 & 1.000 \\ 1.000 & -1.000 & 0.000 \\ 0.000 & 1.000 & -1.000 \end{array}\right]$ |

The map of critical regions is shown in Figure 2 (A). The flexibility in the full design space is also plotted as a heatmap (B). For this purpose, a grid of points within the design space were selected and the minimum distances calculated from the solution of the mp problem.

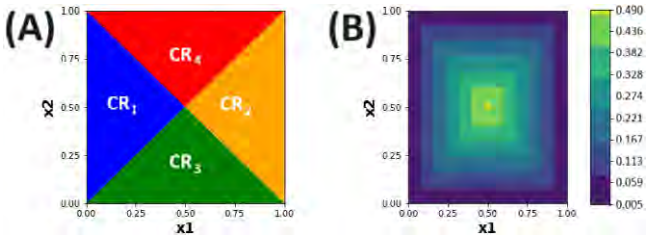



**Figure 2:** Map of critical regions (A) and flexibility design map (B) for minimum design flexibility - first example.

Note that, as expected, all critical regions are in the vicinity of the corresponding nearest bound. This map is useful to identify the nearest bound to any design; yet, by combining this information with the partial minimum distances in Equation 17, the resulting flexibility map (Figure 2B) provides very valuable insight into flexibility. For those points near the bound, the minimum distance is very low; conversely, for those points at the center of the design space, the minimum flexibility becomes increasingly higher. The largest value of the minimum flexibility is found at the center of the box (θ = [0.500, 0.500]), where $d^{min}$ = 0.5 for all active sets.

### Maximum flexibility map

All corners of the feasible space are calculated from the interception of pairs of bounds. These are found at:

$$\begin{bmatrix} \theta^{c,1} \\ \theta^{c,2} \\ \theta^{c,3} \\ \theta^{c,4} \end{bmatrix} = \begin{bmatrix} 0.000 & 0.000 \\ 0.000 & 1.000 \\ 1.000 & 1.000 \\ 1.000 & 0.000 \end{bmatrix} \quad (18)$$

Then, the distance between θ and each of these corners is computed using Equation 11:

$$\begin{bmatrix} d_1^{max} \\ d_2^{max} \\ d_3^{max} \\ d_4^{max} \end{bmatrix} = \theta'\theta \begin{bmatrix} 1 \\ 1 \\ 1 \\ 1 \end{bmatrix} + \begin{bmatrix} 0.000 & 0.000 & 0.000 \\ 0.000 & -2.000 & 1.000 \\ -2.000 & -2.000 & 2.000 \\ -2.000 & 0.000 & 1.000 \end{bmatrix} \begin{bmatrix} \theta_1 \\ \theta_2 \\ 1 \end{bmatrix} \quad (19)$$

At last, the critical regions for all corners are computed via Equations 14 and 15, as listed in Table 2.

**Table 2:** Critical regions for maximum flexibility in first example ($CR^A\theta \leq CR^b$).

| Critical region | Corner | $[CR^A \mid -CR^b]$ |
|---|---|---|
| 1 | $\theta = [0, 0]$ | $\begin{bmatrix} 0.000 & -2.000 & 1.000 \\ -2.000 & 0.000 & 1.000 \\ 1.000 & 0.000 & -1.000 \\ 0.000 & 1.000 & -1.000 \end{bmatrix}$ |
| 2 | $\theta = [0, 1]$ | $\begin{bmatrix} 0.000 & -2.000 & -1.000 \\ -2.000 & 0.000 & 1.000 \\ 1.000 & 0.000 & -1.000 \\ -1.000 & 0.000 & 0.000 \end{bmatrix}$ |
| 3 | $\theta = [1, 1]$ | $\begin{bmatrix} 2.000 & 0.000 & -1.000 \\ 0.000 & 2.000 & -1.000 \\ -1.000 & 0.000 & 0.000 \\ 0.000 & -1.000 & 0.000 \end{bmatrix}$ |
| 4 | $\theta = [1, 0]$ | $\begin{bmatrix} 2.000 & 0.000 & -1.000 \\ 0.000 & -2.000 & 1.000 \\ -1.000 & 0.000 & 0.000 \\ 0.000 & 1.000 & -1.000 \end{bmatrix}$ |

The maps of critical regions and maximum design flexibility are illustrated in Figure 3.

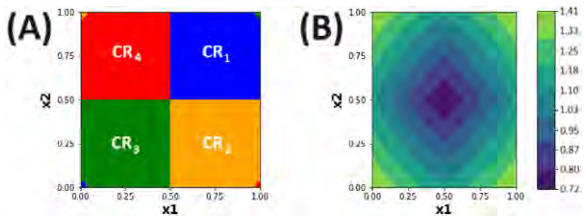



**Figure 3:** Map of critical regions (A) and flexibility design map (B) for maximum design flexibility - first example.

For each corner, the corresponding critical region is in the vicinity of the opposite corner as expected (all corners are highlighted in the same color as the matching critical region in Figure 3A). By combining this information with the partial maximum flexibilities in Equation 18, the maximum flexibility map is delivered as a heatmap in Figure 3B. This is continuous quadratic function of θ. Note that the contours in all critical regions are centered in the opposite, most distant corners. The highest maximum flexibilities are found at the corners, where the maximum distance to the bounds of the feasible space correspond to the opposite corners, as expected ($d^{max} = \sqrt{2}$).

## Hexadecagon

We consider a second 2D example defined via a total of 16 bounds. Its shape will become clear from the analysis of Figures 4 and/or 5.

## Minimum flexibility map

The partial minimum flexibilities were computed for all 16 bounds and the matching critical regions obtained by comparing them. For brevity, these are not listed, and only the maps of critical regions and minimum flexibility are shown in Figure 4.

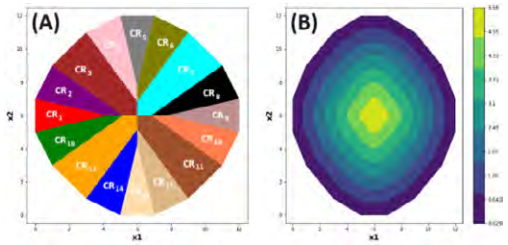



**Figure 4:** Map of critical regions (A) and flexibility design map (B) for maximum design flexibility - second example.

All critical regions extend from the corresponding nearest bound to the boundaries where the partial minimum distances equate those of a neighboring critical region. The minimum design flexibility is null at the bounds of the design space, and as expected increases towards the center of the convex hull. Closer to the center of the convex hull the contours progressively resemble more like a square which is consistent with critical regions 3, 7, 11 and 15 delivering the minimum distance in the vicinity of x = [6.000, 6.000].

## Maximum flexibility map

The partial maximum flexibilities and the corresponding critical regions for all corners were then calculated. For brevity, only the critical region and maximum flexibility maps are shown in Figure 5.

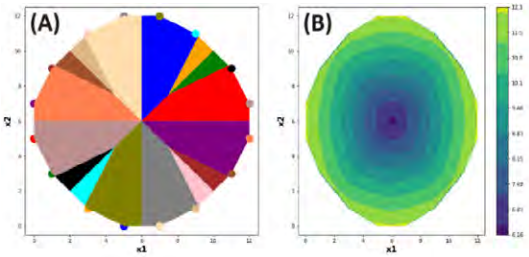



**Figure 5:** Map of critical regions (A) and flexibility design map (B) for maximum design flexibility - second example.

For convenience all corners are highlighted with the same color as the corresponding critical regions. A quick analysis confirms all regions are effectively the most distant to the matching corners. The flexibility map shows that the maximum flexibility increases from the center towards the bounds of the convex hull. Since there are a total of 16 corners, the contours are made of the individual quadratic contours, yielding a more complex, yet fully continuous, map.

## Hypercubes (1D to 10D)

This methodology is particularly attractive for 2D design problems, for which heatmaps can be obtained to provide useful insights on design flexibility. However, it is not constrained by the size of x or even the number of constraints defining the feasible space. The same principles are directly applicable for any design space defined consistently with Equation 1, for which solutions in the format of Equations 17-19 and Tables 1 and 2 are obtained. In this case, for any given θ, the matching critical region must be identified and the minimum or maximum flexibilities determined to provide insights for design.

A total of 10 examples defining boxes between 1D and 10D were defined. These have been defined with the same structure as presented in the first example (Equation 16): restraining the design space between 0 and 1 in the relevant axes. All were successfully solved and validated by the methodology developed.

## CONCLUSIONS AND FUTURE WORK

A new methodology for flexibility assessment in design spaces defined via a set of affine bounds is proposed in this work. The minimum and maximum design flexibilities have been defined as the minimum and maximum distances between a given design and the bounds of the feasible space. This information is useful for design purposes since it quantifies the risk of a given design not complying with the defined design space.

Minimum flexibility is closely related to the distances of individual bounds, while maximum flexibility is associated with the distances to the corners of these convex hulls. Based on this analysis a mathematical framework has been developed to solve problems of this class. Since flexibilities must be computed for all points in the design space, this kind of optimization problem is in fact a multiparametric programming problem. To solve it, the explicit functions for the partial minimum and maximum flexibilities must be calculated, from which the critical regions can be obtained from their comparison. Collectively, these partial flexibilities and the matching critical regions define the flexibility maps, which provide useful information for design. In 2D problems this is particularly relevant since these maps can be shown as heatmaps for effective assessment of flexibility in the full design space.

While the key principles of this methodology have been illustrated in practice, a formal theoretical framework including also the development of algorithms is required. Furthermore, we note that starting with the partial minimum and maximum flexibilities, it is possible not only to calculate the minimum and maximum flexibilities but more broadly, the minimum, average and maximum of these flexibilities, which correspond to a total of 6 potentially flexibility metrics complementing each other. A more detailed examination of the merits and usefulness of these cases will be addressed in our future work.


## ACKNOWLEDGEMENTS

This work was financially supported by CERENA (FCT-UIDB/04028/2025 and FCT-UIDP/04028/2025).


## REFERENCES


1. Grossmann IE, Calfa BA, Garcia-Herreros P. Evolution of concepts and models for quantifying resiliency and flexibility of chemical processes. *Comput. Aided Chem. Eng.* 70:22-34 (2014) doi.org/10.1016/j.compchemeng.2013.12.013
2. Swaney RE, Grossmann IE. An index for operational flexibility in chemical process design. Part I: Formulation and theory. *AIChE Journal* 31:621-630 (1985) doi.org/10.1002/aic.690310412
3. Pistikopoulos EN, Mazzuchi TA. A novel flexibility analysis approach for processes with stochastic parameters. *Comput. Chem. Eng.* 14:991-1000 (1990) doi.org/10.1016/0098-1354(90)87055-t
4. Kabatek U, Swaney RE. Worst-case identification in structured process systems. *Comput. Chem. Eng.* 16:1063-1071 (1992) doi.org/10.1016/0098-1354(92)80024-4
5. Banerjee I, Ierapetritou MG. Feasibility Evaluation of Nonconvex Systems Using Shape Reconstruction Techniques. *Ind. Eng. Chem. Res.* 44:3638-3647 (2005) doi.org/10.1021/ie049294d
6. Sachio S, Kontoravdi C, Papathanasiou MM. A model-based approach towards accelerated process development: A case study on chromatography. *Chem. Eng. Res. Des.* 197:800-820 (2023) doi.org/10.1016/j.cherd.2023.08.016
7. Boukouvala F, Muzzio FJ, Ierapetritou MG. Design Space of Pharmaceutical Processes Using Data-Driven-Based Methods. *J. Pharm. Innov.* 5:119-137 (2010) doi.org/10.1007/s12247-010-9086-y
8. Geremia M, Bezzo F, Ierapetritou MG. A novel framework for the identification of complex feasible space. *Comput. Chem. Eng.* 179:108427 (2023) doi.org/10.1016/j.compchemeng.2023.108427
9. Metta N, Ierapetritou MG. A novel adaptive sampling based methodology for feasible region identification of compute intensive models using artificial neural network. *AIChE Journal* 67 (2020) doi.org/10.1002/aic.17095



© 2025 by the authors. Licensed to PSEcommunity.org and PSE Press. This is an open access article under the creative commons CC-BY-SA licensing terms. Credit must be given to creator and adaptations must be shared under the same terms. See https://creativecommons.org/licenses/by-sa/4.0/

Systems & Control Transactions

**Research Article - Peer Reviewed Conference Proceeding**
ESCAPE 35 - European Symposium on Computer Aided Process Engineering
Ghent, Belgium. 6-9 July 2025
Jan F.M. Van Impe, Grégoire Léonard, Satyajeet S. Bhonsale,
Monika E. Polańska, Filip Logist (Eds.)

PSE PRESS

# A Novel Objective Reduction Algorithm for Nonlinear Many-Objective Optimization Problems

**Hongxuan Wang[a], Andrew Allman[a]***

[a] University of Michigan, Department of Chemical Engineering, Ann Arbor, Michigan, USA
* Corresponding Author: allmanaa@umich.edu

## ABSTRACT

Sustainability is increasingly recognized as a critical global issue. Multi-objective optimization is an important approach for sustainable decision-making, but problems with four or more objectives are hard to interpret due to its high dimensions. In our group's previous work, an algorithm capable of systematically reducing objective dimensionality for (mixed integer) linear Problem has been developed. In this work, we will extend the algorithm to tackle nonlinear many-objective problems. An outer approximation-like method is employed to systematically replace nonlinear objectives and constraints. After converting the original nonlinear problem to linear one, previous linear algorithm can be applied to reduce the dimensionality. The benchmark DTLZ5($I, M$) problem set is used to evaluate the effectiveness of this approach. Our algorithm demonstrates the ability to identify appropriate objective groupings on benchmark problems of up to 20 objectives when algorithm hyperparameters are appropriately chosen. We also conduct extensive testing on the hyperparameters to determine their optimal settings. Additionally, we analyze the computation time required for different components of the algorithm, ensuring efficiency and practical applicability.

**Keywords**: Multi-Objective Optimization, Nonlinear Optimization, Outer Approximation.

## INTRODUCTION

Optimization is an essential mathematical tool for decision making in the chemical industry, enabling solutions of problems in the design, operation, and control of chemical, pharmaceutical and energy processes. Process system optimization is challenging because models of real chemical systems are often complicated, nonlinear and large scale in terms of variables and equations, incorporating both continuous and discrete decisions. The process systems community has been among the leaders in developing powerful theoretical and algorithmic advances in solving the types of challenging optimization problems encountered in decision making for chemical systems [1, 2]. However, most of this effort has been focused on problems containing a single (usually economic) objective [3]. More recently, the chemical industry has come to the forefront as a sector where adopting sustainable practices is essential. To do so requires considering more than just economic drivers for decision making but also include environmental and social objectives during the optimization of chemical engineering process systems.

When considering problems with multiple objectives, there is in almost all cases competition, or tradeoffs, between the different objectives, which can be visualized in a Pareto frontier which presents a set of solutions corresponding to the best one can do in one objective without degrading the others. Multi-objective optimization is an essential tool to generate Pareto frontiers, particularly for problems of two or three objectives [4]. Scalarization approaches, such as the weighted sum or epsilon constraint approach, can be used to generate a set of single-objective optimization problems which rigorously generate Pareto-optimal solutions. This approach enables chemical engineers to simultaneously consider multiple competing objectives and understand their tradeoffs, enabling informed decision-making. However, many disjoint objectives can be thought of as within the purview of "sustainability", and when dealing with more than four objectives (many-objective problems, or MaOPs), a curse of dimensionality emerges. As the number of objectives increases, the computational effort required to solve these problems using rigorous approaches also grows exponentially.

Moreover, visualizing Pareto frontiers in a four or higher dimension space in order to understand tradeoffs and generate a final decision is challenging. Thus, to our knowledge very few works in the process systems literature today formulate and solve high-dimensional MaOP's for sustainable decision making.

To overcome the challenges of objective dimensionality, systematic objective dimensionality reduction for (mixed-integer) linear MaOPs has been previously proposed by our group [5]. For linear problems, optimal solutions always lie on the boundary of the feasible region when the solution is finite. Thus, it is logical to focus the analysis of objective interactions on constraint surfaces. Gradient vectors of the objective functions are projected onto the constraint surfaces. Inner product of the projected vectors and a weighted sum of the constraint interaction strengths are used to determine the total objective correlation strength. Correlation strength is used as edge weight in an objective correlation graph, which consists of nodes corresponding to the different objectives. Finally, a community detection algorithm is applied to identify groups of objectives. For more details about the objective reduction algorithm, please reference our previous works. It has already been successfully used to analyze the correlating and competing nature of a scheduling MaOPs [6]. However, many real-world optimization challenges, particularly in chemical engineering disciplines like process control and system design, are inherently nonlinear. Nonlinear problems introduce additional complexities due to their behavior and interactions, with solutions often not confined to the edges of the feasible region, as well as the potential for locally optimal solutions when the problem is nonconvex, necessitating a more comprehensive approach. Several methods exist for solving mixed-integer nonlinear problems, such as outer approximation [7], generalized benders decomposition [8], and branch and bound [9]. Inspired by these powerful approaches, in this work we extend the dimensionality reduction algorithm to nonlinear MaOPs using an outer approximation-like strategy. The remainder of this paper discusses this approach and is structured as follows. Next, the algorithm for systematically reducing dimensionality of nonlinear MaOPs is described in detail. We then introduce the DZLT5 suite of benchmark MaOP's and discuss why it is an ideal testbed for our algorithm. Then, we present the results of applying our algorithm, making note of the effects of key hyperparameters used in the algorithm. Finally, we provide some concluding remarks and open questions for future work.

# METHODOLOGY

## Nonlinear Dimensionality Reduction Approach

Consider a nonlinear MaOP (Multi-objective Optimization Problem) of the following general form:

$$\min_{x} \{f_1(x), \dots, f_r(x)\}$$
$$s.t. \quad g(x) \leq 0$$

In our previous work [5], we identified that projecting objective cost vectors onto constraint surfaces provided the necessary information for determining groups of correlated objectives. We take a similar approach here, systematically generating approximate linearized constraint surfaces using a first-order Taylor expansion around a feasible fixed point $x^n$ ,as depicted in the equation (1). As additional fixed points are incorporated into the process, the resulting linear constraints progressively provide a closer approximation of the original nonlinear problem when the problem is convex.

$$g(x) \approx g(x^n) + \nabla g(x^n)(x - x^n) \quad (1)$$

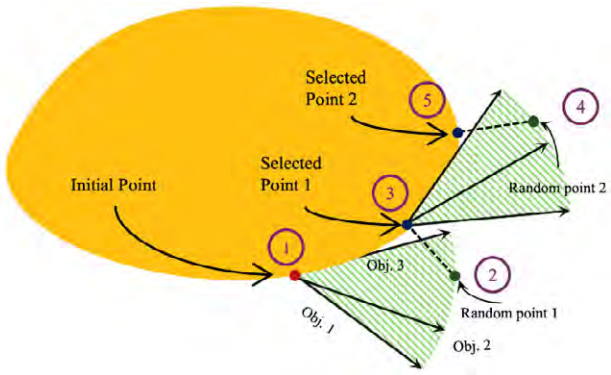



**Figure 1:** How the algorithm choose points. Numbers in the circle shows the sequences of the process.

However, one primary challenge must be addressed to effectively develop this nonlinear method. The challenge involves determining the optimal method for selecting the set of fixed points from which the relaxed linear constraints are derived. We propose a systematic approach that identifies fixed points along the projected gradient descent paths of the objectives. Figure 1 shows how we select the fixed points and the numbers in the purple circle indicated the sequence of the process. It starts from a (set of) initial point $x^n$ on the boundary of $g$. Directions inside the cone of objective gradient vectors indicate directions from the fixed points where the tradeoffs are most likely to occur within this optimization problem, as moving in these directions will improve some objective values. Thus, by strategically selecting new fixed points within the cone of projected objective gradients, new linearized constraints are generated which tend to be concentrated in regions where objective conflicts are most pronounced, that is, along nonlinear

constraints which are active in determining the Pareto frontier.

Unlike linear optimization problems, nonlinear MaOPs can feature single-objective optimal solutions situated within the interior of the feasible region. Therefore, unlike in the linear case, it is crucial to consider the interactions of objectives along constraints where both objective gradients point into the feasible region, which were neglected previouslyWe define a new gradient operator $\nabla f_i(\cdot)_k^*$ , which is equal to the projection of the gradient of objective i onto constraint k if the gradient vector points out of the feasible region, and simply equals the gradient of objective i if the gradient points into the feasible region. Then, for each pair of objectives i and j, the correlation strength along constraint k linearized at fixed point n, $S_{ijkn}$, is:

$$S_{ijkn} = \nabla f_i(x^n)_k^* \cdot \nabla f_j(x^n)_k^* \quad (2)$$

To fully detemine objective correlations, a systematic approach is required for generating new fixed points to use in the generation of linearized constraints. The process for doing so is as follows: first, a random step direction $\Delta$ is chosen that is a conic combination of all projected linearized objectives, such that:

$$\Delta = \frac{\sum_{i=1}^{I} \omega_i \nabla f_i(x^n)_k^p}{\sum_{i=1}^{I} \omega_i} \quad (3)$$

where $\omega_i$ are random values between 0 and 1. A user defined step size parameter $\alpha$ in equation (4) is used to make the fixed point selection more flexible. With this $\Delta$ , a new point (i.e. random point 1 in Figure 1) is obtained: $x^n + \alpha\Delta$. This point may not be feasible to the original problem, so a new feasible point is generated by projecting this point back to the feasible set denoted *X*.

$$x^{n+1} = \text{argmin}_{x \in X} |x - (x^n + \alpha\Delta)|_2^2 \quad (4)$$

In Figure 1, this generates selected fixed point 1 which is the nearest feasible point to the random point 1. This process is repeated applied to the selected fixed points to generate next ones as shown in step 4 and 5 in Figure 1. At each selected fixed point, constraints are linearized and objective correlation strengths are determined using eqn. (2).

Once a sufficient number of fixed points have been generated, we can compile all of the objective correlation strengths into a single value using the same approach as in the linear algorithm:

$$S_{ij}^A = 0.5\left(1 + \frac{\sum_{k=1}^{K}\sum_{n=1}^{N} W_{ijkn} S_{ijkn}}{\sum_{k=1}^{K}\sum_{n=1}^{N} W_{ijkn}}\right) \quad (5)$$

Here, $W_{ijkn}$ is weight that is calculated based on the value of $S_{ijkn}$, taking into account that a competition along a single constraint can cause competition between objectives. We assume that the linearly relaxed constraint space sufficiently approximates the important parts true constraint space for determining objective correlation, enabling the generation of reasonable correlation strengthsThese strengths become the edge weights in an objective correlation graph, which is a fully connected graph where nodes correspond to objectives in the MaOP. Finally, community detection is used on this graph to identify objective groupings for dimensionality reduction.

The nonlinear objective reduction algorithm has two key hyperparameters: the first, as previously described, is the step size to use when generating new fixed points, while the second is the number of fixed points used to determine objective correlation. Determination of the appropriate values to use for each will be assessed using computational experiments that look at, for example, how much new information is added from one additional linearized constraint, and discussed in the results and discussion section.

## DTLZ5($I$, $M$) Problem Set

DTLZ5($I$, $M$) provides MaOPs with a well-defined structure and known objective correlations. Problems from this test set can be of arbitrarily large objective dimensionality It has been widely used to test multi-objective evolutionary algorithms [10], the current state of the art for solving large scale MaOPs. In this problem set, *M* denotes the number of objectives and *I<M* denotes the true dimensionality of the Pareto frontier. All objectives are to be minimized.

$$\min_x \{f_1(x), \ldots, f_M(x)\}$$

$$f_1 = (1+g)\,0.5 \prod_{i=1}^{M-1} cos(\theta_i)$$

$$f_{m=2:M-1} = (1+g)\,0.5 \prod_{i=1}^{M-m} cos(\theta_i) sin(\theta_{M-m+1})$$

$$f_M = (1+g)\,0.5\, sin(\theta_1)$$

$$g = \sum_{i=M}^{M+k-1} (x_i - 0.5)^2$$

$$\theta_{i=1:I-1} = \frac{\pi}{2} x_i$$

$$\theta_{i=I:M-1} = \frac{\pi}{4(1+g)}(1+2gx_i)$$

$$0 \le x_i \le 1, for \ \ldots = 1,2,\ldots,n$$

$$n = M + k - 1$$

All objectives within {f1, . . . , fM−I+1} are positively correlated, while each objective in {fM−I+2, . . . , fM} is conflicting with every other objective in the problem.This

implies that the correct grouping of objectives is to group objectives {f1, . . . , fM−I+1} into a single group, while keeping all remaining I-1 objectives in their own groups. In this work, we choose k = 10, as is consistent with other works using this benchmark problem set. Additionally, the optimal points from the optimization results of individual obejctives of DTLZ5 are used as initial points.

## RESULTS AND DISCUSSION

Our nonlinear dimensionality reduction method has been applied to the DTLZ5 problem set, beginning with DTLZ5(2,3) to assess the feasibility of our algorithm. Our algorithm effectively identified correlated objectives and correctly segmented the multi-objective optimization problem into [f1, f2] and [f3]. This categorization indicates that f1 and f2 are correlated, and both are in competition with f3. This outcome precisely aligns with the specifications defined in the DTLZ5(2,3) problem, confirming the accuracy of our approach.

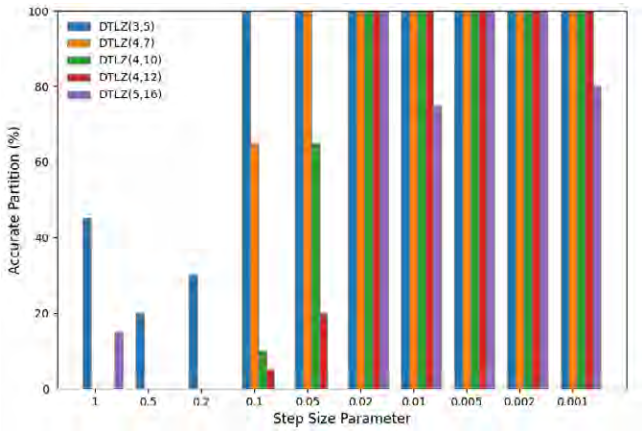



**Figure 2**: Accurate Partition vs Step Size Parameters in different DTLZ5 problems.

However, when testing larger problems such as DTLZ5(3,5) and DTLZ5(4,7), the results are sometimes accurate, but the overall accuracy seemingly decreases as the complexity of the problem increases. This issue may be influenced by the magnitude of the step size hyperparameter used to generate the next selected point. If the step size is too large, it can cause the selected point to fall outside of the region of the feasible space that is active in determining the Pareto frontier, reducing the utility of the linear constraints generated. This effect is consistently observed when selecting fixed points.

To address this, we conducted tests on step size parameters across different DTLZ5 problem sets, as shown in Figure 2. We varied step size parameters from 1 to 0.001 across DTLZ5(3, 5), DTLZ5(4, 7), DTLZ5(4, 10), DTLZ5(4, 12), and DTLZ5(5, 16), using 40 selected fixed points for each objective. Objective groupings for each problem were computed 20 times to mitigate the effects of randomness in step directions. The results show that our algorithm can achieve about 25% or higher accuracy in the DTLZ5(3, 5) tests, even with a large step size parameter. Interestingly, with a step size parameter of 1 in DTLZ5(2, 3), the algorithm still produced high accuracy results, suggesting a high probability of achieving correct results by chance without accurately capturing the conflict zone. When the step size parameter is reduced to 0.1 or lower, the algorithm consistently achieves 100% accuracy, indicating that a smaller step size enhances performance. This trend is also observed in DTLZ5(4, 7), DTLZ5(4, 10), and DTLZ5(4, 12), although the required step size for 100% accuracy decreases as the problem set complexity increases.

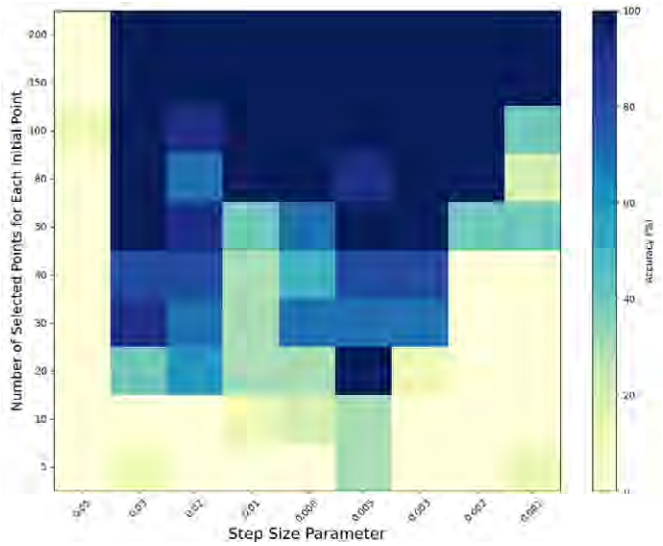



**Figure 3**: Heat map for accuracy of DTLZ(5,20) test results. Each grid in the graph is calculated 10 times with corresponding step size parameters and number of selected points for each starting points.

However, the tests for DTLZ5(5, 16) show relatively lower accuracy when the step size is very small. This suggests that the algorithm's performance can degrade with too small a step size. As the dimension increases, more fixed points are required to move to potential conflict areas. The average random step size direction $\Delta$ also increases with dimensionality. For instance, the average Euclidean distance of random step size direction is about 0.0166 in DTLZ5(3,5), increasing to about 0.0259 in DTLZ5(5,20) with the same step size parameter of 0.03. Therefore, for complex datasets like DTLZ5(5,20), a smaller step size and more selected fixed points are needed to ensure comprehensive mapping of the space and effective location of conflict areas.

To further illustrate the computational performance effected by step size parameter and the number of selected points, a heat map combined with different

selected points and step size parameters are shown in Figure 3. Step size parameter larger than 0.05 would never give a high accuracy results even when 200 selected points are chosen for computation. This matches the conclusion from Figure 2. In this problem set, each variable can feasibly vary between 0 and 1, while from Figure 3, accurate results begin to generate at 0.03. Thus, for this problem it seems a step size of about 3% of the range of the most flexible dimension of the feasible region should be sufficient for most cases in the DTLZ set; however, this finding may be problem-dependent. Moreover, increasing the number of selected points such that the product of the number of steps and step size exceeds the half of longest distances between all the initial points seems to yield good results. A tradeoff clearly emerges similar to that observed in gradient-based optimization: a smaller step size normally will generate higher quality results more reliably, but may require a larger number of iterations, and computational effort, to do so.

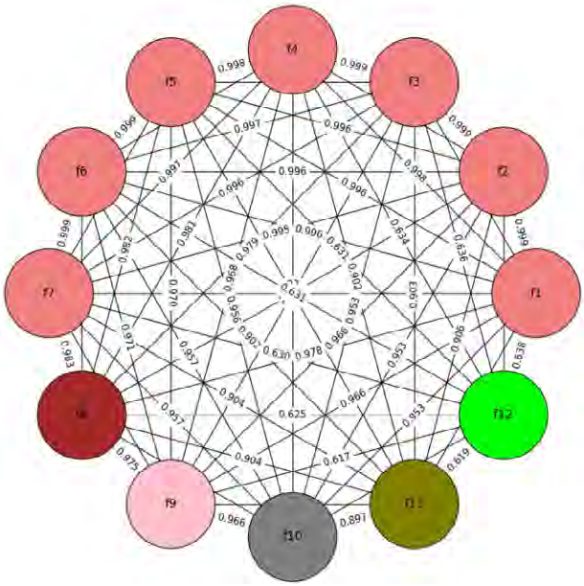



**Figure 4**: Graph results of DTLZ5(6,12). Nodes with the same color indicate that they are in the same group.

After tuning the step size parameter and the number of selected fixed points, the correlating and competing nature of objectives in DTLZ5(5,20) was successfully detected by our nonlinear algorithm. Due to visualization challenges, the graph results of DTLZ5(5,20) are not shown; instead, results from DTLZ5(6,12) are displayed in Figure 4. The lines between different nodes represent the edges indicating the correlation strength between different objectives. Clearly, the largest edge weights, corresponding to pairs of objectives most strongly correlated, occur connecting objectives 1-7, as would be expected for this problem instance.

The time cost of the algorithm for instances of different size was evaluated on a MacBook Air with an M1 CPU and 16GB RAM to assess the algorithm's scalability. In Figure 5, the blue segment illustrates the time spent generating selected points for different optimization problems, while the orange segment indicates the time taken to generate the graph and apply community detection. In this test, each problem includes a total of 240 selected fixed points. Fixed points are generated starting from the optimal solution for each individual objective, which accounts for the slight increase in fixed point generation time as a function of number of objectives. However, the majority of the increase in time as a function of objectives is attibuted to the time required to generate and detect structure in the objective correlation graph. This is consistent with the fact that the number of edge weights calculated is quadratic with the number of objectives, and the community detection algorithm also providing polynomial scaling with number of objectives (graph nodes).

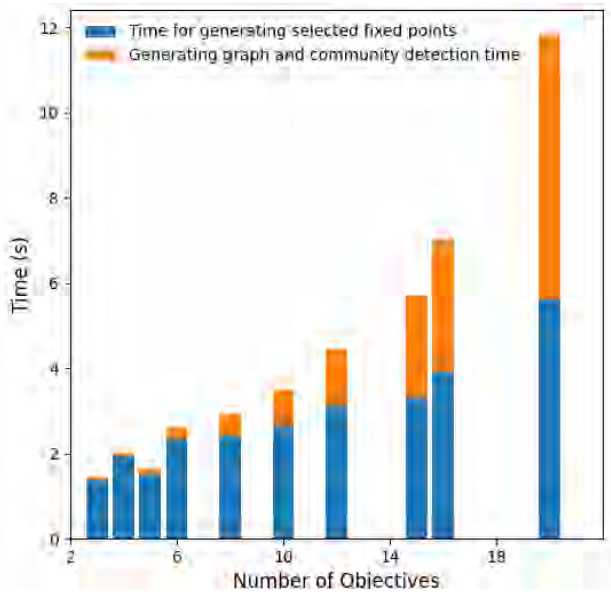



**Figure 5:** Bar graph for time usage of the algorithm with different number of objectives. Total selected points for each of the test is 240.

The relationship between calculation time and the number of selected points is illustrated in Figure 6. To mitigate fluctuations caused by randomness, each data point was calculated 20 times to ensure robustness. As evident, the calculation time increases linearly with the number of selected points, although the slopes vary across different datasets. This trend of increasing slopes corresponds with the observations in Figure 5. Furthermore, the consistent overlap of red and green dots indicates that variations in the step size do not significantly affect the calculation time.

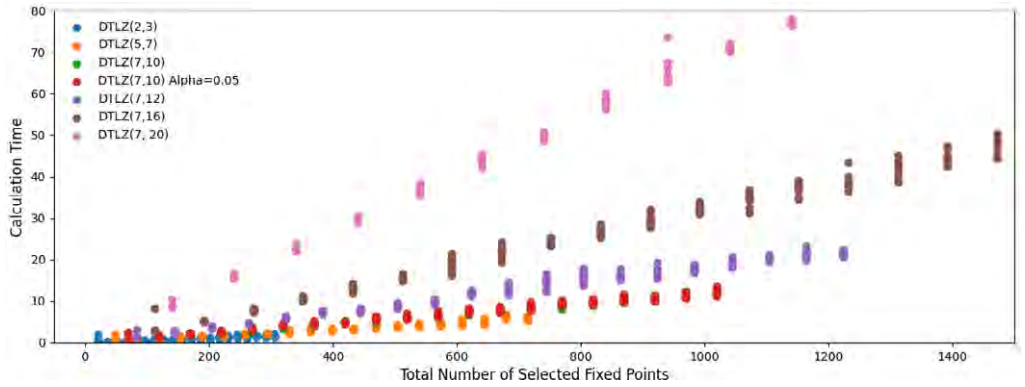



**Figure 6:** Calculation time versus number of selected fixed points in different DTLZ(I,M) problems. Step Size parameter is 0.03 without special annotation.

## CONCLUSION

In this study, we build upon the many-objective dimensionality reduction algorithm developed by our group for linear problems, by introducing a novel algorithm that extends this approach to a nonlinear framework. Utilizing an outer approximation-like method, nonlinear objectives and constraints are converted into linear forms, which are then processed using our existing linear algorithm with minor modifications.

We tested our enhanced algorithm using the DTLZ5(I, M) problem set, a benchmark in many-objective optimization. By carefully adjusting hyperparameters, including the step size and the number of selected fixed points, our algorithm successfully identified the correlating and competing nature of the DTLZ5(I, 20) problem. Additionally, the performance and scalability of the algorithm in terms of computational time is also demonstrated, aligning well with our expectations based on the algorithm's structural design. In the future, we aim to apply this algorithm to problems of practical interest for sustainable decision making in the chemical process industry.

## ACKNOWLEDGEMENTS

Financial support for this work was provided by the National Science Foundation (NSF) CAREER Award (CBET-2237284).

## REFERENCES

1. Sahinidis NV. BARON: A general purpose global optimization software package. *Journal of global optimization*, 8, 201-5 (1996).
2. Wächter A, Biegler LT. On the implementation of an interior-point filter line-search algorithm for large-scale nonlinear programming. *Mathematical programming*, 106,25-57 (2006).
3. Rangaiah GP, editor. Multi-objective Optimization: Techniques and Applications in Chemical Engineering. world scientific (2016).
4. Wu Q, Liu X, Qin J, Zhou L, Mardani A, Deveci M. An integrated multi-criteria decision-making and multi-objective optimization model for socially responsible portfolio selection. *Technological Forecasting and Social Change*, 184, 121977 (2022)
5. Russell JM, Allman A. Sustainable decision making for chemical process systems via dimensionality reduction of many objective problems. *AIChE Journal*. 69(2), e17962 (2023).
6. Wang H, Allman A. Analysis of the correlating or competing nature of cost-driven and emissions-driven demand response. *Computers & Chemical Engineering*, 181, 108520 (2024).
7. Marco AD, Ignacio EG. An outer-approximation algorithm for a class of mixed-integer nonlinear programs. *Mathematical programming*, 36, 307–339 (1986).
8. Arthur MG. Generalized benders decomposition. *Journal of optimization theory and applications*, 10, 237–260 (1972).
9. Evelyn MLB. Branch and bound methods for mathematical programming systems. *In 17 Annals of Discrete Mathematics*, 5, 201–219 (1979).
10. Deb K, Thiele L, Laumanns M, Zitzler E. Scalable Multi-objective optimization test problems. *Proceedings of the 2002 Congress on Evolutionary Computation. CEC'02 (Cat. No. 02TH8600)*. 1, 825-830 (2002).

© 2025 by the authors. Licensed to PSEcommunity.org and PSE Press. This is an open access article under the creative commons CC-BY-SA licensing terms. Credit must be given to creator and adaptations must be shared under the same terms. See https://creativecommons.org/licenses/by-sa/4.0/

Systems & Control Transactions

**Research Article - Peer Reviewed Conference Proceeding**
ESCAPE 35 - European Symposium on Computer Aided Process Engineering
Ghent, Belgium. 6-9 July 2025
Jan F.M. Van Impe, Grégoire Léonard, Satyajeet S. Bhonsale,
Monika E. Polańska, Filip Logist (Eds.)

PSE PRESS

# Applying Quality by Design to Digital Twin Supported Scale-Up of Methyl Acetate Synthesis

**Jessica Ebert[a], Amy Koch[ab]*, Isabell Viedt[ab] and Leon Urbas[ab]**

[a] Technische Universität Dresden, Process-to-Order Group, Process Systems Engineering
[b] Technische Universität Dresden, Process-to-Order Group, Process-to-Order Lab Learning Factory
* Corresponding Author: amy.koch@tu-dresden.de.

## ABSTRACT

A new method for efficient process development is the direct scale-up from laboratory scale to production scale using mechanistic models [1]. The integration of the Quality by Design approach into this scale-up concept may prove beneficial for a variety of product- and process-related aspects. This paper presents a workflow for the digital twin-supported direct scale-up of processes and process plants, which integrates elements of the Quality by Design methodology. To illustrate the concept, the workflow is implemented for the example of an esterification reaction in a stirred tank reactor. Finally, benefits of the implementation of Quality by Design in the direct scale-up using digital twins regarding the product quality and the process development are discussed as well as its limitations.

**Keywords**: scale-up, digital twin, quality by design.

## INTRODUCTION

The trend towards greater product specialization and shorter product life cycles requires the process industry to shorten the time it takes to establish a process (time–to-process) [2]. The direct scale-up from laboratory scale to production scale allows process development to be accelerated, as there is no time-consuming construction of pilot plants and experiments [1]. Especially if high requirements are set for product quality, ensuring product quality should be considered during the process design phase. For this reason, the application of Quality by Design methodology which is common practice in the pharmaceutical industry could be useful in the development of chemical processes. It promises not only to ensure product quality, but also to deepen process understanding and guarantee process safety [3]. Key elements are the definition of the target product quality and the determination of the design space in which the required product quality is assured [3]. Behavioral models of a digital twin support the implementation of the direct scale-up and enables the incorporation of Quality by Design methods. In this paper a concept for a scale-up workflow is demonstrated by the example of the methyl acetate synthesis in a stirred tank reactor.

## BACKGROUND

### Direct Scale-Up

In direct scale-up, process models are used to transfer the process from the laboratory scale to the production scale without intermediate stages. To ensure the scalability, the laboratory plant should be sufficiently similar to the production plant, for example regarding geometry, mass and heat transfer behavior and hydrodynamics. Data from experiments with the lab scale equipment are used to fit the model for both scales. Later, the process model is adapted further to the operational data of the production plant [1], [4].

### Quality-by-Design

Quality by Design is based on the fundamental idea that uniform and consistent product quality is guaranteed by the design of the process [4]. The methodology follows the ICH guidelines Q8 to Q11. It creates an empirical, data-based product and process understanding. First, the Quality Target Product Profile is defined using Critical Quality Attributes (CQAs). These are physical, chemical or biological properties of a product which need to have an appropriate value to ensure the desired product quality [3]. Second, process parameters and material

attributes of the feed substances that significantly affect the product quality are identified. For these Critical Material Attributes (CMAs) and Critical Process Parameters (CPPs), a permissible range is defined to ensure compliance with the CQAs. Thus, the design space is localized within the knowledge space. According to the found design space, the process is monitored, regulated and adapted [3].

## Digital Twin for Scale-Up

ISO 23247-1 [5] defines a digital twin as a digital representation of an observable manufacturing element, i.e. the process plant and the realized processes. Data transfer between the physical and digital object happens automatically in both directions [6]. According to Mädler et al. [7] the operation models of the digital twin may be divided into two sub-models: The transformation model, whose knowledge lies with the plant operator, and the capability model, which is the knowledge of the plant manufacturer [7]. The transformation model comprises the product and the process model. The product model contains information on the properties of the processed and produced substances. The process model describes the processes empirically or mechanistically. The capability model results from the combination of the process and the resource model, which contains the properties of the equipment.

The foundation for the utilization of digital twins for the direct scale-up is presented by Koch et al. [8]: The product-specific transformation model is shared between the laboratory scale plant and the production scale plant. In combination with the corresponding capability model, this results in the operating model. If suitable models are available, the design space can be determined based on experimental data on laboratory scale and then transferred to production scale to avoid expensive experiments on production scale [9].

# CONCEPT

## Workflow for the Integration of Quality-by-Design in the direct Scale-Up

Figure 1 shows the proposed workflow for a direct scale-up using mechanistic behavioral models of a digital twin, incorporating elements of Quality by Design. First, one or multiple mechanistic models are set up for the equipment on both scales. After defining the Quality Target Product Profile, a Global System Analysis (GSA) is performed to identify which model parameters significantly impact the predictions and contribute substantially to their uncertainty. In addition to this, impactful operating variables are identified to support the later determination of CMAs and CPPs. This is followed by an iteration of model-based design of experiments (mbDoE), execution of laboratory-scale experiments and model adaptation. Optionally, one of several competing models is selected (model discrimination). After the validation of the laboratory scale model, parameters of the transformation model including their uncertainty are transferred from the laboratory scale to the production scale. Similarity considerations result in specific values for further model parameters and operating variables. Afterwards, the model for the production plant must also be validated. CPPs and CMAs are determined with the help of a second GSA. The location of the design space within the knowledge space can be located on the laboratory scale and transferred to the production scale. Finally, the operating model of the production plant is used to optimize the process. The Normal Operating Range is set as a subregion of the design space around the optimal operating point

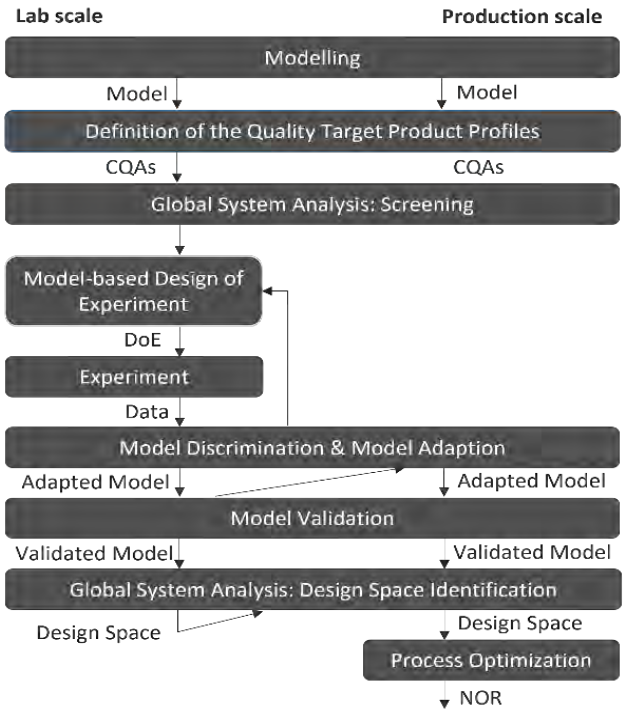



**Figure 1.** Workflow to integrate Quality by Design into a digital twin-supported direct scale-up [10].

# IMPLEMENTATION OF THE CONCEPT

## Introduction of the Use Case

The scale-up concept according to the workflow illustrated in Figure 1 is demonstrated using the esterification of methanol with acetic acid in a stirred tank reactor as an example. The product methyl acetate is used as a solvent for paints or adhesives [12].

$$CH_3OH + CH_3COOH \rightleftharpoons CH_3COOCH_3 + H_2O \quad (1)$$

In the 2 L lab reactor batch experiments are carried out (Figure 2, middle). In contrast, the production reactor

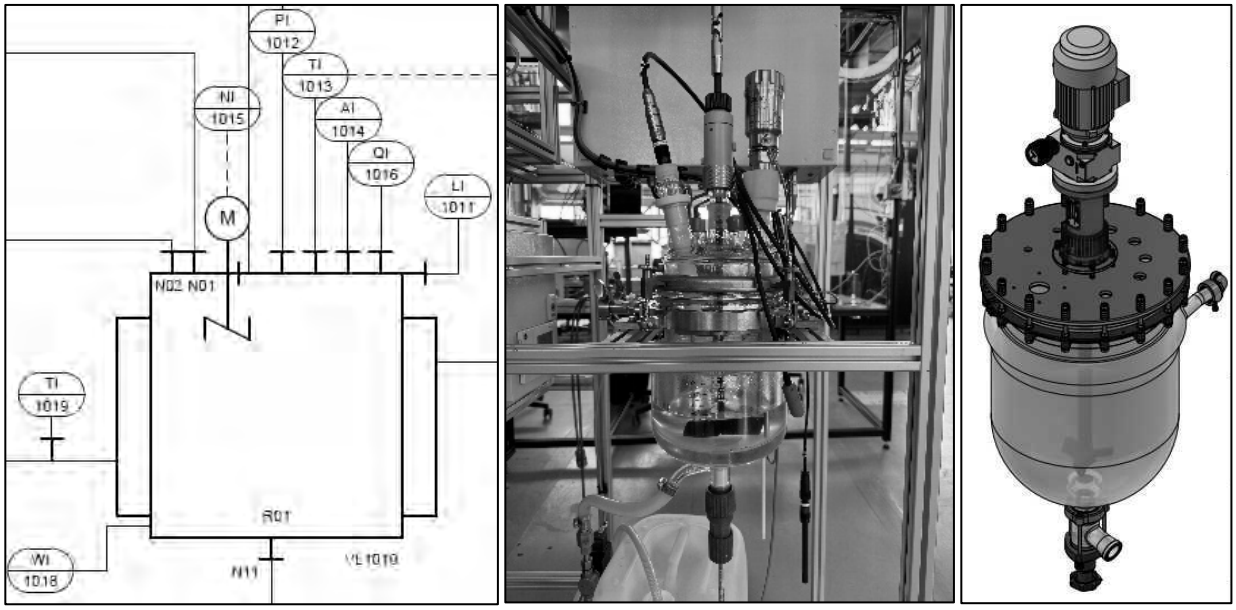



**Figure 2:** P&ID of the stirred tank reactor (left), photo of the laboratory scale reactor (middle) and 3D-model of the production scale reactor (right)

(approx. 50 L) operates stationarily (Figure 2, right).

## Modeling

The reactor is modelled as a cylindrical stirred tank on both scales using the simulation software gPROMS® The mass and energy balance as well as constitutional relationships are set up for this purpose. The kinetic approach for methyl acetate synthesis with the heterogeneous catalyst Amberlyst 15 according to [12] is used (see equation 2). Experimental data from [11] and [12] was also used to validate the simulated behavior in the developed models. Dimensionless numbers such as the Reynolds and Newton number ($Re_{mix}$ and $Ne$) describe the stirring state. To ensure the similarity between the reactors of both scales, common (dimensionless) numbers are used, for instance the volume specific heat transfer area ($A_{spec}$), the specific stirrer performance ($P_{spec}$) or the relation of the height to the diameter of the reactor ($H_{spec}$).

$$r = m_{cat}\,(1.648 \cdot 10^{4}\,\frac{mol}{s\,g}\,e^{\frac{-47.98\frac{kJ}{mol}}{R\,T}}\,x_A x_B - 1.161 \cdot 10^{5}\,\frac{mol}{s\,g}\,e^{\frac{-58.6\frac{kJ}{mol}}{R\,T}}\,x_C x_D) \quad (2)$$

## Definition of the Quality Target Product Profile and GSA for Screening

CQAs are defined in consideration of requirements on the target product quality. The product should contain a minimum molar fraction of methyl acetate ($x_C$) of 1 %. Aiming for an ideal mixture, the Reynolds number $Re_{mix}$ should be higher than $10^4$. As a secondary task, safety requirements are also considered in the CQAs, e.g. the temperature and volume of the reaction mixture ($T$ and $V$) as well as the temperature of the heating fluid ($T_{HM}$). By evaluating scatter plots and variance-based indices resulting from a Monte Carlo simulation, the first GSA shows possible CPPs and CMAs (see Table 1). It also reveals which model parameters are influential on the CQAs and have a high contribution to their uncertainty. For the use case, the activation energies ($E_{A,1}$ and $E_{A,2}$) and the heat transfer coefficient ($k_D$) are found as relevant model parameters as their respective variance-based indices regarding the CQAs exceeded 10 %.

## Experiments, Model Adaptation and Parameter Transfer

By iterating between model-based design of experiments, experiment execution and model adaptation with the maximum likelihood method, the model uncertainty is reduced stepwise as the precision of the model parameters increases. To derive optimal experiments from the model, the D-criterion is used to minimize the variance-covariance matrix of the model parameters. These experiments are simulated with another gPROMS® model with modified parameter values. Afterwards, a normal distributed noise is added on the time series data to represent measurement uncertainties. The reactor model is adapted to fit the resulting experimental data. Model discrimination is not applied in this use case. After that, the model parameters of the transformation model are transferred from the laboratory to the production scale. Further parameters and variables are set for the production

scale model considering similarity between the processes on both scales making sure that the dimensionless numbers equal each other.

## GSA for Design Space Identification and process optimization

A second global system analysis is used to identify CPPs and CMAs for both scales analyzing scatter plots and variance-based indices. A variance-based index of 0 means that the input variable does not affect the output at all while the input variable controls the outcome solely for an index of 1 [13]. If the 1st order variance-based index exceeds 0.1 or there is a clear trend visible in the scatter plot, it is assumed to be a CPP or a CMA. If the total effect is greater than 0.1, it is assumed that the variable contributes significantly to the uncertainty of the investigated CQA. This threshold for the critical value of the variance-based index is set arbitrarily, but the insights resulting out of the analysis of the variance-based indices is reflected in trends visible in the scatter plots.

As Table 1 shows, all CPPs and CMAs that are determined in the second GSA, were already observed as influential operating variables in the screening step. The permissible ranges of the CPPs and CMAs are defined in which the constraints for the QCAs are reached. This reveals the location of the design space within the knowledge space (marked green in Figure 3). A high molar fraction of the educts $x_{A,1}$ and $x_{B,2}$ (CMAs) is needed to reach the target product purity. To guarantee ideal mixing, the stirrer speed $n_{mix}$ (CPP) should be higher than 1 Hz.

Finally, the production process is optimized. In this use case, the yield of methyl acetate relative to methanol should be maximized. Knowing the optimum operating point (marked orange), the Normal Operating Range can be localized (marked light green).

## DISCUSSION, CONCLUSION & OUTLOOK

The proposed workflow was applied successfully to the scale-up of a methyl acetate synthesis in a stirred tank reactor. Although the model presented in the use case has not been validated with real experiments, its predictions show plausible process behaviour.

The integration of the Quality by Design approach into the scale-up of process plants is advantageous in many respects for an effective process scaling. By defining the design space, consistent product quality can be ensured. Furthermore, process safety and robustness are guaranteed. In addition, the Quality by Design methodology deepens process understanding by generating knowledge systematically. This enables a data-based decision about the operating point. Based on this knowledge, the process can be optimized to maximize efficiency and minimize costs [14]. All the advantages are confirmed by results of the use case. The disadvantage of integrating Quality by Design in the direct scale-up is the additional time that is necessary to implement the Quality by Design methods. However, the additional effort can be reduced if digital twins support the process

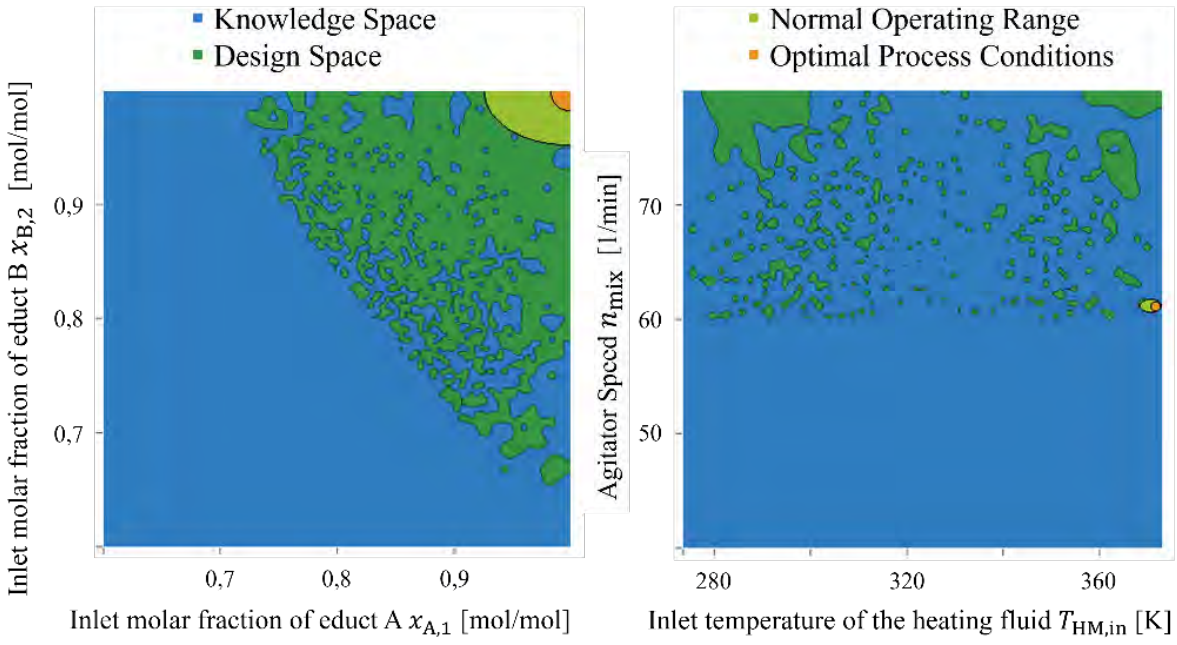



**Figure 3:** Location of the design space and normal operating range within the knowledge space for the production scale reactor (diagram generated with gPROMS®)

development.

To achieve a valid operation model of the digital twin, a large quantity of process data must be generated. The operation model that is build up with the help of the experimental data of the laboratory scale process, needs to be adapted continuously incorporating real time data of the production scale process.

If the data that is used for model adaption and discrimination is incomplete or inaccurate or underlies measurement mistakes, the operational model may not represent the process sufficiently. Thus, not only a high data quantity but also an adequate data quality is required. Another challenge of using digital twins as a tool for process scale-up may be the initial implementation since sensors must be installed at the process plant, a simulation software needs to be set up and a adequate data storage must be made available. As large amounts of data are processed, data security issues must be taken into consideration. Long term use of a digital twin requires maintenance like adding and replacing sensors or updating the simulation software.

In future research projects, the results found for the use case should be validated with measured data, which was not possible as the modular reactors M21 and M22 of the Process-to-Order-Lab-Learning Factory were not operational at the time of this work. The successful application of the workflow should be taken as an opportunity to apply the workflow to other use cases. Furthermore, the workflow could be extended to integrate more Quality by Design methods such as the quality risk analysis and the derivation of a process control strategy

## ACKNOWLEDGEMENTS

The authors would like to thank our partners Merck Electronics KGaA and Siemens AG in the industrial research project Lab2Plant for the fruitful discussions as well as the Process-to-Order Lab Learning Factory at TU Dresden for the information about planned reactor modules M21 and M22.

## REFERENCES

1. T. Furrer, B. Müller, C. Hasler, B. Berger, M. K. Levis, and A. Zogg, “New Scale-Up Technologies for Hydrogenation Reactions in Multipurpose Pharmaceutical Production Plants,” *CHIMIA*, vol. 75, no. 11, p. 948, Nov. 2021, doi: 10.2533/chimia.2021.948.
2. A.-L. Schindel *et al.*, “General approach for technology and Process Equipment Assembly (PEA) selection in process design,” *Chem. Eng. Process. - Process Intensif.*, vol. 159, p. 108223, Feb. 2021, doi: 10.1016/j.cep.2020.108223.
3. Z. Q. Yu, P. S. Chow, and R. B. H. Tan, “Design Space for Polymorphic Co-crystallization: Incorporating Process Model Uncertainty and Operational Variability,” *Cryst. Growth Des.*, vol. 14, no. 8, pp. 3949–3957, Aug. 2014, doi: 10.1021/cg500547m.
4. T. Furrer, M. Levis, B. Berger, M. Kandziora, and A. Zogg, “New Scale-Up Technologies for Multipurpose Pharmaceutical Production Plants: Use Case of a Heterogeneous Hydrogenation Process,” *Org. Process Res. Dev.*, vol. 27, no. 7, pp. 1365–1376, Jul. 2023, doi: 10.1021/acs.oprd.3c00124.
5. ISO 23247-1, “Automation systems and integration — Digital twin framework for manufacturing — Part 1: Overview and general principles,” ISO. Accessed: Apr. 29, 2022. [Online]. Available: https://www.iso.org/standard/75066.html
6. W. Kritzinger, M. Karner, G. Traar, J. Henjes, and W. Sihn, “Digital Twin in manufacturing: A categorical literature review and classification,” *16th IFAC Symp. Inf. Control Probl. Manuf. INCOM 2018*, vol. 51, no. 11, pp. 1016–1022, Jan. 2018, doi: 10.1016/j.ifacol.2018.08.474.
7. J. Mädler, I. Viedt, J. Lorenz, and L. Urbas, “Requirements to a digital twin-centered concept for smart manufacturing in modular plants considering distributed knowledge,” in *Proceedings of the 14th International Symposium on Process Systems Engineering – PSE 2021*, Kyoto, Japan, Jun. 2022.
8. A. Koch, J. Mädler, A. Bamberg, and L. Urbas, “Digital Twins for Scale-Up in Modular Plants: Requirements, Concept, and Roadmap,” in *Computer Aided Chemical Engineering*, vol. 52, Elsevier, 2023, pp. 2063–2068. doi: 10.1016/B978-0-443-15274-0.50328-0.
9. J. Mädler, A. Koch, A. Bamberg, and L. Urbas, “Process Validation in Modular Plants considering the Scale-Up and Prior Knowledge,” in *Computer Aided Chemical Engineering*, vol. 52, A. C. Kokossis, M. C. Georgiadis, and E. Pistikopoulos, Eds., Elsevier, 2023, pp. 2057–2062. doi: 10.1016/B978-0-443-15274-0.50327-9.
10. J. Ebert, “Anwendung von Quality by Design auf das Scale-Up modularer Anlagen,” Diploma Thesis, TU Dresden, 2024.
11. S. Lux, T. Winkler, G. Berger, and M. Siebenhof, “Kinetic Study of the Heterogeneous Catalytic Esterification of Acetic Acid with Methanol Using Amberlyst®15,” *Chemical and Biochemical Engineering Quarterly,* vol. 29, pp549-557, 2015, doi: 10.15255/CABEQ.2014.2083
12. T. Pöpken, L. Götze, and J. Gmehling, “Reaction Kinetics and Chemical Equilibrium of Homogeneously and Heterogeneously Catalyzed

Acetic Acid Esterification with Methanol and Methyl Acetate Hydrolysis," *Ind. Eng. Chem. Res.*, vol. 39, no. 7, pp. 2601–2611, Jul. 2000, doi: 10.1021/ie000063q
13. F. Pianosi, K. Beven, J. Freer, J.W. Hall; J. Rougier, D.B. Stephenson, and T. Wagener, "Sensitivity analysis of environmental models: A systematic review with practical workflow," *Environmental Modelling & Software,* vol. 79, pp. 214-232, Feb. 2016, doi: 10.1016/j.envsoft.2016.02.008
14. N. P. Nadpara, R. V. Thumar, V. N. Kalola, and P. B. Patel, "Quality by Design: A complete review," vol. 2012, no. 17, p. 20.28.

© 2025 by the authors. Licensed to PSEcommunity.org and PSE Press. This is an open access article under the creative commons CC-BY-SA licensing terms. Credit must be given to creator and adaptations must be shared under the same terms. See https://creativecommons.org/licenses/by-sa/4.0/



Systems & Control Transactions

**Research Article - Peer Reviewed Conference Proceeding**
ESCAPE 35 - European Symposium on Computer Aided Process Engineering
Ghent, Belgium. 6-9 July 2025
Jan F.M. Van Impe, Grégoire Léonard, Satyajeet S. Bhonsale,
Monika E. Polańska, Filip Logist (Eds.)

PSE PRESS

# Tune Decomposition Schemes for Large-Scale Mixed-Integer Programs by Bayesian Optimization

**Guido Sand[a*], Sophie Hildebrandt[a,b], Sina Nunes[a], Chung-On Yip[a] and Meik Franke[b]**

[a] Pforzheim University of Applied Science, School of Engineering, Pforzheim, Germany
[b] University of Twente, Faculty of Science and Technology, Enschede, The Netherlands
* Corresponding Author: guido.sand@hs-pforzheim.de.

## ABSTRACT

Heuristic decomposition schemes like moving horizon schemes are a common approach to approximately solve large-scale mixed-integer programs. The authors propose Bayesian optimization as a methodological approach to systematically tune parameters of decomposition schemes for mixed-integer programs. This paper discusses detailed results of three studies of the Bayesian optimization-based approach using hoist scheduling as a case study: Firstly, two objectives of the tuning problem are examined considering sequences of incumbent solutions found by the Bayesian optimization. Secondly, the Bayesian optimization is applied to a set of test instances of the hoist scheduling problem using four types of acquisition functions; they are compared with respect to the convergence of the tuning problem solutions. Thirdly, the scaling behaviour of the Bayesian optimization is studied with respect to the dimension of the space of tuning parameters. The results of the three studies show that the solutions found by the Bayesian optimization converge quickly in smaller and larger tuning parameter spaces using different types of acquisition functions.

**Keywords**: Derivative Free Optimization, Machine Learning, Mixed-Integer Programming

## MOTIVATION

### Decomposition Schemes for MIPs

Heuristic decomposition schemes are a common approach to approximately solve large-scale mixed-integer programs (MIPs) as a sequence of partial MIPs. A typical example are moving horizon schemes applied to scheduling problems. Decomposition schemes usually exhibit parameters which can be used to tune their performance. Examples for parameters of moving horizon schemes are the horizon length and the step size of its movement.

### Existing Tuning Methods

30 publications on decompositions schemes for mixed-integer programs (both linear and non-linear) were analysed with respect to systematic tuning methods. The publication dates range from 2002 to 2025; 26 of the publications are journal papers, 3 are conference papers and 1 is a book section. The mixed-integer programs cover batch scheduling, maintenance scheduling, project scheduling, supply network planning, production routing, bin packing, locomotive assignment, healthcare planning, flowsheet optimization, lot sizing and other optimization problems. The decomposition schemes cover temporal, area, activity, scenario and geographic decomposition as well as rolling horizon and other schemes.

Tuning parameters were clearly identified in 25 publications; in the other 5 publications the existence of tuning parameters could not be decided. Only in 12 publications the tuning parameters were tuned, in 9 of them by grid search [e.g. 1,2,3], in 2 by heuristics and in 1 they were chosen randomly. No publication with an optimization-driven tuning method was found.

### Bayesian Optimization Based Tuning

In a previous paper [4], Bayesian optimization was proposed as a methodological approach to tune decomposition schemes for mixed-integer programs. This approach is reasonable since the tuning problem is a black-box optimization problem with an expensive to evaluate objective function: Each evaluation of the objective function of the Bayesian optimization requires the (approximate) solution of the MIP applying the parametrized decomposition scheme. The mentioned paper demon-

strated by a case study that the proposed approach is feasible and effective in principle. The case study was a mixed-integer hoist scheduling model along with a moving horizon decomposition scheme (see below).

### Scope of this Paper

This paper discusses results of three studies of the Bayesian optimization-based approach using the same case study: Firstly, two objective functions of the tuning problem are examined considering sequences of incumbent solutions found by the Bayesian optimization. (An incumbent solution is the best solution found up to a certain iteration.) Secondly, the Bayesian optimization is applied to a set of test instances of the hoist scheduling problem using four types of acquisition functions; they are compared with respect to the convergence of the tuning problem solutions. Thirdly, the scaling behaviour of the Bayesian optimization is studied with respect to the dimension of the space of tuning-parameters.

## CASE STUDY

### Hoist Scheduling Model

Hoist scheduling is the task of assigning several steps of several jobs to several stations over time. Figure 1 shows an exemplary layout of a batch plant with a hoist (left) and exemplary recipes defining the sequence and duration of steps for two jobs. In addition to the usual job shop scheduling constraints, the hoists must be considered. Hoists transport product carriers between the stations and constrain the solution space due to their finite transportation times. A typical objective of hoist scheduling is makespan minimization. Hoist scheduling problems can be formulated as MIPs.

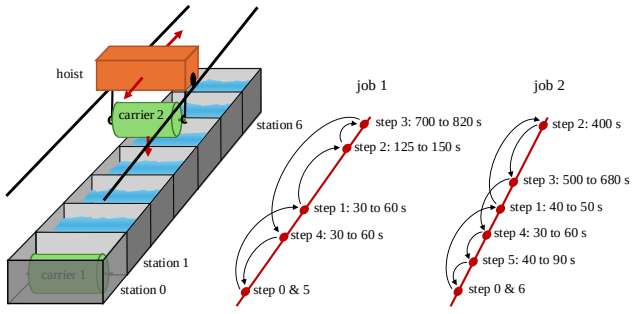



**Figure 1.** Hoist scheduling. Left: Exemplary layout of a batch plant with hoist. Right: Exemplary recipies.

In this paper, the MIP-model by Aguirre at al. [1] is used as a case study. This model considers one hoist, stations with a capacity of one carrier and non-circulating carriers. In the context of this work, it serves as an example for an NP-complete problem, that calls for decomposition schemes for large-scale instances.

### Heuristic Decomposition Scheme

The heuristic decomposition scheme used in this paper is an extension of the moving horizon scheme described by Aguirre et al. [1]. It comprises two sequential phases to schedule jobs from a given list of jobs: a construction phase and an improvement phase.

In the construction phase, jobs 1 to NSJ (number of selected jobs) are scheduled by solving a partial MIP, then jobs 1 to NFJ (number of fixed jobs) are fixed and jobs NFJ+1 to NSJ+NFJ+1 are (re)scheduled, and so on. The number of partial MIPs to be solved is given by the number of jobs divided by NFJ. The construction phase generates a first feasible schedule, which may be improved in the improvement phase.

In the improvement phase, jobs 1 to NRJ (number of released jobs) from the schedule are rescheduled by solving a partial MIP. If the schedule is not improved, jobs 2 to NRJ+1 are rescheduled, and so on. If the schedule is improved, the improvement phase re-starts from the first job in the schedule. The improvement phase terminates if no further improvement is observed. In contrast to the construction phase, the number of partial MIPs to be solved during the improvement phase cannot be predicted.

The tuning parameters NSJ, NFJ and NRJ are integer in nature and have a lower bound of 1. The upper bounds of NSJ and NRJ are the total number of jobs; the upper bound of NFJ is NSJ: NFJ≤NSJ. In addition to the integer parameters, the accepted optimality gap (AOG) of the partial MIPs (termination criterion of the MIP solver) is considered as a continuous tuning parameter within the bounds of 0 % to 100%. Aguirre et al. considered only NSJ and NRJ as tuning parameters; this paper extends the tuning parameter space by NFJ and AOG.

### Architecture of the Tuning Method

Figure 2 illustrates the algorithmic components for the tuning of decomposition schemes for large-scale MIPs and the information exchanged between them.

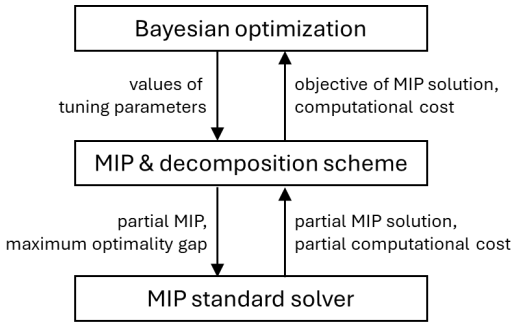



**Figure 2.** Algorithmic architecture for MIP decomposition scheme tuning.

The Bayesian optimization generates the next values of tuning parameters for the decomposition scheme;

the next values are based on previous values of the objective of the MIP solution or the computational cost to apply the decomposition scheme. For the studies in this paper, the implementation SMAC3[1] is used.

Based on the values of the tuning parameters, the decomposition scheme generates a sequence of partial MIPs from the MIP. The MIP and the decomposition scheme are implemented using Pyomo[2].

The MIP standard solver solves the partial MIPs with at least the AOG provided by the Bayesian optimization. It returns the partial MIP solution along with its partial computational cost. For the studies in this paper, CPLEX[3] is used as the MIP standard solver.

## TUNING PROBLEM OBJECTIVES

In the first study two objective functions of the tuning problem are examined considering sequences of incumbent solutions found by the Bayesian optimization.

### Motivation for Different Objectives

Applying heuristic decomposition schemes to large-scale MIPs has two natural and competing objectives: The computational cost shall be minimized while the objective of the MIP shall still be optimized. For the case study at hand, the computational cost is measured by the CPU-time needed to apply the decomposition scheme to the MIP. The MIP objective is to minimize the makespan of the hoist schedule, measured in time units TU.

### Setup of Computational Studies

Heuristic decomposition schemes are useful for large-scale MIPs with computational cost that prohibit their solution. However, the studies in this paper are limited to small-scale MIP-instances that can (exactly) be solved at reasonable computational cost to ensure that all partial MIPs can be solved to proven optimality.

Four instances of the hoist scheduling model comprising six jobs each are considered; the instances differ in the number of steps and stations and in the speed of the hoist.

The number of jobs is kept constant to keep the size of the tuning parameter space constant. In this first study the tuning parameters NSJ und NRJ vary between 1 und 6, while NFJ is set to 1 and AOG is set to 0. This leads to a tuning parameter space with only 36 feasible (integer) solutions, such that a grid search with complete enumeration of all solutions is possible. Only one objective of the tuning problem (computational cost or makespan) is optimized at a time (without limiting the other).

### Computational Results

A grid search in the NSJ-NRJ-space of the tuning problem leads to similar shapes of each of the objective functions for the four instances. Therefore, only the results for instance 1 are discussed in the sequel.

Figure 3 shows the results of the grid search for the computational cost objective combined with the incumbent solutions found by the Bayesian optimization (red line). Note, that only the integer-valued points are feasible while the values of the objective function are interpolated between them to improve the clarity of the figure.

The computational cost objective exhibits multiple minima located at the corners of the tuning parameter space: (1;1), (6;1), (1;6) and (6,6). The Bayesian optimization is initialized at the worst solution (4;4); after finding two local optima it terminates at the global one (1;1). This solution is intuitively reasonable for the computational cost objective, since the partial MIPs in the construction phase and the improvement phase are of minimal size and cheap to solve.

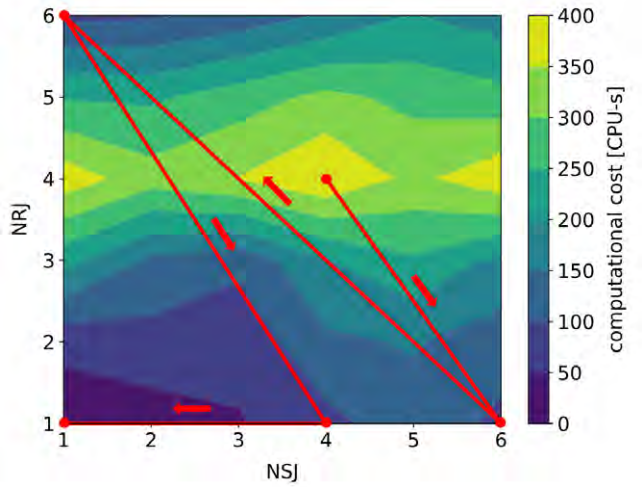



**Figure 3.** Computational cost objective of instance 1 and incumbent solutions found by the Bayesian optimization.

Analogue to Figure 3, Figure 4 shows the results for the makespan objective. The maximum of the makespan objective (1;1) is at the same point as the minimum of the computational cost objective. This exemplifies the competing character of the two objectives and demonstrates the need to balance them appropriately.

Analogue to above, the Bayesian optimization is initialized at the worst solution (1,1). It terminates after the first incumbent solution (6;1). The early termination is obviously favoured by the weakness of the objective function: Since 27 out of 36 solutions are optimal, an optimum is easy to find.

Note, that NSJ=6 or NRJ=6 means that the MIP is neither decomposed in the construction phase nor in the

[1] https://automl.github.io/SMAC3/main/index.html#
[2] https://www.pyomo.org/
[3] https://www.ibm.com/products/ilog-cplex-optimization-studio

improvement phase. The optimality of solutions (6;1), (6,2), … (6,6), (5,6) … (1;6) is intuitively reasonable: Decomposing the MIP bears the risk of losing its optimum, such that by not decomposing it the optimum is secured.

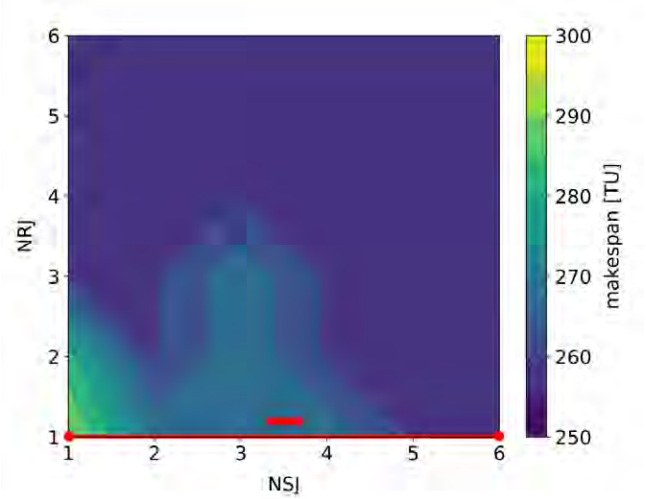



**Figure 4.** Makespan objective of instance 1 and incumbent solutions found by the Bayesian optimization.

## ACQUISITION FUNCTIONS

In the second study the Bayesian optimization is applied to a set of test instances of the hoist scheduling problem using four types of acquisition functions; they are compared with respect to the convergence of the tuning problem solutions.

### Impact of the Acquisition Function

Acquisition functions steer the selection of the next point in the solution space of the Bayesian optimization. Different types of acquisition functions balance the exploitation and the exploration of the search space in different ways. Therefore, the type of acquisition function is assumed to be a design parameter of the Bayesian optimization with a major impact on its performance.

The following four common acquisition functions are applied to the four small-scale instances and the two objective functions from the first study: “expected improvement” (also applied in the first study), “probability of improvement”,” upper confidence bound” and “Thompson sampling”.

### Setup of Computational Studies

For each acquisition function and each objective function, the objective values of the incumbent solutions of the four instances are plotted over the iterations of the Bayesian optimization. To make them comparable, the objective functions are normalized such that the starting point equals 100% and the optimum equals 0%. Note that the optimum in the tuning parameter space is known from the first study. For each iteration, the minimum, the maximum and the mean value of the normalized objective are displayed.

### Computational Results

The results for the acquisitions functions “expected improvement”; “upper confidence bound” and “Thompson Sampling” are similar, while the convergence using the “probability of improvement” function is slower. For the makespan objective the Bayesian optimization converges after 2-3 iterations to an optimum, while for the computational cost objective the number of iterations is higher. (This observation is consistent with study 1.) Therefore, only the results for the computational cost objective and the acquisition functions “probability of improvement” and “expected improvement” are discussed (see Figures 5 und 6).

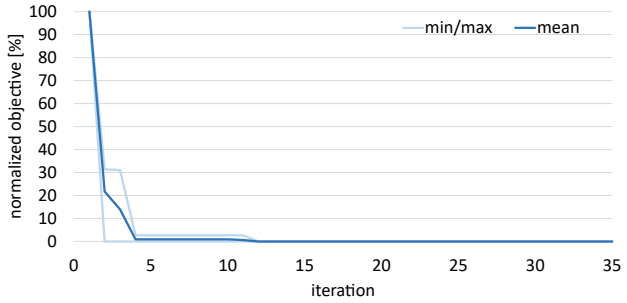



**Figure 5.** Convergence of computational cost objective with acquisition function “expected improvement”.

The acquisition function “expected improvement” considers both, the likelihood of improvement of the next solution and the magnitude of its potential improvement [5]. It balances exploration and exploitation of the tuning parameter space and is therefore well suited for objective functions with multiple local optima.

As Figure 5 shows, the instances converge after 2 to 12 iterations to the global optimum (with a normalized objective of 0%). After 4 iterations the maximum normalized objective over all instances is around 3%. The instances terminate after 14 to 35 iterations. The relevant termination criterion is the maximum number of 16 retries i.e. after 16 iterations no new solution in the tuning parameter space is found.

In contrast to the acquisition function “expected improvement”, the acquisition function “probability of improvement” selects the next solution such that the objective value is most likely to improve [6]. It typically selects the next solution close to the last solutions, such that it behaves more exploitative than explorative.

Applying the acquisition function “probability of improvement” to the case study leads to slower convergence to inferior solutions compared to the other acquisition functions. As Figure 6 shows, the instances terminate after 11 or 13 iterations before the final solution with

normalized objectives between 1% and 13% is reached.

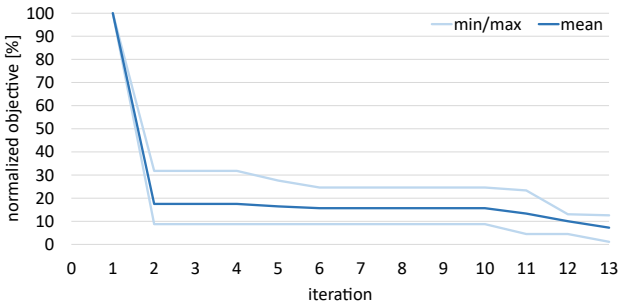



**Figure 6.** Convergence of computational cost objective with acquisition function "probability of improvement".

## TUNING PARAMETER SPACE DIMENSION

The third study analyses the scaling behaviour of the Bayesian optimization with respect to the dimension of the space of tuning parameters.

### Extension of the Tuning Parameter Space

The proposed Bayesian optimization-based approach is particularly useful for tuning parameters spaces of a size that prohibit full grid search. Therefore, the two-dimensional tuning parameter space considered in studies 1 and 2 is extended by two additional dimensions: the integer-valued NFJ and the continuous AOG. (Both were introduced in section "Heuristic Decomposition Scheme" but bound to fixed values in studies 1 and 2.) The same settings as in study 1 were applied.

### Comparative Analysis of the Convergence

To comparatively analyse the convergence speed, the same type of plots with the same normalization is used as in Figures 5 and 6. Figures 7 and 8 show the convergence of both objective functions in the larger tuning parameter space.

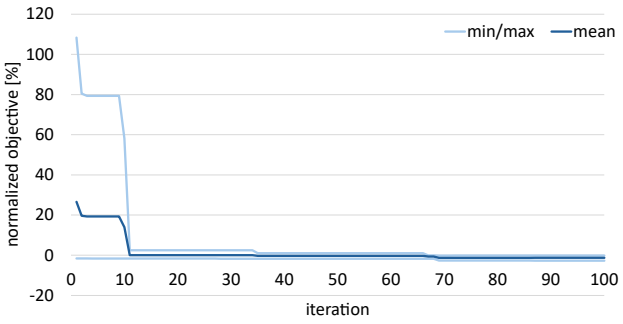



**Figure 7.** Convergence of computational cost objective with four-dimensional tuning parameter space.

As the full grid-search is prohibited, the worst solutions in the tuning parameter space are not know such that they cannot be used to initialize the Bayesian optimization (as in Figures 5 and 6). Instead, arbitrary initialization points were chosen for Figures 7 and 8.

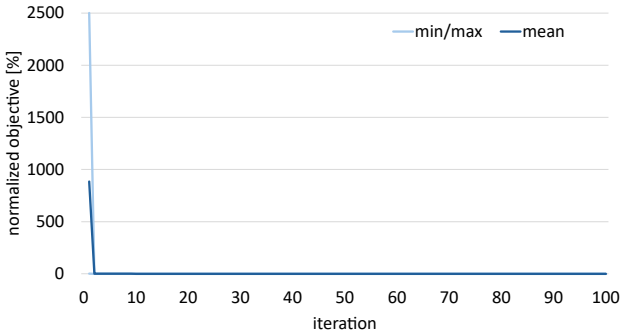



**Figure 8.** Convergence of makespan objective with four-dimensional tuning parameter space.

The worst normalized objective value in Figure 7 is 108% at iteration 1. This shows that the larger search space of this study 3 contains worse solutions than the smaller search space of studies 1 and 2. On the other hand, the Bayesian optimization terminates after 100 iterations at a solution with a normalized objective vale of -3%. This shows that the additional dimensions of the tuning space (NFJ and AOG) provide additional optimization potential that was exploited by the Bayesian optimization.

The convergence speeds in Figures 5 (smaller tuning parameter space) and 7 (large tuning parameter space) are comparable. Figure 7 shows that the maximum normalized objective over all instances is around 3% after 11 iterations (compared to 4 iterations in Figure 5).

Figure 8 shows similar results for the makespan objective than Figure 7 for the computational cost objective: The worst normalized objective in Figure 8 is 2500% (compared to 100% in Figure 6), and the maximum normalized objective over all instances is around 1% already after 2 iterations.

### Comparative Analysis of the Optimized Tuning Parameters

The optimized tuning parameters for the two objectives are shown in Tables 1 and 2.

**Table 1:** Optimized tuning parameters for computational cost objective.

| Instance | NSJ | NRJ | NFJ | AOG |
|---|---|---|---|---|
| 1 | 1 | 1 | 1 | 78% |
| 2 | 4 | 6 | 3 | 86% |
| 3 | 1 | 1 | 1 | 100% |
| 4 | 6 | 6 | 1 | 91% |

**Table 2:** Optimized tuning parameters for makespan objective.

| Instance | NSJ | NRJ | NFJ | AOG |
|---|---|---|---|---|
| 1 | 6 | 2 | 2 | 0% |
| 2 | 3 | 3 | 1 | 2% |
| 3 | 3 | 3 | 1 | 2% |
| 4 | 5 | 5 | 5 | 9% |

For the computational cost objective (see Table 1), most of the values of the integer-valued tuning parameters NSJ, NRJ and NFJ are at their boundaries. This result is reasonable since solving many small or one medium-sized MIP is computationally cheap (compare Figure 3).

The AOG is close to or at 100%, which is also reasonable since the partial MIPs terminate the earlier the larger the AOG is.

For the makespan objective (see Table 2), most of the values of the integer-valued tuning parameters NSJ, NRJ and NFJ are away from their boundaries (contrasting Table 1). This observation can reasonably be explained by the weak optimum of this objective (compare Figure 4).

The AOG is close to or at 0% (also contrasting Table 1). This result is also reasonable since smaller optimality gaps push the MIP solver to better solutions of the partial MIPs.

## CONCLUSIONS AND FUTURE WORK

In this work, a Bayesian optimization-based approach to tune decomposition schemes for MIPs was studied in detail using hoist scheduling as a case study. The results support the following two main conclusions:

Firstly, decomposition schemes comprise tuning parameters which are sensitive to the two natural objectives of decomposing, namely minimizing the computational cost while still optimizing the MIP objective; these two objectives are competing.

Secondly, a reasonable method to tune the parameters of a decomposition scheme is Bayesian optimization due to its following properties:

- The performance of the Bayesian optimization is insensitive against changes of its acquisition function. If exploration and exploitation are not unbalanced, good solutions are found after a few iterations.
- The performance of the Bayesian optimization is insensitive against changes of the parameters of the MIP. The convergence behaviour of different instances of the MIP is similar.
- Multiple local optima and the global optimum in the space of tuning parameters can be found by the Bayesian optimization.
- The Bayesian optimization is efficient in smaller and larger mixed-integer tuning parameter spaces. Its performance in two- and four-dimensional spaces is comparable.

In its present state, Bayesian optimization-based approach exhibits limitations. Future work deals with the approaches to relax them: Multi-objective optimization will be studied; large-scale MIP which cannot be solved to proven optimality will be examined; and methods to deal with multiple MIP-instances will be developed.

## REFERENCES


1. Aguirre A, Méndez C, Sànchez Á, Mier M. Applying MILP/Heuristic Algorithms to Automated Job-Shop Scheduling Problems in Aircraft-Part Manufacturing. *IJIE* 5(10):26-41 (2014) https://incubadora.periodicos.ufsc.br/index.php/IJIE/article/view/3043
2. Kelly JD, Mann JL. Flowsheet decomposition heuristic for scheduling: a relax-and-fix method. *Comp.Chem.Engg.* 28:2193–200 (2004). https://doi.org/10.1016/j.compchemeng.2004.03.009.
3. Paquay C, Limbourg S, Schyns M, Oliveira JF. MIP-based constructive heuristics for the three-dimensional Bin Packing Problem with transportation constraints. *Int.J.Prod.Res.* 56:1581–92 (2018). https://doi.org/10.1080/00207543.2017.1355577.
4. Hildebrandt S, Sand G. Hyperparameter optimization of matheuristics for hoist scheduling. In: ESCAPE34/PSE24. Ed: Manenti F, Reklaitis GV. Elsevier (2024) https://doi.org/10.1016/B978-0-443-28824-1.50488-9
5. Mockus J, Tiesis V, Zilinskas A. The application of Bayesian methods for seeking the extremum. *Towards Global Optimisation* 2:117–129 (1978)
6. Kushner, H J. A New Method of Locating the Maximum Point of an Arbitrary Multipeak Curve in the Presence of Noise. *J. Fluids Eng.* 86(1):97–106 (1964) https://doi.org/10.1115/1.3653121



© 2025 by the authors. Licensed to PSEcommunity.org and PSE Press. This is an open access article under the creative commons CC-BY-SA licensing terms. Credit must be given to creator and adaptations must be shared under the same terms. See https://creativecommons.org/licenses/by-sa/4.0/




Systems & Control Transactions

**Research Article - Peer Reviewed Conference Proceeding**
ESCAPE 35 - European Symposium on Computer Aided Process Engineering
Ghent, Belgium. 6-9 July 2025
Jan F.M. Van Impe, Grégoire Léonard, Satyajeet S. Bhonsale,
Monika E. Polańska, Filip Logist (Eds.)

PSE PRESS

# A Superstructure Approach for Optimization of Simulated Moving Bed (SMB) Chromatography

**Eva Sorensen[a,*], Dian Ning Chia[a], Fanyi Duanmu[a]**

[a] Department of Chemical Engineering, University College London, Torrington Place, London WC1E 7JE, United Kingdom
* Corresponding Author: e.sorensen@ucl.ac.uk

## ABSTRACT

One of the most successful continuous high-performance liquid chromatography (HPLC) processes for drug manufacturing is the Simulated Moving Bed (SMB). SMB is a multi-column, continuous, chromatographic process that can handle much higher throughputs than regular batch chromatographic processes. The process is initially transient, but eventually arrives at a cyclic steady state, which makes optimization very challenging, even more so when superstructure optimization is involved. To simplify the optimization problem, many researchers fixed the SMB structure, optimizing only the continuous variables, so they cannot be considered superstructure optimization. In this work, an SMB superstructure that can simultaneously optimize column structure and operation is proposed. The results showed that the superstructure proposed is reliable, and it is more efficient compared to current optimization approaches if the optimal column structure has to be identified.

**Keywords**: Modelling and Simulations, Process Design, Optimization, Particle Swarm Optimization, gProms, Superstructure, Simulated Moving Bed, Chromatography

## INTRODUCTION

Chromatography is one of the most important separation processes in the pharmaceutical industry, used to purify valuable active pharmaceutical ingredients (APIs). The ability to efficiently extract pure (e.g., 99.9 wt%) APIs is crucial to ensure the health and safety of patients ingesting the medicine, but also to reduce waste and maximise profit. The most commonly used chromatographic process, high-performance liquid chromatography (HPLC), features a tightly packed stationary phase within a column, through which a mobile phase containing the feed mixture is passed. There are two operating modes for HPLC – batch or continuous. Although the continuous process is more complex in terms of design and operation, the pharmaceutical industry is slowly transitioning to adopting continuous processes as this mode can improve both efficiency and productivity.

The most successful continuous HPLC process for drug manufacturing is the Simulated Moving Bed (SMB). SMB is a multi-column, continuous, chromatographic process that can handle much higher throughputs than regular batch chromatographic processes. SMB usually has four sections, the desorbent (D), extract (E), feed (F) and raffinate (R) sections, and simulates a counter-current flow between the stationary and mobile phases through periodical and synchronous switching of the inlet and outlet ports in the direction of fluid flow. Figure 1 illustrates the operating principle for an eight-column SMB (two columns per section, *aka* a 2222 SMB), where the ports move forward (in the direction of fluid flow) by one column after a switch time $t_s$, and finally return to the initial state after eight switches (i.e., after a complete cycle). The process is initially transient but eventually arrives at a cyclic steady state (CSS). Each SMB section can have a different number of columns, which must be determined carefully due to physical limitations (e.g., pressure drop) which may have a significant effect on the separation performance. These limitations pose challenges for the modelling and optimization of an SMB process, as will be briefly discussed below.

Firstly, consider the modelling of an SMB process. To capture both the transient startup stage and the CSS, the most straightforward method is to perform a dynamic simulation, where each cycle in the SMB process is simulated until the CSS is identified [1–3]. This approach is,

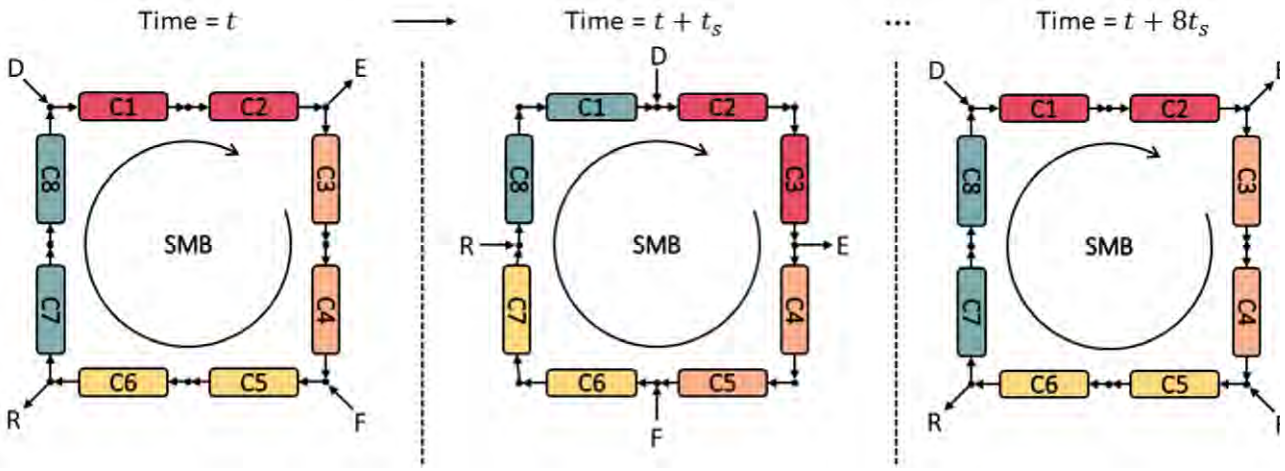



**Figure 1.** Operating procedure of an eight-column SMB (two columns per section), where $t_s$ is the switch time, $C_i$ is column $i$, and D, E, F, R are the desorbent, extract, feed, and raffinate flow rates, respectively. A complete cycle for this structure requires $8t_s$. The circular arrow represents the direction of fluid flow.

however, very time-consuming as CSS is often achieved only after a number of cycles. Information about the transient startup stage is usually redundant when considering optimization; as only the final CSS is of interest for SMB operation. By incorporating the CSS conditions as part of the optimization boundary conditions, the conditions at CSS can be simulated directly, making it faster than dynamic simulation for transient startup. There are two popular ways to include CSS conditions in the boundary conditions: (1) the method by Nilchan and Pantelides [4], where it is assumed that the conditions at the start and end of a cycle are identical, and (2) the method by Kloppenburg and Gilles [5], where the state variables at the outlet of a column are the same as that at the inlet of the next column. However, to incorporate CSS conditions as part of the boundary conditions, a fully discretized model (spatial and temporal domains discretized) is needed, which involves more equations and variables than the partially discretized model (only spatial domain discretized) used for dynamic simulation. It should be noted that the simulation time of both dynamic and direct CSS approaches are highly dependent on the grid discretization; finer grid provides more accurate separation behavior but greatly increases the simulation time, and vice versa. Therefore, whether the dynamic or direct CSS approach is more time-efficient will depend on the discretization grid and method used.

For optimization of SMB, most researchers have conveniently fixed the column structure and optimized only the continuous optimization variables (e.g., [3,6,7]). Only a few studies have considered SMB superstructure optimization, which allows identification also of the column design and arrangement. Kawajiri and Biegler [8–10] explored an SMB superstructure which took into account the standard continuous variables as well as some structural configuration decisions (e.g., the number of columns in each section), but their superstructure was limited to a fixed total number of columns.

This work therefore aims to: (1) discuss and provide solutions for challenges related to handling the number of columns and switch actions in SMB superstructure modelling and optimization, and (2) propose a superstructure approach that allows for simultaneous optimization of the number of columns in each section, as well as the column dimensions (length and diameter) and the switching times and the flow rates. This superstructure optimization problem, which is a mixed integer non-linear programming (MINLP) problem, will determine not only the optimal configuration, but also simultaneously the column design as well as the operating procedure of the SMB process.

## METHODOLOGY

This section will outline the key steps required to construct a superstructure model of an SMB process. Firstly, the superstructure flowsheet must be constructed. In most cases, models are solved with a numerical solver, meaning that the degrees of freedom must be carefully considered when constructing the model (e.g., the number of equations in *if* and *else* branches must be the same). This introduces challenges when handling optimization of the number of columns and port changes, and the solutions to these problems will be discussed. As previously mentioned, the model can be partially or fully discretized depending on the purpose of the study. This work will also discuss the conversion of a partially discretized model into a fully discretized model.

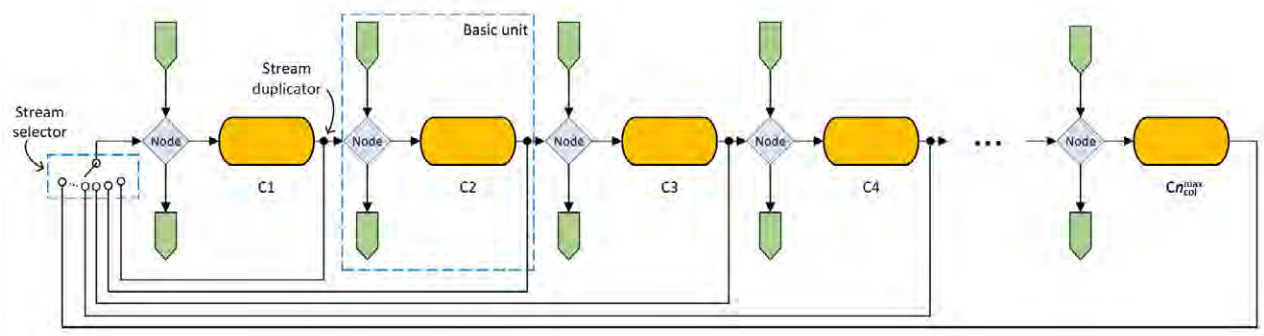



**Figure 2.** Flowsheet of the proposed SMB superstructure made up of $n_{\mathrm{col}}^{\max}$ basic units (node + column).

## Superstructure Flowsheet

The flowsheet of our SMB superstructure is shown in Figure 2. The basic unit is made up of two parts: (1) a node model, where it is modelled as an instantaneous mixer as proposed by Chan et al. [11], followed by (2) a chromatography column model consisting of a transport model (e.g., general rate model or equilibrium dispersive model) and an isotherm model (e.g., linear or Langmuir). The basic unit of node and column is then repeated $n_{\mathrm{col}}^{\max}$ times, where $n_{\mathrm{col}}^{\max}$ is the maximum total number of columns (not number of columns per section) considered in the optimization. This maximum number must be decided *a priori*. The outlet stream of each basic unit (i.e., outlet stream of the column), except for the last basic unit for which the outlet stream is a recycle stream, is connected to a stream duplicator. The stream duplicator does not physically exist, and its existence is solely to duplicate the outlet stream information: for the stream that is sent to the next basic unit (i.e., becomes the inlet stream to the node model) and for a stream selector used to identify the recycle stream location and therefore the optimal number of columns required. Only one stream selector is present in the flowsheet, and it is located prior to the first basic unit. The stream selector connects the recycle stream from the final column (i.e., the recycle stream from column $n_{\mathrm{col}}^{\mathrm{tot}}$) to the inlet of the first basic unit. The other recycle streams that are not selected are treated as redundant streams in the optimization.

## Handle Number of Columns

As previously described, the SMB superstructure flowsheet consists of $n_{\mathrm{col}}^{\max}$ basic units, and this is represented as an array of basic units in the model. When solving the model using numerical solvers, the number of equations cannot change during the simulation/optimization. Therefore, the size of the basic unit array must be fixed *a priori*. Since the number of columns in a section $j$, $n_{col,j}$, is an optimization variable, there are three possible cases: (1) $\sum_{j=1}^{4} n_{col,j} > n_{\mathrm{col}}^{\max}$ which will be treated as an infeasible simulation and discarded, (2) $\sum_{j=1}^{4} n_{col,j} = n_{\mathrm{col}}^{\max}$ where no additional action is required, and (3) $\sum_{j=1}^{4} n_{col,j} < n_{\mathrm{col}}^{\max}$ where there are "redundant" columns that need to be considered. Chia and Sorensen [12] discussed the handling of redundant membrane stages in a membrane superstructure, which is similar in principle to that of an SMB superstructure. Therefore, their strategy where all columns are simulated but the optimal result is collected from the optimal column $n_{\mathrm{col}}^{\mathrm{tot}}$ will be used.

## Handle Port Changes

Referring to Figure 1, a port is the black circle located before each column. For example, the desorbent stream is at port 1 at time $t$, at port 2 at time $t + t_s$, and at port 1 again at time $t + 8t_s$. There are four sections in a typical SMB, and each section has a port number allocated to it at any time. Therefore, a variable $\beta_j$ (where $j$ represents the four sections) is introduced to hold the information about the port number of each section at a given time. During SMB operation, a port moves forward by one column after a switch time $t_s$; hence, the port number should increase by 1 after $t_s$. This change can be captured with an intermediate variable $\beta_j^{\mathrm{raw}}$:

$$\frac{d\beta_j^{\mathrm{raw}}}{dt} = \frac{1}{t_s} \qquad \forall j \in \{1,2,3,4\} \text{ or } \{\mathrm{D},\mathrm{E},\mathrm{F},\mathrm{R}\} \qquad (1)$$

However, Equation 1 will increase the port number beyond the actual total number of columns $n_{\mathrm{col}}^{\mathrm{tot}}$. So, to limit the port number in the range $\left[1, n_{\mathrm{col}}^{\mathrm{tot}}\right]$, a modulo operator where $a \bmod b \equiv a - b \times \left\lfloor \frac{a}{b} \right\rfloor$ is applied:

$$\beta_j = \left\lfloor \left(\beta_j^{\mathrm{raw}} - 1\right) \bmod n_{\mathrm{col}}^{\mathrm{tot}} \right\rfloor \quad \forall j \in \{1,2,3,4\} \text{ or } \{\mathrm{D},\mathrm{E},\mathrm{F},\mathrm{R}\} \qquad (2)$$

With Equation 2, the port number of each section at a given time can be identified, and further actions, such as determining the inlet flow rate of a node at a given time, can be performed using *if-else* statements.

## Discretization of the Superstructure Model

The partially discretized superstructure model,

discretized in the axial direction of the column, has now been constructed. To transform this partially discretized model into a fully discretized model, firstly, all time-variant variables in the partially discretized model must have an additional temporal domain. Then, the initial conditions of the partially discretized model become the boundary conditions for the temporal domain in the fully discretized model. As discussed in the introduction, when formulating the boundary conditions, the CSS condition can be considered as repeating within a cycle [4] or matching inlet-outlet states between columns in a switch [5]. Both options are possible, but the latter allows faster simulation time as it involves fewer equations, hence is applied in this work. To complete the transformation into a fully discretized model, the time-derivative equations must also be transformed into partial derivative equations (e.g., $d\beta_j^{\mathrm{raw}}/dt$ becomes $\partial\beta_j^{\mathrm{raw}}/\partial t$).

Completing the steps above will yield a fully discretized model. The switch time $t_s$ now becomes the upper bound of the temporal domain (i.e., becomes a parameter) and therefore cannot be optimized. To solve this issue, the temporal domain must be normalized. This can be done by introducing a new variable $\tau$, so that $\tau = t/t_s$. This will also transform the range of the temporal domain from $t \in [0, t_s]$ to $\tau \in [0, 1]$. Finally, the partial derivatives need to be transformed with the following equation:

$$\frac{\partial}{\partial t} = \frac{\partial}{\partial(\tau\, t_s)} = \frac{1}{t_s}\frac{\partial}{\partial \tau} \tag{3}$$

After the transformation, the partial derivatives are expressed in terms of $\tau$ and not $t$. Therefore, $t_s$ is freed from the boundary, and returns to becoming a variable that can be optimized (i.e., no longer a parameter).

## MODEL COMPARISON

To demonstrate the performance of the proposed SMB superstructure model, the SMB equations and case study used by Dünnebier et al. [1] is considered. Since this work introduces both partially and fully discretized superstructure models, both models will be considered and compared.

Dünnebier et al. [1] developed a four-zone SMB with two columns in each zone, resulting in a 2222 SMB configuration. The detailed information, including equations of the distributed plug flow and the node, linear isotherm, node equations, and other necessary equations and parameter values, can be found in the literature [1,11], and will therefore not be presented in this work. The maximum allowed number of columns in the superstructure model is set as 12, however, in the optimization only 8 columns will be considered, i.e., 4 columns are "bypassed". This is done to test the methodology and to demonstrate that the redundant 4 columns are not considered in the optimal solution.

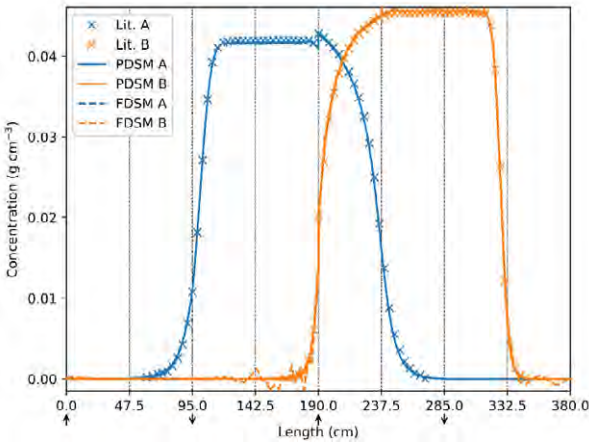



**Figure 3.** Comparison between the steady-state concentration profiles for components A (blue) and B (orange) obtained from literature (Lit.) [1], partially discretized superstructure model (PDSM), and fully discretized superstructure model (FDSM) at the end of a switching time.

The superstructure model in this work is developed in gPROMS. The partially discretized model contains only the spatial domain (i.e., discretization only along the column). A fourth-order orthogonal collocation finite element method (OCFEM) is chosen with ten collocation points. The fully discretized model involves an additional temporal domain. Both spatial and temporal domains in the fully discretized model are described using the fourth-order OCFEM as it can provide a sufficient accuracy with a reasonable computational time (trade-off not shown). All simulations and optimizations are performed on a workstation with a dual Intel Xeon Gold 6226R CPU (64 processors).

The steady-state concentration profiles along a single column for both components A (fructose) and B (glucose) are plotted in Figure 3. Overall, the simulation results from the proposed partially discretized and fully discretized superstructure models are very similar to those from literature. Figure 3 showed only the results for the first eight columns although the superstructure model is set to have 12 columns; the last four columns are bypassed so their results are ignored. The superimposing chromatograms also indicated that the bypassed columns do not affect the optimal results, so the methodology for handling number of columns can be used in optimization. It is noted that some oscillations due to numerical integration appears with the fully discretized model. This could be improved and minimized by using a finer discretization or choosing a more suitable discretization method. In terms of the purity of the products, the difference between the two proposed models is in the order of magnitude of $10^{-4}$ g $g^{-1}$, which is reasonable and more than sufficient for most optimizations. In terms of CPU

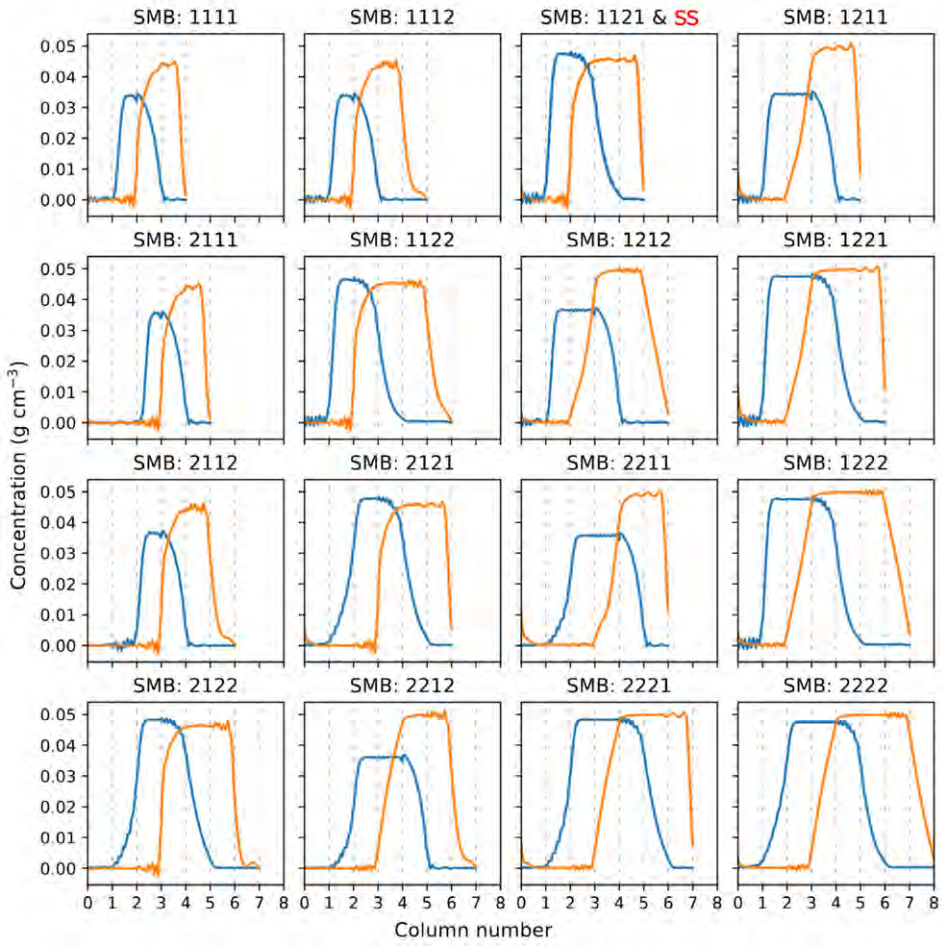



**Figure 4.** Concentration profiles along the columns for the simulated moving bed (SMB) structures investigated, including the optimal design obtained from individual optimization with fixed configuration and superstructure optimization (SS). The numbers in the title indicate the number of columns in the desorbent, extract, feed, and raffinate sections, respectively.

time, the fully discretized model is much faster, with about 8 s per simulation, while the partially discretized model requires 131 s per simulation. This significant difference makes the fully discretized model superior for optimization and cases requiring many simulations (e.g., for global sensitivity analysis).

## SMB OPTIMIZATION

In the following, we will consider superstructure optimization where we simultaneously optimized the number of columns per SMB section, the design of the column (length and diameter) as well as the switch time and flow rates. The model, mixture, and other key parameter values are the same as previously.

In the following, the SMB configurations considered will have one or two columns in each section, which are considered as optimization variables, leading to 16 unique configurations as the maximum number of columns is assumed to be 8 columns (e.g. 1111, 1112, 1122, *etc*). In addition, switch time (500 s to 900 s) and four volumetric flow rates (0.01 $cm^3\ s^{-1}$ to 0.15 $cm^3\ s^{-1}$) are also optimized, leading to nine optimization variables in total (the number of columns for each of the four sections, the switch time and the four flow rates). The objective function considered is to maximize process efficiency defined by the following expression:

$$\text{efficiency} = \frac{\text{throughput}}{\text{rate of solvent consumption} \times \text{total col. volume}}$$

Two constraints are also taken into account: (1) outlet streams should be at least 99 wt% pure, and (2) the pressure drop within each column must be between 13 bar and 100 bar [11]. In terms of the optimizer, particle swarm optimization (PSO) is used due to its robustness and ability to jump out of a local optimum. Fifty particles are used in each iteration, and two stopping criteria are applied: (1) 200 maximum iterations, or (2) the best

objective values remain constant for 20 consecutive iterations, whichever satisfied first.

All concentration profiles for components A and B are plotted in Figure 4, for both individual configurations (i.e., optimization for a fixed column configuration) and for superstructure optimization (SS). Due to the limited space, the optimal designs and objective values for all configurations are not provided. The individual optimization results show that the best configuration is 1121 (i.e., only the feed section has two columns), with an efficiency of 1.086 mg $cm^{-3}$. There is a slight deviation between the individual optimal design for the 1121 configuration and the solution obtained via the superstructure methodology (1.086 vs 1.069 mg $cm^{-3}$) and this is due to local optimality. Note that the concentrations profiles are nevertheless identical in the figure.

## CONCLUSION

This work proposed a novel SMB superstructure, which allows for simultaneous optimization of the number of columns in each SMB section together with other key design variables including column design and operating variables. The modification of the superstructure from a partially discretized model to a fully discretized model was demonstrated and tested, indicating good robustness. The superstructure model was considered to compare superstructure optimization with individual optimization of a fixed column configuration. Both approaches yielded the same optimal result, indicating good efficiency and reliability of the proposed superstructure. The superstructure allows for the direct determination of the optimal process, thus avoiding optimization for each possible column configuration. The proposed superstructure is versatile and can be applied to any type of mass transport model or isotherm used to describe the chromatographic system.

## ACKNOWLEDGEMENTS

The authors wish to acknowledge the financial support given to this research project by Eli Lilly and Company, and the Engineering and Physical Sciences Research Council (EPSRC), grant code EP/T00556/1.

## REFERENCES

1. Dünnebier G, Weirich I, Klatt KU. Computationally efficient dynamic modelling and simulation of simulated moving bed chromatographic processes with linear isotherms. Chem Eng Sci 53(14):2537–46 (1998). 10.1016/S0009-2509(98)00076-1
2. Li S, Kawajiri Y, Raisch J, Seidel-Morgenstern A. Optimization of simulated moving bed chromatography with fractionation and feedback: Part I. Fractionation of one outlet. J Chromatogr A 1217(33):5337–48 (2010). 10.1016/j.chroma.2010.06.031
3. Coelho LCD, Filho NML, Faria RPV, Ferreira AFP, Ribeiro AM, Rodrigues AE. Separation of tartronic and glyceric acids by simulated moving bed chromatography. J Chromatogr A 1563:62–70 (2018). 10.1016/j.chroma.2018.05.052
4. Nilchan S, Pantelides CC. On the Optimisation of Periodic Adsorption Processes. Adsorption 4(2):113–47 (1998). 10.1023/A:1008823102106
5. Kloppenburg E, Gilles ED. A New Concept for Operating Simulated Moving-Bed Processes. Chem Eng Technol 22(10):813–7 (1999). 10.1002/(SICI)1521-4125(199910)22:10<813::AID-CEAT813>3.0.CO;2-G
6. Toumi A, Engell S, Diehl M, Bock HG, Schlöder J. Efficient optimization of simulated moving bed processes. Chem Eng Process Process Intensif 46(11):1067–84 (2007). 10.1016/j.cep.2006.06.026
7. Sumedha M, Bhartiya S. Dual switch simulated moving bed chromatography: An optimal two-fraction yielding separation process. J Chromatogr A 1682:463449 (2022). 10.1016/j.chroma.2022.463449
8. Kawajiri Y, Biegler LT. Large scale nonlinear optimization for asymmetric operation and design of Simulated Moving Beds. J Chromatogr A 1133(1):226–40 (2006). 10.1016/j.chroma.2006.08.037
9. Kawajiri Y, Biegler LT. Nonlinear Programming Superstructure for Optimal Dynamic Operations of Simulated Moving Bed Processes. Ind Eng Chem Res 45(25):8503–13 (2006). 10.1021/ie0601192
10. Kawajiri Y, Biegler LT. Large scale optimization strategies for zone configuration of simulated moving beds. Comput Chem Eng 32(1):135–44 (2008). 10.1016/j.compchemeng.2007.04.009
11. Chan S, Titchener-Hooker N, Sørensen E. Optimal Economic Design and Operation of Single- and Multi-column Chromatographic Processes. Biotechnol Prog 24(2):389–401 (2008). 10.1021/bp070270m
12. Chia DN, Sorensen E. Optimal design of hybrid distillation-membrane processes based on a superstructure approach. Chem Eng Res Des 194:256–79 (2023). 10.1016/j.cherd.2023.04.014

© 2025 by the authors. Licensed to PSEcommunity.org and PSE Press. This is an open access article under the creative commons CC-BY-SA licensing terms. Credit must be given to creator and adaptations must be shared under the same terms. See https://creativecommons.org/licenses/by-sa/4.0/



Systems & Control Transactions

**Research Article - Peer Reviewed Conference Proceeding**
ESCAPE 35 - European Symposium on Computer Aided Process Engineering
Ghent, Belgium. 6-9 July 2025
Jan F.M. Van Impe, Grégoire Léonard, Satyajeet S. Bhonsale,
Monika E. Polańska, Filip Logist (Eds.)

PSE PRESS

# Development of anomaly detection models independent of noise and missing values using graph Laplacian regularization

**Yuna Tahashi[a], and Koichi Fujiwara[a]**

[a] Department of Materials Process Engineering, Nagoya University, Furo-cho, Chikusa-ku, Nagoya, 464-8601, Japan
* Corresponding Author: K. Fujiwara (fujiwara.koichi@hps.material.nagoya-u.ac.jp).

## ABSTRACT

Anomaly detection is a key technique for maintaining process suitability and safety; however, the quality of process data often deteriorates due to missing or noisy values caused by sensor malfunctions. Such data imperfections may obscure real faults. If anomaly detection models are too sensitive to such abnormal data, they may cause false positives resulting in unnecessary alarms, which may obstruct detection of true process faults. Thus, deterioration of the quality of process data may affect process performance and safety. We propose a new anomaly detection method that utilizes graph Laplacian regularization as a loss function considering data-specific temporal relationships. Graph Laplacian regularization is a mathematical tool used in image processing and denoising to smooth data. We assume that successive process data temporally close to each other have similar values and maintain temporal dependencies among variables. In this study, Laplacian regularization imposes significant penalties when the outputs of neighboring samples lose smoothness, under the assumption that neighboring samples keep similar relationships. Such temporal dependencies can be expressed as a graph structure and extracted with the Nearest Correlation (NC) method. To demonstrate the usefulness of the proposed anomaly detection method, we applied it to an anomaly detection problem in a vinyl acetate monomer (VAM) process. The results show that the model with graph Laplacian regularization achieved higher performance than without graph Laplacian regularization in some fault scenarios. It was confirmed that the proposed method is effective for anomaly detection.

**Keywords**: Anomaly detection, Graph Laplacian regularization, Autoencoder, vinyl acetate monomer process

## INTRODUCTION

Process data frequently suffer from imperfections such as missing values or measurement noise due to sensor malfunction. Such data imperfections pose a significant challenge to detection of process anomalies and can lead to false positives or missed rare fault events. Anomaly detection models with high sensitivity may over-detect these faults, leading to interference in detection of true failure events.

Various anomaly detection methods have been developed to detect such faults, such as One-Class Support Vector Machine (OCSVM) and Multivariate Statistical Process Control (MSPC). Although these methods are common and widely used, they are not always applicable for handling complicated fault events due to incompatibility with time-series data or linear models [1,2].

An autoencoder (AE) is a nonlinear expansion of principal component analysis (PCA) and is a type of neural network trained so that the output becomes close to the input. Since MSPC is based on PCA, AE can also be used for anomaly detection [3]. If an AE is trained only on normal process data, a fault event can be detected when reconstruction error (RE) between the input and the output of AE becomes large.

It is, however, difficult for AE, as well as other conventional anomaly detection methods, to appropriately cope with sudden changes in process data, which may cause false alarms and obstruct detection of true fault events in processes. Thus, deterioration of the quality of

process data may affect process performance and safety.

In order to suppress such false alarms and missed fault events caused by sudden changes in data and to improve process suitability and safety, a regularization term in addition to a loss function can be introduced to a training process of an AE model [4].

A graph-based regularization term expresses the relationship between process variables and imposes a penalty when the relationship changes between input and output, which is expected to emphasize abnormal changes in the process data. Graph Laplacian regularization (GLR) has attracted attention for its ability to smooth data, particularly for denoising image data [5], as a simple and useful method that can make the input data according to a graph expressing definitions of smoothness [6-8]. For example, the distance between pixels of image data can be defined as data smoothness. GLR can be applied not only to image data but to any other type of data as long as the data can be expressed as a graph.

In this study, we utilize GLR for anomaly detection to suppress false alarms and missed fault events caused by sudden changes in process data. We propose a new anomaly detection method based on AE with GLR. In the proposed method, a graph-based regularization term is introduced when training an AE model. In addition, the graph-based regularization term can take the smoothness of data expressed as a graph structure.

In order to use GLR, an appropriate graph needs to be constructed. The proposed method adopts, as a graph construction method, the Nearest Correlation (NC) method, which is a structural learning algorithm that considers correlations between variables [9]. Using GLR based on the NC method, it is expected that missed measurements and noise contained in the process data are automatically corrected in terms of correlations between variables, and only significant changes in process characteristics such as fault events are detected.

The use of GLR with the NC method would realize a reliable anomaly detection model that can improve the efficiency and reliability of process monitoring and control in various industrial applications.

In this study, the usefulness of the proposed anomaly detection method is demonstrated through its application to simulation data of a vinyl acetate monomer (VAM) production process, generated by a process simulator provided by Omega Simulation Co., Ltd [10,11].

# METHODS

## Graph Laplacian regularization

The Laplacian is a mathematical operator that measures the degree of curvature or change in a function, quantifying how different the value of a function is from its surroundings.

The Laplacian operator can be extended to graphs, in which case it is called the graph Laplacian, which is used to describe relationships between the nodes of a graph, and in particular to measure the smoothness of features between neighboring nodes. The graph Laplacian $\boldsymbol{L}$ can be defined as

$$\boldsymbol{L} = \Delta - \boldsymbol{A} \tag{1}$$

where $\boldsymbol{A}$ is the adjacency matrix and $\Delta = \sum_j \boldsymbol{A}_{ij}$ is the order matrix.

GLR is a technique that uses the graph Laplacian to impose smoothness constraints on a model. Particularly, it allows the model to take the graph structure into account by adding a penalty so that the differences in output values between neighboring nodes become small. Although GLR has been mainly used in image processing, it can be used for any type of data if the relationship among variables can be expressed as a graph, such as similarity among variables, rules that variables must follow, or temporary relationships among variables in time-series data.

It is assumed that the numbers of data samples and variables are $N$ and $M$, respectively, $\boldsymbol{x}_i, \boldsymbol{x}_j \in \mathbb{R}^N$ are the $i$th and the $j$th variables of the data matrix $\boldsymbol{X} \in \mathbb{R}^{N\times M}$, and $A_{ij}$ is the similarity or the strength of connection between $x_i$ and $x_j$. Here, $A_{ij}$ is the $(i,j)$ element of the adjacency matrix $\boldsymbol{A} \in \mathbb{R}^{M\times M}$ of the graph. For the predictions $\boldsymbol{y}_i, \boldsymbol{y}_j \in \mathbb{R}^N$ from $\boldsymbol{x}_i, \boldsymbol{x}_j$ and the matrix $\boldsymbol{Y} \in \mathbb{R}^{N\times M}$ containing them, the regularization term $R$ based on GLR is defined by the following equation:

$$\begin{aligned} R = \frac{1}{2}\sum_{i,j=1}^{M} A_{ij}\left\|\boldsymbol{y}_i - \boldsymbol{y}_j\right\|^2 &= \sum_{i=1}^{M} \boldsymbol{y}_i \boldsymbol{y}_i \Delta_{i,i} - \sum_{i=1}^{M} \boldsymbol{y}_i \boldsymbol{y}_j A_{ij} \\ &= \mathrm{Tr}(\boldsymbol{Y}\Delta\boldsymbol{Y}^T) - \mathrm{Tr}(\boldsymbol{Y}\boldsymbol{A}\boldsymbol{Y}^T) \\ &= \mathrm{Tr}(\boldsymbol{Y}\boldsymbol{L}\boldsymbol{Y}^T) \end{aligned} \tag{2}$$

By adding this regularization term to the loss function when training the AE model, the similarity among the data can be considered to be within the model.

## Nearest Correlation method (NC method)

To use GLR, a suitable graph needs to be constructed from the data. In this study, we utilize the NC method.

The NC method was originally proposed as a way to detect multiple samples that have similar correlations with the target sample. An illustrated example of the NC method is shown in Figure 1.

$N$ samples are given and a zero matrix $\boldsymbol{S} \in \mathbb{R}^{N\times N}$ is set up. Here, a target sample is $\boldsymbol{x}_1 \in \mathbb{R}^M$. First, $\boldsymbol{x}_1$ is translated to the origin of the space, that is, $\boldsymbol{x}_i' = \boldsymbol{x}_i - \boldsymbol{x}_1$ and $\boldsymbol{x}_1' = 0$. Then, correlation coefficients are calculated for all possible pairs of samples except $\boldsymbol{x}_1'$, such as $\boldsymbol{x}_2 - \boldsymbol{x}_3$, $\boldsymbol{x}_2 - \boldsymbol{x}_4, \cdots$. A weight of 1 is assigned to the pair when

its correlation coefficient exceeds a predefined threshold of $\gamma$. For example, in Fig. 1, samples $\boldsymbol{x_2}$ and $\boldsymbol{x_6}$, $\boldsymbol{x_3}$ and $\boldsymbol{x_4}$ correspond to pairs with high correlation coefficients. That is, 1 is added to $\boldsymbol{S_{2,6}}$, $\boldsymbol{S_{6,2}}$, $\boldsymbol{S_{3,4}}$ and $\boldsymbol{S_{4,3}}$. This process is repeated until all samples have become the target sample. Finally, the matrix $\boldsymbol{S}$ represents the similarity among samples from the viewpoint of correlation. In this study, the obtained matrix $\boldsymbol{S}$ has integer values greater than or equal to 0, which is then transformed into an unweighted matrix consisting only of elements 0 and 1, with all positive values being 1. The resulting matrix is used as the adjacency matrix $\boldsymbol{A}$ of the graph for GLR.

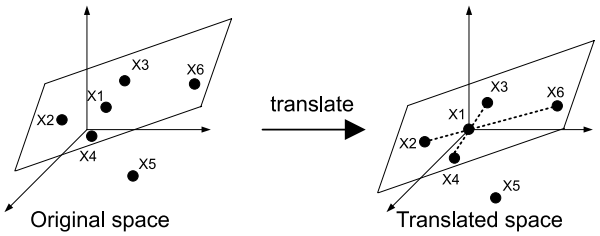



**Figure 1.** Image of NC method

## Proposed method (NCGLR-AE)

In this study, we propose a new anomaly detection method, referred to as NCGLR-AE, which uses GLR and

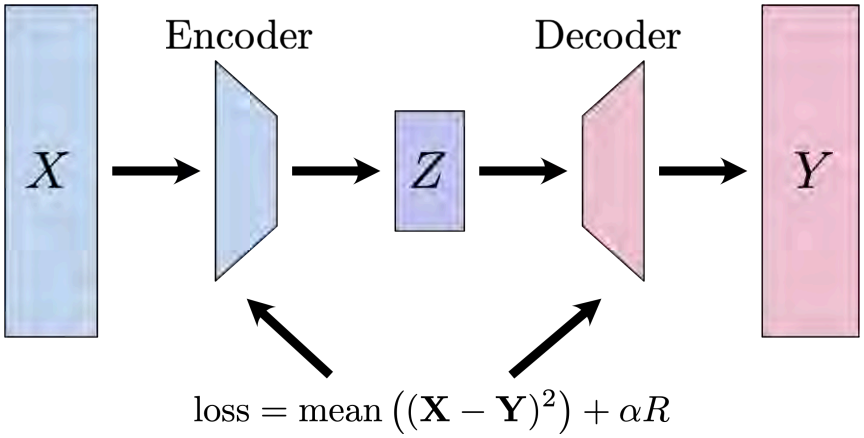



**Figure 2:** Schematic diagram of the proposed anomaly detection method

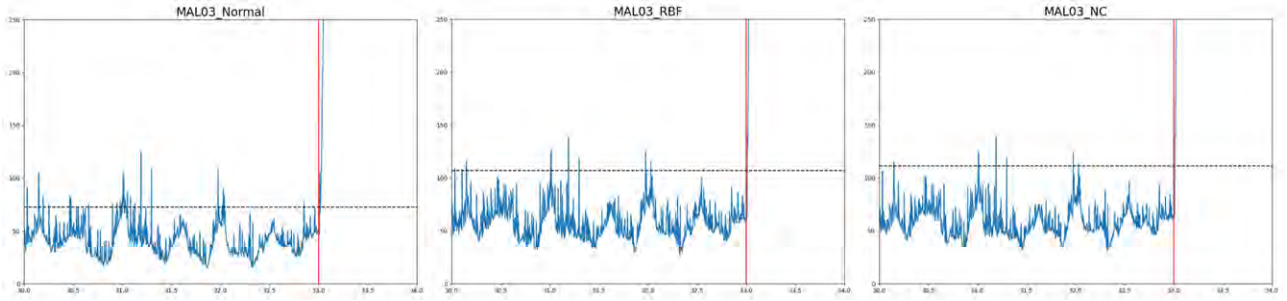



**Figure 3:** RE in VAM process with MAL3

(left: Normal, center: RBF, right: NC)

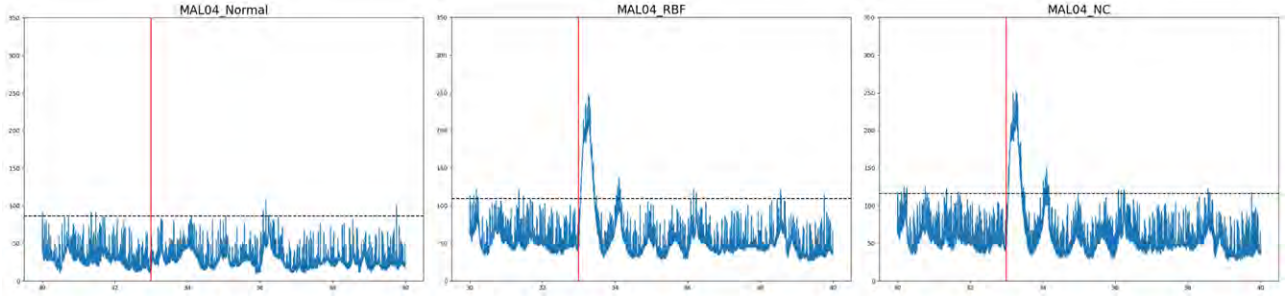



**Figure 4:** RE in VAM process with MAL4
(left: Normal, center: RBF, right: NC)

NC methods during AE training. A schematic diagram of the proposed method is shown in Figure 2. In AE, the input $\boldsymbol{X}$ compress the information into latent variables $\boldsymbol{Z}$ via an encoder. $\boldsymbol{Z}$ is then restored to output $\boldsymbol{Y}$ via a decoder. A graph is created by the NC method with the data variables as nodes from the data matrix $\boldsymbol{X}$. It can be transformed into the GLR $R$ and the AE training is performed with the loss function, defined as

$$\text{loss} = \text{mean}((\boldsymbol{X} - \boldsymbol{Y})^2) + \alpha R \quad (3)$$

where $\alpha$ is a regularization weight.

RE between the input and the output of the trained AE is defined as the anomaly score. A control limit is set as the value at which $\beta$ % is normal with respect to the abnormality score of the training data consisting of normal data only, and the abnormality score calculated from process data. The data are regarded as abnormal only when the abnormality score exceeds the control limit.

The model training procedure of the proposed method is described as follows:

1. Divide the training data $\boldsymbol{X} \in \mathbb{R}^{N \times M}$ into training and validation data so that the order of the time-series does not change.
2. Extract data $\boldsymbol{X}_t \in \mathbb{R}^{B \times M}$ for a batch size $B$.
3. Calculate adjacency matrix $\boldsymbol{A}_t \in \mathbb{R}^{M \times M}$ using the NC method for the variable direction of $\boldsymbol{X}_t$.
4. Input $\boldsymbol{X}_t$ into AE and obtain output $\boldsymbol{Y}_t \in \mathbb{R}^{B \times M}$.
5. Calculate $\boldsymbol{L}_t \in \mathbb{R}^{M \times M}$ from $\boldsymbol{A}_t$ and GLR $R_t$ from $\boldsymbol{L}_t, \boldsymbol{Y}_t$.
6. Calculate the loss function of AE from $\boldsymbol{X}_t$.
7. Extract next data for the next batch size.
8. Repeat steps 3-7 until the validation loss converges.
9. Define the value at which $\beta$ % of the abnormality scores for the training data are normal as the control limit.

# CASE STUDY

## Dataset

Simulated process data generated from the vinyl acetate monomer (VAM) process model was used to assess the performance of the anomaly detection model trained by the proposed method. Forty hours of the VAM process operation data were generated, which included situations where sudden malfunctions occurred 33 hours after the start of measurement. The first 30 hours of data were used for training and the remaining 10 hours for testing. To validate the performance of the model for different types of faults, test data were prepared, including six different faults: faults MAL01 and MAL02, which reduced the feed composition of feedstock ethylene and acetic acid, respectively; MAL03 and MAL04 are malfunctions that reduced the feed pressure of the feedstock ethylene and oxygen, respectively; MAL09 and MAL10 are faults that changed the temperature and pressure of the cooling water, respectively. Sixty-two process variables in the VAM process, measured every 10 seconds, include pressure and flow rate values.

## How to train models and determine thresholds

We employed an autoencoder (AE) as the model for anomaly detection, with a one-layer encoder and a one-layer decoder, and the number of units in the middle layer (30) and the batch size (100) were kept constant for all comparison models.

Taking advantage of the characteristics of time-series data, the graph was constructed under the assumption that data close in time have close values. To calculate the correlations between variables of temporally close data, a graph was constructed using the NC method with the variables as nodes. The GLR was calculated from the adjacency matrix of the graph and added to the loss function during batch training of AE. When validation loss did not decrease for five consecutive times, loss was considered to have converged and AE training was terminated.

In this study, we used "reconstruction error (RE)" as the anomaly score. RE is the square of the error between the input and output values.

In order to compare the performance differences between the graph construction methods, a Gaussian (Radial Basis Function; RBF) kernel, which calculates similarity based on the distance between two points, was employed in addition to the NC method. The Gaussian kernel is calculated by the following equation:

$$A_{ij} = \begin{cases} 1, & \exp\left(-\frac{\|x_i - x_j\|^2}{2\sigma^2}\right) > 0.99 \\ 0, & \exp\left(-\frac{\|x_i - x_j\|^2}{2\sigma^2}\right) \leq 0.99 \end{cases} \quad (4)$$

where $\sigma$ is a hyperparameter that adjusts how far away data can be and still be considered similar; if $\sigma$ is large, a wide range of data points are considered similar. In this case, $\sigma$ was set to 10.

## Results

In this study, we used "False Alarm Rate (FAR)", "Missing Alarm Rate (MAR)" and "Detection Latency (DL)" as evaluation indicators. The definitions of FAR and MAR are given in the following equations:

$$FAR = \frac{False\ Positive}{Number\ of\ Normal\ Samples} \times 100 \quad (5)$$

$$MAR = \frac{False\ Negative}{Number\ of\ Anomalous\ Samples} \times 100 \quad (6)$$

FAR indicates the percentage of samples judged to be abnormal in the normal data before a fault event

**Table 1:** Anomaly detection results for each anomaly scenario. The best value for each test data is shown in bold.

| Malfunction | Model | FAR [%] | MAR [%] | DL [s] |
|---|---|---|---|---|
| MAL01 | - | **0.278** | 0.198 | 52 |
| | RBF | 0.648 | **0.159** | **42** |
| | NC method | 0.648 | **0.159** | **42** |
| MAL02 | - | 0.926 | 0.397 | 103 |
| | RBF | 0.463 | **0.357** | **83** |
| | NC method | **0.370** | 0.397 | 103 |
| MAL03 | - | 3.70 | 0.198 | 44 |
| | RBF | 0.926 | **0.159** | 44 |
| | NC method | **0.741** | **0.159** | 44 |
| MAL04 | - | **0.278** | 99.8 | 11122 |
| | RBF | 0.648 | 94.1 | **212** |
| | NC method | 0.648 | **93.8** | **212** |
| MAL09 | - | 0.0926 | 0.476 | 123 |
| | RBF | 0.0926 | 0.397 | 102 |
| | NC method | 0.0926 | **0.357** | **93** |
| MAL10 | - | 0.185 | **1.67** | **412** |
| | RBF | 0.0926 | 1.74 | 421 |
| | NC method | **0.0** | 1.79 | 452 |

occurred. The lower this indicator, the fewer false detections of abnormalities. MAR indicates the percentage of anomaly data that are incorrectly determined as normal after a fault event occurred. A lower MAR means that anomaly is correctly detected. DL is the time required from the occurrence of a fault event to its detection. DL should be small from the viewpoint of early detection of faults.

Anomaly detection results for each anomaly scenario are shown in Table 1. The best value for each set of test data is shown in bold.

The models with GLR demonstrate significant performance improvements in many anomaly patterns, particularly when graphs were constructed using the NC method. For MAL02, MAL03, and MAL10, the number of false positives was reduced by applying GLR. This indicates that unnecessary alarms were appropriately suppressed, which is expected to reduce operator burden and improve work efficiency.

Figure 3 shows an enlarged view of the MAL03 abnormal score around the normal data. There are several points where the threshold value is exceeded only when GLR is not applied. One possible reason is that the anomaly score fluctuates significantly due to noise when GLR is not applied. This suggests that GLR was effective in removing noise from process data, and that noise removal may enable stable calculation of abnormality scores.

For MAL04 and MAL09, the smallest MAR was achieved with the NC method. Figure 4 shows the MAL04 anomaly score, indicating that the fault event was incorrectly detected without GLR. On the other hand, GLR accurately detected the occurrence of the faults. It is concluded that consideration for the correlation between variables during the training process enabled the accurate detection of fault events. In addition, these results also showed that GLR is useful for time-series data processing.

MAL01 and MAL10, however, had performances that were the same regardless of GLRs, or even better when GLRs were not used. As such, there may be room for improvement in the proposed model.

## CONCLUSION

In this study, an anomaly detection model incorporating graph Laplacian regularization created by the NC method is proposed. Based on the process that data points close in time have close values, it was possible to construct an anomaly detection model that utilizes the properties of time-series data.

The addition of the regularization term successfully improved the anomaly detection rate for many sets of anomaly simulation data compared to cases without the regularization term, and the correlation-aware NC method was effective in detecting anomalies with higher accuracy.

In the future, validation against real data and verification of accuracy will be carried out in order to enable more accurate anomaly detection. In addition, although this study was only validated on AE, future validation will be done on other deep-learning models.

## REFERENCES


1. Schölkopf B, Platt JC, Shawe-Taylor J, Smola AJ, Williamson RC. Estimating the support of a high-dimensional distribution. Neural Comput 13:1443-1471 (2001). https://doi.org/10.1162/089976601750264965
2. MacGregor JF, Kourti T. Statistical process control of multivariate processes. Control Eng Pract 3:403-414 (1995). https://doi.org/10.1016/0967-0661(95)00014-L
3. Venkatasubramanian, V., and King Chan. A neural network methodology for process fault diagnosis. AIChE Journal, 35(12): 1993-2002 (1989). https://doi.org/10.1002/aic.690351210
4. Bergmann P, Löwe S, Fauser M, Sattlegger D, Steger C. Improving unsupervised defect segmentation by applying structural similarity to autoencoders. In: Proc 14th Int Joint Conf Comput Vis Imaging Comput Graph Theory Appl (VISIGRAPP), Vol 5: VISAPP. SciTePress 372-380 (2019). https://doi.org/10.5220/0007364503720380
5. Zeng J, Pang J, Sun W, Cheung G. Deep graph Laplacian regularization for robust denoising of real images. arXiv preprint arXiv:1807.11637 [cs.CV] (2018). https://doi.org/10.48550/arXiv.1807.11637
6. Pang J, Cheung G. Graph Laplacian Regularization for Image Denoising: Analysis in the Continuous Domain. IEEE Transactions on Image Processing 26:1770-1785 (2017). https://doi.org/10.1109/TIP.2017.2651400
7. Hu W, Cheung G, Kazui M. Graph-based Dequantization of Block-Compressed Piecewise Smooth Images. IEEE Signal Processing Letters 23:242-246 (2016). https://doi.org/10.1109/LSP.2015.2510379
8. Liu X, Zhai D, Zhao D, Zhai G, Gao W. Progressive Image Denoising Through Hybrid Graph Laplacian Regularization: A Unified Framework. IEEE Transactions on Image Processing 23:1491-1503 (2014). https://doi.org/10.1109/TIP.2014.2303638
9. Fujiwara K, Kano M, Hasebe S. Correlation-based spectral clustering for flexible process monitoring. J Process Control 21:1438-1448 (2011). https://doi.org/10.1016/j.jprocont.2011.06.023
10. Machida Y, Ootakara S, Seki H, Hashimoto Y, Kano M, Miyake Y, Anzai N, Sawai M, Katsuno T, Omata T. Vinyl acetate monomer (VAM) plant model: A new benchmark problem for control and operation study. IFAC-PapersOnLine 49:533-538 (2016). https://doi.org/10.1016/j.ifacol.2016.07.397
11. Omega Simulation Co., Lid., https://www.omegasim.co.jp, (accessed 2024/07/31)



© 2025 by the authors. Licensed to PSEcommunity.org and PSE Press. This is an open access article under the creative commons CC-BY-SA licensing terms. Credit must be given to creator and adaptations must be shared under the same terms. See https://creativecommons.org/licenses/by-sa/4.0/




Systems & Control Transactions

**Research Article - Peer Reviewed Conference Proceeding**
ESCAPE 35 - European Symposium on Computer Aided Process Engineering
Ghent, Belgium. 6-9 July 2025
Jan F.M. Van Impe, Grégoire Léonard, Satyajeet S. Bhonsale,
Monika E. Polańska, Filip Logist (Eds.)

PSE PRESS

# A Modelling and Simulation Software for Polymerization with Microscopic Resolution

**Shenhua Jiao[a], Xiaowen Lin[a,b], Rui Liu[a] and Xi Chen[a,b]***

[a] State Key Laboratory of Industrial Control Technology, College of Control Science and Engineering, Zhejiang University 310027, Hangzhou China.
[b] Huzhou Institute of Industrial Control Technology 313000, Huzhou China.
* Corresponding Author: xi_chen@zju.edu.cn.

## ABSTRACT

In the domain of process systems engineering, developing software embedded with advanced computational methods is in great demand to enhance the kinetic comprehension and facilitate industrial applications. Polymer production, characterized by complex reaction mechanisms, represents a particularly intricate process industry. In this work, a scientific software is developed for polymerization modelling and simulation with insight on microscopic resolution. From a software architecture perspective, the software is built on a self-developed process modelling platform that allows flexible user customization. A specific design for polymer species with microscopic chain structure information is conducted. From an algorithm perspective, the software offers high-performance solution strategies for polymerization process modelling by utilizing advanced computation approaches. A Ziegler-Natta copolymerization is presented to demonstrate the software's capability in capturing the microscopic structural information of polymers.

**Keywords**: Polymerization Process, Modular Modelling, Software Development.

## INTRODUCTION

In the domain of process systems engineering, developing process modeling software embedded with advanced computational methods is in great demand to enhance the industrial process simulation, synthesis and optimization.

Industrial systems are often characterized by complex process flowsheets and significant uncertainties, leading to the difficulty in establishing a precise mechanism model. Moreover, the application of these models can be diverse, which may involve the calculation of microscope or macroscope quality indicators, the synthesis of process flowsheets, and the optimization of operating conditions. Due to the complexity of modeling and the diverse applications of the models, some customized modeling software for specific processes has been developed and put into practical industrial applications. In some specific industrial scenarios, these specifically designed software can better meet the diversified and flexible requirements of users.

Polymer production is a particularly intricate process industry. There are many difficulties in developing customized modeling software for the polymerization process. First, a qualified software should model basic reactions involving initiation, propagation, chain transfer and termination, etc., each of which contributes to the overall complexity. Distinct polymerization mechanisms, such as free radical and Ziegler-Natta, add further intricacy. Second, accurate quantification of reaction rate constants, and other kinetic parameters also remains a significant challenge. They are hard to measure experimentally. Estimation of these parameters requires extensive engineering experience and industrial data. Moreover, polymers exhibit a wide variety of molecular structures, such as linear, branched, along with complex molecular weight distributions (MWDs). These microscopic indexes, which significantly influence the product properties, are highly sensitive to reaction conditions, monomer types, and catalysts. Therefore, accurate characterization and prediction of them is crucial and require specialized modeling techniques. Last but not least, polymerization models are inherently nonlinear large-scale equations system[1]. The computational cost of

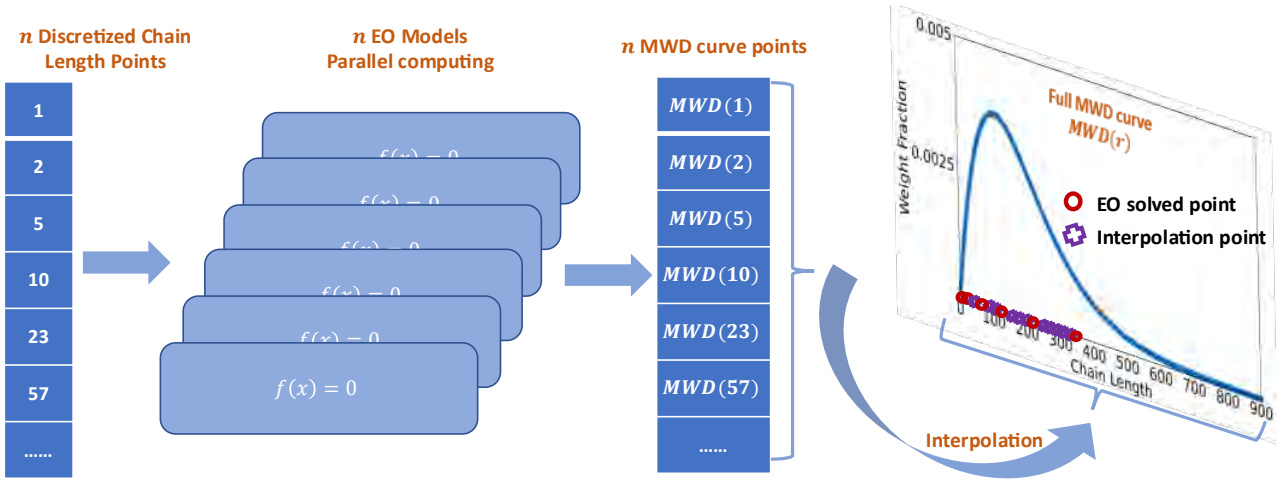



**Figure 1:** A graphic illustration of the solution process for the cumulative MWD is provided. The computation of the full MWD curve is decomposed into *n* sparse systems of linear equations, each with identical topology. These systems are solved to obtain the values of *n* discretized points along the MWD. Using these discretized points, interpolation is applied to reconstruct the full MWD curve. The final MWD curve is constructed from both the discretized points obtained through the solution process and the interpolated points.

solving such models is high. The numerical stability and convergence are also challenging. In light of this, a scientific software is developed for polymerization modelling and simulation with insight on microscopic resolution.

## SOFTWARE ARCHITECTURE

The software is built on a self-developed process modelling platform that allows flexible user customization. It is modularly designed, and each module supports external libraries and secondary development. Pivotal modules, including reaction components, reaction kinetics, process units, process streams and solution strategies, are meticulously constructed and seamlessly integrated.

### Components

The software enables users to define various types of components, including conventional, site-based and polymers. Due to their distinct macroscopic and microscopic representation methods, the corresponding data structures of components in the software are also designed differently. Taking polymer components as an example, their macroscopic properties, such as moments of chain length distribution (CLD) and average molecular weight, as well as microscopic properties, including CLD, molecular weight distribution (MWD), branch structure and monomer composition, are modelled.

Meanwhile, each type of component introduces unique variables that must be solved in the model. Specifically, for all streams, the model needs to solve the flowrate of conventional components, the flowrates of potential, vacant and dead sites of site-based components and moments of polymer distribution.

### Streams

Streams serve as intermediaries between different process units, facilitating the transfer of data structures and solution results of all components. They can also conveniently store various local information that users may wish to retain.

### Units

The software designed a standard unit module for process modelling, which are interconnected through streams. Various unit types and their corresponding functions can be customized, such as continuous stirred tank reactors (CSTR), mixers, and others.

### Kinetics

The designed kinetics module allows for the definition of individual reactions, including the specification of reactants, products, and parameters associated with reaction rates. The defined reaction kinetics can be assigned to reactors and utilized to solve the model. The Arrhenius equation, as shown in Equation 1, is used to calculate the reaction rate $K$, requiring values of the pre-exponential factor $A$, activation energy $E_a$, and reference temperature $T_0$. $R$ is the universal gas constant and $T$ is the temperature.

$$K = A\mathrm{e}^{-\frac{E_a}{R}(\frac{1}{T}-\frac{1}{T_0})} \quad (1)$$

A standard Ziegler Natta reactions library has been developed in this module. The provided polymerization reactions templates, including different kinds of activation, initiation, propagation, chain transfer and deactivation, can be easily called by users. Besides these

reactions, users can also customize various reaction templates.

### Macroscopic process solution strategies

At the flowsheet level, the software provides both an equation-oriented and a sequential-module approach to solve for macroscopic information. The Method of Moment (MoM) is employed to characterize the polymer components throughout the process [2]. As a result, the equation-oriented model will incorporate the balance equations derived from the moment model.

### Microscopic quality indexes solution strategies

The software provides users with both deterministic and stochastic algorithms to predict microscopic quality indexes, particularly the molecular weight distribution. To evaluate cumulative polymer on the stream level, the equation-oriented method is utilized to enable the calculation of cumulative MWD for each stream. For example, in a CSTR with one feed stream and one output stream, the cumulative MWD of the polymer in the output stream is modelled as a weighted sum of the cumulative MWD in the feed stream and the MWD of the newly produced polymer within the CSTR. When solving for the cumulative polymer's MWD of every stream, such equality relationships are systematically established and solved across the entire flowsheet. As shown in Figure 1, efficient solution strategies are adopted during this process. First, the whole MWD curve is discretized into $n$ discrete points. Next, for each discrete point the balance equations model of the whole process is solved. Thus, the dimension of the equations is reduced by a factor of n and we solve $n$ equation models with the exact same topology.

## ALGORITHMS

The software provides users with both deterministic and stochastic algorithms to complete the simulation and computation.

### Stochastic Methods

The SSMC algorithm proposed by our group is used for the modelling and simulation of steady-state polymerization process with complex mechanisms [3]. As illustrated in Figure 2, by utilizing "buffer pool", it decomposed the complex polymerization process into several steps for modelling.

This SSMC algorithm enables the prediction of detailed microscopic structure of polymer. Customized data structures are designed for elaborate polymer chain modeling. Through tracking the formation of every simulated chain, it not only provides MWD information but also offers more detailed insights, such as the number and position of branching in each polymer chain when there involves chain transfer to polymer reaction.

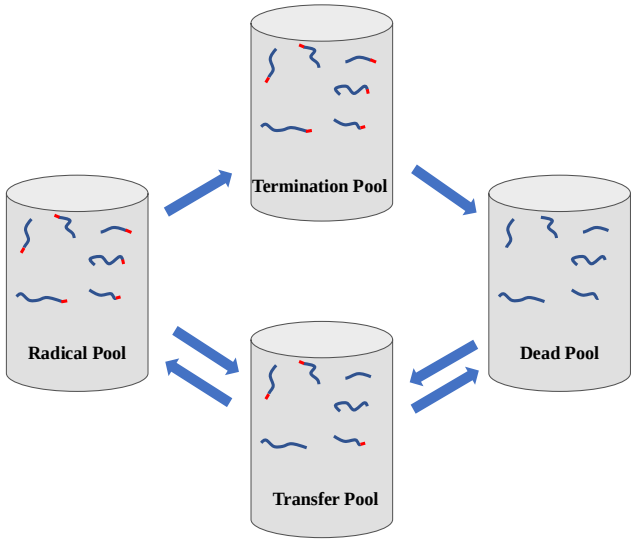



**Figure 2.** Buffer pools and the multistep polymerization model in the SSMC algorithm.

The scheme of this method is shown in Figure 3. It is a general method as long as the moment model can be established and solved by the software. When this algorithm is called in the software, the results from the moment model and the reaction rates from the mechanisms are required, and the microscopic structural information of the polymer is returned as output.

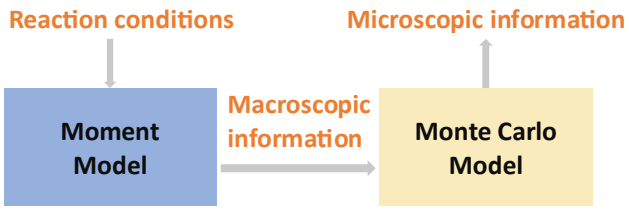



**Figure 3.** Scheme of applying the SSMC algorithm.

Moreover, this SSMC algorithm have an advantage in efficiency compared with traditional Monte Carlo simulation methods which inherently suffer from significant time and computational resource consumption. When the algorithm is implemented in this software as Python code, a modern high-performance code compiler Numba is employed to accelerate Monte Carlo simulations [4]. Numba generates optimized machine code directly from Python code, ensuring improved computational efficiency without compromising the accuracy of the results.

### Deterministic Methods

An orthogonal collocation method with model reformulation strategies for mathematical operations caused by various reactions is involved in the solution algorithms of the software [1]. Theoretically, the number of equilibrium equations of polymer can be infinite if the MWD curve is also inserted in them. This algorithm allows for

the discretization of CLD curve in time and chain length dimensions, thus it significantly decreases the number of equations. It is also applicable for the steady-state considering only chain length dimension.

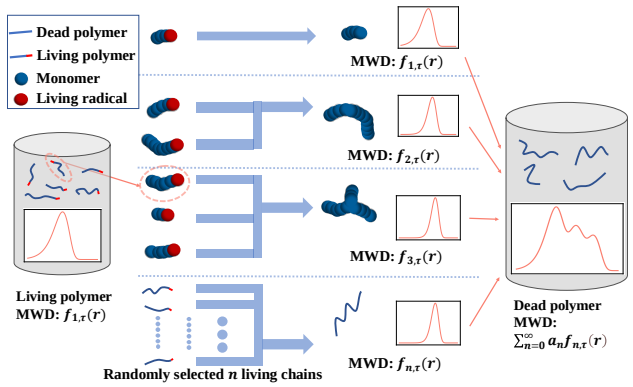



**Figure 4.** Scheme of applying analytical expressions for MWD derivation in the software.

Besides the equation-oriented methods, analytical expressions are derived for the MWDs associated with specific mechanisms. Represented by the Flory distribution, these expressions provide a straightforward way to calculate the MWD. In this method, the classical Flory distribution is extended to a more general form to handle more complex mechanisms, including bi-molecular termination, chain transfer to polymer and reversible reactions. As shown in figure 4, this method defines a general form of probability density functions (PDFs) and basically analyses all the reactions that producing dead polymer and derives the corresponding MWDs. The PDFs is shown in Equation 2, where $n$ and $\tau$ are parameters associated with reaction mechanisms and $r$ is the variable.

$$f_{n,\tau}(r) = \frac{\tau^{n+1} r^n}{n!} e^{-\tau r} \quad (2)$$

The total MWD of all dead polymer is determined as a weighted combination of these MWDs. When this algorithm is called within the software, it requires the mechanisms and results from the moment model as input, and returns the polymer's MWD as output.

## INDUSTRIAL APPLICATION

The software has designed standard functions for defining and solving polymerization models. The core modeling functions are designed for specifying individual modules of the model, including components, streams, units, and kinetics. These functions make the modelling process of each module convenient and efficient. The modelling and simulation steps of this software are illustrated in Figure 5.

An industrial application is next demonstrated by using the software. It is a Ziegler-Natta copolymerization produced by two CSTRs as shown in Figure 6. This case focuses on polymerization kinetics and the microscopic structure of the polymer.

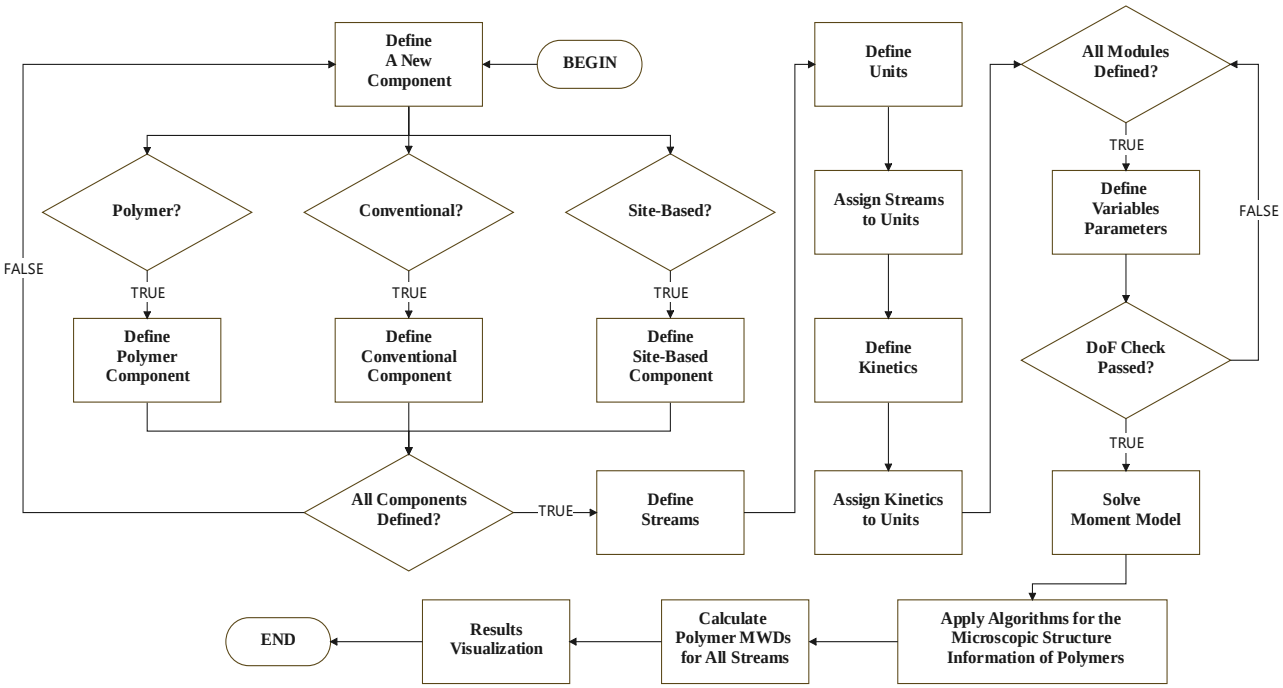



**Figure 5:** The flowchart for the modeling and simulation steps of the software, outlining the sequential process from model definition to simulation execution.

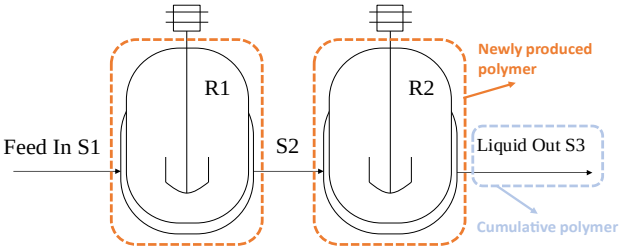



**Figure 6.** The simplified flowsheet of the Ziegler-Natta copolymerization case.

First, we define the components involved in this application. Ethylene and 1-butene are defined as monomers, triethyl aluminum as the cocatalyst, n-hexane as the solvent, and hydrogen as a controlling agent. The site-based component, titanium tetrachloride, is defined as the catalyst, with the potential, vacant, and dead sites being tracked. The number of active sites is set to five. For the olefin polymer, the moments, MWD, and other structure properties are studied.

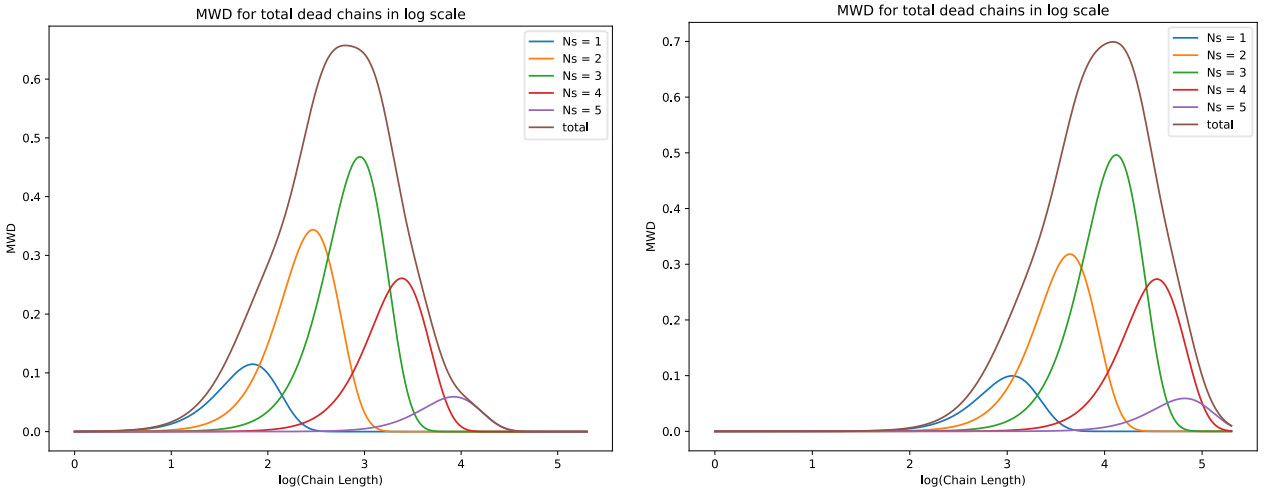
The CSTRs operate under fixed conditions with a constant liquid phase volume. Next, we define the Ziegler-Natta kinetics with reactions occurring on five active sites. The reactions involved in this kinetic model are listed in Table 1. $P_r^*[M]$ denotes living polymer with chain length $r$ and the end monomer $M$. $D_r$ denotes dead polymer with chain length $r$. Values of the pre-exponential factor $A$, activation energy $E_a$, and reference temperature $T_0$ are specified to calculate the corresponding reaction rates. The defined kinetics are then assigned to the two CSTRs.

Eventually, the moment model is established and solved. The results obtained include the concentrations of conventional components, the concentrations of potential, vacant, and dead sites, as well as the moments of the polymer CLD within the two CSTRs. The self-developed algorithms are applied to derive the MWD of newly produced polymer in R1 and R2. The results are plotted in Figure 7, the MWD curves of five activate sites are derived, respectively.

**Table 1:** Reactions involved in the Ziegler-Natta kinetic.

| Description | Chemical Equation |
|---|---|
| Initiation | $P_0^* + C_2H_4 \rightarrow P_1^*[C_2H_4]$ |
| | $P_0^* + C_4H_8 \rightarrow P_1^*[C_4H_8]$ |
| Propagation | $P_r^*[C_2H_4] + C_2H_4 \rightarrow P_{r+1}^*[C_2H_4]$ |
| | $P_r^*[C_2H_4] + C_4H_8 \rightarrow P_{r+1}^*[C_4H_8]$ |
| | $P_r^*[C_4H_8] + C_4H_8 \rightarrow P_{r+1}^*[C_4H_8]$ |
| | $P_r^*[C_4H_8] + C_2H_4 \rightarrow P_{r+1}^*[C_2H_4]$ |
| Transfer to monomer | $P_r^*[C_2H_4] + C_2H_4 \rightarrow D_r + P_1^*[C_2H_4]$ |
| | $P_r^*[C_2H_4] + C_4H_8 \rightarrow D_r + P_1^*[C_4H_8]$ |
| | $P_r^*[C_4H_8] + C_4H_8 \rightarrow D_r + P_1^*[C_4H_8]$ |
| | $P_r^*[C_4H_8] + C_2H_4 \rightarrow D_r + P_1^*[C_2H_4]$ |
| Transfer to hydrogen | $P_r^*[C_2H_4] + H_2 \rightarrow D_r + P_0^*$ |
| | $P_r^*[C_4H_8] + H_2 \rightarrow D_r + P_0^*$ |
| Transfer to cocatalyst | $P_r^*[C_2H_4] + Al \rightarrow D_r + P_0^*$ |
| | $P_r^*[C_4H_8] + Al \rightarrow D_r + P_0^*$ |
| Transfer | $P_r^*[C_2H_4] \rightarrow D_r + P_0^*$ |
| | $P_r^*[C_4H_8] \rightarrow D_r + P_0^*$ |
| Deactivation | $P_r^*[C_2H_4] \rightarrow D_r$ |
| | $P_r^*[C_4H_8] \rightarrow D_r$ |
| | $P_0^* \rightarrow D_0$ |

Last but not least, the microscopic information of cumulative dead polymer in streams S2 and S3 can also be determined. Mathematically, the MWD curve of the final product is a weighted sum of the MWDs of the




(a) CSTR1 (b) CSTR2

**Figure 7:** The MWD results of the dead polymer in R1 and R2 are presented. Each subfigure displays the MWD curves of dead polymer at five sites, along with the MWD curve of the total dead polymer. All curves are plotted on a logarithmic scale.

products from both R1 and R2, as shown in Figure 8.

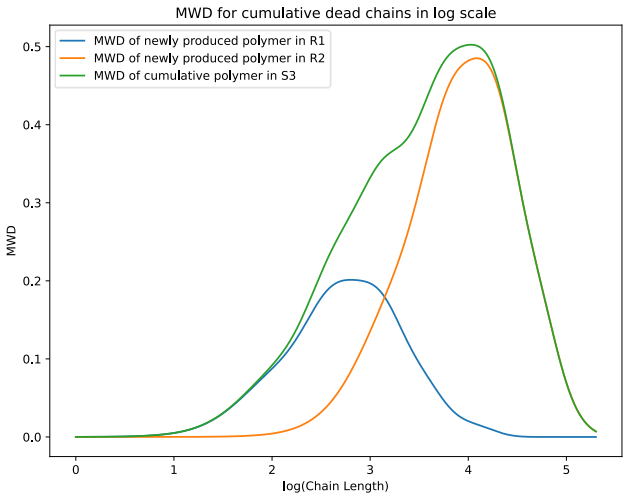



**Figure 8.** The MWD result of the cumulative dead polymer in S3 is shown. The blue and orange lines represent the weighted MWD curves of the newly produced polymer inside R1 and R2, respectively.

## CONCLUSION

A modelling and simulation software for polymerization with microscopic resolution is proposed in this study. The module architecture and self-developed efficient algorithms of this software are introduced in detail. To demonstrate the software's capability in capturing the microscopic structural information of polymers, a Ziegler-Natta polymerization is applied. The insights gained from this work open up opportunities for process analysis and optimization of polymerizations.

## ACKNOWLEDGEMENTS

The authors would like to acknowledge the support of the National Key Research and Development Project (Grant No. 2023YFB3307800) and the State Key Laboratory of Industrial Control Technology, China (Grant No. ICT2024C04).

## REFERENCES

1. Lin X, Chen X, Biegler LT, Feng L-F. A modified collocation modeling framework for dynamic evolution of molecular weight distributions in general polymer kinetic systems. *Chem Eng Sci* 237: 116519 (2021)
2. Mastan E, Zhu S. Method of moments: A versatile tool for deterministic modeling of polymerization kinetics. *Eur Polym J* 68: 139-160 (2015)
3. Liu R, Lin X, Armaou A, Chen X. A multistep method for steady-state Monte Carlo simulations of polymerization processes. *AIChE J* 69: e17978 (2023)
4. Liu R, Armaou A, Chen X. Adaptable Parallel Acceleration Strategy for Dynamic Monte Carlo Simulations of Polymerization with Microscopic Resolution. *Industrial & Engineering Chemistry Research* 60:6173-6187 (2021)

© 2025 by the authors. Licensed to PSEcommunity.org and PSE Press. This is an open access article under the creative commons CC-BY-SA licensing terms. Credit must be given to creator and adaptations must be shared under the same terms. See https://creativecommons.org/licenses/by-sa/4.0/

Systems & Control Transactions

**Research Article - Peer Reviewed Conference Proceeding**
ESCAPE 35 - European Symposium on Computer Aided Process Engineering
Ghent, Belgium. 6-9 July 2025
Jan F.M. Van Impe, Grégoire Léonard, Satyajeet S. Bhonsale,
Monika E. Polańska, Filip Logist (Eds.)

PSE PRESS

# Interval Hessian-based Optimization Algorithm for Unconstrained Non-convex Problems

**Ashutosh Sharma[a], Gauransh Dingwani[b], and Ishan Bajaj[a]***

[a] Indian Institute of Technology Kanpur, Department of Chemical Engineering, Kanpur, Uttar Pradesh, India
[b] Indian Institute of Technology Roorkee, Department of Chemical Engineering, Roorkee, Uttarakhand, India
* Corresponding author: ibajaj@iitk.ac.in.

## ABSTRACT

Second-order optimization algorithms that leverage the exact Hessian or its approximation have been proven to achieve a faster convergence rate than first-order methods. However, their applications on training deep neural networks models, partial differential equations-based optimization problems, and large-scale non-convex problems, are hindered due to high computational cost associated with the Hessian evaluation, Hessian inversion to find the search direction, and ensuring its positive-definiteness. Accordingly, we propose a new search direction based on an interval Hessian and incorporate it into a line-search framework. We apply our algorithm to a set of 210 problems and show that it converges to a local minimum for 70% of the problems. We also compare our algorithm with other approaches. We illustrate that our algorithm is competitive to other methods in finding a local minimum using a smaller number of $O(n^3)$ operations.

**Keywords**: Second-order optimization, Interval Hessian, Line-search framework, Non-Convex optimization.

## 1. INTRODUCTION

We consider the unconstrained optimization problem:

$$\min_{x\in\mathbb{R}^n} f(x)$$

where $f: \mathbb{R}^n \to \mathbb{R}$ is a twice continuously differentiable function, and $n$ is the number of variables. Several first- and second-order methods have been developed to solve the above problem. These algorithms are used in areas like process optimization, communications, machine learning, and signal processing. First-order algorithms, such as steepest descent, stochastic gradient descent, and various adaptive gradient methods, are particularly popular for large-scale problems due to their relatively low computational demands per iteration. Despite their prevalence, first-order methods are limited in that they only guarantee convergence to a first-order stationary point. Thus, these methods can converge to a saddle point rather than a local minimum.

In contrast, second-order optimization algorithms, which utilize the curvature information via the Hessian matrix, provide faster convergence and avoid saddle points. Newton's method, a classic second-order approach, adjusts the gradient direction with a preconditioning matrix derived from the Hessian, achieving convergence to points that meet second-order optimality conditions.

Although Newton's method exhibits impressive convergence characteristics compared to first-order approaches, their broad application to large-scale optimization problems poses significant challenges. First, the memory requirement increases with the square of the number of variables. Second, the Hessian calculation can be expensive. Third, at each iteration, the search direction requires computing the inverse of the Hessian, which requires $O(n^3)$ operations and can be computationally expensive for large $n$. Fourth, Newton's direction for non-convex problems may not be descent at each iteration. However, nonconvexity is ubiquitous in several applications, including, training neural network models, reactor and separation network synthesis, process design, and computational chemistry.

To address these limitations, quasi-Newton methods have been developed as computationally feasible alternatives. Quasi-Newton methods, such as the BFGS algorithm [2], approximate the Hessian using gradients of the previous iteration and thus reduce computational

demands. Sub-sampled Newton methods [5] decrease costs by approximating the Hessian using a subset of data points. Despite these advances, balancing Hessian approximation accuracy with computational tractability remains a fundamental challenge.

Accordingly, we propose a new search direction based on an interval Hessian and incorporate it into a line-search framework. Our approach is inspired by αBB method proposed by Floudas and co-workers [1] to construct a convex underestimator of a twice-differentiable function over an interval $[x^L, x^U]$. Our approach involves using the Hessian of the αBB underestimator. There are three advantages of this approach. First, since the underestimator is convex, its Hessian will always be positive definite. Thus, the search direction is guaranteed to be descent. Second, the same Hessian matrix can be used if the iterates lie in the interval for which the interval Hessian is valid. This results in (1) avoiding computing Hessian at each iteration and (2) the search direction is computed by taking matrix-vector product instead of $O(n^3)$ operations that are typically needed in Newton and Quasi-Newton methods.

## 2. METHODOLOGY

### 2.1. Search Direction

In this article, we propose a variant of the Newton direction to ensure descent at each iteration for non-convex problems. We incorporate the search direction into a line-search framework:

$$x_{k+1} = x_k + \theta_k p_k$$

where $x_k$ is the current iterate, $x_{k+1}$ is the next iterate, $\theta_k$ is the step length, and $p_k$ is the search direction. Our search direction is inspired by the $\alpha BB$ method developed for global optimization of non-convex problems. This method constructs a convex underestimator of a twice continuously differentiable function with the following form:

$$\mathcal{L}(x) = f(x) + \sum_{i=1}^{n} \alpha_i \left(x_i^L - x_i\right)\left(x_i^U - x_i\right)$$

where $\alpha_i \geq 0$. This underestimator is constructed by subtracting a positive term from $f(x)$, making $\mathcal{L}(x)$ a valid underestimator of $f(x)$ within $[x^L, x^U]$. The parameter $\alpha_i$ is calculated to ensure that $\mathcal{L}(x)$ is convex over this interval, which implies that the Hessian of $\mathcal{L}(x)$ is positive semi-definite. Thus, we choose $p_k$ as follows:

$$p_k = -(B_k)^{-1} \nabla f_k \tag{1}$$

where $\nabla f_k = \nabla f(x_k)$ and $B_k = B_{k-1}$ if $x_k$ lies in the interval for which the convex underestimator is valid; otherwise, new variable bounds are constructed and $B_k = \nabla^2 \mathcal{L}_k$. The Hessian of the $\alpha$BB underestimator provides a localized approximation of the objective function's curvature. The relationship between the Hessians of $\mathcal{L}(x)$ and $f(x)$ at $x = x_k$ is:

$$\nabla^2 \mathcal{L}_k = \nabla^2 f_k + 2\Delta$$

where Δ is a diagonal matrix with elements $\alpha_i$. The matrix Δ is referred to as the diagonal shift matrix. For simplicity, we assume a uniform diagonal shift matrix, such that $\alpha_1 = \alpha_2 = \alpha_3 = \cdots = \alpha_n = \alpha$, leading to:

$$\nabla^2 \mathcal{L}_k = \nabla^2 f_k + 2\alpha I$$

where $I$ denotes the identity matrix. Based on the above equation, we conclude that the difference between the Hessian of the function and the $\alpha$BB underestimator depends on $\alpha$. Consequently, the accuracy of computing $\alpha$ determines the search direction quality, which in turn affects the performance of our algorithm.

Maranas and Floudas demonstrated [1] that the underestimator, $\mathcal{L}(x)$, is convex if and only if:

$$\alpha \geq \max\left\{0, -\frac{1}{2} \min_{i, x^L \leq x \leq x^U} \lambda_i \left(\nabla^2 f(x)\right)\right\}$$

where $\lambda_i$ are the eigenvalues of $\nabla^2 f(x)$. Finding $\alpha$ by using the above equation is equivalent to solving a non-convex optimization problem to global optimality, which can require significant computational effort.

To overcome this difficulty, a lower bound on the minimum eigenvalue of the interval matrix, $[\nabla^2 f(x)] \supseteq \nabla^2 f(x), \forall x \in [x^L, x^U]$, is computed. This interval Hessian is then used in further $\alpha$ calculations. In subsequent sections, we explore various approaches to compute $\alpha$ by employing methods with $O(n^2)$ and $O(n^3)$ complexities.

### 2.2. $\alpha$ Calculation Methods

We use three methods to compute the value of lower bound on eigenvalues ($\lambda_{min}$) for a real interval matrix $[A] = \left(\left[\underline{a_{ij}}, \overline{a_{ij}}\right]\right)$. We define following notations useful in computation of $\lambda_{min}$.

$$\underline{A} = \left(\underline{a_{ij}}\right) \text{ and } \overline{A} = \left(\overline{a_{ij}}\right), \Delta a_{ij} = \left(\overline{a_{ij}} - \underline{a_{ij}}\right)/2$$

$$\widetilde{\Delta A} = \left(\widetilde{\Delta a_{ij}}\right), \widetilde{\Delta a_{ij}} = \begin{cases} 0 & \text{if } i = j, \\ \Delta a_{ij} & \text{otherwise} \end{cases}$$

$$A_M = (a_{M,i,j}), a_{M,ij} = \left(\overline{a_{ij}} + \underline{a_{ij}}\right)/2$$

$$\widetilde{A_M} = \left(\widetilde{a_{M,ij}}\right),$$

$$\widetilde{a_{M,ij}} = \begin{cases} \underline{a_{ij}} & \text{if } i = j, \\ a_{M,ij} & \text{otherwise} \end{cases}$$

where, $\Delta A$ is the radius matrix, $\widetilde{\Delta A}$ is the modified radius matrix, $A_M$ is the midpoint matrix, $\widetilde{A_M}$ is the modified midpoint matrix, $\underline{A}$ is the lower vertex matrix and $\overline{A}$ is the upper vertex matrix. The various methods of $O(n^2)$ and $O(n^3)$ complexities to calculate the minimum eigenvalue are given below.

### 2.2.1 Approximate Gerschgorin: Complexity $O(n^2)$

$$\lambda_{min}([A]) \geq \min_i \left[ \underline{a_{ii}} - \sum_{j \neq i} \max\left( \left| \underline{a_{ij}} \right|, \left| \overline{a_{ij}} \right| \right) \right]$$

### 2.2.2. E-Matrix Method: Complexity $O(n^3)$

$$\lambda_{min}([A]) \geq \lambda_{min}\left(\widetilde{A_M} + E\right) - \rho\left(\widetilde{\Delta A} + |E|\right)$$

where E be an arbitrary symmetric matrix, whose value is chosen to be $diag(\Delta A)$ here, $\rho(M)$ denotes the spectral radius of a matrix M, i.e., the maximal absolute eigenvalue and $|E|$ denotes the absolute value taken elementwise.

### 2.2.3. Mori-Kokame Method: Complexity $O(n^3)$

$$\lambda_{min}([A]) \geq \lambda_{min}\left(\underline{A}\right) - \rho\left(\overline{A} - \underline{A}\right)$$

## 2.3. Algorithm

Our algorithm employs a line search technique with the search direction details given in the Section 2.1. The overall framework is outlined in Algorithm 1. We choose two iteration counters, $t$ and $k$. The former serves as the outer iteration counter, and the latter as the inner iteration counter.

We begin by randomly choosing an initial point $x_0$ such that it lies within the interval $[x_0^L, x_0^U]$. The search direction $p_k$ (Eq. (1)) satisfies $\nabla f_k^T p_k < 0$, guaranteeing that it leads to a decrease in the function value. Thus, at each iteration, $f(x_{k+1}) < f(x_k)$.

Once the search direction is determined, we need to decide how far to move in the given direction by choosing an appropriate value of $\theta_k$. We select $\theta_k$ that satisfies the Armijo condition:

$$f(x_k + \theta_k p_k) \leq f(x_k) + c_1 \theta_k \nabla f(x_k)^T p_k$$

where $c_1 \in (0, 1)$. This condition ensures that a sufficiently large decrease in the objective function is achieved. We apply a backtracking line search procedure to find $\theta_k$ that satisfies the Armijo condition.

Our approach leverages interval-based calculations to reduce the need to compute Hessian and its inverse at every iteration. At iteration $k$, if the iterate $x_k$ lies outside the current interval $[x_t^L, x_t^U]$, we update the iteration counter $t$ to $t+1$ and construct an interval of size $\Delta$ around the iterate $x_k$ by setting $x_{t+1}^L = x_k - \frac{\Delta}{2}$ and $x_{t+1}^U = x_k + \frac{\Delta}{2}$. After updating the interval, the interval Hessian is computed using interval arithmetic, the minimum eigenvalue of the interval Hessian is estimated using one of the methods mentioned in section 2.2, and $\nabla^2 L_t$ and its inverse are computed. Thus, at any iteration $t$, depending on the method used to estimate the minimum eigenvalue of the interval Hessian, either one or two $O(n^3)$ operations are performed. On the other hand, at iteration $k$, if the iterate $x_k$ lies inside the current interval $[x_t^L, x_t^U]$, the search direction is updated by taking the product of $(\nabla^2 L_t)^{-1}$ and $\nabla f_k$. Conversely, in Newton's method, Hessian evaluation and its inverse is computed at every iteration. Note that $\nabla^2 L_t$ is a positive-definite matrix, and thus, the search direction is always guaranteed to be descent.

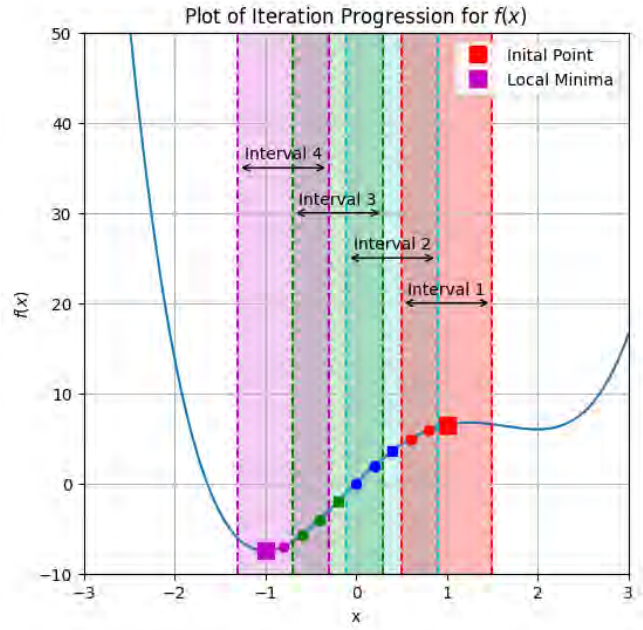



**Figure 1.** Graphical illustration of our proposed algorithm.

Figure 1 demonstrates the iterative mechanics of our approach using a one-dimensional example. The figure illustrates that if the iterates remain within an interval (denoted by a circle marker), the Hessian remains the same, and the search direction is obtained by the matrix-vector product. When an iterate exits the current interval, a new interval is formed around this iterate (denoted by a small square marker), and all the relatively more expensive computations occur.

The algorithm is implemented in C++. We use IBEX for interval Hessian and gradient evaluations and Eigen to compute the matrix inverse.

# 3. COMPETING ALGORITHMS

We compare the performance of our algorithm with the steepest descent, quasi-Newton and the Newton method. The steepest descent amd quasi-Netwon are popular optimization algorithms; their details can be found in a standard optimization textbook [2]. In Newton's method, the search direction, denoted by $p_k^N$, is given by:

$$p_k^N = -(\nabla^2 f_k)^{-1} \nabla f_k$$

At every iteration $k$, finding the search direction requires $O(n^3)$ operations. If the Hessian matrix is positive-definite at the current iterate, $x_k$, then the search

**Algorithm 1** Interval Hessian based line-search method

**Init.** Choose $x_0 \in \mathbb{R}^n, c_1 \in (0,1), \rho \in (0,1), \epsilon_g \in (0,1), \epsilon_H \in (0,1), t = 0$;

**for** $k = 0, 1, 2, \ldots$ **do**

Set $g_k = \nabla f(x_k)$;

**if** $\|g_k\| < \epsilon_g$ and $\lambda_{min}(\nabla^2 f(x_k)) > \epsilon_H$ **then**

**Terminate – Solution found;**

**end if**

**if** $k > iter_{max}$ **then**

**Terminate**

**if** $k = 0$ **then** Set $H_k = \nabla^2 f(x_k)$

**Hessian Modification** (Compute $B_t$, $x_t^L$, $x_t^U$)

**for** $i = 0, 1, 2, \ldots$ **do**

$x_{t,i}^L = x_{k,i} - \Delta/2$

$x_{t,i}^U = x_{k,i} + \Delta/2$

**end for**

Compute interval Hessian $[H_t]$ for the interval $[x_t^L, x_t^U]$ and calculate $\lambda_{min}$ using methods suggested above

Set $B_k = \nabla^2 L_t + \lambda_{min} I_n$

$t \leftarrow t + 1$

**else**

**if** $x_k \in [x_t^L, x_t^U]$ **then**

Use the pre-computed Hessian $B_k = B_{k-1}$

**else**

**Hessian Modification** (Compute $B_t$, $x_t^L$, $x_t^U$)

$t \leftarrow t + 1$

**end if**

**end if**

Find the search direction by solving $p_k = -B_t^{-1} g_k$

Compute step length $\theta_k$ satisfying Armijo condition and set $x_{k+1} = x_k + \theta_k p_k$

**end for**

direction is guaranteed to be descent. On the other hand, if the Hessian is indefinite, then it needs to be modified, requiring additional computations. A simple idea to modify the Hessian is to find a parameter $\tau > 0$ such that $\nabla^2 f_k + \tau I$ is positive definite. Algorithm 2 describes a method to iteratively increase the value of $\tau$ until the matrix becomes positive definite, verified by performing Cholesky decomposition.

**Algorithm 2** Brute-force Diagonal Shift

**Init.** Choose $\tau_0 = 0$;

**for** $i = 0, 1, 2, \ldots$ **do**

**Cholesky Factorization** $LL^T = \nabla^2 f_k + \tau_i I_n$

**if** factorization is completed successfully

$\lambda_{min} \leftarrow \tau_i$ and **terminate**

**else** $\tau_{i+1} \leftarrow \tau_i + 1$

**end if**

**end for**

# 4. RESULTS

We illustrate the performance of our algorithm on two illustrative examples and conduct extensive numerical experiments over a comprehensive set of 210 problems [3]. Specifically, we compare the performance based on the number of Hessian evaluations and $O(n^3)$ operations. Since we estimate the interval Hessian at an iteration $t$, we count equivalent to two Hessian evaluations are performed.

## 4.1. Illustrative Examples

### 4.1.1. Example 1

The objective function is of the following form:

$$f(x_1, x_2) = \sum_{j=1}^{17} \sum_{k=1}^{m_j} \left(t_{j,k} - [\exp(-2jx_2)(0.49 - x_1) + x_1]\right)^2$$

where $m_j$ denotes the number of groups at index $j$ and $t_{j,k}$ is a constant. Figure 2(a) shows the paths taken by

the iterates generated by the steepest descent, quasi-newton BFGS and three variants of our algorithm to calculate $\alpha$ based on the methods described in Section 2.2. For this problem, we used $\Delta = 0.1$. It can be observed that the steepest descent can get stuck at regions with small gradients and is unable to reach a local minimum in 10000 iterations. The BFGS method followed a path similar to the steepest descent but failed to find a descent direction after 9 iterations. This occurs because the quasi-Newton method can fail to find a descent direction for non-convex problems if the Armijo condition is used to find the step size $\theta$ (refer chapter 6 of [2]). On the other hand, all our algorithm variants take almost the same path and converge to the same solution. The Gerschgorin-based method requires 8 Hessian evaluations, 8 $O(n^3)$ operations, and 466 iterations. E-matrix based method requires 317, and the Mori-Kokame method converges in 1125 iterations, requiring 7 and 9 Hessian evaluations and 14 and 18 $O(n^3)$ operations respectively.

### 4.1.2. Example 2

We minimize the function of the form:

$$f(x_1, x_2) = C_A x_1 + C_B x_2 + C_C - \left\{ \sum_{(i,j)\in S} C_{ij} x_1^i x_2^j + \frac{C_D}{1 + x_2} + C_E e^{C_F x_1 x_2} \right\}$$

where $C_A, \ldots, C_F$ and $C_{ij}$ are constants. Figure 2(b) shows the paths taken by the iterates generated by brute force method and three variants of our algorithm corresponding to $\alpha$ calculation methods described in Section 2.2. To illustrate the effect of Hessian evaluations, we use the sleep function with 2 seconds when the Hessian is evaluated. Figure 2(c) shows that all the algorithm variants converge to a better solution in less time than the brute force method.

## 4.2. Benchmarking with Data Profiles

We construct data profiles [4] to systematically benchmark the algorithms. A data profile assesses the absolute performance of an algorithm. It determines the ability of an algorithm to solve an optimization problem within some desirable performance metric. For each problem-algorithm pair $(l, a)$, the data profile $d_a(\delta)$ indicates the proportion of problems solved within $\delta$ metric:

$$d_a(\delta) = \frac{1}{|L|} \text{size}\{l \in L : m_{l,a} \leq \delta\}$$

where $|L|$ represents the total number of problems and $m_{l,a}$ is the performance measure. We evaluate the performance of our algorithm based on Hessian evaluations and the number of $O(n^3)$ operations, as these are the most computationally expensive steps in a second-order optimization method.

A key trade-off in the proposed approach lies in the choice of interval size ($\Delta$). Larger intervals reduce the computations associated with Hessian evaluations and inversion but potentially sacrifice accuracy in $\alpha$ estimates. Conversely, smaller intervals enhance precision and robustness in capturing curvature information but at the cost of increased computational overhead. Additionally, the accuracy of $\alpha$ depends on the method employed. We observed that the Mori-Kokame and E-matrix methods provide more accurate $\alpha$ estimates than the Gerschgorin method. While the former two approaches require $O(n^3)$ operations, the latter requires $O(n^2)$ operations.

Accordingly, to study these trade-offs, we consider six variants of our algorithm by choosing three $\Delta$ values (0.1, 0.5, 1) and three methods to estimate the minimum eigenvalue (section 2.2). We apply the algorithms to a set of 210 problems. The results of the computational experiments are shown in Figure 2 (d), which shows that our algorithm could solve 70% of the problems in less than 300 Hessian evaluations. For 13% of the instances terminated, the algorithm reached the maximum number of iterations (10000), 1.9% stopped due to the time limit (3600 seconds), 9% stopped due to small step size, and 0.9% of cases converged to an iterate where the norm of the gradient was below the threshold but failed to satisfy the minimum eigenvalue condition of the Hessian. The remaining 4.8% of cases involved scenarios where a local minimum did not exist or the algorithm started from points with excessively large function values exceeding the range of data type double.We observe that the E-matrix and Mori-Kokame methods with $\Delta = 0.1$ outperform the Gerschgorin method and converge in a smaller number of iterations.

Next, we compare the performance of our algorithm with Newton's method, employing Algorithm 2 to ensure a positive-definite Hessian matrix. To illustrate the effectiveness of the interval-based approach, we also implement the Gerschgorin method of finding $\alpha$ with $\Delta = 0$. For this computational study, we selected the problems requiring Hessian modifications. Figures 2(e) and 2(f) show the data profiles based on the number of Hessian evaluations and $O(n^3)$ operations, respectively.

We make three key observations. First, the interval-based method for finite values of $\Delta$ performs similarly to the Gerschgorin method with $\Delta = 0$ in terms of Hessian evaluations; however, the former method requires a smaller number of $O(n^3)$ operations. Second, when the computational budget is more than 40 $O(n^3)$ operations, the Gerschgorin-based interval method outperforms the other methods, illustrating the effectiveness of the search direction in navigating the non-convex landscape. Finally, Newton's method with brute force method of modifying the Hessian solves the most problems in least number of Hessian evaluations. Still, it requires a higher number of $O(n^3)$ operations. This can be explained by the fact that the brute-force method adds $\tau$ just enough to make the Hessian positive definite, resulting in a better

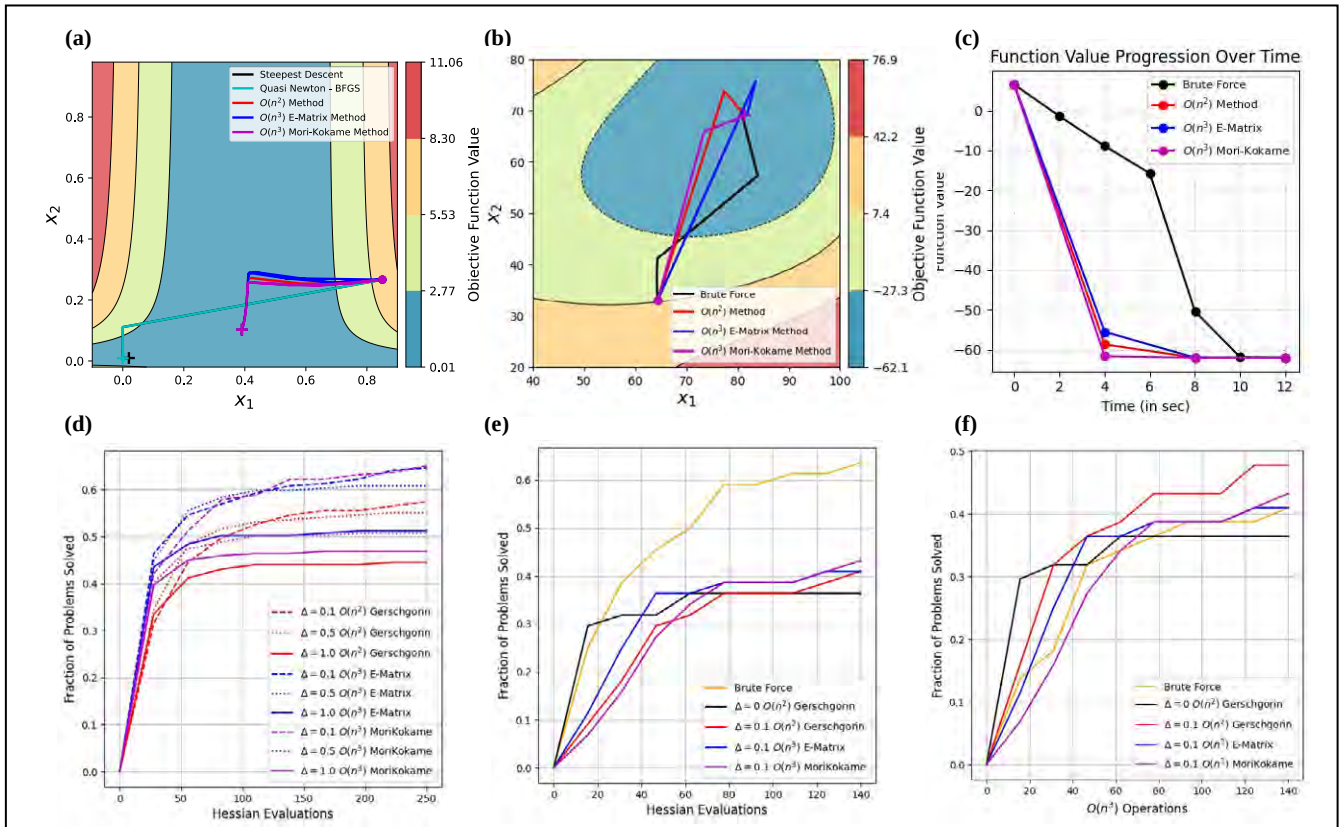



**Figure 2. (a)** and **(b)** compare the paths taken by the iterates generated by various algorithms. **(c)** Function value progression comparison of various algorithms. **(d)** Data profile based on Hessian evaluations for different Δ values and $\alpha$ calculations methods. **(e)** and **(f)** Comparision of our algorithm with other competing algorithms.

search direction. However, this increases $O(n^3)$ operations due to the Cholesky decomposition performed for positive-definiteness verification.

## 5. CONCLUSIONS

In this study, we introduced an interval-based optimization algorithm to find a search direction guaranteed to be descent to find a local minimum of non-convex problems. We show through numerical experiments that our algorithm finds a local minimum for a greater number of problems using less $O(n^3)$ operations compared to Newton's method. The results highlight the potential of our approach to improve the scalability of second-order optimization for complex, real-world applications.

## DIGITAL SUPPLEMENTARY MATERIAL

Supplementary material is uploaded in Living Archive for Process Systems Engineering with ID LAPSE:2025.0005.

## REFERENCES


1. Adjiman C, Dallwig S, Floudas C, Neumaier A. A global optimization method, αBB, for general twice-differentiable constrained NLPs — I. Theoretical advances. *Comput Chem Eng* 22:1137–1158 (1998) https://doi.org/10.1016/S0098-1354(98)00003-3
2. Nocedal, J., & Wright, S. J. NUMERICAL OPTIMIZATION. In Springer eBooks (2006).
3. Puranik, Y., & Sahinidis, N. V. Bounds tightening based on optimality conditions for nonconvex box-constrained optimization. *J Glob Opt*, *67*(1–2), 59–77 (2016) https://doi.org/10.1007/s10898-016-0491-8
4. Moré, J. J., & Wild, S. M. Benchmarking Derivative-Free optimization Algorithms. *SIAM J Opt*, *20*(1), 172–191 (2009). https://doi.org/10.1137/080724083
5. Xu, P., Roosta, F., & Mahoney, M. W. Second-order Optimization for Non-convex Machine Learning: an Empirical Study. In *SIAM eBooks* (pp. 199–207). (2020) https://doi.org/10.1137/1.9781611976236.23



© 2025 by the authors. Licensed to PSEcommunity.org and PSE Press. This is an open access article under the creative commons CC-BY-SA licensing terms. Credit must be given to creator and adaptations must be shared under the same terms. See https://creativecommons.org/licenses/by-sa/4.0/

Systems & Control Transactions

**Research Article - Peer Reviewed Conference Proceeding**
ESCAPE 35 - European Symposium on Computer Aided Process Engineering
Ghent, Belgium. 6-9 July 2025
Jan F.M. Van Impe, Grégoire Léonard, Satyajeet S. Bhonsale,
Monika E. Polańska, Filip Logist (Eds.)

PSE PRESS

# Design Space Exploration via Gaussian Process Regression and Alpha Shape Visualization

**Elizaveta Marich[a,b], Andrea Galeazzi[a,b], Steven Sachio[a,b], Foteini Michalopoulou[a,b], and Maria M. Papathanasiou[a,b]***

[a] Department of Chemical Engineering, Imperial College London, South Kensington Campus, London SW7 2AZ, UK
[b] The Sargent Centre for Process Systems Engineering, Imperial College London, South Kensington Campus, London SW7 2AZ, UK
* Corresponding Author: maria.papathanasiou11@imperial.ac.uk.

## ABSTRACT

This study introduces a novel methodology that combines Gaussian process regression (GPR) with alpha shape design space reconstruction to visualize multi-dimensional design spaces. The proposed GPR surrogate approach incorporates a kernel optimization step, employing a greedy tree search strategy to identify the optimal combinatorial kernel from a selection of base kernels. This approach efficiently evaluates design spaces around specific points of interest, enabling alpha shape reconstruction. The methodology's adaptability is demonstrated through its application to both lower-dimensional (2D and 3D) cases and more complex, higher-dimensional systems (up to 7D), showcasing its scalability and versatility. Its effectiveness is further validated by its ability to generate accurate surrogate models from limited data. Overall, this study presents a robust framework that leverages GPR surrogate modeling and alpha shape reconstruction to facilitate design space evaluation in complex, multidimensional engineering problems.

**Keywords**: Design Space Identification, Surrogate Modelling, Gaussian Process Regression, Alpha Shapes, Kernel Optimisation.

## INTRODUCTION

The development of advanced computational tools and techniques has significantly enhanced the ability to solve challenging high-dimensional chemical engineering problems affected by uncertainty and complexities of chemical processes. Traditional computational tools are often restricted to simpler, lower-dimensional problems mainly due to numerical complexity. In the task of design space (DSp) identification, a major limitation is the substantial computational resources needed to extract the required knowledge from complex mechanistic models. Given that chemical processes are often characterized by intricate systems of equations, surrogate-based methodologies hold significant potential for enabling design space identification of complex and practical industrial scenarios by reducing the need for extensive modeling. Models like High Dimensional Model Representation (HDMR) [1] and Partial Least Squares (PLS) [2] have been directly utilized in DSp evaluation. More recently, Geremia *et al.* [3] analyzed a range of surrogate modeling techniques for DSp and found that the Gaussian Process (GP) is among the best-performing ones.

Despite surrogate models' potential to aid process design and control, producing highly accurate surrogates remains computationally demanding. This is particularly relevant when analyzing problems of increased dimensionality, where computational requirements can scale exponentially with process complexity. Moreover, meaningful analysis and visualization of the design space are crucial in high-dimensional problems to effectively evaluate quality criteria. The presented study aims to investigate the effectiveness of Gaussian process regression as a surrogate modeling technique within the context of multi-dimensional design space identification for enabling visual representation through alpha shape reconstruction.

## BACKGROUND

### Feasibility and Design Space Identification

Design space identification is a form of feasibility

analysis that aims to determine the feasible region of a design space, defined by the set of input variables that ensure the system output meets all specified constraints. The concept of design space identification is particularly relevant in the framework of Quality by Design (QbD), extensively applied in pharma and biopharma [4], which aims to design robust and efficient processes where quality criteria, or Key Performance Indicators (KPIs), are met in product output at varying input conditions. Design space identification is applied in this context to provide a fundamental understanding of the process operative range and is a key tool for enabling more advanced computational techniques for process enhancement, such as flexibility analysis.

The design space problem is formulated as shown in Eq. (1).

$$\begin{aligned} y &= f(\boldsymbol{\theta}) \\ \boldsymbol{\theta}_L \leq \boldsymbol{\theta} &\leq \boldsymbol{\theta}_U \\ g(\boldsymbol{y}) &\leq 0 \end{aligned} \tag{1}$$

where $\boldsymbol{y}$ is the vector of selected KPIs, $f$ is the system model, $\boldsymbol{\theta}$ is the vector of input variables, and $\boldsymbol{\theta_L}$ and $\boldsymbol{\theta_U}$ are the vectors of the lower and upper bounds of such variables, respectively. Finally, $g$ represents the target KPI constraints that must be satisfied.

## Alpha shapes DSp Reconstruction

Various methodologies exist for identifying and visualizing design spaces. Among them, the alpha shape method has demonstrated high accuracy in capturing both convex and non-convex feasibility regions in two- and three-dimensions [5]. Unlike convex hull methods, alpha shapes provide a flexible geometric representation that adapts to the underlying dataset structure. An alpha shape defines a boundary that encapsulates a set of points based on a shape-controlling parameter, the alpha radius $\alpha_r \in [0, +\infty]$. This parameter determines the level of detail in the reconstructed shape, allowing for fine or coarse representations of the feasibility region depending on the dataset $S$ and application requirements [6].

## Gaussian Process Regression

In this study, Gaussian Process Regression (GPR) is employed as a surrogate model to approximate the system function ($f$ in Eq. (1)). GPR is a non-parametric probabilistic approach that assumes the underlying function follows a multivariate Gaussian distribution, characterized by a mean function, $m(x)$, and a covariance function, called kernel, $k(x, x')$. Common kernel functions include the Radial Basis Function (RBF, also known as the Squared Exponential, SE), Rational Quadratic (RQ), Periodic (Per), and Linear (Lin) kernels. This approach enables flexible modeling of complex, non-linear relationships without requiring an explicit parametric form, instead relying on kernel functions to capture dependencies [7]. The kernel function plays a critical role in capturing relationships between data points, allowing GPR to make interpolative predictions. To model complex dependencies, composite kernels, formed by combining base kernels through addition or multiplication, can be employed, generating effective covariance functions while enhancing model expressiveness, as depicted in **Figure 1**.

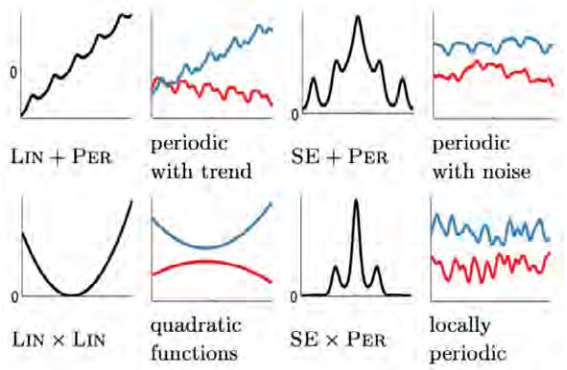



**Figure 1:** Examples of addition and multiplication of base kernels, in black, and the functions they are able to capture, colored, adapted from [8].

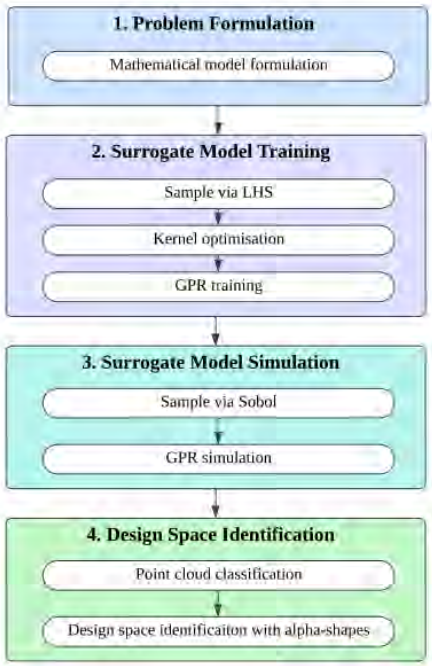



**Figure 2:** Design Space Identification Framework Schematic.

# METHODOLOGY

The methodology proposed in this work, shown in **Figure 2**, is aimed at the identification of the design space of high-dimensional constrained mathematical problems through Gaussian process regression surrogate modeling. In the context of chemical engineering,

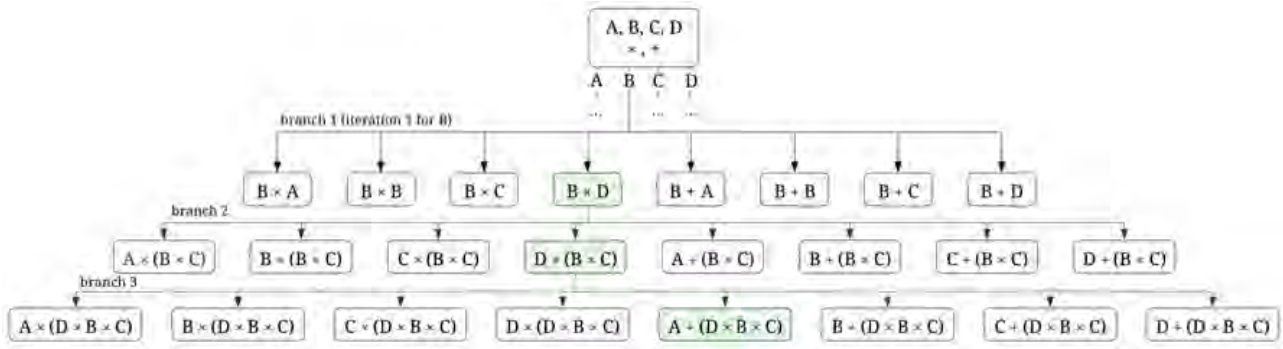



**Figure 3:** Schematic of the kernel optimisation algorithm.

the investigated variables represent design decisions, with the objective function being the process design and/or product specification. This methodology can be integrated as part of the QbD framework by facilitating the exploration of design space and understanding of how process disturbances, process variables, and design variables influence the chemical process and its KPIs.

The computations for this study are conducted in Python and performed using an Intel® Core™ i7–13,700 CPU @ 2.10 GHz. Nevertheless, the proposed framework can be easily implemented and adapted to different programming platforms with minimal changes to the procedure.

## Stage 1: Problem Formulation

The first step of the methodology is defining the objective function, $f(\boldsymbol{x})$, and its constraints, $g(\boldsymbol{x})$, for the analysis. In chemical engineering applications, the objective function may represent the chemical process under investigation or an optimization function that evaluates relevant KPIs. An example of a mathematical problem formulation is presented in **Table 1**.

**Table 1:** Example of a mathematical problem analyzed.

| **The Modified Gomez Function (D=3)** | |
|---|---|
| **Objective function and constraints** | **Search space** |
| $\min f(\boldsymbol{x}) = -\sin(4\pi x_1) + 2sin^2(2\pi x_2) + 4sin^3(\pi x_3)$ <br> $s.t. \quad g_1(\boldsymbol{x}) = f \leq 0$ | $[-1, 1]^3$ |

## Stage 2: Surrogate Model Training and Kernel Optimisation

The problem specifications define the search space within which the knowledge space is sampled using Latin Hypercube Sampling (LHS) for the vector of investigated variables $\boldsymbol{x} = [x_1, x_2, \ldots, x_{n_x}]$ of size $n_x$. The sampled data and computed corresponding outputs constitute the training data on which the surrogate model learns about the system. This training data is thus fed to a kernel optimization algorithm for selecting the best-fit GPR kernel.

The kernel optimization algorithm utilizes a combinatorial method for new kernel construction with a greedy tree search algorithm, as presented by Galeazzi *et al.* [8]. The greedy tree search selects optimal solutions at each step, ensuring the strategy remains computable within reasonable time and computational constraints. New kernels are constructed using four basic kernels (RBF, RQ, Periodic, Linear) and operators (multiplication, addition) to capture intricate model behaviors, as described above. This process is illustrated in the first branch for kernel B in **Figure 3**. Once a branch is composed of all potential kernels, they are evaluated based on the mean absolute error (MAE) parameter, and the kernel with the minimum MAE from the iteration is recorded and used as the basis for generating options in the next branch. This search continues until the user-specified tree depth is achieved, limited to five iterations for this study. All best kernels from each branch are stored, and the final best kernel is selected from this list, thus balancing the model's complexity and performance while mitigating the risk of overfitting that could arise with additional iterations without yielding significant improvements.

## Stage 3: Surrogate Model Testing

To gauge and test the surrogate model performance, after its training, a dense sample set is generated from the benchmark case studies function and MAE and Mean Absolute Percentage Error (MAPE) are re-evaluated for accuracy. Several reference graphs of the true function are generated to provide a visual benchmark, further aiding in the validation of the surrogate's performance. In a practical scenario where a computationally expensive high-fidelity model is implied this step would be skipped. However, in this study, this step is key to understanding the methodology potential.

## Stage 4: Design Space Identification

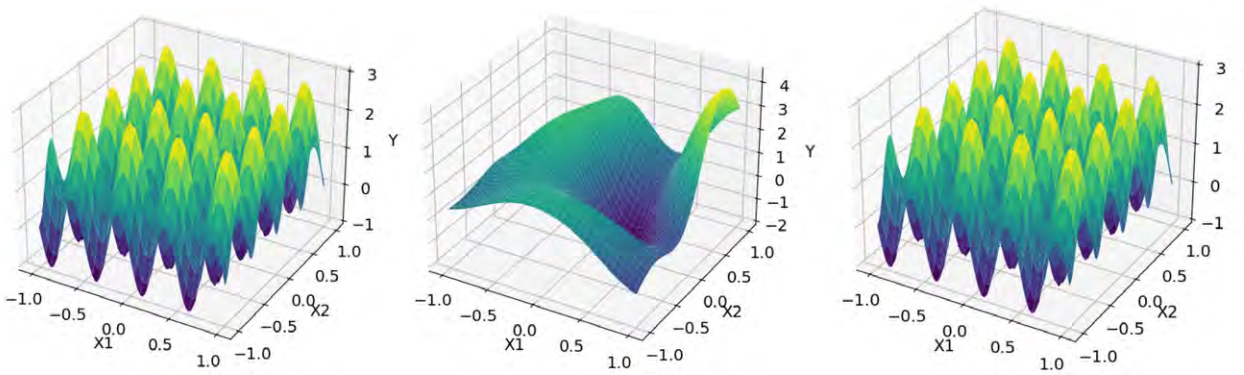



**Figure 4:** (a) Original function, (b) GPR surrogate prediction without kernel optimization, and (c) GPR surrogate prediction with kernel optimization.

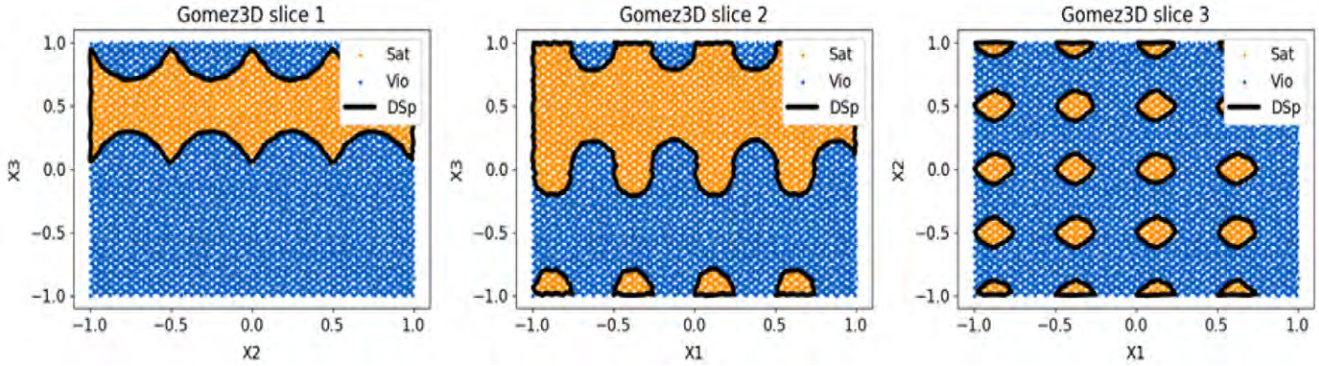



**Figure 5:** Design space (DSp) of the 3D modified Gomez function reconstructed with alpha shapes on 2D slices.

In this stage, the feasibility problem under investigation is developed. In the context of chemical engineering, it involves the selection of design decision variables and KPIs for analysis requirements for which the acceptable region of operation will be defined. In this study, where mathematical functions are employed, the feasibility function is equivalent to the objective function defined in Stage 1, $f(\boldsymbol{x})$, constrained to a user-defined value for DSp evaluation.

The design space is first defined by declaring a nominal point, which is user-selected and can represent any point of interest, such as an optimum. To enable the application of alpha shape reconstruction on higher-dimensional problems, a slicing technique is applied to create lower-dimensional planar slices around the point of interest. As the first stage of DSp identification, the surrogate model is densely resampled around the selected nominal point of interest within the boundaries applied. The slicing function is applied at this stage to create planes for DSp reconstruction. The number of orthogonal slices generated is determined only by the dimensionality of the problem and whether 2D or 3D plots are desired for visualization. Finally, the *dside* package is utilized on each slice for design space identification with alpha shape reconstruction. For a more detailed explanation of the package working principles, the reader is referred to Sachio *et al.* [9].

# RESULTS

## Kernel Optimization in GPR

The quality of design space evaluation is directly linked to the accuracy of predictions made by the surrogate model. Therefore, the initial step in the methodology is to ensure that the GPR can effectively capture even the most intricate relationships within the data. Typically, a basic kernel such as the RBF or Matern 5/2 is employed in GPR analysis. However, this is often insufficient for capturing the complexities of intricate data trends. In chemical engineering, experimentally or computationally collected data often exhibit behaviors that are not characterized a priori, necessitating further analysis to confirm whether the selected kernel is appropriate for the given data type. To avoid this laborious analysis and to create a versatile framework capable of handling any data complexity, kernel optimization was incorporated into the methodology. This optimization allows the construction of a composite kernel, enabling the capture of intricate data trends.

The effectiveness of the developed kernel optimization function was demonstrated using the modified Gomez function, proposed by Geremia *et al.* [3] and shown in **Table 1**. Both the optimized and non-optimized cases

were trained using the same LHS training set of size 38, ensuring that the training set and its size did not influence the accuracy of the surrogate predictions. The original function (**Figure 4.a**), generated using true values, serves as the benchmark for evaluating the GPR surrogate models, illustrating a significant improvement in prediction quality with and without kernel optimization, **Figures 4.c** and **4.b** respectively. This improvement is reflected in the performance metrics reported in **Table 2**, where near-perfect predictions were generated with kernel optimization. GPR training grows cubically as the number of samples increases and this optimization succeeds in reducing the number of training points needed. However, the time required for model training grows linearly with the number of kernels investigated, presenting a trade-off question between computational efficiency and predictive performance.

**Table 2:** Kernel optimization function performance.

| | MAE | $R^2$ | Accuracy | F1 score |
|---|---|---|---|---|
| **Without kernel optimisation** | 1.43 | 0.47 | 73.89% | 73.97 % |
| **With kernel optimisation** | 0.01 | 1.00 | 99.87% | 99.87 % |

## Application to 2D and 3D problems

The application to 2D and 3D case studies is useful in understanding the performance of the proposed methodology and developing heuristics for sample size selection. The latter is of particular importance as with increasing dimensionality the need for balancing computational demand and prediction accuracy arises. Results on the 2D study adapted from Sasena *et al.* [10] showed that a small number of training samples, n = 10D, was sufficient to achieve a 100% F1 score resulting in the DSp being captured fully. However, as expected, with increased dimensionality, and, therefore, problem complexity, the training set requirement increased.

The methodology's efficiency was further validated in the more complex 3D case study using the Modified Gomez function adapted from Geremia *et al.* [3]. As the dimensionality and complexity of the problem increased, a larger number of training samples was required, with an acceptable MAPE achieved only after the fourth incremental increase, where $n = 2(10D) = 60$. As shown in **Table 3**, the model struggled to achieve a good fit with smaller sample sizes, with MAPE ranging from nearly 550% to approximately 140%. This difficulty was primarily due to the surrogate's challenge in capturing the rapid fluctuations in the function's output. A significant improvement in the accuracy of the GPR predictions occurred between the third ($n$ = 53) and fourth ($n$ = 60) iterations. This change is likely due to the search space becoming sufficiently well-sampled, enabling the model to capture the nonlinearities of the original function more effectively, thereby reducing the model's uncertainty. The low standard deviations observed across 10 runs for the $n$ = 60 for MAE (0.00163) and MAPE (0.00521) confirm that the methodology consistently produces reliable and accurate results.

While the metrics generally improved with an increase in the training samples, an exception was noted in the second incremental increase ($n$ = 45), where MAPE increased despite improvements in MAE and $R^2$. This anomaly might be attributed to the overestimation of very small actual values, which disproportionately impacts MAPE due to its sensitivity to such values.

**Table 3:** Methodology results for the 3D case study across different training set sizes, n. Increments refer to the percentile increase of the initial 10D training set.

| Increment | n | MAE | MAPE | $R^2$ |
|---|---|---|---|---|
| Starting | 30 | 1.09952 | 549.45% | 0.67 |
| +25% | 38 | 1.03456 | 441.92% | 0.72 |
| +50% | 45 | 1.01836 | 514.45% | 0.73 |
| +75% | 53 | 0.26165 | 143.90% | 0.98 |
| +100% | 60 | 0.00451 | 1.74% | 1.00 |
| Benchmark | 300 | 0.00002 | 0.01% | 1.00 |

It is important to note that while the methodology is capable of analyzing the system as a 3D problem, as demonstrated by the results for $n$ = 60, 2D planar slicing offers a more understandable visualization of the problem and provides further insights into the method's performance. Such DSp slices are presented in **Figure 5**.

## Application to high-dimensional problems

The results from both 2D and 3D case studies convincingly demonstrate that the proposed methodology utilizing GPR for surrogate modeling and alpha shapes for DSp reconstruction is effective. Based on the analysis of the training size required to encapsulate complex functions, training sample sizes for high dimensional problems were selected following the $2(10D)$ rule.

For higher-dimensional analysis common engineering problems for optimization, listed in **Table 4,** were adapted from Bouhlel *et al.* [11], namely the Gas Transmission Compressor Design (GTCD), Pressure Vessel Design (PVD), and Speed Reducer 7 (RS7) case studies. These cases were chosen because the parameters span different scales, potentially complicating analysis during kernel optimization. Larger-magnitude parameters may disproportionately influence the kernel, causing numerical deviations and reducing model accuracy. However,

the proposed methodology mitigated these issues, achieving high accuracy (**Table 4**) and demonstrating robustness despite parameter variability.

**Table 4:** Methodology results for the high-dimensional case studies.

| Name | D | n | MAE | MAPE | $R^2$ | F1 Score |
|---|---|---|---|---|---|---|
| GTCD | 4 | 80 | 2.79E+01 | 3.86% | 1 | 99.91% |
| PVD | 4 | 80 | 1.20E-02 | 9.09% | 1 | 100.00% |
| RS7 | 7 | 140 | 9.26E-01 | 0.02% | 1 | 92.59% |

The application of the $2(10D)$ rule was effective for 4D cases but proved less efficient in the 7D study, as expected. Higher-dimensional problems typically require exponentially larger training sets, a trend consistent with findings from the 2D and 3D studies. The 7D results exhibited significant deviations across slices, with a tendency for false negatives in half of them, though no false positives were observed. This suggests that the surrogate model struggled to converge optimally in certain slices, indicating that a denser sample set might be needed for accurate design space evaluation. However, this would make alpha shape reconstruction computationally prohibitive. By reducing the 7D problem to 3D through slicing, the methodology enabled DSp evaluation with alpha shapes, demonstrating its efficiency in handling complex design spaces, as shown in **Figure 6**.

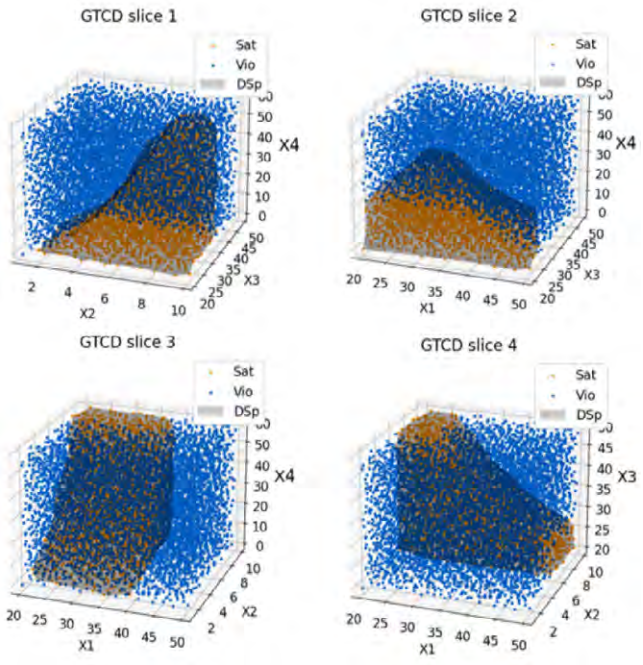



**Figure 6:** DSp of the 4D GTCD Function Reconstructed with Alpha Shapes on 3D Slices.

## CONCLUSIONS

This study presents a methodology that integrates surrogate modeling with alpha shape design space identification to reconstruct complex, high-dimensional design spaces. The framework employs Gaussian Process Regression (GPR) with an optimized kernel selection strategy to capture intricate relationships in complex mathematical systems. GPR enables accurate modeling and representation of feasibility regions, while alpha shape design space identification facilitates the slicing of multidimensional design spaces into two- or three-dimensional projections around a point of interest, allowing for multi-perspective visualization. Its adaptability to different design criteria makes it a powerful tool for evaluating process variations and optimizing design decisions.

The methodology's effectiveness is validated across mathematical problems ranging from two to seven dimensions, demonstrating its scalability and applicability to both low- and high-dimensional challenges.

Ongoing research is focusing on transferring this methodology to real-world problem cases. Future research should tackle refining sample size selection to develop a universal heuristic that balances surrogate model accuracy with GPR computational costs.

## ACKNOWLEDGEMENTS

Funding from the UK EPSRC for the i-PREDICT: Integrated adaptive pRocEss DesIgn and ConTrol (Grant EP/W035006/1) is gratefully acknowledged.

## REFERENCES

1. I. Banerjee and M. G. Ierapetritou, 'Model Independent Parametric Decision Making', Annals of Operations Research, vol. 132, no. 1–4, pp. 135–155, Nov. 2004, doi: 10.1023/B:ANOR.0000045280.55945.e8.
2. P. Facco, F. Dal Pastro, N. Meneghetti, F. Bezzo, and M. Barolo, 'Bracketing the Design Space within the Knowledge Space in Pharmaceutical Product Development', Ind. Eng. Chem. Res., vol. 54, no. 18, pp. 5128–5138, May 2015, doi: 10.1021/acs.iecr.5b00863.
3. M. Geremia, F. Bezzo, and M. G. Ierapetritou, 'A novel framework for the identification of complex feasible space', Computers & Chemical Engineering, vol. 179, p. 108427, Nov. 2023, doi: 10.1016/j.compchemeng.2023.108427.
4. A. S. Rathore and H. Winkle, 'Quality by design for biopharmaceuticals', Nat Biotechnol, vol. 27, no. 1, pp. 26–34, Jan. 2009, doi: 10.1038/nbt0109-26.
5. I. Banerjee and M. G. Ierapetritou, 'A novel feasibility analysis approach based on dimensionality reduction and shape reconstruction',

in Computer Aided Chemical Engineering, vol. 20, L. Puigjaner and A. Espuña, Eds., in European Symposium on Computer-Aided Process Engineering-15, 38 European Symposium of the Working Party on Computer Aided Process Engineering, vol. 20. , Elsevier, 2005, pp. 85–90. doi: 10.1016/S1570-7946(05)80136-1.
6. H. Edelsbrunner and E. P. Mücke, 'Three-dimensional alpha shapes', ACM Trans. Graph., vol. 13, no. 1, pp. 43–72, Jan. 1994, doi: 10.1145/174462.156635.
7. C. E. Rasmussen and C. K. I. Williams, Gaussian processes for machine learning. in Adaptive computation and machine learning. Cambridge, Mass: MIT Press, 2006.
8. A. Galeazzi, F. de Fusco, K. Prifti, F. Gallo, L. Biegler, and F. Manenti, 'Predicting the performance of an industrial furnace using Gaussian process and linear regression: A comparison', Computers & Chemical Engineering, vol. 181, p. 108513, Feb. 2024, doi: 10.1016/j.compchemeng.2023.108513.
9. S. Sachio, C. Kontoravdi, and M. M. Papathanasiou, 'A model-based approach towards accelerated process development: A case study on chromatography', Chemical Engineering Research and Design, vol. 197, pp. 800–820, Sep. 2023, doi: 10.1016/j.cherd.2023.08.016.
10. M. J. Sasena, P. Papalambros, and P. Goovaerts, 'Exploration of Metamodeling Sampling Criteria for Constrained Global Optimization', Engineering Optimization, vol. 34, no. 3, pp. 263–278, Jan. 2002, doi: 10.1080/03052150211751.
11. M. A. Bouhlel, N. Bartoli, R. G. Regis, A. Otsmane, and J. Morlier, 'Efficient global optimization for high-dimensional constrained problems by using the Kriging models combined with the partial least squares method', Engineering Optimization, vol. 50, no. 12, pp. 2038–2053, Dec. 2018, doi: 10.1080/0305215X.2017.1419344.

© 2025 by the authors. Licensed to PSEcommunity.org and PSE Press. This is an open access article under the creative commons CC-BY-SA licensing terms. Credit must be given to creator and adaptations must be shared under the same terms. See https://creativecommons.org/licenses/by-sa/4.0/



Systems & Control Transactions

**Research Article - Peer Reviewed Conference Proceeding**
ESCAPE 35 - European Symposium on Computer Aided Process Engineering
Ghent, Belgium. 6-9 July 2025
Jan F.M. Van Impe, Grégoire Léonard, Satyajeet S. Bhonsale,
Monika E. Polańska, Filip Logist (Eds.)

PSE PRESS

# Langmuir.jl: An Efficient and composable Julia Package for Adsorption Thermodynamics

**Vinicius Santana[c]*, Andrés Riedemann[a], Pierre J. Walker[b] and Idelfonso Nogueira[c]**

[a] Universidad de Concepción, Department of Chemical Engineering, Concepción, Chile
[b] California Institute of Technology, Division of Chemistry and Chemical Engineering, Pasadena, California, USA
[c] Norwegian University of Science and Technology, Department of Chemical Engineering, Trondheim, Norway
* Corresponding Author: vinicius.santana@ntnu.no.

## ABSTRACT

Recent advancements in material design have made adsorption a more energy-efficient alternative to traditional thermally driven separation processes. Accurate modelling of adsorption thermodynamics is crucial for designing and operating equilibrium-limited adsorption systems. High-quality open-source packages like PyIAST, PyGAPsare available for processing adsorption data in Python. They provide a robust set of features for processing and analysing isotherms. However, they have no support for automatic differentiation and are not targeted for performance. Langmuir.jl addresses these limitations by leveraging Julia's composable and differentiable programming ecosystem. Langmuir.jl includes tools for processing adsorption thermodynamics data—loading data, fitting isotherms with most often used models, predictive multicomponent adsorption through Ideal Adsorption Solution Theory (IAST) — and, importantly, enabling accurate derivative calculations through Julia's automatic differentiation libraries, without requiring extensive code adjustments. Furthermore, Langmuir.jl achieves two orders of magnitude faster IAST calculations compared to its Python counterpart, PyIAST.

**Keywords**: Adsorption, Thermodynamics, Differentiable Programming, Open-Source Software

## INTRODUCTION

The separation of fluid mixtures is subject of great attention to chemists and chemical engineers. Traditional methods such as distillation rely on the use of heat to partially vaporize and separate mixtures. Recent advancements in material design have made adsorption a more energy-efficient alternative to traditional thermally driven separation processes [1].

Adsorption is a surface phenomenon that involves the transfer of a substance from a bulk phase of a fluid to the surface of a solid whilst desorption consists of the opposite process. To separate mixtures with this principle, the different affinity of substances (adsorbates) to a solid's surface (adsorbent) is used as driving force. Affinity is linked to the equilibrium concentrations between an adsorbent and adsorbate at a specific temperature. This link is achieved with the well-known adsorption isotherms that seeks to describe the equilibrium relation between bulk concentration, adsorbent concentration and temperature of a fluid or mixture.

Isotherms are fundamental in adsorption as they can be used to describe equilibrium concentrations and to estimate derived quantities such as the Henry coefficient and isosteric heat of adsorption [2]. Classic adsorption isotherms include the Langmuir isotherm, initially developed for gas-phase adsorption on activated carbon, and the simple linear Henry's isotherm. The International Union of Pure and Applied Chemistry (IUPAC) categorizes isotherms into six types based on their shape [3]. With advancements in adsorbents and the discovery of new materials, new isotherms continue to be proposed easily surpassing 20 types today.

When designing adsorption-based separation processes, the typical workflow starts with material characterization and single-component adsorption experiments, as multicomponent adsorption data is challenging to obtain. Single-component data is then fitted to isotherms at different temperatures, enabling the estimation of quantities such as isosteric heat, multicomponent adsorption, and Henry's coefficients, for example. Finally, the predictive capacities of the isotherm and derived

quantities are validated through breakthrough experiments [4].

As the number of isotherms and available data grow with advancements in research and automation, manually performing this workflow becomes increasingly complex, error-prone, and time-consuming. Automating the process with software provides a practical and efficient solution. In the past years, efforts have been made to develop tools that assist users in automating the workflow, enabling the exploration of a broader range of models and potentially enhancing predictive accuracy and process design quality.

While software design has been limited to experts in the past, the advent of high-level dynamically typed programming languages such as Python, Julia and more have made software development possible to a broader range of professionals. In this trend, software for adsorption thermodynamics evolved from statically compiled languages to dynamically typed languages.

IAST++ [5], for example, is an open-source C++ GUI-based software that can fit isotherm data to several models and use the Ideal Adsorbed Solution Theory (IAST) to estimate multicomponent isotherm. Ruptura [4] is also a free and open-source C++ software package for the simulation of gas adsorption breakthrough curves, mixture prediction using IAST-like methods, and fitting of isotherm models' adsorption isotherm data. While C++ is known for its speed and efficient memory management, code syntax is less attractive when compared to high-level languages, which limits cross-collaboration, development, and wider adoption.

Recent advancements in high-level programming languages have led to the development of tools like pyIAST [5] and pyGAPS [6] in Python. PyIAST focuses primarily on providing code interface for initializing and fitting single-component isotherms that can be used for multicomponent prediction through IAST.

In contrast, pyGAPS serves as a "General Adsorption Processing Suite" with a wider range of functionalities. It supports manipulating, storing, visualizing, and processing adsorption isotherms. Its extended feature set includes specific surface area calculations, t- and s-plots, model fitting, IAST calculations, and the estimation of isosteric heat of adsorption from isotherm data.

While Python offers a straightforward and user-friendly environment for software development, particularly with its object-oriented syntax, it often falls short when performance and composability are critical. For instance, the calculation of isosteric heat of adsorption can be performed automatically with exact derivatives, avoiding error approximations and tedious, error-prone derivatives, if automatic differentiation is utilized. However, integrating such functionality directly into tools like pyGAPs could require a significant development effort despite its modular nature. The effort could involve a potential port to a different backend such as JAX or manually writing chain rules for complex operations not supported by numpy-compatible AD frameworks such as autograd – derivatives of root-finding solvers and derivatives of numerical integration routines, for example.

Such a lack of composability in Python often restricts many packages to a specific backend, hindering the adoption and composition of emerging methods from different libraries. The Julia programming language is a language mainly targeted to scientific computing that is known for its composability. It is a fully featured language that can achieve C-like performance native code and, therefore, does not rely heavily on external libraries for numerical computations. Furthermore, it has first-class automatic differentiation support [7]. However, time-to-first execution is a known drawback of JIT compilation in the Julia language. Furthermore, it is a much less popular language than Python, with less mature libraries and a smaller community.

Taking full advantage of Julia's capabilities and its vibrant numerical ecosystem, we present Langmuir.jl: An efficient and composable Julia package for adsorption thermodynamics. Langmuir.jl is part of the Clapeyron-Thermo project that includes the Clapeyron.jl - An Open-Source Fluid Thermodynamics Toolkit in Julia [8] and GCIdentifier.jl – a package for automated group contribution (GC) identification [9].

The remainder of this article is organized as follows: in Section 2, the architecture of Langmuir.jl is explained, as are the isotherm model objects, supported models, core isotherm functions, derived properties, and the use of automatic differentiation. In Section 3, we present case studies of the library and a full workflow for working with adsorption isotherms.

## Adsorption Thermodynamics

To clarify the code structure, it is helpful to briefly introduce the physical meaning and mathematical description of adsorption thermodynamics. This begins with the concept of single-component isotherms and extends to properties derived from their definition. These properties include the isosteric heat, Henry's coefficient, and multicomponent adsorption modeled using the Ideal Adsorbed Solution Theory (IAST).

### Isotherms

Mathematically, the single component adsorption is a smooth, continuous function that defines the loading/solid phase concentration $q_i$ of the component $i$ as a function of bulk concentration $c_i$ or pressure $p_i$ and temperature [4]:

$$q_i = f(c_i, T) \tag{1}$$

To compute the loading, both temperature and bulk concentration must be specified. While other combinations of independent variables are theoretically valid -

such as using solid-phase concentration and temperature as inputs - such cases are less common and involve additional complexity. This approach requires inverting the function $f$, either analytically or by solving a root-finding problem.

The temperature dependence in the isotherm must account for the fact that adsorption is an exothermic process. As temperature increases, the loading $q_i$ decreases. This dependency is typically modeled using parameters that explicitly incorporate the effect of temperature in the affinity parameter, such as in Van't Hoff-like expressions or other temperature-dependent terms in the isotherm equation. The single-site Langmuir isotherm temperature dependency can be written as, for example:

$$q_i = \frac{MKp_i}{1+Kp_i} \tag{2}$$

$$K = K_0\, exp\left(-\frac{E}{RT}\right) \tag{3}$$

## Henry's Coefficient

The Henry coefficient is the slope of the isotherm as the partial pressure tends to zero. Under this condition, adsorbate-adsorbate interactions are negligible, and adsorption is linearly related to the affinity of the adsorbate at a given temperature. Mathematically, it is defined as:

$$H_i = \frac{\partial q_i}{\partial p_i}|p_{i\to 0} \tag{4}$$

Numerically, the Henry coefficient can be determined in one of three ways. The first method involves manually deriving the isotherm and applying the limit $p_i \to 0$, which, while tedious and prone to human and numerical error, would result in an analytical expression. The second approach is automatic differentiation, which provides an accurate result without introducing numerical errors. Lastly, numerical differentiation offers a simpler alternative but can also introduce numerical errors.

## Isosteric Heat of Adsorption

The isosteric heat of adsorption is defined as the differential change in energy when an infinitesimal number of molecules are transferred from the bulk to the adsorbent surface at a fixed temperature, pressure and adsorbent surface area. However, a common way of estimating this quantity is through the Clausius-Clapeyron equation which relates the isosteric heat to the temperature dependence of the adsorption isotherm [2] as follows:

$$q_{st,i} = T\left(V_g - V_a\right)\frac{dp_i}{dT}|_{q_i,A} \tag{5}$$

where $V_g$ is the molar volume of the bulk phase, $V_a$ is the molar volume of the adsorbed phase and $q_{st,i}$ is the isosteric heat. If isotherm is explicit in the loading, one can write:

$$q_{st,i} = -T\left(V_g - V_a\right)\frac{\partial q_i/\partial T|_{p_i}}{\partial q_i/\partial p_i|_T} \tag{2}$$

Similarly to the Henry coefficient, derivatives play an important role in correctly estimating the isosteric heat. This is where the Julia language automatic differentiation support is essential.

## Reduced Grand Potential

Similarly to vapor-liquid equilibrium and the definition of fugacity, adsorption equilibrium has an important quantity used in IAST calculations: the Reduced Grand Potential. It can be defined as:

$$\psi_i = \int_0^{P_{i,0}} \frac{q_i(T,p_i)}{p_i}\, dp_i \tag{3}$$

where $p_i$ is the partial pressure, $T$ is the temperature, $q_i$ is the loading, $\psi_i$ is the grand potential.

This can be obtained analytically for certain types of isotherms. When analytical expressions are not possible, it must be approximated numerically.

# Langmuir.jl Design and Interface

Julia programming adopts a distinct paradigm compared to the object-oriented approach in Python, relying on composite types and multiple dispatch [7]. While a detailed explanation is beyond the scope of this work, in simple terms, multiple dispatch selects the appropriate method or function to execute based on the input types.

The source code of Langmuir.jl follows best practices in Julia programming and is divided into two main components, as illustrated in **Figure 1**.

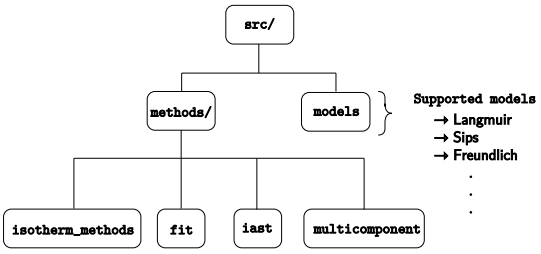



**Figure 1.** Langmuir.jl source-code structure

The *model* component/folder holds all the files that define supported isotherm models' composite types. Those types have all the parameters needed to define the isotherm completely through their fields. Below is an example of the definition of the Langmuir single-site model:

```
@with_metadata struct LangmuirS1{T} <: Iso-
thermModel{T}
    (M::T, (0.0, Inf), "saturation loading")
    (K₀::T, (0.0, Inf), "affinity parameter")
    (E::T, (-Inf, 0.0), "energy parameter")
End
```

The @with_metadata macro in Julia enhances existing code structures by enabling the addition of extra

inputs that generate additional code. In the example provided, `M` represents the saturation loading, `$K_0$` is the affinity parameter, and `E` is the energy parameter. The annotations, such as parentheses and additional characters beside each field, are processed by the macro to define bounds and provide explanatory information for each parameter. This allows the macro to display these details to the user, improving clarity and usability.

The *method* component is subdivided into 4 subcomponents and files: *fit.jl, iast.jl, isotherm_methods.jl and multicomponent.jl*. *isotherm_methods.jl* holds functions dispatched on isotherms to derive properties of interest, such as the Henry coefficient or the spreading pressure. *fit.jl* holds the functions for fitting isotherms using a global optimization approach. *iast.jl* holds the routines for performing the nested-loop IAST and the FastIAS algorithms [10]. Finally, *multicomponent.jl* has the API for unifying multicomponent adsorption prediction given the single component isotherms and bulk conditions of temperature and partial pressures.

## CASE STUDY AND WORKFLOW

This section presents a typical workflow for processing and analyzing isotherm data. The data was obtained from the work of Santana et al. (2024) [11] for an ethane-selective material in an ethane-ethylene mixture, and the results were also compared to what the authors obtained. All the codes for reproducing the results can be found in Langmuir.jl documentation at https://clapeyronthermo.github.io/Langmuir.jl/dev/tutorials/tutorial/.

First, the data is loaded, and then the experimental data is plotted to assess potential isotherms that can fit the data. Then, a model or a set of models is fitted to the data, and the fitting quality is evaluated through a metric and plotted on top of the experimental data. Once the isotherm is obtained, analysis can be performed, such as the isosteric heat of adsorption, Henry coefficient, and multicomponent adsorption estimation with IAST.

### Data loading

The data is assumed to be in a standard file format with comma-separated values and loaded into a Julia-native type - an array. The array is then used to construct an isotherm data instance, an abstraction of the Langmuir.jl isotherm. Below is a code snippet. The data can be found at https://github.com/ClapeyronThermo/Langmuir.jl/tree/main/docs/src/tutorials/sample_data.

```
    using Plots, DelimitedFiles, Langmuir
    ethane_data_path = joinpath(@__DIR__,
"sample_data/ethane_tpl_data.csv")
    ethylene_data_path = joinpath(@__DIR__,
"sample_data/ethylene_tpl_data.csv")
    ethane_data = readdlm(ethane_data_path,
',')
    P_ethane = ethane_data[:, 2]*1e5
    T_ethane = ethane_data[:, 1]
    l_ethane = ethane_data[:, 3]
    d_ethane = isotherm_data(P_ethane,
l_ethane, T_ethane)
    Ts_ethane, lp_ethane = split_data_by_tem-
perature(d_ethane)
```

The function split_data_by_temperature function uses the isotherm_data object and returns all the temperatures in an vector and a 3D array holding the loading and pressure for each temperature. By plotting the loading pressure pairs for two of the temperatures for both ethane and ethylene, we can visualize the isotherm in **Figure 2**.

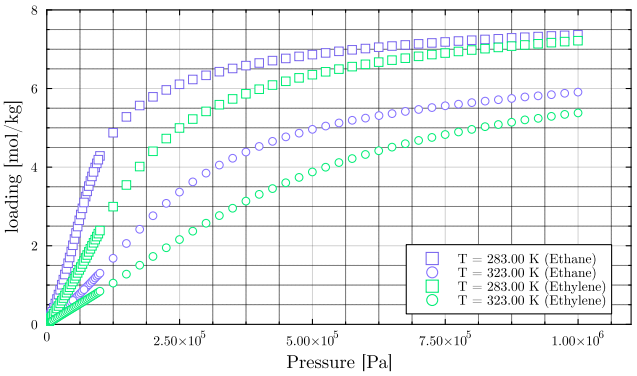



**Figure 2.** Experimental isotherm data for ethane and ethylene at 283.0 K and 323.0 K.

It can be observed that the isotherms are s-shaped, i.e., the derivative of the loading with respect to the pressure has a maximum. For example, in ethane at 283.00 K, the maximum derivative seems to take place for pressures less than $1.25 \times 10^5$ Pa. This behavior is not captured by a single-site Langmuir isotherm. Therefore, a Quadratic isotherm was proposed in the reference manuscript and used in this workflow demonstration.

### Isotherm fitting

To fit the quadratic or any other Isotherm in Langmuir.jl, one can first formulate the isotherm fitting problem by providing the isotherm type, the isotherm data wrapped into the isotherm_data object, a fitting criterion, an initial guess and lower and upper bounds for the parameters by using the IsothermFittingProblem abstraction syntax. If initial guesses and lower or upper bouds are not provided, they are defaulted according to each isotherm – more details found in the package's documentation. The code snippet below shows how to formulate the fitting problem for ethane using the mean squared error as the fitting criterion for loading-pressure data, for example.

```
prob_ethane = IsothermFittingProblem(Quadratic{eltype(d_ethane)}, d_ethane, nothing, abs2, x0_ethane, lb_ethane, ub_ethane)
```

Once the fitting problem is set, an optimizer must be selected for minimizing the objective function. In Langmuir.jl differential evolution, which is a global optimization algorithm, is used through the library BlackBoxOptim.jl. Below is a code snippet showing how to set up the optimizer and perform the fitting for ethane isotherm.

```
alg = DEIsothermFittingSolver(max_steps = 5000, population_size = 50,
logspace = true, verbose = true)
loss_fit_ethane, ethane_isotherm = fit(prob_ethane, alg)
```

After running the fitting for both ethane and ethylene and plotting the corresponding models's loadings with experimental values, we obtained the results shown in **Figure 3**.

The loadings for any model can be obtained by calling the function loading as follows:

```
loading(isotherm, p, T)
```

where p is the pressure, T is the temperature and isotherm is an instance of the supported isotherm models.

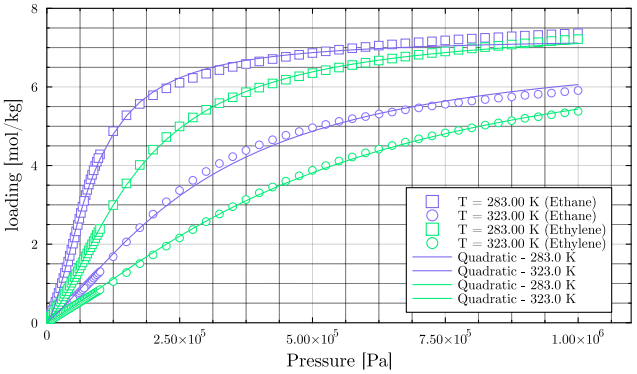



**Figure 3.** Quadratic isotherm fitting vs experimental data at 283.0 K and 323.0 K.

From the fitting results, the isotherm parameters closely match those reported in the reference manuscript. For example, the saturation loading parameter was estimated at 3.68 in the manuscript, while it is 3.64 in this analysis. However, the energy parameters exhibit a more significant discrepancy as it can be seen from **Table 1** and **Table 2**. This discrepancy is due to a different framing of the optimization problem and different optimization strategies. The reference manuscript imposes the same maximum loading capacity for both components and uses a local optimization method. In our case, no such constraint is set, and we use a global optimizer. Finally, without calorimetric data, resolving the accuracy of these values is challenging, as parameter identifiability is limited and suffers from degeneracy when relying solely on loading data for fitting.

**Table 1.** Estimated parameters using Langmuir.jl compared to the ones obtained in Santana et al. (2024) [11] for ethane.

| | $K_A$ | $K_B$ | $E_A$ (kJ/mol) | $E_B$ (k/mol) | $M$ |
|---|---|---|---|---|---|
| Langmuir.jl | $2.51 \times 10^{-7}$ | $2.138 \times 10^{-19}$ | $-6.898$ | $-47.789$ | 3.64 |
| Reference | $3.214 \times 10^{-8}$ | $1.4237 \times 10^{-14}$ | $-12.19$ | $-48.63$ | 3.68 |

**Table 2.** Estimated parameters using Langmuir.jl compared to the ones obtained in Santana et al. (2024) [11] for ethylene.

| | $K_A$ | $K_B$ | $E_A$ (kJ/mol) | $E_B$ (k/mol) | $M$ |
|---|---|---|---|---|---|
| Langmuir.jl | $2.6 \times 10^{-8}$ | $7.13 \times 10^{-19}$ | $-11.79$ | $-41.702$ | 3.83 |
| Reference | $6.282 \times 10^{-8}$ | $8.275 \times 10^{-14}$ | $-9.40$ | $-41.70$ | 3.68 |

## Single component isosteric heat of adsorption using automatic differentiation

The isosteric heat can be derived from the isotherm by using Equation 6. In Langmuir.jl, we leverage forward mode automatic differentiation and dual numbers algebra to obtain the derivatives using ForwardDiff.jl. The molar volume of the gas phase is defaulted to the ideal gas molar volume. For the quadratic isotherms, the isosteric heat varies with the amount adsorbed as it can be seen in **Figure 4**. Changes in temperature also affect the isosteric heat but is not depicted in the Figure.

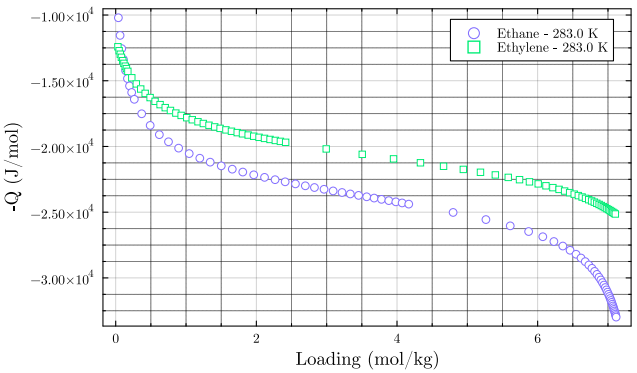



**Figure 4.** Estimated isosteric heat from isotherm vs loading for ethane and ethylene and 283.0 K.

## Multicomponent adsorption with IAST

After obtaining the individual isotherms' parameters for both components, a next step is to use these two isotherms combined to predict the loading in the adsorbent given a mixture of the two components at a certain temperature, pressure and composition. One of the possibles ways to perform such calculations is through the IAST method. To perform IAST calculations in Langmuir, the

two isotherms can first be wrapped into an abstraction named IASTModels where information about the two or more isotherms can be stored and accessed easily:

```
Isotherms = IASTModels(ethane_isotherm, ethylene_isotherm)
```

The loading can be estimated using a similar syntax to the one used for single component isotherm:

```
loading(isotherms, p, T, y)
```

The only difference is that an extra argument (y) must correspond to each component's mole fraction.

### Benchmarking IAST – PyIAST and Langmuir.jl

To compare the efficiency of our proposed solution in Julia with existing Python solutions, a benchmarking test was run to solve an IAST problem in PyIAST and Langmuir.jl, considering the isotherms for ethane and ethylene described above. The IAST problem consists of estimating the solid phase composition of ethane and ethylene given a pressure of 101325.0 Pa, temperature of 323K, and equimolar bulk concentration. The isotherms are quadratic parametrized according to **Table 1** and **Table 2** in Langmuir.jl. Since PyIAST does not support temperature dependency in the parameters, isotherms were fitted to both components at 323.0K and used for running IAST. Therefore, the parameters obtained are not the same as those obtained in Langmuir.jl, but they are close.

PyIAST version 1.4.3 using Python 3.11.5 and Langmuir.jl 0.1.1 with Julia 1.10.7 were used. The calculations were run on a laptop with an Intel i5-1250P 1.7 GHz processor and 16 GB of RAM. PyIAST utilizes scipy.root root-finding solver Levenberg-Marquardt (LM) with default tolerances not shown in the documentation. Langmuir.jl has a built-in implementation of nested loop and FastIAS, as described above. Tolerances (relative and absolute) in Langmuir.jl were set to $1x10^{-7}$. To benchmark PyIAST, the Python library time was used, and the same code ran 10000 times. To benchmark Langmuir.jl, the @benchmark macro in BenchmarkTools.jl library was also used with 10000 samples. The mean and standard deviation of run times are displayed on **Table 3**. The Table shows that Langmuir.jl achieves two orders of magnitude faster calculations for this benchmarking problem.

**Table 3.** Benchmarking of Langmuir.jl and PyIAST (the lower, the better).

| Tool / Solver | Mean run time (μs) | Standard Deviation (μs) |
|---|---|---|
| PyIAST/LM | 206.34 | 164.35 |
| Langmuir.jl /Nested loop | 0.80098 | 1.5670 |
| Langmuir.jl /FastIAS | 0.74962 | 1.1040 |

## CONCLUSIONS AND FUTURE WORK

This work introduces Langmuir.jl, an open-source Julia library for adsorption thermodynamics. To the best of the author's knowledge, it is the first package in Julia to offer such tools. Langmuir.jl benefits from Julia's modern scientific computing environment, known for its user-friendly syntax, efficiency and robust support for differentiable programming. Automatic differentiation, a core feature of Julia, is particularly advantageous for thermodynamics, where derivatives play a critical role, ensuring maintainability and extensibility. Compared with PyIAST, Langmuir.jl presents two orders of magnitude faster calculations in the IAST problem. However, it is placed in a less popular programming language and has fewer features than PyGAPs, for example. Future developments aim to integrate property calculations, such as loading and isosteric heat, into breakthrough curve simulations, similar to the functionality provided by Ruptura software.

## DIGITAL SUPPLEMENTARY MATERIAL

The source code and documentation for Langmuir.jl can be found at https://github.com/Clapeyron-Thermo/Langmuir.jl/tree/main.

## ACKNOWLEDGEMENTS

This publication has been produced with support from the HYDROGENi Research Centre (hydrogeni.no), performed under the Norwegian research program FMETEKN. The authors acknowledge the industry partners in HYDROGENi for their contributions and the Research Council of Norway (333118).

## REFERENCES

1. J.-R. Li et al., “Carbon dioxide capture-related gas adsorption and separation in metal-organic frameworks,” Coord. Chem. Rev., vol. 255, no. 15, pp. 1791–1823, 2011, doi: https://doi.org/10.1016/j.ccr.2011.02.012.
2. H. Pan, J. a Ritter, and P. B. Balbuena, “from the Clausius - Clapeyron Equation,” vol. 7463, no. 11, pp. 6323–6327, 1998.
3. M. A. Al-Ghouti and D. A. Da’ana, “Guidelines for the use and interpretation of adsorption isotherm models: A review,” J. Hazard. Mater., vol. 393, p. 122383, 2020, doi: https://doi.org/10.1016/j.jhazmat.2020.122383.
4. S. Sharma et al., “RUPTURA: simulation code for breakthrough, ideal adsorption solution theory computations, and fitting of isotherm models,” Mol. Simul., vol. 49, no. 9, pp. 893–953, 2023, doi: 10.1080/08927022.2023.2202757.
5. C. M. Simon, B. Smit, and M. Haranczyk, “pyIAST:

Ideal adsorbed solution theory (IAST) Python package," Comput. Phys. Commun., vol. 200, pp. 364–380, 2016, doi: https://doi.org/10.1016/j.cpc.2015.11.016.
6. P. Iacomi and P. L. Llewellyn, "pyGAPS: a Python-based framework for adsorption isotherm processing and material characterisation," Adsorption, vol. 25, no. 8, pp. 1533–1542, 2019, doi: 10.1007/s10450-019-00168-5.
7. J. Bezanson, A. Edelman, S. Karpinski, and V. B. Shah, "Julia: A fresh approach to numerical computing," SIAM Rev., vol. 59, no. 1, pp. 65–98, 2017, [Online]. Available: https://doi.org/10.1137/141000671
8. P. J. Walker, H. W. Yew, and A. Riedemann, "Clapeyron.jl: An Extensible, Open-Source Fluid Thermodynamics Toolkit," Ind. Eng. Chem. Res., vol. 61, no. 20, pp. 7130–7153, 2022, doi: 10.1021/acs.iecr.2c00326.
9. P. J. Walker, A. Riedemann, and Z.-G. Wang, "GCIdentifier.jl: A Julia package for identifying molecular fragments from SMILES," J. Open Source Softw., vol. 9, no. 96, p. 6453, 2024, doi: 10.21105/joss.06453.
10. Z. Qiao, Z. Wang, C. Zhang, S. Yuan, Y. Zhu, and J. Wang, "PVAm–PIP/PS composite membrane with high performance for CO2/N2 separation," AIChE J., vol. 59, no. 4, pp. 215–228, 2012, doi: 10.1002/aic.
11. V. V. Santana et al., "Ethylene Purification by Pressure Swing Adsorption with the Paraffin Selective Metal-Organic Framework—DUT-8," Ind. Eng. Chem. Res., vol. 63, no. 5, pp. 2307–2319, 2024, doi: 10.1021/acs.iecr.3c02808.

© 2025 by the authors. Licensed to PSEcommunity.org and PSE Press. This is an open access article under the creative commons CC-BY-SA licensing terms. Credit must be given to creator and adaptations must be shared under the same terms. See https://creativecommons.org/licenses/by-sa/4.0/



Systems & Control Transactions

**Research Article - Peer Reviewed Conference Proceeding**
ESCAPE 35 - European Symposium on Computer Aided Process Engineering
Ghent, Belgium. 6-9 July 2025
Jan F.M. Van Impe, Grégoire Léonard, Satyajeet S. Bhonsale,
Monika E. Polańska, Filip Logist (Eds.)

PSE PRESS

# Systematic comparison between Graph Neural Networks and UNIFAC-IL for solvent pre-selection in liquid-liquid extraction

**Edgar Ivan Sanchez Medina[a]*, Ann-Joelle Minor[a], and Kai Sundmacher[a,b]***

[a] Max Planck Institute for Dynamics of Complex Technical Systems, Department of Process Systems Engineering, Magdeburg, Saxony-Anhalt, Germany
[b] Otto von Guericke University Magdeburg, Chair of Process systems Engineering, Magdeburg, Saxony-Anhalt, Germany
* Corresponding Authors: sanchez@mpi-magdeburg.mpg.de , sundmacher@mpi-magdeburg.mpg.de

## ABSTRACT

Solvent selection is a critical decision-making process that balances economic, environmental, and societal factors. The vast chemical space makes evaluating all potential solvents impractical, necessitating pre-selection strategies to identify promising candidates. Predictive thermodynamic models, such as the UNIFAC model, are commonly used for this purpose. Recent advancements in deep learning have led to models like the Gibbs-Helmholtz Graph Neural Network (GH-GNN), which overall offers higher accuracy in predicting infinite dilution activity coefficients over a broader chemical space than UNIFAC. This study presents a systematic comparison of solvent pre-selection using GH-GNN and UNIFAC-IL in the context of liquid-liquid extraction. The original GH-GNN model is extended to simultaneously predict organic and ionic systems. This extended GH-GNN model predicts more than 92 % of the logarithmic IDACs with an absolute error of less than 0.3. By comparison, UNIFAC-based models only achieve such accuracy for less than 65 %. A case study is used involving the ionic liquid ethyl-3-methylimidazolium tetrafluoroborate ([EMIM][BF4]) and caprolactam, relevant for the solvolytic depolymerization of polyamide 6. Results indicate a significant correlation in solvent rankings across both methods, with a Spearman's coefficient of 0.62, suggesting that deep learning-based models like GH-GNN are viable alternatives for solvent pre-selection. Additionally, chemical similarity metrics, such as Tanimoto similarity, can assess confidence in solvent rankings, allowing users to determine acceptable risk levels in predictions across a vast chemical space.

**Keywords**: Artificial Intelligence, Machine Learning, Phase Equilibria, Polymers

## INTRODUCTION

Solvents are used in various areas of chemical processes, including reaction and separation units. Selecting appropriate solvents is a complex task that involves decision-making from multiple perspectives. On one hand, the actual thermodynamic performance of the solvents must be considered. On the other hand, the implications of using such solvents must also be considered from environmental and societal perspectives.

From this perspective, the task of predicting solvent properties becomes central to assessing the overall performance of solvents within a specific process system. While important molecular properties can be measured in the laboratory, the vast extension of chemical space makes it inefficient to explore all promising solvent alternatives solely through experimental means. Therefore, predictive thermodynamic models are of key interest during the early stages of process design, especially for those involving solvents.

Pre-selection strategies aim to reduce the time and resources needed during the design of chemical processes by exploring the chemical space and allowing to focus on the most promising solvent candidates. These candidates can then be evaluated using more precise methods and eventually, the top-performer(s), could be investigated experimentally. Typically, the assessment of solvent performance in extraction applications relies on

the prediction of activity coefficients at infinite dilution (IDACs) [1]. Under these conditions, the solvent effect is at its maximum, which is why it is commonly used as a starting point for evaluating and ranking solvent candidates.

In this context, a popular choice is to use the UNIFAC model. However, with the rise of deep learning, novel alternative models have recently been proposed for predicting IDACs, showing overall more accurate predictions [2,3]. One of these alternatives is the so-called Gibbs-Helmholtz Graph Neural Network (GH-GNN), which was originally trained to predict IDACs of organic systems [4], and has also been extended to handle polymer solutions [5].

While the GH-GNN model has been previously used for solvent pre-selection [1], a systematic comparison of the resulting pre-selection to traditional methods is still lacking. Furthermore, given that the GH-GNN model was previously limited to predicting organic systems, we present here a series of extension strategies for expanding the GH-GNN model to simultaneously predict organic systems and mixtures containing ionic liquids (ILs).

This extension is particularly relevant in the context of chemical recycling of polyamide 6, also known as nylon 6, where ionic liquids have been identified as promising candidates due to their non-volatility and catalytic properties, though a complete assessment and process simulation were previously hindered by missing thermodynamic data [8]. The advantage of this approach is elucidated regarding the separation of the monomer caprolactam from the ionic liquid ethyl-3-methylimidazolium tetrafluoroborate ([EMIM][BF4]).

This work is structured as follows. First, the GH-GNN model is briefly described. Then, the extension strategies for systems containing ionic-liquids are presented. Subsequently, using the aforementioned case study, a systematic comparison of solvent pre-selection is conducted by comparing the extended GH-GNN model to UNIFAC-IL. Finally, conclusions and future directions are discussed.

# METHODS

## UNIFAC-IL

The UNIFAC model is a method used to estimate the excess Gibbs energy of a system, which in turn is used to determine the activity coefficients of its components. It operates on the principle of a "solution of groups," where molecules are decomposed into functional groups. This approach simplifies the model by reducing the parameter space from one that requires individual parameters for each unique molecule to one that only needs parameters for each type of group. This reduction in complexity enhances the model's predictive capabilities, allowing it to explore a wider range of chemical systems more efficiently.

Originally, the UNIFAC model was parameterized for predicting organic mixtures. However, extensions of the UNIFAC model to systems that include ionic liquids have also been developed in the past. In this work, we use the UNIFAC-IL extension from [6]. In this extension, a neural recommender system was first trained on experimentally determined IDACs of mixtures containing ionic liquids. Then, this recommender system was used to fill in the missing entries in a previously reported solute-solvent interaction matrix. Finally, the completed matrix was used to regress the binary interaction parameters of the UNIFAC model extended to ionic liquids.

This version of UNIFAC-IL [6] employs the original form of the UNIFAC model, and contains all necessary binary interaction parameters for 22 conventional main groups, 11 cationic main groups and 38 anionic main groups, with overall 102 subgroups. For further details on the model, readers are referred to the original publications mentioned earlier.

## Gibbs-Helmholtz Graph Neural Network

The GH-GNN model was first introduced in [4]. Unlike the UNIFAC model, the GH-GNN model uses a graph representation of molecules, where non-hydrogen atoms are represented as nodes and covalent chemical bonds as edges. Each node and edge in the molecular graph is assigned a vector of binary values containing relevant attributes of the atom or bond, respectively. Information about hydrogen atoms is implicitly included as part of the node features in the graph.

The GH-GNN model consists of two graph neural networks (GNNs) operating at different levels. The first GNN processes molecular graphs to obtain learned representations tailored for the prediction of IDACs. The second GNN operates at the mixture level, using a graph where the learned molecular representations of distinct chemical species in the mixture define the nodes and hydrogen-bonding interactions are represented as edges. These two GNNs are sequentially arranged to predict parameters $K_{1,ij}$ and $K_{2,ij}$ of the following equation derived from the Gibbs-Helmholtz relationship:

$$\ln \gamma_{ij}^{\infty} = K_{1,ij} + \frac{K_{2,ij}}{T} \quad (1)$$

Parameters $K_{1,ij}$ and $K_{2,ij}$ are temperature-independent and specific to the precise solvent-solute combination. As shown in Eq. 1, predicting these two parameters is sufficient to estimate the temperature-dependent IDACs. For further details on the model, readers are referred to the original publication [4].

### Tanimoto similarity for risk level assessment

As demonstrated in the original publication [4], the accuracy of the GH-GNN predictions is correlated with the distance within the chemical space between the

systems observed during training and the systems being predicted. If the distance is relatively short, the predictions tend to be more accurate. Conversely, as the distance increases, the accuracy of the predictions begins to decrease.

The distance between distinct solute-solvent systems can be approximated using the Tanimoto similarity metric, as mentioned in [4]. This metric is designed to estimate the "level of extrapolation" that the GH-GNN must undertake when predicting a system containing a chemical species that was not observed during training (extrapolated species).

The Tanimoto similarity metric is computed by taking the Jaccard distance between the molecular fingerprints of the "extrapolated species" and the set of the $n$ most similar molecules observed during training. This allows the model user to estimate the level of accuracy of the GH-GNN predictions and can inform decisions regarding the level of risk the user is willing to take during the exploration of the chemical space. This feature is not available for models like UNIFAC.

## Solvent pre-selection for liquid-liquid extraction

Measuring the thermodynamic performance of solvents participating in liquid-liquid extraction processes is typically carried out by computing the separation factor [9] defined by Eq. 2

$$K_s = \frac{\gamma_i^R \gamma_j^E}{\gamma_i^E \gamma_j^R} \quad (2)$$

In Eq. 2, the effects of the solvent in the raffinate phase $R$ and the extract phase $E$ are considered. In the case study analyzed here, species $i$ corresponds to the monomer caprolactam, and species $j$ corresponds to the ionic liquid [EMIM][BF4]. Therefore, the ratio $\gamma_i^R/\gamma_i^E$ measures the performance of the solvent within the extraction step, where it is desirable for caprolactam in the extract phase to be as enriched as much as possible while its content in the raffinate phase to be as low as possible. Similarly, the ratio $\gamma_j^E/\gamma_j^R$ measures the performance at the recovery step, where [EMIM][BF4] should be easily separable from the extract phase and preferably move to the raffinate phase.

As a pre-selection metric, the following separation factor at infinite dilution was used, which similarly to Eq. 2 considers the solvent performance at both the extraction and recovery stages:

$$K_s^\infty = \frac{\gamma_{sj}^\infty}{\gamma_{is}^\infty} \quad (3)$$

Eq. 3 results in larger separation factor values for solvents that are easily separable from the raffinate phase (mostly composed by [EMIM][BF4]), while entraining caprolactam as much as possible from the original mixture. This separation factor at infinite dilution was computed for every solvent considering the ambient temperature of 298.15 K, on which the extraction process is assumed to be operated.

# RESULTS

## GH-GNN extension strategies to ionic liquids

Three different strategies were studied to extend the original GH-GNN model from organic systems to ionic liquids. For this purpose, experimental IDAC data reported in the literature for ionic systems was included alongside the data for organic systems originally used to develop the GH-GNN [4]. The ionic liquids dataset corresponds to the compendium of ILThermo (v2.0), originally retrieved by [6] and further processed by [3].

The first extension strategy (S1) involved a complete re-training of the GH-GNN framework using only ionic liquid data. The second strategy (S2) consisted of a pre-training phase of the model using only organic systems, followed by a fine-tuning phase with the ionic liquid data. The third strategy (S3) involved a concurrent re-training of the GH-GNN model using the combined datasets for both organic and ionic liquid systems. In all cases, the same training and test split was used as in the original referenced publications [3,4].

Table 1 compares the three strategies based on the percentage of systems in the test set that are predicted with an absolute error of less than or equal to 0.3.

**Table 1:** Comparison of the percentage of systems predicted with an absolute error less than or equal to 0.3.

| Model | Organic | Ionic liquid |
|---|---|---|
| (Original) GH-GNN | 91.7 % | 16.8 % |
| S1: (IL) GH-GNN | 10.2 % | 94.3 % |
| S2: (pre-trained) GH-GNN | 10.9 % | 94.1 % |
| S3: (concurrent) GH-GNN | 92.4 % | 94.0 % |
| GNN [3] | | 93.8 % |
| Matrix Completion [3] | | 94.1 % |
| UNIFAC (Dortmund) | 64.3 % | |
| UNIFAC-IL [6] | | 50.5 % |

It can be observed that while the original GH-GNN model excels in predicting IDACs for organic systems, its performance when extrapolating to systems with ionic liquids is poor, and is considerably worse than UNIFAC-IL. In contrast, the model developed using the first strategy S1 (i.e., (IL) GH-GNN) achieves high accuracy for ionic liquid systems, even surpassing the GNN model previously reported by [3]. However, when tested for predicting organic systems, the model performs poorly. Analyzing the GH-GNN model extended with the second strategy S2 (i.e., (pre-trained) GH-GNN), the accuracy for predicting organic systems slightly increases, but at the expense of slightly decreasing the accuracy for ionic

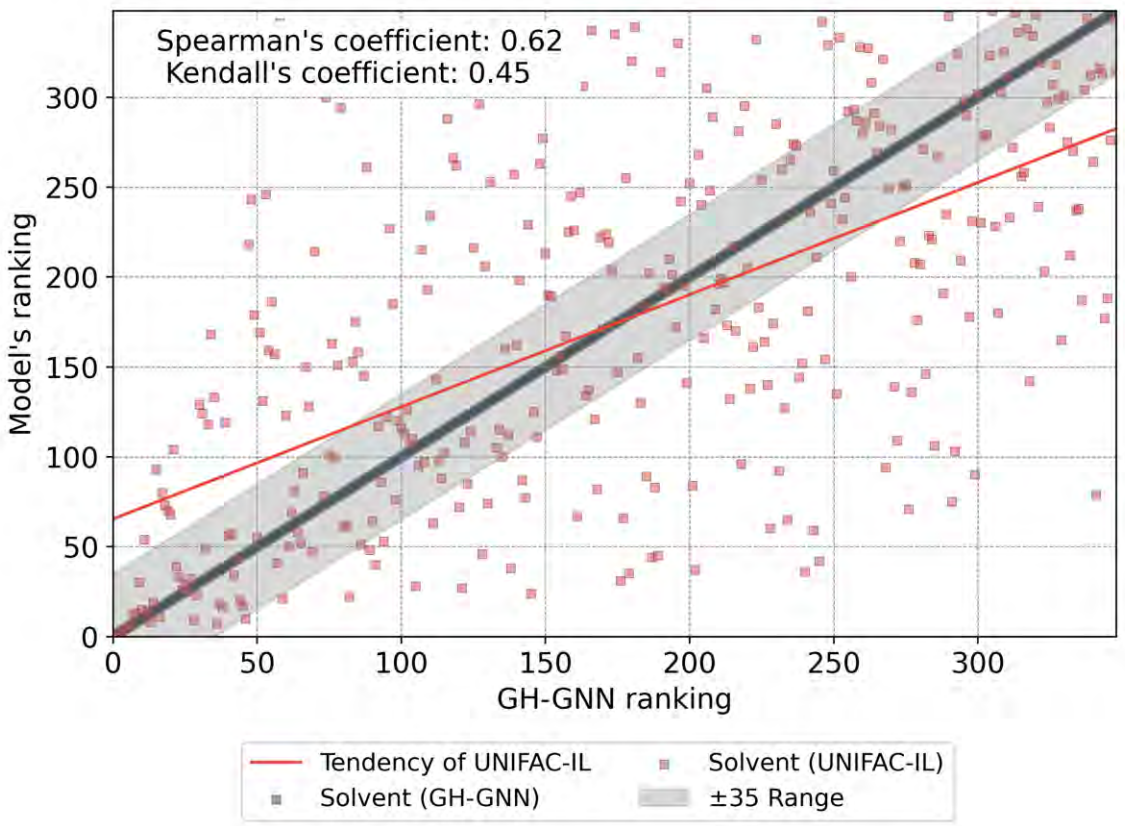



**Figure 1:** Comparison of relative solvent rankings obtained by the GH-GNN model and the UNIFAC-IL model. The linear tendency of the ranking of UNIFAC-IL with respect to the one of GH-GNN is also shown. The gray shaded area indicates ± 35 (10 %) places in the ranking of the GH-GNN.

liquid systems. This mutually exclusive behaviour in accurately predicting either organic or ionic systems highlights the difficulty of exploring vast chemical spaces while extrapolating beyond the types of systems used during training.

Remarkably, the GH-GNN model extended using the third strategy S3 (i.e., (concurrent) GH-GNN) achieves the highest accuracy for predicting organic systems among all compared models, while also performing remarkably well in predicting systems with ionic liquids. Interestingly, as a result of including ionic liquid data, the model's performance in predicting organic systems even surpasses that of the original GH-GNN model. This suggests that the model is able to extract relevant information from systems of organic molecules infinitely diluted in ionic liquids, which is beneficial for capturing effects in organic systems alone. The comparison of the extended (concurrent) GH-GNN model with the UNIFAC models demonstrates the potential of this alternative methods to predict IDACs with significantly higher overall accuracy.

## Comparison of solvent pre-selection between GH-GNN and UNIFAC-IL

The GH-GNN model extended to ionic liquids using the concurrent strategy was employed here to compare solvent pre-selection against UNIFAC-IL. The selection of solvents is aimed at separating caprolactam from ([EMIM][BF4]), a mixture arising in the context of the chemical recycling of polyamide 6. In total, 700 solvents were considered as potential candidates, based on the selection of molecules collected by [7]. Only organic molecules are included among the candidate solvents.

The chemical space that UNIFAC-IL can predict is more restricted compared to that of the GH-GNN model. As a result, the first difference between the methods is encountered: while the necessary IDACs involving all 700 solvents can be predicted by GH-GNN, only the IDACs for 359 solvents are feasible to predict with UNIFAC-IL due to limitations in the "set of functional groups" representation of the molecules and/or the lack of required group binary interaction parameters.

Fig. 1 presents the comparison of the obtained solvent rankings according to GH-GNN and UNIFAC-IL. A Spearman's rank correlation coefficient of 0.62 is obtained between the two rankings, indicating a moderate positive monotonic correlation. When computing Kendall's correlation coefficient for the rankings, a value of 0.45 is obtained, also suggesting a moderate positive correlation. This implies that while the two methods do not rank the solvents identically, there is a substantial level of agreement in their rankings, indicating that they may be capturing similar underlying patterns or properties of the solvents.

However, the exact solvent rankings obtained using GH-GNN and UNIFAC-IL also show significant discrepancies that might influence which solvents are preferred over others. Given that the accuracy of GH-GNN for computing IDACs is significantly higher than that of UNIFAC-IL, it is reasonable to assume that the solvent ranking provided by GH-GNN offers a more reliable description of the physical behaviour.

In total, 42.4 % of the solvents lie within the 10 % (i.e., 35 ranking places) deviation from each method (shaded area in Figure 2). Interestingly, both methods agree on the set of top 7 solvents, which are shown in Table 2. Note that the ranking of these solvents is solely based on their performance according to Eq. 3. Other practical aspects relevant to the application should also be considered in the selection process (e.g., normal boiling points for solvent recovery and environmental properties).

As discussed earlier, the Tanimoto similarity index within the GH-GNN model framework can provide additional insights into the risk or confidence associated with its predictions. For all 7 solvents shown in Tab. 2, the Tanimoto index is relatively high and exceeds the recommended value given in [4] (i.e., 0.35). This suggests a high level of confidence in these predictions. Out of the 349 solvents compared here, only 4 have a Tanimoto metric smaller than 0.35.

## CONCLUSIONS

The procedure of solvent pre-selection is central to the efficient exploration of the vast chemical space, enabling efficient use of resources during the early stages of process design. Predictive thermodynamic methods, such as UNIFAC-based models, are typically employed for this purpose. However, their use is limited by the extent to which the involved molecules can be successfully fragmented into functional groups and the availability of the necessary interaction parameters. The accuracy of such methods is also limited when compared to recent alternatives developed by use of deep learning approaches.

A hybrid graph neural network model, the GH-GNN [4], was here extended to accommodate the simultaneous prediction of organic and ionic systems. Three different extension strategies were compared, and a highly accurate GH-GNN model that can simultaneously predict organic and ionic systems was developed. We demonstrate that while the selection of solvents between UNIFAC-IL and GH-GNN overlaps to a great extent, there are also significant differences that might influence the outcomes of the early stages of process design. The higher accuracy of GH-GNN and larger applicability across the chemical space when compared to UNIFAC-IL, makes the GH-GNN model a potentially more reliable alternative for solvent pre-selection.

In the context of sustainable chemistry, we have chosen a relevant case study for the extraction of the monomer caprolactam from the ionic liquid [EMIM][BF4].

**Table 2:** Top 7 solvents selected by the GH-GNN and UNIFAC-IL. The ranking of the respective solvent for both GH-GNN and UNIFAC-IL is shown. Tanimoto similarity index of the GH-GNN model is also presented.

| Solvent | Rank GH-GNN | Rank UNIFAC-IL | Tanimoto index |
|---|---|---|---|
| Diisononyl adipate | 1 | 3 | 0.88 |
| Eicosane | 2 | 1 | 1 |
| Hexadecane | 3 | 2 | 1 |
| Stearic acid | 4 | 4 | 0.96 |
| Dodecane | 5 | 5 | 1 |
| Tridecyl alcohol | 6 | 6 | 1 |
| Dibutyl sebacate | 7 | 7 | 0.98 |

The top 7 solvents by both GH-GNN and UNIFAC-IL predictions were given for this case study and the Tanimoto index was close to 1 for most of these, showing a high confidence level. The need for such an extraction process arises in the context of chemical recycling of polyamide 6, highlighting the enormous potential of models like GH-GNN to support chemical engineers in developing more powerful and sustainable separation processes.

## ACKNOWLEDGEMENTS

This work was partly supported by the Research Initiative "SmartProSys: Intelligent Process Systems for the Sustainable Production of Chemicals", funded by the Ministry for Science, Energy, Climate Protection and the Environment of the State of Saxony- Anhalt.

## REFERENCES

1. Sanchez Medina, E.I. and Sundmacher, K., 2023. Solvent pre-selection for extractive distillation using Gibbs-Helmholtz Graph Neural Networks. In Computer Aided Chemical Engineering (Vol. 52, pp. 2037-2042). Elsevier.
2. Sanchez Medina, E.I., Linke, S., Stoll, M. and Sundmacher, K., 2022. Graph neural networks for the prediction of infinite dilution activity coefficients. Digital Discovery, 1(3), pp.216-225.
3. Rittig, J.G., Hicham, K.B., Schweidtmann, A.M., Dahmen, M. and Mitsos, A., 2023. Graph neural networks for temperature-dependent activity coefficient prediction of solutes in ionic liquids. Computers & Chemical Engineering, 171, p.108153.
4. Sanchez Medina, E.I., Linke, S., Stoll, M. and Sundmacher, K., 2023. Gibbs–Helmholtz graph neural network: capturing the temperature dependency of activity coefficients at infinite dilution. Digital Discovery, 2(3), pp.781-798.
5. Sanchez Medina, E.I., Kunchapu, S. and Sundmacher, K., 2023. Gibbs–Helmholtz graph neural network for the prediction of activity coefficients of polymer solutions at infinite dilution. The Journal of Physical Chemistry A, 127(46), pp.9863-9873.
6. Chen, G., Song, Z., Qi, Z. and Sundmacher, K., 2021. Neural recommender system for the activity coefficient prediction and UNIFAC model extension of ionic liquid-solute systems. AIChE Journal, 67(4), p.e17171.
7. Qin, S., Jiang, S., Li, J., Balaprakash, P., Van Lehn, R.C. and Zavala, V.M., 2023. Capturing molecular interactions in graph neural networks: a case study in multi-component phase equilibrium. Digital Discovery, 2(1), pp.138-151.
8. Minor, A.J., Goldhahn, R., Rihko-Struckmann, L. and Sundmacher, K., 2023. Chemical recycling processes of Nylon 6 to Caprolactam: Review and Techno-Economic assessment. Chemical Engineering Journal, p.145333.
9. Gmehling, J. and Schedemann, A., 2014. Selection of solvents or solvent mixtures for liquid–liquid extraction using predictive thermodynamic models or access to the Dortmund Data Bank. Industrial & Engineering Chemistry Research, 53(45), pp.17794-17805.

© 2025 by the authors. Licensed to PSEcommunity.org and PSE Press. This is an open access article under the creative commons CC-BY-SA licensing terms. Credit must be given to creator and adaptations must be shared under the same terms. See https://creativecommons.org/licenses/by-sa/4.0/



Systems & Control Transactions

**Research Article - Peer Reviewed Conference Proceeding**
ESCAPE 35 - European Symposium on Computer Aided Process Engineering
Ghent, Belgium. 6-9 July 2025
Jan F.M. Van Impe, Grégoire Léonard, Satyajeet S. Bhonsale,
Monika E. Polańska, Filip Logist (Eds.)

PSE PRESS

# Knowledge Discovery in Large-Scale Batch Processes through Explainable Boosted Models and Uncertainty Quantification: Application to Rubber Mixing

**Louis Berthier[a,b], Ahmed Shokry[a,*], Eric Moulines[a], Guillaume Ramelet[b], Sylvain Desroziers[b]**

[a] Centre de Mathématiques Appliquées (CMAP), Ecole Polytechnique, Institut Polytechnique de Paris, 91120 Palaiseau, France
[b] Explore Team I4.0, Manufacture Française des Pneumatiques Michelin, 63100 Clermont-Ferrand, France
* Corresponding Author: ahmed.shokry@polytechnique.edu.

## ABSTRACT

Rubber mixing (RM) is a vital batch process producing high-quality composites, which serve as input material for manufacturing different types of final products, such as tires. Due to its complexity, this process faces two main challenges regarding the final quality: i) lack of online measurement and ii) limited comprehension of the influence of the different factors involved in the process. While data-driven and machine learning (ML) based soft-sensing methods have been widely applied to address the first challenge, the second challenge, to the best of the author's knowledge, has not yet been addressed in the rubber industry. This work presents a data-driven method for extracting knowledge and providing explainability in the quality prediction in RM processes. The method centers on an XGBoost model while leveraging high-dimensional data collected over extended time periods from one of Michelin's complex mixing processes. First, a recursive feature elimination-based procedure is used for selecting relevant features, which reduces the number of input features used for building the ML model by 82% while improving its predictive performance by 17%. Secondly, SHapley Additive exPlanations (SHAP) techniques are employed to explain the ML model's predictions through global and local analyses of feature interactions. The selected quality-related variables can be leveraged to improve process control and supervision. Finally, an uncertainty quantification (UQ) module, based on Split Conformal Prediction (SCP), is combined with the ML model, providing confidence intervals with 90% coverage and empirically verified theoretical guarantees. This module ensures prediction reliability and robustness in real applications.

**Keywords**: quality monitoring, explainable machine learning, uncertainty quantification, rubber mixing

## I. INTRODUCTION

In the rubber industry, mixing is a key process where raw rubber is blended with several components, such as additives and accelerators, to generate a composite with enhanced properties ideal for the subsequent production of tires. Real-time tracking of the mixing process's quality indicators, such as Mooney viscosity, is currently challenging. The only available methods to obtain their ground truth values are offline sampling and laboratory analyses, which take hours after the batch has been discharged, even though a batch is completed in just 30 minutes. This significant disadvantage hinders efficient process monitoring and control.

Predicting RM quality through physics-based models is also highly challenging. This is due to (i) the nonlinear and heterogeneous nature of the process since it involves several physical, thermal, and chemical transformations, (ii) the varying properties of the feeding raw materials, and (iii) the evolution and degradation of the production machinery status **[1]**. Instead, ML-based softening methods have been widely adopted to achieve this objective: ML models are trained using the process history data to capture the complex relationships between the mixing process variables and the final quality. The trained ML model can be used online as a soft sensor for cheap, real-time quality estimation. In this direction, global modeling techniques have been proposed,

commonly using Partial Least Square **[2]**, Extreme Learning Machine **[3]**, and Artificial Neural Networks models **[4]**. However, they struggle with nonlinearities and local characteristics of the process behavior. To tackle this issue, local modeling techniques have been proposed and can be categorized into three main types:

(1) **Just-in-time Learning (JITL):** each time the online prediction is required, a new ML model is trained. The training uses a few patterns carefully selected from the entire process history data, based on their similarities to the current prediction point. This technique is particularly effective for processes characterized by strong nonlinearities and localities **[3,5]**.

(2) **Ensemble-based method (ENS):** several ML models are trained using different subsets of the process history data. The training subsets can be randomly selected or based on local sub-regions within the input space where the process exhibits distinct local behaviors. The final prediction is then obtained by aggregating the predictions from the individual models. This technique enhances the prediction and its robustness, leveraging the diversity of the ensemble **[4]**.

(3) **Moving Window-based method (MW):** This approach involves training a ML model using past observations up to a certain time window. Unlike JITL, this method effectively handles progressive drifts of the process **[5]**.

Many other approaches have also been developed based on different combinations of the aforementioned types: JITL, ENS, and MW.

Despite their success, all these ML-based softening approaches applied in the rubber industry suffer from remarkable limitations. First, they offer little insight into the underlying physical processes or the influence of conditions on the final quality — an understanding that is crucial for control. Second, they consider basic process variables (e.g., power) as the sole input for the ML model, neglecting critical factors like material characteristics and weather conditions **[1,3,4]**, which can be vital, especially when ultra-quality grades with minimal variation must be achieved. Third, these approaches lack UQ capabilities, which reduces their reliability.

This work addresses these challenges by proposing an explainable and robust ML-based method with UQ to analyze the hidden relationships between final batch quality and influencing factors in RM processes.

## II. CASE STUDY

This study focuses on one of Michelin's RM lines and utilizes a dataset collected over nearly two years of production and comprising 35125 mixing batches. The dataset comprises 316 features, including direct measurements of process variables and engineered features derived from expert knowledge. These features can be categorized into 5 groups (**Table 1**):

(i) Context, such as campaign and batch information
(ii) Process States (PS), such as the mixer's internal temperature and rotor rotation speed.
(iii) Raw material quality (RMQ), such as properties of input materials.
(iv) Weather conditions (WC), such as the ambient temperature and humidity.
(v) Production recipe settings (PRS), such as machines' settings.

**Table 1:** Detailed characteristics of the dataset

| Group | Context | PS | RMQ | WC | PRS |
|---|---|---|---|---|---|
| Number of features | 4 | 99 | 37 | 22 | 154 |
| Range feature identifier: "data_" | 001 - 004 | 005 - 103 | 104 - 140 | 141 – 162 | 183 – 609 |

Moreover, the dataset includes sub-quality targets, represented by rheological parameters like the maximum torque derived from rapid and low-cost tests **[6]**.

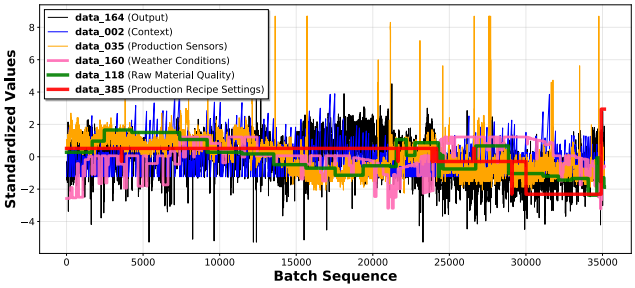



**Figure 1.** Evolution of some features and the sub-quality target over the 35125 batches.

## III. METHODOLOGY

The proposed methodology is built around the XGBoost model, an implementation of gradient-boosting decision trees, and involves four main steps described in the following subsections. For more details about the XGBoost model, we refer to **[7]**. Note that before performing any of these four steps, the available dataset $D = \{(X, y \mid X \in R^{n \times d}, y \in R^{n \times 1})\}$ with $n = 35125$ and $d = 316$, is randomly divided into three subsets for training $(D^T)$, calibration $(D^C)$, and testing $(D^t)$, using a ratio of 70%, 15%, and 15%, respectively where $n^T = |D^T|, n^C = |D^C|$, and $n^t = |D^t|$. This division is done prior to standardization. Importantly, the indices of the patterns included in each of the three subsets strictly remain the same throughout all steps of this study to ensure reproducibility and consistency.

## A. Initial feature selection

Given the high dimensionality of the features measured during the mixing process, selecting informative features relevant to mixing quality is crucial. This step eliminates redundancy, reduces the dimensionality of the input space for the ML model, and ultimately enhances its performance by improving computational efficiency, predictive accuracy, and interpretability.

This work develops a Frequency-based Feature Selection (FFS) method, which relies on a Recursive Feature Elimination (RFE) technique **[8]**. The RFE is a wrapper technique that iteratively excludes features contributing the least to the ML model predictions while minimizing multicollinearity among the features.

The proposed FFS method applies the RFE algorithm $Q$ times. In the $q^{th}$application, a different dataset $D_q^{T\prime}$ is randomly sampled from the original training subset $D^T$, such that $D_q^{T\prime} \subset D^T$, and is used for training a ML model $f_{\theta_q}$, where $\theta_q$ is the model parameters. Then, the RFE iterates, where in each iteration, it calculates an importance score for each feature based on different criteria derived from the ML model's predictions to discard a predefined number $s$ of features with the lowest scores. Although the scores are calculated in a univariate manner, the recursive mechanism of the algorithm effectively induces a multivariate selection process **[8]**. The algorithm terminates once a predefined minimum number of features $d$ is reached, where $d \ll d$.

The $Q$ applications of the RFE techniques yield $Q$ groups of best-selected features which are further analyzed based on frequency: a feature is eventually considered relevant if it appears in at least 80% of the $Q$ selections. In this way, the FFS provides the most informative features $X_* \in R^{n\times\mathcal{K}}$ where $\mathcal{K} \ll d$, and at the same time, guarantees their robustness. The total dataset is then reduced to $D_* = \{(X_*, y \mid X_* \in R^{n\times\mathcal{K}}, y \in R^{n\times 1})\}$, which will be the basis for the next step keeping the same splits for training, calibration and testing.

## B. Refinement of the initially selected features

In the second step, the initially selected set of best features, $D_*$, is refined to reduce its size further. It relies on a SHAP-based Feature Selection (SFS) method. SHAP is a model-agnostic approach that provides local and global interpretability of a ML model $f_\theta$ **[9]**.

For a given query point $x$, SHAP calculates a contribution score $\phi_j$ for each feature $j$, representing its relative impact on the model's prediction. The Shapley value is defined as follows:

$$\phi_j(x) = \sum_{S\subseteq\{1,\dots,\mathcal{K}\}\setminus\{j\}} \frac{|S|!(\mathcal{K}-|S|-1)!}{\mathcal{K}!}\left[v\left(x_{S\cup\{j\}}\right) - v(x_S)\right] \quad (1)$$

where $j \in \{1,\dots,\mathcal{K}\}$ is the index of a feature, $S$ is any subset of features that does not include $j$, and $v(x_S)$ represents the value function of the features in the subset $S$, typically corresponding to the ML model's output when only the features in $S$ are considered. This formulation ensures an equitable allocation of contributions based on all possible combinatorial subsets of features $S$.

For assessing the global importance of features, a global importance index $I_j$ can be calculated for each feature $j$ by averaging the absolute Shapley values obtained over the training set $D_*^T$, as shown in equation (2).

$$I_j = \frac{1}{|D_*^T|}\sum_{i=1}^{|D_*^T|} |\phi_j(x_i)| \quad (2)$$

Next, the $\mathcal{K}$ features are ranked in descending order based on their importance index, where a higher importance index corresponds to a higher rank. In other words, feature $j$ is considered more important than feature $j'$ if $I_j > I_{j'}$. Finally, the ranked feature set denoted as $\boldsymbol{X}^{*\boldsymbol{rnk}} = \{x^1, x^2, \dots, x^l, \dots, x^{\mathcal{K}}\}$ is obtained, where $x^r$ represents the $r-th$ most important feature with respect to the output quality, $y$, among all $\mathcal{K}$ features.

The validation step involves an iterative procedure for training ML models with different feature subsets. Specifically, at the generic $r-th$ iteration, a ML model $f^l$ is trained using the $l$ top-ranked features, where $l \in \{1,2,\dots,\mathcal{K}\}$:

$$\hat{y} = f_\theta^l(\boldsymbol{X}_l^{*rnk})$$

$$\boldsymbol{X}_l^{*rnk} = \{x^1, \dots, x^l\}$$

where $\boldsymbol{X}_l^{*rnk}$ represents the subset of the first $l$ most important features from the ranked set $\boldsymbol{X}^{*rnk}$. The model's performance is then evaluated to assess the effectiveness of these feature subsets in predicting the output $y$.

Finally, the selected subset of top-ranked features corresponds to the smallest subset after which adding more features to the ML model's input does not significantly improve its predictive performance. Consequently, the final dataset can be denoted as $D_+ = \{(X_+, y \mid X_+ \in R^{n\times\ell}, y \in R^{n\times 1})\}$, where $\ell < \mathcal{K}$. Note that, $D_+$ is the final dataset, which will be used to develop and analyze ML models.

Additionally, the same pattern splits initially performed in the first paragraph of **Section III** are strictly maintained to divide the dataset into three subsets: training ($D_+^T$), calibration ($D_+^C$), and testing ($D_+^t$).

## C. Explainability

The explainability of ML models ensures transparency and provides deep insights into their behavior by revealing how predictions are made. This explainability offers valuable information to industry experts, thereby supporting decision-making, particularly in process monitoring and supervision tasks.

While SHAP is used for feature ranking and selection in **Section III-B**, it is also applied to explain the final ML

model $f_\theta^+$ developed using the best features subset $D_+$.

SHAP, a widely used game theory-based tool, provides explainability by coupling an explainer with a trained ML model. It supports (i) global analyses on the entire testing dataset to reveal overall trends and (ii) local analyses for specific instances to detect drifts. Additionally, SHAP visualizes feature interactions using Dependence Plots (DPs).

## D. Uncertainty Quantification

The final step of the proposed approach focuses on the prediction uncertainty of the trained ML model $f_\theta^+$ to enhance its reliability for in-field quality prediction. To achieve this, SCP is employed for UQ due to its advantageous properties, including i) its model-agnostic nature, enabling applicability to any ML model, ii) its distribution-free framework, and iii) its ability to provide mathematical guarantees on the estimated uncertainties.

Relying only on the exchangeability assumption, SCP approximates the true probability, denoted as $P$ in equation (4), ensuring that the estimated prediction intervals achieve the desired coverage level $\delta$ **[10]**. This results in an uncertainty envelope defined by the average quantile value of the non-conformity scores.

$$\delta \leq P\left(y_+^t \in \Gamma_{D_+^C}^{\delta}(X_+^t)\right) \leq \delta + \frac{1}{n^C+1} \qquad (4)$$

where $\Gamma_{D_+^C}^{\delta}$ stands for the prediction set constructed on $D_+^C$.

**Algorithm 1:** SCP Algorithm

**Input:** Calibration set $D_+^C = \{(X_+^C, y^C) \mid X_+^C \in R^{n^C \times l}, y^C \in R^{n^C \times 1}\}$, Coverage level $\delta$, number of splits $\mathcal{S}$, trained ML model $f_\theta^+$.
**Output:** Avg empirical coverage $C^\delta$, avg quantile value $Q^\delta$.

**for** split $s \in \{1, \dots, \mathcal{S}\}$ in **do**
- Shuffle $D_+^C$.
- Split $D_+^C$ into a sub-calibration set $D_{+,s}^{SC} = (X_+^{SC}, y^{SC})_s$ and a validation set $D_{+,s}^V = (X_+^V, y^V)_s$.
- Predict sub-calibration outputs $\hat{y}_s^{SC} = f_\theta^+(X_{+,s}^{SC})$.
- Compute non-conformity scores $A_s = |\hat{y}_s^{SC} - y_s^{SC}|$.
- Calculate the quantile value $Q_s^\delta = quantile(A_s, \delta)$.
- Calculate prediction intervals for each validation point $i \in \{1, \dots, n^V\}$ with $n^V = |D^V|$:
$$\Gamma_{D_{+,s}^{SC}}^{\delta,s}(x_{+,i,s}^V) = \{\hat{y}_{i,s}^V \pm Q_s^\delta\}\ \forall i.$$
- Compute the empirical coverage:
$$C_{\Gamma_{D_{+,s}^{SC}}^{\delta,s}}(X_{+,s}^V) = \frac{1}{n^V}\sum_{i=1}^{n^V} 1_{[y_{i,s}^V \in \Gamma_{D_{+,s}^{SC}}^{\delta,s}(x_{+,i,s}^V)]}$$
- Compute the average empirical coverage:
$$C_s^\delta = \frac{1}{\mathcal{S}}\sum_{k=1}^{\mathcal{S}} C_{\Gamma_{D_{+,s}^{SC}}^{\delta,k}}$$

**end**

Compute the full average empirical coverage: $C^\delta = \frac{1}{\mathcal{S}}\sum_{s=1}^{\mathcal{S}} C_s^\delta$.

Compute the full average quantile value: $Q^\delta = \frac{1}{\mathcal{S}}\sum_{s=1}^{\mathcal{S}} Q_s^\delta$.

The SCP algorithm detailed **above** requires, as inputs, a trained ML model $f_\theta^+$ a calibration dataset ($D_+^C$), and a user-defined value representing a desired coverage level $\delta$ for future predictions. SCP performs its computations over $\mathcal{S}$ iterations, where in each iteration $s \in \{1, \dots, \mathcal{S}\}$ it shuffles the whole calibration dataset then splits it into two subsets: a calibration subset ($D_+^{SC}$) and a validation subset ($D_+^V$). The shuffling and splitting mechanisms enhance robustness and efficiency compared to full CP. This leads to the creation of narrower prediction intervals while mitigating biases that may arise from a single split in full CP.

All in all, SCP is a robust method that offers key statistical properties, including finite-sample coverage, validity, and efficiency. Finite-sample coverage ensures that the constructed prediction intervals maintain their statistical guarantees even with limited data. Validity corresponds to the lower bound $\delta$ and ensures that at least $\delta\%$ of future test observations fall within the prediction sets. Efficiency, defined by the upper bound $\delta + \frac{1}{n^C+1}$, ensures that the intervals remain as tight as possible without being overly conservative.

# IV. RESULTS

As a baseline, the XGBoost model is first constructed using the original dataset $D$. Our model uses 784 estimators as hyperparameters, with a maximum depth of 22 and a learning rate of 0.076. To assess its performance, the Mean Square Error (MSE) and the Coefficient of determination ($R^2$) are used, as defined in equations (5) and (6). In these equations, $y^t \in R^{n^t \times 1}$ represents the ground truth output values in the testing subset, $\bar{y}^t \in R^{1\times 1}$ denotes their mean, and $\hat{y}^t \in R^{n^t \times 1}$ corresponds to their predicted values.

$$MSE = \frac{1}{n^t}\sum_{i=1}^{n^t} (y_i^t - \hat{y}_i^t)^2 \qquad (5)$$

$$R^2 = 1 - \frac{\sum_{i=1}^{n^t} (y_i^t - \hat{y}_i^t)^2}{\sum_{i=1}^{n^t} (y_i^t - \bar{y}^t)^2} \qquad (6)$$

Firstly, the FFS method proposed in **Section III-A** is applied to the original dataset $D$, where the RFE algorithm is executed $Q = 10$ times. This step discards 244 irrelevant or correlated features, resulting in a condensed dataset $D_*$ that includes $\mathcal{K} = 72$ potential features.

Secondly, the SFS method for feature refinement defined in **Section III-B** is applied to the condensed dataset $D_*$ to rank the 72 features. The best subset is then selected according to the impact of the sequential addition of top-ranked features to the ML model's input.

**Figure 2** displays the 72 features ranked in descending order according to their importance, with *data_474* being the most relevant and *data_159* the least relevant to mixing sub-quality. It also illustrates the evolution of the ML model's performance as one of the top-ranked features is sequentially added to its input.

The selection of the optimal subset of top-ranked features $\ell$ is largely influenced by the modeler's trade-off between the desired level of accuracy and model simplicity. In our case, we observe that after the 58th top-

ranked feature, adding more features to the ML model's input does not improve the performance. Finally, the refined dataset $D_+$ comprising the top $\ell = 58$ features is obtained. The corresponding ML model $f_\theta^+$, is then trained and tested using this dataset. Both will be utilized in the subsequent steps for explainability and UQ.

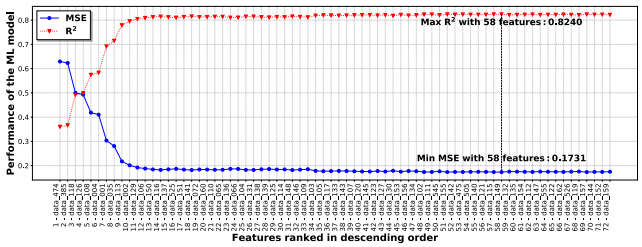



**Figure 2.** Evolution of ML model's performance as a function of the number of top-ranked features included in its input (SFS method).

**Table 2** compares the performance of the ML models developed using step 1 FFS with $D_*$ and step 2 FFS-SFS with $D_+$ of the proposed method to the baseline case, where the original dataset $D$ is used for model development. Compared to the baseline, the FFS step achieves a significant improvement in all three metrics (MSE, $R^2$, and number of features). In comparison to the FFS step, the FFS-SFS step shows a slight improvement in MSE while further reducing the number of features.

**Table 2:** Comparison of ML model performance at each step of the method. **Bold** indicates the best results.

| Dataset used for model development | ML model performance | | Improvement relative to baseline (%) | | |
|---|---|---|---|---|---|
| | MSE | $R^2$ | MSE | $R^2$ | No. of features |
| $D$ ($d$ = 316) | 0.209 | 0.788 | / | / | / |
| $D_*$ ($\mathcal{K}$= 72) | 0.174 | 0.824 | 17% | 4.6% | -77% |
| $D_+$ ($\ell$ = 58) | **0.173** | **0.824** | **17%** | **4.6%** | **-82%** |

A breakdown of the top 58 ranked features identified through Shapley analyses, categorized by the five feature groups, reveals the following distribution: 3 features belong to the Context group, 6 to PS, 31 to RMQ, 12 to WC, and 6 to PRS.

The identification of PRS features as highly important is logical and aligns with most findings in the literature. This is because PRS variables represent control parameters and manipulated machinery settings that can be adjusted to define specific operational regimes or modes, ultimately exerting a strong influence on quality.

Contrary to findings in the literature, numerous and diverse variables are found to significantly influence quality estimation, such as RMQ and WC. Particularly, RMQ features play a crucial role in both quantity and impact, a conclusion further validated by domain experts.

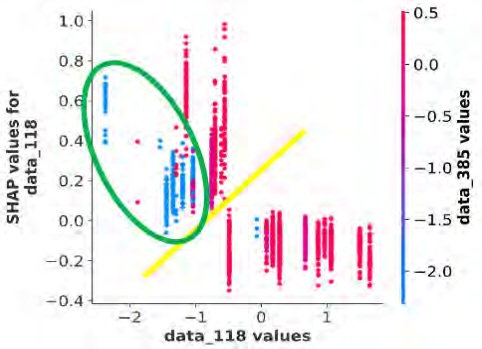



**Figure 3.** SHAP DP of *data_118* against the distribution of feature *data_385*.

Conversely, local analyses using SHAP DPs provide deeper insights into how specific feature ranges contribute to model predictions. As an example, **Figure 3** shows the DP of the second top-ranked feature *data_118* with point colors representing the distribution of the third top-ranked feature *data_385*. It reveals a bimodal behavior in *data_118*, separated by the yellow line. The first one indicates a positive contribution when the feature value is below $-0.75$. In contrast, the second mode exhibits a slightly negative contribution when *data_118* exceeds this threshold. In addition to this bimodal effect, the color distribution based on *data_385* highlights an interaction between both features. Specifically, the green ellipse shows that *data_385* reaches its lowest values almost exclusively when *data_118* is less than $-1$, suggesting a potential relationship between these two features.

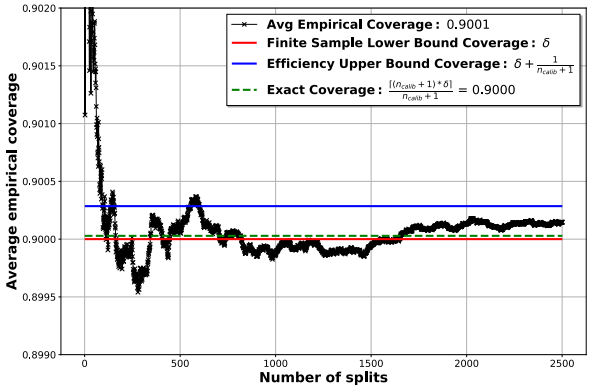



**Figure 4.** SCP convergence and theoretical guarantees with an expected coverage of $\delta = 90\%$.

Finally, regarding the UQ of the model predictions, the SCP method is applied, targeting a coverage level $\delta = 0.9$ while considering multiple splits $\mathcal{S} = 2500$.

The convergence graph in **Figure 4** demonstrates the theoretical guarantees' validation based on the calibration set $D_+^{\mathcal{C}}$. Initially, the average empirical coverage $C^\delta$ lies outside the estimated bounds $[\delta, \delta + \frac{1}{1+n^{\mathcal{C}}}]$ represented by the red and blue lines. However, as the

number of splits increases, $C^{\delta}$ converges within these bounds, aligning with the target coverage level $C^{*} = \frac{\lceil (n^{C}+1)\times\delta \rceil}{n^{C}+1}$.

Statistical properties are upheld during inference as the marginal coverage aligns with the desired level $\delta = 0.9$. Specifically, the testing coverage $C^{t} = 90.09\%$ is achieved with tight confidence intervals, ensuring reliable UQ, as shown in **Figure 5**.

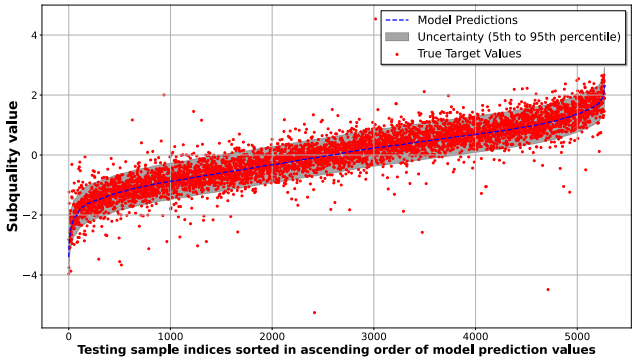



**Figure 5.** SCP uncertainty estimates with a testing coverage of $C^{t} = 90.09\%$

## V. CONCLUSION

This work proposes a data-driven framework for knowledge discovery and the reliable prediction of products' final quality in batch processes, with real application to RM. The proposed FFS and SFS methods for feature selection and refinement effectively address the challenge of high process dimensionality by discarding irrelevant and correlated features. These methods enable identifying the most informative and key features related to batch quality, leading to an 82% reduction in the number of input features while simultaneously enhancing the predictive performance of the ML model by 17% compared to the baseline.

Concerning knowledge discovery, SHAP techniques are harnessed to provide insights into the relationships between the best group of input features, previously identified, and to quantify their global and local impacts on the batch quality. These analyses also revealed the importance of previously overlooked factors in the literature, such as initial material properties and weather conditions, in predicting rubber composite quality.

Finally, the developed SCP-based UQ module can generate reliable confidence intervals with strong mathematical guarantees. This module achieves 90% coverage of the ML model's predictions, ensuring robustness and reliability in real-world industrial applications.

## ACKNOWLEDGEMENTS

The authors acknowledge the support received from Manufacture Française des Pneumatiques Michelin.

## REFERENCES

1. Diancai Yang, Yi Liu, Yugang Fan, and Haiqing Wang. Online prediction of mooney viscosity in industrial rubber mixing process via adaptive kernel learning method. 48th IEEE CDC, pages 404 – 409, 01 (2010).
2. Chunying Zhang, Sun Chen, Fang Wu, and Kai Song. A novel q-based online model updating strategy and its application in statistical process control for rubber mixing. *Chin. J. Chem. Eng.*, 23(5):796–803 (2015).
3. Weiya Jin, Yi Liu, and Zengliang Gao. Fast property prediction in an industrial rubber mixing process with local elm model. *J. App. Poly. Sc.*, 134:45391, 06 (2017).
4. Shuihua Zheng, Kaixin Liu, Yili Xu, Hao Chen, Xuelei Zhang, and Yi Liu. Robust soft sensor with deep kernel learning for quality prediction in rubber mixing processes. *Sensors*, 20(3) (2020).
5. Aysun Urhan and Burak Alakent. Integrating adaptive moving window and just-in-time learning paradigms for soft-sensor design. *Neurocomputing*, 392:23–37 (2020).
6. International Organization for Standardization, ISO 6502-1. Rubber — Measurement of vulcanization characteristics using curemeters — Part 1: Introduction (2018).
7. Tianqi Chen and Carlos Guestrin. XGBoost: A Scalable Tree Boosting System. In Proceedings of the 22nd ACM SIGKDD International Conference on Knowledge Discovery and Data Mining, pages 785–794 (2016).
8. Isabelle Guyon and Andr´e Elisseeff. An introduction to variable and feature selection. *J. Mach. Learn. Res.*, 3(null):1157–1182, 3 (2003).
9. Scott M. Lundberg and Su-In Lee. A unified approach to interpreting model predictions. In Proceedings of the 31st International Conference on Neural Information Processing Systems, NIPS'17, pages 4768–4777 (2017).
10. Anastasios N. Angelopoulos and Stephen Bates. A gentle introduction to conformal prediction and distribution-free uncertainty quantification. CoRR, abs/2107.07511 (2021).

© 2025 by the authors. Licensed to PSEcommunity.org and PSE Press. This is an open access article under the creative commons CC-BY-SA licensing terms. Credit must be given to creator and adaptations must be shared under the same terms. See https://creativecommons.org/licenses/by-sa/4.0/

Systems & Control Transactions

**Research Article - Peer Reviewed Conference Proceeding**
ESCAPE 35 - European Symposium on Computer Aided Process Engineering
Ghent, Belgium. 6-9 July 2025
Jan F.M. Van Impe, Grégoire Léonard, Satyajeet S. Bhonsale,
Monika E. Polańska, Filip Logist (Eds.)

PSE PRESS

# Electricity Bidding with Variable Loads

**Iiro Harjunkoski**[a,b]

[a] Aalto University, Department of Chemical and Metallurgical Engineering, Espoo, Finland
[b] Hitachi Energy Research, Mannheim, Germany
* Corresponding Author: iiro.harjunkoski@aalto.fi.

## ABSTRACT

Processes increasingly need to consider electricity markets, which shifts the traditional demand side management scope towards a more dynamic nature. Instead of only focusing on day-ahead energy trading, demand-side management scope should be broadened towards being able to support the power grid stability during frequency events. This paper studies an artificial example process, similar to the melt-shop process from the steel industry, highlighting the challenges and opportunities of an energy intensive process. We show the potential benefits of having a battery energy storage system on-site, as well as opportunities in lowering the electricity cost by participating in the bidding process of various ancillary products.

**Keywords**: Stochastic Optimization, Renewable and Sustainable Energy, Planning & Scheduling, Energy markets, Battery Energy Storage Systems, Price Uncertainties

## INTRODUCTION

The ongoing and planned electrification of many industries and processes will increase the interdependencies with the power infrastructure due to the increasing electricity demands. This also results in that all disturbances or changes in production processes will directly require countermeasures at the power grid level to maintain stability. As the electricity infrastructure is already facing increasing volatility on the supply side due to the growing number of renewable energy source (RES) generation units, it is also important to tap the potential of the electrification and the flexibility it can enable. Processes will have a strong impact and can also help compensate for the RES-fluctuations, ensuring that the electricity demand and supply are balanced at all times. This opportunity has already been recognized [1] and in this paper we further elaborate on the concept by adding a battery energy storage system (BESS) to support the balancing between the production targets and grid stability.

Apart from the traditional demand-side management [2], which is often based on a day-ahead production scheduling, acknowledging the next day electricity prices – either based on forecasts or actual market clearing prices – electricity bidding offers more opportunities than only forecasting the electricity price and adapting the load accordingly. Large consumers must actively participate in the electricity markets ahead of time and their energy bids will affect the market clearing. Such consumers are called price makers. This mechanism allows to schedule the power plants to ensure sufficient supply, but with increasing RES participation it becomes a challenge to deliver to promise and here industrial loads could potentially participate, also in helping to maintain the grid stability. The main vehicle to deal with large unplanned supply variations is ancillary services [3], which from the consumer point of view means committing to potentially increase or lowering the energy consumption if called upon. This raises the practical question how much the process industries can plan for such volatility as they primarily need to focus on delivering to customers.

A common option – also seen by many RES unit owners – is to invest in BESS to act as a buffer between the consuming load and the power grid. This can also shield the process owner from unwanted and infeasible power volatilities, which can have an immense effect on critical electricity-dependent processes. With such an energy storage system in place, there is an option to use the BESS for offering ancillary services, as well as participating in energy arbitrage trading [4], i.e. benefiting from buying electricity during low prices and selling it back during high prices. This could also help justifying the investment costs. However, the key question is how to

operate such a combined system in a profitable manner, also taking into account the uncertainty over electricity prices. In this paper, we extend the approach in [5], where several energy and ancillary service products are co-optimized taking into account the uncertainty about price developments. The previous approach was targeted at RES/BESS owners, where the forecasted load was relatively stable and mainly consisted of the control system focused on keeping the system running. Here, we change the load behavior to be not a forecasted parameter but a variable and link this to a process schedule, which is co-optimized with the bidding decisions. Much following the concepts in [6], we compare the cases with different combination of products (energy and ancillary products) and different sizes of BESS systems using a simplified stochastic approach, which reduces to a deterministic optimization approach if there is only one price scenario available, which is the case in this paper. The example process is modeled using the resource task network (RTN) [7] approach.

## THE EXAMPLE PROCESS

We introduce a steel-plant like energy-intensive process equipped with electric arc furnaces (EAF) and having four processing stages and two parallel units in the first EAF-stage. The process is shown in Figure 1.

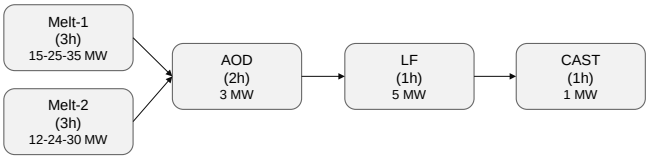



**Figure 1**. Example four-stage energy-intensive process, inspired by the steel-making process

The process durations and electricity consumptions are shown in the figure. Note that the melting process electricity demand increases along the processing time (e.g. 15 MW for hour 1, 25 MW for hour 2 and 35 MW for hour 3 in Melt-1). We can also see that the two EAFs are not equal. The batch size across the processing stage is 25 tons and constant. This example represents a strongly simplified small steel production process and we e.g. ignore the cooling effect caused by waiting times between process stages. We model the process using the discrete-time RTN approach presented in Castro et al. [8], which considered demand-response aspects of a cement plant. The corresponding RTN graph is shown in Figure 2, where we see all resources represented by circles and tasks by rectangles. The resources are: EAFs, argon-oxygen decarburization unit (AOD), ladle furnace (LF) and continuous caster (CAST) and electricity (ELEC). Intermediate product resources are molten metal (MET), the same after AOD (AODMET) and after LF (LFMET). After the casting, we get the final product (SLAB). We refer the interested reader to further process details described in [9] and [10].

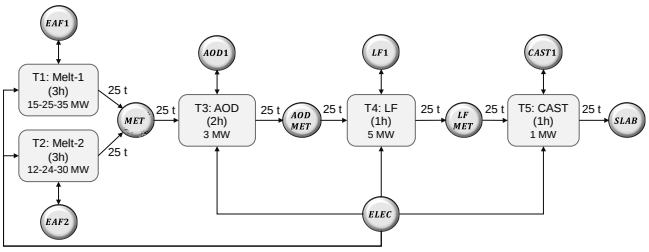



**Figure 2**. RTN graph of the example process

The RTN diagram can be easily converted into an RTN model, which basically has the following structure. We have a number of processing tasks $i$, a set of discrete-time points $t$ and the binary variable, $N_{i,t}$, indicating whether a task $i$ starts at time point $t$. This variable is used in the resource balance equation (1), in which we have ignored the batch size term, as all batches weigh 25 tons. The equation considers the initial resource $r$ amount at time point 1 ($R_r^0$) and else refers to the previous time point $R_{r,t-1}$.

$$R_{r,t} = R_r^0|_{t=1} + R_{r,t-1} + \sum_{i \in I} \sum_{\theta=0}^{\tau_i} \mu_{i,r,\theta} N_{i,t-\theta} + \Pi_{r,t} \; \forall r, t \quad (1)$$

As we use a time discretization of one hour, the actual processing time is represented by the number of time points ($\tau_i$) needed for processing the tasks. The parameter $\mu_{i,r,\theta}$ tracks how much resource $r$ is consumed or produced at each time point $\theta$. The final variable, $\Pi_{r,t}$, indicates interactions with the environment, e.g. electricity purchase in this case. Each resource must stay within given bounds as shown in Eq. (2).

$$R_{r,t}^{min} \leq R_{r,t} \leq R_{r,t}^{max} \quad \forall r \in R, t \in T \quad (2)$$

For electricity the bound is typically zero, unless we have energy storage units available, since all electricity must be purchased at the time of use. Finally, variable definitions are shown in Eq. (3).

$$\pi_t \in \mathbb{R}, R_{r,t} \geq \mathbb{R}^+, N_{i,t} \in \{0,1\} \quad (3)$$

## OPTIMIZING THE PROCESS

In this paper, we focus on a two-day production horizon (48 hours) and assume that the demand of slabs is 500 tons, i.e. 20 batches and that the price per ton ($c_{slab}$) is 2500 EUR. In this case we assume that material, equipment and labor cost is about 70% of the steel price – before electricity costs (considered by a profit factor, $p_{fact} = 0.3$). This also means that there is not so much flexibility to adapt the production according to electricity price deviations. To make the case, we selected a week where the electricity was relatively expensive (DK-2 spot

market on June 28-29th,2023) and assume in this study that the example steel plant is a price-taker and must pay the standard day-ahead market price (normally this is not the case, as will be discussed later). The considered electricity prices are shown in Figure 3 – here we assume "perfect knowledge" and do not involve stochastic elements for the sake of the length of this paper. Note that this corresponds to a maximum of 167 EUR/MWh (about 2-3 times the price of normal industrial energy cost).

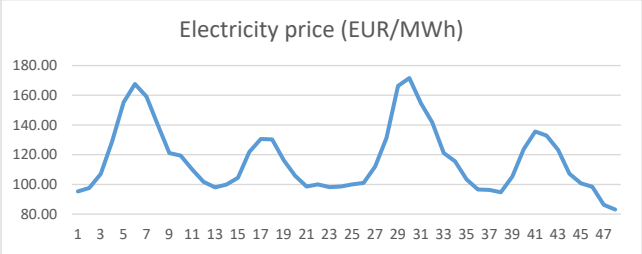



**Figure 3.** Electricity prices for the studied 48-hour period

Let us first optimize the production without considering the electricity price at all – as well as without any energy storage option (worst case). Specifically, we minimize only the makespan ($MS$) which is defined as shown in Eq. (4).

$$MS \geq N_{i,t} \cdot (t + \tau_i - 1) \quad \forall i, t \tag{4}$$

This, as expected, results in a schedule that completely ignores the electricity price.

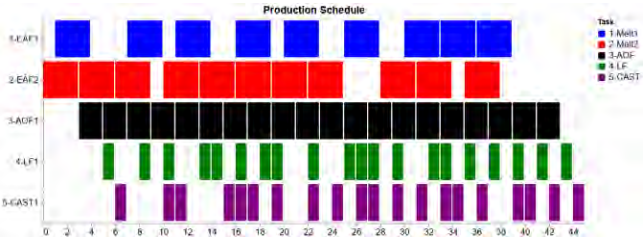



**Figure 4.** Schedule minimizing the makespan

The corresponding Gantt chart is shown in Figure 4 and while the makespan is 45 hours (3 hours of unused production time), this results in a profit of about 182 kEUR after deducting the electricity costs. Note that we enforce the production of minimum 500 tons. If, however, we include the electricity cost into the scheduling objective (Eq. 5),

$$\max \sum_t p_{fact} \cdot c_{slab} \cdot R_{slab,t} - c_{elec,t} \cdot \pi_{elec,t} \tag{5}$$

the results change significantly. The profit increases by 11% to 202 kEUR and the resulting production plan in Figure 5 shows that the full 48 hours are used and the less electricity intensive EAF2 is preferred. Also, one extra batch is produced to increase the profit (total production 525 tons), while simultaneously lowering the electricity costs by 0.6%. This example illustrates that considering the electricity pricing, i.e. doing demand-response has a significant effect on the profitability.

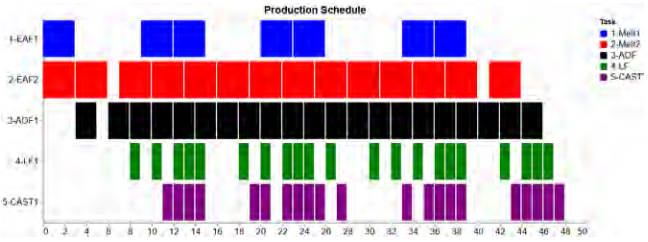



**Figure 5.** Schedule considering electricity cost

If we allow electricity to be stored i.e. by adapting the parameter $R_{r,t}^{max}$ this changes the situation. Having e.g. a 50 MWh battery energy storage system (BESS) unit, which is initially empty, increases the profit by an additional 4.3% to 210 kEUR with minor changes to the production schedule shown in Figure 6. The main change is the time of purchasing as the previous schedule already operates during the cheapest times.

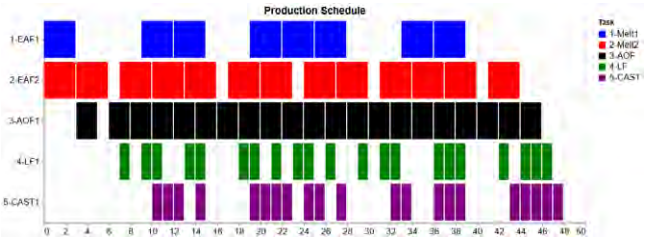



**Figure 6.** Schedule with a BESS of 50 MWh

The use of the BESS capacity correlates well with the electricity price development, as seen in Figure 7, where the storage is filled up during cheaper prices and emptied during peak prices. This shows that it is worth considering both demand-side management scenarios, as well as investing in a BESS, which can shift the electricity purchases to a more profitable period.

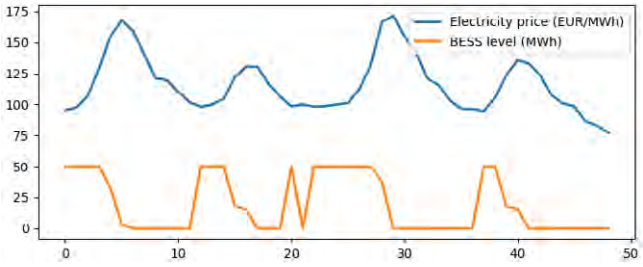



**Figure 7.** Use of BESS capacity w.r.t. electricity price

Optimization results of using three different BESS-sizes is shown in Table 1. As expected, a larger BESS-size increases the profit through the lowered electricity costs. For the two first cases, the production plan did not deviate from the one shown in Figure 5. Here, we cannot analyze the return of investment, but at least provide a

more concrete picture about potential savings (upper bound) of having a BESS installed on site.

**Table 1.** BESS size impact on profit

| BESS size | Profit | Electricity cost |
|---|---|---|
| 0 MWh | 202088.5 | 191661.5 |
| 10 MWh | 203615.2 | 190134.8 |
| 20 MWh | 205621.7 | 188128.3 |
| 50 MWh | 210748.7 | 183001.3 |

## BIDDING TO ELECTRICITY MARKETS

There exists many literature contributions about bidding into various electricity markets [4,5,6] with or without a BESS. The "traditional" market, where industrial consumers have been participating and bidding to, is the electricity market. Typically, large consumers have various electricity contracts, e.g. time-of-use or fixed base tariffs. As mentioned before, here we assume that the example consumer does not impact the final price ("price taker"). Other options that are becoming increasingly important is to bid into ancillary service markets to help stabilizing the power grids during network disturbances, i.e. when the power frequency exits a given threshold (too low or too high). A key requirement here is that ancillary services are always required to be available but mostly not used (in some markets, only 1-2% of the committed capacity is deployed). Therefore, in many markets it is mandatory that the ancillary service capacity be immediately available, i.e. mostly stored within a BESS. Here we build upon the work presented in [5], which discusses a solar power plant combined with a BESS. In this work, we ignore any renewable sources but focus on the process system, discussed in the previous chapter, having an installed BESS capacity (50 MWh), which allows us to participate in the ancillary markets.

We consider two different ancillary markets, where the market M1 requires bidding 36 hours before start of the trading day and market M2 respectively 12 hours before. The products comprise both up and down regulation of the frequency through either injecting (discharging BESS) or extracting (charging BESS) power to/from the grid. We name the products as follows: P1 (up), P2 (down) and P3 (up & down). Product P3 is symmetric and requires exactly same potential capacity (MW) into both directions. The ancillary service capacity cannot be shared by multiple products. For the energy trading, we use only the day-ahead energy market (DAEN).

The modeling is done as follows. We link the RTN model defined above to the model from [5]. The key is the energy balance equation, which basically implies that the amount of energy bought, $x_t^{buy}$, and discharged from BESS, $x_{B,t}^{dc}$, must equal the energy sold, $x_t^{sell}$, charged to BESS, $x_{B,t}^{ch}$, or consumed by a load behind the meter, $X_t^{load}$, as depicted in Eq. (6).

Here, instead of using a fixed load forecast $X_t^{load}$ as was done in [5], we define the load based on the production schedule, i.e. through Eq. (7).

$$x_t^{buy} + \sum_{B \in BESS} x_{B,t}^{dc} \cdot \Delta_t = X_t^{load} \cdot \Delta_t + x_t^{sell} + \sum_{B \in BESS} x_{B,t}^{ch} \cdot \Delta_t \quad \forall t \tag{6}$$

$$\pi_{elec,t} = X_t^{load} \quad \forall t \tag{7}$$

This allows us to directly link a very complex bidding model into the variable load of the generated RTN schedule. We add the first term from the profit function in Eq. (5) into the objective function, which might strongly dominate over bidding profits. Nonetheless, we expect to see some indications of the possible benefits of this co-existence. The electricity cost part (second term in Eq. (5)) is already fully embedded into the bidding scheme. We assume again a BESS configuration with the capacity of 50 MWh, and initial state of charge (SoC) of 50% (25 MWh), which can be fully (dis)charged in 2 hours. Using exactly the same information as in [5], but only considering 48 hours instead of 144, we can now optimize the trading.

The profit increases to 417 kEUR, which is a significant improvement (113%). Figure 8 shows the day-ahead energy market price (DAENprice), which was used earlier, with the ancillary product pricing across the three products and two markets discussed above.

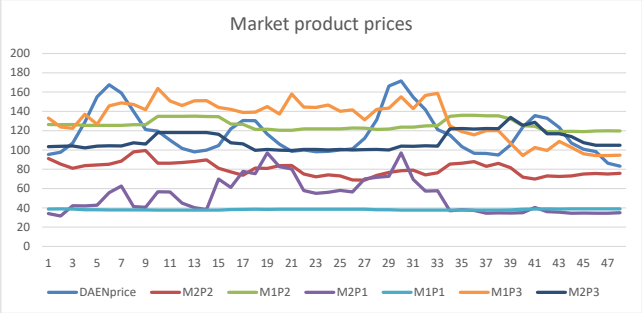



**Figure 8.** Market prices of different products

Using this approach the production schedule remains unchanged and the Gantt chart in Figure 5 is still valid. The trading volumes are shown in Figure 9. Note that energy trading is done in MWh, whereas ancillary products are mainly traded in MW (power).

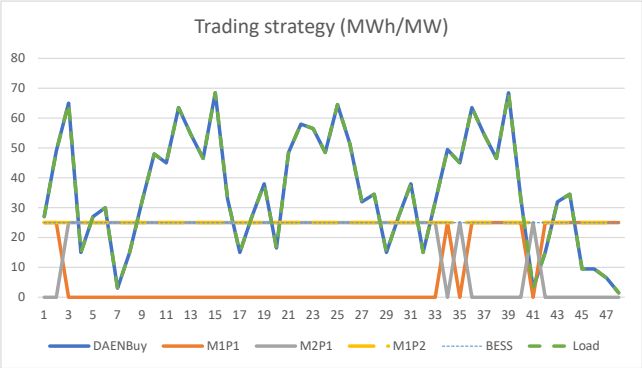


Figure 9. Trading results across multiple markets

Here, we can observe a few facts:

- The energy purchase is 1:1 with the load, i.e. the BESS is not used to shift the electricity demand
- As a consequence, the state of charge (BESS in the figure) is constant and stays exactly in the middle (25 MWh) during the entire planning horizon
- The reason for the above is that the BESS capacity is fully used for trading ancillary services in both directions (25 MW each), which maximizes the trading benefits. Product P3 is not used.

Here we assume the ideal situation that there are no ancillary events, which means that all ancillary trading profits are direct revenues. In this example, the energy purchasing cost is 192 kEUR (as for the 0 MWh case in Table 1) and the earnings from the ancillary service markets 215 kEUR, i.e. the net electricity cost is -23 kEUR. Using the BESS for participating in the ancillary markets would thus completely cover the electricity costs and strongly support the return of investment. However, a more thorough CAPEX estimation would require a more holistic and longer-term studies including seasonal electricity price variations and simulations where ancillary events actually take place, which are out of the scope of this paper.

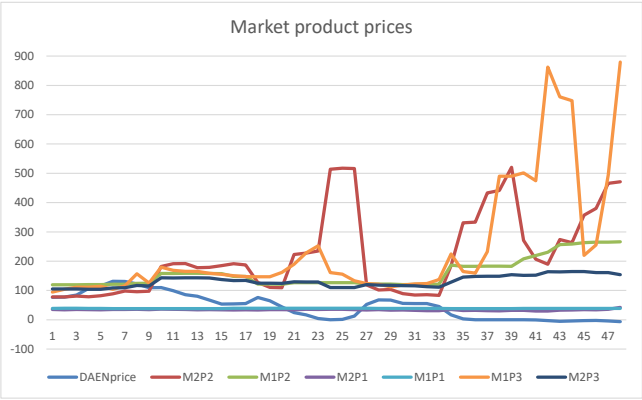


**Figure 10.** Market prices of the second example

## More volatile price profiles

In a second example we study another price profile, which is from the same market but two days later (Figure 10). The volatility of the electricity price (EUR/MWh) is very high (min=-6.62, max=131) and at the end of the time horizon, we can see negative energy prices and very high-prices on the ancillary product P3 (M1P3). Also, compared to the earlier example with an average electricity price of 116 EUR/MWh, in the second example the average price is 45 EUR/MWh, which can be considered more typical.

When running exactly the same problem as earlier, only with the new market prices, the profit increases further by 67% to 696 kEUR. We can also see in Figure 11 that the production schedule is affected and the cheaper or even negative electricity prices at the end of the scheduling horizon are utilized activating the more energy-intensive EAF-1.

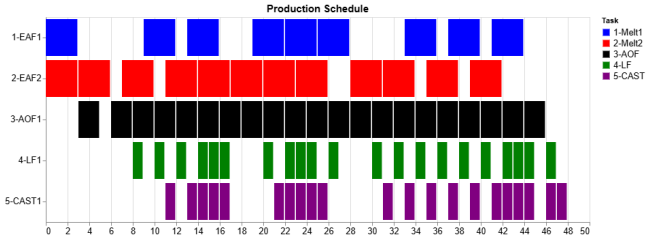


**Figure 11.** Production schedule of the second example

The trading volumes for this volatile example are shown in **Figure 12**, clearly illustrating that now the symmetric product P3 is used as well, especially towards the end of the schedule. We can further observe that the BESS level is slightly adjusted to maximize the trading profit. In general – maybe surprisingly – the ancillary service revenues are so high and do not involve any corrective actions after a true ancillary event that the optimization is keeping the BESS SoC mainly constant in order to leave sufficient headroom for both up/down directions. Thus, in most cases the energy trading is exactly 1:1 with the load at each point of time.

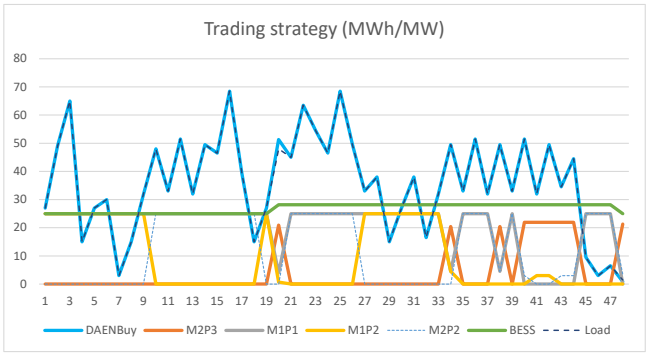


**Figure 12.** Trading volumes for the second example

## CONCLUSIONS

This paper has studied the option of enhancing the traditional demand-side management with BESS utilization and more complex trading schemes, including ancillary services. Both approaches show significant potential. The BESS helps decouple the load and energy purchases, thus reducing trading during the most expensive peak times. If ancillary services are included, the BESS is mainly dedicated to support the enabling of maximum ancillary service trading volumes in both directions. This supports the frequency regulations in various disturbances and ancillary events. The main benefit in the more elaborate trading schemes is that in the two examples ancillary service trading could generate revenues that may fully compensate for the energy costs, making the electricity practically “free”.

However, what we did not address in this short paper were the price uncertainties, which can be easily incorporated into the presented concept. Also, we assumed that all ancillary bids are accepted and did not discuss how an occurring ancillary event would affect the production line and whether e.g. intra-day trading could be used to compensate for these uncertain events. Also, an on-site BESS could also be used to balance possible process disturbances and avoid the resulting demand-peaks. Without having any ancillary events, the production process and energy trading remain practically almost fully decoupled, and one can question the motivation in investing in a BESS. Nevertheless, it is important that future energy-intensive industries also have the capability of, when needed, supporting the grid stability in order to avoid blackouts. As the study shows, this can in ideal situations even be a profitable feature.

## ACKNOWLEDGEMENTS

This paper is dedicated to Prof. Pedro Miguel Castro (1973-2024) acknowledging his remarkable contributions within the areas of planning, scheduling and optimization – some of which are reflected in this paper.

## REFERENCES

1. X. Tang, R. O’Neill, E. Hale, R. Baldick and M. Baldea, "Demand bidding vs. demand response for industrial electrical loads", Computers & Chemical Engineering, vol. 189 (2024) doi: 10.1016/j.compchemeng.2024.108768
2. L. Merkert, I. Harjunkoski, A. Isaksson, S. Säynevirta, A. Saarela, G. Sand, "Scheduling and energy – Industrial challenges and opportunities", Computers & Chemical Engineering, vol. 72, pp. 183-198 (2015), doi: 10.1016/j.compchemeng.2014.05.024
3. Zheng Wang, Chaojie Li, Xiaojun Zhou, Renyou Xie, Xiangyu Li, Zhaoyang Dong, "Stochastic bidding for VPPs enabled ancillary services: A case study", Applied Energy, vol. 352 (2023) doi: 10.1016/j.apenergy.2023.121918
4. N. Padmanabhan, M. Ahmed and K. Bhattacharya, "Battery Energy Storage Systems in Energy and Reserve Markets," in IEEE Transactions on Power Systems, vol. 35, no. 1, pp. 215-226 (2020) doi: 10.1109/TPWRS.2019.2936131
5. F. Hafiz, I. Harjunkoski, M. Eissa, E. Vallarino and S. Picerno, ”Automated Market Bidding for Battery Energy Storage Systems”, CIGRE Session 2024, Paris, France, August 25-30,2024
6. E. Kraft, M. Russo, D. Keles and V. Bertsch. "Stochastic optimization of trading strategies in sequential electricity markets", European Journal of Operational Research, 308 (1), pp. 400 - 421 (2023) doi: 10.1016/j.ejor.2022.10.040
7. C.C. Pantelides, “Unified frameworks for optimal process planning and scheduling”, Second Conf. on Foundations of Computer-Aided Operations, pp. 253-274 (1994)
8. P.M. Castro, I. Harjunkoski and I.E. Grossmann, "New continuous-time scheduling formulation for continuous plants under variable electricity cost", Industrial and Engineering Chemistry Research, 48 (14), pp. 6701-6714. (2009) doi: 10.1021/ie900073k
9. H.S. Lee, S.S. Murthy, S.W. Haider and D.V. Morse “Primary production scheduling at steelmaking industries”, IBM Journal of Research and Development, 40 (2), pp. 231–252. (1997) doi: 10.1147/rd.402.0231
10. I. Harjunkoski and I.E. Grossmann. ”A decomposition approach for the scheduling of a steel plant production”, Computers & Chemical Engineering, vol. 25, pp. 1647-1660 (2001) doi: 10.1016/S0098-1354(01)00729-3

© 2025 by the authors. Licensed to PSEcommunity.org and PSE Press. This is an open access article under the creative commons CC-BY-SA licensing terms. Credit must be given to creator and adaptations must be shared under the same terms. See https://creativecommons.org/licenses/by-sa/4.0/



Systems & Control Transactions

**Research Article - Peer Reviewed Conference Proceeding**
ESCAPE 35 - European Symposium on Computer Aided Process Engineering
Ghent, Belgium. 6-9 July 2025
Jan F.M. Van Impe, Grégoire Léonard, Satyajeet S. Bhonsale,
Monika E. Polańska, Filip Logist (Eds.)

PSE PRESS

# Nonmyopic Bayesian process optimization with a finite budget

**José L. Pitarch[a]*, Leopoldo Armesto[b], and Antonio Sala[a]**

[a] Universitat Politècnica de Valencia, Instituto de Automática e Informática Industrial (ai2), Valencia, Valencia, Spain
[b] Universitat Politècnica de Valencia, Instituto de Diseño y Fabricación (IDF), Valencia, Spain
* Corresponding Author: jlpitarch@isa.upv.es

## ABSTRACT

Optimization under uncertainty is inherent to many PSE applications ranging from process design to RTO. Reaching process true optima often involves learning from experimentation, but actual experiments involve a cost (economic, resources, time) and a budget limit usually exists. Finding the best trade-off on cumulative process performance and experimental cost over a finite budget is a Partially Observable Markov Decision Process (POMDP), known to be computationally intractable. This paper follows the nonmyopic Bayesian optimization (BO) approximation to POMDPs developed by the machine-learning community, that naturally enables the use of hybrid plant surrogate models formed by fundamental laws and Gaussian processes (GP). Although nonmyopic BO using GPs may look more tractable, evaluating multi-step decision trees to find the best first-stage candidate action to apply is still expensive with evolutionary or NLP optimizers. Hence, we propose modelling the value function of the first-stage decision also with a GP, whose data will correspond to virtual evaluations of second-stage decision trees build upon myopic rollouts. Thus, the nonmyopic initial decision can be efficiently optimized via BO and the virtually learned value function. Effectiveness of the approach is demonstrated in a wide benchmark with synthetically generated functions as well as to optimize small batch production with a chemical reactor.

**Keywords**: Optimization, Machine Learning, Batch Process, Algorithms, Design Under Uncertainty, POMDP

## INTRODUCTION

Process optimization in actual applications must deal with uncertainty in exogenous factors (such as weather predictions or market prices), partial and noisy measurements, as well as plant-model mismatch (either parametric or structural). There are widely used techniques to deal with each one of these factors in isolation: multi-stage stochastic optimization offers a good performance-robustness compromise in the case of exogenous and measurable parametric uncertainty [1]; Kalman-based filters and data reconciliation deal with partial and noisy measurements [2]; and extremum seeking [3], modifier adaptation [4], policy search [5], or Bayesian optimization (BO) [6], are typical approaches used to drive the operation point of a real process to its true steady-state optimum by acquiring experimental information. Focusing on the existence of plant-model mismatch and partial information available through measurements, the reader will note that none of the cited approaches include the cost of experimentation (either economic, resource consumption, or number of batches to produce) explicitly. In other words, their objective is just to reach the closest possible neighborhood of true optimum at any cost. But a limit on the experimental budget usually exists in practice. Moreover, with limited budgets one may be interested in finding the best trade-off between an accumulated exploration cost and exploitation performance.

The right way to formulate the problem of finding the best cumulative trade-off on process performance and experimental cost under uncertainty over a finite budget is a Partially-Observable Markov Decision Process (POMDP) whose states are uncertain process beliefs [7]. The general way to approach these problems is evaluating belief trees of candidate actions and plausible observations via dynamic programming, as Monte Carlo Tree Search (MCTS) algorithms do [8]. But their computational cost is prohibitive when the state and action

spaces are of continuous nature.

If such a belief is modeled by a Gaussian process (GP), the nonmyopic BO acquisition functions developed by the machine learning community are a more tractable way to approximate POMDPs. The key idea of nonmyopic BO is to look ahead several steps and compute the best candidate decisions based on an estimation on the cumulative expected value or improvement over the budget horizon [9]. Anyway, optimizing multi-step trees with GPs as states in one shot is also challenging, and rollout algorithms with default myopic BO acquisition functions are normally used to complete the value function estimation after the first lookahead step [10], which can lead to conservative results.

Following this path, recently we proposed a variant tailored for process experimental optimization [11], in which the decision in each action node of the tree is provided by a myopic BO acquisition function from a list of the most widely used in the literature. In this way, the algorithm can dynamically select the most promising acquisition function along the sequence of decisions to optimize the expected value over the decision horizon or budget. We also used Gauss-Hermite Quadrature [12] in each observation node as an efficient way to approximate the value function. Although the approach is much more tractable than other nonmyopic BO in the literature (note that no nested optimizations are involved), its expected optimality proven to be slightly lower due to limiting the first-stage decisions on myopic BO acquisition functions.

To remove such conservativeness, hence unlocking the extra performance that nonmyopic BO can provide in theory but at lower computational costs than the existing proposals in the literature, here we propose *learning the value function of the first-stage decision* also with a GP, whose data will correspond to virtual evaluations of our POMDP decision tree in [11] for the subsequent stages, instead of typical rollouts with expected value or improvement BO. In this way, the first-stage decision can be efficiently optimized via BO with the virtually learned value-function GP. In other words, we use *myopic BO to optimize the nonmyopic BO acquisition function*. Note that evaluating a POMDP decision tree via approximate dynamic programming (ADP) is an expensive function from the computational perspective, which fits into the main hypothesis of BO.

In the next section we briefly summarize the key methods involved in our proposal. Then, we present the nonmyopic BO-POMDP strategy and a basic pseudocode. The proposal is then evaluated in a synthetic benchmark of unconstrained optimization functions, where we also provide the results gathered when comparing to some state of the art nonmyopic and myopic BO. The paper closes with an illustrative application to the Otto-Williams reactor and some remarks.

# METHODS AND PROBLEM STATEMENT

## Hybrid models with Gaussian Processes

The hybrid plant models in this work are understood as a basis of fundamental laws that is then customized to a particular process with gathered experimental data. In this case, instead of incorporating deterministic machine learning sub-models obtained, for instance, with sum-of-squares polynomial regression [13], we employ probabilistic Gaussian Process regression to adjust first-principles predictions to the real data, getting confidence intervals around.

GPs are characterized by a mean function $\mu(x)$ and a covariance generator $\kappa(x_a, x_b) \coloneqq \mathrm{cov}\big(f(x_a) - f(x_b)\big)$, being $f(x)$ the true function whose knowledge is partially unknown. A $GP\{X, Y\}$ is built from input-output data

$$X \coloneqq [x_0, x_1, x_2, \dots, x_n]; \quad Y \coloneqq [y(x_0), y(x_1), \dots, y(x_n)];$$

where measurements are assumed to be $y(x) = f(x) + w$, $w \approx \mathcal{N}(0, \lambda^2)$, being $\lambda$ the noise standard deviation. The a priori mean $\mu(x) \coloneqq 0$ if pure experimental optimization is to be pursued [11], or set to a first-principles model.

Every time new data is gathered, the GP mean and covariance kernel are updated by [14]:

$$\mu(x) = \mu(x) + \kappa(x, X)(\kappa(X, X) + \lambda^2 I)^{-1}\big(Y - \mu(X)\big) \tag{1}$$

$$\kappa(x_a, x_b) = \kappa(x_a, x_b) - \kappa(x_a, X) \cdot (\kappa(X, X) + \lambda^2 I)^{-1} \kappa(x_b, X)^T \tag{2}$$

Moreover, GPs can themselves contain parametric components with adjustable parameters $\theta$, such that $\phi(x)\theta$ is the deterministic prediction by these components. In such a case, the GP covariance kernel becomes

$$\bar{\kappa}(x_a, x_b) \coloneqq \kappa(x_a, x_b) + \phi(x_a)\Sigma_\theta \phi(x_b)^T \tag{3}$$

where $\Sigma_\theta$ is the a priori parameter covariance matrix.

## Myopic Bayesian optimization

The goal of BO is to reach the optimum of a static mapping $f(x)$. In particular, BO proposes the next experiment to actually test by means of optimizing an acquisition function $F(\mathrm{GP}, x)$ with a surrogate model (cheaper to evaluate than $f(x)$), usually a GP built from process data.

The acquisition function $F(\mathrm{GP}, x)$ is the cornerstone of the method, because it defines a certain tradeoff between exploitation of the already acquired knowledge and exploration to improve such a knowledge. There are several well-known heuristics in the BO literature that perform really well and are cheap to optimize [15]: Expected Value; Probability of Improvement; Expected Improvement; Lower-Upper Confidence Bound.

Given a GP, the basic BO algorithm is a one-step optimization and subsequent GP update, as follows:

$$x = \arg\min_{x \in \mathbb{X}} F(\mathrm{GP}, x) \text{ or } x = \arg\max_{x \in \mathbb{X}} F(\mathrm{GP}, x) \tag{4}$$

$$GP \leftarrow GP \oplus \{x, y(x)\} = \{X \cup x, Y \cup y(x)\} \quad (5)$$

This process repeats until some criteria is met, for instance, no improvement observed, number of experiments, o time exhausted. Of course, constraints $g(x) < 0$ can be also realized in BO in straightforward ways [11].

However, the exploitation-exploration tradeoff that these standard functions define is just a myopic heuristic that does not account for the potential gains of optimizing at several steps. There are improved heuristics that look two steps ahead, such as Knowledge Gradient or Predictive Entropy Search [16]. These usually show better performance than the classic ones, but at much higher computational cost. Anyway, none of these considers problem-specific cumulative costs and budgets.

## Multi-stage scenario optimization

Multi-stage scenario optimization (MSSO) [1] is often the approach to approximate complex Markov decision processes. It combines decision optimization with simulation steps on potential scenarios that may realize (sampling from a probability distribution) within a planning horizon. Basically, MSSO builds a tree of sample paths of depth $N$ through possible states and observations. This is the forward-in-time propagation step. Then, state-value functions can be estimated by backward propagation, providing the best decision for each stage.

If such a decision tree is iteratively built, *value functions can be learned* through the evaluations, which might allow generalization across states, i.e., the already visited states or evaluated decisions might tell us something about the value of the ones not visited yet [17].

In this paper we recall the Gauss-Hermite quadrature (GHQ) method [18] to approximate integrals as an efficient way to build sample-paths trees and to estimate state-value functions in POMDPs.

## Problem statement

Assume that a statistical belief of the actual $f(x)$ and $g(x)$ given by GPs is available, constructed from a prior inaccurate model and a set of past data $X_0$,$Y_0$ (e.g. the optimum of the first-principles model tested in the actual plant). Then, there is a finite budget of $N$ experiments or production batches to realize, so that the task is deciding which will be the most promising sequence of decisions $x$ to perform such that they are optimal in some sense related to a POMDP. After each decision $x_k$ ($k = 1, \dots, N-1$) is taken, a process observation $y_k$ will be available, so that an immediate reward or cost $r([X_{k-1}, x_k], [Y_{k-1}, y_k])$ is computed. Compact notation $r(X_k, Y_k)$ is used from now on when the order of the samples does not matter. A terminal cost $J_N(X_N, Y_N)$ will be attained as a result of the last decision $x_N$. Then, the goal is to optimize the expected overall cumulative cost (being $\gamma > 0$ a discount factor)

$$J \coloneqq \mathbb{E}\{\gamma^N J_N(X_N, Y_{f,N}) + \sum_{k=1}^{N-1} \gamma^k r(X_k, Y_{f,k})\} \quad (6)$$

over a set of $N$ future observations of $f(x)$ denoted by $Y_{f,N} \coloneqq \{y_f(x_1), \dots, y_f(x_N)\}$, such that the observations of process constraints $Y_{g,N} \coloneqq \{y_g(x_1), \dots, y_g(x_N)\} < 0$ hold with desired probability threshold, e.g., $2\sigma$ confidence.

## NONMYOPIC OPTIMIZATION STRATEGY

Our proposal of nonmyopic acquisition function approximates the value function of the first-stage decision set $x_0$ by ADP, building scenario trees that branch with some easy-to-compute acquisition functions from myopic BO at the decision nodes and with GHQ points at the observation ones [11]. Evaluating this tree backwards for each first-stage candidate $\tilde{x}_i$ provides the corresponding value-function estimate $\hat{V}_i$, data that serves to fit a GP model of the first-stage value function. The proposed exploration strategy is illustrated in Figure 1 on next page, where the root node has a fixed current belief on the process to be optimized after incorporating previous actual observations, and a value-function belief that is learned dynamically with each subsequent tree evaluation.

Hence, the idea is to progressively improve such a value function model $GP_V\{\tilde{x}, \hat{V}\}$ while performing myopic BO on it to propose new candidates $\tilde{x}_i$. When this learning-optimization process converges (e.g. reaching an input-deviation tolerance or maximum iteration number), the best candidate decision found is tested in the real process and everything repeats for the remaining budget horizon. Algorithm 1 summarizes de proposed procedure.

**Algorithm 1:** Nonmyopic BO acquisition function.

**Global:** $X_0, Y_0, N, H_r, V_0$, optol %Initial data
**1: Create** $GP_c\{X_0, Y_0\}$ %Build root cost GP
**2: For** $k \coloneqq 1$ **to** $N$ **do:**
**3:** **If** $k = 1$ **then** $\tilde{x} \leftarrow X_0$**; otherwise** $\tilde{x} \leftarrow \arg\min_{x \in \mathbb{X}} F(GP_V, x)$ %Value-function BO
**4:** $b = \text{NodeV}(GP_c)$ %Create the root node
**5:** $\bar{H} \leftarrow N - k$ %Reduce prediction horizon
**6:** $b.\text{Expand}(\tilde{x})$ %Branch second-stage tree
**7:** $\hat{V} \leftarrow b.\text{ValueFunction}()$ %Estimate V($\tilde{x}$)
**8:** $GP_V \leftarrow GP_V \oplus \{\tilde{x}, \hat{V}\}$ %Update GP of V(x)
**9:** **If** $|V_0 - \hat{V}| >$ optol **then** $V_0 \leftarrow \min_{\hat{\mathbb{V}}} GP_V$**; Goto 3**
**10: Realize** $x \leftarrow \arg\min_{\tilde{\mathbb{x}}} \min_{\hat{\mathbb{V}}} GP_V$ %Actual experiment
**11: Get** $y_f \leftarrow f(x) + w$ %New observation
**12:** $GP_c \leftarrow GP_c \oplus \{x, y_f\}$; %Update GP of r(X,Y)

Where, abusing notation, $\min_{\hat{\mathbb{V}}} GP_V$ finds the lowest value $[V^*, i_d] = \min GP_V.\hat{\mathbb{V}}$ already in the GP dataset, and $\arg\min_{\tilde{\mathbb{x}}} \min_{\hat{\mathbb{V}}} GP_V$ stands for the $x$-coordinate in the GP data corresponding to such a $V^*$, i.e., $x^* = GP_V.\tilde{\mathbb{x}}[i_d]$.

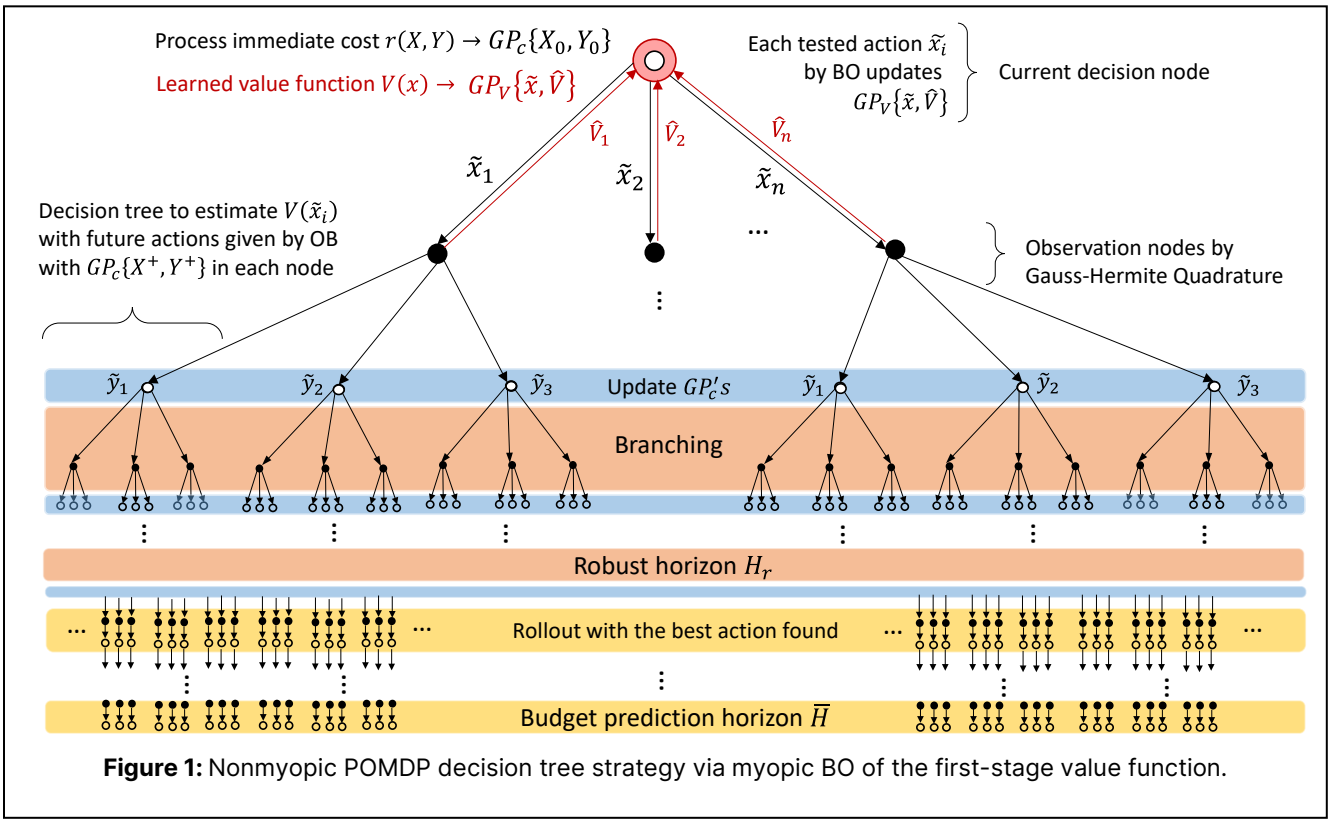



**Figure 1:** Nonmyopic POMDP decision tree strategy via myopic BO of the first-stage value function.

Note that Algorithm 1 here presented is a simple version that does not include process constraints for the sake of clarity, but considering them is straightforward. See our previous work [11] (and references therein) for ideas to deal with constraints in BO-POMDP as well as details and pseudocode on the exploration-decision tree. Moreover, Algorithm 1 assumes a very basic myopic BO in statements 3 and 9, but there is no inconvenience in calling sophisticated software BO packages instead. In fact, Bayesian adaptive direct search (BADS) [19] turned to be a good implementation to realize this higher first-stage BO without worrying on hyperparameter tuning and right covariance-kernel choice for the value-function GP.

## Performance evaluation

To evaluate the proposed nonmyopic optimization strategy, we tested it to optimize the cumulative cost (6) on 100 functions $f(x)$ of two decision variables (normalized to the squared range [-1,1]) and zero mean, synthetically generated from the exponential covariance kernel

$$\kappa(x_a, x_b) = \Sigma \cdot e^{-\frac{\|x_b - x_a\|^2}{2 \cdot \sigma^2}}, \qquad (7)$$

with $\sigma = 0.25$, $\Sigma = 1$, and considering a measurement noise level $\lambda = 0.002$. The problem budget is $N = 10$. Algorithm 1 as well as the proposals of [10] and [11] are both set to branch up to a horizon $H_r = 2$, and the discount factor is set to no discount ($\gamma = 1$).

The average performance got by Algorithm 1, references [10] and [11], as well as myopic BO with typical acquisition functions of negligible computation time (expected improvement, probability of improvement, and expected value) are presented in Table 1 below.

**Table 1:** Average regrets with respect to the best achievable performance (always knowing the true optimum).

| **Method**: | **[10]** | **Alg 1** | **[11]** | **PI** | **EV** | **EI** |
|---|---|---|---|---|---|---|
| **Regret:** | 7.92 | 7.77 | 8.28 | 9.93 | 9.73 | 11.47 |
| **CPU (s):** | 22.3 | 13 | 0.68 | - | - | - |

Algorithm 1 is the one that got lower average regret in the benchmark, followed by our implementation of [10] consisting in a multi-start strategy of a regular grid on the first-stage input space that provides the initial guess to an interior-point NLP optimizer. Furthermore, the average computation load of the proposed Algorithm 1 is about half of the required by [10], as expected because BO is an efficient approach to optimize expensive-to-evaluate functions. Note also that our reduced first-stage exploration strategy [11], although gets a slightly higher regret, it does the work at much lower computation time. Moreover, it outperforms by 15% the best myopic BO tested, and by 30% the usually used expected improvement acquisition function. The evaluation was run in a standard laptop equipped with an Intel Core i7-4510U CPU.

## SMALL-BATCH PRODUCTION EXAMPLE

Next, Algorithm 1 is tested in a simulated chemical batch production process with the Otto-Williams stirred tank reactor. There are two reactants, A and B, whose stream $F_A$ is not controlled but known and $F_B$ is decision variable. The reactor temperature $T_R$ can be set so it is also decision variable. These two define the quality of the product at the reactor outlet once the three chemical reactions are completed. In total, six compounds (or species) exist inside the reactor: 4 products (C, E, G, and P) and the reactants A and B. The equations of the chemical dynamic model and associated parameters are omitted for brevity. See [20] and references therein.

As the mass fraction of the product C is one order of magnitude below the rest of the compounds, a usual gross representation of the process is to consider only the other five species, with the corresponding structural and parametric plant-model mismatch. Then, only two parallel reactions inside the reactor are considered:

$$A + 2B \xrightarrow{r_1} P + E; \quad A + B + P \xrightarrow{r_2} G + E$$

The mass-fraction equations in steady state to act as prior mean $\mu(F_B, T_R)$ for the process belief are:

$$\begin{aligned}
\frac{dX_A}{dt} &\coloneqq \mathrm{F_A} - (\mathrm{F_A} + F_B)\, X_A - (r_1 + r_2)\, \mathrm{V_R} = 0 \\
\frac{dX_B}{dt} &\coloneqq F_B - (\mathrm{F_A} + F_B)\, X_B - (2\, r_1 + r_2)\, \mathrm{V_R} = 0 \\
\frac{dX_E}{dt} &\coloneqq -(\mathrm{F_A} + F_B)\, X_E + 2\, r_1 \mathrm{V_R} = 0 \\
\frac{dX_G}{dt} &\coloneqq -(\mathrm{F_A} + F_B)\, X_G + 3\, r_2 \mathrm{V_R} = 0 \\
\frac{dX_P}{dt} &\coloneqq -(\mathrm{F_A} + F_B)\, X_E + (r_1 - r_2)\, \mathrm{V_R} = 0
\end{aligned} \tag{8}$$

where $\mathrm{F_A} = 1.8275$, $\mathrm{V_R} = 2105$, and the reaction rates:

$$r_1 \coloneqq 1.65 \cdot 10^8\, e^{-\frac{8097}{273+T_R}}\, X_A\, X_B^2$$

$$r_2 \coloneqq 2.61 \cdot 10^{13}\, e^{-\frac{12398}{273+T_R}}\, X_A\, X_B\, X_P$$

The optimization is to sequentially decide the production setpoints $x \coloneqq [F_B, T_R]$ that get the highest cumulative economic benefit at the end of producing $N = 7$ batches of the products P and E with the actual reactor:

$$\max_{F_B, T_R} J \coloneqq \textstyle\sum_{k=1}^{10} \big(X_{P,k}\, \mathrm{P_P} + X_{E,k}\, \mathrm{P_E}\big)\big(\mathrm{F_A} + F_{B,k}\big) - \mathrm{F_A C_A} - F_{B,k} \mathrm{C_B}$$

$$\text{s.t.: } X_{G,k} < 9.5\%; \;\; 3 \le F_{B,k} \le 6\mathrm{kg/s}; \;\; 70 \le T_{R,k} \le 100°\mathrm{C} \tag{9}$$

where $\mathrm{P_p} = 1143.38$ and $\mathrm{P_E} = 25.92$ are product selling prices, $\mathrm{C_A} = 76.23$ and $\mathrm{C_B} = 114.34$ are reactant costs.

The simple non-parametric exponential kernel with $\Sigma_{\kappa_f} = 25$ and $\sigma_f = \sqrt{0.2}$ is chosen to build the GP belief for the immediate economic benefit plant-model mismatch:

$$\kappa_f(x_a, x_b) \coloneqq \Sigma_{\kappa_f}\, e^{-\frac{\|x_b - x_a\|^2}{2 \cdot \sigma_f^2}} \tag{10}$$

Inputs are normalized to $x \in [-1,1]$ to easily interpret the length scale $\sigma_f$. Same kernel class is set up for $\kappa_g(x_a, x_b)$ to model the limit on $X_G$, but with $\sigma_g = \sqrt{0.2}$ and $\Sigma_{\kappa_g} = 0.5$. These values are chosen by mere intuition in accordance with model (8), and no GP-hyperparameter tuning is then performed from run to run with the reactor due to the small batch assumption.

The given measurement noise is $\lambda_f = 0.5$ for the immediate benefit and $\lambda_g = 0.1$ for the constraint on $X_G$.

Algorithm 1 has been set up with $H_r = 3$, optol equal to BADS default tolerance. The first batch is run at $x_0 = [4.62\mathrm{kg\,s^{-1}}, 81.9°\mathrm{C}]$, which is the mean model (8) optimum without violating constraints, whose predicted immediate economic benefit is 157€. However, the actual benefit (noise free) at such a $x_0$ is 176.17€. Note that model (8) is pessimistic so, under non-negligible measurement noise, greedy BO algorithms are not able to see any potential benefit in testing nearby $x_0$ instead of remaining on it.

The actual-reactor optimum batch satisfying constraints provides 188.92€ at $x^* = [4.89\mathrm{kg\,s^{-1}}, 87.64°\mathrm{C}]$, but the goal is not to reach it at any cumulative cost (9).

Table 2 below shows the performance obtained by Algorithm 1 to produce the 7 batches. Myopic BO has been also applied with four widely used acquisition functions: expected improvement, probability of improvement, upper confidence bound, and expected value.

**Table 2:** Regrets with respect to the best achievable performance (computed noise free with the "actual" reactor).

| **Method:** | **Alg 1** | **EI** | **PI** | **UCB** | **EV** |
|---|---|---|---|---|---|
| **Regret (€):** | 44.37 | 56.64 | 74.7 | 48.38 | 76.45 |

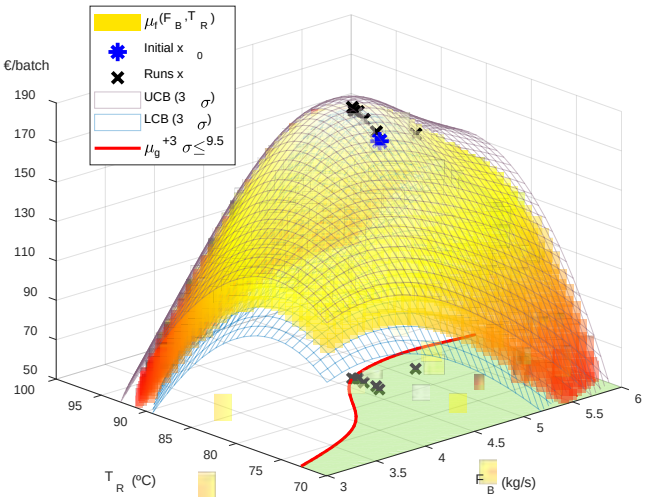



**Figure 2.** Reactor knowledge after producing 7 batches.

For completeness, Figure 2 shows the sequence of batches decided by Algorithm 1 and the final a posteriori belief on the process (mean model (8) plus the GPs fitted to the measured data).

## CONCLUDING REMARKS

This paper proves the advantages of non-myopic BO in process optimization problems of POMDP nature. In contrast to other computationally intensive strategies, we proposed a non-myopic acquisition function that uses efficient myopic BO to evaluate rollout POMDP trees.

In the test with the chemical reactor, our proposal performs better than standard BO, as expected. However, a single run with a particular reactor is not statistically conclusive. Anyway, this "one-chance run" is often the situation in multiproduct industrial plants.

The main performance limitation in practice comes from the ability of the probabilistic belief to represent the actual plant-model mismatch.

## ACKNOWLEDGEMENTS

This work is part of Grants PID2023-146747NB-C21 (SIECMA) and PID2020-116585GB-I00 (LOCPU) funded by MICIU/AEI/10.13039/501100011033 and by ERDF/EU.

## REFERENCES

1. Li C, Grossmann IE. A review of stochastic programming methods for optimization of process systems under uncertainty. *Front. Chem. Eng.* 2:622241 (2021) https://doi.org/10.3389/fceng.2020.622241
2. Bai S, Thibault J, McLean DD. Dynamic data reconciliation: Alternative to Kalman filter. *J. Proc. Cont.*, 16(5):485-498 (2006) https://doi.org/10.1016/j.jprocont.2005.08.002
3. Ariyur KB, Krstic M. Real-time optimization by extremum-seeking control. Wiley & Sons (2003)
4. Bottari A. Real-time optimization modifier adaptation approach using quadratic approximation of the plant-model mismatch function. *J. Proc. Cont.* 136:103180 (2024) https://doi.org/10.1016/j.jprocont.2024.103180
5. Deisenroth MP, Neumann G, Peters J. A survey on policy search for robotics. *Found. & Trends in Rob.* 2(1–2):1-142 (2013) http://dx.doi.org/10.1561/2300000021
6. del Rio Chanona EA, Petsagkourakis P, Bradford E, Graciano JA, Chachuat B. Real-time optimization meets Bayesian optimization and derivative-free optimization: A tale of modifier adaptation. *Comp. & Chem. Eng.* 147:107249. https://doi.org/10.1016/j.compchemeng.2021.107249
7. Smallwood R, Sondik E. The optimal control of partially observable Markov decision processes over a finite horizon. *Oper. Res.* 21:1071–1088 (1973) https://doi.org/10.1287/opre.21.5.1071
8. Świechowski M, Godlewski K, Sawicki B, Mańdziuk J. Monte Carlo tree search: A review of recent modifications and applications. *Artif. Intell. Rev.* 56(3):2497-2562 (2023) https://doi.org/10.1007/s10462-022-10228-y
9. Jiang S, Jiang D, Balandat M, Karrer B, Gardner J, Garnett R. Efficient nonmyopic Bayesian optimization via one-shot multi-step trees. *Adv. Neur. Inform. Proc. Sys.* 33:18039-18049 (2020) https://doi.org/10.48550/arXiv.2006.15779
10. Lam R, Willcox K. Lookahead Bayesian optimization with inequality constraints. *Adv. Neur. Inform. Proc. Sys.* 30:1888 - 1898 (2017)
11. Pitarch JL, Armesto L, Sala A. POMDP non-myopic Bayesian optimization for processes with operation constraints and a finite budget. *Rev. Iber. Autom. Inform. Ind.* 21(4):328-338 (2024) https://doi.org/10.4995/riai.2024.21142
12. Stroud AH, Secrest D. Gaussian Quadrature Formulas. Prentice Hall (1966)
13. Pitarch JL, Sala A, de Prada C. A systematic grey-box modeling methodology via data reconciliation and SOS constrained regression. *Processes* 7(3):170 (2019) https://doi.org/10.3390/pr7030170
14. Rasmussen CE, Williams CK. Gaussian processes for machine learning. Cambridge, MIT press (2006) https://doi.org/10.7551/mitpress/3206.001.0001
15. Frazier PI. Bayesian optimization. *Informs* 255-278 (2018) https://doi.org/10.1287/educ.2018.0188
16. Hernández-Lobato JM, Hoffman MW, Ghahramani Z. Predictive entropy search for efficient global optimization of black-box functions. *Adv. Neur. Inf. Proc. Sys.* 27:918-926 (2014) https://doi.org/10.48550/arXiv.1406.2541
17. Mern J, Yildiz A, Sunberg Z, Mukerji T, Kochenderfer MJ. Bayesian optimized monte carlo planning. *AAAI Conf. Artific. Intell.* 35(13):11880-11887 (2021) https://doi.org/10.1609/aaai.v35i13.17411
18. Abramowitz M, Stegun IA. Handbook of mathematical functions, [Equation 25.4.46], Dover Publications (1972), ISBN: 978-0-486-61272-0.
19. Acerbi L, Ma WJ. Practical Bayesian optimization for model fitting with Bayesian adaptive direct search. *Adv. Neur. Inf. Proc. Sys.* 30:1834-1844 (2017) https://doi.org/10.48550/arXiv.1705.04405
20. Rodríguez-Blanco T. Modifier Adaptation for process optimization with uncertainty. PhD Thesis, Universidad de Valladolid (2017). http://uvadoc.uva.es/handle/10324/28631

© 2025 by the authors. Licensed to PSEcommunity.org and PSE Press. This is an open access article under the creative commons CC-BY-SA licensing terms. Credit must be given to creator and adaptations must be shared under the same terms. See https://creativecommons.org/licenses/by-sa/4.0/



Systems & Control Transactions

**Research Article - Peer Reviewed Conference Proceeding**
ESCAPE 35 - European Symposium on Computer Aided Process Engineering
Ghent, Belgium. 6-9 July 2025
Jan F.M. Van Impe, Grégoire Léonard, Satyajeet S. Bhonsale,
Monika E. Polańska, Filip Logist (Eds.)

PSE PRESS

# Life-Cycle Assessment of Chemical Sugar Synthesis Based on Process Design for Biomanufacturing

**Hiro Tabata[a,b], Satoshi Ohara[c,d], Yuichiro Kanematsu[a], Heng Yi Teah[a], and Yasunori Kikuchi[a,d,e]***

[a] The University of Tokyo, Presidential Endowed Chair for "Platinum Society", Bunkyo-ku, Tokyo, Japan
[b] Osaka University, Graduate School of Engineering Science, Research Center for Solar Energy Chemistry, Toyonaka, Osaka, Japan
[c] The University of Tokyo, Research Center for Advanced Science and Technology, LCA Center for Future Strategy, Meguro-ku, Tokyo, Japan
[d] The University of Tokyo, Department of Chemical System Engineering, Bunkyo-ku, Tokyo, Japan
[e] The University of Tokyo, Institute for Future Initiatives, Bunkyo-ku, Tokyo, Japan
* Corresponding Author: ykikuchi@ifi.u-tokyo.ac.jp.

## ABSTRACT

The growing demand for sustainable alternatives to petroleum-based products drives the development of biomanufacturing using agriculture-based sugars. However, agricultural sugar production faces significant challenges due to limited production capacity and potential negative environmental impacts. This research examines chemical sugar synthesis as an alternative, assessing its environmental impact with conventional agricultural production methods through life cycle assessment. As formaldehyde serves as a primary substrate in chemical synthesis, four production cases were evaluated—comprising two pathways (conventional methods and $CO_2$ capture and utilization (CCU) technologies), each implemented with either fossil fuels or renewable energy sources. The analysis revealed that semi-batch reactors in chemical synthesis substantially reduce environmental impacts compared to batch reactors. Chemical sugar synthesis demonstrated marked advantages in reducing eutrophication, land use change, and water resources consumption across all formaldehyde production methods evaluated. However, the formaldehyde production process was identified as the determining factor in the overall environmental profile. While chemical synthesis offers environmental advantages in several categories, implementing CCU technologies with renewable energy integration remains necessary to reduce climate change impacts and resource consumption. This work demonstrates the potential of optimized chemical sugar synthesis as an alternative to agricultural sugar production and provides direction for future process development.

**Keywords**: Sugar Synthesis, LCA, $CO_2$ Utilization, Renewable Energy, Batch Process, Catalysis, Environment, Fermentation, Matlab, Modelling and Simulations, Process Design

## INTRODUCTION

### Sugar supply in biomanufacturing

The transition away from dependence on fossil fuels is a critical challenge faced by the global community, and the shift toward the production of materials and energy using biomass as a raw material is accelerating. Currently, the most commonly used sources of reducing power and carbon for the bio-based production of valuable substances are sugars (agriculture-based sugars) obtained from crops such as sugarcane and corn. Bioproduction processes utilizing these sugars have been shown to reduce greenhouse gas emissions compared to fossil fuel-based processes [1]. However, the production volume of agriculture-based sugars is insufficient to meet the massive demand for fuels and chemicals, and excessive industrial use of such sugars risks competing with food supply demands [2]. Additionally, concerns have been raised regarding potential decreases in crop yields due to climate change and supply instability arising from geopolitical risks.

### Sugar synthesis and its life-cycle assessment

Against this background, research has been

conducted to synthesize these sugars through catalytic processes that do not rely on agriculture [3]. The chemical synthesis of sugars is achieved by integrating the production of formaldehyde via $CO_2$ reduction with sugar synthesis reactions using formaldehyde as a raw material (Figure 1). Compared to photosynthesis processes that agriculture-based sugars depend on, this method is significantly faster, allows for production near consumption sites, and drastically reduces the consumption of resources such as land and water [4]. As a result, it is expected to address the challenges of raw material supply in bio-production. On the other hand, this method requires more energy compared to conventional agricultural processes, posing challenges in terms of electricity procurement and economic feasibility. Nonetheless, bio-production technologies are essential for the transition to a circular economy, and systems capable of supplying raw materials in large quantities and with stability are equally necessary. Therefore, it is crucial to provide quantitative and objective insights into the changes brought about by the introduction of such technologies, including energy requirements and environmental impacts.

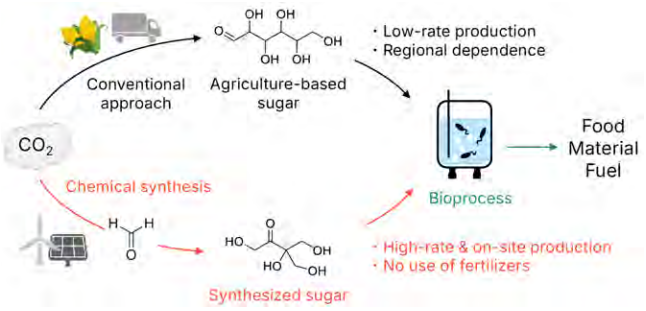



**Figure 1.** A scheme of biomanufacturing using chemically synthesized sugars as the substrates.

In this study, to determine whether the challenges of raw material supply in biomanufacturing can be addressed through the chemical synthesis of sugars, the energy requirements and environmental impacts of each process were evaluated using life-cycle assessment (LCA).

# MATERIALS & METHOD

## Numerical simulation

The time-dependent concentration changes of reactants and products in the chemical reaction were modeled using a set of coupled ordinary differential equations (ODEs). These equations were derived from the reaction rate laws, assuming homogeneous reaction conditions. The system of ODEs was solved numerically using MATLAB (version R2024b, MathWorks, Natick, MA, USA). The ode45 solver, based on an adaptive Runge-Kutta (4,5) method, was employed. The reaction rate constants were taken from the literature [5].

## Life-cycle assessment

### Goal and Scope Definition

The primary goal of this study is to evaluate the environmental impacts associated with the chemical synthesis of sugar using a simulation-based yield of the reaction. The assessment was conducted following the ISO 14040 and ISO 14044 standards. The functional unit was defined as 1 kg of synthesized sugar, and the system boundary encompassed a "cradle-to-gate" approach, including raw material extraction and chemical synthesis.

### System Boundaries

The LCA model encompassed four primary stages: raw material acquisition, chemical reaction (modeled using MATLAB to calculate sugar yield), catalyst removal, and product concentration. For the procurement of formaldehyde as a feedstock for chemical synthesis, two methods of production were considered: conventional production from fossil fuels based on the IDEA database, and production via $CO_2$ capture and utilization (CCU) technologies [6]. As the synthesized sugar product is intended to be used directly as a substrate for bioprocesses following concentration of the product [7], no further purification of the sugar product was considered. Infrastructure development, maintenance, and the transportation of raw materials and final products were excluded from the system boundary, as their contributions were deemed negligible for this study.

### Environmental impact assessment

The life-cycle inventory was calculated using data obtained from the following sources: Material and energy balances were calculated based on stoichiometric equations and simulation results from the material balance and energy consumption for the reaction. Background data such as energy production and chemical manufacturing were sourced from the IDEA ver. 3.4.1 database.

Environmental impacts were assessed using life-cycle impact assessment (LCIA) methods. Global warming potential was evaluated using climate change factors from IPCC 2021 GWP 100a with LULUCF (Land Use, Land-Use Change and Forestry). The other environmental impacts, including eutrophication, land use (transformation), resource consumption, and water resources consumption were assessed using the LIME2 (Life-cycle Impact assessment Method based on Endpoint modeling 2) methodology.

# RESULTS & DISCUSSION

## Kinetic simulation of the formose reaction

The kinetic simulation of the formose reaction were

performed using the mathematical model proposed by Socha et al. (1981) [5], which consists of a system of differential equations describing the concentration changes of formaldehyde and carbohydrates (C2-C7) over time. The model incorporates five key reactions: (1) aldol condensation of formaldehyde with sugars, (2) aldol condensation between sugars, (3) retro-aldol reaction of sugars, (4) Cannizzaro reaction, and (5) saccharinic acid formation.

The simulation was performed using MATLAB to solve the coupled differential equations numerically. The results demonstrated that the total yield of sugars (C2-C7) reached 65.2% under the given reaction conditions (40°C, 200 minutes, initial formaldehyde concentration of 4.5% (w/w)) (Figure 2). This value represents the combined yields of various carbohydrates formed through the complex reaction network. The obtained sugar yield was subsequently used as a basis for mass balance calculations in the sugar synthesis process design.

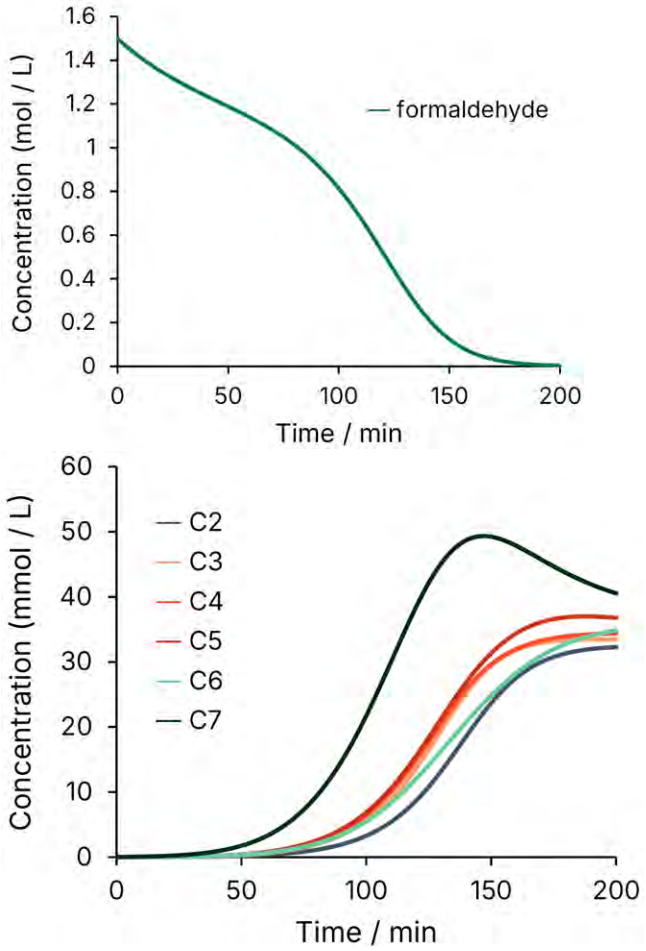



**Figure 2.** Simulation results showing the concentration changes of formaldehyde and each sugar species (C2-C7) during the formose reaction.

## Environmental impact assessment of sugar synthesis

Mass and energy balances were calculated for each process step in the chemical synthesis of sugars, including the thermal reaction, catalyst removal, and the evaporative heating for removal of residual substrate and water solvent. The theoretical energy requirements for heating and evaporation processes were determined using thermodynamic properties. To account for real process conditions, an energy efficiency factor of 70% was applied to calculate the actual energy requirements for each unit operation.

Figure 3 shows the environmental impacts of the sugar synthesis process when using a batch reactor for the formose reaction. The results were categorized into five impact categories: climate change, eutrophication, land use (transformation), resource consumption, and water resources consumption. The impacts were presented as relative contributions (%) of each input: formaldehyde (37% aqueous solution), water, calcium hydroxide, sulfuric acid, and heat energy. As shown in Figure 3, the impact of heat energy was significant in the categories of climate change, land use (transformation), and water resources consumption. The contribution of heat energy was particularly large in these categories, accounting for more than 50% of each impact. In the category of eutrophication, the impact of formaldehyde was dominant, accounting for more than 50% of the total impact. For resource consumption, both formaldehyde and heat energy showed significant contributions.

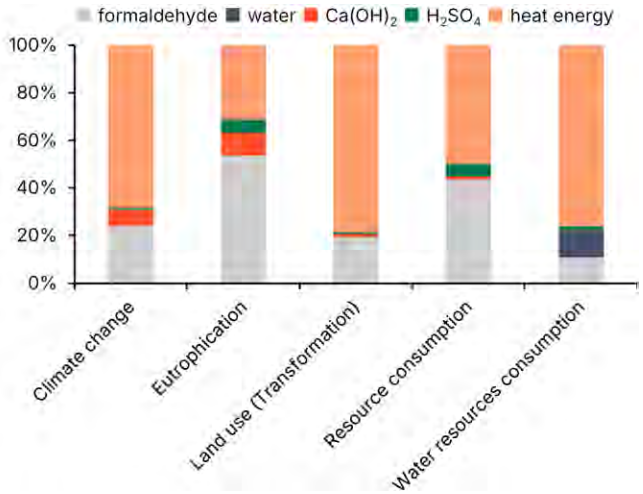



**Figure 3.** Contribution of each input to the environmental impacts (climate change, eutrophication, land use (transformation), resource consumption, and water resources consumption) in the sugar synthesis process using a batch reactor.

Importantly, the formose reaction possesses an autocatalytic reaction cycle [8], allowing for continuous

sugar synthesis by continuously adding formaldehyde during the reaction, that is, by adopting a semi-batch reactor. Therefore, the impact on climate change by adopting a semi-batch reactor was evaluated (Figure 4). The vertical axis shows the GHG emissions per 1 kg sugar produced, and the horizontal axis shows the product concentration. It was revealed that by increasing the product concentration through continuous addition of the substrate, the amount of calcium hydroxide used as a catalyst and the energy required for the concentration process can be significantly reduced. For example, increasing the product concentration to 20% (w/w) can reduce GHG emissions by more than 60% compared to the use of a batch reactor where the product concentration was 4.5%. This reduction is mainly attributed to the decreased energy needed for evaporating water in the concentration process due to the higher sugar concentration, as well as the reduced amount of calcium hydroxide used per unit of sugar produced. These findings demonstrate the effectiveness of the semi-batch reactor in improving energy efficiency and reducing the environmental impact of sugar synthesis.

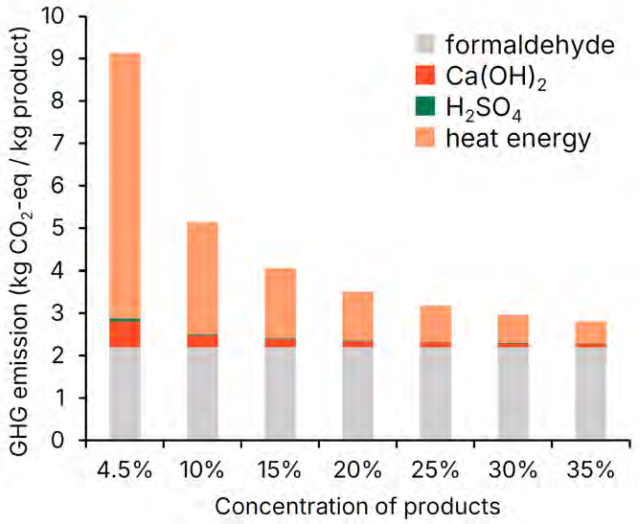



**Figure 4.** Changes in GHG emissions (kg $CO_2$-eq) per input with increasing product concentration when using a semi-batch reactor.

Figure 5 shows the contribution of each impact category when a semi-batch reactor is adopted, and the product concentration is increased to 20% (w/w). As the contribution of heat energy decreased, the contribution of formaldehyde became dominant in each environmental impact. This highlights the significant influence of the formaldehyde production process on the overall environmental performance of sugar synthesis. These findings suggest that improving the manufacturing process of the substrate, formaldehyde, is a crucial factor in reducing the environmental impact of chemical sugar synthesis.

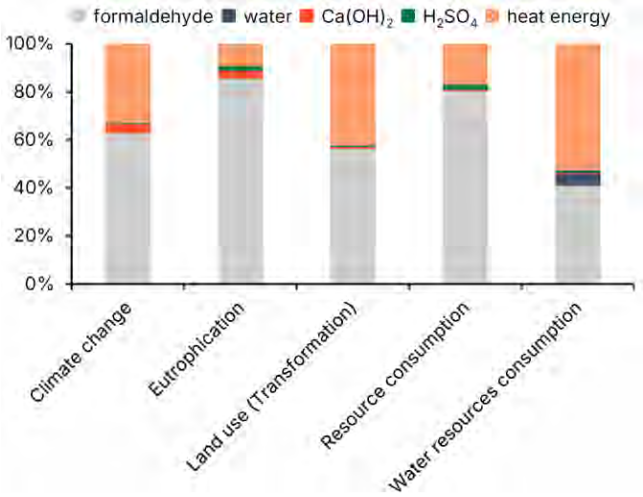



**Figure 5.** Contribution of each input to the environmental impacts (climate change, eutrophication, land use (transformation), resource consumption, and water resources consumption) in the sugar synthesis process using a semi-batch reactor with a product concentration of 20%.

## Changes in environmental impact due to the adoption of $CO_2$ conversion technology

Building upon the previous findings highlighting the significant contribution of formaldehyde to the environmental impact, the environmental impact of formaldehyde production using $CO_2$ as a raw material was evaluated. The assessment employed inventory data from existing literature for the CAMERE process to model $CO_2$ utilization [6]. Figure 6 illustrates a comparison of GHG emissions across different cases. Cases A and B represent conventional formaldehyde production methods. Case A utilized the IDEA database's local heat supply (global) as the emission factor for heat energy, while Case B assumed that heat energy was supplied by renewable energy (geothermal energy). In contrast, Cases C and D represent formaldehyde production via CCU technologies. Case C assumed that the required hydrogen is derived from natural gas, with the heat energy source being the same as in Case A. Case D assumed that the required hydrogen was obtained from water electrolysis powered by geothermal power generation, and also the heat energy was supplied by geothermal. Furthermore, since the carbon source for the sugar produced in Cases C and D was $CO_2$, the calculated emissions took into account the amount of $CO_2$ absorbed.

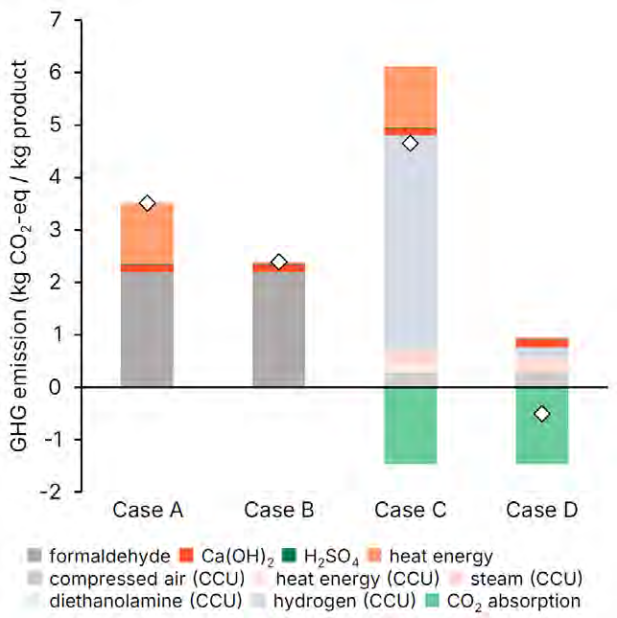



**Figure 6.** Comparison of GHG emissions (kg $CO_2$-eq) per kg of sugar produced under four different cases (Cases A-D). Cases A and B represent conventional formaldehyde production methods, while Cases C and D represent formaldehyde production methods utilizing $CO_2$. Cases A and C assume heat supply mainly from fossil fuels, and Cases B and D assume heat supply from geothermal power generation.

Figure 6 compares the GHG emissions for the four different cases, highlighting the significant impact of the formaldehyde production method. In Case A, which used the current energy supply as energy resources, the GHG emissions were estimated to be approximately 3.5 kg $CO_2$ per 1 kg of sugar. Using renewable geothermal energy for the heat energy in Case B reduced the emissions to around 2.4 kg $CO_2$. However, when $CO_2$ was used as the raw material in Case C, the emissions increased to approximately 4.6 kg $CO_2$, primarily due to the natural gas-derived hydrogen. Despite $CO_2$ uptake, the overall emissions remained high. In stark contrast, Case D, which utilizes hydrogen produced from water electrolysis powered by geothermal energy and uses geothermal energy for heat, achieved a remarkable reduction in emissions, resulting in approximately -0.6 kg $CO_2$. This negative value signifies that the process absorbs more $CO_2$ than it emits (although it is important to note that the synthesized sugar will eventually be emitted as $CO_2$ during its use and disposal, so this does not mean that the emissions are negative over the entire life-cycle). These results clearly demonstrate that while adopting CCU technologies is a promising approach, the introduction of renewable energy is indispensable for maximizing its environmental benefits. Without the integration of renewable energy, the benefits of CCU technologies may be significantly diminished, and could even lead to a higher GHG footprint than conventional methods, as observed in Case C.

## Comparison with agriculture-based sugar

Figure 7 compares the environmental impacts of the four cases (A-D) described in the previous section with those of agriculture-based sugar production across five environmental impact categories. The values are normalized, setting the largest environmental impact among the compared cases to 1 for each impact category. It should be noted that their functional unit differs from that of agriculture-based sugars (glucose in this case) while chemically synthesized sugars are reported to be metabolizable by microorganisms [9] and usable as a raw material for biomanufacturing [7]. The results showed that regardless of the case, the adoption of chemical sugar synthesis technology could significantly reduce environmental impacts in terms of eutrophication, land use (transformation), and water resources consumption. For instance, the impact on eutrophication from chemical synthesis was, at most, approximately 1/10,000th (Case A), and could be as low as approximately 1/24,000th (Case D) of agriculture-based sugar. Similarly, the impact on land use was between approximately 1/70th (Case C) and 1/140th (Case D), and the impact on water resources consumption was between approximately 1/9th (Case A) and 1/30th (Case D) that of agriculture-based sugar. On the other hand, in terms of climate change and resource consumption, the introduction of CCU technologies, premised on the implementation of renewable energy, was essential for reducing environmental impact.

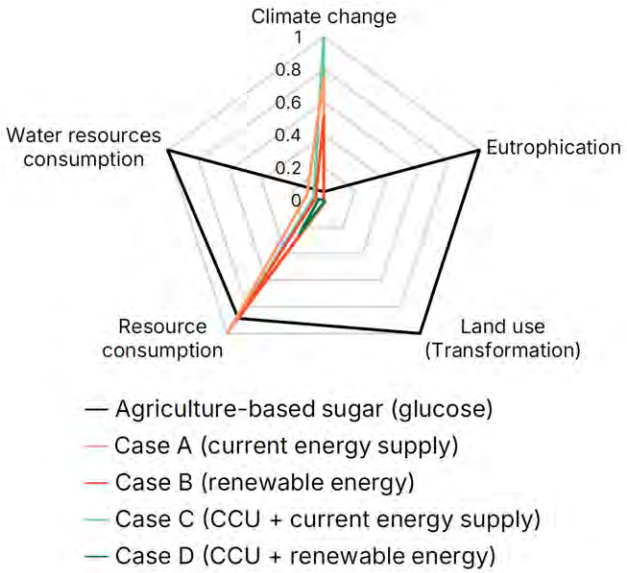



**Figure 7.** A radar chart of indices for all cases of sugar synthesis and agriculture-based sugar, the values of which are normalized as the maximum one in an indicator is set to 1.

## CONCLUSION

This study assessed the environmental impact of chemical sugar synthesis as an alternative to agriculture-based sugar production. The results demonstrated that the chemical synthesis of sugar, particularly when adopting a semi-batch reactor, can significantly reduce environmental impacts in terms of eutrophication, land use, and water resources consumption compared to conventional agriculture-based sugar production. However, the study also highlighted the crucial role of formaldehyde production in the overall environmental footprint. The introduction of CCU technologies for formaldehyde production, premised on the implementation of renewable energy, proved essential for reducing the environmental impact, particularly regarding climate change and resource consumption. Case D, utilizing both CCU and geothermal energy, showed the most promising results among the cases. The findings provide valuable insights for process optimization and future research directions, particularly in the development of more efficient and sustainable formaldehyde production technologies. Further studies should investigate the economic feasibility and scalability of the proposed process, and also focus on a more detailed analysis considering other potential environmental impacts.

The environmental impact of the excessive expansion of agriculture-based sugar utilization has been pointed out in the past. However, as of yet, no replacement methods have been established. In contrast, chemical sugar synthesis is much faster than the agricultural process, and it consumes far fewer resources, such as land and water. This study quantitatively demonstrates the social significance of supplementing sugar production with chemical synthesis processes. Consequently, it is expected to provide new methodologies and perspectives for the field of biomanufacturing, which has been based on the use of agriculture-based sugars, and ultimately for the entire carbon resource recycling system, including food production.

## ACKNOWLEDGEMENTS

This work was supported by New Energy and Industrial Technology Development Organization (NEDO, Grant number JPNP20011), JSPS KAKENHI (Grant Number JP24K23916). Activities of the Presidential Endowed Chair for “Platinum Society” at the University of Tokyo are supported by Mitsui Fudosan Corporation, Sekisui House, Ltd., East Japan Railway Company, and Toyota Tsusho Corporation.

## REFERENCES

1. Brobbey, M., Louw, J., & Goergens, J. Biobased acrylic acid production in a sugarcane biorefinery: A techno-economic assessment using lactic acid, 3-hydroxypropionic acid and glycerol as intermediates. *Chem. Eng. Res. Des.* 193:367-382 (2023) https://doi.org/10.1016/j.cherd.2023.03.034
2. Muscat, A., de Olde, E., de Boer, I., & Ripoll-Bosch, R. The battle for biomass: A systematic review of food -feed -fuel competition. *Glob. Food Secur.-Agric. Policy Econ. Environ.* 25:100330 (2020) https://doi.org/10.1016/j.gfs.2019.100330
3. Cestellos-Blanco, S., Louisia, S., Ross, M., Li, Y., Soland, N., Detomasi, T., Spradlin, J., Nomura, D., & Yang, P. Toward abiotic sugar synthesis from CO2 electrolysis. *Joule* 6:2304-2323 (2022) https://doi.org/10.1016/ .joule.2022.08.007
4. O'Brien, C., Watson, M., & Dowling, A. Challenges and opportunities in converting CO2 to carbohydrates. *ACS Energy Lett.* 7:3509-3523 (2022) https://doi.org/10.1021/acsenergylett.2c01550
5. Socha, R., Weiss, A., & Sakharov, M. Homogeneously catalyzed condensation of formaldehyde to carbohydrates. 7. An overall formose reaction model. *J. Catal.* 67:207-217 (1981) https://doi.org/10.1016/0021-9517(81)90272-4
6. Puhar, J., Krajnc, D., Cucek, L., & Vujanovic, A. Review and environmental footprint assessment of various formalin production pathways. *J. Clean. Prod.* 377:134537 (2022) https://doi.org/10.1016/j.jclepro.2022.134537
7. Tabata, H., Nishijima, H., Yamada, Y., Miyake, R., Yamamoto, K., Kato, S., & Nakanishi, S. Microbial biomanufacturing using chemically synthesized non-natural sugars as the substrate. *ChemBioChem* 25:e202300760 (2024) https://doi.org/10.1002/cbic.202300760
8. Breslow, R. On the mechanism of the formose reaction. *Tetrahedron Lett.* 21:22-26 (1959) https://doi.org/10.1016/S0040-4039(01)99487-0
9. Tabata, H., Chikatani, G., Nishijima, H., Harada, T., Miyake, R., Kato, S., Igarashi, K., Mukouyama, Y., Shirai, S., Waki, & Nakanishi, S. Construction of an autocatalytic reaction cycle in neutral medium for synthesis of life-sustaining sugars. *Chem. Sci.* 14:13475-13484 (2023) https://doi.org/10.1039/d3sc03377e

© 2025 by the authors. Licensed to PSEcommunity.org and PSE Press. This is an open access article under the creative commons CC-BY-SA licensing terms. Credit must be given to creator and adaptations must be shared under the same terms. See https://creativecommons.org/licenses/by-sa/4.0/



Systems & Control Transactions

**Research Article - Peer Reviewed Conference Proceeding**
ESCAPE 35 - European Symposium on Computer Aided Process Engineering
Ghent, Belgium. 6-9 July 2025
Jan F.M. Van Impe, Grégoire Léonard, Satyajeet S. Bhonsale,
Monika E. Polańska, Filip Logist (Eds.)

PSE PRESS

# Decision Support Tool for Sustainable Small to Medium-Volume Natural Gas Utilization

**Patience B. Shamaki[a]*, Pedro H. Callil-Soares[a], and Galo A. C. Le Roux[a]**

[a] University of São Paulo, Department of Chemical Engineering, Polytechnic School, São Paulo, Brazil
* Corresponding Author: shamakipatience@usp.br

## ABSTRACT

This study presents a simple tool to provide decision-makers data that will facilitate informed decisions in selecting utilization for small- to medium-scale utilization of stranded natural gas resources that would otherwise be flared. The methodology involves the simulation of different natural gas utilization technologies on Aspen Plus simulation software and utilizing the results to develop a tool on python that enables the user to assess recoverable valuable products from different natural gas profiles. Ten utilization technologies were implemented and six different natural gas profiles (rich and lean) were used as case studies to ascertain the capabilities of the tool. The results provide the user with the Net Present Values (NPV) of different technologies and the most profitable or infeasible utilization technology. The results also show the potentials of utilizing the gas over flaring. For very small volumes of gas the results favored the compressed natural gas (CNG) with positive NPV, and next electricity production. Small to medium volumes of lean gas favoured the turquoise methanol. Mini- Liquefied Natural Gas (LNG) were the least profitable especially for small volumes. This tool can facilitate the evaluation of several gas profiles to assess the impact of utilizing natural gas over flaring in the sustainable future paradigm.

**Keywords**: Aspen Plus, Methanol, Energy Storage, Carbon Dioxide Capture, Alternative Fuels.

## INTRODUCTION

The global efforts aimed at mitigating carbon emissions include curbing gas flaring. Several initiatives have been introduced by stakeholders, including the World Bank's zero routine gas flaring by 2030, launched in 2015, to achieve this goal of reducing $CO_2$ emissions due to gas flaring. The initiatives led to the development of a gas flaring tracking tool, the Global Gas Flaring Reduction (GGFR) initiatives that foster the development of technologies for the valorization of small natural gas volumes that are routinely flared for safety, logistical, and economic constraints [1]. However, flaring continues to contribute significantly to global emissions, and the last World Bank report observes a reversal of the significant progress made by the GGFR initiatives with an increase in gas flaring volume by 7% [2]. Therefore, innovative solutions are required to facilitate the efficient and sustainable valorization of these otherwise stranded gas volumes to reduce resource waste and curb emissions [3-4].

### Literature review

Numerous studies from oil- and gas-producing countries have evaluated different routes to valorize stranded natural gas resources and avoid flaring. A study that reviewed the different natural gas utilization technologies that can be applied to mitigate flaring showed that gas-to-liquids producing Syncrude, methanol (MeOH) or dimethyl ether (DME), gas-to-wire, which generates electricity and heat in some cases, and natural gas liquid extraction or dry gas liquefaction are economically favorable for small- to medium-scale gas volumes [3]. A detailed World Bank report demonstrates the different technological innovations in the market with the potential to handle small gas volumes that would widely be flared [4]. In the same way, [5] did an environmental and economic analysis of various types of gas feed to group the utilization technologies. This study proposes the integration of data from existing research with new technologies to develop a tool that quickly checks if a gas profile is available for other uses besides flaring.

# METHODOLOGY

## Tool overview

The decision-making tool proposed in this study consists of two parts, described below: the first one, that calculates technology-specific prices, costs and yields, is implemented a priori in ASPEN Plus. The second one, that calculates Net Present Values and obtains the environmental analyses with user-supplied data, is an application programmed in Python. An overview of the tool is exhibited in Fig 1.

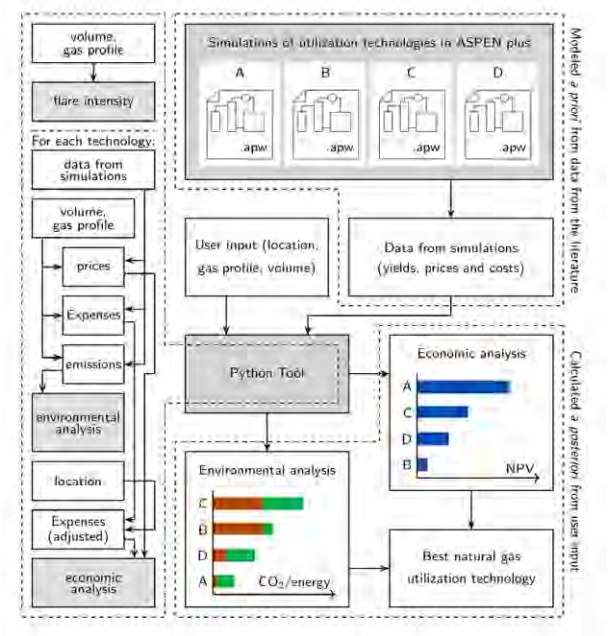



Figure 1. The decision-making tool methodology.

Initially, data from the literature was used to implement simulations of all utilization technologies and pretreatments. These simulations returned capital and operational expenses for a plant with fixed size and yields that could be attainable by each process (and, therefore, the prices of their output streams).

The data obtained through the simulations was then incorporated into the Python tool. This tool reads data supplied by the user (such as gas profile and volume, gas field location, and carbon tax) and calculates, firstly, the emissions if the gas is flared, then, it yields, net present values (NPV) for each utilization technology, considering scale, shipping and installation multipliers (for CAPEX adjustment) and the local discount rate. Besides the NPV, the $CO_2$-equivalent emissions and energy usage are also obtained. For each utilization technology, the cheapest feasible pretreatment was selected, and the economic (NPV) and environmental ($CO_2$ emissions and energy usage) analyses are sorted and presented to the user, who should select the best technology.

## Assumptions

The following assumptions were made in the collection of data and the tool design: Onshore application of technologies, small to medium scale from 0.1 – 20 MMSCFD, Steady state process simulations, HHV values at 15°C and 1 atm, modular units, project implementation of 6-12 months, average gas profile for 10 years, all products are utilized within the vicinity hence transportation costs are not included.

## Data collection

The natural gas field selection was based on the world bank platform for gas flaring monitoring [1]. Gas fields from 5 continents with gas flaring records were selected based on available field data representation as presented in Table 1.

Table 1: Utilization technologies simulation data.

| Process | Conditions | Ref |
|---|---|---|
| Full Fractionation | Dry gas (%):C1-98.9, C2-35, C3-5 | [4,7] |
| NGLs removal | Dry gas (%):C1-98.9, C2-65, C3-5 | [4] |
| Dehydration | Dry gas C3+<5% | [7] |
| LNG | -154°C | [7] |
| CNG | 250bar | [4] |
| G MeOH | S:C=4, 20bar, 850-900°C | [8] |
| T MeOH | 1 bar, 1200°C | [8,9] |
| NGCCT | 7bar, GT: 950°C, ST:480°C, 42 barg | |
| NGCCT+CCS | $CCS_{in}$: 42 bar, $CO2_{in}$ - 0,093, $CO2_{Out}$: 150 bar,98.5% | [10] |
| NGT(CHP)+CCS | 7bar, GT: 950°C, Steam:184°C, 10 barg | [11] |
| NGT(CHP) | Steam:184°C, 10 barg | [12] |
| NGT | 7bar, GT: 950°C | [12,13] |
| NGE | | [4] |

Several reviews on the different valuable products from small scale gas utilization technologies to prevent gas flaring were analysed. This study classified the most common profitable valorization technologies into dry gas liquefaction and compression (mini-LNG, CNG) for storage and transport, gas to liquid/chemicals (methanol was selected) and gas to wire (electricity production) technologies. Ten (10) prospective utilization technologies to obtain valuable products were considered based on available data [2]. These technologies were simulated in Aspen Plus to obtain thermodynamics, mass and energy balance data used for technology assessment. The references used for the different technologies are presented in Table 1.

## Process Simulation

The processes considered were simulated in Aspen plus on a basis of an initial feed gas flowrate of 1 MMSCFD for simplicity. The super structure in Fig 2 represents the different scenarios for simulations carried out using data from the literature as in Table 1.

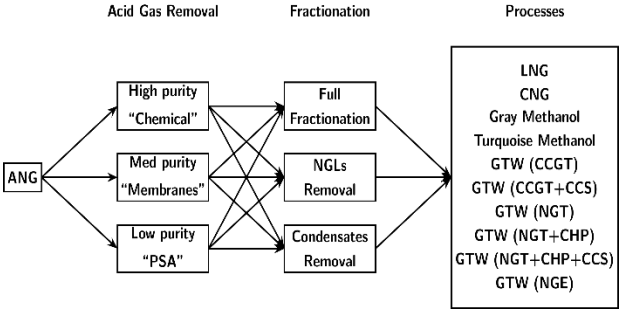


Figure 2. Process case study superstructure.

The Aspen simulation includes the cleaning requirements for different technologies. The acid gas removal and NGLs removal were represented with the SEP component model and the separation parameters obtained from the detailed reporting in the literature [2]. Three acid gas removal purity levels were considered, based on the different purity levels required for different technologies. Similarly, depending on the gas quality, the removal of NGLs may be required for some utilization processes. Thus, different scenarios are simulated for full fractionation into individual products, de-methanization to remove NGLs or basic dehydration (for a clean lean gas) is required for each utilization technology or different valuable products produced.

## Dry gas Storage (Mini-LNG and CNG)

Traditionally, large scale volumes of natural gas are cooled to liquid state at very low temperatures (-145°C to -165°C) for ease and safe transport over long distances where it would be too expensive or infeasible to install. The introduction of the mini-LNG plants facilitates the processing of gas into LNG, the simulation of the LNG plant was carried out based on [2], [3]. CNG can serve as a virtual pipeline, it involves natural gas compression by 250 times (250bar) at ambient temperature. It is used to transport or store gas over short distances for a short period.

## Gas to Wire (Microturbines, Small-scale Engines)

The production of electricity is the most common utilization of natural gas as it accommodates a variety of gas profiles. The use of micro turbines and small gas engines for the combined heat and power process is commonplace in oil and gas production sites. However, this process involves the combustion of the fuel gas which produces $CO_2$. In this study, the application of carbon capture and storage (CCS) was explored. The $CO_2$ mole fraction in the exhaust stream is very low. Hence, for the application of CCS the exhaust gas is recycled to improve the $CO_2$ mole content and less air is required for the combustion as implemented in this work for the NGCCGT with CCS case [4]. Whereas without the application of $CO_2$, the excess gas required is more to maintain the turbine inlet temperature as applied here [5], [6].

## Gas to Liquid/Chemicals (Methanol Synthesis)

The gas to liquid or chemical where natural gas is converted to syngas through steam reforming and subsequently higher hydrocarbons like diesel or the syngas converted to MeOH (Grey methanol), DME or anhydrous ammonia. For small volumes, methanol is usually more profitable and avoids the production of $CO_2$. Equations 2-4 shows the chemical reactions for steam reforming methanol synthesis.

Currently, small-scale $CO_2$ hydrogenation to produces methanol emerges to facilitate renewable (green) methanol. However, green methanol is not cost competitive with conventional methanol. Turquoise methanol (T MeOH) shows the potential to be more competitive. The process involves $CO_2$ hydrogenation using pure hydrogen from methane pyrolysis. Based on Equation 1 methane is split into $H_2$ and solid C. This study applied the technology using a regenerative heat exchanger reactor (RHER) to facilitate heat exchange between reactant, bed and products in a counter-current flow, reducing energy consumption and heat waste as shown in Figure 2.

$$CH_4 \rightarrow 2H_2 + C \quad (1)$$

$$CO + 2H_2 \leftrightarrow CH_3OH \quad (2)$$

$$CO + H_2O \leftrightarrow H_2 + CO_2 \quad (3)$$

$$CO_2 + 3H_2 \leftrightarrow CH_3OH + H_2O \quad (4)$$

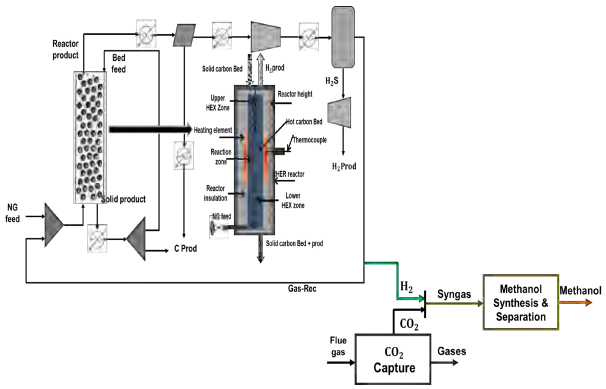


Figure 3. Turquoise Methanol Synthesis.

The RHER uses electricity through ohmic heating. Therefore, when renewable electricity is used the technology does produce $CO_2$ but valuable carbon as a by-product adding to the economic competitiveness of the product. Thus, it is included as an emerging technology in this study based on [7].

## Performance Indices

To evaluate the different technologies, some sustainability (material, energy, economic and environmental) metrics were calculated.

The emission of gas if flared or recoverable products and byproducts if gas is used are calculated based on emission intensity or product yield:

$$CO_{2_{prod}} = \frac{(\%VW_{CO_2})_t}{100\%} + \sum_{y=1}^{Y}\left\{\varepsilon * \frac{(\%C_y)_t}{100\%} * CNM_y\right\} \quad (5)$$

$$E_{CO_2} = \left[(V_{flare})_t * \frac{MW_{CO_2}}{MVC} * K * CO_{2_{prod}}\right] \quad (6)$$

where $CO_{2_{prod}}$ accounts for the $CO_2$ produced from combustion of hydrocarbons in the feed gas and the $CO_2$ components before combustion, $\varepsilon$ is the flare efficiency, y is the index for carbon containing components other than $CO_2$, %VW is the mole concentration of $CO_2$ in the gas stream, t is the time period under consideration CNM is the precursor mole number of carbon. $E_{CO_2}$ is the $CO_2$ emission intensity, $V_{flare}$ is the volume of gas to be flared, MW is the molecular weight, MVC is the molar volume conversion factor and K is the unit conversion factor.

Alternatively, all emissions can be calculated using the heating value and emission factor for each pollutant. This is given by

$$E_i = K * \varepsilon * \sum_{t=1}^{T}\left((V_{flare})_t * HHV * EF_i\right) \quad (7)$$

where $E_i$ is the emission intensity of pollutant, HHV is the higher heating value, $EF_i$ is the emission factor for each pollutant.

The product yield is calculated based on the type of product such as gas, chemical or electricity as follows:

$$Product\ yield(\alpha) = \frac{F_{output}}{F_{input}} = \frac{F_{output} * HHV}{F_{input} * HHV} \quad (8)$$

$$Q_{Prod,mat}(kg/h) = Q_{gas} * \alpha(j) \quad (9)$$

$$Q_{Prod,elect}(kW) = Q_{gas} * \alpha(j) * HHV \quad (10)$$

where $Q$ is the flowrate, $\alpha(j)$ is the product yield for process $j$. The HHV of all NG components was obtained from Aspen Plus and for each gas composition, the summation of the product of each component fraction and its HHV was used.

For this study, the rate of energy consumption, the efficiency, the $CO_2$ equivalent emission or avoided by each technology was also computed:

$$E_{rate} = \frac{E_{input}}{Q_{product}} \quad (11)$$

$$\varepsilon_j = \frac{E_{output}}{E_{input}} * 100\% \quad (12)$$

$$CO_{2_{rate}} = \frac{FCO_{2,product} + FCO_{2,utilities}}{Q_{product}} \quad (13)$$

Likewise, the economics metrics including the capital cost (CAPEX), operating cost (OPEX), rate of returns on investment (ROI), payback period and the production cost were computed:

$$ATCI = CAPEX * \frac{i(1+i)^t}{(1+i)^t - 1} \quad (14)$$

where ATCI is the annualized total capital investment (CAPEX), the annuity factor using the interest $i$ and the time period $t$. The fixed operating cost FOC including the labor cost, general maintenance etc., VOC is the variable operating cost consisting of the energy cost, feed cost, catalyst cost etc. Although in this case, the feed cost is zero being a waste gas.

$$OPEX = FOC + VOC \quad (14)$$

$$Product\ cost = \frac{CAPEX * OPEX}{Q_{product}} = \frac{TAC}{Q_{product}} \quad (15)$$

The total annual cost (TAC) is used to calculate the production cost and the profit, and the profit is used to compute the rate of returns (ROR), and the payback period.

$$Profit = Q_{product} * P_{price} - TAC \quad (16)$$

## Case Studies

To evaluate the capabilities of the model for quick decisions, a few case studies were analyzed, encompassing different sizes (from 0.5 MMSCFD to 20 MMSCFD), geographical locations and gas profiles. The data were selected from the world bank gas flaring tracker [1], six fields were selected. Three of them with a rich gas profile, from Saudi Arabia (SAU), the United States (USA) and the United Kingdom (UK), shown in Table 2, and three of them with a lean gas profile, from Brazil, Australia and Nigeria, shown in Table 3

Besides this analysis, another case study was performed, introducing an increasingly large carbon tax and checking its impact over the models' choices.

# RESULTS

Inline with the user interface presented in Fig S2, the first tab enables the decision maker to initiate the evaluation by providing the profile of the natural gas, the alternatives are provided in the second tab and the user is able to select the preferred result.

The results are presented in the third tab, these results from the evaluation of the model assessing different gas profiles from different locations considered are discussed:

## Rich Gases

Three of the case studies concerned rich gases, that is, gases with a higher concentration of heavier hydrocarbons as shown in Table S1 of the supplementary material.

Despite the physical feasibility of all utilization

technologies with the Saudi gas field, the production of LNG and the usage of Natural Gas Engines are not profitable, with a negative Net Present Value (NPV) of 7.028 million dollars for the former and 4.862 million dollars for the latter. All other utilization technologies can be made profitable through an optimal choice of pretreatment and cleaning processes. The best performing utilization technology was the production of CNG, after chemical Acid Gas removal and simple Natural Gas Liquids removal. This technology yields a positive NPV of 10.377 million dollars.

On the other hand, the gas from the American field can always be profitably explored, regardless of choice of utilization technology, with even the least lucrative choice, LNG production, yielding a modest, but positive, NPV of 7.65 million dollars, after a membrane-based acid gas removal step and after separation of natural gas liquids. Meanwhile, the best choice, turquoise methanol production, exhibits a positive NPV of 72.636 million dollars, using the cheapest acid gas removal technology (PSA) followed by NGL separation.

Finally, the British field shows results very similar to the American ones, when the proportions are taken into account: the least profitable utilization technology is the same (LNG with membrane cleaning and NGL separation), and the most profitable is very similar (also Turquoise Methanol production after NGL separation, but the higher acid gas fraction must be removed through a chemical process, more efficient but also more expensive). The NPVs range from 56.477 million dollars (LNG) to 325.49 million dollars (for the Turquoise Methanol).

## Lean Gases

The other three gas fields analyzed in this work are lean gas fields, that is, with a higher methane content. as shown in Table S1 of the supplementary material.

The Brazilian field can profitably deploy all utilization technologies, with the exception of LNG production. In this situation its NPV is negative and has a value of 2.759 million dollars. On the other hand, the production of CNG is the most profitable choice, with a Net Present Value of 8.292 million dollars. This difference originates from the impurity tolerances of LNG and CNG: while the first must be of higher purity, demanding expensive and complex treatment systems, the second is laxer. Hence, cheaper and simpler technologies can be applied to its purification before usage. Indeed, while the best case for LNG demanded full fractionation and chemical acid gas removal, the most profitable cleaning process for the CNG needed no acid gas removal.

The Australian field also shows the trend of Methanol synthesis being the most profitable choice above a certain gas volume. Despite all choices yielding positive NPVs, the list was headed by Turquoise and Gray Methanol synthesis, with a simple acid gas removal and natural gas liquids separation.

These utilization technologies achieved an NPV of 59.903 million dollars and 57.903 million dollars, respectively. The bottom of the list, as before, is still occupied by the LNG production, with an NPV of 6.584 million dollars.

Lastly, the gas from the Nigerian field is best explored through the synthesis of Methanol: Turquoise and Gray Methanol once again headed the list, with NPVs of 417.56 million dollars and 347.71 million dollars, respectively. The worst, but still profitable, utilization technology for this field is not, however, LNG production as previous examples show, but electricity generation using Natural gas Engines (NGEs).

## Carbon Tax Impact

To assess the economical impacts of a Carbon Capture & Storage technology, 500 new simulations of the United Kingdom gas field described in the previous section were analyzed. Unlike the previous simulations, a Carbon Tax is introduced, spanning from zero to 20 USD/$tCO_2$ emitted. The Net Present Values for different technologies in these circumstances are shown in Figure 3.

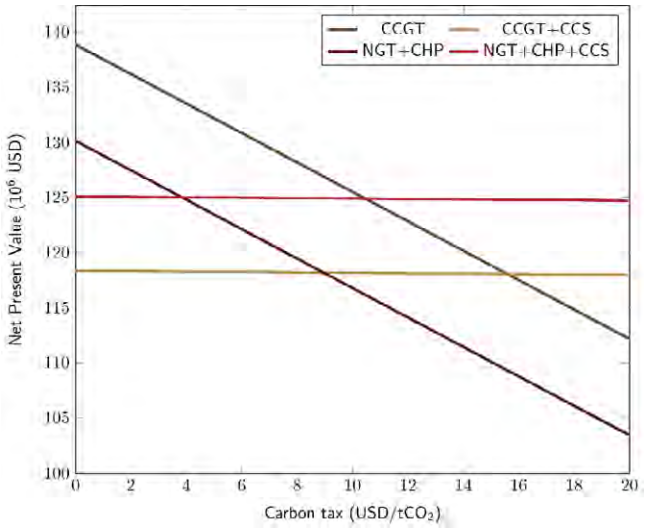



Figure 4. Net Present Values of Gas-To-Wire utilization technologies, with a growing Carbon Tax

It can be observed that, for these Gas-To-Wire technologies, a Carbon Capture system becomes economically superior for a Carbon Tax greater than 10 USD/$tCO_2$.

## CONCLUSION AND FURTHER WORKS

This work presents a tool to provide decision-makers data that will facilitate informed decisions in selecting utilization for small- to medium-scale utilization of stranded natural gas resources that would otherwise be

flared. This would mitigate flaring and reduce waste of valuable resources. The tool also provides data for achieving improved economical performance and sustainability by selecting profitable technology for each gas profile and volume, accounting for the requirements of each one. The application of this tool to a collection of case studies enables quick assessments that impact sustainable future policies, since several scenarios can be assessed before detailed project development. Case study results favored CNG followed by electricity as expected given that they have the least cost. However, CNG can only be applied to short distances within the locality of production. The study also showed the potential for producing clean chemicals, such as emission-free turquoise methanol.

Despite considering location for installation and shipping costs, the uncertain and varying factors (such as product prices and transportation costs) were assumed constant, hence limiting the study. Further works will include the implementation of a stochastic model and the possibility to account for future market movements to greatly improve the tool.

## DIGITAL SUPPLEMENTARY MATERIAL

All source code written for this project is publicly available at GitHub in the following link https://github.com/pedro-callil/flare-alternatives as well as LAPSE:2025.0038

## ACKNOWLEDGEMENTS

This research was financially supported by the Coordination of Superior Level Staff Improvement (CAPES) grant no. 88887.464619/2019-00, PROEX program and RCG2I/FAPESP (2020/15230-5). Galo A. C. Le Roux acknowledges the fellowship from National Council for Scientific and Technological Development CNPq (311550/2022-3). Pedro H. Callil-Soares acknowledges the grant 2023/04683-7, São Paulo Research Foundation (FAPESP), Patience acknowledges Petroleum Technology development fund – Nigeria (PTDF).

## REFERENCES

1. World Bank, “Global Gas Flaring Tracker,” www.worldbank.org. Accessed: Jan. 29, 2025. [Online]. Available: https://www.worldbank.org/en/programs/gasflaringreduction/global-flaring-data
2. World bank, “Global Gas Flaring Tracker Report,” 2024. [Online]. Available: www.worldbank.org
3. A. Khalili-Garakani, M. Iravaninia, and M. Nezhadfard, “A review on the potentials of flare gas recovery applications in Iran,” J Clean Prod, vol. 279, Jan. 2021,
4. H. Darani *et al.*, “Report on Small-scale Technologies for Utilization of Associated Gas,” 2021. [Online]. Available: www.worldbank.org
5. A. Khalili-Garakani, M. Nezhadfard, and M. Iravaninia, “Enviro-economic investigation of various flare gas recovery and utilization technologies in upstream and downstream of oil and gas industries,” *J Clean Prod*, vol. 346. 2022,
6. M. A. Katebah, M. M. Hussein, E. I. Al-musleh, and F. Almomani, “A systematic op-timization approach of an actual LNG plant.,” Energy, vol. 269, p. 126710, Apr. 2023
7. J. Gong, M. Yang, and F. You, “A systematic simulation-based process intensification method for shale gas processing and NGLs recovery process systems under uncertain feedstock compositions,” Comp Chem Eng, pp. 259–275, Oct. 2017, doi: 10.1016/J.COMPCHEMENG.2016.11.010.
8. T. N. Do, H. Kwon, M. Park, C. Kim, Y. T. Kim, and J. Kim, “Carbon-neutral hydrogen production from natural gas via electrified steam reforming: Techno-economic-environmental perspective,” Energy Con M, vol. 279, Mar. 2023, doi: 10.1016/j.enconman.2023.116758.
9. T. Keipi, H. Tolvanen, and J. Konttinen, “Economic analysis of hydrogen production by methane thermal decomposition: Comparison to competing technologies,” *E Con M*, 159: 264–273, (2018),
10. S. Sollai, A. Porcu, V. Tola, F. Ferrara, and A. Pettinau, “Renewable methanol production from green hydrogen and captured CO2: A techno-economic assessment,” *J CO2 Util*, vol. 68, p. 102345, Feb. 2023.
11. D. Barsi, L. Frezza, F. Satta, Y. Luan, and P. Zunino, “Marine Applications and Design of High-Efficiency Small-Scale Gas Turbines,” *Designs (Basel)*, no. 4, Aug. 2024, doi: 10.3390/designs8040066.
12. R. W. Baker, B. Freeman, J. Kniep, X. Wei, and T. Merkel, “CO2 capture from natural gas power plants using selective exhaust gas recycle membrane designs,” *Intl J of GHG Control*, pp. 35–47, Nov. 2017, doi: 10.1016/J.IJGGC.2017.08.016.
13. Aurelia, “Aurelia 400,” Oct. 2024.

© 2025 by the authors. Licensed to PSEcommunity.org and PSE Press. This is an open access article under the creative commons CC-BY-SA licensing terms. Credit must be given to creator and adaptations must be shared under the same terms. See https://creativecommons.org/licenses/by-sa/4.0/



Systems & Control Transactions

**Research Article - Peer Reviewed Conference Proceeding**
ESCAPE 35 - European Symposium on Computer Aided Process Engineering
Ghent, Belgium. 6-9 July 2025
Jan F.M. Van Impe, Grégoire Léonard, Satyajeet S. Bhonsale,
Monika E. Polańska, Filip Logist (Eds.)

PSE PRESS

# Enhancing Batch Chemical Manufacturing via Development of Deep Learning based Predictive Monitoring with Transfer Learning

**Hong Yee Hung[a], Zhao Jinsong[a,*]**

[a] Tsinghua University, Department of Chemical engineering, Beijing, China
* Corresponding Author: jinsongzhao@mail.tsinghua.edu.cn.

## ABSTRACT

Batch chemical processes face significant challenges due to frequent operational shifts and varying conditions, requiring models to be retrained for each new scenario. This high retraining demand limits the scalability of traditional process monitoring systems, making them unsuitable for dynamic batch operations. To address this, we propose a transfer learning-based framework that enhances adaptability by reusing learned features across different batch conditions, reducing the need for extensive retraining. Proposed method integrates Temporal Convolutional Networks (TCNs) for capturing temporal dependencies in batch data and predicting Quality-Indicative Variables (QIVs) to identify deviations. The core innovation lies in transfer learning, enabling the model to adapt to new process variations with minimal updates. This approach ensures robust, accurate monitoring even under evolving conditions. This framework is validated using the IndPenSim penicillin fermentation dataset, which simulates real-world batch process variability. Results show that the transfer learning-enhanced model effectively predicts QIVs and detects deviations across varying control strategies, demonstrating improved adaptability and reduced retraining requirements. This study highlights the potential of transfer learning to revolutionize batch process monitoring by addressing core challenges in dynamic chemical operations.

**Keywords**: Batch Process, Fermentation, Artificial Intelligence, Machine Learning, Process Monitoring, Fault Detection

## 1 INTRODUCTION

The production of high-value-added products like pharmaceuticals, biochemicals, and specialty chemicals heavily relies on batch processes due to their operational flexibility, enabling seamless transitions between various formulations and operating modes within a single facility. However, this flexibility introduces complexities such as intricate process phases and frequent mode switching, which complicate real-time monitoring and control, particularly for quality indicator variables (QIVs) [1]. Since QIVs are often challenging to measure continuously, soft sensors have become a widely adopted solution in industrial settings.

While first-principles models theoretically offer detailed insights into the underlying physicochemical mechanisms, they frequently encounter challenges in modeling the complex nonlinearities and dynamics typical of industrial processes [2]. As an alternative, data-driven methods leverage extensive historical datasets to extract latent features for QIV estimation [3]. Traditional feature extraction approaches include linear methods (e.g., PCA, PLS, ICA) [4,5] and kernel-based variants (e.g., kernel PCA, kernel PLS, SVR) [6], which have shown some efficacy in handling nonlinearity. However, these conventional techniques are often constrained by moderate computational overhead and reduced generalizability when faced with large-scale data and constantly changing operational conditions [7]. This issue becomes especially critical in batch processes, where multi-stage operations, a three-dimensional data structure (time, variables, batches), and multiple operating modes necessitate frequent model reconfiguration, thus restricting their real-time applicability.

Recent advances in deep learning offer promising

avenues for addressing these challenges. Feedforward neural networks and recurrent neural networks (RNNs) exhibit relative strengths in modeling nonlinear and time-varying processes [8], while LSTM networks excel in capturing long-term dependencies [9]. Despite these advantages, LSTM-based methods may still struggle to capture short-term dynamic features between different batch phases and are susceptible to performance degradation under frequent mode transitions and significant batch-to-batch variability [10]. Consequently, transfer learning has gained traction for batch applications, as it facilitates the adaptation of previously acquired knowledge to new modes or new batches, substantially reducing the need for repeated training .

In this context, the present study proposes a soft sensing framework that integrates transfer learning with Temporal Convolutional Networks (TCNs) to achieve both feature extraction and QIV prediction. By introducing a transfer learning mechanism, the model effectively adapts to diverse operating conditions while minimizing retraining efforts. In addition, a variable selection strategy is employed to discard features with limited relevance to QIVs, thereby enhancing predictive accuracy and computational efficiency. The proposed framework addresses the following key challenges:

1. Multi-mode switching: The model can adapt to different operating modes without extensive retraining, addressing batch-to-batch variability.
2. Complex temporal dynamics: TCNs are employed to capture both short-term and long-term dependencies within batch processes.
3. Variable relevance: A variable selection method is introduced to enhance the model's accuracy by focusing on variables that have a strong influence on QIV prediction.

The proposed framework is validated using the IndPenSim penicillin fermentation dataset, which encompasses a variety of control strategies and considerable batch-to-batch variability, thus closely reflecting industrial batch production scenarios. Experimental results indicate that the proposed approach not only captures both short- and long-term temporal dependencies but also sustains robust prediction performance amid frequent mode switching. Consequently, it presents a scalable and readily adaptable solution for real-time QIV prediction and process monitoring in industrial batch operations.

# 2 PRELMINARIES

## 2.1 Benjamini-Hochborg Test

The Benjamini-Hochberg (BH) test controls the false discovery rate (FDR) in multiple hypothesis testing [11]. For soft sensor variable selection, it identifies variables significantly correlated with Quality Indicator Variables (QIVs) by ranking p-values and comparing them to an FDR-adjusted threshold. Variables below the threshold are retained, reducing dimensionality while preserving key features for accurate QIV prediction. Figure 1 illustrates the flow diagram of BH testing.

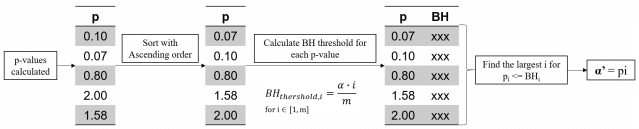



**Figure 1.** Benjamini-Hochberg (BH) program for FDR Control

## 2.2 Temporal Convolutional Network

Temporal Convolutional Networks (TCNs) are deep learning models for sequence modeling that capture both short- and long-term temporal dependencies. Unlike RNNs, which process sequences step by step, TCNs use causal convolutions to ensure predictions depend only on past data. They leverage dilated convolutions to expand their receptive field without requiring deep architectures, and residual connections to stabilize training and mitigate vanishing gradients. TCNs also produce sequence-to-sequence outputs, making them effective for time-series applications in batch processes. Figure 2 shows the TCN framework.

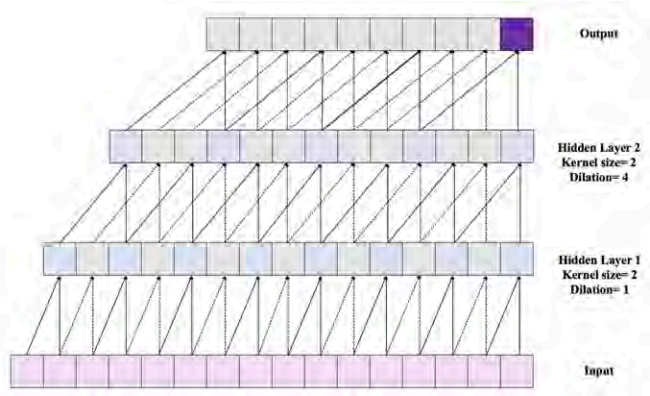



**Figure 2.** Structure of Temporal Convolutional Network

## 2.3 Transfer Learning

Transfer learning reuses knowledge from one task to improve performance on a related but different task [12]. It is particularly useful in batch processes, which often involve variability and multi-mode switching, making it impractical to gather sufficient labeled data for every new condition.

Key components include:

1. Pretrained Feature Extraction: Train a base model on one batch process or condition to capture generalizable patterns.
2. Fine-Tuning: Retrain this model on a smaller dataset from the new condition, reducing data and time

requirements while maintaining accuracy.

Domain Adaptation: Employ methods (e.g., domain-invariant feature extraction) to handle discrepancies between source and target domains. Figure 3 illustrates the transfer learning framework.

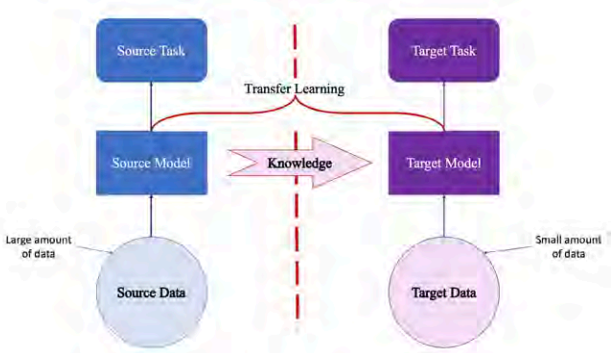



**Figure 3.** Framework of Transfer Learning

# 3 METHODOLOGY

## 3.1 Procedure of Quality Monitoring Framework

The proposed quality monitoring framework follows a two-stage approach, comprising an offline training phase and an online monitoring phase: The proposed quality monitoring framework follows a two-stage approach, comprising an offline training phase and an online monitoring phase:

1. Offline Training Phase

Historical data from past batches under normal conditions are collected, including process variables and Quality Indicator Variables (QIVs). Relevant variables are selected using a mutual information-based method combined with a Benjamini-Hochberg permutation test. A Temporal Convolutional Network (TCN) is trained on the filtered data to capture temporal dynamics, and transfer learning is incorporated for adaptability across different operating modes. Statistical thresholds for fault detection are set using the 3-sigma rule based on model prediction errors.

2. Online Monitoring Phase

Real-time process data are continuously fed into the trained TCN model, which estimates QIVs for comparison with reference profiles or setpoints. Significant deviations outside the 3-sigma thresholds trigger alarms for potential faults. When major process changes occur, transfer learning updates the model with minimal retraining to maintain monitoring accuracy.

A schematic flow chart illustrated the interplay between the offline and online stages in figure 4.

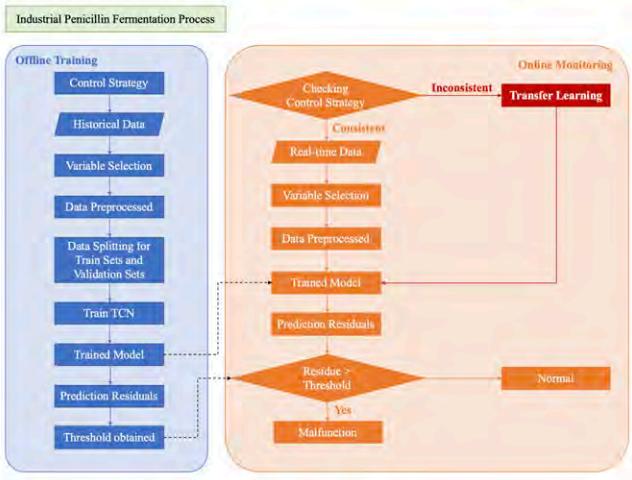



**Figure 4.** The Procedure of Monitoring Framework

## 3.2 Variable Selection by Permutation Test

### 3.2.1 Mutual Information

As an initial step, the mutual information (MI) between each process variable and the QIV is computed. MI measures the shared information between two random variables and captures both linear and nonlinear dependencies. The MI between a candidate variable X and the QIV Y is defined as:

$$I(X;Y) = \iint p(x,y) log \frac{p(x,y)}{p(x)p(y)}\, dx\, dy \quad (1)$$

where $p\,(x, y)$ is the joint probability density of $X$ and $Y$, and $p(x)$, $p(y)$ are their marginal distributions. Variables with high MI values indicate stronger relevance to QIVs, while variables with low MI suggest weaker connections.

### 1.2.2 BH Program-based Permutation Test

Although MI identifies candidate variables, it does not provide a definitive threshold for deciding which variables to keep or discard. To address this, a BH-based permutation test is employed.

The variable selection process begins by removing clearly irrelevant variables (e.g., batch number, condition flag) and computing the mutual information (MI) between each candidate variable $X_k$ and the QIV $Y$. Next, a permutation test is performed by randomly shuffling each $X_k$ multiple times to generate a null distribution of MI values, and a p-value is calculated between $X_k$ and $Y$ based on how often the observed MI exceeds the permuted values. The p-values are then sorted and the Benjamini-Hochberg (BH) procedure is applied to control the false discovery rate (FDR), retaining variables with p-values below the threshold. Finally, the significant variables from the BH test formed the final subset for model development.

Figure 5 illustrates the whole procedure of variable selection proposed by this work.

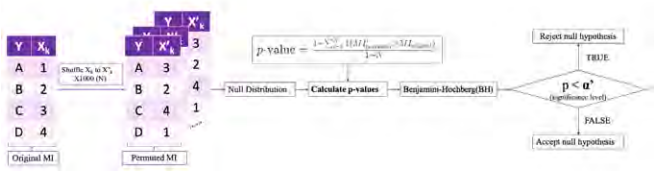



**Figure 5.** Variable Selection through MI Value and BH program -based Permutation Test

## 3.3 Proposed TCN with Transfer Learning Strategy

### 3.3.1 Batch Process Data Preprocessing

Batch processes inherently produce three-dimensional data: batch index, time, and process variables. Traditional data unfolding methods reshape these data into two dimensions, but they may disrupt the inherent structure of batch trajectories, especially when batches vary in length or exhibit phase transitions.

Instead of unfolding all batches onto a single extended axis, this work employed a sliding window approach within each batch. This strategy respects the boundary of each batch by ensuring that a window never overlaps data from different batches. Consequently, it better preserves local temporal correlations and phase-wise characteristics for. Figure 6 shows the strategy of sliding window to cope with the uneven length situation.

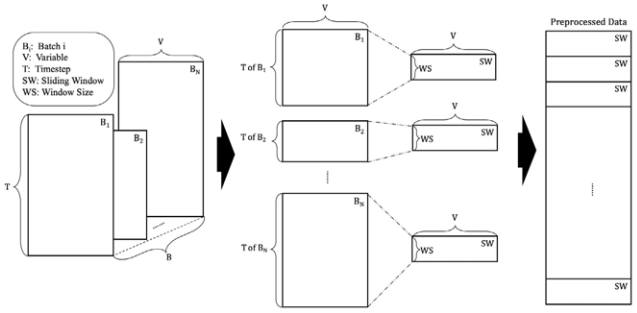



**Figure 6.** Proposed Data Preprocessing Strategy

### 3.3.2 Model Structure and Transfer Learning

The proposed framework involves the following steps after data preprocessing, which ensures synchronization of batch data and standardization of variables. First, a TCN is trained using Normal Operating Condition (NOC) data to capture temporal dependencies and predict Quality Indicator Variables (QIVs).

In this study, Normal Operating Data (NOC data) are used to train the TCN model by minimizing the mean squared error (MSE) between estimated and actual QIV values:

$$min\ MSE = \frac{1}{N}\sum_{i=1}^{N}(\hat{Y}_i - Y_i)^2 \tag{2}$$

where $\hat{Y}_i$ denotes the predicted QIV and $Y_i$ is the true QIV.

To address multi-mode switching and between-batch variability, transfer learning is incorporated into the TCN framework. Once a base TCN model is trained on one operating regime, it can be adapted to new or slightly changed conditions with fewer additional data. The pre-trained TCN is fine-tuned using limited data from a new regime to adapt to changes in operating conditions, such as control strategy variations or raw material differences to validate the transfer learning strategy. Real-time QIV predictions are compared against thresholds derived during training to detect deviations indicative of faults.

### 1.3.4 Process Quality Monitoring

After the TCN model is trained or adapted, it serves as the core of the quality monitoring system:

1. Real-Time QIV Prediction: During operation, the TCN predicts QIV values from incoming sensor data.
2. Threshold Determination: 3-sigma rules (Montgomery, 2012) are applied to the residuals (prediction errors) obtained during the offline training stage. Let the residuals be:

$$e_t = \left|\hat{Y}_t - Y_t\right|^2 \tag{3}$$

Then the control limits can be set as:

$$Threshold = \mu_e \pm 3\sigma_e \tag{4}$$

where $\mu_e$ and $\sigma_e$ are the mean and standard deviation of residuals under normal conditions.

3. Fault Detection: If the residual at time $t$ exceeds these control limits, an alarm is raised to signal a potential fault or deviation from the normal operating condition.
4. Validation with Fault Data: To evaluate fault-detection performance, representative fault scenarios or abnormal batches are introduced, and the detection rate is observed based on the discrepancy of predicted QIVs from normal ranges.

This monitoring approach allows operators to detect process anomalies promptly, maintain product quality, and facilitate proactive adjustments in dynamic batch operations.

# 4 EXPERIMENT

## 4.1 Description of IndPenSim Datasets

The experiments are conducted using the IndPenSim dataset, an industrial-scale penicillin fermentation simulation developed by Goldrick et al. (2019) [13]. Unlike the traditional PenSim benchmark [14], IndPenSim models a 100,000 L bioreactor, bringing it closer to real-world industrial conditions and validated by historical industrial data. Detailed process descriptions and operational specifics can be found at the IndPenSim website and in the original publications [13]. Figure 7 illustrates the summary of IndPenSim.

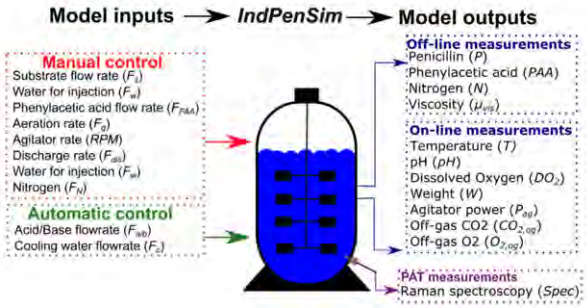



**Figure 7.** Summary of Inputs and Outputs of IndPenSim

This study uses a dataset of 100 simulated batches, with batch lengths ranging from 167 to 290 hours, sampled every 0.2 hours. The first 90 batches represent normal operating conditions and are divided into three groups of 30, each corresponding to a different control strategy. The remaining 10 batches simulate fault conditions to evaluate the fault detection capability. For model training, 20 batches from each control strategy (total of 60 batches) are used, with 30 additional normal batches reserved for evaluation. The 10 fault batches are excluded from training, as the fault conditions and control strategies are unknown. Fault batch data for transfer learning evaluation is generated using a simulator for each control strategy. Detailed batch description and corresponding control strategies are provided in Table 1 and Table 2.

**Table 1:** Batch Description from IndPenSim Datasets.

| Batch No. | Control Strategy | Batch Type |
|---|---|---|
| 1-30 | Recipe Driven Approach | Normal Batch |
| 31-60 | Operators | Normal Batch |
| 61-90 | Advanced Process Control (APC) & Raman Spectroscopy | Normal Batch |
| 91-100 | Unknown | Fault Batch |

**Table 2:** Faulty Batch generated from IndPenSim.

| Fault Batch No. | Control Strategy | Fault Type |
|---|---|---|
| 1 | Recipe Driven Approach | Quality-related |
| 2 | Operators | Quality-related |

## 4.2 Results of Variable Selection

Initially, all 32 process variables are screened based on domain knowledge, removing irrelevant ones not linked to penicillin concentration (QIV) to simplify further analysis. The BH-program-based permutation test is then applied for refined variable selection. Mutual information (MI) values between the retained variables and QIV are computed, and the permutation test evaluates their statistical significance, filtering out weak or insignificant correlations. The final set of highly relevant variables, summarized in Table 3, ensures efficient and effective model development. Figures 8 shows the MI values for the selected variables.

**Table 3:** Screened Variables by Variable Selection.

| Variable No. | Variable description | Unit |
|---|---|---|
| 1 | Aeration rate | L/h |
| 2 | Sugar feed rate | L/h |
| 3 | Acid flow rate | L/h |
| 4 | Base flow rate | L/h |
| 5 | Heating/cooling water flow rate | L/h |
| 6 | Heating water flow rate | L/h |
| 7 | Water for injection/dilution | L/h |
| 8 | Air head pressure | bar |
| 9 | Dumped broth flow | L/h |
| 10 | Substrate concentration | g/L |
| 11 | Dissolved oxygen concentration | mg/L |
| 12 | Vessel Volume | L |
| 13 | Vessel Weight | Kg |
| 14 | pH | / |
| 15 | Temperature | K |
| 16 | Generated heat | kJ |
| 17 | carbon dioxide percent in off-gas | % |
| 18 | PAA flow | L/h |
| 19 | Oil flow | L/hr |
| 20 | Oxygen Uptake Rate | g/min |
| 21 | Oxygen in percent in off-gas | % |
| 22 | Carbon evolution rate | g/h |
| 23 | Penicillin concentration | g/L |

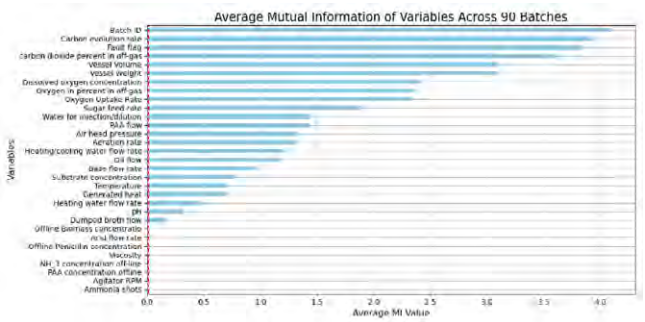



**Figure 8.** Average MI Values of Variables Across 90 batches

## 4.3 Results of Process Monitoring with Transfer Learning

The performance of the proposed TCN-based soft sensor model is evaluated through real-time quality prediction and fault detection. By using normal operating data, the TCN model is trained to predict QIV values. The accuracy of these predictions is illustrated in Figure 9,

which compares predicted QIV trajectories against actual values over time. High fidelity between predictions and true values underlines the model's capability in capturing complex process dynamics.

The model's ability to detect deviations is assessed using fault batches. Figure 10 also shows the residual errors (difference between predicted and measured QIV) alongside the statistically determined control limits based on the 3-sigma rule. Instances where residuals exceed these thresholds indicate faults, demonstrating effective anomaly detection in real-time scenarios.

To validate the adaptability of the proposed framework, the model trained under Control Strategy 1 is adapted to Control Strategy 2 using transfer learning techniques. Figure 11 and 12 depicts the monitoring results after applying transfer learning, showing how the model successfully transitions between different operational strategies with minimal additional training. Table 4 illustrates the Fault Detection Rate (FDR) and False Alarm Rate (FAR) of both without transfer learning and with transfer learning strategy.

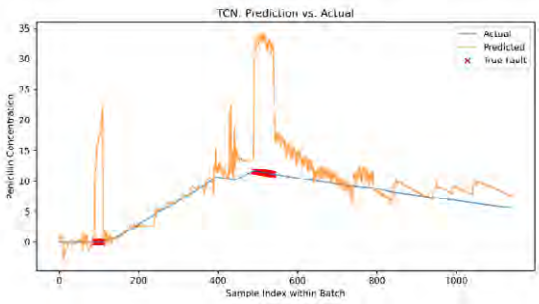



**Figure 9.** Prediction Results of Fault Batch 1

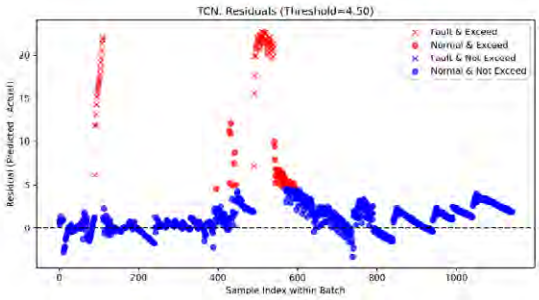



**Figure 10.** Residuals of Fault Batch 1

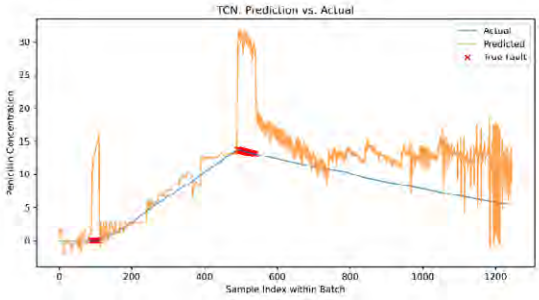



**Figure 11.** Prediction Results of Transfer Learning from Control Strategy 1 to Control Strategy 2 (Fault Batch 2)

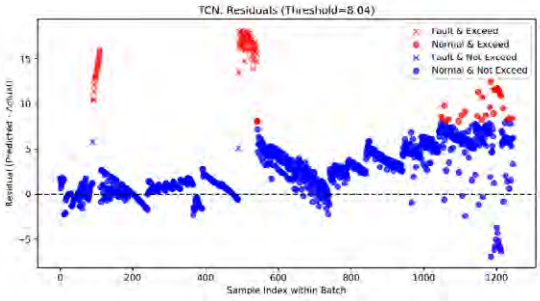



**Figure 12.** Residuals Results of Transfer Learning from Control Strategy 1 to Control Strategy 2 (Fault Batch 2)

**Table 4:** Statistical Results.

| Method. | FDR (%) | FAR (%) |
|---|---|---|
| General | 100.00 | 4.58 |
| Transfer Learning | 97.22 | 2.73 |

## 5 CONCLUSION

This study presents a real-time quality monitoring framework for industrial batch processes, integrating robust variable selection, TCN-based modeling, and transfer learning. It effectively tackles challenges including nonlinear dynamics, multi-phase operations, and batch-to-batch variability. The variable selection method uses mutual information combined with a Benjamini-Hochberg-based permutation test, while TCNs capture complex temporal dependencies and transfer learning enables swift adaptation to different control strategies. A 3-sigma rule–based threshold is employed for real-time fault detection, and experiments on the IndPenSim dataset confirm the framework's enhanced prediction, reliable monitoring, and scalability.

Looking ahead, we plan to incorporate additional sensor types such as images and vibration signals to improve adaptability in complex conditions, explore more sophisticated domain adaptation methods to handle broader operational scenarios, and apply the framework to diverse industrial data to validate its robustness and generality.

## ACKNOWLEDGEMENTS

This work was supported by the National Key R&D Program of China under Grant 2024YFC3013600.

## REFERENCES

1. Kadlec P, Gabrys B, Strandt S. Data-driven soft sensors in the process industry[J]. Computers & chemical engineering, 2009, 33(4): 795-814.
2. Shang H L. A survey of functional principal

component analysis[J]. AStA Advances in Statistical Analysis, 2014, 98: 121-142.
3. Sun Q, Ge Z. A survey on deep learning for data-driven soft sensors[J]. IEEE Transactions on Industrial Informatics, 2021, 17(9): 5853-5866.
4. Keithley R B, Wightman R M, Heien M L. Multivariate concentration determination using principal component regression with residual analysis[J]. TrAC Trends in Analytical Chemistry, 2009, 28(9): 1127-1136.
5. Kaneko H, Arakawa M, Funatsu K. Development of a new soft sensor method using independent component analysis and partial least squares[J]. AIChE Journal, 2009, 55(1): 87-98.
6. Drucker H, Burges C J, Kaufman L, et al. Support vector regression machines[J]. Advances in neural information processing systems, 1996, 9.
7. Liu Y, Gao Z, Li P, et al. Just-in-time kernel learning with adaptive parameter selection for soft sensor modeling of batch processes[J]. Industrial & Engineering Chemistry Research, 2012, 51(11): 4313-4327.
8. Schmidhuber J. Deep learning in neural networks: An overview[J]. Neural networks, 2015, 61: 85-117.
9. Wang K, Gopaluni R B, Chen J, et al. Deep learning of complex batch process data and its application on quality prediction[J]. IEEE Transactions on Industrial Informatics, 2018, 16(12): 7233-7242.
10. Wang Y, Zhang J, Zhu H, et al. Memory in memory: A predictive neural network for learning higher-order non-stationarity from spatiotemporal dynamics[C]//Proceedings of the IEEE/CVF conference on computer vision and pattern recognition. 2019: 9154-9162.
11. Benjamini Y, Hochberg Y. Controlling the false discovery rate: a practical and powerful approach to multiple testing[J]. Journal of the Royal statistical society: series B (Methodological), 1995, 57(1): 289-300.
12. Pan S J, Yang Q. A survey on transfer learning[J]. IEEE Transactions on knowledge and data engineering, 2009, 22(10): 1345-1359.
13. Goldrick S, Ştefan A, Lovett D, et al. The development of an industrial-scale fed-batch fermentation simulation[J]. Journal of biotechnology, 2015, 193: 70-82.
14. Birol G, Ündey C, Cinar A. A modular simulation package for fed-batch fermentation: penicillin production[J]. Computers & chemical engineering, 2002, 26(11): 1553-1565.

© 2025 by the authors. Licensed to PSEcommunity.org and PSE Press. This is an open access article under the creative commons CC-BY-SA licensing terms. Credit must be given to creator and adaptations must be shared under the same terms. See https://creativecommons.org/licenses/by-sa/4.0/

Systems & Control Transactions

**Research Article - Peer Reviewed Conference Proceeding**
ESCAPE 35 - European Symposium on Computer Aided Process Engineering
Ghent, Belgium. 6-9 July 2025
Jan F.M. Van Impe, Grégoire Léonard, Satyajeet S. Bhonsale,
Monika E. Polańska, Filip Logist (Eds.)

PSE PRESS

# Prospective Life Cycle Design Enhanced by Computer Aided Process Modeling: A Case Study of Air Conditioners

**Shoma Fujii[a,b]*, Yuko Oshita[a], Ayumi Yamaki[a], Yasunori Kikuchi[a,b,c]**

[a] The University of Tokyo, Institute for Future Initiatives, Hongo- 7-3-1, Bunkyo-ku, Tokyo, Japan
[b] The University of Tokyo, Department of Chemical System Engineering, Hongo- 7-3-1, Bunkyo-ku, Tokyo, Japan
[c] The University of Tokyo, Presidential Endowed Chari for "Platinum Society", Hongo- 7-3-1, Bunkyo-ku, Tokyo, Japan
* Corresponding Author: shoma.fujii@ifi.u-tokyo.ac.jp

## ABSTRACT

Prospective life-cycle design of emerging technologies is important in discussions of decarbonization and resource circulation strategies. This study demonstrates the role of computer-aided process engineering in reflecting technology information with appropriate granularity and accuracy using air conditioning as a case study. Process simulations involving heat exchangers (indoor/outdoor units), compressors, and expansion valves were developed to model air conditioners to quantify changes in performance and heat exchanger size as existing and alternative refrigerants are introduced. The process simulation results were incorporated into a material flow analysis and life cycle assessment to quantify the change in life cycle greenhouse gas (GHG) emissions through 2050 for each refrigerant installed. The results show that operational emissions dominate the life cycle GHG emissions of air conditioners, that decarbonization of electricity can significantly reduce life cycle GHG emissions, with similar results regardless of which refrigerant is used, and that differences in design policies when alternative refrigerants are introduced strongly affect the breakdown of emissions in 2050.

**Keywords**: Life Cycle Analysis, Interdisciplinary, Modelling and Simulations, Process Design.

## INTRODUCTION

The prospective life cycle design of emerging technologies, combined with Life Cycle Assessment (LCA), Material Flow Analysis (MFA) and Input-Output Analysis (IOA), plays an important role in the design of sustainable societies and business strategies[1]. However, prospective life cycle design is usually not seamlessly linked to technological development. In the example of air conditioners, state-of-the-art development takes place for each component, including the development of new refrigerants and mixture of existing refrigerants[2], clarification and improvement of evaporation and condensation heat transfer phenomena in heat exchangers (evaporators and condensers)[3], design of new compressors[4], improvement of connecting pipes[5], etc. However, this development data is too detailed to be used for life cycle design to build a business strategy. On the other hand, useful indicators such as COP (coefficient of performance) do not show any relationship between design parameters, making it difficult to support decision making.

Figure 1 shows a schematic of the prospective life cycle design of emerging technologies[6] based on seamless analysis from nm to km, using air conditioners as an example. The study of emerging technologies is divided into three major levels: the "materials and components" level (nm to mm level), the "process" level (mm to m level), and the "system" level (m to km level). At the "materials and components" level, taking air conditioners as an example, a variety of research is being conducted. On the other hand, at the "system" level, research is conducted that combines LCA, MFA, IOA and several future scenarios to predict the future, identify gaps between the vision and the predicted future, and identify the need for emerging technologies through back-casting. Computer-aided process engineering is the intermediate process-level research that plays the role of reflecting technical information in system-level analyses with appropriate granularity and precision.

In this study, computer-aided process engineering

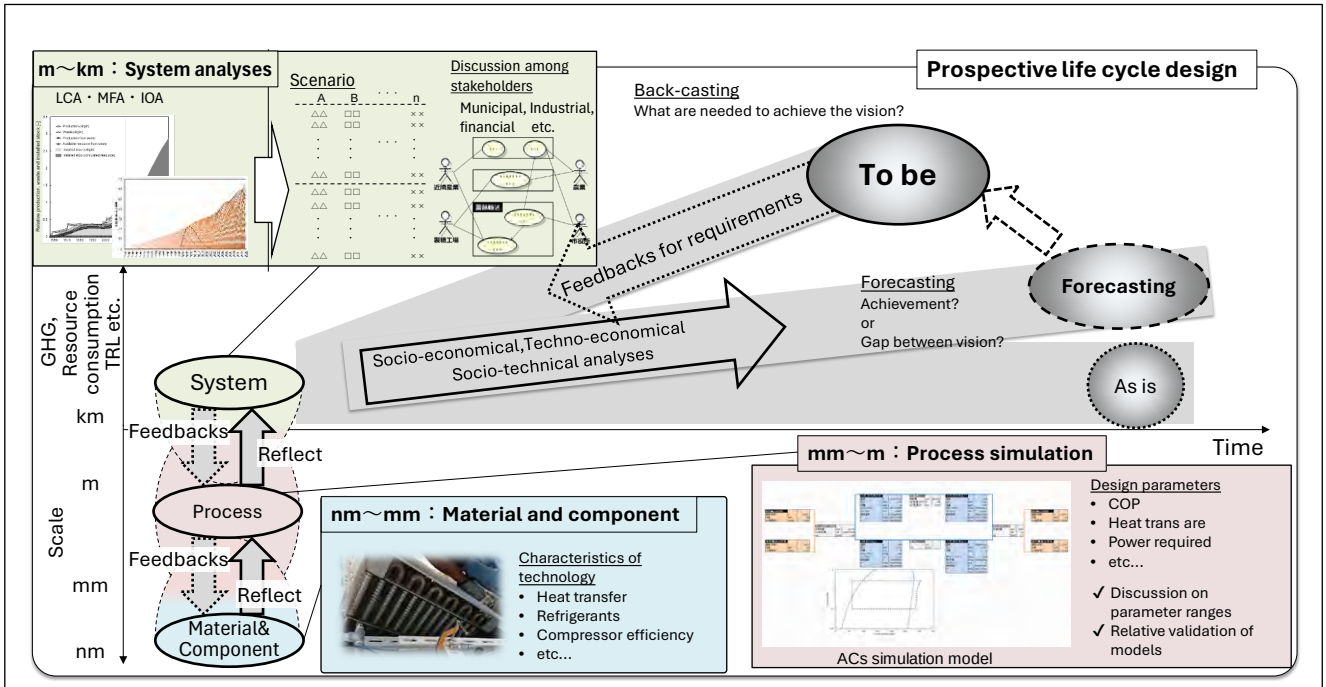



**Figure 1.** Schematic of prospective life cycle assessment for design by seamless analysis from nm~km

is positioned as a function that links technology development and system-level analyses, and a fundamental model combining process simulation of air conditioners, MFA, and LCA was developed to identify the effect of replacing conventional refrigerants with natural refrigerants on life cycle greenhouse gas (GHG) emissions.

## MATERIAL AND METHODOLOGY

Figure 2 shows the linkage diagram among each analysis for prospective life cycle design of air conditioners. Technological data such as like heat transfer coefficient, thermophysical data of refrigerant, design of heat exchangers, efficiency of compressors and fans and the like were aggregated into the process modeling. Figure 3 shows the schematic of process flow diagram of air conditioners. A 2.2 kW air conditioner was simulated as a model machine. In the process modeling, a process flow diagram including heat exchangers for indoor and outdoor, a compressor and an expansion valve was modelled as shown in Figure 3, and for the compressor, the specific enthalpy after compression was calculated assuming an adiabatic efficiency of 90% and for the expansion valve, the refrigerant temperature after expansion was calculated assuming isenthalpy expansion. In the heat exchangers for indoor and outdoor units, the heat exchange process between refrigerants and outdoor air and indoor air was plotted on a temperature-enthalpy diagram, then the UA (overall heat transfer coefficient) values of each heat exchanger were quantified to calculate the relative change in heat exchanger size. The configuration of heat exchangers was based on a typical plate-fin heat exchanger, the number of stages and other sizes have been determined to match the calculated heat transfer area. The refrigerant flow rate was set to give a heat exchange rate of 2.2 kW, which is the performance of the model machine. Based on the determined refrigerant flow rate, the heat exchanger geometry and the pipe length, which was assumed to be 5 m, the pressure losses for the liquid and vapour phases were calculated, respectively. The thermophysical properties of the refrigerant have been calculated using REFPROP10[7]. By using this process modeling, operating power and size of each component for conventional and natural refrigerants could be defined. These results of process simulation were reflected in the MFA and LCA.

In the MFA, statistical data on past and estimated future cooling demand were first incorporated[8,9], then the amount of air conditioners shipped was calculated by balancing the installed stock and the amount of waste estimated by Weibull distribution[10]. Two scenarios were created in which conventional refrigerants continue to be shipped from 2020 to 2050, and a scenario in which $CO_2$ refrigerants are introduced at the same rate as conventional refrigerants from 2030.

In this study, only climate change was considered for the midpoint impact category, since the objective of the LCA in this study is to clarify the impact of refrigerant substitution for the purpose of GWP reduction and changes in electricity emissions intensity on GHG emissions from residential air conditioners in Japan through 2050. The life cycle boundary was set as cradle to gate of conditioned air (manufacturing and operation of air conditioners). The functional unit was defined as cooling

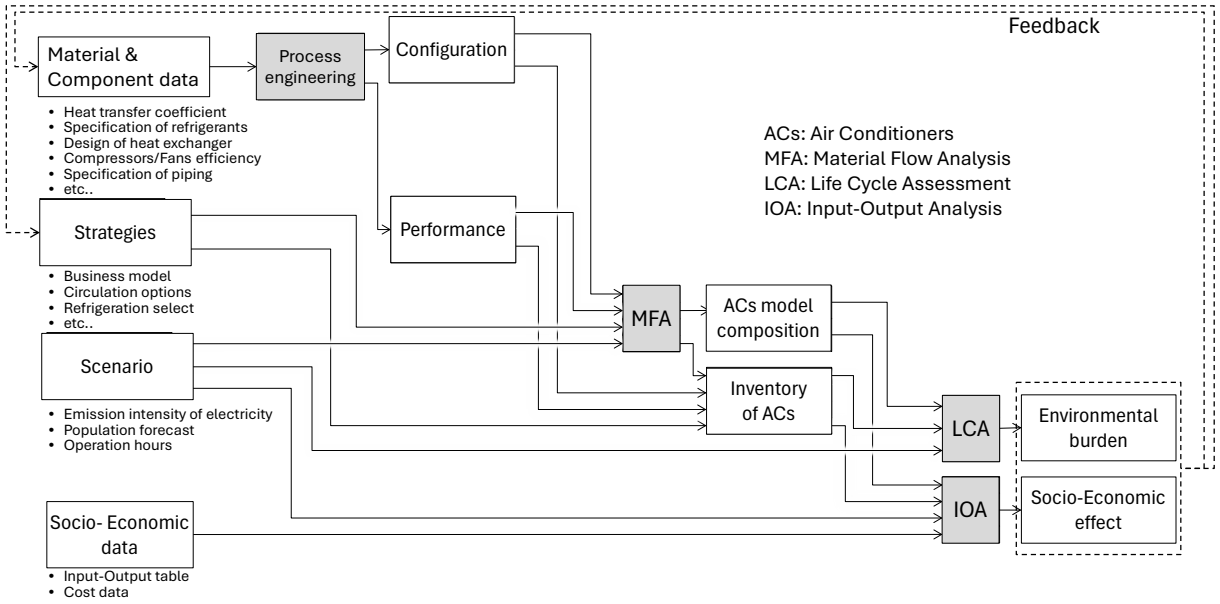



**Figure 2**. Linkage diagram of analyses (Process modeling, Material Flow Analysis, Life Cycle Assessment, and Input Output Analysis) for air conditioners

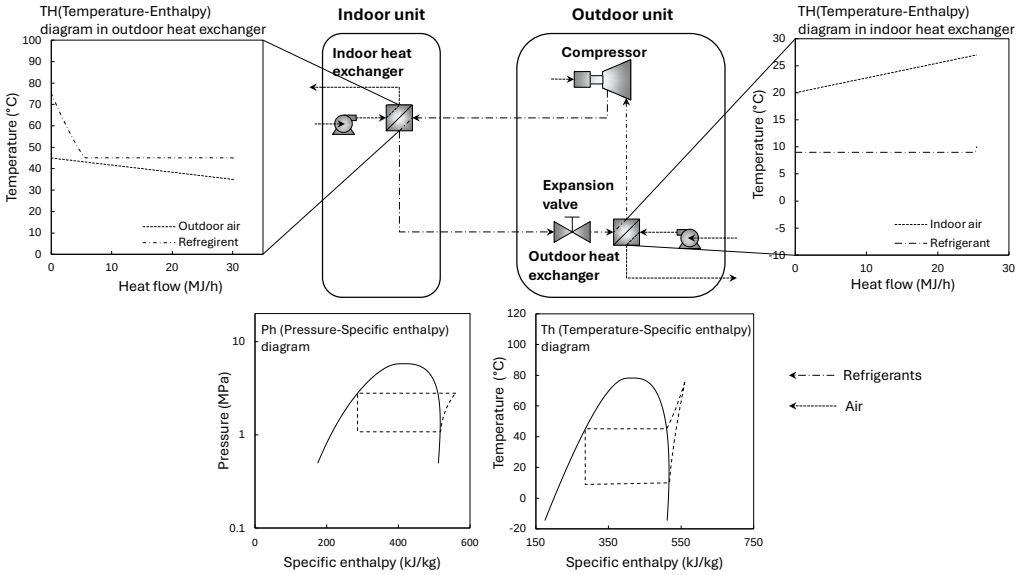



**Figure 3.** Schematic of process flow diagram of air conditioner

and heating by residential air conditioners in Japan through 2050. Inventory data from the manufacture of air conditioners using conventional refrigerant was set[11], and it was assumed that the environmental impact of manufacturing piping and compressors would increase in proportion to the maximum operating pressure ratio with conventional refrigerant when $CO_2$ refrigerant was introduced. Refrigerant leakage was set at 2% per year. Annual power consumption was estimated using performance calculated by the process modeling, annual operation hours, and the results of MFA.

The operating rate was estimated from the energy consumption of air conditioners in the residential sector in the Comprehensive Energy Statistics [12] and the number of units in the market stock calculated by the MFA, and cooling and heating degree days were calculated, then the number of operating days per year was estimated. Annual operating hours were calculated from the operating rate and number of days from 2000 to 2020 and linearly extrapolated to 2050. For electricity emission intensity, two cases were examined: one in which Japan's electricity intensity for the past 10 years is linearly extrapolated to 2050 (almost decarbonized by 2050), and the other in which the intensity in 2020 is maintained.

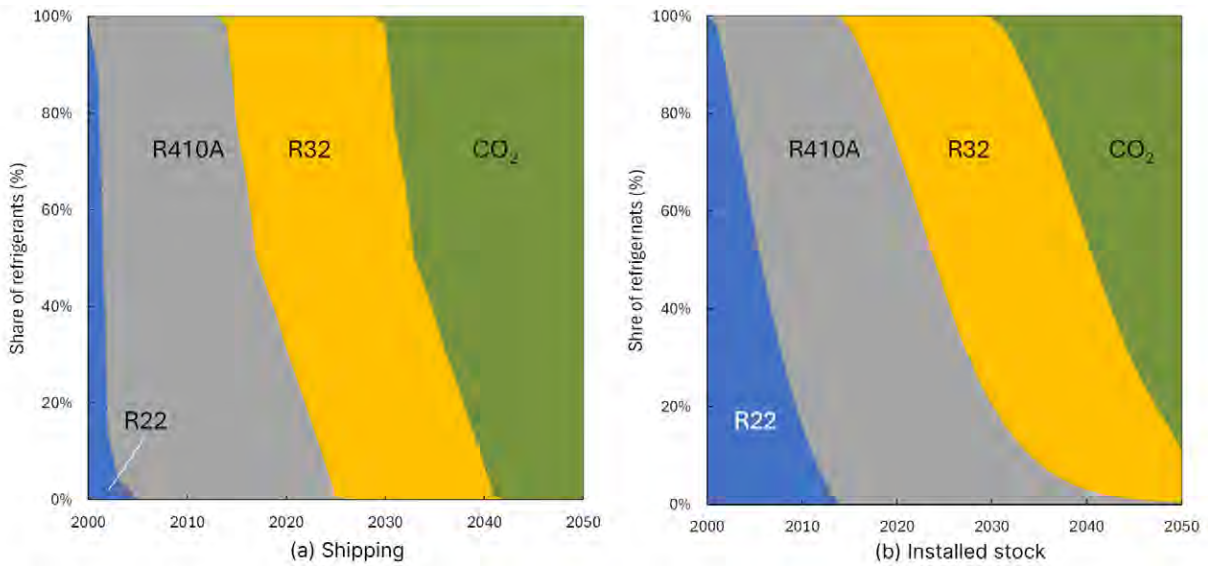



**Figure 4.** Results of material flow analysis of refrigerant when $CO_2$ refrigerant is installed

## RESULTS AND DISCUSSION

Table 1 shows an example of process simulation results for an air conditioner using conventional refrigerant (R32) and $CO_2$ refrigerant. If an air conditioner using $CO_2$ refrigerant is designed to perform the same as an air conditioner using conventional refrigerant, the size of the heat exchanger will be 6 times larger when $CO_2$ is used as the refrigerant. On the other hand, if the heat exchanger of an air conditioner using $CO_2$ refrigerant is designed to be the same size as that of an air conditioner using conventional refrigerant, the COP of an air conditioner using $CO_2$ refrigerant is 30% worse than that of an air conditioner using conventional refrigerant.

Figure 4(b) shows the results of the MFA analysis of the installed stock of refrigerants when $CO_2$ refrigerant is introduced, based on the refrigerant shipment scenario in Figure 4(a). Assuming that $CO_2$ refrigerant shipments begin after 2030 and are introduced at the same rate as conventional refrigerants, $CO_2$ refrigerant will account for 90% of the total in 2050, with the remaining 10% being conventional R32 refrigerant. Using these refrigerant proportions and the results of the process simulation, an LCA up to 2050 was performed.

As illustrated in Figure 5(a), the results of life cycle GHG emissions from 2000 to 2050 are presented for a scenario in which conventional refrigerants continue to be used for air conditioners, and the emission intensity of electricity is equivalent to that of the year 2020. In this scenario, over 90% of the 2050 life cycle GHG emissions are derived from operations. Figure 5(b) presents the results of the life cycle GHG emissions for the electricity decarbonization scenario. A substantial decrease in GHG emissions from operations is estimated, although the emission does not reach zero. This is attributable to the presence of residual electricity emissions intensity at 2050, estimated through linear extrapolation over the past decade, and the persistence of emissions from manufacturing and refrigerant leaks at approximately the same levels.

As illustrated in Figure 5(c), the life cycle GHG emissions from 2000 to 2050 for an air conditioning system designed to utilize a $CO_2$ refrigerant as a substitute for conventional refrigerant, with equivalent performance characteristics, are depicted. The straight lines represent the results for the non-decarbonization scenario, while the area graphs represent the results for the decarbonization scenario. In the non-decarbonization scenario, GHG emissions from operations are the predominant contributor to the total emissions, as estimated in scenarios that utilize conventional refrigerants. In the decarbonization scenario, heat exchangers will increase in size to maintain the same COP as conventional refrigerants. Consequently, GHG emissions derived from the manufacturing phase will account for a greater proportion of total emissions in 2050. In this case, circulation strategies such as heat exchanger recycling play a pivotal role.

**Table 1:** Results of process simulation of air conditioners utilizing conventional refrigerant (R32) and alternative refrigerant ($CO_2$) with two cases

| Refrigerants | Relative COP | Relative size of outdoor unit HEX |
|---|---|---|
| R32 | 100% | 100% |
| $CO_2$ (COP equivalent) | 100% | 574% |
| $CO_2$ (Size equivalent) | 70% | 100% |

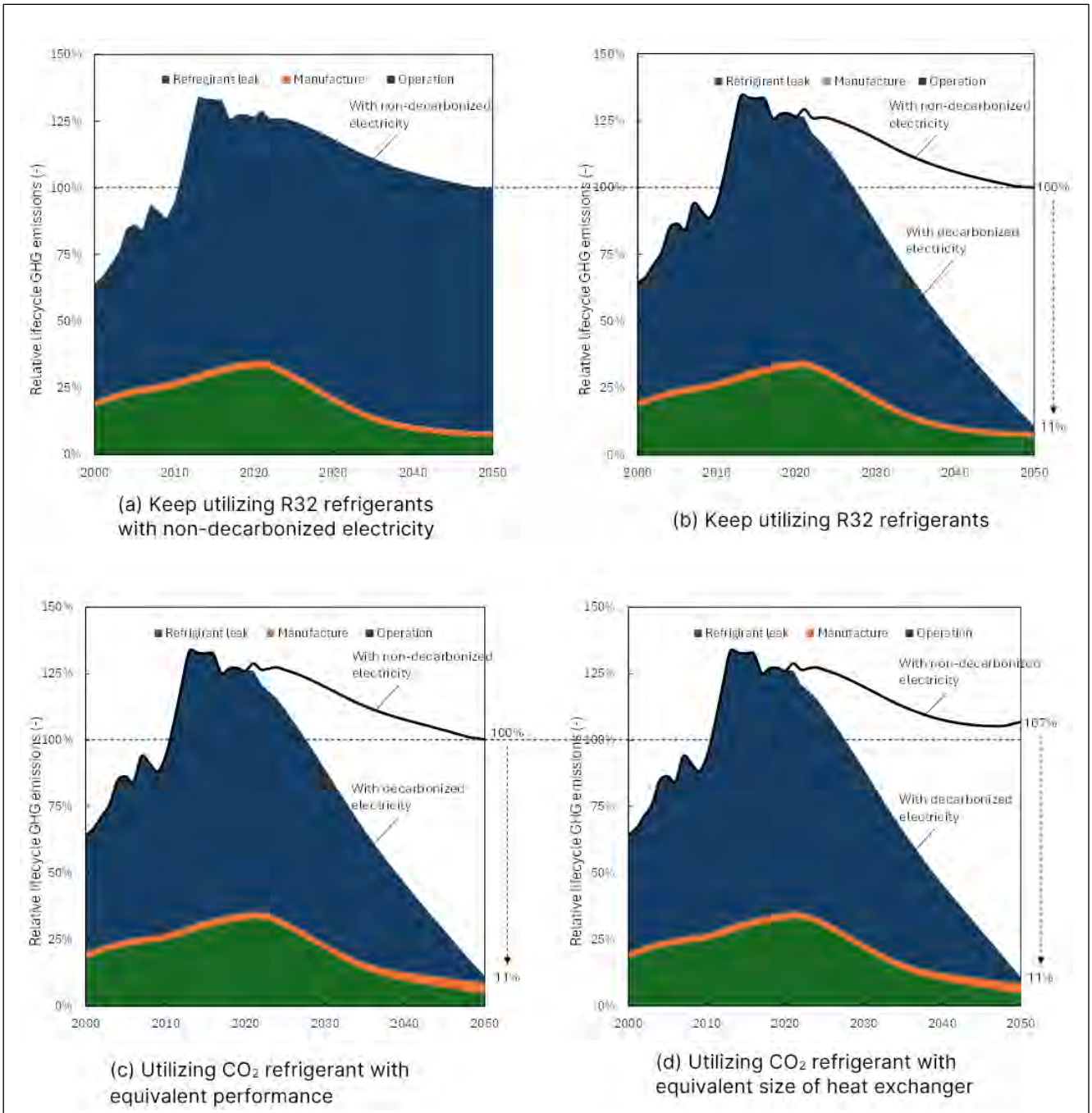



**Figure 5.** Result of life cycle assessment

Figure 5(d) shows the life cycle GHG emissions from 2000 to 2050 for an air conditioning system utilizing $CO_2$ refrigerant with equivalent size of heat exchanger. In this case, the COP of the air conditioner using $CO_2$ refrigerant was worse than that of the air conditioner using conventional refrigerant. In the electricity decarbonization scenario, GHGs derived from electricity consumption are significantly reduced in all cases, so that even if refrigerants are replaced and heat exchangers are enlarged or electricity consumption is increased, total emissions in 2050 would be about the same level as shown in Figure 5(b), (c), and (d), while the non-decarbonization electricity scenario results in increased electricity consumption and accompanying total GHG emissions due to lower performance for the air conditioning system utilizing $CO_2$ refrigerant with equivalent size of heat exchanger as shown in Figure 5(d).

In summary, the dominant factor in the life cycle GHG emissions of air conditioners is derived from electricity consumption, and to move towards carbon neutrality, reducing electricity consumption must be a priority first, and as electricity is decarbonized, the impact of

refrigerants must be considered in the future. As shown in the examples above, computational process simulation can be seamlessly integrated with MFA and LCA to reflect technological information likely to be introduced in the future, while feedback from system analyses can be used to change the strategy of the technology and discuss the feasibility of the technology. Therefore, process engineering plays an important role in prospective life cycle design in resource circulation and decarbonization strategies

## CONCLUSION

In this study, computer-aided process modeling is positioned between technology development and system evaluation to promote feedback from system evaluation by reflecting technical information. The process simulation was developed to visualize the impact of refrigerant substitution by linking MFA and LCA. The results showed that the development of a process simulation that can reflect technological information has the potential to promote discussions on resource circulation and decarbonization strategies.

## ACKNOWLEDGEMENTS

This work was supported by JSPS KAKENHI Grant-in-Aid for Early-Career Scientists (Grant Number JP22K18061), JST COI-NEXT (Grant Number JPMJPF2003), and JST PRESTO (Grant Number JPMJPR2278). This work was conducted in the research unit at the Institute for Future Initiatives at the University of Tokyo: circular economy modeling towards cleaner air supported by DAIKIN Industries, Ltd. The activities of the Presidential Endowed Chair for “Platinum Society” at the University of Tokyo are supported by Mitsui Fudosan Corporation, Sekisui House, Ltd., East Japan Railway Company, and Toyota Tsusho Corporation.

## REFERENCES

1. Kikuchi Y, Nakai M, Kanematsu Y, Oosawa K, Okubo T, Oshita Y, Fukushima Y. Application of technology assessments to co-learning for regional transformation: a case study of biomass energy systems in Tanegashima. *Sustainability* 15:1473-1494 (2020) https://doi.org/10.1007/s11625-020-00801-1
2. Swedish Energy Agency, Tank to Grave Management of new Low-GWP Refrigerants
3. Lv H, Ma H, Mao N, He T. Biling heat transfer mechanism of environmental-friendly refrigerants: A review. *Int. J. Refrig*. 133: 214-225 (2022) https://doi.org/10.1016/j.ijrefrig.2021.10.007
4. Shah N, Park WY, Ding C. Trends in best-in-class energy-efficient technologies for room air conditioners, Energy Reports 7:3162-3170 (2021) https://doi.org/10.1016/j.egyr.2021.05.016
5. Jin T, Li G, Cao Y, Xu R, Shao S, Yang B. Experimental research on applying the copper-clad aluminum tube as connecting tubes of air conditioners. *Energy Build* 97:1–5 (2015) https://doi.org/10.1016/j.enbuild.2015.03.023
6. Fujii S. Development of prospective lifecycle design and assessment method with seamless analysis from nano to kilo level researches, JST PRESTO
7. Lemmon EW, Bell IH, Huber ML, McLinden MO. NIST Standard Reference Database 23: Reference Fluid Thermodynamic and Transport Properties-REFPROP, Version 10.0, National Institute of Standards and Technology, Standard Reference Data Program, (2018)
8. Cabinet Office, Government of Japan, Consumer Confidence Survey (2020)
9. National Institute of Population and Social Security Research. https://www.ipss.go.jp/pp-zenkoku/j/zenkoku2017/pp_zenkoku2017.asp
10. National Institute for Environmental Studies. Lifespan database for Vehicles, Equipment, and Structures. LiVES, (2010)
11. Nishizawa T, Handa Y, Yoneda S, Fang Q, Ohara S, Oshita Y, Fujii S, Kikuchi Y. Hotspot analysis of environmental load at the manufacturing stage of commercial air conditioners(in Japanese). *Proc. 17th Meeting of iLCAj i-A1-01* (2022)
12. Director-General's Secretariat, Agency for Natural Resources and Energy. Comprehensive Energy Statistics (2020)

© 2025 by the authors. Licensed to PSEcommunity.org and PSE Press. This is an open access article under the creative commons CC-BY-SA licensing terms. Credit must be given to creator and adaptations must be shared under the same terms. See https://creativecommons.org/licenses/by-sa/4.0/



Systems & Control Transactions

**Research Article - Peer Reviewed Conference Proceeding**
ESCAPE 35 - European Symposium on Computer Aided Process Engineering
Ghent, Belgium. 6-9 July 2025
Jan F.M. Van Impe, Grégoire Léonard, Satyajeet S. Bhonsale,
Monika E. Polańska, Filip Logist (Eds.)

PSE PRESS

# Solving Complex Combinatorial Optimization Problems Using Quantum Annealing Approaches

**Vasileios K. Mappas[a]*, Bogdan Dorneanu[a], and Harvey Arellano-Garcia[a]**

[a] FG Prozess, und Anlagentechnik, Brandenburgische Technische Universität, Cottbus, Germany
* Corresponding Author: vasileios.mappas@b-tu.de.

## ABSTRACT

Currently, state-of-the-art approaches to solving complex optimization problems have focused solely on methods requiring high computational time and unable to find the global optimal solution. In this work, a methodology based on quantum computing is presented to overcome these drawbacks. The novelty of this framework stems from the quantum computer's architecture and taking into consideration the quantum phenomena that take place to solve optimization problems with specific structure. The proposed methodology includes steps for the transformation of the initial optimization problem into an unconstrainted optimization problem with binary variables and its embedding onto a quantum device. Moreover, different resolution levels for the transformation step and different architectures for the embedding process are utilized. To illustrate the procedure, a case study based on Haverly's pooling and blending problem is examined while demonstrating the potential of the proposed approach. The results indicate that the succinct formulation exhibited higher success rate during the embedding procedure for the different examined architectures, and the quantum annealing solver exhibited the best performance among the various solvers investigated. This highlights the potential of the approach for solving this type of problems with the rapid development and improvement of quantum hardware and expanding it to more complex chemical engineering optimization systems.

**Keywords**: Optimization, Scheduling, Algorithms, Quantum Computing, Quantum Annealing

## 1. INTRODUCTION

Combinatorial optimization (CO) is a branch of mathematical optimization that is applied for a broad set of applications in the fields of industrial engineering, transportation or manufacturing. Finding the global solutions for this type of problems is challenging, due to its NP-hard nature [1].

In real-world applications, processes are described by highly nonlinear and nonconvex expressions leading to an exponential growth of the number of local solutions as the number of variables increases [2].

Several strategies, based on classical optimization techniques, heuristics and neural network methods, have been proposed to solve optimization problems [3]. Nonetheless, these state-of-the-art methods exhibit the following limitations:

1. High computational timeframes are required in deterministic optimization algorithms.
2. Solution quality is not guaranteed in heuristic approaches, leading to suboptimal results.
3. The training and the tuning of the neural networks, as well as the use of small instances of problems affects the solution.

Quantum computing (QC) is a rapidly growing research field and promising technology that differentiates itself from classical computers and utilize quantum phenomena such as entanglement and superposition to perform calculations and simulations. QC is capable of providing polynomial-time solutions for problems in the BQP (bounded error, quantum, polynomial time) complexity class [4].

To address these drawbacks, this contribution proposes a solution framework, based on QC, that involves formulating the original optimization problem as a Quadratic Unconstrained Binary Optimization (QUBO) problem and embedding it onto a quantum device.

The remainder of the contribution is structured as

follows: in Section 2 the methodology for reformulating the CO problem into QUBO is presented. The proposed solution framework is applied for a case study in Section 3. The key results and future work required are summarized in Sections 4 and 5, respectively.

## 2. METHODOLOGY

In the first step, the original CO problem is formulated as a QUBO problem, where continuous and integer variables are transformed into binaries and its formulation is given by:

$$\min_x xQx^T, x \in \{0,1\} \quad (1)$$

where $x$ represents the vector of binary decision variables and $Q$ is a square matrix of constants.

To construct the $Q$ matrix, additional steps are required such as: the transformation of inequality constraints into equalities, the removal of bilinear terms and the introduction of quadratic penalty terms, as shown in Figure 1.

The QUBO problem, defined by Eq. (1), is subsequently solved using Quantum Annealing (QA) in a quantum adiabatic environment. QA is a model of quantum computation that utilizes quantum fluctuations to search for ground state solutions of the CO problem that is encoded as a Hamiltonian by applying a transverse field [5]. Furthermore, QA in D-Wave systems utilizes the QUBO formulation for optimization problems, supports over 5,000 physical qubits, and can efficiently explore the solution space by overcoming local minima.

Apart from QA, the D-Wave suite offers different solution approaches that can be utilized to solve QUBO such as the multistart Tabu search (TS) and qboslv (TN) solvers. TS is based on memory-based strategies, and explores regions of the solution space and prevents the recurrence of recent moves. TN partitions the original problem into smaller sub-problems defined by the algorithm which are solved by simulated annealing (SA). Furthermore, the user can define the size of the sub-problem (TSN-x solver), where x represents the maximum number of variables allowed in each subproblem.

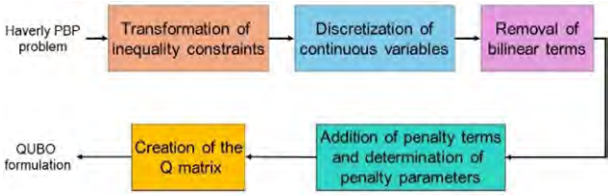



**Figure 1.** Tranformation procedure of the PBP into QUBO

After the QUBO transformation, an embedding procedure onto the QA hardware is required to find the optimal solution, involving mapping the graph described by the QUBO problem as a minor of the graph representing the qubit lattice of the QA system.

To achieve this, Chimera and Pegasus topology unit cells are used to attain connectivity among the qubits which are available in D-Wave systems. These embedding architectures depend on QA hardware design, and parameters such as the largest complete subgraph of an arbitrary problem system (maximal clique size) and the number of nodes in one half of the bipartite cell (shore size).

The benefits of the proposed solution scheme are summarized below:

- The QA framework has the ability to explore the solution space more broadly and not get stuck in a local solution through quantum tunneling.
- Multiple states can be simultaneously explored during the annealing process, reducing the required computational time due to quantum superposition.

## 3. COMPUTATIONAL RESULTS

In this section, a case study based on Haverly's pooling and blending problem (PBP) [6] is examined using the proposed methodology. This problem is selected due to its non-convex nature and the existence of bilinear terms, which can result in multiple local minima. Furthermore, PBPs are easily scalable in terms of complexity, as the problem definition can be readily expanded to include additional streams, products, and pools.

All the simulations are performed in Python, where the NetworkX package is used for creating and analyzing the Chimera and Pegasus graph objects and the D-Wave's Ocean software for embedding and solving the QUBO problem.

The p-formulation of the PBP including three reagent streams, two product streams, and one pool in which two reagents are blended is given by:

$$\min F_A C_A + F_B C_B + F_{Cx} C_C + F_{Cy} C_C + F_X C_X + F_Y C_Y \quad (2a)$$

$$\text{s.t. } F_{px} + F_{py} - F_A - F_B = 0 \quad (2b)$$

$$F_x - F_{Cx} - F_{px} = 0 \quad (2c)$$

$$F_y - F_{Cy} - F_{py} = 0 \quad (2d)$$

$$S_p F_{px} + \mathrm{S_p} F_{py} - \mathrm{S_A F_A} - \mathrm{S_B F_B} = 0 \quad (2e)$$

$$S_p F_{px} + \mathrm{S_C} F_{Cx} - \mathrm{S_x F_x} \leq 0 \quad (2f)$$

$$S_p F_{py} + \mathrm{S_C} F_{Cy} - \mathrm{S_y F_y} \leq 0 \quad (2g)$$

$$F_x - 100 \leq 0 \quad (2h)$$

$$F_y - 200 \leq 0 \quad (2i)$$

where $F_A$, $F_B$, $F_{Cx}$, and $F_{Cy}$ are the feed streams, $F_{px}$ and $F_{py}$ are the pool streams, $F_x$ and $F_y$ denote the product streams, and $S_x$ and $S_y$ represent the product composition. The values of parameters for the examined Haverly

PBP are given in Figure 2.

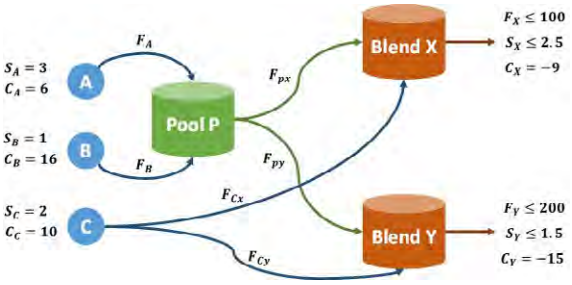



**Figure 2.** Schematic representation of Harvely PBP

Following the steps illustrated in Figure 1, the reformulated PBP can be written as:

$$\min F_A C_A + F_B C_B + F_{Cx} C_C + F_{Cy} C_C + F_x C_x + F_y C_y + P\left\{\left(F_{px} + F_{py} - F_A - F_B\right)^2 + \left(F_x + F_{Cx} - F_{px}\right)^2 + \left(F_y + F_{Cy} - F_{py}\right)^2 + (T_x + \mathrm{S_C F_{Cx}} - \mathrm{S_x F_x} + \Gamma_3)^2 + \left(T_y + \mathrm{S_C F_{Cy}} - \mathrm{S_y F_y} + \Gamma_4\right)^2 + \left(T_x + T_y - S_A F_A - S_B F_B\right)^2 + (F_x - 100 + \Gamma_1)^2 + \left(F_y - 200 + \Gamma_2\right)^2 + \sum_{i=1}^{n_{fpx}} \sum_{j=1}^{n_{sp}} \left(F_{px,i} S_{p,j} - 2T_{x,ij} F_{px,i} - 2T_{x,ij} S_{p,j} + 3T_{x,ij}\right) + \sum_{i=1}^{n_{fpy}} \sum_{j=1}^{n_{sp}} \left(F_{py,i} S_{p,j} - 2T_{y,ij} F_{py,i} - 2T_{y,ij} S_{p,j} + 3T_{y,ij}\right)\right\} \quad (3)$$

where $\Gamma_1 - \Gamma_4$ are the slack variables, $P$ is the penalty parameter, and $T_x$ and $T_y$ are the binary transformation variables for the removal of bilinear terms $S_p F_{px}$ and $S_p F_{py}$, respectively.

In the following, two transformations have been utilized: a verbose transformation, in which the discretized variables are expanded to allow for greater precision, and a succinct transformation, where each variable is constrained to integer values.

In both formulations, the number of binary variables is determined based on the required precision for expressing the continuous variables of the Haverly's PBP. Furthermore, the slack variables introduced to transform the inequality constraints to equalities utilize more qubits compared to the continuous to prevent the imposition of suboptimal values. Based on this protocol, the succinct formulation needed approximately two-thirds fewer binary variables to represent the problem compared to the verbose formulation. This reduction can be attributed to the decrease in the number of transformation variables required to eliminate the bilinear terms present in Eqs. 2e – 2g. Table 1 presents some of the parameters of the resulting succinct and verbose formulations.

Once the QUBO transformation is obtained, the embedding process is employed to insert the reformulated optimization problem into the lattice of qubits that form the quantum processing unit. In this study, the Chimera and Pegasus graphs are used for the embedding. To successfully insert the QUBO to the QA, the value of the maximal clique is required. The maximal cliques for both qubit architectures are obtained using the Bron and Kerboch algorithm [7] and found to be 75 and 30 for the verbose and succinct formulations, respectively, as shown in Table 1.

**Table 1:** Succinct and verbose QUBO characteristics for the Haverly's PBP

| Parameter | Verbose | Succinct |
|---|---|---|
| Binaries for continuous variables | 66 | 63 |
| Binaries for slack variables | 36 | 30 |
| Binaries for transformation variables | 75 | 30 |
| Maximum clique size | 75 | 30 |
| Q matrix size | 177 | 123 |
| Non-zero matrix elements | 7,765 | 3,319 |
| Total binary combinations | $1.9\times10^{53}$ | $1.0\times10^{37}$ |

## 4. RESULTS AND DISCUSSION

All the simulations for the reformulation of the PBP are performed in Python using the D-Wave Ocean toolbox [8], where SA, TS, TN and TSN-x solvers as well as the Pegasus and Chimera topologies are used to solve the succinct and the verbose formulations. As a reference case, the QUBO problem is solved using the Multistart and GlobalSearch solvers available in MATLAB's Global Optimization (GO) toolbox. After the execution of each solver, a sample set is returned and the set with the most occurrences among the collected data is returned as the best solution.

### 4.1 PBP embedding procedure

In this subsection, the performance of the different embedding architectures is examined and compared. Apart form the calculation of the maximum clique value, there are other features that affect the performance of the embedding procedure, such as the number of units, shore size, and the unit's height and width.

In the Chimera graph architecture, two different cases are examined. In the first case, the shore size is fixed to the value of 4 and the height and the width of the graph varied in integer increments from 16 to 26 with the structure remaining symmetric. In the second case, the graph's height and width kept constant to 16 and the shore size varied in integer increments from 4 to 10. In both cases, the probability and the time required to embed the problem system into the Chimera graph are obtained.

It can be observed that the verbose formulation requires a high number of qubits compared to the succinct formulation for a successful embedding, as shown in Figure 3. Furthermore, the verbose architecture failed to embed on any of the Chimera graphs with shore size

equal to 4 and varying graph's height and width.

Figure 4 presents the required wall clock for successful embedding. The succinct architecture exhibits rapid convergence in the range of 20-30 seconds with a standard deviation of 15-30 seconds. On the other hand, the verbose embedding requires higher average embedding times and standard deviations.

It can be concluded that when the embedding is successful, the embedding time will converge, with the rate of convergence being influenced by the system's connectivity.

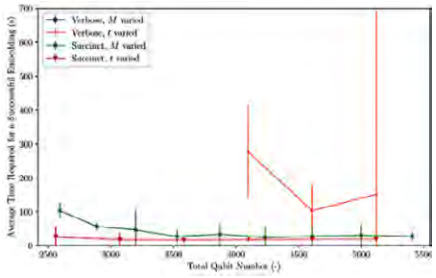



**Figure 3.** Required time for successful embedding in a Chimera graph as a function of qubit number

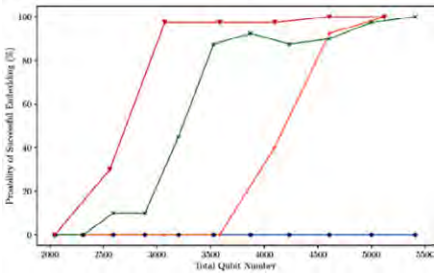



**Figure 4.** Propability for the problem system in a Chimera graph as a funtion of qubit number

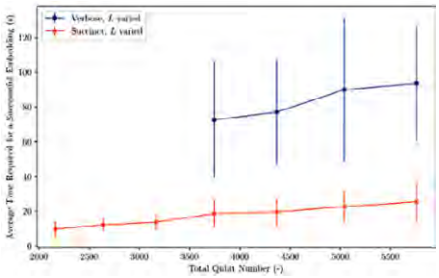



**Figure 5.** Required time for successful embedding in a Pegasus graph as a function of qubit number

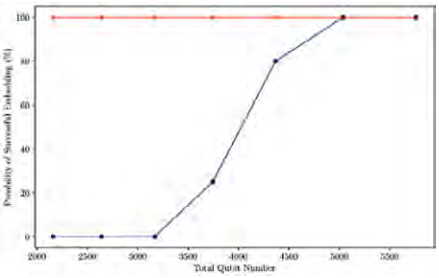



**Figure 6.** Propability for the problem system in a Pegasus graph as a funtion of qubit number

The same procedure is used for the Pegasus configuration where the graph's size parameter is varied in integer increments from 10 to 16. It can be seen that the succinct formulation is successfully embedded for all the sizes, whereas the verbose formulation only when the number of qubits is 3,700 and above, as shown in Figure 5.

Contrary to the behaviour observed for the Chimera embedding, Figure 6 illustrates that the required wall clock time as well as the standard deviation for the embedding step increases with the increase in the number of qubits.

## 4.2 Penalty multiplier value selection

As mentioned in Section 2, a penalty term is introduced during the QUBO transformation procedure to enforce constrained behaviour without the use of constraints. The selection of the appropriate $P$ value is a non-trivial task because there is a trade-off between enforcing constrained behaviour that usually requires large values and retaining the objective function information [9].

For this task, the optimal value of the penalty multiplier was found by solving the verbose and succinct formulations of the problem at different values ranging from 75% to 150% of the optimal objective function value, $\hat{f}^*$ (which is equal to -400), in 5% increments. Each system was solved using 40 calls and the obtained values were processed to yield the unweighted objective function value, given by:

$$\bar{f} = \frac{(\hat{f}-c)}{k} \tag{4}$$

where $c$ is a constant representing the total sum of the constant cross terms from the quadratic penalties and $k$ is a constant ranging from 0.75 to 1.5.

In Figure 7, it can be observed that the succinct formulation of the QUBO problem is solved more easily than the verbose formulation. Furthermore, this effect is most clear in the TN method, while for the TSN-x method is the least evident.

As far as the constraint violation is concerned, the verbose formulation demonstrates lower values compared to the succinct, as shown in Figure 8. Furthermore, SA and TS solvers exhibit the highest and the lowest value for the squared constraint violation, respectively.

It should be noted that none of the solvers returned negative solutions and consequently corresponding all to a setup that would be unprofitable or physically impossible. For each solver, the optimal value of the penalty parameter was obtained by calculating a composite rank that is equally weighted in terms of the objective function value and constraint violations. The obtained results of the ranking method are shown in Table 2.

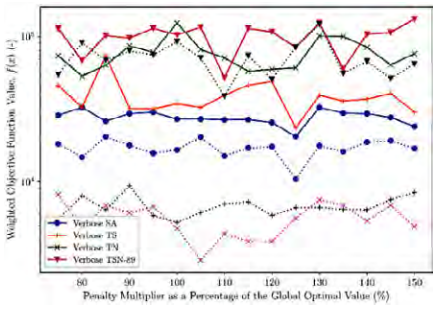



**Figure 7.** Avarage unweighted objective function value

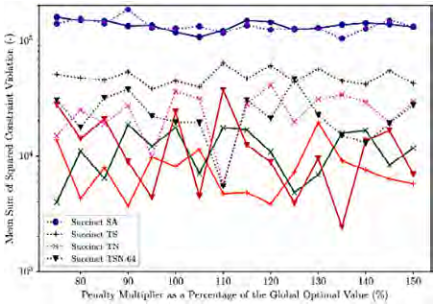



**Figure 8.** Mean sum of squared constraint violation

**Table 2:** Penalty multiplier values $P$ as a % of the objective function values that yielded the lowest composite score

| Formulation | SA | TS | TN | TSN-x |
|---|---|---|---|---|
| Verbose | 125% | 90% | 125% | 135% |
| Succinct | 110% | 95% | 110% | 110% |

## 4.3 QUBO solution

Based on the penalty multiplier values determined in Section 4.2, both the succinct and verbose formulations were created and each problem system is solved using all the aforementioned solvers, using a total of 500 calls and 10,000 initial points. For the GO solvers, the findings indicate that the inclusion of penalty terms enhances the complexity of the resulting system due to the bilinear transformation, thereby making it more challenging to solve.

Tables 3 and 4 present the statistics for the verbose and the succinct of the PBP formulation. It can be seen that the succinct formulation delivers better solutions in terms of the unweighted objective function across all solvers. In particular, this effect is more visible for the TN solver. Furthermore, SA exhibits the best performance for the verbose and the second-best for the succinct formulation among the examined solvers, producing low standard deviations for the unweighted objective function value.

In contrast, the verbose formulation shows better performance in the mean sum of squared violations, except for the case of the TN solver. It can be observed that the succinct formulation exhibits lower performance compared to the verbose at the recovered values of the original objective function.

Based on these findings, the succinct formulation runs into fewer local minima. Therefore, this behaviour can be explained as a result of minimizing toward better underlying solutions but being unable to reduce the error in those solutions.

The TN solver demonstrates better performance in constraint violation and unweighted objective function value compared to the SA solver, as shown in Tables 3

**Table 3:** Summary of results for the verbose formulation of the PBP

| Parameter | SA | TS | TN | TSN-89 | TSN-45 | TSN-23 |
|---|---|---|---|---|---|---|
| Average solving time (ms) | 214 | 596 | 2,087 | 3,039 | 1,875 | 782 |
| Mean of $\bar{f}$ | 6,290 | 14,600 | 24,800 | 30,300 | 23,800 | 36,000 |
| Standard deviation of $\bar{f}$ | 972 | 17,100 | 27,000 | 31,700 | 27,100 | 31,300 |
| Mean of $c$ | 76,240 | 44,990 | 40,961 | 50,174 | 41,436 | 51,999 |
| Standard deviation of $c$ | 81,999 | 74,329 | 73,619 | 79,924 | 73,528 | 73,324 |
| Mean of $f$ | -9.62 | -77.85 | -72.27 | -76.98 | -79.59 | -76.35 |
| Standard deviation of $f$ | 238 | 205 | 254 | 263 | 243 | 271 |

**Table 4:** Summary of results for the succinct formulation of the PBP

| Parameter | SA | TS | TN | TSN-62 | TSN-31 | TSN-16 |
|---|---|---|---|---|---|---|
| Average solving time (ms) | 93 | 587 | 1,514 | 1,480 | 960 | 481 |
| Mean of $\bar{f}$ | 3,340 | 3,900 | 1,620 | 11,400 | 5,560 | 30,700 |
| Standard deviation of $\bar{f}$ | 732 | 1,360 | 625 | 16,700 | 8,690 | 32,900 |
| Mean of $c$ | 81,282 | 76,608 | 28,499 | 64,408 | 52,443 | 59,919 |
| Standard deviation of $c$ | 88,689 | 89,682 | 54,898 | 90,968 | 82,191 | 87,127 |
| Mean of $f$ | -25.02 | 54.75 | -46.43 | -34.15 | -38.06 | -60.16 |
| Standard deviation of $f$ | 241 | 252 | 168 | 158 | 217 | 294 |

and 4. However, the TN solver requires approximately 10 – 15 times more computational time. In the case of the TSN solver, its performance is notably sensitive to the size of the sub-problems, highlighting the pivotal role of subproblem size in achieving optimal solutions.

Overall, the SA solver shows strong performance in terms of the unweighted objective function value and computational time. Therefore, the SA solver is the most promising candidate which is capable of producing good quality results and is suitable for solving QUBO formulation problems successfully.

## 5. CONCLUSIONS

This contribution introduces a quantum approach to formulating and solving CO problems using a QA solution framework. In this work, the procedure for the CO reformulation is showcased as well as embedding and solution of the QUBO reformulation of the Haverly PBP on a quantum machine.

Two QUBO problem formulations, verbose and succinct, are selected and compared. The results revealed that the succinct version of the optimization problem requires smaller value for penalty multipliers and produced better results compared to the verbose formulation.

The numerical experiments have shown that the verbose formulation can be embedded even on very large Chimera graphs. Contrary, the Pegasus architecture is able to successfully handle both succinct and verbose formulations, requiring an average of 25 and 90 seconds, respectively.

The SA solver showed the best performance among the examined solvers in the D-Wave platform and the deterministic GO solvers, although it required high computational time. Furthermore, the results of the TSN-x solver highly depend on the size of subproblem.

This methodology holds the potential for solving efficiently CO problems with the improvement capabilities of the quantum computers in terms of computational power and the availability of the maximum qubits. This approach can be extended to solve chemical engineering applications such as process synthesis and design and production planning and scheduling problems.

As future work, alternative ways for handling bilinear and higher order terms and the transformation of the continuous and integer variables into binaries should be investigated to obtain good quality results in lower computational time.

Additionally, the structure of the optimization problem plays an important role in the solution procedure. Specifically, the embedding algorithm, the sub-problem size and the penalty multiplier values can be optimized, providing the ability of QA systems to offer scaling advantages over traditional heuristics when applied to larger PBPs.

## REFERENCES


1. Zhang C, Wu Y, Ma Y, Song W, Le Z, Cao Z, Zhang J. A review on learning to solve combinatorial optimisation problems in manufacturing. IET Collaborative Intelligent Manufacturing, 5:e12072 (2023) https://doi.org/10.1049/cim2.12072
2. Peres F, Castelli M. Combinatorial optimization problems and metaheuristics: Review, challenges, design, and development. Applied Sciences, 11:6449 (2021) https://doi.org/10.3390/app11146449
3. Blekos K, Brand D, Ceschini A, Chou C-H, Li R-H, Pandya K, Summer A. A review on quantum approximate optimization algorithm and its variants. Physics Reports, 1068:1-66 (2024) https://doi.org/10.1016/j.physrep.2024.03.002
4. Leichtle D, Music L, Kashefi E, Olivier H. Verifying BQP computations on noisy devices with minimal overhead. PRX Quantum, 2:040302 (2021) https://doi.org/10.1103/PRXQuantum.2.040302
5. Yarkoni S, Raponi E, Bäck T, Schmitt S. Quantum annealing for industry applications: Introduction and review. Reports on Progress in Physics, 85:104001 (2022) https://doi.org/10.1088/1361-6633/ac8c54
6. Lotero I., Trespalacios F., Grossmann I. E., Papageorgiou D. J., Cheon M-S. An MILP-MINLP decomposition method for the global optimization of a source based model of the multiperiod blending problem. Computers & Chemical Engineering, 87:13-35 (2016) https://doi.org/10.1016/j.compchemeng.2015.12.017
7. Gupta S. K., Singh D. H., Choudhary J. A review of clique-based overlapping community detection algorithms. Knowledge and Information Systems, 64:2023-2058 (2022) https://doi.org/10.1007/s10115-022-01704-6
8. Ocean Developer Tools, https://docs.ocean.dwavesys.com
9. Ju J., Liu Q. Convergence properties of a class of exact penalty methods for semi-infinite optimization problems. Mathematical Methods of Operations Research, 2020, 91:383-403 https://doi.org/10.1007/s00186-019-00693-7



© 2025 by the authors. Licensed to PSEcommunity.org and PSE Press. This is an open access article under the creative commons CC-BY-SA licensing terms. Credit must be given to creator and adaptations must be shared under the same terms. See https://creativecommons.org/licenses/by-sa/4.0/




Systems & Control Transactions

**Research Article - Peer Reviewed Conference Proceeding**
ESCAPE 35 - European Symposium on Computer Aided Process Engineering
Ghent, Belgium. 6-9 July 2025
Jan F.M. Van Impe, Grégoire Léonard, Satyajeet S. Bhonsale,
Monika E. Polańska, Filip Logist (Eds.)

PSE PRESS

# A Propagated Uncertainty Active Learning Method for Bayesian Classification Problems

**Arun Pankajakshan[a], Sayan Pal[a], Maximilian O. Besenhard[a], Asterios Gavriilidis[a], Luca Mazzei[a], Federico Galvanin[a,*]**

[a] Department of Chemical Engineering, University College London, Torrington Place, London, WC1E 7JE, United Kingdom
* Corresponding Author: f.galvanin@ucl.ac.uk.

## ABSTRACT

Bayesian classification (BC) is a powerful supervised machine learning method for modelling the relationship between a set of continuous variables and a set of discrete variables that represent classes. BC has been successful in engineering and medical applications, including feasibility analysis and clinical diagnosis. Gaussian process (GP) models are widely used in BC methods to model the probability of assigning a class to an input point, typically through an indirect approach: a GP predicts a continuous function value based on Bayesian inference, which is then transformed into class probabilities using a nonlinear function like a sigmoid. The final class labels are assigned based on these probabilities. In this commonly used workflow, the uncertainty associated with the class prediction is usually evaluated as the uncertainty in the GP function values. A disadvantage of this approach is that it does not consider the uncertainty directly associated with the decision-making. In this work, we propagate the uncertainty from the space of GP function values to the class probability space and use this to quantify the uncertainty directly associated with the decision-making process. Additionally, we employ the propagated uncertainty as the objective function in an active learning (AL) method to generate new informative data points for the GP classifier training. We compare the proposed AL method to existing state-of-the-art methods to evaluate its performance.

**Keywords**: Bayesian classification, Gaussian process, active learning, uncertainty propagation.

## 1. INTRODUCTION

Probabilistic learning is key to developing autonomous systems that adapt and make reliable decisions without human intervention [1]. One of the popular probabilistic learning approaches that has key applications in engineering and medical domains is Bayesian classification (BC) [2].

BC involves a probabilistic approach to the classification problem. A classification problem is a supervised machine learning method used to build a functional relationship between a set of input variables and a set of classes or categories related to the input variables. Usually, the classes are labelled using discrete values such as 0, 1, 2 etc. BC has proven successful in applications such as medical diagnosis [3] and feasibility analysis [4], where the uncertainty of model predictions is critical. A popular choice of BC implementation involves BC with Gaussian processes (GPs) [5].

In problems of BC with GPs, the posterior GP model, i.e. the model obtained after data fitting or learning through Bayesian inference [5], provides probability predictions corresponding to the class labels along with an associated uncertainty value. This uncertainty offers meaningful insights into the model and supports the design of learning strategies that utilize it. This field of informed learning process to facilitate efficient training of a GP model with limited informative data is known as active learning (AL) [6]. Therefore, the GP model's ability to quantify uncertainty is closely linked to the learning approach employed in AL.

Two approaches are commonly used for uncertainty quantification in BC with GPs: 1) aleatoric or intrinsic uncertainty associated with the class prediction and 2) uncertainty in the GP model predictions. In 1), the class conditional probability values predicted by the GP model are

used for uncertainty quantification. For instance, extremely low or extremely high probabilities indicate low uncertainty in the outcome predicted by the model while probabilities near 0.5 indicate a presence of high uncertainty. In 2), uncertainty in BC is quantified as the uncertainty around the point estimates of the GP model predictions. The point estimates of the GP model predictions are further transformed into class probabilities for deciding the class label prediction. Both approaches do not consider the uncertainty around the predicted class probabilities which are used in decision-making regarding the class selection. This could lead to slow convergence of the classifier learning process or could result in a classifier model that is not accurately reliable. In this work, we propagate the uncertainty from the predictions of the posterior GP model to the class probability predictions using a linear error propagation rule. This propagated uncertainty is proposed to quantify the uncertainty associated with the BC problem. Further, we employ the propagated uncertainty in an AL framework to generate informative datasets to train the classifier model. This proposed novel AL strategy is compared with the existing methods (methods based on the approaches 1 and 2 discussed above) to demonstrate its usefulness in the context of AL.

## 2. METHODOLOGY

### 2.1 Bayesian binary classification with Gaussian processes

Binary classification involves the problem of assigning one of the two classes (0 or 1) to an input vector $\mathbf{x}$ by predicting the probability $\phi$ of class 1 given $\mathbf{x}$, $\phi = P(c = 1|\mathbf{x})$. This probability can be modelled as $\phi = g(h(\mathbf{x}))$, where $h(\mathbf{x})$ is a latent function, which is a mapping from the inputs $\mathbf{x}$ to continuous real values (latent function values) $y$, and $g$ is the sigmoid transformation defined as $g(y) = 1/1 + e^{-y}$, which is a mapping from the latent function values $y$ to the unit interval $[0,1]$. In Bayesian classification with Gaussian processes, a Gaussian process prior is placed over the latent function $h(\mathbf{x})$.

$$h(\mathbf{x}) \sim \mathcal{N}\big(m(\mathbf{x}), k(\mathbf{x}, \mathbf{x}')\big) \tag{1}$$

As discussed in [5], here the latent function $h$ plays the role of a nuisance function, in the sense that we are not particularly interested in the values of $h$, but rather in $g(h(\mathbf{x}))$. We observe only the inputs $\mathbf{X}$ and the class labels $\mathbf{c}$. Let $\mathbf{X} = [\mathbf{x}_1, \ldots, \mathbf{x}_n]^\intercal$ are the inputs corresponding to $n$ data points. A GP prior is a collection of random variables $\{\mathbf{Y}(\mathbf{x})|\mathbf{x} \in \mathbf{X}\}$ indexed by the set $\mathbf{X}$, where any finite set of $\mathbf{Y}$ follows a joint multivariate Gaussian distribution. A GP prior is fully specified by its mean function $m(\mathbf{x}) = \mathrm{E}[\mathbf{Y}(\mathbf{x})]$ and its covariance function $k(\mathbf{x}, \mathbf{x}') = \mathrm{E}\big[\big(\mathbf{Y}(\mathbf{x}) - m(\mathbf{x})\big)\big(\mathbf{Y}(\mathbf{x}') - m(\mathbf{x}')\big)\big]$. For simplicity, we set the prior mean to zero, i.e., $m(\mathbf{x}) = 0$. For the covariance function, we employed the popular squared exponential covariance function with automatic relevance determination (ARD) distance measure. For the mathematical expression of the squared exponential kernel function, the readers are referred to [5]. We denote all the learned parameters of the covariance function that include the signal variance and the characteristic length scales by the hyperparameter vector $\boldsymbol{\theta}$. With this specification of prior mean and the covariance function, the prior over the latent function is jointly Gaussian. Let $y_\mathrm{i} = h(\mathbf{x}_\mathrm{i})$ and $\mathbf{y} = [y_1, \ldots, y_\mathrm{n}]^\intercal$ denote the latent function values, then the prior takes the form:

$$p(\mathbf{y}|\mathbf{X}, \boldsymbol{\theta}) = \mathcal{N}(\mathbf{0}, \mathbf{K}) \tag{2}$$

where $\mathbf{K}$ is the $n \times n$ covariance matrix with elements defined by $\mathrm{K}_{ij} = k(\mathbf{x}_i, \mathbf{x}_j), i, j = 1, \ldots, n$. Corresponding to each input data point $\mathbf{x}_i$, the probability of observing the class label 1 can be represented using a Bernoulli distribution. That is, given $\mathbf{x}_i$ and $c_i$, $\hat{c}_i = 1 \sim Bernoulli\left(g\big(h(\mathbf{x}_i)\big)\right)$, where $g\big(h(\mathbf{x}_i)\big) = \phi_i$ is the predicted probability of obtaining a class 1. For $n$ independent data points, the likelihood $p(\mathbf{c}|\mathbf{y})$ can be derived from the probability mass function of the individual Bernoulli distributions as:

$$p(\mathbf{c}|\mathbf{y}) = \prod_{i=1}^{n} \left(g\big(h(\mathbf{x}_i)\big)\right)^{c_i} \left(1 - g\big(h(\mathbf{x}_i)\big)\right)^{1-c_i} \tag{3}$$

The posterior distribution over the latent function values $p(\mathbf{y}|\mathbf{X}, \mathbf{c}, \boldsymbol{\theta})$ can be computed from the prior and the likelihood using the Bayesian rule:

$$p(\mathbf{y}|\mathbf{X}, \mathbf{c}, \boldsymbol{\theta}) = \frac{p(\mathbf{y}|\mathbf{X}, \boldsymbol{\theta})}{p(\mathbf{c}|\mathbf{X}, \boldsymbol{\theta})} p(\mathbf{c}|\mathbf{y}) \tag{4}$$

where $p(\mathbf{c}|\mathbf{X}, \boldsymbol{\theta}) = \int p(\mathbf{c}|\mathbf{y})\, p(\mathbf{y}|\mathbf{X}, \boldsymbol{\theta}) d\mathbf{y}$ is the marginal likelihood. The evaluation of the posterior allows to make predictions $h(\mathbf{x}_*)$ for a new test point $\mathbf{x}_*$. However, the computation of the posterior distribution in Equation (4) is analytically intractable due to the non-Gaussian likelihood in Equation (3), which makes the evaluation of the integral on the right-hand side of the marginal likelihood impossible [5]. Owing to this, the training of the GP model (which involves maximizing the marginal likelihood) as well as the inference problem (making predictions based on the sample data, by using the learned hyperparameters) are evaluated using variational inference methods [7]. We employed evidence lower bound (ELBO) [7] as the variational inference loss function for GP model training.

### 2.2 Uncertainty in the inference

Common practices to quantify the uncertainty in the inference of BC with GP model involve either estimating the uncertainty as the variance over the latent function values or estimating it as the variance of the predicted

classification outcomes. For any new input point $\mathbf{x}_*$, the variance over the latent function values can be computed as:

$$\sigma_y^2(\mathbf{x}_*) = k(\mathbf{x}_*, \mathbf{x}_*) - k_*^{\mathrm{T}}\mathbf{K}^{-1}k_* \quad (5)$$

where $k_* = [k(\mathbf{x}_1, \mathbf{x}_*), \ldots, k(\mathbf{x}_n, \mathbf{x}_*)]^{\mathrm{T}}$. With the assumption that the predicted distribution of class labels is the same as the true distribution, the uncertainty of the classification outcome for any new input data point $\mathbf{x}_*$ can be computed as the random variance of the Bernoulli distribution corresponding to predicting a class 1 with a probability $\phi_*$. This variance can be computed as:

$$\sigma_{\hat{c}}^2(\mathbf{x}_*) = \phi_*(1 - \phi_*) \quad (6)$$

## 2.3 The propagated uncertainty

In this work, we quantify the uncertainty around point estimates of the class probability predictions by propagating the uncertainty over the latent function values to the predicted probability values using the linear error propagation rule. The propagated uncertainty is computed as:

$$\sigma_\phi^2(\mathbf{x}_*) = \left(\left.\frac{d\phi}{dy}\right|_{\mathbf{x}_*} \times \sigma_y(\mathbf{x}_*)\right)^2 = \left(\frac{e^y}{(1+e^y)^2}\right)^2 \times \sigma_y^2\Big|_{\mathbf{x}_*} \quad (7)$$

The uncertainty propagation is visually depicted in Figure 1.

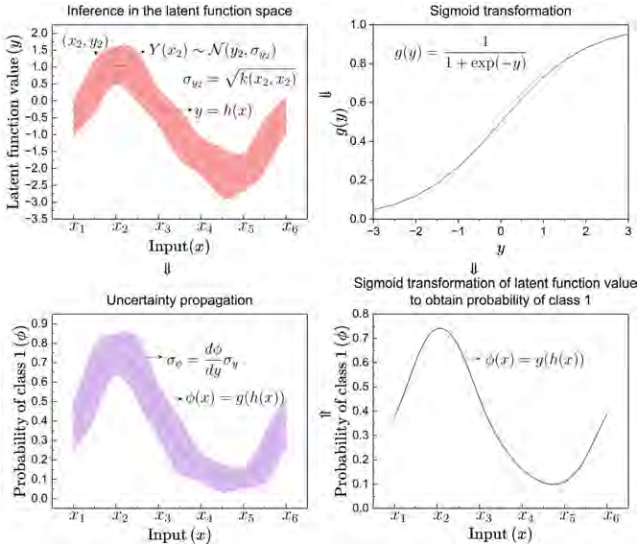



**Figure 1.** Uncertainty propagation to probability space.

## 2.4 Simulation study

A simulation study was designed to compare the performance of the three AL methods: **Method 1** using $\sigma_{\hat{c}}^2(\mathbf{x}_*)$ as the objective function (Equation (6)); **Method 2** using $\sigma_y^2(\mathbf{x}_*)$ as the objective function (Equation (5)) and **Method 3** using the proposed propagated uncertainty, $\sigma_\phi^2(\mathbf{x}_*)$ as the AL objective function (Equation 7). In all the three cases, the design of new experiments using the AL method involved seeking conditions where the corresponding objective function value is a maximum.

The steps involved in the simulation study are summarised in Figure 2. As explained in Figure 2, a classification dataset was first selected as the case study. The second step involved training of a selected classifier model on the full dataset selected in the first step. This trained model was assumed as the "True model" in the simulation study. Next, a limited number of preliminary experiments were designed using design of experiments (DoE) methods and the corresponding class labels were obtained by the simulation of the true model. The preliminary labelled dataset was used to train the GP model which is the test model to compare the AL methods. The GP model was subsequently trained using experiments designed through one of the AL methods.

It is often difficult to evaluate the performance of a classification model based on a single criterion. While accuracy is the simplest criterion, it could be misleading in case of imbalanced class problems. In addition, accuracy is a score based on the final class decision and not based on the statistical quality of model fitting. Therefore, in this work, the performance of the trained GP model was assessed using four different classification metrics: i) accuracy (%), ii) balanced accuracy (%), iii) ROC-AUC score, and iv) cross-entropy loss. The ROC-AUC score provides an aggregate performance measure of the classifier model across all possible threshold values on the predicted probabilities, which are ultimately used to decide class labels. The cross-entropy loss is a score that accounts for the statistical quality of the model fitting, evaluated with the expectation if the predicted class distribution is the same as the true class distribution (which is inferred from the sample data). A brief description of these metrics is provided in Table 1.

In the description of the accuracy and the balanced accuracy metrics, the variables $TP, TN, FP$ and $FN$ respectively indicate the number of true positive, true negative, false positive and false negative datapoints in the binary classification result. True positive are the datapoints that have been labelled as positive by the model (predicted label, $\hat{c} = 1$) and they are actually positive (observed label, $c = 1$), while false positive are the datapoints that have been labelled as positive by the model, but they are actually negative. The same logic applies to the definitions of true negative and false negative datapoints. The values of the metrics accuracy and balanced accuracy range between 0 and 100. The higher the values of these metrics, the better the performance of the classifier model. The ROC-AUC score is defined as the area under the receiver operating characteristic (ROC) curve [8]. The ROC-AUC score ranges from 0 to 1, with a value of 1 indicating perfect classification. The values

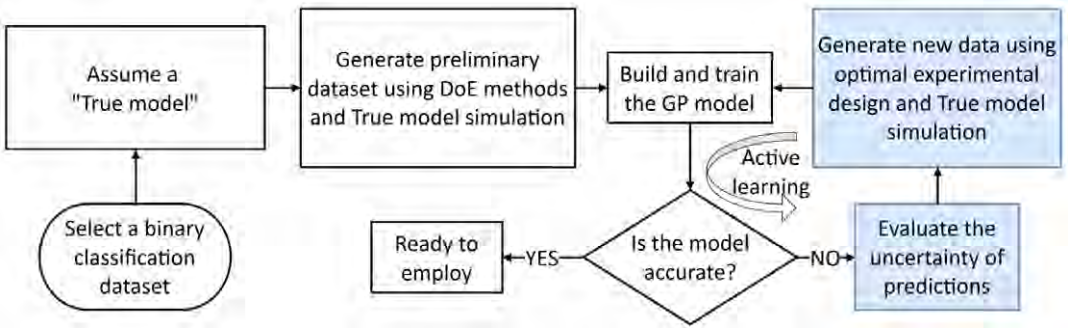



**Figure 2:** Steps involved in the simulation study to compare the different active learning methods.

closer to 1 indicate better classification performance. The cross-entropy loss is defined as the negative log-likelihood of the classifier given the true class labels. A lower cross-entropy loss value indicates better model performance.

**Table 1:** Classification metrics used for performance evaluation.

| Metrics | Description |
|---|---|
| Accuracy (%) | $\frac{TP+TN}{TP+TN+FP+FN}\times 100$ |
| Balanced accuracy (%) | $\frac{1}{2}\left(\frac{TP}{TP+FN}+\frac{TN}{TN+FP}\right)\times 100$ |
| ROC-AUC score | Area under the ROC curve |
| Cross-entropy loss | $-\frac{1}{n}\sum_{i=1}^{n}[c_i \log \phi_i + (1-c_i)\log(1-\phi_i)]$ |

## 3. CASE STUDY

A classification dataset was selected from our recently published work on antisolvent precipitation of ibuprofen particles in a continuous flow precipitator [4]. The classification dataset published in this work consisted of three input variables, which are provided in Table 2. As explained in [4], the dataset was formed from the flow precipitation experiments carried out by varying the inputs provided in Table 2. The experiments resulted in three categories of outcome, which were labelled as: i) class 0 – infeasible experiments, which caused fouling in the flow channels and hindered the particle size measurements, ii) class 1 – partially feasible experiments that caused deposition of fine particles in the flow channels, but produced particle size measurements, and iii) class 2 – fully feasible experiments with no fouling issues. In this work, this multiclass classification dataset was converted to a binary classification problem by treating experiments with class label 1 also as infeasible experiments with label 0. Naturally, the class label 1 was then used to denote all the feasible experiments. The binary classification dataset formed in this way from the original multiclass classification dataset reported in [4] was trained on an SVM model with rbf kernel function. The trained SVM model was assumed as the true model.

**Table 2:** Input variables in classification dataset.

| Input | Bound |
|---|---|
| Antisolvent flow rate (ml/min) | 1 – 4 |
| Antisolvent to solvent flow rate ratio (-) | 1 – 9 |
| Additive concentration (wt.%) | 0 – 3 |

## 4. RESULTS AND DISCUSSION

In the simulation study, eight preliminary experiments were first designed using Sobol sampling method applied to the inputs and their bounds shown in Table 2. Class labels for the preliminary experiments were generated using the true model simulations. The GP model was then trained on the preliminary dataset. Then, twenty-two new experiments were designed one at a time using a specific AL method. To compare the three AL methods, the simulation study included three separate runs, each starting with the same DoE experiments but using different AL methods for the subsequent experiment designs. The results of the simulation study are summarised in Figure 3. In panel (a), the figure provides the scatter plots of marginal histograms of the input condition and the class labels. In each marginal histogram plot, the scatter plot represents the joint distribution of the specific input variable and the class labels. The horizontal histogram represents the class distribution, and the vertical histogram represents the distribution of the specific input variable. In Figure 3 (a), the histograms of Method 2 suggest that the method resulted in an imbalanced classification dataset, with most of the experiments concentrated in the extreme regions (extremely high and extremely low values of the input variables). Upon reviewing the dataset generated in Method 2, a possible explanation is that the

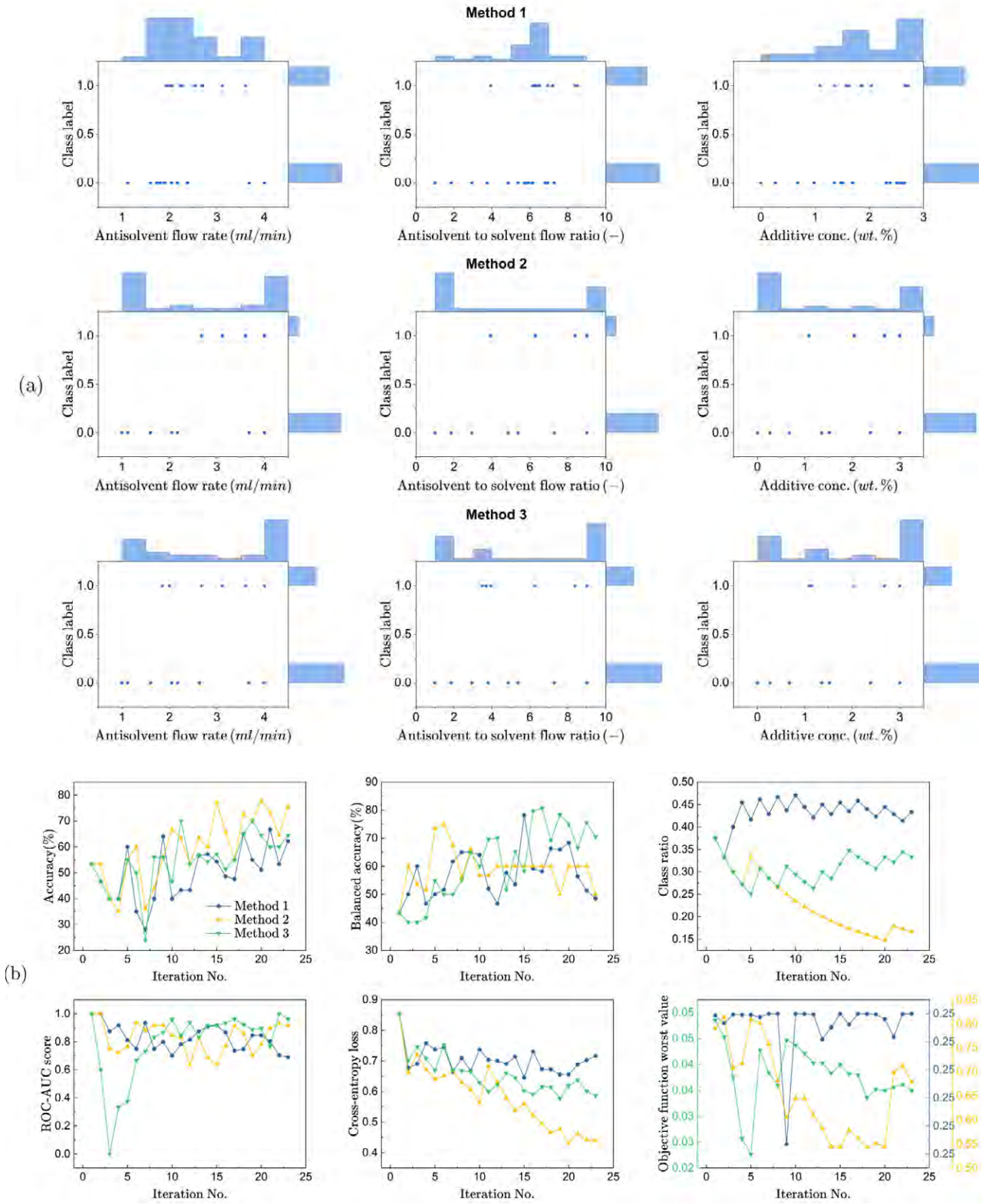



**Figure 3:** Comparison of the AL methods: (a) in terms of experimental design results and (b) in terms of the performance assessed using the classification metrics.

extreme regions were not explored in the initial experiments designed using Sobol sampling. This would have

led to a higher variance at the extreme points, prompting Method 2 to focus on these regions. Figure 3 (a) also indicates that compared to Method 2, the other methods resulted in a more balanced classification, with Method 1 producing the best results. Moreover, we observe that in Methods 1 and 3, the experiments are more evenly distributed, and hence more explorative.

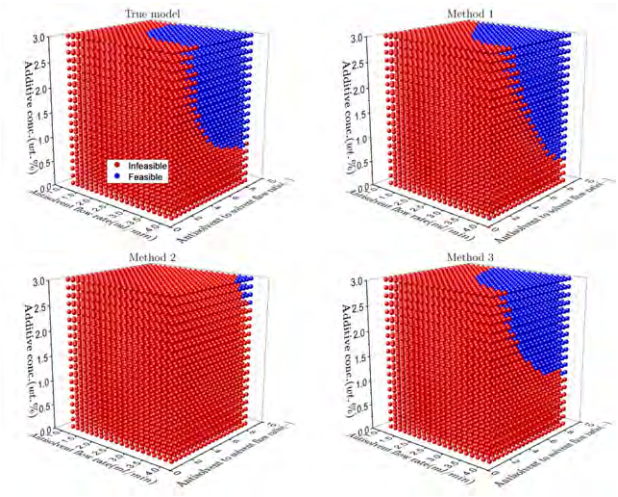



**Figure 4.** Simulations of the classifier models generated using the AL methods vs. the true model behaviour.

In Figure 3(b), the performance of classifier models developed using the three AL methods is evaluated using classification metrics averaged over five-fold cross-validation. While Method 2 shows higher classification accuracy, this is misleading due to the highly imbalanced dataset generated by this method. Balanced accuracy, which accounts for minority class contributions, shows how Method 3 performed best, scoring 70% compared to 48% for Method 1 and 50% for Method 2. Class ratios in Figure 3(b) and marginal distributions in Figure 3(a) reveal that Method 2 sampled many infeasible points, which were correctly classified but added limited learning value. This is evident from the poor decision boundary of Method 2 compared to the true model in Figure 4. Overall, Method 3 outperforms all the others by achieving the highest ROC-AUC score (0.96 compared to 0.91 for Method 2 and 0.69 for Method 1), good class balance (better than Method 2, but worse than Method 1), decreasing cross-entropy loss, and gradual reduction in the propagated uncertainty over the AL iterations. Its final classifier closely aligns with the true model, as shown in the simulation profiles of Figure 4.

## 5. CONCLUSION

We proposed a new method to quantify uncertainty in Bayesian classification. The proposed method focuses on propagating uncertainty from GP model predictions to the space of class probabilities. In a simulation study for binary classification, the method outperformed existing techniques in designing experiments that effectively train classifier models. Further studies will be needed to extend the applicability of the method to multiclass classification problems, and to validate its performance based on actual physical data.

## ACKNOWLEDGEMENTS

This work was supported by the UK Engineering and Physical Sciences Research Council (EPSRC) [grant number EP/V050796/1].

## REFERENCES

1. T. Gamer, M. Hoernicke, B. Kloepper, R. Bauer, and A. J. Isaksson, “The autonomous industrial plant – future of process engineering, operations and maintenance,” J Process Control, vol. 88, 2020.
2. C. K. I. Williams and D. Barber, “Bayesian classification with gaussian processes,” *IEEE Trans Pattern Anal Mach Intell*, vol. 20, no. 12, 1998.
3. B. Kompa, J. Snoek, and A. L. Beam, “Second opinion needed: communicating uncertainty in medical machine learning,” NPJ Digit Med, vol. 4, no. 1, 2021.
4. A. Pankajakshan et al., “MLAPI: A framework for developing machine learning-guided drug particle syntheses in automated continuous flow platforms,” Chem Eng Sci, vol. 302, p. 120780, Feb. 2025.
5. C. E. Rasmussen and C. K. I. Williams, Gaussian processes for machine learning. Cambridge, USA: The MIT Press, 2006.
6. D. D. Lewis and J. Catlett, “Heterogeneous Uncertainty Sampling for Supervised Learning,” in *Proceedings of the 11th International Conference on Machine Learning, ICML 1994*, 1994.
7. D. P. Kingma and M. Welling, “Auto-encoding variational bayes,” in 2nd International Conference on Learning Representations, ICLR 2014.
8. Scikit-learn developers, “Scikit-learn: Machine Learning in Python.” Accessed: Dec. 30, 2024. [Online]. Available: https://scikit-learn.org/stable/modules/model_evaluation.html

© 2025 by the authors. Licensed to PSEcommunity.org and PSE Press. This is an open access article under the creative commons CC-BY-SA licensing terms. Credit must be given to creator and adaptations must be shared under the same terms. See https://creativecommons.org/licenses/by-sa/4.0/

Systems & Control Transactions

**Research Article - Peer Reviewed Conference Proceeding**
ESCAPE 35 - European Symposium on Computer Aided Process Engineering
Ghent, Belgium. 6-9 July 2025
Jan F.M. Van Impe, Grégoire Léonard, Satyajeet S. Bhonsale,
Monika E. Polańska, Filip Logist (Eds.)

PSE PRESS

# Optimizing Individual-based Modelling: A Grid-based Approach to Computationally Efficient Microbial Simulations

**Ihab Hashem[a], Jian Wang[a] and Jan F.M. Van Impe[a]***

[a] BioTeC+ KU Leuven, Department of Chemical Engineering, Gent, Belgium
* Corresponding Author: jan.vanimpe@kuleuven.be.

## ABSTRACT

Individual-based modeling (IbM) has emerged as a powerful approach for studying microbial populations, offering a bottom-up framework to simulate cellular behaviors and their interactions. Unlike continuum-based models, IbM explicitly captures the heterogeneity and emergent dynamics of microbial communities, making it invaluable for studying spatially structured phenomena such as nutrient competition, biofilm formation, and colony interactions. However, IbM faces significant computational challenges, particularly in resolving spatial overlaps during simulations of large microbial populations. Traditional approaches, such as pairwise comparisons or kd-trees, are computationally expensive and scale poorly with population size. The Discretized Overlap Resolution Algorithm (DORA) introduces a novel grid-based solution to overcome these limitations. By encoding spatial information into an occupancy matrix, DORA achieves a time complexity of O(N), enabling efficient resolution of overlaps while maintaining spatial fidelity. To validate its capabilities, we applied DORA to a case study of microbial colony merging. Two scenarios were tested: (1) colonies inoculated 40 µm apart merged at the center due to nutrient depletion, and (2) colonies inoculated 120 µm apart remained separate, with a no-growth zone forming between them. In both cases, DORA replicated observed phenomena with high accuracy and demonstrated linear scalability, significantly reducing simulation time compared to traditional methods. DORA's computational efficiency and scalability position it as a robust tool for large-scale IbM simulations, advancing our ability to study complex microbial systems in diverse ecological and industrial contexts.

**Keywords**: Individual-based modeling, Grid-based algorithm, microbial ecology

## INTRODUCTION

Microbial populations are integral to a wide range of biochemical engineering applications, including wastewater treatment, bioreactor optimization, and the formation of biofilms on industrial and medical surfaces. Understanding and predicting the behavior of these populations require robust modeling frameworks capable of capturing individual cellular behaviors and the emergent dynamics of entire populations. Among these frameworks, Individual-based modeling (IbM) has emerged as a powerful computational framework for studying microbial systems. Unlike continuum-based models, which rely on averaged properties, IbM explicitly captures the behavior and interactions of individual cells, enabling a bottom-up analysis of population-level dynamics. By modeling each cell's local interactions, growth, division, and motility, IbM provides insights into how spatial structure influences social behaviors such as nutrient competition, metabolic cooperation, and quorum sensing [1,2]. These capabilities make IbM particularly valuable in industries where microbial interactions critically impact process performance, stability, and safety, such as food preservation, bioreactor optimization, wastewater treatment, and synthetic biology. By bridging microscale cell behavior with macroscale community dynamics, IbM offers practical insights into microbial processes across diverse natural, medical, and industrial applications [3].

Despite its strengths, IbM faces significant computational challenges, particularly when applied to large

microbial populations. A primary bottleneck lies in resolving spatial overlaps between cells, a critical step in maintaining spatial fidelity during simulations. Traditional methods for resolving overlaps often rely on pairwise comparisons between cells, relying on data structures such as kd-trees. These kd-trees recursively partition the simulation space to reduce the complexity of neighbor searches to O(log N), a substantial improvement over earlier array-based methods with $O(N^2)$ complexity. However, while such complexity is efficient in theory, it still poses a significant computational burden when considering the exponential growth of microbial populations in simulations. This rapid growth exacerbates the demands of spatial overlap resolution, particularly in dynamic simulations where cells grow, divide, and move frequently [4][5].

To address these challenges, we developed the Discretized Overlap Resolution Algorithm (DORA), a novel grid-based method designed to optimize the overlap resolution process. By encoding the spatial information of cells into a grid-based occupancy matrix, which then guides cellular movements, DORA circumvents the need for pairwise comparisons entirely, reducing computational complexity to $O(N^2)$. The algorithm operates in three main steps: (i) forward translation, where the spatial information of cells is encoded into an occupancy matrix; (ii) overlap resolution, which employs a diffusion-like process to iteratively redistribute excess occupancy values; and (iii) backward translation, where the resolved grid data are converted back into movement vectors for individual cells. This grid-based framework hence improves computational efficiency and allows the implementation of large-scale simulations [6].

DORA was integrated into MICRODIMS, an in-house IbM platform [7][8] built on the Repast Simphony toolkit [9]. MICRODIMS provides a flexible framework for simulating microbial growth dynamics, nutrient diffusion, and biofilm formation [10]. The integration of DORA significantly enhanced MICRODIMS's performance and enabled it to handle large-scale simulations of microbial colonies and biofilms within computationally feasible timeframes.

To further test DORA's performance and its applicability under biologically relevant conditions, we introduced a stochastic displacement component prior to the overlap resolution step. This component captures inherent biological variability, such as microbial motility and environmental fluctuations, thereby enhancing the realism of the simulations. As a case study, we applied DORA to simulate the merging of two microbial colonies—a process influenced by complex factors such as the distance between colonies, nutrient availability, and medium diffusivity [8]. This scenario presents a challenging test case for spatial fidelity, requiring the algorithm to accurately capture the conditions under which colony merging occurs. Our results demonstrated that DORA effectively modeled the process, providing high-fidelity representations of colony merging dynamics across different environmental conditions.

## MATERIALS AND METHODS

### The Discretized Overlap Resolution Algorithm (DORA)

Resolving spatial overlaps in IbMs traditionally relies on data structures such as arrays or kd-trees. Arrays store cell positions directly but require computationally expensive pairwise comparisons (complexity $O(N^2)$) [4]. Kd-trees improve efficiency by recursively partitioning space, reducing neighbor searches to O(log N) per query. However, dynamic simulations require frequent tree rebalancing due to cell movement and growth, increasing computational and memory overhead, especially at high cell densities [5].

DORA overcomes these limitations by discretizing the simulation space into an occupancy matrix, avoiding pairwise comparisons entirely and achieving an overall complexity of O(N). Additionally, DORA can incorporate a stochastic motion step before overlap resolution to introduce biologically relevant variability, such as microbial motility.

### Stochastic Motion

Before executing the main steps of the DORA algorithm, a stochastic displacement is applied to each cell. A random displacement vector $(\Delta x,\ \Delta y)$ is sampled from a Gaussian distribution:

$$\Delta x,\ \Delta y \sim N\ (0, \sigma^2) \tag{1}$$

where $\sigma$ represents the standard deviation of the displacement. The new cell positions are calculated as:

$$\mathrm{x}' = \mathrm{x} + \Delta \mathrm{x} \tag{2}$$

$$\mathrm{y}' = \mathrm{y} + \Delta \mathrm{y} \tag{3}$$

subject to the constraints of the simulation environment. This stochastic motion introduces biologically relevant noise into the simulation, simulating random fluctuations in cell movements.

### Forward Translation

The next step maps the spatial attributes of cells onto a discretized occupancy matrix, Ω, which divides the simulation environment into grid units of width w and height h. Each unit in the grid stores a value representing the fraction of its area occupied by cells.

For a cell centered at $(x_c, y_c)$ with radius $r$, its boundaries relative to the grid are calculated as:

$$x_{left/right} = x_c \pm \frac{r}{w} \tag{5}$$

$$y_{bottom/top} = y_c \pm \frac{r}{h} \quad (6)$$

The occupancy of a grid unit $(i, j)$ by cell $k$ is determined by the overlap between the cell and the grid unit, calculated as:

$$\Omega^k_{\{i,j\}} = \frac{horizontal\ overlap \times vertical\ overlap}{w \times h} \quad (7)$$

The horizontal overlap is computed as:

$$\max\left(0, \min\left(\mathrm{i}+1, \mathrm{x}_{\mathrm{right}}\right) - \max\left(\mathrm{i}, \mathrm{x}_{\mathrm{left}}\right)\right) \quad (8)$$

and similarly for the vertical overlap:

$$\max\left(0, \min\left(\mathrm{j}+1, \mathrm{j}_{\mathrm{top}}\right) - \max\left(\mathrm{j}, \mathrm{x}_{\mathrm{bottom}}\right)\right) \quad (9)$$

The total occupancy of grid unit $(i, j)$ is the sum of contributions from all cells overlapping the unit:

$$\Omega[\mathrm{i}][\mathrm{j}] = \sum_{\mathrm{k}} \Omega^k_{ij} \quad (10)$$

Values of $\Omega[\mathrm{i}][\mathrm{j}] < 1$ indicate under-occupied units, $\Omega[\mathrm{i}][\mathrm{j}] = 1$ represents fully occupied units, and $\Omega[\mathrm{i}][\mathrm{j}] > 1$ identifies over-occupied units requiring resolution.

## Overlap Resolution

Overlap is identified wherever $\Omega[\mathrm{i}][\mathrm{j}] > 1$. An excess matrix $E$ is defined to quantify the surplus occupancy:

$$E_{ij} = \max\left(0, \Omega_{ij} - 1\right) \quad (11)$$

The algorithm redistributes excess values iteratively across neighboring grid units within the Von Neumann neighborhood $N_{ij}$, which includes the four adjacent units (up, down, left, and right). The redistribution is governed by:

$$\Omega'_{ij} = \Omega_{ij} - \alpha \times \left(E_{ij} - \frac{1}{4} \sum_{(k,l) \in N_{ij}} E_{kl}\right) \quad (12)$$

where $\alpha$ is a diffusivity factor that ensures numerical stability. A motion tensor $M$ is used to track the directional displacements required to resolve overlaps. For a grid unit $(i, j)$ and a neighboring unit $(k, l)$, the displacement in direction $d$ is updated as:

$$M^d_{ij}(\mathrm{t}+1) = M^d_{ij}(\mathrm{t}) + \alpha \times \frac{1}{4}(E_{ij} - E_{kl}) \quad (13)$$

## Backward Translation

In the final step, the computed displacements in the motion tensor M are translated back to movement vectors for individual cells. For a grid unit $(i, j)$ occupied by a cell, the local movement vector is:

$$\left(v_{x_{ij}}, v_{y_{ij}}\right) = \left(M^{right}_{ij} - M^{left}_{ij}, M^{top}_{ij} - M^{bottom}_{ij}\right) \quad (14)$$

For cells spanning multiple grid units, the overall movement vector is determined by summing contributions from all occupied units:

$$V_x = \sum_{(i,j) \in Cell's grid\ units} v_{x_{ij}} \quad (15)$$

$$V_y = \sum_{(i,j) \in Cell's grid\ units} v_{y_{ij}} \quad (16)$$

To optimize computational efficiency, the simulation dynamically determines the active simulation area, restricting calculations to the region where cells are present. Let $x_c$ and $y_c$ denote the coordinates of all cells. To optimize computational efficiency, the simulation restricts calculations to the active region, defined as:

$$Left, Right = \max(0, \min(x_c) - \Delta), \min(W, \max(x_c) + \Delta) \quad (17)$$

where $\Delta$ represents a buffer margin added around the bounding box to prevent edge effects, and $W$ is the total width of the simulation domain. And similarly, for $Bottom, Top$. The algorithm operates only within the box:

$$\mathrm{B} = \{(x, y) \mid Left \le x \le Right, Bottom \le y \le Top\} \quad (18)$$

By dynamically restricting calculations to $\mathrm{B}$, DORA minimizes unnecessary computations, improving efficiency.

DORA is implemented in the MICRODIMS platform, built on the Repast Simphony toolkit. The simulation environment is discretized into a $600 \times 600$ μm grid with periodic boundary conditions. Cell growth follows Monod kinetics, and substrate diffusion is resolved using the Forward-Time Central-Space (FTCS) scheme. Temporal resolution is achieved by updating cell positions and metabolic processes every 0.01 min.

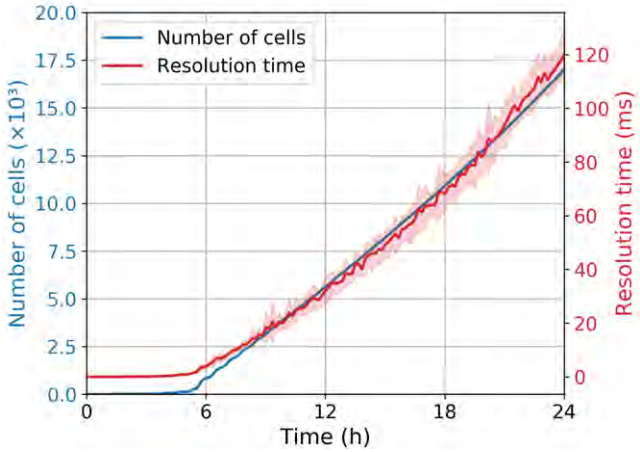
# RESULTS

Modeling cell collisions and resolving spatial overlaps are critical steps in IbM of cells. To test the DORA algorithm's ability to reproduce complex spatial phenomena, we conducted a case study of colony merging, previously explored by Tack et al. [8]. Depending on local conditions, diffusivity, nutrient concentration, inoculation density, and the distance between inocula, colonies close to each other may either merge or remain separate.

## Scenario 1: Merging of Colonies

In the first scenario, we inoculated the medium with two cells positioned 40 μm apart. The results, shown in Figure 1, indicate that the colonies continued to grow until they merged at the center. The DORA algorithm handled spatial resolution effectively during both the growth phase and the merging process, successfully replicating this spatial phenomenon.

In Figure 1(a), we plotted the evolution of the population size and the resolution time required to resolve spatial overlaps at each simulation step over 24 hours. The results represent the mean of 20 simulation runs, with the line thickness indicating the standard deviation. Notably, the growth curve is more linear rather than exponential, which is attributed to the limited diffusivity of the medium. Additionally, the resolution time curve closely follows the population growth, a result of the




(a)



(b)

**Figure 1:** Merging of two colonies: simulation of two colonies inoculated with one cell each, positioned 40 µm apart, and grown for 24 hours. (a) Evolution of the number of cells over time (blue, left y-axis) and the resolution time for resolving overlaps between cells at each time step in milliseconds (red, right y-axis). The lines represent the mean of 20 simulation runs, and the line thickness indicates the standard deviation. (b) Snapshot of the simulation at the end of 24 hours, showing the merging of the two colonies. Microbial cells are shown in green, while black shading represents nutrient concentration. Areas appearing white correspond to depleted nutrient zones.

algorithm's time complexity of O(N). This highlights the efficiency of the DORA algorithm compared to the original array-based overlap resolution method with a time complexity of $O(N^2)$. The reduced computational demands decreased the total simulation time to approximately 10 minutes per run, compared to several hours required in the original simulation.

Another observation is the asymmetry between the two colonies despite the symmetric initial conditions. This can be attributed to the stochastic component incorporated into the DORA algorithm, which introduces variability in spatial dynamics and accounts for the variance observed across the simulation runs.

## Scenario 2: Non-Merging of Colonies

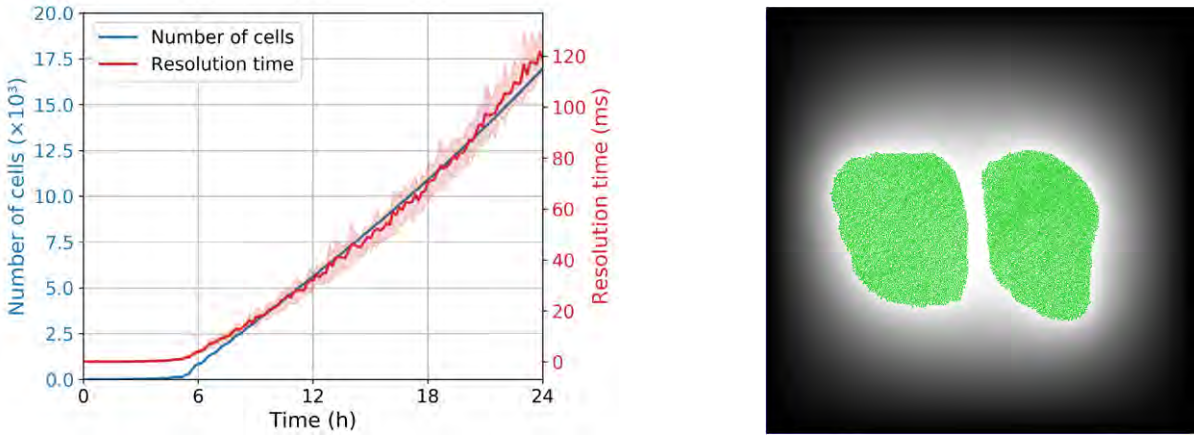
In the second scenario, the two cells were inoculated at 120 µm apart. As shown in Figure 2, the colonies grew by consuming the nutrients in the intercolony region. Due to the larger initial distance, the colonies grew to relatively larger sizes, completely depleting the nutrients between them and creating a no-growth zone in-between that acts as a barrier to merging.

While this scenario is spatially less complex than the merging case, the DORA algorithm successfully replicated the phenomenon. Figure 2(a) presents the mean population size and resolution time for 20 runs, with the standard deviation shown by the line thickness. The growth dynamics and asymmetry between the colonies observed in this scenario were consistent with the first case. The incorporation of stochasticity accounts for the spatial variability and the variance in the results.

The spatial interactions captured by DORA and reproduced in these simulations reflect fundamental microbial behaviors typically observed in structured environments. In such settings, colony growth is shaped by nutrient availability, diffusion constraints, and spatial competition, where interactions occur not only between individual cells but also at the colony level. The observed merging and non-merging results align with previous experimental and modeling studies, which have shown that microbial colonies can either coalesce or remain spatially segregated depending on local resource depletion and diffusivity. For example, studies on Escherichia coli K-12 growing in structured media have demonstrated that higher inoculum densities lead to intensified intercolony competition, often resulting in smaller final colony sizes and the formation of distinct separation zones between neighboring populations.

Beyond computational efficiency, the ability to model colony merging and segregation has implications for understanding microbial coexistence and strain diversity. In natural and engineered microbial ecosystems, spatial structuring plays a crucial role in determining whether different strains or species compete, coexist, or evolve specialized niches. By capturing these interactions, DORA provides a valuable framework for exploring how spatial constraints influence microbial diversity, community stability, and ecological succession.

These results demonstrate that the DORA-based IbM efficiently reproduces both merging and non-merging colony behaviors, maintaining high spatial fidelity while significantly reducing computational overhead. This




(a) (b)

**Figure 2:** Non-merging of two colonies: simulation of two colonies inoculated with one cell each, positioned 120 µm apart, and grown for 24 hours. (a) Evolution of the number of cells over time (blue, left y-axis) and the resolution time for resolving overlaps between cells at each time step in milliseconds (red, right y-axis). The lines represent the mean of 20 simulation runs, and the line thickness indicates the standard deviation. (b) Snapshot of the simulation at the end of 24 hours, showing the two colonies remaining separate and failing to merge. Microbial cells are shown in green, while black shading represents nutrient concentration. A starvation zone emerges between the two colonies, appearing as a white region where nutrients have been fully depleted, preventing further growth and colony merging.

establishes the DORA algorithm as a scalable and reliable tool for modeling complex spatial phenomena in microbial systems.

## CONCLUSION

This study demonstrates the effectiveness of the DORA algorithm in resolving spatial overlaps and replicating complex growth phenomena in microbial simulations. Through the case study of microbial colony merging, DORA was shown to accurately model both merging and non-merging scenarios under varying inoculation distances. By leveraging a grid-based framework with a time complexity of O(N), DORA achieved significant reductions in computational overhead compared to traditional methods, enabling faster simulations without sacrificing spatial fidelity. The incorporation of stochastic components introduced biologically relevant variability, further validating the robustness of the algorithm.

By improving the computational feasibility of large-scale simulations, DORA enhances the applicability of IbMs in biochemical engineering, ecological modeling, and bioprocess optimization.

## ACKNOWLEDGEMENTS

This work was supported by the Research Foundation Flanders (FWO) (project G0B4121N to JVI), by the European Commission within the framework of the Erasmus+ Programme (FOOD4S Erasmus Mundus Joint Master Degree in Food Systems Engineering, Technology and Business 619864-EPP-1-2020-1-BE-EPPKA1-JMD-MOB to JVI), by the European Union's Horizon 2020 research and innovation programme (under the Marie Skłodowska-Curie grant agreement No. 956126 E-MUSE to JW and JVI) and by the European Union's Horizon Europe research and innovation programme (under Grant Agreement No. 101058422 SUPREME - SUstainable nanoPaRticles Enabled antiMicrobial surfacE coatings - to IH and JVI).

## REFERENCES

1. Grimm, V. Ten years of individual-based modelling in ecology: what have we learned and what could we learn in the future? *Ecological Modelling*, 115(2-3), 129–148 (1999). https://doi.org/10.1016/S0304-3800(98)00188-4
2. Esser, D. S., Leveau, J. H., & Meyer, K. M. Modeling microbial growth and dynamics. *Applied Microbiology and Biotechnology*, 99, 8831–8846 (2015). https://doi.org/10.1007/s00253-015-6877-6
3. Hellweger, F.L., Clegg, R.J., Clark, J.R., Plugge, C.M., & Kreft, J.-U. Advancing microbial sciences by individual-based modelling. *Nature Reviews Microbiology*, 14(7), 461–471 (2016). https://doi.org/10.1038/nrmicro.2016.62
4. Kreft, J. U., Picioreanu, C., Wimpenny, J. W., & van Loosdrecht, M. C. Individual-based modelling of biofilms. *Microbiology*, 147(11), 2897–2912 (2001).

https://doi.org/10.1099/00221287-147-11-2897
5. Hellweger, F. L., & Bucci, V. A bunch of tiny individuals—Individual-based modeling for microbes. *Ecological Modelling*, 220(1), 8–22 (2009). https://doi.org/10.1016/j.ecolmodel.2008.09.004
6. Hashem, I., Wang, J., & Van Impe, J. A Discretized Overlap Resolution Algorithm (DORA) for Resolving Spatial Overlaps in Individual-based Models of Microbes. *PLoS Computational Biology* (under review).
7. Verhulst, A., Cappuyns, A., Van Derlinden, E., Bernaerts, K., & Van Impe, J. Analysis of the lag phase to exponential growth transition by incorporating inoculum characteristics. *Food Microbiology*, 28(4), 656–666 (2011). https://doi.org/10.1016/j.fm.2010.07.014
8. Tack, I. L., Logist, F., Fernández, E. N., & Van Impe, J. F. An individual-based modeling approach to simulate the effects of cellular nutrient competition on *Escherichia coli* K-12 MG1655 colony behavior and interactions in aerobic structured food systems. *Food Microbiology*, 45, 179–188 (2015). https://doi.org/10.1016/j.fm.2014.05.003
9. North, M. J., Collier, N. T., Ozik, J., Tatara, E. R., Macal, C. M., Bragen, M., et al. Complex adaptive systems modeling with Repast Simphony. *Complex Adaptive Systems Modeling*, 1(1), 3 (2013). https://doi.org/10.1186/2194-3206-1-3
10. Picioreanu, C., Van Loosdrecht, M. C., & Heijnen, J. J. Mathematical modeling of biofilm structure with a hybrid differential-discrete cellular automaton approach. *Biotechnology and Bioengineering*, 58(1), 101–116 (1998). https://doi.org/10.1002/(sici)1097-0290(19980405)58:1<101::aid-bit11>3.0.co;2-m

© 2025 by the authors. Licensed to PSEcommunity.org and PSE Press. This is an open access article under the creative commons CC-BY-SA licensing terms. Credit must be given to creator and adaptations must be shared under the same terms. See https://creativecommons.org/licenses/by-sa/4.0/



Systems & Control Transactions

**Research Article - Peer Reviewed Conference Proceeding**
ESCAPE 35 - European Symposium on Computer Aided Process Engineering
Ghent, Belgium. 6-9 July 2025
Jan F.M. Van Impe, Grégoire Léonard, Satyajeet S. Bhonsale,
Monika E. Polańska, Filip Logist (Eds.)

PSE PRESS

# A data-driven hybrid multi-objective optimization framework for pressure swing adsorption systems

**Siyang Ma[a], and Jie Li[a]***

[a] Centre for Process Integration, Department of Chemical Engineering, School of Engineering, The University of Manchester, Manchester, the United Kingdom
* Corresponding Author: jie.li-2 @manchester.ac.uk.

## ABSTRACT

Pressure swing adsorption (PSA) is an energy-efficient technology for gas separation, while the multi-objective optimization of PSA is a challenging task. To tackle this, we propose a hybrid optimization framework, which integrates three steps. In the first step, we establish surrogate models for the constraints using Gaussian processes (GPs) and employ multi-objective Bayesian optimization to search for feasible points that satisfy the constraints. In the second step, we establish surrogate models for the objective function and constraints using GPs and utilize constrained multi-objective Bayesian optimization to search for an approximate Pareto front. In the third step, we perform a local search based on the approximate Pareto front. By employing the trust region filter method, we construct quadratic models for each constraint and objective function and refine the Pareto front to achieve local optimality. This framework demonstrates the efficiency of Bayesian optimization and the local optimality of the trust region method. A comparison with the popular evolutionary algorithm, Nondominated Sorting Genetic Algorithm II (NSGA-II), showed that this framework had a higher hypervolume of the Pareto front while halving the runtime and reducing the number of simulations by a factor of 20.

**Keywords**: Pressure swing adsorption, data-driven optimization, machine learning, multi-objective optimization

## INTRODUCTION

Optimizing large-scale partial differential algebraic equation (PDAE) systems has always been a challenging task in chemical engineering. In recent years, there has been an increasing demand for multi-objective optimization of PDAE systems with coupled constraints. Therefore, it is necessary to develop an optimization framework that can be used to solve such problems. The main challenges in optimizing PDAE systems with coupled constraints include:

1. The coupled constraints with PDAEs make it difficult to obtain feasible solutions.
2. Solving PDAEs is very expensive, and satisfactory Pareto fronts need to be obtained within a limited number of solution iterations.
3. The gradient is difficult to obtain, which greatly restricts the use of gradient-based algorithms.

Pressure swing adsorption (PSA) for gas separation is a typical PDAE problem and the most common research subject. Researchers preferred to use Artificial Neural Networks to construct surrogate models and use Nondominated Sorting Genetic Algorithm II (NSGA-II) [1] for solving it [2]. While employing this approach can lead to an enhanced Pareto front, it necessitates the utilization of numerous PDAE problem solutions for acquiring training samples. Recently, Hao et al. [3] developed a hybrid optimization framework efficiently solving unconstrained PSA optimization problems using the Thompson sampling efficient multi-objective optimization (TSEMO) algorithm and DyOS, but it cannot handle PSA problems with coupled constraints. Pini et al. [4] used penalty function method to handle coupled constraints, but the selection of penalty function parameters becomes a new issue.

Therefore, we will develop a hybrid optimization framework that combines the advantages of multi-objective Bayesian optimization and local search to handle large PDAE problems with coupled constraints. This

framework can obtain a satisfactory Pareto front within a limited budget and handle challenging coupled constraints.

## PROBLEM STATEMENTS

A PSA process usually operates cyclically with at least three steps: high-pressure adsorption, low-pressure desorption and pressurisation. Additional steps, such as pressure equalisation, rinse, and purge, are often incorporated to improve process performance. Figure 1 presents an example of the four-step PSA cycle for $CO_2/N_2$ separation from Haghpanah et al. [5], which comprises feed pressurisation, adsorption, blowdown and evacuation.

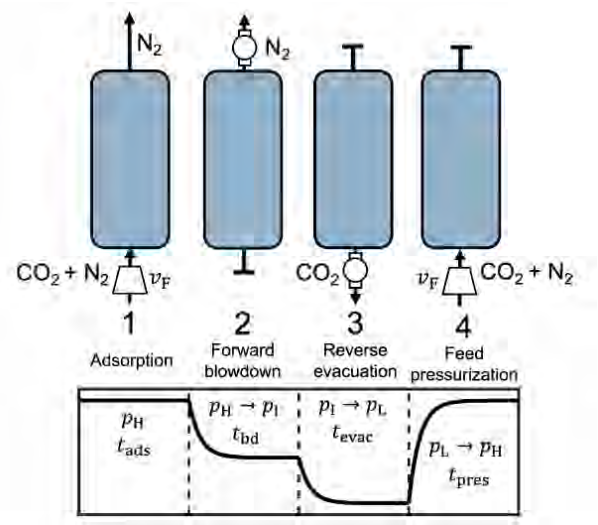



**Figure 1.** Schematic representation of the four-step PSA cycle for $CO_2/N_2$ separation

The problem can be stated as follows,

### Given:

1. The number of adsorption bed, adsorbent layers.
2. Feed conditions such as flow rate, composition, temperature, and pressure.
3. Bed configuration, physical properties of the adsorbent and the corresponding adsorption isotherms.
4. Product purity requirement.

### Determine:

1. The time for each step.
2. Operating conditions, such as operating pressures and flow velocity.

### Assumptions:

- Gas phase follows ideal gas law.
- Non-isothermal adsorption process.
- The bulk flow pattern follows a plug flow model.
- The adsorption equilibrium is described by a dual-site Langmuir model with pure component isotherms dependent on gas phase concentration.
- The mass transfer is described by a linear driving force (LDF) model where the mass transfer resistance is controlled by the molecular diffusion in the macropores.
- The heat of adsorption of each gas component is constant.
- Instantaneous heat transfer between bulk fluid and adsorbent.
- Uniform bed with constant bed void fraction, particle porosity and particle size.
- No radial gradients in concentration, temperature, or pressure.

The objectives are to minimize energy cost and maximize productivity simultaneously while meeting cyclic steady-state (CSS) condition and requirements of product purity and recovery.

The dimensionless form of the PSA rigorous model equations from Liao et al. [6] is used in this work, which is a simplified version from that in Haghpanah et al. [5]. This is because the simplified model effectively captures the full dynamics of the PSA system without loss of accuracy whilst markedly improving simulation efficiency [6]. The PSA model equations are presented in Eqs(1-6). This model consists of PDEs that govern conservation of mass, momentum and bed energy, an ODE for calculating the fractional solid loading, complemented by the dual-site Langmuir adsorption isotherms and the Ergun equation that establishes the correlation between the pressure gradient and the local interstitial velocity. Two additional assumptions are made as follows in the model of Liao et al. [6]:

- The impact of axial dispersion is omitted.
- The column wall temperature is held constant at 298.15K.

$$\frac{\partial y_i}{\partial \tau} = -\frac{\bar{T}}{\bar{P}}\frac{\partial}{\partial Z}\left(\frac{y_i \bar{P}}{\bar{T}}\bar{v}\right) - \Psi\frac{\bar{T}}{\bar{P}}\frac{\partial x_i}{\partial \tau} - \frac{y_i}{\bar{P}}\frac{\partial \bar{P}}{\partial \tau} - \frac{y_i}{\bar{T}}\frac{\partial \bar{T}}{\partial \tau} \quad (1)$$

$$\frac{\partial \bar{P}}{\partial \tau} = -\bar{T}\frac{\partial}{\partial Z}\left(\frac{\bar{P}}{\bar{T}}\bar{v}\right) - \Psi\bar{T}\sum_{i=1}^{n_{comp}}\frac{\partial x_i}{\partial \tau} + \frac{\bar{P}}{\bar{T}}\frac{\partial \bar{T}}{\partial \tau} \quad (2)$$

$$\frac{\partial \bar{T}}{\partial \tau} = -\Omega_1\frac{\partial}{\partial Z}(\bar{v}\bar{P}) - \Omega_2\bar{T}\sum_{i=1}^{n_{comp}}\frac{\partial x_i}{\partial \tau} + \sum_{i=1}^{n_{comp}}(\sigma_i\frac{\partial x_i}{\partial \tau}) + -\Omega_3(\bar{T} - \bar{T}_w) - \Omega_1\frac{\partial \bar{P}}{\partial \tau} \quad (3)$$

$$\frac{\partial x_i}{\partial \tau} = \alpha_i(x_i^* - x_i) \quad (4)$$

$$q_i^* = \frac{q_{sb,i} b_i c_i}{1+\sum_{i=1}^{n_{comp}} b_i c_i} + \frac{q_{sd,i} d_i c_i}{1+\sum_{i=1}^{n_{comp}} d_i c_i} \quad (5)$$

$$\frac{\partial \bar{P}}{\partial Z} = -\frac{150}{4}\frac{1}{r_p^2}\left(\frac{1-\varepsilon}{\varepsilon}\right)^2 \frac{v_0 L}{P_0}\mu\bar{v} + \frac{1.75}{2}\frac{1}{r_p}\frac{1-\varepsilon}{\varepsilon}\frac{v_0^2 L}{P_0}\rho_g|\bar{v}|\bar{v} \quad (6)$$

All decision variables (denoted as x) must satisfy their respective lower and upper bounds (Table 1).

$$x_L \le x \le x_U \quad (7)$$

**Table 1:** Bounds of decision variables.

| Variable | Lower bound | Upper bound |
|---|---|---|
| $t_{ads}$ [s] | 20 | 100 |
| $t_{bd}$ [s] | 30 | 200 |
| $t_{evac}$ [s] | 30 | 200 |
| $P_L$ [bar] | 0.1 | 0.5 |
| $P_I$ [bar] | 0.13 | 3 |
| $P_H$ [bar] | 1 | 10 |
| $v_{feed}$ [m/s] | 0.1 | 2 |

Some logical constraints may be imposed for the operating pressures to avoid unrealistic pressure values.

$$P_I \ge P_L + \Delta P \quad (8)$$

$$P_H \ge P_I + \Delta P \quad (9)$$

where $\Delta P$ is defined as the minimum allowable difference between $P_L$, $P_I$ and $P_H$. In this work, $\Delta P$ =0.01bar. The objectives are to minimize energy cost and maximize productivity simultaneously while meeting CSS condition and requirements of product purity and recovery, which can be calculated below,

$$Purity = \frac{n_{CO_2,out}^{evac}}{n_{CO_2,out}^{evac}+n_{N_2,out}^{evac}} \times 100\% \quad (10)$$

where $n_{CO_2,out}^{evac}$ and $n_{N_2,out}^{evac}$ are the amounts of $CO_2$ and $N_2$ extracted during the evacuation step, respectively.

$$Recovery = \frac{n_{CO_2,out}^{evac}}{n_{CO_2,in}^{pres}+n_{CO_2,in}^{ads}} \times 100\% \quad (11)$$

where $n_{CO_2,in}^{pres}$ and $n_{CO_2,in}^{ads}$ are the amounts of $CO_2$ fed in the pressurization and adsorption steps.

$$CSS\ condition = st(t) - st(t+t_{cycle}) \le \varepsilon \quad (12)$$

where $st(t)$ and $st(t+t_{cycle})$ is defined as the state variables at a given time $t$, and $\varepsilon$ represents the tolerance vector.

$$Productivity = \frac{n_{CO_2,out}^{evac}}{V_{bed} \cdot t_{cycle}} \quad (13)$$

where $V_{bed}$ is the volume of the adsorption bed, and $t_{cycle}$ is the total amount of time required for one complete cycle.

$$Energy\ consumption = \frac{E_{ads}+E_{bd}+E_{evac}+E_{pres}}{m_{CO_2,out}^{evac}} \quad (14)$$

where $E_{ads}$, $E_{bd}$, $E_{evac}$ and $E_{pres}$ are the amounts of energy consumed by the four steps, and $m_{CO_2,out}^{evac}$ represents the mass of $CO_2$ extracted during the evacuation step.

The multi-objective optimization problem (denoted as MOOP) can be stated as follows,

$$\begin{aligned} (\mathbf{MOOP}) \quad & \max \quad Productivity \\ & \min \quad Energy\ consumption \\ \text{s.t.} \quad & \text{Eqs. (1)-(6)} \\ & \text{Eqs. (7)-(14)} \\ & \text{Purity} \geqslant 95\% \\ & \text{Recovery} \geqslant 90\% \\ & \text{Boundary conditions} \end{aligned}$$

The multi-objective optimization (MOOP) is difficult to solve due to the challenge of meeting two coupled constraints and the high cost of simulations. The two constraints, purity and recovery of $CO_2$ product, conflict with each other and are difficult to satisfy simultaneously. Moreover, the expensive PDAE solving process requires the use of efficient surrogate models to reduce optimization time. Therefore, it is necessary to develop a hybrid framework to efficiently optimize the PSA process design.

## HYBRID OPTIMIZATION FRAMEWORK

A hybrid optimization framework is developed to solve the PSA problem. This framework combines multi-objective Bayesian optimization with a trust region algorithm, leveraging the strengths of both to solve expensive constrained multi-objective black-box problems within acceptable computational resources. Multi-objective Bayesian optimization (MOBO) is a global optimization algorithm that constructs surrogate models based on validated data points using a Gaussian process and updates the surrogate model by incorporating new validated points obtained in each iteration. In each iteration, an acquisition function is used as the evaluation criterion to determine the next sampled point for validation. Therefore, multi-objective Bayesian optimization can be used for efficient global search. Conversely, the trust region filter method (TRF) used in this work, constructs a quadratic surrogate model within a region defined by the trust radius to obtain a local optimal solution. The trust radius and center point are then adjusted based on the optimal solution, iteratively, until the hypervolume increment falls below a specified threshold. Therefore, this trust region algorithm is local, deterministic, and derivative-free. The hybrid framework combines these two approaches, executing a "rough to refined" search strategy to efficiently solve expensive black-box problems. Figure 2 shows the overall optimization process.

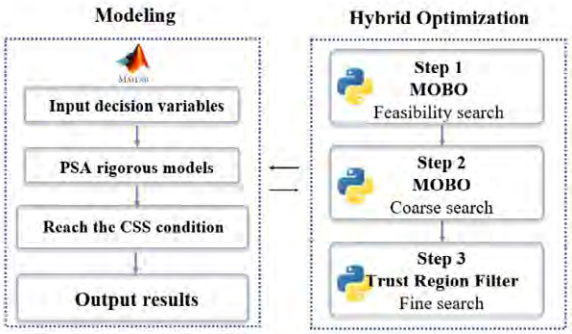



**Figure 2.** The overall PSA process optimization Schematic

The framework consists of three steps:

1. Searching for feasible points under unconstrained conditions using the multi-objective Bayesian optimization algorithm.
2. Searching for a rough Pareto front that satisfies the constraints based on the feasible points.
3. Obtaining an accurate Pareto front based on the rough Pareto front using the trust region method.

In the first step, our objective is to obtain feasible combinations of decision variables (feasible points) that satisfy the constraints. To achieve this, we treat the PSA problem as an unconstrained problem (in this phase, the decision variables remain unchanged, while the objective function becomes the two constraints: purity and recovery). In this way, we can use a multi-objective Bayesian optimization algorithm (e.g., TSEMO [7]) for solving. TSEMO first uses Latin hypercube sampling to randomly sample this black-box problem (in this experiment, 35 initial sampling points are extracted). After obtaining the starting point set, Gaussian surrogate models are constructed for each of the two constraints. After determining the acquisition function, NSGA-II is used for optimization. During the optimization process, we need to add two constraints (purity$\geqslant$95%, recovery$\geqslant$90%) to ensure that the obtained points satisfy the two constraints as much as possible. Then, new data points are validated, and the data set is updated. The new data set is used to construct a new Gaussian surrogate model, and this process repeats iteratively. After multiple iterations, we obtain a set of points that satisfy the constraints of purity and recovery.

In the second step, our objective is to obtain a rough Pareto front concerning energy consumption and productivity. We still use a specialized multi-objective Bayesian optimization (MOBO) to construct a surrogate model for solving this problem. First, we select a reference point $P_{refer}$ (Productivity=0, Energy consumption=600kW·h/ton) and calculate the current hypervolume based on the feasible point set. Then, we use the entire data set to construct Gaussian surrogate models for purity, recovery, energy consumption, and productivity. The hypervolume improvement expectation with constraints is used as the acquisition function. This hypervolume improvement expectation can be expressed as:

$$EHVI_{con} = I_c \cdot EHVI \tag{15}$$

where $I_c$ represents the probability of satisfying the purity and recovery constraints [8], and $EHVI$ represents the hypervolume improvement expectation under unconstrained conditions [9]. We use NSGA-II to optimize the acquisition function and determine the next evaluation point. After simulation, the data set, Gaussian surrogate model, and hypervolume are updated, and this process repeats iteratively. After multiple cycles, we obtain a rough Pareto front.

In the third step, our goal is to optimize the Pareto front. After the two steps of rough search, we have obtained points that satisfy the constraints and a rough Pareto front. However, there great gaps between the points on the Pareto front, and the hypervolume can improve further. Therefore, we need to use local search to further improve the Pareto front. We use the trust region method [10,11] to enhance the Pareto front. First, we select the points on the Pareto front and construct four local quadratic surrogate models (for purity, recovery, energy consumption, and productivity) within a predetermined trust radius. Based on these quadratic surrogate models, we construct a function for hypervolume increment and find the maximum value of hypervolume increment within the trust region. After validation, if the point significantly improves the hypervolume, the trust radius is increased; if the point slightly improves the hypervolume, the trust radius remains unchanged; if the point cannot improve the hypervolume, the trust radius is reduced. The termination conditions are set to an improvement less than $10^{-3}$. After performing this process for each point in the trust region, the algorithm terminates, and we obtain the final Pareto front. Figure 3 shows the workflow of the hybrid optimization framework.

## RESULTS AND DISCUSSION

As a comparison, we use NSGA-II to solve this problem to verify the computational efficiency and accuracy of this framework. In the hybrid optimization framework mentioned above, the first step employs the TSEMO algorithm implemented in MATLAB, while the second and third steps utilize optimization algorithms implemented in Python. The PSA numerical simulation model is solved in MATLAB, and the results are called through MALAB Engine API. All experiments were conducted on an Intel computer with 16 cores and 32GB memory. The Python version used was 3.10.0, and the MATLAB version was 2023a.

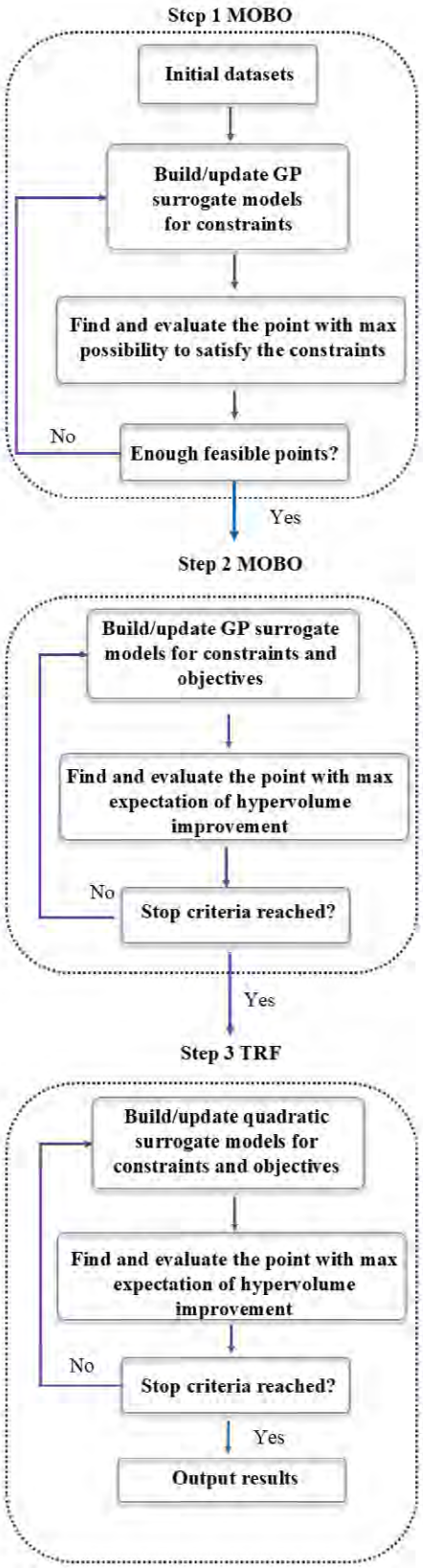



**Figure 3.** Workflow of the hybrid optimization framework

The first step of this hybrid optimization framework is to efficiently search for feasible points using multi-objective Bayesian optimization. In this step, we utilize the TSEMO algorithm as the external optimizer. To initialize the TSEMO algorithm, 35 sets of decision variables were randomly selected using Latin hypercube sampling and numerically simulated to obtain corresponding outputs. These data sets were used to train Gaussian process models. Based on these Gaussian processes, TSEMO evaluates the decision variable combinations that are most likely to satisfy the constraints and performs simulations. Subsequently, the simulation results are added to the entire data set to update the GP model for the next iteration. In this case, we conducted 300 simulations in the first step and recorded the increasing trend in the number of feasible points. When we conducted 300 simulations, we obtained 44 feasible points. However, conducting excessive simulations in the first step would prolong the time for building the Gaussian process model in the second step. Moreover, 44 feasible points are already sufficient to establish the hypervolume reference for productivity and energy consumption. To balance the efficiency of the second step's search, we only use 300 simulations in the first step before proceeding to the second step. In this step, with a wall time of 1.5 hours, an initial Pareto front with a hypervolume of 194.55 was obtained.

In the second step of this hybrid optimization framework, we optimize the original problem based on the feasible points obtained using multi-objective Bayesian optimization (MOBO). Firstly, we calculate the initial hypervolume reference value using the feasible points obtained in the first step. Then, we establish a multi-output Gaussian process model using all the data points. Using the $EHVI_{con}$ acquisition function, we search for the next set of decision variable combinations that are most likely to make progress. After performing simulations, we recalculate the hypervolume and update the data set and Gaussian process for the next iteration. In the second step, we conducted 600 simulations and obtained a rough Pareto front that cannot guarantee local optimality. As the number of simulations increases, the hypervolume also stabilizes and increases. However, after surpassing 500 simulations, the growth trend of the hypervolume noticeably slows down. It can be observed that when the number of simulations reaches 600, the efficiency of improving the hypervolume becomes extremely low. Therefore, we decided to stop the multi-objective Bayesian optimization at 600 simulations and proceed to the third step, where we use a local optimization algorithm to refine the Pareto front. In this step, with a wall time of 5.9 hours, a Pareto front with a hypervolume of 358.13 was obtained.

In the third step, the trust region filter method, a derivative-free local optimization method, will be employed

to enhance the hypervolume. The feasible points on the rough Pareto front obtained in the second step will serve as the starting points for the search. Sampling within the trust region of these points, local quadratic models will be constructed to optimize the hypervolume. After each iteration, the hypervolume will be recalculated, and the process will continue until the convergence condition is met. A total of 5737 simulations were conducted in the local search. In this step, with a wall time of 12.8 hours (8 cores), a Pareto front with a hypervolume of 429.28 was obtained.

To assess the performance of this hybrid optimization framework, we also employed NSGA-II to solve the problem. We utilized NSGA-II to solve the problem three times, selecting the best result from the obtained set. In the process of solving the problem with NSGA-II, a total of 600 iterations were executed. Each iteration consisted of a population of 250, calculated using 8 cores, taking a wall time of 44.3 hours. The resulting hypervolume of the Pareto front obtained was 373.73. Figure 4 shows the Pareto fronts of the hybrid optimization framework and NSGA-II. Table 3 presents a comparative analysis of the optimization performance between the hybrid optimization framework and NSGA-II. The results demonstrate that the hybrid approach yielded a 14% increase in hypervolume and a 62.5% augmentation in the number of Pareto front solutions relative to NSGA-II. The hybrid optimization framework demonstrates the ability to identify feasible points with an energy consumption close to 500 and a productivity of 5, showing superior global search capability compared to NSGA-II under limited wall time. Additionally, the search time of the hybrid optimization framework is only half of the wall time of NSGA-II, indicating significantly higher search efficiency. In summary, the hybrid optimization framework developed in this study effectively addresses the multi-objective optimization problem with coupled constraints.

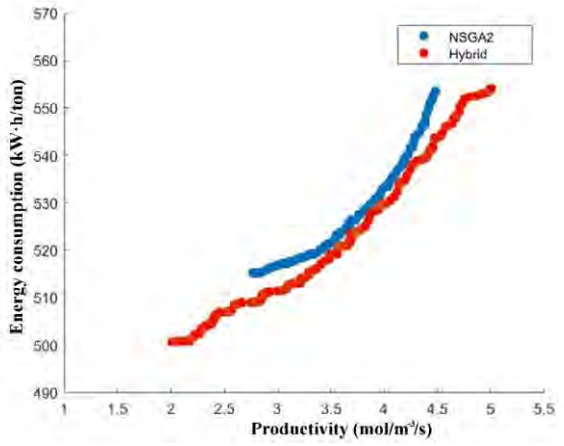



**Figure 4.** Hypervolume comparison between hybrid optimization framework and NSGA-II

**Table 3:** Performance Comparison

| Method | Hybrid optimization framework | NSGA-II |
|---|---|---|
| Wall time (h) | 20.2 | 44.3 |
| CPU time (h) | 109.8 | 364.4 |
| Hypervolume | 429.28 | 376.73 |
| $N_{PF}$ | 143 | 88 |
| $N$ | 6672 | 150000 |

$N_{PF}$ represents the number of points on the Pareto front, and $N$ is the number of rigorous model evaluations conducted.

Compared to the framework developed by Hao et al [3], this hybrid framework has two major advantages. Firstly, this method has improved the coarse search process, making it capable of handling multi-objective optimization problems with coupled constraints. On the other hand, Hao et al's framework [3] can only handle unconstrained multi-objective optimization problems. Secondly, this method uses the trust region method for fine search without using derivative information from dynamic systems, significantly improving computational efficiency. In contrast, Hao et al's framework [3] used the derivative-based DyOS algorithm for deterministic optimization. There are many limitations when using DyOS, including the reduction of decision variables and changes to CSS criteria, which may affect the results.

## CONCLUSIONS

The main challenge in solving the design problems of chemical engineering processes, represented by the PSA process, is the high computational cost. Hence, it is imperative to develop an optimization framework capable of efficiently exploring the Pareto set for design problems. In this work, a hybrid optimization framework was developed, which can efficiently and quickly solve the $CO_2$ capture pressure swing adsorption problem. In the case study of PSA optimization design, this framework has achieved superior Pareto fronts while requiring only half the time compared to NSGA-II. In future research, we will focus on improving the coarse search step of this method to enhance the accuracy and efficiency of the coarse search while increasing compatibility with parallel computing.

## ACKNOWLEDGEMENTS

Siyang Ma would like to thank Yangyanbing Liao and Andrew Wright for their assistance in constructing the PSA model. Jie Li would like to appreciate the financial support from UKRI Impact Acceleration Account (IAA 424).

## REFERENCES


1. K. Deb et al. A fast and elitist multiobjective genetic algorithm: NSGA-II. *IEEE Trans. Evol. Comput.* 6(2):182-197 (2002) https://doi.org/10.1109/4235.996017
2. N. S. Wilkins et al. Optimization of pressure-vacuum swing adsorption processes for nitrogen rejection from natural gas streams using a nitrogen selective metal organic framework. *Can. J. Chem. Eng.* 100(9):2374-93 (2022) https://10.1002/cjce.24469
3. Z. Hao et al. Efficient hybrid multiobjective optimization of pressure swing adsorption. *Chem. Eng. J.* 423:130248 (2021) https://doi.org/10.1016/j.cej.2021.130248
4. W. Adam & R. Pini. Efficient bayesian optimization of industrial-scale pressure-vacuum swing adsorption processes for CO2 capture. *Ind. Eng. Chem. Res.* 61(36):13650-13668 (2022). https://doi.org/10.1021/acs.iecr.2c02313
5. R. Haghpanah et al. Multiobjective optimization of a four-step adsorption process for postcombustion CO2 capture via finite volume simulation, *Ind. Eng. Chem. Res.* 52(11):4249–4265 (2013) https://doi.org/10.1021/ie302658y
6. Y. Liao et al. Simulation and optimisation of vacuum (pressure) swing adsorption with simultaneous consideration of real vacuum pump data and bed fluidisation. *Sep. Purif. Technol.* 358:130354 (2024) https://doi.org/10.1016/j.seppur.2024.130354
7. E. Bradford et al. Efficient multiobjective optimization employing Gaussian processes, spectral sampling and a genetic algorithm. *J. Glob. Optim.* 71(2): 407-438 (2018) https://doi.org/10.1007/s10898-018-0609-2
8. J.R. Gardner et al. Bayesian optimization with inequality constraints. *ICML* 2014:937-945 (2014) https://doi.org/10.5555/3044805.3044997
9. K. Yang et al. Multi-objective Bayesian global optimization using expected hypervolume improvement gradient. *Swarm Evol Comput.* 44:945-956 (2019) https://doi.org/10.1016/j.swevo.2018.10.007
10. B. Manuel et al. Multi-Objective Trust-Region Filter Method for Nonlinear Constraints using Inexact Gradients. arXiv preprint arXiv:2208.12094 (2022) https://doi.org/10.48550/arXiv.2208.12094
11. C. Cartis et al. Improving the flexibility and robustness of model-based derivative-free optimization solvers. *ACM Trans. Math. Software* 45(3):1-41 (2019) https://doi.org/10.48550/arXiv.1804.00154



© 2025 by the authors. Licensed to PSEcommunity.org and PSE Press. This is an open access article under the creative commons CC-BY-SA licensing terms. Credit must be given to creator and adaptations must be shared under the same terms. See https://creativecommons.org/licenses/by-sa/4.0/




Systems & Control Transactions

**Research Article - Peer Reviewed Conference Proceeding**
ESCAPE 35 - European Symposium on Computer Aided Process Engineering
Ghent, Belgium. 6-9 July 2025
Jan F.M. Van Impe, Grégoire Léonard, Satyajeet S. Bhonsale,
Monika E. Polańska, Filip Logist (Eds.)

PSE PRESS

# Multi-Objective Optimization for Sustainable Design of Power-to-Ammonia Plants

**Andrea Isella, Davide Manca***

PSE-Lab, Process Systems Engineering Laboratory, Dipartimento di Chimica, Materiali e Ingegneria Chimica "Giulio Natta", Politecnico di Milano, Piazza Leonardo da Vinci 32, 20133 Milano, Italy
* Corresponding Author: davide.manca@polimi.it.

## ABSTRACT

This work addresses the process design of Power-to-Ammonia plants (*i.e.* ammonia from renewable-powered electrolysis) by a novel methodology based on the multi-objective optimization of the "Three pillars of sustainability": economic, environmental, and social. Specifically, we developed a tool estimating the installed capacities of every main process section typically featured by Power-to-Ammonia facilities (*e.g.*, the renewable power plant, the electrolyzer, energy and hydrogen storage systems, *etc.*) to maximize the plant's "Global Sustainability Score".

**Keywords**: Green ammonia, Decarbonization, Renewable energy, Power-to-X, Three pillars of sustainability

## INTRODUCTION

In 2020, about 185 Mt/y of ammonia were produced worldwide, causing 1% of that year's global greenhouse gas (GHG) emissions [1]. Indeed, more than 96% of today's global hydrogen input for ammonia derives from fossil fuels. Specifically, the most common synthetic pathways for hydrogen feedstocks heading to Haber-Bosch reactors are (i) steam methane reforming, *i.e.* hydrogen from natural gas, accounting for about 70% of global sourcing and emitting from 2.5 to 3 $t_{CO2eq}/t_{NH3}$; (ii) coal gasification, providing 26% of hydrogen feedstocks and emitting ca. 5 $t_{CO2eq}/t_{NH3}$; (iii) partial oxidation of heavy oil, accounting for less than 1%; and (iv) hydrogen from electrolysis, currently representing few isolated cases [2]. The fossil-based routes are classified as "gray" ammonia if no carbon capture and storage (CCS) technologies are implemented or "blue" ammonia if featuring CCS. Conversely, employing hydrogen from electrolysis is defined as "green" ammonia if renewable energy is used to power the electrolyzer, ideally resulting in zero direct carbon emissions. That is why the optimal design of Power-to-Ammonia plants (*i.e.* facilities converting renewable power into green ammonia via water electrolysis) is a topic of significant interest in the recent scientific literature. In particular, the erratic trend of non-dispatchable renewable sources (*e.g.*, solar, wind, *etc.*) leads to several process complications in running (thus designing) such plants: above all, the need for dynamic operations instead of conventional steady-state ones and the demand for buffer mass and energy storage to mitigate the effects of oversupply or shortage occurrences in the renewable inputs. This paper introduces a methodology to optimally design Power-to-Ammonia plants according to the "Three pillars", *i.e.* economic, environmental, and social, "of sustainability". Precisely, the fundamentals of such an approach lie in the works of Scotti *et al.* (2017, 2018) [3,4], as they proposed a solution strategy for the multi-objective optimization (MOO) of sustainability in the conceptual design of conventional (*i.e.* fossil-based, thus operating in stationary conditions) chemical plants. Specifically, this work aims to enhance such an approach by extending it to the much more challenging green process field that calls for an intrinsically dynamic methodology to conceptual design.

## METHODOLOGY

**Figure 1** depicts the investigated Power-to-Ammonia plant's process sections and battery limits (*i.e.* the control volume of the present assessment). Specifically, to achieve an average productivity target of 100 $t_{NH3}$/d, such a facility features (a) a renewable (*i.e.* solar and wind) power plant; (b) an alkaline water electrolyzer; (c) an air separation unit, *i.e.* ASU; (d) a conventional ammonia synthesis loop (*i.e.* Haber-Bosch process); and both

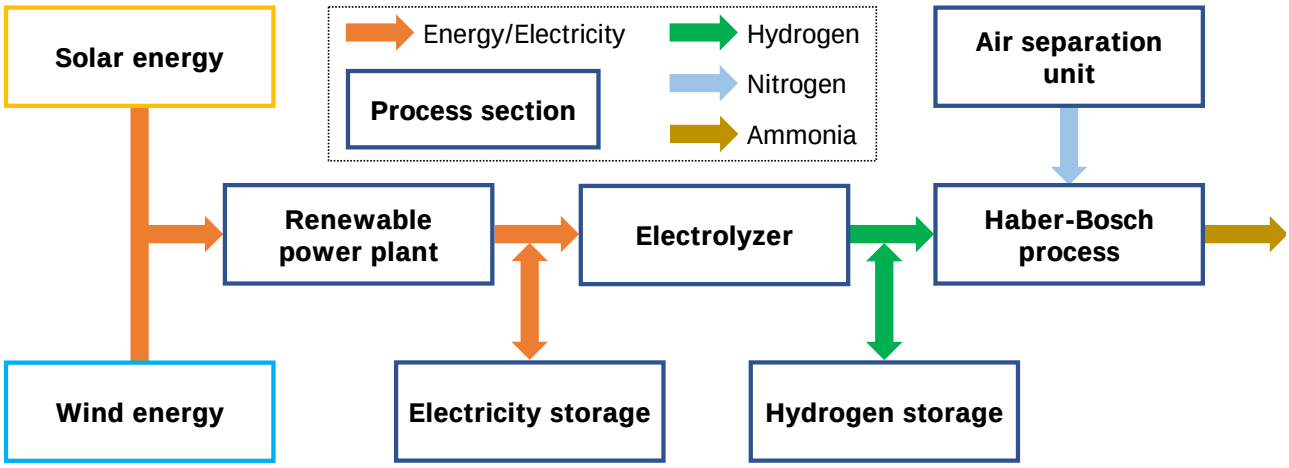



**Figure 1:** Block flow diagram of the assessed Power-to-Ammonia plant.

(e) energy and (f) mass buffer storages (namely, a lithium-ion battery amidst the power plant and the electrolyzer, and hydrogen pressurized tanks amid the electrolyzer and the ammonia plant) to dampen any process discontinuities introduced by solar and wind profiles. Furthermore, an auxiliary electricity supply from the power grid can be provided to meet the electric demand of the ASU, the Haber-Bosch process, and the multistage centrifugal compressors within the hydrogen storage section whenever the renewable electricity inputs exceeding the electrolysis demand are insufficient to power them. Both MATLAB™ R2024 (the power plant, electrolyzer, and storage systems) and UniSim® Design R492 (the ASU and Haber-Bosch process) were used to model the plant according to the renewable inputs, *i.e.* 2023 solar and wind profiles from CAISO (California Independent System Operator) [5], and the optimal policies for flexible mass and electricity storage discussed in Isella and Manca (2025a, 2025b) [6,7]. Accordingly, such process models provide the equation-oriented (in MATLAB™) and black-box (in UniSim®) equality constraints (*e.g.*, mass and energy balances) of the optimization problem. Moreover, the related degrees of freedom are the solar and wind installed capacities (*i.e.* the renewable power plant), determining the energy input to the electrolyzer (and the battery holdup) and thus the hydrogen input to the ammonia synthesis loop (and the hydrogen storage size). Consequently, the resulting capacities for such process sections (conversely, both ASU and Haber-Bosch dimensions are already given according to the high technological maturity of small-scale gray ammonia plants) lead to a "global sustainability score" (GSS) that allows practical comparisons between multiple process configurations. Indeed, the present MOO problem has been approached by the scalarization technique, *i.e.* a solution method aggregating all the different objective functions (namely, the economic, the environmental, and the social ones) into a single one by a suitable scalarization function (in this specific case, their linear combination). Thus, the sustainability metrics formulated for each sustainability pillar are (1) the levelized cost of ammonia, *i.e.* LCOA, for the economic dimension; (2) the global warming potential, *i.e.* GWP, for the environmental dimension (as it counts the cradle-to-grave $CO_2$-equivalent emissions released per mass unit of ammonia product); and (3) the Fire and Explosion Index [8], *i.e.* FEI, for the social dimension. Then, to be scalarized (hence making them comparable with each other), these parameters need to be normalized first through "normalized sustainability indexes":

$$EcoSI_i = \frac{\max(LCOA) - LCOA_i}{\max(LCOA) - \min(LCOA)} \quad (1)$$

$$EnvSI_i = \frac{\max(GWP) - GWP_i}{\max(GWP) - \min(GWP)} \quad (2)$$

$$SocSI_i = \frac{\max(FEI) - FEI_i}{\max(FEI) - \min(FEI)} \quad (3)$$

Where the $i$ subscript denotes the i-th assessed process configuration within the decision space.

As evident from their formulation, all these indexes range from 0 (*i.e.* the least sustainable scenario) to 1 (*i.e.* the most sustainable scenario). Lastly, as mentioned above, the ultimate expression of the GSS (*i.e.* the objective function of the MOO problem, to be maximized) is the linear combination of such indexes, whose coefficients act as user-defined weighting factors for each sustainability pillar:

$$GSS = w_{ECO} \cdot EcoSI + w_{ENV} \cdot EnvSI + w_{SOC} \cdot SocSI \quad (4)$$

Please note that the sum of the weighting factors must always be equal to 1 (*i.e.* 100%) and that, like the normalized sustainability indexes, even the GSS spans in the same sense from 0 to 1.

**Table 1:** Input data for the Power-to-Ammonia model [9].

| | | | |
|---|---|---|---|
| **DATASET** | | | |
| | Location | California | |
| | Year | 2023 | |
| | Solar capacity factor | 26.64% | [-] |
| | Wind capacity factor | 29.66% | [-] |
| | Time discretization | 1 | [h] |
| **TECHNO-ECONOMIC DATA** | | | |
| **Solar** | Lifetime | 25 | [y] |
| | CAPEX | 1119 | [USD/kWe] |
| | OPEX | 1.70% | [CAPEX/y] |
| | GWP | 136.24 | [$kg_{CO2eq}$/MWh] |
| **Wind** | Lifetime | 25 | [y] |
| | CAPEX | 1285 | [USD/kWe] |
| | OPEX | 2% | [CAPEX/y] |
| | GWP | 26.33 | [$kg_{CO2eq}$/MWh] |
| **Electricity storage** | Lifetime | 10 | [y] |
| | CAPEX | 310 | [USD/kWe] |
| | OPEX | 2% | [CAPEX/y] |
| | Charging efficiency | 0.95 | [-] |
| | Discharging efficiency | 0.95 | [-] |
| | Self-discharge rate | 0.007% | [load/h] |
| | GWP | 50 | [$kg_{CO2eq}$/kWh] |
| **Electrolyzer** | Lifetime | 10 | [y] |
| | CAPEX | 700 | [USD/kWe] |
| | OPEX | 2% | [CAPEX/y] |
| | Stack DC consumption | 4.65 | [kWh/$Nm^3_{H2}$] |
| | Maximum load flexibility | 1 | [nominal load] |
| | Minimum load flexibility | 0.1 | [nominal load] |
| | GWP | 0.215 | [$kg_{CO2eq}$/$kg_{H2}$] |
| **Hydrogen storage** | Lifetime | 20 | [y] |
| | CAPEX | 1900 | [USD/$kg_{H2}$] |
| | OPEX | 1% | [CAPEX/y] |
| | P inlet (Electrolyzer) | 30 | [bar] |
| | P outlet ($H_2$ storage) | 200 | [bar] |
| | Electricity consumption | 1.03 | [MWh/$t_{H2}$] |
| | GWP | 200 | [kgCO2eq/$_{kgH2}$] |
| **Air separation unit** | Electricity consumption | 0.08 | [MWh/$t_{N2}$] |
| **Haber-Bosch process** | $NH_3$ target productivity | 4.17 | [$t_{NH3}$/h] |
| | $H_2$ target feed | 0.78 | [$t_{H2}$/h] |
| | Maximum ramp | 100% | [load/h] |
| | Maximum load flexibility | 110% | [nominal load] |
| | Minimum load flexibility | 10% | [nominal load] |
| | Electricity consumption | 0.59 | [MWh/$t_{NH3}$] |
| **Electric grid** | Electricity cost | 100 | [USD/MWh] |
| | GWP | 370 | [$kg_{CO2eq}$/MWh] |

## RESULTS

The optimization problem, as defined in the previous section, is then applied to a Power-to-Ammonia plant showing the features reported in **Table 1**. Both degrees of freedom (*i.e.* the solar and wind installed capacities) are iteratively varied from 0 to 500 MW (according to a 10 MW step size) by a brute-force grid-search method. Multi-objective optimization always requires some human decision-making: in this particular case, such a

feature lies in the weighting factors that the user must assign *a priori* (*i.e.* before the searching phase) according to the emphasis given to each sustainability pillar.

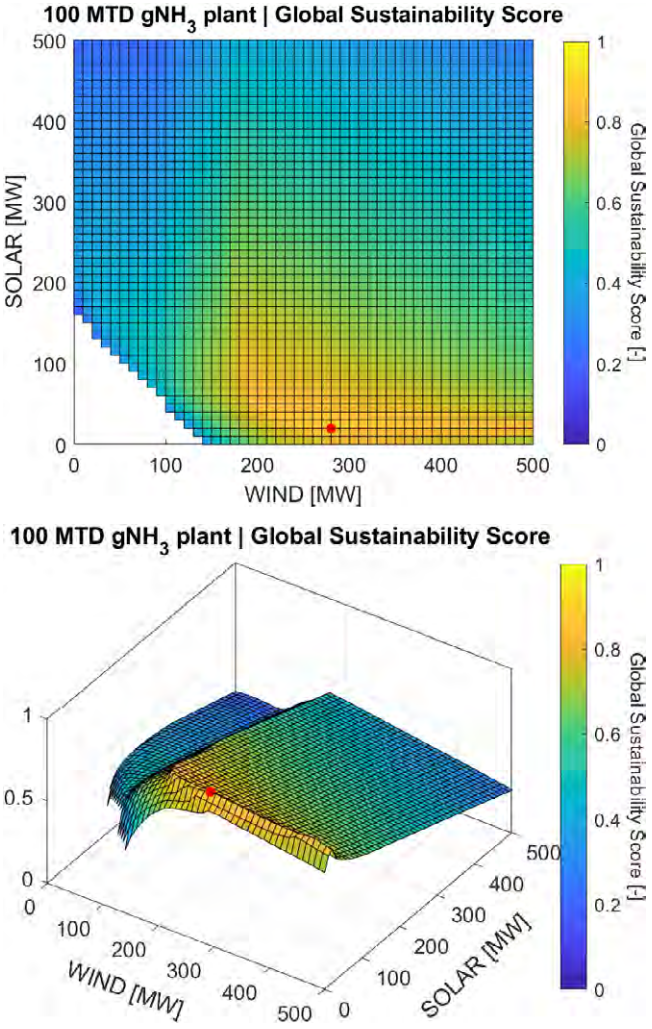



**Figure 2:** 2D (above) and 3D (below) diagrams of the GSS (the red dot corresponds to the maximum, *i.e.* 88.25%).

For example, let us assume: 50% economic; 25% environmental; and 25% social. **Figure 2** shows the two- and three-dimensional topologies of the resulting objective function, while the two panels of **Figure 3** return the main operating profiles of the optimal process configuration. Each pillar aims for a different solution: (A) economic sustainability typically results in a compromise solution on the installed capacity of the renewable power plant as lower ones would imply bigger electrolyzers and storage systems (to process, and mitigate, any energy input made available by the small power plant), and *vice versa*. Specifically, wind power is preferred to solar as its higher availability throughout the day reduces the storage systems' need (hence the size and total costs). (B) Environmental sustainability tends to minimize the renewable power plant sizes as they lead to far higher GWP values than the storage systems. However, the GWP associated with the electrolyzer (as, like its size, increases when the power plant size decreases) counterbalances such a trend, making the optimal power plant slightly more significant than the minimum allowable one. (C) Lastly, social sustainability pushes for huge renewable power plants as they minimize the electrolyzer and hydrogen storage sizes (hence the well-known hydrogen-related process hazards). Consequently, the resulting objective function (see **Figure 2**) displays all these features, though the corresponding weighting factors partially mitigate them. The corresponding optimal GSS is 88.25%, meaning the three sustainability pillars agreed fairly (although not entirely).

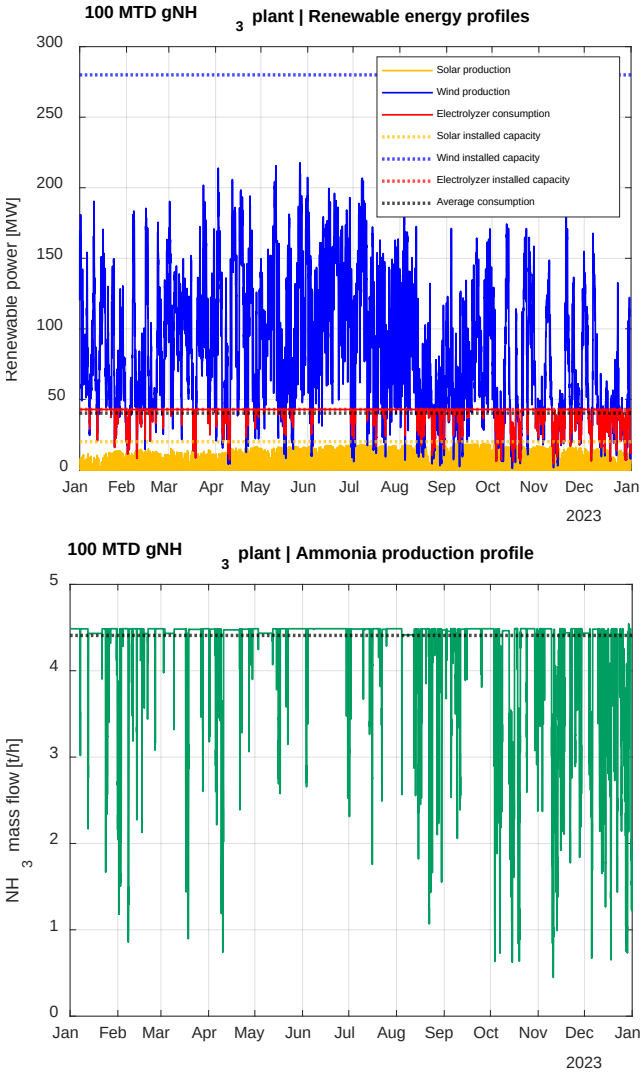
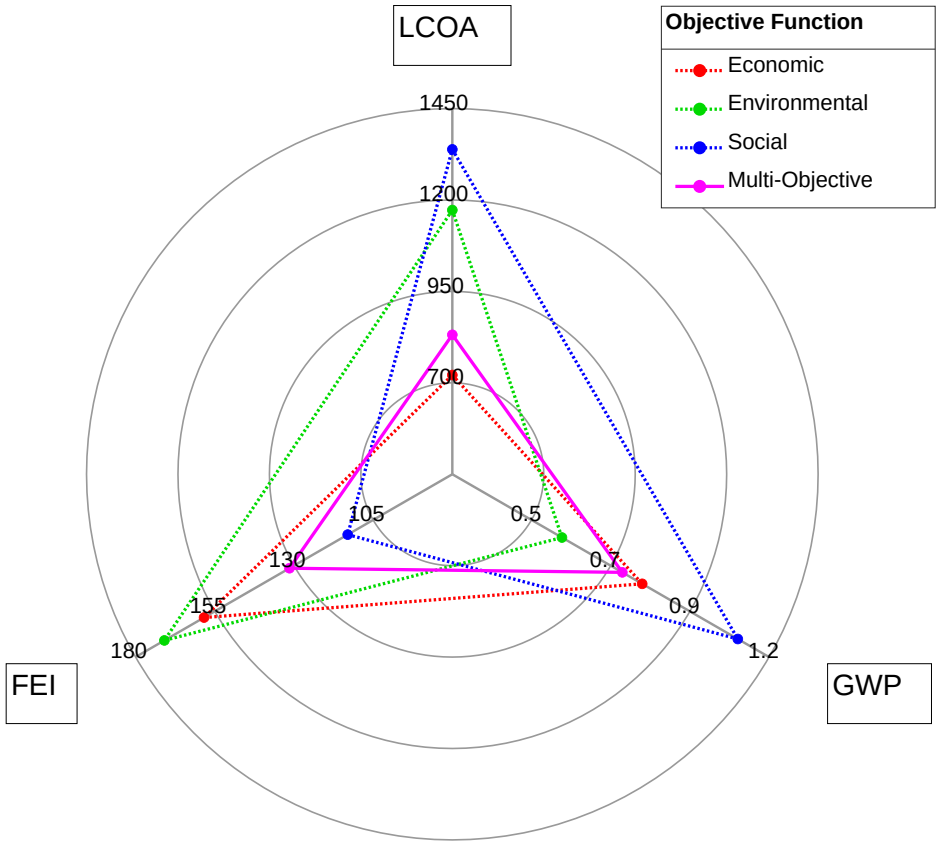



**Figure 3:** Renewable power generation vs. consumption (above) and ammonia production (below) profiles by the optimal Power-to-Ammonia plant process configuration.

Finally, **Table 2** summarizes the installed capacities and sustainability metrics resulting from the optimization

**Table 2:** Main results of the optimal process configuration.

| **Optimal process configuration: 50% economic + 25% environmental + 25% social** | | |
|---|---|---|
| Solar | 20 | [MW] |
| Wind | 280 | [MW] |
| Electrolyzer | 42.87 | [MW] |
| Electricity storage | 2.29 | [MWh] |
| Hydrogen storage | 38.39 | [$kg_{H2}$] |
| LCOA | 871.86 | [USD/$t_{NH3}$] |
| GWP | 0.77 | [$t_{CO2eq}/t_{NH3}$] |
| FEI | 131.40 | [-] |
| GSS | 88.25% | [-] |




problem. Specifically, the optimal process configuration features high wind-power installed capacities and negligible storage sizes (*i.e.* battery and tanks).

As evident from **Table 2**, compared to the economically optimal scenario (*i.e.* the single-objective optimization of the economic dimension only), both environmental and social sustainability improved (−3.5% in GWP and −17% in FEI, respectively) at the expense of the ammonia production cost (+21% in LCOA).

Please also note that solving the three single-objective optimization problems together (economic, environmental, and social) would allow visualizing the Pareto fronts, *i.e.* those points within the decision space whose corresponding objective function values cannot be concurrently improved. This is a traditional "*a posteriori*" technique (meaning that the decision process is postponed after the searching phase; thus, no preference criteria need to be provided "*a priori*"), giving interesting insights on the conciliation among every single objective function. However, the Pareto front approach may be unsatisfactory and confusing for many reasons. Above all, the somewhat chaotic representation of all the solutions explored and the high number of Pareto optimal points (60 out of 2601 process configurations investigated) still leaves too much space for the decision maker's discretion. That is why we opted for the scalarization method:

indeed, as an "*a priori*" technique, it provides the decision criterion (assuming a specific hierarchy of importance in the objective functions according to the weighting factors) before the searching phase, thus allowing for the examination of a unique solution.

## CONCLUSIONS

This work presented a methodology to identify the process design of Power-to-Ammonia plants that best maximizes and harmonizes the three pillars of sustainability: economic, environmental, and social. Resorting to the scalarization method proved to be a successful approach to solving such a multi-objective optimization problem and allowing the users (*e.g.*, academic researchers and industrial stakeholders) to quickly compare the different results arising from the arbitrary choice of the three pillar-related weighting factors. Furthermore, this work stressed the importance of process flexibility in renewable-energy-powered chemical plants to adapt appropriately to the erratic nature of renewable energy sources. Indeed, the higher the process flexibility, the lower the required storage systems' capacities to mitigate the discontinuities in renewable power (hence, the lower the production costs).

## ACKNOWLEDGEMENTS

A.I. acknowledges the contribution of the Italian Ministry of University and Research (MUR) under the PON Research and Innovation 2014-2020 program (Action IV.5 – Doctorates on green topics).

## REFERENCES

1. Isella A, Manca D. GHG Emissions by (Petro)Chemical Processes and Decarbonization Priorities—A Review. *Energies* 15(20):7560 (2022) https://doi.org/10.3390/en15207560
2. Mayer, P, Ramirez A, Pezzella G, Winter B, Sarathy SM, Gascon J, Bardow A. Blue and green ammonia production: A techno-economic and life cycle assessment perspective. *IScience* 26(8):107389 (2023) https://doi.org/10.1016/j.isci.2023.107389
3. Scotti F, Fabricatore N, Sepiacci P, Manca D. A MOO approach towards sustainable process design: integrating the three pillars of sustainability. *Comput. Aided Chem. Eng.* 40:637-642 (2017) https://doi.org/10.1016/B978-0-444-63965-3.50108-2
4. Scotti F, Fabricatore N, Manca D. Multi-objective optimization of sustainability criteria in the design of chemical plants. *Comput. Aided Chem. Eng.* 43:743-748 (2018) https://doi.org/10.1016/B978-0-444-64235-6.50131-5
5. California Independent System Operator. https://www.caiso.com/
6. Isella A, Manca D. A general criterion for the design and operation of flexible hydrogen storage in Power-to-X processes. *Int. J. Hydrogen Energy* 99:649-660 (2025) https://doi.org/10.1016/j.ijhydene.2024.12.228
7. Isella A, Manca D. A framework for the design of battery energy storage systems in Power-to-X processes. *J. Energy Storage* (Under Review)
8. International Labour Organisation. Major Hazard Control: A Practical Manual. I.L.O. (1993).
9. Isella A, Manca D. Integrating economic, environmental, and social sustainability in Power-to-Ammonia plants: A multi-objective optimization methodology. *Comput. Chem. Eng.* 198:109082 (2025) https://doi.org/10.1016/j.compchemeng.2025.109082

© 2025 by the authors. Licensed to PSEcommunity.org and PSE Press. This is an open access article under the creative commons CC-BY-SA licensing terms. Credit must be given to creator and adaptations must be shared under the same terms. See https://creativecommons.org/licenses/by-sa/4.0/



Systems & Control Transactions

**Research Article - Peer Reviewed Conference Proceeding**
ESCAPE 35 - European Symposium on Computer Aided Process Engineering
Ghent, Belgium. 6-9 July 2025
Jan F.M. Van Impe, Grégoire Léonard, Satyajeet S. Bhonsale,
Monika E. Polańska, Filip Logist (Eds.)

PSE PRESS

# Global Robust Optimisation for Non-Convex Quadratic Programs: Application to Pooling Problems

**Asimina Marousi and Vassilis M. Charitopoulos***

Department of Chemical Engineering, The Sargent Centre for Process Systems Engineering, University College London, London, UK
* Corresponding Author: v.charitopoulos@ucl.ac.uk.

## ABSTRACT

Robust optimisation is a powerful approach for addressing uncertainty ensuring constraint satisfaction for all uncertain parameter realisations. While convex robust optimisation problems are effectively tackled using robust reformulations and cutting plane methods, extending these techniques to non-convex problems remains largely unexplored. In this work we propose a method that is based on a parallel robustness and optimality search. We introduce a novel spatial Branch-and-Bound algorithm integrated with robust cutting-planes for solving non-convex robust optimisation problems. The algorithm systematically incorporates global and robust optimisation techniques, leveraging McCormick relaxations. The proposed algorithm is evaluated on benchmark pooling problems with uncertain feed quality, demonstrating algorithm stability and solution robustness. The computational time for the examined case studies is within the same order of magnitude as state-of-the-art. The findings of this work highlight the potential of the proposed algorithm in tackling quadratic non-convex robust optimisation problems, particularly in chemical engineering applications.

**Keywords**: Algorithms, Pyomo, Robust Optimisation, Pooling Problem, Global Optimisation, spatial Branch-and-Bound

## INTRODUCTION

Robust optimisation is widely used to identify worst-case scenarios, ensuring constraint satisfaction under uncertainty or when statistical data is unavailable, as an alternative to scenario-based approaches [1]. The most prevalent solution algorithms for convex problems are robust reformulation and robust cutting planes [2]. Under the assumptions of convex uncertainty set and the problem constraints being concave in the uncertain parameter, both methods can be extended to non-convex problems [3]. Cutting-planes involve sequentially solving an upper-level deterministic problem and lower-level problems to find uncertainty values that cause the maximum constraint violation. For those values, corresponding cuts are added to the upper-level problem. Implementations of cutting-planes can be found in solvers like PyROS [4] and the ROmodel package [5] in Python, which rely on local or global solvers to handle intermediate problems. However, traditional robust cutting-planes are heavily influenced by the performance of the chosen solver, and if the solver fails to converge during a cut-round, the entire algorithm may fail to converge [4]. At the same time, for computationally challenging case studies the cost of solving the problem to global optimality multiple times may be prohibitive.

Nonlinear functions are present in a multitude of chemical engineering problems, especially when data-driven methods are employed, there is a need for systematic techniques that handle non-convex problems under uncertainty [6]. In this study we focus on the class of non-convex quadratic problems, and we leverage spatial Branch-and-Bound (sBB) algorithm. sBB is a deterministic global optimisation algorithm which is suitable for optimisation problems that require branching on the continuous variables. Early application of the sBB in the process systems engineering literature include solving linear fractional and bi-linear problems [7], as well as addressing various NLP and MINLP design problems [8]. sBB algorithms rely on the generation of lower and upper bounds of the objective function over any given variable subdomain. In a minimisation problem, the upper bound value is

selected as a local minimiser in the current subdomain. Depending on the structure of the original problem, different convexification methods can be used to formulate a relaxation of the original problem, corresponding to a lower bounding solution.

Solving non-convex problems to robust optimality requires the connection of the robust algorithms and global optimisation methods. The most prevailing approach to achieve this is by deriving the dual reformulation and using either directly or adaptively a global solver to retrieve a solution [9,10]. Recently, different process case studies have been examined using a local linearisation approach based on an iterative random sampling of the uncertain parameters [11]. The non-convex pooling problem under concave uncertainty is addressed in [3] following two solution paths, reformulation and cutting planes using a global solver. This study proposes a novel spatial Branch-and-Bound algorithm integrated with robust cutting-planes (RsBB) for solving non-convex robust optimisation problems. The proposed algorithm is implemented to solve benchmark pooling problems with uncertain feed quality, using McCormick relaxations [12]. In the RsBB algorithm, robust infeasibility checks are performed at each node of the BB tree. The infeasibility cuts are added both on the original and the relaxed problem. The performance of the proposed RsBB algorithm is compared with and state-of-the-art software in terms of computational efficiency and solution robustness.

## POOLING PROBLEM

The pooling problem is a well-studied benchmark problem in process systems engineering and optimisation communities being non-convex quadratic problem with quadratic constraints. A simple pooling topology is depicted in Fig. 1, where a number of inlet components is mixed into the available pools from which different products are retrieved.

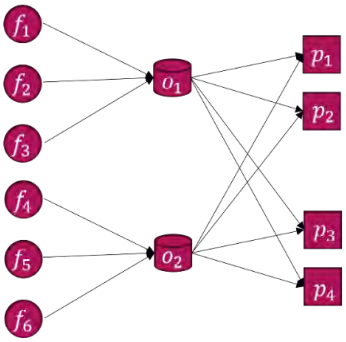



**Figure 1.** Conceptual representation of pooling problem, corresponding to 6 feed components, 2 pools and 4 products.

### Problem definition

Throughout the years several formulations of the pooling problem have been proposed. In this work, we follow the pq-formulation [13] of the standard pooling problem using auxiliary variables. The objective function is to minimise the cost,

$$\min \sum_{ilj} c_i v_{ilj} - \sum_{jl} d_j y_{lj} + \sum_{ji} d_j z_{ij} \tag{1}$$

satisfying constraints on feed availability

$$\text{s.t.} \sum_{lj} v_{ilj} + \sum_{j} z_{ij} \le A_i, \quad \forall i \tag{2}$$

pool capacity

$$\sum_{j} y_{lj} \le S_l, \quad \forall l \tag{3}$$

product demand satisfaction

$$\sum_{l} y_{lj} + \sum_{i} z_{ij} \le D_j, \quad \forall j \tag{4}$$

product quality

$$\sum_{il} C_{ik} v_{ilj} + \sum_{i} C_{ik} z_{ij} \le P_{jk}^{U} f_j, \quad \forall j,k \tag{5}$$

total flow

$$\sum_{l} y_{lj} + \sum_{i} z_{ij} = f_j, \quad \forall j \tag{6}$$

RLT constraints

$$\sum_{i} q_i = y_{lj}, \quad \forall l \tag{7}$$

$$\sum_{i} v_{ilj} = y_{lj}, \quad \forall l \tag{8}$$

and auxiliary constraints.

$$v_{ilj} = q_{il} y_{lj} \; \forall i,l,j \tag{9}$$

**Table 1:** Problem definitions.

| Step | Problem | Notation | Equations |
|---|---|---|---|
| 1st | Original pooling | $\Pi$ | (1)-(9) |
| | Relaxed pooling | $\Pi_R$ | (1)-(8), (10)-(13) |
| 2nd | Quality robustness | $\pi$ | (14), (16)-(18) |

The pq-formulation results in a non-convex problem with quadratic constraints. A convex relaxation is achieved replacing Eq. (9) with the corresponding McCormick envelopes [14] as follows:

$$v_{ilj} \ge \underline{q}_{il} y_{lj} + q_{il} \underline{y}_{lj} - \underline{q}_{il} \underline{y}_{lj}, \quad \forall i,l,j \tag{10}$$

$$v_{ilj} \le \overline{q}_{il} y_{lj} + q_{il} \underline{y}_{lj} - \overline{q}_{il} \underline{y}_{lj}, \quad \forall i,l,j \tag{11}$$

$$v_{ilj} \ge \overline{q}_{il} y_{lj} + q_{il} \overline{y}_{lj} - \overline{q}_{il} \overline{y}_{lj}, \quad \forall i,l,j \tag{12}$$

$$v_{ilj} \le \underline{q}_{il} y_{lj} + q_{il} \overline{y}_{lj} - \underline{q}_{il} \overline{y}_{lj}, \quad \forall i,l,j \tag{13}$$

where $\underline{q}_{il}, \underline{y}_{lj}$ and $\overline{q}_{il}, \overline{y}_{lj}$ correspond to the lower and upper bounds of the complicating variables. The definitions of the problem formulations are displayed in Table 1.

## Uncertainty consideration

In this work uncertainty is introduced in the inlet quality parameters $C_{ik}$ and subsequently in the product quality constraints of Eq. (5). The true value of the uncertain level quality $\tilde{C}_{ik}$ can be formulated as:

$$\tilde{C}_{ik} = C_{ik} + \xi_{ik}\hat{C}_{ik} \tag{14}$$

where $C_{ik}$ represents the nominal value, $\hat{C}_{ik}$ the constant perturbation (which is positive) and $\xi_{ik}$ is a vector of random variables which are subject to uncertainty. The robust counterpart of Eq. (5) for a selected box uncertainty set is derived in Eq. (15).

$$\sum_{il} \tilde{C}_{ik} v_{ilj} + \sum_{i} \tilde{C}_{ik}\, z_{ij} \le P^U_{jk} f_j, \quad \forall \boldsymbol{\xi} \in \mathcal{U}_\infty, \forall j,k \tag{15}$$

Eq.(15) is a semi-infinite constraint which is typically handled either via dual reformulation or robust cutting planes [2]. Following the robust cutting planes, Eq.(15) can be replaced by the quality robustness problem which should be solved $\forall j,k$ quality constraints:

$$\max_{\xi} \phi_{jk} \tag{16}$$

$$s.t. \phi_{jk} = \sum_{il} \tilde{C}_{ik}\, v^*_{ilj} + \sum_{i} \tilde{C}_{ik}\, z^*_{ij} - P^U_{jk} f^*_j \tag{17}$$

$$|\xi_{ik}| \le \Psi, \qquad \forall i,k \tag{18}$$

# METHODOLOGY

## Robust cutting planes

Robust cutting planes approach is an iterative optimisation algorithm. In the first step, the original pooling problem $\Pi$ is solved and the set of solutions $v^*_{ilj}, z^*_{ij}$ and $f^*_j$ is passed in the second-step problems $\pi$. Problems $\pi$ are solved for all $j,k$ maximising the random variable $\xi$ within a selected uncertainty set $\mathcal{U}_\mathrm{p}$. For every $C^*_{ik}$ that $\phi_{jk} > 0$ the equivalent robust cut is added to problem $\Pi$:

$$\sum_{il} C^*_{ik} v_{ilj} + \sum_{i} C^*_{ik} z_{ij} \le P^U_{jk} f_j, \quad \forall j,k \tag{19}$$

The algorithm iterates until no more quality violations are detected, then the algorithm terminates in a robust solution. Depending on the choice of solver for $\Pi$ the solution can be either robust optimal, using a global solver, or robust feasible, using a local solver.

## Robust-spatial-Branch-and-Bound

In the proposed Robust-spatial-Branch-and-Bound algorithm (RsBB), we aim to integrate the robust cutting planes with the spatial Branch-and-Bound (sBB) algorithm. Relying on a local NLP solver, the proposed algorithm is evaluating the robustness of the solutions in a branching tree. The outline of the proposed algorithm is presented in Figure 2. Let the complicating variables $q_{il}$ and $y_{lj}$ be the branching candidates. For the initial variable bounds at the root node, problem $\Pi$ is solved using a local solver. The robustness of the local solution is evaluated solving linear problems $\pi\ \forall j,k$ and the corresponding robust cuts (Eq. (19)) are added both to $\Pi$ and $\Pi_R$if a feasibility violation is detected, i.e. $\phi_{jk} > 0$. The cutting plane algorithm continues at the root node until no more robustness violations are detected. Until this step, the proposed algorithm follows the typical robust cutting plane algorithm.

The following steps of the algorithm correspond the Branch-and-Bound algorithm. Let $q^{R*}_{il}, y^{R*}_{lj}, v^{R*}_{ilj}$ be the solutions of the relaxed linear $\Pi_R$ problem. The branching variable is selected based on the maximum approximation error. Let $x_{br}$ be the branching variable for which:

$$x_{br} = arg\max\{q^{error}_{il}, y^{error}_{lj}\} \tag{20}$$

$$q^{error}_{il} = \sum_{j} v^{R*}_{ilj} - q^{R*}_{il}\, y^{R*}_{lj} \tag{21}$$

$$y^{error}_{lj} = \sum_{i} v^{R*}_{ilj} - q^{R*}_{il}\, y^{R*}_{lj} \tag{22}$$

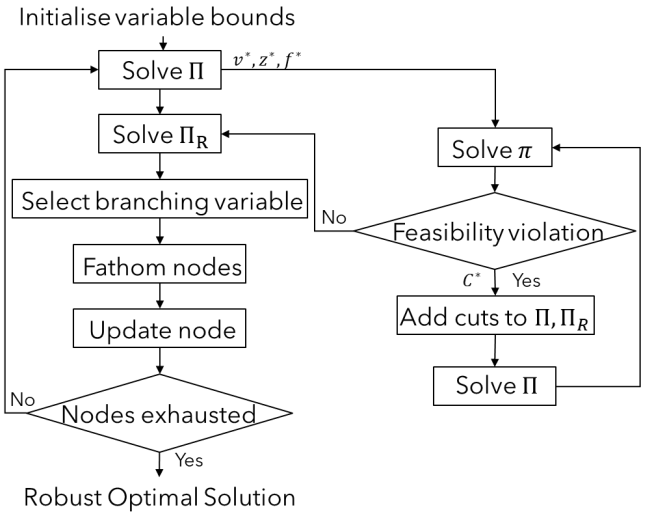



**Figure 2.** The Robust-spatial-Branch-and-Bound algorithm

The branching point is selected as the incumbent solution of the branching variable. Hence the bounds for the first two child nodes the new bounds will be $x_{br} \in X_1 = [\underline{x}_{br}, x^{R*}_{br}]$ and $x_{br} \in X_2 = [x^{R*}_{br}, \overline{x}_{br}]$. Nodes for which the $\Pi_R$ solution is greater than the best-found solution of $\Pi$ are fathomed. The next node is updated as the waiting node with the lowest $\Pi_R$ solution. If the waiting nodes are exhausted, the robust optimal solution of the

problem is obtained.

## COMPUTATIONAL EXPERIMENTS

The RsBB algorithm is evaluated in 10 benchmark pooling instances with varying size, details of the problems can be found in Table 2. For the uncertain inlet quality, we set $\hat{C}_{ik} = C_{ik}$ and examine the results for three different uncertainty sizes, i.e. $\Psi \coloneqq \{0.05, 0.1, 0.15\}$ which correspond to 5%, 10% and 15% allowed perturbation from the nominal inlet quality value. The selected modelling environment is Pyomo v6.7. For the RsBB algorithm HiGHS v.1.5.3 is used as the LP solver and conopt4 as the local NLP solver. The proposed algorithm is compared with PyROS v1.2.8 using Gurobi v11.1 as the LP solver, conopt4 and BARON v23.6.22 as local and global solvers respectively.

**Table 2:** Benchmark pooling problems.

| Problem | #Feeds | #Pools | #Products | #Qualities |
|---|---|---|---|---|
| haverly1-3 | 3 | 1 | 2 | 1 |
| foulds2 | 6 | 2 | 4 | 1 |
| bental4 | 4 | 1 | 2 | 1 |
| bental5 | 13 | 3 | 5 | 2 |
| adhya1 | 5 | 2 | 4 | 4 |
| adhya2 | 5 | 2 | 4 | 6 |
| adhya3 | 8 | 3 | 4 | 6 |
| adhya4 | 8 | 2 | 5 | 4 |

### Results

The proposed algorithm is compared with PyROS solver in Fig.3. PyROS is a built-in solver in Pyomo that is implementing the robust cutting planes algorithm. For each of the 10 benchmark problems, three variants of different uncertainty size were examined resulting to 30 instances in total. The robust optimum is obtained by the RsBB algorithm for all instances. In contrast, using PyROS with local solver conopt4 solves only 10% of the instances to robust optimality and for 40% terminates in a local robust solution. Given that the instances examined are relatively small and represent well-studied benchmarks in the field of global optimisation, PyROS, using the global solver BARON, obtained the robust optimal solution in reduced total computational time compared to RsBB. The instances with the highest CPU time in RsBB correspond to the Adhya problems for $\Psi = 0.05$. Since pooling problems have multiple local optima, introducing uncertainty via robust cutting planes reduces the feasible region and possibly rendering regions with local solutions infeasible.

The impact of the problem size and uncertainty size in the RsBB algorithm is evaluated via Fig.4. Foulds2 problem is double in size of the Haverly2. As expected, in Haverly3 RsBB closes the optimality gap in fewer nodes compared to Foulds2 (Figure 4a, b). Unexpectedly, the optimality gap at root node in Foulds2 is below 15% for all $\Psi$ while above 90% in the Haverly instance. In Foulds2 there is a negative correlation between the uncertainty

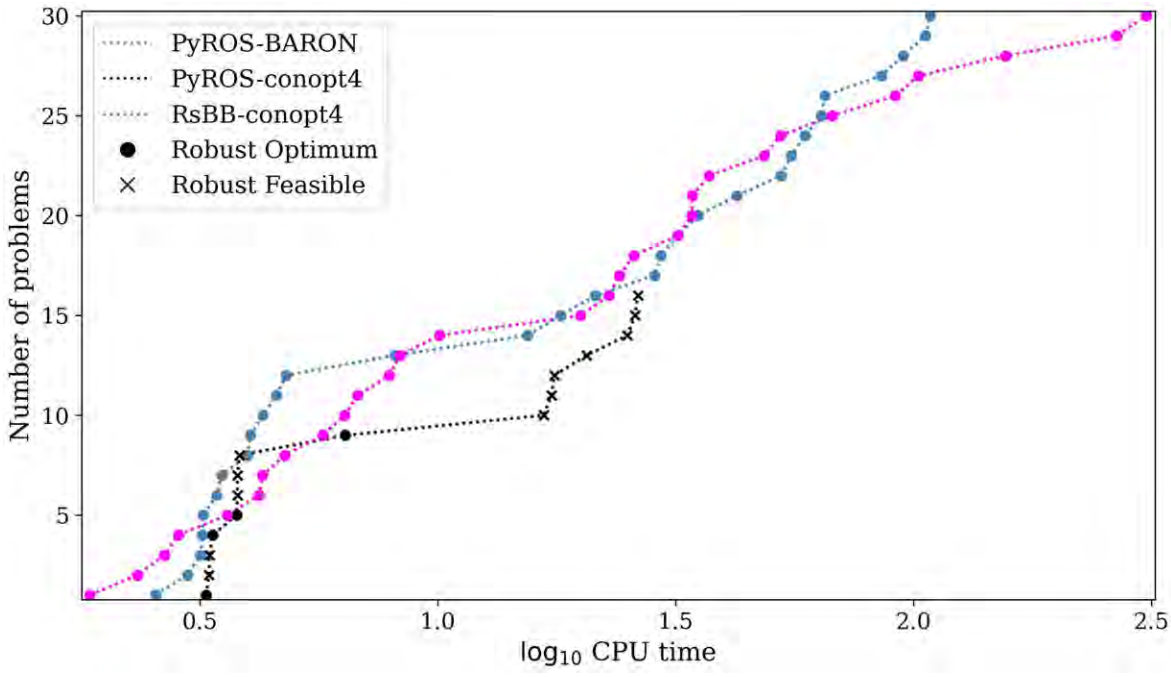



**Figure 3**: Computational time for problems solved by examined algorithms. 30 problems in total, corresponding to 3 different $\Psi$ values for 10 benchmark pooling problems.

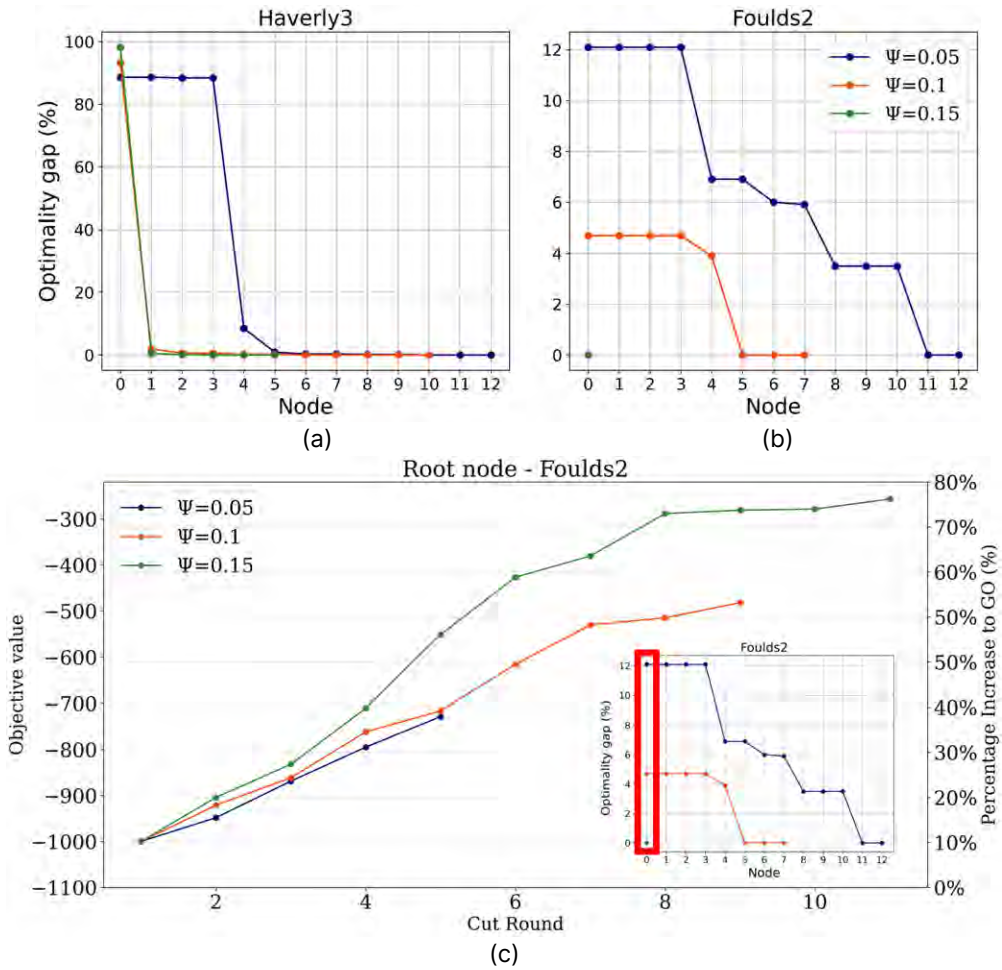



**Figure 4:** a+b) Optimality gap closure at evaluated tree node for Havely3 and Foulds2 problems for varying uncertanty size. c) Objective value decrease at root node of Foulds2 for robust cut iterations.

set size and the optimality gap at the root node, while for $\Psi = 0.15$ the RsBB algorithm terminates at the root node. To elucidate this observation, we focus on the root node of Foulds2 and the iterations of the robust cutting planes in Figure 4c. As the uncertainty size increases, so do the required robust cutting plane iterations to find a robust feasible solution at the root node. At the same time, the increase in robust cut iterations results in a smaller optimality gap. For $\Psi = 0.15$, 12 robust cut iterations are required that result in a robust optimal solution in the root node. Analogously, for $\Psi = 0.1$ 9 robust cut iterations are required for a robust feasible solution in the root node. The added cuts aid the RsBB algorithm to terminate in 7 nodes. To this end, robust cutting planes facilitate the optimality search. For larger uncertainty set size, the corresponding cuts are more restraining the cuts, which allow for an earlier termination of the sBB algorithm. In the same plot the price of robustness can be highlighted. Accounting for 15% increase in the uncertain parameter results in an increase of 75% of the objective value. Even for a 5% increase in the inlet quality increases the cost by almost 40%. Thus, increasing the uncertainty size fortifies the problem against higher uncertainty variations, increases conservativism and at the same time reduces the degeneracy of the problems.

## CONCLUSIONS

In this work, we introduced a novel algorithm by coupling global and robust optimisation methods. The proposed RsBB algorithm integrates the principles of sBB and robust cutting planes to solve non-convex problems with concave uncertain parameters. The performance of the algorithm was evaluated on well-studied benchmark pooling problems with box uncertainty set. The computational results of our study suggest that the proposed method offers stability and guaranteed robust optimality for the examined problems while using a local solver. We observed that using robust cutting planes in the sBB algorithm works as a feasibility bounds tightening method.

Overall, the proposed algorithm is a promising method in tackling non-convex robust optimisation problems. In our future work, we will examine different types of uncertainty sets and extend our method to general non-convex problems.

## ACKNOWLEDGEMENTS

Financial support under the EPSRC grants ADOPT (EP/W003317/1) and RiFtMaP (EP/V034723/1) is gratefully acknowledged by the authors.

## NOMENCLATURE

**Sets:**

| | |
|---|---|
| $i$ | Components |
| $l$ | Pools |
| $j$ | Products |
| $k$ | Qualities |

**Parameters:**

| | |
|---|---|
| $\xi_{ik}$ | Random variable of quality |
| $\Psi$ | Adjustable parameter for the uncertainty size |
| $A_i$ | Upper bound for component availability |
| $D_j$ | Upper bound for product demand |
| $S_l$ | Upper bound for pool size |
| $P_{jk}^U$ | Upper bound for product quality |
| $C_{ik}$ | Nominal inlet quality value |
| $\tilde{C}_{ik}$ | True inlet quality value |
| $\hat{C}_{ik}$ | Perturbed inlet quality value |
| $c_i$ | Component unit price |
| $d_j$ | Product unit price |

**Variables:**

| | |
|---|---|
| $q_{il}$ | Flow of component $i$ entering pool $l$ |
| $y_{lj}$ | Flow from pool $l$ to product $j$ |
| $z_{ij}$ | Flow from component $i$ to product $j$ |
| $f_j$ | Total flow to product $j$ |
| $v_{ilj}$ | Flow of component $i$ entering pool $l$ to product $j$ |

## REFERENCES

1. Dias L S, & Ierapetritou M G. Integration of scheduling and control under uncertainties: Review and challenges. Chem Eng Res and Des, 116, 98–113 (2016).
2. Li, Z., Ding, R, & Floudas, CA. A comparative theoretical and computational study on robust counterpart optimization: I. Robust linear optimization and robust mixed integer linear optimization. Ind Eng Chem Res 50(18), 10567 - 10603 (2011).
3. Wiebe J, CecÍlio I, & Misener R. Robust Optimization for the Pooling Problem. Ind Eng Chem Res 58(28), 12712–12722 (2019).
4. Isenberg NM, Akula P, Eslick JC, Bhattacharyya D, Miller DC, & Gounaris CE. A generalized cutting-set approach for nonlinear robust optimization in process systems engineering. AIChE J, 67: e17175, 5 (2021).
5. Wiebe J, & Misener R. Romodel: modeling robust optimization problems in pyomo. Optim. Eng., 23:1873–1894, 12 (2022).
6. Schweidtmann, A M Bongartz D, Grothe D, Kerkenhoff T, Lin, X, Najman J, & Mitsos, A. Deterministic global optimization with Gaussian processes embedded. Math Program Comput, 13(3), 553–581 (2021).
7. Quesada I, & Grossmann I E. A global optimization algorithm for linear fractional and bilinear programs. J Glob Optim, 6:39–76, 1 (1995).
8. Ryoo H S, & Sahinidis N V. Global optimization of nonconvex NLPs and MINLPs with applications in process design. Comp Chem Eng, 19:551–566, 5 (1995).
9. Li J, Misener R, & Floudas C A. Scheduling of Crude Oil Operations Under Demand Uncertainty: A Robust Optimization Framework Coupled with Global Optimization. AIChE Journal, 58, 2373–2396 (2011).
10. Zhang L, Yuan Z, & Chen B. Refinery-wide planning operations under uncertainty via robust optimization approach coupled with global optimization. Comp Chem Eng, 146, 107205 (2021).
11. Yuan, Y, Li, Z, & Huang, B. Nonlinear robust optimization for process design. AIChE J, 64(2), 481–494 (2018).
12. Mitsos, A, Chachuat, B, & Barton, P I. McCormick-Based Relaxations of Algorithms. SIOPT 20(2), 573–601 (2009).
13. Sahinidis N V, & Tawarmalani M. Accelerating branch-and-bound through a modeling language construct for relaxation-specific constraints. J Glob Optim, 32:259–280, 6 (2005)
14. McCormick GP. Computability of global solutions to factorable nonconvex programs: Part i— convex underestimating problems. Math. Program. 10:1, 10:147–175, 12 (1976).

© 2025 by the authors. Licensed to PSEcommunity.org and PSE Press. This is an open access article under the creative commons CC-BY-SA licensing terms. Credit must be given to creator and adaptations must be shared under the same terms. See https://creativecommons.org/licenses/by-sa/4.0/



Systems & Control Transactions

**Research Article - Peer Reviewed Conference Proceeding**
ESCAPE 35 - European Symposium on Computer Aided Process Engineering
Ghent, Belgium. 6-9 July 2025
Jan F.M. Van Impe, Grégoire Léonard, Satyajeet S. Bhonsale,
Monika E. Polańska, Filip Logist (Eds.)

PSE PRESS

# GRAPSE: Graph-Based Retrieval Augmentation for Process Systems Engineering

**Daniel Ovalle[a†], Arpan Seth[b†], John R. Kitchin[a], Carl D. Laird[a], and Ignacio E. Grossmann[a*]**

[a] Department of Chemical Engineering, Carnegie Mellon University, Pittsburgh, PA 15213, United States
[b] Evonik Corporation, Process Technology and Engineering, Trexlertown, PA 18087, United States
* Corresponding Author: grossmann@cmu.edu.
† These authors contributed equally to this work.

## ABSTRACT

Large Language Models have demonstrated potential in accelerating scientific discovery, but they face challenges when making inferences in rapidly evolving and niche domains like Process Systems Engineering (PSE). To address this, we propose a Graph-based Retrieval-Augmented Generation (RAG) pipeline specifically designed for PSE papers. Our pipeline includes custom document parsing, knowledge graph construction, and refinement to enhance retrieval accuracy. We evaluate the effectiveness of our approach using an automatically generated benchmark consisting entirely of PSE-related questions. The results show that our pipeline outperforms both non-RAG and vanilla RAG implementations in terms of relevant document retrieval and overall answer quality. Additionally, our implementation is fully customizable, allowing users to select the papers most relevant to their specific tasks. This framework is openly available, providing a flexible solution for those working in PSE or similar domains.

**Keywords**: Large Language Model, Retrieval-Augmented Generation, Graph-based Retrieval, Process Systems Engineering

## INTRODUCTION

Large Language Models (LLMs) have shown remarkable capabilities, performing well across a wide range of tasks, including accelerating scientific discovery in different fields. More specifically, in the field of Process Systems Engineering (PSE), LLMs have been adapted to various tasks, including flowsheet generation, the prediction of chemical properties, and infeasibility diagnosis in optimization models [1-2]. Still, off-the-shelf LLMs are inherently limited to the information present in their training data, which may become outdated or fail to cover specialized topics comprehensively [3]. This limitation is particularly relevant in both rapidly evolving and highly specialized fields, like PSE [4].

Retrieval-Augmented Generation (RAG) is an advanced framework that enhances the capabilities of LLMs by integrating them with external knowledge retrieval systems. Unlike standard LLMs, which rely solely on pre-trained knowledge, RAG combines parametric memory (the information encoded in the model's weights) with non-parametric memory (external data sources, such as databases or knowledge repositories). A retriever dynamically identifies and retrieves relevant information from these external sources, presenting it to the model alongside user inputs [5]. This approach enables RAG to provide more accurate, factual, and context-specific responses, while allowing the knowledge base to be updated without requiring model retraining. Such dynamic and interpretable knowledge integration makes RAG particularly valuable for addressing complex, knowledge-intensive tasks. Therefore, the PSE community can benefit from a domain-specific RAG to improve standard LLM performance, while ensuring that the responses remain grounded in truthful and updated information.

Graph-based knowledge structures are powerful tools to study complex and interconnected information, such as the one in scientific domains. Graph RAG enhances traditional RAG frameworks by leveraging knowledge graphs to represent and retrieve interconnected information more effectively. Unlike standard indexed databases that overlook relationships across documents, Graph RAG can be used to construct knowledge

graphs from academic papers, linking entities, concepts, and their relationships. This approach captures the interconnected nature of scientific knowledge, enabling more accurate and context-aware retrieval [6-7]. For example, Graph RAGs have successfully been used in medicine to improve retrieval accuracy and response quality by modeling relationships among diseases, treatments, and outcomes [8].

In this work, we propose a Graph RAG specifically designed to incorporate domain-specific knowledge from PSE. To achieve this, we develop a pipeline that parses academic papers and constructs tailored knowledge graphs from PSE literature. Additionally, we create a benchmark dataset of PSE-specific questions and answers derived from the utilized corpus to evaluate the accuracy and quality of the retrieved information. While copyright restrictions prevent us from publishing graph databases from the model, the pipeline developed in this work is freely accessible through a GitHub repository. This pipeline allows users to fully replicate and customize their selection of papers, enabling the construction of a Graph-based Retrieval Agent for Process Systems Engineering (GRAPSE) that is precisely aligned with their desired body of literature.

## Standard Retrieval-Augmented Generation

RAG is a framework that enables LLMs to infer knowledge from documents that were not directly trained on. This approach leverages the strength of LLMs in abstracting information from text when the relevant content is provided as part of the prompt, often referred to as the context. The primary objective of RAG is to retrieve the most relevant document(s) from a given set based on a user query, ensuring that the retrieved information is passed as context. This enriched prompt, containing both the query and the related context, allows the LLM to perform accurate and informed inference, effectively answering the query [5].

They key part of the RAG framework are embeddings, which are are numeric vector representations of text that encode semantic and contextual information. Words or phrases with similar meanings are positioned closer together in this high-dimensional space, where the distance and angle between vectors represent the degree of similarity. Transformer-based models, unlike traditional embedding methods like TF-DF [9], create contextual embeddings, meaning that the vector representation of a word adapts based on its surrounding context, capturing complex relationships in language.

Once documents have been split, chunks of text are passed through a transformer embedding model, which processes the input and produces high-dimensional vectors that reflect the semantic and contextual meaning of the text. These embeddings are then stored in a vector database, which indexes both the original text and its corresponding vectors. This setup allows for efficient storage and fast retrieval, as the database can perform similarity searches by comparing query embeddings to stored vectors. Typically, a cosine similarity metric is used to determine alignment between vectors.

The chunks corresponding to the vectors with the highest similarity to the embedded query vector are retrieved from the database and provided to the LLM as contextual input. A sketch of a standard RAG methodology is presented in Figure 1.

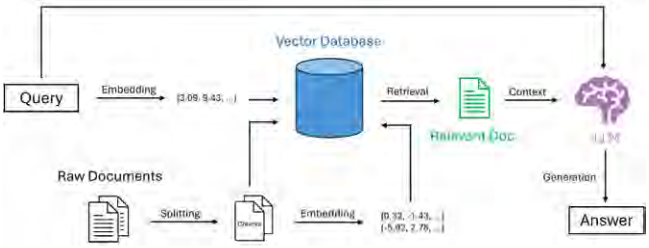



**Figure 1.** Standard Retrieval Augmented Generation pipeline. Raw documents are divided into chunks based on a predefined criterion, often a fixed character length. Each chunk is then converted into a high-dimensional vector using a transformer-based embedding model and indexed within a vector database. Similarly, the query is embedded using the same model to produce its vector representation. A similarity search is performed between the query vector and the vectors stored in the database. The chunks corresponding to the top $k$ most similar vectors are retrieved and incorporated into the prompt as context. This enriched prompt, combining the original query with the retrieved context, is then passed to an LLM for final answer generation.

# METHODOLOGY

The following subsections outline our proposed Graph RAG methodology, detailing the process of transforming raw papers into a refined knowledge graph. For reference, a representation of the entire pipeline is provided in Figure 2.

## Document Parsing

The first step in our approach involves the user selecting the academic papers that will form the knowledge base for the retrieval system. Once the papers are chosen, the pipeline begins by processing each paper, breaking it down into smaller units of information commonly referred to as "chunks". Some traditional RAG methodologies often utilize a fixed character-length chunking strategy, where the chunk size is limited by the maximum input length supported by the embedding model, with overlapping regions between consecutive chunks [5]. While this general approach is applicable to

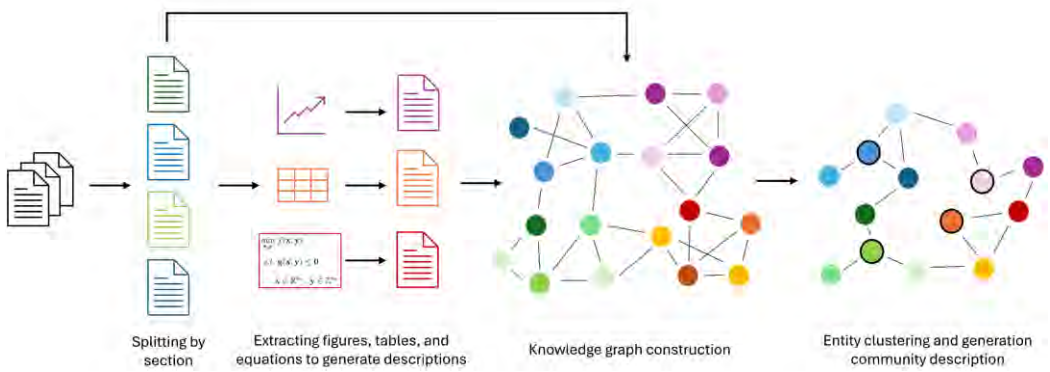



**Figure 2:** Sketch of the proposed Graph RAG pipeline. Raw papers are divided into sections, and each section is analyzed to extract all figures, tables, and equations. A multimodal LLM generates descriptions for these extracted elements, which are then appended to their corresponding sections. From this enriched set of documents, a knowledge graph is constructed, where nodes represent entities identified in the documents, and edges capture their relationships. In the figure, colors denote the topics found in the documents, illustrating the degree of their relation. Similar entities are merged to eliminate duplicates, and a community detection algorithm is applied to group nodes into clusters [7]. Nodes with black borders represent the descriptions generated based on the information within each community. The final knowledge graph is stored in a graph vector database for efficient search and retrieval.

any document, it does not consider the inherent structure of academic papers. Consequently, important ideas may be fragmented across multiple chunks, potentially reducing the retrieval quality.

To address this limitation, our pipeline parses each paper to identify its structural components, such as sections, subsections, and other logical divisions. Instead of relying on arbitrary fixed-size chunking, we allow each section to form its own chunk. This ensures that each chunk represents a self-contained idea or concept, preserving the coherence and contextual integrity of the information.

Academic papers in PSE often include a significant amount of information formatted as equations, tables, and figures. To effectively integrate this knowledge into the retrieval system, we extract these elements and generate detailed text descriptions for each using a multimodal LLM. These descriptions provide contextual information about the purpose, content, and relevance of the equations, tables, and figures, enhancing their interpretability and utility within the knowledge base.

The generated descriptions are not only linked to the specific chunk where the corresponding equation, table, or figure appears but are also associated with all chunks that reference them. For instance, the description of "Figure 1" is attached to both the chunk where the figure resides and all other chunks that mention "Figure 1." This approach ensures that users querying the system can access enriched and cohesive context related to these important elements, regardless of where they are discussed within the academic paper.

## Knowledge Graph Construction

After parsing and processing all the selected papers, the next step of the pipeline is to construct a knowledge graph that integrates and relates the extracted information across the entire body of literature. To achieve this, entities are first identified and extracted from the documents [6]. Tailoring the pipeline to academic literature, entity recognition is constrained to specific categories: papers, solvers, authors, algorithms, institutions, benchmarks, and software. However, this categorization can be customized by users to include additional or alternative categories, allowing greater flexibility and adaptability.

For each identified entity, a detailed description is generated based on the contextual information found in the text. Once these descriptions are established, relationships between entities are inferred and created to form a network [6]. To ensure greater coherence and maintain the integrity of the source information, each chunk from the parsed documents is treated as a separate entity within the graph and linked to the entities extracted from it. The entire knowledge graph construction process is implemented using the Neo4j graph database, enabling efficient storage, querying, and visualization of the interconnected knowledge [10].

## Graph Enhancement

To improve the efficiency of the constructed knowledge graph, the pipeline incorporates a step to group similar entities, reducing redundancy and improving query performance. This step ensures that semantically or contextually identical entities, which may be represented with slight variations (e.g., "Ignacio Grossmann"

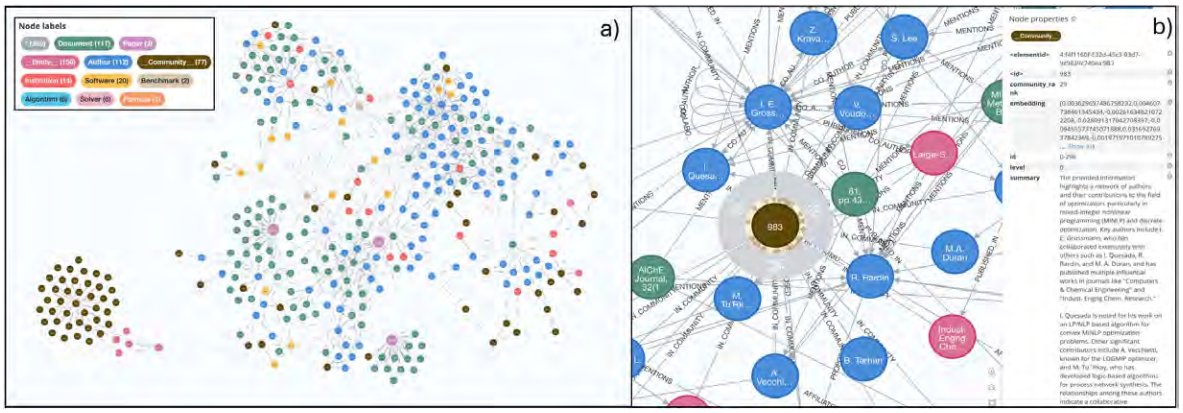



**Figure 3:** Knowledge graph visualization. Figure a) illustrates the complete knowledge graph built from a large collection of PSE papers, with node colors representing various entity types across the network. Figure b) provides a detailed view of a single community within the graph, showing the relationships among entities in the community and the corresponding community description.

vs. "I.E. Grossmann"), are unified into a single node within the graph.

The grouping process begins with a fuzzy search across the recognized entities to identify potential matches based on similarities in names, descriptions, or other attributes. Once potential matches are identified, a clustering algorithm is applied to group these similar entities systematically [7]. The clustering consolidates entities with high similarity scores while preserving entities that are sufficiently different.

Generating communities within a knowledge graph and creating descriptions of these communities play a crucial role in enabling global inference across the graph as seen in Edge et al. [7]. These community summaries provide a foundation for answering high-level, global questions that go above the scope of individual text chunks. By leveraging the Leiden community detection algorithm, the graph is partitioned into clusters of closely related entities, each meaning to represent a distinct theme or area of knowledge within the corpus.

Once communities are identified, generating comprehensive descriptions of each community enhances the ability of the system to perform global query-focused summarization. Analogue to the approach by Edge et al. [7], we separate queries into two distinct vector searches: one local, targeting raw chunks, and one global, focused on community descriptions. By combining the results of the two searches, we create a single retrieved context that simultaneously accounts for both granular details and high-level abstractions. This approach has proven more effective for answering open-ended questions that require various levels of knowledge abstraction [11]. A visualization of the obtained knowledge graphs is provided in Figure 3.

We employed the OpenAI API framework with *ChatGPT-4o-mini* as the generation model, utilized the *text-embedding-ada-002* model for embedding generation, and leveraged Chroma and Neo4j [10] as vector databases. To make sure GRAPSE is easily accessible, all computations were conducted on MacBook Air M1 (16 GB RAM). For all vector searches across the RAG pipelines, we employed similarity search with a threshold of 0.3. The LLMs were used with default settings, except the temperature was set to 0.0, and the same prompts were used uniformly across all pipelines.

## EVALUATION

Evaluating LLM frameworks is a key step in their development, requiring well-defined benchmarks of questions and corresponding metrics. While there are several established benchmarks for LLMs covering topics such as history, reasoning, coding, and math, no such benchmark currently exists for PSE questions. One potential solution is to collect questions from PSE textbooks and tests, but this approach is constrained by copyright issues. Alternatively, manually creating a question set is possible, but it is labor-intensive and would limit users from readily testing their customized pipelines. To address these challenges, we leverage Ragas to automatically generate a benchmark of PSE-specific questions and answers for evaluating retrieval pipeline performance [11]. This method uses the raw documents in the corpus to provide ground truth, enabling reliable assessment of retrieval quality. The metrics employed to evaluate the pipeline are detailed below.

### 1. Context Recall

Context Recall (CR) evaluates how effectively relevant documents or information are retrieved, ensuring no important details are missed. Higher scores, ranging from 0 to 1, indicate better performance by capturing all pertinent material. This metric simplifies evaluation by

breaking the reference answer into individual claims and verifying alignment with the retrieved contexts, eliminating the need for time-intensive direct annotation of reference contexts. CR is calculated using the input, reference answer, and retrieved contexts, emphasizing completeness in retrieval as:

$$CR = \frac{\#\ of\ claims\ in\ reference\ supported\ by\ retrieved\ context}{Total\ \#\ of\ claims\ in\ the\ reference} \quad (1)$$

## 2. Faithfulness

The Faithfulness (F) metric measures the factual alignment of a response with the retrieved context, with scores ranging from 0 to 1, where higher values indicate greater consistency. A response is considered fully faithful when all its claims are supported by the given context. This metric is calculated by identifying individual claims in the response and verifying their support within the retrieved context, ensuring a precise assessment of factual accuracy as:

$$F = \frac{\#\ of\ claims\ in\ response\ supported\ by\ retrieved\ context}{Total\ \#\ of\ claims\ in\ the\ response} \quad (2)$$

## 3. Factual Correctness

Factual Correctness (FC) assesses how accurately a generated response aligns with a given reference, assigning a score between 0 and 1, where higher values indicate better factual consistency. The response and reference are broken into individual claims, and their overlap is evaluated using an LLM. The metric is derived as an F1 score, with true positives representing claims in the response that match the reference, false positives as unmatched claims in the response, and false negatives as reference claims missing from the response. Precision and Recall are combined to compute the final F1 score as:

$$FC = 2\,\frac{Precision \cdot Recall}{Precision + Recall} \quad (3)$$

## 4. Semantic Similarity

Semantic Similarity measures how closely the meaning of a generated response aligns with the ground truth, with scores ranging from 0 to 1, where higher values indicate a stronger semantic match. This metric evaluates response quality by assessing alignment in the semantic embedding space. The ground truth and generated response are transformed into vector representations using the same embedding model, and their similarity is calculated using cosine similarity.

# RESULTS

The entire field of PSE cannot be comprehensively represented through a modest selection of papers due to its wide-ranging diversity in research areas [4]. For the purpose of this work, we based our document selection on the references cited in the *Advanced Optimization for Process Systems Engineering* book by Professor Grossmann [12]. This selection includes 48 papers with the full list available in the GitHub repository. While this is not an exhaustive representation of all research areas within PSE, it serves as an illustrative proof of concept for this study. Importantly, our pipeline is designed to be paper-agnostic, allowing users to customize their selection of documents to suit their specific tasks and apply the methodology accordingly. Our resulting benchmark consists of 577 questions.

## Metric Comparison

We compared four distinct pipelines. The *azure_openai* pipeline represents a straightforward use of the LLM, equivalent to a single, simple API call. The *langchain_basic* pipeline corresponds to a standard RAG implementation, as illustrated in Figure 1. The *graph_db_vector* pipeline performs vector search within the graph database without any additional enhancements. Lastly, the *grapse* pipeline reflects the complete methodology proposed in this work. The results of this comparison are presented in Figure 4.

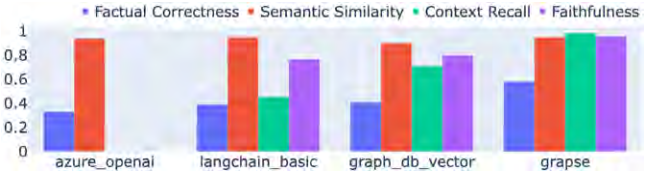



**Figure 4.** Metric comparison for different LLM pipelines performing in a PSE benchmark. Note a score of 1 is the best in all metrics.

Our proposed pipeline consistently achieves the highest scores across all evaluated metrics. The Factual Correctness and Faithfulness metrics are not applicable to the simple LLM call, as it lacks a retrieval mechanism. The Semantic Similarity metric shows minimal variation across pipelines, as it primarily reflects closeness in the embedded space rather than natural language similarity, which explains the uniformly high similarity between responses and queries. The most critical metric, however, is Context Recall, which evaluates the effectiveness of the retrieval mechanism. This metric shows the most significant improvement in our pipeline, demonstrating that the retrieved documents effectively support the generation of accurate answers.

## Q&A

To demonstrate the practical application of our framework, we posed two illustrative questions to our pipeline. The LLM was instructed to provide two distinct types of responses, showcasing the system's flexibility, while maintaining quality and rigor. The questions and corresponding answers are presented in Figure 5.

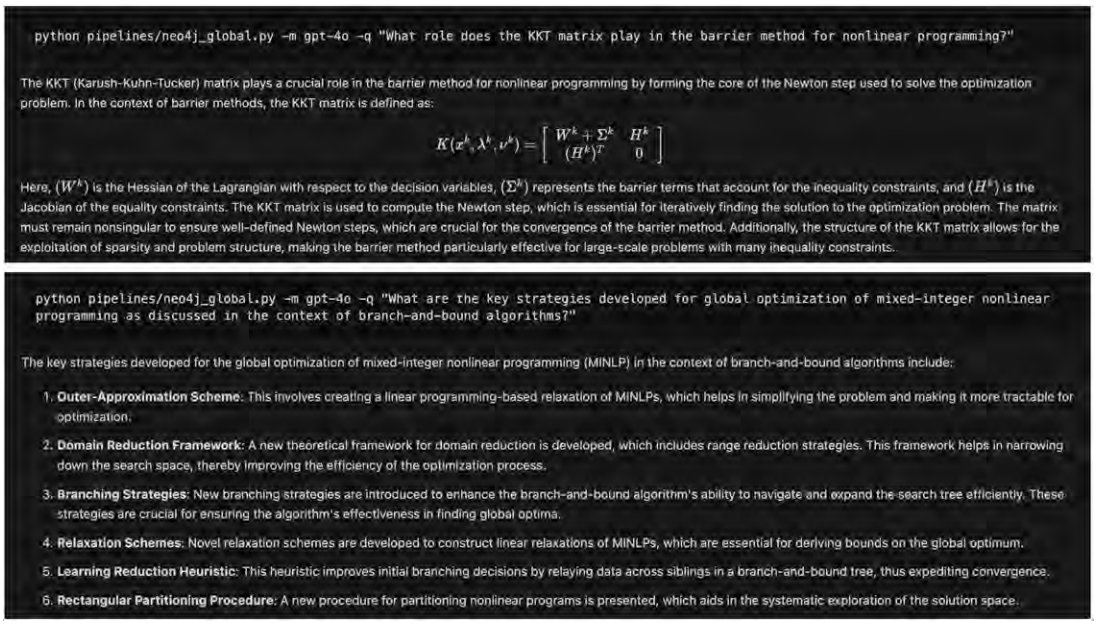



**Figure 5:** Responses generated by our proposed pipeline for two illustrative questions. For the first question the LLM was instructed to provide a concise and mathematically focused answer For the second question, it was prompted to provide a broader and more general explanation.

## CONCLUSIONS

We proposed a graph-based retrieval-augmented generation pipeline specifically designed for PSE papers. The pipeline is fully replicable and customizable to accommodate any papers the user requires. Additionally, we integrated a benchmark generation tool to facilitate the evaluation of the resulting RAGs, potentially paving the way for the creation of PSE question sets. Our pipeline outperforms both non-RAG and vanilla RAG implementations demonstrating its effectiveness. In this paper, we focused on zero-shot prompting to generate and evaluate answers. However, future work will involve integrating this pipeline with reasoning models to further enhance answer quality.

## DIGITAL SUPPLEMENTARY MATERIAL

All the code used in this work can be found in an openly availably GitHub repository: https://github.com/arpanseth/GRAPSE

## ACKNOWLEDGEMENTS

We thank the Center for Advanced Process Decision-making (CAPD) and the Department of Chemical Engineering from Carnegie Mellon University for kindly supporting this work.

## REFERENCES

1. Schweidtmann AM. Generative artificial intelligence in chemical engineering. Nature Chemical Engineering 1.3:193-193 (2024)
2. Hao C, Constante-Flores GE, Li C. Diagnosing infeasible optimization problems using large language models. INFOR: Information Systems and Operational Research 62.4:573-587 (2024).
3. Petroni F. Language models as knowledge bases?. arXiv preprint arXiv:1909.01066 (2019).
4. Pistikopoulos EN, Barbosa-Povoa A, Lee JH, Misener R, Mitsos A, Reklaitis GV, Venkatasubramanian V, You F, Gani R. Process systems engineering-the generation next?. Computers & Chemical Engineering 147: 107252 (2021).
5. Lewis P, Perez E, Piktus A, Petroni F, Karpukhin V, Goyal N, Küttler H, Lewis M, Yih WT, Rocktäschel T, Riedel S. Retrieval-augmented generation for knowledge-intensive nlp tasks. Advances in Neural Information Processing Systems 33:9459-9474 (2020).
6. Hu Y, Lei Z, Zhang Z, Pan B, Ling C, Zhao L. GRAG: Graph Retrieval-Augmented Generation. arXiv preprint arXiv:2405.16506 (2024).
7. Edge D, Trinh H, Cheng N, Bradley J, Chao A, Mody A, Truitt S, Larson J. From local to global: A graph rag approach to query-focused summarization. arXiv preprint arXiv:2404.16130

(2024).
8. Wen Y, Wang Z, Sun J. Mindmap: knowledge graph prompting sparks graph of thoughts in large language models. arXiv. arXiv preprint arXiv:2308.09729 (2023).
9. Leskovec J, Rajaraman A, Ullman JD. Mining of massive data sets. Cambridge University Press (2020).
10. Miller JJ. Graph database applications and concepts with Neo4j. In Proceedings of the southern association for information systems conference. 2324-36:141-147 (2013).
11. Sarthi P, Abdullah S, Tuli A, Khanna S, Goldie A, Manning CD. Raptor: Recursive abstractive processing for tree-organized retrieval. arXiv preprint arXiv:2401.18059 (2024).
12. Es S, James J, Espinosa-Anke L, Schockaert S. Ragas: Automated evaluation of retrieval augmented generation. arXiv preprint arXiv:2309.15217 (2023).
13. Grossmann IE. Advanced Optimization for Process Systems Engineering. Cambridge University Press (2021).

© 2025 by the authors. Licensed to PSEcommunity.org and PSE Press. This is an open access article under the creative commons CC-BY-SA licensing terms. Credit must be given to creator and adaptations must be shared under the same terms. See https://creativecommons.org/licenses/by-sa/4.0/



Systems & Control Transactions

**Research Article - Peer Reviewed Conference Proceeding**
ESCAPE 35 - European Symposium on Computer Aided Process Engineering
Ghent, Belgium. 6-9 July 2025
Jan F.M. Van Impe, Grégoire Léonard, Satyajeet S. Bhonsale,
Monika E. Polańska, Filip Logist (Eds.)

PSE PRESS

# A Fault Detection Method Based on Key Variable Forecasting

**Borui Yang[a,b], Jinsong Zhao[a,b*]**

[a] Department of Chemical Engineering, Tsinghua University, Beijing 100084, China
[b] State Key Laboratory of Chemical Engineering, Tsinghua University, Beijing, China
* Corresponding Author: jinsongzhao@tsinghua.edu.cn.

## ABSTRACT

This paper presents a novel fault detection method based on key variable forecasting models. The approach integrates future forecasts of key variables into a time window, allowing for early fault detection without modifying the offline training phase of the existing fault detection model. By incorporating predicted data into the detection process, the proposed method significantly improves fault detection rates and reduces detection delays. Experiments using the Continuous Stirred Tank Heater (CSTH) system demonstrate the superiority of our method over traditional approaches, showing the advantages of forecasting in enhancing detection performance. However, our results also highlight the dependency of the method's effectiveness on the quality of the forecasting model, suggesting the need for more advanced time-series forecasting techniques. Additionally, the current point forecasting method may not be sufficient in real-world applications, where probabilistic modeling of key variables would provide more reliable detection results. Future research directions will focus on refining forecasting models and exploring probabilistic approaches for more accurate fault detection.

**Keywords**: Fault Detection, Key Variable Forecasting, Artificial Intelligence, Process Monitoring

## INTRODUCTION

With the advancement of industrial production toward digitalization and automation, process monitoring has become an essential technical tool for ensuring the safe and efficient operation of chemical processes [1]. Despite significant advancements in process engineering, the potential for process failures continues to exist. If such faults are not detected and diagnosed at an early stage, they may go beyond control. Over the past decades, various fault detection approaches have been proposed, including model-driven, knowledge-driven, and data-driven methods. Data-driven methods, in particular, have gained prominence, as they rely primarily on large amounts of process data, making them especially relevant with the widespread application of the Internet of Things (IoT). Among these, neural-network-based methods have emerged as a prominent approach. By stacking feature extraction layers and applying nonlinear activation functions between them, deep neural networks exhibit a strong capacity to capture complex, nonlinear patterns. This aligns well with the nature of chemical process variables, which are inherently nonlinear, strongly coupled with control loops, multivariate, and subject to time lags.

In industrial applications, fault detection algorithms rely on the time-series data of key variables. However, statistical methods, such as Principal Component Analysis (PCA) and Partial Least Squares (PLS), face significant limitations. These techniques struggle to capture the temporal dependencies between consecutive data points, are often ill-equipped to handle large-scale datasets, and fail to effectively leverage higher-order information—key shortcomings frequently highlighted in critiques of multivariate process monitoring, such as Multiway Principal Component Analysis (MPCA) [2]. Despite their tremendous success in certain contexts, current statistical analysis technologies still have difficulty utilizing higher-order information for multivariate process monitoring, which limits their ability to model complex, dynamic systems comprehensively [3]. To address this,

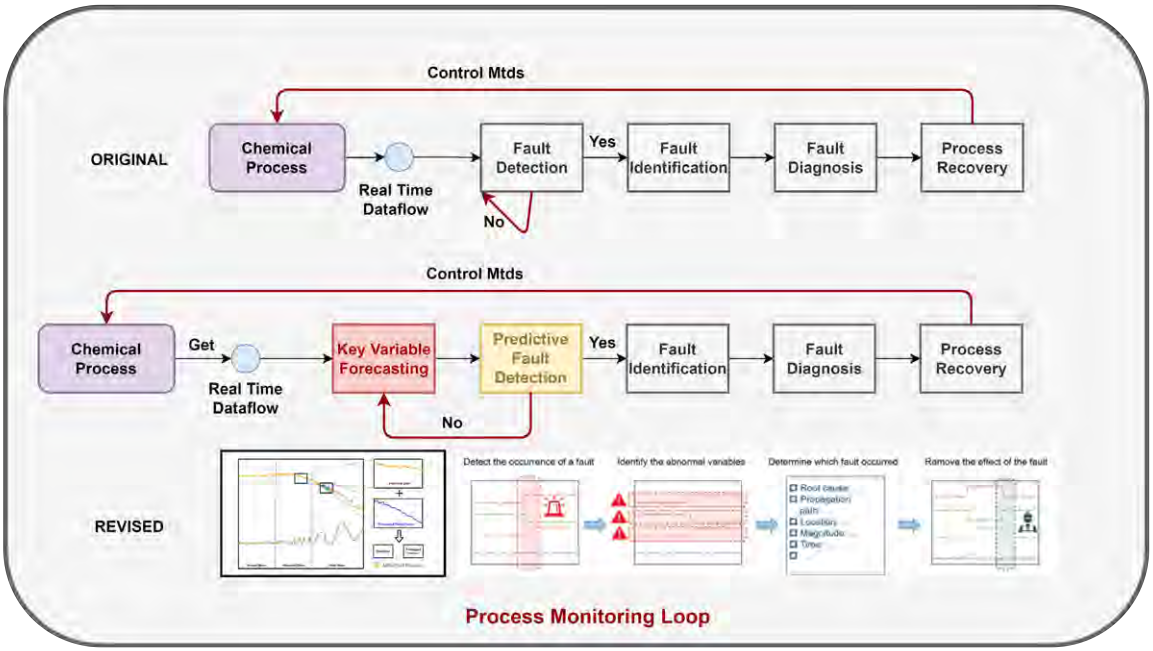



**Figure 1:** Relationship between key variable forecasting and process monitoring.

architectures such as Autoencoders (AE), Convolutional Neural Networks (CNN), and Transformers [4] incorporate the relationships between time points through sliding window sampling. However, this approach can dilute fault signals, leading to delayed fault detection. Most existing methods focus on historical data, but what if we shift the focus from the past to the future? Inspired by the human decision-making process, where adverse future trends are often considered to enable timely responses to unfavorable outcomes, we propose incorporating key variables that have already entered a fault state in future time points into the fault detection model. This proactive inclusion of future fault indicators can significantly improve the timeliness of fault detection.

Building on the aforementioned concept, this work develops and implements a proactive fault detection method based on key variable forecasting. This approach employs predictive models (Transformer and furtherly VCformer) to actively forecast key variables over a future time horizon. The predicted results, combined with historical information, are used as inputs to a variational autoencoder (VAE) to calculate the reconstruction error for fault detection. The detection component of the method is trained using normal operating data, and faults are identified by evaluating the reconstruction error. The forecasting component is trained with mixed data, where the initial part contains normal data, followed by the selective introduction of faults after a certain period, enabling the predictive model to capture both fault evolution trends and normal data characteristics.

The proposed method has been validated on the CSTH dataset, demonstrating that incorporating future information at the current time point significantly enhances early fault detection. However, optimizing the design of the reconstruction loss function and the model architecture is necessary to mitigate false alarms. Introducing future expectations into current assessments shows great potential for advancing early fault detection and diagnosis but also poses challenges, requiring higher performance from key variable forecasting models.

## METHODOLOGY

The proposed methodology consists of two stages: key variable forecasting and subsequent fault detection. A reliable key variable forecasting algorithm is used to extract the trends of key variables from multivariate time-series data, whereas the fault detection algorithm further utilizes the results of predicted key variable in conjunction with the information of existing variables for the over-the-top detection of faults.

The upper loop in Figure 1 illustrates the conventional process monitoring workflow, in which the online detection phase relies on a time window of selected key variables spanning from a previous time point to the current moment. In practical industrial applications, plants often use specific key monitoring variables as the control indicators. If these variables exceed predefined thresholds, an alarm is triggered to notify the operators of the

corrective actions. This suggests that certain key variables play a crucial role in the early detection and control of potential faults. If the evolution of key fault variables can be reliably predicted using an effective forecasting algorithm, future key variable trends can be incorporated into the current decision-making process (i.e., determining whether a fault is occurring). This results in an enhanced revised process-monitoring loop, as depicted in Figure 1. The integration of predicted key variable trends allows for an earlier warning of potential faults, thereby significantly reducing the probability of actual fault occurrences and enhancing overall process safety.

### Key Variable Forecasting Method: VCformer

RNN, Temporal Convolutional Networks (TCN), and Transformer are all neural networks used for modeling time series. Among these, Transformer utilizes the attention mechanism, which allows it to achieve better long-range dependency matching and faster training speeds compared to RNN and CNN. In both chemical process simulations and real industrial processes, key variables often exhibit unidirectional or bidirectional causal relationships owing to the interconnections of physical structures. Several time-series forecasting algorithms have already utilized the attention mechanism to capture these causal relationships, thereby improving the forecast accuracy. Notable examples include Crossformer [5], which employs a two-stage attention mechanism (channel-wise and time-wise), and VCformer [6], which further models the time lag between variables.

### Subsequent Fault Detection

This study uses the traditional method based on Variational Autoencoders (VAE) for fault detection. An Autoencoder (AE) consists of an encoder and a decoder. Given unlabeled data $\mathrm{X} = \{\mathrm{x}^{\mathrm{i}}\}_{\mathrm{i}=1}^{\mathrm{N}}$, the encoder function $\mathrm{f}_\theta$ generates a feature vector $h^i$ in the latent space, and the decoder function $g_\varphi$ reconstructs the latent-space feature vector to obtain the reconstructed vector $\hat{x}^i$ (which contains trainable parameters θ and φ).

$$\hat{x}^i = g_\varphi(h^i) = g_\varphi(\mathrm{f}_\theta(\mathrm{x}^{\mathrm{i}})) \tag{1}$$

The Variational Autoencoder (VAE) employs a directed probabilistic model to characterize the probability distribution of the latent variables. VAE utilizes two separate neural networks to model the mean and variance of the latent variables, which are sampled from a normal distribution. The loss function of the VAE is formulated as follows (n and m are dimensions of x and h respectively):

$$L_{VAE} = \frac{1}{2n} \sum_{i=1}^{n} \left( \|x_i - \hat{x}_i\|_2^2 + \beta \sum_{j=1}^{m} \left( \left(\mu_i^{(j)}\right)^2 + \left(\sigma_i^{(j)}\right)^2 - 1 - \log\left(\left(\sigma_i^{(j)}\right)^2\right) \right) \right) \tag{2}$$

In fault detection, the Negative Variational Score (NVS) is used as the monitoring indicator [7]. Since VAE is a static deep network, it is unable to capture the dynamic correlations and features of time-series variables. Thus, it serves as an ideal baseline method for fault detection afterwards.

## THE PROPOSED METHOD

The proposed Key-Variable-Forecasting-based fault detection algorithm is presented in Table 1.

## APPLICATIONS

In this section, we validate the effectiveness of the proposed fault detection method based on key variable forecasting using the Continuous Stirred Tank Heater (CSTH) as a benchmark, demonstrated in Figure 2. An ablation study is conducted to compare the proposed model with a fault detection algorithm purely based on VAE (No future forecasting information incorporated), highlighting the superiority of our approach. The experiments are implemented on a computing server equipped with an Intel Xeon Gold 5118 CPU and an NVIDIA TITAN RTX GPU.

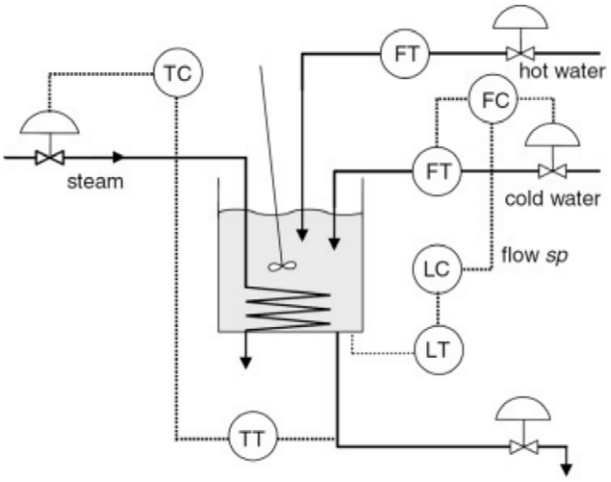



**Figure 2.** Continuous Stirred Tank Heater (CSTH) [8].

CSTH is a typical mixing vessel in chemical processes. The data used in this study originates from the MATLAB Simulink model developed by Thornhill et al. for a CSTH pilot plant. The system operates by supplying a stream of hot water and a stream of cold water into the stirred tank, which is then heated using steam. The water is uniformly mixed, and the outlet water temperature reflects the temperature of the tank.

In this study, five variables are monitored: cold water flow rate (CWflow), cold water valve position (CWValve), tank level (Level), outlet temperature (Temp),

**Table 1:** Pseudo-code of the algorithm.

**Algorithm: Key-Variable-Forecasting-based Fault Detection**

**Key Variable Forecasting**

1 Choose a reliable key variable forecasting model (VCformer).

2 Optimize the model architecture for key variable forecasting.

3 Train and fine-tune the key variable forecasting model to obtain reliable forecasts.

**Fault Detection: Offline Training**

4 Develop a VAE-based feature extractor.

5 Split normal data into training and validation sets, and apply mean centering for normalization.

6 Select a window width w and preprocess the data into a sample matrix, where each matrix has a size of w×v.

7 Use the NVS (-Loss) from the validation dataset and determine the control limits using kernel density es-

**Fault Detection: Online Monitoring**

8 Collect online data and apply mean centering.

9 Preprocess the data into a sample matrix following the same steps as in offline model training.

10 Input the sample matrix into the key variable forecasting model (with a context length of w) to obtain a window for f time points.

11 Extract the last w - t time points from the sample matrix and merge them with the first t predicted sam-cast window to form a new data window of size w×v that incorporates future forecast trends.

12 Input the new w×v data window into the VAE to obtain the NVS.

13 Compare the test sample NVS with the NVS threshold determined in the offline training phase to deter-sample is normal or faulty.

and steam valve position (SteamValve). All measurements are represented as electrical signals in the range of 4–20 mA.

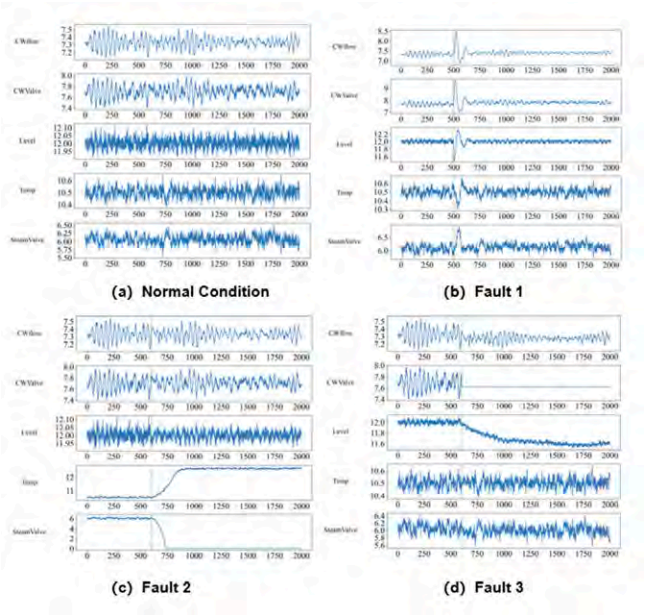



**Figure 3.** Time series data of the five CSTH variables:(a) Under normal operating conditions, (b) Under Fault 1, (c) Under Fault 2, (d) Under Fault 3.

The Simulink program generates data under normal conditions with realistic disturbances, while fault condition data must be generated by manually modifying the program. The CSTH dataset has been widely used as a benchmark in various studies, demonstrating its effectiveness.

In this simulation, due to the limited number of variables, all five variables are extracted as key variables. A total of three types of faults are designed and analyzed, as shown in Table 2. Figure 3 illustrates the temporal variations of each variable under normal operating conditions and the three fault conditions.

## Key Variable Forecasting

To enable the proposed method to learn the dynamic characteristics of the data, Fault 1 data is used as the training dataset when training the key variable forecasting model. This dataset consists of 2400 time points, with the fault introduced at the 2100th time point. Since Fault 1 does not exhibit abrupt changes in variables and does not cause system shutdown, it is well-suited for capturing the dependencies between key variables under both normal and faulty conditions.

The model hyperparameters are set as follows: seq_len = 32, pred_len = 32, encoder_layer = 1, decoder_layer = 1, learning rate = 0.0003, hidden_dim = d_model = 256.

**Table 2:** Fault descriptions in CSTH simulation.

| Fault Num | Description | Type | Usage |
|---|---|---|---|
| 1 | Tank Level | Step Drop | Key Variable Forecasting |
| 2 | Hot water temperature | Slow increase | Fault Detection |
| 3 | Cold water valve | Sticking | Fault Detection |

Figure 4 illustrates the forecasting performance of VCformer for the temperature variable under fault conditions. The model forecasts the values of key variables for the next 32 time points using data from the preceding 32 time points. Mean Squared Error (MSE) and Mean Absolute Error (MAE) are used to quantitatively evaluate the accuracy of the point predictions. Due to its built-in Variable Correlation Attention mechanism, which quantitatively models inter-variable relationships, VCformer achieves the lowest MSE and MAE values compared to methods such as Transformer, DLinear [9], and Crossformer in the forecasting task. It also demonstrates superior capability in capturing short-term dependencies among variables. Detailed quantitative results can be found in Table 3. Through comparative analysis, VCformer exhibits more stable and reliable performance in key variable prediction tasks compared to standard Transformer architectures, RNN-based models, and ARIMA, making it a preferred choice for providing accurate predictions in the subsequent fault detection process.

To further improve the forecasting model's performance, optimizing the regularization term in the loss function to enhance the model's ability to capture short-term variable relationships or designing a new model architecture could be considered.

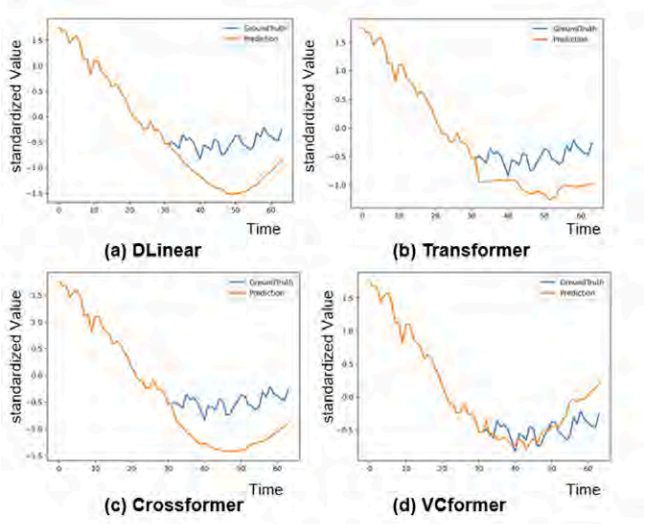



**Figure 4.** Forecasting results of the Steam Valve opening (standardized) at t=100 in the test set.

**Table 3:** Key Variable Forecasting Performance Evaluation (Bold indicates the best model, and the underlined model indicates the second-best model).

| Model | MSE | MAE |
|---|---|---|
| DLinear | 0.3735 | <u>0.3754</u> |
| Transformer | <u>0.2942</u> | 0.4016 |
| Crossformer | 0.3876 | 0.4220 |
| VCformer | **0.2680** | **0.3703** |

## Fault Detection based on Key Variable Forecasting

To demonstrate the improvement in model performance by incorporating future forecasted data, we use the Variational Autoencoder (VAE) as the baseline framework, which lacks the capability to capture the dynamic characteristics of time-series data due to its static latent representation. This limitation stems from VAE's reliance on a fixed encoding-decoding process that does not inherently account for temporal evolution, making it less effective for fault detection in dynamic industrial systems. This study investigates the contribution of the forecasting module to fault detection using the designed Fault 2 and Fault 3 conditions, with detailed fault descriptions provided in Table 1. In both fault conditions, the fault is introduced after 600 samples of normal operation, allowing us to evaluate how well the model transitions from normal to anomalous states under controlled conditions.

During the offline training phase, normal data is split into training and validation sets, with 1500 samples in the training set and 500 samples in the validation set. The test set consists of two groups of data corresponding to the two fault conditions, each containing 1500 sample time points, selected using a sliding window approach. This sliding window technique ensures that the temporal context of the data is preserved, enabling the model to analyze sequential patterns effectively. The model structure is configured as follows: VAE (Encoder: $5 \rightarrow 32 \rightarrow 10$, Reparameterization: $10 \rightarrow 10$, Decoder: $10 \rightarrow 32 \rightarrow 5$). Here, the encoder compresses the 5-dimensional input

**Table 4:** Fault detection performance of all methods for CSTH.

| Model | Fault 2 | | Fault 3 | |
|---|---|---|---|---|
| | Detection Rate | Detection Delay (s) | Detection Rate | Detection Delay (s) |
| PCA | 93.6% | 58 | 90.2% | 88 |
| KPCA | 94.2% | 52 | 91.9% | 73 |
| VAE-base | 94.7% | 49 | 94.1% | 55 |
| VAE-Predictive | **96.0%** | **37** | **95.0%** | **47** |

into a 10-dimensional latent space via an intermediate 32-unit layer, while the decoder reconstructs the data symmetrically, with reparameterization ensuring stable training of the latent variables. The hyperparameters are set as follows: learning rate = 0.0001, beta = 0.001, batch_size = 16, where the low learning rate ensures gradual convergence, beta controls the KL-divergence penalty in the VAE loss, and the small batch size balances computational efficiency with model generalization.

Table 4 compares the results of fault detection without future data incorporation (VAE-base) and fault detection with future forecasted data (VAE-Predictive) in an ablation study. Additionally, the results are compared with classical detection methods such as PCA and Kernel PCA (KPCA). The comparison shows that by incorporating future information ($w$=32, $t$=8), the proposed fault detection method is able to detect faults earlier and achieves a higher fault detection rate (FDR). Specifically, the window size $w$=32 defines the length of the input sequence, while $t$=8 indicates that 8 future time points are forecasted and integrated, enhancing the model's ability to anticipate fault onset compared to purely historical data-driven approaches like PCA and KPCA.

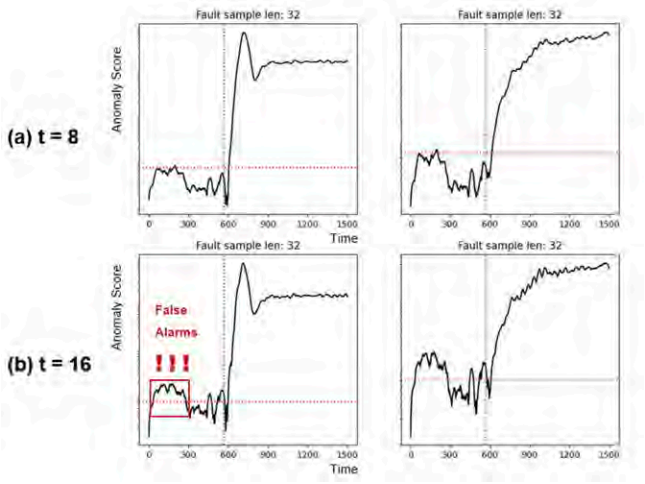



**Figure 5.** The anomaly score over time for the Fault 2 and 3.

Furthermore, we also investigate the impact of the number of future time points $t$ on fault detection. As $t$ increases, the proportion of future information within the new sliding window becomes larger. However, errors in key variable forecasting may also introduce a higher False Positive Rate (FPR) into the detection algorithm. This trade-off arises because forecasting inaccuracies, compounded over longer prediction horizons, can mislead the model into flagging normal variations as faults. By increasing $t$ to 16 (where future data occupies half of the time window length), a significant increase in false alarms is observed, as illustrated in Figure 5. For instance, at $t$=16, the anomaly scores in Figure 5 show more frequent spikes in non-fault regions, reflecting the amplified uncertainty from extended forecasts. This suggests that incorporating future trends may lead to increased fluctuations in diagnostic results, which might necessitate adjustments to the loss function—such as increasing the weight of reconstruction error relative to forecasting error or introducing a penalty term for false positives—to mitigate false positives and stabilize performance.

## CONCLUSIONS

In this paper, we introduce an innovative fault detection framework that leverages key variable forecasting models to enhance diagnostic precision. Our approach begins by employing a forecasting method to predict variable values over an upcoming time window. These predictions are then seamlessly integrated with the current time window data and fed into the detection model. A standout feature of this method is its plug-and-play versatility: it requires no alterations to the original fault detection model during offline training, with future predicted values simply appended to the input time window during online deployment. This elegant design yields superior fault detection rates, reduces detection latency, and can be effortlessly incorporated into existing state-of-the-art (SOTA) models to amplify their effectiveness.

Nevertheless, supplementary experiments reveal that the efficacy of our fault detection model hinges

closely on the accuracy of the forecasting component, underscoring the need for robust time-series forecasting techniques tailored to chemical processes. A further limitation lies in our reliance on point forecasting, which, while effective, falls short of capturing the full complexity of real-world scenarios. In practice, modeling the probability distributions of key variables alongside their point estimates could provide more reliable and confident detection outcomes. This observation paves the way for exciting new directions in our ongoing research.

## ACKNOWLEDGEMENTS

The authors gratefully acknowledge support from the State Key Laboratory of Chemical Engineering and the National Key R&D Program of China (No. 2024YFC3013600).

## REFERENCES

1. Venkatasubramanian V, Rengaswamy R, Yin K, Kavuri SN. A review of process fault detection and diagnosis: Part I: Quantitative model-based methods. Comput Chem Eng 27:293-311 (2003) https://doi.org/10.1016/S0098-1354(02)00160-6
2. Nomikos P, MacGregor JF. Multiway PCA for monitoring batch processes. Chemom Intell Lab Syst 30:97-108 (1995)
3. Qin SJ. Survey on data-driven industrial process monitoring and diagnosis. Annu Rev Control 36:220-234 (2012)
4. Vaswani A, Shazeer N, Parmar N, Uszkoreit J, Jones L, Gomez AN, Kaiser L, Polosukhin I. Attention is all you need. arXiv (2023) https://doi.org/10.48550/arXiv.1706.03762
5. Zhang Y. Crossformer: Transformer utilizing cross-dimension dependency for multivariate time series forecasting. OpenReview (2023) https://openreview.net/forum?id=vSVLM2j9eie
6. Yang Y, Zhu Q, Chen J. VCformer: Variable correlation transformer with inherent lagged correlation for multivariate time series forecasting. arXiv (2024) https://doi.org/10.48550/arXiv.2405.11470
7. An J, Cho S. Variational autoencoder based anomaly detection using reconstruction probability. Spec Lect IE 2:1-18 (2015)
8. Thornhill NF, Patwardhan SC, Shah SL. A continuous stirred tank heater simulation model with applications. J Process Control 18:347-360 (2008) https://doi.org/10.1016/j.jprocont.2007.07.006
9. Zeng A, Chen M, Zhang L, Xu Q. Are transformers effective for time series forecasting?. arXiv (2022) https://doi.org/10.48550/arXiv.2205.13504

© 2025 by the authors. Licensed to PSEcommunity.org and PSE Press. This is an open access article under the creative commons CC-BY-SA licensing terms. Credit must be given to creator and adaptations must be shared under the same terms. See https://creativecommons.org/licenses/by-sa/4.0/



Systems & Control Transactions

**Research Article - Peer Reviewed Conference Proceeding**
ESCAPE 35 - European Symposium on Computer Aided Process Engineering
Ghent, Belgium. 6-9 July 2025
Jan F.M. Van Impe, Grégoire Léonard, Satyajeet S. Bhonsale,
Monika E. Polańska, Filip Logist (Eds.)

PSE PRESS

# Optimizing Industrial Heat Electrification: Balancing Cost and Emissions

**Soha Mousa[a], Dhabia Al-Mohannadi[a]***

[a] Texas A&M University at Qatar, Department of Chemical Engineering, Doha, Qatar
* Corresponding Author: Dhabia.al9mohannadi@qatar.tamu.edu

## ABSTRACT

The electrification of industrial heat is a promising pathway for decarbonization, yet challenges persist in balancing capital costs, operating costs, and emissions reduction. While previous studies have assessed electrification through heat integration and graphical methods, these approaches do not inherently determine the optimal hybrid technology configuration. This study introduces an optimization-based framework that systematically evaluates the cost-optimal allocation of electrified and conventional heating technologies. Formulated as a Mixed-Integer Linear Programming (MILP) model and implemented in Gurobi, the framework minimizes Total Annualized Cost (TAC) while satisfying heat demand, technology constraints, and emissions targets. Applied to an industrial case study, the model compares three scenarios: a fully conventional system relying on steam boilers and fired heaters, a fully electrified system utilizing high-temperature heat pumps, electrode boilers, and electric heaters, and an optimized hybrid system that strategically integrates both conventional and electrified technologies. The results demonstrate that the optimized hybrid system achieves a 75% electrification rate, reducing TAC by 7% compared to previous graphical electrification assessments. The model selects a combination of a high-temperature heat pump and a steam boiler, highlighting the importance of accounting for heat pump cost savings in economic evaluations. Additionally, a comparison with Carbon Capture and Storage (CCS) reveals that partial electrification results in a lower $CO_2$ abatement cost of 131 \$/t$CO_2$, compared to 140 \$/t$CO_2$ for CCS, reinforcing the economic viability of industrial heat electrification. This study provides a systematic optimization framework for guiding industrial electrification decisions and emphasizes the role of carbon taxation, electricity pricing, and renewable energy incentives in shaping cost-effectiveness. The findings underscore the importance of integrating process optimization with techno-economic analysis to accelerate industrial decarbonization.

**Keywords**: Optimization, Renewable and Sustainable Energy, Energy Systems, Technoeconomic Analysis

## INTRODUCTION

The industrial sector is a major contributor to global energy consumption and greenhouse gas (GHG) emissions, with process heat accounting for over half of industrial energy use [1]. Traditionally, industrial heat has been generated using fossil fuel-based technologies, leading to significant $CO_2$ emissions. Decarbonizing industrial heat generation is therefore essential for achieving sustainability targets and reducing reliance on fossil fuels. One of the most promising pathways for industrial decarbonization is electrification, where technologies such as high-temperature heat pumps (HTHPs), electrode boilers (EBs), and electric heaters (EHs) replace conventional systems.

A comprehensive analysis has shown that 78% of industrial energy demand is electrifiable, with potential $CO_2$ reductions of up to 78% as the power sector decarbonizes [3]. Industrial process heating, particularly electrifying industrial boilers, has been identified as a high-impact application, potentially reducing emissions by 19 million metric tons of $CO_2$ equivalent (MMmt$CO_2$e) under a high-renewables energy grid scenario [4]. Gaps remain in developing systematic, cost-effective electrification processes tailored to specific industries, particularly in chemical sectors and high-temperature heat pump

applications [5].

Beyond technological feasibility, policies and economic incentives play a critical role in accelerating industrial electrification [7]. However, transitioning to electrified heat generation presents several key challenges. Matching electrical heating technologies to specific temperature requirements and industrial applications remains complex, as different processes require different heating profiles [6]. Additionally, electrified heating systems often have higher capital and operating costs compared to conventional fossil-fuel-based technologies, making economic feasibility highly dependent on electricity prices and carbon taxation policies [2]. At the same time, there is a pressing need for a systematic framework that optimizes hybrid heat system configurations while leveraging renewable electricity sources to minimize $CO_2$ emissions and enhance sustainability.

## BACKGROUND AND RELATED WORK

Industrial heat electrification has gained significant attention as a key strategy for reducing greenhouse gas emissions and improving energy efficiency in industrial processes. Several studies have explored the techno-economic feasibility of electrification technologies, particularly high-temperature heat pumps (HTHPs), electrode boilers, and electrochemical processes. HTHPs have demonstrated high efficiencies, with coefficient of performance (COP) values ranging from 2.5 to 7 for low-to-medium temperature applications (≤160°C) [8]. However, their adoption remains limited by temperature constraints and high capital costs, restricting their widespread application in high-temperature industrial processes. Recognizing these limitations, Zühlsdorf et al. analyzed the potential for heat pump-based process heat supply at large capacities and temperatures exceeding 150°C, assessing the technical and economic feasibility of integrating heat pumps into industrial systems [9].

Beyond conventional electrification technologies, innovative electrochemical processes are also being explored for cleaner and more energy-efficient industrial applications. Electrochemical synthesis has shown promise in producing ethylene and propylene oxides, providing a cleaner alternative to conventional petrochemical production methods [11]. However, despite their selectivity and efficiency, technical bottlenecks remain, particularly in scaling up these processes for widespread industrial adoption [10]. The integration of electrochemical pathways into industrial heat systems requires further research to address these challenges and enhance their feasibility for large-scale operations.

Several studies have examined the broader implications of industrial electrification on energy systems. Lechtenböhmer et al. found that a fully electrified industry would create significant demand for electricity, which could place major strains on existing power infrastructure [12]. Similarly, Kosmadakis) estimated that high-temperature heat pumps (above 150°C) could meet only 1.5% of industrial heat demand in Europe, underscoring the limitations of single-technology solutions[13]. Bühler et al. investigated the electrification potential in Danish industries, concluding that while up to 80% of heat demand could technically be electrified, economic feasibility remains a major challenge due to high upfront costs and fluctuating electricity prices [14]. These studies highlight the varying degrees of electrification potential across industries but emphasize the need for a more holistic approach that integrates flexibility, cost analysis, and system-level impacts.

Techno-economic analysis (TEA) is commonly employed to evaluate Total Annualized Cost (TAC), Levelized Cost of Heat (LCOH), and $CO_2$ abatement costs, with studies showing that low electricity prices and high carbon taxes are essential for making electrification competitive with fossil-fuel-based systems [16].

Furthermore, individual electrification technologies, optimization-based frameworks have been proposed to evaluate the electrification of industrial heating systems. A multi-period graph-theoretical (P-graph) approach has been applied to assess refinery electrification, optimizing technology selection under different economic and environmental scenarios [18]. Similarly, a deterministic global optimization model has been developed to evaluate solar thermal and photovoltaic (PV) hybridization for industrial process heat, identifying parabolic trough collectors with thermal energy storage as the most cost-effective solution [19]. While these studies provide valuable insights into electrification strategies, they primarily focus on energy sourcing and hybridization, rather than optimizing the allocation of electrified heating technologies within an integrated process heat system.

This study develops an optimized electrification framework for hybrid industrial heat system, integrating heat integration techniques with Mixed-Integer Linear Programming (MILP) optimization. The framework systematically evaluates and allocates heat generation technologies based on TAC, emissions constraints, and technical feasibility. A key contribution is the comparison between previous graphical electrification assessments and an optimization-based approach, demonstrating improvements in hybrid system allocation and cost-effectiveness. The model is applied to an industrial case study, enabling a comparative analysis of full electrification, hybrid heating systems, and conventional fossil-based technologies. By integrating process integration, techno-economic analysis, and carbon taxes, this research provides a comprehensive and practical roadmap for achieving cost-effective and sustainable industrial heat systems.

## OPTIMIZATION FRAMEWORK

Industrial heat electrification presents significant economic and technical challenges, necessitating a systematic approach to determine the most cost-effective integration of electrified and conventional heat generation technologies. While graphical heat integration techniques can provide initial insights, they do not inherently identify the optimal hybrid system allocation that balances cost and emissions reduction. This study introduces an optimization-based framework formulated as a Mixed-Integer Linear Programming (MILP) model, implemented using Gurobi, to achieve a cost-optimal hybrid heat system configuration.

The model is designed to minimize the Total Annualized Cost (TAC) while ensuring compliance with industrial heat demand, technology constraints, and emissions targets. The technologies included are both electrified (High-Temperature Heat Pumps, Electric Boilers, Electric Heaters) and conevtional ones (Steam Boilers and Fired Heaters).

To assess the optimization framework, the model is applied to an industrial case study, generating an optimized hybrid heating system. This system identifies the most cost-effective mix of conventional and electrified technologies for an industrial plant. The optimized system is then compared to scenarios using only conventional technologies (steam boilers and fired heaters) and a fully electrified system (relying solely on HTHPs, EBs, and EHs).

The comparison highlights the trade-offs between capital costs, electricity prices, and carbon taxation policies.

## METHODOLOGY

### Overview

To evaluate the electrification potential of an industrial heating system, a two-stage approach is employed:

- Graphical Analysis Using Heat Integration – Heat recovery is maximized using Pinch Technology, and the Grand Composite Curve (GCC) is generated to determine minimum heating and cooling demands. This step establishes a benchmark for heating utility selection and technology placement.
- Optimization via MILP Model – An MILP-based framework is developed to determine the optimal technology mix that minimizes cost while meeting emissions constraints.

While graphical methods provide valuable initial insights, they do not yield an optimal solution. The MILP optimization model builds upon heat integration findings, ensuring that the electrification strategy is both technically feasible and economically optimal.

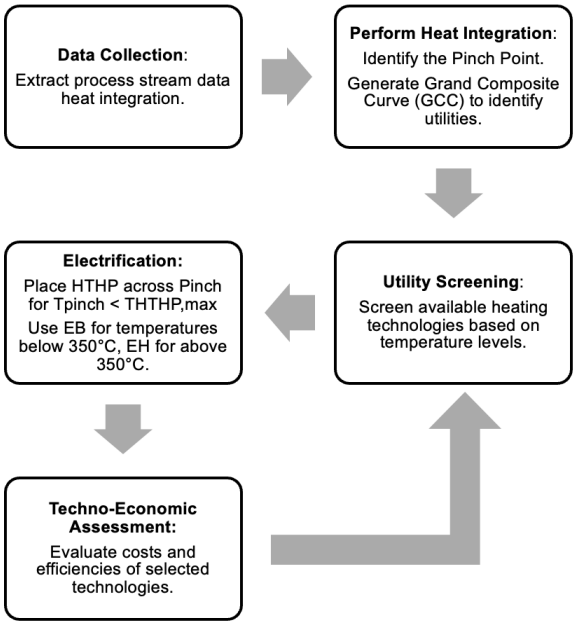



**Figure 1.** Electrification framework.

To evaluate the electrification potential of an industrial heating system, heat integration is first performed to maximize heat recovery and establish a baseline for assessing various heating technologies. Process stream data is extracted, and Pinch Technology is applied to determine minimum heating and cooling demands. The Grand Composite Curve (GCC) is generated, which helps identify utility requirements and guides the selection of suitable utilities based on the required heat load and corresponding temperatures. The GCC also informs the placement of available heat-supplying technologies. By integrating a heat pump and utilizing heat integration, the placement of the heat pump further reduces the minimum utility requirements. Once the technologies are placed and a final system design is achieved, a techno-economic assessment compares the costs and efficiencies of each option, and Technology Readiness Levels (TRL) ensure the feasibility of implementing electrification.

While this approach uses graphical methods to provide insights, it does not yield the optimal solution. Therefore, once the framework is established, it becomes clear that an optimization model, utilizing heat integration as a benchmark, is necessary to achieve the desired optimal outcome.

The MILP optimization model developed in this study determines the optimal allocation of heat generation technologies while ensuring compliance with technical constraints, economic feasibility, and emissions reduction goals.

## Objective Function

The objective function minimizes the Total Annualized Cost (TAC), incorporating:

$$TAC = = \sum(\text{Capital Costs}) + \sum(\text{Operating Costs}) - Cost\ Savings\ from\ Heat\ Recovery \quad (1)$$

where capital costs (CAPEX) account for the investment cost of each technology, and operating costs (OPEX) include electricity and fuel expenditures. $CO_2$ taxes are incorporated to penalize emissions, incentivizing a transition toward low-carbon heat sources.

The decision variables in the model represent the heat supplied by each technology across different temperature levels. Additionally, a binary variable is introduced to govern the usage of HTHPs, ensuring that the heat pump can only operate when its temperature constraints are satisfied.

## Constraints

### Heat Balance Constraint

At each temperature level iii, the total heat supplied by all technologies must satisfy the corresponding heat demand:

$$\sum Qtech, i = Di, \forall \text{i} \quad (2)$$

where $Q_{tech,i}$ is the heat provided by each technology at interval i, and Di represents the industrial process heat demand at the same interval.

### Technology Operating Temperature Constraints

Each heat generation technology is restricted to operate within its maximum allowable temperature range to ensure technical feasibility:

$$Tmax, i \geq Ti, \forall \text{i} \quad (3)$$

where $T_{max,tech}$ is the maximum operating temperature of a given technology, and $T_i$ is the required process temperature at interval i.

### Emissions Constraint

To ensure emissions reduction, the total $CO_2$ emissions fossil fueled technologies must be below a predefined threshold:

$$\sum Econventional \leq \text{Ethreshold} \quad (4)$$

where $E_{conventional}$ represent the $CO_2$ emissions from conventional technologies. And $E_{threshold}$ enforces a cap on total emissions, encouraging greater electrification.

### Piecewise Linearization of Heat Pump COP

The Coefficient of Performance (COP) of heat pumps is a nonlinear function of the heat load and temperature lift, requiring piecewise linearization for integration into the MILP model:

$$COPhthp = f(Qhthp, Tlift) \quad (5)$$

This approximation ensures computational efficiency while capturing nonlinear COP behavior.

The COP curve was approximated using 13 breakpoints, placed at 5 (K) increments across the 0–70 (K) temperature lift range. At the identified optimal solution, the linearization error was 0.6%. A sensitivity analysis was conducted by varying the number of breakpoints (7–13). The results showed that the Total Annualized Cost (TAC) varied by less than 5% across different configurations, while the hybrid technology mix, such as the combination of high-temperature heat pumps (HTHPs) and steam boilers, remained stable. Only minor shifts in heat allocation were observed, with HTHP utilization varying by approximately ±3%. These findings confirm that the model's conclusions are robust to reasonable changes in linearization parameters, reinforcing the validity of the approach.

### Cost Modeling

Conventional equipment cost estimation followed guidelines by Smith (2016) [17]. Cost data is represented through charts showing costs relative to equipment capacity or expressed as a power law of capacity:

$$C_E = C_B(\frac{Q}{Q_B})^M \quad (6)$$

Where $C_E$ is the equipment cost at Q capacity, $C_B$ is the base cost for equipment of $Q_B$ capacity, and M is an equipment type dependent constant.

Capital costs of electrified technologies are estimated using CAPEX factors from the literature.

$$Capital\ Cost = Capacity\ (MW) \times CAPEX\ factor\ (\$/MW) \quad (7)$$

The operating cost includes electricity cost for electric technologies and fuel cost for steam boilers and fired heaters.

The optimization model is solved using Gurobi, and the output includes the optimal technology mix, representing the megawatts of heat supplied by each technology at eachtemperature level, along with the Total Annualized Cost (TAC), total $CO_2$ emissions, and the percentage of electrification achieved.

# CASE STUDY AND RESULTS

This case study builds upon previous work in which heat integration techniques were applied and the assessment of electrification in an industrial plant heating system was performed graphically, following the developed framework shown in Figure 1. The analysis demonstrated a significant reduction in minimum heating and cooling utilities, with the heating utility for the plant after heat integration, Qhmin, at 16.5 MW and the minimum cooling utility, Qcmin, at 26.1 MW. The application of a high-temperature heat pump (HTHP) further lowered the minimum

heating and cooling demands by utilizing waste heat. The study evaluated several scenarios, including partial and full electrification with renewable and conventional electricity, comparing the impacts on operating costs, capital costs, and $CO_2$ emissions.

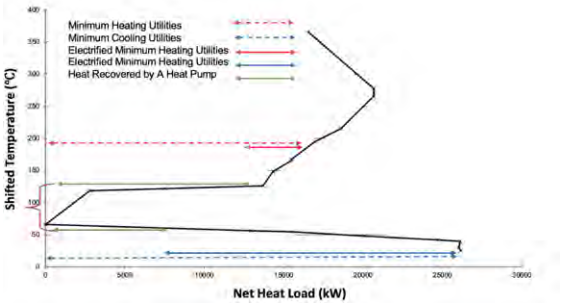



**Figure 2.** GCC of Case Study.

The Partial Electrification with Renewable Electricity scenario is used here as the case study for the optimization model, as it was the best-performing scenario when combining both emissions reduction and economic viability. In this scenario, the integration of an HTHP reduced heating demand by over 83%, resulting in an 80% reduction in emissions and lower annualized costs compared to conventional technologies. This scenario serves as the baseline for the optimization approach in the current study, which aims to evaluate and compare the performance of hybrid heat systems using a multi-criteria optimization model.

**Table 1:** Summary of scenarios results.

| Scenario | $CO_2$ reduction (%) | TAC (MM$/y) |
|---|---|---|
| 100 % electrified | 100 | 7.9 |
| Partial electrification | 83 | 6.1 |
| Partial electrification (Optimized) | 75 | 5.8 |

## DISCUSSION

The The optimization results revealed an optimal hybrid heat system configuration, where 75% of the heating demand was met using electrified technologies. The model selected a combination of a high-temperature heat pump (HTHP) and a steam boiler (SB) as the most cost-effective solution. The preference for a steam boiler over a fired heater was expected, as the steam boiler provides a more economical alternative, particularly when the temperature levels within the case study allowed for full coverage using steam. Similarly, the selection of an HTHP instead of an electrode boiler (EB) was largely influenced by the model's ability to account for heat pump cost savings within the objective function.

Interestingly, previous studies have not explicitly accounted for the cost savings associated with heat pump integration, which may have led to underestimations of electrification's economic feasibility. This omission may explain why electrification has often been perceived as less competitive compared to other decarbonization strategies. In this study, while the reduction in Total Annualized Cost (TAC) was modest (~7%), the computational efficiency and ease of implementation of the optimization model indicate that the trade-off is worthwhile. The limited TAC reduction aligns with expectations, as the capital investment required for electrified technologies remains fixed regardless of optimization. Once a technology falls within a certain capacity range, its investment cost remains relatively unchanged between the optimized and non-optimized cases.

In addition to evaluating full and partial electrification, this study also compared Carbon Capture and Storage (CCS) as an alternative decarbonization strategy. While CCS is a well-established technology, it is capital-intensive and raises concerns regarding the long-term environmental impacts of $CO_2$ sequestration. The results indicate that partial electrification achieved the lowest $CO_2$ abatement cost at 131 \$/t$CO_2$, compared to CCS at 140 \$/t$CO_2$. However, after optimization, the abatement cost increased to 133 \$/t$CO_2$, which can be attributed to the nonlinear relationship between cost and the percentage of electrification. Unlike the trade-off between emissions reduction and electrification percentage, which is relatively linear, the cost vs. electrification percentage relationship is more complex.

Since the optimized scenario resulted in a lower percentage of electrification, it also incurred lower overall costs, but at the expense of higher emissions compared to the non-optimized case. This, in turn, led to a higher abatement cost due to the increased cost per unit of $CO_2$ reduction. Nevertheless, electrification remains a more attractive decarbonization strategy than CCS in this case study, as it offers a lower abatement cost and avoids uncertainties associated with long-term carbon sequestration.

## REFERENCES


1. McMillan, C. A. (2018). Electrification of Industry: Summary of Electrification Futures Study Industrial Sector analysis. https://doi.org/10.2172/1474033
2. Bouckaert, S., Pales, A. F., McGlade, C., Remme, U., Wanner, B., Varro, L., D'Ambrosio, D., & Spencer, T. (2021). *Net Zero by 2050: A roadmap for the global energy sector*. Retrieved February 1, 2025, from https://trid.trb.org/view/1856381
3. Madeddu, S., Ueckerdt, F., Pehl, M., Peterseim, J., Lord, M., Kumar, K. A., Krüger, C., & Luderer, G. (2020). The CO2 reduction potential for the European industry via direct electrification of heat

supply (power-to-heat). *Environmental Research Letters*, *15*(12), 124004. https://doi.org/10.1088/1748-9326/abbd02
4. Schoeneberger, C., Zhang, J., McMillan, C., Dunn, J. B., & Masanet, E. (2022). Electrification potential of U.S. industrial boilers and assessment of the GHG emissions impact. *Advances in Applied Energy*, *5*, 100089. https://doi.org/10.1016/j.adapen.2022.100089
5. Schüwer, D., & Schneider, C. (2018). *Electrification of industrial process heat : long-term applications, potentials and impacts*(pp. 411–422). https://epub.wupperinst.org/files/7037/7037_Schuewer.pdf
6. Masuku, C. M., Caulkins, R. S., & Siirola, J. J. (2024). Process decarbonization through electrification. *Current Opinion in Chemical Engineering*, *44*, 101011. https://doi.org/10.1016/j.coche.2024.101011
7. Veronezi, D., Soulier, M., & Kocsis, T. (2024). Energy solutions for decarbonization of industrial heat processes. *Energies*, *17*(22), 5728. https://doi.org/10.3390/en17225728
8. Arpagaus, C., Bless, F., Uhlmann, M., Schiffmann, J., & Bertsch, S. S. (2018). High temperature heat pumps: Market overview, state of the art, research status, refrigerants, and application potentials. *Energy*, *152*, 985–1010. https://doi.org/10.1016/j.energy.2018.03.166
9. Zühlsdorf, B., Jensen, J. K., & Elmegaard, B. (2018). Heat pump working fluid selection—economic and thermodynamic comparison of criteria and boundary conditions. *International Journal of Refrigeration*, *98*, 500–513. https://doi.org/10.1016/j.ijrefrig.2018.11.034
10. Xia, R., Overa, S., & Jiao, F. (2022). Emerging Electrochemical Processes to Decarbonize the Chemical Industry. *JACS Au*, *2*(5), 1054–1070. https://doi.org/10.1021/jacsau.2c00138
11. Barton, J. L. (2020). Electrification of the chemical industry. *Science*, *368*(6496), 1181–1182. https://doi.org/10.1126/SCIENCE.ABB8061
12. Lechtenböhmer, S., Nilsson, L. J., Åhman, M., & Schneider, C. (2016). Decarbonising the energy intensive basic materials industry through electrification – Implications for future EU electricity demand. *Energy*, *115*, 1623–1631. https://doi.org/10.1016/j.energy.2016.07.110
13. Kosmadakis, G. (2019). Estimating the potential of industrial (high-temperature) heat pumps for exploiting waste heat in EU industries. *Applied Thermal Engineering*, *156*, 287–298. https://doi.org/10.1016/j.applthermaleng.2019.04.082
14. Bühler, F., Zühlsdorf, B., Holm, F. M., & Elmegaard, B. (2019). *The potential of heat pumps in the electrification of the Danish industry* (pp. 51–67). https://backend.orbit.dtu.dk/ws/files/195360531/The_potential_of_heat_pumps_in_the_electrification_of_the_Danish.pdf
15. Bataille, C., Åhman, M., Neuhoff, K., Nilsson, L. J., Fischedick, M., Lechtenböhmer, S., Solano-Rodriquez, B., Denis-Ryan, A., Stiebert, S., Waisman, H., Sartor, O., & Rahbar, S. (2018). A review of technology and policy deep decarbonization pathway options for making energy-intensive industry production consistent with the Paris Agreement. *Journal of Cleaner Production*, *187*, 960–973. https://doi.org/10.1016/j.jclepro.2018.03.107
16. Mousa S., Al-Mohannadi D.M., 2024, A Systematic Electrification Approach: Electrifying Natural Gas Processing for a Net-Zero Future, Chemical Engineering Transactions, 114, 301-306.
17. Smith R., 2016, Chemical Process Design and Integration, Wiley, Hoboken, USA.
18. Sahl, A. B., Orosz, Á., How, B. S., Friedler, F., & Teng, S. Y. (2023). Electrification of oil refineries through multi-objective multi-period graph-theoretical planning: A crude distillation unit case study. *Journal of Cleaner Production*, *434*, 140179. https://doi.org/10.1016/j.jclepro.2023.140179
19. Rastinejad, J., Putnam, S., & Stuber, M. D. (2023). Technoeconomic assessment of solar technologies for the hybridization of industrial process heat systems using deterministic global dynamic optimization. *Renewable Energy*, *216*, 119069. https://doi.org/10.1016/j.renene.2023.119069

© 2025 by the authors. Licensed to PSEcommunity.org and PSE Press. This is an open access article under the creative commons CC-BY-SA licensing terms. Credit must be given to creator and adaptations must be shared under the same terms. See https://creativecommons.org/licenses/by-sa/4.0/



Systems & Control Transactions

**Research Article - Peer Reviewed Conference Proceeding**
ESCAPE 35 - European Symposium on Computer Aided Process Engineering
Ghent, Belgium. 6-9 July 2025
Jan F.M. Van Impe, Grégoire Léonard, Satyajeet S. Bhonsale,
Monika E. Polańska, Filip Logist (Eds.)

PSE PRESS

# Assessing Triviality in Random Mixed-Integer Bilevel Optimization Problems to Improve Problem Generators and Libraries

**Meng-Lin Tsai[a], and Styliani Avraamidou[a*]**

a Department of Chemical & Biological Engineering, University of Wisconsin-Madison, Madison WI, 53706, USA
* Corresponding Author: avraamidou@wisc.edu.

## ABSTRACT

While bilevel optimization is gaining prominence across various domains, the field lacks standardized tools for generating test problems that can effectively evaluate and guide the development of efficient solution algorithms. We define the term "trivial bilevel optimization problem" as a bilevel problem whose high-point relaxation solution is also feasible. These easy-to-solve problems frequently arise in naïve implementations of random bilevel optimization problem generators, significantly impacting the evaluation of bilevel solution algorithms. However, this problem has not been addressed in the literature to our best knowledge. This work introduces a non-trivial mixed-integer bilevel optimization problem generator, NT-BMIPGen, and a problem library, designed to eliminate the generation of trivial bilevel problems. Through analysis of the bilevel problem structure, we identify key factors contributing to problem triviality. Particularly, the upper to lower variable ratios and the number of decoupled lower-level continuous variables increasing two-level competition significantly impact problem triviality. The proposed generator allows users to customize problem structures while ensuring non-triviality by checking the bilevel feasibility of highpoint relaxation. Additionally, we present a library of 105 non-trivial problems to support algorithm development and testing. This work advances the understanding of bilevel problem complexity and provides essential tools for the systematic evaluation of bilevel optimization algorithms.

**Keywords**: Bilevel Optimization, Random Problem Generator, Algorithm Evaluation

## INTRODUCTION

Bilevel optimization, characterized by nested optimization problems, has gained prominence in modeling two-player interactions across various domains, including environmental policy [1], electricity markets [2], hierarchical optimal control [3], supply chain optimization [4], and industrial planning and scheduling [5, 6]. Despite its potential wide applicability, bilevel optimization is not widely utilized as its solution is very challenging, known to be NP-hard [7]. Mixed-integer bilevel optimization problems are even more challenging to solve [8], prompting the development of diverse solution methods, such as Bender's decomposition [9], multiparametric optimization [10, 11], penalty functions [12], and branch-and-bound/cut algorithms [13].

Metaheuristic methods, while not guaranteeing optimality or feasibility in finite time, have gained significant attention for addressing non-linear bilevel problems beyond the reach of deterministic approaches [14]. These problems are often tackled iteratively by alternating between the upper and lower levels, using techniques such as genetic algorithms [15], particle swarm optimization [16], etc. Recently, hybrid approaches have emerged, combining metaheuristics in upper-level with deterministic optimization solvers to handle the lower-level problem within this iterative framework and have guarantees of feasibility [1].

Existing bilevel problem generators and libraries provide valuable resources for testing and evaluating algorithms. For instance, problem generators tailored to specific structures have been developed [17]. A bilevel parametric optimization toolbox (B-POP) is developed with a random problem generator and problem library

[18]. BOBILib [19] offers a comprehensive mixed-integer bilevel problem library containing 2,500 problems. However, due to the diversity in problem types—encompassing different variable types, constraints, and objective functions—the field lacks standardized problem generators or libraries that are adaptable to user-defined problem structures and sizes. While random problem generators are widely used for algorithm evaluation [11], they often result to a significant number of very short solving time bilevel problems [19], limiting their utility for rigorous algorithm testing.

This article presents a non-trivial mixed-integer bilevel optimization problem generator (NT-BMIPGen) and accompanying problem library designed to support the understanding, analysis, and evaluation of bilevel optimization problems. We first outline the problem structure (number of upper/lower variables, binary/continuous, coupled/decoupled variables, and constraints). Next, we examine the concept of problem triviality and its underlying causes. We then present the bilevel problem generator and a bilevel problem library containing 105 problems, highlighting their utility in evaluating diverse non-trivial bilevel problem structures. Finally, we conclude with a discussion of future research opportunities in bilevel optimization.

## GENERAL BILEVEL PROBLEM STRUCTURE

A general Mixed-Integer Bilevel programming problem (B-MIP) can be written in the form of Equation (1). The problem contains two objective functions, an upper-level objective function $F$ and a lower-level objective function $f$. The problem includes both continuous and integer variables, where $\boldsymbol{x}$ is a vector of all continuous variables, $\boldsymbol{y}$ is a vector of all integer variables, subscripts $u$ and $l$ indicate upper- and lower-level variables respectively, and function vectors $\boldsymbol{G}$ and $\boldsymbol{g}$ represent upper- and lower-level constraints respectively.

$$\min_{\boldsymbol{x},\boldsymbol{y}} F(\boldsymbol{x},\boldsymbol{y})$$

$$s.t.\, G(\boldsymbol{x},\boldsymbol{y}) \le 0,$$

$$\boldsymbol{x_l},\boldsymbol{y_l} \in arg\min_{\boldsymbol{x_l},\boldsymbol{y_l}}\{f(\boldsymbol{x},\boldsymbol{y}): g(\boldsymbol{x},\boldsymbol{y}) \le 0\}$$

$$\boldsymbol{x} = \begin{bmatrix}\boldsymbol{x_u}\\ \boldsymbol{x_l}\end{bmatrix}^T, \boldsymbol{y} = \begin{bmatrix}\boldsymbol{y_u}\\ \boldsymbol{y_l}\end{bmatrix}^T,$$

$$\boldsymbol{x} \in R^n, \boldsymbol{y} \in Z^m \qquad (1)$$

Bilevel programming problems couples two distinct optimization problems by embedding the lower-level optimization problem as a constraint of the upper-level optimization problem. A bilevel problem is feasible if both upper- and lower-level constraints ($G$, $g$) are satisfied, and the lower-level problem is solved to global optimality at the selected optimal upper-level variables.

## Coupling bilevel optimization structure

Couplings between the two optimization levels appear linked when upper-level and lower-level variables emerge together in either the constraints and/or objective functions of the problem. Coupled variables, defined as variables that appear in constraint or objective functions that doesn't belongs to their own level, enhance the interaction between the two optimization levels. Coupled variables can manifest as either collaborative or competitive dynamics. In contrast, decoupled variables lack direct interaction with the other level and only exist in their own level but can still increase the overall problem complexity by increasing the complexity of the problem within each level.

To explore the coupling behavior of the bilevel optimization problems, general B-MIPs can be reformulated, without loss of generality, as Equation (2). This form is modified from [16] and can help introduce different B-MIP structures to explore coupling behavior.

$$\min_{\boldsymbol{x},\boldsymbol{y}} F = F_u(\boldsymbol{x_{ud}},\boldsymbol{y_{ud}}) + F_l(\boldsymbol{x_{ld}},\boldsymbol{y_{ld}}) + F_c(\boldsymbol{x_{uc}},\boldsymbol{x_{lc}},\boldsymbol{y_{uc}},\boldsymbol{y_{lc}})$$

$$s.t.\, G_{ud}(\boldsymbol{x_{ud}},\boldsymbol{y_{ud}}) \le 0, G_{uc}(\boldsymbol{x_{ud}},\boldsymbol{x_{uc}},\boldsymbol{y_{ud}},\boldsymbol{y_{uc}}) \le 0$$

$$\boldsymbol{x_{ld}},\boldsymbol{x_{lc}},\boldsymbol{y_{ld}},\boldsymbol{y_{lc}} \in arg\min_{x_{ld},x_{lc},y_{ld},y_{lc}}\{f(\boldsymbol{x},\boldsymbol{y}) = f_l(\boldsymbol{x_{ld}},\boldsymbol{y_{ld}}) + f_c(\boldsymbol{x_{uc}},\boldsymbol{x_{lc}},\boldsymbol{y_{uc}},\boldsymbol{y_{lc}}): g_{ld}(\boldsymbol{x_{ld}},\boldsymbol{y_{ld}}) \le 0, g_{lc}(\boldsymbol{x_l},\boldsymbol{y_l}) \le 0, g_g(\boldsymbol{x_{uc}},\boldsymbol{x_{lc}},\boldsymbol{y_{uc}},\boldsymbol{y_{lc}}) \le 0\}$$

$$\boldsymbol{x} = \begin{bmatrix}\boldsymbol{x_{ud}}\\ \boldsymbol{x_{uc}}\\ \boldsymbol{x_{ld}}\\ \boldsymbol{x_{lc}}\end{bmatrix}^T, y = \begin{bmatrix}\boldsymbol{y_{ud}}\\ \boldsymbol{y_{uc}}\\ \boldsymbol{y_{ld}}\\ \boldsymbol{y_{lc}}\end{bmatrix}^T,$$

$$\boldsymbol{x} \in R^n, \boldsymbol{y} \in Z^m \qquad (2)$$

,where $\boldsymbol{x}$ is a vector of all continuous variables, $\boldsymbol{y}$ is a vector of all integer variables, subscripts $u$ and $l$ indicate upper and lower levels respectively; and subscripts $c$ and $d$ indicates coupled and decoupled respectively as shown in Table 1

**Table 1:** Variable Classification by Type and Coupling.

| | Continuous ($\boldsymbol{x}$) | | | | Binary ($\boldsymbol{y}$) | | | |
|---|---|---|---|---|---|---|---|---|
| | $\boldsymbol{x_{ud}}$ | $\boldsymbol{x_{uc}}$ | $\boldsymbol{x_{ld}}$ | $\boldsymbol{x_{lc}}$ | $\boldsymbol{y_{ud}}$ | $\boldsymbol{y_{uc}}$ | $\boldsymbol{y_{ld}}$ | $\boldsymbol{y_{lc}}$ |
| Upper | ✓ | ✓ | | | ✓ | ✓ | | |
| Lower | | | ✓ | ✓ | | | ✓ | ✓ |
| Coupled | | ✓ | | ✓ | | ✓ | | ✓ |
| Decoupled | ✓ | | ✓ | | ✓ | | ✓ | |

The constraints $G$ and $g$ correspond to the upper and lower constraints respectively, which can be categorized into 5 types based on the type of variables that can appear within them (Table 2). Functions $F$ and $f$ are the

upper and lower-level objective functions, which can also be decomposed into five subtypes based on their structure. A detailed classification of the five types of constraints and objective functions is provided in Table 2.

**Table 2:** Constraints and Objective Function Classification by Type and Coupling.

| | Name | Description |
|---|---|---|
| **Constraints** | | |
| 1 | $G_{ud}(\boldsymbol{x_{ud}}, \boldsymbol{y_{ud}})$ | Upper decoupled |
| 2 | $G_{uc}(\boldsymbol{x_{ud}}, \boldsymbol{x_{uc}}, \boldsymbol{y_{ud}}, \boldsymbol{y_{uc}})$ | Upper coupled |
| 3 | $g_{ld}(\boldsymbol{x_{ld}}, \boldsymbol{y_{ld}})$ | Lower decoupled |
| 4 | $g_{lc}(\boldsymbol{x_{ld}}, \boldsymbol{x_{lc}}, \boldsymbol{y_{ld}}, \boldsymbol{y_{lc}})$ | Lower coupled |
| 5 | $g_g(\boldsymbol{x_{uc}}, \boldsymbol{y_{uc}}, \boldsymbol{x_{lc}}, \boldsymbol{y_{lc}})$ | General |
| **Objective Functions** | | |
| 1 | $F_u(\boldsymbol{x_{ud}}, \boldsymbol{y_{ud}})$ | Upper decoupled upper-level |
| 2 | $F_l(\boldsymbol{x_{ld}}, \boldsymbol{y_{ld}})$ | Lower decoupled upper-level |
| 3 | $F_c(\boldsymbol{x_{uc}}, \boldsymbol{x_{lc}}, \boldsymbol{y_{ud}}, \boldsymbol{y_{lc}})$ | Coupled upper-level |
| $F = F_u + F_l + F_c$ | | Full upper-level |
| 4 | $f_l(\boldsymbol{x_{ld}}, \boldsymbol{y_{ld}})$ | Lower decoupled lower-level |
| 5 | $f_c(\boldsymbol{x_{uc}}, \boldsymbol{x_{lc}}, \boldsymbol{y_{ud}}, \boldsymbol{y_{lc}})$ | Coupled lower-level |
| $f = f_l + f_c$ | | Full lower-level |

## BILEVEL PROBLEM TRIVIALITY

Even though bilevel optimization problems have been proved to be hard to solve, randomly generated bilevel optimization problems are not always hard to solve. As shown in [19], randomly generated problems of the same size and structure have a large range of solving time, some of them can be solved within seconds while some need hours to be solved. Some of the quickly and easily solvable problems are likely trivial and should not be used for algorithm development or evaluation, as they fail to represent the true complexity of bilevel optimization problems. To determine triviality, we solve two single-level problems: the high point relaxation problem (Equation (3)) and the bilevel feasibility check problem (Equation (4)).

### Triviality Check process

High point relaxation problem is a single-level optimization problem optimizing the upper-level objective function over the set of all constraints in the bilevel problem, including both the upper and lower-level constraints, as shown in Equation (3). A bilevel problem is considered trivial if its high-point relaxation is bilevel feasible. To verify bilevel feasibility, we solve the bilevel feasibility check problem, where the upper-level variables' solution is fixed (denoted as $\tilde{\boldsymbol{x}}, \tilde{\boldsymbol{y}}$) and the lower-level problem is solved, as shown in Equation (4). If the upper-level objective $F$ calculated by solutions in Equation (4) equals that in Equation (3), the problem is bilevel feasible.

A bilevel optimization problem is termed trivial if its solution can be obtained by solving these two single-level problems: the high-point relaxation (3), and the bilevel feasibility check problem (4). Both single-level problems are solvable using standard optimization solvers. The high-point relaxation provides the lower bound, and the bilevel feasibility check provides the upper bound to the original bilevel problem. When these bounds are equal, the solution corresponds to the original bilevel problem, and the trivial bilevel problem is solved.

$$\min_{\boldsymbol{x},\boldsymbol{y}} F = F_u(\boldsymbol{x_{ud}}, \boldsymbol{y_{ud}}) + F_l(\boldsymbol{x_{ld}}, \boldsymbol{y_{ld}}) + F_c(\boldsymbol{x_{uc}}, \boldsymbol{x_{lc}}, \boldsymbol{y_{uc}}, \boldsymbol{y_{lc}})$$

$$s.t.\, G_{ud}(\boldsymbol{x_{ud}}, \boldsymbol{y_{ud}}) \le 0, G_{uc}(\boldsymbol{x_{ud}}, \boldsymbol{x_{uc}}, \boldsymbol{y_{ud}}, \boldsymbol{y_{uc}}) \le 0,$$
$$g_{ld}(\boldsymbol{x_{ld}}, \boldsymbol{y_{ld}}) \le 0, g_{lc}(\boldsymbol{x_l}, \boldsymbol{y_l}) \le 0,$$
$$g_g(\boldsymbol{x_{uc}}, \boldsymbol{x_{lc}}, \boldsymbol{y_{uc}}, \boldsymbol{y_{lc}}) \le 0\}$$

$$\boldsymbol{x} = \begin{bmatrix} \boldsymbol{x_{ud}} \\ \boldsymbol{x_{uc}} \\ \boldsymbol{x_{ld}} \\ \boldsymbol{x_{lc}} \end{bmatrix}^T, \boldsymbol{y} = \begin{bmatrix} \boldsymbol{y_{ud}} \\ \boldsymbol{y_{uc}} \\ \boldsymbol{y_{ld}} \\ \boldsymbol{y_{lc}} \end{bmatrix}^T,$$

$$\boldsymbol{x} \in R^n, \boldsymbol{y} \in Z^m \tag{3}$$

$$\min_{\boldsymbol{x_{ld}}, \boldsymbol{x_{lc}}, \boldsymbol{y_{ld}}, \boldsymbol{y_{lc}}} f(\boldsymbol{x}, \boldsymbol{y}) = f_l(\boldsymbol{x_{ld}}, \boldsymbol{y_{ld}}) + f_c(\tilde{\boldsymbol{x}}_{\boldsymbol{uc}}, \boldsymbol{x_{lc}}, \tilde{\boldsymbol{y}}_{\boldsymbol{uc}}, \boldsymbol{y_{lc}}):$$
$$st.\, G_{uc}(\boldsymbol{x_{ld}}, \boldsymbol{y_{ld}}) \le 0, g_{lc}(\boldsymbol{x_l}, \boldsymbol{y_l}) \le 0, g_g(\tilde{\boldsymbol{x}}_{\boldsymbol{uc}}, \boldsymbol{x_{lc}}, \tilde{\boldsymbol{y}}_{\boldsymbol{uc}}, \boldsymbol{y_{lc}}) \le 0,$$
$$\boldsymbol{x} = \begin{bmatrix} \tilde{\boldsymbol{x}}_{\boldsymbol{ud}} \\ \tilde{\boldsymbol{x}}_{\boldsymbol{uc}} \\ \boldsymbol{x_{ld}} \\ \boldsymbol{x_{lc}} \end{bmatrix}^T, \boldsymbol{y} = \begin{bmatrix} \tilde{\boldsymbol{y}}_{\boldsymbol{ud}} \\ \tilde{\boldsymbol{y}}_{\boldsymbol{uc}} \\ \boldsymbol{y_{ld}} \\ \boldsymbol{y_{lc}} \end{bmatrix}^T,$$
$$F = F_u(\tilde{\boldsymbol{x}}_{\boldsymbol{ud}}, \boldsymbol{y_{ud}}) + F_l(\boldsymbol{x_{ld}}, \boldsymbol{y_{ld}}) + F_c(\tilde{\boldsymbol{x}}_{\boldsymbol{uc}}, \boldsymbol{x_{lc}}, \tilde{\boldsymbol{y}}_{\boldsymbol{uc}}, \boldsymbol{y_{lc}})$$

$$\boldsymbol{x} \in R^n, \boldsymbol{y} \in Z^m \tag{4}$$

### Exploring Factors Contributing to Triviality

Bilevel optimization problems with different structures have different implication in the real world. Looking into what is causing the bilevel optimization problem triviality can help us identify what is the critical factors that create complex interactions of the problem. We analyzed various problem structures to identify factors contributing to solution triviality. The problems are generated by using naïve random bilevel problem generation process, which we generate the objectives and constraints using random vectors, as detailed in the problem generator and library section.

#### Continuous bilevel optimization problem

In Figure 3, we varied the number of continuous coupled variables $\boldsymbol{x_{uc}}$ and $\boldsymbol{x_{lc}}$ within the range of 2 to 20

while fixing the general constraints $g_g = 10$. The resulting heatmap illustrates the trivial percentage calculated across 30 test instances, where the trivial percentage is defined as the ratio of number of trivial problems to the total number of tests.

Defining the upper-to-lower variable ratio (ULVR) as the number of upper-level variables divided by the number of lower-level variables, we observed the following trends: when $ULVR > 2$, the trivial percentage is high (above 80%); when $2 > ULVR > 0.5$, the trivial percentage is moderate (20–80%); and when $ULVR < 0.5$, the trivial percentage is low (below 20%).

These trends indicate that the lack of lower-level variables in the problem prevents the lower-level objective from competing with the upper-level objective, resulting in triviality. This finding suggests that increasing lower-level competition with the upper-level can help reduce triviality. To test this hypothesis, we modified the lower-level decoupled continuous variable $x_{ld}$, as introducing such variables complicates the lower-level objective but has no direct impact on the upper-level objective. This creates divergences between the two objectives, causing them to compete, resulting in triviality decreases.

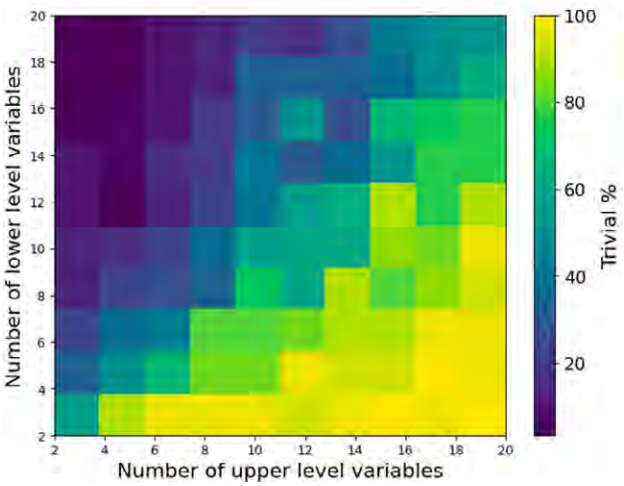



**Figure 3.** Trivial percentage heatmap by varying $\boldsymbol{x_{uc}}$ (2-20) and $\boldsymbol{x_{lc}}$ (2-20) of the continuous bi-level optimization problems. Each structure is tested for 30 times, and the $g_g = 10$ for all instances.

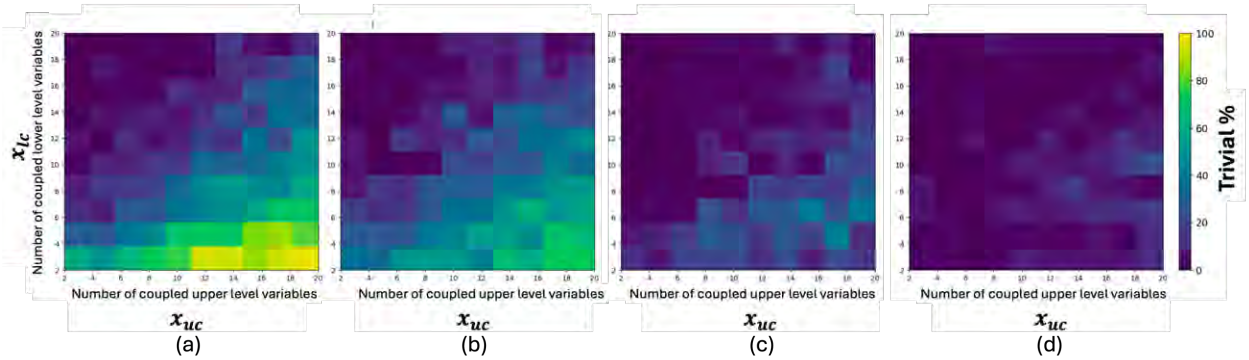



**Figure 1:** Changing $\boldsymbol{x_{uc}}, \boldsymbol{x_{lc}}$ from 2 to 20, fixing Number of decoupled lower level continuous variable $\boldsymbol{x_{ld}}$ at a: 0, b: 1, c: 5, d: 10; $G_{uc} = g_{lc} = g_g = 10$. Each structure is tested for 30 times. As shown by the graph, by changing $\boldsymbol{x_{ld}}$, the triviality decreases. Suggesting Number of decoupled lower level continuous variable is a key factor in triviality.

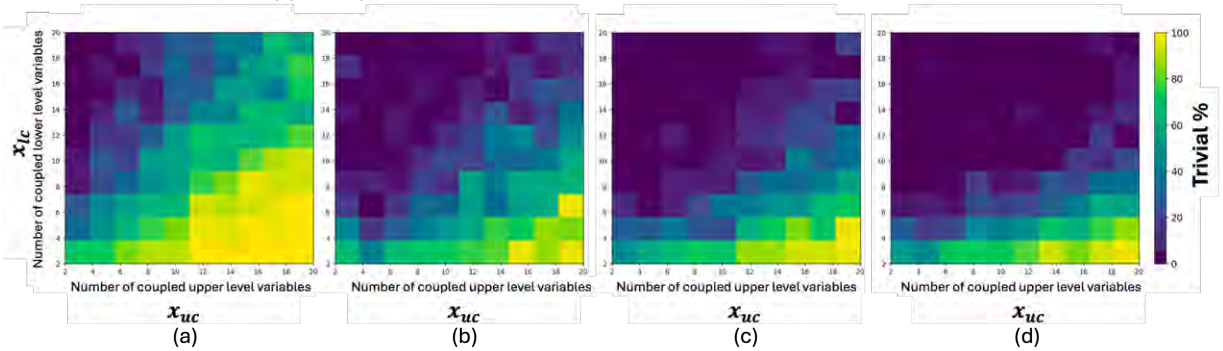



**Figure 2:** Changing $\boldsymbol{x_{uc}}, \boldsymbol{x_{lc}}$ from 2 to 20, fixing Number of binary coupled upper- and binary coupled lower-level variable $(\boldsymbol{y_{uc}}, \boldsymbol{y_{lc}})$ at a: (0,0), b: (2,2), c: (10,10), d: (20,20), $g_g$ is fixed at 20 for each type of constraints. Each structure is tested for 30 times. As shown by the graph, by changing $\boldsymbol{y_{uc}}, \boldsymbol{y_{lc}}$, the triviality decreases. Suggesting

### Continuous bilevel optimization problem with decoupled structure

Figure 2 illustrates the effect of varying the number of pure lower-level decoupled continuous variables ($\boldsymbol{x_{ld}}$) while fixing the values of the coupled variables $\boldsymbol{x_{uc}}$ and $\boldsymbol{x_{lc}}$, and setting the constraints $G_{uc} = g_{lc} = g_g = 10$. Subfigures 2 (a), (b), (c), and (d) represent cases where $\boldsymbol{x_{ld}}$ is set to 0, 1, 5, and 10, respectively. The resulting heatmaps illustrate the trivial percentage across 30 test instances The heatmaps clearly demonstrate that increasing the number of $\boldsymbol{x_{ld}}$ reduces the triviality of the problem. With the addition of just 1 $\boldsymbol{x_{ld}}$, the heatmap results show clear reduction of triviality percentage, as shown in Figure 2 (b). When $x_{ld}$ continuous increases, the percentage of trivial solutions decreases significantly. The triviality percentage goes to near zero in most cases as $x_{ld}$ goes to 10, as shown in Figure 2 (d).

This observation highlights that the number of decoupled lower-level continuous variables plays a crucial role in determining triviality. The results suggest that introducing or increasing $\boldsymbol{x_{ld}}$ enhances the complexity of interactions between levels, reducing the likelihood of trivial solutions.

### Mixed-Integer bilevel optimization problem

Introducing more binary variables also fosters competition between the upper and lower levels. As shown in Figure 3, increasing the number of coupled binary variables reduces triviality; however, the effect is less pronounced compared to the influence of $x_{ld}$ as shown in Figure 2. This effect is less pronounced in the region where the number of continuous coupled lower-level variables $x_{lc}$ is small. We suspect that by only increasing the number of the binary coupled lower-level variables cannot effectively affect the lower-level objective function competence with the upper-level objective function. A minimum amount of the $\boldsymbol{x_{lc}}$ is required to create competence synergetic with the $\boldsymbol{y_{uc}}$, and $\boldsymbol{y_{lc}}$.

Decoupled binary variables also exhibit a similar trend as coupled binary variables, though these results are omitted here for brevity.

In summary, altering the number of variables across different classes significantly impacts the structure of bilevel problems.

## PROBLEM GENERATOR AND LIBRARY

Based on the results in the previous section, we found that naïve implementations of a random bilevel problem generator produce varying levels of triviality depending on the problem's structure. If a problem set with high triviality is used for algorithm testing, it may lead to an overestimation of the solver's capability. To the best of our knowledge, no prior literature has addressed the issue of triviality in generating bilevel optimization problems. Therefore, we developed the random bilevel problem generator, NT-BMIPGen, which can generate non-trivial mixed integer bilevel test problems. The generator cand help the field to generate problems that are non-trivial and truly reflect the ability of the tested algorithm. The generation process is shown in Figure 4.

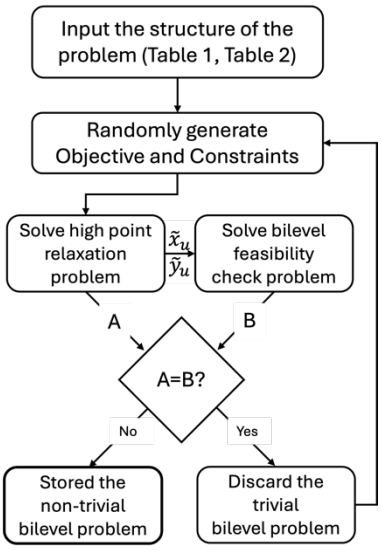



**Figure 4.** Flow diagram showing how random non-trivial bilevel optimization problem generator works.

The user can customize problem structures to explore different forms of two-level interaction by specifying the parameters listed in Table 1 and Table 2. To determine the parameters for the constraints and the objective function, the generator generates a matrix and a vector for each constraint type, along with random vectors for the upper- and lower-level objective subfunctions, based on the number of corresponding variables and constraints number specified.

By default, random parameter values are sampled from a uniform distribution in the range [-10, 10], except for the constraint right hand side vectors, which are restricted to non-negative values in the range [0, 10] to ensure the origin is always feasible. This design ensures the generated problems' feasibility. The continuous variables have a default upper and lower bound of -10 and 10, respectively.

Each problem undergoes a triviality check. The single level subproblems (high point relaxation problem (3) and the bilevel feasibility check problem (4)) are formulated in Pyomo [20] and solved using the Gurobi solver (v11.0.0) [21]. Only non-trivial problems, as verified through this process, are retained and stored with their upper and lower bounds obtained by solving the two subproblems. While the trivial problem is discarded, and the generator will generate another random problem. Each generated problem is stored in a folder, where each matrix and vector are saved in separate CSV files, and

associated parameters and upper and lower bounds solved by the two subproblems are stored in a JSON file. The non-trivial mixed-integer bilevel generator is available at https://test.pypi.org/project/NT-BMIPGen/.

A library with 105 different structure non-trivial B-MIP problems generated from the generator is stored at https://drive.google.com/file/d/185xnM-IG_vziXSDqGIyhSU-HDFgRDr51/view.

## CONCLUSION AND DISCUSSION

This work emphasizes the importance of problem triviality in designing problem generators and using a problem library for bilevel optimization problems, which can lead to the meaningless comparison and evaluation of different solvers, an issue that has been largely overlooked in previous research.

It is worth noting that while the effects of various constraints were also examined, the interaction is more complicated, and no clear trends were observed. A more detailed analysis represents a compelling topic for future research. We acknowledge that our study examines only a limited subset of bilevel problem structures. Future studies will delve into a broader range of bilevel problem structures to gain a deeper understanding of how various parameters influence triviality and its effect on algorithm benchmarking and development.

The proposed bilevel problem generator and library aims to enhance the robustness of continuous and mixed-integer bilevel optimization algorithm testing by ensuring that the generated problems provide a meaningful challenge to the algorithms, and accelerate the development of efficient solvers for complex, real-world bilevel optimization problems.

## ACKNOWLEDGEMENTS

This material is based upon work supported by the Wisconsin Alumni Research Foundation and the Department of Chemical and Biological Engineering at the University of Wisconsin-Madison. Furthermore, we would like to acknowledge the assistance provided by large language models (LLMs), including OpenAI's ChatGPT-4o and Anthropic's Claude 3.5, in the preparation of this manuscript. These tools were used for improving the grammar and fluency of the text, as well as for assistance in coding and commenting.

## REFERENCES

1. Beykal B, Avraamidou S, Pistikopoulos IP, Onel M, Pistikopoulos EN. Domino: Data-driven optimization of bi-level mixed-integer nonlinear problems. J Glob Optim 78:1–36 (2020). https://doi.org/10.1007/s10898-020-00890-3
2. Fampa M, Barroso L, Candal D, Simonetti L. Bilevel optimization applied to strategic pricing in competitive electricity markets. *Comput Optim Appl* 39:121–142 (2008). https://doi.org/10.1007/s10589-007-9066-4
3. Avraamidou S, Pistikopoulos EN. A multi-parametric bi-level optimization strategy for hierarchical model predictive control. *Comput Aided Chem Eng* 40:1591–1596 (2017a). https://doi.org/10.1016/B978-0-444-63965-3.50267-1
4. Yue D, You F. Stackelberg-game-based modeling and optimization for supply chain design and operations: A mixed integer bilevel programming framework. Comput. Chem. Eng. 102:81-95 (2017). https://doi.org/10.1016/j.compchemeng.2016.07.026
5. Avraamidou S, Pistikopoulos EN. A multiparametric mixed-integer bi-level optimization strategy for supply chain planning under demand uncertainty. *IFAC-PapersOnLine* 50(1):10178–10183 (2017b). https://doi.org/10.1016/j.ifacol.2017.08.1766
6. Nikkhah H, Aghayev Z, Shahbazi A, Charitopoulos VM, Avraamidou S, Beykal B. Bi-level data-driven enterprise-wide optimization with mixed-integer nonlinear scheduling problems. Digit Chem Eng 100218 (2025). https://doi.org/10.1016/j.dche.2025.100218
7. Hansen P, Jaumard B, Savard G. New branch-and-bound rules for linear bilevel programming. SIAM J Sci Stat Comput 13(5):1194–1217 (1992). https://doi.org/10.1137/0913069
8. Kleinert T, Labbé M, Ljubić I, Schmidt M. A survey on mixed-integer programming techniques in bilevel optimization. *EURO J Comput* Optim 9:100007 (2021). https://doi.org/10.1016/j.ejco.2021.100007
9. Saharidis GK, Ierapetritou MG. Resolution method for mixed integer bi-level linear problems based on decomposition technique. *J Glob O*ptim 44:29–51 (2009). https://doi.org/10.1007/s10898-008-9291-0
10. Köppe M, Queyranne M, Ryan CT. Parametric integer programming algorithm for bilevel mixed-integer programs. *J Optim Theory* Appl 146(1):137–150 (2010). https://doi.org/10.1007/s10957-010-9668-3
11. Avraamidou S, Pistikopoulos EN. A multi-parametric optimization approach for bilevel mixed-integer linear and quadratic programming problems. *Comput Chem Eng* 125:98–113 (2019). https://doi.org/10.1016/j.compchemeng.2019.01.021
12. Dempe S, Kalashnikov V, Ríos-Mercado RZ. Discrete bilevel programming: Application to a

natural gas cash-out problem. *Eur J Oper* Res 166(2):469–488 (2005). https://doi.org/10.1016/j.ejor.2004.01.047
13. Fischetti M, Ljubić I, Monaci M, Sinnl M. On the use of intersection cuts for bilevel optimization. Math Program 172(1):77–103 (2018). https://doi.org/10.1007/s10107-017-1189-5
14. Camacho-Vallejo J-F, Corpus C, Villegas JG. Metaheuristics for bilevel optimization: A comprehensive review. Comput Oper Res 161:106410 (2024). https://doi.org/10.1016/j.cor.2023.106410
15. Oduguwa V, Roy R. Bi-level optimization using genetic algorithm. Proc IEEE Int Conf Artif Intell Syst (ICAIS) 2002:322–327 (2002). https://doi.org/10.1109/ICAIS.2002.1048121
16. Li X, Tian P, Min X. A hierarchical particle swarm optimization for solving bilevel programming problems. Int Conf Artif Intell Soft Comput 2006:1169–1178. Springer, Berlin, Heidelberg. https://doi.org/10.1007/11785231_122
17. Sinha A, Malo P, Deb K. Test problem construction for single-objective bilevel optimization. *Evol Comput* 22(3):439–477 (2014). https://doi.org/10.1162/EVCO_a_00116
18. Avraamidou S, Pistikopoulos EN. B-POP: Bi-level parametric optimization toolbox. Comput Chem Eng 122:193-202 (2019). https://doi.org/10.1016/j.compchemeng.2018.07.007
19. Thürauf J, Kleinert T, Ljubić I, Ralphs T, Schmidt M. Bobilib: Bilevel optimization (benchmark) Instance Library. Book Abstr PGMO DAYS 2024:121 (2024).
20. Hart, W. E., Laird, C. D., Watson, J. P., Woodruff, D. L., Hackebeil, G. A., Nicholson, B. L., & Siirola, J. D. Pyomo-optimization Modeling in Python (Vol. 67, p. 277). Berlin: Springer. (2017)
21. Gurobi Optimization, LLC. Gurobi optimizer reference manual. (2024). https://www.gurobi.com

© 2025 by the authors. Licensed to PSEcommunity.org and PSE Press. This is an open access article under the creative commons CC-BY-SA licensing terms. Credit must be given to creator and adaptations must be shared under the same terms. See https://creativecommons.org/licenses/by-sa/4.0/



Systems & Control Transactions

**Research Article - Peer Reviewed Conference Proceeding**
ESCAPE 35 - European Symposium on Computer Aided Process Engineering
Ghent, Belgium. 6-9 July 2025
Jan F.M. Van Impe, Grégoire Léonard, Satyajeet S. Bhonsale,
Monika E. Polańska, Filip Logist (Eds.)

PSE PRESS

# Integration of Graph Theory and Machine Learning for Enhanced Process Synthesis and Design of Wastewater Transportation Networks

**Andres Castellar-Freile[a], Jean Pimentel[b], Alec Guerra[a], Pratap Kodate[c], and Kirti M. Yenkie[a]***

[a] Rowan University, Department of Chemical Engineering, Glassboro, New Jersey, USA
[b] Széchenyi István University, Sustainability Competence Center, Győr, Hungary
[c] Indian Institute of Technology, Department of Physics, Kharagpur, India
* Corresponding Author: yenkie@rowan.edu.

## ABSTRACT

Process synthesis is a fundamental step in process design. The aim is to determine the optimal configuration of unit operations and stream flows to enhance key performance metrics. Traditional methods provide just one optimal solution and are strongly dependent on user-defined technologies, stream connections, and initial guesses for unknown variables. Usually, a single solution is not sufficient for adequate decision-making, especially, when properties such as flexibility or reliability are considered in addition to the process economics. Wastewater Treatment network synthesis and design is a complex problem that demands innovative approaches in design, retrofits, and maintenance strategies. Considering this, an enhanced framework for improving reliability in wastewater transportation networks based on graph theory and machine learning is presented. Machine learning models were developed to predict failure probability, where the XGBoost model provided the best predictions. To select the appropriate solution, a trade-off between cost and reliability metrics is presented which is implemented by analyzing the results from the non-dominated solutions obtained for the case study demonstrated in this paper.

**Keywords**: Machine Learning, Graph Theory, Wastewater, Reliability, Optimization, Process Synthesis

## INTRODUCTION

The inadvertent consumption of water resources and the discharge of wastewater from domestic, agricultural, and industrial sectors into natural water bodies have intensified issues concerning water availability, quality, and purity. In this regard, Wastewater Treatment (WWT) is critical to prevent environmental problems and ensure that contaminant concentrations are reduced below the limits established by the governmental authorities before being discharged into the ecosystem [1]. Municipal treatment facilities must have a reliable infrastructure to transport the water from different regions to the WWT plant (pipelines, manholes, and pumping stations), and must select the appropriate technologies to accomplish the WWT goals within reasonable costs. Therefore, Wastewater Treatment Network (WWTN) synthesis and design must incorporate reliability estimation, which in turn results in a complex problem that demands innovative approaches in design, retrofits, and maintenance strategies.

Process synthesis (PS) is crucial to finding the best configuration of unit operations/technologies and stream flows that optimize the parameters of interest. The traditional approach is based on superstructure optimization with solvers such as Mixed-Integer Programming (MIP) or Mixed Integer Non-Linear Programming (MINLP) [2]. However, they strongly depend on user-defined technologies, stream connections, and reasonable initial guesses for the unknown variables. As a result, this approach may miss potential structures that might outperform the selected one and can fail when addressing large-scale problems with complex models [3].

In the case of WWTN synthesis and design, some prior studies have identified limitations, including the inability to identify redundancies, the existence of bypass and recycling streams, the dependency on user-selected technologies, and the identification of just one optimal

solution [4,5]. With the increasing complexity of modern industrial processes, there is a growing demand for more advanced design optimization tools.

Considering this, Graph Theory can be applied to PS using the P-graph framework, which can generate the set of n-best feasible solutions as well as rank them from best to worst for the synthesis problem. In this representation, system units are shown as horizontal bars, while their inputs and outputs, which are the material streams, are depicted as circles. These nodes are connected by arcs that illustrate the material flow within the system [6]. However, even the top-ranked n-best solutions may be impractical in real applications due to insufficient information on structural reliability. This is problematic for systems exposed to unpredictable and extreme events, such as floods and thunderstorms, since anticipating potential failures and maintenance needs is challenging.

Machine learning (ML), a subfield of Artificial Intelligence, offers a promising solution to this problem by estimating reliability using existing data from current WWTNs. ML algorithms are well suited for analyzing vast amounts of data and identifying the complex relationships that exist between process parameters [7]. Herein, two ML algorithms are utilized: Neural Networks (NNs) and Extreme Gradient Boosting (XGBoost). NNs are a series of interconnected nodes, or neurons, separated into distinct layers. NNs learn by iteratively adjusting the network's internal parameters, weights, and biases to minimize the difference between the model's prediction and the actual outcome, also known as the loss function. NNs can model highly non-linear relationships, such as those commonly found in PS. XGBoost is an advanced implementation of the gradient boosting algorithm. It utilizes both the gradient and the Hessian (the second-order derivative) to find the minimum of the loss function. It employs regularization techniques to correct for model overfitting and incorporates parallel computing to accelerate data processing times [7]. As a result, it exhibits high computational efficiency and is still able to provide accurate and insightful results, making it a valuable tool for PS.

In this paper, the integration of Graph Theory and ML for the retrofitting of WWTN considering reliability is presented. The case study is focused on the pipeline network and pumping stations, in which the exhaustive enumeration tools of the P-graph framework are used to determine the feasible set of retrofit alternatives. These solutions are evaluated in terms of reliability and cost, evaluating them in terms of reliability and cost. For the reliability estimation, XGBoost and NNs models were utilized to predict the failure probability of the system components using real data from a municipal WWT facility (reliability can be defined as the complement of failure probability). The novelty of this approach lies in using real data from a WWT plant to predict the failure probability of the transportation system and incorporating this information into the P-graph framework rigorous enumeration algorithms for reliability calculation. Finally, a Pareto set is generated with the optimal retrofitting alternatives, which can be evaluated to find the solution that best fits the case study.

## METHODOLOGY

This section discusses the case study, in which the network synthesis and the P-graph representation of the pipeline network and pumping stations are presented. In addition, the ML models used for estimating the network's failure probability are described. Finally, the framework for reliability estimation is explained, where the ML results are integrated with the P-graph framework.

### Case Study and P-graph Representation

The case study focuses on a simplified pipeline

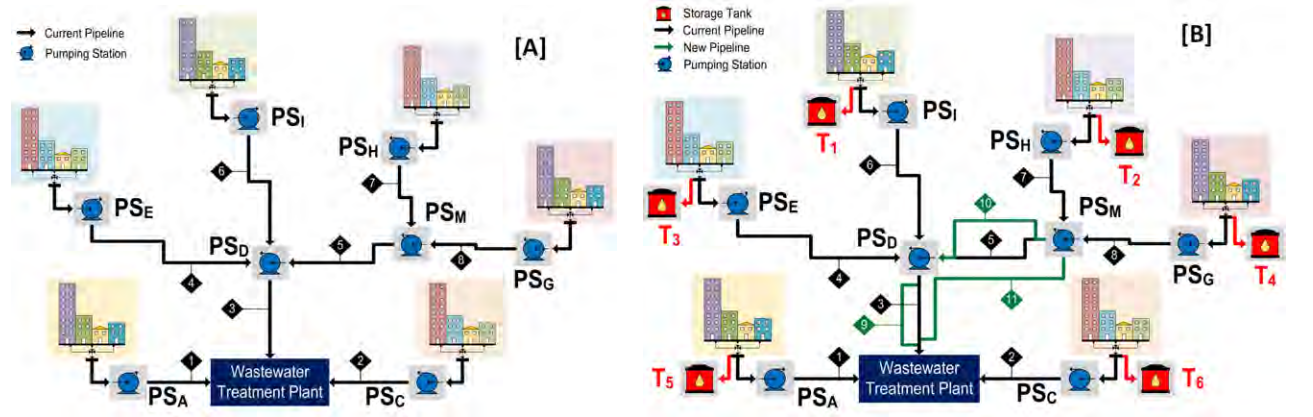



**Figure 1: A.** Base case study for the wastewater treatment pipeline network and pumping stations **B.** Modified pipeline network considering the redundant pipelines (9,10,11) and storage tanks ($T_1$ to $T_6$).

system of a municipal WWT plant with a capacity of approximately 1.6 million gallons per day. The system includes eight pumping stations ($PS_A$, $PS_C$, $PS_D$, $PS_E$, $PS_G$, $PS_H$, $PS_I$, $PS_M$) that collect wastewater from various municipalities through a sewage network. These pumping stations are connected by pipelines that transport the wastewater to the WWT plant as shown in Figure 1A. This system lacks redundancies, meaning there are no alternative routes if a pipeline fails.

Pumping stations $PS_D$ and $PS_M$ are critical as they connect multiple sectors. A pipeline failure between these stations would result in most of the WWTN shutting down. To address this, alternative routes are proposed between pumping stations $PS_D$ and $PS_M$, $PS_D$ and the WWT plant, and $PS_M$ and the WWT plant. Additionally, the installation of tanks ($T_1$, $T_2$, $T_3$, $T_4$, $T_5$, $T_6$) to store wastewater in case of overflow or pipeline failure is evaluated. These tanks are located at pumping stations $PS_A$, $PS_C$, $PS_E$, $PS_G$, $PS_H$, and $PS_I$. Figure 1B illustrates the updated pipeline network, designed to enhance the system's overall reliability.

Figure 2 shows the P-graph structure of the Modified case study, which was adapted from previous work developed by Pimentel et al [8]. The nodes of the main structure are represented in black, additional tanks are shown in red, and additional pipelines are represented in green.

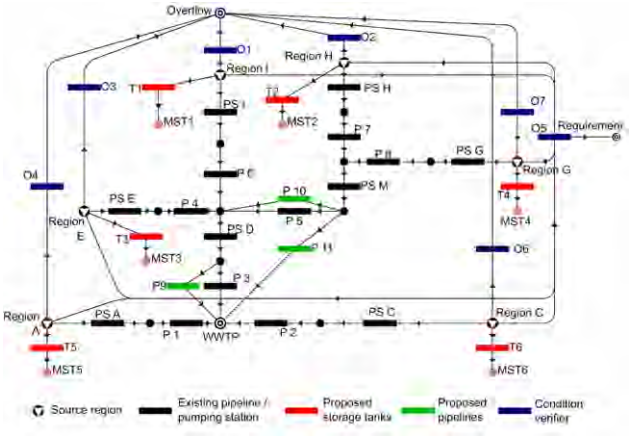



**Figure 2.** P-graph representation of the Modified Case Study.

To assess the feasibility of the system, two additional product nodes are incorporated into the P-graph representation, as shown in Figure 2. The first one, labeled as "Overflow", allows restricting maximum overflow permitted in the system. The second one, labeled as "Requirement", ensures that all water sources are included in the analysis.

## Machine Learning Models

XGBoost and NNs models for regression were developed to predict the failure probability of pipelines. The data provided by the municipal WWT plant includes approximately 250 manholes and 295 pipelines. After data preprocessing, 280 data points were obtained. The features considered for the ML models were pipe size, pipe type (material), segment length, flow rate, flow type (gravity or forced flow), installation date, years since the last inspection, remaining lifespan, population density, and distance from WWT facility. Failure probability values were provided via inspection from experts working at the municipal WWT plant.

For the 'flow type' the values were encoded as follows: gravity flow (0), forced flow (1). Similarly, the 'pipe type' values were encoded in this way: HDPE (1), DIP (2), Steel (3), PVC (4), TCP (5), RCP (6), VCP (7), ACP (8).

For the hyperparameter tuning, the XGBoost model was trained using the following: number of trees = (100, 200, 500, 1000), learning rate= (0.01, 0.05, 0.1, 0.2), maximum depth = (3, 5, 7, 10), subsample = (0.4, 0.6, 0.8, 1.0), colsample by tree = (0.4, 0.6, 0.8, 1.0). In the same way, the regularization for NNs was developed using the following parameters: model neurons = (16, 32, 64, 128), model dropout rate = (0.05, 0.1, 0.2, 0.3), batch size = (10, 20, 30, 40), and epochs = (100, 200, 400, 500). ReLU activation function was used for the NNs model. For both models, cross-validation was implemented.

## Framework for Reliability Estimation

The framework for reliability estimation was developed in a previous work by Pimentel et al [8], in which the objective is to generate a set of retrofitting alternatives for wastewater transportation systems with enhanced reliability. Figure 3 shows the methodology proposed.

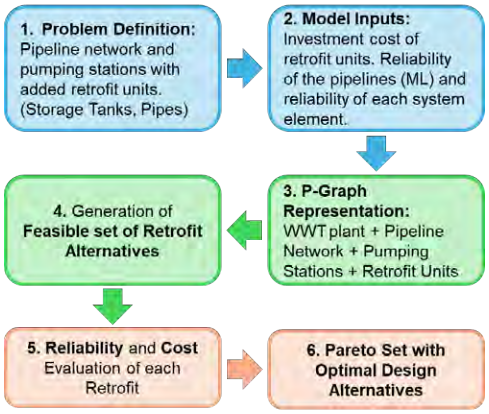



**Figure 3.** Methodology to generate reliable retrofitting alternatives for wastewater transportation systems.

The approach begins with the problem definition by identifying feasible operating units for system expansion. This includes selecting operating units, such as emergency storage tanks, alternative pumping systems, and redundant pipelines that can manage potential failures in

**Table 1:** Pipeline features of the Modified Case Study used for the ML models.

| N | From | To | Remaining Life [years] | Pipe Size [in] | Pipe Type | Segment Length [ft] | Years Since Last Inspection | Original Installation Year | Population Density [pop/mi²] | Flow Type | Flow Rate [Mgal/day] | Distance from WWT plant [km] |
|---|---|---|---|---|---|---|---|---|---|---|---|---|
| 1 | $PS_A$ | Plant | 76 | 30 | 3 | 21918 | 24 | 1976 | 3742.25 | 1 | 0.350 | 10.30 |
| 2 | $PS_C$ | Plant | 52 | 30 | 6 | 17584 | 48 | 1976 | 1208.29 | 0 | 0.320 | 9.66 |
| 3 | $PS_D$ | Plant | 49 | 36 | 6 | 30703.7 | 34 | 1973 | 3541.12 | 1 | 0.990 | 13.20 |
| 4 | $PS_E$ | $PS_D$ | 50 | 30 | 8 | 39623 | 25 | 1976 | 2599.26 | 1 | 0.410 | 8.05 |
| 5 | $PS_M$ | $PS_D$ | 52 | 27 | 6 | 13698 | 48 | 1976 | 1632.96 | 0 | 0.360 | 5.15 |
| 6 | $PS_I$ | $PS_D$ | 67 | 18 | 2 | 76260 | 33 | 1991 | 915.25 | 1 | 0.220 | 21.57 |
| 7 | $PS_H$ | $PS_M$ | 67 | 12 | 8 | 45509 | 33 | 1991 | 634.37 | 1 | 0.110 | 22.69 |
| 8 | $PS_G$ | $PS_M$ | 52 | 18 | 2 | 26576 | 48 | 1976 | 1929.57 | 1 | 0.250 | 16.90 |
| 9 | $PS_D$ | Plant | 100 | 30 | 6 | 30703.7 | 0 | 2024 | 3541.12 | 1 | 0.990 | 25.40 |
| 10 | $PS_M$ | $PS_D$ | 100 | 24 | 6 | 13698 | 0 | 2024 | 1632.96 | 0 | 0.360 | 5.15 |
| 11 | $PS_M$ | Plant | 100 | 24 | 6 | 13698 | 0 | 2024 | 1632.96 | 1 | 0.360 | 30.55 |

the base structure.

Additionally, the investment cost and reliability of each extension unit must be determined for the model inputs. The reliability values are obtained from the ML model, which is integrated with the P-graph framework to obtain the set of n-best solutions based on reliability and cost.

Afterward, all system elements are represented using the P-graph methodology. Based on this structure, retrofitting alternatives (operational sub-structures) are generated by combining different units and integrating them into the base system.

Then, the total cost and reliability of each alternative can be individually determined. The reliability of the retrofitting alternatives is determined by using the reliability formula shown in equation (1):

$$r = \sum_{(x_1,x_2,\ldots,x_n)\in U}\left(\prod_{i=1}^{n} p_i^{x_i}(1-p_i)^{(1-x_i)}\right) \quad (1)$$

Where $p_i$ is the reliability of the network's elements, $x_i$ represents its operational state (failure or operating), and $U$ is the set of operational structures in the problem [6].

Finally, a Pareto set with the best design alternatives (non-dominated solutions) for the problem is created.

## RESULTS AND DISCUSSION

In this section, the data for the case study as well as the assumptions made to solve the problem are presented. Besides, the results for the XGBoost and NNs are shown, from which the better predictions are chosen as inputs in the Framework for Reliability Estimation. Finally, the Pareto set with the best design alternatives for the problem is presented.

### Case Study and P-graph Representation

The case study data is presented in Table 1, in which the features of each segment are described.

Additionally, in Table 2 the annualized cost of each unit operation in the Modified Case Study required for the P-graph framework is presented. The pipelines are denoted as $P_n$, where n is the pipeline number. The storage tanks (from $T_1$ to $T_6$) are assumed to have an annual investment cost of $62,400, a maximum capacity of 250,000 gallons, and a reliability of 0.95. The reliability values for the pumping stations are assumed to be 0.99. The reliability examination for this case study is carried out considering a time horizon of 1 day, consequently, the wastewater transport system must handle 1.6 million gallons. Also, the operational structure's maximum overflow was set at 83,000 gallons, which means that if this value is exceeded, the structure is not feasible.

**Table 2:** Annualized cost of the unit operations (Cost in thousands of USD per year) with their maximum wastewater flow (Flow in millions of gallons per day).

| Unit | Cost [kUSD/y] | Flow [Mgal/day] |
|---|---|---|
| P1, P2, P4 | 0 | 0.860 |
| P3 | 0 | 1.200 |
| P5 | 0 | 0.700 |
| P6, P8 | 0 | 0.310 |
| P7 | 0 | 0.138 |
| P9 | 123.6 | 0.860 |
| P10 | 34.4 | 0.550 |
| P11 | 108.7 | 0.550 |
| PSA, PSC, PSE, PSG, PSH, PSI, PSM | 0 | 0.500 |
| PSD | 0 | 1.200 |

### Machine Learning Models

The XGBoost and NNs results for the case study are presented in Figures 4 and 5, respectively. The metrics used to validate the models were the mean squared error

(MSE) and the coefficient of determination ($R^2$).

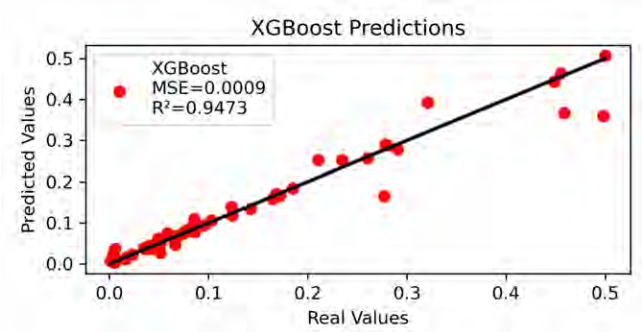



**Figure 4.** XGBoost model for predicting the pipeline failure probability.

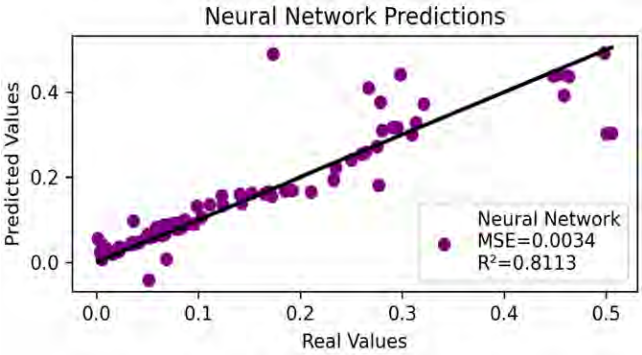



**Figure 5.** NNs model for predicting the pipeline failure probability.

The hyperparameter tuning values for XGBoost provides the following results: Subsample= 0.6, Number of Estimators= 200, Maximum Depth= 5, Learning Rate= 0.1, Colsample by tree= 0.6. For NNs, the following parameter values were obtained after regularization: Model Neurons= 128, Model Dropout Rate= 0.1, Epochs= 400, Batch Size=20

Considering the results for the ML models, XGBoost shows to have better performance than the NNs, which is demonstrated in the $R^2$ value (0.9473 for XGBoost and 0.8113 for NNs) and the lower MSE. The low performance of NNs may be due to the limited amount of data available to train the models. However, we intend to continue training the model with more data obtained from different WWT plants to build a more generalized network.

The predicted values of each model for failure probability and reliability using the features presented in Table 1 are shown in Table 3. To obtain the reliability values for the segments, the failure probability values should be subtracted from 1. From the results obtained for each ML model in Table 3, the failure probability values from the XGBoost model were selected as inputs to the Framework for Reliability Estimation.

Finally, the feature importance results for the XGBoost model are shown in Figure 6. The features with more relevance in the XGBoost model were Years Since Last inspection, Flow Type, and Flow Rate.

**Table 3:** Predicted values of failure probability and reliability for XGBoost and NNs.

| N | XGBoost Failure Probability | NNs Failure Probability |
|---|---|---|
| 1 | 0.2502 | 0.2303 |
| 2 | 0.3223 | 0.6054 |
| 3 | 0.1772 | 0.1993 |
| 4 | 0.2973 | 0.1505 |
| 5 | 0.2940 | 0.7947 |
| 6 | 0.3285 | 0.2375 |
| 7 | 0.2104 | 0.2455 |
| 8 | 0.1480 | 0.2992 |
| 9 | 0.0999 | -0.0417 |
| 10 | 0.0801 | 0.1843 |
| 11 | 0.0106 | -0.0653 |

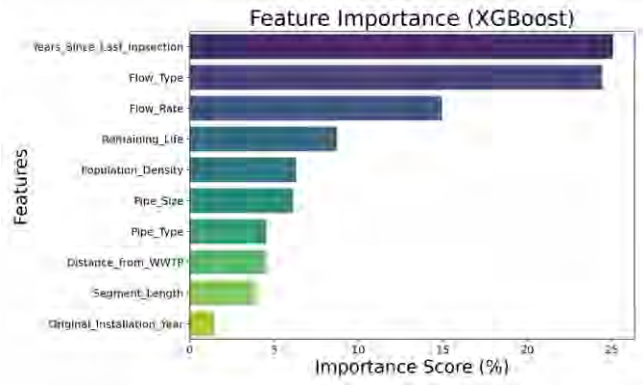



**Figure 6.** Feature importance for the XGBoost model.

## Framework for Reliability Estimation

The results for the non-dominated solution set are obtained from the evaluation of 512 different retrofitting alternatives. The results are shown in Figure 7.

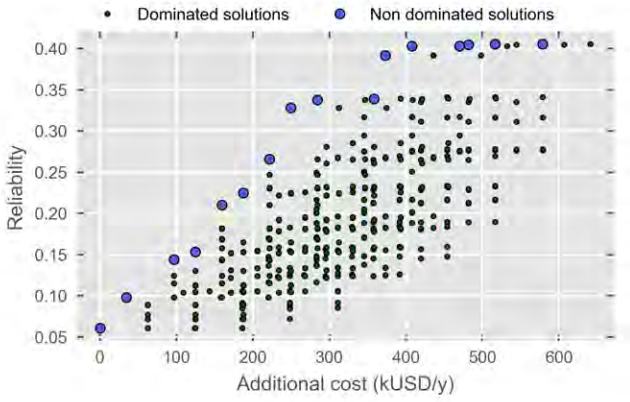



**Figure 7.** Pareto set of solutions for the case study considering Reliability and Annualized cost (USD/y).

In Figure 7 the best solutions regarding cost and reliability are represented by blue circles, while the other solutions are depicted as green circles. Some non-dominated solutions are presented in Table 4.

**Table 4:** Some non-dominated solutions for the case study for reliability and cost metrics. The cost of retrofitting is expressed as kUSD per year.

| Additional Units | Reliability | Cost |
|---|---|---|
| None | 0.061 | 0 |
| $T_2$, $T_4$ | 0.153 | 124.8 |
| $T_2$, $T_4$, $T_6$ | 0.225 | 187.2 |
| $T_1$, $T_6$, $P_{10}$ | 0.210 | 159.2 |
| $T_1$, $T_2$, $T_4$, $T_6$ | 0.328 | 249.6 |
| $T_1$, $T_2$, $T_4$, $T_6$, $P_{10}$ | 0.338 | 284.0 |
| $T_1$, $T_2$, $T_4$, $P_9$, $P_{10}$ | 0.403 | 407.6 |
| $T_1$, $T_2$, $T_3$, $T_4$, $T_6$, $P_9$, $P_{10}$, $P_{11}$ | 0.405 | 578.8 |

In Table 4 it is noted that the most reliable solution is the one with all but one additional unit, but also is the most expensive. On the other hand, the minimum cost is achieved when no additional units are added. In this case, the reliability is low, with a value of 0.061. To select the appropriate solution for the case study, a trade-off between cost and reliability should be considered. By adding four tanks, the reliability value becomes 0.328. This value represents 80% of the maximum reliability value, and the investment cost of 249.6 kUSD/y represents 43.1% of the maximum investment cost, which is 578.8 kUSD/y. For that reason, adding four tanks is one of the best solutions for the case study.

## CONCLUSIONS

In this study, the integration of ML and graph theory in a framework for reliability and cost estimation of WWT networks was presented. The XGBoost model provided better failure probability predictions compared to the NNs model with an $R^2$ value of 0.9473. The low performance of NNs may be due to limited amount of data available to train the models. The features with more relevance in the XGBoost model were Years Since Last inspection, Flow Type, and Flow Rate. The Pareto set showed that to select the appropriate solution, a trade-off between cost and reliability should be considered. Finally, one of the best solutions was adding all the tanks, in which the reliability value was 0.326, which represents 80% of the maximum reliability value, with 43% of the maximum investment cost.

## ACKNOWLEDGEMENTS

This work is supported by the NSF-CBET CAREER under Award #2339588 ("CAREER: Integrating Graph Theory based Networks with Machine Learning for Enhanced Process Synthesis and Design"), 07/01/2024 - 06/30/2029.

Pimentel J. would like to thank the financial support of the Government of Hungary and the European Union Recovery and Resilience Plan within the framework of the Artificial Intelligence National Laboratory Program (RRF-2.3.1-21-2022-00004).

## REFERENCES

1. Yenkie KM. Integrating the three E's in wastewater treatment: efficient design, economic viability, and environmental sustainability. *Curr. Opin. Chem. Eng.*, vol. 26: 131–138 (2019) https://doi.org/10.1016/j.coche.2019.09.002
2. Aboagye EA, Burnham S, Dailey J, Zia R, Tran C, Desai M, Yenkie KM. Systematic Design, Optimization, and Sustainability Assessment for Generation of Efficient Wastewater Treatment Networks. *Water*, vol. 13, no. 9: 1326 (2021) https://doi.org/10.3390/w13091326
3. Chen Q, Grossmann IE. Recent Developments and Challenges in Optimization-Based Process Synthesis. *Annu. Rev. Chem. Biomol. Eng.*, vol. 8, no. 1: 249–283 (2017) https://doi.org/10.1146/annurev-chembioeng-080615-033546
4. Morsy O, Hourfar F, Zhu Q, Almansoori A, Elkamel A. A Superstructure Mixed-Integer Nonlinear Programming Optimization for the Optimal Processing Pathway Selection of Sludge-to-Energy Technologies. *Sustainability*, 15: 4023 (2023) https://doi.org/10.3390/su15054023
5. Padrón-Páez JI, Almaraz SDL, Román-Martínez A. Sustainable wastewater treatment plants design through multiobjective optimization. *Comput. Chem. Eng.*, vol. 140: 106850 (2020) https://doi.org/10.1016/j.compchemeng.2020.106850
6. Friedler F, Orosz Á, Pimentel Losada J. P-graphs for Process Systems Engineering: Mathematical Models and Algorithms. *Cham: Springer International Publishing* (2022) https://doi.org/10.1007/978-3-030-92216-0
7. Zhou ZH. Machine Learning. Springer Singapore (2021) https://doi.org/10.1007/978-981-15-1967-3
8. Pimentel J, Orosz Á, Castellar-Freile A, Yenkie K. Systematic Method of Retrofitting Wastewater Transportation Systems for Enhanced Reliability. *Chem. Eng. Trans.*, vol. 114: 1075–1080 (2024) https://doi.org/10.3303/CET24114180

© 2025 by the authors. Licensed to PSEcommunity.org and PSE Press. This is an open access article under the creative commons CC-BY-SA licensing terms. Credit must be given to creator and adaptations must be shared under the same terms. See https://creativecommons.org/licenses/by-sa/4.0/



Systems & Control Transactions

**Research Article - Peer Reviewed Conference Proceeding**
ESCAPE 35 - European Symposium on Computer Aided Process Engineering
Ghent, Belgium. 6-9 July 2025
Jan F.M. Van Impe, Grégoire Léonard, Satyajeet S. Bhonsale,
Monika E. Polańska, Filip Logist (Eds.)

PSE PRESS

# A Framework Utilizing a Seamless Integration of Python with AspenPlus® for a Multi-Criteria Process Evaluation

**Simon Maier[a,*], Julia Weyand[a], Ginif Kaur[a], Oliver Erdmann[a], and Ralph-Uwe Dietrich[a]**

[a] German Aerospace Center, Institute of Engineering Thermodynamics, Pfaffenwaldring 38-40, 70569 Stuttgart, Germany
* Corresponding Author: simon.maier@dlr.de

## ABSTRACT

Detailed assessment of fuel production processes at an early stage of a project is crucial to identify potential technical challenges, optimize efficiency and minimize costs and environmental impact. While process simulations often are either very rigid and accurate or very flexible and unprecise, informed decision making can only be maintained by establishing a detailed process model as early as possible within the project lifecycle while keeping relevant aspects of the process flexible enough. In this work, we present the development of a framework based on a dynamic interface between AspenPlus® process simulations and Python, enabling enhanced flexibility and automation for process modeling and optimization. This integration leverages the powerful simulation capabilities of AspenPlus® with the versatility of Python for data analysis and optimization, delivering significant improvements in workflow efficiency and process control. By utilizing the dynamic simulation data exchange with Python, extensive parameter studies can be conducted and post-processed for techno-economic and environmental analyses. Furthermore, the interface allows the implementation of complex kinetic models or optimization routines for single process units. An additional extension for heat integration ensures the technical viability of the process route for reliable comparisons of different routes and process configurations. The functionalities are applied to a biomass- and power-based methanol production process including various process designs and operating conditions. To keep the level of detail at a high level, additional Python scripts are implemented securing a proper scaling of process units such as the methanol synthesis reactor system. The process configurations are assessed technically, economically and environmentally.

**Keywords**: Modelling and Simulations, Aspen Plus, Technoeconomic Analysis, Life Cycle Analysis.

## INTRODUCTION

Aspen Plus is a widely used software tool for process flow sheeting and simulation in chemical engineering. Its robust modeling capabilities enable the design, optimization, and analysis of complex chemical processes across a variety of industries. By providing access to comprehensive thermodynamic models and extensive unit operation libraries, Aspen Plus facilitates efficient process development and performance evaluation.

Despite its strengths, Aspen Plus has limitations that may hinder advanced customization and holistic process analysis. The integration of user-defined scripts, while possible through external tools such as Aspen Custom Modeler or Excel, can be cumbersome and lacks native support, limiting flexibility in certain specialized scenarios. Furthermore, the platform's techno economic analysis (TEA) and life cycle assessment (LCA) features often require external tools or manual data extraction and integration. This lack of transparency and seamless workflow can pose challenges for researchers seeking integrated, transparent assessments that combine process simulation, economic evaluation, and environmental impact analysis.

## METHODOLOGY

A simplified illustration of the cost and environmental impact estimation is depicted in Figure 1. Both estimations are based on a detailed process simulation using the commercial AspenPlus® software and Python. Their base functionality is relying on a direct connection with

the simulation via aspenparserDLR [1] as a python-AspenPlus interface. This requires an active AspenPlus® process and hence longer loading times as well as the requirement of AspenPlus® being available on the machine on which the evaluation is conducted. A description of the functionality of pyteea_tea and pyteea_lca can be found elsewhere [2, 3].

## Parameter variation framework

To split the data generation from the evaluation of different process concepts, the tool pyteea_sc, of which the 'sc' stands for simulation control, is developed to conduct externally-controlled parameter variations and extract the simulation data required for subsequent analyses after each run. The major communication in between the tools is shown in Figure 1.

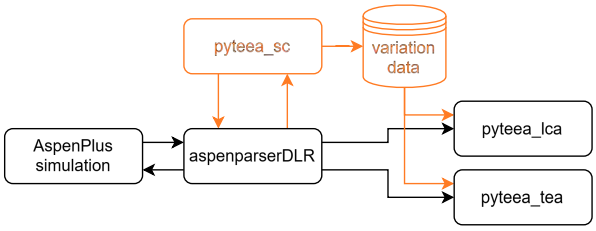



**Figure 1.** Simplified schematic illustration of the utilized tools and their interaction.

Together with the functionality of varying process parameters externally, the tool allows to include and execute user scripts within the parameter runs. This allows to enhance the level of detail and the complexity of certain process steps or to set up own optimization routines which would require a lot of work-arounds in AspenPlus®.

The main program routine of pyteea_sc can be seen in Figure 2. After a main configuration file is read, the major object `SimControl` is initiated. In dependence on the chosen complexity, multiple further configuration files are read to fill the subobjects for the variation run, such as the `linked_objects` which is either an object which communicates with AspenPlus® or a look-up object of a previous variation run. Furthermore, the `process_vars` are initiated, containing a list of process variables and their variation ranges, their paths within the AspenPlus®, as well as their dependencies within each other. The `additional_features` are a list of user defined functions which are being executed with the variation runs. In the `run_options` settings for the data extraction is defined. nformation about the run configuration, as well as information about the variation matrix and the run status:

```
class SimControl:
    linked_objects: list
    process_vars: list
    additional_features: list
    run_options: RunOptions
    var_structure: VarStructure
    var_status: VarStatus

    def run_simulation(self):
       ...
    def export_data(self):
       ...
    def close_simulation(self):
       ...
```

SimControl also allows to define connections between streams from two or more different AspenPlus® files or look-up objects. This functionality comes with a speed advantage since, e.g., a simulation model of an electrolyser requires much less components than a simulation of a hydrocracking process. Hence, the electrolysis can be calculated in a model with limited components and only its resulting hydrogen connected to the hydrocracker model.

Since the communication with AspenPlus® consumes the most time of the whole procedure, as it can be seen in the digital supplementary material, there might be the need to reduce the number of accesses to it. In case of a benchmark run using 'Case1.2_v10.apw' of the Biomass-Gas-and-Nuclear-To-Liquids Simulation Files published by J. Scott and T. A. Adams [4], a short parameter variation took 7:42 min, of which 6:48 min were communicating with AspenPlus® [5]. Therefore, the framework allows to define specific blocks and streams of which all or only limited data is retrieved. In this way the execution time can be significantly be lowered. Yet, this limits the potential of a later setup of the results as a look-up object. In the standard mode, the mass flows for each component is recorded, as well as its molar flow, volume flow, temperature, pressure, vapour fraction, mass density, path, source, and destination. For the different block types, the list differs a lot, since the data from e.g. a Mixer is only its split ratio, and ports, while for a RadFrac unit, also reflux ratio etc. is read.

To ensure a stable execution of the conducted parameter run, the run status after each execution is tracked and the data is only retrieved when it is actually available while a logger records the run status. Nevertheless, in case of unconverged simulation, the data retrieval is skipped the run number is recorded. The list of unconverged simulations can then be executed in a subsequent variation run in order to complete the desired variation matrix. Often, the convergence issues can be overcome in a second run and are originating from an unfavorable order of varied parameters.

After the connection to all simulations or data objects is set up, potential further configuration files for the additional features are read. Eventually, a variation matrix is generated in dependence on potential primary, secondary, etc. parameter relations. The variation matrix is then exported as well as all relevant run settings to ensure the reusability of the run data.

The modular and object-oriented structure of the tool allows to easily include new functionalities and can flexibly work with one or five process parameters, different recorded process units etc. Furthermore, the tools is set up with a clear deviation between input data and functions and allow no hard-coded input.

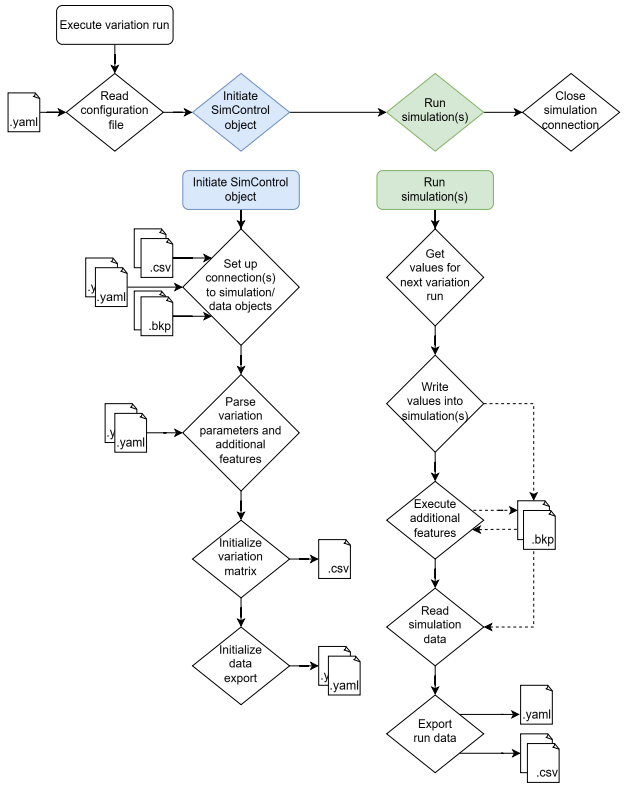



**Figure 2.** Program routine and its major functions and data in- and output.

For the execution of a parameter variation, the values for each single variation parameter are taken from the variation matrix and written into the simulation(s). In case of using look-up objects, the suitable data is prepared in dependence on the given parameters. Then, any additional features are executed. The additional feature which is included in this work is described in the section below. After all simulations converged the simulation data is exported using the aspenparserDLR. To ensure data retrieval for each complete parameter run as well as for each individual simulation run, md5sums are generated based on the run configuration.

## Techno-economic analysis tool

The economic assessment is based on the approach by Peters, Timmerhaus, and West [6] which has been applied in various previous, techno-economic studies [7-9]. A database of reference equipment costs is required to represent any change in the process configurations also in the capital and operational expenditures. Based on the previously described AspenPlus® process model the material and energy flows are used to scale equipment sizes, as well as raw material and by-product streams.

The tool requires a main configuration file which takes plant data input such as lifetime, plant type, operating hours per year, and indirect OPEX cost factors. Together with data coming from various data sources the techno-economic calculations are executed. Currently the tool supports connecting and reading data directly from AspenPlus® simulations, CSV files, YAML files, and JSON files. Once the data is read and parsed from these file input sources, it is further processed in dependence on the reference equipment/raw material/by-products and the costs of the defined product are estimated.

In general, the simulation outputs (material flows, energy flows and equipment dimensions) are employed to calculate capital (CAPEX) and operational expenditures (OPEX) as part of the net production cost (NPC).

## Life cycle assessment tool

The same material and energy flows are also utilized as input for the foreground system of the life cycle inventory (LCI). The background system of the LCI is supplied with data from databases like Ecoinvent or ones created from literature or project partner data. With life cycle impact assessment (LCIA) methods, the environmental impacts are then calculated. Details on the python-based life cycle assessment (pyteea_lca) tool can be found elsewhere [3].

The pyteea_lca tool utilizes the open source LCA framework Brightway2 (Python package) [10]. In order to manage and browse through projects and databases easier and in a more intuitive way the Activity Browser (AB) [11], a graphical user interface (GUI) for Brightway2, can be additionally employed.

To perform the LCA, a configuration file must be set up pointing all additional files which are required for the LCA and defining the general information of the LCA evaluation run. Furthermore, the setup requires a series of YAML files that provide the tool with configurations details, such as linked datasets for Brightway2, functional unit, impact categories from LCIA methods and variation run data.

For conducting the LCA of the generation variation run data batch, a look-up object of that data is initiated reading all the configuration information of the previous parameter run and making it available for the ecological evaluation. Hence, all CSV and YAML files are read, including all stream values (heat-, electricity- and mass flows) for each run, and the variation matrix that describes the varied parameters for each run. These files enable the seamless integration of Aspen Plus® results with pyteea_lca for further analysis. Using the ‘get_current_stream_sizes’ function from pyteea_lca, stream values are extracted from the CSV file and linked to their selected aspen id.

The pyteea_lca tool can either iterate over single runs or run through the whole data batch to perform LCA calculations for each run automatically. After calculating the LCIA results, the tool either generates and stores a single or multiple CSV files. The main result file provides environmental impacts per aspen id.

## Process configurations

The presented tools within this work are applied to the flowsheet model presented by Maier et al. [12]. The study contains the same four process configurations. Two cases which are purely operating with biomass as feedstock, case 1 using bark and case 2 using straw, respectively. Additionally, for both feedstocks a biomass-and-power-based process concept is assessed. In these cases, a PEM electrolyser is integrated providing hydrogen stoichiometrically to the methanol forming reactions. While in previous work the methanol reactor was modelled as an isothermal fixed-bed reactor, in this study a multi-stage quench reactor system is applied.

## Additional feature – Ideal reactor length

As described in section parameter variation framework, another implemented functionality of pyteea_sc is the integration of user scripts which can be included within the parameter variation run.

In this work, an additional feature is implemented that finds the ideal reactor length for each reactor stage in order to prevent over- and underestimation of their size, ensuring that the subsequently calculated costs are properly estimated.

**Table 1.** Reactor dimensioning parameters.

| Parameter | Definition |
|---|---|
| Control parameter | $T_{eq} - T_{out,Ri} = 5 \pm 0.5$ K |
| Control variable | Reactor length |

The routine is using a second RPlug reactor for each reactor stage which is completely oversized to ensure that it reaches equilibrium. A Transfer block ensures that each stage is calculated with the same gas mixture as the regular reactor stage is working with. The methanol formation of each reactor stage over the temperature together with the equilibrium line is given in Figure 3.

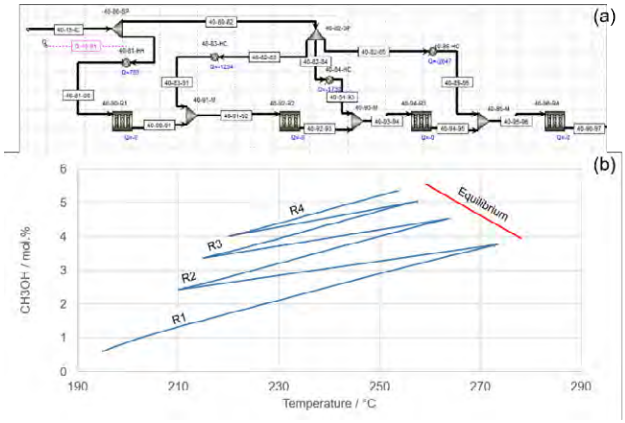



**Figure 3.** Reactor stages in flowsheeting simulation (a); Reaction profiles for all four reactor stages (b)

A Newton algorithm is applied to find the ideal length of reactor including an exiting function when the composition reaches equilibrium in order to prevent the algorithm from running into an asymptotic regime.

# RESULTS & DISCUSSION

## Parameter variation framework

For the conducted parameter variation, the execution time was 36:39 min of which 35:02 min where communication between Python and AspenPlus. If compared to previous approaches for coupling AspenPlus® with a programming software like in the case of Lopez et al. [13], the execution time is much higher which limits the framework's application for operation within larger optimizer routines. For usage in this field, the recording options should be set to a minimum. Especially the implemented additional feature can definitely be improved by that and should be seen as a demonstration of the implementation possibility of user script within the variation loop rather than an ideal solution for reactor design.

Since in the case of this study, the intention of the tool is mainly to make AspenPlus® obsolete for subsequent data analyses such as TEA or LCA, a complete data extraction has been conducted.

## Techno-economic analysis results

Figure 4 shows the techno-economic analysis results for bark and straw and their different process concepts for 100 $MW_{th}$ biomass input.

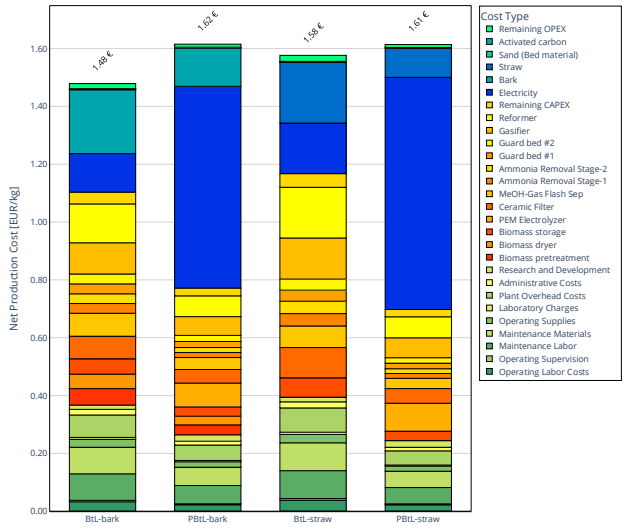



**Figure 4.** Net production costs for the four process concepts.

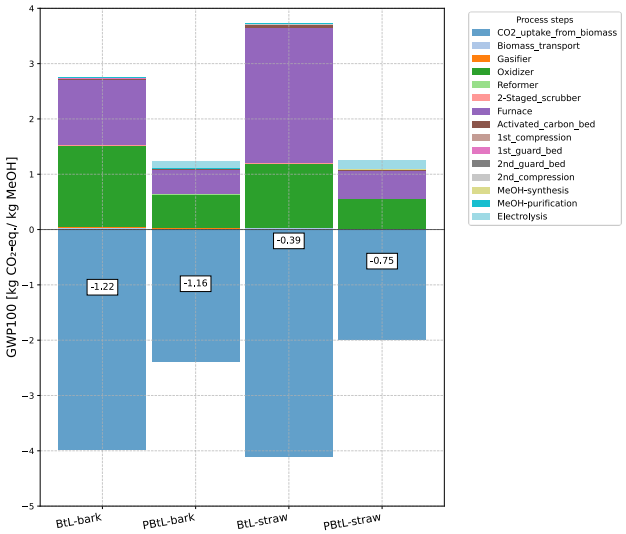



**Figure 5.** LCA results (Cradle-to-Gate) for the four process concepts. Wind energy is assumed as electricity source.

The main aspects which can be identified in Figure 4 are that the net production costs for the power-and-biomass process concepts are higher than their purely biomass-based representative. Main reason is the production of hydrogen at an electricity price of 105 €$_{2023}$/MWh which makes it more expensive than the hydrogen received by biomass gasification. Nevertheless, the implementation of the additional electrolysers nearly doubles the product output of the processes. Hence, even with the very expensive electricity, the PBtL cases are nearly in the same price range as the biomass-based ones.

### Life-cycle analysis results

Using the same simulation data for the ecological analysis of the four process concepts results in the global warming potentials (GWPs) displayed in Figure 5. The figure shows that the processes utilizing bark (BtL-bark & PBtL-bark) have a lower GWP than with straw (BtL-straw & PBtL-straw). Furthermore, when using wind energy as the electricity source, the power-and-biomass based process (PBtL) results in a quite similar GWP in case of bark. In case of straw as a feedstock, the power enhanced process designs results in a 2.2 times higher product yield, which leads to a significant reduction of the process-related emissions since their contribution is divided through a larger amount of product. The gas cleaning steps (reformer, activated carbon bed, 1$^{st}$ guard bed, 2-staged scrubber, 2$^{nd}$ guard bed and 1$^{st}$ compression) and biomass transport (100 km truck transportation) are only contributing 1% for all process concepts and therefore has no significant influence on the GWP. Also, with the MeOH production and purification step (MeOH-synthesis, MeOH-purification and 2$^{nd}$ compression), which are contributing <1%.

The most GWP influencers are the process emissions from the oxidizer flue gas (after biomass gasification) and from furnace (combustion of the purge gas after MeOH-synthesis). These emissions vary depending on the type of biomass. Straw has more emissions from the furnace and bark more from the oxidizer.

## CONCLUSIONS & OUTLOOK

The presented work shows the application of a toolbox which allows extensive process analysis together with the implementation of python-based user scripts. Furthermore, the shown tools allow to divide the process analyses from AspenPlus® simulations, which enables extensive analyses without the need of communicating with AspenPlus® simulations. Hence stability issues of the simulation can be taken care of before the data is further processed. Additionally, the introduction of the parameter run data as an intermediate allows to apply more extensive evaluation features on the data batch opening the whole wide world of python-based data analysis tools for the work with rigorous process simulations in AspenPlus®.

Due to the tool's modular programming approach further objects which allow communication with other simulation or modeling tools could be implemented and included in the list of potential `linked_objects`.

Currently, the tool is completely based on YML files and python scripts and its usability could be improved by including a graphical user interface for the input data definition.

## DIGITAL SUPPLEMENTARY MATERIAL

Digital supplementary material for the mentioned benchmark case is being made public on LAPSE:2025.0042 [5].

## ACKNOWLEDGEMENTS

This research is funded by the German Federal Ministry of Digital Affairs and Transport (BMDV) as part of the Funding Programme Renewable Fuels in the project Methanol-to-Sustainable Aviation Fuels (M2SAF).

## REFERENCES

1. Maier, S. and J. Weyand, aspenarserDLR - A Python-AspenPlus interface. zenodo (2025).
2. Maier, S. and J. Weyand, pyteea_tea - A python-based techno-economic assessment tool. zenodo (2025).
3. Weyand, J. and S. Maier, pyteea_lca - A python-based life cycle assessment tool. zenodo (2025).
4. Scott, J.A. and T.A. Adams, Biomass-Gas-and-Nuclear-To-Liquids Simulation Files. (2018), PSE: PSE Community.
5. Maier, S., A Framework Utilizing a Seamless Integration of Python with AspenPlus® for a Multi-Criteria Process Evaluation - Benchmark case. LAPSE:2025.0042. (2025).
6. Peters, M.S., K.D. Timmerhaus, and R.E. West, Plant Design and Economics for Chemical Engineers. 2002).
7. Albrecht, F.G., et al., A standardized methodology for the techno-economic evaluation of alternative fuels – A case study. Fuel 194: 511-526 (2017) 10.1016/j.fuel.2016.12.003.
8. Maier, S., et al., Techno-economically-driven identification of ideal plant configurations for a new biomass-to-liquid process – A case study for Central-Europe. Energy Conversion and Management 247 (2021) 10.1016/j.enconman.2021.114651.
9. Habermeyer, F., et al., Techno-Economic Analysis of a Flexible Process Concept for the Production of Transport Fuels and Heat from Biomass and Renewable Electricity. Frontiers in Energy Research 9 (2021) 10.3389/fenrg.2021.723774.
10. Mutel, C.L., L. de Baan, and S. Hellweg, Two-step sensitivity testing of parametrized and regionalized life cycle assessments: methodology and case study. Environ Sci Technol 47(11): 5660-7 (2013) 10.1021/es3050949.
11. Steubing, B., et al., The Activity Browser — An open source LCA software building on top of the brightway framework. Software Impacts 3 (2020) 10.1016/j.simpa.2019.100012.
12. Maier, S., R.-U. Dietrich, and Y. Rahmat, Identifying the Ideal Process Configuration for a Green Methanol Production Plant Dependent on Economic Boundary Conditions. 36th International Conference on Efficiency, Cost, Optimization, Simulation and Environmental Impact of Energy Systems (ECOS) (2023). 1422-1431.
13. Muñoz López, C.A., et al., A process simulator interface for multiobjective optimization of chemical processes. Computers & Chemical Engineering 109: 119-137 (2018) 10.1016/j.compchemeng.2017.09.014.

© 2025 by the authors. Licensed to PSEcommunity.org and PSE Press. This is an open access article under the creative commons CC-BY-SA licensing terms. Credit must be given to creator and adaptations must be shared under the same terms. See https://creativecommons.org/licenses/by-sa/4.0/



# Section 6

## Digitalization and AI

Systems & Control Transactions

**Research Article - Peer Reviewed Conference Proceeding**
ESCAPE 35 - European Symposium on Computer Aided Process Engineering
Ghent, Belgium. 6-9 July 2025
Jan F.M. Van Impe, Grégoire Léonard, Satyajeet S. Bhonsale,
Monika E. Polańska, Filip Logist (Eds.)

PSE PRESS

# Optimal Design of Process Equipment Through Hybrid Mechanistic-ANN Models: Effect of Hybridization

**Zaira Jelena Mosqueda-Huerta[a], Oscar Daniel Lara-Montaño[b], Fernando Israel Gómez-Castro[a]*, Manuel Toledano-Ayala[b]**

[a] Universidad de Guanajuato, Departmento de Ingeniería Química, Guanajuato, Guanajuato, México.
[b] Universidad Autónoma de Querétaro, Facultad de Ingeniería, Querétaro, Querétaro, México.
* Corresponding Author: fgomez@ugto.mx.

## ABSTRACT

Artificial neural networks (ANNs) have gained popularity in the last years as tools to develop data-driven models of chemical process units. However, representing a system only with such artificial intelligence models may lead to a loss in the comprehension of the occurring phenomena. Hybrid models allow combining the predictive capabilities of ANNs with the foundational knowledge of rigorous models. This study explores the impact of hybridization in designing and optimizing shell-and-tube heat exchangers, comparing a full ANN-based model with a hybrid model. The hybrid model incorporates ANN predictions for highly nonlinear components, such as heat transfer coefficients, while other calculations are performed using the rigorous Bell-Delaware model. To generate the necessary data, the rigorous model is solved under randomly selected conditions. Using Python, one ANN predicts the exchanger's cost, while another predicts the heat transfer coefficients. Both models are optimized using the differential evolution algorithm. The results indicate that the hybrid model produces designs with an approximately 67% lower standard deviation compared to the full ANN-based model when compared to the rigorous model's cost predictions. This highlights the hybrid model's ability to balance computational efficiency and accuracy, offering a promising approach for process design applications.

**Keywords**: artificial neural networks, hybrid models, optimal design.

## INTRODUCTION

Heat exchangers are essential components in the chemical industry. Among the various types of exchangers, shell-and-tube heat exchangers stand out for their broad acceptance due to their balance between volume and heat transfer area, as well as their ability to operate over a wide range of pressures and temperatures [1]. The design of these exchangers is typically performed using the Bell-Delaware method, a methodology based on highly nonlinear mathematical relationships that involves managing both discrete and continuous variables [2]. Due to the nature of equations that compose Bell-Delaware method, it represents a non-trivial optimization problem [3].

In recent years, artificial intelligence, particularly artificial neural networks (ANNs), has gained relevance in modeling and analyzing industrial process units. Artificial neural networks are data-driven structures widely used to model chemical process units, such as reactors [4] and separation units [5]. These tools allow the prediction of system behavior from data, analyzing how input variables affect system responses. Nevertheless, developing ANN-based models requires training data, which poses challenges in process design where the equipment does not yet exist and real-world data is unavailable. On the other hand, it is crucial to emphasize the importance of avoiding reliance solely on data-based models, as this might overlook the fundamental principles governing system behavior [6]. Hybrid models address this issue by combining the predictive capabilities of ANNs for complex interactions with the foundational knowledge of mechanistic models.

In this context, this work develops an ANN model to predict the cost of a shell-and-tube heat exchanger. Furthermore, a hybrid ANN model (ANN-H) is implemented, combining predictions of heat transfer coefficient

generated by an artificial neural network with the remaining design calculations, represented with the rigorous Bell-Delaware model.

This work focuses on the development and implementation of ANN and ANN-H models for the design and optimization of shell-and-tube heat exchangers. The goal is to explore methodologies for accurately predicting key parameters such as heat transfer coefficients and equipment costs based on design variables. To achieve this, ANN models are trained to analyze and predict complex relationships within the heat exchanger design, while a ANN-H model is developed to integrates the strengths of ANNs with traditional rigorous calculation techniques, such as the Bell-Delaware method. This hybrid approach leverages the ability of ANNs to predict highly nonlinear behaviors while maintaining the fundamental principles provided by mechanistic models, improving the overall accuracy of predictions.

Moreover, the study employs Bayesian optimization algorithms to determine the optimal architecture of the ANN models, ensuring accurate and reliable predictions. Subsequently, metaheuristic optimization algorithms are applied to identify the optimal values of design variables that minimize the heat exchanger cost, providing a comprehensive approach for cost-efficient design.

The results obtained from the ANN and ANN-H models are compared with the outputs of rigorous models to validate the effectiveness and reliability of the proposed methodologies. By integrating advanced machine learning techniques with traditional engineering approaches, this work seeks to bridge the gap between computational efficiency and the accuracy in heat exchanger design, offering an innovative path for process optimization in the chemical industry.

## METHODOLOGY

The study focuses on a heat exchanger with methanol in the shell and seawater in the tubes [5]. Methanol flows with inlet/outlet temperatures of 95 °C and 40 °C, respectively, and a mass flow rate of 27.8 kg/s. Seawater flows through the tubes with inlet/outlet temperatures of 25 °C and 40 °C, and a mass flow rate of 68.9 kg/s. The shell and tubes are made of carbon steel.

The methodology is developed in three main stages: data generation, model development, and optimization.

### Data Generation

To generate the necessary data for the artificial neural network, a shell-and-tube heat exchanger model was developed with 11 decision variables, each bounded by specific lower and upper limits. Among these, four variables are discrete, with their allowable values listed in Table 1, and seven are continuous, as detailed in Table 2.

**Table 1.** Allowed values for discrete design variables.

| Design variable | | Allowed value |
|---|---|---|
| Tube pitch | $P_t$ | $[1.25d_o, 1.5d_o]$ |
| Tube layout angle | $TL$ | $[30°, 45°, 90°]$ |
| Baffle cut | $B_c$ | $[25\%, 30\%, 40\%, 45\%]$ |
| Number of tube passes | $N_p$ | |

**Table 2.** Upper and lower limits for continuous variables.

| **Design variable** | | **Lower limit** | **Upper limit** |
|---|---|---|---|
| Shell diameter | $D_s$ | 0.3 m | 1.5 m |
| Spacing in central baffle | $L_{b,c}$ | 0.2 $D_s$ | 0.55 $D_s$ |
| Initial and final baffle spacing | $L_{b,i}, L_{b,o}$ | 1 $L_{b,c}$ | 1.6 $L_{b,c}$ |
| Diametrical distance of the hole between the shell and baffles | $\delta_{sb}$ | 0.01 $d_o$ | 0.1 $d_o$ |
| Diametrical distance between tubes and baffles | $\delta_{tb}$ | 0.01 $D_s$ | 0.1 $D_s$ |
| Beam tubes diameter | $D_{otl}$ | 0.8 ($D_s$ - $\delta_{sb}$) | 0.95 ($D_s$ - $\delta_{sb}$) |

The design process incorporated five constraints, including operational limits such as maximum pressure drops on both the tube and shell sides, maximum and minimum fluid velocities on the tube side, and a geometric constraint, as outlined in Table 3.

**Table 3.** Constraints used for the STHE design.

| **Variables** | | **Constraint** |
|---|---|---|
| Pressure drop in tubes | Pa | ≤ 70,000 |
| Pressure drop in shell | Pa | ≤ 70,000 |
| Flow rate in tubes | m/s | ≤ 0.5 |
| | | ≥ 3 |
| L/D Ratio | | ≤ 15 |

A total of 50,000 designs were generated randomly by assigning values to the decision variables within their defined ranges for continuous variables and selecting from the permissible values for discrete variables. Of these, only 11,643 designs satisfied the operational and geometric constraints established for the heat exchanger model. The remaining designs, which failed to meet these constraints, were discarded during the data cleaning to ensure the dataset's reliability.

### ANN Model Development and Implementation

The valid dataset comprising 11,643 designs was utilized to train and validate the ANN. In this context, constraint variables served as input features, while the total equipment cost, calculated based on the methodology outlined in [3], was the output target.

The development of the hybrid model involved

replacing the three traditional equations used to calculate the heat transfer coefficient on the tube side with a neural network model. Specifically:

- Equation 1 applies to the laminar flow regime ($Re_t < 2300$).
- Equation 2 is used for the transitional regime ($2300 \leq Re_t \leq 10{,}000$).
- Equation 3 corresponds to the turbulent regime ($Re_t > 10{,}000$).

$$h_t = \frac{k_t}{d_i}\left[1.86\left(\frac{Re_t Pr_t d_i}{L}\right)^{\frac{1}{3}}\right] \quad (1)$$

$$h_t = \frac{k_t}{d_i}\left[\frac{\frac{f_t}{2} Re_t Pr_t}{1.07 + 12.7\left(\frac{f_t}{2}\right)^{0.5}\left(Pr_t^{\frac{2}{3}} - 1\right)}\right] \quad (2)$$

$$h_t = \frac{k_t}{d_i} Re_t^{0.8} Pr_t^{\frac{1}{3}}\left(\frac{\mu_t}{\mu_w}\right)^{0.14} \quad (3)$$

These traditional equations introduce discontinuities at the transitions between Reynolds number domains. To address this, an ANN was employed to provide a smooth and continuous approximation of the overall heat transfer coefficient on the tube side.

Data for training the ANN were generated by randomly sampling values for tube length and diameter, resulting in 13,127 data points. These variables are fundamental inputs to the traditional correlations, ensuring comprehensive coverage of the Reynolds number ranges and enabling the ANN to capture system behavior across all operational domains.

## ANN Architecture Optimization

The optimal ANN architecture was determined using Bayesian optimization, exploring a predefined search space based on the parameters listed in Table 4. This optimization aimed to identify the configuration that maximizes the ANN's performance in terms of accuracy. The same optimization approach was applied to both the traditional and hybrid models to ensure consistency.

**Table 4.** Selection Parameters for ANN Architecture

| Parameter | Values |
|---|---|
| Number of Layers | 1 to 4 |
| Number of Neurons per Layer | 1 to 16 |
| Activation Function | ReLU, ELU, Leaky ReLU |
| Optimizer | Adam, SGD |

Once the optimal architecture was established, the ANN model was implemented in Python, leveraging machine learning libraries to construct and train the network. The model was designed to process the filtered dataset and predict the total equipment cost based on specific input variables for each design scenario.

## Training and Validation

The dataset was partitioned into training and validation sets, with 80% allocated for training and 20% for validation. This split ensured that the ANN could generalize effectively to unseen data. The training-validation process was conducted independently for each modeling approach, reinforcing robust performance and adequate generalization capability.

In the hybrid model, the ANN replaced the segment of the Bell-Delaware model responsible for calculating convective heat transfer coefficients. The ANN's predictions were seamlessly integrated into the overall cost estimation of the heat exchanger, enhancing the model's continuity and accuracy.

## Metaheuristic Optimization of Design Variables

Metaheuristic algorithms were employed through the MEALPHY library to identify the optimal values of the 11 design variables that minimize the heat exchanger cost. These algorithms iteratively explored the design space to converge on the most cost-effective configurations. The optimized design variable values were subsequently utilized in both the traditional and hybrid models to compute and compare heat exchanger costs, facilitating an evaluation of each methodology's predictive capabilities.

## Analysis and Validation

The performance of the ANN and hybrid ANN-H models was assessed by analyzing the accuracy and standard deviation of their predictions. Additionally, the costs calculated for the optimal design variables were compared between both models and validated against the rigorous Bell-Delaware model. This validation ensured that the proposed methodologies are applicable under real-world conditions, demonstrating their reliability and effectiveness in optimizing heat exchanger design.

# RESULTS

This section presents a comparative analysis of the outcomes derived from the two models developed in this study: the Artificial Neural Network (ANN) model and the Hybrid ANN-H model, which integrates the ANN with the rigorous Bell-Delaware model.

## Performance of the ANN Model

The ANN model was trained using a filtered dataset comprising 11,643 entries. The optimal architecture identified consists of an input layer with 16 neurons, followed by two hidden layers containing 10 and 16 neurons,

respectively, and an output layer.

Table 5 illustrates selected cost predictions from the ANN model alongside the corresponding values obtained from the rigorous Bell-Delaware model.

**Table 5.** Heat Exchanger Cost Comparison: Rigorous Model vs. ANN Predictions.

| Rigorous Model Cost [USD/year] | ANN Predicted Cost [USD/year] |
|---|---|
| 22,973.88 | 24,521.90 |
| 29,617.20 | 33,566.61 |
| 20,656.89 | 18,239.29 |
| 17,710.37 | 17,322.07 |
| 23,430.10 | 24,415.09 |
| 24,726.01 | 23,447.56 |
| 27,128.27 | 26,297.71 |
| 31,251.74 | 31,865.45 |
| 21,422.44 | 23,961.10 |
| 37,979.40 | 38,219.78 |

Figure 1 presents a scatter plot comparing the rigorous model costs against the ANN-predicted costs. The average standard deviation between the ANN predictions and the rigorous model costs is 1,079.591 USD/year, indicating a notable variability in the ANN's cost estimations relative to the rigorous model.

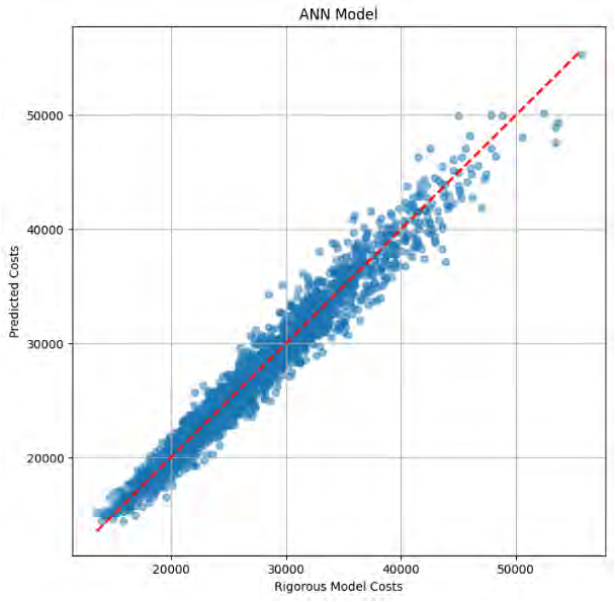



**Figure 1.** Comparison of rigorous model costs and ANN-predicted costs.

## Prediction of Convective Heat Transfer Coefficient

A separate ANN was trained to predict the convective heat transfer coefficient in the tubes using a dataset of 13,125 entries. The optimal architecture for this ANN comprises an input layer with 8 neurons, followed by three hidden layers with 14, 7, and 16 neurons, respectively, and an output layer.

Table 8 provides representative data used for training the ANN predicting the convective heat transfer coefficient.

**Table 6.** Sample Data for ANN Predicting Convective Heat Transfer Coefficient

| $L_t$ [m] | $d_i$ [m] | Flow rate in tubes [m/s] | h [W/m²] |
|---|---|---|---|
| 1.00 | 0.19 | 0.51 | 1662.47 |
| 2.12 | 0.40 | 0.92 | 2304.77 |
| 4.75 | 0.62 | 1.75 | 3519.76 |
| 7.37 | 0.92 | 2.57 | 4430.22 |
| 9.62 | 1.83 | 2.98 | 4346.38 |

Table 7 compares the convective heat transfer coefficients predicted by the ANN-H model with those calculated using the rigorous model. Figure 2 illustrates the relationship between the rigorous model's convective coefficients and those predicted by the ANN-H model. The average standard deviation between the two sets of values is 5.942 W/m²·K, suggesting a closer alignment between the ANN-H predictions and the rigorous model compared to the ANN model's performance in cost predictions.

**Table 7.** Convective Heat Transfer Coefficient Comparison: Rigorous Model vs. ANN-H Predictions

| Rigorous model convective coefficient [W/m²] | Predicted convective coefficient [W/m²] |
|---|---|
| 335.99 | 334.28 |
| 1 662.47 | 1 667.45 |
| 13 044.61 | 13 033.72 |
| 10 297.55 | 10 290.20 |
| 10 726.66 | 10 720.97 |
| 2 652.72 | 2 648.79 |
| 335.99 | 329.62 |
| 10 199.32 | 10 196.65 |
| 8 840.98 | 8 836.88 |
| 9 709.29 | 9 695.50 |

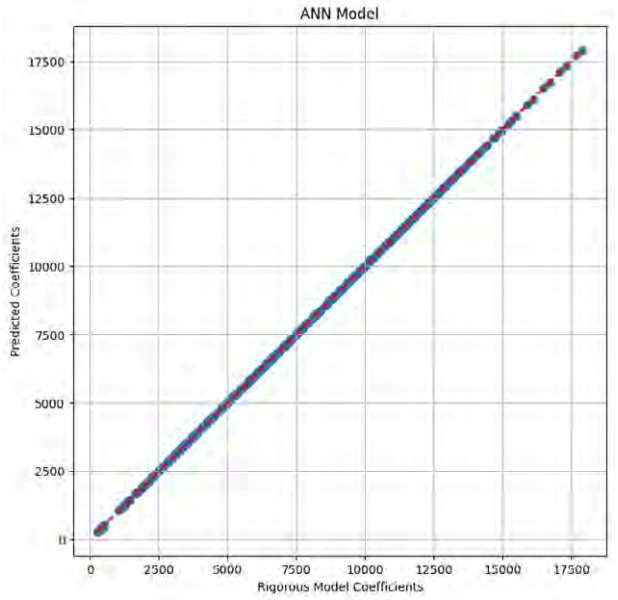



**Figure 2.** Comparison of rigorous model convective coefficients and ANN-H predicted coefficients.

## Performance of the Hybrid ANN-H Model

The Hybrid ANN-H model integrates the ANN to predict the convective heat transfer coefficients, thereby replacing the traditional equations in the rigorous Bell-Delaware model. The cost predictions from the ANN-H model are presented alongside the rigorous model costs in Table 8.

The ANN-H model exhibits an average standard deviation of 348.55 USD/year when compared to the rigorous model, which is significantly lower than the 1,079.59 USD/year observed in the ANN model. This reduction in variability indicates improved consistency and accuracy in cost predictions when utilizing the hybrid approach.

**Table 8.** Heat Exchanger Cost Comparison: Rigorous Model vs. ANN-H Predictions

| Rigorous model cost [USD/year] | ANN- H predicted cost [USD/year] |
|---:|---:|
| 29,617.20 | 30,038.76 |
| 20,656.88 | 21,333.41 |
| 17,710.36 | 18,678.41 |
| 23,430.09 | 23,815.72 |
| 24,726.01 | 25,351.33 |
| 27,128.27 | 27,346.88 |
| 31,251.73 | 31,655.29 |
| 21,422.44 | 21,903.92 |
| 37,979.39 | 38,235.07 |

## Optimization of Design Variables

Table 9 summarizes the optimal values of the design variables obtained through metaheuristic optimization for both the ANN and ANN-H models, along with the corresponding total costs.

**Table 9.** Optimal Design Variables and Costs: ANN vs. ANN-H Models

| Design variable | Optimal value (ANN) | Optimal value (ANN-H) |
|---|---|---|
| Shell diameter | 0.3 m | 0.3 m |
| Tube diameter | $d_o$-0.25in, $d_i$-0.194in | $d_o$-0.25in, $d_i$-0.194in |
| Tube pitch | 1.25 do | 1.25 do |
| Tube arrangement | 45° | 90° |
| Number of passes in the tubes | 1 | 4 |
| Baffle cut percentage | 25% | 45% |
| Spacing in central baffle | 0.2 $D_s$ | 0.2 $D_s$ |
| Initial and final baffle spacing | 1 $L_{b,c}$ | 1.036 $L_{b,c}$ |
| Diametrical distance of the hole between the shell and baffles | 0.01 $d_o$ | 0.1 $d_o$ |
| Diametrical distance between tubes and baffles | 0.01 $D_s$ | 0.09 $D_s$ |
| Beam tubes diameter | 0.948 ($D_s$ - $\delta_{sb}$) | 0.95 ($D_s$ - $\delta_{sb}$) |
| Cost (USD/year) | 13437.20 | 13 404.28 |

Both models suggest similar optimal values for most design variables, with notable differences in the tube arrangement angle and the number of tube passes. Specifically, the ANN model favors a 45° tube arrangement with a single tube pass, whereas the ANN-H model recommends a 90° arrangement with four tube passes. These variations reflect how the ANN-H model's integration of convective coefficient predictions influences the optimization process to achieve lower cost outcomes.

The comparative analysis indicates that the Hybrid ANN-H model consistently demonstrates lower variability in cost predictions compared to the standalone ANN model. The reduced standard deviation in the ANN-H model suggests a closer alignment with the rigorous Bell-Delaware model, thereby enhancing prediction reliability.

Furthermore, the optimization results reveal that while both models converge towards similar solutions for most design variables, the ANN-H model achieves marginally lower total costs. This outcome underscores the potential benefits of integrating ANN with traditional modeling approaches, particularly in achieving more accurate and reliable cost estimations.

## CONCLUSIONS

This study compared an Artificial Neural Network (ANN) model with a Hybrid ANN-H model for the design and cost optimization of shell-and-tube heat exchangers. The results indicate that the Hybrid ANN-H model achieves more accurate cost predictions, evidenced by lower average standard deviations than the standalone ANN model. This improvement is attributed to effectively integrating the rigorous Bell-Delaware model with the ANN, balancing accuracy and computational efficiency.

Despite these advantages, the Hybrid ANN-H model does not consistently match the computational efficiency of the rigorous model across all scenarios. In some cases, it may require additional computational resources, limiting its applicability where rapid calculations are necessary. Nevertheless, the Hybrid ANN-H model remains a viable alternative for scenarios where both predictive accuracy and computational efficiency are critical.

Overall, the findings demonstrate the potential of combining artificial neural networks with traditional engineering methodologies to enhance the design and analysis of industrial process units. This integration offers a balanced approach to managing computational costs while improving prediction accuracy, paving the way for more effective optimization in thermal system design.

## ACKNOWLEDGEMENTS

The authors acknowledge the financial support from Universidad de Guanajuato, Mexico, through project 189/2024. Additionally, CONAHCYT provided financial support through a postdoctoral fellowship granted to Oscar Daniel Lara Montaño (application number 4861420). The resources and academic environment provided by these institutions were fundamental to the successful completion of this research.

## REFERENCES

1. Sinnott RK. Chemical Engineering Design. Butterworth-Heinemann (2005).
2. Shah RK, Sekulic DP. Fundamentals of Heat Exchanger Design. John Wiley & Sons (2003).
3. Lara Montaño OD, Gómez Castro FI, Gutiérrez Antonio C. Comparison of the performance of different metaheuristic methods for the optimization of shell-and-tube heat exchangers. *Comput Chem Eng* 152: 107403 (2021). https://doi.org/10.1016/j.compchemeng.2021.107403
4. [Cerinski D, Baleta J, Mikulčić H, Mikulandrić R, Wang J. Dynamic modelling of the biomass gasification process in a fixed bed reactor by using the artificial neural network. *Clean Eng Technol* 1:100029 (2020). https://doi.org/10.1016/j.clet.2020.100029
5. Jawad J, Hawari AH, Zaidi S. Modeling of forward osmosis process using artificial neural networks (ANN) to predict the permeate flux. *Desalination* 484:114427 (2020). https://doi.org/10.1016/j.desal.2020.114427
6. Sansana J, Joswiak MN, Castillo I, Wang Z, Rendall R, Chiang LH, Reis MS. Recent trends on hybrid modeling for Industry 4.0. *Comput Chem Eng* 151: 107365 (2021) https://doi.org/10.1016/j.compchemeng.2021.107365

© 2025 by the authors. Licensed to PSEcommunity.org and PSE Press. This is an open access article under the creative commons CC-BY-SA licensing terms. Credit must be given to creator and adaptations must be shared under the same terms. See https://creativecommons.org/licenses/by-sa/4.0/



Systems & Control Transactions

**Research Article - Peer Reviewed Conference Proceeding**
ESCAPE 35 - European Symposium on Computer Aided Process Engineering
Ghent, Belgium. 6-9 July 2025
Jan F.M. Van Impe, Grégoire Léonard, Satyajeet S. Bhonsale,
Monika E. Polańska, Filip Logist (Eds.)

PSE PRESS

# Modelling of a Propylene Glycol Production Process With Artificial Neural Networks: Optimization of the Architecture

**Emilio Alba-Robles[a], Oscar Daniel Lara-Montaño[b], Fernando Israel Gómez-Castro[a*], Jahaziel Alberto Sánchez-Gómez[a], Manuel Toledano-Ayala[b]**

[a] Universidad de Guanajuato, Departamento de Ingeniería Química, Guanajuato, Guanajuato, México
[b] Universidad Autónoma de Querétaro, Facultad de Ingeniería, Querétaro, Querétaro, México
* Corresponding Author: fgomez@ugto.mx.

## ABSTRACT

Chemical process models often involve high non-linearity due to thermodynamic and kinetic relationships, with non-convex bilinear terms adding complexity to process optimization. Recently, data-driven models, particularly artificial neural networks (ANNs), have gained traction for representing chemical processing units. The predictive accuracy of ANNs depends on data quality, variable interactions, and network architecture, the latter being an optimization challenge itself. This study proposes and evaluates two strategies to optimize ANN architecture for modeling a propylene glycol production process from glycerol. The process includes a reactor and two distillation columns, with training data generated through simulation in Aspen Plus by varying design and operating variables. Two approaches are compared: random ANN structure generation and architecture optimization using the ant colony algorithm, a method suitable for discrete problems. Decision variables include the number of hidden layers and neurons per layer, with the objective of minimizing mean squared error. Both methods yield ANN predictions with high accuracy ($R^2$ > 99.9%), closely matching simulation data. However, the ant colony algorithm achieves a better fit despite slower convergence, demonstrating its effectiveness in fine-tuning ANN architecture for chemical process modeling.

**Keywords**: Artificial Intelligence, Artificial Neural Networks, Glycerol, Stochastic Optimization, Network Architecture

## INTRODUCTION

Rigorous models for process equipment are built upon well-established physical and chemical principles, such as design equations, mass and energy balances, thermodynamic relationships, and, in some cases, cost equations. These models enable the precise representation of system behavior across various operating conditions, offering a robust foundation for process analysis and optimization.

Despite their advantages—such as high accuracy, clear interpretability, and alignment with physical laws, as highlighted in numerous studies—rigorous models have significant limitations. Researchers have pointed out challenges including the high cost of constructing these models, particularly for large and complex systems. Additionally, they require a deep understanding of the system and often involve extensive fine-tuning to achieve accurate predictions [1]. Moreover, the computational demands of rigorous models can be prohibitive, especially when simulating intricate or highly dynamic processes.

These challenges have accelerated interest in data-driven models, which address many of these limitations. Data-driven science, often referred to as the fourth paradigm [2], is transforming how we approach research and problem-solving. Montáns et al. [3] highlight that, unlike rigorous models, data-driven approaches rely on vast amounts of empirical data to uncover patterns, trends, and insights, bypassing the need for exhaustive system-

specific knowledge. These methods enable faster model development and adaptation, particularly for complex, nonlinear systems.

The development of data-driven models is an area of significant interest in Process Systems Engineering. An example of this can be seen in the work by Kwon et al. [4], where data-driven models are applied to the analysis of processing units for controlling distillation columns. Among the various types of data-driven models, machine learning models stand out due to their ability to identify complex patterns without the need for explicit formulation.

Cavalcanti et al. [5] conducted an extensive review compiling a range of successful studies on the application of Artificial Intelligence (AI) in Process Engineering. This comprehensive study covers various fields, particularly showing how ANNs can replace complex phenomenological models, offering the advantage of reduced computational effort.

For an ANN model to perform satisfactorily, both the quantity and quality of the data used for training must be appropriate. Regarding quantity, the performance of ANN models is enhanced as the amount of data available for training increases [6]. Of course, the number of data points required will depend on the complexity of the system being modeled by the neural network. Likewise, the quality of the information used for training the network is crucial. The use of such strategies for process design applications presents a challenge, as the units necessary for generating data to train the network are not available. One strategy that can be employed under such circumstances is the use of rigorous models for data generation [7].

Recent research has focused on optimizing artificial neural network (ANN) architectures to enhance their predictive performance and computational efficiency. Evolutionary algorithms and metaheuristic approaches have been widely explored to automate the design of ANN structures, allowing for improved adaptability to complex systems [8]. In process modeling applications, strategies incorporating statistical criteria for model selection, such as the Akaike Information Criterion (AIC), have been employed to refine ANN architectures and enhance their predictive capabilities [9].

In this work, ANNs are proposed for modeling chemical processing units, employing two different strategies for architecture optimization. The first strategy relies on randomly generated configurations, while the second utilizes the ant colony optimization algorithm [10]. In both approaches, key performance parameters are recorded to enable a subsequent comparison of their effectiveness. The study begins with an overview of the case study, followed by a detailed description of the methodology used to generate the data and evaluate the proposed optimization strategies. Finally, the results are analyzed and discussed, highlighting the advantages of each approach.

## CASE STUDY

Sánchez-Gómez et al. [11] proposed various production schemes for propylene glycol, including conventional and reactive distillation-based configurations. In this study, the focus is on the conventional processing scheme, which is presented in Figure 1.

The feed to the process consists of a crude glycerol stream, represented as a 1:1 mass ratio mixture of glycerol and water, with a total flow rate of 100 kmol/h. This stream enters a reactor where glycerol reacts with hydrogen to produce propylene glycol. However, a secondary reaction also occurs, forming ethylene glycol as a by-product.

The reactor effluent is separated using a direct distillation sequence, where propylene glycol is obtained as the distillate product from the second column, achieving a molar purity of at least 99%. Further details about the process are provided in the work by Sánchez-Gómez et al. [11]. The initial conditions for the process are given in Table 1.

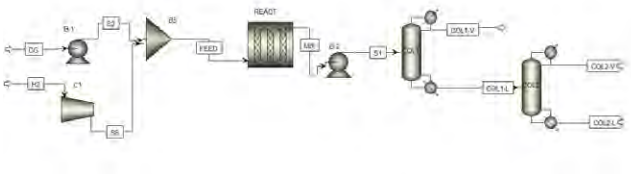


**Figure 1**. Propylene glycol production process from glycerol and hydrogen.

## METHODOLOGY

The analysis has been divided in two stages: (i) data generation, and (ii) development of artificial neural networks. These stages are described below.

### Information Generation

To gather sufficient data for neural network modeling, the analysis begins with an initial simulation in Aspen Plus of the conventional propylene glycol production process (Figure 1), operating under the initial conditions outlined in Table 1. The focus is on modeling the reactor and the two distillation columns using artificial neural networks.

Python programming enables interaction with Aspen Plus simulations [12]. A customized code has been developed to automatically access and modify variables within the simulation, identified as input variables in Table 1. The simulation was executed under various conditions, generating response variable values for 500 random designs.

To define feasible ranges for input variables,

**Table 1:** Manipulated and response variables for sensitivity analysis.

| Reactor | | | |
|---|---|---|---|
| **Manipulated** | **Initial Values** | **Range** | **Response** |
| Diameter | 0.1 m | 1 to 6 m | Heat Load |
| Length | 10 m | 3 to 10 m | Composition |
| Operation temperature | 225 °C | 200 to 250 °C | |
| **Columns 1 and 2** | | | |
| **Manipulated** | **Initial Values** | **Range** | **Response** |
| Number of Stages (NS) | 20 (COL1)<br>40 (COL2) | 10 to 35<br>25 to 50 | Diameter |
| Feed Stage | 5 (COL1)<br>20 (COL2) | From 2 to NS | Composition at bottoms and dome |
| Reboiler Heat Load | 320 kcal/s (COL1)<br>183 kcal/s (COL2) | 157 to 788 kcal/s<br>91 to 457 kcal/s | Condenser heat load |
| Reflux ratio | 0.5 (COL1)<br>2.6 (COL2) | 0.1 to 10 | Temperature at S1, S2, SN and SN-1 |

evaluation intervals were established based on the initial process conditions (Table 1), ensuring the design and operational parameters align with practical standards.

Non-converging or thermodynamically inconsistent simulations were filtered out, leaving a dataset of 351 valid simulations for subsequent economic analysis. For each case, the total annualized cost (TAC) of the process was calculated using Guthrie's method, annualizing equipment costs over 10 years [13].

At the end of this process, the dataset is ready for training and testing the neural networks. An important aspect of the data used to train an artificial neural network is its quality. In this case, the data to be used meets this characteristic, as they come from rigorous simulations conducted in a commercial simulator, Aspen Plus. This simulator is widely recognized in the industry for its ability to accurately and reliably model chemical processes. By using such a simulator, it is ensured that the generated data are representative of actual operational conditions, if adequate datasets and sub-models are employed.

## Development of Artificial Neural Networks (ANNs)

To determine whether the generated data was sufficient, an ANN was developed and trained using Python and the TensorFlow library. For this initial evaluation, a network with two hidden layers, each containing 32 neurons, was employed. The Adam optimization algorithm was used to adjust the weights of the connections between neurons, with the ReLU (Rectified Linear Unit) activation function. In all cases, the output variable was the total annualized cost (TAC) of the equipment being modeled. The dataset was split into training and validation data, using percentages of 80% and 20%, respectively. The results of this preliminary assessment were satisfactory, indicating that the amount of data generated was adequate.

The next step involves identifying the network configuration that minimizes the mean squared error (MSE) of the predictions across the entire dataset. The MSE was quantified using the following objective function:

$$MSE = \frac{1}{n}\sum_{i=1}^{n}(real_i - pred_i)_i^2 \quad (1)$$

Two strategies were evaluated to solve this optimization problem:

(i) Random generation of network architectures.

(ii) A metaheuristic optimization algorithm based on the Ant Colony Optimization (ACO) approach.

### Random Generation

The random generation strategy is widely used as an effective approach for identifying the optimal neural network architecture [14]. This strategy begins by defining the limits for the number of layers and the number of neurons per layer. A code was implemented to randomly generate network architectures within these limits, train them, and evaluate their performance using MSE as the primary metric. Among all evaluated architectures, the one with the lowest MSE was selected. A total of 150 network architectures were tested, with additional performance metrics recorded, such as the coefficient of determination ($R^2$), prediction error percentage, and computation time.

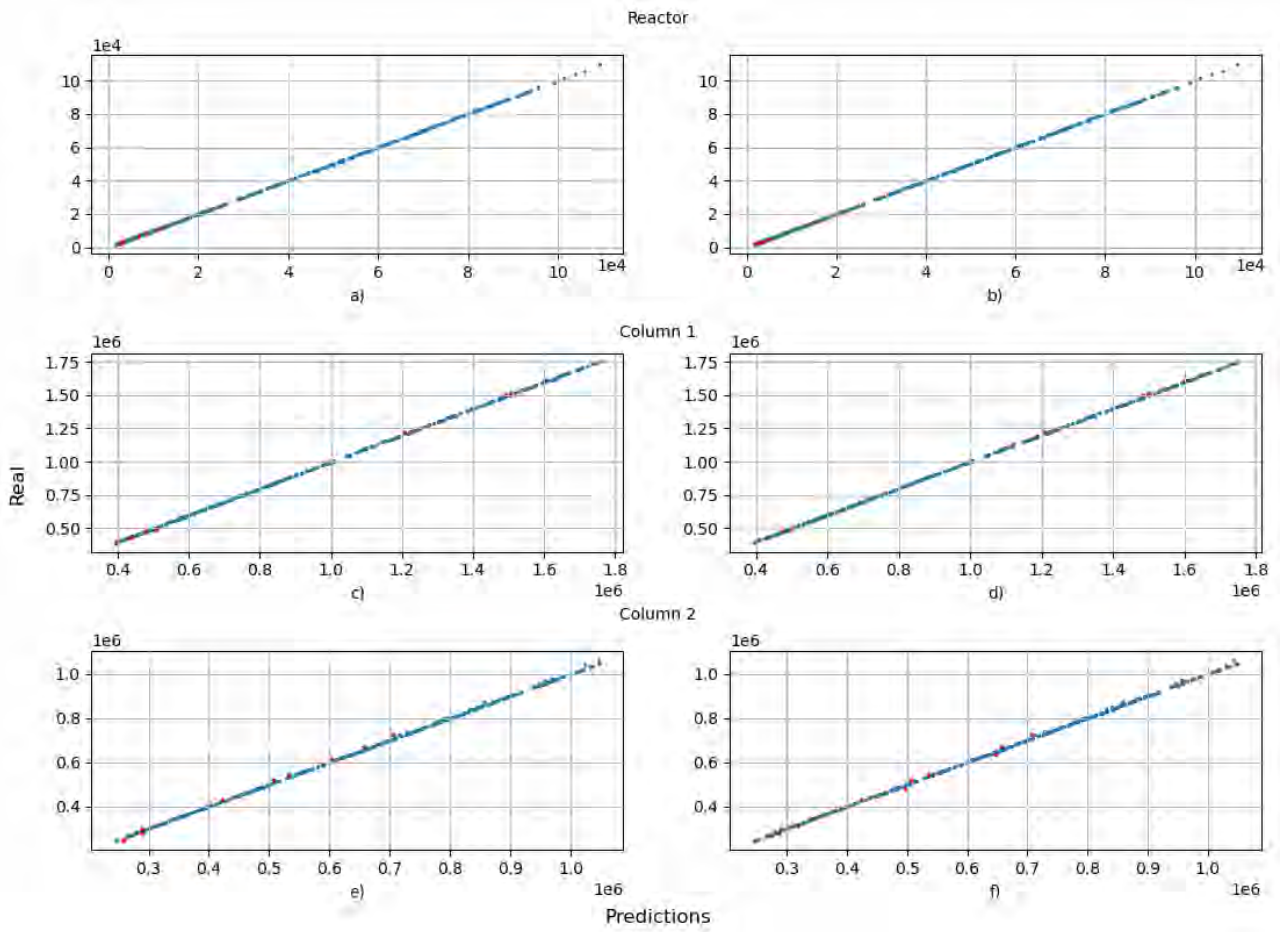



**Figure 2**. Rigorous simulation data (y-axis) vs predictions (x-axis). (a) Reactor with ACO, (b) Reactor with RS, (c) Column 1 with ACO, (d) Column 2 with ACO, (e) Column 2 wirh RS.

### Metaheuristic Optimization Algorithm

Existing ACO algorithm implementations, such as the ACOR algorithm in the *Mealpy* library [15], has been considered. This version of ACOR provides solutions for both integer and continuous variables. However, due to specific needs in this study, the original Ant Colony Optimization algorithm was implemented in Python to address integer-based decisions. The algorithm parameters, along with the ranges for decision variables, are summarized in Tables 2 and 3. These last values were used consistently across both solution strategies.

The number of ants and iterations was set to ensure a total of 150 networks were trained, enabling a fair comparison between the random generation strategy and the metaheuristic approach. Just as in the random generation strategy, metrics such as MSE, $R^2$, prediction error percentage, and computational time were recorded and used to evaluate and compare the performance of both approaches.

## RESULTS

As a result of the analysis conducted six neural network models were obtained, two for each process unit under study, corresponding to each architecture optimization strategy.

Figure 2 shows a comparison of the predictions obtained from both strategies. The data obtained through the Ant Colony Optimization algorithm is presented in the left column, while the corresponding results from Random Search are shown on the right. For each case, the 10 predictions with the highest error percentages can be observed as red points.

**Table 2:** Parameters for the Ant Colony Optimizer.

| Strategy | Iterations | Population | n_best | decay | alpha | beta |
|---|---|---|---|---|---|---|
| ACO | 25 | 6 | 5 | 0.95 | 1 | 1 |
| RG | 150 | - | - | - | - | - |

**Table 3**: Ranges for decision variables.

| Variable | Range |
|---|---|
| Number of layers | [1, 4] |
| Number of neurons | [1, 100] |

Table 4 summarizes the performance measures recorded for each model, as well as the architecture that minimized the MSE. In the last column (Architecture), the first number represents the number of hidden layers, while the information in brackets represents the number of neurons per layer. Among the generated models, only the reactor model obtained through the random search strategy exhibited predictions with an error percentage greater than 5%. In contrast, the remaining models predicted across the entire dataset with an error below 5%. In terms of the values of $R^2$, values higher than 99.9% are obtained for all the cases. However, it is observed that the Ant Colony Optimizer allowed faster convergence, particularly for the model of the second distillation column. It is important to mention that, for both strategies, a high number of neurons per layer are obtained. This is a relevant aspect to be considered for future research, since it is desired to obtain models with a good fitting, but with simpler architectures.

## CONCLUSIONS

In this study, artificial neural networks are used to represent the performance of equipment from a chemical process, particularly the production of propylene glycol from renewable glycerol. Six artificial neural network models were obtained, each achieving accuracy greater than 99%. Several parameters were recorded to analyze their performance and subsequently compare the strategies.

Overall, the random architecture generation strategy yielded slightly better results in terms of MSE and $R^2$. However, the Ant Colony Optimizer required less time than the random search approach to determine the optimal architecture.

## ACKNOWLEDGEMENTS

The authors acknowledge the financial support from Universidad de Guanajuato, Mexico, through project 189/2024. Additionally, CONAHCYT provided financial support through a postdoctoral fellowship granted to Oscar Daniel Lara Montaño (application number 4861420). The resources and academic environment provided by these institutions were fundamental to the successful completion of this research.

## REFERENCES

1. Bikmukhametov T, Jäschke J. Combining machine learning and process engineering physics towards enhanced accuracy and explainability of data-driven models. *Comput Chem Eng* 138: 106834 (2020). https://doi.org/10.1016/j.compchemeng.2020.106834
2. Hey T, Tansley S, Tolle K. The Fourth Paradigm: Data-Intensive Scientific Discovery. Microsoft Research (2009)
3. Montáns FJ, Chinesta F, Gómez-Bombarelli R, Kutz JN. Data-driven modeling and learning in science and engineering. *C R Mécanique* 347: 845–855 (2019). https://doi.org/10.1016/j.crme.2019.11.009
4. Kwon H, Oh KC, Choi Y, Chung YG, Kim J.

**Table 4:** Performance measures recorded for each model.

| Model | MSE | $R^2$ | %e (top1) | Computational time (s) | Architecture |
|---|---|---|---|---|---|
| Reactor AC | 17678.7572 | 0.9999788 | 3.8471 | 12270.27 | 4 [76] |
| Reactor RS | 13854.5483 | 0.9999834 | 8.2299 | 12501.10 | 4 [89] |
| Column 1 AC | 6670628.1656 | 0.9999589 | 4.8744 | 12767.27 | 4 [78] |
| Column 1 RS | 6084556.8997 | 0.9999625 | 1.3685 | 15123.15 | 4 [79] |
| Column 2 AC | 10504337.1583 | 0.9997871 | 4.3230 | 12196.61 | 4, [95] |
| Column 2 RS | 10131389.0314 | 0.9997945 | 3.4354 | 12200.67 | 4 [93] |

Development and application of machine learning-based prediction model for distillation column. *Int J Intell Syst* 36:1970-1997 (2021). https://doi.org/10.1002/int.22368

5. Cavalcanti FM, Kozonoe CE, Pacheco KA, De Brito Alves RM. Application of Artificial Neural Networks to Chemical and Process Engineering. IntechOpen (2021).
6. Aggarwal CC. Neural Networks and Deep Learning: A Textbook. Springer Nature (2023).
7. Mosqueda-Huerta ZJ, Lara-Montaño OD, Toledano-Ayala M, Gómez-Castro FI. Desarrollo de modelos de red neuronal artificial para el diseño de intercambiadores de calor de tubos y coraza. *Avances en Ingeniería Química* 3:PRO75-PRO80 (2024).
8. Ünal HT, Başçiftçi F. Evolutionary design of neural network architectures: a review of three decades of research. *Artif Intell Rev* 55:1723-1802 (2022). https://doi.org/10.1007/s10462-021-10049-5
9. Hernández-Vargas EA, Sánchez-Ramírez E, De La Fuente AR, Calderón-Alvarado MP, Segovia-Hernández JG. Advancing neural network architectures for time series forecasting: A sustainable approach to intensified biobutanol production. *Chem Eng Process* 194:109603 (2023). https://doi.org/10.1016/j.cep.2023.109603
10. Zhao H, Zhang C, Zheng X, Zhang C, Zhang B. A decomposition-based many-objective ant colony optimization algorithm with adaptive solution construction and selection approaches. *Swarm Evol Comput* 68:100977 (2022). https://doi.org/10.1016/j.swevo.2021.100977
11. Sánchez-Gómez JA, Gómez-Castro FI, Hernández S. Design and intensification of the production process of propylene glycol as a high value-added glycerol derivative. *Comput Aided Chem Eng* 52:1915-1920 (2023). https://doi.org/10.1016/B978-0-443-15274-0.50304-8
12. ten Hagen, R. W. AspenPlus Python Interface (Version 2.1) [Computer software] (2022). https://github.com/YouMayCallMeJesus/AspenPlus-Python-Interface
13. Turton R, Shaeiwitz JA, Bhattacharyya D, Whiting WB. Analysis, Synthesis, and Design of Chemical Processes. Pearson Professional (2018).
14. Géron A. Hands-On Machine Learning with Scikit-Learn, Keras, and TensorFlow: Concepts, Tools, and Techniques to Build Intelligent Systems. O'Reilly Media (2019).
15. Van Thieu N, Mirjalili S. MEALPY: An open-source library for latest meta-heuristic algorithms in Python. *J Syst Archit* 139:102871 (2023). https://doi.org/10.1016/j.sysarc.2023.102871

© 2025 by the authors. Licensed to PSEcommunity.org and PSE Press. This is an open access article under the creative commons CC-BY-SA licensing terms. Credit must be given to creator and adaptations must be shared under the same terms. See https://creativecommons.org/licenses/by-sa/4.0/



Systems & Control Transactions

**Research Article - Peer Reviewed Conference Proceeding**
ESCAPE 35 - European Symposium on Computer Aided Process Engineering
Ghent, Belgium. 6-9 July 2025
Jan F.M. Van Impe, Grégoire Léonard, Satyajeet S. Bhonsale,
Monika E. Polańska, Filip Logist (Eds.)

PSE PRESS

# Developing a Digital Twin System Based on a Physics-informed Neural Network for Pipeline Leakage Detection

**Wei-Shiang Lin[a], Yi-Hsiang Cheng[b], Zhen-Yu Hung[b], and Yuan Yao[a]***

[a] Department of Chemical Engineering, National Tsing Hua University, Hsinchu, Taiwan
[b] Material and Chemical Research Laboratories, Industrial Technology Research Institute, Hsinchu, Taiwan
* Corresponding Author: yyao@mx.nthu.edu.tw.

## ABSTRACT

As the demand for resources continues to grow, pipelines have become critical for transporting water, fossil fuels, and chemicals. Monitoring pipeline systems is essential, as leaks can lead to severe environmental damage and safety hazards. This study aims to develop a pipeline leakage detection system based on digital twin technology and Physics-Informed Neural Networks (PINNs). By embedding physical principles, such as the continuity and momentum equations derived from the Navier-Stokes equation, into the neural network's loss function, the model can predict pressure and flow dynamics with high accuracy while adhering to physical constraints. PINNs are particularly advantageous as they require minimal data, maintain physical consistency, and provide reliable interpretations, making them well-suited for addressing pipeline safety challenges. The model is designed to simulate fluid dynamics under normal operating conditions, with deviations in prediction errors signaling potential leaks. Statistical analysis of these errors is used to define control limits, establish rejection regions, and create control charts for leak detection. The detection system is further validated using field data to ensure reliability. By combining physical modeling and neural networks, this approach enhances the accuracy and interpretability of leakage detection, laying a solid foundation for an efficient pipeline monitoring solution.

**Keywords**: Pipeline leakage detection, Physics-informed neural networks, Surrogate model, Industrial safety

## INTRODUCTION

As modern society's demand for energy and resources continues to grow, pipeline transportation has become a critical foundation for industrial and domestic supply. However, pipeline leaks not only pose a significant threat to the environment through severe pollution but also endanger the safety of nearby residents and industrial surroundings. Furthermore, such incidents can compromise the quality of transported materials, with ruptured pipelines potentially leading to product contamination. Therefore, the monitoring and control of pipeline systems are of utmost importance.

Current pipeline leakage detection technologies can be broadly classified into two categories: hardware-based methods and software-based methods [1]. Hardware-based methods utilize equipment to detect leaks and their locations. Common techniques include acoustic sensing, fiber optic cables, ground-penetrating radar, gas injection, and infrared thermography. For example, acoustic sensing detects leaks by capturing the vibrations or sound waves generated by high-pressure fluid escaping from the pipeline and converts these signals into electronic data to analyze the leak's size and location [2]. Fiber optic cables, installed along pipeline lengths, change their transmission characteristics when exposed to liquid. Specially designed hydrophones then detect and analyze these signals to pinpoint the leak's location [3]. Infrared thermography identifies abnormal temperature variations in the pipeline environment through real-time thermal detection [4]. While these methods can achieve high accuracy, they often involve high operational costs, complex maintenance, and limited detection ranges, making them less practical for large-scale pipeline systems.

On the other hand, software-based methods rely on models or algorithms to detect and locate leaks using sensor data (e.g., pressure, flow rate, and temperature).

These methods generally require fewer sensors, resulting in lower maintenance costs. Software-based techniques can be divided into two main categories: model-based and data-driven methods. Model-based approaches use theoretical formulas from fluid dynamics to compare computed and measured values, where significant deviations indicate leaks. An example is the Real-Time Transient Model (RTTM) [5, 6]. Data-driven methods include support vector machines [7], convolutional neural networks [8], and wavelet transforms [9], leveraging machine learning, deep learning, anomaly detection, and time series analysis to learn normal system behavior from historical data and detect anomalies indicative of leaks. Meanwhile, purely data-driven (model-based) approaches often require extensive training data or fail to ensure physical consistency in dynamically changing environments. While effective in handling high-dimensional, nonlinear systems, data-driven methods often lack physical interpretability.

This study aims to develop a Physics-Informed Neural Network (PINN) that combines physical knowledge with data-driven approaches for accurate pipeline leakage detection. PINN, introduced by Raissi et al. [10], consists of a neural network for data fitting and a loss function incorporating physical information. By minimizing both prediction and PDE losses, PINN ensures that the model aligns with real-world data and adheres to physical constraints, offering interpretability and reliability. Automatic differentiation (AD) enables efficient computation of partial derivatives during training. In this study, the Navier-Stokes equations, describing fluid pressure and flow variations in the pipeline, are incorporated into the PINN loss function, capturing pipeline dynamics through continuity and momentum equations to enhance leakage detection accuracy. By utilizing only upstream and downstream flow and pressure sensors, our approach reduces operational costs by eliminating the need for expensive hardware, requires minimal maintenance compared to traditional sensor-intensive techniques, enhances long-range leak detection by leveraging both physical knowledge and machine learning capabilities, and ensures physical interpretability, improving reliability in real-world applications.

## METHODOLOGY

The schematic diagram of the pipeline system is illustrated in Figure 1. This underground pipeline, designed to transport liquid fluids, extends over a total length of 39.68 kilometers.

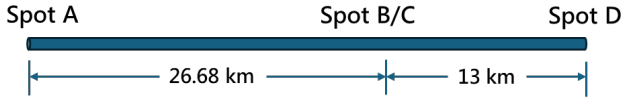



**Figure 1.** Schematic diagram of the pipeline system.

To achieve the goal of leak detection, it is essential to establish an effective leak detection process, with the logic depicted in Figure 2. By training a PINN model using datasets from normal operating conditions, the model is designed to describe the fluid dynamics within a leak-free pipeline. When the input data provided to the model reflects flow rates and pressures under leak conditions, a statistically significant error arises between the model's predictions and the actual values. Therefore, leak occurrence can be detected by applying statistical control to the prediction errors.

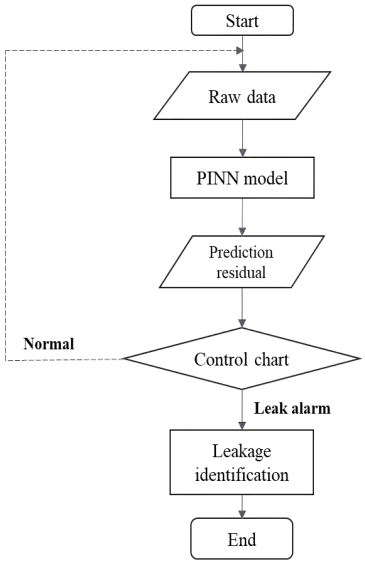



**Figure 2.** Flow chart for leak detection.

### Physics-informed neural networks

To develop a PINN-based surrogate model for predicting pipeline transport variations, it is essential to identify an appropriate physical model and embed it into the loss function to ensure the model adheres to expected physical principles. Considering that the target of this model is to predict the transport behavior of the fluid, the one-dimensional Navier-Stokes equations are employed as the governing equations. These equations describe the motion of fluids (liquids or gases) based on Newton's second law of motion and are derived from the principles of mass conservation and momentum conservation for fluids. The equations are described as follows[11]:

$$\frac{\partial \rho}{\partial t} + \frac{\partial \rho u}{\partial x} = 0 \tag{1}$$

$$\rho \frac{\partial u}{\partial t} + \rho u \frac{\partial u}{\partial x} + \frac{\partial P}{\partial x} + \frac{f \rho u |u|}{2D} = 0 \tag{2}$$

where $u$ is the cross-section averaged velocity (m/s), $\rho$ the density (kg/m$^3$), $p$ pressure (Pa), $f$ (dimensionless) the Darcy friction factor, $D$ (m) pipe diameter.

To establish a PINN model for flow states governed by partial differential equations (PDEs), a deep neural

network (DNN) is first constructed as a surrogate model for solving PDEs. In this study, a feedforward neural network (FFNN) is employed due to its simplicity, which is sufficient for most PDE problems. Considering that the objective at this stage is to identify abnormal transport states, the model must be capable of recognizing the transport state over continuous time under different initial conditions. To enhance the generalization performance of the model, the input layer includes position $x$, time $t$, initial flow velocity condition $u_{IC}$, upstream-downstream pressure difference $\Delta P$, and pressure $P$. The model predicts the output $\hat{u}(x, t, u_{IC}, \Delta P, P, \theta)$, where $\theta$ is a vector containing all weights and biases within the neural network, which are optimized using the gradient descent algorithm during backpropagation. Variables with a hat denote those computed through the neural network. Furthermore, considering that this case involves an inverse problem, the term $f$ in the equations is treated as a model parameter to be estimated.

Ensuring the model's outputs satisfy both real-world data and the physical laws represented by equations (1) and (2) requires minimizing the residuals $g_1$ and $g_2$ as specified in Figure 3. Smaller residual values indicate a high degree of conformity to the underlying physical principles. The time and spatial derivatives are computed using the AD method [12], which eliminates the need for discretizing the computational domain to solve partial differential equations. This approach differs from traditional methods such as the method of characteristics or finite difference methods.

A notable feature of the PINN model is the setup of collocation points, $\{x_f, t_f, u_{ICf}, \Delta P_f, P_f\}$. These points are strategically chosen across different spatial and temporal locations to evaluate the loss based on the problem's requirements. Incorporating these collocation points into the PINN model allows for the calculation of residuals $g_1$ and $g_2$ within the loss function, ensuring that the outputs at these points align with the governing partial differential equations. This enables the neural network to leverage physical knowledge while minimizing the reliance on large datasets of real-world data.

The architecture of the model, as illustrated in Figure 3, consists of an input layer that includes position, time, initial flow velocity condition, upstream-downstream pressure difference, and pressure. The output layer predicts flow velocity. The loss function comprises two components: the error between real-world data and predicted values, and the residual error from the governing partial differential equations. In this study, the weights of these components are set as α = 1 and β = 0.1.

The model configuration includes eight hidden layers, each containing 20 neurons. The activation function tanh introduces nonlinearity. For optimization, a two-stage strategy is applied: initial training is performed using the Adam optimizer, followed by fine-tuning with the L-BFGS-B optimizer to complete the training process.

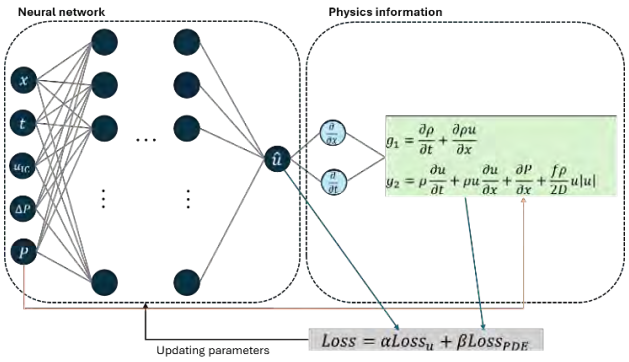



**Figure 3.** Model structure for PINN.

## Dataset splitting and performance evaluation

The dataset used in this study comprises transport data with varying flow rates collected over multiple days of continuous operation. This approach ensures sufficient training of the model and enhances its accuracy and robustness in anomaly detection. The dataset is segmented into fixed windows of 1000 consecutive seconds to create distinct samples, ensuring consistency and precision in the analysis. These samples are further divided into training, validation, and testing sets.

To evaluate the predictive accuracy of the model, the coefficient of determination ($R^2$) and the root mean square error (RMSE) are adopted as evaluation metrics. The $R^2$ measures the model's ability to explain the variance in the data. A value closer to 1 indicates that the model more accurately captures the variability in the data, demonstrating stronger explanatory power. RMSE, on the other hand, quantifies the difference between predicted and actual values in terms of absolute error, providing a direct measurement of the model's accuracy. Lower RMSE values signify that the model's predictions are closer to the actual values, offering a quantitative reflection of the model's predictive performance. By combining these two metrics, the model's performance can be effectively compared, providing a basis for further refinement and improvement.

$$R^2 = 1 - \frac{\sum_{i=1}^{n}(y_i - \hat{y}_i)^2}{\sum_{i=1}^{n}(y_i - \bar{y})^2} \tag{3}$$

$$RMSE = \sqrt{\frac{1}{n}\sum_{i=1}^{n}(y_i - \hat{y}_i)^2} \tag{4}$$

# RESULTS AND DISCUSSIONS

For confidentiality purposes, the flow rate data of the fluid has been normalized. After training the PINN model, the prediction results are shown in Figure 4, which displays the diagonal plots of the actual versus predicted values. In this part, the upstream and downstream flow

rate is separately denoted as Q1 and Q4. The model demonstrates excellent prediction performance for both upstream and downstream flow rates across all datasets, with detailed evaluation metrics provided in Table 1.

Since the dataset includes data from multiple days, variations in transportation conditions or operational states across different days result in the diagonal plots being distributed across different ranges, with each cluster representing data from a specific period. It is important to note that, as the dataset was split into six groups, the calculation of the $R^2$ value may be biased. Specifically, the denominator of $R^2$, i.e., the total sum of squares, is relatively large, making the $R^2$ value closer to 1, which could potentially mislead the results. Therefore, relying solely on $R^2$ to evaluate the model's performance is not entirely accurate. Instead, RMSE provides a more realistic measure of the model's effectiveness. The RMSE values for Q1 are 0.0005, 0.0007, and 0.0004 for the training, validation, and testing datasets, respectively. Similarly, the RMSE values for Q4 are 0.0007, 0.0005, and 0.0005 for the same datasets. These results indicate that the model effectively minimizes prediction errors and achieves an exceptional level of performance.

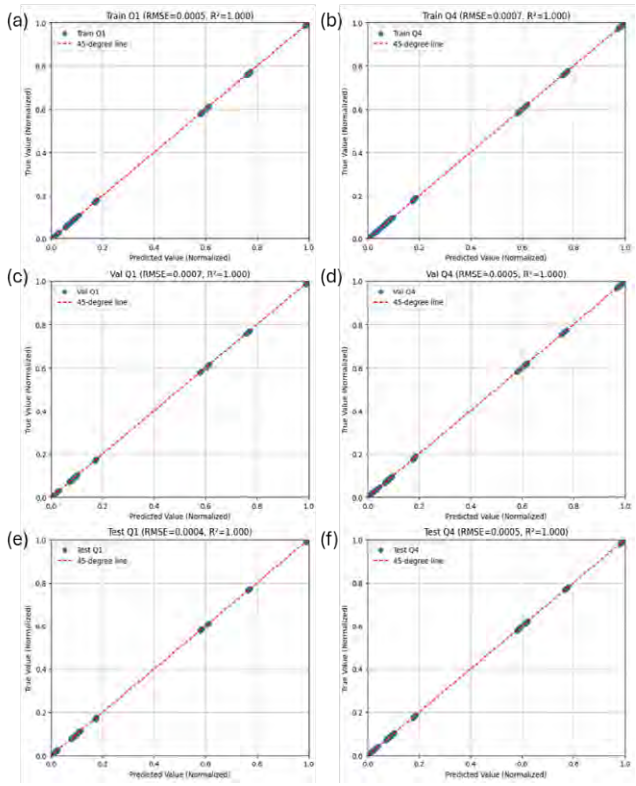



**Figure 4.** Predicted vs. actual values: (a) upstream flow in the train set, (b) downstream flow in the train set, (c) upstream flow in the valid set, (d) downstream flow in the valid set, (e) upstream flow in the test set, and (f) downstream flow in the test set.

**Table 1:** Training, validation, and test performance.

| Dataset | $R^2$(Q1/Q4) | RMSE(Q1/Q4) |
|---|---|---|
| Train | 1.000/1.000 | 0.0005/0.0007 |
| Valid | 1.000/1.000 | 0.0007/0.0005 |
| Test | 1.000/1.000 | 0.0004/0.0005 |

To establish a statistical process control (SPC) chart for anomaly detection, this study selects the validation set for residual sampling. The method involves calculating a range that corresponds to 99.73% of the data distribution, analogous to the 6σ range commonly associated with a normal distribution. This range facilitates subsequent anomaly detection and management. The sampling results are shown in Figures 5 and 6. The residual range of upstream flow lies between -0.0227 and 0.0241, while the residual range of downstream flow is between -0.0272 and 0.0306. These ranges serve as benchmarks for subsequent statistical control, used to detect anomalies based on the model's prediction results. If the residuals of the prediction exceed these ranges, they are considered anomalies, triggering alarms.

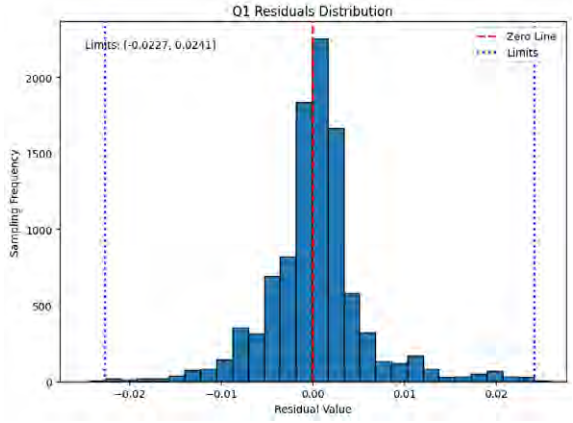



**Figure 5.** Histograms and estmated control limits of the upstream prediction residuals.

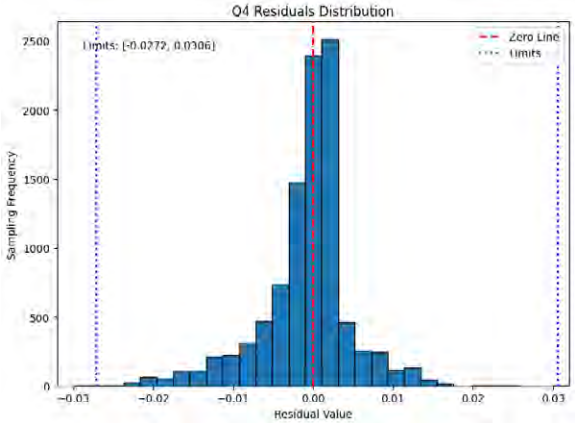



**Figure 6.** Histograms and estmated control limits of the downstream prediction residuals.

Initially, SPC was performed on normal data that the

model had not seen before. Figures 7 and 8 illustrate the monitoring results for upstream and downstream data, respectively. In the control charts, the x-axis represents time, and the y-axis represents the model's prediction residuals. The blue line indicates the actual residual results, while the red dashed lines represent the upper and lower control limits.

From the figures, it is evident that within the selected 1000-second range, the results show that all normal data fall within the in-control range. Additionally, the actual flow rate prediction results over time are shown in Figure 9. For the upstream and downstream flow data, the $R^2$ values reached 1.000 and 0.997, respectively. This demonstrates that the model exhibits high accuracy and reliability in predicting under normal transportation conditions.

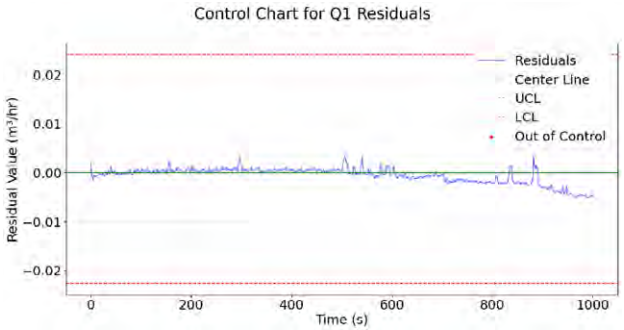



**Figure 7.** Control chart of upstream residuals under normal transportation conditions.

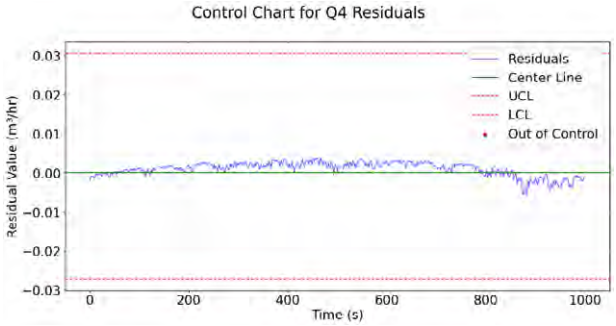



**Figure 8.** Control chart of downstream residuals under normal transportation conditions.

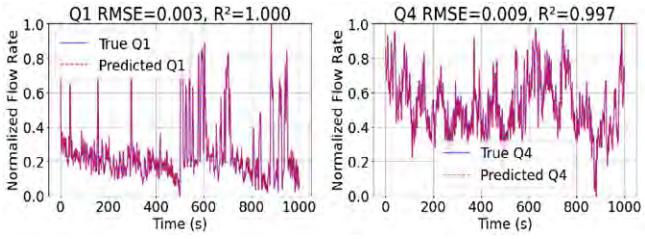



**Figure 9.** Comparison of predicted and true flow rates under normal transportation conditions at different positions in the pipeline system. (a) Flow rate at upstream, and (b) Flow rate at downstream

In the anomaly detection analysis, the statistical control results shown in Figures 10 and 11 clearly reveal abnormal conditions. The upstream data exceed the upper control limit, while the downstream data fall below the lower control limit. A significant number of data points lie outside the control limits, indicating notable differences compared to normal data and suggesting potential anomalies during this time period. Using the control chart, these leakage features can be identified and extracted. Through the above experiments, this study demonstrates the significant impact of leakage events on the distribution of upstream and downstream pressure and flow rate data. The model accurately captures the abnormal behavior during leakage periods.

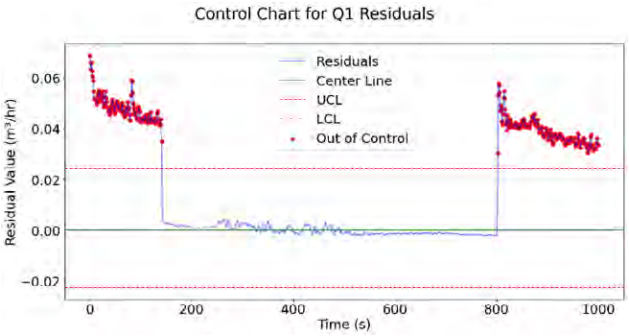



**Figure 10.** Control chart of upstream residuals under leakage conditions.

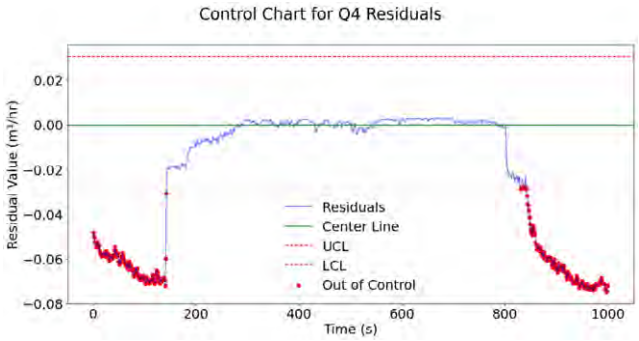



**Figure 11.** Control chart of downstream residuals under leakage conditions.

## CONCLUSIONS

This study developed a pipeline leakage detection system based on Physics-Informed Neural Networks (PINNs), integrating the Navier-Stokes equations of fluid dynamics with deep learning techniques to achieve effective monitoring of pipeline systems. The results demonstrate that the model achieved $R^2$ values close to 1.000. Furthermore, the RMSE values were 0.0005/0.0007 for the training dataset, 0.0007/0.0005 for the validation dataset, and 0.0004/0.0005 for the testing dataset, confirming the high accuracy of its pre-

dictions. Statistical process control chart based on residual analysis, enabling effective differentiation between normal and abnormal states. For normal condition monitoring, the model exhibited strong predictive capability, with residuals from the training, validation, and testing sets remaining within the control limits. For anomaly detection, the model successfully identified the occurrence of leaks, with a significant number of data points exceeding the control limits. By combining the interpretability of physical models with the predictive power of machine learning, this study provides an innovative solution for industrial pipeline safety monitoring, offering a valuable reference for future pipeline system surveillance and diagnosis.

## REFERENCES


1. Yuan J, Mao W, Hu C, Zheng J, Zheng D, and Yang Y. Leak detection and localization techniques in oil and gas pipeline: A bibliometric and systematic review. *Eng Fail Anal* 146:107060 (2023) https://doi.org/10.1016/j.engfailanal.2023.107060
2. Li Z, Zhang H, Tan D, Chen X, and Lei H. A novel acoustic emission detection module for leakage recognition in a gas pipeline valve. *Process Saf Environ Prot* 105:32-40 (2017) https://doi.org/10.1016/j.psep.2016.10.005
3. Tanimola F, and Hill D. Distributed fibre optic sensors for pipeline protection. *J Nat Gas Sci Eng* 1(4-5):134-143 (2009) https://doi.org/10.1016/j.jngse.2009.08.002
4. Manekiya MH, and Arulmozhivarman P. Leakage detection and estimation using IR thermography. *In: 2016 International Conference on Communication and Signal Processing (ICCSP)*. *IEEE*, pp. 1516-1519 (2016) https://doi.org/10.1109/ICCSP.2016.7754411
5. Malekpour A, and She Y. Real-time leak detection in oil pipelines using an Inverse Transient Analysis model. *J Loss Prev Process Ind* 70:104411 (2021) https://doi.org/10.1016/j.jlp.2021.104411
6. Zheng X et al. Leak detection of long-distance district heating pipeline: A hydraulic transient model-based approach. *Energy* 237:121604 (2021) https://doi.org/10.1016/j.energy.2021.121604
7. Qu Z, Feng H, Zeng Z, Zhuge J, and Jin S. A SVM-based pipeline leakage detection and pre-warning system. *Measurement* 43(4):513-519 (2010) https://doi.org/10.1016/j.measurement.2009.12.022
8. Zhou M, Pan Z, Liu Y, Zhang Q, Cai Y, and Pan H. Leak detection and location based on ISLMD and CNN in a pipeline. *IEEE Access* 7:30457-30464 (2019) https://doi.org/10.1109/ACCESS.2019.2902711
9. Xiao R, Hu Q, and Li J. Leak detection of gas pipelines using acoustic signals based on wavelet transform and Support Vector Machine. *Measurement* 146:479-489 (2019) https://doi.org/10.1016/j.measurement.2019.06.050
10. Raissi M, Perdikaris P, and Karniadakis GE. Physics-informed neural networks: A deep learning framework for solving forward and inverse problems involving nonlinear partial differential equations. *J Comput Phys* 378:686-707 (2019) https://doi.org/10.1016/j.jcp.2018.10.045
11. Barnard A, Hunt W, Timlake W, and Varley E. A theory of fluid flow in compliant tubes. *Biophys J* 6(6):717-724 (1966) https://doi.org/10.1016/S0006-3495(66)86690-0
12. Paszke A et al. Automatic differentiation in PyTorch. *In: 31st Conference on Neural Information Processing Systems (NeurIPS)*. (2017)



© 2025 by the authors. Licensed to PSEcommunity.org and PSE Press. This is an open access article under the creative commons CC-BY-SA licensing terms. Credit must be given to creator and adaptations must be shared under the same terms. See https://creativecommons.org/licenses/by-sa/4.0/




Systems & Control Transactions

**Research Article - Peer Reviewed Conference Proceeding**
ESCAPE 35 - European Symposium on Computer Aided Process Engineering
Ghent, Belgium. 6-9 July 2025
Jan F.M. Van Impe, Grégoire Léonard, Satyajeet S. Bhonsale,
Monika E. Polańska, Filip Logist (Eds.)

PSE PRESS

# Rule-Based Autocorrection of Piping and Instrumentation Diagrams (P&IDs) on Graphs

**Lukas Schulze Balhorn[a], Niels Seijsener[b], Kevin Dao[b], Minji Kim[a], Dominik P. Goldstein[a], Ge H. M. Driessen[b], and Artur M. Schweidtmann[a]***

[a] Process Intelligence Research Group, Department of Chemical Engineering, Delft University of Technology, The Netherlands
[b] Fluor BV, Amsterdam, The Netherlands
* Corresponding Author: a.schweidtmann@tudelft.nl.

## ABSTRACT

A piping and instrumentation diagram (P&ID) is a central reference document in chemical process engineering. Currently, chemical engineers manually review P&IDs through visual inspection to find and rectify errors. However, engineering projects can involve hundreds to thousands of P&ID pages, creating a significant revision workload. This study proposes a rule-based method to support engineers with error detection and correction in P&IDs. The method is based on a graph representation of P&IDs, enabling automated error detection and correction, i.e., autocorrection, through rule graphs. We use our pyDEXPI Python package to generate P&ID graphs from DEXPI-standard P&IDs. In this study, we developed 33 rules based on chemical engineering knowledge and heuristics, with five selected rules demonstrated as examples. A case study on an illustrative P&ID validates the reliability and effectiveness of the rule-based autocorrection method in revising P&IDs.

**Keywords**: Autocorrection, P&ID graphs, pyDEXPI

## INTRODUCTION

Undetected errors or suboptimal designs in Piping and Instrumentation Diagrams (P&IDs) can cause financial costs, hazardous situations, unnecessary emissions, and inefficient operation. These errors are currently captured in extensive manual revision processes leading to safe, operable, and maintainable facilities. However, engineering projects often involve hundreds to thousands of P&ID pages, leading to a significant revision workload. With the advent of computer vision-based document digitization [1] and data exchange standards such as the Data Exchange in the Process Industry (DEXPI) [2], opportunities arise for algorithmic support of P&ID development and revision [3].

Several studies have been conducted on error detection and correction in engineering diagrams. These studies can be grouped into rule-based approaches [4] and machine learning (ML)-based approaches [5-8]. Specifically, ML-based approaches function as follows: Dzhusupova et al. [5] detect erroneous designs using computer vision in P&IDs. In contrast, Oeing et al. [6] and Rahmen et al. [7] use node classification on P&ID graphs to detect deviations from common P&ID design. In addition, our previous work proposed a generative artificial intelligence approach that generates corrected P&IDs using a string presentation [8]. The ML-based approaches offer the advantage of automatically learning to detect errors from existing P&ID data. However, ML-based approaches require large-scale data for model training, currently lack explainability due to their black-box nature, and pose a risk of hallucination. Furthermore, ML-based methods do not provide a deterministic guarantee that known errors encountered during training will be detected during inference, posing a risk for safety-critical designs. Conversely, rule-based approaches, grounded in chemical engineering knowledge and heuristics, are beneficial for developing highly accurate error detection and correction methods without the need for large-scale P&ID data. Rule-based approaches detect errors using hard-coded rules. These rules can be formulated based on general engineering logic or safety considerations. Moreover, the derived rules can be accompanied by an explanation. Whereas ML-based approaches still lack

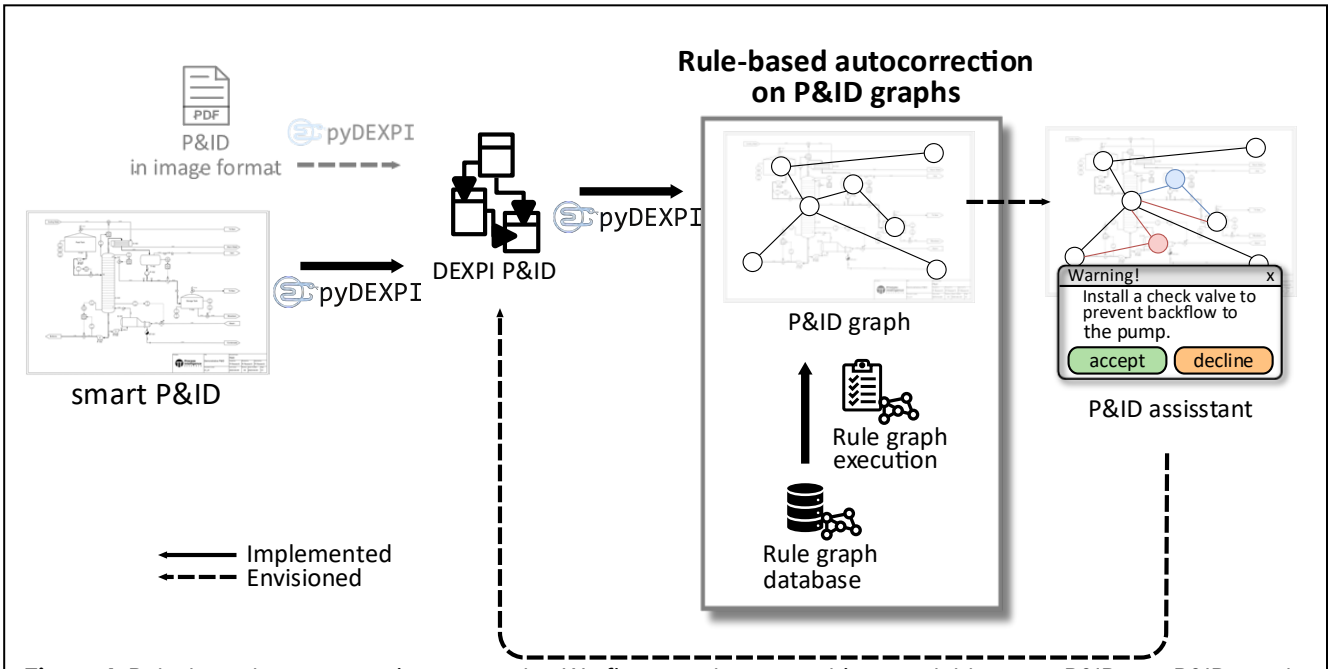



**Figure 1:** Rule-based autocorrection on graphs. We first translate a machine-readable smart P&ID to a P&ID graph. Then, we apply the engineering rules in the form of graph manipulations to the P&ID graph. In future applications, the autocorrection method may be implemented in a P&ID assistant with the human-in-the-loop. Changes can then automatically be updated in the DEXPI P&ID. We envision applying the rule-based autocorrection also on P&IDs in image format via digitization. Steps indicated by solid lines are implemented, steps indicated by dashed lines are envisioned for future projects.

large-scale P&ID data in practice, we expect that a rule-based approach is a good first step for a supporting tool for P&ID revision because it builds trust with the engineer due to the high accuracy and explainability.

Previous rule-based approaches represent P&IDs as graphs and aim to detect errors by identifying abnormal graph patterns [4]. These approaches use graph-based rules to modify P&ID graphs: Once an abnormal graph pattern is identified, specific modifications are applied to correct the P&ID graph. While the previous work is an important contribution toward supporting engineers in P&ID designs, we identify three limitations: (i) Previous methods are not linked to data exchange standards, making their integration into industrial P&ID development difficult, (ii) the literature focuses on digitization errors but neglects engineering errors, and (iii) literature does not account for missing components in P&IDs.

Building on the promising work by [4], we propose a rule-based autocorrection method for DEXPI P&IDs to address the aforementioned limitations. The methodology can be summarized as follows: First, we use our pyDEXPI package [9] to convert a smart P&ID into a graph. Second, rules are formulated based on chemical engineering knowledge and heuristics. These rules are implemented as graphs that describe manipulations to the P&ID graph. Lastly, applying these rule graphs to the P&ID graph completes the autocorrection process.

## RULE-BASED AUTOCORRECTION METHODOLOGY

Figure 1 summarizes our proposed methodology for P&ID autocorrection. First, a smart P&ID is converted into a DEXPI P&ID according to the DEXPI standard. Alternatively, paper-based P&IDs can be digitized. Then, a P&ID graph is generated from the DEXPI P&ID using our pyDEXPI package [9]. We utilize the P&ID graph to facilitate the application of rule graphs which implement various engineering rules for error detection and correction. Next, the rule-based autocorrection yields a corrected P&ID graph. Ultimately, the corrected P&ID graph is presented in a P&ID assistant and transformed back into a DEXPI P&ID. This manuscript focuses on the part from a DEXPI P&ID to a corrected P&ID graph.

### DEXPI P&ID to P&ID graph

The transformation from the DEXPI P&ID to the P&ID graph is achieved through our pyDEXPI package [9]. The pyDEXPI package is a Python implementation of the DEXPI data model, containing data classes that have attribute relationships to encode composition or reference. Furthermore, the pyDEXPI package includes functions for importing and exporting DEXPI data, such as converting a DEXPI P&ID to a P&ID graph. In the P&ID graph, nodes represent P&ID components and directed edges

**Table 1:** List of rules implemented for the case study.

| Rule ID | Rule description | Rule explanation | Implementing the rule is ... |
|---|---|---|---|
| 3 | Do not install a globe valve as a control valve if the pipe diameter is greater or equal to 100 DN (or 4”). | Large globe valves have higher costs compared to other valve types. | suggested. |
| 9 | Install a level instrument on a vessel. | Monitoring the vessel level regularly can prevent accidents caused by overflow. | mandatory. |
| 10 | Install a strainer in the suction line of a pump. | The strainer separates solid matter, which can potentially damage the pump, from the fluid. | suggested. |
| 19 | Install a check valve on a pump's discharge line to avoid backflow. | Backflow is dangerous to the pump because the pump is designed for one-way flow. | suggested. |
| 21 | Install block valves and a drain in the suction and discharge of a pump. | Isolate the pump during maintenance. | mandatory. |

represent pipes and signals. The direction of the edge is determined by the material flow or signal direction. To keep the P&ID graph concise, we only include key P&ID components. Specifically, we include the following components: (i) plant items with a tag, (ii) piping components, such as valves, (iii) actuators, and (iv) process instrumentation. P&ID components not considered mainly store connectivity information which we represent as directed edges.

## Applying rule graphs to a P&ID graph

The rule-based autocorrection method searches for erroneous patterns in P&IDs. If an erroneous pattern is detected, a set of corrections is performed on the pattern. Erroneous patterns and the corresponding set of corrections are collected together in so-called rule graphs. At execution, all rules graphs from a rule graph database are applied sequentially as described in Figure 2.

First, we search for the erroneous graph pattern defined by a rule in the P&ID graph via subgraph isomorphism. The NetworkX package provides a subgraph isomorphism algorithm based on the VF2 algorithm [10]. VF2 is a recursive algorithm that starts by randomly mapping a node from a pattern to a node in the P&ID graph with the same DEXPI class. At each step, the algorithm then tries to include pairs of neighboring nodes in the mapping that also have the same DEXPI class while avoiding previously explored mappings. If the complete pattern is mapped to the P&ID graph, a match is found. There can be multiple matches within a P&ID graph. We extend the work of [4] by incorporating conditions based on conditional statements during the subgraph isomorphism. The conditions allow us to go beyond exact attribute matches and incorporate inequality constraints, ranges, and sets. For example, Rule 3 in Table 1 defines one erroneous P&ID pattern for all line sizes greater or equal to 100 DN (or 4”), instead of defining a separate pattern for every possible line size. Isomorphism conditions are stored as node or edge attributes in the rule graphs.

Second, we correct the P&ID graph according to the rule graph for every match that is found. The graph manipulations include nodes and edges that perform either insertion or deletion. Insertion adds nodes or edges to the P&ID graph, while deletion removes nodes or edges from the P&ID graph. When visualizing a rule graph, insertion is denoted with red and deletion with blue.

A special case involves rules that describe missing components. Here, we search for both the erroneous and the corrected P&ID pattern (i.e., erroneous P&ID pattern with manipulations applied) in the P&ID graph. If a match of an erroneous pattern is included within a match with the corresponding corrected pattern, applying the rule is not necessary because the missing component already exists. However, if a match is found that includes only the erroneous but not the corrected pattern, a component is missing and the graph manipulations should be applied.

Figure 2 (step ④) illustrates an exemplary rule graph to insert a check valve in the pump's discharge line (Rule 19 in Table 1). The rule graph breaks the connection between the pump and the subsequent component “x”. Furthermore, a check valve is added to the graph. Two new connections complete the rule graph: A pipe from the

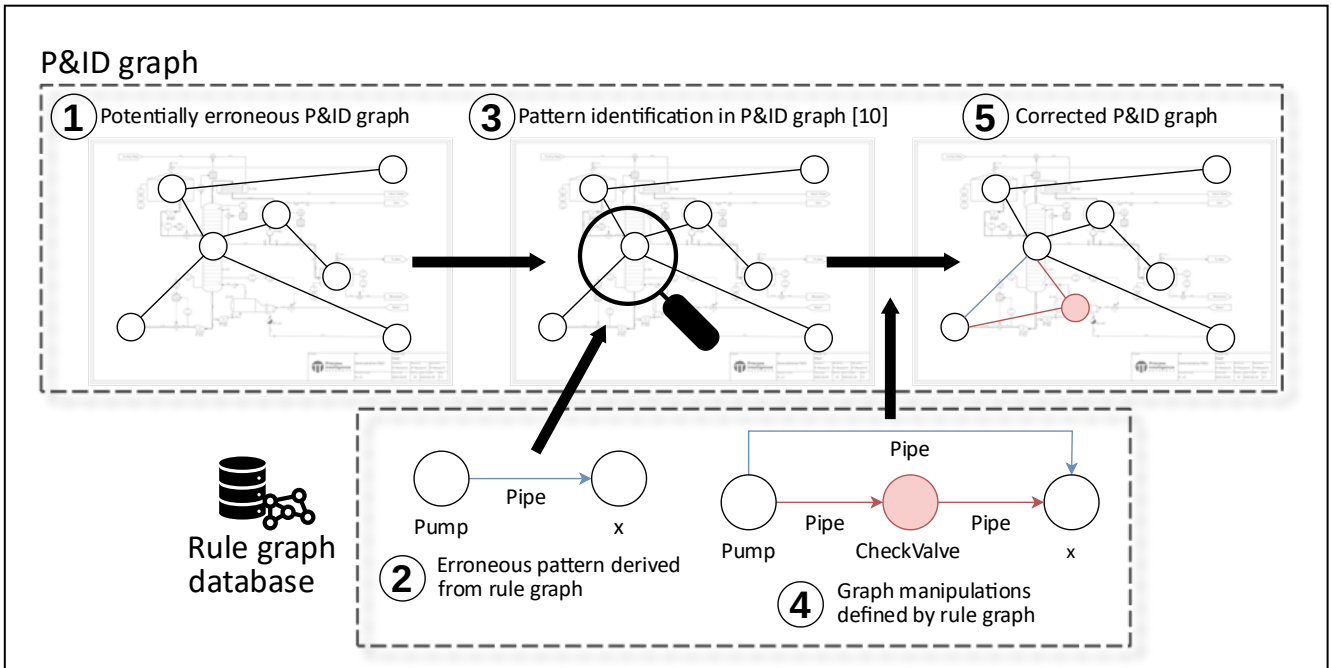



**Figure 2:** Rule graph execution for Rule 19 "Install a check valve in the pump's discharge line". According to P&ID markups, we denote added edges or nodes in red and deletions in blue. Note that for missing components, we search for both the erroneous and the corrected P&ID pattern (i.e., erroneous P&ID pattern with manipulations applied) in the P&ID graph. This is ommitted in the figure for brevity.

pump to the check valve and a pipe from the check valve to the subsequent component. Here, the "x" node can be mapped to any node in the P&ID graph. In addition, a pattern node's DEXPI class can always be mapped to its respective subclasses, i.e., the pump in the rule graph can be mapped to a reciprocating pump in the P&ID graph.

Besides the graph pattern and manipulations, each rule includes further graph attributes: (i) An ID to identify the rule, (ii) the P&ID milestone at which the rule is relevant, for instance, issue for review, issue for design, or issue for construction [11], (iii) a description on how the P&ID should be revised, (iv) an explanation why the P&ID should be revised, (v) the level of recommendation, for instance, the rule is a mandatory revision, a suggestion, or only a consideration, (vi) a boolean stating whether the rule describes a missing component, and (vii) the source of the rule.

In total, we define 33 rules. We define the rules based on engineering heuristics, literature [12], and existing workflows at Flour©. Here, we describe five exemplary rules in Table 1. The output of the methodology developed in this manuscript is a corrected P&ID graph and the meta data of the applied rules as given in Table 1.

## RESULTS AND DISCUSSION

To evaluate the performance of the autocorrection method, we applied the five rules listed in Table 1 in an illustrative case study by the DEXPI initiative (Figure 3). The P&ID includes two pumps, two heat exchangers, and a central vessel, with associated instrumentation for pressure and temperature regulation. The process begins with fluid entering through a pump, passing through a heat exchanger for preconditioning, and then entering a vessel for storage or processing. Post-vessel, the fluid is discharged by another pump and is partly recycled to the vessel. The recycle undergoes additional thermal conditioning for temperature control of the vessel. The resulting P&ID graph consists of 33 nodes and 36 edges. Please note that the case study is not representative for the complexity of a standard P&ID in the process industry.

### Detection and Correction Accuracy

The autocorrection method demonstrates high accuracy in identifying and correcting errors. The method successfully identified all erroneous substructures from the rule graph database, achieving an accuracy of 100%. These substructures were corrected using the corresponding rule graphs. For instance, the vessel is lacking pressure and level control. Rule 9 added a level instrument to the vessel for level control. Additionally, the two pumps are not protected and cannot be isolated for maintenance. Rule 21 facilitates maintenance by isolating the pumps with block valves and drains. To protect the pumps, Rule 10 recommended installing a strainer in the suction line, and Rule 19 suggested placing a check valve in the discharge line. For every applied rule, the method provided an explanation for why the revision was necessary. However, the rule graph database did not address

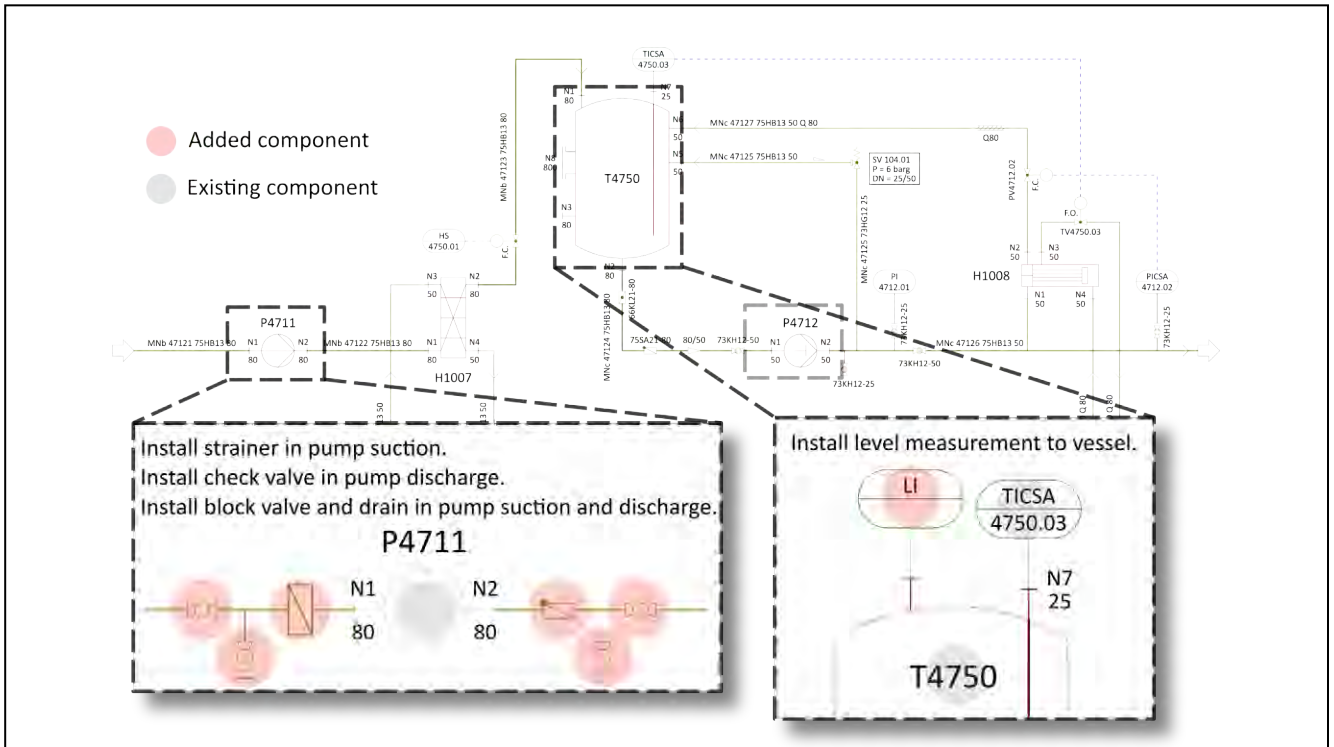



**Figure 3:** Case study for the rule-based autocorrection using the DEXPI v1.3 reference P&ID C01 (https://gitlab.com/dexpi/TrainingTestCases). Note that the P&ID does not reassemble an actual process but acts as a demonstration of the DEXPI data model. The autocorrection method updates pump P4711, pump P4712, and vessel T4750. The same corrections shown for pump P4711 are also applied to pump P4712.

all potential errors; for example, the vessel and heat exchangers were not isolated with block valves and drains, indicating the need for additional rules.

## Computational Performance

The autocorrection method demonstrated computational efficiency. It executed in 0.016 seconds on a laptop equipped with an i7-1185G7 processor (1.8-3.0 GHz) and 16 GB RAM. On average, evaluating a single rule took only 3.2 milliseconds. This performance is significantly faster than manual detection and correction of errors, which can take several minutes to hours, particularly in cluttered P&IDs.

## Discussion

Our findings indicate that the rule-based autocorrection method provides reliable and efficient support for engineers. Its ability to identify and correct errors with deterministic accuracy makes it suitable for safety-critical applications. The rapid execution time also highlights its potential for real-time applications, saving engineers significant time compared to manual reviews. Moreover, the method's integration with smart P&IDs enables it to utilize detailed component attributes, reducing the need for external documentation.

This study emphasizes the importance of applying rules in the correct sequence. For example, applying Rule 21 before Rules 10 and 19 ensures proper placement of strainers and check valves near pumps. Selecting the correct sequence minimizes the risk of overlapping or conflicting corrections.

However, the method's scalability is constrained by the need for manual rule derivation and maintenance. Each rule requires expertise from trained engineers, and as the rule database expands, tracking and managing interactions between rules becomes increasingly complex. In contrast, machine learning-based approaches excel at scaling, offering a promising avenue for future research [3]. Exploring hybrid methods that combine rule-based and ML-based approaches could leverage the strengths of both methodologies [13].

In conclusion, while the rule-based autocorrection method is not a standalone tool, it serves as a valuable support system for engineers, enhancing the accuracy and efficiency of P&ID reviews.

## CONCLUSION

This study presents rule-based autocorrection in DEXPI P&IDs. First, a DEXPI-formatted P&ID is converted into a P&ID graph using pyDEXPI. Subsequently, rule graphs based on chemical engineering knowledge and heuristics are applied to the P&ID graph to detect and rectify errors. The final outcome is a corrected P&ID

graph. We implement five selected rules and test them in a case study. The results show that the autocorrection method has an accuracy of 100% due to the rule-based approach. Therefore, the method is reliable and applicable in safety-critical applications. Besides this, the method detects and corrects errors at a significantly faster rate than humans. This research tackles previous limitations by (i) being compatible with the data exchange standard DEXPI through our pyDEXPI module, (ii) proposing rule graphs embedding engineering experience, and (iii) capturing missing components. However, the rule-based method also comes with limitations. Engineers need to extend and maintain the list of rules. In addition, rules may conflict. Therefore, the order in which we apply the rules and their context is important. Future research should investigate hybrid methods combining rule-based and ML-based for autocorrection. In addition, completing the autocorrection pipeline from Figure 1 by implementing the conversion of P&ID graphs to the DEXPI data model would enable the full integration into existing engineering workflows.

## ACKNOWLEDGEMENTS

We gratefully acknowledge the support provided by Linde GmbH, Linde Engineering and Siemens Aktiengesellschaft (DPG), as well as Flour© and Top Sector Alliance for Knowledge and Innovation (TKI) by the Dutch Ministry of Economic Affairs and Climate (CHEMIE.PGT.2023.033) (LSB).

## REFERENCES

1. Theisen MF, Flores KN, Schulze Balhorn L, Schweidtmann AM. Digitization of chemical process flow diagrams using deep convolutional neural networks. *Digital Chemical Engineering* 6:100072 (2023) https://doi.org/10.1016/j.dche.2022.100072
2. Theißen M, Wiedau M. DEXPI P&ID specification. DEXPI Initiative, version 1.3 (2021)
3. Schweidtmann AM. Generative artificial intelligence in chemical engineering. *Nature Chemical Engineering* 1:193–193 (2024) https://doi.org/10.1038/s44286-024-00041-5
4. Bayer J, Sinha A. Graph-based manipulation rules for piping and instrumentation diagrams. *LEVIA'19* (2019) https://doi.org/10.31219/osf.io/dynqj
5. Dzhusupova R, Banotra R, Bosch J, Olsson HH. Using artificial intelligence to find design errors in engineering drawings. *Journal of Software: Evolution and Process* 35(12) (2023) https://doi.org/10.1002/smr.2543
6. Oeing J, Brandt K, Wiedau M, Tolksdorf G, Welscher W, Kockmann N. Graph learning in machine-readable plant topology data. *Chemie Ingenieur Technik* 95(7):1049–1060 (2023) https://doi.org/10.1002/cite.202200223
7. Mizanur Rahman S, Bayer J, Dengel A. Graph-based object detection enhancement for symbolic engineering drawings. Document Analysis and Recognition – ICDAR 2021 Workshops. 74–90 (2021) https://doi.org/10.1007/978-3-030-86198-8_6
8. Schulze Balhorn L, Caballero M, Schweidtmann AM. Toward autocorrection of chemical process flowsheets using large language models. Computer Aided Chemical Engineering. 53:3109-3114 (2024) https://doi.org/10.1016/B978-0-443-28824-1.50519-6
9. Goldstein DP, Schulze Balhorn L, Schweidtmann AM. pyDEXPI: A Python implementation and toolkit for the DEXPI information model. Unpublished manuscript (2024).
10. Cordella LP, Foggia P, Sansone C, Vento M. A (sub) graph isomorphism algorithm for matching large graphs. *IEEE transactions on pattern analysis and machine intelligence* 26(10):1367–1372 (2004) https://doi.org/10.1109/TPAMI.2004.75
11. Toghraei, M. Piping and instrumentation diagram development. John Wiley & Sons (2019)
12. Woolf P. Chemical Process Dynamics and Controls. Open Textbook Library. University of Michigan Engineering Controls Group (2009) https://books.google.nl/books?id=Op87vwEACAAJ
13. Schweidtmann AM, Esche E, Fischer A, Kloft M, Repke JU, Sager S, & Mitsos A. Machine learning in chemical engineering: A perspective. *Chemie Ingenieur Technik* 93(12), 2029-2039 (2021) https://doi.org/10.1002/cite.202100083

© 2025 by the authors. Licensed to PSEcommunity.org and PSE Press. This is an open access article under the creative commons CC-BY-SA licensing terms. Credit must be given to creator and adaptations must be shared under the same terms. See https://creativecommons.org/licenses/by-sa/4.0/



Systems & Control Transactions

**Research Article - Peer Reviewed Conference Proceeding**
ESCAPE 35 - European Symposium on Computer Aided Process Engineering
Ghent, Belgium. 6-9 July 2025
Jan F.M. Van Impe, Grégoire Léonard, Satyajeet S. Bhonsale,
Monika E. Polańska, Filip Logist (Eds.)

PSE PRESS

# Thermodynamics-informed Graph Neural Networks for Phase Transition Enthalpies

**Roel Leenhouts[a], Sebastien Jankelevitch[a], Roel Raike[a], Simon Müller[b] and Florence Vermeire[a]***

[a] Department of Chemical Engineering, KU Leuven, Leuven, Belgium
[b] Institute of Thermal Separation Processes, Hamburg University of Technology, Hamburg, Germany
* Corresponding Author: florence.vermeire@kuleuven.be.

## ABSTRACT

Phase transition enthalpies, such as those for fusion, vaporization, and sublimation, are vital for understanding thermodynamic properties and aiding early-stage process design. However, measuring these properties is often time-consuming and costly, leading to increased interest in computational methods for fast and accurate predictions. Graph neural networks (GNNs), known for their ability to learn complex molecular representations, have emerged as state-of-the-art tools for predicting various thermophysical properties. Despite their success, GNNs do not inherently obey thermodynamic laws. In this study, we present a multitask GNN designed to predict vaporization, fusion, and sublimation enthalpies of organic compounds. We modified the loss function of the GNN, accounting for the thermodynamic cycle of the three phase transition enthalpies. To train the model, we digitized the extensive Chickos and Acree compendium, which encompasses 32,023 experimental measurements. Two approaches were explored: soft constraints, which guide the model toward thermodynamic consistency, and hard constraints, which enforce fully consistent predictions. The GNN achieved root mean squared errors (RMSEs) of 19.9 kJ/mol for sublimation, 11.0 kJ/mol for fusion, and 16.5 kJ/mol for vaporization enthalpies on the test set. Soft constraints were found to provide a good balance between accuracy and thermodynamic consistency, whereas hard constraints prioritized fidelity at the expense of predictive performance. When compared to the conventional Joback group contribution method the GNN demonstrated an improved accuracy and applicability range. This work underscores the potential of thermodynamics-informed GNNs for predicting thermodynamic properties accurately while maintaining consistency, paving the way for more reliable and efficient computational approaches.

**Keywords**: Graph neural networks, Property prediction, Physics informed, Phase transition enthalpies

## INTRODUCTION

Phase transition enthalpies, such as sublimation, melting, and vaporization enthalpies, have numerous applications for designing process unit operations. For example, they are a crucial part of the energy balances of separation units such as distillation towers or crystallization units. Additionally, phase transition enthalpies can be applied within thermodynamic cycles to predict different thermochemical properties[1],[2]. Measuring these properties is time intensive and costly, therefore it is important to develop predictive methods for fast screening of potential materials.

Different approaches have been used to predict these properties. First principal methods are accurate, in particular for vaporization enthalpies[3], but they are computationally expensive and fall short in crystal structure prediction. On the other hand, empirical methods, such as quantitative structure property relationships (QSPR) [4] and the linear solvation energy relationships (LSER) [5], are commonly used. They can be accurate but have a limited applicability range. Especially for novel components, these empirical methods often lack accuracy. Recent improvements in data availability and computational resources drive the use of machine learning to develop robust and fast models to predict phase transition enthalpies. Graph neural networks have become the state-of-the-art method for molecular property prediction because of their flexibility in molecule representation and their ability to learn deep representations [6]. They have consistently surpassed fixed molecular representation methods [7] and are therefore utilized for analyzing

the properties explored in this study.

One limitation of machine learning algorithms is that they do not inherently imply thermodynamic consistency. Recent studies have investigated the inclusion of these thermodynamic laws in the loss function of deep learning property prediction methods [8],[9] to improve the confidence in black-box models. For phase transition enthalpies, we consider thermodynamic consistency in our models by implying the following:

$$\Delta H_{sub,T} = \Delta H_{fus,T} + \Delta H_{vap,T} \quad (1)$$

Two approaches are reported for the inclusion of this law in the loss function. In the first approach, a regularization term is added to the loss function as a soft constraint, where inconsistent predictions are still allowed but penalized. In the second approach, the loss function is reformulated to only allow consistent predictions or also called hard constraint.

To train our models, we digitized the compendium of Chickos and Acree[10],[11],[12], consisting of 32,023 phase transition enthalpy values measured over 135 years. The performance of the machine learning methods is compared to the Joback group contribution method as implemented in the thermo python package[4]. Additionally, the performance is evaluated by comparing single-task and multi-task models, as well as soft and hard constraint loss functions.

# METHODS

## Phase Transition Enthalpy Database

### Database digitization

The data collected from the works of Chickos and Acree's enthalpy compendium[10],[11],[12] is detailed here. In the compendium for each data point the following metrics were reported: the molecular formula, the CAS-number, the measurement temperature, the enthalpy value, the measurement technique, and the original source. From the CAS-numbers, the InChI and SMILES identifiers were retrieved from the PubChem database[13] and Cactus service[14]. Molecules that include metal atoms were excluded, so the dataset is limited to the following atoms list: C, H, B, Br, Cl, F, I, N, O, P, S, and Si.

Additionally, the enthalpies were converted to the standard state (298 K, 1 atm) using the approach proposed by Chickos et al.[15]. This correction was required, since Equation 1 is only applicable when the three phase enthalpies are at the same temperature. For this correction, heat capacity values were required for the solid, liquid and gas phase. The heat capacities of the solid and liquid phase were computed by the group contribution method from Chickos et al.[15], and for the gas phase, temperature dependent heat capacities were calculated using the RMG software[16]. A list of the heat capacities is provided as part of our Research Data Repository.

### Database characteristics

Analyzing the dataset, Figures 1 and 2 show the distributions of the enthalpy values and molecular weights respectively for the three phase transition enthalpies. The reported fusion enthalpy values were smaller in magnitude and distribution width, which is expected as, compared to the vaporization and sublimation enthalpy, they do not depend on the (higher) enthalpy difference with the gas phase.

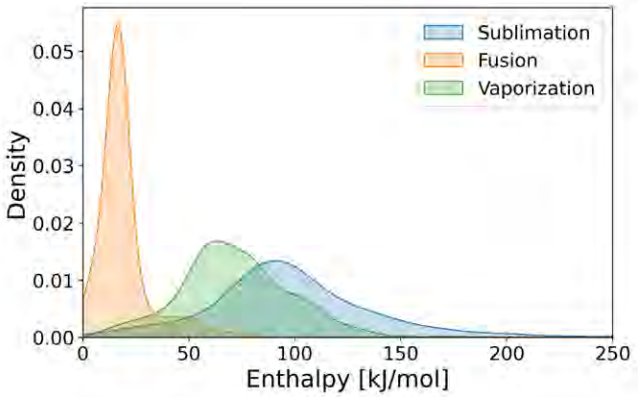



**Figure 1.** Value distribution of the three phase transition enthalpies at 298 K.

The molecular weight distributions for all three enthalpies are showing a widespread, which is critical for training a widely applicable machine learning model. The fusion enthalpy distribution is slightly more shifted to the right, which is inherent for these properties considering organic compounds. For many organic molecules with higher molecular weights, it is not possible to measure vaporization or sublimation enthalpies, since the decomposition temperature will be lower than the boiling point.

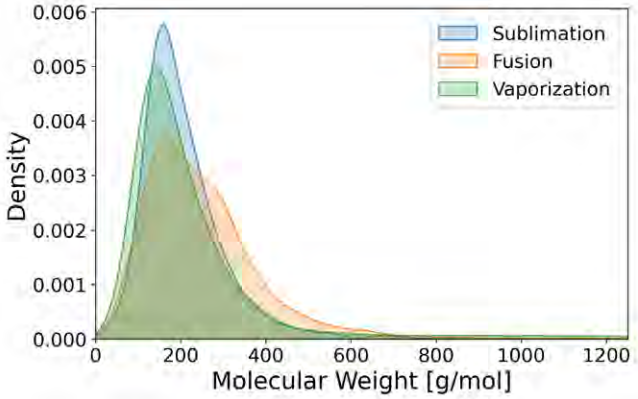



**Figure 2.** Molecular weight distribution of the three phase transition enthalpies.

For data points where all three enthalpies were available, the sum of the fusion and vaporization

enthalpies was compared to the sublimation enthalpy. In Figure 3, a parity plot for this thermodynamic consistency check of the database is shown. It was found that, although the properties are highly correlated, large deviations from the thermodynamic cycle were apparent. It was observed that the experimental sublimation enthalpy is almost consitently higher as compared to the one calculated from the vaporization and fusion enthalpy, with some deviations higher than 50 kJ/mol.

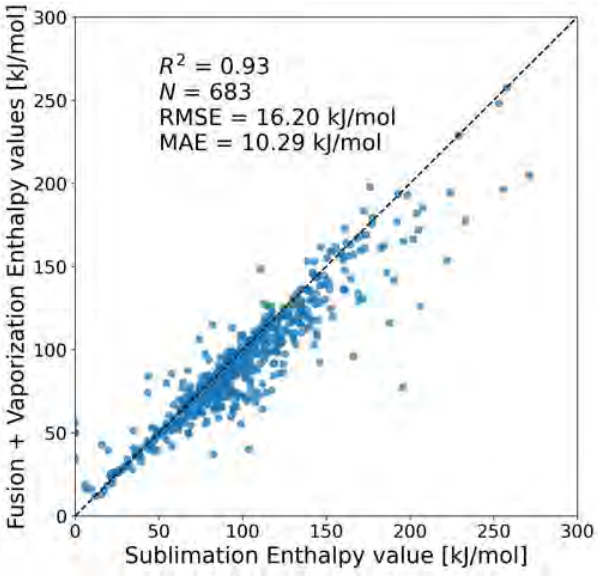



Figure 3. Thermodynamics consistency parity plot for the overlapping values in the phase transition enthalpies at 298 K of the database.

Crystal structures were not reported in the compendium, and different polymorphs could partially account for the observed deviations. Additionally, temperature corrections introduce uncertainty; however, they have been shown to produce acceptable errors and are essential for assessing thermodynamic consistency [11]. The temperature correction for the enthalpy of vaporization introduces an error of 0.016 kJ/(mol K) [11], leading to an uncertainty of 1.6 kJ/mol for a molecule deviating by 100 K from the reference temperature of 298 K. For enthalpies of sublimation and vaporization, an uncertainty of one-third of the total temperature correction can be assumed [11]. As an example, for carbazole, this results in an enthalpy of sublimation of 102.9 ± 1.2 kJ/mol and an enthalpy of fusion of 15.9 ± 3.5 kJ/mol.

The average estimated uncertainties for the temperature correction over the dataset were 0.57, 2.38, and 1.32 kJ/mol for sublimation, fusion, and vaporization enthalpies, respectively. Since sublimation and vaporization enthalpies are commonly reported in the literature at values corrected to 298 K, these uncertainties were averaged only for values that were not reported at 298 K.

Figure 4 shows the distribution of standard deviations for duplicated data points in the dataset before the temperature correction. Duplicates were identified for 1,312 sublimation, 1,143 fusion, and 2,663 vaporization compounds. These standard deviations provide an estimate of experimental uncertainty, specifically aleatoric uncertainty. The average standard deviations are 5.9, 3.3, and 5.4 kJ/mol for sublimation, fusion, and vaporization enthalpies, respectively. This represents the performance limit for a model trained on this data. Notably, the uncertainties introduced by temperature corrections are relatively small compared to experimental uncertainty.

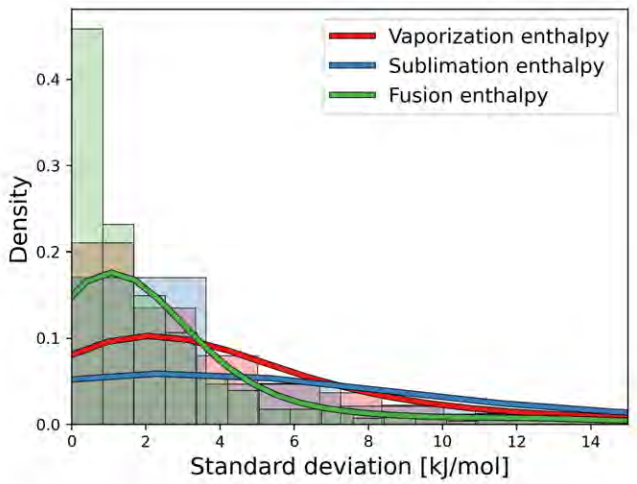



**Figure 4.** A distribution of the standard deviations computed on the duplicated data points in the dataset before the data was adjusted to 298 K.

## Model architecture and training

The graph neural networks (GNNs) were trained using the SolProp repository [2], which focuses on solvation properties and implements directed message passing neural networks (D-MPNN) based on the Chemprop framework [6]. For a detailed explanation, readers are referred to dedicated studies [6],[17]. Figure 5 presents an example model architecture. The model takes a molecular identifier, such as SMILES or InChI, as input and converts it into a featurized molecular graph. This graph representation is then processed by the GNN, which predicts the enthalpy values for phase transitions.

Four different model architectures were trained: single-task, multitask, soft-constraint, and hard-constraint models. The single-task models were trained by initializing three separate neural networks, each focusing on one of the three enthalpy datasets (fusion, vaporization, and sublimation). In contrast, the multitask models used a single GNN with a multi-head output for the multi-layer perceptron (MLP), meaning that a single molecular graph was provided as input, and the network simultaneously predicted all three enthalpies.

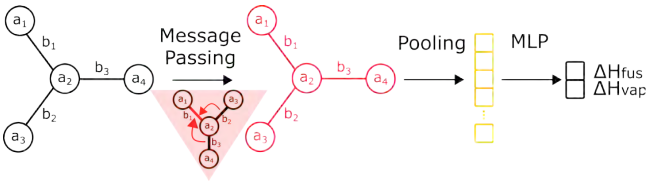



**Figure 5.** Hard-constraint thermodynamics-informed architecture.

The soft-constraint models used a multi-head output for the MLP, but the loss function was modified to include a penalty term that encouraged thermodynamic consistency. This penalty term was scaled by a weight parameter, λ, to balance accuracy in minimizing mean squared error (MSE) while ensuring the enthalpies remained consistent with thermodynamic relationships. After evaluating three values (0.1, 0.01, and 0.001), a λ of 0.01 was found to significantly influence the penalty term without negatively affecting model accuracy. The loss function for soft-constraint models was defined as:

$$\text{Loss} = \sum_{i=1}^{3}\left(y_{i,\text{exp}} - \hat{y}_{i,\text{pred}}\right)^2 + \lambda\left(\Delta\hat{H}_{\text{sub,pred}} - \left(\Delta\hat{H}_{\text{fus,pred}} + \Delta\hat{H}_{\text{vap}}\right)\right)^2 \quad (2)$$

For the hard-constraint models, thermodynamic consistency was strictly enforced within the loss function. Instead of predicting all three enthalpies separately, a single neural network was trained with two outputs: one for fusion enthalpy and one for vaporization enthalpy. The sublimation enthalpy was not directly predicted but was instead computed within the loss function as the sum of the fusion and vaporization enthalpies. The loss function ensured consistency by penalizing deviations from this relationship:

$$\text{Loss} = \left(y_{\text{fus,exp}} - \hat{y}_{\text{fus,pred}}\right)^2 + \left(y_{\text{vap,exp}} - \hat{y}_{\text{vap,pred}}\right)^2 + \left(y_{\text{sub,exp}} - \hat{y}_{\text{fus,pred}} - \hat{y}_{\text{vap,pred}}\right)^2 \quad (3)$$

The dataset was randomly split into a training and validation set (90%) and a test set (10%). Within the training set, a ten-fold cross-validation ensemble was trained to improve model robustness. The standard deviations reported in the results stem from variations between the predictions of the ensemble models. The featurization and hyperparameters remained fixed across all models and were based on prior research in thermodynamic property prediction [17].

### Joback method implementation

The Joback method[4] is a group contribution method that was developed for the prediction of a range of properties among others the vaporization and fusion enthalpy. Here, the implementation from the thermo v0.4.0 python package was used[18]. Predictions were made on the same test set as for the graph neural network. However, the fragmentation algorithm was not able to identify all atoms in the molecules. For the molecules where this was not possible, the predictions were removed from the results, accounting for 16.7% of the compounds in the test set.

Additionally, the Joback method predicts the phase transition enthalpies at the transition temperature, contrary to our method that predicts at the enthalpies at 298 K. Therefore, the fusion and vaporization enthalpies determined with the Joback method, were converted in the same way as the experimental dataset using the approach proposed by Chickos et al.[15]. Since the Joback method was not parametrized for the sublimation enthalpy, this was calculated by the sum of the converted vaporization and fusion enthalpies.

## RESULTS AND DISCUSSION

### Model performance

The model performance is compared for the four different model architectures in Table 1-3 for sublimation, fusion, and vaporization enthalpies respectively. In general, the fusion and vaporization enthalpy were predicted more accurately as compared to the sublimation enthalpy. The best models report an MAE of 13 kJ/mol, 6 kJ/mol, and 8 kJ/mol for the sublimation, fusion, and vaporization enthalpies in the test set respectively.

A similar performance was obtained between the single- and multitask models. A slightly higher RMSE and MAE can be observed for the predictions of the single task models, in particular for sublimation enthalpy. However, these differences are well within the standard deviations between the model ensembles (σ in Table 1-3) which is a measure for the variance contribution to the epistemic uncertainty.

Applying constraints to the multitask model did not lead to a significant improvement in accuracy. Introducing the soft constraint resulted in RMSE and MAE values for all three phase transition enthalpies that remained similar to those of the multitask model. However, when the hard constraint was applied, prediction accuracy declines. Specifically, the RMSE and MAE for the sublimation enthalpy—directly influenced by the hard constraint—increase by more than 10 kJ/mol. This suggests that enforcing thermodynamic consistency through a hard constraint reduces the accuracy of phase transition enthalpy predictions. Moreover, further research is needed to explore the most effective methods for incorporating constraints into neural network training.

Due to the correlation between the three phase transition enthalpies, one would expect a multitask modeling architecture to offer more benefits compared to a single-task model. Additionally, incorporating thermodynamic constraints into the loss function should ideally lead to more accurate predictions. However, as previously discussed, no significant improvements in model accuracy were observed. When comparing model

performance to the average standard deviation from the repeated experiments, the MAE for the fusion and sublimation enthalpies was roughly twice the standard deviation found in the Database Characteristics section. In contrast, the MAE for the vaporization enthalpy was only about 2 kJ/mol from the standard deviation in the dataset, suggesting that the model is close to the aleatoric limit.

A potential explanation for the lower performance of the sublimation and fusion models could be the absence of crystal structure information. The repeated data points in the compendium often came from the same sources or authors, meaning the compounds—and likely their crystal structures—were quite similar. This may have resulted in a low estimate of aleatoric uncertainty. However, further investigation is needed to reach a definitive conclusion.

It is also worth noting that the MAE for the thermodynamic consistency of the experimental data (Figure 3) is 10.3 kJ/mol. While this is not a direct measure of experimental uncertainty, it could offer an indication of its magnitude. Importantly, the MAE for the phase transition enthalpy predictions is lower than 10.3 kJ/mol, except for the sublimation enthalpy.

Lin et al. achieved a RMSE of 4.8 kJ/mol for vaporization enthalpies using first-principles calculations [19], which is notably lower than the standard deviation observed in our data. While our model demonstrates lower accuracy, direct comparison is challenging due to differences in methodologies and test sets. For fusion enthalpies, Chickos et al. reported a prediction error of 6.4 kJ/mol [20], closely matching our model's accuracy. Similarly, Liu et al. used first-principles calculations to estimate sublimation enthalpies, obtaining a mean absolute error (MAE) of 13.5 kJ/mol compared to experimental values [21], which aligns with our model's performance.

**Table 1:** An overview of the model architectures performance for the sublimation enthalpy on the test set.

| Model | RMSE (kJ/mol) | MAE (kJ/mol) | σ (kJ/mol) |
|---|---|---|---|
| Single task | 20.2 | 13.9 | 5.1 |
| Multitask | 19.9 | 13.1 | 3.7 |
| Soft constraint | 19.9 | 13.1 | 1.4 |
| Hard constraint | 30.1 | 24.1 | 2.8 |

**Table 2:** An overview of the model architectures performance for the fusion enthalpy on the test set.

| Model | RMSE (kJ/mol) | MAE (kJ/mol) | σ (kJ/mol) |
|---|---|---|---|
| Single task | 11.0 | 6.3 | 2.1 |
| Multitask | 11.0 | 6.1 | 1.5 |
| Soft constraint | 11.0 | 6.3 | 3.5 |
| Hard constraint | 11.6 | 6.9 | 1.4 |

**Table 3:** An overview of the model architectures performance for the vaporization enthalpy on the test set.

| Model | RMSE (kJ/mol) | MAE (kJ/mol) | σ (kJ/mol) |
|---|---|---|---|
| Single task | 16.2 | 7.3 | 2.8 |
| Multitask | 16.2 | 7.5 | 3.1 |
| Soft constraint | 16.5 | 7.5 | 2.9 |
| Hard constraint | 17.5 | 8.9 | 2.0 |

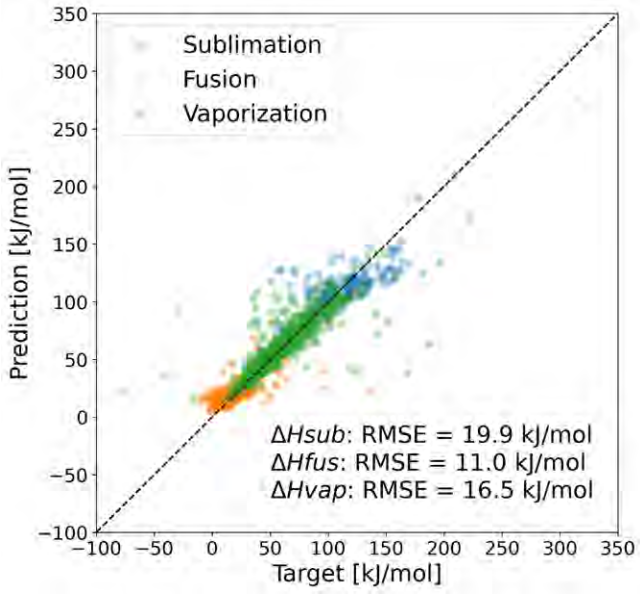



**Figure 6.** Parity plot for the enthalpy predictions made by the SolProp soft-constraint model.

The model predictions for the three phase transition enthalpies are visualized in Figure 6 for the model that includes the soft constraint in the loss function. The majority of the test data is predicted around the parity line, while large deviations are observed for some specific datapoints. The highest deviations for vaporization enthalpy are observed for negative experimental vaporization enthalpies. There were a small group of high molecular weight hydrocarbons for which the temperature correction resulted in a negative value because of the high measurement temperature compared to the reference temperature. Due to the large temperature range the temperature correction is expected to be large too. The low amount of available data for the heavy hydrocarbons and the high uncertainty on the correct can explain the lower performance of the models on this data. We did not find a correlation between the highest errors and the experimental data that showed the highest deviations from thermodynamic consistency in Figure 3, however only 5% of the test set contained experimental measurements for all three phase transition enthalpies. In addition, there was no strong correlation between the epistemic model uncertainties from the model ensemble and the

prediction error.

## Thermodynamic consistency

On top of the model performance, the thermodynamic consistency of the predictions was evaluated. In Figure 7, the predicted sublimation enthalpy is compared to the sublimation enthalpy calculated from the fusion and vaporization enthalpy through Equation 1. The thermodynamic consistency is visualized for the multitask model as well as the model with the soft constraint. The thermodynamic consistency for the model with the hard constraint is omitted from Figure 7 since, as expected from the constraint, the calculated sublimation enthalpy is exactly equal to the predicted sublimation enthalpy.

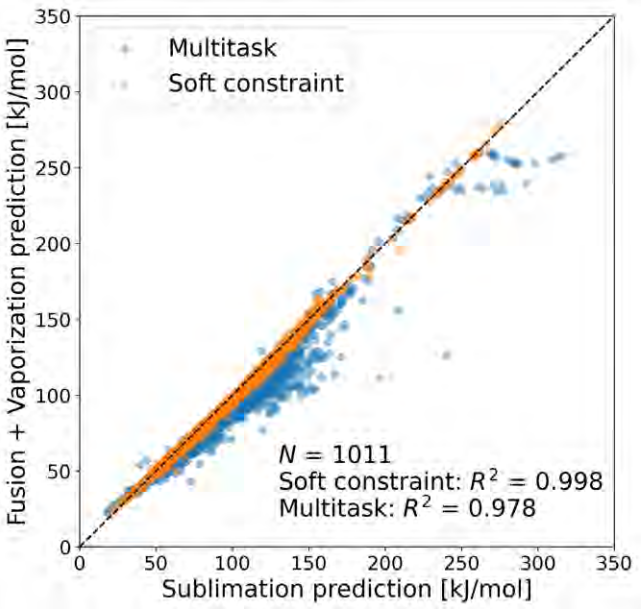



**Figure 7.** Parity plot for the thermodynamic consistency of the multitask and soft constraint model.

The multitask modeling approach already improved the thermodynamic consistency as compared to the experimental measurements with overlapping phase transition enthalpies (**Figure 3**). Yet, the calculated sublimation enthalpy was consistently lower compared to the sublimation enthalpy predicted by the multitask model. The model indeed learned the consistent underestimations that are present in the experimental database. Applying the soft constraint corrects for these discrepancies and a good agreement between calculated and predicted sublimation enthalpy was obtained ($R^2$=0.998). Interestingly, the performance of the model is hardly affected by applying this constraint while the predictions are more consistent. The soft constraint therefore provides a good balance between model performance and consistent predictions. Note that increasing the value of λ in the loss function would result in a higher thermodynamic consistency but at the cost of a lower accuracy of the model.

## Comparison to conventional methods

At last, the performance of our models was compared to the Joback method, which is the conventional way of determining phase transition enthalpies. In Figure 8, a parity plot is given comparing the experimental phase transition enthalpies with the Joback calculations as implemented in the thermo python library. Note that the sublimation enthalpy was determined through the thermodynamic cycle from Equation 1 as it is not directly available from the Joback method.

For fusion and vaporization enthalpies respectively, the RMSEs is the Joback method are 21.8 kJ/mol and 19.4 kJ/mol as compared to 11.0 kJ/mol and 16.5 kJ/mol from our soft constraint model. As such, it is demonstrated that advancements in data availability and computational algorithms can provide a significant improvement in property prediction as compared to conventional methods.

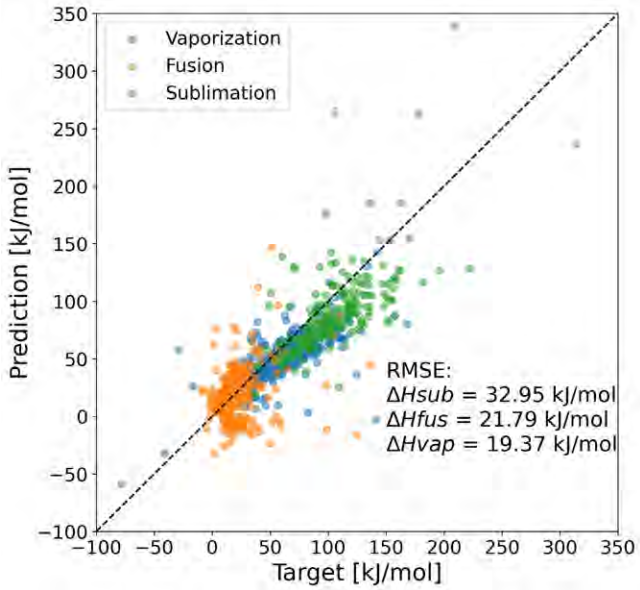



**Figure 8.** Parity plot for the enthalpy predictions made by the Joback method adjusted to standard state[4],[18].

## CONCLUSIONS

In this work, we digitized the compendium of Chickos and Acree for the phase transition enthalpies of sublimation, fusion, and vaporization. The availability of such large and diverse database stimulates the development of deep learning algorithms for the training and prediction of these enthalpies.

Graph neural networks are used to predict these phase transition enthalpies while accounting for thermodynamics. First, no significant improvement in accuracy was found whilst comparing single- and multitask modeling architectures. Additionally, adding a soft-constraint thermodynamics loss function proved to be the best

balance between accuracy and thermodynamic consistency of the predictions. The hard-constraint loss function enforced strict consistency, however at the cost of the accuracy of the model specifically for sublimation enthalpies. A comparison to the Joback method showed an improvement in accuracy and applicability range of the model.

Our graph neural network achieved state-of-the-art performance on sublimation, fusion, and vaporization enthalpies, while adding thermodynamic consistency. This method has the potential to be applied to the screening materials in the early design phase of chemical processes for all three investigated phase transition enthalpies.

## DIGITAL SUPPLEMENTARY MATERIAL

The code repository of the work can be found at the KU Leuven GitLab:

https://gitlab.kuleuven.be/creas/vermeire-group/solprop/-/tree/phase_transition_enthalpies,

and the digitized dataset and static code at KU Leuven Research Data Repository (RDR):

https://doi.org/10.48804/CBHEAB.

## ACKNOWLEDGEMENTS

The authors want to thank W. Acree and J. Chickos for sharing a pdf of their compendium. We acknowledge the Fonds Wetenschappelijk Onderzoek (FWO) for funding (G021924N).

## REFERENCES

1. Zhu, X. , Polyakov, V. R. , Bajjuri, K. , Hu, H. , Maderna, A. , Tovee, C. A. , and Ward, S. C. Building Machine Learning Small Molecule Melting Points and Solubility Models Using CCDC Melting Points Dataset. Journal of Chemical Information and Modeling 2023, 63, 2948–2959.
2. Vermeire, F. H. , Chung, Y. , and Green, W. H. Predicting Solubility Limits of Organic Solutes for a Wide Range of Solvents and Temperatures. Journal of the American Chemical Society 2022, 144, 10785–10797.
3. Lin, S. T. , Chang, J. , Wang, S. , Goddard, W. A. , and Sandler, S. I. Prediction of vapor pressures and enthalpies of vaporization using a COSMO solvation model. Journal of Physical Chemistry A 2004, 108, 7429–7439.
4. [Joback, K. G. A unified approach to physical property estimation using multivariate statistical techniques. 1984
5. Abraham, M. H. and Acree, W. E. Estimation of enthalpies of sublimation of organic, organometallic and inorganic compounds. Fluid Phase Equilibria 2020, 515, 112575.
6. Heid, E. , Greenman, K. P. , Chung, Y. , Li, S. C. , Graff, D. E. , Vermeire, F. H. , Wu, H. , Green, W. H. , and McGill, C. J. Chemprop: A Machine Learning Package for Chemical Property Prediction. Journal of Chemical Information and Modeling 2024, 64, 9–17.
7. Yang, K. , Swanson, K. , Jin, W. , Coley, C. , Eiden, P. , Gao, H. , Guzman-Perez, A. , Hopper, T. , Kelley, B. , Mathea, M. , Palmer, A. , Settels, V. , Jaakkola, T. , Jensen, K. , and Barzilay, R. Analyzing Learned Molecular Representations for Property Prediction. Journal of Chemical Information and Modeling 2019, 59, 3370–3388.
8. Rittig, J. G. and Mitsos, A. Thermodynamics-consistent graph neural networks. Chemical Science 2024, 15, 18504–18512.
9. Specht, T. , Nagda, M. , Fellenz, S. , Mandt, S. , Hasse, H. , and Jirasek, F. HANNA: hard-constraint neural network for consistent activity coefficient prediction. Chemical Science 2024, 15, 19777–19786.
10. Acree, W. and Chickos, J. S. Phase transition enthalpy measurements of organic and organometallic compounds and ionic liquids. sublimation, vaporization, and fusion enthalpies from 1880 to 2015. part 2. C11-C192. Journal of Physical and Chemical Reference Data 2017, 46
11. Acree, W. and Chickos, J. S. Phase Transition Enthalpy Measurements of Organic and Organometallic Compounds. Sublimation, Vaporization and Fusion Enthalpies From 1880 to 2015. Part 1. C1-C10. Journal of Physical and Chemical Reference Data 2016, 45
12. Acree, W. and Chickos, J. S. Phase Transition Enthalpy Measurements of Organic Compounds. An Update of Sublimation, Vaporization, and Fusion Enthalpies from 2016 to 2021. Journal of Physical and Chemical Reference Data 2022, 51
13. Kim, S. , Chen, J. , Cheng, T. , Gindulyte, A. , He, J. , He, S. , Li, Q. , Shoemaker, B. A. , Thiessen, P. A. , Yu, B. , Zaslavsky, L. , Zhang, J. , and Bolton, E. E. PubChem 2025 update. Nucleic Acids Research 2025, 53, D1516–D1525.
14. NCI/CADD Group Chemoinformatics Tools and User Services. https://cactus.nci.nih.gov/ (accessed Jan. 24, 2025).
15. Chickos, J. S. , Hosseini, S. , Hesse, D. G. , and Liebman, J. F. Heat capacity corrections to a standard state: a comparison of new and some literature methods for organic liquids and solids. Structural Chemistry 1993, 4, 271–278.
16. Johnson, M. S. , Dong, X. , Grinberg Dana, A. , Chung, Y. , Farina, D. , Gillis, R. J. , Liu, M. , Yee, N. W. , Blondal, K. , Mazeau, E. , Grambow, C. A. , Payne, A. M. , Spiekermann, K. A. , Pang, H. W. , Goldsmith, C. F. , West, R. H. , and Green, W. H.

RMG Database for Chemical Property Prediction. Journal of Chemical Information and Modeling 2022, 62, 4906–4915.
17. Vermeire, F. H. and Green, W. H. Transfer learning for solvation free energies: From quantum chemistry to experiments. Chemical Engineering Journal 2021, 418, 129307.
18. Joback Group Contribution Method (thermo.group_contribution.joback) — Thermo 0.4.0 documentation. https://thermo.readthedocs.io/thermo.group_contribution.joback.html (accessed Jan. 22, 2025).
19. Lin, S. T. , Chang, J. , Wang, S. , Goddard, W. A. , and Sandler, S. I. Prediction of vapor pressures and enthalpies of vaporization using a COSMO solvation model. Journal of Physical Chemistry A 2004, 108, 7429–7439.
20. Chickos, J. S. , Nichols, G. , and Ruelle, P. The estimation of melting points and fusion enthalpies using experimental solubilities, estimated total phase change entropies, and mobile order and disorder theory. Journal of Chemical Information and Computer Sciences 2002, 42, 368–374.
21. Liu, Y. , Tran, H. , Huang, C. , Rio, B. G. del , Joseph, V. R. , Losego, M. , and Ramprasad, R. Accelerated predictions of the sublimation enthalpy of organic materials with machine learning. Materials Genome Engineering Advances 2025, e84.

© 2025 by the authors. Licensed to PSEcommunity.org and PSE Press. This is an open access article under the creative commons CC-BY-SA licensing terms. Credit must be given to creator and adaptations must be shared under the same terms. See https://creativecommons.org/licenses/by-sa/4.0/



Systems & Control Transactions

**Research Article - Peer Reviewed Conference Proceeding**
ESCAPE 35 - European Symposium on Computer Aided Process Engineering
Ghent, Belgium. 6-9 July 2025
Jan F.M. Van Impe, Grégoire Léonard, Satyajeet S. Bhonsale,
Monika E. Polańska, Filip Logist (Eds.)

PSE PRESS

# Automated Interpretation of Chemical Engineering Diagrams Using Computer Vision

**Maged Eid[a], Giancarlo Dalle Ave[b]**

[a] W Booth School of Engineering Practice and Technology.
[b] Chemical Engineering Department, McMaster University, Canada.
Email addresses: eidm6@mcmaster.ca, dalleagf@mcmaster.ca

## ABSTRACT

This paper presents state-of-the-art object detection and object identification algorithms for digitizing and interpreting chemical engineering diagrams, including, Block Flow Diagrams (BFDs), Process Flow Diagrams (PFDs), and Piping and Instrumentation Diagrams (P&IDs), using computer vision techniques. These diagrams are essential for visualizing plant processes and equipment but are often stored as image-based PDFs, making manual digitization/interpretation labor-intensive and error-prone. The proposed algorithm automates tasks such as detecting unit operations and identifying them using a set of rule-based and predefined approaches including edge and contour-based rules, spatial arrangement rules, and geometric rules. This method avoids data requirements and computational requirements of deep learning approaches, offering a scalable and efficient solution for preliminary extraction of complex process information.

**Keywords**: Chemical Engineering Diagrams, Object Detection, Object Identification, Computer Vision for Chemical Engineering, Optical Character Recognition (OCR), Features Extraction in Diagrams.

## 1. INTRODUCTION

This paper introduces an object detection and identification system designed to interpret chemical engineering diagrams including Block Flow Diagrams (BFDs), Process Flow Diagrams (PFDs), and Piping and Instrumentation Diagrams (P&IDs), which are essential for visualizing material flow, energy transfer, and equipment in chemical processes. The process of manually interpreting these diagrams often requires significant effort, as it is both labor-intensive and susceptible to errors. This not only increases the time and resources needed for analysis but also raises the likelihood of inaccuracies [1]. To address this, the proposed algorithm leverages computer vision techniques to detect key unit operations and identify them based on textual elements. By automating these tasks, the system aims to improve accuracy and speed, reducing reliance on expert analysis and enhancing process design workflows.

A BFD is a simplified representation of a process that outlines the main unit operations and their flow in a highly abstract way. BFDs are often used in the early stages of process design to visualize the overall structure of a process without focusing on details. PFDs, on the other hand, are more complex and detailed than BFDs. They display the relationships between specific unit operations and the flow of materials, PFDs are crucial for understanding the interconnectedness of unit operations and for simulating both individual operations and the entire process. The most detailed level is the P&ID, which reflects the "real" operational state of a process. P&IDs go beyond PFDs to include every piece of equipment, instrument, and control detail, providing a comprehensive view of how the process will operate in practice. The goal is to create a single multipurpose algorithm that can digitize key information by extracting features from these diagrams including automated detection and identification of unit operations, which is the focus of this work.

Predefined computer vision approaches use fixed rules or templates to recognize patterns or symbols in diagrams, offering fast and reliable detection in standardized industries with consistent representation of unit operations, flow paths, and equipment. However, they may struggle with low-quality diagrams, and non-standard, or irregular symbols [2], such as those often present in chemical engineering diagrams. Rule-based approaches, such as edge and contour-based rules, spatial arrangement rules, and geometric rules, leverage domain-

specific knowledge to define tailored rules for detecting and identifying objects, thereby improving detection accuracy. By combining expert insights with predefined, rule-based methods, these approaches ensure flexibility and reliability across diverse scenarios [3]. The proposed algorithms introduce an approach for automating the detection and identification of unit operations in BFDs, PFDs, and P&IDs. Unlike deep learning methods, it does not require manual labeling, making it more easily implementable and adaptable [4][5][6]. The algorithm leverages predefined rules and rule-based approaches to recognize patterns and symbols, enabling consistent performance across diverse and non-standard representations. This approach enhances accuracy and flexibility while streamlining workflows, addressing limitations of past attempts that relied heavily on manual-labor-intensive methods.

## 2. PROJECT METHODOLOGY

This section outlines the workflow for processing chemical process diagrams, from test data acquisition and preprocessing to object detection and identification. Key steps include object detection to isolate elements like unit operations, using OCR to extract labels, and combining these for unit identification.

### 2.1 Data Collection and Preprocessing

The dataset used in this study comprises 100 high-quality diagrams, including PFDs, BFDs, and P&IDs, sourced from various online resources. The primary selection criterion was image clarity and resolution, ensuring minimal noise or distortion. This diverse dataset allowed for comprehensive testing of the model's robustness across diagram types, with a Git repository link provided for access [7].

Performance evaluation focused on object detection and identification efficiency, analyzing metrics such as processing times for the 100 images. To assess the accuracy, a subset of 50 images was manually validated, covering a wide variety of diagrams and characteristics (e.g., different unit operations and types of diagrams). Object detection accuracy was determined by comparing manually counted objects (e.g., unit operations, control loop symbols) with detected ones, while object identification accuracy was validated using domain knowledge of the unit operations and compared to the textual labels assigned by the algorithms.

### 2.2 Algorithm Development

The algorithms presented in this paper aim to process and analyze images by detecting and identifying the main objects within the images. It follows a series of steps designed to identify regions of interest, remove unwanted noise, and highlight the main unit operations in the image. The process includes multiple image processing techniques such as edge detection, contour detection, and the use of OCR for text recognition to effectively detect and identify the different chemical unit operations within the different diagrams.

Object detection and identification focuses on isolating key features and objects within images and labeling them using text in the images, with OpenCV being one of the tools employed for this process [8]. Figure 1 presents pseudo code for the Object Detection algorithm which begins with Canny edge detection to enhance critical boundaries (line 6) [9], followed by contour detection to isolate individual objects based on shape, area thresholds, aspect ratio, and solidity (line 12) [10]. To clean and refine the mask of detected objects, morphological operations like opening and dilation are applied, removing noise, and closing gaps in contours (line 19) [11]. For separating connected components, a distance transform and the watershed algorithm are used, enabling precise segmentation, even in complex scenarios where objects overlap [12].

**Algorithm 1** Image Processing and Contour Detection

```
1  Input: image_dir (directory containing image files)
2  Output: processed images with highlighted contours and separated objects
3  function DETECT_EDGES(image)
4      convert the input image to grayscale
5      smooth the image using Gaussian blur to reduce noise
6      apply Canny edge detection to identify prominent edges
7      return edge-detected image
8  end function
9  function PROCESS_IMAGE(image_path)
10     load the image from the provided file path
11     edges ← DETECT_EDGES(image)          ▷ identify edges in the image
12     contours ← find contours in the edge-detected image
13     for each contour do
14         if the contour meets size and shape criteria then
15             highlight the contour on a separate mask image
16         end if
17     end for
18     use morphological operations to refine the mask and remove noise
19     apply watershed or similar techniques to distinguish overlapping objects
20     return the original image with contours and the refined mask
21 end function
22 function MAIN(image_dir)
23     for each image in image_dir do
24         processed_image, mask ← PROCESS_IMAGE(image)
25     end for
26 end function
```

**Figure 1.** Pseudocode for the object detection algorithm

Figure 2 presents the pseudocode for the Object Identification algorithm. PaddleOCR is employed to extract textual elements from diagrams, while the initial Object Detection algorithm identifies the unit operations [13]. Small objects detected next to one another are merged to account for the possibility that they are different parts of the same object (lines 4-6). The Euclidean distance between the detected text and the detected unit operations is calculated to establish associations, enabling accurate mapping of labels to unit operations. This method allows for localization and detection of components across chemical engineering diagrams.

**Algorithm 2** Object Identification

```
Input: image directory
Output: processed images with identified objects
initialize PaddleOCR model
MERGE_BOUNDING_BOXESbox1, box2
merge boxes by computing min/max coordinates
ARE_BOXES_CLOSEbox1, box2, threshold
return true if distance between centers is below threshold
MERGE_NEARBY_BOUNDING_BOXESword_boxes, threshold
merge nearby boxes based on threshold
DETECT_EDGESimage
apply Canny edge detection after grayscale conversion and blur
PROCESS_IMAGEimage_path, word_boxes
edges ← DETECT_EDGES(image)
contours ← findContours(edges)
word_boxes ← MERGE_NEARBY_BOUNDING_BOXES(word_boxes, threshold)
for each contour in contours do
  if contour area > threshold then
    process contour and match with word boxes
  end if
end for
morph mask, generate main object image
return original_image, main_object, words_cleaned_image
MAINimage_dir
for each filename in image_dir do
  if filename ends with .jpg or .png then
    result ← OCR.OCR(image_path)
    word_boxes ← extract from result
    original_image ← PROCESS_IMAGE(image_path, word_boxes)
    main_object ← PROCESS_IMAGE(image_path, word_boxes)
    words_cleaned_image ← PROCESS_IMAGE(image_path, word_boxes)
  end if
end for
```

**Figure 2.** Pseudocode for the object identification algorithm

## 3. RESULTS AND DISCUSSION

Table 1 shows the computation times for the object detection and object identification algorithms. Overall, the algorithm is fast, offering quick initial results which can speed up digitization workflows.

**Table 1.** Accuracy Distribution for Object Detection and Object Identification.

| Metric | Object Detection | Object Identification |
|---|---|---|
| Average Time per Image (s) | 0.38 | 4.86 |
| Minimum Time (s) | 0.24 | 2.23 |
| Maximum Time (s) | 0.68 | 15.15 |
| Standard Deviation of Time (s) | 0.1 | 2.33 |

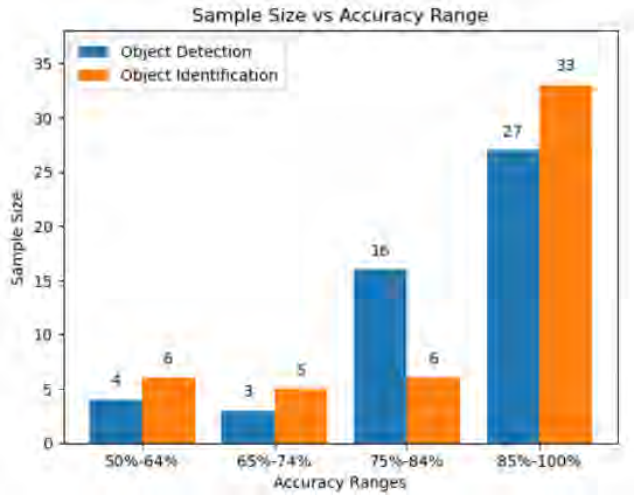



**Figure 3.** Cumulative Time Metrics for Object Detection and Object Identification

Figure 3 summarizes the performance metrics from the manual validation phase of the computer vision models, evaluating accuracy for object detection and identification across the dataset. These results demonstrate the model's effectiveness in detecting and identifying objects within the diagrams. The model achieved strong performance across different accuracy ranges, with the highest sample sizes in the 85%-100% accuracy range. The reason that object identification can have a higher score than object detection is that often multiple objects are mistakenly grouped together (lowering the detection score), however, when analyzing the text of the images multiple labels are assigned to this aggregated space identifying that those operations are all within that space. This evaluation offers insights into the model's consistency for object detection and identification tasks. Specific examples of results are shown below to highlight features of the algorithms' performance as well as situations where the algorithm could be improved.

### 3.1 Object Detection

Figure 4 displays the original and processed images from a BFD. Subfigure 4A shows the original image, while Subfigure 4B presents the results of object detection applied to the same image. The contours and masks are overlaid on the original image, illustrating how the system isolates and identifies key objects. The detected contours are visible, highlighting the effectiveness of the edge detection and contouring methods used. In this example, the accuracy of Object Detection is 100% as it captured all 9 objects within the diagram.

Another example, Figure 5, displays the original and processed images from a PFD. Subfigure 5A shows the original image, while Subfigure 5B highlights the accuracy of the object detection algorithm in handling different object shapes and sizes within the PFD. This visual representation confirms that the system can effectively

manage variations in object appearance and image noise. Some of the drawbacks of the algorithm are visible here as well. The crossing of the streams exiting the central heat exchanger form a closed loop which the algorithm mistakenly identified as belonging to the heat exchanger.

Figure 6 displays the original (A) and processed images (B) from a P&ID. This subfigure demonstrates the algorithm's capability to identify the control aspects of the P&ID and delineate components specific to P&ID diagrams. However, it lacks the ability to capture certain unit operations, such as valves, which will be addressed using template matching techniques in future work. The assigned accuracy of this diagram is 54% as it identifies 19 control icons but misses all 16 valves present in the diagram. P&IDs consistently showed the worst performance in the dataset reflecting their increased complications relative to the other diagrams. Despite some shortcoming, the algorithm shows great flexibility to quickly (<0.5s per image on average) and accurately detect process operations across a wide variety of diagrams with no additional fine tuning required to transition between document types.

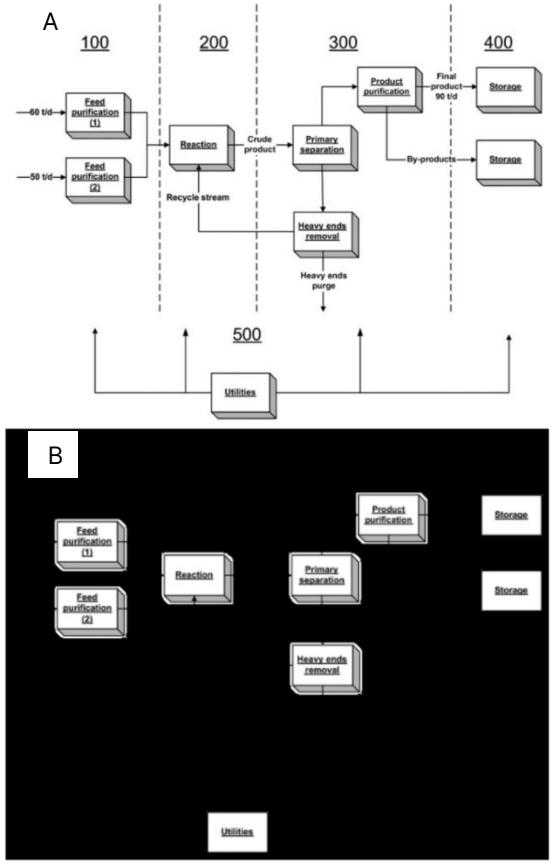



**Figure 4.** (A) Original image of a BFD. (B) Objects detection algorithm output

## 3.2 Object Identification

The object identification algorithm is based on spatial proximity, associating each detected object with its nearest detected word by calculating the Euclidean distance between their center points. In the visual representation (Figures 7 & 8), red dots represent detected words, green dots represent detected objects, and the blue lines are drawn between them to show their assignments. These lines visually indicate which word is linked to which object, based on how close their center points are to each other. A simple example result is shown in Figure 7. In this case, the algorithm clearly connects the text inside the boxes with the boxes themselves. An example of the identification algorithm applied to a PFD can be seen in Figure 8. In this case the object identification algorithm can connect text to label adjacent objects. Lines are drawn between the text box and each of the sub objects which are merged within a unit operation (e.g., each of the tubes in a heat exchanger) to determine which object the label is most likely to belong to. The drawback to the algorithm is that if a unit operation label is too far from the object, it is not connected to it (for example the absorber column on the right). Also, textual elements on the diagrams are often encoded with cryptic names (e.g., REC for the heat exchangers). In practice, these names are often encoded in a standard format and could be converted to more meaningful names with a dictionary.

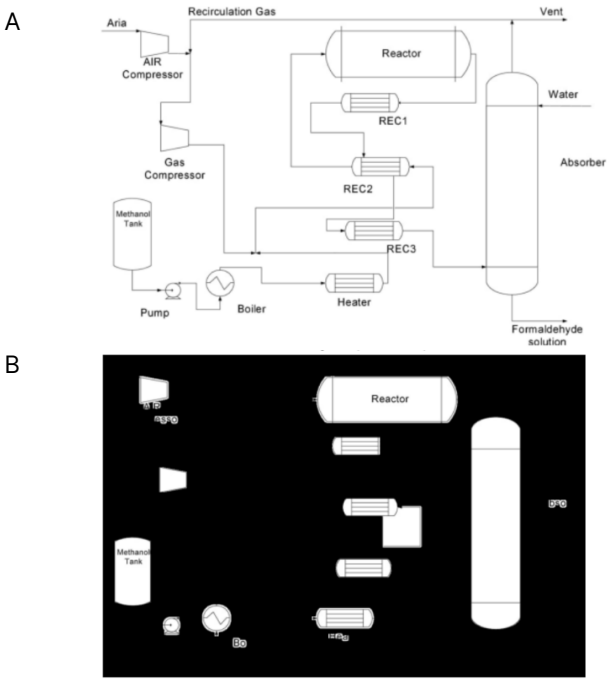


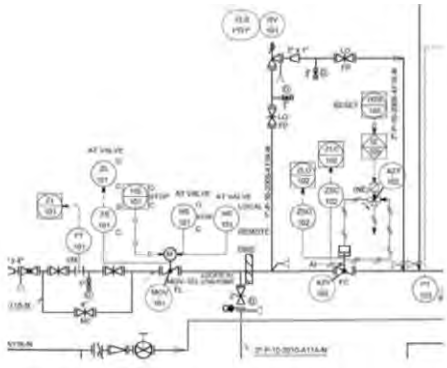

**Figure 5.** (A) Original image of a PFD. (B) Objects detection output from the PFD.

The object identification results demonstrate the algorithm's ability to accurately detect text and associate

it with objects in complex images. High-precision OCR effectively extracts text, with an internal confidence level for reliability of 100%. However, manual validation reveals that in some cases, there may be slight discrepancies between the automated results and the actual text (e.g., chemical formulae containing numbers can get mistaken for text which is “read” incorrectly). One of the major drawbacks to the algorithm is that object identification is based on textual elements in the diagrams, which are often encoded with company- or site-specific naming conventions.

Overall, the system demonstrates fast and accurate detection and text-based identification capabilities, streamlining the preliminary interpretation of chemical engineering diagrams and enhancing workflow efficiency. Compared to deep learning approaches, the proposed algorithm is less computationally intensive, enabling efficient large-scale preliminary data processing. The code processed 100 images with an average of 0.38 seconds for object detection and 4.86 seconds for object identification (on a i7-12700H laptop with 16 GB of RAM and no GPU-based calculations), demonstrating its ability to efficiently handle tasks of varying complexity within a limited timeframe, demonstrating it can help to streamline preliminary digitization workflows at minimal computational expense [14].

A



B

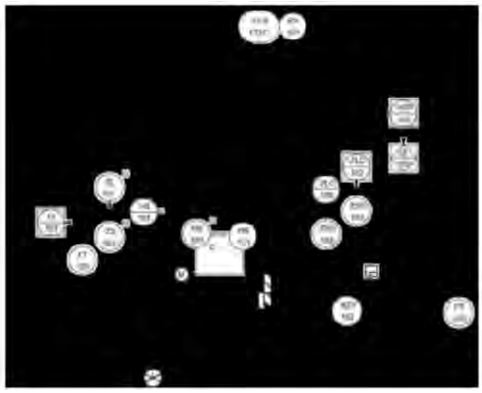


**Figure 6.** (A) Original image of a P&ID. (B) Objects detection output from the P&ID.

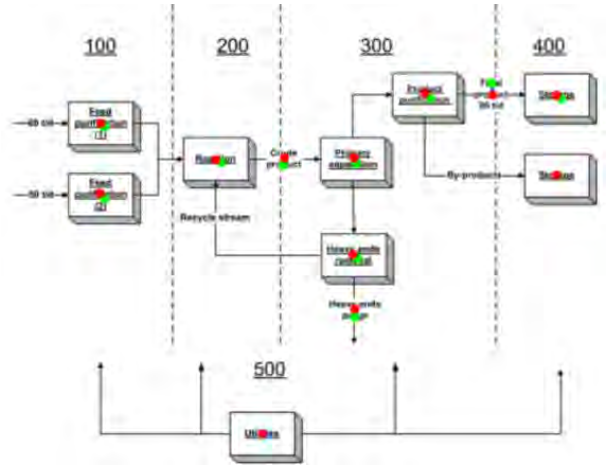



**Figure. 7.** BFD object identification: Red dots mark detected words, green dots mark detected objects, and blue lines show connections between them.



**Figure 8.** PFD object identification: Red dots mark detected words, green dots mark detected objects, and blue lines show connections between them.

## 4. CONCLUSION AND FUTURE WORK

This work presents an object detection and identification system tailored for chemical engineering diagrams, leveraging a combination of rule-based approaches, text extraction, and spatial association. The system quickly and efficiently detects unit operations, establishes connections between text and unit operations to identify objects, and is easily applicable to diverse diagram types, including BFDs, PFDs, and P&IDs. By eliminating the need for manual labeling and relying on predefined rules, the approach is quite flexible streamlining the preliminary interpretation of complex chemical engineering diagrams. Automatically interpreting chemical engineering diagrams reduces the need for manual analysis, significantly saving time and effort. It can improve accuracy by minimizing human errors in identifying process components.

This automation speeds up decision-making,

allowing engineers to focus on optimization rather than diagram interpretation. While the algorithm shows promise, results highlight areas for improvement. Without knowledge of unit operations, it sometimes misidentifies accessory shapes as objects (e.g., recycle loops forming closed shapes). Small objects like valves are often mistaken for noise and filtered out. The object identification relies on linking textual labels to nearby detected objects, but labels often follow site- or application-specific naming conventions.

The next steps involve refining rule-based and predefined approaches, using template matching for smaller objects, and enhancing preprocessing with multi-resolution bounding boxes. Improving OCR with multi-language support, adaptive thresholding, and noise reduction will boost text recognition and object detection. Additionally, the generated data can help integrate deep learning models, further enhancing detection and identification.

## REFERENCES


1. Waller, A., LeDoux, J., & Newstetter, W. What makes an effective engineering diagram? a comparative study of novices and experts.. https://doi.org/10.18260/1-2--22751
2. Yang, L., Zhang, J., Li, H., Ren, L., Yang, C., Wang, J., & Shi, D. (2024). A comprehensive end-to-end computer vision framework for restoration and recognition of low-quality engineering drawings. Engineering Applications of Artificial Intelligence, 133, 108524. https://doi.org/10.1016/j.engappai.2024.108524
3. A rule-based approach for visual pattern inspection. (1988, January 1). IEEE Journals & Magazine | IEEE Xplore. https://ieeexplore.ieee.org/abstract/document/3867
4. Moon, Y., Lee, J., Mun, D., & Lim, S. (2021). Deep Learning-Based Method to Recognize Line Objects and Flow Arrows from Image-Format Piping and Instrumentation Diagrams for Digitization. Applied Sciences, 11(21), 10054. https://doi.org/10.3390/app112110054
5. Deep learning for text detection and recognition in complex engineering diagrams. (2020, July 1). IEEE Conference Publication | IEEE Xplore. https://ieeexplore.ieee.org/document/9207127
6. Kim, H., Lee, W., Kim, M., Yoochan, M., & others. (2021). Deep-learning-based recognition of symbols and texts at an industrially applicable level from images of high-density piping and instrumentation diagrams. Expert Systems with Applications, 183, 115337. https://doi.org/10.1016/j.eswa.2021.115337
7. DalleAveLab. (n.d.). Computer vision chemical simulation: Images. GitHub. https://github.com/DalleAveLab/ComputerVisionChemicalSimulation/tree/main/images
8. Bradski, G. (2000). The OpenCV Library. Dr. Dobb's Journal of Software Tools.
9. Canny, J. (1986). A computational approach to edge detection. IEEE Transactions on Pattern Analysis and Machine Intelligence, 8(6), 679–698. https://doi.org/10.1109/TPAMI.1986.4767851
10. Suzuki, S., & Abe, K. (1985). Topological structural analysis of digitized binary images by border following. Computer Vision, Graphics, and Image Processing, 30(1), 32–46. https://doi.org/10.1016/0734-189X(85)90016-7
11. Haralick, R. M., Sternberg, S. R., & Zhuang, X. (1987). Image analysis using mathematical morphology. IEEE Transactions on Pattern Analysis and Machine Intelligence, 9(4), 532–550. https://doi.org/10.1109/TPAMI.1987.4767941
12. Beucher, S., & Meyer, F. (1993). The morphological approach to segmentation: The watershed transformation. In Mathematical Morphology and Its Applications to Image Processing (pp. 433–441).
13. Du, Y., Li, C., Guo, R., Yin, X., Liu, W., Zhou, J., Bai, Y., Yu, Z., Yang, Y., Dang, Q., & Wang, H. (2020). PP-OCR: A Practical Ultra Lightweight OCR System. arXiv preprint arXiv:2009.09941. Available at: https://arxiv.org/abs/2009.09941 | PaddleOCR Contributors. (2023). PaddleOCR: Awesome multilingual OCR toolkits based on PaddlePaddle. GitHub repository. Available at: https://github.com/PaddlePaddle/PaddleOCR
14. Theisen, M. F., Flores, K. N., Balhorn, L. S., & Schweidtmann, A. M. (2023). Digitization of chemical process flow diagrams using deep convolutional neural networks. Digital Chemical Engineering, 6, 100072. https://doi.org/10.1016/j.dche.2022.100072



© 2025 by the authors. Licensed to PSEcommunity.org and PSE Press. This is an open access article under the creative commons CC-BY-SA licensing terms. Credit must be given to creator and adaptations must be shared under the same terms. See https://creativecommons.org/licenses/by-sa/4.0/




Systems & Control Transactions

**Research Article - Peer Reviewed Conference Proceeding**
ESCAPE 35 - European Symposium on Computer Aided Process Engineering
Ghent, Belgium. 6-9 July 2025
Jan F.M. Van Impe, Grégoire Léonard, Satyajeet S. Bhonsale,
Monika E. Polańska, Filip Logist (Eds.)

PSE PRESS

# Talking like Piping and Instrumentation Diagrams (P&IDs)

**Achmad Anggawirya Alimin[a], Dominik P. Goldstein[a], Lukas Schulze Balhorn[a], and Artur M. Schweidtmann[a]***

[a] Process Intelligence Research Group, Department of Chemical Engineering, Delft University of Technology, Van der Maasweg 9, Delft 2629 HZ, The Netherlands
* Corresponding Author: a.schweidtmann@tudelft.nl

## ABSTRACT

We propose a methodology that allows communication with Piping and Instrumentation Diagrams (P&IDs) using natural language. In particular, we represent P&IDs through the DEXPI data model as labeled property graphs and integrate them with Large Language Models (LLMs). The approach consists of three main parts: 1) P&IDs are cast into a graph representation from the DEXPI format using our pyDEXPI Python package. 2) A tool for generating P&ID knowledge graphs from pyDEXPI. 3) Integration of the P&ID knowledge graph to LLMs using graph-based retrieval augmented generation (graph-RAG). This approach allows users to communicate with P&IDs using natural language. It extends LLM's ability to retrieve contextual data from P&IDs and mitigate hallucinations. Leveraging the LLM's large corpus, the model is also able to interpret process information in P&IDs, which could help engineers in their daily tasks. In the future, this work will also open up opportunities in the context of other generative Artificial Intelligence (genAI) solutions on P&IDs, and AI-assisted HAZOP studies.

**Keywords**: Large Language Models, Knowledge Graph, Graph-based Retrieval Augmented Generation

## INTRODUCTION

Piping and Instrumentation Diagrams (P&IDs) are pivotal in process engineering, serving as comprehensive references across multiple disciplines [1]. For process engineers, daily tasks rely on accurate information retrieved from P&IDs. For example, engineers require accurate information and interpretation of P&IDs during design, HAZOP studies, and operation. However, the intricate nature of P&IDs and the system's complexity pose challenges to extracting information accurately and efficiently. The current approach mainly relies on manually tracing processing lines on PDF or Computer Aided Engineering (CAE) documents, which is time-consuming and prone to errors, leading to loss of production time and potentially hazardous situations.

Recent digitalization efforts in process engineering have brought a more data-centric approach to P&ID development. This advancement, often referred to as "smart" or "intelligent" P&ID, overlays a database on top of process diagrams. Also, recent works proposed the digitization of paper-based P&IDs into smart P&IDs [2]. While each CAE software may use distinct formats, initiatives to improve interoperability are underway. For instance, the Data Exchange in the Process Industry (DEXPI) initiative established a unified, machine-readable format for P&IDs [3]. Leveraging this data exchange standard, our group has developed the pyDEXPI Python package, which implements the DEXPI information model for Python [4]. These developments lay essential groundwork; however, a practical, intuitive implementation is still needed to harness this technology fully and enhance the work experience for process engineers.

Large language models (LLMs) have shown exceptional potential in understanding and processing natural language. The release of GPT-4, which was fine-tuned using reinforcement learning from human feedback (RLHF), marked a significant advancement in tasks such as question-answering and general reasoning [5]. Additionally, retrieval-augmented generation (RAG) systems have made notable progress in reducing hallucinations by enabling LLMs to query information from databases [6]. However, applying these techniques to P&IDs presents

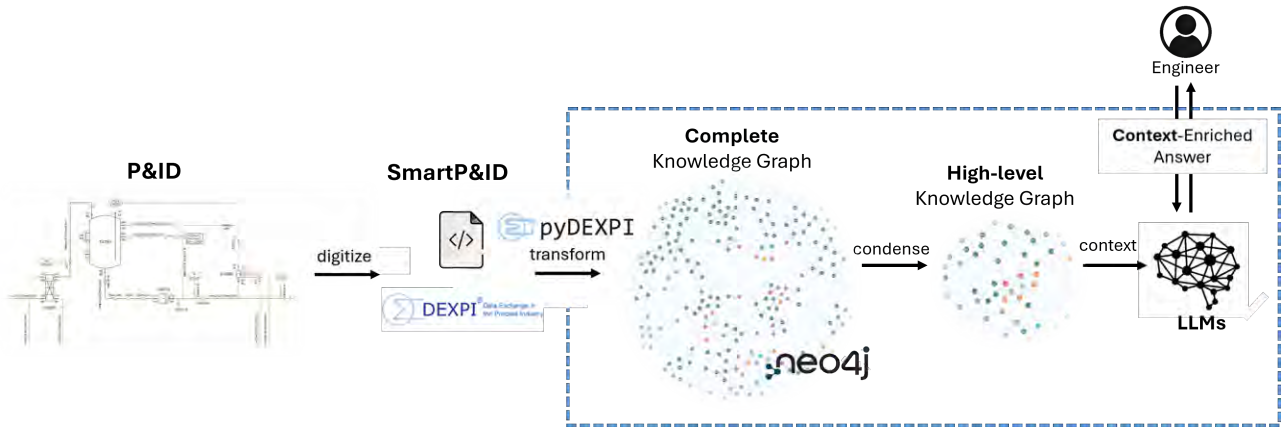



**Figure 1.** This methodology (inside the dashed box) serves as the final element, developed on top and integrated into digitization and contextualization framework. The process begins by digitizing P&ID into smart P&ID using flowsheet digitization tools. The smart P&ID is then transformed into a knowledge graph using the pyDEXPI package. This graph is further condensed into a high-level knowledge graph, which provides contextual input to an LLM for generating context-enriched responses for interaction with the engineer or user.

unique challenges and has not been done yet. As an engineering diagram, P&ID represents the data in both domain and lexical forms. Domain data represents hierarchical information on equipment, piping, and instrumentation, i.e., tubular heat exchangers consisting of a nozzle, shell, and tube bundle. Meanwhile, lexical data captures the interaction relationships between components, i.e., a valve is connected to a tank to regulate inlet flow, while also being connected to an actuator that manipulates the valve opening. This dual nature of P&IDs, involving both structured hierarchy and interlinked relationships, makes effective information retrieval particularly complex.

Building on advancements in process engineering digitalization and LLMs, this work focuses on developing a knowledge graph database derived from P&IDs and its retrieval method. Specifically, DEXPI P&IDs will be transformed into Neo4j labeled property graphs using pyDEXPI. A graph-based RAG technique will then be employed to extract and present relevant information. To ensure LLMs are aware of essential contextual information within P&IDs, high-level representations of P&IDs will be generated and used as context for retrieval. This results in a more intuitive and streamlined approach for process engineers to interact with and retrieve information from P&IDs. Moreover, the integration of P&IDs into foundation models is a key enabler technology for future developments of GenAI applications such as autocorrection of P&D and AI-assisted HAZOPs [7].

## METHOD

This section discusses each of the steps in this methodology, including graph representation, knowledge graph generation, and retrieval method as depicted in **Figure 1**. A DEXPI P&ID sample [3] is used as a case study to demonstrate our approach.

## P&ID GRAPH REPRESENTATION

A graph is an index-free adjacency database consisting of nodes and edges. Nodes represent entities within the dataset, while edges define the relationships between these entities. Due to its flexible structure and intuitive expression, graph databases are widely used in real-world applications, such as social networking, recommendation engines, fraud detection, and knowledge graphs. Graph databases also demonstrated their effectiveness in process engineering to model entire systems like P&IDs [8], [9].

In our data pipeline, smart P&ID in DEXPI format serves as the input, which is parsed using the pyDEXPI package from its XML file into pyDEXPI class instances. The pyDEXPI class framework implements the DEXPI information model in Python; it can be used as a Python package. The graph representation is created by constructing a NetworkX graph from the class instances as pyDEXPI P&ID. The pyDEXPI classes modeled as nodes in this graph representation pertain to the following pyDEXPI packages: 1) equipment, 2) piping, and 3) instrumentation. Meanwhile, edges between these elements are derived from two specific relationships of the pyDEXPI P&ID: domain relationships, which show a child node to the parents, and lexical relationships, which capture the interaction between nodes. The output is a graph showing the network of connection between class instances.

## P&ID KNOWLEDGE GRAPH GENERATION

While the graph captures the structure of the flowsheet, it lacks meaningful semantic context in its raw form. As such, the initial graph representation—comprising Python class instances and their connections—remains abstract and unreadable to LLMs. Semantic information is added to the graph to transform this structure into a readable and functional knowledge graph. This work utilizes a type of knowledge graph called Label Property Graph (LPG) using the Neo4j framework. The LPG graph classifies nodes using the labels and adds key-value pairs as the node properties. This feature is essential to denote different types of components and accommodate the details from the flowsheet.

LPG uses labels as an attribute to distinguish nodes. In our case, multiple labels are employed to classify P&ID components. Node labels are inherited from the pyDEXPI class name and its parent class, which aligns with DEXPI specification. For example, at a higher level, nodes are assigned labels based on their pyDEXPI package, i.e., equipment, piping, or instrumentation. At a more granular level, additional labels are applied according to each component's specific classification, i.e., reciprocatingPump and centrifugalPump. Meanwhile, detailed design information, such as size, operating conditions, tag number, and other specifications, is stored as node properties in key-value pairs. **Figure 2** illustrates an example of a label property graph for a pump, labeled as "equipment" and "reciprocating pump," with its specifications stored as node properties.

The relationship labels in the knowledge graph are also specified following the relationship in pyDEXPI P&ID. Domain relationship labels are remarked as *"has_[componentType]"* or *"is_located_in,"* depending on the direction of the relationship. Meanwhile, the lexical relationship is much more specialized. Material flows were labeled with *"send_to"*; the control structure relationship is represented using words such as *"control," "send_signal_to," "is_logical_end_of,"* and *"measured_by"*.

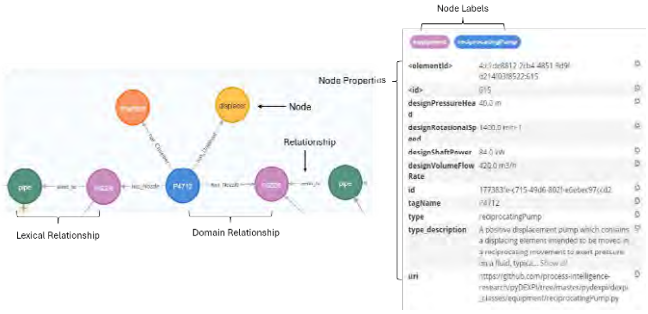



**Figure 2.** LPG structure for a sample of a pump system P&ID. (left) Graph pump node with four child nodes: two nozzles, a displacer, and a pump chamber. The stream enters through the right nozzle and exits at the left. (right) Details of node P4712 with labels of equipment and reciprocatingPump. The node properties contain the pump's specifications.

## GRAPH-BASED RETRIEVAL METHOD

### High-level Graph Context Generation

While the P&ID knowledge graph can be directly used as context for LLMs, extracting information becomes increasingly difficult as the graph's context length and complexity grow. For instance, the illustrative DEXPI flowsheet sample which represents a single page of P&ID with only one tank, two pumps, and two heat exchangers, consists of 212 nodes and 405 relationships. This translates to approximately 67,000 tokens in LLMs, which is inefficient in terms of token usage. The information density in the knowledge graph must be increased to improve efficiency, making the graph more compact and readable for LLMs. The objective is to create high-level graph representations to allow LLMs to focus on the essential structure. This is similar to how engineers read the flowsheet, which develops understanding from a high-level overview of the flowsheet before jumping into details.

Three steps were implemented to create a high-level graph representation:

1. Pruning domain information and connection nodes
2. Condensing low-information nodes
3. Removing non-process-related node properties

These steps reduce the overall complexity while preserving key relationships and concepts. The high-level graph reduces the knowledge graph size from 212 to 53 nodes, 405 to 57 relationships, and tokens usage from approximately 67,000 to 9,000 tokens. The performance of this high-level graph as context will later be compared to the initial complete knowledge graph.

### Chain and Retrieval

The LLM agent was created using the Langchain library. In the chain, the LLM is called using the API key or via a local machine. To enhance the interaction, a memory module is added to allow chat history to become context in LLM's response. As LLM may take time to give a complete response, the stream method is used to show the generated token directly as it is available. For retrieval, the high-level knowledge graph from Neo4j is exported into a graphml file containing information about nodes, relationships, and properties. This file content is then added as context to the engineered system prompt in the chain. In the LLMs, the string from the graphml file is tokenized together with the chat history and user question and passed to the LLM model to generate a history-aware and contextual response.

**Table 1.** Performance comparison of complete and high-level knowledge graph as context across different LLMs. Complete LLMs responses from this study are available in **supporting document**.

| Large Language Models (LLMs) | GPT 4o | | Anthropic Sonnet 3.5 20241022 | | Anthropic Haiku 3 20240307 | | Ollama 3.1: 8B | | Ollama 3.2: 3B | |
|---|---|---|---|---|---|---|---|---|---|---|
| Parameter Number | ~8 x 220B* | | ~175B* | | ~20B* | | ~8B | | ~3B | |
| Context Window | ~128K | | ~200K | | ~200K | | ~128K | | ~128K | |
| **Type of Knowledge Graph** | High-level | Complete | High-level | Complete | High-level | Complete | High-level | Complete | High-level | Complete |
| **Question 1: Reasoning Ability** | | | | | | | | | | |
| Number of major equipment missing in response | 0 | 0 | 0 | 0 | 1 | 1 | NA | NA | NA | NA |
| Flow description accuracy | 90% | 80% | 100% | 50% | 20% | 20% | NA | NA | NA | NA |
| **Question 2: Search Completeness** | | | | | | | | | | |
| Number of retrieved valve | 11 of 11 | 11 of 11 | 11 of 11 | 11 of 11 | 9 of 11 | 9 of 11 | 3 of 11 | 3 of 11 | NA | NA |
| Is valve classified and details given? | Yes | Yes | Yes | Yes | Yes | Yes | No | No | NA | NA |
| **Question 3: Knowledge Inference** | | | | | | | | | | |
| Number of flowsheet specific safety recommendation | 4 | 5 | 6 | 5 | 1 | 4 | 0 | 0 | 0 | 0 |
| Number of generic process safety recommendation | 7 | 3 | 6 | 5 | 6 | 4 | 6 | 6 | 4 | 4 |

NA: The model cannot give an answer based on the given information.

* Estimated by community, no official publication regarding the parameter

## RESULT AND DISCUSSION

In this section, we evaluate our approach's ability to retrieve information from the flowsheet. The model responses are assessed from a series of questions at various configurations of LLM and knowledge graph. The LLMs are varied to determine pipeline performance across different model scales. Additionally, to test our graph condensing method's ability to represent the flowsheet, the model responses from the completed and high-level graphs are also compared.

We designed a series of questions to evaluate distinct aspects, including pattern recognition ability, search completeness, and knowledge inference. The questions are asked sequentially, with each response integrated into the context of the subsequent query to assess how well the model maintains continuity in its analysis. The questions are as follows:

1. *"Describe the process from inlet to outlet."* This question evaluates the model's pattern recognition ability to extract and infer information from the flowsheet.
2. *"List all valves and their specifications."* This question tests the model's capacity for information retrieval and its completeness, specifically its ability to identify and list all valves along with their relevant specifications from the flowsheet.
3. *"Analyze the flowsheet and give recommendations regarding process safety."* This question assesses the model's knowledge inference capability, determining whether it can provide insightful process safety recommendations by leveraging its large corpus of information exposed to LLM during training and information from the flowsheet details.

As provided in **Table 1,** the results showed promising potential for this approach to read, search, and infer information from P&ID. In general, larger LLMs generate more complete and accurate responses. Meanwhile, smaller LLMs have difficulties reading the graph. Besides the current performance, we also see the potential for smaller LLMs, as they are computationally light and relatively affordable to run on local machines and fine-tune for this specific task.

For pattern recognition, as demonstrated in *Question 1*, the model's performance in describing the process is measured by assessing how accurately it follows the flowsheet. A complete score indicates that the model's response correctly traces the process from the inlet to the outlet. A score of 50% signifies that the model only provided a correct description for the first 50% of the process, starting from the inlet. This scoring method is chosen because when large language models (LLMs) make an error early in the response, subsequent parts are likely to be incorrect, as each token is generated based on the preceding tokens. On average, using high-level graph representations improved the model's ability to sequentially describe the process from inlet to outlet by 20% compared to the complete graph. This infers that our condensing methodology to generate high-level graphs better represents the information to improve LLMs' ability to read the P&ID.

The response also reflects the performance of large language models (LLMs) which varies significantly depending on the model size. Larger LLMs generally produce more coherent and accurate responses, whereas smaller LLMs are prone to hallucinations or may refuse to answer altogether. A hallucination occurs when a model generates responses that appear plausible but are factually incorrect, nonsensical, or inconsistent with the given prompt. LLMs are probabilistic models that predict the next word in a sequence, and their accuracy depends heavily on the quality and scope of their training data, as well as the model size. LLMs excel at handling widely popular prompts with established consensus but face challenges on controversial topics or topics with limited data [10]. Additionally, at the cost of computational resources and latency, the model with more parameters tends to have a better performance as it allows for a longer context, which results in better generalization and inferencing [11]. Since all LLMs used in this study are not fine-tuned to read flowsheets in knowledge graph format, the performance represents more of the size of LLMs.

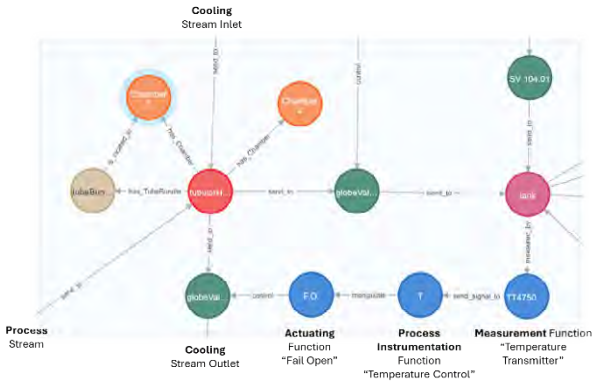



**Figure 3.** Temperature control system in Tank T4750. The tank temperature is measured by the measuring function node TT4750; the measurement signal is then passed to the T process instrumentation function node and actuating function node to the manipulate opening of the globe valve node. The globe valve will control the cooling stream in the tubular heat exchanger to cool the process stream before the tank.

The search completeness results from *Question 2, "List all valves and their specifications,"* demonstrated that both types of knowledge graphs produced the equivalent number of valve retrievals. This indicates that the same amount of information from the flowsheet can be effectively represented using the more compact form of a knowledge graph. Additionally, LLMs with a higher number of parameters showed superior retrieval performance. Notably, all 11 valves were retrieved with detailed information, with Anthropic's Sonnet 3.5 model providing particularly better results. Beyond valve, the LLMs also retrieved the actuators and identified their fail-safe actions. The fail-safe action details were not located directly within the valve node but were instead embedded in the actuating function node, as depicted in **Figure 3**. Despite this, the LLM correctly identified and presented this relevant information. Since all necessary details were included in the system prompt as context, the task essentially information recall.

In the knowledge inference metrics as asked in *Question 3, "Analyze the flowsheet and give recommendations regarding process safety,"* a model that offers more recommendations mentioning specific components of the flowsheet is highly preferred. This indicates that the LLMs are not only able to retrieve information from the flowsheet but also make the inference to the large corpus on which it has been trained. The evaluation shows that using high-level graphs as contexts generally leads to more flowsheet-specific safety recommendations. This aligns with the improvement in pattern recognition observed in the first question; if LLMs can read the pattern, they also generate more relevant recommendations. Below is a sample of Anthropic's Sonnet 3.5 process safety recommendations:

```
1. Pressure Safety:
Current Status:
- One spring-loaded safety valve (SV 104.01) with
set pressure of 6.0 bar
- Design pressures vary from -1 to 60 bar across
equipment
Recommendations:
- Add additional pressure safety valves, espe-
cially around:
  * The centrifugal pump P4711 discharge (60 kW
pump)
  * The reciprocating pump P4712 discharge (84 kW
pump)
- reciprocating pumps are prone to pressure pulsa-
tions
  * Heat exchangers H1007 and H1008 to protect
against thermal expansion
- Install pulsation dampeners around the recipro-
cating pump P4712
- Add pressure indicators and transmitters at more
critical points
```

The results indicate that the Anthropic Sonnet 3.5 is capable of retrieving information on existing safety devices and the design pressure range within the system to formulate relevant recommendations. The recommendations included adding several pressure transmitters at critical locations (though the exact locations were not specified) and installing a pressure safety valve (PSV) on the pump outlet. While the model suggested a PSV, a rupture disc can also be a choice, depending on the fluid, but the recommendation remains relevant as both devices act as pressure protection devices. In addition, the LLMs also highlighted the importance of addressing pressure pulsation in reciprocating pumps, which is

highly pertinent [12]. In the end, the LLMs suggested adding a pressure indicator and transmitter at more critical points. We found this response correct but imprecise; therefore, it's not particularly useful. Other LLMs like GPT-4o and Anthropic Haiku 3 also give process-specific recommendations in their responses but fewer than Anthropic Sonnet 3.5.

Although the results may appear promising, significant challenges remain to be addressed. The field of process engineering demands low tolerance for mistakes due to the risks associated with processing facilities. At the same time, Gen AI models can exhibit hallucinations and can make errors e.g. missing equipment in the response or imprecise response. Therefore, future work will be focused on improving the accuracy and reliability of the tools. This includes experimenting with retrieval methods, refining the knowledge graph schema, integrating a database, and developing more comprehensive evaluation metrics to assess model performance.

## CONCLUSION

We introduced a methodology for intuitive information retrieval and analysis in P&IDs. The methodology encompasses three steps: 1) graph representation of flowsheets using pyDEXPI, 2) knowledge graph generation, and 3) condensing information to a high-level knowledge graph and retrieval using LLMs. We evaluated the model responses across three different metrics: pattern recognition, search completeness, and knowledge inference. The results demonstrated that this approach enables intuitive information retrieval from P&ID using LLMs. The LLMs also showed the potential to read, infer, and generate coherent, contextually accurate information from flowsheets. Additionally, the high-level graph condensing method improved the LLM's ability to retrieve the information from P&ID diagrams. While the current result showed a potential for LLMs to recognize the pattern and infer information from the flowsheet, significant challenges remain to improve the accuracy and reliability in the light of hallucinations of LLMs.

## ACKNOWLEDGEMENTS

We gratefully acknowledge the support provided by Indonesia Endowment Fund for Education Agency LPDP (AAA), Linde Engineering and Siemens AG (DPG), as well as Flour© and Top Sector Alliance for Knowledge and Innovation (TKI) by the Dutch Ministry of Economic Affairs and Climate (CHEMIE.PGT.2023.033) (LSB).

## REFERENCES

1. M. Toghraei, *Piping and instrumentation diagram development*. Hoboken, NJ, USA: Wiley, 2019.
2. F. Theisen, K. N. Flores, L. Schulze Balhorn, and A. M. Schweidtmann, "Digitization of chemical process flow diagrams using deep convolutional neural networks," *Digit. Chem. Eng.*, vol. 6, p. 100072, 2023.
3. M. Theißen and M. Wiedau, *DEXPI P&ID Specification 1.3*, 2021.
4. D. P. Goldstein, A. A. Alimin, L. Schulze Balhorn, and A. M. Schweidtmann, "pyDEXPI: A Python framework for piping and instrumentation diagrams using the DEXPI information model," *ESCAPE35*, 2025.
5. OpenAI, "GPT-4 Technical Report," 2023, *arXiv*: arXiv:2303.08774. Accessed: Oct. 30, 2024. [Online]. Available: http://arxiv.org/abs/2303.08774
6. P. Zhao *et al.*, "Retrieval-Augmented Generation for AI-Generated Content: A Survey," 2024, *arXiv*. doi: 10.48550/ARXIV.2402.19473.
7. A. M. Schweidtmann, "Generative artificial intelligence in chemical engineering," *Nat. Chem. Eng.*, vol. 1, no. 3, pp. 193–193, Mar. 2024, doi: 10.1038/s44286-024-00041-5.
8. J. Morbach, A. Yang, and W. Marquardt, "OntoCAPE—A large-scale ontology for chemical process engineering," *Eng. Appl. Artif. Intell.*, vol. 20, no. 2, pp. 147–161, Mar. 2007, doi: 10.1016/j.engappai.2006.06.010.
9. A. Eibeck, M. Q. Lim, and M. Kraft, "J-Park Simulator: An ontology-based platform for cross-domain scenarios in process industry," *Comput. Chem. Eng.*, vol. 131, p. 106586, Dec. 2019, doi: 10.1016/j.compchemeng.2019.106586.
10. J. Waldo and S. Boussard, "GPTs and Hallucination," *Commun. ACM*, vol. 68, no. 1, pp. 40–45, Jan. 2025, doi: 10.1145/3703757.
11. J. Yang *et al.*, "Harnessing the Power of LLMs in Practice: A Survey on ChatGPT and Beyond," *ACM Trans. Knowl. Discov. Data*, vol. 18, no. 6, pp. 1–32, Jul. 2024, doi: 10.1145/3649506.
12. G. Vetter and F. Schweinfurther, "Pressure pulsations in the piping of reciprocating pumps," *Chem. Eng. Technol.*, vol. 10, no. 1, pp. 262–271, Jan. 1987, doi: 10.1002/ceat.270100132.

© 2025 by the authors. Licensed to PSEcommunity.org and PSE Press. This is an open access article under the creative commons CC-BY-SA licensing terms. Credit must be given to creator and adaptations must be shared under the same terms. See https://creativecommons.org/licenses/by-sa/4.0/



Systems & Control Transactions

**Research Article - Peer Reviewed Conference Proceeding**
ESCAPE 35 - European Symposium on Computer Aided Process Engineering
Ghent, Belgium. 6-9 July 2025
Jan F.M. Van Impe, Grégoire Léonard, Satyajeet S. Bhonsale,
Monika E. Polańska, Filip Logist (Eds.)

PSE PRESS

# Hybrid machine-learning for dynamic plant-wide biomanufacturing

**Shabnam Shahhoseyni[a*], Arijit Chakraborty[b], Mohammad Reza Boskabadi[a], Venkat Venkatasubramanian[b], Seyed Soheil Mansouri[a]**

[a] Department of Chemical and Biochemical Engineering, Technical University of Denmark, DK-2800 Kgs Lyngby, Denmark
[b] Department of Chemical Engineering, Columbia University, New York, NY 10027, United States of America
* Corresponding Author: shabsh@kt.dtu.dk

## ABSTRACT

This study focuses on biomanufacturing case study, i.e. Lovastatin production, employing a hybrid modeling framework that combines mechanistic and data-driven approaches. A time-series dataset was generated using the KT-Biologics I (KTB1) plantwide model, a dynamic simulation of continuous biomanufacturing. The dataset captures critical parameters such as nutrient concentrations and API production. The AI-DARWIN framework was used to develop interpretable machine learning models with constrained functional forms, ensuring both accuracy and clarity. The resulting polynomial-based models reveal key relationships between process variables and system performance, bridging mechanistic insights with data-driven predictions. The models demonstrated reasonable accuracy showing minimal difference between the training and testing errors, highlighting their strong generalization. This work advances hybrid modeling in biomanufacturing by integrating plant-wide mechanistic simulations with interpretable machine learning. The approach ensures both accuracy and transparency while enabling robust process monitoring and control at a 'plant-wide' level, contributing to the broader adoption of hybrid modeling in biomanufacturing.

**Keywords**: Hybrid modeling, Biomanufacturing, Plant-wide modeling, Lovastatin production, Interpretable machine learning.

## 1. INTRODUCTION

The biomanufacturing of high-value products, such as Lovastatin, presents unique challenges due to the complex interplay of biological, chemical, and physical processes [1]. Lovastatin, a widely used cholesterol-lowering drug, is produced through microbial fermentation, where variations in nutrient concentrations, reactor conditions, and downstream processing steps significantly influence its yield and quality. Developing accurate and interpretable models to predict and optimize production outcomes is essential for improving efficiency and meeting stringent quality standards.

Traditional modeling approaches in biomanufacturing often rely on mechanistic models, which are grounded in physical and biochemical laws. Developing these mechanistic models can sometimes be challenging, primarily due to the lack of advanced sensing technologies to gather data (for parameter estimation, model validation, etc.) and a limited understanding of multi-scale phenomenological dynamics. However, data-driven modeling has shown great promise in capturing the behavior of complex systems, if and only, there is sufficient amount of data and right measurement of key characteristic phenomena in a process [2]. So, incorporating domain expertise into the modeling framework is crucial.

Bioprocesses, as a prime example of complex systems, are ideal candidates for data-driven modeling, which help bridge gaps in both theoretical knowledge and practical modeling [3]. Although this approach can handle complex, nonlinear relationships in data, It often lacks transparency, making it difficult to trust and interpret its predictions in regulatory and operational contexts. To address this limitation, hybrid modeling approaches that combine mechanistic models with data-

driven techniques have gained significant attention. By combining numeric AI (machine learning) with symbolic AI, a hybrid AI approach can be developed, resulting in robust, interpretable models suitable for complex systems [4].

KT-Biologics I (KTB1) is a dynamic mechanistic simulation model for continuous biomanufacturing, covering the entire Lovastatin production plant [1]. While effective in capturing process mechanisms, KTB1 has long running times and does not fully clarify how process variables influence the final output, limiting its use for real-time monitoring and optimization. To address these limitations, a hybrid modeling approach integrates mechanistic insights with data-driven modeling. The AI-DARWIN framework [5] enables the discovery of interpretable polynomial models by constraining functional forms, ensuring both accuracy and clarity. This approach accelerates computation, enhances understanding of variable relationships, and improves process control efficiency.

This work develops a hybrid model for Lovastatin biomanufacturing, aiming to create an interpretable representation of the process that captures its dynamic behavior, variable interactions, and plant-wide complexities. The approach begins by generating time-series datasets from the KTB1 model under varying nutrient conditions to systematically examine the effects of key variables, such as lactose and adenine, on Lovastatin production. These datasets feed into the AI-DARWIN framework, which builds explainable ML models, laying the foundation for future optimization of nutrient utilization and enabling knowledge transfer to new process scenarios, such as using different microorganisms or producing alternative products.

## 2. SYSTEM DESCRIPTION

### 2.1. KTB1 Model Description

This model presents a comprehensive framework encompassing both the upstream production and downstream purification of Lovastatin, a target compound produced via fermentation. As depicted in Figure 1, the upstream process begins with the introduction of key raw materials—adenine and lactose—into a mixing unit (M-101). The mixed medium is then continuously fed into a Continuous Stirred-Tank Reactor (CSTR, labeled R-101), where the biomass, predominantly *Aspergillus terreus*, facilitates Lovastatin production.

The fermentation broth exiting the CSTR is directed to a hydro-cyclone separator (HC-101), which plays a pivotal role in separating the mixture into two streams. The first stream, rich in biomass, is partially recycled back to the CSTR to sustain fermentation. The second stream, with lower biomass content (stream 5), is transferred to the downstream process.

In the downstream phase, the focus is on a sequence of separation and purification steps. Centrifugation units (C-101 and C-102) initially remove remaining biomass and dense impurities from the solution. Following centrifugation, the process advances to nanofiltration (NF-101), where Lovastatin is concentrated by retaining larger molecules through steric exclusion while smaller impurities pass through. Figure 1 illustrates the complete process flow for the biomanufacturing of Lovastatin, including both the upstream and downstream operations.

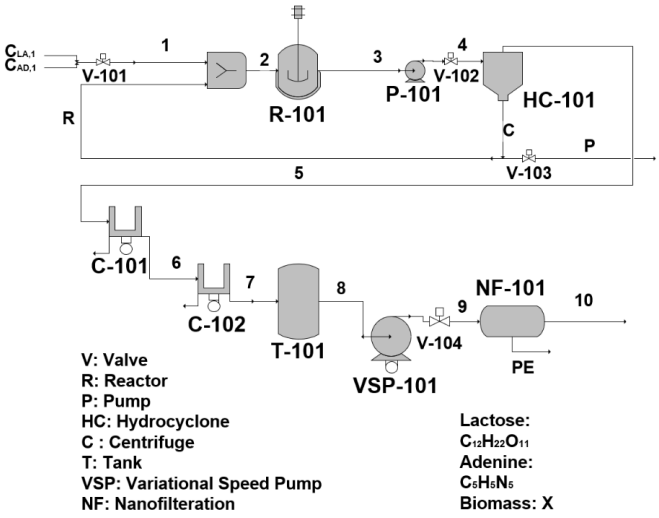



**Figure 1.** Process flow for the biomanufacturing of Lovastatin

#### 2.1.1 Dataset

The datasets used in this study were generated to systematically explore the relationships between nutrient concentrations and Lovastatin API production. Two distinct datasets were created using the KTB1 mechanistic model, each designed to capture specific aspects of the nutrient dynamics in the biomanufacturing process. The datasets include concentrations of various nutrients (such as lactose and adenine), biomass levels in different streams, and the Lovastatin API produced production plant. In these datasets, only one nutrient concentration was varied at a time (by step change) while keeping all other process parameters constant. This method of isolating single variables ensures a controlled environment to study the individual effects of lactose and adenine on Lovastatin production. Each full dataset consists of about 20000 data points. We used 75% for training and 25% for testing, resulting in 15000 training samples and 5000 test samples. Dataset 1 contains information on altering lactose concentration (CLA). And Dataset 2 contains information on altering adenine concentration (CAD). The graphs corresponding to the generated datasets are presented in Figure 2. A step change in lactose at the start of the process, along with a noisy but constant adenine

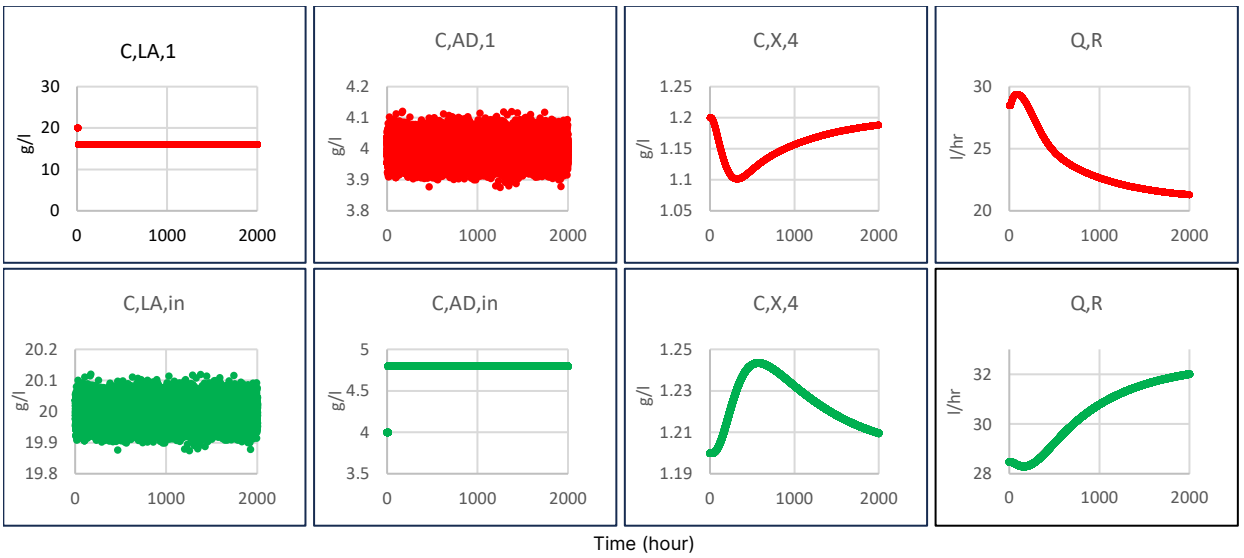



**Figure 2.** Variables in Dataset 1 (in pink) and Dataset 2 (in greens) were varied, with other variables held constant.

input, were introduced to the model. The noise was intentionally added to simulate real-world scenarios, particularly in nutrient supply, where fluctuations are often observed in one of the inputs. Step changes in lactose and adenine, as seen in the first and second datasets, can arise from sensor malfunctions, control system errors, or other process deviations, which are common faults in industrial processes. These variations result in changes to other system variables, such as biomass concentration and flow rates. Figure 2 illustrates how these variations cause dynamic changes in some of the other variables (C,X,4 and Q,R).

## 2.2. AI-DARWIN Framework

The AI-DARWIN framework is a hybrid AI mechanistic model discovery tool designed to uncover interpretable and scientifically valid models from data. Unlike traditional black-box approaches, AI-DARWIN focuses on creating explainable models, ensuring that the resulting mathematical representations are not only accurate but also comprehensible to domain experts. This characteristic makes it particularly suitable for hybrid modeling tasks, such as those encountered in biomanufacturing processes. The framework operates by constraining the model discovery process to specific functional forms, such as polynomials. These constraints allow the generated models to remain aligned with physical laws and domain knowledge, fostering trust and usability in critical applications. By imposing such restrictions, AI-DARWIN ensures that the final models capture essential relationships without unnecessary complexity, making them easier to analyze and validate. For the Lovastatin biomanufacturing process, AI-DARWIN is applied to time-series data generated from the KTB1 mechanistic model. The framework systematically evaluates the dataset to uncover explicit mathematical relationships between input variables, such as nutrient concentrations (e.g., lactose and adenine), and output variables, such as Lovastatin API production. Moreover, normalization using standardization (subtracting the mean of the training data and dividing the difference by the standard deviation of the training data) was used to ensure that all input variables get weighted appropriately

In the context of model optimization and system identification, several frameworks aim to extract meaningful insights from data. One such approach is SINDy [6]. While SINDy is not entirely one-shot (first step of parameter estimation is followed by iteratively sparsifying the coefficients), it comes up with a single best-fit model. AI-DARWIN comes up with multiple options which allow for a broader range of discovery of functional relations between the input variables. This is particularly useful for systems biology models and surrogate models of complex systems. This also can provide a pareto front for further examination of the trade-off between simpler but less accurate models in contrast to complex but more accurate models. Further, AI-DARWIN provides flexibility to incorporate domain-specific constraints, which while limiting in accuracy, reaps rewards in interpretability and eventual robustness over unseen data. The resulting models are expressed in polynomial form, offering a clear interpretation of how each factor influences production outcomes. The generated datasets were used to train the models, with performance assessed using accuracy metrics such as Mean Absolute Error (MAE) and interpretability metrics like $R^2$.

For each dataset, we conducted a series of

modeling steps to predict the concentrations of lactose (C,LA), adenine (C,AD), and lovastatin (C,LOV) in the final stream of the plant (stream #10). Figure 3 shows all the inputs to the model and outputs. However, in AI-DARWIN, we are instructing AI-DARWIN to review all features, select the ones it deems optimal, and potentially arrive at a reduced set of features for the final model.

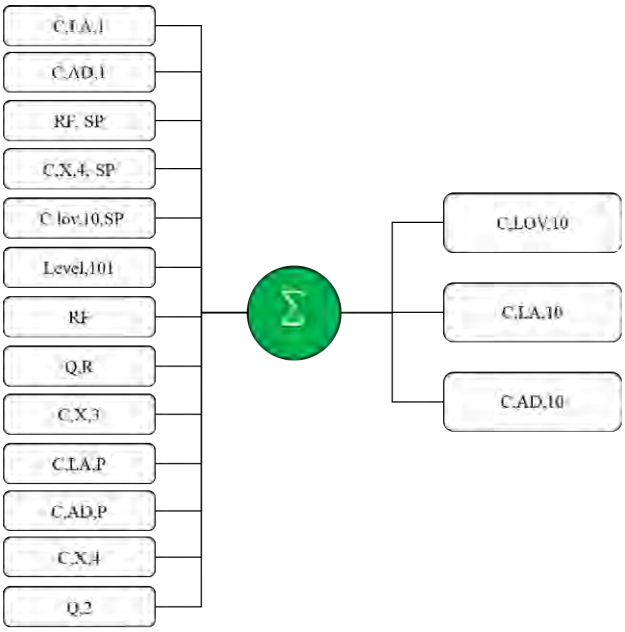



**Figure 3.** All the inputs and outputs of the AI-Darwin framework (C: Concentration, LA: Lactose, AD: Adenine, X: Biomass, LOV: Lovastatin, SP: Setpoint, RF: Recycle factor, Q: flow rate; the numbers represent the streams number at figure 1).

## 3. RESULTS AND DISCUSSION

For each dataset several model architectures were used, and the performance is compared. Table 1 and 2 show selected models developed to predict the concentration of two substrates consumed and the API produced at the outlet of the plant. The results demonstrate that the developed modeling framework effectively captures the complex dynamics of the Lovastatin production plant with low training and testing MAE values, demonstrating high predictive accuracy. Using a combination of mechanistic principles and data-driven modeling, the framework successfully predicts three critical outlet concentrations—C,AD, C,LAC, and C,LOV—at the plant's downstream stage.

For Dataset 1, the models showed strong performance and the minimal error difference between training and testing for all the models suggests strong generalization (Table 1 and Figure 4). The polynomial models, expressed in interpretable forms, highlighted significant contributions from key variables such as 'Q,R' and 'C,LA,1' for predicting adenine concentration, and 'Q,R', 'RF', 'C,X,4', and 'C,AD,P' for predicting lactose and lovastatin concentrations. These terms reflect critical process interactions and nonlinearities inherent in this biomanufacturing system. Adenine concentration in stream 10 (C,AD), being the simplest model, achieves remarkable accuracy ($MAE_{test}$=0.0198), indicating that minimal complexity may suffice for certain targets. In contrast, lactose and lovastatin concentrations (C,LA and C,LOV) include higher-order terms like (C,X,$4^4$) and (C,AD,$P^4$), reflecting more intricate relationships.

These terms suggest significant nonlinearity in the system, consistent with the expected process dynamics. The inclusion of interaction terms, such as (C,X,4)(C,AD,$P^2$), highlights interdependencies between process variables, offering deeper insights into their combined effects on product concentrations. While more complex models (e.g., C,LA and C,LOV) slightly improve accuracy, they may require more computational resources compared to C,AD.

The models developed using Dataset 2 retained this interpretability while incorporating additional interactions and higher-order terms (Table 2 and Figure 5). For example, the C,LA model included interactions like ($RF^2$),(C,X,$4^2$), and (Q,$R^2$), emphasizing the interdependencies between upstream and downstream variables. Similarly, the C,LOV model highlighted the cascading influence of intermediate concentrations, such as C,LA,P on the final product.

The similarity between the MAEs for training and testing sets is due to the relatively large dataset and the low model complexity, which together reduce the risk of overfitting. The large dataset and high sampling

**Table 1.** Model performance on dataset 1 .

| Target | Model | Train MAE | Test MAE |
|---|---|---|---|
| C,AD | $9.72 + 0.25\,(C,LA,1) - 0.56\,(C,LA,1^2)\,(Q,R)$ | 0.0198 | 0.0198 |
| C,LA | $75.4 + 6.45\,(C,X,4^4) - 0.60\,(C,X,4)(C,AD,P^2) + 5.17\,(C,AD,P^3) - 0.94\,(Q,R)\,(RF^2)$ | 0.0785 | 0.0741 |
| C,LOV | $12.04 + 5.17\,(C,X,4^4) - 0.52\,(C,X,4)(C,AD,P^2) + 6.78(C,AD,P^4) - 0.45\,(Q,R)(RF^2)$ | 0.0982 | 0.0971 |

**Table 2.** Model performance on dataset 2 .

| Target | Model | Train MAE | Test MAE |
|---|---|---|---|
| C,AD | $10.18 - 1.75\,(Q,R) \times (RF^2) + 2.06\,(Q,R^4)$ | 0.0158 | 0.0154 |
| C,LA | $77.04 + 3.18\,(C,X,4^4) - 3.21\,(RF^2)(C,X,4^2) + 3.20\,(C,AD,P)\,(Q,R^2) - 2.48\,(C,AD,P^4)$ | 0.0970 | 0.0959 |
| C,LOV | $10.43 - 0.90\,(C,X,4^4) - 0.45\,(RF) + 0.41\,(C,LA,P)(C,X,4) - 0.20\,(C,AD,P^4)$ | 0.0279 | 0.0277 |

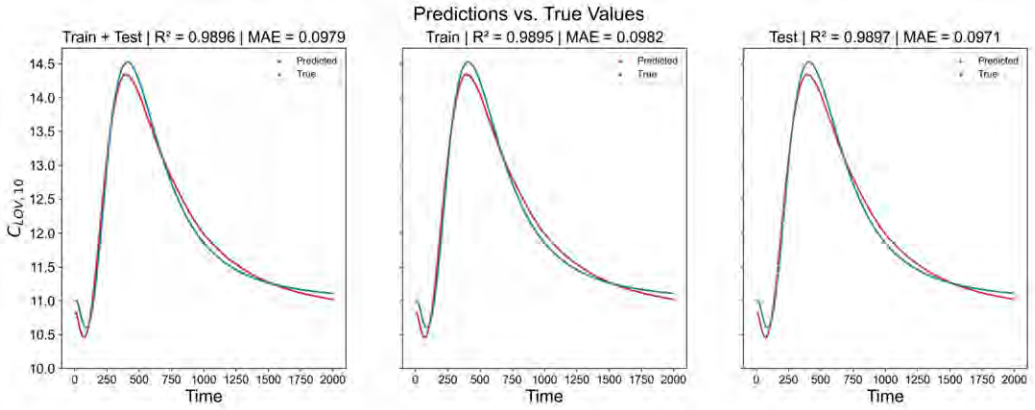



**Figure 4** Model performance on the dataset 1

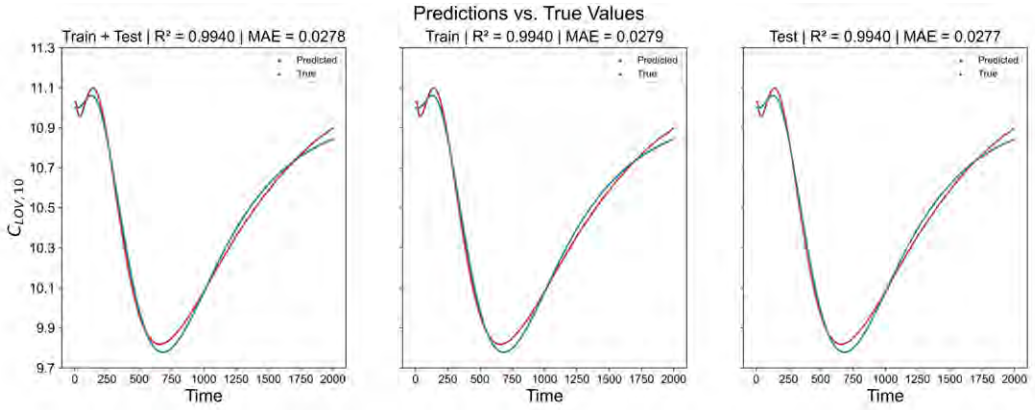



**Figure 5.** Model performance on the dataset 2

frequency could contribute to the observed similarity between training and testing MAEs. However, this sampling strategy reflects realistic process monitoring where frequent measurements are common. The consistent performance across both subsets suggests that the model captures the underlying process behavior without overfitting. Nevertheless, we agree that further validation under different operating conditions would provide a stronger confirmation of generalizability.

Figure 6 presents the sensitivity analysis performed using MAPE. In Dataset 1, the C,AD,P point's distance from the center of the radar chart, represented by the blue line, indicates the highest sensitivity, meaning minor changes in C,AD,P significantly alter the MAPE. Although C,AD,P remain highly influential in Dataset 2 (magenta line), their impact is slightly reduced, which may be attributed to the overall improved fitting performance of the model. Similarly, C,X,4 exhibited significant sensitivity in both datasets, though to a lesser extent than C,AD,P, with Dataset 1 showing a marginally higher sensitivity than Dataset 2. Conversely, RF, Q,R, and C,LA,P demonstrated considerably lower sensitivity in both datasets. Despite slight variations in magnitude, the overall sensitivity patterns regarding biomass concentration were consistent across both datasets, with Dataset 1 showing a slightly higher sensitivity to changes in C,X,4. However, discrepancies in the sensitivities of RF and C,AD,P may arise from the fact that these represent two scenarios modeled for different data conditions (step changes in lactose and adenine, respectively).

This modeling framework demonstrates its capability to model a plantwide biomanufacturing process, laying the groundwork for developing digital twins. The interpretability of the polynomial models facilitates understanding the underlying system dynamics, while the inclusion of complex interactions and nonlinear terms ensures the accuracy needed to capture the intricacies of the process. For models involving biomass concentration at stream 4 (C,X,4 after the fermentation stage) the kinetic models in the KTB1 model can be replaced to calculate biomass concentration in the CSTR for new microorganisms. By transferring the process dynamics knowledge captured in the polynomial models to new scenarios for different products, modeling of new scenarios can also be performed. This idea will be explored in future work, and validation will be required.

Moreover, in the presented study, step changes in lactose and adenine concentrations—representing typical faults encountered in industrial processes—are introduced to the process. Within a broader digital twin framework that includes a fault diagnosis module, once faults are detected and diagnosed, the resulting changes in Lovastatin concentration at the output can be effectively estimated. This estimation can be done using key

process variables, such as flow rates (directly measurable) or biomass concentration (easily calculable), by the models proposed in this study. The biomass concentration can be approximated through a kinetics model within the CSTR. This approach provides an opportunity for the plant to predict the final product concentration—after several units—using operational parameters (recycling factor and flow rate) along with the biomass concentration measured after the fermenter (via the kinetics model) beside nutrient concentrations after the hydro-cyclone.

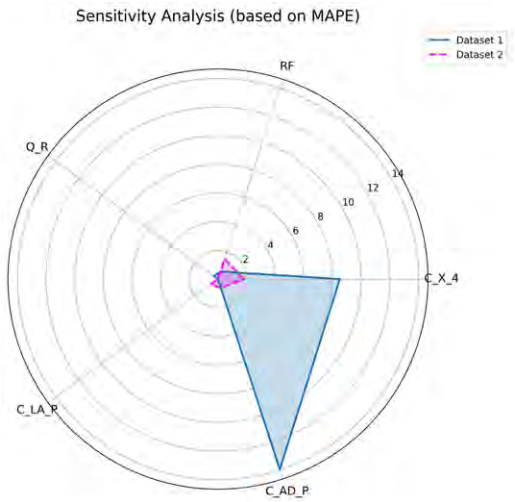



**Figure 6.** Sensitivity analysis of the models developed for lovastatin production using both datasets.

## 4. CONCLUSION

The polynomial models developed in this study accurately capture the complex dynamics of a plantwide bio-manufacturing process, making the framework a valuable tool for advancing digital twins. By incorporating higher-order and interaction terms, the models effectively represent nonlinear relationships and interactions between process variables, enabling predictions under varying operational conditions.

The low MAE values for both training and testing datasets indicate that the models generalize well, balancing accuracy and robustness. Their explicit functional forms provide interpretability, allowing for insight into variable sensitivities and interactions, which is essential for developing digital twins.

Future work will focus on generating more complex datasets by varying multiple variables simultaneously, providing a richer dataset for model development. Additionally, testing more advanced models to ensure the selection of the best, yet simplest, representation would further validate this framework. This approach, coupled with a model selection framework, will optimize the trade-off between accuracy, complexity, and interpretability, expanding the applicability of the models across diverse scenarios. By using polynomial models to determine optimal process setpoints, we can adapt the system for different scenarios, such as changing the microorganism to produce a new product, and transfer insights to new contexts. Additionally, generating natural language explanations from the obtained ML plantwide models by incorporating domain-specific knowledge alongside large language models (LLMs) is part of the vision for future works. This approach could lead to the development of a large knowledge model (LKM) [7] tailored for biomanufacturing. This enhances the interoperability of our obtained models and can be used to generate additional mechanistic insights.

## REFERENCES


1. Boskabadi, M., Ramin, P., Kager, J., Sin, G., & Mansouri, S. S. (2024). KT-Biologics I (KTB1): A dynamic simulation model for continuous biologics manufacturing. Computers and Chemical Engineering, 108770.
2. Venkatasubramanian, V. (2009). Drowning in data: Informatics and modeling challenges in a data-rich, networked world. AIChE Journal, 55(1), 2-8.
3. Shahhoseyni, S., Greco, L., Sivaram, A., & Mansouri, S. S. (2024). A reduced-order hybrid model for photobioreactor performance and biomass prediction. Algal Research, 84, 103750.
4. Chakraborty, A., Serneels, S., Claussen, H., & Venkatasubramanian, V. (2022). Hybrid AI models in chemical engineering – A purpose-driven perspective. Computer Aided Chemical Engineering, 51, 1507-1512. Elsevier.
5. Chakraborty, A., Sivaram, A., & Venkatasubramanian, V. (2021). AI-DARWIN: A first principles-based model discovery engine using machine learning. Computers & Chemical Engineering, 154, 107470.
6. Wentz, J., & Doostan, A. (2023). Derivative-based SINDy (DSINDy): Addressing the challenge of discovering governing equations from noisy data. Computer Methods in Applied Mechanics and Engineering, 413, 116096.
7. Venkatasubramanian, V., & Chakraborty, A. (2025). Quo Vadis ChatGPT? From large language models to large knowledge models. Computers & Chemical Engineering, 192, 108895.



© 2025 by the authors. Licensed to PSEcommunity.org and PSE Press. This is an open access article under the creative commons CC-BY-SA licensing terms. Credit must be given to creator and adaptations must be shared under the same terms. See https://creativecommons.org/licenses/by-sa/4.0/

Systems & Control Transactions

**Research Article - Peer Reviewed Conference Proceeding**
ESCAPE 35 - European Symposium on Computer Aided Process Engineering
Ghent, Belgium. 6-9 July 2025
Jan F.M. Van Impe, Grégoire Léonard, Satyajeet S. Bhonsale,
Monika E. Polańska, Filip Logist (Eds.)

PSE PRESS

# Leveraging Machine Learning for Real-Time Performance Prediction of Near Infrared Separators in Waste Sorting Plant

**Imam M. Iqbal[a]*, Xinyu Wang[a], Isabell Viedt[a,b], and Leonhard Urbas[a,b]**

[a] Technische Universität Dresden, Process-to-Order Group, Chair of Process Control Systems, Dresden, Germany
[b] Technische Universität Dresden, Process-to-Order Group, Process Systems Engineering Group, Dresden, Germany
* Corresponding Author: imam_mujahidin.iqbal@tu-dresden.de.

## ABSTRACT

Many small and medium enterprises (SME) often fail to fully utilize the data they collect due to a lack of technical expertise. The ecoKI platform, a low-code solution that simplifies machine learning application for SMEs, showed a promising answer to the challenge. This study explores the application of ecoKI platform to design process monitoring tools for waste sorting plants. NIR separator data were processed through ecoKI's building blocks to train two neural network architectures—MLP and LSTM—for predicting NIR separation efficiency. The results showed that the models accurately predicted NIR output and effectively identified regions where NIR separation performance declined, demonstrating the potential of data-driven approaches for real-time performance monitoring. This work highlights how SMEs can leverage existing data for operational efficiency and decision-making, offering an accessible solution for industries with limited machine learning expertise. The approach is adaptable to various industrial contexts, paving the way for future advancements in automated, data-driven optimization of equipment performance.

**Keywords**: Machine Learning in Waste Management, Waste Sorting Automation, Performance Monitoring

## INTRODUCTION

Data utilization in SMEs, including waste sorting facilities, is often not maximized, preventing them from fully capitalizing on the data they collect. This underutilization stems from several key challenges. First, SMEs typically have limited technical resources and expertise in data analytics and machine learning, which hinders their ability to process and analyze the vast amounts of data generated by their operations [1]. Second, the integration of advanced data-driven technologies requires significant investment in both time and training, which many SMEs find difficult to accommodate within their existing operational structures [2]. As a result, valuable insights that could drive efficiency improvements, cost savings, and enhanced decision-making remain untapped.

Wang et al. demonstrated that the ecoKI platform is a viable solution for those challenges, as it is a low-code platform, requires no prior machine learning knowledge and is simple to use [3]. EcoKI simplifies the transformation of raw measurement data into actionable insights by providing pre-built building blocks and intuitive interfaces, allowing users to implement advanced machine learning solutions without any programming expertise. This feature makes ecoKI particularly well-suited for SMEs, as it lowers the technical barrier, enabling them to harness their data effectively and implement data-driven solutions with ease.

As part of the EnSort project [4], which aims to enhance automation and energy efficiency in waste sorting plants, this study explores the application of the ecoKI platform to process measurement data into actionable insights. Transforming raw data into real-time performance monitoring tools enables operators to track system efficiency more effectively and detects anomalies. Additionally, these performance measurements can be integrated with advanced automation systems, facilitating operations optimization to achieve energy savings and improved overall performance.

## NEAR-INFRARED SEPARATORS

Near-infrared (NIR) spectroscopy can distinguish non-carbon-black plastic with a very high accuracy, as demonstrated in various studies [5-10]. In a waste sorting plant, the final stage of the sorting section typically comprises NIR separators [11, 12, 13]. These separators are arranged in pairs, consisting of a primary separator and a cleaner separator, as illustrated in Figure 1. Kroell et al. showed that this arrangement generates product with higher purity compared to parallel arrangement [14].

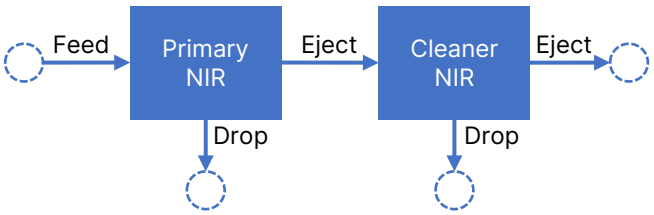



**Figure 1:** NIR Arrangement in Waste Sorting Plant.

The primary NIR separator is designed to maximize the recovery of targeted materials from the waste stream. The cleaner NIR separator, in turn, enhances the purity of the recovered materials by removing unwanted contaminants. Additionally, NIR separators serve a dual function by acting as flow measurement devices, enabling the measurement of the surface flow rate of the material stream.

Multiple datasets (NIR Dataset 1 and 2) were collected from primary-cleaner NIR separator pair in a waste sorting plant located in Northern Europe. The sampling interval of the measurements is 1 minute. Due to the inherent noise in the system, a moving average over the last 5 minutes is applied to smooth the data and improve its reliability.

The system under consideration focuses to separate polypropylene, polyethylene, and their variants, such as polypropylene foil, high-density polyethylene, and polyethylene film. To simplify the analysis and evaluation, the total flow of all targeted materials was calculated from the dataset.

## METHODOLOGY

Machine learning-driven data utilization for performance monitoring has been widely adopted across various fields for maintenance and planning purposes. For instance, Hundi and Shahsavari employed Neural Networks, Random Forests, and Support Vector Machines to estimate power plant performance and identify early-stage equipment malfunctions [15]. In road construction, Cano-Ortiz et al. applied machine learning techniques to assess pavement performance and guide road rehabilitation efforts [16]. Similarly, Gupta et al. used machine learning models to predict the hydrodynamic performance of ships, enabling better estimations of power demand and fuel consumption for planned voyages [17].

The next section will explain how ecoKI platform can be used to develop machine learning models for separation performance prediction.

### Output Prediction

The performance of a primary NIR separator is evaluated based on the amount of targeted material it directs to the cleaner. To predict the outflow, two machine learning model was trained in ecoKI platform and the optimal model was selected based on a balance between complexity and accuracy.

The ecoKI platform offers multiple ready-to-use pipeline templates tailored for different use cases. Each pipeline consists of modular building blocks that represent key steps in the machine learning development process. These blocks provide adjustable options for users with advanced knowledge while also offering default settings for those with limited experience.

In this work, the machine learning models were developed with the Artificial Neural Network (ANN) pipeline. The illustration of the ANN pipeline and its building blocks are presented in Figure 2. The settings for each building blocks are listed in Table 1. The followings sections give a brief explanation on the respective building blocks and their settings.

**Data Reader** first reads the raw dataset. After the user selects the input features and target variable for the machine learning model, the relevant data is extracted from the dataset. Currently, the dataset used for training is the NIR Dataset 1 and the total targeted material flow in the feed stream and eject stream are the input and target variable, respectively.

**Data Sequence Generator** generates input-target sequences based on a defined sequence length to

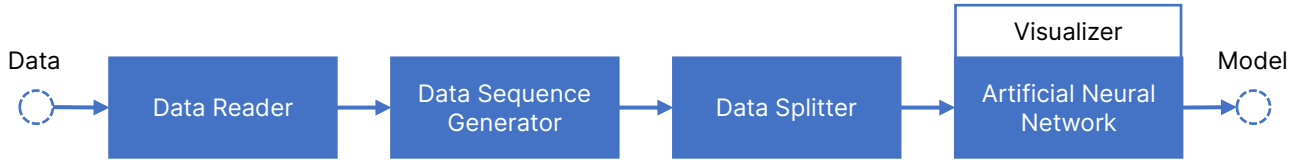



**Figure 2:** Artificial Neural Network Pipeline.

prepare the data for model training. The default value for input step setting is 5 and output step setting is 1, which means the block will pair sequence of five past input data with a one step ahead output.

**Data Splitter** splits the sequence into a training and a test dataset based on the specified fraction. The default setting is 10% of the data is reserved for testing, and the remaining 90% is used for training.

**Artificial Neural Network** block trains an Artificial Neural Network model using the training and test dataset. As of the time of writing, this block supports two ANN models: the Multi-Layer Perceptron (MLP) model and the Long Short-Term Memory (LSTM) model. The neural network structure is fixed with two hidden layers (Layer 1 and 2) positioned between the input and output layers. However, the number of neurons in each hidden layer is adjustable. By default, both hidden layers are set to have two neurons. In this study, both models were used with the default neuron configuration, except for the LSTM model, where Layer 1 was set to four neurons instead of two.

**Visualizer** is connected to the Artificial Neural Network block. It provides graphical representation of the training results, facilitating model evaluation.

**Table 1:** ecoKI Building Blocks Settings.

| Building Block | Setting | Value |
|---|---|---|
| Data Reader | Inputs columns | Target inflow |
| | Feature column | Target outflow |
| Data Sequence Generator | Input steps | 5 |
| | Output steps | 1 |
| Data Splitter | Test fraction | 0.1 |
| Artificial Neural Network | Model | MLP (LSTM) |
| | Layer 1 nodes | 2 (4) |
| | Layer 2 nodes | 2 |

## Disturbance Detection

To detect disturbances or deterioration in NIR performance, the predicted material flow is compared with the actual flow. Since the predictor was developed using disturbance-free data and solely depend on the input stream, any significant discrepancy between the predicted and actual values indicates potential system disturbances.

To evaluate the effectiveness of this tool, a part of NIR Dataset 2 was artificially modified to simulate reduced NIR performance. The alteration was done by changing the actual outflow value with 50% of the inflow. The targeted material outflow in normal and disturbed conditions is shown in Figure 3. Both flow profiles appear similar, despite modifications applied between 21:00 and 22:00 on September 3. This highlights that relying solely on the flow profile is insufficient for anomaly detection, as the changes would likely go unnoticed by operators under normal monitoring conditions. By overlaying the disturbed outflow profile with the predicted normal outflow profile, the operator will be able to clearly observe the range in which the disturbance occurs, as the two lines will not overlap during the disturbance period.

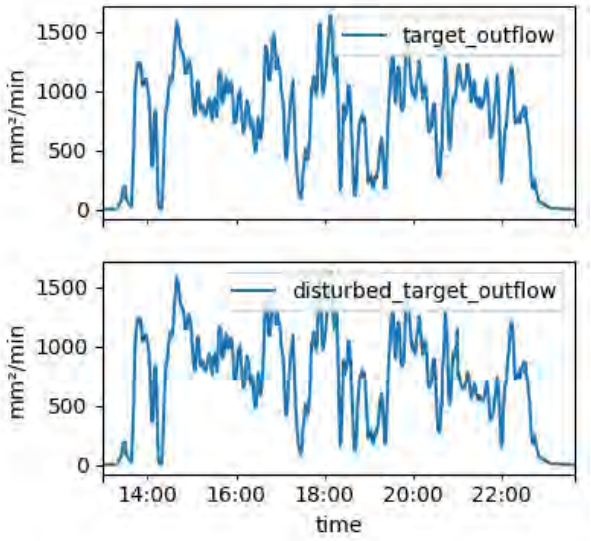


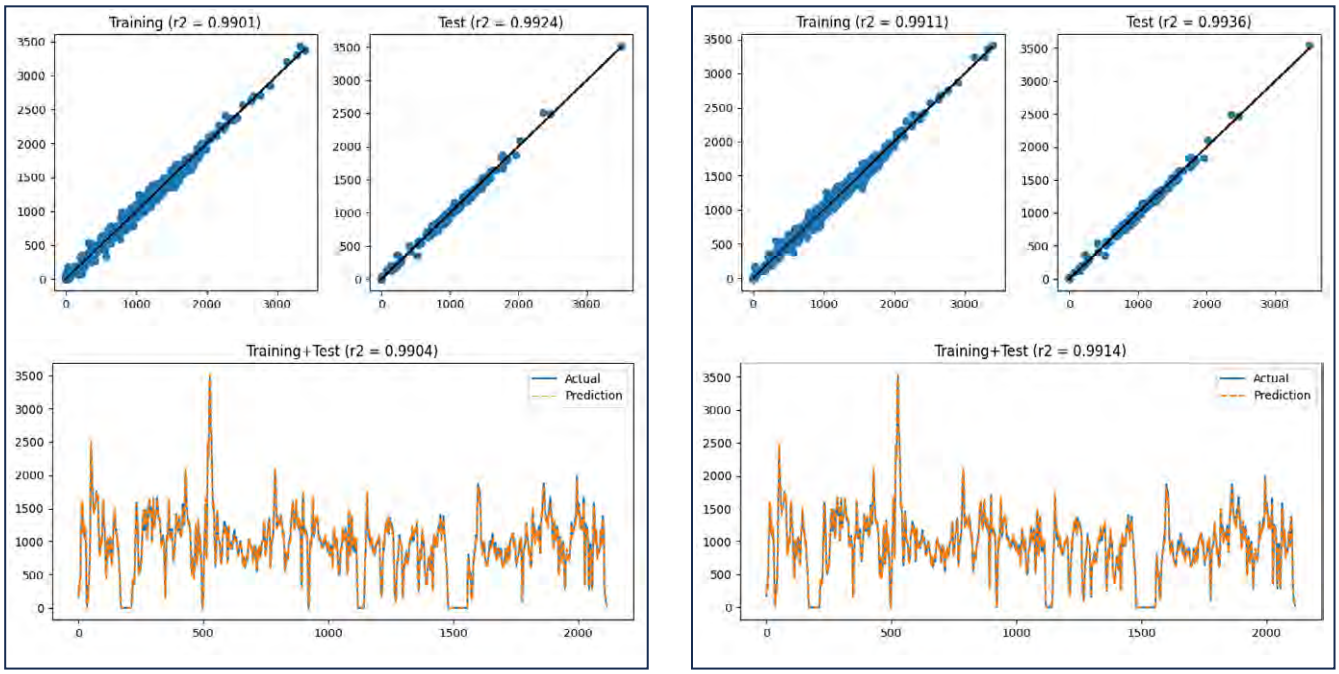

**Figure 3:** Material Outflow Profile on Disturbance Detection (NIR Dataset 2).

# RESULTS AND DISCUSSION

## Output Prediction

The training and testing performance of the MLP and LSTM model are evaluated from ecoKI Visualizer output presented in the left part and right part of Figure 4, respectively. The scatter plot of the training data and the prediction is shown on the top-left and the scatter plot of the test data and the prediction is shown on the top-right. The majority of the data in the training set falls below 2500 mm²/min, while most of the test set data lies below 2000 mm²/min. Despite using the default setting, the generated models demonstrates excellent accuracy as shown by the coefficient of determination. These results imply that ecoKI's automated pipeline effectively optimizes key aspects of model development, enabling users to achieve high-performance predictions without manual fine-tuning. This suggests that even users with minimal expertise in machine learning can leverage ecoKI to develop reliable models, making advanced AI technology more accessible to SMEs. Furthermore, the high accuracy achieved with default settings indicates that ecoKI's pre-configured parameters are well-calibrated for general use cases, reducing the need for extensive trial and error.

The MLP model was ultimately selected as the predictor due to its simplicity, which is evident from the




MLP LSTM

**Figure 4:** LSTM and MLP ecoKI Visualizer. In each model, Top-Right: Training result, Top-Left: Test result, Bottom: Combined result. x and y axis in top plots and y axis in bottom plot are flow in $mm^2/min$, while x axis in bottom plot are the index of the data.

significantly lower number of estimated parameters compared to the LSTM model, as detailed in Table 2. The MLP model, with just 21 parameters, is less complex than the LSTM model, which has 109 parameters. This simplicity not only made the model easier to train but also enhanced its generalization capability. With fewer parameters to optimize, the MLP model was less prone to overfitting, allowing it to generalize more effectively to new, unseen data. This combination of simplicity and robust generalization made the MLP model the preferred choice for the task.

**Table 2:** Machine Learning Model Summary.

| Model | Structure | Trainable Params |
|---|---|---|
| MLP | Dense(2), Dense(2) | 21 |
| LSTM | LSTM(4), Dense(2) | 109 |

## Disturbance Detection

When the actual flow profile is overlaid with the predicted flow profile, as shown in Figure 5 (top), any deterioration in NIR performance becomes immediately apparent. During periods of normal operation, the trained model accurately predicts the outgoing material flow, even when tested on a separate dataset, demonstrating strong generalization capabilities.

The recovery profile, displayed in Figure 5 (bottom), reveals fluctuations, including drops and peaks, corresponding to moments when the machine experienced brief stoppages. These fluctuations are likely due to the cleaner NIR stopping and restarting slightly earlier than the primary NIR. The flat 50% recovery rate near the end of the profile indicates a region where the data has been modified. Approximately 30 minutes before the end, the recovery rate began to decline. However, the flow profile indicates that this behavior is expected as the actual flow match with the predicted flow.

The ability to detect disturbances by comparing actual and predicted flow profiles underscores the practical value of this tool in monitoring and maintaining system performance. By providing real-time insights into deviations from expected behavior, the tool enables early identification of potential issues, allowing operators to take corrective actions before significant disruptions occur. This proactive approach not only enhances process stability but also improves overall efficiency by minimizing unplanned downtime. Furthermore, the tool's strong generalization capability ensures reliable predictions across different datasets, making it a valuable asset for industries seeking to optimize operations with minimal manual intervention.

## How ecoKI Lowers the Barrier for SMEs

As demonstrated in the previous section, ecoKI's default settings achieved a high prediction accuracy, highlighting its ability to generate robust models with minimal input. This is particularly beneficial for SMEs, as ecoKI directly addresses the barriers to adopting machine learning:

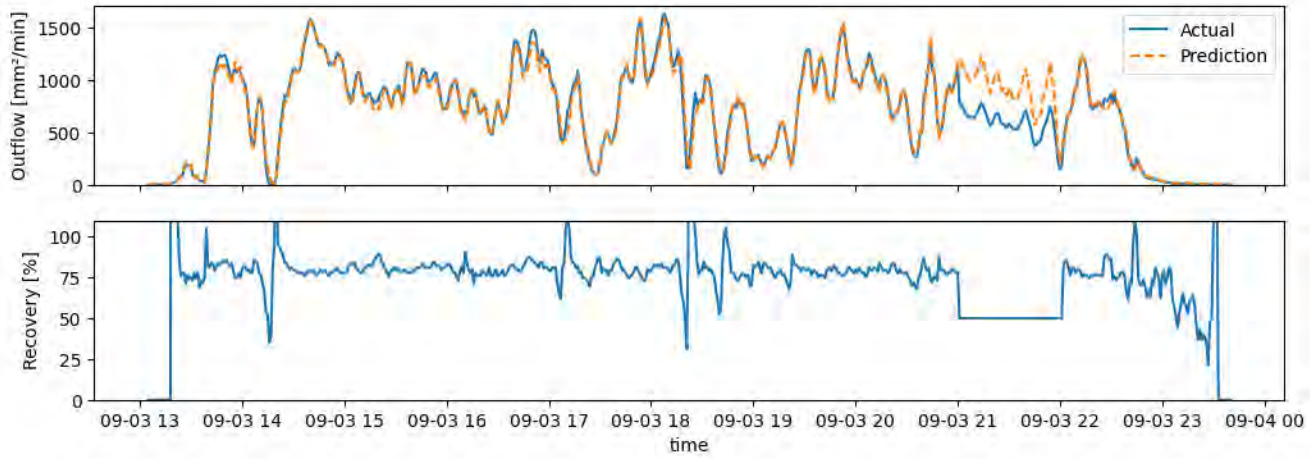



**Figure 5:** Material Outflow Profile on Disturbed System with Prediction Overlay (Top) and Percent Recovery of Targeted Material (Bottom).

- **No-code, automated platform**: Build and deploy accurate models with just a few clicks, as shown by the 99% accuracy.
- **Pre-configured settings**: Default parameters allow users with limited experience to achieve reliable results.
- **Flexibility for advanced users**: Offers customization for experienced users while remaining user-friendly for beginners.
- **Cost-effective, cloud-based solution**: Eliminates the need for expensive infrastructure, making AI accessible to SMEs.
- **Seamless integration**: Easily integrates with existing systems, enabling SMEs to apply AI without disrupting workflows.

By lowering the technical and financial barriers, ecoKI empowers SMEs to utilize their data to develop machine learning models that enhance operational efficiency, reduce downtime, and improve decision-making.

## CONCLUSION

This study successfully demonstrated the application of basic MLP and LSTM models to predict NIR separator output, achieving over 99% accuracy on the training data. The MLP model exhibited strong generalization by accurately predicting outcomes on a separate test dataset. The model's reliance solely on the targeted material feed flow made it effective in detecting instances of performance deterioration in the NIR separator.

The machine learning models were developed using ecoKI's built-in pipeline, building blocks, and default settings for most of the blocks, showcasing the platform's ability to transform raw measurement data into actionable insights without requiring programming expertise. This feature makes ecoKI an ideal solution for small and medium-sized enterprises (SMEs), as it removes the technical barriers to AI adoption and enables businesses to leverage machine learning for operational improvements. The no-code, automated approach, along with pre-configured settings, ensures that even users with limited machine learning experience can develop high-quality models.

While ecoKI proves highly effective for waste sorting applications, it is worth noting its limitations. The platform's model structure offers limited adjustability, which may restrict its use for significantly more complex or customized modeling needs. Nevertheless, ecoKI's approach has significant potential for expansion across various industrial contexts, positioning it as a valuable tool for SMEs seeking to harness machine learning for real-time performance prediction and process optimization.

In conclusion, ecoKI offers a powerful, user-friendly solution for leveraging machine learning to predict the performance of NIR separators in waste sorting plants. By enabling SMEs to tap into AI-driven insights without extensive technical expertise or costly infrastructure, ecoKI paves the way for smarter, more efficient decision-making and process improvement. Future work could explore its scalability and adaptability in diverse industrial settings, cementing ecoKI as a game-changer in the use of machine learning for operational performance prediction.

## DATA AVAILABILITY

The data that has been used is confidential.

## ACKNOWLEDGEMENTS

As part of the Federal Government's seventh energy research program 'Research for an environmentally friendly, reliable and affordable energy supply', research funding is provided by the BMWK and Project

Management Jülich (PtJ) under the title of project EnSort (FKZ 03EN2083B).

## REFERENCES


1. Strljic MM, Vollmann C, Riedel O. Shop-floor service connector - a message-oriented middleware focused on the usability and infrastructure requirements of SMEs developing smart services. ICKII: 37–40 (2020). https://doi.org/10.1109/ICKII50300.2020.9318831
2. Menon S, Shah S. Are SMEs ready for industry 4.0 technologies: an exploratory study of I 4.0 technological impacts. ICCAKM: 203–208 (2020). https://doi.org/10.1109/ICCAKM46823.2020.9051550
3. Wang X, Rani F, Charania Z, Vogt L, Klose A, Urbas, L. Steigerung der energieeffizienz für eine nachhaltige entwicklung in der produktion: Die rolle des maschinellen lernens im ecoKI-projekt. Automation 2024: 825-840 (2024). https://doi.org/10.51202/9783181024379-825
4. Vogt L. https://tu-dresden.de/ing/forschung/bereichs-labs/p2o-lab/projekte/ensort-steigerung-der-energieeffizienz-im-abfall-und-recyclingstoff-sortierprozess-durch-erhoehung-des-automatisierungsgrades?set_language=en
5. Bonifazi G, Capobianco G, Serranti S. A hierarchical classification approach for recognition of low-density (LDPE) and high-density polyethylene (HDPE) in mixed plastic waste based on short-wave infrared (SWIR) hyperspectral imaging. SAA: Molecular and Biomolecular Spectroscopy 198: 115–122 (2018). https://doi.org/10.1016/j.saa.2018.03.006
6. Calvini R, Orlandi G, Foca G, Ulrici A. Development of a classification algorithm for efficient handling of multiple classes in sorting systems based onhyperspectral imaging. J. Spectral Imaging a13 (2018). https://doi.org/10.1255/jsi.2018.a13
7. Chen X, Kroell N, Althaus M, Pretz T, Pomberger R, Greiff K. Enabling mechanical recycling of plastic bottles with shrink sleeves through near-infrared spectroscopy and machine learning algorithms. Resources, Conservation and Recycling 188: 106719 (2023). https://doi.org/10.1016/j.resconrec.2022.106719
8. Duan Q, Li J. Classification of common household plastic wastes combining multiple methods based on near-infrared spectroscopy. ACS EST Eng 1: 1065–1073 (2021). https://doi.org/10.1021/acsestengg.0c00183
9. Xia J, Huang Y, Li Q, Xiong Y, Min S. Convolutional neural network with near-infrared spectroscopy for plastic discrimination. Environ Chem Lett 19: 3547–3555 (2021). https://doi.org/10.1007/s10311-021-01240-9
10. Zheng Y, Bai J, Xu J, Li X, Zhang Y. A discrimination model in waste plastics sorting using NIR hyperspectral imaging system. Waste Management 72: 87–98 (2018). https://doi.org/10.1016/j.wasman.2017.10.015
11. Tanguay-Rioux F, Spreutels L, Héroux M, Legros R. Mixed modeling approach for mechanical sorting processes based on physical properties of municipal solid waste. Waste Management 144: 533–542 (2022). https://doi.org/10.1016/j.wasman.2022.04.025
12. Tanguay-Rioux F, Legros R, Spreutels L. On the limits of empirical partition coefficients for modeling material recovery facility unit operations in municipal solid waste management. Journal of Cleaner Production 293: 126016 (2021). https://doi.org/10.1016/j.jclepro.2021.126016Author
13. Parbat S, Iqbal I, Viedt I, Urbas L. Architecture of digital twin for automating waste and recycling material sorting process. ETFA: 1–4. (2024). https://doi.org/10.1109/ETFA61755.2024.10710670
14. Kroell N, Maghmoumi A, Dietl T, Chen X, Küppers B, Scherling T, Feil A, Greiff K. Towards digital twins of waste sorting plants: Developing data-driven process models of industrial-scale sensor-based sorting units by combining machine learning with near-infrared-based process monitoring. Resources, Conservation and Recycling 200: 107257 (2024). https://doi.org/10.1016/j.resconrec.2023.107257
15. Hundi P, Shahsavari R. Comparative studies among machine learning models for performance estimation and health monitoring of thermal power plants. Applied Energy 265: 114775 (2020). https://doi.org/10.1016/j.apenergy.2020.114775
16. Cano-Ortiz S, Pascual-Muñoz P, Castro-Fresno D. Machine learning algorithms for monitoring pavement performance. Automation in Construction 139: 104309 (2022). https://doi.org/10.1016/j.autcon.2022.104309
17. Gupta P, Rasheed A, Steen S. Ship performance monitoring using machine-learning. Ocean Engineering 254: 111094 (2022). https://doi.org/10.1016/j.oceaneng.2022.111094


© 2025 by the authors. Licensed to PSEcommunity.org and PSE Press. This is an open access article under the creative commons CC-BY-SA licensing terms. Credit must be given to creator and adaptations must be shared under the same terms. See https://creativecommons.org/licenses/by-sa/4.0/



Systems & Control Transactions

**Research Article - Peer Reviewed Conference Proceeding**
ESCAPE 35 - European Symposium on Computer Aided Process Engineering
Ghent, Belgium. 6-9 July 2025
Jan F.M. Van Impe, Grégoire Léonard, Satyajeet S. Bhonsale,
Monika E. Polańska, Filip Logist (Eds.)

PSE PRESS

# Exploring Industrial Text Data for Monitoring Chemical Manufacturing Processes

**Eugeniu Strelet[a,b], Ivan Castillo[a], You Peng[a], Swee-Teng Chin[a], Anna Zink[a], Ricardo Rendall[a], Marco S. Reis[b,*]**

[a] The Dow Chemical Company
[b] Univ Coimbra, CERES, Department of Chemical Engineering, Rua Sílvio Lima, Pólo II – Pinhal de Marrocos, 3030-790 Coimbra, Portugal
* Corresponding Author: marco@eq.uc.pt.

## ABSTRACT

To address the limitations of traditional sensing instrumentation in industrial processes, this work explores the use of industrial text data. Given that current instrumentation often fails to capture the full scope of process-related information, text data resulting from operation of industrial settings (for example: maintenance, inspection and incident reports) can provide valuable insights. This study focuses on accessing the effectiveness of natural language processing (NLP) techniques in retrieving critical information from industrial text data. To achieve this, the classification of Process Safety and Containment Events (PSCE) was used as case study. Overall, we found NLP methods are effective in information retrieval from industrial text data. However, the integration of the embeddings into machine learning (ML) approaches poses some challenges. The complexity of the information encoded in the embeddings makes them too disparate and unique samples of a larger domain, making challenging the training of a ML model.

**Keywords**: Industrial text data, natural language processing, data mining, chemical manufacturing industry, process safety and containment events.

## INTRODUCTION

In the context of chemical manufacturing industry, a wide range of sensor technologies and data collection methods are available to use. These tools serve to provide valuable insights into an array of critical aspects within the industrial process. They encompass the monitoring of physical and chemical phenomena occurring throughout the process, the status of equipment, prevailing process conditions, attributes related to raw materials and product quality, emissions data, logistic issues, and more [1]. This diversity in sensing instrumentation enables us to capture point measurements of essential parameters such as temperature, pressure, pH, and conductivity. Furthermore, it allows for the acquisition of richer data sources, including spectrum, images, vibrations, and sound profiles. Such comprehensive data gathering empowers us to gain a holistic understanding of the complex processes unfolding within the chemical manufacturing.

Despite the abundance of available instrumentation, this falls short in capturing the entirety of process-related information in industrial settings. Typically, sensors are strategically positioned to provide localized snapshots of a given process state, with the assumption that these snapshots are representative and informative of the operation and phenomena taking place. Furthermore, sensors are inherently designed to provide a single or a set of physical and chemical properties, such as a spectral reading of radiation passing through a sample, temperature measurements at a specific location, or reactor pressure data, among others. Moreover, the compensatory actions executed by control systems often effectively conceal process anomalies from sensor detection. Consequently, crucial details pertaining to process health, including issues such as leaks, corrosion, insulation degradation, and other unforeseen events, may remain concealed within the system, eluding their identification.

To address the limitations of existing instrumentation, it is imperative to explore alternative sources of information. One promising solution utilizes text data from inspection reports, incident/event logs, maintenance

records, work order and more that are typically present in industrial setting. These texts information typically encapsulates insights gained by operators, inspectors, or incident management officers (IMOs) during their responsible activities. For example, observations related to unusual noises or vibrations, signs of corrosion or equipment wear, incidents such as leaks, peculiar odors, ongoing maintenance or repair work orders, and activities undertaken on production lines or equipment, all contain valuable information about the production processes. Therefore, textual data analysis can provide valuable insights about current process health and safety monitoring system.

Existing NLP approaches for processing textual data can be broadly categorized into two main groups: context-free methods and context-based methods [2]. Context-free approaches, exemplified by techniques such as bag-of-words (BoW) and term frequency – inverse document frequency (TF-IDF), or machine learning approaches such Word2Vec, etc., primarily rely on word counting or representation without considering contextual relationships. These methods often result in sparse matrices, which can lead to zero-inflation problems. Additionally, frequency-based approaches are notably sensitive to misspellings. On the other hand, context-based NLP such as bidirectional encoder representations from transformers (BERT), generative pre-trained transformer (GPT) and Flair, employ advanced linguistic techniques to analyze and codify the context and semantics of a given text or document. These methods aim to capture the meaning and relationships between words, making them more robust in handling variations and nuances in language [3].

Context-based approaches are typically based on neural networks (NN) structures, often employing either a recurrent NN (RNN) or transformer architectures specifically trained for various text data processing tasks such as text summarization, text generation, topic identification, named entity recognition (NER), classification, etc. Among these tasks, embedding methods play a pivotal role in encoding text data in a limited set of numerical features. In context-based NLP approaches, embeddings are generated not just through counting frequency of the words; instead, they are calculated by weighting the words, so that the semantic meaning is preserved. This preservation of meaning ensures that the context in which words are used is retained, mitigating the risk of information loss. Furthermore, the context-based NLP models are more robust to misspellings. These factors present a significant advantage over frequency-based text processing methods.

One key drawback of these approaches is their substantial data requirements during the training phase. Typically, industrial datasets consist of only hundreds to thousands of observations per text dataset, spanning a time frame of approximately 4 to 5 years, representing the equipment or process life cycle. This limited data volume can indeed pose challenges in training highly effective NLP models. To address such limitation, pretrained models can be utilized. These models have been trained on extensive and diverse textual data from various sources, enabling them to capture broad language patterns and semantics. This training allows the models to exhibit a form of statistical inferred reasoning, effectively interpreting and processing complex text data [4].

Beyond the inherent methodological limitations observed from an NLP perspective in dealing with industrial data, there is a lack of studies within the existing literature that incorporate industrial text data, particularly in the chemical manufacturing domain. In the present study, the primary objective is to evaluate the effectiveness of NLP approaches for information retrieval from industrial text data. Specifically, our research is conducted in the context of predicting Process Safety and Containment Events (PSCE), a critical topic of concern in industrial operations.

The risk estimation of a PSCE has gained significance within the research community. Recent efforts [5] have aimed to predict unplanned events. Notably, the authors employed process data within a risk assessment and surveillance (RAS) framework to monitor the probability of unplanned shutdown events to take place in the near future, detecting high-risk situations ahead of time when there is still time to act and take countermeasures that may prevent their occurrence. However, it is essential to acknowledge that the information derived from process sensing instrumentation has inherent limitations in providing a comprehensive understanding of the process state and health, as discussed earlier in introduction. Therefore, the exploration of alternative sources of information such as available text data can potentially yield new insights for improving the prediction of PSCE, being that in system coverage, robustness or accuracy.

The remainder of this paper is structured as follows. The Data section offers a detailed information about both the simulated and industrial datasets used in this study. In the Methods section, we provide an overview of the data analysis pipeline, and the methods used. The Results section presents the main findings. The Final Remarks section draws some concluding observations.

## DATA

In this study, two distinct text datasets were used: one is a simulated text data generated from GPT model and the other sourced from an industrial process from one of the manufacturing sites owned by the Dow Chemical Company. Both datasets encompass a collection of incident management reports that document relevant events and their severity level.

## Simulated text data

Incident management reports simulated via the GPT-3.5 model resembles the type of information that can be found in an industrial data. Using carefully designed and crafted prompts, the GPT model was instructed to behave as an IMO who is responsible for writing perfect and complete reports about the incidents that may happen at a designated process. In the simulation, five levels of PSCE events were considered with level 1 being the most severe, such as an unplanned event, and level 5 being the least severe one, where neither the production process is jeopardized, nor any personal safety or environmental hazard is present (this is consistent with actual PSCE level categorization). Given such definitions of PSCE levels, the GPT-based IMO had to attribute a PSCE level to each reported incident. The resulting dataset has a total of 1429 simulated reports covering all kinds of PSCE levels from different units and areas of the process. To generate the simulated reports, ChatGPT was prompted with guidelines to use available data from standardization institutions such as American Petroleum Institute (API) and other relevant sources that might aid in assessing severity level of PSCE events.

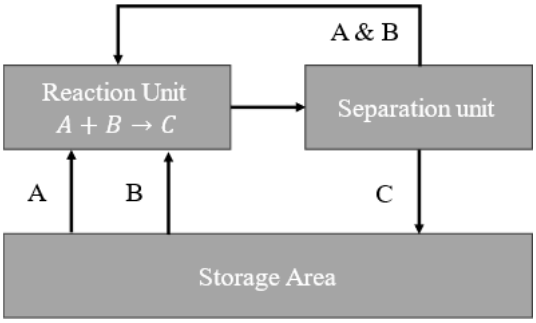



**Figure 1.** Flowchart of the process considered for the simulations of text data.

The process used for simulating the reports was also provided as part of the prompt. It can be described in a simplified version as follows: a system that produces chemical C from chemicals A and B, and consists of a reaction unit, separation unit, and storage areas. In the process, there is a recirculation of chemicals A and B that did not react back to the reactor unit. This process is also summarized in Figure 1. Further considerations are that the chemicals are highly flammable and toxic, Chemical A is in gaseous state, while B and C are liquids.

This dataset is used to establish the benchmark for incident management text data containing reports related to a simplified chemical process, with clear and complete description of the events. Additionally, it served as a proof of concept for the proposed data analysis pipeline.

## Industrial text data

The industrial text data consist of a set of incident management reports with corresponding PSCE levels from a Dow Chemical Company site. These reports contain information introduced by the local IMOs. Overall, these reports present similar characteristics as the simulated data, however, there are also disparities between the reports due to different IMOs, templates or formats used by the local plant. Additionally, these reports contain grammar and spelling errors, abbreviations and site-specific language, involves different writing styles, various functional aggregation levels, and are gathered from multiple processes at a specific site location. Often, incomplete information is available regarding a specific PSCE event. Therefore, it is much more difficult to use for analysis and modeling compared to the simulated reports. For confidentiality reasons no further details can be provided here, and the data were masked before being reported in this paper.

# METHODS

To extract information from textual data, we employed embedding models to convert text into numerical representations first. Then, the numerical embedding vector were used as inputs for a Random Forest (RF) classifier, which predicts the various levels of PSCE events. The following subsections provide an overview of the individual methodologies adopted and data analysis pipeline utilized in this study.

## Embedding Models

Embedding is a process of representing words, phrases, or entire documents as numerical vectors in a high-dimensional feature space. These numerical representations enable the capture of semantic and syntactic relationships between words. The most common embedding techniques are word embedding and document embedding. In this study, document embedding approaches were used. [6]

## Random Forest classifier

The Random Forest classifier is a supervised machine learning method that uses multiple decision trees to predict a class from input features. Each decision tree is constructed by selecting random subsets of the training data, which helps reduce overfitting and increases the model's generalization capabilities. To make a prediction of a class, the random forest algorithm aggregates the results from all the individual trees through majority voting. This ensemble approach improves the model's overall accuracy, stability, and resilience to noise and outliers. [7]

## Data analysis pipeline

One of the premises of the adopted approach is that an efficient information extraction will lead to a

satisfactory performance of the classification pipeline. Thus, the data analysis pipeline consists primarily of two integral stages: (i) information extraction and analysis (ii) classification of PSCE event levels. In the (i) information extraction stage, pretrained NLP models were used to extract pertinent features containing valuable information. Specifically, models from both an open-source python library "Sentence-Transformers" which makes use of BERT architecture [8], and a proprietary model from Azure OpenAI [9] were used. To facilitate effective visualization of the embedding space of the textual data, a dimensionality reduction method named unified manifold approximation and projection (UMAP), was used [10].

After the completion of the information extraction phase, the classification stage (ii) was performed, where the RF model was trained and evaluated, utilizing a total of 100 decision trees. To ensure a rigorous evaluation, our model was trained on 80% of the available data, with the remaining 20% reserved for performance assessment. This data split was executed in a pseudo-random fashion [11], thereby ensuring that both the training and testing subsets maintained a similar representation of the classes. To robustly gauge the model's performance, the model training procedure were repeated 30 times with each iteration having a different 80-20 split of the data set. The evaluation metric employed to assess model performance was the F1-score, as indicated in equation (1). In each iteration, the test and train subsets are the same across different information extraction method.

$$F_1 = 2\frac{precision \times recall}{precision + recall} = \frac{2TP}{2TP + FP + FN} \quad (1)$$

In Equation (1), TP stands for true positives, FP for false positives and FN for false negatives.

## RESULTS

In this section, the main results obtained from the simulated and industrial case studies are presented and discussed.

### Simulated case study

The embeddings for the simulated case study were obtained using the stsb-mpnet-base-v2 model from the Sentence-Transformers python library. UMAP was applied to visualize the simulated dataset, which contains a wide range of events described in the text, as well as different PSCE levels. Figures 2 clearly reflect these distributions. In Figure 2, a gradient of colors indicates that the embeddings effectively encoded relevant information about PSCE levels, although there is some overlap between the levels.

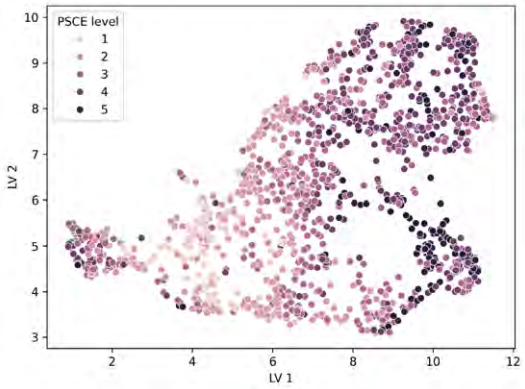



**Figure 2.** UMAP visualization of the Sentence-Transformer embeddings extracted from simulated text data, colored by PSCE Level.

In Table 1, the performance of the Random Forest (RF) model trained on the extracted embeddings is presented in terms of the F1 score. The F1 score is approximately 0.65 for both the training and testing sets. While this performance is not exceptionally high, it is consistent and indicates a low risk of overfitting. This stability suggests that the model is generalizing well to unseen data, even though there is room for improvement in its predictive accuracy.

**Table 1:** Median F1-score of data analysis pipeline applied to simulated case study.

| Training | Test |
|---|---|
| 0.644 | 0.656 |

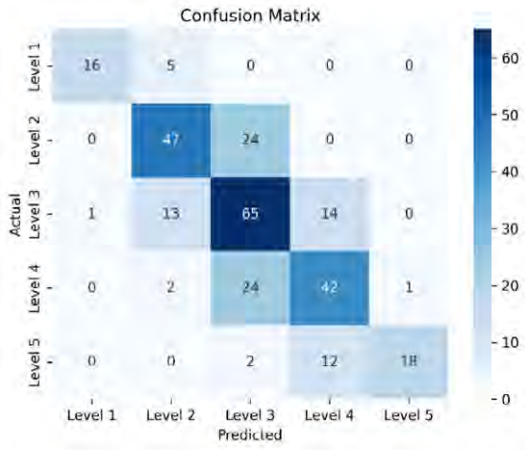



**Figure 3.** Confusion matrix between the actual and predicted PSCE levels, considering one of the testing run from simulated text data.

Upon closer examination of the approach's performance depicted in Figure 3, it becomes evident that the overlap predominantly occurs between adjacent PSCE levels, being consistent with the observations in Figure 2.

For level 1 and 2 PSCEs, the misclassification happens mostly to one level higher (level 2 and 3 respectively) while for level 4 and 5 PSCEs, it is the opposite, misclassification happens mostly to one level lower (level 3 and 4 respectively). For level 3 PSCEs, the misclassification is more balanced between level 2 and 4. Several factors might contribute to this overlap. Firstly, the definitions of the PSCE levels can be somewhat ambiguous near their boundaries. Secondly, the descriptions of events might sometimes be not completely clear or a bit vague. The presence or absence of minor details or the misinterpretation of information can lead to the misclassification of the adjacent PSCE level.

Overall, the results from this case study demonstrate the effectiveness of the proposed processing pipeline. The embeddings successfully encapsulate the relevant information, making them suitable for further data analysis and modeling task. Although the random forest model was not fully optimized, it still managed to classify PSCE levels reasonably well.

## Industrial case study

Applying a similar approach as in the simulated case study to the industrial data, we embedded the text data (using text-embedding-3-large embedding model from OpenAI, this time) and then applied the RF model. Figure 4 shows the UMAP transformation of these embeddings. Unlike the clear separation observed in the simulated case study, the event categories in the industrial data are highly overlapped, making it difficult to distinguish between them.

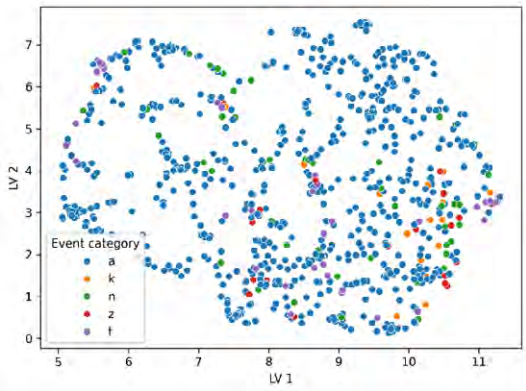



**Figure 4.** UMAP visualization of the Sentence-Transformer embeddings extracted from industrial text data, colored by event category (masked data).

The performance of the RF model is depicted in Table 2. The F1 score for this model stands at approximately 0.18, indicating a very low level of performance. Upon closer examination of Figure 5, it becomes evident that the model predominantly classifies the "a" category as the event category. Additionally, there is a significant imbalance among the classes.

**Table 2:** Median F1-score of data analysis pipeline applied to simulated case study.

| Training | Test |
|---|---|
| 0.182 | 0.179 |

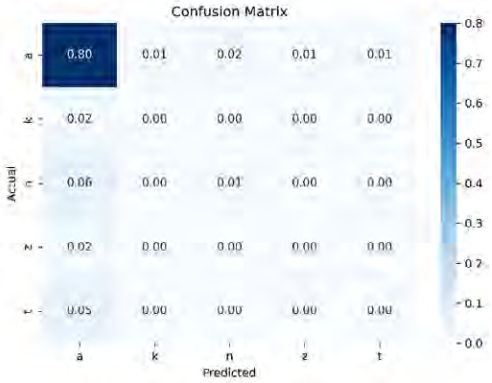



**Figure 5.** Confusion matrix between the actual and predicted event categories, considering one of the testing run of RF model from industrial text data.




**Figure 6.** Confusion matrix between the actual and predicted event categories, considering the LLM based approach and industrial text data.

The approach did not work for the industrial case study due to several contributing factors. Firstly, the complexity of the real-world data far exceeds that of the simulated case study, making it difficult to map the domain accurately (Figure 4). Secondly, the highly unbalanced classes make the classification task nearly impossible, even when we applied resampling. Additionally, the presence of site-specific terminology and potentially incomplete information about the PSCE levels adds additional layer of complexity to the samples.

To address the hypothesis that incomplete information, misspellings, and site-specific language might interfere with performance, a new approach was implemented. This approach involved using a carefully designed prompt in combination with a large language model (LLM), specifically GPT-4 [9], to classify events based on the text data available in the reports. This method proved to be quite effective, achieving an F1

score of approximately 0.78. It performed well across nearly all event categories, except for the "a" and "t" categories, which are closely related and easily confused with each other (see, Figure 6).

The machine learning approach was ineffective due to the complexity of the underlying processes in the generated text data. The considered text data lacked sufficient domain representation to train a high-quality model.

## FINAL REMARKS

In conclusion, we proposed a machine-learning based data analysis pipeline to predict PSCE event level based on text information on 2 different datasets. The proposed workflow works well on the simulated dataset, demonstrating the effectiveness of encoding key information using embedding models. However, the results on the other industrial dataset were not satisfactory. This suggests that the proposed framework was inefficient when the raw text data is originated from a more complex system and wide domain such as chemical manufacturing processes. In this case, the complexity of the underlying phenomena in the real-world case study, combined with low domain representativity and highly imbalanced data, are all possible reasons behind the poor performance. The carefully designed prompts and pre-trained large language models (LLMs) have proven successful on the industrial case study. The extensive training domain of LLMs enhances their capability to extract targeted information, thus retaining key information relevant for classifying PSCE levels. Thus, NLP approaches successfully codified and extracted information from industrial text data. However, integrating these embeddings into ML approaches can be challenging due to limited domain coverage, which is common in industrial text data related to unplanned events. As next steps, a data fusion [11]. approach will be used to integrate text data and process data for the prediction of PSCE.

## REFERENCES


1. Ye, Z., Yang, J., Zhong, N., Tu, X., Jia, J., & Wang, J. Tackling environmental challenges in pollution controls using artificial intelligence: A review. Science of The Total Environment, 699, 134279 (2020) https://doi.org/10.1016/j.scitotenv.2019.134279
2. Wang, C., Nulty, P., & Lillis, D. A Comparative Study on Word Embeddings in Deep Learning for Text Classification. Proceedings of the 4th International Conference on Natural Language Processing and Information Retrieval, 37–46 (2021) https://doi.org/10.1145/3443279.3443304
3. Antons, D., Grünwald, E., Cichy, P., Salge, T. O., & Salge, T. O. The application of text mining methods in innovation research: Current state, evolution patterns, and development priorities. R & D Management, 50(3), 329–351 (2020) https://doi.org/10.1111/radm.12408
4. Manning, C. D. Human Language Understanding & Reasoning. Daedalus, 151 (2), 127–138 (2022) https://doi.org/10.1162/daed_a_01905
5. Rato, T. J., & Reis, M. S. Real-time risk assessment and surveillance for early prediction of unplanned shutdown events. Chemical Engineering Science 282, 119364 (2023) https://doi.org/10.1016/j.ces.2023.119364
6. Mikolov, T., Sutskever, I., Chen, K., Corrado, G. S., & Dean, J. Distributed Representations of Words and Phrases and their Compositionality. Advances in Neural Information Processing Systems 26 (2013) https://papers.nips.cc/paper_files/paper/2013/hash/9aa42b31882ec039965f3c4923ce901b-Abstract.html
7. Breiman, L. Random Forests. Machine Learning, 45(1), 5–32 (2001) https://doi.org/10.1023/a:1010933404324
8. Reimers, N., & Gurevych, I. Sentence-BERT: Sentence Embeddings using Siamese BERT-Networks. Proceedings of the 2019 Conference on Empirical Methods in Natural Language Processing and the 9th International Joint Conference on Natural Language Processing (EMNLP-IJCNLP) 3980–3990 (2019) https://doi.org/10.18653/v1/D19-1410
9. Azure OpenAI. https://learn.microsoft.com/en-us/azure/ai-services/openai/concepts/models
10. McInnes, L., Healy, J., & Melville, J. UMAP: Uniform Manifold Approximation and Projection for Dimension Reduction. arXiv:1802.03426 [Cs, Stat] (2018) http://arxiv.org/abs/1802.03426
11. Strelet, E., Peng, Y., Castillo, I., Rendall, R., Wang, Z, Joswiak, M., Braun, B., Chiang, L., Reis, M. S., Multi-source and multimodal data fusion for improved management of a wastewater treatment plant. Journal of Environmental Chemical Engineering, 111530, (2023), https://doi.org/10.1016/j.jece.2023.111530



© 2025 by the authors. Licensed to PSEcommunity.org and PSE Press. This is an open access article under the creative commons CC-BY-SA licensing terms. Credit must be given to creator and adaptations must be shared under the same terms. See https://creativecommons.org/licenses/by-sa/4.0/




Systems & Control Transactions

**Research Article - Peer Reviewed Conference Proceeding**
ESCAPE 35 - European Symposium on Computer Aided Process Engineering
Ghent, Belgium. 6-9 July 2025
Jan F.M. Van Impe, Grégoire Léonard, Satyajeet S. Bhonsale,
Monika E. Polańska, Filip Logist (Eds.)

PSE PRESS

# Optimal Design and Control of Chemical Reactors using PINN-based frameworks

**Isabela Fons Moreno-Palancas[a]*, Raquel Salcedo Díaz[a], Rubén Ruiz Femenia[a] and José A. Caballero[a]**

[a] University of Alicante, Department of Chemical Engineering, San Vicente del Raspeig, Alicante, Spain
* Corresponding Author: isabela.fons@ua.es.

## ABSTRACT

In an era defined by economic competitiveness and environmental awareness, engineering solutions must maximize profitability, efficiency and sustainability, underscoring the relevance of process optimization and the societal impact any contribution in this research field would bring. In chemical reactor engineering, optimization tasks pose significant challenges due to the highly nonlinear and non-convex nature of reactor models, often involving differential equations. While conventional approaches have proven to be reliable strategies for solving these complex problems, their application becomes impractical as problem size and complexity increase. This work introduces a novel application of Physics-Informed Neural Networks (PINNs) to address constrained optimization problems in reactor engineering and demonstrates the proposed methodology through two illustrative case studies in chemical reactor design and control. In doing so, we highlight the capability of PINNs to efficiently learn optimal reactor patterns and analyse the strengths and limitations of this novel methodology. These findings pave the way for broader adoption of PINN-based techniques in process engineering optimization.

**Keywords**: Constrained Optimization, Reaction Engineering, Machine Learning, Physics-Informed Neural Networks, Differential Equations

## INTRODUCTION

Optimization is crucial in all engineering fields for improving efficiency, reducing costs, and enhancing performance. Focusing on chemical reactor engineering, it helps maximize reaction yields, minimize energy consumption, and ensure safety and environmental compliance, making it essential for both economic and ecological progress.

Optimizing the design and operation of a chemical reactor not only involves achieving specific goals, but also satisfying a set of governing laws and operational constraints. Traditionally, the predominant approach to address these problems relied on mathematical programming, which applies techniques such as gradient descent or branch and bound strategies. Nonetheless, in recent years, genetic algorithms have gained traction as a viable alternative for optimizing complex systems [1]. More recently, reinforcement learning frameworks have emerged as a promising research area [2], particularly in uncertain environments [3]. In this work, we study the application of Physics Informed Neural Networks (PINNs) to solve reactor engineering problems.

PINNs have risen as a promising machine learning approach that integrates domain-specific knowledge, into the network training process [4]. In recent years, the utilization of PINNs has exploded due to its ability to predict complex phenomena when data is scarce or even unavailable, with applications spanning diverse fields, from fluid mechanics to biophysics [5]. Most of its applications involve solving differential equations, where the loss function is constructed from the residual of these equations [6]. Moreover, they have been successfully applied to inverse problems, where unknown parameters of the governing equations are inferred from partial observations [7]. Now the focus points towards extending the application of PINNs beyond simulation and parameter estimation by incorporating optimization objectives into the network training process [8, 9].

In this study, we explore the potential of PINNs in chemical reactor optimization, aiming to provide solutions that satisfy both the governing physical equations

and the desired constraints. This PINN-driven approach poses major challenges, including ensuring feasibility, achieving convergence to optimal solutions, and managing computational resources efficiently. Below, we introduce this novel optimization framework and illustrate its capabilities through two illustrative examples, where we discuss the aforementioned challenges.

## PROBLEM STATEMENT

Chemical reactor optimization aims to design and operate reactors that maximize efficiency, minimize costs or, more broadly, optimize a given objective function $f$, subject to physical laws $h$ and operational constraints $g$. In many cases, these governing equations are represented by ordinary differential equations (ODEs) that describe the evolution of state variables $y$, represented by derivatives $y' = {}^{dy}/_{dx}$. The independent variable $x$ represents a different physical magnitude depending on the case study (e.g., time or reactor length). Only Dirichlet boundary conditions are considered in this work.

A constrained optimization problem can be generally formulated as follows:

$$\begin{array}{lll} min & f(y,x) & \\ s.t., & h(y,y',x)=0 & x \in X \\ & y(x)=bc(x) & x \in \delta X \\ & g(y,x) \le 0 & x \in X \\ & y \in \mathbb{R}^n,\ X \in [x_0, x_F] & \end{array} \quad (1)$$

Solving reactor engineering instances of problem 1 is often challenging, due to the presence of non-linear and non-convex functions, together with stiff ODEs. Furthermore, the optimization problem is typically high-dimensional, characterized by complex interdependencies between decision variables and constraints, especially in large-scale industrial processes. In this context, this work proposes a novel PINN-based framework to assess such challenges.

## METHODOLOGY

The main idea behind using PINNs to solve optimization tasks is to reformulate the original constrained optimization problem into an unconstrained equivalent, whose objective function will ultimately constitute the loss function $\mathcal{L}$ used in the neural network training process to adjust weights $\theta$. Thereby, PINNs integrate physical knowledge by embedding governing equations directly into the neural network's loss function, together with optimization objectives. As derived from Eq. 2, the penalty method is applied to balance individual losses with coefficients $\omega$.

$$\mathcal{L} = \omega_p \mathcal{L}_p + \omega_{bc} \mathcal{L}_{bc} + \omega_{op} \mathcal{L}_{op} + \omega_{ob} \mathcal{L}_{ob} \quad (2)$$

As starting point, a neural network $\hat{y} = \mathcal{N}(x;\theta)$ generates predictions of the state variables $\hat{y}$ taking independent variables $x$ as inputs. Hence, this network works as "ansatz" for solving model equations $h(\hat{y}, \hat{y}', x)$ in problem 1. If needed, derivatives $\hat{y}'$ are computed efficiently and accurately using automatic differentiation.

Then, each term in Eq. 2 is evaluated independently to account for physical and operational constraint satisfaction, as well as for goal minimization.

To ensure network predictions comply with fundamental principles, the physics loss term $\mathcal{L}_p$ in Eq. (3) forces the neural network to satisfy model equations on a set of points $\mathcal{T}_p$ sampled within the domain of the input variables $X$.

$$\mathcal{L}_p(\theta;\mathcal{T}_p) = \frac{1}{|\mathcal{T}_p|} \sum_{x \in \mathcal{T}_p} \| h(\hat{y}, \hat{y}', x) \|_2^2 \quad (3)$$

The integration of the optimization objective in the global loss $\mathcal{L}$ depends on the case study. The definition of $\mathcal{L}_{ob}$ must therefore consider any necessary transformation of function $f(\hat{y}, x)$ to ensure convergence and a smooth training curve (e.g., scaling).

Operational constraints and boundary conditions can be enforced in Eq. 2 expressing the terms $\mathcal{L}_{bc}$ and $\mathcal{L}_{op}$ in the same way as Eq. 3, as shown in Eqs. 4 and 5 respectively. Note that the former guarantees boundary conditions are only satisfied at points $\mathcal{T}_{bc}$ located at the boundary $\delta X$.

$$\mathcal{L}_{bc}(\theta;\mathcal{T}_{bc}) = \frac{1}{|\mathcal{T}_{bc}|} \sum_{x \in \mathcal{T}_{bc}} \| \hat{y} - bc(x) \|_2^2 \quad (4)$$

$$\mathcal{L}_{op}(\theta;\mathcal{T}_p) = \frac{1}{|\mathcal{T}_p|} \sum_{x \in \mathcal{T}_p} \| g(\hat{y}, x) \|_2^2 \quad (5)$$

The preceding approach handles these constraints as "soft constraints" (i.e., the admissible degree of constraint violation is regulated via penalty coefficients $\omega_{bc}$ and $\omega_{op}$). However, they can also be imposed directly or as "hard constraints". In certain cases, operational constraints can be incorporated into the governing equations, as demonstrated in the following section. Alternatively, Dirichlet boundary constraints can be exactly satisfied by modifying the network output, as shown in Eq. 6, following the approach proposed by Lu et al. [10].

$$\hat{y}(x;\theta) = bc(x) + \ell(x)\mathcal{N}(x;\theta) \quad (6)$$

where $\mathcal{N}$ is the network output and $\ell$ is any function satisfying the conditions in Eq. 7.

$$\begin{cases} \ell(x) = 0, & x \in \delta X \\ \ell(x) > 0, & x \in X - \delta X \end{cases} \quad (7)$$

## RESULTS

The proposed methodology is applied to two illustrative examples of reactor engineering by using the library DeepXDE [11]. For comparison purposes, the original optimization models were written in Pyomo and solved applying conventional optimization methods.

## Case Study 1: PFR length optimization

### Problem setup

We first consider the case of cumene production in an isothermal PFR under the elementary reaction $C_3H_6 + C_6H_6 \rightarrow C_9H_{12}$, whose reaction enthalpy is $\Delta H = 9.95 \cdot 10^4\ J/mol$. Arrhenius law is used to calculate reaction rate $r$ as shown in Eq. 8, where $T$ and $n_j$ refer to the temperature and molar flow, respectively, and $\alpha_j$ denotes the stoichiometric coefficient of each species $j$.

$$r_j = \alpha_j r = \alpha_j\, 3500 \exp\left(\frac{-56000}{T}\right) \frac{n_P n_B}{(n_P + n_B + n_c)^2} \tag{8}$$

Aiming to minimize capital and operational costs, the goal is to determine the optimal length $L^*$ required to achieve the desired propene conversion $X_P^* = 0.89$, and the heat flux $Q$ to be removed. The tube cross sectional area is set to $S = \frac{\pi}{4} 1.5^2\ \mathrm{m}^2$ and the feed stream consists of $F^{in} = 324.1\ \mathrm{mol/h}$ at $222°\mathrm{C}$ of a mixture of propene and benzene with mole fractions $x^{in} = [0.659, 0.341, 0]$. The corresponding mass and energy balances are given in Eq. 9. It is worth clarifying that $L^*$ is a trainable variable, while $l$ represents the scaled length $l = L/L^* \in [0,1]$.

$$\frac{dn_j}{dl} = L^* S \alpha_j r \quad \forall\, j \in \{P, B, C\}\ ;\ \frac{dT}{dl} = L^* \frac{dQ/dl - Sr\Delta H}{\sum_j n_j C_{p,j}} \tag{9}$$

### PINN-based optimization

We used a fully connected neural network to predict $\hat{X}_P$ and $\hat{Q}$ taking $l$ as input. The proposed optimization is formulated as a PINN training problem as follows:

$$\mathcal{L} = 10\mathcal{L}_{p1} + \mathcal{L}_{p2} + \mathcal{L}_{bc} + 10\mathcal{L}_{op} + 10^{-4}\mathcal{L}_{ob} \tag{10}$$

$$\mathcal{L}_{ob} = L^* = S n_A^{in} \int_0^1 \frac{1}{r} dl \tag{11}$$

$$\mathcal{L}_{p1} = \sum_{l \in \mathcal{T}_p} \sum_j \left(\frac{d\hat{n}_j}{dl} - \frac{dn_j}{dl}\right)^2 \tag{12}$$

$$\mathcal{L}_{p2} = \sum_{l \in \mathcal{T}_p} \left(\frac{d\hat{Q}_j}{dl} - \frac{dQ}{dl}\right)^2 \tag{13}$$

$$\mathcal{L}_{op} = \hat{X}_P(l=1) - X_P^* \tag{14}$$

$$\mathcal{L}_{bc} = \hat{Q}(l=1) - 0 \tag{15}$$

$$\hat{X}_P = 0 + \mathcal{N}(l;\theta)^T [1 - e^{-l}, 0] \tag{16}$$

While Eqs. 11-15 constitute each one of the terms in Eq. 10, Eq. 16 implies that the initial condition for the first predicted variable (i.e., $\hat{X}_P$) is enforced as a "hard constraint". The coefficients in Eq. 10 were adjusted to achieve a smooth learning curve, which serves as an indicator of a good fit.

### Results

A single-layered neural network with 5 neurons was sufficient to obtain accurate predictions. ODEs were evaluated on a set $\mathcal{T}_p$ containing $100$ samples and Adam optimizer was applied at a learning rate of $10^{-3}$ for $18100$ epochs until the global loss $\mathcal{L}$ dropped below the predefined tolerance of $10^{-5}$. As illustrated in **Figure 1**, the predictive performance stagnates from a certain number of training points. This observation indicates that the selected number of samples is optimal to fully exploit the capacity of the proposed architecture.

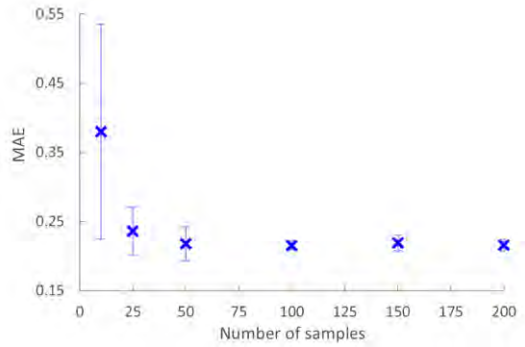



**Figure 1:** Average MAE in prediction of runs with varying number of training points

The output of the PINN was compared to the conventional solution. The latter was obtained by applying orthogonal collocation to discretize the ODEs using the Pyomo DAE extension [12]. The resulting NLP was solved using CONOPT as optimization algorithm.

The results shown in **Figure 2** and **Figure 3** demonstrate that the network accurately replicates reactor dynamics. This observation is further supported by calculating the mean absolute error (MAE) between the network predictions and the Pyomo solution, as reported in **Table 1**, which indicates that the difference is negligible. Both methods also converge to similar reactor length values: $6.34\ \mathrm{m}$ for the PINN solution and $6.38\ \mathrm{m}$ for the Pyomo solution.

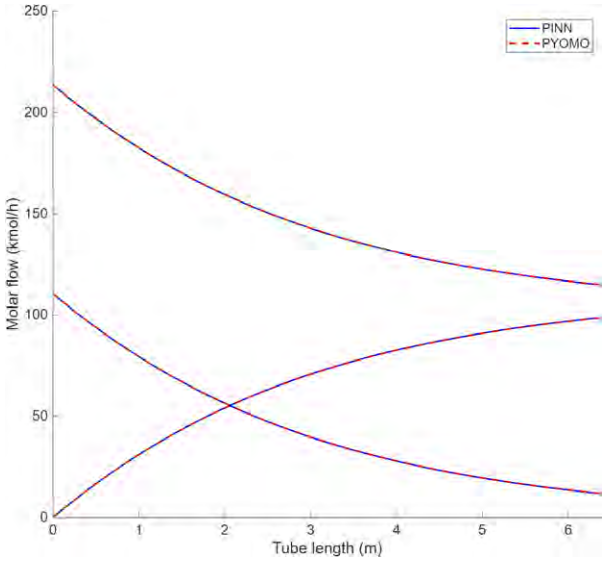



**Figure 2:** Molar profiles in the PFR.

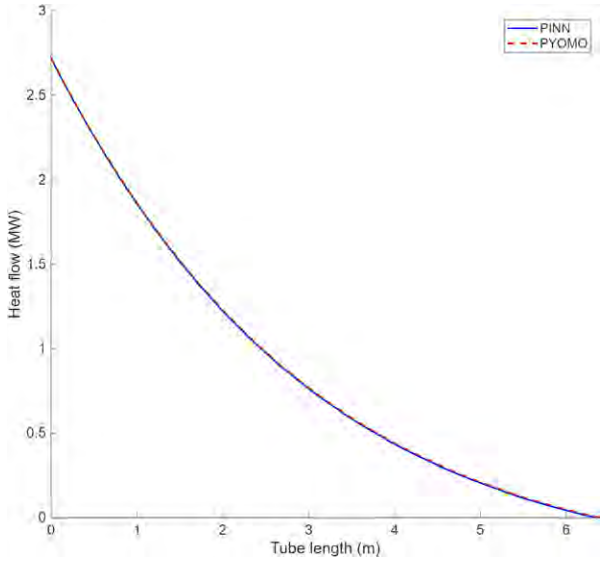



**Figure 3:** Heat flow profile in the PFR.

**Table 1:** Deviation between PINN and Pyomo solutions.

| Compared variable | MAE | Units |
|---|---|---|
| Molar flow | 0,22 | kmol $h^{-1}$ |
| Heat flow | $2{,}24 \cdot 10^{-3}$ | MW |

## Case Study 2: Locus of maximum rates

### Problem setup

Next, the focus is on a batch reactor in which the reversible exothermic reaction $A \leftrightharpoons B$ occurs. For this particular type of reaction, the time required to reach the target conversion $X_A$ can be minimised through precise temperature control ensuring that the reactor consistently operates at the maximum possible reaction rate. This is equivalent to minimising the rate of consumption of species $A$ (i.e., $r_A$), as given by Eq. 17, for each value of $X_A$ through temperature adjustment.

$$r_A = -1{,}79 \cdot 10^5 \, e^{\frac{-1200}{T}} C_A + 1{,}17 \cdot 10^{13} \, e^{\frac{-2400}{T}} \, C_B \qquad (17)$$

The reactor is fed with a solution of pure $A$ in concentration $C_A^0 = 1\ kmol/m^3$ and the temperature cannot exceed $500°C$.

Conventionally, such problems are addressed sequentially: first, by determining the locus of maximum rates $r_A^{max}(X_A)$, and then by numerically solving the integral in Eq. 18. The reader is referred to [13] for further details on the solution procedure.

$$t_{rxn} = C_A^0 \int_0^{X_A^*} \frac{dX_A}{r_A^{max}(X_A)} \qquad (18)$$

### PINN-based optimization

The optimal temperature path following the locus of maximum rates is estimated using a PINN that takes $X_A$ as input and outputs both the temperature $\hat{T}$ that yields the fastest rate of consumption of $A$, and the corresponding value of the latter, $\hat{r}$. A parallel fully connected neural network (PFNN) architecture was preferred to construct an independent network for each output.

The physics-informed loss function used during the PINN training process, as defined in Eq. 19, is composed of the individual loss terms defined in Eqs. 20-22.

$$\mathcal{L} = \omega_{p1}\mathcal{L}_{p1} + \omega_{p2}\mathcal{L}_{p2} + \omega_{ob}\mathcal{L}_{ob} \qquad (19)$$

$$\mathcal{L}_{ob} = \sum_{X_A \in \mathcal{T}_p} \hat{r}_A(X_A) \qquad (20)$$

$$\mathcal{L}_{p1} = \sum_{X_A \in \mathcal{T}_p} \left\| \ln\left(1 - \hat{r}_A(X_A)\right) - \ln\left(1 + r_A(X_A)\right) \right\|_2^2 \qquad (21)$$

$$\mathcal{L}_{p2} = \sum_{X_A \in \mathcal{T}_p} \hat{r}_A(X_A)^2 \cdot 1_{\{\hat{r}_A(X_A) > 0\}} \qquad (22)$$

Unlike the previous example, operational constraints (i.e., temperature bounds) are enforced neither as "soft" nor "hard" constraints, but directly integrating them into Eq. (17) by expressing temperature as:

$$T = T^L + (T^U - T^L)\hat{T} \qquad (23)$$

where $T^L$ and $T^U$ represent feasible temperature bounds and $\hat{T}$ is the scaled temperature, which is the actual prediction of the neural network.

To ensure constraint satisfaction and overcome the risk of ill-conditioned problem when weights in Eq. 19 are large, coefficients $\omega$ were iteratively increased during training following the penalty method [14]. Similarly, residual-based adaptive refinement (RAR) [11] proved an effective technique to improve accuracy by recursively adding sample points in regions where $\mathcal{L}_{p1}$was higher.

### Results

The selected network configuration consists of 3 hidden layers with 10 neurons each for each independent network (i.e., for each output). The penalty method combined with RAR approach was employed during training, using a minimum tolerance of $10^{-5}$ as stopping criterion. At each iteration, Adam optimizer was applied for a maximum of $5000$ epochs at a learning rate of $10^{-3}$, followed by L-BFGS until convergence. The overall training process required $27268$ epochs and $7500$ sample points to evaluate the rate of reaction. The initial training set contained $5000$ samples, and its size was determined following the criteria introduced in the previous case study. The remaining points were subsequently added as a result of RAR algorithm execution.

As in the previous example, the original NLP was solved using the solver CONOPT. Again, the comparison of both solutions shown in **Figure 4** highlights how the PINN-approach effectively reproduces the locus of maximum reaction rates. A quantitative assessment of the error between the conventional and PINN solution is presented in **Table 2**. From this analysis, it is worth noting that the reaction rate computed with Eq. 17 using the optimal temperature predicted by the network, $r(X, \hat{T})$, is

closer to the conventional solution $r(X,T)$ than the actual prediction of the network $\hat{r}$. The presence of large differences of magnitude among the predicted values of the reaction rate might explain the network's difficulties in predicting $\hat{r}$, especially when conversion is close to the target value, since the maximum reaction rate approaches zero in that region. This issue becomes particularly relevant in the evaluation of the reaction time. As **Table 3** illustrates, both methods provide similar estimates for the time required to achieve 50% conversion. However, when considering the entire conversion range, the PINN approach predicts a longer reaction time than the orthogonal collocation-based method. This discrepancy arises because the network slightly underestimates $r_A$ at higher values of $X_A$, and this prediction error is propagated and amplified in the calculation of $t_{rxn}$, as it involves the inverse of the reaction rate.

**Table 2:** Deviation between PINN and conventional solutions for the batch reactor case study.

| Compared variables | MAE | Units |
|---|---|---|
| Temperature | $3{,}46 \cdot 10^{-2}$ | °C |
| $\hat{r}$ and $r(X,T)$ | $5{,}76 \cdot 10^{-4}$ | kmol m$^{-3}$ min$^{-1}$ |
| $r(X,\hat{T})$ and $r(X,T)$ | $1{,}80 \cdot 10^{-7}$ | kmol m$^{-3}$ min$^{-1}$ |

**Table 3:** Comparison of optimal reaction time from PINN and conventional solutions.

| | Pyomo | PINN |
|---|---|---|
| $t_{rxn}$ (h) | 58,6 | 68,4 |
| $t(X_A = 0{,}5 \cdot X_A^*)$ (h) | 3,72 | 3,88 |

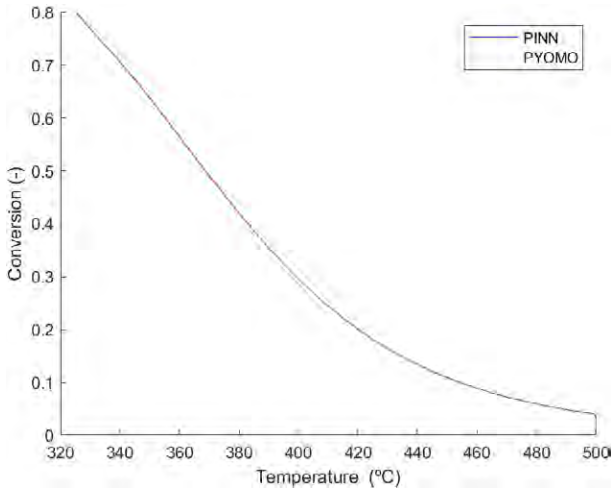



**Figure 4:** Conversion vs. temperature chart following optimal temperature path.

## DISCUSSION

The case studies presented in the previous section proved PINNs are capable of learning the underlying physics of both systems in an unsupervised setting. Moreover, this novel optimization approach provides solutions comparable to those obtained using conventional optimization methods, with the main source of discrepancy arising from the prediction error inherent in neural networks. Given sufficient computational resources, such error can be mitigated by increasing network complexity and decreasing the tolerance threshold.

A key challenge of this methodology lies in the definition of the loss function. Specifically, the individual losses must be carefully formulated to facilitate the learning process and accordingly scaled to prevent significant differences in the order of magnitude among the terms being aggregated. Additionally, the values of the penalty coefficients have a significant impact on the solution, creating a trade-off between the satisfaction of constraints or physical laws and conditioning issues. However, in our numerical examples, we showed how PINN-based optimization can be effectively combined with techniques such as the penalty method and RAR that promote convergence to high-quality solutions.

Due to the non-linear, non-convex nature of this optimization approach, guaranteeing optimality remains challenging when no benchmark solution is available. Nevertheless, the potential of this technique can be significantly enhanced in scenarios where model equations are not perfectly known, but some experimental data is available. This opens promising avenues for future research, where PINNs could be trained to solve optimization problems in a semi-supervised learning setting while also addressing larger-scale problems.

## CONCLUSION

This study delves into the use of physics-informed neural networks (PINNs) for solving chemical reactor optimization problems, demonstrating their potential and underscoring the importance of further research. By integrating governing equations, boundary conditions, and optimization objectives into a single loss function, PINNs provide solutions that are both physically consistent and goal-oriented. The methodology was validated through illustrative case studies, demonstrating its ability to produce results comparable to those of conventional optimization techniques while addressing the inherent challenges posed by non-linearities and non-convexities.

In addition, we employed techniques to enhance training efficiency, including residual-based adaptive refinement (RAR) and the penalty method for enforcing constraint satisfaction. These approaches proved particularly effective for solving more complex instances.

The findings highlight PINNs' flexibility, especially in scenarios where data is scarce or mechanistic models fall short of capturing the system's behavior, paving the way for their application in semi-supervised settings. However, challenges remain in formulating and scaling loss

functions, setting penalty coefficients, and guaranteeing global optimality. Future research should focus on refining these aspects and expanding the framework to tackle larger-scale industrial problems.

PINN-based optimization stands as a promising avenue for advancing chemical reactor engineering, providing a novel approach that bridges data-driven learning and physics-based modeling.

## ACKNOWLEDGEMENTS

The authors gratefully acknowledge financial support from the Spanish Ministry of Science, Innovation, and Universities via the doctoral grant for training university teachers FPU22/01276 and the R&D and Innovation Project PID2021-124139NB-C21.

## REFERENCES

1. Babaqi B.S., Takriff M. S., Othman N.T.A., and Kamarudin S.K. Yield and energy optimization of the continuous catalytic regeneration reforming process based particle swarm optimization. *Energy* 206:118098 (2020) https://doi.org/10.1016/j.energy.2020.118098
2. Petsagkourakis P., Sandoval I.O., Bradford E., Zhang D., del Rio-Chanona E.A. Reinforcement learning for batch bioprocess optimization. *Comput Chem Eng* 133:106649 (2020) https://doi.org/10.1016/j.compchemeng.2019.106649
3. Rangel-Martinez D., Ricardez-Sandoval L. A. A recurrent reinforcement learning strategy for optimal scheduling of partially observable job-shop and flow-shop batch chemical plants under uncertainty. *Comput Chem Eng* 188:108748 (2024) https://doi.org/10.1016/j.compchemeng.2024.108748
4. Raissi M., Perdikaris P., Karniadakis G. E. Physics-informed neural networks: A deep learning framework for solving forward and inverse problems involving nonlinear partial differential equations. *J Comput Phys* 378:686–707 (2019) https://doi.org/10.1016/j.jcp.2018.10.045
5. Ghalambaz M., Sheremet M.A., Khan M.A., Raizah Z., Shafi J. Physics-informed neural networks (PINNs): application categories, trends and impact. *Emerald Publishing*. 34(8): 3131-3165 (2024) https://doi.org/10.1108/HFF-09-2023-0568
6. Lastrucci G., Theisen M. F., Schweidtmann A. M. Physics-informed neural networks and time-series transformer for modeling of chemical reactors. *Computer Aided Chemical Engineering* 53:571–576 (2024) https://doi.org/10.1016/B978-0-443-28824-1.50096-X
7. Kircher T., Döppel F. A., Votsmeier M. Embedding Physics into Neural ODEs to learn Kinetics from Integral Reactors. *Computer Aided Chemical Engineering*. 53:817–822 (2024) https://doi.org/10.1016/B978-0-443-28824-1.50137-X
8. Seo J., Solving real-world optimization tasks using physics-informed neural computing. *Sci Rep* 14:2045-2322 (2024) https://doi.org/10.1038/s41598-023-49977-3
9. Mousa J., Negny S., Ouaret R., Di Pretoro A., Montastruc L. Enhancing Unit Operation Design: Leveraging Neural Networks to Enforce Physical Hard Constraints. *Computer Aided Chemical Engineering*. 53:547–552 (2024) https://doi.org/10.1016/B978-0-443-28824-1.50092-2
10. Chen H., Flores G.E.C., Li C. Physics-informed neural networks with hard linear equality constraints. *Comput Chem Eng*. 189:108764 (2024) https://doi.org/10.1016/j.compchemeng.2024.108764
11. Lu L., Meng X., Mao Z., Karniadakis G. E. DeepXDE: A deep learning library for solving differential equations. *SIAM Review* 63:208-228 (2021) https://doi.org/10.1137/19M1274067
12. Nicholson B., Siirola J. D., Watson J. P., Zavala V. M., Biegler L. T. pyomo.dae: a modeling and automatic discretization framework for optimization with differential and algebraic equations. *Math Program Comput* 10:187–223 (2018) https://doi.org/10.1007/s12532-017-0127-0
13. Fons I, Ruiz R. ReactorApp: a MATLAB toolbox to simulate and optimize chemical reactor networks. (2024) Manuscript submitted for publication.
14. Pestourie L. Lu, Yao R., W., Wang Z., Verdugo F., Johnson S. G. Physics-Informed Neural Networks with Hard Constraints for Inverse Design. *SIAM Journal on Scientific Computing*, vol. 43:B1105–B1132 (2021) https://doi.org/10.48550/arXiv.2102.04626

© 2025 by the authors. Licensed to PSEcommunity.org and PSE Press. This is an open access article under the creative commons CC-BY-SA licensing terms. Credit must be given to creator and adaptations must be shared under the same terms. See https://creativecommons.org/licenses/by-sa/4.0/



Systems & Control Transactions

**Research Article - Peer Reviewed Conference Proceeding**
ESCAPE 35 - European Symposium on Computer Aided Process Engineering
Ghent, Belgium. 6-9 July 2025
Jan F.M. Van Impe, Grégoire Léonard, Satyajeet S. Bhonsale,
Monika E. Polańska, Filip Logist (Eds.)

PSE PRESS

# Text2Model: Generating dynamic chemical reactor models using large language models (LLMs)

**Sophia Rupprecht[a], Yassine Hounat[a], Monisha Kumar[a], Giacomo Lastrucci[a], and Artur M. Schweidtmann[a]***

[a] Delft University of Technology, Department of Chemical Engineering, Process Intelligence Research Group, Van der Maasweg 9, 2629 HZ, Delft, The Netherlands
* Corresponding Author: a.schweidtmann@tudelft.nl.

## ABSTRACT

As large language models have shown remarkable capabilities in conversing via natural language, the question arises in which way LLMs could potentially assist chemical engineers in research and industry with domain-specific tasks. We generate dynamic chemical reactor models in Modelica code format from textual descriptions as user input. We fine-tune Llama 3.1 8B Instruct on synthetically generated Modelica code for different reactor scenarios. We compare the performance of our fine-tuned model to the baseline Llama 3.1 8B Instruct model as well as GPT4o. We manually assess the models' predictions regarding the syntactic and semantic accuracy of the generated dynamic models. We find that considerable improvements are achieved by the fine-tuned model with respect to both the semantic and the syntactic accuracy of the Modelica models. However, the fine-tuned model lacks a satisfactory ability to generalize to unseen scenarios compared to GPT4o.

**Keywords**: Text2Model, Large language models, supervised fine-tuning

## 1 INTRODUCTION

Domain-specific languages for interacting with software tools or for data analysis require scientists and engineers to study the conventions and syntax of such languages [1]. While software-user communication may often rely on a graphical user interface, such as AspenPlus or COMSOL, other tools require users to provide specialized code, e.g., MATLAB Simulink or Dymola. In addition to established programming languages for data analysis and visualization, such as Python or R, studying and applying a multitude of different domain-specific languages can be time- and labor-intensive.

Recent developments in using large language models (LLMs), particularly for code completion, code synthesis [2], and code analysis and interpretation [3] make such LLMs promising assistants for using tools such as modeling environments by converting textual information into domain-specific languages [1]. State-of-the-art multilingual open models for code generation or understanding, such as CodeT5+ [3], are literate in a range of programming languages in addition to natural language. Still, there are domain-specific languages in which pre-trained LLMs might not be proficient yet. The ability of state-of-the-art LLMs to converse in a variety of programming languages motivates leveraging LLMs for the synthesis of domain-specific languages analogously.

While there have been propositions that task-specific performance can be increased by few-shot learning [4], fine-tuning is an established approach to tailor LLMs' responses to specific tasks [5], especially for code synthesis [2]. Previous work by Jacobs and Pollice has shown that it is possible to fine-tune GPT 3.5 to generate input files to ORCA, a programming package specific to the quantum chemistry domain [1]. However, there is a lack of literature that investigates the potential of LLMs to generate dynamic models for chemical reaction systems from descriptions in natural language.

We investigate how fine-tuning an open-source pre-trained LLM on dynamic reactor scenarios written in the domain-specific programming language Modelica affects the semantic and syntactic accuracy of such Modelica models generated by the fine-tuned model. We fine-tune Llama 3.1 8B Instruct to synthesize a full, simulatable

Modelica model based on a textual description of a reactor scenario in the user's prompt. The fine-tuning dataset is generated synthetically from a set of templates of dynamic reactor scenarios. The supervised fine-tuning procedure is conducted using low-rank adaptation [6] as a parameter-efficient fine-tuning technique. We evaluate the results manually on samples randomly generated from the templated scenarios and on cases unseen during training. We compare the results of the fine-tuned model against the baseline Llama 3.1 8B Instruct and GPT4o.

## 2 METHODS

We develop (1) a methodology for the synthetic generation of the fine-tuning dataset (Section 2.1), (2) a supervised fine-tuning procedure (Section 2.2), (3) an evaluation procedure (Section 2.3), and (4) a set of evaluation metrics to assess the investigated models (Section 2.4).

### 2.1 Data generation

The synthetic data used for training and evaluation consists of question-and-answer (Q&A) pairs; the user provides a textual description of a dynamic tank reactor scenario in the question and an LLM is trained to provides a corresponding Modelica script as an answer. The training dataset is synthetically generated from templates of Q&A pairs. The question contains a textual description of a reactor scenario in LaTeX syntax and the corresponding reference answer is a model in Modelica code presented as a string object. To provide further explanatory context, each line of Modelica code in the reference answers is appended with a descriptive comment of the defined parameter, the declared variable, or the expressed physics equation.

The reactor scenarios are designed to convey knowledge about modeling heuristics by independently varying the (a) mode of operation, (b) the reaction taking place, and (c) switching between ODE and DAE systems by removing the constant mixture density assumption. The mode of operations (a) are adiabatic isothermal, non-adiabatic isothermal, isothermal non-adiabatic, non-isothermal non-adiabatic. For ODE systems (constant-density assumption), all four modes of operation are considered; for DAE systems, only the non-adiabatic non-isothermal mode is modeled. For the ODE scenarios, six reaction scenarios (b) are considered per mode of operation: Reversible and irreversible reactions between two, three, and four components, e.g., $\nu_A A + \nu_E E \rightarrow \nu_B B + \nu_C C$, or $\nu_A A \leftrightarrow \nu_B B + \nu_C C$. This yields 24 ODE scenarios in total by combining the variations of (a) and (b). For the single mode of operation (a) considered for DAE systems, two reaction scenarios are modeled: reversible and irreversible four-component reactions. This yields two DAE scenarios and thus 26 templated in total. Note that the stoichiometric numbers are assigned randomly for each template.

For each template, we randomly vary the units of measurement of given parameter values in the input question. The objective is to inspect whether it is attainable to perform direct conversions between non-SI and SI units with zero-shot LLM inference. Though Modelica provides conversion commands, such as from degree Celsius to degree Kelvin and vice versa, variables given in caloric energy units, for instance, must be converted to SI units manually.

We generate 988 Q&A data points of which 790 are used for training and 198 are used for evaluation during training. Each of the 26 synthetic data templates is thus repeated 38 times with arbitrary values of given parameters. The parameter values are real numbers sampled from the range $[10^{-4}, 10^{5}]$ except for stoichiometric numbers, which are integer values between 1 and 15.

### 2.2 Fine-tuning procedure

To enhance model performance in Modelica code generation, we fine-tune an existing LLM to adapt its model weights to better capture the nuances of this specific task. We use the model weights of the baseline Llama 3.1 8B Instruct model from Hugging Face [7].

The results presented in this work are obtained from fine-tuning using an NVIDIA A100 80GB GPU with a batch size of one and a maximum sequence length of 2200 tokens. For tokenization, we re-use the same fast byte-pair-encoding tokenizer as the baseline Llama 3.1 8B Instruct model. We train Llama 3.1 8B Instruct for eight epochs but evaluate the model obtained after four training epochs as indications of overfitting are observed after four epochs. We use linear learning rate scheduling with an initial learning rate of 0.0001. We apply a warmup ratio of 0.1, i.e., the initial learning rate of 0.0001 is reached after 632 steps.

We perform parameter-efficient finetuning by using the low-rank adaptation (LoRA) technique introduced by Hu et al. [6]. We use a rank of eight and scale the accumulated gradient updates that are added to the frozen model weights by a factor of two. We thus effectively update 0.26 % of the trainable 8.03 billion parameters. We do not apply quantization as initial studies have indicated shortcomings likely related to using quantization of model weights.

### 2.3 Evaluation procedure

With the evaluation procedure presented hereafter, we aim to evaluate the effect of the fine-tuning. We evaluate the fine-tuned model, the baseline Llama 3.1 8B Instruct, and GPT4o on two evaluation datasets: The first dataset (1) tests whether the cases presented during training can be reproduced (Section 3.1: Examination of

reproducibility of training scenarios); the second dataset (2) checks whether it is possible to extrapolate to reactor scenarios unseen during training (Section 3.2: Examination of generalization ability).

The first test dataset (1) (Section 3.1) contains entries that are randomly generated from each of the templates used for training with different parameter and variable values. This yields 26 samples in total. The second test dataset (2) (Section 3.2) includes four test cases: (a) a consecutive reaction, (b) two parallel reactions, and (c) a non-constant density system with five reaction participants (the reaction scenarios during training contain four components at the most). In the fourth case (d), we deliberately exclude parameter values that are necessary to fully specify the system. This is to investigate whether the missing parameter values are hallucinated in the models' responses or whether such user-generated errors are detected and addressed in the models' responses.

We perform inference on the baseline Llama 3.1 8B Instruct and the fine-tuned model using the same inference settings each. As a decoding strategy, we apply beam search with multinomial sampling using three beams and a temperature of 0.1. The maximum amount of tokens generated is limited to 4000. Inference is performed on the same machine as for fine-tuning, NVIDIA A100 80GB.

## 2.4 Evaluation metrics

We devise a customized set of evaluation metrics to quantify model performance. We manually evaluate each response given by an LLM (fine-tuned, baseline, GPT4o) by counting the number of occurrences of eight pre-defined error cases. These eight error cases are examining general syntax errors, parameter and variable declaration errors, and errors in the system of equations. A detailed description of the eight error cases is provided below. A simplified example of a user prompt and a potential response by an LLM with errors is displayed in Figure 1. The Modelica code given in the response in Figure 1 contains illustrative examples of seven of the eight error cases that are taken into account in this study.

For parameter and variable declaration errors, we distinguish between four subcases: unit conversion errors (1), declaration syntax errors (2), incorrect parameter values (3), and the usage of undefined variables (4). Errors in the equations section of the produced Modelica model are classified into incorrect equations (5), structural errors in the system of equations (6), and unit conflicts (7). General syntax errors (8) capture errors in the syntax of the model that would lead to compilation errors in the Dymola environment.

Unit conversion errors (1) arise from incorrect attempts to convert to SI units of measurement in cases where values given in the user's prompt are provided in non-SI units. Declaration syntax errors (2) are assigned in cases where Modelica syntax is not respected for

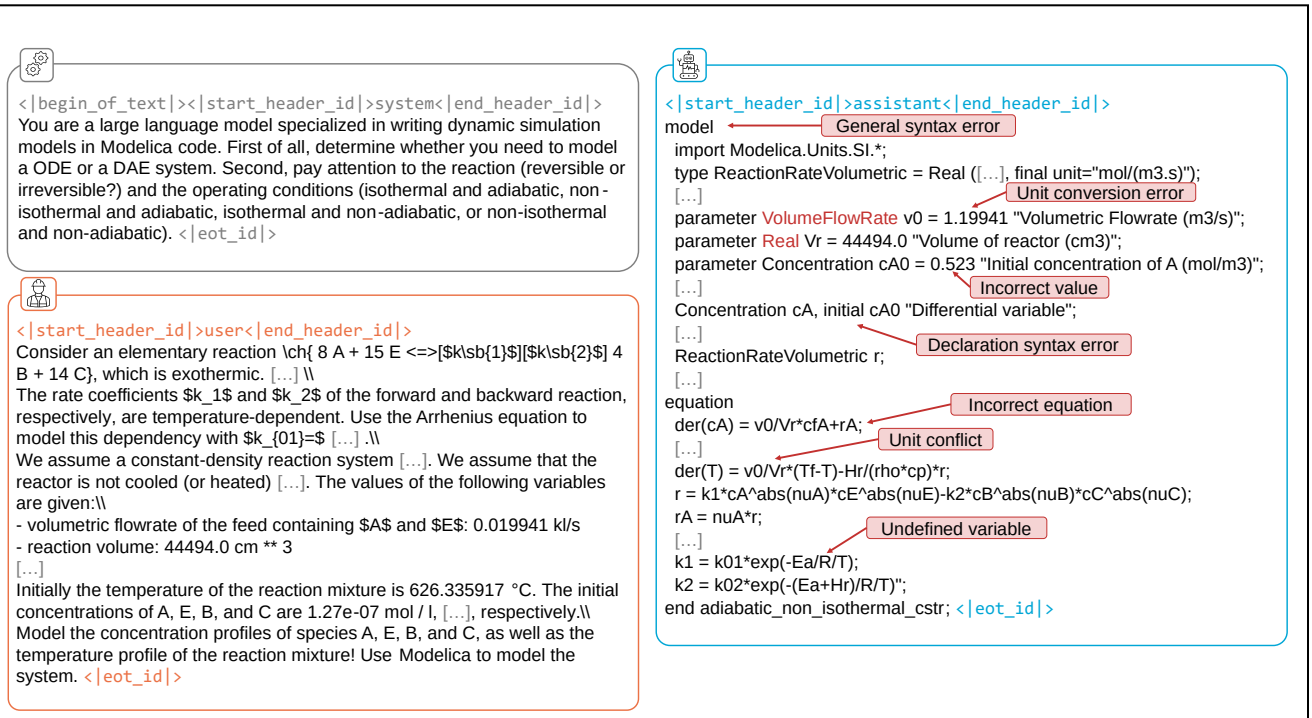



**Figure 1:** System message (top left), example user input (bottom left), and corresponding exemplary response (right). The example input and output are shortened for simplification. The output contains examples of six error cases that are taken into account in this study.

parameter and variable declarations, e.g., in Figure 1, the initial value of cA0 is assigned with the word 'initial', instead of the Modelica convention 'Concentration cA(start=cA0)'. Incorrect parameter values (3) originate from incorrectly transferred values given in the user's question to the output Modelica model. This error category does not punish unit conversion errors, but examines purely fabricated values. Undefined variable errors (4) arise in cases where variables or parameters are used in the equations part of the Modelica model that have not been declared or defined before. Incorrect equations (5) are either physically incorrect or do not respect the constraints given in the users' question, e.g., modeling an adiabatic system although the user requested a non-adiabatic system. Structural errors in the system of equations (6) arise if the defined system of equations is structurally singular, i.e., the defined equations do not allow to determine all of the unknowns. Unit conflicts within the system of equations (7) occur when variables are defined in non-equivalent units of measurement, e.g., using Joules and Calories in the same equation, which do not cancel out. The result is that the lefthand-side value is distorted by an unknown unit conversion factor.

## 3 RESULTS AND DISCUSSION

We examine the results obtained for the two test datasets described in Section 2.3 separately (Section 3.1 and 3.2). In Section 3.1 we present the results for the first test dataset and examine the fine-tuned model's ability to reproduce the reactor scenarios presented during training. In Section 3.2, we asses the second test dataset and inspect the fine-tuned model's ability to extrapolate to reactor scenarios unseen during fine-tuning. We evaluate the fine-tuned Llama 3.1 8B model, the baseline Llama 3.1 8B model before fine-tuning, and GPT4o. For both test datasets, we use the same eight error cases described in Section 2.4 to assess the performance of all three models.

We observe that overall, considerable improvements are achieved by the fine-tuned model compared to the baseline Llama 3.1 8B Instruct for reactor scenarios seen during training (Section 3.1) as well as case studies containing elements unseen during training (Section 3.2). GPT4o shows remarkable performance of Modelica code generation and outperforms the fine-tuned model in cases unseen during training.

### 3.1 Examination of reproducibility of training scenarios

Compared to the baseline Llama 3.1 8B Instruct model, we observe that fine-tuning has a direct influence on both the syntactical correctness of the produced Modelica model and the accuracy of the physics equations. Table 1 presents the absolute number of occurrences per error category (see Section 2.4) for each examined model.

The most prominent error categories of the baseline model are general syntax errors, unit conversion errors in parameter definitions, declaration syntax errors, and incorrect physical equations. On these four error categories, the fine-tuned model yields considerably fewer error cases: General syntax errors are reduced by 73.2 % in the case of the fine-tuned model compared to the baseline model. Unit conversion errors are reduced by 63.4 %, and declaration syntax errors are reduced to zero. In the error category of incorrect equations, the error cases produced by the fine-tuned model are reduced by 65.2 % compared to the baseline model.

The fine-tuned model excels at handling unit conversions from non-SI units in the user's prompt in this first evaluation test set. The responses given by GPT4o contain conversion factors to transparently transform

**Table 1:** Absolute amount of occurrences per error category per model. The test dataset comprises one randomly generated example for each of the 26 reactor scenario templates used for fine-tuning. The baseline model (Llama 3.1 8B Instruct) is fine-tuned and assessed on the same test dataset. GPT4o is assessed on the same test dataset as a benchmark.

| | Parameter and variable declarations | | | | Physics equations | | | General syntax |
|---|---|---|---|---|---|---|---|---|
| | Unit error | Declaration syntax error | Incorrect values | Undefined variables | Incorrect equations | Structural error | Unit conflict | |
| Baseline (Llama 3.1 8B) | 112 | 89 | **0** | 4 | 112 | 6 | 14 | 56 |
| Fine-tuned (Llama 3.1 8B) | **41** | **0** | 17 | 29 | **39** | 14 | **0** | 15 |
| GPT4o | 50 | 27 | 1 | **0** | 42 | **2** | 63 | **4** |

between units while the fine-tuned model is trained towards directly converting between non-SI and SI units if needed. However, the manual unit conversion in GPT4o's responses is not done consistently in 63 cases such that unit conflicts occur in the system of equations. In total, 113 combined error cases are produced by GPT4o in the context of unit conversion for parameter declaration and unit compatibility errors in equations compared to 41 in the case of the fine-tuned model, which is a reduction of 63.7 %. The baseline Llama 3.1 8B Instruct model shows the highest number of error cases in the category unit conversion errors as, in contrast to GPT4o, unit conversions are done less systematically and are thus more error-prone. It should be considered to specifically instruct GPT4o and Llama 3.1 8B Instruct to convert to SI units directly in the system message provided during inference. The decrease of such unit conversion errors in the fine-tuned model gives rise to the assumption that it is reasonable to expect direct unit conversions, however, the fine-tuned model's robustness could benefit from training toward the usage of manual conversion factors instead of direct conversion.

Most notably, the fine-tuned model consistently uses Modelica's built-in variable types, such as Concentration and Density, whereas most of the baseline and GPT4o's responses define parameters and variables as generic Real types. Using generic Real types for parameter definition and variable declarations does not leverage unit checks provided by the Dymola software when attempting to simulate a Modelica model.

Despite the improvements with respect to the physical accuracy of the fine-tuned model, we observe strong shortcomings in the reproducibility of DAE systems. The vast majority of incorrect physics equations produced by the fine-tuned model, 32 out of 39, occur in the two examples requesting DAE systems instead of ODE systems. In the case of the baseline model and GPT4o, physics errors related to DAE systems occur significantly less often with eleven out of 112, and eleven out of 42, respectively. Furthermore, 13 out of 14 structural errors in the system of equations counted in the case of the fine-tuned model occur in the DAE test cases. As merely two of the 26 templated scenarios presented in the training data for fine-tuning contain DAE systems, the decreased performance in the cases of DAE systems during inference could be attributable to this imbalance in the training data. This assumption is supported by the observation that for ODE systems, the fine-tuned model indeed outperforms the baseline model and GPT4o.

A striking difference between the fine-tuned model and both the baseline model and GPT4o is the occurrence of faulty parameter definitions with values that are most likely the result of hallucination. This is observed disproportionately often in the two test cases with DAE systems with eight out of 17 total error cases. We thus hypothesize that hallucinations generally become increasingly frequent the more the test cases deviate from the majority of the training data.

## 3.2 Examination of generalization ability

The fine-tuned Llama 3.1 8B Instruct outperforms its pretrained counterpart on the four test cases that have not been part of the training data. We observe that GPT4o shows a higher physical accuracy of equations than the fine-tuned model. The absolute number of error occurrences per error category is displayed in Table 2.

Most strikingly, the performance of the fine-tuned model is worse than GPT4o in the categories of unit conversion errors in parameter definitions and the accuracy of physics equations. For instance, the reaction rate expressions of parallel and consecutive reactions (cases a and b, see Section 2.3) are not formulated correctly in the responses of both the fine-tuned and the baseline models. In contrast, the responses provided by GPT4o

**Table 2:** Absolute amount of occurrences per error category per model. The test dataset comprises four case studies each containing elements not portrayed in the fine-tuning dataset. The baseline model (Llama 3.1 8B Instruct) is fine-tuned and assessed on the same test dataset. GPT4o is assessed on the same test dataset as a benchmark.

| | Parameter and variable declarations | | | | Physics equations | | | General syntax |
|---|---|---|---|---|---|---|---|---|
| | Unit error | Declaration syntax error | Incorrect values | Undefined variables | Incorrect equations | Structural error | Unit conflict | |
| Baseline (Llama 3.1 8B) | 20 | 39 | 3 | **0** | 25 | 0 | **0** | 9 |
| Fine-tuned (Llama 3.1 8B) | 15 | **0** | **0** | 2 | 14 | 0 | **0** | 1 |
| GPT4o | **5** | 3 | **0** | 1 | **8** | 0 | 1 | **0** |

contain correct rate expressions for both parallel and consecutive reactions. In the case of a requested non-constant density system (case c, see Section 2.3), none of the models examined correctly formulate an algebraic equation for the reaction volume. In the case of left-out parameter values in the user's description (cased d, see Section 2.3), the responses of the fine-tuned model and the baseline model both hallucinate arbitrary values, GPT4o's response defines one parameter arbitrarily and does not define another at all.

We conclude that the fine-tuned model does not show satisfactory ability to extrapolate to scenarios that are not presented during training. Thus, it could be considered to re-train on a wider, more diverse fine-tuning dataset comprising a larger variety of Modelica models with extensive documentation alongside the reference answers. Furthermore, supporting, external knowledge on, e.g., Modelica built-in variable types or textbooks on reactor modelling, could be provided to the LLM via, for instance, retrieval augmented generation (RAG)[8]. Additionally, iterative feedback loops could be implemented by running the produced Modelica script in Dymola and re-routing failed attempts back for improvement.

## 4 CONCLUSIONS

We conclude that it is possible to leverage the potential of LLMs for generating dynamic models of chemical reactor systems from descriptions in natural language. We find that through fine-tuning Llama 3.1 8B Instruct, the syntactic and semantic accuracy of Modelica code generation can be improved compared to the baseline Llama 3.1 8B Instruct model. Compared to GPT4o, the baseline Llama 3.1 8B Instruct model and the fine-tuned counterpart do not show sufficient ability to extrapolate to scenarios unseen during training. We suggest improving model performance through three potential avenues: (1) expanding the fine-tuning dataset, (2) incorporating wider literature and Modelica documentation into the workflow by using RAG, and (3) iterative improvement by leveraging an interface to Dymola. The synthetic generation of a dataset comprising a diverse set of data (1) is labor- and time-intensive, and we also find no evidence of sufficient ability to extrapolate to scenarios not included in the training dataset. We thus suggest providing access to Modelica documentation and literature on reactor modeling (2) as a resource to increase the model's robustness in formulating physically accurate equations and using built-in Modelica variable types. Lastly, simulation of the generated Modelica script could be attempted in Dymola (3) and improved iteratively in case of failure.

## REFERENCES


1. Jacobs PF, Pollice R. Developing large language models for quantum chemistry simulation input generation. *ChemRxiv preprint* (2024) https://doi.org/10.26434/chemrxiv-2024-9g2w2
2. Nijkamp E, Pang B, Hayashi H, Tu L, Wang H, Zhou Y, Savarese S, Xiong C. Codegen: An open large language model for code with multi-turn program synthesis. *arxiv preprint* (2022) https://doi.org/10.48550/ARXIV.2203.13474
3. Wang Y, Le H, Gotmare AD, Bui NDQ, Li J, Hoi SCH. Codet5+: Open code large language models for code understanding and generation. *arxiv preprint* (2023) https://doi.org/10.48550/ARXIV.2305.07922
4. Brown TB, Mann B, Ryder N, Subbiah M, Kaplan J, Dhariwal P, Neelakantan A, Shyam P, Sastry G, Askell A, Agarwal S, Herbert-Voss A, Krueger G, Henighan T, Child R, Ramesh A, Ziegler DM, Wu J, Winter C, Hesse C, Chen M, Sigler E, Litwin M, Gray S, Chess B, Clark J, Berner C, McCandlish S, Radford A, Sutskever I, Amodei D. Language models are few-shot learners. *arxiv preprint* (2020) https://doi.org/10.48550/ARXIV.2005.14165
5. Wei J, Bosma M, Zhao VY, Guu K, Yu AW, Lester B, Du N, Dai AM, Le QV. Finetuned language models are zero-shot learners. *arxiv preprint* (2021) https://doi.org/10.48550/ARXIV.2109.01652
6. Hu EJ, Shen Y, Wallis P, Allen-Zhu Z, Li Y, Wang S, Wang L, Chen W. Lora: Low-rank adaptation of large language models. *arxiv preprint* (2021) https://doi.org/10.48550/ARXIV.2106.09685
7. Hugging Face. meta-llama/llama-3.1-8b-instruct. https://huggingface.co/meta-llama/Llama-3.1-8B-Instruct
8. Lewis P, Perez E, Piktus A, Petroni F, Karpukhin V, Goyal N, Küttler H, Lewis M, Yih W-T, Rocktäschel T, Riedel S, Kiela D. Retrieval-augmented generation for knowledge-intensive nlp tasks. *arxiv preprint* (2020) https://doi.org/10.48550/ARXIV.2005.11401



© 2025 by the authors. Licensed to PSEcommunity.org and PSE Press. This is an open access article under the creative commons CC-BY-SA licensing terms. Credit must be given to creator and adaptations must be shared under the same terms. See https://creativecommons.org/licenses/by-sa/4.0/

Systems & Control Transactions

**Research Article - Peer Reviewed Conference Proceeding**
ESCAPE 35 - European Symposium on Computer Aided Process Engineering
Ghent, Belgium. 6-9 July 2025
Jan F.M. Van Impe, Grégoire Léonard, Satyajeet S. Bhonsale,
Monika E. Polańska, Filip Logist (Eds.)

PSE PRESS

# Enhancing Fault diagnosis for Chemical Processes via MSCNN with Hyperparameters Optimization

**Jingkang Liang[a], GürkanSin[a]***

[a] Process and Systems Engineering Center (PROSYS), Department of Chemical and Biochemical Engineering, Technical University of Denmark (DTU), 2800 Kgs.Lyngby, Denmark
* Corresponding Author: gsi@kt.dtu.dk

## ABSTRACT

Fault diagnosis is critical for ensuring the safety and efficiency of chemical processes, as undetected faults can lead to catastrophic consequences. While deep learning-based methods have shown promise in this field, they often require manual hyperparameter tuning, which is not efficient since they heavily rely on expert knowledge and need iterative trial-and-error. This work introduces a novel approach combining a Multiscale Convolutional Neural Network (MSCNN) with Tree-Structured Parzen Estimator (TPE) for automated hyperparameter optimization to enhance the performance of fault diagnosis for chemical processes. The Multi-Scale Module is to capture complex nonlinear features from the fault data, while the TPE efficiently searches for optimal hyperparameters for MSCNN. An experimental study was carried out on the Tennessee Eastman Process (TE Process) dataset, where the proposed method was benchmarked against state-of-the-art models. The results indicate that the MSCNN-TPE method demonstrated improved performance in terms of precision and recall, achieving 5.26% and 5.63% higher values, respectively, compared to the CNN model. Comparisons of the MSCNN with default hyperparameters further confirmed the effectiveness of these techniques in improving fault diagnosis performance. Additionally, model ensemble technique was explored to further enhance the performance of the model and provide uncertainty estimations. In conclusion, this approach offers a robust and reliable solution for fault diagnosis in the chemical industry, enhancing process safety and efficiency.

**Keywords**: Fault Detection, Machine Learning, Artificial Intelligence

## 1. INTRODUCTION

Fault diagnosis is critical in manufacturing, especially in chemical process, to prevent failures, minimize downtime, and avoid costly repairs and hazardous accidents [1]. With the development of technology, deep learning had been widely used in the field of fault diagnosis for its capability of automatic features extractions and accuracy in diagnosing complex chemical process faults [2].

Bao et al. [3] proposed a fault diagnosis method for chemical processes that combines a deep convolutional neural network (DCNN) with a recurrent neural network (RNN). The application in the Tennessee Eastman (TE) process demonstrated the model's ability to learn dynamic information from raw data in both spatial and temporal domains and achieve high accuracy in identifying abnormal conditions. Lomov et al. [4] proposed to use deep learning architectures, including a novel temporal CNN1D2D model and Generative Adversarial Networks (GANs), for fault detection in the TE process. Souza et al. [5] investigates the development of a fault detection and diagnosis system for TE process using convolutional neural networks (CNNs) and applied transfer learning to address issues of data distribution changes due to alterations in process control strategy. Zhang et al. [6] proposed a fault detection and diagnosis system for complex chemical processes using a bidirectional recurrent neural network (BiRNN) architecture, demonstrating superior performance in fault detection rate (FDR) and fault diagnosis time compared to unidirectional RNNs.

However, the traditional deep learning methods require expert knowledge for hyperparameters tuning to find the optimal hyperparameters for the fault diagnosis

task [7]. This could be time consuming and labour intensive. Liang et al. [8] proposed to use Tree-structured Parzen Estimator (TPE) for hyperparameters optimization in rotating machinery fault diagnosis. Ortiz et al. [9] employed Bayesian optimisation for hyperparameter tuning of machine learning models to achieve high accuracy in fault diagnosis for rotating machinery. Aouichaoui et al. [10] used grid search for hyperparameters tunning for different models and conducted uncertainty estimation methods including bootstrap, ensemble, and dropout to quantify the prediction uncertainty of graph neural networks (GNNs) in chemical property prediction. Nevertheless, research on hyperparameters optimization for fault diagnosis in chemical engineering is limited.

Motivated by the need to overcome the limitations of traditional deep learning-based fault diagnosis approaches which require expert knowledge in tunning hyperparameters, we proposed to utilize MSCNN with Tree-structured Parzen Estimator (TPE) to enhance the performance of fault diagnosis in chemical process. The contributions of this paper are summarized as follows:

1) A novel fault diagnosis framework for chemical process with multi-scale convolutional neural network, leveraging hyperparameters optimization and model ensemble is proposed.

2) Experimental results on TE process indicate the proposed framework outperforms the other comparison methods including PCA, MLP, CNN and MSCNN with default hyperparameters, which highlights the effectiveness of integrating the Multi-Scale module and TPE.

3) Model ensemble technique was conducted to the proposed method, which significantly improved the model performance and provided uncertainty estimations for trustworthy predictions.

The remainder of the paper is organized as follows. Section 2 introduces the methodologies utilized in the proposed method, including the overall proposed workflow, architecture of MSCNN, and introduction of TPE and model ensemble. Section 3 presents the experimental study of the proposed method, using Tennessee Eastman Process (TE process) as case study. Section 4 provides conclusion and future work.

# 2. METHODOLOGIES

## 2.1 Proposed workflow

The proposed workflow mainly consists of 4 steps:

1) Data acquisition and data splitting. The fault data are collected from the simulation and divided into train, validation and test sets.

2) Hyperparameters optimization for MSCNN using TPE. The MSCNN model and training and validation sets are initialized with a specific random seed. The TPE runs 500 trial-and-error iterations automatically to find the optimal hyperparameters set that achieves the highest validation accuracy.

3) Models training. The MSCNN model is trained based on the optimal set of hyperparameters that found by TPE. The trained model is saved for further testing.

4) Model performance testing. The trained MSCNN-TPE model predict the fault type of the given test set samples, and the true positive, false positive and false negative are recorded. Based on this, precision, recall and confusion matrix can be presented to evaluate the performance of the model.

## 2.2 Multi-Scale Convolutional Neural Network

Deep learning has been widely applied in the field of fault diagnosis, with convolutional neural network (CNN) being particularly effective due to their ability to extract hierarchical features. However, traditional CNN often faces challenges in capturing features across multiple scales, which are critical for detecting complex patterns in chemical process data. To address this limitation, a Multi-Scale Convolutional Neural Network (MSCNN) is proposed, as shown in Figure 1.

The key feature of the MSCNN is its ability to extract features at different resolutions through parallel convolutional layers with varying kernel sizes [11]. The one-dimensional fault signal serves as the input to the model, which is processed by a multi-scale convolution module. The module consists of parallel convolutional layer with kernel sizes of 1, 3, and 5. The output of each convolutional layer is computed as follows:

$$z_i^{(j)} = \sum_{k=1}^{K} w_k^{(j)} \cdot x_{i+k-1} + b^{(j)} \quad (1)$$

where $z_i^{(j)}$ is the output of the $j^{th}$ filter at position $i$, $x$ is the input sequence, $w_k^{(j)}$ represents the weights of the $j^{th}$ filter with kernel size $K$, and $b^{(j)}$ is the bias term. The weights and bias are trained with gradient decent.

The outputs of multi-scale convolution module are then concatenated, creating a comprehensive feature representation. A maxpooling operation is applied to the concatenated feature maps to reduce dimensionality while retaining important features. The resulting feature maps are further refined by additional convolutional layers. Finally, the features are flattened and passed through fully connected (FC) layers, followed by a softmax output layer to provide the final diagnostic result, represented as predicted probabilities for each fault class.

The MSCNN is trained using cross-entropy loss function:

$$L(y, \hat{y}) = -\sum_{i=1}^{C} y_i \log(\hat{y}_i) \quad (2)$$

where $C$ is the number of classes (i.e., fault types). $y_i$ is the true label for class $i$, taken from the one-hot encoded target vector (1 for the correct class and 0 for others). $\hat{y}_i$ is the predicted probability output by the softmax layer for class $i$. By minimizing the loss through gradient

decent, the MSCNN achieves optimal fault diagnosis performance.

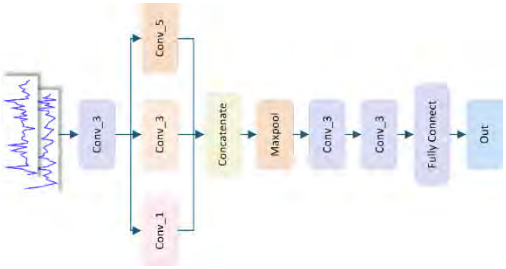



**Figure 1:** Schematic of the MSCNN structure.

## 2.3 Hyperparameters Optimization

To train a model that have the best performance on the validation set, we need to iteratively tune the hyperparameters. Instead of tunning them manually, we proposed to use Tree-structured Parzen Estimator, a Bayesian-based hyperparameters optimization method, to search for optimal hyperparameters automatically, as it has been proven effective in [12].

The search space of the hyperparameters and the default values are shown in Table 1. *Lr* refers to the learning rate of the Adam optimizer in the neural network, whose search space follows a *LogUni* type, which means that the value is uniformly distributed in the logarithmic scale. *Dr* is the drop out rate of the FC layer. *Pre_chan* refers to the channel number of the convolutional layer before the multi-scale module. *Post_chan* represents the channels number of the convolutional layer after maxpool. *Hidden_size* stands for the neurons number in FC layer.

**Table 1:** Hyperparameters Search Space for MSCNN

| Name | Value type | Optional value | Default |
|---|---|---|---|
| Lr | LogUni | [0.0001,0.1] | 0.01 |
| Dr | LogUni | [0.001,0.5] | 0.1 |
| Pre_chan | Choice | 8,16,32,64,128,256,512 | 32 |
| Post_chan | Choice | 8,16,32,64,128,256,512 | 128 |
| Hidden_size | Choice | 25,50,100,200,400 | 100 |

Tree-structured Parzen Estimator (TPE) [13] is utilized to optimize the hyperparameters in this paper. Historical hyperparameters are grouped to “good” set and “bad” set based on their evaluation value, which is the validation accuracy in this paper. The TPE models the likelihood probability of the two groups as follows:

$$p(x|y) = \begin{cases} l(x), & y > y^{\gamma} \\ g(x), & y \le y^{\gamma} \end{cases} \tag{3}$$

where $y$ is the evaluation value of the hyperparameter $x$, $y^{\gamma}$ is the threshold to separate “good” from “bad” observations. By maximizing $l(x)/g(x)$, TPE select the new hyperparameters that have the highest probability to achieve good result relative to a bad one. This strategy allows TPE to search for optimal hyperparameters efficiently compared to manual tunning. In the case study, 500 iterations were conducted, and the searching process took 9 hours and 14 minutes in total.

## 2.4 Model Ensemble

Instead of training a single model for fault diagnosis, we propose to use model ensemble technique to enhance diagnostic results as well as provide uncertainty estimation. For each model in the ensemble, the training and validation dataset are split differently to introduce diversity in the training data, which is different to the bootstrap sampling strategy [10]. In the meantime, each model is initialized with different parameters initialization, which also creates diversity to the models. With different initialization in both data and model, we enable models to learn from different optimization paths. This approach enhances robustness, as a single model may lack the ability to generalize effectively and is more prone to overfitting the data. By aggregating the predictions of multiple models, the ensemble mitigates these limitations and achieves superior overall performance. After training, the predicted probabilities from individual models are averaged to produce the final output, as shown below:

$$p(\hat{y} = c \mid x) = \frac{1}{M}\sum_{m=1}^{M} p(\hat{y} = c \mid x, \theta_m) \tag{4}$$

where $M$ is the number of models, which is set to 100 in this paper, $\theta_m$ is the parameters of the $m^{th}$ model.

# 3. EXPERIMENTAL STUDIES

## 3.1 Dataset Description

The Tennessee Eastman (TE) Process is used as a case study to evaluate the performance of the proposed method. This TE Process dataset, originates from a chemical process simulation by the Eastman Chemical Company, is widely used in the field of fault diagnosis and monitoring in chemical process to serve as a benchmark dataset to test process monitoring and fault diagnosis algorithms.

To be specific, the dataset consists of simulation running with 21 different fault types. For each sample, there are 53 process variables in total, but since the 12$^{th}$ variable remains constant, only 52 variables are considered to serve as input data. Due to the length of the paper, the schematic of the TE Process and the details of the faults can be referred to in [14]. There were 26880 samples in total, training, validation and test sets are separated according to the ratio of 6:2:2. For each fault type, there are 768 samples in the training set, 256 samples in the validation set, and 256 samples in the test set.

## 3.2 Comparison Methods

To highlight the performance of the proposed framework, several comparison methods were carried

**Table 2:** Results of fault diagnosis on the TE Process. P stands for Precision, R stands for Recall, with values expressed as percentages (%). For each fault type, the highest precision and recall are highlighted in bolded.

| | PCA | | MLP | | CNN | | MSCNN | | Proposed | |
|---|---|---|---|---|---|---|---|---|---|---|
| Fault | P | R | P | R | P | R | P | R | P | R |
| 1 | 100 | 98.44 | 87.29 | 99.22 | 100 | 98.83 | 99.61 | **99.22** | **100** | 98.83 |
| 2 | 100 | 96.48 | 98.03 | 97.27 | 100 | 98.05 | 99.21 | 98.44 | **100** | **98.83** |
| 3 | 13.76 | 17.58 | 31.40 | 31.64 | 43.93 | 36.72 | 47.25 | **63.67** | **66.39** | 61.72 |
| 4 | 82.17 | 91.80 | 78.68 | 98.05 | 93.23 | 96.88 | **93.80** | 94.53 | 93.31 | **98.05** |
| 5 | 81.82 | 73.83 | 94.66 | 96.88 | 97.69 | 99.22 | **98.08** | **99.61** | 97.31 | 98.83 |
| 6 | 100 | 100 | 100 | 100 | 100 | 100 | 100 | 100 | **100** | **100** |
| 7 | 100 | 100 | 98.46 | 100 | 99.61 | 99.22 | 100 | 100 | **100** | **100** |
| 8 | 93.95 | 91.02 | 0 | 0 | 92.16 | 96.48 | 97.57 | 94.14 | **98.80** | **96.88** |
| 9 | 19.72 | 16.41 | 22.72 | 35.94 | 43.44 | 41.41 | 57.23 | 37.11 | **61.42** | **60.94** |
| 10 | 27.94 | 22.27 | 61.11 | 64.45 | 57.81 | 86.72 | 77.57 | 82.42 | **83.15** | **86.72** |
| 11 | 23.59 | 26.17 | 0.00 | 0.00 | 72.86 | 79.69 | 65.18 | 79.69 | **79.69** | **81.25** |
| 12 | 86.69 | 83.98 | 65.83 | 92.58 | **98.56** | 80.47 | 95.14 | 91.80 | 96.39 | **93.75** |
| 13 | 95.65 | 94.53 | 78.21 | 95.31 | 94.23 | 95.70 | 97.23 | 96.09 | **97.65** | **97.27** |
| 14 | 87.14 | 82.03 | 84.21 | 93.75 | **98.40** | 96.09 | 96.51 | **97.27** | 97.61 | 95.70 |
| 15 | 17.23 | 23.83 | 21.36 | 24.61 | 44.63 | 51.95 | 51.22 | 49.22 | **57.88** | **66.02** |
| 16 | 27.72 | 21.88 | 46.01 | 47.27 | 62.45 | 55.86 | 66.52 | 59.77 | **73.33** | **68.75** |
| 17 | 84.34 | 92.58 | 84.00 | 90.23 | 91.60 | 93.75 | 92.94 | 92.58 | **95.28** | **94.53** |
| 18 | 96.48 | 85.55 | **99.54** | 84.38 | 95.47 | 90.63 | 95.12 | 91.41 | 96.71 | **91.80** |
| 19 | 49.55 | 64.84 | 66.23 | 58.98 | **78.54** | 62.89 | 76.07 | 69.53 | 74.81 | **76.56** |
| 20 | 57.68 | 60.16 | 61.09 | 74.22 | 82.70 | 76.56 | 79.12 | 76.95 | **86.29** | **83.59** |
| 21 | 56.71 | 36.33 | 63.53 | 63.28 | 76.98 | 75.78 | 74.28 | 80.08 | **78.79** | **81.25** |
| Avg | 66.77 | 65.70 | 63.92 | 68.95 | 82.11 | 81.57 | 83.79 | 83.50 | **87.37** | **87.20** |

out for the same diagnosis task. These methods are described as follows:

1) Principal Component Analysis (PCA). A classical dimensionality reduction technique commonly used in machine learning.

2) Multilayer Perceptron (MLP), which is a simple neural network composed of 4 FC layers, with the neurons number of 512, 256, 128, 64 respectively.

3) Convolutional Neural Network (CNN). A deep learning model adapted by replacing the multiscale module in MSCNN with two sequential convolutional layers, each with a kernel size of 3.

4) MSCNN. The MSCNN model trained with the default hyperparameters shown in Table 1. This model utilizes multiscale features to improve diagnostic performance.

5) MSCNN-TPE (Proposed). The MSCNN model trained with the optimal hyperparameters searched by TPE, which is the proposed method.

The experiments were conducted on a cluster server equipped with an AMD EPYC 9354 CPU and an Nvidia Volta 100 GPU. The models are implemented with the python packages scikit-learn and Pytorch 2.5. The optimizer used was Adam, with a learning rate set to 0.01. A learning rate scheduler was applied, reducing the learning rate by 10% every 10 epochs. Early stopping was employed with a patience of 10, meaning the training process would stop if the validation loss did not decrease for 10 consecutive epochs. By using consistent settings across all methods, this setup ensures a fair comparison between the approaches.

## 3.3 Results and Discussion

### 3.3.1 Evaluation Metrics

To evaluate the performance of the fault diagnosis models, we use precision (P) and recall (R) as the key metrics. These are particularly important in scenarios like fault diagnosis, where both false positives and false negatives can have critical consequences. The calculation of precision and recall are calculated as follows:

$$P = \frac{\mathrm{TP}}{\mathrm{TP+FP}} \tag{4}$$

$$R = \frac{\mathrm{TP}}{\mathrm{TP+FN}} \tag{5}$$

True Positive (TP) refers to a positive sample being correctly classified. False Positive (FP) represents a negative sample but misclassified as positive. False Negative (FN) indicates a positive sample that is misclassified as negative. In plain words, precision measures the proportion of correctly identified positive cases among all predicted positive cases, while recall measures the proportion of actual positive cases that the model successfully identified.

### 3.3.2 Results and Discussion

Table 2 shows the overall diagnostic results of the experiment. Some conclusions can be drawn from it:

**Limited competitiveness of PCA, MLP and CNN.** Both PCA, MLP and CNN have poor precision and recall in many of the fault types, especially on fault type 3,9,11 and 15. Among them, PCA performs the worst, followed by MLP, while CNN shows slightly better results. It is also worth noting that MLP fails to detect fault type 8 and 11 entirely, likely due to its architecture limitations in learning distinguishable features in complex high-dimensional feature spaces.

**Effectiveness of the Multi-Scale module in MSCNN.** Compared to CNN, MSCNN demonstrates

improvements in both precision and recall, particularly for some specific fault types. The average precision and recall of MSCNN (83.79%, and 83.50% respectively) are higher than those of CNN (82.11% and 81.57%), indicating the effectiveness of the integration of multi-scale module.

**Effectiveness of TPE.** The proposed method outperformed all comparison methods in terms of both precision and recall in most of the fault types, indicating its superiority. Specifically, the proposed method achieves an average precision and recall improvement of 3.58% and 3.70% respectively, over MSCNN, indicating the effectiveness of TPE in enhancing model performance.

**Comparison of training loss**. The training and validation losses of different approaches are shown as Figure 2. MLP exhibits the highest training and validation losses, and they can't decrease effectively after the longest training epoch, indicating the insufficient capacity of MLP to extract meaningful features from the data. CNN and MSCNN achieve similar losses, while the validation loss of MSCNN is slightly lower. On the other hand, the proposed method achieves the lowest losses, demonstrating its superior performance on both the training and validation sets, which aligns with the results observed on the test set.

**Analyzing of confusion matrix.** Due to the space limitations, only the confusion matrix of the proposed method is shown in Figure 3. By looking into the confusion matrix, we can have an intuitive analysis about the performance of the model and have insights into which fault types are more challenging to classify and how they are confused with one another.

Overall, the proposed method exhibits a higher number of correctly classified samples along the diagonal compared to MSCNN. Specifically, The TP of fault types 9 and 15 are 156 and 169 respectively— significantly higher than those of MSCNN (95 and 126 respectively). This improvement highlights the proposed method's ability to accurately classify faults. This result also indicated that some specific fault types are more difficult to classify and could be easily confused with one another. The reason could be their similar fault patterns, which make their feature representations highly alike. For example, fault 3 (D Feed Temperature (Stream 2) Step) and fault 9 (D Feed Temperature (Stream 2) Random Variation) exhibits similar characteristics, leading to increased misclassification between them.

**Significance of introduction of model ensemble.** As shown in Table 3 are diagnostic results of some difficult faults of the proposed method before and after using model ensemble. The model number is 100 in the ensemble. We can observe a significant improvement in both precision and recall after model ensemble, highlighting its effectiveness. Moreover, the uncertainty estimation of a fault sample can be calculated from the entropy of the probability distribution, and additional analyses can be provided by looking at the standard deviations, mean and other statistics from the 100 models in the ensemble. This approach provides more reliable result compared to using the prediction from a single model, as it captures the diversity in both model initializations and data splits.

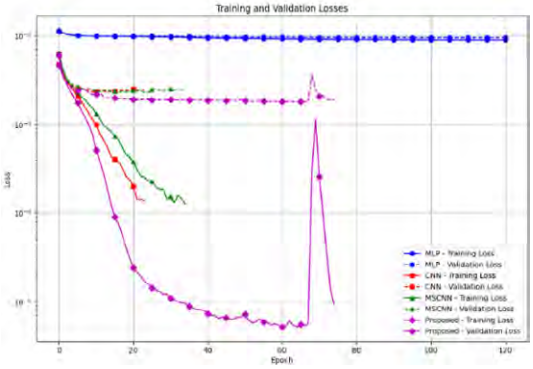



**Figure 2:** Training and validation losses of different approaches.

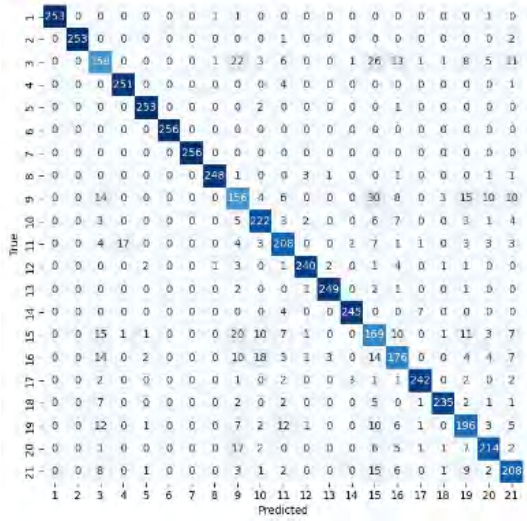



**Figure 3:** Confusion matrix of the proposed method.

**Table 3:** Results before and after model ensemble for difficult faults

| Fault | Proposed-Single | | Proposed-Ensembled | |
|---|---|---|---|---|
| | P | R | P | R |
| 3 | 66.39 | 61.72 | 66.79 | 69.92 |
| 9 | 61.42 | 60.94 | 71.85 | 75.78 |
| 11 | 79.69 | 81.25 | 85.43 | 82.42 |
| 15 | 57.88 | 66.02 | 66.08 | 73.88 |
| 19 | 74.81 | 76.56 | 78.20 | 81.25 |
| Avg | 68.04 | 69.30 | 73.67 | 76.65 |

## 4. CONCLUSION AND FUTURE WORK

To conclude, this paper proposed a fault diagnosis framework that integrates a multi-scale convolutional neural network with hyperparameters optimization and model ensemble to enhance fault diagnosis for complex chemical processes.

Experimental results on TE process indicate the proposed framework outperforms the other comparison methods including PCA, MLP, CNN and MSCNN with default hyperparameters. This shows the effectiveness of the introduction of Multi-Scale module and TPE. Additionally, model ensemble was applied to further improve the fault diagnosis performance and provide uncertainty estimations, enabling more reliable decision-making.

For future study, we aim to further explore model ensemble techniques, compare different models and uncertainty estimation methods, and contribute to trustworthy fault diagnosis that not only focus on the accuracy but also the reliability. Model pruning [15] will also be investigated to reduce model complexity while maintaining a comparable diagnostic performance.

## ACKNOWLEDGEMENTS

This research was funded by the European Union Horizon Europe 2022 Research and Innovation Programme under the Marie Sklodowska-Curie Grant Agreement No. 101119358 (ProSafe).

## REFERENCES

1. Bi X, Qin R, Wu D, Zheng S, Zhao J. One step forward for smart chemical process fault detection and diagnosis. Comput Chem Eng 2022;164:107884. https://doi.org/10.1016/j.compchemeng.2022.107884.
2. Md Nor N, Che Hassan CR, Hussain MA. A review of data-driven fault detection and diagnosis methods: applications in chemical process systems. Rev Chem Eng 2020;36:513–53. https://doi.org/10.1515/revce-2017-0069.
3. Bao Y, Wang B, Guo P, Wang J. Chemical process fault diagnosis based on a combined deep learning method. Can J Chem Eng 2022;100:54–66. https://doi.org/10.1002/cjce.24153.
4. Lomov I, Lyubimov M, Makarov I, Zhukov LE. Fault detection in Tennessee Eastman process with temporal deep learning models. J Ind Inf Integr 2021;23:100216. https://doi.org/10.1016/j.jii.2021.100216.
5. e Souza ACO, de Souza MB, da Silva FV. Enhancing fault detection and diagnosis systems for a chemical process: a study on convolutional neural networks and transfer learning. Evol Syst 2024;15:611–33. https://doi.org/10.1007/s12530-023-09523-y.
6. Zhang S, Bi K, Qiu T. Bidirectional Recurrent Neural Network-Based Chemical Process Fault Diagnosis. Ind Eng Chem Res 2020;59:824–34. https://doi.org/10.1021/acs.iecr.9b05885.
7. Qin R, Zhao J. Adaptive multiscale convolutional neural network model for chemical process fault diagnosis. Chin J Chem Eng 2022;50:398–411. https://doi.org/10.1016/j.cjche.2022.10.001.
8. Liang J, Liao Y, Chen Z, Lin H, Jin G, Gryllias K, et al. Intelligent fault diagnosis of rotating machinery using lightweight network with modified tree-structured parzen estimators. IET Collab Intell Manuf 2022;4:194–207. https://doi.org/10.1049/cim2.12055.
9. Ortiz R, Miranda-Chiquito P, Encalada-Davila A, Marquez LE, Tutiven C, Chatzi E, et al. An Enhanced Modeling Framework for Bearing Fault Simulation and Machine Learning-Based Identification With Bayesian-Optimized Hyperparameter Tuning. J Comput Inf Sci Eng 2024;24:091002. https://doi.org/10.1115/1.4065777.
10. Aouichaoui ARN, Mansouri SS, Abildskov J, Sin G. Uncertainty estimation in deep learning-based property models: Graph neural networks applied to the critical properties. AIChE J 2022;68:e17696. https://doi.org/10.1002/aic.17696.
11. Song Q, Jiang P. A multi-scale convolutional neural network-based fault diagnosis model for complex chemical processes. Process Saf Environ Prot 2022;159:575–84. https://doi.org/10.1016/j.psep.2021.11.020.
12. Loshchilov I, Hutter F. CMA-ES for hyperparameter optimization of deep neural networks. arXiv preprint 2016; arXiv:1604.07269. https://doi.org/10.48550/arXiv.1604.07269.
13. Bergstra J, Bardenet R, Bengio Y, Kégl B. Algorithms for Hyper-Parameter Optimization. Adv. Neural Inf. Process. Syst., vol. 24, Curran Associates, Inc.; 2011.
14. Melo A, Câmara MM, Clavijo N, Pinto JC. Open benchmarks for assessment of process monitoring and fault diagnosis techniques: A review and critical analysis. Comput Chem Eng 2022;165:107964. https://doi.org/10.1016/j.compchemeng.2022.107964.
15. Ruan D, et al. Light convolutional neural network by neural architecture search and model pruning for bearing fault diagnosis and remaining useful life prediction. Sci Rep 2023;13:5484. https://doi.org/10.1038/s41598-023-31532-9.

© 2025 by the authors. Licensed to PSEcommunity.org and PSE Press. This is an open access article under the creative commons CC-BY-SA licensing terms. Credit must be given to creator and adaptations must be shared under the same terms. See https://creativecommons.org/licenses/by-sa/4.0/



Systems & Control Transactions

**Research Article - Peer Reviewed Conference Proceeding**
ESCAPE 35 - European Symposium on Computer Aided Process Engineering
Ghent, Belgium. 6-9 July 2025
Jan F.M. Van Impe, Grégoire Léonard, Satyajeet S. Bhonsale,
Monika E. Polańska, Filip Logist (Eds.)

PSE PRESS

# Picard-KKT-hPINN: Enforcing Nonlinear Enthalpy Balances for Physically Consistent Neural Networks

**Giacomo Lastrucci[a], Tanuj Karia[a], Zoë Gromotka[b], and Artur M. Schweidtmann[a]***

[a] Process Intelligence Research Team, Department of Chemical Engineering, Delft University of Technology, The Netherlands
[b] Mathematical Physics Group, Delft Institute of Applied Mathematics, Delft University of Technology, The Netherlands
* Corresponding Author: a.schweidtmann@tudelft.nl.

## ABSTRACT

Neural networks (NNs) are widely used as surrogate models but they do not guarantee physically consistent predictions thereby preventing adoption in various applications. We propose a method that can enforce NNs to satisfy physical laws that are nonlinear in nature such as enthalpy balances. Our approach, inspired by Picard's successive approximations method, aims to enforce multiplicatively separable constraints by sequentially *freezing* and projecting a set of the participating variables. We demonstrate our Picard-KKT-hPINN for surrogate modeling of a catalytic packed bed reactor for methanol synthesis. Our results show that the method efficiently enforces nonlinear enthalpy and linear atomic balances at machine-level precision. Additionally, we show that enforcing conservation laws can improve accuracy in data-scarce conditions compared to *vanilla* multilayer perceptron.

**Keywords**: Surrogate modeling, Hard-constrained neural networks, Physics-informed neural networks, Constrained learning

## INTRODUCTION

Surrogate modeling plays a crucial role in simplifying and approximating complex physical models, making them suitable for large-scale simulations and optimization studies of industrial relevance. Machine learning models, such as neural networks (NNs), are particularly well-suited for this purpose due to their simplicity and strong regression capabilities [1]. However, despite exceptional advancements in machine learning, issues and skepticism regarding the black-box nature and physical inconsistency of these models hinder the adoption of machine learning-based tools (and, more broadly, artificial intelligence) in industrial applications [2,3]

To mitigate this limitation, significant research has been carried out to enforce known mechanistic relationships between inputs and predictions in NNs. Soft-constrained neural networks represent an approach in which physical equations are included as penalty terms in the loss function [4,5]. This method does not require any modification of the neural network architecture, but it does not guarantee the exact satisfaction of the constraints. When exact adherence to constraints such as closure of balances is required, hard-constrained neural networks become relevant. Models belonging to this class aim to strictly satisfy given equations or symmetries underlying the original system (constrained learning).

Different methodologies have been proposed for constrained learning. For instance, Beucler et al. (2019) and Donti et al. (2019) apply a method known as prediction and completion, where an NN is trained to predict a subset of variables, while the remaining ones are determined by solving a (non)linear system during training [6,7]. Researchers in optimization proposed to learn solutions to constrained optimization problems leveraging Lagrangian duality [8]; however, aspects of this approach still rely on soft constraints. Chen et al. (2021) introduced a projection step to guide the learning process by enforcing adherence to discretized differential equations [9]. Based on a similar concept, Chen, et al. (2024) presented KKT-hPINN to adjust neural network predictions, ensuring compliance with linear algebraic constraints [10]. Recently, Mukherjee and Bhattacharyya (2024) proposed to train constrained neural network using an NLP solver such as IPOPT [11]. Likewise, Schweidtmann et al. (2019) have used deterministic global optimization to compute guaranteed worst-case accuracies of NNs [12]. However, the use of local or global NLP solvers can be memory and

time-intensive for NNs that have a large number of parameters and training data points. Overall, current approaches (1) rely on external solvers that increase the computational cost to train and evaluate the NN or (2) are limited to enforcing linear equality constraints.

To address these challenges, we introduce a computationally efficient method that enforces relevant physical laws in the form of nonlinear algebraic equations. We extend the KKT-hPINN framework by considering local projections and numerical techniques to ensure exact constraint satisfaction at machine-level precision. Drawing inspiration from Picard's successive approximation method for solving nonlinear PDEs, we name our model Picard-KKT-hPINN.

## METHODS

We introduce Picard-KKT-hPINN, a method to enforce algebraic nonlinear constraints, such as energy balances, in NN predictions. It extends the KKT-hPINN approach with local projections and numerical techniques such as variable-freezing, while maintaining computational efficiency.

### Problem statement

Given a dataset $(\boldsymbol{x}_i, \boldsymbol{y}_i)_{i=1,\dots,N}$, representing the input-output behavior of a physical system (e.g., a unit operation), our goal is to train an NN to approximate the underlying model governing this system. In some cases, algebraic equations describing some relationship between input and output are known beforehand. We aim to develop an NN $f_\theta$ such that the predicted output $\hat{\boldsymbol{y}} = f_\theta(\boldsymbol{x})$ satisfies a set of algebraic constraints $c_k(\boldsymbol{x}, \boldsymbol{y}) = 0, k = 1, \dots, N_C$, which may represent conservation laws or design specifications. The number of constraints $(N_C)$ must not exceed the dimensionality of the neural network's output $(N_O)$. This ensures the system is underdetermined $(N_C < N_O)$, allowing the network to learn from the data while adhering to these constraints.

### Background: KKT-hPINN

Chen et al. (2024) proposed a model denoted as KKT-hPINN to enforce linear relationships in NNs [10]. In KKT-hPINN, the (physically inconsistent) prediction of a generic multilayer perceptron is corrected by an orthogonal projection onto the linear feasible region described by a system of linear equations and geometrically defining a hyperplane.

Specifically, the prediction $\hat{\boldsymbol{y}}$ is corrected so as to respect a linear system by solving the following optimization problem:

$$\tilde{\boldsymbol{y}} = \underset{\boldsymbol{y}}{\operatorname{argmin}} \left|\left|\boldsymbol{y} - \hat{\boldsymbol{y}}\right|\right|^2 \quad \text{s.t.} \quad \boldsymbol{A}\boldsymbol{x} + \boldsymbol{B}\boldsymbol{y} = \boldsymbol{b} \tag{1}$$

The corrected, physically consistent, solution $\tilde{y}$ is achieved by solving the Karush-Kuhn-Tucker (KKT) conditions of this optimization problem (Eq. 1), thus the name KKT-hPINN:

$$\tilde{\boldsymbol{y}} = \boldsymbol{A}^*\boldsymbol{x} + \boldsymbol{B}^*\hat{\boldsymbol{y}} + \boldsymbol{b}^* \tag{2}$$

Considering the identity matrix $\boldsymbol{I}$:

$$\begin{aligned} \boldsymbol{A}^* &= -\boldsymbol{B}(\boldsymbol{B}\boldsymbol{B}^T)^{-1}\boldsymbol{A} \\ \boldsymbol{B}^* &= \boldsymbol{I} - \boldsymbol{B}(\boldsymbol{B}\boldsymbol{B}^T)^{-1}\boldsymbol{B} \\ \boldsymbol{b}^* &= -\boldsymbol{B}^T(\boldsymbol{B}\boldsymbol{B}^T)^{-1}\boldsymbol{b} \end{aligned} \tag{3}$$

The projection matrices $(\boldsymbol{A}^*, \boldsymbol{B}^*, \boldsymbol{b}^*)$ are computed analytically owing to the quadratic objective function and linear constraints. This projection acts as a physics-informed activation layer on the network output, providing a computationally efficient approach to enforce linear constraints. However, its applicability is limited to linear systems, making it unsuitable for scenarios with nonlinearities. For instance, while effective for modeling mass balances in chemical engineering, it struggles with enthalpy balances, which often involve nonlinear relationships.

### Local projection

We generalize the linear constraints formulation in Eq. 1 to any nonlinear function in the input vector $\boldsymbol{x}$:

$$c(\boldsymbol{x}, \boldsymbol{y}) = \boldsymbol{B}\boldsymbol{y} + g(\boldsymbol{x}) - \boldsymbol{b} = \boldsymbol{0} \tag{4}$$

Since the input vector is known for every instance, we can consider it as a constant term and define $v(\boldsymbol{x}) = \boldsymbol{b} - g(\boldsymbol{x})$.Moreover, the input vector does not participate as an optimization variable in the projection process and thus $g(\boldsymbol{x})$ can be any nonlinear. Hence, Eq. 4 can be written as:

$$c(\boldsymbol{x}, \boldsymbol{y}) = \boldsymbol{B}\boldsymbol{y} - v(\boldsymbol{x}) = \boldsymbol{0} \tag{5}$$

where $v(\boldsymbol{x})$ is a vector-valued function $v: \boldsymbol{x} \subseteq \mathbb{R}^{N_I} \to \mathbb{R}^{N_C}$. In particular, $v$ is a nonlinear function of the $N_I$-dimensional input to the NN, meaning that its value is instance-dependent (an *instance* is a given datapoint $(\boldsymbol{x}_i, \boldsymbol{y}_i)$). Thus, the value of the constraint must be updated depending on each datapoint instance and can not be defined offline. Additionally, we consider local (*instance-specific*) constraint definition by allowing the matrix $\boldsymbol{B}$ to depend on the output instance $\boldsymbol{y}_i$. To simplify the notation, we define $\boldsymbol{B}_i = \boldsymbol{B}(\boldsymbol{y}_i)$ and $\boldsymbol{v}_i = \boldsymbol{v}(\boldsymbol{x}_i)$ such that:

$$c(\boldsymbol{x}_i, \boldsymbol{y}_i) = \boldsymbol{B}_i\boldsymbol{y}_i - \boldsymbol{v}_i = \boldsymbol{0} \tag{6}$$

This formulation comprises a wider class of functions in respect to the linear case in Eq. 1 and is foundational to handle local nonlinearities.

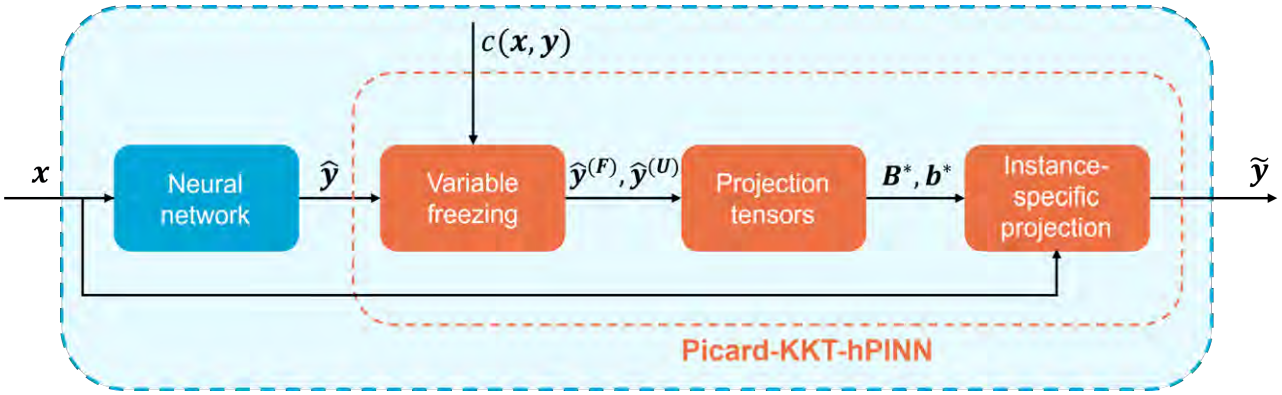



**Figure 1:** Picard-KKT-hPINN consists of a set of non-trainable layers that can be appended on every NN backbone (e.g., multilayer perceptrons, convolutional neural networks, transformers). Multiplicatively separable constraints (Eq. 8) are enforced exactly by partitioning the prediction vector (*variable freezing*). Then, the prediction of the NN is projected onto the feasible space defined by the constraints $c$. The layers composing Picard-KKT-hPINN are differentiable, hence, the NN is trained end-to-end and the architecture is equivalent at training and inference time.

The computational cost to achieve local projection can be reduced by exploiting parallel computing. We perform batch training (with $BS$ being the number of elements in the batch) by building a *rank-3* tensor $\boldsymbol{B} \in \mathbb{R}^{BS \times N_C \times N_O}$ holding a number $BS$ of local $\boldsymbol{B}_i$ matrices. Similarly, we construct a *rank-2* tensor $\boldsymbol{V} \in \mathbb{R}^{BS \times N_C}$ to store the local $\boldsymbol{v}_i$ vectors. The local projection matrices are computed in parallel (Eq. 7), hence reducing the apparent complexity of the most expensive computation, the matrix inversion, from $O(BS \times N^3)$ to $O(N^3)$.

$$\boldsymbol{B}^* = \boldsymbol{I} - \boldsymbol{B}^T(\boldsymbol{B}\boldsymbol{B}^T)^{-1}\boldsymbol{B}$$
$$\boldsymbol{V}^* = \boldsymbol{B}^T(\boldsymbol{B}\boldsymbol{B}^T)^{-1}\boldsymbol{V} \tag{7}$$

More specifically, considering the batch inversion of the tensor $\boldsymbol{B}\boldsymbol{B}^T$, the dimension $N$ is the number of constraints. Assuming to deal with tasks involving $N_C = N < 10^3$, the inversion is performed in a negligible amount of FLOPs in modern hardware. To the best of our knowledge, this dimensionality bound does not limit the applicability of the method for the majority of the surrogate modeling tasks in chemical engineering.

## Picard-KKT-hPINN

Inspired by Picard's successive approximation method for nonlinear partial differential equations (PDEs), we develop a model to exactly enforce nonlinear constraints, including physical balances expressed as algebraic equations (See Figure 1).

### Output partitioning and definition of the constraint class

Given the NN's output vector $\boldsymbol{y} = [y_1, \dots, y_{N_O}] \in \mathbb{R}^{N_O}$, we partition its components as $\boldsymbol{y} = [\boldsymbol{y}^{(F)} \ \ \boldsymbol{y}^{(U)}]$. $\boldsymbol{y}^{(F)}$ is the subvector of *frozen* variables and $\boldsymbol{y}^{(U)}$ is the subvector of *unfrozen* variables, with $\boldsymbol{y}^{(F)} = [y_{j_1}, \dots, y_{j_{N_F}}] \in \mathbb{R}^{N_F}$ and $\boldsymbol{y}^{(U)} = [y_{j_1}, \dots, y_{j_{N_U}}] \in \mathbb{R}^{N_O - N_F}$, with $N_U = N_O - N_F$.

We aim to enforce multiplicatively separable equality constraints of the form:

$$c_k(\boldsymbol{x}, \boldsymbol{y}) = \boldsymbol{B}_k \boldsymbol{y} + F_k\left(\boldsymbol{y}^{(F)}\right) \cdot \boldsymbol{y}^{(U)} - v_k(\boldsymbol{x}) = 0$$
$$k = 1, \dots, N_C \tag{8}$$

The constraint includes some linear function in the output $\boldsymbol{y}$, any nonlinear function $v_k$ in the input $\boldsymbol{x}$, and a scalar multiplication between $F_k$, a nonlinear vector-valued function in the *frozen* variables $\boldsymbol{y}^{(F)}$, and the *unfrozen* variables $\boldsymbol{y}^{(F)}$. Note that $F_k: \mathbb{R}^{N_F} \to \mathbb{R}^{N_U}$.

Steady-state macroscopic conservation principles can be generally formulated as Eq. 8. Thus, the structure of the considered constraint is of interest for engineering and physics-based applications.

More in general, the constraints in Eq. 8 can be formulated in matrix notation as:

$$c(\boldsymbol{x}, \boldsymbol{y}) = \boldsymbol{B}\boldsymbol{y} + F\left(\boldsymbol{y}^{(F)}\right) \cdot \boldsymbol{y}^{(U)} - v(\boldsymbol{x}) = 0 \tag{9}$$

Here, $c(\boldsymbol{x}, \boldsymbol{y})$ is the vector of $N_C$ constraints and $F\left(\boldsymbol{y}^{(F)}\right)$ is an $N_C \times N_U$ matrix. We develop a method to let the NN predictions exactly guarantee constraints belonging to the class in Eq. 9 by *freezing* a partition of the output variables, resembling Picard's iteration method.

### Variables freezing

Given the output $\hat{\boldsymbol{y}}$ of an NN $f_\theta(\boldsymbol{x})$, we aim to guarantee the prediction to satisfy a constraint of the form as in Eq. 9 by projecting the latter onto the feasible space.

The projected prediction $\tilde{\boldsymbol{y}}$ can be computed as the solution of the following nonlinear program (NLP):

$$\tilde{\boldsymbol{y}} = \underset{\boldsymbol{y}}{\operatorname{argmin}} \left|\left|\boldsymbol{y} - \hat{\boldsymbol{y}}\right|\right|^2$$
$$\text{s.t.} \quad c(\boldsymbol{x}, \boldsymbol{y}) = \boldsymbol{B}\boldsymbol{y} + F\left(\boldsymbol{y}^{(F)}\right) \cdot \boldsymbol{y}^{(U)} - v(\boldsymbol{x}) = 0 \tag{10}$$

Instead of relying on an external solver, we reformulate the NLP in Eq. 10 as a quadratic program (QP) solvable analytically. To achieve that, we assume the variables in $\boldsymbol{y}^{(F)}$ as *correct* and thus set them constant. This variable-freezing allows to reformulate Eq. 9 as a linear constraint by defining $\boldsymbol{B}' = \boldsymbol{B}\boldsymbol{y} + F\left(\boldsymbol{y}^{(F)}\right)$:

$$c(\boldsymbol{x}, \boldsymbol{y}) = \boldsymbol{B}'\boldsymbol{y} - v(\boldsymbol{x}) = 0 \tag{11}$$

Since Eq. 11 is the matrix form equivalent of Eq. 6, the local projection is achieved according to Section 2.3 and results in $\tilde{\boldsymbol{y}} = \boldsymbol{B}^*\hat{\boldsymbol{y}} + \boldsymbol{v}^*$,where the projection tensors can be computed exploiting parallel computing during training.

The nonlinear term is handled by projecting only a partition of the output variables. We observe the method to be more efficient when $N_U < N_F$, that is, more variables are projected to guarantee the nonlinear constraints. However, in general, the whole output vector is still potentially projected since linear terms can be present. Such numerical technique resembles Picard's iteration method to solve nonlinear PDEs iteratively (hence, the name Picard-KKT-hPINN), where some variables are kept constant to the previous iteration's value to achieve a linear expression. Similarly, here we exploit the iterative training process to converge towards the ground truth data while guaranteeing the prediction obeys the nonlinear constraint.

## RESULTS AND DISCUSSION

### Case study and constraints

Our proposed method is illustrated on a tubular packed-bed reactor for methanol synthesis, using the same modeling assumptions as in Lastrucci et al. (2024) [13]. The surrogate models involve 10 inputs (inlet temperature, pressure, component flowrates, and coolant flowrate) and 10 outputs (outlet temperature, pressure, component flowrates, and hotspot temperature). The training and test datasets, consisting of 20,000 and 500 data points respectively, are generated by solving the mechanistic model of the reactor implemented in Python under diverse conditions bounded by operational limits derived from flowsheet simulation. Specifically, we simulate the simplified plant for methanol synthesis implemented in the IDEAS library [14] and evaluate extreme recycle conditions to determine those bounds. Hence, each datapoint $(x_i, y_i)$ represents the input-output state variables corresponding to a specific operating scenario. The generated data are intentionally noise-free, as the goal is to develop a surrogate model that faithfully replicates the original mechanistic model. The relevance of this study lies in enabling faster computations, for instance, by eliminating the need for dynamic optimization in flowsheet optimization problems.

We derive algebraic constraints underlying the steady state physical system that we aim to enforce in the surrogate model, such as atomic balance and total enthalpy balance. The system consists of four linear atomic balances (Eq. 12) and one nonlinear equation for the energy balance (Eq. 13):

$$\sum_{i=1}^{N_S} \dot{a}_{ij,in} - \sum_{i=1}^{N_S} \dot{a}_{ij,out} = 0, \qquad j = C, H, O, N \tag{12}$$

$$\sum_{i=1}^{N_S} \dot{n}_{i,in}\tilde{h}_{i,in} - \sum_{i=1}^{N_S} \dot{n}_{i,out}\tilde{h}_{i,out} - \dot{Q} = 0 \tag{13}$$

In Eq. 12, $\dot{a}_{ij,in}$ and $\dot{a}_{ij,out}$ are the molar flowrates of atom $j$ *carried* by species $i$, entering and exiting the reactor, respectively, and $N_S$ is the number of chemical species involved (composed by four atoms, such as carbon, hydrogen, oxygen, and nitrogen). Being the atomic balances linear constraints, they can effectively be enforced using KKT-hPINN [10]. In Eq. 13, $\dot{n}_{i,in}$ and $\dot{n}_{i,out}$ are the molar flowrates of species $i$, $h_{i,in}$ and $h_{i,out}$ are the molar-specific enthalpies and $\dot{Q}$ is the rate of heat transfer out of the system. In general, the specific enthalpy $\tilde{h}_{i,eval} = \tilde{h}_{i,eval}(T_{eval})$ is a nonlinear function of the temperature, depending on the modeling choice for the specific heat at constant pressure $c_P$. Since in the considered case study $\dot{Q} = \dot{n}_c\widetilde{\Delta H}_{ev}(T_c)$ is a function of the input (coolant flowrate, $\dot{n}_c$) [13], the term $\sum_{i=1}^{NS} \dot{n}_{i,in}\tilde{h}_{i,in} - \dot{Q}$ can be regarded as $v_k(\boldsymbol{x})$ in Eq. 8. More importantly, the term $-\sum_{i=1}^{NS} \dot{n}_{i,out}\tilde{h}_{i,out}$ can be seen as the dot-product in Eq. 8, with $F_k\left(\boldsymbol{y}^{(F)}\right) = \tilde{h}_{i,out} = \tilde{h}_i(T_{out})$ and $\boldsymbol{y}^{(U)} = \dot{n}_{i,out}$. Thus, our Picard-KKT-hPINN model can exactly enforce both the atomic (Eq. 12) and the enthalpy balances (Eq. 13).

### Experiments and comparison

We train a shallow Picard-KKT-hPINN consisting of 1 hidden layer with 64 neurons and ReLU activation function, and we compare against a KKT-hPINN and a multilayer perceptron (MLP) with the same backbone architecture. Every model is trained for 50,000 epochs, using the Adam optimizer with a learning rate of $10^{-5}$ and a batch size of 2,000 samples. For reproducibility, the fully connected layers are deterministically optimized from a fixed Glorot initialization [15]. The training time of Picard KKT-hPINN on GPU hardware is comparable to that of MLP and KKT-hPINN, averaging only 15% longer, primarily due to the matrix inversion operation. At inference, the computational time of the three models is equivalent, even on CPU hardware (11th Gen Intel(R) Core(TM) i7-1185G7 @ 3.00GHz, 4 Core(s)).

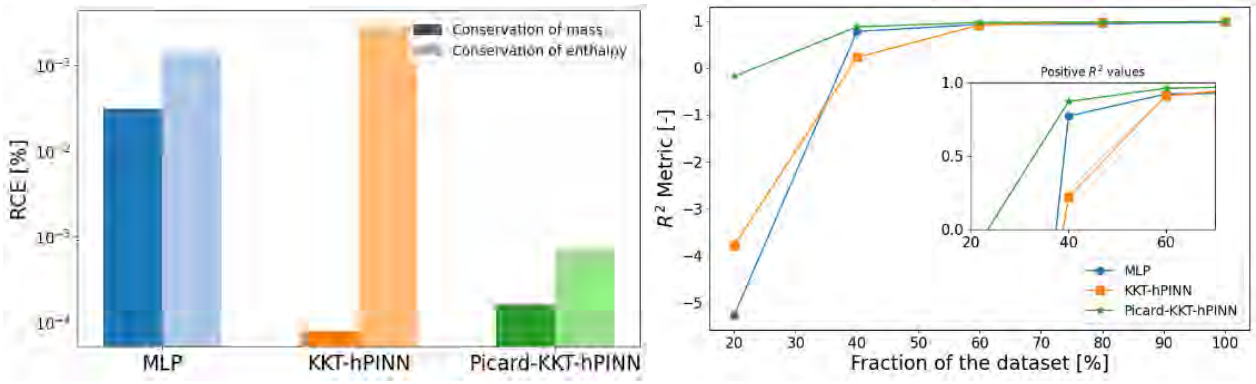



**Figure 2:** Comparison of relative conservation error (RCE) of mass and enthalpy balances (*left*) and model performances in data scarcity conditions (*right*) over the three different models.

**Table 1:** Accuracy comparison over the three different models. We train all the models on a GPU hardware (NVIDIA GeForce RTX 3090).

| | MLP | KKT-hPINN | Picard-KKT-hPINN |
|---|---|---|---|
| $R^2$ [-] | 0.97 | 0.98 | 0.98 |
| MAPE [%] | 0.81 | 0.58 | 0.71 |

The accuracy of the models on the test set is comparable in terms of coefficient of determination ($R^2$) and mean absolute percentage error (MAPE). In Table 1, the metrics are averaged over all the predicted variables in the test set. We do not expect the constraints to increase the accuracy considerably when a traditional MLP is already very accurate.

The focus of the study is to demonstrate the effectiveness of Picard-KKT-hPINN in enforcing both linear and nonlinear constraints. Figure 2 (*left*) shows the relative conservation error of the total mass and enthalpy. The MLP, although very accurate, does not strictly satisfy the balances. As claimed by the authors [10], KKT-hPINN effectively enforces the linear mass balances at machine-level precision (note that the plot is in logarithmic scale), however, the predictions do not strictly satisfy the nonlinear enthalpy balance. Picard-KKT-hPINN, instead, enforces mass and enthalpy balances exactly, reducing the error below 0.001% for both.

In a real-word scenario, the amount of data is often a bottleneck when training *data-hungry* machine learning models such as NNs. We analyze the performance of the models in data scarcity conditions by training on uniformly sampled fractions of the original dataset. We demonstrate that constrained learning can improve model performance in data scarcity conditions (Figure 2, *right*). Specifically, enforcing atomic balance through KKT-hPINN outperforms the MLP when using between 20 and 30% of the original training dataset. When enforcing both atomic and total enthalpy balance with Picard-KKT-hPINN, the model performance shows a positive coefficient of determination ($R^2 \simeq 0.75$) when only 35% of the training dataset is used, while both MLP and KKT-hPINN show a negative $R^2$ in the same data regime.

## CONCLUSION

We propose Picard-KKT-hPINN, a method to ensure that NN predictions adhere strictly to nonlinear algebraic constraints, such as enthalpy balances. Our work extends the recent KKT-hPINN model by Chen, et al. (2024) from linear to nonlinear constraints [10]. Thereby, we address a critical limitation of surrogate models in failing to satisfy fundamental physical principles such as mass and energy conservation.

In our proposed method, we project the NN predictions onto the feasible space defined by mass and enthalpy balances, ensuring the exact satisfaction of these laws. We tested Picard-KKT-hPINN in surrogate modeling tasks, specifically for a methanol synthesis packed bed reactor. The method guarantees atomic and enthalpy balances without adding computational overhead, while also outperforming the accuracy of standard MLPs in data-scarce regimes. These results highlight the potential of Picard-KKT-hPINN to advance the adoption of NNs in relevant chemical engineering applications, including large-scale process optimization and simulation, where developing physically consistent surrogate models is crucial for ensuring both computational efficiency and reliable outcomes.

## ACKNOWLEDGEMENTS

We gratefully acknowledge the support provided by Shell Global Solutions International B.V.

## REFERENCES


1. Kevin McBride and Kai Sundmacher. Overview of surrogate modeling in chemical process engineering. Chemie Ingenieur Technik, 91(3):228–239 (2019) https://doi.org/10.1002/cite.201800091
2. Patrick Bedué and Albrecht Fritzsche. Can we trust ai? An empirical investigation of trust requirements and guide to successful AI adoption. Journal of Enterprise Information Management, 35(2):530–549. (2021) https://doi.org/10.1108/JEIM-06-2020-0233
3. Artur M. Schweidtmann, Jana M. Weber, Christian Wende, Linus Netze, and Alexander Mitsos. Obey validity limits of data-driven models through topological data analysis and one-class classification. Optimization and Engineering, 23(2):855–876. (2021) https://doi.org/10.1007/s11081-021-09608-0
4. M. Raissi, P. Perdikaris, and G.E. Karniadakis. Physics-informed neural networks: A deep learning framework for solving forward and inverse problems involving nonlinear partial differential equations. Journal of Computational Physics, 378:686–707. (2019) https://doi.org/10.1016/j.jcp.2018.10.045
5. Zhiyong Wu, Huan Wang, Chang He, Bingjian Zhang, Tao Xu, and Qinglin Chen. The application of physics-informed machine learning in multiphysics modeling in chemical engineering. Industrial amp; Engineering Chemistry Research, 62(44):18178–18204. (2023) https://doi.org/10.1021/acs.iecr.3c02383
6. Tom Beucler, Michael Pritchard, Stephan Rasp, Jordan Ott, Pierre Baldi, and Pierre Gentine. Enforcing analytic constraints in neural-networks emulating physical systems. Physical Review Letters, 126(9):098302. (2019) https://doi.org/10.1103/PhysRevLett.126.098302
7. Priya L. Donti, David Rolnick, and J. Zico Kolter. Dc3: A learning method for optimization with hard constraints. International Conference on Learning Representations. (2021) https://doi.org/10.48550/arXiv.2104.12225
8. Ferdinando Fioretto, Pascal Van Hentenryck, Terrence WK Mak, Cuong Tran, Federico Baldo, and Michele Lombardi. Lagrangian duality for constrained deep learning. Joint European Conference on Machine Learning and Knowledge Discovery in Databases. (2021) https://doi.org/10.1007/978-3-030-67670-4_8
9. Yuntian Chen, Dou Huang, Dongxiao Zhang, Junsheng Zeng, Nanzhe Wang, Haoran Zhang, and Jinyue Yan. Theory-guided hard constraint projection (hcp): A knowledge-based data-driven scientific machine learning method. Journal of Computational Physics, 445:110624. (2021) https://doi.org/10.1016/j.jcp.2021.110624
10. Hao Chen, Gonzalo E. Constante Flores, and Can Li. Physics-informed neural networks with hard linear equality constraints. Computers & Chemical Engineering, 189:108764. (2024) https://doi.org/10.1016/j.compchemeng.2024.108764
11. Angan Mukherjee and Debangsu Bhattacharyya. On the development of steady-state and dynamic mass-constrained neural networks using noisy transient data. Computers & Chemical Engineering, 187:108722. (2024) https://doi.org/10.1016/j.compchemeng.2024.108722
12. Artur M. Schweidtmann, Dominik Bongartz, Wolfgang R. Huster, and Alexander Mitsos. Deterministic global process optimization: Flash calculations via artificial neural networks. pages 937–942. (2019) https://doi.org/10.1016/B978-0-12-818634-3.50157-0
13. Giacomo Lastrucci, Maximilian F. Theisen, and Artur M. Schweidtmann. Physics-informed neural networks and time-series transformer for modeling of chemical reactors. pages 571–576. (2024) https://doi.org/10.1016/B978-0-443-28824-1.50096-X
14. Lee, A., Ghouse, J. H., Eslick, J.C., Laird, C.D., Siirola, J.D., Zamarripa, M.A., Gunter, D., Shinn, J. H., Dowling, A. W., Bhattacharyya, D., Biegler, L. T., Burgard, A. P., & Miller, D.C. (2021). The IDAES process modeling framework and model library—Flexibility for process simulation and optimization. Journal of Advanced Manufacturing and Processing, 3(3), 1-30. https://doi.org/10.1002/amp2.10095
15. Xavier Glorot and Yoshua Bengio. Understanding the difficulty of training deep feedforward neural networks. Proceedings of the Thirteenth International Conference on Artificial Intelligence and Statistics, Volume 9 of Proceedings of Machine Learning Research, pages 249–256. (2010) https://proceedings.mlr.press/v9/glorot10a.html



© 2025 by the authors. Licensed to PSEcommunity.org and PSE Press. This is an open access article under the creative commons CC-BY-SA licensing terms. Credit must be given to creator and adaptations must be shared under the same terms. See https://creativecommons.org/licenses/by-sa/4.0/




Systems & Control Transactions

**Research Article - Peer Reviewed Conference Proceeding**
ESCAPE 35 - European Symposium on Computer Aided Process Engineering
Ghent, Belgium. 6-9 July 2025
Jan F.M. Van Impe, Grégoire Léonard, Satyajeet S. Bhonsale,
Monika E. Polańska, Filip Logist (Eds.)

PSE PRESS

# AI-Driven Automatic Mechanistic Model Transfer Learning for Accelerating Process Development

**Alexander W. Rogers[a], Amanda Lane[b], Philip Martin[a], and Dongda Zhang[a]***

[a] The University of Manchester, Department of Chemical Engineering, Manchester, UK
[b] Unilever R&D Port Sunlight, Liverpool, UK
* Corresponding Author: dongda.zhang@manchester.ac.uk.

## ABSTRACT

Accurate mechanistic models provide valuable physical insight and are crucial for efficient process scale-up and optimisation, but their identification requires lengthy experimental data collection, model construction, validation and discrimination. Traditional black-box machine learning transfer methods leverage prior knowledge but lack interpretability and physical insights. To address this, we propose a novel approach using artificial neural network feature attribution to automatically locate corrections and symbolic regression to make structural modifications to an inaccurate or low-fidelity mechanistic model. In a comprehensive in-silico case study, the framework adapted a kinetic model from one biochemical system to a different but related one, enhancing predictive accuracy. Integrated within an iterative model-based design of experiments routine, it minimised the number of new experiments required. The study also discusses the impact of the inductive bias trade-off and alternative ways of incorporating prior knowledge to improve performance, highlighting the framework's flexibility and potential for advancing automated knowledge discovery and high-fidelity predictive digital twin design for novel (bio)chemical processes.

**Keywords**: Knowledge Discovery, Dynamic Modelling, Genetic Algorithm, Artificial Intelligence, Biosystems, Model-Based Design of Experiments, Interpretable Machine Learning

## 1. INTRODUCTION

Developing accurate models to predict bioprocess dynamics is vital for commercial process design, scale-up, and control. Kinetic models, formulated as ordinary differential equations (ODEs), incorporate known reaction mechanisms and parameters with physical significance, thus making them interpretable. However, their construction is difficult due to incomplete and uncertain knowledge of biochemical reaction networks. Data-driven methods such as statistical and machine learning models (e.g., artificial neural networks, Gaussian processes, random forests) can capture complex dynamics without explicit mechanistic knowledge. Still, they lack enough interpretability and demand large, high-quality datasets that are experimentally resource-intensive.

Hybrid modelling has emerged as a pragmatic solution when systems are only partially understood and data is limited. Such models combine mass balances and simplified reaction terms with data-driven components to describe unknown kinetics as time-varying parameters. This corrects for structural mismatch and reflects biochemical systems' inherent transient or hysteretic nature.

Transfer learning accelerates model development by updating pre-trained models from related systems. It has proved effective in fields such as image classification, natural language processing, and, increasingly, chemical processes. In bioprocessing, knowledge of one microalgal strain is leveraged to reduce experimentation for mutant strains or the influence of plant hormones to accelerate screening during early bioprocess development while integrated transfer learning and hybrid modelling carry over mechanistic knowledge [1]. The assumption is that the new system's dynamics are sufficiently similar to the source. However, the degree of similarity is often uncertain, while these approaches remain non-interpretable: by only updating the data-driven and mechanistic parameters of an existing hybrid model, the mechanistic model structure remains unchanged, and updates to the embedded data-driven terms are opaque, providing little physical insight into the new system.

In recent years, the push for interpretable,

parsimonious models has led to algorithms that automatically discover governing equations. Sparse identification techniques have been used to elucidate stoichiometry and kinetics in bioprocesses [2]. However, constructing suitable libraries of candidate functions is not always feasible for complex systems. This has motivated symbolic regression (SR) [3], whereby closed-form expressions built from primitive operators (e.g., addition, multiplication) are generated by genetic programming, transformers, reinforcement learning or recurrent neural networks. SR has succeeded in discovering chemical and approximate biochemical mechanistic equations [4] but risks producing non-interpretable local approximations. SR is NP-hard, and when many features are possible, discovering accurate, parsimonious expressions is intractable.

Existing methodologies also demand sampling frequencies beyond typical experimental capabilities, while biomass, substrate, and product measurements may be noisy. This complicates gradient estimation for ODE discovery unless relatively computationally expensive numerical integration is embedded in the fitness function.

Researchers often utilise prior knowledge when exploring new systems. This work, therefore, proposes a framework integrating SR with artificial neural network (ANN) feature attribution to automatically adapt the structure of an existing mechanistic model from literature or a common concept. This will allow the transfer of physical knowledge between different but related systems to rapidly generate accurate predictive models with limited data – a common scenario in bioprocess development.

In Section 4.1, an in-silico case study will demonstrate the framework when prior knowledge is abundant but partially incorrect for the target domain. Moreover, the framework will be combined with a model-based design of experiments (MbDoE) for model discrimination to iteratively refine the model structure while minimising the number of experiments needed to discover the correct equations for the newly investigated system. Section 4.2 will then discuss how the amount of prior knowledge will impact the flexibility and efficiency of the framework.

## 2. METHODOLOGY

A kinetic model represents the rate of change, $\mathrm{d}\boldsymbol{y}/\mathrm{d}t$, in the concentrations of (bio)chemical species, $\boldsymbol{y}$, with respect to time, $t$, as a system of ODEs, $f(\boldsymbol{y}, \boldsymbol{\theta})$, where $\boldsymbol{\theta}$ are the model parameters. The goal of the framework is to take a mechanistic model for a different but related system or a pre-existing low-fidelity mechanistic model and adapt or improve its structure to more accurately fit and make predictions on a new target system. The initial equations, or source model, are denoted by $f_s(\boldsymbol{y}, \boldsymbol{\theta}_s)$, and the adapted equations, or transfer model for the target domain, are denoted by $f_t(\boldsymbol{y}, \boldsymbol{\theta}_t)$.

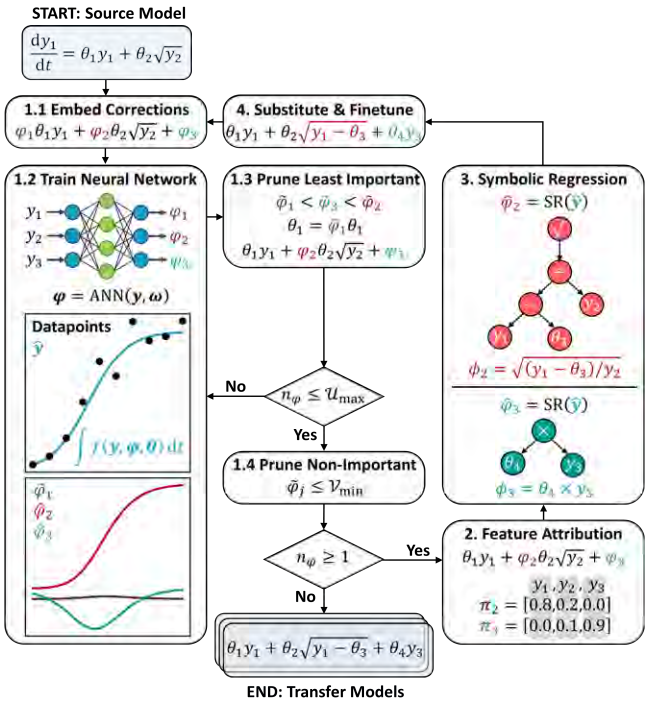



**Figure 1:** ANN attribution guided symbolic regression for dynamic systems. Takes equations for the source model and data for the target domain, and outputs candidate transfer models for model-based design of experiments.

An outline of the framework is depicted in Figure 1. Step 1 identifies which terms need altering by embedding initially unknown correction terms into the kinetic model (Step 1.1). A regularised ANN then learns the relationship between the correction terms and states (Step 1.2), then Steps 1.3-1.4 iteratively prune the corrections with the lowest variance. In Step 2, feature attribution determines which input variables matter most, providing weighting vectors, $\boldsymbol{\pi} = [\pi_1, \pi_2, \pi_3]$, for each feature, $\boldsymbol{y} = [y_1, y_2, y_3]$. Step 3 applies SR to build symbolic corrections guided by $\boldsymbol{\pi}$. Finally, in Step 4, these symbolic corrections are substituted back into the equations and parameters are fine-tuned, yielding $f_t(\boldsymbol{y}, \boldsymbol{\theta}_t)$. Variables $\boldsymbol{y}$ and $t$ are normalised and the source model automatically nondimensionalised; afterwards $f_t(\boldsymbol{y}, \boldsymbol{\theta}_t)$ is automatically re-dimensionalised. Throughout this article, $\hat{\boldsymbol{y}}$ denotes fitted states, $\hat{\boldsymbol{\varphi}}$ fitted corrections, and $\boldsymbol{\phi}$ their symbolic forms or approximations generated by SR. This algorithm's output can be a single model or multiple candidates to be further discriminated by model-based design of experiments (MbDoE).

### 2.1. ANN-Based Algorithm for Locating Structural Corrections

Consider $g_t(\boldsymbol{y}, \boldsymbol{\theta}_t)$ in Eqn. 1a as the target-domain ground-truth equations and $f_s(\boldsymbol{y}, \boldsymbol{\theta}_s)$ in Eqn. 1b as the source equations, where $\boldsymbol{\theta}_t \neq \boldsymbol{\theta}_s$.

$$g_t(\boldsymbol{y}, \boldsymbol{\theta}_t) = \theta_1 \frac{y_1}{y_2 + \theta_2} \frac{y_2}{y_1 + \theta_3} - \theta_4 \frac{y_3}{y_4} \qquad (1a)$$

$$f_s(\boldsymbol{y}, \boldsymbol{\theta}_s) = \theta_1' \frac{y_1 y_2}{y_2 + \theta_2'} - \theta_4' \frac{y_3}{y_1} \tag{1b}$$

$$f_t(\boldsymbol{y}, \boldsymbol{\theta}_t) = \theta_1 \frac{y_1 y_2}{y_2 + \theta_2} \left[\frac{1}{y_1 + \theta_3}\right] - \theta_4 \frac{y_3}{y_1} \left[\frac{y_1}{y_4}\right] \tag{1c}$$

Comparing Eqn. 1a and Eqn. 1b reveals structural errors when using the source model to approximate the ground-truth for the target domain. By inserting $[1/(y_1 + \theta_3)]$ and $[y_1/y_4]$ into Eqn. 1b and re-optimising the parameters, Eqn. 1c and 1a match, illustrating the *simplest* symbolic corrections, $\boldsymbol{\phi}(\boldsymbol{y})$. While these corrections (e.g., $\phi_1(\boldsymbol{y}) = [1/(y_1 + \theta_3)]$, $\phi_2(\boldsymbol{y}) = [y_1/y_4]$) are deduced here by inspection; in practice, they are unknown. Thus, we use an ANN parameterised by a set of weights and biases, $\boldsymbol{\omega}$, as an approximator in Eqn. 2b, to learn $\boldsymbol{\varphi}(\boldsymbol{y})$, embedded into the model as in Eqn. 2c.

$$\min_{\boldsymbol{\theta},\boldsymbol{\omega}} \frac{1}{n_i n_e} \sum_{i=1}^{n_i} \sum_{e=1}^{n_e} \left\| \hat{\boldsymbol{y}}_{i,e}(\boldsymbol{\theta}, \boldsymbol{\omega}) - \boldsymbol{y}_{i,e} \right\|_2 + n_\varphi P(\boldsymbol{y}, \boldsymbol{\omega}) \tag{2a}$$

s. t.

$$\hat{\boldsymbol{\varphi}}(\hat{\boldsymbol{y}}, \boldsymbol{\omega}) = \mathrm{ANN}(\hat{\boldsymbol{y}}, \boldsymbol{\omega}) \tag{2b}$$

$$f_t(\boldsymbol{y}, \boldsymbol{\theta}_t, \boldsymbol{\omega}) = \theta_1 \frac{y_1 y_2}{y_2 + \theta_2} \varphi_1(\boldsymbol{y}, \boldsymbol{\omega}) - \theta_4 \frac{y_3}{y_1} \varphi_2(\boldsymbol{y}, \boldsymbol{\omega}) \tag{2c}$$

$$\hat{\boldsymbol{y}}_{i,e}(\boldsymbol{\theta}, \boldsymbol{\omega}) = \boldsymbol{y}_0^e + \int_0^{t_i} f_t(\boldsymbol{y}, \boldsymbol{\theta}_t, \boldsymbol{\omega})\, \mathrm{d}t \tag{2d}$$

$$P(\boldsymbol{y}, \boldsymbol{\omega}) = \lambda_1 \left\| \frac{\partial \hat{\boldsymbol{\varphi}}}{\partial \hat{\boldsymbol{y}}} \right\|_2 + \lambda_2 \| \hat{\boldsymbol{\varphi}}(\boldsymbol{y}, \boldsymbol{\omega}) - \boldsymbol{b} \|_2 \tag{2e}$$

The transfer model, $f_t(\boldsymbol{y}, \boldsymbol{\theta}_t, \boldsymbol{\omega})$, incorporates ANN-based correction terms, $\boldsymbol{\varphi}(\boldsymbol{y}, \boldsymbol{\omega})$, into the ODEs. The ANN is trained by minimising the mean-square error $\mathcal{L}_{\mathrm{ANN}}(\boldsymbol{\theta}, \boldsymbol{\omega})$ in Eqn. 2a between measured concentrations, $\boldsymbol{y}_{i,e}$, and predictions, $\hat{\boldsymbol{y}}_{i,e}$, obtained by numerically integrating $f_t(\boldsymbol{y}, \boldsymbol{\theta}_t, \boldsymbol{\omega})$ from initial conditions $\boldsymbol{y}_0^e$ to time, $t_i$, where the subscripts $i$ and $e$ are the measurement time interval and experiment number. By automatic differentiation through numerical integration the kinetic parameters $\boldsymbol{\theta}$ and ANN parameters $\boldsymbol{\omega}$ were optimised simultaneously to avoid bias in the estimated corrections. Adaptive Moment Estimation (ADAM) was used to optimise the parameters, as implemented in the *Python* package *PyTorch*.

The $\lambda$-weighted penalty, $P(\boldsymbol{y}, \boldsymbol{\omega})$, in Eqn. 2e is crucial to prevent overfitting. Its first component, the sum of the squares of the elements in the Jacobian, $\partial \hat{\boldsymbol{\varphi}} / \partial \hat{\boldsymbol{y}}$, limits variation in the correction terms, $\hat{\boldsymbol{\varphi}}$, with respect to the fitted states, $\hat{\boldsymbol{y}}$, ensuring only truly influential state variables are retained. Its second component involving a binary vector $\boldsymbol{b}$, pushes additive corrections toward zero and multiplicative ones toward unity, helping to isolate genuine correction locations.

Because correction locations are initially unknown, multiple potential corrections are embedded. Figure 2 illustrates how $\mathcal{D}_{\max}$ sets the initial placement of potential corrections. These, represented by an ANN, are trained together. Unimportant corrections – those with the smallest variance, $\tilde{\varphi}$, over the input domain – are pruned iteratively and the ANN retrained, reducing the number of corrections, $n_\varphi$, until it falls below a pre-defined threshold, $\mathcal{U}_{\max} = 3$. Corrections with variance $\tilde{\varphi} < \mathcal{V}_{\min} = 0.1$ are then also finally removed. On an NVIDIA RTX A1000 GPU, ANN training takes ~20 seconds, so 10 pruning iterations require only a few minutes. Automatic symbolic manipulations using *SymPy* streamline expression modifications throughout.

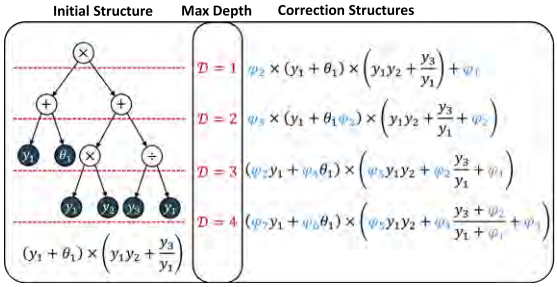



**Figure 2:** Illustration of correction term embedding at various depths ($\mathcal{D}_{\max}$). The initial equation structure (left) transforms into equations with embedded $\varphi_j$ (right). For binary branching trees $n_\varphi = F(\mathcal{D}_{\max}) + \mathcal{D}_{\max}$ where, $F(n)$ is the $n$th entry in the Fibonacci sequence.

## 2.2. Attribution Guided Symbolic Regression to Construct Correction Equations

Not all features are required for every correction term. Integrated Gradients [5] quantifies each feature's, $y_v$, contribution to each fitted correction term, $\hat{\varphi}$. This weights which input features SR should use to construct corrections with the effect of either adding or removing them from the source equations.

$$\mathcal{L}_{\mathrm{SR}}(\phi, \boldsymbol{\theta}) = \frac{1}{n_i n_e} \sum_{i=1}^{n_i} \sum_{e=1}^{n_e} \left( \phi(\hat{\boldsymbol{y}}_{i,e}, \boldsymbol{\theta}) - \hat{\varphi}_{i,e} \right)^2 \tag{3}$$

Once Steps 1 and 2 identify the minimal corrections and key features, in Step 3 SR discovers the symbolic forms, $\phi(\boldsymbol{y}, \boldsymbol{\theta})$, for each correction $\hat{\varphi} = \mathrm{ANN}(\boldsymbol{y}, \boldsymbol{\omega})$. Tournament selection promotes and mutates candidates from a population of expressions using the *Julia* package *SymbolicRegression* [3]. The objective function for fitting corrections is shown in Eqn. 3 as the mean-square-error between the value evaluated by each symbolic expression, $\phi(\hat{\boldsymbol{y}}_{i,e}, \boldsymbol{\theta})$, and the values of the fitted corrections, $\hat{\varphi}_{i,e}$, averaged over each time point, $i$, and experiment, $e$.

After substituting the symbolic corrections into the source equations, yielding the new target equations, the target parameters, $\boldsymbol{\theta}_t$, are then fine-tuned and sparsity in $\boldsymbol{\theta}_t$ promoted by penalising the absolute magnitude, $\|\boldsymbol{\theta}_t\|_2$.

## 2.3. Integrating SR and MbDoE for Model Discrimination

Model-based design of experiments (MbDoE) for model structure discrimination maximises information gain by selecting experimental conditions that maximise differences in predicted responses among model candidates, reducing time and resource expenditure.

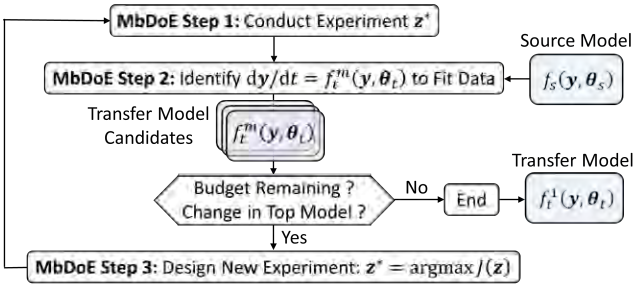



**Figure 3:** Transfer learning integrated with SR-MbDoE.

The SR-MbDoE framework [6] is adapted in Figure 3 to integrate model structure transfer learning. In MbDoE-Step 1, experiments parameterised by $\boldsymbol{z}$ are conducted. MbDoE-Step 2 uses model structure transfer learning to propose different candidate transfer models. In MbDoE-Step 3, so long as the experimental budget has not been exceeded or the equations from one iteration to the next are still being refined, a new experiment is designed by optimising to an objective function, $J(\boldsymbol{z})$.

In model structure transfer learning, SR generates a Pareto set of candidate expressions. These are scored by the derivative in the log-loss with respect to complexity. The top-scoring expressions represent a balance between parsimony and fitting accuracy. By substituting combinations of the top two scoring corrections into the source equations, various candidate transfer models, $f_t^m(\boldsymbol{y}, \boldsymbol{\theta}_t)$, indexed by $m$, are created. In this work, the design variables, $\boldsymbol{z}$, were the initial concentrations of each (bio)chemical species, $\boldsymbol{y}_0$, while the objective function was the Hunter-Reiner criterion.

# 3. BIOPROCESS CASE STUDY

This study considers an in-silico case study representing microalgae cultivation for producing a high-value nutraceutical via carbon substrate consumption. The *source* model, in Eqn. 4, describes the evolution of biomass ($X$), substrate ($S$), and product ($P$) concentration, with the parameters: $\boldsymbol{\theta}_s = (\mu_m, K_S, Y_S, Y_P, \beta)$, where $\mu_m = 0.1\ \mathrm{h}^{-1}$ is the maximum specific growth rate, $K_S = 10\ \mathrm{g\,l}^{-1}$ is the substrate half-saturation constant, $Y_S = 1\ \mathrm{g\,g}^{-1}$ is the growth-dependent substrate yield coefficient, while $Y_P = 0.5\ \mathrm{g\,g}^{-1}$ and $= 0.003\ \mathrm{h}^{-1}$ are the growth-dependent and independent product yield coefficients, respectively.

$$\frac{\mathrm{d}X}{\mathrm{d}t} = \mu_m \frac{S}{S + K_S} X \tag{4a}$$

$$\frac{\mathrm{d}S}{\mathrm{d}t} = -Y_S\, \mu_m \frac{S}{S + K_S} X \tag{4b}$$

$$\frac{\mathrm{d}P}{\mathrm{d}t} = Y_P \mu_m \frac{S}{S + K_S} \cdot X + \beta X \tag{4c}$$

In-silico data for the *target* domain, representing a more productive strain, was generated using the ground-truth model in Eqn. 5. The target model parameters, $\boldsymbol{\theta}_t = (\mu_m, K_S, \mu_d, Y_S, Y_P, \beta, k_d)$, share the same meanings as in the source model but with different values: $K_S = 5\ \mathrm{g\,g}^{-1}$, $\beta = 0.05\ \mathrm{h}^{-1}$. New is a biomass decay constant, $\mu_d = 0.1\ \mathrm{h}^{-1}$, and product reversal rate under substrate-limiting conditions, $k_d = 0.07\ \mathrm{g}^{-1}\,\mathrm{l\,h}^{-1}$, while Eqn. 5 uses Contois, not Monod kinetics, altogether reflecting the physical differences between the source and target systems.

$$\frac{\mathrm{d}X}{\mathrm{d}t} = \mu_m \frac{S}{S + K_S X} \cdot X - \mu_d X \tag{5a}$$

$$\frac{\mathrm{d}S}{\mathrm{d}t} = -Y_S\, \mu_m \frac{S}{S + K_S X} \cdot X \tag{5b}$$

$$\frac{\mathrm{d}P}{\mathrm{d}t} = Y_P \mu_m \frac{S}{S + K_S X} \cdot X + \beta X - k_d X^2 \tag{5c}$$

Batch simulations each run for 144 hours from initial conditions $\boldsymbol{y}_e^0 = (X_{0,e}, S_{0,e}, P_{0,e})$. States $\boldsymbol{y}_{i,e} = (X_{i,e}, S_{i,e}, P_{i,e})$ were recorded every 14 hours with 5% normally distributed noise. This represents practical conditions with measurement uncertainty, and offline data is not frequently collected. Each case study starts with three experiments from different initial conditions. To assess reproducibility and data sensitivity, the framework is re-run ten times, starting from different sets of three experiments generated from different random initial conditions.

# 4. RESULTS AND DISCUSSION

Section 4.1 will demonstrate the robustness of the proposed model structure transfer learning framework, given a detailed but imperfect source model. Section 4.2 will then discuss the impact of the quantity of prior knowledge on the efficiency of the framework.

## 4.1. Scenario with Moderate Inductive Bias

The source model to be modified is given by Eqn. 4. In Section 4.1.1, three initial experiments are used for each of the ten repetitions; Section 4.1.2 extends this with further experiments designed via MbDoE.

### 4.1.1. Single vs Multi-Pass Structure Modification

A single-pass approach first embeds multiple correction terms into the source model, which are then sparingly refined. First, in Step 1 in Figure 1, Eqn. 6 shows where twelve correction terms, $\varphi$, were automatically

embedded into the source model structure. Note that overall specific growth rate, $\mu$, is a shared sub-function. Here $\phi_j^{\mathrm{GT}}$ will denote the *simplest* symbolic corrections when comparing the corrections with the ground truth equations. Comparison with the target ground-truth in Eqn. 5 indicates three key corrections – one for adapting the Monod to the Contois kinetics ($\phi_2^{\mathrm{GT}} = X$), one for biomass decay ($\phi_7^{\mathrm{GT}} = -\mu_d X$) and another for product reversal ($\phi_{12}^{\mathrm{GT}} = -k_d X^2$), while other terms ideally vanish. Note others are possible; should $\phi_7^{\mathrm{GT}} = -\mu_d X$ and $\phi_{12}^{\mathrm{GT}} = -k_d X^2$ then $\phi_3^{\mathrm{GT}} = (S + K_S X - K_S)/S$ or $\phi_4^{\mathrm{GT}} = (S + K_S)/(S + K_S X)$ for example are equally valid, though are not the *simplest*.

$$\frac{\mathrm{d}X}{\mathrm{d}t} = \varphi_6 \mu X + \varphi_7 \tag{6a}$$

$$\frac{\mathrm{d}S}{\mathrm{d}t} = -\varphi_8 Y_S \mu X + \varphi_9 \tag{6b}$$

$$\frac{\mathrm{d}P}{\mathrm{d}t} = \varphi_{11} Y_P \mu X + \varphi_{10} \beta X + \varphi_{12} \tag{6c}$$

$$\mu = \varphi_4 \mu_m \frac{S + \varphi_1}{\varphi_3 S + \varphi_2 K_S} + \varphi_5 \tag{6d}$$

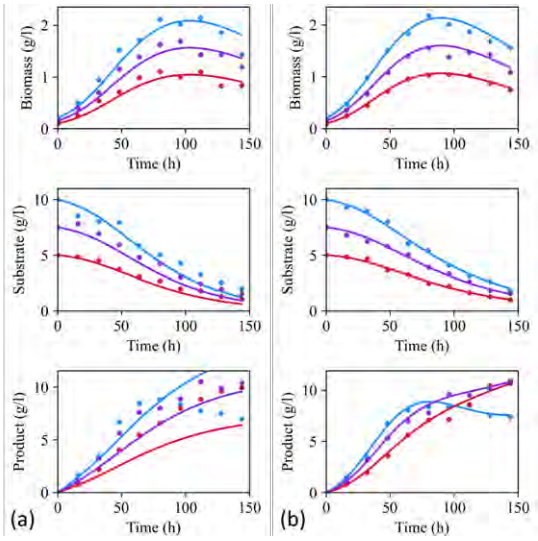



**Figure 4:** Comparison of a model fitting built from one of the random initial experiments after one pass (a) and after three passes (b) of model structure modification.

Across ten repetitions, the source structure was partially corrected in a single pass 10% of the time, where Eqn. 7 illustrates one such partially corrected model; this improves to 50% with sparsity promotion. However, certain terms were often incorrectly inferred: for example, falsely attributing product reversal under substrate-limiting conditions to a product accumulation term that simply diminished towards the end of the batch (i.e., $\phi_{12} = 1.88S$ rather than $\phi_{12}^{\mathrm{GT}} = -k_d X^2$). It could be said that it is prior knowledge that such decay terms should be negligible at the start of the batch; in fact, this information could be incorporated during ANN training but to demonstrate the generality of the method we assume we do not know this.

Now, the equations are returned for further passes to assess whether partially corrected equations can be fully adapted to the target domain. No further passes are required once there are no correction terms with a variance, $\tilde{\varphi}$, greater than the threshold, $\mathcal{V}_{\min}$. Allowing multiple passes of model structure modification raised the success rate from 50% to 80%, illustrating that iteratively refining partially corrected equations is advantageous. For one model, the mean absolute percentage error (MAPE) of fitting improved from 17% to 6.6% as shown in Figure 4a to 4b, once multiple passes discovered the ground truth. Meanwhile, the MAPE of prediction on the unseen experiments dropped from 23% to 10.7%.

### 4.1.2. Model-Based Design of Experiments

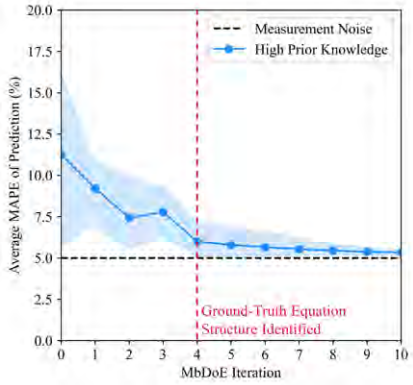



**Figure 5:** The mean absolute percentage error (MAPE) of prediction over each model-based design of experiment (MbDoE) iteration. The shaded region denotes three standard deviations in the MAPEs at each MbDoE iteration over the ten random initialisations, while the markers are the average. Here, multiple passes of structure modification are allowed.

When only a few noisy experiments are available, multiple candidate structures may explain the data equally well. MbDoE identifies experimental conditions for discriminating among those candidates. In Figure 5, given three initial experiments, the average MAPE was 11.2% with a standard deviation of 3.1% across the 10 repetitions. This decreased to 5.3% with a standard deviation of 0.1% after thirteen new MbDoE experiments. Eight out of ten runs achieved a MAPE of 6.0% by the fourth MbDoE iteration, at which point all the runs discovered the ground truth equation structures for the target domain. The product-reversal term ($\phi_{12}^{\mathrm{GT}} = -k_d X^2$) was typically discovered last when it was elucidated that $\phi_{12} = f(X)$ not $\phi_{12} = f(X, S)$ was the simplest correction, highlighting how separating the causal relationship can be difficult when state variables are strongly correlated – such as when one (bio)chemical species reacts to another, and the experiments are poorly designed.

## 4.2. Impact of Prior Knowledge Quantity

The framework's efficiency will be case-dependent. Eqn. 7b replicates the biomass growth model used here, while Eqn. 7a reflects the fundamental assumption that growth is proportional to the current cell population. Starting from a more minimal model will likely require more MbDoE experiments, as more kinetics must be uncovered. However, incorporating more physical knowledge – as in Eqn. 7c with a substrate inhibition term $(K_I/S)$ and a product toxicity term $(P/(P+K_P))$ – increases the risk of introducing incorrect inductive bias, complicating model modification. For a completely new bioprocess, such as a novel strain, it is prudent to start with a simpler source model structure to identify key correction terms, then compare the generated equations with those from higher knowledge source models.

$$\frac{\mathrm{d}X}{\mathrm{d}t} = \mu X \tag{7a}$$

$$\frac{\mathrm{d}X}{\mathrm{d}t} = \mu_m \frac{S}{S+K_S} X \tag{7b}$$

$$\frac{\mathrm{d}X}{\mathrm{d}t} = \mu_m \frac{S}{S+K_S+\frac{K_I}{S}} \cdot X \; - \; \mu_d X \frac{P}{P+K_P} \tag{7c}$$

Prior knowledge can be incorporated beyond the source model structure. Previously, the correction $\phi_{12} = -k_d X^2$ was mistaken as $\phi'_{12} \propto S$ using only the first three experiments. When state variables are strongly correlated – such as when one (bio)chemical species reacts to form another (e.g., $A + 2B \rightarrow C$) – separating the causal relationship becomes more difficult. Fortunately, the framework is highly flexible. In these cases, extra constraints during ANN training are valuable. For example, bioprocess kinetics often follow Eqn. 8, with a growth-dependent term, $\varphi_{GD}(\boldsymbol{y})$, and a growth-independent term, $\varphi_{GI}(\boldsymbol{y})$, (e.g., biomass decay or substrate consumption for maintenance). By providing synthetic data to the ANN that pushes $\varphi_{GI}(\boldsymbol{y})$ to zero when biomass is zero, $\phi_{12} = -k_d X^2$ was reliably identified without MbDoE.

$$\frac{\mathrm{d}\boldsymbol{y}}{\mathrm{d}t} = \mu \cdot \varphi_{GD}(\boldsymbol{y}) + \varphi_{GI}(\boldsymbol{y}) \tag{8}$$

# 4. CONCLUSION

This study introduces a structural transfer learning framework combining symbolic regression (SR) with ANN feature attribution to adapt mechanistic models from literature or common concept for newly investigated systems. Unlike traditional black-box-based transfer learning approaches that only update model parameters, the proposed method modifies the structure of mechanistic models, enabling the discovery of interpretable differential equations. An in-silico bioprocess case study demonstrated the framework's robustness under low-sample frequency, noisy data conditions. Integration with model-based experiment design (MbDoE) minimised experimental effort by efficiently discriminating among candidate transfer models for the new system. Requiring several hyperparameters, the framework offers great flexibility for human-machine interaction, allowing experts to guide model complexity and the interpretability necessary in highly regulated industries. Overall, this general methodology advances automated model discovery for accelerating novel bioprocess development, and within other fast-paced (bio)chemical industries.

# ACKNOWLEDGEMENTS

This research was supported by the Engineering and Physical Sciences Research Council (EPSRC) and Unilever. The authors gratefully acknowledge the crucial financial support and resources provided.

# REFERENCES

1. S. Kay, H. Kay, A.W. Rogers, D. Zhang, Integrating hybrid modelling and transfer learning for new bioprocess predictive modelling, in: CACE, Elsevier, 2023: pp. 259–260. https://doi.org/10.1016/B978-0-443-15274-0.50412-1.
2. G.A. Pimentel, F.N. Santos-Navarro, L. Dewasme, A.V. Wouwer, Elucidation of Macroscopic Stoichiometry and Kinetics of Bioprocesses using Sparse Identification, IFAC 58 (2024) 422–427. https://doi.org/10.1016/j.ifacol.2024.08.373.
3. M. Cranmer, Interpretable Machine Learning for Science with SymbolicRegression.jl, (2023). https://doi.org/10.48550/ARXIV.2305.01582.
4. T. Forster, D. Vázquez, C. Müller, G. Guillén-Gosálbez, Machine learning uncovers analytical kinetic models of bioprocesses, CES (2024) 120606. https://doi.org/10.1016/j.ces.2024.120606.
5. M. Sundararajan, A. Taly, Q. Yan, Axiomatic Attribution for Deep Networks, (2017). http://arxiv.org/abs/1703.01365.
6. A.W. Rogers, A. Lane, C. Mendoza, S. Watson, A. Kowalski, P. Martin, D. Zhang, Integrating knowledge-guided symbolic regression and model-based design of experiments to automate process flow diagram development, CES 300 (2024) 120580. https://doi.org/10.1016/j.ces.2024.120580.

© 2025 by the authors. Licensed to PSEcommunity.org and PSE Press. This is an open access article under the creative commons CC-BY-SA licensing terms. Credit must be given to creator and adaptations must be shared under the same terms. See https://creativecommons.org/licenses/by-sa/4.0/



Systems & Control Transactions

**Research Article - Peer Reviewed Conference Proceeding**
ESCAPE 35 - European Symposium on Computer Aided Process Engineering
Ghent, Belgium. 6-9 July 2025
Jan F.M. Van Impe, Grégoire Léonard, Satyajeet S. Bhonsale,
Monika E. Polańska, Filip Logist (Eds.)

PSE PRESS

# Industrial Time Series Forecasting for Fluid Catalytic Cracking Process

**Qiming Zhao[a,b], Yaning Zhang[c], and Tong Qiu[a,b]***

[a] Department of Chemical Engineering, Tsinghua University, Beijing 100084, China
[b] State Key Laboratory of Chemical Engineering, Tsinghua University, Beijing 100084, China
[c] PetroChina Planning & Engineering Institute, Beijing 100083, China
* Corresponding Author: qiutong@tsinghua.edu.cn.

## ABSTRACT

This study tackles the challenge of accurate yield prediction in fluid catalytic cracking (FCC) units by comparing conventional supervised regression with time series forecasting methods using industrial data collected from the distributed control system (DCS) of an FCC plant. We introduce a shifted forecast paradigm that preserves temporal relationships between predictors and targets. Our preprocessing pipeline, which employs trimmed mean smoothing, addresses common industrial data challenges. Results demonstrate that the forecasting approach significantly outperforms supervised regression, achieving a mean absolute percentage error (MAPE) of 1.56% for 3-hour shifted predictions compared to 6.20% for supervised regression. The model maintains robust performance even with extended shifts during predictions, showing an MAPE of 3.55% for 14-day forecasts. This research provides valuable insights for implementing predictive analytics in industrial FCC operations, demonstrating the superiority of forecasting methods over traditional supervised regression approaches for process yield prediction.

**Keywords**: Machine Learning, Forecasting, Catalytic Cracking, Predictive Modeling

## INTRODUCTION

Fluid catalytic cracking (FCC) is a cornerstone process in modern refineries, playing a crucial role in meeting global energy demands. It enables the efficient conversion of heavy hydrocarbons into lighter and more valuable products, including gasoline and diesel. As crude oil quality continues to decline while global energy demands increase, refineries must navigate intensifying economic and environmental constraints. Under these challenging conditions, process predictive modeling has emerged as an indispensable tool for understanding, controlling, and optimizing the complex behavior of FCC units [1].

Data-driven modeling approaches have gained significant traction in FCC process modeling. These methods excel at capturing complex nonlinearities and interactions and do not require a detailed understanding of the underlying physicochemical phenomena, making them particularly suitable for FCC process modeling [2]. Researchers can leverage the vast amounts of data generated by FCC units to develop empirical models that capture the complex relationships between process variables. By effectively modeling these relationships, operators can make informed adjustments to operating conditions, thereby optimizing performance and enhancing profitability. Machine learning techniques, such as artificial neural networks (ANNs), support vector machines (SVMs), and Gaussian process regression (GPR), have been successfully applied to model various aspects of FCC operation [2]. However, these models often struggle to extrapolate to future operation conditions. Since the FCC process is inherently dynamic and subject to fluctuations over time, effective data-driven modeling requires incorporating time-related information, namely forecasting.

Given these limitations, time series forecasting approaches offer promising alternatives for FCC process modeling. By analyzing temporal dependencies and trends, this modeling approach captures the dynamic nature of the process and provides insights into potential future states. Traditional supervised learning algorithms typically assume independent, identically distributed (IID) inputs [3], and therefore often fail to capture the dynamic nature of industrial processes. In contrast, forecasting

methods emphasize temporal patterns such as seasonality and trends [4], producing more context-aware predictions.

In FCC data, short-term variable relationships remain stable during steady-state operations despite oscillations. However, long-term operations present challenges as operational contexts and system mechanics evolve, complicating the development of consistent input-output mappings. Integrating forecasting techniques with supervised regression methods enhances prediction robustness while accounting for the inherent variability in industrial time series data. Liu *et al.* [5] proposed a hybrid Gaussian Mixture Model (GMM)-Improved Gaussian Process Regression (IGPR) model for time series prediction in industrial processes with varying operating phases and uncertainties. TC-GATN, a novel multivariate time-series forecast model developed by Li *et al.* [6], uses Granger causality-based graph learning and gated recurrent units with self-attention to capture complex nonlinear dependencies in industrial processes, improving prediction accuracy as demonstrated on methanol and chlorosilane datasets. These advancements in industrial time series analysis reflect a broader trend toward more adaptive and context-aware modeling approaches. Nevertheless, their efficacy is predominantly evaluated using moderate-scale systems and datasets, exhibiting more predictable and stable operational characteristics.

In this paper, we develop a shifted forecast paradigm that directly bridges current operational states with future yield predictions of an FCC process. Our approach differs from conventional time series forecasting by explicitly modeling the temporal gap rather than relying on iterative one-step-ahead predictions. The main contributions of this work include: (1) a robust data preprocessing pipeline that addresses common challenges in industrial time series data, including irregular sampling, outliers, and high-frequency fluctuations; (2) a shifted forecast framework that maintains temporal relationships while avoiding the limitations of traditional supervised regression; and (3) comprehensive evaluation of model performance across different prediction shifts, demonstrating its practical utility for industrial applications.

The remainder of this paper is organized as follows. Section 2 describes the data preparation methodology, including variable selection, preprocessing techniques, and dataset organization. Section 3 presents the theoretical framework of our regression and forecasting approaches, with particular emphasis on the shifted forecast paradigm. Section 4 provides detailed experimental results and a comparative analysis of different modeling approaches across various prediction horizons. Finally, Section 5 concludes the paper with a summary of findings and suggestions for future research directions.

# METHODS

Figure 1 shows the framework for developing the prediction model, which consists of two modules: data preparation and regression forecasting.

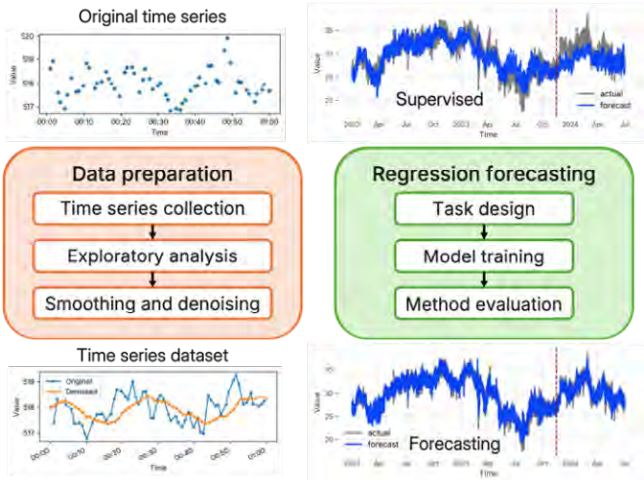



**Figure 1.** Forecast model development framework.

High-quality datasets are generated and then used to build and validate forecast models. The pipelines for data preprocessing and model training are implemented in Python 3.12, using Darts [7], a time series forecasting library.

**Table 1:** Variables in the collected dataset.

| Symbol | Description | Unit |
|---|---|---|
| $T_{\text{feed}}$ | Feed preheat temperature | ℃ |
| $T_{\text{reac}}$ | Reactor temperature | ℃ |
| $T_{\text{regen}}$ | Regenerator riser temperature | ℃ |
| $T_{\text{stripper}}$ | Stripper overhead temperature | ℃ |
| $T_{\text{fractop}}$ | Fractionator overhead temperature | ℃ |
| $T_{\text{naph}}$ | Heavy naphtha extraction temperature | ℃ |
| $T_{\text{LCO}}$ | Light cycle oil (LCO) extraction temperature | ℃ |
| $T_{\text{fracbot}}$ | Fractionator bottoms temperature | ℃ |
| $F_{\text{stripper}}$ | Stripper overhead flow rate | $Nm^3/h$ |
| $F_{\text{feed}}$ | Flow rate of fresh feed | t/h |
| $F_{\text{reflux}}$ | Flow rate of fractionator reflux | t/h |
| $F_{\text{HCO}}$ | Flow rate of heavy cycle oil (HCO) to riser | t/h |
| $F_{\text{recyc_gaso}}$ | Flow rate of recycled stabilized gasoline | t/h |
| COR | Catalyst-to-oil ratio | / |
| $y$ | Diesel yield | wt% |

## Industrial dataset preparation

A typical FCC plant is composed of two core modules: the reactor-regenerator and the downstream

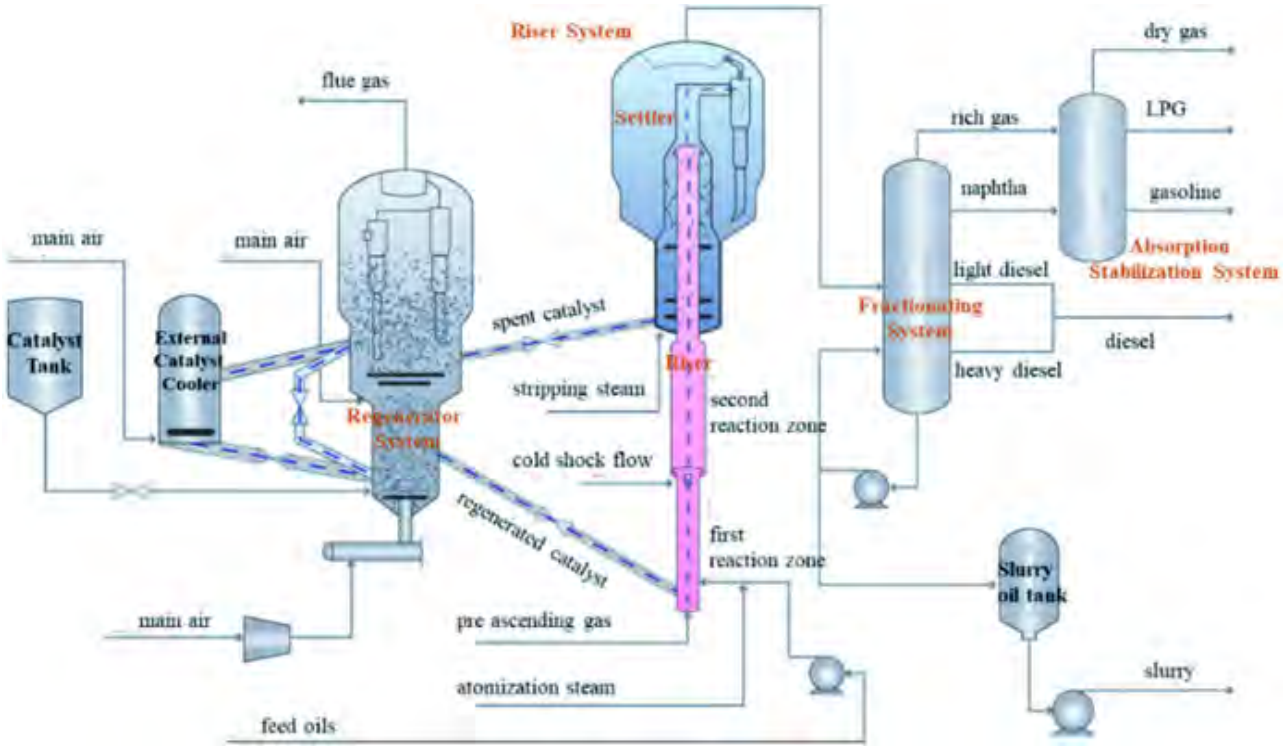



**Figure 2.** A schematic diagram of the FCC unit [8].

product separation system. Raw feedstock is cracked in the riser reactor upon contact with the regenerated catalyst. Subsequently, the cracked mixture is separated into desired products by one or more separation units. In the regenerator, coke is removed by combustion in a controlled process, typically using air. The detailed substance flows are depicted in Figure 2.

We collected time series data from the DCS system in the FCC plant. We preselected variables of interest using domain knowledge, covering the mass flows of feedstocks and products, major operating parameters of the reactor, regenerator, and downstream separation systems like adsorption and distillation columns. A derived variable, catalyst-to-oil ratio (COR), was added to reflect cracking depth, whose values are calculated using an empirical formula. The target variable, diesel yield, is calculated as the mass flow rate ratio of diesel product to fresh feed. Table 1 lists the details of selected variables.

Effective predictive modeling requires robust dataset preparation to ensure data quality and relevance for model training and testing. Data collected from the distributed control system (DCS) may suffer from outliers, irregular sample intervals, and high-frequency fluctuations, hence the need for specific preprocessing methods. These characteristics stem from sensor failures, inconsistent data collection rates, and external measurement influences. Data quality is critical to forecasting performance, and exploratory data analysis (EDA) is necessary for building an effective preprocessing pipeline. Through inspection and visualization, we found the data to be irregularly sampled, with corruptions, outliers, and local oscillations.

To address these challenges, we employed preprocessing techniques to ensure the dataset adhered to the necessary specifications for time series analysis. Irregularly sampled data are aligned to generate a long-form table, facilitating a consistent modeling approach. In time series analysis, rolling window methods—particularly moving averages (or rolling means)—provide an effective approach to smoothing data, helping distinguish signal from noise by minimizing abrupt fluctuations. While simple averaging considers all data points equally, the trimmed mean provides a more robust approach by removing a specified percentage of the most extreme values that could skew the results. The resulting data are aligned and smoothed, and outliers are implicitly removed in this process. This method is called rolling trimmed mean, which can be described as

$$\mathrm{RTM}(p,t,w) = \frac{1}{w-2\lfloor pw \rfloor} \sum_{i=\lfloor pw \rfloor+1}^{w-\lfloor pw \rfloor} x_{(i)} \tag{1}$$

where $t$ represents the current time point, $w$ is the window size, $p$ is the trimming percentage expressed as a decimal, and $x_{(i)}$ represents the $i$-th ordered observations within the window $[t-w+1, t]$ that ends at time $t$.

As a final step, operational parameters are standardized to a similar scale using the z-score method. A temporal split of training and test sets is also carried out,

with the latter taking up 20% of the total data.

## Regression and forecasting

With the dataset prepared, the next phase involves applying time series modeling techniques to forecast future outcomes based on historical data. Among various regression techniques, Bayesian Ridge Regression is selected for its ability to handle multicollinearity and incorporate prior distributions, which helps regularize the model [9]. Bayesian Ridge Regression uses prior distributions for the weights and updates them using observed data. The prior distribution for the weights $w$ is chosen as a normal distribution given by

$$w \sim \mathcal{N}(0, \sigma^2/\lambda) \tag{2}$$

where $\lambda$ is the precision parameter controlling the strength of regularization, and $\sigma^2$ represents the noise variance in the observed data. These hyperparameters are automatically tuned during model training using evidence maximization.

The same regression algorithm is used for different prediction tasks, which can be classified into supervised regression and forecasting. They use the same variable set but with fundamentally different settings in temporal structures and prediction objectives. Supervised regression uses features and lagged versions of them to predict targets, while forecasting methods also use historical values of targets. The forecast model uses two types of input data: the target variable (diesel yield) and covariates (process variables like temperatures and flow rates).

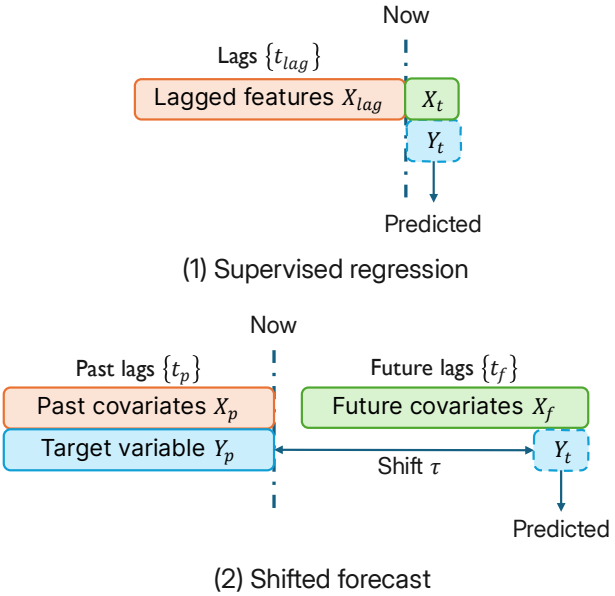



**Figure 3.** Comparison of temporal prediction frameworks illustrating data availability and prediction targets.

Figure 3 illustrates the details of model inputs and outputs, highlighting the difference in the temporal structure. Solid boxes represent available data at prediction time, while dashed boxes indicate predicted values. Vertical dashed lines indicate prediction time points. Past covariates are historical data known up to now, and future covariates are known in the future, at least up to the last forecasted value.

In supervised regression (Figure 3a), the model learns from features $X_t$ and their lagged values to predict a concurrent target variable $Y_t$, where all data is available during training. The model predicts each target independently using lagged features, reflecting a global input-output mapping function.

Conversely, external data are introduced in time series forecasting, which are called covariates. Forecasting makes a distinction between past and future time points relative to the prediction moment. Past covariates are historical data known up to now, and future covariates are known at least up to the last forecasted value (often controlled variables). This approach maintains the temporal ordering essential for time series analysis while avoiding data leakage, as only information available at prediction time is utilized. The lags are chosen to provide local gradients with minimum redundancy:

$$\{t_{lag}\} = \{X_{t-60}, X_{t-30}, X_{t-15}, X_{t-10}, X_{t-5}\} \tag{3}$$

where $t_{lag}$ corresponds to past lags $t_p$ or future lags $t_f$, and $t$ is the timestamp in minutes relative to the end of the corresponding covariate series.

The shifted forecast approach predicts future values by maintaining a fixed time gap between inputs and outputs (Figure 3b). This approach effectively merges lagged inputs (from supervised models) with past covariates (from ordinary forecast models). The temporal difference between past covariates and predicted targets is defined by the prediction shift $\tau$.

A shift of $\tau = 0$ corresponds to one-step-ahead forecasting, where the model leverages data up to the current time point to predict the next value. On industrial datasets with steady states during most periods, the model may degenerate into a naive forecaster that simply repeats the last observation, providing no meaningful information beyond the current state.

Meanwhile, a shifted forecast model with $\tau > 0$ learns to bridge the temporal gap between current information and future outcomes, embedding process information in a way similar to how ordinary supervised regression models learn relationships between input features and output variables. The model implicitly handles slow drifts in process behavior through adaptive corrections of target values with recent historical data.

The models are evaluated with two metrics: mean absolute percentage error (MAPE) and coefficient of variation (CV). In a dataset of n samples, if $y_i$ is the $i$-th target value and $\hat{y}_i$ is the corresponding prediction, MAPE is defined as

$$\text{MAPE}(\mathbf{y}, \hat{\mathbf{y}}) = \frac{1}{n}\sum_{i=0}^{n-1}\left|\frac{y_i - \hat{y}_i}{y_i}\right| \quad (4)$$

as long as the true values are not close to zero.

The coefficient of variation (CV) is also called normalized root mean squared error (NRMSE), which is defined as

$$\text{CV}(\mathbf{y}, \hat{\mathbf{y}}) = \frac{\text{RMSE}}{\bar{y}} = \frac{\sqrt{\frac{1}{n}\sum_{i=0}^{n-1}(y_i - \hat{y}_i)^2}}{\frac{1}{n}\sum_{i=0}^{n-1} y_i} \quad (5)$$

In brief, our method integrates data preprocessing (alignment, outlier removal, standardization), a supervised regression baseline, and a shifted forecast paradigm that explicitly models time gaps between observations and predictions. These experiments directly compare traditional supervised learning and the proposed forecasting method with various data requirements.

## RESULTS AND DISCUSSION

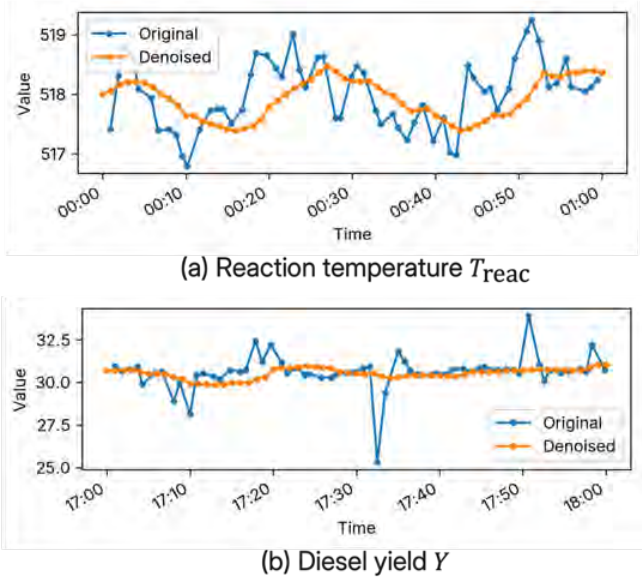
### Data preprocessing

The collected data span two and a half years, from January 2022 to June 2024. Data was sampled approximately once per minute, but the timestamps are not aligned to the minute, and multivariate timestamps are not synchronized. Data points recorded as zero are identified as sensor failures through validation against historical operating ranges. These corrupted readings, comprising approximately 0.12% of the dataset, are removed before further analysis. The dataset undergoes preprocessing using a rolling trimmed mean applied within a 10-minute window. This process involves trimming 5% of extreme values, which effectively smooths the time series and removes outliers, thus preparing it for subsequent modeling. Figure 4 presents examples of original and denoised samples for reaction temperatures and diesel yields.

The denoised temperatures in Figure 4a generally follow the overall trend of the original data but with fewer sporadic deviations. The sharp dip in the original data is significantly reduced in the denoised version, as demonstrated in Figure 4b. The results have smoother and more interpretable trends, providing a good estimate of the system state in the past 10 minutes.

### Model training and validation

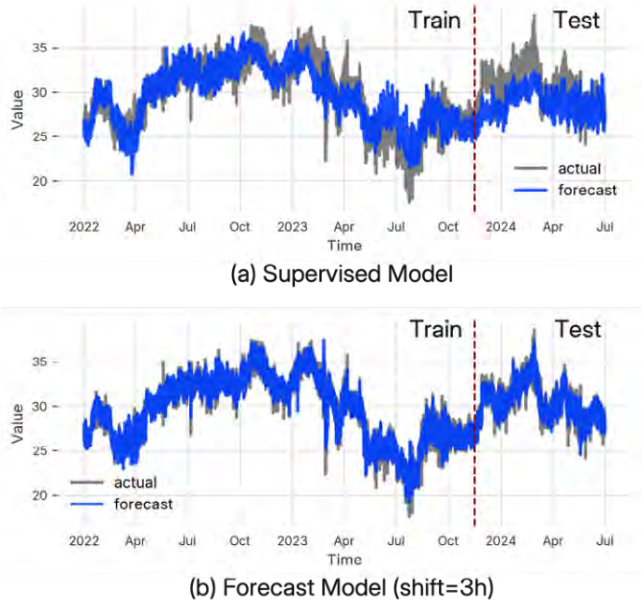
The models are trained on data from approximately April 2022 to late 2023, and their predictions are generated on the full dataset without retraining. The results for the supervised and forecast models are depicted in Figure 5.




(a) Reaction temperature $T_{\text{reac}}$

(b) Diesel yield $Y$

**Figure 4.** Comparison of original and denoised data.




(a) Supervised Model

(b) Forecast Model (shift=3h)

**Figure 5.** Performance of supervised and forecast models on the whole dataset.

The supervised model captures the main trends within the training dataset, maintaining an MAPE of 4.42% during this period. However, its performance deteriorates significantly in the test set, where the MAPE increases to 6.20%, indicating potential overfitting. In contrast, the forecast model maintains consistent performance across both sets, with MAPE values of 1.55% and 1.56% for training and test sets, respectively.

Furthermore, three forecast models are trained and tested using 3-hour, 1-day, and 14-day prediction shifts to evaluate the accuracy and robustness across various timescales. These shifts are chosen for operational relevance, representing short-term process control, daily

planning, and long-term strategic forecasting. Figure 6 compares the performance metrics of these three forecast models, revealing the gradual change of their predictive capabilities across different temporal resolutions.

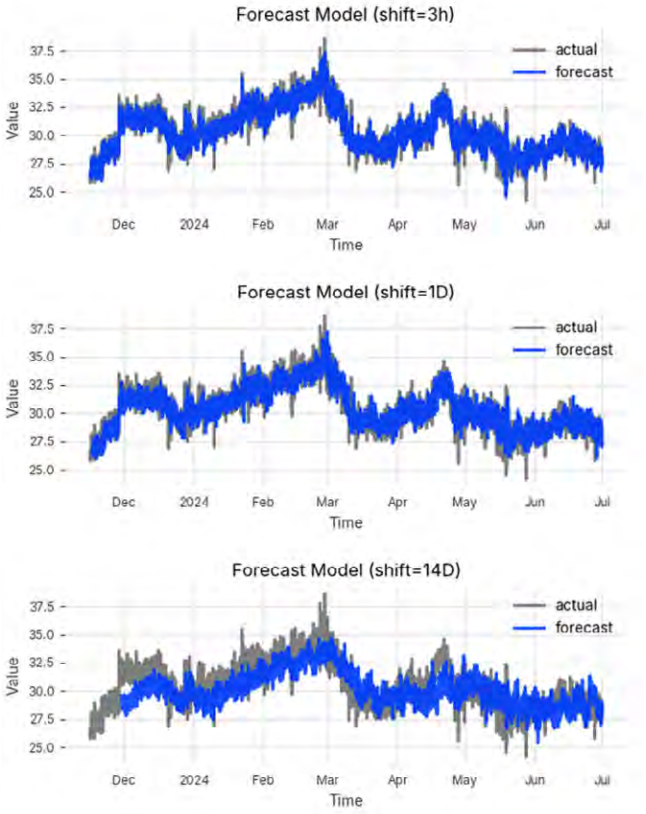



**Figure 6.** Test performance of forecast models using different shifts.

As the shift is prolonged, the model demonstrates reduced accuracy, generally approaching the predictions from the supervised model. However, the forecast model performs much better on the test set, even when predicting the target value 14 days after the known history of diesel yields. This sustained accuracy suggests the successful capture of underlying process relationships rather than simple trend extrapolation.

Table 2 presents the test metrics of different models.

**Table 2:** Test metrics of supervised and forecast models.

| Model | Shift $t_s$ | MAPE (%) | CV |
|---|---|---|---|
| Supervised | / | 6.198 | 7.567 |
| Forecast | 3 hours | 1.564 | 2.120 |
| | 1 day | 2.067 | 2.662 |
| | 14 days | 3.551 | 4.456 |

Forecast models perform better than the supervised one on both metrics, which is reasonable since the inputs to the forecast model are the superset of those available to the supervised one. In real industrial applications, the shift can be selected according to the online data collection mechanism and how often the process states are expected to change.

The forecast model's consistent accuracy validates our approach of explicitly modeling temporal relationships in industrial time series. These results indicate that incorporating historical target values and temporal dependencies is crucial for accurate FCC yield prediction.

## CONCLUSION

This study demonstrates the effectiveness of time series forecasting approaches over supervised regression for predicting FCC diesel yields in industrial settings. The proposed shifted forecast paradigm achieves superior performance across all evaluation metrics, effectively bridging current process states with future operational plans. Experimental results indicate that incorporating historical target values and temporal relationships significantly improves prediction accuracy, with the 3-hour shifted forecast model achieving a 74.8% reduction in MAPE compared to supervised regression (1.56% vs. 6.20%). The model's ability to maintain reasonable accuracy (MAPE of 3.55%) even for 14-day predictions suggests robust learning of process variable correlations. These findings have important implications for industrial applications, enabling more effective process optimization and planning through accurate long-term predictions. The flexibility in selecting prediction horizons makes this approach adaptable to various operational requirements and data collection mechanisms, providing a practical solution for real-world implementation in FCC units.

It is worth noting that feed quality data, such as density and hydrocarbon distribution profiles, were not incorporated in the current model due to the varied and unstable measurement frequency. Future research could incorporate laboratory analysis data, which typically provides more accurate measurements but at much lower sampling frequencies than DCS data. Specifically, integrating laboratory-measured product qualities with high-frequency sensor data could create multi-resolution models that leverage the strengths of both data sources. Further exploration of deep learning methods, particularly transformer architectures that can handle variable-length sequences and capture long-range dependencies, would also be beneficial. Key implementation challenges include handling mixed sampling rates between DCS and laboratory data, managing computational requirements for real-time prediction, and maintaining model interpretability for process engineers. These advancements could potentially extend the application of our forecasting approach to other complex industrial processes facing similar prediction challenges.

## REFERENCES


1. Pinheiro CIC, et al. Fluid Catalytic Cracking (FCC) Process Modeling, Simulation, and Control. *Ind. Eng. Chem. Res.* 51(1):1-29 (2012) https://doi.org/10.1021/ie200743c.
2. Santander O, Kuppuraj V, Harrison CA, Baldea M. An open source fluid catalytic cracker - fractionator model to support the development and benchmarking of process control, machine learning and operation strategies. *Comput. Chem. Eng.* 164:107900 (2022) https://doi.org/10.1016/j.compchemeng.2022.107900.
3. Goodfellow I, Bengio Y, Courville A. Deep Learning. MIT Press (2016).
4. Hyndman RJ, Athanasopoulos G. Forecasting: Principles and Practice. OTexts (2021).
5. Liu T, Wei H, Liu S, Zhang K. Industrial time series forecasting based on improved Gaussian process regression. *Soft Comput* 24(20):15853–15869 (2020) https://doi.org/10.1007/s00500-020-04916-6.
6. Li J, Shi Y, Li H, Yang B. TC-GATN: Temporal Causal Graph Attention Networks With Nonlinear Paradigm for Multivariate Time-Series Forecasting in Industrial Processes. *IEEE Trans. Ind. Inform*. 19(6):7592–7601 (2023) https://doi.org/10.1109/TII.2022.3211330.
7. Herzen J, et al. Darts: User-Friendly Modern Machine Learning for Time Series. *J. Mach. Learn. Res.* 23(124):1–6 (2022).
8. Ni, P, Liu, B, He, G. An online optimization strategy for a fluid catalytic cracking process using a case-based reasoning method based on big data technology. *RSC Adv.* 11(46):28557–28564 (2021) https://doi.org/10.1039/D1RA03228C.
9. Bishop CM, Nasrabadi NM. Pattern recognition and machine learning. New York: Springer (2006).



© 2025 by the authors. Licensed to PSEcommunity.org and PSE Press. This is an open access article under the creative commons CC-BY-SA licensing terms. Credit must be given to creator and adaptations must be shared under the same terms. See https://creativecommons.org/licenses/by-sa/4.0/




Systems & Control Transactions

**Research Article - Peer Reviewed Conference Proceeding**
ESCAPE 35 - European Symposium on Computer Aided Process Engineering
Ghent, Belgium. 6-9 July 2025
Jan F.M. Van Impe, Grégoire Léonard, Satyajeet S. Bhonsale,
Monika E. Polańska, Filip Logist (Eds.)

PSE PRESS

# A White-Box AI Framework for Interpretable Global Warming Potential Prediction

**Jaewook Lee[a], Ethan Errington[a] and Miao Guo[a]***

[a] Department of Engineering, King's College London, London, WC2R 2LS, United Kingdom
* Corresponding Author: miao.guo@kcl.ac.uk

## ABSTRACT

Accurate yet interpretable prediction of Global Warming Potential (GWP) is essential for the sustainable design of chemical products and processes. However, existing studies that utilize molecular structure and physicochemical properties for GWP prediction often suffer from low interpretability, relying on black-box models that obscure the underlying relationships between molecular descriptors and environmental impact. To address this limitation, this study employs a Kolmogorov–Arnold Network (KAN) to derive symbolic equations that establish explicit relationships between molecular properties and GWP. By extracting interpretable mathematical expressions, our approach provides a transparent foundation for decision-making in chemical processes and reaction development. Our comparative analysis of machine learning models—including Random Forest, XGBoost, Deep Neural Networks (DNN), and KAN—reveals that Mordred descriptors outperform MACCS keys in GWP prediction, emphasizing the importance of physicochemical properties. The proposed KAN model achieves predictive accuracy comparable to conventional deep learning methods while maintaining interpretability, facilitating data-driven and transparent sustainability assessments in the chemical industry.

**Keywords**: Global Warming Potential (GWP), Life Cycle Assessment (LCA), Explainable Artificial Intelligence (XAI), Kolmogorov–Arnold Network (KAN), Environmental Impact Prediction

## INTRODUCTION

The chemicals industry, as one of the largest global manufacturing sectors, significantly contributes to global greenhouse gas (GHG) emissions.[1] Major research efforts have been made to design new solutions that decarbonize the way chemical products are made.[2] This requires generating reliable yet transparent predictions of the environmental profiles of chemical products. However, a great deal of information is missing – hindering the extent to which fully informed decision-making can be employed in practice.

Life Cycle Assessment (LCA) provides a standardized framework to evaluate environmental impacts, with Global Warming Potential (GWP) being a key metric. While significant efforts have been made to develop LCA databases for retrospective analysis, they remain incomplete in coverage. The diversity of chemical products, the time-intensive nature of LCA model development, and the variability in available data all contribute to this limitation. Consequently, many chemical products and processes are inadequately represented in current databases, limiting the scope of informed decision-making.

To address these challenges, data-driven predictive models have emerged as an efficient alternative to traditional LCA modelling. In particular, GWP prediction based on molecular structure and physicochemical properties has gained significant attention due to the high availability and reliability of such features.[3-5] These models leverage existing LCA data to identify patterns and estimate GWP values for compounds that lack direct assessment. However, most existing predictive models rely on black-box methodologies, such as deep neural network (DNN), which suffer from low interpretability.

Several studies have attempted to predict LCA impact categories using machine learning models. For example, Zhu et al (2020). developed a DNN-based model capable of predicting multiple LCA endpoints, achieving high accuracy for some categories but significantly lower performance for ecosystem-related metrics.[5] Similarly, Song et al. achieved strong predictive accuracy for Eco-

indicator 99 (Coefficient of Determination ($R^2$) up to 0.87) but reported poor GWP prediction accuracy (only 0.48).[3] These results underscore the need for improved modeling approaches specifically designed for GWP prediction.

A critical limitation of existing GWP predictive models is their reliance on increasingly complex machine learning architectures, such as DNN, to enhance predictive performance. While these models improve accuracy, their complexity significantly reduces interpretability, making it difficult to understand the underlying relationships between input features and GWP predictions. Many of these models function as black boxes, limiting their practical applicability in scientific and regulatory contexts. Although explainable AI (XAI) techniques, such as shapley additive explanations (SHAP), have been applied to provide post-hoc explanations, these methods do not fundamentally improve the transparency of the model itself.[6-9] Instead, they serve as an external layer of analysis rather than integrating interpretability into the core predictive framework, highlighting the need for inherently interpretable modeling approaches.

To address the limitations of black-box models, there is a growing need for white-box modeling approaches that provide both accuracy and transparency. Kolmogorov–Arnold Network (KAN) has recently emerged as a promising alternative to DNNs by offering a compact and interpretable model architecture.[10, 11] Unlike traditional neural networks, KAN can extract generalized equations from data, allowing predictions to be directly linked to chemical properties. This feature makes KAN particularly suitable for applications requiring both predictive power and interpretability, such as GWP estimation.

This study evaluates the effectiveness of KAN in developing an interpretable model for GWP prediction. By leveraging molecular descriptors and KAN's symbolic representations, we provide a transparent alternative to existing machine learning models. This approach enhances interpretability in data-driven environmental assessments, supporting informed decision-making and sustainable chemical design.

# METHODS

Our methodology for GWP prediction follows a structured approach focused on feature engineering, model benchmarking, and white-box modelling.

## Data Collection and Preprocessing

The dataset used in this study is sourced from the Ecoinvent v3.8 database, a widely recognized resource for environmental impact assessment. Our dataset consists of 1,689 GWP values spanning 487 different chemicals, ensuring a diverse and representative chemical space for model training. To mitigate data skewness, we applied log transformation, which reduced the effect of extreme GWP values and improved model stability.

## Feature Engineering

To develop a robust predictive framework, we identified and utilized optimal molecular descriptors that capture key structural and physicochemical properties of chemical compounds. Specifically, we employed MACCS keys, a set of 166 binary features representing fundamental molecular functional groups.[12] And Mordred descriptors, which provide a more comprehensive representation of molecular structure and physicochemical properties.[13] These descriptors capture essential structural and chemical characteristics, allowing for accurate GWP predictions based on molecular information.

## Model Development

Our study evaluates multiple machine learning models, including random forest[14] (RF), extreme gradient boosting[15] (XGBoost), DNN[16], and KAN[10, 11], to compare their performance in GWP prediction. Model performance was assessed using $R^2$ to determine the most effective approach for GWP estimation. Among these, KAN was selected as the primary model to investigate its potential to balance predictive accuracy and interpretability by extracting symbolic equations that describe the relationship between molecular descriptors and GWP.

All computational experiments were conducted using Python (version 3.12) in a macOS environment. Random Forest (RF) and XGBoost models were implemented using the scikit-learn library.[17] DNN and KAN models were developed using the PyTorch framework.[18]

## White-Box Modelling

To enhance transparency, we leveraged KAN's unique architecture to derive explicit mathematical expressions that describe the relationship between molecular descriptors and GWP. We also established a comparative baseline by developing interpretable models using linear regression and RF, both of which are commonly employed for their explainability. Unlike traditional black-box models, this approach allows predictions to be traced back to underlying chemical properties, improving interpretability and decision-making.

By focusing on molecular descriptors, our approach aims to establish a transparent, interpretable, and reproducible methodology for GWP estimation. This ensures that predictions are solely driven by intrinsic chemical properties, allowing for a clear understanding of molecular contributions to GWP.

# RESULTS AND DISCUSSION

## Learning Curve Analysis

Learning curve analysis was performed to

determine the optimal data volume for effective training. The dataset was partitioned into subsets based on ascending GWP values, and model performance was evaluated by incrementally increasing the training dataset size. XGBoost was chosen for evaluation due to its strong predictive performance and computational efficiency. As shown in **Fig. 1**, the highest $R^2$ score was achieved using 0.874 of the available data, after which performance declined due to increased data variability. When using only the data from Fold 1 or 2, negative $R^2$ values were observed. Although the $R^2$ score typically ranges from 0 to 1, it can take negative values when the model performs worse than simply predicting the mean, indicating poor generalisation. To ensure optimal predictive performance while maintaining model robustness, only data with GWP values below 5026.3 kg $CO_2$-eq, corresponding to the upper limit of Fold 8, were included in the training dataset. This threshold was chosen based on the observed sharp decline in model accuracy beyond this point, thereby improving generalizability and reducing the risk of overfitting to extreme values

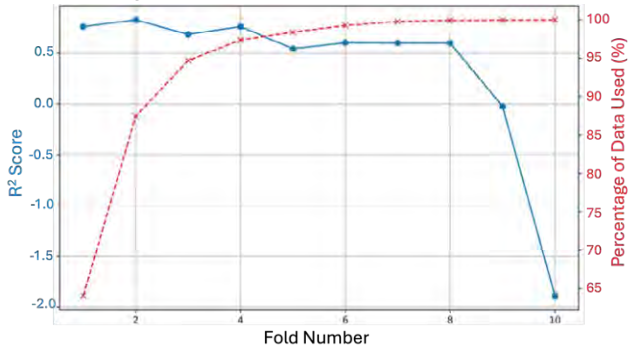



**Fig. 1:** Learning curve analysis through model performance evaluation across different fold numbers.

## Feature Set and Model Performance

We compared the performance of four models—RF, XGBoost, DNN, and KAN—using MACCS keys and Mordred descriptors. **Table 1** shows the $R^2$ prediction results for each model with different features. Mordred descriptors consistently outperformed MACCS keys across all models, with DNN achieving the highest accuracy. This suggests that physicochemical properties captured by Mordred descriptors play a more significant role in GWP prediction than structural fingerprints alone.

**Table 1:** Performance comparison of different models and features for GWP prediction

| | MACCS keys | Mordred |
|---|---|---|
| RF | 0.54 | 0.55 |
| XGBoost | 0.64 | 0.68 |
| DNN | 0.60 | 0.71 |
| KAN | 0.57 | 0.66 |

The results highlight the necessity of incorporating comprehensive physicochemical descriptors for enhanced model performance. The KAN model demonstrated competitive accuracy while maintaining interpretability, making it a viable alternative to DNNs.

## XAI Analysis for Key Feature Identification

To identify the primary factors contributing to GWP prediction, we conducted a post-hoc analysis using the XAI algorithm, SHAP. SHAP quantifies the contribution of each feature to the model's predictions, offering a theoretically grounded approach to explainability in machine learning models.

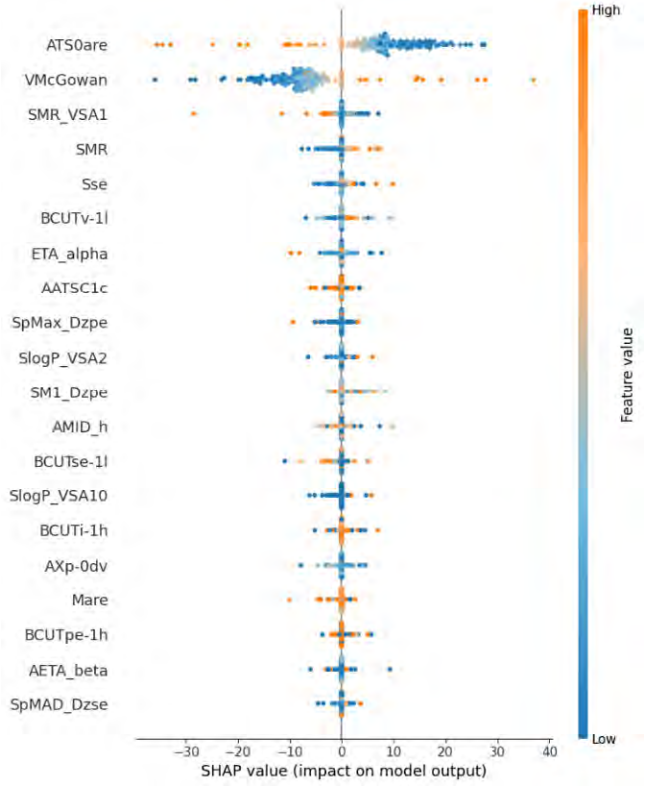



**Fig. 2:** SHAP value distribution for key chemical descriptors, showing their impact on model output.

For this analysis, we examined the DNN model, which achieved the highest predictive accuracy using chemical descriptors, to gain insights into the key molecular properties influencing GWP. As shown in **Fig. 2**, the analysis identified ATS0are and VMcGowan as the most influential descriptors, both exhibiting a strong linear relationship with model outputs. ATS0are, a Mordred descriptor representing the sum of squared atomic electronegativity properties (specifically, Allred-Rochow electronegativity), showed an inverse correlation with GWP. Lower ATS0are values indicate lower molecular electronegativity, which often correlates with increased atmospheric stability, reduced degradation via photolysis, and prolonged greenhouse gas effects. VMcGowan, which quantifies molecular volume based on McGowan's

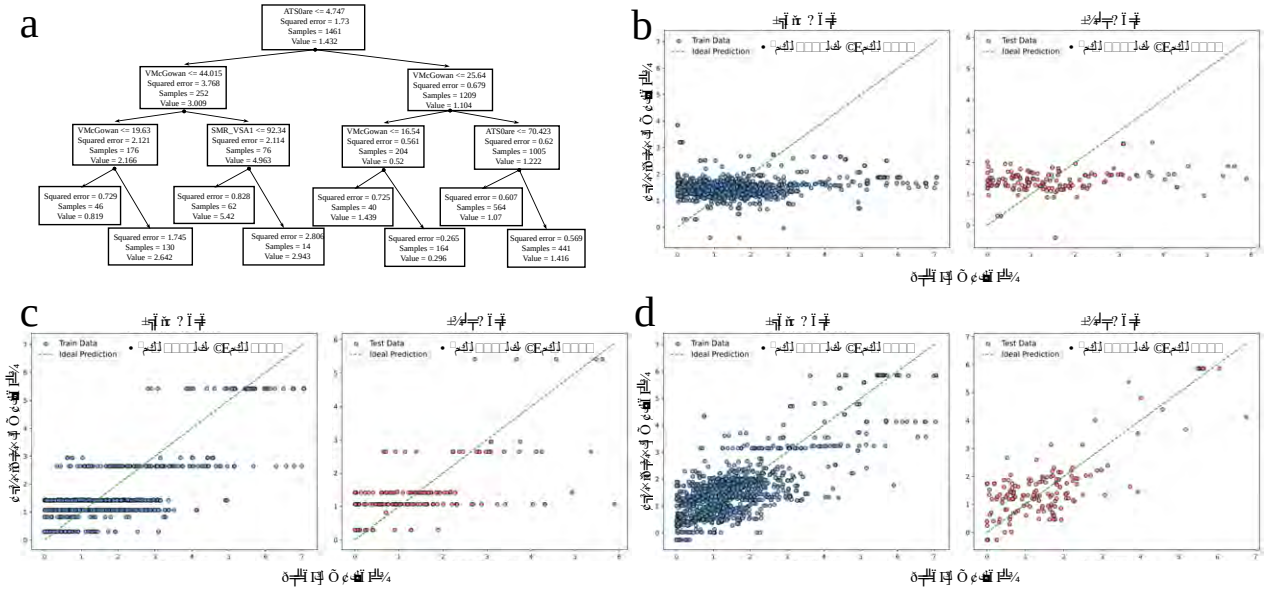



**Fig. 3:** (a) Visualization of the decision tree model trained on key features for GWP prediction. (b) Prediction results for train and test datasets using the linear regression model. (c) Prediction results for train and test datasets using the decision tree model. (d) Prediction results for train and test datasets using the KAN model.

characteristic equation, exhibited a strong positive correlation with GWP. This suggests that larger molecular structures, often associated with higher molecular weights, tend to have prolonged atmospheric lifetimes and greater radiative forcing potential, leading to increased environmental impact. In addition to these primary descriptors, SMR_VSA1, SMR, and SSE ranked as the third, fourth, and fifth most significant features in the model's decision-making process. SMR_VSA1, a van der Waals surface area descriptor weighted by molar refractivity, displayed an inverse relationship with GWP. SMR, representing total molecular refractivity, and SSE, measuring solute excess polarizability, both exhibited positive correlations with GWP, indicating that molecular dispersion forces and polarizability significantly influence environmental impact predictions. These findings highlight the interplay between molecular size, electronic properties, and intermolecular interactions in shaping GWP. Notably, the high correlation between ATS0are and other key descriptors, such as SMR (0.91) and SSE (0.99), suggests that electronegativity-driven features strongly influence GWP predictions. This reinforces the need for white box approaches like KAN to provide explicit, interpretable equations linking molecular descriptors to GWP, ensuring greater transparency in sustainability assessments.

## White-Box Modelling

A white-box modelling approach is proposed to predict GWP scores of chemicals and processes, utilizing the interpretability functions of KAN model.[10, 11] To benchmark the KAN model, we conducted a comparative analysis with two widely used interpretable models: linear regression and decision tree models. To enhance model interpretability, reducing the number of features is as critical as selecting an appropriate model. Therefore, we used the top 20 features identified in **Fig. 2** as inputs for training the white-box models. These features accounted for 87% of the total feature importance, while the remaining features each contributed no more than 1.7%, indicating relatively small influence on model training.

The fundamental benchmark, the linear regression model, produced poor predictive performance, with $R^2$ scores of 0.0598 and 0.0621, and MSE values of 1.6266 and 1.6185 for the training and test datasets, respectively, as shown in **Fig. 3**(b). The mathematical formulation derived from the linear regression model for a given molecule $m$ is provided in Eq. (1):

$$GWP_m = \sum_{i=1}^{20} a_i \cdot x_{m,i} + b \qquad (1)$$

where $x_{m,i}$ represents chemical descriptors, $a_i$ denote regression coefficients, and $b$ is the intercept term representing the baseline GWP. The coefficients derived from the model are summarized in **Table 2**.

Among the descriptors, SpMax_Dzpe has the highest positive coefficient, suggesting that the maximum atomic polarizability along the principal moment of inertia axis is strongly associated with increased GWP. Sse and VMcGowan also exhibit notable positive influences, indicating that solute excess polarizability and molecular volume play key roles in determining GWP. Conversely, SMR_VSA1 has the most significant negative impact, implying that molecular refractivity-weighted van der Waals surface area contributes to lowering GWP.

These observations highlight the limitations of linear

**Table 2:** Coefficients of the linear regression model for GWP prediction.

| Coefficient | Chemical descriptor | Value |
|---|---|---|
| $a_1$ | ATS0are | 0.007946 |
| $a_2$ | VMcGowan | 0.151153 |
| $a_3$ | SMR_VSA1 | -0.800855 |
| $a_4$ | SMR | 0.092298 |
| $a_5$ | Sse | 0.235614 |
| $a_6$ | BCUTv-1l | -0.000368 |
| $a_7$ | ETA_alpha | -0.637297 |
| $a_8$ | AATSC1c | 0.003819 |
| $a_9$ | SpMax_Dzpe | 0.745527 |
| $a_{10}$ | SlogP_VSA2 | -0.003849 |
| $a_{11}$ | SM1_Dzpe | -0.010904 |
| $a_{12}$ | AMID_h | -0.042039 |
| $a_{13}$ | BCUTse-1l | 0.060728 |
| $a_{14}$ | SlogP_VSA10 | -0.042921 |
| $a_{15}$ | BCUTi-1h | -0.054201 |
| $a_{16}$ | AXp-0dv | -0.002186 |
| $a_{17}$ | Mare | -0.119402 |
| $a_{18}$ | BCUTpe-1h | -0.060882 |
| $a_{19}$ | AETA_beta | 0.047351 |
| $a_{20}$ | SpMAD_Dzse | 0.062921 |
| b | - | 1.610488 |

regression in capturing complex, non-linear relationships between molecular descriptors and GWP. Additionally, the presence of collinear features, such as VMcGowan and Sse, suggests potential redundancies in the feature set, which may further restrict the model's predictive capabilities. While the linear regression model offers simplicity and interpretability, its performance remains inadequate for accurate GWP estimation, underscoring the need for more sophisticated modeling approaches that can effectively capture intricate molecular interactions.

The decision tree model, which allows for more complex yet interpretable modelling, yielded the results visualized in **Fig. 3**(a). The boxed structures in the figure represent the decision criteria at each node of the RF model. The tree comprises 15 nodes, with the root node split on ATS6ave, indicating its dominant influence on GWP prediction. Additional splits based on VMcGowan and SMR_VSA1 further indicate the hierarchical importance of these features. As the depth of the tree increases, prediction error decreases, and terminal nodes provide distinct GWP values. However, as depicted in **Fig. 3**(c), the model's predictive performance remains limited, with $R^2$ scores of 0.5978 and 0.3711, and MSE values of 0.6958 and 1.0852 for the training and test datasets, respectively. While the decision tree model captures non-linear patterns to some extent, its predictive performance still falls short of effectively modelling the complex, non-linear behaviour of chemical properties governing GWP. This demonstrates the inherent trade-off between interpretability and predictive accuracy in traditional white-box models.

To address these limitations, we adopted the KAN framework, widely recognized for its capability to represent symbolic expressions, to develop a GWP prediction model.[19] The KAN model captures non-linear relationships between features and GWP by transforming these relationships into interpretable standard functions such as exponential, polynomial, and trigonometric functions. However, if the fitted model is inherently linear, it can be transformed into a linear model through symbolic transformation, distinguishing KAN from conventional non-linear regression models. The development process of this white-box KAN model, including key steps such as fitting, pruning, fine-tuning, and symbolic simplification. In particular, symbolic simplification is a critical process for ensuring model interpretability. During this process, the model fits various candidate symbolic functions—such as sine, cosine, exponential, logarithmic, and power functions—and systematically selects the form that best represents the underlying non-linear relationship in the data. This automated selection ensures that the chosen functions accurately capture the data's structural patterns while maintaining model interpretability.[10]

As shown in **Fig. 3**(d), the model achieved predictive performance with $R^2$ scores of 0.6287 and 0.6433, and MSE values of 0.6352 and 0.6716 for the training and test datasets, respectively. Remarkably, despite being a fully interpretable white-box model, its performance is comparable to or even exceeds that of black-box models developed in previous studies, which achieved accuracies of 0.63 and 0.48.[3, 5] The mathematical expression for the resulting white-box model is presented in Eq. (2) as follows:

$$\mathrm{GWP_m} = \varepsilon \cdot \cos\left(\sum_{i=1}^{15} g_i(x_{m,i}) + \eta\right) + \iota \qquad (2)$$

where $m$ denotes the molecule, and $x_{m,i}$ represents the input molecular descriptors specific to molecule $m$. the parameters $\varepsilon$, $\eta$, and $\iota$ are set to 5.34842491149902, 8.4815278578314, and 4.47257137298584, respectively. Each function $\mathrm{g_i}(x_{m,j})$ is defined in a general form in Eq. (3) as follows:

$$g_i(x_{m,i}) = \alpha_i \cdot func_i(\beta_i \cdot x_{m,i} + \gamma_i) \qquad (3)$$

where $x_{m,i}$ represents the $i$-th molecular descriptor of molecule m. The parameter $\alpha_i$ is a scaling coefficient that determines the magnitude of the transformation, while $\beta_i$and $\gamma_i$ adjust the input values of the function. The function $func_i$ represents a non-linear transformation applied to the descriptor, which can take forms such as sine, cosine, hyperbolic tangent, absolute value, or power functions. The specific functional forms and parameter values used in this model are summarized in **Table 3**. Among the initial 20 descriptors, five—Sse, AATSC1c, SlogP_VSA10, AETA_beta, and SpMAD_Dzse—were excluded during the pruning process of the KAN model. This process systematically removes features that contribute minimally to

the model's predictive performance or exhibit high redundancy with other descriptors.

The function $g_1(x_{m,1})$ is formulated as a scaled hyperbolic tangent function. This structure suggests that $g_1(x_{m,1})$ primarily captures the non-linear effects of ATS0are on GWP, applying a transformation that emphasizes variations within a specific range, while mitigating extreme values through the saturation properties of the hyperbolic tangent function.

The incorporation of a cosine transformation in Eq. (2) allows the model to capture non-linear saturation effects in GWP contributions. This aligns with chemical intuition, reflecting the stabilising effects of certain structural features as they grow larger or more complex. These transformations enable the KAN model to generalise domain-specific knowledge while maintaining interpretability, bridging the gap between predictive accuracy and interpretability. By integrating these features and their transformations, the KAN model delivers a robust framework for understanding the interplay between molecular descriptors and GWP. The result is a white-box model that combines predictive performance with interpretability, adhering to established chemical principles to provide precise forecasts of environmental impact.

**Table 3**: Functional transformations of molecular descriptors in the KAN model

| $g_i$ | $x_{m,i}$ | $func_i$ | $\alpha_i$ | $\beta_i$ | $\gamma_i$ |
|---|---|---|---|---|---|
| $g_1$ | ATS0are | tanh | 0.090 | 2.205 | 3.226 |
| $g_2$ | BCUTv-1l | sin | 0.199 | 2.123 | -6.409 |
| $g_3$ | BCUTse-1l | sin | 0.185 | 0.737 | 5.968 |
| $g_4$ | Mare | sin | -0.192 | 0.914 | -2.037 |
| $g_5$ | BCUTpe-1h | sin | -0.146 | 7.587 | -8.201 |
| $g_6$ | ETA_alpha | cos | 0.032 | 8.995 | 0.996 |
| $g_7$ | SMR_VSA1 | cos | -0.038 | 2.801 | -3.805 |
| $g_8$ | BCUTi-1h | cos | -0.084 | 2.621 | -1.199 |
| $g_9$ | SpMax_Dzpe | cos | -0.051 | 9.357 | -5.015 |
| $g_{10}$ | SlogP_VSA2 | tanh | 0.186 | 0.903 | -1.762 |
| $g_{11}$ | SMR | Abs | 0.007 | 6.364 | -5.575 |
| $g_{12}$ | SM1_Dzpe | Abs | -0.014 | 9.182 | 2.453 |
| $g_{13}$ | VMcGowan | Power (3rd) | 0.016 | -1 | 0.007 |
| $g_{14}$ | AXp-0dv | Power (4th) | 0.003 | -1 | 0.719 |
| $g_{15}$ | AMID_h | Power (2nd) | 0.014 | 1 | 0.083 |

## CONCLUSIONS

This study highlights the effectiveness of KAN based white-box modeling in GWP prediction. By leveraging the KAN model, we developed a predictive framework that effectively captures complex molecular relationships while maintaining interpretability through symbolic equations. Our findings emphasize the crucial role of physicochemical descriptors, particularly molecular electronegativity and volume, in determining GWP values, reinforcing the feasibility of using purely molecular information for environmental impact assessments.

The developed KAN model offers a structured, explainable approach enhancing transparency in environmental impact modeling. By deriving explicit symbolic equations, the model ensures greater interpretability and supports informed decision-making in the sustainable design and evaluation of chemical processes. This interpretability makes the model highly applicable in industrial and regulatory contexts where transparency is essential. Furthermore, our results demonstrate that KAN achieves predictive accuracy comparable to conventional deep learning models while addressing key interpretability challenges in machine learning-based GWP predictions.

## ACKNOWLEDGEMENTS

The authors would like to acknowledge the financial support from the King's College London Net Zero Centre Ph.D. Scholarship scheme.

## REFERENCES

1. L. Torrente-Murciano, J.B. Dunn, et al., Nat. Chem. Eng., 1 (2024) 18-27.
2. M. Peplow, Nature, 603 (2022) 780-783.
3. R. Song, A.A. Keller, S. Suh, Environmental science & technology, 51 (2017) 10777-10785.
4. Y. Sun, X. Wang, N. Ren, Y. Liu, S. You, Environmental Science & Technology, 57 (2022) 3434-3444.
5. X. Zhu, C.-H. Ho, X. Wang, ACS Sustainable Chemistry & Engineering, 8 (2020) 11141-11151.
6. S.J. Silva, C.A. Keller, Artificial Intelligence for the Earth Systems, 3 (2024) e230045.
7. K. Letrache, M. Ramdani, in: 2023 14th International Conference on Intelligent Systems: Theories and Applications (SITA), IEEE, 2023, pp. 1-8.
8. G.P. Wellawatte, P. Schwaller, arXiv preprint arXiv:2311.04047, (2023).
9. S. Lundberg, arXiv preprint arXiv:1705.07874, (2017).
10. Z. Liu, P. Ma, Y. Wang, W. Matusik, M. Tegmark, arXiv preprint arXiv:2408.10205, (2024).
11. Z.Liu, Y. Wang, et al., arXiv preprint arXiv:2404.19756, (2024).
12. J.L. Durant, B.A. Leland, et al., J. Chem. Inf. Comput., 42 (2002) 1273-1280.
13. H. Moriwaki, Y.-S. Tian, N. Kawashita, T. Takagi, Journal of cheminformatics, 10 (2018) 1-14.
14. L. Breiman, Machine learning, 45 (2001) 5-32.
15. T. Chen, C. Guestrin, in: Proceedings of the 22nd acm sigkdd international conference on knowledge discovery and data mining, 2016, pp. 785-794.
16. D. Svozil, V. Kvasnicka, J. Pospichal, Chemometrics and intelligent laboratory systems, 39 (1997) 43-62.

17. F. Pedregosa, G. Varoquaux, et. al., the Journal of machine Learning research, 12 (2011) 2825-2830.
18. A. Paszke, S. Gross, et. al., Advances in neural information processing systems, 32 (2019).
19. B.C. Koenig, S. Kim, S. Deng, Computer Methods in Applied Mechanics and Engineering, 432 (2024) 117397.

© 2025 by the authors. Licensed to PSEcommunity.org and PSE Press. This is an open access article under the creative commons CC-BY-SA licensing terms. Credit must be given to creator and adaptations must be shared under the same terms. See https://creativecommons.org/licenses/by-sa/4.0/



Systems & Control Transactions

**Research Article - Peer Reviewed Conference Proceeding**
ESCAPE 35 - European Symposium on Computer Aided Process Engineering
Ghent, Belgium. 6-9 July 2025
Jan F.M. Van Impe, Grégoire Léonard, Satyajeet S. Bhonsale,
Monika E. Polańska, Filip Logist (Eds.)

PSE PRESS

# Computational Assessment of Molecular Synthetic Accessibility using Economic Indicators

**Friedrich Hastedt[a], Klaus Hellgardt[b], Sophia Yaliraki[a], Antonio del Rio Chanona[a*], Dongda Zhang[b*]**

[a] Imperial College London, Exhibition Rd, South Kensington, London SW7 2BX, United Kingdom
[b] University of Manchester, Oxford Rd, Manchester M13 9PL, United Kingdom
* Corresponding Author: a.del-rio-chanona@imperial.ac.uk, dongda.zhang@manchester.ac.uk

## ABSTRACT

The rapid advancement of computational drug discovery has enabled the generation of vast virtual libraries of promising drug candidates. However, evaluating the synthetic accessibility (SA) of these compounds remains a critical bottleneck. While computer-aided synthesis planning (CASP) tools can provide synthesis routes to the candidate, their computational demands make them impractical for large-scale screening. Existing rapid SA scoring methods, struggle to generalize to out-of-distribution molecules and do not account for economic viability. To address these challenges, we present MolPrice, an accurate and reliable price prediction tool. By introducing a novel self-supervised learning approach, MolPrice achieves robust generalization to diverse molecular structures of various complexities. Our comprehensive analysis of model architectures and molecular representations reveals that substructure-based features strongly correlate with market prices, supporting the relationship between synthetic complexity and economic value. MolPrice performs well on the standard literature SA benchmark, showcasing its ability for SA estimation. MolPrice thus serves as both an accurate molecular price predictor and a rapid synthetic accessibility assessment tool, enhancing the efficiency of modern drug discovery pipelines.

**Keywords**: Molecular Complexity, Machine Learning, Synthetic Accessibility, Virtual Screening, Retrosynthesis

## INTRODUCTION

Generating promising compounds for drug discovery has become increasingly efficient. With the emergence of several open-source tools [1], one can design a whole library of thousands/millions of molecules with desired physical properties in hours.

However, taking these molecules from the virtual library to laboratory testing is a major challenge. This is because the virtual compound needs to be synthesized first, which is costly and time-consuming. Finding synthesis pathways from known building blocks to virtual molecules is a laborious process known as retrosynthesis. Within the past decade, researchers have developed computer-aided synthesis planning tools (CASP) [2] that automate retrosynthetic planning. Whilst these tools are powerful, they are still too slow (~0.5 minutes per molecule). As molecular design routines require a large number of molecular evaluations, CASP tools do not scale [3]. For example, to screen a library of 1 billion molecules within hours, the time scale should be in ms per molecule.

To overcome this issue, researchers have developed efficient scoring systems that can evaluate molecules for *synthetic accessibility* (SA) within milliseconds. The scoring systems classify molecules as either *easy-to-synthesize* (ES) or *hard-to-synthesize* (HS). ES molecules are proceeded for further analysis and HS are usually discarded. Calculated SA scores are based on i) complexity-based indicators [4,5] or ii) retrosynthetic analysis [3,6]. Complexity-based models calculate a score depending on structural indicators such as the presence/absence of functional groups and the number of stereocentres in the molecule [4]. Retrosynthetic-based models predict the output of the slower CASP tool. For example, *Thakkar et al.* [6] attempt to predict whether the CASP tool can successfully find a synthesis route to the molecule. Whilst both methodologies have their merits, they face a significant limitation: the inability to generalize to out-of-distribution molecules. Furthermore, the scoring system is either based on binary classification or

a user-defined scale, lacking physical interpretation.

Inspired by *Sanchez-Garcia et. al.* [7], we propose to assess the synthetic accessibility of a molecule based on its market price. The authors were the first to draw a connection between SA and molecular price. The price prediction model (CoPriNet) presented in [7] accurately recalls the price of purchasable, ES molecules. Similar to other scoring systems, their model fails to generalize to out-of-distribution molecules. In particular, the model is prone to assign a similar price range to both ES and HS molecules. In short, their model cannot distinguish molecular complexity and cannot be used for SA scoring.

This work aims to overcome these challenges by introducing MolPrice, a fast predictive model for molecular price. Using a new self-supervised training methodology, MolPrice learns to distinguish purchasable (ES) molecules from hard-to-synthesize (HS), out-of-distribution molecules. Through systematic analysis of different model architectures and molecular representations, we demonstrate that features capturing substructures strongly correlate with market prices, supporting the fact that synthetic complexity is reflected in economic value. MolPrice can thus be used as an initial starting point for economic analysis (market price of product – reactants).

Finally, MolPrice can be used as an accurate tool for molecular price prediction and as an SA estimation for virtual screening or molecular generation.

# METHODOLOGY

## Model Development

### Data Source

The data was provided by Molport as a snapshot of their purchasable database from March 2024. The database consists of over 5M molecules with their corresponding price in USD per unit weight. Molport provides several prices (by different suppliers) for a range of weights. The first step to obtain a robust dataset is to find a single price value per molecule. We follow the steps below to obtain this database:

1. Molecules that cannot be read by RDKit [8] are filtered out.
2. For each molecule, all corresponding prices are converted from USD per weight to USD per mmol.
3. For each molecule, the lowest price is obtained in USD per mmol.
4. The prices are converted to a logarithmic scale for model training [7].
5. Finally, molecules with a price < 2 USD/mmol on the logarithmic scale are removed (these are mostly stabilizing salts in solution or metals)

The final dataset is plotted in Figure 1.

We acknowledge that over time new molecules may be added to the database. In that case, one can simply retrain the model in a matter of minutes (as outlined in Results and Discussion).

For self-supervised learning, the HS molecules dataset is obtained from *Yu et. al.* [9] consisting of 400K molecules.

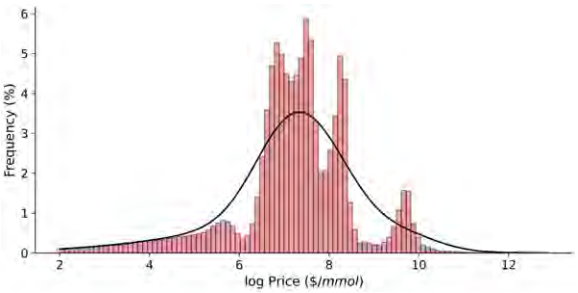



**Figure 1**: Distribution of price dataset

### Model Details

One can use a variety of models for molecular property prediction, the best depending on the specific use case. We screened different molecular featurization schemes and model architectures to select the most accurate and robust model. Particularly, in case of molecular featurization, it is interesting to explore the features that capture the relationship between price and molecule best. This way, we are posing the question whether functional groups or larger molecular moieties determine the economic value of a compound. Below we outline the tested model featurization:

- **Molecular Fingerprints** encode the 2-dimensional molecule in a bit vector. Each bit in the vector indicates the presence or absence of a molecular substructure. Various fingerprint generation algorithms exist. We select four popular algorithms: Morgan (ECFP), Atom-pair, Topological torsion (all three provided by RDKit) and MinHash (Mhfp) [10]. Morgan and Mhfp focus on the circular environment around atoms. Atom-pair considers pairs of atoms and the shortest path between them. Topological torsion considers sequential patterns. One could argue that Morgan/Mhfp best represent functional groups (FGs), atom-pair captures the overall shape of the molecule and topological torsion captures the backbone patterns. The reader is referred to the sources for more detailed information [8,10]. The various fingerprints are then used as input to a multilayer perceptron (MLP).
- **2D Graphs** include the connectivity between atoms in our modelling approach, we explore the direct use of the 2D molecular graph. The graph

features include descriptors for nodes (atom) and edge (bond) features. We use the graph model presented in [6] as the graph neural network (GNN) and as the literature baseline within the results.

- **SMILES** is a text-based representation of a molecule. We explore both the vanilla Transformer and a pre-trained RoBertA model by DeepChem [11]. As a note, the SMILES is tokenized per atom basis.
- **Functional Groups** are features that are constructed through the extended functional groups (EFG) algorithm [12]. Intuitively, EFGs are substructures in the molecule characterizing functionalization such as alcohols, ketones, amides. As molecules have different number of EFGs (different input length), a long-short term memory (LSTM) is a natural modelling choice. As an alternative, one could also construct an EFG fingerprint and use an MLP. This will be investigated in the future.

All models are trained on the MSE loss:

$$L = \frac{1}{M}\sum(y_i - \hat{y}_i)^2, \quad (1)$$

where $y_i$ and $\hat{y}$ are the ground-truth labels and model output, respectively and M is the dataset size. The regression models are compared using mean squared error (MSE), coefficient of determination ($R^2$), Spearman's correlation coefficient ($r_s$) and most importantly, inference time. The selection of time as an evaluation criterion follows naturally from previous arguments; the purpose of *SA* scoring systems is to perform large numbers of evaluations. The Molport dataset is split into 90/5/5 portions for training/validation/testing. This leaves ~500k molecules for validation and testing.

## Self-Supervised Learning

Following model training, the model is still unlikely to generalize to unseen, complex molecules. This is because all molecules in our database are purchasable or in other words, easy to synthesize. Molecules which are not synthesizable (HS) generally will not have a price label since they are not offered by suppliers.

To allow our model to learn price labels for the HS molecules, we use a contrastive learning approach. Particularly, the approach is based on two principles:

First, assuming the model has learnt a good correlation between the *latent* molecule representation and the price, we only need to focus on learning the *latent* representation of the HS molecules. Herein, we define the *latent* representation as the final vector in the model, prior to the readout function. The readout function *f* is defined as $f(\mathcal{R}^N) \rightarrow \mathcal{R}$, that is the function that converts the *latent* representation into the price output. A visual explanation is shown in Figure 2. Following on with this assumption, we freeze the parameters (weights) in the readout function during self-supervised learning. In other words, the only parameters that can be updated during the training, are the parameters that compute the *latent* representation, prior to the readout function.

Second, we assume that each dimension of the *latent* representation follows a Gaussian distribution. The assumption is reasonable as the price distribution of the model output (Figure 3a) is approximate Gaussian (by visual inspection). Using these two principles, we define the loss function for self-supervised learning as:

$$L = \frac{1}{M}\sum_{i\in ES}(y_i - \hat{y}_i)^2 + \lambda \cdot \frac{1}{N}\sum_{j=0}^{N} H_j, \quad (2)$$

$$H_j = \sqrt{\frac{2\sigma_{ES,j}\sigma_{HS,j}}{{\sigma_{ES,j}}^2 + {\sigma_{HS,j}}^2}}\exp\left(-1/4\frac{(\mu_{ES,j}-\mu_{HS,j})^2}{{\sigma_{ES,j}}^2 + {\sigma_{HS,j}}^2}\right), \quad (3)$$

where $H_j$ is the analytical Hellinger distance computed $\forall j \in \{1, \ldots, N\}$ with *N* being the *latent* vector size for Gaussian distributions. In short, the Hellinger distance enforces a separation in the *latent* representation of ES molecules versus HS molecules. The Hellinger distance tends to a minimum of zero when the ES distribution $\mathcal{N}(\mu_{ES,j}, \sigma_{ES,j})$ does not overlap with the HS distribution $\mathcal{N}(\mu_{HS,j}, \sigma_{HS,j})$. Since the parameters of the readout function are not updated during training, a different *latent* vector representation for the HS molecules should lead to a different price. The first term in Eq. 2 is the MSE loss computed over the set of ES molecules and therefore acts as a regularisation term. $\lambda$ is a hyperparameter and was set to a low value of 0.05 by default. By scaling the loss of the Hellinger distance, we do not permit the model to perform poorly on the initial price prediction task. Intuitively, if the two loss terms in Eq. 2 are not conflicting, we should obtain an accurate model for price prediction as well as a model that can distinguish ES from HS molecules.

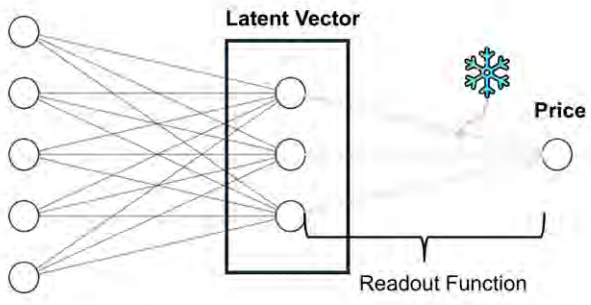



**Figure 2:** Toy example with a latent vector of 3D (N=3). Parameters of the readout functions are frozen.

It is to be noted that there is no theoretical guarantee that the predicted price for the HS molecules will be larger than the predicted price of the ES molecules. This

**Table 1:** Results for different model architectures and molecular featurization schemes on the hold-out test set. The metrics include mean squared error (MSE), coefficient of determination ($R^2$), Spearman's correlation coefficient ($r_s$) and inference time in ms (per single cpu core per molecule)

| Architecture | Feature/Model Type | MSE (↓) | $R^2$ (↑) | $r_s$ (↑) | Inference Time (ms/mol) |
|---|---|---|---|---|---|
| MLP | Atom pair | 0.58 | 0.72 | 0.84 | 1.4 |
| | Topological | 0.61 | 0.71 | 0.84 | 1.4 |
| | Morgan | 0.51 | **0.76** | **0.88** | **1.4** |
| | Mhfp | **0.50** | **0.76** | **0.88** | **1.4** |
| GNN (CoPriNet) | 2D Graph | 0.52 | 0.74 | 0.85 | 21.5 |
| Transformer | SMILES (Vanilla) | 0.88 | 0.58 | 0.72 | 41.1 |
| | SMILES (RoBERTa) | 0.58 | 0.72 | 0.85 | 29.1 |
| LSTM | EFGs | 0.62 | 0.70 | 0.82 | 3.6 |

is because we do not incorporate price labels for the HS molecules and solely rely on the contrastive loss (Eq. 2)

To verify that MolPrice has effectively learnt the difference between ES and HS molecules, we compare its performance to classical SA scoring systems on the test dataset TS1-3 provided in [9], the standard for comparing SA scoring tools.

## RESULTS AND DISCUSSION

### Price Prediction

The results for price prediction on the test set are shown in Table 1. Analysing the performance metrics, the neural network (MLP) with Morgan/Mhfp featurization performs best in terms of MSE, $R^2$ and $r_s$. Particularly, the Morgan/Mhfp featurization is preferred over the two other fingerprints tested (Atom pair and Topological). This can be explained by considering the fingerprint construction algorithm: Both Morgan/Mhfp fingerprints are constructed through circular environments around atoms in the molecule. This featurization resembles functional group (substructure) encoding. On the other hand, atom-pair and topological torsion fingerprints consider the sequential order of atoms in a molecule and fail to fully capture fine-grained details such as functional groups.

The GNN model (CoPriNet) is seen to nearly match the fingerprint MLP models. Possibly this can be explained by comparing the internal model workings: Particularly, the message-passing operation commonly used in GNNs is similar to the circular encoding algorithm (for fingerprint construction). Thus, both model architectures share a certain degree of knowledge.

As expected, the pre-trained Transformer (RoBERTa) model performs better than its vanilla counterpart. The pre-training allows the model to learn the SMILES language prior to the downstream prediction task. Nevertheless, both SMILES-based models fail to outperform the GNN or fingerprint MLP. As SMILES are tokenized per atom basis, the model is not aware of molecular substructures, a piece of information available to both the GNN and MLP.

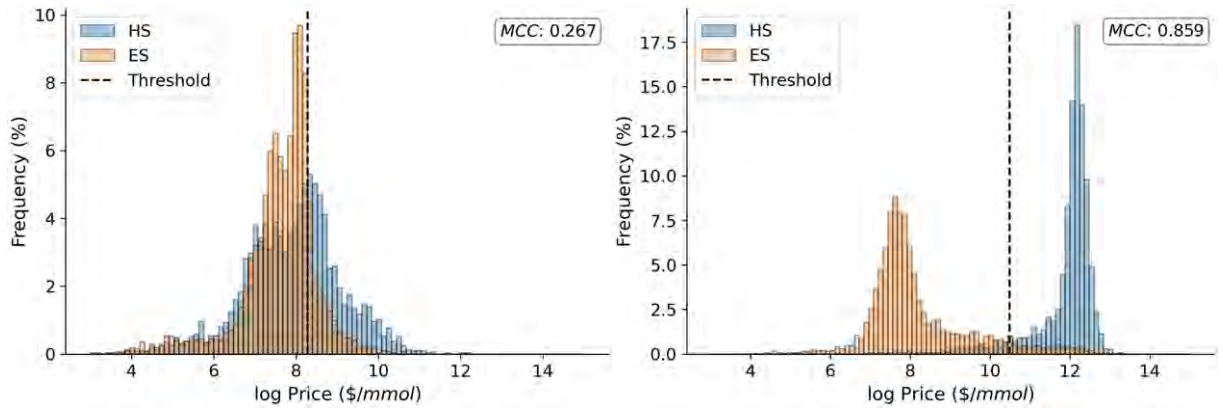
Finally, the extended functional group (EFGs) LSTM is seen to perform acceptably. We believe that the LSTM fails to construct a good latent representation of the molecule due to the sequential input of the EFGs. Instead of using an LSTM, it may be worth constructing a new fingerprint based on EFGs and using an MLP as the model.

Last, a very important factor not yet discussed is the model's inference time. For example, if one wants to screen a database of 1 billion molecules and the scoring takes 1 second per molecule, it would take ~30 years to screen the entire database. From Table 1, we see that the MLP is favourable with a quick inference time of 1.4 ms per molecule (tested on an Intel vPro i9 laptop cpu). The same database could now be screened within 12 days. Both the literature GNN (CoPriNet, literature model) and Transformer models take 20-40x longer for the same task. This is because both models perform a large number of matrix multiplication operations, whereas the MLP only performs 3 overall. The training time of the MLP lies within 30 minutes, whereas both the GNN and Transformer model takes several days, rendering training on a new dataset computationally intensive.

The detailed analysis of different molecular featurization highlights that features capturing substructures correlate well with market prices (Morgan, Mhfp, GNN). This finding underscores the relationship between molecular complexity and market price.

### Learning Synthetic Accessibility

The top two performing models (Mhfp and Morgan) provide the starting point for self-supervised learning. Figure 3 shows the predicted price for both ES and HS molecules before and after self-supervised learning for the Morgan fingerprint. For both Morgan and Mhfp fingerprints, the algorithms learn to assign prices to HS molecules that are different to the ES, purchasable molecule. Empirically, we observe that the model prefers to assign a higher price range to the HS molecules compared to the ES molecules. This is desired, but as outlined previously,




a: Before self-supervised learning b: After self-supervised learning

**Figure 3:** Distributions of ES/HS molecules predicted by MolPrice for Morgan fingerprint. The degree of distribution separation is measured through the Matthews correlation coefficient (MCC).

there is no mathematical guarantee for this observation.

Statistically, the separation between the ES and HS distribution is confirmed in the table below:

**Table 2**: Statistics on HS/ES classification and Price

| **Fingerprint** | **MCC** (↑) | **AUC** (↑) | $\mathbf{R^2}$ (↑) |
|---|---|---|---|
| Morgan | 0.86 | 0.97 | 0.54 |
| Mhfp | 0.89 | 0.98 | 0.73 |

In Table 2, the distribution separation is measured using Matthew's correlation coefficient (MCC) and area under receiver operating characteristic curve (AUC). These two metrics indicate how well MolPrice can distinguish between ES and HS molecules (a binary classification problem). The Mhfp fingerprint slightly outperforms the Morgan fingerprint in both metrics.

More importantly, for the Morgan fingerprint, the MSE loss and Hellinger distance separation were seen to have conflicting objectives. To obtain a higher AUC, the hyperparameter $\lambda$ in Eq. 2 was set to a higher value. This came with a decrease in the accuracy of price prediction for the ES dataset as shown by a lower $R^2$ compared to Table 1. For the Mhfp fingerprint, the $R^2$ only slightly decreased from 0.76 to 0.73. From Table 2, we can deduct that the MLP along with the Mhfp fingerprint results in an accurate price prediction as well as a SA scoring tool.

## Comparison to other SA scoring tools

To confirm that MolPrice is indeed a competitive SA scoring tool, we benchmarked and compared MolPrice to other state-of-the-art SA tools. This analysis is shown in Table 3. From the table, it is seen that MolPrice performs competitively compared to other SA screening tools. Only GASA outperforms MolPrice on the test datasets apart from TS3 – accuracy. While MolPrice is not the top performing model, two things should be kept in mind when analysing the results:

1. GASA and other models were exclusively trained for SA scoring, *i.e.*, the only objective given to the model is the binary classification between ES and HS molecules. MolPrice has to balance between predicting accurate labels for the price as well as learning the difference between the two molecule groups
2. The test sets TS2 and TS3 were curated by using a CASP tool. In short, the HS molecules are labelled as hard-to-synthesize if the CASP tool fails to return a synthesis route for the molecule. It is to note that CASP tools are not perfect and highly depend on the database that it was trained on. Given this, it could be that some molecules that were labelled as ES are

**Table 3:** Comparison of our model MolPrice to other, commonly used SA tools. The test datasets are obtained from [9]. For TS1-3, the area under receiver operating characteristic curve (AUC) is reported as well as the accuracy for TS3. The best performance is highlighted in bold, the second best in italics.

| **Model** | **TS1 (AUC)** | **TS2 (AUC)** | **TS3 (AUC)** | **TS3 (Acc)** |
|---|---|---|---|---|
| *GASA* [9] | **0.999** | *0.881* | **0.850** | *0.759* |
| *SCScore* [5] | 0.881 | 0.487 | 0.575 | 0.511 |
| *SAScore* [4] | 0.989 | **0.919** | 0.772 | 0.664 |
| *RAScore* [6] | 0.919 | 0.865 | 0.790 | 0.701 |
| *MolPrice* (ours) | *0.991* | 0.871 | *0.833* | **0.771** |

actually HS and vice versa.

Given above, it is fair to conclude that MolPrice performs well on these benchmarks. We plan to extend SA testing in future works on case studies as outlined in the next section to solidify the use case of MolPrice of molecular generation and screening.

## CONCLUSION AND OUTLOOK

In this work, we present MolPrice, an accurate tool for both price prediction and synthetic accessibility measurement. MolPrice is based on the Mhfp fingerprint and a fast-to-evaluate MLP, which were carefully selected after exploring a range of model architectures and molecule featurization schemes. Through this exploration, we discovered the importance of molecular substructures for predicting prices, supporting the notion that molecular complexity is reflected in economic value.

By introducing a new contrastive learning approach, we steer MolPrice towards molecules that are out-of-distribution and/or complex.

In the future, we will test MolPrice on different case studies. These case studies will range from multi-objective virtual screening [13] to molecular generation such as in [3]. Furthermore, we want to include MolPrice directly as guidance in retrosynthesis planning. In short, we are interested to see whether MolPrice can steer the synthesis search towards economically viable routes and/or speed up the convergence of the CASP tool.

## DIGITAL SUPPLEMENTARY MATERIAL

MolPrice is hosted on GitHub and usable through https://github.com/fredhastedt/MolPrice

## ACKNOWLEDGEMENTS

This work was supported by the Engineering and Physical Sciences Research Council (EPSRC) funding grant EP/S023232/1.

We thank Molport (https://www.molport.com/) for sharing their private data used for model training.

## REFERENCES

1. Du Y, Jamasb AR, Guo J, et al. Machine learning-aided generative molecular design. *Nat Mach Intell*. 2024;6(6):589-604. doi:10.1038/s42256-024-00843-5
2. Coley CW, Green WH, Jensen KF. Machine Learning in Computer-Aided Synthesis Planning. *Acc Chem Res*. 2018;51(5):1281-1289. doi:10.1021/acs.accounts.8b00087
3. Liu CH, Korablyov M, Jastrzębski S, Włodarczyk-Pruszyński P, Bengio Y, Segler M. RetroGNN: Fast Estimation of Synthesizability for Virtual Screening and De Novo Design by Learning from Slow Retrosynthesis Software. *J Chem Inf Model*. 2022;62(10):2293-2300. doi:10.1021/acs.jcim.1c01476
4. Ertl P, Schuffenhauer A. Estimation of synthetic accessibility score of drug-like molecules based on molecular complexity and fragment contributions. *J Cheminformatics*. 2009;1(1):8. doi:10.1186/1758-2946-1-8
5. Coley CW, Rogers L, Green WH, Jensen KF. SCScore: Synthetic Complexity Learned from a Reaction Corpus. *J Chem Inf Model*. 2018;58(2):252-261. doi:10.1021/acs.jcim.7b00622
6. Thakkar A, Chadimová V, Bjerrum EJ, Engkvist O, Reymond JL. Retrosynthetic accessibility score (RAscore) – rapid machine learned synthesizability classification from AI driven retrosynthetic planning. *Chem Sci*. 2021;12(9):3339-3349. doi:10.1039/D0SC05401A
7. Sanchez-Garcia R, Havasi D, Takács G, et al. CoPriNet: graph neural networks provide accurate and rapid compound price prediction for molecule prioritisation. *Digit Discov*. 2023;2(1):103-111. doi:10.1039/D2DD00071G
8. Landrum G. RDKit: Open-source chemoinformatics. https://www.rdkit.org/docs
9. Yu J, Wang J, Zhao H, et al. Organic Compound Synthetic Accessibility Prediction Based on the Graph Attention Mechanism. *J Chem Inf Model*. 2022;62(12):2973-2986. doi:10.1021/acs.jcim.2c00038
10. Probst D, Reymond JL. A probabilistic molecular fingerprint for big data settings. *J Cheminformatics*. 2018;10(1):66. doi:10.1186/s13321-018-0321-8
11. Ramsundar B, Eastman, Walters P, Pande V, Leswing K, Wu Z. *Deep Learning for the Life Sciences*. O'Reilly Media
12. Lu J, Xia S, Lu J, Zhang Y. Dataset Construction to Explore Chemical Space with 3D Geometry and Deep Learning. *J Chem Inf Model*. 2021;61(3):1095-1104. doi:10.1021/acs.jcim.1c00007
13. Fromer JC, Graff DE, Coley CW. Pareto optimization to accelerate multi-objective virtual screening. *Digit Discov*. 2024;3(3):467-481. doi:10.1039/D3DD00227F

© 2025 by the authors. Licensed to PSEcommunity.org and PSE Press. This is an open access article under the creative commons CC-BY-SA licensing terms. Credit must be given to creator and adaptations must be shared under the same terms. See https://creativecommons.org/licenses/by-sa/4.0/



Systems & Control Transactions

**Research Article - Peer Reviewed Conference Proceeding**
ESCAPE 35 - European Symposium on Computer Aided Process Engineering
Ghent, Belgium. 6-9 July 2025
Jan F.M. Van Impe, Grégoire Léonard, Satyajeet S. Bhonsale,
Monika E. Polańska, Filip Logist (Eds.)

PSE PRESS

# A Physics-Informed Approach to Dynamic Modeling and Parameter Estimation in Biotechnology

**Konstantinos Mexis[a]*, Stefanos Xenios[a], Nikolaos Trokanas[a] and Antonis Kokossis[a]**

[a] National Technical University of Athens, Department of Chemical Engineering, Athens, Greece
* Corresponding Author: konstantinosmexis@mail.ntua.gr.

## ABSTRACT

The increasing complexity of industrial biotechnology demands advanced modeling techniques capable of capturing the intricate dynamics of bioreactors. Traditional regression-based and empirical methods often fall short when confronted with the highly nonlinear behavior and limited experimental data characteristic of bioprocesses. Addressing these challenges requires a more intelligent approach—one that leverages domain knowledge to model complex bioprocess dynamics effectively, even with sparse data, while maintaining interpretability and robustness. In this study, we introduce a process-informed, data-driven methodology for modeling the dynamics of industrial bioreactors, leveraging the capabilities of the rising field of Scientific Machine Learning (SciML). Our approach leverages Physics-Informed Neural Networks (PINNs) to seamlessly integrate domain knowledge encoded in physical laws with sparse experimental data and deep learning techniques, enabling precise simulation and modeling of bioreactor operations. The framework is validated using real-world experimental data, demonstrating its capability for state and space estimation, essential for optimizing biomanufacturing processes. Our findings underscore the potential of Physics Informed Neural Networks to address the challenges of dynamic modeling in bioprocesses, paving the way for the development of intelligent, autonomous, and data-driven solutions in industrial biotechnology. This fusion of data-driven and mechanistic modeling represents a transformative step toward enhancing the efficiency, scalability, and sustainability of modern biomanufacturing practices.

**Keywords**: Machine Learning, Simulation, Dynamic Modelling, Industry 4.0, Intelligent Systems

## INTRODUCTION

The increasing complexity of modern industrial biotechnology underscores the urgent need for advanced modeling and simulation techniques. Many biomanufacturing processes still rely heavily on empirical knowledge and operator expertise, which limits their ability to effectively handle the increasing intricacies and dynamic nature of contemporary bioprocesses. This dependency on traditional methods constrains the scalability, efficiency, and optimization of biomanufacturing, highlighting the need for more data-driven and adaptive approaches. As bioprocess systems become more sophisticated, traditional control strategies struggle to address emerging challenges, including raw material variability, unpredictable biological dynamics, and the imperative for real-time, data-driven decision-making. The advent of Industry 4.0—characterized by digitalization, automation, and intelligent data integration—has initiated a transformative shift towards smarter, more efficient, sustainable, and adaptive bioprocessing systems [4]. Digital transformation in bioprocesses involves integrating multiple technologies, yet the inherent complexity, high dimensionality, and dynamic nature of these systems, driven by numerous interacting parameters, pose significant challenges in optimizing process efficiency, maintaining stability, and maximizing product yields [6].

Artificial Intelligence (AI) is gaining increasing recognition for its potential to revolutionize bioprocesses modeling by effectively leveraging real-world experimental data. Recently, a growing number of AI technologies have been applied in bioprocess optimization and control to enhance the performance of bioprocess. These advancements demonstrate that AI holds great promise

for enhancing bioprocess efficiency, scalability and adaptability, making it a valuable tool for addressing the challenges faced in modern biomanufacturing [6]. However, conventional machine learning approaches, such as neural networks, face significant limitations in this domain due to their reliance on large datasets to achieve optimal performance. In bioreactor applications, the availability of data is often sparse and limited, posing a critical challenge for purely data-driven methodologies. Moreover, traditional neural networks operate as black-box models, lacking the ability to incorporate physical knowledge of the underlying bioprocess, which is essential for ensuring reliability and interpretability in complex biomanufacturing systems.

To address these challenges, in this study, we introduce a novel approach that leverages the principles of Scientific Machine Learning (SciML) to overcome the challenges of bioreactor modeling. Specifically, we employ Physics-Informed Neural Networks (PINNs), a cutting-edge framework that integrates physical knowledge directly into the machine learning process. Unlike traditional neural networks, PINNs embed governing equations, such as mass balance, energy balance, and reaction kinetics, as constraints within the learning architecture. This enables the model to respect the underlying physics of the bioprocess while learning from limited experimental data. In addition to enabling accurate dynamic modeling with limited data, the Physics-Informed Neural Network framework offers the capability to perform parameter estimation directly within its architecture. Traditional methods for parameter estimation in bioprocesses often require extensive experimental data or rely on iterative optimization techniques that can be computationally expensive and time-consuming. In contrast, PINNs naturally incorporate parameter estimation by treating unknown process parameters as trainable variables within the network. We validate our approach using a dynamic model of a batch bioreactor and real-life experimental data. Our demonstration highlights the effectiveness of PINNs in achieving accurate dynamic modeling and parameter estimation, even with very limited experimental data.

# METHODS AND MATERIALS

## Dynamic Model

As a pilot study, we expanded upon the work of [1], which successfully demonstrated the production of recombinant nanobodies with scorpion antivenom activity in Escherichia coli. Nanobodies (VHH), derived from camelid antibodies, were produced intracellularly in E. coli WK6 through fed-batch cultivation, with production yields significantly improved using dynamic modeling techniques [2]. In our study, experimental data from the batch phase of the bioreactor were utilized to develop a predictive model using Physics-Informed Neural Networks (PINNs). The bioreactor is assumed to be an infinitely mixed culture without any transfer limitation. The mass balances for biomass and glucose are given by Eq. (1) and (2):

$$\frac{\mathrm{dX}}{\mathrm{dt}} = \frac{\mu_{max} \cdot S}{K_S + S} \cdot X \quad (1)$$

$$\frac{dS}{dt} = -\frac{1}{Y_{XS}} \cdot \frac{\mu_{max} \cdot S}{K_S + S} \cdot X \quad (2)$$

where X and S are the concentrations of biomass and glucose (in $g/L$), $\mu_{max}$ is the maximum specific growth rate (in $h^{-1}$), $K_S$ is the substrate saturation coefficient (in $g/L$) and $Y_{XS}$ is the yield coefficient of substrate (in $g \cdot cdw/gS$).

## Scientific Machine Learning

Scientific Machine Learning (SciML) is an innovative and rapidly evolving field that merges principles from machine learning (ML) with scientific computing to tackle complex challenges across various domains, including physics, biology, and engineering [5]. This interdisciplinary approach leverages the strengths of both data-driven methods and traditional physics-based models, aiming to enhance predictive capabilities and facilitate data-driven discoveries. This integration enables more accurate simulations and predictions, particularly when the under-lying physics of a system is only partially known or too complex to model explicitly.

By incorporating scientific knowledge, SciML techniques require less data to achieve accurate and robust predictions, which is especially beneficial when collecting large amounts of data is expensive or impractical. Furthermore, these methods maintain interpretability by embedding physical principles and domain knowledge into the models, allowing for better understanding of the underlying processes and greater trust in the predictions they provide.

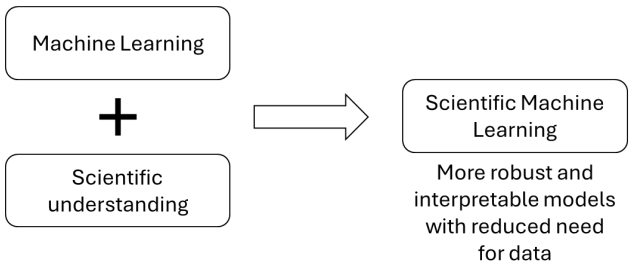



**Figure 1:** Scientific Machine Learning

## Physics-Informed Neural Network

Physics-Informed Neural Networks (PINNs) represent a significant advancement in the intersection of machine learning and computational physics, providing a framework for solving complex mathematical models governed by partial differential equations (PDE).

Introduced in [3], PINNs leverage the capabilities of deep learning to incorporate physical laws directly into the learning process, enabling the networks to approximate solutions to both forward and inverse problems effectively. This approach allows one to automatically find data-driven solutions for PDEs or ODEs. In this paper, we consider parametrized nonlinear system of ODEs given by:

$$\mathcal{F}\left(t, \boldsymbol{y}(t), \frac{d\boldsymbol{y}(t)}{dt}; \boldsymbol{\lambda}\right) = 0 \tag{3}$$

where $\boldsymbol{y}$ represents the state of the dynamic system (i.e., the latent ODE solution) and $\boldsymbol{\lambda} = [\lambda_1, \ldots, \lambda_2]$ are the ODE parameters. In the context of PINNs, a fully connected feed-forward neural network with multiple hidden layers is employed to approximate the solution of the differential equations. The network takes time $t$ as input and outputs:

$$\boldsymbol{y} = f_{\boldsymbol{w}}(t) \tag{4}$$

where $f_{\boldsymbol{w}}$ represents the mapping function learned by the neural network, parametrized by adaptive weights $\boldsymbol{w}$. This setup requires the network to learn to compute the solution of the given ODEs. The neural network in a PINN framework is trained by minimizing a mean squared error (MSE) cost function, typically defined as:

$$MSE = \mathcal{L}_{data} + \mathcal{L}_{physics} \tag{5}$$

where $\mathcal{L}_{data}$ represents the data-based loss term, and $\mathcal{L}_{physics}$ enforces the physical consistency of the solution. These loss terms are formulated as follows:

$$\mathcal{L}_{data} = \frac{1}{N_y}\sum_{i=1}^{N_y}\frac{1}{N_t}\sum_{j=1}^{N_t}\left\|y_i(t_j) - y_i^*\right\|_2^2 \tag{6}$$

$$\mathcal{L}_{physics} = \frac{1}{N_y}\sum_{i=1}^{N_y}\frac{1}{N_{\mathcal{F}}}\sum_{j=1}^{N_{\mathcal{F}}}\left\|\mathcal{F}(y_i(t_j))\right\|_2^2 \tag{7}$$

where, $N_t$,$N_{\mathcal{F}}$ and $N_y$ correspond to the number of training data points, the number of collocation points and the number of outputs of the neural network respectively; $y_i$ is the $i$-th output of the neural network; $y_i^*$ represents the desired $i$-th output, considering the $j$-th data pair $(t_j, y_i^*(t_j))$. The data-based loss term penalizes discrepancies between the network's predictions and the desired outputs from the training data. The physics-based loss term enforces the alignment of the network's outputs with the governing differential equations of the physical system by minimizing the residuals of these equations at a finite set of randomly sampled collocation points. Together, these terms allow the network to approximate the solution of the system's dynamics while adhering to physical laws. By incorporating prior knowledge through the governing equations, the PINN framework reduces the reliance on large datasets, enabling it to perform accurate dynamic modeling and parameter estimation even with sparse data. This integration of theoretical models with experimental data enhances the efficiency and robustness of process modeling, making PINNs particularly suitable for complex, data-limited systems. PINNs can also be employed in a inverse setup to perform parameter estimation of the governing ODEs. In this configuration, unknown parameters within the ODEs are treated as additional trainable variables within the neural network. By incorporating these parameters into the optimization process, the network learns not only the dynamic behavior of the system but also estimates the values of the unknown parameters. This process enables PINNs to infer parameters even in cases where traditional methods struggle due to sparse or noisy data.

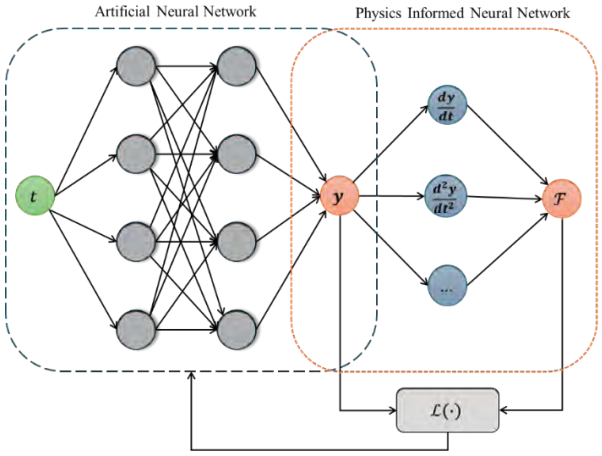



**Figure 2:** Physics Informed Neural Network

## RESULTS

Leveraging experimental data from [1] and the dynamic model described previously, we applied our approach to a batch bioreactor, showcasing the ability of Physics-Informed Neural Networks (PINNs) to accurately capture the system's state-space dynamics and unlock predictive insights, thereby advancing data-driven intelligence in bioprocess modeling. The dataset consists of measurements of biomass and glucose concentrations over time in a batch bioreactor (**Figure 3**).

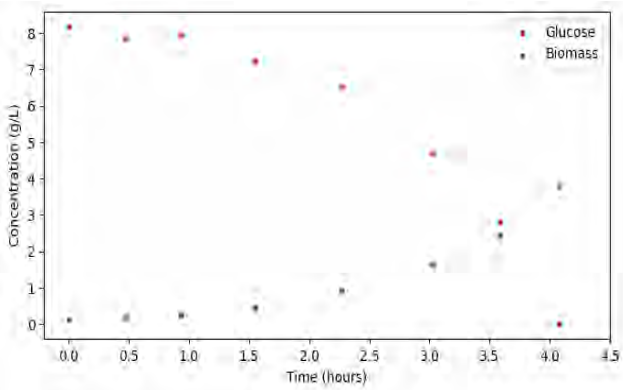



**Figure 3:** Experimental data for batch phase

The results demonstrate that this physics-informed framework effectively overcomes the key challenges of conventional dynamic modeling methods, particularly those arising from sparse and limited experimental datasets. The PINN architecture utilized in this study is a fully connected feed-forward neural network comprising one input layer, three hidden layers (with 64, 1024 and 1024 neurons) and one output layer. The $ReLU$ activation function was applied to the input and final hidden layers, while the $Tanh$ activation function was used for the intermediate layers, a combination that enhanced the network's accuracy and overall performance. The network was trained using the $Adam$ optimizer with a learning rate of $0.0001$ over $30{,}000$ epochs, with early stopping implemented to prevent overfitting.

The network's single input was the time ($t$) variable, and its output layer provided predictions for Biomass ($X$) and Glucose ($S$). To capture the system's underlying dynamics, 50 collocation points were used during training. These points enforced the governing ODEs, ensuring that the PINN not only fit the available data but also adhered to the physical laws governing the system. The PINN was trained by solving the optimization problem:

$$\underset{\boldsymbol{w},\boldsymbol{p}}{minimize}\ \mathcal{L} \tag{8}$$

$$\mathcal{L} = \mathcal{L}_{data} + \mathcal{L}_{physics} \tag{9}$$

where

$$\mathcal{L}_{data} = \frac{1}{2}\cdot\frac{1}{N_y}\left(\sum_{j=1}^{N_y}\left\|X(t_j) - X^*\right\|_2^2 + \sum_{j=1}^{N_y}\left\|S(t_j) - S^*\right\|_2^2\right) \tag{10}$$

and

$$\mathcal{L}_{physics} = \frac{1}{2}\cdot\frac{1}{N_{\mathcal{F}}}\left(\sum_{j=1}^{N_{\mathcal{F}}}\left\|\frac{dX(t_j)}{dt} - \frac{\mu_{max}\cdot S(t_j)}{K_S + S(t_j)}\cdot X(t_j)\right\|_2^2 + \right.$$
$$\left. + \sum_{j=1}^{N_{\mathcal{F}}}\left\|\frac{dS(t_j)}{dt} + \frac{1}{Y_{XS}}\cdot\frac{\mu_{max}\cdot S(t_j)}{K_S + S(t_j)}\cdot X(t_j)\right\|_2^2\right) \tag{11}$$

In the equations (8)-(11), $\boldsymbol{w}$ are the neural network's trainable weights and $\boldsymbol{p}$ are the unknown kinetic parameters of the dynamic model. $\mathcal{L}_{data}$ represents the data-driven loss function, measuring how well the predictions of the model match the experimental data at specific time points. Finally, $\mathcal{L}_{physics}$ represents the physics-driven loss function, which ensures that the model adheres to the physical laws governing the bioprocess system. By minimizing the loss function ($\mathcal{L}$) with respect to both the network weights ($\boldsymbol{w}$) and the unknown kinetic parameters ($\boldsymbol{p}$) of the dynamic model, we simultaneously train the neural network and perform parameter estimation for the dynamic system. Addressing collinearity between network weights and kinetic parameters is essential to ensure that the estimated parameters accurately represent the underlying system dynamics, rather than being influenced by artifacts of the optimization process. Techniques such as regularization, orthogonalization, or introducing additional constraints can help mitigate this issue and improve the robustness of the parameter estimation process.

## Parameter Estimation

We first demonstrate the capability of the PINN to accurately estimate the unknown kinetic parameters of the dynamic model using only a sparse set of measurements. Estimating these parameters is a critical step in effectively modeling and understanding the complex dynamics of bioprocesses, as they govern key aspects such as microbial growth rates and substrate consumption.

By employing the PINN in an inverse configuration, we successfully performed parameter estimation, with the resulting kinetic parameter estimates summarized in next table (**Table 1**).

**Table 1**: Estimated kinetic parameters

| Kinetic parameter | Value |
|---|---|
| $\mu_{max}$ | 0.7267 |
| $K_S$ | 0.1634 |
| $Y_{XS}$ | 0.3983 |

As a reference, the dynamic model calibrated parameters reported in [1] are presented in **Table 2**.

**Table 2**: Model parameters reported in literature

| Kinetic parameter | Min. value | Max. value |
|---|---|---|
| $\mu_{max}$ | 0.67 | 0.87 |
| $Y_{XS}$ | 0.29 | 0.47 |

These findings highlight the ability of PINNs to accurately estimate unknown kinetic parameters, even when experimental data is sparse, showcasing their potential for applications in bioprocess modeling and control. In contrast to traditional parameter estimation approaches, which often require the full trajectory of data—available only at the end of the process—PINNs can achieve accurate parameter estimation using only the available data points at any time during the process. This allows for a more adaptive modeling approach, particularly in bioprocesses where real-time data collection is limited or costly. As a result, kinetic parameters can now be described as dynamic functions of time rather than fixed constants, providing a more realistic and accurate representation of the evolving nature of complex bioprocesses.

## Simulation

In this paragraph, we demonstrate the ability of PINNs to perform accurate simulations of the bioprocess. By leveraging both sparse experimental data and the governing equations of the system, the PINN effectively captures the complex dynamics of the process. Accurate simulation is vital for understanding the system's behavior, predicting outcomes under various operating conditions, and optimizing bioprocess performance. This

capability is particularly important in biomanufacturing, where precise control of dynamic variables such as biomass and substrate concentrations are crucial for achieving consistent product quality and yield. Unlike conventional regression approaches, which rely solely on fitting data and often require large datasets to achieve acceptable accuracy, PINNs integrate prior physical knowledge into the learning process. This integration significantly reduces the dependency on extensive datasets, making PINNs especially well-suited for applications where experimental data is limited or costly to obtain. Furthermore, the physics-based loss function in PINNs ensures that the model predictions adhere to the underlying laws of the system, improving the interpretability and robustness of the simulation results.

The simulation performance of the PINN is evaluated leveraging the mean squared error (MSE) between the predicted state variables and the experimentally measured values for both biomass and glucose. This performance metric provided a quantitative assessment of the model's ability to replicate the observed dynamics of the bioreactor (**Table 3**).

**Table 3**: PINN simulation performance

| Number of data points | Biomass (MSE) | Glucose (MSE) |
|---|---|---|
| 8 | 0.012 | 0.018 |

The low MSE values indicate that the PINN is capable of accurately modeling the dynamics of the batch bioprocess. A key advantage of the PINN also lies in its interpretability, as it incorporates prior process knowledge in the form of governing ODEs directly into the modeling framework.

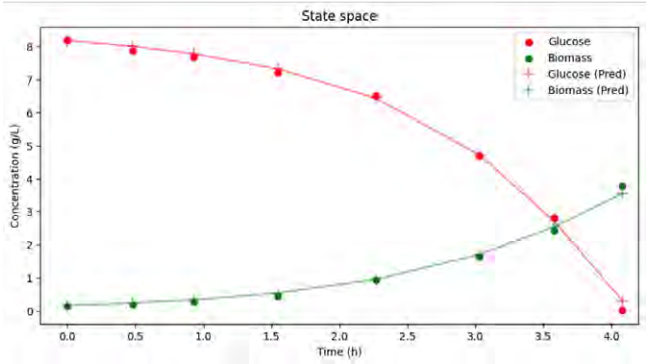



**Figure 4:** PINN simulation results

**Figure 5** presents a comparison of the simulation results obtained by solving the system of ODEs using kinetic parameter values estimated through a traditional regression approach [1] versus the simulation results obtained through PINN. The values of kinetic parameters estimated using standard regression techniques and used for simulating the system dynamics are $\mu_{max} = 0.77$, $K_s = 0.214$ and $Y_{xs} = 0.40$. The results clearly demonstrate that the PINN provides a better fit to the experimental data points compared to the traditional regression-based approach. This improved accuracy in state estimation is achieved because PINNs integrate both sparse experimental data and fundamental process knowledge encoded in the system's governing equations. Unlike pure data-driven methods, which may struggle with limited or noisy datasets, PINNs leverage physical constrants to guyide learning, ensuring consisntesy with known bioprocess dynamics. The superiority of PINNs becomes even more evident in scenarios where fewer experimental data points are available or when modeling occurs in real-time rather than at the end of the process. Traditional regression-based methods typically require a complete dataset spanning the entire process to provide reliable parameter estimates. In contrast, PINNs can extract meaningful insights even from sparse or incomplete data by leveraging the underlying physics of the system.

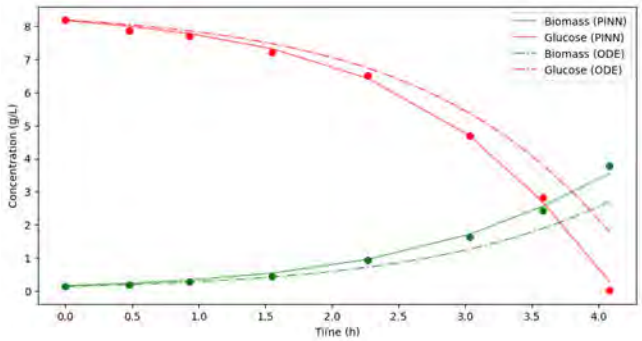



**Figure 5:** Simulation results of PINN and traditional regression approaches

## CONCLUSIONS

Accurate modeling of complex bioprocess systems is hindered by several key challenges. One of the primary issues is the sparse availability of experimental data, as generating comprehensive datasets can be costly and time. Additionally, traditional black-box data-driven methods often lack interpretability, making it difficult to understand and the underlying predictions or to derive actionable insights. "Furthermore, the inherently complex and highly non-linear nature of bioprocesses presents additional challenges, making it difficult to develop robust and accurate models that can effectively capture the intricate and dynamic behaviors involved. n this study, we aim to address these challenges by leveraging Physics-Informed Neural Networks (PINNs), a powerful tool for modeling and simulating the dynamics of complex bioprocesses. By integrating prior knowledge in the form of governing ODEs with sparse experimental data, PINNs offer a robust framework for accurate dynamic modeling and parameter estimation.

The results obtained from a batch bioreactor system highlight the ability of PINNs to capture intricate state-space dynamics, even when data is limited, and to provide interpretable, physics-consistent predictions. Furthermore, the application of PINNs in an inverse setup for estimating kinetic parameters underscores their versatility and effectiveness in addressing one of the key challenges in bioprocess modeling. Compared to conventional regression approaches, PINNs not only reduce the dependency on extensive datasets but also ensure adherence to the physical principles of the system, enhancing both reliability and interpretability.

This integration of machine learning and scientific principles represents a significant step toward more intelligent, data-driven solutions for industrial biotechnology. Future work will focus on extending this approach to more complex bioprocess systems, incorporating real-time data, and exploring adaptive learning strategies to further enhance the scalability and applicability of PINNs in dynamic modeling and control.

## ACKNOWLEDGEMENTS

This project has received funding from the European Union's Horizon 2020 research and innovation programme BIOINDUSTRY 4.0 (grant agreement 101094287)

## REFERENCES

1. Alonso Villela, S. M., Ghezal-Kraïem, H., Bouhaouala-Zahar, B., Bideaux, C., Aceves Lara, C. A., & Fillaudeau, L. Effect of temperature on the production of a recombinant antivenom in fed-batch mode. *Applied Microbiology and Biotechnology*, 105(3), 1017–1030 (2021). https://doi.org/10.1007/s00253-021-11093-5
2. Corrales, D. C., Villela, S. M. A., Bouhaouala-Zahar, B., Cescut, J., Daboussi, F., O'donohue, M., Fillaudeau, L., & Aceves-Lara, C. A. *Dynamic Hybrid Model for Nanobody-based Antivenom Production (scorpion antivenon) with E. coli CH10-12 and E. coli NbF12-10* (pp. 145–150) (2024). https://doi.org/10.1016/B978-0-443-28824-1.50025-9
3. Raissi, M., Perdikaris, P., & Karniadakis, G. E. Physics-informed neural networks: A deep learning framework for solving forward and inverse problems involving nonlinear partial differential equations. *Journal of Computational Physics*, *378*, 686–707 (2019). https://doi.org/10.1016/j.jcp.2018.10.045
4. Isoko, K., Cordiner, J. L., Kis, Z., & Moghadam, P. Z. Bioprocessing 4.0: A Pragmatic review and Future Perspectives. *Digital Discovery*, *3*(9), 1662–1681. (2024). https://doi.org/10.1039/d4dd00127c
5. Salvatore Cuomo, Vincenzo Schiano Di Cola, Fabio Giampaolo, Gianluigi Rozza, Maziar Raissi, and Francesco Piccialli., Scientific Machine Learning Through Physics–Informed Neural Networks: Where we are and What's Next. *J. Sci. Comput*. 92, 3 (2022) https://doi.org/10.1007/s10915-022-01939-z
6. Cheng, Y., Bi, X., Xu, Y., Liu, Y., Li, J., Du, G., Lv, X., & Liu, L. Artificial intelligence technologies in bioprocess: Opportunities and challenges. Bioresource Technology, 369, 128451 (2023). https://doi.org/10.1016/j.biortech.2022.128451
7. Khanal, S. K., Tarafdar, A., & You, S. Artificial intelligence and machine learning for smart bioprocesses. Bioresource Technology, 375, 128826 (2023). https://doi.org/10.1016/j.biortech.2023.128826

© 2025 by the authors. Licensed to PSEcommunity.org and PSE Press. This is an open access article under the creative commons CC-BY-SA licensing terms. Credit must be given to creator and adaptations must be shared under the same terms. See https://creativecommons.org/licenses/by-sa/4.0/



Systems & Control Transactions

**Research Article - Peer Reviewed Conference Proceeding**
ESCAPE 35 - European Symposium on Computer Aided Process Engineering
Ghent, Belgium. 6-9 July 2025
Jan F.M. Van Impe, Grégoire Léonard, Satyajeet S. Bhonsale,
Monika E. Polańska, Filip Logist (Eds.)

PSE PRESS

# Physics-Informed Automated Discovery of Kinetic Models

**Miguel Ángel de Carvalho Servia[a], Ilya Orson Sandoval[a], King Kuok (Mimi) Hii[b], Klaus Hellgardt[a], Dongda Zhang[c], Ehecatl Antonio del Rio Chanona[a*]**

[a] Imperial College London, Department of Chemical Engineering, London, United Kingdom
[b] Imperial College London, Department of Chemistry, London, United Kingdom
[c] The University of Manchester, Department of Chemical Engineering, Manchester, United Kingdom
* Corresponding Author: a.del-rio-chanona@imperial.ac.uk.

## ABSTRACT

The industrialization of catalytic processes requires reliable kinetic models for design, optimization, and control. While white box models are preferred for their interpretability, they demand considerable time and expertise for their construction. This research enhances the ADoK-S framework by embedding prior expert knowledge using mathematical constraints and integrating uncertainty quantification. The improved methodology consists of: (I) a genetic programming algorithm with constraints to produce physically coherent candidate models, (II) a sequential optimization algorithm for parameter estimation, (III) model selection based on the Akaike information criterion (AIC), and (IV) uncertainty quantification of the chosen model's predictions. The refined approach not only requires less data for discovering kinetic models but also ensures physically sound proposals. With the inclusion of uncertainty quantification, the method bolsters prediction reliability, and aids in safer system developments – crucial for decision-making and risk management. These improvements enhance data efficiency, model reliability, and position automated knowledge discovery as a real alternative to traditional kinetic modeling techniques.

**Keywords**: chemical reaction engineering, kinetic model generation, automated knowledge discovery, expert knowledge, uncertainty quantification.

## INTRODUCTION

Catalytic processes stand at the forefront of industrial advancement, and their significance is amplified in the face of climate change and the pressing need to reduce waste and enhance efficiency. In the journey from design to industrialization of catalytic processes, the role of reliable kinetic models is paramount, particularly in the development, optimization, and control of chemical reactors. These models act as the centerpiece of process understanding, enabling the refinement, and scaling of catalytic operations to meet environmental and economic goals.

Yet, the task of developing reliable kinetic models is fraught with challenges. The traditional approach has seen experts making closed-form, interpretable models, known as white box models, from the ground up, guided by physical principles and their domain-specific expertise. Despite their obvious appeal, these models are notoriously cumbersome and time-consuming to develop. As an alternative, the rise of black box models – such as neural networks and Gaussian processes – and hybrid models, which aim to integrate the interpretability of white box models with the flexibility of black box models, has been observed. Nevertheless, these models come with their own caveats, most notably the high volume of data needed for training, which is typically not available in kinetic studies. Moreover, their lack of interpretability raises safety and reliability concerns for deployment in safety-critical processes.

In response to these challenges, a new paradigm has been embraced within the community: automated knowledge discovery or symbolic regression. Symbolic regression, an emerging tool in the field of machine learning and data analysis, offers a novel approach to model discovery. Unlike traditional regression methods that fit predetermined models to data, symbolic regression autonomously searches for mathematical expressions that best describe observed datasets. This method utilizes evolutionary algorithms or other heuristic techniques to explore an extensive space of mathematical constructs, ranging from simple algebraic equations to complex

interactions embodying non-linear behaviors. Its ability to uncover underlying patterns and relationships without pre-specified model structures makes it particularly valuable in scientific research, where it can reveal previously unrecognized phenomena or propose novel theoretical models. As a result, symbolic regression is gaining traction across diverse scientific domains including kinetic modeling, providing a powerful tool for exploratory analysis and advancing our understanding of complex systems.

Techniques such as SINDy (Sparse Identification of Nonlinear Dynamics) and ALAMO (Automated Learning of Algebraic Models for Optimization) have emerged to solve symbolic regression, yet not without limitations. They often depend on significant, accurate prior assumptions about the model structure, are vulnerable to noisy data, and lack a justified model selection routine. These gaps in methodology led the way for the development of ADoK-S and ADoK-W (Automated Discovery of Kinetics using a Strong/Weak formulation of symbolic regression) frameworks, as introduced in the work of de Carvalho Servia et al. [1]. Despite the benefits of this approach, these frameworks were recognized to require enhancements, specifically an uncertainty quantification mechanism for model's predictions and the integration of expert knowledge via mathematical constraints to enrich and ease the model discovery process.

This paper introduces these novel enhancements to the ADoK-S framework, incorporating a sampling-based uncertainty quantification algorithm to evaluate the reliability of a chosen model's predictions – a critical component for the safe design, optimization, and control of processes. Additionally, by assimilating expert knowledge through mathematical constraints, the data requirements for the model discovery phase are reduced. The subsequent sections of this paper are organized as follows: Section 2 revisits the ADoK-S framework, and presents the new methods for uncertainty quantification and constraint handling; Section 3 discusses the case study employed to evaluate the enhanced algorithm, now termed physics-informed ADoK-S (PI-ADoK-S); Section 4 presents the results where PI-ADoK-S improves upon the performance of the unconstrained algorithm; and Section 5 concludes with the study's main contributions.

## METHODOLOGY

In prior works, ADoK-S was presented as a solution to the challenges of conventional modeling paradigms and positioned itself as an alternative to other automated knowledge discovery methodologies such as SINDy and ALAMO [1]. The ADoK-S framework is structured around three main components: (I) a genetic programming (GP) algorithm, which generates candidate models; (II) a sequential optimization algorithm designed for the estimation of parameters in promising models; and (III) a transparent and reasoned model selection routine that utilizes the Akaike Information Criterion (AIC) for determining the best-suited model (for a detailed discussion on the choice of AIC as the criterion of choice, readers are referred to de Carvalho Servia and del Rio Chanona [2]).

ADoK-S implements symbolic regression in its traditional form, often referred to as the strong formulation. This method necessitates the development of rate models to stem from rate measurements, which, being experimentally inaccessible, must be estimated. Following the outlined three-step process, ADoK-S first uncovers the optimal concentration profiles (i.e., a time dependent function), describing the dynamic evolution of species' concentrations in the system. These profiles are then differentiated to approximate the rate measurements of the reaction system. Subsequently, utilizing the same three steps, ADoK-S aims to discover kinetic rate models that best fit these estimated rates. The selected rate model is integrated and compared against the original concentration data. Should the model output prove unsatisfactory – owing to either contradictions of prior knowledge or poor model fitting – ADoK-S offers a closed-loop approach. The modeler can run an optimal experiment, as determined by a Model-Based Design of Experiments (MBDoE) scheme, which is then concatenated with the initial dataset. The Hunter-Reiner criterion is used to find the optimal experiment that maximizes the error between the prediction of two competing models (in this study, the competing models are the best two models found using our methodology) [3]. With the new experimental data, ADoK-S can be iterated, and the subsequent model output examined. This iterative process can continue as required by the modeler or until the experimental budget is exhausted. For a detailed explanation of the ADoK-S algorithm, readers are referred to de Carvalho Servia et al. [1].

Despite favorable results, ADoK-S had its own limitations. Particularly, its lack of a direct and flexible mechanism for injecting prior knowledge through mathematical constraints during the model generation phase, and an absence of a quantifiable measure of the uncertainty in the predictions of the selected rate model. The following subsections delve into these newly incorporated features that have led to the development of PI-ADoK, an improved version of the ADoK-S framework. Figure 1 provides a detailed and visual representation of the workflow of PI-ADoK.

### Inclusion of Mathematical Constraints

The effectiveness of integrating mathematical constraints within a symbolic regression framework has been a subject of debate in the literature. On one hand, studies such as Kronberger et al. [4] indicate that constraints

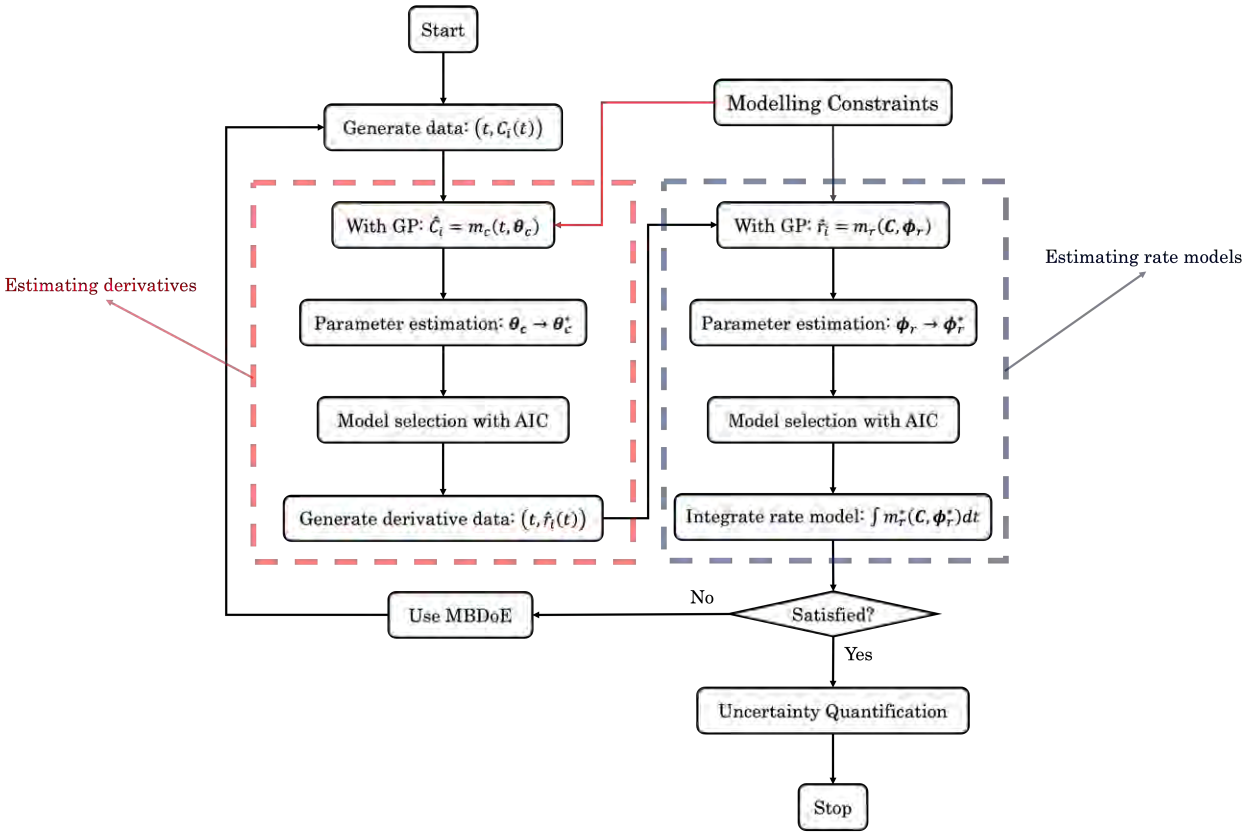



**Figure 1:** Illustration of the PI-ADoK framework, emphasizing its two main tasks: derivative estimation (red box) and rate model generation (blue box). The derivative estimation phase begins with genetic programming to generate candidate concentration models, followed by parameter estimation and model selection based on AIC. These selected models are then numerically differentiated to approximate reaction rates. In the rate-modeling phase, the estimated rates are used to construct kinetic expressions, which are further refined through parameter estimation and model selection. If the current model is insufficient, Model-Based Design of Experiments (MBDoE) suggests new experiments to improve data quality, iterating until a reliable model is obtained. Finally, uncertainty quantification is performed to assess predictive reliability of the best model. Constraints are applied at each step to guide the genetic programming algorithm toward physically meaningful models.

may lead to higher prediction errors on both training and testing datasets. The authors suggest that this could be attributed to slower convergence or a more rapid loss of diversity. However, they also note that the benefits of including constraints may become more relevant in scenarios with higher noise levels. Following up on this, the same authors published Haider et al. [5], investigating case studies with higher noise. Their findings concluded that constraints could aid in identifying better models, characterized by lower prediction errors, though the differences were not statistically significant compared to cases without constraints. On the other hand, other studies like Błądek and Krawiec [6] have demonstrated that in smaller datasets, the inclusion of mathematical constraints can lead to statistically significant improvements compared to a GP algorithm without constraints.

Given the ambiguity in the literature, the necessity for a flexible method to incorporate prior knowledge (which can be extensive in some kinetic studies), and the intuition that including constraints should improve the physical soundness of proposed models, PI-ADoK was developed and benchmarked against the original ADoK-S framework. The integration of mathematical constraints within the GP algorithm is nuanced by a delicate balance of exploration versus exploitation, and the preservation of diversity. GP typically operates in vast search spaces, and constraints can reduce this space and facilitate the exploitation aspect of the argument. However, overly stringent constraints risk premature convergence to suboptimal solutions. Furthermore, maintaining diversity in the population while respecting constraints is a challenging task, that often also leads to early convergence to suboptimal solutions.

With these considerations in mind, our approach to integrating constraints is intentionally straightforward. In PI-ADoK, constraint violation is treated as a penalty in the

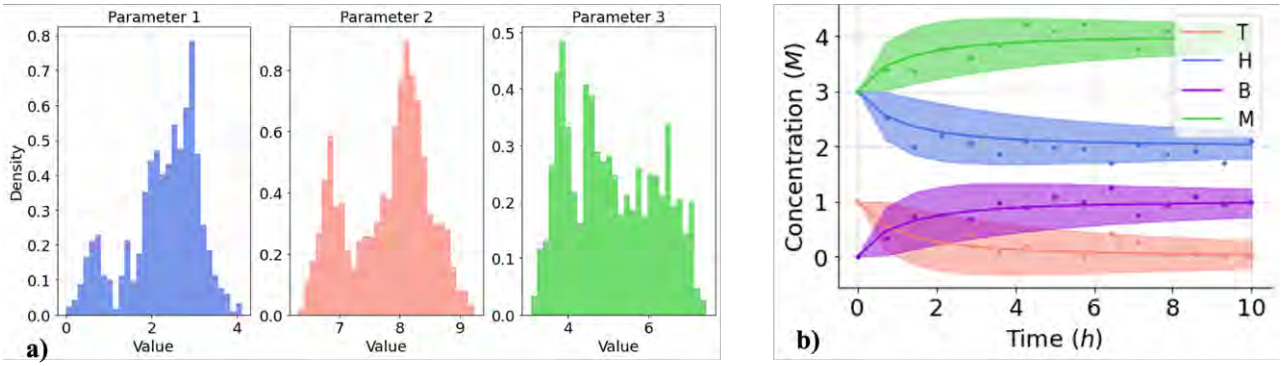



**Figure 2: a)** Histogram of the posterior distribution of the kinetic parameters of the discovered model; **b)** Plot of the in-silico data generated from the seventh experiment along with the average prediction and prediction intervals calculated from 5000 samples, where *T*, *H*, *B* and *M* represent toluene, hydrogen, benzene and methane, respectively.

calculation of a model's performance metric. Specifically, the GP algorithm operates similarly to a standard GP algorithm, with a crucial modification: each constraint acts as a test for candidate models. If a model satisfies the constraints, its performance metric is simply its prediction error. In contrast, if a model fails to meet a constraint, its performance metric is penalized based on the degree of constraint violation and a predefined hyperparameter. This inclusion of hyperparameters allows the modeler to fine-tune the algorithm, ensuring the search space is neither overly constrained, which could yield poor models, nor under-constrained, which could yield physically implausible models.

### Uncertainty Quantification

In uncertainty quantification, various methods range from simpler approximations like Laplace approximations and sigma points to more complex sampling algorithms like Metropolis-Hastings (MH) and Hamiltonian Monte Carlo (HMC). The choice depends on balancing computational efficiency with accuracy. For our purposes, where accuracy is prioritized, we have chosen the MH algorithm for its suitability in propagating uncertainty in kinetic models. MH handles complex, non-linear distributions well, does not require gradient information, and offers flexibility in proposal distributions, making it adaptable for complex models and high-dimensional spaces. While computationally intensive and requiring careful tuning, MH's adaptability and convergence make it a robust choice for uncertainty quantification in complex systems.

The MH algorithm is a Markov Chain Monte Carlo method designed to sample from a complex target distribution, such as a posterior distribution in Bayesian inference. Starting from an initial state, the algorithm iteratively generates a candidate sample from a proposal distribution. It then computes an acceptance probability based on the ratio of the target densities (adjusted by the proposal densities) to ensure detailed balance. If a random draw from a uniform distribution is less than this acceptance probability, the candidate becomes the new state; otherwise, the current state is retained. Over many iterations, this process produces a chain of samples that, after discarding a burn-in period, approximates the target distribution accurately. For more details on MH, see Chib and Greenberg [7].

## CASE STUDY

The case study used for the performance analysis of PI-ADoK is the catalytic toluene hydrodealkylation to benzene, where toluene ($C_6H_5CH_3$) and hydrogen gas ($H_2$) is transformed to benzene ($C_6H_6$) and methane ($CH_4$). The reaction is shown below:

$$C_6H_5CH_3 + H_2 \rightleftharpoons C_6H_6 + CH_4. \quad (1)$$

The kinetic rate model that describes the evolution of the concentrations of $C_6H_5CH_3$, $H_2$, $C_6H_6$ and $CH_4$ through time is shown below. This expression has been directly borrowed from Fogler [8].

$$r = -\frac{dC_T}{dt} = -\frac{dC_H}{dt} = \frac{dC_B}{dt} = \frac{dC_M}{dt} = \frac{K_A C_T C_H}{1+K_B C_B + K_C C_T}. \quad (2)$$

In Equation (2), $C_T$, $C_H$, $C_B$ and $C_M$ represent the concentration of reactants toluene and hydrogen, and of products benzene and methane, respectively. The kinetic parameters of the kinetic rate model are represented by $K_i$ where $i \in [A, B, C]$.

The computational experiments, chosen randomly from a $2^k$ factorial design, are run with the following initial conditions (in molar units): ($C_T(t=0)$, $C_H(t=0)$, $C_B(t=0)$, $C_M(t=0)$) $\in$ {(1, 8, 2, 3), (5, 8, 0, 0.5), (5, 3, 0, 0.5), (1, 3, 0, 3), (1, 8, 2, 0.5)}. For each experiment, the concentration of the reactant and products are recorded 15 times, at evenly spaced intervals between time $t_0$=0 h and $t_f$=10 h. The kinetic parameters were defined as: $K_A$=2 $M^{-1}$ $h^{-1}$,

$K_B$=9 $M^{-1}$ and $K_C$=5 $M^{-1}$.

Gaussian noise is added to the in-silico measurements to simulate a realistic chemical system. The added noise had zero mean and a standard deviation of 0.2 for $C_T$, $C_H$, $C_B$ and $C_M$. This noise addition allows the approximation of the response of a real system.

## RESULTS AND DISCUSSION

Our primary objective was to evaluate if the implementation of constraints could enhance the performance of our discovery algorithm, PI-ADoK-S. For this purpose, we introduced specific constraints at two different stages: the estimation of derivatives and the estimation of rate models. During the derivative estimation phase, the constraints included are: (I) ensuring that the proposed concentration models align with the accurately measured initial conditions of the system, (II) requiring concentration models to converge to a concentration value to simulate equilibrium, (III) ensuring that concentration models do not predict negative concentrations to maintain physical plausibility, and (IV) specific to our case study, ensuring reactant concentrations always decrease while product concentrations always increase. In the rate model estimation stage, we applied the following constraints: (I) ensuring the rate of consumption (or production) of reactants (or products) is consistently negative (or positive), and (II) that these rates should always be decreasing (or increasing) as per the specifics of our case study.

To assess the efficacy of these constraints, we conducted a benchmarking study between the unconstrained ADoK-S and the constrained PI-ADoK-S. Assuming an unlimited experimental budget, we ran as many extra experiments as required to uncover the data-generating rate model presented in Eq. (2) (the extra experiments are determined by solving the Hunter-Reiner criterion – a MBDoE technique for optimal model discrimination [1]). Due to the inherent stochasticity of genetic programming and its sensitivity to initial seeding, we conducted three independent runs. From these, we observed that ADoK-S required 16 experiments to identify the ground-truth model, whereas PI-ADoK-S needed only 10 – representing a 37.5% reduction in experimental effort. However, further investigations – such as ablation studies and exploring the impact of hyperparameters in the constraint penalty – would provide a more in-depth understanding of the methodology itself.

## CONCLUSIONS

This paper introduces PI-ADoK-S, an advancement of the ADoK-S algorithm, featuring the integration of mathematical constraints for prior knowledge injection and an uncertainty quantification method using the Metropolis-Hastings algorithm. The inclusion of constraints streamlines the genetic programming algorithm, significantly reducing the experimental burden by 37.5% on average, though further testing is beneficial for deeper understanding of these results. For instance, additional testing could examine the impact of hyperparameters, individual constraints, and initial DoE strategies on the performance of PI-ADoK. The uncertainty quantification aspect enhances the understanding of the reliability of a certain model's predictions, which can be used to guide future investigative efforts. These improvements underscore PI-ADoK-S as a significant upgrade over ADoK-S, both in terms of efficiency and depth of analysis, marking it as a valuable tool for experts in kinetic modeling and chemical process research.

## ACKNOWLEDGEMENTS

This work was supported by the EPSRC Centre of Doctoral Training for Next Generation Synthesis & Reaction Technology (rEaCt) funding grant EP/S023232/1.

## REFERENCES

1. Miguel Ángel de Carvalho Servia, Ilya Orson Sandoval, King Kuok (Mimi) Hii, Klaus Hellgardt, Dongda Zhang, Ehecatl Antonio del Rio Chanona. The automated discovery of kinetic rate models – methodological frameworks. Digit Discov 3(5):954–968 (2024) https://doi.org/10.1039/D3DD00212H
2. Miguel Ángel de Carvalho, Ehecatl Antonio del Rio Chanona. Model Structure Identification. In: Machine Learning and Hybrid Modelling for Reaction Engineering, Ed: Dongda Zhang, Ehecatl Antonio del Rio Chanona. Royal Society of Chemistry (2023).
3. William Hunter, Albey Reiner. Designs for Discriminating Between Two Rival Models. Technometrics. 1965 Aug;7(3):307-23.
4. Gabriel Kronberger, Fabricio Olivetii de França, Bogdan Burlacu, Christian Haider, Michael Kommenda. Shape-Constrained Symbolic Regression – Improving Extrapolation with Prior Knowledge. Evol Comput 30(1): 75-98 (2022) https://doi.org/10.1162/evco_a_00294
5. Christian Haider, Fabricio Olivetti de França, Bogdan Burlacu, Gabriel Kronberger. Shape-constrained multi-objective genetic programming for symbolic regression. Applied Soft Computing 132: 109855 (2023) https://doi.org/10.1016/j.asoc.2022.109855
6. Iwo Błądek, Krzysztof Krawiec. Solving symbolic regression problems with formal constraints. In: GECCO '19: Proceedings of the Genetic and Evolutionary Computation Conference, Ed: Manuel

López-Ibáñez. Association for Computing Machinery (2019)
7. Siddhartha Chib, Edward Greenberg. Understanding the Metropolis-Hastings Algorithm. Am Stat 49(4):327-335 (1995) https://doi.org/10.2307/2684568
8. H. Scott Fogler. Elements of Chemical Reaction Engineering. Pearson (2016).

© 2025 by the authors. Licensed to PSEcommunity.org and PSE Press. This is an open access article under the creative commons CC-BY-SA licensing terms. Credit must be given to creator and adaptations must be shared under the same terms. See https://creativecommons.org/licenses/by-sa/4.0/



Systems & Control Transactions

**Research Article Peer Reviewed Conference Proceeding**
ESCAPE 35 European Symposium on Computer Aided Process Engineering
Ghent, Belgium. 6-9 July 2025
Jan F.M. Van Impe, Grégoire Léonard, Satyajeet S. Bhonsale,
Monika E. Polańska, Filip Logist (Eds.)

PSE PRESS

# Empowering LLMs for Mathematical Reasoning and Optimization: A Multi-Agent Symbolic Regression System

**Shaurya Vats[a], Sai Phani Chatti[a*], Aravind Devanand[a], Sandeep Krishnan[a], and Rohit Karanth Kota[a]**

[a] Siemens Technology and Services Pvt. Ltd
* Corresponding Author: Bhanu-venkata.chatti@siemens.com.

## ABSTRACT

Understanding data with complex patterns is a significant part of the journey toward accurate data prediction and interpretation. The relationships between input and output variables can unlock diverse advancement opportunities across various processes. However, most AI models attempting to uncover these patterns are not explainable or remain opaque, offering little interpretation. This paper explores an approach in explainable AI by introducing a multi-agent system (MaSR) for extracting equations between features using data. We developed a novel approach to perform symbolic regression by discovering mathematical functions using a multi-agent system of LLMs. This system addresses the traditional challenges of genetic optimization, such as random seed generation, complexity, and the explainability of the final equation. We utilize the in-context learning capabilities of LLMs trained on vast amounts of data to generate accurate equations more quickly. This study presents research on expanding the reasoning capacities of large language models alongside their mathematical understanding. The paper serves as a benchmark in understanding the capabilities of LLMs in mathematical reasoning and can be a starting point for solving numerous complex tasks using LLMs. The MaSR framework can be applied in various areas where the reasoning capabilities of LLMs are tested for complex and sequential tasks. MaSR can explain the predictions of black-box models, develop data-driven models, identify complex relationships within the data, assist in feature engineering and feature selection, and generate synthetic data equations to address data scarcity, which are explored as further directions for future research in this paper.

**Keywords**: Symbolic regression, Large Language Models, Multi-Agent Systems

## INTRODUCTION

The foundation of any machine learning algorithm lies in understanding the mathematics behind it. The entire field of artificial intelligence is built upon mathematical principles, using data as its starting point. Accurately uncovering and interpreting relationships within data is a critical step for advancing tasks in data science and its applications. These relationships often take the form of equations that serve as governing rules, applicable across a wide range of domains, including simulations and industrial processes. To address this critical challenge, we developed a multi-agent system using large language models (LLMs) to effectively uncover these mathematical relationships, enabling advancements across various domains such as simulations and industrial processes.

## SYMBOLIC REGRESSION: AN OVERVIEW

One powerful technique for discovering such relationships is Symbolic Regression[1,2], which identifies mathematical expressions that best describe the relationships between variables in a dataset. This technique can be implemented through various approaches, including genetic optimization[1,2], reinforcement learning[5], recurrent neural networks (RNNs)[5], generative adversarial networks (GANs)[6], and emerging methods. Despite differences in implementation, these methods follow a common set of steps that define symbolic regression as a process: finding, evaluating, and refining relationships to generate interpretable equations.

Symbolic Regression (SR) plays a crucial role in Process Engineering by enabling the discovery of mathematical models that accurately represent complex chemical processes. In process systems, understanding the underlying relationships between variables is essential for optimization, control, and design. SR offers a powerful tool for automatically deriving these models from experimental or simulated data without requiring prior knowledge of the system's functional form. This capability is particularly beneficial in fields like chemical engineering, where processes can be highly nonlinear, dynamic, and data-intensive. By using SR, engineers can gain insights into the fundamental behavior of a process, leading to improved efficiency, better decision-making, and enhanced predictive capabilities for process design and operation.

## FRAMING SYMBOLIC REGRESSION AS A SEARCH PROBLEM

Symbolic regression can be framed either as a learning task[4] or a search problem, where the objective is to identify the optimal equation or parameters within the domain of possibilities. By leveraging **large language models (LLMs)**, the symbolic regression process can be significantly enhanced. LLMs, with their extensive domain knowledge and in-context learning capabilities, have the potential to act as the "brain" of the process, streamlining and optimizing the discovery of symbolic equations. This approach shifts reliance from purely data-driven metrics to a more knowledge-driven framework. The domain of equations can be constrained by the context of the problem statement and the space within which the equation is being searched.

## INTRODUCTION TO MASR FRAMEWORK

To explore this potential, we introduce **MaSR: Multi-Agent Symbolic** Regression, a novel framework that employs LLMs to execute and coordinate the various steps of symbolic regression. In this system, multiple agents, each powered by an LLM, collaborate to handle tasks such as searching for relationships, optimizing equations, and explaining results. By integrating LLMs as the core of the process, MaSR not only automates symbolic regression but also provides interpretable and robust equations for practical applications.

## PROBLEM AND EXISTING SOLUTIONS

Discovering relationships and hidden patterns within datasets is essential for optimization, prediction, forecasting, and other applications.

### Challenges with Existing Models

- The models commonly used for these purposes are often black-box models.
- They are not always well-suited to the specific data being used, as they rely on a limited set of predefined models.
- There is often no mathematical relationship available to effectively link features for tasks like feature selection, synthetic data generation, or feature engineering.
- A lack of physics-based or domain-specific equations ensures constraints are not always adhered to in applications.
- Many transparent models available today are nonlinear and difficult to interpret.
- Traditional models require large amounts of data to perform predictions and learn from the data effectively.

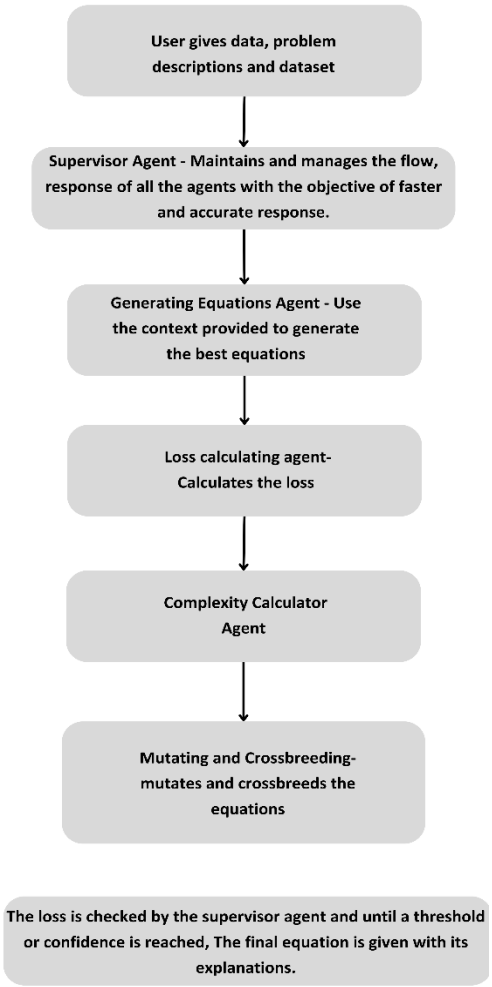



**Figure 1.** Step-wise process of MaSR framework.

Our goal is to derive mathematical equations and

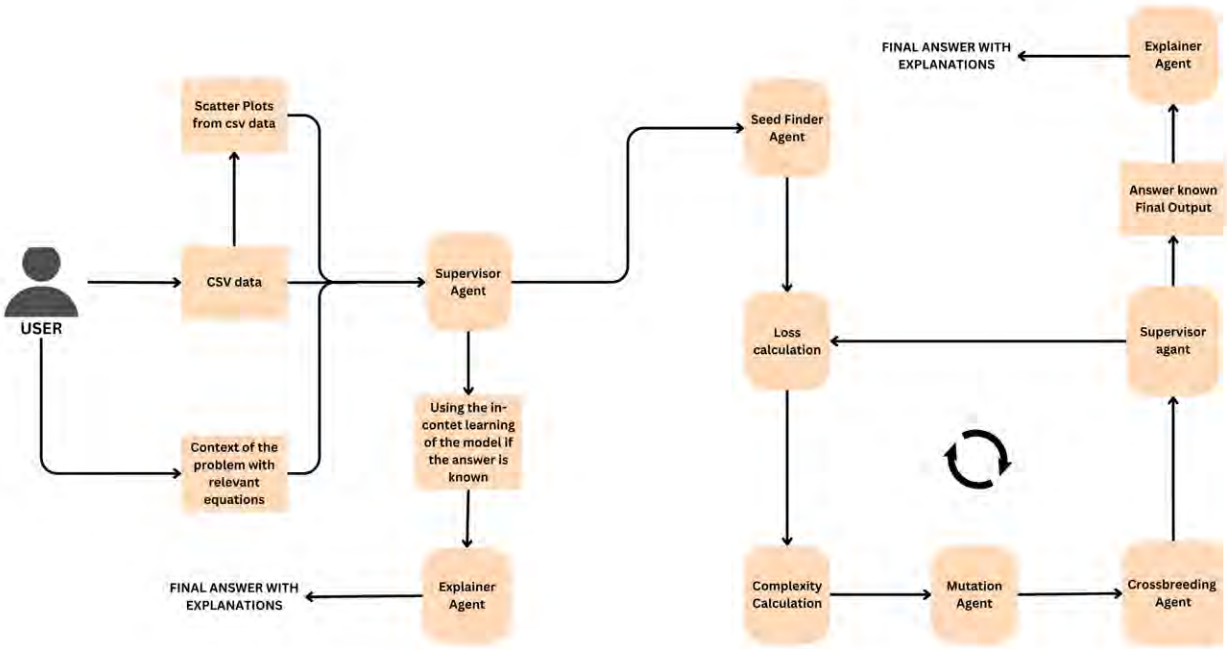



**Figure 2**: This image illustrates the complete workflow of a multi-agent symbolic system. The process begins with the user providing context and a CSV file to the system. The CSV data is transformed into scatter plots, which are then passed to the supervisor agent along with the original CSV data and user-provided context. If the supervisor agent already has knowledge of a relevant equation within its in-context learning capabilities, it directly returns the equation. Otherwise, the data and context are forwarded to the seed finder agent, followed by the loss finder agent, the complexity calculator agent, and finally the mutation and cross-breeding agent. Throughout the process, the supervisor agent continuously evaluates the equation against a loss threshold. Once an equation meets the specified conditions, it is passed to the explanation module, which provides detailed explanations for the equation. The final output includes both the optimal equation and its corresponding explanations.

relationships from data, creating an explainable white-box model for various applications.

## Existing Solutions and Their Limitations

The problem has been addressed using genetic optimization, with several variations and libraries available, including PySR[1], gplearn[2], and SINDy[9]. However, these libraries have the following limitations[8]:

- Random generation of seed functions.
- Managing equation complexity.
- Ensuring the explainability of the final equation.
- Lack of domain-specific knowledge integration.

These limitations are being tackled separately by different methods, such as Pareto-Symbolic Regression[10] and Symbolic GPT[4].

However, no single method currently solves all these problems simultaneously, particularly the challenge of making the equations explainable

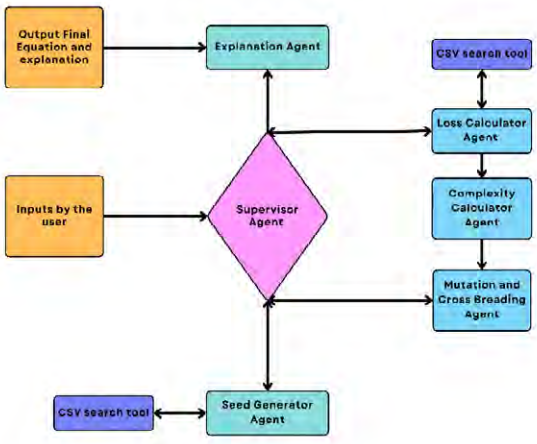



**Figure 3.** Interaction between different agents of MaSR Framework.

## MASR FRAMEWORK

The MaSR framework divides the task into multiple steps, with each step performed by a dedicated agent equipped with specific tools and knowledge bases. These agents collaborate by discarding less accurate or less insightful equations based on metrics such as mean squared error and equation complexity.

The process mimics genetic optimisation and is designed entirely using LLMs to derive relationships from the data.

### Foundation of the MaSR Framework

The framework is built upon the reasoning capabilities of large language models (LLMs), leveraging their in-context learning. Its architecture relies on the in-context learning of LLMs and their ability to effectively identify the seed generation agent. The prompts used in each agent provide the necessary context and instructions. A **sample prompt** from one of the agents (seed finder) is provided below:

"""

### Task:

You are a mathematical equation generator. Your goal is to derive the accurate and complex equations that describe the relationship between the target variable ['target_variable'] and the independent variables ['independent_variables'], based on the provided scatter plot,csv file data and domain knowledge.

### Context:

You have knowledge of ['domain'], including relevant physical and mathematical principles such as dimensional analysis and proportionality. You also have access to:

Data points from a **CSV file** that illustrate the values of all the variables.

**scatter plots** representing the relationship between the independent variables and the target variable.

Equations: ['Equations'].

Available operators: ['Operators'].

Dimensional information: ['Dimensions'].

### Instructions:

1. **Analyze the Data**: Start by analyzing the scatter plot and the data points from the CSV file to understand the relationships between the target variable and the independent variables.

2. **Use Domain Knowledge**: Leverage your understanding of ['domain']}, including fundamental physical and mathematical concepts like distance calculation, to guide your equation formulation.

3. **Generate Equations**: If no existing equation is found, generate up to ['number_of_functions'] possible equations using the operators provided. Start with basic forms and build progressively more complex equations. Incorporate the general proportional relations and dimensional constraints provided.

### Output:

Provide the final ['number_of_functions'] functions as mathematical equations that best describe the relationship between ['target_variable'] and ['independent_variables'].

If an existing equation from the domain of ['domain'] is found, present it as the final solution.

### Output Format:

Return the entire mathematical equations as strings, formatted like this: `"f1(x) = ..."`, `"f2(x) = ..."`, etc as complex and creative as possible.

You must not output python code and must not use mnemonics in the equation it must be from ['target_variable']

and ['independent_variables'].

"""

### Agents and Their Roles

- Seed Function Generator Agent: Generates candidate equations based on the relationships between target and independent variables using the provided data and context.
- Loss Calculator Agent: Evaluates each eqution by calculating the loss to determine its fit to the data.
- Complexity Calculator Agent: Assesses and scores

the complexity of each equation, prioritising simpler models.

- Equation Mutating Agent: Modifies equations to reduce loss and complexity, aiming to improve accuracy.
- Supervisor Manager Agent: Manages the entire process, ensuring effective collaboration among agents to identify the best equation.
- Explainer Agent: Provides detailed insights into the final equation's behaviour and the relationships between the target and independent variables across the domain.

### Framework Overview

The MaSR framework employs a systematic multiagent system of LLMs to discover accurate mathematical relationships from data. These relationships can be utilised for modelling, feature engineering, and feature selection. The framework addresses limitations in existing methods and includes the following key components:

- Hierarchical Structure: A supervisor agent oversees the process, ensuring proper flow of outputs between agents and delivering the final equation with its explanation.
- Agent Responsibilities: Agents handle specific tasks such as seed function generation, loss calculation, complexity evaluation, mutation, and explanation.

### Explainability from MaSR?

The framework explains the final equation by breaking down its terms and coefficients. A simplified example is provided below to demonstrate the output of the MaSR framework:

'''

*To understand this equation, let's define its components first.*
*MD_power: This term represents some measure that depends only on MD, whose value ranges from 3 to 95.*
*SG130: This term stands for another measure depending solely on SG130, ranging from 10 to 570.*
*TemperatureMD: This variable is equal to the expression* (3 * MD_power + 0.845 * SG130) x 0.118 + 36.375), *where MD_power and SG130 take on any values within their respective ranges.*
*Now, let's analyze the equation based on the above definitions.*

*Firstly, observe the multiplicative factor (3) associated with MD_power; since it has a positive sign, increasing MD_power results in higher values assigned to TemperatureMD. Consequently, when working within the context of this problem, larger MD_power values lead to greater temperatures.*
*Next, see the additive component (0.845) linked to SG130; because this term also carries a positive sign, raising SG130 leads to increased values attributed to TemperatureMD. Therefore, more significant values of SG130 imply hotter conditions according to the problem definition.*

*Note the coefficient (0.118) applied directly onto the sum of the previous two terms. Since this constant is positive too, enlarging the outcome originating from the sum generates amplified values of TemperatureMD. Hence, augmenting the total output by a substantial quantity raises the observed temperature.*
*Lastly, consider the additive term (+36.375). Regardless of changes in either MD_power or SG130, this constant consistently contributes a minimum of 36.375 toward the calculation of TemperatureMD.*
*In conclusion, the given equation defines the interplay among factors affecting certain environments' temperatures, namely MD_power and SG130. By raising both MD_power and SG130, the resulting temperature increases proportionally due to the additive properties present in the equation.*
'''

## RESULTS

The paper primarily aims to introduce a novel approach to performing a traditional method. The framework can be adapted with new agents, data sources, and methods to address specific problems. The current architecture was tested against various applications and compared with traditional genetic optimization methods.

1. We evaluated the performance of genetic optimization methods such as gplearn and MaSR to derive the equations governing the physics of industrial chillers. These equations were used as a loss function of ANNs to create a Physics Informed Neural Network (PINNs). Our key observations were as follows:

- The framework's performance, in terms of metrics like the $R^2$ score, was 2% better than the traditional methods.
- The initial equation selected by the seed generation agent adhered to the physics of cooling in chillers.
- The MaSR framework converged to the final equation more quickly and was effective even with a limited or scarce dataset.
- Combining MaSR with traditional genetic

optimization algorithms can enhance the overall performance of Symbolic Regression.

- The final equation derived by MaSR provided an interpretable explanation and aligned with known proportionalities.

2. We validated the framework using 20 Feynman equations, successfully identifying all of them based on the in-context learning capabilities of the underlying models. This method can accurately determine the governing physical equation when it is uncertain. In contrast, other genetic optimization methods without an embedded learning mechanism fail in this regard.

## KEY ADVANTAGES OF MASR

The main differences between our framework and existing solutions are as follows:

Utilizing LLMs: Utilises the in-context knowledge base and domain-specific expertise of LLMs to generate accurate equations quickly, even with sparse data.

- Explainability: Provides detailed explanations and insights from the final equations, fostering transparency and interpretability.
- Guided Seed Generation: Addresses the issue of random seed generation in current methods by guiding the process toward more accurate equations swiftly and efficiently.
- Simplified Complexity: Ensures the final equations are concise and easy to understand, enhancing their explainability and usability.

## CHALLENGES AND LIMITATIONS

The major challenge we faced during the implementation process was accurately enabling the agents to collaborate efficiently while adhering to the workflow. We were able to partially address this by using well-crafted prompts and improving the conditions under which an agent reaches out to another. However, the issue of agents fully understanding and consistently maintaining the workflow for complex tasks remains unresolved and requires further attention.

Another significant issue we encountered was stopping the process when agents reached optimal conditions. To address this, a clear stopping criterion must be defined and strictly enforced through implementation.

In this study, the large language models (LLMs) we explored ranged from multimodal models like Gemini to GPT-based models such as GPT-3.5-Turbo and open-source models like LLaMA 3. We chose to focus on Gemini due to its ability to effectively interpret and process data. To support this, we utilized a combination of Retrieval-Augmented Generation (RAG), structured data in prompts, and scatter plots as data sources. However, passing numerical data to LLMs remains an area that requires significant attention. Ensuring that LLMs can effectively use numerical data in reasoning tasks was a primary objective of this study.

The CrewAI framework we tested for open-source models did not yield the desired results, leading us to switch to LangGraph. We also implemented the system using a structured workflow and conditions crafted for LLMs. Limitations we faced during the implementation included the token size restrictions of both open-source and GPT models, as well as subscription-related challenges with GPT.

## CONCLUSION

This framework explores the combination of logical reasoning with data-driven processes, testing the capabilities of LLMs in reasoning tasks and creating explainable, insightful procedures. The complex tasks performed by the LLMs demonstrate that the system can serve as a starting point for executing intricate

reasoning and tasks requiring coordination. Notably, the multi-agent symbolic regression represents a significant step towards understanding LLM behaviour in such processes.

The method shows promising performance in scenarios where the physics of the system is unknown or when the governing equations are dictated by physical laws embedded in the data. It also examines the reasoning and data interpretation capabilities of LLMs, revealing a key limitation: the inability to fully integrate numerical data into their reasoning and responses. Enhancing the suitability for these tasks involves presenting data in various forms, such as CSV files stored as vector databases, screenshots of data included in prompts, or scatter and insight plots.

The architecture of the supervisor agent has proven to be valuable in aiding complex reasoning, as evidenced by our experiments. Frameworks like CrewAI and LangGraph assist in creating multiagent systems, but the use of a set of LLMs as agents—designed to conditionally exchange responses with other agents and collectively decide on final outputs—has shown promising results. With minor adjustments to prompts and structure, this framework can be adapted to other complex tasks involving data analysis. It holds significant potential across the diverse applications of symbolic regression in today's world.

## REFERENCES

1. Interpretable Machine Learning for Science with PySR and SymbolicRegression.jl https://arxiv.org/abs/2305.01582

2. gplearn-https://github.com/trevorstephens/gplearn
3. In-Context Symbolic Regression: Leveraging Language Models for Function Discovery https://arxiv.org/html/2404.19094v1
4. SmbolicGPT: A Generative Transformer Model for Symbolic Regression https://arxiv.org/abs/2106.14131
5. Generating Symbolic Reasoning Problems with Transformer GANshttps://arxiv.org/abs/2110.10054
6. Langgraph https://www.langchain.com/ langgraph
7. A Comparison of Recent Algorithms for Symbolic Regression to Genetic Programming https://arxiv.org/html/2406.03585v1
8. Discovering governing equations from data: Sparse identification of nonlinear dynamical systems https://arxiv.org/abs/1509.03580
9. AI Feynman 2.0: Pareto-optimal symbolic regression exploiting graph modularityhttps://arxiv.org/abs/2006.10782

© 2025 y the authors. Licensed to PSEcommunity.org and PSE Press. This is an open access article under the creative commons CC-BY-SA licensing terms. Credit must be given to creator and adaptations must be shared under the same terms. See https://creativecommons.org/licenses/by-sa/4.0/



Systems & Control Transactions

**Research Article - Peer Reviewed Conference Proceeding**
ESCAPE 35 - European Symposium on Computer Aided Process Engineering
Ghent, Belgium. 6-9 July 2025
Jan F.M. Van Impe, Grégoire Léonard, Satyajeet S. Bhonsale,
Monika E. Polańska, Filip Logist (Eds.)

PSE PRESS

# Application of Artificial Intelligence in process simulation tool

**Nikhil Rajeev[a], Suresh Jayaraman[a*], Prajnan Das[b], Srividya Varada[a]**

[a] AVEVA Group Ltd, United States of America
[b] Cognizant Technology Solutions U.S. Corporation, United States of America
* Corresponding Author: suresh.jayaraman@aveva.com

## ABSTRACT

Process engineers in the Chemical and Oil & Gas industries extensively use process simulation for the design, development, analysis, and optimization of complex systems. This study investigates the integration of Artificial Intelligence (AI) with AVEVA™ Process Simulation (APS), a next-generation commercial simulation tool. We propose a framework for a custom chatbot application designed to assist engineers in developing and troubleshooting simulations. This chatbot application utilizes a custom-trained model to transform engineer prompts into standardized queries, facilitating access to essential information from APS. The chatbot extracts critical data regarding solvers and thermodynamic models directly from APS to help engineers develop and troubleshoot process simulations. Furthermore, we compare the performance of our custom model against OpenAI technology. Our findings indicate that this integration significantly enhances the usability of process simulation tools, promoting more innovative and cost-effective engineering solutions.

**Keywords**: Artificial Intelligence, Process Design, Machine Learning, Chatbot

## INTRODUCTION

Process simulation is a model-based representation of chemical, physical, and biological processes to analyze, optimize, and design. Process simulation tools are widely used in Chemical, and Oil & Gas industries in various phases of a project. Process simulation can enable the transformation of process engineering as part of the digital twin, an important building block of digital transformation [1]. Simulation and modeling can help accelerate the design cycle of chemical processes. The rapid evolution of Artificial intelligence (AI) and Machine Learning (ML) technologies has significant implications across various domains including engineering. AI and ML technologies have been widely used in various applications of chemical engineering such as process modeling, simulation, control, classification, fault detection and diagnosis [2]. Recent research has focused on integrating AI with process simulation tools to enhance design efficiency [3]. Stergiou et al discuss combining ML algorithms with process simulation tool to optimize plant design parameters, resulting in more efficient and cost-effective chemical production [4]. The application of AI techniques such as Artificial Neural Networks (ANN) is used to model the operation of hydrogen production system [5].

A chatbot is a computer-based program that simulates human conversation with an end user, and they are usually built using AI and Natural Language Processing (NLP) with the goal of interpreting human questions and automating customized responses [6]. ChatGPT (Chat Generative Pre-Trained Transformer) is a recently developed conversational chatbot created by OpenAI [7], and it uses Natural Language Processing (NLP) to generate human-like responses to user input.

This research paper discusses applications of AI in a next-generation process simulation tool using both custom trained model and OpenAI model to answer questions based on the process simulation. The performance of these models is quantified and compared using different types of similarity scores. This innovative approach of integrating AI technology with a next generation process simulation tool is expected to transform AVEVA™ Process Simulation (APS) by making it more user-friendly and efficient, leading to novel and cost-effective solutions in process engineering.

## METHODOLOGY

The architecture of a chatbot encompasses its foundational structure and design principles. It outlines how the chatbot interprets and processes text, influenced by various factors including the domain, use case, type of chatbot, and prompts used [8]. Models in ChatBot utilize NLP engines to process user input and transform it into machine-readable formats; however, traditional NLP engines struggle to fully comprehend human language. To address this limitation, large language models (LLM) were developed to enhance AI's understanding of natural language, enabling the generation of more realistic and coherent human-like text.

### Chatbot architecture

The architecture for implementing the chatbot is illustrated in Figure 1. User input is processed by either a LLM or NLP, which may be a custom-trained model or a pre-trained one, such as OpenAI's Generative Pre-Trained Transformer (GPT) or Google's BERT, LaMDA, and PaLM [9]. The chatbot leverages the LLM to extract relevant information from unstructured textual data through techniques like text classification and entity recognition.

Text classification is essential for identifying user intents by categorizing messages into classes such as inquiries or requests, which guides the chatbot's response strategy. Entity recognition enhances this process by extracting specific information, such as names or dates, from user inputs. Together, these features enable the chatbot to engage in more meaningful, context-aware interactions, significantly improving user satisfaction and overall effectiveness. The unstructured text is then converted into a structured XML format based on user input, which is utilized to build simulations or troubleshoot existing ones. The Next generation process simulation software, AVEVA™ Process Simulation (APS) developed by AVEVA, is used in this work. APS is designed for modeling, simulating, studying thermodynamic behavior and optimizing process operations in industries such as oil and gas, chemicals, and manufacturing.

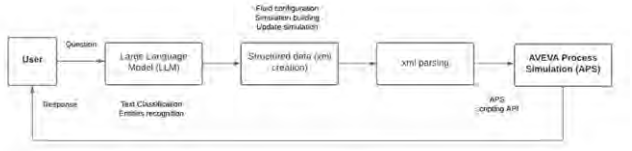



**Figure 1.** Architecture for ChatBot implementation.

The chatbot framework interfaces with the APS through the scripting interface of the process simulator tool, enabling bidirectional communication between the process simulation and the chatbot application using Application Programming Interface (API's) in Python. These API's facilitates tasks such as creating a component slate with thermodynamic models, building simulations, and extracting essential solver and thermodynamic information from the simulation results to help process engineers design, analyze and optimize chemical processes.

### Custom trained model

SpaCy is a Python-based open-source NLP library used to develop custom models. It features built-in pre-trained pipelines and supports tokenization, as well as neural network models for tagging, parsing, named entity recognition (NER), and text classification. In our custom model, text classification and NER are integrated within the pipeline, sharing a token-to-vector layer between the two components. The text classification component categorizes user input into specific types, such as "sim building," "model query," or "fluid building," based on labeled training text. Meanwhile, the NER component identifies and classifies named entities in the text into predefined categories, including models, component names, and thermodynamic methods.

To generate training data for the spaCy model, we utilize Faker, a Python package that creates fake data. The training data patterns are designed to mimic various likely user inputs, and entities are annotated using spaCy's rule-based matching as shown in Figure 2.

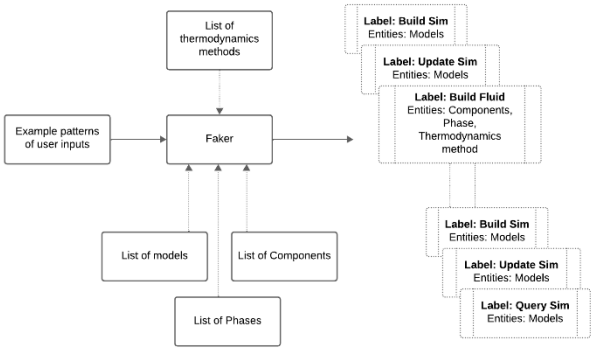



**Figure 2.** Preparation of training data.

The custom training of the spaCy pipeline components is saved as the best model on disk. A simple scoring system, applying equal weights (50-50) to text classification and NER, determines the best model. Once constructed, the NLP pipeline utilizes the pretrained components, allowing user input to be fed into the spaCy pipeline for classification and custom entity identification. Based on this classification, the appropriate XML generation occurs, with named entities represented as XML tags and attributes. From this stage of XML generation onward, the code is consistent between the OpenAI-based model and the custom model. The XML data is then parsed, and the information is sent to the APS through a scripting interface for feedback. Standard

XML template used are presented in the supplementary material.

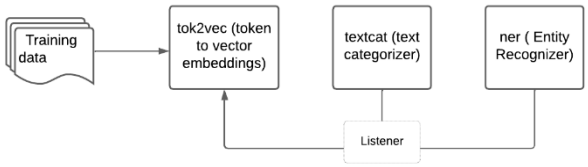



**Figure 3.** SpaCy training pipeline components.

## Pre-trained model

The pretrained GPT-3.5-turbo model is utilized as the base model through the Python API endpoint. Communication with the OpenAI model is facilitated by sending HTTP requests to the API endpoints and receiving corresponding responses.

# RESULTS AND DISCUSSION

To compare the XML results generated by OpenAI and the custom model, it is essential to assess both the structural and content-based similarities. The most effective approach to evaluating the response is by examining both the structural and contextual aspects of the returned XML, such as the similarity of tags and the accuracy of the extracted data. This can be accomplished by establishing a "golden file," which represents the desired XML response, and then comparing the generated XML against this reference. Four metrics have been utilized to assess these differences, each focusing on a distinct aspect of the generated XML file.

## Jaccard similarity

Jaccard similarity quantifies the overlap between two sets. When applied to XML, focusing solely on tags, it evaluates the similarity of the structures between two XML documents. This metric is useful for assessing how closely the structure of a generated XML document aligns with the desired structure. The process involves extracting the unique tags from both XML documents, converting them into sets, and computing the Jaccard similarity, as defined by [10]:

$$J(A,B) = \frac{|A \cap B|}{|A \cup B|} = \frac{|A \cap B|}{|A|+|B|-|A \cap B|} \quad (1)$$

By evaluating both the structural elements of the XML and the data they contain, it enables the assessment of the correctness of the XML structure as well as the accuracy of the data.

## Cosine Similarity

Cosine similarity is employed to assess the similarity between two documents by calculating the cosine value between the term vectors of the documents [11]. This method transforms documents into vectors within a multi-dimensional space, enabling effective comparison of textual data extracted from XML elements. Consequently, cosine similarity is particularly well-suited for evaluating the semantic similarity of text within tags.

## Levenshtein Distance

Levenshtein Distance measures the differences between two sequences, accounting for variations in both equal-length and unequal-length sequences [12]. It determines the minimum number of single-character edits necessary to transform one string into another to identify even the smallest textual differences between two files.

## Case studies

The ChatBot framework is evaluated through a series of case studies designed to simulate real-time user prompts typically posed by process engineers in an industrial setting as presented in supplemented material. The intent, along with the user prompts and associated metrics, is presented in the following section.

## Case study 1

Intent Build a simulation in APS using user prompts in a sentence structure with intentional grammatical errors and typos.

### User Prompts

Prompt 1: Add a source, compressor, valve, pump, valve and sink and connect them. Now update temperature and pressure conditions of source model to 450 K and 250 psi

Prompt 2: Try connecting source, compressor, valve, pump, valve and sink. Also update temperature and pressure of source model to 450 K and 250 psi

Prompt 3: Try connecting source, compressor, valve, pump, valve and sink. Also update T and P of source model to 450 K and 250 psi

Prompt 4: Try connecting source, compressor, valve, pump, valve and sink. Also update temperature and pressure of source model to 100 C and 250 psi1

Prompt 5: Build a simulation with source, valve and sink. Also update temperature and pressure of source model to 100 C and 250 psi

**Table 1:** Metrics for xml generation from user prompts using pre-trained ChatGPT model

| Prompt# | Jaccard Similarity | | Cosine Similarity | Levenshtein Distance |
|---|---|---|---|---|
| | Tags | Data | | |
| 1 | 1 | 0.65 | 0.99 | 6 |
| 2 | 0.63 | 0.51 | 0.99 | 336 |
| 3 | 0.63 | 0.51 | 0.99 | 336 |
| 4 | 1 | 0.65 | 0.99 | 6 |
| 5 | 0.34 | 0.31 | 0.99 | 1246 |

**Table 2:** Metrics for xml generation from user prompts using custom trained model

| Prompt # | Jaccard Similarity | | Cosine Similarity | Levenshtein Distance |
|---|---|---|---|---|
| | Tags | Data | | |
| 1 | 1 | 1 | 1 | 0 |
| 2 | 1 | 1 | 1 | 0 |
| 3 | 0.66 | 0.81 | 0.99 | 38 |
| 4 | 1 | 1 | 1 | 3 |
| 5 | 1 | 1 | 1 | 0 |

## Observation

In the analysis of Prompt #1, both OpenAI and the custom model effectively handled the intentional typographical error. However, with Prompts #2, #3, and #4, OpenAI introduced extraneous and irrelevant sections from the template XML, which negatively impacted both the Jaccard similarity and Levenshtein distance metrics as shown in Table 1 & 2. Despite this, the key information necessary for constructing the simulation in APS was successfully extracted. In contrast, the SpaCy model, which was trained on specific data, did not exhibit this issue and generated a more accurate XML output. For Prompt #5, OpenAI unexpectedly converted units of measure, while the SpaCy model did not. These findings highlight the significant role of sentence structure in the conversion of prompts into structured XML.

## Case study 2

Intent Troubleshoot a built simulation in APS shown in Figure 4, using user prompts in a sentence structure with intentional grammatical errors and typos.

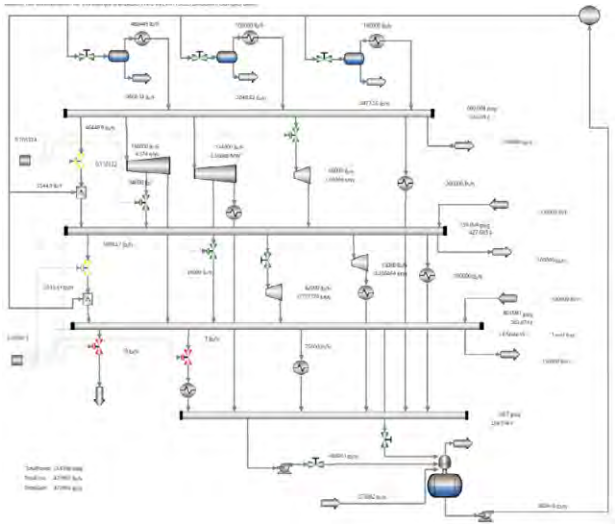


**Figure 4.** Refinery Steam Balance simulation built in APS.

## User Prompts

Prompt 1: Find how many sources, sinks, and valves are present in the simulation

Prompt 2: Find the count the number of sinks, valves and sources1 in the simulation

Prompt 3: Find all Source where temperature is greater than 200 K

Prompt 4: Find all Valves with DP more than 25 kPa

Prompt 5: Can you tell which valves have a DP is greater than 33 kPa

**Table 3:** Metrics for xml generation from user prompts using pre-trained ChatGPT model

| Prompt # | Jaccard Similarity | | Cosine Similarity | Levenshtein Distance |
|---|---|---|---|---|
| | Tags | Data | | |
| 1 | 1 | 1 | 1 | 1 |
| 2 | 1 | 1 | 0.95 | 48 |
| 3 | 1 | 1 | 1 | 1 |
| 4 | 1 | 1 | 1 | 1 |
| 5 | 1 | 0.7 | 0.99 | 236 |

**Table 4:** Metrics for xml generation from user prompts using custom trained model

| Prompt # | Jaccard Similarity | | Cosine Similarity | Levenshtein Distance |
|---|---|---|---|---|
| | Tags | Data | | |
| 1 | 1 | 1 | 1 | 0 |
| 2 | 1 | 1 | 1 | 0 |
| 3 | 0.05 | 0.05 | 0.89 | 283 |
| 4 | 0.5 | 0.5 | 0.92 | 172 |
| 5 | 0.5 | 0.5 | 0.87 | 282 |

## Observation

The OpenAI model successfully extracts the correct information from the APS simulation for prompts #1, #3, and #4, as indicated by the metrics in Table 3. However, for prompt #2, the XML output contains irrelevant information, which negatively impacts the cosine similarity and Levenshtein distance scores as shown in Table 3 & 4. In the case of prompt #5, the OpenAI model generated incorrect tags, specifically "valve1" and "valve2," along with duplicate information in an improper XML format. This error adversely affected the cosine similarity and Levenshtein distance values, ultimately leading to a failure to return a valid response to the user prompt.

The SpaCy model successfully parsed and generated XML for Prompts #1 and #2 when no conditions were included. However, when conditions were introduced, the model failed to generate the relevant sections and was unable to identify the items for Prompts #3 and #5. While the item for Prompt 4 was correctly identified, the associated condition was not parsed accurately. Overall, the SpaCy model performed better with smaller templates but struggled to handle the added complexity introduced by diverse section types.

## Case Study 3

Intent Create a fluid in APS to calculate mixture properties and predict vapor liquid equilibrium using descriptive user prompts

## User Prompts

Prompt 1: Get Vapor fraction for a fluid containing Water, Ethanol, Acetone, and molar composition of 0.5, 0.4, 0.1 using system method NRTL and phase vapor and single liquid equilibrium. Show the fluid details along with mixture liquid density property data at 400k and 200 psi and binary interaction data. Also perform flash calculations at 400 K and 200 psi with the given molar composition.

Prompt 2: Get VF for a fluid with Water, Methanol, Ethanol, Acetone, and molar composition of 0.5, 0.2, 0.2, 0.1 using system method NRTL and one phase vapor liquid equilibrium. Show the fluid details along with mixture density property data at 500 K and 1000 kPa and binary interaction data. Also perform flash calculation at 500 K and 1000 kPa with the same defined composition.

Prompt 3: Get VF for a fluid with Water and Acetone, and molar composition 0.6, 0.4 using method NRTL and phase vapoingle and single liquid. Show the fluid details along with mixture liquid density and binary interaction data. Perform flash at 450 K and 1000 kPa

Prompt 4: Get VF for a fluid with components Methane, Ethane, Water, Butane, and molar composition 0.2, 0.2, 0.4, 0.2 using method SRK and system phase vapor liquid equilibrium.

Prompt 5: Get VF for a fluid with components Methane, Ethane, Water, Butane, and molar composition 0.2, 0.4, 0.2, 0.2 using system method SRK and phase vapor single liquid equilibrium

The information extracted from the prompts are categorized as follows,

1. Component Names
2. System method and Phase
3. Fluid properties – details, mixture properties, interaction parameters
4. Flash conditions – Temperature and pressure (along with unit of measure)

Table 5 presents the information extracted by both the OpenAI and custom models, with "Y" indicating correctly extracted information and "N" representing either incorrect or missing information in the XML format.

**Table 5:** Status of information extracted from user prompts using Custom and OpenAI model

| Category | | 1 | 2 | 3 | 4 |
|---|---|---|---|---|---|
| Prompt 1 | OpenAI | Y | Y | Y | Y |
| | Custom | Y | Y | Y | Y |
| Prompt 2 | OpenAI | Y | N | Y | Y |
| | Custom | Y | Y | Y | Y |
| Prompt 3 | OpenAI | Y | Y | Y | Y |
| | Custom | Y | N | Y | Y |
| Prompt 4 | OpenAI | Y | Y | Y | Y |
| | Custom | Y | Y | N | Y |
| Prompt 5 | OpenAI | Y | Y | N | Y |
| | Custom | N | N | N | N |

**Table 6:** Metrics for xml generation from user prompts using pre-trained ChatGPT model

| Prompt# | Jaccard Similarity | | Cosine Similarity | Levenshtein Distance |
|---|---|---|---|---|
| | Tags | Data | | |
| 1 | 1 | 0.89 | 0.99 | 17 |
| 2 | 1 | 0.89 | 1 | 1 |
| 3 | 1 | 0.85 | 0.99 | 27 |
| 4 | 1 | 0.7 | 1 | 7 |
| 5 | 1 | 0.79 | 1 | 6 |

**Table 7:** Metrics for xml generation from user prompts using custom trained model

| Prompt# | Jaccard Similarity | | Cosine Similarity | Levenshtein Distance |
|---|---|---|---|---|
| | Tags | Data | | |
| 1 | 1 | 1 | 0.99 | 28 |
| 2 | 1 | 1 | 1 | 2 |
| 3 | 1 | 1 | 0.99 | 269 |
| 4 | 1 | 1 | 0.99 | 21 |
| 5 | 0.05 | 0.05 | 0.78 | 948 |

## Observation

OpenAI successfully extracted the information from prompt #1 and generated the XML with the expected unit of measure conversion, matching the XML template. However, for prompts #2, #3, and #4, the phase was extracted as VLLE instead of VLE, which could lead to incorrect results in APS depending on the fluid behavior. Additionally, for prompts #4 and #5, fluid properties were included in the XML and APS results, despite not being requested by the user. It is important to note that while the component names, system method, and flash conditions are correctly extracted from the user prompt, the

phase is inaccurately determined due to the sentence structuring of the prompt.

The custom model successfully predicted the outputs for Prompts #1, #2, and #3. However, Prompt #4 yielded an incorrect result due to an error in parsing the MixturePropertyData tag, which led to a failure during XML parsing. In contrast, Prompt #5 resulted in a complete failure in XML creation, with entities being misclassified as shown in Table 5. Notably, the prompts in question are largely like Prompt #4, differing primarily in sentence structuring and a typo error.

## CONCLUSION

The conversion of user prompts into a standardized XML format provides significant flexibility for modifying underlying APIs, facilitating easier updates to the simulator. This process enables the rapid development of new XML-to-API generators compatible with various simulation tools. Both the custom and pre-trained models can address a variety of challenges when extracting information from prompts, including grammatical errors, typos, repetitive unit operations, abbreviations, and unit of measure conversions. These models successfully convert the extracted data into a structured XML format, which can subsequently be used to generate simulations in APS. However, the quality of the XML output is influenced by factors such as the sentence structure of the prompt, the specificity of model variables, and the units of measure employed. Based on the case studies, it can be observed that the custom model excelled at standard queries, while the OpenAI model handled complex prompts with intricate sentence structures more effectively, despite occasionally introducing unexpected XML changes.

The pretrained GPT-3.5-turbo OpenAI model is readily accessible and easy to use, whereas the SpaCy model, being custom-trained, requires significant investment in terms of labor, cost, and ongoing maintenance as the model needs to be retrained with new datasets.

## DIGITAL SUPPLEMENTARY MATERIAL

The supplementary material can be found with the LAPSE ID: **LAPSE:2025.0019**

## REFERENCES


1. Julien B, Cal D. The role of process engineering in the digital transformation. *Computers & Chemical Engineering* (2021)
2. Zeinab H, Shokoufe T, Mohammad HEA. Application of AI in Chemical Engineering. *InTechOpen* (2018)
3. Venkat V. The promise of artificial intelligence in chemical engineering: Is it here, finally?. *AIChE Journal* 65:466-478 (2018)
4. Konstantinos S, Charis N, Paris V, Elias K, Patrik K, Serafeim M. Enhancing property prediction and process optimization in building materials through machine learning: A review. *Computational Materials Science* 220 (2023)
5. Mohammad A, Bassel S, Mohamed M, Enas S, Maryam A, Abrar I, Muaz R, Abdul O. Progress of artificial neural networks applications in hydrogen production. *Chemical Engineering Research and Design* 182:66-86 (2022)
6. Haley H, Mohannad N, Xinyan H, John G. The role of large language models (AI chatbots) in fire engineering: An examination of technical questions against domain knowledge. *Natural Hazards Research* (2024)
7. Chung L. What Is the Impact of ChatGPT on Education? A Rapid Review of the Literature. *Education Sciences* 410 (2023)
8. Mohannad N. Machine Learning for Civil and Environmental Engineers: A Practical Approach to Data-Driven Analysis, Explainability, and Causality. New Jersey: Wiley (2023)
9. Alipour H, Nick P, Kohinoor R. ChatGPT Alternative Solutions: Large Language Models Survey. arXiv preprint arXiv (2024)
10. Dhiah S. Jaccard Coefficients based Clustering of XML Web Messages for Network Traffic Aggregation. *Journal of Al-Qadisiyah for computer science and mathematic* 11:82-91 (2019)
11. Faisal R, Teruaki K, Masayoshi A. Semantic cosine similarity. 7th international student conference on advanced science and technology ICAST 4 (2012)
12. Seo N, Sangwoo K, Cheonyoung J. A Lightweight Program Similarity Detection Model using XML and Levenshtein Distance. FECS 3-9 (2006)



© 2025 by the authors. Licensed to PSEcommunity.org and PSE Press. This is an open access article under the creative commons CC-BY-SA licensing terms. Credit must be given to creator and adaptations must be shared under the same terms. See https://creativecommons.org/licenses/by-sa/4.0/




Systems & Control Transactions

**Research Article - Peer Reviewed Conference Proceeding**
ESCAPE 35 - European Symposium on Computer Aided Process Engineering
Ghent, Belgium. 6-9 July 2025
Jan F.M. Van Impe, Grégoire Léonard, Satyajeet S. Bhonsale,
Monika E. Polańska, Filip Logist (Eds.)

PSE PRESS

# Hybrid Models Identification and Training through Evolutionary Algorithms

**Ulderico Di Caprio[a], M. Enis Leblebici[a]***

[a] Center for Industrial Process Technology, Department of Chemical Engineering, KU Leuven, Agoralaan Building B, 3590 Diepenbeek, Belgium
* Corresponding Author: muminenis.leblebici@kuleuven.be

## ABSTRACT

Hybrid modelling is widely employed in chemical engineering to generate highly accurate predictions. Such an approach merges first-principle modelling with machine learning techniques to identify and model the epistemic uncertainty from experimental data. Despite its advantages, this still requires cross-domain competencies that are difficult to find in the chemical industry and high human involvement. The possibility of automating the identification and training model would be significantly beneficial for the widespread adoption of hybrid modelling methodology within the chemical industry. This work presents a novel algorithm for the automatic identification of hybrid models (HMs) starting from the first-principle representation of the system, described by differential equation sets. The methodology formulates the problem as mixed-integer programming, identifying the equation running under uncertainty, identifying the machine learning model hyperparameters, and training the latter. The Differential Evolution algorithm drives the identification and training tasks. The methodology is validated in three cases, namely a dynamic reaction system, a dynamic bioreactor and a Lotka-Volterra oscillator deviated with polynomial or MRF equation on different levels, generating 14 validation cases. On all of them, the model correctly identifies the position of the uncertainty and the functional form to approximate it. The methodology returns automatically trained HMs with a mean absolute percentage error in the range of 10%, which is in line with the experimental error of the data. The methodology presented in this work presents a step toward the automatic generation of HMs for dynamic systems and the widespread of this technology in the chemical industry.

**Keywords**: hybrid modelling, automatic identification, epistemic uncertainty, differential evolution, machine learning

## INTRODUCTION

Model accuracy is crucial for effective process design and optimization in the chemical industry. However, model performance often suffers from epistemic uncertainty due to unknown phenomena that current knowledge or analytical techniques cannot fully capture. This uncertainty biases predictions and compromises design quality. Hybrid modelling (HM) has emerged as a promising approach to mitigate these issues by integrating first-principle models (FPMs) with machine learning (ML) methods [1]. Here, experimental data are used to capture unmodeled phenomena in a functional form, thereby enhancing accuracy and providing insights into system behaviour.

In chemical process system engineering, FPMs are typically formulated as differential-algebraic equations that include conservation laws, thermodynamic relations, and other fundamental principles. Each of these equations may run under epistemic uncertainty, making them candidates for correction through a data-driven model (DDM). Constructing an HM requires three steps: (1) identifying the equation affected by epistemic uncertainty, (2) selecting an appropriate DDM structure to capture the unmodeled effects, and (3) training the DDM using available experimental data. The DDM must be sufficiently complex to represent the system accurately while maintaining a number of parameters that align with data availability.

Despite the benefits of HM techniques, their

widespread adoption in the chemical industry is hindered by the need for interdisciplinary expertise in chemical engineering, modelling, and ML. Other fields have benefited from automated ML frameworks that streamline model training and simplify the adoption process. An analogous automated framework for HM could facilitate its broader use, enhancing the interpretability of models and providing new insights into the system dynamics.

Currently, the identification of the epistemic uncertainty location relies heavily on domain expertise and physical insight. While some progress has been made in automating other aspects of HM, the literature lacks a comprehensive methodology for automatically locating epistemic uncertainty. Several studies have explored the selection of DDM structures and hyperparameters using approaches such as integer programming and genetic programming. For example, the ALAMO approach employs quadratic integer programming to approximate unknown physical functions by selecting suitable elementary function candidates and fitting parameters to experimental data [2]. Similarly, Narayanan et al. used genetic programming to approximate the right-hand side of differential equations, aiming to capture the entire physical relationship without additional physical constraints [3]. Furthermore, Willis and von Stosch introduced a mixed-integer linear programming framework that utilizes multivariate rational functions as approximators, validating their method on biochemical reactions and adjusting model complexity based on data availability [4].

In addition to the aforementioned techniques for generating hybrid models (HMs), recent studies have employed symbolic regression (SR) and sparse identification of dynamic systems (SINDy) for data-driven equation discovery [5, 6]. Both methodologies utilize a library of candidate functions to identify underlying equations, producing highly interpretable symbolic representations that approximate the unknown aspects of a system. However, they adopt distinct strategies tailored to different applications. Symbolic regression is typically applied to tabular data, using evolutionary algorithms to construct expression trees of elementary operations. This process identifies the optimal equation configuration that minimizes the discrepancy with experimental data. A notable advantage of SR is its ability to incorporate constraints during optimization, ensuring that the derived models are physically consistent and capable of integrating qualitative information. On the other hand, SINDy is designed for dynamic systems and focuses on uncovering the functional forms governing the temporal evolution of state variables. It employs sparse regression techniques, particularly quadratic optimization, to directly tune model parameters based on state derivative expressions without requiring the explicit solution of differential equations. While both approaches have demonstrated high performance in their respective fields, neither has been systematically evaluated for generating hybrid models in chemical processes.

To our knowledge, no framework exists that can automatically generate a hybrid model solely from an FPM representation and experimental data by simultaneously executing all three HM design steps. Addressing this gap involves solving a mixed-integer programming (MIP) problem that integrates categorical variables (e.g., the location of epistemic uncertainty), discrete variables (e.g., ML hyperparameters), and continuous variables (e.g., DDM fitting parameters). In this paper, we propose an algorithm that automatically identifies the equation affected by epistemic uncertainty, selects the most appropriate DDM hyperparameters, and trains the model using a heuristic global optimization strategy. This approach aims to enhance data efficiency while remaining compatible with the constraints of industrial data availability.

## METHODOLOGY

### The algorithm

The MIP problem to identify and train the HM was solved using the Differential Evolution (DE) algorithm (Scipy v.1.11.3) [7], compatible with integer variables and constraints. For the constraints, the library implements the algorithm proposed by Lampinen [8]. The MIP problem is divided into 3 subproblems, namely 1) the identification of the equation running under epistemic uncertainty, 2) the identification of the most suitable data-driven function structure to capture the said uncertainty from the training data, and 3) training the DDM identifying its continuous parameter values; these three problems are solved simultaneously by the DE. The algorithm employs polynomial equations as the data-driven function. The algorithm can activate each of the monomial terms contained in the polynomial.

The first problem is treated as a discrete optimisation problem, where the discrete variable $P$ sets which equation in the system runs with epistemic uncertainty and should be corrected by the DDM. The discrete variable P varies between 0 and ($N_s$-1), where $N_s$ is the number of equations in the system.

The second solved problem is the structure identification of the data-driven function. The algorithm implements a polynomial function as an approximator by deriving monomial terms from the states of the differential equation, constructing a K-order polynomial, and scaling the exponents of each term within the predefined range *EX_MIN* and *EX_MAX*. This ensures a balanced representation of the system dynamics, enabling accurate approximations while maintaining numerical stability and computational efficiency. This work employed K=4, EX_MIN=0.5 and EX_MAX=2. The structure of the polynomial function to train is selected, activating only certain monomial terms. In the polynomial data-driven function,

each of the monomial terms is multiplied by a continuous and a binary variable

$$M_i = \delta_i w_i \cdot f_i(x_1, x_2, \dots) \quad (1)$$

where $\delta_i \in \{0,1\}$ is the binary variable, $w_i$ is the continuous variable, $x_i$ is the i-th state of the differential equation system and $f_i$ is the polynomial form related to $M_i$. Both $\delta_i$ and $w_i$ of (1) are identified by the DE algorithm; the first is treated as a bounded discrete variable, while the second one is encoded as a bounded continuous variable. This work employed $w_i \in [-5,5]$. The configuration reported in (1) allows for reducing the number of parameters used in the DDM, reducing the overfitting risk in the model training phase. The number of active parameters $\delta_i w_i$ is reduced by limiting the amount of $\delta_i$ values being non-zero. Such a condition is given as a constraint to the DE

$$\sum_i \delta_i < N_{MAX}$$

where $N_{MAX}$ is the maximum cardinality allowed by the optimisation. This work employed $N_{MAX} = 5$.

The Bayesian Information Criterion (BIC) was used as the training loss function to balance the performance of the HM with the structural complexity of the DDM and avoid overfitting the training set. The formulation by Willis and von Stosch was employed in this work [4]. The BIC was computed for each experiment, and the loss function value was calculated as their sum.

The DE algorithm was executed with 300 generations using the default settings of the SciPy implementation. Afterwards, the continuous parameters of the most performant individual were refined using the L-BFGS-B.

The computational complexity of the proposed approach is linear in the number of experiments included in the training set because the most time-consuming part is the resolution of the ODE through numerical solvers.

## The test cases

Three FPMs were employed as test cases to evaluate the performance of the algorithm. These were selected to represent typical dynamic systems in the chemical engineering domain. The first test case, *the reaction system*, is a set of chemical reversible reactions described by the chemical system $A \leftrightharpoons R \leftrightharpoons S$, each running on first-order kinetic in batch conditions assumed isothermal; therefore, described through the set

$$\begin{cases} dC_A/dt = -k_{1,d} \cdot C_A + k_{1,i} \cdot C_R \\ dC_R/dt = k_{1,d} \cdot C_A - k_{1,i} \cdot C_R - k_{2,d} \cdot C_R + k_{2,i} \cdot C_S \\ dC_S/dt = k_{2,d} \cdot C_R - k_{2,i} \cdot C_S \end{cases}$$

with $k_{1,d} = 0.3\ min^{-1}$, $k_{1,i} = 0.1\ min^{-1}$, $k_{2,d} = 0.02\ min^{-1}$, $k_{2,i} = 0.01\ min^{-1}$. The equations were solved with initial conditions in the range [0, 10], with 10 points obtained using the Latin hypercube sampling (LHS).

The second test case is *the Lotka-Volterra oscillator*, described by the system

$$\begin{cases} dx/dt = (1-y) \cdot x \\ dy/dt = (x-1) \cdot y \end{cases}$$

The equations were solved with initial conditions in the range [0, 1], with 10 points obtained using the LHS.

The third evaluation case is *the bioreactor system*, describing the growth of biomass, X, in a continuous bioreactor fed with the nutrient S, influenced by Monod kinetics. The system is described by the equation set

$$\begin{cases} \dfrac{dX}{dt} = \dfrac{\mu_{max} \cdot S}{K_S + S} \cdot X - D \cdot X \\ \dfrac{dS}{dt} = D \cdot (S_{in} - S) - \dfrac{\mu_{max} \cdot S}{K_S + S} \cdot \dfrac{X}{Y_{xs}} \end{cases}$$

with $\mu_{max} = 0.4\ min^{-1}$, $K_S = 0.5\ mol/L$, $S_{in} = 1\ mol/L$, $Y_{xs} = 0.6\ g/mol$ and $D = 0.1\ min^{-1}$. The equations were solved with initial conditions in the range [0.2, 1], with 10 points obtained using the LHS.

Each of the equations in the FPMs was deviated using 2nd-order polynomial or 1st-order MRF functions to mimic the epistemic uncertainty source. The employed parameters were sampled in the range [-1,1]; following that, the output was multiplied by a constant value to enhance the effect of the deviation.

For each validation case, one of the abovementioned deviations was applied to one of the set equations individually. Therefore, the algorithm was validated using 14 cases combining the FPMs and the deviation position. These served as experimental data for the algorithm to identify the position of the epistemic uncertainty and the most suitable data-driven function structure for the HM generation.

Each of the deviated equations was solved using LSODA solver (SciPy v1.11.3). Each of the experiments contained 14 points uniformly sampled in the time range [0,20] min; noise of ±10% was added to the output, mimicking the measurement noise. The test set for the reaction system comprises 5 train points and 5 test points randomly selected. The test set for the Lotka-Volterra oscillator and the bioreactor system comprises 4 points selected to be within the initial conditions convex-hull.

The trained models were evaluated on a test set. The quantitative comparison of the trained HM performance was executed using 1) the coefficient of determination ($R^2$), to evaluate the explained variance of the model, 2) the mean absolute percentage error (MAPE) to have a quantitative deviation of the model from the point weighted on their experimental value, and 3) the mean absolute percentage error (MAE) to have a quantitative deviation of the model prediction from the experiments.

# RESULTS

The results of the identification algorithm are reported differentiated by the test case on which they have

been validated. Tables 1, 2 and 3 report the accuracy of the identified HM on the overall test set, the actual level of the epistemic uncertainty within the equations and the one identified by the algorithm for the reaction system, the Lotka-Volterra oscillator and the bioreactor system, respectively. Figures 1, 2, and 3 report the graphical representation of the model performance on selected experiments contained in the test set, respectively, for the reaction system, the Lotka-Volterra oscillator, and the bioreactor system.

## The reaction system

In the reaction system, the developed algorithm correctly identifies the epistemic uncertainty location within the equations set for all the proposed test conditions (Table 1). Moreover, HMs identified from the algorithm return low prediction errors on the test set.

**Table 1.** Quantitative performance of the identified HM from the algorithm on the test set. The table reports the equation on which the deviation was applied, the one identified by the algorithm, and the obtained metrics.

| *Actual* | | *Identified* | | | |
|---|---|---|---|---|---|
| Level | Deviation | Level | MAPE | MAE | $R^2$ |
| 1 | Poly | 1 | 10.8% | 0.48 | 0.11 |
| | MRF | 1 | 18.4% | 10.53 | 0.59 |
| 2 | Poly | 2 | 15.7% | 7.32 | 0.82 |
| | MRF | 2 | 7.55% | 0.43 | 0.24 |
| 3 | Poly | 3 | 6.07% | 0.27 | 0.29 |
| | MRF | 3 | 6.3% | 0.56 | 0.77 |

Excluding the system deviated on the 1st equation with MRF and the system deviated on the 2nd equation with polynomial, the trained HM predicted the system behaviour with a MAPE error in line with the given experimental error (i.e., ± 10%). The quality of the model is also confirmed by the MAE value, returning low metrics; this highlights how the error is evenly distributed within the entire range without any significant bias toward any area of the output range. On the other hand, in the two cases with high MAPE and MAE, the model cannot accurately predict the output in some experiments contained in the training set. The low amount of data mainly drives this behaviour for a system having 3 states. Performing the convex-hull selection also in this case, the train set comprises 8 points and improved performances; however, this was not included because of poor reliability on the test set.

Despite the low MAPE and MAE values, the $R^2$ obtained on the test set is quite low for some of the cases (e.g., the one with polynomial deviation on the 1st equation or the MRF deviation on the 2nd equation), showing that the trained model has limited capabilities in explaining the variance of the experimental set. We hypothesise that this is driven by the poor ability to identify continuous parameters. The algorithm uses a heuristic approach to identify all the system parameters, but it is quite inefficient for continuous parameters since heuristics do not guarantee the minimisation of the loss function for a given configuration. On the other hand, the continuous parameters can be identified by gradient-based optimisation approaches, improving the quality of the training.

From Figure 1, it is possible to observe how the employed FPM has significant deviations compared to the experimental data, especially for the profile of the reactant S, where it predicts a completely different behaviour. On the other hand, this effect is mitigated by including DDM, which corrects the model prediction and correctly identifies the deviation source. This results in improved model metrics, such as the MAPE decrease of 5 folds. The case reported in Figure 1 runs with epistemic uncertainty on S concentration. S is being generated from something else that is not included in the mathematical system. The mechanistic model of the system closes the mass balance, but in reality, the system description violates this hypothesis. To ensure mass balance, a further investigation of what is causing the S growth is required.

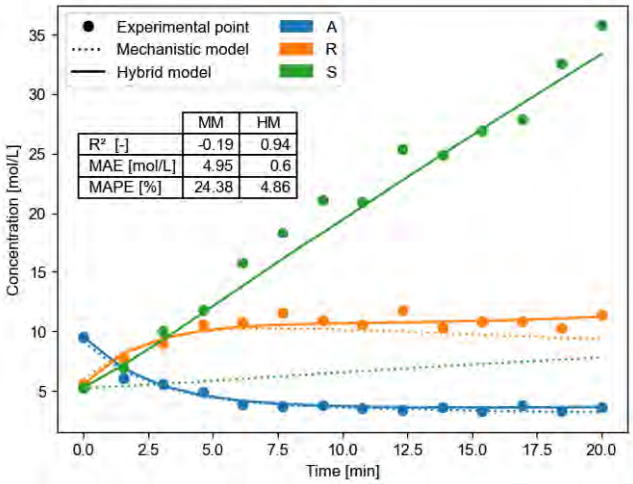



**Figure 1.** First-principles model and hybrid model performance on one of the test examples on the reaction system. The reported experiment is obtained with MRF deviation on the 3rd equation.

## The Lotka-Volterra oscillator

Like the reaction system, also for the Lotka-Volterra case, the developed algorithm performs correct identification of the epistemic uncertainty location both for polynomial and MRF deviation (Table 2). The metrics reported in Table 2 show the enhanced prediction accuracy of the identified HM. For all the validation cases, the HM has low MAPE and MAE with $R^2$ very close to 1, showing how the HM was able to explain the variance of the experimental system completely.

Figure 2 depicts the performance of the mechanistic and HM on one of the test set experiments, having deviation on the 2nd equation with a polynomial function. Here, it is possible to observe how the FPM shows high

deviation on both the variables with error accumulating with time, resulting in a significant shift of the actual and modelled peaks for $t > 7.5\ min$. Additionally, the FPM returns a wrong prediction of peaks amplitude, with a systematic overestimation for both the system states. This behaviour is not observed with the identified HM, returning accurate predictions within the entire simulation time. The HM has effects not only on the peak position but also on their magnitude, which are now correctly predicted. In summary, the HM correctly identifies the behaviour of the test system returning MAPE around 5% and an $R^2$ = 0.98, where the FPM has worse prediction accuracy with an $R^2$=-0.05, indicating that the model returning the average of the points return better prediction than the FPM, and a MAPE around 38%, with a value 7 times higher than the value obtained with the HM predictions.

**Table 2.** Quantitative performance of the identified HM from the algorithm on the test set. The table reports the equation on which the deviation was applied, the one identified by the algorithm, and the obtained metrics.

| *Actual* | | *Identified* | | | |
|---|---|---|---|---|---|
| Level | Deviation | Level | MAPE | MAE | $R^2$ |
| 1 | Poly | 1 | 5.29% | 0.066 | 0.96 |
| | MRF | 1 | 5.51% | 0.068 | 0.95 |
| 2 | Poly | 2 | 5.68% | 0.051 | 0.96 |
| | MRF | 2 | 8.95% | 0.084 | 0.92 |

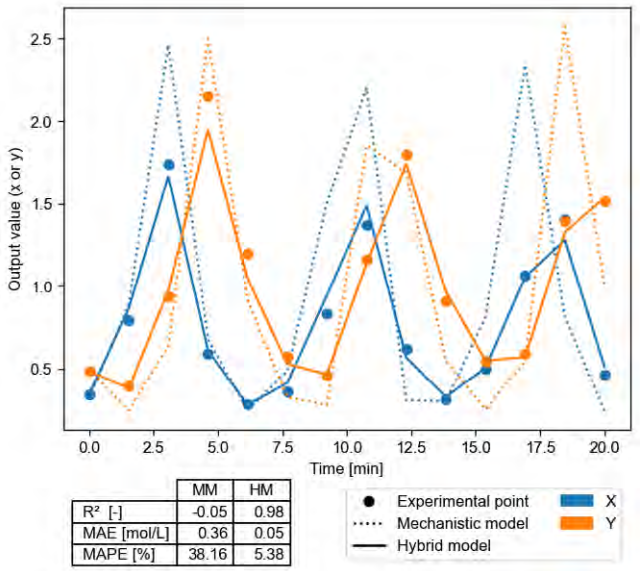



**Figure 2.** First-principles model and hybrid model performance on one of the test examples on the Lotka-Volterra oscillator. The reported experiment is obtained with polynomial deviation on the 2nd equation.

## The bioreactor system

When describing the bioreactor system, the model correctly identifies all the validation cases, with deviations both on biomass growth and substrate profile (Table 3). The source of the epistemic uncertainty has been correctly identified by the algorithm, as well as the approximation for the deviation function. The algorithm did not show any identification bias (i.e., model accuracy or level identification) among the various cases, returning for each of the test case metrics with the same order of magnitude.

**Table 3.** Quantitative performance of the identified HM from the algorithm on the test set. The table reports the equation on which the deviation was applied, the one identified by the algorithm, and the obtained metrics.

| *Actual* | | *Identified* | | | |
|---|---|---|---|---|---|
| Level | Deviation | Level | MAPE | MAE | $R^2$ |
| 1 | Poly | 1 | 6.02% | 0.027 | 0.77 |
| | MRF | 1 | 5.4% | 0.033 | 0.88 |
| 2 | Poly | 2 | 6.87% | 0.042 | 0.8 |
| | MRF | 2 | 6.00% | 0.035 | 0.83 |

Figure 3 depicts one of the test experiments for the case having deviation on the 1st equation described by a polynomial function. Here, the FPM shows significant deviation that is cumulating over time; such behaviour is related to the fact that the numerical resolution of differential equations relies on predicted system state values to run the prediction at the current state, letting the error accumulate over time.

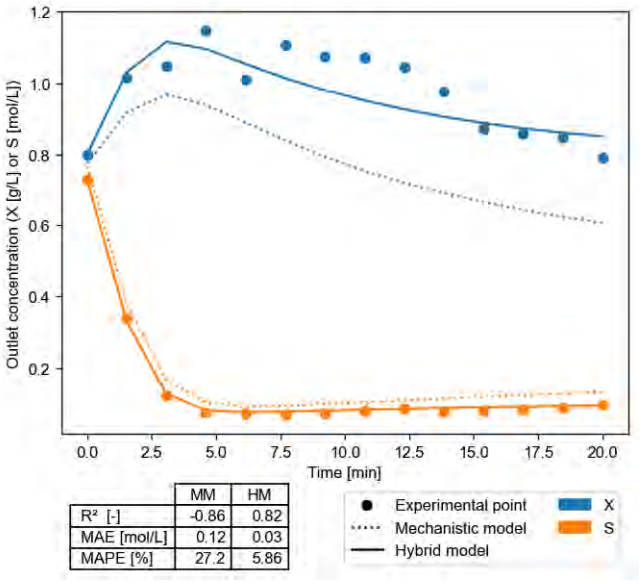



**Figure 3.** First-principles model and hybrid model performance on one of the test examples on the biochemical system. The reported experiment is obtained with polynomial deviation on the 1st equation.

On the other hand, the HM prediction correctly overlaps the experimental points within the entire time range without any significant deviation happening over time, demonstrating the robustness and reliability of the HM obtained with the proposed methodology. It is important to note that both the FPM and the HM identify the same

overall trend, but the HM better identify the change in system behaviour (e.g., the location of the maxima for the X profile), the magnitude of the first derivate of the profile and the plateau location for both the curves. Such an improvement in behaviour prediction resulted in better metrics for the HM over the FPM; the FPM returned a MAPE=27.2% while the $R^2$=-0.86, quantitively proving the poor prediction capabilities of the FPM. On the other hand, the HM results in a MAPE=5.86%, a value around 4.6 times lower than the one obtained for the FPM, and an $R^2$=0.82.

## ALTERNATIVE APPROACHES

A primary limitation of the proposed approach is the need for iterative ODE resolution during parameter identification. This process significantly prolongs identification time and is susceptible to mathematical instabilities, thereby reducing compatibility with derivative-based optimizers. A potential solution to mitigate these issues is the application of SINDy-like techniques [6]. This alternative framework would allow the reformulation of the identification problem using quadratic integer programming to locate epistemic uncertainty while also accommodating multiple model deviations.

## CONCLUSIONS

This work presents an automatic algorithm that identifies and trains hybrid models for dynamic chemical processes. Starting from a first-principle model under epistemic uncertainty, the method integrates missing information from experimental data into a data-driven component. It locates the epistemic uncertainty within the system equations and selects the most suitable data-driven model (DDM) for its mitigation. A constrained mixed-integer Differential Evolution algorithm is used to determine the uncertainty's position along with the hyperparameters and parameters of the DDM.

To work with limited data and minimal experimentation, the method employs a sum of monomial terms as the data-driven function and uses the Bayesian information criterion as the loss function, thereby reducing model complexity and overfitting risk. The approach was validated on a reactive chemical system, a bioreactor with biomass growth, and the Lotka-Volterra oscillator, accurately identifying uncertainty and achieving prediction errors (MAPE) below 10% on unseen cases.

This methodology marks a significant step toward automating hybrid model creation in the chemical industry. Future improvements include integrating deterministic algorithms for continuous parameter identification, testing additional chemical cases, and extending uncertainty identification to model parameters beyond differential equations.

## ACKNOWLEDGEMENTS

The authors acknowledge funding from the KU Leuven project "HyPro - Automatic hybrid digital twins for process modelling" (C3/23/007).

## REFERENCES

1. Schweidtmann AM, Zhang D, Von Stosch M. A review and perspective on hybrid modeling methodologies. *Digit. Chem. Eng.* 10:100136 (2023). doi.org/10.1016/j.dche.2023.100136
2. Wilson ZT, Sahinidis NV. The ALAMO approach to machine learning. *Comput. Chem. Eng.* 106:785–95 (2017).doi.org/10.1016/j.compchemeng.2017.02.010
3. Narayanan H, Bournazou MNC, Gosálbez GG, Butté A. Functional-Hybrid modeling through automated adaptive symbolic regression for interpretable mathematical expressions. *Chem Eng J.* 430:133032 (2021). doi.org/10.1016/j.cej.2021.133032
4. Willis MJ, Von Stosch M. Simultaneous parameter identification and discrimination of the nonparametric structure of hybrid semi-parametric models. *Comput. Chem. Eng.* 104:366–76 (2017). doi.org/10.1016/j.compchemeng.2017.05.005
5. Angelis D., Sofos F., Karakasidis T.E. Artificial Intelligence in Physical Sciences: Symbolic Regression Trends and Perspectives. Arch Computat Methods Eng 30, 3845–3865 (2023). doi.org/10.1007/s11831-023-09922-z
6. Brunton SL., Proctor JL., Kutz JN. Discovering governing equations from data by sparse identification of nonlinear dynamical systems. Proc. Natl. Acad. Sci. 113:3932-3937 (2016). doi.org/10.1073/pnas.1517384113
7. Storn R, Price K. Differential Evolution – a simple and efficient heuristic for global optimization over continuous spaces. *J. Glob. Optim.* 11(4):341–59 (1997). doi.org/10.1023/a:1008202821328
8. Lampinen J. A constraint handling approach for the differential evolution algorithm. Vol. 2, *Proceedings of the 2002 Congress on Evolutionary Computation. CEC'02 (Cat. No.02TH8600)*. 2003. doi.org/10.1109/cec.2002.1004459

© 2025 by the authors. Licensed to PSEcommunity.org and PSE Press. This is an open access article under the creative commons CC-BY-SA licensing terms. Credit must be given to creator and adaptations must be shared under the same terms. See https://creativecommons.org/licenses/by-sa/4.0/



Systems & Control Transactions

**Research Article - Peer Reviewed Conference Proceeding**
ESCAPE 35 - European Symposium on Computer Aided Process Engineering
Ghent, Belgium. 6-9 July 2025
Jan F.M. Van Impe, Grégoire Léonard, Satyajeet S. Bhonsale,
Monika E. Polańska, Filip Logist (Eds.)

PSE PRESS

# Physics-Informed Graph Neural Networks for Modeling Spatially Distributed Dynamically Operated Processes

**Md Meraj Khalid[a,b], Luisa Peterson[a], Edgar Ivan Sanchez Medina[a,*], and Kai Sundmacher[a,b,*]**

[a] Process Systems Engineering, Max Planck Institute for Dynamics of Complex Technical Systems, Sandtorstraße 1, 39106 Magdeburg, Germany
[b] Chair for Process Systems Engineering, Otto-von-Guericke University, Universitätsplatz 2, 39106 Magdeburg, Germany
* Corresponding Authors: sanchez@mpi-magdeburg.mpg.de , sundmacher@mpi-magdeburg.mpg.de.

## ABSTRACT

Modeling process systems by use of partial differential equations is often complex and computationally expensive, especially for inverse problems such as optimization, state identification, or parameter estimation. Data-driven methods typically provide efficient alternatives with lower computational cost. One such method is Graph Neural Networks (GNNs), which can be used to model dynamical systems as graphs. However, dynamic GNNs often face challenges with extrapolation and representability. Integrating mechanistic insights in surrogate models can improve both prediction accuracy and interpretability. This study compares different strategies for embedding physics-based insights into GNNs to model the dynamic behavior of a catalytic $CO_2$ methanation reactor. The hybrid integration of physics-informed GNNs aims to improve the predictive ability and interpretability while reducing the model development time, thereby facilitating faster deployment. Results show that penalizing the predicted change in reactor states from one time step to the next during training reduces the Frobenius error norm of GNN predictions from about 2.2 % to 1.4 %. In contrast, using a traditional physics-based loss function during training results in a Frobenius norm as high as 8.7 %. This highlights the importance of comparing different strategies for embedding physical laws into data-driven models.

**Keywords**: Hybrid modeling, Scientific Machine Learning, Graph Neural Networks, $CO_2$ Methanation

## INTRODUCTION

Process systems are often spatially distributed, dynamic, and exhibit highly nonlinear behavior. Modeling these systems requires the abstraction of process knowledge into a mathematical representation.

Accurate mechanistic models, often represented by mass and energy balances, combined with thermodynamic and kinetic laws, and abstracted as a system of partial differential equations (PDEs), require significant effort in terms of development time. The expertise and deep understanding required for this type of modeling adds to its complexity. Due to the intricate nature of process systems, analytical solutions are rarely achievable, necessitating the use of numerical methods. These methods rely on discretization schemes, in terms of temporal and spatial coordinates of the system. Furthermore, the complexity of problems arising from the numerical treatment increases with finer discretization, especially in inverse applications such as optimization, state identification, or parameter estimation. Despite these challenges, mechanistic models offer significant advantages. Their parametric nature allows sensitivity and scenario analysis, as well as critical flexibility analysis for dynamically operated process systems.

Recent developments in machine learning (ML), especially deep learning (DL) methods, have facilitated surrogate modeling of complex systems. Data-driven models are relatively easy to develop and take less time to build, provided sufficient data is available in both quantity and quality. However, they do require tuning of hyperparameters, which, while not trivial, is generally less time consuming than building mechanistic models from scratch. However, data-driven surrogate models face challenges related to interpretability and the ability to make meaningful extrapolative predictions.

Hybrid methods that integrate ML with knowledge-based models are often referred to as scientific machine

learning (SciML). SciML models leverage the strengths of both mechanistic and data-driven approaches, integrating domain expertise with data-driven insights. They contain embedded physical laws, can be used for extrapolative predictions, and generally provide better interpretability [1, 2].

The principles of modeling of spatially distributed dynamical systems have practical applications in the design and optimization of energy conversion technologies capable of storing renewable energy. Renewable energy plays a critical role in addressing climate change and increasing energy independence, but its intermittent nature presents significant challenges. To overcome these challenges, renewable energy can be converted into other forms, such as chemical energy, to facilitate its long-term storage, transportation, and distribution. One such conversion process is methanation, in which carbon dioxide and hydrogen are converted to methane, with water as a byproduct. The hydrogen, often referred to as green hydrogen, is typically produced by electrolysis of water using renewable energy [3]. This process allows methane to be used as an efficient chemical energy carrier that can be easily stored and transported within the existing infrastructure. The methanation reaction is as follows:

$$\mathrm{CO_2} + 4\,\mathrm{H_2} \rightleftharpoons \mathrm{CH_4} + 2\,\mathrm{H_2O} \tag{1}$$

$CO_2$ methanation is assumed to take place in a one-dimensional polytropic reactor which can be mechanistically described by the mass and energy balances [4]:

$$\frac{\partial X}{\partial t} = -\frac{\mathrm{u}}{\epsilon_\mathrm{R}}\frac{\partial X}{\partial z} + \frac{M_{\mathrm{CO_2}}}{\epsilon_\mathrm{R}\,\rho\,y_{\mathrm{CO_2,in}}}(1-\epsilon_\mathrm{R})\sigma_\mathrm{eff}, \tag{2}$$

$$\frac{\partial T}{\partial t} = -\frac{u_\mathrm{in}\rho_\mathrm{in}C_p}{(\rho C_p)_\mathrm{eff}}\frac{\partial T}{\partial z} + \frac{1}{(\rho C_p)_\mathrm{eff}}\frac{\partial}{\partial z}\left[\Lambda_\mathrm{ax}\frac{\partial T}{\partial z}\right] + \frac{4U}{D\,(\rho C_\mathrm{p})_\mathrm{eff}}(T-T_\mathrm{cool}) - \frac{\Delta H_r}{(\rho C_p)_\mathrm{eff}}(1-\epsilon_\mathrm{R})\sigma_\mathrm{eff}, \tag{3}$$

with the initial and boundary conditions:

$$X|_{z=0} = 0, \quad X|_{t=0} = X_0, \quad T|_{t=0} = T_0, \quad \Lambda_\mathrm{ax}\frac{\partial T}{\partial z} = u_\mathrm{in}\rho_\mathrm{in}C_\mathrm{p}(T-T_\mathrm{cool}), \quad \left.\frac{\partial^2 T}{\partial z^2}\right|_{z=L} = 0. \tag{4}$$

Hereby, $X$ and $T$ denote carbon dioxide conversion and reactor temperature, respectively. $z$ stands for the spatial (axial) and $t$ for the time coordinate. The constants $\epsilon_\mathrm{R}$, $M_{\mathrm{CO_2}}$, $y_{\mathrm{CO_2,in}}$, $u_\mathrm{in}$, $\rho_\mathrm{in}$, $D$ and $L$ describe the specific reactor dimensions and settings. The variables $u$, $\rho$, $\sigma_\mathrm{eff}$, $C_\mathrm{p}$, $\Lambda_\mathrm{ax}$, $U$, $T_\mathrm{cool}$ and $\Delta H_r$ are modeled by algebraic equations.

The initial conditions $X_0$ and $T_0$ are set for a load change scenario where the hydrogen depends on the time-varying renewable energy generation. The synthetic data used in this work, visualized in Figure 1, is generated using the mechanistic model reported above, with the parameter tuned as reported in [5].

This work extends the graph neural network (GNN) study presented in [5] by optimizing the hyperparameters, modifying the network architecture, and exploring different strategies for embedding physical information into the loss function. Three different models are investigated: (i) a baseline GNN, (ii) a GNN incorporating the time derivatives of the data into the loss function, and (iii) a GNN incorporating the underlying physics described by Equations 2 and 3 into the loss function.

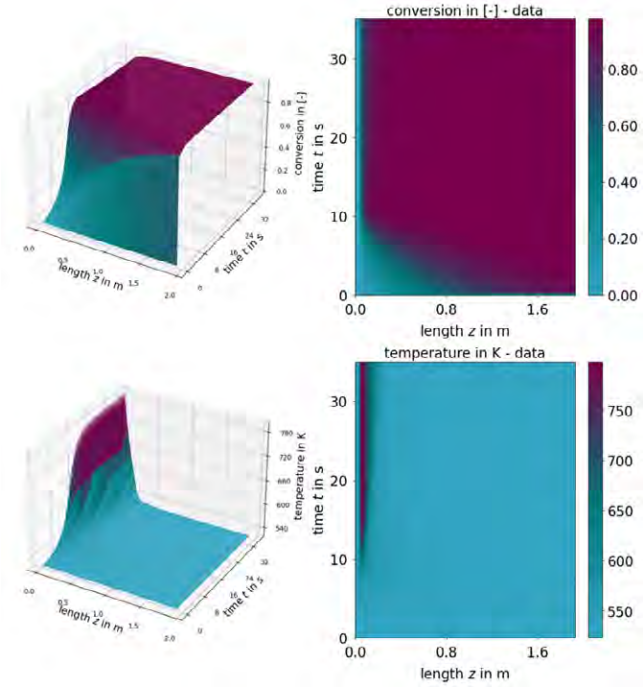



**Figure 1.** Conversion and temperature profiles generated from the mechanistic model and used to train and test GNNs.

## METHODS

### Graph Neural Networks

GNNs, introduced in [6], are a class of DL methods that operate on graphs. GNNs require the system to be represented as a graph '$\mathcal{G}$' with a set of nodes '$V$' and their inter-connectivities as edges '$E$'. A graph is then defined as the tuple of its node attributes and edge attributes along with the information of connectivity $\mathcal{G} = (V, E)$. The individual nodes and edges are denoted as $\mathrm{v}_i \in V$ for the $i^{th}$ node and $\mathrm{e}_{ij} \in E$ for the edge connecting the $i^{th}$ and $j^{th}$ node. The learning in GNNs is based on a message passing strategy where each target node receives the embeddings of all the neighbouring nodes and edges. These embeddings are then aggregated using a permutation invariant operator. Afterwards, this aggregated message is combined with the target node's own embedding using an update function, usually non-linear. This

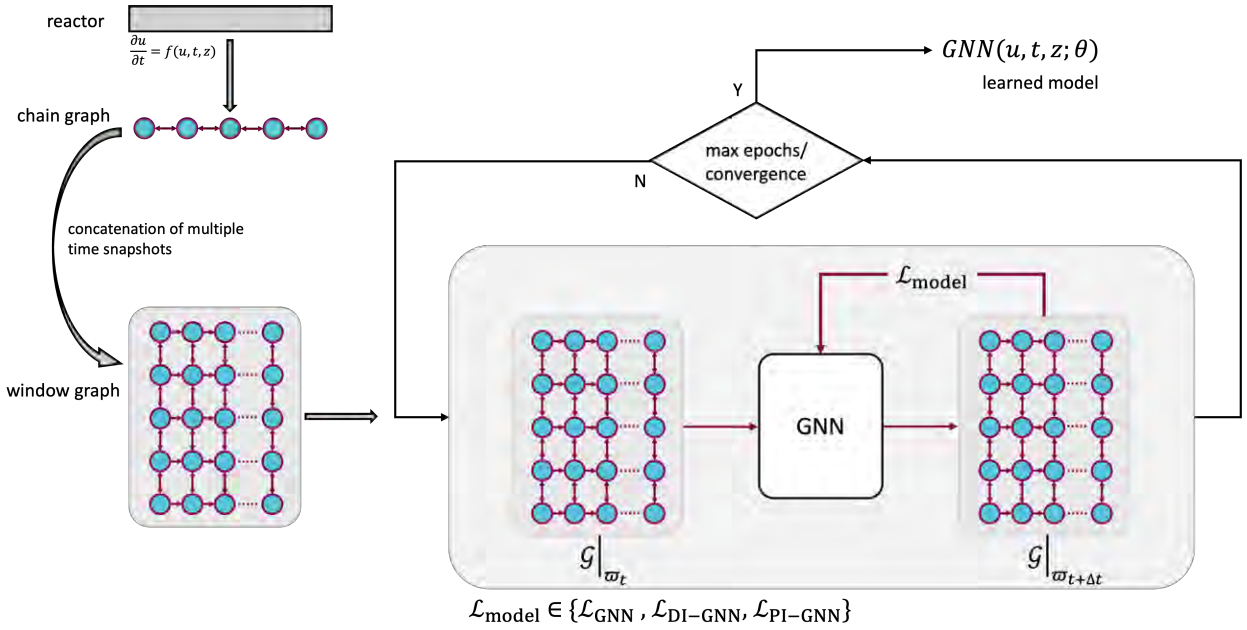



**Figure 2:** Generic schematic diagram of hybrid Graph Neural Networks.

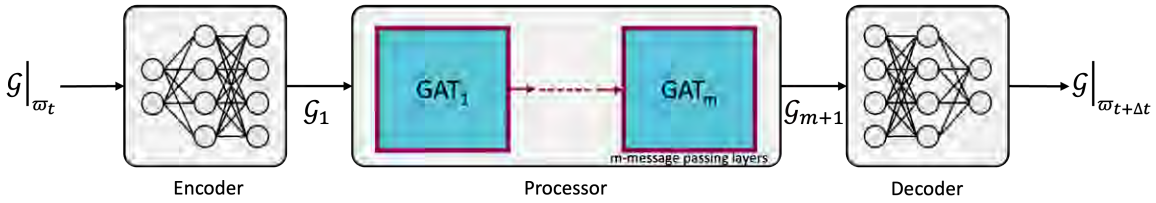



**Figure 3:** Network architecture of Graph Neural Networks.

mechanism, mathematically represented in Equation 5, makes GNNs spatially aware models

$$h_i^{k+1} = \phi\left(h_i^k, \zeta^k(\{h_j^k, \forall j \in \mathcal{N}(i)\})\right). \quad (5)$$

Here, $h$ represents the node embeddings, $\phi$ is the update function, $\zeta$ is the aggregate function, $i$ and $j$ denote the target node $i$ with nodes $j$ in its neighborhood $\mathcal{N}$, $k$ denotes the $k^{th}$ message passing layer.

For spatio-temporal systems, GNNs require the integration of a temporal model to effectively capture their dynamic behavior, leading to the development of spatio-temporal GNNs. Graph attention networks (GATs) [7] are one of these methods, where the message passing equation is modified using an attention coefficient resembling cognitive attention. The mathematical form is given in Equation 6

$$h_i^{k+1} = \phi\left(\sum_{j\in\mathcal{N}(i)} \alpha_{ij}\, \mathcal{W}^k\, h_i^k\right). \quad (6)$$

Here, $\mathcal{W}^k$ stands for the weights matrix at layer $k$ and $\alpha_{ij}$ is the attention coefficient for the connection between node $i$ with its neighboring nodes $j$. The integration of other temporal models, like recurrent neural networks, with GNNs has also been explored in the context of dynamical systems modeling [8].

## Graph representation of dynamical systems

Spatial dependence in systems can be represented structurally using grids for evenly spaced data or meshes for more general arrangements. Graph based models for learning complex physics simulations have been reported in [9-11]. In this work, we represent the dynamical system as a graph, where grid or mesh points are translated into nodes, and their connections are represented by edges. In the case of a methanation reactor, since the system is assumed to be one-dimensional in space, it is represented as a one-dimensional grid or a chain graph, as reported in [5]. Each graph corresponds to a snapshot of the domain at a specific time point. For improved learning, multiple time snapshots or chain graphs are concatenated to form a window graph, as shown in Figure 2. Adjacent nodes at each time point are connected by bi-directional edges, while corresponding nodes in two chain graphs are connected by unidirectional edges from the past to the future. The outputs of the mechanistic model, namely conversion and temperature, are used as node features, while the distances between two

neighboring spatial points are used as edge embeddings. The data is pre-processed using min-max scaling and split sequentially before embedding.

As shown in Figure 3, an encoder-processor-decoder architecture is used for GNN processing. The window graph is passed to an encoder, essentially a multilayer perceptron (MLP), which encodes the node features to the hidden dimension of the architecture. The encoded information is then processed using multiple GAT message passing layers. Finally, a decoder model of structure akin to the encoder is used to get the learned node features back to the original dimensions. The optimized hyperparameters are the hidden dimension of the architecture (228) and the window size (number of chain graphs processed at a time) of 20.

The output from the GNN block is used to calculate the loss function,

$$\mathcal{L}_{\mathrm{GNN}}(\theta) = \sum_{m=1}^{N_t}\sum_{n=1}^{N_z} \| \overline{u}(\varpi_m, z_n) - u(\varpi_m, V_n;\ \theta) \|_2^2. \quad (7)$$

In Equation 7, $\theta$ are the learned parameters of the GNN, $\varpi_m$ is the $m^{th}$ window graph, $V_n$ is the $n^{th}$ node, $N_t$ and $N_z$ denote the total number of window graphs and nodes in each graph, respectively. A stochastic optimization method from [12] with a learning rate of $5 \times 10^{-5}$ is used for GNN-training. This workflow is used in an iterative roll-out manner to predict multiple future time levels.

## Derivative-Informed Graph Neural Networks

The framework of a simple GNN implementation is modified by incorporating the time derivatives of the node features as additional information for the GNN. The architecture is also updated by replacing the MLPs in the encoder and decoder with deep neural networks (DNNs) and including more message-passing steps to enhance the system's awareness of neighboring nodes. Simply using the time derivative information as additional node features does not improve predictions, likely because the model perceives it as additional noise. Therefore, a more robust implementation of the derivative-informed GNN (DI-GNN) was developed by modifying the loss function to incorporate the derivative loss. This approach is based on the hypothesis that, at each time step or for each window graph, although the GNN is informed of the neighboring node embeddings, it remains unaware of how the node embeddings have changed from one time step or window graph to another.

The modified loss function reads:

$$\mathcal{L}_{\mathrm{DI-GNN}}(\theta) = (\gamma_{\mathrm{d}}) \sum_{m=1}^{N_t}\sum_{n=1}^{N_z} \|\overline{u}(\varpi_m, z_n) - u(\varpi_m, V_n;\ \theta)\|_2^2 + (1-\gamma_{\mathrm{d}}) \sum_{m=1}^{N_t}\sum_{n=1}^{N_z} \left\| \frac{d\overline{u}(\varpi_m, z_n)}{dt} - \frac{du(\varpi_m, V_n;\ \theta)}{dt} \right\|_2^2, \quad (8)$$

where $\gamma_{\mathrm{d}}$ denotes the data to derivatives weight.

## Physics-Informed Graph Neural Networks

To make the model truly semi-parametric in nature, the mechanistic model was integrated with the GNN implementation, into a physics-informed GNN (PI-GNN) framework. The modified GNN architecture in DI-GNN was used and the loss function was modified to resemble a physics-informed neural network (PINN) [13]. Ideally in a PINN loss function, the total sum is built of the data loss and physics loss which includes initial conditions loss and boundary conditions loss. In our case, the initial conditions are already satisfied with the first window graph in the train split, while boundary conditions are met within the equation system itself as equations are declared in their discretized form, i.e., as sets of ordinary differential equations (ODEs).

The modified loss function reads:

$$\mathcal{L}_{\mathrm{PI-GNN}}(\theta) = (\gamma_{\mathrm{p}}) \sum_{m=1}^{N_t}\sum_{n=1}^{N_z} \|\overline{u}(\varpi_m, z_n) - u(\varpi_m, V_n;\ \theta)\|_2^2 + (1-\gamma_{\mathrm{p}}) \sum_{m=1}^{N_t}\sum_{n=1}^{N_z} \left\| \frac{d\overline{u}(\varpi_m, z_n)}{dt} - PDE_{\mathrm{sys}(u(\varpi_m, V_n;\ \theta))} \right\|_2^2, \quad (9)$$

where $\gamma_{\mathrm{p}}$ denotes the data to physics weight. $PDE_{\mathrm{sys}}$ denotes the right-hand side of the mechanistic model given by Equations 2 and 3.

## COMPARATIVE ANALYSIS

The comparison between the predictions of the three models is based on the relative Frobenius error between the synthetic data and the model predictions. The Frobenius norm is defined as the square root of the sum of the absolute squares of all matrix elements:

$$\|E\| := \sqrt{\sum_{i=1}^{m}\sum_{j=1}^{n} |E_{ij}|^2}. \quad (10)$$

Each model uses a different GNN architecture and loss function. To reduce computation time and avoid overfitting, we used early stopping, which stops training when validation performance stops improving. This resulted in different training epochs for each model.

Both DI-GNN and PI-GNN are evaluated for two weight factors of 0.5 and 0.7 to evaluate the effect of individual loss terms on the predictions. Table 1 lists the relative Frobenius norms for GNN, DI-GNN ($\gamma_d = \{0.5, 0.7\}$), and PI-GNN ($\gamma_{\mathrm{p}} = \{0.5, 0.7\}$). The profiles predicted by these models have been graphically visualized in Figures 5-7. Out of the simulated time of 35 seconds, the first 20 seconds were used for model training while the remaining 15 seconds were reserved for model testing/performance evaluation. This split has been marked with a horizontal black line on all the figures.

GNNs are able to capture the overall dynamics of the data, but we observe an error propagation with time. This error propagation is reduced in case of DI-GNN, which performs best amongst the three models.

The predictive capability of DI-GNN is influenced by

the data to derivative weight ($\gamma_d$). On increasing the influence of data over derivatives, the DI-GNN theoretically approaches a simple GNN implementation, but because of the presence of an additional derivative loss term, its loss value increases, resulting in poorer predictions than possible with a simple GNN.

PI-GNN performs poorly as compared to simple GNN or DI-GNN, and it is also not trivial to tune. The discretized equations contain non-linear polynomial expressions which are dependent on the discretization of the system, the node distribution in a graph, as well as the number of graphs in the complete domain. The effect of data to physics weight ($\gamma_p$) is opposite to that observed in the case of DI-GNN. One possible cause is that once the model is physics-informed, prioritizing data over physics would make the predictions worse.

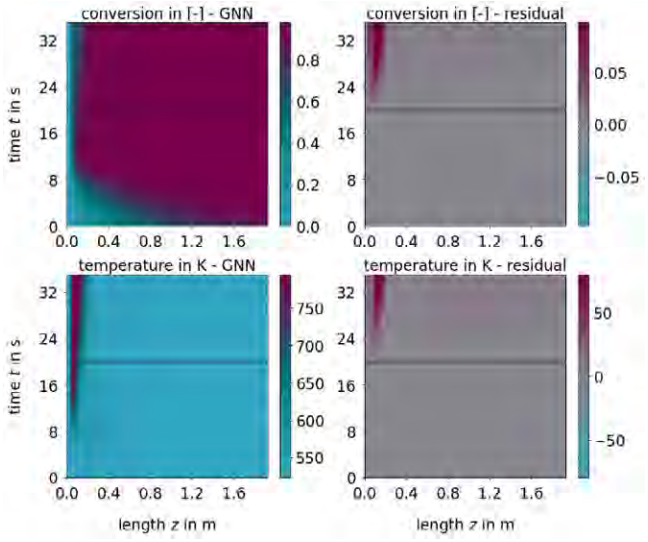



**Figure 5.** Conversion and temperature profiles predicted by the GNN and their comparison to the original data.

**Table 1:** Relative Frobenius Norms

| Method | Weight ($\gamma_-$) | $\|E\|$ for T | $\|E\|$ for X |
|---|---|---|---|
| GNN | - | 2.199 % | 2.165 % |
| DI-GNN | $\gamma_d$ = 0.5 | 1.389 % | 1.077 % |
| | $\gamma_d$ = 0.7 | 2.933 % | 3.845 % |
| PI-GNN | $\gamma_p$ = 0.5 | 8.715 % | 7.015 % |
| | $\gamma_p$ = 0.7 | 4.612 % | 6.755 % |

PI-GNN shows promising results in scenarios where we have sparse experimental data or certain boundary conditions must be explicitly enforced. They also ensure that the physical/scientific limitations are not violated (reactor temperature is below the maximum design temperature, conversion is not above 100%, etc.). But, as shown here, for the construction of surrogate models from mechanistic ones, their development can be cumbersome. The computation time/ epoch required for training of these models also varies with changing complexity ($t_{\mathrm{PI-GNN}} > t_{\mathrm{DI-GNN}} > t_{\mathrm{GNN}}$).

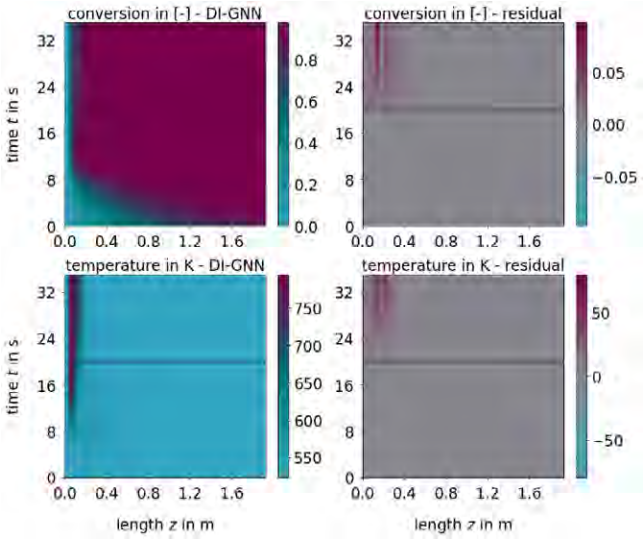



**Figure 6.** Conversion and temperature profiles predicted by the DI-GNN ($\gamma_d$ = 0.5) and their comparison to the original data.

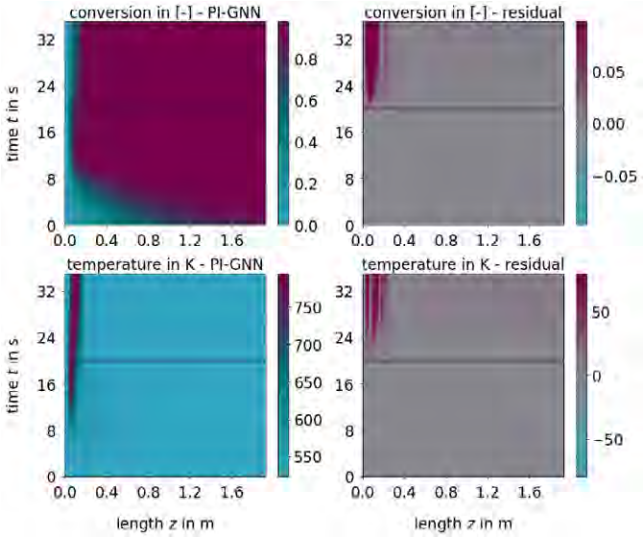



**Figure 7.** Conversion and temperature profiles predicted by the PI-GNN ($\gamma_p$ = 0.5) and their comparison to the original data.

## CONCLUSIONS

Efficient modeling of dynamical systems is critical for insightful predictions and effective decision making. To explore broader process alternatives, a faster model development and deployment pipeline is needed, which can be achieved through surrogate modeling techniques. However, the quality of a surrogate model is highly dependent on the representativeness of the available data. In our case, the training data may not fully capture the dynamics of the system, which could limit the accuracy

and generalizability of the model.

Present implementation of physics-informed models shows comparatively poor predictive capabilities but might outperform other purely data-driven models in scenarios where we have sparse experimental data and in inverse problem constructs for optimization or parametric adaptation of the model. These physically-informed models require more computing resources than a purely data-driven surrogate model. This computational burden can be alleviated by replacing the full mechanistic model with a reduced-order model, an approach particularly relevant for higher-order and multi-dimensional spatial domains.

To maximize the potential of current implementation, further work should ensure thorough hyperparameter optimization for GNN architecture as well as the loss function. The framework can also be extended and evaluated on different dynamical spatio-temporal systems, e.g. fluid mechanics, distribution networks, etc. A well-tuned, parametrized framework should be able to precisely capture the underlying dynamics and be well suited for use in optimization, uncertainty quantification and control.

## DIGITAL SUPPLEMENTARY INFORMATION

The code and data used in this study are available at the accompanying GitHub repository at https://github.com/mmkhalid-pse/hybrid-GNN.

## ACKNOWLEDGEMENTS

Md Meraj Khalid is also affiliated to the International Max Planck Research School for Advanced Methods in Process and Systems Engineering (IMPRS ProEng), Magdeburg, Germany. This work was partly funded by the Bundesministerium für Bildung und Forschung (BMBF) and Project Management Jülich (PtJ) under grant 03HY302R.

## REFERENCES

1. M. von Stosch, R. Oliveira, J. Peres, S. F. de Azevedo. Hybrid semi-parametric modeling in process systems engineering: Past, present and future. Comput. Chem. Eng. 60:86-101 (2014) https://doi.org/10.1016/j.compchemeng.2013.08.008
2. A. M. Schweidtmann, D. Zhang, M. von Stosch. A review and perspective on hybrid modeling methodologies. Digit. Chem. Eng. 100136 (2023) https://doi.org/10.1016/j.dche.2023.100136
3. K. Ghaib, F.-Z. Ben-Fares. Power-to-Methane: A state-of-the-art review. Ren. Sus. E. Reviews 81:433-446 https://doi.org/10.1016/j.rser.2017.08.004
4. R. T. Zimmermann, J. Bremer, and K. Sundmacher. Load-flexible fixed-bed reactors by multi-period design optimization. Chem. Eng. J. 428:130771 (2022) https://doi.org/10.1016/j.cej.2021.130771
5. L. Peterson, A. Forootani, E. I. Sanchez Medina, I. V. Gosea, K. Sundmacher, P. Benner. Towards digital twins for Power-to-X: Comparing surrogate models for a catalytic $CO_2$ methanation reactor. TechRxiv (2024) https://doi.org/10.36227/techrxiv.172263007.76668955/v1
6. M. Gori, G. Monfardini, and F. Scarselli. A new model for learning in graph domains. Proc. 2005 IEEE IJCNN 2: 729–734 (2005) https://doi.org/10.1109/IJCNN.2005.1555942
7. P. Veličković, G. Cucurull, A. Casanova, A. Romero, P. Liò, Y. Bengio. Graph attention networks. ICLR 2018 (2018) https://doi.org/10.48550/arXiv.1710.10903
8. Y. Seo, M. Defferrard, P. Vandergheynst, X. Bresson. Structured sequence modeling with graph convolutional recurrent networks. arXiv (2016) https://doi.org/10.48550/arXiv.1612.07659
9. A. Sanchez-Gonzalez, J. Godwin, T. Pfaff, R. Ying, J. Leskovec, P. W. Battaglia. Learning to simulate complex physics with graph networks. ICML 2020 (2020) https://doi.org/10.48550/arXiv.2002.09405
10. T. Pfaff, M. Fortunato, A. Sanchez-Gonzalez, P. W. Battaglia. Learning mesh-based simulation with graph networks. arXiv (2021) https://doi.org/10.48550/arXiv.2010.03409
11. H. Zhang, L. Jiang, X. Chu, Y. Wen, L. Li, Y. Xiao, L. Wang. Combining physics-informed graph neural network and finite difference for solving forward and inverse spatiotemporal PDEs. arXiv (2024) https://doi.org/10.48550/arXiv.2405.20000
12. D. Kingma and J. Ba. Adam: A method for stochastic optimization. ICLR 2015 (2015) https://doi.org/10.48550/arXiv.1412.6980
13. M. Raissi, P. Perdikaris, G. Karniadakis. Physics-informed neural networks: A deep learning framework for solving forward and inverse problems involving nonlinear partial differential equations. J. Comput. Phys. 378:686-707 (2019) https://doi.org/10.1016/j.jcp.2018.10.045

© 2025 by the authors. Licensed to PSEcommunity.org and PSE Press. This is an open access article under the creative commons CC-BY-SA licensing terms. Credit must be given to creator and adaptations must be shared under the same terms. See https://creativecommons.org/licenses/by-sa/4.0/



Systems & Control Transactions

**Research Article - Peer Reviewed Conference Proceeding**
ESCAPE 35 - European Symposium on Computer Aided Process Engineering
Ghent, Belgium. 6-9 July 2025
Jan F.M. Van Impe, Grégoire Léonard, Satyajeet S. Bhonsale,
Monika E. Polańska, Filip Logist (Eds.)

PSE PRESS

# Network Theoretical Analysis of the Reaction Space in Biorefineries

**Jakub Kontak [a], Jana M. Weber [a]***

[a] Delft University of Technology, Department of Intelligent Systems, Delft, The Netherlands
* Corresponding Author: j.m.weber@tudelft.nl

## ABSTRACT

The analysis of large chemical reaction space sheds light on reaction patterns between molecules and can inform subsequent reaction pathway planning. With the aim to discover more sustainable production systems, it became worthwhile to explicitly model the reaction space reachable from biobased feedstocks. In particular, the space that reactions in integrated biorefineries span for optimised biorefinery planning is of interest. In this work we show a network-theoretical analysis of biorefinery reaction data. We utilise the directed all-to-all mapping between reactants and products to compare the reaction space obtained from biorefineries with the entire network of organic chemistry (NOC). In our results, we find that despite having 1000 times fewer molecules, the constructed network resembles the NOC in terms of its scale-free nature and shares similarities regarding its small-world property. Additionally, we analyse the coverage rate of the biorefinery reaction data and find that many common second and third-level intermediates are present, while the querying strategy leads to a lack of data on value-added refinery end-products and on feedstock molecules, requiring more advanced and combined data querying strategies in the future.

**Keywords**: Biosystems, Refining, Reaction, Algorithms, Planning, Network Science, Reaction Space

## INTRODUCTION

Biorefineries are facilities converting a feedstock-mix of biomass into multiple products through selected processing steps [1], in other words, they produce value-added (bio-)chemicals out of biomass. They comprise a range of (bio-)chemical reactions to cater for the desired refinery product portfolio.

The reaction space that is covered in biorefineries can be complex combining chemical and biological transformations. It is known that a wide range of biomass sources is suitable for the conversion into valuable products through many different routes, which makes the design of optimal biomass conversion pathways a challenging problem [2]. With the aim to design both economical and sustainable refineries, several works focus on biorefinery optimisation approaches where optimal reaction pathways and processes are selected [3-5]. While such works perform a manual preselection of reactions and process units to be considered, the automatization of this task has received notable attention, so that in the future larger (bio-)chemical reaction spaces mined from electronic databases can be evaluated quickly [6-8].

To this end, i.e., reaction pathway planning, but also for automated retrosynthesis planning [9], it became generally necessary to understand the large reaction spaces covered in electronic chemical databases better. Such large chemical reaction space covering millions of molecules are thus analysed intensively.

The reaction space is commonly represented as a graph, where depending on the chosen graph model, molecules are represented by nodes and reactions by edges [10], hyperedges [11], or a second node type [12]. For instance, the work of Jacob & Lapkin performed a holistic statistical analysis on the network of organic chemistry (NOC) to inform on subsequent planning and prediction tasks. In particular, they focused on network characterisation through graph theoretical properties such as degree distributions, pathlengths, wiring pattern and others [10]. They found that the known chemical space organises into a scale-free network, which allowed them to draw conclusions on the likely evolution of the reaction space and molecular participation in synthesis routes across the data space.

Here, we perform a similar network theoretical analysis of the reaction space found in biorefineries and compare it to the chemical reaction space, i.e. the NOC. Insights gained during the analysis of the biorefinery space can improve and speed up the search for promising pathways and identify bottlenecks. In particular, we investigate the following aspects: (i) how is the biorefinery reaction network characterised by network theoretical metrics, (ii) does the biorefinery reaction space exhibit selected similarities to the NOC, and (iii) how (bio-)chemically complete is the biorefinery reaction space investigated in this work with regard to molecules present in the data?

# METHODS

## Data extraction and preprocessing

With more than 46 million recorded reactions and more than 119 million recorded molecules REAXYS is one of the largest databases to investigate reaction spaces [13]. To extract relevant reactions from REAXYS using their web-interface and the Query builder tool, we utilise the "title, abstract and keywords" search with the "contains" parameter set, for the word "biorefiner". The word is not finished on purpose to give the results for both singular and plural forms. Such query provides almost 1300 reactions from the papers that contained the sub-word "biorefiner" in their title, abstract or set of keywords and included information on reactants, products and the number of reaction steps.

During the preprocessing steps, reactions that contain empty reactants or empty product fields are removed. Some of the reactions are recorded as having multiple steps. From this data, we do not know which intermediate molecules are omitted, yet we opt to keep the data due to the relatively small size of the entire biorefinery reaction space.

## Graph model and implementation

The constructed model is a weighted, directed graph connecting reactants and products with directed edges, using an "all to all" wiring scheme, as illustrated for one reaction in **Figure 1**. Each node represents one chemical compound while the edges leaving it represent the reaction that is utilising this molecule as reactant and producing a product at the end of the edge. To distinguish multi-step from single-step reactions for network analysis, we represented the number of reaction steps with the weight of the edge. This way certain properties can still be computed despite the missing intermediates. Duplicate edges are removed, keeping the one with minimal distance in the data. While this representation is a severe simplification as it disregards the polyadic relationships in the data (e.g. multiple reactants are needed to create multiple product(s)), it makes it comparable to other network theoretical studies. We follow these simplification to compare our analysis with the analysis of the NOC [10].

The acquired reaction data is used in the graph model and implemented with Python 3.11. We made use of the NetworkX and powerlaw packages to work with and analyse the graph data [14,15].

**Figure 1.** Illustration of the directed graph model. Nodes represent molecules, edges represent reactant-product relationships. Note that this neglects polyadic and stoichiometric relationships.

## Network analysis metrics

Network metrics are measured to assess the structure of the reaction space and how it compares to the NOC. Here, we focus our analysis on the following network properties.

Firstly, we analyse if the biorefinery network can be classified as scale-free network with similarity to the NOC. We do so by performing statistical testing of the degree distributions. The in-degree is the number of edges incoming to a node and the out-degree is the number of edges outgoing from a specific node. For instance, in **Figure 1**, node B has an in-degree of 0 and an out-degree of two. We first test against an exponential fit and then investigate differences between four heavy-tailed distributions: power law, truncated power law, lognormal and stretched exponential [15]. For the statistical tests the `distribution_compare` method from the powerlaw package is used. We further compare the exponents of the power law fits with those of the NOC.

Secondly, we are interested in understanding if we can expect a "small-world" behaviour in the biorefinery reaction space. This is characterised by the average shortest path scaling proportionally with the logarithm of the number of nodes [10], while also exhibiting high clustering. On average a relatively small number of steps (network edges) connects any two entities (network nodes) in "small-world" networks. We calculate the average shortest path length ($\bar{L}$) in Eq. 2. and the global clustering coefficient ($\bar{C}$) in Eq. 1, which measures the average probability that two vertices connected to a third vertex are also directly connected to each other [10]. We then compare the values with those of the NOC. The metrics are calculated on the weighted, undirected, largest connected component of the network (clustering coefficient) and weighted, directed graph (average path length) respectively.

$$\bar{C} = \frac{3 \times number\ of\ triangles}{number\ of\ triads} \quad (1)$$

$$\bar{L} = \sum_{\substack{u,v \in F \\ u \neq v}} \frac{d(u,v)}{|F|} \quad (2)$$

where a triad consists of two edges that share a vertex , $|F|$ is the set of nodes $u, v$ where the distance $d(u,v)$ between $u$ and $v$ is finite, [18] and $d(u,v)$ is the shortest path from node $u$ to node $v$.

Thirdly, to describe the network topology we consider metrics based on betweenness centrality. We calculate the global central point dominance ($\overline{C_B}$) in Eq. 3 and perform clustering (on the largest connected component of the graph) based on the Girvan-Newman algorithm using betweenness centrality ($c_B$) as edge weights. We choose a suitable number of clusters using a simplified cluster evaluation score ($score_{Cl}$) comparing edges within and between clusters, see Eq. 5.

$$\overline{C_B} = \frac{1}{n-1} \sum_{i \in V} c_B(i^*) - c_B(i) \quad (3)$$

$$c_B(i) = \frac{1}{((n-1)(n-2))} \sum_{s,t \in V} \frac{\sigma(s,t|i)}{\sigma(s,t)} \quad (4)$$

$$score_{Cl} = \frac{1}{g} \sum_{j}^{g} \frac{2\ e_{intra,j}}{e_{inter,j}} \quad (5)$$

where $c_B(i)$ is the normalised betweenness centrality of node $i$, $c_B(i^*)$ is the largest betweenness centrality in the graph, $\sigma(s,t)$ is the number of shortest pathways from node $s$ to node $t$ and $\sigma(s,t|i)$ is the number of shortest pathways from node $s$ to node $t$ that go through node $i$. Further, $g$ is the number of clusters (node groups) and $e_{intra,j}$ and $e_{inter,j}$ are the numbers of intra- (within) and inter- (between) cluster edges given a clustering $j$.

While all metrics are compared to the NOC, the clustering is qualitatively investigated and mapped against referenced molecules of lignocellulosic biorefinery from selected literature [16].

## Coverage analysis

To analyse the coverage of the biorefinery space, we investigate the following aspects: the split of molecules into clusters based on Eq. 5 and the Girvan-Newman algorithm, a quantitative comparison of our detected molecules with platform molecules named in selected literature [16], and the impact of the querying strategy on the completeness of the biobased molecular space.

For the impact of the querying strategy, we compare our naïve query strategy using a REAXYS keyword search with one that targets common feedstock molecules of biorefineries and the reactions that they are listed in. The targeted feedstock molecule search for the lignocellulosic case includes lignin, cellulose and hemicellulose as feedstock molecules, and for the blue biorefinery chitin, chitosan, laminarin, fucoidan and alginic acid as feedstock molecules. The Jaccard similarity coefficient is calculated between molecules found in the different networks. Additionally, we calculate the percentage of how many of the specialised molecules from the targeted search are also picked up by the naïve keyword search.

# RESULTS AND DISCUSSION

Firstly, we present the network-theoretical analysis of the biorefinery reaction space and compare this with the NOC to draw conclusions about the similarities of both data spaces. Secondly, we qualitatively discuss the coverage of the reaction space in the biorefinery network.

## Reaction space

The constructed network consists of 1273 vertices and 2009 edges. It is a disconnected graph separated into 78 components where the largest connected component contains 79.5% of all the nodes. At the same time, the second largest connected component contains less than 1.5 % of all the nodes. This indicates that most of the reaction space is connected and concentrated within a single cluster, suggesting high interconnectivity between those molecules. The remaining molecules form small and unconnected islands of molecular species, connected by one or few reactions.

**Table 1.** Summary of compared metrics between the biorefinery network and the NOC.

| | Global clustering coefficient | Average shortest path length | Central point dominance | In-degree exponent | Out-degree exponent |
|---|---|---|---|---|---|
| NOC | 0.00058 | 6.02 | 0.003719 | 3.0436 | 2.0935 |
| Biorefinery | 0.09001 | 4.77 | 0.009864 | 3.1755 | 2.1651 |

## Network analysis and comparison with NOC

Despite having three orders of magnitude fewer molecules, the constructed network resembles the NOC's topology. The biorefinery network exhibits similarities in scale-free and small-world properties. This could indicate that the sampling strategy (biorefinery reactions are also captured in the NOC) does not destroy the topology and also, that there are intrinsic properties of (bio-)chemical networks that remain unchanged. These could be for instance common numbers of reacting molecular species, common reaction patterns, common reaction

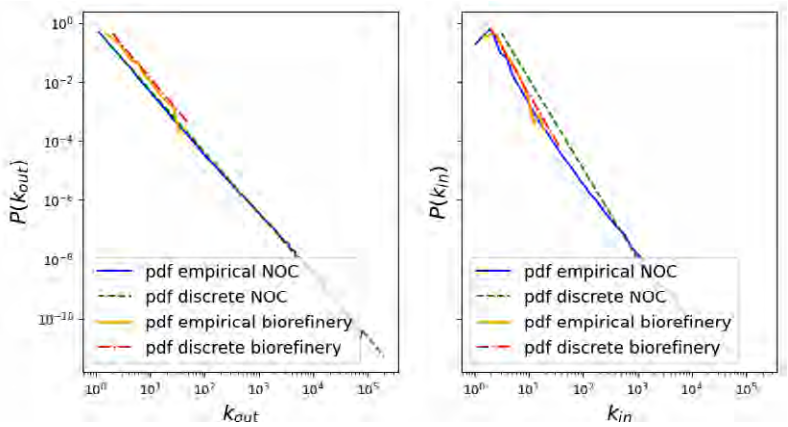



**Figure 2.** Degree distributions of the NOC and biorefinery network as the probability of observing a degree of $k$, using the Python package *powerlaw*. The term pdf empirical denotes the plotted distribution from the observed data, while pdf discrete represents the predicted distribution from power-law model based on the fitted exponent.

publishing practices. The scale-free and small-world properties are discussed in the following sections, while all metrics are provided in **Table 1**.

## Scale-free property

A power law distribution fits the biorefinery network data, which approves the hypothesis that both in- and out-degree are heavy-tailed distributions and to an extend similar to the NOC. Yet, we also identify that other distributions fit our data well.

Both in- and out- degree distribution show a high loglikelihood ratio with a significant p-value of 0.04 (in-degree) and 0.03 (out-degree) for the data to be described by a power law distribution rather than an exponential distribution. This minimum alternative is checked to classify the distribution as heavy-tailed. We illustrate the degree distributions of the biorefinery network as power law fit in **Figure 2**. For the in-degree, further comparisons of the power law distribution against truncated power law, lognormal, or stretched exponential distributions do not lead to statistically significant results. For the out-degree, we see that the lognormal, stretched exponential, and truncated power law distributions are slightly preferred over a power law.

To compare the exponents with those of the NOC, we opt to make use of the power law fit. We find exponents of 3.17 and 2.16 for the in-degree and out-degree respectively. Thus, the respective power law exponents indicate that the network topology can be described as scale-free. Jacob and Lapkin reported an exponent of 3.04 for the in-degree and 2.09 for the out-degree of the NOC [10]. Our findings closely resemble the topology of the NOC. Note that the in-degree distribution deviates from the power law distribution for the in-degree of one, meaning that for those nodes, the power law predicts a higher frequency, which was also seen in the NOC and in further literature [17]. For the in-degree, a $k_{min}$ of three was used for the NOC, while for biorefinery network $k_{min}$ was set to two. For the out-degree, a $k_{min}$ of one was used for fitting the NOC, while for the biorefinery network a $k_{min}$ of two was set.

## Small-world property

We discuss the small-world property based on the global clustering coefficient and the average shortest path length. Connected to these, we also discuss the central point dominance.

The clustering coefficient found in the biorefinery network is 0.09, which is significantly higher than the clustering coefficient of 0.00058 in the NOC. A high clustering coefficient is indicative of the small-world property of a network. In the original work the NOC was described to exhibit the small-world property [10]. We expect that the difference in coefficient is mainly due to our more specialised smaller network, which as a subset of the full NOC is composed of very well-connected molecules and reactions.

The average shortest path length of the biorefinery network is 4.77, while in the NOC an average shortest path length of 6.02 was measured. Besides the average, we illustrate both probability distributions of observing a path with a certain length in **Figure 3**. Commonly, in small-world networks the average shortest path should be approximately the logarithm of the number of nodes, which in the case of the biorefinery network would be $\log_{10} 1273 = 3.10$. Thus, here our network shows longer average path length than normally found in small-world networks.

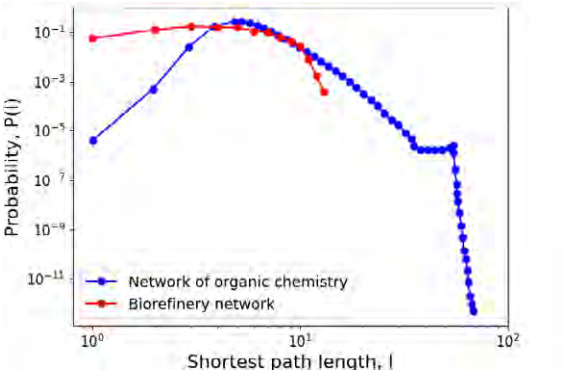



**Figure 3**. Comparison of the probability $P(l)$ of observing the shortest path with length $l$, between the NOC [10] and the network of biorefineries. NOC plot recreated using WebPlotDigitizer.

Lastly, we consider the central point dominance. The central point dominance in the biorefinery network is 0.0099, which is moderately higher than the central point dominance of 0.0037 of the NOC. This suggests that the biorefinery network has a slightly higher centralisation, meaning that a bigger proportion of reactions and pathways in the network go through a central node than in the NOC.

## Coverage of the biobased space

We note that our biobased data space is not significantly fragmented yet lacks some important biorefinery platform molecules as well as feedstocks and end products. This indicates that while our naïve query strategy is successful in mapping general reaction pathways throughout a refinery, to retrieve a holistic picture of all possible molecules and reactions, more advanced query strategies are needed.

### Cluster analysis

We utilise the scoring function described in Eq. 5 to identify the best number of clusters for the biorefinery network. The highest score of 42.92 was achieved with three clusters. We tested values between two and 100 clusters. The clustering based on the Girvan-Newman algorithm is displayed as a schematic overview in **Figure 4**.

Cluster one contains molecular derivatives and pathways mainly from lignin-based feedstock (orange cluster in **Figure 4**). This is not surprising as lignocellulosic biorefineries are one of the major biorefinery classes studied and we can therewith expect them to be highly present and well annotated in REAXYS.

Cluster two contains mostly pathways that produce and utilize 2-methoxy-phenol (yellow cluster in **Figure 4**). 2-methoxy-phenol is also derived from lignin and an important model compound towards the production of green chemicals, flavour molecules such as vanillin, and in the medical sector. We assume that it is very prominent in the network due to its role as important and versatile intermediate.

Cluster three contains a limited number of reactions, all involving 3-methylpyridine as a reactant (green cluster in **Figure 4**). 3-methylpyridine is a precursor for agrochemicals. This cluster is only loosely connected to the remaining space and does not contribute much to the main network characteristics.

We cannot visually detect any fragmentation of the network that clearly separates biorefinery processing steps or types of biorefineries. We note that while we used generic search terms, lignin processing and its associated pathways and derivatives are prominently represented, while other types of biorefineries (e.g. blue biorefinery) do not appear notably in the clusters.



**Figure 4.** Clustering of the biorefinery network using the Girvan-Newman algorithm and three clusters.

### Molecular species coverage

Common biobased feedstock molecules such as hemicellulose or chitosan are lacking in our biorefinery

**Table 2.** Presentation of the network coverage for the lignocellulosic biorefinery molecules from Tey et. al. [16]. It shows how many molecules from the paper are present in the constructed biorefinery network.

| | 1st intermediate | 2nd intermediate | 3rd intermediate | 4th intermediate | Final product |
|---|---|---|---|---|---|
| # species | 3 | 11 | 41 | 33 | 10 |
| # species in data | 2 | 9 | 25 | 11 | 3 |

network. Yet we find that their first, second, and third order derivatives along reaction pathways are present in the biorefinery network. We show in our quantitative analysis based on the platform molecules summarised by Tey et. al. [16] in **Table 2** that 66% of the 1st order intermediates, 82% of the 2nd order intermediate, and 61% of the 3rd order intermediates of lignocellulosic biorefineries are present. This indicates that the naïve query strategy is a sufficient proxy to assemble the data space spanning from 1st to 3rd order intermediates. We find significant less 4th order intermediates and final products in our network. Some products like ethanol and methanol are recorded, yet many more specialised possible biorefinery end products are not present. This, in combination with our cluster analysis, indicates that for fully automated pathway planning, additional effort is needed to query or manually add feedstock and product molecules.

### Database querying strategy

As comparison to our naïve keyword search strategy, we perform targeted molecular search strategies (see the method section coverage analysis) to gain insights on the impact of data acquisition. Both feedstock targeted searches bring networks of about 750 molecules (775 for the lignocellulosic search and 707 for the blue biorefinery search). The Jaccard similarity of the lignocellulosic network and the general biorefinery network in this work is only 8.20% and the Jaccard similarity between the blue biorefinery network and the general biorefinery network in this work is only 2.70%. We find that 20.00% of the molecules in the specialised lignocellulosic network are also part of the general biorefinery network and only 7.36% of the molecules from the specialised blue biorefinery network are present in the general biorefinery network. This indicates that despite the high coverage of common biorefinery 1st to 3rd order intermediates, currently a relatively large space of specialised molecular species at early processing stages of biorefineries remains unexplored by the keyword search strategy. We conclude that a more advanced strategy querying for targeted molecular species and their connecting reactions is needed to obtain a complete picture of possible design options for biorefineries.

## CONCLUSIONS

This paper investigates the reaction space in biorefineries. We present two main contributions. Firstly, this paper characterises the network space through network theoretical metrics and illustrates the topological similarities between the biorefinery reaction space and the NOC. For instance, the analysis of degree distributions shows that the network is scale-free with $\gamma_{in} \approx 3.2$ and $\gamma_{out} \approx 2.2$ resembling the NOC while containing 1000 times less vertices. Secondly, this paper presents evidence that the naïve keyword querying strategy contains many of the important first, second, and third intermediates of lignocellulosic biorefineries. Yet, it also shows that the current network is preliminary, lacking both some specialised products and feedstock molecules, as well as molecules and reactions from different biorefinery types. Our finding that about 80% of the data space is a closely connected network structure, makes this approach very useful for integrated biorefinery planning with the potential of automated reaction pathway optimisation. Our recommendations for future work are to work with a less severe abstraction in the graph data model and to focus on the addition of, in this work identified, bottleneck areas in the data.

## DIGITAL SUPPLEMENTARY MATERIAL

Our code for this work is available at GitHub (https://github.com/Intelligent-molecular-systems/network-analysis-of-biorefineries).

## ACKNOWLEDGEMENTS

JK and JMW would like to acknowledge Benedek Székács for his work on alternative querying strategies that helped inform the analysis in this work.

## REFERENCES

1. Kamm, B, Kamm, MJAM. Principles of biorefineries. *Applied microbiology and biotechnology 64*(2) 137-145 (2004) https://doi.org/10.1007/s00253-003-1537-7
2. Ioannou, I, D'Angelo, SC, Galán-Martín, Á, Pozo, C, Pérez-Ramírez, J, Guillén-Gosálbez, G. Process modelling and life cycle assessment coupled with experimental work to shape the future sustainable production of chemicals and fuels. *Reaction Chemistry & Engineering 6*(7) 1179-1194 (2021) https://doi.org/10.1039/D0RE00451K
3. Voll, A, Marquardt, W. Reaction network flux analysis: Optimization-based evaluation of reaction pathways for biorenewables processing. *AIChE Journal 58*(6) 1788-1801 (2012). https://doi.org/10.1002/aic.12704
4. Ulonska, K, Skiborowski, M, Mitsos, A, Viell, J. Early-stage evaluation of biorefinery processing pathways using process network flux analysis. *AIChE Journal 62*(9) 3096-3108 (2016) https://doi.org/10.1002/aic.15305
5. Zhang, D, del Rio-Chanona, EA, Shah, N. Screening synthesis pathways for biomass-derived sustainable polymer production. *ACS Sustainable Chemistry & Engineering 5*(5) 4388-4398 (2017)

https://doi.org/10.1021/acssuschemeng.7b00429

6. Weber, JM, Guo, Z, Zhang, C, Schweidtmann, AM, Lapkin, AA. Chemical data intelligence for sustainable chemistry. *Chemical Society Reviews 50*(21) 12013-12036 (2021) https://doi.org/10.1039/D1CS00477H
7. Jacob, PM, Yamin, P, Perez-Storey, C, Hopgood, M, Lapkin, AA. Towards automation of chemical process route selection based on data mining. *Green Chemistry 19*(1) 140-152 (2017) https://doi.org/10.1039/C6GC02482C
8. Weber, JM, Guo, Z, & Lapkin, AA. Discovering Circular Process Solutions through Automated Reaction Network Optimization. *ACS Engineering Au 2*(4) 333-349 (2022) https://doi.org/10.1021/acsengineeringau.2c00002
9. Szymkuć, S, Gajewska, EP, Klucznik, T, Molga, K, Dittwald, P, Startek, M, Bajczyk, M, Grzybowski, BA. Computer-assisted synthetic planning: the end of the beginning. *Angewandte Chemie International Edition 55*(20) 5904-5937 (2016) https://doi.org/10.1002/anie.201506101
10. Jacob, PM., Lapkin, A. Statistics of the network of organic chemistry. *Reaction Chemistry & Engineering 3*(1) 102-118 (2018) https://doi.org/10.1039/C7RE00129K
11. Mann, V, Venkatasubramanian, V. AI-driven hypergraph network of organic chemistry: network statistics and applications in reaction classification. *Reaction Chemistry & Engineering 8*(3) 619-635 (2023) https://doi.org/10.1039/D2RE00309K
12. Weber, JM, Schweidtmann, AM, Nolasco, E, Lapkin, AA. Modelling circular structures in reaction networks: Petri nets and reaction network flux analysis. In *Computer Aided Chemical Engineering* 48 1843-1848 (2020) https://doi.org/10.1016/B978-0-12-823377-1.50308-6
13. REAXYS fact sheet. June 2018
14. Hagberg, A, Swart, PJ, Schult, DA. *Exploring network structure, dynamics, and function using NetworkX* (No. LA-UR-08-05495; LA-UR-08-5495). Los Alamos National Laboratory (LANL), Los Alamos, NM (United States) (2008)
15. Alstott, J, Bullmore, E, Plenz, D. Powerlaw: a Python package for analysis of heavy-tailed distributions. *PloS one 9*(1) e85777 (2014) https://doi.org/10.1371/journal.pone.0085777
16. Tey, TO, Chen, S, Cheong, ZX, Choong, ASX, Ng, LY, Chemmangattuvalappil, NG. Synthesis of a sustainable integrated biorefinery to produce value-added chemicals from palm-based biomass via mathematical optimisation. *Sustainable Production and Consumption 26* 288-315 (2021) https://doi.org/10.1016/j.spc.2020.10.012
17. Grzybowski, BA, Bishop, KJ, Kowalczyk, B, Wilmer, CE. The'wired'universe of organic chemistry. *Nature Chemistry 1*(1) 31-36 (2009) https://doi.org/10.1038/nchem.136
18. Bonato A, Chung F. Global clustering coefficients. In: Handbook of Graph Theory. Ed: Gross JL, Yellen J, Zhang P. CRC Press/Taylor and Francis, Boca Raton, FL, 2nd edn. (2014), pp. 1456–1476. https://doi.org/10.1201/9780203490204

© 2025 by the authors. Licensed to PSEcommunity.org and PSE Press. This is an open access article under the creative commons CC-BY-SA licensing terms. Credit must be given to creator and adaptations must be shared under the same terms. See https://creativecommons.org/licenses/by-sa/4.0/



Systems & Control Transactions

**Research Article - Peer Reviewed Conference Proceeding**
ESCAPE 35 - European Symposium on Computer Aided Process Engineering
Ghent, Belgium. 6-9 July 2025
Jan F.M. Van Impe, Grégoire Léonard, Satyajeet S. Bhonsale,
Monika E. Polańska, Filip Logist (Eds.)

PSE PRESS

# Structural Optimization of Translucent Monolith Reactors through Multi-objective Bayesian Optimization

**Onur C. Boy[a], Ulderico Di Caprio[a], Idelfonso B.R. Nogueira[b] and M. Enis Leblebici[a]***

[a] KU Leuven, Center for Industrial Process Technology, Diepenbeek, Belgium
[b] Norwegian University of Science and Technology (NTNU), Department of Chemical Engineering, Trondheim, Norway
* Corresponding Author: muminenis.leblebici@kuleuven.be

## ABSTRACT

Photochemical monolith reactors offer advantages over microreactors by providing high mixing efficiency and surface area to volume ratio while being scalable. However, optimizing monolith design parameters like channel number, shape, and stacking is critical to maximizing light usage and reactor efficiency. This work proposes using Bayesian optimization and COMSOL Multiphysics simulations to automatically design translucent monoliths for photochemical reactions. The goal is to maximize both photochemical space-time yield and space-time yield. Ray tracing simulations were performed while evaluating five different channel geometries (circular, elliptical, triangular, square, and pentagonal) and optimizing parameters, including channel diameter, vertical stacking, shape rotation, and ellipse axis ratio. Results showed a clear trade-off between Space-Time Yield (STY) and Photochemical Space-Time Yield (PSTY), with optimized elliptical channels achieving up to 15.3% improvement in STY with minimal PSTY increase and 9.0% enhancement in PSTY with negligible STY decrease.

**Keywords**: Photochemistry, Photoreactors, Ray tracing, Bayesian Optimization, Monoliths

## INTRODUCTION

Photochemical reactors harness light energy to drive chemical transformation under mild conditions with high energy efficiency [1]. Despite their numerous advantages, including enhanced selectivity and control, reduced organic solvent requirements, renewable energy utilization, and access to novel reaction pathways, industrial adoption remains limited due to several key challenges [2]. The primary obstacles include suboptimal apparent reaction rates, insufficient energy efficiency, and reactor design limitations that impede effective scale-up largely arising from limited light penetration into the reaction environment, leading to low light utilization [3]. While microreactors can partially address these limitations through high surface area-to-volume ratios and improved illumination uniformity [4], their restricted throughput capacity and spatial mismatch between the light source and the reactor channels present significant barriers to industrial implementation. Consequently, there is a pressing need for innovative reactor designs that can effectively balance photon distribution, mass transfer, and scalability considerations.

Monolith reactors offer a scalable approach combining microreactor advantages with industrial throughput. While microreactors excel in mass and photon transfer due to high surface area-to-volume ratios, their scalability limits industrial use. Translucent monolithic structures overcome these limitations, enabling efficient light penetration across reaction channels and achieving substantially higher energy efficiency than conventional designs [6]. However, optimal geometry and opacity are crucial to prevent non-uniform light distribution between surface and reaction regions.

Light scattering in photochemical reactors significantly influences reactor performance through complex light-matter interactions [7]. The geometry of reactor channels, particularly their diameter and spatial arrangement, plays a crucial role in determining photon distribution and utilization efficiency [8].

Ray-tracing simulations can accurately predict photon distribution patterns within a reactor volume. Several studies in the literature have employed ray tracing to optimize the geometrical configurations of photoreactor

systems. Singh et al. conducted a parametric study to optimize the geometry of a photocatalytic monolith reactor, focusing on the optimal aspect ratio of channels and the lamp-to-monolith distance, achieving a maximum photon efficiency of 50% [9]. Athanasiou et al. optimized a photocatalytic reactor design integrating membranes and optical fibers for water purification [10]. Their study identified an optimal intermediate channel thickness of 2 mm, enabling the treatment of 50 $m^3$/day of water with a pressure drop of 1.5 bar. In another study, Martín-Somer et al. investigated reflector geometries for a tubular UV reactor [11]. They demonstrated that parabolic reflectors achieved the highest optical efficiency (65.9%). Jacobs et al. developed translucent monoliths for the degradation of pharmaceutical micropollutants during wastewater treatment. Using COMSOL ray tracing, they optimized the design with 2 mm channel diameter, 2 mm spacing, and 3 vertically stacked rows of channels. The optimized reactor showed significantly improved energy efficiency compared to conventional internally illuminated monoliths [6].

Coupling ray tracing simulations with a gradient-free optimization algorithm, such as Bayesian optimization (BO), can enable the automated design of photochemical reactors. BO can systematically navigate multiple design variables simultaneously - including channel geometry, dimensions, and orientation - while minimizing the number of required simulations. This combined approach offers several advantages over classical optimization approaches where parameter sweep analysis is employed for addressing complex geometrical configurations. These advantages include a continuous design space, rapid identification of optimal design parameters, efficient exploration in high dimensional spaces, and a significant reduction in the experimental effort required for reactor design [12]. Moreover, the flexibility and extensibility of the coupled approach make the optimization process adaptable to various photocatalytic reactor design problems, allowing for the incorporation of additional physical models and design variables.

In this study, the multi-objective optimization of translucent monolithic structures is investigated using ray tracing simulation and Bayesian optimization to maximize the efficiency of the reactor previously studied by Jacobs et al. [6]. To the best of our knowledge, this is the first study to couple ray tracing simulations with Bayesian optimization. The objective function is linearized through space-time yield (STY) and photochemical space-time yield (PSTY) to balance reactor efficiency and energy efficiency, respectively. The effect of weights assigned to STY and PSTY on the optimal configuration is also examined through varying weights. Six channel geometries (circular, elliptic, triangular, square, and pentagonal) are examined along with channel rotation, number of vertically stacked rows, channel diameter, and aspect ratio.

# METHODOLOGY

## Ray Tracing Simulation

COMSOL Multiphysics 6.2 employs nonsequential ray tracing to model complex light-matter interactions in photochemical reactors. The algorithm solves coupled first-order ordinary differential equations for ray position (q) and wave vector (z) components:

$$\frac{dz}{dt} = -\frac{\partial w}{\partial q} \quad (1)$$

$$\frac{dq}{dt} = -\frac{\partial w}{\partial z} \quad (2)$$

The simulation begins by discretizing the geometry and establishing initial ray positions and directions. Primary rays are generated from a source, and when these rays encounter interfaces with different refractive indices, the algorithm computes new directions based on Snell's law and Fresnel's equations: Snell's law describes how light bends when passing between two mediums defined by $n_1$ and $n_2$, and the refractive indices of the two mediums, $\theta_1$and $\theta_2$, the angles of incidence and refraction. Fresnel's equations quantify how much light is reflected and how much is transmitted (refracted) at an interface between two media defined by reflection and transmission coefficients.

Figure 1 shows the 2D geometry of a monolith design example used in this study, implemented in COMSOL, including elliptic channel geometries. The refractive index of the reaction medium is determined by the concentration of photocatalyst, which is 0.0125 mol $TiO_2/m^3$ Water. The wall condition at the outer border of the reactor is set to deactivate any rays that exit the reactor. Number of rays per release is set to 100, and rays are realesed with a canonical ray direction vector with a cone angle of π/6 from the boundary release as it is depicted in Figure 1. The total source power per unit thickness is 50 W/m. Lastly, a deposited ray power is located on channel surfaces to capture the amount of absorbed light by the reaction medium.

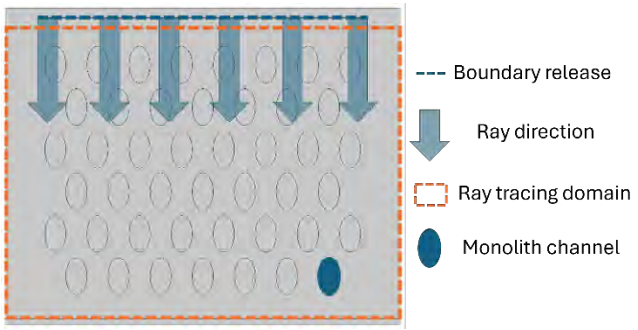



**Figure 1.** 2D geometry of the monolith reactor.

The maximum number of secondary rays was limited to 500,000 to prevent memory overflow. Optimal number

of mesh density is chosen to be the same with Jacobs et al. [6]. A lower limit threshold is also employed to discard secondary rays fall below a certain amount of energy. Table 1 shows the parameters set in the simulation:

**Table 1:** Parameters of ray tracing simulation employed in this work

| Ray tracing parameters | Value |
|---|---|
| Mesh density | 70 elements per $mm^3$ |
| Number of primary rays | 10,000 |
| Limit for secondary rays | 500,000 |
| Refractive index of the 3D-printed material | 1.5403 |
| Refractive index of air | 1 |
| Refractive index of $TiO_2$-Water suspension | 1.335 |
| Wavelength of the Light | 550 nm |
| Source power per unit thickness | 50 W/m |
| Ray release cone angle | π /6 |

## Theoretical Framework

The evaluation of different reactor designs requires a comprehensive thinking on both energy efficiency and reactor performance, as indicated by PSTY and STY, respectively. The energy of a single photon, $E_{photon}$ [J], can be expressed as where $v$ is the speed of light, $h$ is Planck's constant, and $\lambda$ is the wavelength of the absorbed light

$$E_{photon} = \frac{v \cdot h}{\lambda} \quad (3)$$

then, the total amount of absorbed photonic energy divided by the energy of a single photon gives the number of photons absorbed, $\vartheta$, which can be expressed as:

$$\vartheta = \frac{P_{abs}}{E_{photon}} \quad (4)$$

where $P_{abs}$ is the absorbed power by the reaction medium, which is obtained from simulation by integrating deposited power over channel surfaces. Further, dividing $\vartheta$ to Avogadro's number, $N_A$, gives the moles of absorbed photons in $mol \cdot s^{-1}$:

$$\vartheta = \frac{P_{abs} \cdot \lambda}{v \cdot h \cdot N_A} \quad (5)$$

$STY$ is defined as the amount of treated wastewater per unit volume of the reactor. In this study, the quantum yield is assumed to be 2.35%, representing the fraction of absorbed photons that actively contribute to the photodegradation process. To calculate the actual rate of pollutant degradation, the quantum yield is multiplied by the number of absorbed photons (in $mol \cdot s^{-1}$). Once the pollutant degradation rate is obtained, the volume of treated water, expressed in $m^3$ $water.s^{-1}$, can be calculated by dividing the pollutant degradation rate by the pollutant concentration, $C_{pollutant}$ (in $m^3$ $water.s^{-1}$). The value of $C_{pollutant}$ is taken as 0.1 $mol.m^3$ $water^{-1}$. Then, $STY$ (in $m^3$ water. $m^3$ $reactor^{-1}.s^{-1}$), is determined by normalizing this treated water volume by the reactor volume, $V_{reactor}$:

$$STY = \frac{\vartheta \cdot \Phi}{C_{pollutant} \cdot V_{reactor}} \quad (6)$$

Consequently, $PSTY$ is calculated by dividing $STY$ to normalized lamp power, $P_{norm}$ (W). $PSTY$ considers how much energy spent for a unit volume of reactor, and normalized lamp power is calculated by dividing lamp power, $P_{lamp}$, to the reactor volume, $V_{reactor}$. $1\ m^3$ of reactor is taken as reference volume:

$$P_{norm} = \frac{P_{lamp}}{V_{reactor}} \times 1\ m^3 \quad (7)$$

$$PSTY = \frac{STY}{P_{norm}} \quad (8)$$

$STY$ and $PSTY$ provide a robust framework to evaluate reactor designs, enabling a balanced assessment of energy efficiency and performance for optimized photoreactor operation.

## Bayesian Optimization

Bayesian optimization is an efficient method for finding the global optimum of black-box functions that are expensive to evaluate. It combines a probabilistic surrogate model that approximates the objective function and provides uncertainty estimates with an acquisition function that determines the most promising points to evaluate next. The surrogate model is updated as new observations are made, continuously improving its predictions of the underlying function. The algorithm works iteratively by initializing with a few random samples and then fitting the surrogate model to the observed data. At each iteration, it selects the next evaluation point by maximizing an acquisition function that balances exploration (sampling uncertain regions) and exploitation (sampling regions likely to have good values). The acquisition function is a mathematical function used in BO, and it assigns a value to each potential point, indicating how valuable it would be to evaluate that point next.

Expected Improvement (EI) was chosen to guide the optimization process for the remainder of the study due to its adaptive behavior between exploration and exploitation. The loss function is defined as a linear combination of the normalized STY ($STY_{norm}$) and normalized PSTY ($PSTY_{norm}$), as shown in Equation 9. For the normalization process, initial estimates of the minimum and maximum values are based on prior knowledge.

$$Loss = w_{STY} \times STY_{norm} + w_{PSTY} \times PSTY_{norm} \quad (9)$$

$$STY_{norm} = \frac{STY - STY_{min}}{STY_{max} - STY_{min}} \quad (10)$$

$$PSTY_{norm} = \frac{PSTY - PSTY_{min}}{PSTY_{max} - PSTY_{min}} \quad (11)$$

To determine an appropriate weight set ($w_{STY}$, $w_{PSTY}$) for the objective function, the optimization algorithm is executed for varying weight values. The assigned weights range from 0.1 to 0.9, discretized in increments of 0.1, resulting in 9 different weight sets. Each run is initialized with 25 random configurations and iterated for an additional 75 simulations.

**Table 2:** Variables defining the geometry in the ray tracing simulation.

| Variable | Domain | Range |
|---|---|---|
| Characteristic diameter | Real | 1-6.5 |
| Aspect ratio | Real | 0.25-1.75 |
| Number of vertically stacked rows | Integer | 1,2,3 |
| Channel Shape | Categorical | Elliptic, circular, square, triangular, pentagonal, plus-signed |
| Rotation | Real | 0-90 degree |

Variable space is defined as shown in Table 2. Six channel geometries (i.e., circular, elliptic, triangular, square, and pentagonal) are examined along with channel rotation, number of vertically stacked cell rows, characteristic channel diameter, and aspect ratio of ellipses. The characteristic diameter is defined as the diameter for circles, the minor axis length for ellipses, the side length for triangles and squares, and the side length of the cross frame for plus-shaped channels. Analyzed channel shapes are depicted in Figure 2. Python library *scikit-optimize* is utilized for the optimization study. After the simulation is loaded onto a Python interface using MPh v1.2.4, the optimization study is initialized with 25 random points and run for an additional 75 iterations. During each iteration, a COMSOL ray tracing simulation is executed for a new geometrical configuration. The resulting absorbed power is retrieved from the simulation, and the surrogate model is updated before the next evaluation point.

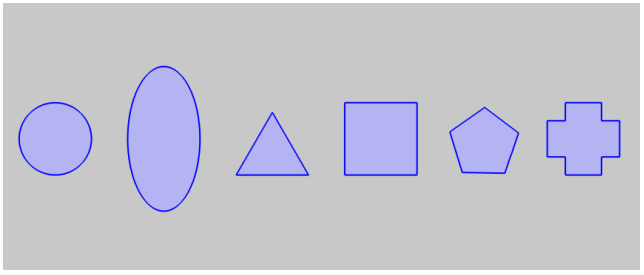


**Figure 2.** Candidate channel shapes

## RESULTS AND DISCUSSION

The geometric configuration of each iteration is recorded, as each represents a valid reactor design. Figure 3 presents the best three solutions for each weight set, distinguished by unique color and marker combinations. As expected, when the weight of STY increases, the best solutions tend to cluster around the bottom-right corner of the figure, where STY is maximized. Conversely, assigning larger weights to PSTY causes the solutions to shift toward the upper-left corner of the figure, resulting in higher PSTY values and lower STY yields. This competing relationship between STY and PSTY is also evident in the figure. Consequently, more balanced solutions are obtained for weights $w_{STY}$=0.5 and $w_{PSTY}$=0.5. These weights are utilized for the remainder of the study. It should be noted that each run may yield different solutions due to the probabilistic nature of the optimization process. Nevertheless, the general trend is consistent across varying weights, and the selected weights are deemed reliable.

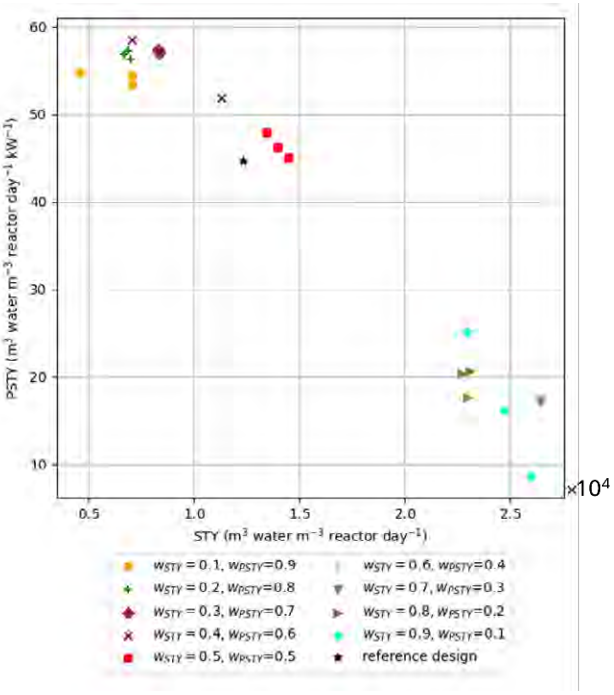



**Figure 3.** effect of weights on STY and PSTY

Following the investigation on the weight effect, a BO optimization with 50 random points and 150 additional simulations was conducted. All candidate points are shown in Figure 4. The STY ranges from approximately 5,000 to 22,500 m³ water/m³ reactor/day, while the PSTY ranges from about 15 to 60 m³ water/m³ reactor/day/kW. As expected, a negative correlation between STY and PSTY is observed, indicating a trade-off between these two parameter. The results are compared to the reference design, shown with a black marker: three unit cells

with 2 mm diameter circular channels, as described by Jacobs et al. [6]. A general trend is observed where larger PSTY values correspond to increased channel volumes. This is attributed to a greater amount of photocatalyst, which can absorb more light energy. However, designs with similar volumes may vary in the amount of absorbed light, demonstrating the impact of geometrical configuration.

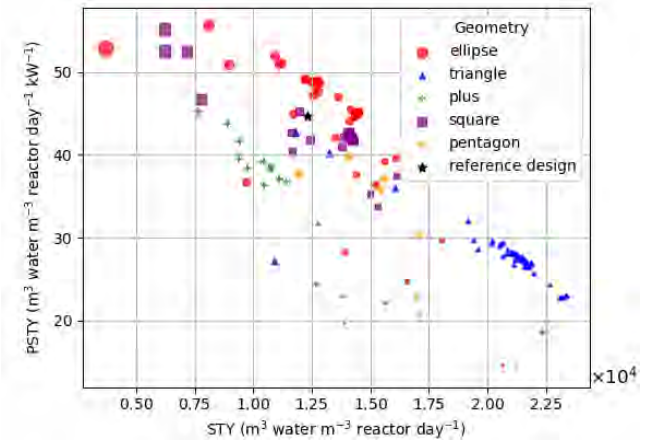



**Figure 4.** Bayesian optimization results (marker sizes proportional to channel volumes.)

Triangular channels are predominantly located in the bottom-right corner of Figure 4, where the STY is maximized. For pentagonal and plus-shaped channel geometries, the results are relatively suboptimal compared to the other geometries. Square channels are positioned in the middle and upper-left regions of the figure, showing some of the highest PSTY values. Elliptic channels dominate the balanced region and are clustered around the reference design, indicating promising solutions.

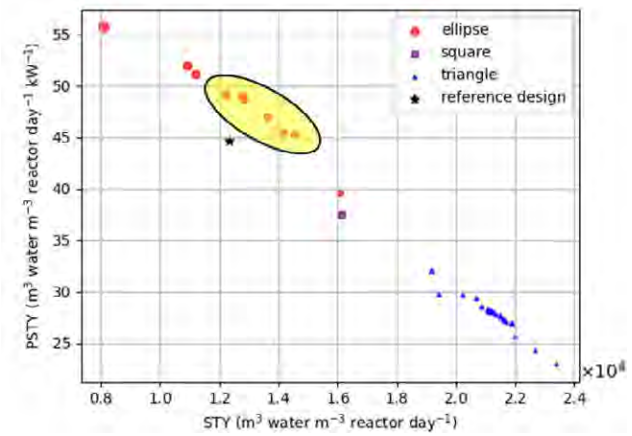



**Figure 5.** Pareto optimal solutions with dominating solutions indicated by the yellow area.

The Pareto front, which represents the non-dominating designs, is plotted separately in Figure 5. Dominating solutions, highlighted in yellow, include points that outperform the reference design in both objectives, as well as those that are slightly worse in one objective. The exact geometrical configurations of the dominating solutions are detailed in Table 3. Each solution is defined by its characteristic diameter (a), aspect ratio for ellipses only (b/a), rotation angle (r), number of vertically stacked rows (N), and total channel volume (V). All dominating solutions feature an elliptic channel shape, with a consistent aspect ratio (b/a) of 1.75 across all configurations, indicating highly elongated ellipses. The rotation angle (r) ranges from 56.4° to 90.0°, reflecting variations in the orientation of the elliptical geometry within the design. The characteristic diameters fall between 1.00 mm and 1.95 mm despite being examined over a broader range of 1.00 mm to 6.50 mm, suggesting that smaller geometries are more favorable. Table 3 also indicates that an optimal design can be achieved with two vertically stacked rows. At one extreme, the optimization study enables a 15.3% increase in STY with only a 1.2% increase in PSTY. Additionally, a roughly 9.0% increase in PSTY can be achieved with a minor reduction in STY at the other extreme. These findings demonstrate the influence of geometrical configuration on the performance of a photo-reactor, and the results emphasize the importance of considering both reaction efficiency and energy efficiency together in reactor design.

**Table 3:** Geometrical configurations of the dominating solutions. (**a**: Characteristic diameter/minor axis length for ellipses, **b/a**: Aspect ratio of the ellipse, **r**: Rotation, **N**: Number of vertically stacked rows, **V**: Total volume of channels, **ΔSTY**: Percent change in STY compared to the reference design, **ΔPSTY**: Percent change PSTY compared to the reference design )

| a (mm) | b/a | r (°) | N | Shape | ΔSTY (%) | ΔPSTY (%) |
|---|---|---|---|---|---|---|
| 1.95 | 1.75 | 90.0 | 2 | Ellipse | -0.6 | 9.1 |
| 1.21 | 1.75 | 57.1 | 3 | Ellipse | 3.6 | 8.7 |
| 1.21 | 1.75 | 56.5 | 3 | Ellipse | 4.1 | 8.1 |
| 1.10 | 1.75 | 56.4 | 3 | Ellipse | 9.6 | 4.8 |
| 1.01 | 1.75 | 56.5 | 3 | Ellipse | 13.0 | 1.7 |
| 1.00 | 1.75 | 81.6 | 3 | Ellipse | 15.3 | 1.2 |

BO is particularly effective for optimizing functions with up to 20 variables. Although this study includes categorical and discrete variables, which make the optimization problem more complex, the total number of variables is much lower than 20. Hence, computational efficiency is not a limiting factor for either BO or the ray tracing simulation, considering that it is a 2D simulation. The proposed methodology can be extended to alternative channel shapes and various types of photoreactors. However, if a more free-form surface controlled by multiple parameters is used, computational

complexity must be considered for 3D simulations, as well as geometrical complexity and reactor dimensions.

## CONCLUSION

This study demonstrates the successful application of Bayesian optimization for designing translucent monolithic photochemical reactors. Through a systematic multi-objective optimization approach considering both STY and PSTY, we identified optimal channel geometries that outperform circular designs. The results revealed important trade-offs between STY and PSTY, with elliptical channels showing the best performances. Two optimized elliptical configurations achieved up to 15.3% improvement in STY with minimal PSTY increase and 9.0% enhancement in PSTY with negligible STY decrease. The methodology established here provides a framework for optimizing photochemical reactor designs using ray tracing-coupled Bayesian optimization. The findings demonstrate that geometric optimization can significantly enhance throughput and energy efficiency in translucent monolithic reactors.

## ACKNOWLEDGEMENTS

Prof. Leblebici gratefully acknowledges the support of KU Leuven C2 project Scalable performant solar cell module for CO2 Reduction Coupled with Organic Synthesis (SPROUT) C2E/23/010.

## REFERENCES

1. Su, Y., Straathof, N. J. W., Hessel, V., & Noël, T. Photochemical transformations accelerated in continuous-flow reactors: Basic concepts and applications. In *Chemistry - A European Journal* (Vol. 20, Issue 34, pp. 10562–10589). Wiley-VCH Verlag. (2014) https://doi.org/10.1002/chem.201400283
2. Loubière, K., Oelgemöller, M., Aillet, T., Dechy-Cabaret, O., & Prat, L. Continuous-flow photochemistry: A need for chemical engineering. *Chemical Engineering and Processing - Process Intensification*, *104*, 120–132. (2016) https://doi.org/10.1016/j.cep.2016.02.008
3. Claes, T., Dilissen, A., Leblebici, M. E., & van Gerven, T. Translucent packed bed structures for high throughput photocatalytic reactors. *Chemical Engineering Journal*, *361*, 725–735. (2019) https://doi.org/10.1016/j.cej.2018.12.107
4. Coyle, E. E., & Oelgemöller, M. Micro-photochemistry: Photochemistry in microstructured reactors. The new photochemistry of the future? In *Photochemical and Photobiological Sciences* (Vol. 7, Issue 11, pp. 1313–1322). Royal Society of Chemistry. (2008) https://doi.org/10.1039/b808778d
5. Leblebici, M. E., Stefanidis, G. D., & van Gerven, T. Comparison of photocatalytic space-time yields of 12 reactor designs for wastewater treatment. *Chemical Engineering and Processing: Process Intensification*, *97*, 106–111. (2015) https://doi.org/10.1016/j.cep.2015.09.009
6. Jacobs, M., Meir, G., Hakki, A., Thomassen, L. C. J., Kuhn, S., & Leblebici, M. E. Scaling up multiphase photochemical reactions using translucent monoliths. *Chemical Engineering and Processing - Process Intensification*, *181*. (2022) https://doi.org/10.1016/j.cep.2022.109138
7. Binjhade, R., Mondal, R., & Mondal, S. Continuous photocatalytic reactor: Critical review on the design and performance. In *Journal of Environmental Chemical Engineering* (Vol. 10, Issue 3). Elsevier Ltd. (2022) https://doi.org/10.1016/j.jece.2022.107746
8. Jacobs, M., Meir, G., Hakki, A., Thomassen, L. C. J., Kuhn, S., & Leblebici, M. E. Scaling up multiphase photochemical reactions using translucent monoliths. *Chemical Engineering and Processing - Process Intensification*, *181*. (2022) https://doi.org/10.1016/j.cep.2022.109138
9. Athanasiou, D. A., Romanos, G. E., & Falaras, P. Design and optimization of a photocatalytic reactor for water purification combining optical fiber and membrane technologies. *Chemical Engineering Journal*, *305*, 92–103. (2016) https://doi.org/10.1016/j.cej.2015.11.080
10. Martín-Sómer, M., Moreira, J., Santos, C., Gomes, A. I., Moreno-SanSegundo, J., Vilar, V. J. P., & Marugán, J. Reflector design for the optimization of photoactivated processes in tubular reactors for water treatment. *Journal of Environmental Chemical Engineering*, *11*(5). (2023) https://doi.org/10.1016/j.jece.2023.110609
11. Singh, M., Salvadó-Estivill, I., & Li Puma, G. Radiation field optimization in photocatalytic df monolith reactors for air treatment. *AIChE Journal*, *53*(3), 678–686. (2007) https://doi.org/10.1002/aic.11093
12. Savage, T., Basha, N., McDonough, J. Machine learning-assisted discovery of flow reactor designs. *Nat Chem Eng* **1**, 522–531 (2024). https://doi.org/10.1038/s44286-024-00099-1

© 2025 by the authors. Licensed to PSEcommunity.org and PSE Press. This is an open access article under the creative commons CC-BY-SA licensing terms. Credit must be given to creator and adaptations must be shared under the same terms. See https://creativecommons.org/licenses/by-sa/4.0/



Systems & Control Transactions

**Research Article - Peer Reviewed Conference Proceeding**
ESCAPE 35 - European Symposium on Computer Aided Process Engineering
Ghent, Belgium. 6-9 July 2025
Jan F.M. Van Impe, Grégoire Léonard, Satyajeet S. Bhonsale,
Monika E. Polańska, Filip Logist (Eds.)

PSE PRESS

# A Novel Symbol Recognition Framework for Digitization of Piping and Instrumentation Diagrams

**Zhiyuan Li[a,b], Jinsong Zhao[a,b]*, Huahui Zhou[c], and Xiaoxin Hu[c]**

[a] Tsinghua University, Department of Chemical Engineering, Beijing, China
[b] State Key Laboratory of Chemical Engineering, Beijing, China
[c] Sinopec Ningbo Engineering Co., Ltd, Ningbo, China
* Corresponding Author: jinsongzhao@tsinghua.edu.cn.

## ABSTRACT

Piping and Instrumentation Diagrams (P&IDs) play a crucial role in the chemical industry, yet they are often stored as scanned images or computer-aided design (CAD) drawings, limiting their seamless integration into modern digital workflows. Consequently, the task of automating P&ID digitization has attracted significant attention from the computer-aided design (CAD) research community. Traditional approaches, which typically rely on conventional object detection techniques, often demand extensive manual annotations to accurately identify and classify the various symbols in P&IDs. In this paper, we proposed a novel framework for automating the recognition of P&IDs. Our method first extracts key features of geometric primitives in CAD drawings through an automated process. Subsequently, a Transformer-based model is employed to predict the layer assignment of these primitives. Following this, an unsupervised clustering method, guided by predefined rules and geometric distances, is applied within each layer type to facilitate the automatic identification of devices, pipes, instrumentation, valves, insulation, and utilities in P&IDs. Extensive evaluation on an annotated dataset comprising 336 authentic P&IDs demonstrates that the proposed semantic annotation method achieves an overall accuracy exceeding 92%. The results of the unsupervised clustering are visualized, demonstrating promising performance and supporting the effectiveness of the proposed method. This study provides valuable insights into the intelligent digitization of P&IDs and lays the groundwork for further advancements in intelligent chemical process design.

**Keywords**: Intelligent Systems, Piping and Instrumentation Diagram, Computer Aided Design

## 1 INTRODUCTION

Piping and Instrumentation Diagrams (P&IDs) play a central role at every stage of chemical engineering design. They serve as an essential tool for communication among engineers, operators, and maintenance personnel by depicting how piping systems connect with industrial processing equipment and how processes are controlled through automated systems. By indicating critical information such as isolation valves and emergency shutdown devices, P&IDs aid operators in executing safe operations and responding effectively in emergencies.

Over the years, millions of P&IDs have been manually generated, scanned, and stored in image formats, encapsulating a wealth of valuable engineering design knowledge [1]. However, analyzing the complex information within these diagrams—due to the intricacy of devices, text, and pipelines—has traditionally required extensive manual effort by engineers. This manual analysis is not only time-consuming but also prone to errors. Therefore, the ability to automatically extract information from P&IDs would significantly enhance productivity and minimize human error. Moreover, since P&IDs are a primary source of design and safety information in chemical engineering, the extracted data can be integrated with intelligent algorithms for process simulation, optimization, and safety analysis, promoting more effective chemical process management and design.

To support digital storage and interoperability, the Digital Exchange of Process and Instrumentation Diagrams (DEXPI) standard [2] was introduced. By defining a comprehensive set of structured data formats based on

eXtensible Markup Language (XML), DEXPI enhances the efficiency and accuracy of engineering processes. In recent years, numerous deep learning-based image recognition algorithms have been developed to convert image-format P&IDs into drawings that comply with the DEXPI standard. For example, Kim et al. proposed a P&ID digitization system that employs two independent Generative Flow Networks (GFL) for recognizing equipment symbols of varying sizes [3]. Despite advances in deep learning-based image recognition, digitization of P&IDs remains challenging due to the high irregularity of ordering and uncertain orientations [4].

Transitioning from these challenges, most traditional P&ID files are created using computer-aided design (CAD) tools, which means that beyond the visible image data, these drawings inherently contain detailed information about the shapes, positions, and layer properties of various geometric primitives (such as lines, arcs, polygons). This fine-grained semantic data can greatly enhance the effectiveness of P&ID recognition by addressing the limitations of traditional methods that rely solely on images. Building on this insight, in this paper we propose a novel intelligent symbol recognition framework that tokenizes various geometric primitives found in CAD drawings, then a Transformer-based model is employed to automatically annotate the layer assignment of these primitives. After that, we apply unsupervised clustering to group the isolated primitives into meaningful symbols (including devices, valves, etc.). Validation on 336 authentic P&IDs demonstrates that our framework achieves an overall accuracy of 0.927 in annotating geometric primitives. The visualization of the clustering results further demonstrates the effectiveness of our approach.

# 2 METHODOLOGY

## 2.1 Data Preprocessing

This paper primarily uses two data sources: CAD drawings and rasterized images. The CAD drawings are in Drawing Exchange Format (DXF), exported from AutoCAD. DXF files employ a vector-based data format, providing detailed attribute information for various geometric primitives and defining the blocks and layers within the drawing. The rasterized images are in Portable Network Graphics (PNG) format, converted from the DXF files. Thus, there is a one-to-one correspondence between the CAD drawings and the rasterized images.

We use the Python library ezdxf to extract the types and layer information of geometric primitives from CAD drawings. The layer information for these geometric primitives is manually created by the designer and typically conveys the specific meaning of the primitives in the P&ID. Therefore, we use the layer information as the semantic label for the primitives. In P&ID drawings, the layers are primarily categorized into 11 distinct categories, the details of which are shown in Table 1.

Next, we utilize the Shapely Python library to convert various types of geometric primitives from the DXF file into Shapely geometric objects. Specifically, straight lines and open polylines are directly converted into LineString objects, while closed polylines are transformed into Polygon objects. For curves in the DXF file, we approximate them with a polyline consisting of 72 endpoints, converting them into either LineString or Polygon objects based on whether they are closed. Subsequently, we employ functions from Shapely to calculate the centroids of the geometric primitives and the minimum distances between each pair of primitives. For each primitive, we identify the 128 nearest geometric primitives as its neighboring nodes and construct the adjacency matrix.

**Table 1.** Common layer definitions in P&IDs.

| Layer name | Definition |
|---|---|
| **Device** | Contour of Physical devices used in the system, such as pumps |
| **Instrument** | Symbol of measuring and controlling instruments |
| **Valve** | Symbol of valves in the system |
| **In-out Signal** | Communication signals for system input and output |
| **Pipeline** | Symbol of the pipework that are used to transport process materials |
| **Control Line** | Symbol of the control lines that are used to carry signals |
| **Insulation** | Symbol of the insulation around piping or equipment |
| **Hot Utility** | Symbol of systems that provide heat |
| **Cold Utility** | Symbol of systems that provide cooling |
| **Arrow** | Symbol of the flow of materials |

## 2.2 Model for Layer Assignment Prediction

### 2.2.1 Backbone Architecture

The backbone architecture of the predictive model is illustrated in Figure 1. PNG images derived from CAD drawings are processed using the pre-trained HRNetV2-W48 model [5] to automatically extract features. Additionally, the previously discussed feature extraction method is used to extract the normalized center coordinates of geometric primitives from the CAD drawings and to construct an adjacency matrix.

Using these normalized coordinates, we project each geometric primitive from the CAD drawing to its corresponding position in the PNG image. We then apply bilinear interpolation-based upsampling to align the feature maps with the positions of the geometric primitives, calculating the feature vectors at each primitive's location. These interpolated feature vectors undergo further linear transformations and ReLU operations to generate the

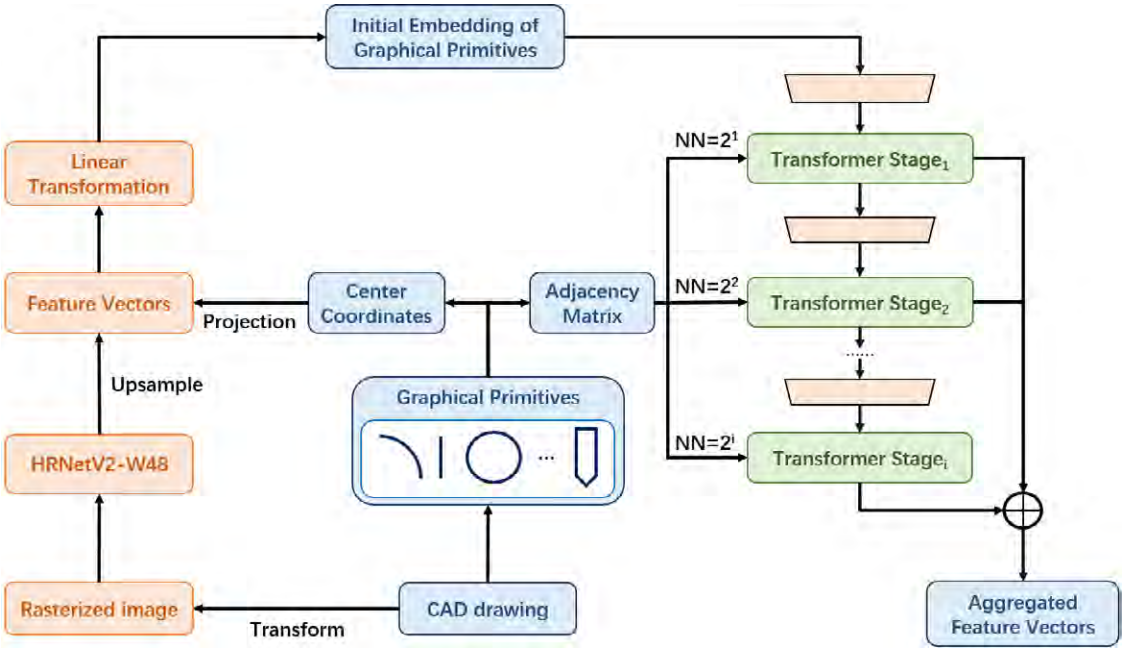



**Figure 1.** Backbone architecture for predicting layer assignment of the geometry primitives.

initial embedding for each geometric primitive. The updated vectors are subsequently processed using a Transformer model that consists of various stages, each stage applies self-attention with spatially localized k-nearest neighbors, enabling the refinement of each primitive's representation using its local features. The features across different stages are then fused by calculating the mean of the output of the Transformer stages.

### 2.2.2 Layer Assignment Prediction Task

The updated vector representations of geometric primitives are then processed using a multi-layer perceptron (MLP) to predict the layer to which each primitive belongs. The MLP model outputs a predicted score for each geometric primitive corresponding to each layer, which is then compared to the actual layer properties of the primitives. The loss function employed is based on the cross-entropy loss function:

$$L_{sem} = -\frac{1}{M}\sum_{m=1}^{M}\sum_{i=1}^{N} y_{i,m} log(p_{i,m}) \quad (1)$$

where $M$ is the total number of geometric primitives, and $N$ is the number of layer categories, $y_{i,m}$ represents whether the $m$-th geometric primitive actually belongs to the $i$-th layer; it is equal to 1 if it does, and 0 if it does not. Additionally, $p_i$ represents the predicted score for the model's prediction of the geometric primitive belonging to the $i$-th layer. In order to overcome the impact of class imbalance, we choose AM-Softmax loss function [6], which introduces an additive margin to the target class's logit. During the inference process, the predicted semantic label is the layer with the highest predicted probability.

## 2.3 Clustering for Symbol Recognition

After assigning layer for the geometric primitives, in order to extract higher-level features, such as the contours of devices, and to better understand the physical process layout, we perform unsupervised clustering for each layer to automatically group isolated geometric primitives into meaningful symbols.

For instances with closed contours, such as equipment, instruments, valves, insulation, and inlet/outlet labels, we apply a Depth First Search (DFS) algorithm to cluster all geometric primitives within the same layer. We assume that if the distance between two geometric primitives is less than the specified threshold, they are considered to intersect. By utilizing a stack to simulate the recursive depth-first search, we group all intersecting geometric primitives into the same cluster, while non-intersecting ones are assigned to separate clusters.

For instances without closed contours, such as pipelines, control lines, cold utilities, and hot utilities, we distinguish instances based on predefined rules. For example, when two perpendicular pipelines intersect, it typically signifies that a main pipeline is branching into two directions. In such cases, the algorithm generates three clusters: one for the main pipeline and two for the branch pipelines. Conversely, if two perpendicular pipelines cross without an intersection point, it suggests that the two pipelines are physically offset. In this scenario, one pipeline may be represented as two straight lines in the drawing. The algorithm identifies collinear segments with distances that are consistent with common knowledge

and merges them into a single cluster.

# 3 EXPERIMENTS

## 3.1 Datasets and Evaluation Metrics

The dataset utilized in this study consists of 336 real P&ID drawings stored in DXF format, each labeled with its corresponding layer assignment. These drawings represent 17 process flows designed for the deep desulfurization of industrial flue gas, providing detailed information about the piping systems, instruments, valves, process topology, and utilities. Although the original versions of these drawings include layer annotations, the naming conventions for the layers are inconsistent. Consequently, we standardized the layer names across the drawings into 11 categories, as detailed in Table 1. Additionally, we converted the drawings from DXF format to PNG format. Prior to being input into the model, each PNG image was cropped into square blocks, each measuring 14m × 14m. The training, validation, and test sets were divided in an 8:1:1 ratio, resulting in 268, 33, and 35 P&ID drawings, respectively.

The Transformer-based layer prediction model we employed has an input dimension of 384 and consists of four layers of self-attention. The number of neighboring nodes utilized by each self-attention layer increases from 2 in the first layer to 4 in the second, 8 in the third, and 16 in the fourth layer. The output dimension is 11, corresponding to the 11 layer categories. During training, the initial learning rate is set to 0.00025, and the Adam optimizer is used with $\beta_1 = 0.9$ and $\beta_2 = 0.999$. Every 20 epochs, the learning rate is reduced to 50% of its previous value. The original momentum is set to 0.1, with momentum decay set to 0.5. The model is trained for 300 epochs. The batch size is fixed to 6, and we trained our model with 6 NVIDIA RTX 4090 GPUs with 1 training sample on each GPU.

We evaluated the effectiveness of the proposed model using the following classic classification metrics:

- Precision: The proportion of correctly predicted instances of a specific layer among all instances predicted as that layer.
- Recall: The proportion of correctly predicted instances of a specific layer among all instances that actually belong to that layer.
- F1 Score: The harmonic mean of precision and recall, considering the balance between these two metrics.
- Accuracy: The proportion of correctly predicted samples out of the total number of samples.

Additionally, we employed a confusion matrix to analyze which geometric elements of the layers are more likely to be mistaken for one another.

## 3.2 Results on Layer Assignment Prediction

The quantitative evaluation results on the test set are presented in Table 2. Figure 2 shows the detailed prediction results for each class in the form of a confusion matrix. The diagonal elements of the matrix represent the number of correctly classified samples, while the off-diagonal elements indicate misclassifications, reflecting the model's ability to distinguish between different categories. It can be seen that our model performs well in overall layer classification for all geometric primitives, achieving an $F_1$ score of 0.9224, with precision of 0.925, recall of 0.9224, and accuracy of 92.7%.

**Table 2.** Evaluation results of the layer prediction model.

| Layer name | $F_1$ | Precision | Recall |
|---|---|---|---|
| **Device** | 0.9249 | 0.9051 | 0.9457 |
| **Instrument** | 0.9643 | 0.9611 | 0.9676 |
| **Valve** | 0.9608 | 0.9606 | 0.9611 |
| **In-out Signal** | 0.9845 | 0.9772 | 0.9919 |
| **Pipeline** | 0.8693 | 0.8487 | 0.8910 |
| **Control Line** | 0.7844 | 0.7977 | 0.7716 |
| **Insulation** | 0.9349 | 0.9496 | 0.9207 |
| **Arrow** | 0.9290 | 0.9290 | 0.9290 |
| **Hot Utility** | 0.3042 | 0.5192 | 0.2151 |
| **Cold Utility** | 0.6973 | 0.7765 | 0.6328 |
| **Total** | 0.9244 | 0.9250 | 0.9224 |

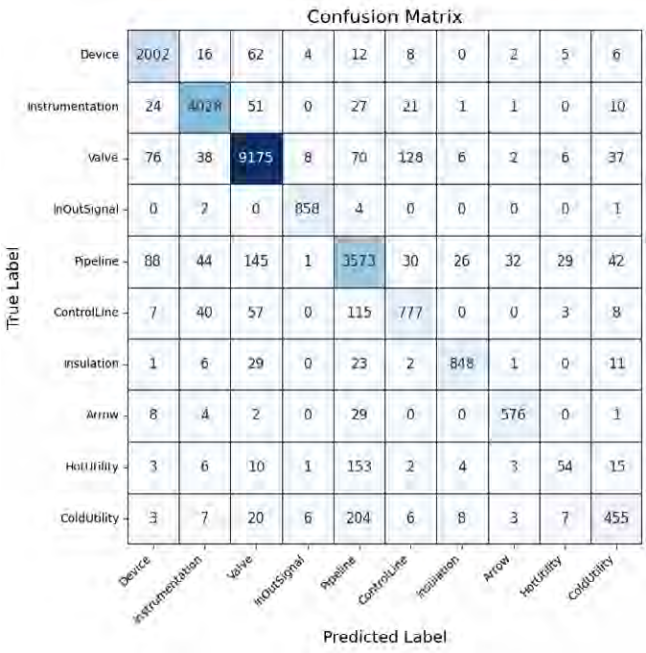



**Figure 2.** Confusion Matrix of Classification Results.

Among the geometric primitives in each layer, the model demonstrates high accuracy in recognizing devices, instruments, valves, inlet/outlet markers, insulation

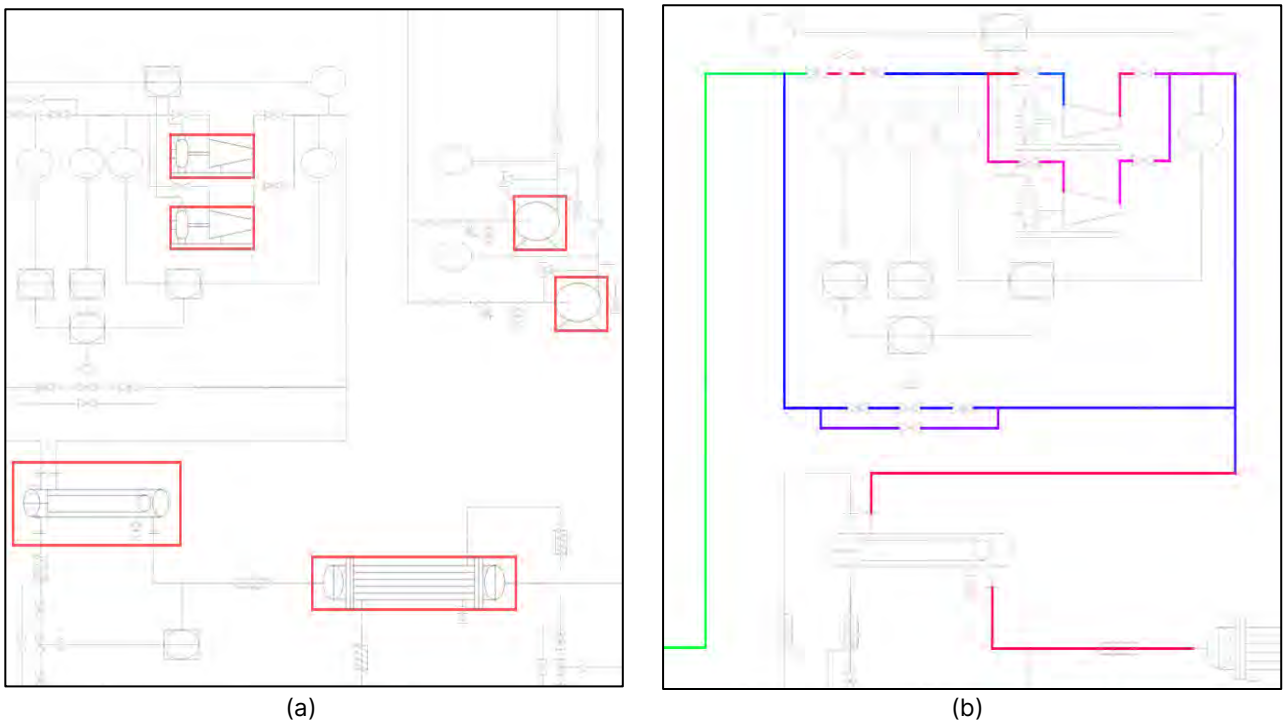
layers, and arrows, with F1 scores exceeding 0.9. We hypothesize that this is due to the relatively standardized shapes of the symbols in these layers and the large number of training samples available.

In contrast, there is room for improvement in the recognition of pipes, control lines, and utilities. This is likely because these layers consist mainly of multiple line segments, which can form highly variable combinations. As indicated by the confusion matrix, some pipelines are misclassified as equipment outlines or valves. Furthermore, the geometric primitives in the control lines, cold utilities, and hot utilities layers are difficult to distinguish from those in the pipeline layer. We believe this is not only because these layers contain fewer geometric primitives than the pipeline layer, but also because they cannot be easily differentiated based solely on the positional information of the geometric primitives. Specifically, the key distinction between control lines and pipes is whether both endpoints of the line segments (or polylines) are connected to control instruments. Similarly, the fundamental criterion for distinguishing between utilities and process material pipelines is whether the transported substance is process material, which requires additional textual information, such as piping codes, from the P&IDs.

## 3.3 Visualization of Clustering Results

The clustering results of the equipment, and pipelines layers are shown in Figure 3, which not only allows us to observe the performance of target recognition for each layer, but also helps assess the clustering precision of different layers. The clustering outcomes for the equipment layers are illustrated in Figures 3(a), respectively. Due to variations in size and distribution density between the equipment and other identified objects, we applied distinct distance thresholds for each layer. For the equipment layer, a larger threshold of 6 units effectively groups adjacent primitives together. While for all other layers, a smaller threshold of 0.001 units ensures more precise clustering by grouping close geometric primitives together, minimizing redundancy and incorrect clustering. From the clustering visualization, we can see that the contours of most equipment and instruments, including instrument interface pipes, are accurately recognized and clearly distinguishable. This demonstrates the strong potential of using a DFS algorithm for closed-contour target recognition.

The clustering results for the pipelines layers are presented in Figures 3(b), respectively. It can be observed that the various pipelines were effectively distinguished according to the established rules. However, some pipelines were not successfully recognized by the layer assignment predictive model, and as a result, their clustering results were not reflected in the drawing. What's more, since the current rule definitions are relatively simplistic, certain specific scenarios, such as the presence of bypass valves on pipelines have not been adequately addressed. In these cases, the bypass pipe should merge with the main pipeline. Consequently, the



(a) (b)

**Figure 3.** (a) Clustering visualization for the equipment layers; (b) Clustering visualization for the pipelines layers.

redundancy in the pipeline clustering results can be reduced by refining the rules.

## 4 CONCLUSION

In this study, we propose a novel intelligent symbol recognition framework for P&ID based on CAD drawings. During the data preprocessing stage, CAD drawings are divided into fine-grained geometric primitives, and an adjacency matrix is constructed based on the distances between these primitives. The symbol recognition framework consists of two stages: layer assignment prediction and symbol recognition. In the layer assignment prediction stage, the classic image recognition framework HRNetV2-W48 is employed to generate feature vectors from the converted PNG images of the CAD drawings, enabling the positional encoding of each geometric primitive. Then, a Transformer-based architecture is utilized to update the encoding of each geometric primitive by leveraging information from the nearest neighbors in the spatial domain. Finally, the membership probability of each geometric primitive to different layers is determined through a linear transformation. In the symbol recognition stage, the symbols with closed contours and open contours are recognized by unsupervised clustering using depth-first search and predefined rule, respectively.

Experimental results showed that the model for layer assignment prediction achieved a multi-class accuracy of 92.7% and an $F_1$ score of 0.9224 on the test set. This indicates the potential of using the Transformer architecture for layer assignment prediction tasks. Unlike traditional object detection frameworks, which perform regression to detect bounding boxes and classify targets within the boxes, this study directly utilizes fine-grained geometric primitive from CAD drawings. It extracts essential geometric features and spatial topology, further refining the embedding representation of geometric primitives using the self-attention mechanism. This approach allows for improved handling of diverse combinations and randomly orientation of the symbols. The effectiveness of unsupervised clustering is demonstrated through visualization, where symbols are accurately clustered according to predefined rules and geometric distances.

Although the experimental results are generally satisfactory, several areas require further improvement. Firstly, the current classification model tends to confuse geometric primitives of pipes, control lines, and utilities across different layers, and some pipes are misidentified as equipment contours or valve components. Secondly, the clustering of pipes, control lines, and utilities may result in redundancy. Finally, the extraction of grounding lines and textual information, and their interrelationships were not addressed in this study. In future work, we plan to develop a model to establish the matching relationships among equipment, instruments, and textual descriptions, thereby automatically forming a process topology network with node descriptions. We believe this study will provide a novel approach to the digitalization of P&ID and contribute to the advancement of intelligent process design, risk analysis, and large language models in the field of chemical engineering.

## ACKNOWLEDGEMENTS

The authors gratefully acknowledge support from the National Key R&D Program of China (2024YFC3013600).

## REFERENCES

1. Paliwal, S., Jain, A., Sharma, M., & Vig, L. (2021). Digitize-PID: Automatic digitization of piping and instrumentation diagrams. In Trends and Applications in Knowledge Discovery and Data Mining: PAKDD 2021 Workshops, WSPA, MLMEIN, SDPRA, DARAI, and AI4EPT, Delhi, India, May 11, 2021 Proceedings 25 (pp. 168-180). Springer International Publishing.
2. Data Exchange in the Process Industry. https://dexpi.org/static/pid_specification_1.4/
3. Kim, B. C., Kim, H., Moon, Y., Lee, G., & Mun, D. (2022). End-to-end digitization of image format piping and instrumentation diagrams at an industrially applicable level. Journal of Computational Design and Engineering, 9(4), 1298-1326.
4. Fan, Z., Chen, T., Wang, P., & Wang, Z. (2022). Cadtransformer: Panoptic symbol spotting transformer for cad drawings. In Proceedings of the IEEE/CVF Conference on Computer Vision and Pattern Recognition (pp. 10986-10996).
5. Sun, K., Xiao, B., Liu, D., & Wang, J. (2019). Deep high-resolution representation learning for human pose estimation. In Proceedings of the IEEE/CVF conference on computer vision and pattern recognition (pp. 5693-5703).
6. Wang, F., Cheng, J., Liu, W., & Liu, H. (2018). Additive margin softmax for face verification. IEEE Signal Processing Letters, 25(7), 926-930.

© 2025 by the authors. Licensed to PSEcommunity.org and PSE Press. This is an open access article under the creative commons CC-BY-SA licensing terms. Credit must be given to creator and adaptations must be shared under the same terms. See https://creativecommons.org/licenses/by-sa/4.0/



Systems & Control Transactions

**Research Article - Peer Reviewed Conference Proceeding**
ESCAPE 35 - European Symposium on Computer Aided Process Engineering
Ghent, Belgium. 6-9 July 2025
Jan F.M. Van Impe, Grégoire Léonard, Satyajeet S. Bhonsale,
Monika E. Polańska, Filip Logist (Eds.)

PSE PRESS

# Enhancing Predictive Maintenance in Used Oil Re-Refining: a Hybrid Machine Learning Approach

**Francesco Negri[a,b], Andrea Galeazzi[c,d], Francesco Gallo[a], Flavio Manenti[b*]**

[a] Itelyum Regeneration S.p.A., Via Tavernelle 19, Pieve Fissiraga, 26854, Italy
[b] Politecnico di Milano, Dipartimento di Chimica, Materiali e Ingegneria Chimica "Giulio Natta", Piazza Leonardo da Vinci 32, Milano, 20133, Italy
[c] Department of Chemical Engineering, Imperial College London, South Kensington Campus, London SW7 2AZ, UK
[d] The Sargent Centre for Process Systems Engineering, Imperial College London, South Kensington Campus, London SW7 2AZ, UK
* Corresponding Author: flavio.manenti@polimi.it

## ABSTRACT

Maintenance is critical for industrial plants to ensure operational reliability and worker safety. In process industries, fouling, the accumulation of solid residues in equipment, poses a significant challenge, causing inefficiencies and productivity losses. Effective modeling of fouling evolution over time is essential for maintenance planning to prevent equipment from operating under suboptimal conditions. Traditional approaches to fouling prediction include equation-based models, which offer high precision but may struggle with continuously changing process boundaries, and machine learning techniques, which are more adaptable but less effective at capturing rapidly evolving trends driven by complex underlying physics. This study introduces an innovative hybrid machine learning approach for predictive maintenance, combining the strengths of both methods. Pressure differential is modeled using an equation-based approach that links pressure data with fouling thickness, while the fouling growth rate is estimated through Gaussian Process Regression (GPR). This hybrid model generates pressure drop profiles with vertical asymptotes that closely mimic real-world behavior. Applied to a vacuum distillation column processing fouling-prone used oil, the proposed predictive method achieves a significant reduction of over 60% in suboptimal operating time compared to the current maintenance strategy, based on a fixed threshold.

**Keywords**: Algorithms, Artificial Intelligence, Industry 4.0, Machine Learning, Process Monitoring

## INTRODUCTION

Maintenance plays a crucial role in industrial plants, directly impacting operations reliability and worker safety. One of the most common and tough challenges tackled with periodic maintenance in process plants is fouling, which is the accumulation of solid deposits in piping, machines, and process equipment, leading to energetic inefficiencies, higher operating costs, and lower productivity [1–3].

Modeling accurately fouling evolution over time is crucial to proper maintenance planning. For this purpose, equation-based models using phenomenological approaches offer precision but may give less satisfactory performances under continuously changing process boundary conditions. Alternatively, machine learning methods, like Gaussian Process Regression, predict fouling trends using process data alone, automatically adapting to evolving conditions. However, these may offer less accurate results with fast-changing profiles following complex underlying physics.

Hybrid machine learning models combine both methods by leveraging the predictive power of machine learning while incorporating physical models to improve accuracy, interpretability, and robustness, especially in complex systems [4].

The aim of this work is to introduce a hybrid machine learning model and use it to enhance the reliability of predictive maintenance techniques applied to vacuum distillation. Complex industrial vacuum distillation equipment working with used oil, a fouling-prone waste feedstock, is considered as a case study.

# METHODS

## Process Operations and Maintenance

Industrial equipment analyzed in this work is part of a used oil regeneration process, currently operational in the Itelyum SpA production plant located in Pieve Fissiraga, Lodi, Italy. The used oil regeneration process is composed of three consecutive steps: *preflash* (PF), *thermodeasphalting* (TDA), and *hydrofinishing* (HDF), with a maximum used oil processing capacity of 130 kt/y.

In the PF section, water and solvents are removed from waste oil under mild vacuum at 120–140°C. The preflashed oil enters the TDA section, where it is heated above 360°C and distilled under strong vacuum using structured packing. This process deasphalts the feedstock, producing bitumen (VISCOFLEX) and fractionating it into gasoil (VGO) and three lubricant base oils: heavy (HLF), light (LLF), and spindle (SLF). All cuts, except bitumen, are then hydrogenated in the HDF section at over 300°C and 100 bar, yielding regenerated products.

The TDA column analyzed in this work suffers from fouling phenomena due to the severe operating conditions and the intrinsic propensity to fouling shown by used oil waste feedstock. The main key performance indicator showcasing this phenomenon is the pressure differential between top and bottom of the column (ΔP), which is carefully monitored during operations to understand when it is more appropriate to perform maintenance of the unit. A typical evolution in time of the ΔP profile specific to the unit of mass is shown in Figure 1 as an example, as a function of dimensionless time τ.

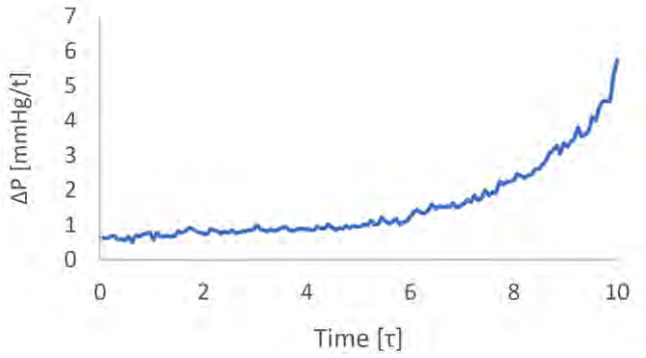



**Figure 1.** Typical TDA column ΔP profile during operations

Currently, maintenance scheduling relies on a condition-based approach, where a shutdown is planned when the pressure drop (ΔP) exceeds a semi-empirical warning threshold [2,3]. This paper introduces an advanced predictive maintenance strategy, leveraging a hybrid machine learning algorithm coupled with an equation-based model, to enhance the reliability and efficiency of maintenance planning.

## GPR Algorithm

Gaussian Process Regression (GPR) is a non-parametric Bayesian approach to regression, widely used in machine learning for its ability to model complex relationships with uncertainty quantification. GPR defines a Gaussian distribution over functions, where predictions are derived as probabilities rather than fixed values, offering flexibility and interpretability. Its key strengths include providing confidence intervals, and capturing nonlinear patterns efficiently [5].

This paper exploits a GPR-based algorithm developed in the work by Galeazzi et al. [1], already tested and validated on complex industrial equipment.The algorithm uses *Linear* (LIN), *Radial Basis Function* (RBF), and *Rational Quadratic* (RQ) kernels. These covariance functions have the following mathematical expressions:

$$k_{LIN}(t,t') = \sigma^2 + t \cdot t' \quad (1)$$

$$k_{RBF}(t,t') = \sigma^2 exp\left(-\frac{(t-t')^2}{2\lambda^2}\right) \quad (2)$$

$$k_{RQ}(t,t') = \sigma^2\left(1+\frac{(t-t')^2}{2\alpha\lambda^2}\right)^{-\alpha} \quad (3)$$

where *k* is the covariance function (or kernel), *t* and *t'* are two points of the input space (time, in this work), $\sigma^2$ is the variance, λ is the length scale parameter, and α is the power of the RQ kernel.

These kernels where chosen since they provided a good balance between prediction reliability when applied to complex industrial datasets, and computational efficiency. Regression models in the algorithm are Gaussian Processes obtained by the combination of these kernels through suitable operators such as *addition (+)* and *multiplication* (·).

The algorithm developed by Galeazzi et al. [1] finds the optimal kernel combination to describe the investigated dataset by applying the following recursive strategy, based on a *greedy search* approach:

- *LIN*, *RBF*, and *RQ* kernels are combined by applying operators (+, ·), obtaining several regression models.
- GPR models are evaluated through an 80/20 train/test split, where 80% of data is used to train the model, and 20% for cross-validation.
- The optimal model is chosen according to the *Mean Absolute Error* (MAE) metric, the best one showing the lowest error.
- Starting from the best kernel combination, the algorithm re-applies the same operators (+, ·), creating new kernel combinations to be tested.

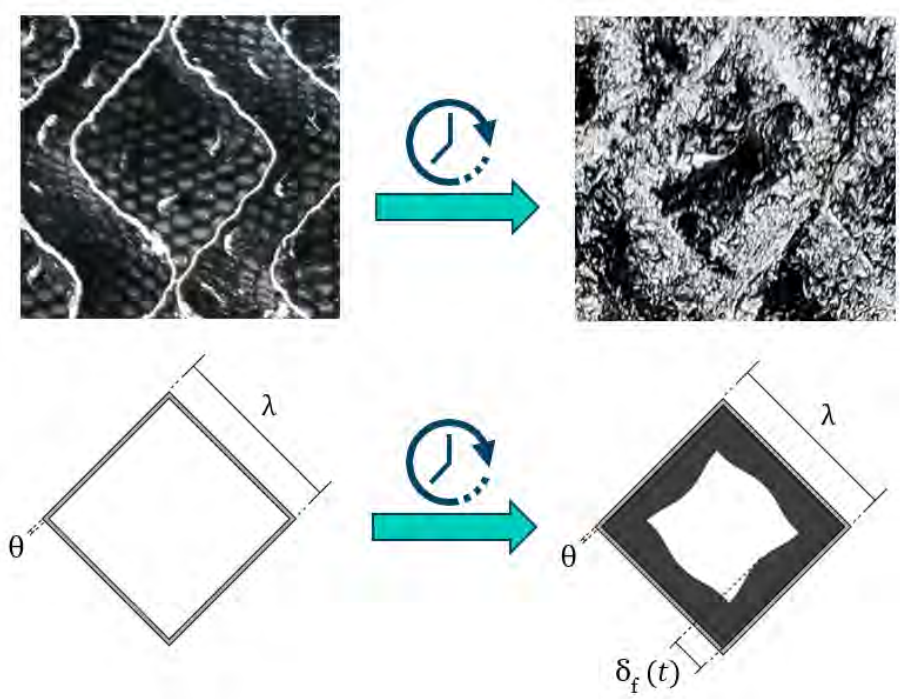



**Figure 2:** Details of the actual structured packing used in the distillation column investigated in this work, and corresponding schematic modeling approach. On the left, packing is represented at the start of run, with characteristic length λ, and thickness θ. On the right, the same equipment is reported during the run, with the addition of the time-dependent fouling thickness $\delta_f(t)$. Geometric parameters are dimensionless.

Regression models created with the kernel combination strategy described here follow a *greedy search* approach, meaning that the search tree is descended by taking the best model at each iteration. This is a compromise between modeling accuracy and computational effort. The algorithm is set to reach a maximum tree depth of five layers, to avoid long computational time and possible overfitting problems, while also ensuring good prediction capabilities. For more details regarding the algorithm, please refer to the work by Galeazzi et al. [1].

## Pressure Drop Model

The algorithm from Galeazzi et al. [1] was effectively applied by Negri et al. [2,3] for predictive maintenance of the same TDA column analyzed in this work. Specifically, they used a GPR algorithm on ΔP datasets to improve maintenance scheduling. While GPR adapted well to the varying used oil composition, providing a robust and reliable maintenance strategy, it gave less accurate results when predicting the steep ΔP increase near end-of-run conditions.

To address this limitation, this paper proposes a hybrid machine learning approach that combines GPR with a tailored ΔP model for the TDA column. This method enhances predictive reliability across the entire time domain, albeit at the cost of reduced generality, as it requires a unit-specific model rather than being universally applicable.

The pressure drop model considered in this work is the one reported for structured packing in the work by Bravo et al. [6], shown in eq. 4.

$$\Delta P = \Delta Z \frac{f \rho_g U_{gs}^2}{S \sin^2(\beta) \varepsilon^2 g_c} \quad (4)$$

where $\Delta P$ is the pressure drop, $\Delta Z$ is the packing height, $f$ is the friction factor, $\rho_g$ is the gas density, $U_{gs}$ is the superficial gas velocity, $S$ is the side dimension of packing corrugation (its characteristic length), $\beta$ is the angle with horizontal for corrugation channel, $\varepsilon$ is the void fraction of the packing, and $g_c$ is the gravity conversion factor (=1.0).

This model is significantly affected by the geometry of the packing. Thus, before applying it to the case of the TDA column, it is necessary to understand how fouling affects geometrical quantities during operations. The effect of fouling in a structured packing can be observed in Figure 2, which shows the packing used in the TDA column and a corresponding schematic modeling view, before the start of run, and after experiencing operations. The scheme shows the characteristic length and thickness of packing, represented by letters λ and θ, respectively. The geometrical quantities shown in the picture, indicated by Greek letters, are made dimensionless by dividing them by a standard side dimension of packing corrugation, $S^0$, to protect Itelyum's industrial secret.

It is possible to see that the main effect of fouling is

the restriction in the cross-sectional area of the packing caused by a growing film, represented by the time-dependent fouling thickness, indicated by the dimensionless parameter $\delta_f(t)$.

The growth in time of this fouling thickness will impact packing void fraction ε, which is a key parameter for pressure drop, as indicated by the formula presented previously in eq. 4. The mathematical relationship showing ε as a function of $\delta_f(t)$ is reported in eq. 5.

$$\varepsilon = \frac{V_{void}}{V_{total}} = \frac{A_{void}\Delta Z}{A_{total}\Delta Z} = \frac{\left(\lambda - 2(\theta+\delta_f)\right)^2}{\lambda^2} = \left[1 - \frac{2}{\lambda}\left(\theta + \delta_f\right)\right]^2 \quad (5)$$

where $V_{void}$, $V_{total}$, $A_{void}$ and $A_{total}$ refer to void and total volume and cross-sectional area, respectively. The proposed expression for ε can be plugged into the model previously shown in eq. 4, obtaining the relationship between ΔP and fouling thickness $\delta_f(t)$.

To simplify the modified ΔP model for the TDA column, the authors assume that the reduction in cross-sectional area due to fouling quickly becomes the dominant factor, a phenomenon which is primarily determined by packing geometry and fouling growth. Thus, all parameters are grouped into a constant, α, except those related to packing geometry (λ, θ, $\delta_f$). This constant also includes the feedstock flowrate, making ΔP specific to the unit mass while protecting Itelyum's industrial confidentiality. The final expressions are shown in Eq. 6 and 7.

$$\Delta P = \frac{\alpha}{\lambda} \cdot \left[1 - \frac{2}{\lambda}\left(\theta + \delta_f(t)\right)\right]^{-4} \quad (6)$$

$$\delta_f(t) = \frac{\lambda}{2} \cdot \left[1 - \left(\frac{\alpha}{\lambda \cdot \Delta P}\right)^{0.25}\right] - \theta \quad (7)$$

The expression in eq. 6 has a vertical asymptote when $\delta_f \rightarrow (\lambda/2 - \theta)$, meaning that pressure drop gradually increases as fouling thickness grows, then it rapidly degenerates to extremely high values when $\delta_f$ approaches the asymptotic limit. Interestingly, this is coherent with the behavior of ΔP in the real industrial system, as shown previously in Figure 1.

This model can be used for predictive maintenance by coupling it with the GPR-based algorithm, by leveraging it to obtain the expected fouling growth rate in the future, something that would hardly be possible to estimate otherwise.

## RESULTS AND DISCUSSION

Maintenance for the TDA column is centered around a key concept: there is a *Normal Operations Limit* (NOL) for the column fixed at 2.5 mmHg/$t_{oil}$ that should not be overcome. Operating the column over this limit should be avoided because the additional stress caused by the high pressure drop makes it less economically advantageous to run the regeneration process. Thus, a proper maintenance strategy should aim at scheduling activities so that the column can be stopped just before this limit, to maximize the acceptable operating range and the economical advantages associated with it. In case the limit is overcome, and the column enters the *Suboptimal Operating Region* (SOR), the timeframe within it should be as low as possible.

### Condition-based Maintenance Strategy

Currently, Itelyum applies a condition-based strategy to schedule maintenance in its plant. This method can be summarized in the following steps:

- TDA column specific ΔP is checked with regular frequency.
- When the pressure drop overcomes a semi-empirical warning threshold of 2 mmHg/$t_{oil}$, maintenance starts being scheduled.
- Typically, there is a time delay of 1 τ (±30%) between scheduling and real maintenance.
- Maintenance should take place before the column overcomes the NOL fixed at 2.5 mmHg/$t_{oil}$.

The biggest limit in this strategy is the aprioristic definition of the warning threshold, which is statically fixed at 2 mmHg/$t_{oil}$ and has no link to the actual operating conditions. While it represents a good rule of thumb to have an approximate idea of the column's behavior, it cannot adapt to the continuously changing composition of used oil waste feedstock, which is something inherently intertwined with fouling behavior. Results from the application of this strategy are shown in Table 1 as an example, where two different runs of the TDA columns are reported and referred to as cases A and B.

Here, $\tau_M$ is the time at which the warning threshold is overcome, and scheduling starts. $\Delta\tau_M$ is the time delay between scheduling and actual maintenance, a period which normally lasts around 1τ, even though unusually long delays do happen, as shown in case B. Finally, $\Delta\tau_{SOR}$ is the timeframe during which the column operates within the Suboptimal Operating Region, a value that should be as low as possible.

It is possible to see that the condition-based strategy is not reliable in consistently providing low permanence within the SOR, with case B showing a residence time within it more than three times higher compared with case A.

**Table 1:** Characteristic times for condition-based maintenance strategy.

| Case | $\tau_M$ | $\Delta\tau_M$ | $\Delta\tau_{SOR}$ |
|---|---|---|---|
| A | 6.48 | 0.69 | 0.48 |
| B | 7.79 | 2.21 | 1.52 |

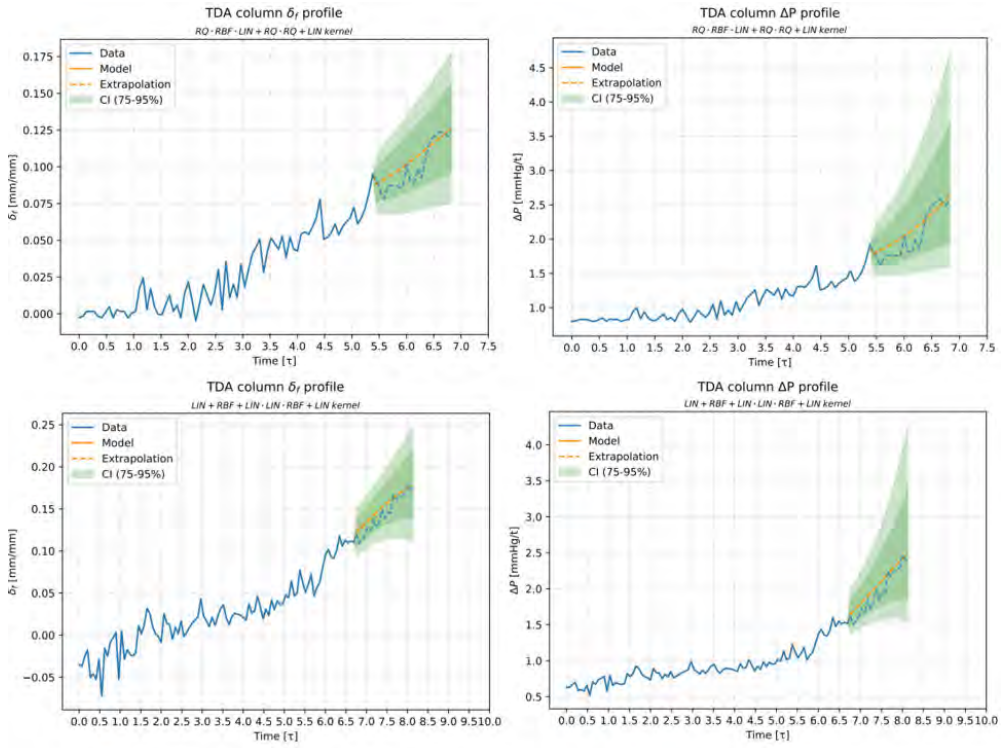



**Figure 3:** Predictions from the forecasting algorithm when NOL overcoming is forecasted ($\tau = \tau_M$). On the left, fouling thickness ($\delta_f$), on the right, pressure drop ($\Delta P$), on the top, case A, and on the bottom, case B.

## Predictive Maintenance Strategy

The authors of this work propose an alternative predictive maintenance strategy to increase the reliability of maintenance scheduling in Itelyum plant, composed of the following steps:

- $\Delta P$ datasets are transformed into equivalent fouling thickness ($\delta_f$) datasets, by applying the formula in eq. 7.
- The GPR-based algorithm is applied to $\delta_f$ datasets following a rolling forecasting approach.
- Algorithm training always starts at $\tau = 0$ and increases at fixed intervals, with a new prediction being performed at every step.
- Prediction horizon has a fixed value of 1.5 $\tau$, which is 50% higher than the average time lag between scheduling and maintenance.
- Forecasting results on $\delta_f$ are transformed back into $\Delta P$ values by applying eq. 6 pointwise to several points of the forecasted probability distributions.
- Maintenance is scheduled for the day in which the algorithm predicts that the most probable value for $\Delta P$ will overcome the NOL.

Graphical outputs from the algorithm at the moment in which overcoming is forecasted ($\tau = \tau_M$) are shown in Figure 3. Here, the best kernel combinations chosen by the algorithm is shown at the top of each graph, the continuous blue line represents the training and cross-validation dataset analyzed by the algorithm, the orange dashed line is the most probable prediction, the dashed blue line represents the validation dataset, the dark and light green shaded areas represent 75% and 95% confidence intervals, respectively.

It is possible to observe both the prediction of $\delta_f$ with its uncertainty, and the corresponding values of $\Delta P$ resulting from the transformation of each forecasted value. Predictions show good accordance between the most probable evolution in time for the investigated variables (orange dashed lines) and real data (blue dashed lines). Moreover, the natural variability of real data is contained within the 95% confidence interval calculated by the regression procedure, confirming the reliability of the model.

Results from the application of this predictive strategy are shown in Table 2, where the same two runs of the TDA column are shown as a comparison with the condition-based strategy. To ensure that the comparison is meaningful, the largest interval between the prediction horizon and the real-life time lag between scheduling and maintenance is taken as value for $\Delta\tau_M$ in each case.

**Table 2:** Characteristic times for condition-based maintenance strategy.

| Case | $\tau_M$ | $\Delta\tau_M$ | $\Delta\tau_{SOR}$ |
|---|---|---|---|
| A | 5.38 | 1.34 | 0.19 |
| B | 6.69 | 2.21 | 0.49 |

When comparing results between Tables 1 and 2, it is clear that the adoption of the predictive maintenance strategy increases significantly the reliability of maintenance scheduling, as highlighted by the systematic and remarkable reduction in the runtime within the SOR for both cases.

This fact is further highlighted in Figure 4, showing the percentage reduction in $\Delta\tau_{SOR}$ parameter for both cases by means of the parameter $R_{SOR}$, defined as follows in eq. 8.

$$R_{SOR} = \frac{\Delta\tau^{P}_{SOR} - \Delta\tau^{CB}_{SOR}}{\Delta\tau^{CB}_{SOR}} \cdot 100 \qquad (8)$$

Where $\Delta\tau^{P}_{SOR}$ and $\Delta\tau^{CB}_{SOR}$ are the timeframe within the SOR for predictive and condition-based strategy, respectively. Reductions of more than 60% for suboptimal operating time are achieved for both cases.

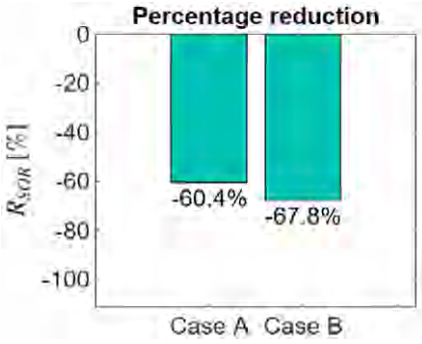



**Figure 4.** Percentage reduction in SOR runtime when shifting from condition-based to predictive maintenance

The significant reduction in suboptimal operating time demonstrates the increased reliability of maintenance planning with the proposed strategy, and robustness across different operating conditions. Additionally, considering the results for the predictions shown previously in Figure 3, it is interesting to notice that the algorithm would have actually avoided the column to enter the SOR altogether in case B, if it wasn't for the exceptionally long time delay between scheduling and maintenance. In case this time lag would have been within the usual value of 1 $\tau$ (±30%), the SOR would have been completely avoided thanks to the algorithm prediction.

## CONCLUSIONS

This study focused on a vacuum distillation system processing used oil, proposing a predictive maintenance strategy. A physics-based model was developed, and a Gaussian Process Regression algorithm was leveraged to forecast fouling thickness ($\delta_f$) evolution.

The hybrid model demonstrated strong alignment with plant data, particularly in the end-of-run region, where ΔP increased rapidly due to packing occlusion. Applying this approach to a predictive maintenance strategy reduced suboptimal operating time by over 60% compared to the current condition-based method in two different cases, offering a more reliable and effective solution for maintenance scheduling.

## REFERENCES


1. A. Galeazzi, F. de Fusco, K. Prifti, F. Gallo, L. Biegler, F. Manenti, Predicting the performance of an industrial furnace using Gaussian process and linear regression: A comparison, Computers & Chemical Engineering 181 (2024) 108513. https://doi.org/10.1016/j.compchemeng.2023.108513
2. F. Negri, A. Galeazzi, F. Gallo, F. Manenti, Application of a Predictive Maintenance Strategy Based on Machine Learning in a Used Oil Refinery, in: F. Manenti, G.V. Reklaitis (Eds.), Computer Aided Chemical Engineering, Elsevier, 2024: pp. 3175–3180. https://doi.org/10.1016/B978-0-443-28824-1.50530-5
3. F. Negri, A. Galeazzi, F. Gallo, F. Manenti, Reshaping Industrial Maintenance with Machine Learning: Fouling Control Using Optimized Gaussian Process Regression, Ind. Eng. Chem. Res. (2025). https://doi.org/10.1021/acs.iecr.4c04550
4. J. Sansana, R. Rendall, I. Castillo, L. de Bruijne, J. Huggins, A. Phillips, M.S. Reis, Hybrid Approach for Advanced Monitoring and Forecasting of Fouling with Application to an Ethylene Oxide Plant, Ind. Eng. Chem. Res. 63 (2024) 10666–10676. https://doi.org/10.1021/acs.iecr.4c00298
5. C.E. Rasmussen, C.K.I. Williams, Gaussian Processes for Machine Learning, The MIT Press, Cambridge, Mass., 2006. https://doi.org/10.7551/mitpress/3206.001.0001
6. J. Bravo, J.A. Rocha, J. Fair, Pressure drop in structured packings, Hydrocarbon Process (1986).



© 2025 by the authors. Licensed to PSEcommunity.org and PSE Press. This is an open access article under the creative commons CC-BY-SA licensing terms. Credit must be given to creator and adaptations must be shared under the same terms. See https://creativecommons.org/licenses/by-sa/4.0/

Systems & Control Transactions

**Research Article - Peer Reviewed Conference Proceeding**
ESCAPE 35 - European Symposium on Computer Aided Process Engineering
Ghent, Belgium. 6-9 July 2025
Jan F.M. Van Impe, Grégoire Léonard, Satyajeet S. Bhonsale,
Monika E. Polańska, Filip Logist (Eds.)

PSE PRESS

# An Integrated Machine Learning Framework for Predicting HPNA Formation in Hydrocracking Units Using Forecasted Operational Parameters

**Pelin Dologlu[a]*, and İbrahim Bayar[b]**

[a] SOCAR Turkey, Digital Transformation Department, Istanbul 34485, Turkey
[b] SOCAR STAR Oil Refinery, Process Department, Aliaga, Izmir 35800, Turkey
* Corresponding Author: pelin.dologlu@socar.com.tr

## ABSTRACT

The accumulation of heavy polynuclear aromatics (HPNAs) in hydrocracking units (HCUs) poses significant challenges to catalyst performance and process efficiency. This study proposes an integrated machine learning framework that combines ridge regression, K-means, and long short-term memory (LSTM) neural networks to predict HPNA formation, enabling proactive process management. For the training phase, weighted average bed temperature (WABT), catalyst deactivation phase—clustered using unsupervised K-means clustering—and hydrocracker feed (HCU feed) parameters obtained from laboratory analyses are utilized to capture the complex nonlinear relationships influencing HPNA formation. In the simulation phase, forecasted WABT values are generated using a ridge regression model, and future HCU feed changes are derived from planned crude oil blend data provided by the planning department. These forecasted WABT values, predicted catalyst deactivation phases, and anticipated HCU feed parameters serve as inputs to the LSTM model for predicting future HPNA levels. This approach allows us to simulate various operational scenarios and assess their impact on HPNA accumulation before they manifest in the actual process. By identifying critical process parameters and their influence on HPNA formation, the model enhances process engineers' understanding of the hydrocracking operation. The ability to predict HPNA levels in advance empowers engineers to implement corrective actions proactively, such as adjusting feed compositions or operating conditions, thereby mitigating HPNA formation and extending catalyst life. The integrated framework demonstrates high predictive accuracy and robustness, underscoring its potential as a valuable tool for optimizing HCU operations through advanced predictive analytics and informed decision-making.

**Keywords**: Heavy Polynuclear Aromatics (HPNAs), Machine Learning, Hydrocracking Unit Optimization, Simulation, LSTM, Catalyst Deactivation

## 1. INTRODUCTION

Hydrocracking is a pivotal unit operation in modern petroleum refining, offering flexibility and high yields of valuable middle distillates and lighter products. By coupling hydrogenation and catalytic cracking, HCUs can process a wide range of feedstocks—from vacuum gas oils to heavier coker feed streams—under severe operating conditions to maximize conversion [1]. However, these severe conditions facilitate the formation of HPNAs as byproducts, which typically contain 11 or more fused aromatic rings. HPNAs present a unique challenge, especially in the latter stages of a catalyst's life cycle, as they can cause critical fouling issues, accelerate catalyst deactivation, and reduce overall process efficiency. The rate of HPNA formation intensifies with increasing conversion levels and the use of heavier feedstocks [2]. Especially as the catalyst approaches the time for regeneration, HPNA accumulation increases very rapidly, making it challenging to manage and optimize unit conditions. Proactively managing HPNA accumulation is thus central to prolonging catalyst life, maintaining product quality, and sustaining high plant profitability.

Recent advances in data analytics and machine

learning have opened up new avenues for tackling this problem. Traditional physics-based or semi-empirical models, while useful, often struggle to capture the highly nonlinear relationships between feed characteristics, operating conditions, and HPNA formation. Machine learning methods—such as artificial neural networks [3], K-means [4], and ensemble techniques—can learn these complex interactions from historical data, yielding more accurate predictions of HPNA buildup under varying future scenarios. Moreover, the integration of multiple models, each specialized in a different task (e.g., forecasting Weighted Average Bed Temperature, clustering catalyst deactivation phases, and predicting HPNA levels), creates a robust predictive framework. The ability to forecast HPNA accumulation before it reaches operationally critical levels enables data-driven decision-making, reducing unplanned shutdowns, streamlining catalyst regeneration cycles, and minimizing downstream fouling costs.

Against this backdrop, the present work introduces an integrated machine learning framework that combines ridge regression, K-means, and LSTM neural networks to model and predict HPNA formation in HCUs. By incorporating both laboratory-based and real-time operational parameters, the framework offers a holistic solution. It not only forecasts HPNA levels but also provides case-study simulations illustrating how variations in operational parameters can drastically alter HPNA accumulation. The study aims to demonstrate how predictive analytics can add tangible value, offering refiners a proactive toolkit for making informed adjustments in feed composition and reactor severity, ultimately balancing higher conversion rates with catalyst longevity and fouling minimization.

## 2. MATERIALS AND METHODS

### 2.1. HPNA Formation Mechanisms

In the hydrocracking process of Heavy Vacuum Gas Oil (HVGO) feedstocks, HPNAs are generated as byproducts. These compounds pose significant challenges by fouling process equipment and shortening the lifespan of catalysts. The rate of HPNA formation intensifies with increasing conversion levels and the use of heavier feedstocks [2]. This issue becomes particularly critical as the catalyst nears the end of its cycle, where HPNA accumulation accelerates rapidly, making it difficult to manage and optimize unit conditions. To maintain the catalyst regeneration process and costs at an optimal level, it is essential to monitor and effectively control HPNA accumulation.

### 2.2. Data Collection and Preprocessing

There are two data frequency types of features: laboratory samples and process values. While process values are continuous, laboratory sample data are collected at irregular intervals; they are collected at different frequencies, such as twice a day or three times a week. Continuous process values are collected as hourly averages and then merged with laboratory sample data. Since this merging is done based on datetime, missing values (NaNs) occur in the laboratory sample data when no sample analysis is available. When NaN values appear due to the nature of laboratory sampling, the corresponding dates are removed from each model's input dataset. Additionally, data from periods when the unit was in shutdown conditions were excluded to ensure consistency in the analysis. All tasks were performed using Python 3.8, and approximately three years of data were used for model training, validation, and testing.

For simulation part, some input parameters for the models which are affected from crude oil change, is calculated from planning department's future crude oil blending plans. Parameters that cannot be derived from these plans are assumed to remain constant, with their last observed values carried forward into the future. A ridge regression model is employed to forecast WABT values, while a K-means clustering model is used for catalyst deactivation modeling. The predicted WABT values, along with the estimated catalyst deactivation phases and the calculated future HCU feed parameters, are then used as inputs for an LSTM model to estimate future HPNA levels.

### 2.3. Catalyst Deactivation Clustering via K-Means

The catalyst in the HCU reactor deactivates over time, undergoing distinct phases that can be clustered using the K-means method. The plant dataset is divided into $k$ categories, with data points in these categories chosen as initial cluster centers. The algorithm assigns each data point to the nearest center, forming clusters, and iteratively updates the centers until convergence is achieved [4]. Six clusters have been identified as the most effective way to categorize the catalyst's deactivation phases from the start of operation to the present, covering approximately three years. Reactor WABT and the cumulative processed feed amount, measured from the catalyst's first day of operation to now, are used to create the clusters for the deactivation phases. The processed feed amount reflects the catalyst's HPNA accumulation, while WABT varies significantly with the HPNA levels. Therefore, these two features are the best inputs for clustering the catalyst deactivation phases due to their strong correlation with HPNA accumulation. Based on these cluster labels, the HPNA sample data is fitted to quadratic functions for each cluster, effectively representing HPNA accumulation while reflecting the key features of catalyst deactivation. This approach captures the deactivation pattern despite some inconsistencies in

laboratory sample points (Figure 1).

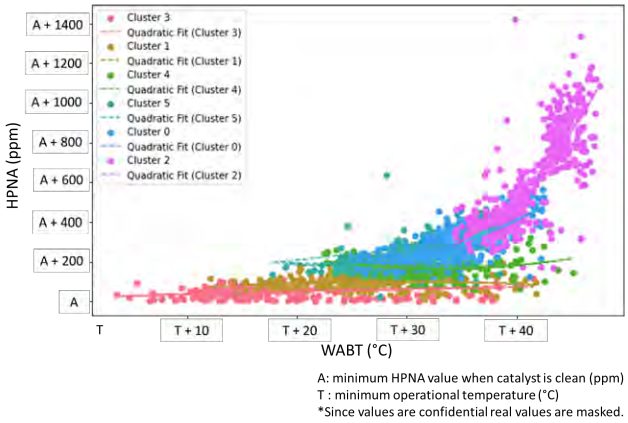



**Figure 1.** K-means clustering model.

## 2.4. WABT Forecasting with Ridge Regression

The WABT in HCU's reactors is a key operational parameter that directly influences conversion rates and catalyst deactivation. Since HPNA formation—and consequently catalyst deactivation—is inevitable over time, engineers increase reactor temperatures to maintain a consistent conversion rate. However, this increased severity also accelerates HPNA formation. Therefore, for simulating future plant operations and predicting HPNA formation, it is essential to accurately forecast the WABT profile in the reactors.

Ridge regression, a popular method for estimating parameters in multivariate regression, is applied to model the relationship between WABT, HPNA accumulation, and other influencing factors, particularly in the presence of collinearity. By adding a regularization term to prevent overfitting, ridge regression can enhance prediction accuracy despite its limitations, such as reduced interpretability and lack of variable selection [5]. The WABT prediction model uses the following inputs: ten-day moving average of HCU feed sulfur content, cumulative processed feed amount, one-day average flow of HVGO from the crude oil unit to the HCU, four-day moving average of HCU feed nitrogen content, and denoised heavy coker gas oil (HCGO) flow from the delayed coker unit to the HCU, lagged six hours. These features were selected based on their established influence on reactor temperature dynamics and catalyst aging. Smoothing the input data is necessary because WABT is highly sensitive to these variables, and smoothing makes the model more robust.

The model is trained on historical plant data spanning three years, with the test set comprising 20% of the dataset. The model's test set performance metrics are $R^2$ = 0.57 and Mean Absolute Percentage Error (MAPE) = 0.46%. Figure 2 shows the model's predictive performance by comparing actual and predicted values for both the training and test datasets over time. The close alignment of the predicted (blue and red) and actual (green and purple) values suggests that the model captures overall trends effectively, though some deviations remain, particularly in regions of high variability. The general upward trend in later timestamps indicates that the model adapts well to changes over time. However, minor fluctuations between actual and predicted values may point to areas where the model struggles with short-term variability. Despite these imperfections, the relatively low MAPE suggests the model maintains strong predictive accuracy. The model successfully captures WABT trends, which are crucial for estimating future HPNA accumulation and enabling proactive process adjustments, and it serves as an input for the simulation to forecast HPNA accumulation under varying future process conditions.

## 2.5. LSTM Model for HPNA Prediction

As the catalyst approaches the end of its cycle, the HPNA amount in the output feed of HCU reactors increases due to the cumulative effect of catalyst deactivators. Therefore, the HPNA profile—comprising previous HPNA samples—serves as an indicator for the current HPNA amount. Given the dynamic behavior of this process, time series modeling is crucial, as the problem is inherently time-dependent. Furthermore, the absence of data from previous catalyst life cycles makes it even more challenging to learn from and accurately model this behavior.

LSTM networks, a type of recurrent neural network,

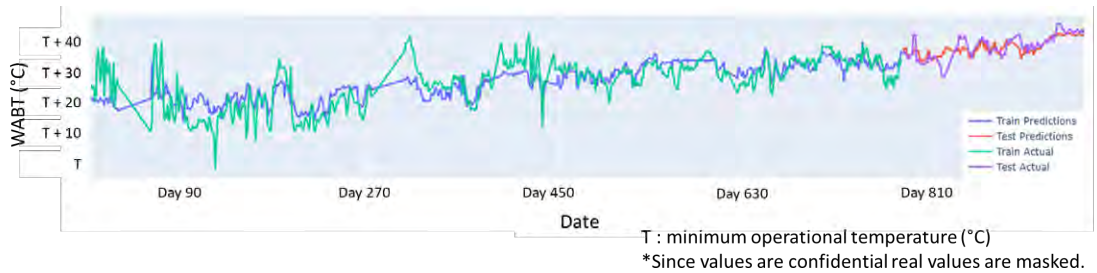



**Figure 2.** WABT prediction model.

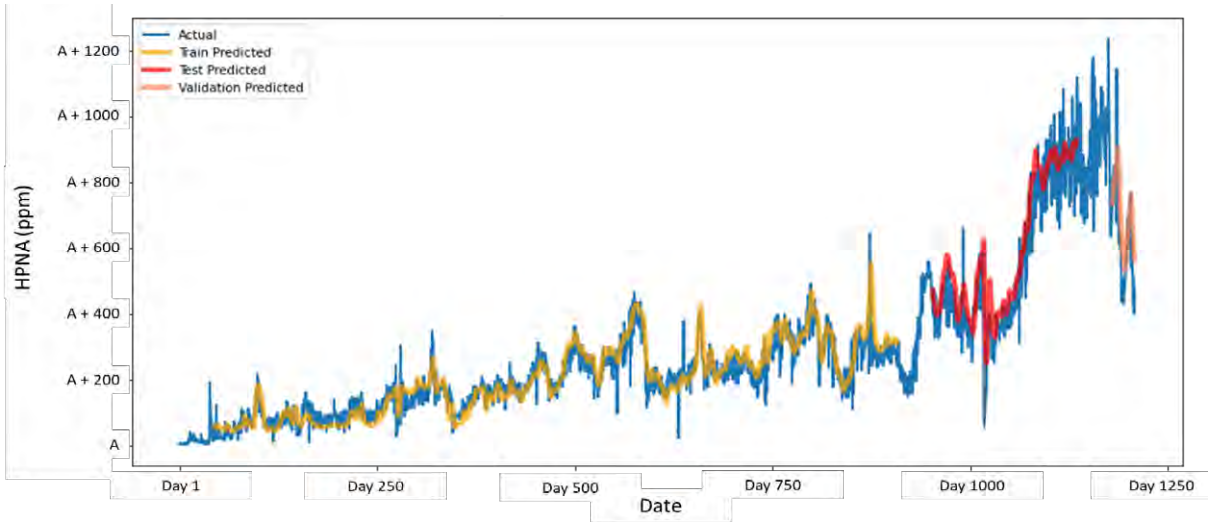



**Figure 3.** LSTM model performance.

are particularly well-suited for such time series problems. LSTMs introduce gating mechanisms to effectively learn dependencies in sequential data, making them ideal for modeling the nonlinear dynamics of chemical processes and catalyst behavior [3]. Studies have demonstrated the effectiveness of LSTM models in handling complex dynamics in chemical processes, further validating their potential for modeling processes like HPNA accumulation.

After conducting correlation analysis, the best parameters for the prediction of HPNA amount in the output flow of HCU's reactors were identified as the 98% distillation temperature of HCGO, reactor's WABT, sulfur and nitrogen content in the HCU feed. However, the initial results were unsatisfactory, as real historical outputs were not directly incorporated into the predictions. This limitation arose because the LSTM model relied only on an abstract representation of past states. To address this, the HPNA refitted feature—reflecting catalyst deactivation and detailed in Section 2.3—was also included as an input.

The model was trained using these five inputs, with the target being the HPNA amount in the HCU output flow. To predict the target variable, the LSTM neural network architecture was implemented using the Keras/TensorFlow framework. Before model development, the dataset, spanning approximately three years, was scaled using the MinMaxScaler to normalize all features. The data was then split chronologically into training (80%) and testing (20%) subsets without shuffling, preserving the time dependency. A sliding window approach was adopted to capture temporal dependencies. Specifically, a window length of 90 time steps (corresponding to one and a half months of data, with two samples per day) was used to create training sequences. Each sequence of 90 time steps was used to predict the target value at the subsequent time step. A batch size of 8 was chosen to balance memory constraints and training stability. The LSTM architecture consisted of two stacked LSTM layers, each with 64 units and a dropout of 0.2, followed by a dense layer of 32 neurons (ReLU activation) and a final output neuron. The model was trained with a mean squared error loss function and the Adam optimizer. Early stopping (with a patience of 2) and an exponential decay learning rate scheduler (triggered after 10 epochs) were employed, using a portion of the data to monitor validation loss during each epoch. To ensure no data leakage between validation and testing steps, an additional one-month validation set was used as unseen data to evaluate model performance with 80 mean absolute error. Figure 3 displays the LSTM model's performance in predicting HPNA accumulation trends. Gaps appear in each prediction set because the initial data from the sliding window is used to predict the last value. The model demonstrates a strong ability to track HPNA trends, with predictions aligning closely to actual values. This enables process engineers to anticipate HPNA formation and take preventive measures proactively.

## 3. SIMULATION RESULTS OF CASE STUDIES

Beyond merely predicting current HPNA levels, a key advantage of this integrated approach lies in its capacity to forecast the future performance of the HCU. By incorporating the planning department's projections for crude oil blends, models' some of parameters influenced by changing feedstocks can be accurately estimated.

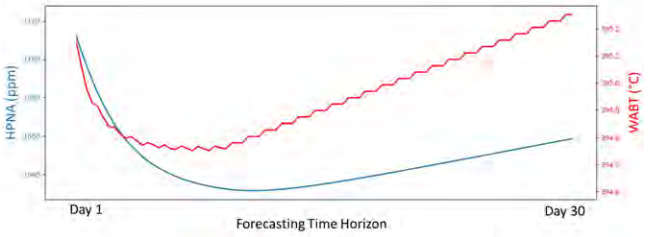
These forecasts serve as critical inputs to the three-model framework—the ridge regression model for WABT prediction, the K-means clustering method for catalyst deactivation phases, and the LSTM network for future HPNA estimation—thereby enabling process engineers to proactively adjust feed compositions or operating conditions. Such targeted interventions not only help mitigate HPNA formation but also extend catalyst life. In addition, the models provide insights into how various parameters affect both HPNA levels and WABT, empowering users to make informed decisions and fine-tune process settings. In Figure 4, the influence of adjusting these parameters on each model's output is illustrated as case studies.

The base case (Figure 4.a) represents the standard operational scenario, with no adjustments to input parameters within one month. At the initial point, there is a decrease due to the residual effects of the moving window size (one and a half months) still influencing the LSTM model, which forecasts one month. Once a steady-state condition is reached, HPNA accumulation increases, and WABT rises over time, reflecting the natural progression of catalyst deactivation in the HCU under current operating conditions.

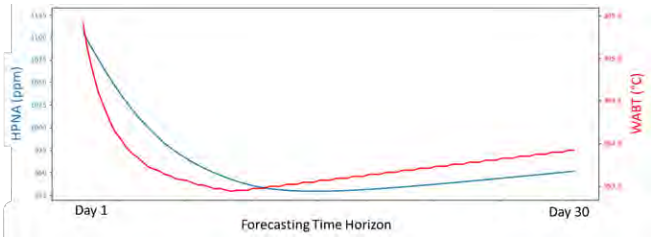
In the case of Figure 4.b, the sulfur content in the HCU feed is increased by 0.46 %wt. This leads to a reduction in cracking reactions due to the presence of sulfur-containing compounds, resulting in a lower temperature. Consequently, both HPNA accumulation and WABT decrease more rapidly, leading to lower final levels of HPNA and WABT compared to the base case. These findings suggest that the observed reduction in HPNA accumulation and WABT is not directly caused by the sulfur increase itself, but rather by the decreased cracking conversion due to sulfur retention in the diesel fraction, which helps maintain overall conversion levels. This mechanism ultimately mitigates fouling and improves operating conditions.

Reducing the flow of HCGO by 47.5 $m^3$ results (Figure 4.c) in a notable slowdown in HPNA accumulation. Correspondingly, WABT remains lower and more stable over time. This indicates that reducing HCGO flow mitigates fouling and slows catalyst deactivation, providing a potential strategy for process optimization.

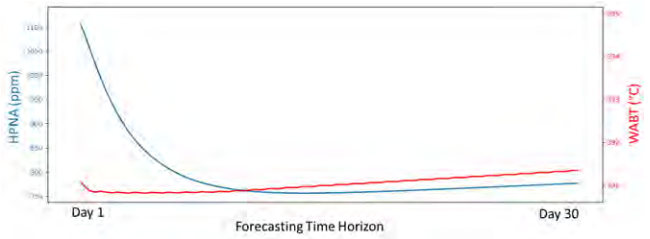
An increase in nitrogen content in the HCU feed by 55 ppm (Figure 4.d) leads to a significant acceleration in HPNA formation, as indicated by the steep rise. However, WABT remains relatively unchanged, suggesting that while nitrogen compounds strongly influence HPNA buildup, they do not significantly impact WABT in the short term. This highlights the critical importance of controlling feed nitrogen content to manage catalyst performance and minimize long-term fouling effects.



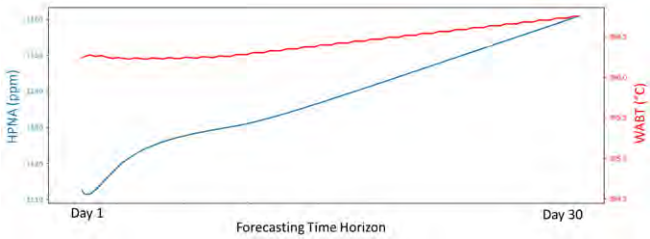

**a)** base case.



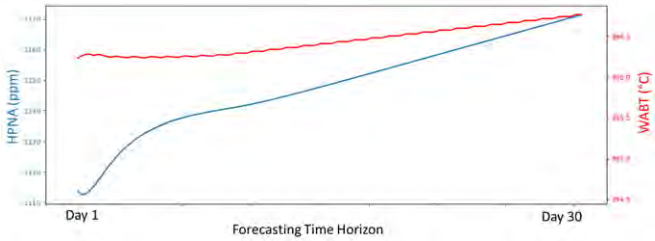

**b)** sulfur amount in the HCU feed increases by 0.46 %wt.



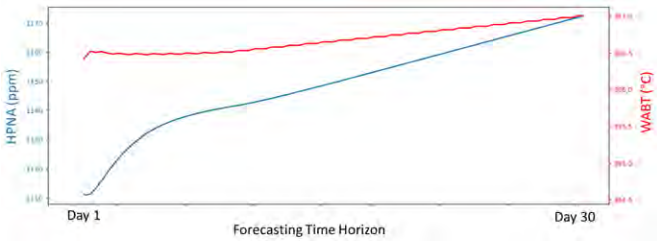

**c)** HCGO flow decreases by 47.5 $m^3$.




**d)** nitrogen amount in the HCU feed increases by 55 ppm.




**e)** 98% distillation temperature of HCGO decreases by 15 °C.




**f)** HVGO flow increases by 42.5 $m^3$.

**Figure 4.** Simulation results for each case studies.

When the 98% distillation temperature of HCGO is reduced by 15°C (Figure 4.e), HPNA accumulation continues significantly, while WABT remains relatively stable. This case highlights the effectiveness of reducing heavier components in the feed to mitigate fouling and improve catalyst performance, as the lower temperature likely decreases the presence of high-molecular-weight components that contribute to HPNA formation.

Lastly, increasing the HVGO flow rate by 42.5 $m^3$ (Figure 4.f) results in an increase in HPNA accumulation, implying that heavier feed fractions contribute more significantly to HPNA precursor formation. These findings highlight the critical role of feed composition and process conditions in controlling HPNA buildup within the HCU, providing valuable insights for optimizing unit operation and extending catalyst life.

## 4. CONCLUSIONS

This study demonstrates the effectiveness of a multi-model, machine learning-based approach for predicting HPNA accumulation in hydrocracking units, providing refineries with a proactive strategy for managing catalyst health. By integrating ridge regression for WABT forecasting, K-means clustering for catalyst deactivation phases, and a LSTM model for HPNA projection, the framework captures the complex, time-dependent interactions that drive HPNA formation. The case studies highlight how variations in feed properties, process parameters, and operating conditions influence HPNA accumulation trends, offering insights that can inform operational adjustments to mitigate fouling and extend catalyst life.

While the model was trained using three years of historical data from a specific hydrocracking unit, its underlying methodology is not confined to a single facility. The approach—integrating machine learning framework for temperature forecasting, catalyst deactivation clustering, and HPNA prediction—can be generalized to other HCUs with appropriate modifications. However, challenges such as differences in feedstock composition, process severity, and catalyst formulations may necessitate model retraining or recalibration. Despite these variations, the overall framework offers a transferable, data-driven strategy that can be adapted for predictive maintenance and process optimization across multiple refining operations.

Future research could focus on incorporating advanced optimization algorithms to provide real-time control recommendations, further bridging the gap between predictive analytics and operational decision-making. Additionally, expanding the dataset to include multiple catalyst cycles or integrating kinetic models could enhance the robustness and generalizability of the predictions. Overall, the results underscore the potential of an integrated data-driven strategy to enhance catalyst performance, improve process economics, and maintain the reliability of hydrocracking operations in a rapidly evolving refining landscape.

## ACKNOWLEDGEMENTS

The authors would like to acknowledge Alp Eren Vedin and Berkay Er for their valuable contributions and insightful discussions that helped shape the development of this study.

## REFERENCES

1. J. Ancheyta, S. Sánchez, and M. A. Rodríguez, “Kinetic modeling of hydrocracking of heavy oil fractions: A review,” Catal. Today, vol. 109, no. 1–4, pp. 76–92, Nov. 2005, doi: 10.1016/J.CATTOD.2005.08.015.
2. A. L. N. Mohammed, “Polynuclear Aromatic Formation in Hydrocracker and their Impact on Catalyst Stabiliy,” Stud. Surf. Sci. Catal., vol. 53, no. C, pp. 349–361, Jan. 1989, doi: 10.1016/S0167-2991(08)61076-9.
3. F. Yang, M. Xu, W. Lei, and J. Lv, “Artificial Intelligence Methods Applied to Catalytic Cracking Processes,” Big Data Min. Anal., vol. 6, no. 3, pp. 361–380, 2023, doi: 10.26599/BDMA.2023.9020002.
4. W. Tian, G. Ji, S. Wang, Z. Cui, and S. Sun, “Intelligent Soft Measurement of Catalyst Activity during a Polyethylene Reaction Based on Mechanistic Modeling and Deep Learning,” Ind. Eng. Chem. Res., vol. 63, no. 26, pp. 11353–11364, Jul. 2024, doi: 10.1021/acs.iecr.4c00410.
5. N. Jha, H. Kumar Tanneru, S. Palla, and I. Hussain Mafat, “Multivariate analysis and forecasting of the crude oil prices: Part I – Classical machine learning approaches,” Energy, vol. 296, p. 131185, Jun. 2024, doi: 10.1016/J.ENERGY.2024.131185

© 2025 by the authors. Licensed to PSEcommunity.org and PSE Press. This is an open access article under the creative commons CC-BY-SA licensing terms. Credit must be given to creator and adaptations must be shared under the same terms. See https://creativecommons.org/licenses/by-sa/4.0/



Systems & Control Transactions

**Research Article - Peer Reviewed Conference Proceeding**
ESCAPE 35 - European Symposium on Computer Aided Process Engineering
Ghent, Belgium. 6-9 July 2025
Jan F.M. Van Impe, Grégoire Léonard, Satyajeet S. Bhonsale,
Monika E. Polańska, Filip Logist (Eds.)

PSE PRESS

# Optimization of Shell and Tube Heat Exchangers Using Reinforcement Learning

**Luana P. Queiroz[a,b,c*], Olve R. Bruaset[c], Ana M. Ribeiro[a,b], Idelfonso B. R. Nogueira[c]**

[a]LSRE-LCM – Laboratory of Separation and Reaction Engineering - Laboratory of Catalysis and Materials, Faculty of Engineering, University of Porto, Rua Dr. Roberto Frias, Porto, 4200-465, Portugal
[b]ALiCE – Associate Laboratory in Chemical Engineering, Faculty of Engineering, University of Porto, Rua Dr. Roberto Frias, Porto, 4200-465, Portugal
[c]Chemical Engineering Department, Norwegian University of Science and Technology, Trondheim, 793101, Norway
* Corresponding Author: up201700139@edu.fe.up.pt.

## ABSTRACT

This work presents a model for optimizing shell-and-tube heat exchanger design using Q-learning, a reinforcement learning technique. An agent is trained to interact with a simulated environment of a heat exchange model, iteratively refining design configurations to maximize a reward function. This reward function balances heat exchanger effectiveness and pressure drop, emphasizing designs that minimize pressure drop. Results showed that simpler configurations consistently achieved higher rewards, despite complex designs offering better heat transfer efficiency.

**Keywords**: heat exchanger, reinforcement learning, design optimization, machine learning

## INTRODUCTION

Heat exchangers are essential components across industries, facilitating heat transfer between fluids of differing temperatures [1]. Since their development in the early 20th century for industrial steam generators and power plant condensers, their applications have expanded into refrigeration, automotive cooling, waste heat recovery, and petrochemical processes [2]. The optimization of heat exchangers is directly connected to the energy and operational costs [3]. Thus, linking this equipment to important performance parameters. However, traditional design methods often rely on iterative manual processes that fail to guarantee optimal solutions due to the complexity of influencing parameters [4].

Recent advancements in Scientific Machine Learning (SciML) offer promising avenues for addressing these challenges. By integrating scientific principles with machine learning, SciML has shown potential in optimizing intricate systems like heat exchangers [5]. For instance, reinforcement learning (RL), a branch of SciML, can be utilized to identify optimal designs by exploring vast solution spaces without manual intervention. For example, a Scopus search using "heat exchanger" and "machine learning" revealed 259 studies, the narrower term "q-learning," an RL technique, yielded just five results. Research highlights, such as Wang et al. (2023) [6], demonstrate the potential of machine learning and computational fluid dynamics to enhance heat transfer in finned heat pipe radiators by optimizing parameters like fluid flow and thermal efficiency. By leveraging machine learning models trained on CFD simulation data, the authors identified design configurations that significantly enhanced thermal performance while maintaining manufacturability. This approach highlights the value of integrating machine learning with traditional physics-based methods to tackle the complexities of heat exchanger optimization.

Studies leveraging machine learning for heat exchanger optimization have explored diverse methods. For instance, Nevin et al. (2023) [7] employed Gaussian Process Regression and Random Forest models to enhance performance with turbulator inserts. In contrast, Keramati et al. (2022) [8] applied Deep Reinforcement Learning to optimize heat exchanger geometry, balancing heat transfer efficiency with reduced pressure drop. While these techniques have made notable advances, commercial optimization tools like Aspen EDR and HTRI Heat Exchanger Suite are still widely used in industry. These tools typically rely on meta-heuristics to solve

design problems, which, while effective, are often computationally intensive and require significant time for design iteration [9, 10]. This work differentiates itself by applying Q-learning, a simpler yet efficient reinforcement learning method, to optimize shell and tube heat exchangers, offering a potential for faster design evaluation and reduced computational time compared to traditional methods. The study focuses on maximizing a reward function defined by heat exchanger effectiveness and pressure drop. Despite limited precedent in applying Q-learning to this field, the findings from this exploratory work provide a foundation for further development.

# BACKGROUND

## Shell and Tube Heat Exchangers

Shell and tube heat exchangers are versatile and widely used in industrial applications due to their scalability, durability, and flexibility. In these exchangers, one fluid flows through a bundle of tubes, while another fluid circulates around the tubes within a shell. This arrangement enables heat transfer, where the hotter fluid warms the cooler one or vice versa. The efficiency of this process depends on factors like the overall heat transfer coefficient, heat transfer surface area, and the temperature gradient between fluids [1].

To optimize heat transfer, shell and tube exchangers incorporate numerous small tubes within a single shell. Baffles inside the shell direct the fluid in a serpentine path, creating turbulence that enhances heat transfer by breaking up thermal boundary layers on the tube surfaces [1]. Figure 1 illustrates a typical shell and tube heat exchanger with a one-shell pass and one-tube pass configuration, showing the internal structure and flow arrangement.

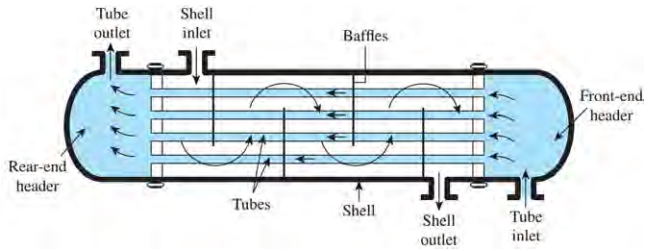



**Figure 1.** Shell and tube heat exchanger with one-shell pass and one-tube pass scheme.[1]

The flexibility of shell and tube heat exchangers allows for various configurations tailored to specific operational needs. These designs, combined with their ability to withstand high pressure and temperature, make them ideal for chemical processing, power generation, and petrochemical production [1]. This work employs the effectiveness-NTU (ε-NTU) method to evaluate the performance and design of such heat exchangers.

## Performance-indicating Parameters

The heat transfer rate (q) in a shell and tube exchanger is often calculated using the rate equation:

$$q = UA_s\Delta T_{lm} \quad (1)$$

where *U* is the overall heat transfer coefficient, $A_s$ is the total surface area for heat transfer, and $\Delta T_{lm}$ is the log mean temperature difference (LMTD). However, when only inlet temperatures are available, the effectiveness-NTU method simplifies the process by introducing dimensionless parameters like NTU (number of transfer units) and heat capacity ratios to directly estimate the exchanger's effectiveness (ε) [10].

The relationship for effectiveness in a single-shell pass shell and tube exchanger is:

$$\varepsilon_1 = \frac{2}{1 + C_r + \sqrt{1 + C_r^2}\,\frac{1 + exp\,(-\Gamma)}{1 - exp\,(-\Gamma)}} \quad (2)$$

where $C_r$ is the heat capacity ratio $C_r = C_{min}/C_{max}$, and $\Gamma = NTU\sqrt{1 + C_r^2}$. For exchangers with multiple shell passes, the generalized effectiveness equation is:

$$\varepsilon = \frac{\left(\frac{1-\varepsilon_1 C_r}{1-\varepsilon_1}\right)^n - 1}{\left(\frac{1-\varepsilon_1 C_r}{1-\varepsilon_1}\right)^n - C_r} \quad (3)$$

High effectiveness values indicate efficient heat transfer, making these parameters crucial for assessing exchanger performance. Additional considerations, such as temperature profiles and pressure drop, provide a comprehensive evaluation.

The pressure drop (ΔP) is critical for evaluating performance, calculated using the *Darcy-Weisbach* equation [12]:

$$\Delta P = f\frac{v^2}{2}\frac{L}{d_i} \quad (4)$$

Here, $\Delta P$ is the pressure drop across the tubes; f is the friction factor; and L is the total length of the pipes, calculated as the length of each pipe (l) multiplied by the number of shell passes (n): L = l · n. The friction factor is determined using the *Colebrook* equation [12]:

$$\frac{1}{\sqrt{f}} = -2\log\left(\frac{\frac{e}{d_i}}{3.7} + \frac{2.51}{Re\sqrt{f}}\right) \quad (5)$$

where *e* is the absolute roughness of the pipes, and *Re* is the Reynolds number. The Reynolds number describes the flow patterns of a fluid, indicating whether the flow is laminar or turbulent. For fluid flow within a pipe, it is defined as [13]:

$$Re = \frac{v d_i \rho}{\mu} \quad (6)$$

where $\mu$ is the fluid viscosity.

These equations provide the foundation for evaluating heat exchanger performance by calculating key metrics such as effectiveness, temperature profiles, and pressure drop. In this work, these parameters play a central role in assessing and optimizing heat exchanger designs through the application of Q-learning.

## Reinforcement Learning

Reinforcement learning (RL) is a machine learning technique where an agent interacts with an artificial environment to maximize cumulative rewards, based on the Markov Decision Process (MDP) [14]. The MDP provides a mathematical framework for decision-making, particularly suited to dynamic programming and optimization challenges [15].

In an MDP, the agent observes the current state $S_t$ , selects an action $A_t$, and receives a reward $R_t$+1 alongside a new state at each time step [16]. Transitions between states follow the Markov Property, where the next state depends only on the current state and action. A visual representation of this process is illustrated in Figure 2.

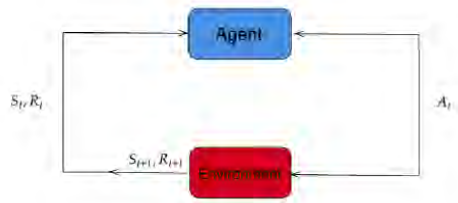



**Figure 2.** A simplified representation of MDP.

The agent's goal is to maximize total return over time by optimizing its policy $\pi$ (a|s), which determines the probability of taking action a in state s. Value functions are key to RL, estimating the expected return for a policy π. Iterative evaluation and policy improvement enable the agent to identify the optimal policy $\pi *$, maximizing returns.

While models of the environment can simplify this process, RL often relies on experience, where episodes of states, actions, and rewards guide learning [16].

## Q-Learning

Q-learning, introduced by Watkins (1989), is a reinforcement learning algorithm based on Temporal Difference (TD) learning. It estimates an optimal decision strategy for infinite-horizon problems without requiring an environmental model [17, 18]. Q-learning adopts an off-policy approach within TD learning, meaning that the optimal value function derives from actions chosen independently of the current policy $\pi$ (a|s) [16]. The updating rule proposed by *Watkins* (1989) is [17]:

$$Q\ (S_t, A_t) \leftarrow\ Q\ (S_t, A_t) + \alpha[T_{t+1} + \gamma\ max_a Q(S_{t+1}, A_{t+1}) - Q(S_t, A_t)] \quad (7)$$

Here, α is the learning rate, γ is the discount factor, and $max_a Q(S_{t+1}, A_{t+1})$ represents the estimated optimal future reward. A Q-table, as shown in Table 1, stores these values to guide the agent's decisions.

**Table 1:** A simple schematic of a Q-table.

| | $A_1$ | $A_2$ | ... | $A_n$ |
|---|---|---|---|---|
| $S_1$ | $Q\ (S_1, A_1)$ | $Q\ (S_1, A_2)$ | ... | $Q\ (S_1, A_n)$ |
| $S_2$ | $Q\ (S_1, A_1)$ | $Q\ (S_1, A_2)$ | ... | $Q\ (S_1, A_n)$ |
| ... | ... | ... | .... | ... |
| $S_m$ | $Q\ (S_m, A_1)$ | $Q\ (S_m, A_2)$ | .... | $Q\ (S_m, A_n)$ |

The agent balances exploration (trying new actions) and exploitation (choosing the best-known actions) using the ϵ-greedy method. Exploration probability ϵ decreases over time, transitioning from exploration to exploitation.

Q-learning's adaptability and effectiveness make it a powerful tool for solving dynamic decision-making problems, enabling agents to learn optimal strategies through continuous experience.

# METHODOLOGY

The development and execution of the Python program for this work were conducted on the following computer setup:

- Hardware:
  - Processor: 1.4 GHz quad-core Intel Core i5
  - Memory (RAM): 8 GB 2133 MHz LPDDR3
  - Storage: 256 GB
- Operating System: macOS Sonoma V. 14.4.1
- Development Environment:
  - IDE/Editor: Virtual Studio Code V. 1.88.0
  - Python Version: Python 3.9.18
  - Key Libraries and Frameworks: NumPy, Matplotlib, SciPy, Gym, Pandas, Os

## Database

To enable Q-learning and train the model, a database containing the necessary input parameters for the heat exchanger had to be provided. Since experimental data was not available, this database was artificially created using randomly selected values with reasonable intervals. For simplicity, all fluids were assumed to be water. The required input data included inlet mass flow ($\dot{m}$), overall heat transfer coefficient (U), heat capacities (Cp), and inlet temperatures (T) for both the hot and cold fluids. The intervals set for each parameter were chosen based on plausible values, as shown in Table 2.

**Table 2:** Model input parameters with corresponding intervals.

| Parameter | Interval |
|---|---|
| U [W/$m^2$K] | [400, 1500] |
| $\dot{m}_{hot}$ [kg/s] | [0.2, 1.5] |
| $\dot{m}_{cold}$ [kg/s] | [0.2, 1.5] |
| $C_{p.hot}$ [kJ/kgK] | [3.8, 4.5] |
| $C_{p.cold}$ [kJ/kgK] | [3.8, 4.5] |
| $T_{hot}$ [°C] | [70, 200] |
| $T_{cold}$ [°C] | [10, 30] |

The database was created using a for-loop that generated 100 examples, which were stored in a DataFrame1. These data points were then randomly selected by the program during each training step.

## Heat Exchanger Calculations

A core component of the program calculates key performance parameters:

**Effectiveness (ε):** Calculated using the ε-NTU method, considering the number of shell and tube passes. The program implements the necessary equations for single and multiple shell passes.

**Pressure Drop (ΔP):** Calculated using the Darcy-Weisbach equation, with the friction factor determined using the Colebrook equation and the Reynolds number.

**Temperature Profiles:** Calculated by solving discretized versions of the energy balance PDEs for the tube and shell sides, including a stabilizing thermal diffusion term.

The calculate_performance() function takes input parameters (from the database and chosen action) and predefined fluid/tube properties (Table 3) to compute these performance metrics. The hot fluid was consistently assigned to the tube side and the cold fluid to the shell side.

**Table 3:** Predefined parameters for the shell and tube side.

| Parameter | Tube side | Shell side |
|---|---|---|
| Type of fluid | Water | Water |
| Density, $\rho$ $[kg/m^3]$ | 997 | 997 |
| Dynamic viscosity, $\mu$ $[Pa \cdot s]$ | $10.52 \cdot 10^{-3}$ | $10.52 \cdot 10^{-3}$ |
| Thermal conductivity, $\kappa$ $[W/m \cdot K]$ | 0.61 | 0.61 |
| Internal diameter of tubes, $d_i$ $[m]$ | $20 \cdot 10^{-3}$ | |
| Outer diameter of tubes, $d_o$ $[m]$ | $22 \cdot 10^{-3}$ | |
| Tube length, $l$ $[m]$ | 1 | |

## Q-Learning Implementation

The Q-learning algorithm was implemented through a structured framework consisting of an environment, an agent class, and a systematic training process:

Environment Class The reward function combines the effectiveness factor (ε) and pressure drop (ΔP) to evaluate the performance of the heat exchanger. By adjusting the pressure drop to a scale of [0, 22] psi, the model is incentivized to maximize ε and minimize ΔP, promoting optimal design outcomes with high efficiency and low energy loss. The step() function calculates the next state, reward, and a stop criterion based on maximum steps per episode and steps since reward increase. The reset() function initializes the environment for each new data point.

$$reward = \varepsilon + \frac{1}{\Delta P_{psi}} \quad (8)$$

**Table 4:** Total number of configurations based on the action space.

| Tube passes / Shell passes (n) | 2n | 4n | 6n |
|---|---|---|---|
| 1 | (1,2) | (1,4) | (1,6) |
| 2 | (2,4) | (2,8) | (2,12) |
| 3 | (3,6) | (3,12) | (3,18) |

**Agent** Class Implements the Q-learning agent. It initializes with a learning rate (0.1), discount factor (0.9), and epsilon value (0.1). The choose_action() function uses the ε-greedy policy for action selection. The update() function updates the Q-table based on the Q-learning update rule.

**Training Process (training.py):** The training process follows these steps:

1. Read heat exchanger parameters from the database.
2. Initialize the agent and environment.
3. Iterate through episodes (50) and data points (10 per episode).
4. For each data point:
   - Randomly select heat exchanger parameters.
   - Reset the environment.
   - While the stop criterion is not met:
     - Agent chooses an action using ε-greedy.
     - Environment performs the action and returns the next state, reward, etc.
     - Agent updates the Q-table.
5. Store best-performing data points, cumulative rewards, and trained agents.

## RESULTS

The implementation of the program required approximately 48 hours on the specified computer, averaging under one hour per episode. The average reward per episode is shown in Figure 3.

Performance varied significantly across episodes due to the reset of training for each new episode, which provided insight into diverse configurations. The training aimed to optimize performance for specific parameters, achieving near-optimal designs through 5000 simulation steps per episode.

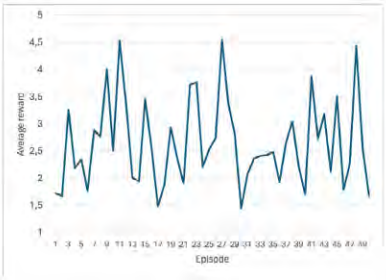



**Figure 3.** Average reward for each episode of the training procedure.

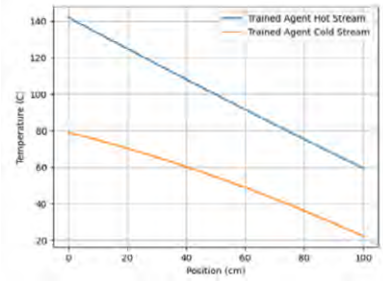



**Figure 4.** Temperature profile for the best performing epoch within data point 10, episode 27.

## Best and Worst Performing Episodes

Episode 27 achieved the highest reward, with an average score of 4.549. Within this episode, data point 10 reached a peak reward of 10.450. The details are presented in Table 5, and the corresponding temperature profile is illustrated in Figure 4.

**Table 5:** Properties of the best performing epoch within data point 10, episode 27.

| Properties | Hot fluid | Cold fluid |
|---|---|---|
| Reward | 10.450 | |
| Effectiveness factor, $\varepsilon$ [-] | 0.687 | |
| Pressure drop, $\Delta P$ [psi] | 0.706 | |
| Overall heat transfer coefficient, U [W/$m^2$K] | 683 | |
| Inlet mass flow, $\dot{m}$ [kg/s] | 0.218 | 0.358 |
| Heat capacity, $C_p$ [kJ/kgK] | 4.392 | 3.891 |
| Inlet temperature, $T_{in}$ [ºC] | 142 | 22 |
| Action, (nº shell passes, nº tube passes) | (1,2) | |

The heat exchanger achieved 69% effectiveness with minimal pressure drop (0.7 psi), using a configuration of one shell pass and two tube passes. Although higher effectiveness might be expected for better performance, the reward function heavily penalizes high-pressure drops, making this configuration optimal. The temperature profiles indicate consistent energy conservation principles, with the hot stream cooling from 142°C to 59°C and the cold stream heating from 22°C to 79°C.

In contrast, episode 30 recorded the lowest reward, averaging 1.450. Data point 2, with a reward of 0.780, stands out as the poorest performer due to a high-pressure drop of 190 psi despite achieving 75% effectiveness. This pressure drop renders the configuration impractical for real-world applications. The suboptimal results highlight the importance of balancing effectiveness and pressure drop for optimal design.

## Optimal Design Insights

Analysis of the top-performing epochs identified the (1, 2) configuration as the most effective design. This configuration consistently achieved superior rewards due to a favorable balance between moderate effectiveness (~69%) and minimal pressure drop (~0.7 psi). Although designs with additional shell or tube passes offered higher effectiveness, they incurred significantly higher pressure drops, reducing their overall performance scores.

## Comparative Analysis

Simpler configurations like (1, 2) outperformed more complex designs, demonstrating the trade-off between heat transfer efficiency and system practicality. The reward system penalized configurations with excessive pressure drops, reinforcing the preference for designs that optimize both criteria.

# CONCLUSION

This work proposed a novel framework for optimizing heat exchanger design using Q-learning, showcasing the integration of Scientific Machine Learning (SciML) with heat exchanger optimization. The model was built upon fundamental heat transfer principles and the ε-NTU method, enabling a thorough performance evaluation based on effectiveness and pressure drop across the heat exchanger.

Q-learning was chosen for its capability to operate without a precise system model, relying instead on trial-and-error exploration to navigate the design space. The model's training process incorporated an environment, an agent, and a structured training sequence, with the agent iteratively maximizing the reward function by exploring various design configurations.

The findings revealed that the simplest design was identified as optimal within the model's constraints, primarily due to the reward function's emphasis on minimizing pressure drop over maximizing heat transfer effectiveness. This outcome underscores the critical role of reward function design in guiding optimization priorities. A comparative analysis demonstrated that while more intricate designs improved heat transfer efficiency, they yielded lower reward scores due to higher pressure drops.

Future improvements to the framework should focus on enhancing its versatility and realism. These enhancements include incorporating a broader range of fluid types, integrating more detailed and accurate heat transfer equations, expanding the diversity of design configurations, and refining the reward function to balance multiple performance parameters more effectively. Additionally, leveraging real-world datasets for training and validation will increase the model's reliability and applicability, paving the way for more robust and practical optimization outcomes.

## ACKNOWLEDGEMENTS

This work was supported by national funds through FCT/MCTES (PIDDAC) UI/BD/154743/2023; FCT/MCTES (PIDDAC): LSRE-LCM, UIDB/50020/2020 (DOI: 10.54499/UIDB/50020/2020) and UIDP/50020/2020 (DOI: 10.54499/UIDP/50020/2020); and ALiCE, LA/P/0045/2020 (DOI: 10.54499/LA/P/0045/2020).

## REFERENCES

1. Balaji C, Srinivasan B, Gedupudi S. “Chapter 7 - Heat exchangers”. In: Heat Transfer Engineering: Fundamentals and Techniques. Academic Press, 2021, pp. 199–231. https://doi.org/10.1016/B978-0-12-818503-2.00007-1
2. Theodore L. Heat transfer applications for the practicing engineer. John Wiley & Sons, 2011, pp. 3–5. ISBN: 978-0-47-064372-3.
3. Caputo AC, Pelagagge PM, Salini P. Heat exchanger design based on economic optimisation. *App Therm Eng* 28:1151-1159 (2008) https://doi.org/10.1016/j.applthermaleng.2007.08.010
4. Saxena R, Yadav S. Designing Steps for a Heat Exchanger. *Int J Eng Res Tech* 2:943-959 (2013).
5. Iwema J. “Scientific Machine Learning”. In: Wageningen University & Research (Jan. 2023). URL: https://sciml.wur.nl/reviews/sciml/sciml.html
6. Wang Y, Ma Y, Chao H. Machine learning and computational fluid dynamics-based optimization of finned heat pipe radiator performance. *J Build Eng* 7 8:107612 (2023) https://doi.org/10.1016/j.jobe.2023.107612
7. Celik N, Tasar B, Kapan S, Tanyildizi V. Performance optimization of a heat exchanger with coiled-wire turbulator insert by using various machine learning methods. *Int J Therm Sci* 192:108439 (2023). https://doi.org/10.1016/j.ijthermalsci.2023.108439
8. Keramati H, Hamdullahpur F, Barzegari M. Deep reinforcement learning for heat exchanger shape optimization. *Int J Heat Mass Transfer* 194:123112 (2022)https://doi.org/10.1016/j.ijheatmasstransfer.2022.123112
9. Handibag R, Potdar DU, Jadhav A. Thermal design of tube and shell heat exchanger and verification by HTRI software. *Int J Eng Res Tech* 9:525-530 (2020).
10. Janaun J, Kamin NH, Wong KH, Tham HJ, Kong VV, Farajpourlar M. Design and simulation of heat exchangers using Aspen HYSYS, and Aspen exchanger design and rating for paddy drying application. In *IOP Conference Series: Earth and Environmental Science* 36:1:012056 (2020)
11. Incropera FP et al. Fundamentals of Heat and Mass Transfer. 6th ed. John Wiley & Sons, 2007, pp. 686–699. ISBN: 978-0-471-45728-2.
12. Mohammed Rabeeh V, Vysakh S. Design of Shell and Tube Heat Exchanger Using MATLAB and Finding the Steady State Time Using Energy Balance Equation. *Int J Adv Mech Eng* 4:95-100 (2014), pp. 95–100. ISSN: 2250-3234. URL: https://www.ripublication.com/ijame-spl/ijamev4n1spl_12.pdf
13. Papaevangelou G, Evangelides C, C Tzimopoulos C. A new explicit relation for friction coefficient f in the Darcy-Weisbach equation. In: *Proc 10th Conf Protect Restor Environ*. 166:6-9 (2010).
14. Niranjan K. “Elements of Fluid Flow”. In: Engineering Principles for Food Process and Product Realization. Cham: Springer International Publishing, 2022, pp. 23–50. https://doi.org/10.1007/978-3-031-07570-4_2
15. Yamin Kao et al. “A dynamic approach to support outbreak management using reinforcement learning and semi-connected SEIQR models”. In: BMC Public Health 194 (2024). https://doi.org/10.1186/s12889-024-18251-0
16. Feinberg EA, Shwartz A. Handbook of Markov decision processes: methods and applications. Vol. 40. Springer Science & Business Media, 2012.
17. Sutton RS, Barto AG. Reinforcement learning: An introduction. 2nd ed. MIT press, 2018, pp. 47–68, 119–138. ISBN: 978-02-62039-24-6.
18. Watkins CJCH. “Learning from delayed rewards”. (May 1989)
19. Clifton J, Laber E. Q-learning: Theory and applications. *Annual Review of Statistics and Its Application* 7 (2020), pp. 279–301.

© 2025 by the authors. Licensed to PSEcommunity.org and PSE Press. This is an open access article under the creative commons CC-BY-SA licensing terms. Credit must be given to creator and adaptations must be shared under the same terms. See https://creativecommons.org/licenses/by-sa/4.0/



Systems & Control Transactions

**Research Article - Peer Reviewed Conference Proceeding**
ESCAPE 35 - European Symposium on Computer Aided Process Engineering
Ghent, Belgium. 6-9 July 2025
Jan F.M. Van Impe, Grégoire Léonard, Satyajeet S. Bhonsale,
Monika E. Polańska, Filip Logist (Eds.)

PSE PRESS

# Multi-Agent LLMs for Automating Sustainable Operational Decision-Making

**Emma Pajak[a], Abdullah Bahamdan[a], Klaus Hellgardt[a], Antonio del Río-Chanona[a,*]**

[a] Imperial College London, Department of Chemical Engineering, London, United Kingdom.
* Corresponding Author: a.del-rio-chanona@imperial.ac.uk.

## ABSTRACT

Operational decision-making in Process Systems Engineering (PSE) has achieved high proficiency at specific levels, such as supply chain optimization and unit-operation optimization. However, a critical challenge remains: integrating these layers of optimization into a cohesive, hierarchical decision-making framework that enables sustainable and automated operations. Addressing this challenge requires systems capable of coordinating multi-level decisions while maintaining interpretability and adaptability. Multi-agent frameworks based on Large Language Models (LLMs) have demonstrated significant promise in other domains, successfully simulating traditional human decision-making tasks and tackling complex, multi-stage problems. This paper explores their potential application within operational decision-making for PSE, focusing on sustainability-driven objectives. A realistic Gas-Oil Separation Plant (GOSP) network is used as a case study, mimicking a hierarchical workflow that spans from initial back-of-the-envelope multi-objective optimization for cost-emissions trade-offs to a negotiation phase reflecting upper management decision-making, and culminating in high-fidelity simulations to validate operational setpoints at the plant level. This workflow serves as a canvas to assess the benefits of multi-agent LLMs, including their ability to integrate multi-layered decisions, enhance the explainability of strategies, and streamline automation in PSE workflows. The results demonstrate the potential of multi-agent LLMs to address the integration challenge in PSE, supporting sustainable and efficient operational decisions. Beyond GOSPs, this research highlights promising applications of multi-agent LLMs across process engineering, contributing to the vision of hierarchical, automated decision-making for the 'plant of the future,' where diverse models and tools operate within an intelligent, unified framework.

**Keywords**: operational decision-making, large language models (LLMs), sustainability, optimization.

## INTRODUCTION

Operational decision-making (ODM) is pivotal in Process Systems Engineering (PSE), serving as the foundation for optimizing the performance, efficiency, and sustainability of industrial processes. In an era where industries face mounting pressure to achieve net zero emissions while maintaining cost-effectiveness, the necessity for robust ODM frameworks has become increasingly critical. Optimization in PSE is conducted at multiple hierarchical levels: system-wide optimization enhances supply chain efficiency by managing the flow of materials, information, and funds; plant-wide optimization focuses on improving operational efficiency within individual plants, such as utility management; and unit operation optimization targets specific processes like reactor performance. Despite these layered approaches, a significant challenge remains—the automation and seamless integration of multi-layered decision-making processes. As industrial systems grow in complexity, there is a need for automated tools that can unify these layers, providing operators with rapid access to comprehensive insights or suggestions. Such automation not only promises substantial cost savings but also facilitates significant reductions in emissions, thereby driving industries toward more sustainable and economically viable operations.

An increasing number of studies are emerging that focus on leveraging Generative Artificial Intelligence (GenAI) within PSE [1]]. GenAI encompasses a range of technologies, including Large Language Models (LLMs),

which are advanced AI systems trained on vast amounts of text data to understand and generate human language. LLMs have found applications in PSE such as supporting the automatic generation of P&IDs [2], and fault detection and diagnosis in chemical processes [3].

## Multi-Agent LLMs

Multi-agent LLMs are a development in GenAI that extends the capabilities of individual language models by orchestrating multiple specialized LLMs, known as agents, to collaborate on complex tasks [4]. Studies indicate that multi-agent LLM systems have the potential to surpass single-agent approaches in both accuracy and complex problem-solving capabilities [5]. In tasks replicating human behavior, multi-agent architectures have demonstrated substantial accuracy gains, with some findings suggesting a direct correlation between the number of agents and overall performance [5]. The "More Agents Is All You Need" approach (Agent Forest) further shows that increasing the number of instantiated LLM agents through sampling and voting can boost accuracy, particularly on difficult tasks [6]. Meanwhile, the Mixture-of-Agents (MoA) approach leverages iterative collaboration among multiple models to address more intricate problems, outperforming single agents on benchmarks such as AlpacaEval 2.0, MT-Bench, and FLASK [7].

Building on these performance advantages, multi-agent LLMs excel in advanced multi-step problems through agent specialization: specialized agents can be developed and dedicated to distinct subtasks or areas of expertise, avoiding reliance on a single model for all problem aspects. Hence, multi-agent systems are inherently modular and thus flexible, making them easier to reconfigure as operational needs evolve. Adding or updating agents—each responsible for a particular function—can often be done with minimal disruption to the broader system. This adaptability ensures that multi-agent LLM frameworks remain robust and scalable, even in rapidly changing industrial or research environments.

Multi-agent LLMs have already seen application across a wide range of industries [8]. For example, ChatDev integrates different phases of the software development lifecycle into a unified communication system using LLM agents. It enhances collaboration through multi-turn dialogues, chat chain organization, and dehallucination, improving software design, coding, and debugging [9]. Compared to its single-LLM counterpart, GPT-Engineer, ChatDev achieves higher Quality (0.3953 vs. 0.1419) and Consistency (0.8021 vs. 0.7887). These results demonstrate that multi-agent systems can outperform single-agent systems, particularly in managing complex, multi-stage tasks [9].

More recent works have demonstrated the implementation of multi-agent systems in process engineering contexts. For example, industrial automation of control systems has been explored using multi-agent frameworks with LLM-based agents, incorporating validation and reprompting architectures to improve accuracy, adapt to dynamic disturbances, and enhance reliability in complex operational environments [10].

## Study Aim

Although multi-agent LLMs have demonstrated success across various industries and are beginning to gain traction in PSE, there remains a substantial opportunity to harness their capabilities specifically for ODM. By leveraging their capacity for complex problem-solving and coordination of multi-step tasks through specialized agents, these systems could serve as a decision-support tool that fully automates and integrates ODM. This, in turn, unlocks significant cost savings and emission reductions, supporting PSE operations in meeting global sustainability targets. This work investigates the application of multi-agent LLM systems for ODM in PSE. This study explores how these systems can represent multiple stakeholders across the decision-making landscape to address the complexities of hierarchical workflows, and focuses on the following key areas:

- **Integration:** Assessing how multi-agent LLMs can integrate the different layers of decision-making, from management to operator level.
- **Negotiation:** Investigating the potential of agents to simulate realistic stakeholder negotiations, addressing trade-offs between competing business units and goals such as economic performance and sustainability.
- **Automation:** Exploring how multi-agent LLMs can reduce human intervention while maintaining transparency and explainability, ensuring that the system's decisions are interpretable and actionable.

Together, these focal points aim to assess the feasibility and transformative potential of multi-agent LLMs in enabling sustainable, efficient, and intelligent decision-making within PSE.

# METHODOLOGY

To explore the potential of multi-agent LLM systems for operational decision-making, it is essential to select a case study that is both realistic and representative of industrial challenges. This curated case study draws inspiration from production planning in the oil and gas industry, a sector characterised by extensive, interconnected supply chains and complex, interdependent decision-making processes that are needed of sustainable operations. The detailed case study, optimization formulation, and HYSYS flowsheet can be found in the work by Bahamdan et al. [11]. This example not only captures multi-layered workflows typical of PSE but also integrates simulation and optimisation components, making it an ideal

testbed for assessing LLMs' tool usage. Furthermore, the cost-emissions trade-off provides a compelling scenario to explore LLM agent negotiation, mirroring real-world industrial decision-making dynamics.

## Gas-Oil Separation Plant (GOSP) Case Study

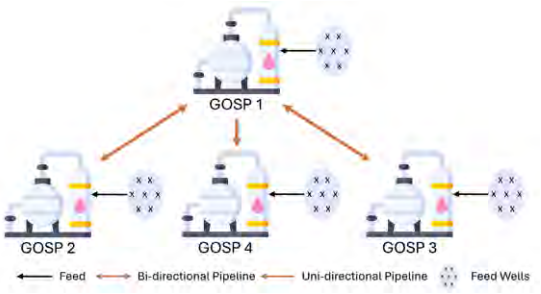



**Figure 1.** Schematic of four interconnected GOSPs connected by uni- and bi-directional pipelines.

This study focuses on the midstream sector of the oil and gas supply chain, which forms the logistical backbone, facilitating the production, processing, and transfer of products. This sector comprises a network of Gas-Oil Separation Plants (GOSPs) that separate oil, gas, and water phases, remove impurities, and ensure products meet customer specifications. These facilities are interconnected via swing pipelines to optimize operations and handle disturbances effectively. A simplified network of four GOSPs, as illustrated in Figure 1, is considered for this study. Each GOSP processes feedstock from a dedicated cluster of production wells. Although all wells within a cluster produce oil of the same grade, feed quality varies slightly but remains within acceptable limits.

Typical GOSPs consist of three main sections: crude oil, associated gas, and oily water. Each incorporates a series of separation vessels and energy-intensive rotating equipment, which contribute significantly to emissions in fossil-based fuel production. This case study builds on recent work that employs state-of-the-art, data-driven methods to decarbonize and optimize GOSP networks by utilizing swing pipelines.

## Hierarchical Decision-Making Workflow

Building on the previously defined 4 GOSP system, this case study examines the production planning process of a typical oil and gas company involving multiple stakeholders from different organizations. Within industry, the production planning process typically follows the following structure. A month in advance, a central planning group receives government-issued monthly production targets. An upstream team uses advanced reservoir simulations to determine optimal production capacities for each well, coordinating with midstream planners to ensure processing systems are ready. Once all parties agree on production targets and midstream capacities, the decision is finalized. Afterwards, separate organizations for production and environmental compliance monitor real-time data to make necessary adjustments for the remainder of the planning period.

Closely mirroring the status quo of industry, this study's production planning process takes the following structure. The objective of the ODM workflow is to determine an operational setpoint for a given schedule, defining the system's cost and emissions through a three-stage decision-making process. The '**Initial Analysis**' stage employs Multi-Objective Optimization (MOO) to balance cost and emissions, generating a Pareto front of operational set points. As Operating Expenses (OPEX) are primarily driven by the power consumption of major equipment, a low-fidelity surrogate was trained on plant operation data to avoid expensive, iterative runs of a process simulation. The surrogate outputs the power consumption of the four major rotating equipment that represent 90% of the total power consumption, which is used as a proxy for cost. Emissions, including scope 1 (flaring and venting) and scope 2 (indirect emissions from power generation) are calculated by using mass balances to determine surplus gas. Model constraints include design capacities for the GOSPs and swing pipelines, material balances, and flow direction of swing pipelines. This problem is formulated as a Mixed-Integer Linear Program (MILP), determining the optimal feed rate for each facility, as well as the swing pipe configuration. The **'Strategic Selection**' involves choosing an operational setpoint from the Pareto front by evaluating trade-offs between cost and emissions, aligning with the management's strategic priorities and considering market and regulatory factors. Finally, the '**Operational Realization**' stage implements the chosen setpoint in system operations, transitioning from theoretical optimization to practical application while accounting for operational uncertainties such as equipment performance variations and external disruptions.

## Multi-Agent LLM Framework

### LLMs and Architecture

The workflow employs two LLM models, both deployed locally using Ollama on an RTX 3060 GPU. Llama-3.1 8B is used for reasoning and decision-making tasks, such as debate evaluation and argument generation. For tasks requiring tool integration, the Llama-3-Groq-8B-Tool-Use model is used, which is fine-tuned for structured tool use and function calling. This model scores 89% overall accuracy on the Berkeley Function Calling Leaderboard used for benchmarking LLM tool usage [12]. The agentic system was implemented using LangGraph, selected for its ability to build workflows around a graph structure. In this framework, agents are represented as nodes, and edges define the routing logic, making the workflow intuitive and easy to visualise. Multi-agent LLM

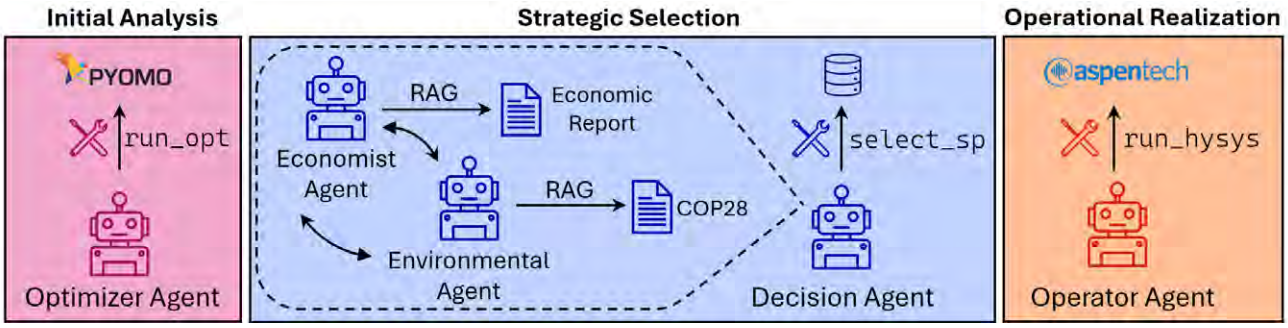



**Figure 2:** Multi-agent LLM workflow: Initial Analysis - The Optimizer Agent utilizes `run_opt` to calculate the Pareto front for a user-given schedule; Strategic Selection - Decision Agent reviews a debate between RAG-enhanced Economist and Environmental Agent and uses `select_sp` to choose the set point; Operational Realization - Operator Agent takes operational parameters at selected setpoint and runs GOSP system using `run_hysys`.

architectures refer to the connections, or edges, that direct workflows between agents [13]. Different architectures are suited to different tasks. For example, sequential architectures are simple and efficient, making them ideal for workflows with clearly defined stages. This workflow employs an architecture that combines the sequential structure to address each decision-making layer systematically and incorporates a cycle for the setpoint debate between Environmental and Economist agents. This design enables focused negotiation, improving decision quality through iterative exchanges without unnecessary complexity.

## Agents and Tools

The workflow relies on three specialized tools to facilitate decision-making and system simulation, as summarised in Table 1.

**Table 1:** Workflow tools and their functionalities.

| Tool | Description |
|---|---|
| `run_opt` | Takes the initial feed, executes Pyomo-based MOO, and returns Pareto front. |
| `choose_sp` | Takes setpoint identifier, retrieves the Pareto front, and returns the selected operational parameters. |
| `run_hysys` | Takes finalized operating schedule, runs a HYSYS simulation, returns key unit operations power consumption and OPEX. |

The framework also integrates Retrieval-Augmented Generation (RAG), which enhances LLM responses by incorporating external documents or knowledge bases, enabling a more informed and contextually relevant output [14]. Both the Environmental and Economic agents employed RAG to strengthen their arguments. The Environmental agent referenced sustainability-focused documents, such as the COP28 report [15]. Meanwhile, the Economic agent had access to economic and corporate documents to support its arguments.

**Table 2:** Overview of agent roles in the workflow.

| Agent | Role Description |
|---|---|
| Optimisation Agent | Extracts the ICF from user input and runs the `run_opt` tool to compute the Pareto front, balancing cost and emissions. |
| Economic Agent | Advocates for cost minimisation in the debate phase. |
| Environmental Agent | Advocates for emissions reduction, using RAG on documents such as COP28 in the debate phase. |
| Decision Agent | Evaluates arguments, selects the setpoint, and retrieves operational parameters with `choose_sp` tool. |
| Operator Agent | Uses `run_hysys` to run operations and validate cost and emissions. |

## Agentic Workflow Description

Figure 2 illustrates the agentic workflow aligned with the three-stage decision-making process. It begins with the Optimisation Agent, which extracts the Initial Condition Factors (ICF) from the user prompt and uses its `run_opt` tool to execute a Pyomo-based MOO. This generates a set of feasible operational configurations for the GOSP which forms a Pareto front representing the trade-off between cost and emissions.

The Economic and Environmental Agents then engage in a structured debate to select the operating setpoint. The Economic Agent advocates for cost minimization, while the Environmental Agent prioritises emissions reduction, using RAG with sources like COP28 to support its arguments. Each agent presents two arguments in turn, advocating for their preferred setpoint.

Next, the Decision Agent evaluates the debate transcript to select the winning setpoint based on argument quality. Using the `choose_sp` tool, it retrieves the corresponding operational parameters from the Pareto front. The Operator Agent uses these parameters with the `run_hysys` tool to interact with the HYSYS simulation,

set stream values, and retrieve power consumption data to calculate the actual OPEX for the chosen configuration.

## RESULTS

The multi-agent LLM framework successfully executed the entire operational workflow in all trials. Upon receiving a user prompt with the latest ICF schedule, the Optimizer Agent generated the Pareto front using the `run_opt` tool. Subsequently, the Decision Agent evaluated the arguments presented by the Economist and Environmentalist agents to select the optimal operational setpoint. Finally, the Operator Agent applied the parameters from the chosen configuration to operate the GOSP network. Across ten runs, the agentic workflow had an average runtime of 79.2 seconds on an RTX 3060 GPU.

### Agent Debate and Decision-Making Process

To evaluate the multi-agent LLM framework's responsiveness to evolving information, two distinct runs were conducted under identical ICF schedules with differing informational inputs. From the back-and-forth exchange between the agents, two quotes are presented to highlight some of the more significant arguments.

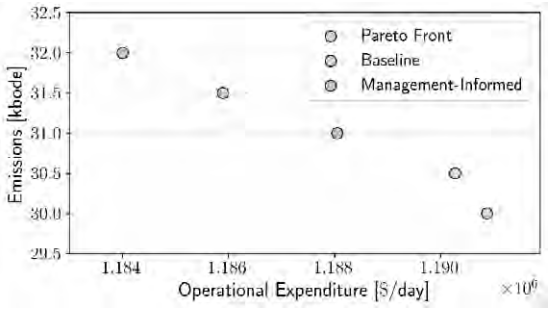



**Figure 3.** Pareto front illustrating the trade-off between operational costs and emissions. Each point represents a feasible operational configuration for the GOSP network.

### Baseline Run

In the initial run, no additional economic directives were provided. The agents engaged in a debate focused solely on balancing emissions and operational costs. The Environmentalist Agent cited global sustainability commitments, emphasizing recent international agreements:

> `At COP28, Parties emphasized the importance of accelerating emissions reductions and promoting a just transition for energy systems worldwide. If we fail to make ambitious choices now, we risk undermining these global commitments.` **`-Environmental Agent`**

Influenced by these arguments, the Decision Agent opted for a setpoint that minimised emissions, resulting in the highest operational cost among available options.

### Second Run (With Economic Directive)

In the next run, an "Economic Directive" document was introduced to the Economist Agent via RAG. This directive stipulated a soft constraint on operational costs of 1,188,500 [$/day], from upper management. Equipped with this information, the Economist Agent adjusted its arguments to align with the new budgetary constraint:

> `Given upper management's directive to keep costs below $1,188,500 per day, we must explore a more balanced trade-off. Setpoint 3 adheres to the strict budget while mitigating emissions.` **`-Economist Agent`**

Consequently, the Decision Agent adopted a setpoint that achieved a balanced compromise between emissions and costs, ensuring compliance with the managerial cost threshold while still addressing environmental concerns. This outcome marked a clear departure from the earlier sustainability-focused solution, illustrating how new information can prompt a recalibration of priorities in the workflow, resulting in a shift in outcome.

Overall, these findings highlight the adaptability of the multi-agent LLM framework. When presented with evolving objectives—be it a sustainability pledge linked to COP28 or a budgetary mandate from upper management—the agents' internal debate naturally reorients toward fulfilling the most pressing constraint. In doing so, the system demonstrates how LLMs, when integrated into an orchestrated multi-agent workflow, can reconcile environmental imperatives with operational costs, integrating new information into decision-making processes. A workflow like the one presented in this work could integrate into the production planning cycle, enabling real-time adjustments to operational parameters to optimize the alignment between planned and actual performance.

## CONCLUSION

In line with this study's aim to explore the potential of multi-agent LLMs for ODM in PSE, our findings demonstrate the efficacy of these frameworks within the midstream sector of the oil and gas supply chain. By leveraging multi-agent LLMs, the framework effectively integrates complex, multi-level decision-making processes in an automated and highly interpretable manner, dynamically adapting to evolving operational constraints and directives. This highlights the ability of multi-agent LLMs to navigate trade-offs, balancing sustainability and economic objectives.

Presented as a decision-support tool to complement human expertise, the multi-agent LLM framework accelerates stakeholder alignment by providing a structured and interpretable approach to complex decision-making. In real deployments, domain experts will remain vital to validating final setpoints, and ensuring adherence to plant safety protocols, corporate objectives, and

operational constraints. Although multi-agent LLMs are rapidly advancing, they still face challenges, such as scalability, model alignment, and governance.

### Future Work

One key direction is expanding argument quality and industrial relevance through RAG by integrating dynamically updated reference documents (e.g., industry standards, real-time news) and proprietary materials (e.g., sustainability reports, financial data). Incorporating live economic or environmental metrics would enhance both precision and relevance. Another focus is generalization and scalability: by adjusting the `run_opt` tool and the MILP, the workflow could handle different numbers of GOSPs of varying capacities. To further validate the benefits of multi-agent LLMs for ODM in PSE, work should explore their use in other sectors, e.g., chemical manufacturing.

Introducing additional agent roles (e.g., Regulatory Agent, Safety Manager) and enabling agents to learn from prior runs or user feedback would enrich the decision-making process. User interaction and overrides also warrant attention, allowing domain experts to review and override decisions, supported by access to Pareto fronts, and debate transcripts. Finally, assessing the framework's robustness under incomplete or conflicting information is critical to ensure feasible outcomes. Addressing ethical and interpretability concerns is equally important for building trust, requiring alignment with ethical standards and clear explanations of agent reasoning.

## ACKNOWLEDGEMENTS

We gratefully acknowledge financial support from BASF SE and the EPSRC Centre for Doctoral Training in Next Generation Synthesis & Reaction Technology (EP/S023232/1).

## REFERENCES

1. Decardi-Nelson B, Alshehri AS, Ajagekar A, You F, Generative AI and process systems engineering: The next frontier. *Comput Chem Eng*, 187:108723 (2024) doi: 10.1016/j.compchemeng.2024.108723.
2. Hirtreiter E, Balhorn LS, Schweidtmann AM, Towards automatic generation of Piping and Instrumentation Diagrams (P&IDs) with Artificial Intelligence. *AIChE J* 70: e18259 (2024), doi: 10.1002/aic.18259.
3. Khan A, Nahar R, Chen H, Flores GEC, Li C, FaultExplainer: Leveraging Large Language Models for Interpretable Fault Detection and Diagnosis. Dec. 19, 2024, *arXiv*: doi: 10.48550/arXiv.2412.14492.
4. Guo T *et al*. Large Language Model based Multi-Agents: A Survey of Progress and Challenges. Apr. 19, 2024, *arXiv*: doi: 10.48550/arXiv.2402.01680.
5. Sreedhar K, Chilton L. Simulating Human Strategic Behavior: Comparing Single and Multi-agent LLMs. Jul. 02, 2024, *arXiv*: doi: 10.48550/arXiv.2402.08189.
6. J. Li, Q. Zhang, Y. Yu, Q. Fu, and D. Ye, "More Agents Is All You Need," Oct. 11, 2024, arXiv: doi: 10.48550/arXiv.2402.05120.
7. J. Wang, J. Wang, B. Athiwaratkun, C. Zhang, and J. Zou, "Mixture-of-Agents Enhances Large Language Model Capabilities," Jun. 07, 2024, arXiv: doi: 10.48550/arXiv.2406.04692.
8. X. Li, S. Wang, S. Zeng, Y. Wu, and Y. Yang, "A survey on LLM-based multi-agent systems: workflow, infrastructure, and challenges," Vicinagearth, vol. 1, no. 1, p. 9, Oct. 2024, doi: 10.1007/s44336-024-00009-2.
9. C. Qian et al., "ChatDev: Communicative Agents for Software Development," in Proceedings of the 62nd Annual Meeting of the Association for Computational Linguistics (Volume 1: Long Papers), L.-W. Ku, A. Martins, and V. Srikumar, Eds., Bangkok, Thailand: Association for Computational Linguistics, Aug. 2024, pp. 15174–15186. https://aclanthology.org/2024.acl-long.810
10. [J. Vyas and M. Mercangöz, "Autonomous Industrial Control using an Agentic Framework with Large Language Models," Nov. 08, 2024, arXiv: doi: 10.48550/arXiv.2411.05904.
11. Bahamdan A, Shah N, del Rio-Chanona A. Surrogate Based Mixed Integer Linear Programming Model for Decarbonization of an Integrated Gas-Oil Separation Network. *Comput Aided Chem Eng*, 53:2209–2214 (2024). doi: 10.1016/B978-0-443-28824-1.50369-0.
12. Hugging Face Llama-3-8B. https://huggingface.co/Groq/Llama-3-Groq-8B Tool-Use.
13. T. Händler, "Balancing Autonomy and Alignment: A Multi-Dimensional Taxonomy for Autonomous LLM-powered Multi-Agent Architectures," Oct. 05, 2023, arXiv: doi: 10.48550/arXiv.2310.03659.
14. P. Lewis et al., "Retrieval-augmented generation for knowledge-intensive NLP tasks," in Proc 34th Int Conf on Neural Information Processing Systems, in NIPS '20. Red Hook, NY, USA: Curran Associates Inc., Dec. 2020, pp. 9459–9474.
15. "Summary of Global Climate Action at COP 28 | UNFCCC." https://unfccc.int/documents/636485.

© 2025 by the authors. Licensed to PSEcommunity.org and PSE Press. This is an open access article under the creative commons CC-BY-SA licensing terms. Credit must be given to creator and adaptations must be shared under the same terms. See https://creativecommons.org/licenses/by-sa/4.0/



Systems & Control Transactions

**Research Article - Peer Reviewed Conference Proceeding**
ESCAPE 35 - European Symposium on Computer Aided Process Engineering
Ghent, Belgium. 6-9 July 2025
Jan F.M. Van Impe, Grégoire Léonard, Satyajeet S. Bhonsale,
Monika E. Polańska, Filip Logist (Eds.)

PSE PRESS

# On the role of artificial intelligence in feature oriented multi-criteria decision analysis

**Heyuan Liu[a,b], Yi Zhao[a]*, and Francois Maréchal[a]**

[a] Industrial Process and Energy Systems Engineering (IPESE), Ecole Polytechnique Fédérale de Lausanne, Sion, Switzerland
[b] MSc&T AiViC, École Polytechnique, Palasieau, France
* Corresponding Author: yi.zhao@epfl.ch.

## ABSTRACT

Balancing economic and environmental goals in industrial applications is critical amid challenges like climate change. Multi-objective optimization (MOO) and multi-criteria decision analysis (MCDA) are key tools for addressing conflicting objectives. MOO generates viable solutions, while MCDA selects the optimal option based on key performance indicators such as profitability, environmental impact, safety, and efficiency. However, large datasets pose a challenge in selecting the preferred solution during the MCDA process This study introduces a novel machine learning-enhanced MCDA framework and applies the method to analyze decarbonization solutions for a European refinery. A stage-wise dimensionality reduction method, combining AutoEncoders and Principal Component Analysis (PCA), is applied to simplify high-dimensional datasets while preserving key spatial features. Geometric analysis techniques, including Intrinsic Shape Signatures (ISS), are employed to refine the identification of typical configurations for baseline evaluations. Once typical configurations are identified, Large Language Models (LLMs) are utilized to enhance decision-making by providing contextual problem explanations and generating weight proposals for the weighted sum method, ensuring alignment with decision criteria. This framework is designed to support stakeholders in making informed, transparent decisions in complex, uncertain environments.

**Keywords**: Artificial Intelligence, Key performance indicator, Machine Learning, Multi-Criteria Decision Analysis

## INTRODUCTION

In chemical engineering, balancing economic and environmental goals is crucial amidst challenges like climate change. To address conflicting objectives, tools like multi-objective optimization (MOO) [1] and multi-criteria decision analysis (MCDA) [2] are utilized. MOO generates a range of viable solutions on Pareto fronts, while MCDA helps select the most suitable option considering key performance indicators (KPIs) like profitability, environmental impact, safety, and efficiency. These tools aid in making informed decisions amidst complex trade-offs and uncertainties. However, the vast number of solutions generated by MOO presents a significant challenge, as it is impractical for human decision-makers to compare and analyze all configurations manually. This raises a critical question: how can preferred solutions be effectively selected from such a large solution database?

The selection process is generally divided into two steps: first, identifying typical configurations from the database, and second, selecting preferred configurations from this identified set based on MCDA.

To identify typical configurations, data-driven approaches have garnered significant attention, particularly those utilizing clustering methods [3]. These methods analyze the solution space by dividing it into several clusters instead of examining the entire dataset. This approach effectively captures the global distribution of the data by segmenting it into distinct groups. However, existing clustering techniques are generally based on selected KPIs of each configuration, like operating costs, which are typically calculated under uncertain market conditions. Configurations should instead be analyzed based on their inherent features, where each feature represents an independent dimension such as the material and energy flows describing the configuration. Notably,

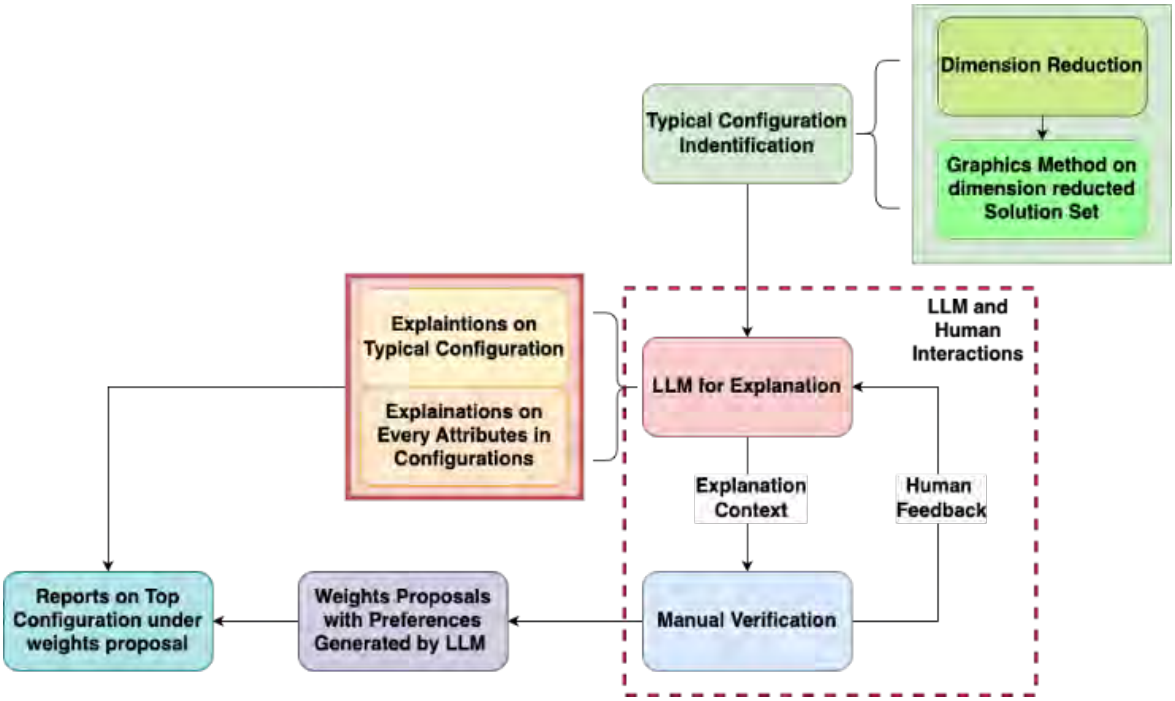



**Figure 1.** Method of feature-oriented MCDA processes

two different configurations may share the same KPIs despite being fundamentally distinct. Consequently, KPI-based clustering may fail to accurately represent the underlying differences among configurations. In addition, a notable drawback of the traditional clustering method is the neglect of intra-cluster distributions. The loss of local features within clusters can significantly impact the depth and accuracy of the analysis.

For preferred solution selection, the weighted sum method [4] remains the most popular approach in both research and industry. This method involves assigning a weight to each KPI, computing the score of each solution, ranking the scores, and selecting the top configurations as optimal solutions. Despite its widespread use, this approach suffers from several limitations:

**Lack of Diversity:** Due to the inherent properties of Multi-Objective Optimization (MOO), solution datasets often contain repeated configurations. As a result, the top-ranked solutions derived from the weighted sum method frequently share the same configuration, leading to a lack of diversity in the selected solutions.

**Limited Individual-Oriented Decision Making:** The subjective nature of weight assignments also poses challenges for accommodating diverse perspectives, which can hinder personalized or individual-oriented decision-making. The core of the weighted sum method lies in the assignment of weights to each KPI, which translates user preferences into quantifiable metrics. This process often requires domain expertise, making it challenging to generalize. Furthermore, the assigned weights are highly influenced by the individual expert's subjective preferences, introducing bias into the decision-making process.

**Difficulty in weight collection:** Gathering accurate and reliable weights for KPIs is a significant challenge. The process requires domain expertise and often lacks sufficient data support, making it difficult to establish objective and robust weight assignments.

To address these issues, a novel method is proposed that utilizes machine learning techniques, specifically Large Language Models (LLMs), to enhance the MCDA process under uncertain market conditions. The weight proposals for the weighted sum method are generated using the LLM model by incorporating specific preferences, eliminating the need for random identification or sole reliance on expert judgment. The primary contribution of this work lies in applying advanced machine learning methods to capture both global and local features in the solution space while leveraging LLMs for weight generation and MCDA.

## METHODS AND MATERIALS

The method is outlined in Figure 1, beginning with the identification of typical configurations, followed by the application of an LLM model to generate weight proposals for different KPIs to support the selection of preferred configurations.

### Typical Solution Identification

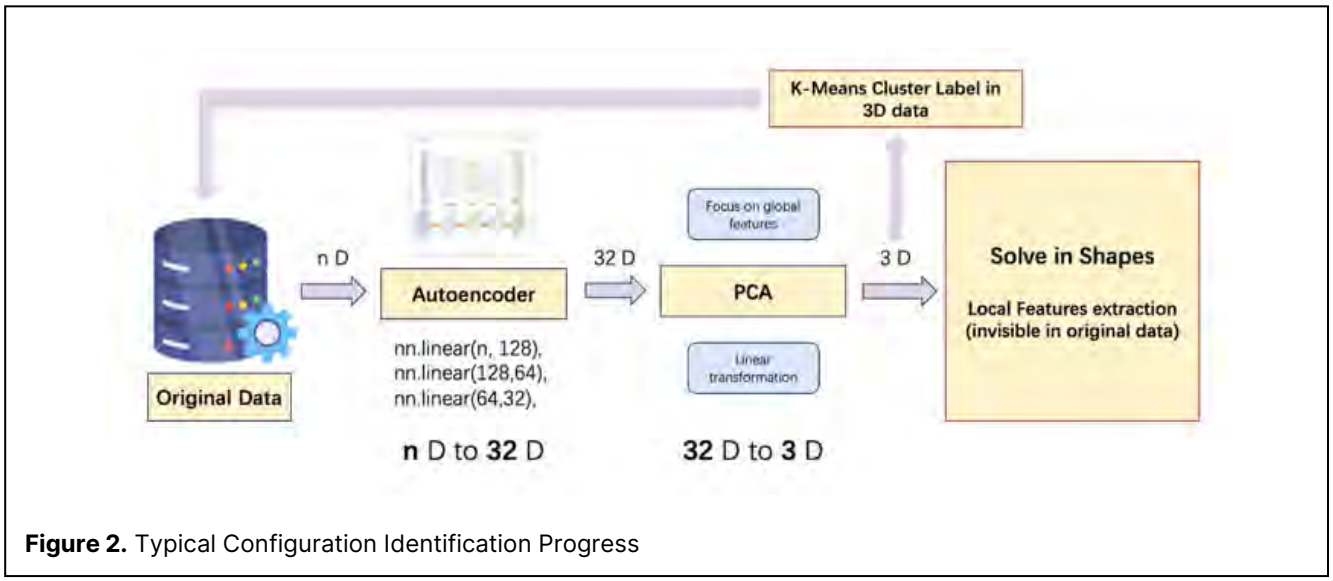



**Figure 2.** Typical Configuration Identification Progress

In complex energy systems, configurations often involve a vast number of features, making them a high dimension space impractical for manual analysis. Dimension reduction serves as an effective strategy to address this issue by simplifying the scale of the data while retaining its essential features. Clustering methods are then applied in dimension reduction datasets to identify the representative configurations, as shown in Figure 2.

## Dimension Reduction

In this study, the Linear Combiner (LC) is proposed, a two-stage dimensionality reduction approach combining AutoEncoder [5] and Principal components analysis (PCA) [6] to enhance clustering performance on high-dimensional datasets. The PCA can identify the linear connections in the resulting dataset in linear space. However, the feature space exhibits non-linear relationships due to interdependencies. The Autoencoder captures the complex, nonlinear structures of the data by reducing the input dimensionality to an intermediate dimensional latent space. Subsequently, PCA is applied to further reduce this latent representation to 3 dimensions, effectively preserving the most significant linear features while eliminating redundant information.

To validate the effectiveness of the approach, its ability to preserve the essential spatial distribution characteristics of the data after dimensionality reduction is evaluated. Clustering is performed in a three-dimensional space, and the resulting cluster labels are projected back to the original high-dimensional space, which is assessed using two metrics: the Davies-Bouldin Score (DB Score) [7] and the Calinski-Harabasz Index (CH Index) [8].

## Clustering based on the graphical method

In the pursuit of identifying the most representative solutions within the dataset, cluster centroids obtained through the K-Medoids method are selected as the reference case. However, empirical observations revealed critical limitations in this approach. The derived cluster centers proved overly dependent on intra-cluster density distributions, occasionally failing to encapsulate the essential characteristics that define typical configurations across the entire solution space. This realization motivated the development of a more robust identification strategy.

Building on the prior dimensionality reduction of the dataset into three-dimensional embeddings, graphical are used to extract latent spatial patterns that reveal structural relationships and density variations hidden in high-dimensional data. This 3D projection creates a visually interpretable landscape, where topological properties and neighborhood continuity can be algorithmically quantified, offering a more robust criterion for identifying typical configurations beyond centroid proximity. To achieve this, an advanced technique from graphics and computer vision—Intrinsic Shape Signatures (ISS) [9], is employed, providing a unique perspective to better understand the dataset's structure and identify typical configurations.

## LLM for MCDA

To effectively integrate Large Language Models (LLMs) into Multi-Criteria Decision Analysis (MCDA), the first step is to enable the LLM (e.g., ChatGPT series [10]) to comprehend the dataset. This involves providing the model with a curated subset of typical configurations rather than the entire dataset, as processing large datasets directly is impractical. The LLM is tasked with generating explanations for each attribute in the dataset, enhancing its reasoning ability through structured prompts and human verification. By manually verifying the explanations provided by the LLM, one can assess whether the LLM has properly understood the dataset. This allows the LLM to interpret the data contextually and provide meaningful

insights, paving the way for subsequent weight generation and decision-making processes.

## Data set interpretation

The reasoning ability of LLMs is crucial for accurate dataset interpretation. To enhance this capability, hierarchical explanation mechanisms and structured prompting are implemented to improve depth, accuracy, and reliability. Additionally, a human verification mechanism is introduced, enabling experts to review and validate AI-generated outputs at key stages. This interactive process identifies and corrects potential errors or biases while refining the model's reasoning through iterative feedback. By integrating human oversight, the framework ensures reliable, domain-aligned outputs, significantly enhancing the system's robustness and credibility.

**Hierarchical Explanation**:

A hierarchical explanation approach is applied, instructing the large language model (LLM) to first categorize attributes into their respective subcategories, and then provide detailed explanations for each attribute based on its assigned category. This method is beneficial because it enforces a structured organization of data, increasing the inductive bias, reducing hallucination, and enabling clear verification of each reasoning step. The overall workflow (Figure 3) proceeds as follows: (1) Identify attributes that require explanation. (2) Classify attributes into relevant subcategories. (3) Provide detailed explanations for each attribute under its subcategory. (4) Present the final output by listing each attribute's classification alongside its detailed explanation.

Meanwhile, a verified explanation ensures the stakeholders without mathematical expertise can interpret and validate decisions, which is particularly useful in a diverse disciplinary team.

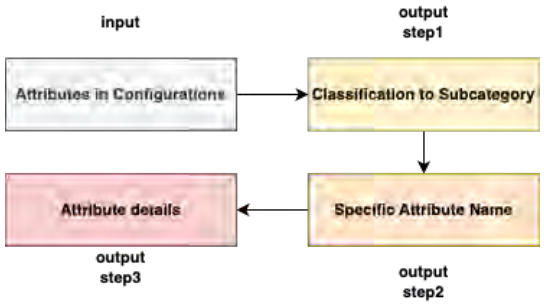



**Figure 3.** Hierarchical Explanation for increasing the reasoning ability of the LLM agent

**Prompts Structure**: To further enhance the reasoning process, a structured prompting framework is designed inspired by the Chain of Thought (CoT) and its related research [11], which has demonstrated significant improvements in reasoning tasks. This framework involves 3 independent LLM agents proposing distinct strategies, each addressing specific aspects of the problem. These strategies are then evaluated through a voting mechanism by a panel of 5 additional LLM agents, ensuring an unbiased assessment. The most effective strategy is subsequently selected and refined into an optimal solution, integrating the strengths of individual proposals while minimizing potential biases and limitations. Notably, all 8 experts involved in this process are distinct LLM agents.

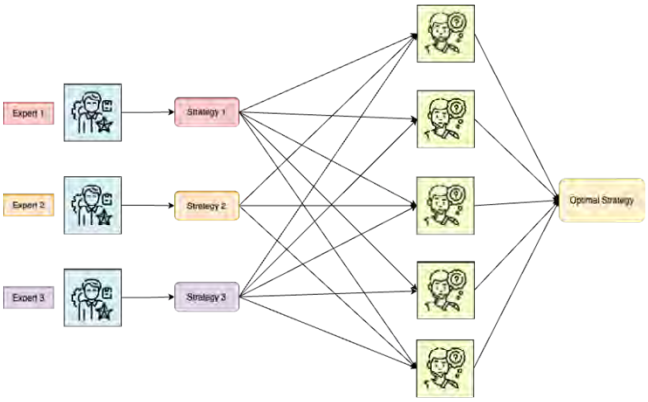



**Figure 4.** Prompts Structure with 3 experts for strategy generating and 5 experts for voting

## Weights Proposals Generation

For weight generation, three key inputs are utilized, including user-defined preference settings, typical configurations identified in previous sections, and explanations generated by LLMs. This process leverages the structured prompting framework introduced earlier, which guides the weight assignment in a manner analogous to group-based decision-making mechanisms. Specifically, the framework facilitates the aggregation of preferences and the systematic integration of insights from the three inputs, ensuring a balanced and well-informed weight assignment process.

Traditional weight generation in MCDA often relies on expert input, which presents several challenges, including the need for domain expertise, difficulty in collecting reliable weight proposals, and potential bias from individual preferences. Moreover, integrating multiple expert opinions into a coherent weighting scheme remains a complex task. In contrast, LLMs offer a more flexible and scalable alternative. With their extensive training in diverse knowledge sources, LLMs can generate weight proposals more efficiently, accommodate various preference settings, and reduce dependence on subjective expert judgment. This approach enhances efficiency and consistency in decision-making while allowing for greater adaptability across different application scenarios.

# CASE STUDY

The method is applied to rank solutions for decarbonizing petroleum refining processes. The case study is

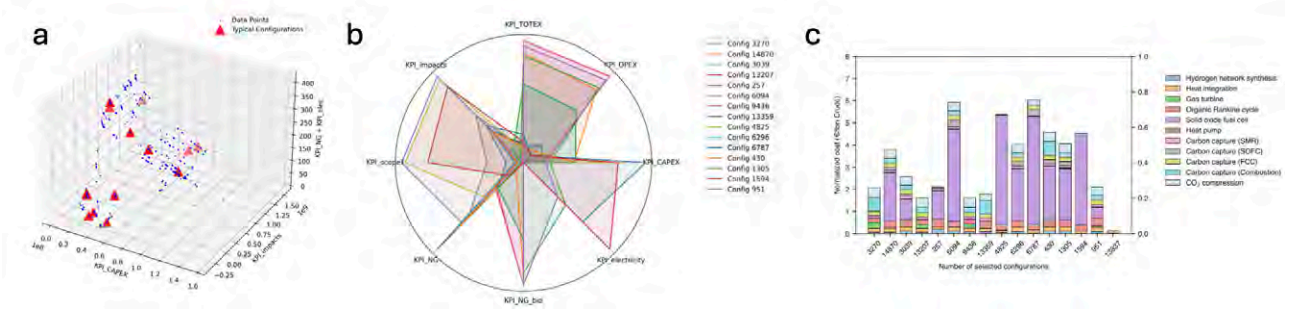



**Figure 5:** (a) Clustering results visualized in a 3D solution space using KPI_CAPEX, KPI_impacts, and the sum of KPI_NG, and KPI_elec. **(b)** Selected configurations displayed in a radar graph with key KPIs. **(c)** Selected configurations represented by features, indicating the size of different decarbonization technologies implemented in the refinery.

based on a superstructure of refining processes integrating various decarbonization technologies, including energy efficiency measures, carbon capture and storage, low-carbon hydrogen, and renewable energy resources. A total of 16,000 decarbonization configurations are generated using a MILP formula to balance the trade-offs between investment, electricity and natural gas consumption, and $CO_2$ emissions (Scope 1 and Scope 2). Solutions are derived under a wide range of market and other conditions, considering factors such as natural gas and electricity prices, carbon pricing policies, and electricity carbon footprint. Each of the 16,000 configurations represents an optimal solution for a specific set of input conditions.

Each configuration is represented by two data sets: KPIs and features. The KPI set includes total cost (KPI_TOTEX), operating costs (KPI_OPEX), annualized investment (KPI_CAPEX), and resource consumption metrics such as natural gas, biogas, and electricity usage (KPI_NG, KPI_NG_bio, and KPI_electricity), along with scope 1 and scope 2 emissions (KPI_scope1 and KPI_scope2). These KPIs are derived from the material and energy flows as well as the installed units, which constitute the configuration's features. Unlike KPIs, which vary based on different conditions, features remain constant for a given configuration.

# RESULTS

## Typical configuration identification

Figure 5(a) visualizes the dimension-reduced dataset, with 16 clustering centers highlighted by red triangles, identified using the graphical methods described in the method section. Clustering performance is quantified using established metrics. The selected configurations are further presented by their KPIs (Figure 5(b)) and features, such as the installed capacity of decarbonization technologies (Figure 5(c)). This provides a clearer representation, demonstrating that the selected configurations are distinct in both KPIs and features.

## Preferred configuration selection

Dataset interpretations were first generated independently by LLM, incorporating hierarchical explanation and structured prompting to enhance its reasoning ability. However, as shown in Figure 6, three key misinterpretations were identified in the initial LLM explanation: (1) *KPI_impacts* should only include scope 1 and 2 emissions, (2) *KPI_CAPEX* should be annualized, and (3) Heat Exchange Variables should be treated solely as intermediate computational values. Notably, despite lacking predefined conditions, the LLM correctly avoided assigning weights to Heat Exchange Variables. After manual feedback alignment, the second iteration showed a significantly improved understanding of the dataset and problem, leading to a more accurate interpretation.

Following the correct understanding achieved through human alignment with the LLM-generated context, Figure 7 presents an example of the complete weights-generation process. From the outset, the priority was set to "Focusing on the Environmental Impact." The deduction progress in weights generation follows the structure of the prompts we designed in the previous section, prompting experts to vote on various KPIs. After consolidating the voting results, higher weights were allocated to KPIs most strongly tied to environmental impact, while moderate values were assigned to other attributes like CAPEX and OPEX. This iterative, feedback-driven approach demonstrates how the LLM can integrate expert judgment and maintain alignment with an overarching priority—namely, reducing environmental impact—within its weights-generation process.

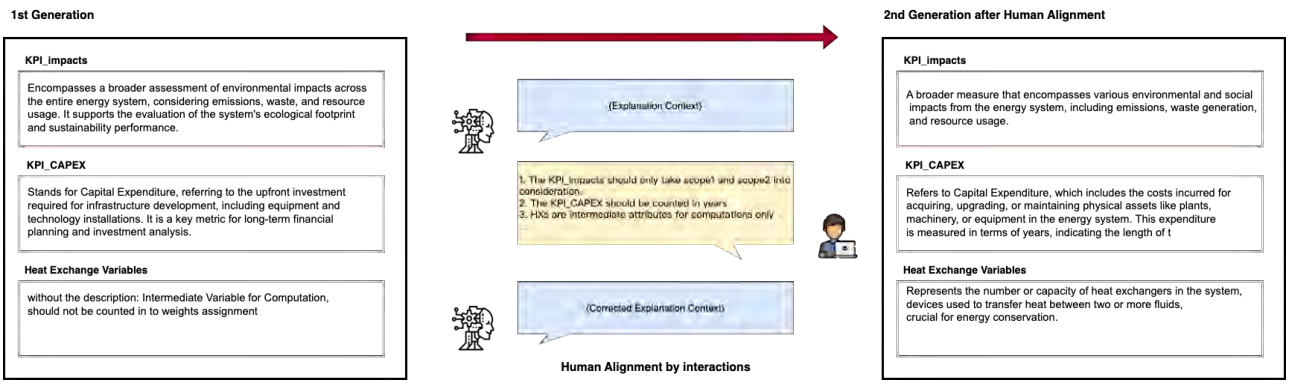



**Figure 6:** The Human Alignment progress in case study to ensure the AI-generated context trustworthy

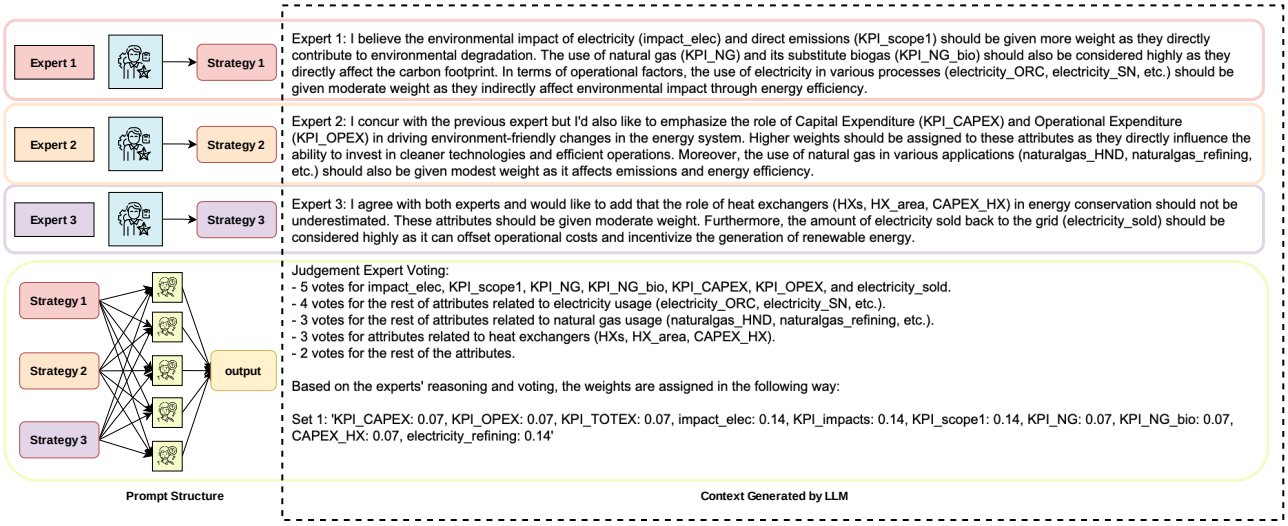



**Figure 7:** The Deduction Progress of generating the weights proposals withthe preferrence is setted as the "focus on Environmental Impact" and the weights proposal is listed in Set 1.

Figure 8 presents the ranking results obtained from the weighted sum method, with weights generated by the LLM agent as illustrated in Figure 8. The top-ranked configurations (e.g., Configurations 257, 4825, and 1594) exhibit varying ranking weighted sum scores under the focus on "Environmental Impact," as they are identified as typical configurations. Figure 5(b-c) highlights the corresponding KPIs and features of these configurations, revealing distinct characteristics and orientations that contribute to their differentiation within the solution space.

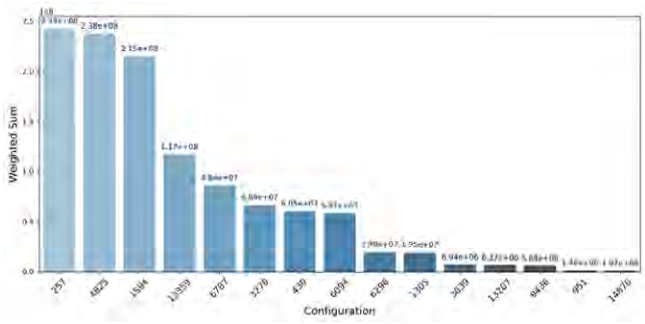



**Figure 8.** Typical Configuration weighted sum scores are computed with weights generated by LLM.

## DISCUSSION

This study presents a feature-oriented MCDA framework with machine learning method that addresses key challenges in selecting preferred solutions from large industrial datasets. First, by integrating dimensionality reduction and geometric analysis, our approach effectively captures both global and local structural features, enhancing decision-making transparency and robustness. Second, through hierarchical explanation, prompt engineering, and human verification, the LLM-assisted explanation and weight generation process reduce reliance on subjective expert input, ensuring consistency, efficiency, and adaptability in preference-based decision-making across diverse industrial applications.

Applied to refinery decarbonization, our framework successfully identifies representative solutions while ensuring diversity and interpretability in high-dimensional solution spaces. Additionally, the AI-driven methodology leverages Large Language Models (LLMs) with enhanced

reasoning ability to provide context-aware explanations for decision attributes and generate weight proposals aligned with user preferences. This approach reduces reliance on subjective expert input and improves decision-making efficiency. This scalable, interpretable, and adaptable solution demonstrates its applicability to complex multi-criteria decision-making problems.

## ACKNOWLEDGEMENTS

The author thanks TotalEnergies for their financial support and valuable discussion about this research.

## REFERENCES

1. Zhao, Y., Hagi, H., Delahaye, B., & Maréchal, F. (2024). A holistic approach to refinery decarbonization based on atomic, energy and exergy flow analysis. Energy, 296, 131117.
2. Wang, J. J., Jing, Y. Y., Zhang, C. F., & Zhao, J. H. (2009). Review on multi-criteria decision analysis aid in sustainable energy decision-making. *Renewable and sustainable energy reviews*, *13*(9), 2263-2278.
3. Nolzen, N., Lademann, A., Roskosch, D., Moret, S., Seele, H., Baader, F. J., & Bardow, A. (2024). Low-regret decisions for the steam supply in the chemical industry. In *ESCAPE-34 PSE-2024*.
4. Dawes, R. M., & Corrigan, B. (1974). Linear models in decision making. *Psychological bulletin*, *81*(2), 95.
5. Wang, Y., Yao, H., & Zhao, S. (2016). Auto-encoder based dimensionality reduction. *Neurocomputing*, *184*, 232-242.
6. Jolliffe, I. T., & Cadima, J. (2016). Principal component analysis: a review and recent developments. *Philosophical transactions of the royal society A: Mathematical, Physical and Engineering Sciences*, *374*(2065), 20150202.
7. Davies, D. L., & Bouldin, D. W. (1979). A cluster separation measure. *IEEE transactions on pattern analysis and machine intelligence*, (2), 224-227.
8. Caliński, T., & Harabasz, J. (1974). A dendrite method for cluster analysis. *Communications in Statistics-theory and Methods*, *3*(1), 1-27.
9. Zhong, Y. (2009, September). Intrinsic shape signatures: A shape descriptor for 3D object recognition. In *2009 IEEE 12th international conference on computer vision workshops, ICCV Workshops* (pp. 689-696). IEEE.
10. Brown, T., Mann, B., Ryder, N., Subbiah, M., Kaplan, J. D., Dhariwal, P., ... & Amodei, D. (2020). Language models are few-shot learners. *Advances in neural information processing systems*, *33*, 1877-1901.
11. Wei, J., Wang, X., Schuurmans, D., Bosma, M., Xia, F., Chi, E., ... & Zhou, D. (2022). Chain-of-thought prompting elicits reasoning in large language models. Advances in neural information processing systems, 35, 24824-24837.

© 2025 by the authors. Licensed to PSEcommunity.org and PSE Press. This is an open access article under the creative commons CC-BY-SA licensing terms. Credit must be given to creator and adaptations must be shared under the same terms. See https://creativecommons.org/licenses/by-sa/4.0/



Systems & Control Transactions

**Research Article - Peer Reviewed Conference Proceeding**
ESCAPE 35 - European Symposium on Computer Aided Process Engineering
Ghent, Belgium. 6-9 July 2025
Jan F.M. Van Impe, Grégoire Léonard, Satyajeet S. Bhonsale,
Monika E. Polańska, Filip Logist (Eds.)

PSE PRESS

# Selection of Fitness Criteria for Learning Interpretable PDE Solutions via Symbolic Regression

**Benjamin G. Cohen[a,b], Burcu Beykal[a,c], and George M. Bollas[a,b]***

[a] University of Connecticut, Department of Chemical and Biomolecular Engineering, Storrs, CT, USA
[b] University of Connecticut, Pratt & Whitney Institute for Advanced Systems Engineering, Storrs, CT, USA
[c] University of Connecticut, Center for Clean Energy Engineering, Storrs, CT, USA
* Corresponding Author: george.bollas@uconn.edu

## ABSTRACT

Physics-Informed Symbolic Regression (PISR) offers a pathway to discover human-interpretable solutions to partial differential equations (PDEs). This work investigates three fitness metrics within a PISR framework: PDE fitness, Bayesian Information Criterion (BIC), and a fitness metric proportional to the probability of a model given the data. Through experiments with Laplace's equation, Burgers' equation, and a nonlinear wave equation, we demonstrate that incorporating information theoretic criteria like BIC can yield higher fidelity models while maintaining interpretability. Our results show that BIC-based PISR achieved the best performance, identifying an exact solution to Laplace's equation and finding solutions with $R^2$-values of 0.998 for Burgers' equation and 0.957 for the nonlinear wave equation. The inclusion of the Bayes D-optimality criterion in estimating model probability strongly constrained solution complexity, limiting models to 3-4 parameters and reducing accuracy. These findings suggest that a two-stage approach-using simpler complexity metrics during initial solution discovery followed by a post-hoc identifiability analysis may be optimal for discovering interpretable and mathematically identifiable PDE solutions.

**Keywords**: Genetic Algorithm, Machine Learning, Algorithms, Artificial Intelligence, Modelling

## INTRODUCTION

Understanding dynamical system models, their solutions, and potential failures is critical, especially in safety, health, and security. Traditionally, symbolic models with identifiable parameters, input-output relationships that provide tractable logic, and physically meaningful terms have established trust in deployed models [1]. However, these techniques to establish trust are ineffective for machine-learned models. Consequently, while machine learning has motivated advancements in understanding black-box model decisions [2], the simplicity and clarity of concise symbolic expressions make them inherently more straightforward to understand than their deep learning counterparts.

Dynamical system models often take the form of differential equations (DEs). When properly built and used, DEs enable engineers and scientists to predict future or hidden states while also explaining the underlying phenomena which drive system dynamics. Thus, DE-based system models are crucial for making informed decisions in process design and control.

Because of their importance, significant effort has been dedicated to simplifying and solving systems of PDEs [3,4]. Various methods for DEs include identifying coordinate transformations to simplify dynamics [5], linearizing models for rapid prediction and control, and finding analytical solutions to replace differential equations with algebraic relationships where possible. Depending on the DE and its application, different methods may be preferred. However, among the most challenging DEs to manage are those that include partial differential equations (PDEs).

Prominent in fluid flow, chemical reactions, and biological systems [6], PDEs can exhibit complex dynamics that make identifying solutions difficult. Common approaches for discovering PDE solutions are challenging to implement and require highly specialized skills and knowledge. Often PDE models can be linearized to leverage linear PDE theory, and Taylor series expansions can be used to find solutions via perturbation theory or finite differences among other methods. However, these

solution paths are subject to strict convergence and stability conditions that are difficult to meet.

Alternatives to traditional methods are emerging from the field of machine learning [7]. Large foundation models for physics can help predict dynamics across various domains. Focusing on smaller problems, tools like DeepONets can learn neural operators that map inputs to outputs [8], while physics-informed machine learning methods can learn solutions to PDEs with known initial/boundary conditions [9, 10]. Although many of these tools are changing the way PDEs are solved, they often fall into the same pitfalls as other use cases of machine learning: the solutions they produce lack interpretability.

One exception to the lack of interpretability in machine learning for PDEs is physics-informed symbolic regression (PISR) [11, 12]. PISR leverages symbolic regression (SR) to produce solutions to PDEs in symbolic form. Previous works have shown that PISR can learn exact analytical solutions to PDEs when they exist and provide good approximations with physically meaningful terms when analytical solutions do not exist [11, 12]. Therefore, as an approach to simplify PDEs into explicit algebraic relationships, PISR is particularly attractive when model trust is important.

An important aspect of building model trust is to ensure that all model parameters are mathematically identifiable [1]. In this work, we explore various information-theoretic criteria as fitness metrics within PISR, beyond the metrics used in [11, 12], to learn interpretable solutions to PDEs that are simple, and concise. We examine the effect of the fitness criterion (loss function) within PISR on the discovered solutions through three examples: Laplace's equation, Burgers' equation, and a nonlinear wave equation.

The remainder of this paper is structured as follows: First, the PISR method and motivating examples will be introduced along with three fitness criteria. Following the methods, the results of our experiments are presented and briefly discussed. Finally, the paper concludes with a summary of the results and findings.

## Methods

The goal of PISR is to discover an explicit mathematical relationship that provides tractable logic from coordinate inputs to state outputs, ensuring consistency with a known PDE. This is achieved using symbolic regression. As the symbolic regressor generates different expressions, their derivatives are determined using automatic differentiation and evaluated against the known PDE. A solution with good fitness will have derivatives that satisfy the PDE, while those of an unfit solution are unlike to agree with that PDE. The symbolic regressor can take advantage of different fitness metrics to search for an optimal solution to a known PDE.

## Symbolic Regression

In this work, genetic programming (GP) is used to perform the symbolic regression. GP is an evolutionary algorithm that operates on a population of mathematical expressions, represented as binary expression trees, to explore the space of feasible expressions. Each individual in the population is constructed using an argument set and a primitive set. The argument set includes all arguments for the final model, while the primitive set is comprised of all mathematical operations that can appear in the model.

Genetic operators, along with evolutionary pressure from the selected fitness criterion and a tournament selection, iteratively evolve a population of expressions towards optimal fitness. Tournament selection is implemented using the selTournament method from the open-source evolutionary algorithm framework DEAP [13]. The genetic operators used can be categorized into crossover and mutation. In each generation, the population selected for offspring generation through tournament selection is subjected to these operators.

Crossover, an exploitative process, shuffles subexpressions from two individuals to create two offspring. The crossover operator used here is DEAP's cxOnePoint [13]. Complementary to crossover, mutation is an exploratory process that makes random changes to a single individual to generate one offspring. Each expression used to generate offspring is operated on by one of four operators each generation: mutShrink, mutInsert, mutNodeReplacement, and mutUniform from DEAP's library [13]. This combination of mutation operators helps explore the symbol space while reducing bloat, or the tendency of symbolic regression to evolve overly complicated expressions.

Once the population of offspring is generated using genetic operations, they are added to the total population along with a hall of fame that is made of the fittest individuals ever evolved. To promote diversity, some individuals are randomly removed. Before the next tournament selection can begin, fitness values must be calculated for any new individuals.

## Fitness Metrics

Fitness metrics are crucial in ensuring that the evolutionary pressure from the tournament selection process eliminates unfit individuals. However, different fitness measures may yield different solutions for the same PDE. Therefore, it is important to investigate the effect of different fitness criteria on the solutions learned for PDEs using PISR. Here, we introduce three fitness criteria used in the discovery of solutions to PDEs in this work.

### PDE Fitness

The first fitness criterion is the simplest PISR fitness metric, $\mathcal{L}_{PDE}$, which is defined in Equation 1. $N_C$ represents the number of collocation points at which the nonlinear

PDE $F\left(x, u(x), D^{\alpha^1}u(x), D^{\alpha^2}u(x), \ldots, D^{\alpha^m}u(x)\right) = 0$, written using multi-index notation, is evaluated in the $n$-dimensional domain $X \subseteq \mathbb{R}^n$. The variables $\lambda_0$, $\lambda_j$, $N_{BCs}$, $N_{BC_j}$, and $\Gamma_j$ respectively represent hyperparameters for the PDE, hyperparameters for each boundary condition, the number of boundary conditions, the number of collocation points on the $j^{\text{th}}$ boundary condition, and the $j^{\text{th}}$ boundary condition. The goal of $\mathcal{L}_{PDE}$ is to capture how well an expression represents a PDE and its initial and boundary conditions.

$$\mathcal{L}_{PDE} = \lambda_0 \sum_{i=1}^{N_C} F(\mathbf{x}_i, u(\mathbf{x}_i), \ldots)^2 + \sum_{j=1}^{N_{BCs}} \lambda_j \sum_{k=1}^{N_{BC_j}} \Gamma_j(\mathbf{x}_k, u(\mathbf{x}_k), \ldots)^2 \quad (1)$$

To calculate $\mathcal{L}_{PDE}$, the derivatives of the expression being evaluated must be determined. In this work, we used the automatic differentiation tool CasADi [14] to obtain exact derivatives quickly and efficiently. Next, those derivatives must be used to evaluate $F$ at the $N_C$ collocation points and each $\Gamma_j$ at the $N_{BC_j}$ collocation points. **Table 1** shows a symbolic evaluation of $F = u_t - \alpha u_{xx} = 0$ with constant $\alpha$ for two different expressions, demonstrating how $\mathcal{L}_{PDE}$ can be determined.

**Table 1:** Example of symbolic evaluation of $F = u_t - \alpha u_{xx}$ for different expressions when $\alpha$ is a constant.

| $u$ | $u_t$ | $u_{xx}$ | $F$ |
|---|---|---|---|
| $t - \alpha x^3$ | $1$ | $-6\alpha x$ | $1 + 6\alpha^2 x$ |
| $\exp(-\alpha\omega^2 t)\sin(\omega x)$ | $-\alpha\omega^2 u$ | $-\omega^2 u$ | $0$ |

## Bayesian Information Criterion

A limitation of $\mathcal{L}_{PDE}$ is that it only evaluates how well the proposed expressions satisfy the PDE and boundary conditions at the collocation points. While this is crucial for obtaining accurate solutions to PDEs, it is also important to consider the complexity of the relationships between the input coordinates and the state output. $\mathcal{L}_{PDE}$ does not provide safeguards against excessing model complexity, meaning the symbolic regressor can quickly suffer from expression bloat and learn overly complicated expressions that are difficult to interpret and understand.

One potential remedy to this limitation is to use the Bayesian Information Criterion (BIC) [15]. The BIC is an information-theoretic criterion that helps mitigate model complexity by balancing the fitness of the expression in terms of both its agreement with the PDE and its complexity. Equation 2 calculates the BIC, where $N_{points}$ represents the weighted number of collocation points used (given by $\lambda_0 N_C + \sum_{j=1}^{N_{BCs}} \lambda_j N_{BC_j}$), and $k$ denotes the model node complexity, which is determined by counting the number of nodes in the expression tree.

$$\mathcal{L}_{\text{BIC}} = N_{points} \log \mathcal{L}_{PDE} + k \log N_{points} \quad (2)$$

## Probability of Solution

The BIC is often a powerful criterion for identifying concise and descriptive expressions in symbolic regression. However, in many cases, simply balancing model complexity and fit does not guarantee that the model is identifiable. To ensure that each model parameter is mathematically identifiable based on the information provided, an additional term must be used.

A strong candidate for this additional term is the Bayes D-optimal criterion, $\Psi_D$ [16]. $\Psi_D$ is an information-theoretic criterion that uses the determinant, denoted as $|\cdot|$, of the Fisher Information Matrix (FIM) to give insight into the precision of parameter estimates. It can help determine if a model is identifiable, meaning that there exits a unique parameter set defining the optimal solution [16]. $\Psi_D$ also appears in the derivation of the BIC but is omitted in its final form due to asymptotic assumptions.

The FIM can be calculated using the sensitivity matrix $\mathbf{Q} = \nabla_{\boldsymbol{\theta}} \mathcal{L}_{PDE}$, where $\boldsymbol{\theta}$ is the vector of parameters proposed by the symbolic regressor. Typically, the sensitivity matrix is calculated with a variance term to account for noise in the data. However, in PISR, since there is no data, this variance term is omitted, implicitly assuming a variance of $1$. With $\mathbf{Q}$ defined, we can now introduce the third fitness criterion, $\mathcal{L}_{BIC,\Psi_D}$, as shown in Equation 3. This criterion is proportional to approximate probability of the PDE given the model $m$ at the maximum likelihood estimator $\widehat{\boldsymbol{\theta}}$, $p(F|m)$, which is derived using the same process as the derivation of the BIC.

$$\mathcal{L}_{BIC,\Psi_D} = \mathcal{L}_{BIC} - \log\left|\mathbf{Q}^{\mathrm{T}}\mathbf{Q}\right| \quad (3)$$

## Test Cases

With the fitness criteria established, the performance of PISR using each criterion must be assessed. This evaluation was conducted using three two-dimensional second-order PDEs. For each criterion and PDE pair, PISR was run 50 times, with support from a $30 \times 30$ grid of collocation points. The PDEs and boundary conditions were evaluated on this grid, and each run produced a hall of fame containing the 10 most fit evolved solutions. The experiments were executed on an Intel® Xeon® W7-2495X processor across 10 threads.

Solution evaluation was carried out on a $50 \times 50$ gird of points, where the true solution at each point was computed either using an exact analytical solution or a numerical method. The symbolically regressed models were compared using three metrics: mean-squared error (MSE) against the ground truth, the $R^2$-value against the ground truth, and model parameter complexity, $N_p$, defined as the number of parameters in the model.

## Laplace's Equation

The first PDE investigated was Laplace's equation, a second-order linear PDE with an exact analytical solution for the boundary conditions specified in Equation 4. Laplace's equation is a fundamental PDE in process

systems engineering, as it models many steady-state phenomena such as heat transfer and diffusion. The domain for this PDE, as explored in this study, was $(x, y) \in [0,1] \times [0,1]$. The primitives used to discover solutions to Laplace's equation were $\{+, -, \exp, \sin, \sinh\}$, with arguments $\{x, y\}$. The tuning parameters for $\mathcal{L}_{PDE}$ were selected as $\boldsymbol{\lambda} = [0.001, 0.8, 0.8, 80, 0.8]$.

$$\begin{aligned} u_{xx} + u_{yy} &= 0 \\ u(x,y) &= 0 \quad \text{when } x = 0 \\ u(x,y) &= 0 \quad \text{when } x = 1 \\ u(x,y) &= \sin(2\pi x) \quad \text{when y} = 0 \\ u(x,y) &= 0 \quad \text{when y} = 1 \end{aligned} \tag{4}$$

### Burgers' Equation

The second PDE explored in this work was Burgers' equation, which is often used to describe one-dimensional viscous fluid flow. It is a quasi-linear second-order PDE in two dimensions and does not have an exact strong form analytical solution. The domain considered in this work was $(x, t) \in [0,10] \times [0,10]$. The primitives used to discover solutions to Burgers' equation were $\{+, \times, \exp, \sin, \sinh, u_{diff}\}$, where $u_{diff}$ is the solution to the diffusion equation with the same initial and boundary conditions in Equation 5, solved using eigenfunction expansion. For more details on the method of the primitive set selection see [12]. The arguments used were $\{x, t\}$, and the tuning parameters for $\mathcal{L}_{PDE}$ were $\boldsymbol{\lambda} = [1, 0.8, 0.8, 0.8]$.

$$\begin{aligned} u_t - 0.1u_{xx} - 0.2uu_x &= 0 \\ u(x,0) = \exp -0.2(x-5)^2 \quad &\text{when } t = 0 \\ u_x(0,t) &= 0 \quad \text{when } x = 0 \\ u_x(10,t) &= 0 \quad \text{when } x = 10 \end{aligned} \tag{5}$$

### Nonlinear Wave Equation

The third and final PDE explored in this work was the nonlinear wave equation, which is commonly used to model waves in shallow water. It is a nonlinear second-order PDE in two dimensions and, like Burgers' equation, does not have an exact analytical solution. The domain considered in this work was $(x, t) \in [0,1] \times [0,1]$. The primitives used to discover solutions to the nonlinear wave equation were $\{+, \times, \exp, \sin, \sinh, \mathrm{u_{linwave}}\}$, where $u_{linwave}$ is the analytical solution to the linear wave equation with the same initial and boundary conditions in Equation 6. The arguments used were $\{x, t\}$, and the tuning parameters for $\mathcal{L}_{PDE}$ were $\boldsymbol{\lambda} = [0.1, 0.8, 0.8, 80]$.

$$\begin{aligned} u_{tt} - u^2 u_{xx} &= 0 \\ u(x,0) = \frac{1}{2}\sin(3\pi x) \quad &\text{when } t = 0 \\ u(0,t) &= 0 \quad \text{when x} = 0 \\ u(1,t) &= 0 \quad \text{when } x = 1 \end{aligned} \tag{6}$$

## RESULTS AND DISCUSSION

The results of our experiments demonstrate that the selection of fitness criterion can significantly influence the solutions discovered using PISR. When model complexity is considered during exploration, PISR tends to return models with fewer parameters. Moreover, when PISR produces models with more parameters, those trained with complexity considerations align better with the solution to the PDE compared to those trained without considering complexity. When a metric of identifiability, or the ability for all parameter values in a model to be uniquely identified given the available information, is incorporated into the fitness criterion, PISR is more likely to return models with only a few parameters and those models tend to perform as well or worse than models learned using other fitness metrics.

### Results: Laplace's Equation

These relationships between fitness metrics and the discovered solutions are particularly clear for Laplace's equation. Laplace's equation, with the boundary conditions shown in Equation 4, has an exact analytical solution, allowing the learned solutions to be compared symbolically with the exact solution. PISR successfully learned the exact solution to Laplace's equation using $\mathcal{L}_{PDE}$ and $\mathcal{L}_{PBIC}$ as fitness metrics, but not when using $\mathcal{L}_{BIC,\Psi_D}$.

Although PISR did learn exact analytical solutions to Laplace's equation, on average, the models discovered across the 50 runs for each fitness criteria did not perfectly match an analytical solution. **Figure 1** illustrates the average MSE values at different model parameter complexities. This figure also shows the number of models returned at each parameter complexity for the different fitness metrics.

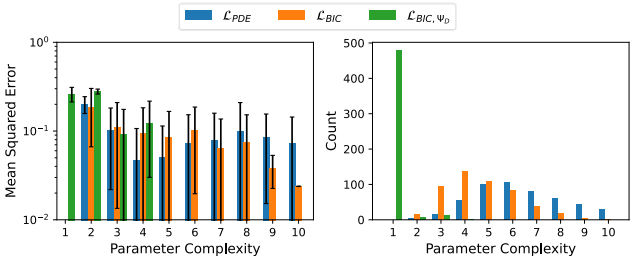



**Figure 1:** Left: Average MSE values per model parameter complexity for Laplace's equation solution discovery. Right: Count of learned models with different parameter complexities.

The results show that the selection of fitness criteria has little impact on the quality of the solutions when models have only a few parameters. However, the fitness criteria did affect the likelihood of a learned model have a small number of parameters, with stricter definitions of complexity leading to more models with fewer parameters. As the number of parameters in a model increases, $\mathcal{L}_{BIC}$ tends to yield the best solutions on average. Notably, no model learned using $\mathcal{L}_{BIC,\Psi_D}$ had more than 4 parameters.

While limiting model complexity may be advantageous for building models that are easy to interpret, it can also impede the discovery of better models. By including the $\Psi_D$ term in the fitness, the symbol space is constrained to consider only expressions that are mathematically identifiable. This constraint may make it more difficult to discover models that fit the underlying PDE well, as it restricts access to certain regions of the symbol space in which useful intermediate expressions may lie.

## Results: Burgers' Equation

The results from the Burgers' equation experiments tell a similar story to those from Laplace's equation. The best-learned models using each of the three fitness criteria are shown in **Table 2**. Since Burgers' equation does not have an exact analytical solution, all metrics of agreement with the ground truth were compared to the solution computed using the method of lines.

**Table 2:** Best models learned for Burgers' equation using different fitness criteria. The MSE and $R^2$-values are calculated using the solution calculated using the method of lines as the ground truth.

| Fitness | Model | MSE $\times 10^4$ | $R^2$ |
|---|---|---|---|
| $\mathcal{L}_{PDE}$ | $u_{diff}[x - 0.189t \cdot u_{diff}(x, 17.317), t]$ | 3.850 | 0.996 |
| $\mathcal{L}_{BIC}$ | $u_{diff}[x - 0.167t \cdot u_{diff}(x - 0.066x, t), t]$ | 1.796 | 0.998 |
| $\mathcal{L}_{BIC,\Psi_D}$ | $u_{diff}[x - 0.174t \cdot u_{diff}(x, x + t), t]$ | 4.466 | 0.995 |

As in the previous experiment, $\mathcal{L}_{PDE}$ and $\mathcal{L}_{BIC}$ produced better solutions than $\mathcal{L}_{BIC,\Psi_D}$. The best model was discovered using $\mathcal{L}_{BIC}$. Furthermore, the best solutions learned using all three fitness criteria have similar structures shown in **Table 2**.

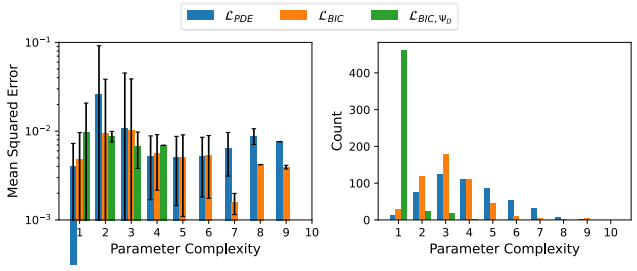



**Figure 2:** Left: Average MSE values per parameter complexity Burgers' equation solution discovery. Right: Count of learned models with different parameter complexities.

To better understand the average performance of the discovered solutions for Burgers' equation, **Figure 2** displays the average MSE values at different model parameter complexities, along with the number of models returned at each parameter complexity for the different fitness metrics. Analysis of these plot reveal the same trends as those discussed for **Figure 1**.

## Results: Nonlinear Wave Equation

The third PDE explored was the nonlinear wave equation, which proved more challenging to solve using PISR than the other two PDEs. This increased difficulty in solution discovery is reflected in the learned models, which . **Table 3** presents the model parameter complexities, $N_p$, node complexities, $k$, as well as the MSE and $R^2$-values of the best solutions discovered using the three fitness metrics. These complexity measures were chosen because the learned solutions are long and difficult to interpret, although still have fewer parameters than solutions learned using neural networks.

**Table 3:** Characteristics of best models learned for Burgers' equation using different fitness criteria. The MSE and R2-values are calculated using the solution calculated using the method of lines as the ground truth.

| Fitness | $N_p$ | $k$ | $MSE$ | $R^2$ |
|---|---|---|---|---|
| $\mathcal{L}_{PDE}$ | 5 | 40 | 0.020 | 0.941 |
| $\mathcal{L}_{BIC}$ | 5 | 27 | 0.015 | 0.957 |
| $\mathcal{L}_{BIC,\Psi_D}$ | 3 | 19 | 0.125 | 0.633 |

These solutions are significantly more (node) complex than those learned for the previous two PDEs. Nevertheless, all three best solutions use fewer than 10 parameters, and PISR with $\mathcal{L}_{PDE}$ and $\mathcal{L}_{BIC}$ returned models with $R^2$-values greater than 0.9. With more time, effort, and hyperparameter optimization, it is possible even better symbolic solutions exist within the explored symbol space. Once again, PISR using $\mathcal{L}_{BIC}$ yielded the best model among the fitness metrics considered.

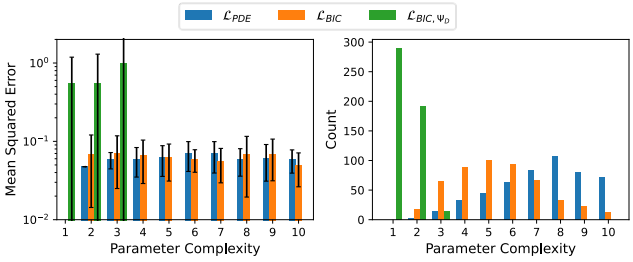



**Figure 3:** Left: Average MSE values per parameter complexity of Wave equation solution discovery. Right: Count of learned models with different parameter complexities.

**Figure 3** shows the average MSE values at different model parameter complexities and the number of models returned at each model parameter complexity for the

three fitness criteria. Consistent with the results from the other two cases, the results shown in the right-side plot of **Figure 3** follow a similar pattern with respect to the number of models learned at each parameter complexity. However, unlike the other two cases, solutions learned using $\mathcal{L}_{BIC}$ do not, on average, perform better than those learned using $\mathcal{L}_{PDE}$ as the parameter complexity increases. At low parameter complexity, solutions learned using $\mathcal{L}_{BIC,\Psi_D}$ perform worse than those discovered using other fitness metrics.

## CONCLUSIONS

PISR is an approach for learning symbolic, interpretable solutions to PDEs. Its efficacy varies depending on the type of PDE and it can struggle to find a balance between interpretability and accuracy in representations to solutions of complex PDEs. Its performance can be influenced by the selection of a fitness criterion. In this work, we demonstrate that using an information-theoretic fitness criterion can help learn higher-fidelity solutions to PDEs. Penalizing model complexity can promote simpler, more easily interpreted solutions. However, using metrics that incorporate model identifiability can constrain the symbol space, potentially hindering solution discovery.

This tension between model fit and simplicity is difficult to balance. While mathematically identifiable solutions are often desired, our findings suggest it may be more effective to use symbolic regression with less stringent metrics, such as parameter or node complexity, and to access mathematical identifiability post hoc, only after candidate solutions have been discovered.

## ACKNOWLEDGEMENTS

This project was sponsored by the Pratt & Whitney Institute of Advanced Systems Engineering (P&W-IASE) of the University of Connecticut and Pratt & Whitney; and the National Institutes of Health [NIH P42 ES027704]. Any opinions expressed herein are those of the authors and do not represent those of the sponsor. The manuscript contents are solely the responsibility of the grantee and do not necessarily represent the official views of the NIH. Further, the NIH does not endorse the purchase of any commercial products or services mentioned in the publication.

## REFERENCES

1. F.-G. Wieland, A.L. Hauber, M. Rosenblatt, C. Tönsing, J. Timmer. On structural and practical identifiability. *Curr Opin Syst Biol* 25:60-69 (2021)
2. A. Adadi, M. Berrada. Peeking Inside the Black-Box: A survey on Explainable Artificial Intelligence (XAI). *IEEE Access* 6:52138-52160 (2018)
3. J. Guckenheimer, P. Holmes. Nonlinear Oscillations, Dynamical Systems, and Bifurcations of Vector Fields. Spring New York (1983)
4. S.J. Farlow. Introduction to Partial Differential Equations. Dover Publications (1993)
5. Z. Liu, M. Tegmark. Machine Learning Hidden Symmetries. *Phys Rev Lett* 128(18):180201 (2022)
6. B.G. Cohen, B. Beykal, G.M. Bollas. Physics-informed genetic programming for discovery of partial differential equations from scarce and noisy data. *J Comput Phys* 514:113261 (2024)
7. S.L. Brunton, J.N. Kutz. Promising directions of machine learning for partial differential equations. *Nat Comput Sci* 4(7):483-494 (2024)
8. L. Lu, P. Jin, G. Pang, Z. Zhang, G.E. Karniadakis. Learning nonlinear operators via DeepONet based on the universal approximation theorem of operators. *Nat Mach Intell* 3(3):218-229 (2021)
9. M. Raissi, P. Perdikaris, G.E. Karniadakis. Physic-informed neural networks: A deep learning framework for solving forward and inverse problems involving nonlinear partial differential equations. *J Comput Phys* 378:686-707 (2019)
10. M. Pförtner, I. Steinwart, P. Henning, J. Wenger. Physics-Informed Gaussian Process Regression Generalizes Linear PDE Solvers. *ArXiv* (2022)
11. I.G. Tsoulos, I.E. Lagaris. Solving differential equations with genetic programming. *Genet Program evolvable Mach* 7(1):33-54 (2006)
12. B.G. Cohen, B. Beykal, G.M. Bollas. Physics-Informed Symbolic Regression for Partial Differential Equations: The Forward and Inverse Problem. *J Comut Phys* (Submitted)
13. F.A. Fortin, F.M. De Rainville, M.A.G. Gardner, M. Parizeau, C. Cagné. DEAP: Evolutionary Algorithms Made Easy. *J. Mach. Learn. Res.* 31(1):2171-2175 (2012)
14. J.A.E. Andersson, J. Gillis, G. Horn, J.B. Rawlings, M. Diehl. CasADi: a software framework for nonlinear optimization and optimal control. *Math Program Comput* 11(1):1-36 (2019)
15. G. Schwarz. Estimating the Dimension of a Model. *Ann. Stat.* 6(2):461-464 (1978)
16. L. Han, Z. Zhou, G.M. Bollas. Model-Based Analysis of Chemical-Looping Combustion Experiments. Part I: Structural Identifiability of Kinetic Models for NiO Reduction. *AIChE J* 62:2419-2431 (2016)

© 2025 by the authors. Licensed to PSEcommunity.org and PSE Press. This is an open access article under the creative commons CC-BY-SA licensing terms. Credit must be given to creator and adaptations must be shared under the same terms. See https://creativecommons.org/licenses/by-sa/4.0/



Systems & Control Transactions

**Research Article - Peer Reviewed Conference Proceeding**
ESCAPE 35 - European Symposium on Computer Aided Process Engineering
Ghent, Belgium. 6-9 July 2025
Jan F.M. Van Impe, Grégoire Léonard, Satyajeet S. Bhonsale,
Monika E. Polańska, Filip Logist (Eds.)

PSE PRESS

# Towards Self-Tuning PID Controllers: A Data-Driven, Reinforcement Learning Approach for Industrial Automation

**Kyle Territo[a], Peter Vallet[a], and Jose Romagnoli[a*]**

[a] Louisiana State University, Department of Chemical Engineering, Baton Rouge, Louisiana, United States

## ABSTRACT

As industries embrace the digitalization of Industry 4.0, the abundance of process data creates new opportunities to optimize industrial control systems. Traditional Proportional-Integral-Derivative (PID) controllers often require manual tuning to address changing conditions. This paper introduces an automated, adaptive PID tuning method using historical data and machine learning for a continuously evolving, data-driven approach. The method centers on training a surrogate model using historical process data to replicate real system behavior under various conditions. This enables safe exploration of control strategies without disrupting live operations. An RL (Reinforcement Learning) agent interacts with the surrogate model to learn optimal control policies, dynamically responding to the plant's state, defined by variables like operational conditions and measured disturbances. The agent adjusts PID parameters in real-time, optimizing metrics such as stability, response time, and energy efficiency. After training, the RL agent is deployed online to monitor and adjust PID controllers in response to real-time deviations. The system continuously integrates new data to refine the surrogate model and RL agent, ensuring adaptability to long-term process changes. This continuous learning enhances resilience and scalability, maintaining optimal performance in dynamic environments. By combining data-driven modeling with RL, this method automates PID tuning, maximizing process data utility and aligning with Industry 4.0 principles. It reduces manual oversight while improving efficiency, reliability, and sustainability, addressing the challenges of increasingly complex and data-rich industrial systems.

**Keywords**: Surrogate Model, Industry 4.0, Intelligent Systems, Process Control, Machine Learning

## 1. INTRODUCTION

In recent years, advancements in machine learning and artificial intelligence have transformed industries by enabling systems that can learn, adapt, and operate autonomously. Technologies like self-driving cars and autonomous drones exemplify the potential of data-driven decision-making to improve efficiency, safety, and performance in complex environments. Yet, while such innovations have gained traction in consumer and transportation sectors, their application to industrial operations remains mostly underexplored. Industrial facilities, particularly in manufacturing and process industries, face similar challenges of dynamic conditions, complex systems, and a demand for optimal performance. Current control systems often rely heavily on manual oversight and static configurations, leaving them ill-equipped to handle evolving demands. This raises a provocative question: If a car can navigate city streets autonomously, why can't a plant adapt and optimize itself in real time? The answer lies in the integration of adaptive control systems with the wealth of process data available in modern industrial environments. By leveraging machine learning and reinforcement learning, it becomes possible to create "self-driving" plants that monitor their own states, respond dynamically to disturbances, and continuously improve over time.

Proportional-Integral-Derivative (PID) controllers are fundamental to industrial automation, providing a straightforward yet effective method to maintain desired

process variables (PVs) through proportional, integral, and derivative adjustments. However, traditional tuning methods, such as Ziegler-Nichols, are often inadequate for dynamic or nonlinear environments [1]. In addition, this method pushes the plant to its stability limits in order to find the ultimate gain—a necessary component for its controller parameter calculations. Model Predictive Control (MPC) represents a significant step forward, using mathematical models to predict system behavior and optimize control actions, excelling in multivariable and constrained systems. Despite these advantages, MPC relies on accurate models and high computational resources, making it less adaptable to rapidly evolving industrial conditions [5]. Emerging techniques in machine learning (ML) and reinforcement learning (RL) offer dynamic adaptability by leveraging data-driven models to learn and optimize control strategies, reducing reliance on explicitly defined physical or mathematical models [3][6]. Contrary to traditional optimization techniques, RL learns optimal policies through direct interaction with the environment—guided by a custom reward function—making it well suited for complex, high dimensional, and uncertain systems. By integrating these approaches, adaptive PID tuning leverages surrogate models for safe strategy exploration and RL agents for real-time parameter optimization, enabling continuous learning and improved resilience under varying conditions [2]. This method aligns with Industry 4.0 principles, utilizing IoT and big data to enhance control systems for modern industrial processes [4].

This paper presents a step toward such a vision by introducing an automated and adaptive method for PID controller tuning, combining historical process data and artificial intelligence to drive optimal performance across diverse operating conditions. The format of this paper will consist of an overview of the process pipeline for this implementation followed by a case study of a demethanizer unit.

## 2. PROPOSED ADAPTIVE CONTROL PIPELINE

### 2.1 Data Collection/ Data Preprocessing

The data collection process is a critical step in developing a robust surrogate model, particularly because the quality and diversity of the data significantly influence the model's ability to generalize. Diverse data is essential to ensure the model can accurately capture the wide range of behaviors and dynamics in the system it is designed to emulate. Inadequate data diversity can lead to overfitting, where the model performs well on the training data but poorly on unseen scenarios. To mitigate this, it is crucial to collect data representing various operating conditions, disturbances, and system responses. This diversity allows the model to learn from a broader spectrum

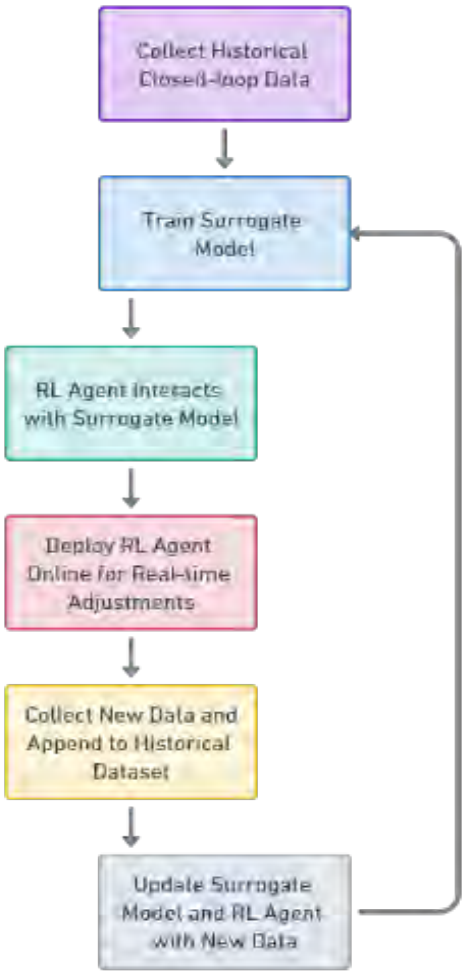



***Figure 1:*** Pipeline for Adaptive Control

of scenarios, enhancing its predictive accuracy and reliability when deployed in real-world applications. For this surrogate model, the data requirements are specific and targeted. The model relies on frames of data associated with setpoint (SP) changes, as these transitions encapsulate critical information about system behavior. *Each frame must include detailed operating conditions, measured disturbances, and, most importantly, labeled controller parameters such as the proportional gain ($Kc$) and integral time ($Ti$).* If PID controllers were too be tuned as well, $T_D$ values will have to be collected as well. These labeled parameters are vital for the model to associate the controller's configuration with the resulting system dynamics. The data collection process begins with a thorough analysis of historical data. The first step is to filter out frames of data corresponding to instances where SP changes occurred. This filtering is crucial as it isolates the dynamic segments most relevant for training the surrogate model. However, historical data may not always be sufficient in terms of volume or diversity. If gaps exist, manual experimentation will be necessary. This involves intentionally perturbing the system to induce SP

changes under a controlled range of operating conditions. Such self-perturbation ensures the acquisition of an adequate variety of frames to capture the full scope of system behavior. By combining historical data and carefully designed manual experiments, the data collection process can yield a comprehensive and diverse dataset for training the surrogate model effectively. After compiling the dataset, preprocessing begins with cleaning to remove missing values and outliers, ensuring data integrity. Next, features are individually normalized to a uniform range, preventing scale imbalances and enhancing model accuracy and training efficiency.

## 2.2 Building Surrogate Model

After collecting and preprocessing the historical data, the development of the initial surrogate model for the plant can commence. A feedforward neural network will be constructed using PyTorch. PyTorch was selected as the deep learning framework due to its flexibility, automatic differentiation capabilities, and extensive support for optimization techniques. The neural network will have three sections: the input layer, hidden layers and output layers. The input layer will take a combination of relevant features, including static characteristics of the step response, such as operating conditions, measured disturbances, and controller parameters, all of which influence the system's transient and steady-state behavior. To enhance the model's capacity for learning intricate patterns in the data, multiple hidden layers will be incorporated, each utilizing non-linear activation functions. Each hidden layer contained 64 neurons as a result of our hyperparameter optimization of the model. This design choice allows the network to generalize well across different operating conditions and adapt to variations in system dynamics. The output layer will generate the predicted PV response, providing an efficient approximation of the plant's behavior.

## 2.3 Training a RL Agent

The reinforcement learning (RL) framework consists of an agent and an environment. The **agent**, implemented using the Proximal Policy Optimization (PPO) algorithm from Stable Baselines3, interacts with the environment to learn optimal control strategies. PPO was chosen for its stability and efficiency in handling continuous control tasks and high-dimensional state spaces. The agent iteratively adjusts controller parameters based on reward signals that assess system performance. The **environment** provides the agent with observations reflecting the system's state and allows it to modify controller parameters. A pretrained surrogate model of the plant is integrated into the environment, enabling rapid testing and refinement of strategies without relying on computationally expensive simulations or real-world interactions. The **state** represents the system's current condition and includes the same input features as the surrogate model, excluding controller parameters, which are adjusted by the agent. The action is the update to the controller parameters, carefully constrained—perhaps within historical controller settings of the plant. The **reward function** drives the learning process by evaluating the PV response after an action. It assigns a numerical score based on key performance metrics, including the Integral of Squared Error (ISE), rise time ($T_R$), settling time ($T_S$), overshoot (OS), and control effort (CE):

$$R = -ISE[\alpha + (\beta * T_R) + (\gamma * T_S) + (\delta * OS) + (\varepsilon * \mathrm{CE})] \quad \boldsymbol{Eqn.1}$$

To prioritize specific objectives, weight factors ($\alpha, \beta, \gamma, \delta, \varepsilon$) adjust the relative importance of each metric. For instance, if minimizing settling time or overshoot is critical, their corresponding weights can be increased. ISE was chosen as the basis as it effectively quantifies overall control performance.

## 2.4 Online Implementation and Updating

Once the agent is trained on the surrogate model, it can be deployed online to monitor and interact with the system in real time. The agent continuously observes the process for significant changes in the state of the selected controller. When such a change is detected, the agent is tasked with recommending a new set of controller parameters, which can then be applied to the controller in real time. During its online operation, the agent also collects new data whenever a SP change occurs, storing these frames for future use. Once a sufficient amount of data has been accumulated, the surrogate model can be updated, and the agent can update its policy accordingly. This iterative approach ensures the pipeline remains adaptive, enabling the system to evolve and improve over time as new behaviors and conditions are encountered. An overview of the process pipeline is shown in ***Figure 1***.

# Case Study: Demethanizer HYSYS Simulation

In this case study, transient plant data was gathered from a HYSYS simulation of a demethanizer unit within an LNG production system (***Figure 2***). The demethanizer column (T-100) is the central unit in this separation process, consisting of a 30-stage multicomponent distillation column with a reboiler (E-103). This unit is designed to separate the methane, the lightest component, from the heavier portion of the gas. For this reason, the CRR plant has to operate under cryogenic conditions with a nominal temperature in the top tray of approximately -116°C. Among the different control loops in the process, the temperature controllers have a key role in ensuring

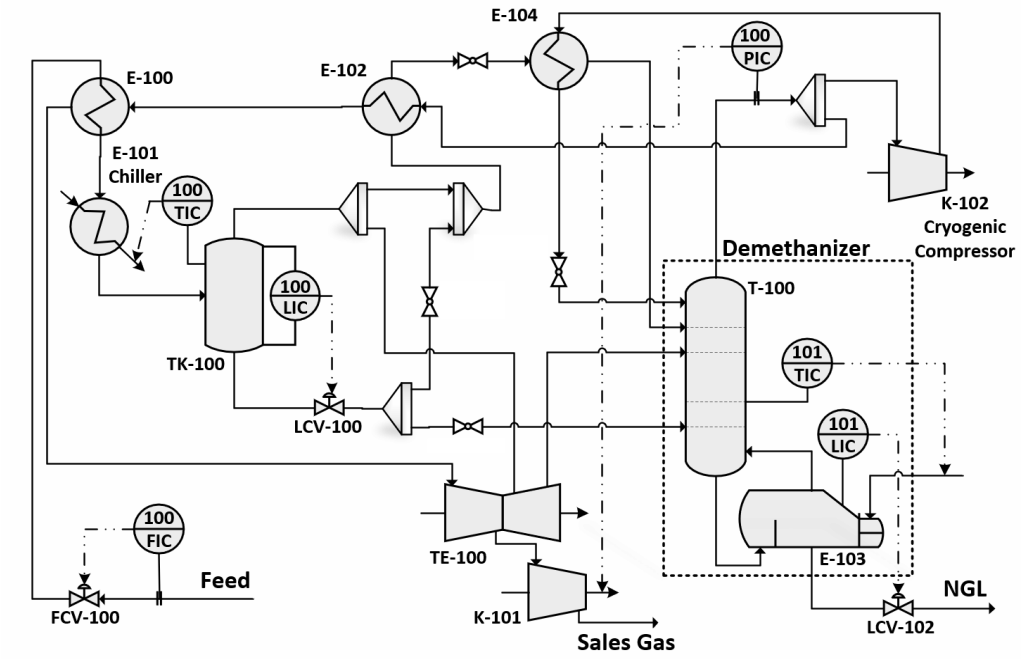



**Figure 2:** Schematic of the demethanizer unit

the product specifications in terms of ethane recovery and methane impurity in the bottom product of the demethanizer. The indirect control of ethane recovery is achieved by regulating the temperature in the separator upstream of the demethanizer and manipulating the cooling fluid flowrate of the chiller (E-101). The control of methane composition in the column bottom product is attained by manipulating the rebuilder's duty. The tuning of these valves are critical. However, different load changes and disturbances can affect the quality of the control—often leading to manual tuning efforts. The proposed strategy was implemented to automatically update all main controllers of the unit. Only results involving the composition controller (XIC-100) and ethane recovery control (ERIC-100) are shown here (controllers not depicted in ***Figure 2***).

The data collected was for different measured disturbances: change in feed temperature, change in feed pressure, and change in feed primary mole fraction (D1, D2, D3 respectfully) as well as a variety of tuning constants. These values can be seen in ***Tables A.1 and A.2*** of the *Appendix*. Again, this data is PV response data to a SP change under the specific combination of the state {KC, TI, D1, D2, D3}. The surrogate model was then trained in this simulation in order to have an initial model to represent the plant. It is important to note that the model will only be as good as the data that it is trained on—the more extensive data collected the more robust the predictions will be. From this initial model, a PPO agent will interact with it by subjecting random bounded state values (D1, D2, D3) and taking a control action. Each time an action is taken, one episode is completed, and

the reward is collected based on the step response metrics and ***Eqn. 1***. For example, fast control has lower weights on overshoot compared to tight control. In this case, four controller policies were inquired: fast, slow, tight, and ISE. These four policies were learned and tested for composition control (XIC-100), and the results are shown in ***Figure 3.*** The initial settings are shown in the blue series to have a baseline for comparison. Then each agent was subjected to the same state change and called upon to make a control adjustment. The green, yellow, purple, and red series show the PV responses for the control adjustments for the respective control policies. In addition, the models are validated by showing the neural network predictions in the colored dashed lines in each subplot. Each agent successfully learns the appropriate control actions required to meet the specified control objectives while subjected to a constant operational state for each case. The recommendations vary based on the selected policy: the *Fast Policy* suggests a gain of 2.51 and an integral time of 1; the *Slow Policy* advises a gain of 1 and an integral time of 17; the *Tight Policy* recommends both a gain and integral time of 1; and the *ISE Policy* prescribes a gain of 1.96 and an integral time of 4.37.

The next test was to see how a controller behaves within a chosen control objective to different states. In the first case, tight control was chosen for the composition controller (XIC-100). The controller was then tested with different states as shown in ***Table 1***. Here,

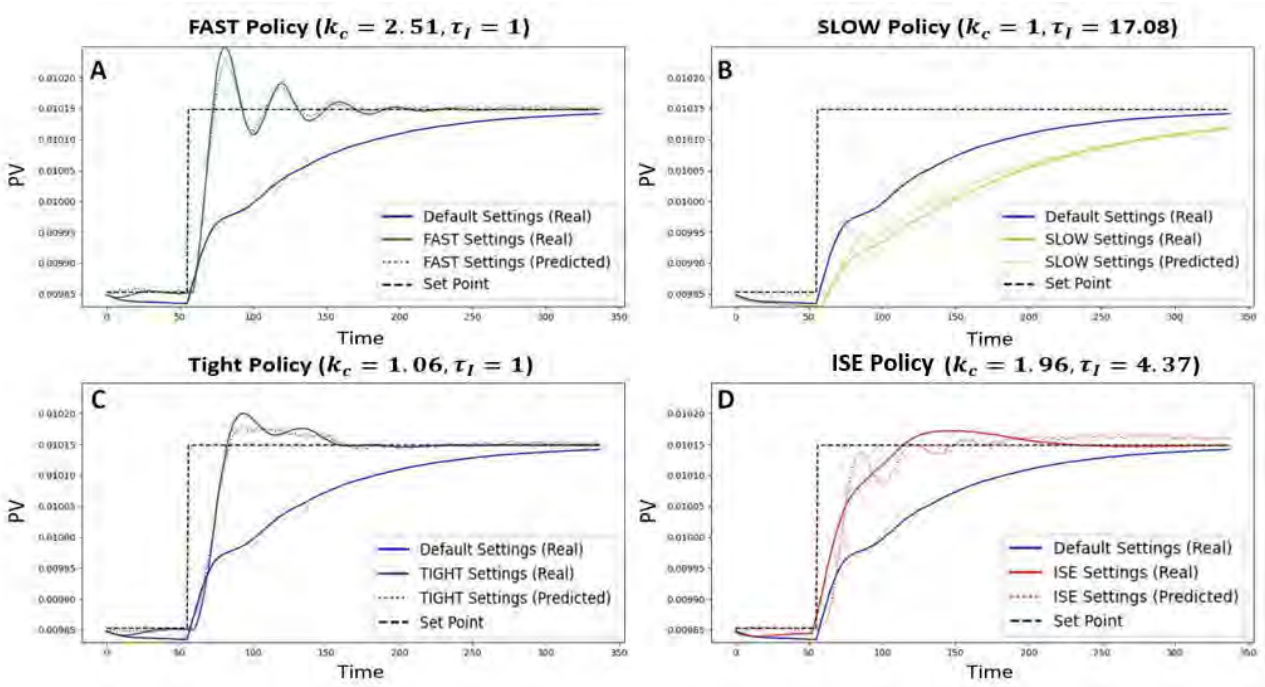



***Figure 3***: Different control policies learned via the reinforcement learning agent subjected to different reward function weights. **A.** *Fast control policy*. **B.** *Slow control policy*. **C.** *Tight control policy*. **D.** *ISE based control policy*.

***Table 1:*** Tight Control Agent for Composition (XIC-100) Results

| Trial | Description | State | Kc | Ti (min.) |
|---|---|---|---|---|
| 1 | Min | {31.5, 6004, 0.842658} | 1.0335 | 1 |
| 2 | Max | {35, 6320, 0.842686} | 1.1923 | 1 |
| 3 | Avg | {33.25, 6162, 0.842672} | 1.122 | 1 |
| 4 | Min -1% | {31.185, 5943.96, 0.834231} | 1 | 3.1314 |
| 5 | Max +1% | {35.35, 6383.2, 0.851113} | 1.2142 | 1 |

***Table 2:*** ISE Control Agent for Ethane Recycle Control (ERIC-100) Results

| Trial | Description | State | Kc | Ti (min.) |
|---|---|---|---|---|
| 1 | Min | {31.5, 6004, 0.842658} | 0.004 | 0.04051 |
| 2 | Max | {35, 6320, 0.842686} | 0.004 | 0.04270 |
| 3 | Avg | {33.25, 6162, 0.842672} | 0.004 | 0.04173 |
| 4 | Min -1% | {31.185, 5943.96, 0.834231} | 0.004016 | 0.04 |
| 5 | Max +1% | {35.35, 6383.2, 0.851113} | 0.004 | 0.04319 |

different state configurations were chosen in order to test the robustness of the predictions. The configurations are as follows: the minimum bounds of the state, the maximum bounds, the average of the bounds, +1% of the maximum bounds, and -1% of the minimum bounds—with the bounds being the limits of the training data. By doing so, the interpolative and slight extrapolative abilities of the proposed agent can be studied. From these results, the controller was able to fine tune its gain and integral time in order to best stay on track with the learned policy. In most cases, the policy learned to just slightly adjust the gain value with the exception of the minimum -1% entry where the integral time was slightly adjusted. It makes sense here knowing that the minimum kc value that the model was trained on was 1, so the agent learned that it had to start adjusting the ti value. For the second example, a general ISE policy was learned for the ethane recovery control. The adaptive controller was subjected to the same changes in state as previously mentioned. The agent updates are shown in ***Table 2***. As observed, the

agent learned to fine tune the integral time in this case in order to best maintain the optimal policy for the changes in state with the exception of the -1% of the minimum bound again. Where—in this case—the ti value hit the minimum value of 0.04 and the kc value had to take more of the responsibility of the control action.

## CONCLUSION

This research presents a robust framework for adaptive PID controller tuning, combining data-driven surrogate models and reinforcement learning to address the challenges of dynamic industrial environments. By utilizing historical process data, the surrogate model accurately mimics system behavior, enabling safe and efficient exploration of control strategies. The reinforcement learning agent, trained with a customizable reward function, optimizes controller performance in real-time, adapting to varying operating conditions and process demands.

The application to a demethanizer unit demonstrates the method's flexibility and effectiveness, showcasing its ability to align with specific control objectives, whether fast, slow, or precise responses are required. More results and use cases will be sought after, but the preliminary results affirm the framework's capacity to adapt to evolving plant conditions, ensuring reliability and efficiency through continuous learning and optimization.

Looking forward, the approach has potential for broader application across complex industrial processes, where enhanced robustness of surrogate models and advanced reward functions can unlock even greater adaptability. This research represents a step toward fully autonomous control systems, laying the groundwork for the realization of "self-driving" industrial plants that continuously monitor, optimize, and improve themselves in real time.

## ACKNOWLEDGEMENTS

We extend out gratitude to ExxonMobil for their research collaboration and support. We also wish to acknowledge the Process Systems Engineering group at LSU, led by Dr. Romagnoli, for guidance and expertise. Additionally, we would like to thank the LSU Chemical Engineering Department for the facilities and resources to complete this research.

## APPENDIX

***Table A.1:*** XIC-100 Training States (72 unique SP changes)

| KC | Ti (min.) | D1 | D2 | D3 |
|---|---|---|---|---|
| 1 | 1 | 31.5 | 6004 | 0.842658 |
| 3 | 10 | 35 | 6320 | 0.842686 |
| 5 | 20 | / | / | / |

***Table A.2:*** ERIC-100 Training States (72 unique SP changes)

| KC | Ti (min.) | D1 | D2 | D3 |
|---|---|---|---|---|
| 0.004 | 0.04 | 31.5 | 6004 | 0.842658 |
| 0.005 | 0.05 | 35 | 6320 | 0.842686 |
| 0.006 | 0.06 | / | / | / |

## REFERENCES

1. Åström, K. J., & Hägglund, T. (2006). *Advanced PID control*. ISA.
2. Cheng, M., Zhao, X., Dhimish, M., Qiu, W. and Niu, S., "A Review of Data-driven Surrogate Models for Design Optimization of Electric Motors," in *IEEE Transactions on Transportation Electrification*
3. Goodfellow, I., Bengio, Y., & Courville, A. (2016). *Deep learning*. MIT Press.
4. Lu, Y. (2017). "Industry 4.0: A survey on technologies, applications, and challenges." *Computers in Industry*.
5. Qin, S. J., & Badgwell, T. A. (2003). "A survey of industrial model predictive control technology." *Control Engineering Practice*.
6. Sutton, R. S., & Barto, A. G. (2018). *Reinforcement learning: An introduction*. MIT Press.

© 2025 by the authors. Licensed to PSEcommunity.org and PSE Press. This is an open access article under the creative commons CC-BY-SA licensing terms. Credit must be given to creator and adaptations must be shared under the same terms. See https://creativecommons.org/licenses/by-sa/4.0/



Systems & Control Transactions

**Research Article - Peer Reviewed Conference Proceeding**
ESCAPE 35 - European Symposium on Computer Aided Process Engineering
Ghent, Belgium. 6-9 July 2025
Jan F.M. Van Impe, Grégoire Léonard, Satyajeet S. Bhonsale,
Monika E. Polańska, Filip Logist (Eds.)

PSE PRESS

# *CompArt*: Next-Generation *Comp*artmental Models for Complex Systems Powered by *Art*ificial Intelligence

**Antonello Raponi[a*], Zoltan Nagy[a]**

[a] Purdue University, Davidson School of Chemical Engineering, 47907 West Lafayette, Indiana, USA
* Corresponding Author: araponi@purdue.edu.

## ABSTRACT

Compartmental models are widely used to simplify the analysis of complex fluid dynamics systems, yet subjective compartment definitions and computational constraints often limit their applicability. The CompArt algorithm introduces an AI-driven framework that automates compartmentalization in Computational Fluid Dynamics (CFD) simulations, optimizing both accuracy and efficiency. By leveraging unsupervised clustering techniques such as Agglomerative Clustering, CompArt identifies coherent flow regions based on velocity and turbulent kinetic energy dissipation rate, ensuring a data-driven, physically consistent segmentation. The methodology integrates a connectivity-based clustering strategy, where compartments are dynamically optimized using the Silhouette score and adjacency matrix. This approach enables the reduction of high-resolution 3D CFD simulations into a network of interconnected sub-systems, significantly lowering computational costs while preserving system heterogeneity. The framework was tested on turbulent stirred tank simulations at 200 and 400 RPM, demonstrating its ability to capture both large-scale flow structures and fine-scale turbulence features. At higher RPM, increased mixing leads to a more fragmented dissipation pattern, which the model successfully adapts to. With scalability up to industrial scale meshes (~1M cells) and full automation of hyperparameter selection, CompArt enhances the applicability of CFD compartmental models in crystallization, multiphase flow, and process optimization. By bridging AI-driven clustering with physical modelling, this novel framework streamlines CFD simulations, making real-time industrial applications feasible without sacrificing predictive accuracy.

**Keywords**: Artificial Intelligence, Computational Fluid Dynamics, Mixing, Industry 4.0, Process Design

## INTRODUCTION

Compartmental models have long been a cornerstone, offering a simplified yet effective framework for analyzing and simulating complex processes [1]. These models divide a system into interconnected compartments, each representing a sub-region with uniform properties, such as temperature, concentration, or velocity. By reducing a continuous system into discrete, manageable units, compartmental models facilitate the study of phenomena such as mass transfer, reaction kinetics, mixing dynamics and their interplay.

The strength of compartmental models lies in their ability to provide insightful approximations while significantly reducing computational demands compared to full-scale three-dimensional (3D) simulations. They are widely applied in fields such as reactive crystallization, multiphase flow, and pharmaceutical manufacturing, where understanding process heterogeneity and scaling effects is critical [2–4]. However, despite their utility, compartmental models face significant limitations that constrain their broader applicability and accuracy.

One major challenge is the reliance on expert judgment to define the number, size, and connectivity of compartments [5]. This process is often subjective, time-intensive, and prone to inconsistencies, particularly for systems with high spatial complexity. Additionally, traditional compartmental models struggle to preserve fine-scale heterogeneity, leading to oversimplified representations that may overlook critical interactions within the system.

Another limitation lies in their adaptability. Classical approaches are often tailored to specific scenarios,

requiring extensive reconfiguration when applied to new processes or scales. This lack of flexibility reduces their utility in dynamic, industrial contexts where process conditions and requirements frequently change.

Finally, the integration of multiple governing variables, such as velocity, turbulent energy dissipation rate, and temperature, remains a challenge. While these factors are crucial for accurately describing complex systems, incorporating them into compartmental models without introducing prohibitive computational costs is a significant hurdle [6].

Addressing these limitations is crucial to enhance the predictive power, scalability, and versatility of compartmental models, ensuring they remain a relevant and powerful tool in modern chemical engineering applications.

## CompArt algorithm

CompArt is an innovative approach to modelling complex systems, based on Computational Fluid Dynamics (CFD) simulations. CFD plays a crucial role in various industries such as chemical engineering, pharmaceuticals, and energy, where understanding fluid flow, heat transfer, and mass transport is vital for optimizing process performance. However, simulating large-scale 3D systems is computationally expensive, which limits their real-time applicability in industrial applications. The CompArt project addresses this challenge by exploiting artificial intelligence (AI) to reduce computational costs without compromising the fidelity of the simulation results.

## Objectives

The primary goal of the CompArt project is to innovate the way complex systems are modelled. A central ambition of the project is the integration of unsupervised AI-driven clustering techniques to automate the compartmentalization process. Traditionally, determining the optimal number of compartments for a CFD simulation has relied heavily on expert knowledge, requiring iterative manual adjustments to balance computational cost and simulation accuracy [7]. By using AI, CompArt automates this process, enabling the system to autonomously define the most suitable number of compartments based on input parameters. This not only reduces the dependence on domain-specific expertise but also enhances the consistency and efficiency of the modelling process.

Scalability is another cornerstone of the project. By representing the 3D system as a network of interconnected sub-systems, CompArt provides a structured way to reduce the computational burden associated with CFD simulations. Each compartment is characterized by uniform properties, such as velocity or turbulence dissipation rates, which significantly simplifies the mathematical complexity of the problem. This reduction allows for real-time simulations, even in industrial contexts where rapid decision-making is essential.

Finally, CompArt places a strong focus on preserving the heterogeneity and spatial characteristics of the system. While simplifying the model, the framework ensures that the inherent complexity of the system, such as variations in flow dynamics or reactive processes, is not lost. This attention to detail is particularly critical in applications like crystallization, where system heterogeneity plays a vital role in determining the outcome of processes. By maintaining these features, CompArt strikes a balance between computational efficiency and the fidelity required for accurate simulations.

# METHODOLOGY

## Simulation Setup and Governing Equations

To test the proposed methodology, simulations are performed on 3D stirred tanks. The simulations use the Reynolds-Averaged Navier-Stokes (RAS) approach with the $k-\varepsilon$ turbulence model. The governing equations include the incompressible Navier-Stokes equations, along with transport equations for turbulent kinetic energy ($k$) and its dissipation rate ($\varepsilon$)

$$\frac{\partial \boldsymbol{u}}{\partial t} + \boldsymbol{u}\cdot\nabla\boldsymbol{u} = \nu_t\nabla^2\boldsymbol{u} - \frac{1}{\rho}\nabla p + \boldsymbol{g} \quad (1)$$

$$\frac{\partial k}{\partial t} + \boldsymbol{u}\cdot\nabla k = \Gamma_{t,k}\nabla^2 k + \frac{P}{\rho} - \varepsilon \quad (2)$$

$$\frac{\partial \varepsilon}{\partial t} + \boldsymbol{u}\cdot\nabla\varepsilon = \Gamma_{t,\varepsilon}\nabla^2\varepsilon + \frac{C_{\varepsilon 1}\varepsilon}{k}\frac{P}{\rho} - \frac{C_{\varepsilon 2}\varepsilon^2}{k} \quad (3)$$

$$\nu_t = \frac{C_\mu k^2}{\varepsilon} \quad (4)$$

The Navier-Stokes equations describe the motion of an incompressible, Newtonian fluid, where turbulence effects are modeled through the turbulent viscosity ($\nu_t$). This additional viscosity accounts for the enhanced momentum diffusion due to turbulent eddies, which cannot be directly resolved in a Reynolds-Averaged Navier-Stokes (RAS) framework.

The turbulent kinetic energy equation ($k$) quantifies the energy associated with turbulent velocity fluctuations. It includes terms for production ($P$), which arises from the mean velocity gradients, dissipation ($\varepsilon$), which represents the conversion of turbulent energy into thermal energy, and diffusion ($\Gamma_t$) to account for spatial transport of turbulence.

The turbulent dissipation rate equation ($\varepsilon$) governs the rate at which turbulent kinetic energy is dissipated into smaller scales.

## AI-driven Clustering for Compartmentalization

Clustering plays a pivotal role in compartmentalization by grouping cells in the mesh based on similar characteristics. Several clustering methods were considered,

including k-means and DBSCAN. However, we focused on using Agglomerative Clustering, which is an unsupervised neural network that maps high-dimensional data onto a lower-dimensional (embedded) space, preserving the topological relationships in the input data. This algorithm is well-suited for clustering spatial data in CFD simulations, as it can efficiently handle the inherent complexity of fluid dynamics and capture system heterogeneity.

The AI-driven model autonomously determines the optimal number of clusters based on the user-defined input parameters, such as velocity and turbulent kinetic energy dissipation rate, using the Silhouette score as a quantitative metric. The Silhouette score evaluates the quality of clustering by measuring how similar a data point is to its cluster compared to other clusters, indicating the cohesion and separation of the clusters.

### Feature Processing and Connectivity

In CFD simulations, the fluid domain is represented as a mesh of interconnected cells, and dividing this mesh into meaningful compartments requires a robust understanding of cell connectivity. To achieve this, a connectivity matrix is constructed to capture the relationships between neighboring cells efficiently. Leveraging parallel computation, the matrix is built using a sparse format, significantly reducing the computational time and making the process suitable for large-scale meshes. Once the connectivity is established, the input features, such as velocity and turbulent dissipation rate, are normalized. This normalization, performed using standard scaling techniques, prepares the data for effective clustering. To enhance the accuracy of the Agglomerative Clustering algorithm, key hyperparameters are optimized using the Silhouette score, automating the process and eliminating the need for expert-driven adjustments. This streamlined approach ensures efficient and reliable compartmentalization of complex systems, paving the way for broader application in industrial simulations.

## RESULTS

The results underscore the effectiveness of unsupervised algorithms in clustering CFD data, accurately identifying zones with differing velocities, as shown in Figure 1. However, velocity alone is insufficient to capture the complexity of processes like reactive crystallization [8], where the turbulent kinetic energy dissipation rate plays a crucial role in flow dynamics and system behavior. By incorporating both velocity and turbulence dissipation as input features, the clustering algorithm produces a more refined segmentation, effectively capturing system heterogeneity.

The velocity and turbulence dissipation rate fields at 200 and 400 RPM, shown in Figure 1, were processed using the CompArt algorithm to generate dynamically optimized compartments. The compartmentalization strategy was guided by two key criteria: the silhouette metric, ensuring well-defined clusters, and cell connectivity, preserving the physical consistency of adjacent regions. The resulting segmentation effectively captures both large-scale flow structures and fine-scale turbulence features. At 200 RPM, turbulence dissipation is more localized near the bottom and walls, whereas at 400 RPM, the enhanced mixing leads to a greater number of high-dissipation regions.

A crucial observation is the ability of the algorithm to adapt to changes in the flow and turbulence fields as the RPM increases. At 200 RPM, the region with the highest variation in velocity and turbulence is concentrated near the impeller. However, as the rotational speed increases, the system becomes globally more turbulent, leading to the formation of strong gradients, particularly in stagnant zones (below the impeller) and at the interface between the bulk fluid and the wall (wall effect). Even for an expert, it would be challenging to manually delineate these zones accurately, whereas CompArt successfully identifies them. A particularly evident example is the stagnant fluid region below the impeller. In crystallization processes, this reactor zone can lead to Critical Quality Attributes (CQA) of the product that do not meet specifications, as particles in this region can grow or agglomerate due to prolonged residence times.

Another notable feature of CompArt is its ability to define clusters composed of just a few layers of cells. In both cases, a distinct compartment is observed wrapping around the impeller shaft. It is important to note that, although at lower magnitudes, the shaft also rotates at a certain velocity, thereby exchanging momentum with the surrounding fluid. This characteristic is captured by the algorithm, enabling the monitoring of processes such as secondary nucleation or agglomeration, which are directly linked to turbulent kinetic energy dissipation near moving walls.

These findings highlight the robustness of the CompArt framework in systematically identifying meaningful compartments while preserving spatial heterogeneity and flow physics. By integrating data-driven clustering with physical constraints, this methodology provides an efficient and adaptive approach for reducing CFD complexity while maintaining predictive accuracy.

## CONCLUSIONS

The CompArt framework demonstrates a significant advancement in the compartmental modelling of fluid dynamics systems by integrating AI-driven clustering techniques with CFD simulations. Through the application of Agglomerative Clustering, the methodology effectively partitions the computational domain into meaningful

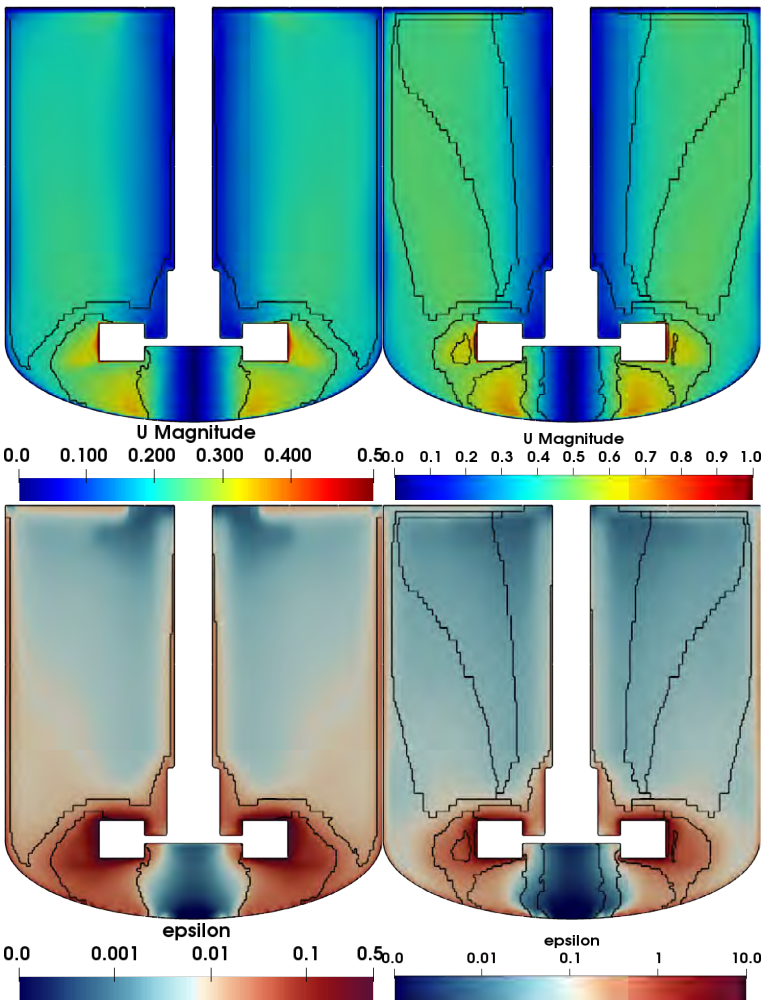



**Figure 1:** Velocity (*top row*) and turbulence dissipation rate (*bottom row*) compartmentalized fields at 200 RPM (*left*) and 400 RPM (*right*). The compartmentalization was performed using the CompArt algorithm.

compartments, preserving the spatial heterogeneity and critical flow structures. This novel approach addresses the key limitations of traditional compartmental models by eliminating the reliance on expert-driven segmentation and enhancing the adaptability of the model across different process conditions.

One of the primary strengths of CompArt is its ability to autonomously determine the optimal number of compartments based on quantitative metrics such as the Silhouette score, ensuring well-defined and physically relevant clusters. Additionally, the framework's capacity to incorporate multiple variables, such as velocity fields and turbulent kinetic energy dissipation rates, allows for a more accurate representation of flow dynamics, which is crucial in applications like crystallization and multiphase flow systems.

The studies at different rotational speeds (200 and 400 RPM) illustrate the robustness of the approach. The model successfully captures key flow features, such as the formation of strong turbulence gradients near stagnation zones and wall regions, which are critical in industrial applications. The ability of the algorithm to detect small-scale but significant structures, such as the interaction of the impeller shaft with the surrounding fluid, further underscores its capability to enhance predictive accuracy.

By reducing computational complexity while maintaining fidelity, the CompArt framework provides a scalable and efficient tool for industrial CFD simulations. Its automation, adaptability, and accuracy make it a promising solution for optimizing process performance in various engineering domains, facilitating real-time decision-making and improved process control.

## ACKNOWLEDGEMENTS

This material is based upon work partially supported by the National Science Foundation (NSF) under Grant No. 2132142.

## REFERENCES


1. N. Jourdan, T. Neveux, O. Potier, M. Kanniche, J. Wicks, I. Nopens, U. Rehman, Y. Le Moullec, Compartmental Modelling in chemical engineering: A critical review, Chem Eng Sci 210 (2019). https://doi.org/10.1016/j.ces.2019.115196.
2. M. Öner, C. Bach, T. Tajsoleiman, G.S. Molla, M.F. Freitag, S.M. Stocks, J. Abildskov, U. Krühne, G. Sin, Scale-up Modeling of a Pharmaceutical Crystallization Process via Compartmentalization Approach, in: Computer Aided Chemical Engineering, Elsevier B.V., 2018: pp. 181–186. https://doi.org/10.1016/B978-0-444-64241-7.50025-2.
3. E. Kougoulos, A.G. Jones, M.W. Wood-Kaczmar, A hybrid CFD compartmentalization modeling framework for the scaleup of batch cooling crystallization processes, Chem Eng Commun 193 (2006) 1008–1023. https://doi.org/10.1080/00986440500352022.
4. M. Öner, S.M. Stocks, J. Abildskov, G. Sin, Scale-up Modeling of a Pharmaceutical Antisolvent Crystallization via a Hybrid Method of Computational Fluid Dynamics and Compartmental Modeling, in: 2019: pp. 709–714. https://doi.org/10.1016/B978-0-12-818634-3.50119-3.
5. F. Bezzo, S. Macchietto, C.C. Pantelides, A general methodology for hybrid multizonal/CFD models: Part I. Theoretical framework, Comput Chem Eng 28 (2004) 501–511. https://doi.org/10.1016/j.compchemeng.2003.08.004.
6. E. Kougoulos, A.G. Jones, M. Wood-Kaczmar, CFD modelling of mixing and heat transfer in batch cooling crystallizers aiding the development of a hybrid predictive compartmental model, Chemical Engineering Research and Design 83 (2005) 30–39. https://doi.org/10.1205/cherd.04080.
7. A. Querio, M. Shiea, A. Buffo, D.L. Marchisio, Comparison between Compartment and Computational Fluid Dynamics Models for Simulating Reactive Crystallization Processes, Ind Eng Chem Res (2024). https://doi.org/10.1021/acs.iecr.4c01483.
8. A. Raponi, R. Achermann, S. Romano, S. Trespi, M. Mazzotti, A. Cipollina, A. Buffo, M. Vanni, D. Marchisio, Population balance modelling of magnesium hydroxide precipitation: Full validation on different reactor configurations, Chemical Engineering Journal 477 (2023) 146540. https://doi.org/10.1016/j.cej.2023.146540.



© 2025 by the authors. Licensed to PSEcommunity.org and PSE Press. This is an open access article under the creative commons CC-BY-SA licensing terms. Credit must be given to creator and adaptations must be shared under the same terms. See https://creativecommons.org/licenses/by-sa/4.0/




Systems & Control Transactions

Research Article - Peer Reviewed Conference Proceeding
ESCAPE 35 - European Symposium on Computer Aided Process Engineering
Ghent, Belgium. 6-9 July 2025
Jan F.M. Van Impe, Grégoire Léonard, Satyajeet S. Bhonsale,
Monika E. Polańska, Filip Logist (Eds.)

PSE PRESS

# ML-based adsorption isotherm prediction of metal-organic frameworks for carbon dioxide and methane separation adsorbent screening

**Dongin Jung[a], Hyeon Yang[a], Donggeun Kang[a], Donghyeon Kim[a], Siuk Roh[a] and Jiyong Kim[a]***

[a] Sungkyunkwan University (SKKU), Department of Chemical Engineering, Suwon, Republic of Korea
* Corresponding Author: jiyongkim@skku.edu.

## ABSTRACT

The efficient separation of carbon dioxide ($CO_2$) and methane ($CH_4$) is crucial for chemical processes, including biogas upgrading and natural gas purification. Metal-organic frameworks (MOFs) have gained significant attention as promising adsorbents for these processes due to their high porosity and tunable structures. Estimating the adsorption capacity of MOFs is essential for screening high performing adsorbents. While molecular simulations are commonly used to estimate the adsorption capacities, their computational intensity acts as a bottleneck in screening MOF adsorbents. In this study, we propose a machine learning (ML)-based framework for the high-throughput prediction of adsorption isotherms for $CO_2$ and $CH_4$ in MOFs. A graph neural network (GNN) model was developed to predict adsorption capacities, effectively replacing the time-consuming molecular simulations. The GNN model processes the structural graphs of MOFs, capturing their spatial configurations, such as surface structure and pore characteristics, which are closely related to adsorption performance. Based on the adsorption capacities predicted by the GNN model, an isotherm model was derived to characterize the adsorption behavior of the MOFs. This framework enables the rapid and reliable screening of MOFs with superior adsorption performance for $CO_2/CH_4$ separation, offering a computationally efficient approach that paves the way for broader applications of MOFs in carbon dioxide separation technologies.

**Keywords**: Adsorption, Machine Learning, Carbon Dioxide Capture

## 1. INTRODUCTION

The separation of carbon dioxide ($CO_2$) and methane ($CH_4$) from gas mixtures is a critical process in chemical processes such as biogas upgrading [1]. Efficient separation of these gases is essential for enhancing biomethane purity, reducing greenhouse gas emissions, and improving the sustainability of energy production. Pressure swing adsorption (PSA) is one of the most widely used techniques for gas separation, relying on porous solid adsorbents to selectively capture $CO_2$ from gas mixtures. The performance of PSA largely depends on the properties of the adsorbent, including its adsorption capacity and selectivity. Therefore, the development of high-performance adsorbents is crucial for improving the efficiency of $CO_2/CH_4$ separation. Metal-organic frameworks (MOFs), characterized by high porosity and structural tunability, have emerged as promising candidates for PSA adsorbents owing to their outstanding adsorption capacities and selectivity [2]. The modular nature of MOFs, which allows flexible design of their chemical composition and physical structure, enables tailored designs for specific gas separation applications. However, this tunability poses a challenge in efficiently identifying materials optimized for specific separation processes.

Traditional methods for determining MOF adsorption properties, such as molecular simulations and experimental measurements, are both time-intensive and computationally expensive, especially when screening large datasets [4]. Machine learning (ML) has recently emerged as a powerful alternative, enabling rapid and accurate predictions of MOF adsorption properties. By reducing computational costs and accelerating analysis,

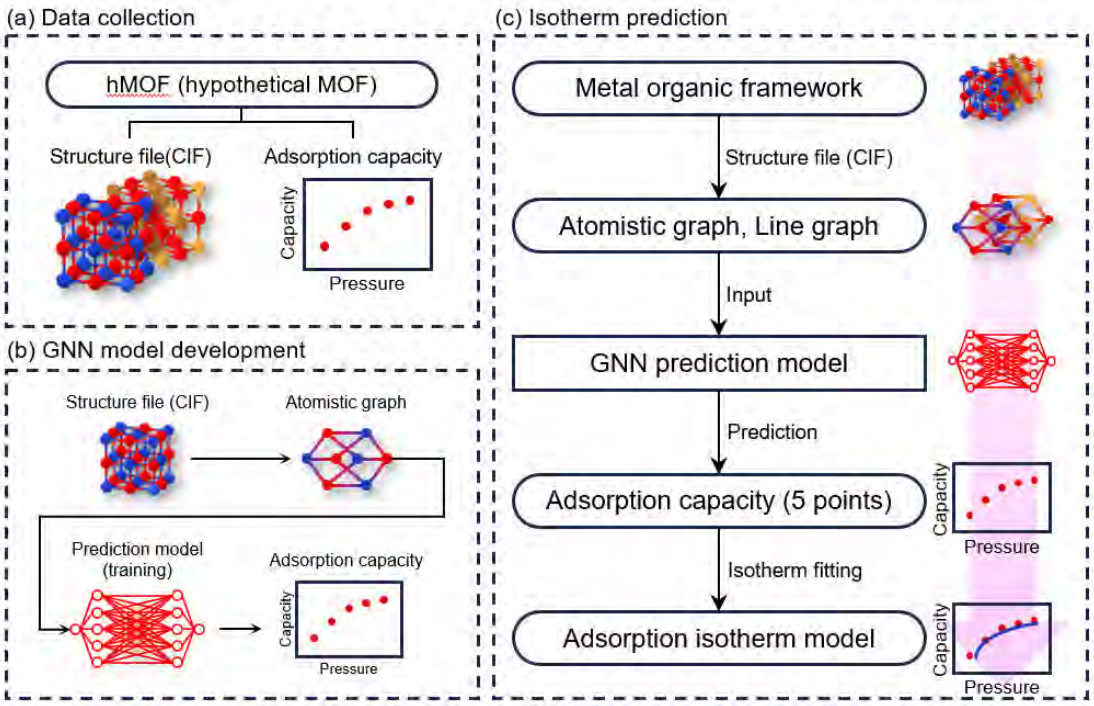



**Figure 1:** Research overview

ML provides a transformative approach for efficiently screening MOFs across diverse applications. Among ML approaches, graph neural network (GNN) stand out as a highly effective and specialized method for predicting MOF properties. Unlike conventional ML models, which rely on predefined descriptors or simple structural representations, GNN directly process chemical structures as graphs, where atoms are represented as nodes and bonds as edges [5]. This unique capability allows GNN to inherently capture both atomic- and bond-level features while preserving the spatial and topological complexity of MOFs. As a result, GNN excel in modeling the intricate relationships between structural characteristics and adsorption behavior, making them exceptionally suited for analyzing the complex and diverse architectures of MOFs.

This study introduces a framework for predicting the adsorption isotherms of $CO_2$ and $CH_4$ in MOFs. Using graph representations of MOFs, the GNN model predicts adsorption capacities. These predictions are subsequently processed by the pyAPEP software, which fits adsorption isotherms using established models such as the Langmuir or Dual-Site Langmuir equations [6].

By leveraging advanced GNN model and large-scale MOF datasets, this study provides a scalable framework for predicting $CO_2$ and $CH_4$ adsorption isotherms with reduced computational costs.

## 2. METHOD

### Data collection

In this study, we used the hypothetical MOFs (hMOF) dataset from the MOFX database to train the model. The MOFX database is a comprehensive repository that consolidates diverse datasets of MOFs, including both hypothetical and experimentally synthesized structures [7]. It provides Crystallographic Information Files (CIFs) containing atomic coordinates and structural properties, along with adsorption and textural property data. Such detailed information is instrumental in facilitating the screening of MOFs for adsorption-based applications.

The hMOF dataset, comprising 137,953 hypothetical MOF structures, was selected from the MOFX database for the present study [8]. These structures were computationally generated by systematically combining a diverse set of 102 building blocks, including metal nodes and organic linkers, to explore a wide range of potential MOF configurations. The resulting hypothetical structures represent the diverse structural and chemical properties of MOFs.

In this study, preprocessing was applied to filter out structures unsuitable for adsorption studies. MOFs lacking methane adsorption data were removed, and those with a pore limiting diameter (PLD) smaller than 3.3 Å were excluded. The PLD represents the smallest pore diameter of an adsorbent, and if it is smaller than the gas molecules, adsorption cannot occur as the molecules cannot enter the pores. Since this dataset is used to

train a model for predicting $CO_2$ adsorption capacity, information on MOFs that are physically incapable of adsorbing $CO_2$ must be excluded. Therefore, a 3.3 Å constraint, corresponding to the molecular diameter of $CO_2$, was applied to filter out such structures. After preprocessing, 112,351 MOFs remained as training data. The dataset was then split into training, validation, and test sets with a ratio of 0.8:0.1:0.1. CIFs of the hMOF structures were utilized to construct graph-based representations, where atoms and bonds correspond to nodes and edges, respectively. These graph representations served as input data for training the GNN model.

The adsorption data of $CO_2$ and $CH_4$ from the hMOF dataset were used as target values for model training, which were computed using Grand Canonical Monte Carlo (GCMC) simulations at 298 K across multiple pressure conditions [9]. We obtained five adsorption data points for each gas, with $CO_2$ adsorption data including simulation results at pressures of 0.01, 0.05, 0.1, 0.5, and 2.5 bar, and $CH_4$ adsorption data including simulation results at pressures of 0.05, 0.5, 0.9, 2.5, and 4.5 bar. The TraPPE (Transferable Potentials for Phase Equilibria) force field was employed to model molecular interactions for the adsorption gases, and the UFF (Universal Force Field) was used for the MOF structures. Each simulation included 1,000 initialization cycles for system equilibration, followed by 1,000 production cycles to gather adsorption data.

## GNN model development

We developed a GNN model to predict the adsorption capacities of $CO_2$ and $CH_4$ for MOFs, based on the Atomistic Line Graph Neural Network (ALIGNN) architecture. ALIGNN combines atomistic and line graph representations to effectively capture structural and bond-level interactions within MOFs, enabling accurate predictions of material properties [10].

In the atomistic graph representation, atoms are represented as nodes and bonds as edges. For this study, 8 atomic features were used: column number, atomic radius, ionization energy, electronegativity, electron affinity, valence electrons, atomic volume, and block (outermost shell). Edge features, representing bond distances, were encoded using a radial basis function (RBF) expansion with a cutoff of 8 Å. To ensure structural completeness, a periodic 12-nearest-neighbor configuration was applied during graph construction.

The line graph representation complements the atomistic graph by treating interatomic bonds as nodes and bond angles as edges. Bond angles were encoded using RBF features and propagated with bond distance features through Edge-gated Graph Convolutions. Alternating convolutions between atomistic and line graphs allowed ALIGNN to efficiently update atom, bond, and bond-angle features, capturing both local and higher-order structural relationships in MOFs.

The ALIGNN architecture consisted of 4 ALIGNN layers and 4 graph convolution (GCN) layers, each with 256 hidden nodes. Initial bond and bond angle features were embedded into a 64-dimensional space using 80 RBF features for bond distances and 40 RBF features for bond angles. Final atom-wise representations were averaged and passed through a linear layer to generate regression outputs. This robust architecture enabled ALIGNN to capture both local and higher-order structural relationships in MOFs, allowing accurate prediction of adsorption capacities across various pressure conditions.

## Adsorption isotherm fitting

To construct adsorption isotherms for each MOF, the predicted adsorption capacities at five pressure points were fitted using the pyAPEP software package. pyAPEP is a comprehensive software designed for adsorption process simulations, automating data processing and fitting adsorption isotherms to enable accurate modeling of gas adsorption behavior [6].

pyAPEP employs a well-designed algorithm to automatically determine the most suitable isotherm model for a given pressure-uptake dataset. This is achieved by optimizing parameters, minimizing errors, and selecting the best-fitting model from five established options: Langmuir, Freundlich, Sips, Quadratic, and Dual-Site Langmuir. Each model is described by the following equations:

Langmuir model: $q(P) = \frac{K_1 K_2 P}{1+K_2 P}$ (1)

Freundlich model: $q(P) = K_1 P^{K_2}$ (2)

Sips model: $q(P) = \frac{K_1 K_2 P^{K_3}}{1+K_2 P^{K_3}}$ (3)

Quadratic model: $q(P) = K_1 \frac{(K_2+2K_3 P)P}{1+K_2 P+K_3 P^2}$ (4)

Dual-site Langmuir model: $q(P) = K_1 \frac{K_2 P}{1+K_2 P} + K_3 \frac{K_4 P}{1+K_4 P}$ (5)

This approach efficiently generates adsorption isotherms from limited data, providing a robust basis for analyzing and screening MOFs based on their adsorption performance.

## Model validation

To validate the generalizability of the model, the CRAFTED dataset, which provides adsorption data for 690 experimentally synthesized MOFs extracted from the CoREMOF2014 database, was utilized [11]. This dataset includes simulated adsorption data performed for the adsorption of $CO_2$ with two fields (i.e., UFF and DREIDING), six partial charge schemes (i.e., no charge, Qeq, EQeq, PACMOF, MPNN, and DDEC), at three temperatures (i.e., 273, 298, 323 K).

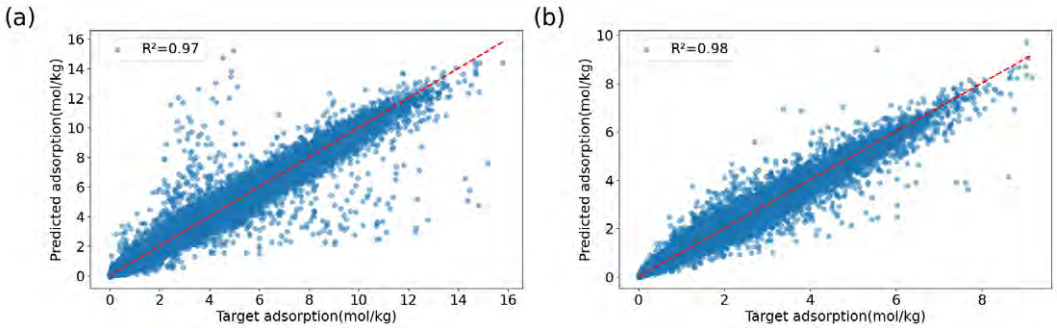



**Figure 2:** Comparison of target vs predicted adsorption capacities for (a) carbon dioxide adsorption with model accuracy ($R^2$ = 0.97), (b) methane adsorption with model accuracy ($R^2$ = 0.98)

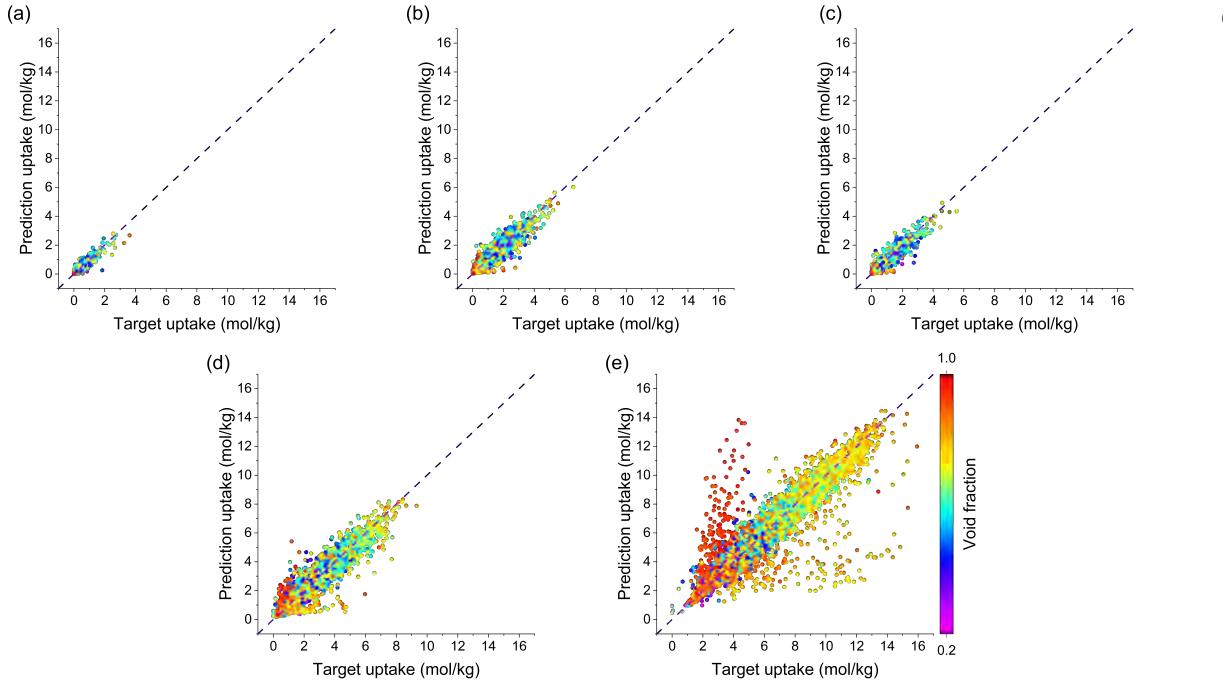



**Figure 3:** The plots of target vs predicted $CO_2$ adsorption capacity colored by void fraction at five pressure points
(a) 0.01 bar, (b) 0.05 bar, (c) 0.1 bar, (d) 0.5 bar, (e) 2.5 bar

To ensure compatibility with the GNN model's training conditions, adsorption data simulated with the UFF force field, EQeq partial charge calculation method, and a temperature of 298 K were selected. Based on this simulated data, simulated adsorption isotherms were fitted and compared with the isotherms predicted by the GNN framework.

## 3. RESULT ANALYSIS

### Model accuracy

We evaluated the accuracy of the adsorption prediction models for $CO_2$ and $CH_4$ using the coefficient of determination ($R^2$), which measures the proportion of variance in the target values explained by the predictions. $R^2$ scores range from 0 to 1, with higher values indicating greater predictive accuracy. The evaluation results showed $R^2$ scores of 0.97 for $CO_2$ and 0.98 for $CH_4$, demonstrating the explanatory power of the prediction models in estimating adsorption capacities for both gases. Additionally, Figure 2 illustrates the alignment between the target and predicted adsorption capacities, highlighting the high accuracy of the models.

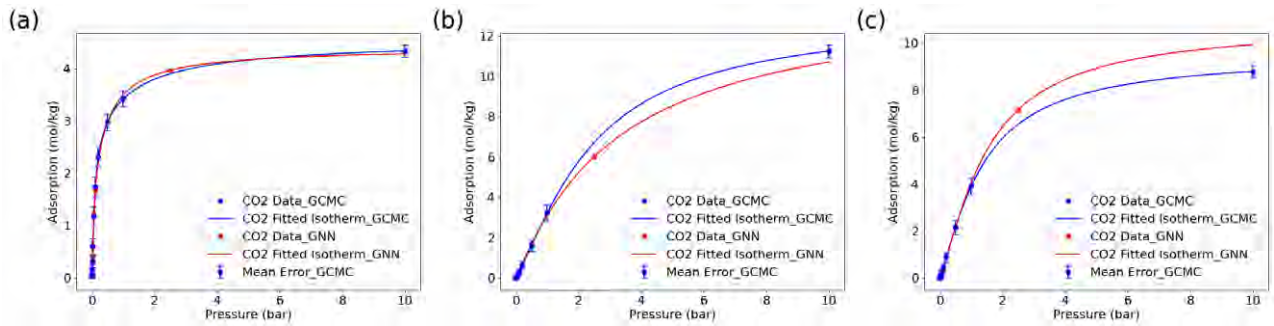



**Figure 4:** Three examples of CRAFTED dataset validation results: GCMC vs. GNN $CO_2$ isotherm

**Table 1.** $R^2$ scores for each pressure point for $CO_2$ adsorption model

| Pressure (bar) | $CO_2$ model ($R^2$ score) |
|---|---|
| 0.01 | 0.88 |
| 0.05 | 0.92 |
| 0.1 | 0.93 |
| 0.5 | 0.94 |
| 2.5 | 0.88 |

**Table 2.** $R^2$ scores for each pressure point for $CH_4$ adsorption model

| Pressure (bar) | $CH_4$ model ($R^2$ score) |
|---|---|
| 0.05 | 0.92 |
| 0.5 | 0.95 |
| 0.9 | 0.95 |
| 2.5 | 0.94 |
| 4.5 | 0.94 |

In addition to overall accuracy, Table 1 and 2 provides $R^2$ scores for each pressure point across the two gases, offering a detailed assessment of model performance. While the $CH_4$ model maintained consistently high $R^2$ scores across all pressure points, the $CO_2$ model exhibited lower accuracy at some pressure points. For example, at 0.01 bar and 2.5 bar, the model exhibited $R^2$ score of 0.88

To investigate the factors responsible for the lower accuracy of the $CO_2$ model at specific pressure points, we analyzed the textural properties of MOFs with significant prediction errors. Among the textural properties, void fraction, which is known to have a significant association with adsorption, was identified as the property most strongly influencing the model's predictive performance. The analysis revealed that MOFs with large prediction errors were predominantly those with high void fractions. The relationship between target and predicted $CO_2$ adsorption capacities at five pressure points is visualized in Figure 3, with void fraction represented as a color gradient. At 2.5 bar, the structures with the most significant prediction errors were mostly MOFs with void fractions greater than 0.8. This pattern suggests that the unique structural characteristics of MOFs with high void fractions are not fully captured by the current GNN model. This limitation is interpreted as resulting from the graph representation of MOFs, where a cutoff distance of 8 Å is used to define connections between atoms, assuming bonds exist between the 12 nearest neighbors within this range. For MOFs with high void fractions, the relative distances between atoms are often larger, making the graph representation less effective at capturing their structural features. These findings highlight the need to refine the model into a more robust framework that ensures high accuracy across diverse MOF characteristics.

## Computational efficiency

To demonstrate the computational efficiency of our model, we compared its performance with molecular simulations by analyzing the time required for adsorption data generation. In GCMC simulations, generating adsorption data for a single pressure point requires approximately 8.6 hours [12].

While the initial training process for the GNN model requires 31.5 hours for $CO_2$ and 16.5 hours for $CH_4$, this is a one-time computational cost. Once trained, the model is capable of rapidly predicting adsorption data for any given MOF. This makes the proposed framework advantageous for handling large-scale datasets compared to GCMC simulations. This advantage is particularly significant in high-throughput screening processes, where predicting adsorption properties for a vast number of MOFs is required.

## CRAFTED dataset validation

Figure 4 presents the validation results comparing the GNN-predicted and GCMC-simulated isotherms for MOFs included in the CRAFTED dataset. The results indicate a strong alignment between the two isotherms. However, minor discrepancies are observed at comparatively high-pressure ranges. For example, Figure 4 (b) and (c) show noticeable deviations at pressures above 2 bar. The reason for this discrepancy is attributed to the absence of high-pressure adsorption data in the training

set.

These results demonstrate the generalizability of the proposed framework in accurately predicting the adsorption behavior of diverse MOFs.

## 4. CONCLUSION

This study proposed a GNN-based framework utilizing the ALIGNN to predict adsorption isotherms for $CO_2$ and $CH_4$ in MOFs. We developed a GNN model to predict adsorption capacities using a large-scale dataset of hypothetical MOFs and applied an isotherm fitting algorithm to rapidly and accurately fit adsorption isotherms based on the predicted capacities. The developed model demonstrated high predictive accuracy. The computational efficiency of the framework was validated by comparing its calculation time with that of molecular simulations, highlighting its comparative advantage. Furthermore, the framework's generalizability to experimentally synthesized MOF datasets was confirmed through validation.

Consequently, the proposed framework is expected to be utilized for rapid high-throughput screening of MOF adsorbents. Future research should be directed toward developing a model capable of capturing complex MOF structures and establishing a framework that demonstrates high generalizability to diverse MOFs.

## REFERENCES


1. Zhang, Y., Sunarso, J., Liu, S., & Wang, R. (2012). Current status and development of membranes for CO2/CH4 separation: A review. International Journal of Greenhouse Gas Control, 12, 84–107. https://doi.org/10.1016/j.ijggc.2012.10.009
2. Furukawa, H., Cordova, K. E., O'Keeffe, M., & Yaghi, O. M. (2013). The Chemistry and Applications of Metal-Organic Frameworks. Science, 341(6149). https://doi.org/10.1126/science.1230444
3. Baumann, A.E., Burns, D.A., Liu, B. et al. Metal-organic framework functionalization and design strategies for advanced electrochemical energy storage devices. Commun Chem 2, 86 (2019). https://doi.org/10.1038/s42004-019-0184-6
4. Choudhary, K., Yildirim, T., Siderius, D. W., Kusne, A. G., McDannald, A., & Ortiz-Montalvo, D. L. (2022). Graph neural network predictions of metal organic framework CO2 adsorption properties. Computational Materials Science, 210, 111388. https://doi.org/10.1016/j.commatsci.2022.111388
5. Reiser, P., Neubert, M., Eberhard, A., Torresi, L., Zhou, C., Shao, C., Metni, H., Van Hoesel, C., Schopmans, H., Sommer, T., & Friederich, P. (2022). Graph neural networks for materials science and chemistry. Communications Materials, 3(1). https://doi.org/10.1038/s43246-022-00315-6
6. Ga, S., An, N., Joo, C., & Kim, J. (2023). pyAPEP: An all-in-one software package for the automated preparation of adsorption process simulations. Computer Physics Communications, 291, 108830. https://doi.org/10.1016/j.cpc.2023.108830
7. Bobbitt, N. S., Shi, K., Bucior, B. J., Chen, H., Tracy-Amoroso, N., Li, Z., Sun, Y., Merlin, J. H., Siepmann, J. I., Siderius, D. W., & Snurr, R. Q. (2023). MOFX-DB: An Online Database of Computational Adsorption Data for Nanoporous Materials. Journal of Chemical & Engineering Data, 68(2), 483–498. https://doi.org/10.1021/acs.jced.2c00583
8. Wilmer, C., Leaf, M., Lee, C. *et al.* Large-scale screening of hypothetical metal–organic frameworks. *Nature Chem* **4**, 83–89 (2012). https://doi.org/10.1038/nchem.1192
9. Wilmer, C. E., Farha, O. K., Bae, Y., Hupp, J. T., & Snurr, R. Q. (2012). Structure–property relationships of porous materials for carbon dioxide separation and capture. Energy & Environmental Science, 5(12), 9849. https://doi.org/10.1039/c2ee23201d
10. Choudhary, K., & DeCost, B. (2021). Atomistic Line Graph Neural Network for improved materials property predictions. Npj Computational Materials, 7(1). https://doi.org/10.1038/s41524-021-00650-1
11. Oliveira, F. L., Cleeton, C., Ferreira, R. N. B., Luan, B., Farmahini, A. H., Sarkisov, L., & Steiner, M. (2023). CRAFTED: An exploratory database of simulated adsorption isotherms of metal-organic frameworks. Scientific Data, 10(1). https://doi.org/10.1038/s41597-023-02116-z
12. Ga, S., An, N., Lee, G. Y., Joo, C., & Kim, J. (2024). Multidisciplinary high-throughput screening of metal–organic framework for ammonia-based green hydrogen production. Renewable and Sustainable Energy Reviews, 192, 114275. https://doi.org/10.1016/j.rser.2023.114275



© 2025 by the authors. Licensed to PSEcommunity.org and PSE Press. This is an open access article under the creative commons CC-BY-SA licensing terms. Credit must be given to creator and adaptations must be shared under the same terms. See https://creativecommons.org/licenses/by-sa/4.0/




Systems & Control Transactions

**Research Article - Peer Reviewed Conference Proceeding**
ESCAPE 35 - European Symposium on Computer Aided Process Engineering
Ghent, Belgium. 6-9 July 2025
Jan F.M. Van Impe, Grégoire Léonard, Satyajeet S. Bhonsale,
Monika E. Polańska, Filip Logist (Eds.)

PSE PRESS

# Data-Driven Soft Sensors for Process Industries: Case Study on a Delayed Coker Unit

**Wei Sun[a], James G. Brigman[b], Cheng Ji[a], Pratap Nair[b], Fangyuan Ma[a], Jingde Wang[a,*]**

[a] College of Chemical Engineering, Beijing University of Chemical Technology, 100029, North Third Ring Road 15, Chaoyang District, Beijing, China
[b] Ingenero Inc. 4615 Southwest Freeway, Suite 320, Houston TX 77027, USA
* Corresponding Author: jingdewwang@mail.buct.edu.cn.

## ABSTRACT

This research addresses the challenges associated with data-driven soft sensors in industrial applications, where successful implementations remain limited. The scarcity of practical applications can be attributed to variable operating conditions and frequent disturbances in real-time processes. Industrial data are often nonlinear, dynamic, and highly unbalanced, complicating efforts to capture the essential characteristics of underlying processes. To tackle these issues, we propose a comprehensive solution for industrial application, that encompasses feature selection, feature extraction, and model updating. Feature selection aims to pinpoint the independent variables that have a substantial impact on key performance indicators, including quality, safety, efficiency, reliability, and sustainability. By doing so, it simplifies the model and boosts its predictive accuracy. The process begins with screening variables based on process knowledge, followed by a thorough analysis of correlation and redundancy to eliminate redundant information, which can burden computational resources and degrade prediction accuracy. We propose a mutual information-based algorithm for feature selection that assesses the relevance and redundancy among process variables through a comprehensive correlation function. This algorithm ranks variables by their importance using a Greedy search method to identify the optimal set of variables. After selecting the optimal variables, feature extraction is carried out to derive internal features from this set and establish a relationship between these latent features and the output variables. Given the intricate nature of industrial processes, we employ deep learning techniques, specifically Long Short-Term Memory (LSTM) networks, which are a type of Recurrent Neural Network (RNN) well-suited for capturing long-term dependencies in sequential data. LSTMs excel at modeling temporal correlations due to their ability to maintain memory states that allow for learning from sequential data over extended periods. To address short-term nonstationary features resulting from process disturbances, we incorporate a differential unit into the latent layer of the LSTM network. Once trained, the model is updated during online applications to incorporate gradual changes in equipment and reaction agents. Quality-related data, although typically available only post-measurement, can be leveraged to fine-tune model parameters, ensuring sustained predictive accuracy over time. To validate our approach, we present a case study on a delayed coker unit, yielding promising long-term predictions for tube metal temperature and showcasing the potential of our methodology for industrial applications.

**Keywords**: quality prediction, feature selection, feature extraction

## 1.INTRODUCTION

In chemical production, quality variables serve as indicators of plant operating status and are directly linked to product quality and production efficiency. However, the online acquisition of these quality variables isn often challenging due to limitations in measurement methods and the high cost of instrumentation. To address this challenge, soft sensor technology has been developed to

indirectly estimate quality variables through easily measurable secondary variables such as temperature, pressure, and flow rate [1-2].

Effective selection of secondary variables is a crucial prerequisite for ensuring the performance of soft-sensing models. Distributed control systems can be used to collect a large number of variables, while inputting all of them into the model to establish a correlation with quality variables would increase computational complexity, and the introduction of irrelevant variables would also affect the model prediction performance [3]. Operators can initially determine the range of relevant variables based on their process knowledge, but in front of complex actual chemical processes and control networks, their understanding of the relationships between variables is still insufficient [4]. Therefore, a series of correlation analysis methods have been introduced to assess the degree of correlation between each pair of secondary variables and the quality variable. The Pearson correlation coefficient, a classic correlation analysis tool in machine learning, can effectively measure the linear relationship between candidate features and the target variable [5]. However, chemical processes are typically nonlinear, and some key variables are difficult to identify effectively through linear analysis methods [6]. For the nonlinear relationships between variables, information theory methods, represented by Mutual Information (MI), show significant advantages [7]. One limitation of MI is that its value is unbounded, making it difficult to determine an objective threshold to judge whether the correlation between variables is significant. To address this issue, Ji et al. proposed estimating the MI threshold through random sequences generated by the Monte Carlo method [8]. Estevez et al. introduced a variable selection method based on normalized MI to standardize MI to a range of 0 to 1 [9]. To improve the accuracy of MI estimation, Reshef et al. proposed the Maximal Information Coefficient (MIC) based on MI [10]. MI can be seen as a quantification of the degree of information overlap between secondary variables and quality variables. However, at the same time, variables with high MI values may also have information overlap, i.e., redundancy. The above methods can screen out a series of variables with the strongest correlation with quality variables, but they neglect the information redundancy between variables. Information theory also provides a theoretical basis for the calculation of redundancy between variables. The Maximum Relevance Minimum Redundancy (mRMR) algorithm was proposed from an information-theoretic perspective to measure the correlation and redundancy between variables [11]. Based on this, Xiao et al. proposed an mRMR method based on neighborhood MI [12]. Yin et al. proposed a feature selection method based on Maximum Dynamic Relevance and Minimum Redundancy [13]. Bennasar et al. proposed a joint MI maximization method to measure the importance of candidate features based on conditional MI [14]. However, these methods only consider the information redundancy between secondary variables and ignore their common redundancy with quality variables. Ji et al. considered common information redundancy and proposed a variable selection method based on conditional information entropy, which was validated in the soft-sensing of ethylene components [15]. However, it has limitations in ranking the importance of secondary variables and still does not obtain the optimal set of secondary variables. Che et al. proposed a feature selection method based on Maximum Relevance and Minimum Common Redundancy, which comprehensively considers the correlation and redundancy information between variables to rank the importance of candidate features [16]. Although this method can objectively calculate the ranking of the importance of candidate features, it does not provide a method for determining the optimal feature subset in different machine learning tasks.

To more comprehensively consider the importance and information redundancy of secondary variables in the selection of secondary variables for soft-sensing tasks, this paper introduces the Maximum Relevance and Minimum Common Redundancy feature extraction algorithm based on MI in the variable selection for soft sensor modeling. It establishes an objective evaluation function that comprehensively considers variable correlation and redundancy, updates the set of secondary variables through the Greedy search algorithm to determine the ranking of their importance, and ultimately obtains the optimal set of secondary variables by evaluating the information gain of the secondary variables for predicting the target variable. Then the optimal variable set is input into Long Short-Term Memory (LSTM) networks to extract the nonlinear and temporal features from sequential data and establish mapping relationship with the target variable. To validate the effectiveness of the proposed method, a case study was conducted on a delayed Coker unit at an actual chemical enterprise. The results demonstrate a promising potential for real-time estimation of quality variables in chemical production.

## 2. BACKGROUND

### 2.1 Information theory

Information theory is a mathematical theory proposed by American scholar Shannon, which provides an explanation for the information content of signals and their transmission based on probability theory and mathematical statistics. Due to its clear statistical significance, it is widely used in measuring the correlation and redundancy of variables in industrial processes [17]. The information content of a signal can be measured by the information entropy in Equation (1),

$$\mathrm{H}(X) = \sum_{x \in X} -p(x)\log\left(p(x)\right) \quad (1)$$

where $p(x)$ is the marginal distribution of variable $x$. When extending information entropy to two-dimensional variables, the shared information between them can represent their degree of correlation, which can be calculated using Mutual Information (MI) [18], as shown in Equation (2),

$$\mathrm{I}(X,Y) = \sum_{x \in X}\sum_{y \in Y} p(x,y) log \frac{p(x,y)}{p(x)p(y)} \quad (2)$$

where $p(x,y)$ represents the joint probability distribution of $x$ and $y$, and $p(x)$ and $p(y)$ represent the marginal distributions of $x$ and $y$, respectively, which can usually be approximated using kernel density estimation [19]. According to Equation (2), if the variables are independent, the MI value is 0; the stronger the correlation between the variables, the larger the MI value. In research, the MI values between each variable and the target variable are often used as the basis for ranking variable importance. However, when measuring the correlation between multidimensional variables using information content, redundant information must be considered, as variables with high correlation may not cover more information about the target variable. Taking a ternary variable as an example, when variables $X_1, X_2$ are known, the information content of the target variable $Y$ is,

$$\mathrm{H}(Y|(X_1,X_2)) = H(Y) - I(X_1,Y) - I(X_2,Y) + I(X_1,X_2,Y) \quad (3)$$

where $I(X_1,X_2,Y)$ is the common mutual information among the three variables, also representing the common redundancy among them. From Equation (3), even if variable $X_2$has a strong correlation with the target variable, if its redundancy with variable $X_1$ and target variable $Y$ is also high, it does not necessarily mean that it is highly important for predicting the target variable. Therefore, in variable selection for soft sensors, both correlation and redundancy need to be considered comprehensively to rank the importance of predictor variables and select the optimal set of auxiliary variables. To this end, the MI-based correlation-redundancy feature selection algorithm adopted in this paper is based on the above information theory knowledge, which constructs a correlation evaluation function to measure the importance of each auxiliary variable and determine the optimal variable set. The specific calculation and implementation steps are introduced in Sections 3.

### 2.2 Long short-term memory neural networks

The dynamics of industrial processes are abundant in process data and must be explicitly taken into account to enhance the effectiveness of process monitoring. To this end, recurrent neural networks (RNNs) are frequently utilized to capture these dynamics by transitioning through hidden states. However, as the time-step accumulates, conventional RNNs may fail to maintain the long-term temporal dependencies of the process. A well-recognized variant of RNNs that can address this issue is the LSTM unit, which excels at extracting long-term temporal dependencies. Its advantage lies in the gate-controlled memory transitions, which can be formulated as follows,

$$i_t = \sigma(W_i \cdot [h_{t-1}, x_t] + b_i) \quad (4)$$

$$f_t = \sigma\left(W_f \cdot [h_{t-1}, x_t] + b_f\right) \quad (5)$$

$$g_t = tanh\left(W_g \cdot [h_{t-1}, x_t] + b_g\right) \quad (6)$$

$$o_t = \sigma(W_o \cdot [h_{t-1}, x_t] + b_o) \quad (7)$$

$$C_t = f_t \odot C_{t-1} + i_t \odot g_t \quad (8)$$

$$h_t = o_t \odot tanh(C_t) \quad (9)$$

where $i_t, f_t, o_t$ stand for the input gate, forget gate, and output gate, respectively, $x_t$ is the input at the current time step, $g_t$ is the current candidate state, $C_t, C_{t-1}$ are the memory cells of the current and last time step, $h_t, h_{t-1}$ are the hidden states of the current and last time step, $W., b.$ are the weight and bias, and $\sigma, tanh$ are sigmoid and tanh activation functions. With the gate structure, irrelevant information of hidden states from the previous time step can be forgotten and useful information from the current time step can be retained by the memory cell, making the LSTM unit more effective in extracting long-term time dependency.

## 3.THE PROPOSED MI-BASED FEATURE SELECTION ALGORITHM FOR DATA-DRIVEN QUALITY PREDICTION

The correlation-redundancy feature selection algorithm based on mutual information adopted in this paper takes into account both the correlation among variables and information redundancy to determine the optimal set of auxiliary variables. For the initial set of auxiliary variables $W$ and the quality variable $Y$, this method aims to obtain the optimal variable set $S$ through a correlation evaluation function. The calculation formula is as follows,

$$f(x_i) = \frac{I(x_i,Y)}{I(Y,Y)} - \frac{CI(x_i,S,Y)}{I(Y,Y)} \quad (10)$$

This function consists of two parts. The first part is the ratio of the mutual information between the candidate variable $x_i$ and the target variable $Y$ to the information entropy of the target variable $Y$. It reflects the degree of correlation between the candidate variable $x_i$ and the target variable $Y$. The second part is the proportion of the redundant information $CI(x_i,S,Y)$ among the candidate variable $x_i$, the already selected set of auxiliary

variables $S$, and the target variable $Y$, relative to the information contained in the target variable $Y$. This part reflects the degree of redundancy of the candidate variable $x_i$. The calculation of redundant information is as follows,

$$CI(x_i,S,Y)=\frac{I(x_i,S)}{Max\{I(x_i,\mathrm{S}),\mathrm{I}(x_i,Y),I(S,Y)\}}\times Min\{I(x_i,Y),I(S,Y)\}(11)$$

In summary, this evaluation function comprehensively considers the correlation between each variable $x_i$ and the target variable $Y$, the maximum redundancy between $x_i$ and $S$, as well as the minimum common redundancy among $x_i$, $S$, and $Y$. A higher value of this function indicates a greater importance of the candidate variable $x_i$ for predicting the target variable $Y$. Additionally, the value of this correlation evaluation function is related to the order of variable input. Therefore, this paper adopts a greedy search algorithm to ensure that the variable selected in each round maximizes the value of the correlation evaluation function, thereby more comprehensively and objectively ranking the importance of each auxiliary variable. Meanwhile, after selecting a sufficient number of auxiliary variables, the coverage of information for the target variable $Y$ reaches saturation, and adding more auxiliary variables will not introduce new information, i.e., the correlation evaluation function decreases near zero, thereby finally determining the optimal set of auxiliary variables.

The modeling and implementation steps of the proposed method are shown in Figure 1. The training data is normalized, and the Mutual Information (MI) values between each variable and the quality variable are calculated using Equation (2). The variable with the maximum MI is taken as the initial value of the undefined set $S$, while the remaining variables, excluding this one, are taken as the initial value of $W$. Then, based on the correlation evaluation function in Equation (10), a greedy search approach is used to iteratively calculate the importance of each auxiliary variable in $W$, and $S$ and $W$ are updated accordingly, until the value of the correlation evaluation function decreases to 0. This determines the final set of auxiliary variable features, $S$. Subsequently, a soft sensor model is established based on the ranked auxiliary variables. During online testing, the optimal auxiliary variables determined during the training phase are selected, standardized based on the mean and variance of the training data, and input into the offline-trained soft sensor model to obtain real-time predictions of the target variable. The Mean Absolute Error (MAE), Root Mean Square Error (RMSE), R2, and mean absolute percentage error (MAPE) metrics are calculated to evaluate the prediction performance of the soft sensor model.

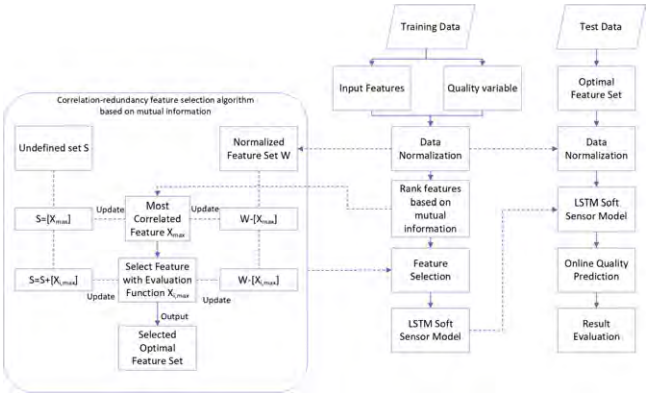



**Figure 1.** Flowchart of the proposed MI-based correlation-redundancy feature selection and soft sensor method.

## 4.CASE STUDY

In this section, data from a delayed Coker unit of an operating factory is investigated to evaluate the proposed method. The delayed Coker unit is a critical component in the refining industry to convert heavy residual oils into lighter, more valuable products. One of the key parameters that significantly influences the performance and reliability of these units is the Tube Metal Temperature (TMT). This temperature represents the heat level within the tubes of the Coker, where the cracking process takes place. An accurate and online estimation on TMT is necessary to enable insights like determination of coking in tubes and drive correct actions, for optimal operating conditions, preventing tube damage, and maintaining high product quality while minimizing costs.

In this case study, 438,049 data points from January 1, 2020 to March 1, 2024 are collected, in which data from ten complete production cycles before 2023 are applied to build the proposed feature selection and soft sensor model and data from the latest one year are employed as test set.

While the range of relevant variables can be identified using the expertise and experience of operators, the significance of these variables for prediction and the redundancy among them may not be fully addressed. To address this problem, the proposed correlation-redundancy feature extraction algorithm based on MI is first applied to all available variables to select an optimal subset of auxiliary variables. Then, a soft sensor model is established using the selected variables.

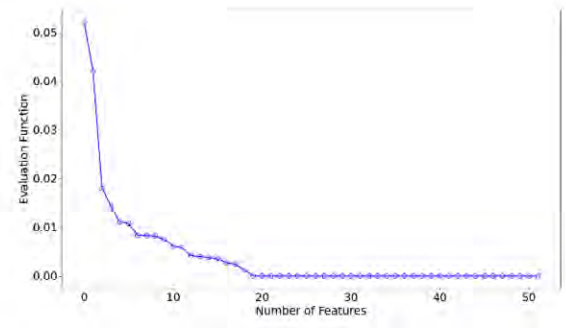



**Figure 2.** Variation of the evaluation function with the number of features.

Using all available variables as inputs, a Greedy search algorithm is employed to iteratively calculate a correlation evaluation function to obtain the importance ranking of each variable. The variation of the evaluation function with the number of features after sorting is shown in Figure 2. It can be observed that as the number of auxiliary variables increases, the amount of information conducive to predicting the target variable continuously grows, and the evaluation function gradually decreases. When the number of auxiliary variables reaches 20, the evaluation function drops to 0, reaching an inflection point, indicating that adding more variables will not introduce new information. Thus, the optimal set of auxiliary variables is finally determined.

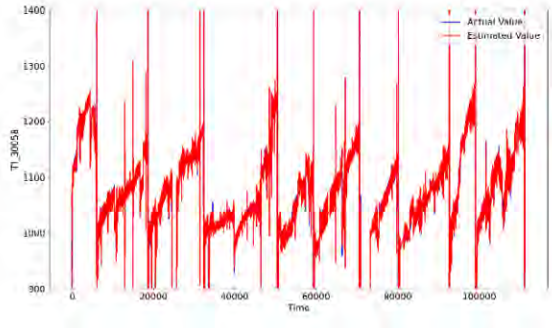



**Figure 3.** The prediction result for TMT.

Using the auxiliary variables determined based on the results in Figure 2, an LSTM-based soft-sensing model is established for online testing using the whole year data in 2023. The online prediction results for TMT are shown in Figure 3. It can be observed that the auxiliary variables selected using the method proposed in this paper can fit the true trend of the quality variable, providing reliable process information to operators and valuable guidance for their online operational decisions. The prediction evaluation metrics for each model are presented in Table 1. It can be seen that the R2 values obtained using our method are all above 0.98, and various error metrics are below 3%. This is attributed to the method's ability to effectively reduce information redundancy among variables while maximizing the coverage of quality variable information.

**Table 1:** The evaluation for prediction results dated from January 9, 2023 to January 30, 2024 except the period from March 15 to May 2, 2023.

| period | 1 | 2 | 3 | 4 | 5 | 6 | 7 | 8 | 9 |
|---|---|---|---|---|---|---|---|---|---|
| Date | 2023/ | 2023/1/ | 2023/5 | 2023/7 | 2023/8/ | 2023/9/1 | 2023/10/ | 2023/11/ | 2023/12/ |
| Start | 1/9 | 31 | /2 | /3 | 3 | 2 | 15 | 27 | 19 |
| Data | 2023/ | 2023/3/ | 2023/7 | 2023/8 | 2023/9/ | 2023/10/ | 2023/11/ | 2023/12/ | 2024/1/3 |
| End | 1/31 | 15 | /3 | /3 | 12 | 15 | 27 | 19 | 0 |
| MAE | 0.010 | 0.011 | 0.006 | 0.012 | 0.016 | 0.019 | 0.010 | 0.013 | 0.016 |
| RMSE | 0.015 | 0.019 | 0.013 | 0.019 | 0.023 | 0.025 | 0.018 | 0.019 | 0.021 |
| MAPE | 0.004 | 0.004 | 0.003 | 0.005 | 0.007 | 0.024 | 0.004 | 0.005 | 0.006 |
| R2 | 0.987 | 0.971 | 0.995 | 0.981 | 0.977 | 0.999 | 0.981 | 0.991 | 0.984 |

## 5.CONCLUSIONS

In conclusion, this study tackles the auxiliary variable selection challenge in soft sensor modeling for chemical processes by introducing a mutual information-based relevance-redundancy feature selection algorithm. This algorithm thoroughly evaluates the correlations and redundancies among variables to obtain an optimal feature set for prediction. By leveraging LSTM networks, the study effectively captures the complex patterns and temporal dependencies present in industrial data, thereby enhancing the predictive accuracy of the soft sensor models. Furthermore, a model update mechanism is integrated to maintain the accuracy and reliability of the models over time. The effectiveness of this comprehensive approach is illustrated through a case study on a delayed Coker unit. Overall, this study offers a robust and objective strategy for auxiliary variable selection in soft

sensor modeling, significantly improving model predictive performance and laying the groundwork for optimizing and controlling chemical processes.

## ACKNOWLEDGEMENTS

The authors would like to acknowledge the financial support from the National Natural Science Foundation of China (Grant # 22278018).

## REFERENCES

1. Kadlec P, Gabrys B, Strandt S. Data-driven soft sensors in the process industry[J]. Computers & Chemical Engineering, 2009, 33: 795-814.
2. Souza F A A, Araújo R, Mendes J. Review of soft sensor methods for regression applications[J]. Chemometrics and Intelligent Laboratory Systems, 2016, 152: 69-79.
3. Wang Z X, He Q P, Wang J. Comparison of variable selection methods for PLS-based soft sensor modeling[J]. Journal of Process Control, 2015, 26: 56-72.
4. Ji C, Sun W. A review on data-driven process monitoring methods: Characterization and mining of industrial data[J]. Processes, 2022, 10(2): 335.
5. Pearson K. VII. Mathematical contributions to the theory of evolution. — III. Regression, heredity, and panmixia[J]. Philosophical Transactions of the Royal Society A, 1896(187): 253-318.
6. Sun K, Huang S H, Wong D S H, et al. Design and application of a variable selection method for multilayer perceptron neural network with LASSO[J]. IEEE Transactions on Neural Networks and Learning Systems, 2017, 28(6): 1386-1396.
7. Vergara J R, Estévez P A. A review of feature selection methods based on mutual information[J]. Neural Computing & Applications, 2014, 24: 175-186.
8. Ji C, Ma F, Wang J, et al. Profitability related industrial-scale batch processes monitoring via deep learning based soft sensor development[J]. Computers & Chemical Engineering, 2023, 170: 108125.
9. Estevez P A, Tesmer M, Perez C A, et al. Normalized Mutual Information Feature Selection[J]. IEEE Transactions on Neural Networks and Learning Systems, 2009, 20(2): 189-201.
10. Reshef D N, Reshef Y A, Finucane H K, et al. Detecting novel associations in large data sets[J]. Science, 2011, 334(6062): 1518-1524.
11. Freeman C, Kulić D, Basir O. An evaluation of classifier-specific filter measure performance for feature selection[J]. Pattern Recognition, 2015, 48(5): 1812-1826.
12. Xiao L, Wang C, Dong Y, et al. A novel sub-models selection algorithm based on max-relevance and min-redundancy neighborhood mutual information[J]. Information Sciences, 2019, 486: 310-339.
13. Yin K, Zhai J, Xie A, et al. Feature selection using max dynamic relevancy and min redundancy[J]. Pattern Analysis and Applications, 2023, 26(2): 631-643.
14. Bennasar M, Hicks Y, Setchi R. Feature selection using joint mutual information maximisation[J]. Expert Systems with Applications, 2015, 42(22): 8520-8532.
15. Ji C, Ma F, Wan J, et al. A Conditional Entropy Based Feature Selection for Soft Sensor Development in Chemical Processes[J]. Chemical Engineering Transactions, 2023, 103: 61-66.
16. Che J, Yang Y, Li L, et al. Maximum relevance minimum common redundancy feature selection for nonlinear data[J]. Information Sciences, 2017, 409: 68-86.
17. Shannon C E. A mathematical theory of communication[J]. Bell Labs Technical Journal, 1948, 27(3): 379-423.
18. Kraskov A, Stögbauer H, Grassberger P. Estimating mutual information[J]. Physical Review E—Statistical, Nonlinear, and Soft Matter Physics, 2004, 69(6): 066138.
19. Moon Y I, Rajagopalan B, Lall U. Estimation of mutual information using kernel density estimators[J]. Physical Review E, 1995, 52(3): 2318.

© 2025 by the authors. Licensed to PSEcommunity.org and PSE Press. This is an open access article under the creative commons CC-BY-SA licensing terms. Credit must be given to creator and adaptations must be shared under the same terms. See https://creativecommons.org/licenses/by-sa/4.0/



Systems & Control Transactions

**Research Article - Peer Reviewed Conference Proceeding**
ESCAPE 35 - European Symposium on Computer Aided Process Engineering
Ghent, Belgium. 6-9 July 2025
Jan F.M. Van Impe, Grégoire Léonard, Satyajeet S. Bhonsale,
Monika E. Polańska, Filip Logist (Eds.)

PSE PRESS

# Streamlining Catalyst Development through Machine Learning: Insights from Heterogeneous Catalysis and Photocatalysis

**Parisa Shafiee[a], Mitra Jafari[a], Julia Schowarte[a], Bogdan Dorneanu[a], Harvey Arellano-Garcia[a,*]**

[a] FG Prozess- und Anlagentechnik, Brandenburgische Technische Universität Cottbus-Senftenberg, Cottbus, Germany
* Corresponding Author: arellano@b-tu.de.

## ABSTRACT

Catalysis design and reaction condition optimization are considered the heart of many chemical and petrochemical processes and industries; however, there are still significant challenges in these fields. Advances in machine learning (ML) have provided researchers with new tools to address some of these obstacles, offering the ability to predict catalyst behaviour, optimal reaction conditions, and product distributions without the need for extensive laboratory experimentation. In this contribution, the potential applications of ML in heterogeneous catalysis and photocatalysis are explored by analysing datasets from different reactions, including Fischer-Tropsch synthesis and photocatalytic pollutant degradation. First, datasets were collected from literature. After cleaning and preparing the datasets, they were employed to train and test several models. The best model for each dataset was selected and applied for optimization.

**Keywords**: Catalysis, Machine Learning, Modelling, Optimization, Alternative Fuels, Environment, Fischer-Tropsch Synthesis, Photocatalysis

## INTRODUCTION

Developing catalysts (heterogeneous and photocatalysts) and selecting the optimum reaction conditions are considerable challenges. In this process, complex variables need to be addressed, including active material selection, catalyst structure design, or operating parameter optimization [1]. All these tasks require considerable effort in lab and numerous reaction tests, which are not only energy- and time-intensive but also costly. Recent advances in Machine Learning (ML) provide scientists with powerful tools to model and predict the behavior of catalysts, optimize reaction conditions, and forecast product distributions [2]. These methods leverage large datasets and employ sophisticated algorithms, significantly reducing the energy, time, and money spent in laboratory research. By using ML to model and optimize the processes, researchers can now identify patterns, simulate complex reactions, and generate previously unattainable insights. ML enables correlation analysis to uncover relationships between various parameters and catalyst performance. Predictive models, trained on existing data, can forecast the effectiveness of new materials. Additionally, ML provides data-driven insights that offer valuable guidance for catalyst design and optimization [3].

This work introduces a comprehensive framework unifying various aspects of catalyst development and optimization, addressing a significant gap in existing research. The framework's novelty lies in its holistic approach, integrating multiple aspects of catalytic processes, including catalyst formulation, structure, preparation, activation, and operating conditions. Unlike previous studies focusing on individual aspects, this integrated approach provides a more complete understanding of catalyst behavior across diverse catalytic processes: environmental pollutant degradation using photocatalysts, and Fischer-Tropsch Synthesis (FTS) for liquid fuel and jet fuel production, respectively, using heterogeneous catalysts.

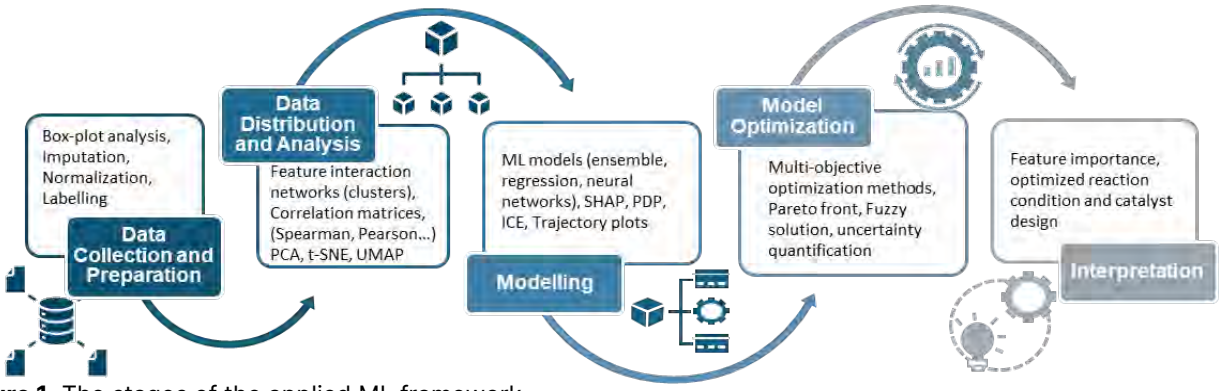



**Figure 1.** The stages of the applied ML framework.

## METHODOLOGY

First the data is collected from literature. The datasets are categorized based on different features like catalyst formulation, catalyst characterization, activation, and reaction conditions with the goal of predicting catalyst performance. To prepare the datasets, the data is cleaned, labelled, imputed and normalized. Techniques such as Spearman correlation matrices, dendrograms, pair plots, and dimensionality reduction methods are applied to uncover relationships between descriptors and catalyst performance. The data is then employed to train and test several models. Performance metrics such as root mean square error (RMSE), mean absolute percentage error (MAPE), Akaike Information Criterion (AIC), and coefficient of determination ($R^2$) are used to assess model accuracy. Given the non-linear nature of the models, RMSE was selected as the primary evaluation metric for model selection, while R2 is reported as a complementary measure to provide additional context. After selecting the best model, it is used for optimization to find the optimum point with the highest catalysis performance. Figure 1 illustrates this framework, and the subsequent subsections provide a more detailed description of each step in the process.

### Data Collection and Preparation

The three datasets used in this work are for perfluorooctanoic acid (PFOA) degradation with photocatalysis, FTS for liquid fuel production, and FTS for jet fuel production.

**Table 1.** Number of descriptors and target responses in the different datasets of three case studies.

| Reaction | Descriptors | Target Responses |
|---|---|---|
| PFOA photocatalysis | 9 | 2 |
| FTS for liquid fuel | 26 | 2 |
| FTS for jet fuel | 21 | 2 |

The data is manually extracted from literature. The derived data is classified as descriptors and target responses as mentioned in Table 1. These descriptors are different parameters describing the catalyst formulation, catalyst characterization, catalyst activation, and reaction conditions.

The data is prepared using standard methods. These steps include removing outliers with box-plot analysis, labeling through label encoding or one hot labeling, imputing missing data using methods such as Soft Impute, k-nearest neighbours (KNN), etc., and normalizing to improve data quality.

### Data Distribution and Analysis

Cluster analysis and Spearman correlation analysis were also used to examine the relationship between features.

In the datasets with a large number of datapoints, principal component analysis (PCA) was used to reduce the dimension of the experimental datasets. PCA transforms high-dimensional data into a lower-dimensional space, preserving key patterns and relationships by identifying directions (principal components) that capture maximum variance in the data.

### Modelling

Several ML algorithms (models) including Random Forest, CatBoost, Boosted Gradient, Artificial Neural Networks (ANN) etc. are used to predict the target responses. The performance of the models is evaluated and compared using the performance metrics mentioned above. Important features were identified using Shapley Additive Explanations (SHAP) and Partial Dependency Diagram (PDP) techniques.

### Optimization

The Non-dominated Sorting Genetic Algorithm II (NSGA-II) was used for multi-objective optimization to find the optimum conversion and selectivity as target responses [4]. This method helps to identify the optimum points on the Pareto front. Subsequently, a Fuzzy-based

method selected a balanced solution using membership functions with parameters [0.2, 0.5, 0.8] from normalized data. Here, 0.2 sets the minimum acceptable value, 0.5 the ideal target, and 0.8 the upper limit. The solution maximizing the minimum satisfaction score ensured both objectives remained strong without trade-offs, aligning with multi-criteria decision-making [5]. The most important descriptors for the best solution are determined and compared with the experimental data.

## RESULTS AND DISCUSSION

### Photocatalysis of PFOA

The database for the case study of photocatalytical PFOA degradation consists of 127 datapoints, with two target responses and nine descriptors. One-hot labeling is used to convert categorical data to numerical data. For dealing with missing data, five different imputation methods were tested like Stochastic Within-Zone (SWZ), Robust Principal Component Analysis (RPCA), smallest squares, Automatic JMP imputing and mean Python imputing, as well as the removal of these points. Before running the model, the data is also normalized.

The data distribution shows mostly similar patterns, yet some unique distributions result from the different imputation methods. A prominent example (pH) is shown in Figure 2. Further differences include: The smallest squares method leads to additional peaks in higher regions for pH and degradation in comparison to SWZ and RPCA. Automatic JMP and mean Python distributions are highly similar, with a prominent brooding of pH- and defluorination-distributions. The mean Python method shows a distribution for light type and degradation as similar to the method, where all missing values were removed. Yet, this last method shows the broadest distribution for all descriptors and target responses. Thus, it can be concluded that the data distribution is biased.

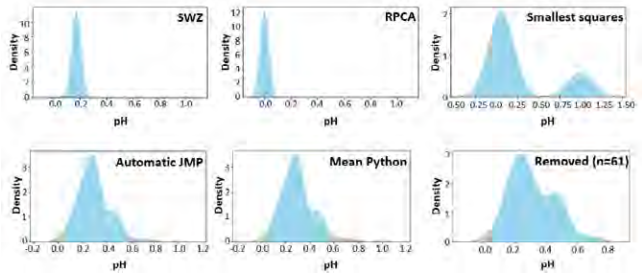



**Figure 2.** Data distribution with different imputation methods.

Pearson correlation analysis reveals that the imputation method plays an important role in the linearity, as this correlation specifically measures linear relationships between two variables. It can be noticed that there is very little linear correlation in this photocatalytic dataset. In general, the correlation is more positively linear for the defluorination (here correlation to treatment time and pH), which might be attributed to a higher number of missing values. For degradation, the correlation is mostly negatively linear, especially for the variables such as catalyst amount, initial PFOA concentration and in some cases pH.

Spearman correlation analysis is conducted as well. Compared to Pearson, Spearman reveals fewer negative correlations overall, indicating that the data has significant non-linear relationships not captured by the linear correlation. Furthermore, for all imputation methods (beside of missing value removal) a much stronger negative correlation between degradation and initial PFOA concentration is depicted. This is found for the defluorination response as well in Automatic JMP, mean Python and removal methods. For SWZ, RPCA and smallest square imputations no positive correlations, as in the case with Pearson, can be found and treatment time shows a highly negative correlation with defluorination.

The model screening runs 5 times and model optimization is conducted using 10 loops of hyperparameter optimization (GridSearch). Based on high $R^2$ and low RMSE values. the best result for predicting the degradation response is achieved with the KNN model (SWZ-imputation) and partly with the Neuronal Boosted model (removal of missing data). The defluorination response is captured well with the Neuronal Boosted model (SWZ, RPCA and Automatic JMP imputations).

Best results for the response degradation are obtained with SWZ imputation and the KNN model ($R^2$=0.843, RMSE=0.004), while the defluorination response is captured well by the SWZ imputation and Neuronal Boosted model ($R^2$=0.987, RMSE=0.021), as well as by Automatic JMP imputation with the Neuronal Boosted model ($R^2$=0.998, RMSE=0.009). For comparison, with a simple linear regression model, an average $R^2$ of 0.8 for the defluorination response can be reached (RMSE and MAE<1, AIC=-2 to 45).

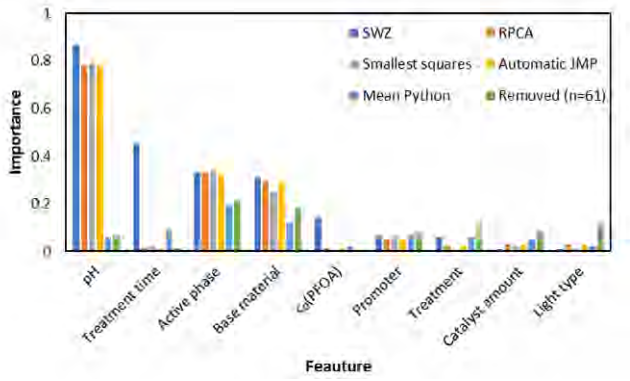



**Figure 3.** Feature importance with linear regression model for defluorination response with different imputation methods.

The importance of each feature on the defluorination response for the linear regression model is shown in Figure 3, where slight changes can be seen with each imputation method. Main features that influence PFOA defluorination are the pH and the nature of the catalyst (active phase, base material). Linked to the latter is the light type. Interestingly, treatment time plays a minor role in most imputation methods, which highlights the biased data (only small treatment times reported). Beside of the latter (due to bias), the results match other publications on this topic regarding photocatalysis of PFOA [6]. A more theoretical and compound-based approach for the defluorination of Per- and Polyfluoroalkyl Substances (PFAS) has been reported by Raza et al. [7].

## FTS for Liquid Fuel Production

A dataset of 96 datapoints is used to model and optimize liquid fuel production using FTS. This dataset includes 26 features consisting of catalyst formulation, characteristics, and operational conditions. As for the targets, CO conversion and $C_{5+}$ selectivity are chosen to represent the liquid fuel production.

To prepare the dataset, after removing the outliers, label encoding is used to change the categorical data to numerical data. Similarly to the previous case study, different methods are used for imputation of the missing data; among them, automated imputation in JMP has shown the best performance and is selected for this dataset. Then data is normalized for the effect of features to be comparable.

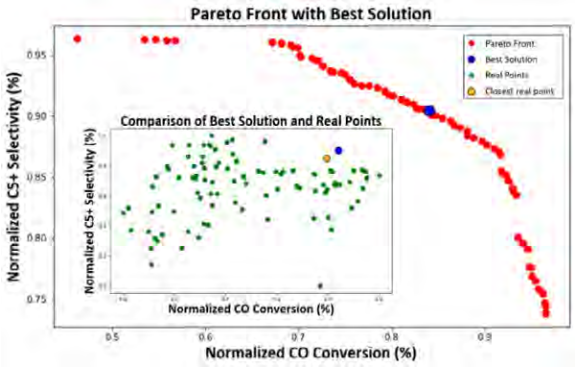



**Figure 4.** Pareto front with Fuzzy-based solution for normalized CO conversion and $C_{5+}$ selectivity.

To find the best model for describing the behaviour of the dataset, 5 different models are tested and compared, including: XGBoost, LightGBM, Gradient Boosting, CatBoost, and Random Forest. To compare the performance of these models, different criteria, described in the previous sections are used. Among the models, CatBoost had the best performance with $R^2$, MSE, RMSE, and MAE equal to 0.95, 0.003, 0.057, 0.041, respectively for CO conversion and 0.88, 0.004, 0.063, 0.035 for $C_{5+}$ selectivity.

The CatBoost model is then used for optimization. The aim was to optimize the CO conversion and $C_{5+}$ selectivity. The Pareto front with the optimal Fuzzy solution, as well as the comparison of the best solution and the real data, are depicted in Figure 4.

Since the data was normalized in the preparation step, to recover the real data, de-normalization is carried out. The best Fuzzy solutions for CO conversion and $C_{5+}$ selectivity are 76.24 % and 81.89 %, respectively. The best Fuzzy solution is also compared with the experimental values and the closest point is also detected [8]. The values for these two points are summarised in Table 2.

**Table 2.** Descriptor values for the best optimum point and closest real point.

| Descriptor | Best Solution | Closest Real Point |
|---|---|---|
| Support | ZSM-5 | ZSM-5 |
| Active metal | Cobalt | Iron |
| Active metal loading (%) | 16.66 | 18.00 |
| $H_2$/CO ratio | 2 | 2 |
| Zeolite $SiO_2/Al_2O_3$ ratio | 19.31 | 280.00 |
| Calcination temperature (°C) | 371.55 | 450.00 |
| Calcination time (h) | 3.10 | 8.00 |
| Pore volume ($cm^3/g$) | 0.58 | 0.17 |
| Meso-pore volume ($cm^3/g$) | 0.16 | 0.13 |
| Reduction temperature (°C) | 402.66 | 420.00 |
| Reduction time (h) | 1.84 | 10.00 |
| Reaction temperature (°C) | 241.38 | 280.00 |
| Reaction pressure (bar) | 19.91 | 19.00 |
| Time on stream (h) | 67.78 | 34.46 |
| Loading of catalyst (g) | 1.34 | 0.50 |
| $C_{5+}$ selectivity (%) | 81.89 | 78.20 |
| CO conversion (%) | 76.24 | 72.40 |

## FTS for Jet Fuel Production

To develop a ML method for modelling and optimizing jet fuel production through FTS, a dataset of 41 datapoints from 10 recent research papers was collected. The data was manually extracted and included 21 features related to catalyst formulation and operating conditions. The model targets included $C_8$-$C_{16}$ selectivity and CO conversion rate.

The data was prepared by removing outliers using box-plot analysis, imputing missing data with methods such as Soft Impute and KNN, and normalization to improve data quality. Cluster analysis and correlation matrix methods were also used to examine the relationship between features.

Several ML algorithms including Random Forest, CatBoost, Boosted Gradient, and ANN were evaluated to predict $C_8$-$C_{16}$ selectivity and CO conversion. The CatBoost model showed the best performance using metrics such as $R^2$, RMSE, and MAPE. Important features were

identified using SHAP and PDP techniques.

These analyses showed that the $H_2$/CO ratio, the reaction temperature, and the catalyst specific surface area had a significant impact on the selectivity and conversion rate. For example, higher reduction temperature and moderate active metal loading led to improved catalyst performance.

The NSGA-II algorithm was used to simultaneously optimize selectivity and conversion. This method helped to identify the optimal points on the Pareto front. Then, the optimal parameters including active metal loading, reduction temperature, reaction temperature, and $H_2$/CO ratio were determined. The results were evaluated using statistical indices and comparison with experimental data.

**Table 3.** Value of the features for best solution point

| Parameter | Best solution | Closest Real Point |
|---|---|---|
| Active metal | Iron | Iron |
| Promoter | Yes | Yes |
| Active metal loading (%) | 50.5 | 100.0 |
| Promoter loading (%) | 5 | 6 |
| Average pore size of catalyst (nm) | 4.25 | 4.24 |
| Specific surface area of catalyst ($m^2$/g) | 283.8 | 14.6 |
| Specific surface area of support ($m^2$/g) | 504.0 | 458.4 |
| Acidity of support (μmol/g) | 1040 | 465.8 |
| Active metal particle size (nm) | 12.30 | 11.44 |
| Calcination time (h) | 4 | 4 |
| Calcination temperature (°C) | 450 | 450 |
| Reduction atmosphere | $H_2$/CO | $H_2$/CO |
| Reduction time (h) | 6.5 | 10.0 |
| Reduction temperature (°C) | 407.5 | 350.0 |
| Reaction temperature (°C) | 265 | 250 |
| Reaction pressure (bar) | 39.45 | 20.00 |
| Loading of catalyst (g) | 1.6 | 0.5 |
| $H_2$/CO ratio | 1.25 | 2.00 |
| Time on stream (h) | 99 | 60 |
| $C_8$-$C_{16}$ selectivity (%) | 36.86 | 30.00 |
| CO conversion (%) | 49.32 | 50.00 |

Statistical analyses showed that properties such as active metal loading and specific surface area of the catalyst had a significant effect on catalyst performance. For example, increasing the metal loading by about 15 % increased the selectivity, but loading beyond this value led to a decrease in performance. In addition, properties such as support acidity and surface area played a key role in improving the $C_8$-$C_{16}$ selectivity.

The CatBoost model showed the best performance with an accuracy of $R^2$=0.82 for CO conversion and $R^2$=0.84 for $C_8$-$C_{16}$ selectivity. This model had higher accuracy than other methods such as Neural Networks and Random Forests and was able to better analyze the complex relationships between properties and responses. Also, the use of model interpretability techniques such as SHAP helped to better understand the effect of the properties.

The $H_2$/CO ratio had a nonlinear effect on selectivity. Increasing this ratio to 2 improved the $C_8$-$C_{16}$ selectivity, but higher values produced lighter products. Also, the reaction temperature between 245 °C and 260 °C provided the optimal conditions for jet fuel production.

It was found that the specific surface area of the catalyst and the support acidity played an important role in increasing the selectivity. Catalysts with mesoporous structure and moderate acidity performed best. These features helped to improve the chain reactions and reduce light by-products.

Additionally, the Fuzzy satisfaction levels for solutions obtained using a multi-objective genetic algorithm were evaluated. The optimized parameters achieved a MSE of 0.015 and an $R^2$ of 0.70, indicating high accuracy. The best compromise solution offered 36.48 % $C_8$-$C_{16}$ selectivity, 48.95 % CO conversion, and a Fuzzy satisfaction level of 0.99, suggesting a well-balanced trade-off. Further refinement used the minimize function from the SciPy optimization library to match target values of 36.48 % $C_8$-$C_{16}$ selectivity and 48.95 % CO conversion. The optimized input features, shown in Table 3, closely matched these targets with predicted values of 36.86 % and 49.32 %, respectively. This accuracy validates the robustness of the models and the optimization process. The optimal parameters were identified as a reduction temperature of 407.5 °C, a reaction temperature of 265 °C, a reaction pressure of 39.45 bar, and a $H_2$/CO ratio of 1.25. These values provided a balance between selectivity and conversion. The results obtained were in good agreement with the experimental data and confirmed the effectiveness of the applied framework.

## CONCLUSIONS

In this work, an applied ML framework is used for modeling and optimizing different datasets on photo-catalysis and heterogeneous catalysis.

For the photocatalytic degradation of PFOA the importance of data quality is highlighted, as biased data influenced the efficiency of the modelling procedure. Reliable (in-house generated) experimental data for photocatalysis is recommended for ML processes. Regardless of this, the influence of different imputation methods is presented, which can be considered in future applications. Additionally, the resulting feature importance for defluorination is in accordance with recent literature.

Moreover, the applied ML framework provides a

powerful tool for the rational design of FTS catalysts and operating conditions to maximize liquid and jet fuel production, respectively. For liquid fuels, zeolite $SiO_2/Al_2O_3$ ratio, pore volume, and reaction temperature and pressure are identified as key parameters. In the case of jet fuel production, $H_2/CO$ ratio, temperature, and surface area are key to jet fuel selectivity. Multi-objective optimization was used to identify optimal catalysts and FTS operating conditions.

In the case of liquid fuel production, the CatBoost model is the best model and can predict the dataset satisfactorily. After using this model for optimization, the best solution for maximizing the CO conversion and $C_{5+}$ selectivity are also obtained.

The ML framework not only predicts outcomes but also guides experimental efforts by identifying key parameters for catalyst optimization. It reconciles conflicting trends in literature and contributes to the FTS mechanism debate. Moreover, for experimentalists, it offers a practical tool for understanding performance limits, focusing on achievable improvements, and predicting optimal parameters without extensive trial-and-error.

For the next step, the identified optimal catalysts with the best optimized solutions will be tested experimentally to check their performance. This can be used both for model verification/validation and for actual catalysis optimization. For further work, the suggested framework will also be used for datasets of other catalytic reactions, expanding its applicability and ensuring robustness in diverse reaction conditions.

## ACKNOWLEDGEMENTS

This project has been funded as part of the PyroBioFuel project within the Long-Term Joint European Union – African Union Research and Innovation Partnership on Renewable Energy (LEAP-RE), co-financed by the Horizon 2020 programme of the European Union and the German Federal Ministry of Education and Research (Bundesministerium für Bildung und Forschung – BMBF), under grant agreement number 03SF0678 and MyReacAvFu project, financed by the German Federal Ministry of Economic Affairs and Climate Action (Bundesministerium für Wirtschaft und Klimaschutz – BMWK), under grant agreement number 03EI5447A.

## REFERENCES

1. Choung S., Park W., Moon J., Han JW. Rise of Machine Learning Potentials in Heterogeneous Catalysis: Developments, Applications, and Prospects. *Chem. Eng. J* 2:152757 (2024) https://doi.org/10.1016/j.cej.2024.152757
2. Benavides-Hernández J., Dumeignil F. From Characterization to Discovery: Artificial Intelligence, Machine Learning and High-Throughput Experiments for Heterogeneous Catalyst Design. *ACS Catal.* 14:11749-79 (2024) https://doi.org/10.1021/acscatal.3c06293
3. Shafiee P., Dorneanu B., Arellano-Garcia H. Improving Catalysts and Operating Conditions Using Machine Learning in Fischer-Tropsch Synthesis of Jet Fuels ($C_8$-$C_{16}$). *Chem Eng J Adv* 9:100702 (2025) https://doi.org/10.1016/j.ceja.2024.100702
4. Deb, K., Pratap, A., Agarwal, S., Meyarivan, T. A fast and elitist multiobjective genetic algorithm: NSGA-II. IEEE Trans. Evol. Comput 6(2), 182–197 (2002) https://doi.org/10.1109/4235.996017
5. Sánchez-Orgaz, S., Pedemonte, M., Ezzatti, P., Curto-Risso, P. L., Medina, A., & Hernández, A. C. Multi-objective optimization of a multi-step solar-driven Brayton plant. Energy Convers. Manage., 99, 346-358(2015) https://doi.org/10.1016/j.enconman.2015.04.077
6. Navidpour AH., Hosseinzadeha A., Huang Z., Li D., Zhou JL. Application of Machine Learning Algorithms in Predicting the Photocatalytic Degradation of Perfluorooctanoic Acid. *Catal Rev* 66:687-712 (2022) https://doi.org/10.1080/01614940.2022.2082650
7. Raza A., Bardhan S., Xu L., Yamijala SS., Lian C., Kwon H., Wong BM. A Machine Learning Approach for Predicting Defluorination of Per-and Polyfluoroalkyl Substances (PFAS) for Their Efficient Treatment and Removal. *Environ Sci Technol Lett* 6:624-9 (2019) https://doi.org/10.1021/acs.estlett.9b00476
8. Baranak M., Gürünlü B., Sarıoğlan A., Ataç Ö., Atakül H., Low Acidity ZSM-5 Supported Iron Catalysts for Fischer–Tropsch Synthesis. *Catal today* 207:57-64 (2013) https://doi.org/10.1016/j.cattod.2012.04.013

© 2025 by the authors. Licensed to PSEcommunity.org and PSE Press. This is an open access article under the creative commons CC-BY-SA licensing terms. Credit must be given to creator and adaptations must be shared under the same terms. See https://creativecommons.org/licenses/by-sa/4.0/



Systems & Control Transactions

**Research Article - Peer Reviewed Conference Proceeding**
ESCAPE 35 - European Symposium on Computer Aided Process Engineering
Ghent, Belgium. 6-9 July 2025
Jan F.M. Van Impe, Grégoire Léonard, Satyajeet S. Bhonsale,
Monika E. Polańska, Filip Logist (Eds.)

PSE PRESS

# A Novel Approach to Gradient Evaluation and Efficient Deep Learning: A Hybrid Method

**Bogdan Dorneanu[a], Vasileios K. Mappas[a], and Harvey Arellano-Garcia[a]***

[a] Brandenburgische Technische Universitat Cottbus-Senftenberg, FG Prozess- und Anlagentechnik, Cottbus, Germany
* Corresponding Author: arellano@b-tu.de.

## ABSTRACT

Deep learning faces significant challenges in efficiently training large-scale models. These issues are closely linked, as efficient training often depends on precise and computationally feasible gradient calculations. This work introduces innovative methodologies to improve deep learning network (DLN) training in complex systems. A novel approach to DLN training is proposed by adapting the block coordinate descent (BCD) method, which optimizes individual layers sequentially. This is combined with traditional batch-based training to create a hybrid method that harnesses the strengths of both techniques. Additionally, the study explores Iterated Control Random Search (ICRS) for initializing parameters and applies quasi-Newton methods like L-BFGS with restricted iterations to enhance optimization. By tackling DLN training efficiency, this contribution offers a comprehensive framework to address key challenges in modern machine learning. The proposed methods improve scalability and effectiveness, especially for handling complex real-world problems. Examples from Process Systems Engineering illustrate how these advancements can directly enhance the training of large-scale systems.

**Keywords**: Artificial Intelligence, Machine Learning, Numerical Methods.

## INTRODUCTION

Deep learning, a specialized subset of machine learning, utilizes artificial neural networks with multiple layers to model and learn intricate patterns from large datasets. Unlike traditional machine learning, which often relies on manually engineered features, deep learning autonomously extracts hierarchical representations of data through its layered architecture. This capability enables it to address highly complex problems in domains such as image and speech recognition, natural language processing, drug discovery, and genomics [1]. By learning directly from raw data, deep learning reduces the need for domain-specific feature engineering, offering remarkable flexibility and scalability.

Despite this transformative potential, deep learning faces several challenges. One of the primary obstacles is computational complexity. Training deep neural networks (DNNs) requires substantial resources, including high-performance GPUs and significant memory capacity for data storage. These requirements make deep learning both resource- and cost-intensive. Additionally, deep models demand large amounts of data to achieve high accuracy, posing a limitation in fields where data collection is sparse or expensive.

Optimization of deep learning models presents another significant challenge. Training involves tuning numerous hyperparameters (i.e., learning rates, layer configurations), which is both time-consuming and computationally demanding. Various optimization techniques, including stochastic gradient descent (SGD) or ADAM have been developed, to improve training efficiency and convergence. However, the process remains difficult due to the complexity of deep architectures.

Despite these challenges, significant advancements continue to improve the robustness and efficiency of deep learning systems. The training of deep learning networks (DLNs) involves optimizing a loss function to minimize the difference between model prediction and actual targets. Backpropagation, introduced by Rumelhart et al. [2], remains the foundational algorithm for training DLNs, efficiently calculating gradients using the chain rule. However, backpropagation faces challenges such as vanishing gradients in deep networks, which slow or halt

learning [3]. Techniques like batch training and optimization methods such as stochastic gradient descent (SGD) or ADAM have been developed to address these issues, improving convergence and computational efficiency. Recent advances include block coordinate descent (BCD) [4], which updates parameters layer by layer to reduce computational overhead, and its application in binary neural networks for resource-constrained devices.

While the algorithmic logic of such methods is implementation-agnostic, the practical deployment of deep learning frameworks can benefit significantly from modern software engineering practices. Object-oriented programming (OOP) facilitates modular and reusable code structures, which are particularly valuable for building and scaling complex deep learning systems. Frameworks like TensorFlow or PyTorch adopt OOP principles to encapsulate components such as layers, optimizers, and loss functions, facilitating scalability and distributed training [5]. These innovations collectively address the growing complexity of DLNs while improving training efficiency and adaptability across diverse hardware environments. The proposed framework, while using algorithmic innovations of BCD and ICRS, leverages the advantages of OOP to create a flexible and extensible platform. The following sections will detail the algorithmic aspects of the approach, and where relevant, highlight how OOP principles contribute to its practical implementation.

## METHODOLOGY

This contribution introduces a novel approach to deep learning optimization by addressing key limitations in traditional methods, particularly in computational efficiency, scalability, and flexibility. Unlike conventional techniques such as SGD and ADAM, which optimize all parameters simultaneously and often struggle with the complexity of deep networks, the proposed framework illustrated in Figure 1 leverages a Block Coordinate Descent (BCD)-based strategy.

This method dynamically identifies and optimizes the most influential layers using sensitivity measures [3], ensuring computational resources are allocated effectively. The modularity enabled by the proposed OOP design allows to easily swap and configure different BCD variants, such as those using different sensitivity measures or layer selection strategies.

To further enhance global exploration and avoid local minima, the framework integrates Iterated Control Random Search (ICRS) [6], a global optimization technique that efficiently explores non-convex parameter spaces. By combining ICRS for initial exploration with BCD for layer-specific refinement, the framework achieves more robust convergence and improved training stability for complex neural architectures. Additionally, the framework incorporates object-oriented design to overcome the modularity and adaptability of existing deep learning tools. The ICRS optimizer is implemented as a separate class that can be easily integrated with other components of the framework due to the well-defined interfaces of the OOP design. Similarly, different optimization algorithms (Table 1) are encapsulated within dedicated classes, adhering to a common interface, facilitating easy swapping and comparison of optimization strategies. The framework is implemented in Python 3.11 on an AMD Ryzen 9 7950X 16-core processor with 56GB RAM.

It is important to clarify that the algorithm depicted in Figure 1 represents the computational flow of the proposed hybrid training approach and is, in principle, independent of any specific programming paradigm. The core logic of BCD and ICRS could be implemented in various ways. However, an OOP approach is chosen to enhance code organisation, reusability and maintainability. Specifically, the framework is structured around classes representing different layers, optimizers and training strategies. This facilitates easy swapping and modification of individual components without affecting the rest of the system.

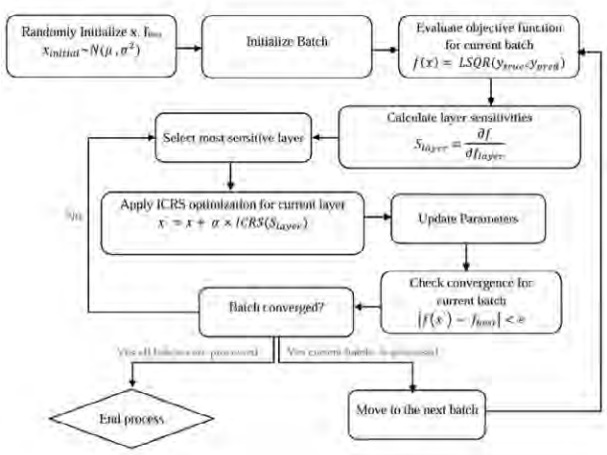



**Figure 1.** OOP deep learning network training algorithm

**Table 1:** Optimization methods

| Optimizer | Type |
|---|---|
| ADAM | Stochastic gradient-based |
| L-BFGS | Quasi-Newton gradient-based |
| Barzilai-Borwein | Gradient-based |
| ICRS | Derivative free |

## CASE STUDIES

To evaluate the performance of the proposed deep learning framework, two datasets from the UCI Machine Learning Repository [7] are utilized: the combined cycle power plant (CCPP) dataset, and the steel industry energy consumption (SIEC). The CCPP dataset consists of

9,568 samples with four features and one target variable. This dataset captures data from a CCPP where electricity is generated through gas and steam turbines working in tandem, making it a well-suited benchmark for regression tasks in industrial energy systems.

The SIEC dataset contains 35,040 samples with fifteen features and one target variable. The data is collected from a smart small-scale steel industry in South Korea at 15-minute intervals over a year, providing a high-resolution temporal dataset suitable for time-series forecasting and energy efficiency analysis.

For the CCPP dataset, a fully connected deep learning network was implemented, with an input layer of four neurons (one per feature), followed by hidden layers with varying configurations (i.e., 5,5,5; 10,10,10, etc.) and an output layer consisting of a single neuron for predicting power output. Each layer type (input, hidden, output) is implemented as a separate class, allowing for easy modification of layer parameters and the addition of new layer types without affecting other parts of the network.

To further enhance performance, four distinct block-selection strategies were explored: most sensitive layer selection, random layer selection, forward sequential selection, and ping-pong directional updates. The model's accuracy was assessed using the coefficient of determination ($R^2$), mean squared error (MSE), and mean absolute error (MAE).

For the SIEC dataset, a similar architecture is adopted with fifteen input neurons in the input layer and sensitivity-based block selection is employed to adaptively refine layer-wise updates. Various activation functions, including sigmoid, Tanh, ReLU and Leaky ReLU activation functions, are tested in the hidden layers for both datasets, to evaluate their impact on learning dynamics. Each activation function is implemented as a distinct class. This allows for easy experimentation with new activation functions by simply creating a new class that implements the required interface, without modifying the core network architecture.

Hyperparameters for both datasets were tuned to ensure effective and stable learning and included parameters such as batch subset size set to 1.1 times the number of network parameters and sensitivity tolerance adjusted to 10 times the projected gradient tolerance. The tuning process involved systematically exploring different combinations of learning rates, batch sizes, etc. to optimize model performance.

## RESULTS AND DISCUSSION

### The CCPP dataset

The first stage of evaluating the performance of the proposed DLN training framework looked into the different types of activation functions, while keeping the network architecture and hyperparameters constant.

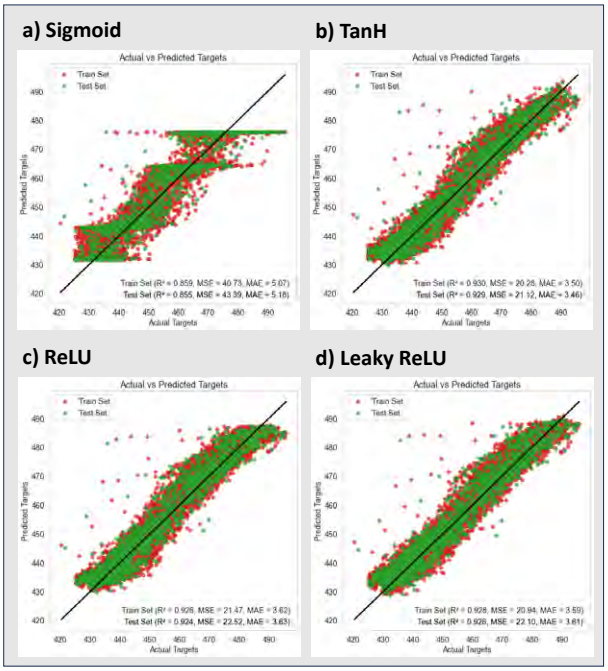



**Figure 2.** Performance comparison for various activation functions

As illustrated in Figure 2, Tanh emerges as the most reliable activation function, achieving high $R^2$ values (0.929 for the test set) and low MSE/MAE across multiple runs. LeakyReLU performs comparably but exhibits slightly higher variability in predictions. ReLU shows good performance but has more scattered test points compared to Tanh and LeakyReLU. Sigmoid performs the worst due to higher residual variance and non-uniform distributions. Visualizations of actual versus predicted values confirm that Tanh and LeakyReLU produce predictions closer to the diagonal line, indicating more accurate fits. Residual plots further demonstrate that Tanh has more uniform residuals with fewer outliers compared to other activation functions.

To ensure robustness, multiple runs are conducted with randomized test sets for Tanh and LeakyReLU. This approach assesses whether these activation functions maintain consistent performance across different data splits. Results confirm that Tanh consistently outperforms LeakyReLU in terms of stability and accuracy, with slightly higher $R^2$ values and lower MSE/MAE on average. For example, in one run, Tanh achieves an $R^2$ of 0.930 on the test set compared to 0.926 for LeakyReLU. Additionally, Tanh exhibits tighter clustering of residuals around zero across runs, suggesting better generalizability. Further, the impact of different block selection strategies on deep learning model performance strategies have been examined.

Figure 3 illustrates the different layers selected by each of the four approaches considered. The findings revealed that the most sensitive layer method consistently

outperformed the other strategies across the performance metrics. This method demonstrated the highest and most consistent $R^2$ values for both training and test sets, while also exhibiting lower and more uniform MSE and MAE values across multiple runs. Notably, the Most Sensitive Layer approach showed the lowest standard deviation in $R^2$, MSE, and MAE, indicating superior robustness and stability compared to the other methods.

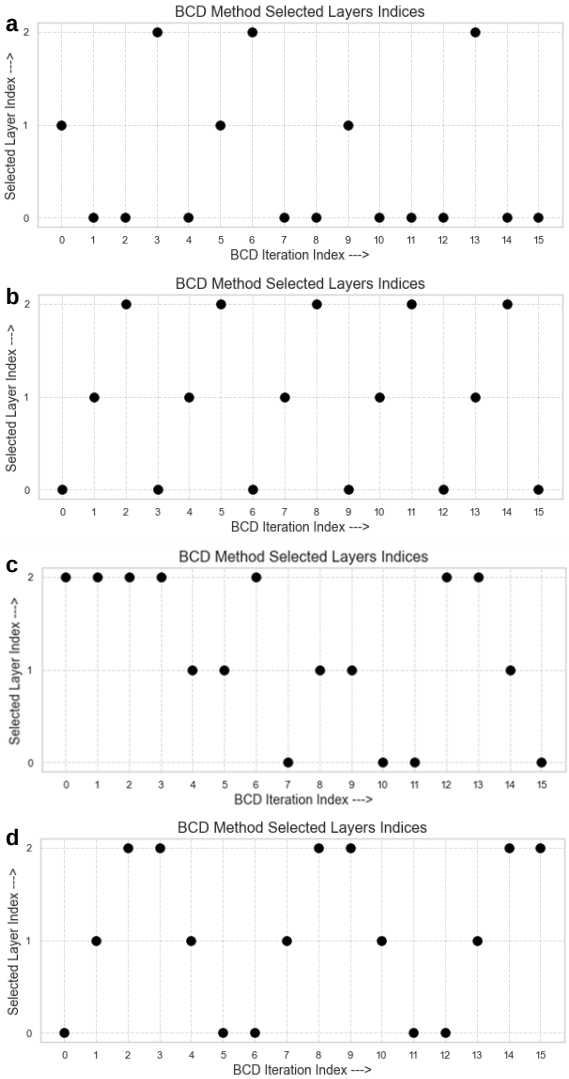



**Figure 3.** Selection of layers for the BCD using: a) most sensitive layers; b) random layer; c) forward sequentially; and d) ping-pong directionality approach.

The results suggest that the most sensitive layer method is better suited for handling variations in handling input data compared to the other methods, making it the most robust and reliable strategy for optimizing the performance of the deep learning model. To investigate the influence of the four optimization algorithms, and their integration with the BCD, a batch shell method is employed to improve model performance. BCD divides the dataset into mini-batches, optimizing each batch separately, while the Batch Shell Method focuses on layer-by-layer optimization, prioritizing the Most Sensitive Layer in the network.

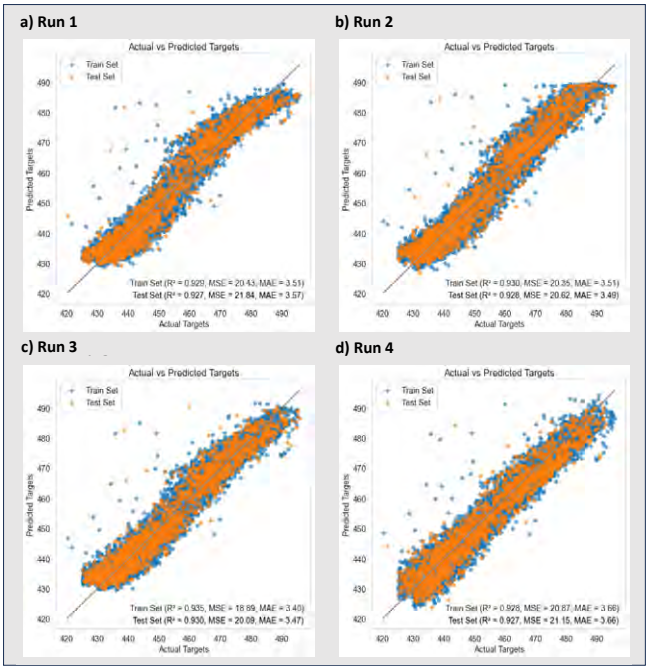



**Figure 4.** Performance comparison for four runs with ICRS for the CCPP dataset

A randomized test set approach is employed to compare ICRS and L-BFGS across five runs, revealing comparable performance but slight differences in consistency (Figure 4). ICRS achieves test $R^2$ values ranging from 0.921 to 0.931, with MSE between 19.79 and 23.27 and MAE between 3.46 and 3.60, while L-BFGS shows test $R^2$ values from 0.914 to 0.931, MSE between 20.01 and 25.53, and MAE between 3.44 and 3.80. Although both optimizers perform well, ICRS demonstrates slightly better stability across runs, particularly in residual distributions.

When combining these optimization methods with BCD and Batch Shell, ADAM provides faster convergence due to its adaptive learning rates but is more sensitive to noisy gradients in smaller datasets or complex models. In contrast, L-BFGS achieves slightly higher accuracy but requires longer training times due to its computational intensity in approximating curvature information. The Batch Shell Method emerges as a promising approach for improving layer-specific optimization by targeting the Most Sensitive Layer, especially when combined with robust optimizers like ICRS or L-BFGS. This integration ensures that the model benefits from both global optimization strategies (e.g., ADAM) and targeted improvements in layer-specific sensitivity (via Batch Shell).

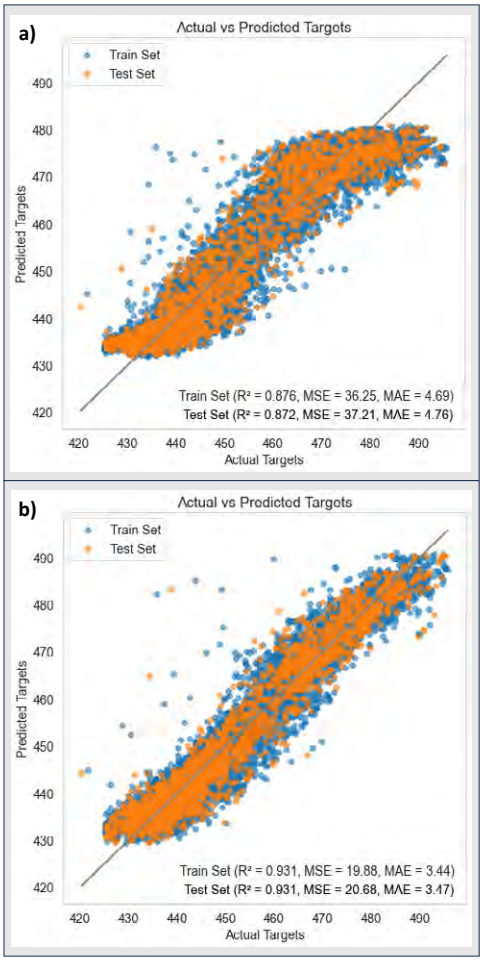



**Figure 5.** Performance comparison for model training using the CCPP dataset: a) without integration of ICRS with BCD; and b) with integration of ICRS with BCD.

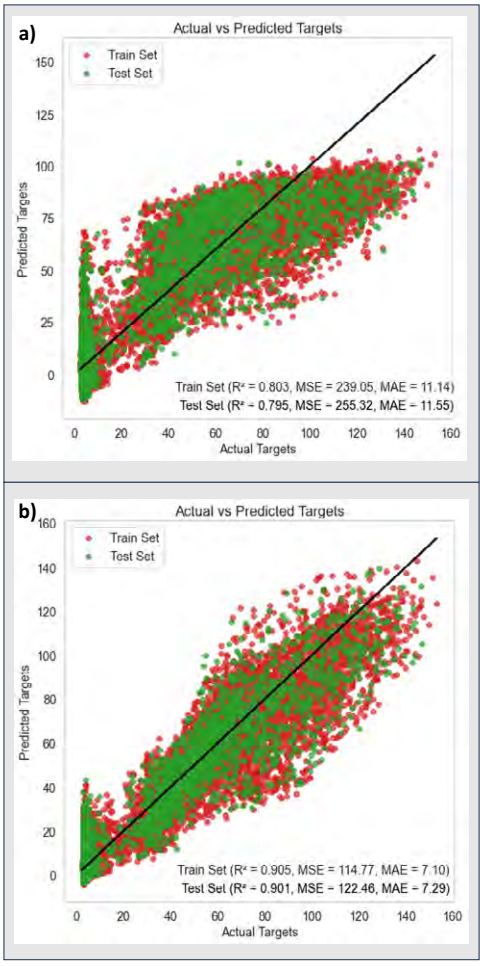



**Figure 6.** Performance comparison for model training using the SIEC dataset: a) without integration of ICRS with BCD; and b) with integration of ICRS with BCD.

Overall, the study highlights that combining advanced optimization techniques with structured learning strategies can significantly enhance deep learning performance for predictive tasks.

To assess the implementation of the BCD as a key optimization strategy, this sequential procedure to optimize model parameters layer by layer has been integrated with the ICRS to enhance the initialization of parameters and improve convergence in high-dimensional spaces. Using the CCPP dataset, the model trained with BCD and ICRS achieved $R^2$ values of 0.931 on both training and test sets, demonstrating superior accuracy compared to the model trained without BCD, which yielded $R^2$ values of 0.876 and 0.872 for training and test sets, respectively.

As shown in Figure 5, the BCD-ICRS combination significantly enhances model convergence and improves training efficiency.

BCD's layer-specific optimization, coupled with the robust parameter initialization provided by ICRS, allows the model to converge to a higher accuracy faster than training without BCD, reducing the computational cost of achieving optimal performance.

## The SIEC dataset

The procedure was subsequently applied to the SIEC dataset. Similarly to the results for the CCPP case study, the most sensitive layer approach showed a more uniform distribution of performance metrics compared to the other methods, both in training and testing phases.

Furthermore, the integration of the ICRS optimizer with the BCD method demonstrated strong performance across various block selection strategies, as illustrated in Figure 6. These results demonstrate that the targeted layer optimization provided by the BCD improves the accuracy and robustness of the SIEC model, showcasing the adaptability of this method to the specific characteristics of this dataset. The performance improvement, while specific to the SIEC data, suggests the potential of

BCD for generalizable application in complex system modelling, as also evidenced by the similar benefits observed with the CCPP dataset (Figure 5), albeit with different data characteristics.

Overall, the object-oriented framework proved effective for both datasets by leveraging modularity and advanced optimization techniques. A core contribution of this work is demonstrating the algorithmic advantages of the proposed hybrid approach. In this prototype implementation, training the SIEC dataset with L-BFGS took ~220 minutes, while BCD-ICRS achieved comparable results in just 35 minutes (6x speedup). For the CCPP dataset, L-BFGS required ~35 minutes, whereas ICRS converged in 7 minutes (5x acceleration). These results validate the method's efficiency gains with substantial empirical improvements. While GPU-accelerated frameworks can train similar models in seconds, the focus is on advancing algorithmic efficiency, which remains critical for large, high-dimensional problems, where solver performance is a key bottleneck [8].

## CONCLUSIONS

This work introduces a novel hybrid deep learning training framework that addresses key challenges in optimizing complex neural networks. While object-oriented programming is prevalent in modern deep learning solutions, our approach distinguishes itself through the novel integration of BCD and ICRS, allowing for modular experimentation with layer-specific optimization strategies. BCD enables sequential, resource-efficient layer optimization, while ICRS provides robust initial parameters, enhancing convergence in high-dimensional spaces. This combination improves scalability and computational efficiency while offering a customizable environment adaptable to diverse architectures and datasets.

The framework's ability to integrate batch-based processing with adaptive optimization methods underscores its ability to handle large-scale DLNNs. Empirical validation on CCPP and SIEC datasets from the UCI Machine Learning Repository demonstrates significant improvements in training efficiency, accuracy, and robustness over conventional methods, setting a new benchmark for industrial applications. Its modularity allows users to easily adjust network configuration and integrate additional layers without extensive programming, making it highly adaptable for various datasets or applications.

Current work focuses on extending this framework to additional datasets and domains to further validate its scalability and generalizability. Future efforts will implement the hybrid approach in CUDA to fully quantify its practical impact on deep learning workloads, particularly for complex models where second-order optimization remains computationally challenging. Additionally, integrating automated hyperparameter tuning and exploring real-time applications in industrial settings will provide valuable insights into optimizing deep learning models for practical use cases.

Moreover, automatic network architecture configuration will enable the framework to dynamically adjust its architecture, such as the number of layers, neurons per layer, and activation functions, based on the characteristics of the dataset and the optimization goals. Exploring real-time architecture reconfiguration during training could provide valuable insights into dynamic optimization strategies, allowing models to adapt to changing data distributions or computational constraints in industrial applications. While this presents significant implementation challenges, advancements in adaptive learning algorithms and hardware acceleration may make such dynamic reconfiguration feasible in future research.

## REFERENCES


1. Manakitsa N et al. A review of machine learning and deep learning for object detection, semantic segmentation, and human action recognition in machine robotic vision. *Technol.* 12:15 (2024)
2. Rumelhart DE et al. Learning representations by backpropagation errors. *Nature* 323:533-536 (1986)
3. Zhang S et al. Hierarchical multi-scale parametric optimization of deep neural networks. *Appl. Intell.* 53:24963-24990 (2023)
4. Liu M et al. An Improved ADAM optimization algorithm combining adaptive coefficients and composite gradients based on randomized block coordinate descent. *Comput. Intell. Neurosci.* 2023:4765891 (2023)
5. Lodhi YR, Shukla SVS. Applying object-oriented principles to machine learning frameworks for improved scalability. *IJSCI* 1:10-17 (2024)
6. Li B et al. ICRS-Filter: A randomized direct search algorithm for constrained nonconvex optimization problems. *CHERD* 106:178-190 (2016)
7. Dua D and Graff C. UCI Machine learning repository. Irvine, CA: University of California, School of Information and Computer Science (2019) Retrieved from: https://archive.ics.uci.edu/ml
8. Byrd RH, Hansen SL, Nocedal J, Singer Y. A stochastic quasi-Newton method for large-scale optimization. *SIAM J Optim.* 2:1008-1031 (2016)



© 2025 by the authors. Licensed to PSEcommunity.org and PSE Press. This is an open access article under the creative commons CC-BY-SA licensing terms. Credit must be given to creator and adaptations must be shared under the same terms. See https://creativecommons.org/licenses/by-sa/4.0/




Systems & Control Transactions

**Research Article - Peer Reviewed Conference Proceeding**
ESCAPE 35 - European Symposium on Computer Aided Process Engineering
Ghent, Belgium. 6-9 July 2025
Jan F.M. Van Impe, Grégoire Léonard, Satyajeet S. Bhonsale,
Monika E. Polańska, Filip Logist (Eds.)

PSE PRESS

# A Comparative Analysis of Industrial MLOps prototype for ML Application Deployment at the edge devices

**Fatima Rani[a,b,*], Fenin Jose[a,b], Lucas Vogt[a,b], and Leonhard Urbas[a,b]**

[a] Faculty of Electrical and Computer Engineering, Chair of Process Control Systems & Process Systems Engineering Group, TUD Dresden University of Technology, 01069 Dresden, Germany

[b] Process-to-Order-Group, TUD Dresden University of Technology, 01069 Dresden, Germany
* Corresponding Author: fatima.rani@tu-dresden.de

## ABSTRACT

This paper introduces a prototype for constructing an edge AI system utilizing the contemporary Machine Learning Operations (MLOps) concept. By employing microcontrollers such as the Raspberry Pi as hardware, our methodology includes data scrubbing and machine learning model deployment on edge devices. Crucially, the MLOps pipeline is fully developed within the ecoKI platform, a research platform for ML/AI applications. In this study, we thoroughly investigate the performance of our ecoKI platform by comparing it with the established Edge Impulse platform. We deployed the ML model with different weight quantization methods, such as FP32 and INT8, to compare accuracy variations and inference speed between these two platforms and quantization strategies on edge devices. In our experiments, we identified that the average accuracy performance of the ecoKI platform is 3.61% better than the edge impulse. Moreover, real-time AI processing on edge devices enables microcontrollers, even those with limited resources, to effectively handle tasks in areas such as predictive maintenance, process optimization, quality assurance, and supply chain management.

**Keywords**: Artificial Intelligence, Industry 4.0, Energy Efficiency, Machine Learning, Big Data, Edge Intelligence.

## INTRODUCTION

Presently, Edge AI is a rapidly growing field combining edge computing principles with artificial intelligence (AI) to enable the execution of AI algorithms directly on edge devices. This eliminates the need to transmit and process data on remote servers. Thereby This significantly reduces latency and improves the efficiency of AI-driven applications. By processing data closer to its source, Edge AI supports faster decision-making and enhances real-time functionality. According to recent market analysis [1], the global Edge AI hardware market, estimated at $24.2 billion in 2024, is projected to reach approximately $55 billion by 2029. This growth is driven by the increasing adoption of Internet of Things (IoT) devices across various industries, including smart homes, industrial automation, healthcare, agriculture, and transportation.

While edge computing has existed for years, the integration of AI has recently fueled the development of Edge AI [2]. Many IoT devices lack the computational power to handle complex processing tasks and, therefore, often rely on cloud-based solutions that can be costly and time-intensive. Edge AI addresses this limitation by enabling on-device data processing and reducing dependence on external data centers. Additionally, industries increasingly focus on lightweight vision inspection systems designed for specific tasks, moving away from bulkier automated optical inspection (AOI) machines. These streamlined edge device-based solutions offer advantages such as real-time insights, reduced physical space requirements, and simplified setups. However, several challenges remain in fully realizing the potential of Edge AI. One major issue is the limited availability of detailed performance benchmarks, particularly for processing large datasets or high-resolution images.

## RELATED WORK

Recent studies have evaluated the performance of various Edge AI devices for deep learning applications, particularly object detection, highlighting how different

accelerators like GPUs and TPUs provide viable alternatives to traditional cloud-based processing [3]. Evaluations focused on throughput, power consumption, cost-effectiveness, accuracy, and latency [4,5]. Edge devices with AI chips demonstrated significant performance improvements compared to traditional edge devices. However, the choice of device depends on specific application requirements, as performance varies across different architectures and precision levels [6]. While some devices, like the Jetson AGX Orin and Intel NUC, showed promising results, others, like the Raspberry Pi, exhibited limitations in processing speed [7]. These comparative analyses provide valuable insights for selecting appropriate edge AI devices based on specific use cases and performance needs.

## .METHODOLOGY & DATASET

### A) Methodology

To derive our main insights, we perform a comparative analysis of industrial Edge MLOps platforms, specifically Edge Impulse and the ecoKI Platform. We follow contemporary MLOps practices [8,9], including model optimization and deployment on edge devices. "Lastly, we compare performance characteristics using an evaluation matrix consisting of the ROC curve, precision, recall, and F1 score. Based on this methodology, we elaborate on our findings about the pros and cons of both platforms in the next sections.

### B) Dataset

In line with the objectives of evaluation studies, aligning the experiment's goals with a suitable dataset is crucial. In this work, our initial task involved selecting an appropriate dataset and preparing a trained model. Given our primary focus on wearable devices, we selected a dataset tailored to this domain. To further enhance the analysis, we incorporated a dataset capable of detecting 12 distinct sleep positions with finer granularity under energy-efficient constraints [10]. Leveraging accelerometer data from wearable devices across various timeframes, this dataset supports detailed position inference, offering insights valuable for both sleep quality analysis and energy-efficient wearable solutions.

## EVALUATION

### A) Edge Impulse

Edge Impulse [11], a leading AI development platform, enables intelligence on any edge device. There are several steps to perform a complete inference in the Edge impulse platform and for the deployment.

#### i. Data acquisition

For the sleep dataset, a CSV wizard was used to load the data from a .csv file into the Edge Impulse platform

#### ii. Create Impulse

Creating an impulse is central to Edge Impulse, combining features, data pre-processors, neural network architectures, and desired outputs. Raw data undergoes signal processing to extract features, which are subsequently used by learning blocks for tasks such as classification or regression. Signal processing includes DSPs and FFTs to reduce noise and generate intermediate inputs for learning. Then, spectral analysis and classification were selected for accelerometer data, and raw data was converted into processed features using FFT to enhance model complexity and learning capability.

#### iii. Signal Processing Block

In Edge Impulse, spectral features processing is used to extract frequency, power, and signal characteristics from accelerometer data, leveraging FFT to decompose signals into frequency components.

This approach filters unwanted frequencies, analyzes patterns, and reduces model size for efficient and reliable machine learning. Here, the pre-processing block has been used spectral features for the sleep classification data. This SP block extracts a signal's frequency, power, and other characteristics.

#### iv. Learning Block

The learning block defines the neural network architecture, comprising a fully connected model with a 63-neuron input layer, two hidden layers (80 and 40 neurons), and a 12-class output layer as depicted in the Figure 1.

The result of the classifier for training data set for model FP32 is shown in Figure 2 and corresponding metric in table 1. The on-device performance can be seen in Figure 3 with accuracy and its loss.

Similarly, the result of the classifier for training data set for model int8 is depicted in Figure 4 and corresponding metric in table 2. The on-device performance can be seen in Figure 5 with accuracy and its loss.

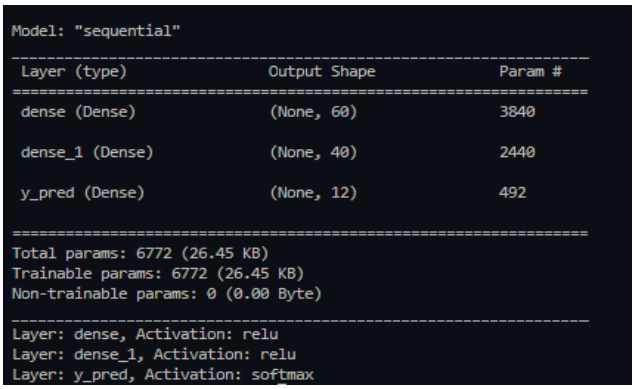



**Figure 1.** Deep Neural Network architecture used in Edge Impulse platform.




**Figure 2.** Validations result of DNN unoptimised (float32) model in Edge Impulse platform.

**Table 1:** Metrics **(validation set of unoptimized (float32) model).**

| METRIC | Value |
|---|---|
| Area under ROC Curve | 1.00 |
| Weighted avg. Precision | 0.98 |
| Weighted avg. Recall | 0.97 |
| Weighted avg. F1 score | 0.97 |




**Figure 3.** On-device performance of unoptimised (float32) model.




**Figure 4.** Validation result of DNN Quantized(int 8) model in Edge Impulse platform.

**Table 2:** Metrics **(validation set of quantised (int8) model).**

| METRIC | Value |
|---|---|
| Area under ROC Curve | 1.00 |
| Weighted avg. Precision | 0.96 |
| Weighted avg. Recall | 0.94 |
| Weighted avg. F1 score | 0.93 |




**Figure 5.** On device performance of Quantized(int 8) model.

## v. Model Test Result

Generally, quantization reduces model weight precision, potentially impacting performance, with options like quantized (INT8) and unoptimized (Float32) models offering varying accuracy.

In Edge impulse, model testing involves selecting the different versions, either unoptimized (float32) or quantized (int8) via the platform; the result of each has been presented in Tables 3 and 4 correspondingly.

**Table 3:** FP_32 accuracy, Metrics for Classifier test results.

| Accuracy: 90.39% | |
|---|---|
| **METRIC** | **Value** |
| Area under ROC Curve | 1.00 |
| Weighted avg. Precision | 0.98 |
| Weighted avg. Recall | 0.97 |
| Weighted avg. F1 score | 0.97 |

**Table 4:** int_8 accuracy, Metrics for Classifier test results.

| Accuracy: 88.21% | |
|---|---|
| **METRIC** | **Value** |
| Area under ROC Curve | 1.00 |
| Weighted avg. Precision | 0.96 |
| Weighted avg. Recall | 0.94 |
| Weighted avg. F1 score | 0.93 |

## vi. Model Deployment

The model offers versatile deployment options, including a standalone C++ application, board-specific binaries for devices like Nordic Thingy:91, or downloadable Keras (.h5) and TFLite formats. Testing confirms successful performance even on resource-constrained hardware such as the Raspberry Pi 2 (ARM V7).

**Table 5:** Metrics comparison for FP32 and Int8 quantization of ML model deployment result at Edge Impulse.

| Model quantization | File size | Ram usage | Inference time | Accuracy |
|---|---|---|---|---|
| FP 32 | 11MB* | 128KB | 0ms | 90.39 |
| INT_8 | 11MB* | 128KB | 0ms | 88.21 |

*11 MB is the file size of the build not the whole zip.

# B) ecoKI Platform

The ecoKI platform follows a streamlined workflow from data preparation to deployment: data loading, selection, train-test splitting, hyperparameter tuning, neural network training, and time series visualization. This systematic process ensures efficient and effective implementation of the ecoKI-Platform.

## i. ecoKI Data Reader

The ecoKI data reader building block enables seamless data integration through multiple input methods: local CSV files, MongoDB databases, or Dataverse integration [12]. This versatile approach ensures compatibility with diverse data sources, streamlining the entire workflow while maintaining optimal efficiency.

## ii. Data Selection

In ecoKI platform, the front end provides the functionality of data selection. This process not only enhances data quality by removing noise and redundancies

but also reduces computational overhead, enabling more efficient processing and analysis.

### iii. Split train and test data

In ecoKI, the front end provides the functionality of splitting data into training and testing because selecting input and output features is essential. This selection ensures ecoKI preprocesses the data into the required format for seamless analysis.

### iv. Train and predict NN multi-class

Then, ecoKI performs training and testing via the dashboard using a fully connected neural network with customizable activation functions, epochs, and neuron counts. Upon completion, it generates the model (.h5), weights, parameters, and a TFLite model for inference, as can be seen in Figure 6.

```
Layer (type)                 Output Shape              Param #
=================================================================
input_1 (InputLayer)         [(None, 3)]               0

dense (Dense)                (None, 10)                40

dense_1 (Dense)              (None, 20)                220

dense_2 (Dense)              (None, 40)                840

dense_3 (Dense)              (None, 12)                492

dense_4 (Dense)              (None, 12)                156

=================================================================
Total params: 1748 (6.83 KB)
Trainable params: 1748 (6.83 KB)
Non-trainable params: 0 (0.00 Byte)
_________________________________________________________________
Layer: input_1, Activation: None
Layer: dense, Activation: relu
Layer: dense_1, Activation: relu
Layer: dense_2, Activation: relu
Layer: dense_3, Activation: relu
Layer: dense_4, Activation: softmax
```

**Figure 6.** Deep Neural Network architecture (classification) used in ecoKI platform.

### v. Time series visualizer

The final step involves generating data for analysis supported by visualization capabilities integrated into this module, as illustrated in Figure 7 (a). This feature allows for exploring key insights by presenting critical data points in an accessible and interpretable format. Through comprehensive visualization tools, users can effectively analyze trends, patterns, and relationships within the data, enabling more informed decision-making and a deeper understanding of the results.

### vi. Model Test Result

Model evaluation in ecoKI is conducted using comprehensive testing metrics, including a confusion matrix to assess classification accuracy and detailed performance measures such as Mean Squared Error (MSE), accuracy, precision, recall, and F1 score. The results can be seen in Figure 7. b and c. These metrics provide a holistic understanding of the model's performance, capturing its predictive accuracy and ability to balance false positives and negatives. This rigorous evaluation ensures the reliability and effectiveness of the trained model in real-world applications.

### vii. Model Deployment

The ecoKI platform provides a TFLite model in FP32 format, designed for seamless integration and deployment. The model can be wrapped using C++ or Python wrappers to enable inference, which serve as interfaces to invoke the TFLite interpreter; the model result is shown in Table 6.

**Table 6:** Model deployment result on ecoKI platform.

| Model quantization | File size | Ram usage | Inference time | Accuracy |
|---|---|---|---|---|
| FP 32 | 9.53KB | 128KB | 0.1ms | 94% |

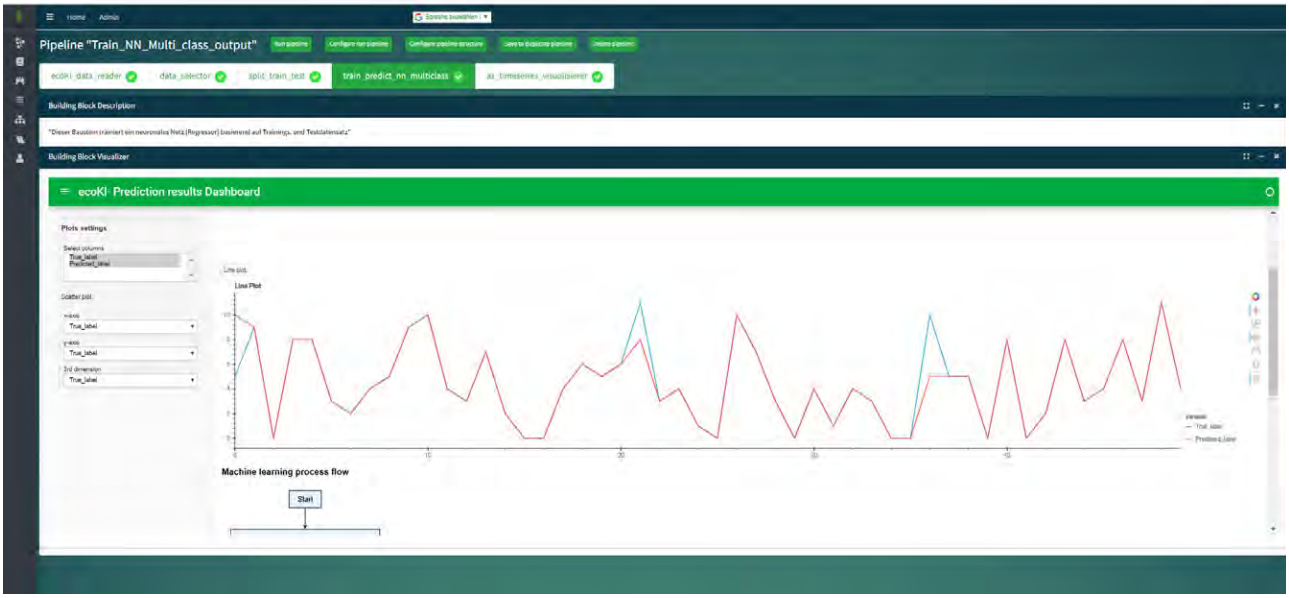
## DISCUSSION AND CONCLUSION

In the rapidly evolving field of machine learning at the edge, platforms like ecoKI and Edge Impulse provide powerful tools for efficient model development and deployment. Both platforms offer robust features tailored to specific needs, but they differ in their approaches, strengths, and limitations.

On the one hand, ecoKI excels in comprehensive data preprocessing, handling various data formats seamlessly, and offering advanced features such as ModelCheckpoint and dynamic learning rate adjustments.

*ModelCheckpoint* ensures the model or its weights are saved at specific intervals in checkpoint files, enabling training to resume from a saved state if needed. It offers flexibility by allowing users to save only the best-performing model based on a monitored metric or to save the model at the end of every epoch, regardless of performance. Users can define 'best performance' by selecting the metric to monitor and determining whether it should be maximized or minimized. In contrast, the dynamic learning rate adjustments allow for a dynamic reduction of the learning rate when the monitored metrics show no improvement for a specified number of epochs. This adaptive learning rate reduction, typically by a factor of 2–10, helps models to overcome stagnation and enhances convergence, ultimately improving training efficiency and model performance by 3.61% for the FP32 model compared to Edge impulse. ecoKI's flexible workflow also supports detailed hyperparameter tuning and real-time data processing. However, larger datasets may require more setup and computational resources.

On the other hand, Edge Impulse provides a user-




**(a)**

| index | pred0 | pred1 | pred2 | pred3 | pred4 | pred5 | pred6 | pred7 | pred8 | pred9 | pred10 | pred11 |
|---|---|---|---|---|---|---|---|---|---|---|---|---|
| True_0 | 576 | 0 | 0 | 0 | 0 | 0 | 0 | 0 | 0 | 0 | 0 | 0 |
| True_1 | 0 | 598 | 0 | 0 | 0 | 0 | 0 | 0 | 0 | 0 | 0 | 0 |
| True_2 | 0 | 0 | 611 | 0 | 0 | 0 | 0 | 0 | 0 | 0 | 0 | 0 |
| True_3 | 0 | 0 | 0 | 599 | 0 | 0 | 0 | 0 | 0 | 0 | 0 | 0 |
| True_4 | 0 | 0 | 0 | 0 | 569 | 0 | 0 | 0 | 0 | 0 | 0 | 0 |
| True_5 | 0 | 0 | 0 | 0 | 0 | 146 | 0 | 0 | 0 | 0 | 469 | 0 |
| True_6 | 0 | 0 | 0 | 0 | 0 | 0 | 618 | 0 | 0 | 0 | 0 | 0 |
| True_7 | 0 | 0 | 0 | 0 | 0 | 0 | 0 | 594 | 0 | 0 | 0 | 0 |
| True_8 | 0 | 0 | 0 | 0 | 0 | 0 | 0 | 0 | 595 | 0 | 0 | 0 |
| True_9 | 0 | 0 | 0 | 0 | 0 | 0 | 0 | 0 | 0 | 606 | 0 | 0 |
| True_10 | 0 | 0 | 0 | 0 | 0 | 41 | 0 | 0 | 0 | 0 | 583 | 0 |
| True_11 | 0 | 0 | 0 | 0 | 0 | 0 | 0 | 0 | 3 | 0 | 0 | 592 |

**(b)**

| Index | Metric | 0.0 | 1.0 | 2.0 | 3.0 | 4.0 | 5.0 | 6.0 | 7.0 | 8.0 | 9.0 | 10.0 | 11.0 |
|---|---|---|---|---|---|---|---|---|---|---|---|---|---|
| 0 | MSE | 0.0 | 0.0 | 0.0 | 0.0 | 0.0 | 0.07 | 0.0 | 0.0 | 0.0004 | 0.0 | 0.00088 | 0.0004 |
| 1 | Accuracy | 1.0 | 1.0 | 1.0 | 1.0 | 1.0 | 0.929 | 1.0 | 1.0 | 0.9995 | 1.0 | 0.4411 | 0.9995 |
| 2 | Precision | 1.0 | 1.0 | 1.0 | 1.0 | 1.0 | 0.78 | 1.0 | 1.0 | 0.9949 | 1.0 | 0.2727 | 1.0 |
| 3 | Recall | 1.0 | 1.0 | 1.0 | 1.0 | 1.0 | 0.237 | 1.0 | 1.0 | 1.0 | 1.0 | 0.707 | 0.9949 |
| 4 | F1 | 1.0 | 1.0 | 1.0 | 1.0 | 1.0 | 0.364 | 1.0 | 1.0 | 0.9974 | 1.0 | 0.0882 | 0.9974 |

**(c)**

**Figure 2:** a) The front-end dashboard of the EcoKI platform provides an intuitive interface for visualizing test data and b) test predictions, enabling comprehensive validation of model performance. It includes a confusion matrix offering insights into classification accuracy. c) Additionally, model metrics such as Mean Squared Error (MSE), accuracy, precision, recall, and F1 score are evaluated and displayed to ensure thorough performance assessment.

friendly interface for rapid model development and de ployment, which is especially suited for edge devices. Its support for lightweight quantized models and pre-built learning blocks enhances efficiency as it provides the standalone C++ model and TFlite interpreter. That is the reason it supports many hardware configurations. However, it has limitations in handling complex data pipelines and high-performance inference tasks. In summary, ecoKI offers flexibility and deep data integration, while Edge Impulse excels in ease of use and edge deployment efficiency. The ultimate choice depends on specific research needs and deployment requirements. The results of this study could be extended in future research by expanding the number of compared MLOps platforms and the number and variety of the used metrics. Furthermore, these platforms' scaling and reliability characteristics

require further investigation to make decisive statements about their capabilities.

## ACKNOWLEDGEMENTS

This work was funded by the German Federal Ministry for Economic Affairs and Climate Action (BMWK) under grant number 03EN2047C.

## DECLARATION OF AI-ASSISTED TECHNOLOGIES

While preparing this manuscript, the authors used AI tools to improve language and readability. They carefully reviewed all content, taking full responsibility for the research work and ideas presented in this publication.

## REFERENCES

1. Marketsandmarkets.https://www.marketsandmarkets.com/Market-Reports/edge-ai-hardware-market-158498281.html
2. Singh R, & Gill S. S. Edge AI: a survey. Internet of Things and Cyber-Physical Systems, 71-92 (2023).
3. Rohit C, Sant R, Nawade S, Vedhant V, & Gupta V. Exploring edge artificial intelligence: A comparative study of computing devices for deployment of object detection algorithm. INCET, pp. 1-5 (2023).
4. Su W, Li L, Liu F, He M, & Liang X. AI on the edge: a comprehensive review. Artificial Intelligence Review, 55(8), 6125-6183 (2022).
5. Amanatidis, P., Iosifidis, G., & Karampatzakis, D. (2021, November). Comparative evaluation of machine learning inference machines on edge-class devices. PCI,pp. 102-106,2(021).
6. Garcia-Perez A, Miñón R, Torre-Bastida A. I, & Zulueta-Guerrero E. Analysing edge computing devices for the deployment of embedded AI. *Sensors*, *23*(23), 9495 (2023).
7. Samsuri M. H, Yuen S. L, Lau P Y, Wong C. W, Kamarudin N A, Hussin Z, & Ho, H W. Comparative Performance Analysis of Edge-AI Devices in Deep Learning Applications. ICIEA, pp. 1-6 (2024). https://ieeexplore.ieee.org/document/10665079
8. Rani F, Chollet N, Vogt L, & Urbas L. Industrial Edge MLOps: Overview and Challenges. CACE, 53, 3019-3024 (2024). https://doi.org/10.1016/B978-0-443-28824-1.50504-4
9. Rani F, Khaydarov V, Bode D, Hasan I. H, & Urbas, L. MLOps Practice: Overcoming the Energy Efficiency Gap, Empirical Support Through ecoKI Platform in the Case of German SMEs. PAC- World Global Conference (2023).
10. IEEE Dataset. https://ieeedataport.org/documents/sleep-position-classification-using-single-abdominal-accelerometer
11. Janapa Reddi V, Elium A, Hymel S, Tischler D, Situnayake D, Ward C, & Quaye J. Edge impulse: An mlops platform for tiny machine learning. MLSys, 5. (2023).
12. Rani F, Wang X, Mutlu I, & Urbas L. A Centralized MongoDB-Based Repository Design for IIoT Data: The ecoKI Project. IFAC-PapersOnLine, 56(2), 3184-3189 (2023). https://doi.org/10.1016/j.ifacol.2023.10.1454

© 2025 by the authors. Licensed to PSEcommunity.org and PSE Press. This is an open access article under the creative commons CC-BY-SA licensing terms. Credit must be given to creator and adaptations must be shared under the same terms. See https://creativecommons.org/licenses/by-sa/4.0/



Systems & Control Transactions

**Research Article - Peer Reviewed Conference Proceeding**
ESCAPE 35 - European Symposium on Computer Aided Process Engineering
Ghent, Belgium. 6-9 July 2025
Jan F.M. Van Impe, Grégoire Léonard, Satyajeet S. Bhonsale,
Monika E. Polańska, Filip Logist (Eds.)

PSE PRESS

# The Smart HPLC Robot: Fully Autonomous Method Development Guided by A Mechanistic Model Framework

**Dian Ning Chia, Fanyi Duanmu, Luca Mazzei, Eva Sorensen, Maximilian O. Besenhard***

Department of Chemical Engineering, University College London, Torrington Place, London WC1E 7JE, United Kingdom
* Corresponding Author: m.besenhard@ucl.ac.uk

## ABSTRACT

Developing ultra- or high-performance liquid chromatography (HPLC) methods for analysis or purification requires significant amounts of material and manpower, and typically involves time-consuming iterative lab-based workflows. This work demonstrates in two case studies that an autonomous HPLC platform coupled with a mechanistic model that self-corrects itself by performing parameter estimation can efficiently develop an optimized HPLC method with minimal experiments (i.e., reduced experimental costs and burden) and manual intervention (i.e., reduced manpower). At the same time, this HPLC platform, referred to as Smart HPLC Robot, can deliver a calibrated mechanistic model that provides valuable insights into method robustness.

**Keywords**: Industry 4.0, Modelling and Simulations, Optimization, Genetic Algorithm, Batch Process, Self-driving, Autonomous, Digital Twin, Mechanistic Model, Chromatography

## INTRODUCTION

One of the most important analysis and purification methods in the fine chemical and pharmaceutical industry is liquid chromatography [1]. The degree of separation necessary for success is dictated by the affinity of the solutes (i.e., the dissolved molecules) towards the solid phase (i.e., the adsorbent). The greater the affinity of the solute for the solid phase, the slower its movement through the chromatography column, resulting in a later elution. Considering a column with a fixed solid phase, one of the most significant factors affecting the affinity of the solute is solvent composition, where the solvent in HPLC processes is typically a mixture of organic and inorganic solvents. The simplest way to operate an HPLC process is through isocratic elution, where the solvent composition remains constant throughout the operation. However, isocratic elution often has limitations, such as long process time (the time taken for the last component to elute) or the inability to satisfactorily resolve a complex mixture. An alternative mode of operation is gradient elution, where the solvent composition varies over time. This approach introduces additional degrees of freedom, such as the initial and final solvent composition, the duration of the composition change, and the number of gradient steps, adding complexity to the process. Even so, gradient elution is generally preferred for complex mixtures due to its enhanced ability to resolve components more efficiently and quickly [2].

Developing gradient based HPLC methods usually requires significant material and manpower, and typically involves time-consuming and iterative laboratory-based workflows. Recent technological advancements now enable fully computer-controlled workflows; these allow not only automated but also streamlined autonomous (that is, self-driven) HPLC method development, with minimal to no human intervention (employing robotic solutions for iterative workflows [3]). In this article, we summarize two recent applications of autonomous processes; readers are referred to Tom et al. [3] for a comprehensive review of the concepts of autonomous processes in laboratories (coined as self-driving laboratories in the review article). Boelrijk et al. [2] and Dixon et al. [4] demonstrated the potential of autonomy for developing HPLC methods. Both authors achieved autonomy of gradient method development via the following steps:

1. **Initial Small Experimental Campaign,** e.g. as in Boelrijk et al. via random input parameter selection [2] or Dixon et al. via Latin Hypercube Sampling (LHS)[4].
2. **Fit the data-based surrogate model** using experiments performed in step 1.

3. **Optimize the HPLC process** using the surrogate model, where the optimizer **suggests the next experiment(s)** to perform. Both authors used Bayesian optimization aimed to optimize gradient methods regarding time, and number of resolved peaks.
4. **Run model-guided additional real experiments** and **analyze key indicators in-silico** (=computationally), e.g., peak height, peak width, retention time. The key indicators are analyzed by a surrogate model and are automatically sent to the optimizer (used in the next step); no manual interpretation is required.
5. **Repeat steps 2 and 3** until reaching stopping criteria.

Both groups demonstrated that satisfactory optimal results could be achieved autonomously with the help of in-silico surrogate models. However, surrogate models rely on data to be informative and effective, making them less efficient in the early stages. Due to their data-driven nature, they may not accurately reflect known physical phenomena, limiting their ability to provide reliable guidance, especially when only a few experiments are available for model training and development.

To address the above-mentioned issue, **this work proposes an autonomous process guided by a mechanistic model** for knowledge-driven (instead of purely data-driven) decision-making. One of the challenges when using a mechanistic model is to find a set of good parameters (e.g., isotherm parameters) that can represent the real experimental results (e.g., chromatogram) sufficiently well. Therefore, a parameter estimation step is added to the previously mentioned automation step (see discussion for Figure 2 in the methodology section). This framework, here called "Smart HPLC Robot", is an intelligent platform enabling the development of an optimized HPLC method with minimal experiments while simultaneously delivering a calibrated mechanistic model that provides valuable insights into method robustness. Importantly, since mechanistic models are physics-based and not tied to a specific objective function, they can be applied to optimization tasks with different objectives and provide reliable predictions beyond the range of experimental settings used for training (i.e., extrapolation). Once model parameters are properly determined and experimental conditions remain consistent (e.g., using the same mixture), mechanistic models offer better adaptability, require fewer calibration experiments, and do not need retraining, unlike the data based surrogate models used in previous works.




**Figure 1**. Communication protocol of Smart HPLC Robot.

## METHODOLOGY

The Smart HPLC Robot features mechanistic simulations and an autonomous process; thus, it requires efficient communication between laboratory equipment and chromatography simulators. The developed autonomous workflow, including the communication between model and HPLC system, is illustrated in Figure 1 and discussed in this section. In addition, the working principles (shown in Figure 2) will also be discussed.

### Communication Protocol

The user interface is developed in Python, which also bridges the communication between equipment and simulators. As shown in Figure 1, the current project is developed with Agilent equipment and simulators such as gPROMS and CADET (https://cadet-web.de/), but it is not limited to those and can be integrated with other systems, provided that users adhere to a standard communication framework. To integrate equipment from different manufacturers, users can leverage, for example, Application Programming Interfaces (APIs) to efficiently establish communication and exchange key values.

In this project, the communication protocol for Agilent OpenLab is written in C# (left part in Figure 1). Therefore the equipment control sequences (e.g., modifying experimental input sequence and executing sequence) are all implemented in C# for better compatibility and operation efficiency. A C# web API facilitates seamless data exchange by providing a standardized communication interface while isolating equipment control sequences. The right part of Figure 1 illustrates the communication between the Python framework and simulators. Currently, gPROMS and CADET are supported, and the communications with Python are via gO:Python and CADET-Python, respectively.

### Working Principle

The working principle of the Smart HPLC Robot can be divided into two main steps as shown in Figure 2: (1) the preparation step (a one-time execution) and (2) the mechanistic loop (i.e., mechanistic model-guided autonomous method development). The former requires configuring the Smart HPLC Robot and performing initial experiments, and the latter involves parameter estimation for model calibration and optimization for the generation of new experiments. This section will detail each step together with associated challenges and solutions.

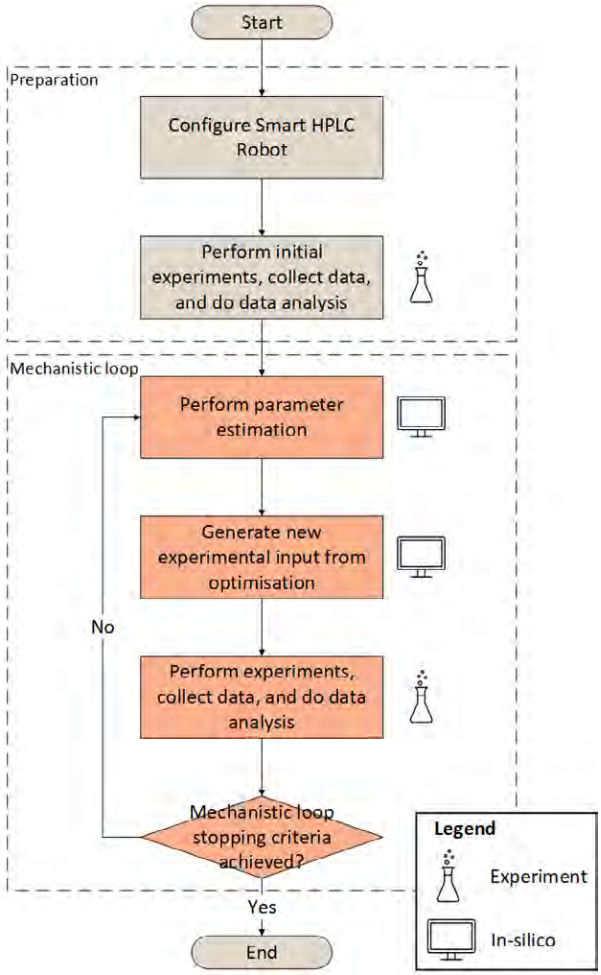



**Figure 2.** Smart HPLC Robot working principle. All steps are performed autonomously after the initial manual configuration of the robot (e.g., input column dimension, model selection, optimization settings).

## Preparation

In contrast to using machine learning [2,4], the mechanistic model framework used in this work requires prior knowledge of the number of components in the system for model development. This step is more straightforward with a mass spectrometer than an ultraviolet (UV) detector, as a UV detector cannot distinguish overlapping components, leading to inaccurate method development. When using a UV detector (as done here), it is recommended to perform preliminary experiments at low flow rates and a low initial organic solvent fraction and low gradients. This approach can, theoretically, maximize the separation of components with the current system, providing an initial understanding of the number of components that can be resolved from the (potentially) unknown mixture.

Besides the number of components, other information, e.g., column dimensions, selection of isotherms and mass transport model, and parameter estimation/optimization settings, including boundaries of parameter estimation/optimization variables and objective functions, is also required for configuring the mechanistic model of the Smart HPLC Robot. Most information can be obtained from equipment manufacturers or is based on the aim of the task. The boundaries of variables are crucial to the success of the HPLC method development, but they are often tricky to determine. For design variables, such as flow rates, percentage of organic solvent, and column temperature, the boundaries are often defined as the equipment physical limitations. Isotherm parameters, on the other hand, lack clear boundaries. The Smart HPLC Robot conducts a basic boundary analysis using Sobol sampling across an initial input search space (HPLC settings), typically with broad boundaries. This process helps identify regions with a higher likelihood of yielding optimal results, as indicated by the objective function's quantification of the HPLC method quality. Hence, shrinking the search space for the subsequent parameter estimation step, leading to an improved efficiency.

Once all necessary information is provided, users can execute the program and the robot will do all other steps without further human interference. The first automated step is to generate and perform a user-defined number of initial experiments generated from sampling methods (e.g., LHS or factorial design). The number of initial experiments is a trade-off between accuracy of prediction and experimental burden. For the low-parameter mechanistic models used thus far, four experiments provided a good foundation

## Model Calibration and Validation Loop

The mechanistic model's initial training (parameter estimation) will begin once the Smart HPLC Robot completes the initial experiments and sends the results to Python. The first step in the loop is to estimate the parameters for the selected isotherm(s) (e.g., linear isotherm or Langmuir isotherm) based on the user-defined objective functions (e.g., maximum likelihood method or least square method). In this step, all experiments, including initial experiments and those generated in the mechanistic loop, will be taken into account.

Once calibrated with the best available parameter estimates, the mechanistic model computationally optimizes the HPLC method settings (i.e., the inputs such as flow rate, initial and final mobile phase composition, and gradient time) based on the selected method objectives (such as achieving sufficient resolution for all or selected components in the shortest possible time). Therefore, selecting an appropriate objective function is crucial to yield the desired HPLC method.

Once computational optimization is complete, the HPLC system will automatically execute the updated

method (using the optimum inputs) and return key data (including UV absorbance, retention time, and peak width, i.e., the method results) to Python. The latter aims to validate whether the computed optimum has been achieved and to determine if a sufficiently robust HPLC method now meets the stopping criteria. If not, it serves as a new experiment to refine the mechanistic model parameters and rerun the computational optimization. The stopping criteria may include factors like reaching the maximum iterations or no further method improvement. Once met, the Smart HPLC Robot reports the validated model and optimal HPLC method settings. In most cases, the mechanistic loop requires multiple iterations. During the parameter estimation step, both stochastic and deterministic optimizers carry the risk of yielding worse isotherm parameters than the previous iteration (stochastic optimizers due to inherent randomness and deterministic ones due to sensitivity to initial values).Therefore, the newly estimated model parameters will be compared with the previous best values, and only those yielding an improved estimation of parameters (reduced error between experiment and model calculation) will be used to update the model.

## RESULTS AND DISCUSSIONS

Two case studies were performed in this work: (1) an in-silico system case study to quantify the performance of the Smart HPLC Robot, and (2) a real world case study for initial showcase. The simulations for both case studies were performed using the CADET-Core simulator. The mass transfer model used is the native Equilibrium Dispersive Model, and the isotherm model is a non-native linear isotherm coupled with the Linear Solvent Strength (LSS) theory:

$$\text{Linear isotherm: } q_i = a_i\, C_i \qquad \forall i = 1, \dots, n \qquad (1)$$

$$\text{LSS theory: } a_i = a_{0.i} \exp\left(-S_{s,i}\, \phi\right) \quad \forall i = 1, \dots, n \qquad (2)$$

where $n$ is the number of components in the mixture, $q$ is the equilibrium concentration in the stationary phase, $C$ is the concentration in the liquid phase, $a$ is the Henry coefficient, $a_0$ and $S_s$ are the numerical constants in LSS theory, and $\phi$ is the organic solvent composition (i.e., volumetric fraction of the organic modifier in the solvent).

In both case studies, initial experimental conditions are generated via LHS, which are then performed either in-silico using the aforementioned model or sent to the instruments (see setup in later section) to perform real experiments. A virtual column is used in the in-silico system case study, while the Agilent Poroshell 120 EC-C18 column (G7104C096) is used in the real world case study. The column information is summarized in Table 1.

Parameter estimation is then performed in-silico by minimizing the mean of the relative errors ($EE_{PE}$) [5] via genetic algorithm (using Python package "geneticalgorithm2"):

**Table 1**. Information of the columns in the case studies.

| Parameters | In-silico | Real |
|---|---|---|
| Col. length (mm) | 150 | 100 |
| Col. radius (mm) | 5 | 3 |
| Total porosity (-) | 0.645 | 0.840 |
| Internal porosity (-) | 0.189 | 0.160 |
| Particle radius (μm) | 2.50 | 1.35 |

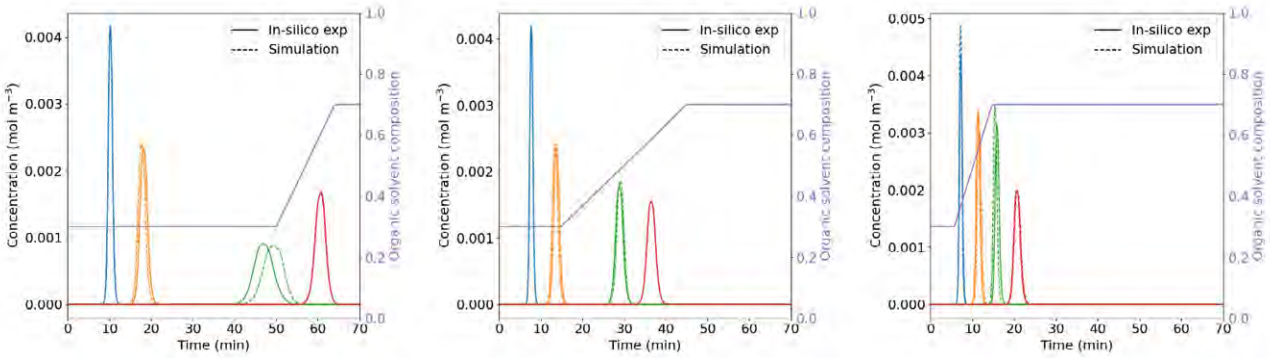
$$EE_{PE} = \frac{1}{n}\sum_{i=1}^{n}\left(\frac{\left|t_{R,i}^{\text{sim}} - t_{R,i}^{\text{exp}}\right|}{t_{R,i}^{\text{sim}}} \times 100\right) \quad \forall i = 1, \dots, n \qquad (3)$$

where $t_R^{\text{sim/exp}}$ are the simulation (using the mechanistic model)/experimental retention times. The parameters that are varied to minimize the model error $EE_{PE}$ are $a_{0,i}$ and $S_{s,i}$.

Next, the isotherm parameters in the simulation model are updated with those obtained from the parameter estimation step before performing optimization. The optimizer used is also a genetic algorithm. During optimization, the objective function (note that this is not the same as the objective function in parameter estimation) is to minimize the method time (i.e., the retention time of the last eluting component) subject to a critical resolution constraint (i.e., the smallest resolution of all component pairs) of at least 1.5. The critical resolution is calculated considering the peak asymmetry and peak width at 0.135 peak height as suggested by Boelrijk et al. [2]. The optimization variables (and model inputs) are the flow rate, gradient start time, and gradient change duration. The gradient starting and ending volume fractions are fixed at 0.3 and 0.7 for the in-silico system case study, and 0.5 and 1.0 for the real world case study (but could also be optimized). The "optimal" experimental conditions are then performed in the HPLC platform considered, and the model parameter estimation and HPLC method optimization steps are repeated until the stopping criteria are satisfied. Here, a simple stopping criterion of a maximum of four mechanistic loops was used in both case studies.

### (1) In-silico System Case Study

An in-silico system is used as a case study so that the performance of the Smart HPLC Robot can be analyzed quantitatively as the true values of the parameters involved are all known. A four-component mixture is considered. In this case study, simulations and in-silico (i.e., virtual) experiments are carried out using the simulation model described above without considering any uncertainties in the model parameters. Note that for the in-silico experiments, the isotherm parameters are pre-defined and fixed. Therefore, theoretically, the parameter




*(a) Worst parameter estimation case* *(b) Best parameter estimation case* *(c) Final optimized condition*

**Figure 3.** Chromatograms of simulation and in-silico experiments obtained from (a,b) parameter estimation and (c) optimization. All chromatograms are obtained at the last mechanistic loop (loop 4).

estimation should be capable of yielding the true isotherm values, but the optimizer cannot guarantee global optimality, so there is still a small deviation of about 4% absolute average difference in this case study. The parameter estimation (see Equation 3 for the objective function) is performed on all previously executed experiments, and Figures 3a and 3b show the bad and good cases, respectively. It is clearly seen that the simulation and in-silico experiment chromatograms for "fast" (i.e., short method time) cases have greater similarities (i.e., indicating better predictions of the isotherm parameters), which benefits the objective function as this is to minimize the method time.

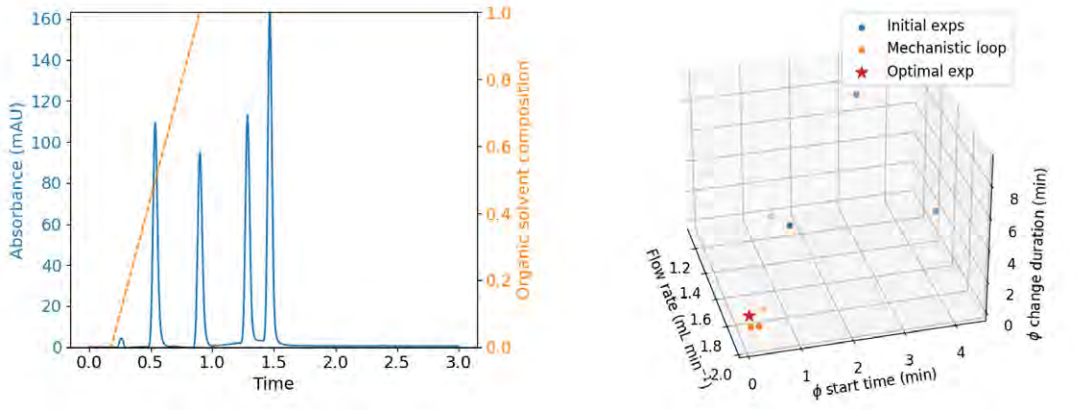
Figure 3c shows the optimized chromatogram for the in-silico experiment and the associated simulation. The results deliver two main takeaways: (1) the chromatograms nearly overlapped, indicating a fairly accurate prediction of isotherm values; (2) all components are completely resolved with a short/minimum gap between adjacent components, illustrating a good quality of the optimized experiment condition.

## (2) Real World Case Study

Having validated the performance of the Smart HPLC Robot, a real world case study is carried out to demonstrate its applicability to laboratory-based experiments. The simulations are performed using the same mechanistic model as for the in-silico system case study, and the real experiments are carried out with an Agilent 1260 Infinity II system. The system is equipped with a quaternary pump (G7104C), an online sample manager set (G3167AA) that consists of an auto-sampler and an online valve configured for off-line sampling, a multicolumn compartment with thermostat (G7116A), and a variable wavelength detector (G7114A). The UV absorbance is recorded at a wavelength of 254 nm and a frequency of 5 Hz. The needle is set to draw the sample at 100 µL $min^{-1}$, eject at 400 µL $min^{-1}$, and an equilibration time of 1.2 s. A four-component sample is used as model sample, with an injection volume of 1 µL.

Compared to the in-silico case study, two new challenges arise for real system. Firstly, the raw experimental data from Agilent provides UV absorbance, and calibration is required to convert absorbance to concentration, but this requires prior knowledge of each component which is sometimes unavailable. Therefore, as done in Case Study 1, component retention times are used as the sole performance indicator for parameter estimation (see Equation 3). The second challenge is that numerical diffusion may contribute significantly to the band broadening in the simulation if the discretization grid of the column is not fine enough. Conversely, a fine discretization may increase the computational burden, leading to a long simulation time. To obtain accurate retention times and peak widths within a short time, this work uses a loose discretization grid to estimate only the retention time, and the peak widths are extracted directly from the experiments. In the first iteration, the peak width of each component is based on the average from initial experiments, and the chromatogram is approximated by a Gaussian curve centered on the retention time. In subsequent iterations, the previous iteration's peak width is used, enabling progressive self-correction and refinement of the method.

As the simulation and experiment generate different profiles (concentration vs absorbance), only the final optimal experimental results are shown in Figure 4a. It is noted that the first small peak is the solvent front, which is not considered a component during parameter estimation and optimization. After four iterations of the mechanistic loop, the method time is minimized to about 1.49 min while achieving complete separation (critical resolution $\geq 1.5$) of all components, which is 49% to 78% faster compared to the initial experiments. In Figure 4b, the distribution of all experiments performed is plotted together. It shows that the initial experiments are spread across the search space and are away from the final optimal experiment, showing how simulations helped eliminate the real




*(a) Optimal chromatogram* *(b) Experiment propagation*

**Figure 4.** Key indicators of the real system case study: (a) The optimal chromatogram obtained from real experiment; (b)The propagation of the experiments throughout the whole automation process.

experiments that are otherwise needed to finally arrive at the optimal point. Also, note that the optimized experiments are close to each other, indicating that they have similar performances. Therefore, the goal is not necessarily to develop a perfect model, but rather a robust method that achieves reliable results. Ideally, this would be complemented by a well-calibrated mechanistic model, which can provide added value, such as enabling sensitivity studies and further refining the process.

## CONCLUSIONS

This work has presented an autonomous HPLC method development program coupled with a mechanistic model, here termed the Smart HPLC Robot. Unlike literature methods, which rely solely on a data-driven approach, incorporating a mechanistic model retains the physics of the system, providing valuable insights and enabling easy model reuse. Throughout the process, the model automatically calibrates itself using real-time data feedback, making it a digital HPLC twin.

The Smart HPLC Robot's performance was validated through an in-silico case study, demonstrating its ability to accurately predict isotherm model parameters and optimize HPLC methods. In a real-world case study, it efficiently explored the search space, improving the HPLC method (e.g., minimizing method time). Notably, the goal of the Smart HPLC Robot is to deliver an optimal method, not a perfect model.

To conclude, the Smart HPLC Robot has two main benefits: (1) reduction in experimental costs and burden through efficient search space exploration, and (2) reduced manpower by enabling self-driven method development until “satisfaction” compared to traditional iterative experimental workflow through automation.

## ACKNOWLEDGEMENTS

We gratefully acknowledge funding from UCL's Impact Acceleration Account, which supported this project, as well as Eli Lilly for their specific support and Agilent for their valuable contributions, all of which were vital to the success of this work

## REFERENCES

1. Besenhard MO, Tsatse A, Mazzei L, Sorensen E. Recent advances in modelling and control of liquid chromatography. *Curr Opin Chem Eng* 32:100685 (2021). 10.1016/j.coche.2021.100685
2. Boelrijk J, Ensing B, Forré P, Pirok BWJ. Closed-loop automatic gradient design for liquid chromatography using Bayesian optimization. *Anal Chim Acta* 1242:340789 (2023). 10.1016/j.aca.2023.340789
3. Tom G, Schmid SP, Baird SG, Cao Y, Darvish K, Hao H, et al. Self-Driving Laboratories for Chemistry and Materials Science. *Chem Rev* 124(16):9633–732 (2024). 10.1021/acs.chemrev.4c00055
4. Dixon TM, Williams J, Besenhard M, Howard RM, MacGregor J, Peach P, et al. Operator-free HPLC automated method development guided by Bayesian optimization. *Digit Discov* 3(8):1591–601 (2024). 10.1039/D4DD00062E
5. Tirapelle M, Besenhard MO, Mazzei L, Zhou J, Hartzell SA, Sorensen E. Towards A Digital Twin for Analytic HPLC. In Texas, US; 2023.

© 2025 by the authors. Licensed to PSEcommunity.org and PSE Press. This is an open access article under the creative commons CC-BY-SA licensing terms. Credit must be given to creator and adaptations must be shared under the same terms. See https://creativecommons.org/licenses/by-sa/4.0/

Systems & Control Transactions

**Research Article - Peer Reviewed Conference Proceeding**
ESCAPE 35 - European Symposium on Computer Aided Process Engineering
Ghent, Belgium. 6-9 July 2025
Jan F.M. Van Impe, Grégoire Léonard, Satyajeet S. Bhonsale,
Monika E. Polańska, Filip Logist (Eds.)

PSE PRESS

# Predicting Surface Tension of Organic Molecules using COSMO-RS Theory and Machine Learning

**Flora Esposito[a], Ulderico Di Caprio[a], Bruno Rodrigues[c], Florence H. Vermeire[b], Idelfonso B.R. Nogueira[c], and M.Enis Leblebici[a,*]**

[a] Center for Industrial Process Technology, Department of Chemical Engineering, KU Leuven, Agoralaan Building B, 3590 Diepenbeek, Belgium
[b] KU Leuven, Department of Chemical Engineering, Celestijnenlaan 200F-bus 2424, Leuven 3001, Belgium
[c] Department of Chemical Engineering; Norwegian University of Science and Technology, Gløshaugen, Trondheim, 7034, Norway
* Corresponding Author: muminenisleblebici@kuleuven.be.

## ABSTRACT

Surface tension is a fundamental property at the liquid/gas interface, influencing phenomena such as capillary action, droplet formation, and interfacial behavior in chemical engineering processes. Despite its significance, experimental determination of surface tension is time-intensive and impractical for in silico-designed compounds. Predictive models are essential for bridging this gap. This study expands on Gaudin's COSMO-RS-based model, which assumes uniform molecular orientation at the surface, by testing its predictive capability across broader temperatures (5–50°C) and developing a hybrid model combining first-principle and machine learning insights to improve Gaudin's model predictions. The HM employs a serial configuration where COSMO-RS predictions serve as inputs alongside molecular descriptors, derived using the Mordred library. SHAP analysis guides feature selection, enhancing model interpretability. An artificial neural network refines predictions, optimized via Bayesian optimization for architecture and hyperparameters. Using a diverse dataset of 85 organic molecules, the HM demonstrates improved accuracy, reducing various metrics compared to standalone first-principle predictions.

**Keywords**: COSMO-RS, Machine Learning, Hybrid Modeling, Surface tension, First-Principle modeling.

## INTRODUCTION

Surface tension is a key property at the liquid/gas interface and plays an important role in various chemical engineering processes, including liquid flow and transport through porous media. This property is responsible for various phenomena, such as capillary action, droplet formation, and the behavior of liquid interfaces. Surface tension has practical applications in various fields, e.g., thin layer technologies, sol–gel technologies, phase separation techniques, drug carriers and treatment of raw materials [1]. Experimental measurement results for this property require specialized equipment and are time-consuming, therefore predictive models for surface tension are essential. Moreover, significantly different surface tension values for a given compound can arise from the method used (e.g., Wilhelmy plate, Du Noüy ring, maximum bubble pressure, dropweight, or hanging-drop) and the liquid purity [2]. Additionally, a transition to a greener chemical industry requires the development of innovative and sustainable solvents. Utilizing an in-silico model enables the pre-screening of these materials without the need for experimental procedures, thereby accelerating process development. Therefore, reliably predicting surface tension values for candidate compounds is essential. Numerous predictive models have been proposed in the literature for surface tension, e.g. neural network regression and graph machine regression [2], Quantitative Structure-Property Relationship (QSPR) models [3], combination of group-contribution and machine learning (ML) models [4]. These rely on large datasets and maintain reliability only within the boundaries of their training data. Moreover, they do not incorporate any underlying physical principles of the system. Quantum chemistry-based models are highly effective in predicting a wide range of physicochemical properties of organic compounds. The Conductor-like Screening Model for Real Solvents (COSMO-RS) method,

introduced by Andreas Klamt in 1995, integrates unimolecular quantum chemical calculations with exact statistical thermodynamics [5]. This approach enables the prediction of chemical potentials in liquids, which can be used to derive various thermodynamic equilibrium properties, without relying on experimental data. For example, COSMO-RS can be used to compute interfacial tension, which represents the free energy per unit surface area required to maintain an interface between two condensed phases. However, accurately predicting surface tension remains a significant challenge for COSMO-RS [6]. Recently, Gaudin proposed a COSMO-RS based model to predict surface tension ($\sigma$) of pure liquids [7]. Gaudin's approach is employed in this work and explained in the Methodology paragraph of this manuscript. Briefly, this method assumes uniform molecular orientation, meaning that every surface segment has an equal probability of being exposed. While originally tested on a limited set of molecules at 20°C, this study aims to (1) evaluate its predictive performance across a broader temperature range and (2) develop a Hybrid Model (HM) that combines COSMO-RS predictions with molecular descriptors to estimate experimental surface tension for more robust predictions. By integrating domain knowledge, HMs improve system understanding while requiring less data than purely ML models. This approach enhances reliability and offers a high benefit-to-cost ratio for complex systems [8]. In this work, a serial HM is employed, where the first-principle model (FPM) predictions are used as an input for the ML model together with molecular descriptors. The ML model then predicts the experimental surface tension value.

# METHODOLOGY

## First Principle predictions

Gaudin proposed a COSMO-RS based model to predict surface tension ($\sigma_{sim}$) of pure liquids [7]. The model is described by

$$\sigma_{sim} = -\frac{\Delta G_{sim}}{S_{sim}}, \quad (1)$$

where $\sigma_{sim}$ (mN/m) is the simulated surface tension, $\Delta G_{sim}$ (kcal/mol) is the COSMO-RS simulated Gibbs free energy of self-solvation and $S_{sim}$ (Å$^2$) is the molecular flat surface. The implicit assumption of this model is that the molecular orientation at the surface is neglected: any surface segment has the same probability to be exposed at the surface. However, this assumption may not be true for compounds where specific molecular orientations are energetically favored. In such cases, surface segments with lower desolvation energy are more likely to be exposed. Both the authors of this work and Gaudin suggest that deviations in surface tension predictions stem from this simplified hypothesis.

## Data gathering

The experimental surface tension data, used for model training, has been retrieved online (surface-tension.de website). The dataset contains values for 85 organic molecules. These molecules vary from small, simple compounds to larger, complex structures, with molecular weights ranging from 18.02 g/mol (water) to 260.8 g/mol (hexachlorobutadiene). The dataset includes hydrocarbons, halogenated compounds, alcohols, and nitrogen-containing molecules. Additionally, there are compounds with oxygen-containing functional groups, such as ethers, esters and ketones. The molecules exhibit a broad range of polarities, with polar compounds contrasting nonpolar hydrocarbons. Structural complexity also varies, including linear alkanes, aromatic rings, and cyclic compounds. This chemical diversity makes the dataset suitable for exploring a wide range of physical and chemical properties. The Gibbs self-solvation free energy ($\Delta G_{sim}$) and molecular surfaces ($S_{sim}$) were caulcated from COSMOTherm software (version 24.0.0) using the BP-TVZP parameterisation, as suggested by Gaudin. Simulations were conducted over a temperature range of 5 to 50 °C, with increments of 5 °C for $\Delta G_{sim}$ predictions. Molecular flat surface data were extracted from the COSMO file of each molecule. A comparison between the simulated surface tensions in this study and those from Gaudin's work revealed strong agreement. Error metrics have been calculated point by point for $\Delta G_{sim}$, $S_{sim}$ and $\sigma_{sim}$, at T = 20 C, at which Gaudin results are available. The maximum absolute error observed was 0.66 kcal/mol for $\Delta G_{sim}$, 8.41 Å$^2$ for $S_{sim}$ , and 6.74 mN/m for the $\sigma_{sim}$. The maximum absolute percentage error observed was 8% for $\Delta G_{sim}$, 5% on the $S_{sim}$ and 11% for $\sigma_{sim}$. The coefficient of determination ($R^2$) for $\sigma_{sim}$, $S_{sim}$ and $\Delta G_{sim}$ is 0.989, 0.999 and 0.991 respectively. The small deviations observed could be due to slightly different parametrization in older versions of COSMOTherm or to the chosen molecules conformer.

## Features selection and data preprocessing

The developed model is a HM where the FPM is the one reported in Eq 1 and the ML part is composed by an Artificial Neural Network (ANN). The starting point of the ML part is the Simplified Molecular Input Line Entry System (SMILES) of the molecules. SMILES strings were stored from COSMOTherm along with simulation results, but can be easily retrieved from RDKit library as well. The SMILES strings are processed using the RDKit library (version 2024.9.4) in Python to generate chemical structures, substructures, and conformations, represented as text-based connection tables (MOL files). The resulting MOL files are subsequently analyzed with the Mordred library (version 1.2.0) in Python to compute molecular descriptors [9]. 37 2D descriptors are calculated, among which four are selected as inputs for the model. The

calculated descriptors concern the molecule aromaticity, structure, geometry, polarity. They were chosen for their potential influence on surface tension. Deviations in flat surface measurements are already expected due to polarity and may also result from molecular geometry, weight, hydrophobicity, and aromaticity. Feature selection is conducted iteratively using SHAP analysis, a game-theoretic approach that explains machine learning model predictions by assigning contribution values (SHAP values) to each feature [10]. This method helps identify which features drive the predictions and whether their influence positively or negatively affects the predicted surface tension. The SHAP (version 0.46.0.) library in Python has been used for the analysis. The selection process begins with training a neural network with a randomly chosen structure (e.g., three hidden layers with 30 nodes per layer) and evaluating its performance on test set metrics. In each iteration, the least important feature identified through SHAP analysis is removed, and the model is retrained. This process continues until the model achieves satisfactory performance, i.e. a MSE lower than that of a standalone FPM. This procedure is shown in Figure 1. The final selected features are the atom and bond polarizability, the average molecular weight, and the number of double bonds in Kekulized structure. In addition to these features, the COSMO-RS simulated surface tensions and the corresponding temperature are also used as model input. The dataset is therefore composed of molecular descriptors, temperatures, and surface tension calculations at every temperature. Given 85 molecules and temperatures ranging from 5 to 50°C with a step of 5°C, the dataset is composed of 850 examples and 6 features: simulated surface tension, temperature, atom and bond polarizability, average molecular weight and the number of double bonds in kekulized structure. The molecules have been organised by CAS Number and the test set has been randomly selected, while making sure that the molecules appearing in the test set are not included in the training set. For simplicity, the first 680 rows, e.g. the first 68 molecules of the dataset are used as training set and the remaining 170 rows, e.g. 17 molecules are used as test set. The data is then standardized prior to model training using a standard scaler in scikit learn (version 1.6.1) library.

## Model development

The workflow of the HM is given in Figure 2. Once the FPM calculations are completed, literature data gathered and features selected, the ANN can be trained for predicting experimental values of surface tensions from 5 to 50°C. The trained neural network is built and optimized in Keras library (version 3.5.0) in Python. The loss function is represented by the mean squared error (MSE). Activation function is Leaky Rectified Linear Unit (Leaky ReLU) with $\alpha$ = 0.01 for all layers, except the output one which has a linear activation function. The number of layers, neurons per layers and learning rate of the ANN are optimized through a Bayesian optimization (BO). The number of hidden layers to be chosen by the optimizer ranges from 2 to 5, while the number of nodes per layer ranges from 5 to 100 with a step of 3. The learning rate minimum and maximum boundaries were $10^{-4}$ and $10^{-2}$ respectively. During BO, the dataset is divided into training, validation, and test subsets. The test set comprises the last 17 molecules in the dataset, while the validation set is formed by randomly selecting 7 molecules (corresponding to 70 rows) from the training set across temperatures ranging from 5 to 50 °C. The loss function is the MSE on the validation set. After identifying the optimal network structure, the molecules initially used for validation are reintegrated into the training set, ensuring that the test set remains entirely unseen by both the model and the optimizer throughout the process. The proposed structure is formed by three hidden layers. The number of nodes per layer is 17,65,59 respectively and the learning rate is 0.00184. The model prediction accuracy is evaluated on various metrics both on training and test set e.g. the Mean Absolute Error (MAE), Mean Absolute Percentage Error (MAPE), MSE, the Root Mean Squared Error (RMSE), and the $R^2$. The same evaluation metrics are also used to compare the FPM standalone prediction accuracy.

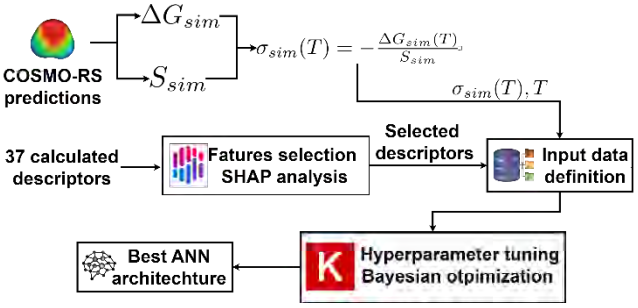



**Figure 1:** Training workflow. Self-solvation energies and molecular flat surfaces are obtained from COSMO-RS predictions, and surface tension is subsequently calculated. A total of 37 molecular descriptors are computed. Feature selection is carried out using SHAP analysis through an iterative process. Upon completion, the selected descriptors, simulated surface tension, and corresponding temperature constitute the input dataset. Hyperparameter tuning is then conducted to identify the optimal model architecture.

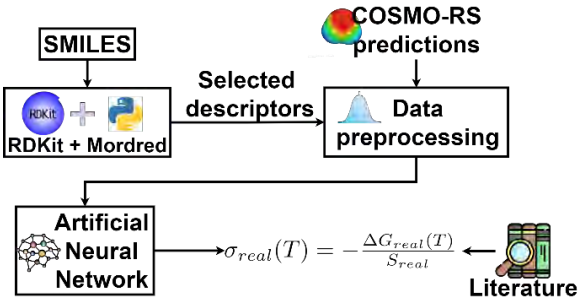



**Figure 2:** HM model workflow. Mol files are retrieved from SMILES in RDKit library. Molecular descriptors are calculated from Mordred library. Surface tensions, temperatures and descriptors are provided to an ANN which can predict temperature-dependent surface tensions experimental data.

## RESULTS

### Model prediction accuracy

Figure 3 shows a comparison of the predicted surface tension using Gaudin standalone model, the developed HM and experimental values. The left plot shows the parity plot for a range of temperatures from 5 to 50°C, while the right one shows predictions for a temperature of 25°C for the HM only, middle point of the selected temperatures. Looking at the standalone FPM, for some, less polar molecules, e.g. cyclohexane, 1-chlorobutane, dodecane, carbon tetrachloride, 1-nitropropane, Gaudin approximation seems to hold. Nevertheless, some molecules that show strong hydrogen-bonding association may orient in a specific way at the interface, with consequent deviations from experimental measurements. Overestimated surface tension is indeed evident for molecules above the 20% error line. These are methanol, ethanol, water, formamide, glycol, propanol and 2-propanol. 5 of these are also cited as overestimated outliers in Gaudin's paper. Overall, apart from the molecules mentioned above, the standalone FPM slightly underestimates surface tension. This trend is visible in the clustering of green data points below the parity line. Focusing on the HM model predictions, instead, all the points, for both training and test sets, fall within the 20% error region, showing the improved accuracy of the HM compared to the FPM. The plots demonstrate that the ANN effectively corrects the deviations of the FPM, even for the aforementioned polar molecules that exhibit significant discrepancies from the experimental values. Table 1 presents Gaudin's standalone model metrics for predicting surface tension, along with the percentage improvement in these metrics when the FPM is compared to the HM test set performance. The decrease of all the error metrics and the outstanding increase of the $R^2$ confirm that the HM offers a significant improvement in predictive performance.

**Table 1:** FPM metrics and corresponding percentage improvement achieved when compared to the HM test set metrics.

| Metric | FPM | Improvement (%) |
|---|---|---|
| MAE | 5.99 mN/m | -75.6% |
| MAPE | 17.95 % | -78.9% |
| MSE | 70.25 $mN^2/m^2$ | -95.0% |
| RMSE | 8.3816 mN/m | -77.8% |
| $R^2$ | 0.4281 | +111.0% |

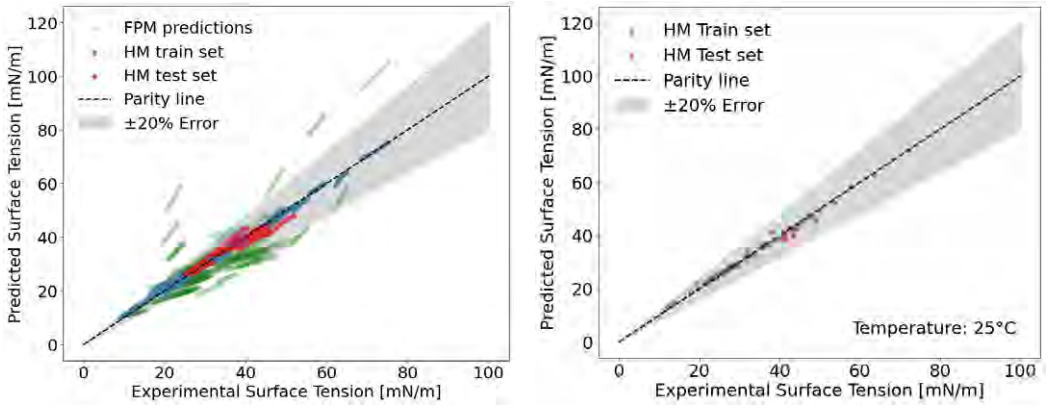



**Figure 3**: Comparison between the FPM, the HM developed in this work and experimental data. The left plot shows results of surface tension calculations from 5 to 50 °C. The green points represent the FPM model predictions. Blue and red points represent the HM train and test dataset, respectively. The black dashed line represents the ideal scenario where predicted values perfectly match experimental values, indicating a model with no error. The gray shaded region shows a ±20% error margin, providing a visual reference for acceptable prediction deviations. The right plot shows a parity plot of the simulated vs experimental surface tension at 25 °C for the HM only.

Table 2 shows the HM metrics, both for training and test set. The training set metrics highlight the model accuracy on known data, indicating excellent fit. For the test set, the metrics remain robust, also demonstrating good agreement with experimental data.

**Table 2:** HM metrics on training and test sets.

| Metric | Train | Test |
|---|---|---|
| MAE | 0.60 mN/m | 1.4619 mN/m |
| MAPE | 2.27% | 3.77% |
| MSE | 0.6281 $mN^2/m^2$ | 3.4852 $mN^2/m^2$ |
| RMSE | 0.7925 mN/m | 1.8669 mN/m |
| $R^2$ | 0.99 | 0.90 |

## SHAP analysis

Figure 4 shows a SHAP violin plot for the presented model. In the violin plot shown, SHAP values are plotted for the features evaluated on the test set, with the horizontal axis representing the SHAP value (i.e., the impact on the model's output) and the vertical axis listing the features. The shape of each violin represents the distribution of SHAP values for a feature across the dataset, highlighting variability in its impact.

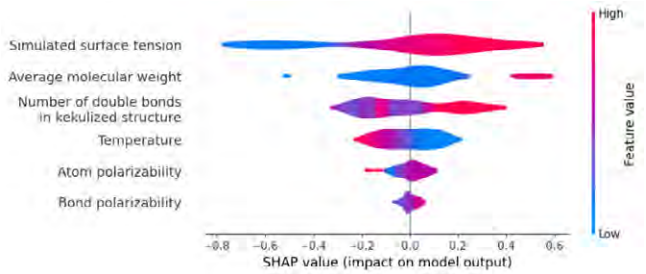



**Figure 4:** SHAP analysis violin plot. Simulated surface tension is the most relevant feature, bond polarizability the least relevant one.

Additionally, the color gradient within each violin indicates the corresponding feature value, with red denoting high feature values and blue denoting low feature values. This dual representation allows for an intuitive understanding of both the direction and magnitude of feature contributions to the model predictions. For the developed HM, the simulated surface tension is the most influential feature, with higher simulated surface tension (red) generally increasing the model's predictions and lower values (blue) reducing them. The widespread indicates a substantial variability in its impact. The average molecular weight of a molecule is nothing else than the sum of molecular weights of its elements divided by the number of elements. It is strictly correlated with the molecular weight, which can affect the hydrophobicity of a molecule, thus affecting how it behaves at a liquid interface. However, the effect can vary depending on the compound's structure and functional groups. For example, if the molecule is large but contains hydrophobic regions, it may reduce surface tension by disrupting water's hydrogen bonding network. Conversely, molecules with hydrophilic groups and higher molecular weights may increase surface tension by reinforcing interfacial interactions. The average molecular weight feature shows a less pronounced but consistent positive influence on predictions when its values are high, while lower values have little to no effect. Aromaticity can be defined in a multitude of ways. Moreover, 'aromatic' moieties in structures can be represented in Kekulé form using alternating single and double bonds [11]. Double bonds introduce rigidity and delocalized π-electron systems, which can affect molecular interactions. Molecules with a higher number of double bonds in the Kekulized structure could exhibit increased molecular polarizability, which can contribute to higher surface tension. Additionally, these aromatic systems may alter the hydrophobicity or hydrophilicity of a molecule, further affecting how it behaves at liquid interfaces. The number of double bonds in kekulized structure feature has a balanced influence, with higher values slightly increasing the predictions and lower values reducing them. The spread of SHAP values suggests moderate variability in its impact. High temperatures tend to lower the prediction values, while lower temperatures slightly increase them. This behavior aligns with expectations. As temperature rises, the self-solvation energy slightly increases (e.g. becomes less negative). Since surface tension is calculated as the negative ratio of the self-solvation energy to the molar surface (which is temperature-independent), an increase in temperature results in a decrease in surface tension. Polarizability measures how easily the electron cloud around an atom can be distorted by external electric fields. It affects the strength of van der Waals forces, which play a significant role in determining surface tension. Atomic polarizability is a parameter depending on the ease of deforming the valence electron clouds of a chemical species. Mordred iterates over all atoms and bonds of a molecule and then return the sum of all atomic and bond polarizabilities as a total value. Molecules with higher atom polarizability often exhibit stronger intermolecular attractions, potentially increasing surface tension. Similar to atom polarizability, bond polarizability refers to the distortion of electron density within bonds. It influences the molecule's ability to interact with neighboring molecules. While its direct impact on surface tension may be weaker compared to atom polarizability, it can contribute to intermolecular forces. The variability indicates a modest but significant influence. Atom and bond polarizability exhibit a narrower range of SHAP values, indicating a limited impact overall.

## CONCLUSIONS

A HM to accurately predict surface tension of organic molecules from 5 to 50°C has been presented. This study highlights the value of integrating first-principle and data-driven methods to enhance prediction. Nevertheless, the developed HM was trained on a relatively small dataset consisting of 68 molecules. The authors of this work have parallelly revisited a comprehensive but largely inaccessible, due to its outdated digital format, dataset of over 2000 surface tension measurements, transforming it into a machine-readable format to eliminate manual transcription errors. The experimental data utilized in this work originates from Jasper's compilation [12]. The dataset will be used for model training in future work. Moreover, the authors are currently working at an improved, physics-informed, version of the current model. In order to prove previous assumption on deviation source, 53 pseudo-experimental self-solvation free energies have been found from dGsolvDB1 dataset [13]. Through the FPM, calculations of the real molecular surface can be performed. The ANN can be therefore trained to also predict the deviation between the flat surface and the real one, in order to show how restrictive this hypothesis can be. Additionally, developing a model capable of pointing the sources of FPM deviations and addressing them could be highly beneficial. Such a model could then be adapted and extended to a wider range of applications.

## ACKNOWLEDGEMENTS

FE, UDC, MEL acknowledge funding from the KU Leuven project HyPro (C3/23/007) and VLAIO project FAST (HBC2021.0974).

## REFERENCES

1. A. Roosta, P. Setoodeh, and A. Jahanmiri, "Artificial neural network modeling of surface tension for pure organic compounds," *Ind Eng Chem Res*, vol. 51, no. 1, pp. 561–566, Jan. 2012, doi: 10.1021/ie2017459.
2. V. Goussard et al., "Predicting the Surface Tension of Liquids: Comparison of Four Modeling Approaches and Application to Cosmetic Oils," *J Chem Inf Model*, vol. 57, no. 12, pp. 2986–2995, Dec. 2017, doi: 10.1021/acs.jcim.7b00512.
3. E. J. Delgado and G. A. Diaz, "A molecular structure based model for predicting surface tension of organic compounds," *SAR QSAR Environ Res*, vol. 17, no. 5, pp. 483–496, Oct. 2006, doi: 10.1080/10629360600933913.
4. Y. Lei, Y. Shu, X. Liu, X. Liu, X. Wu, and Y. Chen, "Predictive modeling on the surface tension and viscosity of ionic liquid-organic solvent mixtures via machine learning," *J Taiwan Inst Chem Eng*, vol. 151, Oct. 2023, doi: 10.1016/j.jtice.2023.105140.
5. A. Klamt, "Conductor-like Screening Model for Real Solvents: A New Approach to the Quantitative Calculation of Solvation Phenomena," *J. Phys. Chem*, vol. 99, pp. 2224–2235, 1995, doi: 10.1021/j100007a062.
6. C. Nieto-Draghi et al., "A General Guidebook for the Theoretical Prediction of Physicochemical Properties of Chemicals for Regulatory Purposes," *Chem Rev*, vol. 115, no. 24, pp. 13093–13164, Dec. 2015, doi: 10.1021/acs.chemrev.5b00215.
7. T. Gaudin, "Exploring direct prediction of surface tension from COSMO-RS theory," *Chem Phys Lett*, vol. 706, pp. 308–310, Aug. 2018, doi:10.1016/j.cplett.2018.06.036.
8. J. Glassey and M. von Stosch, Hybrid Modeling in Process Industries, First edition. New York: CRC Press, 2018.
9. H. Moriwaki, Y. S. Tian, N. Kawashita, and T. Takagi, "Mordred: A molecular descriptor calculator," *J Cheminform*, vol. 10, no. 1, Feb. 2018, doi: 10.1186/s13321-018-0258-y.
10. S. M. Lundberg and S.-I. Lee, "A Unified Approach to Interpreting Model Predictions," in Advances in Neural Information Processing Systems, I. Guyon, U. Von Luxburg, S. Bengio, H. Wallach, R. Fergus, S. Vishwanathan, and R. Garnett, Eds., Curran Associates, Inc., 2017.
11. S. J. Cyvln and I. Gutman, "Kekulé Structures and their Symmetry Properties," *Comp. & Maths. with Appls*, vol. 12, pp. 859–876, 1986.
12. J. J. Jasper, "The Surface Tension of Pure Liquid Compounds," *J Phys Chem Ref Data*, vol. 1, no. 4, pp. 841–1010, 1972, doi: 10.1063/1.3253106.
13. Y. Chung, F. H. Vermeire, H. Wu, P. J. Walker, M. H. Abraham, and W. H. Green, "Group Contribution and Machine Learning Approaches to Predict Abraham Solute Parameters, Solvation Free Energy, and Solvation Enthalpy," *J Chem Inf Model*, vol. 62, no. 3, pp. 433–446, Feb. 2022, doi: 10.1021/acs.jcim.1c01103.

© 2025 by the authors. Licensed to PSEcommunity.org and PSE Press. This is an open access article under the creative commons CC-BY-SA licensing terms. Credit must be given to creator and adaptations must be shared under the same terms. See https://creativecommons.org/licenses/by-sa/4.0/



Systems & Control Transactions

**Research Article - Peer Reviewed Conference Proceeding**
ESCAPE 35 - European Symposium on Computer Aided Process Engineering
Ghent, Belgium. 6-9 July 2025
Jan F.M. Van Impe, Grégoire Léonard, Satyajeet S. Bhonsale,
Monika E. Polańska, Filip Logist (Eds.)

PSE PRESS

# Hybrid model development for Succinic Acid fermentation: relevance of ensemble learning for enhancing model prediction

**Juan Federico Herrera-Ruiz[a], Javier Fontalvo[a], Oscar Andrés Prado-Rubio[a]***

[a] Departamento de Ingeniería Química, Universidad Nacional de Colombia – 170003 Manizales, Colombia
* Corresponding Author: oaprador@unal.edu.co

## ABSTRACT

Sustainable development goals have spurred advancements in bioprocess design, driven by improved process monitoring, data storage, and computational power. High-fidelity models are essential for advanced process system engineering, yet accurate parametric models for bioprocessing remain challenging due to overparameterization, often resulting in poor predictive accuracy. Hybrid modeling, combining parametric and non-parametric methods, offers a promising solution by enhancing accuracy while maintaining interpretability. This study explores hybrid models for succinic acid fermentation by *Escherichia coli*, a critical process for sustainable bio-based chemical production. The research presents a structured exploration of hybrid model architectures and their robustness under varying conditions. Experimental data were preprocessed to remove noise and outliers, and hybrid model structures were developed with differing levels of hybridization (from one to all reaction rates). Kinetic parameters were recalibrated and compared against original values. Machine learning algorithms, including Artificial Neural Networks, Support Vector Machines, and Gaussian Processes, were tested, with tuning strategies applied to original or recalibrated parameters. Due to a considerable variability in individual model performance for validation, an ensemble learning approach was proposed to enhance robustness. Results demonstrate that despite not solving the overparametrization issues, all hybrid models outperform the original parametric model, with the best-performing hybrid model achieving a 52.3% lower RMSE of validation, avoiding overfitting. Ensemble approaches further improved predictions, reducing RMSE by up to 62.3% compared to individual parametric models. This highlights hybrid modeling's potential to enhance bioprocess prediction accuracy, even with limited data, supporting future advancements in bioprocess scale-up, digitalization, and sustainable biorefinery implementations.

**Keywords**: Modelling, Fermentation, Modelling and Simulations, Machine Learning, Reaction Engineering, Hybrid modelling, Succinic Acid, Kinetics.

## 1. INTRODUCTION

Succinic Acid is considered as one of the key molecules to pave the way for sustainable bio-based production of chemicals. Succinic acid is used to produce over 30 commercially available products, including food ingredients and additives, commodity chemicals like polymers (PBS), solvents and other organic acids and even pharmaceutical intermediates [1].

The increasing focus on sustainable development goals has spurred significant research into bioprocesses optimization, particularly through technological advancements in process monitoring, data storage, and computational capabilities. These developments, combined with modelling techniques and simulation tools, are driving substantial advances on digitalization of biomanufacturing. In this context, hybrid modelling has emerged as a powerful approach, combining parametric and non-parametric methods to mitigate their individual drawbacks. Parametric kinetic models for succinic acid fermentation tend to be overparameterized and uncertain, leading to poor predictive performance [2,3], presenting prediction

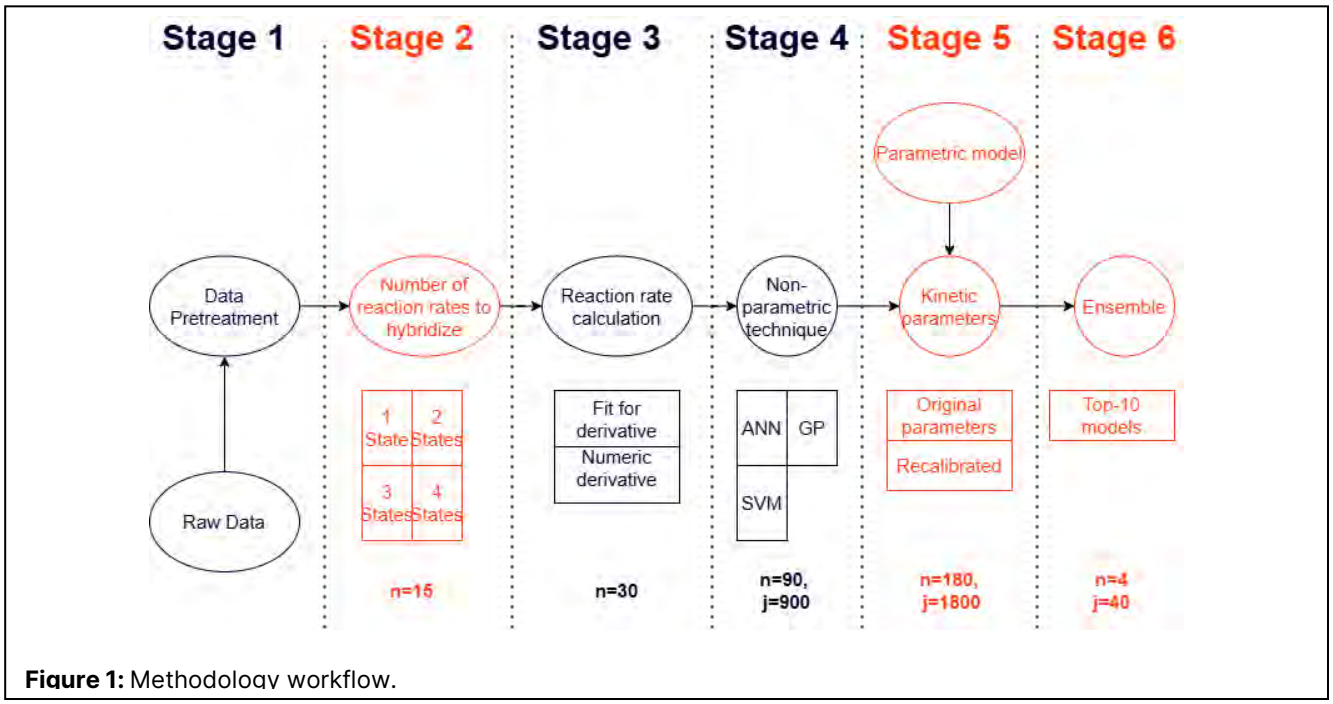



**Figure 1:** Methodology workflow.

errors up to 30% in key variables such as biomass and product concentrations [4]. Hybrid modelling has been successfully applied to describe fermentations, reducing errors in industrial settings up to 50% when compared against parametric models [5]. Therefore, hybrid modelling rises as an alternative to increase accuracy and precision for describing succinic acid fermentations.

This study focuses on developing a hybrid model to harness limited experimental data and improve states' predictions of succinic acid fermentation by *Escherichia coli* [6]. To achieve this objective, model structures and nonparametric techniques were systematically constructed and investigated. Different levels of hybridization were tested, ranging from 1 to 4 reaction rates replaced by either Artificial Neural Networks (ANNs), Support Vector Machines (SVMs), and Gaussian Processes (GPs). Ensemble learning was proposed to enhance predictive capabilities, due to high variability between predictions of individual models and poor performance. This paper is structured as follows: section 2 presents the methodology for constructing the hybrid models, detailing data pretreatment and model structure choices. In section 3 results are shown, comparing different model structures and their combinations. Finally, section 4 provides the conclusions of this investigation.

## 2. METHODOLOGY

Figure 1 presents the workflow proposed in the present work. Stages colored in orange represent structural decisions made to develop the model and stages presented in dark blue represent numeric decisions. Mass balances constitute the parametric knowledge incorporated to the hybrid model whereas reaction rates are replaced by nonparametric techniques. In the lower part of Figure 1, *n* refers to the number of model structures involved in the stage, while j refers to the total number of possible trained models. Notice that the sequential stages from 2 to 5 correspond to model structures building and do not mean those models were trained in each stage. The total number of models trained were 1800 in Stage 5.

### 2.1 Data Pretreatment

The experimental data was taken from the original paper [6]. First, outliers were detected and removed following established methodologies [7]: i) Outliers were identified using a moving median window of three datapoints and ii) if an outlier was identified, this was replaced using the Savitsky-Golay polynomial approach. Then, data augmentation was performed to enhance the predictive capabilities of the ML algorithms. Originally, experiments ranged from 21 to 37 experimental datapoints and the data augmentation procedure was done, so each experiment had 50 datapoints for each variable. Experiments were separated in training and validation in the same partitions as the original authors [6].

### 2.2 Reaction rate hybridization

In Stage 2, a decision is made to quantify how many and which reaction rates will be replaced by non-parametric model. There are a total of 15 possible combinations of reaction rates replaced by non-parametric techniques.

As such, the reaction rate of a state is replaced by a

non-parametric technique, as exemplified in eq. 1 for Succinic Acid ($SA$):

$$\frac{dSA}{dt} = f(t, S_{in}) \quad (1)$$

where $f(t, S_{in})$ represents the output of a non-parametric technique that receives time ($t$) and initial substrate concentration $S_{in}$ as inputs.

## 2.3 Reaction rate calculation

Reaction rates are used to train the non-parametric techniques chosen in Stage 4. To approximate these rates two different approaches were tested: i) a sigmoidal fit for substrate, succinic and acetic acid, and a polynomial fit for biomass were implemented, and then derived to obtain the reaction rate, and ii) the numeric derivative was calculated using the smoothed experimental data. This procedure yields 30 different model combinations to evaluate.

## 2.4 Non-parametric technique

In Stage 4, the non-parametric technique used to describe the reactions rates replaced in Stage 2 and calculated in Stage 3 is chosen. In this work, Artificial Neural Networks (ANN), Support Vector Machines (SVM), and Gaussian Processes (GP) were tested for each hybrid model. Notice that the same non-parametric technique was used for all the reaction rates, not considering mixtures such as one reaction rate modeled using GPs and other using ANNs. Therefore, there are 90 model combinations to evaluate. Each combination was trained 100 times, yielding 900 different trained models. Hyper-parameters were optimized using MATLAB 2024b® built-in functionalities.

### Hybrid Model structure

#### 2.1.1. Parametric model

For the succinic acid fermentation, the original researchers proposed a model to describe biomass growth, succinic and acetic acid production, and substrate consumption composed by 4 ODE's and 16 parameters. The biomass growth is expressed using a modified Monod expression (eq. 2) incorporating the product and substrate inhibition terms proposed by Levenspiel [8]. Cell lysis was considered, and it's expressed in eq. 3:

$$\mu = \mu_{max} \cdot \left(\frac{S}{S+k_S}\right) \cdot \left(1 - \frac{SA}{SA_{crit}}\right)^p \cdot \left(1 - \frac{S}{S_{crit}}\right)^n \quad (2)$$

$$k_L = k_{l,max} \cdot \left(\frac{k_l}{S+k_l}\right) \quad (3)$$

$$\frac{dX}{dt} = (\mu - k_L) \cdot X \quad (4)$$

where, $S$ the substrate concentration, $SA$ the succinic acid concentration, $X$ represents the biomass concentration, $\mu$ is the specific growth rate, $\mu_{max}$ the maximum specific growth rate, $SA_{crit}$ the critical succinic acid concentration for inhibition, $p$ the power constant of succinic acid inhibition, $S_{crit}$ the critical substrate concentration for inhibition, $n$ the power constant of substrate inhibition..

Product formation of Succinic Acid and Acetic Acid was described using Luedeking-Pirett expressions, shown in eqs 5 and 6, where $AA$ represents the acetic acid concentration, $\alpha_{SA}$ and $\alpha_{SA}$ represent the growth associated constants for $AA$ and $SA$ respectively, whereas $\beta_{AA}$ and $\beta_{SA}$ represent the non-growth associated constants for $AA$ and $SA$, respectively.

$$\frac{dSA}{dt} = \alpha_{SA} \cdot \frac{dX}{dt} + \beta_{SA} \cdot X \quad (5)$$

$$\frac{dAA}{dt} = \alpha_{AA} \cdot \frac{dX}{dt} + \beta_{AA} \cdot X \quad (6)$$

Substrate consumption depends on two terms: one associated with biomass growth (eq. 7) and a term associated with biomass maintenance (eq 8). The substrate consumption rate is shown in eq. 9:

$$w = \frac{1}{Y_{X/S}} + \frac{\alpha_{SA}}{Y_{SA/S}} + \frac{\alpha_{AA}}{Y_{AA/S}} \quad (7)$$

$$z = \frac{\beta_{SA}}{Y_{SA/S}} + \frac{\beta_{AA}}{Y_{AA/S}} + m_{e,X} \quad (8)$$

$$\frac{dS}{dt} = -(w \cdot dX + z \cdot X) \quad (9)$$

where $Y_{X/S}$,$Y_{SA/S}$,$Y_{AA/S}$ represent the yields for biomass, succinic acid and acetic acid respectively. $m_{e,X}$ represents the cell maintenance coefficient of substrate consumption.

#### 2.1.2. Remaining Kinetic Parameters values

For the hybrid model consolidation, the kinetic parameters that remain in the mass balances, after replacing the reaction rates predicted by the ML technique in Stage 4, are evaluated in two different schemes:

- Keeping the original values proposed by the authors.
- Recalibrating the kinetic parameters.

This final procedure yields 180 model combinations, and 1800 models trained.

#### 2.1.3 Ensemble learning approach

In preliminary simulations, high variability in predicted outputs and poor performance of individual models were observed. To address this issue and improve model performance, an ensemble approach was implemented by algebraically averaging predictions. Specifically, 100 models were trained for each model structure, and the top 10 models were selected and evaluated based on their performance. From these, the best combinations were identified for cases involving the replacement of 1, 2, 3, and 4 reaction rates. This process resulted in the selection of 4 model structures and a total of 40 trained models, which were ultimately used for

predictions.

### 2.1.4 Computational Aspects

Simulations were conducted on a commercial laptop with an Intel(R) Core (TM) i7-10510U CPU 1.80GHz, 2304 Mhz with 4 cores, 8 GB of RAM and no dedicated GPU. Calculations were performed in Matlab 2024a®. Models were trained in parallel with training times ranging from 9 up to 49 hours.

To compare the results of the different models, the RMSE reduction was calculated, as seen in eq 10:

$$RMSE_{reduction} = \frac{RMSE_{Parametric\ Model} - RMSE_{Hybrid\ Model}}{RMSE_{Parametric\ Model}} \quad (10)$$

## 3. RESULTS

Figure 2 shows the SA concentration in a validation experiment for the parametric model, when only the SA reaction rate is replaced using GPs.

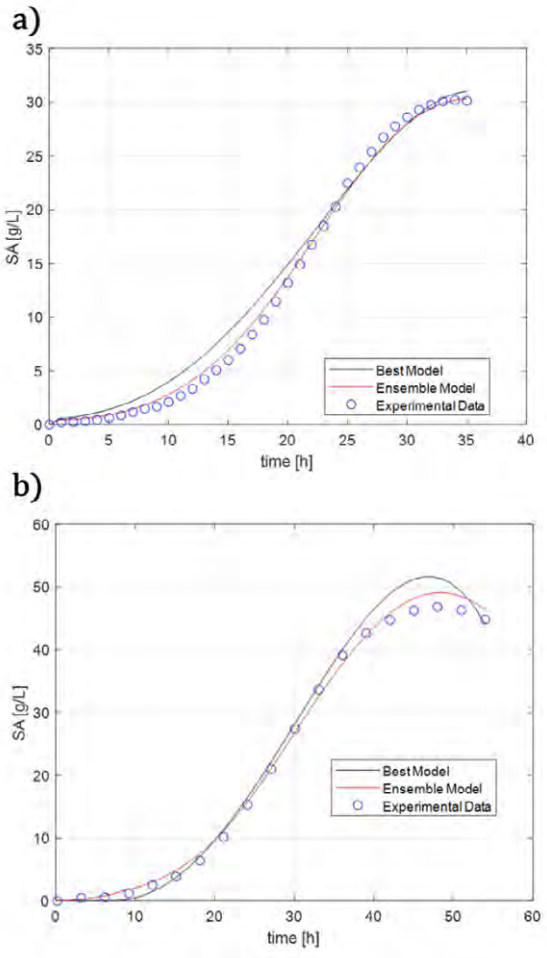



**Figure 2.** Best individual model fit and ensemble predictor when replacing only the SA reaction rate . a) initial concentration of 40g/l of Xylose. b) concentration of 60g/l of Xylose.

As seen in Figure 2, the best individual model (GPs, numeric derivatives for reaction rates and no kinetic parameter recalibration) correctly predicts the general trends and values of experimental data, but the ensemble model (GPs, numeric derivatives for reaction rates and no kinetic parameter recalibration) is closer to them. Consequently, the parametric model has an RMSE of 7.03, while the best individual fit has an RMSE of 6.68 and the ensemble prediction presents an RMSE of 6.37. Although both the best individual model and the ensemble model perform better than the parametric one, the ensemble approach yields a significantly better RMSE, with an RMSE reduction of 9.9% against the 4.9% yielded by the best individual fit. Overall, ensemble approaches show prediction errors in the validation set ranging from 5% to 14% lower when compared to the best individual models, with the greatest gains observed when replacing all four reaction rates.

Figure 3 shows the ensemble model and its confidence intervals when using GPs and replacing only the SA reaction rate. Confidence intervals are built using the lowest and highest prediction of SA within the ensembled models for each sample time. The median confidence interval presents a 10% deviation from the ensemble model's prediction. Higher deviations are seen for lower times, whereas the model's confidence intervals become narrower as the time advances, becoming as narrow as 2.3%. As a result, 94% of the experimental datapoints lie inside the confidence interval with all the points outside of it being in fermentation times less than 4 hours, signaling that the ensemble model is robust enough to average the weaknesses and strengths of individual models while accurately describing the dataset.

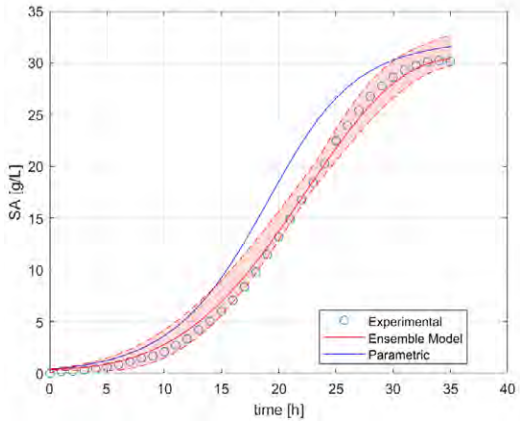



**Figure 3.** Ensemble predictor uncertainty when replacing only the SA reaction rate

Figure 4 presents the profiles obtained for the ensemble models when replacing SA, and X for ANNs and using numeric derivatives in validation experiments. It is noteworthy that despite the similarities in the profiles, the Hybrid Models have different performances, with an

RMSE of 5.68 (RMSE reduction of 27.1%) for the hybrid model with the original parameters and 5.22 (RMSE reduction of 34.8%) for the hybrid model recalibrating the other initial parameters.

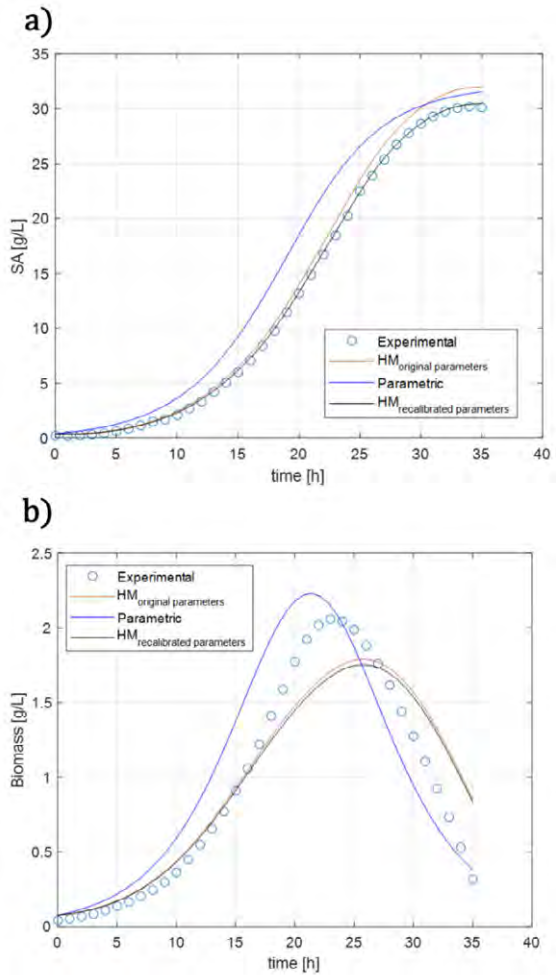



**Figure 4.** Performance of the ensemble models when replacing SA, and X for ANNs and using numeric derivatives. a) Succinic Acid for an initial concentration of 40 g/L of Xylose. b) Biomass for an initial concentration of 60 g/L of Xylose. HM stands for "Hybrid Model".

As seen in Figure 4, the Hybrid models represent more accurately the behavior of SA, whereas the parametric model tends to overpredict concentrations. Nonetheless, the Hybrid Model that uses the original kinetic parameters results in higher final SA concentrations than both the parametric model and the experimental data. For biomass, the parametric model tends to overestimate concentrations and predicts the biomass peak earlier than the experimental data shows, with a steep descent that results in an underestimation of the biomass concentrations. Hybrid Models perform better up until the 20h mark, where the Hybrid Models deviate, predicting lower concentrations and a lower peak displaced around 5h. After the predicted peak, the Hybrid Models tend to predict higher concentrations than both the parametric model and experimental data.

When recalibrating the kinetic parameters, their values differed on average 14.9% when compared against the original ones. The mass balances show high dependency between one another, therefore replacing reaction rates could provide better description for a specific variable while worsening other predictions.

Table 1 shows the RMSE reduction in validation classified by number of reaction rates and machine learning technique for the best ensemble models. The best ensemble models for the three machine learning techniques are as follows, with all of them using numeric derivatives and recalibrating kinetic parameters:

- Replacing only one reaction rate (SA).
- Replacing two reaction rates (SA and AA)
- Replacing three reaction rates (SA, AA and X)

**Table 1**: Percentage of RMSE reduction in validation experiments classified by number of reaction rates replaced and nonparametric technique used.

| Black Box Technique | 1 rate | 2 rates | 3 rates | 4 rates |
|---|---|---|---|---|
| ANN | 20.9% | 34.8% | 61.4% | 62.3% |
| GP | 15.6% | 29.8% | 50.9% | 57.0% |
| SVM | 13.3% | 27.1% | 40.5% | 47.3% |

As expected, for all machine learning techniques, the model predictions improve by increasing the number of reaction rates replaced. However, there are diminishing returns each time, since the biggest performance gains are seen when jumping from 2 to 3 reaction rates, reducing RMSE around 50% for all cases. This is due to the states interact between each other in the model, therefore, a better description of one state does not necessarily translate into better description of the other states. This occurs despite recalibrating the remaining model parameters, as can be seen in Figure 3 for biomass.

Generally, ANNs perform better than SVMs and GPs for all cases. However, the performance of ANNs and GPs is comparable, with latter needing fewer intensive calculations. When replacing the four reaction rates, GPs reduce the RMSE 57%, with ANNs presenting a 62.8% reduction despite taking almost 5 times larger training time (9 hours versus 45 hours). SVMs have comparable performance to the other two machine learning techniques up to replacing two states, however the performance gains when using three or more are less than what GPs and ANNs present.

Despite gaining better performance when replacing more reaction rates, the structure of the model becomes

less parametric and approaches more to a full non-parametric technique. This means that the model loses interpretability and explainability in exchange for more numeric precision. Moreover, the performance gains seen from three to four reaction rates replaced are small, signalling diminishing returns.

## 4. CONCLUSIONS

The results of this study underscore the transformative potential of hybrid modeling in succinic acid fermentation by *Escherichia coli*. The hybrid models demonstrated superior predictive accuracy, achieving RMSE reductions of up to 62.3% when replacing four reaction rates, significantly outperforming traditional parametric models. Also, the individual hybrid models suffer from low robustness during validation, making necessary the use of ensemble learning, which is not commonly use in ML applications. Ensemble approaches provided higher accuracy, by leveraging the strengths of the individual models while minimizing their weaknesses. Ensemble approaches could be very useful for developing bioprocesses because they are usually less sensitive to noisy data, making them more robust than traditional models. Among the non-parametric techniques tested, Artificial Neural Networks (ANNs) delivered the highest accuracy but at a greater computational cost, whereas Gaussian Processes (GPs) provided comparable performance with reduced complexity, making them an efficient alternative. The recalibration of kinetic parameters emerged as a critical factor for optimizing model performance, particularly when paired with numeric derivatives for reaction rate calculation. While increasing the number of replaced reaction rates improved numerical precision, this came at the expense of model interpretability, with diminishing returns observed beyond three reaction rates. Besides using black box techniques to replace reaction rates does not solve the issue of overparametrization of kinetic models in bioprocesses which might lead to overfitting and poor prediction capabilities in the validation sets. However, it has been shown that using ensemble approaches helps to reduce models' individual weaknesses and enhance their strengths, therefore increasing and enhancing prediction capabilities, as seen by better predictions in the validation set with reduced predictor uncertainty.

## ACKNOWLEDGEMENTS

This work was funded by the Sistema General de Regalías de Colombia (SGR) fund, through the Project BPIN: 2022000100035.

## REFERENCES

1. Dai Z, Guo F, Zhang S, Zhang W, Yang Q, Dong W, et al. Bio-based succinic acid: an overview of strain development, substrate utilization, and downstream purification. Biofuels, Bioproducts and Biorefining 2020;14:965–85. https://doi.org/10.1002/bbb.2063.
2. de Azevedo CR, Díaz VG, Prado-Rubio OA, Willis MJ, Préat V, Oliveira R, et al. Hybrid Semiparametric Modeling: A Modular Process Systems Engineering Approach for the Integration of Available Knowledge Sources. Systems Engineering in the Fourth Industrial Revolution, Wiley; 2019, p. 345–73. https://doi.org/10.1002/9781119513957.ch14.
3. Leonov P. Bio-succinic acid production from alternative feedstock. Denmark Technical University, 2022.
4. F. Vigato, J.M. Woodley, M. Alvarado-Morales, Modeling the effect of CO2 limitation in continuous fermentation for biosuccinic acid production, Journal of CO2 Utilization 79 (2024) 102651. https://doi.org/10.1016/j.jcou.2023.102651.
5. P. Shah, M.Z. Sheriff, M.S.F. Bangi, C. Kravaris, J.S. Il Kwon, C. Botre, J. Hirota, Deep neural network-based hybrid modeling and experimental validation for an industry-scale fermentation process: Identification of time-varying dependencies among parameters, Chemical Engineering Journal 441 (2022). https://doi.org/10.1016/j.cej.2022.135643
6. Chaleewong T, Khunnonkwao P, Puchongkawarin C, Jantama K. Kinetic modeling of succinate production from glucose and xylose by metabolically engineered Escherichia coli KJ12201. Biochem Eng J 2022;185:108487. https://doi.org/10.1016/j.bej.2022.108487.
7. Sánchez-Rendón JC, Morales-Rodriguez R, Matallana-Pérez LG, Prado-Rubio OA. Assessing Parameter Relative Importance in Bioprocesses Mathematical Models through Dynamic Sensitivity Analysis, 2020, p. 1711–6. https://doi.org/10.1016/B978-0-12-823377-1.50286-X.
8. Levenspiel O. The monod equation: A revisit and a generalization to product inhibition situations. Biotechnol Bioeng 1980;22:1671–87. https://doi.org/10.1002/bit.260220810.

© 2025 by the authors. Licensed to PSEcommunity.org and PSE Press. This is an open access article under the creative commons CC-BY-SA licensing terms. Credit must be given to creator and adaptations must be shared under the same terms. See https://creativecommons.org/licenses/by-sa/4.0/



Systems & Control Transactions

**Research Article - Peer Reviewed Conference Proceeding**
ESCAPE 35 - European Symposium on Computer Aided Process Engineering
Ghent, Belgium. 6-9 July 2025
Jan F.M. Van Impe, Grégoire Léonard, Satyajeet S. Bhonsale,
Monika E. Polańska, Filip Logist (Eds.)

PSE PRESS

# Reinforcement learning for distillation process synthesis using transformer blocks

**N. Slager[a], M.B. Franke[a,*]**

[a] Sustainable Process Technology Group, Department of Chemical Engineering, Faculty of Science and Technology, University of Twente, Drienerlolaan 5, 7522 NB Enschede, The Netherlands
* Corresponding Author: m.b.franke@utwente.nl.

## ABSTRACT

A reinforcement learning framework is developed for the synthesis of distillation trains. The rigorous Naphtali-Sandholm algorithm for equilibrium separation modeling was implemented in JAX and coupled with the benchmarking Jumanji RL library. The vanilla actor-critic agent was successfully trained to build distillation trains for a seven-component hydrocarbon mixture. A transformer encoder structure was used to apply self-attention over the agent's observation. The agent was trained on minimal data representation containing quantitative component flows and relative volatility parameters between present components. Training sessions involving $5{\cdot}10^4$ episodes ($3{\cdot}10^5$ column designs) were typically run in under 60 minutes. While training was fast and reliable with appropriate tuning of the hyperparameters, further improvements are needed in the generalizability performance for similar separation problems.

**Keywords**: Artificial Intelligence, Machine Learning, Process Synthesis, Distillation, Optimization, Reinforcement learning, Transformer Blocks

## INTRODUCTION

The field of process systems engineering (PSE) has witnessed significant advancements through the combination of machine learning (ML) techniques with traditional PSE methods. Among these, reinforcement learning (RL) has emerged as a promising approach [1], due to its capacity to tackle sequential decision-making problems inherent to process synthesis. Notably, Midgley (2020) [2] pioneered RL in PSE for process synthesis with the introduction of the Distillation Gym, an open-source platform designed for optimizing distillation train configurations simulated in ChemSep/COCO for user-defined multicomponent feeds. This foundational work was further developed by van Kalmthout et al. (2022) [3], who integrated Aspen Plus for rigorous process modeling within the RL framework. However, major improvements were not achieved due to the insufficient data transfer speed and (un)reliability of the RL/Aspen Plus interface.

Considering flowsheet synthesis involving multiple unit operations and recycles, Göttl et al. (2021) [4] proposed a two-player game framework in which an RL agent competes against itself to generate profitable flowsheets involving multiple unit operations simulated using short-cut models. Building on this, Göttl et al. (2023) [5] explored the generalizability of RL methods by applying them to azeotropic distillation case studies. Using similar process simulation models, Khan et al. (2022) [6] integrated RL with mathematical programming (MP) to allow RL agents to design unit operation sequences while optimizing these sequences via MP.

Recent efforts have addressed challenges related to simulation accuracy and computational efficiency. For instance, Wang et al. (2023) [7] proposed an RL framework coupled with IDEAS as a process simulator. Gao et al. (2023) [8] addressed the issues of slow and inaccurate process simulators by introducing transfer learning. In their approach, the RL agent is pretrained on short-cut process models to facilitate rapid learning, followed by fine-tuning training on rigorous simulations using DWSIM for improved accuracy. Reynose-Donzelli et al. (2024) [9] applied policy masking techniques to simplify the RL agent's learning process while leveraging Aspen Plus for simulations.

The need for process flowsheet data embedding to create meaningful data representations for the RL agent has been widely acknowledged. Stops et al. (2022) [10] emphasized the creation of meaningful flowsheet data

embeddings using graph neural networks (GNNs). Göttl et al. (2023) [5] used MLP-mixer methods. Seidenberg et al. (2023) [11] introduced knowledge graphs to represent flowsheet object-relation dynamics more concretely. Wang et al. (2023) [7] exploited the well-established convolutional neural network (CNN) agent architecture.

These studies collectively underscore the versatility and potential of RL in PSE, from distillation train optimization to generalized flowsheet synthesis and novel approaches to data representation and simulation efficiency. This growing body of work highlights RL's promise in addressing complex, real-world challenges in process synthesis engineering. Yet, challenges remain both in developing a thorough understanding of the RL agent's performance and integration of fast, reliable, and accurate process simulators in the proposed RL applications.

This work continues the search for optimal RL performance through combining rigorous process modeling with the existing open-source benchmarking Jumanji [12] platform for RL applications, leveraging the use of state-of-the-art RL agent features combined with effective data embedding through transformer blocks. Jumanji is developed in JAX, which is a layer on top of Python and developed for machine learning purposes by Google DeepMind. JAX provides explicit features including parallel computing on GPU backends, Just-In-Time (JIT) compilation, and automatic differentiation. These features are used in this work to simulate equilibrium-based separation processes in JAX, seamlessly integrating with Jumanji.

The choice for transformer data embedding as an alternative to the aforementioned embedding techniques has been made to explore its capacity for the given purpose and optimally exploit parallel computing in JAX. It is explored how the transformer architecture operates on a variety of information representation in terms of quality and quantity.

# METHODOLOGY

The work involved the implementation of the rigorous Naphtali and Sandholm (N&S) algorithm into JAX for simulating multi-component equilibrium separation and coupling this algorithm with the RL framework for distillation train sequencing. The N&S algorithm is an equation-grouping-by-stages procedure and exploits the NR iteration for finding the non-linear solution vectors. Finding the Jacobian for the NR iterations either numerically or analytically is traditionally a tedious process involving significant computational effort. In the current work, the JAX library has been leveraged to use automatic differentiation (AD) for finding the Jacobian in a highly efficient and accurate way.

**Table 1:** Data representation in the initial observation by the RL agent.

| **Component** | **C3** | **I-C4** | **C4** | **C5** |
|---|---|---|---|---|
| Fraction | 0.143 | 0.143 | 0.143 | 0.143 |
| **Component** | **C-C5** | **C6** | **T-C4** | **$R_{tot}$*** |
| Fraction | 0.143 | 0.143 | 0.143 | 1 |

*$R_{tot}$ gives the ratio of the current total stream quantity over the initial feed to the train instead of the current stream absolute flow value to minimize steep gradients during training.

## RL framework

The RL problem is formally defined by the Markov decision process (MDP). The MDP can be described by the tuple M ={S,A,P,R} where S is the collection of states describing the environment, A contains the possible actions for the agent to take in the environment, P is the transition function describing the system dynamics via the probability of space action trajectories, and R is the reward function. The agent runs an episode which is a series of time steps. In each time step, the agent observes the current state upon which it selects an action to let the environment transition to a new state and receive a reward for the chosen action from the environment. The episode is finalized once the terminal state is reached. The agent learns to maximize the reward.

In this framework, the state observation is an available component stream to be separated. The agent decides on the column design parameters for the observed stream, after which it receive a financially based reward for the generated separation. The episode is terminated once the minimum number of columns has been completed to recover all components in the initial feed as pure products based on binary separation. This termination condition is chosen as it is deemed not reasonable to built additional columns for the presented easy-to-separate mixture.

### State space

The state space contains all possibly flowsheet configurations of the multi-component separation train. State representations are stored in a stream table structure wherein the connectivity of separation units and stream information is represented. This potentially includes component flow quantities, column design parameters, column installed and operating costs, and stream revenues if a product purity criteria is met.

### Observation space

Given the Markov property, the observation of a current state should provide all information relevant to the RL agent to inform its decision upon action taking. It is considered that all information to build a distillation column is contained in the quantity and quality of the feed stream. The origin of such a feed stream in terms of preceding column passes is therefore irrelevant in this approach and information about existing flowsheet top-

ology is not contained in the observation. Table 1 gives the data presented with only the stream composition in the initial observation (see Figure 1).

**Table 2:** Design parameter windows and discretization for the multi-variable discrete action space

| | Lower | Upper | Steps |
|---|---|---|---|
| Stage number | 5 | 85 | 81 |
| Reflux ratio | 0.1 | 10 | 30 |
| Distillate ratio | 0.01 | 0.99 | 150 |
| Feed location* | 0.2 | 0.85 | 30 |

* The feed location is defined as the column fraction above the feed

### Action space

While several literature studies focused on hierarchical action space structures, a simplified approach is used in this work. Each time step will generate at least one non-pure outflow stream as long as there are still more than two feed components present. These outflows are systematically acted upon by the agent, either until the product purity constraint is met for all streams or if the maximum number of columns allowed has been built.

For a given observed single stream, the agent must decide on the column design parameters including number of trays, distillate rate, reflux ratio, and feed location. A multi-discrete action space has been exploited where each action involves adapting the four design parameters. The chosen feasible parameter bounds and the number of discretization steps are summarized in Table 2. The given discretization gives roughly 11M possible action values combinations for a single column design. Action masking is used to control the different number of discretization steps for each design parameter. The small discretization step size for the distillate ratio was chosen to potentially allow the agent to achieve optimal purity close to the minimum requirement (95%).

### Reward definition

The RL agent aims to maximize a cumulative award. It is essential to effective learning that the reward definition accurately captures the environment dynamics. For a flowsheet configuration, reward can be expressed in financial terms through the potential revenues of product streams minus the installed and operating costs.

$$Reward = Revenue - (C_{installed} + C_{operating}) \quad (4)$$

The installed costs were estimated using the Marshall & Swift index correlations and operating costs are considered for heating and cooling in the reboiler and condenser, respectively. The cost correlations for both contributions are detailed in the supplementary material.

The same revenue value is chosen for all components, regardless of possible deviations in market values to prevent introducing bias during learning. A hypothetic constant product revenue of 20$/kmol has been selected.

### RL agent architecture

The agent architecture has been adopted from the Jumanji library [12] and features state-of-the-art functionalities. The actor-critic baseline agent uses bootstrapping for the objective function, preventing it from collapsing. The advantage is used for update estimates, and an entropy term is introduced to favor exploration.

### Data embedding

The transformer architecture is implemented as an encoder structure with self-attention to the input sequences. The structure allows for addressing the relative importance of input parameters with respect to the overall input for the system dynamics. The transformer encoder takes in a query (Q), key (K), and value (V). Scaled dot self-attention is applied over Q and K and a SoftMax function is used to create the attention weights. The weights are multiplied with V to obtain a weighed value representation indicating the relative importance of the vector entries in Q to focus on the most relevant information from the sequence to take its next action.

Q, K, and V are all the same for the encoder transformer and contain the observation of the environment. Learnable weight matrices are introduced for Q, K, and V to transform the observation into a higher dimensional representation before entering the self-attention mechanism. Trainable parameters are the Q, K, and V weight matrices, the feedforward NN layers, and the linear transformation layers. The agent learns by calculating the update for each of the parameters via the gradient of the loss function with respect to the parameters. The parameter updates are applied for the critic and actor network.

## SCOPE

A case study is selected where a multi-component hydrocarbon mixture needs to be separated into >95% pure product streams. The components are listed in Table 3 and have been chosen for their reasonable relative volatilities, rather than representing a potential real system. Non-ideality is not considered in the algorithm. Feed streams are always considered to be liquid at boiling point. Heating and cooling duty costs are based on standard cooling water, even though this may not be realistic for the light boiling components present in the initial feed.

The rigorous algorithm takes in the number of stages, feed location, distillate rate, reflux ratio, feed rate, operating pressure, and feed composition. The algorithm has been tested for its reliability and speed as function of number of components in multi-component systems. It was chosen to initiate random feeds with and

find reasonable column designs for these feeds using the Fenske-Underwood-Gilliland shortcut method. These column design were then evaluated using the rigorous algorithm. For batches containing 1000 random initiated feeds for a given number of components, it was found that full convergence for all columns in a batch could no longer be guaranteed with more than nine components present. It was deemed reasonable to verify the RL framework performance using a seven-component mixture to introduce separation complexity while guaranteeing reliable and stable performance of the separation algorithm.

**Table 3:** Components considered in the multi-component separation train.

| Component | BP@1 atm | CAS | Not. |
|---|---|---|---|
| propane | $-42\ ^oC$ | 74-94-6 | C3 |
| isobutane | $-12\ ^oC$ | 72-28-5 | I-C4 |
| n-butane | $-1\ ^oC$ | 106-97-8 | C4 |
| n-pentane | $36\ ^oC$ | 109-66-0 | C5 |
| cyclopentane | $49\ ^oC$ | 287-92-3 | C-C5 |
| n-hexane | $69\ ^oC$ | 110-54-3 | C6 |
| 2,2,3-trimethyl butane | $81\ ^oC$ | 464-06-2 | T-C4 |

**Table 4:** Hyperparameter settings used for the RL framework.

| Agent | | Transformer network | |
|---|---|---|---|
| Learning rate | 0.4e-3 | Blocks | 1 |
| Bootstrap factor | 0.95 | Heads | 1/2/4 |
| Entropy term | 0.1 | Key size | 32 |
| Discount factor | 1.0 | MLP-layer size | 512 |
| **Training** | | | |
| Batch size | 32 | | |
| Episode steps | 6 | | |

## RESULTS

The goal for the agent was to construct a flowsheet in which all seven components are recovered as purified product streams using six separation units producing 2000 kmol/hr total pure product. When trained on a fixed feed composition, the agent was well capable of doing so, given that the framework hyperparameters were appropriately chosen. While the hyperparameter settings can be tuned over a wide range, findings for fixed sets of the hyperparameter as given in Table 4 are presented. The choice for these fixed parameter values is informed by the settings for different games with similar RL networks as provided within the Jumanji library.

Figure 1 shows the episode return as function of episode number or time. In the base case, training is done on basis of quantitative component flow observation ($\phi$)

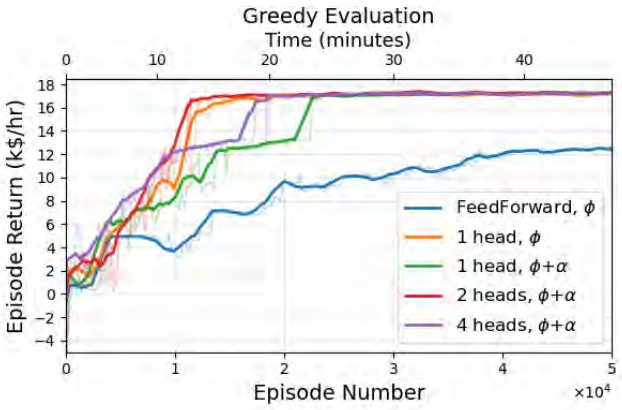



**Figure 1:** Episode return using argmax over the policy parameters as function of episode number (lower axis) or time (upper axis). $\phi$ for training on quantitative component flows observation. $\phi + \alpha$ for training on additional relative volatility data.

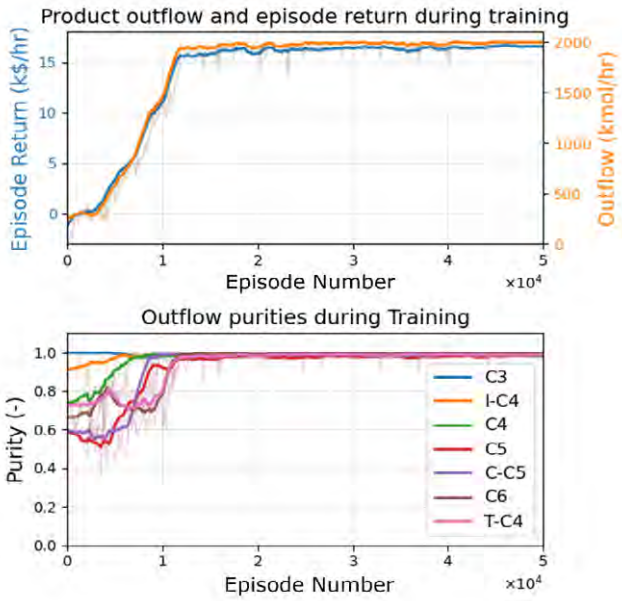



**Figure 2:** Training progression profiles in terms of cumulative episode return (Fig 2A), total product recovery during training (Fig 2A), and outflow purity development during training (Fig 2B) for 2 heads $\phi + \alpha$ (Figure 1).

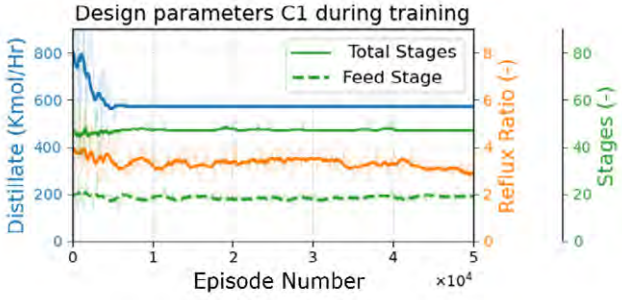



**Figure 3:** Separation column design parameter of the first column in the sequence profiles during training.

using single head attention. In the absence of a transformer encoder (feedforward network), the agent was not able to learn how to produce all outflows as products with six columns. The impact of adding the relative volatilities to the observation space is illustrated ($\phi + \alpha$) in combination with the number of attention heads. It is observed that the fastest learning was achieved for the observation space of form $\phi + \alpha$ in combination with two heads. The effectiveness of multi-head attention is however not easily quantified as also the training parameter set size changes upon adding additional attention heads in the current setup. Having four attention heads shows decreased learning performance indicated by the slowdown in convergence towards full product recovery.

Figure 2A shows the total molar outflow of streams being product streams and the episode return. The episode return corresponds to the cumulative reward received by the agent for completing one flowchart of 6 columns. The product outflow strongly correlates with the episode return as the agent receives high reward for producing product streams. It can be expected that the reward increases if the agent would more closely approach the purity constraint by tuning the design parameters for a converged flowsheet. However, such reward optimization is hardly observed for the current training (flat purity profiles once seven components are recovered as product streams), indicating the potential need for reward shaping to achieve better static optimization. Figure 2B showcases, however, that the agent was able to learn the purity constraint of >95 mol% on product flows, based on the reward definition.

Figure 3 provides an exemplary plot based on the first column in the flowchart for the learned design parameter tuning by the agent. The variation remains larger for the reflux ratio, and feed location which is due to the larger discretization steps for both parameters (see Table 1).

## Flowchart benchmarking

The performance of the RL agent was validated through the generation of benchmark flowcharts in Aspen Plus. The comparison of episode return is done for the flowchart generated by the agent and two flowcharts where either all distillate or bottom streams are >95% pure products. The comparison is summarized in Table 3. The column number of stages, feed locations, and distillate rates are determined using the DWSTU model in Aspen Plus. The reflux is determined using a purity design spec after converting the DWSTU models into RADFRAC models. The comparison shows that the episode return obtained by the agent is competitive with the values found for the benchmark flowcharts. It must be noted that the DWSTU involves a shortcut method for which the dynamics might be different compared to the reward function on which the agent was trained.

**Table 5:** Flowchart episode return comparison between RL-generated and Aspen Plus optimized designs and learned flowsheet column design parameters. $RR$ is reflux ratio, $D$ is distillate rate (kmol/hr), $N_{tot}$ and $N_f$ is total and feed stage number, respectively.

| RL | Distillates | Bottoms |
|---|---|---|
|  |  |  |
| 17.3 k$/hr | 17.2 k$/hr | 15.8 k$/hr |

**Column design parameters RL flowchart**

| | $RR$ | $D$ | $N_{tot}$ | $N_f$ |
|---|---|---|---|---|
| **C1** | 2.8 | 572 | 47 | 19 |
| **C2** | 1.6 | 296 | 82 | 51 |
| **C3** | 1.7 | 296 | 35 | 20 |
| **C4** | 3.2 | 287 | 42 | 13 |
| **C5** | 2.3 | 570 | 55 | 24 |
| **C6** | 2.3 | 283 | 79 | 35 |

* Using argmax over the policy params

## Inference

RL is believed to be capable of outperforming other optimization approaches for its inference properties. Where traditional approaches optimize problem-specific, the RL approach involves the optimization of its policy to make the right decisions under the given circumstances. As such, new problems following a similar problem definition as the problem trained for may be solvable by the RL agent using its trained policy. This inference property has been tested in the current work to provide some insight into how well the agent is capable of generalizing between similar problems. Since the agent was trained on a fixed initial feed composition, inference can be tested by introducing random distributions for the feed composition and see how well the agent is capable of obtaining an optimal reward for these distributions.

**Table 6:** Inference capacity of the trained networks in Figure 1.

| **Policy** | **Mean reward** (k$/h) | **Mean product outflow** (kmol/h) |
|---|---|---|
| $\boldsymbol{random}$ | -1.9 | 470 |
| $\boldsymbol{1\ head, \phi}$ | 3.3 | 504 |
| $\boldsymbol{1\ head, \phi + \alpha}$ | 3.8 | 562 |
| $\boldsymbol{2\ head, \phi + \alpha}$ | 2.6 | 463 |
| $\boldsymbol{4\ head, \phi + \alpha}$ | 3.8 | 532 |

The episode return for 100 randomly sampled feed distributions with a minimum fraction of 0.05 for each component was evaluated for the trained policies in Figure 1. The results are in Table 6. The trained policy outperforms the random policy in terms of episode return

but there is hardly a gain in product recovery and also no strong correlation between number of heads vs performance is found.

## CONCLUSIONS

With the implementation of rigorous modeling into JAX, seamlessly integrated with the Jumanji framework, this work demonstrates the potential of combining RL with rigorous simulation methods for process synthesis. The RL agent successfully handles the complexity of the optimization problem, managing an extensive action space containing 11 million possible action values for a single state. Flowsheet convergence toward full product recovery was typically achieved after evaluating fewer than 20,000 episodes (or six-column flowcharts). The simplified approach of using a non-hierarchical action space and single-stream observations highlights that RL does not necessarily require massive data input for optimal learning. However, the need for meaningful data representation was indicated, as flowchart convergence was not achieved without a transformer encoder. While transformer structures are renowned for their parallel multi-head attention, adding more attention heads did not necessarily improve learning performance.

Further improvements are needed to enhance the inference performance of the trained policy. While there was a slight improvement in reward gain between the trained and random policies, the overall performance remains unsatisfactory. One possible way to improve generalizability could be to train the agent on random feed distributions for given multi-component mixtures, rather than relying on fixed compositions as is currently done.

The major limitation from a process synthesis perspective lies in the feedforward structure of the generated flowchart. Process synthesis relevance could be enhanced by incorporating a variety of unit operations along with the presence of recycle streams. Additionally, challenges are likely to arise in achieving convergence of the rigorous model when non-idealities are introduced.

## DIGITAL SUPPLEMENTARY MATERIAL

Supplementary information on the code accessibility, hardware usage, and reward function definition can be found at https://psecommunity.org/LAPSE:2025.0026.

## REFERENCE


1. Mowbray, M. et al. Industrial data science-a review of machine learning applications for chemical and process industries. React. Chem. Eng. 7:141-1509 (2022) https://doi.org/10.1039/D1RE00541C
2. Midgley LI. Deep reinforcement learning for process synthesis. arXiv preprint (2020) arXiv:2009.13265
3. van Kalmthout SC, Midgley LI, and Franke MB. Synthesis of separation processes with reinforcement learning. arXiv preprint 4:32-42 (2022) arXiv:2211.04327, 2022
4. Göttl Q, et al. Automated Flowsheet Synthesis Using Hierarchical Reinforcement Learning: Proof of Concept. Chem. Ing. Tech. 4:32-42 (2020) https://doi.org/10.1234/56789.10
5. Göttl Q, et al. Deep reinforcement learning uncovers processes for separating azeotropic mixtures without prior knowledge. arXiv preprint (2023) arXiv:2310.06415, 2023
6. Khan AA, Lapkin, AA. Designing the process designer: Hierarchical reinforcement learning for optimisation-based process design. Chem Eng Process Process. Intensif. 180:108885 (2022) https://doi.org/10.1016/j.cep.2022.108885
7. Wang D, et al. A coupled reinforcement learning and IDAES process modeling framework for automated conceptual design of energy and chemical systems.. Energy Adv. 2:1735-1751 (2023) https://doi.org/10.1039/D3YA00310H
8. Gao Q, et al. Transfer learning for process design with reinforcement learning. Comput. Aided Chem. Eng. 52:2005-2010 (2023) https://doi.org/10.1016/B978-0-443-15274-0.50319-X
9. Reynoso-Donzelli S, Ricardez-Sandoval LA. A reinforcement learning approach with masked agents for chemical process flowsheet design. AIChE Journal 71:e18584 (2024) https://doi.org/10.1002/aic.18584
10. Stops L, et al. Flowsheet generation through hierarchical reinforcement learning and graph neural networks. AIChE Journal 69:e17938 (2023) https://doi.org/10.1002/aic.17938
11. Seidenberg JR, Khan AA, Lapkin, AA. Boosting autonomous process design and intensification with formalized domain knowledge. Comput. Chem. Eng. 169:108097 (2023) https://doi.org/10.1016/j.compchemeng.2022.108097
12. Bonnet C, et al. Jumanji: a diverse suite of scalable reinforcement learning environments in JAX. arXiv preprint (2023) arXiv:2306.09884



© 2025 by the authors. Licensed to PSEcommunity.org and PSE Press. This is an open access article under the creative commons CC-BY-SA licensing terms. Credit must be given to creator and adaptations must be shared under the same terms. See https://creativecommons.org/licenses/by-sa/4.0/




Systems & Control Transactions

**Research Article - Peer Reviewed Conference Proceeding**
ESCAPE 35 - European Symposium on Computer Aided Process Engineering
Ghent, Belgium. 6-9 July 2025
Jan F.M. Van Impe, Grégoire Léonard, Satyajeet S. Bhonsale,
Monika E. Polańska, Filip Logist (Eds.)

PSE PRESS

# Physics-informed Data-driven control of Electrochemical Separation Processes

**Teslim Olayiwola[a], Kyle Territo[a], and Jose Romagnoli[a*]**

[a] Louisiana State University, Department of Chemical Engineering, Baton Rouge, Louisiana, United States
* Corresponding Author: jose@lsu.edu

## ABSTRACT

Optimizing the operational conditions of electrochemical separation systems to achieve higher separation efficiency remains a complex challenge due to their nonlinear and dynamic nature. In this work, we proposed a Reinforcement Learning (RL)-based control framework to address this challenge. By applying various RL algorithms, we trained an RL-based controller that adapts to different system configurations and conditions. Also, the trained model learns the optimality between the removal efficiency and energy consumption. Overall, this approach autonomously learns the optimal operational parameters, significantly improving ion removal efficiency. The proposed RL-based control system enhances the performance of electrochemical system, providing a versatile and adaptive solution for optimizing separation across multiple electrochemical technologies. This work demonstrates the potential of RL in advancing the design and control of sustainable water purification systems.

**Keywords**: Reinforcement Learning , Separation, Intelligent Systems, Process Control, Machine Learning

## 1. INTRODUCTION

Water is one of the most essential and valuable natural resources, critical to sustaining all forms of life [1]. However, water scarcity remains a critical global challenge, with projections indicating that the average per capita supply of clean water will decline by one-third within the next 20 years [2,3]. Efforts from governments, industries, and academia have increasingly focused on developing advanced separation processes to address this issue. Desalination has emerged as a viable solution for converting brackish and seawater into potable water, but many desalination technologies are energy-intensive and capital-demanding [4,5]. Broadly, these technologies include pressure-driven, electrically driven, and thermal-driven processes [5]. Examples include reverse osmosis (RO) and ultrafiltration for pressure-driven processes, electrodialysis and capacitive deionization for electrically driven processes, and distillation for thermal-driven processes [5,6]. Although significant advancements in desalination technologies over the past decade have enhanced their reliability and reduced capital costs, high energy consumption remains a major concern, especially in regions with limited energy resources.[7] While RO dominates other desalination technologies, electrically driven processes like electrodialysis (ED) are particularly advantageous for low salinity/brackish water desalination, low pressure requirements and decentralized water treatment due to their modular design [6,8].

Electrochemical processes, such as ED, are well-positioned to play a critical role in addressing water scarcity in specific scenarios, such as brackish water treatment, and in supporting sustainable mineral supply chains and nutrient cycle management [9]. The design of ED systems involves numerous factors, including applied voltage, current density, feed ion concentration, ion type, and ion-exchange membrane (IEM) properties, as well as trade-offs in unit size (e.g., number of stacks) [10]. These parameters collectively influence separation efficiency, energy consumption, and overall costs. However, optimizing ED is challenging due to the intricate interactions among these parameters and their effects on system performance. Addressing these complexities requires precise, adaptable, and rapid control tools capable of real-time optimization to ensure high water quality and energy efficiency.

To achieve real-time control of chemical processes, researchers have increasingly turned to advanced

algorithms such as Reinforcement Learning (RL). Unlike traditional control methods, RL algorithms are robust to nonlinearities arising from operational irregularities and complex process dynamics [11]. RL eliminates the need for complete prior understanding of these intricate processes by learning optimal control strategies through trial-and-error interactions between the agent and its environment. This adaptability has led to RL's widespread application in engineering fields, including reactor design [12], distillation [13], and separation [14]. However, despite its potential, RL has been underutilized in electrochemical separation processes. Notably, recent studies by Moon et al. [14,15] have focused primarily on membrane capacitive deionization, which has been shown to consume more energy (i.e., have lower energy efficiency) compared to electrodialysis (ED).

The present study examines the implications of incorporating RL-based control strategies in ED operations. Specifically, we evaluate the performance of different RL algorithms in maintaining high separation efficiency at low energy consumption under dynamic operating conditions (Figure 1). We explore reward functions designed for both single-objective and multi-objective optimization. The goal is to develop a controller capable of achieving performance metrics close to 99% separation efficiency and 0.3 kWh/m³ specific energy consumption. The RL control framework employs a numerical model to predict system states—such as separation efficiency and energy consumption—based on dynamic actions like applied voltage and operational time. By leveraging these advanced AI controllers, this work aims to enhance water quality, improve process efficiency, and reduce operational costs, thereby addressing the complexities inherent in electrochemical separation systems.

## 2. METHODOLOGY

The implemented framework "OptiDial" in this study is elucidated in Figure 1. Initially, a numerical modeling technique that approximate the working principle of the electrodialysis (ED) process is proposed. Afterwards, the set up and training of the AI-based controller is outlined.

### 2.1 Physics-based modeling

To model the physical processes happening in the electrochemical system, we adopted the physics model from our previous work [10]. This complex and non-linear dynamical system is modeled as a tank with inflow and outflow into main compartment and selectively through the membrane into the adjacent compartment. Thus, for an electrochemical device system as shown in Figure 2 with diluate ($dc$) and concentrate ($cc$) compartments component mass balance with concentration $C_i$ in the cell compartment with volume $V_i^k$ at a volumetric flowrate $Q_i$ and reservoir tank with volume $V_i^T$ is given as follows in equation (1) – (3). Herein, there is a flow across the membrane (anion exchange membrane, a; cation exchange membrane, c) with diffusion coefficient Da/c and thickness $l_{a/c}$ upon application of voltage E which resulted into ohmic drop across the two fluid compartment ($E_{ohm}^{cc}$, $E_{ohm}^{dc}$), ohmic drop across the membrane ($E_{mem}$) and electrodes ($E_{anode}$, $E_{cathode}$). Upon solving the coupled ordinary differential equations presented in equations (1) – (3), the desalination metrics such as ion removal efficiency (SR) and specific energy consumed (EC) are computed as in equations (4) – (5).

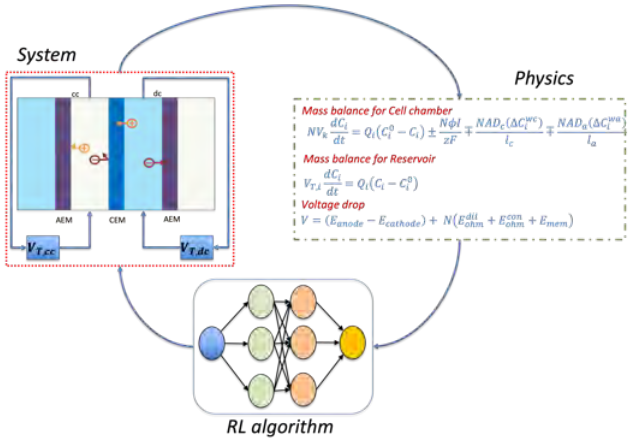



**Figure 1:** The architecture of "OptiDial", a reinforcement learning-based real-time control of electrodialysis.

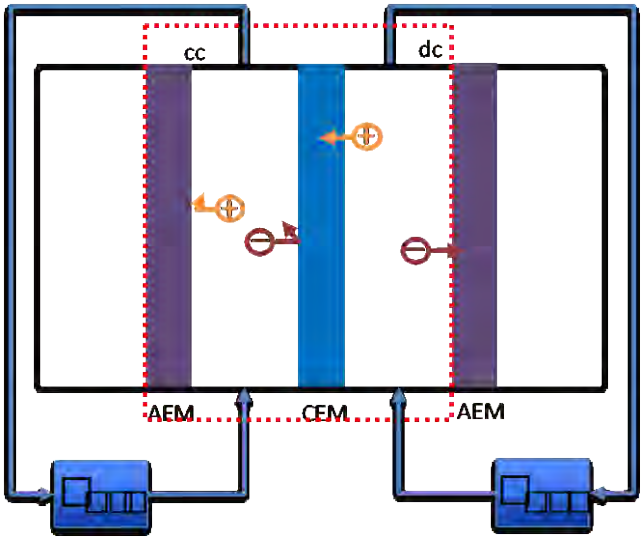



**Figure 2.** Schematic representation of the electrodialysis device. The red outline highlights a stack composed of a concentrate compartment, a diluate compartment, and alternating anion exchange membranes and cation exchange membranes.

$$NV_i^k \frac{dC_i}{dt} = Q_i(C_i^{in} - C_i) \pm \frac{N\phi I}{zF} \mp \frac{NAD_a}{l_a}(C_{cc}^{wa} - C_{dc}^{wa}) \mp \frac{NAD_c}{l_c}(C_{cc}^{wc} - C_{dc}^{wc}) \quad (1)$$

$$V_i^T \frac{dC_i^{in}}{dt} = Q_i\left(C_i - C_i^{in}\right) \quad (2)$$

$$E = (E_{anode} - E_{cathode}) + N \cdot \left(E_{ohm}^{cc} + E_{ohm}^{dc} + E_{mem}\right) \quad (3)$$

$$SR = 1 - \frac{C_{dc}^f}{C_{dc}^{in}} \quad (4)$$

$$EC = \frac{E \cdot \int I dt}{V_{dc}^T} \quad (5)$$

## 2.2 Reinforcement Learning Framework

### Theory

Reinforcement Learning (RL) is a branch of machine learning where an agent learns to make decisions by interacting with an environment to maximize a cumulative reward [16]. Unlike supervised learning, RL does not rely on labeled data but instead uses trial-and-error to discover an optimal policy [17]. The agent's actions influence future states and rewards, making RL particularly suited for sequential decision-making tasks. Generally, the core components of RL (as shown in Figure 3) include the agent, environment, state, action, reward, and policy [16,17].

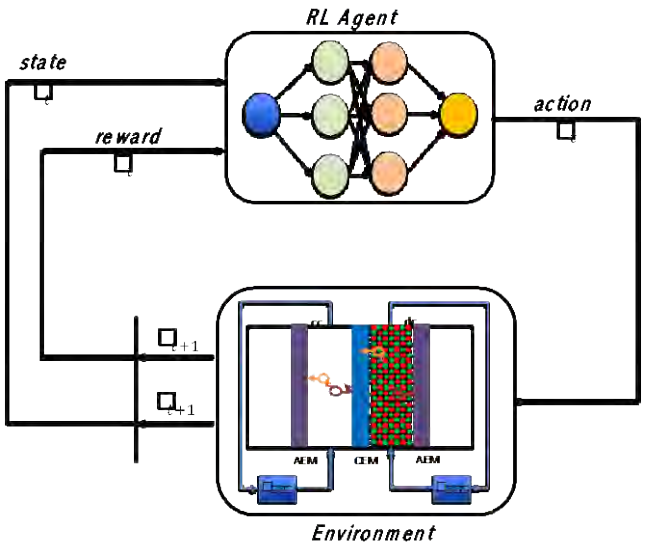



**Figure 3:** Schematic workflow of the RL-coupled electrochemical desalination process.

### Problem set up

In this work, we will focus mostly on the proximal policy optimization (PPO), Soft Actor Critic (SAC), and Advantage Actor Critic (A2C) algorithms. Though the RL models have a similar framework and are data-driven models but differs in their training algorithm. For example, the PPO algorithm maximizes the gradient of an expected reward function while the A2C containing two components an actor (policy, which selects actions to maximize cumulative rewards) and critic (a value function, which evaluates the quality of the chosen actions) maximizes the expected cumulative reward by combining two components. Lastly, the SAC maximizes the expected cumulative reward while incorporating an additional term for entropy to encourage exploration.

During the learning process, the RL agent interacts with the environment (approximated by the numerical model) and explores different action values based on the observations from the numerical model to maximize the reward function. See Table 2 for the range of action and state parameters. The action in this work considers key operational parameters such as the number of stacks ($N$), applied voltage ($E$) operational time ($T_{tot}$), volume of the diluate reservoir tank ($V_{dc}^T$) and volume of the concentrate reservoir tank ($V_{cc}^T$). Meanwhile, we adopted the salt removal efficiency ($SR$), specific energy consumed ($EC$), final effluent concentration from diluate tank ($C_{dc}^f$), and final effluent concentration from concentrate tank ($C_{cc}^f$). As the RL agent requires a reward function to direct the training process, we created a reward function (F1, F2, F3) that attempts to enhance the desalination metrics such as SR and EC as defined in eq 6 – 8. In this work, the RL environment is inherited the gym environment provided in the OpenAI Gym python library.

$$\text{F1: } R(t) = \alpha \cdot SR \quad (6)$$

$$\text{F2: } R(t) = \alpha \cdot SR + \beta \cdot {}^{EC}/_{10} \quad (7)$$

$$\text{F3: } R(t) =\cdot SR + \beta \cdot \left(1 - {}^{EC}/_{10}\right) \quad (8)$$

### Training and Testing

Once the RL environment and variables are defined, model training is the next. In this work, we trained the RL model with the three RL algorithms (PPO, SAC, A2C) and three reward functions under the same condition (30,000 epochs and $10^{-3}$ learning rate). Herein, we used the RL algorithms implementation in stable-basline3 for easy reproducibility [18]. Throughout training, the RL algorithm iteratively refines its policies to achieve improved SR and/or EC while considering the complex interplay of these variables. Afterward, the trained RL agent recommends optimized action values ($N$, $E$, $T_{tot}$, $V_{dc}^T$, $V_{cc}^T$) during the testing step.

**Table 1:** Parameters of the RL environment employed in training the agent.

| Parameters | Variable | Range |
|---|---|---|
| Action | N | 20 – 80 |
| | E | 0.1 – 2.0 V |
| | $V_{conc}^T$ | 0.1 – 2.0 m$^3$ |
| | $V_{dil}^T$ | 0.01 – 0.5 m$^3$ |
| States | SR | 0 – 1 |
| | EC | 0 – 10 KWh/ m$^3$ |
| | $C_{conc}^f$ | 0 – 1000 mol/m$^3$ |
| | $C_{dil}^f$ | 0 – 1000 mol/m$^3$ |

**Table 2:** Range employed in the sensitivity study.

| Variable | Range |
|---|---|
| N | 5 – 100 |
| E | 0.1 – 2.0 V |
| $V_{conc}^{T}$ | 0.2 – 2.0 m$^3$ |
| $V_{dil}^{T}$ | 0.01 – 0.6 m$^3$ |
| $C_{conc}^{f} = C_{dil}^{f}$ | 500 – 1000 mol/m$^3$ |

**Algorithm 1:** Training algorithm for the RL model.

**Parameters:**

- Action: $N$, $E$, $T_{tot}$, $V_{dc}^{T}$ , $V_{cc}^{T}$.
- State: $SR$, $SEC$, $C_{dc}^{f}$, $C_{cc}^{f}$.
- Reward: as defined in eq. 6 – 8.
- Termination: $SR \geq 0.99$ or $EC \leq 0\ KWh/m^3$.

**Algorithm:**

*Step 1: Initialize Agent*
Set up RL agent with an initial policy & parameters.

*Step 2: Observe Current State*
Agent observes the state of the system

*Step 3: Choose Action*
Select an action from the action space

*Step 4: Simulate Environment*
Apply action to the numerical model to predict the next state.

*Step 5: Compute Reward*
Calculate the reward using one of the 3 functions.

*Step 6: Update Policy*
Update the agent's policy using the reward & state feedback.

*Step 7: Convergence Check*
If the policy has converged, terminate the process. If not, repeat from Step 2.

## 3. RESULTS AND DISCUSSION

### 3.1 Physics-based modeling

Before applying the numerical model for real-time control, it is crucial to evaluate whether the model aligns with experimentally observed trends. A sensitivity analysis was conducted to validate model accuracy and reliability, ensuring an accurate representation of electrodialysis (ED) system behavior. The analysis identified key factors affecting predictions and explored variable ranges and magnitudes within the system. Systematic variations in the number of stacks, applied voltage, concentrate reservoir volume, and diluate reservoir volume were analyzed to assess their impact on critical ED performance metrics, such as salt removal (SR) and specific energy consumption (SEC). The parameter ranges for this study are outlined in Table 2, and the sensitivity results are shown in Figure 4.

The results confirmed consistency with theoretical trends within the specified boundary conditions. For example, SR and SEC increased with the number of ED stacks, as predicted by theoretical equations and prior studies. Adding more unit cells improves ion removal capacity but demands higher energy. Similarly, increasing applied voltage showed a comparable trend, with higher energy enabling more efficient ion removal in agreement with experimental data from Karimi et al. [19]. In contrast, increasing the diluate reservoir size reduced SR and SEC, likely due to a larger volume being retained rather than processed. The concentrate reservoir size had a minimal effect on these metrics. Additionally, higher feed concentrations led to lower separation efficiency owing to reduced diffusion of ions through the IEMs and increased energy demands [20,21]. These observations align closely with experimental findings, demonstrating the robustness and reliability of the numerical model in capturing the complex dynamics of the ED system.

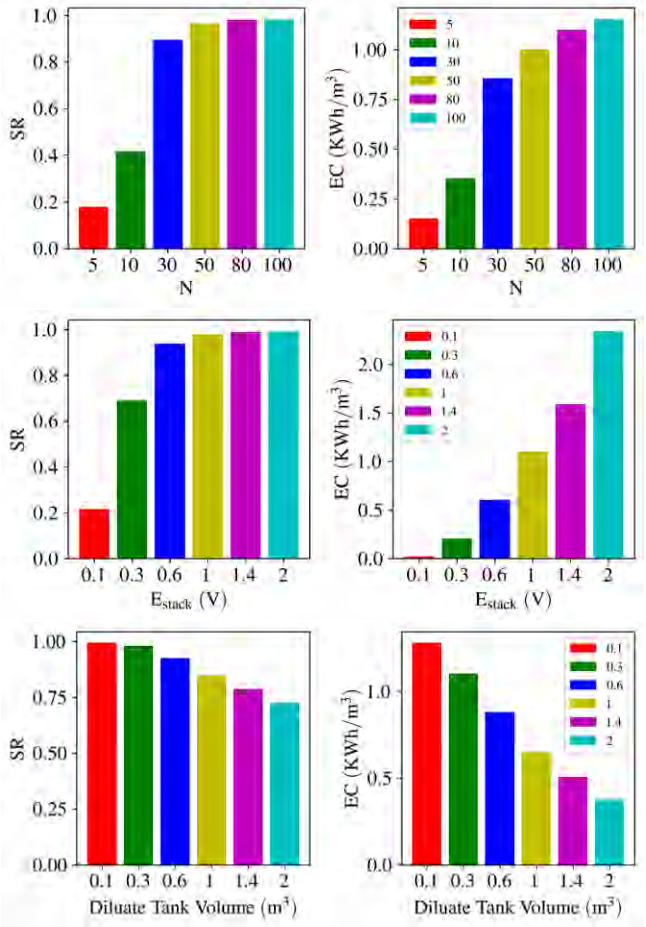



**Figure 4:** Sensitivity analysis of the mathematical model subject to the number of ED stacks, applied voltage, and volume of diluate tank volume.

In summary, a further correlation analysis using the Pearson coefficient as shown in Figure 5 revealed a positive correlation between SR and parameters such as

the number of stacks (N), stack energy ($E_{stack}$), and treatment time ($T_{tot}$), while a negative correlation was observed between SR and feed concentration, as well as diluate and concentrate reservoir sizes. For SEC, a similar relationship was identified, except that feed concentration exhibited a positive correlation with energy consumption.

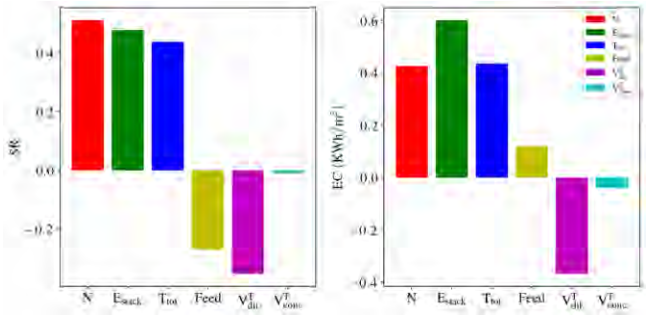


**Figure 5.** Correlation analysis of the ED parameters and the performance metrics.

## 3.2 Reinforcement Learning

To optimize the electrodialysis (ED) system, three RL algorithms (PPO, SAC, and A2C) were trained over 30,000 episodes, with one step per episode, under different reward scenarios. These included a single-objective reward function (F1) focused on salt removal (SR) and multi-objective reward functions (F2 and F3) incorporating SR and specific energy consumption (SEC). As shown in Figure 6, the A2C algorithm consistently outperformed PPO and SAC, achieving a reward exceeding 0.9 and 1.8 for single and multi-objective, respectively translating to >90% separation efficiency within the first 5,000 episodes for F1. Under multi-objective reward functions, A2C demonstrated faster convergence and higher rewards, further establishing its superior performance.

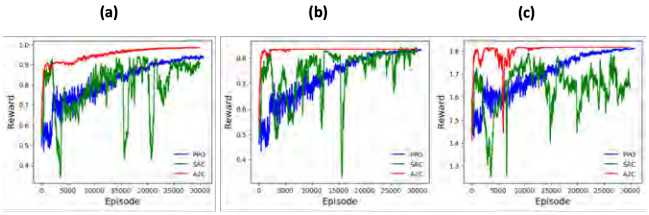



**Figure 6:** Mean reward improvement during the training process for different reward functions a) F1 b) F2 c) F3.

However, as shown in Figure 7, focusing on a single objective (F1) led to higher energy consumption (EC) as the controller prioritized maximizing SR without accounting for energy trade-offs. By contrast, the multi-objective reward functions (F2 and F3) enabled the controller to balance SR and EC simultaneously, achieving better overall system performance.

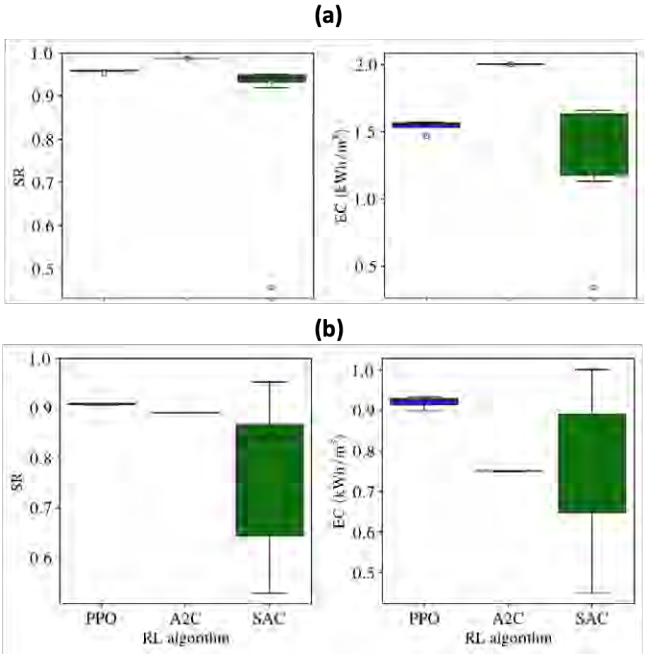



**Figure 7:** Boxplot of the RL-controller performance based on reward function a) F1 and b) F3.

**Table 3:** Statistics of the evaluated results.

| 6/23/2025 12:24:00 PMReward | Algorithm | SR | EC |
|---|---|---|---|
| F1 | PPO | 0.959 ± 0.002 | 1.545 ± 0.030 |
| | A2C | 0.988 ± 0.000 | 2.002 ± 0.000 |
| | SAC | 0.892+/- 0.153 | 1.329 ± 0.410 |
| F2 | PPO | 0.904 ± 0.003 | 0.877 ± 0.033 |
| | A2C | 0.892 ± 0.000 | 0.751 ± 0.000 |
| | SAC | 0.942 ± 0.037 | 1.353 ± 0.380 |
| F3 | PPO | 0.908 ± 0.001 | 0.921 ± 0.011 |
| | A2C | 0.892 ± 0.000 | 0.751 ± 0.000 |
| | SAC | 0.771 ± 0.143 | 0.772 ± 0.177 |

## 4. CONCLUSION

In this work, we have introduced reinforcement learning framework named “OptiDial” to optimize electrodialysis (ED) performance by balancing salt removal (SR) and specific energy consumption (SEC). The A2C algorithm demonstrated superior performance across both single and multi-objective reward functions, excelling in achieving high SR and low SEC simultaneously. Sensitivity to reward design highlighted the importance of multi-

objective optimization for real-world applicability. These findings underline the potential of RL-based approaches to effectively manage complex trade-offs in ED systems, paving the way for more efficient and adaptive desalination processes. While this study focuses on RL-based optimization, a direct comparison with nonlinear model predictive control (NMPC) is an important next step. We plan to explore this comparison in another publication, providing a deeper analysis of constraints, safety considerations, and performance trade-offs between RL and NMPC for ED control.

## ACKNOWLEDGEMENTS

We would like to thank U.S. Department of Energy, Office of Science, under the Office of Basic Energy Sciences Separation Science program under award no. DE-SC0022304 for the funding support.

## DATA AVAILABILITY

The datasets and code generated during this study are available at GitHub: https://github.com/Enthusiastic-Teslim/separationML. We adopted RL algorithms implemented in https://github.com/DLR-RM/stable-baselines3.

## APPENDIX

The section contains additional information from the manuscript.

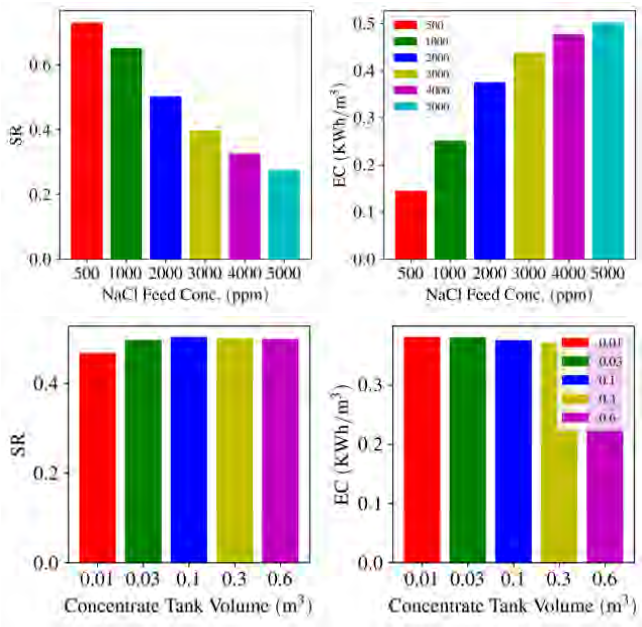



**Figure A1:** Sensitivity analysis of the mathematical model subject to the feed concentration and concentrate tank volume.

## REFERENCES

1. Elsaid, K. et al. Environmental impact of desalination technologies: A review. Science of The Total Environment 748, 141528 (2020).
2. Cao, X. et al. A New Method for Water Desalination Using Microbial Desalination Cells. Environ. Sci. Technol. 43, 7148–7152 (2009).
3. UNESCO, UN-Water & Programme, W. W. A. The United Nations World Water Development Report 3 :: water in a changing world. (2009).
4. Shannon, M. A. et al. Science and technology for water purification in the coming decades. Nature 452, 301–310 (2008).
5. Curto, D., Franzitta, V. & Guercio, A. A Review of the Water Desalination Technologies. Applied Sciences 11, 670 (2021).
6. Alkhadra, M. A. et al. Electrochemical Methods for Water Purification, Ion Separations, and Energy Conversion. Chem. Rev. 122, 13547–13635 (2022).
7. Matsuura, T. Progress in membrane science and technology for seawater desalination — a review. Desalination 134, 47–54 (2001).
8. Sauvet-Goichon, B. Ashkelon desalination plant — A successful challenge. Desalination 203, 75–81 (2007).
9. Campione, A. et al. Electrodialysis for water desalination: A critical assessment of recent developments on process fundamentals, models and applications. Desalination vol. 434 121–160 (2018).
10. Olayiwola, T., Briceno-Mena, L. A., Arges, C. G. & Romagnoli, J. A. Synergizing Data-Driven and Knowledge-Based Hybrid Models for Ionic Separations. ACS EST Eng. (2024) doi:10.1021/acsestengg.4c00405.
11. Dutta, D. & Upreti, S. R. Artificial intelligence-based process control in chemical, biochemical, and biomedical engineering. The Canadian Journal of Chemical Engineering 99, 2467–2504 (2021).
12. Ma, Y., Zhu, W., Benton, M. G. & Romagnoli, J. Continuous control of a polymerization system with deep reinforcement learning. Journal of Process Control 75, 40–47 (2019).
13. Patel, K. M. A practical Reinforcement Learning implementation approach for continuous process control. Computers & Chemical Engineering 174, 108232 (2023).
14. Yoon, N., Park, S., Son, M. & Cho, K. H. Automation of membrane capacitive deionization process using reinforcement learning. Water Research 227, 119337 (2022).
15. Ullah, Z., Yun, N., Rossi, R. & Son, M. Reinforcement Learning and Machine Learning Controllers for Enhancing Water Quality and Process Efficiency in

Electrochemical Desalination. ACS EST Water 4, 5482–5491 (2024).
16. Sutton, R. S. & Barto, A. G. Reinforcement Learning: An Introduction. (MIT Press, Cambridge, Massachusetts, 2018).
17. Shakya, A. K., Pillai, G. & Chakrabarty, S. Reinforcement learning algorithms: A brief survey. Expert Systems with Applications 231, 120495 (2023).
18. Raffin, A. et al. Stable-Baselines3: Reliable Reinforcement Learning Implementations. Journal of Machine Learning Research 22, 1–8 (2021).
19. Karimi, L., Ghassemi, A. & Zamani Sabzi, H. Quantitative studies of electrodialysis performance. Desalination 445, 159–169 (2018).
20. Zoungrana, A. & Çakmakci, M. Optimization of the reverse electrodialysis power output through the ratio of the feed solutions salinity. IET Renewable Power Generation 15, 769–777 (2021).
21. Gubari, M. Q., Zwain, H. M., Alekseeva, N. V. & Baziyani, G. I. Features of feed concentration and temperature effects on membranes operation in electrodialysis systems – a review. J. Phys.: Conf. Ser. 1973, 012178 (2021).

© 2025 by the authors. Licensed to PSEcommunity.org and PSE Press. This is an open access article under the creative commons CC-BY-SA licensing terms. Credit must be given to creator and adaptations must be shared under the same terms. See https://creativecommons.org/licenses/by-sa/4.0/



Systems & Control Transactions

**Research Article - Peer Reviewed Conference Proceeding**
ESCAPE 35 - European Symposium on Computer Aided Process Engineering
Ghent, Belgium. 6-9 July 2025
Jan F.M. Van Impe, Grégoire Léonard, Satyajeet S. Bhonsale,
Monika E. Polańska, Filip Logist (Eds.)

PSE PRESS

# A Novel AI-Driven Approach for Parameter Estimation in Gas-Phase Fixed-Bed Experiments

**Rui D. G. Matias[a,b], Alexandre F.P. Ferreira[a,b], Idelfonso B.R. Nogueira[c], Ana M. Ribeiro[a,b,*]**

[a]Laboratory of Separation and Reaction Engineering–Laboratory of Catalysis and Materials (LSRE-LCM), Department of Chemical Engineering, University of Porto, Porto, 4200-465, Portugal
[b]ALiCE–Associate Laboratory in Chemical Engineering, Faculty of Engineering, University of Porto, Porto, 4200-465, Portugal

[c]Chemical Engineering Department, Norwegian University of Science and Technology, Sem Sælandsvei 4, Kjemiblokk 5, Trondheim, 793101, Norway

* Corresponding Author: apeixoto@fe.up.pt

## ABSTRACT

The transition to renewable energy sources, such as biogas, requires purification processes to separate methane from carbon dioxide, with adsorption-based methods being widely employed. Accurate simulations of these systems, governed by coupled PDEs, ODEs, and algebraic equations, critically depend on precise parameter determination. While traditional approaches often result in significant errors or complex procedures, optimization algorithms provide a more efficient and reliable means of parameter estimation, simplifying the process, improving simulation accuracy, and enhancing the understanding of these systems. This work introduces an Artificial Intelligence-based methodology for estimating the isotherm parameters of a mathematical phenomenological model for fixed-bed experiments. The separation of $CO_2$ and $CH_4$ is used as case study. This work develops an algorithm for parameter estimation for the system's mathematical model. The results show that the validated model has a close fit with experimental results.

**Keywords**: Adsorption, Optimization, Artificial Intelligence, Parameter Estimation

## INTRODUCTION

The need to reduce greenhouse gas emissions has driven the shift toward renewable energy sources such as biogas. However, to use biogas as a substitute for natural gas, it must undergo a purification process to separate methane from carbon dioxide. Adsorption-based separation processes are standard methods for biogas separation. Fixed-bed systems form the fundamental step for many separation processes in this context [1].

Parameter estimation is a usual step in developing mathematical models which affects not only the model prediction in itself, but also the future use of the model in process control and optimization.

By solving a system of coupled Partial Differential Equations, Ordinary Differential Equations, and Algebraic Equations, it is possible to accurately simulate fixed-bed units used in these processes [1, 2]. However, a rigorous simulation and, consequently, a better understanding of the intrinsic phenomena governing these systems, such as adsorption isotherms, film and particle mass transfer, energy transfer phenomena, among others, heavily depends on the parameter values [3]. These parameters can be estimated using well-known mathematical correlations or trial and error. However, these methods often introduce significant errors [4]. For a more accurate determination, an optimization algorithm can be employed to find the best set of parameters that minimize the difference between the simulation and experimental data, thereby providing a better representation and understanding of the real process.

Different optimization methodologies can be employed for this purpose. For example, deterministic methods are known for ensuring convergence to an optimal solution, but the starting point selection significantly impacts their performance [5]. In contrast, meta-heuristic techniques are often preferred for their adaptability and efficiency since they do not rely on predefined initial

conditions [6]. However, these approaches may not always guarantee finding the optimal solution for every problem.

Within the field of Artificial intelligence, Reinforcement Learning (RL) emerges as self-supervised technique. RL uses a trial-and-error algorithm, guided by rewards, to help agents learn optimal behaviors, mapping situations to actions to maximize long-term rewards [7]. RL excels at handling delayed feedback, where actions impact both immediate and future outcomes, enabling effective long-term planning. However, RL faces challenges in balancing exploration (seeking new optimal actions) and exploitation (using current knowledge to maximize rewards). Striking this balance is critical, as premature exploitation can lead to suboptimal solutions, while excessive exploration delays progress [8].

Recent advancements, including algorithms like Deep Deterministic Policy Gradient (DDPG), have expanded RL's reach by using deep neural networks for high-dimensional action spaces. This has driven success in multiple fields, including robotics, games, and industrial optimization by a more efficient management of delayed rewards and refining exploration-exploitation [9, 10].

This work introduces an AI-based approach for estimating adsorption isotherm parameters in the mathematical model of fixed-bed experiments for $CH_4/CO_2$ separation. Using a DDPG agent in a Reinforcement Learning algorithm, this methodology addresses the common limitations of deterministic methods by leveraging a deep neural network capable of balancing exploitation and exploration, aiming to optimize the fit between simulated results and experimental data by minimizing the error between the two datasets, thereby enhancing the accuracy and predictive capability of the model.

## MATERIALS AND METHODS

### Objective

Adsorption in a fixed bed unit can be described through a mathematical model that includes the mass, energy, and momentum balances that govern the process. Proper modeling of the equilibrium data is critical for effective process design. Using three different approaches, the main objective of this work is to determine the parameter set, $\theta$, of the Extended Langmuir isotherm (Equation 1) that, when incorporated into the mathematical model (available in [1]) for simulating the gas composition in fixed-bed experiments, enables accurate reproduction of experimental data, and achieves a close-to-optimal fit between simulated and experimental results.

$$q_i = q_{sat,i}\frac{b_i P_i}{1 + \Sigma_{1=1}^{n}(b_i P_i)} \quad (1)$$

### Experimental Dataset

This work used experimental data collected by Ferreira and colleagues [1] , using MIL-53(Al) as the adsorbent for the $CH_4/CO_2$ separation in fixed-bed experiments. The dataset comprises 17 breakthrough experiments conducted under varying feed composition and pressure (from 0.1 to 4 bar) conditions, all at constant temperature (303 K). The conditions can be consulted in Tabel SI.1. At the start of each breakthrough experiment, the column, initially filled with He, was fed with either pure gas or with a gas mixture of $CO_2$ and $CH_4$. Once the column reached saturation under the specified feed conditions the inlet stream was switched to helium at the same total flow rate to initiate the regeneration step. The dataset includes 7 experiments with pure $CO_2$, 7 with pure $CH_4$, and 3 with varying mixtures of $CO_2/CH_4$.

Since all experiments were conducted at the same temperature, the estimated parameters were $q_{sat,CO2}$, $q_{sat,CH4}$, $b_{\infty,CO2}$ and $b_{\infty,CH4}$. The parameters $b_{CO2}$ and $b_{CH4}$ can be calculated using Equation 2, based on a constant value of $(-\Delta H_i)$ obtained from the literature: 26000 J·mol$^{-1}$ for $CO_2$ and 18300 J·mol$^{-1}$ for $CH_4$ [11].

$$b_i = b_{\infty,i}\, exp\left(\frac{-\Delta H_i}{R_g T}\right) \quad (2)$$

Ferreira et al. [1] obtained the adsorption isotherms parameters through breakthrough experiments. The adsorbed amount of gas was calculated using breakthrough curve data from adsorption and desorption experiments. For adsorption, the area under the breakthrough curve was integrated and subtracted from the total gas fed into the column. For desorption, the area under the curve was directly integrated. Comparing both adsorbed amounts (adsorption and desorption), one can verify whether the mass balance closes. These values were normalized by dividing by the dry adsorbent mass, yielding the adsorbed amount per mass unit of adsorbent.

Subsequently, the Extended Langmuir Isotherm parameters were determined using the Generalized Reduced Gradient Nonlinear Solver by fitting the experimental data for adsorbed amounts to the Extended Langmuir Equation, using the partial pressures from each experiment. The parameters obtained can be consulted in Table 1 and were used as reference values for this work.

### Reinforcement Learning Algorithm

The RL setup requires defining: (1) the Environment, representing the system where actions are applied; (2) the Reward, which guides the algorithm's learning process; (3) the State, reflecting the environment's response to an action; (4) the Agent, the decision-making component of the RL algorithm; and (5) the Actions, indicating how the algorithm interacts with the environment.

The action represents how the RL agent affects the environment to maximize the reward. In this work, the action is the set of parameters, $\theta$, that needs to be

estimated. The action must be constrained between a lower ($Act_{min}$) and an upper bound ($Act_{max}$) and an initial guess must be given ($Act_0$).

The agent is the core of the RL algorithm, responsible for learning from past trials (exploitation) and exploring new possibilities (exploration) to maximize long-term rewards by deciding the next action to take. The selection of the best agent depends on the desired policy, observation space, action space, and learning process. For this project, since a deterministic policy is preferred over a stochastic one, both the observation and action spaces are continuous, and the objective function is too complex for a simpler Q-learning process so a deep neural network-based agent was chosen, a Deep Deterministic Policy Gradient agent was selected.

The tuning of the neural networks responsible for the agent is crucial, as their hyperparameters play a key role in balancing exploration and exploitation.

## Parameter Estimation

All the work was done on a computer with a processor 13th Gen Intel(R) Core (TM) i7-13700F 2.10 GHz, 32 GB of RAM and a graphic card NVIDIA GeForce RTX 4070.

The first approach tried replicating the method described in [1], replacing the used solver with the RL algorithm. This enabled the direct adjustment of the Extended Langmuir model for each experiment with the experimental values of $q_{CO2}$ and $q_{CH4}$, obtained after mass balance, as previously described.

In this approach, the Environment is defined as the calculation of the predicted $q_{CO2}$ and $q_{CH4}$ values for all experiments using Equation 1. The Action corresponds to the set of parameters to be applied in Equation 1, while the State represents the Mean Squared Error (MSE) between the calculated and experimental $q_{CO2}$ and $q_{CH4}$ values. In RL, the reward is typically designed to be maximized. However, since the objective is to minimize the error between experimental and simulated data, the Reward is defined as the negative of the MSE between the simulated and experimental results.

This entire approach was implemented in MATLAB. After the training, the parameter set that best minimized the MSE was used to simulate the 17 breakthrough experiments and the error between the experimental and simulated dataset was compared with the one obtained with the reference parameters.

The second and third approaches involved the direct adjustment of parameters based on the breakthrough curves simulations. The Environment is the simulation of the breakthrough experiments used for training, utilizing the parameter set provided by the agent in each trial. The simulations were conducted in the gPPROMS environment (Process Systems Enterprise, London, UK) and numerically solved using the orthogonal collocation on finite elements method, with second-order polynomials and 115 intervals, using the phenomenological model available at [1, 2]. The RL Algorithm was implemented in MATLAB.

As mentioned, RL algorithms typically aim to optimize a problem by maximizing the reward. Since the goal is to minimize the difference between experimental and simulated data, the reward is the negative of the error between the two datasets. The number of comparison points per experiment is denoted as $N_{\text{points}}$. Since this value varies across experiments, a weighting factor, $\omega$, is applied to normalize the MSE between experiments.

Equation 3 shows the objective function ($f_{obj}$) to be minimized and Equation 4 the Long-Term Reward ($\text{Rew}_{\text{LT}}$) that the agent aims to maximize. In these equations, $y$ corresponds to the molar composition of a determined component, $j$ represents the experiment number, $N_{exp}$ is the total number of experiments, $k$ is the time corresponding to the simulated and experimental points, $T$ is the total duration of the experiment, and $i$ represents 1 and/or 2 (depending on the type of experiment) corresponding to $CO_2$ and $CH_4$, respectively.

$$f_{obj} = \sum_{j=1}^{N_{exp}} \omega_j \left[ \frac{1}{N_{points,j}} \sum_{k=1}^{T} \left( \sum_{i=1}^{2} (y_{k,exp,i} - y_{k,sim,i})^2 \right) \right] \quad (3)$$

$$\text{Rew}_{\text{LT}} = \sum_{\text{trial}=1}^{\text{N}_{\text{trials}}} \text{Rew}_{\text{trial}} = \sum_{\text{trial}=1}^{\text{N}_{\text{trials}}} - f_{obj_{trial}} \quad (4)$$

To ensure consistency in the rate of change for each parameter across trials, the action generated by the agent is normalized in a range between -1 and 1. Before being sent to the environment, the action is re-normalized, converting it into a set of parameters suitable for simulating the experiments. This helps nullify the high difference in the order of magnitude between the parameters to be estimated.

To reduce computational effort, 6 experiments were selected from the dataset of 17. These included 2 experiments with pure $CO_2$, 2 with pure $CH_4$, and 2 binary experiments. The RL algorithm focused on maximizing the long-term reward for these 6 breakthrough curves during training by maximizing the reward function in each trial. Once the optimal $\theta$ was identified for these experiments, it was used to simulate the remaining experiments, and the objective function was evaluated across all experiments to assess the methodology's results.

The primary difference between approaches two and three lies in the range of the search for the optimal set of parameters, specifically in the range of the action. The first and second approaches aimed to improve the results obtained by the authors of the base article. To achieve this, a range of ±20% around the reference

values was used as the upper and lower limits for the action to be taken in each trial. The reference values served as the initial guess. The third methodology was implemented to assess the RL algorithm's ability to find the optimal set of parameters without prior knowledge of the system. In this case, a broader range of exploration was allowed for each parameter. The initial guess was set as the mean value of the action limits. The action limits for each approach can be consulted in Table SI.4.

# RESULTS

## Agent

A DDPG agent is an actor-critic RL agent that, using neural-networks, searches for an optimal policy that maximizes the expected cumulative long-term reward. The actor takes observations and returns the corresponding action that maximizes the long-term reward. The critic takes observations and actions as inputs and returns the corresponding expectation of the long-term reward.

The architecture and structure used are based on the one presented in [1], with some adaptations. The actor is a feedforward neural network with three fully connected layers. The first two dense layers have 256 neurons each, followed by ReLU activations. The final dense layer has 4 neurons, and its output is transformed using the Tanh activation function. The critic is a multi-input architecture with two neural network branches. Both input features through a fully connected layer with 256 neurons. The outputs of these branches are concatenated and passed through a ReLU activation, followed by a fully connected layer with 256 neurons and a subsequent ReLU activation. The agent uses an Ornstein–Uhlenbeck noise function to develop an exploration policy.

The hyperparameters were manually tuned following a sensitivity analysis, in which each of the main hyperparameters was varied within a specified search range. Although relevant, it was observed that hyperparameter manipulation within the selected tuning range had little impact on the algorithm's performance. Therefore, the agent was kept as small as possible without compromising its predictive capabilities. A more detailed description of the agent, as well as the process of hyperparameter tuning and selection, is provided in the SI.

## Parameters Estimation

On the first approach, 500,000 trials were used to estimate $\theta$. Despite the extensive number of iterations, the best parameter set only managed to reduce the error by 8% on the breakthrough curves compared to the reference parameters. Thus, while this methodology is more straightforward than the next two, it does not offer significant advantages to the standard approach, as it requires the same previous work, is more time-consuming and provides no meaningful improvements in accuracy.

For the second approach, the search for the optimal set of parameters was conducted over 350 trials, with the best result achieved at trial number 276. The obtained $\theta$ reduced the objective function by 26% for the training experiments and by 28% across all experiments. However, to achieve this result, all the manual work done in [1] to find the initial guess and a small margin of search must still be performed. This approach proved to be a valid methodology for achieving high accuracy, allowing for fine-tuning of the parameters, although exhaustive work is still required.

For the third approach, the search was done for 350 trials, with the best result achieved at trial number 119. The obtained $\theta$ resulted in a 15% reduction in the objective function for the training experiments and a 31% reduction in the objective function across the entire set of experiments, indicating a substantial improvement in the alignment between the simulated and experimental data. More significantly, this result demonstrates that the RL algorithm can map the surface area of the objective function and identify a function minimum, surpassing the derivative-based solver used in the reference work.

Table 1 summarizes the parameter sets obtained from each approach, the reference values used for process simulation, and the objective function obtained with each methodology. Table S.I.5 provides a more detailed analysis of the results. These results highlight the effectiveness of approach number 3. It resulted in the set of parameters that most significantly reduced the global error between the experimental and simulated datasets and was the only approach that improved the fit for the pure $CH_4$ experiments when compared to the reference work. Additionally, this methodology does not rely on all the previous work already done by the authors, like approach one and two, allowing a broad exploration of each parameter without prior knowledge of the system and, so, can be applied directly after experimental work.

**Table 1:** Reference and Estimated Parameters and objective function value obtained via Approach (Ap.) 1, 2 and 3

| $\boldsymbol{\theta}$ | Units | Ref. | Ap.1 | Ap.2 | Ap.3 |
|---|---|---|---|---|---|
| $q_{sat,CO2}$ | [mmol g$^{-1}$] | 6.38 | 6.76 | 7.65 | 6.46 |
| $q_{sat,CH4}$ | [mmol g$^{-1}$] | 7.38 | 6.87 | 6.48 | 6.86 |
| $b_{\infty,\mathrm{CO2}}$ | [Pa$^{-1}$] | 1.55 | 1.40 | 1.24 | 1.67 |
| $b_{\infty,\mathrm{CH4}}$ | [Pa$^{-1}$] | 8.07 | 8.87 | 9.68 | 8.74 |
| $\boldsymbol{f_{obj}}$ $(\times 10^3)$ | | 3.06 | 2.82 | 2.19 | 2.11 |

To evaluate the exploration behavior over trials, Figure SI.1 displays the action values assigned per trial in this approach. It demonstrates that the algorithm initially explores the entire parameter space. However, as iterations progress, it begins to focus more on a specific region,

prioritizing exploration in that area to identify a minimum. This underscores the algorithm's ability to explore the parameter space effectively while simultaneously learning to refine its search for optimal solutions.

When analyzing the evolution of the objective function over the trials (Figure 1), two main conclusions can be taken that coincide with the two main concepts of Reinforcement Learning. Firstly, a clear trend of reduction in the objective function emerges as the RL agent begins to learn. This demonstrates the agent's ability to leverage past experiences to maximize long-term rewards (exploitation). This learning process is further corroborated by the convergence observed in Figure SI.1 for all actions. Secondly, significant fluctuations in the objective function are still evident, even after numerous trials. These fluctuations can be attributed to the algorithm's continued exploration of the parameter space and the high sensitivity of the simulation to small parameter changes.

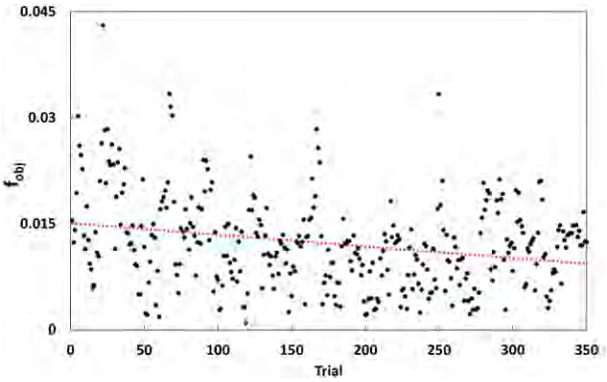



**Figure 1:** Evolution of the Objective Function Across Iterations: Objective function per iteration (•) and Trendline of the objective function (·····)

To assess the impact of these small fluctuations of the parameters set on the objective function, a sensitivity analysis was conducted. The 17 breakthrough experiments were simulated using the parameter set obtained on the third approach, adjusted by multiplication factors of ± 0.01, 0.1, 1, 5, and 10%. The objective function values for the full set of experiments, corresponding to each parameter set, are presented in Table SI.6.

This analysis is particularly relevant as it leads to several conclusions. Firstly, as mentioned previously, even small changes in the parameter set can result in significant variations in the objective function. For instance, decreasing the parameters by just 1% can increase the objective function by 38%. However, increasing all the parameters by the same 1% can reduce the objective function, demonstrating no straightforward correlation. This conclusion is supported by the results in Table SI.7, which presents the outcomes of a sensitivity analysis similar to the one described earlier. However, in this case, only a 1% variation was applied to each parameter individually. Even such a small change of 1% can lead to a 10% increase in the objective function.

This underscores the challenges faced by the RL algorithm in mapping the objective function surface, given its high sensitivity to minor parameter changes. Nonetheless, it also highlights the effectiveness of the algorithm in learning from past trials and converging toward an optimal region, as evidenced by Figure 1. These results also indicate that the best parameter set achieved with approach 3 does not correspond to the global minimum, as evidenced by better outcomes obtained after incrementing all parameters by 1%, 0.1%, and 0.01%. This was somewhat expected after analyzing Figure 1. While there is a clear trend of reducing the objective function across trials, the best result occurred at trial 119 out of 350. This suggests that the result was achieved more due to exploration than exploitation. Furthermore, since the RL algorithm did not immediately converge to the region of this trial, that area was not thoroughly explored, preventing further refinement of the result. This explains the presence of better outcomes near the identified optimum that were not found by the algorithm.

Finally, to evaluate the capability of the new set of parameters on predicting the adsorbed amount on every experiment, the Extended Langmuir Isotherms were plotted and the MSE values between the experimental (obtained in [1] after mass balance) and calculated (using both the reference parameters and those obtained from approach 3) $q_{CO2}$ and $q_{CH4}$ were determined (Table SI.8 ,Figures SI.2 and SI.3) . Although the new parameter set improves the fit between predicted and experimental adsorbed amounts for some experiments (especially for pure $CH_4$ experiments), it globally increases the MSE from $3.97\times10^{-3}$ to $5.87\times10^{-3}$. This leads to the conclusion that this methodology does not improve the precision of the model in predicting the adsorbed amount. However, the adjustment of the simulated breakthrough curves to the experimental data is still enhanced by the new parameter set (Figure SI.4), as previously discussed. This improvement can be attributed to the ability of the new parameters to compensate for inaccuracies in other parameters of the mathematical model. Thus, while the prediction of the adsorbed amount is negatively affected, the overall adjustment benefits from this compensation. This is another advantage of using a broad range of search.

To assess the algorithm's reproducibility, approach 3 was repeated. After 207 trials, the objective function was reduced by 7%. Although this result did not match the previous outcome (likely due to earlier success driven by exploration), it confirms that the RL algorithm reliably identifies a set of parameters for the Extended Langmuir Equation that accurately simulates fixed-bed experiments for $CH_4/CO_2$ separation. Additionally, the same trends observed in Figures 1 and SI.1 were visualized when repeating the methodology, highlighting the

capability to replicate the behavior of the training.

## CONCLUSIONS

This work introduces an AI-based methodology using Reinforcement Learning to estimate parameters in the mathematical model of gas-phase fixed-bed experiments for $CO_2$ and $CH_4$ separation and minimize the error between simulated and experimental breakthrough data.

Using the same DDPG agent, three approaches were tested. In the first, the RL algorithm replaced the traditional solver to determine Extended Langmuir isotherm parameters that best fit the experimental adsorbed amounts obtained from breakthrough curves. In the second and third approaches, the RL agent directly provided parameters for breakthrough curve simulations. The key difference lies in parameter exploration: the second approach used literature values as an initial guess with a limited search range, while the third treated it as a zero-knowledge problem, allowing wide parameter exploration without prior system knowledge.

While RL, like other meta-heuristic approaches, does not guarantee global optimality, it offers a flexible framework that adaptively explores and exploits the search space. By incorporating learning into the exploration process, RL can reduce the number of iterations typically required by standard meta-heuristic methods. Despite its simplicity and lack of manual work required after the experimental phase, the third approach delivered the best results. It reduced the global error between experimental and simulated data by 31% after just 119 iterations, when compared with the parameters obtained using the Generalized Reduced Gradient. The new set of parameters can compensate for misadjustments in other system parameters, which was not possible when obtaining the parameters by adjusting the Extended Langmuir Equation to only the adsorbed amount. Using RL as an optimization algorithm proved to be an efficient, reproducible, and highly effective method for parameter estimation. It exhibited strong iterative learning and thorough exploration of the objective function surface, successfully identifying a set of parameters that align the mathematical model with the experimental data.

## DIGITAL SUPPLEMENTARY MATERIAL

For a more detailed explanation and analysis of the methodology and results, the Digital Supplementary Materials referenced throughout the work can be consulted here.

## ACKNOWLEDGEMENTS

This work was supported by national funds through FCT/MCTES (PIDDAC): LSRE-LCM, UIDB/50020/2020 (DOI: 10.54499/UIDB/50020/2020) and UIDP/50020/2020 (DOI: 10.54499/UIDP/50020/2020); and ALiCE, LA/P/0045/2020 (DOI: 10.54499/LA/P/0045/2020).

## REFERENCES

1. Ferreira, A.F.P., et al., Methane purification by adsorptive processes on MIL-53(Al). Chemical Engineering Science, 2015. 124: p. 79-95.
2. Da Silva, F.A., J.A. Silva, and A.E. Rodrigues, General package for the simulation of cyclic adsorption processes. Adsorption, 1999. 5(3): p. 229-244.
3. Won, W., S. Lee, and K.S. Lee, Modeling and parameter estimation for a fixed-bed adsorption process for CO2 capture using zeolite 13X. Separation and Purification Technology, 2012. 85: p. 120-129.
4. Weber Jr, W.J. and K.T. Liu, DETERMINATION OF MASS TRANSPORT PARAMETERS FOR FIXED-BED ADSORBERS. Chemical Engineering Communications, 1980. 6(1-3): p. 49-60.
5. Schwaab, J.C.P.M., Análise de Dados Experimentais: I. Fundamentos de Estatística e Estimação de Parâmetros. Editora E-papers.
6. Lin, M.-H., J.-F. Tsai, and C.-S. Yu, A Review of Deterministic Optimization Methods in Engineering and Management. Mathematical Problems in Engineering, 2012. 2012(1): p. 756023.
7. Nian, R., J. Liu, and B. Huang, A review On reinforcement learning: Introduction and applications in industrial process control. Computers & Chemical Engineering, 2020. 139: p. 106886.
8. Sutton, R.S. and A.G. Barto, Reinforcement Learning: An Introduction. 2018: A Bradford Book.
9. Lillicrap, T., Continuous control with deep reinforcement learning. arXiv preprint arXiv:1509.02971, 2015.
10. Tan, H. Reinforcement Learning with Deep Deterministic Policy Gradient. in 2021 International Conference on Artificial Intelligence, Big Data and Algorithms (CAIBDA). 2021.
11. Rallapalli, P., et al., Sorption studies of CO2, CH4, N2, CO, O2 and Ar on nanoporous aluminum terephthalate [MIL-53(Al)]. Journal of Porous Materials, 2011. 18(2): p. 205-210.

© 2025 by the authors. Licensed to PSEcommunity.org and PSE Press. This is an open access article under the creative commons CC-BY-SA licensing terms. Credit must be given to creator and adaptations must be shared under the same terms. See https://creativecommons.org/licenses/by-sa/4.0/



# Section 7

## CAPEing with Societal Challenges (Green Deal, Energy Transition)

Systems & Control Transactions

**Research Article - Peer Reviewed Conference Proceeding**
ESCAPE 35 - European Symposium on Computer Aided Process Engineering
Ghent, Belgium. 6-9 July 2025
Jan F.M. Van Impe, Grégoire Léonard, Satyajeet S. Bhonsale,
Monika E. Polańska, Filip Logist (Eds.)

PSE PRESS

# Engineering the Final Frontier: The Role of Chemical and Process Systems Engineering in Space Exploration

**Edwin Zondervan**

[a] Twente University, Drienerlolaan 5, Enschede 7522NB, the Netherlands. e.zondervan@utwente.nl

## ABSTRACT

Space exploration demands the integration of multiple scientific and engineering disciplines, with chemical engineering and process systems engineering playing pivotal roles. This paper examines their critical contributions to propulsion systems, life support mechanisms, and advanced materials essential for space missions. Recent advancements in chemical propellants and rocket fuels, illustrated by SpaceX and NASA missions, have significantly improved propulsion efficiency and safety. Chemical engineering is vital in developing air purification, water recycling, and bioregenerative life support systems, ensuring astronaut survival and mission sustainability. Additionally, creating heat-resistant, lightweight materials enhances spacecraft durability under extreme space conditions. Process systems engineering (PSE) complements these efforts by integrating, simulating, and controlling complex systems. PSE ensures reliable subsystem integration and uses predictive analytics and advanced modeling for mission planning and risk mitigation. Automation and control systems are essential for maintaining operations with minimal human intervention. The synergy between these fields is evident in in-situ resource utilization (ISRU) technologies, which extract and process local resources on extraterrestrial bodies, reducing reliance on Earth supplies and enhancing mission viability. Despite significant progress, challenges remain. Addressing harsh space environments, ensuring long-duration mission sustainability, and advancing energy sources and materials are ongoing research areas. This presentation underscores the indispensable roles of chemical and process systems engineering in overcoming space exploration challenges.

**Keywords**: Space exploration, chemical engineering, process systems engineering

## 1. INTRODUCTION

A few years ago, I read somewhere in a popular magazine about the *Mars Oxygen In-Situ Resource Utilization Experiment* (MOXIE). A project by NASA where a mobile reactor was landed on Mars. The equipment could capture carbon dioxide and convert it into oxygen. The start of a science fiction story! Such equipment could be used in terraforming (making Mars suitable for humans to live). The chemical engineer in me was also thinking about how such equipment had to be completely autonomous and that communication with Earth would lead to large delays (the average distance between Mars and Earth is 140 million miles). This probably required a big deal of *control systems engineering*. At that time, I was still working at Bremen University (Germany), and one of my colleagues, Lucio Colombi Ciacchi, was also thinking about how *chemical engineering* could be of importance in space exploration. He was reasoning that if men wanted to live on the moon or Mars, for that matter, shooting rockets with construction materials into space would be hard to impossible. In other words, materials should be locally produced. As a materials scientist, Colombi Ciacchi was especially interested in developing electrochemical processes to make metal alloys; see, for example, [1].

I also got back in touch with Volker Hessel, one of my former colleagues at Eindhoven University (the Netherlands), who moved to Australia and took up a new research direction. Hessel was very much interested in exploring how space conditions (e.g., vacuum, no gravity, extreme pressures/temperatures) affected and/or could be used to benefit the design of new pharmaceuticals [2,3].



**Figure 1:** Manufacturing equipment could be much lighter than on earth because of the moon's gravity. The first things you would want to make would be mining devices to speed up production. After that you would make the things you need for a power grid, including solar panels. You might also make robots that are remotely operated by humans on earth for general maintenance tasks. The last thing to produce would be rockets since they don't offer much for base expansion and self sufficiency. Heat shields are heavy so a rocket could launch off earth without one and then one made on the moon could be attached. Taken from [4]

You can imagine that my attention to this topic was caught, and I was looking around for possibilities to hook up or launch some projects that linked chemical engineering to space exploration. Figure 1 shows an artist's impression of how a lunar industrial site could look.

It turned out that there are not so many direct references to chemical engineering in space [5,6]. I found inspiration in a short chapter that Isaac Asimov wrote in 1989 in "*The Tyrannosaurus Prescription and 100 Other Essays*" [7]. Chapter 6 deals with the future of chemical engineering, where he concludes that "orbital chemical engineering" is a new and spacious branch of the field in which engineers deal with new situations and new problems. For sure, we can hope that finding new solutions will make the 21$^{st}$ century as different from the 20$^{th}$ as the twentieth is from Roger Bacon's 13$^{th}$!

When sharing my enthusiasm about this with my colleagues, I often was answered with frowning eyebrows and replies like, "Let us first try to find solutions for the problems we have on earth". When reaching out to students to probe if they would be interested in researching the topic, they'd politely thank me and preferred to stay with a more conventional topic.

Maybe a focus on solving Earth's problems is indeed more appropriate. But there already exists something like a space economy. In 2022, OECD countries spent 75 billion US dollars on space-based systems [8]. That means especially satellites. More than 100 countries have already managed to launch satellites into space. These satellites provide information on climate variables (e.g., methane emissions in landfills), and this data is used, of course, to monitor and control greenhouse gas emissions globally. Satellites also support our critical infrastructures on Earth (transport, energy, food supply, and law enforcement). Especially via communication and positioning instruments. Although most of the spending still comes from governments, more and more commercial space activities commence. In other words, space exploration also contributes to solving problems on Earth.

I got stuck with the question: What kind of problems might we encounter when doing space exploration, and what type of solutions could chemical engineering offer to such problems? It stayed with being a question until I submitted an abstract to the ESCAPE, which was accepted. Not hindered by any knowledge, the accepted abstract forced me to look into the matter, so here we go!

Space exploration is a paramount scientific and engineering pursuit that involves overcoming numerous challenges. Chemical and process systems engineering are critical in developing the technologies necessary for successful and sustainable space missions.

This paper explores the significant contributions of these fields to space exploration, focusing on propulsion systems, life support mechanisms, materials engineering, systems integration, simulation, automation, and in-situ resource utilization (ISRU).

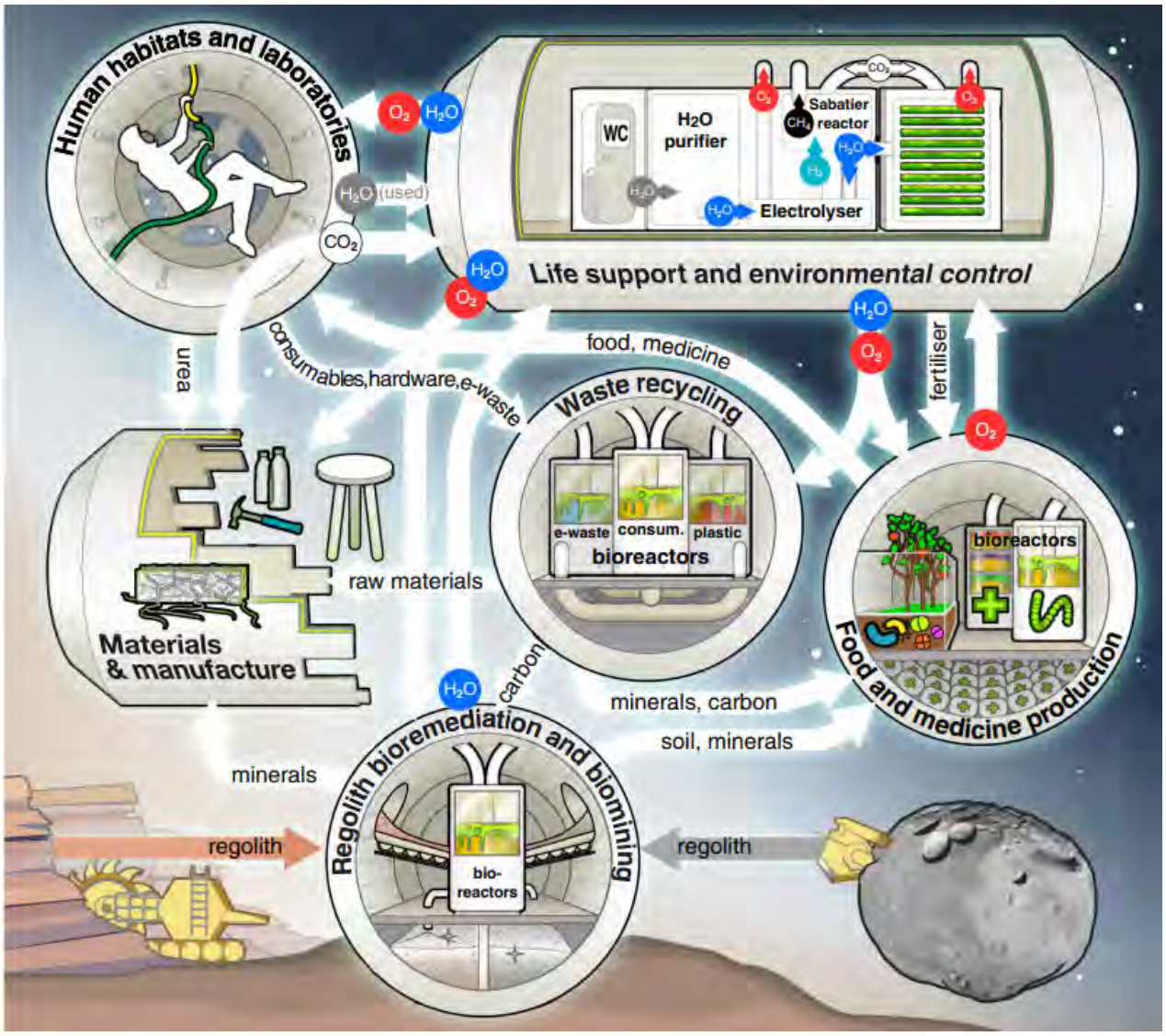



**Figure 2:** Impression of a biotechnology based life support system in an agnostic space environment. This figure was taken from [9]

## 2. CHEMICAL ENGINEERING IN SPACE EXPLORATION

### Role of Chemical Engineering

Chemical engineering involves the application of chemical processes and principles to create and optimize products and systems. In space exploration, chemical engineering is vital for developing propulsion systems, life support technologies, and advanced materials.

### Propulsion Systems

Propulsion systems are fundamental to space travel. Chemical engineers develop and optimize rocket fuels and propulsion technologies to enhance efficiency and safety. Innovations in chemical propellants, such as liquid hydrogen and oxygen, hypergolic fuels, and ion propulsion systems, have revolutionized space travel. Case studies from SpaceX and NASA missions illustrate these advancements' practical applications and benefits. For instance, SpaceX's Falcon 9 and NASA's Space Launch System (SLS) utilize advanced chemical propellants for higher performance and safety (You might think of hypergolic fuels or ion propulsion systems).

### Life Support Systems

Life support systems are essential for maintaining astronaut health and safety. Chemical engineers design air purification systems that remove carbon dioxide and other contaminants from the spacecraft environment.

Water recycling systems convert wastewater into potable water, ensuring a sustainable water supply. Bioregenerative life support systems, which include the cultivation of plants for food and oxygen production, have also been developed by chemical engineers. These technologies are critical for long-duration missions, such as those planned for Mars exploration. Figure 2 renders an impression of a life support system, see also [9], basically (re)cycling water, oxygen, and carbon dioxide, mining regolith (space rock), and then producing materials, food, medicine, and fertilizer.

### Materials Engineering

Materials engineering, a subset of chemical engineering, focuses on developing materials that can withstand the extreme conditions of space. Engineers create heat-resistant and lightweight composites and alloys for spacecraft construction. These materials must endure high radiation levels, temperature fluctuations, and mechanical stresses. Innovations in materials engineering enhance the structural integrity and durability of spacecraft, ensuring mission safety and longevity.

## 3. PROCESS SYSTEMS ENGINEERING IN SPACE EXPLORATION

### Role of Process Systems Engineering

Process systems engineering (PSE) focuses on designing, integrating, optimizing, and controlling complex systems. In space exploration, PSE is crucial for ensuring the reliability and efficiency of spacecraft systems.

### Systems Integration

Systems integration involves the seamless combination of various subsystems, such as power, life support, and thermal management. PSE ensures that these subsystems work together reliably and efficiently. Redundancy and reliability are critical as any subsystem failure can jeopardize the mission. PSE methodologies, including systems engineering principles and integration frameworks, are employed to achieve this goal.

### Simulation and Modeling

Simulation and modeling are essential tools in PSE. They provide a means to plan missions, assess risks, and

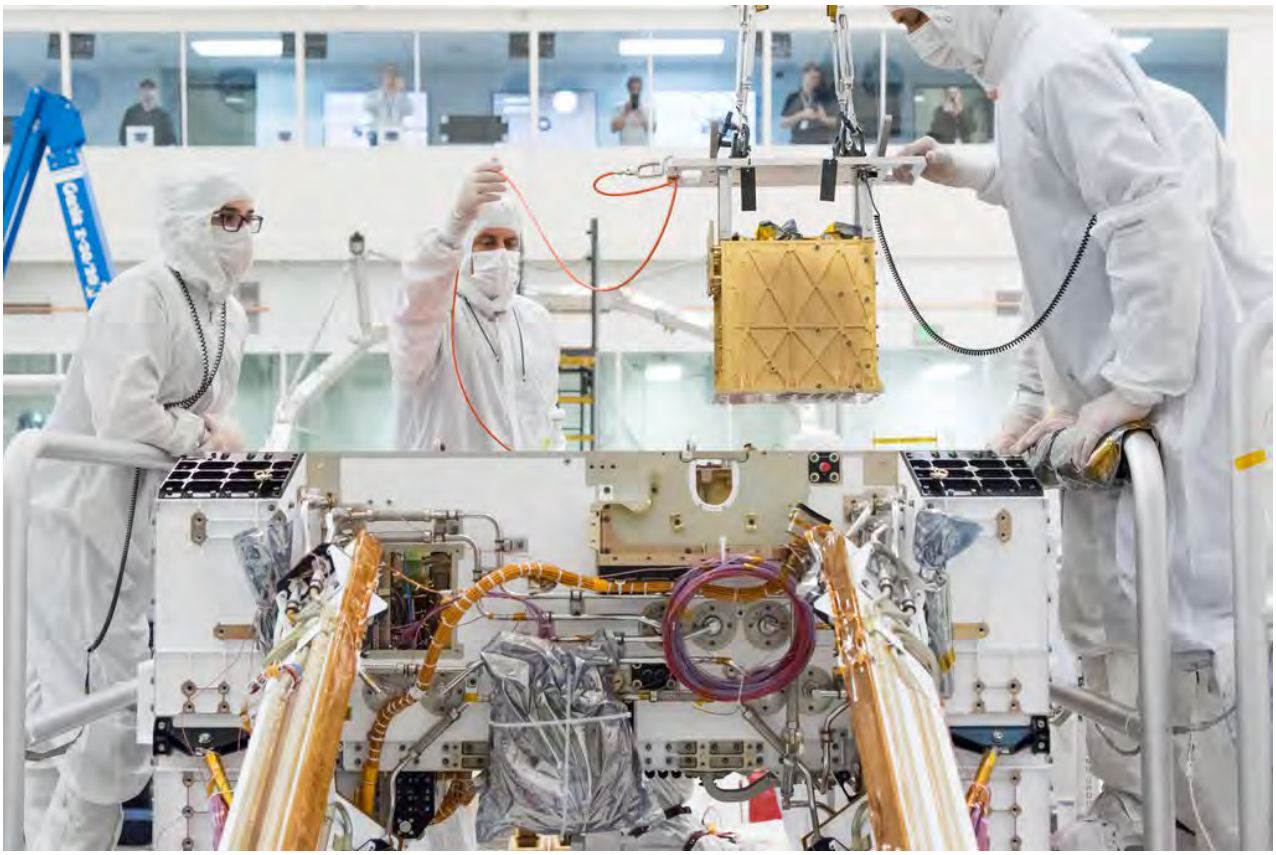


**Figure 3:** MOXIE (Mars Oxygen In-situ Resource Utilization Experiment) is lowered into the chassis of NASA's Perseverance in 2019. During the mission, MOXIE extracted oxygen from the Martian atmosphere 16 times, testing a way that future astronauts could make rocket propellant that would launch them back to Earth.
Credit: NASA/JPL-Caltec

optimize systems. Predictive analytics and advanced modeling techniques allow engineers to anticipate potential issues and develop effective mitigation strategies. For example, thermal modeling ensures that a spacecraft can maintain optimal temperatures in the harsh environment of space, while life support models simulate the long-term sustainability of air, water, and food systems.

### Automation and Control

Automation and control systems are critical for maintaining spacecraft operations and habitat environments with minimal human intervention. PSE develops automated control systems that manage various functions, such as navigation, thermal regulation, and life support. These systems enhance mission efficiency and reduce the risk of human error. Examples include automated docking systems used by the International Space Station (ISS) and autonomous rovers deployed on Mars.

## 4. SYNERGISTIC APPLICATIONS

### Combined Use in Life Support Systems

The integration of chemical and process systems engineering is particularly evident in life support systems. Chemical processes are used to purify air and recycle water, while PSE integrates these processes into a reliable and efficient system. Case studies, such as the ISS life support systems, demonstrate how these disciplines work together to ensure sustainability.

### In-Situ Resource Utilization (ISRU)

ISRU involves extracting and processing local resources on extraterrestrial bodies, such as the Moon and Mars, to produce water, oxygen, and building materials. Chemical engineering develops the extraction and processing techniques, while PSE integrates these processes into a coherent system. For instance, lunar regolith can be processed to extract oxygen, which can then be used for life support and propulsion. Efficient ISRU systems reduce reliance on Earth-supplied resources and enhance mission viability. With Figure 3, I am returning to my opening statement. Figure 3 shows MOXIE, the reactor that can convert captured carbon dioxide from Mars's atmosphere into oxygen. A lighting example of reactor engineering (chemical engineering) and automation and control (process systems engineering).

### Advanced Manufacturing and Repair

Advanced manufacturing technologies, such as 3D printing, are crucial for space exploration. These technologies enable the in-situ production of tools, spare parts, and even habitats using local materials. Chemical engineering develops the materials and processes for 3D printing, while PSE ensures the integration and reliability of these manufacturing systems. This capability is vital for long-duration missions where resupply from Earth is not feasible.

### Illustrative example: distillation on the Moon

NASA and other space agencies are making plans to develop ISRU technologies on the moon, including distillation. Distillation could be used to purify water (that is available in lunar ice) or extract oxygen, water or other byproduct after regolith is treated chemically (e.g. via hydrogen reduction, carbon thermal reduction or molten salt electrolysis). It might also be useful as part of a process to locally produce rocket fuels.

But distillation on the moon poses several (chemical engineering) challenges. For example:

- The Moon's gravity is about 1/6th of Earth's, which could affect the separation of liquids and vapors during distillation. However, this is a manageable issue with the proper equipment design;
- The Moon has no atmosphere, meaning distillation would need to occur in a pressurized, controlled environment to prevent liquids from boiling away instantly in the vacuum.
- Lunar temperatures range from extremely cold (-173°C at night) to very hot (127°C during the day). Distillation systems would need robust thermal insulation and temperature control to function effectively.
- Distillation requires energy to heat liquids. On the Moon, energy would likely come from solar panels or nuclear power sources, both of which are feasible but require careful planning.
- Equipment would need to be lightweight, durable, and capable of operating in harsh conditions. Transporting materials to the Moon is expensive, so efficiency is critical.

PSE can tackle lunar distillation challenges through a structured, holistic approach. It uses system modeling and simulation to predict performance and address low-gravity issues like phase separation.

PSE integrates distillation with power, water extraction, and life support systems for optimal resource and energy use. It optimizes designs to balance mass, efficiency, and reliability for lunar operations. Risk analysis identifies failure points and incorporates safeguards for harsh environments. Automated control systems enable real-time monitoring and adjustment, reducing human intervention.

And, PSE designs gravity-independent solutions using centrifugal force, capillary action, or pressure gradients. It also ensures sustainability and validates designs through microgravity and lunar simulations for reliable

performance.

## 5. CHALLENGES AND FUTURE DIRECTIONS

### Technical Challenges

Space exploration faces numerous technical challenges, including harsh environmental conditions, long-duration mission sustainability, and system reliability.

Engineers must develop technologies that can withstand high radiation, extreme temperatures, and mechanical stresses. Ensuring the durability and efficiency of life support systems, propulsion systems, and materials is paramount.

### Future Research Areas

Future research must address the development of new energy sources, advanced materials, and sustainable life support systems. Innovations in biotechnology, such as bioengineered organisms for life support, and the application of artificial intelligence (AI) in process systems engineering, hold promise for future space missions. AI can optimize system performance, predict failures, and enhance automation.

### Potential Breakthroughs

Potential breakthroughs include the integration of biotechnology and AI in space exploration. Bioengineered organisms could be used to produce food, oxygen, and other essential resources. AI-driven process systems could enhance the reliability and efficiency of spacecraft systems. These innovations could revolutionize space exploration, making long-duration missions more feasible and sustainable.

## 6. CONCLUSION

Chemical engineering and process systems engineering are indispensable for the success and sustainability of space missions. These fields contribute to the development of propulsion systems, life support technologies, materials, systems integration, simulation, automation, and ISRU. As humanity continues to push the boundaries of space exploration, innovations in these disciplines will be crucial in overcoming the challenges of the final frontier. The collaboration between chemical engineering and PSE will play a pivotal role in ensuring the success of future space missions, making it possible to explore and inhabit new worlds.

## REFERENCES


1. M. Avila, C. Heinicke, L. Colombi Ciacchi, A. Dekorsy, S. Fehrler, K. Rezwan, N. Sieroka, K. Tracht, C. Verseux, A vision for human mars exploration made in Bremen, 44th COSPA Scientific Assembly, 16-24 July, 2022.
2. M. Varon Hoyos, V. Hessel, E. Salas, J. Culton, K. Robertson, A. Laybourn, M. Escriba-Gelonch, N. Cook, M. de Zwart, Supply chain sustainability in outer space: lessons to be learnt from remote sites on earth, 2024, Processes, 12, pp. 2015.
3. K. Brinkert, C. Zhuang, M. Escriba-Gelonch, V. Hessel, The potential of catalysis for closing the loop in human space exploration, (2023), Catalysis today, 423, pp. 114242.
4. Lunar industrialization, from webpage: http://ffden-2.phys.uaf.edu/webproj/212_spring_2019/Cole_Sudkamp-Walker/1026563465cb8145247993/how.html (accessed January 2025)
5. A. Lobmeyer and B. Meneghelli, Chemical engineering in Space, 6th World Congress of Chemical eEngineering, Melbourne, Australia, 23-27 September 2001.
6. V.J. Inglezakis, D. Rapp, P. Razis, A.A. Zorpas, Chemical engineering beyond earth: astrochemical engineering in the space age, 2023, Sustainability, 15. Pp. 13227.
7. I. Asimov, The Tyrannosaurus Prescription and 100 Other Essays, 1989, Prometheus books: Chapter 6, The future of chemical engineering, p. 37.
8. OECD (2023), The Space Economy in Figures: Responding to Global Challenges, OECD Publishing, Paris, https://doi.org/10.1787/fa5494aa-en.
9. R. Santomartino, N.J.H. Averesch, M. Bhuyan, C.S. Cockell, J. Colangelo, Y. Gumulya, B. Lehner, I. Lopez-Ayala, S. McMahon, A. Mohanty, S.R. Santa Maria, C. Urbaniak, R. Volger, J. Yang, L. Zea, Towards sustainable space exploration: a roadmap for harnessing the power of microorganisms,Nature Communications | (2023) 14:1391



© 2025 by the authors. Licensed to PSEcommunity.org and PSE Press. This is an open access article under the creative commons CC-BY-SA licensing terms. Credit must be given to creator and adaptations must be shared under the same terms. See https://creativecommons.org/licenses/by-sa/4.0/




Systems & Control Transactions

**Research Article - Peer Reviewed Conference Proceeding**
ESCAPE 35 - European Symposium on Computer Aided Process Engineering
Ghent, Belgium. 6-9 July 2025
Jan F.M. Van Impe, Grégoire Léonard, Satyajeet S. Bhonsale,
Monika E. Polańska, Filip Logist (Eds.)

PSE PRESS

# Green Solvent Alternative for Extractive Distillation of 1,3-Butadiene

**João P. Gomes[a]*, Rodrigo Silva[b], Clemente Nunes[c] and Domingos Barbosa[a]**

[a] LEPABE / ALiCE, Faculty of Engineering, University of Porto, Rua Dr Roberto Frias, 4200-465 Porto, Portugal.
[b] Repsol Polímeros, S.A., Sines, Portugal.
[c] CERENA, Instituto Superior Técnico, Av. Rovisco Pais 1, 1049-001 Lisboa, Portugal.
* Corresponding Author: joaopedrosilvagomes998@gmail.com.

## ABSTRACT

The separation of 1,3-butadiene from $C_4$ hydrocarbon mixtures is a crucial step in the production of synthetic rubbers and plastics. Conventional extractive distillation methods using solvents, like N,N-dimethylformamide (DMF), have proven effective but presents significant health and environmental challenges. This study explores the feasibility of using propylene carbonate (PC) as a green solvent alternative for butadiene extractive distillation, leveraging its environmentally friendly properties and industrial compatibility. Simulations were conducted using Aspen Plus®, employing the Non-Random Two-Liquid (NRTL) model coupled with the Redlich-Kwong equation of state to describe phase equilibrium. Results indicate that PC integrates seamlessly into existing processes, achieving comparable operational stability and butadiene separation efficiency with minimal modifications. A significant design improvement was the elimination of the methylacetylene separation column in the PC process, which simplified the overall configuration and reduced cooling water requirements by approximately 43 tonnes per hour. This change resulted in a 0.4% reduction in utility costs. While PC's higher boiling point requires operational adjustments, such as the use of higher medium-pressure steam, the overall energy consumption was 3.7% lower than with DMF. These findings demonstrate that PC is a viable and sustainable alternative for butadiene recovery processes, offering economic, operational, and environmental benefits.

**Keywords**: 1,3-Butadiene, Extractive distillation, Green solvent, Propylene carbonate, Process simulation, Aspen Plus

## INTRODUCTION

1,3-Butadiene (butadiene) is a critical feedstock to produce synthetic rubbers and plastics, including styrene-butadiene rubber, polybutadiene rubber, and latex. It is primarily obtained as a by-product of steam cracking processes. However, its separation from $C_4$ hydrocarbon mixtures poses a significant challenge due to the close boiling points of the components within these mixtures. Conventional distillation requires an impractically high number of trays and high reflux ratios, making it unfeasible. Consequently, extractive distillation has become the primary technique for separating butadiene, leveraging the selective solubility and enhancement of relative volatility by using appropriate solvents that facilitate the separation process.

Commonly used solvents for extractive distillation include N,N-dimethylformamide (DMF), N-methyl-2-pyrrolidone (NMP) and acetonitrile. Each of these solvents offers distinct advantages and limitations [1-5]. Although highly successful in separating butadiene from other $C_4$ hydrocarbons, these solvents pose significant health and environmental risks. Their use has been linked to adverse human health effects, including skin irritation, liver damage and an increased risk of cancer. Additionally, these solvents might bioaccumulate in ecosystems, posing serious threats to wildlife habitats and species. Identifying and mitigating these risks is essential to ensure safer and more sustainable industrial processes [6,7].

The economic, health and environmental challenges associated with conventional extractive distillation solvents have driven growing interest in simulation-based studies to optimize the process. Simulation tools, like As-

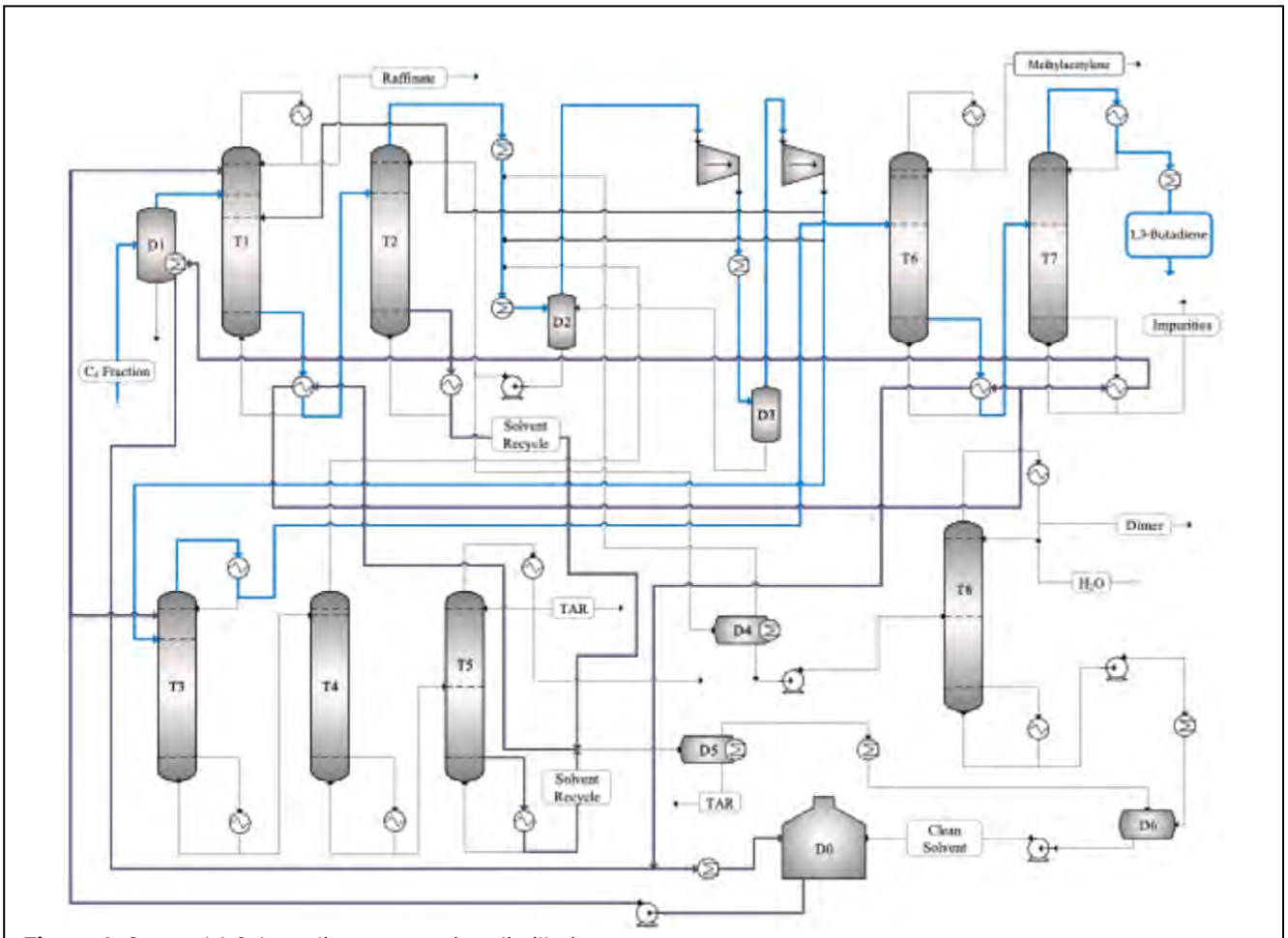



**Figure 1:** General 1,3-butadiene extractive distillation process.

pen Plus®, offer a robust framework for modeling extractive distillation processes, enabling the integration of mass and energy balances, phase equilibrium data, and complex distillation modeling. Advanced thermodynamic models, such as the Non-Random Two-Liquid (NRTL) model coupled with the Redlich-Kwong (RK) equation of state, are often employed to account for the non-ideal behavior of complex mixtures. These simulations not only facilitate accurate predictions of process behavior but also support the design and optimization of distillation columns and overall process efficiency. Previous studies have used computer-aided simulations to investigate the performance of conventional solvents, such as DMF, NMP, and acetonitrile, in extractive distillation processes for separating butadiene from crude $C_4$ mixtures [8,15].

Recent research has identified propylene carbonate (PC) as a promising green solvent for butadiene recovery, offering a viable alternative to conventional solvents like DMF and NMP, which may pose significant health and environmental risks [13]. While PC exhibits slightly lower selectivity, it provides an optimal balance between selectivity, cost-effectiveness, and industrial compatibility. Moreover, its favorable environmental, health, and safety (EHS) profile aligns with regulatory frameworks such as REACH (Registration, Evaluation, Authorization, and Restriction of Chemicals), which governs chemical use in the European Union. Additionally, the CEFIC (European Chemical Industry Council) emphasizes the need for sustainable and safer chemical alternatives, reinforcing the relevance of this study.

Building on these findings, this study aims to evaluate the feasibility of integrating PC into an existing butadiene recovery process with minimal modifications, ensuring that its adoption does not significantly disrupt current industrial operations or increase capital expenditures. A simulation approach using Aspen Plus® software is employed to model the extractive distillation process, comparing the performance of PC with the conventional DMF based process. Furthermore, the study assesses potential energy efficiency improvements, contributing to a more sustainable and economically viable butadiene production process.

Butadiene extraction is a multistep procedure that can be divided into four main sections (as it can be seen in Figure 1): first and second extractive distillation units, conventional distillation unit, and solvent purification

section. These stages work synergistically to achieve efficient butadiene separation while simultaneously enabling the recovery and reuse of the solvent. To improve process efficiency, the hot solvent from the bottoms of the stripping columns is integrated into a heat recovery circuit, where it is utilized to preheat subsequent distillation column streams. This heat integration significantly reduces total energy consumption.

In the first extractive distillation unit, the feed is introduced into the first column, where components with higher relative volatility than butadiene, such as 1-butene, are removed as overhead products. The bottom stream, enriched with butadiene and other less volatile components, including acetylene compounds, is directed to a stripper. In the stripper, hydrocarbons and impurities are separated from the solvent, producing a side stream containing purified butadiene and minor quantities of acetylene compounds. This side stream is subsequently fed into a second extractive distillation column, which removes remaining low-volatility impurities, achieving higher purity of 1,3-butadiene as the overhead product.

The conventional distillation section complements the process by refining by-products such as methylacetylene (propyne) and *cis*-2-butene. Additives, such as *tert*-butyl catechol (TBC) and silicone, are commonly employed to inhibit butadiene polymerization during the distillation process. However, due to the complexity and multiple pathways involved in polymerization mechanisms, its formation was not included in the current simulation. The so-called “popcorn” polymerization of butadiene, which occurs under specific reaction conditions in the presence of oxygen, remains a critical consideration. While this aspect was not addressed in the present study or in other similar studies, it represents a significant factor that should be incorporated into future analyses to ensure a more comprehensive evaluation of the process.

The final stage of the process involves solvent purification. A small fraction of the stripper’s bottom stream is directed to a distillation column for solvent recovery.

The feed composition plays a vital role in defining key process parameters. **Table 1** shows a representative feed composition stream, which was used in this simulation.

## Methodology

The process flow diagram (PFD) depicted in **Figure 1** illustrates a standard configuration for a butadiene extraction plant, showcasing the typical steps and equipment involved in the extraction process. The system was designed to process an average $C_4$ feed of 10,000 kg/h under normal operating conditions. Operating conditions and feed specifications were derived from typical industrial data, ensuring the simulation accurately mirrored realistic scenarios. The composition of the $C_4$ mixture and DMF solvent entering the first extractive distillation column is shown in **Table 1**.

**Table 1:** Composition of the fresh $C_4$ mixture and solvent.

| **$C_4$ mixture Component** | **wt%** |
|---|---|
| Propane | 0.03 |
| Propadiene | 0.03 |
| Methylacetylene | 0.02 |
| 1,2-Butadiene | 0.25 |
| 1,3-Butadiene | 44.98 |
| *cis*-2-Butene | 4.26 |
| *trans*-2-Butene | 5.41 |
| *iso*-Butene | 20.72 |
| 1-Butene | 13.67 |
| n-Butane | 4.98 |
| *iso*-Butane | 4.98 |
| Ethylacetylene | 0.09 |
| Vinylacetylene | 0.49 |
| n-Pentane | 0.09 |
| **DMF Solvent** | **wt%** |
| DMF | 97.00 |
| TAR | 2.50 |
| Dimer | 0.50 |
| Water | 0.00 |

The NRTL model, coupled with the RK equation of state, was selected as the thermodynamic framework to handle the complex, non-ideal behavior of the chemical systems involved. This combination is particularly effective for polar compounds, systems with strong molecular interactions, and highly non-ideal mixtures, such as those encountered in extractive distillation processes. Accurate vapor-liquid equilibrium (VLE) calculations were primarily based on binary interaction parameters obtained from the Aspen Plus® database. However, for certain pairs, where parameters were unavailable, the COSMO-RS (Conductor-like Screening Model for Real Solvents) model was employed. COSMO-RS, known for its accuracy in predicting molecular interactions, was utilized to estimate new parameters, ensuring robust and reliable VLE predictions for these systems [16]. Previous research has established the usefulness of COSMO-RS for estimating phase equilibrium parameters in extractive distillation systems, including its application to butadiene purification using polar solvents, where it offered reliable predictions of solution non-ideality and VLE behavior [17].

The integration of the new solvent into the simulation model began by closely aligning it with the existing DMF-based simulation. This approach minimized process modifications, ensuring a direct and reliable comparison of energy consumption in the subsequent analysis.

## Results

**Figure 2** presents the calculated temperature profile and the butadiene mass composition in the liquid for the first extractive distillation column (T1 in **Figure 1**). As expected, the temperature changes most rapidly at the top and bottom of the column and in the vicinity of the solvent feeding point and the $C_4$ fraction feeding point for the extractive distillation. Due to having a lower selectivity than DMF, PC simulation needed a solvent to feed ratio higher than DMF (6.8:1.0 for DMF and 7.6:1.0 for PC). Yet, PC showed a similar affinity behavior in the separation of butadiene, resulting in similar operational procedure.

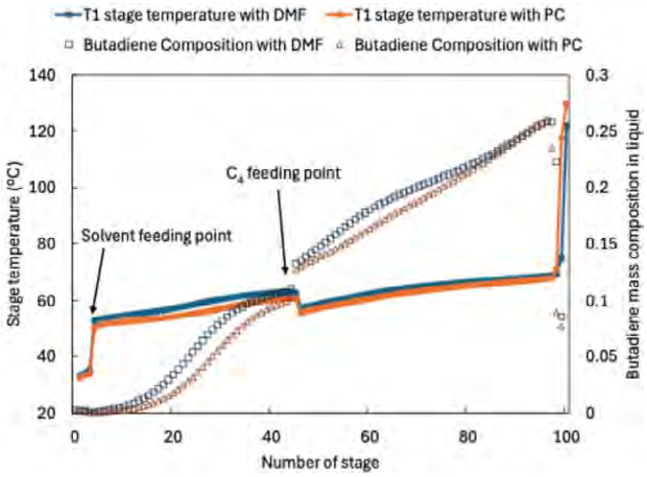



**Figure 2:** T1 stage temperature and butadiene composition for DMF and PC simulations.

The theoretical number of trays was determined by initially considering the actual number of trays in the distillation columns and systematically reducing them until significant differences in composition and temperature were observed between adjacent stages. This iterative approach ensured that only effective stages, which contribute meaningfully to the separation process, were included in the final design. If a stage exhibited negligible differences in these parameters compared to adjacent stages, it was deemed ineffective contributing little to the separation process. Such stages were excluded from the final design as they added unnecessary complexity to the simulation. This approach is particularly critical in complex systems, such as the one studied here, which involves multiple recycles and interconnected units (**Figure 1**). Reducing the number of ineffective stages helps to streamline the simulation, improving computational efficiency and model convergence. Moreover, removing non-contributing stages minimizes the potential for numerical instability, which is often a concern in simulations with extensive recycle loops and highly coupled systems. By ensuring that, only effective stages were included, and the simulation more accurately represented the operational behavior of the distillation columns, leading to more reliable results.

The implementation of PC as a solvent demonstrated that methylacetylene is insoluble in PC, thereby eliminating the need for column T6 (**Figure 1**) in the separation process. This significantly simplified the process design, as methylacetylene was effectively removed in the raffinate stream from the first extractive distillation column and directed towards other production facilities. In these facilities, methylacetylene may, for example, undergo hydrogenation, preventing adverse effects in subsequent process steps. This modification alone resulted in a 0.4% reduction in utility costs, primarily due to an estimated savings of 43 tonnes per hour in cooling water consumption.

A critical challenge associated with PC as a solvent is its high normal boiling point (242°C) compared to DMF (153°C). This requires operating at lower pressures (as low as -0.8 barg) to accommodate the thermal limitations of existing equipment. However, not all distillation columns in the process can operate under vacuum conditions. Specifically, the first stripper, responsible for separating the solvent from butadiene and acetylene compounds, cannot operate at reduced pressures due to operational constraints imposed by the positive displacement compressor downstream. In contrast, the second stripper (T5 in **Figure 1**) is capable of operating under these conditions, allowing for partial adaptation of the process to the use of PC.

Additionally, a conventional DMF-based process primarily relies on low-pressure (LP, 5 barg) and medium-pressure (MP, 12 barg) steam for heating. However, the implementation of PC required a higher hot utility, which was successfully met by employing higher medium-pressure steam (MP+, 18 barg). This adaptation was critical to avoid the use of high-pressure steam, thereby minimizing infrastructural modifications and maintaining the feasibility of the process. Additionally, PC showed similar behavior to DMF within the general solvent circuit, where hot solvent from the bottom of strippers was used to heat other column streams and equipment, as shown in **Figure 1** (blue line).

Overall, the transition to PC as a solvent demonstrated high compatibility with the existing butadiene plant configuration, achieving the desired separation performance (butadiene product 99.6 wt%) with minimal process modifications. In terms of utility consumption, PC required slightly higher electricity usage due to its higher solvent-to-feed ratio compared to DMF (**Figure 3**). However, despite using higher pressure steam, the total heat consumption in the PC simulation was 3.7 % lower than in the DMF process.

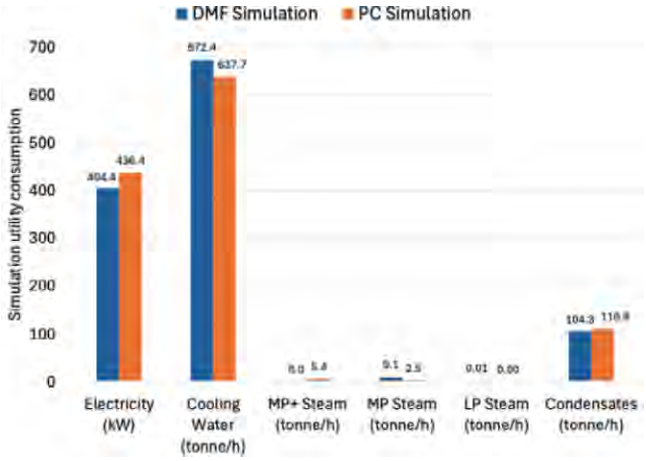



**Figure 3.** DMF and PC simulation's utilities consumptions.

**Table 2** highlights the key operational rates and ratios for the DMF and PC simulations, providing insight into their comparative performance within the same process framework. The data indicates that PC solvent values align closely with those of DMF, confirming that PC integrates seamlessly into the existing process configuration with minimal adjustments. Notable differences include a slightly higher solvent-to-$C_4$ feed ratio for PC, which compensates for its lower selectivity relative to DMF. Furthermore, the reflux-to-feed ratio in the downstream columns (T5 and T8) is lower for PC, contributing to reduced energy consumption in some sections of the plant.

Despite these differences, PC achieves similar operational stability and butadiene separation efficiency, illustrating its strong compatibility with the existing process. Moreover, the elimination of column T6 in the PC simulation, due to the insolubility of methylacetylene in PC, further simplifies the process and reduces operational complexity. Overall, these results underscore PC's potential as a viable and sustainable alternative to DMF, offering operational consistency with additional energy and process efficiency benefits.

## CONCLUSION

This study explored the use of PC as a green solvent alternative for the extractive distillation of butadiene, comparing its performance to the conventional DMF process. The results demonstrated that PC is highly compatible with the existing butadiene recovery configurations, requiring only minor process adjustments to achieve similar separation efficiency. Although PC exhibited slightly lower selectivity, necessitating a higher solvent-to-feed ratio, it maintained comparable operational stability and achieved the desired butadiene purity of 99.6 wt%.

Overall, PC proved to be a viable and sustainable alternative to DMF, offering notable operational, environmental, and economic advantages while minimizing the need for infrastructural modifications. Its implementation has the strong potential to enhance energy efficiency and reduce the environmental footprint of butadiene recovery processes. Future studies should focus on validating these findings under industrial-scale conditions and exploring the long-term stability and performance of PC in continuous operations.

## ACKNOWLEDGEMENTS

This work was financially supported by: (a) Fundação para a Ciência e a Tecnologia (FCT) through the Ph.D. Grant PRT/BD/153600/2022; (b) National funds through FCT/MCTES (PIDDAC): LEPABE, UIDB/00511/2020 (DOI: 10.54499/UIDB/00511/2020) and UIDP/00511/2020 (DOI: 10.54499/UIDP/00511/2020), ALiCE, LA/P/0045/2020 (DOI: 10.54499/LA/P/0045/2020); CERENA – Centro de Recursos Naturais e Ambiente, CERENA (UIDB/04028/2020), and CQE (UIDB/00100/2020 and UIDP/00100/2020).

**Table 2:** Operational conditions.

| Equipment | Parameter | DMF Simulation | PC Simulation |
|---|---|---|---|
| - | $C_4$ fraction feed rate | 10.07 | 10.07 |
| T1 | Solvent / $C_4$ | 6.75 | 7.55 |
| T1 | Reflux / Solvent | 0.12 | 0.14 |
| T2 | Reflux / Solvent to T1 | 0.06 | 0.06 |
| - | Butadiene rate in $C_4$ + Recycle stream of T4 | 5.03 | 4.72 |
| T3 | Solvent / Feed | 1.90 | 1.99 |
| T3 | Reflux / Solvent | 0.53 | 0.53 |
| T5 | Reflux / Solvent to T3 | 0.12 | 0.06 |
| T6 | Reflux / Feed | 1.02 | - |
| T7 | Reflux / Feed to T6 | 4.87 | 4.67 |
| T8 | Reflux / Feed | 0.43 | 0.35 |

## REFERENCES


1. J. V. Oliveira, A. M. C. Uller. Solubility of pure 1,3-butadiene and methyl propene and their
2. mixtures in pure n-methyl-2-pyrrolidone and in its aqueous solutions. *Fluid Phase Equilib.* 1996, 118(1), 133–141
3. S. Takao, Oil Gas 1979, 77, 81–82
4. P. M. Mathias, J. R. Elliott Jr. and A. Klamt. Butadiene purification using polar solvents. Analysis of solution nonideality using data and estimation methods. *Ind. Eng. Chem. Res.* 2008, 47(15), 4996–5004
5. R. A. Meyers, Handbook of Petrochemical Production Processes, 1st ed., *McGraw-Hill*, New York 2005
6. K. Kindler, H. Puhl, US Patent, 6 337 429 B1, 2002
7. Kerton, F. Alternative solvents for green chemistry. *RSC Publishing*. 2009, 131(33)
8. Warner, J. C. Reaction: exploring the chemistry frontier in water-borne vessels. *Chem*. 2008 4(9), 2010–2012
9. Z. Lei, R. Zhou and Z. Duan. *Chem. Eng. J.* 2002, 85, 379-386
10. Tripathi N, Xu Q, Palanki S. Modeling and simulation of the 1,3-butadiene extraction process at turndown capacity. *Chem Eng Technol* . 2019, 42, 1–10
11. Lei Z, Zhou R, Ding Z, Chen B. Azeotropic distillation: A review of mathematical models. *Comput Chem Eng.* 2002, 26, 1213–1221
12. Wang, Hongyou & Zhou, Rongqi & Duan, Zhanting. Solvent improvement for separating C4 with ACN. Computers & Chemical Engineering. 2002, 26, 1213-1221
13. Jalali F, Saffari R. Simulation and optimization in 1,3-butadiene process from C4-CUT using genetic algorithm. in: Marquardt W, Pantelides C, editors. Computer Aided Chemical Engineering. 16th European Symposium on Computer Aided Process Engineering and 9th International Symposium on Process Systems Engineering. 21st ed. Elsevier; 2006, 901-906
14. Yang X, Yin X, Ouyang P. Simulation of 1,3-butadiene production process by dimethylformamide extractive distillation. *Chin J Chem Eng.* 2009, 17, 27–35
15. Kim, Y., Kim, S. & Lee, B. Simulation of 1,3-butadiene extractive distillation process using N-methyl-2-pyrrolidone solvent. *Korean J. Chem. Eng.* 2012, 29, 1493–1499
16. J. Gomes, R. Silva, C. Nunes, D. Barbosa. Towards sustainable industrial processes: A preselection method for screening green solvents for 1,3-butadiene extraction. Submitted to *Sustainability*
17. Klamt, A. & Eckert, F. (2000). COSMO-RS: a novel and efficient method for the a priori prediction of thermophysical data of liquids. Fluid Phase Equilibria, 172(1), 43–72



© 2025 by the authors. Licensed to PSEcommunity.org and PSE Press. This is an open access article under the creative commons CC-BY-SA licensing terms. Credit must be given to creator and adaptations must be shared under the same terms. See https://creativecommons.org/licenses/by-sa/4.0/




Systems & Control Transactions

**Research Article - Peer Reviewed Conference Proceeding**
ESCAPE 35 - European Symposium on Computer Aided Process Engineering
Ghent, Belgium. 6-9 July 2025
Jan F.M. Van Impe, Grégoire Léonard, Satyajeet S. Bhonsale,
Monika E. Polańska, Filip Logist (Eds.)

PSE PRESS

# Modelling and Analysis of $CO_2$ Electrolyzers Integrated with Downstream Separation Processes via Heat Pumps

**Riccardo Dal Mas[a], Andrea Carta[a], Ana Somoza-Tornos[a], and Anton A. Kiss[a]***

[a] Delft University of Technology, Department of Chemical Engineering, Van der Maasweg 9, 2629 HZ Delft, Netherlands
* Corresponding Author: A.A.Kiss@tudelft.nl

## ABSTRACT

The electrification of chemical processes and carbon capture and utilisation represent two promising approaches to improve efficiency and decrease carbon emissions of the process industry. The development of electrolyzers has gathered momentum in the last decades, allowing for the possible introduction of renewable electrons into carbon dioxide-based chemicals manufacture. While the performance of the electrolyzers is subject to improvements driven by the experimental community, the generation of waste heat is unavoidable due to the electrical resistances and process inefficiencies within the electrochemical cells. The possibility of re-using this waste heat has not been investigated within the realm of carbon dioxide electrolyzers. Here we show the potential of upgrading this waste heat by means of a heat pump, for its utilisation in the downstream processing of formic acid obtained from carbon dioxide electroreduction. We found that the waste heat represents roughly 62% of the power input to the electrochemical cells and it can be upgraded from 35 °C to 112 °C to drive the extractive distillation of formic acid and water. For a system producing 25 kt/y of formic acid, this results in the electrification of 60% of the separation energy duty, yielding a decrease in carbon dioxide emissions of 39-58% for the downstream processing, while the addition of a heat pump has a payback period of ~4.4 years in the base case.

**Keywords**: Process Design, Carbon Dioxide, Electrification, Process Integration, Heat Pump

## INTRODUCTION

Several strategies can be deployed to reduce the environmental burden of manufacturing processes, specifically for chemicals. Among these strategies, of prime importance is the substitution of fossil inputs with renewable ones, whether it be electricity, biomass, or carbon dioxide. To enable this, productions based on electrolysis have significant potential, as they exploit renewable electricity to drive the reactions and allow for the conversion of carbon dioxide. Both experimental efforts and techno-economic assessments are directing the concerted development of the field of carbon dioxide electrolysis [1-2].

However, electrolyzers generate waste heat due to ohmic and kinetic losses, which are overcome through the application of an overpotential. Notably, heat management for electrolyzers remains under-explored, particularly when referring to the realm of low temperature carbon dioxide electrolysis. Conversely, the field of water electrolysis has seen some research in this [3], but, as hydrogen production lacks significant downstream processing, the possibilities of waste heat utilisation in the plant are limited.

This is not true for carbon dioxide electrolysis, especially when yielding liquid products relying on thermal separations. As the waste heat is at low temperature, it cannot be directly exploited to drive the separations. To tackle this obstacle, heat pumps can be employed to upgrade the waste heat to useful temperature levels, thus enabling heat integration and further diminishing the need for fossil fuels in the separation section of the plant. An additional challenge is represented by the typical room temperature operation of carbon dioxide electrolyzer currently developed at the lab scale. This would imply a very high temperature lift for the heat pump, thus diminishing its performance. However, recent literature shows that optimal operation would lie between 60 and 70 °C [4], which can be more readily exploited by a heat pump.

## PROBLEM STATEMENT

This study aims at assessing the potential of upgrading the waste heat from the electrolyzer via heat pump to drive the product recovery and purification processes. To showcase this, we have selected the production of formic acid, since it can be obtained with good performance through carbon dioxide electrolysis [5]. By designing the different parts of the process – electrolyzer stacks, separation processes, and heat pump – and combining them together, we have obtained a complete flowsheet for the integrated plant. This has allowed for the quantification of the reduction in the external load for the thermal separation and, consequently, of the carbon dioxide emissions of the process.

This work constitutes a proof of concept for the potential upgrade of waste heat from the electrolyzers, reporting preliminary results. The inclusion of a heat pump in the process is evaluated based on economics and environmental (carbon dioxide emissions) performance. However, the complete techno-economic assessment of the process, together with further heat integration and overall process optimization, are out of scope for this study.

## METHODOLOGY

A process to produce formic acid (HCOOH) from carbon dioxide and water comprises three main parts, as shown in the block flow diagram of Figure 1: the electrolyzer stacks, the formic acid-water separation and the heat pump. To support the design, we simulated this process at steady state using Aspen Plus®. Considering the formic acid market [6], the plant is sized to produce 25 kt/y of FA at 85 wt.%, with 100% utilisation based on 8000 h/y of operation.

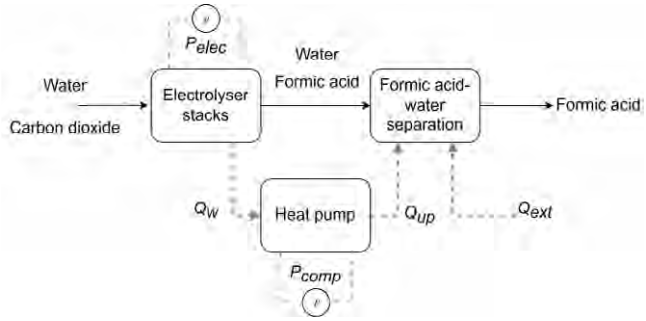



**Figure 1.** Block flow diagram for the process, highlighting the three sections in which the system can be broken down. The main material and energy flows are also displayed.

A three compartment electrolyzer, based on the set up of Yang et al. [7], is chosen, as it reduces the complexity of the process by yielding directly formic acid instead of the formate salt, obtained from the combination of the product and the cation of the electrolyte. To design the electrolyzer, we considered several trade-offs between major decision variables, namely the cell voltage, the current density, the faradaic efficiency and the product concentration in the outlet stream [8]. The current density determines, for a given production capacity, the electrolyzer size required, and its dependence on the cell voltage can be obtained by fitting experimental data [7]. The availability of experimental data up to 4 V for the polarization curve provides an upper limit to the investigated cell voltage ranges.

The waste heat $Q_W$ developed by the electrolyzers is calculated using in Eq. 1, where $i_k$ is the partial current for product $k$ ($i_k = FE_k\ i$, with $FE_k$ Faradaic efficiency for product $k$, and $i$ total current), $E_{cell}$ is the total cell voltage, and $E_{tn,k}$ is the thermoneutral voltage for product $k$ (i.e. the voltage such that the cell would have isothermal operation) [3]. The waste heat, together with the total power input to the cell $P_{cell}$, determines also the cell efficiency $\epsilon$, as expressed in Eq. 2.

$$Q_W = \sum_k i_k (E_{cell} - E_{tn,k}) \quad (1)$$

$$\epsilon = \frac{P_{cell} - Q_W}{P_{cell}} \quad (2)$$

The separation of formic acid from water is based on the work of Ramdin et al. [9], where it is carried out through extractive distillation with 2-methyltetrahydrofuran. Notably, this separation technology keeps the main reboiler temperature at 106 °C, which is key to enable a more efficient performance for the heat pump. Since the goal of this work is to demonstrate the potential of upgrading the waste heat, systematic improvements to the downstream processing are out of scope.

The selection of the heat pump technology is limited to the mechanically-driven ones in order to maximise the electrification of the process via the compressor power input. The investigation space is thus reduced to vapor compression and compression resorption heat pumps [10]. Due to the scope constraints of this work, the implementation of compression resorption heat pumps, which might result in higher efficiency, is deferred to future studies. We have analyzed the performance of different working fluids, with the goal of maximising the coefficient of performance ($COP$) of the system, as defined in Eq. 3, where $Q_{up}$ is the upgraded heat flow and $P_{comp}$ is the power input to the compressor.

$$COP = \frac{Q_{up}}{P_{comp}} \quad (3)$$

Simplified economics, based on the Total Annualised Costs ($TAC$, see Eq. 4) have been exploited for the design of the electrolyzer.

$$TAC = \mathrm{OPEX} + \frac{CAPEX}{lifetime} \quad (4)$$

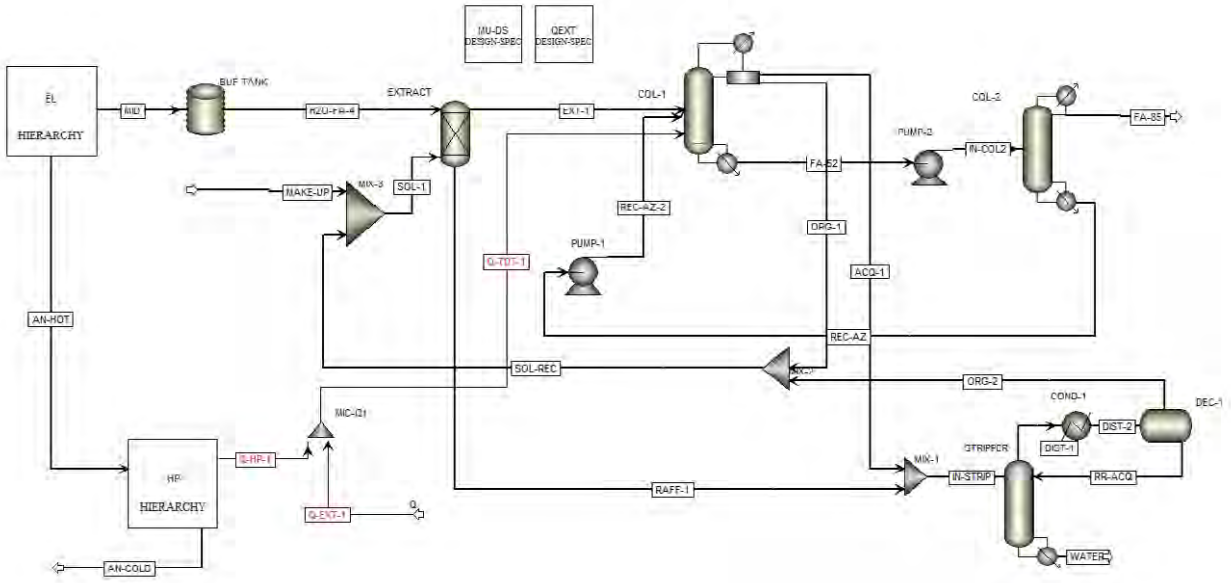



**Figure 2.** Aspen Plus® flowsheet for the process, showing the separation system and the two hierarchical blocks containing the electrolyzers and the heat pump models.

Moreover, the payback period for the heat pump has been calculated to evaluate the investment from an economic perspective (compressor and heat exchangers capital costs estimated according to [11]). Carbon dioxide emissions per unit product, based on the energy demand and its origin, provide support and context for the decisions on design and the benefits of upgrading the waste heat by means of the heat pump.

The Aspen Plus® implementation of the model rests on the choice of different thermodynamic packages for different parts of the flowsheet, namely: ELECNRTL for the electrolyzer stacks and balance of plant; UNIQUAC-HOC for the formic acid-water separation; and REFPROP for the heat pump, tailoring each of these models to the specific application. The REFPROP library contains several, fluid-specific models based on fundamental equations of state, as discussed in [12].

## RESULTS AND DISCUSSION

The flowsheet for the whole process, as developed in Aspen Plus®, is reported in Figure 2, which displays the downstream separation, while the electrolyzers and the heat pump are included in hierarchy blocks. The electrolyzer is modelled in Excel, which is embedded as a calculator block in the Aspen Plus® simulation, while the heat pump is modelled as a closed loop vapor compression system (evaporator, compressor, condenser, and expansion valve). The following sections present first the results for the electrolyzer design, followed by the heat pump selection and the heat integration in the process. Finally, simplified metrics to evaluate the carbon dioxide emissions and the economic performance of the design are described and discussed.

### Electrolyzer design

The design of the electrolyzer has been defined through an optimisation of the different trade-offs discussed in the previous section. The sensitivity of the cell voltage which allows to minimise the $TAC$, based on the electricity price and the electrolyzer cost, is shown in Figure 3.

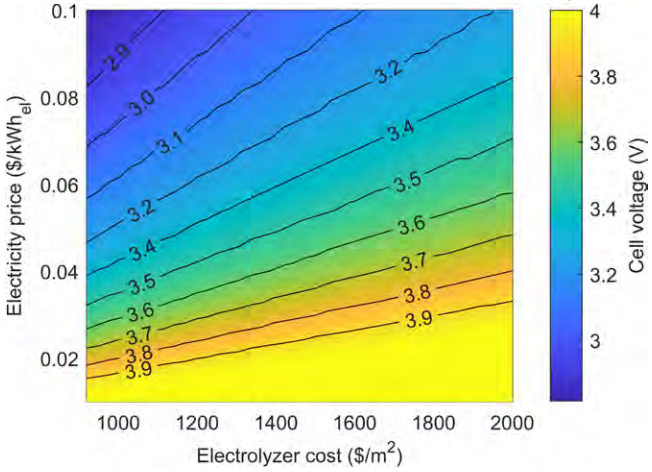



**Figure 3.** Cell voltage that minimises total annualised costs as a function of electrolyzer and electricity cost.

Cheap electricity (below 0.03 $/kWh$_{el}$) would favor operation at maximum voltages, regardless of the electrolyzer cost, because the current density, a function of the cell voltage, is pushed to higher values, resulting in smaller, and thus cheaper, reactors. This effect can also be observed at constant electricity price, with an increasing trend in the optimal voltage with higher electrolyzer prices, thanks to the inverse proportionality between cell voltage and electrolyzer area required. The capital costs

of the electrolyzer do not become dominant in the range considered (based on [13]), therefore the optimal operation is not found at lower voltages.

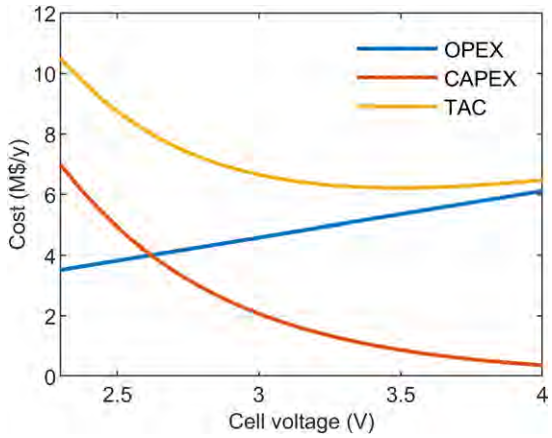



**Figure 4.** Trade-off between OPEX and CAPEX for the electrolyzer as a function of the cell voltage (electricty price: 0.05 $/kWh$_{el}$; electrolyzer cost: 1500 $/m$^2$).

For the base case values of 0.05 $/kWh$_{el}$ and 1500 $/m$^2$ for electricity price and electrolyzer cost, respectively, the trade-off between OPEX and CAPEX is displayed in Figure 4. The OPEX are linearly dependent on the cell voltage, for a given production capacity, while the CAPEX decrease with $E_{cell}$, since the current density rises, leading to smaller units. An optimum value of the cell voltage can be identified, as ~3.5 V, which corresponds to a current density of ~130 mA/cm$^2$. Table 1 summarizes the design variables chosen, as well as some relevant design parameters and process inputs.

**Table 1:** Main process design variables chosen, together with the carbon intensity of relevant energy sources. $FE$ is Faradaic efficiency. The subscript *th* and *el* distinguish between thermal and electrical energy.

| Stream | Value | Units of measure |
|---|---|---|
| Cell voltage | 3.5 | V |
| $FE$ (HCOOH) | 90% | (-) |
| $FE$ (CO) | 2% | (-) |
| $FE$ ($H_2$) | 8% | (-) |
| Product concentration (middle compartment outlet) | 10% | w/w |
| Electrolyzer lifetime | 5 | years |
| Electrolyzer temperature | 50 | °C |
| Carbon intensity MP steam | 237 | gCO2/kWh$_{th}$ |
| Carbon intensity electricity (grid, EU-27)[15] | 251 | gCO2/kWh$_{el}$ |
| Carbon intensity electricity (renewables)[16] | 19 | gCO2/kWh$_{el}$ |

The choice of the cell voltage determines also the amount of waste heat available for upgrading via the heat pump, according to Eq. 1. This effect is shown in Figure 5, which on the right y-axis reports both the total power input to the electrolyzers and the available waste heat as a function of the cell voltage, while the left y-axis shows the electrolysis cell energy efficiency (Eq. 2). This highlights how the design of the electrolyzer has cascade effects on the performance of the rest of the process, as the electrolyzer efficiency could be improved, but this would increase the demand for external energy inputs for the downstream separation in the integrated system. For the cell voltage chosen, ~8.3 MW of waste heat is obtained, while the cell operates at ~38% efficiency.

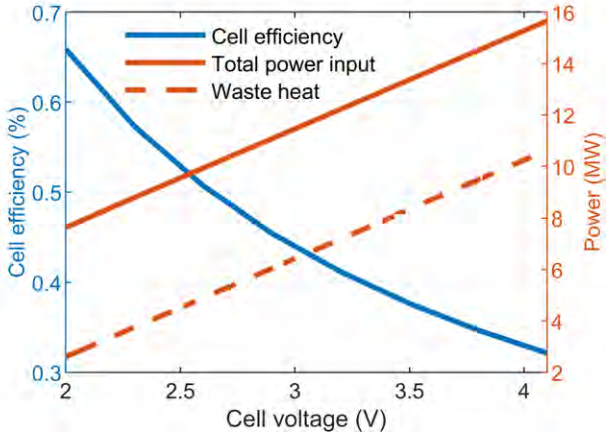



**Figure 5.** System trade-off showing the total power input to, and the waste heat developed by, the electrolyzers, as a function of the cell voltage. The cell efficiency vs. the voltage is also provided.

## Heat pump selection and heat integration

The waste heat available can be upgraded by means of a heat pump. The performance of the heat pump, measured by the $COP$, is strongly dependent on the temperature lift required, defined as the difference between the temperature of the upgraded heat and that of the waste heat. In our case, based on the electrolyzer operating temperature of 50 °C, electrolyte return temperature of 40 °C, and reboiler temperature of 106 °C, the temperature lift is 77 °C (35 °C to 112 °C).

After screening different working fluids, we have identified a vapour compression heat pump using HFO-1233zd and one using ammonia as a suitable candidates, due to their performance, appropriate critical temperature, and low global warming potential and ozone depletion potential [14]. Based on the conditions, the heat pump can reach a COP of ~2.8-3.1, employing compressors requiring ~4-4.5 MW$_{el}$, and leading to upgraded heat of ~12-13 MW$_{th}$ at the desired temperature. The results presented below are based on the ammonia case, as they are substantially the same for HFO-1233zd.

**Table 2:** Impact of different heat pump technologies and working fluid on the upgraded heat and on carbon dioxide emissions for the downstream processing (DSP). Note that the emissions do not represent the full carbon footprint of the product.

| Heat pump | Working fluid | COP | Electricity source | Carbon dioxide emissions DSP ($kgCO_2$/kg product) | Carbon dioxide reduction (%) |
|---|---|---|---|---|---|
| No | N/A | N/A | N/A | 2.55 | N/A |
| Yes | Ammonia | 3.06 | Offshore wind | 1.07 | -64% |
| Yes | Ammonia | 3.06 | Grid | 1.56 | -42% |

The reboiler heat duties for the azeotropic distillation and the vacuum distillation (COL-1 and COL-2 in Figure 2) are 13.5 $MW_{th}$ and 7 $MW_{th}$, respectively. Figure 6 summarizes the main energy flows among the three sections of the system: it is possible to observe that the upgraded heat covers the vast majority of the duty of the azeotropic distillation column (COL-1), leaving COL-2 to be supplied by external heat. The heat pump thus accomplishes the dual goal of providing cooling to the electrolyzer system, and delivering high temperature heat to the separation. Electricity constitutes ~70% of the energy inputs to the process, while the upgraded heat covers ~60% of the thermal duties.

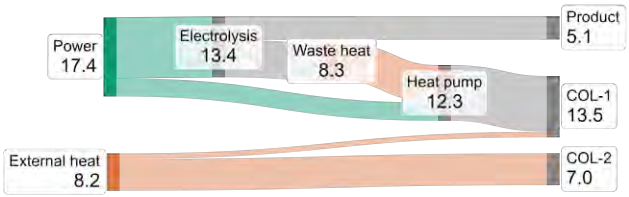



**Figure 6.** Sankey diagram displaying the energy flows (in MW) in the system. Electric energy is shown as green, while thermal energy is represented in orange.

## Emissions and economic metrics

Table 2 provides a comparison between the case of implementation of a heat pump versus a system in which the separation duty is fully provided via an external source (steam boiler with natural gas). The results show that the heat pump allows for significant improvements in the carbon dioxide emissions of downstream process, with a reduction of -58% when using fully renewable electricity (based on median offshore wind emissions [16]) and -39% when connected to a national grid (assuming the current average grid emissions for the European Union-27 [15]). This reduction in emissions results from a decrease in the primary energy input through the energy multiplying effect of the heat pump.

While the heat pump brings benefits from the environmental perspective regardless of the source of the electricity, economic considerations should not be overlooked for its widespread adoption. Therefore, we have calculated the payback period for the addition of the heat pump to the system, as displayed in Figure 7 for different scenarios of electricity and fuel prices. The figure shows that the investment is paid back in less than ~4.5 years, except for when electricity is expensive (0.09 $\$/kWh_{el}$). In this case, the investment is not attractive, as the additional electricity input to the system for the heat pump compressor does not offset the reduced primary energy demand. Furthermore, it can be observed that the system is sensitive to increases in the fuel prices, given that the payback period for scenario 4 (electricity price of 0.05 $\$/kWh_{el}$ and fuel price of 0.045 $\$/kWh_{th}$) is about half of that for scenario 1 (same electricity price, 0.03 $\$/kWh_{th}$ for fuel).

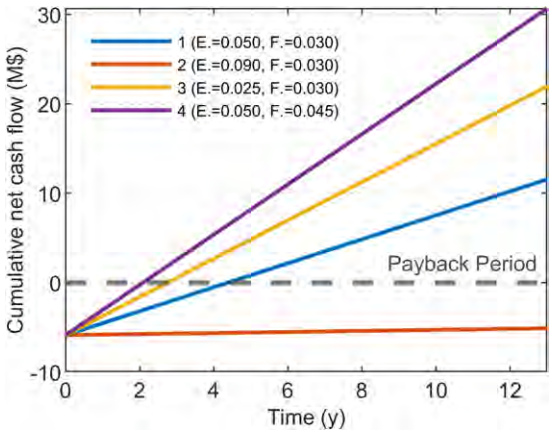



**Figure 7.** Cumulative net cash flow over a plant lifetime of 20 years for the investment in the heat pump, showing different scenarios based on the electricity (E.) and fuel (F.) price (reported in $\$/kWh_{el}$ and $\$/kWh_{th}$, respectively).

## CONCLUSIONS AND FUTURE WORK

This work shows how the waste heat from the electrolyzer can be upgraded for heat integration, thus reducing the need for external energy inputs for the separation of products. This type of assessment can be extended to other processes operating with electrolyzers and similar conditions, including those downstream of water electrolysis for hydrogen generation.

Moreover, the application of a multi-pronged

electrification strategy, in which renewable electrons are used to both drive reactions and the energy integration of the system, is demonstrated. This is key in the perspective of the reduction of carbon dioxide emissions, as it offsets the use of conventional heating media in the downstream separations by ~60% and increases electricity inputs to 70% of the total energy demand. Additionally, the economic performance of the heat pump would justify the increased capital investment, given that the payback period is a few years, with the exception of higher electricity prices.

These results justify future work on a detailed techno-economic assessment of the whole process, including a system-wide optimisation to find the best design and operating conditions under different sets of inputs (electricity price, renewable electricity availability, heat pump technology). Moreover, the potential for waste heat upgrade in other electrolysis-based processes merits further investigation.

## REFERENCES


1. O'Brien CP, Miao RK, Shayesteh Zeraati A, Geonhui L, Sargent EH, and Sinton D. CO2 Electrolyzers. *Chem. Rev.* 124 (7): 3648–93. (2024) https://doi.org/10.1021/acs.chemrev.3c00206.
2. Somoza-Tornos A, Guerra OJ, Crow AM, Smith WA, Hodge BM. Process Modeling, Techno-Economic Assessment, and Life Cycle Assessment of the Electrochemical Reduction of CO2: A Review. *iScience* 24 (7): 102813. (2021) https://doi.org/10.1016/j.isci.2021.102813.
3. Van Der Roest E, Bol R, Fens T, Van Wijk A. Utilisation of Waste Heat from PEM Electrolyzers – Unlocking Local Optimisation. *Int. J. Hydrog. Energy*. 48 (72): 27872–91. (2023) https://doi.org/10.1016/j.ijhydene.2023.03.374.
4. Hurkmans, JW, Pelzer HM, Burdyny T, Peeters J, Vermaas DA. Heating Dictates the Scalability of $CO_2$ Electrolyzer Types. *EES Catal.* (2025) https://doi.org/10.1039/D4EY00190G.
5. Fernández-Caso K, Díaz-Sainz G, Alvarez-Guerra M, Irabien A. Electroreduction of CO2 : Advances in the Continuous Production of Formic Acid and Formate. *ACS Energy Lett.* 8 (4): 1992–2024. (2023) https://doi.org/10.1021/acsenergylett.3c00489.
6. Hietala J, Vuori A, Johnsson P, Pollari I, Reutemann W, Kieczka H. Formic Acid. In: Ullmann's Encyclopedia of Industrial Chemistry, edited by Wiley-VCH, 1st ed., 1–22. Wiley. (2016) https://doi.org/10.1002/14356007.a12_013.pub3.
7. Yang, H, Kaczur JJ, Sajjad SD, Masel RI. Performance and Long-Term Stability of CO2 Conversion to Formic Acid Using a Three-Compartment Electrolyzer Design. *J. CO2 Util.*, 42, p. 101349. (2020) https://doi.org/10.1016/j.jcou.2020.101349
8. Thijs, B, Rongé, J, Martens JA. Matching Emerging Formic Acid Synthesis Processes with Application Requirements. *Green Chem. 24* (6), 2287–2295. (2022) https://doi.org/10.1039/D1GC04791D.
9. Ramdin, M, Morrison ART, De Groen M, Van Haperen R, De Kler R, Irtem E, Laitinen AT, Van Den Broeke LJP, Breugelmans T, Trusler JPM, De Jong W, Vlugt TJH. High-Pressure Electrochemical Reduction of CO2 to Formic Acid/Formate: Effect of pH on the Downstream Separation Process and Economics. *Ind. Eng. Chem. Res.* 58 (51): 22718–40. (2019) https://doi.org/10.1021/acs.iecr.9b03970.
10. Kiss, Anton A., and Carlos A. Infante Ferreira. Heat Pumps in Chemical Process Industry. 1st ed. CRC Press. (2016)
11. Towler, G. P.; Sinnott, R. K. Chemical Engineering Design: Principles, Practice, and Economics of Plant and Process Design. 2nd ed. Butterworth-Heinemann: Boston, MA. (2013)
12. Huber ML, Lemmon EW, Bell IH, McLinden MO. The NIST REFPROP Database for Highly Accurate Properties of Industrially Important Fluids. *Ind. Eng. Chem. Res.* 61 (42): 15449–72. (2022) https://doi.org/10.1021/acs.iecr.2c01427.
13. Jouny, M, Luc W, Jiao F. General Techno-Economic Analysis of CO $_2$ Electrolysis Systems. *Ind. Eng. Chem. Res. 57* (6), 2165–2177. (2018) https://doi.org/10.1021/acs.iecr.7b03514.
14. Mateu-Royo, C, Navarro-Esbrí J, Mota-Babiloni A, Amat-Albuixech M, Molés F. Theoretical Evaluation of Different High-Temperature Heat Pump Configurations for Low-Grade Waste Heat Recovery. *Int. J. Refrig.*, *90*, 229–237. (2018) https://doi.org/10.1016/j.ijrefrig.2018.04.017.
15. European Environment Agency. https://www.eea.europa.eu/en/analysis/indicators/greenhouse-gas-emission-intensity-of-1?activeAccordion=
16. U.S. Department of Energy. Wind Vision: A New Era for Wind Power in the United States. (2015)



© 2025 by the authors. Licensed to PSEcommunity.org and PSE Press. This is an open access article under the creative commons CC-BY-SA licensing terms. Credit must be given to creator and adaptations must be shared under the same terms. See https://creativecommons.org/licenses/by-sa/4.0/




Systems & Control Transactions

**Research Article - Peer Reviewed Conference Proceeding**
ESCAPE 35 - European Symposium on Computer Aided Process Engineering
Ghent, Belgium. 6-9 July 2025
Jan F.M. Van Impe, Grégoire Léonard, Satyajeet S. Bhonsale,
Monika E. Polańska, Filip Logist (Eds.)

PSE PRESS

# Optimization of Sustainable Fuel Station Retrofitting: A Set-Covering Approach considering Environmental and Economic Objectives

**Daniel Vázquez*, Raul Calvo-Serrano**

IQS School of Engineering, Universitat Ramon Llull, Via Augusta 390, 08017 Barcelona, Spain
* Corresponding Author: daniel.vazquez@iqs.url.edu.

## ABSTRACT

In this work, we propose a mixed-integer linear programming (MILP) model that optimizes economic and environmental objectives by retrofitting fuel stations for the case study of Spain. The model contains set-covering constraints that ensure that there is at least one retrofitted fuel station within a radius of 20 kilometers of each retrofitted fuel station. The results indicate that by retrofitting fuel stations to allow for electric vehicles, both economic and environmental objectives improve, while showing which power plants would be tasked with the increase in electricity production to satisfy the increased electric demand.

**Keywords**: Life Cycle Assessment, Supply Chain, Optimization, Renewable and Sustainable Energy, Technoeconomic Analysis

## INTRODUCTION

To improve the sustainability of the transport sector, there is a global tendency to promote more environmentally friendly modes of transportation, in alignment with the Sustainable Development Goals (SDGs), particularly SDG 13, which focuses on climate change action. This shift is essential given that the transport sector is one of the largest contributors to greenhouse gas emissions globally, and transitioning to cleaner transportation options is a critical step toward mitigating climate change. Electric vehicles (EVs), if powered by renewable energy, are a promising solution to reduce emissions significantly. In response to these developments, many countries are implementing policies and incentives to encourage the adoption of EVs, including subsidies for EV purchases, investments in charging infrastructure, and stringent emission standards for conventional vehicles. This trend has led to a surge in EV adoption, which may reduce the reliance on traditional fuel stations in the future. However, the existing network of fuel stations, strategically located and familiar to consumers, offers a unique opportunity to support the EV transition. Retrofitting these fuel stations into EV charging stations not only profits from their advantageous locations and existing infrastructure but also facilitates a smoother transition for current consumers [1].

We propose a mixed-integer linear programming (MILP) optimization model based on the set-covering problem to determine which fuel stations are best suited for retrofitting and to evaluate the impact of this conversion on economic and environmental objectives compared to a baseline scenario with no retrofitting. The set-covering approach ensures that the retrofitted stations can adequately serve EVs within a specified radius, addressing the limited range issue of current electric vehicles. These types of models are common in supply chain and energy systems modelling [2].

This methodology is applied to a case study in Spain, utilizing a comprehensive dataset of all existing fuel stations. Given the NP-hard nature of the set-covering problem, an initial filtering step is employed to reduce the problem's size. Subsequent optimization is performed under various assumptions, such as the source of electricity and local demands of transport usage, using bi-objective optimization techniques. The model aims to minimize economic costs and $CO_2$ equivalent emissions, employing a life-cycle assessment (LCA) framework [3].

The results indicate that retrofitting a relatively small fraction (~10%) of the fuel stations satisfies set-

covering constraints, ensuring sufficient coverage for EV users. Notably, even considering retrofitting costs, both the economic and environmental optima coincide in a full electrification of the vehicle float.

## PROBLEM STATEMENT

The objective is to model and optimize the economic and environmental impacts of retrofitting existing standard fuel stations into EV charging stations in Spain, compared to a baseline case where no retrofitting is allowed. Thus, part of the energy system of the country is also modeled through the locations and capacities of existing power plants. The problem can be summarized through the following bi-objective optimization problem (1).

$$\begin{aligned} &\min\ \{obj^{eco}(x,y), obj^{env}(x,y)\} \\ &s.t. \\ &h(x,y) = 0 \\ &g(x,y) \leq 0 \\ &x \in \mathbb{R}^n, y \in \{0,1\} \end{aligned} \tag{1}$$

where $obj^{eco}, obj^{env}$ represent economic and environmental objectives, $x$ represent continuous variables, $y$ represent Boolean variables, $h(x,y)$ indicate equality constraints, and $g(x,y)$ indicate inequality constraints. Boolean variables are required to include set-covering constraints and other logical requirements detailed in the modeling section. For the economic objectives we consider the total cost, and for the environmental objective, we use the global warming potential from the IPCC2021 method (GWP). The temporal scope is one year.

## OPTIMIZATION MODEL

### Sets

We will use three main sets to model the system, these being, the set of fuel stations that can be retrofitted, $s \in S$, the set of power plants that could provide electricity to the retrofitted fuel stations, $p \in P$, and the set of autonomous regions in Spain, $r \in R$.

We define subsets depending on the type of power plant, specifically, if they are wind-offshore ($P^{WO}$), coal ($P^{C}$), gas ($P^{NG}$), waste ($P^{W}$), biomass ($P^{B}$), hydropower ($P^{H}$), solar ($P^{S}$), oil ($P^{O}$), or nuclear ($P^{N}$). We define a multi-set, $GS_{s,r}$, which maps which fuel stations are in each autonomous region.

### Variables

The model includes the following continuous variables: $e_{p,s}^{RF}$ indicates the amount of electricity produced in power plant $p$ that will be sent to retrofitted fuel station $s$ [GWh], $e_p^{DE}$ refers to the electricity produced in power plant $p$ to satisfy the country's demand of electricity [GWh], $e_p^{TP}$ refers to the total amount of electricity produced in power plant $p$ [GWh], $e_r^{EC}$ refers to the electricity available in autonomous region $r$ to be used to charge electric vehicles, $e_s^{SEC}$ refers to the electricity available in fuel station $s$ to be used to charge electric vehicles, $d_r^{EC}$ refers to the amount of kilometers traveled using electric cars in autonomous region $r$ [$\times 10^3$ km], and $d_r^{NC}$ refers to the amount of kilometers traveled using conventional combustion engine cars in autonomous region $r$ [$\times 10^3$ km].

Regarding binary variables, we consider two. $w$ indicates if we activate or de-activate the set-covering constraints, while $y_s$ indicates if we retrofit fuel station $s$ ($y_s = 1$) or not ($y_s = 0$).

### Parameters

$D_{s,s'}^{SC}$, refers to a binary parameter that has a value of 1 if fuel stations $s$ and $s'$ are within a given distance valid for the set-covering problem, $D_{s,s'}^{S}$, refers to the distance between two fuel stations [$10^3$ km], $D_{p,s}^{PS}$ refers to the distance between each power plant and each station [$10^3$ km], $GWP_p^{PP}$ refers to the GWP of generating electricity in power plant $p$ [$\mathrm{tCO_2eq/GWh}$], $GWP^{EC}$ refers to the GWP of using an electric car without counting the fuel [$\mathrm{tCO_2eq}/10^3$ km], $GWP^{NC}$ refers to the GWP of using a standard car [$\mathrm{tCO_2eq}/10^3$ km], $\bar{E}_p$ refers to the maximum amount of electricity that power plant $p$ can produce [GWh], $E^{EC}$ refers to the required electricity for traveling using an electric vehicle [$\mathrm{GWh}/10^3\mathrm{km}$], $B_r^D$ refers to a demand of distance that must be fulfilled in each autonomous region $r$ [$10^3$ km], $B^E$ refers to the demand of electricity of the country, not counting inclusion of new electric vehicles [GWh], $C^{RF}$ refers to the cost of retrofitting a fuel station [M€], $C^{NC}$ refers to the cost of traveling using a standard vehicle [M€/$10^3$ km], and $C^{WO}$, $C^{C}$, $C^{NG}$, $C^{W}$, $C^{B}$, $C^{H}$, $C^{S}$, $C^{O}$, and $C^{N}$ refer to the levelized cost of each type of electricity [M€/GWh].

### Equations & Constraints

#### Objective functions

We consider both an economic and an environmental objective, calculated as shown in (2) and (3).

$$\begin{aligned} obj^{eco} = &\sum_{s\in S} C^{RF} y_s + \sum_{r\in R} C^{NC} d_r^{NC} + \sum_{p\in P^{WO}} C^{WO} e_p^{TP} + \\ &\sum_{p\in P^{C}} C^{C} e_p^{TP} + \sum_{p\in P^{NG}} C^{NG} e_p^{TP} + \sum_{p\in P^{W}} C^{W} e_p^{TP} + \\ &\sum_{p\in P^{B}} C^{B} e_p^{TP} + \sum_{p\in P^{H}} C^{H} e_p^{TP} + \sum_{p\in P^{S}} C^{S} e_p^{TP} + \sum_{p\in P^{O}} C^{O} e_p^{TP} + \\ &\sum_{p\in P^{N}} C^{N} e_p^{TP} \end{aligned} \tag{2}$$

$$\begin{aligned} obj^{env} = &\sum_{r\in R} d_r^{NC} GWP^{NC} + \sum_{r\in R} d_r^{EC} GWP^{EC} + \\ &\sum_{p\in P} GWP_p^{PP} e_p^{TP} \end{aligned} \tag{3}$$

The economic objective includes the cost of retrofitting plants, producing electricity required both for the country's demand and for the electric vehicles, and the cost of using standard combustion cars for traveling distances. The environmental objective includes the

emissions from the electricity production, the emissions of using standard combustion cars for traveling distances, and the emissions of electric vehicles for traveling distances, without counting the electricity itself to avoid double counting.

### Set-covering constraints

The set-covering constraints make use of the Boolean parameter $D^{SC}_{s,s'}$, to make sure that there each retrofitted fuel station has at least one another retrofitted fuel station at the stipulated distance. In this work, the stipulated distance is 20 km. We also allow the model to not retrofit any station at all, thus ignoring the set-covering constraints. For this, we use the following equations (4,5):

$$\sum_{s' \in S} D^{SC}_{s',s} \geq w \quad \forall s \in S \tag{4}$$

$$w \geq y_s \quad \forall s \in S \tag{5}$$

### Electricity balances

The total electricity produced in a power plant is given by (6).

$$e^{TP}_p = e^{DE}_p + \sum_{s \in S} e^{RF}_{p,s} \quad \forall p \in P \tag{6}$$

The electricity that can be used in a retrofitted fuel station is the amount that is sent from each power plant, subtracting a 3%/1000 km loss in transport (7).

$$e^{SEC}_s = \sum_{p \in P} e^{RF}_{p,s} \cdot (1 - 0.03 D^{PS}_{p,s}) \quad \forall p \in P \tag{7}$$

The aggregation of electricity produced for electric vehicles in an autonomous region is given by (8).

$$e^{EC}_r = \sum_{s \in GS_{s,r}} e^{SEC}_s \quad \forall r \in R \tag{8}$$

We also limit the amount of electricity that each retrofitted gas station can receive from non-dispatchable technologies (wind and solar) to a 40% of the total it receives (9), in order to at least simulate part of the availability problems that non-dispatchable technologies present.

$$\sum_{p \in (P^{WO} \cup P^{S})} e^{RF}_{p,s} \leq 0.40 \cdot \sum_{p \in P} e^{RF}_{p,s} \quad \forall s \in S \tag{9}$$

If a fuel station is not retrofitted, it cannot be used to fuel electric vehicles (10)

$$e^{RF}_{p,s} \leq \bar{E}_p \cdot y_s \quad \forall s \in S, p \in P \tag{10}$$

You cannot produce more electricity in a power plant than its maximum capacity (11)

$$e^{TP}_p \leq \bar{E}_p \quad \forall p \in P \tag{11}$$

A lower bound of 1 GWh is set to the electricity used to charge electric vehicles, so to ensure that all retrofitted stations are used to charge electric vehicles (12).

$$e^{SEC}_s \geq y_s \quad \forall s \in S \tag{12}$$

### Demand constraints

The demand of electricity of the country must be fulfilled notwithstanding the introduction of electric vehicles (13).

$$\sum_{p \in P} e^{DE}_p = B^E \tag{13}$$

To fulfill the transportation demand, we must specify how electricity is converted through kilometers in electric vehicles, using (14).

$$d^{EC}_r = e^{EC}_r / E^{EC} \quad \forall r \in R \tag{14}$$

The transportation demand is fulfilled through electric and non-electric vehicles (15).

$$B^D_r = d^{NC}_r + d^{EC}_r \quad \forall r \in R \tag{15}$$

### Domain of the variables

All continuous variables, except for $obj^{eco}, obj^{env}$, are positive real variables ($\mathbb{R}^+$). The objective function variables are real variables ($\mathbb{R}$). Variables $w$ and $y_s$ are binary variables ($\{0,1\}$).

## Data gathering and assumptions

For the geographical coordinates, enumeration, and label of the existent fuel stations in Spain, we use the API offered by the Spanish Ministry of Industry and Tourism[4], through GET requests. A total of 11,733 fuel stations were found in the original dataset. Due to the set-covering problem being NP-hard, we reduced the size of the dataset by filtering out the fuel-stations that do not belong to major companies in Spain in order to reduce the solving time. The reduced dataset contains 5,866 fuel stations.

We obtain the geographical coordinates, primary fuel, and capacities of the power plants from the World Resources Institute [5]. We assume 8,000 h of possible production of electricity per year for the power plants. We model intermittency through the assumption that only 40% of the electricity used in electric vehicles can come from non-dispatchable technologies (9).

To calculate the distance among the different fuel stations, as well as between power plants and fuel stations, we use Haversine equation. While this distance is the shortest distance between two points in the Earth, and due to that is not really the distance that vehicles would have to traverse between two fuel stations, we balance that through the fact that for the set-covering, a small limit of 20 km is set for two fuel-stations to be able to fulfill the constraint. Considering that electric vehicles have an autonomy of >200 km, we consider that this proximity between retrofitted fuel stations would be enough to ensure availability.

The cost parameters for the electricity are sourced from a work by the European Commission [6], and the amount of kilometers traveled in the country per autonomous region has been calculated from a Spanish




**Figure 1**. Map showing the location of the possible gas stations to retrofit, as well as the power plants available to produce the electricity required in them. The legend indicates the types of power plant and gas stations. The number between parenthesis indicates the number of plants/gas stations that are considered in the study.

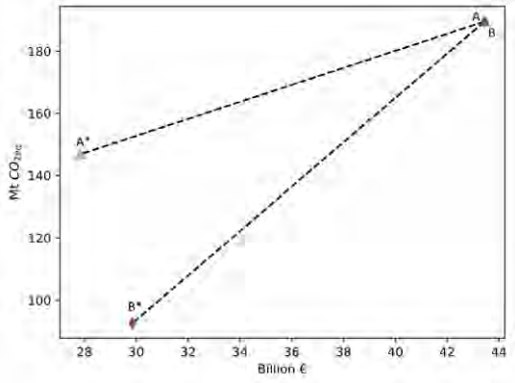



**Figure 2**. Results of the four optimization problems run. A and A* refer to the optimization of the economic objective without and with retrofitting, respectively. B and B* refer to the optimization of the environmental objective without and with retrofitting, respectively.

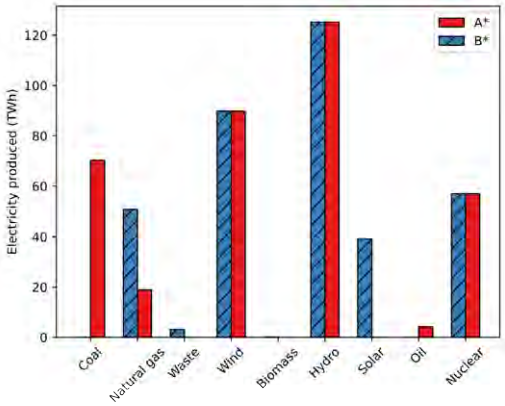



**Figure 3**. Electricity mix obtained for the economic optimum scenario (A*) and the environmental optimum scenario (B*).

newsletter [7], considering an average consumption of six liters of gasoline per 100 km traveled. The price of fuel for standard cars is considered as 0.771 €/l, without counting taxes. The cost of retrofitting a fuel station ($3,988,900) is sourced from the work of Feng and Khan [8], and does not consider on-site power storage. For the environmental impacts, we use the Ecoinvent database[9] 3.9.1 cutoff, using the IPCC2021 GWP method. For the case of electric cars, we take the GWP of the car subtracting the electricity needed to fuel it, since we are considering it in the model through equation (14).

In **Figure 1**, we show the location of each power plant and fuel station considered in this work.

## RESULTS AND DISCUSSION

We perform two optimizations per objective, for a total of four optimization runs. For each objective, we consider a scenario where we forbid retrofitting ($w \leq 0$) in order to obtain a comparison of how much the inclusion of electric vehicles modifies the results. The scenarios considered are therefore A and A*, where we optimize the economic objective without and with retrofitting, and B and B*, where we optimize the environmental objective without and with retrofitting. The results obtained are shown in Error! Reference source not found..

As shown in the figure, when we do not allow retrofitting in the model, both solutions (points A and B) are very close, changing only a bit the optimal electric mix obtained. However, when we allow retrofitting (points A* and B*), and thus, electric vehicles, both solutions immediately get better in both objectives. Compared to their base cases, A* improves 36% its economic objective and 22% its environmental objective, while B* improves 31%

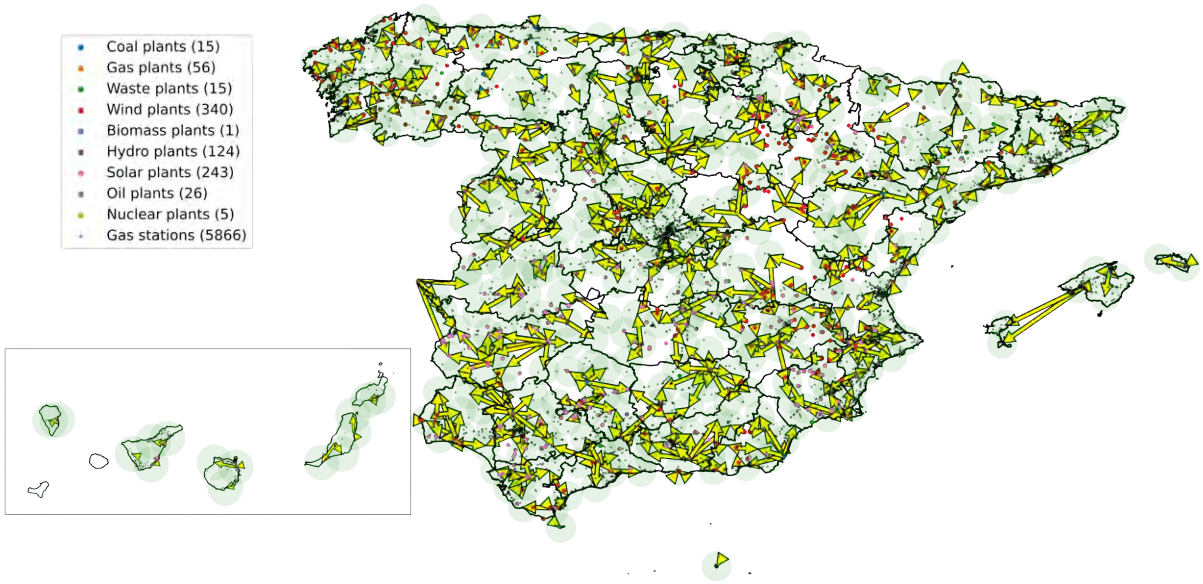



**Figure 4**. Economic optimum result (A*). Green circles indicate service area of each retrofitted station. Yellow arrows indicate from which power plant is electricity generated for each retrofitted fuel station.

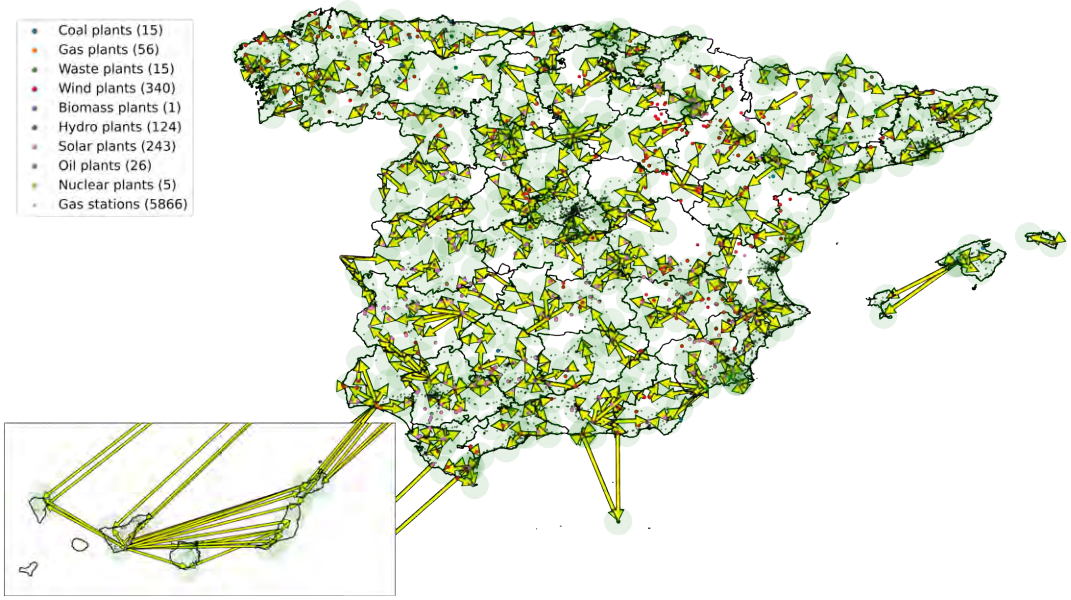



**Figure 5**. Environmental optimum result (B*). service area of each retrofitted station. Yellow arrows indicate from which power plant is electricity generated for each retrofitted fuel station.

its economic objective and 51% its environmental objective.

Notably, in both A* and B*, the model chooses to electrify the vehicle fleet completely, since that alternative is cheaper and more environmentally friendly than standard combustion vehicles, even with the cost of retrofitting the fuel stations needed.

Focusing on the scenarios where we allow retrofitting of fuel stations, the electric mix optimized to account for both the electricity demand of the country and the demand from the electric vehicles is shown in **Figure 3**.

While the electricity mixes are very similar, focusing on renewable energy available in the country with a low levelized cost of electricity, there certain differences between the environmental and economic optimums. While the economic optimum employs oil and coal, which are economic but contaminant, the environmental optimum uses solar and waste, as well as raising the use of natural gas, which while being a fossil fuel, has a lower GWP than that of coal and oil.

In **Figure 4** and **Figure 5** the supply chain results of the economic (A*) and environmental (B*) optima are

shown. It is important to mention that, in the model, certain electricity transport options which are currently not possible were not limited. For example, in the environmental optimum, there is transport from the mainland to the Canary Islands, which is not currently possible. However, it is noteworthy that even with losses that are proportional to the distance that electricity is transported, the model chooses to generate electricity in the peninsula and transport it to the islands. The number of retrofitted stations also varies between the solutions. For the economic optimum, 412 fuel stations are retrofitted, to fulfill the set-covering constraint. However, in the environmental optimum, this number rises to 477.

It is important to note that, due to data not being available, there was no upper limit to the number of cars that any fuel station can serve in a year. For a more precise model, an upper bound would need to be set to each fuel station that limits the amount of service that it can provide per year.

## CONCLUSIONS AND LIMITATIONS

The model shows that it is possible to reduce both the economic and environmental objective through an implementation of retrofitted fuel stations and electric vehicles. Specifically, the cost and GWP are reduced from 43.44 billion € and 189.55 million tonnes of CO2eq. to 27.83 billion € and 146.80 million tonnes of CO2eq. when minimizing the cost (scenarios A and A*), and from 43.44 billion € and 189.55 million tonnes of CO2eq. to 29.85 billion € and 92.57 million tonnes of CO2eq. when minimizing the cost (scenarios B and B*).

However, the results of this study must be taken as an ideal case due to the assumptions followed during its modeling. Namely, the consideration of steady state indicates that although Spain has enough electricity production capacity to satisfy a full electric fleet, electricity demand and production dynamics are not considered, hence assuming that the country has the instantaneous capacity required to provide electric energy at a given point in time.

In summary, future work will focus on the dynamic aspect of the model, including generation profiles of the different electricity technologies, as well as realistic upper limits for the service that each fuel station can provide at a given time.

## ACKNOWLEDGEMENTS

D.V. acknowledges financial support from grant PID2023-151826OA-I00 funded by MICIU/AEI/10.13039/501100011033 and ERDF/EU.

## REFERENCES

1. N. Ghosh, S. Mothilal Bhagavathy, and J. Thakur. Accelerating electric vehicle adoption: techno-economic assessment to modify existing fuel stations with fast charging infrastructure, *Clean Techn Environ Policy* 24 10:3033–3046 (2022) https://doi.org/10.1007/s10098-022-02406-x
2. Á. Galán-Martín, D. Vázquez, S. Cobo, N. Mac Dowell, J. A. Caballero, and G. Guillén-Gosálbez. Delaying carbon dioxide removal in the European Union puts climate targets at risk. *Nature Communications* 12 1:6490–6490 (2021) https://doi.org/10.1038/s41467-021-26680-3
3. A. Azapagic. Life cycle assessment and its application to process selection, design and optimisation. *Chemical Engineering Journal* 73 1: 1–21 (1999) https://doi.org/10.1016/S1385-8947(99)00042-X
4. Ministry of Industry and Tourism, Spain. API fuel stations. Accessed: Dec. 20, 2024. [Online]. https://sedeaplicaciones.minetur.gob.es/ServiciosRESTCarburantes/PreciosCarburantes/help/operations/PreciosEESSTerrestres#response-json
5. L. Byers et al. A Global Database of Power Plants. Accessed: Dec. 20, 2024. [Online] https://www.wri.org/research/global-database-power-plants
6. European Commission. Directorate General for Energy. and Trinomics. Cost of energy (LCOE): energy costs, taxes and the impact of government interventions on investments : final report. *LU: Publications Office* (2020). https://data.europa.eu/doi/10.2833/779528
7. Cores. Boletín Estadístico de Hidrocarburos. Cores, Spain, 317, (2024). https://aop.es/wp-content/uploads/2024/06/boletin-est-hidrocarburos-317-abril-2024.pdf
8. J. Feng and A. M. Khan. Accelerating urban road transportation electrification: planning, technology, economic and implementation factors in converting gas stations into fast charging stations. *Energy Syst* (2024) https://doi.org/10.1007/s12667-023-00638-4
9. G. Wernet, C. Bauer, B. Steubing, J. Reinhard, E. Moreno-Ruiz, and B. Weidema. The ecoinvent database version 3 (part I): overview and methodology. *Int J Life Cycle Assess* 21 9:1218–1230, (2016), https://doi.org/10.1007/s11367-016-1087-8

© 2025 by the authors. Licensed to PSEcommunity.org and PSE Press. This is an open access article under the creative commons CC-BY-SA licensing terms. Credit must be given to creator and adaptations must be shared under the same terms. See https://creativecommons.org/licenses/by-sa/4.0/



Systems & Control Transactions

**Research Article - Peer Reviewed Conference Proceeding**
ESCAPE 35 - European Symposium on Computer Aided Process Engineering
Ghent, Belgium. 6-9 July 2025
Jan F.M. Van Impe, Grégoire Léonard, Satyajeet S. Bhonsale,
Monika E. Polańska, Filip Logist (Eds.)

PSE PRESS

# Optimizing Heat Recovery: Advanced Design of Integrated Heat Exchanger Networks with ORCs and Heat Pumps

**Zinet Mekidiche[a], Juan A. Labarta[a,b], José A. Caballero[a,b*]**

[a] Institute of Chemical Process Engineering, University of Alicante, Carretera de S. Vicente s.n. 03690, Alicante, Spain.
[b] Chemical Engineering Department, University of Alicante, Carretera de S. Vicente s.n. 03690, Alicante, Spain.
* Corresponding author: caballer@ua.es

## ABSTRACT

A comprehensive model has been developed to design heat exchanger networks integrated with organic Rankine cycles (ORCs) and heat pumps, aiming to optimize energy efficiency. The model focuses on two key objectives: first, using heat pumps to reduce dependency on external services by enhancing heat recovery within the system; second, utilizing ORCs to recover residual heat or generate additional energy. To achieve optimal performance, the model requires careful selection of fluids for both ORCs and heat pumps, and the determination of optimal operating temperatures for maximum efficiency. The heat exchanger network is designed to be flexible, with non-fixed inlet and outlet temperatures, while simultaneously optimizing the number and operating conditions of ORCs and heat pumps. This approach reduces costs related to external services, electricity, and equipment such as compressors and turbines. Ultimately, the model facilitates the design of a heat exchanger network that efficiently utilizes residual heat and integrates other energy streams, thus improving both operational efficiency and sustainability. It demonstrates the potential for incorporating ORCs into systems that manage various energy streams, extending beyond just residual heat.

**Keywords**: Electrification Strategies, Green Heat Integration, Low-Carbon Technology, Eco-Friendly Heat Recovery.

## INTRODUCTION

In recent years, the optimization of heat recovery networks has become a key focus in efforts to improve energy efficiency and reduce environmental impact in industrial systems. The integration of Organic Rankine Cycles (ORCs) and heat pumps into these networks offers a promising solution by recovering waste heat and converting it into usable energy, thereby reducing the reliance on external energy sources. However, the successful implementation of this approach depends on the careful selection of system components, including fluids for the ORCs and heat pumps, as well as the determination of optimal operating conditions. In this study, we explore several case studies that illustrate the potential of these technologies in different industrial settings, highlighting their impact on cost reduction, energy efficiency, and sustainability.

## CASE OF STUDY

### 1. Integration of Heat Recovery and Heat Pumps

A base case study was analyzed to illustrate the effectiveness of the proposed methodology. The process system included a hot stream (H1) and a cold stream (C1) with defined inlet and outlet temperatures (Table 1). This system has been previously studied by Holiastos & Manousiouthakis [1] to consider the introduction of heat pumps and heat engines. We assume that there are contracts with a utility plant that provided vapor in different conditions and prices as shown in Table 2. Prices are calculated using the approach proposed by Turton et al. [2] using gas natural prices from Eurostat [3].

**Table 1.** Process Streams Data

| Name | Tin [°C] | Tout [°C] | Fcp [MW/°C] |
|---|---|---|---|
| H1 | 106 | 176 | 0.52 |
| C1 | 146 | 76 | 0.32 |

**Table 2.** Utilities Streams Data

| Name | Tin [°C] | Tout [°C] | Cost [k$/MW·y] |
|---|---|---|---|
| LP Steam | 150 | 149 | 666,43 |
| MP Steam | 200 | 199 | 700,42 |
| HP Steam | 250 | 249 | 831,42 |
| Cooling Water | 20 | 25 | 23,5 |

## 2. Initial Results

In the base case, the total utility cost was calculated at **18,797.4 k$/y** without additional optimization. MP Steam was the primary utility with a consumption of 18.72 MW, followed by LP Steam at 8.08 MW and cooling water at 12.80 MW (Figure 1)

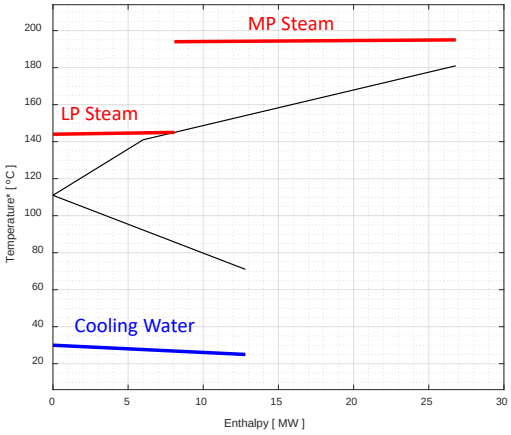



**Figure 1.** Analysis of Utilities on the Grand Composite Curve

## 3. Optimization with Re-Flashing:

The first optimization step involved re-flashing MP Steam (200 °C) into LP Steam (150 °C) (Figure 2). By recovering 2.246 MW of LP Steam, the utility cost was reduced by **1,496.8 k$/y**, representing a **7.96%** cost reduction. (Figure 3)

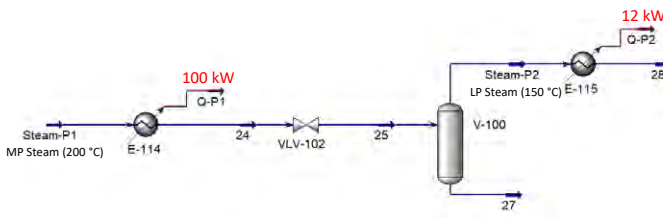



**Figure 2.** Re-flashing diagram in Aspen HYSYS.

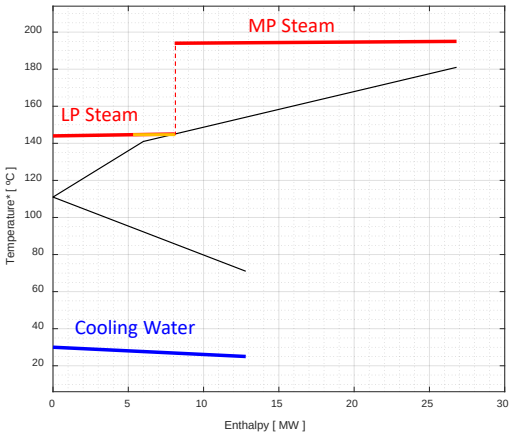



**Figure 3.** Analysis of Utilities on the Grand Composite Curve after re-flashing the MP Steam to LP Steam.

## 4. Optimization with Heat Pump:

A heat pump was introduced to enhance energy efficiency further to reduce the remaining LP Steam consumption (from 8.08 MW to 2.25 MW). The heat pump, operating between a hot stream at ~150 °C and a cold stream at ~90 °C, optimized using GAMS, required 1.259 MW of electrical work and contributed to recovering 5.83 MW of heat. This configuration reduced the total utility cost to **14,813.2 k$/y**, reducing additional costs while maintaining process requirements, representing a **21.02%** cost reduction. (Figure 4 and 5).

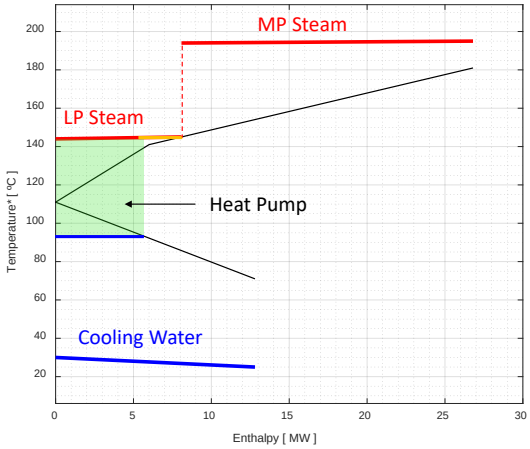



**Figure 4.** Analysis of Utilities on the Grand Composite Curve after re-flashing the MP Steam to LP Steam (the green section qualitatively illustrates how to add a heat pump)

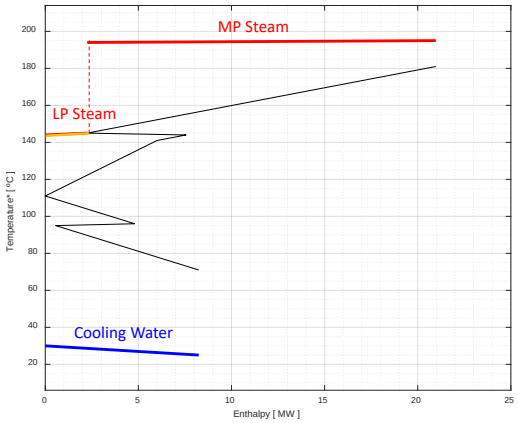



**Figure 5.** Analysis of Utilities on the Grand Composite Curve after adding the first heat pump.

For optimization in GAMS, the Pinch Location Methodology [4,5] was employed, enabling the calculation of utility costs for streams with variable temperature and/or flow rates. The heat loads associated with heat pumps or heat engines were correlated using second-order polynomials, with correlation coefficients exceeding 0.995 in all cases. The problem was solved to global optimality

This example demonstrates the proposed methodology's capability to integrate heat pumps and re-flashing processes, significantly improving heat recovery, reducing energy costs, and promoting system sustainability.

## 5. Integration of an ORC

Before incorporating the second heat pump, a simulation was performed to explore the integration of an Organic Rankine Cycle (ORC) below the pinch point. Under these conditions, the simulation indicates that approximately **0.70 MW** can be recovered using benzene as the working fluid.

While this amount of energy recovery is relatively small and does not appear to offer significant economic benefits, an interesting opportunity exists to enhance the ORC's performance. By extending the heat pump's operating range to higher values, the ORC can utilize the hot water generated by the utility system. This, however, comes at the expense of requiring additional cooling water.

For instance, by specifying an ORC capable of expanding to around **14 MW**, we obtain the configuration of Figure 6.

This example highlights the potential for combining heat pumps and ORCs to maximize energy recovery. Such an approach optimizes the utilization of thermal resources within the system, showcasing the flexibility and benefits of integrating ORCs in conjunction with other thermal management strategies.

Using the available data, it is possible to calculate the amount of hot water (in MW) generated from the saturated liquid after utilizing both MP and LP steam (Figure 7)

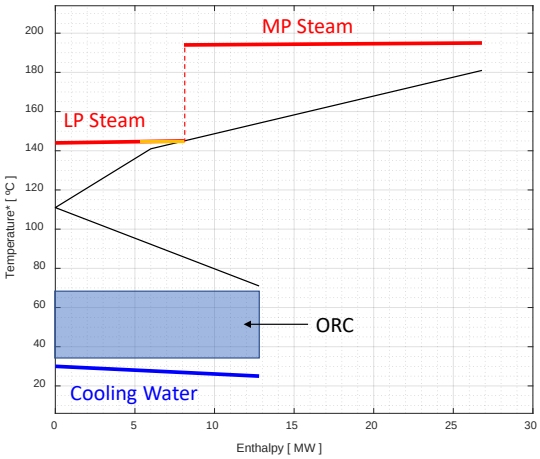



**Figure 6.** Analysis of Utilities on the Grand Composite Curve (the blue section qualitatively illustrates how to add an ORC)

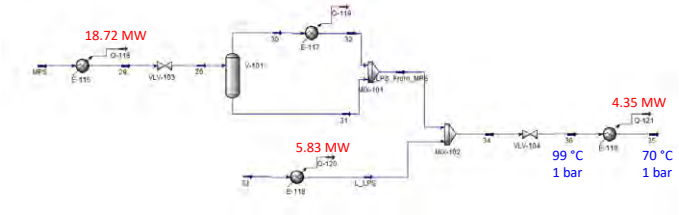



**Figure 7.** Simulation of the amount of hot water (in MW) generated from the saturated liquid in Aspen HYSYS.

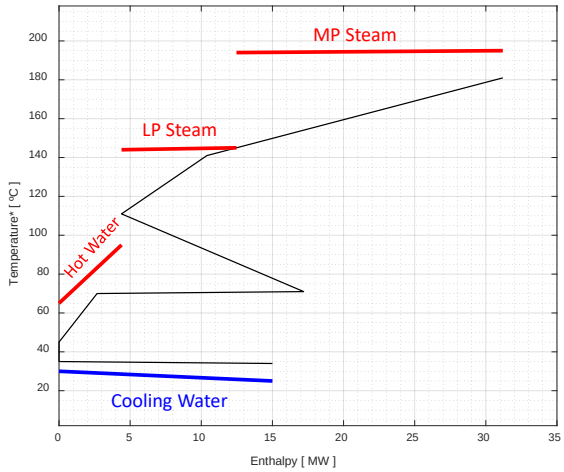



**Figure 8.** Analysis of Utilities on the Grand Composite Curve after adding an ORC.

As illustrated in the schematic, the system can recover 4.35 MW of hot water at 99°C (1 bar) and reduce it to 70°C (1 bar). However, with the extended ORC design, the recovery is limited to **approximately 0.85 MW**, which

is relatively low.

This configuration reduced the total utility cost to **17,840.4 k$/y**, reducing additional costs while maintaining process requirements, representing a **5.09%** cost reduction. (Figure 8)

## 6. Integration of an ORC after the heat pump.

This study evaluates the feasibility of implementing an Organic Rankine Cycle (ORC) operating between temperatures of approximately 65 °C and 40 °C. (Figure 9) Tests conducted with benzene as the working fluid have demonstrated feasibility within these temperature ranges. The system focuses on recovering approximately **8 MW** from residual streams, optimizing the energy utilization of the process.

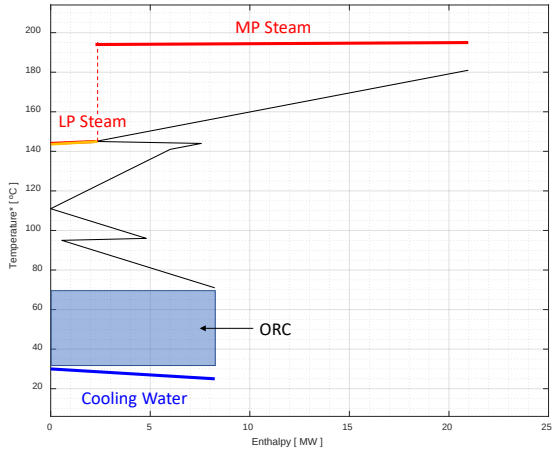



**Figure 9.** Analysis of Utilities on the Grand Composite Curve after adding the first heat pump (the blue section qualitatively illustrates how to add an ORC)

Additionally, it has been identified that by expanding liquid water from the condensation of low-pressure (LPS) and medium-pressure steam (MPS) to atmospheric conditions, up to **2.75 MW** of hot water can be generated. This recovered heat can be utilized as an additional thermal utility. (Figure 10)

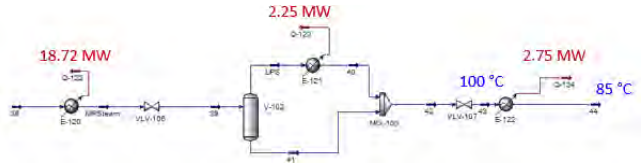



**Figure 10.** Simulation of the amount of hot water (in MW) generated from the saturated liquid in Aspen HYSYS.

Based on these findings, the implementation of an ORC with 10.3 MW thermal power in the condenser is proposed. Although this increases cooling water consumption, it generates **0.58 MW** of electricity (Figure 11). This approach represents a technically and economically attractive solution to maximize energy utilization in industrial processes through the integration of recovery and energy conversion technologies.

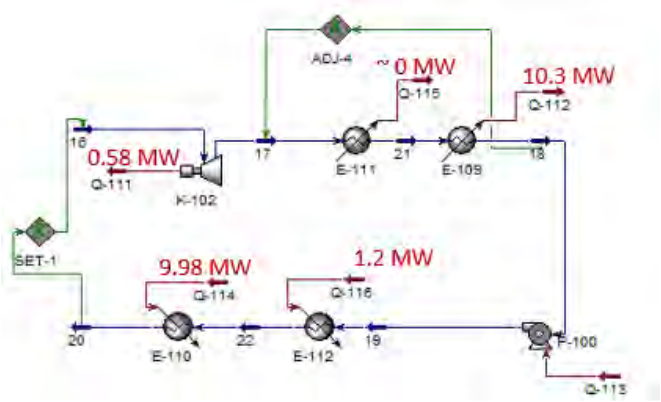



**Figure 11.** Simulation of the ORC in Aspen HYSYS.

By implementing this configuration, the total utility cost was reduced to **14,168.7 k$/y**, representing a **24.60%** decrease in costs while ensuring compliance with process requirements and limiting additional expenditures (Figure 12)

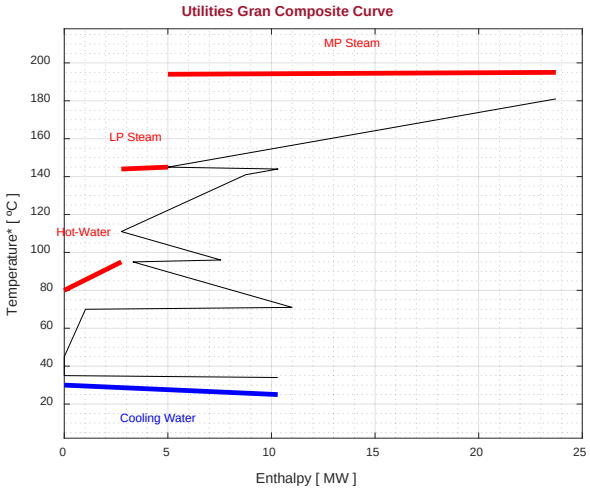



**Figure 12.** Analysis of Utilities on the Grand Composite Curve after adding a heat pump and ORC.

## CONCLUSION

In conclusion, the integration of Organic Rankine Cycles (ORCs) and heat pumps into heat exchanger networks presents a promising approach for improving energy efficiency and reducing operational costs. The optimization of both the internal and external energy flows within a system can significantly lower the reliance on external energy services, minimizing the overall energy consumption and reducing carbon emissions. This method shows great potential for industrial applications,

especially when considering the wide range of energy streams that can be recovered, such as residual heat, and used to generate power or preheat fluids.

However, there are practical limitations in applying this approach in real-world industry, particularly when it comes to selecting the right operating conditions for ORCs and heat pumps, as well as ensuring that the integration with existing systems is efficient. The modeling complexity can also increase as the number of variables grows, making it crucial to optimize not just the design but the operation of these systems in real-time.

Heat recovery, such as from steam, has a significant impact on the energy requirements of a utility system in an industrial plant. When a heat recovery strategy is implemented, the plant's energy system is affected as the amount of energy supplied externally to meet thermal demands is reduced. Specifically, heat recovery from steam can reduce the need for additional heat provided by conventional energy sources like natural gas or coal, which decreases the demand for fossil fuels and reduces the system's carbon footprint. However, this type of recovery can also affect the amount of energy the utility system must provide to maintain thermal balance in other areas of the process. For example, if recovered heat is used to preheat feed fluids to a distillation column or heat exchanger, the plant's heating system will require less energy to generate the necessary heat, but the pumping or generation systems may need to be adjusted to handle flow or pressure variations.

Therefore, it is essential to model the impact of heat recovery on the overall energy requirements of the utility system. It should be evaluated how this recovery influences the energy consumption of pumps, generators, or cooling units, and how different energy flows within the system are balanced to optimize consumption and minimize operating costs.

## ACKNOWLEDGMENTS

The authors gratefully acknowledge financial support by the Ministry of Science and Innovation from Spain under the project (PID2021-124139NB-C21, SUS4Energy)

## REFERENCES

1. Holiastos K, Manousiouthakis V. Minimum hot/cold/electric utility cost for heat exchange networks. Comput Chem Eng 2002;26:3–16.
2. Turton, R.J., Bailie, R.C., Whiting, W.B., Shaeiwitz, J.A., Bhattacharyya, D. (2018). Analysis, Synthesis and Design of Chemical Processes - United States Edition, fourth ed, Prentice Hall, Boston.
3. Eurostat. (2025). *Eurostat database*. European Commission. https://ec.europa.eu/eurostat/web/main/data/database
4. Quirante N, Caballero JA, Grossmann IE. A novel disjunctive model for the simultaneous optimization and heat integration. Comput Chem Eng 2017;96:149–68. https://doi.org/10.1016/j.compchemeng.2016.10.002
5. Quirante N, Grossmann IE, Caballero JA. Disjunctive model for the simultaneous optimization and heat integration with unclassified streams and area estimation. Comput Chem Eng 2018;108:217–31. https://doi.org/10.1016/j.compchemeng.2017.09.013

© 2025 by the authors. Licensed to PSEcommunity.org and PSE Press. This is an open access article under the creative commons CC-BY-SA licensing terms. Credit must be given to creator and adaptations must be shared under the same terms. See https://creativecommons.org/licenses/by-sa/4.0/



Systems & Control Transactions

**Research Article - Peer Reviewed Conference Proceeding**
ESCAPE 35 - European Symposium on Computer Aided Process Engineering
Ghent, Belgium. 6-9 July 2025
Jan F.M. Van Impe, Grégoire Léonard, Satyajeet S. Bhonsale,
Monika E. Polańska, Filip Logist (Eds.)

PSE PRESS

# $CO_2$ recycling plant for decarbonizing hard-to-abate industries: Empirical modelling and Process design of a CCU plant- A case study.

**Jose Antonio Abarca*, Stephanie Arias-Lugo, Lucia Gomez-Coma, Guillermo Diaz-Sainz and Angel Irabien**

Departamento de Ingenierías Química y Biomolecular, Universidad de Cantabria, ETSIIT, Avenida de los Castros s/n, 39005, Santander, Spain.
* Corresponding Author: joseantonio.abarca@unican.es

## ABSTRACT

Climate change, driven by increasing $CO_2$ emissions, necessitates innovative mitigation strategies, particularly for hard-to-abate industries. Carbon Capture and Utilization technologies offer promising solutions by capturing $CO_2$ from industrial flue gases and converting it into value-added products. Among capture methods, membrane separation stands out for its compact design, energy efficiency, and scalability. Following capture, $CO_2$ can be converted into chemicals like formic acid using electrocatalytic processes, enabling energy storage from renewable sources. This study proposes the design of an industrial demonstrator for a $CO_2$ recycling plant targeting hard-to-abate sectors such as textile and cement industries. The system integrates polymeric membranes for $CO_2$ capture and a 100 $cm^2$ electrochemical reactor for $CO_2$ electroreduction into formic acid. Experimental data from both stages are used to develop predictive models based on artificial neural networks (ANN), optimizing system performance. Case studies reveal that $CO_2$ concentration at the capture inlet significantly impacts plant design. For a textile plant with 3.5% $CO_2$ emissions, a four-stage membrane system is required, resulting in higher CAPEX and OPEX. Conversely, a cement plant with 12% $CO_2$ emissions requires only two stages to achieve the target $CO_2$ concentration of >75 %, reducing costs by over 60%. Sensitivity analysis highlights the critical role of inlet $CO_2$ concentration on the membrane area and system stages. The findings underscore the feasibility of modular membrane systems tailored to emission characteristics, paving the way for sustainable $CO_2$ recycling processes adaptable to various industries. This integrated approach offers a pathway to mitigate emissions while generating valuable chemical products.

**Keywords**: Process Design, Carbon Dioxide Capture, Modelling, Optimization, Electrocatalysis, Formic acid

## INTRODUCTION

Climate change has emerged as one of the most important challenges that society faces nowadays. Increasing anthropogenic $CO_2$ emissions is one of the main causes driving this phenomenon. In this sense, several strategies have been proposed to mitigate $CO_2$ emissions. Some of these are related to the use of renewable energy sources or improving energy efficiency. However, some industries inherently produce $CO_2$ as a by-product of their production processes, making conventional approaches insufficient to eliminate emissions. In such cases, alternative strategies must be explored, including Carbon Capture and Utilization (CCU) technologies [1].

Two stages are involved in this decarbonization approach. First, $CO_2$ is captured from industrial gas effluent. In the second stage, it is converted into value-added chemicals. To achieve efficient separation of $CO_2$ from industrial flue gas streams and prevent its release into the atmosphere, various capture technologies have been developed. These include absorption, adsorption, membrane capture, and cryogenic separation [2,3].

Among these technologies, membrane separation has garnered significant attention due to its compact

design, energy efficiency, simplicity, and ability to overcome selectivity limitations [4]. Additionally, the modularity of membrane systems enhances their scalability, making them a promising solution for industrial $CO_2$ capture. Polymeric membranes are particularly well-suited for separating $CO_2$ from other compounds in post-combustion streams, which typically contain $CO_2$, $N_2$, $O_2$, and traces of CO or NOx [5].

Once captured, $CO_2$ is directed to the conversion stage. In this context, the electroreduction of $CO_2$ ($ERCO_2$) into value-added products has emerged as one of the most promising $CO_2$ conversion processes, offering significant economic and environmental benefits [6]. This technology converts $CO_2$ into various chemical products, such as formic acid, methanol, and ethylene, via an electrocatalytic process that supplies an external voltage to generate electron flux between two electrodes. Furthermore, it enables the storage of energy from renewable sources in the form of chemical bonds [7].

Integrating these two stages presents a significant challenge for the industrial implementation of $CO_2$ recycling plants, where $CO_2$ is first captured and subsequently converted [1]. To address it, this work proposes the design of an industrial demonstrator for a $CO_2$ recycling plant. This system employs polysulfone membranes for $CO_2$ capture, followed by conversion into formic acid through $ERCO_2$ targeting the decarbonization of hard-to-abate industries such as textile or cement.

The study focuses on empirically modeling both the $CO_2$ capture and electroreduction systems using neural networks, resulting in an integrated predictive model for the entire $CO_2$ recycling process. This model aims to optimize the performance of the capture-conversion system, thereby paving the way for developing a sustainable process for $CO_2$ capture and its conversion into formic acid. Furthermore, the model is designed to adapt to the specific conditions and needs of different industries.

# METHODOLOGY

## Experimental set-up

Two experimental setups are used to provide the data required for constructing the empirical model for each stage. For $CO_2$ capture, hollow fiber membrane modules (Airrane, MCH-1006A) with an active area of 1822 $cm^{-2}$, 2000 fibers, and 110 µm thickness are utilized. The concentrated $CO_2$ is collected in the permeate, which is released at ambient pressure. Various operational variables are evaluated to determine the separation performance; i) pressure applied, ii) $CO_2$ inlet flow rate, and iii) $CO_2$ inlet concentration. Capture experiments are carried out at least twice using synthetic and real gas mixtures from two industrial sources (textile and cement). These flue gas sources differ in $CO_2$ concentration, reflecting the variability in industrial emissions.

For the conversion stage, a 5 $cm^2$ commercial lab-scale three-compartment electrochemical reactor (Dioxide Materials and Membranes International, Inc), consisting of a $Bi_2O_3$ cathode, an $IrO_2$ anode, with a central compartment formed by ion exchange resins (Amberlite), a CEM (Nafion) and an AEM (Sustainion). The reactor is fed with deionized water to the anode and central compartment, while humified $CO_2$ is supplied to the cathode. This is utilized to investigate the effects of key process variables. A factorial experimental design is implemented to analyze three operational parameters: (i) $CO_2$ inlet flow rate, (ii) humidity of the $CO_2$ feed, and (iii) applied current density, identified as critical variables [8]. Additional factors, such as the water flow rate into the central compartment and the anolyte inlet flow rate, are evaluated based on information from the literature [9]. To ensure robust input data for the model, all experimental tests are performed at least in duplicate.

## Model deployment

Two independent neural-network-based empirical models are developed using Neural Designer [10] (Artificial Intelligence Techniques, Ltd.). These models generate numerical expressions based on the input data collected during experimental work with the membrane modules and the commercial reactor. The input variables and their corresponding ranges are detailed in Table 1:

**Table 1:** Variables and value ranges for input variables in the Artificial Neural Network (ANN) models.

| Model | Variable | Range |
|---|---|---|
| Capture | Pressure (bar) | 3-6 |
| Capture | Inlet flowrate (ml $min^{-1}$ $cm^{-2}$) | 0.17-0.55 |
| Capture | $CO_2$ inlet concentration (%) | 0.5-35 |
| $ERCO_2$ | Central water flow rate (ml $min^{-1}$) | 0.12-0.17 |
| $ERCO_2$ | Current density (mA $cm^{-2}$) | 45-200 |
| $ERCO_2$ | Cathode water feed (g $h^{-1}$) | 0.5-3 |
| $ERCO_2$ | $CO_2$ flowrate (ml $min^{-1}$) | 1500-2000 |
| $ERCO_2$ | $CO_2$ concentration (%) | 75-100 |

## Case study

An optimization problem is proposed for the functioning of an industrial demonstrator plant, where the electrochemical reactor serves as the central element. In this case, the $CO_2$ capture process must be optimized to supply $CO_2$ under specific conditions to the 100 $cm^2$ electrochemical reactor. The critical variables of the reactor must also be optimized to maximize formic acid

production. The overall cost is established as the objective function to minimize, considering both the CAPEX and OPEX of the recycling plant.

$$OF = CAPEX + OPEX \quad (1)$$

$$CAPEX = (AreaR \cdot Rc + AreaM \cdot Mc)/5 \quad (2)$$

$$OPEX = Ecost + Ccost - FA \cdot FAp \quad (3)$$

In these equations, AreaR represents the reactor's geometric area ($m^2$), and AreaM refers to the total membrane area required for $CO_2$ capture ($m^2$). The respective costs, Rc (Reactor cost, 27,000 € $m^{-2}$) and Mc (Membrane cost, 5,500 € $m^{-2}$), are based on previous acquisition costs per square meter. Ecost and Ccost represent the energy cost from the conversion stage and the compression cost required in each separation stage, respectively. FA denotes the amount of formic acid produced, and FAp is its market price (4,100 € $t^{-1}$).

The CAPEX evaluates the cost of constructing the $CO_2$ recycling plant, taking into account both the membrane area required for $CO_2$ capture and the fixed cost of the 100 $cm^2$ reactor, annualized over 5 years. On the other hand, the OPEX includes the electricity cost (based on Spanish electricity prices) for the $ERCO_2$ process, the compression cost for the capture stage, and the savings associated with the formic acid produced, which can either be sold or used in industry.

The optimization problem is subject to constraints related to product quality, model, or process input requirements (as shown in Table 2). This leads to a constrained non-linear optimization minimization problem (MINLP), which is addressed using the General Algebraic Modeling System (GAMS, GAMS Development Corporation, Washington, DC, USA). A reduced gradient algorithm is employed to solve the MINLP, with the CONOPT solver used to obtain the optimal solution.

**Table 2:** Constrained variables of the case study optimization problem

| Constrain | Variable | Range |
|---|---|---|
| Model Capture | Pressure | 3-6 |
| Model $ERCO_2$ | Central water flow rate (ml $min^{-1}$) | 0.13-0.34 |
| Model $ERCO_2$ | Current density | 45-200 |
| Input $ERCO_2$ | $CO_2$ inlet concentration (%) | 75-100 |
| Input $ERCO_2$ | $CO_2$ flowrate (ml $min^{-1}$) | 1500-2000 |
| Product Quality | Formic acid concentration (g $L^{-1}$) | 80-130 |

Two industries are considered for the case studies: a textile plant, where the $CO_2$ content in the flue gas stream is 3.5 %, and a cement industry that emits 12 % of $CO_2$ in its post-combustion stream. Additionally, a sensitivity analysis regarding the $CO_2$ concentration in the inlet of the $CO_2$ capture is conducted to evaluate the economical viability of installing this $CO_2$ recycling plant in diverse industries with varying $CO_2$ emissions.

# RESULTS

## Model deployment

The $CO_2$ capture predictive model is developed using a machine learning approach, where experimental data is utilized to establish the architecture of the artificial neural network (ANN). As shown in Figure 2.a, the resulting ANN comprises several interconnected components: (i) a scaling layer to normalize input values, (ii) a perceptron layer that processes the inputs using a mathematical function derived from the experimental data, (iii) an un-scaling layer that restores the output values to their original dimensions, and (iv) a bounding layer that constrains the final output within the model's confidence intervals. The selection and optimization of neurons is performed through an iterative process designed to achieve the best possible alignment with the provided data, thereby constructing an accurate and efficient ANN. The neural network architecture comprises three neurons in the scaling layer, seven and two for the subsequent perceptron layers (with hyperbolic and linear activation functions), and two neurons in each un-scaling and bounding layer. As seen in Figures 1.c-d, the predictive model's adjustment for the two output variables achieves an $R^2$ value exceeding 0.99, demonstrating high accuracy.

The Gradient Boosting Variable Importance highlights the contribution of each input variable to the final output, effectively capturing the system's nonlinearities (Figure 2.b). For the permeate flow rate, the inlet pressure emerges as the most influential factor (0.544), followed by the inlet flow rate (0.332). In contrast, these variables have a negligible impact on the $CO_2$ outlet concentration, which is primarily determined by the inlet $CO_2$ concentration (0.964).

For the $CO_2$ conversion predictive model, a similar methodology is followed, as detailed in previous works [8]. Another input variable is introduced in this case: the inlet $CO_2$ concentration, which corresponds to the $CO_2$ concentration at the capture stage outlet. The target variable in this model is the formate concentration obtained. When analyzing the importance of each input variable with the Gradient Boosting Variable Importance, two input variables stand out as the most influential on the target variable, the current density and $CO_2$ inlet concentration.

The development of the ANN enables the creation of an empirical mathematical model that establishes the relationship between input and output variables. The

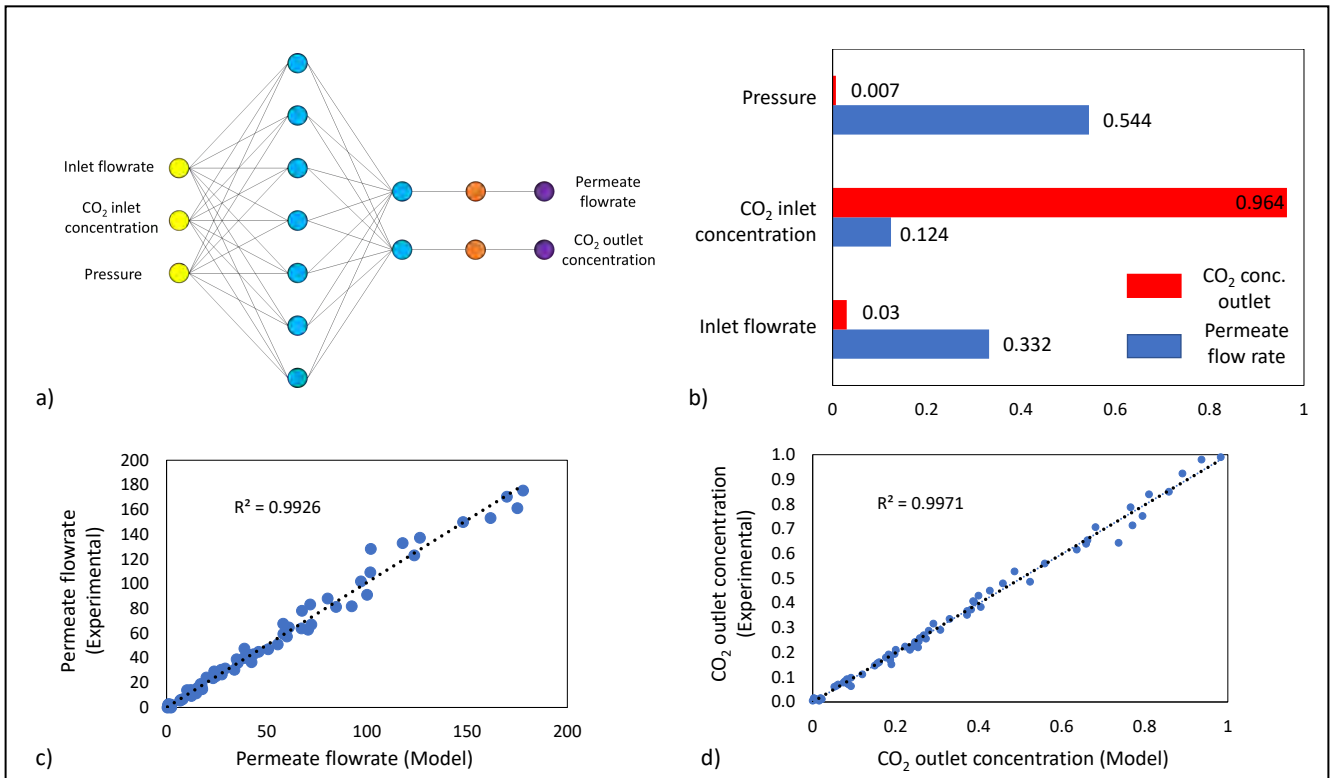



**Figure 1: a)** ANN architecture for the $CO_2$ capture predictive model using membranes, **b)** Gradient Boosting variable importance coefficient chart of the input variables regarding the two target variables of the model, **c)** Model adjustment to experimental data for the permeate flow rate, and **d)** Model adjustment to experimental data for the $CO_2$ outlet concentration.

mathematical expressions defining the ANN's architecture are manually derived and integrated as model equations within the optimization problem described below.

## Case Study

The optimization problem focuses on designing an industrial demonstrator for decarbonizing hard-to-abate industries. The system consists of two stages: $CO_2$ capture using polymeric membranes and $CO_2$ conversion to formic acid via $ERCO_2$. The design is centered around the $ERCO_2$ reactor, which has an active area of 100 $cm^2$.

Two different scenarios are proposed for implementing the system: the case of the textile industry, the $CO_2$ concentration is 3.5 %, while for the cement industry, it rises to 12 %. This variation directly impacts the overall design of the $CO_2$ recycling plant, although both scenarios target the same product quality.

For the textile industry case, the optimal design for the capture stage involves four different membrane stages to achieve the required 75 % $CO_2$ concentration at the inlet of the $ERCO_2$ [11]. Four membrane separation stages are arranged in series, using the polymeric membrane modules employed in the experimental testing, as shown in Figure 2. The total membrane area is 27.7 $m^2$, operating at 3 bar pressure. The membranes feed the $ERCO_2$ with 1569 ml $min^{-1}$ of gas at a $CO_2$ concentration of 90.9 %. The $ERCO_2$ reactor operates at 200 mA $cm^{-2}$, producing 137.2 g $L^{-1}$ of formic acid. The system CAPEX is estimated at 30,524 € $y^{-1}$, with the membrane cost being the biggest contributor. On the other hand, the compression cost, primarily associated with the $CO_2$ capture stage is the main contributor to the OPEX. Ultimately, the total yearly cost for the recycling plant, representing the objective function, is calculated at 36440 € $y^{-1}$.

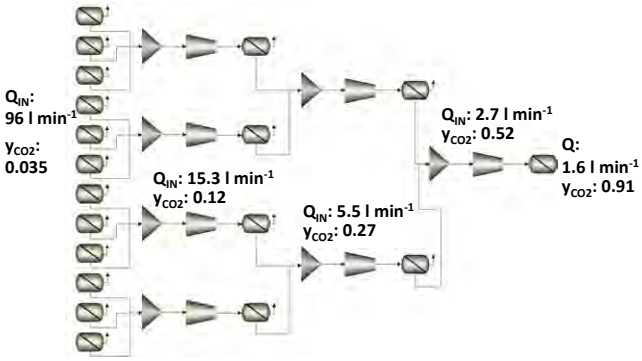



**Figure 2:** Schematic diagram for the capture stage of the $CO_2$ recycling plant for the textile industry case study.

As observed in the model evaluation, the $CO_2$ concentration in the flue gas at the capture inlet is one of the most impactful variables in achieving the desired $CO_2$

concentration at the outlet. In this sense, the next case study evaluates the cement industry, where the initial $CO_2$ concentration is 12 %. The optimal design for the $CO_2$ recycling plant in this case consists of 2 stages in series, as seen in Figure 3. The total membrane area is reduced compared to Case Study 1 to 8.2 $m^2$, and it achieves a $CO_2$ concentration of 95.9 % with a 1640 ml $min^{-1}$ flow rate. The $ERCO_2$ is operated at 200 mA $cm^{-2}$, resulting in a formic acid concentration of 130.27 g $L^{-1}$. The CAPEX is notably reduced to 9074 € $y^{-1}$, with the membrane cost is cut by 70 %. OPEX is also lower, as less gas volume is treated by the membrane modules, resulting in reduced compression costs. Overall, the total cost is 12,359 € $y^{-1}$, which is a 66 % reduction compared to the overall cost for the textile industry case, confirming the significant impact of the $CO_2$ inlet concentration on the overall $CO_2$ recycling plant design.

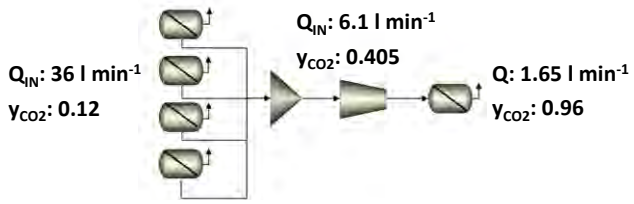



**Figure 3**: Schematic diagram for the capture stage of the $CO_2$ recycling plant for the cement industry.

One of the benefits of membrane separation for $CO_2$ capture is the system's modularity, which allows it to adapt to varying $CO_2$ concentrations at the capture in let. As observed in both case studies, the $CO_2$ concentration is a critical variable in the system's design to achieve the target $CO_2$ concentration before the $ERCO_2$. A sensitivity analysis is performed to determine the effect of this input variable in the membrane area required to achieve the target $CO_2$ concentration (>75 %). This analysis helps identify which emission sources are suitable for capture without oversizing the membrane system. It also serves as a preliminary estimate for evaluating other $CO_2$-emitting industries, such as biogas plants, thermal power plants, or large chemical plants.

A sensitivity analysis is carried out to evaluate the membrane area and the number of capture stages needed to achieve the target $CO_2$ concentration with different $CO_2$ concentrations at the inlet. As seen in Figure 4, as the inlet $CO_2$ concentration increases, the membrane area required decreases significantly. Notably, a small increase in concentration yields a substantial reduction in the membrane area when operating with highly diluted $CO_2$ streams. However, when the $CO_2$ stream is less diluted, increasing the concentration results in a smaller reduction in the total membrane area required.

The membrane area directly impacts the CAPEX of the system. Therefore, a higher $CO_2$ concentration in the inlet stream leads to lower capital investment for the $CO_2$ recycling plant. Additionally, the number of membrane stages decreases as the $CO_2$ concentration increases, affecting the OPEX, as fewer stages result in lower compression costs.

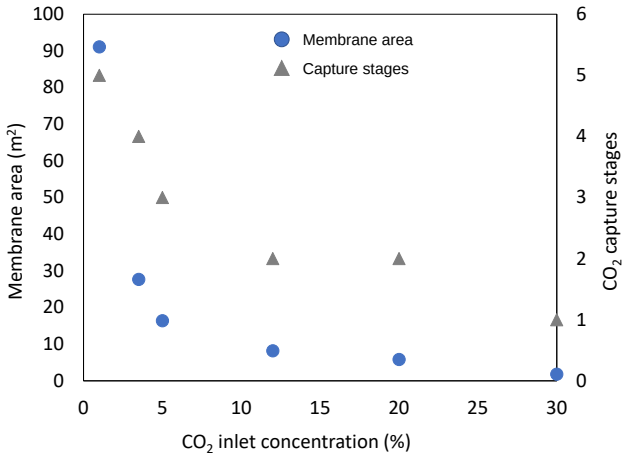



**Figure 4**: Sensitivity analysis results for evaluating the influence of the inlet $CO_2$ concentration on the membrane area and stages of the $CO_2$ capture system.

## CONCLUSIONS

The integration of $CO_2$ capture and conversion presents a viable solution for reducing emissions in hard-to-abate industries such as textiles and cement. This approach not only mitigates $CO_2$ emissions but also facilitates the conversion of captured $CO_2$ into value-added products like formic acid, offering economic and environmental benefits.

The $CO_2$ concentration of $_2$ in the inlet stream is a critical factor that significantly impacts the design and cost of the system. Higher $CO_2$ concentrations reduce the required membrane area and the number of capture stages, leading to lower capital (CAPEX) and operational (OPEX) expenditures. This underscores the importance of adapting the system design to the specific characteristics of each industrial emission source. The modularity of membrane systems makes them highly adaptable to varying $CO_2$ concentrations and emission profiles. Sensitivity analyses confirm that even small increases in inlet $CO_2$ concentration can drastically reduce the required membrane area, particularly in highly diluted streams. This adaptability makes the technology suitable for a wide range of industries, including biogas plants, thermal power plants, and chemical manufacturing facilities.

Overall, the proposed $CO_2$ recycling system offers a scalable and sustainable pathway for decarbonizing industrial processes. It demonstrates the potential to address climate change challenges while generating

economic value through the production of high-demand chemical products.

## ACKNOWLEDGEMENTS

The authors fully acknowledge the financial support received from the Spanish State Research Agency (AEI) through the project PLEC2022-009398 (MCIN/AEI/10.13039/501100011033 and Union Europea Next Generation EU/PRTR), and SODERCAN through the project SOSCEM (SODERCAN 2024 Fomento de la Economía Circular)

The present work is related to CAPTUS Project. This project has received funding from the European Union's Horizon Europe research and innovation programme under grant agreement No 101118265.

Jose Antonio Abarca gratefully acknowledges the predoctoral research grant (FPI) PRE2021-097200.

## REFERENCES

1. Rafiee A., Rajab Khalilpour K., Milani D., Panahi M., Trends in $CO_2$ conversion and utilization: A review from process systems perspective, *J Environ Chem Eng* 6:5771–5794 (2018). https://doi.org/10.1016/j.jece.2018.08.065.
2. Mikulčić H., Skov I.R., Dominković D.F., Wan Alwi S.R., Manan Z.A., Tan R., Duić N., Hidayah Mohamad S.N., Wang X., Flexible Carbon Capture and Utilization technologies in future energy systems and the utilization pathways of captured $CO_2$, *Renewable Sustainable Energy Rev.* 114:109338 (2019). https://doi.org/10.1016/J.RSER.2019.109
3. Wilberforce T., Baroutaji A., Soudan B., Al-Alami A.H., Olabi A.G., Outlook of carbon capture technology and challenges, *Sci Total Environ* 657:56–72 (2019). https://doi.org/10.1016/j.scitotenv.2018.11.424.
4. He X., Fu C., Hägg M.B., Membrane system design and process feasibility analysis for $CO_2$ capture from flue gas with a fixed-site-carrier membrane, *Chem Eng J* 268:1–9 (2015). https://doi.org/10.1016/j.cej.2014.12.105.
5. Han Y., Ho W.S.W, Polymeric membranes for $CO_2$ separation and capture, *J Memb Sci* 628: 119244 (2021). https://doi.org/10.1016/j.memsci.2021.119244.
6. Rumayor M., Dominguez-Ramos A., Perez P., Irabien A., A techno-economic evaluation approach to the electrochemical reduction of $CO_2$ for formic acid manufacture, *J $CO_2$ Util* 34: 490–499 (2019). https://doi.org/10.1016/J.JCOU.2019.07.024.
7. Abarca J.A., Díaz-Sainz G., Merino-Garcia I., Irabien A., Albo J., Photoelectrochemical $CO_2$ electrolyzers: From photoelectrode fabrication to reactor configuration, *J Energy Chem* 85:455–480 (2023). https://doi.org/10.1016/j.jechem.2023.06.032.
8. Abarca J.A., Coz-Cruz M., Díaz-Sainz G., Irabien A., Modelling and stochastic optimization of a three-compartment electrochemical reactor for $CO_2$ electroreduction to formic acid using neural networks, in: COMPUTER AIDED CHEMICAL ENGINEERING, Elsevier B.V., pp. 2827–2832 (2024). https://doi.org/10.1016/B978-0-443-28824-1.50472-5.
9. Yang H., Kaczur J.J, Sajjad S.D., Masel R.I., Performance and long-term stability of $CO_2$ conversion to formic acid using a three-compartment electrolyzer design, *J $CO_2$ Util* 42: 101349 (2020). https://doi.org/10.1016/J.JCOU.2020.101349.
10. Abarca J.A., Díaz-Sainz G., Merino-Garcia I., Albo J., Irabien A., Statistical modeling of electrodes manufacture for $CO_2$ electroreduction to value-added products., in: COMPUTER AIDED CHEMICAL ENGINEERING, Elsevier B.V.: pp. 3061–3066 (2023). https://doi.org/10.1016/B978-0-443-15274-0.50488-1.
11. Díaz-Sainz G., Abarca J.A., Alvarez-Guerra M., Irabien A., Exploring the impact of partial pressure and typical compounds on the continuous electroconversion of $CO_2$ into formate, *J $CO_2$ Util* 81:102735 (2024). https://doi.org/10.1016/j.jcou.2024.102735

© 2025 by the authors. Licensed to PSEcommunity.org and PSE Press. This is an open access article under the creative commons CC-BY-SA licensing terms. Credit must be given to creator and adaptations must be shared under the same terms. See https://creativecommons.org/licenses/by-sa/4.0/



Systems & Control Transactions

**Research Article - Peer Reviewed Conference Proceeding**
ESCAPE 35 - European Symposium on Computer Aided Process Engineering
Ghent, Belgium. 6-9 July 2025
Jan F.M. Van Impe, Grégoire Léonard, Satyajeet S. Bhonsale,
Monika E. Polańska, Filip Logist (Eds.)

PSE PRESS

# Techno-economic Assessment of Sustainable Aviation Fuel Production via $H_2/CO_2$-Based Methanol Pathway

**Pierre Guilloteau[a], Hugo Silva[b], Anders Andreasen[bd], Niklas Groll[a], Anker Degn Jensen[c], Gürkan Sin[a*]**

[a] Technical University of Denmark (DTU), Process and Systems Engineering Center (PROSYS), Department of Chemical and Biochemical Engineering, Kgs Lyngby, Denmark
[b] Ramboll Energy, Energy Transition - Process Department, København S, Denmark
[C] Technical University of Denmark (DTU), Catalysis and High Temperature Engineering Center (CHEC), Department of Chemical and Biochemical Engineering, Kgs Lyngby, Denmark
[d] Presently at ORS Consulting, Borgergade 66 st th, 6700 Esbjerg, Denmark
* Corresponding Author: gsi@kt.dtu.dk

## ABSTRACT

To achieve long-term greenhouse gas neutrality in aviation, replacing fossil aviation fuels with Sustainable Aviation Fuels (SAF) from renewable sources is essential. A SAF production process from renewable hydrogen and carbon dioxide, was designed using Aveva Process Simulation, followed by comprehensive economical assessments. The designed process leads to an annual production of 37kt of SAF, with 97% of the molecules featuring a carbon chain length between 8 and 16. This output indicates a robust and targeted production capability. With an in-depth optimization of the methanol reactor, it was found that the profitability of the plant aligns with other SAF studies, demonstrating a Minimum Selling Price of Product of $2.46/kg after Heat Integration. In terms of economic profitability, the production of SAF using the methanol pathway appears to be an alternative to other SAF production pathways such as Fischer-Tropsch process but resides dependent on the evolution of $H_2$ production technologies, novel SAF production processes and environmental regulations. Despite this, the price remains higher than the current cost of fossil jet fuels, posing a competitive challenge.

**Keywords**: Alternative Fuels, Modelling and Simulations, Methanol, Technoeconomic Analysis

## INTRODUCTION

To limit global warming to 1.5°C, the Paris Agreement of 2015 established goals for reducing greenhouse gas emissions [1]. The transportation sector is a major contributor to emissions, and the aviation field is no exception, accounting for 2.5% of global emissions [2]. By 2025, SAF production will be predominant through the Hydrotreated Esters and Fatty Acids (HEFA) pathway, which will account for 99% of production (42.1 Mt). The HEFA process can reduce greenhouse gas emissions by up to 85% compared to fossil jet fuels, whereas Power-To-Liquid processes have the capability to achieve a 100% reduction [3]. One Power-To-Liquid pathway involves using renewable hydrogen and carbon dioxide to produce methanol, which can then be converted into SAF using the ExxonMobil process [4]. Although SAF production from $H_2$ and $CO_2$ is still under development, it is necessary to evaluate the economic potential of this process. This study explores the process design, optimization and economic viability of the production of SAF from $H_2$ and $CO_2$.

## MATERIAL AND METHODS

### Process Design

The production of SAF from $H_2$ and $CO_2$ consists of 4 main steps: methanol is first formed based on equation 1. Secondly it is turned into dimethyl ether and further to olefins through the Methanol-To-Olefins (MTO) process (equations 2 and 3). Olefins are then converted into longer olefins in the Mobil-Olefins-to-Gasoline-and-Distillate (MOGD) process (equation 4) and finally converted to paraffins through hydrogenation (equation 5).

$$CO_2 + 3\,H_2 \leftrightarrow CH_3OH + H_2O \quad (1)$$

$$2\,CH_3OH \leftrightarrow CH_3OCH_3 + H_2O \quad (2)$$

$$n\,CH_3OCH_3 \leftrightarrow 2\,(CH_2)_n + n\,H_2O \quad (3)$$

$$2\,(CH_2)_n \leftrightarrow C_{2n}H_{4n} \quad (4)$$

$$C_{2n}H_{4n} + H_2 \leftrightarrow C_{2n}H_{4n+2} \quad (5)$$

The process is modelled using the equation-based software Aveva Process Simulation 2024 (APS). The sizing of equipments is based on basic Chemical Engineering Principles and APS modelling assumptions. The process is designed with the following objectives: 37kt/year of kerosene with a purity of 91.3% of C8-C16 Hydrocarbons. The choice of quantity is based on the average value of kerosene from existing and future SAF production projects [5,6]. The purity is based on the percentage of non-desired products from the High Biofuel Blends in Aviation Final Report [7]. Additionally, Liquefied Petroleum Gas (LPG), gasoline and diesel are co-products of the process. Furthermore, Heat Integration (HI) was performed on the major hot and cold streams of the process with a heat duty higher than 200kJ/s.

## Sensitivity analysis

While the process of SAF production and its reactions are studied in the literature, the impact of key design parameters is often neglected, especially for the methanol formation reactor in a SAF production process. An in-depth sensitivity analysis was performed on the methanol reactor to optimize the conversion of reactants. Sensitivity analysis was performed on the temperature, pressure, and reactor design (diameter, length, number of tubes).

## Economical Assessment

The economical assessment was performed on the process for different scenarios. A Matlab script of a Discouted Cash Flow Rate (DCFR) model for Monte-Carlo simulations is used based on 7 input parameters: price of reactants ($H_2$ and $CO_2$), price of Kerosene Fixed Capital Cost (FCI), Working Capital (WC), Operational Cost (OPEX) and Income Tax Rate. The plant is located in Denmark with a lifetime of 20 years.

## Input parameters

### Fixed Capital Investment

The Fixed Capital Investment (FCI) includes the purchase of equipments and their installation. The price of a single piece of equipment is taken from APS 2024 and based on the Chemical Engineering Plant Cost Index (CEPCI) of 2022 (816.0) [8]. This library uses a factorial method considering the Lang factors for the cost of purchase and installation of equipments. The fixed capital cost is calculated using the following formula:

$$C_f = f_L * C_e \quad (6)$$

Where $f_L$ is the Lang factor and $C_e$ is the total delivery cost of all the major equipment items.

The Lang factor is already implemented in Aveva and set to $f_L$=*5.93* for the total capital investment which is the recommended value from Aveva for a fluids processing plant. The total capital cost is equal to the sum of the FCI and the working capital calculated directly from APS. This investment in cost is divided over the first two years.

### Operational Cost (OPEX)

The cost of operations includes the heating and cooling of the streams, the electricity furnished to the process and the cost of raw material and catalyst (assumed to be replaced every 2 years). The cooling of streams is assumed to be done with water or glycol while the heating is assumed to be from steam (low pressure at 160°C, medium pressure at 184°C and high pressure at 254° C) [9]. These costs include the operating costs to generate the utility and the price of the circulated cooling or heating system. Moreover, based on the Danish grid, the cost of electricity is taken as 0.095$/kWh [10]. Operational cost also includes the price of raw material. Finally, the economic assessment needs to take the price of products into account. The perturbation and distribution of reactant and kerosene prices are based on a list of current literature values. The lower, average and upper values are presented in Table 1.

**Table 1:** Lower, average and upper values used for the uncertainty analysis [11-13]

| Parameter | Lower value | Average value | Upper value |
|---|---|---|---|
| $H_2$ price ($/kg) | 1.27 | 3.00 | 10.13 |
| $CO_2$ price ($/kg) | 0.06 | 0.10 | 1.27 |
| Kerosene price ($/kg) | 0.86 | 3.25 | 6.06 |

## Output parameters

Five outputs parameters are studied with their uncertainty:

- The Return of Investment (ROI) is taken as the average of the annual net profit calculation divided by the total investment capital.
- The Payback Period (PBP) is obtained by dividing the FCI by the average of annual operating cash flow.
- The Net Present Value (NPV) is equal to the sum of present worth of annual cash flow of each year of the plant life.
- The Discounted Cash Flow Rate (DCFR) is the iterated discount rate corresponding to a NPV

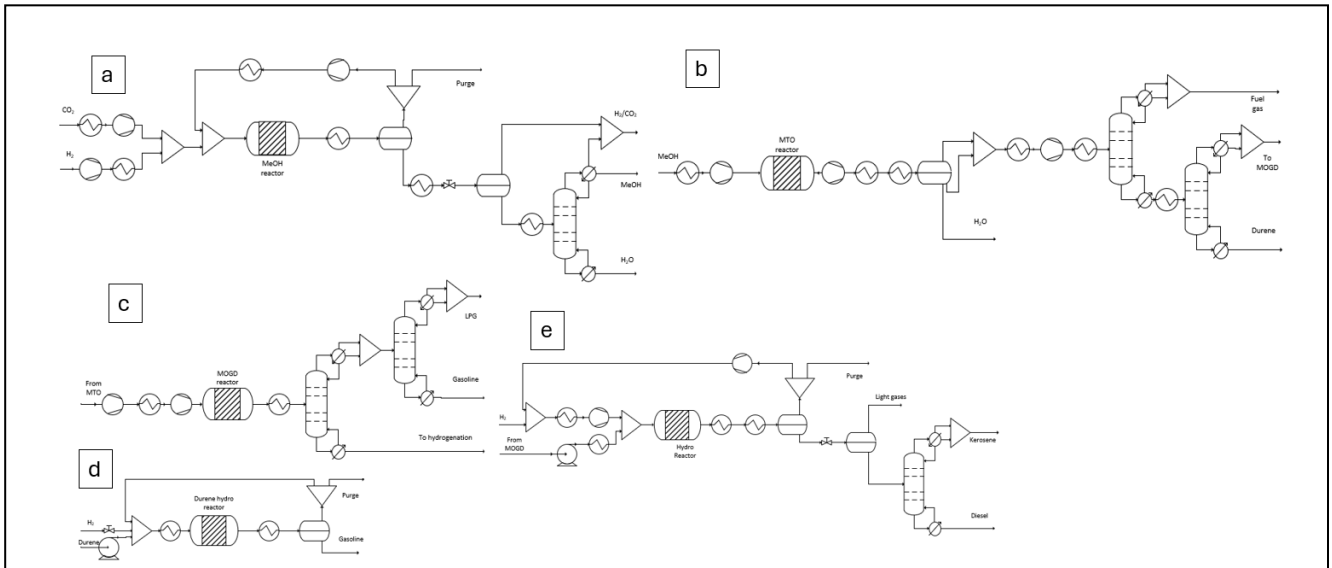



**Figure 1:** Complete process of the production of kerosene from $H_2$ and $CO_2$: Formation of methanol (a), Methanol-To-Olefins (b), Mobil-Olefins-To-Gasoline-and-Distillate (c), Durene Hydrogenation (d), Olefins Hydrogenation (e)

equal to zero.

- The Minimum Selling Price of Product (MSEP) is the price of SAF corresponding to an NPV equal to zero.

The Monte-Carlo simulations are done with 500 iterations and returns the average and standard deviation of each value. The perturbations and distributions for the Monte-Carlo Analysis are presented in table 2. For reactant and product prices, a lognormal distribution has been chosen to fit with the range of prices found in literature [11-13]. Additionally a Latin Hypercube Sampling function is applied to the input parameters to represent their distribution within the minimum and maximum values.

**Table 2:** Perturbation and distribution of inputs parameters for uncertainty and sensitivity analysis of the economical assessment

| Parameter | Perturbation (%) | | Distribution |
|---|---|---|---|
| FCI | -30 | +30 | Normal |
| WC | -20 | +50 | Uniform |
| $H_2$ price | -60 | +230 | Lognormal |
| $CO_2$ price | -40 | +1170 | Lognormal |
| Kerosene price | -70 | +90 | Lognormal |
| OPEX | -30 | +30 | Normal |

# RESULTS AND DISCUSSION

## Final process

The final process is presented in figure 1. In a boiling-water reactor, $H_2$ and $CO_2$ are first converted into methanol and water which are then separated in a distillation column. A kinetic model based on Froment et al. work is implemented [14] over a $Cu/ZnO/Al_2O_3$ catalyst. The second part from methanol to SAF is based on the conversion models from Ruokonen's work [11]. Four reactors are implemented using the zeolite catalyst HZSM-5: the conversion of methanol to olefins (b), the formation of higher olefins (c), the hydrogenation of durene to form a part of the gasoline (d) and the hydrogenation of olefins to form kerosene and diesel (e). Additionally, the ratio kerosene/reactants is based on Ruokonen's work [11] for a production of 37kt of kerosene for 66kt of $H_2$.

## Sensitivity Analysis

### Comparison with experiment

A Sensitivity Analysis was performed on the methanol formation reactor. First the kinetic model needs to be validated with experimental data. The $CO_2$ hydrogenation (equation 8) and Reverse Water Gas Shift (equation 9) are considered to model the methanol formation:

$$CO_2 + 3\,H_2 \leftrightarrow CH_3OH + H_2O \quad (8)$$

$$CO_2 + H_2 \leftrightarrow CO + H_2O \quad (9)$$

As the kinetic model from Froment et al. fits with the experimental data, the model implemented in Aveva Process Simulation is compared with the model implemented by Froment et al. [14]. This comparison is performed for a laboratory scale plug flow reactor with a feed composed of 4 mol% of CO, 82 mol% of $H_2$, 3 mol% of $CO_2$ and 11 mol% inert. The results are presented in Table 3.

The implementation on Aveva fits with the referenced model and therefore with the experimental data. The applied model can be the subject of further studies.

**Table 3:** Comparison of the component fraction at the outlet of the methanol reactor for the model implemented in APS and the model implemented by Froment et al. [14]

| Component | APS model | Froment et al. model |
|---|---|---|
| CO | 0.030 | 0.030 |
| $CO_2$ | 0.021 | 0.021 |
| $H_2$ | 0.801 | 0.801 |
| $CH_3OH$ | 0.023 | 0.023 |
| $H_2O$ | 0.011 | 0.011 |

## Key-design parameters

The key-design parameters of the methanol formation reactor are studied to optimize the carbon conversion to methanol. The initial design is based on the Luyben et al. model of the methanol formation [15]. The methanol formation reaction being exothermic, the reactor is modelled as tubular with an external utility to cool down the fluid. The diameter of the tubes is set as D=0.03675 m, the smallest diameter available, to maximize the heat exchange, with a heat transfer coefficient of 244 $kcalh^{-1}m^{-2}K^{-1}$ [15]. The volume is calculated from the Gas Hourly Space Velocity used in the literature GHSV=3.348 $kg/kg_{cat}/h$ [15]. Hence, for a number of tubes $N_t$=4000, the length of the reactor is L=4 m with a feed of 66kt/year of $H_2$ and 480 kt/year of $CO_2$. Moreover, the pressure drop inside the reactor is assumed to be equal to 1 bar.

The evolution of carbon conversion with the pressure inside the reactor is plotted figure 2. The carbon conversion is defined as the following:

$$conv = \frac{n_{in}(CO_2) - n_{out}(CO_2)}{n_{in}(CO_2)} \quad (10)$$

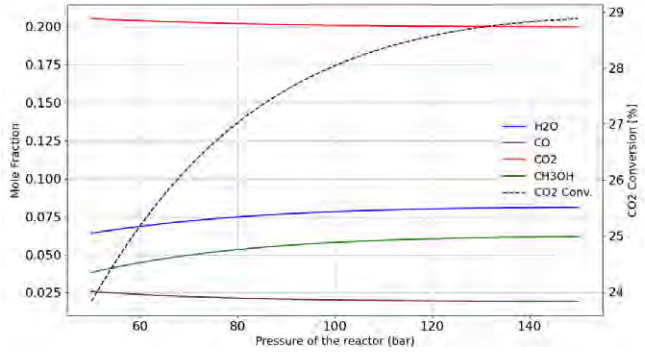



**Figure 2.** Evolution of the gas composition and the carbon conversion at the outlet of the methanol reactor with the inlet pressure at fixed temperature ($T_{feed}$=423.15K)

The carbon conversion increases with the pressure of the reactor. However, the conversion stabilizes after 150 bar. Hence, P=110bar is chosen to optimize the conversion while lowering the operational cost.

Additionally, the evolution of the carbon conversion is studied figure 3 with the variation of temperature. The carbon conversion increases with the temperature of the reactor until 540K before decreasing due to the main reaction of $CO_2$ hydrogenation being exothermic and the competitive reaction (Reverse Water Gas Shift) being endothermic.

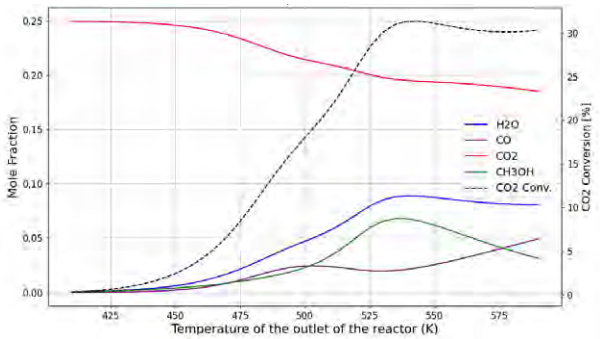



**Figure 3.** Evolution of the gas composition and the carbon conversion at the outlet of the methanol reactor with the outlet temperature (P=110bar, $T_{feed}$=423.15K)

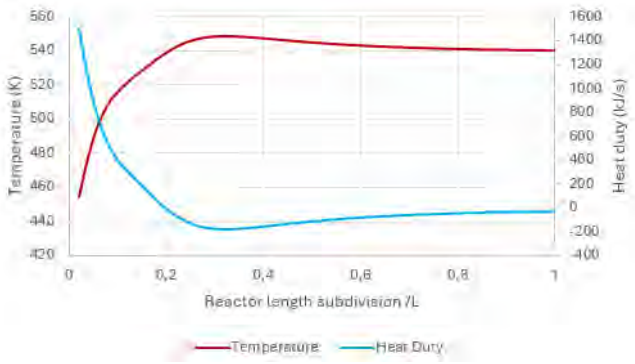



**Figure 4.** Evolution of the temperature and heat transfer duty inside the methanol formation reactor ($Duty_{tot}$=1465 kJ/s)

**Table 4:** Key-design parameters of the methanol formation reactor

| Parameter | Value |
|---|---|
| Pressure (bara) | 110 |
| $T_{out}$(K) | 540 |
| Number of tubes | 4000 |
| Diameter of the tubes (m) | 0.03675 |
| Length of the tubes (m) | 4 |
| Volume ($m^3$) | 17 |
| Catalyst | Cu/ZnO/Al2O3 |
| Catalyst mass (kg) | 15 054 |
| Catalyst volumic mass ($kg/m^3$) | 1 775 |

Consequently, the utility of the reactor is modelled to obtain an outlet temperature of the reactor equal to

540K. The evolution of temperature and heat transfer inside the final model of reactor is presented figure 3 while the final reactor design parameters are presented in table 4. All the parameters listed in Table 4 influence the final conversion, and their optimal values were determined through univariate analysis. However, an additional assessment considering their interdependencies could improve the optimization process.

### Heat Integration

The cumulative heats are presented in figure 5. As no pinch point exists, the heat exchangers are combined freely if heat is transferred from warm streams to cold streams (with threshold set to $\Delta T_{min}$ = 10K). The resulting optimization of cost after Heat Integration is presented in table 5.

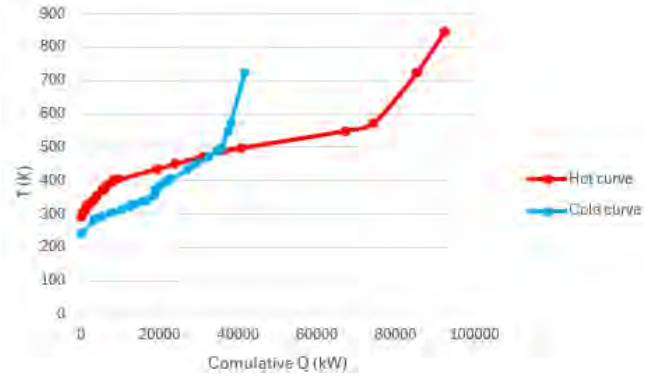



**Figure 5.** Cumulative heat of the hot and cold streams

**Table 5:** Reduction of duties and cost after HI

| | Duty reduction (kW) | Cost reduction ($million/year) |
|---|---|---|
| Cooling | 39 701 | 0.43 |
| Heating | 39 701 | 2.33 |
| **Total** | **79 401** | 2.76 |

## Economic Analysis

The economical analysis is performed for the overall process from the purchase of $H_2$ and $CO_2$ to the retailing of kerosene and its co-products. The mean value of the input parameters for the Monte-Carlo simulation are presented in table 5. The resulting distribution is plotted in figure 6 and 7 and matches with the expected distribution from table 2 for all 7 inputs parameters.

Figure 8 and Table 6 show the results of the economic assessment. The value of MSEP ($2.46/kg) fits with previously published values [11-13] but remain however higher than $0.68/kg the current price of fossil-based kerosene in Denmark [16]. Additionally, the purchase of hydrogen accounts for 78% of the total OPEX with an extremely wide range of price values (see Table 1). This results in a high standard deviation of all the output parameters.

**Table 6:** Mean Value of the input parameters for the economic assessment

| | $million | $million/year |
|---|---|---|
| FCI | 144.9 | |
| Working Capital | 22.6 | |
| **Total CAPEX** | 167.5 | |
| Utility | | 15.3 |
| Raw materials | | 249.1 |
| **Total OPEX** | | **264.4** |
| **Sales** | | **304.2** |

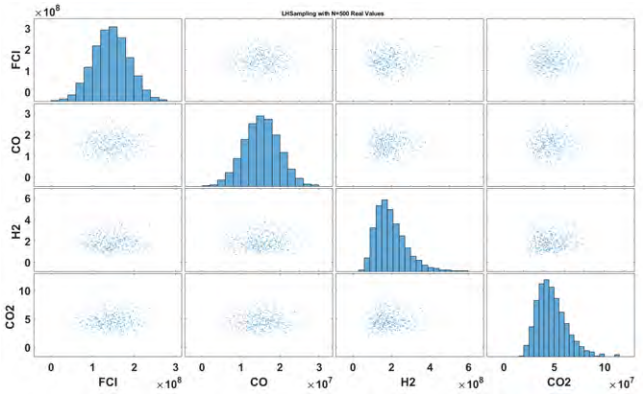



**Figure 6.** Real value distribution of the first 5 input parameters for the Monte-Carlo simulation

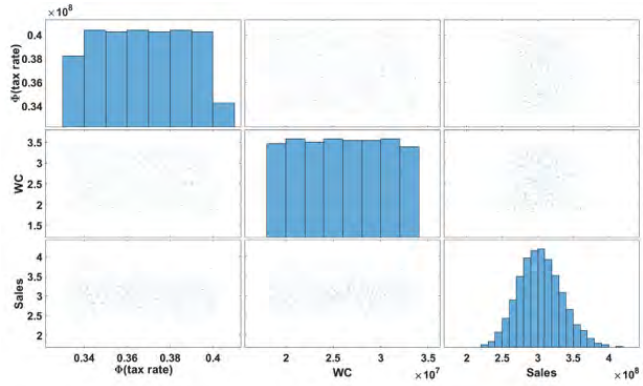



**Figure 7.** Real value distribution of the last 5 input parameters for the Monte-Carlo simulation

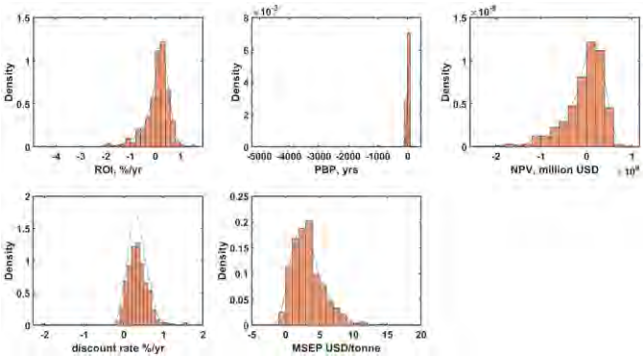



**Figure 8.** Density value of the ouput parameters of the Monte-Carlo simulation (N=500)

**Table 7:** Avearge and Standard Deviation of the ouput parameters of the Monte-Carlo simulation (N=500)

| | Average | Standard deviation |
|---|---|---|
| ROI (%/year) | 0.09 | 0.47 |
| PBP (years) | 5.87 | 50.52 |
| NPV ($million) | -50.5 | 448.2 |
| MSEP ($/kg) | 2.46 | 2.30 |

## CONCLUSION

The process design of SAF from $H_2$ and $CO_2$ appears to be a promising process for the development of alternative fuels. As the quantity of raw materials mainly impacts the final price of SAF, the conversion into methanol must be the subject of an in-depth study. A boiling-water reactor with V=17m³, P=110bara and $T_{out}$=540K is chosen for the final design.

While the Minimum Selling Price of the produced kerosene ($2.46/kg) falls into the range of previous techno-economic assessments, it remains non-competitive against fossil-based aviation fuels. Additionally, a significant sensitivity to the price of hydrogen leads to considerable uncertainty on the result. Hence, the economic viability of SAF is highly dependent on innovations in performance, cost-breakdown electrolyzer technologies along with governmental regulation on fossil-based kerosene usage. Finally, novel concepts for Sustainable Aviation Fuel (SAF) synthesis could potentially reduce aviation fuel production costs, opening pathways for more sustainable air transportation in the future.

## ACKNOWLEDGEMENTS

The authors gratefully acknowledge the financial support provided by Ørsted for this research.

## REFERENCES

1. The Paris Agreement (2015) The Paris Agreement | UNFCCC
2. D.S. Lee et al. The contribution of global aviation to anthropogenic climate forcing for 2000 to 2018. Atmospheric Environment 244 (2021) http://dx.doi.org/10.1016/j.atmosenv.2020.117834
3. Energistyrelsen. Technology data. Renewable fuels (2017).
4. A. A. Avidan. Gasoline and Distillate Fuels From Methanol. Mobil Research and Development Corporation (1988) https://doi.org/10.1016/S0167-2991(09)60524-3
5. Green kerosene to be produced in Hamburg from 2026 (2022) Green kerosene to be produced in Hamburg from 2026 | News | Hamburg Business
6. Jangada project (2024) https://www.hy2gen.com/jangada
7. Alexander Zschocke. High Biofuel Blends in Aviation (HBBA). ENER/C2/2012/ 4201 Deutsche Lufthansa (2012) https://books.google.dk/books/about/High_Biofuel_Blends_in_Aviation_HBBA.html?id=HQf6swEACAAJ&redir_esc=y
8. CEPCI values. (2024) https://www.training.itservices.manchester.ac.uk/public/gced/CEPCI.html?reactors/CEPCI/index.html
9. Shaeiwitz Turton. Analysis, Synthesis and Design of Chemical Processes (2016). Analysis Synthesis and Design of Chemical Processes 5th Edition | Richard Turton | West Virginia University
10. Electricity prices in Denmark (2024). https://www.dst.dk/en/Statistik/emner/miljoe-og-energi/energiforbrug-og-energipriser/energipriser
11. Jenna Ruokonen et al. Modelling and Cost Estimation for Conversion of Green Methanol to Renewable Liquid Transport Fuels via Olefin Oligomerisation. Processes 9 (2021) https://doi.org/10.3390/pr9061046
12. Maria Fernanda Rojas-Michaga et al. Sustainable aviation fuel (SAF) production through power-to-liquid (PtL): A combined technoeconomic and life cycle assessment (2023) https://doi.org/10.1016/j.enconman.2023.117427
13. Patrick Schmidt et al. Power-to-Liquids as Renewable Fuel Option for Aviation: A Review. Chemie Ing Technik 90:127-140 (2018) https://doi.org/10.1002/cite.201700129
14. K.M.Vanden Bussche, G.F. Froment. A SteadyState Kinetic Model for Methanol Synthesis and the Water Gas Shift Reaction on a Commercial Cu/ZnO/Al2O3Catalyst. Journal of Catalysis 161 (1996). https://doi.org/10.1006/jcat.1996.0156
15. William L. Luyben. Design and Control of a Methanol Reactor/Column Process. Ind. Eng. Chem. Res 49 (June). https://doi.org/10.1021/ie100323d
16. Jet A1 price Denmark (2024). https://jet-a1-fuel.com/price/denmark

© 2025 by the authors. Licensed to PSEcommunity.org and PSE Press. This is an open access article under the creative commons CC-BY-SA licensing terms. Credit must be given to creator and adaptations must be shared under the same terms. See https://creativecommons.org/licenses/by-sa/4.0/



Systems & Control Transactions

**Research Article - Peer Reviewed Conference Proceeding**
ESCAPE 35 - European Symposium on Computer Aided Process Engineering
Ghent, Belgium. 6-9 July 2025
Jan F.M. Van Impe, Grégoire Léonard, Satyajeet S. Bhonsale,
Monika E. Polańska, Filip Logist (Eds.)

PSE PRESS

# Assessing the Environmental Impact of Global Hydrogen Supply through the Lens of Planetary Boundaries

**Jesmyl-Elisa Cordova-Cordova[a], Carlos Pozo[a]***

[a] Departament d'Enginyeria Química, Universitat Rovira i Virgili, Av. Països Catalans 26, 43007 Tarragona, Spain
* Corresponding Author: carlos.pozo@urv.cat

## ABSTRACT

Hydrogen is increasingly recognized as a crucial energy carrier for a low-carbon future. However, most studies on clean hydrogen production devote limited attention to the entire supply chain. This study evaluates the sustainability of 800 combinations of hydrogen production and transportation methods, comparing their environmental impacts against the geophysical limits defined by the Planetary Boundaries framework. Findings reveal that no supply chain alone can make the current economy sustainable, yet powering water electrolysis with bioenergy and carbon capture and storage can meet the $CO_2$-based planetary boundaries. The analysis also underscores the need for decarbonization efforts in the hydrogen transportation sector, as certain options could offset the benefits of clean hydrogen production.

**Keywords**: Life Cycle Analysis, Planetary Boundaries, Absolute environmental sustainability, Hydrogen

## INTRODUCTION

Most of current hydrogen production is centralized, with large-scale hydrogen plants, often located near natural gas reserves or industrial hubs, dominating global production. However, as global decarbonisation efforts accelerate and hydrogen is increasingly recognised as a crucial energy carrier for the transition to a low-carbon future, decoupling of production and demand become more likely. Regions with abundant renewable energy resources are positioned to produce green hydrogen at lower costs, while other industrialized regions have high hydrogen demand but limited local production capacity.

This potential paradigm shift is not yet reflected in the literature, where most research efforts still focus on hydrogen production alone. Few studies have examined the complete hydrogen supply chain, integrating both production and transportation. This leaves unanswered important questions about the real impact of large-scale hydrogen production, which can hamper a rapid transition towards a global hydrogen economy.

In addition, recent life cycle assessment (LCA) studies for hydrogen production and end uses are mostly limited to benchmarking alternatives. While these studies provide valuable insight regarding the best performing alternatives, they do not address the fundamental question of whether said options are sustainable in absolute terms.

To address this gap, we investigate the sustainability of different technologies for hydrogen production and transportation in a global context, comparing the impacts produced by multiple supply chain alternatives against the geophysical limits provided by the Planetary boundaries (PB) framework [1]. PBs are safe environmental limits within which humanity can operate to ensure the stability and resilience of Earth's systems. Each boundary is associated with quantitative limits on specific control variables that help monitor its state. Crossing these boundaries increases the risk of destabilizing critical processes that regulate the planet, potentially leading to irreversible environmental changes. Hence, comparing impacts of hydrogen supply chains against PBs is crucial to properly assess the potential consequences of adopting a hydrogen economy for the planet.

## METHODOLOGY

### Hydrogen Supply Chain Pathways

The present study evaluates the environmental performance of various hydrogen supply chains (i.e., production and transportation) options on a global scale. Specifically, we base our analysis on the 2021 hydrogen demand data provided by the International Energy

Agency (IEA) [2], which accounts for a total of 94 Mt. This demand is distributed across six regions: Europe (EU), China (CN), India (IN), the Middle East (ME), the United States (USA), and the Rest of the World (RoW).

We analyse 32 hydrogen production methods (see Figure 1a), including steam reforming using biogas or natural gas (Business-As-Usual (BAU)) as feedstock, as well as water electrolysis (WE) powered by various energy sources, such as bioenergy with carbon capture and storage (BECCS) or wind energy. We also explore the potential of producing hydrogen from waste materials, such as plastic waste, aluminium scrap, rice husks, and residues from other processes, using methods like gasification, aluminium combustion, or dark fermentation.

In addition, we model hydrogen transportation with the aim of understanding how the introduction of this activity would affect the Earth System in terms of PBs. This requires tracking (i) hydrogen state, and (ii) the transportation mean used of each alternative.

For the former, three options are considered: compressed hydrogen gas, liquid hydrogen, and hydrogen chemically bonded to another compound to form a stable liquid, the so-called Liquid Organic Hydrogen Carrier (LOHC). LOHCs are molecules that can absorb and release hydrogen through hydrogenation and dehydrogenation reactions, behaving as a storage media for hydrogen transportation. Hydrogen transportation as a LOHC can be addressed in two different ways. On the one hand, a linear transportation of the LOHC, which, upon dehydrogenation, results in the transportation of two compounds, hydrogen and the precursor of the corresponding LOCH, using the same transport. Alternatively, the precursor could be recirculated for reuse, reducing this way its overall consumption. This second option is considered for two compounds: dibenzyl toluene (DBT) and toluene.

For the transportation mean, hydrogen can be transported in any of the previous state-form alternatives. This can be done *via* pipeline, truck, and shipping. However, not all hydrogen state and transportation method combinations are viable. For instance, transporting liquid hydrogen *via* pipeline is highly energy-intensive due to the extreme cooling required to maintain its liquid state. Additionally, pipelines would require expensive insulation and frequent maintenance to prevent ice formation around pipes, valves, and vents. Therefore, this option is excluded. Similarly, compressed hydrogen *via* shipping is less feasible than liquid hydrogen, as the latter minimizes boil-off losses and requires less volume and weight. As a result, the three transportation means are available for all the LOHCs (i.e., 3·(5+2) = 21), but only two alternatives are considered for the other hydrogen-state forms (2·2 = 4).This results in a total of 25 transportation options, which, combined with the 32 production methods, yield a total of 800 alternative hydrogen supply chains. For simplicity, this study assumes that hydrogen production and transportation, over 500 km, occur within the same region where demand arises. However, a sensitivity analysis on transport distance is also performed to ascertain the potential influence of this parameter in the assessment.

## LCA and Planetary Boundaries

Next, the resulting 800 alternatives are assessed using the Planetary Boundaries-Life Cycle Impact Assessment (PB-LCIA) framework, an absolute environmental sustainability assessment (AESA) method, bridging conventional LCA principles with the concept of PBs. This requires following the four interconnected phases of the general LCA methodology.

In the first phase, the scope and goal of the study are defined. In this case, the goal is to quantify the absolute environmental sustainability level of different hydrogen supply chain alternatives, adopting an attributional approach with a cradle-to-gate perspective, i.e., considering processes from raw material extraction to hydrogen production and transportation. The functional unit is the annual hydrogen demand in 2021 for each region provided by the IEA, measured in million tonnes per year.

In the second phase, primary inputs and outputs — energy, raw materials, byproducts, and emissions— flowing in and out of the system (i.e., crossing its defined boundaries) are quantified. To this end, mass and energy balance information is gathered from previous studies. Then, this information is combined with the corresponding background activity data from ecoinvent v3.8 to calculate the so-called life cycle inventories (LCIs). This procedure was automated using the Activity Browser interface for Brighway2 open-source LCA software. In all cases, the “Allocation at the point of substitution” (APOS) system model was used.

Since hydrogen production and transportation are assumed to take place within the same region, the study accounts for location-specific environmental impacts. However, the regional classification in the ecoinvent v3.8 database does not align directly with the IEA regionalization, from which hydrogen demand data are sourced. To address this, distinct ecoinvent lumped regions (e.g., Rest of Europe (RER)) are used to model background activity impacts. When specific data for an activity is unavailable at the lumped-region level, data from a representative country within that region (e.g., Germany (DE)) are used instead. If no country-specific data are available, "Rest of the World" (RoW) data are used.

The third phase of the LCA involves assessing the damage produced by the LCIs in different environmental categories. In this case, ten control variables referring to eight Earth-System processes related to the PBs are considered. The PB-LCIA framework is used to express LCIs as impacts caused on the corresponding control

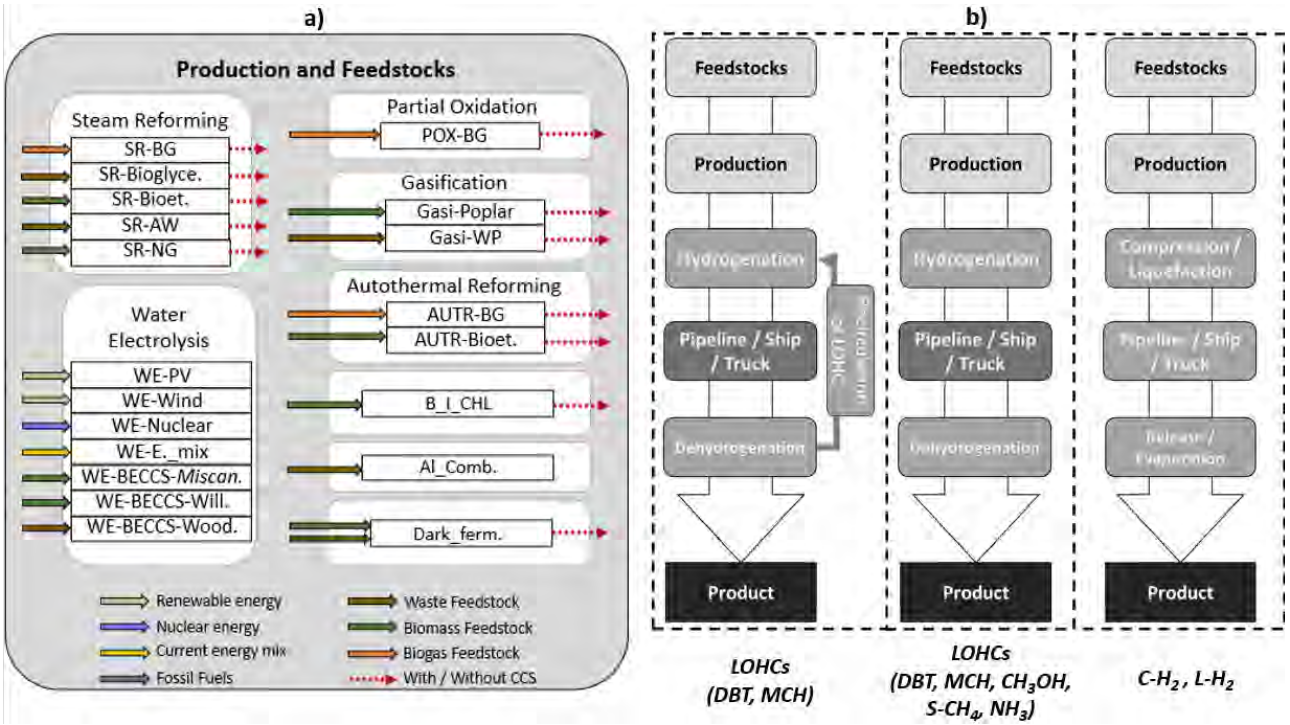



**Figure 1:** Panel (a) shows all the production alternatives studied and their main feedstocks, differentiated by colours. Panel (b) illustrates the three concepts considered for hydrogen transportation (from left to right): transportation as LOHC with precursor recirculation, transportation as LOHC with precursor delivery at destination, and transportation as hydrogen. CCS: carbon capture and storage; SR-BG: steam reforming from biogas; SR-bioglyce.: steam reforming from bioglycerol; SR-Bioet.: steam reforming from bioethanol; SR-AW: steam reforming from alcohol waste; SR-NG: steam reforming from natural gas; POX-BG: partial oxidation from biogas; Gasi-Poplar: poplar gasification; Gasi-WP: waste polymer gasification; AUTR-BG: autothermal reforming from biogas; AUTR-bioet.: autothermal reforming from bioethanol; B_I_CHL: biomass iron-based chemical looping; Al_Comb.: aluminum combustion; Dark_ferm.: dark fermentation; WE: water electrolysis; PV: photovoltaic; Wind: wind turbine onshore; E._mix: current energy mix; BECCS: bioenergy with carbon capture and storage ; Miscan.: Miscanthus; Will: willow; Wood: woodchips; LOHCs: liquid organic hydrogen carriers; DBT: dibenzyl toluene; MCH: methylcyclohexane; $CH_3OH$: methanol; S-$CH_4$: synthetic methane; $NH_3$: ammonia; C-$H_2$: compress hydrogen; L-$H_2$: liquid hydrogen.

variables by means of appropriate characterisation factors (CF). This can be expressed in mathematical terms as follows. The environmental impact caused by alternative $s$ on control variable $b$ ($EI_{b,s}$) is calculated with Eq. (1):

$$EI_{b,s} = \sum_{f} LCI_{s,f} \cdot CF_{b,f} \cdot FU \quad \forall\, b, s \tag{1}$$

where $LCI_{s,f}$ represents the quantity of elementary flow $f$ associated with the production and/or supply of one kilogram of hydrogen in alternative $s$, $CF_{b,f}$ is the CF translating the impact of one unit of elementary flow $f$ into control variable $b$, and $FU$ denotes the functional unit in consistent units (i.e., kilograms of hydrogen per year). CFs developed by Ryberg et al. [3] are employed for all the control variables studied expect for BII, for which the CFs by Galán-Martin et al. [4] are used.

In the fourth phase, results are interpreted, and recommendations are made. This is where the PBs framework demonstrates its full usefulness, as it provides quantitative limits to ascertain whether the activity under analysis can be deemed sustainable or not. To this end, results are compared against absolute limits derived from the PB framework, which defines the level to which principal Earth-system processes can be disturbed before triggering irreversible damage. We note that some Earth-system processes have clear thresholds beyond which critical changes would happen, while others do not. However, even when no precise tipping point exists, increasing stress can still lead to cumulative and potentially irreversible damage, triggering cascading effects on other systems. To address this, an uncertainty zone is defined around each control variable boundary, recognizing that the exact point of irreversible change is not always clear.

Additionally, the planet itself naturally contributes towards each control variables; this is called the natural background level (NBL). Hence, the available 'environmental budget' for human activities, the so-called safe operating space (SOS), is obtained by subtracting the

NBL from the corresponding threshold of the PB: here, the limit between the safe and the uncertainty zone.

On the other hand, PBs are defined at a global scale, but this study assesses only a single sector. To overcome this mismatch in scope, previous studies have employed downscaling methods, although this is a controversial approach that can yield varying conclusions depending on the specific downscaling methodology used. To avoid this, we simulate the global anthropogenic impact of the whole economy ($IMP^{GLO}$) that would result from replacing the BAU scenario for the hydrogen sector ($IMPT^{BAU}$) by each of the 800 alternatives for hydrogen production and transportation ($IMPT^{ALT}$).

$$IMP_{b,s}^{GLO} = IMP_{b}^{CUR} - IMP_{b}^{BAU} + IMP_{b,s}^{ALT} \quad \forall\, b, s \tag{2}$$

Here, $IMP_{b,s}^{GLO}$ provides the global impact of the whole economy on control variable $b$ after substitution of alternative $s$; $IMP_{b}^{CUR}$ corresponds to the current impact of the whole economy on control variable $b$; $IMP_{b}^{BAU}$ is the impact of the BAU scenario for hydrogen supply on control variable $b$; and $IMP_{b,s}^{ALT}$ is the impact of hydrogen supply alternative $s$ on control variable $b$.

Finally, in order to ascertain whether a scenario is environmentally sustainable in absolute terms, the PB footprint (PBF) [6] is calculated by comparing the (predicted) global anthropogenic environmental impact $IMP_{b,s}^{GLO}$ with the SOS, as shown in Eqs. (3-4).

$$LT_{b,s}^{GLO} = \begin{cases} 0 \quad if \quad \dfrac{IMP_{b,s}^{GLO}}{SOS_b} < 1 \\ \dfrac{IMP_{b,s}^{GLO}}{SOS_b} \quad otherwise \end{cases} \quad \forall\, b, s \tag{3}$$

$$PBF_s = \frac{\sum_b LT_{b,s}^{GLO}}{|B|} \tag{4}$$

Here, the global level of transgression ($LT_{b,s}^{GLO}$) is given by the quotient between the global anthropogenic impact $IMP_{b,s}^{GLO}$ (for control variable $b$ under alternative $s$) and the $SOS$ for each control variable $b$ ($SOS_b$). PBs not transgressed after sector substitution, are assigned a $LT_{b,s}^{GLO}$ value of 0 is assigned, thus prioritising solutions that can meet multiple boundaries concurrently. Finally, the summation of the transgression level for each control variable $b$ (under alternative $s$) is divided by $|B|$, which corresponds to the number of control variables considered (ten in this study). This is equivalent to assuming equal weights regardless of the transgression level, i.e., all control variables are deemed equally important.

## RESULTS AND DISCUSSION

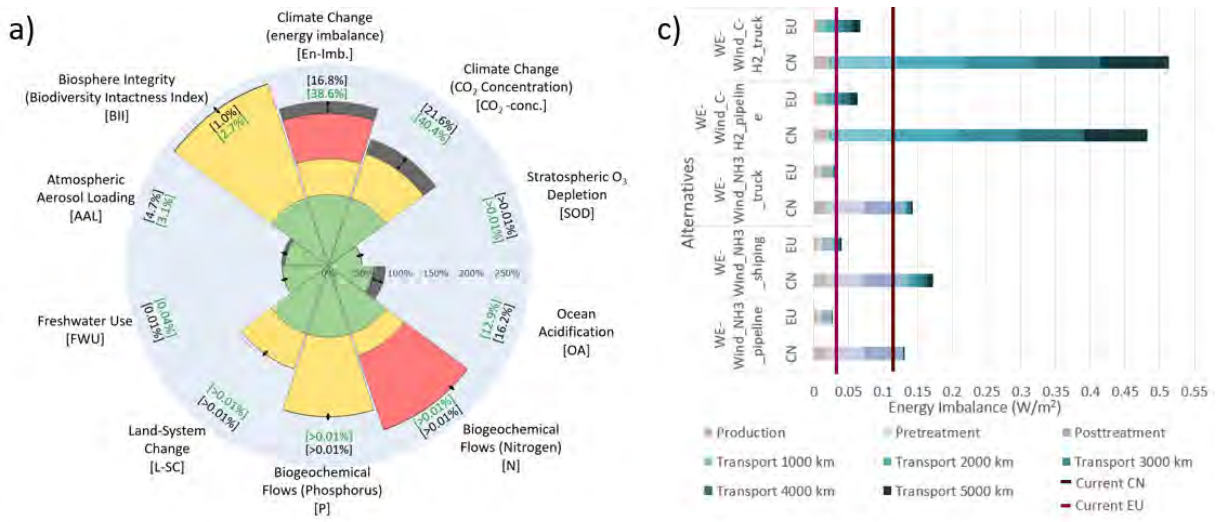
To provide some context, we start by analysing the current impacts of the global economy onto the PBs (Figure 2a). This is a relevant analysis since, arguably, already-transgressed boundaries should be prioritized when designing alternative systems and technologies. As can be seen in the figure, only four PBs are currently met: SOD, OA, FWU and AAL (see Figure 2 caption for acronyms). From the remaining control variables, four lie in the uncertainty zone (i.e., $CO_2$-conc., P flow, LSC and BII), while the other two are severely transgressed, reaching the high-risk zone.

Currently, hydrogen is responsible for more than 15% of the impacts incurred at global scale on $CO_2$-base control variables ( En-Imb., $CO_2$-conc., and OA, see black labels in the figure), while showing minor contributions (i.e., below 5%) to impacts on AAL and BII, and smaller than 0.01% in the remaining control variables. However, when hydrogen impacts are compared against the SOS (green labels), it can be seen that global hydrogen supply represents 39%, 40%, and 13% of the maximum impacts allowed at the global level in En-Imb., $CO_2$-conc., and OA, respectively. This reveals a concerning situation since it is hard to envision that the remaining economic sectors can successfully operate within the remaining SOS for these control variables. The situation is even more worrisome when considering that some of the PBs associated with these control variables have already been crossed at the global level (see Figure 2a). On the other hand, small contributions are observed towards the remaining control variables, all of them more strongly linked to other anthropogenic activities, mainly agriculture [5]. This situation might worsen in the coming years due to the expected increase in hydrogen demand.

We next turn our attention to the alternatives studied (Figure 2b), finding that only 205 out of the 800 hydrogen supply chains considered exhibit a lower PBF than the BAU scenario. As an example, the BAU scenario, predominantly based on steam reforming from natural gas, remains a better option than WE given that the current electricity mix is still largely based on fossil fuels.

There is no hydrogen supply chain that alone can make the current economy sustainable: additional efforts will be required from other sectors. The alternative with the lowest PBF (0.90) is WE-BECCS with Miscanthus, which meets the SOS limits for the $CO_2$-base control variables. However, growing biomass feedstock exerts increasing pressure on the Biodiversity Intactness Index (BII) due to land use impacts, though this boundary remains within the uncertainty zone (from 268% to 288% of the SOS). Additionally, biomass combustion contributes to NMVOC emissions, increasing pressure on the Atmospheric Aerosol Loading (AAL) boundary, but without exceeding the uncertainty zone (from 66% to 86%).

AI_Comb. emerges as a slightly better option production than WE with PV and wind turbines, primarily due to avoided impacts associated with aluminium scrap management. However, this effect shows asymmetric contributions across regions (results not shown owing to space limitation). Negative impacts (i.e., lower than zero)




b)

| Production | Transport | En-Imb | CO2-conc. | SOD | OA | N | P | L-SC | FWU | AAL | BII | PBF | Rank |
|---|---|---|---|---|---|---|---|---|---|---|---|---|---|
| WE-BECCS_Miscan. | C-H2_pipeline | 48% | -6% | 47% | 18% | 245% | 211% | 152% | 65% | 86% | 288% | **0.90** | 1 |
| WE-BECCS_Miscan. | L-H2_truck | 50% | -5% | 47% | 19% | 245% | 211% | 152% | 65% | 89% | 288% | **0.90** | 3 |
| WE-BECCS_Miscan. | NH3_pipeline | 198% | 153% | 47% | 69% | 242% | 211% | 152% | 65% | 79% | 271% | **1.23** | 42 |
| Al_Comb. | C-H2_pipeline | 205% | 161% | 47% | 71% | 242% | 211% | 152% | 65% | 67% | 266% | **1.24** | 51 |
| WE-E._mix | MCH_pipeline | 241% | 199% | 47% | 84% | 242% | 211% | 152% | 65% | 78% | 269% | **1.31** | 409 |
| WE-Wind | C-H2_pipeline | 210% | 166% | 47% | 73% | 242% | 211% | 152% | 65% | 74% | 267% | **1.25** | 63 |
| WE-PV | C-H2_pipeline | 215% | 171% | 47% | 75% | 242% | 211% | 152% | 65% | 76% | 268% | **1.26** | 82 |
| BAU | | 230% | 187% | 47% | 80% | 242% | 211% | 152% | 65% | 66% | 268% | **1.29** | 206 |

**Figure 2:** a) Analysis of the current situation. Current impacts of the whole economy are depicted against boundaries on the different control variables, with different colours depending on whether they lay within the SOS (green), in the uncertainty zone (yellow), or in the high-risk zone (red). The contribution from the hydrogen supply chain is highlighted with dark grey sectors, with black labels providing their contribution to current impacts. Green labels in the same panel show the share of the SOS by the current hydrogen supply chain. b) Level of transgression achieved by the global economy when replacing the BAU hydrogen supply chain by selected scenarios. Each row in the heatmap corresponds to a different alternative scenario, as described by the label of the first (hydrogen production) and second (transportation alternative) columns. Underlined values in the heatmap indicate that the impact on the control variable of this alternative is lower than the BAU scenario. The two last columns provide (from left to right) the PBF and the ranking of the alternative (from the lowest to the highest PBF). c) Impacts on the energy imbalance control variable of supplying current hydrogen demand in China and Europe over different distances with selected alternatives. Stacked bars breakdown the impacts by production, pretreatment, transportation mean (considering different potential distances), and posttreatment alternatives.

on $CO_2$-based control variables are achieved in all regions except in India, where the reliance on fossil fuels for electricity generation offsets the benefits of aluminium recycling.

Regarding transportation (Figure 2b), C-$H_2$ via pipeline is the most favourable option as it eliminates the need for conversion (e.g., hydrogenation-dehydrogenation reactions for LOHCs) or conditioning (e.g., liquefaction for L-$H_2$). For example, certain LOHCs such as DBT would transgress planetary boundaries like OA, while others like $CO_2$-concentration could shift from the uncertainty zone to the high-risk zone (results not shown). The AAL control variable also increase for all cases using LOHCs, specially for DBT, MCH, and $CH_3OH$. This is primarily due to the energy-intensive nature of pretreatment processes such as compression, liquefaction, and hydrogenation.

In $CO_2$-based control variables, as well as in BII, S-$CH_4$ and $NH_3$ alternatives show the highest contributions from post-treatment, highlighting this stage as a key bottleneck in these transportation pathways. Notably, if S-$CH_4$ and $NH_3$ were directly used as fuels (i.e., avoiding $H_2$ regeneration) their contribution from transport would almost be on pair with those from C-$H_2$ or L-$H_2$. In addition, this would have the added benefit of avoiding the need to update the transport infrastructure, as required for C-$H_2$. This suggests that S-$CH_4$ and $NH_3$ could serve as competitive alternatives to hydrogen in energy applications, providing comparable performance while reducing transport and infrastructure needs. This is only a viable

option in energy applications and not in cases where hydrogen is used as a chemical feedstock.

Finally, the largest contribution in the supply chain depends on the combination of production and transportation alternatives. For instance, in purple hydrogen (WE-nuclear), electrolysis contributions range from 0.5% to 37.5%, depending on the transportation method. Conversely, in alternatives such as WE-BECCS, the negative impacts from production are substantial enough to offset all positive transportation impacts. On the other hand, transport distance and regional factors are also crucial parameters. As an example (Figure 2c), we find that WE-wind combined with C-$H_2$ in China is a better alternative than BAU only for distances below 1,000 km, due to the energy required for hydrogen recompression every 250 km. For context, the breakeven distance for Europe is 2,500 km. Therefore, hydrogen decarbonization must be accompanied by simultaneous electricity mix decarbonization, which may follow different pathways and timelines across regions.

## CONCLUSIONS

Our results uncover the potential threats of maintaining the current hydrogen supply chain, which requires an excessive environmental budget: standalone, almost 40% of the Safe Operating Space in some control variables. Shifting Natural gas Steam reforming with Carbon Capture Storage or green hydrogen could reduce the damage to critical $CO_2$ control variables, leaving room for other hard-to-abate economic sectors to operate. However, decarbonisation efforts such as Water Electrolysis combined with Bioenergy with Carbon Capture Storage could still worsen Biodiversity Intactness Index or Nitrogen flows. In addition, recycling waste (e.g., aluminium scrap or plastic waste) to produce hydrogen can mitigate environmental burdens without jeopardising the Biodiversity Intactness Index (as Water Electrolysis combined with Bioenergy with Carbon Capture Storage does), or threatening the resources of critical materials required for the construction of electrolysers, photovoltaic panels, or wind turbines. Finally, when formulating policies for the hydrogen economy, these must also consider transportation means, as they could negate the efforts made in hydrogen production. Overall, this highlights the need to optimize hydrogen supply chains holistically.

## ACKNOWLEDGEMENTS

This publications and other results have the support of the predoctoral program AGAUR-FISDUR (2023 FISDUR 00189) of the Secretariat of Universities and Research of the Department of Research and Universities of the Generalitat of Catalonia and the European Social Plus Fund. The authors acknowledge grants PID2021-123511OB-C33, and PID2021-124139NB-C22 funded by MCIN/AEI/10.13039/501100011033 and by "FEDER, UE", grant TED2021-129851B–I00 funded by MCIN/AEI/10.13039/501100011033 by the European Union NextGenerationEU/PRTR, and grant CNS2023-144890 funded by MICIU/AEI/10.13039/501100011033 and by the European Union NextGenerationEU/PRTR.

## REFERENCES

1. Rockström J, Steffen W, Noone K, Persson Å, Chapin FS, Lambin E, Lenton TM, Scheffer M, Folke C, Schellnhuber HJ, Nykvist B, de Wit CA, Hughes T, van der Leeuw S, Rodhe H, Sörlin S, Snyder PK, Costanza R, Svedin U, Falkenmark M, Karlberg L, Corell RW, Fabry VJ, Hansen J, Walker B, Liverman D, Richardson K, Crutzen P, Foley J. Planetary Boundaries: Exploring the Safe Operating Space for Humanity. *Ecology and Society*, *14*(2) http://www.jstor.org/stable/26268316
2. International Energy Agency, I. *Global Hydrogen Review 2023*. www.iea.org (2023)
3. Ryberg MW, Owsianiak M, Richardson K, Hauschild MZ. Development of a life-cycle impact assessment methodology linked to the Planetary Boundaries framework. *Ecol Indic* **88**, 250–262 (2018) https://doi.org/10.1016/j.ecolind.2017.12.065
4. Galán-Martín A, Tulus V, Díaz I, Pozo C, Pérez-Ramírez J, Guillén-Gosálbez G. Sustainability footprints of a renewable carbon transition for the petrochemical sector within planetary boundaries. *One Earth* **4**, 565–583 (2021). https://doi.org/10.1016/j.oneear.2021.04.001
5. Sterner, T. Barbier EB, Bateman I, Van Den Bijgaart I, Crépin AS, Edenhofer O, Fischer C, Habla W, Hassler J, Johansson-Stenman O, Lange A, Polasky S, Rockström J, Smith HG, Steffen W, Wagner G, Wilen JE, Alpízar F, Azar C Carless D, Chávez C, Coria J, Engström, Jagers SC, Köhlin G, ,öfgren A, Pleijel H, Robinson A. Policy design for the Anthropocene. *Nat Sustain* **2**, 14–21 (2019). https://doi.org/10.1038/s41893-018-0194-x https://doi.org/10.1234/56789.10

© 2025 by the authors. Licensed to PSEcommunity.org and PSE Press. This is an open access article under the creative commons CC-BY-SA licensing terms. Credit must be given to creator and adaptations must be shared under the same terms. See https://creativecommons.org/licenses/by-sa/4.0/



Systems & Control Transactions

**Research Article - Peer Reviewed Conference Proceeding**
ESCAPE 35 - European Symposium on Computer Aided Process Engineering
Ghent, Belgium. 6-9 July 2025
Jan F.M. Van Impe, Grégoire Léonard, Satyajeet S. Bhonsale,
Monika E. Polańska, Filip Logist (Eds.)

PSE PRESS

# Integration of Direct Air Capture with $CO_2$ Utilization Technologies powered by Renewable Energy Sources to deliver Negative Carbon Emissions

**Calin-Cristian Cormos[a]*, Arthur-Maximilian Báthori[a], Angéla-Mária Kasza[a,b], Maria Mihet[b], Letitia Petrescu[a], Ana-Maria Cormos[a]**

[a] Babes-Bolyai University, Faculty of Chemistry and Chemical Engineering, Chemical Engineering Department, 11 Arany Janos, Postal code: 400028, Cluj-Napoca, Romania
[b] National Institute for Research and Development of Isotopic and Molecular Technologies - INCDTIM, 67-103 Donat, Postal code: 400293, Cluj-Napoca, Romania
* Corresponding Author: calin.cormos@ubbcluj.ro.

## ABSTRACT

Reduction of greenhouse gas emissions is an important environmental element to actively combat the global warming and climate change. In view of reducing the $CO_2$ concentration from the atmosphere, the Direct Air Capture (DAC) options are promising technologies in delivering negative carbon emissions. The integration of renewable-powered DAC systems with the $CO_2$ utilization technologies can deliver both negative carbon emissions as well as reduced energy and economic penalties of overall decarbonized processes. This work evaluates the innovative energy- and cost-efficient potassium - calcium looping cycle as promising direct air capture technology integrated with various $CO_2$ catalytic transformations into basic chemicals / energy carriers (e.g., synthetic natural gas, methanol etc.). The integrated system will be powered by renewable energy (in terms of both heat and electricity requirements). The investigated DAC concept is set to capture 1 Mt/y $CO_2$ with about 75 % carbon capture rate. Up to 50 % fraction of the captured $CO_2$ stream will be then catalytically converted into the Synthetic Natural Gas (SNG) or methanol using the green hydrogen produced by the water electrolysis (using renewable power), the rest being sent to geological storage. As the results show, the integrated DAC - $CO_2$ utilization system, powered by renewable energy, has promising performances in terms of delivering negative carbon emissions, promoting the utilization of renewables and reducing ancillary plant energy consumptions.

**Keywords**: Carbon Dioxide Capture, Renewable and Sustainable Energy, Modelling and Simulations, Energy Efficiency, Process Design, $CO_2$ utilization

## 1. INTRODUCTION

Combating the global warming and climate changes are matters of great importance globally. To achieve climate neutrality by 2050, several key technical options are envisaged such as increasing the share of renewable energy sources (e.g., solar, wind, biofuels etc.) to gradually replace the fossil fuels, large-scale implementation of the Carbon Capture and Utilization (CCUS) technologies, improving overall energy efficiencies of both production and utilization steps etc. The integration of renewable energy sources with the CCUS & DAC technologies is very promising in delivering negative carbon emissions as well as replacing the fossil energy for future low-carbon applications [1]. The negative carbon emission is a key environmental element for achieving the climate neutrality in order to balance the still remaining positive emission systems and the hard-to-decarbonize processes.

This work evaluates the innovative potassium - calcium looping cycle as DAC system integrated with various $CO_2$ catalytic transformations (e.g., synthetic natural gas, methanol etc.). Conceptual design, modelling and simulation, model validation followed by the energy optimization done by thermal integration analysis, were relevant engineering tools used to assess and optimize the mass and energy balances for quantification of the key

techno-economic and environmental performance indicators. As shown, the proposed integrated systems have promising performances (e.g., negative $CO_2$ emissions). However, significant technological developments are still needed to advance this innovative technology from the current state of the art to relevant industrial sizes as well as to improve the overall techno-economic indicators [2].

## 2. PLANT CONFIGURATION, DESIGN ASSUMPTIONS AND ENERGY INTEGRATION ANALYSIS

The innovative DAC system based on a potassium - calcium looping cycle involves the following technological steps with the correspondent chemical reactors [3]:

- Air contactor for $CO_2$ capture from air using an alkaline potassium hydroxide aqueous solution:

$$CO_2 + 2KOH \rightarrow K_2CO_3 + H_2O \;\; \Delta H = -95.8\ kJ/mole \quad (1)$$

- Causticization reactor for the carbonate precipitation and alkaline solvent regeneration:

$$K_2CO_3 + Ca(OH)_2 \rightarrow 2KOH + CaCO_3 \; \Delta H = -5.8\ kJ/mole \quad (2)$$

- Calcination reactor for the thermal release of captured $CO_2$ and sorbent regeneration:

$$CaCO_3 \rightarrow CaO + CO_2 \quad \Delta H = +178.3\ kJ/mole \quad (3)$$

- Slaker reactor for the hydration of quick lime (regeneration of causticization agent):

$$CaO + H_2O \rightarrow Ca(OH)_2 \;\; \Delta H = -63.9\ kJ/mole \quad (4)$$

Excepting the calcination of calcium carbonate (which requires a significant thermal energy consumption), the rest of involved chemical reactions are exothermic having a positive influence on overall plant energy consumption. The calciner is operated in oxy-combustion mode using biomass (renewable fuel). The overall configuration of the combined potassium - calcium looping cycle used for DAC purposes is shown in Figure 1.

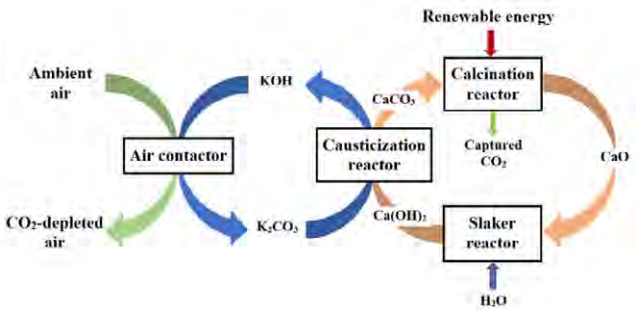



**Figure 1.** Innovative potassium - calcium looping cycles for the direct air $CO_2$ capture (DAC).

Up to 50 % ratio of captured $CO_2$ is then catalytically converted into Synthetic Natural Gas (SNG) or methanol using green hydrogen produced by renewable power water electrolysis [4]. The chemical reactions used in the $CO_2$ utilization concept are the following:

- SNG production (Sabatier process):

$$CO_2 + 4H_2 \leftrightarrow CH_4 + 2H_2O \quad \Delta H = -165\ kJ/mole \quad (5)$$

- Methanol production:

$$CO_2 + 3H_2 \rightarrow CH_3OH + H_2O \quad \Delta H = -49.8\ kJ/mole \quad (6)$$

Figure 2 presents the conceptual layouts of the SNG (left) and methanol (right) production plants using the captured $CO_2$ (from various industrial sources or DAC as the case of this work) and the green hydrogen (produced from the renewable-powered water electrolysis).

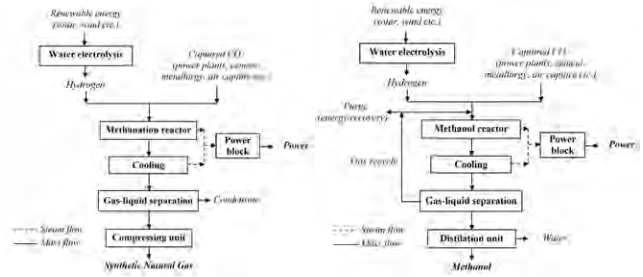



**Figure 2.** SNG (left) & methanol (right) production plants.

Table 1 presents the main design assumptions of the investigated innovative DAC - $CO_2$ utilization concepts.

**Table 1:** Key design assumptions of integrated DAC plant with several $CO_2$ utilization options.

| Unit | Design parameter |
|---|---|
| Air contactor | Solvent: KOH solution (2 kmole/m$^3$)<br>Packing surface: 210 m$^2$/m$^3$<br>Operation temperature: 20-30°C<br>$CO_2$ capture rate: 75 % |
| Causticization reactor | Operational mode: fluidization bed<br>Operation temperature: 80-100°C<br>Calcium retention rate: 90 %<br>$CaCO_3$ pellet size: >0.85 mm |
| Calcination reactor | Operational mode: fluidization bed<br>Operation temperature: 900-950°C<br>$CaCO_3$ decomposition rate: 98 %<br>Energy consumption: 4.8 GJ/t $CO_2$ |
| Slaker reactor | Operation temperature: 300°C<br>Conversion yield: 85 % |
| $CO_2$ drying and compressing | Tri-ethylene-glycol (TEG) moisture removal system<br>Captured $CO_2$ quality (vol. %): >95% $CO_2$, <2000 ppm CO, <250 ppm $H_2O$, <100 ppm $H_2S$, <4% non-condensable gases (nitrogen, hydrogen, argon etc.)<br>Compressor efficiency: 85 %<br>Delivery pressure: 120 bar |

| | |
|---|---|
| Water electrolysis for $H_2$ production | Specific electricity consumption: 54 kWh/kg $H_2$<br>Hydrogen purity: 99.90 % vol. |
| SNG synthesis | Ni-based catalyst<br>Reactor temperature & pressure: 300°C & 50 bar<br>Reactor model: Kinetic<br>Thermal mode: heat exchanger (steam generation)<br>SNG delivery pressure: 60 bar |
| Methanol synthesis | Cu/ZnO/$Al_2O_3$ catalyst<br>Reactor temperature & pressure: 220°C & 80 bar<br>Reactor model: Kinetic<br>Thermal mode: heat exchanger (steam generation)<br>Methanol purity (after distillation): 99.9 % wt. |
| Rankine (steam) cycle | HP steam temperature & pressure: 565°C & 120 bar<br>LP steam temperature & pressure: 250°C & 3 bar<br>Steam turbine efficiency: 90 %<br>Final expansion pressure: 45 mbar |
| Heat exchanger network | Temperature difference: 10°C<br>Pressure drops: 2 - 4 % from inlet pressure |
| Thermodynamic package | Soave-Redlich-Kwong (SRK) |

To optimize energy efficiency, a detailed thermal integration analysis using the pinch methodology was performed for both DAC and $CO_2$ utilization main plant subsystems [5] (without considering the total site analysis). As an illustrative example, Figure 3 presents the correspondent hot and cold composite curves (HCC and CCC) for the sorbent calcination reactor within DAC plant which is showing a significant heat recovery potential (in form of steam generation - see the cold composite curve) from the available heat sources (hot process streams).

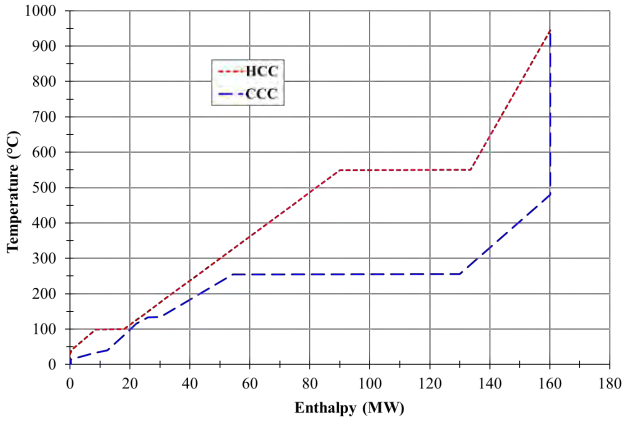



**Figure 3.** Thermal integration analysis of DAC calciner.

## 3. RESULTS AND DISCUSSIONS

The developed models for the combined DAC system and $CO_2$ utilization routes were validated by comparison to available industrial / experimental data. In this respect, the key performance indicators resulted from simulation results of main plant sub-systems were used. For instance, in relation with the involved chemical reactors, the following technical performance indicators were used: conversion rates of various chemical reactions, $CO_2$ capture and utilization rates, DAC calciner thermal duty and sorbent make-up ratio etc. Table 2 presents the comparison of experimental vs. simulated key performance indicators for the integrated DAC - $CO_2$ utilization systems [3-4,6]. As noticed, no significant differences were observed. Therefore, the developed models of integrated DAC - $CO_2$ utilization concepts are validated.

**Table 2:** Validation of developed DAC - $CO_2$ utilization systems.

| Key indicator | Experimental | Simulated |
|---|---|---|
| DAC $CO_2$ capture rate (%) | 70.00 - 75.00 | 75.00 |
| Thermal duty for sorbent regeneration (MJ/kg $CO_2$) | 4.50 - 5.25 | 4.80 |
| DAC sorbent regeneration rate (%) | 95.00 - 98.00 | 98.00 |
| Sorbent make-up rate (%) | 1.00 - 5.00 | 2.00 |
| Power consumption water electrolysis (kWh/kg) | 50.00 - 55.00 | 54.00 |
| $CO_2$ conversion rate for SNG plant (%) | 90.00 - 99.00 | 99.00 |
| $CO_2$ conversion rate for methanol plant (%) | 90.00 - 99.00 | 97.25 |

The overall assessment methodology used for the techno-economic and environmental evaluation as well as the used key performance indicators of the integrated $CO_2$ capture and utilization system were described in details in another paper [4]. For the DAC system, woody biomass was used in the calcination reactor under oxy-combustion conditions (the required oxygen was provided by an integrated cryogenic air separation unit). Considering the thermal operation of the DAC calcination reactor, the overall captured $CO_2$ stream is about 1.5 Mt/y covering both the $CO_2$ captured from air (1 Mt/y) and the $CO_2$ generated from the biomass oxy-combustion process (0.5 Mt/y). The process flow modeling and simulation was done using ChemCAD software [7] for all integrated DAC - $CO_2$ utilization concepts. Table 3 presents the most important techno-economic performance indicators of the evaluated renewable-based DAC system.

**Table 3:** DAC performance indicators.

| Key performance indicator | U.M. | Value |
|---|---|---|
| Captured $CO_2$ flowrate | t/h | 187.50 |
| Biomass input to calciner (pre-dried to 10 % moisture) | t/h | 35.70 |
| Oxygen input to calciner | t/h | 48.20 |
| Power output | $MW_e$ | 23.50 |
| $CO_2$ capture rate | % | 75.00 |
| Specific power consumption per captured $CO_2$ | kWh/t | 315.00 |
| Specific thermal energy per captured $CO_2$ | kWh/t | 1400.00 |
| Captured $CO_2$ quality specification | % vol. | 97.4 % $CO_2$, 2.58 % $N_2$ + Ar, 200 ppm $H_2O$ |
| Specific investment cost per captured $CO_2$ | €/t | 1022.10 |
| Operational and Maintenance (O&M) costs | €/t | 55.82 |

The levelized cost of captured $CO_2$ for the investigated biomass-based DAC concept is about 166 €/t. This calculated value is in line with other estimations presented in the literature (for the same high-temperature DAC technology and similar plant capture capacity) which ranged between 120 - 400 €/t [3,8]. Comparing with the current EU $CO_2$ prices of about 60 - 70 €/t [9], the investigated DAC technology has significantly higher values, but it is expected that in with the further decrease of renewable energy prices (e.g., green power), improving the technological and commercial expertise of DAC processes (to reduces capital and operational costs), the proposed technology will become economically viable.

To assess the overall influence of different cost components (e.g., capital and operational costs, biomass cost, interest rate, plant availability factor etc.) on the levelized cost of captured $CO_2$ for the evaluated DAC plant, a sensitivity analysis was performed. Figure 4 presents the sensitivity analysis for the evaluated biomass-based DAC concept. The analysis shows, somehow expected for these systems, that the DAC capital cost has the highest influence on the captured $CO_2$ cost followed by the interest rate and the plant availability factor.

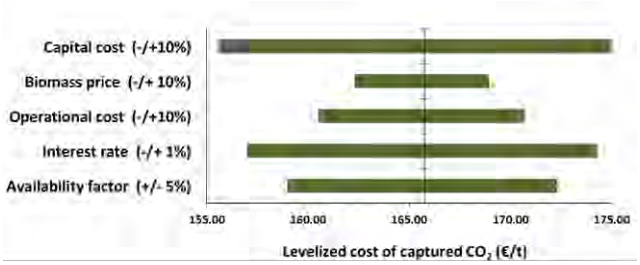



**Figure 4.** Sensitivity analysis of the levelized cost of captured $CO_2$.

In addition, the influence of $CO_2$ transport and storage cost was evaluated (see Figure 5). This key economic indicator is very important for any CCUS project. One can notice that the $CO_2$ transport and storage cost has an important influence on the overall DAC economics.

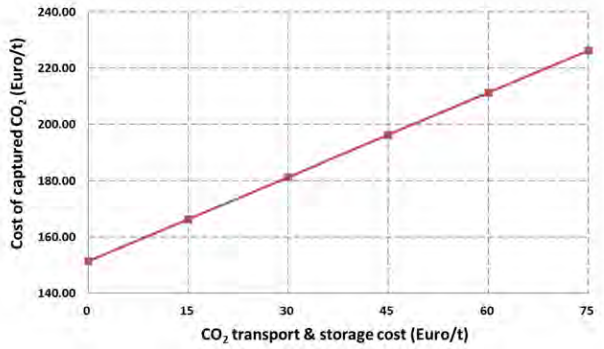



**Figure 5.** Influence of the $CO_2$ transporty and storage cost.

The cumulative cash flow analysis is a very important tool for evaluation of any project along its entirely life (construction, commissioning, operation and decommissioning). Figure 6 presents the cumulative cash flow analysis for the evaluated biomass-based DAC system.

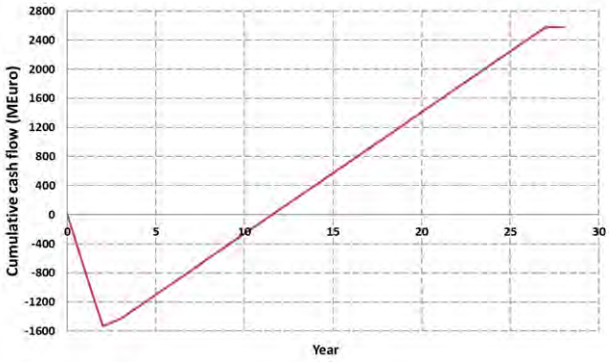



**Figure 6.** Cumulative cash flow analysis for the DAC concept.

Following the biomass-fuelled DAC plant, a relevant fraction of captured $CO_2$ (up to 50 %) is then catalytically transformed into SNG or methanol (MeOH) using green hydrogen produced from renewable-based water electrolysis. As for DAC concept, both $CO_2$ utilization technologies were modeled and simulated using process flow modeling software ChemCAD. The resulted mass and energy balances were then subsequently used for the overall techno-economic and environmental evaluation. Table 4 presents the main techno-economic performance indicators for the integrated DAC - $CO_2$ utilization options. From the technical and specific $CO_2$ emissions (at plant level), both $CO_2$ utilization options are very attractive. For

instance, both $CO_2$ and $H_2$ conversion rates are very high. In addition, the overall $CO_2$ emissions at the plant level are very close to zero. Considering the overall carbon value chain, the specific $CO_2$ emissions are negative for both investigated energy carriers / chemicals (not considering further utilization of SNG and methanol).

**Table 4:** Integrated DAC - $CO_2$ utilization routes key techno-economic performance indicators.

| Performance indicator | U.M. | SNG | MeOH |
|---|---|---|---|
| SNG / methanol thermal output | $MW_{th}$ | 500.00 | 70.00 |
| $CO_2$ conversion rate | % | 99.00 | 97.25 |
| $H_2$ conversion rate | % | 98.00 | 99.00 |
| Cumulative energy efficiency | % | 58.70 | 54.10 |
| Specific $CO_2$ emissions (at plant level) | kg/kg | 0.05 | 0.04 |
| Specific $CO_2$ emissions (for the overall chain) | kg/kg | -2.58 | -1.30 |
| Specific capital investment per SNG / MeOH output | €/t | 2160.25 | 640.10 |
| Operational and maintenance costs | €/t | 734.91 | 1065.89 |
| Levelized cost of SNG / MeOH | €/t | 1324.86 | 926.52 |

From the economic point of view, both SNG / MeOH production costs are higher than the corresponded fossil-based options [4,10]. For instance, the SNG price is about 25.3 €/GJ which is significantly higher than the historical natural gas prices (6 - 8 €/GJ) but somehow comparable with current EU natural gas price of about 12 - 13 €/GJ [11]. A sensitivity analysis was also performed for SNG plant to see the influence of various economic elements (e.g., capital cost, green hydrogen cost, operational cost, interest rate, electricity price etc.) on the SNG production cost. As Figure 7 shows, the most important influence is observed for the green hydrogen cost followed by the operational and maintenance cost.

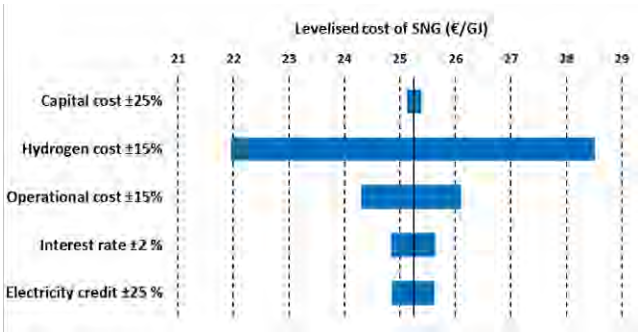



**Figure 7.** Sensitivity analysis of SNG production cost.

For the methanol case, a similar situation than the SNG case is observed, the methanol production price is about 400 - 600 €/t in case of fossil-based methanol [12-13] vs. about 926 €/t for this analysis (green methanol produced with air captured $CO_2$ and renewable energy sources). To assess the effect of $CO_2$ price / $CO_2$ emission tax on green methanol production cost, Figure 8 presents the variation of net present value (NPV). As can be noticed, the green methanol production from captured $CO_2$ can become economically viable (NPV zero or positive) at $CO_2$ emission cost of higher than 230 €/t (currently, this value is about 65 €/t, according to the European Union, Emission Trading System - EU-ETS [14]).

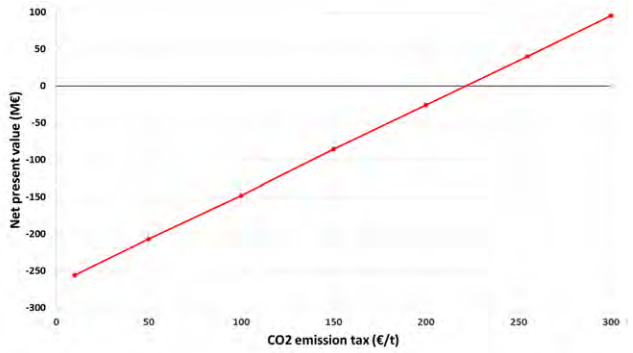



**Figure 8.** Net present value variation of methanol production cost vs. $CO_2$ price.

However, for both evaluated $CO_2$ utilization concepts, it is expected that the overall economics to be improved with expected reduction of the renewable energy prices, increase of $CO_2$ emission taxes as well as further technological improvements [15]. The presented analysis is emphasizing also the importance of developing renewable hydrogen supply chain in deployment of $CO_2$ utilization technologies [16]. It must be noted one strategically important aspect, namely the ability of the investigated green hydrogen $CO_2$ utilization concepts to tackle the inherent time variability of the solar and wind applications by producing storable chemicals that can be used either in energy applications and chemical processes [17]. In addition, the further technological developments (e.g., more efficient water electrolysis systems, improved mass and energy integration of DAC technology, better $CO_2$ utilization catalysts, process intensification etc.) will have a positive influence on economics of these processes.

## 4. CONCLUSIONS

The present work evaluated the techno-economic and environmental performances of an innovative renewable-based DAC system integrated with the $CO_2$ utilization routes to produce SNG and methanol. A wide range of process engineering tools (e.g., conceptual design, mathematical modeling and simulation, mass and energy process integration, techno-economic and

environmental assessment etc.) were used in the evaluation of the integrated DAC - $CO_2$ utilization concepts.

As the results show, the integrated DAC - $CO_2$ utilization systems, powered by renewable energy (biomass and renewable electricity), have promising technical performances in terms of delivering high energy efficiencies (54 - 59 %), negative carbon emissions for the overall value chain (- 2.58 to -1.3 kg/kg), boosting the utilization of renewable energy, reducing ancillary energy consumptions (e.g., for sorbent thermal regeneration), emphasizing the mass and energy integration potential etc. However, the economics of the investigated DAC - $CO_2$ utilization concepts is not yet fully viable in comparison to the current fossil-based similar systems (e.g., natural gas, fossil methanol) but several further developments (e.g., higher penetration of renewable-based hydrogen systems, improved processes and catalysts etc.) could significantly help to improve the economic indicators.

## ACKNOWLEDGEMENTS

This work was supported by a grant of the Ministry of Research, Innovation and Digitization, CCCDI - UEFISCDI, project number: PN-IV-P8-8.1-PRE-HE-ORG-2024-0228, within PNCDI IV.

## REFERENCES

1. García-Bordejé E, González-Olmos R. Advances in process intensification of direct air $CO_2$ capture with chemical conversion. *Prog Energy Combust Sci* 100:101132 (2024) https://doi.org/10.1016/j.pecs.2023.101132
2. Jiang L, Liu W, Wang RQ, Gonzalez-Diaz A, Rojas-Michaga MF, Michailos S, Pourkashanian M, Zhang XL, Font-Palma C. Sorption direct air capture with $CO_2$ utilization. *Prog Energy Combust Sci* 95:101069 (2023) https://doi.org/10.1016/j.pecs.2022.101069
3. Keith DW, Holmes G, St. Angelo D, Heidel K. A process for capturing $CO_2$ from the atmosphere. *Joule* 2:1573-1594 (2018) https://doi.org/10.1016/j.joule.2018.05.006
4. Cormos CC. Deployment of integrated Power-to-X and $CO_2$ utilization systems: Techno-economic assessment of synthetic natural gas and methanol cases. *Appl Them Eng* 231: 120943 (2023) https://doi.org/10.1016/j.applthermaleng.2023.120943
5. Smith R. Chemical process design and integration. second edition, Wiley, Hoboken, USA (2016)
6. Kamkeng A, Wang M, Hu J, Du W, Qian F. Transformation technologies for $CO_2$ utilisation: Current status, challenges and future prospects. *Chem Eng J* 409:128138 (2021) https://doi.org/10.1016/j.cej.2020.128138
7. Chemstations, ChemCAD - Chemical Process Simulation. http://www.chemstations.net
8. Daniel T, Masini A, Milne C, Nourshagh N, Iranpour C, Xuan J. Techno-economic analysis of direct air carbon capture with $CO_2$ utilisation. *Carbon Capture Sci Technol* 2:100025 (2022) https://doi.org/10.1016/j.ccst.2021.100025
9. Trading economics, EU carbon prices. https://tradingeconomics.com/commodity/carbon
10. Tregambi C, Bareschino P, Hanak DP, Mancusi E, Montagnaro F, Pepe F. Techno-economic assessment of a synthetic methane production process by hydrogenation of carbon dioxide from direct air capture. *Int J Hydrogen Energy* 48:37594-37606 (2023) https://doi.org/10.1016/j.ijhydene.2023.06.289
11. European Union, EU Natural Gas Prices. https://tradingeconomics.com/commodity/eu-natural-gas
12. INTRATEC, Methanol Prices. https://www.intratec.us
13. International Renewable Energy Agency (IRENA), Innovation Outlook - Renewable Methanol (2021)
14. EMBER - Coal to clean energy policy, Daily carbon prices. https://ember-climate.org/data/carbon-price-viewer
15. Baskaran D, Saravanan P, Nagarajan L, Byun HS. An overview of technologies for capturing, storing, and utilizing carbon dioxide: Technology readiness, large-scale demonstration, and cost. *Chem Eng J* 491:151998 (2024) https://doi.org/10.1016/j.cej.2024.151998
16. Tasleem S, Bongu CS, Krishnan MJ, Alsharaeh EH. Navigating the hydrogen prospect: A comprehensive review of sustainable source-based production technologies, transport solutions, advanced storage mechanisms, and CCUS integration. *J Energy Chem* 97:166-215 (2024) https://doi.org/10.1016/j.jechem.2024.05.022
17. Ahmad A, Khan S, Chhabra T, Tariq S, Javed MS, Li H, Naqvi SR, Rajendran S, Luque R, Ahmad I. Synergic impact of renewable resources and advanced technologies for green hydrogen production: Trends and perspectives. *Int J Hydrogen Energy* 67:788-806 (2024) https://doi.org/10.1016/j.ijhydene.2023.06.337

© 2025 by the authors. Licensed to PSEcommunity.org and PSE Press. This is an open access article under the creative commons CC-BY-SA licensing terms. Credit must be given to creator and adaptations must be shared under the same terms. See https://creativecommons.org/licenses/by-sa/4.0/



Systems & Control Transactions

**Research Article - Peer Reviewed Conference Proceeding**
ESCAPE 35 - European Symposium on Computer Aided Process Engineering
Ghent, Belgium. 6-9 July 2025
Jan F.M. Van Impe, Grégoire Léonard, Satyajeet S. Bhonsale,
Monika E. Polańska, Filip Logist (Eds.)

PSE PRESS

# Towards Sustainable Processing Of Municipal Household Organic Waste: The Role Of Energy Mix Grids

**Christian Ottini[a,b], Gwenola Yannou-Le Bris[a,b], Sandra Domenek[a,b] and Felipe Buendia[a,b]***

[a] Université Paris-Saclay, INRAE, AgroParisTech, UMR SayFood, 91120 Palaiseau, France
[b] Fondation AgroParisTech, Chaire CoPack, 91120 Palaiseau, France
* Corresponding Author: felipe.buendia-kandia@inrae.fr

## ABSTRACT

The reduction and recovery of organic fraction of municipal solid waste is a major challenge for contemporary society. It requires the establishment of regional strategies with minimized environmental impact. This study employs life cycle assessment to evaluate the respective environmental performances of the current French system based on incineration, and those of alternative systems including (i) anaerobic digestion with composting and (ii) composting for biowaste treatment under different energy scenarios. The environmental impacts of Parisian biowaste are calculated by considering incineration technologies in the area, the French energy mix in 2022, the average European energy mix in 2022 and the projected French energy mix for 2030. The results show that the proportion of fossil-based sources in the energy mixes significantly influences the environmental performance of waste management systems. Energy mixes based in high-carbon fossil sources dependency tend to favour incineration-based processing systems. This is driven by the significant volume of credits allocated to the alternative energy produced from waste treatment. It is therefore essential for processing system design projects to account for planned changes in the energy mix in order to accurately assess the future impact of waste management strategies.

Keywords: Life Cycle Analysis, Biowaste, Circular Bioeconomy, Composting, Anaerobic Digestion, Energy Efficiency, Municipal Household Waste Management.

## INTRODUCTION

The significance of waste management in European legislation reflects the environmental challenges posed by the vast quantities of waste requiring treatment. Annually, more than 2 billion tonnes of municipal solid waste are generated, with 32-34% comprising the organic fraction of municipal solid waste (OFMSW) in Europe [1,2]. To address the critical need for sustainable management of organic solid waste, several studies [3–5] have examined the environmental assessment of various technological alternatives that can be mobilised for this purpose. Previous research has highlighted the sensitivity of the environmental performance of biowaste reprocessing technologies to energy mixes.

Slorach et al. [3] compared incineration, composting and anaerobic digestion technologies for food waste in the United Kingdom (UK). Their study showed better environmental performance for the anaerobic digestion treatment with a particular sensitivity of the results to the energy mix. They found out that when anaerobic digestion and incineration are credited with displacing wind or solar energy, both treatment options become net contributors to Global Warming Potential and Fossil Depletion, as the associated credits are lower compared to those for the grid electricity. As highlighted by Soimakallio et al. [4] differences in actual research questions, methodological choices, and data set selection have a significant impact on the outcomes of life cycle assessment (LCA) studies for energy systems. These inconsistencies make it challenging to compare the findings of various studies and may lead to uncertainties in the conclusions. These results were confirmed by Dastjerdi et al. [5] in a systematic review. The article states that one of the most investigated sources of uncertainty was the source of avoided electricity and assumptions for energy recovery.

The aim of this work is to assess the environmental performance of current and potential systems for

managing OFMSW in the Parisian region. To the best of our knowledge, the case of France has not been studied from this perspective. The scenarios evaluated are mainly incineration, composting, and anaerobic digestion with composting (AD-co). In the first part, the comparison of the French and European scenarios was evaluated. In the second part of this work, the influence of the energy mix planned in France for 2030 vs. that of 2022 on the environmental performance of the OFMSW treatment system was studied. Results aim to provide actionable insights to policymakers and waste management operators.

## METHODOLOGY

Figure 1 illustrates the perimeter of the data used in

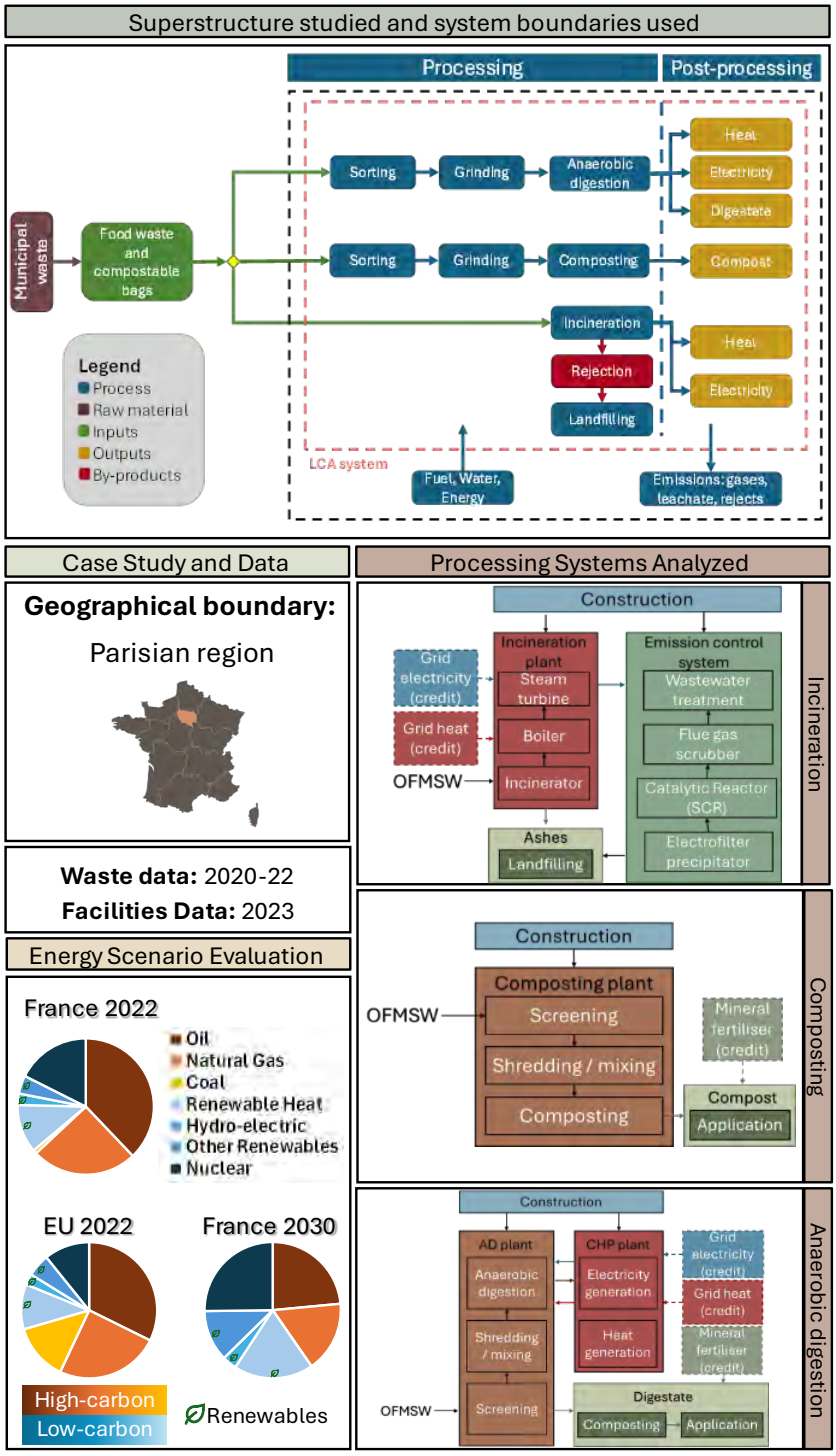



**Figure 1**. Schematic representation of the study boundaries and considered cases.

this study, including energy mix scenarios and the perimeters of the global system and sub-systems compared. LCA was conducted using the OpenLCA 2.3.1 software with the Ecoinvent 3.9.1 database. The four phases of LCA have been followed as standardized by ISO 14040/44. The functional unit was defined as the treatment of 1 kg of OFMSW. A review of recent publications [5-8] guided the selection of the 12 most relevant environmental categories for this field as shown in Figure 2. Impacts were normalized according to the highest absolute value per category for better visibility. The impact assessment method chosen is: ReCiPe (H) 2016 [6] (LCIA method 2.1.1).

For the analysis, three energy mixes were considered: i) France 2022 (current energy mix), ii) 2030 future scenario (projected energy mix), and iii) Average European Union (EU) energy mix in 2022 (as the comparison system). The details of these energy mixes are provided in the supplementary material (Tab. S1-3). To isolate the impact of the national energy grids, including the expected changes in the national energy grid for 2030, consistent process efficiencies have been applied throughout the study for the same technologies across all scenarios. This approach ensures that the analysis focuses solely on the influence of the different energy mix grids analysed. The Parisian OFMSW was characterised in terms of volume using data supplied by the operator, and its composition was established using literature data on composition [7]. A detailed description can be found in Tab. S4-5.

The incineration process of OFMSW was simulated using the modelling tools provided by Doka et al. [8]. After data collection, the detailed Parisian plant inventories have been summarized in Tab. S4 and used in the assessment. It is important to note that incineration facilities in Paris are highly optimized, including their dry ash treatment. The energy produced by incineration has been discounted from the LCA as a credit.

For the composting process, the inventory was retrieved from Lu et al. [9]. The compost has been allocated by means of substitution and the system is credited against the avoided production of mineral nitrogen (calcium ammonium nitrate), phosphate (diammonium phosphate) and potassium fertilizer. For that, the characterization of the compost composition was performed as proposed by Boldrin et al. [10] and detailed in Tab. S6. To credit the various fertilizer substitutions used in the study, the replaced quantity was calculated using Eq. S1-3.

For the anaerobic digestion process, the inventory was retrieved from the literature [11]. Using annual OFMSW production data for greater Paris, the required sizes for the AD-co and Combined Heat and Power (CHP) unit were calculated using the Ecoinvent inventory and scaled up with Eq. 1.

$$E_2 = E_1\left(\frac{C_2}{C_1}\right)^{0.6} \quad (1)$$

where:

$E_1$ environment impact of the smaller plant

$E_2$ environment impact of the larger plant

$C_1$ plant capacity of the smaller plant

$C_2$ plant capacity of the larger plant.

The produced biogas, without upgrade to biomethane, has been considered to be burned in a CHP unit. Its calorific value was credited for the energy displaced, and the digestate through Eq. S4-6.

## RESULTS AND DISCUSSION

The results clearly highlight the significant influence of the different energy mix grids on the environmental performance of waste treatment system.

Figure 2a and 2b illustrate the midpoint impact assessment of the studied technologies. These graphs were constructed by subtracting the environmental credits (avoided impacts) of each technology from their generated impacts. Figure 2a compares the midpoint impact assessment of the three technologies for the French (2022) and average EU (2022) energy grid mixes. Concerning fossil resource scarcity (FRS), the energy credits from displacement are sufficient to make incineration and AD-co net negative-impact processes under the studied grid mixes (60% fossil for France, 70% for the EU). This is due to energy production rates of 0.81 kWh/FU for incineration and 0.753 kWh/FU for AD-co. Incineration emerges as the best option, followed by AD-co, with a greater relative benefit in the EU context. Composting, which consumes resources like fuel and energy, does not gain sufficient offset from fertilizer displacement, resulting in a net environmental impact.

Aquatic environmental impacts, including freshwater ecotoxicity (FWEc), eutrophication (FWEu), and marine ecotoxicity (MEc), vary significantly across different contexts. In France, AD-co consistently performs best, while composting ranks as intermediate. Incineration exhibits the highest impacts due to the release of toxic compounds from combustion, flue gas washing, and phosphate emissions from fly ash. In the EU context, similar trends are observed for ecotoxicity. However, freshwater eutrophication improves substantially for incineration (-581%) and AD-co (-311%), which is attributed to the displacement of coal-based energy production.

For global warming (GW) it can be seen that incineration is the least polluting option, followed by AD-co and lastly, composting. For France and the EU, a difference of -12.16 and -13.72% is observed for incineration and anaerobic digestion respectively. It's important to point out that even if seemingly small, this difference in the impact for one kg when related to the annual production of 440kt in France creates a difference of 2 million

$CO_2$eq. saved per year for the incineration and 1.85 $CO_2$eq. for anaerobic digestion.

Human health impacts, measured through carcinogenic (HCT) and non-carcinogenic toxicity (HNCT) (1,4-DCB eq. and kg $NO_x$-eq.), show that AD-co consistently demonstrates superior performance, while incineration ranks lowest despite filtration systems, due to combustion-generated toxic compounds.

For ozone formation related impacts (OF-HH and OF-TE), composting presented the highest impact due to unfiltered $NO_x$ and NMVOC emissions, with the lack of biofilters resulting in direct atmospheric exchange of

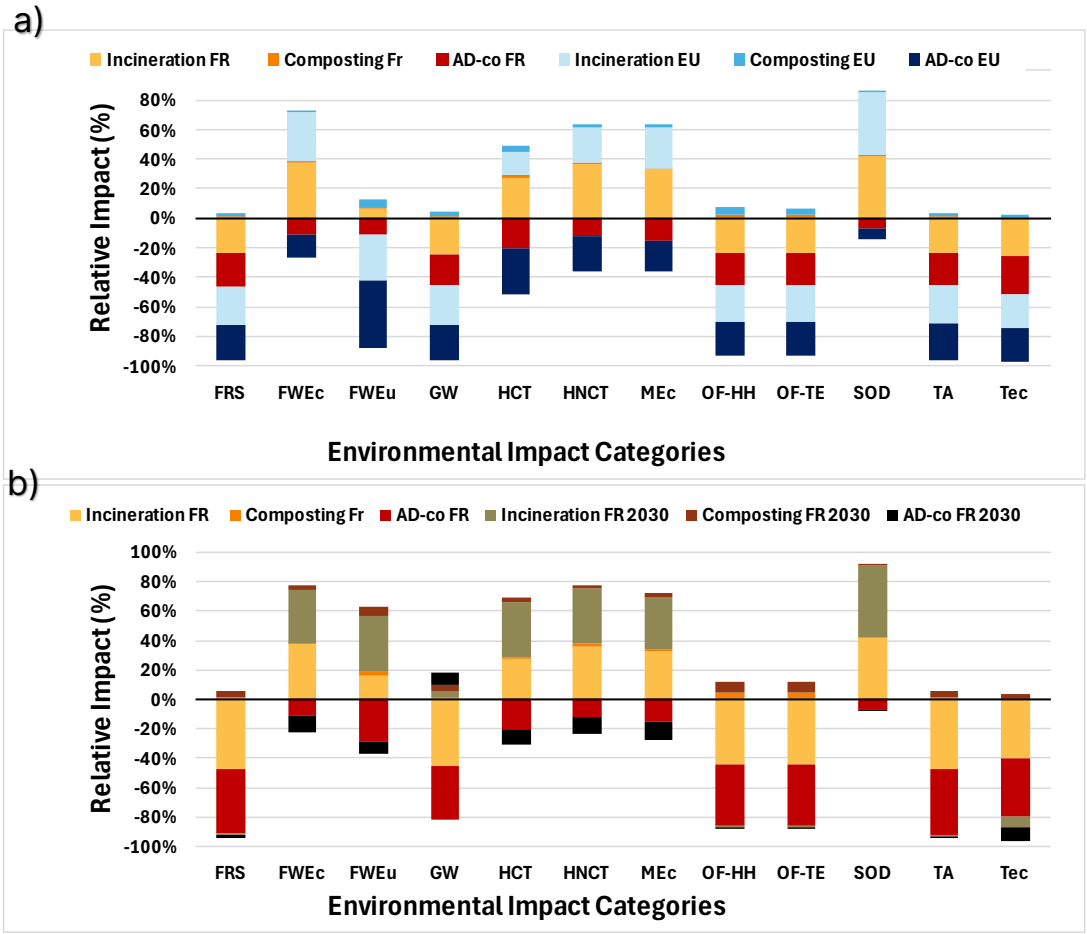



**Figure 2**. Environmental impacts with credits of the various processing technologies in the Parisian region a) using the French (2022) and European (2022) energy mix and b). using the current (2022) and projected French (2030) energy mix Terrestrial Acidification (TA), Global Warming (GW), Stratospheric Ozone Depletion (SOD), Ozone formation-Human health (OF-HH), Ozone formation-Terrestrial ecosystems (OF-TE), Human carcinogenic toxicity (HCT), Human non-carcinogenic toxicity (HNCT), Freshwater Eutrophication (FWEu), Freshwater Ecotoxicity (FWEc), Marine Ecotoxicity (MEc), Terrestrial Ecotoxicity (TEc) and Fossil Resource Scarcicity (FRS).

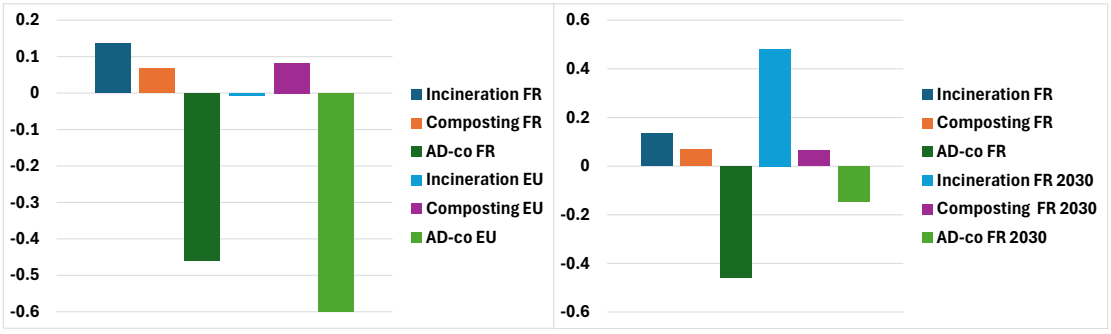



**Figure 3.** Environmental single score for different energy mix grids: a) France vs EU and b) France today vs 2030.

these compounds.

Regarding stratospheric ozone depletion (SOD) (kg CFC11-eq.), AD-co showed the least impact, with energy displacement creating environmental credits, while incineration's energy credits prove insufficient to offset continuous ozone-depleting compound production.

For terrestrial impacts, the analysis of acidification (TA) and ecotoxicity (TEc) (measured in kg $SO_2$-eq. and 1,4-DCB eq. emitted to industrial soil) reveals that composting demonstrates the highest impact, primarily due to fuel combustion during operations and energy production. Both AD-co and incineration benefit significantly from energy displacement credits, which effectively reduce their environmental impact in these categories.

Figure 2b present the comparison of the midpoint impact assessment of the three technologies with regards to the actual French energy mix grid and the 2030 horizon is shown. The reduction in high-carbon fossil fuel based technologies share from 60 % to 42 % drastically reduce the environmental credits of the three waste treatment technologies, revealing significant shifts in technology performance with the projected changes in energy mix composition. For fossil resource scarcity (FRS), the impact order changed, now Ad-co is the least impacting technology, followed by Incineration. The same results are found for freshwater ecotoxicity (FWEc), eutrophication (FWEu) and marine ecotoxicity (MEc). AD-co is the least impacting technology bringing credits; while composting and incineration result in higher environmental impacts. A slight reduction of -4 % to -14 % in the impact category of freshwater ecotoxicity is observed, primarily due to the increased share of energy co-generation using biogas. However, freshwater eutrophication and marine ecotoxicity show significant increases for incineration (130 % and 10.6 % respectively) and AD-co (70 % and 21 % respectively), linked to reduced energy displacement credits.

The global warming (GW) analysis for 2030 demonstrated perhaps the most dramatic shift, with a 108 % to 122 % relative increase for incineration and AD-co respectively. This shift transforms incineration from saving 16 million tonnes $CO_2$eq. to producing 1.38 million tonnes $CO_2$eq. annually, while AD-co shifts from saving 13.5 million tonnes $CO_2$eq. to producing 3 million tonnes $CO_2$eq.

Despite these increases, the analysis of human toxicity impacts shows that AD-co maintains its environmental advantage, even after experiencing a 46 % increase in human carcinogenic (HCT) and 7 % increase in non-carcinogenic toxicity (HNCT) impacts. Incineration follows a similar trend but to a lesser extent, with 37 % and 2 % increases respectively.

Fig. 3 presents the aggregated end-point environmental single score, they have been produced following ReCiPe 2016 [6] methodology. The analysis highlights how energy mix differences lead to varying technological preferences. In the EU context, with its higher fossil fuel dependency, AD-co emerges as the least impacting technology available, followed by incineration and lastly composting.

However, the French context, with its less carbon-based energy mix, shows a different trend: AD-co remains the preferred option, but composting becomes more favourable than incineration due to reduced energy displacement credits. This trend becomes even more pronounced in the 2030 scenario, where AD-co maintains its position as the least environmentally impacting system despite losing a significant share of positive impact. Composting emerges as a valuable alternative with relatively small environmental impact, and incineration becomes one order of magnitude more impacting than composting and two orders more impacting than AD-co.

## CONCLUSIONS

This study provides valuable insights into waste treatment technologies through two perspectives. In the context of Paris, the life cycle assessment demonstrated that anaerobic digestion with composting (AD-co) emerges as the most environmentally favourable option, followed by composting, with incineration showing the highest environmental impact. This hierarchy is maintained when the share of high-carbon sources in the energy mix is reduced. However, the decarbonisation of the mix increases the final impact of incineration and progressively reduces the interest of anaerobic digestion with composting.

The analysis of environmental impacts in different energy mix scenarios revealed a critical insight: the perceived advantages of WtE plants are largely artificial, created by avoided impacts in carbon-intensive energy contexts. As energy grids transition toward low-carbon renewable sources, this artificial benefit will decrease, highlighting the urgent need to shift toward alternative treatment systems like AD-co and composting. This relationship between waste treatment technologies and energy resources demonstrate how the environmental performance of waste management systems is intrinsically linked to the energy mix grid.

The specific impact assessment shows that AD-co consistently maintains its environmental advantage across different scenarios, while incineration's performance significantly deteriorates in lower-carbon energy contexts. For instance, in the 2030 scenario, AD-co remains the most environmentally sound option, despite reduced benefits from energy displacement, while incineration becomes notably less favourable, showing impacts two orders of magnitude higher than AD-co.

Based on these findings, some recommendations to the policymakers can be formulated: consider the projected changes in energy mix when planning long-term

waste management infrastructure, prioritize the development of AD-co facilities due to their consistent environmental benefits across different energy scenarios, and gradually transition away from incineration in regions with increasingly renewable energy mixes. Additionally, policymakers should consider incorporating composting facilities in their plans as complementary infrastructure to AD-co, particularly in areas with limited space or resources for AD-co implementation. Future studies should also consider technological advancements and various system configurations to provide a more comprehensive understanding of treatment options.

While these findings provide crucial environmental insights, it's important to recognize that a comprehensive assessment of waste processing systems must also incorporate economic and social dimensions to develop truly sustainable and practical solutions.

## DIGITAL SUPPLEMENTARY MATERIAL

In the supplementary material, all the inventories and calculations can be found.
https://psecommunity.org/LAPSE:2025.0013

## REFERENCES


1. Kaza S, Yao L, Bhada-Tata P, Van Woerden F. What a Waste 2.0: A Global Snapshot of Solid Waste Management to 2050. What a Waste 2.0: A Global Snapshot of Solid Waste Management to 2050.
2. European Environment Agency. Bio-Waste in Europe: Turning Challenges into Opportunities. Bio-Waste in Europe: Turning Challenges into Opportunities. Publications Office (2020).
3. Slorach PC, Jeswani HK, Cuéllar-Franca R, Azapagic A. Environmental and economic implications of recovering resources from food waste in a circular economy. Sci. Total Environ. 693:133516 (2019) https://doi.org/10.1016/j.scitotenv.2019.07.322.
4. Soimakallio S, Kiviluoma J, Saikku L. The complexity and challenges of determining ghg (greenhouse gas) emissions from grid electricity consumption and conservation in lca (life cycle assessment) – a methodological review. Energy 36:6705–6713 (2011) https://doi.org/10.1016/j.energy.2011.10.028.
5. Dastjerdi B, Strezov V, Rajaeifar MA, Kumar R, Behnia M. A systematic review on life cycle assessment of different waste to energy valorization technologies. J. Clean. Prod. 290:125747 (2021) https://doi.org/10.1016/j.jclepro.2020.125747.
6. Huijbregts MAJ, Steinmann ZJN, Elshout PMF, Stam G, Verones F, Vieira M, Zijp M, Hollander A, Van Zelm R. ReCiPe2016: a harmonised life cycle impact assessment method at midpoint and endpoint level. Int. J. Life Cycle Assess. 22:138–147 (2017) https://doi.org/10.1007/s11367-016-1246-y.
7. Beylot A, Muller S, Descat M, Ménard Y, Villeneuve J. Life cycle assessment of the french municipal solid waste incineration sector. Waste Manag. 80:144–153 (2018) https://doi.org/10.1016/j.wasman.2018.08.037.
8. Gabor D. LCI calculation tools for regionalised waste treatment: 5 excel workbooks. Zurich Switz. (2017).
9. Lu HR, Qu X, El Hanandeh A. Towards a better environment - the municipal organic waste management in brisbane: environmental life cycle and cost perspective. J. Clean. Prod. 258:120756 (2020) https://doi.org/10.1016/j.jclepro.2020.120756.
10. Boldrin A, Hartling KR, Laugen M, Christensen TH. Environmental inventory modelling of the use of compost and peat in growth media preparation. Resour. Conserv. Recycl. 54:1250–1260 (2010) https://doi.org/10.1016/j.resconrec.2010.04.003.
11. Slorach PC, Jeswani HK, Cuéllar-Franca R, Azapagic A. Environmental sustainability of anaerobic digestion of household food waste. J. Environ. Manage. 236:798–814 (2019) https://doi.org/10.1016/j.jenvman.2019.02.001.



© 2025 by the authors. Licensed to PSEcommunity.org and PSE Press. This is an open access article under the creative commons CC-BY-SA licensing terms. Credit must be given to creator and adaptations must be shared under the same terms. See https://creativecommons.org/licenses/by-sa/4.0/




Systems & Control Transactions

**Research Article - Peer Reviewed Conference Proceeding**
ESCAPE 35 - European Symposium on Computer Aided Process Engineering
Ghent, Belgium. 6-9 July 2025
Jan F.M. Van Impe, Grégoire Léonard, Satyajeet S. Bhonsale,
Monika E. Polańska, Filip Logist (Eds.)

PSE PRESS

# Repurposing Existing Combined Cycle Power Plants with Methane Production for Renewable Energy Storage

**Diego Santamaría*, Antonio Sánchez, Mariano Martín**

Department of Chemical Engineering, University of Salamanca, Plz Caidos 1-5, 37008, Salamanca, Spain.
* Corresponding Author: diegosg@usal.es.

## ABSTRACT

Energy storage is essential for transitioning to a renewable system based on renewable sources. To meet this challenge, Power-to-X technologies are attracting more attention. This work explores converting the excess of electric energy obtained from wind or solar sources into hydrogen and then into methane leveraging existing natural gas infrastructure for easier storage and transport. The process involves two stages: Firstly, the methane production step using Power-to-X technologies during excess renewable energy periods and, secondly, the electricity generation step during high demand with $CO_2$ capture for reuse in methane synthesis, forming a closed carbon loop. In this way the Power-to-X process is integrated with repurposed combined cycle power plants (CCPPs) creating a Power-to-methane-to-power system. Two approaches are evaluated: oxy-combustion, which simplifies process $CO_2$ purification and air combustion, which needs a more complex $CO_2$ purification, such as amine absorption or PSA systems. The results show that ordinary combustion capturing $CO_2$ by amines is the most profitable process, especially when it is assumed that the oxygen produced by the electrolyzer is sold. For a CCPP with a nominal capacity of 400MW, the cost of electricity production ranges from 450 $/MWh to 490 $/MWh when the income from oxygen sales is neglected. If the oxygen produced can be fully absorbed by the market, the electricity production cost decreases to 250 $/MWh and 300 $/MWh.

**Keywords**: Process Design, Carbon Capture, Energy Storage, Hydrogen, Methane.

## INTRODUCTION

Renewable energy sources (RES) are transforming power systems and will be predominant in the years to come. For example, by 2030, an increase of more than 90% in the electricity generation from RES is expected with solar PV and wind being the leading technologies. However, these generation alternatives fluctuate according to the weather conditions, causing a paradigm shift from the current steady-state systems. Therefore, energy storage technologies will be required to ensure a stable power grid and the balance between electricity production and demand at every time. Different alternatives have been proposed, which can be classified as follows: mechanical, chemical, electrochemical, and electrical.

Among them, hydrogen is emerging as a highly attractive option. According to the current predictions, by 2050, the global demand for hydrogen could increase up to 585 Mtpa under a Net Zero scenario. However, some significant challenges are associated with hydrogen utilization highlighting the low volumetric energy density and the difficult storage conditions. Thus, for medium/long-term storage horizon, the use of hydrogen as such is not considered the most suitable option. Other chemicals produced from hydrogen have been proposed to overcome its issues. These options offer beneficial conditions in terms of volumetric energy density, storage and transport conditions, etc. allowing an effective deployment as grid-scale energy storage system. Among these chemicals, methane, methanol, and ammonia emerge as the most promising options. Although methane is a gas, with the difficulties associated with this phase, this component is attracting attention due to the possibility of using the existing natural gas infrastructure to handle this hydrogen carrier. This allows storage and transport of significant amounts of green methane to address the challenges associated with an energy system with a high

penetration of renewables. The use of methane as energy storage system involves two main steps. The first one is related to the production of methane using Power-to-X processes in time periods with high energy production. Subsequently, a second step is the back transformation into electricity with the possibility of capturing $CO_2$ to synthesize again methane as required.

In this field, Xiang et al. [1] evaluated the implementation of the carbon capture technology in a natural gas combined cycle power plant coupled with oxy-combustion. A simple condensation step is selected as $CO_2$ separation alternative due to the oxy-combustion conditions. An extended work including two $CO_2$ capture retrofits in natural gas power plants in presented by Strojny et al. [2]. In particular, amine absorption and calcium looping have been investigated. Other works have assessed the production of methane through $CO_2$ methanation. For instance, Blanco et al. [3] evaluated the potential implementation of Power-to-methane processes in the European Union using a life cycle assessment approach. However, a comprehensive analysis of the two stages to introduce green methane as energy storage has not yet been performed.

Therefore, in this work, a holistic process design analysis of the Power-to-methane-to-power is developed to be integrated as grid-scale energy storage system. Specifically, the integration of this technology with existing combined cycle power plants is proposed to repurpose current infrastructure, thereby reducing the capital costs associated with the energy transition. In the first stage, devoted to methane production, $CO_2$ (from carbon capture) is combined with green hydrogen produced from water electrolysis using renewable energy (wind and PV solar). This stage will take place in periods with high renewable generation (exceeding demand). The second stage is related to the production of electricity from the previously produced methane. This will take place during periods when renewable generation is not sufficient to meet demand. In this case, the existing combined cycles are evaluated by coupling carbon capture technologies. Two different approaches have been evaluated. Firstly, the use of oxy-combustion together with a simple carbon capture unit (condensation). A second option is to maintain the existing air combustion but with a more complex carbon capture technology (amines or pressure swing adsorption in this case). The captured $CO_2$ is stored to be used in the methanation section as required. Therefore, this comprehensive approach demonstrates the potential of green methane as an efficient solution for grid-scale energy storage, enabling the repurposing of natural gas-based infrastructure to support the transition to a sustainable energy system.

## PROCESS ANALYSIS

This work compares three methane combustion processes. The first two utilize conventional combustion (air-based combustion), which requires a carbon capture system due to the high nitrogen content in the exhaust gases. These processes differ in their carbon capture technology: one employs amine absorption technology, while the other uses PSA systems. The third process replaces air with pure oxygen (oxy-combustion), resulting in exhaust gases mainly composed of $CO_2$ and water.

The diagram of each process can be seen in Figure 1, Figure 2 and Figure 3.

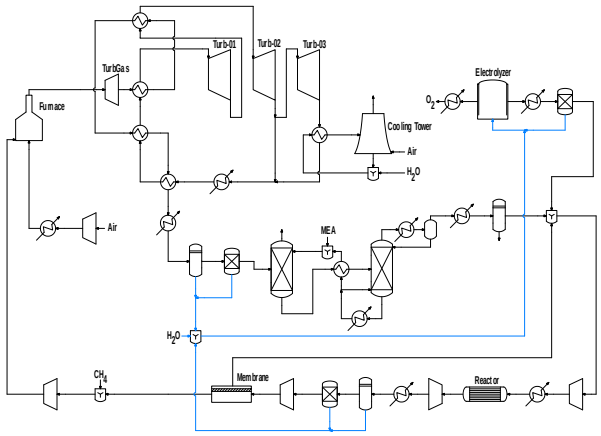



**Figure 1.** Process flow diagram of process using ordinary combustion and absorption as carbon capture system.

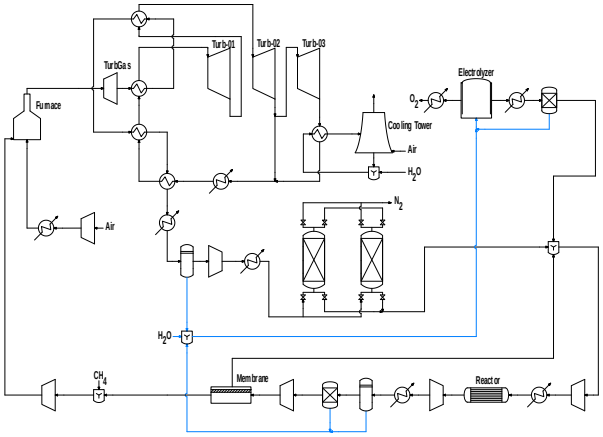



**Figure 2.** Process flow diagram of process using ordinary combustion and adsorption with PSA as carbon capture system.

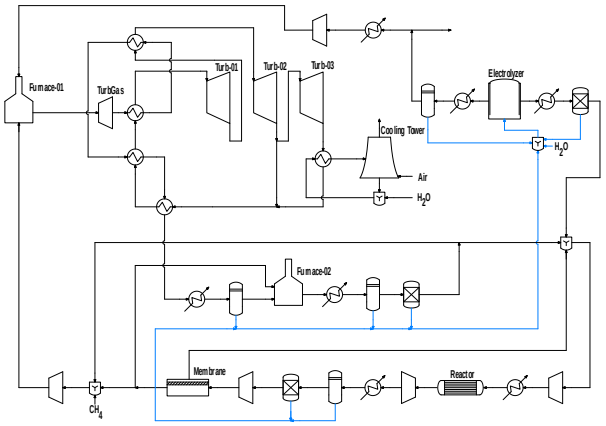



**Figure 3.** Process flow diagram of process using oxy-combustion.

## Process Description

The processes can be divided into four sections. 1) the combined cycle power plant where electricity is produced by burning methane. 2) The second one consists of capturing or purifying CO2. 3) The third one corresponds to renewable hydrogen production by an electrolyzer. 4) Finally, the reaction of H2 and CO2 to produce methane. The methane generated in this section is used as feed of the first. Thereby, the cycle can be closed. The different sections are described as follows.

### Combined Cycle Power Plant

The Combined Cycle Power Plant is composed of two thermodynamic cycles to maximize efficiency. The first one is the Brayton cycle, which takes place in a gas turbine and the second one is the regenerative Rankine cycle, which involves a system of steam turbines (high-pressure, medium-pressure, and low-pressure turbines). Although the reuse of existing CCPPs is proposed, they are also modeled to create a complete model.

The operation of a CCPP begins by introducing the feed, which has been previously conditioned, into the combustion chamber. The composition of the feed varies depending on the modeled processes, but the treatment is the same for all the cases: the feed stream must be compressed and its temperature adjusted to the required level. The combustion chamber is modeled as adiabatic where complete combustion is ensured by adding an excess of comburent. Moreover, an inert substance must be introduced with the comburent to prevent the furnace temperature from exceeding the critical limit of 1600 ºC and avoid material problems. For ordinary combustion the oxygen is already mixed with nitrogen from the air. However, in the case of oxy-combustion, pure oxygen is mixed with $CO_2$ from combustion exhaust gases to achieve the conditions required.

The gas turbine is modeled as a polytropic expansion process with an efficiency of 85%. After passing through the gas turbine, the exhausted gases, which still contain significant thermal energy, are utilized as a heat source for reheater and preheater in the regenerative Rankine cycle with reheating.

In the Rankine cycle, the steam exiting the low-pressure turbine is condensed using a water refrigeration cycle with a cooling tower. The performance of the tower is modeled using Mickey's method [4]. The increment of temperature is limited to 8-10 ºC following rules of thumb to ensure a proper operation. In the cooling tower, the water temperature is reduced by evaporating a fraction of the water so to compensate this lost make-up water is required. To calculate it, the air humidity and water temperature in the cooling tower must be considered.

In general, the equipment of CCPP is the same for all alternative processes, but the following subsections are different for each one.

### $CO_2$ Separation

The $CO_2$ separation section is designed to be integrated with existing CCPPs, creating a closed carbon loop to prevent emission into the atmosphere. Various treatments methods for the exhaust gases are proposed, including the following. When the methane is burned using air as the comburent the exhaust gases are composed mainly of $CO_2$, $H_2O$, a small amount of $O_2$ (as previously it was introduced in excess) and a large amount of $N_2$. Nitrogen acts as an inert component and must be separated from the $CO_2$ to enable a proper operation of methanation. To reach the $CO_2$ purification two technologies are evaluated: adsorption with PSA system and amine absorption system.

Adsorption with PSA system. The process flow diagram can be seen at Figure 1. The PSA columns use as adsorbent material zeolite 13 X [5]. This process is modeled using a Langmuir solid-gas adsorption isotherm. Mainly, the nitrogen can cross the bed while the $CO_2$ is captured. It can be assumed the small amount of oxygen in inlet gases is not trapped, since the adsorption capacity of zeolite 13 X for oxygen is minimal [6]. Then, the $CO_2$ is sent to the methane production section and the not captured gases ($N_2$, $H_2O$, $O_2$) are released into the atmosphere.

Amine absorption system. The process flow diagram is shown at Figure 2. This system consists of two columns. The first one is the absorption column where the exhaust gases from the gas turbine brought into contact with amine solution of 20 % monoethanolamine (MEA). The non-absorbed gases are released into the atmosphere. The amine solution rich in $CO_2$ is heated and sent to the second column or stripping column. Here the $CO_2$ is desorbed from the amine solution and a pure steam of $CO_2$ is reached. Then, the amine solution is mixed with fresh amine solution to make up for losses and refeed to

the first column. The model of this section is based on first principles and industrial data.

In contrast, the exhaust flue gases of oxy-combustion are only composed of $CO_2$, $H_2O$ and $O_2$. The flow diagram of this process can be seen at Figure 3. In this case the $CO_2$ must be also purified. The water is easily removed by condensation and the elimination of the oxygen is done by sending the gases to a second combustion chamber where extra methane is added to ensure the complete remotion of oxygen. The chamber combustion temperature is limited thanks to the large amount of $CO_2$ there is in the inlet steam. After this step, the humidity steam is reduced by condensation to reach a better operation of methane production.

### Renewable hydrogen production

The hydrogen is produced through water electrolysis and is the same for all alternative processes. Since it is proposed that the electricity used for electrolysis came from renewable energy sources such as wind or solar, the hydrogen produced can be considered green hydrogen. The water required for this operation is provided by the various drying operations throughout the system, minimizing the need for external water. Nowadays, several types of electrolyzers are available: Proton Exchange Membrane (PEM), Anion Exchange Membrane (AEM), Alkaline and Solid Oxide Ceramic (SOEC). Among them, PEM technology is selected due to the high purity of gases produced, its advanced commercial maturity and its short start-up time [7].

The electrolyzer generates two streams, one contains mainly hydrogen and the other contains oxygen. Both streams are subjected to a drying process to remove the residual water. The hydrogen stream is mixed with the $CO_2$ previously purified while the intended use of the oxygen depends on the analyzed process. The oxygen obtained under ordinary combustion process can be sold. However, the oxygen obtained under oxy-combustion process is used as a comburent in this process. In this way, the oxygen is completely integrated in the process.

### Methane production

The $CO_2$ stream, the hydrogen stream and the recirculation steam are mixed and compressed to reach the methanation reactor conditions. The methanation reactor is a fixed bed reactor with thermal control. A nickel-based catalysis is used. The reactions for methane production are shown below, eqs 2, 3, 4. The reactor behavior is modeled using equilibrium conditions. The typical temperature range is between 250 ºC and 400 ºC and the pressure is up to 20 bar [8].

$$CO + 3H_2 \rightleftarrows CH_4 + H_2O \quad (2)$$

$$CO_2 + H_2 \rightleftarrows CO + H_2O \quad (3)$$

$$CO_2 + 4H_2 \rightleftarrows CH_4 + 2H_2O \quad (4)$$

The outlet reactor stream is expanded into a gas turbine and cooled to remove water by condensation. As there is hydrogen in this stream, it is recovered and recirculated to the methane production by a membrane separation. Finally, the purified methane is sent to the CCPP combustion chambre, closing the cycle.

### Optimization procedure and Techno-economic analysis

The processes are modeled using mass and energy balances, thermodynamic equilibria, experimental data and rules of thumb and they are optimized to maximize the electricity production and minimize the energy consumption derived of the process. For this purpose, a NLP is solved for each of the suggested cases. The objective function is the same for all cases, see eq (1), and the objective is to maximize the electrical efficiency of the cycle. The problem is formulated as a MINLP, which is decomposed into three NLP. The first one modeled the process using ordinary combustion with absorption as the carbon capture technology. This model contains 1491 variables and 1279 equations. The second one also employs ordinary combustion but using adsorption with a PSA system for carbon capture, in this case 1045 variables and 1202 equations. Finally, the third one models the oxy combustion process, which contains 1379 variables and 1229 equations.

$$OBJ = Max\ (W_{generated} - W_{consumed}) \quad (1)$$

The capital cost of every piece of equipment is calculated with a function of a characteristic variable such as power for turbines or area for heat exchanges. This characteristic variable also indicates which option of equipment is the most suitable and if it is necessary to add a new unit because the capacity of the previous one is excesses. The investment cost is estimated from the unit costs using the factorial method [9]. To perform the scale-up analysis, the different Spanish CCPP capacities have been used. The Spanish CCPPs can be categorized into three distinct capacity ranges: 400 MW, 800 MW, and 1200 MW with small deviation. Each group of a CCPP typically has a capacity of 400 MW, which means that the different types of power plants usually comprise 1, 2, or 3 groups, respectively, although there are also groups with a capacity of 800 MW.

## RESULTS

The methodology has been applied to the Spanish CCPPs which are located in the peninsular territory, in total there are 30 plants. Figure 4 illustrates the evolution of electricity production cost for various groups of power plants when the oxygen generated as a byproduct during the electrolysis process is sold. Among the analyzed

processes, the most profitable is the ordinary combustion with absorption for carbon capture, followed by ordinary combustion process with PSA systems for carbon capture and finally oxy-combustion process.

A remarkable point of this figure is the significant impact of economies of scale on electricity production costs. Specifically, as the size of the groups of power plant increases, the production cost per unit of electricity decreases. Another important aspect is the important difference in electricity production costs between the ordinary combustion processes and the oxy-combustion process. For ordinary combustion processes, the electricity production cost ranges between 250 $/MWh and 300 $/MWh for CCPP groups with a nominal capacity of approximately 400 MW and between 90 $/MWh and 120 $/MWh for CCPP groups with a nominal capacity of around 800 MW. In contrast, the electricity production cost for oxy-combustion process is higher, approximately 470 $/MWh for 400 MW CCPP groups and 270 $/MWh for 800 MW CCPP groups.

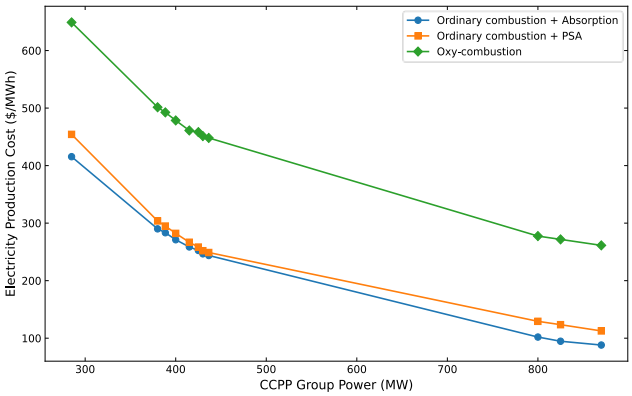



**Figure 4.** Comparation of electricity cost obtained with the different alternatives processes when the oxygen produced in the electrolyzer as subproduct is sold.

The reason for that big difference is due to the utilization of oxygen. In the oxy-combustion process, the oxygen produced during electrolysis is consumed completely for methane combustion, eliminating the option of selling it. In the ordinary combustion processes, it is assumed that all the oxygen generated as a byproduct is sold, which provides an additional revenue line that offsets the electricity production cost. This difference in oxygen utilization has a profound impact on the economic results of the processes, making the ordinary combustion configurations more cost-effective under these assumptions.

To take into account the effects of oxygen sales on electricity production costs, Figure 5 presents the costs under the assumption that the oxygen generated during the electrolysis process is not sold. In this scenario, the electricity production costs for the oxy-combustion process remain unchanged, as the oxygen produced in this process is already consumed entirely for methane combustion. However, the electricity costs for the processes based on ordinary combustion increase significantly, bringing them much closer to the costs of the oxy-combustion process. Without the additional revenue from selling oxygen, the cost advantage of these processes diminishes substantially. Figure 5 also shows an interesting trend for larger groups of power plants. Specifically, for groups with a nominal capacity exceeding 800 MW, the cost dynamics begin to change, and the oxy-combustion process emerges as the most profitable option. This suggests that, at larger scales, the oxy-combustion process offers significant economic advantages. However, only 7% of CCPP groups in Spain have a capacity higher than 800 MW, limiting the scope of this benefit.

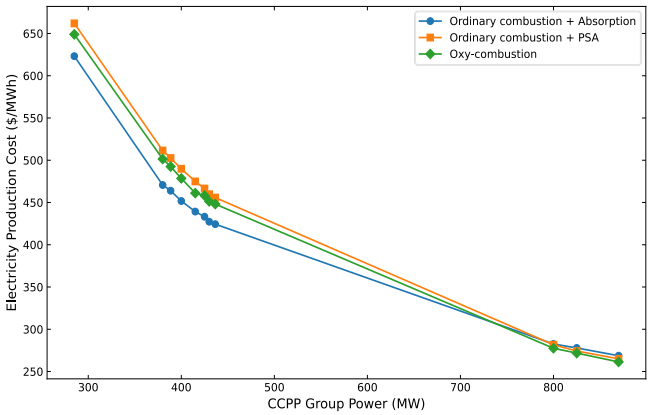



**Figure 5.** Comparation of electricity cost obtained with the different alternatives processes when any subproduct is sold.

The yields of this process have been calculated according to the following equations (5, 6, 7) and the results can be seen in Table 1.

$$\eta_{CCPP} = \frac{Power\ generated\ tubines\ CCPP}{LHV_{CH_4} \cdot F_{CH_4}} \quad (5)$$

$$\eta_{PtG} = \frac{LHV_{CH_4} \cdot F_{CH_4}}{W_{aux.met.} + W_{electrolyzer} + W_{carbon\ capture}} \quad (6)$$

$$\eta_{process} = \frac{Power\ generated}{Power\ consumed} \quad (7)$$

A typical CCPP usually achieves an efficiency ranging between 55% and 62% [10]. Processes based on ordinary combustion fall within this range, while the efficiency of the oxy-combustion process is lower. However, this trend is inverted when Power-to-Gas efficiency is analyzed. Although the oxy-combustion process requires the same hydrogen production as ordinary combustion processes, it eliminates the need for a carbon capture system, which improves the performance process. As a result, the best PtG efficiency results are achieved with oxy-combustion process (39.78%). The global efficiency of the processes analyzed is relatively similar, ranging

between 17.56% and 14.98%.

**Table 1:** Efficiencies of the processes.

| | Ordinary C. + Absorption | Ordinary C. + PSA | Oxy-combus-tion |
|---|---|---|---|
| $\eta_{CCPP}$ (%) | 65.39 | 65.65 | 43.28 |
| $\eta_{PtG}$ (%) | 32.56 | 34.06 | 29.68 |
| $\eta_{process}$ (%) | 18.14 | 20.88 | 11.65 |

## CONCLUSIONS

Different processes to integrate renewable energy with CCPP as energy storage systems are optimized and evaluated. The current CCPP could be part of this type of system by coupling the new sections of hydrogen production, carbon capture and methane production. Renewable energy (wind or solar) is employed to produce hydrogen by a PEM electrolyzer when there is an excess in the electric grid. Then it is mixed with CO2 purified to generate methane, which is again burned at the combustion chamber in the CCPP. The three processes are optimized and modeled using the first principles, thermodynamics equilibria, rules of thumb. Next, the cost estimation studies are performed and, finally, a scaling study using as base the capacity of the Spanish CCPP.

A large difference exists between the electricity production cost in ordinary combustion processes and oxy-combustion process. For a CCPP group with nominal power of 400 MW ordinary combustion processes reach a production cost of 250 -300 $/MWh and around 470 $/MWh for oxy-combustion processes. However, the difference is reduced when it is considered that oxygen cannot be sold, and the production cost is approaching the oxy-combustion ones.

The process global efficiencies are not particularly high (14.98% - 17.56%), but they demonstrate the potential of these technologies as a viable alternative for energy storage. This highlights the importance of future development and optimization of these processes to expand the number of options available for integrating renewable energy into the storage energy system.

## ACKNOWLEDGMENTS

This work was supported by the Regional Government of Castilla y León (Junta de Castilla León) and by the Ministry of Science and Innovation MICIN and the European Union NextGenerationEU / PRTR (H2MetAmo project - C17.I01.P01.S21).

## REFERENCES

1. Xiang Y, Cai L, Guan Y, Liu W, Han Y, & Liang Y. Study on the configuration of bottom cycle in natural gas combined cycle power plants integrated with oxy-fuel combustion. *Appl Energy* 212:465-477 (2018). https://doi.org/10.1016/j.apenergy.2017.12.049
2. Strojny M, Gładysz P, Hanak D P, Nowak W. Comparative analysis of CO2 capture technologies using amine absorption and calcium looping integrated with natural gas combined cycle power plant. *Energy* 284:128599 (2023). https://doi.org/10.1016/j.energy.2023.128599
3. Blanco H, Codina V, Laurent A, Nijs W, Maréchal F, Faaij A. Life cycle assessment integration into energy system models: An application for Power-to-Methane in the EU. *Appl Energy* 259: 114160 (2020). https://doi.org/10.1016/j.apenergy.2019.114160
4. Guerras LS, Martín M. On the water footprint in power production: Sustainable design of wet cooling towers. *Appl Energy* 263:114620 (2020). https://doi.org/10.1016/j.apenergy.2020.114620.
5. Martín-Hernández E, Guerras LS, Martín M. Optimal technology selection for the biogas upgrading to biomethane. *J. Clean. Prod.* 267:122032 (2020). https://doi.org/10.1016/j.jclepro.2020.122032
6. Chue KT, Kim JN, Yoo YJ, Cho SH, Yang RT. Comparison of activated carbon and zeolite 13X for CO2 recovery from flue gas by pressure swing adsorption. *Ind. Eng. Chem. Res.* 34(2):591-598 (1995). https://doi.org/10.1021/ie00041a020.
7. Akyüz ES, Telli E, Farsak M. Hydrogen generation electrolyzers: paving the way for sustainable energy. *Int. J. Hydrogen Energy* 81: 1338-1362 (2024). https://doi.org/10.1016/j.ijhydene.2024.07.175.
8. Stangeland K, Kalai D, Li H, Yu Z. CO2 methanation: the effect of catalysts and reaction conditions. *Energy Procedia* 105: 2022-2027 (2017). https://doi.org/10.1016/j.egypro.2017.03.577.
9. Sinnott R, Gavin T. Costing and project evaluation. In: Chemical Engineering Design Ed: Butterworth-Heinemann. Elsevier (2019).
10. IPIECA. Combined-Cycle Gas Turbines. 2022. https://www.ipieca.org/resources/energy-efficiency-compendium-online/combined-cycle-gas-turbines-2022#

© 2025 by the authors. Licensed to PSEcommunity.org and PSE Press. This is an open access article under the creative commons CC-BY-SA licensing terms. Credit must be given to creator and adaptations must be shared under the same terms. See https://creativecommons.org/licenses/by-sa/4.0/



Systems & Control Transactions

**Research Article - Peer Reviewed Conference Proceeding**
ESCAPE 35 - European Symposium on Computer Aided Process Engineering
Ghent, Belgium. 6-9 July 2025
Jan F.M. Van Impe, Grégoire Léonard, Satyajeet S. Bhonsale,
Monika E. Polańska, Filip Logist (Eds.)

PSE PRESS

# On the Economic Uncertainty and Crisis Resiliency of Decarbonization Solutions for the Aluminium Industry

**Dareen Dardor[a,b,] *, Daniel Flórez-Orrego[a], Reginald Germanier[c], Manuele Margni[b], and François Maréchal[a]**

[a] Industrial Process and Energy Systems Engineering, Ecole Polytechnique Fédérale de Lausanne, EPFL, Sion, 1950, Switzerland
[b] Institute of Sustainable Energy, School of Engineering, University of Applied Sciences and Arts Western Switzerland (HES-SO), Sion, 1950, Switzerland
[c] Novelis Switzerland S.A., Sierre 3960, Switzerland
* Corresponding Author: dareen.dardor@epfl.ch

## ABSTRACT

The aluminium industry emits approximately 1.1 billion tonnes of $CO_2$-eq annually, contributing about 2% of global industrial emissions. Decarbonization pathways aim to achieve net-zero emissions by 2050, but this requires making decisions today for technologies having lifetimes of 20 – 25 years, based on uncertain economic assumptions, particularly given the volatility of energy prices. Traditional price forecasting models often fail to anticipate major disruptions, such as the 2022 energy crisis. This work applies Monte-Carlo Analysis (MCA) to evaluate the financial stability of decarbonization pathways under energy crisis scenarios and report on the resilience of the alternative solutions. In the modelled secondary aluminium production facility, direct electrification is assumed for lower temperature furnaces of annealing heat treatments or preheating, while the study defines the decarbonization options based on the melter furnace technology, a key bottleneck in terms of load and viable technological alternatives with roof temperatures exceeding 1,000°C. In this study, four decarbonization pathways characterized by unique melting furnace solutions are analyzed, namely: an oxyfuel scenario using natural gas with carbon capture, a biomass-based approach relying on syngas, a hydrogen-based solution utilizing onsite electrolysis, and a plasma-based system with torches for melting. These options are compared to a natural gas baseline. Differences in electrification levels and reliance on imported energy sources result in varied economic resilience under price shocks that can occur during different times of the plant's life. Results obtained for a set of initial price levels at moderate or crisis energy price profiles revealed a more resilient oxyfuel scenario, followed by biomass utilization, and finally the all-electric scenarios utilizing either hydrogen or plasma. For instance, the oxyfuel option demonstrates a 54% probability of negative incremental Net Present Value (iNPV) with reference to the base case under both crisis and moderate price profiles. Conversely, the biomass scenario was found to have a 95-98% likelihood of economic loss under similar conditions while the all-electric solutions were at 100% likelihood of loss regardless of the initial price or profile. This is because electricity prices start at a higher baseline than combustible fuels and spike dramatically during crisis events. This analysis highlights the importance of considering energy price volatility and the need for diversified energy sources when developing decarbonization strategies for the aluminium industry.

**Keywords**: Aluminium, Decarbonization, Energy Prices, Crisis Modelling, Monte-Carlo Analysis.

## INTRODUCTION

Increasing global warming effects have urged heavy industries to actively reduce greenhouse gas (GHG) emissions, targeting net zero by 2050. The aluminium sector emits approximately 1.1 billion tonnes of GHG

annually, representing 2% of global industrial emissions [1]. The primary energy source for aluminium remelting furnaces is fossil natural gas; while rolling processes consume electricity whose embodied emissions depend on geographical location. Decarbonization strategies for aluminium include biomass gasification, power-to-gas, direct electrification of furnaces, and carbon capture. While most of these technologies have lifetimes of 20 – 25 years, decisions on their installment must be made during the early stages of design. Prices and future availability of utilities depend on many economic and geopolitical inter-related aspects. Another influencing value is the cost of continuing to emit GHG which could directly translate to an imposed carbon tax [2] or a defined social cost of negatively impacting the environment [3]. Hence, future uncertainty in energy prices must be accounted for in today's decisions.

Price forecasting models, while useful, are often inaccurate, failing to account for significant events like the 2022 energy crisis [4–6]. Historical data shows that predictions can significantly underestimate or overestimate actual prices due to unpredictable market factors. This is because the market is not only a function of demand and supply but is also dependent upon numerous geopolitical factors which are simply unpredictable in the long term. Nonetheless, prices are a major influencing factor on decision-makers' choices towards industry decarbonization, which necessitates the development of a systematic methodology to deal with such uncertainty.

Monte-Carlo analysis (MCA) is a stochastic mathematical technique for global sensitivity and risk or uncertainty evaluations. It is mainly used to quantify the simultaneous impact of various parameters on a performance indicator using hundreds of thousands of model inputs. One study used MCA to explore decarbonization strategies in the steel industry [7]. The authors used MCA to examine the effects of factors such as hydrogen prices, the investment costs of reduction furnaces, and associated emissions on the adoption of hydrogen in steel production. Their analysis identified hydrogen price as the most critical factor. Similarly, another study evaluated the impact of natural gas price uncertainty on the economic feasibility of offshore power hubs with carbon capture systems for Floating Production, Storage, and Offloading facilities (FPSOs). By generating stochastic price profiles, the researchers calculated incremental net present values (iNPVs) for various configurations and found that profitability was highly sensitive to operational delays, as longer delays increased the likelihood of losses due to opportunity costs and depreciation [8]. Similarly, MCA could be used in evaluating the economic stability of different decarbonization configurations developed for the aluminium industry. In this regard, this work adopts stochastic and deterministic methodologies to more accurately model the effect of energy price uncertainty, especially during times of economic crisis, on potential decarbonization pathways for secondary aluminium production. The work integrates Process Systems Engineering (PSE) methodologies by combining mixed-integer linear programming (MILP) with MCA to evaluate uncertainty in industrial energy systems. The developed framework provides a systematic approach for assessing economic risk in decarbonization pathways, offering a decision-support tool based on PSE principles for process optimization under uncertainty.

## METHODS

The methodology developed in this work starts by modeling a typical secondary aluminium production plant and a set of energy conversion systems associated with different decarbonization pathways within the OSMOSE platform [9]. Herewith, a MILP optimization approach is applied to generate a list of optimal system configurations under specified economic scenarios using a defined set of current energy price levels. Finally, MCA is performed to estimate the probability of each solution incurring higher costs than the base case over a 25-year lifetime, incorporating random price fluctuations and crisis-like price profiles. This hybrid deterministic-stochastic approach aligns with PSE methodologies, enabling more robust decision-making in the face of industrial uncertainties.

First, a typical secondary aluminium production process is modeled based on Novelis' production facility in Sierre, Switzerland, consisting of a cast house, and a rolling mill for subsequent treatment and coil rolling [10]. The process begins with preheating pure aluminium ingots to around 250°C in the preheater, to prevent explosion risks during melting, this step accounts for approximately 5% of the plant's total natural gas consumption. In the melter, where around 49% of the facility's natural gas is consumed, pure and scrap aluminium are melted at approximately 660°C and then superheated to 700°C. The holder furnace, which uses 4% of the plant's natural gas, acts as a buffer for the direct chill casting (DCC) process, where the aluminium solidifies gradually by dissipating heat into a water sink. The cast ingots undergo surface treatment before being sent to the pusher furnace for annealing, which consumes 25% of the plant's natural gas, followed by hot and cold rolling processes. Finally, the coils are subjected to further heat and chemical treatment in the annealing continuous line (ACL), which accounts for 17% of the natural gas consumption. While conventional facilities rely on fossil natural gas to fuel these furnaces, several decarbonization alternatives can be explored, utilizing diverse energy sources. This work evaluates several of these alternatives. A simplified schematic of the potential decarbonization options is presented in **Figure 1**. The energy conversion technologies and furnaces were modeled in detail using software tools

such as Aspen Plus®, supplemented by data from industrial system audits and commercial technology specifications. All optimized scenarios, except the base case, employ fixed electrification solutions for the preheating, annealing, and holding furnaces. Thus, the optimization focuses on the melter furnace, identified as the technological bottleneck in decarbonizing secondary aluminium production. The following scenarios define the range of solutions explored:

1. **Base Case:** This represents the current baseline operation of the plant, where all furnaces rely on fossil natural gas combustion.
2. **Oxyfuel CCS:** Implements an oxyfuel combustion system for the melter furnace, where natural gas is burned in oxyfuel burners, followed by post-combustion carbon capture and sequestration through transportation and injection. Oxygen for the process is supplied by an on-site air separation unit (ASU).
3. **Bio-Syngas:** Utilizes oxyfuel combustion of bio-syngas, a mixture of CO, $H_2$, and $CO_2$ gases, produced via on-site biomass gasification for the melter furnace. Oxygen is supplied using an on-site ASU.
4. **Hydrogen:** Employs air combustion of hydrogen in the melter furnace, with hydrogen generated on-site using a proton exchange membrane (PEM) electrolyzer.
5. **Plasma:** Adopts an electric aluminium melting solution using plasma torches for the melter furnace, with nitrogen plasma gas supplied via an on-site ASU.

This structured approach ensures that each decarbonization pathway addresses the specific challenges posed by the melter furnace while considering diverse energy resources and technologies.

Furthermore, MCA is applied to assess the economic feasibility of these defined decarbonization pathways for aluminium production compared to the natural gas-based baseline (Base Case). Two modes of price evolution are modeled: moderate price trends, representing natural market fluctuations, and crisis scenarios, simulating sudden price spikes followed by gradual recovery. An example of the generated price profiles is illustrated in Figure 2 (moderate trends) and Figure 3 (crisis scenarios).

**Table 1:** Initial energy prices and crisis mode multipliers

| Resource | Initial Price | Peak multiplier |
|---|---|---|
| Natural gas | 0.04 (€/kWh) | 7 |
| Electricity | 0.10 (€/kWh) | 3 |
| Biomass | 0.06 (€/kWh) | 3 |
| $CO_2$ tax | 100 (€/t$CO_2$) | N/A |

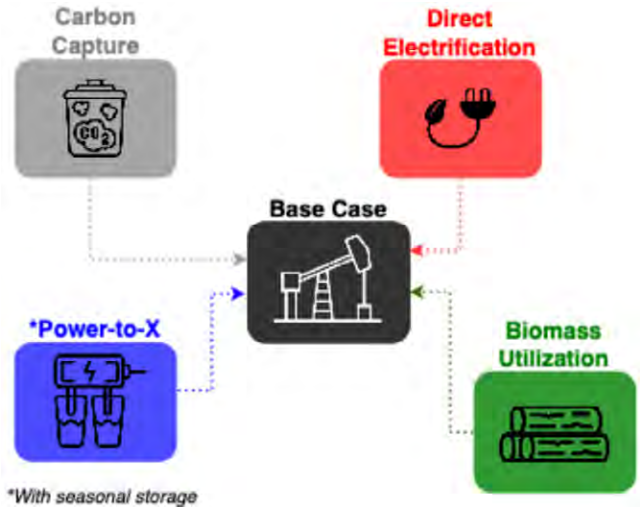



**Figure 1.** Simplified schematic of aluminium decarbonization scenarios investigated in this work.

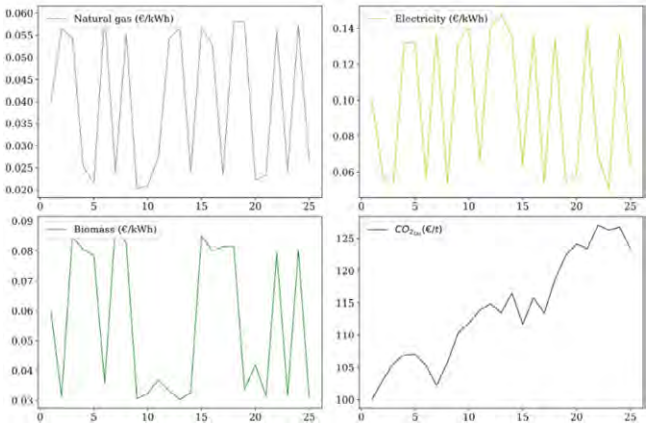



**Figure 2.** MCA sample of a set of stochastic energy price profiles over a lifetime of 25 years.

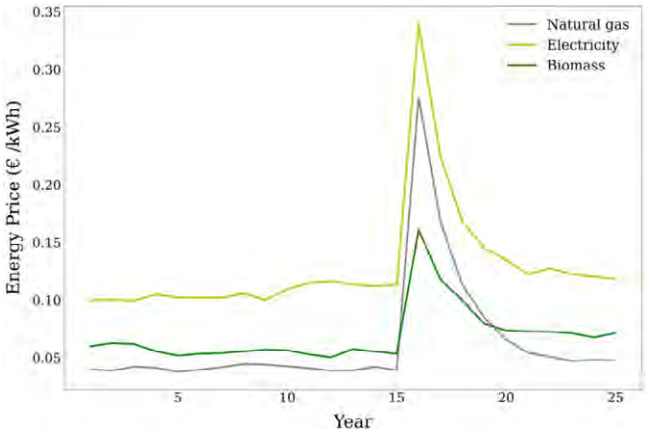



**Figure 3.** MCA sample of a set of energy price shock profiles over a lifetime of 25 years.

## Initial Price Trends and Profiles

The simulation begins by defining initial energy and commodity prices for key resources, as shown in Table 1.

Next, price evolution is modeled as follows:

1. **Moderate Price Trends:** Prices fluctuate annually based on a normal distribution with a 5% standard deviation around the previous year's price. These profiles represent natural market dynamics without major disruptions and are shown in Figure 2.
2. **Crisis Scenarios:** A random crisis year is selected between years 2 and 20. During this year, prices experience sudden spikes, defined by resource-specific peak multipliers. Prices then gradually stabilize post-crisis at levels 20% higher than the initial price. An example of these crisis-induced profiles is illustrated in Figure 3.

The price profiles in this study are generated using pseudo-random numbers sampled from statistical distributions implemented by Python's NumPy random number generator. The following equations provide more insight into how the profiles are generated:

- **Moderate Trends:**

$$P_y = P_{y-1} \cdot (1 \pm random\ variation) \quad (1)$$

In this case, the random variation is sampled from the range defined by `varin=(0.3, 0.5)`, representing deviations of 30% to 50% of the initial or previous year's price. This range ensures variability while maintaining realistic fluctuations in the moderate trend profiles. Additionally, for each resource price profile, a trend probability parameter ($P_{trend}$) determines the likelihood of following a predefined trend. In the current simulation, $P_{trend} = 0.5$, meaning there is a 50% probability that the price will follow the specified trend ("up," "down," or "none"). The remaining 50% of the time, prices deviate randomly, ensuring variability in the generated profiles.

- **Crisis Mode:**

o Pre-crisis:

$$P_y = P_{y-1} \cdot Normal\ (1, 0.05) \quad (2)$$

Smaller fluctuations in prices before the crisis are modeled using random multipliers sampled from a normal distribution $Normal\ (1, 0.05)$, which ensures prices fluctuate around the previous year's value with a mean of 1 and a standard deviation of 0.05, reflecting natural market variability.

o Crisis year:

$$P_y = P_{y-1} \cdot Peak\ multiplier \quad (3)$$

During the crisis year, prices experience sharp spikes, modeled using predefined peak multipliers (e.g., 7 for natural gas, 3 for electricity, and 2 for biomass).

o Post-crisis:

$$P_y = P_{y-1} - (P_{y-1} - P_{post-crisis}) \cdot Decline\ Rate \cdot Normal\ (1, 0.05) \quad (4)$$

After the crisis, prices gradually stabilize toward a defined post-crisis level, calculated as a fixed percentage above the initial price (e.g., 20% higher, as set in this simulation). The decline rate, set to 0.5, in this case, controls how quickly prices approach the post-crisis level.

## Cost Calculation and NPV Evaluation

For both modes, the Base Case and decarbonization scenarios are evaluated as follows for the defined parameters listed in Table 2:

1. **Annual Cost Profiles:**
   - o Resource costs (natural gas, electricity, etc.) are multiplied by respective consumption flows to calculate operational expenses (OPEX).
   - o Capital expenditures (CAPEX) are distributed as 60% in the first year and 40% in the second year.
2. **Net Present Value (NPV):**
   - o Total Expenditures ($TOTEX_y$) include CAPEX and OPEX for each year.
   - o Discounted cash flows are calculated using:

$$NPV = \sum_{y=1}^{N} \frac{TOTEX_y}{(1+i)^y} \quad (5)$$

   where $i = 6\%$ is the discount rate.
3. **Incremental NPV (iNPV):**
   - o $iNPV = NPV_{decarb} - NPV_{base\ case}$
   - o The likelihood of loss ($iNPV < 0$) is calculated over 10,000 Monte Carlo iterations.

**Table 2:** Simulation settings for both moderate and crisis modes

| Parameter | Value |
|---|---|
| Discount rate (i) | 6% |
| Plant lifetime (N) | 25 years |
| Annual Operating hours | 8,760 h |
| Monte-Carlo iterations | 10,000 |

By combining moderate and crisis price profiles, the approach quantifies the economic stability of decarbonization pathways, highlighting the influence of market volatility and extreme price shocks on incremental net present value. This dual-mode simulation provides a probabilistic framework for decision-making under uncertainty.

# RESULTS

First, the performance of the defined decarbonization routes is assessed relative to the Base Case. **Figure 4** illustrates the energy load distribution and the equivalent carbon footprint (including scope 1 and 2 emissions) for the various alternatives. Among the scenarios, the

Bio-Syngas route achieves the lowest carbon footprint, at approximately -2.80 $kgCO_2/tAl$, due to the net-negative impact of sequestering biogenic carbon used in the melter furnace. The all-electric options result in a footprint of around 30 $kgCO_2/tAl$, primarily driven by the indirect emissions associated with the electricity grid. In contrast, the Oxyfuel CCS scenario has slightly higher emissions, at approximately 55 $kgCO_2/tAl$, which is attributed to both indirect electricity emissions and loss of some direct $CO_2$ during furnace operation prior to capture.

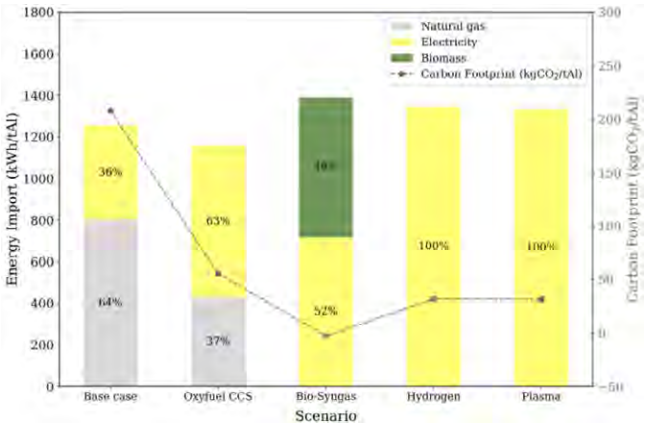



**Figure 4.** Energy load distribution and equivalent carbon footprint of aluminium decarbonization options.

Next, the iNPVs of the different scenarios are evaluated for both moderate and crisis price fluctuations over 10,000 Monte-Carlo samples and the resulting distributions are plotted in **Figure 5**. It is evident that moderate price fluctuations generally result in broader iNPV ranges than crisis price profiles while the average iNPV value for both modes is observed to be similar. The Oxyfuel CCS is the least economically volatile solution at a 54% likelihood of loss regardless or moderate or crisis modes, followed by the Bio-Syngas option at around 95-98% likelihood of loss. Both electrification solutions are significantly negative in terms of iNPVs with reference to the natural gas driven base case. With a 100% likelihood of loss quantifying the economic risk associated with complete electrification.

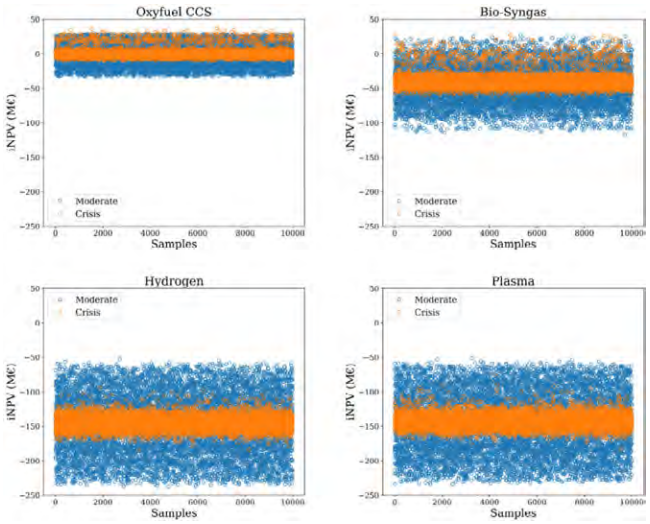



**Figure 5.** Resilience comparison of the decarbonization options in case of moderate or crisis price profiles.

To better understand the statistical distribution of iNPV results**, Figure 6** presents a box plot of iNPVs for the different decarbonization scenarios, highlighting the variability under moderate and crisis conditions. The boxes represent the interquartile range (IQR), while data points outside the whiskers, calculated as values smaller than Q1–1.5×IQR or larger than Q3+1.5×IQR, are considered outliers and plotted as dots. The outliers observed in the iNPV distributions, particularly under crisis scenarios, are closely linked to the timing of energy price spikes and their impact on operational costs. Both higher-than-average and lower-than-average outliers tend to occur when the crisis happens early in the project lifetime, specifically in Year 2. This timing coincides with a period where discounting effects are less pronounced, which intensifies the influence of energy price volatility on economic performance outcomes. The exact reasons for the dual behavior, positive and negative outliers, remain complex and may depend on several factors, including the severity of the spike, the recovery rate of energy prices, and other influential aspects. This result, however, highlights Year 2 as a critical period where energy price dynamics have an exaggerated impact on iNPV.

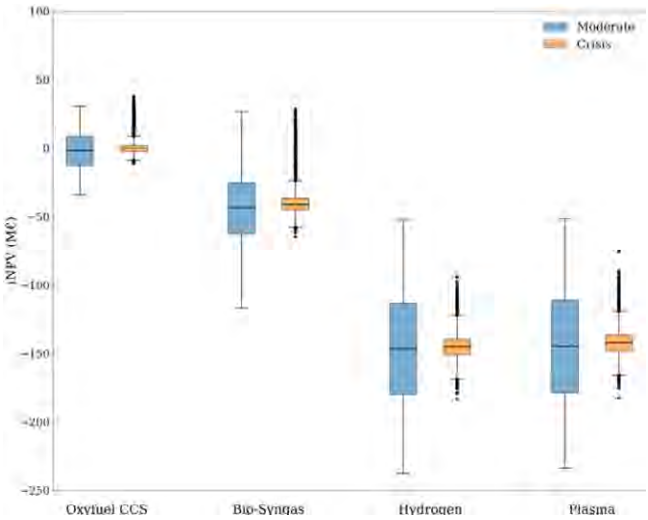



**Figure 6.** Box plot distribution of the likelihood of loss results for the decarbonization options.

Due to the apparent coupling of natural gas and electricity prices the economic risk for the Oxyfuel CCS solution seemed to remain constant at 54% for a fixed set of initial energy prices no matter the mode of energy price profiles (moderate or crisis). Hence, a sensitivity analysis over the likelihood of loss when varying initial prices of electricity and $CO_2$ tax was conducted following moderate price fluctuations. From **Figure 7**, it is seen that the breakeven initial $CO_2$ tax for this solution increases from around 170 €/t$CO_2$ for cheaper electricity (at an initial price of 0.1 €/kWh$_{EE}$) to 380 €/t$CO_2$ at double the initial electricity price following a directly proportional correlation.

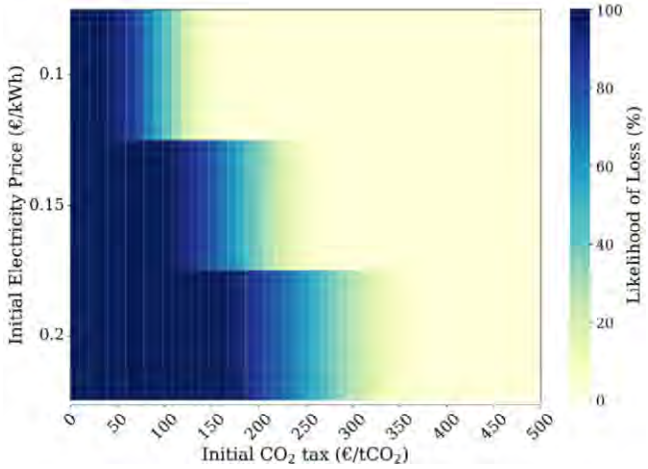



**Figure 7.** Economic risk of the Oxyfuel CCS configuration as a function of the initial values of $CO_2$ tax and electricity price.

## CONCLUSION

This study highlights the critical role of economic uncertainty and energy price volatility in shaping the viability of decarbonization pathways for secondary aluminium production. By combining Monte Carlo Analysis with mixed-integer linear programming, the work leverages PSE tools to provide key insights into the resilience of various technological configurations under moderate and crisis scenarios. The findings emphasize that decarbonization strategies heavily reliant on electricity are particularly vulnerable to price shocks, leading to a 100% likelihood of economic loss compared to the natural gas baseline. In contrast, the Oxyfuel CCS scenario exhibits greater economic resilience, maintaining a constant 54% likelihood of loss across both modes of price evolution, suggesting its potential as a transitional pathway. However, these conclusions must be taken with caution as they are heavily influenced by the low initial natural gas price of 0.04 €/kWh, mainly due to fossil subsidies, which currently makes it a more economically favorable energy source. If renewable electricity becomes significantly cheaper in the future, the relative economic performance of electrification-based solutions could improve, shifting the results of this comparative evaluation. This work provides a probabilistic framework to guide policymakers and industry stakeholders in navigating market uncertainties and emphasizes the importance of preparing diversified and adaptive decarbonization strategies.

## ACKNOWLEDGEMENTS

The authors would like to thank the Net Zero Lab consortium for funding this work in the context of the project goals of decarbonizing secondary aluminium production.

## REFERENCES

1. IAI. Greenhouse Gas Emissions – Aluminium Sector [Internet]. 2024 [cited 2024 Jul 19]. Available from: https://international-aluminium.org/statistics/greenhouse-gas-emissions-aluminium-sector/
2. European Commission. The Functioning of the European carbon market in 2021. 2022.
3. Rennert K, Errickson F, Prest BC, Rennels L, Newell RG, Pizer W, et al. Comprehensive evidence implies a higher social cost of CO2. Nature. 2022;610:687–92.
4. Craig PP, Gadgil A, Koomey JG. What Can History Teach Us? A Retrospective Examination of Long-Term Energy Forecasts for the United States. Annu Rev Energy Environ. 2002;27:83–118.
5. Koomey J, Craig P, Gadgil A, Lorenzetti D. Improving Long-Range Energy Modeling: A Plea for Historical Retrospectives. The Energy Journal. 2003;24:75–92.

6. Sohn I. Long-term energy projections: What lessons have we learned? Energy Policy. 2007;35:4574–84.
7. Lee H. Decarbonization strategies for steel production with uncertainty in hydrogen direct reduction. Energy. 2023;283:129057.
8. Flórez-Orrego D, Albuquerque C, Da Silva JAM, Freire R, De Oliveira Junior S. Offshore Utility Systems for FPSOs: A Techno-Environomic Assessment Considering the Uncertainty About the Natural Gas Price. Front Chem Eng. 2022;4:853749.
9. Dardor D, Flórez-Orrego D, Terrier C, Ribeiro ME, Lopez M, Maréchal F. ROSMOSE: A Web-based Optimization Tool to Aid Decision-making for the Design and Operation of Industrial and Urban Energy Systems. ECOS 2023 [Internet]. Las Palmas de Gran Canaria; 2023. Available from: https://infoscience.epfl.ch/record/303487
10. Florez Orrego DA, Dardor D, Germanier R, Maréchal F. A systemic study for enhanced waste heat recovery and renewable energy integration towards decarbonizing the aluminium industry. 36th international conference on efficiency, cost, optimisation, simulation and environmental impact of energy systems-ECOS 2023. 2023.

© 2025 by the authors. Licensed to PSEcommunity.org and PSE Press. This is an open access article under the creative commons CC-BY-SA licensing terms. Credit must be given to creator and adaptations must be shared under the same terms. See https://creativecommons.org/licenses/by-sa/4.0/



Systems & Control Transactions

**Research Article - Peer Reviewed Conference Proceeding**
ESCAPE 35 - European Symposium on Computer Aided Process Engineering
Ghent, Belgium. 6-9 July 2025
Jan F.M. Van Impe, Grégoire Léonard, Satyajeet S. Bhonsale,
Monika E. Polańska, Filip Logist (Eds.)

PSE PRESS

# A Data-Driven Conceptual Approach to Heat Pump Sizing in Chemical Processes with Fluctuating Heat Supply and Demand

**Thorben Hochhaus[a#*], Johannes Wloch[a#], Marcus Grünewald[a], and Julia Riese[b]**

[a] Ruhr University Bochum, Laboratory of Fluid Separations, Bochum, Germany
[b] Paderborn University, Fluid Process Engineering, Paderborn, Germany
[#] Thorben Hochhaus and Johannes Wloch contributed equally to this work.
[*] Corresponding Author: thorben.hochhaus@fluidvt.rub.de.

## ABSTRACT

Heat pumps play a crucial role in decarbonizing the chemical industry. The integration and sizing of heat pumps in chemical processes is a challenging task in multi-product chemical processes due to the fluctuating waste heat supply and heat demand. Integrating heat pumps may require a retrofit of the utility system. Mathematical optimization is a useful tool to tackle this challenge by enabling the analysis of correlation between relevant system parameters and equipment sizing. This study demonstrates the utilization of mathematical optimization and parameter studies for utility system equipment sizing addressing fluctuating heat supply and demand profiles.

**Keywords**: Energy Systems, Batch Systems, Optimization, Renewable and Sustainable Energy, Energy Storage

## INTRODUCTION

To achieve the goal of climate neutrality by 2045, Europe must cut down $CO_2$ emissions significantly [1]. This initiative directly impacts the chemical and pharmaceutical industries, which account for a substantial share of energy usage and related $CO_2$ emissions [2]. One potential approach to lower these emissions is the electrification of chemical and pharmaceutical processes, ideally powered by renewable electricity with a smaller carbon footprint, for instance, through the integration of heat pumps [3]. Pharmaceutical processes are often multi-product plants where heat is supplied using heating and cooling circuits. In these cases, heat is supplied centrally to the utility system. When integrating heat pumps, not only the correct sizing of the heat pump must be determined but also a possible retrofit of the utility system, additional components such as heat storages and backup systems and optimal operation must be considered. This results in a complex integration problem. Mathematical optimization is a method that can solve complex problems like the aforementioned. Different problem types have been solved in the context of utility system optimization for chemical processes. The scope of this paper is to give a brief overview of mathematical optimizations in different applications of utility systems. We further analyse optimal equipment sizing for a utility system in a multi-product plant with fluctuating waste heat supply and heat demand. By using mathematical optimization and parameter studies, we analyse the correlation between system parameters such as specific investment cost or heat profile characteristics and equipment sizing.

## LITERATURE REVIEW

The optimization of utility systems without the integration of heat pumps is a topic that has been extensively studied. A utility system should deliver mostly electricity and heat. Papoulias and Grossmann developed a MILP to minimize costs of a utility system that provides electricity and steam in the context of a chemical plant and to derive the optimal structure of equipment and operation [4]. Other work included nonlinear equations of cost functions and operational constraints, resulting in a MINLP for optimizing the utility system [5]. Mitra et al. optimized operation of an existing utility system under fluctuating electricity prices. Solving the resulting MILP requires precise knowledge of the flexibility parameters of the components. [6]

Several studies also optimize the design and

operation of utility systems including heat pumps with respect to minimizing costs. Bischi et al. linearized non-linear performance curves of equipment to minimize costs using a MILP [7]. Baumgärtner et al. developed a model for a low-carbon utility system incorporating heat pumps. By accounting for time-dependent emission factors, a MILP was employed to analyze the trade-off between economic and environmental impacts. [8] Prendl et al. examined the sizing and operation of a heat pump and heat storage within heat exchanger networks, aiming to minimize total annual costs using a MILP [9].

As previously mentioned, integrating heat pumps into chemical processes poses significant challenges. It may be worthwhile looking at different sectors which also implement heat pumps in their utility system to find possible analogies. One such sector is the residential sector where various methods for heat pump integration and equipment sizing are studied, including mathematical optimization. Molyneaux et al. solved the problem of choosing between centralized and decentralized heat pump integration for district heating in residential buildings using a multi-objective optimization. They compared different systems using multi-objective optimization regarding economic and ecological parameters. [10] Rinaldi et al. determined the optimal size of a system which includes photovoltaic, battery storage and a heat pump for residential buildings by minimizing the total cost. The heat pump enables the system to increase the utilization of electricity generated by the photovoltaic system. Furthermore, the heat pump can be operated flexibly to reduce operating costs, leveraging the building's thermal inertia, as heat only needs to be provided over the course of the day rather than at specific times. [11] Renaldi et al. also analyzed a residential heating system including a heat pump and a thermal storage, by minimising the total costs using a MILP. They considered flexible heat pump operation with upper and lower operating bounds for the heat pump. [12]

A few optimisation approaches compare the solution of mathematical optimization with rules of thumb. Alay et al. use a mathematical approach to optimize the design of a hybrid ground source heat pump for different case studies. The results of the optimization have been compared afterwards with an existing rule of thumb regarding the percentage of the total heat demand covered directly by the heat pump. It became evident that results of the optimisation could not confirm the rule of thumb but rather also vary in a range for different case studies. Furthermore, they highlighted that rules of thumb are often restricted to a specific sector, as general conditions, such as the ratio of cooling to heating, can vary significantly depending on the sector. [13] Fischer et al. examined existing heuristic sizing methods of thermal energy system components like heat pumps and heating storage depending on the operation mode of the heat pump (monovalent, monoenergetic and bivalent). They applied mathematical optimization to minimize total cost for different case studies in the residential sector, taking variable electricity prices into account and compared the results with the heuristic rules. They found sufficient agreement between the heuristic-based design and mathematical optimization approach. Moreover, they underline that the heat demand profile has the greatest impact on sizing. [14]

This further motivates investigating the impact of heat profiles on component sizing within other sectors, such as the chemical industry. In non-continuous chemical processes in particular, the heat demand profiles are not as characteristic as in the building sector and can therefore present an additional challenge for deriving sizing methods for heat pumps. In order for heat pumps to be integrated in chemical processes such as non-continuous processes, their flexibility parameters must be available. Sadjjadi et al. underline the importance of developing methods for sizing and operational strategies of large-scale heat pumps for industrial applications [15]. Part-load efficiencies are relevant to model the flexibility of heat pumps. However, Xu et al. point out that there is no uniform standard for part-load efficiency calculations of heat pumps [16]. Walden et al. used an approach to determine heat pump part-load efficiency by taking the individual component part-load efficiencies into account. They compared this approach to a standard approach which calculates the part-load efficiency by means of a degradation coefficient. [17]

This brief literature review illustrates that equipment sizing for processes requiring flexible operation, such as non-continuous chemical processes, presents a significant challenge. Mathematical optimization proves to be a valuable method to address this complexity, and to analyze the impact of fluctuating heat supply and demand profiles on equipment sizing and operation while incorporating the flexibility characteristics of components.

## PROBLEM STATEMENT

Using mathematical optimization in combination with robust parameter studies allows for the sizing equipment of a utility system and is applied to an application in a multi-product chemical process with resulting fluctuating waste heat supply and heat demand in this work.

To analyze the impact of fluctuating waste heat supply and heat demand, an exemplary scenario has been analyzed as depicted in Figure 1. This can be a typical energy supply system to multiple batch processes with fluctuating heat and cooling demand. Batch operated processes often require heating and cooling intervals following fixed patterns to produce the desired product. These patterns can vary for different products considering heating and cooling duties as well as their duration.

Additionally, batch plants can be multi-product plants without fixed production schedules which can lead to further fluctuations in heat supply and demand.

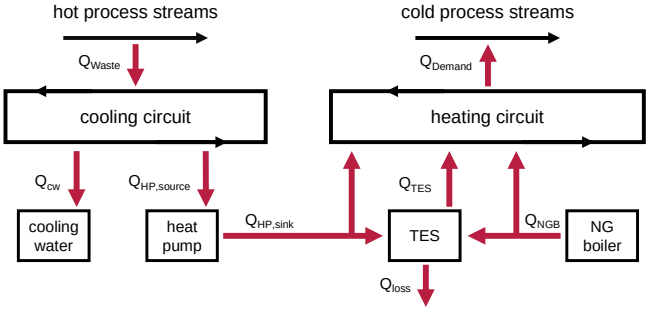



**Figure 1.** Schematic of the examplary utility system.

We assume a brownfield scenario for the chemical process side where heat is supplied to cold process streams using a heating circuit at a supply temperature of maximum 105 °C e.g. through thermal oil or steam. A cooling circuit is used to collect waste heat from the processes at a return temperature of minimum 25 °C e.g. through thermal oil or cooling water. We assume the holdup in the system to be in the range of 15 minutes. To ensure normal operation, the energy demand of the process system must be met by the energy supply for every 15-minute period. The necessary heating and cooling duties are supplied centrally to the heating and cooling circuits.

For the utility side, three technologies are available for a new investment. Firstly, a natural gas boiler which can be used to supply heat to the heating circuit by burning natural gas. Secondly, a vapor compression heat pump which can be used to upgrade waste heat from the cooling circuit to the heating circuit by using electricity to drive the compressor. Lastly, a thermal energy storage can be used to store thermal energy supplied by the natural gas boiler or heat pump and supply it to the heating circuit.

We use a synthetic profile with fluctuations around a mean to emulate a fluctuating heat demand and waste heat profile. The fluctuations are evoked by normally distributed random noise and small and large spikes with normally distributed random amplitude and time between spikes. These fluctuations are assumed to result from fluctuating heating and cooling demand from process streams which must be met by the different utility components. Although we assume a multi-product batch system on the process side, we assume the heating and cooling demand to follow similar patterns. Thus, the cooling duty profile differs from the heating duty profile only by assuming a lag of 15 minutes, as shown in the supplementary material.

## MODEL FORMULATION

The impact of fluctuating demand profiles on equipment sizing was examined using a MINLP to determine the minimum total annual cost. For this purpose, we used simple energy balance models that incorporate efficiency correlations and operational constraints for all components of the utility system. This reduces computational effort and allows for a general system comparison without technology specific characteristics. Including operational expenditure and investment cost allows for minimization of total annual costs. The equations used to model the utility system as well as underlying operational constraints are described in more detail in the following sections and in the supplementary material.

### MINLP

The MINLP formulation minimizes the objective function $c$ subject to sets of linear and nonlinear equality and inequality constraints, represented by $g$ and $f$, respectively. The decision variables include binary variables $x$ and continuous variables $y$.

$$\min_{x,y} c(x,y) \tag{1}$$
$$\text{s.t. } g(x,y) = 0$$
$$f(x,y) \leq 0$$
$$x \in \{0,1\}^m,\ y \in \mathbb{R}^n$$

The component and system constraints must be satisfied for each time interval $t$. Since energy supply and demand must be balanced in 15-minute intervals, this condition applies to every 15-minute timestep within the optimization time horizon of 48 hours.

### Heat Pump

We consider the heat pump (HP) to be a closed-cycle mechanical vapor compression HP. It can be operated with load flexibility concerning its sink duty $\dot{Q}_{HP,sink}(t)$ in a range of 40-100% of the nominal sink duty $\dot{Q}_{HP,sink,nom}$. A constant part-load efficiency is assumed by using a constant coefficient of performance (COP).

To account for operational constraints, we used minimum uptime and downtime constraints. We used binary variables to indicate startups and shutdown and summation constraints to ensure minimum uptime and downtime of the HP. Additionally, we added constraints on the time between load shifts of the HP to account for real world operational challenges during load shifts.

### Natural gas boiler

For the natural gas boiler (NGB), we used a simple model consisting of boiler efficiency ($\eta_{NGB}$) as well as the same operational constraints as for the HP. The duty of the NGB $\dot{Q}_{NGB}(t)$ is allowed to range from 20-100% of the

nominal duty $\dot{Q}_{NGB,nom}$. Again, we assume no decrease in efficiency during partial load.

The same operational constraints were applied for the NGB as for the HP. Binary variables indicate startup and shutdown of the NGB as well as load changes. Limitations for minimum uptime, minimum downtime and time between load changes were implemented analogically. This was done due to a lack of experimental data as well as the motivation to compare different heat supply system configurations instead of a detailed technological comparison. This also ensures that no unbiased preference is given to one component over the other. It follows that the primary distinction between the heat pump and natural gas boiler is the heat pumps supply of cooling duty and different efficiencies for heat supply.

### Thermal energy storage

The simple energy model for the thermal energy storage (TES) includes charging ($\eta_{TES,ch}$) and discharging efficiencies ($\eta_{TES,dis}$) to account for non idealities during charging and discharging. The energy level at the beginning and at the end of the time horizon of optimization is assumed to be 50% of the maximum storage capacity. Moreover, we assume an operating range of 0-100% of the nominal capacity of the TES ($C_{TES,nom}$). The charging and discharging rates of the TES are limited in correlation to the nominal TES capacity. Heat loss $\dot{Q}_{TES,loss}(t)$ to the environment was modeled as a linear efficiency of the actual storage level $C_{TES}(t)$ and efficiency factor $\eta_{TES,loss}$.

### System

The heat demand $\dot{Q}_{heating}(t)$ given by the fluctuating demand profile must be provided to the heating circuit by a combination of the three possible components HP, NGB and TES. Similarly, the waste heat $\dot{Q}_{cooling}(t)$ must be removed from the cooling circuit either by the HP or through cooling water $\dot{Q}_{cw}(t)$. It follows that the HP is limited by the waste heat supply.

### $CO_2$ emissions

As costs for $CO_2$-emission certificates are rising significantly and are expected to still rise in the future, we considered $CO_2$-emissions during operation of the HP and NGB, $e_{HP}(t)$ and $e_{NGB}(t)$ respectively. For the heat pump we used emission factors for electricity $EF_{CO_2,el}$ assuming the compressor is driven by electricity. Likewise, the emission factor of natural gas $EF_{CO_2,NG}$ was used for calculating the emissions of the NGB.

### Cost functions

The minimization of total annual costs (TAC) requires the consideration of operating expenditure (OPEX) as well as investment cost (CAPEX). We are assuming that all components are greenfield and use specific cost factors $f_{inv,i}$ for the HP, NGB and TES. We do not consider operating costs for the TES and only consider costs for $CO_2$-emissions, the required electricity of the heat pump, natural gas as well as costs for cooling water.

## CASE STUDIES

The MINLP has been solved in Python using Gurobi [18]. In the first case study (CS 1), current cost factors for equipment and operation have been used to find the optimal equipment sizing. The profile and cost parameters as well as operating limitations are shown in the supplementary material. Equipment sizing is significantly impacted by the economic parameters as well as the parameters affecting component flexibility. In the case of CS 1, the operational cost of the natural gas boiler combined with costs for cooling water are lower than the operational costs of a heat pump.

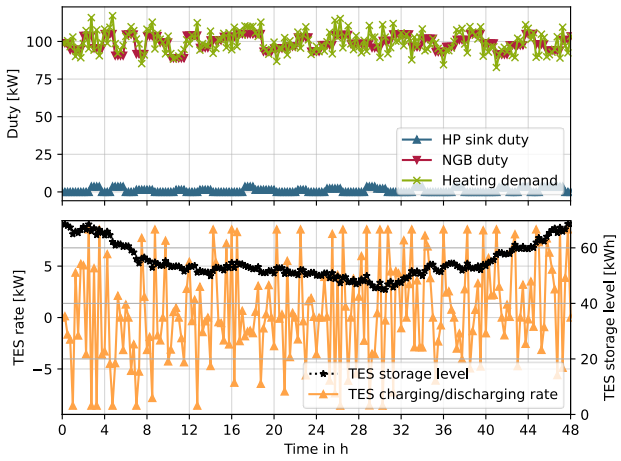



**Figure 2.** Operation and sizing results for CS 1.

Nevertheless, a small heat pump is used to improve the flexibility of the system as shown in Figure 2. NGB and HP are both constraint to a maximum of one load change per hour. With a fluctuating heat demand changing every 15 minutes, this results in heat surplus or heat deficit supplied by the NGB and HP. This mismatch of heat supply and demand can be reduced by shifting the load changes of the HP to time periods where no load shift is allowed for the NGB and vice versa. The remaining mismatch is met by charging and discharging the TES. This subsequently leads to the required storage size. The maximum allowable charging and discharging rates are a function of the nominal storage capacity. Thus, the required storage capacity is directly influenced by the fluctuating heat demand and the flexibility of the other components. In case of no restrictions on load changes of HP and NGB, no TES might be required. On the other hand, with fewer load changes allowed, the required storage capacity increases. Moreover, it is evident that the TES is operated such that the storage level is lower than the

starting and ending level. This is likely because the thermal energy loss is a function of the current energy stored in the energy storage. By reducing the energy stored in the storage, the energy loss is reduced.

In case study 2 (CS 2), we conducted a parameter study to determine the effect of varying specific HP investment cost on equipment sizing. As shown in Figure 3, for low specific investment costs, the heat pump is preferred over the natural gas boiler. The TES is used to buffer the supply and demand mismatch which result from load change restrictions of the HP. High specific investment cost led to a small HP design. This requires higher TES capacity to buffer the mismatch between heat supply and demand, because load changes of the HP only have a small contribution. In cases where the operational and investment costs of the HP exceed those of a NGB, the HP may nonetheless be favored due to its ability to provide cooling services. This characteristic contributes to a reduction in costs associated with cooling water consumption.

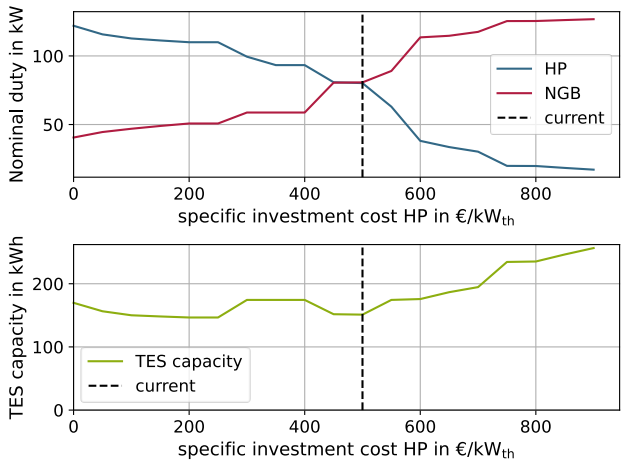



**Figure 3.** Impact of specific HP investment cost on equipment sizing.

To further examine the impact of different economic and profile parameters on equipment sizing, we conducted a parameter study in case study 3 (CS 3). The sensitivity parameter ranges are shown in the supplementary material. As depicted in Figure 4, there is a strong correlation between the standard deviation of the demand profile and the required capacity of the TES. For cases with restrictions on load shifts for the HP and NGB, the TES is required to buffer the resulting mismatch between heat supply and demand. For current price ratios of electricity to natural gas and lower investment cost of the NGB favor the NGB over the HP. The TES is required to buffer the mismatch between heat supply and demand resulting from load shift limitations of the NGB. As shown in Figure 4, for a price ratio of 1.5, the HP has lower operational costs and is therefore preferred over the NGB. With increasing standard deviations, the NGB and TES are utilized to buffer profile fluctuations. At a standard deviation of around 33, a new trend can be identified. The nominal heat duty of the NGB increases significantly and the required TES capacity is reduced. In profiles with standard deviations greater than 33, low waste heat supply and peaks in heat demand appear at the same time. In these cases, the HP can not be used to supply heat which requires the NGB and TES to buffer the mismatch. The NGB requires lower investment costs for the same output heat duty than the TES and is therefore preferred over the TES.

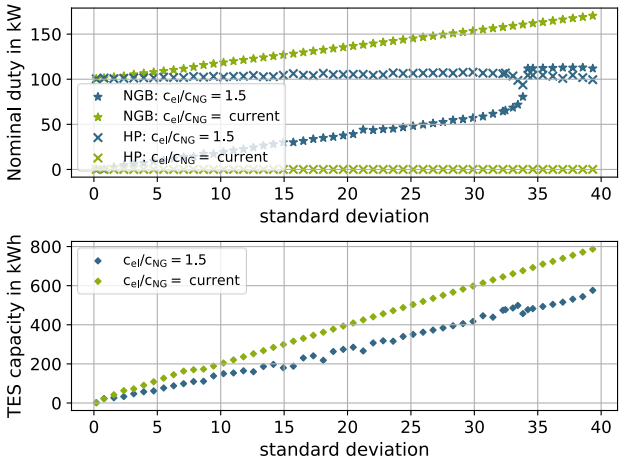



**Figure 4.** Correlation between the standard deviation of the demand profile and nominal TES capacity for different ratios of operating costs.

## CONCLUSION

In the present study, we analyzed the impact of fluctuating waste heat supply and heating demand in the context of chemical processes on utility equipment sizing. It is evident that equipment sizing is a complex task which is affected by many different aspects such as profile and cost parameters as well es equipment constraints. Parameter studies may support understanding the dependencies in a utility system and identifying economically feasible conditions. They can also help in identifying change points in optimal solutions e.g. for different degrees of fluctuations in the demand profile.

From our view, it is important to conduct further research on equipment flexibility parameters, since equipment sizing for fluctuating profiles is significantly dependent on equipment flexibility. Moreover, different types of profile fluctuations can be studied such as step profiles and seasonal profiles. Comparing statistical parameters of real-world profiles and synthetic profiles or combinations of synthetic profiles may help in qualitatively identifying the best combination and sizing of equipment.

## DIGITAL SUPPLEMENTARY MATERIAL

Detailed description of the model, parameters for the different case studies and figure of exemplary waste heat supply and heat demand. LAPSE:2025.0011

## ACKNOWLEDGEMENTS

This work was funded by the Federal Ministry for Economic Affairs and Climate Action (BMWK) within the project WinPro (project funding reference number 03EN2115A).

## REFERENCES

1. United Nations, Paris Agreement. United Nations Framework Convention on Climate Change (2015) https://unfccc.int/sites/default/files/english_paris_agreement.pdf
2. Wolf S. Integration von Wärmepumpen in industrielle Produktionssysteme. Universität Stuttgart (2017) http://dx.doi.org/10.18419/opus-9593
3. Kiss AA, Smith R. Rethinking energy use in distillation processes for a more sustainable chemical industry. *Energy* 203:117788 (2020) https://doi.org/10.1016/j.energy.2020.117788
4. Papoulias SA, Grossmann IE. A structural optimization approach in process synthesis-I. *Comput. Chem. Eng.* 7:659-706 (1983) https://doi.org/10.1016/0098-1354(83)85022-4
5. Bruno JC, Fernandez F, Castells F, Grossmann IE. A Rigorous MINLP Model for the Optimal Synthesis and Operation of Utility Plants. *Chem. Eng. Res. Des.* 76:246-258 (1998) https://doi.org/10.1205/026387698524901
6. Mitra S, Sun L, Grossmann IE. Optimal scheduling of industrial combined heat and power plants under time-sensitive electricity prices. *Energy* 54:194-211 (2013) https://doi.org/10.1016/j.energy.2013.02.030
7. Bischi A, Taccari L, Martelli E, Amaldi E, Manzolini G, Silva P, Campanari S, Macchi E. A detailed MILP optimization model for combined cooling, heat and power system operation planning. *Energy* 74:12-26 (2014) https://doi.org/10.1016/j.energy.2014.02.042
8. Baumgärtner N, Delorme R, Hennen M, Bardow A. Design of low-carbon utility systems: Exploiting time-dependent grid emissions for climate-friendly demand-side management. *Appl. Energy* 247:755-765 (2019) https://doi.org/10.1016/j.apenergy.2019.04.029
9. Prendl L, Schenzel K, Hofmann R. Simultaneous integration of heat pumps and different thermal energy storages into a tightened multi-period MILP HENS superstructure formulation for industrial applications. *Comput. Chem. Eng.* 147:107237 (2021) https://doi.org/10.1016/j.compchemeng.2021.107237
10. Molyneaux A, Leyland G, Favrat D. Environomic multi-objective optimisation of a district heating network considering centralized and decentralized heat pumps Energy 35:751-758 (2010) https://doi.org/10.1016/j.energy.2009.09.028
11. Rinaldi A, Soini MC, Streicher K, Patel MK, Parra D. Decarbonising heat with optimal PV and storage investments: A detailed sector coupling modelling framework with flexible heat pump operation. *Appl. Energy* 282:116110 (2021) https://doi.org/10.1016/j.apenergy.2020.116110
12. Renaldi R, Kiprakis A, Friedrich D. An optimisation framework for thermal energy storage integration in a residential heat pump heating system. *Appl. Energy* 186:520-529 (2017) https://doi.org/10.1016/j.apenergy.2016.02.067
13. Alavy M, Nguyen HV, Leong WH, Dworkin SB. A methodology and computerized approach for optimizing hybrid ground source heat pump system design. *Renew. Energy* 57:404-412 (2013) https://doi.org/10.1016/j.renene.2013.02.003
14. Fischer D, Lindberg KB, Madani H, Wittwer C. Impact of PV and variable prices on optimal system sizing for heat pumps and thermal storage. Energy Build. 128:723-733 (2016) https://doi.org/10.1016/j.enbuild.2016.07.008
15. Sadjjadi BS, Gerdes JN, Sauer A. Energy flexible heat pumps in industrial energy systems: A review. *Energy Rep.* 9:386-394 (2023) https://doi.org/10.1016/j.egyr.2022.12.110
16. Xu Z, Li H, Xu W, Shao S, Wang Z, Gou X, Zhao M, Li J. Investigation on the efficiency degradation characterization of low ambient temperature air source heat pump under partial load operation. IJR 133:99-110 (2022) https://doi.org/10.1016/j.ijrefrig.2021.10.002
17. Walden JVM, Stathopoulos P. The impact of heat pump load flexibility on its process integration and economics. J. Clean. Prod. 462:142643 (2024) https://doi.org/10.1016/j.jclepro.2024.142643
18. Gurobi Optimization, LLC. Gurobi Optimizer Reference Manual. (2024) https://www.gurobi.com

© 2025 by the authors. Licensed to PSEcommunity.org and PSE Press. This is an open access article under the creative commons CC-BY-SA licensing terms. Credit must be given to creator and adaptations must be shared under the same terms. See https://creativecommons.org/licenses/by-sa/4.0/



Systems & Control Transactions

**Research Article - Peer Reviewed Conference Proceeding**
ESCAPE 35 - European Symposium on Computer Aided Process Engineering
Ghent, Belgium. 6-9 July 2025
Jan F.M. Van Impe, Grégoire Léonard, Satyajeet S. Bhonsale,
Monika E. Polańska, Filip Logist (Eds.)

PSE PRESS

# Optimization of prospective circular economy in sewage sludge to biofuel production pathways via hydrothermal liquefaction using P-graph

**Safdar Abbas[a]*, Paraskevi Karka[b], and Stavros Papadokonstantakis[a]**

[a] TU Wien, Institute of Chemical, Environmental and Bioscience Engineering, Vienna, Austria
[b] University of Groningen, Engineering and Technology Institute Groningen (ENTEG), Faculty of Science and Engineering, Groningen, Netherlands
* Corresponding Author: safdar.abbas@tuwien.ac.at

## ABSTRACT

Hydrothermal liquefaction (HTL) has proven to be an appropriate technology for converting sewage sludge into a valuable resource for renewable energy generation. This study focuses on a prospective analysis of various technological scenarios for sewage sludge-to-fuel pathways via HTL, co-located with a wastewater treatment plant, in support of a circular economy perspective. Four technological foreground scenarios and three prospective background scenarios aligned with the Paris agreement's climate targets REMIND-SSP2-Base (projecting a 3.5°C temperature rise by the end of the century), PKBudg1150 (aiming to limit the rise to below 2°C), and PKBudg500 (targeting a cap below 1.5°C) are analyzed for sewage sludge-to-fuel conversion in 2030, 2040, and 2050. The superstructure problem of the possible combinations of the developed scenarios is solved using the P-graph studio which is based on the branch and bound approach. The goal of this study is to maximize the objective function (OF) by accounting the credits from avoided GHG emissions, the market value of recovered products, while subtracting operational costs and GHG emission penalties incurred during the biocrude production and upgrading processes. The optimal solution shows a potential OF equal to 858 €/ton of sewage sludge for Pkbudg500 under technological foreground scenario 2 by 2040. The P-graph approach demonstrates that HTL treatment of sewage sludge provides an alternative production pathway within the circular economy concept, capable of identifying optimal and near-optimal solutions for addressing trade-offs between future socio-economic policies and practical implementation for 2030, 2040, and 2050, which are often difficult to monetize.

**Keywords**: Prospective circular economy, integrated assessment models, shared socio-economic pathways, sewage sludge, hydrothermal liquefaction.

## INTRODUCTION

Sludge from wastewater treatment plants is a major source of urban waste and the circular economy approach has demonstrated its effectiveness in the waste-to-energy sector as a method to extract value from waste while minimizing fossil fuel consumption [1]. Transforming this sludge into fuels for the transportation sector via HTL can substantially support the renewable energy targets in Europe, presenting an eco-friendly and cost-effective solution over traditional waste management practices [2]. Regarding the market acceptance, the use of sustainable advanced biofuels produced from biocrude is viewed as essential in the shift towards renewable energy, offering a pathway to quick emission reduction while requiring minimal alterations to the existing fossil crude infrastructure [1,3]. As sustainability concerns continue to rise, environmental impacts are gaining increasing attention. Prospective life cycle assessment (pLCA) has emerged as a valuable tool for estimating future environmental performance by accounting for the advancement of current and emerging technologies. It considers both the foreground system e.g., improvements of the investigated technology, and the background systems

such as raw material and energy market developments [4]. Regarding the evolution of background systems, the integrated assessment model (IAM), based on shared socioeconomic pathways (SSPs), provides a framework for analyzing climate-related scenario outcomes [6]. One such IAM, the regional model of investment and development (REMIND), describes transformation pathways within the interconnected energy-economy-land-climate system [5]. Addressing climate change requires two key approaches: mitigation, which focuses on reducing greenhouse gas emissions, and adaptation, which involves adjusting economies and societies to meet climate goals [6,7]. Additionally, biogenic carbon removal is increasingly recognized as an essential aspect of mitigation and remains an important area for future exploration. This study employs the SSP2 narrative, known as the "middle-of-the-road" pathway, serving as a useful starting point for exploring solutions that integrate climate mitigation and adaptation while also addressing broader societal objectives throughout the 21st century [7,5,8,9].

The open source LCA tool, activity-browser (AB), modifies the Ecoinvent 3.9.1 database to align with socioeconomic and climate-oriented SSP projections, specifically REMIND-SSP2-Base, Pkbudg1150, and Pkbudg500, for the years 2030, 2040, and 2050 [10].

This study focuses on the conversion of sewage sludge into biofuel using the HTL process, as illustrated in Figure 1. Four distinct technological scenarios for converting sewage sludge to biofuel via HTL are analyzed, as detailed in Table 1. Despite the growing interest in HTL for biofuel production, there remains a gap in the literature regarding a comprehensive, prospective analysis that integrates both economic and environmental factors. The core of this study is the use of prospective assessment to identify the most suitable technological production pathway by considering the economic balance between future demand and the market value of products, alongside externality costs related to GHG emissions and future operating costs (OPEX). To address this, the P-graph framework, combined with prospective assessment, facilitates rigorous superstructure design and efficiently identifies optimal and near-optimal solutions for mid-to long-term scenarios [11,12,13].This approach offers a practical tool for decision-makers to assess trade-offs among technological options, accounting for future socio-economic policies and implementation goals for 2030, 2040, and 2050, which would otherwise be challenging to evaluate both economically and environmentally.

## MATERIALS AND METHODS

### Technological foreground scenarios

The HTL-based foreground system for sewage sludge valorization, shown in Figure 1, is analyzed across four scenarios as detailed in table 1. In scenarios 1 and 3, natural gas is used to heat the HTL unit, while biomethane is the heating source in scenarios 2 and 4, maintaining a temperature of 347°C [1,3,14]. This process converts sewage sludge into fractions by weight: 42% biocrude, 28% aqueous phase, 24% solids and ash, and small amount of gases [3,14,18]. The solid residues are assumed to be disposed of in a landfill. Other technological options involve recovering valuable nutrients, such as phosphorus, or producing a combined fertilizer product from these solids. While this could enhance sustainability and circular economy concepts, further research is needed to evaluate the technical and economic viability of this option, which is beyond the scope of the current study [3,14,18].

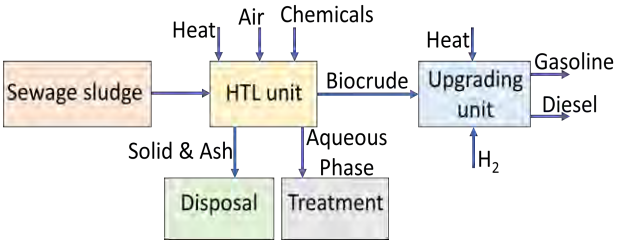



**Figure 1.** Sewage sludge to biofuel conversion via HTL process.

The aqueous phase treatment varies between scenarios. In scenarios 1 and 3, the aqueous phase, containing effluent water, dissolved organics, ammonia, and metal salts, is treated with lime to raise its pH to 11, releasing ammonia gas. This ammonia is then combusted catalytically in a thermal oxidation unit with a natural gas-air mixture [3,14,18]. In contrast, scenarios 2 and 4 employ dewatering to increase the organic content of the aqueous phase from 7.5% to 45% [3,14,18], followed by anaerobic digestion to produce biogas. After purification, the biomethane generated is used onsite in the HTL and biocrude upgrading units, with any surplus treated as an additional biomethane product. The hydrogen required for upgrading the biocrude differs across scenarios. In scenarios 1 and 2, hydrogen is generated via steam methane or biomethane reforming, while in scenarios 3 and 4, it is produced through electrolysis. The upgraded biocrude is ultimately converted into biogasoline and biodiesel as the primary products, with biomethane included as an additional product in scenarios 2 and 4. The production pathways for sewage sludge-to-biofuel are modeled using P-Graph studio to identify optimal configurations from both economic and environmental perspectives. The analysis evaluates four alternative technological pathways under various future scenarios spanning the years 2030 to 2050. The optimization goal is to maximize the objective function (OF), as defined in Equation (1) [12]. A cradle-to-gate approach is employed in this

study to conduct a prospective life cycle assessment (LCA), calculating both the greenhouse gas (GHG) emissions avoided by replacing fossil fuels and the GHG emissions generated during the hydrothermal liquefaction (HTL) process. In this analysis, sewage sludge is assumed to carry no environmental burden, as it originates from wastewater treatment plants (WWTP), where all associated impacts are already allocated. For the alternative approach to biofuel production via HTL, this study specifically examines non-biogenic emission sources, such as chemical inputs and energy consumption. The inputs for converting sewage sludge to biocrude via HTL, upgrading biocrude to biofuels, are detailed in Table 2 and illustrated in Figure 1. Comprehensive life cycle inventories (LCI) for these scenarios are based on data from Karka et al. (2024), Snowden-Swan et al. (2017) and Tews et al. (2014). For cradle-to-gate fossil fuel emissions, the study relies on a prospective LCI database accessed through the open-source software AB.

$$OF = GHG\ avoided\ emissions * C + MV\ product - OPEX - GHG\ emitted\ emissions * C \quad (1)$$

In Equation 1, the term 'OF' does not represent the monetary profit of the entity operating the sludge-to-biofuels facility. Instead, it denotes an objective function that integrates economic aspects (market value minus operational costs) and environmental factors (credits for avoided greenhouse gas emissions minus penalties for emitted greenhouse gases). Both components are monetized to formulate a unified single-objective problem, thereby avoiding the complexity of a bi-objective approach. In OF the term *GHG avoided emissions* refers to the greenhouse gas emissions avoided through the displacement of fossil fuels by biofuels. This is determined by multiplying the annual production of biofuels (e.g., tons of bio-gasoline per year) by the cradle-to-gate emission factor of the fossil fuel being replaced (e.g., tons of $CO_2$-equivalent per ton of fossil gasoline). These avoided emissions are then multiplied by the carbon tax *C*, measured in €/ton of $CO_2$-equivalent, to calculate the monetary credits for avoided emissions (€/year). Carbon tax values for 2030, 2040, and 2050 are sourced from the REMIND-SSP2-base, PKBudg1150, and PKBudg500 scenarios [5,15,17].

The term *MV product* is calculated as the revenue generated by biofuel production. This is obtained by multiplying the market price of the biofuel (€/ton), as predicted by the REMIND model for specific years and background scenarios, by the annual production volume (tons/year) for each technological pathway [15,17]. Operating costs *OPEX* include the annual expenses (€/year) associated with biofuel production, considering only the future costs of energy sources such as natural gas and electricity. These costs are derived from REMIND model projections for 2030, 2040, and 2050 under the REMIND-SSP2-base, PKBudg1150, and PKBudg500 scenarios. Material costs for inputs like lime or chemicals, listed in Table 2, are excluded due to insufficient data in the REMIND framework, which primarily focuses on energy-economy modeling [15,17].

The term *GHG emitted emissions* represent the cradle-to-gate greenhouse gas output generated during biofuel production (tons of $CO_2$-equivalent/year). These emissions are multiplied by the carbon tax (€/ton of $CO_2$-equivalent) to calculate emission penalties (€/year). Annualized capital costs are not included in this analysis, as their assessment would require a detailed technology learning framework, which is beyond the scope of this study.

## Data Collection

The data used in Equation 1, including avoided emission credits, market values of biofuels, operating costs, and emission penalties, is available in the GitHub repository [15]. For convenience, the repository can be accessed directly via this link:[https://github.com/safdar-abbas123/Availability-of-data-for-prospective-circular-economy?tab=readme-ov-file].

### Framework of scenarios' modelling using the P-graph software

The P-graph framework is a combinatorial optimization tool based on five core axioms [12,16]. These axioms establish the combinatorially feasible process structures within the P-graph software. Axiom 1 states that every product must be included in the structure. Axiom 2 specifies that a material has no ancestors in the structure only if it represents a raw material. Axiom 3 ensures that every operating unit in the structure is defined in the synthesis problem. Axiom 4 requires that each operating unit in the structure has at least one direct path leading to the final product. Axiom 5 dictates that if a material is part of the structure, it must either be an input to or an output from at least one operating unit in the system [12,16]. These axioms provide mathematically precise guidelines regarding the structural requirements of a problem [12,16]. They are particularly effective in narrowing the structural search space for optimization, allowing the focus to remain on analysing feasible configurations. Figure 2 illustrates the general P-graph structure used to optimize the sewage sludge system. In the first layer, sewage sludge is converted to biocrude via hydrothermal liquefaction (HTL), with heating for the HTL unit provided by either natural gas or onsite-produced biomethane. The second layer involves the upgrading of biocrude, with hydrogen supplied either from natural gas or biomethane through a steam methane reformer (SMR) or electrolysis. In the third layer, product recovery takes place. Four different technological foreground pathways and three prospective background scenarios are considered for the years

**Table 1.** Scenario description for sewage sludge to biofuel conversion via HTL process included in superstructure.

| Scenarios | Heating source in HTL Unit | $H_2$ source in upgrading Unit | Aqueous phase treatment | Products |
|---|---|---|---|---|
| Scenario 1 | Natural gas | SMR* | Thermal treatment | Gasoline, Diesel |
| Scenario 2 | Biomethane | SBMR** | Anaerobic digestion | Gasoline, Diesel, biomethane |
| Scenario 3 | Natural gas | Electrolysis | Thermal treatment | Gasoline, Diesel |
| Scenario 4 | Biomethane | Electrolysis | Anaerobic digestion | Gasoline, Diesel, biomethane |

SMR*: Steam methane reforming
SBMR**: Steam bio-methane reforming
Note: (Sources of these scenarios are mainly from Karka et al. (2024), Snowden-Swan et al. (2017) and Tews et al., 2014).

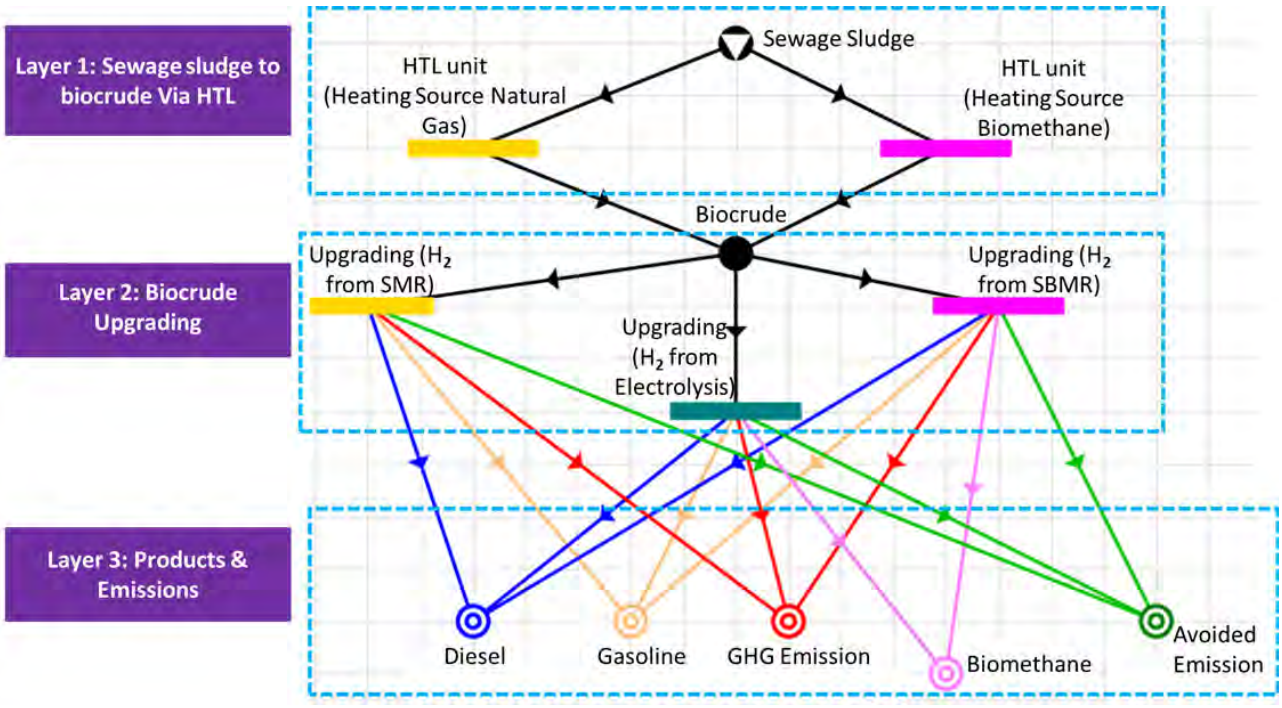



**Figure 2.** Generic model of sewage sludge to biofuel production using P-graphs: Layer 1 sewage sludge to biocrude via HTL; Layer 2 biocrude upgrading with $H_2$ sources from SMR, electrolysis, and SBMR; Layer 3 products and emissions.

2030, 2040, and 2050. A total of 36 scenarios are incorporated into a superstructure to find the optimal and near-optimal production pathways.

## RESULTS AND DISCUSSIONS

Figure 3 illustrates the optimal and near-optimal solutions for various technological production pathways, modelled using P-graph, across different prospective scenarios for the years 2030, 2040, and 2050. The optimal solution (Scen 2) achieves the highest OF of 858 €/ton of sewage sludge in 2040 under the optimistic REMIND-SSP2-Pkbudg500 scenario, which aims to limit global temperature rise to below 1.5°C. In this technological pathway, biomethane is used in HTL and the biocrude upgrading units. This pathway generates significant revenue from biofuel production (917€/ton of sewage sludge) and credits for avoided GHG emissions through the displacement of fossil fuels (200€/ton of sewage sludge). These benefits outweigh the associated costs, including penalties for cradle-to-gate non-biogenic GHG emissions, primarily resulting from material inputs, as shown in Table 2, during sewage sludge-to-biofuel production via HTL (-253€/ton of sewage sludge) and OPEX (-6€/ton of sewage sludge). The substantial objective function (OF) margin in this pathway is attributed to the optimal alignment of technology and market conditions, maximizing both environmental and economic performance.

**Table 2.** Material inputs for sewage sludge to biofuel conversion via HTL process.

| Material input | Processing unit | Amount |
|---|---|---|
| Dewatered sludge | HTL Unit | 4158 kg/hr |
| Air | HTL Unit | 4418 kg/hr |
| Natural gas or biomethane | HTL Unit | 221 m3/hr |
| Chemical organic | HTL Unit | 18.7 kg/hr |
| Electricity, medium voltage | HTL Unit | 160.4 kWh |
| Biocrude | Upgrading unit | 1767 kg/hr |
| Hydrogen | Upgrading unit | 96 kg/hr |

Note: (Sources of these material inputs are mainly from Karka et al. (2024), Snowden-Swan et al. (2017) and Tews et al., 2014).

The first near-optimal solution yields a slightly lower OF of 804 €/ton of sewage sludge, also in 2040 under the REMIND-SSP2-Pkbudg500 scenario. In this case, scenario 4 is used, where biomethane is utilized in the HTL unit, but electrolysis is employed for the biocrude upgrading unit. While this pathway generates the biofuel revenues (922 €/ton of sewage sludge) and identical avoided GHG credits (200 €/ton of sewage sludge), it incurs the GHG emission penalties (-267 €/ton of sewage sludge) and significantly increased OPEX (-51 €/ton of sewage sludge) due to the additional electricity use. These increased costs reduce overall OF profitability compared to the optimal solution.

Further reductions in OF are observed in the second and third near-optimal solutions, which use technological foreground scenario 2 as also the best solution but under different background scenario years. The second near-optimal solution, under the REMIND-SSP2-Pkbudg500 scenario for 2030, achieves a OF of 735 €/ton of sewage sludge. In this scenario, revenue from biofuel production is (781 €/ton of sewage sludge), and avoided GHG credits drop to (135 €/ton of sewage sludge), reflecting less favorable conditions compared to the optimal solution. Costs include GHG emission penalties (-170 €/ton of sewage sludge) and OPEX (-11 €/ton of sewage sludge). The third near-optimal solution, also using scen 2, occurs in 2050 under the REMIND-SSP2-Pkbudg500 scenario and achieves a OF of 728 €/ton of sewage sludge. Biofuel revenues is (765 €/ton of sewage sludge), while avoided GHG credits fall to (130 €/ton of sewage sludge). Associated costs include GHG emission penalties (-162 €/ton of sewage sludge) and OPEX (-5 €/ton of sewage sludge). The stack bar charts for these solutions demonstrate that the main drivers of OF are revenues from biofuel production and credits for cradle-to-gate avoided GHG emissions. Scenario 2 performs well under the REMIND-SSP2-Pkbudg1150 and REMIND-SSP2-Base scenarios; however, it achieves the highest objective function (OF) in REMIND-SSP2-Pkbudg500, as indicated by the optimal and near-optimal solutions shown in Figure 3.

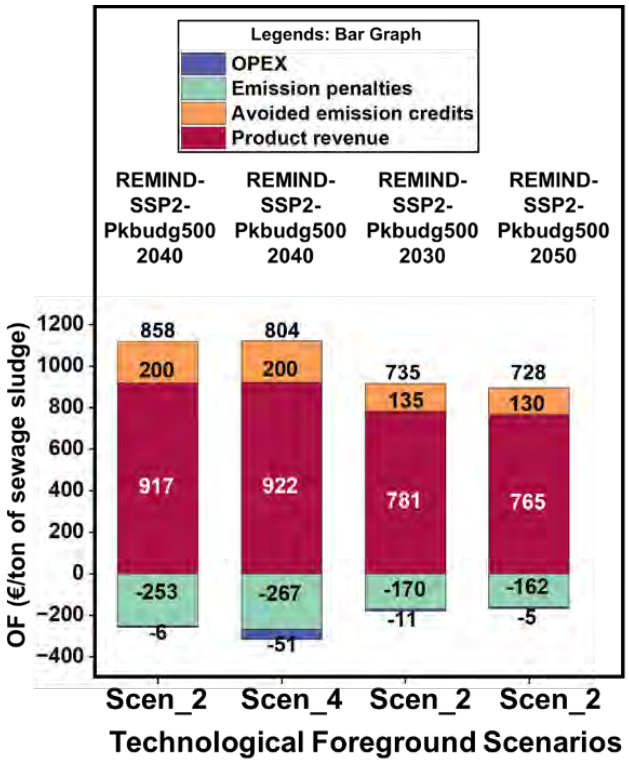



**Figure 3.** The set of optimal and near optimal solution of different technological foreground scenarios. The bar graph presents the optimal and near optimal solution achieved under the highly optimistic scenario REMIND-SSP2-Pkbudg500 for the year 2030, 2040 and 2050.

Despite costs like GHG emission penalties and OPEX, these revenue streams maintain OF profitability. The key driver for both optimal and first near-optimal solutions in the REMIND-SSP2-Pkbudg500 scenario is the higher biofuel market value in 2040, as outlined in GitHub repository [17]. This increase in biofuel prices significantly boosts revenue, making 2040 the most profitable year. However, biofuel OF are projected to decline in 2050, even under the highly optimistic REMIND-SSP2-

Pkbudg500 scenario, due to reduced demand as the transportation sector increasingly shifts towards electric vehicles and cleaner fuel sources, reducing the reliance on biofuels [5].

## CONCLUSIONS

The superstructure-based optimization of sewage sludge conversion to biofuel via HTL, using the P-graph framework combined with prospective assessments, offers valuable insights for circular bioeconomy approaches. The optimal and near-optimal solutions provide valuable guidance for stakeholders offering multiple technological production pathways under various socioeconomic scenarios for the years 2030, 2040, and 2050. The optimal solution recommends the conversion of sewage sludge to biocrude through HTL, followed by upgrading biocrude to biofuel, with biomethane being used in both stages. However, a key limitation of P-graphs is its reliance on predefined process structures, which restricts its ability to automatically explore alternative configurations outside the given set. For instance, the present study can be populated with more scenarios regarding the HTL aqueous phase treatment, alternative uses of sewage sludge, and biocrude upgrading product diversification. Despite this, the study illustrates the systematic development and assessment of scenarios, guiding future developments in waste-to-energy conversion and supporting long-term sustainability goals.

## ACKNOWLEDGEMENTS

We gratefully acknowledge financial support by TU Wien global budget for PhD research.

## REFERENCES

1. E. M. Lozano, S. Løkke, L. A. Rosendahl, and T. H. Pedersen, “Production of marine biofuels from hydrothermal liquefaction of sewage sludge. Preliminary techno-economic analysis and life-cycle GHG emissions assessment of Dutch case study,” Energy Conversion and Management: X, vol. 14, no. October 2021, 2022, https://doi:10.1016/j.ecmx.2022.100178
2. K. Kohansal et al., “Automotive sustainable diesel blendstock production through biocrude obtained from hydrothermal liquefaction of municipal solid waste,” Fuel, vol. 350, no. June, pp. 1–13, 2023, https://doi:10.1016/j.fuel.2023.128770
3. L. J. Snowden-Swan et al., “Conceptual Biorefinery Design and Research Targeted for 2022: Hydrothermal Liquefaction Processing of Wet Waste to Fuels,” Pnnl-27186, vol. 27186, pp. 1–40, 2017.
4. N. Thonemann, A. Schulte, and D. Maga, “How to conduct prospective life cycle assessment for emerging technologies? A systematic review and methodological guidance,” Sustainability (Switzerland), vol. 12, no. 3, pp. 1–23, 2020, https://doi:10.3390/su12031192
5. L. Baumstark et al., “REMIND2.1: transformation and innovation dynamics of the energy-economic system within climate and sustainability limits,” Geosci Model Dev, vol. 14, no. 10, pp. 6571–6603, 2021, https://doi:10.5194/gmd-14-6571-2021
6. B. C. O’Neill et al., “A new scenario framework for climate change research: The concept of shared socioeconomic pathways,” Clim Change, vol. 122, no. 3, pp. 387–400, 2014 https://doi:10.1007/s10584-013-0905-2
7. O. Fricko et al., “The marker quantification of the Shared Socioeconomic Pathway 2: A middle-of-the-road scenario for the 21st century,” Global Environmental Change, vol. 42, pp. 251–267, 2017, https://doi:10.1016/j.gloenvcha.2016.06.004
8. S. Abbas, “Background Scenario Explanation,” Mar. 2024. doi: 10.5281/zenodo.8281192.
9. R. Sacchi, “PRospective EnvironMental Impact AsSEssment,” 2024. [Online]. Available: https://github.com/polca/premise
10. R. Sacchi, A. Dirnaichner, and C. Mutel, “Release 1.7.2 Romain Sacchi, Alois Dirnaichner, Chris Mutel,” 2023.
11. R. R. Tan, M. F. D. Benjamin, C. D. Cayamanda, K. B. Aviso, and L. F. Razon, “P-Graph Approach to Optimizing Crisis Operations in an Industrial Complex,” Ind Eng Chem Res, vol. 55, no. 12, pp. 3467–3477, 2016, https://doi:10.1021/acs.iecr.5b03205
12. Y. Van Fan, J. J. Klemeš, T. G. Walmsley, and B. Bertók, “Implementing Circular Economy in municipal solid waste treatment system using P-graph,” Science of the Total Environment, vol. 701, 2020, https://doi:10.1016/j.scitotenv.2019.134652
13. R. R. Tan, C. D. Cayamanda, and K. B. Aviso, “P-graph approach to optimal operational adjustment in polygeneration plants under conditions of process inoperability,” Appl Energy, vol. 135, pp. 402–406, 2014, https://doi:10.1016/j.apenergy.2014.08.089
14. P. Karka, I. Johannsen, and S. Papadokonstantakis, “Hydrothermal liquefaction integrated with wastewater treatment plants - life cycle assessment and technoeconomic analysis of process system options,” Sustain Energy Fuels, vol. 8, no. 15, pp. 3438–3451, 2024, https://doi:10.1039/d3se01211e
15. S. Abbas, “safdarabbas123/Availability-of-data-for- prospective-circular-economy: Initial release,”

Dec. 2024, Zenodo. https://doi:10.5281/zenodo.14294389
16. F. Friedler, Á. Orosz, and J. P. Losada, P-graphs for process systems engineering. Springer, 2022.
17. S. Abbas, “Future price of biomass, Electricity,” Apr. 2024. https://doi:10.5281/zenodo.10937931
Tews, I., Zhu, Y., Drennan, C. V., Elliott, D., Snowden-Swan, L. J., Onarheim, K., Solantausta, Y., & Beckman, D. (2014). Biomass direct liquefaction options: technoeconomic and life cycle assessment. Pacific Northwest National Laboratory, July, 62. https://www.osti.gov/biblio/1184983

© 2025 by the authors. Licensed to PSEcommunity.org and PSE Press. This is an open access article under the creative commons CC-BY-SA licensing terms. Credit must be given to creator and adaptations must be shared under the same terms. See https://creativecommons.org/licenses/by-sa/4.0/



Systems & Control Transactions

**Research Article - Peer Reviewed Conference Proceeding**
ESCAPE 35 - European Symposium on Computer Aided Process Engineering
Ghent, Belgium. 6-9 July 2025
Jan F.M. Van Impe, Grégoire Léonard, Satyajeet S. Bhonsale,
Monika E. Polańska, Filip Logist (Eds.)

PSE PRESS

# Model-based Operability and Safety Optimization for PEM Water Electrolysis

**Beatriz Dantas[a], Sahithi S. Akundi[b,c,d], Yuanxing Liu[b,c,d], Austin Braniff[a], Shayan S. Niknezhad[b], Faisal Khan[c,d], Efstratios N. Pistikopoulos[b,d], Fernando V. Lima[a] and Yuhe Tian[a,*]**

[a] Department of Chemical and Biomedical Engineering, West Virginia University, Morgantown, WV, USA
[b] Texas A&M Energy Institute, Texas A&M University, College Station, TX, USA
[c] Mary Kay O'Connor Process Safety Center, Texas A&M University, College Station, TX, USA
[d] Artie McFerrin Department of Chemical Engineering, Texas A&M University, College Station, TX, USA
* Corresponding Author: yuhe.tian@mail.wvu.edu.

## ABSTRACT

In this paper, we present a systematic approach to quantify the safe operating window of a proton exchange membrane water electrolysis (PEMWE) system considering energy intermittency and varying hydrogen demand. The PEMWE model has been developed based on first principles, with the polarization curve validated against a lab-scale experimental setup. The impact of key operational variables is investigated which include voltage, inlet temperature, and water flowrate (utilized for both feed and system cooling). Emphasis is given on operating temperature, a safety-critical variable, as its elevation can pose significant hydrogen safety risks within both the electrolyzer cells and the storage system. The impact of temperature on process safety is quantified via a risk index considering the fault probability and consequence severity. Process operability analysis is employed to assess the achievability of a safe and feasible region for design and operations. This analysis provides a comprehensive framework to optimize PEMWE systems for enhanced operational flexibility and robust performance with application to modular hydrogen production using renewable energy sources.

**Keywords**: Operability Analysis, Risk Assessment, Water Electrolysis, Sustainable Hydrogen Production

## 1. INTRODUCTION

In recent years, the transition of the energy grid to hydropower, wind, and solar photovoltaics has gained significant attention. Renewable sources are at the core of energy transition and remain among the most critical factors in the process of industrial decarbonization. However, their output is intermittent with daily and seasonal variability, which may lead to fluctuations in energy supply [1, 2]. Advancements in electrolysis technologies, such as proton exchange membrane water electrolysis (PEMWE) systems, are critical in addressing the challenges of integrating renewable energy sources for hydrogen production [3, 4]. PEMWE stands out among other technologies (e.g., solid oxide electrolyzers and alkaline electrolyzers) due to its simplicity, reversible operation, higher current densities supported, and ability to supply highly pure hydrogen. These attributes make PEMWE a promising option for coupling with intermittent renewable energy sources, contributing to the decarbonization of various sectors such as transportation, industry, and power generation [5, 6]. Despite these advancements, significant research gaps remain in how to effectively characterize the operability of a PEMWE system. These include: (i) the lack of integrated performance analysis (and metrics) for PEMWE accounting for operability, safety, productivity, etc.; and (ii) the lack of a systematic approach to quantify the safe PEMWE operating window under conditions of energy intermittency and varying hydrogen demand.

To address these challenges, this work presents a systematic approach that integrates operability and safety analysis to quantify the safe operating window of a PEMWE system while ensuring high-efficiency hydrogen production. Section 2 provides a detailed PEMWE process description to motivate the research developments. Section 3 outlines the methods in terms of operability and risk assessment. Section 4 presents a case

study demonstrating the practical application and effectiveness of the methodology framework in enhancing PEMWE system safety and operability.

## 2. PEMWE CASE STUDY

### 2.1 Process Description

In this work, we consider the PEMWE system as conceptualized in Figure 1a. The PEMWE design and operations are based on the reference experimental setup given in Figure 1b [6, 7]. Specifically, water is supplied to the anode at a controlled temperature and flow rate, serving a dual purpose as both a reactant and a coolant. Within the anode, water moves through the diffusion layer to reach the catalyst site, where the anodic electrochemical reaction occurs as described in Eq. (1). During this reaction, water interacts electrochemically with electrons from the current to produce oxygen and hydrogen ions. The oxygen ions at the anode combine to form oxygen molecules, while the hydrogen ions diffuse through the membrane to the cathode, where pairs of $H^+$ ions combine to form hydrogen molecules as described in the cathodic reaction in Eq. (2). The oxygen and hydrogen molecules generated then exit the catalyst layer via the diffusion layer. The overall reaction is presented in Eq. (3).

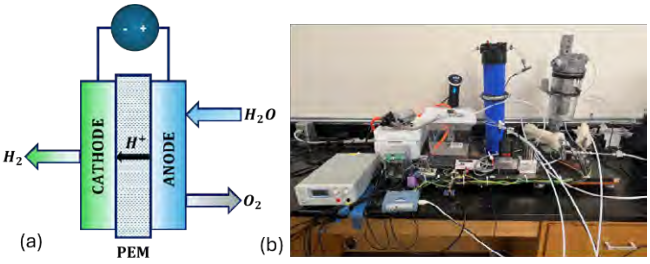



**Figure 1**: PEMWE system. (a) Schematic representation. (b) Experimental setup.

$$\text{Anode: } H_2O \longrightarrow \frac{1}{2}O_2 + 2H^+ + 2e^- \quad (1)$$

$$\text{Cathode: } 2H^+ + 2e^- \longrightarrow H_2 \quad (2)$$

$$\text{Overall Reaction: } H_2O \longrightarrow \frac{1}{2}O_2 + H_2 \quad (3)$$

### 2.2 Research Objectives

The manipulated variables for this PEMWE system are considered as: (i) makeup water flowrate – which is used for both feed inlet and system cooling, and (ii) voltage – reflecting the varying electricity availability considering the scenario of electrolyzer powered by renewable energy sources. Disturbance exists at the makeup water inlet temperature. To assess the PEMWE performance, the output variables are selected as $H_2$ production flowrate and power consumption. Temperature is the safety-critical variable to be further correlated with the process risk calculation. Temperature elevation can pose significant hydrogen safety risks within both the electrolyzer cells and the storage system.

Key research objectives of this work include:

- Model-based analysis to characterize the entire PEMWE safe and feasible operating region for input and output variables.
- Systematic identification of the optimal input operating region under disturbances, based on the desired level of outputs (maximum hydrogen production rates).

## 3. AN INTEGRATED OPERABILITY AND SAFETY OPTIMIZATION APPROACH

A methodology framework has been developed in our prior work to incorporate risk considerations into steady-state operability-based process design [8]. This section provides a brief overview on the key methods (i.e., process operability analysis and risk assessment), before applying the framework to study the PEMWE system in Section 4.

### 3.1 Process Operability Analysis

Process operability analysis is employed to quantify the achievability of a safe and feasible operating region at the early design stage. Several approaches have been proposed to tackle the challenges of feasibility and flexibility, including evaluating and integrating these factors within process design optimization and operations [9] and employing probabilistic identification of the design space [10]. The steady-state operability framework used in this study accounts for the impact of process design variables and varying operating conditions on the outputs to address the complexities of chemical processes [11, 12]. Figure 2 illustrates a schematic for performing a generalized steady-state operability analysis. This process starts by defining the input variables' upper and lower bounds, which define the Available Input Set (AIS). The process model, represented by $M$, is then applied to the AIS to determine the resulting output variables, which constitute the Achievable Output Set (AOS). Next, the Desired Output Set (DOS) is specified to include the target output values for the system. Through inverse mapping ($M^{-1}$), the input requirements needed to achieve the entire DOS region, if possible, are identified and referred to as the Desired Input Set (DIS). Additionally, by incorporating the Expected Disturbance Set (EDS), the AOS is adjusted to account for shifts across the specified range of disturbances, reflecting how these disturbances impact the achievable outputs. The feasible regions within DIS and DOS are labeled as DIS* and DOS*, respectively.

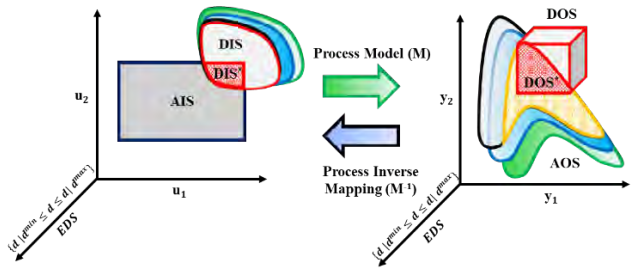



**Figure 2:** Schematic of the process operability concepts at steady-state.

## 3.2 Risk Assessment

The risk model can be established as a function of safety-critical variables in the process, inspired by the methodology described in [13]. Here, let $x$ represent these safety-critical variables, such as states. The risk index, $RI$, is defined in terms of the deviation of $x$ from the standard design or operating conditions, denoted by μ. Eq. (4) specifies $RI$ as the product of the fault probability, $P(x)$, and the consequence severity, $S(x)$. Additional insights into using $RI$ for real-time risk monitoring and management are provided in [14].

$$RI = P(x) \times S(x) \tag{4}$$

Fault Probability: The fault probability is determined using Eq. (5) for the case when $x \geq \mu$. The formulation incorporates a probability density function based on the mean (μ) and standard deviation ($\sigma$) of the safety-critical variables ($x$). This approach leverages the three-sigma rule ($\mu \pm 3\sigma$), meaning that roughly 99.7% of values are expected to lie within three standard deviations from the mean.

$$P(x) = \phi\left[\frac{x-(\mu+3\sigma)}{\sigma}\right] = \int_{-\infty}^{x} \frac{1}{\sqrt{2\pi}\sigma} e^{-\frac{[t-(\mu+3\sigma)]^2}{2\sigma^2}} dt, \quad \text{when } x \geq \mu \tag{5}$$

Consequence Severity: Eq. (6) is applied to measure consequence severity, which intensifies notably as the deviation of $x$ from three-sigma region increases.

$$S(x) = 100^{\frac{x-(\mu+\mu\sigma)}{x-\mu}}, \text{ when } x \geq \mu \tag{6}$$

# 4. PEMWE CASE STUDY: RESULTS AND DISCUSSIONS

This section presents the stepwise procedure to analyze the operability and safety of the PEMWE system.

## 4.1 First-Principles Process Modeling

The first-principles electrolyzer model provided in AVEVA™ Process Simulation is used in this case study. Modifications to the model are made to better align with the parameters of the experimental system (Fig. 1b). The polarization curve is a fundamental starting point in the study of PEMWE system, providing insights into the electrochemical performance of the cell under varying operating conditions. Table 1 provides the core electrochemical equations governing the PEMWE system, covering the open circuit voltage, activation overpotential, and ohmic overpotential.

In estimating the polarization curve, parameters with high impact on the stack's electrochemical behavior are carefully calibrated using experimental data. To ensure robustness, we conducted a sensitivity analysis to identify which parameters significantly affect the model's output and are well-represented by the experimental data. These include the exchange current densities for the anode ($i_{o,an}$) and cathode ($i_{o,ca}$). Table 2 presents both the design specifications and the estimated parameters for the PEMWE system. Table 3 presents the electrochemistry parameters. The optimal exchange current density values are determined to be $i_{o,an} = 3.62 \times 10^{-6}\ A \cdot cm^{-2}$ for the anode and $i_{o,ca} = 8.20 \times 10^{-6}\ A \cdot cm^{-2}$ for the cathode. Constants $\alpha_{an}$ and $\alpha_{ca}$, which represent the charge transfer coefficients for the anode and cathode, respectively, are adopted from literature values of 2 and 0.5. Figure 3 presents the polarization curve results, showing great agreement with experimental data.

## 4.2 Risk Modeling

Although the reaction is endothermic, heat is generated due to the Joule heating effect [6]. As a result, effective thermal management becomes crucial for safe PEMWE operation, as excessive heat buildup can lead to equipment failure and hazardous conditions. Applying high current densities increases electrolysis and heat generation, which risks damaging critical components like the membrane and electrodes or leads to a thermal runaway condition. Additionally, hydrogen is highly flammable. The leaks or improper handling can lead to explosive atmospheres.

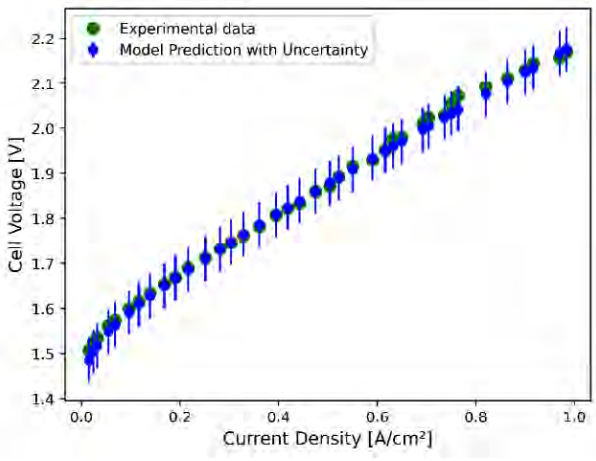



**Figure 3:** Parameter estimation results of the polarization curve.

**Table 1:** Electrochemistry equations of the PEMWE System.

| Electrochemistry | |
|---|---|
| **Open circuit voltage** | $V = E_{oc} + V_{act} + V_{\mathrm{ohm}}$ |
| | $E_{oc} = E_o + \frac{RT}{2\mathrm{F}} \ln \frac{p_{\mathrm{H_2}} p_{\mathrm{O_2}}^{0.5}}{p_{\mathrm{H_2O}}}$ |
| | $E_o = 1.229 - E_T(T - 298)$ |
| **Activation overpotential** | $V_{act} = \frac{RT}{\alpha_{an} F} \sinh \frac{i}{2i_{o,an}} + \frac{RT}{\alpha_{ca} F} \sinh \frac{i}{2i_{o,ca}}$ |
| **Ohmic overpotential** | $V_{\mathrm{ohm}} = \tau_m \frac{i}{\sigma_m}$ |
| | $\sigma_m = (M_a \lambda_m - M_b) \exp\left[M_c \left(\frac{1}{303} - \frac{1}{T}\right)\right]$ |

**Table 2:** Design and Estimated Parameters of the PEMWE System.

| Variable | Unit | Value |
|---|---|---|
| $\boldsymbol{P}$ | $Bar$ | 1.2 |
| $\mathbf{T_{in}}$ | ℃ | 20 |
| $\boldsymbol{\tau_m}$ | $\mu m$ | 254 |
| $\boldsymbol{A}$ | $cm^2$ | 50 |
| $\boldsymbol{N_c}$ | – | 4 |
| $\boldsymbol{\lambda_m}$ | – | 10.5 |
| $\boldsymbol{\alpha_{an}}$ | – | 2 |
| $\boldsymbol{\alpha_{ca}}$ | – | 0.5 |
| $\boldsymbol{i_{o,an}}$ | $A/cm^2$ | $3.62 \times 10^{-6}$ |
| $\boldsymbol{i_{o,ca}}$ | $A/cm^2$ | $8.20 \times 10^{-6}$ |

**Table 3:** Electrochemistry Parameters of the PEMWE System [13].

| Variable | Unit | Value |
|---|---|---|
| $\boldsymbol{E_T}$ | – | 0.0009 |
| $\boldsymbol{M_a}$ | – | 0.005114 |
| $\boldsymbol{M_b}$ | – | 0.00326 |
| $\boldsymbol{M_c}$ | – | 1268 |

In this study, the operating temperature is selected as the safety-critical variable, as its increase can pose significant risks to both the electrolyzer cells and the hydrogen storage system. The impact of temperature is quantified using the risk index previously presented, incorporating both fault probability and consequence severity to comprehensively assess safety risks. Figure 4 illustrates the risk quantification, with a mean temperature (μ) of $318.15\,K$ and a standard deviation ($\sigma$) of 5 K, defining the three-sigma range ($\mu + 3\sigma$) up to $333.15\,K$. Given a high-risk threshold temperature within this value, the calculated risk index of 0.5 underscores the need for urgent risk management.

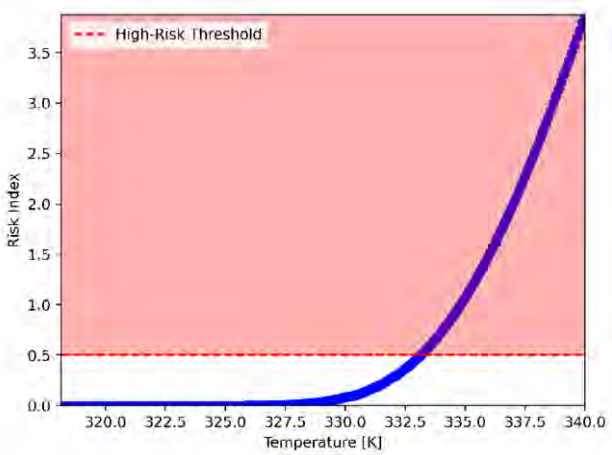



**Figure 4:** Risk evaluation

## 4.3 Operability and Safety Analysis – Forward Mapping

Forward mapping calculates the possible output space based on a given set of inputs (see Table 4). This analysis aims to provide valuable insights into how the system performs under varying conditions, such as fluctuations in renewable energy supply and demand-driven operations. The variables selected in this framework are designed to characterize these conditions. For example, makeup water is included as a manipulated variable as it serves as the raw material for hydrogen production and a key component of the system's cooling resources. Voltage is selected as the other manipulated variable to capture the impact of renewable energy source intermittency on system performance. The feed inlet temperature is considered as disturbance due to its potential variability, which may result from changes in ambient temperature or fluctuations in the cooling system.

**Table 4:** PEMWE System Input Variables.

| Input/Disturbance Variables | Physical Description | Available Range | Unit |
|---|---|---|---|
| $\boldsymbol{Q}$ | Makeup water | $0.01 - 1.2$ | $L/min$ |
| $\boldsymbol{T_{in}}$ | Voltage | $1.4 - 2.2$ | $V$ |
| $\boldsymbol{V}$ | Feed inlet temperature | $293.15 - 333.15$ | $K$ |

Figure 5a illustrates the space discretization employed based on the available input ranges. Figure 5b shows the corresponding outputs, which include hydrogen flow, outlet temperature, the ratio of hydrogen power (the power required by the electrolyzer per unit of hydrogen produced), and the risk index, as indicated in the

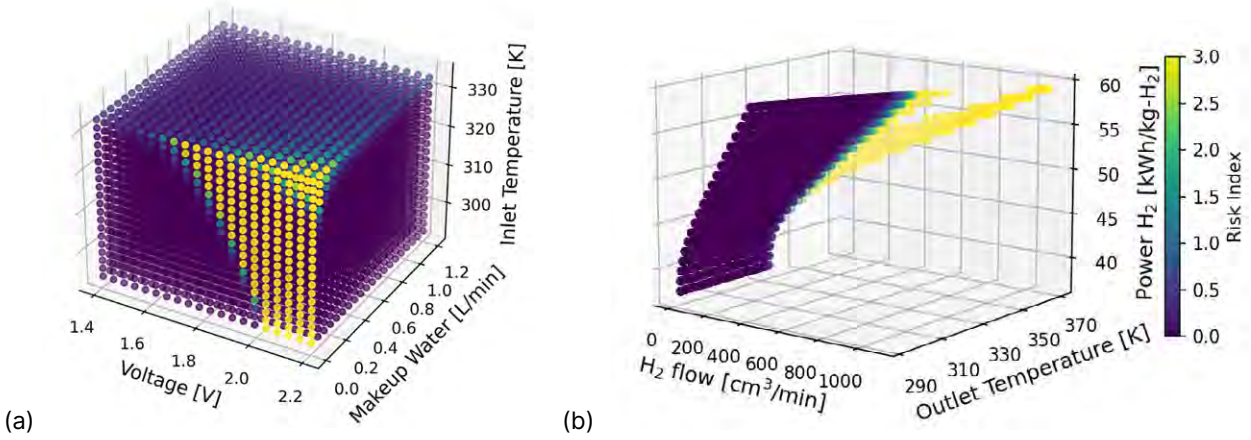



**Figure 5:** Forward mapping assessment for the PEMWE System. (a) Available input set (AIS). (b) Achievable output set (AOS).

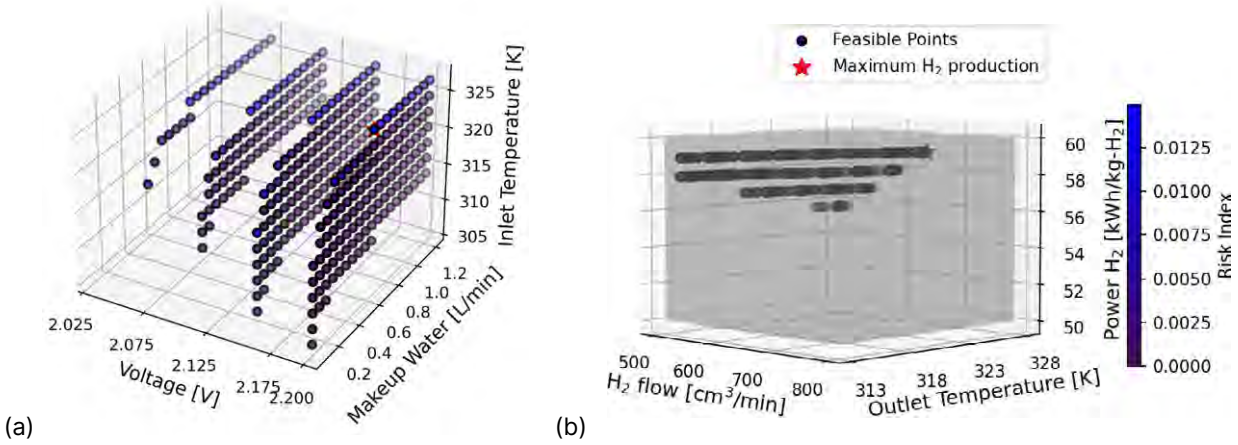



**Figure 6:** Inverse mapping assessment for the PEMWE System. (a) Feasible input set. (b) Feasible output set.

colormap. The high-risk region ($RI \geq 0.5$) results from a combination of inefficient cooling and elevated voltages in response to higher temperature disturbances, as depicted by the green-yellow regions in the colormap. This map enables to identify all possible configurations for the given high-risk scenarios, providing valuable insights for selecting set points in closed-loop operations. Notably, the achievability of these configurations is independent of the specific control law employed.

## 4.4 Operability and Safety Optimization – Inverse Mapping

Based on the entire operational space of the PEMWE system obtained via forward mapping, we further perform inverse mapping to evaluate whether the system can operate within a desired region. We identify the specific input conditions required to achieve the targeted hydrogen productivity while maintaining safety. Table 5 summarizes the target region for electrolyzer operation, derived from previous knowledge of the forward mapping results.

**Table 5:** PEMWE System Desired Output Set (DOS).

| Output Variables | Physical Description | Desired Range | Unit |
|---|---|---|---|
| $\boldsymbol{T_{out}}$ | Outlet temperature | $313.15 - 328.15$ | $K$ |
| $\boldsymbol{H_2\ Flow}$ | Hydrogen production | $500 - 800$ | $cm^3/min$ |
| $\boldsymbol{Power\ H_2}$ | Power $H_2$ | $50 - 60$ | $kWh/kg - H_2$ |

Figures 6a and 6b illustrate the feasible region from the input and output perspectives, respectively. Notably, within the feasible box, multiple points can be selected to achieve the desired target. The optimum point for

maximizing hydrogen production is identified as $T_{out} = 328.1\,K$, $H_2\,Flow = 650\,cm^3/min$, and $Power\,H_2 = 58.96\,kWh/kg - H_2$, with inputs of $Q = 0.63632\,l/min$, $V = 2.2\,V$ and $T_{in} = 326.83\,K$, which corresponds to a risk index of $0.01495$. This design not only achieves the highest hydrogen production but also adheres to the specified safety constraint ($RI < 0.5$).

## 5. CONCLUDING REMARKS

This work introduces a framework that integrates both forward and inverse mapping to optimize the operability and safety of PEMWE systems. Ongoing research is focused on implementing a multi-parametric model predictive controller (mp-MPC) to further enhance real-time control and safety performance based on the obtained regions from operability analyses.

## 6. ACKNOWLEDGEMENTS

The authors acknowledge the financial support from NSF RETRO Project CBET-2312457, NSF GRFP DGE-110268, Department of Chemical and Biomedical Engineering at West Virginia University, Mary O'Connor Process Safety Center and Energy Institute at Texas A&M University.

## REFERENCES

1. Wadim Strielkowski, Lubomír Civín, Elena Tarkhanova, Manuela Tvaronavic˘iene˙, and Yelena Petrenko. Renewable Energy in the Sustainable Development of Electrical Power Sector: A Review. Energies, 14(24):8240, 2021.
2. Lizica Simona Paraschiv and Spiru Paraschiv. Contribution of renewable energy (hydro, wind, solar and biomass) to decarbonization and transformation of the electricity generation sector for sustainable development. Energy Reports, 9:535–544, 2023.
3. Muhammad Amin, Hamad Hussain Shah, Anaiz Gul Fareed, Wasim Ullah Khan, Eunhyea Chung, Adeel Zia, Zia Ur Rahman Farooqi, and Chaehyeon Lee. Hydrogen production through renewable and non-renewable energy processes and their impact on climate change. International Journal of Hydrogen Energy, 47(77):33112–33134, 2022.
4. Mahdi Sharifzadeh, Nathanial Cooper, Hans Van'T Noordende, and Nilay Shah. Operational strategies and integrated design for producing green hydrogen from wind electricity. International Journal of Hydrogen Energy, 64:650–675, 2024.
5. D.S. Falcão and A.M.F.R. Pinto. A review on PEM electrolyzer modelling: Guidelines for beginners. Journal of Cleaner Production, 261:121184, 2020.
6. Gerald S. Ogumerem and Efstratios N. Pistikopoulos. Parametric optimization and control for a smart Proton Exchange Membrane Water Electrolysis (PEMWE) system. Journal of Process Control, 91:37–49, 2020.
7. Yuanxing Liu, Sahithi Srijana Akundi, Austin Braniff, Beatriz Dantas, Yuhe Tian, Shayan S Niknezhad, Faisal I Khan, and Efstratios N Pistikopoulos. Cyber-physical systems in chemical and energy pro- cesses. In Methods in Chemical Process Safety, volume 8, pages 215–241. 2024.
8. Beatriz Dantas, Austin Braniff, Sahithi S. Akundi, Yuanxing Liu, Shayan S. Niknezhad, Faisal I. Khan, Efstratios N. Pistikopoulos, Fernando V. Lima, and Yuhe Tian. An operability-based approach for integrated process design, operations, and risk management. In Methods in Chemical Process Safety, volume 8, pages 115–131. Elsevier, 2024.
9. Huayu Tian, Jnana Sai Jagana, Qi Zhang, and Marianthi Ierapetritou. Feasibility/flexibility-based optimization for process design and operations. Computers & Chemical Engineering 180 (2024): 108461.
10. Gabriele Bano, Pierantonio Facco, Fabrizio Bezzo, and Massimiliano Barolo. Probabilistic Design space determination in pharmaceutical product development: A Bayesian/latent variable approach. AIChE Journal 64, no. 7 (2018): 2438-2449.
11. Fernando V. Lima and Christos Georgakis. Input-output operability of control systems: The steady-state case. Journal of Process Control, 20(6):769–776, 2010.
12. Victor Alves, San Dinh, John R. Kitchin, Vitor Gazzaneo, Juan C. Carrasco, and Fernando V. Lima. Opyrability: A Python package for process operability analysis. Journal of Open Source Software, 9(94):5966, 2024.
13. Huizhi Bao, Faisal Khan, Tariq Iqbal, and Yanjun Chang. Risk-based fault diagnosis and safety management for process systems. Process Safety Progress, 30(1):6–17, 2011.
14. Moustafa Ali, Xiaoqing Cai, Faisal I. Khan, Efstratios N. Pistikopoulos, and Yuhe Tian. Dynamic risk-based process design and operational optimization via multi-parametric programming. Digital Chemical Engineering, 7:100096, 2023.

© 2025 by the authors. Licensed to PSEcommunity.org and PSE Press. This is an open access article under the creative commons CC-BY-SA licensing terms. Credit must be given to creator and adaptations must be shared under the same terms. See https://creativecommons.org/licenses/by-sa/4.0/



Systems & Control Transactions

**Research Article - Peer Reviewed Conference Proceeding**
ESCAPE 35 - European Symposium on Computer Aided Process Engineering
Ghent, Belgium. 6-9 July 2025
Jan F.M. Van Impe, Grégoire Léonard, Satyajeet S. Bhonsale,
Monika E. Polańska, Filip Logist (Eds.)

PSE PRESS

# Multi-Stakeholder Optimization for Identification of Relevant Life Cycle Assessment Endpoint Indicators

**Dat Huynh[a], Oluwadare Badejo[a], Borja Hernández[b], Marianthi Ierapetritou[a]***

[a] Department of Chemical and Biomolecular Engineering, University of Delaware, Newark, Delaware, United States of America
[b] Chemical and Energy Technology Department, Universidad Rey Juan Carlos, Calle Tulipan s/n, Móstoles, Madrid, Spain
* Corresponding Author: mgi@udel.edu.

## ABSTRACT

Endpoint indicators provide a concise representation of environmental impacts by aggregating multiple midpoint indicators into a single value. Traditional endpoint weighting systems, however, are often limited by biases introduced through panel reviews and a lack of robustness in scientific process models. Additionally, they typically fail to account for the preferences of key stakeholders, including industry, government, and the public. This work addresses these limitations by developing an endpoint indicator that incorporates stakeholder preferences and minimizes dissatisfaction. A multi-stakeholder optimization framework was formulated to achieve this goal, employing distance, downside risk, and conditional value at risk as objective functions. Stakeholder preferences were derived from emissions data for industry, federal spending on environmental issues for government, and public surveys for societal input. Results highlight regional variations in midpoint indicator weightings across Texas, California, Delaware, and the United States. Furthermore, the influence of public and government preferences reveals a prioritization of human health concerns over environmental impacts. This framework offers a novel approach to creating endpoint indicators that align with stakeholder priorities, promoting more inclusive and collaborative environmental decision-making.

**Keywords**: Life Cycle Assessment, Multi-Stakeholder Optimization, Risk Assessment

## INTRODUCTION

Life Cycle Assessment (LCA) is used to evaluate the environmental effects of products and processes. Several Life Cycle Impact Assessment (LCIA) methods such as TRACI and ReCiPE have been developed to quantify impacts[1, 2]. They employ midpoint indicators that relate the impact of an activity on specific environmental sectors. For example, kg $SO_2$-eq relates to acidification and kg N-eq for eutrophication in TRACI v2.1[2]. All environmental flows are measured relative to a basis, which serves as the primary causal factor. Additionally, ReCiPe also employs endpoint indicators that are a linear combination of midpoint indicators, with weights assigned based on relative physical impact.

Endpoint indicators aggregate relevant midpoint indicators to reflect broader societal impacts, such as human health, ecosystem quality, and resource depletion. While there is a physical basis for some of these endpoint indicators, their weights are mostly subjective and may not necessarily align with the interests of stakeholders. One example is the human development index (HDI) of the United Nations where three indicators (life expectancy, education index, and the income per capita) are grouped into the HDI with a fixed weight[3]. These weights can change between regions and the stakeholders' preferences.

Eco-Indicator 99 weighting for endpoint indicator was determined by a panel survey to weigh the importance of human life loss, extinction of plant species, and resource depletion[4]. The authors remarked that this panel is not necessarily reflective of society. The Institute of Environmental Science at Leiden University developed the CML method which does not provide endpoint indicators and states that any aggregation needs to be thoroughly explained[4]. The ReCiPe method provides three types of aggregation for endpoint indicators: individualistic, hierarchist, and egalitarian[5]. These

aggregations are based on Cultural Theory from the work of Thompson and are used to represent certain assumptions[5, 6]. The individualistic approach assumes a 20-year horizon with optimistic developments, the hierarchist approach aligns with current science over 100 years, and the egalitarian approach spans 1000 years with pessimistic assumptions and highest impact damages. The endpoint value varies based on the approach and assumptions made.

There are some limitations in the use of midpoint and endpoint indicators. The weighting for endpoint indicators is often done by an expert panel, which can result in biases and not accurately reflect stakeholder preferences[7]. In other instances when endpoint indicators are based on science modeling, the aggregation for different midpoint categories results in a loss of accuracy due to the lack of robustness of endpoint models[7].

In lieu of expert weighting or model-based aggregation, we propose an endpoint indicator that considers the environmental impacts important to stakeholders. By considering all stakeholders in the evaluation of the metric, we hope the framework would increase buy-in, particularly for policymaking. This metric is essential for setting policy that prevents burden-shifting between different environmental impacts. Consequently, a multi-stakeholder optimization approach with risk objective functions is formulated to develop an LCA endpoint metric. The multi-stakeholder framework allows for every perspective to be considered. Risk metrics are extensively used within the financial industry to minimize and mitigate extreme losses. In this context, they are used to minimize stakeholder dissatisfaction.

A data-driven, multi-stakeholder framework has been developed to enable the creation of LCA endpoint metrics that accommodate the diverse needs of stakeholders, including businesses, governments, and the public.

## METHODOLOGY

In this work, we consider the use of the following TRACIv2.1 midpoint indicators: acidification, ecotoxicity, climate change (GWP), human health (cancer and non-cancer), particulate matter (PM), smog formation, and ozone depltion. An endpoint indicator is a linear combination of the midpoint indicators as shown in equation 1, where $EP$ is the endpoint indicator value, $p_j$ is the weight for midpoint indicator *j,* and $f_j$ is the impact of midpoint indicator $j$.

$$EP = \sum_j p_j f_j \quad (1)$$

The main contribution of this work is to provide a method for determining the weighting factors of the midpoint indicators that will satisfy the needs of multiple stakeholders. To do so, first the stakeholder preferences are generated from data. A multi-stakeholder optimization function is generated to determine the optimal weighting function that minimizes stakeholder dissatisfaction.

### Stakeholder Preference Generation

There are three stakeholders: Industry, Public, and Government. For the public preferences, the results from a Gallup poll surveying 1,016 adults living in the United States were used[8]. Human health indicators and the remaining environmental indicators were split based on the number of correspondents who indicated that healthcare was a problem they worried about a fair amount or more. The remaining environmental indicator preferences were determined similarly by correlating responses with indicators. For the government preferences, the EPA 2024 Fiscal Year budget was used[9]. The EPA has strategic goals that were correlated with midpoint indicators. The preferences were generated as the fraction of money allocated to each strategic goal. For any indicators that are broken down into additional sub-indicators, such as Ecotoxicity, the weights are allocated uniformly.

For industry stakeholders, their preferences are built based on midpoint indicator impacts as calculated by their point-source air emissions. The point source air releases are obtained from the National Emissions Inventory (NEI), which contains information on point source emissions for every state in the United States[10]. The NEI consists of criteria air pollutants/precursors (CAPs), hazardous air pollutants (HAPs), and greenhouse gas emissions (GHGs). Point sources are facilities that have a large number of emissions from a fixed point. The NEI also reports nonpoint, on-road, nonroad, and fire sources. These alternative sources are smaller in magnitude than the point sources and are harder to attribute a stakeholder to. Consequently, only point sources from the NEI are used in this analysis. The NEI labels all point source data into facility types, which will serve as the basis for the industrial stakeholders. After the emissions for each pollutant type are identified, the midpoint impacts are calculated using the characterization factors from TRACIv2.2[11]. For substances in the NEI that are not found in the TRACI database, surrogate molecules are used as needed. Note that eutrophication is not considered in the optimization. Eutrophication can be calculated according to the spatial characterization factors provided by Henderson et al.; however, this consists of water emissions which can theoretically be determined by the national phosphorus inventory and national nitrogen inventory[12-14]. However, the water inventories do not have information on individual point sources. Therefore, we cannot attribute these emissions to any single stakeholder, and they are on a different basis than the air

emissions.

The stakeholder preferences are calculated from the midpoint impact values in the following way. Consider the matrix with elements $a_{i,j}$ where $i$ is the stakeholder and $j$ is the impact factor. The first transformation normalizes each column with respect to the total midpoint impact value, i.e. $a^1_{i,j} = \frac{a_{i,j}}{\sum_i a_{i,j}}$. The second transformation consists of normalizing each row with respect to the total TRACI impact across all impact categories, i.e. $a^2_{i,j} = \frac{a^1_{i,j}}{\sum_j a^1_{i,j}}$. We assume that if each stakeholder were to make an endpoint indicator as outlined in equation (1), then their desired weighting, $p_j$, will be proportional to their respective midpoint impacts. Therefore, we consider the preferred weightings for stakeholder $i$, $p_{i,j}$, to be equivalent to $a^2_{i,j}$. The preferred stakeholder weightings serve as parameters in our multi-stakeholder optimization problem.

## Multi-Stakeholder Model Formulation

There are three optimization objectives considered in the work, corresponding with Euclidean distance (ED), Conditional Value at Risk (CVaR), and downside risk (DSR) approaches. The three objective functions are different measures of stakeholder dissatisfaction, which should be minimized.

The Euclidean distance approach is equivalent to minimizing the sum of the stakeholder dissatisfaction. The distance approach minimizes the following objective function:

$$ED = \Sigma_s \Sigma_j k_s \left(p_{s,j} - p_j^*\right)^2 \qquad (2)$$

where $p_{s,j}$ is the preference for midpoint indicator$j \in J$ of stakeholder $s \in S$, $p_j^*$ is the optimum preference for midpoint indicator $j$, and $k_s$ is the stakeholder coefficient. The stakeholder coefficient is used to normalize the weighting between the industry, public, and government sectors. This is required because there are many industry stakeholders and only one public and one government stakeholder considered in this work. The goal of the distance approach is to simply minimize the sum of Euclidean distances between all stakeholders and the optimal preference.

In the CVaR approach, the expected dissatisfaction of the top c% dissatisfied stakeholders is minimized. $c$ is an arbitrary cutoff value, which is selected as 2.5 in this work. This objective function attempts to reduce the dissatisfaction of the stakeholders who will be most affected by the new endpoint metric[12]. The Conditional Value at Risk approach minimizes the following objective function:

$$CVaR = \frac{1}{(1-c)|S|} \sum_{s \in S} \psi_s + VaR \qquad (3)$$

where $\sum_j \left(\left(p_{s,j} - p_j^*\right)^2 - VaR\right) \leq \psi_s$ and $\psi_s$ is the amount of dissatisfaction above the VaR. , $p_{s,j}$ is the preference for midpoint indicator$j \in J$ of stakeholder $s \in S$ and $p_j^*$ is the optimum preference for midpoint indicator $j$. Both $\psi_s$ and $VaR$ are positive continuous variables. The Value at Risk, VaR, which represents $(1-c)$ percentile of dissatisfaction.

Downside Risk specifies a specific dissatisfaction level $L$. All stakeholder dissatisfaction greater than L is summed into the metric. The objective minimizes all stakeholder dissatisfaction above a specific level. The downside risk is given the following objective function:

$$DSR = \Sigma_s \phi_s \qquad (4)$$

where $\sum_j \left(\left(p_{s,j} - p_j^*\right)^2 - L\right) \leq \phi_s$ and $\phi_s$ is the amount of dissatisfaction above L, $p_{s,j}$ is the preference for midpoint indicator $j \in J$ of stakeholder $s \in S$ and $p_j^*$ is the optimum preference for midpoint indicator $j$.

The full optimization problem is formulated as follows:

$$\min f\left(p_j^*\right) \qquad (5)$$
$$s.t.\ \sum p_j^* = 1$$

where $f(p_j^*)$ corresponds to the corresponding objective function and $p_j^*$ are positive continuous variables corresponding to the ideal endpoint indicator weightings, that sum to 1. Additional inequalities are required for the CVaR and DSR approaches and are added as needed.

# CASE STUDY DESCRIPTION

The optimization problem was formulated and solved in Excel as an NLP using the Excel Solver plug-in with the GRG Nonlinear method. All computations were performed on a Mac M1 Pro @ 3.2 GHz CPU and 16.0 GB of RAM. The case study considers solving for endpoint indicator weights using the three objective functions described above. First, the state of Delaware is studied in depth. The endpoint indicators, risk by sector, and a sensitivity analysis on risk level are performed. To assess the effect of geography, the differences between the weightings are calculated from data for Texas, California, and Delaware, as well as the entire United States. These states were chosen as Texas and California have the largest GDP and large manufacturing sectors, while Delaware is a smaller state with manufacturing capacities. This is compared against the United States in aggregate. These results do not consider the effect of the public and of the government as stakeholders in the model. Finally, the effect of non-industry participants is considered by

increasing the stakeholder coefficients for these entities.

## RESULTS

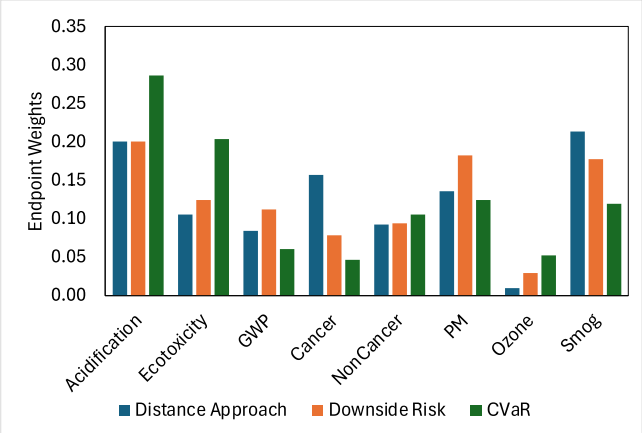



**Figure 1.** Endpoint indicator weights for the distance, downside risk (L = .15), and CVaR (c = 2.5%) objective functions for the state of Delaware.

The weights for the state of Delaware using distance, downside risk, and CVaR are obtained solving the optimization problem given in Equation 5. The resulting values $p_j^*$ are presented in Figure 1. The CVaR approach has higher weighting for acidification, ecotoxicity, and ozone depletion compared to the downside risk and distance approaches. CVaR has lower weighting for global warming potential (GWP), cancer, and smog. The downside risk approach with a dissatisfaction level of 0.15 has weights in between the distance approach and CVaR for a majority of indicator values. This effect is due in part to the low risk tolerance and medium risk tolerance set for CVaR, and downside risk, respectively. Additionally, the distance approach does not consider risk and therefore has the highest risk tolerance. Global warming potential and particulate matter (PM) are exceptions where downside risk has higher weighting.

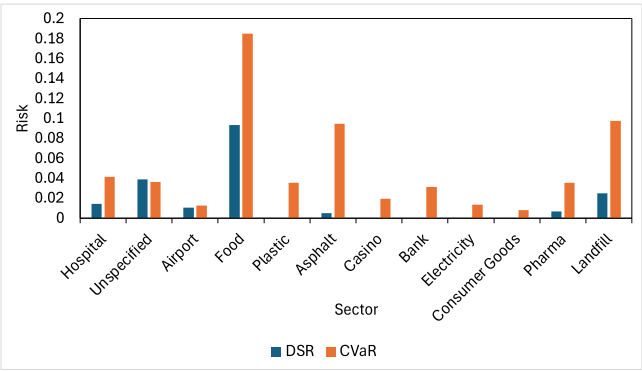



**Figure 2.** Risk levels for the downside risk and CVaR approach for unsatisfied sectors for the state of Delaware

There are 23 sectors considered in Delaware. At the prescribed dissatisfaction level, there are a number of sectors with dissatisfaction levels above the enforced limit. This is equivalent to risk. In the downside risk approach, there are 7 unsatisfied stakeholders with dissatisfaction levels above the dissatisfaction limit. In the CVaR approach, there are 12 unsatisfied stakeholders. The sectors' risks are shown in Figure 2. The lower risk tolerance in the CVaR approach accounts for the higher number of stakeholders and higher overall risk per sector compared to the downside risk approach.

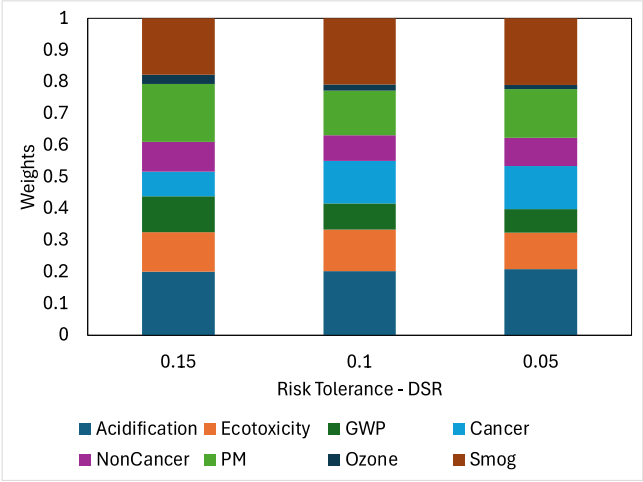



**Figure 3.** Endpoint indicator weights as a function of risk tolerance level for downside risk in the state of Delaware

A sensitivity analysis was performed on the risk tolerance level to understand the impact on endpoint indicator weights as shown in Figure 3. Decreasing the risk tolerance level results in smog, and cancer weights to increase. In contrast, global warming potential, particulate matter, and ozone decrease. Particulate matter and smog have the greatest contribution towards the total dissatisfaction. For particulate matter, there are two stakeholders with high dissatisfaction, food and asphalt. In contrast, smog affects a larger number of stakeholders but with relatively lower levels of dissatisfaction. Adjusting the weight of smog will result in higher cumulative stakeholder satisfaction than for particulate matter. For ecotoxicity, 0.1 relative to 0.15 risk tolerance has higher weights; however, 0.05 relative to 0.15 has a lower risk tolerance. The weighting for ecotoxicity is summed from several sub-indicators consisting of air, water, and soil emissions to water, resulting in no clear trend. When the risk tolerance was set above 0.2, there was no risk. Because there is no unique solution in this case, those results are omitted as there are multiple solutions.

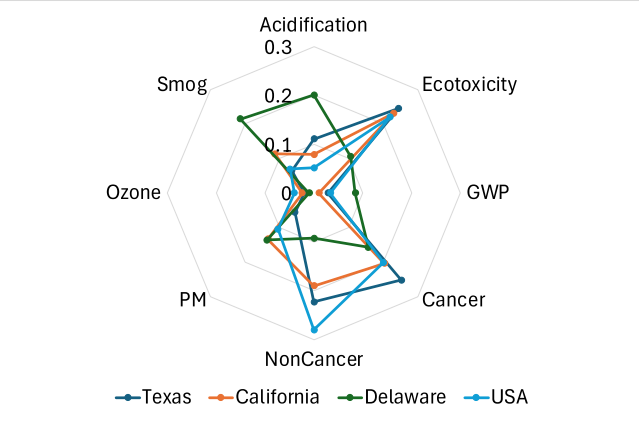



**Figure 4.** Endpoint indicator weights for Texas, California, Delaware, and the entire United States of America using the Euclidean distance approach

The endpoint indicator weights were calculated for Texas, California, Delaware, and the entire United States as a whole, as shown in Figure 4. The results reveal distinct regional variations in environmental impacts across Texas, California, Delaware, and the United States as a whole. Particulate matter impacts were notably lower in Texas compared to other regions. Delaware exhibited the lowest ecotoxicity values but had the highest acidification and smog endpoint weights. While ozone depletion and global warming potential carried relatively smaller weights across all regions, Delaware recorded a higher GWP weighting compared to the other states. Notably, the United States aggregated values were generally lower than those of individual states across most indicators, with the exception of non-carcinogenic effects, which were higher in the national assessment. These results highlight the spatial heterogeneity of environmental impacts and the importance of location-specific considerations in chemical engineering applications and policymaking.

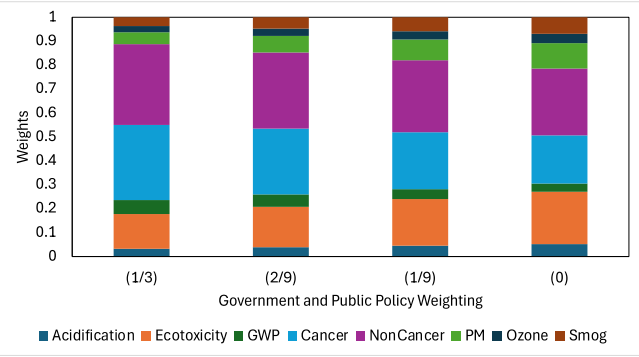



Figure 5. Endpoint indicator weights as a function of government and public policy stakeholder influence for the United States using the Euclidean distance approach

Figure 5 highlights the impact of varying public and government influence on endpoint indicators coefficients as determined using the Euclidean distance approach. As the influence of public and government preferences increases, the emphasis on cancer and non-cancer health risks increases significantly. This trend reflects the strong prioritization of these indicators, as supported by EPA spending and public survey data—92% of EPA spending is allocated to protecting public health and ensuring safe drinking water[9]. Similarly, the weighting of GWP rises with greater public and government influence, while the importance of other categories diminishes. Under the scenario with one-third weighting, each for the government and public, cancer and non-cancer health indicators account for 65% of the total weight. Even without government and public policy intervention, these indicators remain the most significant, representing 48% of the weight. This somewhat unexpected result underscores the dominant influence of regulatory compliance and societal priorities, which favor human health outcomes over broader environmental emissions.

## CONCLUSIONS

This work formulated a multi-stakeholder optimization problem to determine optimal midpoint indicator weightings for the creation of an endpoint indicator that minimizes dissatisfaction between all stakeholders. The Euclidean distance, downside risk, and conditional value at risk objective functions were minimized to do so. Industry, government, and public environmental impact preferences were generated from national emissions data, EPA funding, and public opinion data, respectively. The framework develops a unifying metric that can facilitate collaboration among stakeholders, promoting collective action towards environmental protection. It must be noted that the preference generation procedure in this work results in an inherently dynamic endpoint indicator. Emissions data, EPA fiscal budgets, and public opinion are constantly changing with time. The multi-stakeholder approach aims to minimize dissatisfaction between all stakeholders which optimizes agreement at the present time period. In context of policymaking, time inconsistency refers to the tendency for the optimal solution to any policy problem will be unlikely to remain the optimal solution throughout time, requiring new policies to be created. This is, in part, due to the dynamic nature of people's preferences.

Future work will focus on integrating this framework into policy-driven optimization models, such as cap-and-trade systems, where midpoint indicator impacts can be exchanged among stakeholders. This model will develop a pareto frontier of profits and environmental impacts with the goal of encouraging synergies between stakeholders via the novel endpoint indicator. Additional efforts will include refining the methodology for

determining preferences for midpoint indicators and tailoring the framework to capture regional variations by developing state-specific preferences. These advancements aim to further enhance the applicability and impact of this approach in fostering sustainable decision-making and environmental stewardship.

## ACKNOWLEDGEMENTS

The authors gratefully acknowledge financial support from the National Science Foundation under award number NSF-2134471.

## REFERENCES

1. Huijbregts, M.A.J., et al., ReCiPe2016: a harmonised life cycle impact assessment method at midpoint and endpoint level. The International Journal of Life Cycle Assessment, 2017. **22**(2): p. 138-147.
2. Bare, J.C., TRACI: The tool for the reduction and assessment of chemical and other environmental impacts. Journal of industrial ecology, 2002. **6**(3-4): p. 49-78.
3. Programme, U.N.D., Human Development Report 2023/2024. 2024: United Nations.
4. Smurthwaite, M., et al., A review of the LCA literature investigating the methods by which distinct impact categories are compared. Environment, Development and Sustainability 2023 26:8, 2023-06-14. **26**(8).
5. Huijbregts MAJ, S.Z., Elshout PMF, Stam G, Verones F, Vieira MDM, Van Zelm R, ReCiPe2016. A harmonized life cycle impact assessment method at midpoint and endpoint level. Report I: characterization. 2016, National Institute for Human Health and the Environment: Bilthoven
6. Michael Thompson, R.J.E., Aaron Wildavsky, Mary Wildavsky, Cultural Theory. 1990, Boulder, CO: Westview Press.
7. Bare, J.C., et al., Midpoints versus endpoints: The sacrifices and benefits. The International Journal of Life Cycle Assessment, 2000. **5**: p. 319-326.
8. Evans, M.C. Seven Key Gallup Findings About the Environment on Earth Day. 2024.
9. FY 2024 Annual Performance Report. 2024, United States Environmental Protection Agency.
10. Houyoux, M., National Emissions Inventory, U.S.E.O.o.A.a.R.O.-O.o.A.Q.P.a.S. (OAQPS), Editor. 2020.
11. Bare, J., et al., Tool for the Reduction and Assessment of Chemical and other Environmental Impacts (TRACI). US Environmental Protection Agency: Washington, DC, USA, 2012.
12. Henderson, A.D., et al., Modeling spatially resolved characterization factors for eutrophication potential in life cycle assessment. The international journal of life cycle assessment, 2021. **26**(9): p. 1832-1846.
13. National Inventory of Reactive Nitrogen, U. EPA, Editor. 2018: U.S. Environmental Protection Agency: Environmental Dataset Gateway.
14. National Inventory of Phosphorus, U. EPA, Editor. 2019: U.S. Environmental Protection Agency: Environmental Dataset Gateway.

© 2025 by the authors. Licensed to PSEcommunity.org and PSE Press. This is an open access article under the creative commons CC-BY-SA licensing terms. Credit must be given to creator and adaptations must be shared under the same terms. See https://creativecommons.org/licenses/by-sa/4.0/



Systems & Control Transactions

**Research Article - Peer Reviewed Conference Proceeding**
ESCAPE 35 - European Symposium on Computer Aided Process Engineering
Ghent, Belgium. 6-9 July 2025
Jan F.M. Van Impe, Grégoire Léonard, Satyajeet S. Bhonsale,
Monika E. Polańska, Filip Logist (Eds.)

PSE PRESS

# Lignocellulosic Waste Supply Chain Network Design for Sustainable Aviation Fuels Production through Solar Pyrolysis

**Stavroula Zervopoulou[a*], Stavros Papadokonstantakis[a], Mika Järvinen[b], and Muddasser Inayat[b]**

[a] Vienna University of Technology, Institute of Chemical, Environmental and Bioscience Engineering, Faculty of Technical Chemistry Getreidemarkt 9, A-1060 Vienna, Austria
[b] Aalto University, Energy Conversion and Systems Research Group, Department of Energy and Mechanical Engineering, School of Engineering, Sähkömiehentie 4J, 02150 Espoo, Finland
* Corresponding Author: stavroula.zervopoulou@tuwien.ac.at

## ABSTRACT

This study optimizes the Sustainable Aviation Fuel Supply Chain Network (SAFSCN) in the Czech Republic, using wheat straw as feedstock. It integrates geospatial data, transportation logistics, and economic feasibility, applying mixed-integer linear programming (MILP) to optimize pyrolysis plant locations and minimize costs. Sensitivity analysis varied wheat production growth by ±0.1% and ±0.2%. Results confirm Sustainable Aviation Fuel (SAF) production is technically and economically viable, with costs projected to decline up to 30.64% and revenues rising 49.07% from 2030 to 2050 due to technological advancements, improved logistics, and economies of scale. The findings underscore the critical role of SAF in achieving EU aviation decarbonization targets and highlight the importance of efficient supply chain planning for scaling SAF production.

**Keywords**: Biomass, Biofuels, Sustainable Aviation Fuel, Supply Chain Network Model, Optimization

## INTRODUCTION

The EUROCONTROL main report [4] outlines long-term forecasts for flights and $CO_2$ emissions across three scenarios—low, base, and high. In the base scenario, Europe's aviation sector is expected to grow significantly, with flights increasing by 44% from 2019 levels, reaching 16 million annually by 2050. This growth in flights will drive a corresponding rise in fossil fuel demand, resulting in millions of gigatons of $CO_2$ emissions from aviation. According to Wang et al., renewable aviation fuel holds the highest potential for reducing $CO_2$ emissions, while biomass is the only renewable energy source capable of capturing $CO_2$ emissions. This makes biomass-based fuel production a promising option for achieving a net-zero carbon balance through $CO_2$ fixation via photosynthesis [18]. Similarly, Martinez-Valencia emphasizes that the production of renewable fuels is critical for global efforts to reduce greenhouse gas emissions [11]. This aligns with the Eurocontrol report, which identifies scaling up the production, distribution, and use of Sustainable Aviation Fuels (SAFs) as a key strategy to help the aviation industry achieve net-zero $CO_2$ emissions by 2050. In the base scenario, SAFs are projected to contribute 41% of the necessary emission reductions. While there is no single solution, the long-term impact of SAF scaling is expected to be the largest, with operational improvements providing more immediate benefits, alongside contributions from governments and regulators [4]. To address the growing $CO_2$ emissions from aviation, the European Union introduced the ReFuelEU Aviation Regulation, which aims to reduce greenhouse gas emissions by promoting SAF usage. Starting in 2025, aviation fuel suppliers will be required to provide a minimum SAF blend of 2% at EU airports, with this percentage increasing over time. By 2030 and 2050, the required SAF blend is expected to reach 6% and 70%, respectively, with 35% of this coming from synthetic aviation fuels (e-fuels). This regulation is projected to cut $CO_2$ emissions by more than 60% by 2050 compared to 1990 levels, playing a crucial role in the EU's broader decarbonization efforts [7]. The Renewable Energy Directive II (RED II) provides a comprehensive

framework for promoting renewable energy in the EU, with a focus on advanced biofuels (second-generation biofuels), which are derived from non-food feedstocks such as straw, nut shells, and husks. This distinction helps reduce competition with food crops and mitigates the risk of indirect land-use change [6]. Currently, Sapp's research on seven certified processes under ASTM D7566 allows up to 50% SAF blends with fossil jet fuel [15]. SAFs must ensure low lifecycle carbon emissions, renewability, and sustainability, avoiding competition with food production, ecosystem harm, and deforestation, while also being economically viable. Masum et al. highlight the importance of developing an efficient supply chain for large-scale SAF production and distribution. A comprehensive approach involves key elements like feedstock availability, optimization of production pathways by exploring technological options, assessing infrastructure and logistics for transporting feedstocks to pyrolysis plants and bio-oil to refineries, and ultimately utilizing Supply Chain Optimization Modeling. Mixed-integer linear programming (MILP) models can simulate and optimize the supply chain over time, aiding decisions on facility locations, transportation routes, and inventory management to minimize both costs and environmental impact [12].

Our study presents a comprehensive approach to optimizing a Sustainable Aviation Fuel Supply Chain Network (SAFSCN), with a focus on the Czech Republic.

## METHOD

This study outlines a SAF supply chain network, with the process divided into four stages. In Stage 1, geospatial data including wheat production and developed area data (2002-2023) from the Czech Statistical Office [1], administrative boundaries (Nomenclature of Territorial Units for Statistics - NUTS 3) provided by the EUROSTAT website [2], road distances between regions cities (point in the map) and refineries, Direct Normal Irradiance (DNI) data from SOLARGIS [17], and the locations and capacities of existing refineries are gathered. For this study, wheat straw is chosen as the feedstock for SAF production, aimed at replacing a portion of Jet A-1 fuel. In Stage 2, the methodology followed for the wheat straw estimation was first to calculate the dry matter production of wheat which is 90% [10]. Then, the yield (production/developed surface) was calculated for each year and the straw quantification estimation was calculated by using the residues-to-product ratio (RPR) empirical function by Scarlat et al., 2010 as reported by Karan & Hamelin [10, 16]. The RPR is as follows:

$$RPR = -0.3629*\ln(Y)+1.6057\ 0.28 \quad (1)$$

where Y is the Yield, and this function derived best-fit logarithmic function curves for RPR by plotting the values for RPR and crop yield based on data available in the literature. This approach determines the theoretical potential of straw production, by using the following formula as reported in the Karan and Hamelin study [10]:

$$\text{Straw Production} = \text{RPR} * \text{Yield} * \text{Surface area} \quad (2)$$

For estimating available straw production, it is important to take into account crucial parameters such as the removal rate of residues from the terrain and the amount that is used in competitive uses. Removal rates must be sustainable in order to protect soil quality, biodiversity, and erosion control, and in this study, the sustainable removal rate of wheat and rye residues is 40% [17], and the amount of straw needed for animal bedding is 16% of the collectable crop [14]. The formula that was followed to calculate the available potential straw production is as follows:

$$\text{Available residues} = \text{Theoretical potential (dry matter)} - \text{Removal rate \%} - \text{Competitive uses \%} \quad (3)$$

This approach is based on the approach mentioned by Elbersen et al. [3] and has been applied to the AdvanceFuel Horizon Project [8]. Using the historical data, forecasting of feedstock for the short-mid term (2030) and long term (2050) was performed by applying the 'Commission' method. In this method, the production area of wheat was forecasted based on the annual growth percentage of these crops given in Agricultural Outlook 2023-35 [2]. For the crop period 2013-2023, the annual growth percentage of soft wheat was 0.1% for the period of 2013-2023 and 2023-2035. This growth rate was applied to project wheat production areas for 2030 and 2050. Crop production was then estimated by multiplying the projected production areas by the average yield of these crops, which was derived from a historical dataset spanning 22 years. For this study, a sensitivity analysis was conducted by varying the annual growth rate (AGR) of wheat production within a range of ±0.1% and ±0.2% from the historical data. This approach accounts for potential fluctuations in productivity due to factors such as climate variability, thereby enhancing the robustness of the results.

In the present study, an initial quantitative assessment of SAF production was conducted based on the availability of feedstock, as outlined above. The calculations followed the material flow from dried feedstock to the final SAF product, utilizing a system coupling fast pyrolysis with solar energy, as proposed in the CIRCULAR FUELS project and presented in Figure 1 [9].

The SAF demand was forecasted for 2030 and 2050, considering the required minimum SAF blending

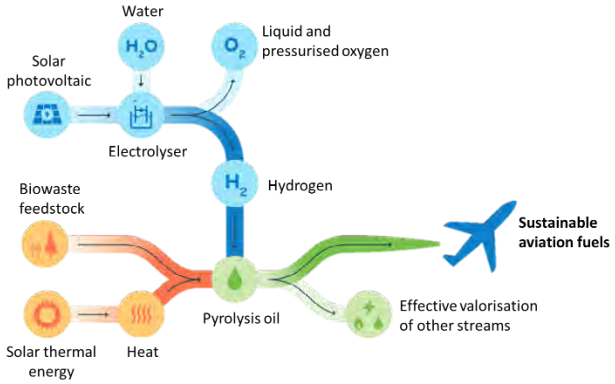



**Figure 1.** The Circular Fuels project process shows the conversion of renewable feedstock to sustainable aviation fuel (CIRCULAR FUELS).

targets of 6% by 2030 and 35% (with 70% of SAF, including at least 35% synthetic aviation fuels or e-fuels) by 2050, as outlined in Annex IX of the ReFuelEU Aviation regulation [7]. The Jet A-1 supply projections for 2030 and 2050 are based on EUROCONTROL's main report, using the base case scenario, which predicts a 14% increase in flight activity over 2019 levels by 2030 and a 44% increase by 2050 [4]. The analysis then assessed whether the SAF quantities required to meet the ReFuelEU regulation targets for 2030 and 2050 would be sufficient to satisfy demand. In Stage 3, potential sites for the pyrolysis plant are identified by calculating a trade-off score that balances feedstock capacity and DNI. First, the transportation cost of feedstock is calculated and normalized for different regions, taking into account straw availability and a distance constraint of up to 150 km. Then, a combined score function is applied to compute a trade-off score, incorporating the two normalized factors: transportation cost and DNI. This function helps assess how transportation costs and solar energy potential contribute to the overall system performance, allowing for a balanced decision. The weights used for this evaluation were 0.7 for transportation cost and 0.3 for DNI. The function operates by multiplying the normalized transportation and DNI scores by their respective weights, and then summing them to obtain the final trade-off score. This score, which ranges from 0 to 1 (assuming normalized scores between 0 and 1), provides an integrated metric where 0 represents the least favorable scenario (either high transportation costs or low solar potential) and 1 indicates the optimal combination (low transportation costs and high solar potential).
The combined score is calculated as:

$$\text{Combined score} = (\text{weight transport} \times \text{transportation normalized}) + (\text{weight DNI} \times \text{DNI normalized}) \quad (4)$$

For the final selection of plant sites, a two-thirds capacity constraint was implemented to ensure that each selected plant receives a minimum amount of straw to maintain operational efficiency. By enforcing this threshold, the algorithm avoids underutilized plants and prioritizes locations with sufficient biomass supply.

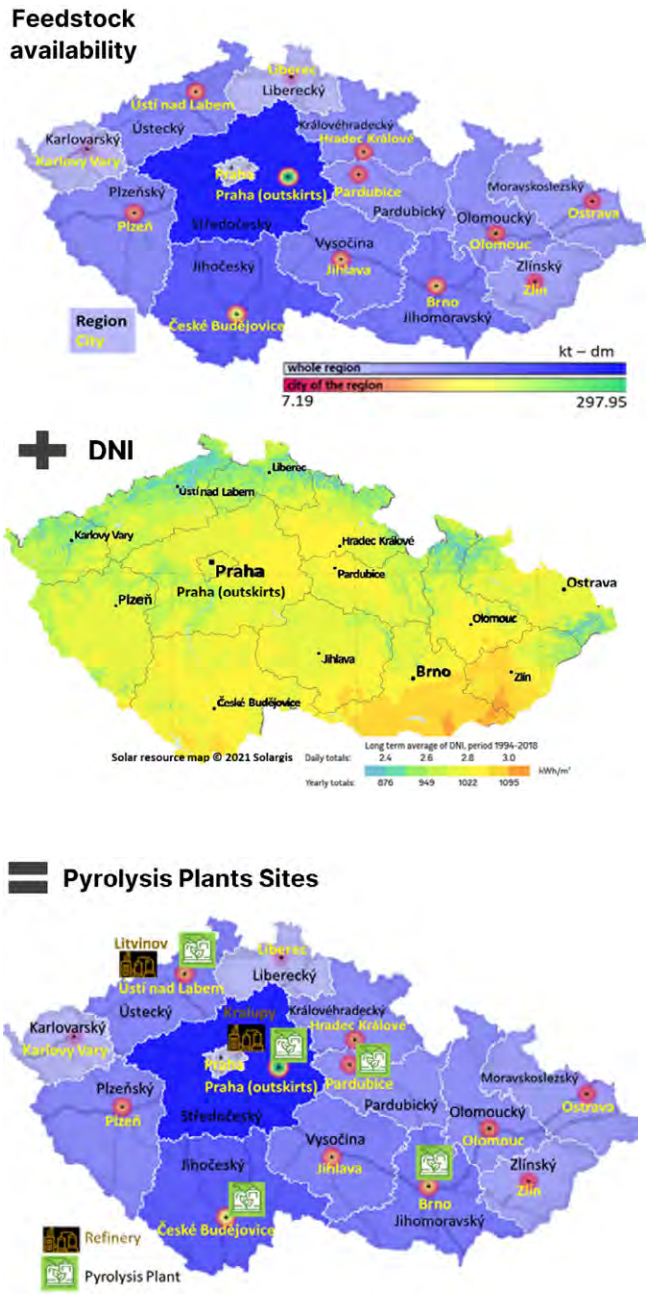



**Figure 2.** Selected pyrolysis plant sites, by using a trade-off score between feedstock capacity and DNI for 2030.

Mennicken et al. reported that when calculating transportation costs in Europe using straight-line distances, it is recommended to apply a correction factor (detour index) ranging from 1.1 to 1.3. In this study, a correction factor of 1.1 was applied [13]. In Stage 4, the supply chain network model was run to provide the optimal allocation of feedstock to the potential pyrolysis plant sites and bio-oil to the nearest refinery. Finally, the OPEX,

CAPEX breakdown, Revenues per site, and SAF replacement satisfaction in 2030 and 2050 were calculated.

## Supply Chain Network Model

The model in this study represents a three-stage supply chain for converting feedstock into SAF. It begins with straw collection from the regions, then transported to a storage facility where it is stored until needed for processing, which is located in the plant site area. The available straw of each region is transported to one plant site only. At the plant site, the feedstock undergoes initial treatment processes to prepare it for pyrolysis. Solar energy is utilized to support sustainable operations at the plant. In the pyrolysis plant, a wastewater treatment plant is located for treating the aqueous phase, where the purified water is used in the electrolysis. The pyrolysis plant includes two upgrading steps to begin refining the pyrolysis oil. Following the upgrading process, the resulting bio-oil is transported to the nearest refinery, where it undergoes further processing in a distillation column to produce biofuels, including SAF, biodiesel, and biogasoline. Each stage of the supply chain is interconnected through truck transportation, with transportation costs calculated in both directions. A 30% discount is applied to return trips. For this study, a plant capacity of 300 kt was assumed. It is assumed that the available straw in each region is concentrated at the regional city center to facilitate the calculation of distances. The plant sites are established in regions with the highest combined scores and are designated according to the names of these regions.

The objective function seeks to minimize the total costs, which include feedstock, transportation, storage, operational, and capital expenditure costs associated with pyrolysis plants, while accounting for the revenue generated from biochar and SAF.

### Index Sets:

R = {r|region in the country}

RF = {rf| refinery in the county}

### Decision Variables:

$X_r$ = 1 if r has a plant, otherwise 0

$Y_{r,r'}$ = 1 if the straw is transported from region r′ to plant in region r, otherwise 0.

$Z_{r,rf}$ = 1 if HDO from r is transported to rf; otherwise, 0.

### Parameters:

$DNI_r$ = Direct Normal Irradiance at a region

$S_r$ = biomass availability in a region

$S_p$ = available straw in a plant

$TC_{r,r'}$ = Full-truck transport cost per km with TC capacity

TC = Truck capacity (tn)

$CT_{r,r'}$ = Transportation cost per km per tn ($TC_{r,r'}$ / TC)

$D_{2,r,r'}$ = Two directions distance between r and r′ ϵ R

BD = Bulk density of biomass (kg/m³)

SC = Storage and loading cost per m³

CAP = Maximum straw processing plant capacity (kt)

$CAP_{rf}$ = Maximum refinery capacity (bbl)

$TC_{r,rf}$ = Transportation cost per km of a full tanker truck with TTC capacity

TTC = Tanker truck capacity (gallons)

$CT_{r,rf}$ = Transportation cost per km per bbl ($TC_{r,rf}$ / TTC*α)

$D_{2,r,rf}$ = Two directions distance between regions r and rf ϵ R

HDO = bio-oil (bbl)

α = Convector factor from gallons to barrels

γ = Conversion factor for SAF

δ = Conversion factor for HDO

Biochar and SAF selling price (€)

### Objective function:

$$min[\sum_{r,r' \in R, r \neq r'} r, r' Yr, r' * S_r * D_{2r,r'} * CT_{r,r'} + \sum_r BD * S_p * SC + \sum_{r,rf} Z_{r,rf} * HDO_r * D_{2,r,rf} * CT_{r,rf} + \sum_r (OPEX + CAPEX)] - \sum_r (Biochar\ revenues + SAF\ reveneues)] \quad (5)$$

### Constraints:

Feedstock Supply: $S_{min}*Y_r \leq \sum_r X_r*S_r \leq S_{max}*Y_r, \forall r$ (6)

Region Supply: $\sum_r X_r \leq 1, \forall r$ (7)

*Ensures that each region supplies biomass to only one plant.*

Straw Utilization: $\sum_r S_p \leq \sum_r S_r$ (8)

*Ensures the straw used in all plants does not exceed the total straw supply.*

Straw Allocation: $\sum_r Y_{r,r'} * S_r \leq CAP, \forall r$ (9)

*Ensures that the allocation of straw from each region to a plant does not exceed the plant's capacity.*

Trade-off Score: $X_r$ * Combined score ≥ Tmin (10)

Two-Thirds Plant Capacity: $S_r \geq 2/3 * Smax, \forall r$ (11)

Transportation Distance: $D_{r,r'} \leq 150, \forall Y_{r,r'}=1$ (12)

*Ensures transportation distances do not exceed 150 km for regions where biomass is transported.*

SAF Production: $\sum_r \gamma * S_p \geq$ SAF DEMAND (13)

*Ensures that the total SAF production meets the demand.*

HDO Refinery Capacity: $\sum_r \delta * S_p \leq \sum_{rf} CAP_{rf}$ (14)

*Ensures that the HDO produced at all plants does not exceed the total refinery capacity.*

Refinery Transportation: $\sum_{rf} Z_{r,rf} = 1, \forall p$ (15)

*Ensures that each region where a plant is located sends its produced HDO to exactly one refinery.*

Solar Collector Energy Production: energy produced by solar collectors must meet or exceed the daily thermal energy requirement for the pyrolysis process.

num collectors needed * energy per collector per day kWh ≥ total thermal energy kWh per day (16)

*The installed electrolyzer and PV systems must be sufficient to meet the hydrogen production demand.*

electrolyzer capacity kW ≥ ($H_2$ needed per year / operating hours per year) (17)

pv capacity kW ≥ [($H_2$ needed per year * production efficiency)/operating hours per year] (18)

## RESULTS

By executing the Supply Chain Network Model code in Python, the optimal locations for the pyrolysis plant in 2030 and 2050 for all the cases (AGR ±0.1% and ±0.2% from the historical data) and bio-oil transportation to the nearest refinery are presented in Figure 3.

In the short to mid-term (2030), the model does not exhibit sensitivity, as it selects the same plant sites. However, in the long term (2050), the model demonstrates sensitivity by selecting different plant sites. In all scenarios, the plant sites in Praha (outskirts) and České Budějovice are consistently chosen. Additionally, the results indicate a well-optimized and scalable pyrolysis-based SAF production system with high straw utilization (94–100%) across all cases, as presented in Table 1.

Refinery capacities remain sufficient to handle bio-oil production, supporting seamless integration into existing fuel infrastructure.

Despite fluctuations in biomass availability, SAF production consistently meets 6% and 35% of Jet A-1 fuel demand for 2030 and 2050 respectively, highlighting supply chain resilience.

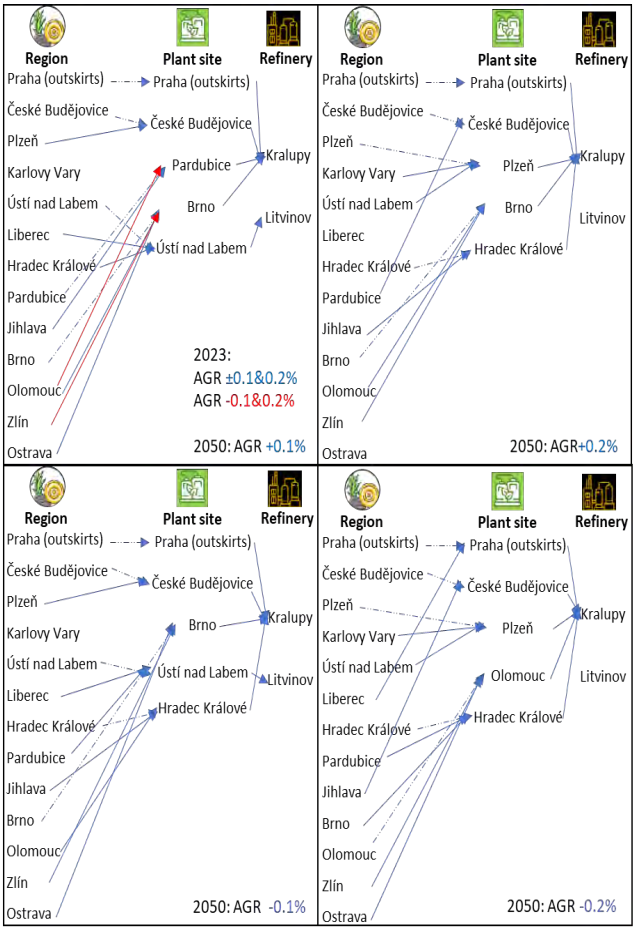



**Figure 3.** The three-supply chain network for 2030 and 2050. The dashed lines do not represent straw transportation but rather indicate that the straw from a region is utilized at the plant site located within the same region.

**Table 1:** Estimated wheat straw utilization and SAF production plant in 2030 and 2050 for all the cases.

| | Straw Utilized % | | SAF produced (kt) | |
|---|---|---|---|---|
| | 2030 | 2050 | 2030 | 2050 |
| AGR+0.1% | 94.4% | 94.4% | 199.05 | 202.1 |
| AGR -0.1% | 98.6% | 98.5% | 204.3 | 200.1 |
| AGR+0.2% | 94.4% | 93.7% | 200.1 | 205.2 |
| AGR -0.2% | 98.5% | 100% | 202.5 | 197.4 |

Total cost shows a downward trend over time, suggesting improved cost efficiency due to technological advancements. Specifically, in 2030 cases the economic feasibility is maintained, with total costs ranging from €755M to €884M, while biochar and SAF revenues contribute up to €214M, while in 2050 cases the total costs vary between €542M and €613M, while biochar and SAF revenues contribute up to €319M, ensuring economic feasibility. Praha (outskirts) consistently emerges as the most economically viable plant site location for all the cases. Solar collectors play a crucial role in meeting heat

demand, reducing external energy dependence, and ensuring sustainability.

Overall, the analysis confirms that the current strategy is robust, adaptable, and viable for long-term SAF production, while also highlighting a cost-effective approach with strong long-term profitability and energy security.

## CONCLUSION

This study confirms that SAF production in the Czech Republic is both technically and economically viable. The total costs are projected to decline by up to 30.64% from 2030 to 2050, while revenues are estimated to increase by approximately 49.07% over the same period. Strategic site selection based on feedstock availability, transportation costs, and solar energy potential enhances efficiency, with Praha outskirts emerging as a key production hub. CAPEX and OPEX (total cost) estimates show declining costs over time, especially with advancements in solar collectors and energy efficiency improvements.

The results align with EU decarbonization goals, demonstrating that SAF, supported by optimized supply chain networks, can play a pivotal role in reducing aviation emissions. Continued investment in SAF infrastructure, technological advancements, and regulatory support will be essential to ensuring a sustainable and cost-effective transition to greener aviation fuels.

## ACKNOWLEDGEMENTS

The authors wish to gratefully acknowledge the support of the Horizon Europe Circular Fuels project 101118239, funded by the European Climate, Infrastructure and Environment Executive Agency (CINEA), which funds this research.

## REFERENCES

1. Czech Statistical Office. https://csu.gov.cz/home
2. European Commission. Agricultural outlook for markets, 2023-2035. DG Agriculture and Rural Development, Brussels (2023) https://doi.org/10.2762/722428
3. Elbersen B, Startisky I, Hengeveld G, Jeurissen L, and Lesschen J. Outlook of spatial value chains in EU28–Deliverable 2.3 of Biomass Policies Project. Alterra–Part of Wageningen UR, Wageningen, the Netherlands and Laxenburg, Austria (2015)
4. EUROCONTROL. EUROCONTROL Aviation Outlook 2050 (2022) https://www.eurocontrol.int/publication/eurocontrol-aviation-outlook-2050
5. EUROSTAT. https://ec.europa.eu/eurostat/web/nuts
6. European Parliament and Council of the European Union. Directive (EU) 2018/2001 of the European Parliament and of the Council of 11 December 2018 on the promotion of the use of energy from renewable sources (recast). Official Journal of the European Union, L328, 82–209 (2018) https://eur-lex.europa.eu/legal-content/EN/TXT/?uri=CELEX:32018L2001
7. European Parliament and Council of the European Union. Regulation (EU) 2023/2405 of the European Parliament and of the Council of 18 October 2023 on ensuring a level playing field for sustainable air transport (ReFuelEU Aviation). Official Journal of the European Union, L202, 1–378 (2023) https://eur-lex.europa.eu/legal-content/EN/TXT/?uri=CELEX:32023R2405
8. Hoefnagels R, and Germer S. Supply potential, suitability and status of lignocellulosic feedstocks for advanced biofuels. D2. 1 Report on lignocellulosic feedstock availability, market status and suitability for RESfuels (2018)
9. European Commission. Circular Fuels Horizon Project: Production of sustainable aviation fuels from waste biomass by coupling of fast pyrolysis with solar energy (2022) https://cordis.europa.eu/project/id/101118239
10. Karan S K, and Hamelin L. Crop residues may be a key feedstock to bioeconomy but how reliable are current estimation methods? Resources, Conservation and Recycling, 164, 105211 (2021) https://doi.org/https://doi.org/10.1016/j.resconrec.2020.105211
11. Martinez-Valencia L., Camenzind D, Wigmosta M, Garcia-Perez M, and Wolcott M. Biomass supply chain equipment for renewable fuels production: A review. Biomass and Bioenergy, 148, 106054 (2021) https://doi.org/10.1016/j.biombioe.2021.106054
12. Masum F H, Coppola E, Field J L, Geller D, George S, Miller J L, Mulvaney M J, Nana S, Seepaul R, Small I M, Wright D, and Dwivedi P. Supply chain optimization of sustainable aviation fuel from carinata in the Southeastern United States. Renewable and Sustainable Energy Reviews, 171, 113032 (2023) https://doi.org/10.1016/j.rser.2022.113032
13. Mennicken E, Lemoy R, and Caruso G. Road network distances and detours in Europe: Radial profiles and city size effects. Environment and Planning B: Urban Analytics and City Science, 51(1): 174-194 (2024) https://doi.org/10.1177/23998083231168870
14. Monforti F, Bódis K, Scarlat N, and Dallemand J.-F. The possible contribution of agricultural crop

residues to renewable energy targets in Europe: A spatially explicit study. Renewable and Sustainable Energy Reviews, 19: 666-677 (2013) https://doi.org/10.1016/j.rser.2012.11.060
15. Sapp M. ASTM approves new SAF production pathway called Catalytic Hydrothermolysis Jet, Biofuels Digest 5 In press, https://www.biofuels digest.com/bdigest/2020/02/19/astm-approves-new-saf-production-pathway-called-catalytic-hydrothermolysis-jet (2020)
16. Scarlat N, Martinov M, and Dallemand J.-F. Assessment of the availability of agricultural crop residues in the European Union: Potential and limitations for bioenergy use. Waste Management, 30(10), 1889-1897 (2010) https://doi.org/10.1016/j.wasman.2010.04.016
17. SOLARGIS. https://solargis.com
18. Wang M, Dewil R, Maniatis K, Wheeldon J, Tan T, Baeyens J, and Fang Y. Biomass-derived aviation fuels: Challenges and perspective. Progress in Energy and Combustion Science 74: 31–49 (2019) https://doi.org/10.1016/j.pecs.2019.04.004

© 2025 by the authors. Licensed to PSEcommunity.org and PSE Press. This is an open access article under the creative commons CC-BY-SA licensing terms. Credit must be given to creator and adaptations must be shared under the same terms. See https://creativecommons.org/licenses/by-sa/4.0/



Systems & Control Transactions

**Research Article - Peer Reviewed Conference Proceeding**
ESCAPE 35 - European Symposium on Computer Aided Process Engineering
Ghent, Belgium. 6-9 July 2025
Jan F.M. Van Impe, Grégoire Léonard, Satyajeet S. Bhonsale,
Monika E. Polańska, Filip Logist (Eds.)

PSE PRESS

# Resource and Pathways Analysis for Decarbonizing the Pulp and Paper Sector in Quebec

**Marie-Hélène Talbot[a]*, and Mélissa Lemire[a]**

[a] Hydro-Quebec, Quebec, Canada
* Corresponding Author: talbot.marie-helene@hydroquebec.com.

## ABSTRACT

Decarbonizing industries could significantly increase electricity demand, necessitating strategic grid expansion. This study evaluates the impact of decarbonizing the Pulp and Paper Sector under four 2050 scenarios: carbon capture, biomass-based, direct electrification, and indirect electrification. A bottom-up approach is employed to estimate 2020 final energy demand by heat grade and subsector. Both final and primary energy demand systems are modeled, accounting for the efficiencies of end-use technologies and primary energy transformation processes. The analysis compares primary renewable energy demand (electricity and biomass) normalized per ton of equivalent $CO_2$ avoided against a business-as-usual scenario. It also considers the requirements for wood residues, organic waste, and $CO_2$ storage. The carbon capture scenario, while low in electricity demand, requires significant organic waste for renewable natural gas production and 2.6 Mt of $CO_2$ storage to offset direct and indirect emissions, making it the least feasible due to uncertainties around carbon storage in Quebec. Among the remaining scenarios, the direct electrification stands out by offering the lowest primary energy demand. It combines heat pumps with electric boilers for steam production and lime kilns are converted to a plasma-based solution. The study also includes a sensitivity analysis highlighting the potential of energy efficiency measures to ease the burden of decarbonization.

**Keywords**: Decarbonization, Energy Conversion, Modelling and Simulations, Planning, Carbon Capture, Pulp and Paper

## INTRODUCTION

Achieving net-zero emissions by 2050 will require significant adaptations in industries, increasing pressure on electric grids. Forecasting industrial energy demand is important for electric utilities and requires a deep understanding of each sector. In Quebec, Canada, the pulp and paper sector (PPS) may need to make major adjustments to reduce GHG emissions from fossil fuel combustion, which accounted for 12% of total industrial emissions in 2020. The PPS has several abatement solutions to choose from, including installing carbon capture units, shifting to sustainable natural gas, increasing biomass use, electrifying process heat, or using hydrogen for indirect electrification.

Besides these solutions, which can be combined, the PPS could further contribute to the energy transition. The chemical and semi-chemical pulp subsector emits significant biogenic $CO_2$ from the combustion of residual liquor and lime regeneration. This biogenic $CO_2$ could be used to produce synthetic fuels and/or generate negative emissions to offset unavoidable GHG emissions [1]. These pathways are known as Bioenergy with Carbon Capture and Utilization (BECCU) and Bioenergy with Carbon Capture and Storage (BECCS). The possibility of contributing to BECCU and BECCS, along with the existing biomass supply chain value and the fact that most of the sector's GHG emissions can be easily abated with existing solutions, the PPS is well-positioned to play a key role in decarbonization. Therefore, multiple decarbonization scenarios for the PPS should be evaluated, particularly regarding their impact on electric grids.

This study explores scenarios involving the adoption of different end-use technologies to achieve net-zero emissions by 2050. Key performance indicators assess the impact on the electric grid and biomass resources. The study aims to provide insights based on a bottom-up approach to guide electric system capacity expansion.

## METHODOLOGY

The methodology relies on publicly reported GHG emissions data [2]. Using a bottom-up approach, the final energy demand for low, medium, and high-grade heat is estimated for 2020 for two subsectors: semi-chemical and chemical pulp mills, and other categories. Low-grade heat is required for pulp bleaching, medium-grade heat for washers and evaporators, and high-grade heat for lime kilns. To estimate the evolution of energy demand, a useful energy approach is employed in the Low Emissions Analysis Platform (LEAP), considering an annual growth rate of 1% and the efficiencies of current and alternative end-use technologies. Based on energy demand, the software estimates primary energy demand, considering transformation process efficiencies.

### Scenarios

A business-as-usual (BAU) scenario serves as a baseline, with four simplified scenarios modelled using constant useful energy. The end-use technologies per subsector and heat grade are illustrated in Figure 1. The first scenario, the carbon capture (CC) scenario, involves minimal adaptation of end-use technologies, relying on carbon capture and storage to achieve net-zero. A blend of 20% renewable natural gas (RNG) and 80% natural gas replaces natural gas. RNG is produced from organic waste, including food, agricultural, livestock residues, landfill sites, and wastewater. Light fuel oil and heavy fuel oil are replaced with liquefied gas blend. The carbon capture units are directly installed as post-combustion equipment on boilers and lime kiln to offset emissions from burning natural gas.

The subsequent scenarios involve significant adaptations of end-use technologies, converting them to biomass-based, direct electrification, and/or indirect electrification technologies. For low- and medium-grade heat, heat pumps (HPs) and high-temperature heat pumps (HTHPs) are prioritized, as they can effectively upgrade waste heat to produce hot water and steam. The proportion of process heat that can be supplied by heat pumps depends on factors like location, timing, temperature and flow rate of both waste and process heat streams. Marina et al. [3] estimated that heat pumps could supply up to 69% of process heat below 200°C in European PPS, though excluding (Semi-) Chemical Pulp Mills. For the entire sector, up to 65% is set for low- and medium-grade heat. Since recovery boilers already provide steam, HTHPs supply 45% of medium-grade heat in (Semi-) Chemical Pulp Mills. A sensitivity analysis complements the results to account for uncertainties. For the biomass-based (BIO) scenario, efficient bark boilers supply the remaining heat, with enhanced efficiency from crushing and drying processes using low-grade waste heat. For the direct (DE) and indirect (IE) electrification scenarios, electric boilers provide the remaining heat. For high-grade heat, a gasified biomass lime kiln is selected in the BIO scenario, though alternatives like torrefied biomass, pulverized wood or lignin exist [4], with gasified biomass being widely adopted in Finland [1]. For the DE scenario, an electrified plasma calcination process is selected [5], and for the IE scenario, a hydrogen-fired lime kiln is selected. Finally, while adoption of end-use technologies is not constrained by regional electric capacities, but wood residues are limited to current availability.

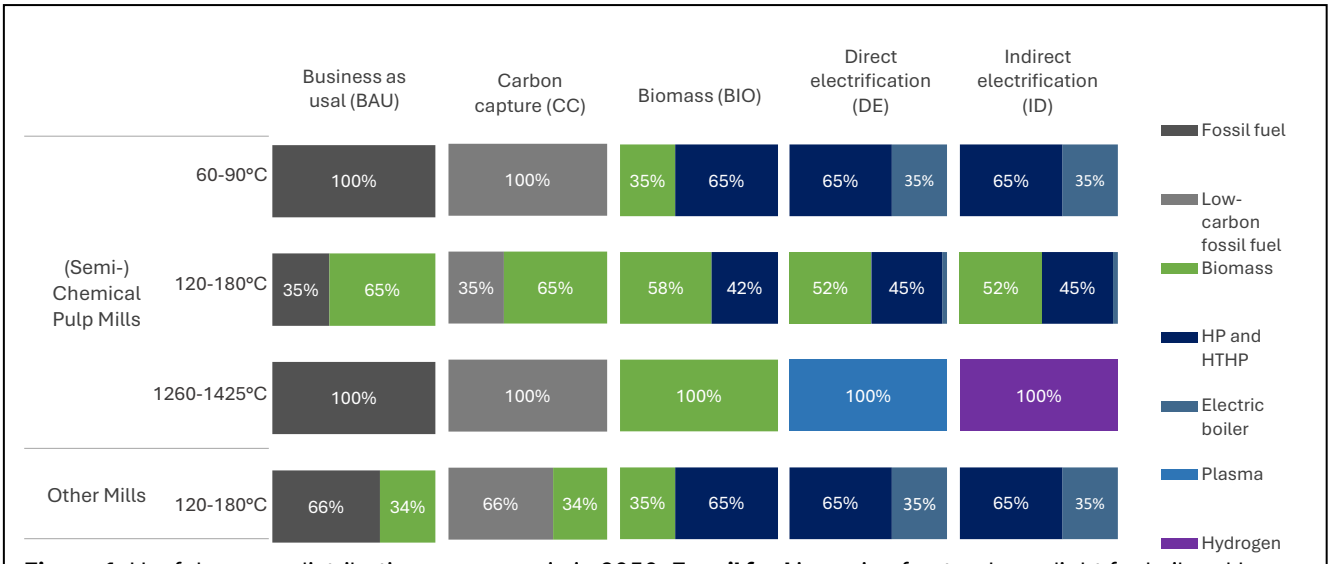



**Figure 1:** Useful energy distribution per scenario in 2050. **Fossil fuel** is a mix of natural gas, light fuel oil and heavy fuel oil. **Low-carbon fossil fuel** is a mix of natural gas, renewable natural gas and liquified natural gas blend. **Biomass** is a mix of residual liquor, wood bark and decentralized biogas. **HP, HTHP** and **EB** refer to heat pump, high temperature heat pump, and electric boiler.

## Final energy demand

The final energy demand system includes both current and alternative end-use technologies. For low and medium-grade heat, current technologies are fossil fuel-fired, bark, and recovery boilers, while alternatives include efficient bark boilers, electric boilers, HPs, and HTHPs. For high-grade heat, the current technology is a fossil fuel lime kiln, while alternatives include gasified biomass, plasma-based solution, and hydrogen. Efficiencies and auxiliary energy requirements are listed in Table 1, using a low heating value (LHV) of 19 MJ/kg for wood residues. The final energy demand system also includes carbon capture technology, with an efficiency of 95% and energy requirements of 333 $kWh_{el}$/t for capture and conditioning with a membrane separation technology Zanco et al. [6]. This simplified approach may differ for lime kilns due to variations in $CO_2$ concentration and scale [7, 8].

Direct emissions are estimated by LEAP, following the IPCC AR5. Quebec's electricity grid, mainly powered by renewables, has a GHG emissions intensity of about 0.3% of Europe's average in 2023 [9, 10]. Emissions from imported non-renewable electricity are small, but by 2050, all imports are assumed to be 100% renewable.

**Table 1:** End-use technologies parameters

| End-use technology | Efficiency | Auxiliary energy requirements |
|---|---|---|
| Low and medium-grade heat | | |
| Boiler | | |
| Fossil fuel | 75%[11] | N/A |
| Bark | 70%[11] | N/A |
| Recovery | 65% [12, 13] | N/A |
| Bark (efficient) | 80% [14] | Crushing: 32 $kWh_{el}$/t[1] |
| Electric | 99%[11] | N/A |
| Heat pump | | |
| HP | 300%[3] | N/A |
| HTHP | 250%[3, 15] | N/A |
| High-grade heat | | |
| Lime kiln | | |
| Fossil fuel | 53%[16] | N/A |
| Gasified biomass | 41%[4] | Drying: 465 $kWh_{th}$/t[4] Grinding: 278 $kWh_{el}$/t[4] |
| Hydrogen | 56%[4] | N/A |
| Plasma-based | 55%[16] | N/A |

[1]Electric consumption of a bark crusher per dry ton of pine wood residues, based on vendor data.

## Primary energy demand

The primary energy demand system includes centralized energy solutions such as natural gas, gas blend with RNG, liquefied gas blend, 100% renewable electricity, and green hydrogen. For the liquefied gas blend, energy for liquefaction, truck transport, and fugitive emissions are neglected due to data limitations, though it represents only 2% of final energy demand in the CC scenario. Green hydrogen is produced using alkaline electrolysers, with liquefaction and transport by trucks for storage and distribution. Decentralized energy solutions like wood residues, residual liquor, biogas from wastewater streams, are also included. Transformation processes and distribution efficiencies as well as fugitive GHG emissions are listed in Table 2. Fugitive emissions for natural gas are relatively low and have been estimated at 0.93%(vol.) by the CIRAIG [17], while those for RNG are considered negligible. The primary energy demand system also includes direct air capture technology, with an energy requirement of 2514 $kWh_{el}$/t [18], to offset the fugitive emissions of natural gas.

**Table 2:** Transformation processes and distribution parameters

| Energy produced | Requirements | Primary energy |
|---|---|---|
| Green hydrogen | 1.37 $kWh_{in}/kWh_{out}$ [19] | Renewable electricity |
| RNG[1] | 1.47 $kWh_{in}/kWh_{out}$ 0.05 $kWh_{in}/kWh_{out}$ | Organic waste Renewable electricity |
| **Energy distributed** | **Efficiency** | **GHG emissions** |
| Renewable electricity | 93%[20] | - |
| Natural gas | 96%[17, 21] | 13.5 $g_{CO2eq}/MJ_{consumed}$[17] |
| Green hydrogen | 95%[22] | 11.6 $g_{CO2eq}/g_{H2leaking}$[23] |
| Natural gas blend | 96%[17, 21] | 10.8 $g_{CO2eq}/MJ_{consumed}$[17] |

[1]The organic waste requirements are based on a theoretical assessment, assuming 50% average carbon content, a LHV of 5.55 kWh/kg, and a carbon conversion fraction of 0.85. The electricity requirement was estimated at 5% of the product's LHV.

## Key performance indicators

Resource indicators, along with the reduction of GHG emissions, differences in biomass demand and $CO_2$ storage requirements, are calculated for each scenario. The GHG Performance Indicator (GPI) assesses the marginal renewable energy - electricity, biomass, or both - required per ton of GHG emissions avoided, as expressed in Equation 1. This indicator is evaluated by heat grade, subsector, and globally, relative to the BAU scenario.

$$GPI_i = \frac{E_i - E_{i,baseline}}{GHG_{baseline} - GHG}, \quad (1)$$

where E is the primary energy demand in MWh, GHG is the 100-year GWP emissions in ton of equivalent $CO_2$, i is the resource of interest (electricity, biomass or total).

## RESULTS AND DISCUSION

The sector's thermal energy consumption in 2020 is estimated at 23 $TWh_{th}$, and its distribution by usage is illustrated in Figure 2.

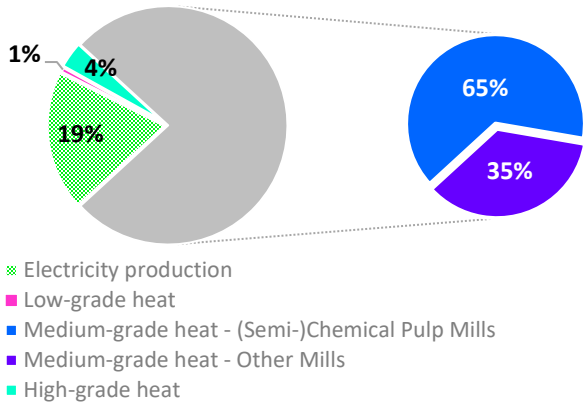



**Figure 2.** Distribution of the thermal energy consumption by usage.

Most consumption is attributed to steam used in various processes, with the remainder used for low- and high-grade heat in processes and on-site electricity production. The main fuels consumed in the (Semi-) Chemical Pulp Mills are residual liquor (63%), natural gas (25%), and wood residues (9%). For the Other Mills, the main fuels are natural gas (52%) and wood residues (37%). The use of gas directly fired in Through Air Dryers is neglected, slightly overestimating steam consumption. It is assumed that electricity production is fueled by wood residues and residual liquor.

### Resource analysis

Figure 3 illustrates the marginal primary energy demand for each scenario and its breakdown by source. All scenarios achieve a 98-99% reduction in 100-year GWP direct emissions and a 96-100% reduction in indirect emissions. Residual GHG emissions result from the combustion of large amounts of biomass - wood residues and residual liquor – emitting biogenic methane and nitrous oxide. Only the CC scenario requires $CO_2$ storage, with 2.2 Mt to offset direct emissions and 0.4 Mt for indirect emissions.

The CC scenario requires more energy due to electricity needed by the carbon capture technology and RNG production, along with about 3.2 TWh of organic waste for RNG production. The other scenarios are fossil-free and more efficient than the baseline, but they required additional electricity, mainly for direct electrification. The DE and IE scenarios, the adoption of direct electrification technologies releases 4.7 TWh of wood residues that were used in bark boilers. Lastly, the IE scenario requires an additional 0.6 TWh for electrolysis to supply five lime kilns.

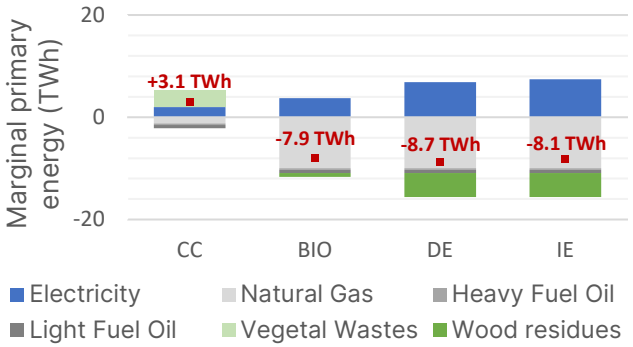



**Figure 3.** Marginal primary energy (red square) and its breakdown per source compared to the baseline.

The total, electric and biomass GPIs are reported in Table 3. The DE scenario have the highest biomass GPI, but with a relatively high electric GPI. Overall, the total GPI is the lowest, meaning that the DE can decarbonized effectively the PPS.

**Table 3.** Total, electric and biomass GPI in MWh/t per scenario.

| | CC | BIO | DE | IE |
|---|---|---|---|---|
| $GPI_{total}$ | +2.0 | +1.1 | +0.6 | +0.9 |
| $GPI_{electric}$ | +0.7 | +1.4 | +2.6 | +2.8 |
| $GPI_{biomass}$ | +1.2 | -0.3 | -1.9 | -1.9 |

To better understand what influences the GPIs, the total, electric and biomass GPI are breakdown by heat grade and subsector in Figure 4.

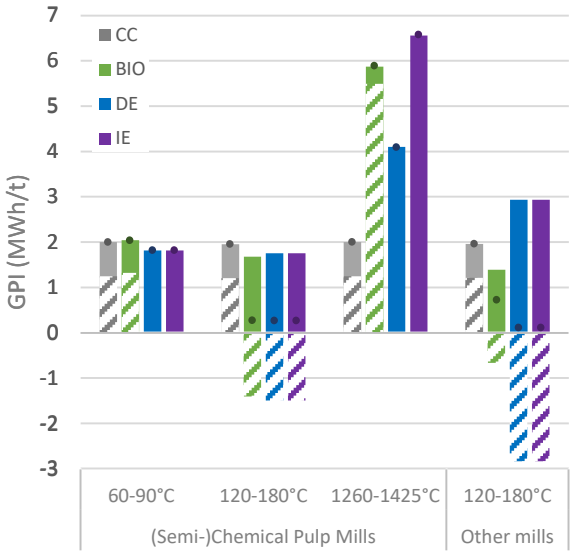



**Figure 4.** GHG performance indicator for electricity (solid bars), biomass (hatched bars) and total (dot).

The highest total GPI is for high-grade heat, reflecting that the usage is harder to abate than the others. The

CC scenario achieves the lowest total GPI, but $CO_2$ storage remains uncertain and the organic waste resource used to produce RNG is also limited - 25% of it is used in the CC scenario, based on the 2021 Quebec biomass inventory [24]. Therefore, the CC scenario's decarbonization solutions should be reserved for hard-to-abate industrial applications and residual emissions. The DE scenario ranks second, but it has the highest electric GPI across all heat grades and subsectors. The BIO scenario, relying mainly on wood residues, ranks third, with the lowest electric GPI and no need for additional biomass, as wood residues are redirected from steam production via HTHPs.

## Sensitivity analysis

The sensitivity of three uncertain variables on the GPI is assessed in Table 4 using a one-at-a-time technique with lower and upper bound for each variable:

1. The proportion of heat provided by heat pumps, with bounds of 25% and 85%.
2. The reduction in energy demand from energy efficiency measures (EEMs), excluding heat pumps, with bounds of 10% and 20%. EEMs are apply to electricity for equipment (lighting, motors, compressors, etc.) and steam demand in (Semi-) mChemical Pulp Mills only.
3. The proportion of RNG in the gas blend, with bounds of 10% and 20%, including the change in natural gas fugitive emissions.

**Table 4**: Sensitivity analysis of variables on the GPI.

| **Scenarios** | **$\Delta GPI_{electric}$ (%)** | | **$\Delta GPI_{biomass}$ (%)** | |
|---|---|---|---|---|
| | LB | UB | LB | UB |
| 1. Proportion of heat from HP and HTHP vs boilers | | | | |
| | 25% | 85% | 25% | 85% |
| BIO | OB | +13% | OB | -185% |
| DE | +40% | -9% | - | - |
| IE | +36% | -9% | - | - |
| 2. Reduction of electricity and steam consumption | | | | |
| | 10% | 20% | 10% | 20% |
| CC | -18% | -19% | -18% | -51% |
| BIO | -16% | -19% | 45% | 324% |
| DE | -12% | -24% | - | - |
| ID | -11% | -22% | - | - |
| 3. Proportion of RNG in the gas blend | | | | |
| | 10% | 30% | 10% | 30% |
| CC | +7% | -7% | -50% | +50% |

OB: Out of bounds

The sensitivity analysis results provide valuable insights: EEMs and waste heat recovery with heat pumps could significantly reduce additional electricity and limit unnecessary grid expansion. EEMs cutting steam and electricity demand of electric equipment by 10% and 20% could reduce additional electricity demand by 11%-18% and 18%-24%, respectively, depending on the scenario. EEMs should be implemented before or alongside electrification of process heat to reduce decarbonization's burden. They must also align with the chosen decarbonization pathway for effectiveness. Heat pump adoption is crucial in limiting electric demand. If heat pumps provide 25% of the process heat, additional electricity increases by 40% for the DE scenario, while providing 85% of the heat reduces additional electricity demand by 9%. These differences highlight the importance of characterizing the potential of heat pumps to minimize the capacities of electric boilers as much as possible.

The sensitive analysis shows that the proportion of RNG represents a trade-off between the organic waste demand and $CO_2$ storage requirements, both limited resources. At 30% RNG, organic waste demand rises to 37% of the available resource in Quebec for 2021. At 10% RNG level, $CO_2$ storage requirements to offset indirect emissions rises by 13% due to natural gas fugitive emissions.

# CONCLUSION

This study provides a comprehensive analysis of the decarbonization pathways for the PPS and their impact on resource in Quebec. The results indicate that while all scenarios lead to 98-99% reductions in GHG emissions, the strategies employed have varying levels of efficiency. The CC scenario is notable for its low electricity demand and costs but requires uncertain $CO_2$ storage and large amounts of organic waste for RNG production. Carbon capture and RNG should be reserved for the hardest-to-abate applications among all industries. Further work is needed to determine whether the lime kiln falls into this category. The DE scenario, with a total GPI of 0.6 MWh/t, uses the least combined electricity and biomass to avoid one ton of $CO_2$. The sensitivity analysis highlights key variables like EEMs, heat pump integration, and the proportion of RNG in gas bend. EEMs and heat pumps are critical for minimizing grid expansion, and aligning EEMs with decarbonization pathways is vital for an effective energy transition. Future research should focus on cost-effectiveness assessments and expanding the model to optimize resource allocation across Quebec's major industries.

# REFERENCES


1. Lipiäinen, S., E.-L. Apajalahti, and E. Vakkilainen, Decarbonization Prospects for the European Pulp and Paper Industry: Different Development Pathways and Needed Actions. Energies, 2023. **16**.
2. Québec GHG inventory, L.c.l.c.c. Ministère de

l'Environnement, Faune et Parcs, Editor. 2024.
3. Marina, A., et al., An estimation of the European industrial heat pump market potential. Renewable and Sustainable Energy Reviews, 2021. **139**: p. 110545.
4. Kuparinen, K. and E. Vakkilainen, Green pulp mill: renewable alternatives to fossil fuels in lime kiln operations. BioResources, 2017. **12**(2): p. 4031-4048.
5. Svensson, E., H. Wiertzema, and S. Harvey, Potential for Negative Emissions by Carbon Capture and Storage From a Novel Electric Plasma Calcination Process for Pulp and Paper Mills. Frontiers in Climate, 2021. **3**.
6. Zanco, S.E., et al., Postcombustion CO2 Capture: A Comparative Techno-Economic Assessment of Three Technologies Using a Solvent, an Adsorbent, and a Membrane. ACS Engineering Au, 2021. **1**(1): p. 50-72.
7. Onarheim, K., et al., Performance and costs of CCS in the pulp and paper industry part 1: Performance of amine-based post-combustion CO2 capture. International Journal of Greenhouse Gas Control, 2017. **59**: p. 58-73.
8. Onarheim, K., et al., Performance and cost of CCS in the pulp and paper industry part 2: Economic feasibility of amine-based post-combustion CO2 capture. International Journal of Greenhouse Gas Control, 2017. **66**: p. 60-75.
9. Hydro-Québec, Taux d'émission de GES associés aux approvisionnements résiduels en électricité. 2023.
10. European Environment Agency. Greenhouse gas emission intensity of electricity generation, EU level. 2025 14 Feb 2025; Available from: https://www.eea.europa.eu/en/analysis/indicators/greenhouse-gas-emission-intensity-of-1/greenhouse-gas-emission-intensity-of-electricity-generation-eu-level?activeTab=570bee2d-1316-48cf-adde-4b640f92119b.
11. Schoeneberger, C., et al., Electrification potential of U.S. industrial boilers and assessment of the GHG emissions impact. Advances in Applied Energy, 2022. **5**: p. 100089.
12. Cloutier, J.-N., P. Dontigny, and L. Beaudoin, Ultra high solids black liquor using the electromagnetic induction heating technology. International Chemical Recovery Conference, 2010. **2**: p. 268-284.
13. Vakkilainen, E.K., Boiler processes. Steam generation from biomass, 2017: p. 57-86.
14. Sharpe, D. and W.D.K. Association, Comparing waste wood boilers. 2002.
15. Arpagaus, C., et al., High temperature heat pumps: Market overview, state of the art, research status, refrigerants, and application potentials. Energy, 2018. **152**: p. 985-1010.
16. Lefvert, A. and S. Grönkvist, Smarter ways to capture carbon dioxide – exploring alternatives for small to medium-scale carbon capture in Kraft pulp mills. International Journal of Greenhouse Gas Control, 2023. **127**: p. 103934.
17. CIRAIG, Profil environnemental du gaz naturel distribué au Québec. . 2020.
18. House, K.Z., et al., Economic and energetic analysis of capturing CO2 from ambient air. Proc Natl Acad Sci U S A, 2011. **108**(51): p. 20428-33.
19. U.S. Department of Energy (DOE). Technical Targets for Liquid Alkaline Electrolysis. March 11, 2025].
20. Hydro-Québec, Building the Future, in Annual report. 2023.
21. Brun, K., The US Natural Gas Compression Infrastructure: Opportunities for Efficiency Improvements. 2018, University Turbine Systems Research Symposium.
22. Muñoz, I., Literature review on climate effects and leakage rates in a hydrogen economy. 2023.
23. Sand, M., et al., A multi-model assessment of the Global Warming Potential of hydrogen. Communications Earth & Environment, 2023. **4**(1): p. 203.
24. WSP, INVENTAIRE DE LA BIOMASSE DISPONIBLE POUR PRODUIRE DE LA BIOÉNERGIE ET PORTRAIT DE LA PRODUCTION DE LA BIOÉNERGIE SUR LE TERRITOIRE QUÉBÉCOIS. 2021, for the Ministère de l'Énergie et des Ressources naturelles.

© 2025 by the authors. Licensed to PSEcommunity.org and PSE Press. This is an open access article under the creative commons CC-BY-SA licensing terms. Credit must be given to creator and adaptations must be shared under the same terms. See https://creativecommons.org/licenses/by-sa/4.0/



Systems & Control Transactions

**Research Article - Peer Reviewed Conference Proceeding**
ESCAPE 35 - European Symposium on Computer Aided Process Engineering
Ghent, Belgium. 6-9 July 2025
Jan F.M. Van Impe, Grégoire Léonard, Satyajeet S. Bhonsale,
Monika E. Polańska, Filip Logist (Eds.)

PSE PRESS

# Methanol and Ammonia as Green Fuels and Hydrogen Carriers: A Comparative Analysis for Fuel Cell Power Generation

**Antonio Sánchez[a*], Elena C. Blanco[a], and Mariano Martín[a]**

[a] Department of Chemical Engineering, University of Salamanca, Spain, 37008, Spain
* Corresponding Author: antoniosg@usal.es.

## ABSTRACT

Methanol and ammonia are key energy carriers in a decarbonized society. This study assesses their use in power generation via two pathways: direct utilization as green fuels in fuel cells or as hydrogen carriers. Using these chemicals as hydrogen carriers achieves higher efficiencies (around 40%) due to the maturity of hydrogen fuel cells, resulting in electricity costs around 700 €/MWh compared to 1200 €/MWh for direct utilization. While hydrogen offers lower electricity production costs, efficiency advancements in methanol and ammonia fuel cells could enhance their competitiveness. Additionally, for scenarios involving transportation and power generation, methanol and ammonia prove economically viable, particularly for distances exceeding 3000 km. Consequently, both are crucial for addressing hydrogen-related challenges in the new renewable energy systems.

**Keywords**: Process Design, Energy Storage, Hydrogen, Fuel Cells, Methanol, Ammonia

## INTRODUCTION

The energy sector, responsible for around 75% of greenhouse gas emissions, requires a significant shift to achieve global climate goals. The integration of renewable energy sources, particularly wind and solar, is expected to increase substantially in the coming years. However, these technologies face challenges mainly related to their variability, which could disrupt grid stability. Additionally, sectors like heavy transport, shipping, and industrial heating are difficult to electrify directly. In this context, hydrogen is emerging as a promising solution to address these issues due to its versatility and potential to decarbonize hard-to-abate industries.

According to Bloomberg [1], hydrogen and its derivatives could reduce up to one-third of global emissions, with a projected capacity to meet 24% of global final energy demand by 2050. Hydrogen's challenges, such as low volumetric energy density and complex storage conditions, have led to the exploration of hydrogen-derived products with methanol and ammonia being the most prominent. These chemicals offer easier storage and transport options and are gaining attention for use in energy storage, power generation, and as alternative fuels in sectors such as maritime transport and aviation.

Ammonia and methanol can be used for different applications through two approaches: as green fuels or as hydrogen carriers [2]. When used as green fuels, they are synthesized from green hydrogen and directly utilized in end-use sectors. Alternatively, they can function as hydrogen carriers, simplifying the storage and transport of hydrogen. In this case, methanol and ammonia are first synthesized, then decomposed or reformed to release hydrogen for final applications. In this last option, methanol steam reforming and ammonia decomposition emerge as the key technologies for hydrogen production from these two liquid carriers.

For power generation, methanol and ammonia can be used in two pathways. The thermochemical approach involves combusting methanol or ammonia, mainly, in gas turbines, sometimes requiring co-fuels to stabilize combustion. Alternatively, electrochemical methods employ methanol or ammonia in fuel cells, known as Direct Methanol Fuel Cells (DMFC) and Direct Ammonia Fuel Cells (DAFC). While promising, these technologies face energy efficiency challenges today that require further research.

Another option is using methanol and ammonia as intermediaries to generate hydrogen, which is then used in hydrogen fuel cells. This approach benefits from the higher efficiency of hydrogen fuel cells but introduces added process complexity, energy losses, and costs.

Research has mainly focused on optimizing catalysts and reactor designs for processes like methanol reforming and ammonia decomposition, as well as improving fuel cell materials and configurations. However, there is limited comprehensive analysis from a process system engineering perspective of these X-to-Power alternatives using fuel cells. Therefore, this work addresses the gap by systematically evaluating five process alternatives: direct methanol and ammonia fuel cells, methanol reforming and ammonia decomposition coupled with hydrogen fuel cells, and direct hydrogen use in fuel cells. A technical and economic evaluation is performed, introducing detailed reactor modeling, to provide comprehensive insights into the deployment of this power generation technology.

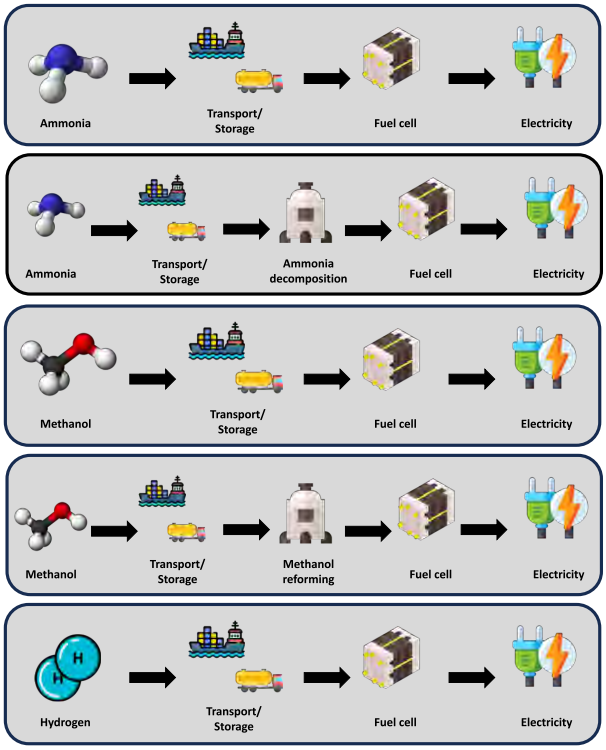



**Figure 1:** Overview of the analyzed alternatives [3]

## PROCESS ALTERNATIVES

This study evaluates two distinct methods for utilizing methanol and ammonia in power generation with fuel cell technology. The first approach directly introduces these compounds into fuel cells, while the second uses them as hydrogen carriers. In the latter option, hydrogen is generated from methanol or ammonia before being fed into a fuel cell. A third alternative is also examined, where hydrogen is directly utilized as a fuel for comparative purposes. A schematic representation of these approaches is provided in Figure 1.

### Methanol based alternatives

The first method involves the direct use of methanol in a direct methanol fuel cell (DMFC), which operates with an aqueous methanol solution (1 M) and air. In the DMFC, methanol reacts at the anode to produce carbon dioxide, protons, and electrons, while oxygen at the cathode reacts with protons to form water according to the following reactions.

$$CH_3OH + H_2O \rightarrow CO_2 + 6H^+ + 6e^- \quad (1)$$

$$6H^+ + 6e^- + \frac{3}{2}O_2 \rightarrow 3H_2O \quad (2)$$

The system operates at a temperature of 333 K under atmospheric pressure. Effluents from the DMFC are processed to separate carbon dioxide, water, and methanol. Gaseous $CO_2$ can be recycled to methanol synthesis, while water and methanol are reintegrated into the fuel cell feed. The cathode effluent undergoes similar separation to recycle water and adjust methanol composition.

In the second alternative, methanol is reformed to produce hydrogen, which is then fed into a solid oxide fuel cell (SOFC). The reforming process involves steam reforming of methanol in a fixed-bed, adiabatic, catalytic, membrane reactor, producing hydrogen, carbon dioxide, and small amounts of carbon monoxide. $Cu/ZnO/Al_2O_3$ is the selected catalyst due to its favorable catalytic activity, rapid kinetics, high selectivity, and cost-effectiveness. The following reactions are involved in the methanol steam reforming unit:

$$CH_3OH + H_2O \rightleftharpoons CO_2 + 3H_2 \quad (3)$$

$$CO + H_2O \leftrightharpoons CO_2 + H_2 \quad (4)$$

$$CH_3OH \leftrightharpoons CO + 2H_2 \quad (5)$$

The process operates at 600 K and 10 bar with a steam-to-methanol ratio of 1.5. A Pd-Ag membrane separates hydrogen from the reforming mixture, and the remaining stream is further processed. To maintain the endothermic reforming reactions, heat is supplied through intermediate heating stages (interheaters between adiabatic reaction stages). This involves burning a fraction of methanol and utilizing the flue gases for heating.

Hydrogen generated is then introduced into an SOFC, which operates at 800°C. This technology has been selected for its high level of efficiency, exploiting the high temperature of the hydrogen obtained in the reforming stage. The high-temperature outlet gases are used to heat the incoming streams, and the remaining energy is utilized in an organic Rankine cycle (ORC) to maximize energy recovery. Refrigerant R134a is selected as

working fluid in this work. The SOFC has an electrical efficiency of 60%, and its fuel utilization ratio is set at 80%.

## Ammonia based alternatives

The first alternative explored with regards to ammonia utilization is the direct ammonia fuel cell (DAFC). In this study, an alkaline membrane fuel cell has been selected since it allows operation at low temperature. Ammonia reacts at the anode to produce nitrogen, water, and electrons, while oxygen reacts at the cathode to form hydroxyl ions. The following reactions take place in the DAFC unit:

$$2NH_3 + 6OH^- \rightarrow N_2 + 6H_2O + 6e^- \quad (6)$$

$$3H_2O + 6e^- + \frac{3}{2}O_2 \rightarrow 6OH^- \quad (7)$$

The process operates at 368 K under ambient pressure, with air at 50% relative humidity. A fraction of the ammonia permeates the anion exchange membrane (referred to as crossover), undergoing oxidation at the cathode to produce nitrogen oxide (NO). A selective catalytic reduction (SCR) unit is used to remove nitrogen oxides from the cathode effluent. The anode effluent, primarily ammonia, water, and nitrogen, is cooled to separate and recycle ammonia.

In the second ammonia-based method, ammonia is decomposed in a fixed bed, adiabatic, catalytic membrane reactor to produce hydrogen, which is then fed into a SOFC. The reaction is endothermic, requiring high temperatures (900 K) and a pressure of 10 bar. $Ni/Al_2O_3$ is the selected catalyst due to its economic advantages and satisfactory performance. The following reaction is performed in the ammonia decomposition process:

$$2NH_3 \leftrightharpoons N_2 + 3H_2 \quad (6)$$

To enhance the performance of the decomposition reaction, a Pd-Ag membrane separates hydrogen in situ, improving equilibrium conditions. A sequence of four reactors along with their respective heat exchangers has been implemented to supply the required energy for the reaction. A fraction of ammonia is combusted to provide the necessary energy in the decomposition section. Hydrogen produced is heated and introduced into the SOFC, similar to the methanol reforming case. Waste heat from the SOFC is also used in an ORC to improve the energy efficiency of the overall process.

## Hydrogen based alternative

In the final alternative, hydrogen is directly fed into a SOFC. The process is similar to the hydrogen utilization stages of methanol and ammonia as hydrogen carriers. Hydrogen is preheated to 800°C, and the high-temperature SOFC exhaust gases are used, in a first stage, to heat the inlet streams and, finally, for energy recovery via an ORC.

## Solution Procedure

A detailed 1-D differential equation model is included to evaluate the performance of the reactor units (ammonia decomposition and methanol steam reforming). With this information, all alternatives are modeled using a nonlinear programming (NLP) approach in GAMS, optimizing system operation under an economic objective function. Mass and energy balances, equilibrium conditions, detailed 1-D differential equation models, etc. are used to represent the different units involved. Capital (CAPEX) and operating (OPEX) costs are estimated using established correlations for the chemical industry. For the calculation of the operating cost, the main inlet parameter is the cost of the fuel. For methanol, the baseline price is set to 1200 €/t, for ammonia, 1060 €/t and, for hydrogen, 5 €/kg. All cases are modeled for a fuel cell with a power capacity of 1 MW. In addition, an integrated assessment of the transportation of these chemicals and their subsequent transformation into power (using the proposed alternatives) is performed. To compute the transportation cost for each chemical, an average value is taken from the literature for the different alternatives.

# RESULTS AND DISCUSSION

The result section presents the key operating variables for four analyzed alternatives that utilize ammonia and methanol as hydrogen carriers, along with a baseline scenario using hydrogen directly in a fuel cell.

**Table 1:** Main operating variables for power production using methanol/ammonia as hydrogen carriers.

| Variables | Methanol | Ammonia |
|---|---|---|
| % inlet fuel to combustion | 22.5 | 25.5 |
| % $H_2$ recovery in the membrane | 78.8 | 96.1 |
| Final reactor conversion (%) | 97.3 | 97.5 |
| kg $H_2$ /kg fuel | 0.11 | 0.12 |
| Net power (kW) | 1106 | 1108 |
| Energy efficiency (%) | 35.8 | 42.3 |
| Energy yield (kWh/kg) | 2.00 | 2.18 |

Both methanol reforming (600 K) and ammonia decomposition (900 K) are endothermic reactions requiring significant heat input. To achieve standalone operation, a fraction of the fuel (20–25%) is combusted to meet these thermal requirements. Ammonia decomposition demands more fuel combustion due to its higher operating temperature (as shown in Table 1). The reactor configuration based on a multibed reactor ensures nearly complete conversion of methanol and ammonia (around 97% in both cases). However, hydrogen recovery varies between processes attributed to differences in permeability and partial pressures in the membrane. Consequently,

the hydrogen yield is 0.11 kg $H_2$/kg methanol (58% of maximum potential) and 0.12 kg $H_2$/kg ammonia (67% of maximum). This operating results directly influence the energy efficiency of the process. Methanol-based systems achieve 36% efficiency, while ammonia-based systems reach 42%, mainly due to the better performance in the production of hydrogen from ammonia.

**Table 2:** Main operating variables for power production using methanol/ammonia/hydrogen as green fuels.

| Variables | Methanol | Ammonia | Hydrogen |
|---|---|---|---|
| Net power (kW) | 1000 | 885.7 | 1000 |
| Energy efficiency (%) | 26.5 | 16.8 | 52.9 |
| Energy yield (kWh/kg) | 1.46 | 0.86 | 17.6 |

Methanol and ammonia can also be used directly in fuel cells. The fuel cell efficiencies achieved are 23.3% for methanol and 15% for ammonia (reaching the global efficiencies of Table 2). These efficiencies are significantly lower than those of hydrogen fuel cells (60% of the selected SOFC). The overall energy efficiency of the process (including other units apart from the fuel cell) is 26% for methanol, 17% for ammonia, and 53% for hydrogen. Therefore, despite the more complex processes in hydrogen carrier alternatives, they remain competitive due to the lower efficiencies of the current DMFC and DAFC technologies.

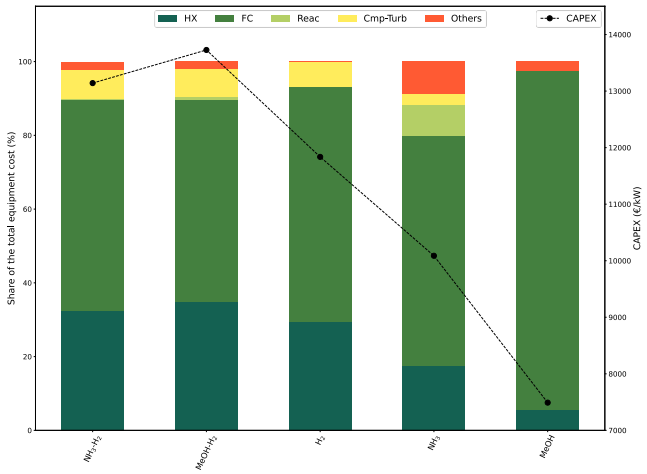



**Figure 2.** Total CAPEX and its distribution [3]

A systematic economic evaluation of the proposed alternatives has also been performed. The CAPEX for the systems studied ranges from 7,000 to 14,000 €/kW (as shown in Figure 2). Processes employing methanol or ammonia as hydrogen carriers exhibit higher investment costs compared to direct fuel cell technologies, mainly due to the added complexity introduced by methanol reforming or ammonia decomposition. Among these, the DMFC represents the least capital-intensive option, as it operates with minimal additional equipment beyond the fuel cell. However, alternatives with lower CAPEX have reduced energy efficiencies according to Tables 1 and 2, presenting a trade-off that becomes evident in the operating costs, as discussed below. The distribution of CAPEX shows that the fuel cell unit accounts for the majority of the investment, ranging from 55% to 92% of the total cost. Heat exchangers also constitute a significant portion of CAPEX in methanol reforming and ammonia decomposition processes, given their critical role in managing the thermal demands of these systems.

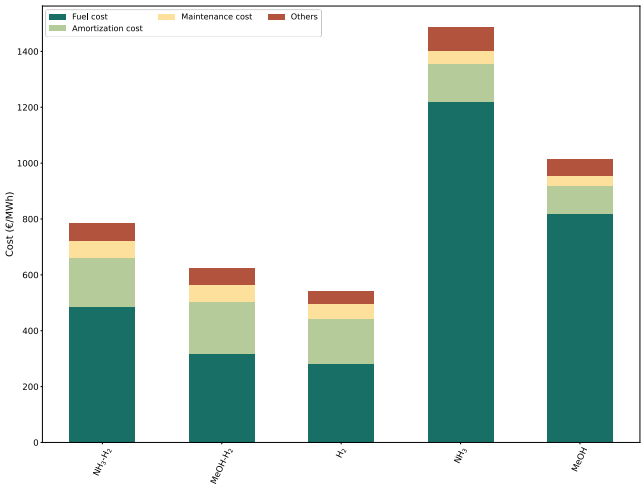



**Figure 3.** OPEX of the different alternatives with its breakdown [3]

When compared to other power generation technologies, the CAPEX for methanol and ammonia fuel cell systems is considerably higher. For instance, renewable technologies like PV panels (810 €/kW), onshore wind turbines (1178 €/kW), biomass-based systems (1998 €/kW), and concentrated solar power (3950 €/kW), as well as traditional sources like natural gas combined cycle plants (924–1386 €/kW) and nuclear plants (6470–7394 €/kW), all show significantly lower CAPEX. The elevated capital costs of methanol/ammonia fuel cell systems arise from two main factors: the high cost of fuel cells, which are still maturing and expected to become more affordable, and the lack of economies of scale due to their relatively small-scale application (in this study 1 MW capacity).

Figure 3 presents the operational costs for the analyzed alternatives. In contrast to CAPEX, the OPEX of systems using methanol/ammonia as hydrogen carriers is lower than that of direct ammonia or methanol fuel cell systems. For hydrogen carrier-based configurations, the OPEX is approximately 500–800 €/MWh, whereas for direct ammonia or methanol usage, the OPEX ranges from 1000–1500 €/MWh. The higher energy efficiency of

hydrogen carrier alternatives offsets their increased CAPEX, leading to comparatively lower operating costs. Fuel costs dominate the OPEX, especially for systems where methanol or ammonia is directly used as green fuels, contributing over 80% of total operational expenses. Thus, the reduction of the production cost of green methanol and ammonia will be a critical driver for the broader adoption of these power generation pathways.

Compared to current electricity generation costs, methanol and ammonia systems are more expensive. For example, renewable systems such as solar PV (60–100 €/MWh), onshore wind (40–80 €/MWh), and biogas (90–170 €/MWh) are more cost-effective. However, methanol and ammonia are employed as energy carriers/storage systems, involving the chemical production and the back transformation into electricity, which inherently leads to higher costs. When viewed as energy storage options, methanol and ammonia offer competitive costs compared to other storage technologies. For instance, pumped hydro costs range from 185–278 €/MWh for short-term applications but escalate to 2778–3704 €/MWh for seasonal storage. Similarly, battery storage costs range from 370–556 €/MWh for short-term and 37037–41667 €/MWh for seasonal applications [4].

In addition, a sensitivity analysis is performed for two critical parameters: fuel cell energy efficiency and the price of methanol/ammonia. Hydrogen fuel cells currently achieve approximately 60% efficiency, while direct ammonia and methanol fuel cells achieve around 15% and 25%, respectively. These efficiency differences significantly affect economic performance. Hydrogen fuel cells, being more developed, are expected to see moderate improvements (up to around 80%). However, direct methanol/ammonia fuel cells are in earlier stages of development, with potential for significant efficiency gains. The economic performance of the proposed system is analyzed under different energy efficiency scenarios showing the results in Figure 4. For direct methanol fuel cells, achieving an efficiency of 47% would make them competitive with systems based on methanol reforming and hydrogen fuel cells. Similarly, direct ammonia fuel cells would need to reach 43% efficiency.

Fuel cost is a dominant factor in the overall electricity cost, as indicated in Figure 3. Green methanol and ammonia prices vary widely, influenced by production methods. Future projections estimate prices of 231–583 €/t for methanol and 285–350 €/t for ammonia by 2050 [5]. If methanol and ammonia prices drop below 400 €/t, electricity costs could range between 400 and 600 €/MWh, narrowing the gap between direct and hydrogen-based systems. Direct methanol systems, in particular, could become more economically competitive, potentially outperforming hydrogen-based alternatives.

The previous results are circumscribed to the process itself. At this point, hydrogen as such shows the best economic performance with the lowest operating cost. However, the main limitations about the use of hydrogen come from its storage and transport conditions.

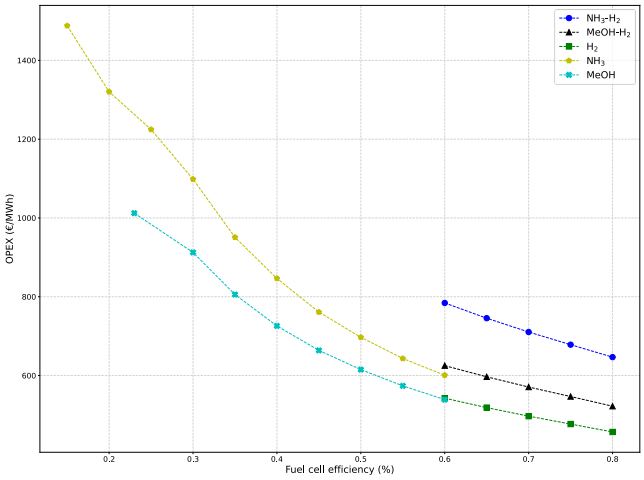



**Figure 4.** Operating cost versus fuel cell efficiency [3]

For shorter distances, the percentage of the transportation cost in the total cost remains low in all cases. Therefore, as hydrogen shows the best operating cost in the transformation stage, this is the technology with the best global performance. In the case of rail transport or shipping, hydrogen transport is not considered due to the difficulties associated and the lack of data for these alternatives. As distance increases, the transport costs associated with hydrogen experiments notably increase, higher than in the case of methanol or ammonia. For example, when transported by truck over 3000 km, the transportation cost represents around 70% of the total cost for hydrogen. Consequently, the total cost of the system exceeds the cost values associated with ammonia and methanol. In the case of truck transport, the transition point is around 400 km, where the use of methanol as hydrogen carrier is recommended. Regarding pipelines, the hydrogen transportation cost is significantly lower than the case of truck, shifting the transition point to around 3000 km. Hence, methanol and ammonia demonstrate great potential in applications where transportation and/or storage is critical.

## CONCLUSIONS

A systematic evaluation compares methanol and ammonia as green fuels or hydrogen carriers for electricity generation via fuel cells. Ammonia and methanol as hydrogen carriers demonstrate superior technical and economic performance today, with overall energy efficiency of 35–40% compared to 15–25% for direct alternatives. This efficiency translates to lower operating costs (600–800 €/MWh). While hydrogen fuel cells

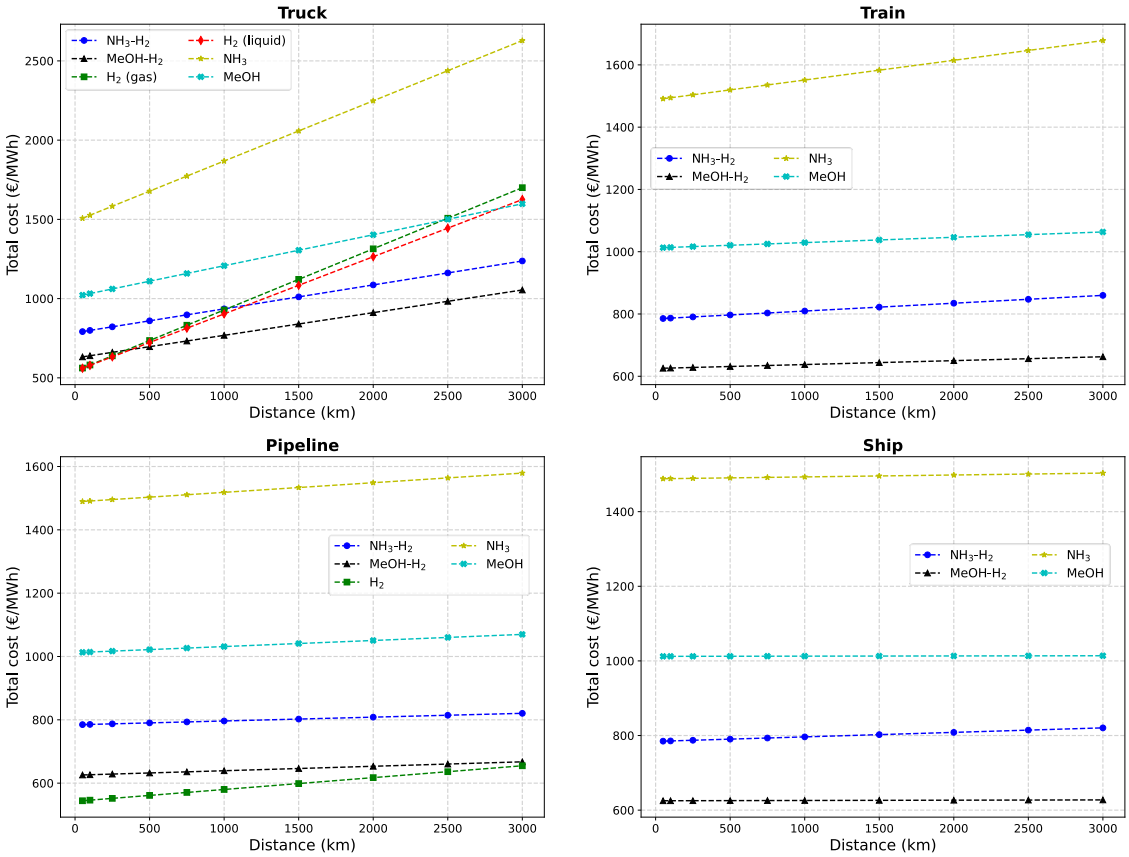



**Figure 5:** Total cost of transportation and power production [3]

exhibit higher efficiency in power generation, transportation costs favor methanol and ammonia, particularly for long distances. With potential efficiency improvements for direct alternatives, methanol and ammonia are positioned as critical solutions for long-term energy storage and transportation challenges.

## ACKNOWLEDGEMENTS

This work was supported by the Regional Government of Castilla y León (Junta de Castilla y León) and by the Ministry of Science and Innovation MICIN and the European Union NextGenerationEU/PRTR(H2MetAmo project-C17.I01.P01.S21). The authors acknowledge Programa Investigo JCYL fellowship to Elena C. Blanco.

## REFERENCES

1. BloombergNEF. Hydrogen economy outlook. 2020, URL: https://about.bnef.com/blog/hydrogen-economy-offers-promising-path-to-decarbonization/.
2. Tawalbeh M, Murtaza SZ, Al-Othman A, Alami AH, Singh K, Olabi AG. Ammonia: A versatile candidate for the use in energy storage systems. Renew Energy 194:955–77 (2022) https://doi.org/10.1016/j.renene.2022.06.015
3. Sánchez A, Blanco EC, Martín M. Comparative assessment of methanol and ammonia: Green fuels vs. hydrogen carriers in fuel cell power generation. Appl Energy 374: 124009 (2024) https://doi.org/10.1016/j.apenergy.2024.124009
4. Schmidt O, Melchior S, Hawkes A, Staffell I. Projecting the future levelized cost of electricity storage technologies. Joule 3(1):81–100 (2019) http://dx.doi.org/10.1016/j.joule.2018.12.008
5. Fasihi M, Weiss R, Savolainen J, Breyer C. Global potential of green ammonia based on hybrid PV-wind power plants. Appl Energy 294:116170 (2021) http://dx.doi.org/10.1016/j.apenergy.2020.116170

© 2025 by the authors. Licensed to PSEcommunity.org and PSE Press. This is an open access article under the creative commons CC-BY-SA licensing terms. Credit must be given to creator and adaptations must be shared under the same terms. See https://creativecommons.org/licenses/by-sa/4.0/

Systems & Control Transactions

**Research Article - Peer Reviewed Conference Proceeding**
ESCAPE 35 - European Symposium on Computer Aided Process Engineering
Ghent, Belgium. 6-9 July 2025
Jan F.M. Van Impe, Grégoire Léonard, Satyajeet S. Bhonsale,
Monika E. Polańska, Filip Logist (Eds.)

PSE PRESS

# The Green Hydrogen Supply Chain in The Brazilian State of Bahia: A Deterministic Approach

**Leonardo O. S. de Santana[a]*, Gustavo S. dos Santos[a], Fernando L. P. Pessoa[a], and Ana P. Barbosa-Póvoa[b].**

[a] SENAI CIMATEC University, Department of Computational Modeling, Salvador, Bahia, Brazil
[b] University of Lisbon, Instituto Superior Técnico, Lisbon, Portugal
* Corresponding Author: leosantana049@gmail.com

## ABSTRACT

Hydrogen is a key element in the global transition toward a low-carbon economy, with green hydrogen offering significant potential to decarbonize industries and energy systems. This study focuses on designing and optimizing a green hydrogen supply chain (HSC) for the state of Bahia, Brazil, using a deterministic Mixed-Integer Linear Programming (MILP) model. The model evaluates 24 scenarios combining production sites, storage technologies, transportation methods, and energy sources, minimizing the Total Sustainable Cost (TSC). The TSC integrates financial and environmental costs, monetizing $CO_2$ emissions using international carbon pricing. Results indicate that economies of scale play a critical role allowing the minimization of the financial costs while achieving lower greenhouse gas (GHG) emissions compared to other scenarios. The study emphasizes the importance of aligning production strategies with regional renewable energy resources to enhance both cost-effectiveness and sustainability. Future research should incorporate stochastic approaches to address uncertainties in hydrogen demand, energy availability, and market dynamics.

**Keywords**: Green Hydrogen Supply Chain, Optimization, Brazil Case Study, Environmental Concerns, Scenarios Analysis

## INTRODUCTION

The rising greenhouse gas (GHG) emissions have led to a significant shift in energy production, distribution, and consumption. To facilitate this transition—replacing fossil fuels with renewable sources—it is essential to understand the role of energy storage in the supply chains (SC) of the future energy mix [1]. In this setting, Hydrogen is an energy carrier with significant potential to decarbonize key sectors. The optimization of hydrogen supply chains (HSC) has gained considerable attention from the Process Systems Engineering (PSE) community over the last decade [2]. Several studies address SC uncertainty, while others use capacitated facility location problem models based on deterministic data. Although deterministic models offer a solid foundation for SC design, they do not account for uncertainties and imperfect information about future business environments, limiting their capacity to predict performance in varying scenarios [3-4].

In this context, Brazil emerges as a relevant player in green hydrogen production due to its abundant wind and solar resources. However, the deployment of a complete SC is necessary to produce, transport, store, and distribute this low-carbon fuel [5]. This work explores these challenges and develops a deterministic approach to design and plan a green hydrogen supply chain (GHSC) for the Brazilian State of Bahia.

## PROBLEM STATEMENT

As a deterministic capacitated facility location problem, this work aims to design optimal investments in the GHSC to meet the demand of Bahia's oil refinery, according to the superstructure in figure 1. The demand cluster requires 200 MW (29 kt/year) of hydrogen, according to a previous study developed at SENAI-CIMATEC [6].

**Given:**

(i) A predefined hydrogen demand $D_j$ for $j = 1$ (representing the refinery).

(ii) Possible facility locations (7 locations in Bahia).

(iii) Scenarios involving energy sources (solar, wind, or grid), storage options (liquefied or compressed), and transportation methods (trucks or pipelines).

**Determine the optimal:**

(i) Hydrogen production plant locations and capacities $x_i$.
(ii) Storage and transportation methods for each production plant.
(iii) Energy sources used at each production plant.

**Objective:** Minimize the Total Sustainable Cost (TSC), which is the sum of financial and environmental costs. The environmental cost is represented as a weighted function of $CO_2$ emissions, monetized using the international carbon credit price.

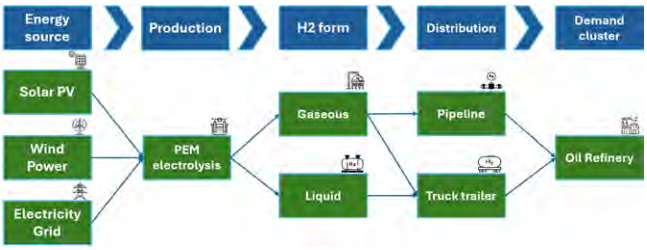



**Figure 1**: Model superstructure.

## METHODOLOGY

The cost and emissions data were obtained using the Decision-Making Model for Hydrogen (DMMH2) software developed by SENAI-CIMATEC University [7]. This software calculates the Levelized Cost of Hydrogen (LCOH) across all stages of production, storage, and transportation for different production scales, incorporating inputs such as capacity availability for wind and solar plants, as well as electricity prices for grid-powered plants. Emissions data are also considered. The model estimates annual costs based on a comprehensive database that includes both literature sources and supplier data [8].

The capacity factors for renewable energy generation at each site are derived from historical data provided by the National Electric System Operator (ONS) for the year 2024. Regarding $CO_2$ emissions, fugitive hydrogen emissions were not considered in this study. Instead, emissions were estimated based on life cycle assessment (LCA) data available in the literature for each stage of the supply chain, including PEM electrolysis, gaseous and liquid storage, as well as transportation via trucks and pipelines.

Distances (in kilometers) between the production plants and the demand point were included for both pipelines and trucks. These were calculated using Google Earth (with a 5% safety margin to account for potential deviations in pipeline routing) and Google Maps for road-based transportation routes, Figure 2 indicates the localization of each possible hydrogen plant (1 to 7) and the demand point (A) for the study case. Additionally, the analysis assumes the construction of new hydrogen pipelines, incorporating their associated costs into the model.

Capacity factors for wind and solar power plants were obtained from the Brazilian National Electric System Operator [9]. The capacity factors were regionally specific and calculated based on the locations of wind and solar plants near the hydrogen production sites. Table 1 summarizes the location, primary energy source, and distances between production plants and the demand point and average capacity factor. Figure 3 presents the monthly capacity factor.

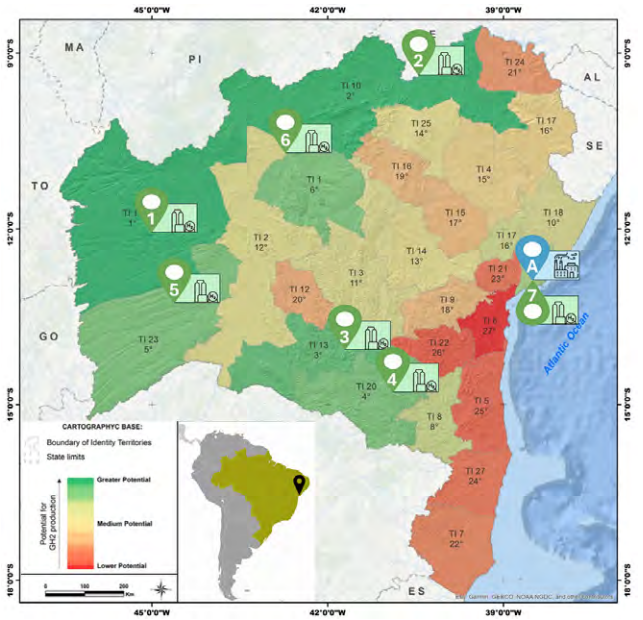



**Figure 2:** Geographic Map of Hydrogen Production Plants and Demand Points in Bahia.

The optimization problem incorporated these data inputs to evaluate 24 scenarios (7 potential plant locations, 2 storage technologies, and 2 transportation methods), with each scenario representing a different logistical and renewable energy availability. Table 2 provides additional information, such as electricity prices, carbon emissions prices, operational hours, and other relevant parameters.

These inputs directly feed into the Mixed-Integer

**Table 1**: Distances Between Hydrogen Production Plants and Demand Point.

| Plant Number | Plant Location | Primary Energy Source | Distance (km) | | Capacity Factor (Average) |
|---|---|---|---|---|---|
| | | | Truck | Pipeline | |
| 1 | Barreiras | Solar PV | 815 | 735 | 34% |
| 2 | Juazeiro | Solar PV, Wind Power | 460 | 441 | 45% Wind Power 30% Solar PV |
| 3 | Brumado | Wind Power | 490 | 392 | 42% |
| 4 | Vitória da Conquista | Grid | 469 | 364 | - |
| 5 | Tabocas do Brejo Velho | Solar PV | 742 | 618 | 34% |
| 6 | Xique-Xique | Wind Power | 540 | 523 | 29% |
| 7 | São Francisco do Conde | Grid | 0 | 0 | - |

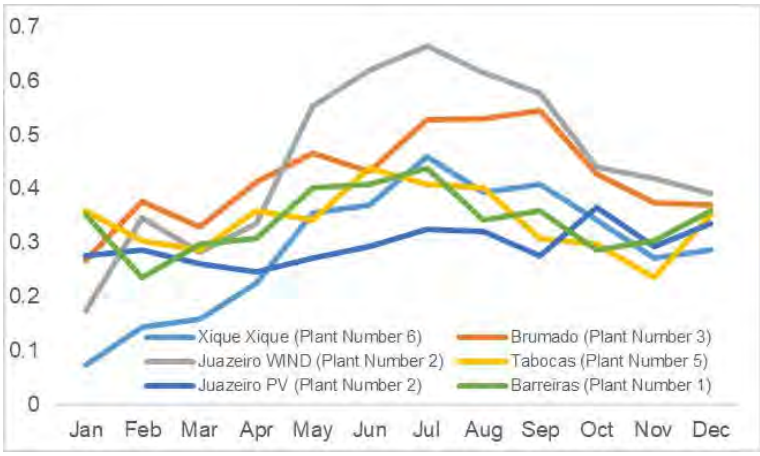



**Figure 3:** Monthly Capacity Factor.

**Table 2:** Software Inputs.

| Information | Input | Reference |
|---|---|---|
| Bahia's electricity price | US$ 0.10/ kWh | [10] |
| Carbon Emissions Price | US$ 74.40/ kgCO2eq | [11] |
| Operating Hours | 8000 h/year | DMMH2 default |
| Cylinder Type | Type I | DMMH2 default |
| Pipeline Type | 20" 100% H2 | DMMH2 default |
| Plant Capacity Factor | 100% | DMMH2 default |
| WACC | Brazil: 0.089 | DMMH2 default |

Linear Programming (MILP) model, described in section "Mathematical Modelling", where the regression data ($A_i$, $B_i$, $C_i$, $D_i$) are used to calculate the TSC for each scenario. This integration ensures that the optimization process accounts for both economic and environmental considerations. The regression coefficients were derived using Microsoft Excel's "SLOPE" function, which determines the slope of the linear regression line, and the "INTERCEPT" function, which calculates the corresponding intercept. These calculations were performed using cost and emissions data extracted from the DMMH2 software.

## OPTIMIZATION FRAMEWORK

### Problem Description

The optimization aims to minimize the TSC of the GHSC. This is achieved by determining the optimal locations, energy sources, storage, and transportation methods to supply the full hydrogen demand of Bahia's oil refinery. Each scenario $i$ is defined by:

- One energy source (solar, wind, or grid).
- One storage technology (liquefied or compressed hydrogen).
- One transportation method (truck or pipeline).

### Mathematical Modelling

The sustainable cost for each scenario is given by the scalarization function:

$$min\ TSC = \sum_{i=1}^{n} SC_i(x_i) \quad (1)$$

$$SC_i(x_i) = TC_i(x_i) + E_i(x_i) \quad (2)$$

where:

- $TC_i(x_i) = A_i x_i + B_i$: Total financial cost as a function of decision variables $x_i$.
- $E_i(x_i) = C_i x_i + D_i$: Environmental cost, where $w$ is the weight given to emissions.
- $A_i, B_i, C_i, D_i$: Regression parameters for each scenario $i$.

**Constraints:**

- Hydrogen production from all selected plants must equal the refinery's demand:

$$\sum_i x_i = D_j,\ \forall j = 1\ ;\ D_j = 200\ MW \quad (3)$$

- Hydrogen production is an integer variable:

$$x_i \in \mathbb{Z}^+,\ \forall i \quad (4)$$

- Hydrogen production is constrained by its maximum capacity and is dependent on whether the plant is selected:

$$x_i \leq 200 Y_i,\ \forall i \quad (5)$$

  - Binary decision variables $Y_i$ indicate whether a specific scenario is selected:

$$Y_i \in \{0,1\},\ \forall i \quad (6)$$

This model was implemented using Python due to its flexibility and the availability of robust libraries for mathematical programming. The formulation of the MILP problem was conducted using Pyomo. For solving the optimization problem, GLPK was selected as solver, given its efficiency in handling large-scale MILP problems and its advanced features for parameter tuning and performance improvement. The solver configuration included default precision settings, with adjustments made to the time limit to ensure computational feasibility while maintaining the accuracy of the results. This computational framework facilitated the integration of regression data and allowed for efficient scenario evaluation across all 24 cases.

## RESULTS & DISCUSSION

The results obtained are presented in Table 3. The minimization of the Total Sustainable Cost (TSC) revealed only one viable scenario, scenario 8, characterized by maximum production capacity. This outcome is attributed to the economies of scale inherent in hydrogen production, where increasing production capacity significantly reduces financial costs. Consequently, the cost equations consistently achieve their minimum value at 200 MW.

Scenario 8, with a TSC of USD 5.88/kg $H_2$, was identified as the optimal solution. It features a plant located in Juazeiro, a region with high wind energy potential, and utilizes gaseous hydrogen distributed via pipeline. This configuration benefits from reduced financial costs due to the favorable wind energy profile of the location.

A sensitivity analysis (Figure 4) varying the demand constraint reinforces this finding. For most demand scenarios, Scenario 23 emerges as the optimal solution in terms of TSC, except for the 200 MW capacity case, where Scenario 8 remains the best option.

Figure 5 provides a snapshot of the results. While Scenario 23 demonstrates the lowest Levelized Cost of Hydrogen (LCOH), it shares the same hydrogen form and distribution method (Liquefied and pipeline) as Scenario 8 but differs in plant location (S. Francisco do Conde) and primary energy source (Grid). However, Scenario 8 achieves significantly lower GHG emissions than Scenario 23, highlighting the trade-off between financial and environmental considerations, and the considerable difference at TSC.

The results underscore the impact of economies of scale on GHSC optimization. By prioritizing maximum production capacity, the model leverages cost advantages that make large-scale production the most financially viable option. However, the practical implementation of such solutions remains challenging, requiring substantial investments in infrastructure and technology, particularly concerning the construction of new pipeline networks.

Furthermore, the comparison between Scenarios 8 and 23 highlights the importance of considering both financial and environmental metrics. While Scenario 23 minimizes LCOH, its reliance on electricity from the grid results in higher GHG emissions, emphasizing the environmental trade-offs of different SC configurations.

Additionally, scenarios relying on grid electricity exhibited significantly higher LCOH values due to the elevated electricity prices in Brazil. Despite these variations, the hydrogen cost ranges presented in this study align with values reported in the literature [12,13] for optimal configurations. This work reinforces the importance of evaluating the hydrogen supply chain (HSC) within specific production and usage contexts, providing valuable insights for guiding the development of the hydrogen market while reducing uncertainties from project planning to physical deployment.

## CONCLUSION

This study develops a deterministic MILP model to optimize the HSC for Bahia, focusing on supplying 200 MW of hydrogen to its oil refinery. The model evaluates 24 scenarios involving combinations of production sites, storage technologies, transportation methods, and energy sources, aiming to minimize the TSC, which integrates financial and environmental metrics. The results highlight the importance of economies of scale in reducing the financial costs of hydrogen production. The

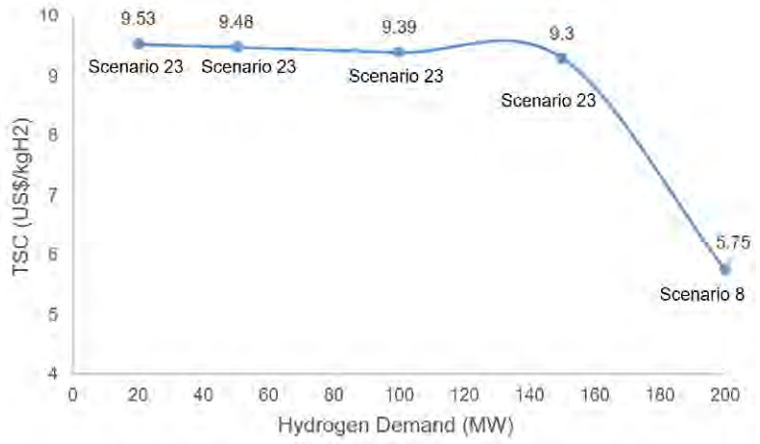



**Figure 4:** Sensitivity analysis.

**Table 3**: Study Case Results.

| Scenario | TSC (US$/kgH2) | Plant Capacity (MW) | Plant location | Energy source | H2 Form | Distribution |
|---|---|---|---|---|---|---|
| 8 | 5.75 | 200 | Juazeiro | Wind Power | Gaseous | Pipeline |
| 23 | 9.2 | 200 | São Francisco do Conde | Grid | Gaseous | Pipeline |

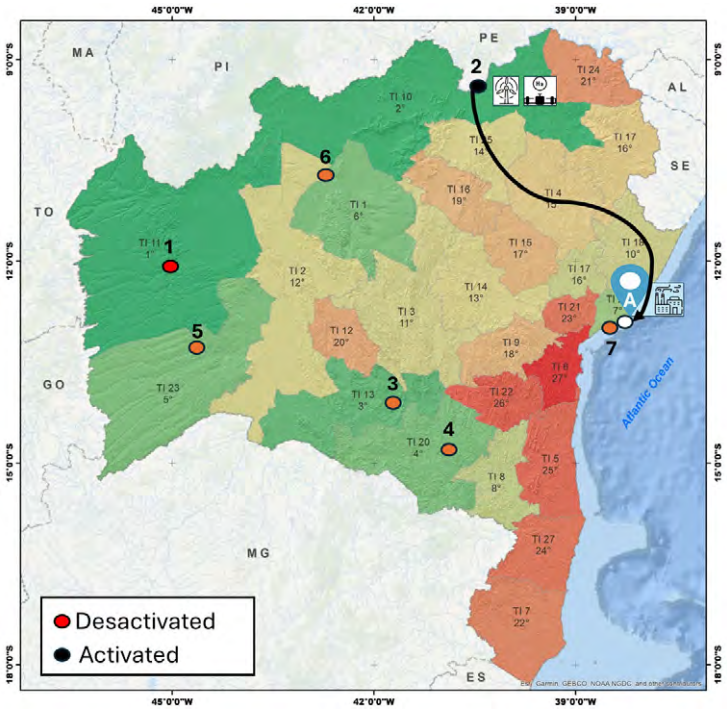



**Figure 5:** Result Snapshot.

optimal scenario identified a production plant located in a region with high wind energy potential, leveraging renewable energy to achieve cost-effectiveness and sustainability. However, trade-offs between financial and environmental metrics were observed, demonstrating the need for balanced decision-making to meet both economic and decarbonization goals.

Future research should address uncertainties in

HSC design, enhancing resilience to market and operational variability while advancing decarbonization strategies. Moreover, the integration of multi-objective optimization could provide more robust solutions, accounting for variations in renewable energy availability, hydrogen demand, and carbon pricing. Expanding the analysis to include sector coupling, such as heat and power integration, may further enhance the practical application and sustainability of GHSCs. Additionally, exploring parameter sensitivity and socio-political factors would enhance the robustness and relevance of the study.

## ACKNOWLEDGEMENTS

We acknowledge the Green Hydrogen Competence Center of SENAI CIMATEC University for its financial support; FCT - Foundation for Science and Technology, I.P under the project UIDB/00097/2020; and the Open project Open Research Project of the State Key Laboratory of Industrial Control Technology, China (Grant No. ICT2024B07).

## REFERENCES

1. Ibrahim Y, Abraham EJ, Al-Mohannadi DM. A Systematic Analysis of Economic and Environmental Trade-Offs in Hydrogen Supply Chains with Resilience Considerations. 53:2401-2406 (2024) https://doi.org/10.1016/B978-0-443-28824-1.50401-4
2. Efthymiadou M, Charitopoulos V, Papageorgiou L. Hydrogen infrastructure planning for heat decarbonisation in Great Britain. 52:3025-3030 (2023) https://doi.org/10.1016/B978-0-443-15274-0.50482-0
3. Li L, Manier H, Manier M. Hydrogen supply chain network design: An optimization-oriented review. Renewable and Sustainable Energy Reviews, 103: 342-360 (2024) https://doi.org/10.1016/j.rser.2018.12.060
4. Klibi W, Martel A, Guitouni A. The design of robust value-creating supply chain networks: A critical review. European Journal of Operational Research, 203; 2; 283-293 (2010). https://doi.org/10.1016/j.ejor.2009.06.011
5. Jacquot V, Pantel C, Bourjade S, Muller C. A Bilevel Framework for Environmental and Economic Optimisation of Hydrogen Supply Chains. Computer Aided Chemical Engineering, 53; 907-912 (2024). https://doi.org/10.1016/B978-0-443-28824-1.50152-6
6. SENAI-CIMATEC. Atlas H2V Bahia. (2023).
7. Pessoa F. L. P & Santos, G. S.. DMMH2 - Decision-Making Model for Hydrogen. BR512024005206-2. (2025)
8. Santos, G. Modelo para Tomada de Decisão das Rotas de Produção do Hidrogênio. Universidade SENAI CIMATEC. 2024. 10.13140/RG.2.2.22624.80642
9. ONS. https://www.ons.org.br/Paginas/resultados-da-operacao/historico-da-operacao/fator-capacidade.aspx
10. CNI. https://perfildaindustria.portaldaindustria.com.br/estado/ba
11. Investing.com. https://br.investing.com/commodities/carbon-emissions-streaming-chart
12. Van der Spek, M., Banet, C., Bauer, C., Gabrielli, P., Goldthorpe, W., Mazzotti, M., Munkejord, S. T., Røkke, N. A., Shah, N., Sunny, N., Sutter, D., Trusler, J. M., & Gazzani, M. (2022). Perspective on the hydrogen economy as a pathway to reach net-zero $CO_2$ emissions in Europe. Energy & Environmental Science, 15(1034-1077). https://doi.org/10.1039/d1ee02118d
13. Younas, M., Shafique, S., Hafeez, A., Javed, F., & Rehman, F. (2022). An overview of hydrogen production: Current status, potential, and challenges. Fuel, 316, 123317. https://doi.org/10.1016/j.fuel.2022.123317

© 2025 by the authors. Licensed to PSEcommunity.org and PSE Press. This is an open access article under the creative commons CC-BY-SA licensing terms. Credit must be given to creator and adaptations must be shared under the same terms. See https://creativecommons.org/licenses/by-sa/4.0/



Systems & Control Transactions

**Research Article - Peer Reviewed Conference Proceeding**
ESCAPE 35 - European Symposium on Computer Aided Process Engineering
Ghent, Belgium. 6-9 July 2025
Jan F.M. Van Impe, Grégoire Léonard, Satyajeet S. Bhonsale,
Monika E. Polańska, Filip Logist (Eds.)

PSE PRESS

# Design of a policy framework in support of the Transformation of the Dutch Industry

**Jan van Schijndel[a]*, Rutger de Mare[a], Nort Thijssen[a] and Jim van der Valk Bouman[a]**

[a] QuoMare, Kampenringweg 45A, Gouda 2803PE, The Netherlands
*Corresponding Author: janvanschijndel@quomare.com

## ABSTRACT

In 2022 the Dutch Energy System used some 2700 PJ of energy. Some 86% of its input was natural gas, crude oil and coal. The other 14% were renewables. A network of power-generation units, refineries and petrochemical complexes converted fossil resources into heat (700 PJ), power (400 PJ), transportation fuels (500 PJ) and chemicals (400 PJ). Some 700 PJ were lost due to conversion and transport. $CO_2$ emissions were 160 Mt in 2022 of which 65 Mt by industry and 30 Mt by mobility. Transformation of this system into a Net Zero $CO_2$ system calls for replacement of fossil resources by renewable heat, power and carbon. Decarbonisation of heat & power for residential and mobility is well underway at the moment. However, decarbonisation of industry and recarbonisation of shipping & aviation fuels, as well as recarbonisation of feeds for chemicals, is hampering progress. This paper concludes that current policies, predominantly based on trading $CO_2$ emission certificates (ETS) is insufficient for industry to justify investment decisions. A carbon tax of 100 €/t $CO_2$ on top of ETS prices (currently some 70 €/t $CO_2$) is still insufficient for viable business cases. This paper shows that a combination of mandated production volumes for renewable fuels supported by opex subsidies, investors' willingness to accept lower costs of capital, off-takers' willingness to pay higher prices for green products and producers' willingness to accept lower returns on their investment, may drive industry towards viable business cases. Financial support comes from government through their return of extra $CO_2$ tax income and income from sales of ETS certificates to producers, off-takers and investors (risk mitigation assurances). This paper shows how QuoMare's TDES (Transformation of the Dutch Energy System) is deployed to outline a policy framework that provides robust incentives to industry to invest in decarbonisation and recarbonisation projects.

**Keywords**: Mixed-Integer Multi-Period Linear Programming, Decision Support System, Optimal Policy Making

## INTRODUCTION

In 2022, the Dutch energy system emitted some 160 Mt $CO_2$: 20 Mt $CO_2$ by residential, 30 Mt $CO_2$ by mobility, 20 Mt $CO_2$ by agriculture (mostly $CO_2$ equivalents due to $CH_4$ & $N_2O$ emissions), 25 Mt $CO_2$ by electricity producers and 65 Mt $CO_2$ by industry [1].

The larger industrial $CO_2$ emitters are: Tata Steel (12 Mt $CO_2$), fertilizer producers Yara & OCI (6 Mt $CO_2$), refineries (18 Mt $CO_2$), naphtha crackers (6 Mt $CO_2$) and the chemical industry (23 Mt $CO_2$). These $CO_2$ emissions are classified as scope-1 & scope-2 emissions. Refineries produce 10 Mt transportation fuels that yield the 30 Mt $CO_2$ mobility emissions mentioned above. From a refinery point of view these $CO_2$ emissions qualify as scope-3 emissions.

Scope-1 and scope-2 $CO_2$ emissions need to be decarbonised. Recarbonisation of fuels will address scope-3 $CO_2$ emissions. In a fossil free scenario, cracker feedstocks face a similar recarbonisation challenge.

This paper shows that decarbonisation and recarbonisation are lacking economically viable business cases. Hence, the challenge is to design a policy framework that supports the energy transition stakeholders (producers, product off-takers, investors and government) to build viable business cases for the transformation of the Dutch industry. This paper outlines how such a framework can be developed by using network

optimisation principles with dedicated focus on the petrochemical sector (refineries, crackers, chemical industry). This paper builds on the TDES functionality presented at ESCAPE34, Florence, June 2-6, 2024 [2].

## DECARBONISATION ECONOMICS - GENERAL

### Tata Steel

Tata Steel operates two Blast Furnaces (BF's) and is evaluating the economics to replace these BF's by two Direct Reduction of Iron (DRI) facilities to eliminate its 12 Mt/a $CO_2$ emissions. DRI can be done by either $CH_4$ & CCS or by $H_2$. The DRI - $H_2$ option calls for an investment of 6 bln € (assuming a capital intensity of 850 € per ton of steel) and 0,5 Mt/a of green $H_2$ (variable opex of 2.5 bln €/a assuming @ 5000 €/ton $H_2$).

### Fertilizer manufacturing (OCI & YARA)

Decarbonisation of 3 Mt/a $NH_3$ production by $H_2$ calls for 0,5 Mt/a green $H_2$ to avoid 6 Mt/a $CO_2$ emissions. The corresponding electrolyser investment is 3 bln € and calls for 25 TWh electricity @ 80 €/MWh (2 bln €/a).

### Refineries

Crude intake by the Dutch refineries is currently some 52 Mt/a with reported $CO_2$ emissions of 18 Mt/a. It is assumed that these $CO_2$ emissions can largely be removed by Carbon Capture & $CO_2$ Storage (CCS) in the North Sea @ capital intensity of 500 € per ton $CO_2$ (9 bln €) and variable opex of 100 €/ton $CO_2$ (1,8 bln €/a).

### Naphtha crackers

The main feedstock for the Dow, Shell and Sabic crackers in the Netherlands is naphtha with some 4 Mt/a of ethylene and some 6 Mt/a of other lower olefins & aromatics as output. The cracking furnaces are fired by the $CH_4$ product stream (2 mln t/a), resulting in some 6 Mt/a $CO_2$ emissions. These emissions can be eliminated by ATR (Auto Thermal Reforming) of $CH_4$ into $H_2$ & $CO_2$ combined with CCS. The ATR-CCS capex is estimated at 3.7 bln €. Variable opex of 1.05 bln € is for the additional intake of steam, oxygen and natural gas for the reformer and utilities to capture and sequester $CO_2$.

### Chemical Industry

Olefins and aromatics are upgraded into industrial chemicals and polymers. Some 8,4 Mt/a $CH_4$ is consumed for the production of (high temperature) heat and power. The resulting 23 Mt/a of $CO_2$ emissions can be avoided by a combination of industrial heat pumps & e-boilers (20 TWh E-power @ 80€/MWh) and 1 mln ton/a $H_2$ firing (@ 5000 €/ton $H_2$) to meet the high temperature requirements. Capex for heat-pumps & boilers is estimated at 1.1 bln €.

### Break Even $CO_2$ Emission Trading Scheme (ETS) Prices

Total Annualised Costs (TAC's) have been calculated to test the economic viability of decarbonisation technologies discussed above. TAC is the sum of costs of capital (on annuity basis, but for simplicity sake set at 6% of capital expenditure), fixed opex for operations and maintenance (set at 4% of capex) and variable opex being feedstock costs and utility costs. The Break-Even ETS price is the price to be paid for an ETS certificate to match the TAC per ton of $CO_2$ to be captured. From the Break-Even ETS prices summarised in Table 1 below, it may be concluded that apart from CCS to remove and store $CO_2$ ex refinery furnaces, other technologies lack a solid business case to justify implementation. The projected $CO_2$ price of 220 €/ton by 2050 for ETS certificates (Figure 1) is simply too low. ETS certificate pricing is expected to increase from 70 €/ton $CO_2$ in 2025 to some 220 €/ton $CO_2$ in 2050 based on supply-demand unbalances for ETS certificates as predicted by TNO [5].

**Table 1:** Summary Break-Even ETS prices

| | TATA Steel | OCI & YARA | Refineries | Crackers | Chemicals |
|---|---|---|---|---|---|
| CO2 emissions 2022 (Mt/a) | 12 | 6 | 18 | 6 | 23 |
| | | | | | |
| Decarbonsation technology | DRI - H2 | H2 | CCS | ATR - CCS | E & H2 |
| Capex (bln €) | 6,0 | 3,0 | 9,0 | 3,7 | 1,1 |
| Cost of Capital (bln €/a) | 0,36 | 0,18 | 0,54 | 0,22 | 0,07 |
| Fixed Opex (bln €/a) | 0,24 | 0,12 | 0,36 | 0,15 | 0,04 |
| Variable Opex (bln €/a) | 2,50 | 2,00 | 1,80 | 1,05 | 6,60 |
| TAC (bln €/a) | 3,10 | 2,30 | 2,70 | 1,42 | 6,71 |
| | | | | | |
| Break Even ETS price (€/ton CO2) | 258 | 383 | 150 | 237 | 292 |

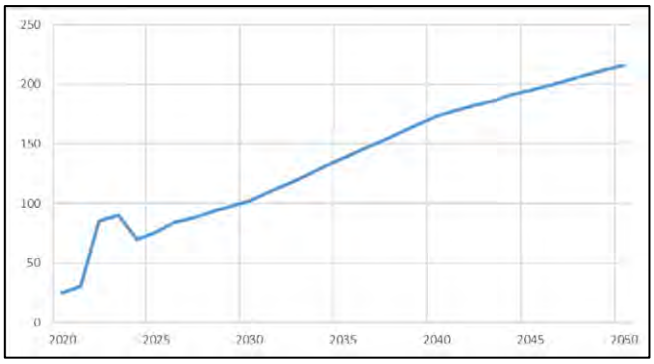



**Figure 1:** Projected cost ETS certificates in €/ton $CO_2$

## RECARBONISATION ECONOMICS - GENERAL

Recarbonisation projects for the production of renewable transportation fuels and feeds for the naphtha crackers will also be difficult to justify economically. As an example, the economics for the production of biomethanol are outlined in Figure 2 below. Typically, methanol prices range between 400 €/ton and 500 €/ton. The example shows that a Break-Even Value of 770 €/ton

methanol would be needed for a Return on Investment (ROI) of 0% and some 900 €/ton to deliver an ROI of 5%. ROI is the ratio between annual Net Income After Tax (NIAT) and project investment (capex) and a key-indicator for the profitability of a capital project.

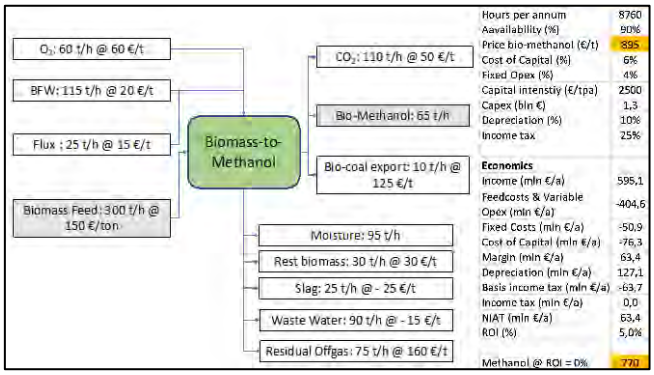



**Figure 2**: Biomass To Methanol Economics

## TDES & INDUSTRY TRANSFORMATION SCOPE

Transforming the Dutch industry sector into a system that is largely based on renewable energy resources in an economically viable manner, requires a systemic analysis of a large set of decarbonisation and recarbonisation investment options. To this end, QuoMare developed TDES (Transformation Dutch Energy System).

TDES is an optimisation methodology based on an MP-MILP (Muli-Period Mixed Integer Linear Programming) algorithm that evaluates a set of decarbonization & recarbonisation investment options (integer variables) on a year-to-year basis from today towards 2050, together with unit capacities (continuous variables) and subject to various constraints (like $CO_2$ reduction targets, availability of resources and product demand). The objective is to determine a lowest cost transformation pathway.

The combined decarbonisation & recarbonisation challenge and option space for petrochemicals is outlined in Figure 3.

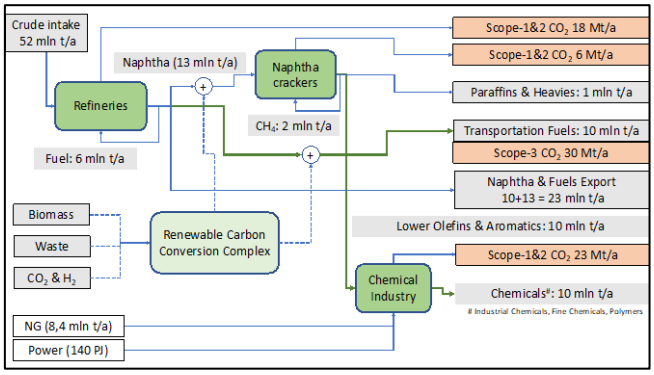



**Figure 3:** Decarbonisation & Recarbonisation Petrochemicals

To address the 47 Mt $CO_2$/a scope-1 & scope-2 decarbonisation challenge for petrochemicals, TDES may select technologies based on electrification (heat pumps, e-boilers), carbon capture & storage (CCS) or burning $H_2$ rather than $CH_4$.

To address the 30 Mt $CO_2$/a scope-3 recarbonisation challenge for petrochemicals, TDES has access to a portfolio of process technologies converting renewable carbon from biomass, waste and $CO_2$ into transportation fuels and feeds for chemicals. Process technologies modelled in TDES as per Figure 4 below include fermentation, hydrogenation, reforming, torrefaction, and gasification of biomass & waste streams into syngas. Renewable syngas can also be produced by the RWGS (Reverse Water Gas Shift) technology: reactivating $CO_2$ with green $H_2$ into CO & $H_2O$. Syngas is subsequently converted through either Fischer-Tropsch synthesis or methanol synthesis into transportation fuels and cracker feedstocks. Pyrolysis of recycled plastics is another route to produce renewable cracker feedstocks.

TDES is based on QuoMare's proprietary TEACOS framework (Techno-Economic Analysis of Complex Option Spaces). See below.

Please find below some comments on TDES validation, uncertainty & constraint analysis and broader concept applicability.

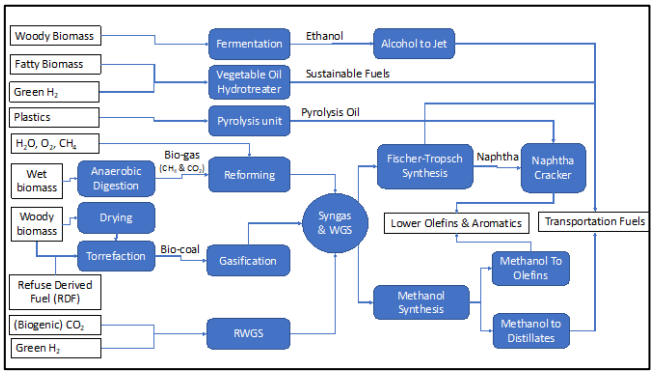



**Figure 4:** Superstructure Renewable Carbon Conversion Complex

TDES has been validated through various studies with institutions in the Netherlands: Institute for Sustainable Process Technology; Sustainable Industry Laboratory of University of Utrecht; Department of Economic Affairs of the Dutch Government.

TDES uses the Monte-Carlo functionality to address both parameter uncertainties and to evaluate scenarios in a systematic manner. This combination supports so-called "no-regret investment decisions". Likewise, also policy uncertainties are addressed by a structured Monte-Carlo and scenario analysis.

While TDES identifies economically viable transformation pathways within given set of constraints like feedstock availabilities, throughput capacities and product demand, TDES simultaneously also acknowledges

potential barriers to conversion technology implementation, such as technological readiness levels (TRL), supply chain limitations like mode-of-transport, and societal acceptance issues (e.g. no onshore windmills in a particular region).

Although TDES is specific to the Dutch context, it can easily be adapted to other countries or regions as TDES is 100% data driven. Heat, power and carbon demand data by residential, mobility, agriculture and industry sectors (production of steel, fertilizers and chemicals) are combined with yields and expense data of the conversion units to calculate feedstock and utility requirements. This clearly enhances the broader concept applicability.

## TEACOS

TEACOS is an optimization framework based on Multi-Period Mixed-Integer Linear Programming [3]. TEACOS has four general building blocks, as shown below.

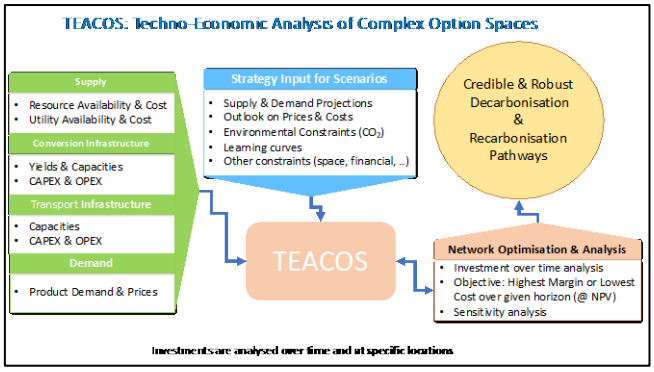



**Figure 5:** High level overview of TEACOS

These building blocks together represent a classical supply or value chain with temporal and spatial granularity: both location and timing aspects are included. TEACOS can either maximize the Net Present Value (NPV) of the supply chain margin or minimize the NPV of supply chain costs, both over the time horizon imposed, meanwhile respecting boundary conditions and environmental constraints. Sensitivity analyses by the Monte-Carlo functionality demonstrate the robustness of transition pathways and detect tipping points to understand the relative attractiveness of the investments over time. The mathematics (MP-MILP) behind TEACOS and its deployment have been described in a decarbonisation study for the industrial cluster of the Port of Rotterdam [4].

## DESIGN OF A POLICY FRAMEWORK

The Dutch government is well aware of the lack of economically viable business cases limiting progress towards the Net Zero $CO_2$ target in 2050. In principle, government has 3 degrees of freedom: imposing mandates, levy/charge additional $CO_2$ taxation and providing subsidies. However, such an approach is rather directive and collaboration with industry & infrastructure companies is probably more effective.

To this end, government is engaging with key industry partners (including TATA Steel, OCI & YARA and the petrochemical sector) with the aim to conclude tailor-made decarbonisation and recarbonisation agreements ("Maatwerk Afspraken" in Dutch).

Obviously, the Dutch government is key stakeholder in this process due to their commitment to deliver $CO_2$ reduction targets agreed upon within the European Community (55% reduction in 2030 and 100% reduction in 2050, both relative to the Dutch reference emission of 220 Mt $CO_2$ in 1990). Apart from the Dutch government and their industrial partners, there are two other important stakeholders: product off-takers and investors.

Figure 6 below shows how these stakeholders may work together to develop viable business cases.

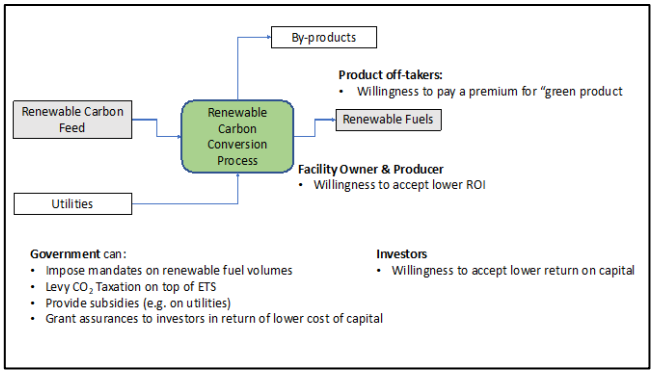



**Figure 6:** Stakeholder Analysis & their degrees of freedom

Product off-takers may be willing to pay a price premium for decarbonised and/or recarbonised products, which entitles them to market "green products". Investors' willingness relates to accepting a lower return on their investment by demanding a lower WACC (Weighted Average Cost of Capital). This usually comes with the requirement that the Dutch government provides them with sufficient assurances that reduce/minimize their risk of "losing" their investment. Producers contribute to a viable business case by accepting a lower Return on Investment (ROI): 5% rather than 10%.

Apart from imposing mandates on the production of renewable transportation fuels, the Dutch government has tax measures to play with. They may decide to impose an additional $CO_2$ tax on top of the $CO_2$ price to be paid for ETS certificates. Government may also grant income tax waivers or tax-holidays for producers. Another degree of freedom is the provision of subsidies on process utilities lowering operating expenses like costs of power, Natural Gas and CCS entrance fees.

As TDES selects those options that minimise the net present value of accumulated system costs over the 2020-2050 time-horizon, post-processing is needed to identify economically viable conditions for industry. The policy framework outlined above together with TDES results is used to find that combination of price premia, WACC reductions and subsidies that will bring decarbonisation and recarbonisation projects over time (2025 – 2050 horizon) sufficiently into "the money" within constraints imposed: $CO_2$ reduction targets; availabilities of renewable feeds; and mandates on renewable transportation fuels.

In the decarbonisation space, the Dutch government is clearly in the lead in view of the scope-1 and scope 2 $CO_2$ reduction ambitions. They orchestrate how their ETS-1 income (some 10 bln € per year with ETS certificates valued at 150 €/ton) can be redistributed as subsidies to the various industry segments, to create a viable business case in combination with price premia.

In case of recarbonisation, the Dutch government facilitates and supports industrial initiatives in getting recarbonisation projects towards Final Investment Decisions (FID) with a budget of some 4,5 bln € (30 Mt/a $CO_2$ scope-3 emissions @ 150 €/ton).

## DEPLOYMENT POLICY FRAMEWORK - RESULTS

### Outcome decarbonisation analysis

Table 2 below shows the results of the TDES decarbonisation optimisation. The table captures the situation in 2050. In case of TATA, the DRI option with $H_2$ has been chosen. For OCI & YARA, both green and blue $H_2$ have been included in the option space. For the refineries, blue $H_2$ has been shown to be less attractive than CCS. For the crackers, upgrading the $CH_4$ product stream through ATR into blue $H_2$ with $CO_2$ captured and stored proved the better decarbonisation option compared to electrification of the cracking furnaces. Most of the lower heat requirements of chemical production units can be met by industrial heat pumps and e-boilers with 1 Mt/a of $H_2$ to satisfy high temperature demand.

The benefits entry is based on the avoidance of buying ETS certificates @ 150 €/ton $CO_2$ plus extra revenues for green products. Within the stakeholder frame, product premia assumptions have been made for the off-take of green steel (50 €/ton) and ammonia (120 €/ton); government subsidies have been assumed for utilities: a renewable power discount of 40 €/MWh for power needed for $H_2$ production (partly reflecting the compensation for high electricity network costs in the Netherlands), a discount of 30 €/ton for $O_2$, a discount of 75 €/ton for NG and a discount of 25 €/ton $CO_2$ on the $CO_2$ feed-in tariff. Furthermore, investors are assumed to be willing to lower their fees for lending capital by 2% in absolute terms backed by government risk assurance terms (WACC of 4% rather than typically 6%).

This results in Net Income After Tax (NIAT) improvements for all industry partners bringing the ROI at/above the 5% threshold.

The reference NIAT entry refers to the NIAT without the benefits from variable opex subsidies, premia from green products, tax holiday and lower cost of capital.

The "zero-sum" section shows how each stakeholder may contribute to a sufficiently attractive decarbonisation project. The negative values are the off-takers, investors and government contributions: off-takers pay a premium for green, investors accept a lower return on capital they lend and government provide subsidies. Together they provide a margin improvement that turns the reference NIAT positive with an ROI above the 5% threshold the manufacturing stakeholder is willing to accept.

**Table 2:** Decarbonisation outcome

| | TATA Steel | OCI & YARA | Refineries | Crackers | Chemicals |
|---|---|---|---|---|---|
| CO2 emissions 2022 (Mt/a) | 12 | 6 | 18 | 6 | 23 |
| Decarbonsation technology | DRI - H2 | H2 | CCS | ATR - CCS | E & H2 |
| Capex (bln €) | 6,0 | 3,0 | 9,0 | 3,7 | 1,1 |
| Cost of Capital (bln €/a) | 0,36 | 0,18 | 0,54 | 0,22 | 0,07 |
| Fixed Opex (bln €/a) | 0,24 | 0,12 | 0,36 | 0,15 | 0,04 |
| Variable Opex (bln €/a) | 2,50 | 2,00 | 1,80 | 1,05 | 6,60 |
| TAC (bln €/a) | 3,10 | 2,30 | 2,70 | 1,42 | 6,71 |
| | | | | | |
| Variable Opex subsidies (bln €/a) | 1,13 | 1,13 | 0,27 | 0,63 | 3,30 |
| | | | | | |
| **Economics** | | | | | |
| Premium green product (€/ton) | 50 | 120 | | | |
| Benefits (bln €/a) | 2,15 | 1,26 | 2,70 | 0,90 | 3,45 |
| Variable Opex (bln €/a) | 1,37 | 0,87 | 1,53 | 0,42 | 3,30 |
| Fixed Costs (bln €/a) | 0,24 | 0,12 | 0,36 | 0,15 | 0,04 |
| Cost of Capital (bln €/a) | 0,24 | 0,12 | 0,36 | 0,15 | 0,04 |
| Margin (bln €/a) | 0,30 | 0,15 | 0,45 | 0,19 | 0,06 |
| Depreciation (bln €/a | 0,60 | 0,30 | 0,90 | 0,37 | 0,11 |
| Basis income tax (bln €/a) | -0,30 | -0,15 | -0,45 | -0,19 | -0,05 |
| Income tax (bln €/a) | 0,00 | 0,00 | 0,00 | 0,00 | 0,00 |
| NIAT (bln €/a) | 0,30 | 0,15 | 0,45 | 0,19 | 0,06 |
| ROI (%) | 5,0% | 5,0% | 5,0% | 5,0% | 5,3% |
| **Reference NIAT (bln €/a)** | -1,30 | -1,40 | 0,00 | -0,52 | -3,26 |
| | | | | | |
| Zero-Sum check: | | | | | |
| Contribution Offtakers (bln €/a) | -0,35 | -0,36 | 0,00 | 0,00 | 0,00 |
| Contribution Investors (bln €/a) | -0,12 | -0,06 | -0,18 | -0,07 | -0,02 |
| Contribution Government (bln €/a) | -1,13 | -1,13 | -0,27 | -0,63 | -3,30 |
| Margin improvement (bln €/a) | 1,60 | 1,55 | 0,45 | 0,71 | 3,32 |
| Sum | 0,00 | 0,00 | 0,00 | 0,00 | 0,00 |

### Outcome recarbonisation analysis

TDES shows that the HVO (Hydrotreatment of Vegetable Oil), WPO (Waste Plastics to Oil), BTL (Biomass To Liquids) and PTL (Power to Liquids) processes deliver the best configuration for the recarbonisation of cracker feedstocks and transportation fuels. The basis for this TDES optimisation are constraints imposed on the production of renewable fuels mandated by the EU for aviation (Sustainable Aviation Fuel, SAF) and for shipping (Sustainable Marine Gasoil, SMG) as per Table 3 below. The availability of renewable feedstocks listed in Table 4 is another set of constraints used by TDES to determine

the best combination of renewable feeds and processes to deliver renewable transportation fuels (7,5 Mt/a in 2050) and renewable cracker feeds (3,8 Mt/a pyrolysis oil ex WPO-unit). Table 4 lists envisaged feedstock availabities in 2050 on the basis of a conversion efficiency (thermal efficiency) of 70% for lipids, ligno and RDF (Refuse Derived Fuel) and 75% for plastics.

**Table 3:** Renewable share as mandated by ReFuelEU for aviation fuels & FuelEU for shipping fuels

| | 2030 | 2040 | 2050 |
|---|---|---|---|
| Bio-based SAF (Mt/a) | 0,25 | 1,25 | 2,00 |
| E-SAF (Mt/a) | 0,05 | 0,50 | 1,50 |
| Total SAF (Mt/a) | 0,30 | 1,75 | 3,50 |
| Bio-based SMG | 0,10 | 1,50 | 4,00 |
| Total renewable fuels (Mt/a) | 0,40 | 3,25 | 7,50 |

**Table 4:** Feedstock availabilities (Mt/a)

| | LHV (GJ/ton) | 2030 | 2040 | 2050 |
|---|---|---|---|---|
| Lipids | 30 | 4,0 | 5,0 | 6,0 |
| Plastics | 40 | 1,3 | 2,7 | 5,0 |
| Lignocellulose | 12 | 2,0 | 2,4 | 7,0 |
| RDF | 25 | 0,5 | 1,0 | 2,0 |
| Biogenic $CO_2$ | 0 | 1,3 | 3,2 | 6,3 |

Table 5 below shows the ROI target of 5% is attained by the optimal combination of price premia and opex subsidies. The "zero-sum" analysis shows the importance of government-industry partnering. Reference prices are based on a crude oil price of 80 $/bbl with product-crude spreads assumed for naphtha, kero and gasoil of 20 $/bbl, 10 $/bbl and 5 $/bbl respectively, with corresponding bbl-factors of 8,3 bbl/ton, 8,4 bbl/ton and 7,5 bbl/ton respectively.

Note that Table 5 shows that in 2050 only 75% of the 10 Mt/a target renewable fuel volume (50/50 split over SAF/SMG) is realised. This is in accordance with the mandates imposed and availabilities of renewable feed volumes, but insufficient for the Net Zero $CO_2$ goal in 2050. Hence, additional volumes of $CO_2$ removal or negative emissions are needed as compensation.

Furthermore, note that product price premia to bring projects for producers into the money are significant: some 40% – 55% on top of the reference price for HVO & BTL fuels and even 150% for SAF from the PTL process. It will be difficult for producers to conclude long-term offtake agreements needed for FID based on those premia. Hence, assuming an ETS-2 $CO_2$ price of 150 €/ton by 2050 and the replacement of 7,5 Mt/a fossil fuels by renewables, the ETS-2 budget of some 3.4 bln €/a can be redistributed as opex subsidies to producers (1,8 bln €/a) and compensation to off-takers (1,6 bln €/a) to limit their contribution to the transportation fuels recarbonisation challenge. On average, the 1.6 bln €/a would lower price premia by some 200 €/ton. However, this would still be insufficient to attract PTL investments for production of E-SAF.

**Table 5:** Recarbonisation status by 2050

| | HVO | WPO | BTL | PTL |
|---|---|---|---|---|
| Capacity (Mt/a) | 3,2 | 3,8 | 2,3 | 2,0 |
| Investment (bln €) | 3,2 | 5,7 | 6,9 | 4 |
| | | | | |
| Reference Price (€/ton) | 755 | 839 | 640 | 755 |
| Premium (€/ton) | 285 | 0 | 345 | 1148 |
| Product Price (€/ton) | 1040 | 839 | 985 | 1903 |
| | | | | |
| Income (bln €/a) | 3,33 | 3,19 | 2,26 | 3,81 |
| Feedstock & Variable Opex (bln €/a) | 3,18 | 2,53 | 1,46 | 4,43 |
| Variable Opex subsidies (bln €/a) | 0,27 | 0,31 | 0,09 | 1,14 |
| Fixed Costs (bln €/a) | 0,13 | 0,23 | 0,28 | 0,16 |
| Cost of Capital (bln €/a) | 0,13 | 0,23 | 0,28 | 0,16 |
| Margin (bln €/a) | 0,16 | 0,51 | 0,35 | 0,20 |
| Depreciation (bln €/a) | 0,32 | 0,57 | 0,69 | 0,40 |
| Basis for income tax (bln €/a) | -0,16 | -0,06 | -0,35 | -0,20 |
| Income tax (bln €/a) | 0,00 | 0,00 | 0,00 | 0,00 |
| NIAT (bln €/a) | 0,16 | 0,51 | 0,35 | 0,20 |
| ROI (%) | 5% | 9% | 5% | 5% |
| | | | | |
| Zero-Sum Check | | | | |
| Contribution offtakers (bln €/a) | -0,91 | 0,00 | -0,79 | -2,30 |
| Contribution Banks (bln €/a) | -0,06 | -0,11 | -0,14 | -0,08 |
| Contribution Government (bln €/a) | -0,27 | -0,31 | -0,09 | -1,14 |
| Delta Margin Producers (bln €) | 1,25 | 0,42 | 1,03 | 3,52 |
| Sum | 0,00 | 0,00 | 0,00 | 0,00 |

## SUMMARY & CONCLUSIONS

Based on 2022 $CO_2$ emission data, the Dutch industry is facing a $CO_2$ decarbonisation target of 65 Mt/a. In addition, the envisaged domestic offtake of 10 Mt/a fuels for aviation and shipping sets a longer term recarbonisation target of 30 Mt/a of $CO_2$.

Within the current scheme of $CO_2$ reduction policies, largely driven by the Emission Trading Scheme, both decarbonisation and recarbonisation project options are insufficiently competitive relative to "business as usual": they do not result in attractive business cases, e.g. with a Return of Capital (ROI) of 10%. $CO_2$ emission Break Even values range between 150 €/ton and 380 €/ton for decarbonisation projects (delivering an ROI of 0%).

A policy framework is presented that builds on the TDES decarbonisation and recarbonisation results for the Dutch industry over the 2025-2050 time horizon. These

results are obtained within set of constraints imposed on the MP-MILP problem: $CO_2$ reduction targets, mandated production of renewable fuel volumes and given availiablities of renewable feedstocks. This policy framework allows industry and government to jointly explore and agree how their degrees of freedom (opex subsidies, price premia, lower WACC) contribute to the development of economically viable business cases for industry with an ROI of 5% (typically an ROI of 10% would be needed for industries to take a FID).

Decarbonisation of the Dutch industry calls for an investment of some 23 bln€ over the 2025-2050 timeframe. This is equivalent to 350 €/ton $CO_2$ avoided. Corresponding Total Annualised Cost average out at some 16 bln €/a, equivalent to 250 €/ton $CO_2$ avoided. Some 6,5 bln€/a opex subsidies are needed together with 1 bln€/a price premia and lower costs of capital to turn decarbonisation industry projects viable for an ROI of 5%. Part of the ETS-1 revenues of some 10 bln€/a would cover funding.

The mandated recarbonisation of 7,5 Mt/a aviation and shipping fuels by 2050 calls for an investment of some 14 bln € (some 625 €/ton $CO_2$ avoided). Corresponding Total Annualised Cost are some 10 bln €/a (some 450 €/ton $CO_2$ avoided). Significant price premia of some 530 €/t on average on top of the average fuel price of 720 €/ton together with opex subsidies of some 1.5 bln €/a are needed for an ROI of 5%. ETS-2 revenues of 4,5 bln € (30 Mt/a @ 150 €/ton) are insufficient to compensate the 5,5 bln €/a for price and opex support. The economics of the PTL process producing E-SAF is the main contributor to this unbalance.

The extension of TDES with this policy framework provides a powerful tool supporting government-industry discussions in an interactive and transparent manner. on the so-called “Maatwerk” agreements as to arrive at economically viable cases for industry to meet their 95 Mt/a CO2 reduction target.

The TDES functionality is currently being extended to cover European policies related to CBAM (Carbon Border Adjustment Mechanism policy imposing $CO_2$ taxes on fossil-based imports from outside Europe), PPWD (the Plastic & Paper Waste Directive addressing impact on volume and pricing of plastics & paper recycling as circular feedstocks for naphtha crackers) and the Clean Industrial Deal (policies that aim to compensate for high electricity distribution network costs and high energy prices in general).

## REFERENCES


1. EBN infographic over 2022, issued January 2024;
2. Jan van Schijndel, Rutger de Mare, Nort Thijssen, Jim van der Valk Bouman, TDES Transformation of the Dutch energy System, Proceedings of the 34th European Symposium on Computer Aided Process Engineering / 15th International Symposium on Process Systems Engineering, Elsevier;
3. J. van Schijndel, 2019, Energy System Modelling in support of the Energy Transition, 29th European Symposium on Computer Aided Process Engineering, Elsevier, p. 1621-1626;
4. J. Davelaar, 2023, Accelerating the Energy Transition: Determining No-Regret Transition Pathways in the Port of Rotterdam, Proceedings International Conference on Operations Research (OR 2023), Springer;
5. Personal communication with Sebastian Hers, Research Analyst, TNO.



© 2025 by the authors. Licensed to PSEcommunity.org and PSE Press. This is an open access article under the creative commons CC-BY-SA licensing terms. Credit must be given to creator and adaptations must be shared under the same terms. See https://creativecommons.org/licenses/by-sa/4.0/




Systems & Control Transactions

**Research Article - Peer Reviewed Conference Proceeding**
ESCAPE 35 - European Symposium on Computer Aided Process Engineering
Ghent, Belgium. 6-9 July 2025
Jan F.M. Van Impe, Grégoire Léonard, Satyajeet S. Bhonsale,
Monika E. Polańska, Filip Logist (Eds.)

PSE PRESS

# Green Hydrogen Supply Chains Design in Portugal: Economic Efficiency vs Water Sustainability

**Tânia Pinto-Varela[a] , João Imaginário[a], Nelson Chibeles-Martins[b,c]**

[a] Centro de Estudos de Gestão, Instituto Superior Técnico, Universidade Lisboa, Lisboa, Portugal
[b] NOVA MATH, Centro de Matemática e Aplicações, Faculdade de Ciências e Tecnologia, Universidade Nova de Lisboa, Caparica, Portugal
[c] Departamento de Matemática, Faculdade de Ciências e Tecnologia, Universidade Nova de Lisboa, Caparica, Portugal
* Corresponding Author: tania.pinto.varela@tecnico.ulisboa.pt

## ABSTRACT

This study designs a green hydrogen supply chain for Portugal, focusing on minimizing both economic costs and water stress. The research uses a multi-objective simulated annealing algorithm to address the trade-offs between the two objectives. The process of producing hydrogen via electrolysis is highly water-intensive, posing a challenge in water-scarce regions like southern Portugal. The study considers Portugal's uneven water distribution, renewable energy availability and, different hydrological conditions across districts. An aggregate indicator, Water Stress Index (TWSI), quantify the pressure on water resources covering all the Portugal´s districts in a single score. This study explores four scenarios, a baseline scenario, a green hydrogen scenario using only renewable energy, drought conditions, and increased demand in major cities with drought conditions. The quasi pareto front illustrates the trade-offs between supply chain cost and TWSI, enabling decision-makers to select solutions tailored to local priorities. The findings highlight the importance of adaptable and robustness infrastructure to overcome both environmental and demand challenges.

**Keywords**: Green hydrogen supply chain, multi-objective, simulated annealing, water stress.

## INTRODUCTION

As the world pursues solutions to reduce carbon emissions and combat climate change, green hydrogen has emerged as a critical component of the clean energy transition. Produced through renewable energy-powered electrolysis, green hydrogen is a versatile and emissions-free fuel that offers a pathway to decarbonize hard-to-abate sectors such as heavy industry, transportation, and energy storage. Countries like Portugal, with rich renewable resources, are well-positioned to lead in green hydrogen production. However, the process of producing hydrogen via electrolysis is highly water-intensive, presenting challenges in water-scarce regions, particularly in southern Portugal where droughts are common.

Current research on green hydrogen supply chains (HSC) has largely focused on optimizing economic objectives, such as production cost minimization, while addressing safety and environmental impact through mixed integer linear programming (MILP) approaches [1]. The author explored multi-objective approaches, considering the trade-off between cost and sustainability goals, considering the global warming potential (GWP). The results have shown how hydrogen supply chains can achieve economic efficiency alongside some environmental benefits. In 2019, Câmara, et al. [2] used multi-objective, multi-period, stochastic, MILP model to design and plan an HSC considering uncertainty over the availability of primary energy sources.

The aim of this study is to design a green hydrogen supply chain, applied to Portugal, considering economic and water stress minimization, using multi-objective Simulating Annealing. A quasi pareto front is characterized showing the trade-off between both objective functions. Four scenarios are explored, with disruptive aspects (e.g. water scarcity, increase urban demand) to illustrate how the hydrogen supply chains can overcome the strain on water resources while meeting economic targets and satisfy the demand, highlighting the robustness of the Portuguese supply chain, and offering insights for

sustainable hydrogen production. This study aims to support policymakers and industry leaders in building a robust, efficient hydrogen infrastructure for Portugal that aligns with both economic and environmental objectives.

## The Problem

Portugal's hydrological landscape is marked by uneven water distribution across its regions, which presents specific challenges for green hydrogen production due to the highwater consumption of the electrolysis process. Portugal is divided into eight main hydrographic regions (HRs), each with distinct levels of water availability influenced by regional precipitation patterns and water basin characteristics. The water availability in each district was estimated considering the hydrological availability for each district, along with the values of the monthly and annual standard deviation. The uneven distribution of water resources requires careful planning to avoid exacerbating water stress, particularly in areas where drought and low precipitation levels already impact local water availability. Portugal's water resources are further influenced by the presence of Strongly Regulated Flows (SRFs) in certain river basins. Those allows to stabilize water supplies by controlling flow rates through dams and reservoirs. While SRFs can offer greater water stability, they also introduce constraints that must be integrated into hydrogen production to ensure sustainable water management.

Electrolysis is characterized by its reliance on water and electricity. Through electrolysis, water is split into hydrogen and oxygen using an electric current, if renewable sources are used the process is emissions-free. The average water consumption for hydrogen production via electrolysis is estimated between 10 to 22 liters of water per kilogram of hydrogen produced. In this study is used 16 liters/kilogram as a mean value, allowing the comparison of hydrogen production strategies across regions with different levels of water availability.

The availability of renewable energy sources also plays a critical role in ensuring that hydrogen production remains sustainable. Portugal's solar, wind and hydro energy outputs, are very different among each district. Producing hydrogen with grid electricity, or a mix of renewable and non-renewable sources, would reduce the overall environmental benefits of the supply chain, making it essential to focus on maximizing hydrogen produced with dedicated renewable sources.

## Model

A multi-objective Simulating Annealing is known, for handling complex problem and computational burden. This meta-heuristic mimic the physical process of annealing metals, where a material is heated and then gradually cooled to reach a stable, low-energy configuration. The gradual cooling allows the model to explore the solution space extensively and avoid local optima. In this work, a multi-objective Simulated Annealing algorithm (MOSA) is developed. The MOSA follows several steps, Figure 1. Two objectives' functions area used: the total cost of the supply chain, followed by the water stress index. The aim is to minimize the hydrogen supply chain design cost, ensuring the hydrogen production is economically feasible, and simultaneously minimize the environmental impact on water resources, which are particularly scarce in Portugal's southern regions.

**Total Costs:** Which stand, respectively, for Production Plants Capital Cost (PPCC), Biomass Transportation Cost, (BTC), Primary Energy Sources Cost (PESC), Hydrogen Transportation Cost (HTC) and Hydrogen Refuelling Stations Capital Cost (HRSCC).

$$Minimize\ TCSC = PPCC + PESC + HTC + HRSCC \quad (1)$$

**Water Stress Index:** Given Portugal's regional disparities in water availability, minimizing water stress is essential to ensure that hydrogen production does not exacerbate local water scarcity. The water stress metric used in this model is based on the Water Stress Index (WSI), an environmental assessment tool that quantifies the pressure on water resources, [3]. The WSI for each district is calculated by adjusting the water withdrawal-to-availability ratio (WTA) considering hydrological characteristics. Instead of optimizing the WSI of each district individually, the model employs an aggregate objective function to consolidate all district-level WSI values into a single representative metric: the Total Water Stress (TWS). Achieved by computing the geometric mean of the WSI values across all districts, ensuring a balanced and holistic evaluation of water stress at a regional level. The TWS provides a single metric that guides decision-making towards minimizing the overall impact on water resources across Portugal.

$$\text{Minimize } TWS = \left(\prod_{i=1}^{n} WSI_i\right)^{\frac{1}{n}} \quad (2)$$

The model generates a quasi pareto front, capturing the trade-offs between TWS and Cost, providing decision-makers with information to evaluate and select solutions that best align with regional resource availability, economic constraints, and sustainability goals, ensuring a flexible and informed approach to water resource management. E.g. In water-scarce regions, water conservation may be prioritized, while in water-abundant areas, cost reduction could prevail.

# CASE STUDY: HYDROGEN SC IN PORTUGAL

The case study designs a hydrogen SC in Portugal to meet district demand while minimizing costs and water stress.

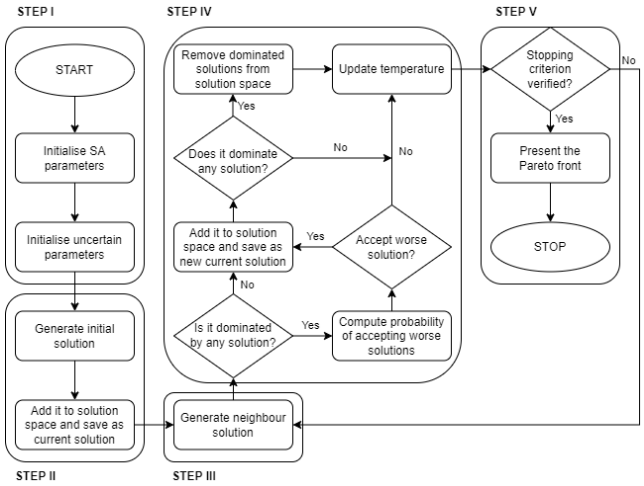



**Figure 1.** Multi-objective simulated annealing.

The study is set in mainland Portugal, considering the different hydrological conditions across eighteen districts, its characterization available in Figure 7 and delineated with a lighter line in all Portugal's figures**.** The electrolysis is the method for hydrogen production, because is the most used and is water-intensive process. The renewable energy sources (wind, solar, and hydro) as primary energy sources (PES) to produce energy for electrolysis, is considered, alongside grid power. Demand is estimated considering the population of each district and satisfied by hydrogen at Hydrogen Fueling Stations (HFS). The model integrates TWS to assess the environmental impact of water consumption, considering the presence of Strongly Regulated Flows (SRFs). The exportation and importation of hydrogen between district is allowed, only after its own demand satisfied. Higher producer of hydrogen may export hydrogen for districts with low production to face its demand. A MOSA algorithm is used to make the trade-off between both objective functions. The characterization of quasi pareto front allows decision-makers to select design of HSC that best fit their priorities. To evaluate the hydrogen SC robustness, four scenarios were developed. Each scenario represents different conditions for hydrogen production and distribution.

**Scenario A - Baseline** scenario exploring the trade-offs between cost and water stress.

**Scenario B - Green Hydrogen Supply Chain** focus on a green hydrogen SC powered only by renewable energy sources (wind, solar, hydro), excluding grid power.

**Scenario C - A drought scenario**, reduce the water availability by 10% of the baseline.

**Scenario D - Increased Demand in Major Cities** (Porto and Lisboa) combined with the water scarcity of scenario C.

Data: The model uses data on water runoff, water availability per district, renewable energy production by district, and hydrogen demand by district.

Multi-objective approach with objective functions: Economic) The model minimizes the total supply chain cost: production plants capital costs, primary energy source costs, hydrogen transportation costs, hydrogen refuelling stations capital costs; Total Water Stress) The water stress function is characterized by the calculation of two step: 1) the raw ratio of water use to availability and adjusts for regional factors using the variation factor and the presence of SRFs; 2) the resulting water stress index is aggregated into a single value (TWS) using the geometric mean.

Parameters: The MOSA parameters are tuned through experimentation, considering factors like number of iterations, initial temperature, cooling rate, and final temperature.

## Results and Discussion

The research provides a comprehensive analysis of the challenges and trade-offs in designing a sustainable green hydrogen supply chain in Portugal. The use of a multi-objective optimization model, combined with scenario analysis, offers valuable insights for decision-makers in the energy sector. The study underscores the importance of considering both economic and environmental factors in the development of a robust and efficient hydrogen infrastructure.

Given the extensive number of solutions in the quasi pareto fronts, obtained for each scenario, Figure 6, four representative solutions were selected from each scenario to characterize their outcomes. These solutions are even distributed along the quasi pareto front.

A deeper understanding the SC dynamics each solution was analysed considering: the hydrogen SC design and transportation network, Figures 2-5; district classification as importer/exporter, Table 1 and Figures 2-5; PES portfolio consumption, Table 2. The hydrogen transportation network, Figures 2-5. In each scenario a deeper analysis is taken considering the fours solutions along the respective quasi pareto front.

**Scenario A**: The quasi pareto front, Figure 6, shows a clear trade-off, where lower water stress is achieved at the expense of increased costs. Viana do Castelo, Guarda, and Lisboa are the key exporter regions, producing more hydrogen than their local demand, as in Figure 2. The transportation network changes across the four solutions (being network of the two solutions on the right-hand side of the curve the same), but these three regions remain consistent exporters, Table 1. Initially, Viana do Castelo and Guarda export to several districts, but Lisboa becomes the dominant exporter in the later solutions, shown the wider arrow in Figure 2. The portfolio of primary energy sources is shown in Table 2. A low use in hydropower across the solutions, at expense of a higher grid power consumption.

**Scenario B**: Costs are generally lower than in

scenario A, but the Total Water Stress (TWS) is higher, Figure 6. This is due to the increased reliance on hydropower, Table 2. Bragança, Viseu, Coimbra, Santarém, Portalegre, and Évora become key exporters, with Bragança being the largest. Viana do Castelo and Faro become self-sufficient, producing only enough hydrogen to meet their own demand, Table 1. The transportation network shifts to accommodate the new exporters. The network design has two main topologies, Figure 3, and Bragança becomes a major supplier. The primary energy resources portfolio, shown in Table 2, denotes higher percentage of hydropower, which is related with the increase of TWS, Table2.

**Table 1:** District classification as importer (I), exporter (E) or self-sufficient (S) for each scenario.

| | Scenario | | | |
|---|---|---|---|---|
| | **A** | **B** | **C** | **D** |
| Viana do Castelo | E | S | I | I |
| Braga | I | I | I | I |
| Porto | I | I | I | I |
| Vila Real | I | I | I | E |
| Bragança | I | E | I | E |
| Aveiro | I | I | E | I |
| Viseu | I | E | I | I |
| Guarda | E | I | I | E |
| Coimbra | I | E | I | I |
| Castelo Branco | I | I | I | E |
| Leiria | I | I | E | E |
| Santarém | I | E | I | I |
| Portalegre | I | E | I | E |
| Lisboa | E | I | I | I |
| Setúbal | I | I | I | I |
| Évora | I | E | E | I |
| Beja | I | I | I | E |
| Faro | I | S | I | I |

**Scenario C**: Both the total cost and TWS are significantly higher compared to the baseline scenario, illustrating the impact imposed by limited water availability, Figure 6. Aveiro, Leiria, and Évora emerge as key exporters, with Leiria being the largest producer. Only in the solution on the right-hand of the quasi pareto front (solution IV), Viana do Castelo, Braga and Lisboa become self-sufficient, until then are importers district. The transportation network shows Leiria playing a major role in supplying a wide range of districts, Figure 4. There's a slight increase in the use of grid electricity, while the use of hydropower also increases, Table 2.

**Scenario D:** The quasi pareto front shows a substantial increase in both cost and TWS compared to all other scenarios, Figure 6. Vila Real, Bragança, Guarda, Castelo Branco, Leiria, Portalegre, and Beja are exportes, beeing Vila Real and Portalegre the larger, ones. Slight changes are shown in transportation network as we progress towards higher costs, Figure 5. The primary energy sources portfolio shows a high user of wind power, followed by the grid, hydro and finally solar, Table 2.

The analysis of previous scenarios highlights the impact of its characteristics in the hydrogen supply chain designs. For instance, in Scenario C, the networks emphasize reducing water stress by relocating production away from drought-affected regions, even if this increases the overall costs. In Scenario D, the networks illustrate how increased urban demand reshapes the supply chain, with production hubs shifting more attention to Lisbon and Porto to optimize logistics.

The Figures 2 to 5 offer a visual representation of the trade-offs captured by the quasi pareto front and demonstrate the model's flexibility in addressing complex, multi-objective optimization challenges in Portugal's green hydrogen supply chain design.

To better understand the trade-off between total supply chain cost and water stress, a deeper discussion and guidance will be conducted.

## DISCUSSION AND GUIDANCE

The restrictions on grid power access in Scenario B demonstrated the model's capability to maximize green hydrogen production, with wind accounting for over 50% of the primary energy source portfolio, followed by hydro and the remaining share from solar (Table 2). However, despite a similar cost distribution, the model did not achieve a lower water stress level compared to the baseline scenario. These findings suggest that while prioritizing green hydrogen production is feasible, it requires careful water management in water-scarce regions, as TWS cannot be reduced to the same extent as in the baseline scenario.

Furthermore, under drought conditions, the model efficiently redistributed production to regions with more stable water supplies, as observed in Scenario C, thereby mitigating the severe impact on production costs. The trade-off between cost and water stress led to increase reliance on grid energy to off-set drought effects.

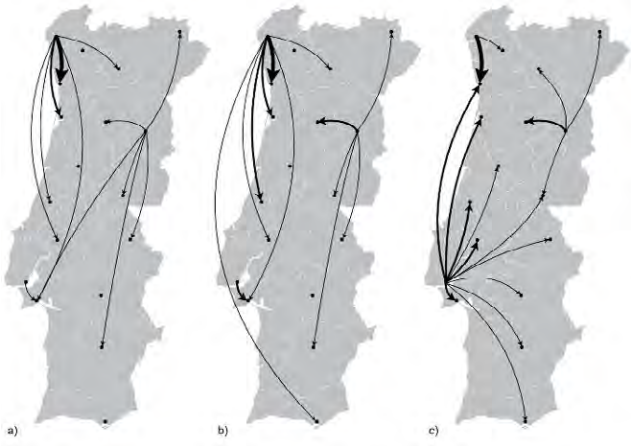



**Figure 2.** Scenario A. a) Transportation network for solution I. b) Transportation network for solution II. c) Transportation network for solutions III and IV.

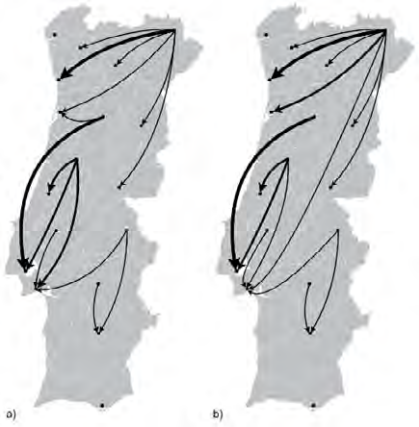



**Figure 3.** Scenario B. a) Transportation network for solution I. b) Transportation network for solutions II, III, IV.

Scenario D was the one that stood out from the rest, as shown in Figure 6. This scenario must overcome simultaneously the water scarcity and increase in demand. As result, has shown higher costs and higher water stress indicator. This analysis highlights how increasing demand, particularly in resource-constrained urban areas, puts significant pressure on the hydrogen supply chain. It underscores the urgent need for adaptable and robust infrastructures able to handle both environmental, economic challenges and demand fluctuations. Notably, most of the hydrogen produced was green, likely due to the higher overall TWS.

Regardless of the scenarios, the structure (design) of the hydrogen distribution chain remains robust. However, there is a noticeable variation in the amount of hydrogen produced in each district, along with a different utilization of the portfolio of primary energy sources.

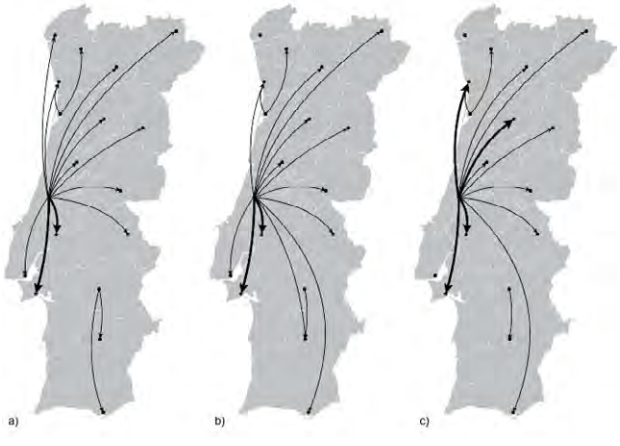



**Figure 4.** Scenario C. a) Transportation network for solution I. b) Transportation network for solution II. c) Transportation network for solutions III and IV.

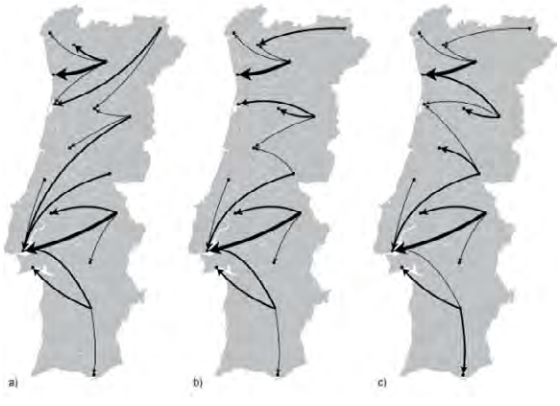



**Figure 5.** Scenario D. a) Transportation network for solution I. b) Transportation network for solution II. c) Transportation network for solutions III and IV.

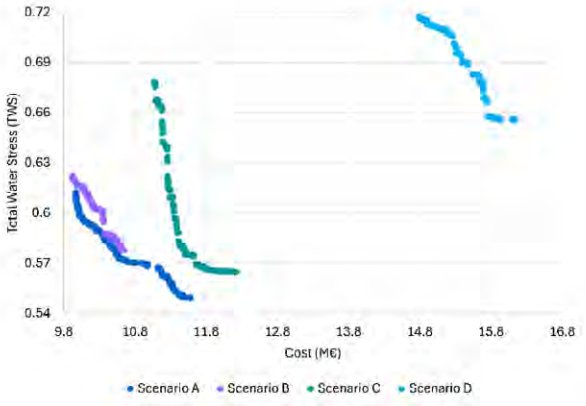



**Figure 6.** Quasi pareto front of the scenarios.

**Table 2:** Distribution of primary energy consumption portfolio for each scenario.

| Scenario | Energy Source | Solution I | II | III | IV |
|---|---|---|---|---|---|
| A | Wind | 53% | 47% | 41% | 39% |
| | Solar | 6% | 6% | 5% | 5% |
| | Hydro | 10% | 10% | 6% | 6% |
| | Grid | 31% | 38% | 47% | 50% |
| B | Wind | 59% | 56% | 55% | 53% |
| | Solar | 19% | 18% | 18% | 18% |
| | Hydro | 21% | 25% | 26% | 29% |
| | Grid | 0% | 0% | 0% | 0% |
| C | Wind | 28% | 27% | 25% | 24% |
| | Solar | 7% | 7% | 7% | 7% |
| | Hydro | 7% | 8% | 8% | 9% |
| | Grid | 58% | 58% | 60% | 60% |
| D | Wind | 51% | 48% | 48% | 46% |
| | Solar | 11% | 9% | 9% | 8% |
| | Hydro | 19% | 19% | 18% | 18% |
| | Grid | 18% | 23% | 26% | 29% |




**Figure 7.** Portugal Districts

## CONCLUSIONS

The work presented focuses on designing a green hydrogen supply chain in Portugal, considering the trade-offs between economic efficiency and water sustainability. The study uses a multi-objective simulated annealing algorithm to minimize both the total supply chain cost and the environmental impact on water resources, mainly in the water-scarce southern regions of Portugal. Lower water stress is generally achieved at the expense of increased costs. The quasi pareto fronts provide to the decision-makers with a framework to select solutions based on local priorities under different scenarios. The research highlights the significant impact of water availability on the hydrogen supply chain. Drought conditions (scenario C) lead to significantly higher costs and water stress. The model adapts by shifting production to regions with more stable water supplies, though this increases costs. Restriction to renewable energy sources (scenario B), lead to generally lower costs, but water stress is higher due to increased reliance on hydropower. This highlights the need for careful water management even when prioritizing green hydrogen production. The model demonstrates its ability to reallocate production and adjust the consumption of primary energy sources in response to varying conditions, such as drought, increased demand or both, which puts significant pressure on the hydrogen supply chain, leading to higher costs and water stress. This emphasizes the need for adaptable infrastructure capable of handling both environmental challenges and demand fluctuations.

## ACKNOWLEDGEMENTS

This work is financed by Portuguese funds through the Foundation for Science and Technology (FCT) I.P., under project: UIDB/00097/2020, UIDP/00097/2020 (CEGIST).

This work is funded by national funds through the FCT - Fundação para a Ciência e a Tecnologia, I.P., under the scope of the projects UIDB/00297/2020 and UIDP/00297/2020 (Center for Mathematics and Applications).

## REFERENCES

1. Almaraz,S, Azzaro-Pantel, C, Montastruc, L, Pibouleau, L, Senties, O, Assessment of mono and multi-objective optimization to design a hydrogen supply chain. *International Journal of Hydrogen Energy*, 38: 14121–14145, 11 (2013). https://doi.org/10.1016/j.ijhydene.2013.07.059
2. Câmera D.,Pinto-varela T., Barbosa-Povoa A.; Multi-objective optimization approach to design and planning hydrogen supply chain under uncertainty: A Portugal study case, *Computer Aided Chemical Engineering*, 46, Pages 1309-1314 (2019), https://doi.org/10.1016/B978-0-12-818634-3.50219-8
3. Pfister, S, Koehler, A, Hellweg, S, Assessing the environmental impacts of freshwater consumption in LCA, *Environmental Science and Technology*, 43:4098–4104, 6 (2009). https://doi.org/10.1021/es802423e

© 2025 by the authors. Licensed to PSEcommunity.org and PSE Press. This is an open access article under the creative commons CC-BY-SA licensing terms. Credit must be given to creator and adaptations must be shared under the same terms. See https://creativecommons.org/licenses/by-sa/4.0/

Systems & Control Transactions

**Research Article - Peer Reviewed Conference Proceeding**
ESCAPE 35 - European Symposium on Computer Aided Process Engineering
Ghent, Belgium. 6-9 July 2025
Jan F.M. Van Impe, Grégoire Léonard, Satyajeet S. Bhonsale,
Monika E. Polańska, Filip Logist (Eds.)

PSE PRESS

# Life Cycle Assessment of Synthetic Methanol Production: Integrating Alkaline Electrolysis and Direct Air Capture Across Regional Grid Scenarios

**Ankur Singhal[a] and Pratham Arora[a]***

[a] Indian Institute of Technology Roorkee, Department of Hydro and Renewable Energy, Roorkee, Uttarakhand, India
* Corresponding Author: pratham.arora@hre.iitr.ac.in.

## ABSTRACT

A transition to low-carbon fuels is integral in addressing the challenge of climate change. An essential transformation is underway in the transportation sector, one of the primary sources of global greenhouse gas emissions. The electrofuels that represent methanol synthesis via power-to-fuel technology have the potential to decarbonize the sector. This paper outlines a critical comprehensive life cycle assessment for electrofuels, with this study focusing on the production of synthetic methanol from renewable hydrogen from water electrolysis coupled with carbon from the direct air capture (DAC) process. This study has provided a comparison of the environmental impacts of synthetic methanol produced from grids of five regions (India, the US, China, Switzerland, and the EU) with conventional methanol from coal gasification and natural gas reforming. The results from this impact assessment show a high dependency of environmental scores on the footprint of the grid. Switzerland, with its limited usage of fossil fuels in grid electricity, has shown the least environmental damage in most of the impact categories in comparison to more non-renewable grids like India and China. Interestingly, conventional methanol has proved to be more environmentally friendly when compared with non-renewable grids like India and China in most of the impact categories.

**Keywords**: Alternative Fuels, Aspen Plus, Carbon Dioxide Capture, Energy, Environment, Hydrogen

## INTRODUCTION

The drive for reducing greenhouse gas (GHG) emissions has resulted in a global focus on sustainable fuels, with synthetic methanol among other potential alternatives to fossil fuels. Synthetic methanol combined with hydrogen ($H_2$) and carbon dioxide ($CO_2$) can be a pathway for decarbonizing the transportation and chemical feedstock production sector. Sustainable methanol paths rely on hydrogen generation by alkaline electrolysis and $CO_2$ capture through direct air capture (DAC) technologies. At the same time, fossil fuels demonstrate their continued relevance to world economies, and despite global endeavors to slash emissions, those typical mitigation methods are falling short of the ambitious targets set by the Paris Agreement. Synthetic fuel production is a promising avenue of study to fill this gap when paired with net carbon-negative technologies like DAC [1]. With ubiquitous $CO_2$-scrubbing technology, concentrated $CO_2$ streams are achievable for fuel production. Carbon dioxide is hence considered a renewable feedstock since it is non-depleting [2], [3], [4]. However, extraction and refining of the isolated carbon dioxide stream requires a significant amount of energy, which can further contribute to environmental damage scores. Hence, it can be stated that carbon capture and utilization (CCU) methods do not explicitly yield the environmental benefits one might assume, necessitating careful assessment. This often stems from the fact that these processes generally require substantial input energy. A detailed life cycle assessment (LCA) will be essential for elucidating the environmental footprints of synthetic methanol and discovering sustainable production pathways.

The studies at carbon capture plants combined with renewables for methanol manufacture present an intentional approach to reduce GHG emissions and

transition to sustainable production of chemicals. The studies [5], [6] analyze the economic and environmental performance of DAC and its environmental guide in the field of methanol production. In the work by [7] more of these arguments are fleshed out by comparing power-to-fuel and power-to-DAC approaches and providing evidence for the efficiency of DAC to facilitate climate change mitigation in Ireland. Biernacki et al. [8], who also consider the environmental impacts of using renewable electricity to produce methanol, further demonstrate the integration of renewable energy into the chemistry industry. Through a detailed assessment of CCU technology development, the research by [9] emphasizes that life cycle assessment (LCA) is fundamental to maximizing these technologies for environmental and economic sustainability. The research publications [10], [11], [12], [13] have examined green methanol production from $CO_2$ and renewable hydrogen, highlighting the significance of process design and the use of renewable energy sources in fuel production.

The literature thus far has much interest in the LCA of synthetic methanol and its precursors. However, most of these studies are too geographically limited, neglecting to model changes in grid mixes and lacking sufficient attention to the co-optimization of end-use electricity use. Most importantly, the differences in the carbon intensity of the electricity grid between countries and the resulting variability in environmental impacts remain largely unaddressed.

The present work can contribute to overcoming the existing research gaps by providing a detailed cradle-to-grave LCA of synthetic methanol and emphasizing the evaluation of electricity sources used for hydrogen production from alkaline electrolysis. This research analysis focuses on the impacts of electricity grids of five large-scale regions, namely India, China, Switzerland, Europe, and the USA, representing a wider range of electricity grid carbon intensities. Combining Aspen Plus modeling for process-level simulations with region-specific LCA data, this research depicts the regional environmental trade-offs related to electricity utilization depending on the grid. Moreover, this study seeks other routes for reducing ecological footprints, such as renewable energy incorporation and optimized electrolysis performance.

This work is significant because it features both the methodological rigor of high-resolution integration of Aspen Plus process simulations with geographically explicit LCA and the scenario-based assessment of regional electricity grids, yielding actionable insights for policymakers and industrial stakeholders. Instead of generalizing a single electricity input or assumed constant, this research serves as a dynamic model of grid mixes to enable a more realistic evaluation of the environmental viability of synthetic methanol.

This study is critical in closing urgent knowledge gaps in the literature. This work leverages advanced modeling and assessment tools to help inform sustainable energy pathways and aid in the decision-making for the low-carbon transition.

## METHODOLOGY

The methodology for assessing the environmental sustainability of synthetic methanol production combines process simulation, life cycle assessment (LCA), and comparative analysis. Hydrogen from alkaline electrolysis and subsequent conversion to methanol through hydrogen and $CO_2$ was modeled in Aspen Plus for process simulation and energy balance calculations. Parameters like electrolyzer operations, energy requirements, and process operations efficiency were specifically modeled to simulate hydrogen production in Aspen Plus.

The carbon dioxide used for methanol manufacturing was obtained from direct air capture (DAC) technologies. Plant data for DAC was imported from several literature sources ([14], [15], [16]), which allowed us to quickly disaggregate energy usage, material requirements, and $CO_2$ capture efficiencies. Using the LCA methodology, the above inputs were parametrically modeled to account for realistic operating situations, allowing for a comprehensive analysis of DACs' contribution to the overall environmental footprint.

Life cycle assessmentAn LCA was conducted following the ISO 14040 and 14044 frameworks using the SimaPro 9.6.0.1 software and various Ecoinvent databases. A cradle-to-grave system boundary was defined, including all stages from raw material extraction and energy inputs through methanol production and final use. Environmental impacts were evaluated using the ReCiPe 2016 impact assessment method with GWP, fossil resource depletion, and other impact categories of interest. The electricity consumption for hydrogen production has been modeled under five regional grid scenarios, i.e., India, China, Switzerland, Europe without Switzerland (EU), and the United States of America (USA) using the Ecoinvent database for country energy mix. The above geographical areas were chosen to capture a wide range of carbon intensity of the electricity grid, from coal-heavy grids to high-renewable generation grids across the globe.

The results from the LCA were contextualized by evaluating the LCA outcomes for synthetic methanol against conventional methanol production pathways, namely coal gasification and natural gas reforming. All these conventional pathways data were obtained from the Ecoinvent database in SimaPro to ensure consistency and comparability. Combining Aspen Plus simulations with region-specific life cycle assessment (LCA) enabled a high-fidelity examination of the environmental trade-offs of synthetic methanol production. This study draws

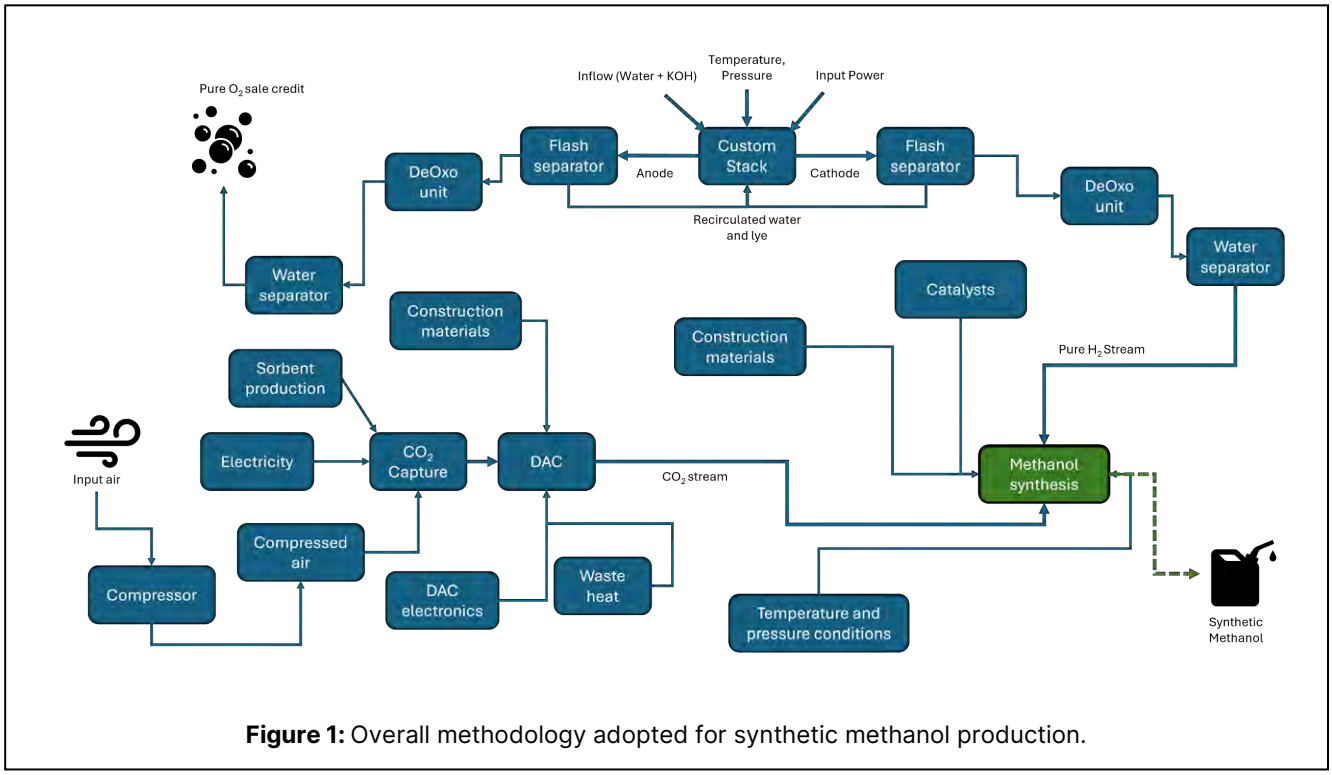



**Figure 1:** Overall methodology adopted for synthetic methanol production.

on available DAC data from credible literature sources and compares the results across regional grid scenarios and conventional production pathways to inform comprehensive insights into the potential for decarbonization and the hazards associated with transitioning to sustainable methanol production. The overall production methodology is depicted in Figure 1.

## Hydrogen production

The hydrogen production for this study has been modeled as a 500 kW electrolyzer in Aspen Plus, along with various balance of plant components. The hydrogen production modeling aims to obtain a purity greater than 99.99% to make industrially suitable hydrogen. As shown in Figure 1, the stack has been custom-modeled using the Aspen Custom Modeler at 25 bars of pressure and at a temperature of 75°C. This work has significantly used the semi-empirical polarization curve model developed by Sánchez et al. [17], [18] to generate a customized model for an alkaline electrolyzer stack in the Aspen Custom Modeler. This model has robustly described the electrochemical behavior of the alkaline water electrolyzers, incorporating critical resistive, kinetic, and thermodynamic phenomena for hydrogen production.

The Aspen Plus model is focused on efficiency and environmental effects, simulating the combined alkaline electrolysis for hydrogen production. Water and a lye solution are electrolyzed at the system's cathode and anode, producing hydrogen and oxygen molecules. This approach recycles the leftover water and lye produced at the two electrodes back to the stack (B1) to minimize the waste of resources and to maintain permanent operation. During recirculation, the recirculating streams are cooled using two shell-and-tube heat exchangers (IC-R1 and IC-R2) to maintain ideal operating temperatures for the stack to enhance system performance.

A de-oxygenation kinetic reactor unit operates on the cathode side to remove any oxygen impurities from the hydrogen product stream. This reactor facilitates the controlled reaction of surplus hydrogen and oxygen impurities to create water. This process creates high-purity hydrogen at 99.9958% purity that has high industrial utilization after extraction from the water stream. For oxygen purification at the anode side, a similar purification process is implemented via oxygen extraction as a product for real-world use. This recovery not only provides a potential financial benefit by valuing the by-product oxygen, but it also reduces the environmental impacts associated with the oxygen production processes, aligning with sustainable and resource-efficient concepts.

The model results show that approximately 59 units (kWh) of electricity are required to produce 1 kg of pure hydrogen. Similarly, 9.3 kilograms of makeup water is required to produce one kilogram of pure hydrogen.

## Carbon capture

This analysis's DAC plant construction and operating data are based on Climeworks' work [14]. The carbon capture is based on the temperature-vacuum swing adsorption method. The plant's capacity is four kilotons (kt) $CO_2$ per year with an operational life of 20 years. The plant's construction is divided into collector, processing,

land requirement, and hall and tank units. The land requirement for this 4-kt/year plant is taken as 1045 $m^2$. The LCI also considers the materials required to manufacture, operate, and maintain DAC systems. The existing plant comprises eight collection containers, each containing six $CO_2$ collectors and a processing unit. The materials are procured and processed according to industry requirements, including steel, stainless steel, aluminum, copper, concrete, insulation, and polymers. Considering global recycling rates (e.g., 70% for copper and 85% for steel), the LCI includes recycling rates for key metals, such as copper, steel, and aluminum. Plastics and insulation hand disposed of in landfilling or waste incinerator techniques are examples of non-metallic materials. For conventional production, end-of-life scenarios are considered to avoid burdens, accounting for the environmental credit through co-generated heat and energy in the waste treatment. The energy requirements for this plant have been fulfilled by waste heat from chemical industries and electricity. The waste heat requirement has been taken as 1.55 MJ and 0.55 kWh of electricity for extracting 1 kilogram of $CO_2$ [15], [16], [19]. The sorbent type for carbon capture was taken as zeolite powder. The solid low-temperature sorbent consumption requirement was 0.788 g/kg of $CO_2$ captured [19].

### Methanol production

Several interconnected procedures are used in the $CO_2$ hydrogenation process to produce methanol, increase productivity, and reduce environmental effects. A low-temperature powder sorbent DAC system is used to capture $CO_2$ at the start of the process. The methanol production for this study is based on research done by [20]. For every kilogram of methanol produced, the process consumes 1.446 kg of $CO_2$, 0.208 kg of $H_2$, and 2.173 kWh of electricity. The product is 1 kg of 95.3% pure methanol [20]. In the synthesis of methanol, the streams of $CO_2$ and $H_2$ are compressed and heated to 6.5 MPa and 210°C, respectively, before being fed into an adiabatic fixed-bed catalytic reactor with a Cu/Zn/Al catalyst installed based on the Aspen model by [20]. The reaction produces water and methanol; unreacted gases are recycled to increase conversion efficiency. However, during the separation process, there are minor losses of $CO_2$ (36.32 kg/h) and $H_2$ (9.64 kg/h). The purification process involves treating about 281 kg of water every hour, and a distillation column refines the resulting methanol stream.

## RESULTS, DISCUSSION, AND CONCLUSIONS

The underlying energy mix in each location drives notable trends in the Life Cycle Impact Assessment (LCIA) results for methanol production across different energy grids. In addition to traditional production techniques like coal gasification and natural gas reforming, the comparison covers the United States, Switzerland, India, the European Union, and China grids. Particulate matter generation, ionizing radiation, ozone depletion, global warming potential, and other essential impact categories were assessed. The observed differences in environmental impacts can be explained by the energy grid performance of each region, which reflects the proportion of nuclear, renewable, and fossil fuels in its electricity generation portfolio.

Compared to the grids in the United States, Switzerland, and the European Union, the global warming potential (GWP) of the Chinese and Indian grids is significantly more enormous. For instance, the Chinese grid records 11.51 kilograms $CO_2$ eq per kilogram of methanol, whereas the Indian grid displays 15.93 kg $CO_2$ eq. On the other hand, the Swiss grid exhibits a net carbon sequestration effect, with a negative GWP of -0.97 kg $CO_2$ eq. The negative values indicate the avoided emissions due to the sale of purified oxygen. This discrepancy can be linked to China's and India's heavy reliance on coal and other fossil fuels, which raise $CO_2$ emissions significantly when energy is generated. Coal makes up more than half of the electrical mix in China, and in India, it makes up around 70%. Conversely, Switzerland's energy mix is primarily composed of nuclear and hydroelectric power, which are nearly carbon-neutral and account for its negative GWP numbers.

Across all grids, stratospheric ozone depletion is typically minimal, but it is marginally higher in areas where a significant portion of fossil fuels are used. The Swiss grid reports 0.000002 kg CFC11 eq, while the Indian grid displays the highest amount at 0.000005 kg CFC11 eq. Though in small proportions compared to past emissions from refrigerants and aerosols, burning fossil fuels emits chlorinated chemicals that can damage the ozone layer. Switzerland contributes very little to ozone depletion because of its emphasis on clean energy sources, primarily hydropower and nuclear energy [21].

Impacts of ionizing radiation differ significantly; the EU grid has the second-highest figure at 2.84 kBq Co-60 eq, while the Swiss grid has the highest at 3.57 kBq Co-60 eq. Since ionizing radiation is released during the extraction, processing, and disposal of nuclear fuel, this pattern is consistent with the high percentage of nuclear power in Switzerland and the EU. On the other hand, because of its restricted use of nuclear energy, the Indian grid exhibits far lower ionizing radiation at 0.23 kBq Co-60 eq. There are noticeable differences in the creation of particulate matter and ozone, two processes that affect air quality and human health. The highest ozone generation values are seen in the Chinese and Indian grids, with the Chinese grid recording 0.03754 kg NOx eq and the Indian grid recording 0.04195 kg NOx eq. Similarly, the Indian grid has the largest particle matter generation

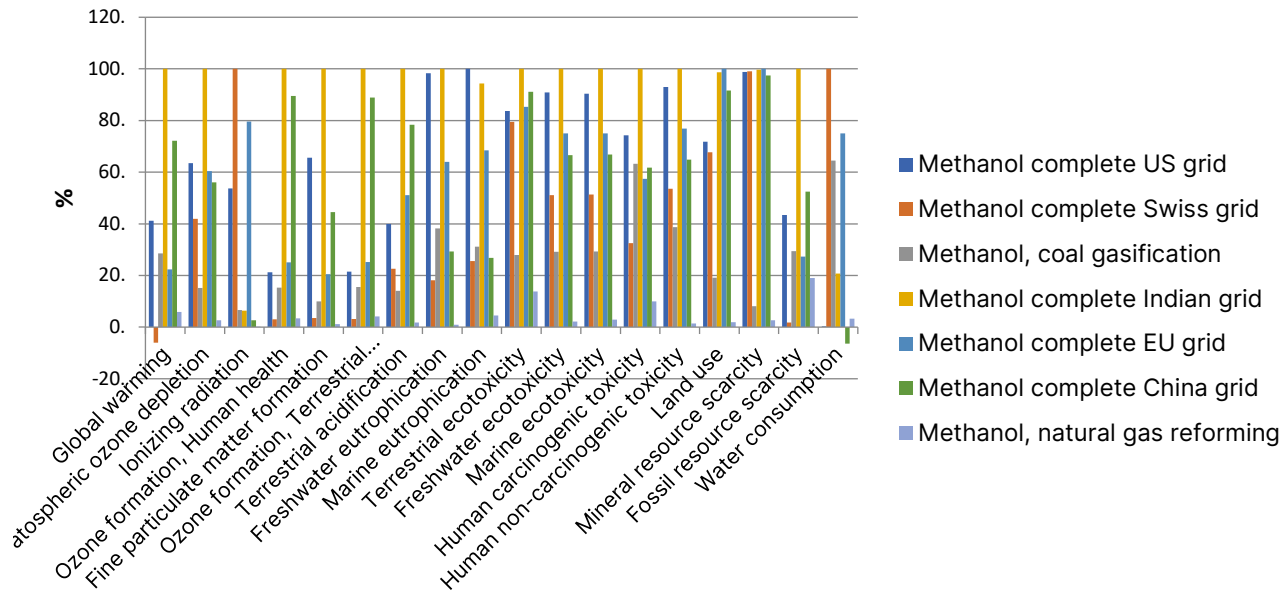



**Figure 2:** Life cycle impact results for synthetic and conventional methanol compared across various grids.

(0.04575 kg PM2.5 eq). These outcomes are caused by nitrogen oxides (NOx) and fine particles released while burning coal and other fossil fuels. With 0.00126 kg NOx eq for ozone formation and 0.00159 kg PM2.5 eq for particulate matter formation, the Swiss grid, on the other hand, has the lowest values in these categories because of its clean energy mix. An overall comparison of all the impact categories for various region-based grids for synthetic methanol and conventional methanol (natural gas reforming and coal gasification) is depicted in Figure 2. The significant impact that energy mixes have on environmental effects is highlighted by the comparative Life Cycle Impact Assessment (LCIA) for methanol production across several energy grids. Due to their carbon-intensive energy generation, grids that rely heavily on coal and other fossil fuels, like those in China and India, have far higher global warming potential (GWP), ozone formation, and particulate matter formation. On the other hand, networks that use cleaner energy sources—such as Switzerland's combination of nuclear and hydroelectric power—achieve low or even negative GWP values, which indicates net carbon sequestration. Furthermore, the effects of ionizing radiation and stratospheric ozone depletion correspond with the frequency of nuclear power and fossil fuel burning, respectively, in local grids. These results highlight how important it is to switch to low-carbon and renewable energy sources to lessen the adverse environmental effects of methanol production, especially in areas that rely significantly on coal and other fossil fuels.

## ACKNOWLEDGEMENTS

We thank the Ministry of Education, Govt. of India, for awarding the Prime Minister's Research Fellowship.

## REFERENCES

1. N. von der Assen, J. Jung, and A. Bardow, “Life-cycle assessment of carbon dioxide capture and utilization: avoiding the pitfalls,” Energy Environ Sci, vol. 6, no. 9, p. 2721, 2013, doi: 10.1039/c3ee41151f.
2. T. Sakakura, J.-C. Choi, and H. Yasuda, “Transformation of Carbon Dioxide,” Chem Rev, vol. 107, no. 6, pp. 2365–2387, Jun. 2007, doi: 10.1021/cr068357u.
3. M. Aresta, Ed., Carbon Dioxide as Chemical Feedstock. Wiley, 2010. doi: 10.1002/9783527629916.
4. F. T. Zangeneh, S. Sahebdelfar, and M. T. Ravanchi, “Conversion of carbon dioxide to valuable petrochemicals: An approach to clean development mechanism,” Journal of Natural Gas Chemistry, vol. 20, no. 3, pp. 219–231, May 2011, doi: 10.1016/S1003-9953(10)60191-0.
5. M. Fasihi, O. Efimova, and C. Breyer, “Techno-economic assessment of CO2 direct air capture plants,” J Clean Prod, vol. 224, pp. 957–980, Jul. 2019, doi: 10.1016/j.jclepro.2019.03.086.
6. D. Huisingh, Z. Zhang, J. C. Moore, Q. Qiao, and Q. Li, “Recent advances in carbon emissions reduction: policies, technologies, monitoring, assessment and modeling,” J Clean Prod, vol. 103, pp. 1–12, Sep. 2015, doi:

10.1016/j.jclepro.2015.04.098.
7. D. Casaban and E. Tsalaporta, “Life Cycle Assessment of a Direct Air Capture and Storage plant in Ireland,” Jul. 14, 2023. doi: 10.21203/rs.3.rs-3145370/v1.
8. P. Biernacki, T. Röther, W. Paul, P. Werner, and S. Steinigeweg, “Environmental impact of the excess electricity conversion into methanol,” J Clean Prod, vol. 191, pp. 87–98, Aug. 2018, doi: 10.1016/j.jclepro.2018.04.232.
9. J. Artz et al., “Sustainable Conversion of Carbon Dioxide: An Integrated Review of Catalysis and Life Cycle Assessment,” Chem Rev, vol. 118, no. 2, pp. 434–504, Jan. 2018, doi: 10.1021/acs.chemrev.7b00435.
10. T. Cordero-Lanzac et al., “A techno-economic and life cycle assessment for the production of green methanol from CO2: catalyst and process bottlenecks,” Journal of Energy Chemistry, vol. 68, pp. 255–266, May 2022, doi: 10.1016/j.jechem.2021.09.045.
11. T. Cordero-Lanzac et al., “A CO2 valorization plant to produce light hydrocarbons: Kinetic model, process design and life cycle assessment,” Journal of CO2 Utilization, vol. 67, p. 102337, Jan. 2023, doi: 10.1016/j.jcou.2022.102337.
12. S. C. Galusnyak, L. Petrescu, D. A. Chisalita, and C.-C. Cormos, “Life cycle assessment of methanol production and conversion into various chemical intermediates and products,” Energy, vol. 259, p. 124784, Nov. 2022, doi: 10.1016/j.energy.2022.124784.
13. A. Sternberg, C. M. Jens, and A. Bardow, “Life cycle assessment of CO 2 -based C1-chemicals,” Green Chemistry, vol. 19, no. 9, pp. 2244–2259, 2017, doi: 10.1039/C6GC02852G.
14. S. Deutz and A. Bardow, “Life-cycle assessment of an industrial direct air capture process based on temperature–vacuum swing adsorption,” Nat Energy, vol. 6, no. 2, pp. 203–213, Feb. 2021, doi: 10.1038/s41560-020-00771-9.
15. T. Terlouw, K. Treyer, C. Bauer, and M. Mazzotti, “Life Cycle Assessment of Direct Air Carbon Capture and Storage with Low-Carbon Energy Sources,” Environ Sci Technol, vol. 55, no. 16, pp. 11397–11411, Aug. 2021, doi: 10.1021/acs.est.1c03263.
16. D. Casaban and E. Tsalaporta, “Life cycle assessment of a direct air capture and storage plant in Ireland,” Sci Rep, vol. 13, no. 1, Dec. 2023, doi: 10.1038/s41598-023-44709-z.
17. M. Sánchez, E. Amores, L. Rodríguez, and C. Clemente-Jul, “Semi-empirical model and experimental validation for the performance evaluation of a 15 kW alkaline water electrolyzer,” Int J Hydrogen Energy, vol. 43, no. 45, pp. 20332–20345, Nov. 2018, doi: 10.1016/j.ijhydene.2018.09.029.
18. M. Sánchez, E. Amores, D. Abad, L. Rodríguez, and C. Clemente-Jul, “Aspen Plus model of an alkaline electrolysis system for hydrogen production,” Int J Hydrogen Energy, vol. 45, no. 7, pp. 3916–3929, Feb. 2020, doi: 10.1016/j.ijhydene.2019.12.027.
19. R. Gonzalez-Olmos, A. Gutierrez-Ortega, J. Sempere, and R. Nomen, “Zeolite versus carbon adsorbents in carbon capture: A comparison from an operational and life cycle perspective,” Journal of CO2 Utilization, vol. 55, p. 101791, Jan. 2022, doi: 10.1016/j.jcou.2021.101791.
20. N. Badger, R. Boylu, V. Ilojianya, M. Erguvan, and S. Amini, “A cradle-to-gate life cycle assessment of green methanol production using direct air capture,” Energy Advances, vol. 3, no. 9, pp. 2311–2327, Aug. 2024, doi: 10.1039/d4ya00316k.
21. IEA, “World Energy Statistics and Balances, https://www.iea.org/data-and-statistics/data-product/world-energy-statistics-and-balances,” IEA, Paris, 2024.

© 2025 by the authors. Licensed to PSEcommunity.org and PSE Press. This is an open access article under the creative commons CC-BY-SA licensing terms. Credit must be given to creator and adaptations must be shared under the same terms. See https://creativecommons.org/licenses/by-sa/4.0/



Systems & Control Transactions

**Research Article - Peer Reviewed Conference Proceeding**
ESCAPE 35 - European Symposium on Computer Aided Process Engineering
Ghent, Belgium. 6-9 July 2025
Jan F.M. Van Impe, Grégoire Léonard, Satyajeet S. Bhonsale,
Monika E. Polańska, Filip Logist (Eds.)

PSE PRESS

# Waste-heat upgrading from alkaline and PEM electrolyzers using heat pumps

**Aldwin-Lois Galvan-Cara[a,b] and Dominik Bongartz[a,b]***

[a] KU Leuven, Department of Chemical Engineering, Leuven 3001, Belgium
[b] EnergyVille, Genk 3600, Belgium
* Corresponding Author: dominikbongartz@alum.mit.edu.

## ABSTRACT

The use of waste heat from electrolysis can significantly increase process efficiency. Alkaline and PEM electrolyzers, the most mature technologies, produce low-temperature waste heat. Most studies focus on using this waste heat for low-temperature applications like district heating. Alternatively, this waste heat can be upgraded to a temperature that can be usable in the chemical industry, e.g., for steam generation. The combination of an alkaline electrolyzer with a heat pump has been recently investigated to supply both hydrogen and medium-temperature heat. Optimizing electrolyzers for both hydrogen and heat production (combined design) has been shown to have advantages over optimizing for hydrogen only and upgrading the waste heat a posteriori (separate design). However, the effects of electrolyzer pressure and hydrogen compression were not considered, and it remains unclear if similar benefits apply to PEM electrolyzers. This work further analyzes the combined system (i.e., electrolyzer with a heat pump) by including hydrogen compression and comparing alkaline and PEM electrolyzers. The results show that designing with waste-heat utilization in mind benefits both alkaline and PEM at low and high pressures. The combined design allows up to 10% cost reduction and up to fourfold reduction in $CO_2$ emissions compared to the separate design. However, this benefit is constrained by the maximum achievable current density, particularly for PEM. Despite this limitation, the combined system can effectively supply hydrogen and heat across various energy price scenarios, making it a promising solution for hydrogen supply and industrial electric heating.

**Keywords**: Hydrogen, Electric heating, Energy, Modelling, Optimization

## INTRODUCTION

Waste-heat recovery from alkaline and PEM electrolyzers has been widely studied for low-temperature heat applications (below 100°C), like district heating [1]. However, upgrading electrolyzer waste heat to meet medium-temperature heat demand (e.g., up to 200°C) is less explored, despite recent advancements in heat pump technologies that enable reaching these temperature levels [2]. Moreover, waste-heat utilization is usually added a posteriori after optimizing the electrolyzer for hydrogen production only, which may limit its benefits.

In our previous work [3], we recently explored the advantages of designing an atmospheric alkaline electrolyzer for waste-heat utilization, optimizing for both hydrogen and heat production. This new design approach provided further benefits over using the waste heat a posteriori. Additionally, upgrading waste heat to higher temperatures via heat pumps was found to be preferable over direct use at lower temperatures (e.g., district heating) when heat at both temperatures is required.

However, this previous study did not consider the effects of electrolyzer pressure or the integration with downstream processes: In most industrial applications, hydrogen is required at high pressures (e.g., up to 250 bar for chemical synthesis [4]), requiring a compression step and thus increasing cost and energy demand. Moreover, the same analysis should be extended to PEM electrolyzers, another well-established technology that is drawing increasing interest thanks to its potential for flexible operation.

In this work, we thus further investigate the potential

of combined systems to supply both hydrogen and medium-temperature heat. To address the aforementioned shortcomings, we analyze the impact of electrolyzer operating pressure, incorporate hydrogen compression, and compare alkaline and PEM electrolyzers.

## SYSTEM DESCRIPTION

The combined system consists of three main units, i.e., a water electrolyzer, a multi-stage compressor with intercooling and a heat pump. The electrolyzer is composed of 26 modules, each one capable of producing 72 kg/h of hydrogen [3]. The hydrogen is subsequently compressed to the required pressure in the multi-stage compressor. Finally, a closed-loop compression heat pump is used to upgrade the electrolyzer waste heat to a higher temperature level. Potential working fluids for achieving the target temperature lift include $CO_2$, argon, and air.

Such a combined system is able to supply around 1.9 t/h of hydrogen at 75 bar (suitable for methanol production [4]) and heat at 120°C (capable of producing low-pressure steam [2]), thus being an alternative to other electric heating technologies, such as direct electric boilers or air-source heat pumps.

For low-pressure (LP) electrolysis (alkaline and PEM at 1 bar), a multistage compressor with 5 stages is used, whereas for high-pressure (HP) electrolysis (PEM at 30 bar), a single-stage compressor is used. Intercooling to 35°C is considered between stages and before and after the compression step.

## METHODOLOGY

### Model

The backbone of the mathematical model is based on our previous work [3], which includes the polarization curve of an alkaline electrolyzer, the thermal model of the electrolyzer stack, and the efficiency-based model of different electric heating technologies (heat pump and direct electric boiler). The heat pump, operating at 40% of the maximum COP (i.e., Carnot cycle), achieves COP values ranging from 2.2 to 5.2.

For this work, the polarization curve [5] and Faraday efficiency [6] of a PEM electrolyzer and a multi-stage compressor model based on a fixed isentropic efficiency per stage are added. The molar enthalpies and entropies are computed using data from the CoolProp library [7]. Therefore, the effect of the pressure is captured in the electrolyzer and the compression stage.

### Performance evaluation

The performance is evaluated according to two indicators: the levelized cost of hydrogen (LCOH) and the net $CO_2$ emissions ($NetCO_2$).

The LCOH (Equation (1)) evaluates the total hydrogen production expenses over the system's lifetime (20 years) considering revenue from heat sales. Electrolyzer investment costs are taken from Cooper et al. [8], and replacement costs at the end of the tenth year are considered. Electricity and heat prices are based on the average EU-27 prices (2016-2020) [9]. The rest of model parameters are taken from our previous work [3].

$$\mathrm{LCOH} = \frac{\mathrm{CAPEX} + \sum_{j=1}^{N} (\mathrm{OM} + \mathrm{OPEX} - \mathrm{SALES}) \cdot (1+i)^{-j}}{\sum_{j=1}^{N} (m_{\mathrm{H_2}}) \cdot (1+i)^{-j}} \quad (1)$$

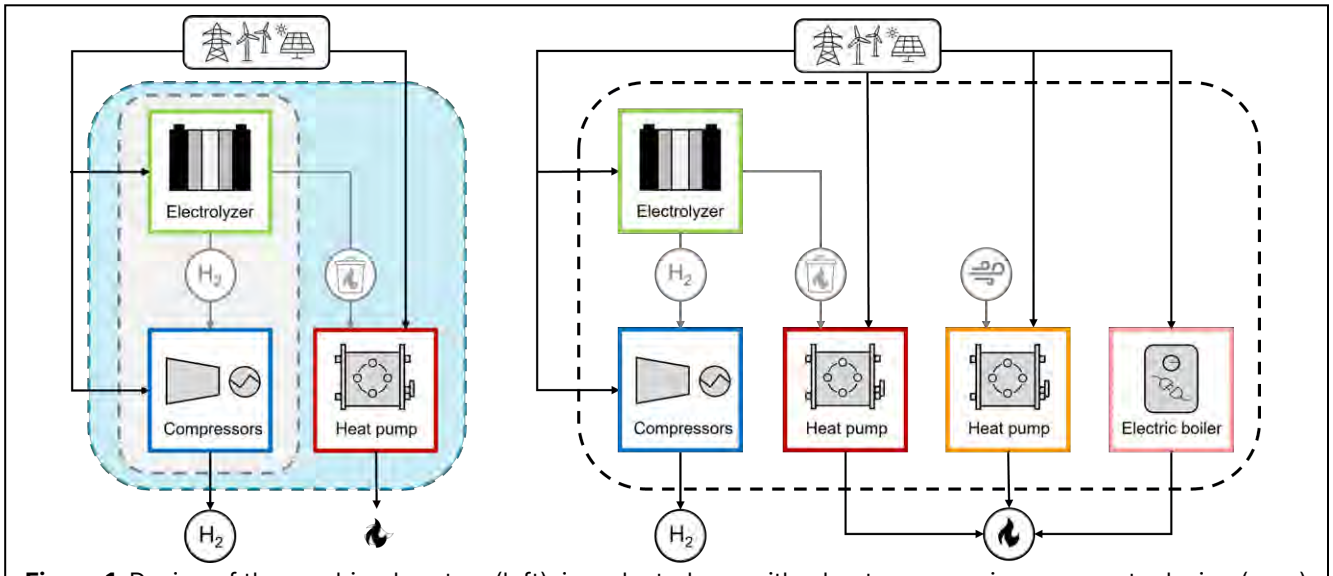



**Figure 1.** Design of the combined system (left), i.e., electrolyzer with a heat pump, using a separate design (gray) and a combined design (blue), and superstructure diagram of the hydrogen and heat supply network (right). The indicated areas refer to the system boundary considered in the optimization. The circled outputs are fixed.

The $NetCO_2$ (Equation (2)) accounts for the emissions due to electricity consumption of the different units *u* (i.e., electrolyzer, compressors, etc.) and the emissions avoided due to the heat output from electric heating technologies (i.e., heat pump and direct electric boiler), which is assumed to replace heating via natural gas.

$$\mathrm{NetCO_2} = \frac{\mathrm{Em_{ele}}(\sum_u P_u) - \mathrm{Em_{gas}}(\sum_u Q_u)}{m_{H2}} \quad (2)$$

For simplicity, the cooling requirements in the compression unit are excluded from the evaluation as they are small compared to those of the electrolyzer (up to 14% of the waste heat). However, the higher temperature level of the heat from compressor intercooling (140-150°C) makes it a potentially valuable additional heat source, which could further enhance system efficiency.

## System design and optimization

We compare the conventional separate design of the combined system, i.e., a posteriori coupling (see Figure 1 left, gray box), with the combined design approach that explicitly incorporates waste-heat utilization (blue box). In both design approaches, we optimize the system for both cost and emissions.

Additionally, we use a superstructure optimization problem to determine the optimal hydrogen and heat supply network, considering various electric heating alternatives, namely air-source heat pumps and direct electric boilers (see Figure 1 right). A hydrogen-to-heat demand ratio of one is considered, where the hydrogen energy content is computed using the higher heating value (HHV).

The electrolyzer optimization variables and the main model parameters are given in Table 1 and Table 2, respectively. Note that the COP of the heat pump is determined by the electrolyzer operating temperature and the sink temperature [3].

**Table 1:** Electrolyzer optimization variables.

| Variables | Alkaline | PEM |
|---|---|---|
| Temperature | 50-90°C | 50-90°C |
| Current density | 0.2-1 A $cm^{-2}$ | 0.5-3 A $cm^{-2}$ |

**Table 2:** Summary of the main model parameters.

| Variable | Value |
|---|---|
| Compressor isentropic efficiency | 0.8 |
| Electric boiler efficiency | 0.98 |
| Discount rate | 5% |
| O&M | 2% of the CAPEX |
| Operating hours | 8000 h/y |
| Electricity price | 79.2 €/MWh |
| Heat price | 30.7 €/MWh |
| Electricity emission factor | 0.164 kg/MWh |
| Heat emission factor | 0.244 kg/MWh |

# RESULTS AND DISCUSSION

## Designing for waste-heat utilization

### Optimal combined system designs

The performance of combined systems optimized using the different design approaches are shown in Figure 2. The results are consistent with our previous work on atmospheric alkaline electrolyzers only [3]: also for LP and HP PEM electrolyzers, the separate design leads to suboptimal solutions, whereas the combined design allows optimal trade-offs between cost and emissions, depending on the heat output of the system.

In terms of the electrolyzer operating conditions, the combined design leads to more compact electrolyzers with higher current densities, because the additional waste heat can be valorized. Moreover, operating at a higher pressure increases the optimal current density.

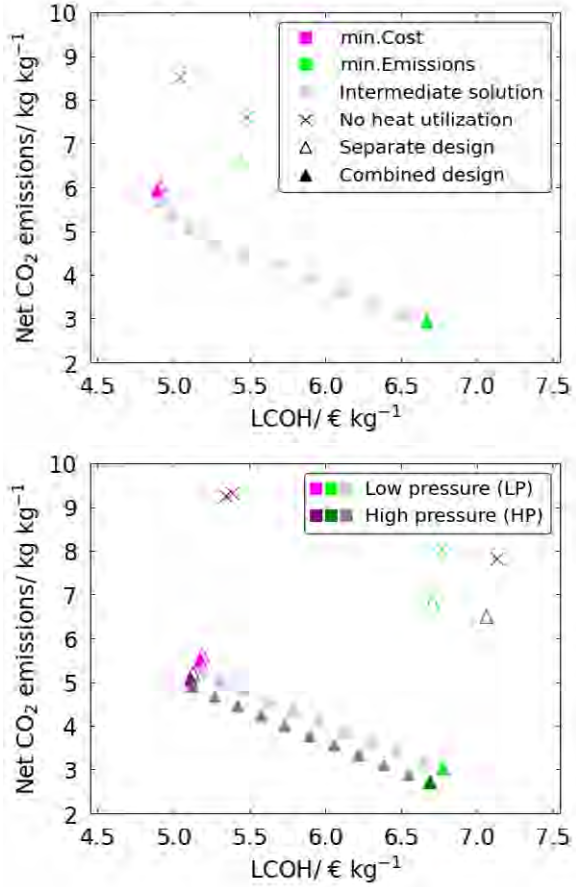



**Figure 2.** Trade-off between levelized cost of hydrogen (LCOH) and net $CO_2$ emissions for the combined system with alkaline (top) and PEM (bottom) electrolyzers. Both cost and emissions are given per kg of hydrogen and consider sales revenues and avoided burden, respectively, for the generated heat.

When minimizing costs, the combined systems

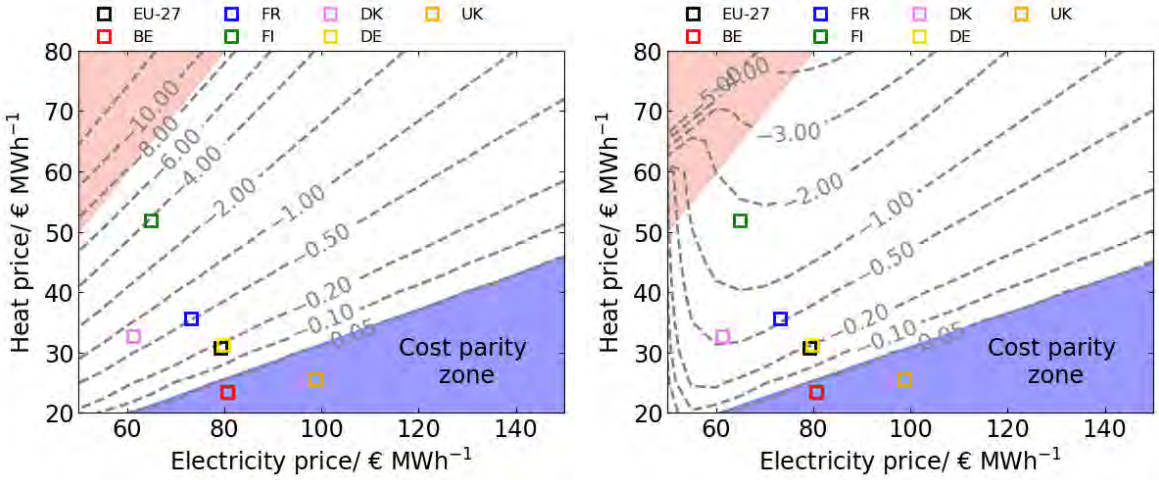



**Figure 3.** Percentage cost reduction of the combined design over the separate design of the combined system based on alkaline (left) and HP PEM (right) at different energy prices. The blue area indicates the area where both designs have the same cost. The red area indicates an area of unlikely price combinations, in which the heat price is higher than the electricity price. The squares indicate average price in different EU countries in 2016-2020 [9].

based on PEM are more expensive than those based on alkaline, mainly due to their higher CAPEX. Remarkably, HP PEM allows lower cost than LP PEM because (i) the increase in CAPEX due to the pressure factor of 1.2 is offset by an 80% reduction in compression costs (saving nearly 40 M€), and (ii) the higher waste heat available resulting from operation at higher current density is valorized via the heat pumps.

When minimizing emissions, the combined designs allow significant emission reductions but are generally more expensive than the separate designs (filled vs. unfilled green triangles). This is because in the separate designs, the optimizer selects an electrolyzer with the highest efficiency in terms of electricity consumption (highest temperature and lowest current density), significantly reducing the electrolyzer OPEX in exchange of a slight increase in CAPEX. However, for HP PEM, the increase in CAPEX is substantially higher due to the pressure factor, making it more expensive than in the combined design.

### Cost benefits over a posteriori coupling

The observed benefit of combined design over separate design holds across various energy price scenarios, especially when electricity prices are low and heat prices are high (see Figure 3). This is evident in the alkaline system, where straight contour lines are observed. However, for PEM systems, curved contour lines appear due to the upper bound on current density.

The higher the current density in the combined design compared to the separate design, the higher the benefit. For alkaline, optimal current densities are typically achieved in the middle of the allowable current density range. In contrast, for PEM, the optimal current densities often reach the upper bound, limiting the system's heat output and, consequently, the heat sales. This limitation is more pronounced in the HP PEM system, where higher current densities are required (Figure 3 right). This suggest that to fully unlock the potential of waste-heat utilization from electrolysis, even higher achievable current densities would be desirable.

### Emission benefits over a posteriori coupling

The analysis across various $CO_2$ emission factors show similar results: The combined design outperforms the separate design, especially at low electricity emission factors and high heat emission factors (up to fourfold reduction). While designing with waste-heat utilization in mind offers limited advantages at low heat emission factors (e.g., heat from biomass), heat is currently still mainly supplied by fossil sources like natural gas. Thus, the combined design remains beneficial in most current scenarios.

## Hydrogen and heat supply networks

### Optimal supply networks

The cost-optimal hydrogen and heat supply networks to supply a methanol production process and generate steam are depicted in Figure 4. The combined system is the main heat supplier in all the optimal networks, which showcases the potential of the system to contribute to industrial electric heating.

There are no significant differences between the different electrolyzer systems. In all optimal combined systems, the electrolyzer operates at the highest temperature and current density allowed. The slight discrepancy in the amount of heat supplied is due to the different polarization curve (alkaline vs. PEM) and the different

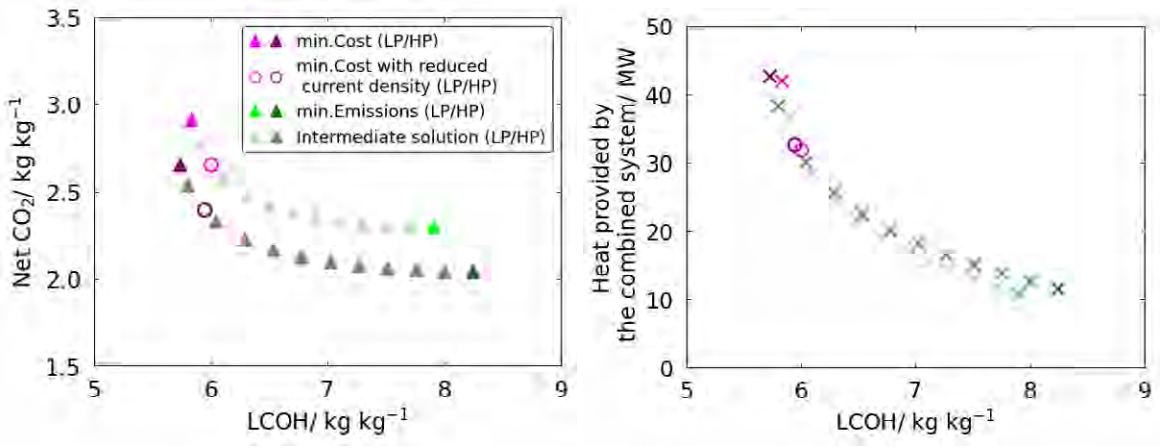



**Figure 5.** Optimal hydrogen and heat supply networks based on PEM: Pareto front (left) and heat contribution of the combined system in the Pareto-optimal solutions (right).

operating pressure (LP vs. HP).

The air-source heat pump supplies the remaining heat. This technology is preferred over the direct electric boiler for better efficiency and cost advantages from economies of scale.

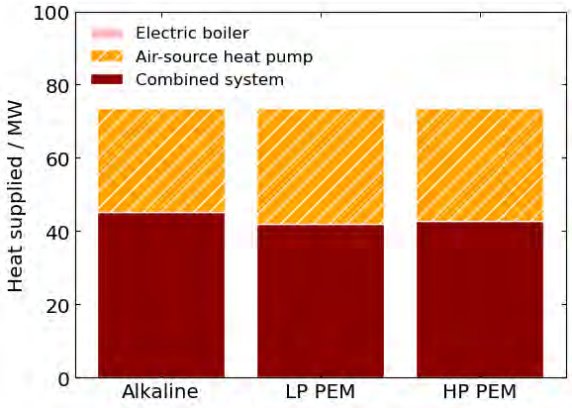



**Figure 4.** Cost-optimal heat supply networks when using different electrolyzers.

In this work, different heat pumps are considered for each heat source. However, utilizing a heat pump with multiple heat sources (e.g., waste heat, compressor intercooling, and ambient air), could further enhance efficiency, reduce reliance on a single heat source, and increase process reliability. Nonetheless, a cost analysis is necessary to ensure an effective heat supply.

## Contribution of the combined system

The cost of the supply network is significantly affected by the amount of heat supplied by the combined system (see Figure 5). While reducing its heat output (i.e., decreasing current density) can lower the net emissions, it also substantially increases costs.

The cost reduction potential compared to the minimum emissions solution depends on the upper bound of the current density. When considering a reduced upper bound of current density (0.7 A/cm2 for alkaline and 2 A/cm2 for PEM), the cost-optimal solutions result in a higher minimum cost (unfilled circles in Figure 5). Therefore, further advances in electrolyzer development to operate at higher current densities are desirable.

## Sensitivity analysis

A sensitivity analysis is conducted to assess the impact of electrolyzer investment costs and energy prices (i.e., electricity and heat) on the optimal supply network design and cost. The combined hydrogen and heat supply network is re-optimized for each parameter value.

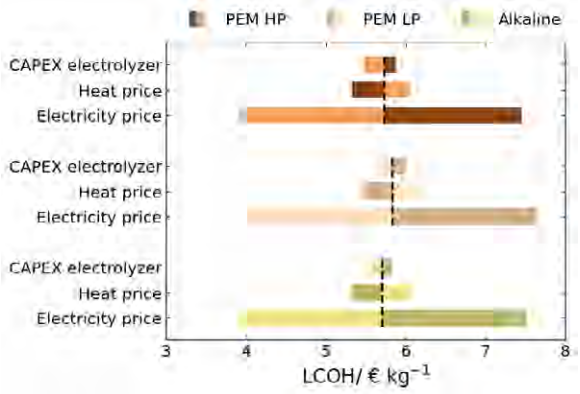



**Figure 6.** Influence of ±30% changes in the electrolyzer CAPEX, heat price and electricity price on the optimal levelized cost of hydrogen.

The optimal combined system design remains unaffected by these parameters, indicating the robustness of the system across a wide range of scenarios. Nonetheless, the resulting cost varies depending on the specific

parameter being considered (see Figure 6).

Electricity price has the biggest impact due to the high contribution of OPEX in the cost breakdown. Conversely, investment cost has the lowest influence because of the lower contribution of CAPEX.

The influence of electricity and heat prices is similar across the three electrolyzer systems. However, the investment cost has a greater influence on PEM compared to alkaline systems, as PEM are more expensive.

## CONCLUSIONS

The combined system, i.e., electrolyzer with a heat pump, was analyzed for supplying hydrogen to a methanol production process while producing heat suitable for steam production. Waste-heat upgrading from alkaline and PEM electrolyzers offer similar benefits, with the choice depending on the hydrogen needs. Alkaline electrolyzers are cost-effective for large-scale production, while PEM electrolyzers, despite higher upfront costs, provide higher hydrogen purity and flexibility.

Optimizing electrolyzers for both hydrogen and heat production is more beneficial than using the waste heat a posteriori from an electrolyzer optimized solely for hydrogen production. This new approach leads to more compact electrolyzers with higher current densities, reducing costs by up to 10% and $CO_2$ emissions by four times. Therefore, increasing the maximum achievable current densities can improve waste-heat utilization. The effect of the electrolyzer operating pressure is not significant, as the increase in CAPEX is offset by the reduced compression requirements (about 80% cost reduction).

The combined system is always selected over alternative electric heating technologies in the optimal hydrogen and heat supply networks. Notably, its optimal design remains consistent despite uncertainty in electrolyzer investment cost and energy prices, with electricity price having the biggest impact. Conversely, electrolyzer investment cost has the lowest impact, being higher for PEM than for alkaline.

Further research can investigate the detailed coupling of electrolyzers and heat pumps using flowsheet models. This analysis will help retrofit existing electrolyzer installations and contribute to the optimal waste-heat utilization of future energy systems.

## ACKNOWLEDGEMENTS

The authors gratefully acknowledge funding through Internal Funds KU Leuven (STG/22/060).

## REFERENCES

1. van der Roest E, Bol R, Fens T, van Wijk A. Utilisation of waste heat from PEM electrolysers – Unlocking local optimisation. *Int J Hydrogen Energy* 48(72):27872-27891 (2023) https://doi.org/10.1016/j.ijhydene.2023.03.374
2. Klute S, Budt M, van Beek M, Doetsch C. Steam generating heat pumps – Overview, classification, economics, and basic modeling principles. *Energy Convers Manag* 299:117882 (2024) https://doi.org/10.1016/j.enconman.2023.117882
3. Galvan-Cara AL, Bongartz D. Rethinking electrolyzer design for optimal waste-heat utilization. Submitted for publication (2024). Preprint: https://doi.org/10.1149/OSF.IO/BCVW4
4. Mucci S, Mitsos A, Bongartz D. Power-to-X processes based on PEM water electrolyzers: A review of process integration and flexible operation. *Comput Chem Eng* 175:108260 (2023) https://doi.org/10.1016/j.compchemeng.2023.108260
5. Chung DH, Graham EJ, Paren BA, Schofield L, Shao-Horn Y, Mallapragada DS. Design space for PEM electrolysis for cost-effective H2 production using grid electricity. *Ind Eng Chem Res* 63 (2024) https://doi.org/10.1021/acs.iecr.4c00123
6. Yodwong B, Guilbert D, Phattanasak M, Kaewmanee W, Hinaje M, Vitale G. Faraday's efficiency modeling of a proton exchange membrane electrolyzer based on experimental data. *Energies* 13(18):4792 (2020) https://doi.org/10.3390/en13184792
7. Bell, I. H., Wronski, J., Quoilin, S. & Lemort, V. Pure and pseudo-pure fluid thermophysical property evaluation and the open-source thermophysical property library CoolProp. *Ind Eng Chem Res* 53, 2498–2508 (2014) https://doi.org/10.1021/ie4033999
8. Cooper N, Horend C, Röben F, Bardow A, Shah N. A framework for the design & operation of a large-scale wind-powered hydrogen electrolyzer hub. *Int J Hydrogen Energy* 47(14):8671-8686 (2022) https://doi.org/10.1016/j.ijhydene.2021.12.225
9. Vieren E, Demeester T, Beyne W, et al. The potential of vapor compression heat pumps supplying process heat between 100 and 200 °C in the chemical industry. *Energies* 16(18):6473 (2023) https://doi.org/10.3390/en16186473

© 2025 by the authors. Licensed to PSEcommunity.org and PSE Press. This is an open access article under the creative commons CC-BY-SA licensing terms. Credit must be given to creator and adaptations must be shared under the same terms. See https://creativecommons.org/licenses/by-sa/4.0/



Systems & Control Transactions

**Research Article - Peer Reviewed Conference Proceeding**
ESCAPE 35 - European Symposium on Computer Aided Process Engineering
Ghent, Belgium. 6-9 July 2025
Jan F.M. Van Impe, Grégoire Léonard, Satyajeet S. Bhonsale,
Monika E. Polańska, Filip Logist (Eds.)

PSE PRESS

# A Techno-Economic Optimization Approach to an Integrated Biomethane and Hydrogen Supply Chain

**Sandra Cecilia Cerda Flores[a*], Catherine Azzaro-Pantel[a], and Fabricio Nápoles Rivera[b]**

[a]Laboratoire de Génie Chimique, Université de Toulouse, CNRS, INPT, UPS, Toulouse France
[b]Posgrado de Ingeniería Química, Universidad Michoacana de San Nicolás de Hidalgo, Morelia, Michoacán, México
* Corresponding Author: sandracecilia.cerdaflores@toulouse-inp.fr

## ABSTRACT

One of the proposed strategies to reach net-zero goals is the diversification of a country's energy mix and transition to technologies that favour the mitigation of greenhouse gas emissions, while decreasing dependency on conventional fuels. This work presents a mathematical model that describes key production routes for two proposed energy transition vectors, biomethane and hydrogen, expressed as a Mixed-Integer Linear Problem (MILP). The supply chain is optimized with the objective of maximizing the profits from the global supply chain. The problem is formulated as an allocation problem, with production distributed between biomethane and hydrogen markets. The case study focuses on a region in Mexico where second-generation biomass for biogas production is abundant, while hydrogen is produced from biomethane using steam methane reforming. The results highlight the importance of balancing resource allocation in shared supply chains. With a production ratio of 60% biomethane and 40% hydrogen, a Levelized Cost of Hydrogen (LCOH) of 2.07 €/kWh and a Levelized Cost of Biomethane (LCBM) of 0.17 €/kWh are obtained, resulting in total hydrogen and biomethane production of 12,563 GWh/year and 72,374 GWh/year, respectively.

**Keywords**: Optimization, Environment, Hydrogen, Renewable and Sustainable Energy, Supply Chain

## 1. INTRODUCTION

A country's energy consumption is closely linked to its economic growth. Despite efforts to reduce greenhouse gas emissions by integrating green technologies to meet energy demands, energy consumption remains heavily reliant on fossil fuels. On a global scale, oil and gas production is projected to increase by 27% and 25% by 2030 [1]. According to the findings of the Intergovernmental Panel on Climate Change (IPCC) in 2018, limiting global temperature rise to no more than 1.5°C requires nations worldwide to achieve net-zero emissions by 2050 [2]. To reach this goal, different pathways have been proposed, which include the use of various technologies to decarbonize hard-to-abate sectors [3]. These sectors, which account for 30% of global emissions, encompass industry applications such as cement, plastics, and steel, as well as heavy-duty transport. Among the proposed technologies for decarbonization, biomethane and hydrogen have emerged as promising solutions, supported by the extensive research into their production technologies and associated limitations. Biogas is obtained from organic waste, and its process occurs naturally in landfills when it decomposes and produces methane, which is twenty times more damaging to the atmosphere than carbon dioxide [4]. Hydrogen production is currently dominated by steam methane reforming (SMR) using natural gas. Since SMR is a well-established technology, using biomethane obtained from biogas offers an attractive alternative for hydrogen production [5]. The use of biomass for methane and hydrogen production fosters a circular economy by reincorporating waste into the value chain [6], significantly reducing greenhouse gas (GHG) emissions. Waste-to-energy systems provide dual benefits: improved waste management and enhanced energy security, as the production and consumption of the resulting product can be located within the same geographic region. To address some of the challenges that arise from the network design of these technologies, various approaches have been proposed.

For instance, the application of a multi-objective optimization approach for biogas supply chains that considers the upgrading of biogas to biomethane reduces environmental impact and enhances applicability to different end-users. However, this also leads to higher production costs [7]. Additionally, some studies have considered inorganic waste sources to obtain a range of products in addition to electricity, such as syngas [8], incorporating the minimization of GHG emissions. A key advantage of biogas production is its feedstock flexibility, making it a more reliable energy source compared to the inherent variability of wind and PV energy [9]. In parallel, there is extensive research on hydrogen supply chains [10-12], which determines key components for the optimal supply chain design (energy source, production technology, storage, transportation, end-use). For green hydrogen production, the prominent technology used is electrolysis, relying on electricity production from renewable energy sources (RES). However, production costs and availability are highly dependent on the geographical region. Some frameworks have been developed to integrate dual product demands within a single supply chain network, such as hydrogen and methane through Power-to-Hydrogen (which transforms energy into hydrogen) and Power-to-Methane concepts (which produces methane through methanation) [13]. These approaches aim to provide fuel supply at a lower carbon-cost, while mitigating the impact from RES fluctuations. In the present study, biomethane and hydrogen are considered as products from a shared supply chain, which uses second generation waste as biomass source, a strategy particularly relevant to avoid the use of energy crops. Biogas is produced through anaerobic digestion and subsequently upgraded to biomethane. Hydrogen is generated via SMR, with biomethane being allocated between market demand and hydrogen production based on a specified distribution ratio. The interdependency of these products is analysed using a techno-economic approach through a set of equations that consider resource allocation and distribution, as well as cost constraints.

### 1.1 Methodology

The framework for the techno-economic assessment for biomethane and hydrogen production consists of three steps. First, the potential biomethane and hydrogen markets are analysed, considering the demand for each product. In the case of biomethane, its use in the domestic sector and electricity production sector is considered. Two hard-to-abate sectors are identified for hydrogen: the heavy-duty transport sector and the steel sector. The second step comprises the formulation of the mathematical model, which is based on the superstructure shown in **Figure 1**. Finally, the supply chain is optimized considering the maximization of global profits as the objective function.

The mathematical model incorporates mass balance equations in a steady-state configuration. The supply chain considers the following echelons: biomass is obtained from location ***f*** and processed into biogas using technology ***j*** in location ***l***. Biofertilizer is obtained as a by-product and can be sold in demand market ***q.*** Biogas is upgraded using technology ***k*** in location ***m***. The upgraded biogas, or biomethane, is sold at demand market ***p***. Biomethane that is not sent to the demand market ***p*** is used to produce hydrogen, which is produced using technology ***r***. As this results in gaseous-state hydrogen, a liquefaction step is needed, using technology ***lq***, to store liquid hydrogen in storage tank ***s*** and to be able to transport it in liquid form to location ***h***, where it is regasified to be distributed through the refuelling station ***rf***. The mathematical model is formulated as a mixed integer linear programming model (MILP). Since this is a preliminary assessment, uncertainty in the process was not considered. The supply chain is modelled as an allocation problem, where a percentage of the obtained biomethane will be sold to the demand market and the other percentage is used to produce hydrogen.

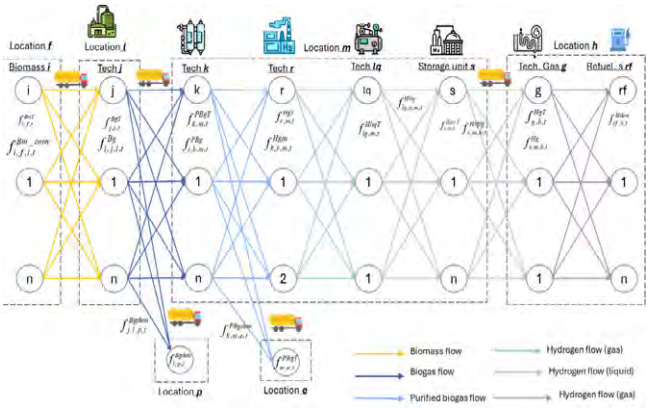



**Figure 1.** Proposed superstructure for the biomethane and hydrogen supply chain.

## 2. MATHEMATICAL MODEL

### 2.1 Biogas and Hydrogen Production

The total amount of biomethane ($f_{k,m,t}^{PBg_T}$) using technology ($k$) at location ($m$) must be equal to the sum of biogas from every biomass source ($i$) purified at location ($m$) using technology ($k$). It should also be equal to the amount of biomethane ($f_{k,m,p,t}^{PBg_market}$) needed to satisfy market ($p$) and the amount of biomethane allocated for hydrogen production ($f_{k,m,t}^{BgH}$).

$$f_{k,m,t}^{PBg_T} = \sum_i f_{i,m,k,t}^{PBg}, \forall (k \in K, m \in M, t \in T) \quad (1)$$

$$f_{k,m,t}^{BgH} = x \sum_i f_{i,m,k,t}^{PBg} \forall (k \in K, m \in M, t \in T) \quad (2)$$

$$f_{k,m,t}^{PBg_T} = \sum_p f_{k,m,p,t}^{PBg_market} + \sum_i f_{i,m,k,t}^{BgH}, \forall (k \in K, m \in M, t \in T) \quad (3)$$

The balance in the storage unit STOR of type s in location m at time *t* is given by the difference between the flows that go into the storage unit and the mass flows leaving the storage unit.

$$STOR_{s,m,t} = STOR_{s,m,t-1} + \sum_{lq} f_{lq,s,m,t}^{Hliq} - \sum_h f_{s,m,h,t}^{Hlqrf} \quad \forall (s \in S, m \in M, t \in T) \quad (4)$$

To make sure that the liquid hydrogen flow to and from the storage unit u at production site m during time t is within the storage unit capacity limit, the following restriction is applied:

$$SCap_{s,m,t}^{\min} \cdot \gamma_{s,m}^{s} \leq STOR_{s,m,t} \leq SCap_{s,m,t}^{\max} \cdot \gamma_{s,m}^{s} \quad (5)$$

$SCap_{s,m,t}^{min}$ and $SCap_{s,m,t}^{max}$ represent the minimum and maximum storage capacities for the storage tank type *s* at location *m* in time *t*.

## 2.2 Economic objective

The total profit (*Pft*) considers the revenue (*T_Rev*) obtained from sales for each product minus the total costs from the supply chain, which include fixed costs (*T_FC*), variable costs (*T_VC*), and transport costs (*Tr_C*).

$$Profit = Total_{Revenue} - Total_{Costs} \quad (6)$$

The fixed costs (*FC*) for each process *X* involved in the supply chain are calculated by multiplying the annualization factor *K* by the parameter *C*F and the binary variable y, which dictates whether the process technology *X* will be installed or not.

$$FC[processX] = KX_{x,t} \cdot CF_{x,t} \cdot y_{x,t} \forall t \quad (7)$$

The annualization factor K is calculated as follows:

$$k_{x,t} = \left[\frac{(1+\alpha_x)^n \cdot \alpha_x}{(1+\alpha_x)^n - 1}\right] \quad (8)$$

In this expression, *x* refers to the production technology, *α* is the discount rate set at 10%, and *n* is the plant lifetime (20 years). The variable costs are computed by the product of the parameter *VC* by the mass flow relevant to the conversion process at each stage. For instance, considering the SMR process, the parameter $VC_{m,r,t}^{ref}$ is multiplied by the mass flow $f_{k,m,r,t}^{Hgas}$ , that is used for hydrogen production.

$$VC^{ref} = \sum_k \sum_m \sum_r \sum_t CV_{m,r,t}^{ref} \cdot f_{k,m,r,t}^{Hgas} \quad (9)$$

Transport costs consider fuel, labour, and maintenance costs, multiplied by the demand flows, taking into account the distance between the production site and the demand market. The total costs are the sum of the fixed, variable, and transport costs.

$$TotalCosts = Total_{FC} + Total_{VC} + Total_{TR} \quad (10)$$

Finally, the levelized costs for biomethane and hydrogen respectively LCOH and LCBM are calculated as follows:

$$LCOH = \frac{Total\ hydrogen\ production\ costs}{Annual\ hydrogen\ production} \quad (11)$$

$$LCBM = \frac{Total\ biomethane\ production\ costs}{Annual\ biomethane\ \ production} \quad (12)$$

The mathematical model is expressed as a Mixed-Integer Linear Problem (MILP). This was solved using CPLEX 22 within the GAMS environment. The model consists of 83 blocks of equations and 70 blocks of variables. The supply chain is optimized with the objective of maximizing the profits from the global supply chain. The problem is expressed as an allocation problem, with production distributed between biomethane and hydrogen markets.

# 3. CASE STUDY

The mathematical model is applied to a case study in Mexico, focusing on the country's central region. The states selected play a significant role in the agricultural sector, resulting in a high availability of residues that can be used as feedstock for biogas production. For market demands, biomethane is considered a substitute for natural gas in energy production. Regarding hydrogen, market trends in Mexico highlight its potential to decarbonize the heavy-duty transport sector and some hard-to-abate industries, such as steel and ammonia production. In this case study, the heavy-duty transport sector was considered. GHG emissions from road transportation in Mexico contribute to 34% of the total emissions [14]. With current tendencies suggesting increased investment in the industry sector in the country, this number is expected to grow even further.

# 4. RESULTS

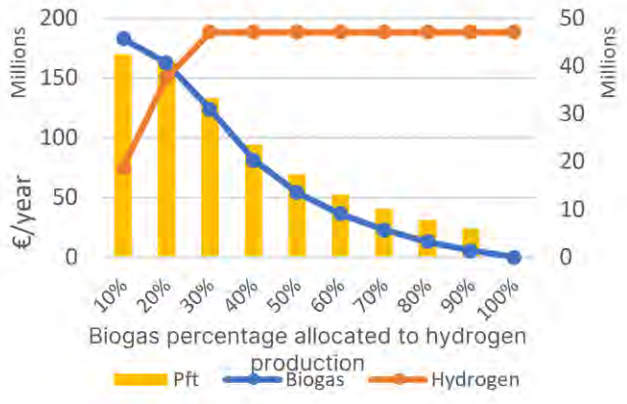



**Figure 2.** Revenue per product

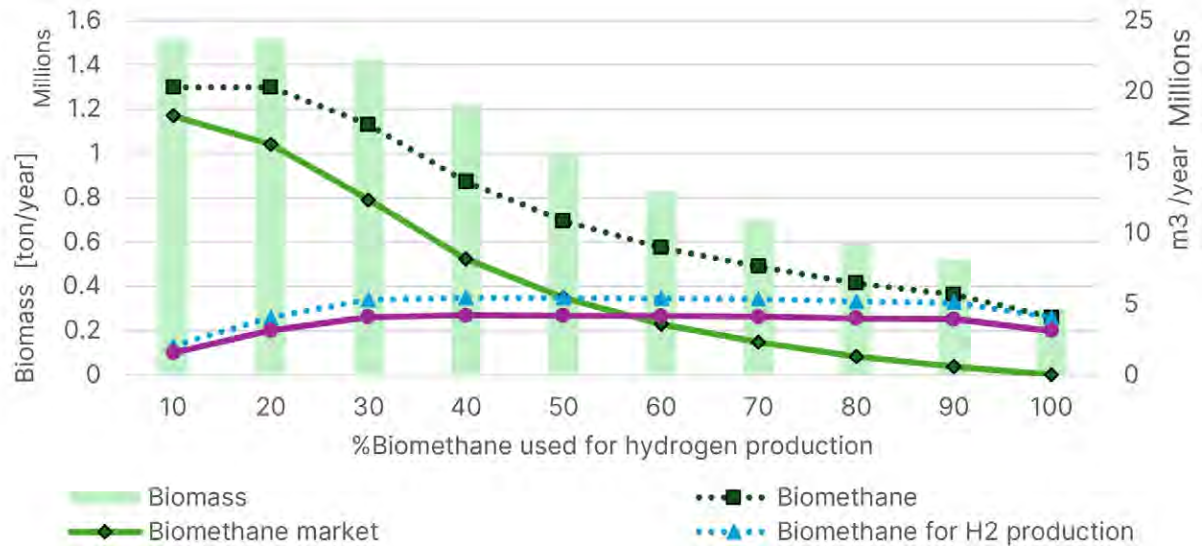



**Figure 3.** Impact of Biomethane Allocation on Hydrogen and Biomethane Production.

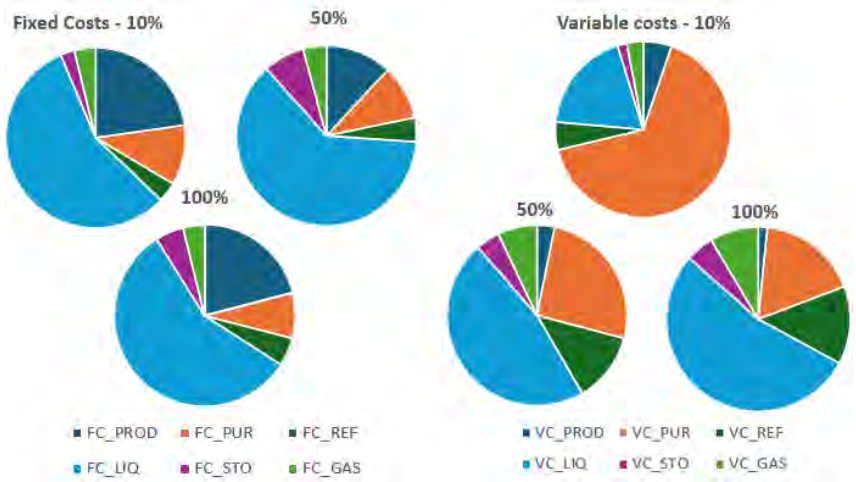



**Figure 4.** Share of Fixed and Variable costs.

**Figure 2** illustrates a clear trend, showing the profit for each allocation scenario. As the quantity of biogas allocated to hydrogen production increases, profits decrease significantly. Biomethane revenue decreases as the amount of biomethane allocated for hydrogen production rises, which aligns with the concept of economy of scales. This concept refers to the cost advantages with the increase in production. However, hydrogen revenue remains constant, from 30% of biomethane allocation for hydrogen production onwards. The main reason for this trend is the inflated cost of hydrogen production, specifically, its liquefaction, which is a crucial step needed to store and transport from the production site to refuelling stations.

This is further demonstrated in **Figure 3**, which shows that with a higher percentage of biomethane being used for hydrogen production, the overall of biomass required for the supply chain is adjusted to maintain profitability. This decrease helps in controlling costs associated with hydrogen production. As it can be observed in **Figure 4**, when hydrogen is produced from 10% biomethane, the fixed costs for the liquefaction technology take up more than half of the overall capital costs. This contribution remains constant up to the point where all biomethane is used to produce hydrogen. Yet, in terms of operational costs, the main contributor is the cost from upgrading biogas to biomethane. As hydrogen production increases, these costs become negligible compared to those associated with hydrogen liquefaction.

**Figures 5 and 6** present the levelized costs in terms of energy, considering that 1 $m^3$ of biomethane and 1 $m^3$ of hydrogen gas have a Low Heating Value (LHV) of 10 kWh/$m^3$ [15] and 3 kWh/$m^3$ [16], respectively. Under these assumptions, the highest LCBM for this supply chain reaches 1.04 €/kWh, while the highest LCOH amounts to 5.06 €/kWh. In **Figure 5**, an exponential trend

is noticeable from allocating 40% to the biomethane market onwards. Since the revenue from biomethane is higher than that from hydrogen, the optimization strategy seeks to limit its production. Considering the LCOH (**Figure 6**), this value decreases as more biomethane is used in production but stabilizes between 2€/kWh to 1.6€/kWh from scenario D onwards, maintaining a constant profitability in the system.

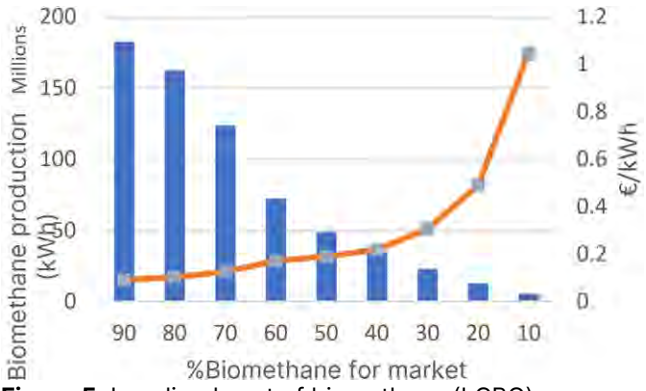



**Figure 5.** Levelized cost of biomethane (LCBG)

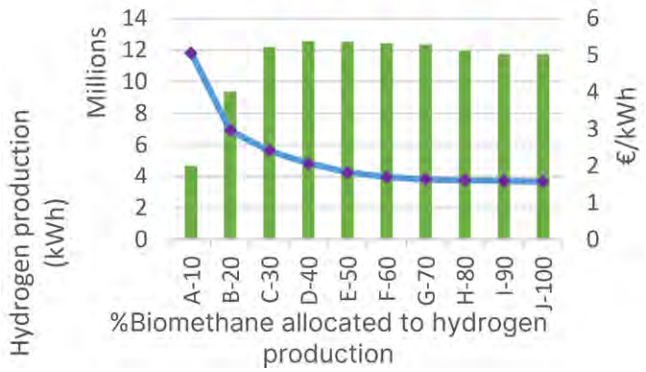



Figure 6. Levelized cost of hydrogen (LCOH)

**Figure 7** provides a schematic representation of the supply chain design resulting from scenario "D", covering six of the most industrialized and energy-driven cities (labelled 1 to 6). The network integrates biogas upgrading, hydrogen production, transport, and refuelling infrastructure to support a sustainable energy transition. In this scenario,1,224,103 tons of biomass are collected at each of the locations, consisting of 3% from organic waste, 11% from cow manure, and 86% from wastewater. To maintain profit margins, biomass is obtained, transformed to biogas and upgraded to biomethane within the same locations where biomethane is distributed. The upgrading technology used to produce biomethane is High-Pressure Water Scrubbing (HPWS), obtaining 8,173,563 $nm^3$ of biomethane to be sold to the demand market, while 4,8249,93 $m^3$ are used to produce hydrogen by SMR, representing a 60-40 ratio. From this configuration 4,187,805 $m^3$ of hydrogen are regasified at the refuelling stations. Hydrogen production plants, storage, and refuelling stations are installed at all locations, and hydrogen distribution prioritizes the demand of the most industrialized cities, locations 1 and 6. The LCBM presents a value of 0.17 €/kWh, while the LCOH is 2.07 €/kWh.

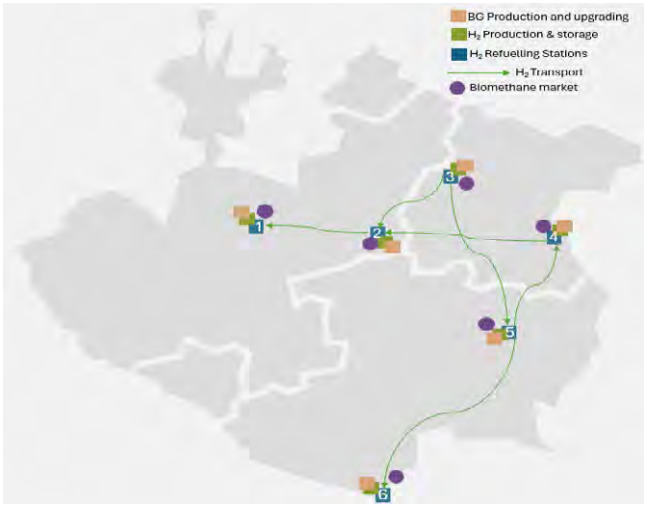



**Figure 7.** Supply chain design for scenario "D".

## 5. Conclusions

The techno-economic optimization for a biomass and hydrogen supply chain is considered for a case study in Mexico. The objective function is profit-maximization of the global supply chain. It is well-established that hydrogen production is an expensive process, compared to biomethane production. Therefore, the optimization problem is formulated as an allocation problem, to distribute the quantity of biomethane that is used for hydrogen production. These results emphasize the importance of balancing resource allocation in shared supply chains. A production scenario with 60% biomethane and 40% hydrogen offers a balanced cost-effectiveness for both products with a LCOH of 2.07 €/kWh and an LCBM of 0.17 €/MWh, with total hydrogen and biomethane production of 12,563 GWh/year and 72,374GWh/year, respectively. While the LCBM is slightly higher than average LCOE for biomethane (0.1 €/MWh [17]), the hydrogen costs are quite further from average LCOH costs in literature. This can be explained by the relatively low demand for hydrogen considered for this case study. However, costs can be reduced through government subsidies, carbon taxes to incentivize the use of cleaner energy sources, as well as considering the optimization of energy-intensive processes. Furthermore, there is a need to conduct an environmental evaluation of the supply chain to assess the impacts of these products on various environmental indicators. One key indicator is water use throughout the supply chain, as water is required at multiple stages, including biogas production in digesters, upgrading biogas to biomethane, and hydrogen production. The comparison between producing hydrogen from biomethane

through SMR, and producing green hydrogen through electrolysers, which relies on fresh water, is a critical consideration, particularly in water-stressed regions. The use of life cycle assessment to evaluate this (and other) environmental indicators will further allow the evaluation of the supply chain from a multi-objective perspective and enrich the discussion of the integration of these technologies, while ensuring compliance with energy policies and sustainability goals.

## ACKNOWLEDGEMENTS

The authors acknowledge the financial support from the Mexican Secretary of Science, Humanities, Technology and Innovation (SECIHTI), Toulouse INP, and IEM-SySEM.

## REFERENCES

1. McKinsey & Company. *Global energy perspective 2024*. McKinsey & Company (2024).
2. Tollefson, Jeff. "IPCC says limiting global warming to 1.5°C will require drastic action." *Nature*, vol. 562, no. 7726, Oct. 2018, pp. 172
3. Fankhauser, S., Smith, S. M., Allen, M., Axelsson, K., Hale, T., Hepburn, C., ... & Wetzer, T. The meaning of net zero and how to get it right. *Nature Climate Change*, *12*(1), 15-21 (2022).
4. Rafiee, A., Khalilpour, K. R., Prest, J., & Skryabin, I. Biogas as an energy vector. *Biomass and Bioenergy*, *144*, 105935 (2021).
5. Kumar, R., Kumar, A., & Pal, A. Overview of hydrogen production from biogas reforming: Technological advancement. *International Journal of Hydrogen Energy*, *47*(82), 34831-34855 (2022).
6. Sharma, S., Basu, S., Shetti, N. P., & Aminabhavi, T. M. Waste-to-energy nexus for circular economy and environmental protection: recent trends in hydrogen energy. *Science of the Total Environment*, *713*, 136633 (2020).
7. Díaz-Trujillo L, Nápoles-Rivera, F. Optimization of biogas supply chain in Mexico considering economic and environmental aspects. *Renewable energy*, *139*, 1227-1240 (2019).
8. Mohammadi, Maryam, and Iiro Harjunkoski. "Performance analysis of waste-to-energy technologies for sustainable energy generation in integrated supply chains." *Computers & Chemical Engineering* 140 (2020): 106905.
9. Csedő, Zoltán, József Magyari, and Máté Zavarkó. "Biofuel supply chain planning and circular business model innovation at wastewater treatment plants: The case of biomethane production." *Cleaner Logistics and Supply Chain* (2024): 100158.
10. Almaraz, Sofía De-León, et al. "Hydrogen supply chain optimization for deployment scenarios in the Midi-Pyrénées region, France." *International journal of hydrogen energy* 39.23 (2014).
11. Li, Lei, Hervé Manier, and Marie-Ange Manier. "Integrated optimization model for hydrogen supply chain network design and hydrogen fueling station planning." *Computers & Chemical Engineering* 134 (2020)
12. Kim, Sunwoo, et al. "Techno-economic analysis for design and management of international green hydrogen supply chain under uncertainty: An integrated temporal planning approach." *Energy Conversion and Management* 301 (2024).
13. Carrera, Eduardo, and Catherine Azzaro-Pantel. "Bi-objective optimal design of Hydrogen and Methane Supply Chains based on Power-to-Gas systems." *Chemical Engineering Science* 246 (2021).
14. IEA. Mexico Energy Profile, IEA, Paris https://www.iea.org/reports/mexico-energy-profile (2023). Licence: CC BY 4.0
15. IEA . *Outlook for biogas and biomethane: Prospects for organic growth* . https://www.iea.org/reports/outlook-for-biogas-and-biomethane-prospects-for-organic-growth (2020).
Licence: CC BY 4.0
16. IEA. (n.d.*). Global average levelized cost of hydrogen production by energy source and technology, 2019 and 2050 – Charts – Data & Statistics*.https://www.iea.org/data-and statistics/charts/global-average-levelised-cost-of-hydrogen-production-by-energy-source-and-technology-2019-and-2050
Licence: CC BY 4.0
17. ENGIE. *Geographical analysis of biomethane potential and costs in Europe in 2050* (2021).

© 2025 by the authors. Licensed to PSEcommunity.org and PSE Press. This is an open access article under the creative commons CC-BY-SA licensing terms. Credit must be given to creator and adaptations must be shared under the same terms. See https://creativecommons.org/licenses/by-sa/4.0/



Systems & Control Transactions

**Research Article - Peer Reviewed Conference Proceeding**
ESCAPE 35 - European Symposium on Computer Aided Process Engineering
Ghent, Belgium. 6-9 July 2025
Jan F.M. Van Impe, Grégoire Léonard, Satyajeet S. Bhonsale,
Monika E. Polańska, Filip Logist (Eds.)

PSE PRESS

# On Optimisation of Operating Conditions for Maximum Hydrogen Storage in Metal Hydrides

**Chizembi Sakulanda[a], Thokozani Majozi[a*]**

[a]School of Chemical and Metallurgical Engineering, University of the Witwatersrand, Johannesburg, South Africa
* Corresponding Author: Thokozani.majozi@wits.ac.za

## ABSTRACT

The climate crisis continues to grow as an existential threat. Establishing reliable energy resources that are renewable and zero-carbon emitting is a critical endeavour. Hydrogen has emerged as one such critical resource due to its high gravimetric energy density and near-abundant availability. However, it suffers from low volumetric energy density and is incredibly challenging to store and transport. The metal hydride, a solid-state storage method, provides a viable solution to the current limitations. Storage is achieved through the chemical absorption of hydrogen into a porous metal alloy's sublattice. But its challenging thermodynamic functionality leaves a gap between the ideal storage capacity that current industry requires and the limited capacity that reusable metal hydrides currently provide. This work used mathematical modelling to determine optimal operating conditions for a metal hydride in order to maximise hydrogen storage capacity. Computational fluid dynamics is used to simulate the coupled heat and mass transfer that occurs during the absorption process into the metal alloy. The finite volume method is used to discretise governing equations, and the alternating direction implicit method is used for numerical solutions as it proved the most stable platform to conduct analyses. An initial investigation into numerical grid sizing is conducted to determine the optimal node allocation. The impact of the hydride bed thickness and supply pressure are varied and optimised. The alloy $MmNi_{4.6}Al_{0.4}$ is used in the investigation.

**Keywords**: Metal Hydride, Optimisation, Computational Fluid Dynamics

## INTRODUCTION

The climate crisis is an anthropological concern that has had an ever-increasing level of importance in the 21st century. The 2015 Paris Agreement, signed by 196 nations, sought to ideally limit the global temperature increase at 1.5 °C [1]. However, in 2022, the Intergovernmental Panel on Climate Change (IPCC) stated that efforts implemented between its 2022 sitting and the 2015 agreement significantly undershot the targets to reach a 1.5 °C limit [2]. The South African government announced strategies to introduce more renewable power production into its energy sector. However, South Africa is not yet meeting its nationally determined contribution to reach the goal of limiting global warming by 1.5 °C [3].

South Africa has sufficient renewable resources to power a transition to zero-emissions power production, but clean energy integration remains a critical issue. 70% of local project developers working in the renewable energy sector found that the limited physical and institutional capacity to integrate the growing number of renewables into the resource mix are a significant hinderance to the country's transition away from fossil fuels [4].

With its natural abundance and high gravimetric energy density, hydrogen has been positioned as a critical player for 21st century decarbonisation ambitions [5]. Despite its growing attention, there remain some key practical hurdles for the mass adoption of hydrogen. This is due to its low volumetric energy density and difficulty when it comes to storage. An area of growing attention is solid-state storage and that is because it provides a solution to the volumetric energy density shortfall that hydrogen suffers from [6]. The metal hydride is among these solid-state storage solutions.

### Background and motivation

Metal hydrides are a very attractive storage pathway for the emerging hydrogen market for several

reasons. The primary is their potential for high storage density. In addition to that, metal hydrides are often recyclable and their formation occurs at safe operational pressures. Once formed, they are also easy to store and can easily by transported [7].

Figure 1 below provides a representation of how the hydrogen molecule approaches the alloy surface and is eventually absorbed into the bulk lattice. The general reaction formula for the formation of a metal hydride where M is the metal, MH is the hydride, x is the hydrogen concentration and Q is the heat released is as follows [8]:

$$M(s) + \frac{x}{2}H_2(g) \leftrightarrow MH_x(g) + Q \quad (1)$$

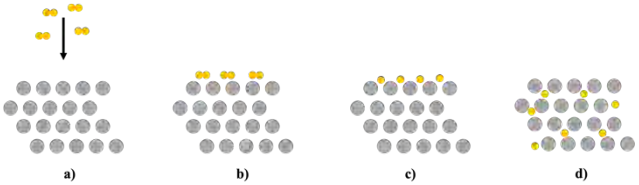



**Figure 1.** Step-by-step visualisation of hydrogen absoprtion process

Extensive work has gone into mathematically modelling the metal hydride. Understanding the interplay between heat generation and storage capacity is key to ensuring this technology can be adopted into industrial use [9]. Equation 1 shows that heat is a critical component to the hydrogen absorption and desorption cycle, the former being an exothermic reaction and the latter endothermic. A good control of the thermodynamic functions of the metal hydride is critical for reaching any attainable goal of maximising its storage potential.

Therefore, this research aims to develop a two-dimensional model that will accurately simulate a metal hydride system with which an optimisation can be performed.

The prescribed objectives are to:

i. Develop a mathematical model for the heat and mass transfer within the metal hydride reactor using given parameters.
ii. Compare the results of the developed model with existing literature and validate model results.
iii. Investigate the effect of varying particular variables.
iv. Conduct an optimisation on the identified variables.

## Literature Review

Metal hydrides can be distinguished into two classifications, interstitial and non-interstitial. The divergence between interstitial and non-interstitial is not drastic but significant enough in that it results in the two classifications having different storage potentials and operating conditions [6]. During the absorption and desorption cycle, very little change occurs to the metal's surface when dealing with an interstitial hydride. The non-interstitial is dependent on the decomposition and recombination of the hydride as a whole. While interstitial hydrides typically have a lower storage density than non-interstitial, they are generally recyclable unlike non-interstitials. It is for this reason that interstitials are perused more commonly in research [6].

Figure 2 shows the general trend across metal hydrides. There is a directly correlative relationship between storage capacity and heat of formation. The lower the storage capacity of a hydride results in a lower the heat of formation and similarly the converse bears true.

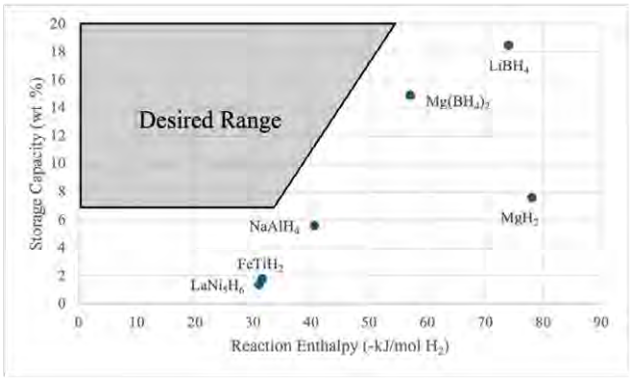



**Figure 2.** Comparison of different metal hydrides' potential storage density and reaction enthalpies [8]

There is a broad range of metal alloys used to make metal hydrides. Among the many metals and alloys used, a classification of three distinct groups can be formed. These three are intermetallics (Eg. $LaNi_5H_6$), magnesium-based hydrides (Eg. $MgH_2$) and complex hydrides (Eg. $LiBH_4$, $NaAlH_4$) [7]. The former group is typically interstitial while the latter two groups are often non-interstitial. Some metrics considered when reviewing the classifications are storage capacity, temperature and recyclability. Some conservative estimations suggest that hydrides need only reach a storage capacity of 2 wt.% for stationary applications [10]. Other investigations peg this minimum to be higher with at least 5 wt.% [8]. The US Department of Energy outlines an ultimate gravimetric density target for any hydrogen fuelled light-duty vehicles to be 6.5 wt. % [11].

Unlike complex hydrides and magnesium hydrides, intermetallics have much more suitable operating conditions. In fact, most academic literature models some kind of intermetallic hydride [9]. This is due to their manageable working temperature and pressure ranges, fast kinetics and reusability. However, their benefits are counteracted by their low storage capacity; often, they do not manage to exceed 2 wt.%. Ultimately, their workability supersedes their storage deficiency. The most common alloy that is investigated is the lanthanum penta-nickel

($LaNi_5$) [12]. $LaNi_5$ is often cited for having a high production cost due to the lanthanum. To circumvent this, some investigations use a cheaper rare-earth mischmetal mixture as a replacement for pure lanthanum [19, 20]. This work conducted its investigation with the alloy $MmNi_{4.6}Al_{0.4}$. It is understood that its ideal storage capacity limit resides somewhere between 1 - 1.4 wt.% [13, 14].

## MATHEMATICAL MODEL

The absorption/desorption cycle of a metal hydride is a process that involves both heat and mass transfer. It is a two-phase system with the gas phase covering the hydrogen and solid phase covering the hydride bed within the storage vessel. This results in the reactor vessel being a discontinuous medium. However, conservation equations that model heat and mass transfer in a porous medium are intended for a continuous medium. To allow the applicability of these equations, the scale of examination is shifted from microscopic to macroscopic. To do this phase averaging is implemented. This allows the average volume, over which heat and mass transfer takes place, to be larger than the individual bed pores [15].

A standard cylindrical vessel with external cooling is considered – see Figure 3. The heat and mass transfer are modeled in two dimensions, the radial and axial flow. Figure 3 shows two reactor geometries. Figure 3A has hydrogen fed through an axial inlet and its hydride bed occupies the full breadth of the vessel. It is modelled asymmetrically for ease. Figure 3B is an expansion on the axisymmetric condition. The geometry potentially offers a much more even distribution of the hydrogen gas and with it an even generation of heat across the hydride bed [14, 16]. This work makes use of Figure 3B geometry.

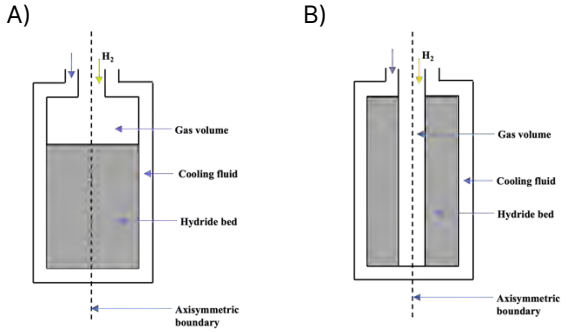



**Figure 3.** A simple diagram of the two most common reactor geometries

An initial starting point for the thermal governing equation, are the following:

$$\varepsilon\rho_g C_{pg}\frac{\partial T_g}{\partial t} = \frac{1}{r}\frac{\partial}{\partial r}\left(\varepsilon\lambda_{ge} r\frac{\partial T_g}{\partial r}\right) + \frac{\partial}{\partial z}\left(\varepsilon\lambda_{ge}\frac{\partial T_g}{\partial z}\right) - \rho_g C_{pg} v_{gr}\frac{\partial T_g}{\partial r} - \rho_g C_{pg} v_{gz}\frac{\partial T_g}{\partial z} + H_{gs}(T_g - T_s)S - mC_{pg}(T_g - T_s) \quad (2)$$

$$(1-\varepsilon)\rho_s C_{ps}\frac{\partial T_s}{\partial t} = \frac{1}{r}\frac{\partial}{\partial r}\left((1-\varepsilon)\lambda_{se} r\frac{\partial T_s}{\partial r}\right) + \frac{\partial}{\partial z}\left((1-\varepsilon)\lambda_{se}\frac{\partial T_s}{\partial z}\right) + H_{gs}(T_g - T_s)S + m(\Delta H^o + C_{pg}T_g - C_{ps}T_s) \quad (3)$$

Equations 2 and 3 are the thermal balance of the gas and solid phase, respectively [15, 17].

The mathematical formation of the governing equations is established with the following assumptions taken into consideration:

i. The gas phase within the vessel and hydride bed exhibits ideal gas behaviour
ii. The local thermal equilibrium hypothesis is taken to be true
iii. Radiative heat transfer is negligible
iv. Viscous dissipation and compression work are considered negligible
v. Hydride porosity, permeability and heat conductivity remain unchanged during absorption cycle

Of the assumptions, one that provides an immediate simplification to the heat transfer model is the local thermal equilibrium assumption. This allows for the temperature within the gas and solid phase along any radial and axial length at any given time to be the same. This, therefore, eliminates the need for two thermal balances and reduces it down to a single thermal equation:

$$(\rho C_p)_e\frac{\partial T}{\partial t} = \frac{1}{r}\frac{\partial}{\partial r}\left(\lambda_e r\frac{\partial T}{\partial r}\right) + \frac{\partial}{\partial z}\left(\lambda_e\frac{\partial T}{\partial z}\right) - \rho_g C_{pg} v_{gr}\frac{\partial T}{\partial r} - \rho_g C_{pg} v_{gz}\frac{\partial T}{\partial z} + m(\Delta H + T(C_{pg} - C_{ps}) \quad (4)$$

$$(\rho C_p)_e = \varepsilon\rho_g C_{p_g} + (1-\varepsilon)\rho_s C_{p_s} \quad (5)$$

$$\lambda_e = \varepsilon\lambda_{ge} + (1-\varepsilon)\lambda_{se} \quad (6)$$

Another assumption that is commonly used is that of ignoring pressure effects within the vessel and, by extension, ignoring the effect of convective heat transfer. To determine if this assumption is applicable to this investigation, a dimensionless ratio seen in Equation 7 helps identify if the effect of gaseous flow can be neglected or not [18]. If N is found to be much less than 1, then ignoring pressure effects will have a negligible effect on the results of the simulation.

$$N = \frac{\lambda_e \cdot M \cdot L_{gas}^2 \cdot \mu}{\frac{\partial P_{eq}}{\partial T}\cdot\Delta H\cdot\rho_g\cdot K\cdot L_{heat}^2} \quad (7)$$

The continuity equation and reaction kinetics for this system are given by Equations 8 - 12. Equations 8 and 11 are similar in that the former records mass absorption and the latter hydrogenation. There are instances where the thermal equation's heat generation term makes use of the hydrogenation model – see Equation 14. Equation 12 shows a modified van't Hoff equation which accounts for varying hydrogen concentration and hysteresis [9, 14]. The benefit of the model employed in this work is its generality for porous multiphase systems [15]. Its specificity comes in the form of the thermo-physical properties

shown in Table 1.

$$m_{abs} = C_a \exp\left(-\frac{Ea}{RT}\right) \ln\left(\frac{P}{P_{eq}}\right)(\rho_{ss} - \rho_s) \quad (8)$$

$$(1-\varepsilon)\frac{\partial \rho_s}{\partial t} = m_{abs} \quad (9)$$

$$\frac{dx}{dt} = \sigma \frac{(p-p_{eq})}{p_{eq}} \frac{(x-x_f)}{(x_o-x_f)} \exp\left(\frac{-E_a}{RT}\right) \quad (10)$$

$$\varepsilon \frac{\partial \rho_g}{\partial t} + \nabla \cdot \left(\rho_g \underset{v}{\rightarrow}\right) = (\rho_{ss} - \rho_s)(1-\varepsilon)\frac{dx}{dt} \quad (11)$$

$$lnP_{eq} = \frac{\Delta H}{R_g T} - \frac{\Delta S}{R_g} + (\emptyset \pm \varphi) tan\left[\pi\left(\frac{\left(\frac{H}{M}\right)}{\left(\frac{H}{M}\right)} - \frac{1}{2}\right)\right] \pm \frac{\beta}{2} \quad (12)$$

The following are the boundary conditions used:
Reactor axis

$$\frac{\partial T}{\partial r}(z, 0, t) = 0 \quad (13a)$$

Reactor base

$$-\lambda_e \frac{\partial T}{\partial z}(H, r, t) = h\big(T(H, r, t) - T_f\big) \quad (13b)$$

Reactor lateral area

$$-\lambda_e \frac{\partial T}{\partial r}(z, R, t) = h\big(T(z, R, t) - T_f\big) \quad (13c)$$

**Table 1:** Alloy and hydrogen thermo-physical properties [15, 18]

| | |
|---|---|
| **Alloy properties** | |
| Density (kg/m$^3$), $\rho_s$ | 8400 |
| Specific heat (J/kg.K), $C_{ps}$ | 419 |
| Effective thermal conductivity (W/m.K), $\lambda_e$ | 1.6 |
| Porosity, $\varepsilon$ | 0.5 |
| Effective saturated density (kg/m$^3$), $\rho_{ss}$ | 4259 |
| Effective initial density (kg/m$^3$), $\rho_s$ | 4200 |
| Activation energy (J/kg.K), $E_a$ | 21170 |
| Entropy (J/mol $H_2$.K), $\Delta S$ | 107.2 |
| Enthalpy (J/mol $H_2$), $\Delta H$ | 28000 |
| **Hydrogen properties** | |
| Thermal conductivity (W/m.K), $\lambda_{ge}$ | 0.127 |
| Specific heat (J/kg.K), $C_{pg}$ | 14183 |
| Density (kg/m$^3$), $\rho_g$ | 0.084 |
| Molar mass (kg/mol), $M_{H_2}$ | 2x10$^{-3}$ |
| Dynamic viscosity (Pa.s), $\mu$ | 8.9x10$^{-6}$ |
| **Constants** | |
| Gas constant (J/mol.K), R | 8.314 |
| Reaction constant (s$^{-1}$), $\sigma$ | 75 |
| Slope factor, $\emptyset$ | 0.35 |
| Constant, $\varphi$ | 0.15 |
| Hysteresis factor, $\beta$ | 0.2 |

## NUMERICAL METHOD

A critical component of computational fluid dynamic work is the discretisation technique used to solve the governing equations. Initially, this work sought an exploration of the possibilities between the finite difference method (FDM) and finite volume method (FVM) [19, 20]. In literature, there are diverging paths with many opting for FVM and few opting for FDM [8]. This work settled on using node-centred FVM. MATLAB was the chosen software to conduct the work.

The conductive terms after the FVM treatment can be seen in Equation 14. Note the hydrogenation modified heat generation term.

$$(\rho C_p)_e \frac{\partial T}{\partial t} = \frac{1}{r_P}\left(r_E \lambda_e \frac{T_E - T_P}{r_E - r_p} - r_W \lambda_e \frac{T_P - T_W}{r_P - r_E}\right) + \left(\lambda_e \frac{T_N - T_P}{Z_N - Z_p} - \lambda_e \frac{T_P - T_S}{Z_P - Z_S}\right) + \frac{\Delta\rho \cdot (1-\varepsilon)\Delta H}{M_{H_2}} \frac{dx}{dt} \quad (14)$$

In addition to the discretisation method, there is a need to select a solution technique for solving these governing equations. On this matter, there is typically one of two ways that can be selected – explicit solutions or implicit solutions. This investigation sought to determine the most beneficial option between using explicit and implicit solution methods [19-21]. The solution which provided the best numerical stability was the implicit solution, specifically the alternating-direction implicit (ADI) method. The application of this is shown in Equation 15 and 16. A tridiagonal matrix algorithm is then utilised. The Dirichlet boundary condition is directly applied, and the Robin boundary conditions are treated with a difference approximation [19, 22].

Radial step:

$$(\rho C_p)_e \frac{T_{i,j}^{n+1/2} - T_{i,j}^{n}}{\Delta t/2} = \frac{1}{r_P}\left(r_E \lambda_e \frac{T_E^{n+1/2} - T_P^{n+1/2}}{r_E - r_p} - r_W \lambda_e \frac{T_P^{n+1/2} - T_E^{n+1/2}}{r_P - r_E}\right) + \left(\lambda_e \frac{T_N^{n} - T_P^{n}}{Z_N - Z_p} - \lambda_e \frac{T_P^{n} - T_S^{n}}{Z_P - Z_S}\right) + Q \quad (15)$$

Axial step:

$$(\rho C_p)_e \frac{T_{i,j}^{n+1} - T_{i,j}^{n+1/2}}{\Delta t/2} = \left(\lambda_e \frac{T_N^{n+1} - T_P^{n+1} + 1}{Z_N - Z_p} - \lambda_e \frac{T_P^{n+1} - T_S^{n+1}}{Z_P - Z_S}\right) + \frac{1}{r_P}\left(r_E \lambda_e \frac{T_E^{n+1/2} - T_P^{n+1/2}}{r_E - r_p} - r_W \lambda_e \frac{T_P^{n+1/2} - T_E^{n+1/2}}{r_P - r_E}\right) + Q \quad (16)$$

## RESULTS

Using the criterion of Equation 7, it was determined that it is suitable for this work to neglect the effect of gaseous flow and neglect convective heat transfer.

An appreciable baseline figure to remember for comparison is an estimation on how much hydrogen would be stored in a high-pressure (350 bar) gas vessel without a packed hydride bed. At a volume of 8.41x10$^{-5}$ m$^3$, radius of 7.5x10$^{-3}$ m and length of 4.75x10$^{-1}$ m, and with the aid of the ideal gas equation, an estimated 2.39x10$^{-3}$ kg can be stored in such a vessel. A vessel of steel composition would result in a storage capacity

somewhere in the region of 0.6 wt.%. A lighter composite of aluminium and carbon fibre, as is increasingly used [23], would raise this to a potential capacity of 0.8 wt.%

### Grid sizing

Before testing the effect of operating conditions, an important consideration is the effect of the numerical grid size used for the simulation. A base 20x200 grid is initially selected. An investigation into varying the gride size across a predetermined range of values was conducted. The adjustment of the radial resolution has a more prominent impact than the axial resolution variation. Figure 3 below shows how increasing nodal points in both the axial and radial direction increases storage capacity. This is understandable as coarser numerical grids often lead to higher inaccuracies.

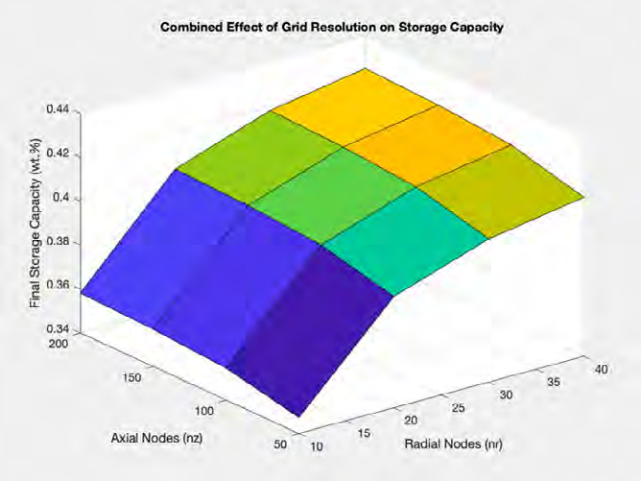



**Figure 3.** 3D plot of the effect of axial and radial nodes numbering on storage capacity

A preliminary optimisation run saw that the Δstorage convergence threshold of 0.5% change was reached at a 270x1295 grid size and yielded 0.448 wt.% capacity.

### Supply pressure and bed thickness

Supply pressure plays a critical role in the attempt to maximise storage. Equation 10 shows how the difference between the P and $P_{eq}$ is a driving force for absorption. Like the grid sizing, pressure was varied across a predetermined range. Table 2 shows that larger supply pressures allow for more hydrogen to be absorbed. The optimisation simulation found convergence at 43.2 bar with a storage of 0.411 wt.%.

In addition to supply pressure, this investigation tested the reactor bed thickness. Something helpful to consider is the surface area/volume ratio. An increased radius increases the required surface area across which the hydrogen must diffuse. Increasing the diffusion area increases the diffusion resistance and ultimately limits the amount absorbed – see Table 3. An optimisation was also run for bed thickness, but the convergence criterion was not met. However, the plotting did indicate that a maximum storage of just over 0.4 wt.% was reached between 0.005m and 0.01m.

**Table 2:** Varied supply pressure and the impact on storage capacity

| Pressure (bar) | Wt.% |
|---|---|
| 5 | 0.016 |
| 10 | 0.096 |
| 15 | 0.186 |
| 20 | 0.270 |
| 25 | 0.337 |
| 30 | 0.390 |

**Table 3:** Varied bed thickness and the impact on storage capacity

| Radius (m) | Wt.% |
|---|---|
| $5x10^{-3}$ | 0.390 |
| $75x10^{-3}$ | 0.169 |
| $10x10^{-2}$ | 0.092 |
| $15x10^{-2}$ | 0.037 |

## CONCLUSIONS

The metal hydride is a promising hydrogen storage pathway. The developed heat and mass transfer modelled for this investigation, simulated on the $MmNi_{4.6}Al_{0.4}$ alloy, yielded stable and comparable results to that seen in literature. The peak storage capacity values achieved in this work, while just under half of what is understood to be the ideal threshold, were appreciable enough for this investigation. It is also lower than the comparably sized high-pressure gas storage vessel.

The intention to store hydrogen at safe and operable pressures which will aid its transportation and storage characteristics remains a significant hurdle to overcome. The metal hydride, at least the intermetallic kind, is still not yet a fully viable route but its promise remains alive. This work produced valuable insight into the effect that numerical grid sizing, supply pressure and bed thickness have on gas absorption for hydride operating.

## ACKNOWLEDGEMENTS

Thank you to the National Research Foundation for funding this work (UID47440).

## REFERENCES

1. United Nations Climate Change. The Paris Agreement. [Online] Available at: https://unfccc.int/process-and-meetings/the-paris-agreement/the-paris-agreement.

2. United Nations. UN climate report: It's 'now or never to limit global warming to 1.5 degrees. [Online] Available at: https://news.un.org/en/story/2022/04/1115452.
3. Climate Transparency & Energy Systems Research Group. Climate Transparency Report: Comparing G20 Climate Action, Climate Transparency. University of Cape Town (2022)
4. Renaud, C., Tyler, D. E., Roff, A. & Steyn, D. G. Accelerating renewable energy industrialisation in South Africa: What's stopping us? *Meridian Economics* (2020).
5. Barretoa, L., Makihiraa, A. & Riahi, K. The hydrogen economy in the 21st century: a sustainable development scenario. *International Journal of Hydrogen Energy* 28:267-284 (2003).
6. Chen, Zhen; Ma, Zhongliang; Zheng, Jie; Li, Xingguo; Akiba, Etsuo & Li, Hai-Wen. Perspectives and challenges of hydrogen storage in solid-state hydrides. *Chinese Journal of Chemical Engineering* 29:1-12 (2021).
7. Sakintuna, B., Lamari-Darkrimb, F. & Hirscher, M. Metal hydride materials for solid hydrogen storage: A review. *International Journal of Hydrogen Energy* 32:1121-1140 (2007).
8. Dornheim, M. Thermodynamics of Metal Hydrides: Tailoring Reaction Enthalpies of Hydrogen Storage Materials. In: Thermodynamics - Interaction Studies - Solids, Liquids and Gases. Ed.J. C. Moreno-Pirajan. Intechopen (2011)
9. Mohammadshahi, S., Gray, E. & Webb, C. A review of mathematical modelling of metal hydride systems for hydrogen storage applications. *International Journal of Hydrogen Energy* 41:3470-3484 (2016).
10. Modi, P. & Aguey-Zinsou, K.-F. Room Temperature Metal Hydrides for Station and Heat Storage Applications: A Review. *Frontiers in Energy Research* 9:616115 (2021).
11. Office of Energy Efficiency & Renewable Energy. DOE Technical Targets for Onboard Hydrogen Storage for Light-Duty Vehicles. [Online] Available at: https://www.energy.gov/eere/fuelcells/doe-technical-targets-onboard-hydrogen-storage-light-duty-vehicles
12. Rusman, N. & Dahari, M. A review on the current progress of metal hydrides material for solid-state hydrogen storage applications. *International Journal of Hydrogen Energy* 41:12108-12126 (2016.).
13. Singh, R. K., Gupta, B. K., Lototsky, M. & Srivastava, O. On the synthesis and hydrogenation behaviour of MmNi5−xFex alloys and computer simulation of their P–C–T curves *Journal of Alloys and Compounds*. 373:208-213 (2004).
14. Muthukumar, P., Madhavakrishna, U. & Dewan, A. Parametric studies on a metal hydride based hydrogen storage device. *International Journal of Hydrogen* 32:4988-4997 (2007).
15. Whitaker, S. Simultaneous Heat, Mass, and Momentum Transfer in Porous Media: A Theory of Drying. In: Advances in Heat Transfer. Ed. J. P. Hartnett & T. F. I. Jr. Academic Press, INC (1977).
16. Hasnain, M., Sezer, H. & Mason, J. H. Modeling heat and mass transfer in metal hydride hydrogen storage systems: Impact of operating parameters and reactor geometry. *International Journal of Hydrogen* 71:1045-1055 (2024).
17. Ben Nasrallah, S., Jemni, A. Heat and Mass Transfer Model in Metal-Hydride Reactors. *International Journal of Hydrogen Energy* 22:67-76 (1997).
18. Chaise, A., Marty, P., Rango, P. d. & Fruchart, D. A simple criterion for estimating the effect of pressure gradients on hydrogen absorption in a hydride reactor. *International Journal of Heat and Mass Transfer* 52:4564-4572 (2009).
19. Patankar, S. V. Numerical Heat Transfer and Fluid Flow. Hemisphere Publishing Corporation/McGraw-Hill Book Company (1980)
20. Ozisik, M. N., Orlande, H. R., Colaco, M. J. & Cotta, R. M. Finite Difference Methods in Heat Transfer. CRC Press 2017
21. Roache, P. J. Computational Fluid Dynamics Hermosa Publishers (1972)
22. Smith, G. H. Numerical Solution of Partial Differential Equations: Finite Difference Methods. Oxford University Press (1985).
23. Xu, Y., Zhou, Y., Li, Y. & Ding, Z. Research Progress and Application Prospects of Solid-State Hydrogen Storage Technology. *Molecules* 29:1767 (2024).

© 2025 by the authors. Licensed to PSEcommunity.org and PSE Press. This is an open access article under the creative commons CC-BY-SA licensing terms. Credit must be given to creator and adaptations must be shared under the same terms. See https://creativecommons.org/licenses/by-sa/4.0/



Systems & Control Transactions

**Research Article - Peer Reviewed Conference Proceeding**
ESCAPE 35 - European Symposium on Computer Aided Process Engineering
Ghent, Belgium. 6-9 July 2025
Jan F.M. Van Impe, Grégoire Léonard, Satyajeet S. Bhonsale,
Monika E. Polańska, Filip Logist (Eds.)

PSE PRESS

# Integrating Renewable Energy and $CO_2$ Utilization for Sustainable Chemical Production: A Superstructure Optimization Approach

**Tianen Lim[a], Yuxuan Xu[a], and Zhihong Yuan[a]***

[a]State Key Laboratory of Chemical Engineering, Department of Chemical Engineering, Tsinghua University, Beijing 100084, China
* Corresponding Author: zhihongyuan@mail.tsinghua.edu.cn.

## ABSTRACT

Climate change, primarily caused by the excessive emission of greenhouse gases, particularly carbon dioxide ($CO_2$), has intensified global efforts toward achieving carbon neutrality. In this context, renewable energy and $CO_2$ utilization technologies have emerged as key strategies for reducing reliance on fossil fuels and mitigating environmental impacts. In this work, a superstructure model is developed to integrate renewable energy network and chemical production processes. The energy network integrates wind, solar, and biomass energy, complemented by storage systems to enhance reliability and reduce reliance on external power sources. The reaction network features various pathways that utilize $CO_2$ as a raw material to produce high value-added chemicals such as polyglycolic acid (PGA), ethylene-vinyl acetate (EVA), and dimethyl carbonate (DMC), allowing for efficient conversion and resource utilization. A mixed-integer linear programming (MILP) model is formulated to minimize production costs while optimizing energy and reaction pathways. This research supports the green transition of the chemical industry by optimizing the integration of renewable energy and $CO_2$-based chemical processes, promoting more sustainable production practices.

**Keywords**: sustainable chemical production, HRES, $CO_2$ utilization, superstructure optimization, MILP

## INTRODUCTION

Global climate change, driven by the excessive emission of greenhouse gases, particularly carbon dioxide ($CO_2$), represents a critical challenge of the 21st century. According to the World Meteorological Organization's (WMO) Greenhouse Gas Bulletin, the global average surface carbon dioxide concentration had reached 420 ppm in 2023, marking an 11.4% increase over the past 20 years [1]. The rapid growth in energy demand, coupled with the finite nature of fossil fuel reserves and their high carbon footprint, underscores the urgent need for a transition to renewable energy sources and implement sustainable development strategies [2]. In the context of China's dual carbon goals, aiming to peaking carbon emissions by 2030 and achieving carbon neutrality by 2060, the emphasis on green chemistry and sustainable production has gained unprecedented importance. These efforts aim to balance economic development with environmental protection, ensuring a sustainable future.

Hybrid renewable energy systems (HRES) have demonstrated significant potential as a solution to enhance the stability and efficiency of renewable energy supply by integrating multiple sources such as solar, wind, and biomass energy. These systems effectively mitigate the intermittency challenges associated with individual renewable sources, contributing to a more reliable and resilient energy network [3]. Meanwhile, the utilization of $CO_2$ as a raw material for high-value chemicals presents a strategic approach to both reduce carbon emissions and foster the circular carbon economy [4]. This approach not only decreases reliance on fossil fuels but also enhances the economic viability of sustainable chemical production by converting $CO_2$ into valuable products like polymers and organic compounds.

However, existing studies often focus either on optimizing renewable energy integration or on specific $CO_2$ conversion technologies, rarely addressing an integrated

approach that combines renewable energy utilization with $CO_2$ conversion in a unified production network. To address this gap, this study develops a novel superstructure model that integrates a hybrid renewable energy system with a chemical production network to optimize the conversion of $CO_2$ into high-value chemicals. In detail, we focus on designing processes driven by renewable energy and optimizing the pathways for $CO_2$ conversion into high-value chemicals including polyglycolic acid (PGA), ethylene-vinyl acetate (EVA), and dimethyl carbonate (DMC). By bridging the gap between renewable energy integration and green chemical production, this research offers valuable insights into achieving carbon neutrality and promoting sustainable production practices.

## MODELING

### Modeling of Hybrid Renewable Energy System (HRES)

The designed HRES in this study consists of two main components: power generation and thermal generation. The superstructure of the HRES is shown in Figure 1. In the power generation section, the system integrates wind power (P1), photovoltaic power (P2), concentrated solar power (P3a,3b), combined cycle gas turbine (P4) technology, and is complemented by battery storage. The thermal generation section includes biomass energy technologies, coal-fired heating (P8) systems, and electric boiler (P9) systems. Biomass undergoes gasification to produce syngas (P5), serving as a dual source for electricity (P6) and heat (P7).

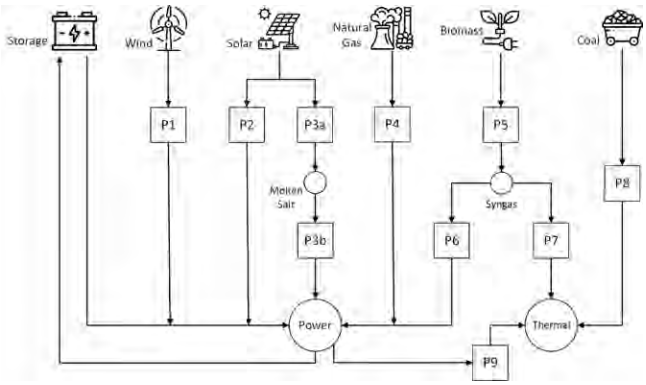



**Figure 1.** Superstructure of the hybrid renewable energy system (HRES).

Wind power and photovoltaic power are among the most widely adopted renewable energy technologies. Wind turbines harness wind energy to produce electricity, while photovoltaic panels directly convert sunlight into electrical power. Despite being environmentally friendly, both of these technologies have significant fluctuations in power generation, often requiring integration with more stable technologies or combined with battery storage. Battery storage facilitates load balancing by storing surplus electricity during off-peak periods and releasing it during peak demand, effectively balancing the energy load and enhancing system reliability. Concentrated solar power (CSP) employs reflective mirrors to concentrate sunlight, generating thermal energy that can be stored via molten salt energy storage (MSES). This thermal storage capability ensures a continuous power supply even during periods without sunlight, improving the dependability of solar energy. The combined cycle gas turbine (CCGT) technology generates electricity by combining gas and steam turbines, using natural gas as the primary fuel. In the context of the HRES, CCGT serves as a reliable supplementary energy source, compensating for any shortfall in renewable energy generation when renewable sources cannot meet demand. Biomass energy offers a dual-purpose solution by generating both electricity and heat through biomass gasification, contributing to a flexible and renewable energy mix. Coal-fired heating generates thermal energy through coal combustion, acting as a transitional technology within the HRES until low-carbon alternatives become more viable. The electric boiler efficiently utilizes surplus electricity during low-demand periods or peak renewable output, enhancing system efficiency and minimizing energy waste.

Each technology in the HRES will be mathematically modeled to evaluate its performance and cost, including both power generation and thermal generation. Technology performance will be assessed considering raw material consumption, installed capacity, and operational efficiency. Energy production costs will be analyzed by integrating raw material, investment, and operational expenses into the cost model. Additionally, the model incorporates dynamic constraints on $CO_2$ emissions, aiming to gradually phase out high-emission technologies and align with global carbon neutrality targets.

### Modeling of Chemical Production Network (CPN)

In the chemical production network (CPN), this study mainly focuses on three products: polyglycolic acid (PGA), ethylene-vinyl acetate copolymer (EVA), and dimethyl carbonate (DMC). PGA is a synthetic polymer with exceptional biodegradability and biocompatibility, widely applied in the pharmaceutical industry and biodegradable plastics [5]. EVA is a versatile polymer known for its flexibility and toughness even at low temperatures, strong adhesion, and stress-cracking resistance, commonly used in applications like footwear materials and packaging molds [6]. DMC is a low-toxicity, environmentally friendly organic compound with applications in polymer synthesis, solvents, and electrolytes [7]. The main raw materials for the production network include $CO_2$, $H_2$, and

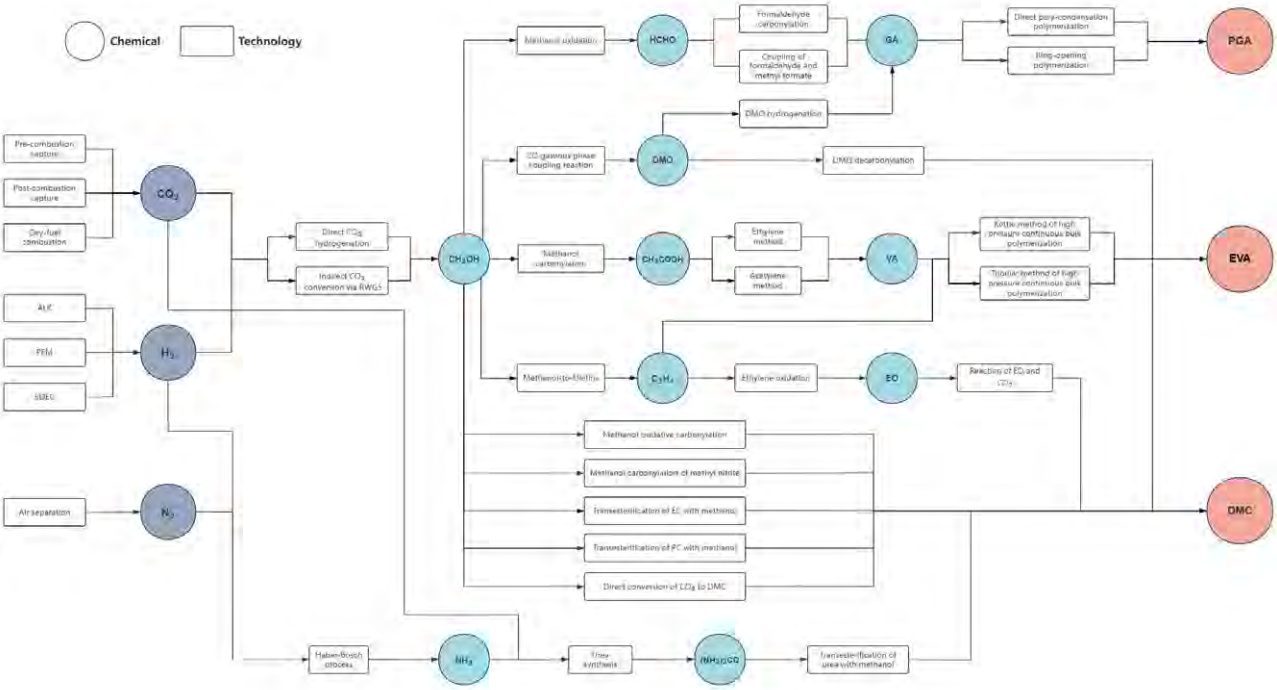



**Figure 2:** Superstructure of the chemical production network (CPN). The figure presents various technological pathways for producing the three main products: PGA, EVA, and DMC. The connections between different chemicals represent the possible pathways from one intermediate chemical to the next.

$N_2$. $CO_2$ can be captured using various methods, while hydrogen is produced through water electrolysis, and nitrogen is typically obtained via air separation technology.

To optimize the conversion of raw materials into final products, a superstructure model encompassing multiple technological options has been developed, as shown in Figure 2. In this model, various technological alternatives may act as substitutes or complements. The selection of a specific technology for each intermediate chemical is mutually exclusive, ensuring only one option is selected for each production step. However, the model allows for multiple technological pathways to produce final products, enhancing the system's design flexibility and operational robustness.

Each technology within the production network is mathematically modeled to represent the chemical conversion and mass balance for both inputs and outputs. Numerous constraints are incorporated to ensure the feasibility and rationality of the model's results, including limitations on feedstock availability, process efficiency, product demand, and network structural constraints. The cost assessments consider investment costs, as well as operational expenses, such as catalyst costs, utility costs, and raw material costs. To estimate these costs, a simplified process simulation approach using Aspen Plus V14 is adopted. This approach focuses on the key stages of chemical production, providing approximations for investment costs and energy demands while avoiding overly complex process details. Investment cost estimation utilizes Aspen Process Economic Analyzer (APEA) V14, while energy consumption, including electricity and thermal demands, is directly assessed through the simulation model. By-products generated during production are treated as additional revenue, which is subtracted from the overall costs. Chemical prices are referenced from market data for cost calculations.

## Integration of HRES and CPN

The integration of HRES and CPN is achieved through the coupling of energy supply and the operational demands of CPN. Electricity generated by the HRES powers key chemical processing equipment, such as pumps, compressors, and mixers, ensuring stable operation and precise process control. Meanwhile, thermal energy is widely employed in heating systems and heat exchange equipment across the production network, meeting the temperature regulation and reaction requirements critical for chemical synthesis.

The energy balance of the integrated system is governed by the energy conservation equations, as represented by Equations (1) and (2).

$$P_{wind,t} + P_{PV,t} + P_{CSP,t} + P_{CCGT,t} + P_{synburn,t} + P^{Out}_{battery,t} = P_{CPN,t} + P^{In}_{battery,t} + P_{cur,t} \quad (1)$$

$$Th_{synburn,t} + Th_{coalburn,t} = Th_{CPN,t} \quad (2)$$

## Optimization Model and Assumptions

### Model Assumptions

1. The relationships between chemical inputs and outputs, as well as the material and energy flows within processes, are simplified and modeled using linear functions.

2. Electricity and heat supplied by the HRES are assumed to be delivered without losses.

3. Transportation and storage costs for raw materials, intermediates, and final products are neglected.

4. A 20-year operational lifecycle is assumed, consistent with the typical lifespan of chemical production facilities.

5. Data sampling is performed at monthly intervals, resulting in 240 discrete time points over the 20-year period.

6. Historical wind and solar energy data for the Qinghai region, China, are used for the HRES analysis, with monthly averages applied to represent each time step.

7. It is assumed that existing CCGT units are already in place and do not require new construction, so the CCGT cost is limited to the operating cost only.

8. Annual chemical production volumes, energy consumption, and thermal demand are assumed to fluctuate randomly within a 10% range.

9. A linear annual reduction in $CO_2$ emissions from CCGT and coal-based heating is enforced, achieving full decarbonization by the ninth operational year.

### Overall Optimization Model

The objective of the optimization model is to minimize the total cost, which includes costs associated with both the HRES and CPN, as shown in Equations (3)-(5). To ensure the accuracy and feasibility of the results, the model incorporates several constraints, as previously discussed. Equation (6) defines the conversion between input and output flow rates for a chemical process technology, which is modeled as a linear relationship. Equation (7) represents the demand constraint for the final products, ensuring that the production quantity of each product meets the specified demand. Equation (8) ensures that only one technological route can be selected for one intermediate chemical to the next.

$$\min obj = C_{HRES} + C_{CPN} \tag{3}$$

$$C_{HRES} = C_{wind} + C_{PV} + C_{CSP} + C_{CCGT} + C_{battery} + C_{bio} + C_{coal} \tag{4}$$

$$C_{CPN} = C_{cap} + C_{operation} + C_{raw} - R_{byprod} \tag{5}$$

$$Output_{P,T} = \alpha_{P,T} \cdot Input_{P,T} \tag{6}$$

$$Flow_P^{final} \geq Demand_P^{final} \tag{7}$$

$$\sum_T x_T^{PP'} = 1 \tag{8}$$

The model was developed using the General Algebraic Modeling System (GAMS) with the CPLEX solver. The model involves 61,555 single equations and 9,037 single variables, including 272 discrete variables.

## RESULTS AND DISCUSSION

### Optimal Route for CPN

The optimization results of the CPN provided insights into the integration of raw material acquisition, intermediate production, and final product synthesis. The optimized network structure, shown in Figure 3, illustrates the production pathways and the selection of related technologies from raw materials to final products. In the optimized network, $CO_2$ is sourced through post-combustion capture, while $H_2$ is generated via alkaline water electrolysis. Methanol emerged as a critical intermediate, enabling the synthesis of various target chemicals through versatile conversion pathways. It is generated through the indirect conversion of $CO_2$ and $H_2$ via the Reverse Water-Gas Shift (RWGS) reaction.

The PGA production pathway begins with methanol participating in a CO gaseous phase coupling reaction to generate dimethyl oxalate (DMO). Subsequently, DMO undergoes hydrogenation to produce glycolic acid (GA), which is polymerized through a ring-opening process to yield the final PGA product. For EVA production, methanol is first converted into formic acid, which is further processed into vinyl acetate (VA) via an acetylene-based reaction. Parallelly, the methanol-to-olefins process produces ethylene. Finally, VA and ethylene react through the tubular method of high-pressure continuous bulk polymerization to produce EVA. In the DMC production route, methanol engages in a transesterification reaction with ethylene carbonate (EC), directly yielding the target product. Notably, the ammonia production route, although included in the network design, was not selected in the optimization. This decision is primarily driven by the high costs associated with using large quantities of green hydrogen, which makes this route economically unfeasible. Overall, the results underscore the significance of methanol as a pivotal intermediate and highlight the economic considerations inherent in the selection of sustainable technologies for chemical production.

### Power and Thermal Generation by HRES

The energy required for the CPN is supplied by the HRES. Figure 4 shows the results of HRES power generation. The system primarily relies on wind energy, which, as expected, exhibits significant fluctuations. To address this variability, a smaller portion of the total energy comes from solar power, which, although still subject to fluctuations, provides more stable generation compared to wind energy. This dual-source approach enhances the

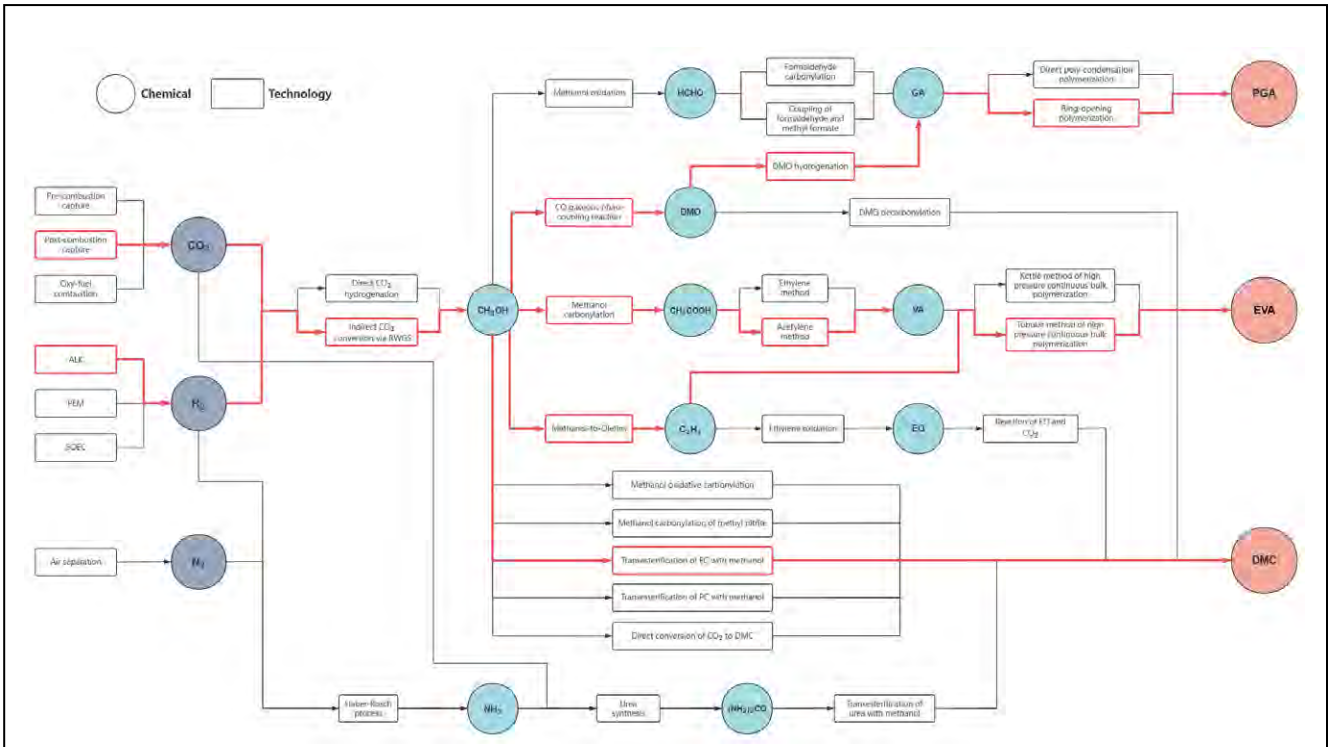



**Figure 3.** Optimized Chemical Production Network Structure.

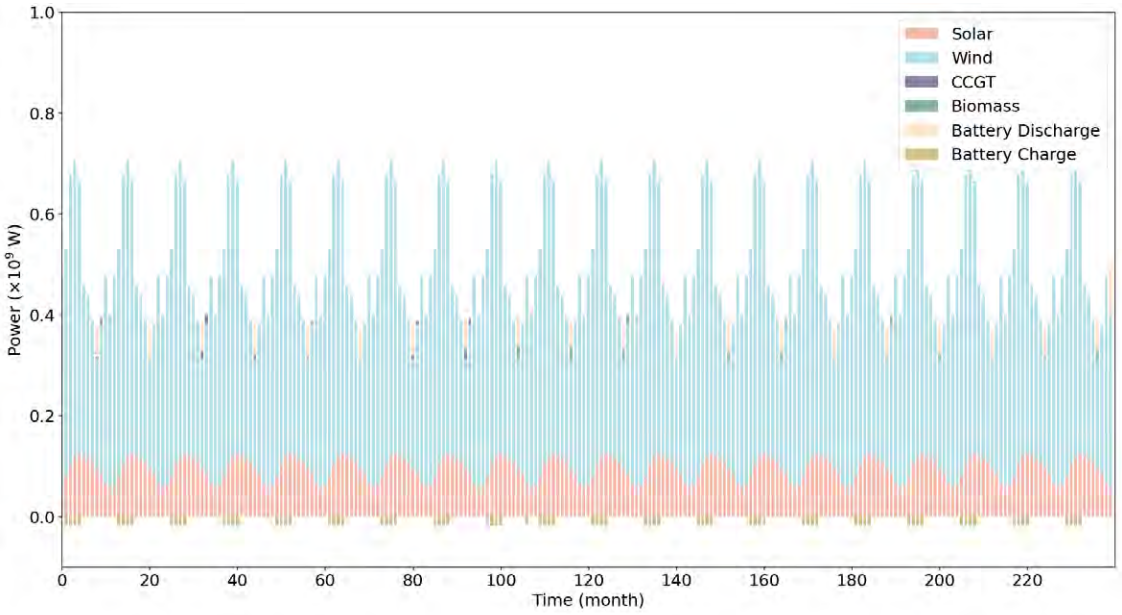



**Figure 4:** Power generation results of HRES. The positive values represent the power generation and discharging portions of the HRES, while the negative values reflect the charging portions.

overall reliability of the power supply. During periods of excess energy, part of the surplus is stored in batteries, while a larger portion is directed to the electric boilers for heat generation, improving the efficiency of electricity utilization. When energy demand exceeds the available renewable generation, the system prioritizes the use of stored energy in batteries to maintain stability. In the initial phase, CCGT technology is used as a supplementary source to bridge the gap. However, as $CO_2$ emission constraints become more stringent, the model gradually reduces reliance on CCGT and transitions towards biomass energy, a more sustainable and low-emission alternative.

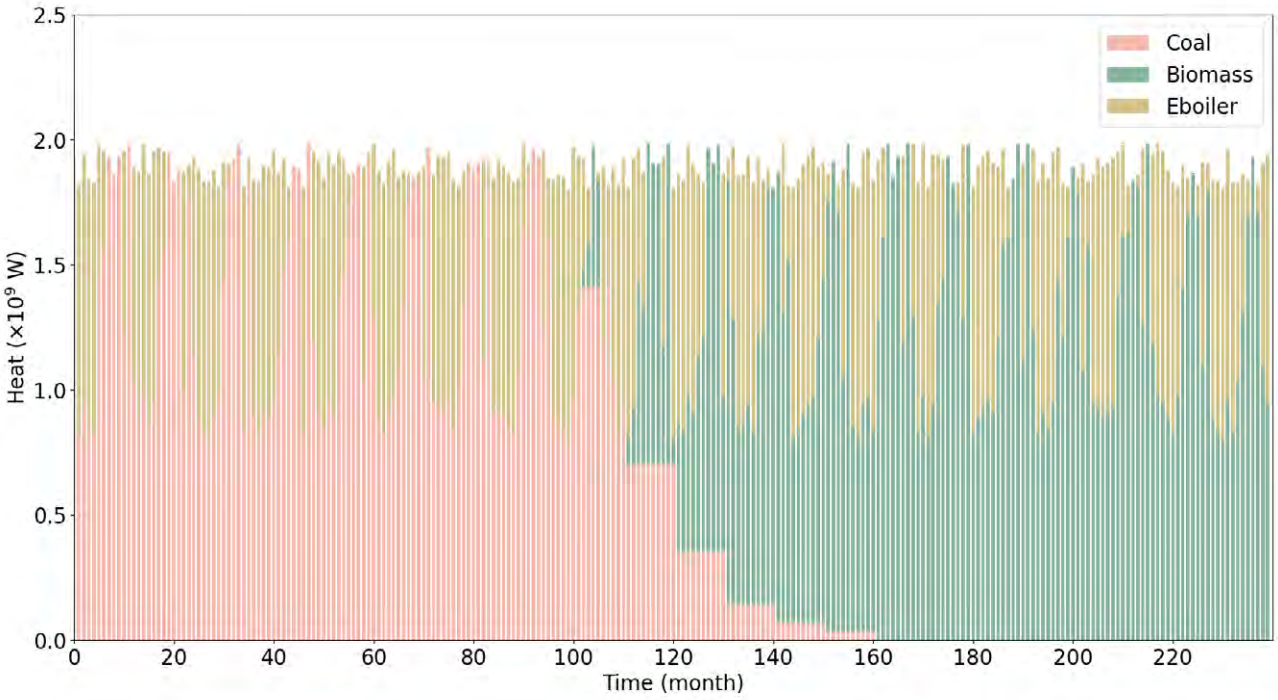



**Figure 5.** Thermal generation results of HRES.

On the other hand, CSP technology was not selected due to its relatively high costs.

The thermal energy generation results, as illustrated in Figure 5, follow a similar trend. In the early stages, the system primarily relies on electric boilers and coal-based heating technology to meet heating demands. Over time, driven by $CO_2$ emission constraints, the model progressively shifts to a combination of electric boilers and biomass energy for heat production. This transition aligns with the goal of reducing carbon emissions and moving towards more sustainable technologies over time.

## Costs of HRES and CPN

The total costs of the HRES and the CPN are crucial in assessing the economic feasibility and efficiency of the integrated system. Table 1 provides an overview of the average power and thermal demands of the CPN, along with the corresponding costs for both the CPN and HRES required to meet these demands. The CPN has production targets of 100,000 tons of PGA, 400,000 tons of EVA, and 400,000 tons of DMC. To meet these production targets, the CPN requires an average power demand of approximately 382.9 MW and a thermal energy demand of 189.6 MW. The total combined cost, represented by the objective function value, amounts to approximately $7.39 billion.

The higher cost of the HRES is largely due to significant initial investments in renewable energy technologies, including wind turbines, solar panels, and energy storage systems. In contrast, the lower cost of the CPN is partly driven by the revenue generated from by-products, which effectively offsets overall production costs. Both the HRES and the CPN are integral components of the overall cost structure, with neither playing a dominant role in the total cost.

**Table 1:** Energy demand of CPN with costs of HRES and CPN.

| Term | Value |
|---|---|
| Average Power demand (W) | $3.829\times10^{8}$ |
| Average Thermal demand (W) | $1.896\times10^{8}$ |
| CPN cost ($) | $3.039\times10^{9}$ |
| HRES cost ($) | $4.349\times10^{9}$ |
| Objective function ($) | $7.388\times10^{9}$ |

## CONCLUSION

In this study, a novel superstructure optimization framework integrating hybrid renewable energy systems (HRES) with chemical production networks (CPN) was developed to address global energy and green chemical production challenges. This approach considers both energy and material flows, enabling a more comprehensive decision-making process for sustainable chemical production. The optimization provides valuable insights into the selection of efficient production technologies for the CPN and the optimal configuration of HRES technologies. The results highlight the ability to create a resilient and

flexible energy supply by combining renewable sources with supplementary technologies such as CCGT and biomass, ensuring a stable and reliable power and heat supply for chemical processes. Additionally, the utilization of $CO_2$ as a feedstock is emphasized as a critical strategy for reducing carbon emissions while contributing to the production of high-value chemicals, further promoting the transition to a sustainable, low-carbon economy.

Despite its contributions, this study has some limitations. The model is based on historical renewable energy data and assumes monthly-averaged values, which may not fully capture real-time fluctuations in energy availability. Additionally, the optimization is conducted within a deterministic framework, meaning that uncertainties in energy supply, raw material prices, and market demand are not explicitly accounted for. Future research will focus on expanding green chemical production pathways, particularly by utilizing $CO_2$ as a feedstock for chemical synthesis. Additionally, incorporating uncertainty factors related to renewable energy availability, raw material supply and product demand will be vital for enhancing the robustness and reliability of the model. By addressing these uncertainties, the aim is to develop more resilient and cost-effective solutions that facilitate the transition toward a carbon-neutral chemical production sector, aligning with global sustainability goals.

## ACKNOWLEDGEMENTS

The authors gratefully acknowledge the financial support from the National Natural Science Foundation of China under Gant U24B6016.

## REFERENCES

1. World Meteorological Organization, WMO Greenhouse Gas Bulletin No.20 (2024).
2. Taghavi M, Lee CJ. Development of novel hydrogen liquefaction structures based on waste heat recovery in diffusion-absorption refrigeration and power generation units. *ENERGY CONVERS MANAG* 302: 118056 (2024).
3. Thirunavukkarasu M, Sawle Y, Lala H. A comprehensive review on optimization of hybrid renewable energy systems using various optimization techniques. *RENEW SUST ENERG REV* 176: 113192 (2023).
4. Zhang Z, Pan SY, Li H, et al. Recent advances in carbon dioxide utilization. *RENEW SUST ENERG REV* 125: 109799. (2020).
5. Samantaray PK, Little A, Haddleton DM, et al. Poly (glycolic acid) (PGA): A versatile building block expanding high performance and sustainable bioplastic applications. *GREEN CHEM* 22(13): 4055-4081 (2020).
6. Han DH, Choi MC, Nagappan S, et al. Ethylene vinyl acetate (EVA)/poly (lactic acid) (PLA) blends and their foams. *MOL CRYST LIQ CRYST* 707(1): 38-45 (2020).
7. Kumar P, Srivastava VC, Štangar UL, et al. Recent progress in dimethyl carbonate synthesis using different feedstock and techniques in the presence of heterogeneous catalysts. *CATAL REV* 63(3): 363-421 (2021).

© 2025 by the authors. Licensed to PSEcommunity.org and PSE Press. This is an open access article under the creative commons CC-BY-SA licensing terms. Credit must be given to creator and adaptations must be shared under the same terms. See https://creativecommons.org/licenses/by-sa/4.0/



Systems & Control Transactions

**Research Article - Peer Reviewed Conference Proceeding**
ESCAPE 35 - European Symposium on Computer Aided Process Engineering
Ghent, Belgium. 6-9 July 2025
Jan F.M. Van Impe, Grégoire Léonard, Satyajeet S. Bhonsale,
Monika E. Polańska, Filip Logist (Eds.)

PSE PRESS

# An Integrated Approach for the Sustainable Water Resources Optimization

**Michaela C. Zaroula[a], Emilia M. Kondili [a*], John K. Kaldellis[b]**

[a] Optimisation of Production Systems Lab, Mechanical Engineering Department, University of West Attica
[b] Soft Energy Applications and Environmental Protection Lab., Mechanical Engineering Department, University of West Attica
* Corresponding Author: ekondili@uniwa.gr

## ABSTRACT

Ensuring access to clean water, preserving water reserves, and meeting energy needs are fundamental for sustainability and a priority for global organizations like the UN and EU. The Mediterranean, particularly Greece, faces severe water imbalances due to rising demand, prolonged droughts, and seasonal tourism pressure. This over-exploitation of water resources threatens agriculture, employment, and regional sustainability. Addressing these challenges, this study analyzes the water-energy nexus in high-stress areas and develops an optimization model for sustainable water resource management. The model integrates sectoral demands, energy consumption, and seasonal variability to improve efficiency while balancing economic and environmental constraints. Additionally, it incorporates demand forecasting to align water use with ecosystem sustainability, reducing environmental impacts. By providing a systematic framework for decision-makers, this research supports the development of long-term, resilient water management strategies, ensuring efficient resource allocation in vulnerable regions. The findings will contribute to sustainable water policies and infrastructure planning.

**Keywords**: water resources, water-energy nexus, water sustainability, optimisation, mathematical model

## 1. INTRODUCTION

Water is vital for human survival, socio-economic development, and ecological balance. However, global water scarcity is intensifying due to rising demand and the impacts of climate change. Approximately 844 million people currently lack access to safe drinking water, and nearly 2 billion live in areas of high water stress. By 2050, water demand is expected to rise by 30%, further straining resources and exacerbating challenges in already water-stressed regions [1].

The Mediterranean region, home to over 500 million people, is particularly vulnerable to these challenges. Renewable water resources are estimated at 1,500 km³ annually, but their distribution is highly uneven: 74% is available in the north, 21% in the east, and only 5% in the south. Agriculture, which accounts for over 65% of the region's water withdrawals, is especially at risk from shortages, jeopardizing food security and economic stability [2]. In Greece, seasonal and geographic dynamics compound the issue. The influx of tourists during the summer months significantly increases water stress, particularly in island regions where reserves are already limited. Overexploitation of aquifers has led to the depletion of water reserves, with negative impacts on agriculture, biodiversity, and local economies. Reduced irrigation capacity has contributed to declining agricultural productivity and a shrinking workforce in the sector. These issues are further exacerbated by climate change, which causes prolonged droughts, increased temperatures, and the salinization of freshwater sources, severely diminishing the availability of potable water [2].

Another critical factor is the water-energy nexus, reflecting the interdependence between water and energy systems. Globally, water systems—including supply, treatment, distribution, and wastewater management—consume approximately 7% of total electricity. Drinking water treatment requires energy inputs ranging from 0.4–3 kWh/m³, while seawater desalination, increasingly relied upon in arid regions, demands 3.9–4.3 kWh/m³, making it one of the most energy-intensive processes. This interconnection highlights the need for integrated

strategies that address both water and energy demands efficiently [3].

Sustainable water management is essential for addressing these challenges. Optimization techniques like linear programming, mixed-integer programming, and dynamic simulations enhance resource allocation, reduce losses, and lower energy consumption. Studies show these models can cut leakage rates by up to 30% and achieve 15–20% energy savings in urban water systems [4]. Recognizing the urgency, the EU has prioritized water optimization in its 2030 agenda, promoting smart management technologies like real-time monitoring to reduce inefficiencies and expand clean water access to 70 million citizens [5]. These measures align with sustainability goals and mitigate climate change impacts.

This study explores advanced optimization techniques to balance water resource allocation and energy consumption while adhering to sustainability goals. By integrating innovative tools and approaches, it aims to deliver actionable solutions for sustainable water management, ensuring resilience and alignment with broader climate and development objectives.

## 2. CURRENT SITUATION

### 2.1. Global and economic impact of water scarcity

Despite notable advancements in water management technologies and infrastructure, water scarcity continues to be a pressing global challenge and is recognized as one of the most critical risks for the coming decade. Globally, over 2 billion people are living in regions of high water stress, with projections indicating that this number will increase due to population growth, urbanization, and climate change. Additionally, 1 billion people lack access to clean and safe drinking water, leading to significant health crises, including 3.4 million deaths annually caused by water-related diseases [6].

Agriculture consumes over 80% of global freshwater resources, making it the most vulnerable sector to water shortages, especially in arid and semi-arid regions where irrigation is critical for food production [7]. Urbanization and industrial activities further exacerbate the strain on water availability, highlighting the urgent need for sustainable water resource management. The financial repercussions of droughts, which often exacerbate water scarcity, are substantial. In the United States, annual drought damages are estimated between $2 billion and $6 billion, while in the European Union, these losses amount to approximately $3 billion annually [8]. These costs represent 0.05% to 0.1% of the GDP, though in particularly severe years, the economic burden can rise dramatically, impacting multiple sectors, including agriculture, industry, and domestic water use [9].

### 2.2. Water scarcity in Mediterranean and Greece

The Mediterranean region is home to over 500 million people, with population growth and trends varying across the 24 countries in the area. Between 2008 and 2018, the population increased by **11%**, adding further strain to the region's already limited water resources [1]. The annual water requirement in the Mediterranean, estimated to range between 500 and 1000 $m^3$ per capita, has risen due to the combined pressures of population growth, urbanization, and the expansion of irrigated agriculture [10]. Currently, the region is classified as "water-poor," with less than 1000 $m^3$ of water available per person annually. According to United Nations projections, this water scarcity will intensify, potentially affecting 250 million people by 2040 [1].

Greece possesses a sufficient overall supply of water resources; however, significant challenges remain in ensuring their efficient utilization and management. This is particularly true given the country's distinct geographical features and climatic variability. Greece generates approximately 72 $km^3$ of renewable freshwater annually, while its annual water consumption stands at about 9.5 $km^3$. Water consumption is also heavily influenced by land use patterns, with agriculture being the dominant user. Depending on the district, agricultural water usage ranges from 11% to 92%, with a national average of approximately 74% [11].

## 3. WATER-ENERGY NEXUS

### 3.1. The dynamic interdependence of the water-energy nexus

Water and energy are intricately interconnected, forming a complex relationship that varies at local and regional levels. Communities rely on water for a wide range of purposes, including residential, commercial, industrial, recreational, and agricultural activities. In urban water systems specifically, energy plays a critical role in every stage of the water management cycle, from intake and purification to transmission, distribution, sewage collection, treatment, recycling, and discharge back into natural waterways. This interdependence becomes even more evident as an increase in water demand directly drives a required to manage these resources efficiently [12].

For instance, one study [13] highlighted that groundwater abstraction for drinking water requires significantly higher energy consumption compared to surface water abstraction, demonstrating the energy demands of different water sources. Similarly, research [14] in Germany found that reducing fossil fuel production contributed to alleviating water stress, emphasizing the interconnection between energy policies and water resources. The importance of minimizing energy use in

water and wastewater treatment systems has also been underscored [15], as this can yield substantial environmental and economic benefits. Furthermore, factors such as water use patterns, topography, climate, and operational efficiencies significantly influence energy intensities in water purification processes, highlighting the need for tailored strategies to optimize energy use in specific contexts[16].

### 3.2. Navigating challenges and innovations in the water-energy nexus

The intricate balance between water and energy resources presents significant challenges that are often compounded by trade-offs inherent in their interdependence. For instance, desalination, a vital water source in arid regions, is highly energy-intensive, raising concerns about its environmental and economic sustainability, especially in energy-scarce areas. Similarly, thermoelectric power generation, which relies heavily on water for cooling, is vulnerable to water shortages, particularly in regions experiencing droughts or increased competition for water resources. These examples illustrate how actions to secure one resource can inadvertently strain the other, emphasizing the need for integrated and sustainable approaches to resource management [17].

To address these challenges, technological innovations offer promising solutions. Advances in energy-efficient desalination technologies, such as reverse osmosis membranes with enhanced permeability and durability, are helping to reduce the energy footprint of water production. Similarly, adopting renewable energy sources, such as solar and wind power, for water management processes like pumping, desalination, and wastewater treatment significantly mitigates the reliance on fossil fuels, thereby reducing greenhouse gas emissions. Additionally, smart water systems that incorporate IoT and big data analytics enable real-time monitoring and optimization of water distribution networks, minimizing energy losses and improving overall efficiency [18, 19].

## 4. OPTIMISATION

### 4.1. Optimising water supply systems within the water-energy nexus

Efficient design, management, and planning of water supply systems with a focus on the water-energy nexus can preserve resources and reduce avoidable costs in investments, operations, and management. However, optimization challenges in this nexus have primarily been addressed from either a water or energy perspective, with limited studies focusing on their simultaneous optimization [20, 21].

To bridge these gaps, recent research emphasizes integrative frameworks for dual optimization of water and energy. Multi-objective models have been developed to minimize costs, improve resource efficiency, and mitigate environmental impacts, enabling decision-makers to optimize both systems concurrently and achieve a more sustainable and resilient nexus [22, 23].

One notable strategy is the application of mixed-integer linear programming (MILP) and graphical methods to identify optimal solutions. MILP-based models provide precision and adaptability, accommodating complex interdependencies between water supply systems and energy demands. Similarly, graphical optimization techniques, such as composite curves, visually represent resource flows and help pinpoint the minimum water and energy requirements for a given demand, as demonstrated in case studies like Spain's water-energy nexus [23].

### 4.2. Integrated approaches, challenges and future directions

Integrated approaches are particularly effective in urban areas, where centralized and decentralized systems coexist. Platforms like resilience.io employ agent-based modeling to simulate the spatiotemporal dynamics of resource demand and supply [22]. These simulations facilitate informed planning by considering factors such as demographic changes, urbanization, and renewable energy integration. Moreover, technological innovations play a vital role in optimizing the water-energy nexus. Renewable energy-powered water treatment facilities and decentralized systems have emerged as promising solutions to address resource constraints. For instance, integrating solar-powered desalination systems can significantly reduce energy consumption in water-scarce regions [23]. Despite progress, several challenges remain in advancing nexus optimization. Key issues include the lack of comprehensive datasets, computational limitations in large-scale models, and the need to account for uncertainties such as climate variability and fluctuating resource demands. Future research should prioritize several key areas to advance understanding and practical solutions within the water-energy nexus. First, there is a pressing need to develop adaptive and scalable models that incorporate stochastic variables and scenario-based analyses, allowing for more accurate predictions and better handling of uncertainties. Second, improving data availability and quality is crucial to enhance the accuracy of models and support informed decision-making processes. High-resolution, reliable data can help identify trends, assess resource dependencies, and tailor solutions to specific contexts [24, 25].

## 5. MATHEMATICAL MODEL

### 5.1. Description

Water resource management in Greece faces significant challenges, especially in regions heavily influenced

by tourism. Seasonal peaks during the summer tourist season create high water demand, intensifying the strain on limited water supplies. Furthermore, water extraction and distribution systems are energy-intensive, adding an additional layer of complexity due to environmental and economic considerations. As a result, a strategic approach is required to ensure the efficient and sustainable use of available resources.

To address these challenges, this study presents a linear optimization model designed to optimize water resource allocation while balancing costs, energy consumption, and environmental sustainability. The model integrates sectoral water demands, energy consumption, and seasonal variability to achieve a cost-effective and sustainable solution. Specifically, it is tailored for application in Greece, where water scarcity, tourism-driven seasonal demand, and high energy costs create significant management challenges. Regions such as the Greek islands (e.g., Crete, Cyclades) and mainland agricultural zones (e.g., Thessaly) serve as potential case studies for validating the model's effectiveness in optimizing water allocation and energy use.

The optimization model aims to minimize the total cost of water allocation, taking into account the direct costs of sourcing and distributing water, as well as the energy costs incurred during extraction and distribution. By applying this approach, the model provides a systematic framework for improving water management in high-demand regions, ensuring long-term sustainability while addressing socio-economic and environmental constraints.

The objective function is mathematically expressed as:

$$Z = \sum_{t=1} \sum_{i=1}^{n} \sum_{j=1}^{m} \left( C_{i,j}^{t} * x_{i,j}^{t} + E_i * P_i * x_{i,j}^{t} \right) \quad (1)$$

Where:

- Z: total cost to minimize
- t: index of the time periods (peak, off-season)
- i: index of water sources (i=1,…,n)
- j: index of water demand sectors (j=1,…,m)
- $C_{i,j}^{t}$ : cost per unit of water ($/m³) from source i for sector j in season t
- $x_{i,j}^{t}$: volume of water allocated (m³) from source i to sector j in season t
- $E_i$: energy intensity of water source i (kWh/m³)
- Pi: energy cost for source i ($/kWh)

This function ensures that the water sourcing and energy costs are optimized over all sources, sectors, and seasons. In this model, t represents different time periods, specifically seasonal variations (e.g., peak and off-season demand). Thus, the total cost Z reflects the overall annual expenditure for water allocation and energy use, ensuring cost-effective and sustainable water distribution throughout the year.

## 5.2. Constraints

### 5.2.1. Water availability constraint

The total water extracted from each source i during season t cannot exceed its seasonal availability$W_i^t$, which is influenced by natural recharge rates, legal extraction limits, and infrastructure capacity. In Greece, the touristic season significantly amplifies water demand, especially in island regions and coastal areas. This seasonal surge often coincides with lower rainfall periods, intensifying stress on local water resources. The constraint ensures that extraction levels remain sustainable, balancing the needs of permanent residents and seasonal visitors without compromising long-term water availability. Planning for peak tourist seasons is critical to preventing overexploitation and ensuring sufficient reserves for off-peak periods.

$$\sum_{j=1}^{m} x_{i,j}^{t} \leq W_i^t, \ \forall \ i,t \quad (2)$$

### 5.2.2. Sectoral demand constraint

The total water allocated to each sector j during season t must at least meet its dynamic seasonal demand$D_j^t$. This demand is driven by factors such as peak tourist influx, crop-specific irrigation needs, and domestic water consumption. By ensuring sectoral demands are met, this constraint supports economic activities, such as agriculture and tourism, while safeguarding basic human needs. It also accounts for sector-specific priorities during water shortages; ensuring essential services like healthcare or food production are not compromised.

$$\sum_{i=1}^{n} x_{i,j}^{t} \geq D_j^t \ , \ \forall \ j,t \quad (3)$$

### 5.2.3. Energy sustainability constraint

The total energy required for water extraction and distribution must not exceed the allowable energy threshold $E_{max}$. This includes energy from renewable and non-renewable sources, factoring in energy efficiency and carbon reduction strategies. Energy sustainability is critical to managing the water-energy nexus, reducing operational costs, and achieving climate goals.

$$\sum_{t=1} \sum_{i=1}^{n} \sum_{j=1}^{m} \left( E_i * x_{i,j}^{t} \right) \leq E_{max} \quad (4)$$

### 5.2.4. Environmental sustainability constraint

The environmental impact of water sourcing, expressed as $I_i$, must remain within acceptable ecological limits $I_{max}$. The coefficient $I_i$ represents the environmental impact per cubic meter of water extracted from source i. It can be measured in terms of greenhouse gas emissions

(kg $CO_2/m^3$), water quality degradation (e.g., pollutant levels per $m^3$), or ecosystem disturbance (e.g., groundwater depletion rates). By enforcing this constraint, the model ensures that water sourcing remains within ecologically sustainable limits.. Adherence to this constraint helps minimize the degradation of natural habitats, ensure compliance with environmental regulations, and maintain biodiversity.

$$\sum_{t=1}\sum_{j=1}^{m} x_{i,j}^{t} * I_i \leq I_{max} \ , \ \forall i \quad (5)$$

### 5.2.5. Infrastructure capacity constraint

Each water source has an infrastructure capacity ($F_i$) limiting the maximum water that can be extracted during season t. This constraint considers the physical limits of pumps, pipelines, and storage facilities, as well as maintenance schedules and potential downtime. By enforcing these limits, the constraint prevents overloading of infrastructure and ensures its longevity. It also emphasizes the importance of planned infrastructure upgrades to accommodate future water demands without jeopardizing system reliability.

$$\sum_{j=1}^{m} x_{i,j}^{t} \leq F_i, \ \forall \ i,t \quad (6)$$

### 5.2.6. Non- negativity constraint

The non-negativity constraint ensures that all decision variables in the optimization model take non-negative values. In the context of water resource management, this constraint guarantees that the volume of water allocated from each source to each sector remains physically meaningful and prevents unrealistic negative values in calculations.

$$\sum_{j=1}^{m} x_{i,j}^{t} \leq F_i, \ \forall \ i,t \quad (7)$$

## 6. CONCLUSIONS AND FUTURE STEPS

### 6.1. Conclusions

This study presents an integrated optimization model for sustainable water resource management, addressing water scarcity challenges in regions like Greece and the Mediterranean. Seasonal demand fluctuations, climate change, and rising energy costs for water extraction and distribution intensify these issues. By analyzing the water-energy nexus, this research highlights the interdependencies between water availability, energy use, and economic sustainability, emphasizing the need for multi-objective resource management.

The model enhances water allocation efficiency while balancing economic, energy, and environmental factors. It considers sectoral demand variations, infrastructure constraints, and future consumption trends, ensuring resilient and adaptive distribution. Using multi-objective optimization, it maximizes resource efficiency, reduces losses, and promotes equitable distribution. Integrating renewable energy sources such as solar desalination and wind-assisted distribution can further enhance sustainability and reduce operational costs.

While this study primarily focuses on the model's formulation and theoretical framework, future research will focus on applying the model to real-world case studies. The next steps involve validating its effectiveness using data from Greek regions with high seasonal water demand, such as Aegean Islands. This practical application will allow for a detailed assessment of the model's performance in optimizing water allocation and minimizing environmental impact.

Future research should strengthen the water-energy nexus, embedding energy-efficient technologies like smart grids and wastewater recycling into water systems. Sectoral prioritization must be improved to ensure schools, hospitals, and homes receive priority during scarcity, supported by real-time data analytics. Advances in machine learning and AI-driven forecasting will improve demand predictions, while climate-resilient strategies and early warning systems will enhance preparedness. Expanding hybrid renewable energy solutions will further mitigate reliance on fossil fuels. By integrating these innovations, water-energy optimization can enhance resilience, sustainability, and socio-economic stability in water-stressed regions.

## ACKNOWLEDGEMENTS

This research has been funded under the investment support action "Flagship actions in interdisciplinary scientific areas with a special interest in the connection with the productive tissue" / Emblematic Action of Green Islands in the framework of the circular economy (NHSOS) – TAEDR-0537029. The action is implemented within the framework of the National Recovery and Resilience Plan Greece 2.0 with funding from the European Union - NextGenerationEU.

## REFERENCES

1. Vinci, G., Maddaloni, L., Mancini, L., Prencipe, S. A., Ruggeri, M., & Tiradritti, M. (2021). The health of the water planet: Challenges and opportunities in the mediterranean area. An overview. Earth, 2(4), 894-919.
2. Sorlini, S., Rondi, L., Pollmann Gomez, A., & Collivignarelli, C. (2015). Appropriate technologies for drinking water treatment in Mediterranean countries. Environmental Engineering & Management Journal (EEMJ), 14(7).
3. Subramani, A., Badruzzaman, M., Oppenheimer, J., & Jacangelo, J. G. (2011). Energy minimization strategies and renewable energy utilization for desalination: a review. Water research, 45(5),

1907-1920.
4. Ahmad, S., Jia, H., Chen, Z., Li, Q., & Xu, C. (2020). Water-energy nexus and energy efficiency: A systematic analysis of urban water systems. Renewable and Sustainable Energy Reviews, 134
5. Taylor, P. (2013). National Stakeholder Consultations on Water: Supporting the Post-2015 Development Agenda. The Post-2015 Water Thematic Consultation.
6. WWAP (UNESCO World Water Assessment Programme). The United Nations World Water Development Report 2019: Leaving No One Behind; UNESCO: Paris, France, 2020.
7. Dalezios, N. R., Angelakis, A. N., & Eslamian, S. (2018). Water scarcity management: part 1: methodological framework. International Journal of Global Environmental Issues, 17(1), 1-40.
8. Europea, C. (2007) Addressing the challenge of water scarcity and droughts in the European Union. Commu- nication from the Commission to the European Parliament & the Council, COM (2007), 414.
9. Kirby, M., Bark, R., Connor, J., Qureshi, M. E., & Keyworth, S. (2014). Sustainable irrigation: How did irrigated agriculture in Australia's Murray–Darling Basin adapt in the Millennium Drought?. Agricultural Water Management, 145, 154-162.
10. Rossano, C., Milstein, A., Nuccio, C., Tamburini, E., & Scapini, F. (2020). Variables affecting the plankton network in Mediterranean ports. Marine Pollution Bulletin, 158, 111362.
11. Panagopoulos, A., & Giannika, V. (2023). Study on the water resources and the opportunities for sustainable desalination & minimal/zero liquid discharge (MLD/ZLD) practices in Greece (Eastern Mediterranean). Sustainable Water Resources Management, 9(4), 106.
12. Rezaei Kalvani, S., & Celico, F. (2024). Analysis of Pros and Cons in Using the Water–Energy–Food Nexus Approach to Assess Resource Security: A Review. Sustainability, 16(7), 2605.
13. Lechón, Y., De La Rúa, C., & Cabal, H. (2018). Impacts of decarbonisation on the water-energy-land (WEL) nexus: a case study of the spanish electricity sector. Energies, 11(5), 1203.
14. Heinrichs, H. U., Mourao, Z., Venghaus, S., Konadu, D., Gillessen, B., Vögele, S., Linssen J., Allwood J.,Kuckshinrichs W., Robinius M., Stolten D. (2021). Analysing the water and land system impacts of Germany's future energy system. Renewable and Sustainable Energy Reviews, 150, 111469.
15. Gude, V. G. (2015). Energy and water autarky of wastewater treatment and power generation systems. Renewable and sustainable energy reviews, 45, 52-68.
16. ] Lam, K. L., Kenway, S. J., & Lant, P. A. (2017). Energy use for water provision in cities. Journal of cleaner production, 143, 699-709.
17. Fan, J. L., Kong, L. S., Wang, H., & Zhang, X. (2019). A water-energy nexus review from the perspective of urban metabolism. Ecological modelling, 392
18. Aivazidou, E., Banias, G., Lampridi, M., Vasileiadis, G., Anagnostis, A., Papageorgiou, E., & Bochtis, D. (2021). Smart technologies for sustainable water management: An urban analysis. Sustainability, 13(24), 13940.
19. Ahmed, F. E., Khalil, A., & Hilal, N. (2021). Emerging desalination technologies: Current status, challenges and future trends. Desalination, 517Santhosh, A., Farid, A. M., & Youcef-Toumi, K. (2014). Real-time economic dispatch for the supply side of the energy-water nexus. Applied Energy 122, 42-52.
20. Santhosh, A., Farid, A. M., & Youcef-Toumi, K. (2014). The impact of storage facility capacity and ramping capabilities on the supply side economic dispatch of the energy–water nexus. Energy, 66.
21. Wang, X., van Dam, K. H., Triantafyllidis, C., Koppelaar, R. H., & Shah, N. (2019). Energy-water nexus design and operation towards the sustainable development goals. Computers & Chemical Engineering, 124, 162-171.
22. Prabhakar, S., & Bandyopadhyay, S. (2023). Graphical Optimisation of Supplying Water and Energy in a Water-Energy Nexus System. Chemical Engineering Transactions, 103, 307-312.
23. Ghassemi, A., & Scott, M. J. (2021). A mathematical approach to improve energy-water nexus reliability using a novel multi-stage adjustable fuzzy robust approach. In Progress in Intelligent Decision Science: Proceeding of IDS 2020 (pp. 115-123). Springer International Publishing.
24. Ghassemi, A., & Scott, M. J. (2021). A mathematical approach to improve energy-water nexus reliability using a novel multi-stage adjustable fuzzy robust approach. In Progress in Intelligent Decision Science: Proceeding of IDS 2020 (pp. 115-123). Springer International Publishing.

© 2025 by the authors. Licensed to PSEcommunity.org and PSE Press. This is an open access article under the creative commons CC-BY-SA licensing terms. Credit must be given to creator and adaptations must be shared under the same terms. See https://creativecommons.org/licenses/by-sa/4.0/



Systems & Control Transactions

**Research Article - Peer Reviewed Conference Proceeding**
ESCAPE 35 - European Symposium on Computer Aided Process Engineering
Ghent, Belgium. 6-9 July 2025
Jan F.M. Van Impe, Grégoire Léonard, Satyajeet S. Bhonsale,
Monika E. Polańska, Filip Logist (Eds.)

PSE PRESS

# Optimization of hydrogen system deployment via environmental and economic life cycle assessment

**Alessandro Poles[a], Catherine Azzaro-Pantel[a], Henri Schneider[b], Renato Luise[c]**

[a] Laboratoire de Génie Chimique, Université Toulouse, CNRS, INPT, Toulouse, France
[b] Laboratoire Plasma et Conversion d'Énergie, INPT, Toulouse, France
[c] European Institute for Energy Research, Emmy-Noether Straße 11, Karlsruhe, Germany
alessandro.poles@toulouse-inp.fr, catherine.azzaropantel@toulouse-inp.fr, henri.schneider@laplace.univ-tlse.fr, Renato.Luise@eifer.org

## ABSTRACT

Hydrogen is increasingly recognized as a key player in future energy systems. However, its production technologies—Steam Methane Reforming (SMR) and electrolysis—present trade-offs. SMR, the dominant method, is cost-effective but has a significant carbon footprint, emitting substantial greenhouse gases (GHGs). In contrast, electrolysis, powered by renewable energy sources, offers a cleaner alternative, albeit at a higher cost. While current hydrogen system optimizations primarily focus on cost reduction and GHG mitigation, they often neglect broader environmental impacts. This paper addresses the challenge of modeling a hydrogen supply chain (HSC) that achieves strong environmental performance at a relatively affordable cost. To this end, a supply chain design optimization is coupled with Life Cycle Assessment (LCA). The novelty of this work lies in the integration of multiple LCA indicators in the supply chain design optimization, rather than focusing solely on costs and Global Warming Potential. The model employs a multi-period (2025–2050) mixed-integer linear programming (MILP) formulation, implemented in the General Algebraic Modeling System (GAMS) environment, using CPLEX as the solver. The Bourgogne-Franche-Comté region is used as a case study to illustrate the framework. Initial optimization results highlight how varying the focus on different parameters can lead to distinct solutions and provide insights into the interactions between indicators. Future research will aim to reduce the dimensionality in multi-objective optimization to improve efficiency while maintaining environmental sustainability in the development of hydrogen networks.

**Keywords**: Hydrogen Supply Chain, Life Cycle Assessment, Green Energy, Multi-criteria assessment

## INTRODUCTION

In the context of energy systems, hydrogen has emerged as a key component of the future energy mix. However, hydrogen production technologies, such as Steam Methane Reforming (SMR) and electrolysis, present significant trade-offs between costs and greenhouse gas (GHG) emissions. SMR currently dominates the market due to its lower production cost, but leads to high GHG emissions. In contrast, electrolysis, when powered by renewable energy, offers a lower-carbon alternative, though at a higher cost. Most existing hydrogen system optimizations focus on reducing costs and minimizing GHG emissions, often overlooking broader environmental considerations.

The central research question addressed by this study is: How can a multi-criteria environmental approach improve the optimal design of hydrogen production systems by including a wider range of environmental factors, and how can the interrelations between these criteria inform more sustainable decision-makers?

To answer this question, this study integrates hydrogen supply chain design with life cycle assessment (LCA). The optimization will be based on Mixed Integer Linear Programming (MILP) and incorporate LCA indicators using the ReCiPe2016 method to calculate environmental indicators. A case study in the French region of Bourgogne-Franche-Comté will illustrate the application of the proposed framework, addressing both industrial and mobility-related hydrogen demand.

## LITERATURE REVIEW

### Hydrogen supply chain

For the production of hydrogen, the most developed technologies include SMR, electrolysis, and gasification, each with significant trade-offs. Today hydrogen is primarily produced via SMR, as the technology is well-established in the market and offers a relatively low production cost (~2 €/kg$H_2$ [1]), despite its substantial greenhouse gas emissions (10-19 kg$CO_2$/kg$H_2$ [1]). Electrolysis is expected to grow and eventually overtake SMR-based technology, as it offers low-carbon alternatives to produce hydrogen, provided that its electricity requirement is met by renewables [2]. Low-temperature electrolyzers, such as alkaline, and proton exchange-membrane (PEM) electrolyzers, are commercially available, while high-temperature solid-oxide electrolyzers remain at the demonstration stage: alkaline and PEM electrolyzers have lower capital costs than solid-oxide electrolyzers; however, electrolysis remains significantly more expensive than fossil fuel-based production (4-9 $/kg$H_2$ [3]). In this study, PEM electrolyzers are considered as the low-carbon option, due to their relatively high efficiency and fast reaction time [4].

Hydrogen can then be transported and/or stored in two forms: liquified hydrogen ($LH_2$) or compressed hydrogen ($CH_2$). A third option, solid interstitial storage, remains at the research and development stage and is not considered in this study. Each of these two options has distinct advantages and disadvantages, depending on transportation infrastructure, distance, and final user requirements. Hydrogen transportation can be carried out via tanks ($CH_2$ or $LH_2$) or gas pipelines, which may be specifically designed for pure $CH_2$ or retrofitted natural gas pipelines, in which methane is enriched with $CH_2$. A promising alternative is the use of ammonia as hydrogen carrier, which is not covered in this study.

All these phases are important when designing and optimizing a supply chain. To understand the environmental impact of each step, LCA is an effective approach for analyzing the entire supply chain. In addition, a Life Cycle Cost approach can complement the analysis.

## Life Cycle Assessment

LCA is crucial when dealing with problems involving extended lifespans and/or the integration of different sectors collaborating towards a shared goal. The literature review highlights that, despite existing studies covering multiple indicators [5-9], current optimization efforts for hydrogen energy systems primarily target cost reduction and greenhouse gas emission minimization, relegating the other parameters to a secondary role. As a result, broader multi-criteria environmental analyses are quite limited [10].

# METHODOLOGICAL FRAMEWORK

The study follows a structured approach to organize the analysis and optimization process. The evaluated supply and distribution chains are summarized in Figure 1. Various energy sources – wind, photovoltaic (PV), hydro, and the national grid – are considered for hydrogen production via electrolysis, in comparison to SMR with and without Carbon Capture and Storage (CCS). Storage options include compression and liquefaction, while transportation is analyzed through pipelines, tanker trucks, and tube trailers. The final users considered in the study are the mobility sector (hydrogen refueling stations, HRS) and industry.

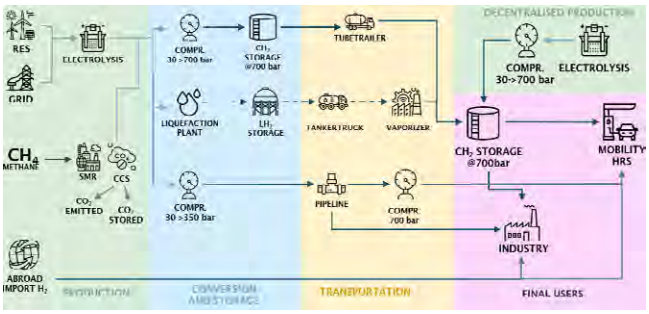



**Figure 1.** Considered actors in the modeling of the supply and distribution chain [11]

A comprehensive LCA was conducted, considering each system component to quantify the environmental impacts associated with each phase.

## Environmental LCA model

Only the main assumptions for the LCA model will be presented. The Functional Unit (FU) , i.e. the service(s) provided, is defined as the amount of hydrogen (1 kg $H_2$) delivered for either mobility or industrial use. The energy requirement for electrolysis, 55 kWh/kg$H_2$ [11,12], was applied to a certain quantity of hydrogen produced to take into account losses during storage and transportation. After considering these losses, the required hydrogen output from the production plant for each kg of hydrogen delivered to the end-user was 1.17 kg. Furthermore, a 4% energy loss was factored into the production process, resulting in a total gross energy demand of approximately 67 kWh/kg$H_2$ for each functional unit of hydrogen delivered. Additionally, the material and resource requirements for the electrolyzer stack and balance of plant (BOP) components, as reported in [13], were incorporated into the LCA study as input data. These values are provided in Table 1 and 2, and refer to a single 1 MW PEM electrolyzer.

To obtain values relevant to the Functional Unit, the total hydrogen production capacity for each production chain (source+electrolysis) over its lifetime was calculated. For each energy plant installation, a lifetime value (in years) and a *Load Factor* (*LF*) [14] were selected based on literature in order to compute the total number of operating hours of the power plant over the chosen

lifetime. Consequently, the total hydrogen production was calculated for each type of plant, as shown in Table 3: this value was then used to allocate the resource quantities per kg of hydrogen produced.

**Table 1.** Material inventory for Balance-of-Plant components for 1 MW PEM Electrolyzer

| Material | Amount [kg] |
|---|---|
| Titanium | 528 |
| Aluminum | 27 |
| Stainless steel | 100 |
| Copper | 4.5 |
| Nafion | 16 |
| Activated Carbon | 9 |
| Iridium | 0.75 |
| Platinum | 0.075 |

**Table 2.** Material inventory for stack of 1 MW PEM Electrolyzer

| Material | Components | Unit | Value |
|---|---|---|---|
| Steel | Container, pump, etc. | kg | 13700 |
| Stainless steel | Air blast chiller | kg | 1100 |
| Copper | Transformer, rectifier, PLC, etc. | kg | 5900 |
| Aluminum | Transformer, rectifier | kg | 1000 |
| Polyethylene | Vessel, pipping, tank | kg | 300 |
| Display panels | 17 inch, Eco Invent 3.3 | - | 1 |
| Concrete | Infrastructure | kg | 5600 |

**Table 3** Resource allocation factors

| Source | Lifetime [years] | LF [%] | Lifetime [hours] | H2 produced during lifetime [t] | Allocation factor/kgH2 |
|---|---|---|---|---|---|
| Wind turbine | 20 | 24% | 42048 | 627.1 | 1.595e-6 |
| Solar PV | 30 | 13% | 34164 | 509.5 | 1.963e-6 |
| Hydro | 100 | 25% | 219000 | 3266.1 | 3.062e-7 |

Using these values, the different hydrogen production pathways were modeled on the LCA software SimaPro (version 9.6.0.1, equipped with EcoInvent 3.10 libraries), along with hydrogen production through SMR with and without CCS, as carbon-rich alternatives.

The same approach was applied to transportation options (pipelines and road truck transport), and conversion technologies including compression to either 350 or 700 bar, and liquefaction.

For Life Cycle Impact Assessment (LCIA), the most commonly used methodology in the relevant literature [15] is ReCiPe midpoint, most often in the hierarchical version. To ensure consistency with the majority of existing studies, ReCiPe 2016 midpoint (H) was selected (version 1.13), for comparison purposes. However, other methodologies, such as Environmental Footprint (EF), will also be used to provide a broader perspective and align with recent impact assessment recommendations.

## LCA results

A total of 15 environmental indicators were considered in the study, but only some of them will be presented for illustration purpose. An initial analysis of the output results from the LCA software SimaPro quantifies the lower climate change impacts associated with renewable energy sources in hydrogen production (Figure 2).

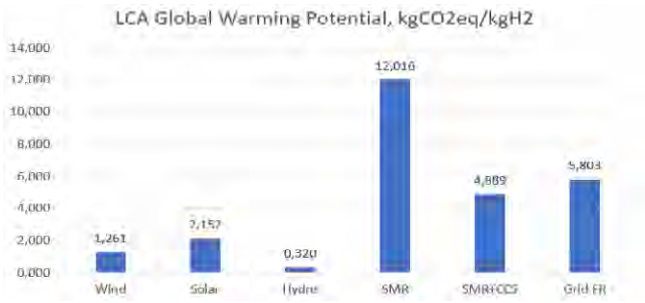



**Figure 2.** $CO_2$-eq emission by producing 1 kg of hydrogen by source (please note that the French electrical grid has low $CO_2$ emissions due to its heavy reliance on nuclear energy, abundant hydroelectric resources, growing integration of renewable energies, and policies promoting low-carbon electricity generation)

A similar pattern was observed for the ozone, water and fossil depletion indicators, with methane-based technologies exhibiting the greatest impacts (Figure 3).

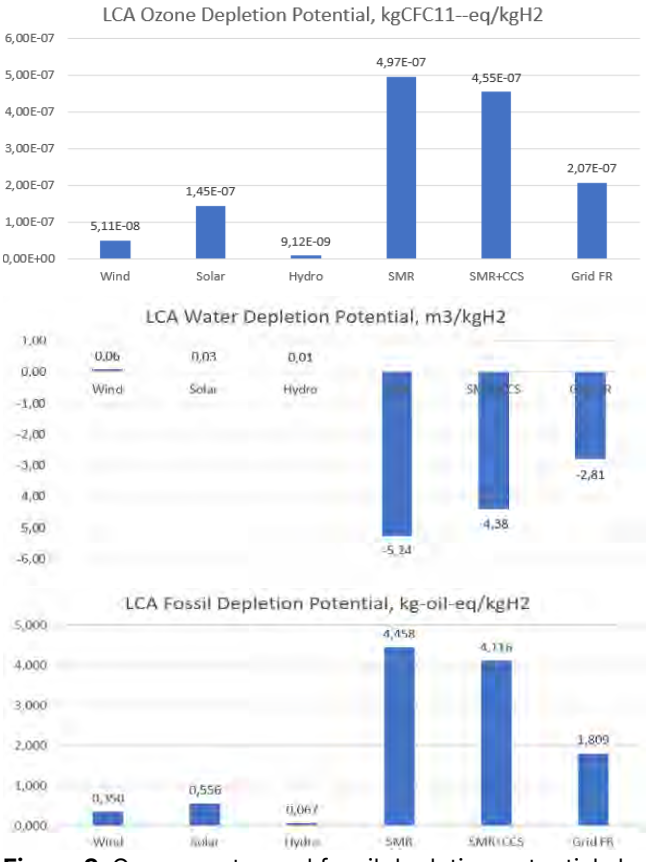



**Figure 3.** Ozone, water and fossil depletion potentials by source, LCA

Indicators such as metal depletion potential, freshwater eutrophication, and particle matter formation potential showed more comparable effects across the different production sources (Figure 4).

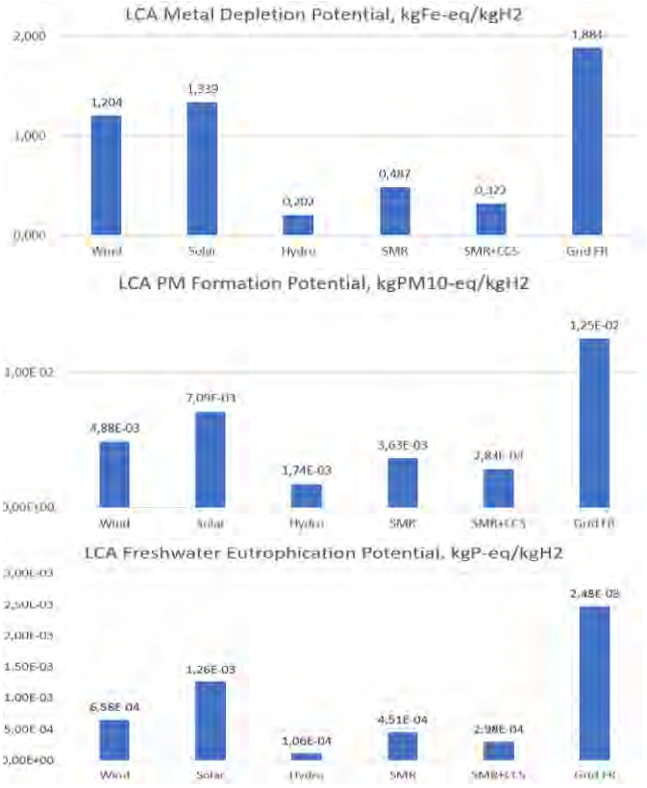



**Figure 4.** LCA values for Metal depletion, PM formation, and Freshwater eutrophication potentials by source

The urban land occupation indicator highlights the significantly larger surface area required for solar-based Hydrogen production (Figure 5).




**Figure 5.** LCA Urban Land Occupation by source, m2/kgH2

For the optimization part these results, specific to each production, transport and conversion method, were integrated in the framework of the supply chain as a whole. It will be the software duty to select the better pathway for the FU, i.e. the kg of hydrogen.

## Supply chain optimization

The model developed in this study extends the work of [11], with the key innovation being the integration of the LCA framework into an existing optimization model for hydrogen deployment in France. The optimization problem is structured as a multi-period, mono-objective model, divided into five-year intervals. The model is implemented in the GAMS® modeling language, using the CPLEX 12 solver. Additional details on the parameters, formulas, and constraints are provided in [11].

## Modeling framework

The first step involved a geographical discretization: the territory of France was divided in its regions, with each region further subdivided into grids corresponding to the 91 French *départements*, to perform single-region studies. In this work, the case of Bourgogne-Franche-Comté is presented as an example (Figure 6). Each grid was equipped with a set of data summarizing, among other factors, the forecasted hydrogen demand from 2025 to 2050, availability of resources, trading route capacity, and renewable energy potential for new installations [11,12].

- Production methods are covered by SMR and green electrolysis. The French electric grid and abroad imports are also considered as energy and hydrogen wells. Three plant sizes are considered: large, small, and on-site, depending on the required quantity.
- Conversion for transport and storage includes compression units (up to 350 or 700 bar) and liquefaction plants.
- For transportation, tanker trucks, tube trailers and pipelines are considered.
- Maximum and minimum capacities for production, transportation and storage are introduced as constraints.
- Data on capital costs and operation and maintenance for production plants are considered, as well as for pipelines. For road transportation, truck fuel economy, driver wages, and load/unload times are taken into account.
- A series of constraints and compatibility checks complete the model structure. For example, no on-site power plants can be coupled with liquified hydrogen production, to avoid missing economies of scale for LH2; there are also controls on the matching between an energy source and a production method (no SMR plant powered by RES, or electrolysis plant powered by $CH_4$).

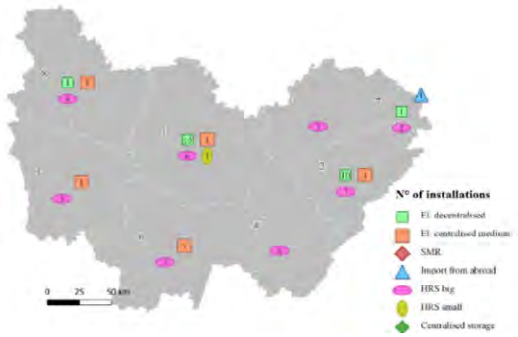



**Figure 6.** Geographical discretization of the region Bourgogne-Franche-Comté. Simulation results in period 2 (2030-2034) from [11]

Each phase of the supply chain corresponds to a separated calculation for each of the parameters evaluated (cost and environmental indicators). Each indicator presents three contributions to its total value: production (P), transportation (T) and conversion (C). Let $Env_x$ be the generic indicator, its calculation is expressed as in Eq. (1):

$$Env_x Total = PEnv_x + CEnv_x + TEnv_x \quad (1)$$

Each one of the $Env_x$ terms was subject of a dedicated optimisation.

The investment cost of the facilities (*FCC*) (Eq. (2)) includes the capital cost for each facility (respectively, *PCC*, *SCC* and *FSCC*) for the installed number of each facility: production (NP), storage (NS), and refueling stations (NFS). These factors are divided by a learning factor (*LearnFt*) to account for cost reductions due to mass production and market penetration of certain technologies (e.g., electrolyzers). They are then discounted to year *n* to reflect their present value (Eq. (3), with *i* as the discount rate.

$$FCC_t = \frac{1}{LearnF_t} \sum_{ig} \left( \sum_{pj} PCC_{pij} NP_{pijgt} + \sum_{sj} SCC_{sij} NS_{sijgt} + \sum_{fj} FSCC_{fkj} NFS_{fkjgt} \right) \quad (2)$$

$$FCC_n = FCC_0 \frac{1}{(1+i)^n} \quad (3)$$

The optimisation criterion is the total cost (TSCTotal), which consists of the sum of investment costs and the sum of the total yearly operating costs (TOC):

$$TSCTotal = \sum_t (FCC_t) + \sum_n TOC_n \quad (4)$$

The total cost then allows for the determination of the Levelized Cost of Hydrogen (LCOH) based on the hydrogen production.

In the first phase, the methodology focused on a single-criteria optimization framework, resulting in 16 scenarios, each illustrating how minimizing a specific criterion impacts the other categories. This phase is essential for understanding the behavior of the criteria, providing a solid foundation for the subsequent development of a multi-objective approach and multi-criteria decision-making, which will be the natural progression of the study.

## Optimization results

The results are organized in a table with a color scale (green-yellow-red) highlighting the performance of each scenario (Figure 7). Each column represents a different scenario, with the objective function to be optimized indicated at the top of the columns. The diagonal shows the minimum values for each parameter. A greener column indicates better overall performance in terms of the indicators.

Validation of the obtained values was performed by comparing them with similar studies analyzing the proposed indicators. Despite minor discrepancies due to differences in the database, LCA method, or update year, the order of magnitude for the various parameters

| Parameter object of the optimisation --> | LCOH | GWP | ODP | AP | FEP | MEP | HTTP | PMFP | ETP | IRP | POFP | ALO | ULO | WDP | MEP | FDP |
|---|---|---|---|---|---|---|---|---|---|---|---|---|---|---|---|---|
| Total Cost [M€] | 2403 | 3117 | 2951 | 4043 | 2891 | 3739 | 3668 | 4137 | 3869 | 4470 | 4396 | 2920 | 2843 | 4005 | 3445 | 3921 |
| LCOH [€/kgH2] | 4,67 | 6,03 | 5,73 | 7,86 | 5,62 | 7,27 | 7,13 | 8,04 | 7,52 | 8,69 | 8,54 | 5,67 | 5,53 | 7,78 | 6,69 | 7,62 |
| GWP [kgCO2/kgH2] | 1,98 | 1,61 | 1,66 | 4,04 | 1,62 | 3,04 | 3,58 | 4,47 | 4,26 | 2,98 | 4,72 | 1,82 | 2,11 | 5,07 | 1,74 | 3,47 |
| ODP, ozone depletion [kgCFC-eq/kgH2] | 8,83E-08 | 6,13E-08 | 5,82E-08 | 1,58E-06 | 5,83E-08 | 1,06E-06 | 1,12E-06 | 1,74E-06 | 1,47E-06 | 1,12E-06 | 2,48E-06 | 5,86E-08 | 1,91E-07 | 1,41E-06 | 6,56E-08 | 8,34E-08 |
| AD, Acidification potential [kgP-eq/kgH2] | 1,29E-02 | 9,92E-03 | 1,02E-02 | 7,81E-03 | 9,96E-03 | 7,95E-03 | 8,56E-03 | 7,90E-03 | 8,87E-03 | 8,41E-03 | 8,66E-03 | 1,08E-02 | 1,11E-02 | 1,87E-02 | 1,02E-02 | 1,22E-02 |
| FEP, freshwater eutrophication [kgP-eq/kgH2] | 8,45E-04 | 6,38E-04 | 6,14E-04 | 1,37E-03 | 6,15E-04 | 1,10E-03 | 1,10E-03 | 1,45E-03 | 1,33E-03 | 1,19E-03 | 2,06E-03 | 6,14E-04 | 7,30E-04 | 2,18E-03 | 6,59E-04 | 9,41E-04 |
| MEP, marine eutrophication [kgN-eq/kgH2] | 7,83E-04 | 6,19E-04 | 6,15E-04 | 5,65E-04 | 6,02E-04 | 5,29E-04 | 5,90E-04 | 5,82E-04 | 6,26E-04 | 5,50E-04 | 6,68E-04 | 6,57E-04 | 7,51E-04 | 1,77E-03 | 7,03E-04 | 6,13E-04 |
| HTP, human toxicity [kg1,4-DB-eq/kgH2] | 1,51 | 1,10 | 1,05 | 0,94 | 1,06 | 0,94 | 0,91 | 0,94 | 1,01 | 1,02 | 1,19 | 1,05 | 1,23 | 3,42 | 1,16 | 2,01 |
| PMFP, PM formation [kgPM10-eq/kgH2] | 6,02E-03 | 5,04E-03 | 5,13E-03 | 3,95E-03 | 5,05E-03 | 4,12E-03 | 4,31E-03 | 3,93E-03 | 4,27E-03 | 4,33E-03 | 4,35E-03 | 5,41E-03 | 5,51E-03 | 7,96E-03 | 5,19E-03 | 5,48E-03 |
| ETP, ecotoxicity [kg1,4-DB-eq/kgH2] | 0,64 | 0,54 | 0,52 | 0,43 | 0,52 | 0,47 | 0,43 | 0,42 | 0,41 | 0,52 | 0,59 | 0,52 | 0,64 | 1,53 | 0,54 | 1,14 |
| IRP, ionising radiation [kBqU235/kgH2] | 2,92 | 2,78 | 2,37 | 2,14 | 2,37 | 2,00 | 2,27 | 2,19 | 2,25 | 1,94 | 2,32 | 2,37 | 4,05 | 16,10 | 3,94 | 2,84 |
| POFP, photochemical oxidant formation [kgNVMOC] | 9,90E-03 | 8,01E-03 | 8,72E-03 | 8,13E-03 | 8,36E-03 | 7,32E-03 | 9,59E-03 | 8,98E-03 | 1,01E-02 | 6,71E-03 | 5,41E-03 | 9,85E-03 | 9,97E-03 | 1,29E-02 | 8,36E-03 | 8,21E-03 |
| ALO, agricultural land occupation [m2] | 0,09 | 0,07 | 0,06 | 0,17 | 0,06 | 0,13 | 0,13 | 0,18 | 0,16 | 0,14 | 0,25 | 0,06 | 0,09 | 0,38 | 0,09 | 0,07 |
| ULO, urban land occupation [m2] | 0,33 | 0,15 | 0,14 | 0,22 | 0,14 | 0,17 | 0,17 | 0,23 | 0,26 | 0,20 | 0,35 | 0,14 | 0,09 | 0,30 | 0,14 | 0,17 |
| WDP, water depletion [m3] | 0,17 | 0,24 | 0,21 | 0,53 | 0,21 | 0,47 | 0,17 | 0,38 | 0,14 | 0,79 | 2,18 | 0,22 | 0,18 | 0,12 | 0,34 | 0,43 |
| MDP, metal depletion [kgFe-eq/kgH2] | 1,09 | 0,94 | 0,92 | 1,09 | 0,92 | 1,05 | 0,98 | 1,10 | 1,04 | 1,15 | 1,53 | 0,92 | 0,97 | 1,66 | 0,92 | 1,14 |
| FDP, fossil depletion [kgoil-eq/kgH2] | 0,56 | 0,46 | 0,48 | 1,63 | 0,46 | 1,15 | 1,52 | 1,91 | 1,87 | 0,97 | 1,27 | 0,53 | 0,62 | 1,47 | 0,50 | 0,40 |

**Figure 7:** Optimisation results

showed a high level of consistency [16-19].

The table first reveals a wide variation in the results across the different performance indicators, highlighting the significant potential for optimization.

When comparing the obtained results with the EU's standard for low carbon hydrogen, which allows a maximum of 3.38 kg of $CO_2$-equivalent ($CO_2e$) emissions per kilogram of hydrogen produced and distributed, we see that 10 scenarios remain well below this threshold.

An analysis of results reveals a clear trade-off between cost and GHG minimization. The least expensive solution, while economically favorable, demonstrates a poor overall performance across several environmental indicators.

In contrast, the solution optimized for the minimization of Global Warming Potential (GWP) involves a notable increase in costs, although it yields favorable results for other environmental indicators. Among the various scenarios evaluated, good performances were observed for GWP, Ozone Depletion, and Metal Depletion, primarily driven by a higher proportion of renewable hydrogen production. Conversely, the worst outcomes, particularly for Photochemical Oxidant Formation and Water Depletion, stem from a higher reliance on imported hydrogen and grid electricity, both of which exhibit less favorable life cycle assessment (LCA) parameters compared to green hydrogen.

Finally, the table shows that optimizing solely the "cost-GHG" pair is insufficient, and that other criteria must be considered in the optimization process. It is difficult to go further at this stage without a thorough analysis of the corresponding supply chain structure.

## CONCLUSIONS AND PERSPECTIVES

This study presents a methodological framework for the comprehensive analysis of hydrogen supply chains by integrating Life Cycle Assessment (LCA) with optimization techniques. The proposed approach enables a systematic evaluation of various environmental and economic parameters, offering a more detailed understanding of the trade-offs involved in different hydrogen production pathways. The primary contribution of this work lies in the optimization of individual indicators, highlighting the potential for Multi-Objective Optimization (MOO) to simultaneously improve the performance across various environmental and economic parameters.

The next phase of the research will then focus on MOO to identify optimal trade-offs. Given the computational challenges of MOO (not feasible with the whole group of 16 LCA indicators at once), the study will explore methods to reduce dimensionality without sacrificing the quality of results. This could include analyzing the behavior similarities among different indicators, as revealed by the preliminary results (Figures 2-3-4). This will ensure that the optimization process remains efficient while maintaining its robustness, ultimately offering valuable insights for the design of sustainable and economically viable hydrogen supply chains.

## ACKNOWLEDGEMENTS

This work was supported by a French government grant managed by the Agence Nationale de la Recherche under the France 2023 program, reference ANR-22-PEHY-0019

## REFERENCES

1. Does Hydrogen have a place in the energy transition? É. Beeker (2014), strategie.gouv.fr/sites/strategie.gouv.fr/files/atoms/files/na-fs-hydrogene-anglais.pdf
2. Green hydrogen: Energizing the path to net zero, Deloitte (2023), deloitte.com/global/en/issues/climate/green-hydrogen.html
3. Making the breakthrough: Green hydrogen policies and technology costs, International Renewable Energy Agency, Abu Dhabi, irena.org/media/Files/IRENA/Agency/Publication/2020/Nov/IRENA_Green_Hydrogen_breakthrough_2021.pdf
4. M. El-Shafie, Hydrogen production by water electrolysis technologies: A review, Results in Engineering Vol. 20 (2023), 101426, ISSN 2590-1230, 10.1016/j.rineng.2023.101426S
5. Sadeghi et al., Comparative economic and life cycle assessment of solar-based hydrogen production for oil and gas industries, Energy Vol. 208 (2020), 118347, 10.1016/j.energy.2020.118347
6. J.C. Koj, et al., Environmental impacts of power-to-X systems - A review of technological and methodological choices in Life Cycle Assessments, Renewable and Sustainable Energy Reviews Vol. 112 (2019), 865-879, 10.1016/j.rser.2019.06.029
7. J. Wilkinson et al., Review and meta-analysis of recent life cycle assessments of hydrogen production, Cleaner Environmental Systems Vol. 9 (2023), 100116, 10.1016/j.cesys.2023.100116
8. S. Krishnan et al., Prospective LCA of alkaline and PEM electrolyser systems, Int. J. H. Energy Vol. 55 (2024), 26-41, 10.1016/j.ijhydene.2023.10.192
9. G. Zhao et al., Life cycle assessment of H2O electrolysis technologies, Int. J. H. Energy Vol. 45 (2020), 23765-781, 10.1016/j.ijhydene.2020.05.282
10. N. Sabio et al., Holistic minimization of the life cycle environmental impact of hydrogen infrastructures using multi-objective optimization and principal component analysis, Int. J. H. Energy Vol. 37 (2012), 5385-5405, ISSN 0360-3199, 10.1016/j.ijhydene.2011.09.039.

11. R. Luise, Développement par approche ascendante de méthodes et d'outils de conception de chaînes logistiques « hydrogène décarboné » : application au cas de la France, Toulouse INP, 10/2023, theses.fr/2023INPT0083
12. RTE Réseau de Transport d'Electricité. Futurs énergétiques 2050, Rapport complet, 2022
13. Sharma et al., Integration of life cycle assessment with energy simulation software for PEM electrolysis, Procedia CIRP Vol. 90 (2020), 176-181, 10.1016/j.procir.2020.02.139
14. Share of average plant load factor in France, statista.com
15. A. Sola et al., Green Hydrogen and supply chain. A critical assessment of the environmental impact, Adv. Sust. Systems Vol. 9 (2025), 2400708, 10.1002/adsu.202400708
16. T. Terlouw et al., Future hydrogen economies imply environmental trade-offs and a supply-demand mismatch, Nature communications Vol. 15 (2024), 7043, 10.1038/s41467-024-51251-7
17. Silva Ortiz et al., Environmental Assessment of Liquid Hydrogen Production Routes, Chemical Engineering Transactions Vol. 109 (2024), 583-588, 10.3303/CET24109098
18. G. Naumann et al., Dynamic life cycle assessment of European electricity generation based on a retrospective approach, Energy Conversion and Management Vol. 311 (2024), 118520, 10.1016/j.enconman.2024.118520
19. A. Mio et al., Sust. Analysis of Hydrogen Production Processes, Int. J. H. Energy Vol. 54 (2024), 540–553, 10.1016/j.ijhydene.2023.06.122

© 2025 by the authors. Licensed to PSEcommunity.org and PSE Press. This is an open access article under the creative commons CC-BY-SA licensing terms. Credit must be given to creator and adaptations must be shared under the same terms. See https://creativecommons.org/licenses/by-sa/4.0/



Systems & Control Transactions

**Research Article - Peer Reviewed Conference Proceeding**
ESCAPE 35 - European Symposium on Computer Aided Process Engineering
Ghent, Belgium. 6-9 July 2025
Jan F.M. Van Impe, Grégoire Léonard, Satyajeet S. Bhonsale,
Monika E. Polańska, Filip Logist (Eds.)

PSE PRESS

# Taking into account social aspects for the development of industrial ecology on a territory

**Maud Verneuil[a], Sydney Thomas[a], Marianne Boix[a*]**

[a] Toulouse INP, CNRS, Université Paul Sabatier, Laboratoire de Génie Chimique, UMR 5503, 4 Allée Emile Monso, 31432 Toulouse, France
* Corresponding Author: marianne.boix@toulouse-inp.fr

## ABSTRACT

Industrial ecology appears to be a significant means of reducing carbon dioxide emissions from industry. However, beyond flow management, eco-industrial parks can also contribute to a socio-economic transition on a regional scale. Usually, multi-criteria optimization models use economic and environmental criteria in the decision-making process. This article looks at the integration of social criteria in these models, and more broadly at the issues involved in measuring the social impact of an eco-industrial park. The aim of this article is to take a different approach to social indicators, by highlighting the key success factors of an eco-industrial park, such as cooperation within a collective but also between the different scales making up the system. This work is based on bibliographical research and semi-structured interviews with stakeholders in the field. What's more, the process of developing social indicators, particularly participatory ones, seems to be a strong catalyst in the construction of relationships and their dynamics. Finally, the metric of social indicators also has its limitations, which should be considered if we are to be able to address the various issues in a systemic way and potentially envisage other ways of taking into account the social aspect of an eco-industrial park.

**Keywords**: Eco-industrial park, social indicators, relational dimension, co-building

## 1. INTRODUCTION

The technical, economic and environmental benefits of industrial ecology have already been demonstrated through multi-criteria optimization models [1]. Optimization models make possible to implement synergies according to economic and environmental criteria. Numerous studies have proposed several criteria such as: $CO_2$ emissions, Net Present Value or other economic ones, and today the reorganization of industry into eco-industrial parks appears to be a significant way of reducing carbon dioxide emissions into the atmosphere [2]. However, it appears less common to consider eco-industrial parks as an opportunity to modify socio-economic landscapes on a territorial scale.

The aim of this article is therefore to highlight the social impact that a territorial planification of cooperation can have on a territory and conversely. This impact will be assessed in a case study using social indicators such as job creation. This case study is about the development of offshore wind energy expertise in the port of Port-La-Nouvelle in South of France with the port of Sète as a rear base. The aim is to assess the capacity of the port of Sète to host component manufacturing and anchor system storage activities, by evaluating the economic, environmental and social impacts of this approach. We will then highlight the criteria chosen and assess their relevance and limitations, particularly with regard to the social aspect.

To this end, we will define the needs and challenges of an industrial and territorial ecology approach with a relational and human point of view. Semi-directive interviews with players in the field and researchers who have studied this issue will enable us to highlight the complexity of this system and the parameters that determine its success.

In another time, we will examine the real added value of social indicators on this relational dimension, in particular by studying the way in which social indicators are implemented. Indeed, beyond the indicator itself, the

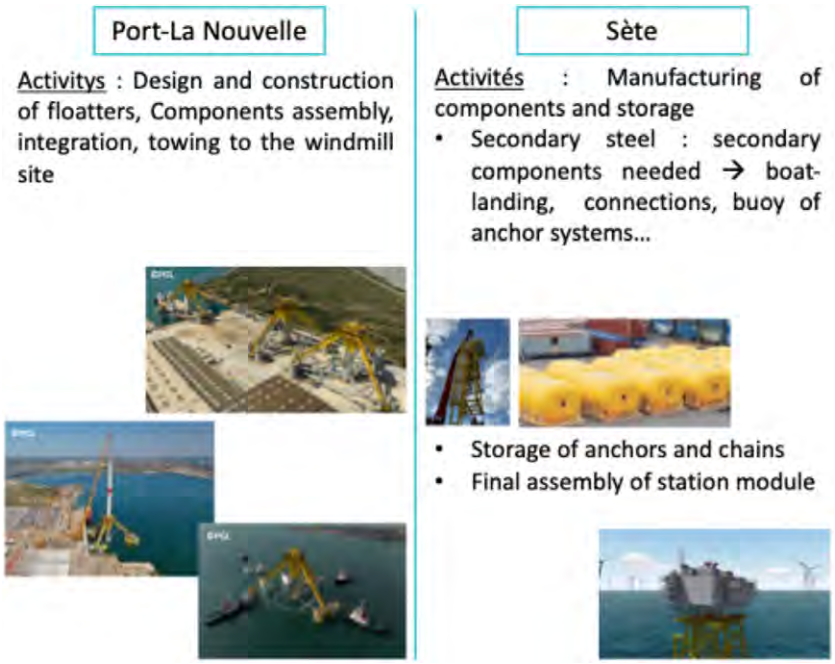



**Figure 1:** Illustration of the different activities to implement in the sites of Port-La-Nouvelle and Sète

process chosen for its elaboration has a real influence on the indicator itself, as well as on the ability of users to appropriate it. We therefore need to consider which process seems most effective in enabling the use of social indicators to provide a new perspective on the context of an industrial and territorial ecology approach.

Finally, we will highlight the limits of metrics based on social indicators, and question their ability to capture a complex, multidimensional social environment [3]. We will also explore the possibility of using other concepts and tools to account for social reality, and assess their relevance to industrial and territorial ecology.

## 2. CASE STUDY

The proposed case study concerns the development of a regional port scheme with the port of Port-La-Nouvelle as a hub for floating offshore wind energy and the port of Sète as a rear base. The aim of the study is to assess the suitability of the port of Sète as a base for manufacturing components and storing anchoring systems (Figure 1). Various scenarios are proposed for evaluation, based on economic, environmental and social criteria.

In this article, we take one of the proposed activities as an example.

Components manufactured in Béziers need to be transported to Sète for finishing stages. Three transport scenarios are proposed:

- Road transport
- Rail transport
- River transport

The criteria presented in Table 1 will enable us to assess the impact of the three scenarios.

**Table 1:** Criteria chosen for the transport scenario

| Economic criterion | Environmental criterion | Social criterion |
|---|---|---|
| C1 Transport costs | C2 Human health | C5 Job creation |
| | C3 Ecosystem quality | |
| | C4 Resources | |

The environmental criteria were selected using the SIMAPRO life-cycle analysis software and the Eco-indicator 99 (E) V2.10 method, which uses end-point indicators. This method has been chosen because it allows for a limited number of criteria and therefore better readability of the results even if the uncertainty increases.

The social criterion was chosen in consultation with the actors of the region, which wanted to measure the contribution of this new activity in terms of employment and dynamization of their territory (attractivity).

The Electre I multicriteria decision aid methodology has been chosen to compare the different scenarios and to propose which one is the best compromise regarding the weights accorded to the criteria by the different actors.

## 3. RESULTS

Tables 2 and 3 show the performance matrix based on criteria reported on Table 1, with different weights affected for each player.

**Table 2:** Manufacturer's performance chart

| Criteria | C1 | C2 | C3 | C4 | C5 |
|---|---|---|---|---|---|
| **Weights** | **3** | **2** | **1** | **2** | **2** |
| Road | 91 | 0,3 | 7,9 | 2,9 | 15 |
| Rail | 68 | 8,5 | 9,7 | 9,5 | 5 |
| Waterway | 62 | 6,3 | 9,7 | 8,2 | 10 |

**Table 3:** Local authorities' performance chart

| Criteria | C1 | C2 | C3 | C4 | C5 |
|---|---|---|---|---|---|
| **Weights** | **1** | **1** | **1** | **1** | **6** |
| Road | 91 | 0,3 | 7,9 | 2,9 | 15 |
| Rail | 68 | 8,5 | 9,7 | 9,5 | 5 |
| Waterway | 62 | 6,3 | 9,7 | 8,2 | 10 |

The results that emerge from this study differ according to the weight attributed by the different stakeholders involved in the project.

According to ELECTRE approach and based on the weights affected using the different interviews, the best option is selected for each actor.

For manufacturers, rail transport is the preferred option, while for the general public, road transport is preferable.

From the point of view of social indicators, this method has its limits.

Firstly, in the context of a multi-criteria optimization model, the loss of qualitative information is very high. The context and its complexity are not taken into account. What's more, the job creation criterion is questionable, as it doesn't highlight the quality of the jobs and doesn't measure the real contribution to the region. We may well wonder what will happen to these jobs once the finishing activity is over.

In conclusion, this type of modeling, incorporating indicators with a social dimension, can be used to guide strategies. It also highlights the divergent viewpoints of stakeholders, thanks to the weights assigned to each criterion. This divergence of interests, objectivized by a mathematical model, can form the basis for discussion between stakeholders, and enable each to understand the stakes of the other. Nevertheless, we can't claim to take the social dimension of the situation into account. To understand social issues, we need to consider the context and its complexity. In order to emphasize and to understand the challenges into the consideration of social aspects in such territorial projects, we propose a new definition of the multi-actor compound of territorial projects.

## 4. KEY FACTORS FOR ECO-INDUSTRIAL PARKS

Given the limitations of the above case study, we turned our attention to the needs and challenges of an eco-industrial park in the context of trying to imagine new synergies to enhance the attractivity of a territory. Figure 2 shows the representation of the structure of an eco-industrial park with this multi stakeholder point of view.

This representation was drawn up on the basis of interviews with two consultancies specializing in industrial and territorial ecology, as well as with 5 industrial and territorial ecology coordinators employed by local authorities.

This representation reveals a complex, multidimensional system with 3 different strata:

- The operational level: made up of manufacturers and their internal ecosystems.
- Tactical level: the park and its key players (local community members, industrialists, park managers and institutions).
- Strategic level: with a more macro-systemic vision (politicians and external stakeholders).

It's interesting to note that some players belong to different scales, both tactical and strategic. For example, a farmer may generate flows that will feed the park. They will therefore be involved in the system, while at the same time having an activity outside the park. The aim of this diagram is to highlight the diversity of players with potentially divergent interests who are brought into contact with each other.

Following this observation, we asked ourselves what ingredients would enable this structure to operate ona good way.

Kalundborg is Europe's benchmark industrial ecology park. The success of this park seems to be linked, among other things, to good communication and the implementation of collaborative relationships between players [4]. What's more, following interviews with one employee of a private company, two park managers and five project managers, it seems obvious that it's socio-economic, human and organizational factors that either block or enable an industrial and territorial ecology approach to develop [5].

Figure 3 summarizes the keys to success identified by the players in the field, according to the park's life stage.

During the reflection phase, it became clear that a detailed analysis of the area was essential. This enables us to determine whether the area is economically and demographically dynamic enough to make such a project viable. The job market and local political will are also key factors.




**Figure 2:** Representation of an eco-industrial park as a multi-stakeholder system

In the start-up phase, the third-party player appeared to be a mainstay.

In the sustainability phase, the trio of communication, trust and cooperation is the key to a healthy collective. In fact, these 3 elements are essential at all stages of the process, and not just during the sustainment phase.

## 5. SOCIAL INDICATORS HELPFUL FOR ECO-INDUSTRIAL PARKS

Having highlighted the key social aspects that enable an eco-park to function, it seems worthwhile to examine the relevance of social indicators as a tool for steering such initiatives.

Social indicators can be approached from different angles. They can be used as external communication tools, evaluation and management tools, decision-making tools or impact measurement tools.

One of the angles chosen in this article concerns the notion of performative social sustainability indicators. These are indicators that raise the ambitious question "what kind of world do we want to create?" [3]. The performative approach allows us to adopt a "real relational orientation towards the causes and conditions that shape outcomes."

This approach aims to question the system, the way it works, as well as highlighting its dysfunctions. For example, this type of indicator can question the potential presence of a space for the expression of divergent points of view.

In addition, the previous chapter highlighted the importance of relationships within a collective, and in particular the need to build a climate of trust and cooperation led by a third-party actor who will be able to animate the industrial and territorial ecology approach throughout the life of the park. It therefore seems essential to pay particular attention to the stakeholders involved in this approach, and to give them the space to express their needs and interests. The method used to construct social indicators plays a decisive role in this process.

Indeed, a constructivist perception of social indicators makes it possible to involve eco-park stakeholders in the process. This involves understanding how individuals have constructed their vision of the world, and enables a more refined approach to the complexity of situations and therefore potential dysfunctions [6].

It turns out that a constructivist vision encourages the implementation of indicators via participatory processes that will enable stakeholders to appropriate these tools and perceive the benefits of using them. However, this approach involves qualitative methods such as interviews and narratives, which can be time-consuming to process.




**Figure 3:** Field analysis of keys to success

## 6. DISCUSSION

It seems that social indicators can bring real added value to the management of industrial and territorial ecology initiatives. They can give an account of a process and its malfunctions, and thus enable the implementation of corrective actions with the aim of developing the trust and cooperation essential to the smooth running of the system. By way of example, we can propose park-wide indicators such as: the composition of governance bodies, the organization and frequency of informal exchanges, the presence of a third-party actor, the existence of collective mediation, and the presence of rules for preserving the confidentiality of strategic data [7]. These indicators are intended to measure the collective dynamic and assess the framework conducive to secure exchanges enabling trust and cooperation.

However, beyond the mere proposal of indicators, their development process seems to be the most impactful contribution. Indeed, the inclusion of stakeholders in their construction generates exchanges that encourage the expression of each party's issues. This space for dialogue is itself a creator of the collective: "The dialogue process must be seen as much more than a selection of indicators. Above all, it creates an opportunity for collective learning and debate between stakeholders, enabling them to perceive the range of issues at stake, and to learn what is important to others, and why." This iterative process of discussion, revision, and validation of indicators not only refines the assessment tools but also strengthens relationships among actors, promoting a culture of transparency, cooperation, and shared governance.

Industrial and territorial ecology can thus be seen as a means of "providing a technical, organizational, or economic response to a challenge felt by the players involved (public and private). Industrial Ecology is therefore no longer an objective in itself (as has often been the case during the many experiments carried out in France), but it constitutes an innovative solution to resolve a problem relating to the management of waste, a resource, energy production, or even the economic development of the territory" [8]. The contextualization of these indicators within the framework of industrial ecology implies that their impact extends beyond operational efficiency and includes socio-economic resilience. By adopting this perspective, stakeholders can integrate social sustainability considerations into their strategies, ensuring that industrial symbiosis initiatives align with broader societal values.

Nevertheless, indicators generate "a simplification of complex social realities into abbreviated symbols for easy communication." This simplification can facilitate the implementation of rather top-down forms of governance, which will focus their attention on the consumer and the market and turn away from questions about the social sustainability of the system such as "worker well-being, industrial equity, and engaged, positive relationships with external communities." The risk of reductionism highlights the need for reflexivity in indicator design. If indicators merely serve to rationalize existing power structures or validate pre-established narratives, they

may obscure deeper systemic issues and reinforce inequitable dynamics.

The political nature of the indicator then needs to be questioned, as claiming that it only describes and analyzes is a mistake. An indicator is a choice, a choice to make certain realities visible and others invisible. It is important to clearly identify the intention behind the choice of indicators and to iteratively question their meaning and objectives. This vigilance is a way of shedding light on manipulative commercial practices, known as Greenwashing. Indeed, isn't taking social issues into account a way for industries to justify themselves and show that they are “repairing,” thereby feeding the myth of sustainable development? If social indicators are merely used as a performative mechanism rather than a genuine tool for progress, they risk being reduced to symbolic gestures rather than catalysts for substantive change.

Furthermore, the integration of social indicators into industrial and territorial ecology can serve as a bridge between quantitative and qualitative assessment frameworks. Traditional environmental and economic models rely heavily on measurable data, but social dimensions require interpretive approaches that capture the nuances of human interactions, trust, and collaboration. Thus, a hybrid methodology that combines quantitative metrics with qualitative insights is necessary to ensure a holistic understanding of industrial ecosystems. This would enable a more inclusive evaluation process that incorporates the lived experiences of various stakeholders.

This study constitutes a key step in our process of developing a generic methodology to design and optimize flows in eco-industrial parks. Indeed, when taking into account several criteria in an optimization model, environmental and economic aspects are the most commonly used and the most easily quantified. The social criterion, however, is more important at a territorial scale and can vary significantly depending on the different actors involved. This study shows which criteria can be chosen and emphasizes the need to conduct preliminary interviews before formulating the problem. Engaging with stakeholders early in the process ensures that the indicators reflect the diversity of perspectives, allowing for a co-built and contextually relevant problem formulation.

Ultimately, the development of social indicators in industrial and territorial ecology is not merely an exercise in measurement but a fundamental practice of participatory governance. As industry and policymakers seek to balance ecological imperatives with economic viability, the social dimension must not be relegated to the background. The success of eco-industrial initiatives depends on the extent to which they integrate social trust, cooperation, and equity into their core frameworks. By fostering inclusive dialogue, continuously refining indicators, and ensuring their alignment with real-world social dynamics, we can create industrial ecosystems that are not only efficient and sustainable but also just and resilient.

## 7. CONCLUSION AND PERSPECTIVES

An eco-industrial park cannot function without particular attention to the links between the various players. Communication, trust and cooperation are the foundations of an effective collective. Social indicators can be used to assess the parameters conducive to this type of climate. We have also found that their participative elaboration has a strong potential to transform the collective.

Ultimately, social indicators in the context of industrial and territorial ecology raise questions about the management of common goods within a territory. The governance of the commons can be approached in ways other than metrics. Elinor Ostrom's work sets out fundamental principles for the management of common goods [9]. Moreover, the notion of principles and values [10] can also be seen as an alternative to social indicators. The idea here is to focus on the collective's values, what it wishes to defend and the principles that will flow from them.

These different avenues of reflection lead the collective, in our case an eco-park, to question the social impact it wishes to have on a micro, meso and macro scale.

In conclusion, this reflection on social indicators highlights a profound question: what impact do we wish to have on the world?

## ACKNOWLEDGEMENTS

This project has been accompanied by Region Occitanie that is fully thanked for the case study. It has been funded by PETRA grant through Defi Clé Circulades and Université de Toulouse.

## REFERENCES

1. Boix, M., Montastruc, L., Azzaro-Pantel, C., & Domenech, S. (2015). Optimization methods applied to the design of eco-industrial parks : A literature review. *Journal of Cleaner Production*, *87*, 303-317. https://doi.org/10.1016/j.jclepro.2014.09.032
2. Thomas, S., Boix, M., & Negny, S. (2024). Stratégies de décarbonation pour l’écologie industrielle, *19ème Congrès SFGP 2024, Deauville, France.*
3. Hale, J., Legun, K., Campbell, H., & Carolan, M. (2019). Social sustainability indicators as performance. *Geoforum*, *103*, 47-55. https://doi.org/10.1016/j.geoforum.2 019.03.008
4. Diemer, A., & Rubio, M. E. M. (2016). L’écologie industrielle et territoriale peut-elle s’affirmer

comme un véritable modèle de développement durable pour les pays du Sud ? *Revue Francophone du Développement Durable*, 1, 52-71.
5. Gobert, J., & Brullot, S. (2018). La mobilisation du capital territorial pour le développement d'une logique d'Écologie industrielle et territoriale: *Revue d'Économie Régionale & Urbaine*, *Décembre*(5), 881-904. https://doi.org/10.3917/reru.175.0881
6. Shek, D. T. L., & Wu, F. K. Y. (2018). The Social Indicators Movement : Progress, Paradigms, Puzzles, Promise and Potential Research Directions. *Social Indicators Research*, *135*(3), 975-990. https://doi.org/10.1007/s11205-017-1552-1
7. Faucheux, S., & Nicolaï, I. (2022). Indicateurs de Développement Durable dans les entreprises : Vers un contrat social? *Encyclopédie du Développement durable, 4D, 2009. hal-01799295*
8. Brullot, S., Junqua, G., & Zuindeau, B. (2017). Écologie industrielle et territoriale à l'heure de la transition écologique et sociale de l'économie. *Revue d'Économie Régionale & Urbaine*, *Décembre* (5), 771-796. https://doi.org/10.3917/reru.175.0771
9. Holland, G., & Sene, O. (2010). Elinor Ostrom et la Gouvernance Economique. *Revue d'économie politique*, *120*(3), 441-452. https://doi.org/10.3917/redp.203.0441
10. Buclet, N. (2012). Territoire, innovation et développement durable : L'émergence d'un nouveau régime conventionnel ?: *Revue d'Économie Régionale & Urbaine*, *décembre*(5), 911-940. https://doi.org/10.3917/reru.115.0911

© 2025 by the authors. Licensed to PSEcommunity.org and PSE Press. This is an open access article under the creative commons CC-BY-SA licensing terms. Credit must be given to creator and adaptations must be shared under the same terms. See https://creativecommons.org/licenses/by-sa/4.0/



Systems & Control Transactions

**Research Article - Peer Reviewed Conference Proceeding**
ESCAPE 35 - European Symposium on Computer Aided Process Engineering
Ghent, Belgium. 6-9 July 2025
Jan F.M. Van Impe, Grégoire Léonard, Satyajeet S. Bhonsale,
Monika E. Polańska, Filip Logist (Eds.)

PSE PRESS

# Life cycle assessment of a post-combustion $CO_2$ capture unit through chemical absorption

**Agathe Gabrion[a], Sydney Thomas[a], Marianne Boix[a*], and Stéphane Negny[a]**

[a] Laboratoire de Génie Chimique, UMR 5503, Toulouse INP/ CNRS/ UPS, 4 Allée Emile Monso, 31432 Toulouse Cedex 4, France
* Corresponding Author: Marianne.boix@ensiacet.fr

## ABSTRACT

This study evaluates the environmental impact of carbon capture technology in the context of reducing industrial $CO_2$ emissions within Eco-Industrial Parks (EIP). The primary focus is on the post-combustion absorption process, which uses solvents like monoethanolamine (MOA) to capture $CO_2$ before it is released into the atmosphere. The captured $CO_2$ is either stored or utilized to prevent further contribution to climate change. The study employs a Life Cycle Assessment (LCA) methodology to compare the environmental impacts of two scenarios: one with $CO_2$ capture and the other with the direct release of $CO_2$ into the atmosphere. The LCA considers inputs, outputs, energy requirements, and materials needed for the $CO_2$ absorption process. The functional unit of the assessment is 1000 tons of $CO_2$, to standardize comparisons between both scenarios. Results show that the $CO_2$ absorption process significantly reduces the impact on climate change, capturing over 80% of the $CO_2$ from the stream. In terms of climate change, the absorption process has a much lower environmental impact than releasing $CO_2$ into the atmosphere. However, other ecological impacts, such as resource use and ecotoxicity, are higher in the absorption process due to the materials required and the solvents used. In conclusion, while the $CO_2$ absorption process offers clear climate benefits, it introduces additional environmental challenges. Future studies should explore alternative carbon capture technologies and extend the scope to include $CO_2$ storage impacts and a broader range of LCA tools for more detailed assessments.

**Keywords**: Life Cycle Analysis, Carbon Dioxide Capture, Absorption, Decarbonization

## INTRODUCTION

Human activities are acknowledged to have an impact on the environment ever since the pre-industrial era. This influence on the climate, referred to as climate change, is mainly caused by the burning of fossil fuel [1]. Indeed, large amounts of carbon dioxide ($CO_2$) and other greenhouse gases are released in the atmosphere and act as traps for the sun's heat radiating from the surface of our planet.

Industrial activities are a major factor in climate change, given the amount of greenhouse gases released into the Earth's atmosphere from fossil fuel burning and from the energy required for industrial processes. In an attempt to reduce the environmental impact of the industry on climate change, many technologies are studied and considered.

This study focuses on one of these technologies – carbon capture. Carbon capture refers to the process of trapping $CO_2$ particles before or after the combustion of fossil fuels. Next, the carbon is used or stored in order for it not to reach the atmosphere, where it would be trapped and have a serious impact on climate change, as mentioned previously. This whole process is referred to as Carbon Capture, Utilization and Storage (CCUS). Carbon capture is declined into multiple technologies. This study focuses only on amine absorption, which is described in the next part.

In this study, the process of carbon capture is seen as part of a bigger project aiming at reducing the $CO_2$ emissions of the industry referred as an Eco-Industrial Park (EIP). Indeed, the process is studied in the context of an EIP in order to determine whether setting it up is more or less valuable in terms of ecological impact than the current situation consisting on releasing the greenhouse gases into the atmosphere.

To properly conduct this study, it was necessary to consider various factors of ecological impacts. Indeed, carbon absorption through an amine lowers the amount of $CO_2$ released in the atmosphere but on the other hand, the use of amine as a solvent comes with its share of degradation. For instance, the release of amine in the atmosphere is known to have several impacts such as on human health for instance.

Therefore, it was necessary to involve many different criteria in order to compare the ecological impact of a carbon capture and the ecological impact of the release of industry-produced greenhouse gases. To do so, the Life Cycle Analysis (LCA) method was chosen to assess the environmental impacts of both scenarios. This paper aims at presenting a methodology applicable to any technology in order to determine its environmental impact in the context of an EIP. After explaining the methodology, a case study will be made on post-combustion carbon absorption.

## POST-COMBUSTION ABSORPTION PROCESS DESCRIPTION

$CO_2$ absorption refers to the process in which a liquid solvent absorbs the $CO_2$ contained in a gas stream. In order to capture and separate $CO_2$ from the stream gas, the process of absorption requires solvents with high $CO_2$ binding capacity [2]. A recurrent solvent used for this purpose is a monoethanolamine (MOA) aqueous solution, given its high reactivity with $CO_2$ and its low price for production [3].

In this study, the absorption process was simulated with the Fives ProSim© software. The process is part of the software database and is set to treat 3073 tons of stream gas per hour (Figure 1).

## GOAL AND SCOPE OF THE LIFE CYCLE ASSESSMENT

Having clearly defined the $CO_2$ absorption process in the previous part of this study, this next part is intended to thoroughly define the goal and the scope of the LCA. This exercise is crucial in the LCA methodology as it ensures that the LCA has been performed consistently.

This LCA is conducted in order to quantify the environmental impact of a $CO_2$ absorption process including the design stage of the process. Ultimately, the goal is to define whether this process has an environmental benefit

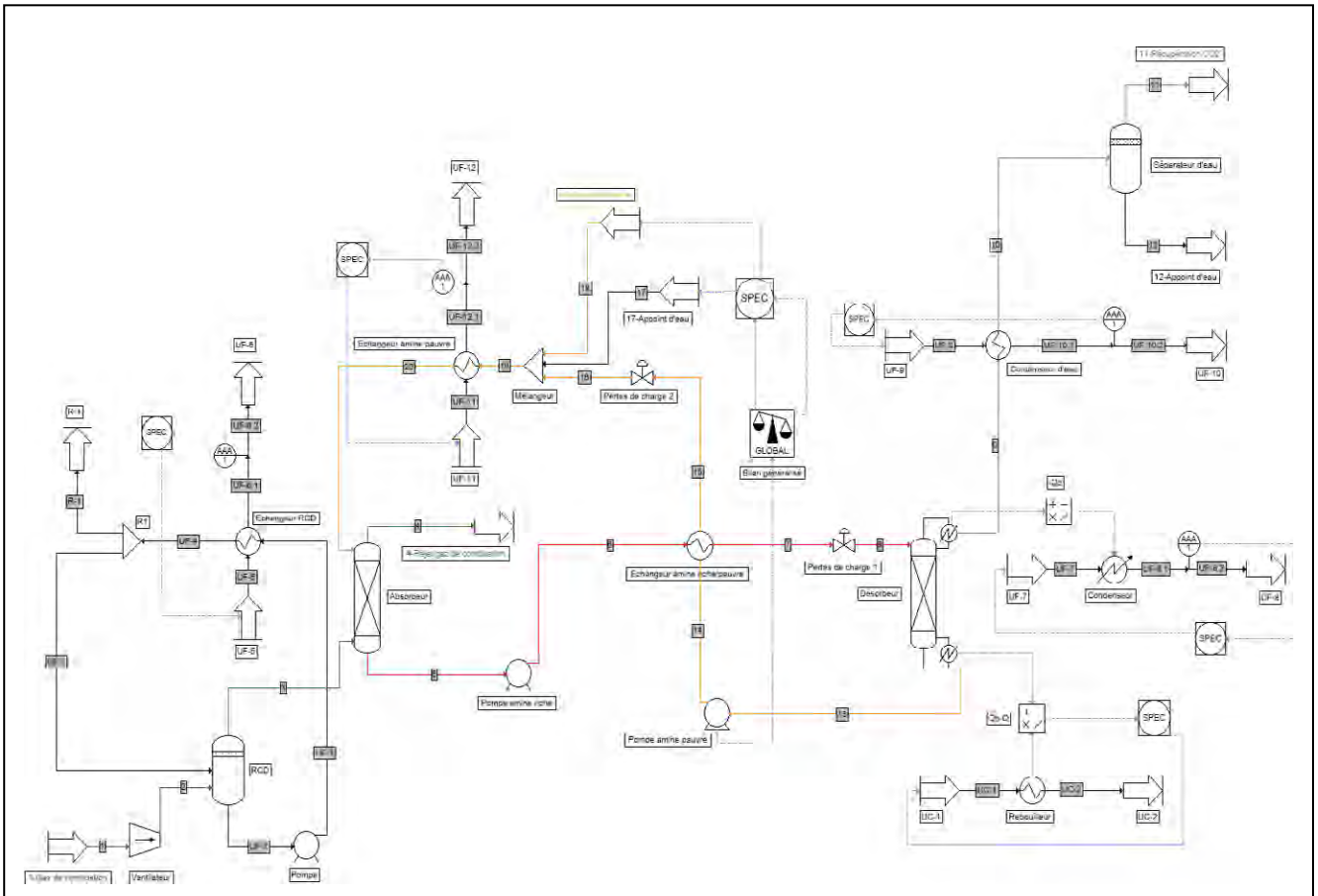



**Figure 1:** Schematic representation of the absorption process

over the gases release in the atmosphere.

In order to compare the impact of the $CO_2$ absorption process to the release of the $CO_2$ in the atmosphere, a functional unit is to be defined. The functional unit refers to any quantifiable unit in which the process' footprint is measured. Choosing a functional unit enables objective comparisons across all the elements considered. The functional unit selected for this study is 1000 tons of $CO_2$ collected at the outlet of the plant and treated or released in the atmosphere. In the context of the absorption process, the functional unit refers to the amount of $CO_2$ contained in the treated stream, whereas in the context of the release in the atmosphere, the functional unit refers to the amount of $CO_2$ contained in the released stream.

The scope defines the stages of the life of the $CO_2$ absorption process considered for the LCA. The usual scope would be cradle-to-grave because it covers every stage of the life of the process. However, this study does not include the last stage of the life of the process – waste disposal. Indeed, the disposal of the outputs of the process are considered, but not the disposal of the raw materials used to build the process in itself. The scope can then be referred to as cradle-to-use [4].

## LIFE CYCLE INVENTORY

The life cycle inventory for the $CO_2$ absorption process consists of the input and output streams, the materials needed to build the process and the energy required to run the process.

### Streams and energy requirements

In order to get an accurate representation of the input required to run the process and the outputs generated, a simulation of the $CO_2$ absorption process was run on Fives ProSim©. The block diagram featured in Figure 2 shows the results of this simulation.

This simulation provided values on the input and output streams as well as the energy requirements of the $CO_2$ absorption process. However, not every stream has to be considered for the LCA. Some hypotheses were made in order to conduct the LCA.

### Assumptions

First, the nitrogen contained in the input stream n°1 and the output stream n°4 are not considered because the amount in both streams is equal, meaning the amount of nitrogen entering the process is equal to the amount exiting the process. Only a trace is exiting the process through R-1 stream, which was considered in the LCA. Moreover, whether stream gas is treated through the $CO_2$ absorption process or released into the atmosphere, the amount of nitrogen released in the atmosphere is *in fine* the same.

Next, the utility streams were not considered either in the LCA because it can be considered as recycled. Indeed, the output and input streams carry the same amount.

Lastly, streams n°1 and n°11 are not considered for the LCA. The input stream n°1 is not considered in the LCA, as the purpose of the $CO_2$ absorption process is to treat said stream by separating the $CO_2$ from the other gases. The output stream n°11 is not considered either because it is the final product of the $CO_2$ absorption process, meaning the stream that contains the $CO_2$

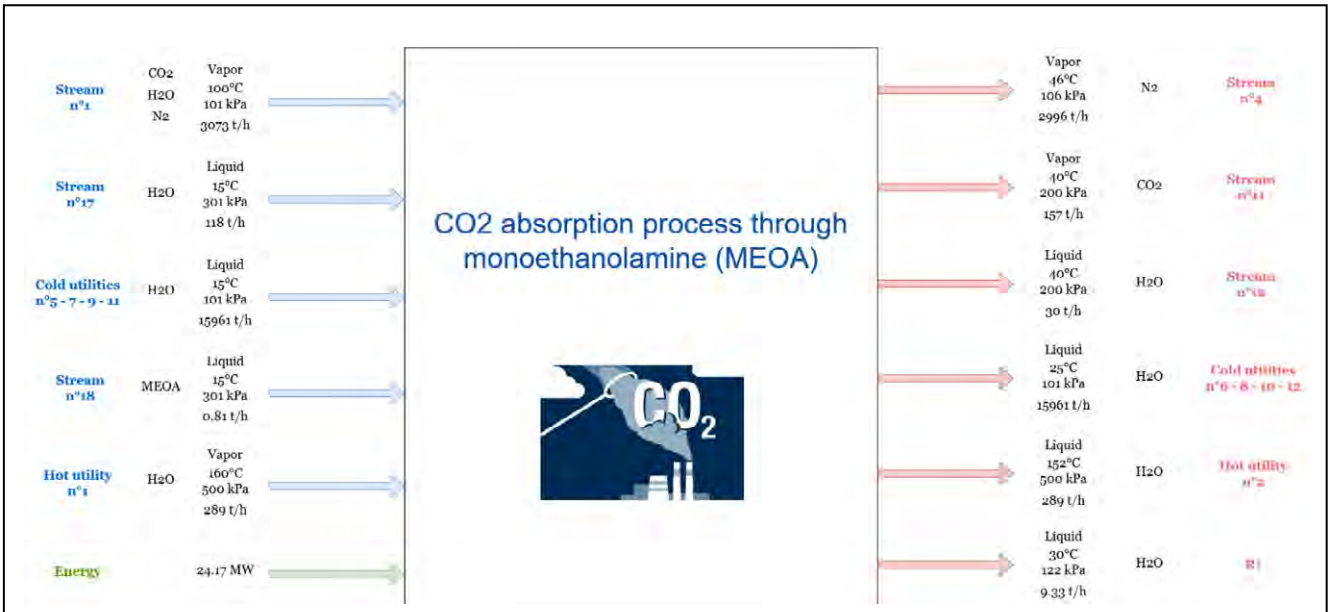



**Figure 2:** Block diagram of the results of the simulation of the $CO_2$ absorption process

separated for the other gases. This stream will then undergo a separate process, which does not fall into the scope of this study.

## Materials for process design

In order to get a rough idea of which materials were required to build the installation of the $CO_2$ absorption process, a Large Language Model was used. This tool provided an estimation of the amount of materials needed for each part of the process, as well as the amount of $CO_2$ treated by the process before the installation requires being replaced. The amount of materials was then brought back to 1000 tons of $CO_2$ to match the functional unit of the LCA. The final results used for the LCA are given in Table 1.

**Table 1:** Materials needed to build the process for 1000T of $CO_2$ treated

| Building materials | Amount needed (Ton) |
|---|---|
| Stainless steel | 0.1683 |
| Nickel-based alloy | 0.0700 |
| Packing materials | 0.0333 |
| Sealing materials | 0.0050 |

# RESULTS AND ANALYSES

The LCA was executed with the SimaPro© software. Figures 3 and 4 show the impacts of respectively the $CO_2$ absorption process and the release of stream gas in the atmosphere. The method Environmental Footprint was used in the software in order to obtain these two diagrams.

Impacts of both strategies to deal with $CO_2$ can be compared when considering the *Climate Change* category. Indeed, the impact of the release of stream gas is around 28kPt when the impact of the $CO_2$ absorption process is around 6.5kPt, meaning more than 4 times lesser than the direct release. 1 Pt is equivalent to the mean annual impact of a European inhabitant for the considered category. This is easily explained by the fact that more than 80% of the $CO_2$ contained in the stream gas is captured when going through the process.

However, the other categories have a greater impact when the stream gas is undergoing the $CO_2$ absorption process than when it is directly released. The analysis of the stream gas by SimaPro© can be discussed, as it appears that the stream gas, composed of 1000 tons of $CO_2$ and 728 tons of water, only impacts the *Climate Change and Water Use categories*.

The LCA was conducted using SimaPro© software. Figures 3 and 4 illustrate the environmental impact of $CO_2$ absorption and direct emissions, respectively, using the Environmental Footprint method.

Additionally, the energy required for the absorption process contributes to its environmental footprint. Future work should explore optimizing energy consumption to further reduce negative impacts. Another aspect to consider is solvent management. Amine-based solvents degrade over time, leading to waste generation. Implementing solvent regeneration techniques could enhance sustainability. Furthermore, alternative solvents with lower environmental impacts should be investigated.

## Integration in an optimization model

This study has been integrated into a previous optimization study (Boix et al., 2024) carried out to model and design the best exchanges of steam in an eco-industrial park. A set of companies operates processes that require vapor, electricity, and water. The objective is to determine the optimal configuration of exchanges between these companies that minimizes both cost and carbon emissions. The decision variables in the mathematical model include all inter-company flows (their existence and physical properties) as well as the sizing of necessary equipment.

A multi-objective optimization approach is applied to an Eco-Industrial Park (EIP) incorporating new facilities to assess their impact on greenhouse gas (GHG) emissions. These facilities include:

- An optimal steam network
- A Hybrid Power System (HPS)
- A $CO_2$ capture unit as modelled in the previous paragraph.

These elements are integrated into the optimization model, which is formulated as a multiperiod Mixed Integer Linear Programming (MILP) approach based on [5, 6]. The study by [7] on Yeosu Industrial Park is used as a case study to demonstrate the applicability of an optimization approach for a steam exchange network in a real industrial complex. The study identifies 15 industries, categorized into two groups: producing companies and consuming companies.

Producing industries generate steam, while consuming industries rely on external steam sources. Each industry has specific steam requirements, varying in type and quantity. The types of steam include:

- Very High-Pressure Steam (THP)
- High-Pressure Steam (HP)
- Medium-Pressure Steam (MP)
- Low-Pressure Steam (BP)

Since demand fluctuates throughout the year, it is divided into four periods based on seasons:

- t1: Spring (April to June)
- t2: Summer (July to September)

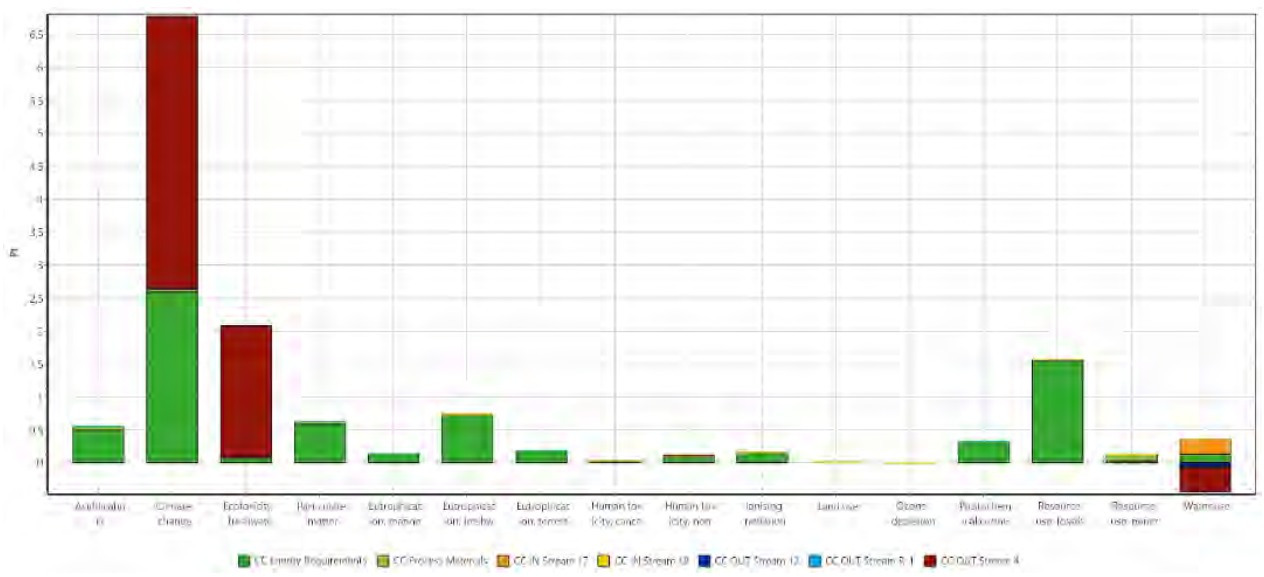


**Figure 3:** Diagram of the impacts of the $CO_2$ absorption process across different categories

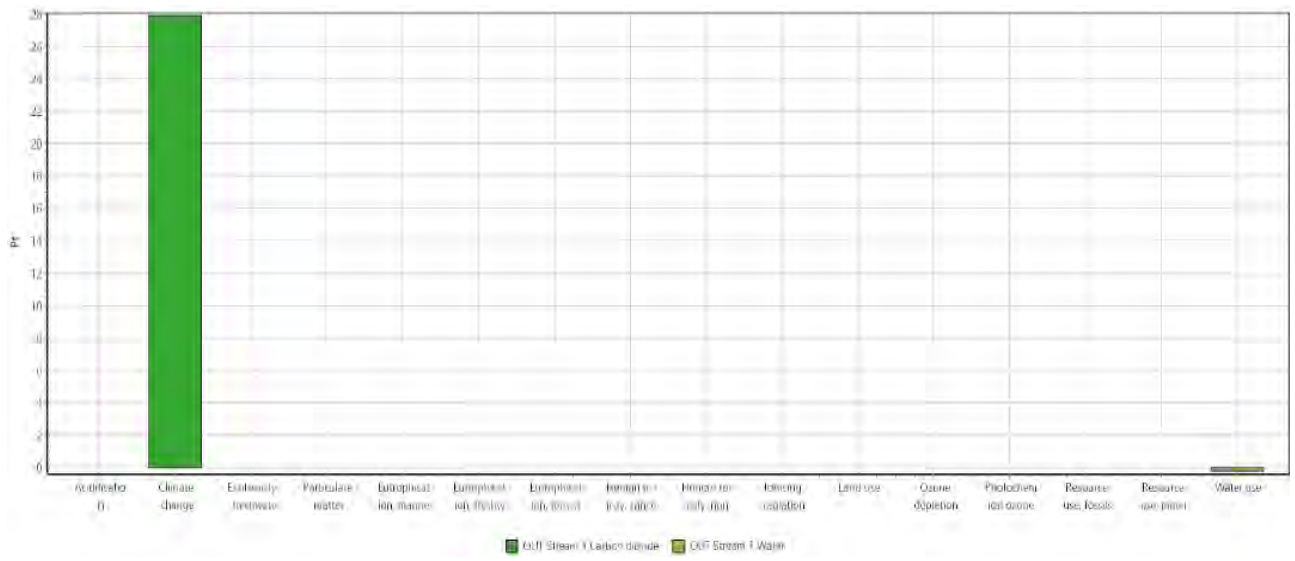


**Figure 4:** Diagram of the impacts of the release of stream gas across different categories

t3: Autumn (October to December)

- t4: Winter (January to March)

The first step in the optimization process involves defining the flue gas to be treated. Several simplifying assumptions are made:

1. The flue gas stream is considered a binary mixture comprising 14% $CO_2$ and 86% $N_2$.
2. The greenhouse gas (GHG) emissions from boilers consist solely of $CO_2$.
3. The flue gas temperature is assumed to be reduced to 25°C.

Using these assumptions, the model calculates the flue gas flow rate to be treated based on the GHG emissions generated by the boilers. This approach provides a structured framework for optimizing industrial symbiosis while integrating cost-efficient and environmentally friendly strategies. According to Table 2, it can be observed that the integration of such a unit in an eco-industrial park can lead to a decrease of GHG emissions of

more than 60% with a little increase of the cost of approximatively 0.4%. The total annual cost refers to the operating cost and also the investment linked to the $CO_2$ capture unit, it includes OPEX and CAPEX.

**Table 2:** Results of the integration of the carbon capture unit in the eco-industrial park

| | **Without $CO_2$ capture** | **With $CO_2$ capture** |
|---|---|---|
| Total annual cost (G$/yr) | 1899 | 1906 |
| Total GHG emissions ($TCO_{2eq.}$/yr) | 10416 | 3304 |

An attention must be paid to the modeling of news processes to be integrated into optimization model and especially with environmental impacts. We suggest that each new technology brick must be carefully modeled in order to quantify environmental impacts before being integrated into an optimization model.

## CONCLUSION AND PERSPECTIVES

Using SimaPro© software, this study demonstrated that $CO_2$ absorption significantly reduces climate change impact compared to direct emissions. Within an EIP, implementing $CO_2$ capture could enhance sustainability efforts. However, increased impacts on ecotoxicity and resource consumption warrant further consideration.

Future research directions include:

- Exploring alternative carbon capture technologies such as adsorption or membrane separation.
- Assessing the environmental impact of $CO_2$ storage.
- Extending the LCA scope to include $CO_2$ sequestration.
- Evaluating different LCA tools for a more comprehensive impact assessment.
- Investigating process improvements to enhance efficiency and sustainability.
- Studying economic feasibility to determine the long-term viability of $CO_2$ capture solutions.
- Investigating policy incentives and industrial cooperation strategies to improve the adoption of carbon capture technologies.

By addressing these considerations, future studies can contribute to the development of more sustainable industrial practices, ultimately mitigating climate change while minimizing adverse environmental effects.


## ACKNOWLEDGEMENTS

This work was supported by a government grant managed by the Agence Nationale de la Recherche under the France 2030 program, under the reference ANR-22-PESP-0004.


## REFERENCES


1. Haut Conseil pour le Climat, Rapport annuel (2024)
2. Wang, P. et al. (2024) 'Advances in life cycle assessment of chemical absorption-based carbon capture technologies', Separation and Purification Technology, 346, p. 127252. Available at: https://doi.org/10.1016/j.seppur.2024.127252.date).
3. Putta, K.R. *et al.* (2016) '$CO_2$ absorption into loaded aqueous MEA solutions: Kinetics assessment using penetration theory', *International Journal of Greenhouse Gas Control*, 53, pp. 338–353. Available at: https://doi.org/10.1016/j.ijggc.2016.08.009.
4. Cradle-to-Gate: What is it & How does it work in LCA?' (no date) *Ecochain*. Available at: https://ecochain.com/blog/cradle-to-gate-in-lca/.
5. Boix, M. et al., (2024) Decarbonization strategies by industrial ecology, Computers Aided Process Engineering, Volume 53, 3445-3450, ISSN 1570-7946, https://doi.org/10.1016/B978-0-443-28824-1.50575-5.
6. Boix, M. et al., (2023). How to design cooperative sustainable industrial systems? Computers Aided Process Engineering, Volume 50, 959-964, ISSN 1570-7946, https://doi.org/10.1016/B978-0-323-88506-5.50148-0.
7. Kim et al., (2010). S., Kim, Yoon, S.-G., Chae, S. H. & Park, S., 2010, Economic and environmental optimization of a multi-site utility network for an industrial complex. J. Env. Manag. 91, 690–705.



© 2025 by the authors. Licensed to PSEcommunity.org and PSE Press. This is an open access article under the creative commons CC-BY-SA licensing terms. Credit must be given to creator and adaptations must be shared under the same terms. See https://creativecommons.org/licenses/by-sa/4.0/

Systems & Control Transactions

**Research Article - Peer Reviewed Conference Proceeding**
ESCAPE 35 - European Symposium on Computer Aided Process Engineering
Ghent, Belgium. 6-9 July 2025
Jan F.M. Van Impe, Grégoire Léonard, Satyajeet S. Bhonsale,
Monika E. Polańska, Filip Logist (Eds.)

PSE PRESS

# Dynamic Simulation and Life Cycle Assessment of Energy Storage Systems Connecting Variable Renewable Sources with Regional Energy Demand

**Ayumi Yamaki[a], Shoma Fujii[ab], Yuichiro Kanematsu[c], and Yasunori Kikuchi[abc]***

[a] The University of Tokyo, Institute for Future Initiatives, Tokyo, Japan
[b] The University of Tokyo, Department of Chemical System Engineering, Tokyo, Japan
[c] The University of Tokyo, Presidential Endowed Chair for "Platinum Society" Organization for Interdisciplinary Research Project,, Tokyo, Japan
* Corresponding Author: ykikuchi@ifi.u-tokyo.ac.jp

## ABSTRACT

To achieve carbon neutrality, the installation of variable renewable energy (VRE) has been accelerated. However, the inherent variability of VRE can be mitigated through the installation of energy storage. This study aims to evaluate life cycle impacts of energy storage systems utilizing batteries, hydrogen storage, or thermal energy storage. A model of the energy storage systems with VRE was developed, and the annual energy flow simulations were conducted. The energy storage system targeted in this study assumed that all energy derived from VRE was stored in the energy storage and supplied to consumers. The amount of electricity to-be-sold from the energy storage system, based on the capacity of VRE and the installed energy storage, was calculated. A life cycle assessment was performed to evaluate the greenhouse gas (GHG) emissions, abiotic resource depletion (ARD), and intensity of GHG and ARD as life cycle impacts. The smallest life cycle impacts varied depending on the type and scale of energy storage. This quantitative evaluation of the energy supply capacity and the environmental impacts of the energy storage systems could provide valuable insights for designing efficient energy storage systems integrated with VRE, tailored to regional energy supply requirements.

**Keywords**: Batteries, Hydrogen, Thermal energy storage

## INTRODUCTION

The installation of variable renewable energy (VRE) has expanded around the world to promote the transition to a sustainable society, although ensuring a stable electricity supply from VRE remains challenging due to its inherent variability. To accelerate the penetration of VRE, projects are underway to install energy storage technologies, such as batteries, hydrogen ($H_2$) storage, and thermal energy storage (TES).

Selecting the appropriate energy storage technology requires careful consideration of multiple factors. The life cycle greenhouse gas (LC-GHG) of different storage systems is evaluated [1–3]. However, their types and scales should be designed based on regional characteristics because an improperly sized system can lead to increased LC-GHG [4]. There are studies to evaluate the installation of specific energy storage technologies under certain conditions [5], but comparing different storage types remains challenging. To address this, a comprehensive model is needed to assess the performance and environmental impacts of various energy storage options while considering regional conditions, such as VRE installation potential, under a consistent functional unit.

This study developed a model for evaluating environmental impacts of the energy storage systems in a region, based on an existing model by Yamaki et al. [6]. The energy storage systems assumed to include batteries, $H_2$ storage, and TES, which were evaluated using life cycle assessment (LCA). These systems were designed as new energy supply solutions to mitigate the variability of wind energy as a representative VRE source and connect to

the grid. The energy storage systems incorporating batteries, $H_2$ storage, and TES are referred to as a battery system, $H_2$ system, and TES system, respectively.

The model of the energy storage system was constructed to simulate the annual energy flows. We calculated the amount of electricity that could be sold from the energy storage system and analyzed their life cycle impacts. For life cycle impacts, LC-GHG, abiotic resource depletion (ARD), and greenhouse gas (GHG) and ARD intensities were evaluated. We discuss the applicability and implications of these energy storage systems.

## MATERIALS AND METHODS

### Model of the Energy Storage Systems

The model of the energy storage systems is shown in Figure 1. Figure 1(a) shows the energy and material flows of the energy storage systems targeted in this study. In energy storage systems, wind energy is assumed to be stored and supplied as electricity.

In the battery system, electricity is assumed to be generated by wind turbines (WTs), stored in batteries, and supplied to meet demand. In the $H_2$ system, $H_2$ is assumed to be produced by electrolyzers using electricity generated in WT. The $H_2$ is then stored as liquefied $H_2$ in tanks and converted into electricity in fuel cells. In the TES system, wind energy is directly converted into thermal energy through wind-thermal energy converters ($WEC_{th}$s), stored in molten salts, and later used to generate steam in a heat exchanger, which drives a steam turbine for electricity production. A $WEC_{th}$ directly converts wind-derived rotational energy into thermal energy [4].

Figure 1(b) expresses the wind speed profile assumed for the energy flow simulations in this study. The meteorological data referred to Cape Erimo in Hokkaido prefecture, which has the highest average wind speed in Japan [7]. Figure 1(c) shows the electricity demand curve for Hokkaido prefecture [8].

LCA was performed on a cradle-to-grave basis, covering energy storage and related facilities, under the assumption of installing a new energy storage system. The LCA covered the batteries and WTs in the battery

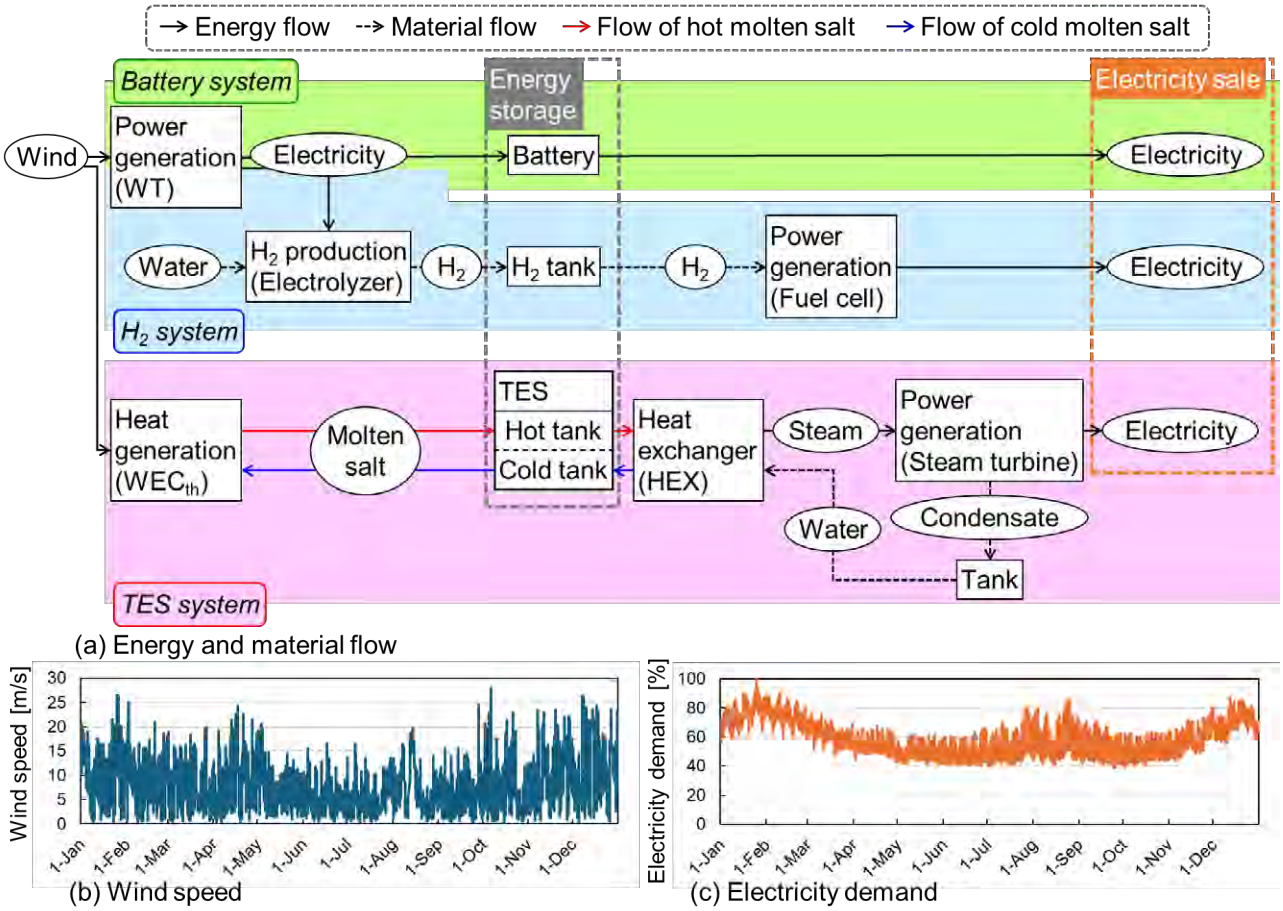



**Figure 1:** Model of energy storage systems. (a) Energy and material flows of the energy storage systems. (b) Wind speed at Erimo cape in Hokkaido prefecture. (c) Electricity demand in Hokkaido prefecture.

system; the $H_2$ tank, electrolyzer, fuel cell, and WTs in the $H_2$ system; and the molten salt, its tanks, heat exchanger, steam turbine, and $WEC_{th}$ in the TES system.

## Energy Flow Simulations

The model developed in this study assumed that all power and heat derived from wind energy were stored in energy storage and supplied as electricity to consumers. The simulations were conducted using Microsoft Excel with energy flows calculated on an hourly basis from 00:00 on January 1 to 24:00 on December 31.

$$Q_{\mathrm{storage}}(t) = Q_{\mathrm{storage}}(t-\Delta t) + Q_{\mathrm{in}}(t) - Q_{\mathrm{out}}(t) - Q_{\mathrm{leakage}}(t) \quad (1)$$

In equation (1), $Q_{\mathrm{storage}}(t)$ represents the energy stored in the targeted energy storage at time *t*, while $Q_{\mathrm{in}}(t)$ is the input energy supplied from wind energy. If electricity or heat generation from wind energy exceeded the energy storage capacity, the excess energy was assumed to be curtailed. $Q_{\mathrm{out}}(t)$ is the output energy from the energy storage, which is calculated based on the electricity sold. The electricity demand curve used in this study is shown in Figure 1(c). $Q_{\mathrm{leakage}}(t)$ represents energy leakage from energy storage, which includes battery self-discharge, $H_2$ leakage, and heat loss. The parameters for the energy flow simulations are extracted from the references [1–4,6,9,10].

The amount of electricity sold is adjusted to occur in periods of zero $Q_{\mathrm{storage}}(t)$, and the electricity sales value represents the maximum electricity that the targeted energy storage system could supply. The simulation also imposed the constraint that energy for selling electricity at time *t* was assumed to be stored at time *t*–Δ*t* in this simulation, as indicated in equation (2).

$$Q_{\mathrm{out}}(t) \leqq Q_{\mathrm{storage}}(t-\Delta t) \quad (2)$$

This study presents the value of electricity sales as a result of total electricity sold over the year. To ensure the energy storage system could supply electricity continuously over multiple years, it was assumed that the stored energy levels at 0:00 on January 1st and at 24:00 on December 31st were the same. This applied to the amounts of charged electricity in the battery, the $H_2$ in the $H_2$ tank, and the temperature and quantity of molten salt in the TES tank.

## Analysis Settings

An LCA was conducted to evaluate the cradle-to-grave impacts of energy storage and related facilities, assuming the installation of a new energy storage system. The LCA covered power and heat generation facilities powered by wind energy, as well as components specific to each energy storage system. For the battery system, lithium-ion batteries were assessed. The $H_2$ system included components such as a $H_2$ tank, an alkaline electrolyzer, and solid oxide fuel cells (SOFC). The scale of the electrolyzer was adjusted according to the capacity of WT and $H_2$ tank. The TES system encompassed the molten salt, its tanks, heat exchanger, and steam turbine.

The functional unit was the annual wind speed shown in Figure 1(b). Foreground data for the LCA was derived from energy flow simulations, while background data, such as materials for the energy systems, were extracted from the Japanese LCA database, the inventory database for environmental analysis version 3.4.1 (IDEA) [11]. The quantities of materials used for production and operation were extracted from the references [1–3,6,10,12–15]. LC-GHG and ARD were calculated by adding the GHG emission and ARD across all stages of the life cycle from production to disposal of the facilities.

The GHG and ARD intensities were expressed as LC-GHG and ARD per electricity sold. Although GHG emissions are reduced by VRE installation, ARD would increase due to the use of rare metals required for energy storage systems. Therefore, it is essential to evaluate both GHG emissions and ARD.

# RESULTS AND DISCUSSIONS

## Annual Energy Flow and Electricity Sold from the Energy Storage Systems

Energy flow simulations for the energy storage systems were conducted to calculate annual electricity sales under varying capacities of WT/$WEC_{th}$ and energy storage. The maximum potential electricity sales were determined for each combination of energy storage capacity and WT/$WEC_{th}$ installations.

Figure 2(a) shows the hourly variation in stored energy and electricity sales, whose demand curve was assumed as shown in Figure 1(c), for a system with 15 GWh-energy storage and 100 MW-wind energy. To maximize electricity sales, the stored energy was depleted to near-zero levels, adhering to the constraints defined in equation (2). Wind-derived energy was curtailed when the energy storage system reached full capacity.

As shown in Figure 2(b), electricity sales increased with larger WT/$WEC_{th}$ and energy storage installations but plateaued or declined with excessive storage capacity. With smaller storage systems, the electricity sales rose as the storable energy, $Q_{\mathrm{in}}(t)$, increased. However, due to the finite availability of wind energy, $Q_{\mathrm{in}}(t)$ cannot grow indefinitely, even with larger storage facilities. The output energy, $Q_{\mathrm{out}}(t)$, is constrained by operational limitations, including the depth of discharge (DoD) in batteries, $H_2$ gasification in a $H_2$ tank, and heat release in the TES system. Excessive energy storage installations led to inefficiencies, as stored energy could not be fully utilized. In TES systems, for example, molten salt stored in the cold tank at 290°C continuously released heat.

These findings suggest that to maximize the effective utilization of stored energy, energy storage

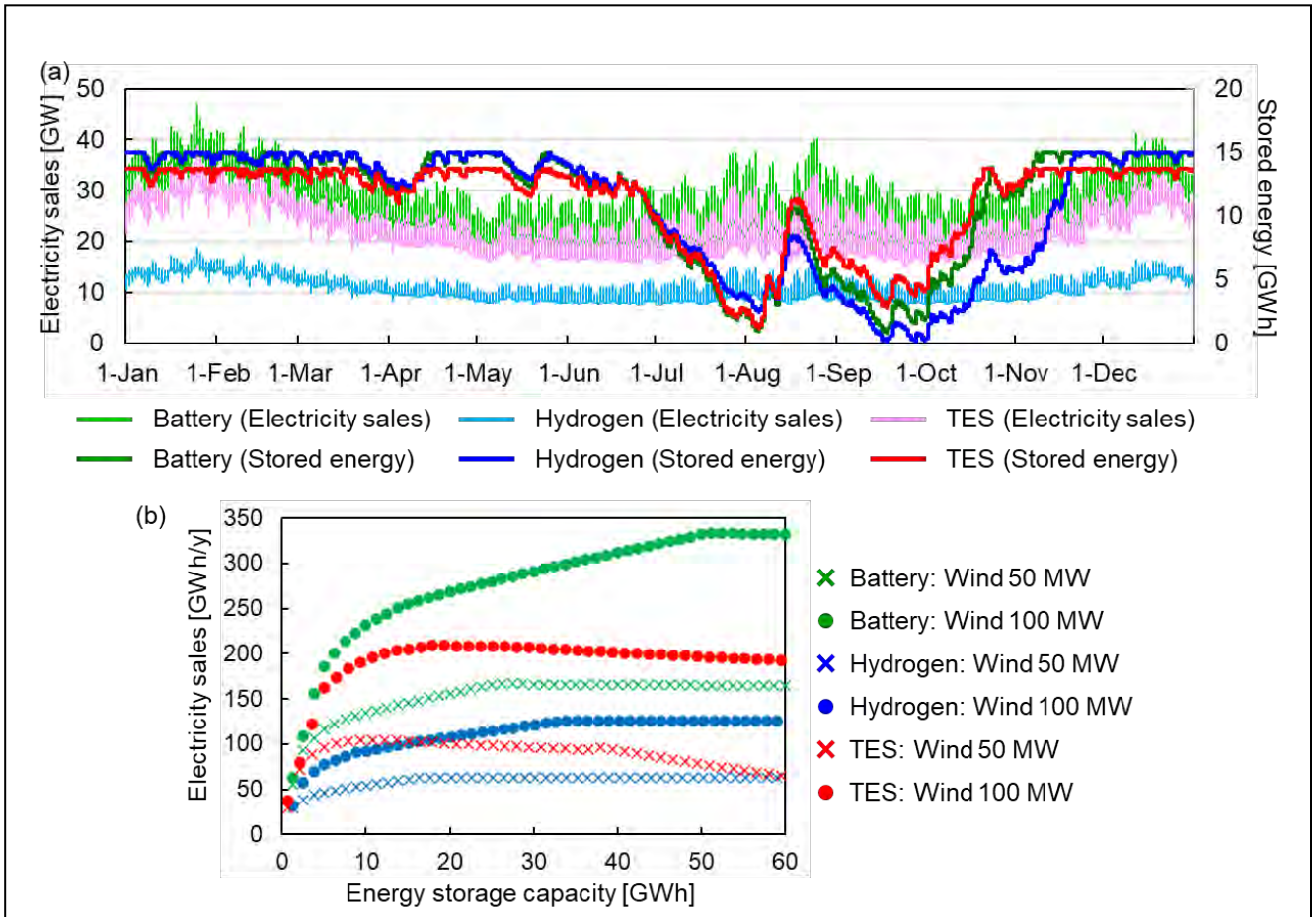



**Figure 2:** Results of energy flow simulations. (a) Hourly variation of the energy storage systems with 15 GWh energy storage and 100 MW class wind energy. (b) Electricity sold from the energy storage system.

capacities must be carefully balanced with the scale of WT/WEC$_{th}$ installations. Over-provisioning energy storage can lead to diminished returns due to storage inefficiencies and energy losses.

## Life Cycle Impacts of the Energy Storage Systems

Life cycle impacts of the energy storage systems were evaluated for various capacities of WT/WEC$_{th}$ and energy storage. LC-GHG and ARD were calculated considering the full life cycle—from production to disposal—of WT/WEC$_{th}$, energy storage, and other related utilities. The related utilities included an electrolyzer and fuel cell in the $H_2$ system, as well as a steam turbine and heat exchanger in the TES system. The GHG and ARD intensities, which were expressed LC-GHG and ARD per unit electricity sold respectively, are shown in Figure 3.

GHG intensities were compared in Figure 3 (a). In all systems, GHG intensities were high with small energy storages due to the large impact of WT/WEC$_{th}$ production. With a moderate number of large energy storage facilities, GHG intensities decreased as electricity sales increased. Conversely, excessive energy storage installations (except in the $H_2$ system) led to increased GHG intensities due to the high GHG emissions from the producing energy storage facilities. In the battery and TES systems, large wind energy installations reduced GHG intensities as electricity sales increased without a corresponding rise in LC-GHG. In the $H_2$ system, GHG intensities remained nearly constant regardless of the scale of WT and $H_2$ tanks. As the scale of WT and $H_2$ tanks increased, electricity sales grew; however, GHG emissions from production of electrolyzers and fuel cells also increased due to the need for large equipment.

The ARD intensities of the energy storage systems are shown in Figure 3 (b). Similar to GHG intensities, ARD intensities were high with very small or excessively large energy storage capacities. Appropriate energy storage capacities resulted in the lowest ARD intensities. Among the systems with 100 MW-wind energy, the TES system demonstrated the lowest ARD intensity.

## Applicability of the Energy Storage Systems

For large-scale WT/WEC$_{th}$ and energy storage

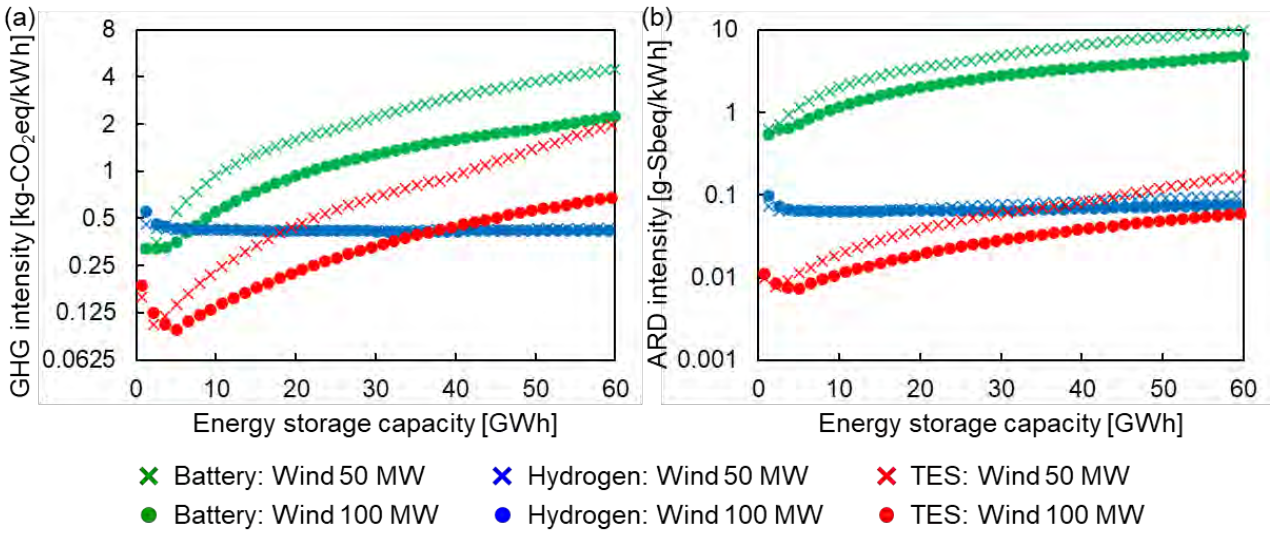



**Figure 3:** Life cycle impacts of the energy storage systems. (a) GHG intensity. (b) ARD intensity.

installations, $H_2$ or TES systems were more suitable due to their lower life cycle impacts compared to battery systems. Selecting the optimal energy storage system requires considering regional energy demands, including H2 for fuel and industry and heat for residential and industrial use. This study facilitates a quantitative assessment of the environmental performance of energy storage systems, encompassing their operation and offering insights into detailed energy storage installation planning.

Each scenario in this study analyzed only one type of energy storage. If a significant amount of VRE-derived electricity is supplied directly without an energy storage system, electricity from the energy storage system must be shut down frequently to meet the electricity demand. Long startup times may fail to supply electricity promptly during demand spikes. This highlights the need for a hybrid energy storage technology to ensure a stable and responsible electricity supply. System designs must account for both load-following capabilities and environmental impacts. While batteries offer fast response times, their LC-GHG and ARD are higher compared to $H_2$ storage and TES. Designing hybrid systems can achieve a balance between stable energy supply, operational flexibility, and minimizing environmental impacts. Enhancing the model developed in this study could support designing such integrated systems.

In this analysis, all facilities were assumed to be disposed of without recycling. Recycling energy storage components offers significant opportunities for improvement [16]. Additionally, operational adjustments could further optimize energy storage system performance [6]. Although the optimizations in this study are not comprehensive, the simulations conducted here demonstrate the potential for designing energy storage systems with low environmental impacts and high efficiency.

The installation of energy storage systems can also deliver broader societal and economic benefits. In regions where these systems are installed, life cycle impacts can be reduced, and the risk of blackouts from natural disasters minimized. Moreover, establishing new facilities such as energy storage systems could create jobs for operation and maintenance. Local socio-economic effects of adopting new technologies can be assessed using Input-Output (IO) models [17]. The energy storage system installation is expected to stimulate the local economy and drive regional revitalization. This study can provide quantitative parameters for analyzing these local socio-economic effects. Thus, energy storage systems may offer diverse applicability, contributing not only to carbon neutrality but also to regional development and resilience.

## CONCLUSIONS

In this study, we developed a model for energy storage systems integrated with VRE and conducted annual energy flow simulations alongside an LCA. The study provided a quantitative comparison of various energy storage technologies, evaluating electricity sales and life cycle impacts based on regional energy demands and storage system characteristics.

Designing energy storage systems in a given region should consider the electricity supply capacity, as this determines the energy demand that the system can meet. The minimum GHG and ARD intensities also depend on the type and scale of the storage system, underscoring the importance of designing systems considering

regional requirements.

Advancements in energy storage technology and operational strategies can enhance efficiency and adaptability to VRE variability. These systems have broad applications, from supporting carbon neutrality to regional revitalization. This study provided a framework for LCA of energy storage systems including operational considerations and would support to design of energy storage systems that are both environmentally sustainable and operationally effective.

## ACKNOWLEDGEMENTS

This study was financially supported by the New Energy and Industrial Technology Development Organization (NEDO) (Grant number, JPNP21026). This research contained the achievements of the JST-MIRAI Program Grant Number JPMJMI19C7, JST COI-NEXT (JPMJPF2003), JST PRESTO (Grant Number JPMJPR2278), JSPS KAKENHI (Grant Number JP21H03660), JSPS KAKENHI Grant-in-Aid for Early-Career Scientists (Grant Number JP22K18061), and the Environment Research and Technology Development Fund (Grant Number JPMEERF20243G01) of the Environmental Restoration and Conservation Agency of Japan. Activities of the Presidential Endowed Chair for "Platinum Society" at the University of Tokyo are supported by Mitsui Fudosan Corporation, Sekisui House, Ltd., the East Japan Railway Company, and Toyota Tsusho Corporation.

## REFERENCES

1. Rahman MM, Gemechu E, Oni AO, Kumar A. The greenhouse gas emissions' footprint and net energy ratio of utility-scale electro-chemical energy storage systems. Energy Convers Manag. 2021;244: 114497. doi:10.1016/j.enconman.2021.114497
2. Ozawa A, Kudoh Y, Kitagawa N, Muramatsu R. Life cycle CO2 emissions from power generation using hydrogen energy carriers. Int J Hydrogen Energy. 2019;44: 11219–11232. doi:10.1016/j.ijhydene.2019.02.230
3. Oró E, Gil A, de Gracia A, Boer D, Cabeza LF. Comparative life cycle assessment of thermal energy storage systems for solar power plants. Renew Energy. 2012;44: 166–173. doi:10.1016/j.renene.2012.01.008
4. Yamaki A, Fujii S, Kanematsu Y, Kikuchi Y. Life cycle greenhouse gas emissions of cogeneration energy hubs at Japanese paper mills with thermal energy storage. Energy. 2023;270: 126886. doi:10.1016/j.energy.2023.126886
5. Wang Y, Wang B, Chu C-C, Pota H, Gadh R. Energy management for a commercial building microgrid with stationary and mobile battery storage. Energy Build. 2016;116: 141–150. doi:10.1016/j.enbuild.2015.12.055
6. Yamaki A, Fujii S, Kanematsu Y, Kikuchi Y. Comparative life cycle assessment of energy storage systems for connecting large-scale wind energy to the grid. J Chem Eng Japan. 2024;57. doi:10.1080/00219592.2024.2406316
7. Japan Meteorological Agency. Historical meteorological data. [cited 13 Mar 2025]. Available: https://www.data.jma.go.jp/stats/etrn/index.php
8. Hokkaido Electric Power Network, Inc. Download histrical electricity usage data. [cited 13 Mar 2025]. Available: https://denkiyoho.hepco.co.jp/area_download.html
9. Connexx systems. Large Capacity Energy Storage System/Container-Type. Available: https://www.connexxsys.com/products/c-type-ess/
10. Inomata A, Hashimoto S, Yamanouchi K, Yamamoto T. Hydrogen StorageDevelopment of Liquefied Hydrogen Terminal. 2020;182: 20–23.
11. National Institute of Advanced Industrial Science and Technology. Inventory Database for environmental analysis version 3.4.1. 2024.
12. Krishnan S, Koning V, Theodorus de Groot M, de Groot A, Mendoza PG, Junginger M, et al. Present and future cost of alkaline and PEM electrolyser stacks. Int J Hydrogen Energy. 2023;48: 32313–32330. doi:10.1016/j.ijhydene.2023.05.031
13. Bicer Y, Khalid F. Life cycle environmental impact comparison of solid oxide fuel cells fueled by natural gas, hydrogen, ammonia and methanol for combined heat and power generation. Int J Hydrogen Energy. 2020;45: 3670–3685. doi:10.1016/j.ijhydene.2018.11.122
14. Morimoto K, Yamashita S, Watanabe D. Hydrogen liquefaction and storage system. J Jpn Weld Soc. 2019;88: 56–62. doi:10.2207/jjws.88.56
15. Wang Y, Liu J, Ma X, Ouyang Y, Zhu D, Zhang Y. Numerical investigation on the thermal performance of a molten salt tank under different electric heating method. Sol Energy Mater Sol Cells. 2024;278: 113183. doi:10.1016/j.solmat.2024.113183
16. Kikuchi Y, Suwa I, Heiho A, Dou Y, Lim S, Namihira T, et al. Separation of cathode particles and aluminum current foil in lithium-ion battery by high-voltage pulsed discharge Part II: Prospective life cycle assessment based on experimental data. Waste Manag. 2021;132: 86–95. doi:10.1016/j.wasman.2021.07.016
17. Oshita Y, Heiho A, Ouchida K, Kanematsu Y, Fukushima Y, Kikuchi Y. Analyzing Socio-economic effect induced by technology implementation on

available renewables: A case study of tanegashima, japan. J Life Cycle Assess Jpn. 2019;15: 360–376. doi:10.3370/lca.15.360

© 2025 by the authors. Licensed to PSEcommunity.org and PSE Press. This is an open access article under the creative commons CC-BY-SA licensing terms. Credit must be given to creator and adaptations must be shared under the same terms. See https://creativecommons.org/licenses/by-sa/4.0/



Systems & Control Transactions

**Research Article - Peer Reviewed Conference Proceeding**
ESCAPE 35 - European Symposium on Computer Aided Process Engineering
Ghent, Belgium. 6-9 July 2025
Jan F.M. Van Impe, Grégoire Léonard, Satyajeet S. Bhonsale,
Monika E. Polańska, Filip Logist (Eds.)

PSE PRESS

# Optimisation of Carbon Capture Utilisation and Storage Supply Chains Under Carbon Trading and Taxation

**Hourissa Soleymani Babadi[a] and Lazaros G. Papageorgiou[a]***

[a] The Sargent Centre for Process Systems Engineering, Department of Chemical Engineering, University College London (UCL), Torrington Place, London WC1E 7JE, UK
* Corresponding Author: l.papageorgiou@ucl.ac.uk

## ABSTRACT

In recent years, several strategies have been developed to reduce the carbon dioxide ($CO_2$) released into the atmosphere. Carbon Capture, Storage and Utilisation (CCUS) is one of the proposed solutions. However, CCUS systems are expensive to install and operate. Furthermore, most studies in the literature have focused on $CO_2$ utilisation and storage separately, without accounting for the effects of other $CO_2$ emission management strategies. To address this gap, a Mixed Integer Linear Programming (MILP) framework for a supply chain network is developed in this work, incorporating $CO_2$ storage, utilisation, permit trading, and carbon emission taxation. Multi-criteria decision analysis (MCDA) techniques are implemented to select $CO_2$-based products for $CO_2$ utilisation. The MILP framework is set to achieve the maximum environmental and economic performance using a Multi-Objective Optimisation (MOO) approach. This involves using the ε-constraint method as a solution procedure to minimise the total cost of the supply chain network while maximising $CO_2$ reduction. A case study of supply chains in Germany is conducted to demonstrate the applicability of the model. The game theoretical Nash approach is successfully applied to determine the fair trade-off between the two objectives.

**Keywords**: CCUS Supply Chains, Multi Objective Optimisation, CO2 Trading and Taxation, Game theoretical Nash Approach.

## INTRODUCTION

The UN's International Panel on Climate Change states that the rise in $CO_2$, which constitutes the majority of greenhouse gas emissions, contributes to global warming and climate change. As a result, scientific research and governmental policies have been working towards the reduction of $CO_2$ emissions in processes across the board. Carbon Capture Utilisation and Storage (CCUS) is considered to be one of the solutions to lower greenhouse gas emissions. New CCUS routes, such as utilising $CO_2$ in the production of fuels, chemicals, and building materials, have the potential to use 5 Gt/year of $CO_2$ [1]. However, this is a challenging task due to the economic costs of developing CCUS products and technologies. Many products can be produced from $CO_2$ conversion, but not all these $CO_2$ utilisation reactions have the potential to be implemented profitably at scale. Therefore, implementing cost-effective CCUS supply chain networks at scale will be beneficial in overcoming the high cost of $CO_2$ combating development.

## LITERATURE REVIEW

Multi-Criteria Decision Analysis (MCDA) is a decision-making methodology that evaluates and ranks a set of $CO_2$-based products by considering multiple criteria, including environmental, social, and economic aspects. Pacheco et al. [2] conducted a comprehensive assessment of the techno-economic, environmental, and social aspects of 122 $CO_2$-based chemical compounds. Implementing six different MCDA methods, methanol, dimethyl ether, methane and a couple of other candidates were identified as the best products.

Hasan et al. [3] developed a CCUS network aimed at reducing $CO_2$ emissions in the United States by 50-80% while minimising the overall cost, incorporating the revenue generated from utilising $CO_2$ in enhanced oil recovery. The approach involved optimising the selection of the emission sources, capture processes and

materials, pipelines, as well as the $CO_2$ utilisation/storage amount. Zhang et al. [4] proposed a superstructure in Northeastern China that includes underground storage and the utilisation of $CO_2$ through several possible conversion paths. Although $CO_2$ conversion may generate a carbon-neutral cycle, the result emphasised the increased costs with more $CO_2$ utilisation. A multi-objective optimisation framework was proposed by Leonzio et al. [5] for CCUS deployment, considering cost as the economic performance measure and $CO_2$ reduction as the environmental performance measure.

In addition to CCUS, various methods exist for carbon emission management, such as introducing carbon pricing. Carbon pricing can take different forms, including carbon taxes or carbon emissions permit trading. The European Union Emissions Trading System (EU ETS), established in 2005, is the oldest cap-and-trade system. This system works by imposing a cap (limit) on the $CO_2$ that can be emitted from each emission source. Within this cap-and-trade framework, emission sources can buy or sell carbon emission permits to achieve their emission reduction targets in the most cost-effective way [6,7]. Considering the $CO_2$ market within the scope of carbon management, Zhang et al. [8] developed a mathematical model integrating CCS and carbon trading. Various price levels for excess emissions exceeding the allocated allowances across several power plants in Qatar were considered. To ensure fair competition among these plants, the game theoretic Nash approach was applied to optimise the cost of CCS infrastructure.

In this work, MCDA methods were employed to identify suitable $CO_2$ utilisation products. Drawing inspiration from the models proposed by Zhang et al. [4] and Zhang et al. [8], a framework was developed for CCUS supply chains incorporating carbon trading and taxation aspects. The ε-constraint method was used to achieve both $CO_2$ reduction maximisation and cost minimisation of the supply chain network. Furthermore, to determine the fair trade-off between the two objectives, the game theoretical Nash approach was applied. A case study focusing on supply chains in Germany was carried out to evaluate the performance of the model.

## PROBLEM STATEMENT

Each emission source has a maximum allowable $CO_2$ emission limit. As shown in the **Figure 1**, the remaining emissions must be managed through CCUS or non-physical carbon management platforms. The first platform involves the physical $CO_2$ supply chain network, where emissions are captured and sent to utilisation or storage sites. The second platform is the non-physical $CO_2$ management system, which allows trading $CO_2$ permits between emission sources or paying a tax to release an excessive amount of $CO_2$ into the atmosphere.

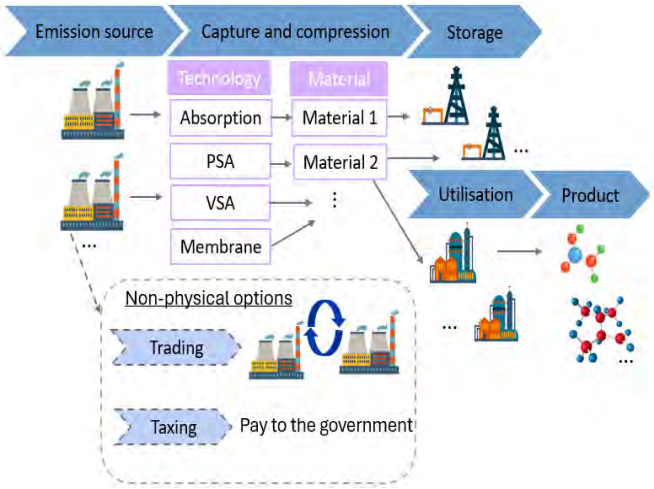



**Figure 1.** Superstructure of CCUS supply chains under carbon trading and taxation.

The overall supply chain can be stated as follows:

**Given:** (a) emission sources with their location, annual $CO_2$ emission and flue gas compositions; (b) combinations of technologies for $CO_2$ capture and compression with the corresponding materials and cost parameters; (c) cost parameters for the $CO_2$ transportation via pipelines; (d) locations of $CO_2$ storage and utilisation sites, their capacities, and the products produced at each utilisation site; (e) for all $CO_2$ utilisation pathways: unit production costs, selling prices, reactions and conversion rates of products; (f) $CO_2$ permit price; (g) carbon tax rate.

**Determine:** (a) $CO_2$ flow rate to be captured from each selected source; (b) $CO_2$ capture technology and material for each selected source; (c) storage and utilisation sources to be used and the amount of $CO_2$ to be utilised/stored; (d) production quantity of each product; (e) pipeline network connecting source and storage/utilisation sites; (f) the quantity of $CO_2$ permit traded between the emission sources; (g) the amount of $CO_2$ released into the atmosphere, with the corresponding tax payment made to cover this release; (h) cap percentage for each emission source; (i) the cost of: flue gas dehydration, $CO_2$ capture and compression, transportation, $CO_2$ storage, $CO_2$ permit trading, and the tax payment; (j) Pareto optimal solutions; (k) game-theoretical Nash approach solution.

**So as to** (a) minimise the total cost; (b) maximise the total $CO_2$ reduction.

**Assumptions:** (a) capture plants and $CO_2$ sources are located in the same place; (b) only one technology-material combination can be selected for $CO_2$ capture at each source; (c) $CO_2$ transportation is possible just through pipelines; (d) the production and selling price of the $CO_2$-based products are fixed; (e) carbon trading occurs within the domestic platform of a country, with no credits being bought or sold internationally; (f) the carbon

tax rate is fixed and uniform across emission sources; (g) a flexible cap is considered for each emission source; (h) carbon permits are traded at a single price.

## METHODOLOGY AND MATHEMATICAL FORMULATION

### Methodology

Using the combination of four common MCDA methods in the CCUS field (TOPSIS, MARCOS, EDAS, VIKOR) returns a ranked list of all alternative $CO_2$-based products based on their scores [9]. Each MCDA method determines the rankings using a mathematical scoring system that calculates the distance of each data point from the ideal and negative ideal solutions.

Regarding the supply chain aspect of this paper, the overall problem was formulated as a Mixed Integer Linear Programming (MILP) model which integrates process, tax and trading constraints in addition to accounting for cost calculations. A brief outline of some of the model equations is next given. To facilitate the mathematical formulation, the indices and sets are used as follows: $i \in I$ represents the emission sources, $j \in J$ the $CO_2$ capture technologies-materials, $k \in K$ the storage and utilisation sites and $p \in P$ represents the $CO_2$-based products. Furthermore, subset $S \subset K$ is especially for the storage site.

### Mathematical Formulation

**Objective functions:** The supply chain problem is formulated as an MOO model with two objective functions. The first objective, total cost ($Cost$), is minimised and includes the cost of each emission source, $CostI_i$ , the production cost of the $CO_2$-based products, $PRC_p$, and the revenue from selling the products, $Re_p$ (see equation (2)). The second objective considers the maximisation of the total amount of $CO_2$ reduction ($CR$), calculated as the sum of the $CO_2$ captured and sent to the storage and utilisation sites, $CK_{ik}$ (see equation (4)).

$$min \quad Cost \tag{1}$$

$$Cost = (\sum_{i\in I} CostI_i) + \left(\sum_{p\in P} PRC_p - Re_p\right) \tag{2}$$

$$\max \quad CR \tag{3}$$

$$CR = \sum_{i\in I, k\in K} CK_{i,k} \tag{4}$$

**Cost calculation:** The supply chain cost for each emission source is calculated using equation (5) which consists of several components: the cost of flue gas dehydration, $FDC_{i,j}$; the investment and operational cost of $CO_2$ capture and compression, $CIC_{i,j}$ and $COC_{i,j}$; the investment and operation cost of transportation, $TIC_{i,k}$ and $TOC_{i,k}$; the cost of $CO_2$ storage, $SC_{i,k}$; the cost of $CO_2$ permit trading, $CTC_i$; and the tax payment. Ravi et al. [10] provided detailed mathematical formulations for calculating the costs of flue gas dehydration, $CO_2$ capture and compression, transportation, and $CO_2$ storage. All these cost components depend on the amount of $CO_2$ captured and sent to storage and utilisation sites ($CK_{ik}$). The tax payment is calculated by multiplying the tax rate per tonne of $CO_2$ emissions (denoted as the parameter $Tax$), by the amount of excess $CO_2$ emissions subject to taxations, $TaxC_i$.

$$CostI_i = \left(\sum_{j\in J} FDC_{i,j} + CIC_{i,j} + COC_{i,j}\right) + \left(\sum_{k\in K} TIC_{i,k} + TOC_{i,k}\right) + \left(\sum_{k\in S} SC_{i,k}\right) + CTC_i + (TaxC_i \cdot Tax) \quad \forall i \in I \tag{5}$$

**$CO_2$ Mass balance:** Equation (6) represents the $CO_2$ mass balance for each emission source. Considering variable emission cap for each source, only (1-$\varphi_i$ ) percent of the total emissions, $E_i$, from each emission site, can be released into the atmosphere without any consideration. According to the cap, $\varphi_i E_i$ is the amount of $CO_2$ emission that each emission source should manage using the available options: capturing and sending $CO_2$ to the storage and utilisation sites, $CK_{ik}$; trading $CO_2$ by selling $CO_2$ permits to other domestic emission sources, $Tr_{ii'}$, or buying the $CO_2$ permits from the domestic sources, $Tr_{i'i}$. Another option exists that allows the emission source to pay tax for excess $CO_2$ emissions ($TaxC_i$).

$$\varphi_i E_i = \sum_k CK_{ik} + \sum_{i'} (Tr_{i'i} - Tr_{ii'}) + TaxC_i \quad \forall i \in I \tag{6}$$

**Trading and taxing constraints:** Each emission source is not allowed to sell carbon permits to other plants while it is paying taxes and/or buying $CO_2$ permits from the domestic market. This is facilitated through constraints (7) and (8), in which $B$ is a big number, and the binary variable $H_i$ equals one when an emission source pays a tax and/or purchases permits for excess $CO_2$ emissions. Furthermore, more than 50% of the $CO_2$ emissions are constrained to be managed through physical CCUS (see equation (9)).

$$TaxC_i + \sum_{i'\in I} Tr_{i'i} \le B\, H_i \qquad \forall i \in I \tag{7}$$

$$\sum_{i'\in I} Tr_{ii'} \le B\,(1 - H_i) \qquad \forall i \in I \tag{8}$$

$$0.5 \sum_{i\in I} \varphi_i\, E_i \le CR \tag{9}$$

**Process constraints:** Equations (10) to (13) represent some of the process constraints in the model. For each emission source, at most one capture technology and material can be selected, as shown in constraint (10). To ensure $CO_2$ will be captured only if at least one storage and/or utilisation site is chosen, equation (11) is used in which $B$ is a big number. The binary variables, $X_{ij}$ and $Y_{ik}$, are equal to one when $CO_2$ is captured from the emission source $i$ with the capture technology material $j$ and sent to the storage and/or utilisation site $k$. The quantity

of the captured $CO_2$ is calculated in (12). The symbol $FR_{ij}$ represents the fraction of $CO_2$ captured from each emission source, which is constrained by an upper-bound $f_j^u$ specific to each capture technology and material, as can be seen in constraint (13).

$$\sum_{j\in J} X_{ij} \leq 1 \quad \forall i \in I \tag{10}$$

$$CK_{ik} \leq B\, Y_{ik} \quad \forall i \in I, k \in K \tag{11}$$

$$\sum_{k\in K} CK_{ik} = \sum_{j\in J} E_i \cdot FR_{ij} \quad \forall i \in I \tag{12}$$

$$FR_{ij} \leq f_j^u\, X_{ij} \quad \forall i \in I, j \in J \tag{13}$$

## SOLUTION APPROACH

### ε-Constraint method

An ε-constraint method [11] is applied to solve the multi-objective optimisation problem. By keeping one objective as the objective function and the other as a constraint (see formulation (14)), along with equations (2) and (4) to (13), the obtained solutions produce Pareto optimal points, any of which can be selected for the CCUS supply chain.

$$min \quad Cost \tag{14}$$
$$s.t. \quad CR \geq \varepsilon\,;$$

### Nash game-theoretic approach

The Nash bargaining approach represents a fair solution for the economic and environmental aspects of the supply chain, given the status quo point. Using this approach, the objective is to maximise the product of the deviations of the optimisation variable cost from the maximum cost ($cost^{quo}$) and the deviation of the optimisation variable $CR$ from the minimum $CO_2$ reduction ($CR^{quo}$) shown in equation (15).

$$Max \quad \mu = (cost^{quo} - cost)\,(CR - CR^{quo}) \tag{15}$$

The nonlinearity of the above equation causes challenges. To address this, logarithmic operation and separable programming approach are applied by defining piecewise linear functions of $n$ prespecifies grid points, converting the objective function into equation (16). By defining SOS2 variables ( $z1_n$ and $z2_n$) and the corresponding values for the cost and $CO_2$ reduction at each grid point ( $\widetilde{cost}_n$ and $\widetilde{CR}_n$ respectively) the nonlinearity is handled. Gjerdrum et al. [12] provides a comprehensive description of game-theoretic Nash approach formulation and linearisation of the Nash objective function. Maximising the Nash variable, $\mu'$, subject to equations (2), (4) to (13), and (16) results in a fair solution for both objectives.

$$Max \quad \mu' = \sum_n z1_n\, ln(cost^{quo} - \widetilde{cost}_n) + \sum_n z2_n\, ln(\widetilde{CR}_n - CR^{quo}) \tag{16}$$

## CASE STUDY

To demonstrate the applicability of the proposed MOO model, a case study of a supply chain network in Germany is conducted. This supply chain network considers 70 power plants with three power generation sources, including coal, oil and gas, as well as 19 storage sites and five utilisation sites. Each utilisation site can either directly convert $CO_2$ to specific products or use the $CO_2$ in the production process of that product.

The required data for the emission sources regarding the estimated power generation and latitude and longitude of the power plants are collected from the Global Power Plant Database [13]. Afterwards, $CO_2$ emission data are obtained for these emission sources using plant efficiency and emission factors. The total $CO_2$ emission from these 70 sources is 77562 kt/year. An emission management range of 60–80% is considered. Twelve combinations of absorption, membrane, PSA, and VSA-based technologies with different materials are considered for $CO_2$ capture and compression. Each material-technology combination has upper and lower bounds on the input $CO_2$ composition it can handle. In this study, the upper bound on the fraction of $CO_2$ that can be captured, $f_j^u$, assumed to be 90%.

By applying the MCDA methods, 70 $CO_2$ utilisation products and pathways are compared across ten criteria, such as product demand, market value, technology readiness level, and others. Methane, cement, and ethylene ranked among the top choices and are selected as the $CO_2$-based products for the supply chain network of this paper. $CO_2$ curing in the cement industry especially improves the mechanical properties of cement-based products and transforms $CO_2$ into thermochemically stable carbonates. In Germany, where cement production is one of the main sources of $CO_2$ emissions, capturing and reusing $CO_2$ within cement plants is particularly beneficial. Among the five considered utilisation sites, two of them can produce ethylene, two of them methane and only one of them can be used for cement.

## RESULTS AND DISCUSSION

The multi-objective optimisation of the developed MILP model is implemented using Gurobi 11.0.0 in GAMS 46.1.0 with an optimality gap set to 0.1%, using a Dell workstation with Intel® Core™ i9-10980XE CPU @ 3.0 GHz and 128 GB RAM. First, the MOO problem is solved using the ε-Constraint method by fixing $\varepsilon$ to 13 values between $CR_{eps}^{min}$ and $CR_{eps}^{max}$. The value for $CR_{eps}^{min}$ is obtained through a single optimisation with the objective of

cost minimisation, and the value for $CR_{eps}^{max}$ is obtained with the objective of maximising the $CO_2$ reduction. The MOO model consists of 21,011 equations and 24,902 variables, of which 2,660 are discrete variables. The entire process to find Pareto optimal solutions (see **Figure 2**) with different values of ε takes 90.8 s CPU time with an average of 6.9 s for each iteration. The total cost of the supply chains gradually increases as the amount of $CO_2$ reduction increases.

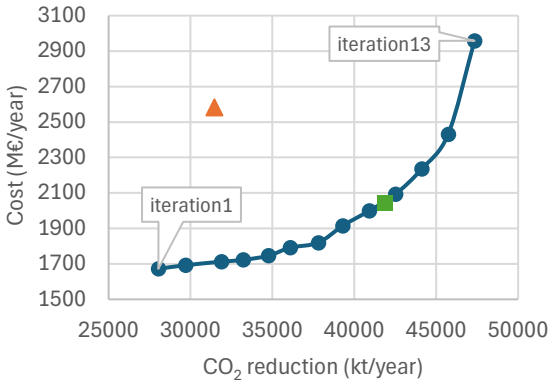



**Figure 2.** Pareto front and the Nash approach solution: • Pareto optimal; ▲ ($CR^{quo}$ , $cost^{quo}$ ); ■ Nash result.

**Figure 3** illustrates the contribution of each component of the supply chain network to the total cost for some iterations on the Pareto curve. It is important to note that since trading is restricted to the domestic market, the cost of $CO_2$ permit trading incurred by buyers will be offset by the benefit for the emission sources who sell the permits. Therefore, the net contribution of carbon trading to the total cost of the supply chain network is zero. On another note, the cost of flue gas dehydration, along with the cost of carbon capture and compression, is high, and this creates a trade between cost minimisation and $CO_2$ reduction because $CO_2$ capture is one of the bottlenecks of the process. The production cost of $CO_2$-based products is another economic concern for CCUS. However, the revenue obtained from selling these products can offset the economic challenges of the utilisation processes. The cost of $CO_2$ storage has a negligible effect on the total costs.

**Table 1** represents the amount of $CO_2$ being covered across different supply chain sections in some iterations that have been chosen to demonstrate the progress of the solver. As $CO_2$ reduction increases, the contribution of $CO_2$ utilisation and storage grows, while $CO_2$ emissions managed through tax payments decrease. By the final iteration on the Pareto front, the amount of $CO_2$ emissions covered by tax payments reaches zero. However, due to capacity limits for the storage and utilisation sites, $CO_2$ trading is an important component of $CO_2$ management to provide the $CO_2$ mass balance.

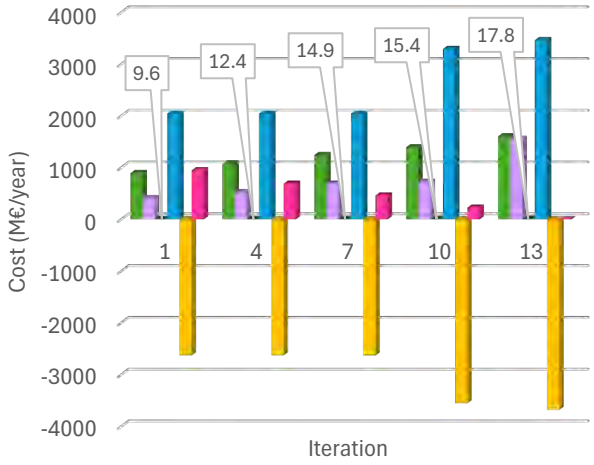



**Figure 3.** Cost breakdown for selected iterations of the ε-Constraint method: total cost of ■ flue gas dehydration and carbon capture and compression; ■ transportation; ■ storage; ■ production of $CO_2$-based products; ■ revenue from selling the products; ■ taxes.

**Table 1.** Management paths for $CO_2$ emissions (Mt/year) in selected iterations and Nash equilibrium.

| | Utilisation | Storage | Permit trading | Tax payment |
|---|---|---|---|---|
| **1** | 10.4 | 17.6 | 8.6 | 18.9 |
| **4** | 10.4 | 22.8 | 10.3 | 13.8 |
| **7** | 10.4 | 27.4 | 11.8 | 9.2 |
| **10** | 14.1 | 28.4 | 13.3 | 4.5 |
| **13** | 14.7 | 32.7 | 13.6 | 0.0 |
| **Nash** | 14.6 | 27.2 | 13.5 | 5.1 |

In order to find the point where cost and $CO_2$ reduction are at equilibrium, the game theoretic Nash approach is implemented in the GAMS using the Gurobi solver. The model consists of 21,015 equations and 24,933 variables, of which 2,660 are discrete variables. The number of grid points for the linearisation in equation (16) is 15, the CPU time required to obtain the solution is 6.3 s, and the relative gap obtained was 0.1%. The quo stat point is obtained with a single objective optimisation in a scenario where trading is not allowed, and all emission sources must manage 80% of their total $CO_2$ emissions. **Table 1** represents the amount of $CO_2$ being covered through different supply chain sections when the Nash equilibrium strategy is considered. The Nash solution is presented in **Figure 2** with a total cost of 2046.6 M€/year (see **Table 2** for the cost breakdown values) and a $CO_2$ reduction value of 41859.8 kt/year, of which 35% is achieved through $CO_2$ utilisation and 65% through storage. Among the 70 emission sources, 10 participate in the CCUS,

using 7 storage sites and 3 utilisation sites to produce 1,660 kt/year of $CO_2$-based ethylene and cure 1,1791.9 kt/year of cement. s

**Table 2.** Total cost breakdown of the Nash result.

| Cost breakdown | (M€/year) |
|---|---|
| Dehydration, capture and compression | 1357.9 |
| Transportation | 634.5 |
| Storage | 14.8 |
| Production of $CO_2$-based products | 3461.5 |
| Tax payment | 256.3 |
| Revenue from selling the products | 3678.3 |

## CONCLUSIONS AND FUTURE WORK

A multi-objective MILP modelling framework is presented for the optimisation of carbon capture utilisation and storage supply chains, which is applied to a case study in Germany. The MOO model demonstrates that the total cost of the proposed supply chain network increases nonlinearly with increasing $CO_2$ reduction quantities. As a guide to decision-makers, the Pareto front of these trade-offs is found. The fair trade-off between these two objectives is determined using the game theoretical Nash approach, and the resulting solution is selected as the optimal strategy in this study. This strategy achieves a $CO_2$ emissions reduction of approximately 54% from the examined sources, corresponding to ca. 7% of $CO_2$ of current German emissions. The estimated cost of €2 billion corresponds to ca. 0.05% of German GDP. This is achieved by sending two-thirds of mitigated $CO_2$ emissions into storage and utilising another third for the production of cement and ethylene. These results rely on assumptions about production, capture, compression, storage and transportation costs, which could affect the profitability of the chosen $CO_2$ management framework. More investigations and technical progress in these areas will enhance the cost efficiency of the optimal $CO_2$ management framework.

## REFERENCES


1. Baroudi HA, Awoyomi A, Patchigolla K, Jonnalagadda K, Anthony E. A review of large-scale $CO_2$ shipping and marine emissions management for carbon capture, utilization, and storage. Applied Energy 287:116510 (2021).
2. Pacheco KA, Bresciani AE, Alves RM. Multi-criteria decision analysis for screening carbon dioxide conversion products. *J CO2 Util* 43:101391 (2021).
3. Hasan MMF, Boukouvala F, First EL, Floudas CA. Nationwide, regional, and statewide $CO_2$ capture, utilization, and sequestration supply chain network optimization. *Ind Eng Chem Res* 53:7489-7506 (2014).
4. Zhang S, Zhuang Y, Liu L, Zhang L, Du J. Optimization-based approach for $CO_2$ utilization in carbon capture, utilization, and storage supply chain. *Comp Chem Eng* 139:106885 (2020).
5. Leonzio G, Foscolo PU, Zondervan E. Multi-objective optimization of CCUS supply chains for European countries with higher carbon dioxide emissions. *Phys Sci Rev* 8:1593-1620 (2023).
6. EU Emissions Trading System (EU ETS) — ICAP Carbon Action. https://icapcarbonaction.com/en/ets/eu-emissions-trading-system-eu-ets [Accessed 21 Oct 2024].
7. European Commission Climate Action. https://climate.ec.europa.eu/eu-action/eu-emissions-trading-system-eu-ets_en [Accessed 07 Aug 2024].
8. Zhang D, Alhorr Y, Elsarrag E, Marafia AH, Lettieri P, Papageorgiou LG. Fair design of CCS infrastructure for power plants in Qatar under carbon trading scheme. International Journal of Greenhouse Gas Control 56:43-54 (2017).
9. Opricovic S, Tzeng GH. Compromise solution by MCDM methods: a comparative analysis of VIKOR and TOPSIS. *Eur J Oper Res* 156:445-455 (2004)
10. Ravi NK, Van Sint Annaland M, Fransoo JC, Grievink J, Zondervan E. Development and implementation of supply chain optimization framework for $CO_2$ capture and storage in the Netherlands. *Comp Chem Eng* 102:40-51 (2017).
11. Haimes Y. On a bicriterion formulation of the problems of integrated system identification and system optimization. *IEEE Trans Syst Man Cybern* 1(3):296–297 (1971)
12. Gjerdrum J, Shah N, Papageorgiou LG. Transfer prices for multienterprise supply chain optimization. *Ind Eng Chem Res* 40:1650–1660 (2001)
13. World Resources Institute. https://www.wri.org/research/global-database-power-plants [Accessed Aug 2024].



© 2025 by the authors. Licensed to PSEcommunity.org and PSE Press. This is an open access article under the creative commons CC-BY-SA licensing terms. Credit must be given to creator and adaptations must be shared under the same terms. See https://creativecommons.org/licenses/by-sa/4.0/




Systems & Control Transactions

**Research Article - Peer Reviewed Conference Proceeding**
ESCAPE 35 - European Symposium on Computer Aided Process Engineering
Ghent, Belgium. 6-9 July 2025
Jan F.M. Van Impe, Grégoire Léonard, Satyajeet S. Bhonsale,
Monika E. Polańska, Filip Logist (Eds.)

PSE PRESS

# Evaluation of Energy Transition Pathways for Industries with Low-Temperature Heat Demand: The Case of Laundry and Syrup Sectors

**Juliette M. Limpach[a*], Muhammad Salman[a], Daniel Florez-Orrego[b], François Maréchal[b] and Grégoire Léonard[a]**

[a] Chemical Engineering, University of Liège, Liège Sart Tilman, 4000, Belgium.
[b] IPESE group, Federal Polytechnic School of Lausanne, Sion, Switzerland.
* Corresponding Author: juliette.limpach@uliege.be

## ABSTRACT

Industries with low-temperature heat demand, such as laundry and syrup sectors, heavily rely on natural gas-fired boilers, posing challenges to achieving net-zero emissions by 2050. Like hard-to-abate sectors, they must explore energy transition strategies, including heat recovery, fuel substitution, or carbon capture, to reduce $CO_2$ emissions. This paper evaluates the potential of energy transition in these sectors through case studies, using a mixed integer linear programming (MILP) approach. The analysis focuses on three key performance indicators (KPIs): specific energy consumption, $CO_2$ reduction, and variable costs. By 2050, the adoption of heat pumps and waste valorization emerge as the most promising solutions for the syrup and laundry sectors. Specifically, the use of heat pumps reduces energy demand by at least 50%, while on-site biofuel production can fully replace natural gas consumption, thus eliminating dependency on external energy sources. The analysis highlights the importance of sector-specific strategies to meet climate targets, offering a pathway for low-temperature heat industries to reduce emissions while addressing economic and technological constraints.

**Keywords**: Energy Management, Process Design, Energy Systems, Alternative Fuels, Renewable and Sustainable Energy

## 1. INTRODUCTION

The goal of achieving net zero emissions by 2050 has driven European industries to intensify their efforts toward implementing $CO_2$ reduction strategies. While hard-to-abate sectors like steel, cement, glass, and lime production, etc., characterized by high-temperature energy demands, are the focus of much attention, other sectors characterized by lower emissions and typically low to moderate temperature heat demands are often overlooked. However, these sectors collectively contribute a substantial share of the total industrial emissions of a country [8]. The potential of energy transition to low-emission pathways in these sectors needs to be detailed.

In this study, two low-temperature (low-T) industries, syrup manufacturing, and laundry, are selected as case studies to demonstrate a methodological approach for addressing the energy transition in low-T industries. Key strategies leading to reduced emissions in such industries include heat recovery (via Heat Pumps), fuel substitution (e.g., hydrogen, biofuels), electrification (electric boilers), and $CO_2$ capture (CC). Previously, other research also explored energy transitions in low-T industries [2][5]. Lastly, Best Available Techniques (BAT) documents also provide valuable insights into how such industries can reduce energy consumption (European Commission. Joint Research Centre, 2019). Although previous research tried to explore the potential of these pathways for low-T industries, a comprehensive techno-economic comparison, ranking these technologies from a future energy scenario point of view, is still lacking.

This study examines the potential energy savings and required investments associated with various energy transition strategies in low-T industries through a

detailed techno-economic comparison. Multiple energy transition pathways, including fuel switching, CC, electrification, and heat recovery, are evaluated using key performance indicators (KPIs) such as relative energy consumption, total emissions, and total cost. Furthermore, a superstructure-based optimization is conducted to rank these pathways under different future energy scenarios, which dictate the prices of energy commodities and emissions. This comprehensive approach provides a robust analysis, supporting informed decision-making to identify the pathways that will play a crucial role in reducing emissions in low-T sectors under future scenarios.

# 2. METHODOLOGY

## 2.1 Process Description

This study analyzes two key sectors: laundry and syrup production, selected from industries located in the Liège Province, Belgium. By focusing on one food industry and one sanitation-related industry, the analysis highlights sector-specific opportunities for transitioning to more sustainable energy solutions.

The **laundry sector** cleans textiles using water, air, and energy. A standard cleaning cycle includes pre-washing (30-45°C), washing (45-60°C), rinsing (20°C), spinning, and drying (70-120°C). For healthcare textiles, an additional disinfection step (60-90°C) may be incorporated, achieved through thermal treatment or chemical agents. When chemical disinfection is used, a neutralization stage is required to restore fabric pH, followed by rinsing to remove residual chemicals before spinning and drying. Washing typically employs hot water, heated directly by natural gas (NG) boilers or indirectly via steam through heat exchangers, while cold water is used during rinsing to remove detergent residues. Drying occurs in two phases: mechanical dewatering (spinning or compression) followed by thermal drying, where hot air, often heated by steam, removes the remaining moisture from the textiles [1].

The **syrup production** sector, which can be linked to the sugar industry, is more complex regarding its processes. Two types of syrup can be considered: one made directly from fruit and the other from cereals. The primary distinction between these two lies in the intermediate process. The fruit-based syrup requires cooking, while the cereal-based syrup involves hydrolysis. In both cases, it begins with the cultivation and harvesting of crops. In the plant, the initial step involves preparing the raw materials—either washing, cutting, or milling—requiring electricity consumption [10]. Then, both hydrolysis and cooking demand an energy source to achieve a medium temperature of approximately 100°C. Following these steps, the product undergoes filtration, typically involving mechanical technologies like decantation. The filtrate is then concentrated (80-120°C), transforming the fruit juice or cereal mixture into syrup. The common method for juice concentration is evaporation, particularly quadruple-effect evaporation [9]. This technology reduces energy demand for evaporation by approximately four times, as it recycles the energy from the produced steam. This step is nevertheless energy intensive. Finally, refining (105°C), cooling (65°C), and packaging (65°C to 15°C) can occur.

## 2.2 Superstructure Development

To conduct the optimization analysis, a general superstructure is developed for both industries, incorporating many possible energy transition options. Blueprints (BPs) are first created as equation-based models that include detailed mass and energy balances, as well as cost parameters for each process. These BPs are derived from BAT documents and relevant literature. BPs for all processes in both industries, along with available energy transition options, are integrated into the superstructure.

The superstructure contains the following options for energy transition in both sectors; 1) Heat recovery (via utilization of heat pumps, recovering heat from external and internal sources), 2) Fuel-switching (bio-fuels and $H_2$) 3) Electrification and cogeneration 4) Solid and Liquid waste valorization and 5) CC.

The energy demand in the syrup and laundry sectors is primarily met using NG boilers and electricity. Therefore, the base case configuration for each sector involves a NG-fired boiler with an assumed efficiency of 80% for steam generation. Both can implement fuel substitution, electrification, heat recovery, and CC.

There is considerable flexibility in the choice of fuel for boilers, with options including hydrogen, biomass, biogas, and other alternatives to reduce $CO_2$ emissions associated with NG combustion. Additionally, these boilers can be electrified to achieve similar outcomes. Liquid waste can be treated in water treatment units, where biogas is recovered through anaerobic digestion. Given that water treatment plants are already required in both sectors, biogas is readily accessible. For the syrup sector, solid waste, such as peels, rooted feedstocks, and cereal residues, can be composted to produce biomass. This biomass can either be used as a solid fuel for boilers or as an input for biomethanation. Through biomethanation, organic matter is converted into a combustible biogas, which can be further refined into biomethane. However, solid waste is often prioritized for reuse in crop cultivation, which may limit its availability for energy production. Bio-sourced fuels, regardless of their origin, can thus supply boilers, reducing the reliance on fossil fuels. Additionally, the produced gases can be used to power cogeneration units, thereby improving overall energy efficiency.

Heat recovery is another important option for these sectors. It can be achieved through heat pumps (HP),

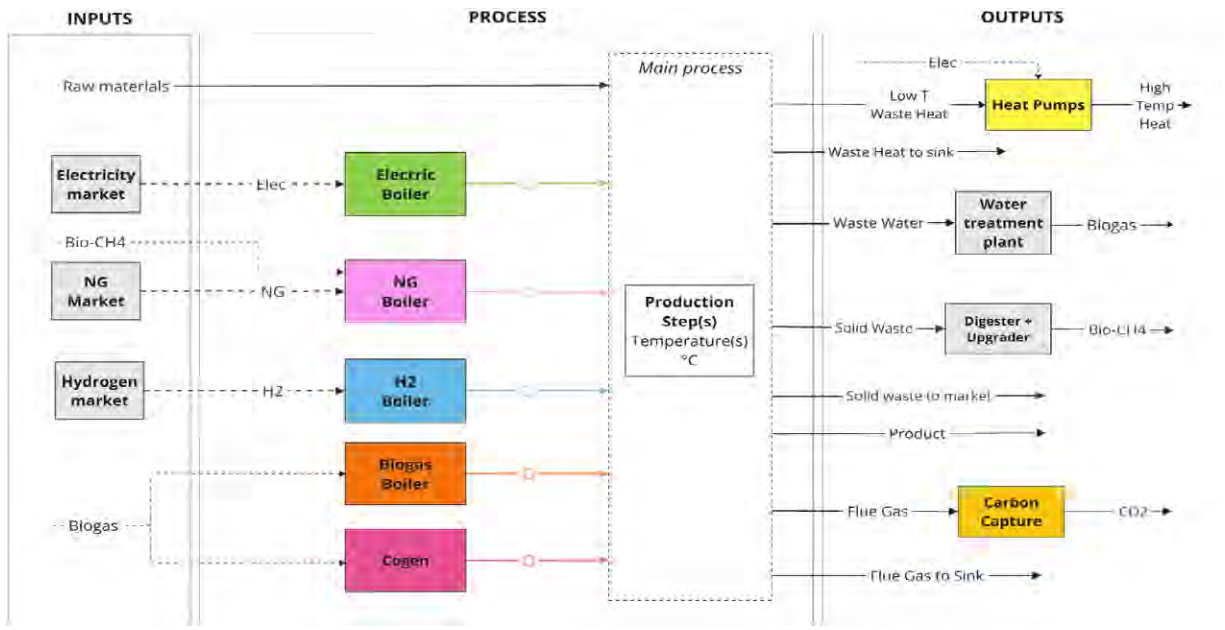



**Figure 1.** A general superstructure for the energy transition

which capture and reuse waste heat, further optimizing energy performance. Depending on the availability of a heat source inside or outside of the process, these are described as internal or external HP.

Lastly, the potential role of CC should be considered: if NG boilers are retained, CC may be necessary to achieve net-zero emissions by 2050. In this context, CC refers to a post-combustion capture process based on chemical absorption using amine solvents.

Figure 1 illustrates a general superstructure for the energy transition in these sectors incorporating all the options discussed above.

Assumptions are made regarding the efficiency and performance of key technologies. For fuel substitution, it is assumed that green electricity operates with an energy efficiency of 90–100%, while green hydrogen is characterized by an energy density of 34 MWh/t with an energy efficiency close to 90%. Biofuels such as biomass and biogas, are considered less efficient, with a thermal efficiency of 70% [3]. In the context of heat recovery, HP functioning within a temperature range of 100°C to 200°C are expected to achieve a coefficient of performance (COP) ranging between 2 and 3 [12]. For CC, post-combustion technologies are assumed to capture at least 90% of $CO_2$ emissions, with energy requirements estimated between 0.9 and 1.4 MWh/t of $CO_2$ captured [6].

## 2.3 Optimization Problem and KPIs

Once the superstructure is developed, the next step is to solve the optimization problem. For this, the Osmose Lua optimization framework [11]. a tool to optimize process and energy systems, is utilized to solve mixed-integer linear programming (MILP)-based formulation containing objective functions of total specific cost and emissions. It optimizes the superstructure of the BPs models, serving as a decision-support tool to identify the most effective $CO_2$ reduction strategy tailored to each sector's specific needs.

The evaluation of various strategies for each sector is based on three KPIs: specific $CO_2$ emissions, specific energy consumption, and specific variable costs.

The two objective functions employed for the evaluation are specific variable cost (€/t of materials) and specific emissions ($tCO_2$//t of materials) and the MILP problem to be solved is outlined in equations (1-4).

$$Annual\ CAPEX_{n,i} = \sum_u \left( CAPEX(u_{ref}) \cdot \left(\frac{s}{s_{ref}}\right)^{0.6} \cdot \frac{CEPCI_{2023}}{CEPCI_{ref}} \cdot i \cdot \frac{(i+1)^n}{(i+1)^{n-1}} \right) \quad (1)$$

$$Annual\ OPEX = \sum_u \left( \sum_e \left( C_{e_u} \cdot \dot{Q}_{e_u} \right) + \left( C_{em_u} \cdot \dot{m}_{em_u} \right) \right) \cdot hr \quad (2)$$

$$\min Cost \left( \frac{€}{ton\ of\ material} \right) = \frac{Annual\ OPEX + Annual\ CAPEX}{ton\ of\ product\ per\ year} \quad (3)$$

$$\min Emissions \left( \frac{ton\ of\ CO_2}{ton\ of\ material} \right) = \frac{\sum_u (\dot{m}_{em_u}) \cdot hr/1000}{ton\ of\ material\ per\ year} \quad (4)$$

CAPEX is annualized over 25 years ($n$) with a 3% discount rate ($i$), $u$ is the unit, $s$ the unit size, $ref$ the reference unit for CAPEX calculations. For OPEX calculation, $C$ represents cost, $e$ the energy source, $\dot{Q}$ energy, $\dot{m}$ mass flow rate, $em$ emissions, and $hr$ total operating hours (8000). CAPEX excludes constant equipment costs across configurations, and OPEX omits raw material costs, as they remain unchanged.

Equation (2) treats energy and emission costs as

input variables, based on future energy projections. The electrification scenario from EnergyVille's Paths2050 study (TIMES-BE) has been selected to provide marginal production costs for electricity, hydrogen, and natural gas, along with $CO_2$ emission costs [7]. This choice favors renewable energy and more particularly electricity use. Table 1 gives a detailed view of the cost. Carbon taxes are evaluated at 350 €/t$CO_2$ for 2050.

**Table 1:** Marginal production costs of energy commodities, based on the Paths2050 study electrification scenario for 2050 [7]

| Price (€/MWh) | Electricity | $H_2$ | Natural Gas |
|---|---|---|---|
| | 56 | 78 | 35 |

## 3. RESULTS AND DISCUSSIONS

### 3.1 Blueprint Validation

Table 2 compares the specific energy consumption derived from the BPs and the data available in the literature. The calculated values fall within the range reported in the literature, confirming the validity of the mass and energy balances for the syrup and laundry sectors.

**Table 2:** Specific energy demand comparison for BPs model and literature [1] [4]

| Sector | Unit | BP model | Literature |
|---|---|---|---|
| Syrup | MWh/t fruits-cereals | 0.23-0.26 | [0.05; 0.6] |
| Laundry | MWh/t laundry | 2.21 | [1.3; 4.6] |

### 3.2 KPI evaluation

First, the specific energy demand and Scope 1 emissions for the laundry and syrup sectors are analyzed for each pathway toward achieving net-zero emissions. The results are presented in Figure 2.

In the laundry sector, the base case scenario consumes 2.21 MWh/t of laundry and generates 0.4 t$CO_2$/t of laundry. Transitioning to hydrogen or electrification results in similar energy demands, with less than 10% variation, due to comparable efficiencies with NG. Nevertheless, electricity and hydrogen offer the advantage of eliminating Scope 1 emissions. Biogas has the same advantage (as it gives biogenic emissions that are not accounted for) but leads to a 20% increase in energy demand compared to NG boilers. In contrast, the laundry sector can adopt CC without going for fuel substitution. This approach results in the highest energy demand but still emits approximately 10% of the $CO_2$ produced from NG, due to capture efficiency. Lastly, external HP use reduces the base case energy consumption by more than half, achieving 0.87 MWh per ton of product, while maintaining zero Scope 1 emissions. Alternatively, a simple electrification with no HP also decreases energy demand (but to a lower extent) and reaches zero scope 1 emissions. In conclusion, for the laundry sector, heat recovery offers the greatest benefits: HP strongly reduce energy demand, also decreasing Scope 2 emissions associated with electricity consumption.

For the syrup sector, the base scenario depicts an energy consumption of 0.26 MWh/t of cereals and 0.05 t$CO_2$/t of cereals. Among the transition pathways, the highest energy demand is associated with CC, then NG substitution by biogas, primarily due to the relatively low efficiency of biogas considered in this study. These paths increase energy consumption by at least 20% while achieving $CO_2$ emission reductions of 50% to 90% compared to the base case. Conversely, the lowest energy demand is linked to internal HP utilization with NG, resulting in a 65% reduction in energy demand. To combine energy consumption reduction while minimizing reliance on NG, HP can also be coupled with cleaner energy sources such as electricity, hydrogen, or biogas. The valorization of biogas from biodigesters, when combined with HP, already achieves a 15% reduction in energy consumption and eliminate Scope 1 $CO_2$ emissions. In the food industry, internal HP enable heat recovery from the cooling process to warm water for cooking purposes. More particularly, quadruple effect evaporation exhibits advantages for HP use. The use of electricity and hydrogen eliminates Scope 1 emissions while maintaining energy consumption levels close to the base case, with only a 5% to 10% variation.

Next, the economic results are discussed. Figure 3 provides the installation and operational costs associated with deploying new units in the laundry and syrup sectors for each pathway. The variable costs linked to the operation of NG boilers in the base case scenario are calculated at 230 €/t for laundry processing and 29 €/t for cereal production. The laundry sector demonstrates the lowest operational costs when utilizing biogas (93% reduction). Biogas is assumed to be produced and used onsite, incurring mainly capital costs for the digester and minimal operating expenses. The laundry sector is expected to integrate biogas production within its existing wastewater treatment plants, which should generate sufficient biogas to meet energy demands. A sensitivity study should be done to assess plant capacity, validate biogas availability, and refine energy requirements for anaerobic digestion, where additional costs are primarily limited to electricity for mixing and pumping. Following biogas, electricity use also demonstrates greater cost-effectiveness compared to the base case scenario, resulting in a cost reduction of nearly 50% with electrification and up to 70% with the integration of HP, despite their higher capital investment compared to conventional boilers. This observation aligns with the 2050 "EnergyVille" scenario proposed by VITO, which prioritizes

electrification as a key pathway for defossilisation. In contrast, CC is the least economically favorable option. The laundry sector's has a relatively low $CO_2$ emissions capacity, resulting in an increase in the specific capital expenditure per ton of $CO_2$ captured. In comparison with considering the cost of $CO_2$ allowances, the investment required for CC remains too high to be economically viable for this sector.

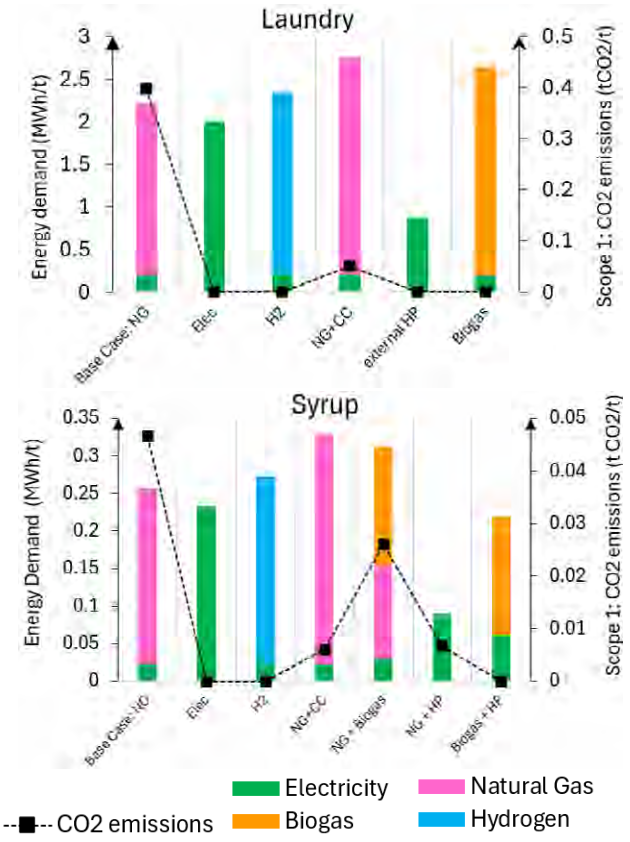



**Figure 2.** Specific energy consumption and $CO_2$ emissions in the laundry and syrup sectors based on energy choices

The analysis of the syrup production sector reveals conclusions analogous to those observed in the laundry sector. Biogas and electricity exhibit the lowest production costs among the evaluated energy sources. Biogas is still considered to be derived from solid waste, leading to low additional cost, while electricity remains more economical than both hydrogen and NG. CC is slightly more economically viable in the syrup sector compared to the laundry sector. This is primarily attributed to the production scale, which generates approximately 86,000 tons of $CO_2$ per year for syrup production, in contrast to 4,000 tons of $CO_2$ per year for the laundry sector. Given this higher volume of emissions, CC is more cost-effective than purchasing CO2 quotas, with a 34% cost reduction compared to the base case.

Overall, based on the KPI analysis, the transition strategies for the sectors under study are highlighted.

The analysis identifies bio-based resources and electrification as the most viable pathways, given their low to moderate process temperature requirements.

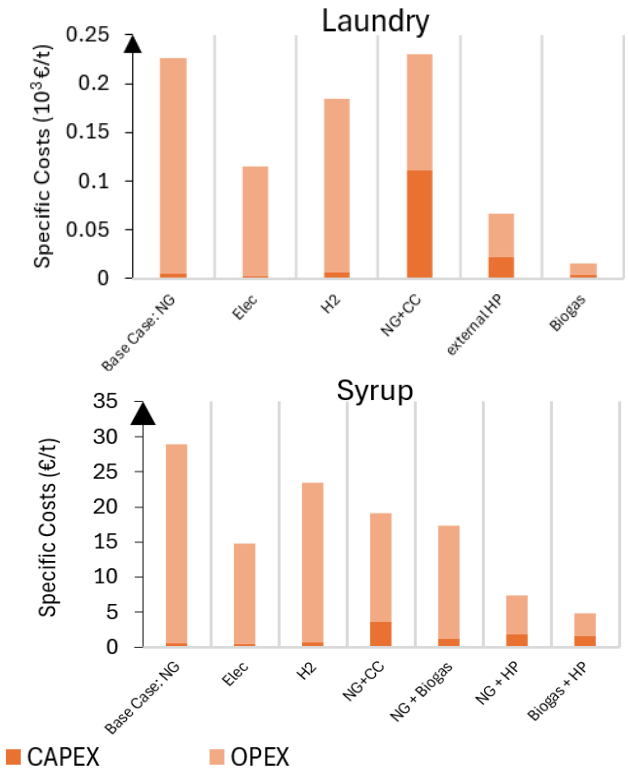



**Figure 3.** Specific costs in the laundry and syrup sectors based on energy choices

Fuel substitution emerges as a viable alternative for the transition. Each form of fuel substitution eliminates Scope 1 $CO_2$ emissions, with the most economically advantageous option being the valorization of solid or liquid waste to produce biogas, even if it requires more energy. In addition, electrification and HP integration present major opportunities for energy transition. Electrification provides higher energy efficiency compared to NG or hydrogen-based systems while eliminating direct $CO_2$ emissions. HP further enhance this advantage by enabling efficient waste heat recovery, reducing overall energy consumption.

Sector-specific differences can still be addressed. In the syrup sector, internal HP are used to recover on-site waste heat, and their efficiency is modeled using Carnot assumptions. Conversely, the laundry sector employs external HP, for which a COP of 3 is assumed, reflecting typical temperature lifts from an ambient temperature source of 20°C to a process requirement below 120°C. As COP values vary according to process conditions, their fluctuation directly impacts the electricity consumption of HP. While unfavorable COPs

can increase electricity use, ongoing technological advancements are expected to improve COP, enhancing the efficiency and cost-effectiveness of this approach.

## 4. CONCLUSIONS & PERSPECTIVES

This study explores the transition pathways for the laundry and syrup sectors toward net-zero emission objectives using the Osmose Lua optimization framework based on MILP. Energy transition strategies analyzed hydrogen utilization, bio-based resources, electrification, CC and HP integration.

Bio-based fuel substitution is particularly relevant for sectors with low-T demand when on-site resources, such as wastewater or solid waste, can produce biofuels, enabling direct reductions in Scope 1 $CO_2$ emissions. Electrification and HP integration offer efficient, cheap, and clean alternatives to fossil fuel use, with facilitating waste heat recovery in the case of HP. Technological improvements in HP, especially in COP, could further enhance its competitiveness. Hydrogen, while efficient and $CO_2$-reducing, faces barriers like infrastructure needs (facility retrofitting, revaluation of transport, storage logistics) and high costs, making it less viable for low-temperature sectors. $H_2$ and CC are deemed less favorable options for the future of the low-T sector. The substantial capital expenditures required for CC are disproportionate relative to the moderate emissions levels of the industries.

As a result, to achieve net-zero Scope 1 emissions in low-temperature industrial sectors by 2050 will likely require a multi-pronged approach combining bio-based fuel substitution, HP integration, and/or electrification. Looking ahead, Effective strategies will depend on sector constraints and energy price trends, with continuous reassessment and scenario-based planning crucial for identifying viable pathways.

## ACKNOWLEDGEMENTS

The authors thank the Belgian Energy Transition Fund (TRILATE project).

## REFERENCES

1. CTTN-IREN, Ademe. La blanchisserie industrielle et l'energie (2002)
2. Flórez-Orrego D, Domingos M, Maréchal F. Heat pumping and renewable energy integration for decarbonizing brewery industry and district heating, in: 33rd European Symposium on Computer Aided Process Engineering, Computer Aided Chemical Engineering. Elsevier, pp. 3177–3182. (2023) https://doi.org/10.1016/B978-0-443-15274-0.50507-2
3. Eo JW, Kim MJ, Jeong IS, Cho L,Kim SJ, Park S, Kim DH, Enhancing thermal efficiency of wood pellet boilers by improving inlet air characteristics Energy 228, 120475 (2021) https://doi.org/10.1016/j.energy.2021.120475
4. European Commission. Joint Research Centre, Giner Santonja G, Karlis P, Stubdrup K, Brinkmann T, Roudier S, Best Available Techniques (BAT) Document for the Food, Drink and Milk Industries. Industrial Emissions Directive 2010/75/EU (Integrated Pollution Prevention and Control), Publications Office (2019) https://data.europa.eu/doi/10.2760/243911
5. Griffin PW, Hammond GP, Norman JB, Industrial decarbonisation of the pulp and paper sector: A UK perspective, Applied Thermal Engineering, Volume 134, Pages 152-162, ISSN 1359-4311 (2018) https://doi.org/10.1016/j.applthermaleng.2018.01.126
6. Kim S, Léonard G, $CO_2$ Capture Technologies and Shortcut Cost Correlations for Different Inlet $CO_2$ Concentrations and Flow Rates. 1. Chemical Absorption. (2024) http://dx.doi.org/10.2139/ssrn.4967576
7. Laguna JC, Moglianesi A, Vingerhoets P, Nijs W, Lodewijks P, PATHS 2050- scenarios towards a carbon-neutral belgium by 2050 (2023)
8. Rissman J. Decarbonizing Low-Temperature Industrial Heat in the U.S. (2022)
9. Sogut Z, Ilten N, Oktay Z, Energetic and exergetic performance evaluation of the quadruple-effect evaporator unit in tomato paste production, Energy, Volume 35, Issue 9, Pages 3821-3826, ISSN 0360-5442, (2010) https://doi.org/10.1016/j.energy.2010.05.035.
10. Trends Tendances, En visite chez Meurens, le sirop à toutes les sauces (2019) https://trends.levif.be/entreprises/en-visite-chez-meurens-le-sirop-a-toutes-les-sauces-en-images/
11. Yoo MJ, Lessard L, Kermani M, Maréchal F, Osmose Lua – An Integrated Approach to Energy Systems Integration with LCIA and GIS. In K. V Gernaey, J. K. Huusom, & R. Gani (Eds.), *Computer Aided Chemical Engineering* (Vol. 37, pp. 587–592). Elsevier(2015)
12. Zühlsdorf B, Annex 58 High-Temperature Heat Pumps (No. HPT-AN58-2). HPT TCP (2023)

© 2025 by the authors. Licensed to PSEcommunity.org and PSE Press. This is an open access article under the creative commons CC-BY-SA licensing terms. Credit must be given to creator and adaptations must be shared under the same terms. See https://creativecommons.org/licenses/by-sa/4.0/



Systems & Control Transactions

**Research Article - Peer Reviewed Conference Proceeding**
ESCAPE 35 - European Symposium on Computer Aided Process Engineering
Ghent, Belgium. 6-9 July 2025
Jan F.M. Van Impe, Grégoire Léonard, Satyajeet S. Bhonsale,
Monika E. Polańska, Filip Logist (Eds.)

PSE PRESS

# Impact of energy sources on Global Warming Potential of hydrogen production: Case study of Uruguay

**V. Olave[a]*, J. Pineda[a], V. Larnaudie[b], and M. Corengia[c]**

[a] Universidad Tecnológica del Uruguay, Unidad Tecnológica de Energías Renovables, Durazno, Durazno, Uruguay
[b] Universidad de la Republica, Depto. De Bioingeniería, Instituto de Ingeniería Química, Montevideo, Montevideo, Uruguay
[c] Universidad de la Republica, Instituto de Ingeniería Química, Facultad de Ingeniería, Montevideo, Montevideo, Uruguay
* Corresponding Author: vitoria.olave@utec.edu.uy.

## ABSTRACT

In 2022, Uruguay launched its green hydrogen roadmap, due to its renewable energy potential, water availability, and favorable logistics to position itself as an exporter of green hydrogen and derivatives. The energy source for water electrolysis is a key factor in both the final cost and the environmental impact of hydrogen production. In this context, this study evaluates the environmental impact of hydrogen production via water electrolysis, powered by 150 MW of new power sources (solar, wind, and hybrid farms) in Uruguay, all connected to the national grid. A life cycle assessment (LCA) was conducted using OpenLCA software and the Ecoinvent database, with 1 kg of hydrogen as the functional unit and the system boundaries included power generation and the electrolysis system. The analysis focused on global warming potential (GWP), considering different scenarios for the grid energy mix and the inclusion or exclusion of surplus energy as carbon credits. The wind plant is the option that generates the highest energy output and surplus while requiring the least energy purchase from the Uruguayan grid, due to its higher capacity factor. Regarding GWP, it is also the alternative with the lowest environmental impact, with annual average emissions ranging from 0.84 to 1.02 kg $CO_2$/kg $H_2$ not considering carbon credits (CC) and between 0.2 and -1.87 kg $CO_2$/kg $H_2$ when CC are considered. These values represent emissions based on grid connection during the years with the highest proportion of renewable and fossil sources, respectively.

**Keywords**: Hydrogen, Life Cycle Analysis, Renewable and Sustainable Energy

## INTRODUCTION

Several countries have recently developed strategies to advance green hydrogen as a feedstock or energy carrier. Hydrogen has the potential to play a fundamental role in the energy transition, contributing to the decarbonization of sectors like transport and industry.

In 2022, Uruguay launched its green hydrogen roadmap, outlining its plan to promote this emerging market [1]. The country has the capacity to become a producer of green hydrogen derivatives for export due to the potential and complementarity of its renewable energy sources (solar and wind), an electricity matrix with a high share of renewable sources, its availability of water, and favorable logistics [1].

Low-carbon hydrogen currently represents less than 0.1% of global demand, but its use is projected to grow by 6% annually by 2030, according to the International Energy Agency. This underscores the need for low-emission hydrogen production pathways to meet increasing demand while reducing environmental impact [2].

In this context, life cycle assessment (LCA) plays a crucial role in evaluating and comparing the environmental performance of different production methods. A key LCA metric is Global Warming Potential (GWP). GWP index converts greenhouse gas emissions into $CO_2$ equivalents, offering a standardized and widely used measure in environmental studies [3].

Electrolysis-based hydrogen is expected to offer significant environmental benefits, particularly when powered by low-carbon electricity [4]. On average, renewable hydrogen cases exhibited a 68–92% reduction in GWP compared to conventional systems such as coal

gasification and natural gas steam methane reforming [3]. However, the high energy requirements for water electrolysis makes the source of electricity a crucial factor. Emissions associated with electric energy consumption are thus the primary contributors to the environmental impact of hydrogen production [5].

Latin America and the Caribbean (LAC) are developing a hydrogen certification system to establish environmental and social sustainability criteria for clean and low-carbon hydrogen. This framework aims to set greenhouse gas (GHG) emissions thresholds and transparently report energy sources, production technologies, and certified attributes. Methodologies for measuring GHG emissions should align with international ISO standards [6]. For example, China categorizes hydrogen emissions into low-carbon (up to 14.51 kg $CO_2$eq/kg $H_2$), clean (4.9 kg $CO_2$eq/kg $H_2$), and green (below 4.9 kg $CO_2$eq/kg $H_2$) [7]. Similarly, the European Union's CertifHy Green Hydrogen standard requires at least a 60% reduction in GHG emissions compared to natural gas-based steam methane reforming, roughly 4.37 kg $CO_2$eq/kg $H_2$ [8].

The literature reports significant variations in the environmental impact of hydrogen production depending on the energy source, scope of analysis, and methodologies used [2, 3, 9] . For example, studies report that hydrogen produced from wind systems shows GWP values ranging from 0.03 to 5.10 kg $CO_2$eq/kg $H_2$, while photovoltaic systems range from 0.37 to 7.50 kg $CO_2$eq/kg $H_2$ [3]. In the case of hydrogen production using grid electricity in countries with low renewable penetration, the carbon footprint could reach values between 17.2 and 41.4 kg $CO_2$eq/kg $H_2$ [2].

Comparing hydrogen production methods, it was found that biomass gasification ranks highest technically and financially due to high energy and exergy efficiency and low production costs, but it performs poorly environmentally and socially due to high GWP. Wind electrolysis ranks second, offering the best environmental and social performance with the lowest emissions. Solar electrolysis has the weakest technical and financial performance but shows results closer to the wind in environmental and social metrics [10].

Solar and wind energy, when used independently, are limited by their intermittent generation. When combined, they provide benefits such as smoothing output fluctuations, resulting in a more stable energy supply. Additionally, the combined production of wind and solar can be optimized to align with specific demand profiles, effectively addressing variations in energy requirements. To identify the optimal combination of both energy sources for achieving more stable energy generation, many authors use the standard deviation as a metric. This method quantifies how closely the output data cluster around the mean value [11].

This study aims to assess the impact of different energy sources on GWP of hydrogen production in Uruguay. Specifically, it compares solar, wind, and hybrid solar-wind systems connected to the grid, evaluating different grid energy mix scenarios. It also analyses the effect of including or excluding surplus energy from renewable energy plants as carbon credits.

The production of wind and solar energy in Uruguay is quite stable when comparing annual values, but the electric grid relies in high shares of hydropower. The annual rain in this part of South America is strongly dependent on the climate phenomenon El Niño–Southern Oscillation (ENSO), directly impacting energy generation.

## METHODOLOGY

The system evaluated includes a 50 MW PEM electrolyzer, operating at its nominal capacity continuously, 365 days a year, and the installation of 150 MW of new power sources. Three configurations for power production were analyzed: (1) photovoltaic, (2) wind, and (3) hybrid (solar + wind) farms. In all cases, connection to the national power grid was assumed to ensure a reliable and uninterrupted energy supply for plant operation. Energy storage technologies (such as batteries or similar) are not considered.

Different yearly electricity mix scenarios (EMS) were analyzed to assess the environmental impact of hydrogen. The EMS data (Table 1) is based on the average generation of the Uruguayan energy mix over the past five years [12]. The selected data represents different years in Uruguay, influenced by periods of high availability of water and drought, which are key factors directly affecting the composition of the country's electricity matrix.

For the solar and wind generation, hourly data of real plants close to Paysandú region was employed in all the analysis and simulations [13].

The reason to consider the production of new plants hourly, whereas the electric grid composition is considered as an yearly average, is that the first depends on hour to hour availability of resources and the second one depend on seasonal effects. The focus is not on evaluating these specific years, but rather on assessing how different electricity mix compositions may impact GWP.

**Table 1:** Uruguayan Electricity shares for each year

| | Thermal Fossil (%) | Thermal Biomass (%) | Hydropower (%) | Wind (%) | Solar (%) |
|---|---|---|---|---|---|
| EMS_2019 | 2 | 15 | 50 | 30 | 3 |
| EMS_2020 | 6 | 20 | 30 | 40 | 4 |
| EMS_2021 | 15 | 17 | 33 | 31 | 4 |
| EMS_2022 | 9 | 17 | 39 | 32 | 3 |
| EMS_2023 | 8 | 24 | 27 | 37 | 4 |

To determine the shares of renewable energy sources in the hybrid generation scenario, the minimum standard deviation was the metric used to search for the most stable generation. Details of this methodology can be found in the literature [14].

The environmental impact of the different case studies was assessed through a LCA using OpenLCA 2.3.1 software and the Ecoinvent 3.10 database. The analysis was conducted following the IPCC 2013 methodology.

Among the impact categories that can be analyzed by LCA (human health, environmental, resource depletion, etc.), this work focused on the 100-year GWP, using the carbon dioxide as emissions metric. This metric converts greenhouse gas emissions into $CO_2$ equivalents, providing a clear understanding of a system's overall emissions. Additionally, most studies in the literature on this topic utilize this impact category, making future comparisons more straightforward.

Regarding system boundaries, a "cradle-to-gate" approach was considered, including power generation and the electrolysis system used for hydrogen production. As the Ecoinvent database does not include a PEM electrolyzer, the life cycle inventory for the primary materials and energy required to construct a 1 MW PEM electrolyzer (including balance of plant (BOP) components) was taken from the literature [15, 16]. The construction of the electrolyzer was assumed to scale linearly. The electrolyzer's efficiency (70%) and production rate were considered constant over its entire lifetime. The lifetimes of the stack and BOP were assumed to be 7 and 20 years, respectively. For this analysis, 1 kg of produced hydrogen was considered the functional unit.

The main goal of this analysis was to compute the GWP of hydrogen production by electrolysis for each scenario (photovoltaic, wind, and hybrid) including and excluding carbon credits when selling any surplus energy to the national grid.

For the case of carbon credits, it is assumed that all the available energy can be taken by the grid, getting a limit value of change in the GWP by this strategy. If the grid could not take all the energy due to operational restrictions, an intermediate value of GWP between the scenarios with and without carbon credits should be expected.

## RESULTS

Figure 1 compares the energy generation, purchase, and surplus of three power plant configurations (solar, wind, and hybrid), all with a new generation power capacity of 150 MW at the same location in Uruguay. The energy generated by these systems is used for hydrogen production through the electrolysis process.

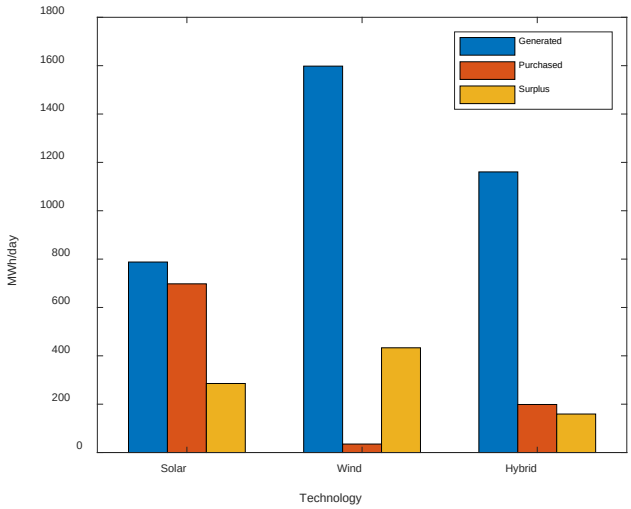



**Figure 1:** Generation, purchase, and surplus energy for a solar, wind, and hybrid park

It can be observed from Figure 1 that the wind farm is the most efficient in terms of energy generation due to its higher capacity factor (0.44) when compared to solar (0.22) and hybrid (0.32) farms. This is attributed to favorable wind conditions in Uruguay most of the year. This installed capacity almost fully meets the energy demand of the electrolysis system (50 MW) for hydrogen production, significantly reducing the need to purchase energy from the National Interconnected System (NIS). Additionally, the generation of surplus energy is considerable and exceeds that of the other systems, highlighting its potential for integration with the power grid, energy storage, or other uses for the plant.

According to the results obtained through the standard deviation method, to achieve a more balanced energy generation at the studied location, a hybrid park with a composition of 54% photovoltaic energy and 46% wind energy is required. This system has a lower capacity factor than the wind plant. However, it provides more stable energy generation throughout the day by combining both complementary technologies. The surpluses generated are moderate, reflecting better synchronization with the demand of the electrolysis system.

The solar plant shows the most significant hourly variability in energy generation due to its direct dependence on solar irradiation. In this regard, this system is limited in consistently meeting the hydrogen plant's energy demand. Additionally, the solar plant produces significant surplus energy during peak solar irradiation hours. This is an opportunity for integration with other systems, including energy storage solutions.

Figure 2 shows the GWP associated with hydrogen production through water electrolysis, evaluating different energy sources: the Uruguayan power grid, a solar plant, a wind plant, and a solar-wind hybrid plant. The

analysis considers five scenarios (EMS_2019, EMS_2020, EMS_2021, EMS_2022, EMS_2023) reflecting the variability in the composition of Uruguay's energy matrix between 2019 and 2023. Additionally, two approaches are examined: with carbon credits derived from the surplus energy generated by the plants and without carbon credits.

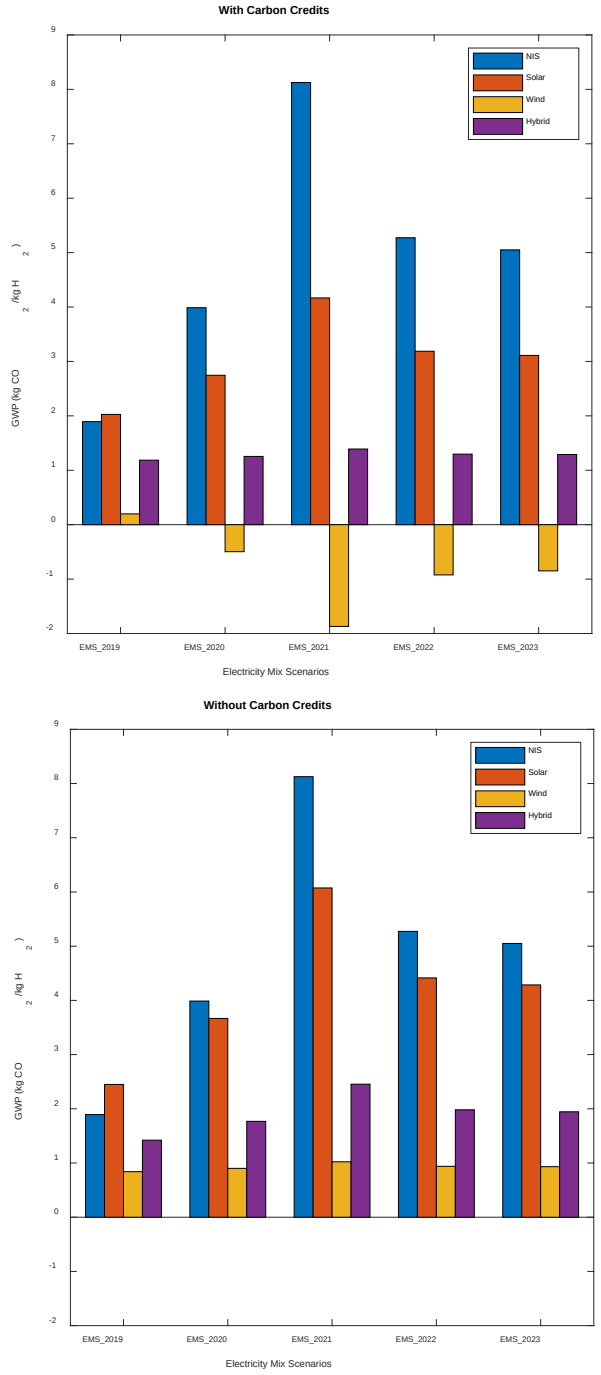



**Figure 2:** GWP for hydrogen production considering different energy souces (NIS, solar, wind and hybrid parks) and electricity mix scenarios.

The NIS showed its lowest environmental impact in 2019 due to a highly renewable energy matrix. However, starting in 2020, the share of fossil fuels and biomass increased in the energy mix significantly raising the GWP. All renewable plants evaluated are connected to the NIS, which means that the GWP is also directly influenced by the composition of the national electricity matrix.

In the case of the solar plant, its GWP in EMS_2019 was higher than that of the NIS, even when considering carbon credits. This is due to the low proportion of fossil fuels in the energy mix that year. It was predominantly composed of hydro and wind power, energy sources with a lower environmental impact than solar energy.

However, as the share of fossil fuels in the NIS mix increased, the GWP of the solar plant became more competitive, achieving lower values than those of the NIS. This is confirmed when comparing the contribution of different energy sources to total emissions. For instance, the solar plant generates an average of 787.8 MWh/day and purchases 697 MWh/day from the NIS.

In the EMS_2019, the solar system contributed 53% of total emissions, while the NIS accounted for 42%. In the EMS_2021, the NIS share rose to 76.7%, while the photovoltaic system's contribution decreased to 21.4%.

Among all evaluated scenarios, the wind plant consistently exhibits the lowest environmental impact. It generates an average of 1598 MWh/day, purchasing only 35.11 MWh/day from the NIS. In the EMS_2019, the wind plant accounted for 80% of total emissions, while the NIS contributed 6.2%. In the EMS_2021, these proportions shifted to 66.7% and 22.9%, respectively. Incorporating carbon credits, the wind plant achieves negative GWP values in the scenarios with a higher share of fossil fuels and biomass in the energy mix (2021–2023), due to the wind system's ability to offset emissions through the carbon credits generated by its energy surpluses.

The hybrid system combines the characteristics of solar and wind systems, resulting in an intermediate environmental impact. Although its GWP is slightly higher than that of the wind plant, it remains significantly lower than that of the NIS and the solar plant, especially when carbon credits are considered.

When carbon credits are not considered, the year with the highest share of renewable energy in the electricity matrix coincides with the lowest GWP for all the analyzed plants. However, this dynamic changes when carbon credits are incorporated. In the case of the wind plant, the lowest GWP is observed in the year with the highest share of fossil fuels in the energy mix, as this plant requires minimal energy from the NIS, and the surpluses generated fully offset the impact of fossil energy consumption associated with hydrogen production and even more, throughout the year. A similar behavior is observed in the hybrid plant, although this effect is limited to five months of the year, when energy surpluses reach

high levels. During these months, the GWPs for EMS_2020 – EMS_2023 are lower than those of EMS_2019. In contrast, this effect is not present in the solar plant due to its greater dependence on energy purchased from the NIS and its higher environmental impact.

**Table 2:** Annual average, maximum and minimum monthly generation (G), and its respectively energy purchased from the NIS (P); and energy surpluses (S) for renewable parks connected to the grid.

| | **G** | **P** | **S** | **Month** |
|---|---|---|---|---|
| **Minimum** (MWh/day)* | | | | |
| Solar | 368.1 | 834.8 | 2.9 | Jun |
| Wind | 1330.9 | 119.3 | 250.8 | Feb |
| Hybrid | 955.6 | 258.2 | 13.8 | Jun |
| **Maximum** (MWh/day)* | | | | |
| Solar | 1171.2 | 593.2 | 564.5 | Dec |
| Wind | 1755.0 | 0 | 555.0 | Oct |
| Hybrid | 1433.4 | 98.0 | 331.5 | Dec |
| **Annual Average** (MWh/day ) | | | | |
| Solar | 787.8 | 697.6 | 285.5 | |
| Wind | 1598.0 | 35.1 | 433.1 | |
| Hybrid | 1160.5 | 198.7 | 159.3 | |

* Monthly minimum and maximum energy generation.

**Table 3:** GWP for hydrogen production, considering scenarios EMS_2019 (1) and EMS_2021 (2) without (w/o CC) and with (w CC) carbon credits.

| | **Solar** | | **Wind** | | **Hybrid** | |
|---|---|---|---|---|---|---|
| **GWP (kg $CO_2$/kg $H_2$)** - Minimum | | | | | | |
| | w/o CC | w CC | w/o CC | w CC | w/o CC | w CC |
| 1 | 1.96 | 1.96 | 0.85 | 0.48 | 1.14 | 1.12 |
| 2 | 6.30 | 6.28 | 1.47 | -0.20 | 2.48 | 2.39 |
| **GWP (kg $CO_2$/kg $H_2$)** - Maximum | | | | | | |
| | w/o CC | w CC | w/o CC | w CC | w/o CC | w CC |
| 1 | 2.93 | 2.09 | 0.86 | 0.03 | 1.64 | 1.15 |
| 2 | 6.01 | 2.24 | 0.86 | -2.85 | 2,15 | -0.06 |
| **GWP (kg $CO_2$/kg $H_2$)** - Annual Average | | | | | | |
| | w/o CC | w CC | w/o CC | w CC | w/o CC | w CC |
| 1 | 2.45 | 2.03 | 0.85 | 0.20 | 1.42 | 1.18 |
| 2 | 6.07 | 4.16 | 1.02 | -1.87 | 2.45 | 1.39 |

Table 2 presents the annual average, monthly maximum and minimum values for energy generation (G) and its respectively energy purchased from the NIS (P); and energy surpluses (S) to solar, wind, and hybrid parks.

Table 3 shows the GWP associated with the cases presented in Table 1, evaluated under the extreme scenarios of the electricity grid composition: (1) EMS_2019 and (2) EMS_2021, characterized by a maximum share of renewable and fossil fuels sources, respectively. Additionally, it includes cases without (w/o CC) and with (w CC) carbon credits.

When comparing the months of minimum and maximum wind energy generation w/o CC in Table 3, the GWP showed an almost negligible increase in EMS_2019. This is attributed to the high percentage of renewable sources in the energy mix that year, and the fact that no energy purchases from the NIS were required during the month of maximum generation. In EMS_2021, the GWP decreased approximately 42% since no energy purchases from the NIS were needed during the month of maximum generation. When incorporating the surpluses generated in both years as carbon credits, the GWP is reduced by 94% in EMS_2019 and by 1330% in EMS_2021. The substantial reduction in EMS_2021 is due to the high share of fossil fuels in the NIS, whose impact is offset by the carbon credits generated by the wind system.

For the solar plant, when comparing the months of minimum and maximum generation w/o CC, the GWP shows a 49% increase in EMS_2019 and a 4.6% reduction in EMS_2021. This is attributed to the higher environmental impact of the photovoltaic system compared to the NIS in EMS_2019 and the lower relative impact of the photovoltaic system compared to the NIS in EMS_2021. When including the energy surpluses generated, the GWP increases by 6.6% in EMS_2019 and decreases significantly by 64% in EMS_2021, reflecting the variation in impact between the photovoltaic system and the NIS across the years. On the other hand, the hybrid plant exhibits an intermediate behavior between the solar and wind systems.

When comparing scenarios w CC and w/o CC for the solar and hybrid systems in the same year, it is observed that the reduction in GWP is almost negligible during months of minimum energy generation. This is due to the low surpluses generated during these periods and the higher environmental impact associated with the photovoltaic system. However, during months of maximum generation, a significant reduction is recorded in both cases, with a more pronounced effect for the hybrid system, especially in EMS_2021. In the case of the wind plant, a considerable reduction in environmental impact is observed during both minimum and maximum generation months. This can be attributed to the higher energy surpluses generated and the inherently lower environmental impact of this system. Additionally, negative GWP values were obtained for the wind system when carbon credits were considered.

In all the evaluated cases, electricity generation was the main contributor to the environmental impact of hydrogen production, varying depending on the production technology used. In 2019, this contribution was lowest in the wind system (86%), followed by the hybrid system (92%) and the solar system (95%). In the year with the

highest share of fossil fuels in the NIS energy mix, there was a slight increase of approximately 3% in this contribution across all cases.

The impact of water treatment is lower than 1% for all cases. For the electrolysis system, the impact varies between approximately 10 and 2.5% when using the wind and photovoltaic systems, respectively. This impact is primarily associated with the materials used in the production of the stack, such as platinum and titanium, as well as the electricity required for its production. These factors were also identified as the main contributors to environmental impact by other authors. Additionally, they reported electricity generation contribution rates ranging from 78–97% for electrolysis using wind energy and 88–99% for electrolysis using photovoltaic energy [3].

The results obtained in this study for the GWP are within the range reported in the literature [3] for the different evaluated case studies. The differences can be attributed to various factors: the system boundaries, the connection of renewable energy generation plants to the NIS (which exhibits different energy mixes depending on the country), and the inclusion or exclusion of carbon credits for the generated energy surpluses. Variations in GWP across different studies have also been reported by several authors in previous research [3, 9].

Moreover, the values found in this study align with the ranges established by European and Chinese organizations [7, 8] for green hydrogen in wind and hybrid systems. In the case of solar energy, the results depend on the composition of the electricity matrix. Hydrogen production by solar energy complemented with energy form the NIS demonstrates greater vulnerability to the effects of climate change, since it affects directly the availability of water to produce hydropower.

## CONCLUSION

The results obtained in this study indicate that the wind plant is the most efficient alternative in terms of energy generation due to its higher capacity factor compared to the other systems. This plant requires the least energy purchase from the NIS and generates the most significant amount of energy surpluses. When carbon credits are considered, these surpluses significantly reduce the environmental impact, even achieving negative GWP values.

In contrast, the solar system exhibited a higher GWP than the electrical grid in scenarios where the grid had a high proportion of low-emission sources, such as hydropower and wind. However, in contexts where the share of non-renewable sources in the grid increased, the relative impact of the solar system decreased, though it did not reach the competitiveness levels observed in the hybrid and wind systems.

The hybrid system demonstrated greater stability in energy generation compared to exclusively solar or wind plants. However, its lower capacity factor relative to the wind system limited its energy production and surplus generation, which in turn increased the energy purchase from the NIS. As a result, it presented an intermediate GWP between the solar and wind systems.

The environmental impact associated with energy generation for the electrolysis process is a critical aspect to evaluate, as it plays the most significant role in the overall impact of hydrogen production, contributing between 78% and 99%, depending on the energy source used. On the other hand, energy surpluses generated by renewable plants offer a crucial opportunity to reduce environmental impact by creating carbon credits, considering that the electrical grid can be integrated and utilize these surpluses effectively.

An important aspect to be evaluated in future studies is the GWP associated with energy storage, either in batteries or as hydrogen, to enable the plant to operate independently from the grid.

## REFERENCES


1. Ministerio de Industria, Energía y Minería. Green Hydrogen Roadmap in Uruguay. https://www.gub.uy/ministerio-industria-energia-mineria/comunicacion/noticias/green-hydrogen-roadmap-in-uruguay.
2. Maniscalco MP, Longo S, Cellura M, Miccichè G, Ferraro M. Critical review of life cycle assessment of hydrogen production pathways. Environments 11:108 (2024) https://doi.org/10.3390/environments11060108.
3. [Cho HH, Strezov V, Evans TJ. A review on global warming potential, challenges and opportunities of renewable hydrogen production technologies. Sustainable Materials and Technologies 35:00567 (2023) https://doi.org/10.1016/j.susmat.2023.e00567.
4. Iyer RK, Prosser JH, Kelly JC, James BD, Elgowainy A. Life-cycle analysis of hydrogen production from water electrolyzers. Int J Hydrogen Energy 81:1467–1478 (2024) https://doi.org/10.1016/j.ijhydene.2024.06.355.
5. Kanz O, Bittkau K, Ding K, Rau U, Reinders A. Review and harmonization of the life-cycle global warming impact of PV-powered hydrogen production by electrolysis. Front Electron 2: 711103 (2021) https://doi.org/10.3389/felec.2021.711103.
6. Inter-American Development Bank. Guide for the Implementation of a Hydrogen Certification System in Latin America and the Caribbean. https://publications.iadb.org/en/publications/english/viewer/Guide-for-the-Implementation-of-a-Hydrogen-Certification-System-in-Latin-America-

and-the-Caribbean.pdf
7. Liu W, Wan Y, Xiong Y, Gao P. Green hydrogen standard in China: Standard and evaluation of low-carbon hydrogen, clean hydrogen, and renewable hydrogen. Int J Hydrogen Energy 47:24584–24591 (2022) https://doi.org/10.1016/j.ijhydene.2021.10.193.
8. CERTIFHY. https://www.certifhy.eu/.
9. Valente A, Iribarren D, Dufour J. Harmonised life-cycle global warming impact of renewable hydrogen. J Clean Prod 149:762–772 (2017) https://doi.org/10.1016/j.jclepro.2017.02.163.
10. Acar C, Dincer I. Comparative assessment of hydrogen production methods from renewable and non-renewable sources. Int J Hydrogen Energy 39:1–12 (2014) https://doi.org/10.1016/j.ijhydene.2013.10.060.
11. Weschenfelder F, Pires GN, Araújo AC, de Castro O, Ribeiro CM, Villa AA, Araújo AM. A review on the complementarity between grid-connected solar and wind power systems. J Clean Prod 257:120617 (2020) https://doi.org/10.1016/j.jclepro.2020.120617.
12. Ministerio de Industria, Energía y Minería. Balance Energético Nacional. https://ben.miem.gub.uy.
13. ADME. https://adme.com.uy/index.php.
14. Heide, D., Von Bremen, L., Greiner, M., Hoffmann, C., Speckmann, M., & Bofinger, S. Seasonal optimal mix of wind and solar power in a future, highly renewable Europe. Renewable Energy, 35(11): 2483-2489 (2010) https://doi.org/10.1016/j.renene.2010.03.012
15. Bareiß K, de la Rua C, Möckl M, Hamacher T. Life cycle assessment of hydrogen from proton exchange membrane water electrolysis in future energy systems. Appl Energy 237:862–872 (2019) https://doi.org/10.1016/j.apenergy.2019.01.001.
16. Koj JC, Zapp P, Wieland C, Görner K, Kuckshinrichs W. Life cycle environmental impacts and costs of water electrolysis technologies for green hydrogen production in the future. Energy Sustain Soc 14:64 (2024) https://doi.org/10.1186/s13705-024-00497-6.

© 2025 by the authors. Licensed to PSEcommunity.org and PSE Press. This is an open access article under the creative commons CC-BY-SA licensing terms. Credit must be given to creator and adaptations must be shared under the same terms. See https://creativecommons.org/licenses/by-sa/4.0/



Systems & Control Transactions

**Research Article - Peer Reviewed Conference Proceeding**
ESCAPE 35 - European Symposium on Computer Aided Process Engineering
Ghent, Belgium. 6-9 July 2025
Jan F.M. Van Impe, Grégoire Léonard, Satyajeet S. Bhonsale,
Monika E. Polańska, Filip Logist (Eds.)

PSE PRESS

# An Optimization-Based Law of Mass Action Precipitation/Dissolution Model

**Chris A. Laliwala[a], Oluwamayowa O. Amusat[b], and Ana I. Torres[a]***

[a] Carnegie Mellon University, Department of Chemical Engineering, Pittsburgh, PA, USA.
[b] Lawrence Berkeley National Laboratory (LBNL), Berkeley, CA, USA.
* Corresponding Author: aitorres@cmu.edu.

## ABSTRACT

Rare earth elements (REE) and many other critical minerals are necessary for the manufacturing of modern everyday technologies, including microchips, batteries and electric motors. Recovery of these materials typically involves aqueous systems which can be modeled as chemical equilibrium problems. One common method for solving these problems is the law of mass action approach (LMA), where a system of non-linear equations involving the equilibrium constants is solved. However, despite being theoretically simple, these problems are in practice very difficult to solve. Currently, the use of iterative heuristics based on saturation indices to decide on which species and reactions to include in the calculations is the state of the art to arrive at a solution. Here, we present an optimization-based alternative to solve chemical equilibria problems involving precipitation/dissolution reactions without the need for such heuristics. Our approach is first validated against the LMA software MINTEQ and PHREEQC for a number of case studies, and then applied to a novel REE recovery process reported in the literature. Overall, our approach was found to have close agreement with MINTEQ and PHREEQC, and we were able to successfully replicate the reported yield and purity for the published REE process.

**Keywords**: Critical Minerals, Precipitation/Dissolution Models, Optimization.

## INTRODUCTION

Rare earth elements and critical minerals are among the most challenging materials to acquire for many modern technologies, often requiring complex processing and extraction methods. Recovery of these minerals, either from ores or unconventional feedstocks such as end-of-life products, involves processes where chemical equilibrium calculations are essential. Chemical equilibria problems are typically solved in one of two ways [1]: either by minimizing the Gibbs free energy of the system (the GEM approach) or by solving a system of non-linear equations involving the equilibrium constants (the law of mass action approach, LMA). GEM methods rely on thermodynamic data that is not always available [1], thus making the older LMA approach the more widely used. However, despite the widespread use and popularity of the LMA approach, it tends to fail when many precipitating species are involved [1].

To address these issues, many LMA software applications use heuristics based on saturation indices to decide on the addition/removal of species and reactions from calculations [1]. For instance, the state-of-the-art software PHREEQC and MINTEQ employ an iterative heuristic approach involving saturation indices ($SI$) [2-4]. The $SI$ represents the saturation of the solution with respect to a particular solid and can be used to determine if precipitation will occur at equilibrium. It is defined as follows [2-4]:

$$SI = Q_{r,sp} - K_{r,sp} \quad (1)$$

In this approach, the equilibrium concentration of the aqueous species in solution is first calculated by ignoring all possible precipitates. Next, the saturation index for each possible precipitate is calculated. The precipitate with the most positive $SI$ is then forced into equilibrium (i.e. $SI = 0$). Next, the equilibrium concentrations of all the aqueous species are re-calculated, followed by the calculation of all saturation indices for all remaining possible precipitates. If they are all undersaturated (i.e. $SI < 0$),

the process is complete. Otherwise, the precipitation procedure is repeated.

In this work, we present an optimization-based approach for solving chemical equilibria problems involving precipitation/dissolution reactions. Our approach models the precipitation reactions as inequality constraints which allows for the prediction of the precipitated species and the final solution state without the need for saturation indices heuristics [2-4]. This approach offers an initial implementation of an alternative formulation that could in the future be used in conjunction with GEM approaches.

## OPTIMIZATION PROBLEM FORMULATION

The objective function of our precipitation model formulation is to minimize the square difference between the ion product $Q_{r,sp}$, defined over the actual concentration in solution, and the solubility constant $K_{r,sp}$, defined over the equilibrium concentrations in the solution,

$$z = \sum_{r \in N_{rxn,sp}} \left(\log(K_{r,sp}) - \log(Q_{r,sp})\right)^2 \quad (2)$$

where $N_{rxn,sp}$ is the set of precipitation/dissolution reactions. By adding in the following constraints, this objective function allows the identification of the species that should precipitate (i.e. $Q_{r,sp} = K_{r,sp}$) and those that should not (i.e. $Q_{r,sp} \leq K_{r,sp}$):

$$\log(Q_{r,sp}) = \sum_{i \in I_{r,products}} \alpha_{i,r} \log\left(C_i^f\right) \ \forall r \in N_{rxn,sp} \quad (3)$$

$$\log(Q_{r,sp}) \leq \log(K_{r,sp}) \ \forall r \in N_{rxn,sp} \quad (4)$$

where $I_{r,products}$ is the set of products formed in reaction $r$. Eq. (3) computes the ionic product based on the actual concentration in the solution; its upper bound is defined by the solubility product (Eq. 4).

Equilibrium conditions are imposed in all reactions that do not involve solids as shown in Eq. (5):

$$\log(K_{r,aq}) = \sum_{i \epsilon I_{r,products}} \alpha_{i,r} \log\left(C_i^f\right) - \sum_{i \epsilon I_{r,reactants}} \alpha_{i,r} \log\left(C_i^f\right) \ \forall r \in N_{rxn,aq} \quad (5)$$

where $\alpha_{i,r}$ is the stoichiometric coefficient of species $i$ in reaction $r$, $C_i^f$ is the equilibrium concentration of species $i$, and $N_{rxn,aq}$ is the set of all aqueous reactions. We use the logarithmic form(s) in Eq. (3) to (5) to minimize numerical issues.

The set of restrictions is completed with the inclusion of mass and concentration balances to calculate the final concentration/ mass of species:

$$C_i^f = C_i^0 + \sum_{r \in N_{rxn,i}} \alpha_{i,r} X_r \ \forall i \in I_{aq} \quad (6)$$

$$m_i^f = m_i^0 + \sum_r^{N_{rxn,i}} \alpha_{i,r} X_r V \ \forall i \in I_{sp} \quad (7)$$

where $C_i^0$ is the initial concentration of species $i$, $N_{rxn,i}$ is the set of all reactions involving species $i$, $X_r$ is the extent of reaction $r$, $I_{aq}$ is the set of all aqueous species, $m_i^0$ is the initial amount of solid species $i$, $V$ is the volume of solvent, and $I_{sp}$ is the set of all precipitates.

The problem was implemented in Python and solved with IPOPT utilizing the linear solver MA57. The model was scaled with custom scaling parameters and the tolerance was set to 1E-12.

## MODEL VALIDATION

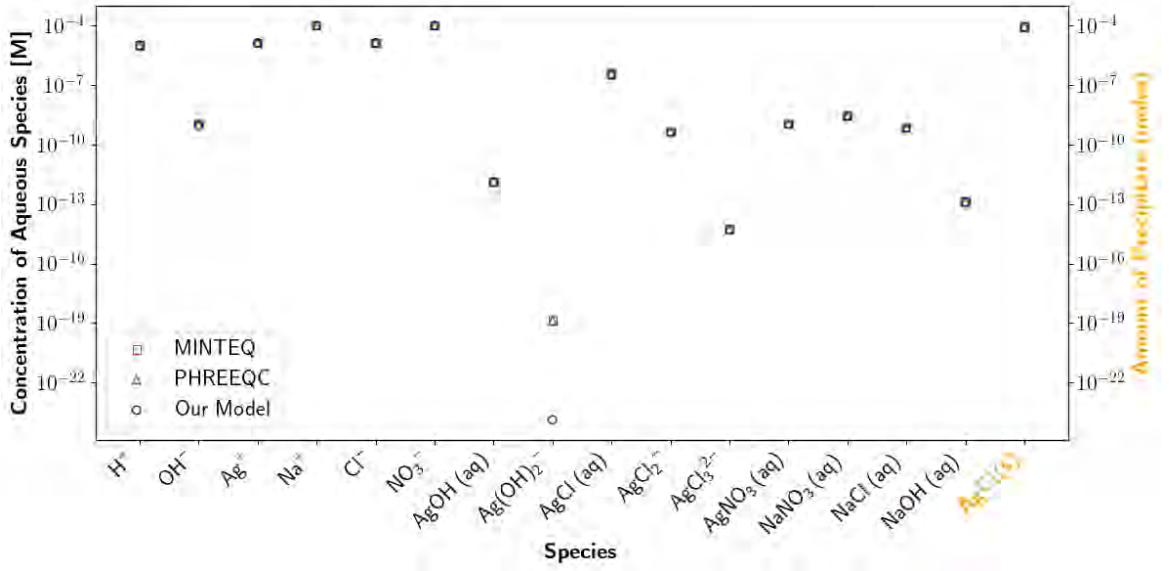



**Figure 1.** Comparison of predicted final concentrations for aqueous species, and predicted final amounts of precipitate formed between MINTEQ, PHREEQC, and our model for Case 1.

To validate our model, we compared the results of several case studies against those from MINTEQ [2,3] and PHREEQC [4], two LMA-based software applications that predict equilibrium calculations based on saturation indices heuristics.

## Case 1: Ag-Cl-$NO_3$ ionic system

For the first case study, we consider a system containing $Ag^+$, $Cl^-$ and $NO_3^-$, with initial concentrations for each species of $1 \times 10^{-4} M$ and a pH of 5. For this system, MINTEQ predicts the formation of 15 aqueous species and one precipitate. The predicted final concentrations and precipitate formed for our model, MINTEQ, and PHREEQC are all shown in Figure 1. All three models show close agreement for the amount of precipitate formed and the final concentrations of all aqueous species with the exception of $Ag(OH)_2^-$.The largest relative difference between our model and PHREEQC, and our model and MINTEQ (excluding $Ag(OH)_2^-$) is 4.9% (for $AgCl_2^-$) and the average one is 1.14%. For $Ag(OH)_2^-$, it was found that both PHREEQC and MINTEQ predicted very similar final concentrations. While our model predicted a lower final concentration, all three models predicted an essentially zero final concentration.

## Case 2: Na-K-Ca-Mg-Cl-$SO_4$ ionic system

For our second validation case, we considered a system based on a subset of the primary ions typically found in water treatment. We intentionally leave carbonate ions out. For the initial concentration in Table 1, MINTEQ predicted 21 aqueous species and one possible precipitate.

**Table 1.** Initial concentration of ions in Case 2.

| Species | Initial Concentration [M] |
|---|---|
| Na+ | $3.35 \times 10^{-4}$ |
| K+ | $4.09 \times 10^{-4}$ |
| Ca2+ | $3.24 \times 10^{-2}$ |
| Mg2+ | $1.23 \times 10^{-4}$ |
| Cl- | $3.33 \times 10^{-4}$ |
| SO42- | $2.50 \times 10^{-2}$ |

The comparisons of the final predicted concentrations of the aqueous species and amount of precipitate formed for all three models are shown in Figure 2. As can be seen in the figure, there is excellent agreement between our model and PHREEQC for all species. However, for species containing $OH^-$, MINTEQ consistently predicted a lower final concentration, and for species containing $H^+$, MINTEQ consistently predicted a higher final concentration than both PHREEQC and our model.

The relative differences between our model and PHREEQC, and our model and MINTEQ are larger than for case 1. However, similar differences are found if the predictions from PREEQC and MINTEQ are compared with each other.

Additional simulations adding carbonate to the ions pool to more accurately represent water treatment processes were performed. The results, not presented here, also show excellent agreement and will be discussed at the conference.

## Case 3: Na-K-Ca-Mg-Cl-$SO_4$-Fe ionic system

Finally, we validated our model in a setting where multiple precipitates are possible. For this, $1 \times 10^{-6} M$ of

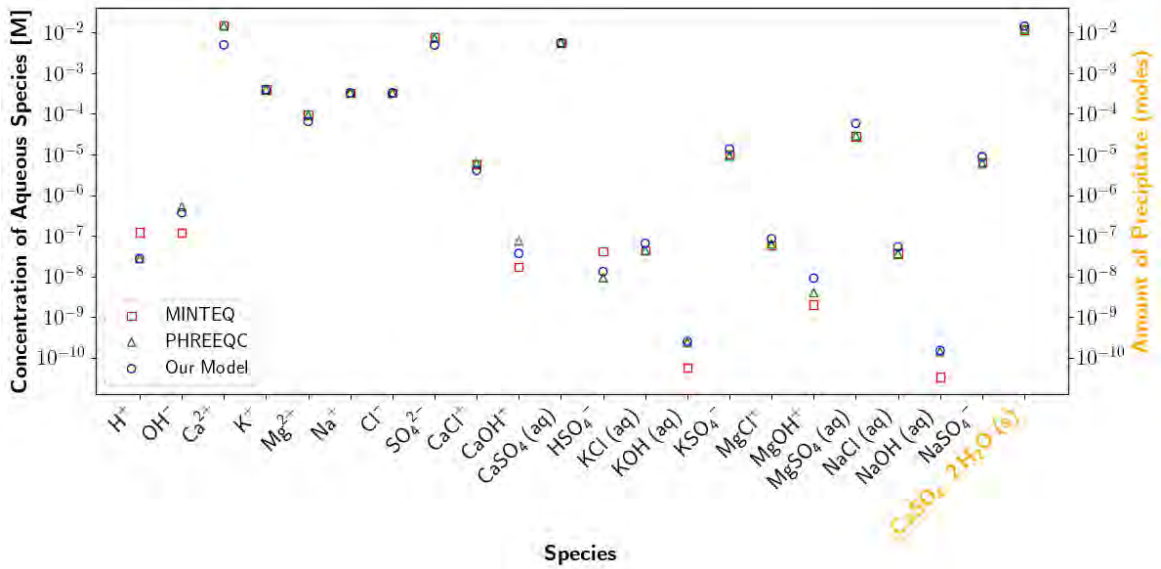



**Figure 2.** Comparison of predicted final concentrations for aqueous species, and predicted final amounts of precipitate formed between MINTEQ, PHREEQC, and our model for Case 2.

$Fe^{3+}$ was added to the initial system of ions shown in Table 1. With this change, MINTEQ predicts 31 different aqueous species and seven potential precipitates: $CaSO_4 \bullet 2H_2O$(s) (gypsum), $Fe(OH)_{2.7}Cl_{0.3}$(s), $Fe(OH)_3$(s) (ferrihydrite), FeO(OH)(s) (goethite), $Fe_2O_3$(s) (hematite), $KFe(SO_4)_2(OH)_6$(s) (k-jarosite), and $Mg(Fe)_2O_4$(s) (magnesioferrite). Comparisons of the final predicted concentrations of the aqueous species and the predicted amount of precipitate formed with the three models are shown in Figure 3. As can be seen, there is good agreement between our model and MINTEQ on the final species concentrations, while PHREEQC slightly underpredicted the final concentrations for many of the aqueous species. For the precipitates, it was found that while all three models predicted the formation of the same amount of gypsum at equilibrium, PHREEQC and MINTEQ also predicted the formation of hematite, while our model predicted the formation of magnesioferrite. None of the models predicted any $Fe(OH)_{2.7}Cl_{0.3}$(s), ferrihydrite, goethite, or k-jarosite to form at equilibrium.

The difference in the predicted final concentration of the precipitates can be attributed to MINTEQ and PHREEQC's reliance on the iterative saturation indices heuristic to determine which species precipitate. This heuristic also implicitly assigns an order in which the species precipitate, which can lead to the exclusion of species that might form under simultaneous equilibrium. In contrast, our model does not rely on such heuristics, as the equilibrium conditions of all possible precipitates are incorporated within the optimization problem. However, to further establish the reliability of our approach, future work needs to involve experimental validation.

## CMI PROCESS CASE STUDY

### Process Description

As a proof of concept on how our model can be used for modeling and future optimization of critical mineral processing, we applied it to a novel REE recovery process developed by the Critical Materials Innovation Hub (CMI) [5,6].

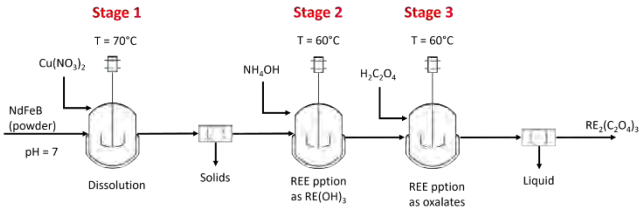



**Figure 4.** Depiction of the CMI process [5,6].

The CMI process is depicted in Figure 4. The process uses a series of dissolution and precipitation reactions to recover rare earth elements as rare earth oxalates from end-of-life (EOL) rare earth permanent magnets (REPM) [5,6]. In the first stage, the NdFeB feed in powder form is dissolved in a solution of copper nitrate salts. This leads to the formation of precipitates containing the iron and boron contaminants ($Cu_3(BO_3)_2$, $Fe(OH)_3$), which are subsequently filtered from the solution. In the next stage, ammonium hydroxide is added to the solution to increase the pH. This leads to the formation of rare earth hydroxides and the conversion of some of the remaining iron in solution into iron hydroxides. Next, in stage 3, oxalic acid is added to the solution. This leads to the formation of soluble iron-ammonium

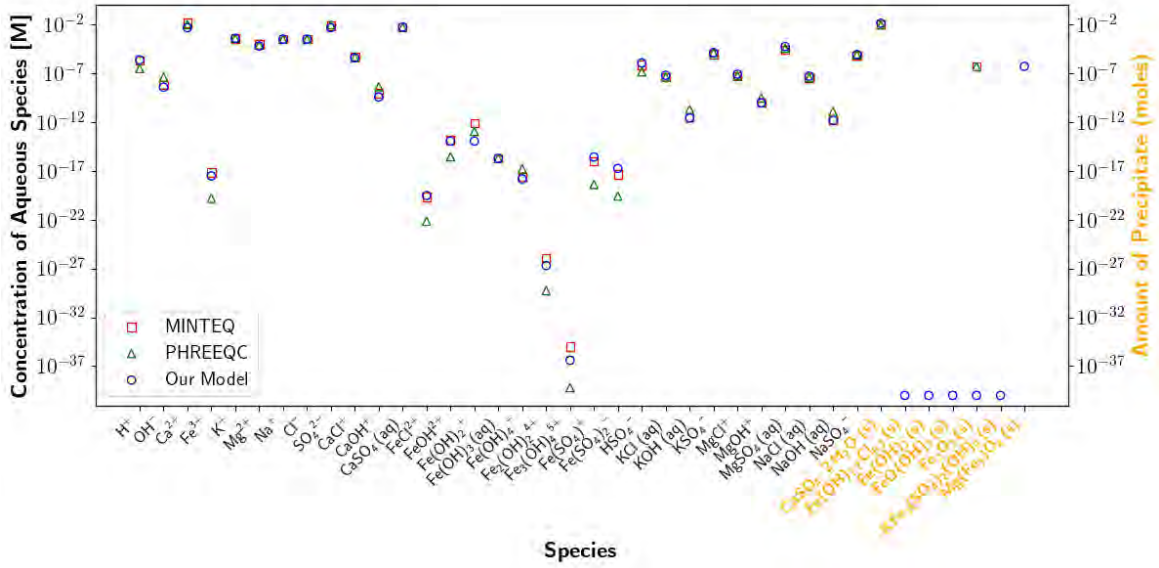



**Figure 3.** Comparison of predicted final concentrations for aqueous species, and predicted final amounts of precipitate formed between MINTEQ, PHREEQC, and our model for Case 3.

oxalate and insoluble rare earth oxalate. The rare earth oxalate precipitate is subsequently separated from the solution.

## Simulation Results

In the paper, a yield of >98% of REEs recovered as rare earth oxalates, and a final purity >99%, was reported for a feedstock consisting of REPM swarf [6]. While the paper also reported REE recoveries from other feedstocks,

REPM swarf was specifically selected for this case study because it consists exclusively of pure REPM material. This eliminates the need to account for mass transfer limitations caused by casing materials, which are a concern in feedstocks like shredded HDDs.

Although the overall yield was reported, some important parameters were not. These include: the final pH of stage 2 and the amount of oxalic acid added to the solution in stage 3. Thus, a sensitivity analysis was conducted on these important parameters to determine if the reported yield and purity could be recreated. To simulate the process, our precipitation model was utilized for stages 1, 2, and 3. Ideal separation between solids and liquids was assumed for all separation steps.

The results of the sensitivity analyses are shown in Figures 5 and 6. It was found that the reported yield and purity could be successfully replicated with our model. Furthermore, the reported yield was found to occur over a range of pH values, and for four out of five of the initial concentrations of oxalic acid that were simulated (0.045M, 0.09M, 0.135M, and 0.18M). The reported purity was also found to occur over a range of pH values and for three out of 5 of the initial concentrations of oxalic acid that were simulated (0.09M, 0.135M, and 0.18M).

As can be seen in Figure 5, increasing the amount of oxalic acid added to the solution in stage 3 was found to increase the amount of neodymium recovered. Additionally, it was also found that increasing the final pH of stage 2 (by adding more ammonium hydroxide) increased the recovery of neodymium, but only up to a point. Increasing the pH past 7 was found to lead to a decrease in the amount of neodymium recovered for all initial concentrations of oxalic acid except for 0.015M.

Figure 6 depicts the effects of the amount of oxalic

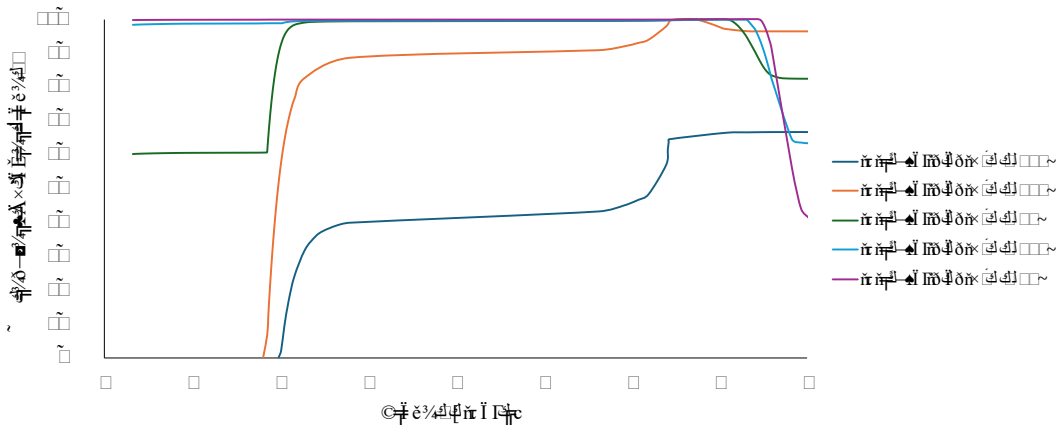


**Figure 5.** Simulation results for the CMI process. Increasing the pH of stage 2 led to an increased recovery of Nd-oxalate up to a point.

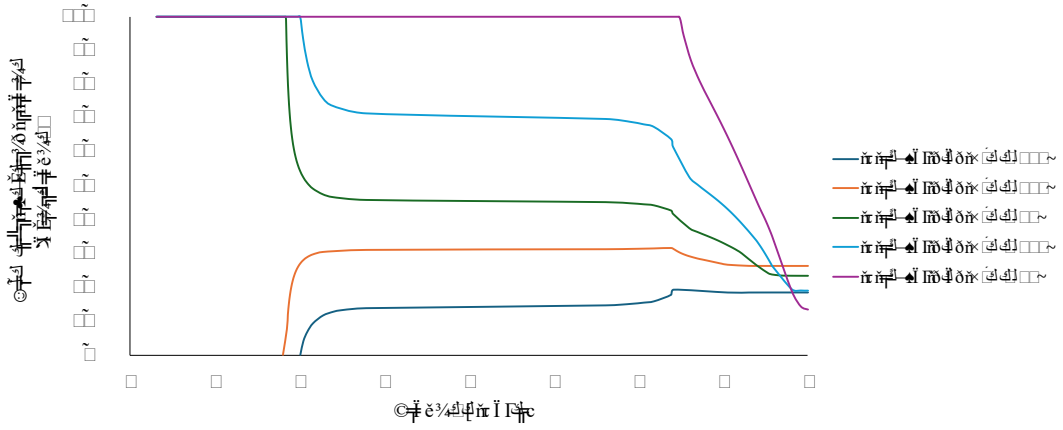


**Figure 6.** Simulation results for the CMI process. Increasing the pH of stage 2 led to a decrease in the purity of the precipitate.

acid added in stage 3, and the pH of stage 2 on the purity of the recovered precipitate. It was found that while increasing the pH of stage 2 led to an increase in the amount of precipitate formed (up to a pH of 7), it also led to a decrease in the purity of the precipitate. This can be attributed to more iron hydroxide being precipitated out of solution as the pH was increased.

Overall, our results suggest that there is room for optimization of the reaction conditions, for example, to find those that minimize acid consumption while keeping the desired purity and yields.

## CONCLUSION

In this work, an initial implementation of an optimization-based approach for solving precipitation/dissolution reactions utilizing equilibrium relations is presented. We first present three case studies to show that the predictions from this model are in good agreement with LMA-based software: MINTEQ and PHREEQC. Then we present a proof of concept where our model is applied to the CMI process [5,6]. By conducting sensitivity analyses on the uncertain parameters of the model, we were able to replicate the paper's reported yield and purity, suggesting that our model is capable of modeling aqueous equilibrium systems accurately.

## DIGITAL SUPPLEMENTARY MATERIAL

Code utilized in this paper will be available at https://github.com/prommis/prommis.

## ACKNOWLEDGMENTS

This effort was funded by the U.S. Department of Energy's Process Optimization and Modeling for Minerals Sustainability (PrOMMiS) Initiative, supported by the Office of Fossil Energy and Carbon Management's Office of Resource Sustainability.

## DISCLAIMER

This project was funded by an agency of the United States Government. Neither the United States Government, nor any agency thereof, nor any of their employees, nor any of their contractors, subcontractors, or their employees, make any warranty, express or implied, or assumes any legal liability or responsibility for the accuracy, completeness, or usefulness of any information, apparatus, product, or process disclosed, or represents that its use would not infringe privately owned rights. Reference herein to any specific commercial product, process, or service by trade name, trademark, manufacturer, or otherwise does not necessarily constitute or imply its endorsement, recommendation, or favoring by the United States Government, any agency thereof, or any of their contractors or subcontractors. The views and opinions of authors expressed herein do not necessarily state or reflect those of the United States Government, any agency thereof, or any of their contractors. The Lawrence Berkeley National Laboratory (LBNL) is managed and operated by the University of California (UC) under U.S. Department of Energy Contract No. DE-AC02-05CH11231. Sandia National Laboratories is a multi-mission laboratory managed and operated by National Technology and Engineering Solutions of Sandia, LLC., a wholly owned subsidiary of Honeywell International, Inc., for the U.S. Department of Energy's National Nuclear Security Administration under contract DE-NA-0003525.

## REFERENCES

1. Allan M.M. Leal, Dmitrii A. Kulik, William R. Smith, Martin O. Saar. An overview of computational methods for chemical equilibrium and kinetic calculations for geochemical and reactive transport modeling. *Pure Appl. Chem.* 89:597-643 (2017) https://doi.org/10.1515/pac-2016-1107
2. Jerry D. Allison, David S. Brown, Kevin J. Novo-Gradac. MINTEQA2/PRODEFA2, a geochemical assessment model for environment systems: version 3.0 user's manual (1991)
3. Jon P. Gustafsson. Visual MINTEQ 4.0 user guide (2022)
4. David L. Parkhurst, C.A.J. Appelo. User's guide to PHREEQC (version 2)- a computer program for speciation, batch-reaction, one-dimensional transport, and inverse geochemical calculations (1999) https://doi.org/10.3133/wri994259
5. Nighat A. Chowdhury, Sidi Deng, Hongyue Jin, Denis Prodius, John W. Sutherland, Ikenna C. Nlebedim. Sustainable recycling of rare-earth elements from NdFeB magnet swarf: techno-economic and environmental perspectives. ACS Sustain. Chem. Eng. 9:15915-15924 (2021) https://doi.org/10.1021/acssuschemeng.1c05965
6. Denis Prodius, Kinjal Gandha, Anja-Verena Mudring, Ikenna C. Nlebedim. ACS Sustain. Chem. Eng. 8:1455-1463 (2020) https://doi.org/10.1021/acssuschemeng.9b05741

© 2025 by the authors. Licensed to PSEcommunity.org and PSE Press. This is an open access article under the creative commons CC-BY-SA licensing terms. Credit must be given to creator and adaptations must be shared under the same terms. See https://creativecommons.org/licenses/by-sa/4.0/



Systems & Control Transactions

**Research Article - Peer Reviewed Conference Proceeding**
ESCAPE 35 - European Symposium on Computer Aided Process Engineering
Ghent, Belgium. 6-9 July 2025
Jan F.M. Van Impe, Grégoire Léonard, Satyajeet S. Bhonsale,
Monika E. Polańska, Filip Logist (Eds.)

PSE PRESS

# Sustainable Aviation Fuels Production via Biogas Reforming and Fischer-Tropsch Integrated with Solid Oxide Electrolysis

**Muhammad Nizami[a], Konstantinos Anastasakis[a]***

[a] Department of Biological and Chemical Engineering, Aarhus University, Hangøvej 2, Aarhus 8200, Denmark
* Corresponding Author: kanastasakis@bce.au.dk .

## ABSTRACT

Sustainable aviation fuels (SAFs) can be pivotal, gradually replacing fossil kerosene and lowering carbon emissions without changing the existing infrastructure. One of the pathways to produce SAFs is through the Fischer-Tropsch synthesis (FTS) process. The present work proposes an integrated process of sustainable aviation fuel production from biogas through a reforming process, Fischer-Tropsch (FT), and a solid oxide electrolysis (SOEC) process. Aspen Plus v14 is used to build an integrated kinetic process model for biogas reforming, FTS and hydrocracking. The technical evaluation is assessed with several key performance indicators, such as carbon efficiency and process efficiency. In addition, two scenarios are investigated in this study for $H_2$ supply from SOEC before and after reforming. The output products consist of kerosene and diesel since the tail gas and naphtha are recycled to the reformer to maximize SAF production. The simulation results show that the carbon efficiency of the integrated process is between 96.3% and 96.5%. Meanwhile, the process efficiency is between 40.1% and 40.9%. The process efficiency can be further improved by investigating the options for heat integration, with subsequent economic and environmental analysis to determine the production cost of SAFs and the $CO_2$ reduction potential compared to conventional aviation fuel. In addition, projection cost analysis is needed to determine the decline in the cost of fuel production in the future.

**Keywords**: sustainable aviation fuels, biogas reforming, Fischer-Tropsch process, solid oxide electrolysis

## 1. INTRODUCTION

The aviation industry is essential for the fast and efficient transportation of people and goods, making it crucial for international business and tourism. However, this sector contributes greenhouse gas (GHG) emissions significantly, releasing around one billion tons of $CO_2$ annually—about 2.5% of global energy-related $CO_2$ emissions. One of the strategies to achieve carbon neutrality in the aviation sector is the adoption of Sustainable Aviation Fuel (SAFs) [1].

A viable method for producing SAFs is the Fischer-Tropsch (FT) process. This method converts syngas into liquid fuels whose composition depends on pressure, temperature, syngas composition, and catalyst type. The FT synthesis can occur at low temperatures (LTFT) and high temperatures (HTFT). The LTFT process is operated at 210–260 °C with a cobalt catalyst, which produces long-chain hydrocarbon. Meanwhile, the HTFT process is operated at 310–340 °C with an iron catalyst, which generates short-chain hydrocarbons [2].

The syngas, which is a mixture of CO, $H_2$, $CO_2$, and $H_2O$, can be produced from a thermochemical conversion process at a high temperature of 900 °C with several routes: reverse water gas shift, steam reforming, and autothermal reforming, with the primary feedstock is natural gas or biogas along with steam or hydrogen. Biogas is an attractive resource because it has carbon sources from methane and $CO_2$, which can be transformed into syngas through steam reforming process [3]. In addition, due to the awareness of Power-to-X (PtX) technologies, this can expand to green hydrogen production from the electrolysis process (e.g., solid oxide electrolysis), which can fulfill the syngas requirement for the FT process [4].

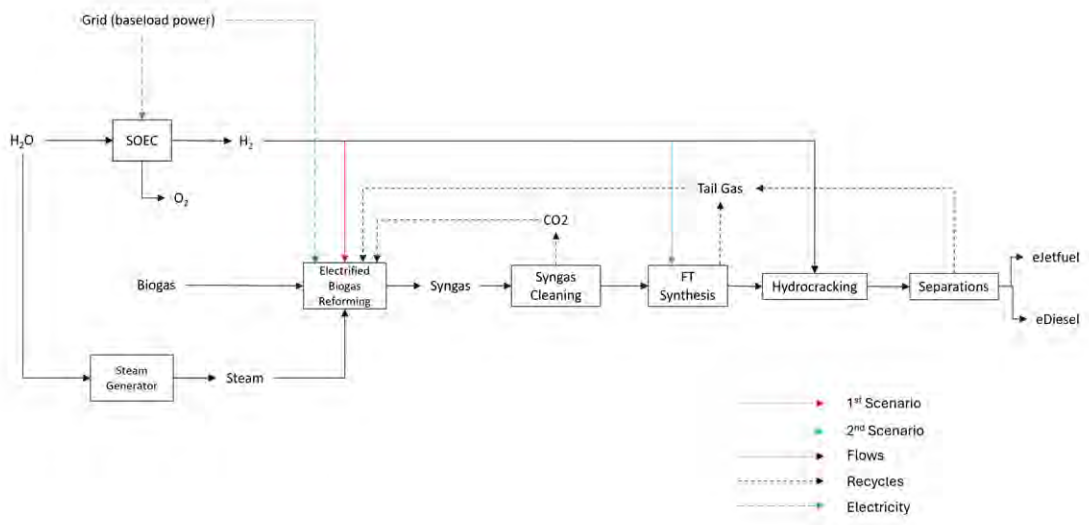



**Figure 1.** Schematic of the system.

Existing studies in process modeling of sustainable aviation fuel through the Fischer-Tropsch process typically focus on a $CO_2$ source from flue gas and ambient air. For instance, Paulsen et al. performed techno-economic assessments of jet fuel production integrated, reverse water gas shift (RWGS), Fischer-Tropsch, and electrolysis process with $CO_2$ source from ambient air through high-temperature direct air capture (HTDAC). It demonstrated that the energy efficiency is up to 39% with specific energy consumption of up to 156 $MJ/kg_{Jet\ fuel}$ [4]. In another $CO_2$ source, Marchese et al. conducted the process modeling of integrated RWGS and co-electrolysis process with the Fischer-Tropsch process to produce the liquid fuels with $CO_2$ source from biogas through MEA absorption. The results show that plant efficiency is 75.8% for co-electrolysis and 70.1% for RWGS [5]. However, these studies do not utilize the methane from biogas as the input to maximize the yield of liquid fuels.

This work aims to develop a rigorous process model of SAF production through the FT process with solid oxide electrolyzer and electrified biogas reforming, which utilize the $CH_4$ and $CO_2$ from biogas as the primary feedstock and the output products consisting of kerosene and diesel. Hydrocracking is employed to crack the wax, and the resulting tail gas and naphtha are recycled to the reformer to maximize the fuel yield. Kinetic models are developed for all reactors (reformer, FT, and hydrocracking) and validated with experimental data.

# 2. METHODOLOGY

## 2.1. Process description

The integrated process model is developed for SAF production via the Fischer-Tropsch process with syngas sources generated from electrified biogas reforming. Two scenarios are investigated in this study. In the first scenario, biogas, steam, and hydrogen from SOEC are input to the steam reforming reactor. Biogas and steam are fed into the reforming reactor, with the additional required hydrogen being input before the FT reactor in the second scenario. The first and second scenarios are presented in Fig. 1.

## 2.2. Process Simulation

The process simulation is developed using Aspen PLUS v14 with Peng-Robinson (biogas reforming and electrolysis), Soave-Redlich-Kwong (Fischer-Tropsch and hydrocracking), and E-NTRL (syngas cleaning) EOS's, as the thermodynamic models. The Aspen simulation workbook (ASW) is employed to solve the complex kinetic model of FT and solid oxide electrolyzer cell (SOEC). The process models developed in this study are illustrated in Fig. 2 (biogas reforming) and Fig. 3 (FT process with hydrocracking and separation).

### 2.2.1 Electrified Biogas Reforming

The electrified biogas reforming along with steam input to produce the syngas was simulated in multi-tubular plug flow reactor (PFR) at P = 20 bar and T = 950 °C. Electrified reformer employs resistance heating to replaces the fired heater, with heating elements powered by an external electricity source to heat the reactor. In terms of energy efficiency, the electrified reformer demonstrated better efficiency compared to conventional fired reformers [3]. A commercial Ni-$CeO_2$/$MgAl_2O_4$ catalyst is selected with LHHW kinetic model that combine steam methane reforming, $CO_2$ reforming, and water gas shift (WGS) reactions developed by Park et al. [6].

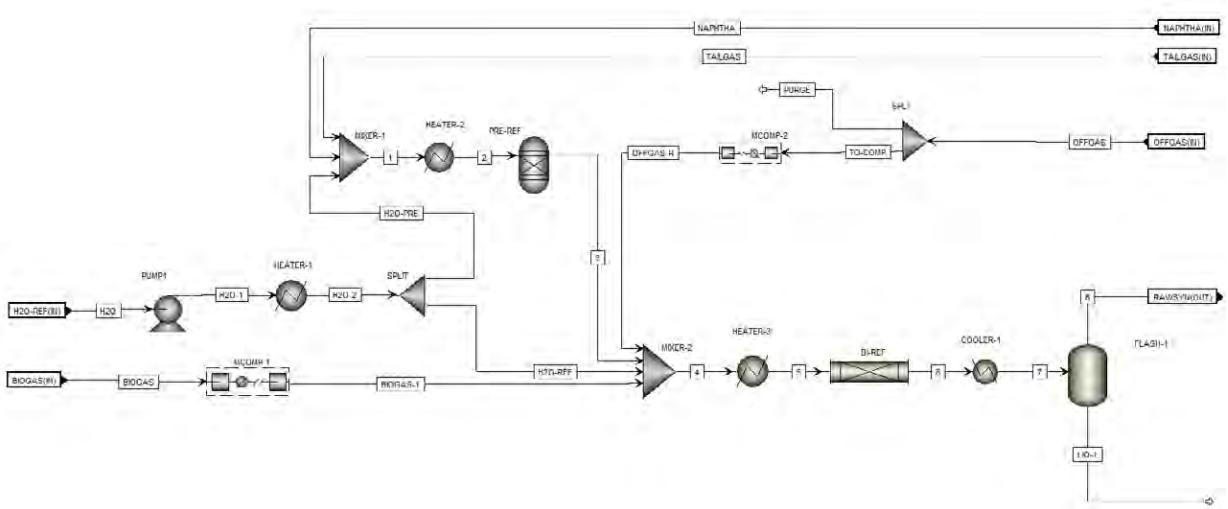



**Figure 2.** Process Simulation of Biogas Reforming

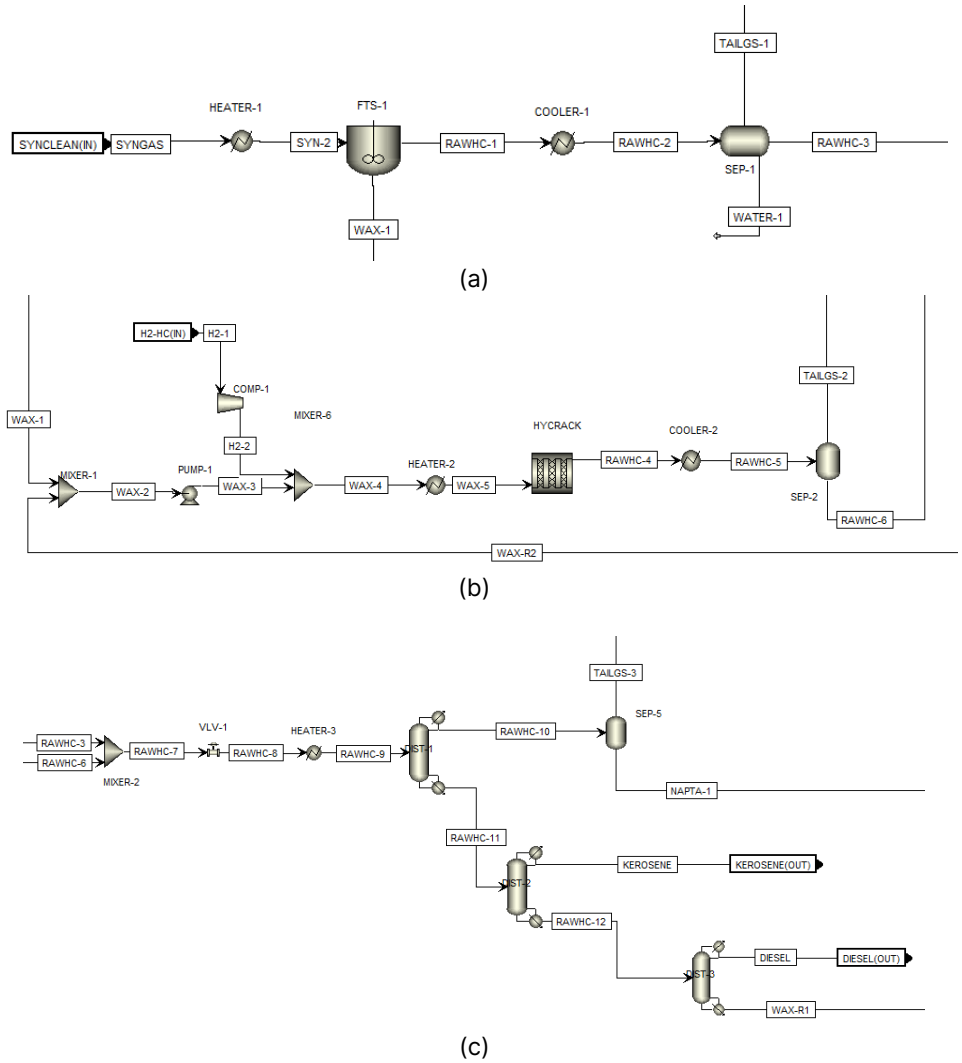



**Figure 3.** Process Simulation of (a) Fischer-Tropsch with (b) Hydrocracking and (c) Separation

### 2.2.2 Solid Oxide Electrolyzer

The solid oxide electrolyzer cell (SOEC) unit is modeled as the stoichiometric reactor at 750 °C and P = 1.15 bar with an $H_2O$ conversion of 60%. The fraction of hydrogen produced from the electrolyzer is recycled back to the stack, and it is adjusted by design specifications so the steam concentration in the feed of the stack is at 90%. The modeling of the electrolytic cell, which is applied in the Aspen Plus stoichiometric reactor, is assisted by the Aspen simulation workbook (ASW). The detailed mathematical model of electrolytic cells is presented by AlZahrani and Dincer [7].

### 2.2.3 Fischer-Tropsch and Hydrocracking

A low-temperature Fischer Tropsch (LTFT) with a cobalt-based catalyst is employed in the process model from the syngas with an H2/CO ratio of around 2.1. The process is modeled in a slurry-bubble column reactor (SBCR) with an operating pressure of 20 bar and a temperature of 230 °C [8]. The SBCR can be modeled as the continuous stirred tank reactor (CSTR) in Aspen Plus, assisted by the Aspen simulation workbook. In general, the reaction follows this highly exothermic reaction:

$$CO + 2H_2 \rightarrow -(CH_2) - + H_2O \quad \Delta H = -150 \frac{kJ}{mol} \quad (1)$$

The term of $-(CH_2)-$ is described as the monomer product through the polymerization process, and the water is a side product of the process. The FTS process is modeled based on chain growth probability and the olefin/paraffin ratio which is presented by Todic et al. with CO conversion per pass = 52.5% [8].

A heavier hydrocarbon in wax produced from the FT reactor is sent to a hydrocracking process to maximize the jet fuel yield. The hydrocracking model with silica-alumina catalyst was simulated in the plug-flow reactor at P = 30 bar and T = 367 °C, assisted by the Aspen simulation workbook. The hydrocracking kinetic model is based on the study by Bhutani et al., 2006 [9].

### 2.2.4 Additional processes

There are additional processes besides reforming, SOEC, and the FT process, e.g., $CO_2$ capture, pre-reforming, and distillation columns, which are needed for a comprehensive evaluation of the biogas-to-jet fuel process.

Syngas cleaning is employed to remove $CO_2$ from the syngas, which is recycled back into the reforming reactor. The MEA absorption process, a well-established industrial process, is used, with a $CO_2$ recovery of 90% and specific heat consumption of 3.5 MJ per kg-$CO_2$ [10].

The raw synfuel from FT and hydrocracking are sent to three stages of distillation columns to separate the tail gas, naphtha, kerosene, diesel, and wax at atmospheric conditions. The tail gas and naphtha are recycled back to the pre-reforming reactor which is operated at P = 20 bar and T = 400 °C and simulated in Gibbs reactor at adiabatic conditions to produce additional CO and $H_2$ from $C_{2+}$. The wax is sent to the hydrocracking reactor along with wax from the FT process.

## 2.3. Performance Indicators

The performance indicators from the proposed process are calculated based on the mass and energy balance, as presented below:

- Carbon conversion ratio, also known as carbon efficiency ($\eta_C$), is defined as the ratio of the carbon atoms in the hydrocarbon after reforming and the Fischer-Tropsch process relative to carbon atoms in the biogas feedstock, as presented in Eq. (2):

$$\eta_C = \frac{\dot{n}_{C,hydrocarbons}}{\dot{n}_{C,feedstock}} \quad (2)$$

- Hydrogen efficiency ($\eta_H$) is defined as the ratio of the hydrogen atoms in the hydrocarbon products relative to the hydrogen atoms in the water for SOEC process, as presented in Eq. (3):

$$\eta_H = \frac{\dot{n}_{H,hydrocarbons}}{\dot{n}_{H,feedstock}} \quad (3)$$

- Process efficiency ($\eta_P$) represents the ratio of the energetic content of hydrocarbon products relative to the energetic content of biogas and the total energy input of the system, including the electrified reforming power, SOEC power, and process power consumption, as shown in Eq. (4):

$$\eta_P = \frac{\dot{m}_{hydrocarbon} \times LHV_{hydrocarbon}}{\dot{m}_{biogas} \times LHV_{biogas} + P_{SOEC} + P_{reforming} + P_{process}} \quad (4)$$

# 3. RESULTS

The integrated modeling of the FT process with electrified biogas reforming considers biogas feedstock volume flow of 45 million $m^3$/year, and the mole fraction is 60% $CH_4$ and 40% $CO_2$. This flow corresponds to 5,544 kg/hr. The validation of the FT process was carried out using mole fraction against the carbon number, as shown in Fig. 4, along with experimental data from Todic et al.[8]. As it can be appreciated there is a good correlation between the model predictions and experimental data for hydrocarbons with up to 15 carbons. Unfortunately, there were no experimental data for long chain hydrocarbons.

Table 1 highlights mass and energy balance of FT fuel process in two scenarios. After recovering and recirculating unreacted $CO_2$ from the syngas cleaning process via MEA absorption, tail gas, and naphtha from FT and separation process, the hydrocarbon output is 2,132 kg/hr of kerosene and 648 kg/hr of diesel meanwhile in the second scenario, the hydrocarbon output is 2,137 kg/hr of kerosene and 648 kg/hr of diesel. In addition, the total electricity consumption for electrified reforming, SOEC, and other processes in the first and second scenarios are 38.9 MW and 37.9 MW, respectively.

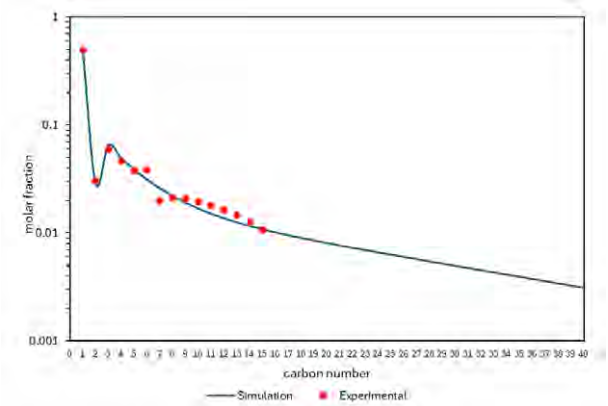



**Figure 4.** The Molar fraction of FT products with Experimental validation

Regarding energy input, the first scenario requires larger electricity consumption (27.9 MW) compared to the second scenario (27.1 MW) due to the electrified reforming consuming more electricity with hydrogen input sent to reforming. It differs from the second scenario, where hydrogen input is sent directly to the FT reactor to fulfill syngas requirements ($H_2/CO \approx 2.1$) for the FT process. However, in the SOEC, electricity consumption is slightly elevated due to the reaction of hydrogen with $CO_2$ in the reformer within the first scenario, which consequently reduces hydrogen output. The electricity requirement for electrified biogas reforming is two times higher than that of the SOEC process because the SOEC process is only employed to supply the lack of hydrogen produced from reforming. In addition, the hydrogen requirement for hydrocracking, supplied by the SOEC, is significantly lower than hydrogen requirement for the reforming process.

**Table 1:** Key Performance Indicators of the FT fuel

| Parameter | 1st Scenario | 2nd Scenario |
|---|---|---|
| Material input (kg/hr) | | |
| Biogas flow rate | 5,544 | 5,544 |
| Process Water | 9,674 | 9,609 |
| Material output (kg/hr) | | |
| Kerosene | 2,132 | 2,137 |
| Diesel | 648 | 648 |
| Energy input (MW) | | |
| Biogas heat flow | 27.2 | 27.2 |
| Electricity input | 38.9 | 37.9 |
| Energy output | | |
| Kerosene | 22.2 | 22.3 |
| Diesel | 4.4 | 4.4 |
| Electricity input (MW) | | |
| Electrified reforming | 27.9 | 27.1 |
| SOEC | 8.9 | 8.7 |
| Compressor | 2.01 | 2.01 |
| Pump | 0.07 | 0.07 |

The performance indicators assessed in this study, include carbon conversion, hydrogen and process efficiencies. As presented in Fig. 5, the overall (kerosene and diesel) carbon conversion efficiency between the two scenarios is relatively the same, around 96%. The carbon loss is in the purge, associated with $CO_2$ recirculation from the syngas cleaning process and tail gas recirculation from the FT process. The total hydrogen efficiency is approximately 27%, significantly lower than carbon conversion efficiency, due to the abundance of water lost after water separation from syngas in reforming and syncrude in the FT process.

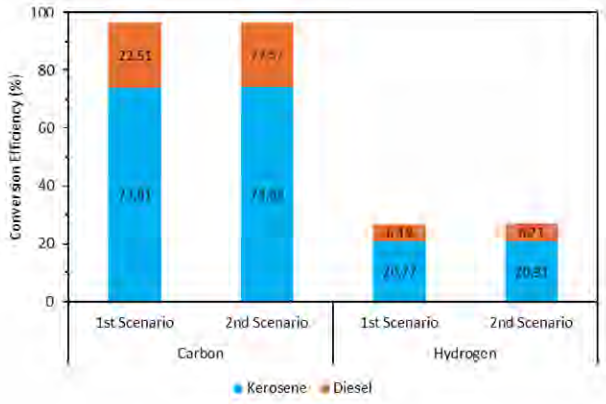



**Figure 5.** Carbon and Hydrogen Conversion Efficiency from Two Scenarios

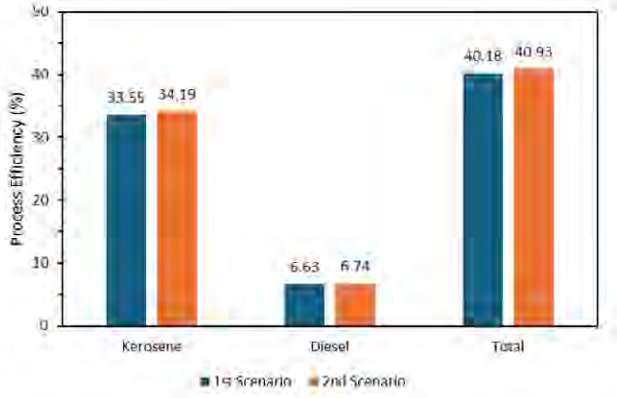



**Figure 6.** Process Efficiency from Two Scenarios

Overall, the process efficiency as shown in Fig. 6 is calculated at approximately 40% due to the large electricity consumption in electrified reforming and SOEC processes. The comparison between the two scenarios reveals insights into mass and energy balances, particularly focusing on process efficiency of two scenarios. The results show that the second scenario exhibits slightly better overall process efficiency, with stable hydrocarbon production, while slightly reducing total electricity consumption. For further analysis, the developed model featuring the two scenarios needs to incorporate heat integration, which will change the electricity consumption and process efficiency. In addition, economic and

environmental assessments are conducted to determine the production cost and carbon reduction potential compared to conventional aviation fuel.

## 4. CONCLUSION

The study evaluated two scenarios of sustainable aviation fuels (SAFs) production from biogas upgrading and the Fischer-Tropsch process, with focus on carbon utilization, process efficiency, and electricity consumption. Rigorous kinetic process models for all involved processes were developed to enhance the accuracy and flexibility of the evaluation. Based on the developed models, the two scenarios achieve stable production of kerosene and diesel. However, providing hydrogen at the inlet of the FT unit (after the reformer) resulted in lower electricity consumption compared to the scenario where the additional hydrogen required for FT is supplied directly at the reformer. In addition, the carbon conversion efficiency remains high (96%), indicating high carbon utilization for hydrocarbon production.

In future work, the study will expand on economic implications to assess the cost of SAF production compared to conventional aviation fuels. In addition, the environmental impact will be assessed via life-cycle assessment to determine the potential of carbon reduction from the whole process.

## ACKNOWLEDGEMENTS

This work was supported by Energiteknologisk Udviklings og Demonstrations Program (EUDP) under the "FrontFuel: Sustainable aviation fuel to implement green transition" project, grant number: 43514-21301.

## REFERENCES

1. International Energy Agency. Aviation 2025. https://www.iea.org/energy-system/transport/aviation#programmes (accessed January 29, 2025).
2. Wang B, Ting ZJ, Zhao M. Sustainable aviation fuels: Key opportunities and challenges in lowering carbon emissions for aviation industry. Carbon Capture Science & Technology 2024;13:100263. https://doi.org/10.1016/j.ccst.2024.100263.
3. From TN, Partoon B, Rautenbach M, Østberg M, Bentien A, Aasberg-Petersen K, et al. Electrified steam methane reforming of biogas for sustainable syngas manufacturing and next-generation of plant design: A pilot plant study. Chemical Engineering Journal 2024;479:147205. https://doi.org/10.1016/j.cej.2023.147205.
4. Paulsen MM, Petersen SB, Lozano EM, Pedersen TH. Techno-economic study of integrated high-temperature direct air capture with hydrogen-based calcination and Fischer–Tropsch synthesis for jet fuel production. Appl Energy 2024;369:123524. https://doi.org/10.1016/j.apenergy.2024.123524.
5. Marchese M, Giglio E, Santarelli M, Lanzini A. Energy performance of Power-to-Liquid applications integrating biogas upgrading, reverse water gas shift, solid oxide electrolysis and Fischer-Tropsch technologies. Energy Conversion and Management: X 2020;6:100041. https://doi.org/10.1016/j.ecmx.2020.100041.
6. Park N, Park M-J, Baek S-C, Ha K-S, Lee Y-J, Kwak G, et al. Modeling and optimization of the mixed reforming of methane: Maximizing CO2 utilization for non-equilibrated reaction. Fuel 2014;115:357–65. https://doi.org/10.1016/j.fuel.2013.07.035.
7. AlZahrani AA, Dincer I. Thermodynamic and electrochemical analyses of a solid oxide electrolyzer for hydrogen production. Int J Hydrogen Energy 2017;42:21404–13. https://doi.org/10.1016/j.ijhydene.2017.03.186.
8. Todic B, Bhatelia T, Froment GF, Ma W, Jacobs G, Davis BH, et al. Kinetic Model of Fischer–Tropsch Synthesis in a Slurry Reactor on Co–Re/Al 2 O 3 Catalyst. Ind Eng Chem Res 2013;52:669–79. https://doi.org/10.1021/ie3028312.
9. Bhutani N, Ray AK, Rangaiah GP. Modeling, Simulation, and Multi-objective Optimization of an Industrial Hydrocracking Unit. Ind Eng Chem Res 2006;45:1354–72. https://doi.org/10.1021/ie050423f.
10. Pratschner S, Hammerschmid M, Müller S, Winter F. Off-grid vs. grid-based: Techno-economic assessment of a power-to-liquid plant combining solid-oxide electrolysis and Fischer-Tropsch synthesis. Chemical Engineering Journal 2024;481:148413. https://doi.org/10.1016/j.cej.2023.148413.

© 2025 by the authors. Licensed to PSEcommunity.org and PSE Press. This is an open access article under the creative commons CC-BY-SA licensing terms. Credit must be given to creator and adaptations must be shared under the same terms. See https://creativecommons.org/licenses/by-sa/4.0/



Systems & Control Transactions

**Research Article - Peer Reviewed Conference Proceeding**
ESCAPE 35 - European Symposium on Computer Aided Process Engineering
Ghent, Belgium. 6-9 July 2025
Jan F.M. Van Impe, Grégoire Léonard, Satyajeet S. Bhonsale,
Monika E. Polańska, Filip Logist (Eds.)

PSE PRESS

# Socioeconomic Impacts and Land Use Change of Integrating Biofuel Production with Livestock Farming in Brazil: A Computable General Equilibrium (CGE) Approach

**Igor L. R. Dias[a,c]*, Matheus S. Lacerda[b], Geraldo B. Martha Jr[c], Terezinha F. Cardoso[d], Ana C. M. Jimenez [d], Tassia L. Junqueira[d], Flávia Barbosa[e], Adriano P. Mariano[a], Antonio Bonomi[d], Marcelo P. Cunha[b]**

[a] Faculdade de Engenharia Química (FEQ), Universidade Estadual de Campinas (UNICAMP), Campinas, SP, Brazil
[b] Instituto de Economia (IE), Universidade Estadual de Campinas (UNICAMP), Campinas, São Paulo, Brazil
[c] Embrapa Digital Agriculture, and Graduate Programs in Energy Systems Planning (UNICAMP, Faculdade de Engenharia Mecânica, FEM) and on Economic Development (UNICAMP, IE), Campinas, São Paulo, Brazil
[d] Brazilian Biorenewables National Laboratory (LNBR), Brazilian Center for Research in Energy and Materials (CNPEM), Campinas, São Paulo, Brazil
[e] INESC TEC, Faculty of Engineering, University of Porto, Porto, Portugal
* Corresponding Author: i261185@dac.unicamp.br.

## ABSTRACT

Sugarcane bioenergy is a reality in Brazil, comprising the production of ethanol and bioelectricity. Sugarcane bioenergy can reduce greenhouse gas (GHG) emissions as compared to fossil fuels. However, there are concerns about the possible implications caused by the expansion of sugarcane production, the displacement of mainly pastureland, but also other croplands, and the potential for indirect land use changes. A promising strategy to enlarge sugarcane bioenergy in Brazil without compromising the cattle industry is to integrate both activities, converting extensive livestock production systems into more intensive ones. The objective of this study is to model and evaluate the socioeconomic impacts and land use change considering the expansion of ethanol production in two scenarios. The first scenario, referred to Business as Usual (BAU), comprises of sugarcane bioenergy and extensive livestock production, without any integration between the two. The second scenario, Integrated Sugarcane-Bioenergy and Livestock (ISBL) in Brazilian agriculture, considers the integration between these activities. To achieve this goal, a computable general equilibrium (CGE) model for the Brazilian economy was implemented. The Brazilian input-output matrix (main data for the model) was estimated for 2021. The closure and the shocks were set to 2031, with an estimated increase of 75% in ethanol production. Additionally, a technological efficiency gain of 5% was considered for the livestock sector within the ISBL system. Our modeling results show that the ISBL scenario is economically more efficient, as a higher gross domestic product and output level were obtained. The aggregate employment level of the economy also increased. Even considering that the integration of sugarcane bioenergy and livestock production took place only in these activities, positive socioeconomic impacts were noticed across other sectors of the economy.

**Keywords**: Ethanol, Biomass, Modelling and Simulations, Renewable and Sustainable Energy, Energy Policy

## 1 INTRODUCTION

The increasing global pressure to reduce greenhouse gas (GHG) emissions and increase sectors' efficiency have driven significant transformations in energy consumption patterns and production models. In this context, biofuels emerge as a strategic solution, particularly ethanol, whose use can reduce up to 90% of $CO_2$ equivalent emissions compared to gasoline [1]. However, the expansion of biofuel production in Brazil faces complex challenges, ranging from direct environmental impacts, such as those related to the intensive use of

agrochemicals and biomass burning, to indirect ("leakage") impacts, such as the displacement of traditional agricultural activities with potential pressures on native ecosystems and to food security [2].

The fulfillment of international emission control agreements is directly linked to reducing deforestation in Brazil, as the agricultural and land-use sectors are the main contributors to GHG emissions in the country, accounting for ca. 75% of Brazil's emissions in 2021 [3]. Indirect land use changes (ILUC), for example driven by ethanol expansion, are a point of consideration, as they might pose pressures to expand deforestation in the Cerrado and Amazon biomes, compromising the achieved levels of GHG emission reductions in addition to the impacts to biodiversity and the environment. Also, displaced livestock and agricultural activities may face output constraints, jeopardizing economic output, employment levels, and food security. In this context, public and private initiatives targeting sustainable intensification approaches have gained relevance and are creating opportunities to transform the externalities of agricultural production into economic, social, and environmental advantages.

Thus, expanding biofuel production, combining the environmental benefits of being a cleaner fuel with the possibility of reducing environmental impacts, becomes a key strategy for Brazil. The integration of sugarcane production with livestock and bioenergy can enhance the efficient use of existing pasture areas and potentially recover degraded pastures, without compromising the level of production.

The integration of biofuel production with livestock farming offers several advantages to the Brazilian economy. Among them, it allows for the use of existing infrastructure and the production of co-products from biorefinery, contributing to the reduction of feeding costs for confined livestock and, at the same time, reducing the need for new areas for raising animals. This allows producers to diversify their activities and maximize the use of their land, creating a more sustainable and efficient economic cycle. Also, backward and forward spillover effects are expected in this process, benefiting other sectors in the economy.

Therefore, the main research question to be addressed in this work is expressed as follows: what are the socioeconomic and land use impacts of the expansion of ethanol production in Brazil, and how does this transformation potentially influence the production levels of the main agricultural sectors, the gross domestic product (GDP), and employment in the country?

## 2 METHODS

The method adopted in this study is based on the development and application of a Computable General Equilibrium (CGE) model for the Brazilian economy, implemented using the GEMPACK v.12 interface with the MINIMAL version [4]. The following key assumptions establish the fundamental framework for the analysis, providing a clear foundation for projecting the effects of ethanol production expansion:

- *Period under analysis:* The study considered a 10-year period, given the fact that the effects of the integration between sugarcane production for bioenergy and livestock farming, as well as changes in land use and agricultural practices, involve costs and require more complex planning, which demands a longer time horizon. Thus, it was focused on the projections and impacts of ethanol production expansion from 2021 (admitted as the first recovered economic year after the Covid-19 crisis in 2020) until 2031. Ethanol expansion followed RenovaBio's target as a policy scenario [5].
- *Input-Output Matrix:* The study utilized the Input-Output Matrix (IOM) for 141 sectors of the Brazilian economy, providing a detailed analysis of the economic impacts of ethanol production expansion across various productive sectors and supply chains. The IOM was estimated for the year 2021, ensuring an up-to-date representation of sectoral interactions.
- *Ethanol Production:* The study considered a 75% increase in hydrated ethanol production, according to the projections established by RenovaBio [5]. This increase was modeled within the IOM, evaluating the effects on other sectors of the economy.
- *Gasohol Usage:* For analytical purposes, it was assumed that there would no substantial changes in the use of gasohol, allowing the isolation of the impacts of expanding hydrated ethanol production, without external interference related to changes in gasohol usage policies.
- *Total Land in Brazil:* Given the government's commitment to achieving zero deforestation by 2030, it is assumed, as a limiting condition, that no additional land beyond the total available in 2021 will be accessible to any economic sector. Consequently, the expansion of ethanol production will not lead to new deforestation or conversion of native vegetation areas. On the contrary, its expansion should be based only on displacing other agricultural activities, as degraded pastureland [6].

### 2.1 Description of scenarios

To analyze the impacts of expanding ethanol production in Brazil, two distinct scenarios were defined: the

BAU (Business as Usual) Scenario and the ISBL (Integrated Sugarcane-Bioenergy and Livestock) Scenario. Each of these scenarios reflects different development trajectories, considering the growth assumptions of the ethanol sector, land use, and interactions with other economic activities, such as livestock farming.

### 2.1.1 The BAU Scenario

This scenario assumes continuity of the current model, with bioenergy production from sugarcane and extensive livestock farming without integration between the activities, representing the most likely production pattern in Brazil.

### 2.1.2 The ISBL Scenario

This scenario proposes the integration of sugarcane production for bioenergy with livestock farming, aiming at more efficient land use and intensification of production. It is assumed that all the released pasturelands will be used for sugarcane production.

## 2.2 Technological efficiency change

To estimate the change in technological efficiency between a representative cattle management system in Brazil and an integrated system, we analyzed the variation in total production cost per carcass between the two models. It was assumed that the unit total cost serves as a good technological indicator, as it reflects the use of primary factors (land, labor, and capital), input consumption, and productivity.

Brazilian cattle farming in 2021 is characterized by the following data: pastureland covers 161.7 million hectares [7]; the total cattle herd consists of 224.6 million heads, with 27.7 million slaughtered annually [8]; among these, 6.5 million are finished in feedlots [9]. Annual beef production reaches 7.456 million tons of carcass equivalent. Based on these figures, the estimated average stocking rate in Brazil is 1.3 heads per hectare. Additionally, it was assumed that conventional management in Brazil involves pasture renewal every five years.

The ISBL system, on the other hand, consists of a first-generation ethanol plant with vinasse biodigestion for electricity generation [10-12]. The selected plant capacity was 4 million tons of sugarcane per year (4MTC/year), which is considered close to the optimal capacity for the biorefinery [13]. This corresponds to a sugarcane plantation area of 64.5 thousand hectares and an annual ethanol production of 345 million liters. Furthermore, it was assumed that soybeans are grown during sugarcane reform and processed at the plant, with by-products such as soybean meal used in animal feed. It was also assumed that all cattle are finished in feedlots, leading to an annual beef production of 60 thousand tons of carcass equivalent [13].

Based on these data and assumptions, production costs were estimated using a techno-economic model developed by Embrapa Digital Agriculture. The estimated cost for the conventional Brazilian system, considering an exchange rate of 1 USD = 6 BRL and a historical average of key input prices in the model, was 3.2 USD/kg of carcass equivalent. In the integrated system, this cost was lower, reaching 2.8 USD/kg of carcass equivalent. When accounting for the total carcass production in each system, this cost variation translates into a -5% difference, indicating an improvement in technological efficiency in the integrated system compared to the conventional one.

## 2.3 Closure of the General Equilibrium Model

For both scenarios, exogenous variables were defined for the general equilibrium model closure, as presented by Horridge (2001) [4]:

- Exchange rate (local currency/foreign currency);
- Wage rate, adjusted by the Consumer Price Index (CPI);
- Gross rate of return;
- Total land area available;
- Ordinary change in the import tax rate;
- Ordinary change in the domestic tax rate, except for the hydrated ethanol sector;
- Use of composite goods by the investment sector;
- Use of composite goods by the government;
- World prices, measured in foreign currency;
- Quantity shift in foreign demand;
- All primary factors augmenting technical change;
- Industrial production of hydrated ethanol and gasohol.

As established, a 75% shock in hydrated ethanol production was applied to both scenarios. In addition to this initial shock, a sensitivity analysis considering variations relative to the original shock of ±50% (e.g. 37.5% and 112.5% range) was modeled. Based on these results, the mean and standard deviation were calculated. Using Chebyshev's theorem, a confidence interval of 88.9% was determined, considering three standard deviations [14].

In the ISBL scenario, in addition to the hydrated ethanol shock, an additional -5% shock was applied to all primary factors augmenting technical change in the livestock sector, as previously estimated. Furthermore, in ISBL, land allocated to agricultural crop sectors was defined as exogenous, replacing the ordinary change in the domestic tax rate for these sectors, which became endogenous.

# 3 RESULTS

In the analysis of the results, the percentage variations in primary factors, total output, household consumption, exports, and domestic taxes and macoeconomics were assessed for key sectors of the Brazilian economy directly related to the study. The analysis was conducted for the BAU and ISBL scenarios, with the difference between them (ISBL – BAU) referred to as Delta.

## 3.1 Primary factors (land, capital, and labor)

The projected increase in ethanol production directly impacts Brazilian agriculture. To assess the effects of this growth on primary factors in the sector, we analyzed changes in sugarcane, corn, soybean, and livestock production, which account for the largest land area usage in the country (Figure 1).

In the BAU scenario, the expansion of sugarcane cultivation required a reduction in land used by other agricultural sectors, even though in different proportions (Figure 1A). This shift highlights the ongoing trade-off between biofuel production and food supply. Although the percentage variations appear small, particularly for corn and soybeans, their absolute impacts are significant.

In the ISBL scenario, there was a more pronounced reduction in land allocated to livestock, a direct consequence of increased efficiency through the adoption of cattle confinement in integrated systems. The freed-up land was almost entirely redirected to sugarcane production without affecting the areas allocated to other crops, which remained constant in the model closure. Additionally, the ISBL system required less land for sugarcane cultivation compared to BAU, likely due to improved efficiency in other primary factors within the sector (Figures 1B and 1C).

The increase in ethanol production also led to a higher demand for labor and capital in the sugarcane sector in both scenarios, with a slightly greater increase in ISBL compared to BAU (Figures 1B and 1C). A similar trend was observed for the corn and soybean sectors, although the rise in primary factors was more pronounced in the ISBL scenario. For the livestock sector, variations in these factors were minimal in both scenarios. However, in ISBL, the variation was even smaller, with a negative impact on capital stock, reflecting improvements in the sector's technological efficiency.

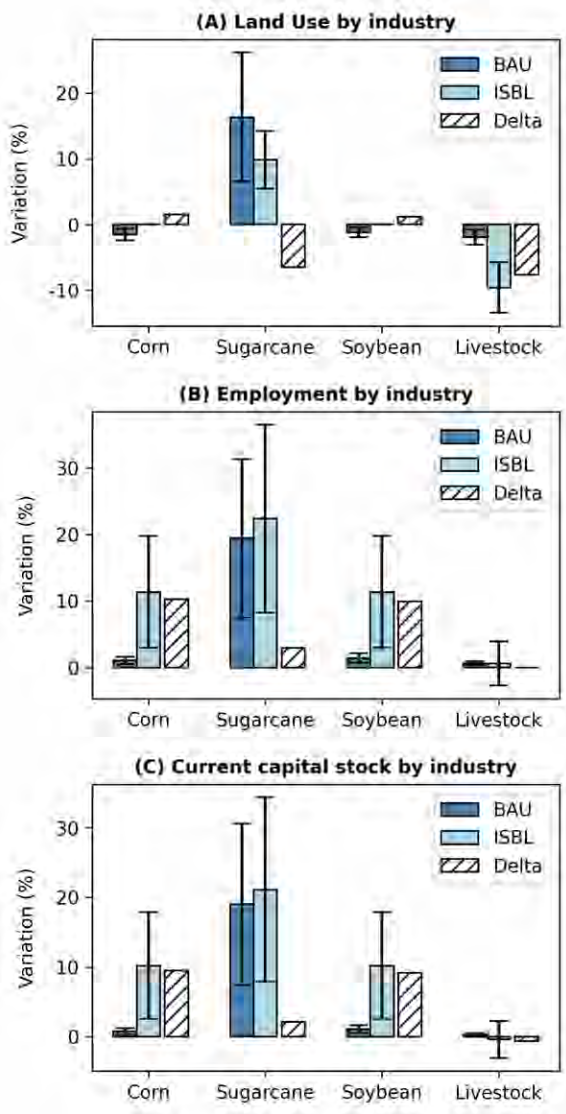



**Figure 1.** Variation in the primary factors of some sectors of the economy. For BAU and ISLB, the 89% confidence interval is indicated.

## 3.2 Total output

Another important aspect of the general equilibrium analysis is the total output across sectors (Figure 2). In addition to sugarcane, corn, soybean, and livestock sectors, the analysis also included beef production and certain fuels, such as gasoline A and anhydrous ethanol. The production of these sectors, along with many others, increased in the scenario projecting a 75% expansion of hydrated ethanol. While the difference between ISBL and BAU scenarios is small for sugarcane production, it becomes more pronounced in other sectors, particularly for corn, soybeans, and beef.

Furthermore, an increase in the production of other fuels is observed, likely as a consequence of the higher productive use in other economic sectors that require these fuels in their pure form.

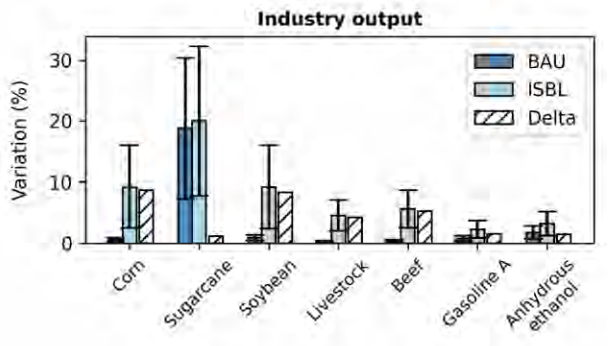



**Figure 2.** Variation in total production in some sectors of the economy.

## 3.3 Household consumption and exports

Household consumption in the beef sector showed a significant increase in the ISBL scenario, while it remained practically unchanged in BAU (Figure 3A). On the other hand, the consumption of gasoline A and anhydrous ethanol decreased in both scenarios, with a more pronounced reduction in ISBL. This decline is likely explained by the increase in exports of these fuels (Figure 3B).

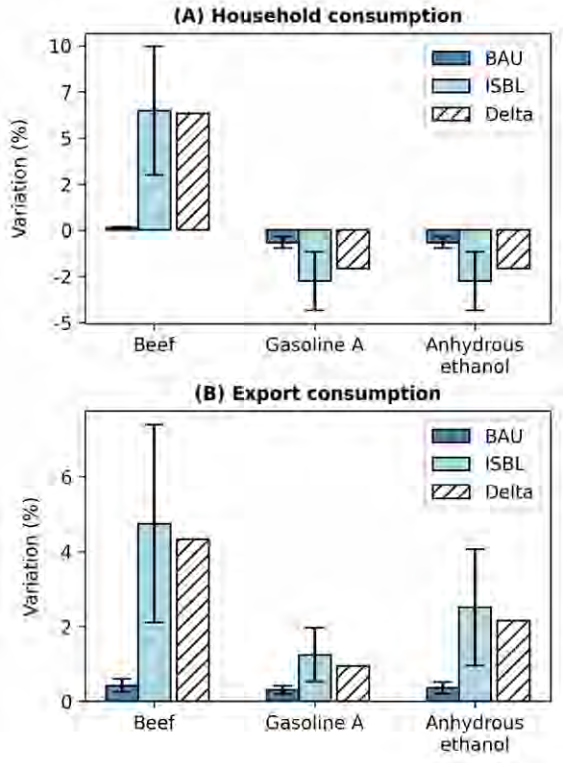



**Figure 3.** Variation in household (A) and export consumption (B) in some sectors of the economy.

## 3.4 Domestic rate taxes

To facilitate the increase in hydrated ethanol production, domestic tax rates on this product were treated as endogenous variables in the ISBL scenario. Consequently, a reduction in the ordinary tax rate of -0.47 would be required for hydrated ethanol in both the BAU and ISBL scenarios. In the ISBL scenario, to validate the premise that sugarcane expansion would occur exclusively over pastureland, it would also be necessary to reduce taxes on agricultural products (Table 1).

**Table 1.** Variation of ordinary change in the domestic tax rate in some sectors of the economy.

| Industry sector | Mean | Confidence interval |
|---|---|---|
| Hydrated ethanol | -0.47 | [-0.62, -0.32] |
| Corn | -0.16 | [-0.28, -0.04] |
| Soybean | -0.17 | [-0.29, -0.05] |

## 3.5 Macroeconomic results

Figure 4 presents the macroeconomic results of the BAU and ISBL systems after the shocks were applied, considering the proposed closure. In both scenarios, there was an increase in aggregate employment, real GDP, real household consumption, export volume index, and import volume index (Figure 4). However, when comparing the scenarios, ISBL exhibited a more significant increase than BAU.

These results suggest that a policy of expanding ethanol production over time could be beneficial to the Brazilian economy under the tested conditions and assumed premises. Additionally, it is noteworthy that land prices increased more in the ISBL scenario (18%) compared to BAU (4%).

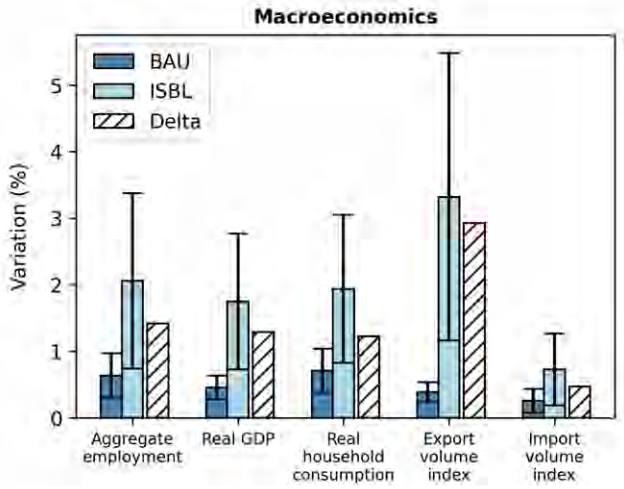



**Figure 4.** Variation in macroeconomic parameters.

# 4 CONCLUSIONS

In comparison to the business-as-usual (BAU) scenario, the ISBL scenario, under the evaluated conditions

and assumptions, demonstrates higher economic efficiency and overall positive effects to other sectors.The integrated scenario makes more rational use of production factors, leading to an increase in productivity driven by technical efficiency gains. Additionally, the ISBL scenario stands out for presenting more substantial real economic growth, reflected in the increase in GDP. This scenario illustrates the potential of an initiative that can contribute to mitigating the impacts on native vegetation areas, showcasing significant potential for the recovery of degraded pastures in Brazil.

Future research is expected to disaggregate the cattle farming sectors in order to distinguish between confinement and pasture systems relative to the broader livestock sector. Furthermore, incorporating greenhouse gas emission levels from each of the economic sectors included in the model will be crucial for constructing a more complete and detailed emissions balance. This approach will allow for a more precise and comprehensive assessment of the environmental impacts associated with each production system, contributing to the understanding of their ecological and economic implications.

Finally, this study demonstrated that the expansion of ethanol production in Brazil, while representing a significant opportunity to strengthen the energy and agricultural sectors, also presents complex challenges to socioeconomic and environmental aspects. The analysis of indirect land use change (ILUC) impacts reveals that the growing demand for ethanol may lead to the intensification of agricultural production, altering the balance between different sectors of the economy and affecting land use in ways that generate both benefits and environmental costs. Additionally, the positive effects on GDP and employment emphasize the opportunities of pursuing and promoting sustainability approaches, balancing bioenergy production with environmental preservation and social well-being. In summary, for Brazil to solidify its position as a leader in ethanol production, it will be essential to adopt strategies that integrate productive efficiency, environmental protection, and social inclusion to ensure a trajectory of sustainable development in the long term.

## ACKNOWLEDGEMENTS

The authors gratefully acknowledge the financial support received from FAPESP (2017/11523-5), CNPq (140029/2022-2), and CAPES (88887.829970/2023-00). Additionally, we extend our appreciation to the team of Embrapa Digital Agriculture for their contribution and support in successfully executing this research project.

## REFERENCES

1. UNICA – União da Indústria de Cana-de-Açúcar e Bioenergia (2025). https://unica.com.br/
2. Sparovek, G.; Maule, R. F.; Burgi, R. Integração cana-pecuária: geração de valor social e ambiental. Visão Agrícola, 5(8), 84–88 (2008).
3. SEEG – Sistema de Estimativas de Emissões e Remoções de Gases de Efeito Estufa (2025). https://seeg.eco.br/
4. Horridge, M. MINIMAL - a Simplified General Equilibrium Model (2001). https://www.copsmodels.com/minimal.htm
5. Empresa de Pesquisa Energética (EPE). Plano Decenal de Expansão de Energia 2031 – Oferta de Biocombustíveis. Rio de Janeiro: EPE (2021). http://www.epe.gov.br/pt
6. Nogueira, G. P.; et al. Supplying the ethanol demand for 2030 in Brazil as a land-based climate change mitigation alternative: Implications on greenhouse gases emissions. Science of The Total Environment, 951, 175782 (2024)
7. MAPBIOMAS. Plataforma MapBiomas: uso e cobertura (2025). https://plataforma.brasil.mapbiomas.org
8. IBGE – Instituto Brasileiro de Geografia e Estatística. PPM Pesquisa da Pecuária Municipal 2021 (2021).
9. Anualpec. Anualpec 2022: Anuário da pecuária brasileira (2022).
10. Jimenez, A. C. M.; et al. Different approaches to sugarcane vinasse use and management in Brazil: A technical, economic, and environmental analysis. Biomass and Bioenergy, 193, 107603 (2025).
11. Bonomi, A.; et al. Virtual Biorefinery – An Optimization Strategy for Renewable Carbon Valorization. *Springer International Publishing*, Switzerland (2016).
12. Junqueira, T. L.; et al. Techno-economic analysis and climate change impacts of sugarcane biorefineries considering different time horizons. Biotechnology for Biofuels, 10(1) (2017).
13. Dias, I. L. R.; et al. Economic Optimization of Sugarcane-livestock Integration for Bioenergy Expansion in Brazil. Chemical Engineering Transactions, 109, 151–156 (2024).
14. Burfisher, M. E. Introduction to computable general equilibrium models. Cambridge University Press (2021).

© 2025 by the authors. Licensed to PSEcommunity.org and PSE Press. This is an open access article under the creative commons CC-BY-SA licensing terms. Credit must be given to creator and adaptations must be shared under the same terms. See https://creativecommons.org/licenses/by-sa/4.0/



Systems & Control Transactions

**Research Article - Peer Reviewed Conference Proceeding**
ESCAPE 35 - European Symposium on Computer Aided Process Engineering
Ghent, Belgium. 6-9 July 2025
Jan F.M. Van Impe, Grégoire Léonard, Satyajeet S. Bhonsale,
Monika E. Polańska, Filip Logist (Eds.)

PSE PRESS

# Optimal Hydrogen Flux in a Catalytic Membrane Water Gas Shift Reactor

**Nabeel S. Abo-Ghander[a], Filip Logist[b]**

[a] Department of Chemical Engineering, Interdisciplinary Center for Refining & Advanced Chemicals, King Fahd University of Petroleum & Minerals, Dhahran 31261, Saudi Arabia.
[b] BioTeC+, Department of Chemical Engineering, KULeuven, Gebroeders de Smetstraat 1, 9000 Ghent, Belgium.
* Corresponding Author: naboghander@gmail.com.

## ABSTRACT

A one-dimensional homogeneous reactor model for a cocurrent flow nonadiabatic catalytic membrane reactor operating water gas shift reaction (WGSR) is developed. The model is used to predict the performance of the reactor and estimate the optimal hydrogen flux profiles required to maximize the CO conversion, and control the temperature rise due to the exothermicity. Under the optimized condition, the secured optimal hydrogen flux is found to be a bang-bang type suggesting constructing reactors of different hydrogen permeabilities. To control the reactor temperature, the activity of the reaction side is diluted by distributing axially certain fractions of inert solid, i.e. 0.35, 0.45 and 0.50. The total volume fraction of the inert solid required to maintain the temperature at 320°C (593.15 K) is 0.50 and the profile is obtained to be a singular-arc type with an observed maximum activity at the reactor inlet.

**Keywords**: Modelling, Optimization, Reaction Engineering, Simulation, Membranes, water gas shift reaction, membrane reactor, bang-bang controller, singular-arc controller, optimal hydrogen flux, inert solid distribution

## INTRODUCTION

Hydrogen is considered to be a potential future replacement for fossil fuel [1]. It is produced industrially by steam reforming of hydrocarbons or water gas shift reaction. Both processes are thermodynamically-limited whose conversion is favored by operating the reactions in nonconventional catalytic reactors such as membrane reactors. In membrane reactors, the $H_2$ production can be boosted via in-situ separation which takes place when hydrogen permeative membranes are installed. Two main types of catalysts have been developed over the years for the water gas shift reaction. The first one, which has been used for many years, is an iron–based catalyst on which CO is oxidized in the presence of steam to hydrogen and $CO_2$ at a temperature range of 350–500°C [2]. This catalyst is known to be a high-temperature water gas shift reaction catalyst. The second one is a copper-based catalyst on which the reaction is operated at a temperature range of 150-250°C, and the catalyst is referred to as a low-temperature water gas shift reaction catalyst [3]. For these two types of catalysts, various mathematical reaction rate expressions were developed based on power-law kinetic models, Eley–Rideal, and Langmuir–Hinshelwood kinetic models [4]. An excellent review with a summary of different kinetic models is given by Saeidi et al [5] and Shahid et al [1].

As far as the reactor modelling is concerned, numerous mathematical models were proposed for the water gas shift reactor accounting for the changes in molar flowrates of species, reactor temperature and pressure with different degrees of sophistication [6-8]. Those models were used to conduct parameter sensitivity analysis, predictions, and optimization of reactor performance.

In this work, the theory of optimal control is applied to a cocurrent flow nonadiabatic catalytic membrane WGSR to optimally design for suitable hydrogen fluxes required to maximize the CO conversion and controlling the temperature inside this reactor. This problem has not been yet addressed in the literature for membrane reactors and the results presented in this study can greatly assist in providing rigorous decisions about the proper set-up of the reactor configurations required to achieve the set goals.

## KINETICS AND REACTION RATE LAW

Water gas shift reaction is described by the following stoichiometric equation:

$$CO + H_2O \Leftrightarrow H_2 + CO_2 \; \Delta H^0_{298} = -41.1 \frac{kJ}{mol} \quad [1]$$

The reaction is moderately exothermic, reversible, and its conversion can be favored by operating at low temperatures in conversional fixed bed reactors. The kinetic expression of the water gas shift reaction expressed in mol/ (kg cat ×s) on a commercial Cu/ZnO/$AlO_3$ catalyst is given in terms of the component partial pressure as follows [9,10]:

$$r = 82.4 \times 10^3 \, exp\left(-\frac{47400}{RT}\right)\left[p_{CO}p_{H_2O} - \frac{p_{H_2}p_{CO_2}}{K_{eq}}\right] \quad [2]$$

The equilibrium constant can be estimated using:

$$K_{eq} = exp\left(\frac{4577.8}{T} - 4.33\right) \quad [3]$$

## REACTOR CONFIGURATION

The co-current configuration of the catalytic membrane water gas shift reactor utilized in this study is depicted in Figure 1. The reactor is composed of two main concentric tubes separated by a highly selective hydrogen permeative membrane wall extending along the axial distance of the reactor.

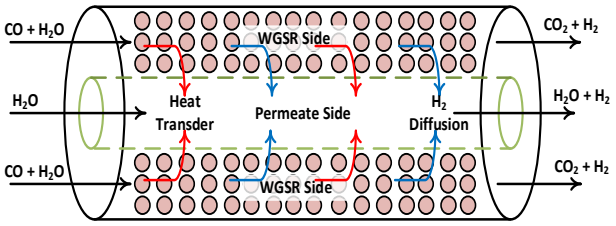



**Figure 1:** Co-current configuration of the catalytic membrane water gas shift reactor.

On the outer side, a copper-based catalyst is used to pack the bed allowing low-temperature water gas shift reaction to take place. The feed to this side is mainly composed of carbon monoxide, steam and inert gases introduced at a temperature of 200°C and a pressure of 1.5 atm. While the reaction takes place in the outer tube, both hydrogen and heat are produced, and exchanged with the permeate side.

On the inner side, pure steam at a temperature of 120°C is introduced. It is used to create an appreciable driving force along the membrane reactor and purge the diffused hydrogen out of the reactor.

## REACTOR MATHEMATICAL MODELLING

The reactor model equations are derived considering the assumptions of steady-state operation of both sides of the reactor, ideal gas behavior, plug-flow reactor model, negligible effect of the catalyst deactivation, adiabatic reactor external wall, negligible diffusional resistances, highly selective hydrogen permeative membranes are installed, the pressure drop on the reaction side is estimated using Ergun's equation, and negligible pressure drop on the permeate side. The governing equations of the reactor are given as:

Mole balance:

$$\frac{dn_i}{dz} = \sigma_i r \rho_s (1-\varepsilon)(1-u_1)A_c - 2\pi R_3 \psi_i u_2 \quad [4]$$

Energy balance:

$$\frac{dT}{dz} = \frac{[-\Delta H(T)]r\rho_s(1-\varepsilon)(1-u_1)A_c - 2\pi R_3 U(T-T') - \sum_{i=1}^{n} 2\pi R_3 \psi_i u_2 \int_{T'}^{T} C_{pi} dT}{\sum_{i=1}^{n} n_i C_{pi}} \quad [5]$$

Pressure drop:

$$\frac{dP}{dz} = -\frac{G}{\rho D_p g_c}\left(\frac{1-\varepsilon}{\varepsilon^3}\right)\left[\frac{150\mu(1-\varepsilon)}{D_p} + 1.75G\right] \quad [6]$$

On the permeate side, the equations are given by:

$$\frac{dn_i'}{dz} = 2\pi R_3 u_2 \quad [7]$$

$$\frac{dT'}{dz} = \frac{2\pi R_3 U(T-T') + \sum_{i=1}^{n} 2\pi R_3 \psi_i u_2 \int_{T'}^{T} C_{pi} dT}{\sum_{i=1}^{n} n_i' C_{pi}'} \quad [8]$$

The boundary conditions are defined at the reactor inlet for the cocurrent configuration as follows:

At $z = 0$:

$$n_i = n_{i0} \qquad T = T_0 \qquad P = P_0 \quad [9]$$

$$n_i' = n_{i0}' \qquad T' = T_0' \quad [10]$$

In the above reactor model equations, two control variables are included, namely the inert solid volume fraction $u_1$ and hydrogen flux $u_2$. The volume inert solid fraction is a dimensionless variable defined as the ratio of the volume of the inert solid to the total solid fraction present on the reaction side, while the hydrogen flux is defined as moles of hydrogen exchanged per unit time per unit surface area. Both variables are determined numerically based on prescribed performance measures. Additionally, the phi parameter $\psi_i$ introduced in the model equations owns a value of one for hydrogen and zero otherwise. The overall heat transfer coefficient $U$ between the reaction side and permeate side is estimated using a composite wall correlation.

## MATHEMATICAL FORMULATION OF THE OPTIMIZATION PROBLEMS

The optimization problems can be stated as follows:

Let $U_1$and $U_2$ be the set of all admissible profiles of solid volume fraction and hydrogen flux, respectively.

The optimization problems encountered in this study is to compute $u_1(z) \in U_1$ and/or $u_2(z) \in U_2$ such that a performance measure is minimized without violating the governing model equations of the catalytic membrane WGSR and/or any other specified equality or inequality constraints.

Three objective functions are considered in this study for the membrane catalytic reactor and defined as conversion of carbon monoxide achieved in the reaction side, temperature cost at the reactor exit, and variation cost of the temperature inside the reactor with respect to a set temperature, i.e. 320°C. The mathematical representation is given as:

$$J_1(x,u_1,u_2) = \frac{n_{CO}^f - n_{CO}}{n_{CO}^f} \quad [11]$$

$$J_2(x,u_1,u_2) = [T(L) - T_R]^2$$

$$[12] J_3(x,u_1,u_2) = [T(L) - T_R]^2 + \int_0^L (T - T_R)^2 dz \quad [13]$$

The mathematical formulation of the optimization problem can be stated as follows:

$$\underset{x,u_1,u_2}{Min}\ J_i(x,u_1,u_2) \qquad i \in \{1,2,3\} \quad [14]$$

Subject to:

$$F(x,u_1,u_2) = 0 \quad [15]$$

The conversion of carbon monoxide is multiplied by "-1" to convert the maximization problem to minimization in Eq [11]. Eq [15] is a vector representing the conservation nonlinear algebraic equations of the reactor model equations obtained by discretizing the ordinary differential equations using Hermite-Simpson collocation technique.

The hydrogen flux along the WGSR expressed in mol/(m$^2$×s) is the main optimal profile to be determined. The bound is set to be:

$$0.5 \le u_2 \le 8.0 \quad [16]$$

The hydrogen recovery defined as cumulative molar flowrate of hydrogen diffused to the permeate side with respect to CO fed to the reactor is controlled by setting a hard constraint given by the following nonlinear algebraic equation:

$$n'_{H_2}(L) - n^R_{H_2} = 0 \quad [17]$$

The hydrogen recovery is varied in this study between two limits, i.e. 1.25 and 1.75 mol/s.

The inert solid volume fraction is introduced to the optimization problems in order to control the temperature inside the reactor. The total volume fraction of the inert solid is defined along the dimensionless axial distance as:

$$\bar{u}_1 = \int_0^{1.0} u_1(\zeta) d\zeta \quad [18]$$

The total volume fraction of the inert solid is varied assuming the values of 0.35, 0.45 and 0.50 and the bound on the solid volume fraction is given by:

$$0.0 \le u_1 \le 1.0 \quad [19]$$

A summary of the optimization problem addressed in this work and the reactor design and operational parameters are given in Tables 1 and 2, respectively. The optimization problems are solved numerically using SNOPT.

**Table 1:** Optimization problem set-up

| Problem | Case No. | Objective function | Control variables | $H_2$ recovery constraints |
|---|---|---|---|---|
| 1 | 1 | $J = J_1$ | $H_2$ flux | NA |
| | 2 | $J = 0.01J_1 + 0.99J_2$ | $H_2$ flux | NA |
| | 3 | $J = J_2 + J_3$ | $H_2$flux | NA |
| 2 | 1 | $J = J_1$ | $H_2$ flux | 1.25 mol/s |
| | 2 | $J = J_1$ | $H_2$ flux | 1.75 mol/s |
| 3 | 1 | $J = J_2 + J_3$ | $H_2$ flux & inert volume fraction | NA |

**Table 2:** Reactor design and operating parameters

| Parameter | Numerical value | Unit |
|---|---|---|
| Reactor length | 3.0 | m |
| Reactor inner radius | 0.05 | m |
| Stainless steel thickness | $2.0\times10^{-3}$ | m |
| Membrane thickness | $1.0\times10^{-6}$ | m |
| Reactor outer radius | 0.08 | m |
| Diameter of catalyst particles | $6.0\times10^{-3}$ | m |
| Catalyst density | 2500 | Kg/m$^3$ |
| Bed porosity | 0.55 | -- |
| *Reaction Side* | | |
| Feed molar flowrate | 5.0 | mol/s |
| *Feed composition* | | |
| CO | 0.2749 | -- |
| $H_2O$ | 0.3165 | -- |
| $CO_2$ | 0.1198 | -- |
| $H_2$ | 0.2686 | -- |
| $N_2$ | 0.0202 | -- |
| Feed temperature | 473.15 | K |
| Feed pressure | 1.5 | atm |
| *Permeate side* | | |
| Steam molar flowrate | 25.0 | mol/s |
| Steam feed temperature | 393.15 | K |
| Steam feed pressure | 1.0 | atm |

## Without catalyst dilution

For the first optimization problem, the objective functions considered were the conversion of CO in the reactor, a linear combination of the conversion of CO and

the exit temperature cost with a weight of 0.99 and 0.01, and a temperature cost combining the temperature inside the reactor and at the exit point. The optimization problems were solved for the optimal $H_2$ flux profiles with no constraints on the $H_2$ recovery.

In Figure 2, the conversion of carbon monoxide and the equilibrium conversion are plotted against the dimensionless axial distance for all scenarios. It is observed that the CO conversion inside the membrane reactor is higher than those of the equilibrium due to the hydrogen permeation. The maximum conversion observed is when the objective function is the conversion of CO, while the second highest is observed when the temperature of the reactor is controlled inside the reactor and at the exit. The reduction in CO conversion in the reactor when the temperature is controlled, is due to the low $H_2$ recovery, i.e. less $H_2$ diffused from the reaction side to the permeate side. In all three optimization scenarios, the estimated reactor conversions are >~ 95%.

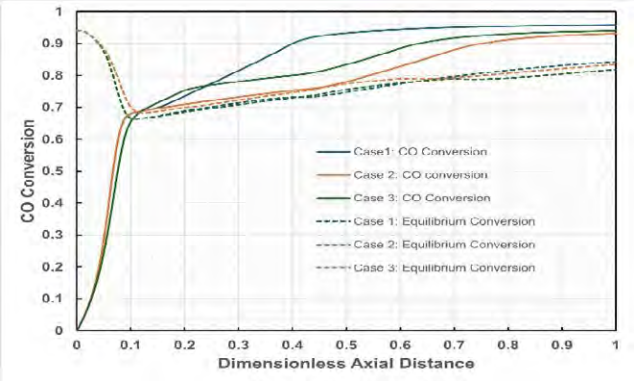



**Figure 2:** CO conversion and equilibrium conversion profiles for the cases of maximizing CO conversion, minimizing exit and reactor temperature.

The optimal hydrogen flux profiles expressed in mole/($m^2$×s) are plotted vs. the dimensionless reactor distance in Figure 3 for all optimization problems.

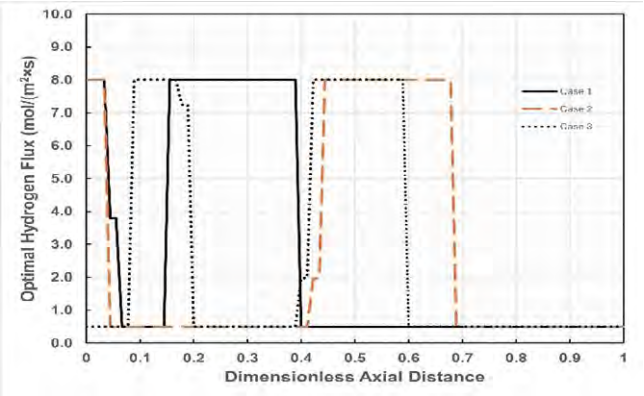



**Figure 3:** Optimal $H_2$ flux profiles based on maximizing CO conversion, minimizing exit and reactor temperature.

All the three control profiles computed are **bang-bang** type with no singular intervals due to the fact that the Hamiltonian for the reactor depends affinely on the hydrogen flux. The hydrogen flux alternates between 8.0 mole/ ($m^2$×s) and 0.5 mole/ ($m^2$×s) representing two types of membrane reactors with high and low $H_2$ permeation rates achieved by the installation of $H_2$ membranes with different fluxes. To maximize the conversion of CO, it is observed that maximum hydrogen flux is required at the reactor inlet, while minimum hydrogen flux is required when the reactor temperature is to be controlled. At the reactor outlet, a low hydrogen flux is required as the conversion of CO approaches completion.

In Figure 4, the temperature profiles on the reaction side are plotted along the dimensionless axial distance. The reactor temperature increases due to the reaction, then decreases due to heat exchange with the permeate side. For a set temperature of 320°C (593.15K), It is observed that the maximum deviation is depicted when the CO conversion is maximized. However, this deviation decreases as the objective function is redefined to include the temperature deviation terms in cases 2 and 3.

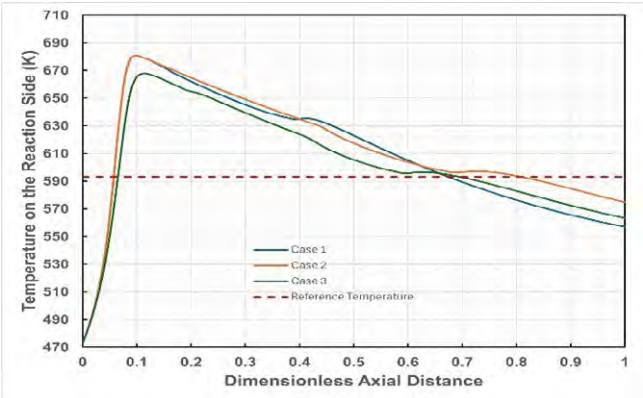



**Figure 4:** Temperature profiles based on maximizing the CO conversion, minimizing exit and reactor temperature.

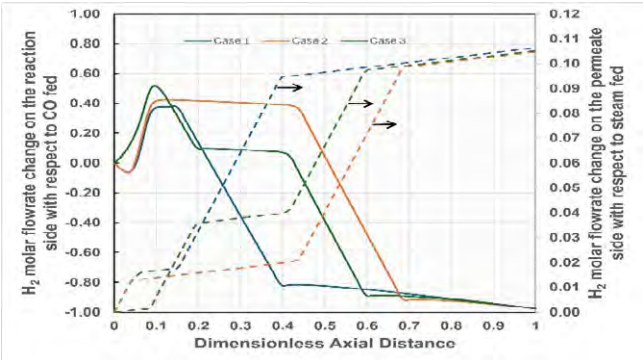



**Figure 5:** Change in $H_2$ molar flowrate profiles on the reaction side and permeate.

The fractional change of the molar flowrates of hydrogen on the reaction side and the permeate side are plotted against the dimensionless distance in Figure 5.

On the reaction side, the molar flowrate of hydrogen decreases within the fractional length of ~0.05 due to the maximum hydrogen flux of 8.0 mol/($m^2$×s) for the case of maximizing the CO conversion, increases due to production by the reaction, then decreases due to the diffusion. When reactor temperature is controlled, hydrogen is maintained inside the reaction side as much as possible as this suppresses the progress of the reaction. On the permeate side of the reactor, it is observed that the sharpest and fastest change is obtained when the CO is maximized where most of hydrogen is recovered within 0.40 fractional length.

In Figure 6, the conversion of CO is plotted along the dimensionless axial distance for unlimited hydrrogen recovrery, 1.25 mol/s, and 1.75 mol/ s. In all cases, the conversion of the carbon monoxide increases along the reactor with a significant difference for the case where the $H_2$ recovery is maximum, i.e. no constraint is set on $H_2$ recovery.

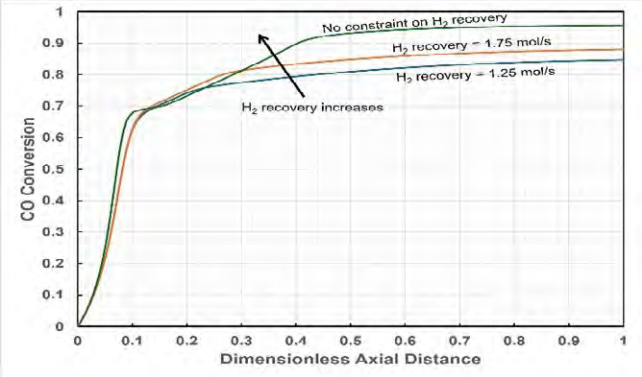



**Figure 6:** Influence of $H_2$ recovery on the CO conversion.

In Figure 7, the molar flowrate of diffused $H_2$ on the permeate side is plotted against the dimensionless axial distance.

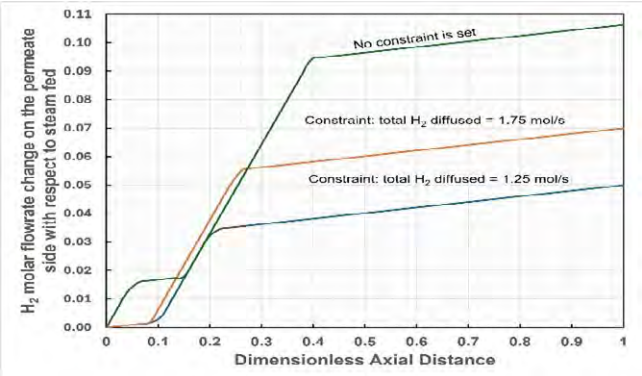



**Figure 7:** Influence of hydrogen recovery on hydrogen flowrate on the permeate side.

All curves show that $H_2$ molar flowrate increases inside the permeate side due to the flux through the membrane but the one with no $H_2$ flux limitation gives the highest $H_2$ recovery in the membrane reactor.

## With catalyst dilution

To control the temperature inside the reactor so that it does not exceed 320°C (593.15K), an inert solid is axially distributed. The distribution profiles of the inert solid for total average amounts of 0.35, 0.45 and 0.50, and the corresponding CO conversion profiles are shown in Figure 8.

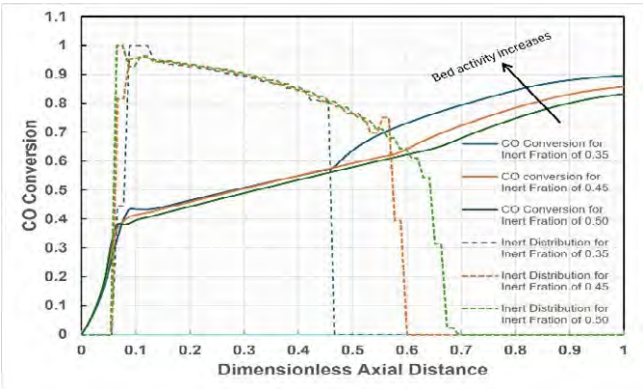



**Figure 8:** Optimal solid inert distribution and the corresponding CO conversion profiles.

At the reactor entrance, it is required to have the catalytic bed fully active indicated by zero inert solid volume fraction. This causes a ramp in the reactor temperature from the feed temperature to the required set temperature as shown in Figure 9.

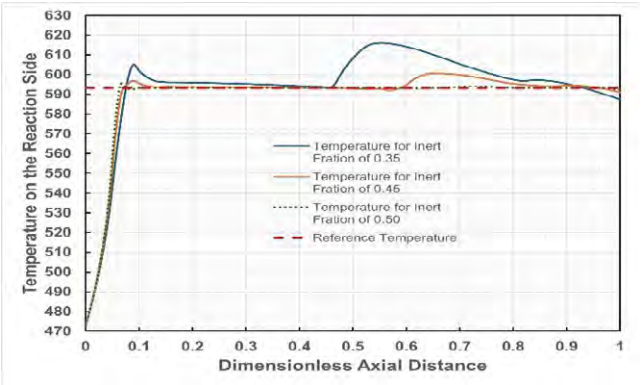



**Figure 9:** Temperature profiles for total inert solid fraction of 0.35, 0.45 and 0.50.

A peak is then formed at which the bed is made to be inactive by setting the volume fraction of the inert solid to unity. This causes the generated reaction heat rate to be zero and only heat exchange between the reaction side and the permeate side takes place. After that, a decreasing inert solid fraction profile is utilized to adjust the temperature to get close to 320°C. The average solid volume fraction of 0.35 gives the highest temperature

deviation compared to the other two scenarios of 0.45 and 0.50 as most of the inert solid is used to reduce the temperature in the reaction side and none is left to maintain the temperature close to 320°C. The optimal inert solid distribution profiles on the reaction side are a **min-max-singular-min** types recommending the utilization of a catalytic membrane reactor with four activity zones, i.e. fully active bed followed by an inactive bed followed by a mixed catalyst bed and finally an active bed.

## CONCLUSION

A 1D homogeneous steady-state reactor model for a membrane catalytic water gas shift reactor was developed. The model was used to secure the optimal $H_2$ flux required to maximize the yield conversion and controlling the temperature along the reactor axial distance. In addition, the reactor model was used to optimize the distribution of the inert solid required to maintain the temperature of the reactor not exceeding 320°C (593.15K) and eliminating the hot spot formed due to the reaction exothermicity. The maximization of CO conversion requires hydrogen flux to be maximum at the reactor entrance as this shift the thermodynamic equilibrium and achieving higher conversion. The scenario was the opposite when the temperature is to be controlled where minimum hydrogen flux is needed at the reactor entrance so that the reaction progress is suppressed and amount of heat released is minimized, too. The hydrogen optimal flux profile is a bang-bang controller type with five switching points indicating that membrane reactors with different permeability must be used. The inert solid distribution used to control the temperature inside the reactor shows that a singular arc must be implemented where a fully active bed has to be used at the entrance to favor the temperature rise to the set temperature.


## ACKNOWLEDGEMENTS

The Author would like to acknowledge Interdisciplinary Research Center for Refining and Advanced Chemicals, King Fahd University of Petroleum & Minerals, Dhahran, Saudi Arabia for the financial support for this work through Project # INRC2319.


## NOMENCLATURE

$A_c$: cross-sectional area of the reaction side, [m2].
$C_{pi}$: heat capacity of species i (reaction side), [J/(mol×K)].
$C_{pi}^{'}$: heat capacity of species i (permeate side), [J/(mol×K)].
$D_p$: Particle diameter, [m].
$G$: mass velocity on the reaction side, [Kg/(m2×s)].
$n_i$: molar flowrate of species i, [mol/s].
$n_i^{'}$: molar flowrate of species i, [mol/s].
$P$: pressure on the reaction side, [atm].
$P_0$: feed pressure on the reaction side, [atm].
$P^{'}$: pressure on the reaction side, [atm].
$P_0^{'}$: feed pressure on the reaction side, [atm].
$R_3$: external radius of the inner cylinder, [m].
$T$: temperature on the reaction side, [K]
$T_0$: feed temperature on the reaction side, [K]
$T^{'}$: temperature on the reaction side, [K]
$T_0^{'}$: feed temperature on the reaction side, [-]
$u_1$: inert solid profile on the reaction side, [-].
$u_2$: H2 flux profile on the reaction side, [mol/(m2×s)].
$z$: axial distance, [m].
$\sigma_i$: stoichiometric no. of component i, [-].
$\mu$: gas viscosity on the reaction side, [Pa×s].
$\varepsilon$: void fraction of the reaction side, [-].
$\rho$: gas density on the reaction side, [Kg/m3].
$\Delta H(T)$: heat of reaction, [J/ mol].

## REFERENCES


1. Shahid MZ, Farooqi AS, Fajri K, El-Adawy M, Hamdy M, Farooqi AS, Abdelaziz OY, Hossain MM, Nemitallah MA. Clean hydrogen production via sorption enhanced water gas shift reaction: A comprehensive review. Int J Hydrogen Energy 2025; 100:1483–512. https://doi.org/10.1016/J.IJHYDENE.2024.12.400
2. Kumar P, Akpan E, Ibrahim H, Aboudheir A, Idem R. Kinetics and Reactor Modeling of a High Temperature Water−Gas Shift Reaction (WGSR) for Hydrogen Production in a Packed Bed Tubular Reactor (PBTR). Ind Eng Chem Res 2008;47:4086–97. https://doi.org/10.1021/ie071547q
3. Ayastuy JL, Gutiérrez-Ortiz MA, González-Marcos JA, Aranzabal A, González-Velasco JR. Kinetics of the Low-Temperature WGS Reaction over a CuO/ZnO/Al2O3 Catalyst. Ind Eng Chem Res 2005; 44:41–50. https://doi.org/10.1021/ie049886w
4. Mendes D, Chibante V, Mendes A, Madeira LM. Determination of the Low-Temperature Water−Gas Shift Reaction Kinetics Using a Cu-Based Catalyst. Ind Eng Chem Res 2010; 49:11269–79. https://doi.org/10.1021/ie101137b
5. Saeidi S, Fazlollahi F, Najari S, Iranshahi D, Klemeš JJ, Baxter LL. Hydrogen production: Perspectives, separation with special emphasis on kinetics of WGS reaction: A state-of-the-art review. Journal of Industrial and Engineering Chemistry 2017;49:1–25. https://doi.org/10.1016/J.JIEC.2016.12.003
6. Brunetti A, Caravella A, Barbieri G, Drioli E. Simulation study of water gas shift reaction in a membrane reactor. J Memb Sci 2007;306:329–40. https://doi.org/10.1016/J.MEMSCI.2007.09.009
7. Ding OL, Chan SH. Water–gas shift reaction – A 2-D modeling approach. Int J Hydrogen Energy

2008;33:4325–36. https://doi.org/10.1016/J.IJHYDENE.2008.05.087
8. Piemonte V, De Falco M, Favetta B, Basile A. Counter-current membrane reactor for WGS process: Membrane design. Int J Hydrogen Energy 2010;35:12609–17. https://doi.org/10.1016/J.IJHYDENE.2010.07.158
9. Choi Y, Stenger HG. Water gas shift reaction kinetics and reactor modeling for fuel cell grade hydrogen. J Power Sources 2003;124:432–9. https://doi.org/10.1016/S0378-7753(03)00614-1
10. Francesconi JA, Mussati MC, Aguirre PA. Analysis of design variables for water-gas-shift reactors by model-based optimization. J Power Sources 2007;173:467–77. https://doi.org/10.1016/J.JPOWSOUR.2007.04.048.

© 2025 by the authors. Licensed to PSEcommunity.org and PSE Press. This is an open access article under the creative commons CC-BY-SA licensing terms. Credit must be given to creator and adaptations must be shared under the same terms. See https://creativecommons.org/licenses/by-sa/4.0/



Systems & Control Transactions

**Research Article - Peer Reviewed Conference Proceeding**
ESCAPE 35 - European Symposium on Computer Aided Process Engineering
Ghent, Belgium. 6-9 July 2025
Jan F.M. Van Impe, Grégoire Léonard, Satyajeet S. Bhonsale,
Monika E. Polańska, Filip Logist (Eds.)

PSE PRESS

# Solar-Driven Hydrogen Economy Potential in the Greater Middle East: Geographic, Economic, and Environmental Perspectives

**Abiha Abbas[a,b], Muhammad Mustafa Tahir[a], Jay Liu[c], Rofice Dickson[b*]**

[a] Department of Chemical and Metallurgical Engineering, School of Chemical Engineering, Aalto University, P.O. Box 11000, FI-00076 Aalto, Finland
[b] Department of Chemistry & Chemical Engineering, SBA School of Science and Engineering, Lahore University of Management Sciences (LUMS), Lahore, 54792, Pakistan
[c] Department of Chemical Engineering, Pukyong National University, Busan, Republic of Korea
* Corresponding Author: rofice.dickson@aalto.fi

## ABSTRACT

The production of hydrogen from solar energy has surged in popularity in recent years, driven by global initiatives to combat climate change. The Greater Middle East (GME) region, with its favorable geographical position, offers considerable potential for solar-based hydrogen generation. This study combines Geographic Information System (GIS) spatial analysis and the Analytical Hierarchy Process (AHP) with data-driven optimization models to assess land suitability and hydrogen production potential within the region under various scenarios. Findings highlight that water availability is the primary limiting factor, followed closely by road accessibility in determining land suitability for hydrogen production. According to the AHP analysis, only 3.8% of the GME region is highly suitable for such initiatives. Projections suggest that by 2050, the region could achieve a total hydrogen production capacity of up to 1590 Mt/y, potentially avoiding around 4586 Mt of $CO_2$ emissions if all highly suitable land is utilized effectively. Furthermore, the levelized cost of hydrogen (LCOH) is expected to decrease to a range of $2.56-4.17/kg, while green ammonia and methanol costs are anticipated to fall between $0.56-0.79/kg and $0.67-0.93/kg, respectively. This study offers valuable insights that contribute significantly to the global hydrogen discourse and provides essential guidance for policymakers aiming to develop comprehensive strategies for advancing the hydrogen economy in the GME region.

**Keywords**: Optimization, GAMS, Modelling and Simulation, Energy Management, Hydrogen, GIS-MCDM

## INTRODUCTION

The Greater Middle East (GME) region, encompassing the Middle East, Türkiye, Iran, Iraq, North Africa, Central Asia, and the Caucasus, is strategically located within the global sunbelt and possesses significant potential for solar-driven hydrogen production. For these nations, hydrogen presents an opportunity to decrease dependence on fossil fuels while positioning themselves as major exporters to burgeoning hydrogen markets in the EU, Japan, and South Korea, all of which are actively investing in this sector. Saudi Arabia aims to capture 10% of the global hydrogen market by 2030 [1], while Egypt targets a market share of 4-8%. Additionally, various countries in the region have set ambitious hydrogen production goals and initiated several large-scale projects [2]. Despite these advancements, the green hydrogen industry in the GME remains nascent, with uncertainties surrounding the future dynamics of energy trade in this evolving economy. This raises critical questions about which countries will emerge as dominant players and their capacity to meet both local and global hydrogen demands. To address this, it is essential to first estimate the hydrogen production potential of the region by evaluating the

suitable land area, accompanied by a technical, economic, and environmental evaluation for a broader perspective.

Several studies have examined the hydrogen potential of countries in this region, most of which utilize GIS analysis to identify suitable land areas [3,4]. However, accurately estimating hydrogen production potential requires precise data acquisition, such as hourly solar profiles, which are crucial for making informed decisions regarding solar and electrolyzer operations. The complexity of handling such extensive data often limits these analyses to single locations or a few major cities within a country. Furthermore, only a handful of studies address economic factors, and even fewer incorporate an environmental perspective. In this study, GIS-AHP analysis is employed to estimate the amount of suitable land available for hydrogen production. Additionally, data-driven optimization models are utilized to facilitate hydrogen production estimates on a larger scale. This research considers thirty countries in the GME region, evaluating their hydrogen potential alongside key metrics such as the levelized cost of hydrogen (LCOH), levelized cost of ammonia (LCOA), and levelized cost of methanol (LCOM). The potential for $CO_2$ emissions reduction is also assessed through Life Cycle Assessment (LCA) analysis.

## METHODOLOGY

The study area comprises thirty countries with a total area of 29,544,619 km$^2$. A spatial resolution of 1km x 1km was selected, yielding 29.5 million alternatives (locations) as candidates for suitable sites in the GME region. To determine the most appropriate sites, six key criteria were examined: solar resource availability, proximity to water bodies and waterways, topographical slope, land use, and land cover, accessibility to roads, and proximity to protected or restricted areas. An AHP analysis was then performed which compares all these factors pairwise and assigns weights to them based on their relative importance. The AHP extension tool within ArcMap software was employed to guarantee the accuracy of calculations. The consistency matrix and the scores assigned to each criterion are detailed in the supplementary material.

A data-driven optimization model was employed to estimate the annual hydrogen production potential (AHPP) and the LCOH using a two-stage approach. In the initial stage, 100 locations within the GME region were randomly selected, and their hourly solar profiles were sourced from the Global Solar Atlas. The optimization model was then executed for these locations, yielding optimized data such as electrolyzer operating hours, solar-to-electrolyzer ratios, and power loss. Based on the specific power output of these locations, they were categorized into ten distinct intervals. Average feature values for each interval were calculated, leading to the development of a predictive model. In this model, each location is first assigned to an interval based on its PVOUT and subsequently assigned the average feature values corresponding to that interval. All analyses were conducted for the years 2024 and 2050 under two distinct scenarios. In Case 1 (conservative scenario), it was assumed that each location would be utilized only partially, at a rate of 5% for hydrogen projects. This scenario considered a 2 MW solar plant paired with a 1 MW electrolyzer. In Case 2, an optimistic scenario was evaluated, assuming full utilization of the available area (100% coverage). For this scenario, a 38 MW solar plant with a 19 MW electrolyzer was proposed.

The power ($P_{t,m}$) produced by the solar plant at time *t* in month *m* is estimated as follows:

$$P_{t,m} = \emptyset_{t,m} \times C, \quad \forall\, t \in T, \forall\, m \in M, \tag{1}$$

where $\emptyset_{t,m}$ is temporal photovoltaic power output (kWh/kWp) data for the time *t* in the month *m*. $C$ is the capacity of the solar plant and the primary decision variable in the model.

The power supplied to the electrolyzer can neither exceed its capacity ($\delta$) nor fall below its minimum threshold power ($\alpha$). This is modeled as:

$$P_{t,m} \leq \delta, \quad \forall\, t \in T, \forall\, m \in M, \tag{2}$$

$$P_{t,m} \leq B_{t,m}, \quad \forall\, t \in T, \forall\, m \in M, \tag{3}$$

$$P_{t,m} \geq \alpha \times \delta - \varepsilon \times (1 - B_{t,m}), \forall\, t \in T, \forall\, m \in M, \tag{4}$$

where $B_{t,m}$ represent binary variables to allow power to the electrolyzer and $\varepsilon$ represents the upper bound for power to the electrolyzer according to the Big-M formulation method.

The amount of hydrogen ($H_{t,m}$) produced by the electrolyzer at time *t* in month *m* is estimated as:

$$H_{t,m} = \eta \times P_{t,m}, \quad \forall\, t \in T, \forall\, m \in M, \tag{5}$$

where $\eta$ is the electrolyzer efficiency. The total annual hydrogen (*TH*) produced is calculated as follows:

$$TH = \sum_{t,m} H_{t,m} \times d_m, \tag{6}$$

where $dm$ is days in month *m*.

A discounted cash flow model is formulated for the economic analysis. The LCOH in $/kg is defined as:

$$LCOH = \frac{NPV\ of\ total\ costs}{NPV\ of\ hydrogen\ production}, \tag{7}$$

where *NPV* is the net present value. The *NPV* of total costs and hydrogen production is estimated as follows:

$$NPV\ of\ total\ costs = \sum_{n=0}^{20} \frac{CAPEX+OPEX}{(1+r)^n}, \tag{8}$$

where CAPEX and OPEX are the capital and operating expenditure, respectively.

$$NPV\ of\ hydrogen\ production = \sum_{n=1}^{20} \frac{TH}{(1+r)^n}, \tag{9}$$

where *r* is the internal rate of return and *n* is the project life. Notably, *CAPEX* incurs at $n = 0$ (construction period) and *OPEX* and hydrogen production occur at $1 \leq n \leq 20$.

An estimation of the levelized cost of energy (LCOE) was used to estimate the LCOA and LCOM. The total lifecycle costs (TLCC) and annual power (AP) output are estimated using:

$$TLCC = \sum_{n=0}^{20} \frac{CAPEX + OPEX}{(1+r)^n}, \quad (10)$$

$$AP = \sum_{n=0}^{20} \frac{PVOut \times C \times 365}{(1+r)^n}. \quad (11)$$

The LCOE is then calculated using (10) and (11) as:

$$LCOE = \frac{TLCC}{AP}. \quad (12)$$

The raw material and utility demand for each derivative is estimated using process simulations as described in our previous studies [5]. The final cost of the derivatives was estimated using equations (7-9).

All assumed parameters are given in the supplementary material.

To evaluate the environmental impact of hydrogen in comparison to gasoline, a cradle-to-grave life cycle assessment (LCA) was conducted. This study quantified the potential reduction in carbon emissions achievable by transitioning to solar-driven hydrogen as an alternative to gasoline, referring to this reduction as "avoided $CO_2$ potential" for both conservative and optimistic scenarios. For inventory scaling, 1 kg of hydrogen was utilized as the functional unit. The energy produced from hydrogen, estimated at approximately 120–142 MJ/kg, was converted into its gasoline equivalent of 44–46 MJ/kg, based on usage in a typical fuel-efficient vehicle that consumes 70 grams of fuel per kilometer. The LCA was carried out using SimaPro V8.2.3, employing the CML-IA baseline V3.03 characterization method.

## RESULTS & DISCUSSION

GIS analysis indicates that water availability is the primary factor influencing land suitability for hydrogen production in the GME region, particularly in the Middle Eastern and North African countries. Overall, about 57% of land is considered unsuitable for the deployment of solar-driven hydrogen production facilities. Locations within a 10 km radius of water bodies are deemed suitable, while those further away are not. Among the thirty countries studied, fourteen have less than 50% of their land with accessible water resources. Another constraint is the land slope which should be below 5° to facilitate the large-scale deployment of solar panels. Among the thirty countries analyzed, five—Tajikistan, Kyrgyzstan, Lebanon, Armenia, and Türkiye—have less than 50% of their land suitable due to slope constraints. Approximately 86% of the total land in these regions is suitable for solar panel installation.

When selecting optimal sites, the proximity to roads is a crucial constraint to consider since hydrogen needs to be transported to the end user. Any location that is within 500m of roads or more than 10 km away from them was considered unsuitable for this analysis. Overall, approximately 40% of the total land in the GME region is considered unsuitable for hydrogen production when factoring in proximity to roads. Analysis of the land cover and land use data revealed that approximately 88% of the GME region consists of barren or open land, characterized by minimal man-made infrastructure or restricted/protected areas. This type of land is particularly well-suited for hydrogen facilities. As a result, this constraint has not significantly affected the overall suitability of the land for such projects.

The AHP analysis results, illustrated in **Figure 1**, categorized the GME region into four suitability levels" highly suitable, moderately suitable, low suitable, and not suitable. The results revealed that only 3.8% (about 1.2 million $km^2$) of the land is highly suitable, satisfying all the constraints. It is important to highlight that Saudi Arabia distinguishes itself in the region by having the highest number of optimal sites for hydrogen production. In contrast, the Central Asian states face challenges due to their rugged terrain and slope, resulting in a lower availability of suitable land. North African countries, on the other hand, encounter limitations related to water availability, which restricts their land suitability for solar-driven hydrogen production. An exception is Morocco with a high proportion of suitable land.

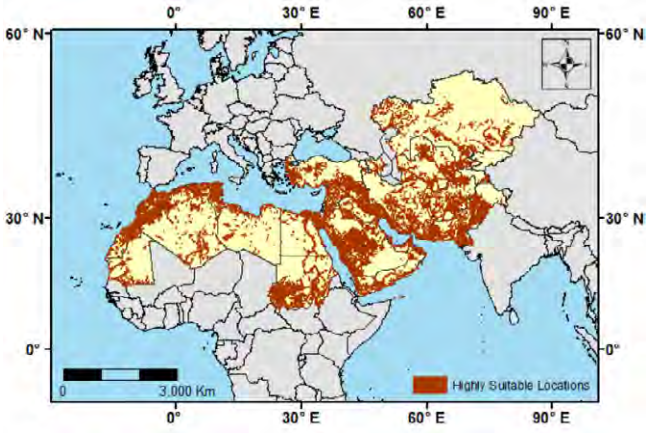



**Figure 1** Highly suitable locations identified through the AHP analysis.

### Hydrogen Production Potential

To estimate the hydrogen production potential of the GME region, the land area identified as highly suitable through the AHP analysis is utilized. Figure 2 illustrates the annual hydrogen production potential for each country in 2024, along with projections for 2025. For smaller nations such as Armenia, Bahrain, Lebanon, and Qatar, the potential remains below 1 Mt/y even under the 100% coverage scenario. In scenario one, all countries

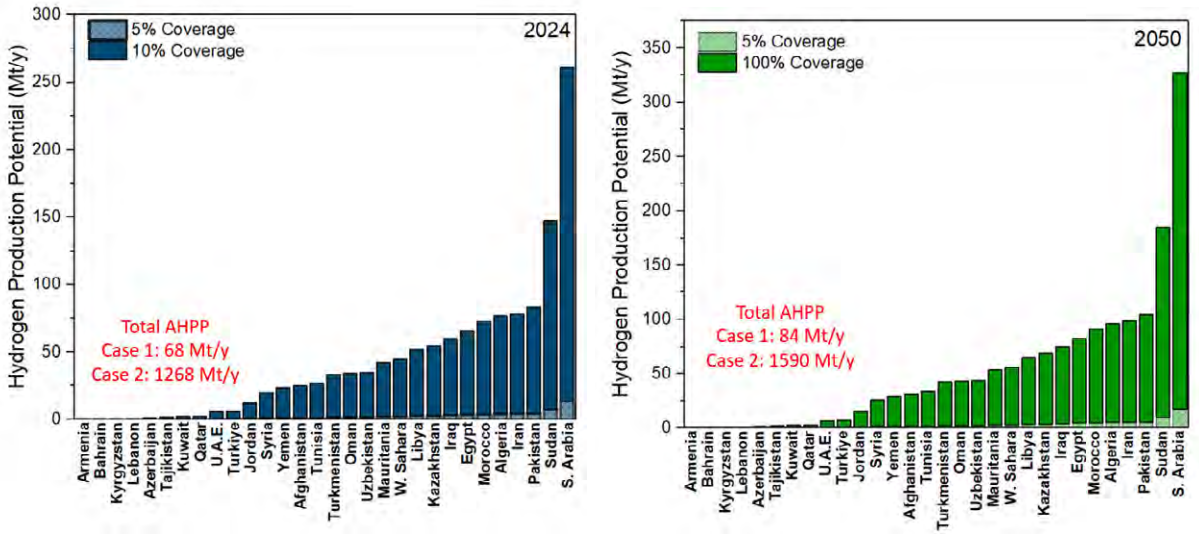



**Figure 2:** Annual Hydrogen Production Potential (AHPP) of thirty countries in the GME region for Case 1 (5% Coverage) and Case 2 (100% Coverage) for 2024 and 2050.

remain below 15-17 Mt/y, indicating that even with minimal land use, these nations can be self-sufficient in meeting their hydrogen needs. The cumulative potential for this scenario totals 68 Mt/y in 2024 and increases to 84 Mt/y by 2050. In a more optimistic scenario (case 2), the region's hydrogen production potential rises significantly to 1268 Mt/y in 2024 and reaches 1590 Mt/y by 2050. Among the countries analyzed, Saudi Arabia stands out with the highest production potential, projected to reach approximately 327 Mt/y by 2050. Meanwhile, Pakistan, Morocco, and Egypt are expected to achieve production potentials of 104 Mt/y, 91 Mt/y, and 82 Mt/y respectively in this optimistic scenario. According to IRENA, global hydrogen demand is projected to reach 450 Mt/y by 2050 [6], with about one-third of this demand expected to be met through international trade. Given these figures, it is evident that the GME region is poised to play a crucial role in capturing a significant share of the global hydrogen market.

## Levelized Cost of Products

A location that is deemed highly suitable based on the aforementioned constraints does not necessarily imply that it is also economically viable. The LCOH serves as the economic indicator for assessing the feasibility of a location by examining the total expenses in the production of hydrogen. Figure 3 illustrates the current and projected ranges of LCOH in the GME region.

The LCOH in the region ranges from 4.6 $/kg to 16.4 $/kg. However, if we consider only the highly suitable locations in the region, Egypt, Saudi Arabia, and Libya have the lowest LCOH of about 4.70, 4.73, and 4.75 $/kg, respectively. On the other hand, Kazakhstan shows the highest LCOH of 7.84 $/kg in 2024. Projections for 2050 indicate that the LCOH range will decrease to 2.5 to 9.1 $/kg with Egypt showing the lowest LCOH while Kazakhstan has one of the highest. Despite the potential for hydrogen production in the region, the LCOH remains higher than that of grey hydrogen produced from fossil fuels, which are still more readily available and affordable in this region. The extent to which a country can lower the CAPEX for solar panels and electrolyzers—through measures such as reducing import taxes—will play a crucial role in facilitating the region's transition to a green hydrogen economy. North African and Middle Eastern countries benefit from abundant solar resources, resulting in relatively lower LCOH in these areas. However, water scarcity may hinder them from fully utilizing this potential. In contrast, Central Asian states have access to good water supplies but face significant challenges due to limited solar resources and challenging topography, which could restrict development. Countries situated between these two extremes—such as Iran, Iraq, Pakistan, Afghanistan, and Turkey—enjoy a favorable balance of both solar and water resources, positioning them well for potential growth in green hydrogen production.

Hydrogen derivatives like Ammonia and Methanol have a significant global market and utilizing green hydrogen to produce these can save up a lot of $CO_2$ emissions. In addition to being valuable products themselves, these chemicals can easily be transported internationally and can serve as cost-effective hydrogen carriers. Figure 3 illustrates the LCOA and LCOM for 2024 and 2050. For highly suitable locations, green ammonia is expected to cost between 0.96-1.38$/kg in 2024 and 0.56-0.79$/kg by 2050 while green LCOM ranges from 1.12-1.59 $/kg in

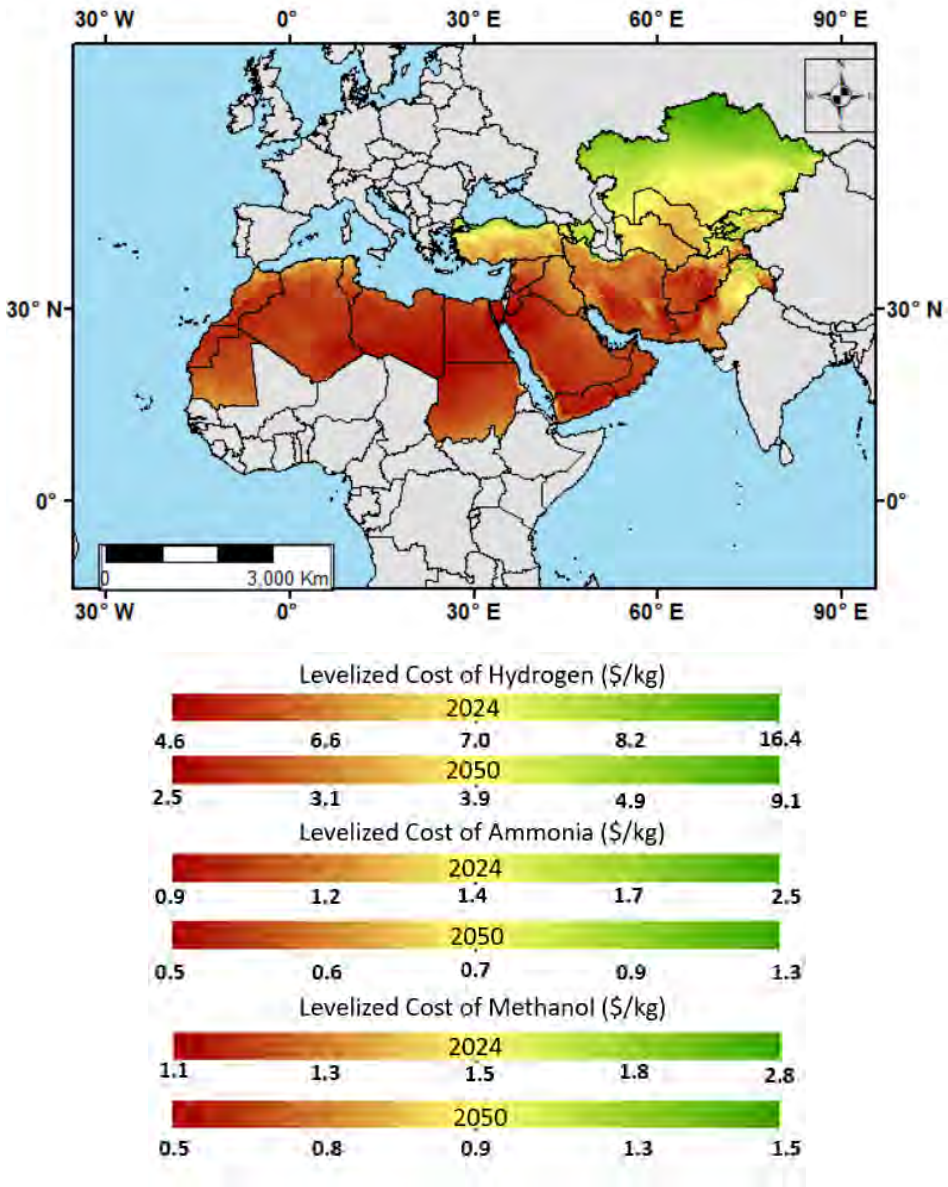



**Figure 3**: Levelized cost of hydrogen, ammonia, and methanol in the GME region for 2024 and 2050.

2024 and is expected to decrease to 0.67-0.93 $/kg by 2050.

**Table 1** $CO_2$ avoided potential for Case 1: 5% coverage and Case 2: 100% coverage for 2024 and 2050.

| Year | Case | $CO_2$ avoided potential (Mt/y) |
|---|---|---|
| 2024 | 1 | 481 |
| | 2 | 3655 |
| 2050 | 1 | 603 |
| | 2 | 4586 |

## $CO_2$ Avoided Potential

The LCA analysis was conducted to quantify the $CO_2$ emissions that could be avoided by substituting gasoline with green hydrogen. The total potential for $CO_2$ emissions reduction in the two scenarios is presented in **Table 1**. For the year 2024, the region has the potential to avoid between 481 and 3655 Mt/y of $CO_2$, depending on whether highly suitable locations are utilized partially (5%) or fully (100%) for hydrogen projects, respectively. By 2050, these values could increase to between 603 and 4586 Mt/y, assuming improved production efficiency of electrolyzers and solar panels. These findings highlight the significant opportunity for the region to achieve its net-zero targets through the adoption of green hydrogen across various sectors. Notably, most countries in the region are self-sufficient and will not need to rely on imported hydrogen to realize this potential.

## CONCLUSION

An integrated approach combining GIS-MCDM analysis, along with data-driven optimization models, was employed to assess the hydrogen potential of the GME region through technical, economic, and environmental evaluations. The GIS analysis identified proximity to water resources as the primary constraint affecting land suitability, particularly in North African and Middle Eastern countries. In contrast, Central Asian states face challenges due to rugged topography that renders much of their land unsuitable. Additionally, proximity to roads emerged as another significant factor impacting land suitability. After conducting the AHP analysis, it was determined that only 3.8% of the GME region is classified as highly suitable for solar-driven hydrogen projects, with Saudi Arabia, Sudan, and Pakistan identified as the top three countries with the most favorable land conditions. However, not all suitable locations are economically viable. The LCOH results indicate that Egypt and Libya have very low LCOH due to their excellent solar resources. The region also possesses the potential to produce green ammonia and methanol, which are valuable chemicals with a strong global market demand. Overall, the hydrogen potential suggests that the GME region could capture a significant share of the global hydrogen market, particularly serving European Union countries and Asia-Pacific nations like Japan and Korea that are actively investing in hydrogen economies. Furthermore, it can meet its net-zero targets by integrating green hydrogen across various sectors. However, establishing a robust hydrogen economy will require significant government efforts and investments. This transition may only be feasible if green hydrogen projects become profitable, which hinges on achieving economies of scale in electrolyzer production and reducing costs in the coming years.

## DIGITAL SUPPLEMENTARY MATERIAL

Details of the AHP analysis as well as all the assumed parameter values in the optimization code are given in the digital supplementary material.

## ACKNOWLEDGEMENTS

This work was supported by the National Research Program for Universities (NRPU), Research and Development Division, Higher Education Commission of Pakistan (20-14827/NRPU/R&D/HEC/2021). This research was also supported by Aalto University through project number 96310047.

## REFERENCES

1. James Burgess. COP27: Saudi Arabia targets Europe, Asia-Pacific in global hydrogen push 2022. https://www.spglobal.com (accessed April 24, 2024).
2. International Energy Agency (IEA). National Hydrogen Strategy 2023. https://www.iea.org/policies/16971-national-hydrogen-strategy (accessed April 24, 2024).
3. Touili S, Alami Merrouni A, Azouzoute A, El Hassouani Y, Amrani A. A technical and economical assessment of hydrogen production potential from solar energy in Morocco. Int J Hydrogen Energy 2018;43:22777–96. https://doi.org/10.1016/j.ijhydene.2018.10.136.
4. Messaoudi D, Settou N, Negrou B, Settou B, Mokhtara C, Amine CM. Suitable Sites for Wind Hydrogen Production Based on GIS-MCDM Method in Algeria, 2021, p. 405–12. https://doi.org/10.1007/978-981-15-6595-3_52.
5. Dickson R, Akhtar MS, Abbas A, Park ED, Liu J. Global transportation of green hydrogen via liquid carriers: economic and environmental sustainability analysis, policy implications, and future directions. Green Chemistry 2022;24:8484–93. https://doi.org/10.1039/d2gc02079c.
6. International Renewable Energy Agency. Accelerating hydrogen deployment in the G7: recommendations for the Hydrogen action pact. 2022.

© 2025 by the authors. Licensed to PSEcommunity.org and PSE Press. This is an open access article under the creative commons CC-BY-SA licensing terms. Credit must be given to creator and adaptations must be shared under the same terms. See https://creativecommons.org/licenses/by-sa/4.0/



# Section 8

## CAPE Education and Knowledge Transfer

Systems & Control Transactions

**Research Article - Peer Reviewed Conference Proceeding**
ESCAPE 35 - European Symposium on Computer Aided Process Engineering
Ghent, Belgium. 6-9 July 2025
Jan F.M. Van Impe, Grégoire Léonard, Satyajeet S. Bhonsale,
Monika E. Polańska, Filip Logist (Eds.)

PSE PRESS

# Food for thought: Delicious problems for Process System Engineering (PSE) courses

**Daniel R. Lewin***

Department of Chemical Engineering, Technion I. I. T., Haifa 32000, Israel
* Corresponding Author: dlewin@technion.ac.il.

## ABSTRACT

Active learning is widely recognized as an effective teaching approach that can improve classroom outcomes. This is enabled by providing the time for students to apply new knowledge, make mistakes, correct them, and repeat the process until mastery is achieved. One way to implement active learning is through the flipped classroom paradigm. However, to be effective, active learning depends on providing students with a variety of open-ended problems, ranging in difficulty from introductory to advanced levels. This paper presents four food-themed problems for use in numerical methods and process control courses:

1. *Formulating Willy Wonka's new chocolate bar*: An introductory linear programming problem focused on translating verbal descriptions into mathematical models.

2. *Optimal production for the Matrix Pizza company*: A more advanced mixed-integer linear programming problem involving multiple scheduling scenarios.

3. *Optimal frying time for fried ice cream production*: A transient heat transfer problem modelled by an initial-value partial differential equation.

4. *Control system design for Uncle Kane's pancake batter machine*: A control design problem involving uncertain process models and the selection of an appropriate operating mode and PI controller design.

These problems aim to engage students in practical, problem-solving activities central to the active learning process.

**Keywords**: Chemical engineering education, flipped classroom, active learning.

## 1. INTRODUCTION

Active learning is widely accepted as a collection of teaching paradigms that have the best potential to yield improved learning outcomes in classroom settings [1-3]. Traditional lecture-centred teaching often struggles to engage students effectively in a discipline characterized by complex processes and systems [4]. By incorporating active learning techniques such as peer instruction [2], problem-based learning [5], and gamification [6-7], educators can enhance student engagement, critical thinking, and real-world application of concepts [8-9].

Adopting the flipped classroom paradigm [10-11], which moves traditional lecture-based transfer of information to online lessons completed by students in advance of class activities, frees class time for the aforementioned student-centred activities. To adopt active learning, some class time needs to be allocated for students to experiment with the application of the newly acquired knowledge, giving them time to make mistakes, correct their errors, try again, and repeat this process as necessary. This cyclic activity is a variant of Kolb's [12] ideas about the cognitive processes involved in learning. One way to allocate time for effective learning would be to adopt the flipped classroom.

To be effective, this form of learning relies on the availability of sufficient open-ended problem sets to provide students with a rich source of practice materials. These should encompass a range of difficulty: from introductory level to "final exam level" and beyond. To that

end, this paper presents a set of problems with an arbitrary common theme close to the author's heart ("the best way to a man's heart is through his stomach"), mostly intended to be utilized in a course on numerical methods, with one extra problem designed for a course on "good old" process control.

## 2. EXAMPLE FOOD-RELATED PROBLEMS FOR PSE COURSES

With "food, glorious food" as a theme, the four example problems presented in this paper are:

1. *Optimal formulation of Willy Wonka's new chocolate bar*. This is an introductory linear programming (LP) problem, which gives students practice in translation of a verbal description into a mathematical formulation, and its solution.
2. *Optimal production for the "Matrix Pizza" company*, a bakery providing quality pizzas to a college campus in mid-West USA. This is a more advanced mixed integer linear programming (MILP) problem including alternative scenarios that need to be accounted for in the optimal scheduling solution.
3. *Optimal frying time for "fried ice cream."* This is a transient heat transfer problem that is defined as an initial value partial differential equation (IVPDE) that needs to be solved numerically.
4. *Control system design for Uncle Kane's continuous pancake batter machine*. This is a single input – single output (SISO) control problem presented as a set of alternative operating modes, each with its own uncertain model description. The student needs to select the operating mode and design a suitable PI controller that meets required specifications.

Each of the above four example problems will be discussed next, focusing on the problem definition, the degree of difficulty, and the learning objectives. Because of space limitations, only sketches of the solutions will be presented here. Full solution outlines to all four problems will appear in the full version of this paper.

### 2.1 Optimal formulation of Willy Wonka's new chocolate bar

**Problem definition:** Willy Wonka has hired you to formulate a new chocolate bar called "Super-Choc," weighing 100 grams. The bar consists of sugar, and two types of chocolate: African and Belgian. The optimal mass of each component needs to be specified to minimize costs, while meeting the following five requirements:

1. Each bar should contain no more than 60 grams of chocolate
2. The amount of African chocolate should not exceed the amount of Belgian chocolate by more than 10 grams.
3. The bar's Sweetness (S) should not exceed 30 units per bar, where each gram of African chocolate reduces S by 0.3 unit (relative to sugar), while each gram of Belgian chocolate raises S by one unit.
4. The bar's Mouth Feel (M) should be at least 40 units. Each gram of African chocolate increases M by 2.2 units, while each gram of Belgian chocolate raises M by one unit.
5. The bar's Luster (L) should be at least 70 units. Each gram of African chocolate increases L by one unit, while each gram of Belgian chocolate raises L by 3.9 units.

If the cost of Belgian chocolate is three times the cost of African chocolate, and the cost of sugar can be neglected, compute the optimal composition of a bar of "Super-Choc."

**Degree of difficulty**: A practice problem to train basic application of LP methodology.
**Learning objectives**: The student will demonstrate the ability to develop an LP based on a written problem description, and to graphically solve the LP to obtain the optimal solution.
**Sketch of solution**: Defining $x_1$ and $x_2$ as the mass in grams, of African and Belgian chocolate, respectively, the problem as defined can be translated to the following LP:

$$\begin{aligned}
&\min_{x_1,x_2} J = x_1 + 3x_2 \quad \text{(B costs 3 times more than A)} \\
&\text{Subject to:} \\
&x_1 + x_2 \le 60 \quad \text{(chocolate content of at most 60 g)} \\
&x_1 - x_2 \le 10 \quad \text{(A content must be up to 10 g more than B)} \\
&-0.3x_1 + x_2 \le 30 \quad \text{(S must be at most 30)} \\
&2.2x_1 + x_2 \ge 40 \quad \text{(M must be at least 40)} \\
&x_1 + 3.9x_2 \ge 70 \quad \text{(L must be at least 70)} \\
&x_1, x_2 \ge 0
\end{aligned} \tag{1}$$

The graphical solution is shown in Figure 1, indicating that the active constraints are those on M and L, and that 56% of the optimal bar is sugar!

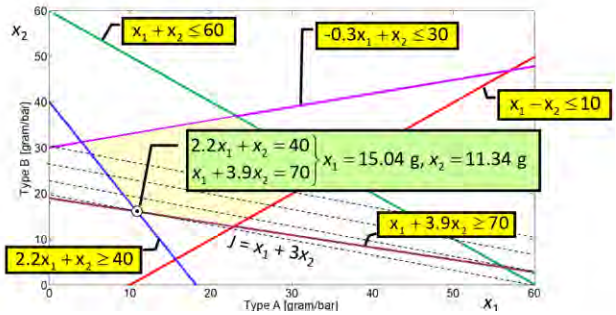



**Figure 1.** Graphical solution for Willy Wonka's chocolate

bar formulation.

## 2.2 Optimal production for the "Matrix Pizza" company

**Problem definition**: "Matrix Pizza" is a pizza bakery that provides quality pizza pies to the college campus in mid-West USA. The bakery produces three types of pizza pies: **Matrix Special**, sold for \$10/pie, **Matrix Pro**, sold for \$7/pie, and **Matrix College**, sold for \$5/pie. The three types of pizza differ only in the toppings, as listed in Table 1.

**Table 1:** Recipes for the Pizzas (quantities of each topping, in grams, on each pizza).

| | Special | Pro | College | Cost (\$/kg) |
|---|---|---|---|---|
| Price (\$/pie) | 10 | 7 | 5 | |
| Tomatoes (g) | 200 | 250 | 350 | 2 |
| Mozzarella (g) | 200 | 250 | 350 | 2 |
| Parmesan (g) | 100 | 100 | 0 | 15 |
| Olives (g) | 100 | 100 | 0 | 20 |
| Tuna (g) | 100 | 0 | 0 | 10 |

In addition to the cost of the toppings, the production costs of the pizza pies also need to account for staff costs estimated at \$1 per pizza pie, as well as operating and maintenance costs of the pizza oven, estimated at \$1,000 per oven per week. For each oven installed, the production capacity is 1,000 pizzas per week. There is no limit on the number of pizza pies that can be produced in the bakery per day, so long as the daily demands, listed in Table 2, are not exceeded on a weekly basis. Your tasks are:

(a) Formulate a MILP whose solution is the optimal quantities of each type of pizza that should be produced each week, including the number of ovens that should be installed in the bakery to maximize profits.
(b) Solve the MILP formulated in step (a).
(c) The college's football team is planning to hold home games each Saturday night. How will this affect the optimal solution if the home games change the pizza demand on Saturdays according to Table 3.

**Table 2:** Typical Demand (pizzas/day for each type).

| Day | Special | Pro | College |
|---|---|---|---|
| Monday | 20 | 60 | 60 |
| Tuesday | 0 | 80 | 80 |
| Wednesday | 0 | 60 | 140 |
| Thursday | 20 | 80 | 160 |
| Friday | 40 | 40 | 120 |
| Saturday | 140 | 60 | 20 |
| Sunday | 100 | 100 | 20 |
| Weekly Total | 320 | 480 | 600 |

**Table 3:** Revised Demand on Saturdays (pizzas/day for each type).

| Day | Special | Pro | College |
|---|---|---|---|
| Saturday | 340 | 160 | 120 |

**Degree of difficulty**: A more advanced MILP problem.
**Learning objectives**: The student will demonstrate the ability to develop a MILP based on a written problem description, and to either solve the problem graphically or using the Simplex method.
**Sketch of solution**: (a) Formulation of the problems as set as a MILP; (b) Solution using a MILP solution method such as Branch-and-bound or by using the Simplex method on separate scenarios.

## 2.3 Optimal frying time for "fried ice cream."

**Problem definition**: "Fried ice cream" is the house specialty of the "Sea Waves" restaurant, overlooking Haifa bay. A portion of ice cream is wrapped in pastry dough and deep-frozen. Just before serving, it is deep fried for a short time in high-temperature oil. A typical portion of "fried ice cream" is shown in Figure 2. You have been hired by the chef to provide an estimate of the time needed to fry the pastry-wrapped ice cream such that the pastry is crispy, and the ice-cream stays frozen.



**Figure 2.** Fried ice cream

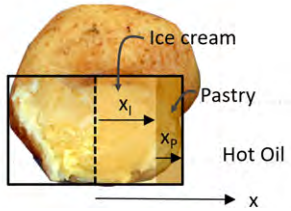



**Figure 3.** Coordinate system

A mathematical model is set up to compute the temperature of the pastry and ice cream as functions of time and position. For simplicity, a one-dimensional model is constructed making use of symmetry, as shown in Figure 3:

$$\text{For ice cream: } \frac{\partial T_I}{\partial t} = \alpha_I \frac{\partial^2 T_I}{\partial x^2},\ T_I(x,0) = T^0,\ 0 \le x \le x_I \qquad (2)$$

$$\text{For pastry: } \frac{\partial T_P}{\partial t} = \alpha_P \frac{\partial^2 T_P}{\partial x^2},\ T_P(x,0) = T^0,\ x_I < x \le x_P \qquad (3)$$

The following boundary conditions apply:

$$@\ x = 0:\ \frac{\partial T_I}{\partial x} = 0 \qquad @\ x = x_I:\ \alpha_I \frac{\partial T_I}{\partial x} = \alpha_P \frac{\partial T_P}{\partial x}$$

$$@\ x = x_I:\ T_I(x_I,t) = T_P(x_I,t) \qquad @\ x = x_P:\ \frac{\partial T_P}{\partial x} = \beta\left(T_{oil} - T_P(x_P,t)\right)$$

**Degree of difficulty**: This problem tests the ability to apply numerical methods for the solution of initial value partial differential equations (IVPDEs).
**Learning objectives**: The student will demonstrate the ability to discretize an IVPDE and its boundary conditions and solve it to ensure a stable numerical solution.
**Sketch of solution**: Development of discretized approximation of the original PDE using a backward difference approximation for the time-differential term to impart unconditional stability on the numerical solution (Crank-Nicolson's method).

### 2.4. Control system design for Uncle Kane's continuous pancake batter machine.

**Problem definition**: Uncle Kane, the famous chemical engineer and expert chef, has developed a continuous process for the production of pancake batter. A controlled stream of liquid, consisting of milk, eggs, and vanilla, $F_1$, is fed to a mixing vessel together with a continuous stream of solid feed consisting mostly of flour and sugar, $F_2$. Uncle Kane has noticed that the frequency of the sound made by the mixer head is related almost linearly to the viscosity of the mixture, which also affects its quality. He has developed an automatic control system that uses a microphone to measure the sound in the mixing vessel, which sends a feedback signal to a controller that manipulates the control valve installed on stream $F_1$. The control system is illustrated schematically in Figure 4.

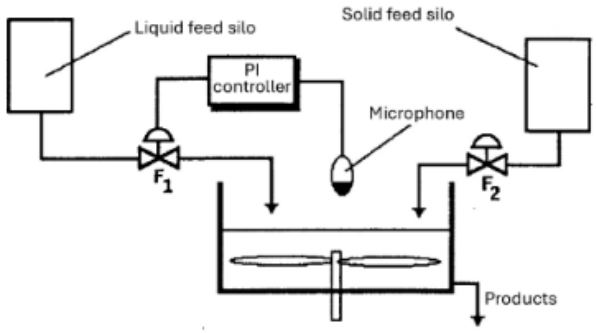



**Figure 4.** Uncle Kane's continuous pancake batter production unit.

After much soul-destroying research, Uncle Kane has succeeded in developing a model relating the flowrate of $F_1$ to the frequency of sound picked up by the microphone, $\phi$:

$$\frac{\phi}{F_1}(s) = p(s) = \frac{K_p(-\alpha s + 1)}{(\tau s + 1)^2} e^{-\theta s} \qquad (4)$$

**Table 4:** Parameters for the model in Eq.(4) as a function of the flow rate $F_2$.

| $F_2$ (kg/h) | $K_p$ | α(s) | τ(s) | θ(s) |
|---|---|---|---|---|
| 750 | $0.9 \le K_p \le 1.1$ | 5 | 5 | 1 |
| 1,000 | $2 \le K_p \le 4$ | 1 | 1 | 0.2 |
| 1,250 | $0.8 \le K_p \le 7.2$ | 5 | 5 | 1 |

His experimental work has also discovered three possible operating points for the production unit, each around a given flow rate of the solid feed, F2. Table 4 presents values of the model parameters in Eq.(4) at each operating point. Design a PI controller to control $\phi$ by manipulating $F_1$ so that the following specifications are satisfied: (a) Robust stability; (b) Bandwidth of the Internal Model Controller (IMC) filter of at least 0.3 rad/sec; (c) Maximizing production.

**Degree of difficulty**: A typical problem in robust control design.

**Learning objectives**: The student will demonstrate the ability to adequately represent the model uncertainty for design purposes and use it to compute PI controller parameters, designed via the IMC parametrization, that meet all the specifications.

**Sketch of solution**: (a) Development of multiplicative approximation accounting both for parametric uncertainty and the consequence of 1st order model implied by the requirement of PI control; (b) Computing stability limit in terms of the time constant of the IMC filter; (c) Usage of these tools to determine the most suitable operating mode and corresponding PI controller tuning.

## 3. INTEGRATION WITH THE FLIPPED CLASS PARADIGM

It would be appropriate to discuss how the problems presented here could be incorporated into the flipped classroom paradigm. While organizational, evaluation and student feedback are addressed in our published papers [10,11], a full version of the paper would provide space to cover these issues in more details.

## 4. DISCUSSION

The use of active learning in engineering education, particularly in courses involving numerical methods and process control, offers numerous benefits over traditional lecture-based teaching [10,11]. Active learning strategies, such as problem-based learning (PBL), peer instruction, and gamification, have been shown to improve student engagement, critical thinking, and long-term retention of knowledge [1-3]. The example problems introduced in this paper, which leverage the flipped classroom paradigm, not only align with these findings but also offer a practical framework for implementing active learning in technically demanding fields such as PSE. They offer a diverse and engaging way to introduce students to fundamental concepts in optimization, heat transfer, and control system design. By utilizing scenarios that range from the formulation of a new chocolate bar to the design of a control system for a pancake batter machine, students are exposed to real-world problems that require both analytical rigor and creative problem-solving skills. This thematic approach—framed around the relatable and engaging concept of food production—appeals to students' interests and can foster a deeper connection to the material, leading to improved motivation and learning outcomes.

### 4.1 Active learning and student engagement

A central goal of active learning is to increase student participation and engagement in the learning

process, which can be particularly challenging in disciplines like PSE where abstract concepts and complex systems are common. Traditional teaching methods often rely on passive learning, where students listen to lectures and absorb information, usually without the opportunity to immediately apply their knowledge for themselves. In contrast, implementing the flipped classroom paradigm, transfers the responsibility of covering the lecture materials to the students as pre-class preparation, and reallocates in-class time for active, hands-on problem-solving.

The problems outlined in this paper facilitate this active learning model by encouraging students to work through open-ended, real-world challenges. This type of problem solving not only reinforces technical knowledge but also helps develop critical thinking, adaptability, and decision-making skills. As students work through problems such as optimizing pizza production or controlling the frying time of ice cream, they learn to balance conflicting objectives, and select appropriate methods for solving complex, dynamic problems. By solving problems iteratively and experimenting, students can internalize the underlying concepts more deeply, improving their ability to transfer this knowledge to new and unfamiliar contexts.

## 4.2 Problem complexity and cognitive development

The problems presented span a broad spectrum of difficulty, catering to students at different levels of expertise. The introductory LP problem on chocolate bar formulation, for example, provides a relatively simple application where students practice translating verbal descriptions into mathematical models. This offers an excellent opportunity for students to gain foundational skills in optimization. On the other hand, more advanced problems—such as the MILP problem for pizza production and the control system design for the pancake batter machine—challenge students to apply more sophisticated mathematical techniques and consider the implications of uncertainty, robustness, and system dynamics.

This range of problem complexity is essential for promoting cognitive development and ensuring that students progress from basic to advanced levels of understanding. By providing a series of problems that increase in complexity, students are able to gradually build their knowledge and skills while reinforcing their learning through multiple iterations. This approach mirrors Kolb's [12] experiential learning cycle, where concrete experience is followed by reflective observation, abstract conceptualization, and active experimentation. Furthermore, the inclusion of open-ended problems allows students to explore different solution paths, promoting deeper cognitive engagement with the material. In the case of the MILP problem for the Matrix Pizza company, for instance, students must navigate the intricacies of balancing resource constraints, demand forecasts, and cost optimization, while considering alternative production schedules. This requires not only mathematical proficiency but also the ability to model and solve real-world optimization problems with multiple variables and constraints.

## 4.3 Interdisciplinary learning and real-world applications

One strength of the food-themed problems is their ability to connect mathematical and engineering concepts to real-world applications. Using familiar scenarios like chocolate bar formulation or fried ice cream production helps students understand the practical implications of the methods they are learning. This connection is vital in engineering education, where students may struggle to relate abstract concepts to real-world problems.

The interdisciplinary nature of the problems also helps students link different areas of study. For example, the optimal frying time problem applies numerical methods to heat transfer, while the control system design for the pancake batter machine highlights the importance of robustness in engineering design. These problems demonstrate that real-world challenges often require skills from multiple fields, enriching students' chemical engineering education.

By framing problems around food production, the paper shows that complex engineering concepts can be communicated in an engaging and accessible way. This approach encourages students to think beyond traditional boundaries and explore diverse applications of chemical engineering.

## 4.4 Limitations and future directions

While the approach described in this paper has considerable promise, there are several limitations that should be considered. One challenge is ensuring that students have the necessary background knowledge to tackle more advanced problems. For example, while the introductory problems on linear programming and optimization may be accessible to students with a basic understanding of mathematics, the more complex problems involving MILP and robust control system design may require additional support in terms of prerequisite knowledge or instructional resources.

Another limitation is the time required for students to engage with these open-ended problems. The flipped classroom paradigm depends on students completing preparatory work outside of class, which may not always be feasible for all students, particularly those who struggle with self-directed learning. To mitigate this, instructors can provide additional support, such as pre-class tutorials, practice exercises, or discussion forums, to ensure students feel confident in their ability to solve the problems [10,11]. Additionally, incorporating peer

collaboration into the learning process—such as through group problem-solving sessions—could help foster a more supportive and dynamic learning environment [2].

Future research could explore the specific impacts of these types of problems on student outcomes, such as academic performance, engagement, and retention of knowledge. It would also be valuable to assess how students respond to the food-themed problems, or other themes, in terms of motivation and interest, and whether these themes contribute to a greater sense of relevance and enjoyment in the learning process.

Finally, one could expand the problem sets presented here to include even more interdisciplinary scenarios, incorporating areas such as environmental sustainability and even space exploration applications [13]. This would not only broaden the applicability of the problems but also encourage students to think about engineering challenges in a more holistic and interconnected way.

## CONCLUSIONS

The use of active learning strategies, particularly within the context of the flipped classroom paradigm, offers significant potential for improving student engagement and learning outcomes in process systems engineering courses. By presenting food-themed problems that span a range of difficulty levels and disciplines, this approach allows students to develop critical thinking, problem-solving, and technical skills in a more interactive and experiential way. Although there are challenges to implementing this approach, the potential benefits for both student learning and motivation are considerable, and future research should explore the broader impacts of such active learning strategies in engineering education. The author has used all of the exercises presented here over decades of teaching with great success. Each of them was used just once in exams and repeatedly since then in the classroom as open-ended practice problems. In the last 10 years, the incorporation of the flipped classroom paradigm in his teaching has released additional contact time to utilize for open-ended problem solving using exercise problems like the ones showcased in this paper.

## REFERENCES


1. Bloom BS. (1968). Learning for mastery. *UCLA - CSEIP - Evaluation Comment*, 1(2):1-12.
2. Crouch CH and Mazur E. (2001). Peer instruction: Ten years of experience and results, *American Journal of Physics*, 69 (9): 970-977.
3. Freeman S, Eddy SL, McDonough M, Smith MS, Okorafor N, Jordt H, and Wenderoth MP (2014). Active learning Increases student performance in science, engineering, and mathematics. *PNAS*, **111**(23): 8410-8415.
4. Rodríguez M, Díaz I, Gonzáles EJ and Gonzáles-Miquel M (2018). Motivational active learning: an integrated approach to teaching and learning process control, *Education for Chemical Engineers*, 24, 7-12.
5. Woods DR. (1996). Problem-Based Learning for Large Classes in Chemical Engineering, *New Directions for Teaching and Learning*, 68, 91-99.
6. de Paz Carmona H and Borgues Chinea E. (2021). Gamifying education: a practical example in chemical engineering, *VIII Jornadas Iberoamericanas de Innovacíon Educativa en el Ámbito de las TIC y las TAC*, Las Palmas de Gran Canaria.
7. Díaz I, Gonzáles EJ, Gonzáles-Miquel M, and Rodríguez M (2024). Application of serious games in chemical engineering courses, *Education for Chemical Engineers*, 46, 22-32.
8. Au N, Bayles T, Ross J. (2008). Exposing chemical engineering students to real world problems: health care and renewable energy systems, *Proc. of the ASEE Annual Conference*.
9. Garnier G (2014) Grand challenges in chemical engineering, *Frontiers in Chemistry*, 2, 1-3.
10. Lewin DR and Barzilai A. (2022). The Flip Side of Teaching Process Design and Process Control to Chemical Engineering Undergraduates – and Completely Online to Boot, *Education for Chemical Engineers*, 39, 44-57.
11. Lewin DR and Barzilai A (2023). A Hybrid-Flipped Course in Numerical Methods for Chemical Engineers, *Comput. Chem. Eng.*, 172, 108167.
12. Kolb D. (1984). *Experimental Learning as the Science of Learning and Development*. Prentice Hall, Englewood Cliffs, NJ.
13. Zondervan E. (2025) Engineering the final frontier: the role of chemical and Process Systems Engineering in space exploration, *Proc. Of ESCAPE-35*, Ghent, Belgium.



© 2025 by the authors. Licensed to PSEcommunity.org and PSE Press. This is an open access article under the creative commons CC-BY-SA licensing terms. Credit must be given to creator and adaptations must be shared under the same terms. See https://creativecommons.org/licenses/by-sa/4.0/




Systems & Control Transactions

**Research Article - Peer Reviewed Conference Proceeding**
ESCAPE 35 - European Symposium on Computer Aided Process Engineering
Ghent, Belgium. 6-9 July 2025
Jan F.M. Van Impe, Grégoire Léonard, Satyajeet S. Bhonsale,
Monika E. Polańska, Filip Logist (Eds.)

PSE PRESS

# The flipped classroom: The good, the bad, and the ~~ugly~~ surprising

**Daniel R. Lewin[a]*, Nilay Shah[b], and Abigail Barzilai[c]**

[a]Department of Chemical Engineering, Technion I. I. T., Haifa 32000, Israel
[b]Department of Chemical Engineering, Imperial College, London, UK
[c]Centre for the Promotion of Learning and Teaching, Technion, Haifa 32000, Israel
* Corresponding Author: dlewin@technion.ac.il.

## ABSTRACT

Three different implementations of the flipped class paradigm were used to teach Chemical Engineering students at Imperial College London (ICL) in the 2023-24 academic year: (1) The 3rd year elective course *Introduction to Numerical Methods (INM)* taught in its entirety in flipped format (the "good"); (2) The 2nd year core course on *Process Dynamics and Control (PDC)*, with the first half of the course on process dynamics taught in traditional lecture format, and the second half on process control taught in flipped format (the "bad"); and (3) a one-week workshop on heat integration, taught as part of a 3rd year core course on *Process Design (PD)*, taught in flipped format (the "surprising"). This paper describes these three implementations in detail and presents and analyzes the responses from student surveys intended to ascertain students' perceptions about the level of their satisfaction with the flipped class approach and the degree to which they achieved mastery of the taught materials. The actual learning outcomes are also analysed, that is, the exam results in the case of the first two courses, and the performance of the students on their design project, for the last course. The paper ends with conclusions and recommendations concerning how the flipped class paradigm should be implemented, depending on the classroom situation for which it is intended.

**Keywords**: Chemical engineering education, flipped classroom, active learning.

## 1. INTRODUCTION

In the 2023-24 academic year, the lead author of this paper was on sabbatical at London's Imperial College Department of Chemical Engineering, where he taught or co-taught three undergraduate courses, using variations of the flipped class paradigm, where lecture materials are viewed as preparation by students, and the class time is largely used for cooperative problem solving and exercises to build mastery:

(a) The 3rd year elective course *Introduction to Numerical Methods, INM* (the "good"), which used "flipping" in each week of the course. This implementation most closely followed the flipped class paradigm implemented at the Technion [1, 2].
(b) The 2nd year core course *Process Dynamics and Control, PDC* (the "bad") consisting of six weeks covering process dynamics, taught by conventional lecturing, followed by five weeks covering process control, taught with a flipped approach.
(c) The workshop on heat integration, taught as part of the 3rd year core course *Process Design, PD* (the "surprising"), which was an integral part of the process design course. It involved three online lessons completed by the students in advance of class activity, with each online lesson associated with a hands-on problem-solving class meeting, to a total of seven contact hours held during a single week of the course.

The reader is probably curious why we have used the epithets "good," "bad," and "surprising" for the three courses, and we promise that all will be clear by the end of the paper. The flipping paradigm proposed by Lewin and Barzilai [1,2] involves three phases, repeated in each week: Phase 1 – *Online Lesson*, Phase 2 – *Class Meeting*, and Phase 3 – *Active Tutorial*. Because sufficient contact time was unavailable at ICL, the implementations there combined the second and third phase into one class

meeting which focused mainly on active tutorial work by the students.

David Kolb [3] famously postulated a continuous cycle of cognitive processes employed by learners to perceive and process information: from concrete experience to reflective observation, to abstract conceptualization, and finally to active experimentation, although he accepted that most learners favor one cognitive learning process over the others. Benjamin Bloom [4] observed that moving from passive, lecturer-centered teaching to active, student-centered learning can improve learning outcomes by one standard deviation.

The flipping paradigm has been adopted with documented success by the lead author in all the courses he has taught at the Technion. With this rich and successful experience behind him, it is not surprising that he requested that all three of his courses taught at Imperial College would be delivered in flipped format, even though the department had experienced disappointing results when flipping had been tried there previously. To their credit, the management supported the principle of allowing the author to teach with his approach.

## 2. COURSE DESCRIPTIONS

Curricula, learning outcomes, and investment expected from both teachers and students for the three courses that were taught in "flipped" format at ICL will be detailed in the full paper. These closely resemble similar courses taught at the Technion as described in Lewin and Barzilai [1,2]. In the space available here, we shall focus on distinguishing between the degree to which the flipping paradigm was implemented in the three courses.

### 2.1 Introduction to Numerical Methods

The first part of the course provides instruction on the basic building blocks of numerical methods, with the second part focusing on the application of those tools for the solution of numerical problems associated with engineering applications (Riggs [5], Carnahan et al. [6]). The course taught at ICL was a version of the hybrid flipped course developed and taught at the Technion in 2022 that was described by Lewin and Barzilai [2].

### 2.2 Process Dynamics and Control

The first part of the course provides the tools to develop first principles and empirical process models. In the second part of the course, the derived models are used to design simple control systems to meet desired closed-loop performance specifications (Seborg et al. [7]). The first part of the course was taught in regular lecture format, which included demonstration of applications of the taught materials, as well as assigned problem sets for the students to try on their own. However, this lecturer-centered teaching did not provide time for students to work problems for themselves in scheduled class time. The second part of the course was taught in flipped format, in which each week, students prepared for the class meeting by watching online lessons in advance. In the class meetings, time was provided for students to solve hands-on exercises for themselves. Unless such active tutorials are offered to students, there is no way to assess their degree of mastery in the formative stage (during the studies). We are left only in testing their mastery in the summative stage (i.e., by exams).

### 2.3 Workshop on Heat Integration

The workshop provides students with instruction in the principles and rules governing the "pinch" design of heat exchanger networks (HENs) and their practical application (Seider et al. [8]). On the completion of the workshop, students are expected to be able to apply all the methodologies taught to perform efficient heat integration in the framework of their design projects. The materials were divided into three lessons taught in flipped format, covering (a) Introduction to HEN synthesis: Targeting and basic HEN design; (b) Advanced HEN design: Heat loops, stream splitting and threshold problems; (c) Heat and power integration: Extracting flowsheet data for HEN synthesis, the usage of the Grand Composite Curve for utility management, and efficient integration of process units within a HEN.

## 3. METHODS

### 3.1 Research Questions

**RQ1.** What was the level of students' approval for the usage of flipping? Was this perception different for those students who engaged more with the course resources and activities, compared to those who engaged less?

**RQ2.** Did the students who engaged most with the course resources and activities achieve better learning outcomes than those who engaged less?

**RQ3.** Which of the three versions of flipping achieved the best results, and why?

### 3.2 Research Methods

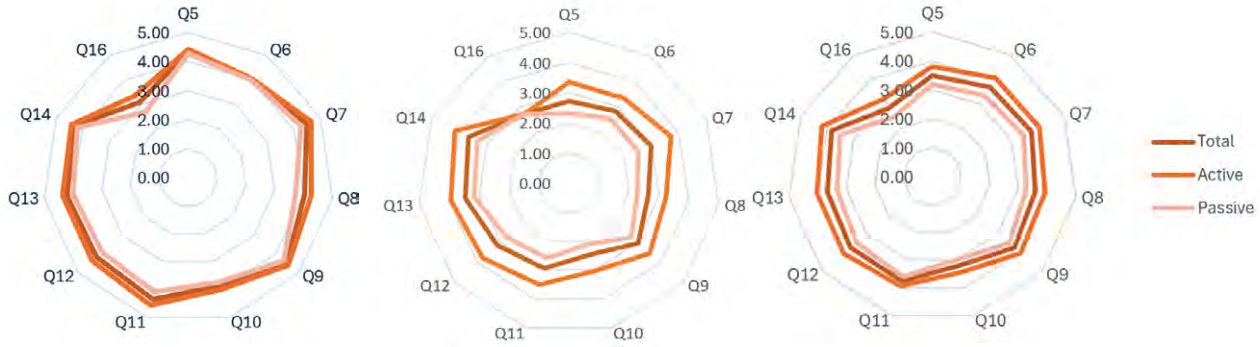
Two measures were used to assess effectiveness of the flipping approach as implemented at ICL: (a) The three course cohorts were asked to respond to surveys in which students provided self-assessment of the degree of their engagement with the course components, the degree of satisfaction with the flipped class approach, as well as their estimated degree of learning and mastery. (b) Learning outcomes of the three courses were analyzed, and where relevant, compared with the results of previous years.

**Table 1:** Categorization as "active" students according to response.

| | *INM*, the "good" | *PDC*, the "bad" | *PD*, the "surprising" |
|---|---|---|---|
| No. of registered students | 29 | 140 | 138 |
| No. of responders | 25 (86%) | 105 (75%) | 108 (78%) |
| What was your degree of participation in the following activities? | | | |
| **Q1.** Online lessons (OL) completed | Completed all OLs | Completed all OLs | Completed all OLs |
| **Q2.** Class meetings (CMs) attended | Attended at least 5 out of 10 CMs | Attended at least half of 5 CMs | Attended at least 1 out of 3 CMs |
| What was your degree of active participation in the following activities? | | | |
| **Q3.** Engagement while watching online lessons | Watched some clips repeatedly | Not asked | Watched all clips at least once |
| **Q4.** Degree of active participation in CMs | Tried to solve some or all the class problems | Tried to solve problems in at least half of the CMs | Tried to solve most or all of the class problems |
| No. of "Active" students | 14 (56%) | 41(39%) | 52 (48%) |

**Table 2:** Listing of survey questions regarding students' perceptions of flipped classroom.

| | | |
|---|---|---|
| **Q5.** | Flipped classroom (FC) is more appropriate than traditional teaching | ❶ |
| **Q6.** | FC improved my ability to learn | |
| **Q7.** | FC motivated me to take an active role in my learning | |
| **Q8.** | FC encouraged me to learn more effectively | |
| **Q9.** | FC was a valuable learning experience | |
| **Q10.** | I want to expand my learning opportunities with more courses using FC | |
| **Q11.** | The online lessons (OLs) were helpful in clarifying the course material | ❷ |
| **Q12.** | The OLs prepared me adequately for class meetings | |
| **Q13.** | The in-class activities in the class meetings (CMs) were engaging and interactive | |
| **Q14.** | The CMs helped me to apply concepts I learned from OLs | |
| **Q15.** | List the resons why the CM was effective to your learning (or not) | |
| **Q16.** | What was the level of confidence in your mastery after CMs? | ❸ |




(a) *INM*, the "good" (b) *PDC*, the "bad" (c) *PD*, the "surprising"

**Figure 1:** Summary of responses to the surveys in the three courses, differentiating between the total class and the "active" and "passive" groups.

## 4. SURVEYS RESPONSES: RESULTS AND DISCUSSION

The first four survey questions are intended to gauge the degree of responder engagement in the components of the flipped courses. The first two ascertain the extent of the responder's passive engagement, that is, what percentage of the Online Lessons (OLs) were completed, and class meetings attended. The third and fourth establish the responder's degree of active engagement, that is, for the OLs, were the video clips viewed partially, just once, or often several times to improve understanding, and in the class meeting problem-solving exercises, did the responder just listen to the presented solution, or try to solve a few, most, or all the problems. As shown in Table 1, the responses to these questions distinguish between two approximately equal groups: the so-called "active" students, i.e., those that meet given levels of engagement with the online resources and class meeting exercises, and those that do not, who are termed "passive" students.

The remaining survey questions, listed in Table 2, were intended to ascertain, from each responder: Group ❶ (Q5-Q10), the degree of agreement with several statements concerning the flipped class paradigm as implemented, Group ❷, the degree of agreement with statements concerning the effectiveness of the online lessons and class meetings (Q11-Q14), and Group ❸, their perception of the level of confidence in their understanding of the course material (Q16). Except for Q15 and Q16, the responses were on a Likert scale of 1-5, with 1 = strongly disagree, 2 = disagree, 3 = neither agree nor disagree, 4 = agree, and 5 = strongly agree. Q15 asks the responders to indicate the reasons why the class meeting was effective for their learning or not. For Q16, the scale was: 1 = not at all confident, 2 = somewhat confident, 3 = confident, 4 = very confident, and 5 = extremely confident.

The students' responses to all three surveys are summarized in the radar plots of Figure 1, which shows the average scores returned for three categories of students: The scores for the "active" and "passive" students, on either side of the scores for the entire class. The polar plots provide a visual comparison of the degree of approval for the flipped class paradigm for the three courses; the degree of approval in each course is in proportion to the area encircled by the plots:

(a) The largest area indicating relatively high approval was expressed in the "good" course, where the responses to most questions indicate "agreement" (the "active" students returned an average score of 4.3), with statistically indistinguishable responses for the "active" and "passive" students, with the exception of their degree of confidence in mastery, where "active" students are significantly more confident than "passive" students.

(b) The smallest area indicating relatively low approval was expressed in the "bad" course, with the largest differences between the responses of the "active" and "passive" students out of the three courses: The average responses of the "active" students indicated "agreement" with positive opinions (average score of 3.5), while for the "passive" students, the average indicated disagreement. The average student opinion that their level of confidence was only "somewhat confident."

(c) The survey results indicate that the "surprising" course was perceived somewhere between the other two courses, where again, one can observe that the "active" students were statistically more positive in their opinions than the "passive" ones.

## 5. LEARNING OUTCOMES

For the "good" and "bad" courses, both of which included an examination as the main grade component, this is straight forward, and these are presented and discussed. For the "surprising" course, in which there was no final exam, but rather, a group project, we bring the group project grade distribution of the project component that involved heat integration, with a comparison with its distribution from the previous year, when heat integration was taught by regular lecturing alone. A passing grade at ICL is 40%, with grades of 70% and above being considered 1st Class Honors (the highest grade).

### 5.1 Learning outcomes for the "good" course (INM)

Going by the responses from the first four questions of the corresponding survey (See Table 1) and the lecturer's own observations, most students were actively engaged during the entire semester. Figure 2 presents the exam grade distribution for this course, showing that given this level of motivation in the class, it is not surprising that all the students passed the exam, with an average grade of 71%. The grade distribution is multimodal, indicating that the class is roughly divided into three equally sized groups, one which excelled, one which did well by ICL standards, and one last group who passed the exam with basic capabilities. This pleasing outcome is indicative of a well-prepared exam, which accomplished a clear separation of the course participants by abilities.

### 5.2 Learning outcomes for the "bad" course (PDC)

In this case, most of the students (61%) were not actively engaged during the entire semester. Figure 3 shows the exam grade distribution for this course, indicating that given the relatively low level of engagement

in the class, it is not surprising that the overall class performance was poor, with an average of 50%; 41 out of 149 students failed the exam (28%), with 21 scoring above 70%. Indeed, the primary lecturer reports that this is the worst performance in the course in all the years that she has taught it. As shown in Figure 3, the distribution can be decomposed into a bimodal distribution using the method of Lewin [9], which computes the parameters of two weighted normal distributions that best fit the overall grade distribution: for the better-performing students with an average of 63%, and for the underperformers with an average of 35%. The better-performing students constitute 64% of the class, with the remaining 36% being the underperformers, which can explain the high failure rate. Students cannot realistically expect to achieve mastery in a course if they do not engage, whichever method is used to teach it.

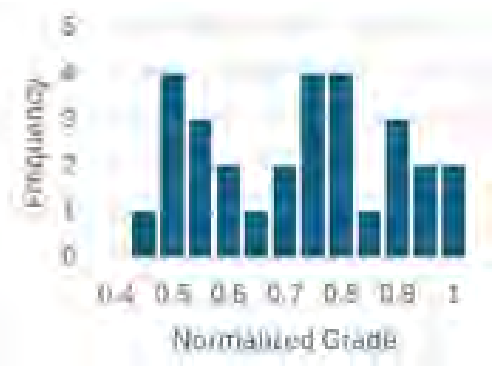



**Figure 2.** Exam grade distribution for *Introduction to Numerical Methods* (the "good" course).

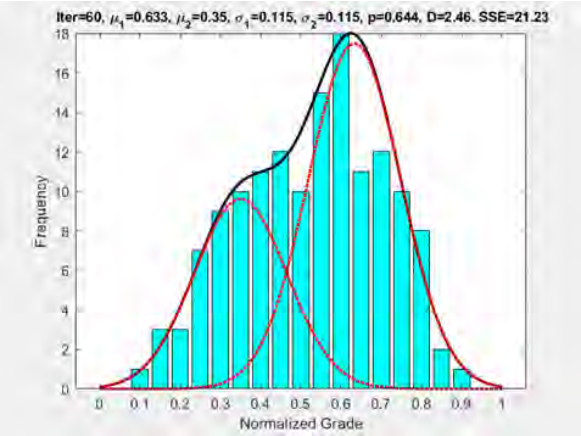
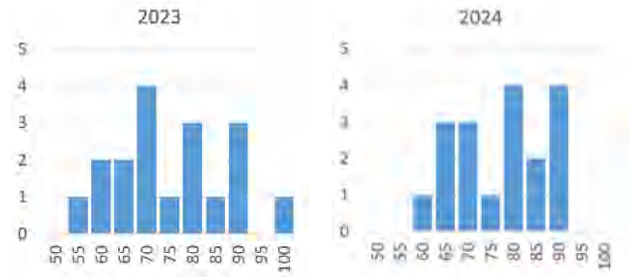



**Figure 3.** Exam grade distribution for *Process Dynamics and Control* (the "bad" course).

## 5.3 Learning outcomes for the "surprising" course (Workshop on Heat Integration)

About half of the students (48%) were actively engaged during the workshop. It is of interest to compare the team grade distribution for the design project's heat integration component awarded last year, when the subject was taught using face-to-face lectures, with this year's grade, in which the subject was instructed by the one-week flipped workshop. As shown in Figure 4, this year's distribution is slightly narrower (the standard deviation has dropped from 12.4% to 10.0%), with a slightly higher average grade (the average has increased from 75.3% to 77.2%). However, this small improvement is not statistically significant.




(a) (b)

**Figure 4.** Grades for the L5 component (heat integration) of the design project: (a) for 2023 (last year), (b) This year's (2024) grades following flipped workshop participation.

## 6. ADDRESSING THE RESEARCH QUESTIONS

The three research questions can now be addressed:

**RQ1.** *For all three courses, what was the level of approval for the usage of flipping? Was this perception different for those students who engaged more with the course resources and activities, compared to those who engaged less?*

We can state that most students perceive the flipped class teaching method positively, with the "active" students perceiving this to a greater extent than the "passive" ones. The least positive perceptions were for PDC, which was not flipped in its entirety.

**RQ2.** *Did the students who engaged most with the course resources and activities achieve better learning achievements than those who engaged less?*

Students that are more engaged with their studies usually achieve better outcomes than those who engage less. The most striking example was seen in the results of the final exam for PDC (see Figure 3), where the class can be divided into high- and low-performing subsets according to the degree of their engagement.

**RQ3.** *Which of the three versions of flipping achieved the best results, and why?*

Based on the survey and outcomes data, the best results were achieved in the elective course INM. This was the only course out of the three that adopted flipping in its entirety and was taught to a relatively small group of committed students. This experience indicates that if the student body come fully onboard, the approach has the capacity to be extraordinarily successful. Again, based both on survey and outcomes data, the lowest level of approval for the flipping method and the poorest outcomes were received by PDC, principally because many of the students opted not to engage with the course. Going by the survey results, the one-week flipped workshop on heat integration was well received by the students, who implemented the materials taught in the workshop successfully into their projects at least as well as with previous experience with the course and certainly more uniformly across the entire class.

## 7. CONCLUSIONS

We have reported the outcomes from a year of flipped teaching at ICL. The three undergraduate courses taught were different variations of the flipped paradigm that has been run successfully at the Technion in Israel: (1) a 3rd year elective course on numerical methods taught in its entirety in flipped format (the "good"); (2) the 2nd year core course on process dynamics and control, with the first half of the course on process dynamics taught in traditional lecture format, and the second half on process control taught in flipped format (the "bad"); and (3) a one-week workshop on heat integration, taught as part of a 3rd year core course on process design, taught in flipped format (the "surprising"). The four main takeaways from this study are as follows:

- If a decision to "flip" a course has been made, the decision should be concerning the entire course. The least successful implementation of flipping reported in this study was the one in which the first half of the course was delivered as lecture-based, with no significant effort being made to ensure students are mastering the topics being taught, and the second half was given by "flipped class." The switch between the two modes caused about half of the students to simply give up on the entire course and rely on cramming a few days before the exam, leading to an abnormally high failure rate.
- In contrast, the elective course on numerical methods, taught as a "flipped" course in its entirety was a clear success – the small class of 29 students were actively engaged to the point that an attempt to differentiate between the perceptions of the most and least engaged students did not produce results of statistical significance.
- The flipped workshop on heat integration was another success, where even the least engaged students perceived that the flipped approach improved their learning. Indeed, the students' approval of the flipped class paradigm was generally good, despite the unusually intensive way it was applied, ergo the epithet "the surprising".
- To obtain reliable results in student perception surveys, it is imperative to separate the responders into those who significantly engage with the course resources and activities, and those who engage less or not at all. High- and low-engagers often become high- and low-performers, respectively, and the perceptions of these two groups can be significantly different.

We have presented these results and our conclusions to assist any lecturer who is considering applying flipping in his or her classroom with useful tips and information.

## REFERENCES


1. Lewin DR, Barzilai A. The flip side of teaching process design and process control to chemical engineering undergraduates – and completely online to boot. *Educ. for Chem. Eng.* 39:44-57 (2022).
2. Lewin DR, Barzilai A. A hybrid-flipped course in numerical methods for chemical engineers. *Comput. Chem. Eng*. 172, 108167 (2023).
3. Kolb D. *Experimental learning as the science of learning and development*. Prentice Hall, Englewood Cliffs, NJ (1984).
4. Bloom BS. The 2-sigma problem: The search for methods of instruction as effective as one-to-one tutoring. *Educational Researcher*, 13(6): 4-16(1984).
5. Riggs JB. *An Introduction to Numerical Methods for Chemical Engineers*, Texas Tech University Press, Lubbock, Texas (1988).
6. Carnahan B, Luther HA, Wilkes JO. *Applied Numerical Methods*, John Wiley and Sons, New York, NY (1969).
7. Seborg DE, Edgar TF, Mellichamp DA, Doyle III FJ. *Process Dynamics and Control*, 4th Edition, John Wiley and Sons, New York, NY (2017).
8. Seider WD, Lewin DR, Seader JD, Widagdo S, Gani R, Ng KM. *Product and Process Design Principles: Synthesis, Analysis and Evaluation*, 4th Edition John Wiley and Sons, New York, NY (2017).
9. Lewin DR. What can we learn from exam grade distributions? *Int. Journal for the Scholarship of*

*Teaching and Learning*, 15(2), Article 7 (2021).

© 2025 by the authors. Licensed to PSEcommunity.org and PSE Press. This is an open access article under the creative commons CC-BY-SA licensing terms. Credit must be given to creator and adaptations must be shared under the same terms. See https://creativecommons.org/licenses/by-sa/4.0/



Systems & Control Transactions

**Research Article - Peer Reviewed Conference Proceeding**
ESCAPE 35 - European Symposium on Computer Aided Process Engineering
Ghent, Belgium. 6-9 July 2025
Jan F.M. Van Impe, Grégoire Léonard, Satyajeet S. Bhonsale,
Monika E. Polańska, Filip Logist (Eds.)

PSE PRESS

# Digital Shadow of a Pilot Scale Packed Batch Distillation Column for Real-Time Operator Training- and Support

**Mads Stevnsborg[a], Krist V. Gernaey[a], and Jakob K. Huusom[a]***

[a] Technical University of Denmark, Department of Chemical and Biochemical Engineering, Kgs. Lyngby, Denmark
* Corresponding Author: jkh@kt.dtu.dk.

## ABSTRACT

Digital twins and digital shadows are frequently used terms by industry and academia to describe data-centric models that accurately depict a physical system intended for process monitoring and control. Processes restricted by a low degree of automation rely greatly on operator competencies in key decision-making; a digital shadow can here assist as a guidance tool [1-4]. This work presents a practical implementation of a digital shadow to support operators running a pilot scale-packed batch distillation column at the Technical University of Denmark (DTU) primarily used in education and teaching activities [5]. This operation is selected due to inherent unsteady process dynamics that are controlled by a set of manual valves, which the student operator must continuously balance to meet purity constraints without disrupting the operation. This realisation employ a modular software architecture, separated into four distinct modules compiled into Docker images and independently deployed. These facilitate real-time connection with the equipment via OPC-UA endpoints, process model analysis via HTTP/HTTPS requests, and a dashboard UI presenting the data accessible through any web browser. The final module is realised as a Python package that stores thermodynamic models and is published on the internal GitLab registry for more straightforward utilisation across multiple projects. The advantages of this implementation strategy are flexibility and speed, allowing for continuously updating process models and directly employing them in various projects.

**Keywords**: Digital Shadow, Industry 4.0, Operator Support, Pilot Scale, Packed Batch Distillation

## INTRODUCTION

Today, digitalisation and Industry 4.0 are terms used prolifically in chemical- and biochemical engineering research. It describes various activities that ultimately focus on expanding automation and optimisation in different aspects of manufacturing and research processes. Enhancing data contextualisation and application of data-driven methods in process development and regular operation are both activities associated with digitalisation [1]. Today, the most common and significant barriers to implementation of digitalisation concepts relates to an immature digital infrastructure, data security concerns and complex systems integration. This makes data consolidation and utilisation across various sources challenging and restrict the compliance with the Internet of Things (IoT) and Big Data architectures [2]. Since the digital twin and digital shadow concepts rely heavily on these enabling technologies in practice, most chemical and biochemical manufacturers are generally committed to improving or expanding their respective digital infrastructure [1]. However, there is still an overall challenge in correctly scoping and quantifying the cost/benefit of these digitalisation projects which limit widespread adoption [1-4]. For systems of a lower automation level that rely heavily on employing operators in crucial operation steps, there is an increased focus on developing methods and tools that assist the operator in decision-making during operation [5]. In this work such example is developed for a digital shadow that is intended as support for student operators in an education setting for a pilot scale batch distillation process. Batch distillation is an old and proven volatility-based separation technology that is most frequently employed today in alcoholic beverage production and in the recovery of aromatic compounds and solvents [6]. These processes exhibit a

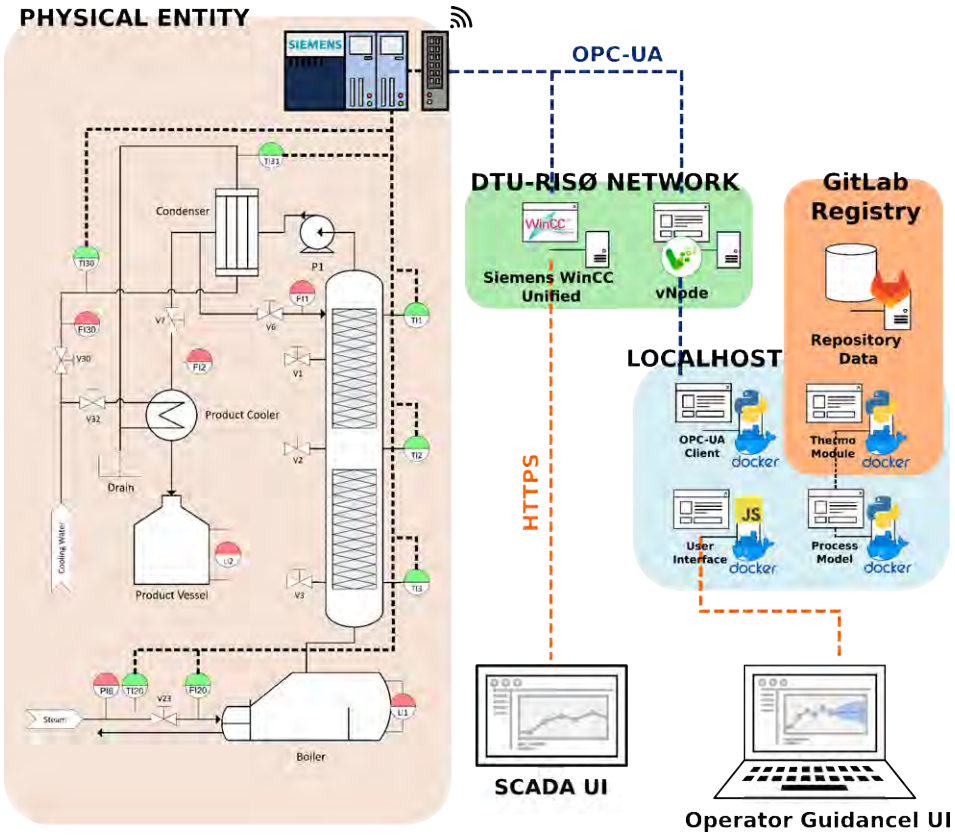



**Figure 1:** The P&ID of the packed batch distillation column at DTU-KT. The connection to the central digital infrastructure is also displayed, and all digital signals are denoted with dashed lines. The digital shadow modular architecture is also depicted with the installable module dependency connected to the central GitLab registry.

continuous transient behaviour as the product is extracted from the otherwise closed system. While most processes have automated flow control and duty utilisation, the central operation is dictated by the operators who specify desired reflux ratios. The Department of Chemical Engineering at the Technical University of Denmark (DTU-KT) manages a manually operated pilot scale packed batch distillation column primarily employed for education purposes and solvent recovery. The unit is included in the digital retrofitting activities described by Jones et al. in 2022 [7].

## MATERIAL AND METHODS

The pilot scale packed batch distillation column at DTU-KT separates a well-documented water-ethanol binary system that forms a high-boiling azeotrope at approximately 92 mol% ethanol. The exercise aims to teach engineers about managing flow rates, reflux ratios, and heating/cooling duty to collect an ethanol product of sufficient purity. The pilot scale equipment consists of a 100L steam-heated boiler (T1) connected to a glass column with an inner diameter of 10 cm. The column is fitted with Mellapak™250Y for a total height of 1.68 m. Atop the column sits a total condenser connected to a pump (P1) that returns the condensate to the column as reflux or to a product tank (T2). The unit is augmented with a total of 13 sensors, of which 6 x temperature (TI) sensors and 1 x flow meter (FI) are logged online with an additional 3 x flowmeters, 2 x level indicators (LI) and 1 x pressure sensor (PI) are read by operators offline. The simplified PI&D for the setup is presented in Figure 1. The initial boiler contains a mixture of approximately 80L 30w% Ethanol. The operator is responsible for manipulating the reflux ratio and the steam- and cooling duty to maximise the recovery and purity of ethanol over an operation period of approximately 2 hours at atmospheric pressure. The digital infrastructure is addressed in a later section.

## MATHEMATICAL MODELS

Even though the unit operation is operated frequently at DTU-KT, the collected data is of limited usability for unit characterisation and model development. This is primarily due to vital analogue information pertaining to flow rates, liquid levels and liquid composition being omitted from the digitally stored data. Therefore, reconstructing mass- and energy balances is challenging

and requires several simplifying assumptions regarding the process operation characteristics. As a result, this caveat limits the applicability of data-driven and hybrid methods due to a lack of data volume. Furthermore, since the operators are instructed to select a specific reflux ratio and keep this constant, it produces a dynamic profile that becomes very similar across experimental runs. The lack of variability in the dataset ultimately limits the effectiveness of using supervised learning methods such as neural networks to derive the operational characteristics, even if a sufficient data volume is available. This work puts emphasises on delivering mathematical models for the given process. Therefore, simple equilibrium-based models have been employed and deemed sufficiently accurate for the application. The future prospect of employing data-centric models is discussed later.

Separation of the water-ethanol binary at atmospheric pressure can confidently be modelled as an ideal vapour phase and non-ideal liquid phase using the modified Raoult's law. The mixture's vapour-liquid phase equilibrium (VLE), Antoine parameters and binary interaction coefficients are presented by Kamihama et al. [8]. The component heat capacities, densities, and latent heat of vaporisation are modelled using fitted 3rd-order polynomial functions with respect to a reduced temperature. The polynomial function is depicted in equation 1. Coefficients are fitted using saturated temperature data from CRC 101st ed.

$$f(T_r) = A + BT_r + CT_r^2 + DT_r^3 \quad (1)$$

The separation efficiency of structured packaging material Mellapak™ 250Y [9] depends on a flow number (*F*) calculated based on the vapour flow rate in an empty column and the vapour density shown in equation 2.

$$F = \omega \cdot \left(\frac{g}{A_c}\right) \sqrt{\frac{T}{P \cdot M_{w,g}}} \quad (2)$$

$$\mathrm{HETP} = a \cdot \log\,[1+F] \cdot \left[\frac{F}{s}\right]^p + x_0 \quad (3)$$

This is a function on the vapour flow rate in an empty column, $\omega \cdot (g/A_c)$ , and the vapour's molar weight, $M_{w,g}$. The flow number takes a value in the interval 0.5 – 3.5, corresponding to packaging material attaining an equilibrium tray equivalent height (HETP) of 0.32/m – 0.45/m. This results in an expected number of equilibrium trays (NETP) between 3.73 and 5.25 for a packed column height of 1.68m. A surrogate model is fitted to the HETP curve provided by Sulzer in Figure 2. to readily determine the packaging material's separation efficiency from estimating the boil-up ratio and vapour composition. Here, the F values refer to a flow number, while the coefficients $a$, $p$, $s$, and $x_0$ are coefficients that are determined by fitting equation 3. to the data presented in the Sulzer data sheet for Mellapak 250Y packing at 960 mbar [9]. The fitted expression is presented in equation 4.

$$\mathrm{HETP} = 0.0634 \cdot \log\,[1+F] \cdot \left[\frac{F}{313}\right]^{30.3} + 0.315 \quad (4)$$

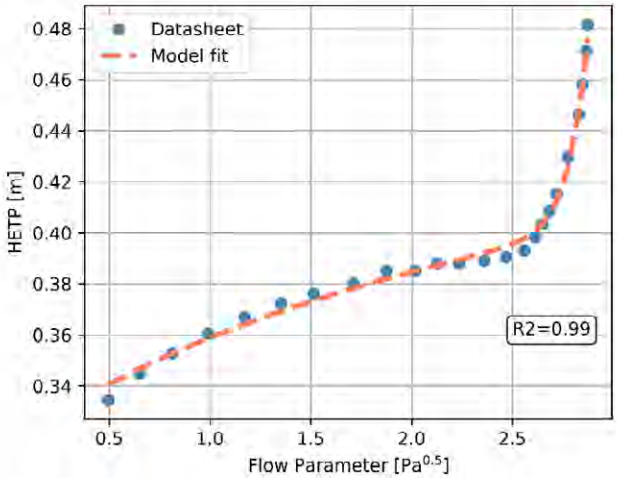



**Figure 2.** Reported Mellapak 250Y separation as a function of the characteristic flow number.

Currently, the operator is guessing the condensate's total volumetric flow rate and perform incremental adjustments from a visual inspection of the condenser hold-up to balance the flows. Approximating the volumetric condensate flow rate can alleviate this task while simultaneously predicting changes from boiler duty or reflux ratio modifications. This can give rise to more accurate control adjustments that allow for possibly operating at variable reflux ratios, improving the process's energy efficiency. If the steam condensation supplies only heat to evaporate the boiler mixture, the estimated vapour flow rate leaving the boiler can be readily estimated from online sensors with equation 5.

$$V_{est.} = \frac{\Delta H_{vap}^{steam} \cdot FI_{20}}{\Delta H_{vap}^{boiler}} \quad (5$$

From the vapour flow rate and estimated vapour composition, the flow number and NETP can be readily determined from the online sensor readings. In combination with user inputs regarding the reflux ratio and estimation of the condensate composition, it is possible to construct a McCabe-Thiele diagram for the operation, as depicted in Figure 4. In addition, the cooling duty in the condenser is employed to estimate energy efficiency $\eta$. It is also employed to estimate the product's composition and thereby track an estimate of the recovered liquid's purity and the remaining amount of ethanol to purify.

## RESULTS AND IMPLEMENTATION

Digital shadows and digital twins are frequently attributed as flexible model realisations that satisfy multiple stakeholders across research and manufacturing and

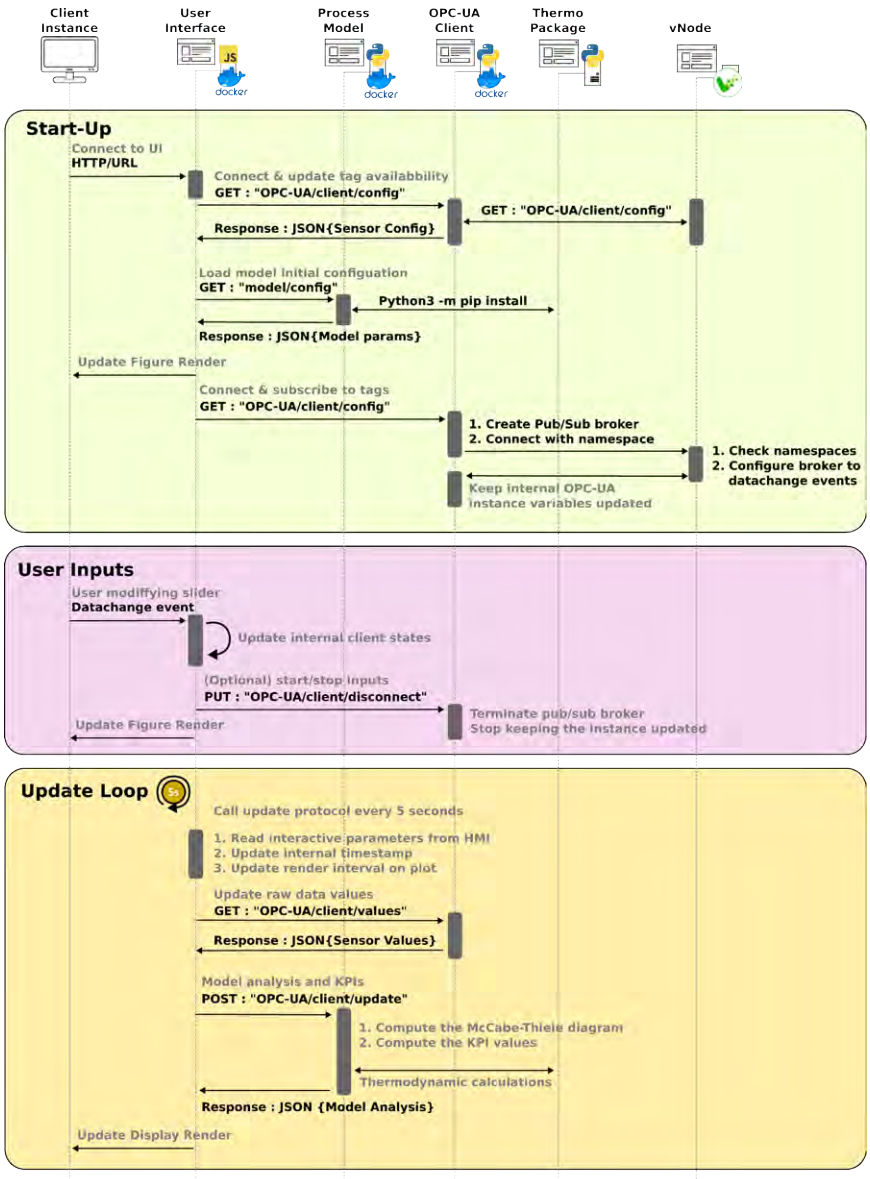



**Figure 3:** A summarised sequence diagram for the packed batch distillation column core functionality. Here, the various resources are depicted in a column format, with the interactions depicted as prompted connections.

interface easily with physical equipment [2,4]. Consensus is that the best approach is to follow a standardised implementation paradigm that link multiple smaller model realisations and software resources together in a central environment. This work adopts a microservice-oriented approach to realising the software implementation. In addition, the workflow adopts the DevOps development paradigm often utilised in conventional software development [10]. The various modules/services developed in this project are version-controlled using git (v2.36.1) and distributed through GitLab with continuous integration and continuous delivery (CI/CD) pipeline compiling Docker images and package installables. The software is structured into four modules, as depicted in Figure 1. Each module functionality is compartmentalised individually using Docker (v24.0.6) except the thermodynamic module, which is configured as a Python installable dependency. The Docker images are configured as a collection using Docker Compose (v2.22.0). This results in a software collection where each module can deploy independently but allows communication between modules in the collection, as depicted in Figure 3. The UI is developed using Next.js (v13.5.0) with Redux (v4.2.1) state management, Materials-UI library components and D3.js (v7.8.5) visual rendering. The connection, storage and model backend is developed in Python (v3.10.15) and deployed using the FastAPI (v0.103.2) and Uvicorn (v0.18.3) libraries. The connection manager is a general-purpose

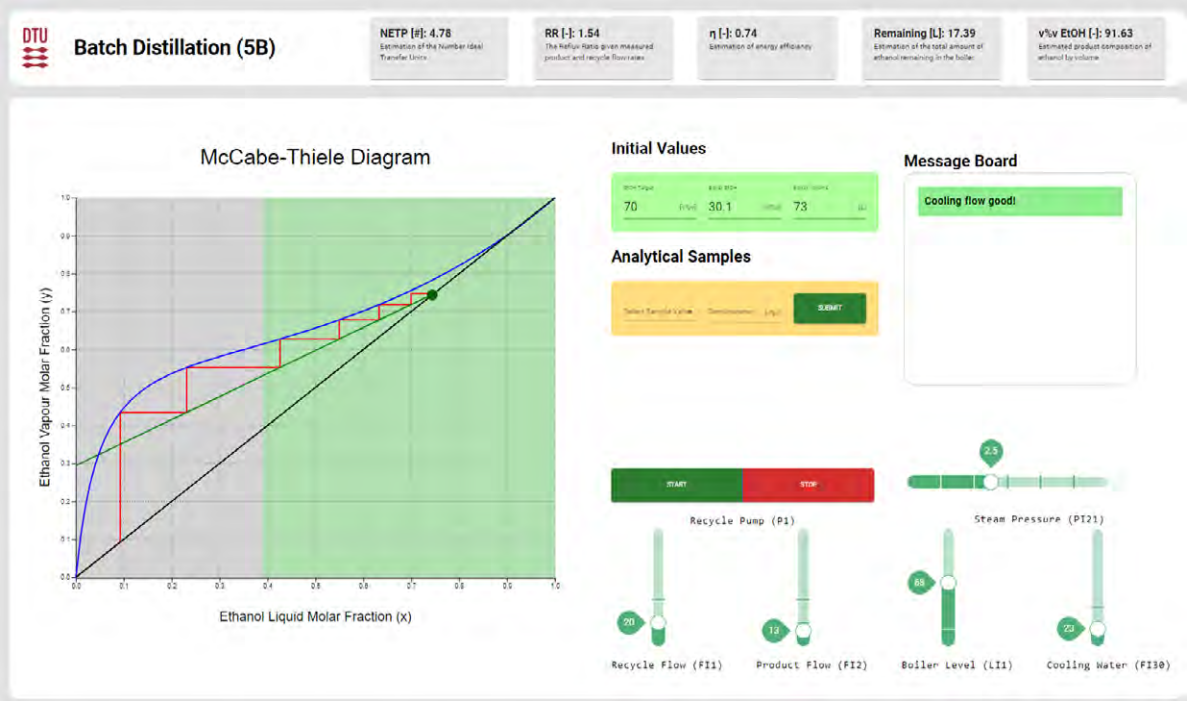



**Figure 4:** Screen capture of the UI for the pilot scale packed batch distillation column. This cas depicts an operation with an initial boiler content of 73 L and approximately 30 vol% ethanol.

OPC-UA client developed in Python and designed to integrate specifically with DTU-KT pilot equipment connected to the vNode intermediary [7]. The operator accesses the UI dashboard through a web browser on a device connected to the secure network. The UI then manages calls to the various API that establish connection and process model functionalities based on the operator interactions through the UI. All logic concerning model prediction and estimation is compartmentalised with Docker, and all functionality is exposed to the software architecture by a REST API construction. The UI updates the relevant elements based on user interaction and automated update loops. The operator interacts with the logic through the UI abstraction. This interface includes a graphical rendering of the current operational state with a summary of key performance indicators as a McCabe-Thiele diagram, depicted in Figure 4. A series of sliders and buttons are also presented to the operator, which she can use to update the offline sensor values quickly. The UI detects the change in slider position and sends the information to the database, where it is stored next to raw sensor inputs and model analysis. The updated user inputs are used in the succeeding API calls to provide updated trajectories on the McCabe-Thiele diagram. From the online temperature sensor measurements, the molar vapour and liquid compositions are determined for the boiler (TI04), middle column (TI02), and top of the column (TI01), assuming phase equilibrium. The online steam flow rate (FI20) and saturated steam temperature (TI20) also provide an online estimate of the applied heat duty. Combined, it is possible to estimate the boil-up rate and flow number readily. Thus, it is possible to provide an estimation of the HETP and NETP from the Sulzer reference sheet [9]. The operator can update the value of the three offline liquid flow meters depicting reflux (FI1), product (FI2) and cooling water (FI30), respectively, with a slider-based input system on the UI. Also, the boiler (LI1) and product tank (LI2) level indicators are updated with a slider input block. Additional performance metrics such as the condenser duty, reflux ratio (RR), and material balance can then be computed and displayed with the online and offline sensor measurements.

## DISCUSSION

This work achieves a practical realisation of a digital shadow for a pilot scale packed batch distillation using a modular implementation approach akin to a microservice architecture which follow a modular architecture suggested in recently published literature [4,7]. In the current configuration, the thermodynamics models are implemented in parallel to the system models and separated into a dedicated thermodynamic installable package. This allows for better utilisation of these models and data across multiple projects for different processes. In this case study, the central objective is not the effectiveness and usability of the final software solution. Instead, focus is placed on the development and delivery process,

evaluating the relative ease of modification and expansion to the presented proof-of-concept. With the modular implementation, updating or substituting the first-principles model, in this case, will be more straightforward if implemented as an API resource accessible with communication protocols such as HTTP/HTTPS. As data is collected throughout multiple runs and analytical data is properly contextualised and stored next to the online measurements in a digital and easy-to-query environment, complete or partial data-driven methods in state estimation will be possible in the future. The OPC-UA connection module is sufficiently generic, which has significantly streamlined integrating connection and delivery of other projects at DTU-KT. The selection of the KPIs employed in this work is based entirely on the authors' perceptions. It is important to include the users in the development loop to effectively continue the development of a digital shadow such as the one presented in this case study. Following the DevOps cycle, the next steps are operations and performance evaluation. Operator support and guidance tools do not have to be overly complicated to be effective. Since this exercise is also leveraged in chemical engineering education, the aim is equally to enhance the learning outcome of the exercise. Ideally, the more complex UI can allow the engineer to experience theoretical material employed on real systems in real-time and observe how the dynamic operation affects the various KPIs. Here, the results are largely qualitative, focusing mostly on delivering a platform that leverages the model-based and domain competencies in a format that generates value. With the infrastructure in place, a succeeding project can more easily implement new metrics or compare against future data for a quantitative assessment of the model accuracy, KPI usefulness, etc. Most of the cases explored in this area are centred on bio-based manufacturing. However, this case illustrates a modular approach to developing digitalisation tools, which can arguably be leveraged for other process types as well.

## CONCLUSION

It is possible to develop and implement a digital shadow for real process equipment using the micro-service software architecture. The case study delivers a proof-of-concept digital shadow that is of an appropriate- and feasible scope given the process description. The application employs a rudimentary model that could offer some model-based support for operators running the packed batch distillation column at DTU-KT. This guidance system focuses on lowering the barrier for operators to report offline sensor values, providing the operator with enhanced insight into the operation state, and improving offline data collection. Future developments will focus on collaborating with the operators to drive the next development steps in a direction that best suits the use-case of this digitalisation tool.

## ACKNOWLEDGEMENTS

The authors of this work acknowledge the efforts of students and staff at DTU-KT and express our gratitude to the Novo Nordisk Foundation for funding through grant NNF19SA0035474.

## REFERENCES

1. Udugama et al., Digital Twin in biomanufacturing: challenges and opportunities towards its implementation, *Syst. microbiol. biomanuf*, 3:1, 257-274, (2021),
2. Borgosz et al., Industrial internet of things: What does it mean for the bioprocess industries?, *BioChem Eng J.*, 201, 109122, (2024)
3. Stark et al., Hybrid digital manufacturing: Capturing the value of digitalization, *J. Oper. Manag*, 69:6, 890-910, (2023)
4. Boschert et. al., On the Importance of Simulation and Digital Twin for Industrial Applications, *Digital Twins, simulation, and the metaverse*, 95-117, (2024)
5. Bähner et al., Challenges in Optimization and Control of Biobased Process Systems: An Industrial-Academic Perspective, *Ind. Eng. Chem. Res*, 60:42, 14985-15003, (2021),
6. Díaz-Quezada et al., Model-based workflow for sustainable production of high-quality spirits in packed column stills, *Comput Chem Eng*, 192, 108910, (2025),
7. Jones et al., Pilot Plant 4.0: A Review of Digitalization Efforts of the Chemical and Biochemical Engineering Department at the Technical University of Denmark (DTU), *Comput. Aided Chem. Eng*, 49:1, 1525-1530, (2022),
8. Kamihama et al., Isobaric Vapor–Liquid Equilibria for Ethanol + Water + Ethylene Glycol and Its Constituent Three Binary Systems, *JCED*, 57:2, 339-344, (2012),
9. Sulzer Ltd., Structured Packings: Energy-efficient, innovative & profitable, *Technical Report, Sulzer Ltd*, (2024)
10. Koren et al., Implementing DevOps Practices in CPPS Using Microservices and GitOps, *ETFA*, 1-4, (2023),

© 2025 by the authors. Licensed to PSEcommunity.org and PSE Press. This is an open access article under the creative commons CC-BY-SA licensing terms. Credit must be given to creator and adaptations must be shared under the same terms. See https://creativecommons.org/licenses/by-sa/4.0/



Systems & Control Transactions

**Research Article - Peer Reviewed Conference Proceeding**
ESCAPE 35 - European Symposium on Computer Aided Process Engineering
Ghent, Belgium. 6-9 July 2025
Jan F.M. Van Impe, Grégoire Léonard, Satyajeet S. Bhonsale,
Monika E. Polańska, Filip Logist (Eds.)

PSE PRESS

# Teaching Automatic Control for Chemical Engineers

**Miroslav Fikar*, Lenka Galčíková**

Slovak University of Technology in Bratislava, 812 37 Bratislava, Slovakia
* Corresponding Author: miroslav.fikar@stuba.sk.

## ABSTRACT

In this paper, we present our recent advances and achievements in automatic control course in the engineering study of cybernetics at the Faculty of Chemical and Food Technology STU in Bratislava. We describe the course elements and procedures used to improve teaching, learning, and administration experience. We discuss on-line learning management system, various teaching aids like e-books with/without solutions to practice examples, computer generated questions, video lectures, choice of computation and simulation tools. The course is provided in the presence form of study for about 20 students, but it relies on on-line tools and methods. Starting from this academic year, flipped design of the course was designed. We describe our experience in the preparation of such a change and some initial feedback from the students. The course concentrates on input/output linear approximation of processes in chemical and food technology and discusses poles/zeros, process dynamics, frequency and time methods, closed-loop system, design and tuning of PID controllers, root-locus analysis. Although the majority of laboratory exercises is performed using simulation tools, we also provide easy-to-use laboratory device that can be given to all students to work either at school or at home.

**Keywords**: Education, Process Control, MATLAB, Students' Feedback

## INTRODUCTION

The rapid advancements in information technologies have affected engineering education, particularly in the fields of chemical engineering and automatic control. This trend was even strengthened during and after the Covid-19 pandemic.

The course on automatic control is a core component in master programs in the field of cybernetics. The students usually define it as a difficult one, due to heavy use of mathematics, physics, and chemical engineering principles. In addition, IT skills (programming and simulation languages) are needed as well. Therefore, it is of utmost importance to try to improve the learning experience of the students and, at the same time, to maintain the depth of the studied topics.

One innovative approach to enhance student engagement and learning outcomes is the flipped classroom model [3,4,8]. In this model, traditional lectures are replaced with online video lectures that students can watch at their own pace outside of class. In-class time is then used for active learning activities, such as problem-solving, discussions, and group work. This approach has been shown to be effective in promoting deeper understanding and critical thinking skills.

This paper shares our experience and shows an overview of the structure and methods used to improve teaching, learning, and administrative tasks for the course on automatic control for master students at the Faculty of Chemical and Food Engineering, STU in Bratislava.

## PROGRAM AND COURSE CONTENTS

The course *Theory of Automatic Control I* is taught at the Institute of Information Engineering, Automation, and Mathematics in the first semester of the master study in the program *Automation and Information Engineering in Chemistry and Food Industry* accredited under the field of Cybernetics. The program is thus focused on applications control and IT in process industries. It contains several main branches represented by a series of courses:

- Theory of automatic control: fundamentals, state-space methods, multivariable control, process control, robust control, intelligent control, MPC.

- Modeling: fundamental models, identification, separation processes, data processing, machine learning, process optimization.
- Technical means of automation: sensors, actuators, PLC, DCS, visualization, HMI.
- IT: web programming, databases, object-oriented programming, git, LaTeX.

Students that enroll in the program all come from chemical engineering bachelor programs at the faculty but have different levels of knowledge in cybernetics and automatic control. About 10-20% of them completed the bachelor program Process Control and are advanced, but the rest of them are students mostly with chemistry, biology, food or chemical technology backgrounds and with no previous experience with control. Therefore, the institute organizes mini-courses on MATLAB and Python programming, data treatment, and IT skills at the beginning of the first semester.

The course is planned with 2 hours of lectures and 3 hours of seminars/exercises per week and its contents is as follows:

- Mathematical modeling of continuous-time systems: general principles of modeling, linearization, deviation variables, state-space representation.
- Input-output properties: from states to I/O representation, from transfer function to states.
- Poles, zeros, process dynamics.
- Frequency characteristics: complex numbers, frequency responses.
- Control performance: time, frequency, integral indices, poles and zeros.
- Closed-loop system: structures, components, stability, regulation, tracking problems.
- PID controller: review, types, properties, anti-windup, bumpless transfer.
- Root-locus techniques for analysis and design.
- PID controller tuning.

This is a fairly standard course content for the introductory course in automatic control. As it is taught at the chemical engineering faculty, all students have knowledge and experience with standard engineering mathematics and physics, steady-state material and enthalpy balances, chemical engineering fundamentals.

The processes selected for modelling and control are built on this knowledge and include mainly heat exchangers and water tanks. They are used repeatedly in different course topics. A simple heat exchanger can be represented by a first-order transfer function, and a series of them can be used for linear systems of higher order. Two or more water tanks (without pumps) represent stable nonlinear processes, suitable for linearisation, comparison of linear and nonlinear behaviour. If a pump is included, it results in unstable integrating process that needs to be stabilised using feedback control. We note that specific control of more complicated processes is studied in the third semester in the course Theory of Automatic Control III (advanced process control).

## STUDY SYSTEM AND SUPPORT

The course frontend is provided using LMS Moodle that has been in use at the faculty since 2005. Therefore, teachers have a good knowledge of the system. The most used activities/sources are files, links to videos, assignments, and quizzes. Institute courses provide full read access to all teachers - the aim is to know about material and ways how it is provided to students - to increase compatibility level between courses. In addition, limited read access is provided for anonymous course guests (https://elearn.uiam.sk/course/view.php?id=95).

The backend to the course is maintained in Gitlab repository of the institute. This covers LaTeX sources to all study materials, MATLAB and Python sources to scripts. This helps to follow the evolution of the course and facilitates transitions between instructors.

Starting from this school year, flipped design has been used. Since Covid19 times, lectures have been recorded. The most recent 2 hours lecture recordings (approx. 20 hours total) were cut into smaller logical pieces (5-10 minutes each) and uploaded to YouTube. One or two Moodle Lesson activities were then prepared from every lecture and there are one or more questions after each video. Each Lesson begins with definition of its objectives and aims for students. This activity must be completed prior to the actual week. The experience from the first year shows that the average duration of this individual activity takes about 3 hours. Students can repeat the lesson questions, and the best result is used for grading. Knowledge of the material shown in lecture recordings is required in the final oral exam.

As the flipped-design classroom requires students to dedicate significant time to preparing in advance individually, it makes the flipped design a good candidate for putting all students with different backgrounds on the same level. This way, the students get familiar with novel topics at their own pace, and they apply the acquired knowledge in practice at school during active tutorials and seminars.

Instead of the traditional lecture, students come to Active tutorial, supervised by the lecturer. The first part of the Active tutorial reviews the Lesson, student results and their errors in question answers. Then, the lecturer states problems that students try to solve. Students are

encouraged to work in groups, discuss together. There are two types of PDF documents available: unsolved problems with blank space to be filled and the same information with complete solutions. Therefore, students can review again the solutions provided by the lecturer. The level of complexity is chosen in such a way that no computer solutions/simulations are needed, a mobile phone or pocket calculator suffices.

The seminars are held in groups of approximately 10 students in computer laboratories, where every student works with their computer. The teaching assistant follows up on the topic from Active tutorial and gives tasks to the students. Some of the tasks are focused on manual derivations and mathematical analysis to improve students' critical and technical thinking. The teaching assistant strongly leads this part. Most of the tasks are focused on programming and simulations performed in MATLAB. During this part, the students are actively engaged, and the teaching assistant provides technical support.

Regarding the grading of the seminar, students obtain 2 assignments during the semester, and they have approximately 2 weeks to work on them at home and to submit a protocol. At the end of the semester, the students take the final test using MATLAB and MATLAB Simulink. The grade from seminars is calculated as the arithmetic mean from the two assignments and the final test.

Study materials of the course consist of selected parts from the monograph [6]. Of course, the material is standard, and any appropriate feedback control book can be used. In addition, an electronic textbook specially tailored to this course is also provided. Each chapter corresponds to one course topic, and it is divided into:

1. Topic goals, overview and summarization of the theory - this is related to the lecture recordings.
2. Examples - this corresponds to problems treated in Active tutorials.
3. Practice examples - this is the topic for the seminars with the teaching assistant.
4. Problems, MATLAB and Python snippets - supplementary information for interested students.

The individual chapters are used during the seminars. In that case, practice examples in the respective Moodle topic do not contain solutions. However, documents available for download within Moodle course also provide the full version with solutions. This helps both students (if they want to review) and if there is a replacement for a teaching assistant.

The overall course grade consists of completion of Lessons (15%), seminars (25%), and oral exam (60%).

## ELECTRONIC QUIZZES AND QUESTIONS

Assessment of student knowledge can be realized in Moodle using questions. A collection of questions can form Moodle activity Quiz, or it can be part of the Lesson activity. The Quiz question bank supports various plugins - the standard ones are for example true/false, multichoice, short answer, matching, numerical, calculated, drag-and-drop, matching. The Lesson module can use only a few of them, and, unfortunately, for the time being, it is not possible to have only a single question bank for both Quiz and Lesson.

Among other contributed plugins for the Quiz activity, STACK questions have proven to be very beneficial for our engineering the course. STACK [7] is a powerful open-source assessment system for mathematics and related disciplines, designed to enable students to answer questions with mathematical expressions. STACK uses the Computer Algebra System (CAS) Maxima [5] to evaluate the answers. It can accept equivalent expressions (random order of terms, factorization, etc.), it provides controlled randomization and inspection of deployed variants, multipart questions, customized feedback and response trees.

Figure 1 shows an example of a STACK question on inverse Laplace transform. The student specifies the answer which is immediately evaluated to show how it will be interpreted by the system. Therefore, the student can check the answer for correctness before the actual evaluation. Such questions can greatly improve the learning experience.

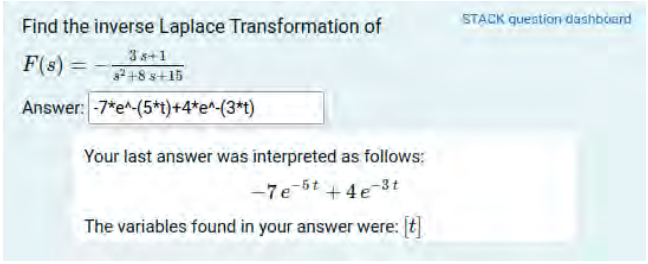



**Figure 1.** Inverse Laplace transform question using STACK.

Due to current shortcomings of the Lesson module, we generate multiple variants of numerical multichoice or short answer questions outside of Moodle using our solution based on MATLAB and XML [1]. MATLAB (or any other language) can be used as a scripting and templating engine to generate automatically many identical questions with different numerical values. Every question then consists of two input files: template XML file with placeholder for numerical values at appropriate places and computational part that generates suitable random sets and prepares the numerical values. MATLAB scripts then generate a desired type and number of questions

and produce an output neutral XML file. Then, XSLT processor is employed to generate a desired output format - this can be for example PDF to be printed (paper quiz with versions for students and for teachers) as well as import XML format suitable for Moodle -- for both Quiz and Lesson activities. One of such random questions is provided to a student using the Cluster and Random question within the page features of the Lesson activity (Figure 2).

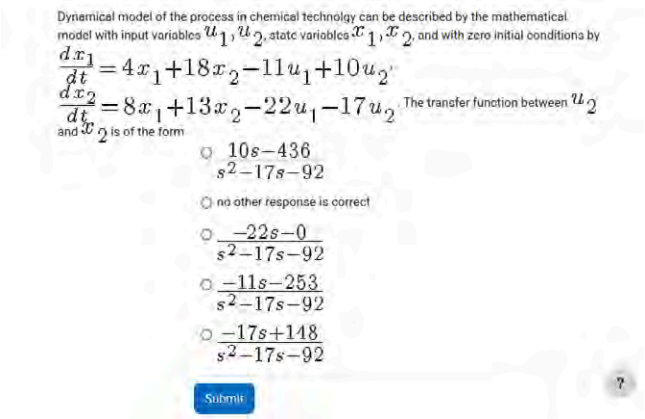



**Figure 2.** A randomly generated question in Lesson module using MATLAB, XML and XSLT.

## REAL-TIME EXPERIMENTS




**Figure 3.** Flexy2 device.

Although most of the semester work is based on simulations, we also devote some time for real-time experiments. Flexy2 device [2], shown in Figure 3, is used to demonstrate practically some steps in process control: selection of signals, observation of dynamical behavior, model estimation, PID controller design.

Flexy2 is a simple dynamical system with one input and one output. The manipulated variable is air flow from a computer fan that propels an air column in an upward vertical direction. The effect of air flow is measured by a flexible sensor that is deployed in the air column. The output variable is electrical resistance of the flexible sensor based on a degree of bend that is caused by hydrodynamic push of air. Figure 4 shows normalized step responses for steps of different magnitude and direction.

The device has a nonlinear behavior, with some minor oscillations at higher air speed. Its small dimensions make it suitable as a portable device and students can borrow it to work at home. Its API is provided both in MATLAB and Python. Both manual and automatic operations are available, the two tuning knobs at the device are programmable, they can be used for manual control or for tuning of controller parameters.

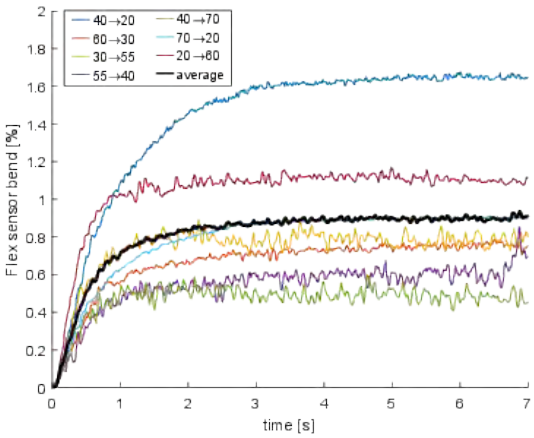



**Figure 4.** Normalized step responses of Flexy2 device.

Students are expected to measure the step responses of the process, estimate its model, design PID controllers using Ziegler-Nichols and SIMC methods, and observe/quantify control performance. Therefore, these experiments usually take place at the end of the semester when they have covered all these topics theoretically.

## FEEDBACK BY STUDENTS

This section provides an overview of the students' feedback collected weekly during the semester, as well as one final survey at the end of the semester.

The main aim of the weekly survey is to examine the students' satisfaction with the subject and teaching process. Feedback is nonmandatory, anonymous, and is collected at the end of every lecture/Active tutorial and seminar. Besides other questions, we ask students to rate the clarity and appropriateness of the presented topic on a scale from 1 (worst) to 5 points (best). In 2023, when the lectures had the standard format, we collected 62 answers during the semester with an average score of 4.76 and a minimum value of 3. One year later, after introducing the Active tutorials, we collected 77 feedbacks with an improved average score of 4.95 and a minimum value of 4.

Students can provide verbal feedback as well, but they usually do not dedicate much time to a deeper

evaluation at the end of every lecture or seminar. Therefore, we created one final survey at the end of the semester, focused on the novel form of the automatic control theory course. The feedback was provided from 10 students. The questions are as follows:

1. How do you evaluate the difficulty of the course?
2. How do you evaluate the coverage of the course by study literature?
3. How do you evaluate the novel format of lectures – Active tutorial?
4. How do you evaluate the format of seminars?
5. To what extent do you think it is possible to work on seminars independently without the guidance of a teacher?

First, we asked students about their opinion on the difficulty of the course on a scale from 1 (very easy) to 5 points (very difficult), see Figure 5. 70% of students rated the difficulty with 4 points, and the remaining 30% rated the difficulty with 3 points, which supports our experience that students usually see this course as a difficult one.

We were also curious about students' opinion about the coverage of the course by study literature on a scale from 1 (worst) to 5 points (best), see Figure 6. 50% of students were satisfied with the study materials and rated them with 5 points, and 40% of students rated them with 4 points.

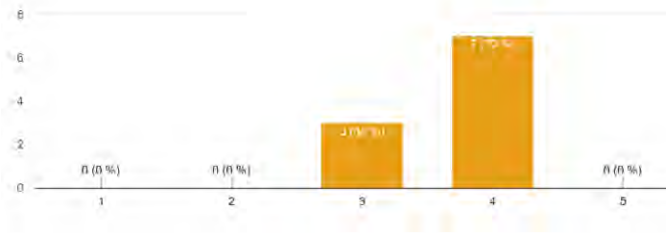


**Figure 5.** Evaluation of the course difficulty (1 – very easy, 5 - very difficult).

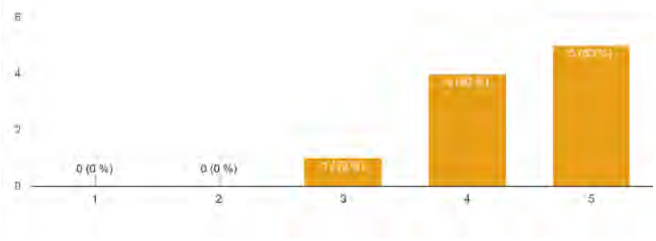


**Figure 6.** Evaluation of the study literature (1 - worst, 5 - best).

In the third question, we asked students to evaluate the format of the Active tutorial on a scale from 1 (worst) to 5 points (best). Although in this feedback, the evaluation is more distributed, majority, i.e., 70% of students rated the Active tutorial format with 4 points, see Figure 7. There was also the ability to write a comment about the novel format of the lectures. Most of the students were satisfied, but they complained about the increased time they needed to dedicate to the course:

*"It was more time-consuming, but I personally liked it because I could take good notes right away. I would probably watch the lectures again before the exam anyway."*

*"It's very time-consuming, it practically doubles the lecture time, and I only fully understand it in class. The recordings are great - you can always return to the topic, and they complement the lectures in class nicely."*

*"I prefer it over a regular lecture."*

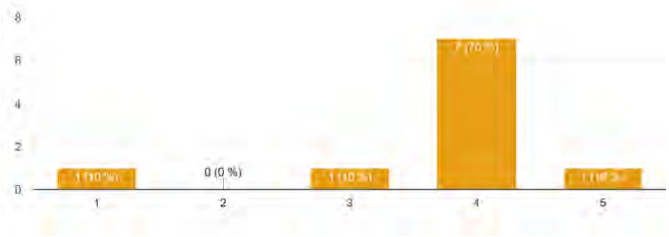


**Figure 7.** Evaluation of the Active tutorial (1 - worst, 5 - best).

In the last two questions we asked about the seminars. First, students evaluated the format of the seminars on a scale from 1 (worst) to 5 points (best), see Figure 8. Here, students expressed their satisfaction, i.e., 90% of students rated the seminars with 5 points and the rest rated them with 4 points.

Finally, we asked students about their opinion on the ability to work independently during seminars, because our aim was to decrease the necessity to lead the students and to support them mostly in work with MATLAB. The students could evaluate the independence during seminars on a scale from 1 (need for lots of support) to 5 points (totally independent), see Figure 9. The evaluation in this question is distributed, but most of the students, i.e., 60%, evaluated the independency with 3 points. The reason behind this is probably that many students studied bachelor's degrees with mostly chemical backgrounds and with no previous experience with automatic control. Students were able to leave a comment to this question, and support our reasoning of the lack of independence during seminars:

*"Many things were new to me and some I barely remembered, so I didn't even know how to start with*

*some tasks. Some questions were perhaps a little complicated and asked about things I hadn't encountered much before."*

*"The exercises were great and over time they became easier to understand. At first, everyone is of course a little lost, but over time, people get into it and start to understand the context and connections."*

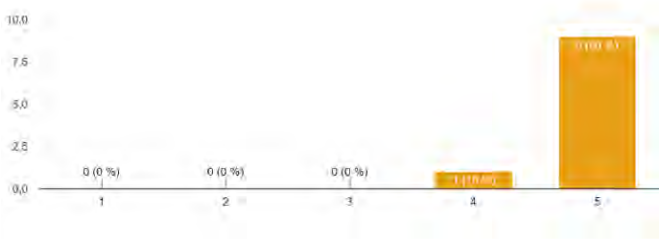



**Figure 8.** Evaluation of the seminars (1 - worst, 5 - best).

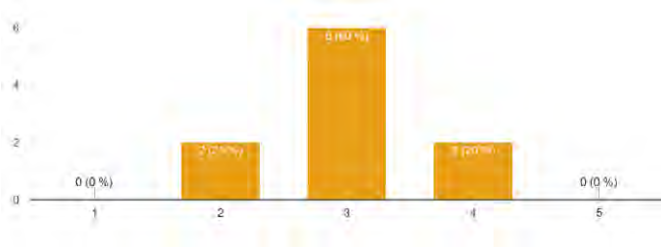



**Figure 9.** Opinion on independence during seminars (1 - need for lots of support, 5 - totally independent).

To summarize, the students see the course as quite a difficult one. Despite this fact, they rate its quality and study materials highly. The novel format of Active tutorials is more time-demanding, but students prefer it over a standard lecture.

## CONCLUSION

This paper presents our experiences and provides an overview of the structure and methods employed to enhance teaching and learning in a master's-level course on automatic control. By leveraging innovative teaching strategies, such as flipped classrooms, active tutorials, real-time experiments, and digital tools like Moodle, we successfully improved the quality of education and student engagement. The course structure integrates mainly theoretical background together with practical applications, supported by comprehensive study materials and hands-on learning through simulations and portable laboratory devices.

The students' feedback indicates a positive response to the novel teaching methods despite the recognized difficulty of the course. Students appreciate the new format, even though it demands significant time and effort. Moreover, introducing the Active tutorials led to improvement in the results of the course weekly survey when comparing this academic year with the previous one.

## ACKNOWLEDGEMENTS

This research is funded by the Cultural and Educational Grant Agency (006TUKE-4/2024), by the European Commission (FrontSeat, 101079342), and by EU RePower project VAIA (FS-Match, 09I01-03-V04-00024).

## REFERENCES

1. Fikar M, On automatic generation of quizzes using MATLAB and XML in control engineering education. Tech. Rep. 348, UIAM FCHPT STU (2007).
2. Kalúz M, Klaučo M, Čirka Ľ, Fikar M, Flexy2: A portable laboratory device for control engineering education. In: 12th IFAC Symposium Advances in Control Education, Philadelphia, USA. 159–164 (2019).
3. Lewin DR, Teaching PSE mastery during, and after, the COVID-19 pandemic. *Computers and Chemical Engineering* 160, 107741 (2022).
4. Lewin DR, Barzilai A, The flip side of teaching process design and process control to chemical engineering undergraduates. *Education for Chemical Engineers* 39, 44–57 (2022).
5. Maxima, a computer algebra system. https://maxima.sourceforge.io/ (2023)
6. Mikleš J, Fikar M, Process Modelling, Identification, and Control. Springer, Berlin (2007).
7. Sangwin CJ, Assessing elementary algebra with STACK. *International Journal of Mathematical Education in Science and Technology* 38 (8), 987–1002 (2008).
8. Talbert R, Flipped Learning. A Guide for Higher Education Faculty. Stylus Publishing (2017).

© 2025 by the authors. Licensed to PSEcommunity.org and PSE Press. This is an open access article under the creative commons CC-BY-SA licensing terms. Credit must be given to creator and adaptations must be shared under the same terms. See https://creativecommons.org/licenses/by-sa/4.0/

Systems & Control Transactions

**Research Article - Peer Reviewed Conference Proceeding**
ESCAPE 35 - European Symposium on Computer Aided Process Engineering
Ghent, Belgium. 6-9 July 2025
Jan F.M. Van Impe, Grégoire Léonard, Satyajeet S. Bhonsale,
Monika E. Polańska, Filip Logist (Eds.)

PSE PRESS

# Teaching Computational Tools in Chemical Engineering Curriculum in Preparation for the Capstone Design Project

**D. Kamel, A. Tsatse, S. Badmos***

Department of Chemical Engineering, University College London, Torrington Place, WC1E 7JE London, UK
* Corresponding Author: s.badmos@ucl.ac.uk.

## ABSTRACT

UCL Chemical Engineering ensures graduates are digitally literate by integrating computational tools like gPROMS, Aspen Plus, and GAMS into the undergraduate curriculum. Students in the first year of undergraduate program use GAMS to solve simple simulation and optimization problems and gPROMS for solving ordinary differential equations (ODEs) in reactor design problems. In the second year, students start using Aspen Plus to simulate more complex chemical process units, interpret and discuss results obtained and justify any differences observed between experimental data and computational results. They use GAMS to simulate and optimize a process flowsheet with considerations of the implications of proper initialization procedures and strategies for obtaining optimal parameters and gPROMS for advanced reactor and separator problems. The computational knowledge acquired in the first two years prepares students for the third-year capstone design project where they use the various tools in designing and simulating their processes during the preliminary, conceptual and detail designs. The computational resources available to students and the additional supports provided by educators help the students succeed on the design project in the third year. This work outlines strategies for delivering the computational tools required for modules in the first two years of the undergraduate program and the application of the knowledge in the third-year design project. It demonstrates how complex process systems engineering (PSE) problems are taught, student support and resources available, and feedback for continuous improvement. It presents some challenges faced due to the use of generative AI tools and how this can be addressed.

**Keywords**: Education, Aspen Plus, GAMS, gPROMS, Process Design, GenAI

## INTRODUCTION

Computational tools are present in most, if not all, Chemical Engineering programmes according to Molaei Chalchooghi and Sorensen [2]. In the digital era we live in, universities prioritise that their graduates are digitally literate, able to use a variety of digital tools. These computational tools could range from process simulators, programming languages, computer packages etc., and are widely used both in academia and industry for solving several problems, from the solution of very simple algebraic equations to the optimisation of complex (i.e. highly non-linear and non-convex) processes and flowsheets [3]These tools include, but are not limited to, Aspen Plus [4], GAMS [5], gPROMS [6], ChemCAD [7], MATLAB [8], Python [9] etc. Some of these tools, among others, are widely used in Chemical Engineering programmes, due to their ease of use, accessibility, availability of teaching and learning materials and resources [10], however, the choice of tools to be used depends on the application, the level of the students etc.

Computational tools in chemical engineering are essential for process design, simulation and optimization and for solving complex problems [11]. Tools like Aspen Plus can be used to model chemical processes, simulate plant operations, and optimize process conditions. These simulators allow engineers to design and test process configurations before physical implementation, reducing cost and risk. While gPROMS ModelBuilder can be used for dynamic simulation and optimization, parameter estimation, experimental design etc, General Algebraic Modelling System (GAMS) is designed to solve large scale

optimization problems. Within the Chemical engineering program, it can be used for process optimization, production planning and scheduling, heat integration and energy management through heat exchanger networks optimization, process synthesis and economic evaluation of processes.

This work explores the approach to teaching computational tools in the first two years of undergraduate chemical engineering program at UCL. It discusses the design of teaching methods, assessment strategies and feedback, along with the development of learning resources and the challenges encountered. Additionally, it highlights the collaborative efforts between students and staff in enhancing computational education and addressing learning difficulties, ensuring students are well-prepared for the third-year capstone design project and beyond.

## COMPUTATIONAL TOOLS TEACHING, ASSESSMENT AND FEEDBACK APPROACHES

### Teaching Approaches and resources

In the department, students are taught how to select the most suitable software for a given problem; and how to use this software effectively in their work before proceeding to solve more challenging problems in their future careers. In addition, teaching staff regularly evaluate the material delivered, to ensure that the concepts and topics discussed align with current research directions and the constantly evolving industrial needs.

The teaching approach includes a combination of lectures, video tutorials, and guided problem-solving sessions, ensuring students have multiple avenues for learning and understanding these tools. Supporting resources such as tutorial videos and lecture slides have been developed to cater to diverse learning needs and allow for self-paced learning.

In the first year of the undergraduate program, students are introduced to GAMS (General Algebraic Modeling System) and gPROMS Model Builder as part of the Computational Modelling and Analysis module. These tools are fundamental in developing computational problem-solving skills relevant for the chemical engineering degree program early in the curriculum. For GAMS, they learn how to solve various problems, starting from basic systems of equations to more applied cases such as simple flash calculations and refinery blending problems. The problems are carefully designed to expose students to different solvers, including constrained non-linear systems (CNS), linear programming (LP), and non-linear programming (NLP) solvers. By working through these exercises, students gain a good foundation in optimization and numerical methods, while developing a good understanding of how different mathematical formulations are applied to practical engineering problems.

For gPROMS, students are taught how to solve basic ordinary differential equations (ODEs) before progressing to more complex problems involving batch and continuous stirred tank reactors (CSTRs). This provides them with an understanding of dynamic systems and the ability to simulate basic reactor problems.

In the second year, students build on their foundational knowledge by tackling more advanced problems using GAMS. They are tasked with solving process design challenges involving complex flowsheets that typically include a flash column, a reactor, heat exchangers, and separation units. The entire process flowsheet is implemented in GAMS, requiring students to integrate multiple unit operations into a cohesive optimization framework. This includes defining an objective function, such as maximizing product yield as well as economic potential or minimizing energy consumption with the use of relevant optimization solvers. Through these activities, students further develop their programming and modeling skills and become more aware of process design and optimization concepts that are relevant to real-world engineering practice.

Additionally, Year 2 introduces students to Aspen Plus in the Separation Processes module in three lectures, integrated within the module curriculum. During these lectures the students are introduced to the Aspen plus as a simulation tool and its application in chemical engineering. They begin by learning to model basic processes, such as heaters, coolers, short cut distillation models (DSTWU), and liquid-liquid extraction. These foundational exercises build their confidence to tackle more complex operations, including rigorous distillation with RadFrac. As the course progresses, students explore advanced tools within Aspen Plus, such as sensitivity analysis for optimization and economic feasibility studies to assess the viability of process designs.

The teaching approach and computational topics covered during the year 1 ,2 and 3 are summarised in Figure 1. This approach ensures that students are equipped with the skills needed to select the most suitable computational tools for specific problems and reflect on their results before their third year capstone design project.

During their studies, students have continuous access to online learning material for all the computational tools used across the entire curriculum (i.e. AspenPlus, gPROMS, GAMS and MATLAB). The material for each of the tools includes how-to videos and step-by-step presentations that explain various concepts and processes, and how these can be implemented and solved using the respective tool. The material is updated regularly to make sure it aligns with the theory taught, or any new elements added, as well as updated versions of the software. For instance, material on how to consider

distributed models in gPROMS, and relevant examples thereof, is available for students to download, study and apply in their own time. Relevant material is available online also for aspects that are not formally considered or assessed as part of any of the taught modules, such as solids processing, so that students can refer to this if they need to consider these aspects as part of an open-ended project. Postgraduate students also make use of these resources as needed in their research and taught modules.




**Figure 1.** Distribution of PSE related tasks and available support over the curriculum.

This supporting material provides additional resources that are useful to the students especially for their projects in 3rd year, when they need to consider processes not previously covered in individual taught modules [1].

## ASSESSMENT APPROACHES

### Assessments Approaches

In all modules discussed in the previous section, assessed projects and team reports evaluate whether the learning outcomes are met, whilst tutorials for the relevant computational tools take place before the release of the material for which the software is required (e.g. project, coursework etc.). In addition, computational help desk sessions are scheduled before the respective assessment deadline so that support by staff is provided to students who may be facing difficulties with the specific software used.

In Year 1, in Process Modelling and Analysis module, students apply their computational knowledge through assessments that account for 50% of the overall module grade. These assessments include both coursework and project designed to evaluate their knowledge of using GAMS and gPROMS for programming and modelling. The problems presented to students cover a wide range of applications, including but not limited to application of some numerical methods, process flowsheeting with recycles, sensitivity analysis, convergence analysis, and simulation of steady-state and dynamic operations by solving relevant ordinary differential equations (ODEs).

In Year 2, as part of the Process Design Principles module, students undertake a project that constitutes 60% of the overall module grade. In this project, students use GAMS and Aspen Plus to design a complete process plant. The project involves solving a complex problem with multiple design variables, where the primary objective is typically to maximize the economic potential of the process and obtain a stream table for the process. Students are required to compare results obtained in GAMS with that of ASPEN and comment on the discrepancy observed. Within this assessment, students perform sensitivity analyses to identify the optimal set of operating parameters that achieve the best economic potential. This task requires the application of advanced features in GAMS, such as the use of flow-control structures (e.g., while loops), enabling them to handle iterative calculations effectively. The project provides students with hands-on experience in tackling design problems and reinforces their understanding of process design, optimization, and modelling using computational tools. Refer to **Table 1** for Computational tool used in year 1 and year 2 as part of different modules' assessments. These assessments are designed to not only test students' technical understanding of the computational tools but also to develop their problem-solving skills and confidence in applying these tools to real-world chemical engineering challenges.

### Artificial Intelligence (AI) Tools and Assessment

Technological advancement has introduced unique challenges in assessment involving the use of computational tools, particularly with the increasing accessibility of AI tools that can generate code in common programming languages such as Python and MATLAB with high accuracy. One of the primary challenges is the potential misuse of these AI tools by students to generate code required as part of their assessment. While these tools could be valuable aids, their misuse can diminish students' critical thinking and proficiency in using the tools. For instance, rather than developing a good understanding of model implementation in these software, students might rely solely on AI-generated solutions.

The situation is further aggravated by the flexibility offered to students in some assessments, where they are free to choose the software or tools they prefer. In these instances, the use of AI assistance could undermine the intended learning outcomes if assessments are not carefully designed.

**Table 1:** Computational tools used in different modules in Year 1 and 2.

| Year of study | Module name | Computational tools used |
|---|---|---|
| Year 1 | Process Modelling and Analysis, | GAMS and gPROMS Model Builder |
| | Design and Professional skills I | GAMS |
| Year 2 | Separation Processes | ASPEN PLUS and gPROMS Model Builder |
| | Process Design Principles | ASPEN PLUS and GAMS |
| | Design and Professional Skills II | ASPEN PLUS and GAMS |

To address this, educators need to adopt strategies that ensure assessments meet their educational goals even when students have access to AI tools. Assignments should be structured in a manner that integrates critical analysis, interpretation of results, and the ability to explain the rationale behind specific computational approaches. For example, tasks that require students to debug, modify, or evaluate AI-generated code can shift the focus back to understanding the implementation rather than just copying the generated codes. Similarly, incorporating reflective components, where students justify their approach to solving a problem, can help educators gauge their understanding.

UCL has also provided a guideline on how generative AI (GenAI) can be used ethically in assessments. Students must acknowledge where and how they have used GenAI in any piece of work they are submitting, and where GenAI is used inappropriately, this is considered academic misconduct that will be referred to the appropriate panels.

## FEED BACK APPROACHES

The application of computational tools is integrated within the curriculum of different modules as presented in **Table 1**. Students' feedback is collected formally three times per modules as part of CMD (continuous module dialogue). UCL's approach to gathering and responding to student feedback prioritizes anonymity and open communication, ensuring students felt comfortable sharing their experiences and suggestions.

To collect feedback effectively, Mentimeter slides are used, which allow students to present their feedback anonymously. This method was chosen to encourage honest communication, ensuring that students could express their views without hesitation [12]. By using this approach, a wide range of perspectives on the students' learning experiences are gathered, along with the challenges they faced, and their suggestions for improvement. After collecting feedback on learning experiences and challenges, the module coordinator analyses the responses and the proposed actions for developing the delivery of computational tools were collaboratively discussed with the teaching team. To maintain transparency, response slides are uploaded to Moodle, ensuring all students have access to the comprehensive overview of the improvements made based on their feedback.

Student feedback over four years for the *Computational Modelling and Analysis* module (Year 1) showed positive responses, with low response rates of 29%, 26%, 27%, and 41%. 75% found the materials useful, and 66% said tutorials met expectations. Feedback led to improvements, enhancing student confidence. Future efforts will address challenges to improve learning outcomes further.

## APPLYING COMPUTIONAL TOOLS IN THE CAPSTONE DESIGN PROJECT

During the Capstone Design Project, students apply the knowledge of computational tools they have developed over their first two years of study to design and optimize a chemical plant. The project is structured into four main stages: Appraise, Select, Unit Design I, and Unit Design II. Computational tools are used in the first three stages the details of which are provided in this section.

In the Appraise stage, students begin by developing a mathematical model of the process plant. Using GAMS, they solve the mass and energy balances for the entire process. This enables them to produce a comprehensive stream table for the flowsheet and estimate the energy requirements for the plant.

In the Select stage, students create a detailed Process Flow Diagram (PFD) and simulate the entire process in Aspen Plus. This simulation helps them assess the initial feasibility of the process and apply heat integration principles to optimize energy recovery for the overall plant, improving efficiency and sustainability.

Finally, during the Unit Design I (UDI) stage, students focus on the detailed design of a major process unit, such as a reactor or a separator. For separation columns, they use Aspen Plus, leveraging its robust capabilities in simulating and designing such systems. For reactor design, students are given the flexibility to choose from various computational tools as they wish. Commonly chosen tools include gPROMS, Python, MATLAB, and Polymath, each offering distinct capabilities for modelling and optimization of chemical processes. For more information on the design project stages, refer to Nayak-Luke et al. [13]

## TEACHING APPROACHES OF COMPUTATIONAL TOOLS IN THE DESIGN PROJECT

In the context of the Capstone Design Project, our teaching approach includes providing structured technical support sessions to assist students in overcoming computational challenges. These sessions are designed to address the diverse technical difficulties faced by students, ensuring that they can effectively simulate and analyze their chemical engineering processes using computational tools.

To facilitate effective learning, the technical support sessions are conducted in small groups of 10-15 students. This group size allows for personalized attention, fostering student engagement and encouraging active participation. Each session is repeated four times depending on the size of the cohort to accommodate different groups of students, ensuring consistent delivery of content across all sessions. The structure of these sessions is informed by educational frameworks [14] and aligned with the key aspects of teaching.

In preparation for each session, we create a forum where students could submit their questions in advance. This approach enabled the teaching team to identify the key issues to be addressed during the session, optimizing the use of time and ensuring that the most pressing concerns were covered. Additionally, this forum allows students who might be hesitant to ask questions during the session to voice their concerns anonymously, fostering a more inclusive learning environment.

The main challenges encountered during these sessions included maintaining consistent content delivery across different groups and addressing all student questions within the limited time available. Moreover, managing the varying levels of simulation skills among students required careful formulation of responses to ensure that all students could understand and apply the information, regardless of their progress.

While the primary focus of the sessions is to provide computational support, an equally important objective is to bridge the gap between theoretical knowledge and practical application. By interpreting the results generated by the computational tools, students are encouraged to critically evaluate whether the outcomes were reasonable in the context of the theoretical concepts they had learned in previous years. This integration of theory and practice is crucial for developing a deep understanding of chemical engineering principles.

Following each session, a comprehensive Frequently Asked Questions (FAQs) document addressing the main points discussed is uploaded. This resource is made available to all students, including those who are unable to attend the sessions or those that had fewer questions asked during their session. The FAQs document serves as a reference, allowing students to revisit key concepts and solutions as they progress through their design projects

## STUDENT-STAFF COLLABORATIONS IN DEVELOPING THE RESOURCES FOR COMPUTATIONAL TOOLS

UCL is committed to fostering staff-student collaboration through projects aimed at enhancing the quality of teaching and learning across departments. The need for student-staff partnership in teaching and learning and its benefit has been documented in literature [15]. In summer 2024, the Faculty of Engineering Sciences funded a project in the Department of Chemical Engineering at UCL to address specific areas where students expressed a need for additional support in computational tools. One such project involved a student developing computational resources over two months, focusing on topics that posed challenges for their peers. These resources included: step-by-step guides (in PowerPoint and Word format) on retrieving experimental data from Aspen, instructions on implementation of column internals for distillation columns, detailed troubleshooting workflows for resolving issues in AspenPlus for increasingly complex chemical processes, and guidelines for configuring more advanced process intensifications in AspenPlus, specifically reactive distillation columns. These materials were made available students on the department's online learning system (Moodle) to provide accessible and structured support for students across all cohorts. They are designed to assist students with coursework and project and to enhance understanding of advanced process simulation topics. Additionally, a similar summer project was undertaken by another student to develop resources aimed at simplifying basic modeling concepts and learning videos and slides on GAMS and gPROMS. The developed materials from this project included: sample GAMS and gPROMS codes for fundamental modeling tasks, troubleshooting tips for common errors in GAMS, and a collection of exercise problems tailored to engineering applications. These materials have also been made available to students on the online learning platform.

The active involvement of students in developing these resources not only addresses immediate learning gaps but also promotes continuous improvement in the teaching of computational tools. This collaboration highlights the value of leveraging student perspectives to improve learning resources and accessibility, while simultaneously equipping them with practical skills in computational problem-solving that could be developed further in the future.

## CONCLUSION

This paper outlined the integration of computational tools within the undergraduate chemical engineering curriculum at UCL, specifically in preparation for the third-year Capstone Design Project. It presents the approach to teaching these tools, the assessments, the feedback received from students and how it is responded to, and the various support mechanism provided to facilitate their learning.

Students are introduced to computational tools in their first year, where they apply them to solving fundamental chemical engineering problems in process modeling and simulation which they further develop in their second year by tackling more complex problems involving process design and optimization. This prepares them for them for the capstone design project in the third year.

The rapid advancement of artificial intelligence presents new challenges in higher education, particularly regarding academic integrity and the potential over-reliance of students on AI-generated solutions. Addressing these concerns requires the careful design of assessments that emphasize critical thinking and problem-solving, ensuring that students develop the deep understanding necessary for professional practice.

By continuously refining the integration of computational tools and adapting teaching strategies to evolving technological trends, chemical engineering education can better equip students with the skills needed for both research and industrial applications.

## REFERENCES


1. Tsatse AK, Sorensen E. Teaching strategies for the effective use of computational tools within the Chemical Engineering curriculum. Computer Aided Chemical Engineering 52:3501-3506 (2023) https://doi.org/10.1016/B978-0-443-15274-0.50559-X
2. Chalchooghi MM, Sorensen E. Supporting the use of PSE computational tools across a chemical engineering program. Computer Aided Chemical Engineering. 44: 1651-1656 (2018) https://doi.org/10.1016/B978-0-444-64241-7.50270-6
3. Gani R, Chen X, Eden MR, Mansouri SS, Martin M, Mujtaba IM, et al. Challenges and Opportunities for Process Systems Engineering in a Changed World. Computer Aided Chemical Engineering. 49:7-20 (2022) https://doi.org 10.1016/B978-0-323-85159-6.50002-6
4. Aspentech (2024). Aspen Plus USA, Aspen Technology.Inc.,https://www.aspentech.com/en/products/engineering/aspen-plus [Accessed 27/10/2024]
5. GAMS (2024). https://www.gams.com [Accessed 27/10/2024]
6. Siemens Process Systems Engineering (2022). gPROMS, https://www.psenterprise.com/products/gproms/process, 1997-2022.
7. CHEMCAD (2024) https://chemstations.com/chemcad. [Accessed 30/01/2025]
8. Mathworks (2024). https://uk.mathworks.com/products/matlab.html [Accessed 27/10/2024]
9. Python (2024) https://www.python.org/ . [Accessed 30/01/2025]
10. Udugama IA, Atkins M, Bayer C, Carson J, Dikicioglu D, Gernaey K V. Digital tools in chemical engineering education: The needs and the desires. Education for Chemical Engineers.44:63-70 (2023) https://doi.org/10.1016/j.ece.2023.05.002
11. Pistikopoulos EN, Barbosa-Povoa A, Lee JH, Misener R, Mitsos A, Reklaitis G V., et al. Process systems engineering – The generation next? Computers and Chemical Engineering. 147(2021). https://doi.org/10.1016/j.compchemeng.2021.10725
12. Corelli A. Direct vs. Anonymous Feedback: Teacher Behavior in Higher Education, with Focus on Technology Advances. Procedia Soc Behav Sci. 195:52-61 (2015) https://doi.org/10.1016/j.sbspro.2015.06.329
13. Nayak-Luke R, Odunsi A, Badmos S, Pollock, M. Teaching, assessing and operational sustainability in UCL's chemical engineering capstone design project. In *Proceedings of the 8th International Symposium for Engineering Education* Article 2126 University of Strathclyde (2022).
14. Cowan J. Teaching for quality learning at university – By John Biggs & Catherine Tang. British Journal of Educational Technology.43:93-100(2012) https://doi.org/10.1111/j.1467-8535.2012.01317_3.x
15. Bovill A. Student–staff partnerships in learning and teaching: An overview of current practice and discourse' Journal of geography in higher education. 43: 385–398 (2019) https://doi.org/10.1080/03098265.2019.1660628



© 2025 by the authors. Licensed to PSEcommunity.org and PSE Press. This is an open access article under the creative commons CC-BY-SA licensing terms. Credit must be given to creator and adaptations must be shared under the same terms. See https://creativecommons.org/licenses/by-sa/4.0/




Systems & Control Transactions

**Research Article - Peer Reviewed Conference Proceeding**
ESCAPE 35 - European Symposium on Computer Aided Process Engineering
Ghent, Belgium. 6-9 July 2025
Jan F.M. Van Impe, Grégoire Léonard, Satyajeet S. Bhonsale,
Monika E. Polańska, Filip Logist (Eds.)

PSE PRESS

# Closing the loop: customized coding courses and chatbots embedded in a virtual lab to teach bioprocesses

**Fiammetta Caccavale[a], Carina L. Gargalo[a], Krist V. Gernaey[a], and Ulrich Krühne[a*]**

[a] Process and Systems Engineering Center (PROSYS), Department of Chemical and Biochemical Engineering, Technical University of Denmark, Søltofts Plads, Building 228A, 2800 Kgs. Lyngby, Denmark
* Corresponding Author: ulkr@kt.dtu.dk.

## ABSTRACT

Current progress in digitalization has led to a wide interest in learning more from available data. Advanced data analytics can be achieved through commercially available software; however, learning to program allows for more flexibility and, ultimately, more freedom in the potentially tailor-suited investigation. Among other programming languages, Python is one of the most requested, in industry and research alike. To intensify the earlier efforts and create both a pedagogical framework to teach programming to (bio)chemical engineers, and provide students with the opportunity to ask questions, we explore the integration of sPyCE and FermentAI into BioVL, a virtual laboratory for teaching (bio)processes, previously implemented by the authors. sPyCE is an open-source series of Python courses tailored to (bio)chemical engineers, FermentAI is a chatbot trained to answer questions about fermentation processes. The main goal of this work is to enable students to (i) learn (bio)processes and how to model them, and (ii) ask questions to a chatbot to clarify their doubts. We believe that the Python tutorials will enable students with different backgrounds and programming skills to learn how to model (bio)processes. Moreover, the chatbot will enable students to ask for clarification right away, without having to search for an answer or wait for a teacher to reply.

**Keywords**: Education, Industry 4.0, Virtual Laboratories, Programming, Chatbots.

## INTRODUCTION

Education 4.0 uses cutting-edge technology and automation to transform learning and work. It encourages creativity and non-traditional thinking. It prepares students for Industry 4.0 by focusing on a broad range of skills and harnessing technological and pedagogical innovation [1-2]. It also aims to empower learners to tackle many new challenges. Among the skills taught under this paradigm, programming and the use of artificial intelligence (AI) are the most requested.

Along with the constant development of new and advancing technologies, comes the need for a qualified workforce [3]. One of the increasingly mandatory requirements is to suitably educate future engineers for Industry 4.0 and its demands. Therefore, it is necessary to improve the quality of education in (bio)chemical engineering processes and increase students' engagement [4].

By fostering a culture of continuous learning and leveraging digital tools and resources, learners can improve their expertise, strive towards excellence, and contribute to the advancement of the field.

One of the ways educators can contribute to this is by teaching students how to code. Integrating coding in the (bio)chemical engineering curriculum is paramount [5], especially with regards to the four following aspects:

- Data analytics: (bio)chemical engineers frequently handle large amounts of data, and coding can automate the data analysis process, making it more efficient.
- Process modelling and simulation: coding skills are increasingly necessary for creating and working with process simulations. (Bio)chemical engineers frequently create models of (bio)chemical processes using coding to simulate different




(a) (b)

**Figure 1:** BioVL platform. Figure (a) Shows the BioVL interface; Figure (b) illustrates the development of the interface based on Bloom's taxonomy (Bloom, 1956).

process design scenarios.

- Optimization: (bio)chemical processes involve complex systems that need to be optimized; we can optimize complex (bio)chemical systems using even pre-existing coding algorithms.
- Sensors and automation: it is currently becoming mandatory for (bio)chemical engineers to possess coding skills to effectively design, modify, and troubleshoot automated systems.

Research suggests that personal tutoring is the most effective mode of learning [6]. However, while it is generally unsustainable in higher education [7], it can be implemented on digital platforms through intelligent tutoring systems, such as generative AI chatbots. This is possible thanks to the recent advancements in AI, which have led researchers to investigate its feasibility, reliability, and validity in many fields, including education.

To train engineers willing to take on the challenge, we previously implemented sPyCE [5], an open-source series of Python courses tailored to (bio)chemical engineers, covering topics such as design of chemical reactors, stoichiometry, data pre-processing, data analysis, and various machine learning methods, from supervised to unsupervised learning and including both classification and regression examples.

We also implemented FermentAI [8], an intelligent tutoring system provided as a chatbot trained to answer questions about fermentation processes.

In order to intensify the previously carried out efforts and provide both a pedagogical framework to teach programming to (bio)chemical engineers and give students the opportunity to ask questions and clarify any doubts regarding their learning material, we explore the integration of sPyCE and FermentAI into BioVL [9], a virtual laboratory for teaching (bio)processes, previously implemented by the authors.

FermentAI was previously used by leveraging a dataset composed of exam questions (and answers) from a master's degree course offered by the Technical University of Denmark (DTU). However, the dataset was enriched with broader fermentation and modelling information for this work. This enables the model to answer questions that students might have when learning how to work with the fermentation models available on the BioVL platform.

The main goal of the work presented in this article is to enable students to (i) learn (bio)processes and how to model them, and (ii) ask questions to a chatbot regarding their doubts. We believe that the Python tutorials, given the stimulant material used along with gamification, is an engaging and insightful way to learn to model (bio)processes. Moreover, this will also enable students with different backgrounds - within the (bio)chemical engineering field - and programming skills to better understand the models available in BioVL, without having to search for additional material. The chatbot will allow students to ask for clarification right away, without any time delay. Therefore, this work aims to provide one centralized platform where all learning aids are available to students.

## MATERIALS AND METHODS

### BioVL: A platform for teaching fermentation processes

BioVL [9], available at http://www.biovl.eu, is an e-learning platform designed to teach (bio)processes. It aims to teach students how to build both simple and more

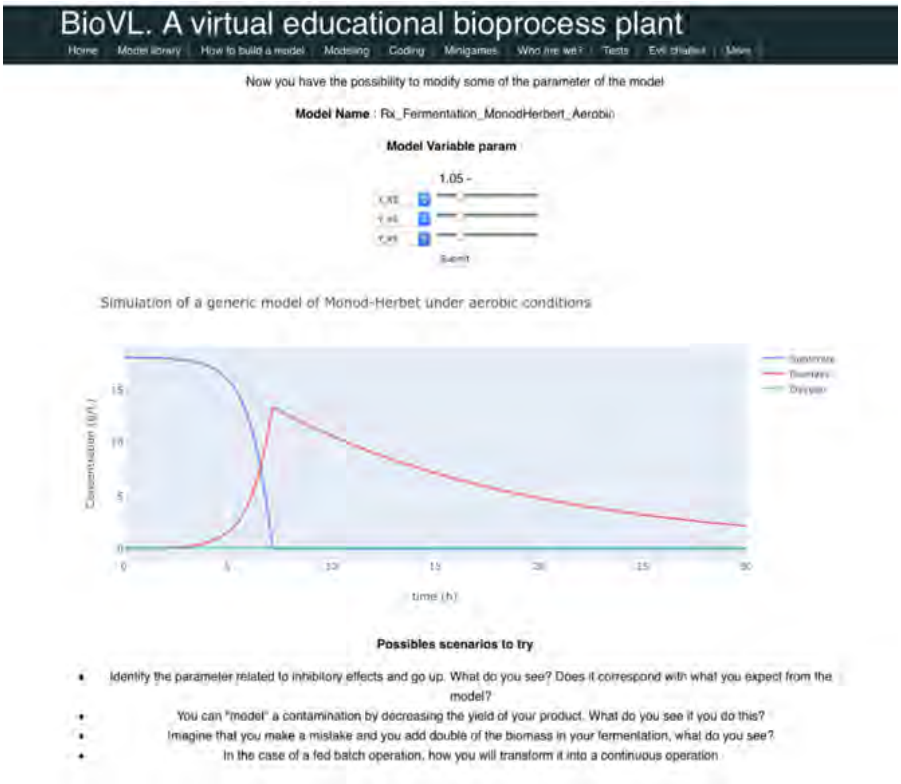



**Figure 2:** BioVL platform that shows how to interactively modify the parameters of a model in the platform (figure adapted from [9]).

complex models.

Figure 1 (a) presents the BioVL home page, while Figure 1 (b) introduces how the interface was developed according to Bloom's taxonomy [10]. The model library contains well-known and used models, such as Monod kinetics (aerobic and anaerobic), *E. coli* (aerobic, batch and fedbatch) and *S. cerevisiae* (aerobic, batch and fedbatch). The experience provided to the students is interactive; in fact, they can learn how different parameters affect the models by tuning the parameters directly on the platform. An example of this is presented in Figure 2.

Of note is that, although BioVL was originally developed aiming to teach (bio)processes (see more details in [9]), the authors have envisioned it to be a suitable centralized and customizable platform to support and e-teach a broader range of content taught in the (bio)chemical engineering curriculum· This provides the motivation behind the work performed for this manuscript: to build on the available platform and expand the capacities enabled. In fact, although the platform already contained a page on which students could train in coding (http://www.biovl.eu/coding), no tailored programming introduction was provided. Therefore, the platform assumed the user to have already an intermediate level of programming skills.

## Educational tools for (bio)chemical engineers: sPyCE and FermentAI

The work presented in this manuscript aims to reduce the expected prerequisites and introduce a tab on the website (www.biovl.eu/spyce) that links to sPyCE [5], an already implemented and abundantly tested series of Python courses tailored for (bio)chemical engineers. This series currently includes two Python courses, "Chemical Reaction Engineering in Python" and "AI for Chemical Engineers". Both courses are open-source and can be downloaded freely by everybody. The first course has been successfully embedded in the curriculum of a B.Eng. course at DTU since the fall semester of 2022. The second course has been tested in various special courses with students at DTU.

In an effort to support students willing to learn about fermentation models independently, the platform also includes FermentAI [8], a chatbot trained to answer questions about fermentation processes. The purpose of introducing the chatbot to the platform is to provide instant 1:1 tutoring support to students, enabling them to quickly ask FermentAI. Students can use the chatbot to answer any question they have about fermentation, or regarding the models provided on the platform. Possible questions

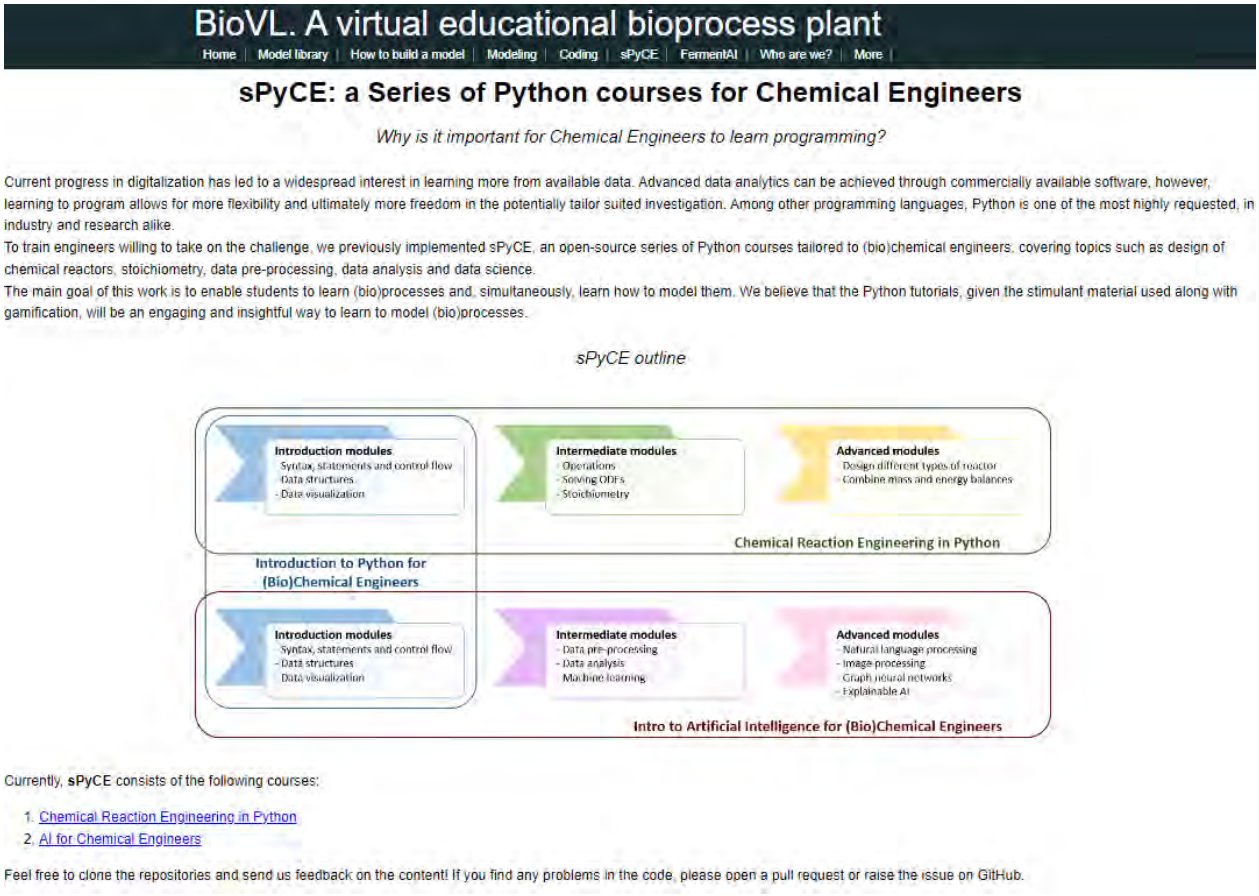



**Figure 3:** Developed tools embedded into BioVL. The Figure presents how sPyCE is integrated into the platform.

could be, for example, about parameter ranges or clarifying why changing an initial substrate amount results in changes in the final yield.

## RESULTS AND DISCUSSION

Figure 3 shows how sPyCE is embedded into BioVL. It is introduced on the website as a new tab, to facilitate students in finding it. First, a description of sPyCE is provided, as well as a contextualization of the motivation behind creating Python courses for (bio)chemical engineers. Afterward, the series outline is introduced, showing the two courses that belong to it.

The first two modules, which introduce the basics of Python, are shared between the courses, enabling students to freely choose the course they want to take to learn this programming language. The GitHub repositories that host the code are then linked at the bottom of the page.

FermentAI is also embedded in the platform as a separate tab, following sPyCE. The chatbot's interface is shown in Figure 4. In the example provided, the user asked about the most well-known fermentation process. The chatbot can be also used to ask further information about the models provided in BioVL. Figure 2 showed a simulation of a generic model of Monod-Herbert. In this case, FermentAI could be used to ask further questions about this fermentation, such as how does it work under aerobic compared to anaerobic conditions. Alternatively, FermentAI could be asked about the effect of a change in the initial parameters on the final concentration.

Although students' feedback has not been yet collected to evaluate this initiative, embedding these tools in a virtual laboratory aims to boost students' understanding by providing further support throughout each stage of their learning.

## CONCLUSION

Digitalization is revolutionizing the field of engineering, empowering it with enhanced efficiency, quality, and scalability. Implementing digital technologies such as AI, robotics, and big data analytics optimizes production processes and enables real-time (or near real-time) decision-making. The examples pursued in our work

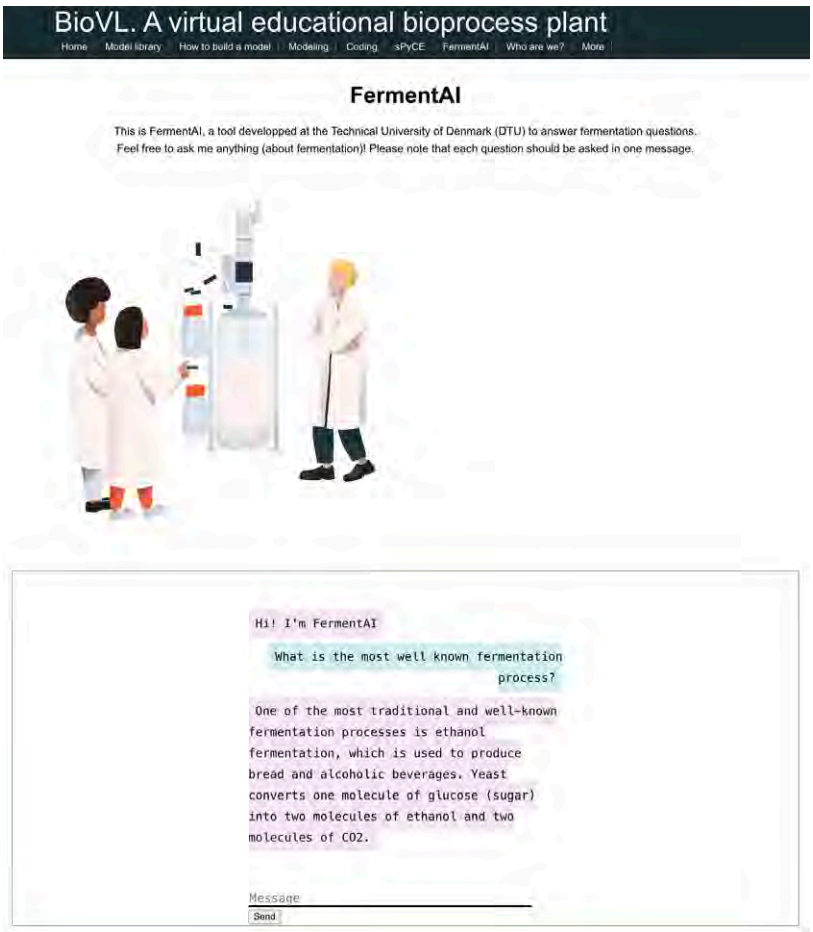



**Figure 4:** Developed tools embedded into BioVL. The Figure shows the chatbot available, FermentAI.

demonstrate the endless possibilities that lie in embracing and implementing the new tech avenues. However, there are some issues and challenges that still need to be addressed, such as how digitalization and its enabling technologies can not only prepare engineers for the biomanufacturing industry but also empower future engineers for Industry 4.0. This work strives to push the boundaries towards this goal, by leveraging technologies such as programming and AI, to facilitate knowledge transfer and improve the platforms that enable it.

More specifically, a previously developed platform, BioVL, is enriched with further capabilities. In fact, sPyCE, a series of Python courses tailored to chemical engineers has been added to the platform, facilitating students who want to learn to program. Furthermore, to provide instant 1:1 tutoring to students, we deploy FermentAI, a chatbot trained to answer fermentation questions, on the platform. The aim of this initiative is to leverage new technologies to facilitate the learning process and provide support to students throughout each stage of their learning.

## LIMITATIONS

The current version of FermentAI is based on questions from a course at DTU. Although the dataset is enriched with broader fermentation and modelling information for this work, further expansion of the database used by FermentAI to retrieve the relevant information would be highly beneficial, and it is therefore planned for the near future. For this reason, we are continuously collecting more questions which will then be answered by experts to enrich the database. We created a survey where both experts and readers can suggest questions to be added to the model. The survey is available here: https://forms.gle/R8NvhgwXouEpem7a7; we welcome any suggestion or further comment related to this work.

The tools added to BioVL have not been evaluated by students yet. This is planned to be performed in connection with the Dig4Bio project, as further explained in the next Section.

## FUTURE PERSPECTIVES

This work is meant to represent a stepping stone to

bring digital tools to other universities and audiences. In fact, the models and tools added to BioVL will be used and extensively evaluated by students and other researchers in three European Universities: DTU, TU Berlin and the Instituto Superior Técnico in Lisbon as part of the European project, Dig4Bio. This thorough evaluation will ensure that the tools are useful, and the users are able to leverage sPyCE and FermentAI to learn (bio)processes in a more efficient manner. This also aims to limit the possible impediments, such as the lack of programming skills or getting stuck with one specific doubt, in achieving this goal.

## DIGITAL SUPPLEMENTARY MATERIAL

BioVL is available at http://www.biovl.eu. sPyCE currently includes two open-source Python courses available at: www.github.com/FiammettaC/Chemical-Reaction-Engineering-in-Python and https://github.com/FiammettaC/AI-for-Chemical-Engineers. The code and interface used to build and deploy FermentAI is available at https://github.com/FiammettaC/FermentAI.

## ACKNOWLEDGEMENTS

Funding was provided by (i) the Novo Nordisk Foundation, grant number NNF22OC0080136 - Real-time sustainability analysis for Industry 4.0 (Sustain4.0); (ii) Technical University of Denmark (DTU) and Novonesis (formerly Novozymes), Denmark; and, (iii) Dig4Bio, European Union under the Horizon Europe research and innovation programme with the grant agreement 101159993, within the HORIZON-WIDERA-2023-ACCESS-02-0 call.

## REFERENCES

1. Moraes, E. B., Kipper, L. M., Hackenhaar Kellermann, A. C., Austria, L., Leivas, P., Moraes, J. A. R., & Witczak, M. (2023). Integration of industry 4.0 technologies with education 4.0: Advantages for improvements in learning. Interactive Technology and Smart Education, 20(2), 271–287. https://doi.org/10.1108/ITSE-11-2021-0201
2. Hariharasudan, A., & Kot, S. (2018). A scoping review on digital english and education 4.0 for industry 4.0. Social Sciences, 7(11), 227. https://doi.org/10.3390/ socsci7110227
3. Chakraborty, S., Gonzalez-Triana, Y., Mendoza, J., & Galatro, D. (2023). Insights on mapping industry 4.0 and education 4.0. Frontiers in Education, 8, 1150190. https: //doi.org/10.3389/feduc.2023.1150190
4. Caccavale, F., Gargalo, C. L., Gernaey, K. V., & Krühne, U. (2024a). Towards education 4.0: The role of large language models as virtual tutors in chemical engineering. Education for Chemical Engineers, 49, 1–11.
5. Caccavale, F., Gargalo, C. L., Gernaey, K. V., & Krühne, U. (2023a). Spyce: A structured and tailored series of python courses for (bio) chemical engineers. Education for Chemical Engineers, 45, 90–103.
6. Bloom, B. S. (1984). The 2 sigma problem: The search for methods of group instruction as effective as one-to-one tutoring. Educational researcher, 13(6), 4–16.
7. Lewin, D. R., & Barzilai, A. (2023). A hybrid-flipped course in numerical methods for chemical engineers. Computers & Chemical Engineering, 172, 108167. https://doi.org/ https://doi.org/10.1016/j.compchemeng.2023.108167
8. Caccavale, F., Gargalo, C. L., Gernaey, K. V., & Krühne, U. (2024b). FermentAI: Large language models in chemical engineering education for learning fermentation processes. In Computer aided chemical engineering (pp. 3493–3498, Vol. 53). Elsevier.
9. de las Heras, S. C., Gargalo, C. L., Caccavale, F., Kensington-Miller, B., Gernaey, K. V., Baroutian, S., & Krühne, U. (2023). From paper to web: Students as partners for virtual laboratories in (bio) chemical engineering education.
10. Bloom, B. S. (1956). Taxonomy of educational objectives: The classification of educational goals (handbook one). David McKay, New York, NY.

© 2025 by the authors. Licensed to PSEcommunity.org and PSE Press. This is an open access article under the creative commons CC-BY-SA licensing terms. Credit must be given to creator and adaptations must be shared under the same terms. See https://creativecommons.org/licenses/by-sa/4.0/



Systems & Control Transactions

**Research Article - Peer Reviewed Conference Proceeding**
ESCAPE 35 - European Symposium on Computer Aided Process Engineering
Ghent, Belgium. 6-9 July 2025
Jan F.M. Van Impe, Grégoire Léonard, Satyajeet S. Bhonsale,
Monika E. Polańska, Filip Logist (Eds.)

PSE PRESS

# Beyond ChatGMP: Improving LLM generation through user preferences

**Fiammetta Caccavale[a], Carina L. Gargalo[a], Krist V. Gernaey[a], Ulrich Krühne[a*], and Alessandra Russo[b]**

[a] Process and Systems Engineering Center (PROSYS), Department of Chemical and Biochemical Engineering, Technical University of Denmark, Søltofts Plads, Building 228 A, 2800 Kgs. Lyngby, Denmark
[b] Department of Computing, Imperial College London, London, UK
* Corresponding Author: ulkr@kt.dtu.dk.

## ABSTRACT

Prompt engineering – improving the command given to a large language model (LLM) – is becoming increasingly useful in order to maximize the performance of the model and therefore the quality of the output. However, in certain instances, the user is not able to enrich the prompt with additional and personalized details, such as the preferred tone and length of generated response. Therefore, it is useful to create models that learn these preferences and implement them directly in the prompt. Current state-of-the-art inductive logic programming (ILP) systems can play an important role in the development and advancement of digitalization strategies. For example, they can be used to learn personal preferences of users without sacrificing human interpretability of the learned outcomes. These systems have recently witnessed the development of data efficient, robust, and human interpretable algorithms and systems for learning predictive models from data and background knowledge. In this paper, one of these systems, ILASP (inductive learning of answer set programs), is used to develop a proof of concept of how personal preferences of groups of students participating in an interview exercise can be learned to tailor and improve the generated response of a LLM used in an educational context.

**Keywords**: Intelligent Systems, Machine Learning, Artificial Intelligence, Education, Industry 4.0.

## INTRODUCTION

One of the primary issues concerning the application of artificial intelligence (AI) in education is the reliability and transparency of the information it generates. In particular, widely accessible generative AI models such as large language models (LLM) are designed to deliver responses even when the correctness of those responses might be questionable. A known phenomenon currently occurring with available chatbots is hallucination, meaning that the model provides incorrect or misleading information. To mitigate this issue, a possible solution could be to reduce the generative abilities of these models by opting for more conservative hyperparameter settings. Among these there is temperature, which controls the randomness of the output. Higher values produce more creative results, while low temperature produces more deterministic and conservative outputs. Other hyperparameters that control the randomness and length of the generated answer are top p, token length and max tokens. Top p computes the cumulative probability distribution, setting a cut off when the distribution exceeds the value. For example, a top p value of 0.3 means that only the tokens comprising the top 30% probability mass are considered. Researchers can use all these hyperparameters to tune how creative or long a response should be, having more control over the generative process. Another strategy for increasing the control over the generation of the LLM is prompt engineering. In this case, the AI model could be combined with more interpretable techniques to enhance the prompts given to the LLM.

The Department of Chemical and Biochemical Engineering at the Technical University of Denmark (DTU) offers a course in Good Manufacturing Practices (GMP). As part of the course, students are required to participate in an audit exercise, in which they take on the role of an auditor investigating a company about its good manufacturing practices. In the audit exercise, the company is fictional and is represented by the teachers. After a few

years of participating in this exercise, teachers have agreed to test the replacement of the physical teacher with ChatGMP [1], an AI-powered digital audit tool to represent the fictional company. The chatbot, tested at DTU in the spring of 2024, proved to be considered a viable alternative by both teachers and students. To be noted is that part of the role of a teacher in educating students is also to understand the personal differences of each student and leverage them to help students achieve the best learning outcome. For example, in the audit exercises the teachers normally deduce whether students prefer to have an elaborate or straight-to-the-point answer and try to act accordingly. Moreover, they would perhaps try to help students in case they realized that they do not understand the answer provided, for example, by repeating it but in a simplified manner. Additionally, teachers would also detect whether students missed asking very important questions for the positive outcome of the exercise. In fact, not asking some important questions could result, in this exercise, in the students not obtaining the correct documents that they need to write an audit report. However, most commonly available chatbots would reply to each user and each question in the standard format, without taking these differences and learned knowledge about the students into account.

An approach that can automatically extract knowledge from given examples and therefore could be used to address both the interpretability and the lack of personalization challenges expressed above is inductive logic programming (ILP). The field of ILP has been subjected to substantial advancements over the course of the past ten years. These systems are capable of automatically extracting knowledge (expressed as logic program) from given examples and domain-specific prior knowledge. The aim of ILP systems is to learn models that together with existing background knowledge, explain labeled data [2-4]. An advantage of these models is that they are easily expressed in plain English and are inherently interpretable. This means that they can be explained to a human user, which in turn can facilitate a closer interaction between humans and machine.

This work aims to investigate the use of ILP to learn user preferences and provide a proof of concept on how these can be injected into the prompt given to ChatGMP. To achieve this, we investigate three main use cases: (1) detect whether students have missed some important question in their audit preparation work, (2) analyze if there are some repetitive questions that the students are asking, and (3) extract user preferences to personalize the response generated by the LLM. Overall, the aim of these investigations is to extract insights and improve the question-answering process. This will be done by (i) providing valuable feedback to the students, (ii) further improving the model's responses, and (iii) learning user preferences to tailor the audit exercise to each individual group of students.

## BACKGROUND

Current state-of-the-art ILP systems such as ILASP (inductive learning of answer set programs) [2] and FastLAS [5] can learn a broad range of interpretable models using answer set programming (ASP) [6]. ASP is a purely declarative language for representing and reasoning about knowledge. Typically, real-world problems are addressed by manually encoding them into ASP programs, followed by computing answer sets, which serve as solutions to the original issues. Due to its expressiveness and ability to efficiently find solutions, ASP is gaining increasing interest in the industry [7].

Cutting-edge ILP systems, to automatically derive models from labeled data, utilize input answer sets that represent positive or negative solution examples of a real-world problem and, alongside existing knowledge, learn ASP programs that encode the original problem. ILP has been effectively utilized in numerous real-world applications, including bioinformatics and chemoinformatics [8-10], natural language processing [11], and web mining [12]. Specific cases within chemistry and engineering include interactive exploration of chemical fragments [13], uncovering hydrogen-bonding patterns in crystals [9], drug design [14] and mining pump control systems. These methodologies highlight the capabilities of ILP in different fields and applications, including education.

## MATERIALS AND METHODS

This work aims to take the experiment performed with the creation of ChatGMP a step further. In fact, it aims to present a proof of concept on how the responses generated by ChatGMP could be improved through the use of ILP.

### Data

To leverage a pre-trained LLM on a specific task, domain specific data needs to be collected and curated.

The data used in this work is mainly collected from the audit exercises performed during the GMP course; the audits were performed and video recorded in the spring semesters of 2022 and 2023, summing up to 35 audits of approximately 45 minutes length each. The audios were then extracted from the videos in Python. To detect the different speakers and therefore being able to identify the questions (asked by the students) and the answers (formulated by the teacher), diarization, a process of automatically partitioning an audio recording into segments that correspond to different speakers, was performed. The speaker segmentation was then used to extract the text through a speech-to-text model. Then all

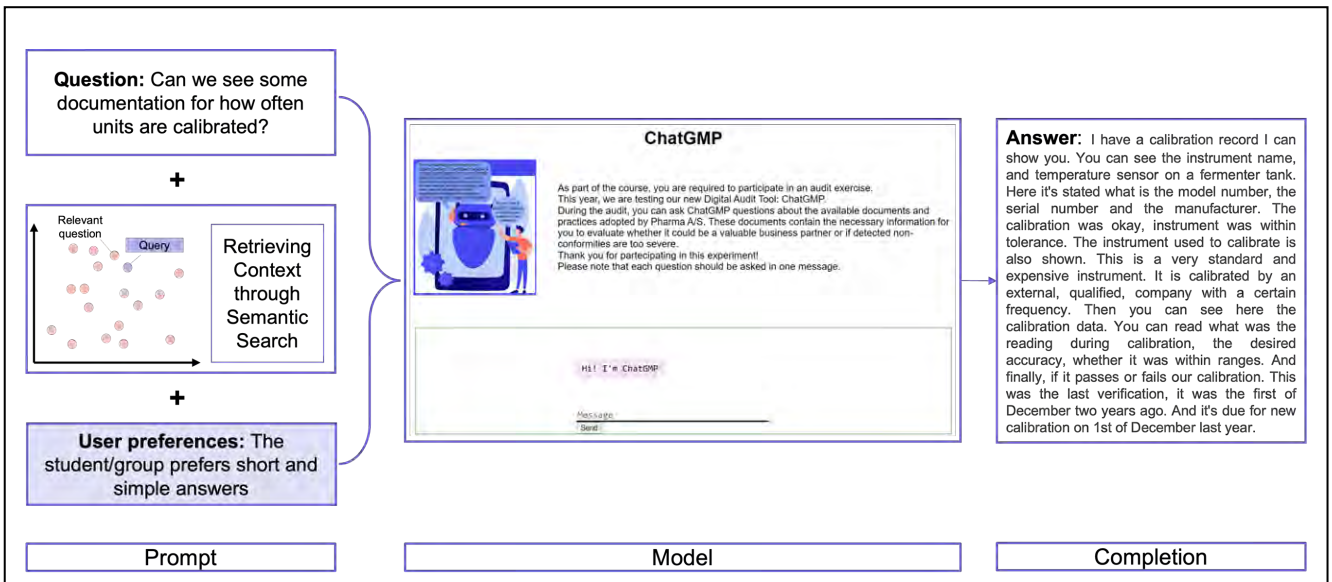



**Figure 1:** Schematics of the prompt given to ChatGMP. ChatGMP is prompted to open the "Calibration record" document, and summarizes it to the students. Here, the prompt is enriched with user preferences, which are weak constraints learned in ILASP. Figure is adapted from [1].

the students' questions were merged, therefore resulting in a document with the question-answer pairs. To ensure the highest quality of data to be used as model input, the resulting text documents (one for each audit performed), were manually checked and edited when necessary. Finally, the curated documents containing the question-answer pairs were concatenated and saved in a JSON file, for easiness of use. Further details can be found in [1].

## ChatGMP Model

ChatGMP is a question-answering (QA) LLM based on a pre-trained model and delivered to the students through an interactive user interface. The LLM component is based on a pre-trained model, FLAN-T5 base [15].

The prompt includes the question asked by the student group performing the audit and is enriched with some context, which contains the response to the question. The context is retrieved through semantic search by calculating the cosine similarity between the query question and the most similar question in the corpus. The LLM then generates an answer to the question asked based on the context provided. Further details are discussed in [1].

## ILP tasks and objectives

For the logic-based part, ILASP is used to learn rules concerning the cases investigated (missing and repetitive questions) and weak constraints to understand the preferences of each group of students. These preferences might concern, for example, the length or level of detail of the questions that they ask, the topic that they focus on more, whether they repeat questions or they are missing fundamental questions to achieve a high grade. The objective of this project is to automatically feed this information and therefore enrich the prompt given to ChatGMP with the weak constraints and user preferences learned. In this manner, ChatGMP could personalize the response based on the user. This process is shown in Figure 4.

The three different cases investigated are:

- *Missing questions*: To achieve a good performance in the audit report, there are two very specific questions (i.e. reference questions) that should be asked. We vectorize both the reference questions and the asked questions and we calculate the cosine similarity between them. Then, based on the similarity between the reference questions and the asked questions, we learn rules to establish whether the group of students asked all questions ("correct" label), if they asked one of them ("semi-correct" label) or if they did not ask any of the reference questions ("wrong" label). The aim of this use case is to directly assess the quality of the questions prepared by the students by checking whether some important questions have not been asked by the group of students, inevitably resulting in a lower grade. Students will then receive feedback on their list of questions, spurring them to further reflection.
- *Repetitive questions*: In the audit exercise, students might not understand a concept and ask for further details or repeat the same question more than once. We assume that question

repetition means that the answer given by the teacher/ChatGMP was inadequate, being either incomplete or not understood by the students. Therefore, we want to predict if students will ask questions with high similarity (repeating one question) to evaluate the understanding of the students. The aim of this use case is to gain deeper insight into the understanding of the students and adjust the agent's answer accordingly, by providing additional details or improving on the quality of the future generated answers.

- *User preferences*: In this case, we want to learn both general rules to achieve a good performance (e.g. questions about a specific topic are to be preferred to another one to maximize performance), as well as personal preferences of the groups, such as length and complexity of the questions, order of the topics, in order to better engineer the prompt given to the LLM for the answer generation. The aim of this use case is to learn user preferences to personalize the responses provided by ChatGMP according to each groups' individual traits and favorable factors.

The examples provided to ILASP were automatically generated using Python and extracted from historical audits recorded in the spring of 2022 and 2023. Explaining the formalism behind ASP is out of the scope of this work. However, from the provided code and learned rules it is possible to extract and discuss some general patterns and insights on the audits.

## RESULTS AND DISCUSSION

The goal of this study is to improve the prompt given to ChatGMP with user preferences learned in ILASP. These rules are easily translatable to natural language and therefore can be appended to the prompt.

Regarding the first case investigated, whether the students are missing important questions, ILASP founds the following rule:

```
relevant(V1) :- similarity(V1,V2); V2 > 62.
```

Provided the given examples and the label for the three classes ("correct", "semi-correct" and "wrong"), ILASP was able to automatically calculate the threshold for differentiating the classes. V1 indicates the reference question (either D1 or D2, since we have two relevant questions that the students should ask). V2 is the cosine similarity between V1 and the asked question. This means that if the cosine similarity between the asked question and the reference question is less than 62, the reference question was not asked. When the example is "correct", it means that the group managed to ask both the reference questions needed. "Semi-correct" means that one of the two questions was asked, while "wrong" indicates that the students did not ask any of the reference questions.

For detecting repetitive questions, the following rule was learned:

```
repeat :- success(V1,V2); repetition(V1,V2,V3); V3 > 60.
```

In this example, V1 and V2 indicate the question sequence (e.g., question 1 and question 2), and V3 is the cosine similarity between the two. Therefore, if two questions in have high cosine similarity, it means that the question is repeated. Here, the threshold learned is 60, so if the cosine similarity of two consequent questions is higher than 60, it indicated that students might be asking the same questions again, maybe because they did not understand the first answer provided by the chatbot.

This rule is useful to extract because, by calculating this similarity of the questions asked by the students, we can learn whether students did not understand an answer given by ChatGMP, so asked a similar question, and inject this information in the prompt of the LLM.

In this case, a possible prompt could be:

- "Please answer the <QUESTION> based on the given <CONTEXT> in a more elaborate manner, since students seem not to have understood the previous response".

This would ensure a more elaborate, complete and perhaps simplified answer from ChatGMP. On the other hand, it is also possible that the chatbot did not understand the question in the first place and therefore prompting it to re-elaborate the answer might lead to a better response. This approach would hopefully lead the students to understand the response and get the answer they were inquiring.

These two use cases are particularly important because the knowledge extracted by ILASP can be helpful when building a chatbot. In fact, detecting whether some questions are missing or if the students did not understand something would enable us to provide feedback back to the students and help them. This would thus ensure that the students have understood and learned the necessary material. This is of the utmost importance, since students' learning should be the ultimate goal. Thus, AI should not be blindly used to replace tasks to save time and resources but rather to help the educator with the automation of repetitive tasks while still ensuring that students reach the learning objectives.

In the last case, concerning user preferences, these are the rules learned:

```
:~ question_type(V1, review), number_questions(V1,
V2).[-V2@3, V1, V2]
 :~ question_type(V1, logistics), number_ques-
tions(V1, V2).[V2@1, V1, V2]
```

This investigation aims to learn the personal preferences of students, for example by learning the preferred number of questions (if many or few) and the length of the outcome. It does it by learning weak constraints. In the learned rule, V1 is the topic of the question, which is defined among 7 topics related to GMP, which are: management, training, quality assurance, quality control, maintenance, production, review and logistics. ILASP learned that the topic is the most important indicator for performance, followed by the number of questions that were asked about the topic. Additionally, how complex the questions are, and the level of details are also relevant considerations.

According to the learned preferences of each user, a possible prompt could be engineered by adding the following request:

- "Please answer the <QUESTION> based on the given <CONTEXT> *in a short and precise manner*".
- "Please answer the <QUESTION> based on the given <CONTEXT> *to include more information*".
- "Please answer the <QUESTION> based on the given <CONTEXT> *and recommend the students to ask more about maintenance*".

Using the weak constraints learned, every prompt could be tailored for the individual student or group of students interacting with the chatbot. This approach also enables to extract which topics, historically, lead to the best results (e.g., grades in the report). This means that, for example, if students ask more questions about logistics, they will get higher grades in the audit report. So, ChatGMP could also use this information to provide feedback to students on some topics they are missing or did not gather enough information about.

Although this study only provides a proof of concept and the ILP approach was not yet integrated into ChatGMP, it aims to give an example of how the prompt of an LLM could be improved through interpretable and reliable insights, incorporating use preferences and tailoring the prompt to the individual user.

## CONCLUSION

AI chatbots are increasingly being used in various contexts, including in education. It is necessary to ensure ethical applications of these models in order to safeguard students, as well as provide the correct and relevant information. Additionally, every student is different, and therefore the responses provided by an LLM should be tailored accordingly, to enhance the learning experience and leverage this individuality. This study provides a proof of concept on how ILASP can be used to learn rules and weak constraints in an audit exercise scenario. This results in the ability to enrich the prompt given to the LLM by including feedback, such as missing questions and lack of understanding, and user preferences. This enables the prompt to be tailored according to the individual user interaction, personalizing the responses and providing instant feedback to students.

## FUTURE PERSPECTIVES

In the near future the second (repetitive questions) and third (user preferences) use case will be combined and further developed to enrich the prompt of ChatGMP. This will ensure that the LLM will receive further information on how to answer the questions. Moreover, by learning the user preferences, the length, complexity and level of details contained in the generated answer can be calibrated based on individual preferences. Once the investigated cases will be integrated into the pipeline of ChatGMP, the role of the chatbot will therefore be to understand how the interaction is evolving, so that it can adapt its answers to improve the learning and aid students further. This is a dynamic approach, since the interaction will be observed in real time rather than a posteriori.

## DIGITAL SUPPLEMENTARY MATERIAL

The ILASP code used is open-source and can be found on GitHub at github.com/FiammettaC/ILP-user-preferences. ChatGMP is published and its code and data are available at github.com/FiammettaC/ChatGMP.

## ACKNOWLEDGEMENTS

Funding was provided by (i) the Novo Nordisk Foundation, grant number NNF22OC0080136 - Real-time sustainability analysis for Industry 4.0 (Sustain4.0); (ii) Technical University of Denmark (DTU) and Novonesis (formerly Novozymes), Denmark; and, (iii) European Union under the Horizon Europe research and innovation programme with the grant agreement 101159993, within the HORIZON-WIDERA-2023-ACCESS-02-0 call.

## REFERENCES

1. Caccavale, F., Gargalo, C. L., Kager, J., Larsen, S., Gernaey, K. V., & Krühne, U. (2024). ChatGMP: a case of AI chatbots in chemical engineering education towards the automation of repetitive tasks. *Computers and Education: Artificial Intelligence*, 100354.

2. Law, M., Russo, A., & Broda, K. (2019). Logic-Based Learning of Answer Set Programs. Lecture Notes in Computer Science (including subseries Lecture Notes in Artificial Intelligence and Lecture Notes in Bioinformatics), 11810 LNCS, 196–231. https://doi.org/10.1007/978-3-030-31423-1_6
3. Muggleton, S., & De Raedt, L. (1994). Inductive logic programming: Theory and methods. The Journal of Logic Programming, 19, 629–679.
4. Law, M., Russo, A., & Broda, K. (2015). Learning weak constraints in answer set programming. Theory and Practice of Logic Programming, 15(4-5), 511–525. https: //doi.org/10.1017/S1471068415000198
5. Law, M., Russo, A., Bertino, E., Broda, K., & Lobo, J. (2020). FastLAS: Scalable Inductive Logic Programming Incorporating Domain-Specific Optimisation Criteria. Proceedings of the AAAI Conference on Artificial Intelligence, 34(03), 2877–2885. https://doi.org/10.1609/aaai.v34i03.5678
6. Gelfond, M., & Lifschitz, V. (1988). The stable model semantics for logic programming. ICLP/SLP, 88, 1070–1080.
7. Erdem, E., Gelfond, M., & Leone, N. (2016). Applications of answer set programming. AI Magazine, 37(3), 53–68.
8. Agrafiotis, D. K., Bandyopadhyay, D., Wegner, J. K., & Van Vlijmen, H. (2007). Recent advances in chemoinformatics. Journal of Chemical Information and Modeling, 47(4), 1279–1293. https://doi.org/10.1021/ci700059g
9. Ando, H. Y., Dehaspe, L., Luyten, W., Van Craenenbroeck, E., Vandecasteele, H., & Van Meervelt, L. (2006). Discovering h-bonding rules in crystals with inductive logic programming. Molecular pharmaceutics, 3(6), 665–674.
10. Begam, B. F., & Kumar, J. S. (2012). A study on cheminformatics and its applications on modern drug discovery. Procedia engineering, 38, 1264–1275.
11. Muggleton, S. (1993). Inductive logic programming: Derivations, successes and shortcomings. Lecture Notes in Computer Science (including subseries Lecture Notes in Artificial Intelligence and Lecture Notes in Bioinformatics), 667 LNAI(1), 21–37. https://doi.org/10.1007/3-540-56602-3_125
12. Lisi, F. A. (2007). Building rules on top of ontologies for the semantic web with inductive logic programming. arXiv preprint arXiv:0711.1814.
13. Costa, V. S., Fonseca, N. A., & Camacho, R. (2008). Logchem: Interactive discriminative mining of chemical structure. 2008 IEEE International Conference on Bioinformatics and Biomedicine, 421–426.
14. Kaalia, R., Srinivasan, A., Kumar, A., & Ghosh, I. (2016). Ilp-assisted de novo drug design. Machine Learning, 103, 309–341.
15. Chung, H.W., Hou, L., Longpre, S., Zoph, B., Tay, Y., Fedus, W., Li, Y., Wang, X., Dehghani, M., Brahma, S. and Webson, A., (2024). Scaling instruction-finetuned language models. Journal of Machine Learning Research, 25(70), pp.1-53.

© 2025 by the authors. Licensed to PSEcommunity.org and PSE Press. This is an open access article under the creative commons CC-BY-SA licensing terms. Credit must be given to creator and adaptations must be shared under the same terms. See https://creativecommons.org/licenses/by-sa/4.0/



Systems & Control Transactions

**Research Article - Peer Reviewed Conference Proceeding**
ESCAPE 35 - European Symposium on Computer Aided Process Engineering
Ghent, Belgium. 6-9 July 2025
Jan F.M. Van Impe, Grégoire Léonard, Satyajeet S. Bhonsale,
Monika E. Polańska, Filip Logist (Eds.)

PSE PRESS

# Teaching Digital Twins in Process Control Using the Temperature Control Lab

**Alexander W. Dowling*, Molly Dougher, Madelynn J. Watson, Hailey G. Lynch, Zhicheng Lu, and Daniel J. Laky**

University of Notre Dame, Department of Chemical and Biomolecular Engineering, Notre Dame, IN 46556, United States
* Corresponding Author: adowling@nd.edu.

## ABSTRACT

Process control can be one of the most exciting and engaging chemical engineering undergraduate courses! This paper describes our experience transforming *Chemical Process Control* into *Data Analytics, Optimization, and Control* at the University of Notre Dame (second semester required course in the junior year). Our modern course is built around six hands-on experiments in which students practice data-centric modeling and analysis using the Arduino-based Temperature Control Lab (TCLab) hardware. We argue that state-space dynamic modeling and optimization are more critical for educating modern chemical engineers than topics such as frequency domain analysis and controller synthesis emphasized in many classical undergraduate control courses. All the course material is available online at https://ndcbe.github.io/controls.

**Keywords**: Process Control, Education, Dynamic Modelling, System Identification, Model Predictive Control, Pyomo, Process Monitoring, Process Operations, Industry 4.0

## INTRODUCTION

This paper describes several innovations in the undergraduate chemical engineering required process controls course at the University of Notre Dame, including:

- Hands-on experiential learning,
- State-space modeling,
- Advanced data analytics,
- Optimization for decision-making, and
- Model predictive control (MPC) and state estimation.

Through this perspective, we frame key concepts from process control – modeling, feedback, and optimization – through the lens of digital twins, which a recent U.S. National Academies report [1] defines as follows (emphasis ours):

*"A **digital twin** is a set of **virtual information constructs** that mimics the structure, context, and behavior of a **natural**, **engineered**, or **social system** (or **system-of-systems**), is **dynamically updated** with data from its physical twin, has a **predictive capability**, and **informs decisions that realize value**. The **bidirectional interaction** between the virtual and the physical is central to the digital twin."*

**Figure 1** shows the overarching themes for the course. The interplay between the physical and information realms in feedback control closely echoes key themes in the digital twin paradigm.

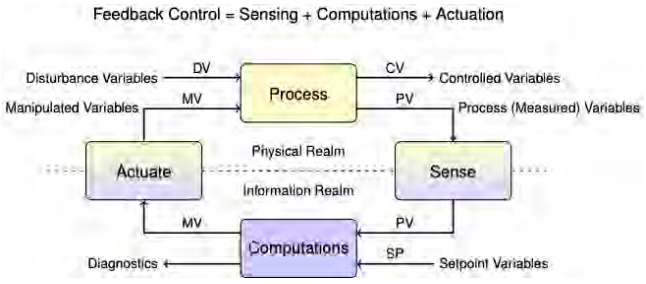



**Figure 1.** Feedback control, realized through integrating the physical and information realms, is the central organizing concept in the course.

### Temperature Control Lab

The course is organized around the Temperature Control Lab (TCLab) [2-5], an inexpensive Arduino device (shown in **Figure 2**) that enables experiential learning. Each student purchases a TCLab device instead of a textbook, as all course material is available online at

https://ndcbe.github.io/controls. Using the TCLab, students:

- Perform step and sine wave tests;
- Identify state-space models via nonlinear regression (with uncertainty quantification);
- Use simulation to tune various classical control algorithms, e.g., on/off control, PI(D) control;
- Implement open-loop and closed-loop model predictive control;
- Learn about state estimation from an optimization perspective; and
- Compare the above-described control algorithms for following the temperature profile for tempering dark chocolate using the TCLab as the physical system

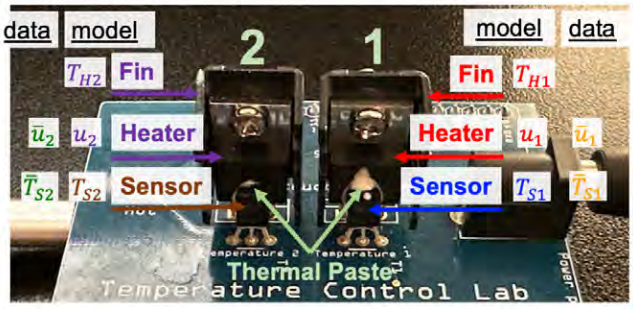



**Figure 2.** Photo of the TCLab hardware with two channels, each consisting of a heater, fin, and sensor. There is visible manufacturing variability in the thermal paste for each channel (and device). As such, each student has a hardware system that exhibits slightly different dynamics.

## Broader Curriculum Context

At Notre Dame, chemical engineering undergraduates enroll in process controls (3 credits) in the second semester of their junior year. As prerequisites, students complete a four-semester calculus sequence, a dedicated linear algebra course, and a department-taught required course on numerical methods and applied statistics. Students concurrently take *Transport II (Heat and Mass)* with process controls. Students enroll in *Chemical Reaction Engineering* in their first semester senior year and capstone *Chemical Process Design* in their final semester. Currently, our students learn MATLAB and Python during their first year through a college-wide required course. Python programming is further taught in the sophomore-required course *Numerical and Statistical Analysis*.

## State-Space Modeling and Data Analytics

Most process control courses focus on frequency domain analysis [6]. While the frequency domain perspective provides beautiful insights into certain aspects of controls (e.g., time delays and responses to periodic inputs), it requires significant time to (re)teach Laplace transformations. Moreover, students often struggle with the abstract nature of frequency domain analysis and have difficulty connecting these concepts with modeling in other core chemical engineering courses.

Compared to this classical treatment, we emphasize mathematical modeling, numerical methods, and applied statistics. The course emphasizes building state-space dynamic models from experimental data, as described below, which naturally complements the (partial) differential (algebraic) equation models taught in transport, kinetics, and thermodynamics. We (anecdotally) find that students conceptually understand state-space modeling, as it is grounded in core chemical engineering concepts, such as mass and energy balances. Moreover, we use advanced data analytics techniques such as nonlinear regression to train these physics-based state-space models from data and characterize the prediction uncertainty.

## Learning Objectives and Organization

The semester learning goals are:

1. Develop mathematical models for dynamical systems from data and first principles using modern statistical methods (in Python);
2. Predict dynamical system performance using numerical methods (in Python);
3. Analyze, implement, tune, and debug feedback controllers using the hands-on laboratory (in Python);
4. Formulate and solve optimization problems for decision-making (in Python); and
5. Demonstrate mastery of at least two of the above skills in an open-ended group project.

The course content and assessments are organized into three parts, as described in the following sections. Students individually complete two homework assignments and six hands-on laboratory assignments, each with significant data analysis and interpretation components. Students take one in-class exam during the semester to assess individual mastery. In place of a final exam, students complete an open-ended group project.

# PART 1: DATA-CENTRIC MODELING OF DYNAMICAL SYSTEMS (4 WEEKS)

Our assessments emphasize data analysis, computer-aided problem-solving, and open-ended discussion questions to connect theoretical concepts from lectures (75 minutes, twice each week) with hands-on activities using the TCLab. Students attend a dedicated 50-

minute laboratory session in a computer classroom once a week to start the new laboratory assignments with easy access to the teaching team when questions arise. Lectures in this part of the course emphasize simulation to understand the performance of (non)linear systems of ordinary differential equations (ODEs).

## Homework 1

Homework 1 reviews key concepts from this later course, especially mathematical modeling, numerical solutions to initial value problems, nonlinear regression, uncertainty quantification (e.g., covariance and correlation matrices), uncertainty propagation, and numerical solutions to systems of nonlinear equations. See our previous work on innovations in modernizing this pre-requisite course. [7-8] Course material is available at https://ndcbe.github.io/data-and-computing.

## Lab 1: Step Test

In the Lab 1 assignment, students perform a step test (**Figure 3**) using their TCLab hardware. Students then practice three methods – graphical analysis, simulation trial-and-error, and nonlinear regression – to build a first-order dynamic model for a single channel of their TCLab hardware:

$$C_p \frac{\mathrm{d}T_1}{\mathrm{dt}} = U_a(T_{amb} - T_1) + \alpha P_1 u_1 \quad (1)$$

where $T_1$ is the average temperature of heater/sensor one, $T_{amb}$ is the ambient temperature, $C_p$ is the heat capacity, $U_a$ is the heat transfer coefficient between the sensor/heat body and the environment, $\alpha$ is a system calibration constant, $P_1$ is the maximum power setting for heater one, and $u_1$ is the percentage of available power for heater one. We reformulate this as a first-order linear model without a time delay using the deviation variable $T'_1 = T_1 - T_{amb}$:

$$\frac{C_p}{U_a}\frac{\mathrm{d}T'_1}{\mathrm{dt}} = -T'_1 + \frac{\alpha P_1}{U_a}u_1 \quad (2)$$

Here $\tau = C_p\, U_a^{-1}$ is the time constant and $K = \alpha P_1 U_a^{-1}$ is the gain. Through discussion questions, students reflect on the pros and cons of each model-building approach and brainstorm ways to handle noisy data.

## Lab 2: Model Identification

In the Lab 2 assignment, students perform a sine wave test with their TCLab hardware. Using their step test (Lab 1) and sine test (Lab 2) data, students build a second-order dynamic model:

$$C_p^H \frac{\mathrm{d}T_{H,1}}{\mathrm{dt}} = U_a\left(T_{amb} - T_{H,1}\right) + U_b\left(T_{S,1} - T_{H,1}\right) + P_1 u_1 \quad (3)$$

$$C_p^S \frac{\mathrm{d}T_{S,1}}{\mathrm{dt}} = U_b\left(T_{H,1} - T_{S,1}\right) \quad (4)$$

where the superscripts (and subscripts) $H$ and $S$ denote the heater and sensor, respectively, and $U_b$ is the heat transfer coefficient between the heater and sensor.

Throughout the Lab 2 assignment, students explore the pros and cons of step tests (**Figure 3**) and sine tests (**Figure 4**) and the two model choices (first- and second-order dynamic models). Specifically, students find that the single-state model is reasonable for the step test data, whereas the two-state model is superior for the sine test data. The two-state model incorporates natural delays in the system due to thermal inertia by considering two different temperatures (sensor and heater/fin). The sine test, which is inherently more dynamic, emphasizes the importance of (approximating) delays. Moreover, the students concurrently take *Heat and Mass Transfer*, which empowers them to connect our state-space modeling course with the broader chemical engineering curriculum and appreciate the physical differences between these two models. On a more applied note, Lab 2 shows the importance of multi-start initialization for nonlinear regression and how simultaneously regressing data from two types of experiments (sine and step tests) results in a model with lower parameter and prediction uncertainty.

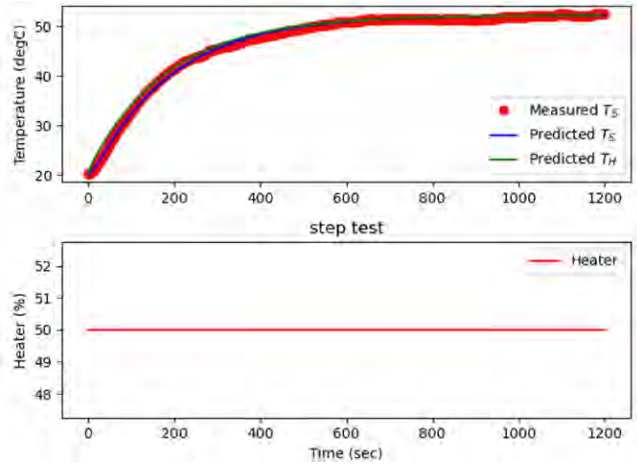



**Figure 3.** Parameter estimation results for the step test in Lab 1.

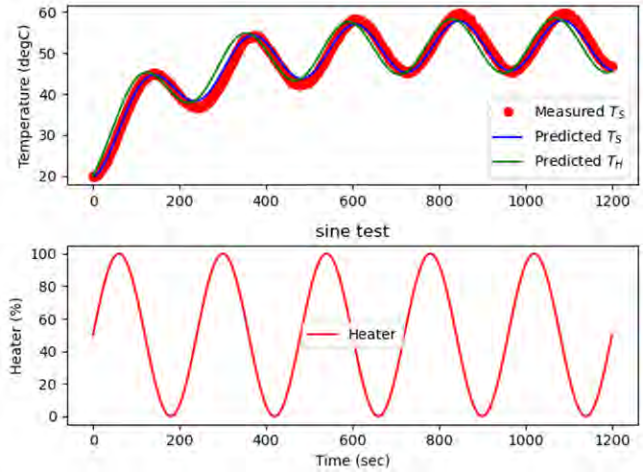



**Figure 4.** Parameter estimation results for the sine test in Lab 2.

## PART 2: FEEDBACK CONTROL (4 WEEKS)

As a motivating example throughout the semester, students compare different control strategies to follow a piecewise linear temperature profile that mimics the process of tempering dark chocolate. This example is well-suited to the temperature range of the TCLab (from ambient to approximately 65 °C). Moreover, students can easily relate to this example and appreciate how other forms of temperature control, e.g., polymerase chain reaction (PCR) or (bio)manufacturing, are relevant to their career interests.

### Lab 3: Relay (On/Off) Control

In Lab 3, students implement a simple relay (on/off) controller with a deadband (**Figure 5**). As a pre-lab exercise, students use their mathematical model from Lab 2 to tune the deadband parameter via simulation. The lab assignment focuses on implementing the controller, quantifying the controller performance, and comparing the performance to the simulation. As a final exercise in Lab 3, students use two relay controllers. One controller tracks the chocolate tempering temperature profile in channel 1. In contrast, the other controller tracks a constant temperature setpoint (30 °C) in channel 2. Through discussion questions, students contemplate potential challenges with independently controlling both channels, which interact due to their proximity.

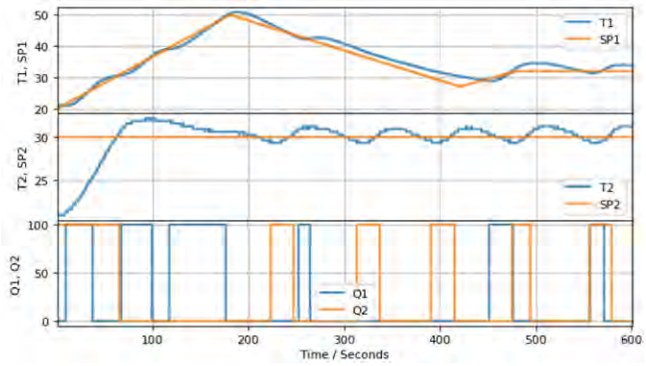



**Figure 5.** TCLab hardware results using relay (on/off) control in Lab 3. Top/Middle: channel 1/2 temperature data and setpoints. Bottom: controller actions.

### Lab 4: PI Control

In Lab 4, students explore two proportional-integral (PI) control implementations: a "textbook" position-form PI controller and a more practical velocity-form PI controller with anti-windup reset and bumpless transfer. As a pre-lab exercise, students use their mathematical model from Lab 2 to tune the gains in both PI controllers by analyzing the eigenvalues of the closed-loop dynamical system. Students then test both controllers and quantify their performance. Thus, this lab introduces students to arguably the most ubiquitous low-level controller in (bio)molecular/chemical processes, emphasizing the power of model-based controller design and analysis. Moreover, in the complementary lectures, students learn how to use linearization to analyze the local dynamics of nonlinear systems.

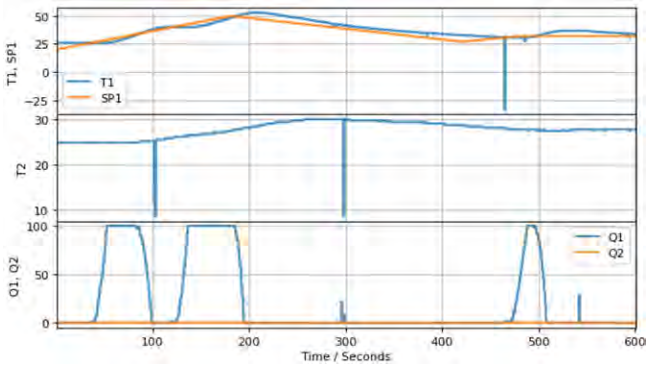



**Figure 6**. TCLab hardware results using PI control in Lab 4. The TCLabs occasionally drop data, which provides a good "real world" lesson: data are messy, and hardware is imperfect!

## PART 3: OPTIMIZATION (4 WEEKS)

Few of our undergraduate alumni are practicing control engineers, but many (anecdotally) regularly use data analytics for decision-making in their professional careers. Thus, we emphasize optimization as a framework for data-driven decision-making. In some of our favorite lectures, we introduce students to linear programming using production planning examples, e.g., blending in a refinery. Students are amazed to see how optimization easily applies to business-relevant analyses, such as pricing the marginal value of overtime labor or additional supplies or determining the best way to change blending operations to accommodate a new product (e.g., mid-grade fuel) or environmental regulations.

### Homework 2: Introduction to Pyomo

In Homework 2, students practice optimization modeling and problem-solving using Pyomo [9], an open-source algebraic modeling environment. Specifically, we focus on two examples – product blending and portfolio management under uncertainty – to appeal to diverse career interests. In the portfolio optimization example, students analyze time-series closing day prices for five funds to compute the covariance of their daily return rate. Students then use quadratic programming to calculate the Pareto optimal trade-off between expected return and volatility (risk). These examples help students appreciate the importance of modeling, data analytics, and optimization for business decisions.

### Lab 5: Open-Loop Optimal Control

Equipped with an operational understanding of Pyomo, in Lab 5, students compute the open-loop, optimal time-varying heating profile $u(t)$ to track the dark chocolate tempering temperature set point. Specifically, students use Pyomo.DAE [10] to formulate and solve the dynamic optimization problem using their model from Lab 2:

$$\min_{u} \int_{t_0}^{t_f} \left( \left\| T_S^{SP}(t) - T_S(t) \right\|^2 + w \left\| T_S^{SP}(t) - T_H(t) \right\|^2 \right) dt \quad (5)$$

$$\text{s.t. } C_p^H \frac{\mathrm{d}T_H}{\mathrm{dt}} = U_a(T_{amb} - T_H) + U_b(T_S - T_H) + Pu(t) + d(t) \quad (6)$$

$$C_p^S \frac{\mathrm{d}T_S}{\mathrm{dt}} = U_b(T_H - T_S) \quad (7)$$

$$T_H(t_0) = T_{amb} \quad (8)$$

$$T_S(t_0) = T_{amb} \quad (9)$$

$$\frac{du}{dt} \leq \dot{u}_{max} \quad (10)$$

$$\frac{du}{dt} \geq \dot{u}_{min} \quad (11)$$

where the superscript $SP$ denotes the setpoint, $d(t)$ is the disturbance (often set to zero), and $\dot{u}_{max}$ and $\dot{u}_{min}$ are the maximum and minimum rate of change of the control action, respectively.

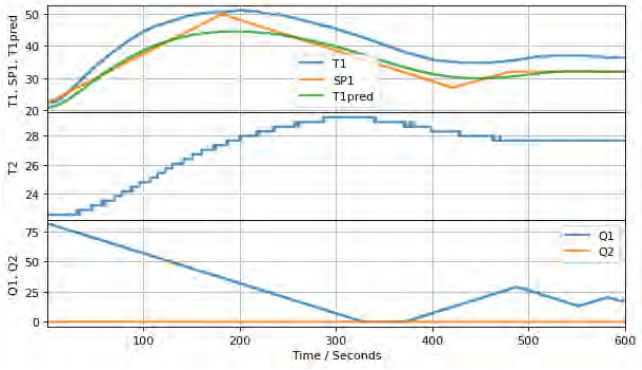



**Figure 7**. TCLab hardware results using open-loop optimal control in Lab 5.

In Lab 5, students execute the open-loop optimal solution with their TCLab hardware and compare their results to the model prediction (**Figure 7**). While much of the code is provided, students add a ramping constraint on the control input $u(t)$ and analyze the impact of this limitation (Equations 10-11). Through discussion questions, students explain why their open-loop optimal solutions make sense from a physical perspective.

Through examples in lectures, students learn how to use Pyomo.DAE to numerically solve boundary value problems with (partial) (differential) algebraic equations. This provides students with modeling tools for other classes, such as *Heat and Mass Transfer*, *Chemical Reaction Engineering*, and *Chemical Process Design*, in addition to our semester final project.

## Lab 6: Model Predictive Control

In Lab 5, students learn that while open-loop optimization can provide a physically sensible plan, without feedback, model mismatch can cause subpar hardware performance compared to other control strategies (e.g., Lab 3, Lab 4). This motivates Lab 6, which focuses on model predictive control (MPC). We describe this to students as essentially putting the optimization formulation from Lab 5 inside of a for loop and repeating the optimization as new measurements become available.

But there is a catch! The preferred TCLab model has one measured state, $T_{S,1}(t)$, and one unmeasured state, $T_{H,1}(t)$. To initialize the optimal planning problem, we need to estimate the unmeasured state. Thus, the TCLab example motivates state estimation, which we pose as an optimization problem:

$$\min_{d(t)} \int_{t_0}^{t_f} (\|\bar{T}_s(t) - T_S(t)\|^2 + w\|d(t)\|^2) dt \quad (12)$$

$$\text{s.t. } C_p^H \frac{\mathrm{d}T_H}{\mathrm{dt}} = U_a(T_{amb} - T_H) + U_b(T_S - T_H) + Pu(t) + d(t) \quad (13)$$

$$C_p^S \frac{\mathrm{d}T_S}{\mathrm{dt}} = U_b(T_H - T_S) \quad (14)$$

$$T_H(t_0) = T_{amb} \quad (15)$$

$$T_S(t_0) = T_{amb} \quad (16)$$

Specifically, we infer the unmeasured disturbance and heater temperature $T_{H,1}(t)$ by minimizing the deviation between the measured sensor temperature $\bar{T}_s$ and the model prediction $T_S$.

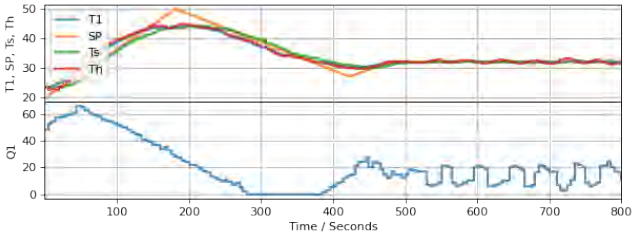



**Figure 8**. TCLab hardware results using MPC in Lab 6.

Lab 6 builds up these concepts by individually solving the optimal planning and state estimation problems separately. Finally, we integrate these to form a complete MPC demonstration (**Figure 8**). The data integration between the state estimation and control optimization problems is nuanced and benefits from advanced

programming concepts, e.g., Object Oriented Programming. As such, the students are provided with most of the code for Lab 6.

Thus, the Lab 6 assignment focuses on running the MPC scheme with their TCLab hardware and critically analyzing the results. Specifically, students are asked to quantitatively compare the performance of the four control strategies studied throughout the semester (Labs 3, 4, 5, and 6) on the same dark chocolate tempering problem. Students then discuss the pros and cons of each approach. Finally, the students describe a real-world application of receding horizon optimal control, state estimation, or both. Many of our students use this to share their creativity or interests. Popular answers include self-driving cars, supply chain management, and financial trading.

## SEMESTER PROJECT (3 WEEKS)

In place of a final exam, teams of three or four students work on a final project incorporating at least two of the class learning objectives. Many groups are very creative, with past project topics including analysis of university sustainability projects (e.g., solar or geothermal energy), glucose modeling for diabetes management, and trajectory planning for a submarine. We use the final three class periods for short presentations. During the two preceding weeks, we hold 6- to 7-minute project consultation meetings with each team during lectures. This has the bonus of introducing students to open-ended projects, meeting preparation, time management, and note-taking skills, which are especially helpful for their capstone projects the following year.

## CONCLUSIONS AND OUTLOOK

In summary, we have reorganized Process Control around six hands-on laboratory experiments, transforming the course from classical frequency domain analysis to emphasize dynamic state-space modeling, data analytics, and optimization for decision-making. The TCLab experiments enable us to distill the course into two key concepts:

1. The importance of feedback (**Figure 1**), both in classical control applications (e.g., temperature regulation) as well as many systems from daily life (e.g., cruise control).
2. The utility of predictive mathematical models for engineering [12].

We argue this modern take on process controls is better suited for today's chemical engineers, especially as the profession diversifies into new application areas and technologies. Moreover, these two key concepts capture the ethos of digital twins, which we believe will play a significant role in the future of engineering. Furthermore, we encourage students who find specific topics especially exciting, such as dynamic modeling, optimization, or statistical analysis, to pursue a technical elective in this area in their final year at Notre Dame.

We conclude by describing several opportunities for future refinement and customization. In parallel to exploring these refinements, we are exploring ways to measure student outcomes to assess the efficacy of the new course organization.

### What about time delays?

One of the great strengths of frequency domain analysis is the ability to model and design control systems to mitigate time delays. Moreover, time delays are especially important in traditional chemical engineering applications (e.g., fluid flowing in a pipe) and newer frontiers (e.g., systems biology). One option is to augment the state-space model with additional states to approximate the time delay. In essence, the two-state TCLab model does this by considering the lag in heat transfer from the heater/fin to the sensor. Another option is to introduce delay differential equations.

### Lost Insights from the Frequency Domain?

While we argue that the state-space perspective is more intuitive for most chemical engineering students, we also acknowledge that frequency domain analysis provides an important modeling perspective. The sine test experiment (Lab 2) starts to introduce these ideas. One opportunity is to expand this course section further to introduce Fourier analysis as a tool for analyzing periodic data. We hypothesize this data analysis perspective would be more engaging for students.

### Advanced Data Science Topics

The TCLab experiments can also be extended to introduce advanced data science topics. For example, time series analysis techniques could be introduced to go beyond standard independent and identically distributed Gaussian error assumptions for systems identification and instead consider auto-correlated measurement errors. This semester, we introduced maximum likelihood estimation to provide students with a more foundational understanding of nonlinear regression and introduce a core concept in many machine learning workflows. Similarly, the course content can be extended to consider more sophisticated uncertainty quantification methods, e.g., Bayesian inference or nonlinear confidence regions. Moreover, we use the TCLab example in our hands-on workshops to introduce Pyomo.DoE, an open-source tool for model-based design of experiments [11]. We have also begun exploring the TCLab as a motivating system for hybrid models to quantify model misspecification [13].

### Advanced Process Control Topics

In a Lab 3 extra credit exercise, students use their Lab 1 to 3 data to build and estimate a four-state model

that captures the interacting dynamics of the two channels in the TCLab (see **Figure 2**). This more sophisticated model motivates advanced topics such as estimability analysis and model-based design of experiments. We encourage students to presume this or other advanced process control topics as final projects. For example, students are encouraged to develop two PI controllers for one channel to follow the dark chocolate tempering profile while the other maintains a constant, elevated temperature (similar to Lab 2 with relay control). This reenforces ideas of interacting control systems. Another project idea includes model-free (e.g., Ziegler-Nichols) PID controller tuning. Some ambitious groups may even try to extend the state estimation formulation in Lab 6 for fault detection, such as determining when a hair dryer starts to blow on the TCLab.

## ACKNOWLEDGEMENTS

Many course design ideas this paper presents originated with Prof. Jeffery Kantor. Jeff spent over five years conceptualizing, testing, and refining this course and creating much of the content in our online textbook. Jeff passed away in 2023. This paper is dedicated to him.

## REFERENCES

1. National Academies of Sciences, Engineering, and Medicine. Foundational research gaps and future directions for digital twins. Washington, DC: The National Academies Press. (2024) https://doi.org/10.17226/26894
2. Oliveira PM and Hedengren JD. An APmonitor temperature lab PID control experiment for undergraduate students. *2019 24th IEEE International Conference on Emerging Technologies and Factory Automation (ETFA)* 790-797 (2019) 10.1109/ETFA.2019.8869247
3. Park J, Martin RA, Kelly JD, Hedengren JD. Benchmark temperature microcontroller for process dynamics and control. *Comput Chem Eng* 135:106736 (2020) https://doi.org/10.1016/j.compchemeng.2020.106736
4. de Moura Oliveira PB, Hedengren JD, Rossiter JA. Introducing digital controllers to undergraduate students using the TClab Arduino kit. *IFAC PapersOnLine* 53(2):17524-9 (2020) https://doi.org/10.1016/j.ifacol.2020.12.2662
5. Hedengren JD and Kantor J. Computer programming and process control take-home lab. *CACHE Newsletter* (2020)
6. Seborg DE, Edgar TF, Mellichamp DA, Doyle III FJ. Process Dynamics and Control. John Wiley & Sons (2016)
7. Boukouvala F, Dowling A, Verrett J, Ulissi Z, Zavala V. Computational notebooks in chemical engineering curricula. *Chemical Engineering Education* 54(3):143-150 (2020)
8. Dowling A. Training all chemical engineers in computing and data science. *2019 AIChE Annual Meeting* (2019) LAPSE:2019.1133
9. Bynum ML, Hackebeil GA, Hart WE, Laird CD, Nicholson BL, Siirola JD, Watson JP, Woodruff DL. Pyomo – Optimization Modeling in Python. Springer (2017)
10. Nicholson B, Siirola JD, Watson JP, Zavala VM, and Biegler LT. Pyomo.DAE: A modeling and automatic discretization framework for optimization with differential and algebraic equations. *Math Prog Comp* 10(2):187-223 (2018) https://doi.org/10.1007/s12532-017-0127-0
11. Wang J, Dowling AW. Pyomo.DOE: An open-source package for model-based design of experiments in Python. *AIChE J* 68(12):e17813 (2022) https://doi.org/10.1002/aic.17813
12. Agi, D.T., Jones, K.D., Watson, M.J., Lynch, H.G., Dougher, M., Chen, X., Carlozo, M.N., Dowling, A.W. Computational toolkits for model-based design and optimization. *Current Opinion in Chemical Engineering*, 43, 100994 (2024) https://doi.org/10.1016/j.coche.2023.100994
13. Eugene, E.A., Jones, K.D., Wang, J., Gao, X., Dowling, A.W. Learning and Optimization Under Epistemic Uncertainty with Bayesian Hybrid Models. *Computers & Chemical Engineering*, 179, 108430 (2023). https://doi.org/10.1016/j.compchemeng.2023.108430

© 2025 by the authors. Licensed to PSEcommunity.org and PSE Press. This is an open access article under the creative commons CC-BY-SA licensing terms. Credit must be given to creator and adaptations must be shared under the same terms. See https://creativecommons.org/licenses/by-sa/4.0/



Systems & Control Transactions

**Research Article - Peer Reviewed Conference Proceeding**
ESCAPE 35 - European Symposium on Computer Aided Process Engineering
Ghent, Belgium. 6-9 July 2025
Jan F.M. Van Impe, Grégoire Léonard, Satyajeet S. Bhonsale,
Monika E. Polańska, Filip Logist (Eds.)

PSE PRESS

# An integrated VR/MR and flipped classroom concept for enhanced chemical and biochemical engineering education

**Marcos Fallanza[a], Antonio Dominguez-Ramos[a], and Seyed Soheil Mansouri[b]***

[a] Department of Chemical and Biomolecular Engineering, University of Cantabria, Santander, Cantabria, Spain
[b] Department of Chemical and Biomolecular Engineering, Technical University of Denmark, Lyngby, Denmark
* Corresponding Author: seso@kt.dtu.dk

## ABSTRACT

The integration of mixed reality (MR) and virtual reality (VR) into Chemical, Biochemical, and Biomolecular Engineering (CBB) education presents an opportunity to address one of today's most pressing pedagogical challenges: sustaining student attention and engagement. Traditional "magistral" approaches often tend to limit the adoption of interactive methodologies. By contrast, MR/VR technologies can heighten immersion and practical intuition, capturing learner focus more effectively than conventional lectures. Yet, if deployed as superficial, isolated demonstrations, these tools may fail to support deep conceptual understanding and risk supplanting core course content. This work proposes a flipped-classroom model that deliberately embeds MR/VR exercises throughout the typical CBB curriculum. The methodology emphasizes a human-in-the-loop concept, whereby the educator strategically orchestrates virtual simulations and real-world problem-solving, reinforcing theoretical concepts through hands-on digital experiences. We address challenges related to scaling this approach, highlighting the importance of aligning content across multiple years and conducting cost-benefit assessments. Preliminary efforts indicate high student acceptance and potential for enhanced learning outcomes. By blending MR/VR with proven instructional strategies, CBB educators can better equip graduates with the skills and engagement needed for success in an evolving industrial landscape.

**Keywords**: Education, Mixed Reality, Virtual Reality, Flipped Classroom, Human-in-the-loop

## 1. BACKGROUND AND CONTEXT

Teaching Chemical, Biochemical and Biomolecular Engineering (CBB), as well as other engineering degrees has a "quantum-like behaviour" as a system. At the same time, there are two different super positioned teaching states: a) the teaching resources, both in terms of hardware and software are extremely different from those available in 1800s and not even a few decades ago b) the teaching methodology, in which magistral lessons still represents a large share of the teaching methods in our time. As it can be understood, current teaching resembles a superposition state because "the old & the new" live simultaneously, this is, the classical magistral methodology from centuries ago, and the modern resources (internet resources, LLMs, TV displays, etc.).

As reimagined in figure 1, it is clear that "much has changed or nothing at all" as this classical magistral teaching means the "minimum energy state", at which all systems tend to be. The integration of mixed reality (MR) and virtual reality (VR) technologies into CBB engineering education offers potentially promising avenues for enhancing student engagement, intuition and comprehension of practical concepts. Very recently, it came to our knowledge the next idea: "Attention is the new oil" [1]. We cannot agree more with this idea. The current generation of permanent staff at European universities were probably motivated by the fact of better professional prospects. However, even if this idea remains at any percentage of the today's enrolled students, the lack of attention is more evident than ever. The use of tablets and laptops do allow the student to connect to Internet resources, download documents, use CBB related software

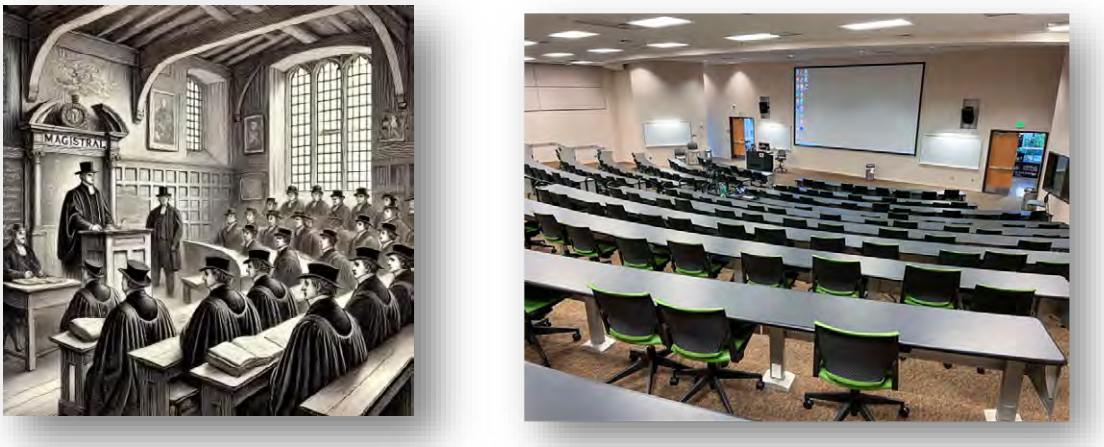



**Figure 1:** On the left, an AI reimagination of magistral course back in the early days of the university, which clearly resembles the picture on the right, which belongs to modern universities in the XXI century.

including spreadsheets, create presentations, chat with AI-based LLMs, etc. But this use of computers is indeed such a temptation to the less motivated students. It is nearly impossible to grab the attention more than the time typically predefined in conferences such as TED Talks, which are basically in the range of 18 min, being favored those of 5 minutes [2]. This means that the long presentations from magistral lessons must adapt and evolve to short-high impact ones.

MR and VR have emerged in universities as hardware-based teaching alternatives to improve the way undergraduate students reach competences in several science domains ranging from medicine to engineering. Literature is full of references about the prospects of the benefits of using MR and VR in university teaching. However, there is an existing risk that MR and VR can supplant the real content of CBB engineering courses. Their use by the teaching staff is expected to regain the attention momentum and serve as augmentative tool that enhance, rather than replace, current existing teaching methodologies. That is, they need to be adapted with a human-in-the-loop concept and social learning theory principles.

Current implementations of MR and VR are often isolated within single topic and lack interoperability with the broader curriculum, resulting in partial educational experiences with ill-defined learning designs that fail to exploit the interconnected nature of CBB engineering disciplines. Their use is essentially limited to individual sessions within courses in which it is an activity with probably low-added value. This siloed approach impedes the development of a cohesive understanding of wide topics ranging from chemical reactor design to heat transfer and limits the potential for integrated learning.

The effective incorporation of MR/VR necessitates the seamless integration of existing teaching materials, including presentations, lecture videos, and textual resources with current modern methodologies. By embedding and blending MR/VR experiences within the current variety of existing methodologies, chemical engineering educators can create enriched learning environments that cater to diverse cognitive preferences without discarding proven instructional methodologies.

Table 1 shows an overview of different current modern methodologies plenty used as well as their pros and cons in relation with the attention. In general, it is possible to combine or blend different methodologies with MR/VR. However, each integrated approach has their own advantages and problems. In this work, we do propose the unique features that can be derived from the combination of MR/VR with the flipped classroom approach. Next is discussed a formal definition of the mentioned integration.

The advent of bringing digital tools such MR/VR into the university classroom to provide a more accessible education to a growing interest in process industries has led to a few fundamental questions around CBB engineering education. However, as previously discussed there has been research indicating that MR/VR tools alone are not completely fulfilling students' learning needs and learning outcomes across bloom taxonomy [3]. One major challenge is to regain students' attention to pursue better learning outcomes by using the MR/VR learning environment and primarily using these tools to create a real-world intuition.



**Figure 2**: A selection of picture of individual Chem Eng students in the process of desassembling a heat exchanger (HX) unit, created to fit the front of the classroom. The size of the HX unit was sized in a previous exercise.

To address this situation, we do propose the integration of the flipped-classroom with MR/VR to devise a learning design that combines MR/VR technologies into flipped classroom models within CBB Engineering education. This framework emphasizes pre-class exposure to traditional content, enabling students to acquire foundational knowledge through established resources. The flipped classroom approach proposes quite a series of advantages that fits very well the integration of MR/VR tools in CBB Engineering. First, the available content can be approached by the students at any time. This gives the flexibility to learn on the way or at more convenient times during the day. Being recorded, student can fit their own pace, which is typically avoided during magistral lessons. Indeed, this is connected to higher grades of self-learning and autonomous learning. Once the students have acquired the knowledge, they are ready to test, experience and feel the application of these concepts on their own under a AR/MR experience. Second, the use of MR/VR in the classroom requires intrinsically the interaction between the students and the teaching staff. The students are clearly guided during the MR/VR activity with a process that demands interaction with the students and the mixed or virtual environments. Third, under proper developments, students can be engaged in a collaborative environment in which they may need to help each other to solve the challenges of the MR/VR activity in which they are involve, in a similar way in which they do in real CBB teaching labs.

Therefore, the set of pre, post and in-class sessions leverage MR/VR to provide immersive, interactive experiences that reinforce, contextualize and deepen in the practical application of the learned theoretical concepts.

The prospect of extending the approach throughout the degree or master facilitates a consolidated practice, which in turn favors the current expectation of students. For instance, students might engage in virtual simulations of chemical reactors to explore reaction kinetics, thermodynamics, and mass transfer phenomena in a controlled and manipulable environment. This holistic educational strategy may align better with industry expectations, preparing students to navigate the multifaceted demands of the professional market and developing the expected digital competences highly demanded by industrial partners. Indeed, in many CBB Engineering degree programs, the foundational sequence begins with Material and Energy Balances, followed by core courses such as Thermodynamics, Fluid Mechanics, Heat Transfer, and Reaction Engineering. More advanced or specialized topics like Biochemical Processes, Process Control, and Plant Design typically appear later in the curriculum. **We do propose in this work that an integrated MR/VR and a flipped-classroom strategy can be used to strengthen student engagement and conceptual understanding** through a holistic hands-on experience integrated along the whole curriculum.

## 2. HOW TO SOLVE CURRENT LIMITATIONS: METHODOLOGY

In our view, a significant challenge lies in bridging the gap between an efficient integration of application of MR/VR technologies with well-established teaching practices. Often, these MR/VR technologies are introduced as engaging but superficial, low-added value demonstrations, lacking alignment with specific learning outcomes and unbalanced cost-benefit implications for educational

institutions. To transcend this limitation, MR/VR must be deliberately deployed to facilitate deep conceptual understanding and practical skill development, rather than serving as mere visual spectacles. Figure 4 shows an example of a heat exchanger unit modelled in Unity. The role of the educator plays a more-than-ever important role, a human-in-the-loop, as they can bridge the gap in a way that learning outcomes can be effectively reached.

The proposed methodology to solve current limitations uses the principles of flipped classroom as the basis to integrate MR/VR as explicit exercises to mimic real-world situations. However, connecting the MR/VR exercises to the curriculum must be done in such way that iteratively, learn, implement and practice principles are adhered. So, our view in this work is that MR/VR tools are valuable tools in a human-in-the-loop context.

First, it is quite difficult to tackle this integration without a proper team. Considering the starting point based on the experience of the teaching team must be properly addressed. Second, the team must discuss the scale-up process. We have identified that a drastic transition from full-magistral lessons to flipped classroom may emerge into a plethora of problems. Mainly, because the classical contents should be prepared to be ready to be adopted to flipped classrooms and MR/VR activities in which the contents prepared in advanced are considered in the blending process rather than be stacked. In this sense, it means that the flipped content cannot be understood without the MR/VR content and vice versa. Otherwise, MR/VR integration would be simply an incremental part of the contents. Third, it is important that contents are used as uniform as possible along individual courses and years. This is quite relevant because of potential crossed unmatched signals. Using the integrated flipped classroom and MR/VR during the first year and then radically extirpated from the remaining years can surely provide a negative experience in the students, as they may feel more attracted by these methodologies, which the main element for its implementation.

As a result, the transition towards the integration of MR/VR into flipped classroom means that actions must be taken at different tiers, which are discussed next:

- Tier 1: integration at program level: we do believe that the effectiveness of this approach is rooted in the possibility to extend it proportionally alongside a full program, for example the 4 years of a CBB degree. This way, the students can understand that using MR/VR is not a mere set of "fireworks" but an effective tool to integrate CBB concepts in a more efficient way.
- Tier 2: integration at module level: using a heat exchanger unit in a typical 101 course of Chemical Engineering using this approach and later on (1 yr. later) using "just slides" to describe the behaviour of the unit within a 100% classical magistral lessons methodology can lead to unwanted situations. Students may feel this point really discouraging, loosing the human-in-the-loop factor.
- Tier 3: integration at course level: similarly, to the tier 2 integration, it can be also discouraging the fact that a heat exchange course faces two different methodologies. This situation may arise when the coordination level of the course is not adequate.

All said, we do not propose that a full program (bachelor degree, master degree or PhD program) must transit to a full the integration of MR/VR in flipped classroom in a single year. What we are really proposing here is that partially fulfilling cherry-picked courses with MR/VR content without a well-thought strategy may entail negative effects. This is especially true as long-term strategy. As firstly discussed, the key element here is to regain the student's attention by more appealing ways of active learning. The main negative effect is perceiving the new tools as another distraction instead of an attraction. Consequently, we consider that the main risk of this approach is the lack of momentum to implement the aforementioned integration. Everything said, there must be a reasonable period of time to transit to the steady state of the integration.

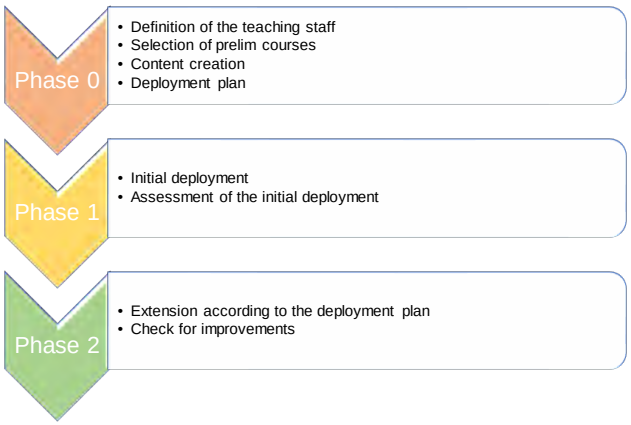



**Figure 3**: A deployment plan of the proposed methodology

We do propose that a reasonable strategy as depicted in figure 3, divided into 3 phases. During phase 0, it is critical to define the teaching staff involved in the plan, being convenient that they can have some degree of responsibility regarding the contents of the courses preliminary selected. Also, it is important the contents can be created with certain anticipation. As a results of this, the team can propose a deployment plant, which should be the deliverable from phase 0. In a later stage corresponding to phase 1, according to the deployment



**Figure 4***:* A simplified example of a heat exchanger in Unity and the final experience in XR.

plan, the teaching staff must initiate the integration of MR/VR with the flipped classroom in the selected courses. It is critical here that the intensity of the learning outcomes can be evaluated as a prior move to phase 2. It is far way more important to complete a proper assessment of the phase 1 than move to phase 2. Finally, once the appropriateness of phase 1 has been achieved, it is possible to move to phase 2, in which a relevant fraction of the courses integrates this approach. The penetration of the methodology into a program must be chosen carefully to promote acceptability among the teaching staff involved in the whole program.

From a methodological point of view, it is also important to provide a skeleton to design in a robust way the integration of MR/VR in the flipped classroom approach according to the deployment plan of phase 0. Next, we discuss the way in which this can be done and the main tips to avoid pitfalls:

- Strong bound between the pre-class material, the in-class material and the post-class material. Students find extremely confusing using different references to the same concepts. This is strongly avoided in magistral lessons as it is usually the same individual the one using all those concepts. However, in our approach, the individual responsible for creating the MR/VR contents must be the teaching staff or at least must be in close contact to the ones creating them. This disconnection may lead to a common pitfall: the MR/VR activity can be about the different elements that belongs to the assembling of a heat exchanger, but the pre-class concept did not mention the very basic elements that form the unit (shell, tubes, headers, etc.). In this sense, this should reinforce the pre-class content rather than being an extension. So, when applied to the aforementioned example, the MR/VR activity must be used to visualize the elements such as the tubes and the shells, which can be difficult using just videos and/or pictures. But the MR/VR activity should not be used to explain what and why the tubes and shell are needed.
- Define and identify clear learning outcomes from every MR/VR activity. While assembling/disassembling a heat exchange unit can be a fun activity for the students (as it would be for any interested individual in CBB), a clear set of learning outcomes must be defined and identified by the teaching staff. This is certainly a relevant issue: learning outcomes clearly identified such as "*understanding the role of shell & tubes in a heat exchanger*" is critical. This means that they can see clearly the dimensions, the numbers of passes, the deflectors, etc. their relative proportions, the challenging related to choosing the shell or tube side, etc. The wrong outcome would be that they found the activity fun because of the possibility of grabbing and throwing the elements of the heat exchanger.
- Evaluation. It is high debatable if the MR/VR activities should deserve a separate piece of evaluation. In our view, to guarantee the coherence of the proposal, it is not advisable to include specific evaluation for the MR/VR activities themselves. The basis for this claim lays on the fact that MR/VR activities are envisaged as an element to improve the intensity of the learning outcomes and the way to reach them. This means that they should be helpful at answering questions such as those practised in the MR/VR activity "is the sizing of this heat exchanger reasonable?". It would be pitfall to try to recreate the MR/VR

activity and assess that one as a separate piece

**Table 1:** A comparison among methodologies with a brief description, pros and cons.

| Methodology | Description | Pros | Cons |
|---|---|---|---|
| Learning-by-Doing | Students learn through direct experience, such as experiments, simulations, or projects, reflecting on their actions and outcomes | The level of attention of high as the students must be focused on the direct experience | The lack of external drivers apart from deadlines may be an issue |
| Problem-based Learning | Students tackle real-world problems in groups, fostering critical thinking, research, and collaboration | The need to work in groups promotes attention | Difficulties for more introvert students |
| Project-based Learning | Students work on extended projects that require applying knowledge to produce a concrete deliverable, often integrating multiple disciplines | The need to work in groups promotes attention | Difficulties for more introvert students, enhanced by a longest contact time due to the project duration |
| Flipped Classroom | Students study theoretical content at home / library (videos, readings) and use classroom time for active problem-solving, discussions, or hands-on activities | Effective discussion time that requests full attention | Low quality or engagement contents disrupt the use of time at home /library |
| Gamification | The use of game-like elements (points, badges, challenges) in learning to boost engagement and motivation | High engagement factor | The game over the content |

Another aspect to the implementation of VR/MR tools is the cost of implementing as opposed to stand alone benefits. An economic assessment of implanting VR/MR tools must be carried out in the context of CBB engineering education [4]. An important issue is the adaption of these without a thoughtful learning design and their integration with other teaching methodologies involving a human teacher may bear substantial economic and adverse learning outcomes.

## 3. FUTURE PROSPECTS AND ON-GOING WORK

The integration of MR/VR technologies within a flipped classroom paradigm can enhance learning outcomes by providing experiential learning opportunities that complement traditional content delivery without any partial withdrawal. The educator's role is even more relevant than ever due to the need of integrating and blending new tools in the CBB engineering course mix with a clear learning design that objectives fulfill learning outcomes. By focusing on the alignment of these technologies with curricular objectives, we can cultivate chemical engineering professionals equipped with both the theoretical acumen and practical skills necessary to excel in a technologically advancing field such as CBB engineering.

On-going efforts suggests preliminary that a proper combination as shown in Figure 2 can be appropriate and the student's acceptance of the tools is high or very high. Furthermore, a use case demonstration is planned at University of Cantabria as a launchpad of this approach. This will enable to evaluate the effectiveness of the approach in conjunction with learning outcomes.

## 4. ACKNOWLEDGEMENTS

Marcos Fallanza and Antonio Dominguez-Ramos acknowledge the financial support of the University of Cantabria for the project PR_35 "Innovación en la formación de ingenieros: Ingeniería inmersiva con herramientas de simulación CFD".

## REFERENCES

1. Scott Galloway. https://www.profgalloway.com/attentive/
2. TED TALK, https://help.ted.com/hc/en-us/articles/360038669354-Why-do-we-need-to-keep-talks-within-18-minutes
3. S. Caño de las Heras, B. Kensington-Miller, B. Young, V. Gonzalez, U. Krühne, S. S. Mansouri, S. Baroutian. Benefits and challenges of a virtual laboratory in chemical and biochemical engineering: Students' experiences in fermentation. *J Chem Educ* 98(3):866-875 (2021) https://doi.org/10.1021/acs.jchemed.0c01227
4. V. V. Kumar, D. Carberry, C. Beenfeldt, M. P. Andersson, S. S. Mansouri, F. Gallucci. Virtual reality in chemical and biochemical engineering education and training. *Educ Chem Eng* 36:143-153 (2021)

© 2025 by the authors. Licensed to PSEcommunity.org and PSE Press. This is an open access article under the creative commons CC-BY-SA licensing terms. Credit must be given to creator and adaptations must be shared under the same terms. See https://creativecommons.org/licenses/by-sa/4.0/



Systems & Control Transactions

**Research Article - Peer Reviewed Conference Proceeding**
ESCAPE 35 - European Symposium on Computer Aided Process Engineering
Ghent, Belgium. 6-9 July 2025
Jan F.M. Van Impe, Grégoire Léonard, Satyajeet S. Bhonsale,
Monika E. Polańska, Filip Logist (Eds.)

PSE PRESS

# From Sugar to Bioethanol – Simulation, Optimization, and Process Technology in One Module

**Jan Schöneberger[a]* and Burcu Aker[b]**

[a] Berliner Hochschule für Technik, Sustainable Process Engineering, Department VIII, Berlin, Germany
[b] Chemstations, a Datacor company, Houston, Texas, USA
* Corresponding Author: Jan.Schoeneberger@BHT-Berlin.de.

## ABSTRACT

This work gives a detailed description of the models, methods, and equipment used in a bachelor's degree lab course. The connections between simulation results and real-world data are highlighted and tools for making the models useful for process design tasks are portrayed. The models cover the production chain for fuel-grade bioethanol, starting from the fermentation of sugar with yeast. In only one semester (14 weeks with 180 minutes per week) the students achieve to produce high-purity ethanol. Some exemplary results of the process designs and their comparison to the realized intermediate and final products are given together with production cost data.

**Keywords**: Batch Process, Ethanol, Education, Batch Distillation, Biofuels, Data Reconciliation

## INTRODUCTION

The Green Processes Lab module, part of the Green Engineering study program at Berlin University of Applied Science (BHT), trains students to simulate, optimize, and implement an industrially relevant sustainable process within a single semester. The selected process is a fuel-grade bioethanol production, with a minimum purity of 99.8 wt.%, using readily available supermarket feedstocks: sugar and yeast.

In earlier modules of the program, students engage with fundamental unit operations, including vessel reactor (fermentation), batch distillation, batch rectification, filtration, centrifugation, dryer, and adsorber. These operations are extensively covered in theoretical lectures, mathematical modeling, and predefined experiments, ensuring a solid understanding of their behavior. Working in teams, students design their processes in five steps with minimal restrictions, aside from safety regulations and two key constraints: They must use only existing equipment, and each process step is limited to a duration of 180 minutes, including the 30-minute set-up, shutdown and cleaning phase. The groups compete to develop the most cost-effective process maximizing bioethanol yield while minimizing resource consumption—specifically sugar, yeast, and electricity. The time constraint adds complexity, demanding meticulous simulation and process planning.

To tackle this challenge, students utilize the commercial flowsheet simulator CHEMCAD. This software offers fundamental unit operation models and a robust thermodynamic engine for calculating physical properties of pure substances and mixtures. However, the models require parametrization based on the available equipment. Students achieve this through reaction rate regression and data reconciliation, leveraging data from previous experiments and a limited number of newly designed trials.

The parametrized models serve as the foundation for optimizing the economic objective function. Given the stepwise nature of the process, optimizing all process parameters simultaneously is extremely difficult. Instead, teams integrate different optimization strategies refining individual steps while maintaining overall process coherence. This encourages strong intra-group communication, as each member is responsible for a specific process stage. The course can be carried out with four groups, five participants each. Thus, one student is responsible for one process step.

By the end of the semester, each group successfully produced a measurable quantity of bioethanol while tracking the resource consumption. Utility consumption was recorded at each step enabling a precise calculation of specific product costs, facilitating comparisons among

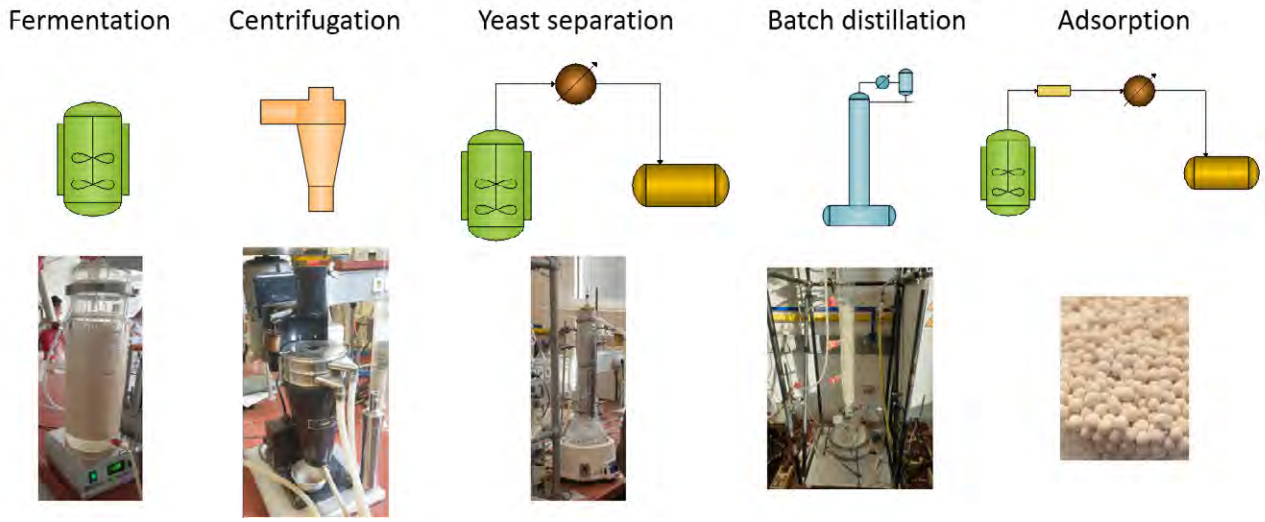



**Figure 1:** Sequence of the process steps with the corresponding CHEMCAD icon and available lab equipment.

groups and against commercially available bioethanol.

## PROCESS EQUIPMENT

Figure 1 illustrates the sequence of process steps alongside the corresponding CHEMCAD icons, which represent the utilized model and the available laboratory equipment. This section provides a summary of the key equipment parameters.

### Vessel reactor with temperature control

The fermentation takes place in a cylindrical glass vessel with a usable volume of six liters. Temperature control is achieved through a double-jacketed system, where water circulates via a thermostat. The water temperature is maintained at 30°C, closely matching fermenter temperature. A magnetic stirrer ensures thorough mixing. The vessel remains sealed, besides a tube that directs the produced gas through a gas meter to the atmosphere.

Liquid samples can be collected from the bottom of the vessel for analysis. Glucose and dry matter are measured using optical measurement methods, while the ethanol content is later determined by gas chromatography. However, an estimate for the current ethanol concentration can be approximated from the gas production rate.

At the end of the fermentation step the reactor contents are harvested and frozen to prevent further glucose conversion. The energy required for freezing and unfreezing is not accounted for in the analysis.

### Tubular centrifuge

The bulk amount of yeast is separated in a tubular centrifuge. The tube has an inlet diameter $d_i$ of 14.5 mm, an inner diameter $d_0$ of 43.5 mm, a length $L$ of 188 mm, and can rotate at speeds up to $n = 25{,}000$ revolutions per minute (RPM). The dry matter content of the feed and the products can be analysed with a high accuracy evaporation scale. At this point the ethanol in the separated centrifugate is replaced by taxed ethanol in compliance with German customs regulations.

### Heated glass bulb with condenser

The intermediate product is purified from yeast and glucose in a single stage distillation conducted in a heated glass bulb with a condenser. Two glass bulbs, each with a volume of three liters and a 500 W heating device are available for the process. To prevent foam from entering the water-cooled condenser, an empty glass column is placed on top of the bulb.

The ethanol content of the distillate is measured by analyzing the refractive index of the liquid. At the end of this step, a sample of the distillate is analyzed in a gas chromatograph to detect and quantify any contamination with methanol or other alcohols.

### Packed batch column

The plant used to increase the ethanol content consists of a four-liter pot, a column with an internal diameter of 50 mm and a height of 1,200 mm, a condenser with integrated reflux control by a magnetic valve, a guard condenser, a product cooler, and three receiver tanks, which can be connected by a magnetic valve. The column was packed with Raschig rings up to a height of 1,000 mm. The pot can be heated with a maximum duty of 1,800 W, although flooding in the condenser occurs earlier, at around 600 W.

Labview™ is used to control the plant and to visualize the measured temperature profiles, the volume rate and the temperature increase of the cooling water, and the added heat duty. The Labview™ screen and a sketch of the column are depicted in Figure 2.



**Figure 2.** Automated batch distillation plant.

## Adsorption plant

The remaining water is adsorbed on the molecular sieve KÖSTROLITH ® 3AK. 120g of this zeolite are allocated in the heated glass column of the adsorption plant.

The ethanol-water mixture is transported by a gear pump to a bulb, where it is evaporated using heat from a thermal oil which is maintained at 180°C by a thermostat. The temperature profile in the column is monitored to detect the breakthrough of water. The vapor from the top of the column is condensed and the liquid product is collected in another bulb. The purity of the product is quantified by a high accuracy density measurement.

The zeolite is regenerated in a drying cabinet, where it is completely regenerated over around six hours at 230°C until no more water is adsorbed on it.

# PROCESS MODELS

Rigorous process models are used to design the process steps and to assess their performance after execution. The models are based on mass and energy balances and on phase equilibrium calculation when applicable.

## Fermentation

The fermenter is modelled as a perfectly mixed reactor. The species carbon dioxide $CO_2$, ethanol $C_2H_5OH$, water $H_2O$, alpha-D-glucose $C_6H_{12}O_6$, and biomass $X$ are considered in the material balances. Only one reaction is taken into account, the growth of biomass with the simultaneous production of ethanol. The mass-based stoichiometry is given in equation (1) using the yield coefficients for ethanol production $Y_{P/S}$ and for biomass production $Y_{X/S}$.

$$C_6H_{12}O_6 \rightarrow Y_{P/S}\, C_2H_5OH + Y_{X/S}\, X + \left(1 - Y_{\frac{P}{S}} - Y_{X/S}\right) CO_2 \qquad (1)$$

The structure of the reaction rate, given in equation (2), is taken from Fogler [1]. The rate uses the mass-based concentrations $c_i$.

$$\dot{r}_1 = \mu_{max} \left(1 - \frac{c_{C_2H_5OH}}{c_{C_2H_5OH}^{tox}}\right)^{0.52} \frac{c_X\, c_{C_6H_{12}O_6}}{K_S + c_{C_6H_{12}O_6}} \qquad (2)$$

The reaction rate is implemented in the vessel reactor model in CHEMCAD.

## Centrifugation

The separation efficiency of the centrifuge is estimated by balancing centrifugal force, lifting force and drag force. This leads to equation (3) for the separation grain diameter $d_T$.

$$d_T = \frac{1}{2\,\pi\, n} \cdot \sqrt{\frac{18\,\eta}{\Delta\rho} \cdot \frac{4\dot{V}}{\pi d_0^2 L} \cdot \frac{d_0}{d_i}} \qquad (3)$$

## Evaporation

The MESH equations (material balances M, equilibrium conditions E, sum equations S and heat balance H) are used to model the evaporation of ethanol and water in the heated glass bulb. The five components mentioned in the Fermenter section are balanced. The caloric properties of the biomass are estimated with the properties of water. The phase equilibrium (K-values / $K_i$) is calculated with the non-random two liquid model (NRTL) from Renon and Prausnitz [2]. In the equations 4 – 10 $x_i$ refers to the molar liquid fraction, $y_i$ to the molar vapor fraction, $M$ to the molar hold-up, $\dot{Q}$ to the heat duty added or removed, $U$ to the inner energy $h$ to the enthalpy, and $V$ to the vapor flow. The indices L and V refer to liquid and vapor.

$$\text{M:}\quad \frac{d(x_i M_L)}{dt} = -y_i V \qquad (4)$$

$$\text{E:}\quad y_i = K_i x_i \qquad (5)$$

$$T_V = T_L \qquad (6)$$

$$P_V = P_L \qquad (7)$$

$$\text{S:}\quad 1 = \sum_{i=1}^{NC} x_i \qquad (8)$$

$$1 = \sum_{i=1}^{NC} y_i \qquad (9)$$

$$\text{H:}\quad \frac{dU_L}{dt} = \dot{Q} - h_V V \qquad (10)$$

The MESH equations are solved in CHEMCAD using the vessel reactor unit operation.

## Packed batch column

The batch column is modelled by solving a set of the MESH equations, with a number of MESH sets equal to the number of theoretical plates. Therefore, the equations 4 and 10 are modified by adding a vapor flow from the lower plate, a liquid flow from the upper plate and by subtracting the liquid flow to the lower plate. The resulting differential-algebraic equation system is solved in the CHEMCAD unit operation batch column. To include non-integer values for the number of theoretical plates Murphree tray efficiencies are used. Heat losses over the column are estimated for each stage with equation (11), where $k$ is the heat transfer coefficient. At the last stage the reboiler duty is added, at the first stage the

condenser duty is removed.

$$\dot{Q}_{\mathrm{HeatLoss}} = k \cdot A_{Stage} \cdot \left(T_{Ambient} - T_{Stage}\right) \quad (11)$$

### Adsorption

The adsorption of water on the zeolite is modelled by assuming a water free adsorbent as initial condition, spherical particles of equal size, and a linear adsorption isotherm. The approximated solution to the partial differential equation system proposed by Rosen is used to calculate the dynamic behaviour of the gas phase concentrations. For further details, see Sattler`s textbook [3].

## PROCESS STEPS

Each process step can only be performed once, making detailed planning of the entire process essential. Process models are developed, fitted to data from preliminary experiments, and used to design the individual process steps.

### Feedstock and product requirements

The sugar alpha-D-glucose monohydrate is used as feedstock, because its concentration in an aqueous mixture with ethanol is easier to measure compared to other sugars. Besides water, the only other feedstock is fresh yeast with a dry matter content of around 30% by weight.

The ethanol concentration in the fuel-grade bioethanol product must exceed 98.7% by weight [4].

### Preliminary experiments

Preliminary experiments are performed to determine missing model parameters. Most of these parameters are obtained by reconciliation of measured data. However, for the design of the fermentation process, the solubility of the sugar, the yeast, and their mixture in water are critical. These parameters are determined through trials which are not directly related to the later process steps.

### Data reconciliation

Data reconciliation is a powerful tool for estimating missing model parameters. It involves using measured data and correcting it by applying conservation equations. This is required because the mathematical models, where these parameters are used follow these fundamental laws, whereas measure data commonly is subject to errors and may not. The models that are used during the data reconciliation are described in the section on process models.

### Reaction kinetics and yield coefficients

A fermentation trial is carried out in the previously described vessel reactor. The concentrations of glucose, yeast, and ethanol are monitored over time. Additionally, the $CO_2$ production rate is measured. A comparison of the initially added glucose with the produced ethanol and the increased amount of yeast at the end of the experiment produces the yield coefficients. The reaction kinetic parameters in equation (2) are determined using the reaction rate regression tool implemented in CHEMCAD.

### Mechanical yeast separation

Although the separation grain diameter can be calculated using equation (3), where all parameters are known, the mechanical yeast separation can not be calculated a priori. The unknown property in this case is the particle size distribution of the yeast in the mixture, which cannot be measured directly. Instead, the remaining amount of yeast in the intermediate product is analyzed.

### Column start-up and total reflux profiles

Several important simulation parameters can be retrieved from the temperature profiles of the column start up. The curves from a preliminary experiment are shown in Figure 3. The next sections will refer to these profiles.

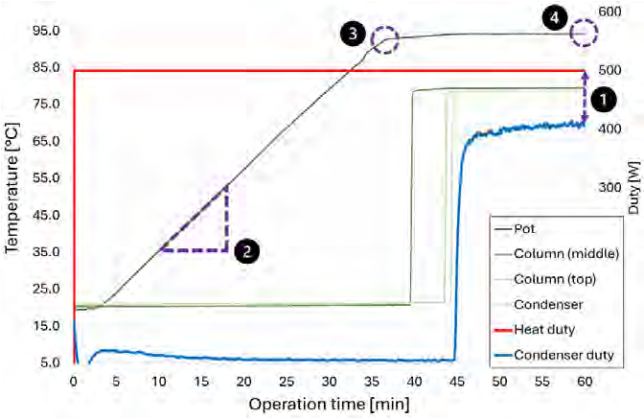



**Figure 3.** Temperature profiles during start-up.

### Heat losses

Heat losses occur in all process steps, but they are particularly significant in the packed distillation column, where they lead to an increased reflux stream and impact the separation efficiency. These losses can be estimated by comparing the heat added to the pot with the heat removed by the cooling water in the condenser. At total reflux the difference of these values gives the overall heat loss (arrows at Point 1 in Figure 3). The heat loss from the pot can be estimated separately by analyzing the heat-up curve (Point 2 in Figure 3).

### Column hold-up

The liquid hold-up in the packing and in the condenser directly influence the dynamic behavior of the batch distillation. These factors must be included in the model to make reasonable predictions of the product concentration in the distillate and receiver tanks.

Fortunately, they can be estimated from the total reflux experiment. Initially, all the column content is allocated in the pot, and its composition is known or can be derived from the temperature profiles during the heat-up

phase (Point 3 in Figure 3). Temperature and composition in the pot change over time and reach a steady state once the total reflux profile is fully established (Point 4 in Figure 3). This change in composition is a result of the transfer of mass from the pot into the column.

The correlation between the hold-up and the temperatures at Points 3 and 4 in Figure 3 is not trivial but can be determined through data reconciliation. However, no direct differentiation between the hold-up in the packing and the hold-up in the condenser is possible. Therefore, one of these parameters should be fixed to a reasonable value during the data reconciliation.

## Separation efficiency

The number of equilibrium stages in the packed column, defined by the modified equation system 4-10, can be estimated using the McCabe-Thiele method, i.e. drawing steps into the x-y equilibrium diagram (Figure 4). This graphical method is not very accurate, often resulting in a non-integer value for the last stage, which is hard to read precisely from the diagram. Additionally, the energy balance is neglected, which is not a valid assumption for columns with considerable heat losses. Consequently, the separation efficiency is estimated by rigorous simulation using Murphree tray efficiencies.

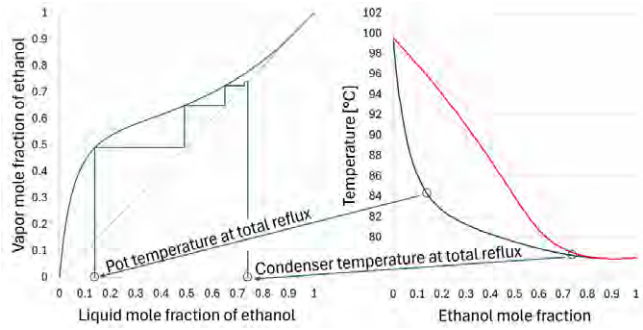



**Figure 4.** McCabe Thiele method for estimating the number of equilibrium stages in the packed column.

Graphically these efficiencies mean, that the step of an equilibrium tray is not drawn until the equilibrium line but ends at a certain percentage (the Murphree efficiency of the tray) of the full distance. The estimation from the McCabe Thiele method still gives a good initial guess for the data reconciliation.

Heat loss, hold-up, and separation efficiency are coupled in a highly non-linear manner, so they must be regressed together. This simultaneous regression is performed using the data reconciliation tool implemented in CHEMCAD. The measured values to be matched include the pot and condenser temperatures, as well as the heat loss over the packed column. Samples can be drawn from the pot and condenser to determine their composition, but these values correlate with the respective temperatures in the case of a binary mixture. The measurements are still used to verify the accuracy of the method.

## Adsorber capacity

The particle diameter and the adsorption isotherms for the zeolite are commonly provided by the vendor, but the packing porosity and the effective diffusivity must be estimated to apply Rosen`s equation. While the packing porosity can be read from volume measurements, the effective diffusivity requires a trial run. The final missing parameter in the adsorber model can be estimated from the breakthrough curves of water.

## Fermentation

The validated model for the conversion of glucose to ethanol, yeast, and carbon dioxide in the given fermenter can be used to maximize the amount of ethanol produced at minimum costs in a 150-minute run. The decision variables include the initial amounts of yeast and glucose, as well as additional glucose fed to the fermenter at any time later in the run. The feedstock content in the fermenter is limited by its solubility. While the operational costs, such as electricity consumption for stirring and cooling remain fixed, feedstock costs directly impact the profitability of the process.

## Yeast removal

The two steps of yeast removal offer little room for optimization but impose constraints to the amount of fermenter broth that can be produced during the fermentation step. Additionally, the liquid volume of the batch distillation plant`s pot is limited, which restricts the amount of condensate generated in the evaporation step. This step also determines the initial ethanol concentration for the distillation and, consequently the maximum product purity achievable with the existing column.

## Distillation

The distillation column has only one degree of freedom during operation: the reflux ratio. In theory, the heat duty added to the pot could be adjusted, but due to the risk of flooding, it is fixed at a safe value.
Nevertheless, designing the distillation step is challenging because the reflux ratio can be adjusted dynamically. Instead of optimizing a single value, the goal is to determine an optimal trajectory over the 150-minute runtime or, alternatively, a sequence of operational steps.
The objective function is also complex. While the operation costs don't vary much (600 W over 150 minutes plus heat-up time), a key decision involves determining how much product should be collected and at what concentration. Product batches of varying volumes and concentrations can be collected in the receiver tanks, adding another layer of optimization.

## Adsorption

Finally, the water content in the product batches

must be removed in the adsorption step, which is the bottleneck of the overall production process. While this step does not feature any decision variables, detailed planning is essential to ensure that all the product from the distillation column is processed efficiently. Due to heat-up and cool-down times, only two adsorption runs can be performed in the 180-minute timeframe.

## RESULTS

All groups successfully produced bioethanol with the required purity. The utilized electrical energy was similar for all groups, but the final product mass varied significantly, ranging from 50g to 200g depending on the process design. Figure 5 presents an example of the fermentation step, comparing the planned concentration trajectories (model) with the measured values. In this specific case the students have decided for a fed-batch strategy. A similar comparison for the distillation step is shown in Figure 6. The primary cost driver in the process is the glucose feedstock, with overall operational expenditures ranging from €20 to €50 per group. The overall student feedback on the project was very positive.

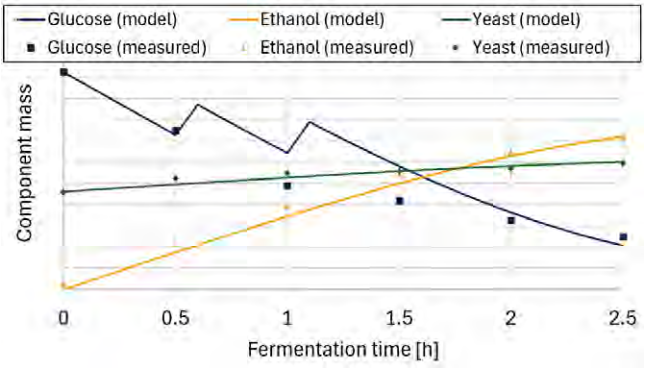



**Figure 5.** Exemplary results of the fermentation step.

## SUMMARY

This work provides a detailed overview of the materials and methods used for a university course during which students produce bioethanol in a demanding competition. It shares key insights from the course, highlighting both challenges and successes. The study emphasizes the importance of mathematical modelling and the challenges in aligning modeled data with measured data. A key takeaway is that while the models may not perfectly capture reality, they are essential for a successful process design, particularly for inexperienced engineers transitioning from academia to industry.

Each student has an individual project, but this project is connected to those from the other group members. Providing reasonable guesses for data that is required in the other projects is very challenging, but also a great learning experience, especially if the guess was good.

This case study shows how combining modelling tasks and experimental tasks and merging them to a project that follows a red thread leads to an extraordinary learning experience for the students. It is intended to motivate the design of similar courses.

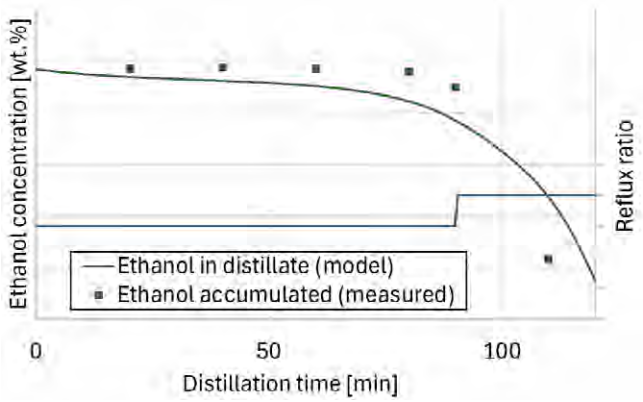



**Figure 6.** Exemplary results of the distillation step.

## DIGITAL SUPPLEMENTARY MATERIAL

The CHEMCAD simulation files for the modelling of the fermentation step, the open distillation step and the batch distillation step are available as digital supplementary material:

https://psecommunity.org/LAPSE:2025.0016
https://psecommunity.org/LAPSE:2025.0017
https://psecommunity.org/LAPSE:2025.0018

Furthermore, a tutorial like detailed description of how to parametrize the batch column model in CHEMCAD can be found on the Chemstations website:

https://www.datacor.com/hubfs/Estimating_Simulation_Parameters_for_Batch_Columns.pdf

## REFERENCES


1. H.S. Fogler. Elements of Chemical Reaction Engineering. Prentice Hall (2016).
2. H. Renon, J.M. Prausnitz, Local Compositions in Thermodynamic Excess Functions for Liquid Mixtures. *AIChE Journal* 14-1:135-144 (1968)
3. K. Sattler. Thermische Trennverfahren. Wiley-VCH (2001).
4. Automotive fuels – Ethanol as a blending component for petrol – Requirements and test methods DIN EN 15376 (2014)



© 2025 by the authors. Licensed to PSEcommunity.org and PSE Press. This is an open access article under the creative commons CC-BY-SA licensing terms. Credit must be given to creator and adaptations must be shared under the same terms. See https://creativecommons.org/licenses/by-sa/4.0/

Systems & Control Transactions

**Research Article - Peer Reviewed Conference Proceeding**
ESCAPE 35 - European Symposium on Computer Aided Process Engineering
Ghent, Belgium. 6-9 July 2025
Jan F.M. Van Impe, Grégoire Léonard, Satyajeet S. Bhonsale,
Monika E. Polańska, Filip Logist (Eds.)

PSE PRESS

# Exergy Examples for the Chemical Engineering Classroom

**Thomas A. Adams II**[a]*

[a] Norwegian University of Science and Technology, Department of Energy and Process Engineering, Trondheim, Norway
* Corresponding Author: thomas.a.adams@ntnu.no

## ABSTRACT

This work explores several examples of how the thermodynamic concept of exergy can be used in the chemical engineering classroom. Examples include using exergy to determine thermodynamic and monetary value of utilities, to identify better heat exchanger network designs, to aid in work-heat integration applications such as heat pumps and organic Rankine cycles, to scope out realistic energy integration cases, and to assess how well chemical potential is being used and managed. The examples are presented in one connected context that makes it easy to see how exergy analyses can be useful across many aspects of chemical and energy industry supply chains.

**Keywords**: Exergy, Education, Energy Efficiency, Process Design

## INTRODUCTION

Exergy is an interesting thermodynamic property that is especially useful for the design, analysis, and optimization of energy systems. Although there are competing definitions of exergy, I believe the definition of Moran et al. [1] is the most general and the easiest for process systems engineers to understand (emphasis mine):

### Definition of Exergy

> Exergy is the **maximum** theoretical work obtainable from an overall system consisting of a system and the environment as the system comes into equilibrium with the environment (passes to the dead state).

The text definition can be written mathematically in a form understandable to process systems engineers:

$$e = \max_{\mathcal{P}} w \tag{1}$$

where $e$ is the exergy, $\mathcal{P}$ is a process that brings the system into equilibrium with the environment, and $\mathbb{P}$ is the set of all possible processes such that $\mathcal{P} \in \mathbb{P}$. [2]. Note that "the system" can include a process, device, unit operation, heat, or a substance.

Exergy arises from the ways in which the system differs from the environment, such that some process $\mathcal{P}$ can be made to exploit those differences. For example, if a fluid has a higher pressure than the environment, a turbine can be used to produce work by passing the fluid through the turbine into the environment (the reverse direction is also possible [2]). If a substance is hotter than the surrounding environment, a Carnot engine can convert the higher temperature heat from the substance into work and use the environment as the sink for the lower-temperature waste heat (or its reverse [3]). Chemical potential, phase differences, concentration differences, gravity, and other forms of energy can all be exploited for some kind of work production [4], and the exergy is the maximum work theoretically possible using a perfect, reversible, frictionless, lossless process. In this form, exergy is both a measure of quantity and quality of energy simultaneously. For example, 1 kJ of heat at 100°C has less exergy than 1 kJ of heat at 200°C, even though they have the same energy.

To the process systems engineer, and especially to the process designer, this property makes exergy useful for process design, optimization, and analysis. Exergy is a good proxy for value. For example, the exergies of utilities are directly correlated with their market prices [4], exergy losses in flowing systems correlate very well system complexity [5], and exergy can also be used as a proxy for capital cost, making it particularly suitable as an objective in optimal process design problems [6]. It is excellent for debottlenecking, benchmarking, and identifying value and thermodynamic limits. It also works in reverse: exergy is also the thermodynamic minimum work

required to take material and energy from the environment and create high value products. This is particularly useful for modern relevant chemical engineering applications such as direct air capture of $CO_2$, desalination, cryogenic air separation, resource extraction, green hydrogen production from water ("un-combustion of hydrogen"), $CO_2$ conversion into fuels like synthetic methane ( "un-combustion of natural gas"), and environmental remediation.

Despite all these potential uses to the system engineer, exergy is not traditionally taught much in chemical engineering education. It has little to no mention in most major chemical process design textbooks including those by Smith [7], Towler and Sinnot [8], and Peters, Timmerhaus, and West [9]. The 3rd edition of Seider et al. [10] uses the terms "availability" and "2nd law analysis" to express some of the same fundamental concepts, but is relegated to the supplementary material rather than the actual print.

Exergy is a difficult concept for both students and educators. Students need to understand enthalpy and entropy, and many of its benefits to engineering decision making can only be exploited at the senior level or higher. Nevertheless, it can be used at lower levels for analysis purposes, especially when students simply look-up / are given exergy values and skip the difficult computation portion (the book Exergy Tables [4] is simply a compendium of look-up values for students to use, shortcutting the more difficult computational portion). To make this easier, this work provides several examples of how it can be used in the classroom in a variety of contexts.

## CLASSROOM EXERGY EXAMPLES

### Example 1: Exergy as Proxy for Value

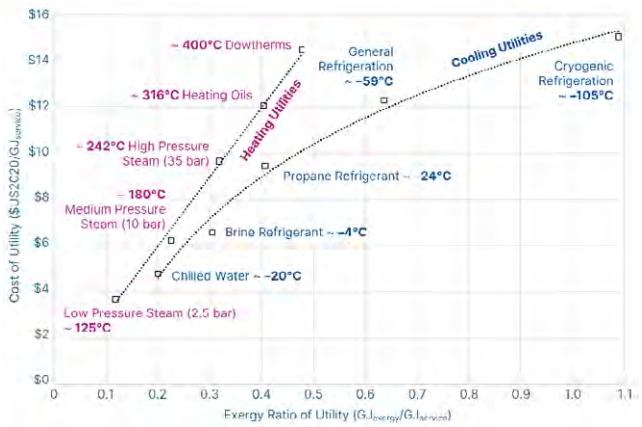



**Figure 1:** The cost of a utility as a function of its exergy ratio using 78°C as $T_{\text{ref}}$ and the assumed average operating temperatures shown. Adapted from [4].

Exergy is an excellent proxy for value and can be used to estimate the market value of cold or hot utilities at any temperature. This is especially convenient when the designer has enough degrees of freedom to choose the temperature of the desired utility. For example, Deng et al. [4] suggested the existence of a so-called "plant ambient" temperature of 78°C that arises from the statistical cost of utilities presented in Seider et al. [10]. The statistical value/cost of heating and cooling services is effectively zero at 78°C and increases as temperature moves away (up or down) from it. Essentially, 78°C statistically arises as the temperature at which something has zero thermal value on average in chemical plants, and all other deviations from there cost money to achieve. As far as utilities are concerned, 78°C is a better definition of "environmental temperature" for a chemical plant than 25°C. Consequently, Deng et al. [4] showed that the cost of utilities is strongly correlated with exergy using 78°C as the reference temperature ($T_{\text{ref}}$), as shown in Figure 1:

The correlation for the cost of hot utilities $C_{\text{heat}}$ is [4]:

$$C_{\text{heat}} = 29.9\ \text{USD}_{2020} R_{\text{ex}} \tag{1}$$

where $R_{\text{ex}}$ is the exergy ratio of the utility at temperature $T$ in °C (sometimes called the exergy quality) which is the amount of exergy of that utility using 78°C as the environmental reference temperature expressed per unit of thermal energy received or delivered by the utility. $\text{USD}_{2020}$ means US dollars in the year 2020. For heat at $T \geq T_{\text{ref}}$ this is:

$$R_{\text{ex}} = 1 - \frac{273.15+T_{\text{ref}}}{273.15+T} \tag{2}$$

For example, heating services at 200°C would have an exergy ratio of 0.258 $\text{GJ}_{\text{exergy}}$ per $\text{GJ}_{\text{heat}}$ and cost 7.71 $\text{USD}_{2020}$ per $\text{GJ}_{\text{heat}}$ purchased. For cold, the exergy ratio is the exergy the heat sink (the cooling sink / utility) at temperature $T$ per unit of thermal energy moved from the hot source to the cold utility. The definition of $R_{\text{ex}}$ switches for $T \leq T_{ref}$:

$$R_{\text{ex}} = \frac{273.15+T_{\text{ref}}}{273.15+T} - 1 \tag{3}$$

and is expressed in $\text{GJ}_{\text{exergy}}$ per $\text{GJ}_{\text{cooling}}$. The corresponding cost of cooling utilities again applies when $R_{\text{ex}}$ is calculated using 78°C for $T_{\text{ref}}$:

$$C_{\text{cool}} = 14.75\ \text{USD}_{2020} + 6.31\ \text{USD}_{2020} \ln R_{\text{ex}} \tag{4}$$

For example, a cooling sink at –40°C (e.g. refrigeration) has an exergy ratio of 0.506 $\text{GJ}_{\text{exergy}}$ per $\text{GJ}_{\text{cooling}}$ and cost 10.5 $\text{USD}_{2020}$ per $\text{GJ}_{\text{cooling}}$ provided. It is very straightforward for students to quickly connect exergy, temperature, and value with these equations for all sorts of uses.

### Example 2: Pinch Analysis & Heat Integration

Consider the balanced composite curves shown for a proposed heat exchanger network (HEN) that meets the minimum energy targets in Figure 2 (left). The red lines indicate the profile of the hot streams of the HEN and the blue lines indicate the cold streams. The heating

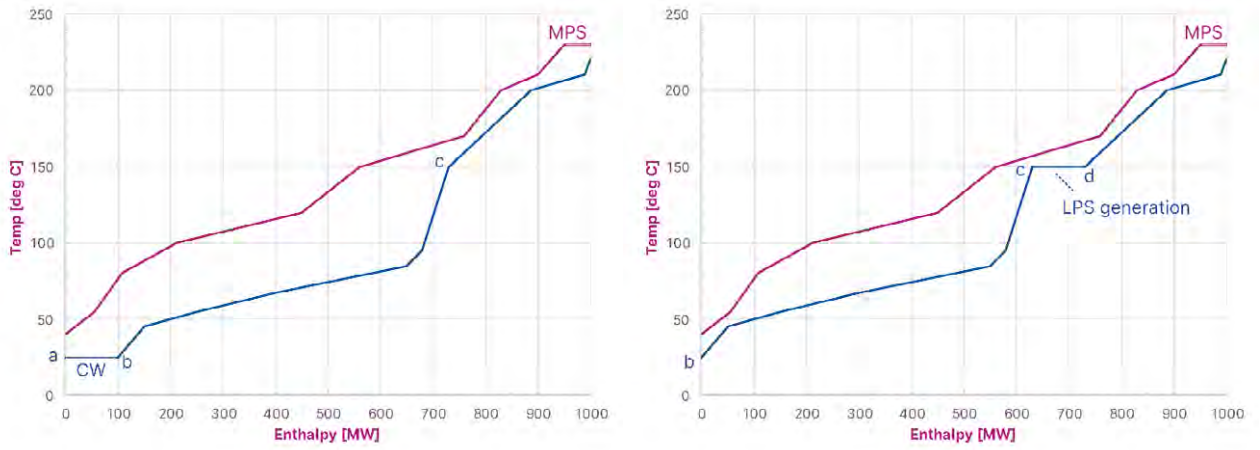



**Figure 2:** (left) Balanced composite curves of a proposed heat exchanger network resulting from classic methods. (right) A suggested improvement by a student.

utility is medium pressure stream (MPS) as shown, and the cooling utility is cooling water (CW), line segment **ab**. This balanced composite curve is typical of one that would be developed with classic minimum energy targeting methods as described in various popular textbooks [7, 10, 11] and taught in many undergraduate courses.

The student can take another step further and evaluate the exergy value or cost of the utilities. Whether selecting the plant ambient or environmental ambient as the reference case, the exergy of the required utilities can be computed, and their market value approximated from equations (1)-(4). Here, the cost of cooling is about 3.85 $USD_{2020}$/GJ and at 100 MW (the width of line **ab**) would cost about 12 million $USD_{2020}$/year. Then the student can identify an improvement to the system which still meets the minimum energy requirements, but has better exergy or monetary value, which are directly correlated.

The general idea is to identify low hanging fruit on the composite curve such that utility loads can shift to places in the HEN with lower cost. For example, a student could suggest that a new HEN could be made with the balanced composite curve shown in Figure 2 (right) by shifting line segment **bc** to the left until a minimum approach temperature other constraint has been reached. In this case, all 100 MW of cooling can be removed, and **bc** shifted all the way to the left. The student can replace the 100 MW of cooling with 100 MW of low-pressure steam (LPS) **generation** at 150°C (segment **cd**). The curves are tighter now for hot-side temperatures around 50°C and 160°C, meaning that the HEN might be more complex and require more heat exchanger area (due to smaller temperature driving forces). But it might be worth it because the utility value improvement is enormous. Instead of spending money on cooling, we can **generate** value up to 16 million USD/year instead of spending 12 million USD/year.

This is simple way to connect many topics relating to energy quantity, quality, economics, thermodynamics, HEN design, and optimization all at once in the classroom. You can immediately see how this can be integrated into the objective functions of optimal heat exchanger network design for more complex class material [6].

## Example 3: Work-Heat Integration

Continuing that example, perhaps we do not want to make LPS because we have no need for it or way to sell it, but we could instead use that steam to produce work. A student can immediately estimate the upper bound work production potential of recovering 100 MW at 150°C against our actual environmental temperature (let us choose the common $T_{\mathrm{ref}}$ of 25°C). From equation (2), the exergy ratio of that recovered heat is about 0.295, meaning that one could produce a theoretical maximum of 0.295 GJ of work per GJ of heat recovered. For 100 MW of waste heat recovered, this is 29.5 MW of work. That is certainly a large enough potential to considering the idea further.

A student can then use exergy to set a few more benchmarks about how the system could work in practice. First, LPS is generally too weak to produce much work in a steam cycle, so at 150°C we might consider an organic Rankine cycle (ORC). Figure 3 shows an example of how a simple ORC might work using R113 as a working fluid on a Temperature-Enthalpy-Exergy diagram. Thermo-mechanical exergy ($e^{\mathrm{tm}}$, blue lines) is computed using $T_{\mathrm{ref}}$ of 25°C and the following equations for thermo-mechanical exergy of a substance [2]:

$$e_1^{\mathrm{tm}} = \begin{cases} (h - h_{\mathrm{ref}}) - T_{\mathrm{ref}}(s - s_{\mathrm{ref}}) & p \geq p_{ref} \\ (2h_* - h - h_{\mathrm{ref}}) - T_{\mathrm{ref}}(s - s_{\mathrm{ref}}) & p \leq p_{ref} \end{cases} \quad (5)$$

where $h$, $s$, and $p$ are the intensive enthalpy, entropy, and pressure of the point of interest; $h_{\mathrm{ref}}$, $s_{\mathrm{ref}}$, and $p_{\mathrm{ref}}$ are the

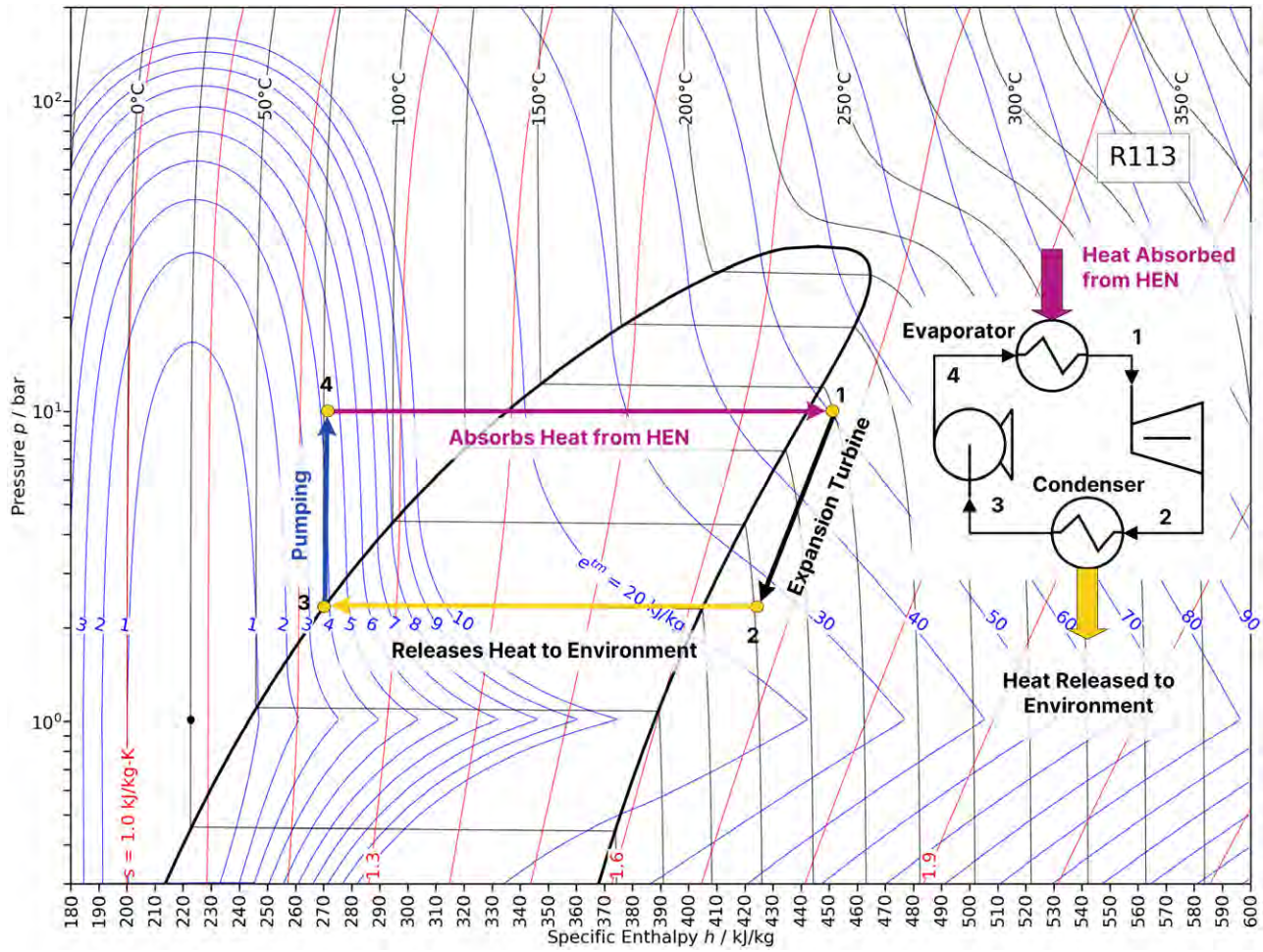



**Figure 3:** The pressure-enthalpy-entropy diagram for R113 (adapted from [2]), with the working fluid state changes overlaid with coloured arrows. The inset shows the corresponding ORC design with corresponding streams.

intensive enthalpy, entropy, and pressure at the reference conditions (the reference pressure chosen is $p_{\text{ref}}$= 1 atm); and $h_* = h(p_{\text{ref}}, s)$.

Using Figure 3 or equation (5), the student can quickly select some good starting points for an ORC design. The student has chosen point **1** to be the highest pressure that R113 can get while being slightly superheated and at the maximum possible 150°C (about 10 bar, see Table 1 for approximate stream conditions), since this is the temperature of our sink. This student selected the pressure of Point **2** to be the lowest pressure R113 can get along a path of isentropic expansion such that the temperature is still high enough to dump heat to the environment via the condenser. For example, we could decide we want to use cooling towers and so maybe we would pick a temperature of, say, 40°C. The lower the temperature, the more work produced, but then the higher the cost for cooling in the condenser.

**Table 1.** Approximate stream conditions for the ORC shown in Figure 3.

| **Stream** | **1** | **2** | **3** | **4** |
|---|---|---|---|---|
| $T$ °C | 150 | 101 | 78 | 78 |
| $P$ bar | 10 | 2.1 | 2.1 | 10 |
| $h$ kJ/kg | 450 | 425 | 272 | 272 |
| $e^{\text{tm}}$ kJ/kg | 51 | 26 | 4 | 4 |
| $E$ MW | 28.7 | 14.6 | | |

However, remembering example 2, the point of this was to avoid cooling towers, so the student chose a point at 2.1 bar such that phase change occurs close to the plant ambient temperature so that heat removal in the condenser is basically free. Point **3** is chosen as simply the point at which the R113 is fully condensed. Point **4** is point where the pressure returns to 10 bar isentropically. This line of thinking is simple and quick enough such that points can be chosen by hand and sketched with a pencil on an exam.

The student can quickly determine key several metrics by reading off the diagram or using more rigorous formulas (see Table 1). For example, the flow rate of the working fluid is quickly determined by the enthalpy difference between points 4 and 1 ($h_4 - h_1$ = 178 kJ of heat adsorbed per kg of R113, which at 100 MW absorbed is 562 kg/s of R113).

The exergy at point **1** is about 51 kJ/kg, which at the system flow rate is about 29 MW. This is a good check because it cannot be higher than the theoretical maximum exergy of the 100 MW heat of 29.5 MW exergy we computed earlier. Given the limited precision of Figure 3, it means our choice for point **1** is very good and there is little room for improvement by changing the conditions. Note that for this sketch, the work required by the pump ($h_4 - h_3$) is too small to be considered within the precision of this analysis.

The work produced by the turbine is simply the enthalpy difference between points **1** and **2** ($h_1 - h_2$ = 25 kJ/kg, which for 562 kg/s of R113 is 14 MW). That's a sizeable amount of work and perhaps worth pursuing. Note however, that the work produced by the turbine is also the thermo-mechanical exergy difference between point **1** and point **2** ($e_1^{\text{tm}} - e_2^{\text{tm}}$ = 25 kJ/kg also). We can see immediately since point **2** has a thermo-mechanical exergy of $e_2^{\text{tm}}$ = 26 kJ/kg that we are not using, we are leaving about half of our potential value on the table with this ORC.

It is instructive for the student to compute some useful metrics such as the energy efficiency ($\eta_{\text{en}}$) and the exergy efficiency ($\eta_{\text{ex}}$), noting that work is pure exergy:

$$\eta_{\text{en}} = \frac{\text{Power Produced}}{\text{Heat Supplied}} = \frac{14\ \text{MW}}{100\ \text{MW}} = 14\% \qquad (6)$$

$$\eta_{\text{ex}} = \frac{\text{Exergy Produced}}{\text{Exergy Supplied}} = \frac{14\ \text{MW}}{29.5\ \text{MW}} = 47\% \qquad (7)$$

The metrics show that although percentage of the waste we convert to power is relatively small (14%), we recover 47% of the **value**, which is quite good for low quality waste heat! Considering all the metrics together, the student can conclude that (1) the 150°C waste heat is sufficiently large to be meaningful, (2) the ORC design captures about half the value of that heat, which is also meaningful, and (3) there is still much room to improve the design with changes like a lower turbine outlet pressure or an economizer. The process of sketching out design concepts, linking them to thermodynamic states, and then computing and analyzing important metrics relating to energy and exergy is an important take-away skill set for any student approaching any kind of energy engineering problem.

## Example 4: MPS Generation by Combustion

Let's continue that example but focus on the MPS utility requirement. Utility steam generation usually requires natural gas or some other fossil fuel combustion to produce. A student can quickly estimate the cost and exergy value of this steam (50 MW at 230°C) using equations (1) – (4) to be about 14 million USD/yr with an exergy value relative to 25°C of 18.6 MW. Suppose the student should design a boiler process to create this steam from natural gas, and proposes a design shown in Figure 4, with stream conditions in Table 2 determined by Aspen Plus V14 simulation (see end of paper for downloadable link). To deliver heating services by condensing at about 230°C we need steam at 29 bar, and we should make it superheated to 235°C as a safety margin. The steam flow can be determined via the latent heat of vaporization of steam at 29 bar knowing that we need 50 MW of heating service. The rest of the stream rates are determined by other design requirements such as complete combustion of the natural gas, maximum combustion zone temperature, a minimum driving force temperature in the boiler heat exchanger, and assumed conditions about the condensed steam that returns to the boiler in a closed loop.

**Table 2.** Approximate mass and exergy flows for the boiler process shown in Figure 4.

| **Stream** | F (kg/s) | $e^{\text{ch}}$ (MJ/kg) | $e^{\text{tm}}$ (MJ/kg) | $E$ (MW) |
|---|---|---|---|---|
| **1** | 2.68 | 48.3 | - | 129 |
| **2** | 2.68 | 48.3 | 0.013 | 129 |
| **3** | 225 | - | - | - |
| **4** | 225 | - | 0.007 | 1.6 |
| **5** | 227 | 0.009 | 0.063 | 16.4 |
| **6** | 27.7 | 0.049 | 0.207 | 7.1 |
| **7** | 27.7 | 0.049 | 0.209 | 7.2 |
| **8** | 27.7 | 0.526 | 0.964 | 41.3 |
| Blow. 1 | 44 kW | | | 0.04 |
| Blow. 2 | 2.2 MW | | | 2.23 |
| Pump | 10 kW | | | 0.01 |

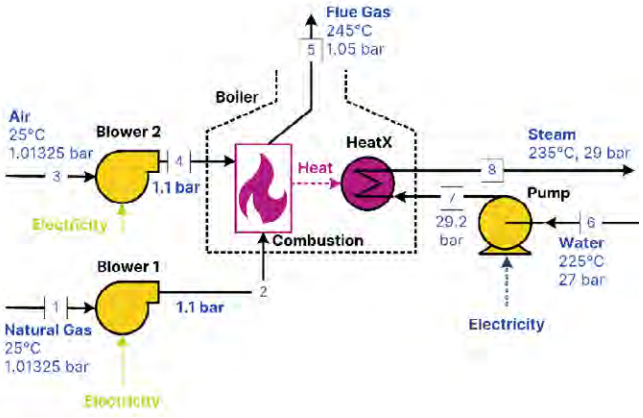



**Figure 4.** A proposed boiler for generating MPS (29 bar steam slightly superheated to 235°C) which can be used to deliver heat at about 230°C as it condenses.

The thermo-mechanical exergy of the relevant streams can be quickly determined through equation (5) or found in tables such as in the book Exergy Tables [4]. Similarly, the chemical exergy ($e^{\text{ch}}$) of the streams (the

work potential associated with chemical bonds, phase, and its chemical composition difference against the environment), can also be found in Exergy Tables to be 831.7 MJ/kmol (or 48.27 MJ/kg) of US Average Pipeline Natural Gas. From this information, the total exergy flows ($E$, the sum of thermo-mechanical and chemical exergy) can be computed and shown in a Sankey diagram (Figure 5). Exergy efficiency also can be computed with equation 7 ($\eta_{\text{ex}} = 31\%$).

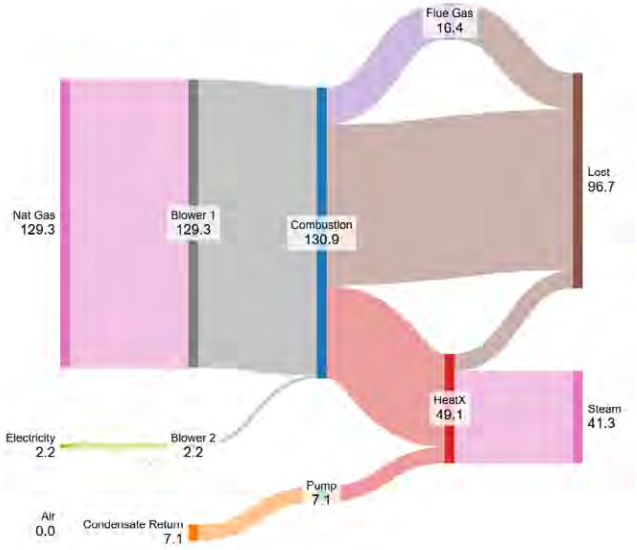



**Figure 5.** Exergy flows in MW of the boiler process of Figure 4. Generated at Sankeymatic.com.

The Sankey diagram is an excellent teaching tool to visualize the exergy flow (the energetic **value**) through the system. The student can immediately see the relatively small importance of the electricity compared to the chemical exergy of the natural gas. The condensate return (stream 6) matters too. The losses though are the most telling. For example, a sizeable amount of heat is lost in the flue gas, identifying this as a possible place to capture that heat for some purpose and recover a decent amount of value of up to 16.4 MW. Again, the exact values do not matter so much; using different reference conditions or different approximations for exergy will still result in a diagram that looks very much the same with the same analytic usefulness to the engineer.

However, most of the exergy lost is through exergy destruction in the combustion step. In other words, combustion as a process inherently destroys much of the chemical exergy value in the fuel. This has bigger picture concerns in the world of power production in which most transportation mechanical power and municipal electric power is produced from fossil fuels via combustion. Now the student can see the connection between combustion and how well the natural gas is used. This is an opportunity to start larger discussions into sustainability and modern technologies like fuel cells that are not limited by combustion and therefore can theoretically better use our fossil-fuel resources via non-combustion approaches to heating and power.

## Example 5: Heat Pumps

With that note, we can continue the example further by considering whether we can avoid combustion entirely. Looking at the balanced composite curves in Figure 2 (right), we might be able to use a heat pump to take the waste heat from our new 100 MW heat sink at 150°C (with 29.5 MW of exergy) and upgrade it to a heat source at 230°C, potentially replacing the need for some or all of the 50 MW of MPS generation from natural gas.

The student can immediately scope this out with exergy because the 29.5 MW waste heat exergy is higher than the 20.4 MW of exergy needed to provide 50 MW of 230°C heat to our HEN cold streams. In theory, there is more than enough exergy available from the waste heat to convert it to a high temperature heating utility by using **theoretically perfect and fully reversible machines**. In fact, we would only need to recover about 20.4 / 29.5 = 69% of the exergy of our waste heat to replace all MPS needs. Of course, the practical reality can be quite different. Nevertheless, this proposed match is potentially suitable from an exergy perspective and deserving of a closer look.

One option is a chemical heat pump, which uses chemical loop where an endothermic reaction absorbs the low temperature waste heat, and then later the reaction is run in reverse exothermically to release heat at a higher temperature. This process requires relatively little work and is mostly powered by the waste heat [12], so it is a good option when electricity is expensive or has a high carbon footprint. A recent study considered several candidate chemical systems and recommended an optimal design using an isopropanol-acetone-hydrogen chemical heat pump that could take waste heat at 150°C and produce heat at 225°C (very close to this example) with an exergy efficiency (relative to 25°C) of about 33% and a coefficient of performance of about 18% [13]. This is a meaningful amount of exergy recovery for something that is powered almost entirely by waste heat. In other words, instead of using cooling water for this HEN, or instead of building an ORC, this chemical heat pump would convert the 100 MW waste heat at 150°C to about 18 MW at 230°C, reducing the MPS production load by 36% and its associated greenhouse gas emissions from natural gas combustion. The student can then estimate if this concept is worth it by considering the exergy flows and cost as predicted by exergy discussed earlier.

Mechanical heat pumps could be another option, in which a meaningful (but not huge) amount of work is used to upgrade waste heat to higher temperatures. If we had access to low cost and/or low carbon-footprint electricity, this might be a good way to avoid natural gas

combustion for MPS production. However, most so-called "high temperature" mechanical heat pumps operate at ranges well below our targeted application [14] with the next frontier going up to the 200°C range [15]. Unfortunately we need to go to 230°C with an 80°C temperature lift, something that has not been well-proven yet but is under active study.

However, based on some of the highest temperature mechanical heat pumps that have been studied, we can make some estimates using exergy. An ammonia-water absorption-compression heat pump can reach temperatures of 230°C, although perhaps not with this high of a temperature lift. Regardless, based on studies at similar temperatures [16], at best we could expect a coefficient of performance of about 3 in a future system. For a mechanical heat pump, this is:

$$COP = \frac{high\ temperature\ heat\ produed}{work\ consumed} \quad (8)$$

So, for A COP of 3 we would need 16.7 $MW_{el}$ of electric work (which is 16.7 MW of pure exergy) to produce 50 MW of 230°C heat, and by energy balance we would consume 33 MW, or 33% of the 150°C waste heat (so there is amply supply). The student can quickly compute the exergy efficiency of the mechanical heat pump to be:

$$\eta_{ex,mhp} = \frac{20.4\ \mathrm{MW}_{230\mathrm{C,heat}}}{(0.33)29.5\ \mathrm{MW}_{150\mathrm{C,heat}}+16.7\ \mathrm{MW}_{\mathrm{el}}} = 77\% \quad (9)$$

This is a high number and is a good use of high-exergy electricity—much higher than the 31% exergy efficiency from natural gas combustion, and higher than the chemical heat pump to boot. In fact, this is even better than if we used a resistance-type electric heating system (which has 100% energy efficiency!), because the exergy efficiency of that would be only 20.4 MW / 50 MW = 41%. Thus, although the technology has not been well studied yet for this application, there is a real potential value in it.

## Other Energy and Sustainability Examples

Some other interesting classroom examples include:

- **Direct Air Capture of $CO_2$.** Exergy Tables lists the chemical exergy of $CO_2$ at about 19.8 kJ/mol [4], which is the **maximum** amount of work that could be produced by taking pure $CO_2$ at 25°C and 1 atm and exploiting the concentration difference with the environment (at hundreds of ppm levels). However, it is also the reverse; it is the thermodynamic **minimum** work required to extract pure $CO_2$ from the atmosphere at 25°C and 1 atm. Good classroom discussions can follow which compare existing DAC technologies to this bound, or cross-compare against other kinds of $CO_2$ mitigation or capture technologies.
- **$CO_2$ Compression for Transport.** $CO_2$ captured from power plant exhaust or other process streams is generally high-purity $CO_2$ near environmental temperature and pressure. The next step usually is compression to supercritical conditions for pipeline transport (often for sequestration). The $e^{\mathrm{tm}}_{\mathrm{CO2}}$ at common pipeline conditions (120 bar, 30°C) is about 220 kJ/kg [4], meaning that $e^{\mathrm{tm}}_{\mathrm{CO2}}$ is a great lower bound on the work required to do the compression. Students can use this benchmark to compare quality of compression train designs or for broad-level analyses that place it in a larger picture of $CO_2$ mitigation technology options for many different supply chains.
- **Liquefied natural gas (LNG) and liquid hydrogen ($LH_2$).** Exergy Tables [4] lists chemical and thermo-mechanical exergy for many transport fuels. For example, $e^{\mathrm{tm}}_{\mathrm{LNG}}$ is roughly 1.1 MJ/kg, which is about 2% of its chemical exergy. $e^{\mathrm{tm}}_{\mathrm{LH2}}$ is about 12 MJ/kg, a whopping 10% of its chemical exergy. These are the thermo-dynamic minimum work requirements to liquify each fuel in preparation for transport, highlighting the substantial energy penalty required. It illustrates one major problem with switching from LNG supply chains to $LH_2$ supply chains since 10% of the chemical value of the $H_2$ must be spent just to prepare it for transport. This is an interesting, big-picture way of seeing the global problem. It also is a great launch point for discussing cold exergy, since some of that work can be recaptured during regasification.

## FINAL NOTES

There is a longstanding debate as to how much importance should be placed on the concept of exergy. Some perhaps place it on too-high of a pedestal with other thermodynamic concepts such as Gibbs or Helmholtz free energies. Thermo-mechanical exergy appears very similar in structure to those fundamental properties, but in the final analysis, exergy lacks the deeper thermo-chemical nuance owing to its dependence on non-arbitrary reference conditions which are very difficult to define and ultimately are always changing [4]. Thus, some argue passionately over the "correct" reference conditions and use cases. Others reject exergy entirely in favour of similar approaches like lost-work analysis (entropy generation), citing the various ambiguities in exergy analysis and the reliance on a subjective determination of what **precisely** constitutes "the environment" [17]. The reader is referred to work by Gößling-Reisemann for a historical overview of this ongoing debate [18].

In my view, the value of exergy is in its usefulness to us process systems engineers. For the examples we have given, it does not truly matter if one person choses slightly different environmental reference conditions than

another, thus arriving at different actual values of exergy, because differences in the precise values of exergy ultimately do not hinder its usefulness. If I use exergy as a proxy for cost in a design optimization problem, I can get very good optimal design results that will end up being a very good design, regardless of those precise choices. If I use exergy for a thermodynamic bound on my performance, my real performance will never get very close to the perfect theoretical limit anyway, but it remains very helpful in my continual strive to improve my process and approach this bound. It is still very useful for identifying bottlenecks and energy integration opportunities even if the measured size of that opportunity changes a little bit depending on who is doing the asking. The point is in the identification, in the doing, and in the outcomes, not the final metric. My suggestion to the educator is to continually present the material in the context of how it helps the designer make good decisions and focus less on the exact values of the numbers themselves.

## DIGITAL SUPPLEMENTARY MATERIAL

The Aspen Plus V14 simulation used in this work is archived in LAPSE and freely downloadable at:

https:/psecommunity.org/LAPSE:2025.0027

## ACKNOWLEDGEMENTS

No funding was received for this work.

## REFERENCES

1. Moran MJ, Shapiro HN, Boettner DD, Bailey MB. Fundamentals of Engineering Thermodynamics, 8th ed.; Wiley: NJ, 2014. ISBN 978-1118412930
2. Adams TA II, Gundersen T. Thermo-mechanical exergy of a substance below environmental pressure. *Ind Eng Chem Res* 63:6286-6296 (2024). https://doi.org/10.1021/acs.iecr.4c00007
3. Adams TA II. Thermo-mechanical exergy of a substance in cold applications approaching absolute zero. *Sys Control Trans* 3:2-9 (2024). https://doi.org/10.69997/sct.129960
4. Deng L, Adams TA II, Gundersen T. Exergy Tables. McGraw-Hill: New York (2023)
5. Ibrić N, Adams TA II, Gundersen T. Synthesis of heat-integrated water networks with exergo-economic criteria. *Chem Eng Trans* 103:805-810 (2023). https://doi.org/0.3303/CET23103135
6. Ibrić N, Adams TA II, Gundersen T. Exergo-economic optimization of heat-integrated water networks. *Thermal Sci Eng Prog* 55:102883 (2024). https://doi.org/10.1016/j.tsep.2024.102883
7. Smith R. Chemical Process Design and Integration, 2nd Edition. Wiley: West Sussex (2016).
8. Towler G, Sinnot R. Chemical Engineering Design. 6th Edition. Butterworth-Heinemann: Oxford (2020).
9. Peters MS, Timmerhaus KD. Plant Design and Economics for Chemical Engineers, 5th Edition. McGraw-Hill: New York (2004).
10. Seider WD, Seader JD, Lewin DR, Widago S. Product and Process Design Principles 3rd Edition. Wiley: New Jersey (2009).
11. Kemp, IC. Pinch Analysis and Process Integration, 2nd Edition. Elsevier-BH (2006)
12. Krishnadoss R, Adams TA II. Integration of a Chemical Heat Pump with a Post-Combustion Carbon Capture Adsorption Unit. *Syst Control Trans* 3: 484-489 (2024). https://doi.org/10.69997/sct.128149
13. Krishnadoss R, Dyrland IA, Adams TA II. Design and optimization of alcohol-ketone-hydrogen chemical heat pumps. *Submitted to Comput Chem Eng* (2025). https://psecommunity.org/LAPSE:2025.0009
14. Jiang J, Hu B, Wang RZ, Deng N, Cao F, Wang CC. A review and perspective on industry high-temperature heat pumps. *Renew Sus Energy Rev* 161:112106 (2022). https://doi.org/10.1016/j.rser.2022.112106
15. Hamid K, Sajjad U, Ahrens MU, Ren S, Ganesan P, Tolstorebrov I, Arshad A, Said Z, Hafner A, Wang CC, Wang R, Eikevik TM. Potential evaluation of integrated high temperature heat pumps: A review of recent advances. *App Thermal Eng* 230:120720 (2023). https://doi.org/10.1016/j.applthermaleng.2023.120720
16. Jensen JK, Markussen WB, Reinholdt L, Elmegaard B. On the development of high temperature ammonia-water hybrid absorption-compression heat pumps. *Int J Refrig* 58: 79-89 (2015). https://doi.org/10.1016/j.ijrefrig.2015.06.006
17. Chen D, O'Connell JP, Seider WD. Thermoeconomic analyses of $sCO_2$ power cycles. *AIChE J* 70:e18502 (2024). https://doi.org/10.1002/aic.18502
18. Gößling-Reisemann S. Entropy production and resource consumption in life-cycle assessments. Chapter in: Thermodynamics and the Destruction of Resources, eds: Bakshi BR, Gutowski TG, Sekulić DP, Cambridge University Press: New York (2011).

© 2025 by the authors. Licensed to PSEcommunity.org and PSE Press. This is an open access article under the creative commons CC-BY-SA licensing terms. Credit must be given to creator and adaptations must be shared under the same terms. See https://creativecommons.org/licenses/by-sa/4.0/



Systems & Control Transactions

**Research Article - Peer Reviewed Conference Proceeding**
ESCAPE 35 - European Symposium on Computer Aided Process Engineering
Ghent, Belgium. 6-9 July 2025
Jan F.M. Van Impe, Grégoire Léonard, Satyajeet S. Bhonsale,
Monika E. Polańska, Filip Logist (Eds.)

PSE PRESS

# Teaching of Process Design Courses – The CMU experience, trends and challenges

**Ana I. Torres and Ignacio E. Grossmann***

Department of Chemical Engineering, Carnegie Mellon University, Pittsburgh, PA, USA
* Corresponding Author: grossmann@cmu.edu

## ABSTRACT

Carnegie Mellon University (CMU) has a strong tradition and expertise in Chemical Process Systems Engineering. This short article comments on the CMU PSE-related courses and describes in more detail our approach to teaching Chemical Process Design. We discuss (i) our emphasis on proposing processes related to energy and sustainability and (ii) some of the challenges that are currently faced when teaching this course.

**Keywords**: Process Design, Education

## INTRODUCTION

Process design has been the traditional capstone course for chemical engineering. It is generally the course where the material learned in previous semesters is integrated and applied to a major design project. A major component of this course is decision-making since students have to select the process technology, the flowsheet configuration, and its operating parameters. Modern educational trends emphasize process invention [1] (i.e., synthesis of flowsheets) and the teaching of systematic techniques for design. These include synthesis strategies (e.g., hierarchical decomposition, separation synthesis, heat exchanger networks, energy integration, and water networks), process simulation tools to perform the mass and energy balances, detailed modeling tools for chemical reactors and separators, and economic evaluation.

Process design projects are also ideal for introducing emerging topics such as energy, decarbonization, and sustainability and environmental justice which are becoming highly relevant in the professional education of chemical engineering students. In our experience, students have been highly motivated by design projects that focus on these areas, which in turn can help increase enrollments in chemical engineering.

In this paper, we provide an overview of the Process Systems Engineering related courses offered at CMU and describe, in detail, our approach to teaching Process Design.

## PROCESS SYSTEMS ENGINEERING COURSES TAUGHT AT CMU

Dating back to the pioneering vision by Professor Arthur Westerberg in the late 70s, Process Systems Engineering (PSE) is a major research and education strength of the Chemical Engineering Program at Carnegie Mellon University. Currently, five tenure track faculty members (Biegler, Gounaris, Grossmann, Laird, Torres) focus their research on PSE. They maintain an active research environment, seminar series, the CAPD industrial consortium [2], and a cohort of graduate students at the master's and doctorate levels. The CAPD faculty have written several textbooks in the area [3-7] .

While many chemical engineering programs struggle to cover design courses with tenure-track faculty [8] within a curriculum, our strength in this area of Chemical Engineering allows us to cover design-related courses with specialists. This tenure-track faculty is complemented by adjunct faculty with extensive industrial experience who actively participate in teaching design courses covering practical topics such as process safety.

At CMU, the Chemical Process Systems Design course is the major engineering design experience required by ABET [9]. This course represents 12 units, where one unit expects one hour per week of work and is taught during the fall semester of the senior year (fourth year). Then, students take Chemical Product Design (9

units) in the spring semester of their senior year. These courses build on previous courses that include two design-related courses: Unit Operations (9 units) in the junior year and Unit Operations Laboratory (9 units) in the senior year, and two PSE-related mini-courses (6 units each): Numerical Methods and Machine Learning for Chemical Engineering and Optimization Modeling and Algorithms taken during the fall semester of the junior year. The PSE sequence is completed by Chemical Engineering Process Control (9 units) taken in the senior spring semester.

At the graduate level, we regularly offer three PSE-related courses: Advanced Process Systems Engineering (A-PSE), Process Systems Modeling/Design and Optimization of Sustainable Processes (PSM), and Computational Methods for Large Scale Process Design & Analysis (CMPMO).

A-PSE covers the fundamentals and algorithms of optimization techniques for linear and nonlinear programming, mixed-integer linear and nonlinear programming, generalized disjunctive programming, flexibility analysis, and stochastic programming. It also covers the application of these techniques to the synthesis of heat exchanger networks, distillation sequences, water networks, and process flowsheets as well as the planning and scheduling of batch and continuous processes.

PSM is a long-standing course targeted at masters-level students that covers the simulation and optimization of complex flowsheets using Process Simulation Software. Starting in 2025, this course has been reformulated to (i) introduce these topics in the context of sustainable process design and (ii) improve the process de-sign, simulation, and evaluation skills for those graduate students who come to the PhD program without a strong Process Design background. PSM currently covers modeling simulation evaluation and optimization of state-of-the-art technologies for the conversion of biomass and waste to fuels and chemicals, electrification of chemical processes, the use and storage of energy from intermit-tent non-programmable sources (including batteries, hydrogen, and chemicals), and carbon capture, among others. The course is also offered as an elective for under-graduate senior and PhD students. Currently, all students have the same assignments regardless of whether they did the full PSE sequence at CMU or not.

CMPMO deals with the underlying computer-aided design techniques for steady-state and dynamic simulation, numerical solution and decomposition strategies for large systems of sparse nonlinear algebraic equations, stiff ordinary differential equations, strategies

for mixed algebraic/differential systems and computer architectures for process systems.

In addition, more specialized courses are offered in an intermittent fashion as Special Topics courses: Nonlinear Optimization in Process Systems Engineering is aimed at graduate-level students and is based on the textbook in [4]. It covers methods for solution and optimization for engineering systems described by nonlinear algebraic and/or differential equations. Production and Supply Chain Optimization also targets graduate students and aims to familiarize them with popular decision-making contexts related to production and supply chain optimization and with the numerical optimization methods (both model-based and metaheuristics-based) employed in such settings.

## OUR APPROACH TO TEACH CHEMICAL PROCESS SYSTEMS DESIGN

As with many capstone design courses, Chemical Process Systems Design covers screening process alternatives and computational strategies for preliminary material and heat balances in large chemical processes, including preliminary sizing of process equipment. A key part of the course is evaluating the economics of alternative flowsheet configurations and technologies. Currently, the teaching team comprises two tenure-track faculty, one adjunct faculty, and four teaching assistants (TAs), who are usually PhD students. Class size has oscillated over time and is currently at 50-60 students per cohort.

The course involves lectures and a major project. The main topics in the lectures include techniques for the conceptual design of chemical processes, preliminary process calculations, systematic methods for pro-cess synthesis and energy recovery, economic evaluations of competing processes, fundamentals of flowsheet simulation, and design and scheduling for batch pro-cessing. These topics are covered in the textbook that is used in this course, “Systematic Methods of Chemical Process Design” [3]. Students are also given as references the textbooks by Seider at al [11], Towler and Sinnot [12] and Turton et.al [13]. Students are given two tests that are graded: the first on preliminary mass and energy balances and equipment sizing to prepare them for memo 2; the second on economic evaluation and pro-cess synthesis to prepare them for their final report, project memo 3.

The project itself, for more than a decade, has been defined with input from Dr. Jeff Siirola an expert in process design, former Technology Fellow at Eastman Chemical Company, and current Professor of Engineering Practice at Purdue and Adjunct Faculty at Carnegie Mellon University. The project is organized around the design of a process for a hypothetical “Andrew Corporation” that requests their team of engineers within the Special Projects Group to study a novel processing approach. For example, the 2022 course dealt with the design of a blue hydrogen plant, the 2023 course with chemical depolymerization of PET plastics, and the 2024 course with polyolefin depolymerization.

Students are required to work in a self-selected team of four people. All teams are given the same memo with a brief description of the project, design specifications, and constraints such as production rate, product purity, available feedstocks, location, and economic data. It is important to note that the project is a new unsolved problem, so each team must conduct a literature review and gather data on relevant technologies and chemistries, process conditions, etc., to come up with their own solution. After the preliminary literature review, each team is expected to postulate a superstructure with the major alternatives they have found and, from it, extract a process flowsheet with all the major pieces of equipment and approximate operating conditions.

Students are asked to solve the mass and energy balances for that flowsheet by considering simplified (linear) models for the unit operations prior to using commercial process simulators. Formulating these equations and solving them using simple spreadsheets serves the purpose of teaching the students approximation techniques to allow them to quickly screen design alternatives by generating reasonable first guesses. These first guesses help in building intuition and greatly simplify subsequent rigorous modeling in commercial simulators. We use Aspen Plus as the process simulation software. At CMU, Aspen Plus is also taught as part of the Design Course; this is, students do not generally have prior expo-sure to the software.

In addition, students must perform heat integration using pinch analysis and perform an economic evaluation to determine the net present value or breakeven point of their proposed design. We use and teach commercial software (Synheat, Aspen Energy Analyzer, As-pen Process Economic Analyzer) to facilitate calculations. Safety analysis is covered via a Failure Modes and Effects Analysis (FMEA). Starting in 2024, students are also required to perform a gate-to-gate emission evaluation. To this end, we use EPA's GREENSCOPE tool [10], whose use and logics is also introduced during lectures.

To mock a real engineering position, each team is assigned a TA or faculty member who acts as the project manager to whom the students report progress on a weekly basis. The TA/ faculty member also provides guidance to the students on establishing appropriate goals and planning doable tasks to meet the project objectives. It is worth noting that teams create their flowsheets/designs throughout the course and do not share them with other groups. Hence, their proposed flowsheets differ despite addressing the same design project.

We evaluate the designs by requesting students to submit three reports in the form of memos. The literature search and flowsheet development are reported in Memo 1, preliminary mass and energy balances in Memo 2, and full economic evaluation, gate-to-gate environ-mental assessment, and FMEA analysis in Memo 3. Finally, students give a final oral presentation to summarize their major findings in the design project, which is judged by the TAs, faculty members, and people from industry. We invite industrial colleagues (usually members of the CAPD center) to attend these final presentations. Students are given 5 minutes for the presentation with 5 minutes for questions. The short 5-min presentations force the students to highlight their major results, findings, and recommendations to an industrial audience. The fact that real engineers judge their designs and presentations greatly motivates the students and adds reality to the design experience. The evaluation of the course itself is completed by weekly short homework exercises that assess what was covered in the week and two midterm exams that assess the students' performance at the individual level.

## THE GOOD, THE BAD AND THE CHALLENGES

From the activities described above, the CMU Process Systems Design experience is clearly a challenging one. Feedback from the students indicates that they tend to spend more than the 12-hour expectation, typically 17 hours on average. A number of factors may influence this perception, some of which are discussed below. Despite the time commitment, students find this course to be one of the most valuable ones. As examples, the following sentences are copied verbatim from the 2023 and 2024 faculty and course evaluations (FCEs):

> "I personally thought that while Memo was a ton of work and involved an overwhelming time commitment, it was definitely one of the most useful assignments Ive done in the ChemE curriculum so far in actually preparing us for the future. "

> "While this class was a ton of work I really learned a lot (...) The material is important to a career in chemical engineering, and the skills feel transferable."

> "This course was a lot of work, but I am happy with what I learned from it. It was clear to see the importance and relevance of the coursework with content even from intro tied in. Thank you."

Personal interaction with the students indicates that focusing the project on current topics of relevance, such as clean energy, decarbonization, and sustainability, is, in general, very well received. The positive reception seems to be linked to two facts. One is that these topics are becoming highly relevant in the Chemical Engineering job postings, and being knowledgeable of the newer technologies differentiates them from other applicants. The

second one is that designing novel processes adds the innovation edge that is common in the final projects of other engineering disciplines; this innovation edge is missed if we pick known designs of commodity chemicals as the case study. The downside of selecting novel processes is that some of the operations required to model and simulate them are not well covered in Chemical Engineering curricula, not only at CMU, but to the best of our knowledge across the USA. In addition, commercial simulators do not really have advanced models for non-traditional components such as different types of biomasses. As an example, the polymer recycling processes considered in the last two years required solid processing operations which students were not familiar with; verbatim comments from the FCEs are as follows:

> "Handling of Solids for the project is really problematic when important solid separators are not taught in class."

> "... solids modeling is so difficult in ASPEN and very little was done analytically. "

As faculty, we may argue or expect senior students to be able to learn about novel operations from literature independently. However, for reasons that are not clear to us, self-learning is a barrier for our students.

Another major challenge we face when teaching the process design course is the increasing reduction of fundamental chemical engineering courses (e.g. thermodynamics, fluid mechanics, heat and mass transfer, unit operations) at the expense of the introduction of new courses. Some of these courses are related to new chemical engineering areas (e.g. biological engineering and nanomaterials) and some to general education requirements. These new courses certainly enrich students' education; however, this decrease in fundamentals impacts the design course teaching as one must cover additional basic topics that would have been taken for granted 10-15 years ago. At this point, we as instructors phase the dilemma of cutting process design material, thus lowering the educational value of the course, or phase increasingly lower FCEs as our course is perceived as being too demanding. The latter not only lowers the morale of faculty but also affects faculty's careers as in most American universities, FCEs are one of the main metrics taken into account for faculty reappointment and promotion. In our view, this trend of decrease in fundamentals could be reversed by assigning more hours per week to the design course, e.g., in our case at CMU, for example from 12 to 15 hours. This has been our de facto approach.

From our perspective, the trend in lower process design skills seems to be happening across many ChemE programs. This comment is supported by the authors' observation of our graduate student cohort, including those who come to CMU to pursue MS and PhDs in the PSE at the graduate level. Most of these students have excellent analytical skills and are very well-trained in programming. Many of them are also familiar with the use of commercial process simulators. However, a worrisome problem is that, more commonly than not, students are unable to distinguish between conceptual design and plant design or have the intuition to critically assess whether the result of a simulation makes sense or not. In terms of process evaluation, most students have been exposed to cost correlations to estimate equipment purchase costs. Still, not too many know how to go from equipment purchase cost to installed equipment cost or which terms should be included in operating expenses. We hypothesize that this might be the result of the shift from tenure to non-tenure track faculty reported in [8]. It is only those departments that have faculty in process systems engineering that a regular faculty member teaches the design course. We believe this is a worrying trend because it means that the faculty will increasingly become unable to teach this core course in undergraduate chemical engineering. We very much hope that this trend will be reversed in the future.

## REFERENCES


1. Biegler LT, Grossmann IE, Westerberg AW. Issues and trends in the teaching of process and product design. *AIChE J.*, 56 1120-1125 (2010) https://doi.org/10.1002/aic.12256
2. Carnegie Mellon University Center for Advanced Process Decision-making https://capd.cheme.cmu.edu/
3. Biegler LT, Grossmann IE, Westerberg AW. Systematic Methods of Chemical Process Design, Prentice-Hall (1998)
4. Biegler LT, Nonlinear Programming: Concepts, Algorithms, and Applications to Chemical Engineering. SIAM (2010).
5. Grossmann IE. Advanced Optimization for Process Systems Engineering. Cambridge University Press (2021).
6. Bynum ML, Hackebeil GA, Hart WE, Laird CD, Nicholson BL, Siirola JD, Watson JP, Woodruff DL, Pyomo—Optimization Modeling in Python. Springer (2021).
7. Tawarmalani M, Sahinidis NV, Convexification and Global Optimization in Continuous and Mixed-Integer Nonlinear Programming: Theory, Algorithms, Software, and Applications. Kluwer Academic Publishers (2002).
8. Ford LP, Cole J, Dahm KD, Vaughen BK, Jamieson MV, Landherr L, Silverstein DL, Vogel TJ, West CW, Thiel SW. How We Teach: Capstone Design Paper presented at 2023 ASEE Annual Conference & Exposition, Baltimore, Maryland (2023). https://nemo.asee.org/public/conferences/327/pap

ers/37520/view
9. ABET Criteria for Accrediting Engineering Programs 2024 2025 https://www.abet.org/accreditation/accreditation-criteria/criteria-for-accrediting-engineering-programs-2024-2025/ Accessed January 2025.
10. US Environmental Protection Agency Assessing Chemical Process Sustainability with GREENSCOPE https://www.epa.gov/chemical-research/assessing-chemical-process-sustainability-greenscope Accessed January 2025.
11. Seider WD, Lewin DR, Seader JD, Widagdo S, Gani R, Ng KM. Product and Process Design Principles: Synthesis, Analysis and Evaluation. Wiley (2016)
12. Towler G, Sinnot R. Chemical Engineering Design: Principles, Practice and Economics of Plant and Process Design. Butterworth-Heinemann (2021).
13. Turton R. Shaeiwitz JA, Bhattacharyya D, Whiting WB. Analysis Synthesis and Design of Chemical Processes. Prentice Hall (2018).

© 2025 by the authors. Licensed to PSEcommunity.org and PSE Press. This is an open access article under the creative commons CC-BY-SA licensing terms. Credit must be given to creator and adaptations must be shared under the same terms. See https://creativecommons.org/licenses/by-sa/4.0/



Systems & Control Transactions

**Research Article - Peer Reviewed Conference Proceeding**
ESCAPE 35 - European Symposium on Computer Aided Process Engineering
Ghent, Belgium. 6-9 July 2025
Jan F.M. Van Impe, Grégoire Léonard, Satyajeet S. Bhonsale,
Monika E. Polańska, Filip Logist (Eds.)

PSE PRESS

# Integrated Project in the Master of Chemical Engineering and Materials Science at the University of Liège

**Marie-Noëlle Dumont[a*], Marc Philippart de Foy[a], Grégoire Léonard[a]**

[a] Department of Chemical Engineering, Faculty of Applied Sciences, Campus Liège Sart-Tilman, University of Liège, Belgium
* Corresponding Author: mn.dumont@uliege.be

## ABSTRACT

The Integrated Project in the Master of Chemical Engineering and Materials Science at the University of Liège (ULiège) aims to consolidate technical knowledge and promote the acquisition of soft skills by integrating various chemical engineering disciplines. The project focus on the design of an industrial process and is divided into five parts: individual work on mass balances and literature reviews, detailed modeling of thermodynamics and key unit operations, sensitivity studies, process integration, and report to a general audience. Key learning outcomes include developing critical thinking, addressing complex multidisciplinary topics, and understanding the role of science and technology in society. Students enhance their soft skills in project management, teamwork, and effective communication in English. Regular interactions with industry and academic experts, along with support from the ULiège Soft Skills Team, ensure comprehensive development. Evaluation includes both technical and soft skills assessments, with individual and group performance contributing to final grades. This project, running for several years, is highly regarded by students for its rigorous and instructive nature, preparing them well for their future careers.

**Keywords**: Education, Process Design, Modelling and Simulations, Interdisciplinary

## INTRODUCTION

In many universities, courses are given independently of each other and it can be observed that students tend to focus on each course and each exam separately, missing the overarching links between disciplines. However, integration into applied projects of different but related disciplines (such as catalysis, reaction engineering, chemical thermodynamics, separation processes or process system engineering among others...) is key for the training of future chemical and process engineers. Indeed, most chemical processes include reaction, separation and/or purification steps, pumps and/or compressors, heat exchangers... However, modeling these is only possible with the choice of an appropriate thermodynamic method and adequate kinetics. It is thus important that students are taught these disciplines and are able to integrate them for designing a relevant and efficient process, while justifying each choice and simplification. This approach is called for by industry, international education evaluators, and often by university authorities as well [1].

The project described in the present paper forces students to consider different disciplines as part of a coherent whole necessary to solve a given process design problem inspired by an industrial case study. Previous work has shown that process design is being taught in most Chemical Engineering curricula, and that it often includes teamwork activities in addition of individual mastery of the disciplines [2]. A recent work has surveyed the practices and the usual teaching methods regarding process design, evidencing the central importance of this topic in the chemical engineering education. It also highlighted common lines but also differences in approaches among universities [3]. In this paper, we present the Integrated Project offered to chemical engineering students at the University of Liège. We first describe the general context of the project and its objectives. Then, the teaching methods for technical skills are presented following the yearly progression of the work, and a specific focus set on soft skills development is highlighted.

## PROJECT'S CONTEXT AND OBJECTIVES

This project is offered to senior students in

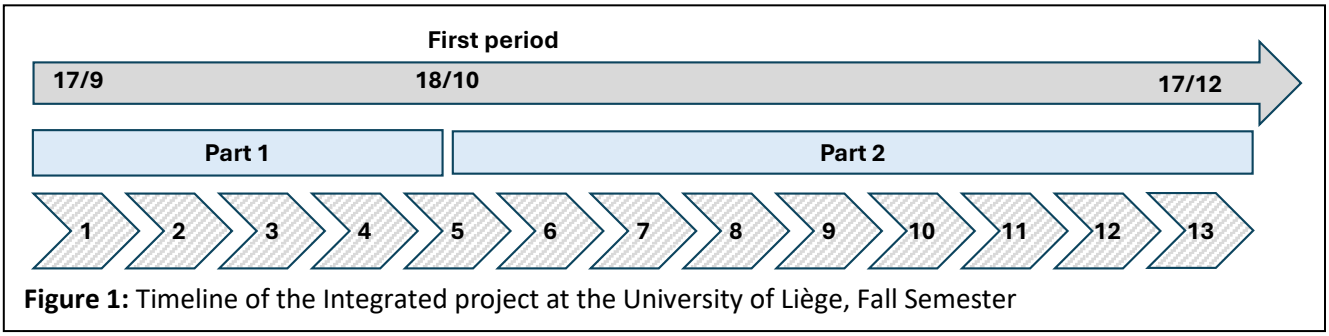



**Figure 1:** Timeline of the Integrated project at the University of Liège, Fall Semester

Chemical Engineering and Material Science at the University of Liège, i.e. a number of students usually ranging between 10 and 20. It was designed about 10 years ago and has evolved with the objective of confronting students with a less academic situation, more akin to what they will encounter in the industrial world. Groups are defined randomly, although the teaching team may intervene to make sure that the final student distribution respects some equity principles with respect to the student's background, e.g. Erasmus students are reasonably split among the groups. A new theme is proposed each year by a different industrial expert identified among the Department's network and who is accepting to provide some follow-up during the year. The initial definition is extremely broad: "propose a process to produce XX tons per year of YY product with ZZ purity." The technical key learning outcomes for the project are listed as follows [4]:

- Consolidate technical knowledge by integrating and linking the different disciplines of chemical engineering and integrate these disciplines within one unique project.
- Acquire critical thinking and ability to challenge and validate assumptions made. This includes the acquisition of a gut feeling for orders of magnitude typical of engineers.
- Address complex and multi-disciplinary topics centered on chemical industry.
- Develop knowledge about current hot topics in chemical engineering and increase the awareness about the role of science & technology in society.
- Use powers of judgment as engineers in order to work with complex and possibly incomplete information, to recognize discrepancies and to deal with them
- Recognize the need for information, find and provide information

Beyond the process design and the integration of technical skills, the development of soft skills is another major goal of this project. There, the key learning outcomes are also presented to the students, as follows [4]:

- Ability to work in large groups (between 7-12 students, random selection of members).
- Management of project and deadlines.
- Writing of technical reports in English, with written feed-back from teachers after each report.
- Communication to scientific and non-scientific audience: technical presentations to teachers, and final presentation to a larger audience with general engineering background.
- Communication in English, written and oral (all group members must talk).

The Integrated Project spans the entire academic year, from the first week of classes in September to the last week in May, with a break during the exam session from the end of December to early February. Each project is handled by a group of 6 to 12 students and accounts for 10 credits in an academic year that contains 60 credits. In this paper, we illustrate the Integrated Project of the 2024-2025 academic year, which is dedicated to the synthesis of Vinyl Chloride Monomer (VCM), a topic proposed by INOVYN.

## TEACHING METHODS

The Integrated Project is supervised by a whole teaching team gathering 7 Professors of the Chemical Engineering and Material Science + Energy Engineering curricula. A teaching assistant is present to support the project logistics (planification of teaching sessions, communication with the students…) but is not involved in the technical supervision. Additionally, a support is provided by the University of Liège's soft skills team, composed of two psychologists with experience in social psychology of groups and organizations.

Teaching methods include a few hours (about 20 hours spread over the year) of theoretical courses with Professors or external experts, but mostly group work by students and face-to-face interactions between a Professor and a sub-group of students. Plenary meetings gathering all student groups and the whole teaching team take place every month to ensure consistency and follow-up on the groups' progress. The respective share of these teaching activities depends on the moment of the

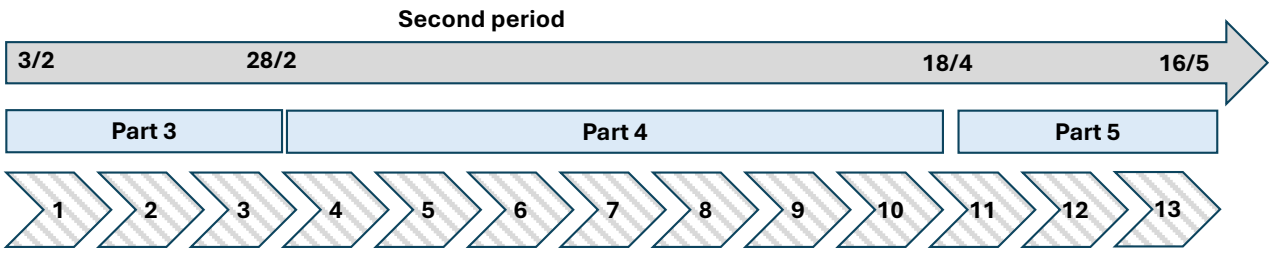


**Figure 2:** Timeline of the Integrated project at the University of Liège, Spring Semester

year and on the discipline covered at that time. The project is indeed divided into 5 parts, each concluding with a final report and presentation. At the University of Liège, an academic year consists of two semesters (two periods) of 13 weeks of classes, each followed by an exam session. The first semester starts on September 15th, and the second on February 3rd. The distribution of the different parts is presented in Figures 1 & 2.

## Part 1: Individual Work

### Individual Work on Mass Balances and Literature Reviews

In the first phase of the Integrated Project, students engage in individual work focusing successively on mass balances and literature review. This phase aims to establish a solid foundation for the subsequent stages of the project and individual deliverables (reports) are expected so that each student has to commit from the very beginning. Each student is indeed responsible for conducting a comprehensive mass balance for the synthesis of Vinyl Chloride Monomer (VCM), ensuring a thorough understanding of the material inputs and outputs involved in the process. Additionally, each student performs a detailed literature review to gather relevant information on the chemical and process engineering aspects of VCM production. This includes reviewing existing technologies, process conditions, and recent advancements in the field. The mass balance analysis as well as the literature review last respectively about 1 and 2 weeks.

### Consolidation of results and project planning

Following the individual efforts, students consolidate their findings in group sessions. These collaborative meetings are designed to integrate individual results, allowing for the identification of common themes and discrepancies. The groups then plan the next steps of the project, setting clear objectives and timelines. This phase lasts about 1 week and culminates in a presentation where students showcase their mass balance results, literature review insights, and initial process design concepts. This structured approach ensures that all participants have a robust understanding of the project's foundational elements before progressing to more complex modeling and integration tasks.

## Part 2: Detailed Models for Thermodynamics, Process Techno-Economics, Kinetics, Reactors, Separation, and Unit Operations

In the second phase of the Integrated Project, students focus on developing detailed models for key unit operations, including thermodynamics, reaction kinetics, and separation processes. This phase is crucial for understanding the fundamental aspects of the process and preparing for the integration phase.

From this second part onwards, students will freely divide into 3 different sub-groups, each of them being followed-up by a Professor:

- Thermodynamics, energy balances and process costing,
- Kinetics and Reaction Engineering
- Separation and Unit Operations

Each sub-group is responsible for a part of the project but of course, close interactions between the subgroups are necessary for the successful completion of the tasks. Regular progress reports presentations (about every 2-3 weeks) are made to share the results with the teaching team.

**Thermodynamics, energy balances and process costing:** Students begin by selecting appropriate thermodynamic models to describe the behavior of pure components and mixtures within the process operating ranges. They evaluate properties such as density, heat capacity, enthalpy, and vapor pressure. The selection of thermodynamic methods for real systems involves comparing real solution properties to ideal solutions and discussing the differences. Validation of these models is essential, requiring consistency checks based on thermodynamic relations and comparison with at least one other data source. Relevant phase equilibria for pure components and mixtures are characterized, and appropriate thermodynamic models are selected and validated with experimental data. Students also perform initial energy balances and evaluate the rough profitability of the process, creating a proper Process Flow Diagram (PFD).

**Kinetics and Reaction Engineering:** This section involves determining kinetic laws and mechanisms,

selecting catalysts, and designing reactors. Students explore kinetic laws and parameters available in the literature. They propose reaction mechanisms that align with suggested reaction rate laws and demonstrate these laws, explaining any simplifications made. The design and modeling of reactors are performed using Matlab or Python, where students establish mass and energy balances, compute concentration and temperature profiles, and evaluate yield and selectivity. Heat exchange is also considered, usually initiated by a comparison between isothermal and adiabatic approaches and followed by making the link with the types of reactors identified in the literature or from discussion with the industry.

**Separation and Unit Operations:** Students design and model separation equipment and heat exchangers. They define the separation tasks, including flow rates, compositions, and conditions like pressure and temperature limits. Using first short cut equations, then McCabe-Thiele diagrams, students determine the required number of theoretical stages and design the height and diameter of columns. They also model and size heat exchangers, considering constraints such as volume, length, pressure drop, and velocity. Preliminary designs are rated using methods like Kern and Bell-Delaware, and the results are compared to ensure accuracy.

## Part 3: Sensitivity Studies and Model Validation

In the third phase, students focus on performing sensitivity studies and validating the models developed in Part 2. This phase aims to refine the process models and ensure their robustness by evaluating the impact of key process parameters. Moreover, from a soft skills point of view, it is noted that the sub-groups are modified between phase 2 and phase 3 in line with what was announced to students at the beginning of the project. Each student is required to change topics and work with different team members, ensuring a comprehensive understanding of the entire process. This change of subgroups has several objectives. First, it is intended to foster the acquisition of new technical skills (it is not wished to form specialists in one single discipline in this course). Second, this enhances knowledge transfer as students know from Part 2 that the model they develop will be then used by others in Part 3, and it forces them to keep all other students continuously informed about their choices and difficulties. Finally, it helps developing critical thinking as students in Part 3 have to validate the assumptions and results reached by their peers in Part 2.

**Thermodynamics, energy balances and process costing:** if needed, students refine their thermodynamic models by validating the models against additional data sources and ensuring consistency with thermodynamic principles. Moreover, they gather the inputs from all subgroups into the process flow diagram that they then use to refine energy balance and profitability estimates performed in Part 2. This task also comes with the first steps towards process design optimization.

**Kinetics and Reaction Engineering:** In this phase, sensitivity analyses are conducted to optimize reactor performance, considering factors such as feed composition and operating conditions. This involves software tools like Matlab or Python to simulate scenarios and optimize the reactor design. Students also validate their kinetic models and have to identify potential mass and heat transfer limitations related to their choice of catalyst. This step is crucial for ensuring that the kinetic models are reliable and can later be used for process optimization.

**Separation and Unit Operations:** Students conduct sensitivity studies on the separation processes and unit operations designed in Part 2. They evaluate the impact of variations in flow rates, compositions, and operating conditions on the performance of separation equipment and heat exchangers. This involves using tools like Aspen Plus or Aspen Exchanger Design and Rating (EDR) to simulate different scenarios and optimize the design. Students validate their models by comparing the results with experimental data from the literature and ensuring that the assumptions made in the design are reasonable. This step helps to identify the most critical parameters and optimize the separation processes for better performance and cost efficiency. For the rating of the heat exchanger design, the work is supported by a professor from the energy engineering program, which is very instructive as it forces chemical engineering students to interact with non-chemical engineers.

## Part 4: Process Integration

In the fourth phase, students focus on integrating the various components of the process into a cohesive and optimized global flowsheet in Aspen Plus. This phase is critical for ensuring that all elements of the process work together efficiently and effectively.

**Global Process Flowsheet:** Students begin by combining the sub-models developed in previous parts into a comprehensive global process flowsheet in Aspen Plus. This involves refining the models and identifying key variables that impact the overall process performance. The goal is to create a detailed and accurate representation of the entire VCM production process.

**Optimization of Process Operating Conditions:** Students work towards optimizing the process operating conditions to enhance efficiency and reduce costs. This includes topological optimization, where the layout of the process is adjusted for optimal performance, and parameter optimization, where specific operating conditions are fine-tuned. Techniques such as pinch analysis are applied for heat integration, ensuring that energy usage is minimized, and heat recovery is maximized.

**Cost Evaluation:** A detailed cost evaluation of the

process is conducted, building on the initial assessments made in previous parts. Students analyze both capital expenditures (CAPEX) and operating expenses (OPEX) to determine the overall economic feasibility of the VCM production process. They also need to come up with a first cash flow diagram of the process that will be used to evaluate the impact of CAPEX, utilities, raw material and product price, process performances... on profitability.

**Environmental Impact and Life Cycle Assessment (LCA):** Students develop a life cycle thinking approach to assess the environmental impact of the VCM production process. This includes evaluating the process from a cradle-to-grave perspective, considering factors such as raw material extraction, production, usage, and disposal. The goal is not to perform a full LCA, but to identify opportunities for reducing the environmental footprint and improving the sustainability of the process.

**Literature Review:** An extended literature review is initiated again, now to compare the results obtained from the process models with existing data in the literature. This helps validate the efficiency and effectiveness of their VCM production process. Key Process Indicators (KPIs) such as $t_{CO2}/t_{VCM}$, $kWh/t_{VCM}$, and $t_{Cl2}/t_{VCM}$ are used for ease of comparison. Students also identify technological alternatives and potential improvements to the process, considering factors such as raw material efficiency, energy consumption, and environmental impact.

### Part 5: Report to a General Audience

In the fifth and final phase of the Integrated Project, students focus on summarizing their work and presenting it to a broader audience. This phase involves updating and validating the project's results, concluding the extended literature review, and considering the broader societal implications of the VCM production process. Regarding this last point, students consider a broader societal overview, assessing the environmental footprint, costs, raw materials use, safety, market conditions, recyclability, toxicity and alternative manufacturing pathways and product replacement solutions. This holistic approach ensures that the VCM production process is evaluated not only from a technical perspective but also in terms of its societal and environmental impact.

The final report is concise, limited to 15 pages and written in the form of a journal article for online publication (see results of the five previous years, [5]). It describes the context of the project and the technical challenge, presents a summary of the main technical results, and validates these results by comparing them to the literature. The report also includes the results of the cost evaluation and the LCA approach. It is designed to be understandable for external readers with a background in chemical engineering. A few days after report submission, students then present their findings in front of the Chemical Engineering Department of ULiège and external experts. The presentation needs to be professional yet engaging, with a maximum duration of 30 minutes per group. The presentation slides are reviewed in advance by the industrial partner to ensure that no confidential information is divulged. An industrial agreement is also required before publishing the project's final article.

Students are encouraged to present results clearly, with enough details, and discuss their impacts critically. They are reminded to follow communication guidelines for both the report and presentation, ensuring that their work is well-documented and easily understandable.

## SOFT SKILLS DEVELOPMENT

### Additional Lectures

Several "theoretical" lectures are given to students throughout the year. These lectures are either technical and aim to transfer the knowledge needed to solve the technical tasks of the project or dedicated to learning soft skills or reflection. All courses are given by a lecturer specialized in the field. Some courses are also attended by energy engineering students, enriching discussions by bringing together students from different backgrounds.

The first type of course includes process design theory (hierarchical approach), economic evaluation, heat exchanger design and introduction to LCA. These technical skills are not yet mastered by students in their first year of the master's program, but they are necessary to successfully complete the integrated project.

Other courses are also given, linked to the development of non-technical skills such as literature research or scientific writing and presentation. At the start of the project, a lecture is also given on Fermi's questions, where students learn how to solve problems by focusing on orders of magnitude as a first approach. During the fourth part of the project, when the students already have an overview of the process and are integrating all parts into a single flowsheet, an experienced chemical engineer gives a presentation on industrial project management. This session is particularly appreciated by the students, as it enables them to have a very fruitful exchange with a professional about industrial work. The final sessions organized as part of the project are two discussions on ethics and sustainability, led by ULiège's SPIRAL group. The aim of these two sessions is to raise questions and encourage dialogue and reflection on less technical subjects that are also essential for the future chemical engineers taking part in the project.

A visit to the industrial partner's production plant is also planned, usually in Spring. This visit enables students to see the equipment they have designed over the course of the year in real-life conditions, and to observe how the chemical plant operates. The visit is also an opportunity to talk to industrial partners, and to get a better idea of the day-to-day operation of the process, which

the students did not necessarily consider during process design. The visit usually lasts a day, enabling the process to be studied in detail and showing students what working in industrial companies is really looking like.

### Group Sessions with ULiège Soft Skills Team

During the year, students are supervised by the ULiège Soft Skills team. As said, this team is made up of two psychologists specialized in group management. At least five sessions are organized over the course of the year, where these specialists present the important concepts of group management, and where students can reflect and discuss about their own group dynamics. Discussion is always encouraged at these sessions, as it helps first to highlight and then to solve any problems that may arise during the year.

At the end of Part 1, the Soft Skills team helps students to build up their sub-groups based on the characteristics of each student. A session is then organized a month later to discuss how the group is functioning and to help students communicate better if necessary. At the end of Part 2, a session is organized during which the students watch the recording of their own presentation, then discuss it with the "soft skills" team and possibly a few teachers. Two further sessions are organized in the second semester, on group communication and problem-solving. At the end of the year, a final debriefing of the project is carried out with the Soft Skills team and the two teachers coordinating the teaching team. On the one hand, this debriefing enables the professors to see what the problems and positive points were, so to improve for the next year, and on the other, it helps students to summarize everything they have learned over the year and realize what their abilities and problems were. This forms a good basis for future group work, which they will most probably have in their careers. The Soft Skills team is also always available during the year to help students with any problems they may have, either as a group or individually.

These sessions are also used to discuss the student's peer-evaluation. Part of the final grade for the project is indeed awarded to this assessment done in groups (for details of the evaluation methods, see [4]). This evaluation is based on a discussion between the students, supervised by the Soft Skills team. A grade is assigned to each student, which is then approved by the whole group. This assessment is new from 2024-2025, and replaces the usual peer assessment that was done by each student individually. The aim here again is to open a discussion on each student's work and contribution to the life of the group, and to discuss each student's contributions and shortcomings to give constructive feedback on his or her contribution to the group's work.

## CONCLUSION

The Integrated Project in the Master of Chemical Engineering and Materials Science at the University of Liège offers a unique opportunity for students to develop both technical and soft skills essential for their future careers. By working on industrial case studies, such as the synthesis of Vinyl Chloride Monomer (VCM) this year, students face real-world challenges that prepare them for complex industrial situations. The project emphasizes the integration of chemical engineering disciplines, detailed process modeling and optimization of operating conditions, while considering economic and environmental impacts. Regular interactions with industry and academic experts, along with support from the ULiège Soft Skills Team, ensure comprehensive student development. In conclusion, this rigorous and instructive project is highly valued by students and provides solid preparation for their professional future.

## REFERENCES


1. Léonard G., Belboom S., Toye D., Dumont M.-N., Léonard A., Heyen G. Recent Evolutions and Trends in the Use of Computer Aided Chemical Engineering for Educational Purposes at the University of Liège. Comput. Aided Chem. Eng. 40: 2941-2946 (2017) https://doi.org/10.1016/B978-0-444-63965-3.50492-X
2. Lewin D., Kondili E., Cameron I., Léonard G., Mansouri S., Martins F., Ricardez-Sandoval L., Sugiyama H., Zondervan E. Agile process systems engineering education: What to teach, and how to teach. Comp. & Chem. Eng. 170: 108134 (2023) https://doi.org/10.1016/j.compchemeng.2023.108134
3. Lewin D., Adams T., Bongartz D., Léonard G., Mansouri S., Martins F., Mujtaba I., Zondervan E. Teaching Process Design – Quo Vadis? Comput. Aided Chem. Eng. 53: 3505-3510 https://doi.org/10.1016/B978-0-443-28824-1.50585-8
4. University of Liège. Integrated Project course description (2024-2025). https://www.programmes.uliege.be/cocoon/20242025/en/cours/PROJ0012-1.html
5. Chemical Engineering Department, University of Liège. Integrated Project (2024-2025). https://www.chemeng.uliege.be/cms/c_4912130/en/chemeng-integrated-project-m1



© 2025 by the authors. Licensed to PSEcommunity.org and PSE Press. This is an open access article under the creative commons CC-BY-SA licensing terms. Credit must be given to creator and adaptations must be shared under the same terms. See https://creativecommons.org/licenses/by-sa/4.0/




Systems & Control Transactions

**Research Article - Peer Reviewed Conference Proceeding**
ESCAPE 35 - European Symposium on Computer Aided Process Engineering
Ghent, Belgium. 6-9 July 2025
Jan F.M. Van Impe, Grégoire Léonard, Satyajeet S. Bhonsale,
Monika E. Polańska, Filip Logist (Eds.)

PSE PRESS

# Computer-based Chemical Engineering Education for Green and Digital Transformation

**Zorka Novak Pintarič, Miloš Bogataj, and Zdravko Kravanja***

University of Maribor, Faculty of Chemistry and Chemical Engineering, Maribor, Slovenia
* Corresponding Author: zdravko.kravanja@um.si

## ABSTRACT

This paper examines the current state of green and digital integration in traditional chemical engineering education, focusing on how artificial intelligence (AI) can enhance learning. A review of curricula shows that sustainability principles, such as green chemistry, circular economy, and resource efficiency, are often confined to electives rather than core courses. Likewise, digital skills are introduced at a basic level, with limited exposure to AI, especially machine learning, and advanced process optimization. The paper emphasizes the need for a structured approach to integrating sustainability and digitalization into core subjects, supported by interdisciplinary learning. It also explores AI's role in transforming education, particularly in predictive modeling, process optimization, and adaptive learning. The study provides recommendations for redesigning the traditional chemical engineering curriculum to strengthen green and digital transformation.

**Keywords**: Education, Artificial Intelligence, Optimization, Green Transition, Digitalization

## INTRODUCTION

The mission of chemical engineering higher education, particularly computer-aided chemical engineering, is to equip students with the knowledge and skills they need to drive the green and digital transformation. The EFCE Bologna recommendations emphasize data management and digitalization tools as fundamental components of informatics in the first cycle and place a general focus on digitalization at the second cycle [1].

While chemical engineering programs certainly include elements of green and digital engineering, their systematic integration into core subjects is often implicit, making them less visible to students and industry [2]. In fact, the definition of what 'green content' entails is not precisely established. It can encompass the formal 12 principles of green chemistry [3], the 12 principles of green engineering [4], and the 17 sustainable development goals (SDG) [5], as well as more specific topics such as the circular economy, industrial symbiosis, environmental protection, production technologies with reduced environmental impact, sustainable materials and catalysts and related areas.

The curriculum analysis at our institution shows that only a few green engineering principles, such as maximizing efficiency and integrating energy flows, are explicitly covered. Others appear indirectly through case studies but lack systematic integration. Digital skills are mostly limited to spreadsheet-based data processing, basic programming, and process simulation and optimization. Green and digital topics are explored more deeply in project work, advanced studies, electives, and final theses.

Artificial Intelligence (AI), a key driver of digitalization, presents an opportunity to enhance both digital and green engineering education. It is already significantly impacting education by transforming teaching methods and driving advancements in chemical engineering curricula, especially in PSE/CAPE related courses. However, the interdisciplinary complexity of AI poses challenges, as students need a solid foundation in programming, data science, and statistics, and more importantly, they should acquire skills for the right comprehension and interpretation of solutions they obtained using AI tools. For effective integration, AI should be introduced gradually [6], balancing technical skills with critical thinking, creativity, and ethical awareness while maintaining core engineering fundamentals.

This article examines the readiness of higher education institutions to equip chemical engineering

students for the digital and green transition, along with the challenges they face and the strategies they employ to address them.

## CHALLENGES AND CONCEPTS FOR GREEN AND DIGITAL TRANSFORMATION

The main challenge of our society is how to efficiently and effectively address severe global issues—population growth, depletion of non-renewable resources, and environmental and societal degradation. The community strives for sustainable development in general, with a particular focus on sustainable chemical and biochemical industries. To reverse the negative climate trends, the European Commission launched the European Green Deal in 2020 [7] and initiated the foundation of the European Climate Pact [8], with the main goal of making the EU climate-neutral by 2050. Probably the two main related topics are green and digital transformations, which are happening in the EU at an increasing pace, demanding faster and faster economic, social, and personal adaptation. This brings a need for the continuous refinement of the education system, focused on more efficient teaching methods and the introduction of relevant topics and outcomes that students should acquire to be able to face current and future professional challenges.

At the level of the European Federation of Chemical Engineering (EFCE), this transformation is managed through 20 working parties (WPs). The Education WP is primarily focused on teaching methods, topics, and outcomes, while the CAPE WP concentrates on the development and application of process systems engineering (PSE) concepts, algorithms, modelling, and tools. Additionally, there are seven sections, with the Energy and Sustainability section predominantly focused on green transformation.

To cope with current challenges and needs, EFCE recently issued a renewed recommendations for chemical engineering study programs, the EFCE Bologna Recommendations 2020 [1], which can serve as a guide for developing new or adapting current study programs. It can also be used by professionals to assess their missing knowledge and skills, helping them identify areas for their supplementary lifelong learning.

The programming outcomes follow an arrangement introduced by the EUR-ACE® Framework Standards [9], from knowledge to understanding, engineering analysis, engineering design, investigations, engineering practice, making judgements, communication and team-working, and lifelong learning, structured hierarchically over the first and second cycles by applying Bloom's taxonomies. As the first cycle typically provides students with basic knowledge and skills, the first four taxonomy levels are predominantly in place—knowledge, comprehension, application, and analysis. The second cycle aims to deepen knowledge and skills by incorporating synthesis and evaluation. At the doctoral (third) cycle, it is evident that the highest levels should be applied, enabling students to develop new knowledge and innovative skills for novel engineering applications or enhancing existing ones.

The traditional basic structure of higher education chemical engineering core curriculum [10] is sketch on Figure 1 in black colour. It starts with fundamentals of science and natural sciences like mathematics, physics and chemistry, continuous with engineering fundamentals based on mass and energy balances, transport phenomena as well as separation and reaction engineering and process control. At the second cycle, a process systems approach is introduced, with the primary learning outcome being the synthesis of knowledge in subjects such as process design, dynamics and optimization, culminating in the student project course. The doctoral level is dedicated to generating new knowledge through the application and advancement of cutting-edge methods, as well as the development of novel approaches based on computer-based chemical engineering.

Green, sustainability, and circularity, also regenerative principles related to chemical engineering study programs, are listed together with the four basic components and five branches of AI in Table 1. The reader can find a more detailed description and explanation in the given references. The challenge is how to integrate the principles and AI components into chemical engineering study programs and to what extent. Some principles are simple, others complex, and all interrelated, with varying complexity across AI components. For teaching and study, they should be hierarchically classified using Bloom's taxonomies.

## INTEGRATING GREEN AND DIGITAL TRANSFORMATION IN CHEMICAL ENGINEERING EDUCATION

Transforming the traditional chemical engineering curriculum to equip graduates for the demands of a green, digital, and resilient economy is a critical challenge. Larger universities with substantial student populations have addressed this by establishing specialized programs or modules such as Data Science in Chemical Engineering (Purdue), Machine Learning in Process Engineering (Imperial College), Chemical and Biochemical Engineering (DTU) to mention just a few. They pilot AI-driven projects, including digital twins for process control, machine learning for experiment optimization, neural networks for predicting thermodynamic properties, among others. Smaller institutions, meanwhile, must integrate these topics into existing courses.

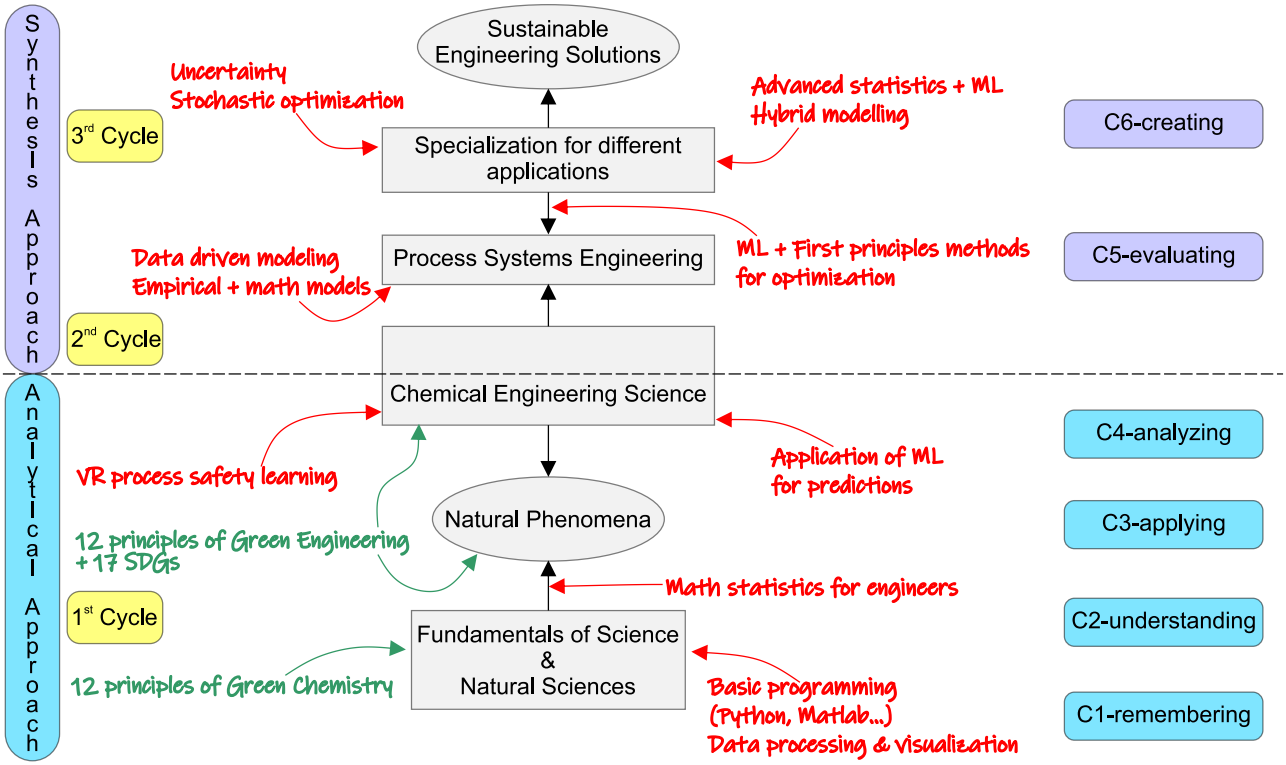



**Figure 1:** Traditional chemical engineering core curriculum (black), upgraded for green (green) and digital transformation (red). Bloom's taxonomy: Analytical Approach (C1-C4), Synthesis Approach (C5-C6)

**Table 1**: Green, sustainability and circularity principles, and basic components and branches of AI

| | |
|---|---|
| Principles of green chemistry [3] | i) Prevention, ii) atom economy, iii) less hazardous chemical syntheses, iv) designing safer chemicals, v) safer solvents and auxiliaries, vi) design for energy efficiency, vii) use of renewable feedstocks, viii) reduce derivatives, ix) catalysis, x) design for degradation, xi) real-time analysis for pollution prevention, xii) inherently safer chemistry for accident prevention |
| Principles of green engineering [4] | i) Inherent rather than circumstantial, ii) prevention instead of treatment, iii) design for separation, iv) maximize efficiency, v) output-pulled versus input-pushed, vi) conserve complexity, vii) durability rather than immortality, viii) meet need, minimize excess, ix) minimize material diversity, x) integrate material and energy flows, xi )design for commercial "afterlife", xii) renewable rather than depleting |
| Engineering sustainability principles [11,12] | i) Contribute to building a sustainable society, present and future, ii) apply professional and responsible judgement and take a leadership role, iii) do more than just comply with legislation and codes, iv) use resources efficiently and effectively, v) seek multiple views to solve sustainability challenges, and vi) manage risk to minimise adverse impact to people or the environment. |
| Core circularity principles [13] | i) Eliminate waste and pollution, ii) circulate products and materials, and iii) regenerate nature |
| Basic AI components and branches [14] | *Components*: i) learning, ii) reasoning and decision making, iii) problem solving and iv) perception<br>*Branches*: i) machine learning, ii) deep learning, iii) natural language processing, iv) robotics and v) fuzzy logic |

Several decades ago, bioengineering and other life science related courses, such as biochemistry, biotechnology, bioreaction engineering, biocatalysis, microbiology, genetic engineering etc., were thoroughly integrated into traditional chemical engineering curricula. However, green content remains largely absent in core courses like transport phenomena, materials, process design, control, and optimization. Illustrative examples in these areas continue to focus predominantly on base industries, which are largely fossil-based.

Digitalization in curricula has been limited to basic tools, such as spreadsheets, introductory programming, process simulation or optimization based on first-principles models using software like Aspen or GAMS. Basic

statistical concepts, including hypothesis testing, receive little attention. Topics like artificial intelligence and its subsets (e.g., machine learning, digital twins) are almost entirely absent at the first and second levels. The same applies to other emerging technologies, such as the Internet of Things (IoT) and blockchain, except for the occasional use of generative AI for text writing. Topics like environmental protection, sustainable development, and the circular economy are primarily confined to elective courses, student projects, and final theses.

The foundational textbooks for chemical and process systems engineering, primarily written in the 1970s and 1980s, remain staples in chemical engineering education, while those on the green transition and digitalization are scarce. This lack of resources has slowed the integration of these emerging topics into curricula. Meanwhile, the shift from traditional textbooks to digital learning platforms for self-paced learning of digital content is becoming increasingly evident.

Group of experts identified key areas for integrating machine learning into research and industry, including materials and catalyst design, industrial analysis, process dynamics and control, and optimization [15]. The challenge lies in selecting suitable courses and defining graduates' roles, whether as users or developers of machine learning tools. Given the field's interdisciplinary nature, they must master both traditional engineering principles and essential digital skills for the future [16].

To tackle these challenges, we present examples of how green chemical engineering and digitalization can be integrated both vertically and horizontally into selected traditional courses (green and red in Figure 1), aligning with key topics from the EFCE Bologna Recommendations [1]. This list is not exhaustive; the examples serve as initial suggestions, and we encourage readers to contribute ideas to enrich the discussion. We advocate integrating the proposed topics into existing subjects instead of adding numerous new courses, as shown in the following examples. A modular approach with pilot projects, electives, and project-based learning allows a gradual transition without overwhelming faculty and students.

## Fundamentals of science and natural sciences

Chemistry, physics, and bio-courses should explicitly incorporate all 12 principles of green chemistry into the curriculum, ensuring their clear visibility and practical applications.

Computer programming should include an introduction to a general-purpose programming language, e.g. Python, computing platform, e.g. MATLAB, and preferably also modelling environment, e.g. GAMS along with fundamental libraries for data visualization. It should also cover basic machine learning models, such as linear regression and decision trees, with applications in engineering problem-solving.

Mathematical statistics for engineers should cover hypothesis testing, regression analysis, statistical inference, and data analysis for process monitoring and optimization.

## Chemical engineering fundamentals

These courses need to identify ways to explicitly emphasize the 12 principles of green engineering, the 17 SDGs, as well as more advanced principles of circular, restorative and regenerative economics.

Process balances should incorporate the visualization of mass and material flows using modern tools like Sankey diagrams. It should also include the formulation of mass balances for recycling and material reuse processes, emphasizing closed-loop systems and minimizing material losses.

Heat and mass transfer should focus on developing predictive models to evaluate efficiency, integrating experimental data with machine learning algorithms. It should include, for example, the use of recycled insulation materials, supported by case studies on energy efficiency improvements. Additionally, it should explore waste heat recovery technologies in industrial settings.

Thermodynamics should incorporate the application of machine learning for predicting thermodynamic properties of fluids, phase equilibria, and chemical reaction equilibria. It should also integrate data-driven models with classical thermodynamic equations of state to enhance prediction accuracy.

Separation processes should incorporate the use of digital twins to simulate and optimize distillation, absorption, and extraction processes. It should also include case studies on energy-efficient separation techniques.

Reaction engineering should include the prediction of reaction kinetics based on experimental data using data-driven models. It could also integrate advanced algorithms to optimize reactor design and operational conditions, with a focus on sustainable reaction pathways.

## Core chemical engineering applications

Chemical process safety could integrate operator training in virtual reality (VR), root-cause analysis to enhance emergency response planning and risk mitigation, and blockchain for secure data management, compliance tracking, and supply chain transparency.

Process optimization for chemical engineering at first cycle should include not only single-objective linear and nonlinear optimization but also statistical analysis, multivariate analysis, multi-objective optimization, and data-driven modeling of complex phenomena and units. It could introduce the integration of such empirical models with mathematical models to improve process efficiency.

## Process systems engineering

Process dynamics should encompass mechanistic,

data-driven, and hybrid models, considering both continuous and discrete data due to digitalization. Analysis can be performed using dynamic simulators, computing platforms (e.g., MATLAB, Mathematica), or general-purpose languages like Python. From a control perspective, classical linear controllers, model-based approaches, and AI-driven strategies for nonlinear control should be explored. Additionally, machine learning can enhance adaptive control, real-time fault detection, predictive maintenance, and forecasting.

Process design could incorporate machine learning for selecting optimal process flowsheets, including tools for generating alternative solutions that minimize waste and energy consumption. It should also emphasize life cycle assessment (LCA) to evaluate the environmental impact of different design options.

Advanced process optimization should encompass mixed-integer linear and nonlinear programming, integrating first-principle models with machine learning models to enhance predictive capabilities. It should incorporate multi-objective optimization techniques linking statistical techniques with process optimization for sustainable and efficient system design. The PhD level could explore stochastic optimization methods that incorporate uncertainty quantification and probabilistic modeling.

## PERSPECTIVES AND CHALLENGES OF ARTIFICIAL INTELLIGENCE IN CHEMICAL ENGINEERING EDUCATION

Artificial intelligence (AI) is transforming industry and academia, making its integration into chemical engineering education essential. Tailored approaches for undergraduate and graduate programs maximize the potential of AI while addressing the specific challenges.

At the undergraduate level, the introduction of AI tools can enhance fundamental chemical engineering subjects such as thermodynamics, reaction engineering and process control. The benefits of integrating AI at this stage are many. Students are exposed to cutting-edge technologies early on, which improves their problem-solving skills and prepares them for the demands of industry. In addition, AI can personalize learning through adaptive educational platforms and allow students to address their weaknesses in core subjects. However, challenges include the steep learning curve of AI tools and the risk of students relying too much on algorithms without grasping the underlying principles of chemical engineering. A recent study on implementation of generative artificial intelligence in chemical engineering education [17] clearly indicates that a balance between traditional engineering principles and AI applications is crucial to avoid such pitfalls. For lecturers, the inclusion of AI requires curriculum redesign and professional development to ensure effective teaching. Lecturers need to be able to handle AI tools themselves and contextualize their applications in chemical engineering. This increases their workload but also provides opportunities for collaborative research with students on AI-driven projects, which encourages academic innovation.

At the graduate level, AI can drive specialized research and innovation. Advanced topics such as data-driven modeling, optimization, and predictive maintenance can be integrated into courses. The benefits of AI at the graduate level go beyond skill development and also foster interdisciplinary collaboration. Graduate students can work at the intersection of AI, chemistry and engineering, exploring novel solutions to industry challenges. However, there are still pitfalls, such as the possibility of over-fitting models or misinterpreting AI-generated results due to an insufficient understanding of the principles of data science. This requires a solid foundation in statistics and programming, which may require additional courses or self-directed learning. For educators, integrating AI at the graduate level provides an opportunity to advance their research agendas and obtain funding in emerging fields. However, it also requires significant effort to keep pace with rapidly evolving AI technologies and their applications. Collaboration between faculty in chemical engineering, computer science and data science departments can alleviate some of these challenges and promote a holistic approach to AI education.

Looking to the future, the role of AI in chemical engineering education is poised to grow. Advances in generative AI, real-time data analytics, and digital twins will continue to transform the curriculum. Students will be able to interact with AI tutors, design processes in virtual environments and contribute to AI-powered research projects. While these developments are very promising, ethical considerations, such as data privacy and algorithmic bias, must be carefully considered. It is clear that integrating AI into the chemical engineering curriculum represents both a challenge and an opportunity. By thoughtfully incorporating AI tools into the undergraduate and graduate curriculum, educational institutions can prepare their students to lead and shape the future of chemical engineering and raise a generation of engineers who are not only technically proficient, but also adaptable and innovative.

It is not difficult to imagine all the benefits that digitalization and artificial intelligence will bring to the learning processes in chemical engineering. From the students' perspective, these will certainly include personalized learning with an increasing presence of virtual reality. This ranges from digital twins of the phenomena and processes studied to digital twins of entire courses and eventually even the lecturers — why not? From the lecturers' perspective, before we are replaced by digital twins, AI will enable data-driven curriculum

improvements, advanced teaching materials with virtual and augmented reality demonstrations, early warning systems to detect student learning difficulties, and curriculum progress tracking, among other things.

However, it is important to emphasize that due to digitalization and/or artificial intelligence, it will be crucial for chemical engineering students to acquire sound skills in data processing (e.g. data mining, data crunching and pre-processing, understanding data bias and variability, feature engineering, ethical and legal considerations, etc.) as well as in processing, analysis and, most importantly, in assessing the validity and significance of the results obtained.

## CONCLUSION

This study highlights the lag in integrating green and digital competencies into the core chemical engineering courses. Systematic teaching materials, both traditional and digital, are essential for educators and students. As a novel approach, we propose the incorporation of green and digital content across the entire vertical structure of chemical engineering education, aligned with EFCE Bologna recommendations—spanning from fundamental sciences through chemical engineering principles to process systems engineering. To support this transition, we encourage the development of common guidelines, e.g. by EFCE, EURECHA or other professional associations, enriched with clear instructions for embedding green and digital competencies into chemical engineering curricula, equipping future engineers with the necessary skills to drive sustainable and digital transformation.

## ACKNOWLEDGMENT

The authors gratefully acknowledge the support of the Slovenian Research and Innovation Agency ARIS (programme P2-0414 and project J2-60044).

## REFERENCES

1. European Federation of Chemical Engineering. EFCE Bologna Recommendations (2020).
2. Wu Y, Huang J, Zhou L, Zhang X, Gao Y, Fan H, Xin Z. The green engineering education in chemical engineering curriculum at East China University of Science and Technology. *Education J* 10:83-90 (2021).
3. Anastas PT, Warner JC. Green Chemistry: Theory and Practice, Oxford University Press (1998)
4. Anastas PT, Zimmerman JB. Design through the twelve principles of green engineering, *Env. Sci. and Tech.*, 37: 94A-101A (2003)
5. United Nations, https://sdgs.un.org/goals
6. Venkatasubramanian V. Teaching artificial intelligence to engineers: experience for a 35-year-old course. *Chem. Eng. Educ.* 56:231-240 (2022).
7. European Commission, The European Green Deal https://shorturl.at/ckAHG
8. European Union, European Climate Pact, https://shorturl.at/Ljt0p
9. ENAEE, EUR-ACE® Framework Standards and Guidelines, https://shorturl.at/fdmOw
10. Klemeš, JJ, Kravanja Z, Varbanov PS, Lam HL. Advanced multimedia engineering education in energy, process integration and optimisation. *Appl. Energy*, 101; 33–40 (2012)
11. Engineering Council, Guidance on Sustainability, https://shorturl.at/StZnZ
12. Bogle D, Seaman M, The six principles of sustainability, Engineering Council, https://shorturl.at/DbJ1T
13. Ellen MacArthur Foundation, Circular economy principles, https://shorturl.at/0nncd
14. SOCI, The Basic Components and Branches of AI https://shorturl.at/skLKg
15. Daoutidis P, Lee JH, Rangarajan A, Chiang L, Gopaluni B, Schweidtmann AM, Harjukonski I., Mercangöz M, Georgakis C, Machine learning in process systems engineering: challenges and opportunities. *Comput. Chem. Eng*. 181 (2024).
16. Proctor M, Chiang L. Data science and digitalisation for chemical engineers. *The Chemical Engineer*, 983 (2023).
17. Keith M, Keiller E, Windows-Yule C, Kings I, Robbins P. Implementation and evaluation of generative artificial intelligence (GAI) in chemical engineering education. *Educ. Chem. Eng*. (2025).

© 2025 by the authors. Licensed to PSEcommunity.org and PSE Press. This is an open access article under the creative commons CC-BY-SA licensing terms. Credit must be given to creator and adaptations must be shared under the same terms. See https://creativecommons.org/licenses/by-sa/4.0/



Systems & Control Transactions

**Research Article - Peer Reviewed Conference Proceeding**
ESCAPE 35 - European Symposium on Computer Aided Process Engineering
Ghent, Belgium. 6-9 July 2025
Jan F.M. Van Impe, Grégoire Léonard, Satyajeet S. Bhonsale,
Monika E. Polańska, Filip Logist (Eds.)

PSE PRESS

# Novel PSE applications and knowledge transfer in joint industry - university energy-related postgraduate education

**A. S. Stefanakis[a], D.Kolokotsa[a] , E. Kapartzianis[a], J. Bonis[a], E. Kondili[b]*, J.K. Kaldellis[c]**

[a] Helleniq Energy, 17th km National Rd. Athens – Corinth, Aspropyrgos 193 00, Greece.
[b] Optimisation of Production Systems Laboratory, University of West Attica, P. Ralli & Thivon Street, 12244, Egaleo, Greece.
[c] Soft Energy Applications and Env. Protection Lab., University of West Attica, P. Ralli & Thivon Street, 12244, Egaleo, Greece.
* Corresponding Author: ekondili@uniwa.gr.

## ABSTRACT

The field of Process Systems Engineering (PSE) is undergoing a renaissance through the integration of artificial intelligence (AI) and machine learning (ML). This transformation is driven by the vast availability of industrial data and advanced computing power, enabling the practical application of sophisticated ML models. These models enhance PSE capabilities in design, control, optimization, and safety. The progress of ML and ever-present data collection address previously intractable problems, particularly in system integration and life-cycle modeling. ML-powered predictive algorithms are augmenting traditional control systems, showing potential in supply chain optimization and increasing operational resilience. Additionally, ML-driven fault prediction and diagnostics are enhancing process safety systems, allowing for predictive maintenance and minimizing risks of accidents. A case study of the collaboration between the University of West Attica and Helleniq Energy through the MSc program in Oil and Gas Process Systems Engineering showcases the practical application of advanced technologies and knowledge transfer, emphasizing the importance of blending AI with traditional PSE education.

**Keywords**: Artificial Intelligence, Machine Learning, Education, Knowledge Transfer, Oil and Gas.

## INTRODUCTION

The field of process systems engineering (PSE) has long been characterized by a deep theoretical foundation. Pioneers like George Stephanopoulos [1] and David Himmelblau [2] laid the initiative. A lot of other researchers have laid the groundwork, exploring the potential of early artificial intelligence (AI) concepts to model and optimize complex industrial processes. However, these ambitious ideas often outstripped the available computing power and the quantity and quality of data. The models were constrained, not by theory, but by practical limitations. Today, the situation is dramatically different. The confluence of vast industrial data repositories and highly accessible cloud computing has created a fertile ground for the practical application of sophisticated machine learning (ML) models augmenting PSE modelling capabilities. This is driving a renaissance in PSE, transforming how we approach design, control, optimization and safety within the process industry.

### The Dawn of Data-Driven Process Systems Engineering

The maturation of ML, combined with ubiquitous data collection, allows for previously intractable problems to be addressed. The most intractable problem in PSE is the integration of systems in a life-cycle model of the process.

In PSE, the focus is shifting to two key areas:

1. Advanced Control and Optimization
2. Fault Detection and Diagnosis or Enhanced Process Safety and Reliability

A description of this trend as expressed by academia can be found in [12], [13].

### Advanced Control and Optimization

Traditional control systems, typically implemented on Distributed Control Systems (DCS) and Advanced

Control Systems (APC) using real-time operating systems, are being augmented by ML-powered predictive algorithms. These algorithms, often implemented as neural networks and deep learning architectures, can handle the complexities of large-scale systems more effectively than classical methods. While full plant-wide optimization remains a challenge, progress is being made in areas such as supply chain optimization. This is supported by research and industrial adoption, showing a clear potential to boost efficiency, reduce costs and increase operational resilience. Academic institutions (see for example [5]) are actively researching supply chain optimization using ML, seeking to understand how algorithms can predict demand, optimize production scheduling and manage inventory effectively. This area showcases a clear transition towards more intelligent manufacturing and is currently being implemented on pilot scales within various industries.

Reluctance of market participants has resulted in applications which have different origins towards autonomy (mostly arbitrary and team driven).

In the area of Reinforcement learning controls there are examples of:

1. Off-line reinforcement learning optimization (AIO) by IMUBIT (www.imubit.com)
2. Other similar to IMUBIT partial efforts toward real time AI augmented optimization (YOKOGAWA- KBC, ASPENTECH, C3.AI etc.) depending on the application.
3. Online gain adapting controllers by Honeywell, ExxonMobil and Yokogawa.

Information currently can be obtained mainly by their patents and traced back to theory as the descriptions are usually very detailed and can be easily compared with Google Reinforcement Learning (RL) models or among them all [8], [9], [10], [11].

It is very much of a coincidence indicating the difficulty of the problem that Anderson controller described in [2] is also tested today by some companies like Honeywell and Yokogawa in laboratory environments.

Of course, this list is by no means exhaustive but gives the dynamics of the problem, i.e very few companies are involved because of the difficulty of the subject but the development thrives in this area (there are patents and products). Note that development is mostly associated with academia for all the above companies.

## Fault Detection and Diagnosis or Enhanced Process Safety and Reliability

Process safety systems, implemented on Programmable Logic Controllers (PLCs) and also known as Interlock or Emergency Shutdown Systems, are now being enhanced with ML-driven fault detection and diagnosis. Most of industrial applications are given as ad-hoc cases for special equipment e.g. furnaces, compressors, mixers or individual unit emergency s/d. Details can be found in [6] on the internet. While still ad-hoc, a systematic Abnormal situation management system is of paramount importance as described for example in [7]. Comparison in [7] of 7 methods with 10 criteria concludes that no one can serve more that 70% of the criteria and no criterion can be served by more than half of the methods. This adds to theoretical complexity as much as safety requirements add to the implementation of the methods. For example, explainability criterion clearly can be fulfilled by expert systems but not by neural networks. Alternatives to these criteria are still evolving.

Fault Detection and Diagnostics (FDD) in reliability is especially impactful in asset performance management, where ML is used to predict failures in rotating machinery and other critical assets. Predictive maintenance allows companies to take proactive measures, minimizing the risks of accidents and avoiding production losses by maintenance planning. ML algorithms learn from sensor data (vibration, temperature, pressure) to identify patterns indicating potential failures, enabling preventive maintenance interventions. This is vital for preventing catastrophic events and ensuring a smooth production process.

Currently there are vast alternatives for predictive maintenance applications and large machinery equipment provide ML software as a standard part of their machines (for monitoring by both client and manufacturer). Still reinforcement learning equipment switching is not provided yet to the clients.

Most market participants employ ML for advice to operations with statistical ML methods, providing ML libraries (in edge i.e. field computers) with particular case studies.

An important field for continuous plants is the ML augmented procedural automation standards (ISO 106) and implementations which automate the step-wise procedures required in starting-up and shutting-down.

## The Challenges of Interdisciplinary Integration

While the potential benefits of ML in PSE are clear, several significant challenges hinder its widespread adoption. These challenges mainly concern education at any level (undergraduate, postgraduate, continuing). This problem has been already pinpointed e.g. in [4] by defining a partial role of a “process data scientist”. Also, in [3] where it is noted that there is a tendency to rush off and teach courses that are cookbook-style offerings, where students learn to mechanically apply different software packages without a deeper understanding of the fundamentals knowing not only how to apply but also why to apply.

Currently with a relatively narrow industrial application environment a bonus starting point is also “where to

apply" with industrial applications guiding theoretical analysis efforts with a dynamic curriculum.

The integration of PSE with ML and data engineering presents a triple challenge:

1. Understanding Process Systems Engineering Fundamentals: The first challenge resides in the complexity of PSE itself, requiring a deep understanding of chemical, physical, and thermodynamic principles. This alone is a demanding discipline. Students need a robust foundation in process modeling, simulation and control theory to grasp the notion of industrial processes.

2. Mastering Machine Learning Techniques: ML, while powerful, is also a complex discipline that requires familiarity with statistical modeling, algorithm design and optimization. This understanding is paramount for applying ML correctly and understanding its limitations, ensuring that ML is being used in a suitable way and not only as a black box.

3. Developing Data Engineering Skills: The sheer volume of data generated by modern industrial processes demands a proficiency in data engineering. This involves skills in database management, cloud computing, data preprocessing, data architecture and data governance. Without the ability to effectively handle and structure data, advanced ML algorithms cannot reach their full potential.

These are three distinct disciplines, each with its own language, frameworks and modes of thinking. To fully leverage the power of ML in PSE, there needs to be a convergence of these disciplines, and reframing of classical engineering principles to incorporate the new methodologies. This requires a shift in education methodologies, moving past siloed subjects and into an integrated approach.

A similar shift is expected from an industry point of view because of low inventory of both experience and head count. Both represent hurdles which can be surpassed by educational means only and beyond classical business measures per se.

## The Need for Rapid Adaptation

The pace of technological change demands that the PSE field adapts quickly. While new generations, are adept at hands-on learning and readily embracing new technologies, seasoned engineers may find this transition overwhelming. The ability of companies and academia to adapt to the changes of incorporating the new technologies and the development of novel talent will be the main factors for the survival of businesses in the coming years.

Evolution of similar systems like APC may predict that AI will mature in the next decade (50 years as other PSE systems).

Having noticed that, it is also clear that the arguments expressed for AI in [1] in 1986 are still valid:

1. Limited by complexity 1986 – Still a problem in 2025
2. Limited by computing power 1986 – Still a problem for combinatorial or factorial size processes in PSE.
3. Limited by data (Industry is not mature) 1986 – still a problem but Digital transformation is underway, and data quality is an issue followed by data marketing problems.
4. Not existing market pull (conceptually successful, implementation and workflow limited) 1986 – Still a problem if AI hype is removed but cloud facilitates development. ML for PSE might help but General AI for PSE is rather not yet. AutoML slowly evolves to be an option for ad-hoc model building.
5. High hanging fruits for the period 1986– Multivariable Predictive Control took over the low hanging fruits 1995-2005 – Still a problem in 2025 to maintain MPC apps and a new high hanging challenge is integration of MPC with Scheduling and Supply chain Optimization on a theoretical and practical ground.

The rapid adaptation of AI by the companies and academia is required because of the momentum of Digital transform. As an example of such efforts, currently, a change management project supports the digital transformation of the Helleniq Energy Group, introducing an extensive training program for engineers and technical personnel. More than 12k manhours training in 2023 and approximately 30k manhours training for 2025, are spent for several digital transformation tools applications (Asset Management, Digital OPS/HSE, HC Supply Chain, Energy Management Cyber Security etc.). This momentum was not present in the distant 1986 or even 2016 and presents a large factor of evolution.

Still, the development of theory is not yet complete and Autonomous plants are a distant vision.

## Future Trajectory: Plant-Wide Intelligence

The future of AI in PSE lies in the development of intelligent plant-wide optimization and fault detection and diagnosis models.

A partial example is discussed in [5] where academic and industrial experience have put reinforcement learning methods in chemical plant scheduling. Operations continue with these models for years already.

These systems will leverage ML to optimize every aspect of the production process, from resource allocation to energy management and maintenance, and provide real-time diagnostics, enabling highly reliable operations.

# A CASE STUDY IN COLLABORATION: ACADEMIA AND INDUSTRY PARTNERSHIP

The Master of Science Postgraduate Program (MSc)

"MSc in Oil and Gas Process Systems Engineering" began its first cycle in April 2019. The MSc is implemented by a scientific team from the Department of Mechanical Engineering at the University of West Attica (UNIWA), who have significant and long-standing experience in reputable postgraduate programs in the energy field, with the support of Hellenic Petroleum and, until recently, the Aspropyrgos Municipality.

The Program, which awards a Master of Science - MSc in Oil and Gas Process Systems Engineering, focuses on:

- Industrial systems and hydrocarbon processing (H/C),
- Production, storage, supply chain of liquid and gaseous hydrocarbons, and
- Optimization of processes and production planning/control of hydrocarboNIns.

The MSc is a full-time program, lasting four (4) academic semesters, equivalent to 120 ECTS, and includes:

- Attendance of ten courses (out of 13 offered in total),
- Completion of a research master's thesis, and
- Completion of a two-month internship in an industry or organization.

Currently, one hundred students are being trained, while many of the MSc instructors come from Helleniq Energy Group: over twenty subject matter experts - production and process engineers with PhD teaching courses such as Basics of Refinery Operations, Process Safety, Natural Gas Processing - Transportation and Distribution, Supply Chain Management in Oil and Gas Industries, Optimization and Decision Making in Oil and Gas Process Industry, etc. This is a unique competitive feature as it transfers genuine knowledge and valuable real-world experience to the MSc students. This is especially pronounced during their thesis preparation, where the collaboration becomes even closer with the allocation of industrial research subjects to be investigated by the students.

From the highly successful course of the Postgraduate Program so far, it is concluded that there are excellent prospects for further development. In the next steps, the Postgraduate Program will design fully English-taught courses to meet the educational needs of company executives and hydrocarbon organizations abroad. Today the Course is bilingual, with teaching to be carried out in Greek but the Assignments, Dissertation and most of the educational material to be in English. Additionally, already implemented activities that will be further strengthened in the Program include scheduled lectures by field experts, as well as selected high-specialization and know-how seminars. The program runs exclusively with the physical presence of students and instructors/professors. However, recent COVID experience had inspired the preparation of e-learning material. Therefore, some of the highly specialised or wide interest courses may also be carried out in distant mode, allowing wider participation from executives of hydrocarbon companies and local municipalities.

With the expansion of Helleniq Energy Group's activities into other energy fields (RES, green hydrogen production) and its pioneering role in energy issues beyond Greece, joint actions with the laboratories of UNIWA, which also have a long history and specialization in modern energy issues, can be expanded.

This article highlights the ongoing collaboration between the Helleniq Energy, the largest energy company in Greece and a leading university UNIWA. This partnership is facilitating the transfer of knowledge in the practical implementation of advanced technologies through postgraduate and potential doctoral programs. These programs will enhance the understanding of novel AI implementation within the process industry.

The collaboration provides real-world industrial data for testing and implementation, promoting the education of students by offering a unique insight to the real application of the academic taught principles and enabling faster adaptation for the industrial partners.

This type of collaboration acts as a catalyst, accelerating the implementation of innovative AI solutions within industry, while also enabling a deeper theoretical understanding for all sides involved.

## Practical aspects of the case study

The artificial intelligence has been introduced in both UNIWA and Helleniq Energy with a pace corresponding to Helleniq Energy Digital Transformation so that firm steps are presented to the students as a supplement in particular courses. A faster pace would be possible but was deemed overwhelmingly evolving and difficult to bottle in a comprehensive course. A significant feature of the process is that AI is a bridge between fossil fuels technology and green fuels technologies enabling the persistence of the latter reducing costs and improving efficiency which enables energy transformation. So, digital and energy transformation go hand in hand and AI is augmenting capability down this path.

Furthermore, and in addition to initial efforts, a course in AI is planned with considerations from all involved subjects. The MSc program evolves and targets AI-augmented contemporary industrial needs.

## AI lectures in MSc program: already in place

Methods for exploiting and utilizing the readily available data are presented in various modules of the MSc course. The most extensive and systematic amalgamation of conventional engineering approaches with novel data-driven techniques, is found in the “Advanced Process Control and Digital Transformation” module, that contains lectures, tutorials, as well as a reverse MATLAB PC-lab, which is split between control systems synthesis and analysis, and ML methodologies. Namely, although the module focuses on real-world control systems, both

classical and advanced, it also entails lectures on measurements and real-world data-cleaning, ML (supervised, unsupervised, reinforcement learning), ensemble methods and actual case studies. A couple of reverse labs are on supervised learning and reinforcement learning. The agile methodology is introduced, to break the project into phases and emphasize on the continuous collaboration and improvement, by following a cycle of planning, executing, and evaluating. The goal of this approach to teach Process Control through a modern prism, is to provide students with practical skills and foster real-life intuitions.

Current efforts focus involve a number of seminars on the subject at hand:

1. A Seminar on the application of statistical modeling in maintenance. A predictive maintenance (and asset management in general) related subject outline, the theory and ML methods used as well as the target and scope of Industrial applications. The predictive maintenance applications of Helleniq Energy are discussed as examples of applications.

2. One Seminar on the application of reinforcement learning in Control and Scheduling applications with an outline of the methods used. These two areas of PSE have distinct scientists in both academia and industry and completely different understanding depending on the origin, be it control or scheduling. Again, examples of blending and unit operations (FCC unit) of Helleniq Energy are used from the control point of view with examples in MATLAB. In the future the Scheduling point of view will be incorporated.

3. A Seminar after supply chain and process design courses for supply chain integration. The focus is on historical evolution of machine learning especially in PSE but also recent advances, Process monitoring examples, emphasis on better quality inference with ML, reinforcement learning theory and current use in the industry, fault detection and diagnosis not only in predictive maintenance but in all process, equipment rotating or static and finally operating procedures (start-up, shutdown)

4. A seminar focused on non-technical aspects of AI as it is applied in Refinery unit optimization. For non-technical people reading the press, there is a lot of simplifications and analogies for AI and ML which are misleading. Also, General AI in PSE or even AI is rather just an intention yet (2025). A grounded fact is ML for PSE. So, there is a need of specifying where and how existing systems are augmented and how the augmentation would produce benefits without the need for programming or Machine learning fundamentals.

### AI in MSc program evolution: Enrichment with AI courses

A plan for a course in “ML applications in PSE in Oil and Gas” which will not replace references inside particular courses but rather setup a basic understanding of breadth and depth of ML applications. Several other courses are known in the academia including that of V. Venkatasubramanian [3]

The plan involves the following considerations:

1. Preparatory course: Two courses are proposed by V. Venkatasubramanian [3] namely undergraduate and postgraduate. To cover for the scenario of continuing education students, a two-month preparatory course with basic elements (ML methods, PSE subjects and uses) in the postgraduate (MSc) will replace and enhance the current seminar covered subjects. A special focus on all three elements (PSE, ML Programming, Data Engineering) will be characterizing this effort.

2. An elective course will cover applications of AI in PSE expanding all the subjects of preparatory course and focusing in current (growing) applications in Industry as well machine learning (see for example Kumar and Cerrillo [4]) as outlined in the following:

a. Machine Learning subjects for Process Monitoring, Advice and Predictions

i. Classification techniques
ii. Regression techniques
iii. Ensemble Learning, Boosting, Random Forests
iv. Deep Neural Networks
v. Deep Belief Networks and Classifiers

b. Reinforcement Learning, theory, applications and offline/online RL agents for control and scheduling integration.

c. Applications in PSE

i. Optimization of Unit operations and Blending
ii. Fault Detection and Diagnosis in rotating equipment
iii. Fault Detection and Diagnosis in process equipment
iv. Procedural automation augmented with AI
v. Scheduling and Control integrated and augmented with AI
vi. Quality and Quantity Inferentials augmented with AI.
vii. Large Language models as operator/engineering and predictive maintenance advisors

These courses are under review for the next year starting with the preparatory course but current status of AI in the industry and academia forces their introduction as soon as possible. It is well understood that as applications are evolving, a dynamic curriculum should be anticipated and a process in the curriculum for its improvement should be built in.

## CONCLUSIONS

### Paradigm of Continuous Improvement Culture: Continuous process performance improvement and optimization

The "MSc in Oil and Gas Process Systems Engineering", is a Paradigm of Academia and Industry Partnership in Greece and EU, providing sustainable and continuous

improvement culture in both industry and university [14].

The MSc Program is well designed to enhance the academic program of West Attika University, but also to support the sustainable development and operation of the Helleniq Energy Group business areas, covering continuously and in an advanced way the educational needs of its Technical Personnel.

The long-lasting expertise acquired in the Oil & Gas sector, is transferred to the academia through the pool of knowledge of its experts and their valuable contribution.

Technical experts of almost all the business units of Helleniq Energy Refineries, actively support the program with lectures, industrial case studies and thesis work supervision.

It is of paramount importance in this point to emphasize that the inspiration of AI and ML introduction in the Aspropyrgos Refinery of Helleniq Energy SA has been provided by the detailed, enthusiastic and thorough investigation of the state of the art in these issues that has been carried out for the successful implementation of an intensive highly specialised course in the above MSc Course, delivered by one of the authors of the present paper and embraced from the whole team and the management of the company.

Furthermore, one more invaluable reciprocal benefits of the MSc Course should be recalled, namely the high quality of the education that is provided to the technical personnel of the company, as well as the development – through the Course of excellent quality instructors that will in their own turn educate the rest of the company's technical personnel.

During its six years of operation the PG Course has been educating 120 professionals, mostly working in the hydrocarbons field. Almost 40 of them have already graduated and have advanced their career in petroleum and natural gas industries. On the other hand, the knowledge acquired form the graduates has been implemented through the implementation of advanced methods and tools for the design, operation and optimization of the processes and supply chains.

To conclude, the convergence of ML, cloud computing, and vast datasets is revolutionizing process systems engineering. The challenge lies in integrating these new tools and skills into the core of the PSE discipline, thus creating a new kind of engineer. This will require cross-disciplinary education, industry-academia partnerships, and a commitment to embracing the potential of AI to unlock unprecedented levels of efficiency, safety, and sustainability in industrial operations. The ability to adapt is going to be paramount for the industry and academia..

## REFERENCES


1. Stephanopoulos, G. (1986). Artificial Intelligence in Process Engineering. Chemical Engineering Education, 20(4), 182-192.
2. Hoskins, J. C., & Himmelblau, D. M. (1992). Process control via artificial neural networks and reinforcement learning. Computers & chemical engineering, 16(4), 241-251.
3. Venkatasubramanian, V. (2022). Teaching artificial intelligence to chemical engineers: experience from a 35-year-old course. Chemical Engineering Education, 56(4), 231-240.
4. Kumar, A., & Flores-Cerrillo, J. (2022). Machine Learning in Python for Process Systems Engineering: Achieve Operational Excellence Using Process Data. MLforPSE.
5. Hubbs, C., Can Li, Sahinidis, N., Grossmann, I.,, Wassick, J. (2020). A deep reinforcement learning approach for chemical production scheduling. Computers and Chemical Engineering 141, 4 October 2020, 106982
6. https://www.yokogawa.com/special/artificial-intelligence/, https://process.honeywell.com/us/en/solutions/experion-pks/experion-halo,
7. Venkatasubramanian, V. et al (2003). A review of process fault detection and diagnosis - Part I,II,3 Computers and Chemical Engineering 27 (2003) 293-311, 313-326, 327-346.
8. For Yokogawa controller - Matsubara, T., Gomez, V., Kappen, H. (2014) Latent Kullback Leibler Control for Continuous-State Systems using Probabilistic Graphical Models. Conference: Proc. of the 30th Conference on Uncertainty in AI (UAI)
9. ExxonMobil US PATENT Jun.20, 2019 DRL adaptive tuning of PID controls
10. IMUBIT US PATENT Nov.10 2022: WO 2022/235314 A1
11. ASPENTECH US PATENT Nov 17,2022: US 2022/0365497 A1
12. Pistikopoulos et. Al. (2023). Process Systems Engineering – The generation next? Computers & Chemical Engineering Volume 147, April 2021, 107252
13. Mitsos et. Al (2021). Machine Learning in Chemical Engineering A Perspective. Chemie Ingenieur Technik 93, No 12,2029-2039.
14. Kondili, E.M., Kaldellis, J.K., Demenagas, E., Stefanakis, A.(2020), Knowledge Transfer, Experiences and Prospects from the Collaboration between an Energy Company and the University, CAPE Volume 48, Pages 2029 - 2034



© 2025 by the authors. Licensed to PSEcommunity.org and PSE Press. This is an open access article under the creative commons CC-BY-SA licensing terms. Credit must be given to creator and adaptations must be shared under the same terms. See https://creativecommons.org/licenses/by-sa/4.0/




Systems & Control Transactions

**Research Article - Peer Reviewed Conference Proceeding**
ESCAPE 35 - European Symposium on Computer Aided Process Engineering
Ghent, Belgium. 6-9 July 2025
Jan F.M. Van Impe, Grégoire Léonard, Satyajeet S. Bhonsale,
Monika E. Polańska, Filip Logist (Eds.)

PSE PRESS

# Sociotechnical Transition: An Exploratory Study on the Social Appropriability of Users of Smart Meters in Wallonia.

**Boissézon Elisa**[a*]

[a] University of Mons, Department of Social Pedagogy and Andragogy, Mons, Belgium
* elisa.boissezon@umons.ac.be.

## ABSTRACT

Optimal and autonomous daily use of new technologies isn't a reality for everyone. In a societal context driven by sociotechnical transitions [1] many people lack access to digital equipment and skills, preventing their participation in digital social life, including energy services. Our exploratory and phenomenological research, guided by European Union directives [2], explores the social appropriation [3] of new technologies during the deployment of smart meters in Wallonia. The study investigates social behaviour of audiences with support during smart meter installation and identifies barriers to technology appropriation. In an exclusively qualitative approach, the field surveys aim to determine to what extent individual participatory forms [4][5] and collective forms [8][9] of support, through active pedagogies like experiential learning [6][7], can include digitally vulnerable users. The central role of field professionals as interfaces [10] is also highlighted within the service relationship [11] that connects, on one hand, the end consumers and, on the other hand, the organization responsible for deploying the smart meters. While our study does not directly utilize CAPE methods and tools, it investigates the current social implications of digitalization.

**Keywords**: Sociotechnical Transition, Social Appropriability, Smart Meters.

## A SOCIOTECHNICAL CONTEXT

### The sociotechnical transition

The innovations developed to deal with the climate challenges of our century raise several questions regarding the adoption of new transition technologies by households with very diverse socio-economic realities and digital skills. In this context, energy transition is carried out alongside the digital transition, making them complementary [12]. Therefore, Socio-technical transitions differ from technological transitions in that they include changes in user practices and institutional (e.g., regulatory and cultural) structures, in addition to the technological dimension [1]. For instance, the need for innovation in managing complex energy systems [12] is reflected, among other things, in EU directives mandating 80% smart grid deployment by 2020 across its territories [13]. Despite practical challenges, this deployment is crucial for achieving the EU's energy transition goals: renewable energy investment, energy efficiency, and energy sobriety [2].

### The deployment of smart meters in Wallonia

In Wallonia, the deployment of smart meters follows the European directives on energy transition. According to the decree of July 19, 2018, the smart meter is defined as an electronic system that can measure the energy taken or injected by adding information that a conventional meter does not provide, that can transmit and receive data in the form of electronic communication, and that can be operated remotely (...) (art. 2, 29°bis). However, the numerous investments in technology for ecological sustainability and energy efficiency raise questions about end-user technological adoption. Literature suggests that with increasing household innovations, service provisions will become more self-organized by individuals (or communities), limiting professional intervention to key moments [14]. Therefore, users, including the most vulnerable, will need to be able to familiarize themselves with these devices for autonomous use post-service provision.

### Smart meters and their users

Besides concerns about electromagnetic waves and privacy, users doubt the intelligent nature of the technology [15]. While technology outcomes depend on users, their digital skills often do not evolve at the same pace as the technological advancements, leading to dependence rather than empowerment [3][16]. Thus, studies highlight user difficulties in understanding device data and using complementary tools like websites or platforms. Users also struggle with complex data presentations via multiple graphs, units in kWh, etc. [17]. In the wake of these results, the issue of digital inequalities emerges, encompassing aspects related to access, use, and digital participation in the social life of users.

### Digital divide in Wallonia

The digital divide is multifaceted and occurs at three levels: access to ICT, use of ICT and digital skills, and active participation in social life via ICT, such as e-services. In Wallonia, the digital divide is significant. According to the Digital Maturity Barometer of Walloon Citizen, in 2023, 6% of individuals lacked access to digital devices [18]. Beyond the material dimension, it has been observed that having access to the internet (...) does not guarantee full and complete practice, that is, autonomous and effective (...) and is therefore not synonymous with greater equality. However, digital practices are not self-evident and require 'digital skills' [19]. Digital exclusion is an important factor to consider in the deployment of smart meters, especially for vulnerable populations. Not all their users have internet access or digital devices to manage their consumption data or use online tools.

### Using smart meters through digital divide

According to the Walloon legislator [20] the deployment of smart meters in Wallonia primarily targets households in payment default, one of the objective indicators of energy poverty [21]. Digital inequalities, linked to poverty, exacerbate this issue, as those experiencing energy poverty are often most affected by the digital divide [22]. When resources are limited, digital inclusion is not a priority and may lead to debt for acquiring equipment, training, etc. [23]. Furthermore, digital skills vary widely based on income, age, socioeconomic status, sociodemographic characteristics, education, employment status, illiteracy or disability [24][25]. In 2021, 32,2% of households faced energy poverty [21]. Considering those elements, it seems more than appropriate for energy professionals, as well as users, to consider diverse public profiles to ensure effective smart meter deployment (profiles, needs, expectations, etc.) while supporting the population.

## THE SOCIAL APPROPRIATION OF TECHNOLOGIES

### The interface situation and the service relationship

In the context of the deployment of smart meters, the support relationship involves an interface situation with devices for the public, managed by professionals [10]. The interface situation forms a triangular relationship between the public (client-experimenter, client of a service relationship, user, local partner, manager, decision-maker, etc.), devices (technical objects, management devices, and organizational structures), and professionals (actors positioned at the boundaries of different dimensions and responsible for managing the uncertainties arising from them). This interface situation links various social worlds (users, professionals, organizations, etc.) and their respective issues through which energy exists [10].

The backdrop of this interface relationship between the client and the professional in the context of the deployment of smart meters can be framed by the service relationship which is defined as a triangular relationship bringing together a professional (holder of a skill requested for the accomplishment of a 'repair'), an object to be repaired, and its owner (requesting the skill of this professional for the purpose of repair). The realization of the service here requires the involvement and cooperation of both parties. In this sense, the service participates in a social relationship through the confrontation and mutual adjustment it demands from each of its parties [11][26]. Therefore, field professionals act as intermediaries between the device, the public, and themselves. However, despite theoretical preparations for user support, real-world challenges arise due to the unique characteristics of users, such as socioeconomic status, sociodemographic characteristics, social inequalities, etc.

### From acceptability to appropriability

The introduction of technologies in the energy market faces several challenges since their logic are not necessarily compatible with social logics [27]. Moreover, these technologies are based on standardized conceptions of social practices [27] and their use assumes that their users possess skills they do not necessarily have [19]. Engineering sciences use the concept of social acceptability of the technological devices [27], which allows for the analysis of the mechanisms governing the anchoring of a project or decision within a social dynamic without reducing them to the formal institutional framework [28]. However, this concept is questioned in the scientific literature since to reason in terms of social acceptability is to shift the responsibility to the target public to adopt or not the concerned technologies. It is to consider that only the social dimension plays a role in realizing the potentials invested in the technologies [29]. Nevertheless, given that the reluctance to engage with

technologies is more complex than just a socioeconomic barrier, the technical dimension must also be considered. Thus, it is more appropriate to speak of social appropriability which encompasses a set of complex processes: the technical culture of users, their social representations, the origin of the innovation and the means by which it was presented to its users, the practices and uses of the innovation, the type of communication that accompanies it, the users' lifestyle and their relationship to comfort, their previous technical experiences, the collective dynamics in which they are involved, etc. [30].

## SOCIAL APPROPRIATION THROUGH PARTICIPATION

### User participation in the service relationship

In response to the challenges related to the process of social appropriability of technologies, the service literature highlights positive aspects of user participation in the service relationship [4][5][14]. In this context, consumer participation, in the broad sense, characterizes an involvement (physical and/or mental) in the process of producing the company's product or service [4]. In Wallonia, smart meter deployment involves a standardized support protocol, inviting the client to participate in system demonstrations or satisfaction online surveys. However, user participation is not guaranteed. To engage users, the system must be able to interest them, engage them, or also socialize clients who have different perceptions of participation: the idea is thus to develop a flexible and evolving system, integrating options, services, and communication supports to remove potential barriers to participation [4]. Moreover, when the public adheres to the support system, positive effects of client participation include increased productivity, leveraging consumer know-how for innovation, strengthened company attachment, a sense of freedom of choice, power transfer to users, alignment with client preferences, and improved service quality [4][5][14].

### User participation against social inequalities

Active public involvement presents numerous advantages in addressing digital inequalities, especially when user participation is viewed through the lens of active pedagogies. Firstly, experiential learning, through a meaningful practice, is essential in the context of training adult learners in the use of ICT: the 'learning-by-doing' and 'do-it-yourself' approaches appear even more important as the primary goal of adult learners in training is not to assimilate theoretical and technical concepts, but rather to concretely learn to use certain aspects of ICT for activities carefully selected based on daily concerns [7]. Secondly, social proximity also plays a crucial role in individuals' digital usage [7]. Indeed, group learning in mastering ICT represents a significant advantage [8] considering that bringing people together around the same table and involving them in a common project promotes meeting and socialization, as well as collaboration and informal learning among learners, which are essential dimensions for the successful completion of ICT training [6]. These advantages are important to consider for vulnerable and/or precarious populations, who are often isolated and lack support assistance. Similarly, the group effect represents a significant asset when support is aimed at non-voluntary or hard-to-reach individuals [9], which are populations also affected by the deployment of smart meters in Wallonia.

### The sociotechnical transition through user participation

Through participation, the consumer, who was previously passive towards services, becomes a 'prosumer' or, in other words, a consumer who participates and engages alongside companies [31]. Additionally, participation seems to restore a central role to clients by considering the human factor in support processes, regarding real-life experiences from the field. Thus, this approach redefines individuals as 'users' rather than just 'consumers' or 'clients'. However, considering user support in smart meter deployment solely through the lens of participation is not sufficient. User engagement depends on numerous factors, with the central question ultimately being the meaningfulness of using the technologies in question. In fact, user engagement depends on the meaningfulness of technology use. Considering that, the Reflexive Practice theory [32] emphasizes that autonomy and systematic thinking lead to relevant practice changes [33]. This principle also applies to the deployment of smart meters and their sustainable use in the daily management of household energy.

## METHODOLOGY

The present research focuses on the support provided to the public in the context of deployment of smart meters in Wallonia in an exploratory and phenomenological perspective. Considering all the elements reviewed and presented in the conceptual framework, our research question is as follows: do the current support mechanisms for the public (individual or collective) enable the social appropriability of smart meters in Wallonia?

To achieve this, data collection was conducted using semi-structured interviews with four samples: non-requesting users (N=10), requesting users (N=17), field professionals (N=5) and mixed profiles users (N=10). The investigation of individual public support was conducted with reference to the following indicators, derived from scientific literature on engagement, including the use of ICTs: digital inequalities, perception, attitude, motivation, voluntarism, sense of social justice, trust, user postures,

and relationship to energy. On the other hand, collective support was observed through the conduct of focus groups workshops.

Data analysis and processing were conducted using a hybrid method that combines general inductive analysis [34] with analysis using conceptual categories [35], with the aim of identifying potential links between (sub-)categories through updating coherences [35]. In addition, the data collected from field professionals were analyzed using thematic analysis [35].

# RESULTS

## Individual support

The linking of conceptual entities for individual support highlighted differences in the social appropriability of smart meters and associated online tools between sample 1 (non-requesting users) and sample 2 (requesting users). First, digital inclusion was linked to educational attainment, with half of sample 1, who were experiencing digital inequalities or disconnection, having no higher education degrees. The level of digital inclusion among participants also appeared to impact their proactivity in engaging with the technology. Thus, the results show that in sample 2, all of whom were digitally included, 15 individuals were proactive in using the smart meter and associated online tools, compared to only one person in sample 1. User voluntarism also appears as a determining variable in the process of social appropriability of technologies. Three relationships were identified between voluntarism and amotivation, the level of proactivity, as well as trust. Indeed, the results showed that among the non-voluntary participants regarding the deployment of smart meters, 5 individuals exhibited signs of amotivation to use the technology, compared to only one amotivated person in sample 2, which consisted of voluntary users. Additionally, among the 10 individuals in the non-voluntary sample, only one person showed signs of proactivity, compared to 12 proactive individuals in the voluntary sample. Furthermore, within the non-voluntary sample, 7 out of 10 individuals exhibited signs of distrust towards both the technology (the smart meter and associated online tools) and the organization overseeing the deployment of these technologies. Additionally, in this group, 8 out of 10 individuals showed signs of prescribed (default) trust, partly due to digital inequalities that hinder their access to relevant information. Conversely, 14 out of 17 individuals in the voluntary sample felt confident about the smart metering system at all levels (technical, organizational, and the expertise of field professionals), with 7 individuals exhibiting prescribed (default) trust. Finally, two relationships were observed between users' usage stance towards the smart meter, including the associated online tools, and on the one hand, their relationship with energy, and, on the other hand, their attitude towards technological change. First, all 5 individuals in sample 1 who were experiencing digital inequalities or disconnection adopted a disinterested usage stance towards the smart meter and associated online tools. Additionally, out of the 10 individuals in sample 1, 2 showed some interest in the technological change but considered its use not a priority in their daily lives. In contrast, within sample 2, which consists of individuals digitally included, 10 out 17 adopted a non-priority usage stance, while 7 were disinterested. Second, regarding the attitude towards technological change, 5 out of 10 individuals in the sample 1 who adopted a potential contributor usage stance (volunteers for involvement in the support management process), 4 of them had a positive view of the deployment of smart meters. Within sample 2, among the 9 out the 17 individuals who adopted the same potential contributor stance, 4 also had a positive view of the change.

## The perspective of field professionals

In addition to field surveys with users, interviews were conducted with field professionals to explore their experiences of individual support within the deployment of smart meters. The thematic analysis of the data highlighted several themes related to their role in the service relationship. First, training: generally, technicians receive standardized technical training for the smart meter installation, but not for using associated online tools. While their technical training is well-received, technicians often didn't feel fully prepared for field contingencies. Second: fieldwork. Technicians must adopt multiple roles beyond technical tasks, including communication and social interaction, and adapt to the unique profiles of individuals they encounter (vulnerabilities, inequalities, delicate situations, etc.). This necessitates continuous hands-on-training, often self-directed or peer-supported. Third, application of training: despite having a standardized support protocol, the level of support provided varies widely, from 'fully applied, with additional personal contributions' to 'not applied at all'.

## Collective support

The data analysis collected from sample 4 (mixed profiles users) highlighted four relationships between conceptual entities for collective support. The first relationship is situated at the level of experiential learning, between pedagogical demonstration and the active participation of users supported in collective workshops. The results showed that among the 5 out of 10 individuals experiencing digital inequalities, all left with a higher sense of digital competence thanks to their active participation during the pedagogical demonstration (handling of a real smart meter, moments of exchanges and sharing, exploration of guides and brochures, discovery of online tools, etc.). Additionally, for the 2 more digitally

experienced individuals of the group, the workshop served as a constructive reminder. The second relationship is situated between pedagogical demonstration and the collective participation of users during the workshops. For all group members, collective participation in the pedagogical demonstration facilitated new theorical and technical learning. As well, 8 out of 10 individuals reported a positive customer experience. The third relationship is situated between pedagogical demonstration and the collective participation of users during the workshops. The third identified relationship relates to group effect, between the interactions and social support experienced by users during the workshops. Indeed, thanks to the interactions and sharing of experiences, 7 out of 10 individuals felt social support during their active participation in the workshop. The fourth and final relationship for collective support is between collective participation and the evolution of users' energy management. At the end of the workshops, among the 8 out of 10 individuals who had a positive customer experience, 5 left with the intention to improve their home energy system through new practices or by utilizing digital tools. Moreover, the 2 digitally vulnerable individuals in the group left the workshops with a renewed interest in using the smart meter and associated online tools, which they had previously given up.

## DISCUSSION AND CONCLUSION

Overall, our research findings align with the scientific literature and support the issues highlighted by the scientific community in the field of social appropriability of technologies. Therefore, we answer our research question both affirmatively and negatively. Yes, the current support systems (individual or collective) in Wallonia enable the social appropriability of smart meters for digitally proficient individuals and/or those interested in digital matters. However, the standardized support systems do not facilitate the social appropriability of technologies for less digitally proficient and/or digitally vulnerable individuals. Nevertheless, our results highlight the importance of local and collective support, which seems to be effective in this context. In conclusion, our research has highlighted the importance of supporting the public from a holistic perspective that considers the unique profiles of individuals. It also underscores the significance of technician training, particularly through practical cases, to ensure quality support. Furthermore, it is essential to promote the development of local and participatory support protocols, paying special attention to vulnerable populations, who are often overlooked by statistics or sociotechnical transition scenarios.

## ACKNOWLEDGEMENTS

We would like to express our sincere thanks to Prof. Willy Lahaye for his guidance and promotion throughout the course of this research. We also acknowledge the financial support provided by the University of Mons and the Walloon distribution network operator ORES. Special thanks to our colleagues from the Department of Social Andragogy and Pedagogy for their constructive discussions and suggestions. Additionally, we offer our heartfelt gratitude to all the participants of this research (ORES collaborators, users, technicians, etc.). Finally, we also extend our sincere thanks to the anonymous reviewers fort their thorough review and helpful comments, which significantly improved the quality of this paper.

## REFERENCES

1. Markard J, Raven R, Truffer B. Sustainability transitions: An emerging field of research and its prospects. *Research Policy* 41: 955-967. (2012). https://doi.org/10.1016/j.respol.2012.02.013
2. Dufournet C, Marignac Y. https://negawatt.org/IMG/pdf/180421_diapo_scenario-europeen.pdf
3. Zélem MC. Économies d'énergie : Le bâtiment confronté à ses occupants. *Annales des mines - Responsabilité et environnement* 90: 26-34. (2018). https://hal.science/hal-01757795
4. Benoit-Moreau F, Bonnemaizon A, Cadenat S. La participation ordinaire : Mieux comprendre le vécu du consommateur pour faciliter son adhésion. *Revue française de gestion*, 39: 151-166. (2013) https://doi.org/10.3166/RFG.234.151-166
5. Cadenat S, Bonnemaizon A, Benoit-Moreau F, Renaudin V. Regards sur la co-production du client : comment les entreprises nous font-elles participer ? *Décisions Marketing* 70: 9-24 (2013)
6. Brotcorne P, Valenduc G. (2008). http://www.ftu-namur.org/fichiers/Comp%C3%A9tences%20num%C3%A9riques%20et%20in%C3%A9galit%C3%A9s.pdf
7. Brotcorne P, Valenduc G. Les compétences numériques et les inégalités dans les usages d'internet : Comment réduire les inégalités ? *Les cahiers du numérique*, 5: 45-68 (2009)
8. Bernaud J-L, Lhotellier L, Sovet L, Arnoux-Nicolas C, Pelayo F. PSYCHOLOGIE DE L'ACCOMPAGNEMENT : CONCEPTS ET OUTILS POUR DÉVLELOPPER LE SENS DE LA VIE ET DU TRAVAIL. Dunod (2015).
9. Turcotte D, Lindsay J. L'INTERVENTION SOCIALE AUPRES DES GROUPES. La Chenelière inc (2008).
10. Cihuelo J, Jobert A. Conclusion générale : Energie et situations d'interface. In: ÉNERGIE ET TRANSFORMATIONS SOCIALES : ENQUÊTES SUR LES INTERFACES ÉNERGÉTIQUES. Lavoisier

(2015).
11. Gadrey J. Les relations de service et l'analyse du travail des agents. *Sociologie du travail* 3: 381-389. (1994) https://doi.org/10.3406/sotra.1994.2183
12. Geoffon P. Comment transition numérique et transition écologique s'interconnectent-elles ? *Annales des Mines – Responsabilité et environnement* 87: 17-19. (2017) https://doi.org/10.3917/re1.087.0017
13. Directive EU 2009/72/EC.
14. Bovaird T. Beyond Engagement and Participation: User and Community Coproduction of Public Services. *Public Administration Review*, 67: 846-860. (2007)
15. Peters D, Axsen J, Mallett A. The role of environmental framing in socio-political acceptance of smart grid: The case of British Columbia, Canada. *Renewable and Sustainable Energy Reviews* 82: 1939-1951. (2018). https://doi.org/10.1016/j.rser.2017.06.020
16. Zélem MC, Beslay C, Gournet R. Pas de « smart cities » sans « smart habitants ». *Les cahiers du développement urbain durable* 15: 45-60. (2013).
17. Poumadère M, Mays C, Schneider N, Bertoldo R, Boso À, Oltra C, Prades A, Espluga-Trenc J. Entre consommation durable et vie quotidienne : Les premiers balbutiements du compteur communicant en France et en Espagne. In: SOCIOLOGIE DE L'ÉNERGIE : GOUVERNANCE ET PRATIQUES SOCIALES. Ed : Paris, France. CNRS (2015)
18. Agence du numérique. (2023). https://assets.ctfassets.net/myqv2p4gx62v/6kN44GYisA6wrFrlxpcye4/1e65606903b9d069bc4bfdd39a84ee3c/Barome_tre-DW-Maturite_-Nume_rique-Citoyens-2023-Complet.pdf
19. Ottaviani E. Les fractures numériques : Comment réduire les inégalités. *Citoyenneté & Participation* 267: 1-20. (2016).
20. Walloon Region. Decree of July 19, 2018. M.B. September 6, 2018.
21. Meyer S, Coene J. (2023). https://media.kbs-frb.be/fr/media/10490/Barom%C3%A8tre%20Pr%C3%A9carit%C3%A9%20Energ%C3%A9tique%202023%20DEF
22. Frérotte P. La précarité énergétique : Un cercle vicieux ? Une analyse de Philippe Frérotte. *Citoyenneté & Participation* 324: 1-28 (2018).
23. Valenduc G. Les nouveaux visages de la fracture numérique. In : Pauvreté en Belgique : Annuaire 2013. Ed. : Acco Éditions (2013).
24. Brotcorne P, Ponnet K. (2024). https://media.kbs-frb.be/nl/media/11919/Barom%C3%A8tre%20de%20l%27Inclusion%20Num%C3%A9rique%202024_Publication
25. Brotcorne P. Mariën I. (2020). https://en.calameo.com/read/0017742954bec89c77172?authid=OClWTGwXHtBZ
26. Cihuelo J. La relation de service au croisement de logiques marchande et organisationnelle. In : ÉNERGIE ET TRANSFORMATIONS SOCIALES : ENQUETES SUR LES INTERFACES ÉNERGÉTIQUES. Lavoisier (2015).
27. Zélem MC, Beslay C. SOCIOLOGIE DE L'ÉNERGIE : GOUVERNANCE ET PRATIQUES SOCIALES. CNRS Editions (2015).
28. Gendron C. Penser l'acceptabilité sociale : Au-delà de l'intérêt, les valeurs. *Communiquer* 11: 117-129. (2014). https://doi.org/10.4000/communiquer.584
29. Zélem MC. Les effets pervers de la sobriété énergétique : Une écologisation contrainte des modes de vie. *Environnement et citoyenneté* 55: 70-80. (2016). https://doi.org/10.4000/revss.2001
30. Barthe J-F, Beslay C, Minoustchin M. Acceptabilité et appropriation sociale de la flexibilité énergétique par les consommateurs. In : SOCIOLOGIE DE L'ÉNERGIE : GOUVERNANCE ET PRATIQUES SOCIALES. Ed : Paris, France. CNRS (2015)
31. Trespeuch L. (2017). https://www.researchgate.net/publication/320739139_La_participation_du_consommateur_antecedents_et_consequences_proposition_d'un_modele_integrateur_applique_au_cas_du_crowdfunding
32. Schön DA. Quotations. A Symposium on Schön's Concept of Reflective Practice : Critiques, Commentaries, Illustrations. *Journal of Curriculum and Supervision* 5: 6-9. (1989).
33. Perrenoud P. Peut-on changer par l'analyse de ses pratiques. *Cahiers pédagogiques* 346: 14-16. (1996).
34. Blais M, Martineau S. L'analyse inductive générale : description d'une démarche visant à donner un sens à des données brutes. *Recherches qualitatives* 26: 1-18. (2006). https://doi.org/10.7202/1085369ar
35. Paillé P, Mucchielli A. L'ANALYSE QUALITATIVE EN SCIENCES HUMAINES ET SOCIALES. Armand Colin (2016).

© 2025 by the authors. Licensed to PSEcommunity.org and PSE Press. This is an open access article under the creative commons CC-BY-SA licensing terms. Credit must be given to creator and adaptations must be shared under the same terms. See https://creativecommons.org/licenses/by-sa/4.0/



Systems & Control Transactions

**Research Article - Peer Reviewed Conference Proceeding**
ESCAPE 35 - European Symposium on Computer Aided Process Engineering
Ghent, Belgium. 6-9 July 2025
Jan F.M. Van Impe, Grégoire Léonard, Satyajeet S. Bhonsale,
Monika E. Polańska, Filip Logist (Eds.)

PSE PRESS

# Smart Manufacturing Course: Proposed and Executed Curriculum Integrating Modern Digital Tools into Chemical Engineering Education

**Montgomery D. Laky[a], Gintaras V. Reklaitis[a], Zoltan K. Nagy[a], and Joseph F. Pekny[a*]**

[a] Purdue University, Davidson School of Chemical Engineering, West Lafayette, IN, USA
* Corresponding Author: pekny@purdue.edu.

## ABSTRACT

The paradigm shift into an era of Industry 4.0, also referred to as the fourth Industrial Revolution, has emphasized the need for intelligent networking between process equipment and industrial processes themselves. This has brought on an age of research and framework development for smart manufacturing in the name of Industry 4.0 [1]. While the physical and digital advancements towards smart manufacturing integration are substantial the inclusion of engineers themselves amongst this shift is often less considered [2]. There are educational efforts in Europe to create and implement smart manufacturing curriculum for non-traditional or adult learners already integrated in the workforce, but attention is also needed on a next generation smart manufacturing curriculum for pre-career students [3]. We, the teaching team of CHE 554: Smart Manufacturing at Purdue University, developed and implemented a curriculum geared towards the training of undergraduate, graduate, and non-traditional students in methods of smart manufacturing as they apply directly to industrial scenarios. Through this elective course, taught primarily through the context of chemical engineering but enrolling students from other disciplines, we introduce concepts not covered in its entirety by the core engineering curriculum. Our course includes but is not limited to material on data reconciliation, machine learning, chemometrics, data-driven fault detection, digital twin development, and process optimization. Further, these concepts are executed through the context of open-source Python packages, enabling the accessible and practical application of smart manufacturing in the form of assignments and in the context of professional application in the future [4,5]. The integration of modern tools and Python libraries connects academic solutions to industrial challenges with industrial practice becoming evident for students who would otherwise be unaware of these resources. With the creation and implementation of the Purdue University Smart Manufacturing elective course, we help develop a uniquely prepared and technologically educated generation of engineering students capable of bringing Smart Manufacturing capabilities to industry. This helps catalyze smart manufacturing knowledge transfer where all enrolled students are given the tools to apply their knowledge mastery to their specific engineering discipline and industrial application.

**Keywords**: Industry 4.0, Fault Detection, Artificial Intelligence, Interdisciplinary, Model Predictive Control, Digital Twin, Process Optimization

## INTRODUCTION

Industrial revolutions have consistently marked transformative eras of technological advancement, shaping the modern world. Industry 4.0, also known as the Fourth Industrial Revolution, is no exception [1]. This era has witnessed an unprecedented integration of novel technologies into manufacturing, aimed at making processes more sustainable, robust, customizable, and profitable. However, despite the transformative potential of these technologies, their adoption is not always met with universal success. Even in companies that

enthusiastically embrace Industry 4.0, a critical gap often arises. Students entering the workforce frequently lack exposure to the technologies and concepts foundational to Industry 4.0. This unawareness highlights the opportunity for academic institutions to prepare graduates with concepts that allow them to immediately contribute to industrial engineering and manufacturing.

Purdue University has long been recognized as a leader in fostering experiential learning through co-ops, internships, and other opportunities for industrial engagement. However, sending graduates into the chemical manufacturing workforce during an era defined by Industry 4.0 necessitates equipping them with relevant skills for evolving industrial landscapes. To equip students properly, universities must critically evaluate their core curricula and integrate data-centric and digitally focused material alongside traditional engineering education, transitioning academic programs into the realm of Education 4.0 [7]. Recognizing this need, Purdue's Davidson School of Chemical Engineering leveraged its strong process systems engineering community to develop an innovative elective course: Smart Manufacturing. This course is designed with several features that enhance accessibility across physical, generational, computational, and disciplinary boundaries. By welcoming a diverse range of learners—from different ages, backgrounds, and disciplines—this elective provides an inclusive platform to engage with Industry 4.0 concepts. The course has successfully run for six semesters at Purdue University and continues to evolve, reflecting technological advancements to ensure students remain at the forefront of smart manufacturing education.

The following sections of this article will explore the course's key features, assignments, and guiding philosophies that contribute to its success, making it a valuable and adaptable model for other institutions aiming to bridge the gap between academia and the demands of Industry 4.0.

## COURSE DESCRIPTION

### Course Philosophy

This course surveys the tools and techniques which are relevant to support the multiple levels of technical decisions that arise in modern integrated operation of manufacturing resources in the chemical, petrochemical and pharmaceutical industries. The real time generation and sharing of associated data and knowledge via relevant IT methodology and the effective use of this information in the various levels of the process operations management hierarchy are currently termed Industry 4.0 (Europe) and Smart Manufacturing (US). The topics covered in the course span all the technical components and decision levels in the operations decision hierarchy. Topics include the role of on-line and at-line process measurements, elements of sensor network design, information systems to support process operations, plant data reconciliation, detection and diagnosis of process faults, condition-based monitoring of plant assets, plant wide control, real time process optimization, production planning and scheduling, and supply chain management. Each topic is addressed by first summarizing the basic role and scope of that component, then discussing the elements of the decision problem, and outlining some representative tools available to address that decision problem. Each major topic includes a lecture given by an industrial practitioner who offers a perspective on the state of industrial practice.

### Learning Outcomes

The Smart Manufacturing elective communicates a short list of learning outcomes to each student to serve as a target for the minimum goals that should be achieved over the course of the semester. They are as follows:

- Explain the key decisions that are made at each level of the operational hierarchy of an integrated process system.
- Define what the various types of manufacturing and enterprise data are, how they are generated and managed and what their functions are in supporting these decisions.
- Explain the role of models in supporting the decisions made at each level of the operational hierarchy.
- Evaluate and improve a plant wide control system for a given manufacturing system.
- Identify condition-based monitoring of a manufacturing system, how it is performed and what its outcomes should be.
- Explain the nature and role of planning and scheduling models and tools as applied at the plant and supply chain levels.

### Critical Features

The success of the Smart Manufacturing elective can be attributed to several strategic course and curriculum design decisions. A few key elements that distinguish this course and contribute to its ongoing success are particularly noteworthy.

Firstly, offering this course exclusively online as an asynchronous learning opportunity enables access for engineers who are already in the field or industry, often with several years of professional experience. This format allows them to explore Industry 4.0 tools and gain insights relevant to their roles without the need to enroll in a traditional, in-person degree program. Such flexibility

is particularly valuable for experienced professionals, including older generations of engineers, who might otherwise find it challenging to engage in further education.

Another unique aspect of the course is the deliberate emphasis on open-source software packages, particularly those based in Python. These packages are integrated into various assignments and projects, ensuring that students gain proficiency in tools that remain accessible after their time at Purdue. This approach significantly enhances the transferability and adaptability of the skills learned, enabling integration into the industrial workflows of their (future) employers.

Finally, a critical factor in the course's success is the commitment to frequent and thorough updates to the curriculum. As the field of smart manufacturing evolves, new tools emerge, existing software packages improve, and industry standards shift. Staying current with these advancements is essential for a course centered on cutting-edge technologies. Regular updates ensure that students are equipped with the most relevant and advanced knowledge, keeping pace with the rapidly changing landscape of smart manufacturing. These foundational principles—broad accessibility, the use of open-source tools, and a commitment to staying at the forefront of technological advancements—are integral to the continued success and impact of the Smart Manufacturing elective.

## Course Audience

The Smart Manufacturing elective is a 500-level elective course (for both undergraduate- and graduate-level students) offered through the School of Chemical Engineering although students across departments and education levels are encouraged to enroll. As a result, our student body actively enrolled in the course spans undergraduate, graduate (Master's and Ph.D.), and adult learners across multiple departments ranging from Industrial Pharmacy to Mechanical Engineering to Industry.

# PROJECT DESCRIPTIONS

## Data Reconciliation

The efficiency, safety, and overall success of chemical manufacturing operations rely on several critical factors, including robust process controls, effective monitoring, and sound process design. When sensors or process controls fail, undetected deviations can result in costly operational disruptions and potentially catastrophic safety incidents. As a result, one critical function of an operator and/or engineer is the ability to reconcile data and detect deviations. This concept appears in three of the course projects, however in this homework assignment, students are asked to approach data reconciliation through the lens of statistics, emphasizing confidence interval calculations and error minimization. The chosen application for communicating this technique was methanol synthesis reconciliation of flowrate data, represented as the network shown in Figure 1.

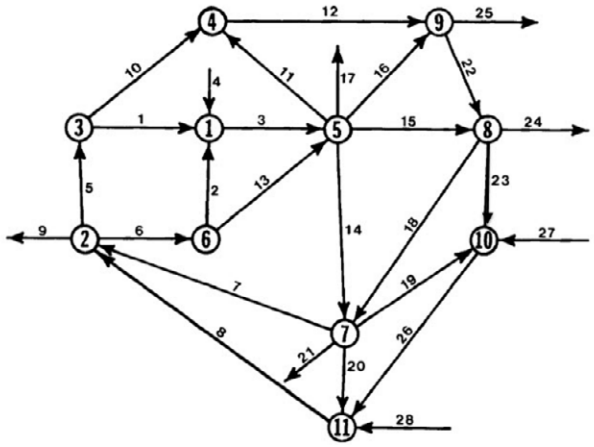



**Figure 1.** Network representation of process steam system for a methanol synthesis unit [Seth and Heenan, 1986].

After designing a simple optimization problem from the stream networks material balances, students reconcile the data by minimizing the error between the actual and desired stream flowrates. After this error function validation, students are asked to calculate the upper and lower bounds of specific stream flowrates that would have to be reached to trigger a fault. The magnitude of this range being determined by the established confidence interval.

## Chemometrics and Fault Detection

Process monitoring can allow for deviation detection when coupled with various data handling tools. However, variable correlation that enables the association of cause with effect cannot be effectively determined with all the same tools. In a homework assignment, students are asked to apply Principal Component Analysis (PCA) and Partial Least Squares (PLS) to a sensor-based dataset which contains a known fault. Students are asked to leverage the chemometric tools to identify the onset time of the fault, the associated variables, and suggest a sound engineering reason for the fault. The process schema and associated points of data collection are represented in Figure 2.

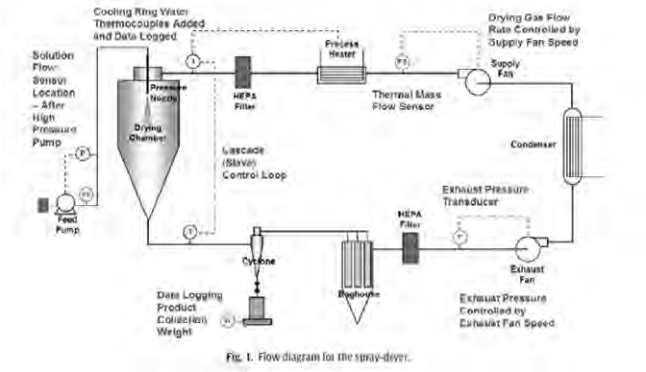



**Figure 2.** Spray-dryer flow diagram, [Garcia-Munoz S & Settell D, 2009].

This project serves as one of the most unifying projects because regardless of engineering discipline, the core descriptor of an engineer is the ability to think critically, and problem solve. Unlike other assignments where accuracy is determined by exact numerical values, this assignment is more open in terms of what is given full credit and not. One example would be after identifying that the greatest contributions to fault data were the variables "Outlet Temperature" and "Cyclone Differential Pressure" a potential engineering explanation could be but not limited to:

- Temperature sensor failure leading to fault in the cascade control loop around the spray dryer
- Clogging in the cyclone filter leading to a pressure build up and subsequent process temperature increase upstream
- Temperature sensor failure leading to unregulated temperature control, altering process conditions enough to change particle size, impacting cyclone performance

## Digital Twin Development and Process Optimization

In the age of Industry 4.0, engineers have seen a boom in the leveraging of process modeling capabilities for applications such as design space analysis, sensitivity analysis, and process optimization. However, no catch all parameters exist that can make these process models universal for all systems. As a result, the development of digital twins is required for the robust consideration of these application spaces. In pharmaceutical manufacturing specifically such analyses aid in time to submission, reduced process uncertainty in a highly regulated market and other market specific benefits. As a result, this assignment asks students to consider the critical drug substance unit operation, crystallization. One key advancement in process modeling, particularly in the context of accessible education, was the development of the open-source, python-based software package, PharmaPy. Laid out in full detail, as a component of a complimentary course, by Laky D, et al. (2023) this crystallization assignment asks students to leverage the model libraries available in PharmaPy to progress through:

- Model Discrimination
- Parameter Estimation

Students then finalize the development of a system/species specific digitial twin which is then applied to single and multiple objective process optimization. Since students have previously been introduced to confidence interval calculations and error minimization in the first assignment, the learning curve for parameter estimation is reduced and allows for students to more fully engage with the process of model discrimination, and digital twin development without being a barrier to entry. Additionally, conducting this assignment through the usage of Jupyter notebooks reduces the computational learning curve for students that are beginners and novices in Python based coding [8]. An example of one of the process optimization prompts is illustrated in Figure 3, where students are asked to optimize a cooling temperature profile (linear and quadratic) to either minimize or maximize a predetermined set of critical quality attributes for drug substance manufacturing.

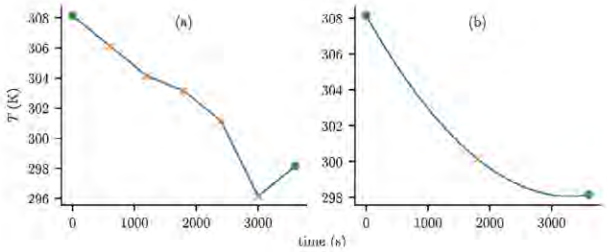



**Figure 3.** Examples of piecewise linear (a) and quadratic (b) temperature profiles. Internal points are equidistant decision variables marked orange 'x' symbols.

## Machine Learning

The influence of artificial intelligence (AI) and machine learning (ML) are widespread, impacting many aspects of modern life, particularly in manufacturing. These technologies offer significant potential for growth, enabling advancements in decision-making processes and accelerating the pace at which those decisions are made. At the early stage of launching the Smart Manufacturing elective, AI and ML were still emerging, especially in terms of their representation in academic literature. Consequently, our machine learning-based assignment was intentionally designed to be straightforward. Students were tasked with exploring two distinct datasets: one related to regression (solubility

data) and another focused on classification (drug product quality data). Using these datasets, students developed machine learning models tailored to each scenario, providing a practical introduction to AI/ML applications in manufacturing.

Future iterations of this assignment will incorporate more advanced and challenging evaluations of AI and ML applications in the context of manufacturing. For example, a potential assignment could involve analyzing *in-situ* concentration trends as determined from raw analytical data using a machine learning model, and comparing the results to a chemometric based model such as PLS regression. A critical aspect of this evaluation is the ability to determine trade-off points, resource intensity, and overall payoffs when comparing the two choices.

This approach explores the ongoing trend of using Industry 4.0 tools to address persistent manufacturing challenges while fostering an understanding that no single tool is universally applicable. Such assignments aim to enhance students' ability to make informed, scientifically grounded decisions, a critical skill for all engineers working in manufacturing and industry-based roles.

### Planning and Scheduling

Engineering process planning and scheduling is a long-established and critical aspect of process design and operation, essential for effective resource allocation and timing. While this skill is a common component of undergraduate engineering curricula (typically addressed in design courses), it is often taught with unbounded or flexible constraints. In contrast, industrial planning and scheduling problems are often highly constrained, requiring optimization procedures that can identify and explore this smaller feasible space. To bridge this gap, the penultimate assignment in this course involves a self-guided development of a knapsack problem [6]. Students are provided with specific constraints to follow, but the application and subject matter of their knapsack problem are entirely self-determined. This approach encourages students to critically evaluate real-world situations where a knapsack formulation would be valuable, such as equipment budgeting or resource allocation. As part of the assignment, students are required to construct a branch-and-bound tree for their problem, offering a visual representation of their solution process. Additionally, students are introduced to the concept of NP-completeness and other advanced algorithmic concepts, which are often absent from traditional undergraduate education but are increasingly relevant in modern industrial manufacturing.

### Final Project

The planning and scheduling assignment serves as a capstone for the course prior to the final project. It emphasizes how every decision an engineer makes in manufacturing has upstream and downstream impacts. While engineers are often responsible for individual operations, decisions ranging from sensor placement to data handling, model building, and final planning and scheduling are interconnected. The final project is designed to reinforce these ideas by challenging students to think holistically about how Industry 4.0 advancements can positively influence the manufacturing environment. Students are asked to propose an engineering problem or application and develop a solution using at least two of the concepts introduced during the course. This open-ended approach fosters creativity, critical thinking, and a deeper understanding of how these tools can interact to address complex engineering challenges effectively.

Past project examples have included:

- PCA evaluation for identifying UV wavelength unique to a specific molecule coupled with PLSR for in-situ concentration modeling
- Machine learning evaluation of fitted kinetic parameters for pattern detection of parameter coupling
- Plantwide control schema coupled with sensor prioritization via scheduling decision making
- Batch versus continuous manufacturing evaluations following the development of a reaction with isolation process digital twin
- Fault detection from historic wind farm data and proposed process control schemas for switching between energy systems in the case of successful fault detection

Through these strategically designed assignments, students are equipped to think beyond isolated tasks, understanding how their decisions contribute to the broader manufacturing process and how moving forward they can leverage modern tools to improve industrial operations. In unique cases, this project gives non-traditional students the opportunity to apply smart manufacturing techniques to their real-life plant data and current vocational challenges to test the appropriate digital tools and innovate new workflows for their given industrial discipline.

## ADJACENT COURSE DEVELOPMENT

Integration of the software tool PharmaPy into the Smart Manufacturing elective catalyzed student inquiries about process modeling outside of software encountered in undergraduate education like flowsheet packages. Encouraged by this and developed alongside an additional course offered at Purdue University through the school

of chemical engineering is CHE 553 - Pharmaceutical Process, Development and Design. This course focuses on similar process systems engineering challenges but dives deeper into pharmaceutical processes only and covers multiple unit operations, all using PharmaPy within Jupyter notebooks [8].

## CONCLUSIONS

As digitalization increases in industry, the preparation of students for the new challenges of manufacturing in the Industry 4.0 era is paramount. We present six modules that address industrially relevant problems which can be solved with the implementation of smart manufacturing techniques. Such approaches do not exist within the inherited and established core curriculum across engineering, and in particular chemical engineering. The introduction of such modules in parallel with the curriculum and teaching philosophy presented in this manuscript have proven to successfully advance the industrial preparedness of undergraduate, graduate, and non-traditional students at Purdue University.

The Smart Manufacturing elective described in this manuscript can be readily developed by other universities. Manufacturing-based alumni can offer guest lectures to connect course concepts to practice. A Smart Manufacturing course is valuable for advanced undergraduate, graduate, and practitioner learning. Given the rapid pace of technology change, instructors should be prepared to evolve the course and assignments. Purdue University offers the Smart Manufacturing course as an elective every semester to 20-40 students.

## REFERENCES


1. Zhou R, Le Cardinal, J. Exploring the Impacts of Industry 4.0 From a Macroscopic Perspective. International Conference on Engineering Design. Delft, The Netherlands (2019)
2. Davis J, Edgar T, Graybill R, Korambath P, Schott B, Swink D, … & Wetzel J. Smart Manufacturing. *Annual Review of Chemical and Biomolecular Engineering* (2015)
3. Assante D, Caforio A, Flamini M, & Romano E. Smart Education in the Context of Industry 4.0. *IEEE Global Engineering Education Conference* (2019)
4. Garcia-Munoz S. https://github.com/salvadorgarciamunoz/pyphi.
5. Casas-Orozco D, Laky D, Wang V, Abdi M, Feng X, Wood E, … & Nagy ZK. PharmaPy: An object-oriented tool for the development of hybrid pharmaceutical flowsheets. *Computers & chemical engineering* (2021)
6. Pekny JF. Algorithm Architectures to Support Large Scale Process Systems Engineering Applications Involving Combinatorics, Uncertainty, and Risk Management. *Computers and Chemical Engineering*. 26:2:239-267 (2002)
7. Hernandez de Menendez M, Escobar C, Morales-Menedez, R, Engineering education for smart 4.0 technology: a review. *International Journal on Interactive Design and Manufacturing* 14:3 (2020)
8. Laky D, Casas-Orozco D, Abdi M, Feng X, Wood E, Reklaitis GV, Nagy ZK, Using PharmaPy with Jupyter Notebook to teach digital design in pharmaceutical manufacturing. *Computer Applications in Engineering Education*. 31:6:1662-1677 (2023)
9. Garcia-Munoz S & Settell D, Application of multivariate latent variable modeling to pilot-scale spray drying monitoring and fault detection: Monitoring with fundamental knowledge. *Computers and Chemical Engineering*. 33:2106-2110 (2009)



© 2025 by the authors. Licensed to PSEcommunity.org and PSE Press. This is an open access article under the creative commons CC-BY-SA licensing terms. Credit must be given to creator and adaptations must be shared under the same terms. See https://creativecommons.org/licenses/by-sa/4.0/




# Section 9

## PSE4Food and Biochemical

Systems & Control Transactions

**Research Article - Peer Reviewed Conference Proceeding**
ESCAPE 35 - European Symposium on Computer Aided Process Engineering
Ghent, Belgium. 6-9 July 2025
Jan F.M. Van Impe, Grégoire Léonard, Satyajeet S. Bhonsale,
Monika E. Polańska, Filip Logist (Eds.)

PSE PRESS

# Valorization of suspended solids from wine effluents through hydrothermal liquefaction: a sustainable solution for residual sludge management

**Carlos E. Guzmán Martínez [a], Sergio I. Martínez Guido [a], Valeria Caltzontzin Rabell [a], Salvador Hernández [b], and Claudia Gutiérrez Antonio [a]***

[a] Universidad Autónoma de Querétaro, Facultad de Ingeniería, Querétaro, Querétaro, México
[b] Universidad de Guanajuato, Departamento de Ingeniería Química, Guanajuato, Guanajuato, México
* Corresponding Author: claudia.gutierrez@uaq.mx

## ABSTRACT

The growing concern over the environmental impacts of the wine industry has driven the search for sustainable technologies to manage its waste, particularly the residual sludge generated during effluent treatment. This sludge, rich in organic matter, represents a significant source of pollution if not properly treated. However, their energy content allows them to turn this environmental liability into an asset through innovative valorization. Hydrothermal liquefaction (HTL) emerges as a promising technology in this context. This process allows the direct conversion of residual sludge into high-energy-value liquid biofuels. Unlike other treatment methods, HTL can process wet biomass without needing prior drying, making it particularly suitable for managing sludge from wine effluents. Thus, this research aims to evaluate the conversion of residual sludge derived from wine effluent treatment into biofuels through a hydrothermal liquefaction simulation, integrating this process into a sustainable biorefinery for levulinic acid and bioethanol production. The methodology considers the determination of the composition and treatment of the wine effluent to define a case study. The biorefinery processes, as well as the HTL, are designed and simulated in Aspen Plus V.14, and also they are evaluated technically and economically. As a result, levulinic acid, sustainable aviation fuel, bioethanol, propylene glycol, and electrical energy are produced. In addition, the biorefinery reduces the effluent's Chemical Oxygen Demand (COD) by 99%. In conclusion, valorizing suspended solids from wine effluents through HTL is technically and economically feasible.

**Keywords**: Hydrothermal liquefaction, Biorefinery, Wine effluents, Sludge valorization, Aspen Plus V.14.

## INTRODUCTION

The winemaking industry releases large quantities of waste, being wine effluents between them. According to Buitron et al. (2019) [1], the ratio of wastewater per liter of wine produced is 2-4. Due to its features, the effluent is treated by using biological processes, such as anaerobic fermentation [1]; unfortunately, the organic material remotion in wastewater generates considerable quantities of sludge, which represents a significant source of pollution if it is not adequately treated [2]. Sludge derived from effluent treatment can be valorized to generate new products. In the literature, several alternative processes for treating sludge are reported. These processes are feasible from a technical point of view, but they fail to reach economic viability. In this context, the concept of biorefinery arises. A biorefinery is an implemented process involving unit operations aiming to transform raw materials, mainly biological ones, into a wide range of value-added products, biofuels, energy, or renewable materials [3].

Among the value-added products, levulinic acid is highlighted. The National Renewable Energy Laboratory identifies 12 essential chemical compounds, which are value-added products that can be produced from sugars through biological or chemical conversions; among these

compounds is levulinic acid. This component presents enormous economic potential because it is a raw material of various industrially important chemicals, such as methyl-tetrahydrofuran [4]. Besides, levulinic acid is a value-added product used in producing nylon, synthetic rubbers, plastics, and pharmaceuticals.

On the other hand, biofuels and chemicals, bioethanol, sustainable aviation fuel, and propylene glycol are of interest due to their wide applications in the industrial sectors. Bioethanol is a liquid biofuel from renewable biomass sources such as agricultural waste, winery effluent, and lignocellulosic residues. Its increasing use in the energy matrix addresses the need to reduce dependence on fossil fuels and lower greenhouse gas emissions, thereby contributing to climate change mitigation and energy sustainability [5]. Moreover, propylene glycol and dipropylene glycol are used as an antifreeze liquid in airplane engines. Employing ethylene oxide hydration and propylene oxide hydration can produce a mixture of glycols that have an industrial value [5]. Finally, sustainable aviation fuel is the best alternative for decarbonizing the aviation sector.

Therefore, this work proposes using sludge derived from wine effluent treatment to produce levulinic acid, bioethanol, propylene glycol, and sustainable aviation fuel. To the authors' knowledge, this approach has not been reported in the literature. For this, a biorefinery is modeled and simulated, considering hydrothermal liquefaction; this last technology is a promising solution to transform wet biomass, such as sludge, into valuable bio-oil, offering advantages like waste volume reduction, energy recovery, and decrement of greenhouse gas emission [6].

## METHODOLOGY

The research is divided into six stages:

1. Definition of a case study. It consists of considering a calculous base that represents an actual situation; according to that, the process feed stream is chemically characterized using literature searching.
2. Development of a conceptual design for biorefinery. It proposes the products obtained from the raw material stream and the unit operations needed to reach them.
3. Compilation of thermodynamic and chemical kinetic data. Through a literature search, chemical kinetic parameters and equations are joined to describe reactors' behavior. In addition, thermodynamic parameters are taken to guarantee a close approach to actual process performance. Carlson algorithm has been employed to define thermodynamic models in each unit operation [7].
4. Aspen Plus V.14 simulation. Using rigorous models, the conceptual design of biorefinery is simulated in Aspen Plus V.14.
5. Parametric analysis. Sensitivity analyses are carried out for each unit operation to define the final values of manipulated variables.
6. Technical and economic evaluation. Technic and economic parameters are calculated to evaluate the biorefinery performance. These are described by equations (1 - 12). Equipment costs are estimated by using the Guthrie method [8]. In addition, chemical oxygen demand (COD) is calculated using Aspen Plus V. 14 as a technical and environmental indicator.

$$rec = \frac{oms}{fms} \quad (1)$$

$$cv = \frac{r_{in} - r_{out}}{r_{in}} \quad (2)$$

$$Yd = \frac{pmf}{tpm} \quad (3)$$

$$pmr = \frac{mp}{rmm} \quad (4)$$

$$PFT = (Ah)(psale - rmc - UC_T) - (\mathrm{k})(\mathrm{EC}) \quad (5)$$

$$psale = \sum_1^j \left((mp_j)(pp_j)\right) \quad (6)$$

$$rmc = \sum_1^g \left((rmm_g)(prmm_g)\right) \quad (7)$$

$$UC_T = \sum_1^i UC_i \quad (8)$$

$$k = \frac{i(1+i)^n}{(1+i)^n - 1} \quad (9)$$

$$EC = C_2 = C_1\left(\frac{I_2}{I_1}\right) \quad (10)$$

$$C_{BM} = C_P^{\circ}(B_1 + B_2 F_M F_P) \quad (11)$$

$$Log_{10} C_P^{\circ} = K_1 + K_2 Log_{10}(\mathrm{A}) + K_3 (Log_{10}(\mathrm{A}))^2 \quad (12)$$

Where: rec = component recuperation, oms = output mass flow (kg/h), fms = feed mass flow (kg/h), cv =conversion, $r_{in}$ = reactant input to process (mol/h), $r_{out}$ = reactant output to process (mol/h), Yd = Yield, pmf = moles of desired product formed (mol), tpm = theoretical product moles (mol), pmr = product mass ratio, mp = product mass flow (kg/h), rmm = raw material mass flow (kg/h), PFT= Annual profit (USD/y), Ah = hours per year (8,766 h/y), PSALE = product sale (USD/h), RMC = raw material cost (USD/h), UCT = Utilities total cost (USD/h), k = annualization factor, EC = Equipment cost (USD), pp = product price (USD/kg), prmm = raw material price (USD/kg), UC = Utility cost, i = interest rate (10 %), n = project life period (20 years), $C^{\circ}_p$ = Equipment base cost (USD), A = capacity or measurement parameter for the equipment, ($K_1$, $K_2$, $K_3$, $B_1$, $B_2$,) = Guthrie's constants, $F_M$ = material factor, $F_P$ = pressure factor, $C_{BM}$ = module cost (USD), $C_1$ = Equipment cost at reference time (USD), $C_2$ =

Cost of equipment in the desired time (USD), $I_1$ = Reference time cost index, $I_2$ = Desired Time Cost Index. Subscripts: j = product stream, g = raw material stream, i = utility. It is important to mention that utility costs are calculated by using Aspen Plus V.14 software.

Table 1 shows the wine effluent composition. The solids, which are considered the sludge's main components, are represented by cellulose ($C_6H_{10}O_5$), hemicellulose ($C_5H_8O_4$), lignin ($C_{7.3}H_{13.9}O_{1.3}$), and lees (dead yeast, $CH_{1.83}O_{0.56}N_{0.17}$) [9].

**Table 1:** Comparison between wine effluent and treated water.

| Parameter | Wine effluent | Treated water |
|---|---|---|
| Mass Flow (kg/h) | 10,000 | 4,333.16 |
| Water (% mass) | 71.76 | 99.99 |
| Ethanol (% mass) | 7.39 | 0 |
| Glucose(% mass) | 5.26 | 0 |
| Solid (% mass) | 15.59 | 0 |
| COD (PPM) | 210,052 | 32.19 |

Figure 1 represents the conceptual biorefinery. Wine effluent is fed to process through a decanter tank (DCT-01), where some solids are separated from the liquid matrix. NRTL is employed as a thermodynamic model for this unit operation. The remaining solids in the liquid phase are sent to the centrifuge (CN-01). This equipment uses NRTL as thermodynamic model. Liquid flow coming from CN-01 goes to reactive distillation column # 1 (RD-01); on the other side, the solids from CN-01 are mixed with those coming from DCT-01 to be pumped and heated for reaching the operational conditions in hydrothermal liquefaction reactor (R-01).

The liquid phase of water, ethanol, and glucose feeds RD-01. Inside the reactive column reactions (1) and (2), are carried out, Table 2. The kinetic parameters are taken from the literature [4]. Glucose is transformed to 5-Hydroximetilfurfural, then converted to levulinic acid and formic acid. For RD-01 modeling, the Rad Frac block and NRTL thermodynamic model are employed. The RD-01 top releases ethanol and water to a conventional distillation column (DC-03). Moreover, the stream coming from the RD-01 bottom is constituted by levulinic, formic, and sulphuric acids; this stream is fed to DC-01, a conventional distillation column that separates formic acid from the acid mixture.

DC-01 is modeled by Rad Frac block and uses NRTL as a thermodynamic model. DC-01 bottoms are directed to DC-02, where levulinic acid is separated from the mixture that contains the catalyst, $H_2SO_4$. DC-02 is simulated with the same rigorous models as DC-01. The catalyst is recirculated to RD-01.

DC-03 purifies the water by releasing all the organic compounds, mainly ethanol and traces of formic acid, from its top. From the DC-03 bottom, treated water is obtained. The thermodynamic model employed is Wilson, and Rad Frac block is used.

RD-02 receives the diluted ethanol, 53.94 % mass from DC-03, and propylene oxide as raw material. Inside this reactive column, reactions (3) and (4) are carried out [5], Table 2. The water reacts with propylene oxide to get propylene glycol. In addition, propylene oxide reacts with propylene glycol to produce dipropylene glycol. Rad frac block and NRTL thermodynamic model are used. Kinetic parameters are obtained from the literature [5]. On the RD-02 top, bioethanol production is reached, while glycols are released on the RD-02 bottom. It is important to mention that the glycol stream is coupled to the organic Rankine cycle, which uses R235FA as a working fluid to get electrical power; this aims to reduce electrical utility consumption.

**Table 2:** Reactions carried out in reactive distillation columns.

| Reaction | # |
|---|---|
| $C_6H_{12}O_6 \xrightarrow{H_2SO_4} C_6H_6O_3 + 3H_2O$ | (1) |
| $C_6H_6O_3 + 2H_2O \rightarrow C_3H_8O_3 + CH_2O_2$ | (2) |
| $C_3H_6O + H_2O \rightarrow C_3H_8O_2$ | (3) |
| $C_3H_6O + C_3H_8O_2 \rightarrow C_6H_{14}O_3$ | (4) |

R-01 is represented by the RBatch block and Peng-Robinson thermodynamic model. The solid compounds are transformed into biogas, bio-oil, and aqueous phase [10-11]. Operational conditions reached by R-01 are 400 °C and 220 bar. Reactions are described in Table 3. The kinetic parameters are taken from the literature [12].

Once products are obtained from R-01, they are separated using Flash Tank #1 (FL-01). FL-01 is modeled through a Sep block and NRTL thermodynamic model. Operational conditions are 20 °C and 1 bar.

The biogas and aqueous phases are considered by-products. The bio-oil is sent to the up-grading process in reactor #2 (R-02), the hydrotreatment. R-02 is a batch reactor, represented by RBatch block and Peng-Robinson thermodynamic model. It operates at 450 °C and 20 MPa. The reactions involved are those shown in Table 4. Kinetic parameters are taken from the literature [13]. At the end of this unit operation, residual gas (mainly $H_2$), biofuel, and aqueous phase are obtained. The mixture goes to Flash Tank #2 (FL-02).

A Sep block represents FL-02 and uses the NRTL thermodynamic model. Operation conditions are 30 °C and 1.52 bar. The biofuel stream is fed to conventional distillation column #4 (DC-04). DC-04 separates naphtha from the top and sustainable aviation fuel (biojet fuel) by the column bottoms. This column uses a Rad frac block and BK-10 as thermodynamic models.

**Table 3:** Reactions carried out in hydrothermal liquefaction reactor.

| Reaction | # |
|---|---|
| $C_{73}H_{139}O_{13} \rightarrow 0.4475C_{12}H_{16}O + 0.8525H_2O + 1.93CH_4$ | (5) |
| $C_{73}H_{139}O_{13} \rightarrow 0.4068C_{14}H_{12} + 1.3H_2O + 1.6045CH_4$ | (6) |
| $C_{73}H_{139}O_{13} \rightarrow 0.3729C_{15}H_{14}O + 0.9271H_2O + 1.7063CH_4$ | (7) |
| $C_{73}H_{139}O_{13} \rightarrow 0.6885C_8H_8O + 0.6115H_2O + 1.7923CH_4$ | (8) |
| $C_{73}H_{139}O_{13} \rightarrow C_6H_6 + 3.95H_2 + 1.3CO$ | (9) |
| $C_{73}H_{139}O_{13} \rightarrow 0.7417C_8H_8O + 0.1397C_6H_{10}O_4 + 2.0138CH_4$ | (10) |
| $C_6H_{10}O_5 \rightarrow C_5H_4O_2 + CO + 2H_2O + H_2$ | (11) |
| $C_6H_{10}O_5 \rightarrow C_5H_8O_3 + CO_2 + H_2$ | (12) |
| $C_6H_{10}O_5 \rightarrow 0.48C_8H_{18} + 2.16CO_2 + 0.68H_2O$ | (13) |
| $C_6H_{10}O_5 \rightarrow 0.4286C_9H_{20} + 2.1429CO_2 + 0.7143H_2O$ | (14) |
| $C_6H_{10}O_5 \rightarrow 0.3871C_{10}H_{22} + 2.129CO_2 + 0.7419H_2O$ | (15) |
| $C_6H_{10}O_5 \rightarrow C_2H_6O + C_2H_4O + CO + CO_2$ | (16) |
| $C_6H_{10}O_5 + 3H_2O \rightarrow 2CH_2O_2 + 2C_2H_4O_2 + 2H_2$ | (17) |
| $C_3H_8O_4 \rightarrow C_5H_4O_2 + 2H_2O$ | (18) |
| $C_3H_8O_4 \rightarrow C_5H_8O_3 + O_2$ | (19) |
| $C_3H_8O_4 \rightarrow 0.4C_8H_{18} + 1.8CO_2 + 0.4H_2O$ | (20) |
| $C_3H_8O_4 \rightarrow 0.3571C_9H_{20} + 1.7857CO_2 + 0.4286H_2O$ | (21) |
| $C_3H_8O_4 \rightarrow 0.3226C_{10}H_{22} + 1.7742CO_2 + 0.4516H_2O$ | (22) |
| $C_3H_8O_4 \rightarrow 2C_2H_4O + CO_2$ | (23) |
| $C_3H_8O_4 \rightarrow C_2H_6O + 3CO + H_2$ | (24) |
| $C_3H_8O_4 + 2H_2O \rightarrow CH_2O_2 + 2C_2H_4O_2 + H_2$ | (25) |
| $CH_{1.83}O_{0.56}N_{0.17} \rightarrow 0.09C_4H_5N + 0.49H_2 + 0.48CO + 0.08C_2H_5ON$ | (26) |
| $CH_{1.83}O_{0.56}N_{0.17} \rightarrow 0.06C_4H_4N_2 + 0.05C_4H_9N + 0.57H_2 + 0.56CO$ | (27) |
| $CH_{1.83}O_{0.56}N_{0.17} + 0.34H_2O \rightarrow 0.2667C_3H_6O_3 + 0.17NH_3 + 0.1C_2H_4O$ | (28) |
| $CH_{1.83}O_{0.56}N_{0.17} \rightarrow 0.0647C_8H_{18} + 0.4824CO + 0.0776H_2O + 0.17NH_3$ | (29) |
| $CH_{1.83}O_{0.56}N_{0.17} \rightarrow 0.0579C_9H_{20} + 0.4789CO + 0.0811H_2O + 0.17NH_3$ | (30) |
| $C_6H_{12}O_6 \rightarrow C_5H_4O_2 + CO + 3H_2O + H_2$ | (31) |
| $C_6H_{12}O_6 \rightarrow C_5H_8O_3 + CH_2O_2 + H_2O$ | (32) |
| $C_6H_{12}O_6 \rightarrow 0.48C_8H_{18} + 2.16CO_2 + 1.68H_2O$ | (33) |
| $C_6H_{12}O_6 \rightarrow 0.4286C_9H_{20} + 2.1429CO_2 + 1.7143H_2O$ | (34) |
| $C_6H_{12}O_6 \rightarrow 0.3871C_{10}H_{22} + 2.129CO_2 + 1.7419H_2O$ | (35) |
| $C_6H_{12}O_6 \rightarrow C_2H_6O + C_2H_4O + H_2 + 2CO_2$ | (36) |

## RESULTS

As the study case, the wine effluent generated in a year by the Baja, California, Mexico wine industry is considered because this Mexican State generates 80% of national production [14,15]. Table 1 shows the study case's effluent characterization and the mass flow rates. Moreover, Table 5 shows the obtained products through the biorefinery scheme.

According to Table 5, water, glycols, bioethanol, biogas, and levulinic acid represent 58.12%, 23.9%, 6.5%, 3.89%, and 2.94% of the total production, respectively. These results are consistent with the inputs; the most abundant compound in wine effluents is water, which justifies that water has the highest value. The percentage of glycols comes from the reaction between the attached water in the diluted ethanol stream at the DC-03 dome outlet and the supplied propylene oxide. Although the solid presence is higher than ethanol and glucose in wine effluent, bioethanol and levulinic acid production are more significant than the biofuels (naphtha and sustainable aviation fuel) from sludge hydrothermal liquefaction. The cause is that not all solids produce bio-oil to upgrade to biofuels because they have both aqueous phase and biogas production; thus, bioethanol and levulinic acid production are more significant than liquid biofuels.

**Table 4:** Reactions carried out in bio-oil hydrotreatment reactor.

| Reaction | # |
|---|---|
| $C_{12}H_{10}O + 9H_2 \rightarrow C_{12}H_{28} + H_2O$ | (37) |
| $C_{12}H_{10}O + 8H_2 \rightarrow C_{12}H_{24} + H_2O$ | (38) |
| $C_{14}H_{12} + 9H_2 \rightarrow C_{14}H_{30}$ | (39) |
| $C_{14}H_{12} + 10H_2 \rightarrow 2C_7H_{16}$ | (40) |
| $C_6H_6 + 4H_2 \rightarrow C_6H_{14}$ | (41) |
| $C_6H_6 + 3H_2 \rightarrow C_6H_{12}$ | (42) |
| $C_8H_8O + 6H_2 \rightarrow C_8H_{18} + H_2O$ | (43) |
| $C_8H_8O + 5H_2 \rightarrow C_8H_{16} + H_2O$ | (44) |
| $C_{15}H_{14}O + 10H_2 \rightarrow C_{15}H_{32} + H_2O$ | (45) |
| $C_{15}H_{14}O + 9H_2 \rightarrow C_{15}H_{30} + H_2O$ | (46) |
| $C_4H_5N + 4H_2 \rightarrow C_4H_{10} + NH_3$ | (47) |
| $C_4H_5N + 3H_2 \rightarrow C_4H_8 + NH_3$ | (48) |
| $C_4H_4N_2 + 6H_2 \rightarrow C_4H_{10} + 2NH_3$ | (49) |
| $C_4H_4N_2 + 5H_2 \rightarrow C_4H_8 + 2NH_3$ | (50) |
| $C_4H_9N + 2H_2 \rightarrow C_4H_{10} + NH_3$ | (51) |
| $C_4H_9N + H_2 \rightarrow C_4H_8 + NH_3$ | (52) |
| $C_5H_4O_2 + 6H_2 \rightarrow C_5H_{12} + 2H_2O$ | (53) |
| $C_5H_4O_2 + 5H_2 \rightarrow C_5H_{10} + 2H_2O$ | (54) |
| $C_5H_8O_3 + 5H_2 \rightarrow C_5H_{12} + 3H_2O$ | (55) |
| $C_5H_8O_3 + 4H_2 \rightarrow C_5H_{10} + 3H_2O$ | (56) |

**Table 5:** Product mass flow

| Product | Mass flow (kg/h) |
|---|---|
| Biogas | 290.32 |
| Naphtha | 90.14 |
| Sustainable aviation fuel | 158.22 |
| Levulinic acid | 219.05 |
| Bioethanol | 485 |
| Water | 4,333.16 |
| Glycols | 1,781.68 |
| Formic acid | 93.5 |
| Residual gas | 5.03 |

Table 6 shows the technical indicators obtained. It is essential to highlight the conversion of solids and glucose that reach 100%. This means finding a sustainable solution for managing all residual sludge in treating wine effluents is possible. Water recuperation seems to have a low value; however, a water mass flow is consumed in glycol production, and another part goes to the aqueous phase, with the mass balance of ethanol, in the sludge hydrothermal liquefaction. The glycol yield is attractive because it is greater than 95 %. The levulinic acid yield may not seem good enough. However, it has to be highlighted that the reaction to obtain levulinic acid involved the production of formic acid, so it represents an attractive yield for reaching a value higher than 50%.

The ratios obtained in Table 6 give the impression that they are too small, though as shown in Table 1, the mass flow of wine effluent is several times greater than the obtained products. In addition, water is the main component of wine effluent, and it does not directly contribute to almost all products except glycol production; it

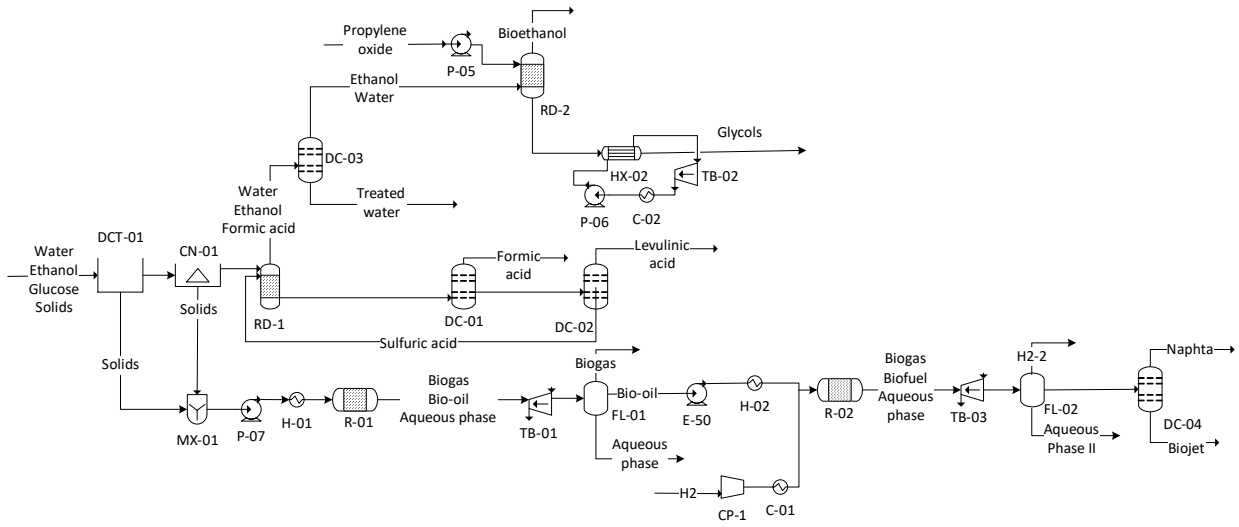



**Figure 1:** Biorefinery scheme. Where DCT=Decanter tank, CN= Centrifuge, RD= Reactive distillation column, DC= Distillation column, R= reactor, FT= Flash tank, MX= Mixer, TB=Turbine, C= condenser, P= Pump, CP= Compressor, HX= Heat exchanger, MX= Mixer.

provokes ratios that seem too insignificant. It does not happen with glycol production, where water is a reactant.

**Table 6:** Technical indicators

| Parameter | Value |
|---|---|
| $rec_{Water}$ | 60.38 % |
| $rec_{Ethanol}$ | 65.63 % |
| $cv_{Glucose}$ | 100 % |
| $cv_{Solids}$ | 100 % |
| $Yd_{Levulinic\ acid}$ | 64.63 % |
| $Yd_{Glycol}$ | 97.21 % |
| $pmr_{Biogas}$ | 0.029 |
| $pmr_{Naphtha}$ | 0.009 |
| $pmr_{Biojet}$ | 0.0158 |
| $pmr_{Levulinic\ acid}$ | 0.0219 |
| $pmr_{Bioethanol}$ | 0.0485 |
| $pmr_{Water}$ | 0.4333 |
| $pmr_{Glycols}$ | 0.1782 |
| $pmr_{Formic\ acid}$ | 0.0093 |
| $pmr_{Residual\ gas}$ | 0.0005 |
| COD removed | 99.99% |

For finishing the technical parameters, the COD reduction in treated water is so attractive because it is under the Official Mexican Standards (NOM-001-SEMARNAT-2021 and NOM-127-SSA1- 2021) that stipulate a COD level lower than 75 ppm is adequate to human use.

On the other hand, Table 7 shows the economic indicators. Regarding raw material cost, $H_2$ constitutes 50.2 % of the total, and the propylene oxide cost completes the balance. In product sales, levulinic acid gives the 86.89 % of the total, glycols the 8.86%, and bioethanol the 1.89%. Considering utility cost, the reboiler in RD-01 spent 91.52 % of the total; it is due to there being a large quantity of water and ethanol mass that has to be evaporated to separate it from the matrix with glucose, sulphuric acid, and formic acid; besides, it presents a higher reflux ratio, 20. these features consume too much energy, 136,043.28 kW.

**Table 7:** Economic indicators

| Parameter | Value |
|---|---|
| Raw material cost (USD/h) | $129.75 |
| Product sale (USD/h) | $31,010.08 |
| Levulinic acid (USD/kg) | $123 |
| Glycols (USD/kg) | $1.76 |
| Bioethanol (USD/Kg) | $1.21 |
| SAF (USD/kg) | $2.44 |
| Naphtha (USD/kg) | $1.56 |
| Biogas (USD/kg) | $1.39 |
| Utilities cost (USD/h) | $1,507.88 |
| Equipment cost (USD) | $51,335,863.95 |
| Annual equipment cost (USD/y) | $6,029,891.32 |
| Total annual cost (USD/y) | $20,385,357.23 |
| Profit (USD/y) | $251,449,023.39 |

Regarding equipment cost, RD-01 represents the most expensive by using 41.45 % of the total, followed by R-01, the hydrothermal liquefaction reactor, with 23.51%, and R-02, the bio-oil hydrotreatment reactor. RD-01 has the highest cost due to its size and operational pressure, contributing to a more considerable equipment thickness.

## CONCLUSIONS

This research presents the technical and economic feasibility of obtaining biofuels and value-added molecules through a biorefinery scheme. Different products, such as levulinic acid, bioethanol, biogas, glycols, naphtha, sustainable aviation fuel, and formic acid, are obtained from this biorefinery. This shows that the valuation of wine effluents and their sludge is possible using a biorefinery scheme.

Regarding the economic analysis, it is clear that levulinic acid production is essential in reaching the economic feasibility of wine effluent and its sludge valorization. However, expanding the range of generated products enhances the economic condition of the process, particularly when including biofuels, whose market price is lower than other higher-value-added products.

The presented strategy provides an efficient solution for waste management in the wine industry. However, a similar approach can be implemented for other sludge types. Moreover, this strategy contributes to the transition toward a circular economy by turning waste into energy-rich and value-added products.

## ACKNOWLEDGEMENTS

The authors appreciate the financial support provided by SECIHTI through the Carlos Eduardo Guzmán Martínez postdoctoral scholarship (Call: 2022 (1). Project: 2397403). Moreover, the authors appreciate the financial support of Bioproducts Sustainable Production Processes Research Group of Engineering Faculty, and the National Laboratory SECIHTI of Solid Biofuels (BIOENER) (Support LNC-2023-40).

## REFERENCES

1. Germán B, Francisco MV, and Felipe O. Biogas Production from a Highly Organic Loaded Winery Effluent Through a Two-Stage Process. BioEnergy Res., pp. 714–721 (2019).
2. Ciniza DR, et al. Mesophilic and thermophilic anaerobic co-digestion of winery wastewater sludge and wine lees: an integrated approach for sustainable wine production. Journal of environmental management, 203, 745-752 (2017).
3. Satya NN, Devesh KS, Bhushon RD, and Sunil KK. Potential and perspective of castor biorefinery. In Waste biorefinery (pp. 623-656) (2018).
4. José SS, Heriberto AG, Eduardo SR, and Juan SH. Innovative reactive distillation process for levulinic acid production and purification. Chemical Engineering Research and Design, 183, 28-40 (2022).
5. Carlos GM, Agustin CM, and Fabricio NR. Economic and environmental comparison of bioethanol dehydration processes via simulation: reactive distillation, reactor–separator process, and azeotropic distillation. *Clean Technologies and Environmental Policy*, *21*, 2061-2071. (2019)
6. Ya W, Donghai X, Mingxin X, Peiyao Z, Liangliang F, Lijian L, and Krzysztof K. Hydrothermal liquefaction of municipal sludge and its products applications. Science of The Total Environment, 168-177. (2024)
7. Eric C, Don't gamble with physical properties for simulations, Chemical engineering progress, 92(10), 35-46, (1996).
8. Richard T, Richard Bailie, Wallace W, and Joseph S. Analysis, synthesis, and design of chemical processes. Pearson Education, (2008).
9. Robert W, and Victoria P, Development of an ASPEN PLUS physical property database for biofuels components (No. NREL/TP-425-20685), National Renewable Energy Lab. (NREL), Golden, CO (United States), (1996).
10. Shengfei D, Ziyu L, and Xiaoyi Y. Hydrothermal liquefaction of biomass for jet fuel precursors: A review. Chinese Chemical Letters, 35(8), (2024).
11. Authilingam S, Sivakumar S, Kannappan P, Ramachandran S, Rajasree S, and Jayaseelan A. Review hydrothermal liquefaction aqueous phase as a valuable resource for biofuels, bio-hydrogen, and valuable bio-chemicals recovery. Chemosphere, 283, 131248. (2021).
12. Wahab M, Patrick B, and Konstantinos A. A kinetic process model for sewage sludge hydrothermal liquefaction in Aspen Plus: Model validation with pilot-plant data and scale up. Energy Conversion and Management, 302, 118136. (2024).
13. Suping Z, et al. Lumping kinetic model for hydrotreating of bio-oil from the fast pyrolysis of biomass. Energy Sources, Part A: Recovery, Utilization, and Environmental Effects, 31(8), 639-645, (2009).
14. https://www.oiv.int/es/what-we-do/country-report?oiv
15. https://uvayvino.org.mx/html/docs/produccion_consumo_vino.pdf

© 2025 by the authors. Licensed to PSEcommunity.org and PSE Press. This is an open-access article under the Creative Commons CC-BY-SA licensing terms. Credit must be given to the creator, and adaptations must be shared under the same terms. See https://creativecommons.org/licenses/by-sa/4.0/



Systems & Control Transactions

**Research Article - Peer Reviewed Conference Proceeding**
ESCAPE 35 - European Symposium on Computer Aided Process Engineering
Ghent, Belgium. 6-9 July 2025
Jan F.M. Van Impe, Grégoire Léonard, Satyajeet S. Bhonsale,
Monika E. Polańska, Filip Logist (Eds.)

PSE PRESS

# Adaptable dividing-wall column design for intensified purification of butanediols after fermentation

**Tamara Janković[a], Siddhant Sharma[b], Adrie J.J. Straathof[a] and Anton A. Kiss[a,b]***

[a] Delft University of Technology, Department of Biotechnology, Delft, The Netherlands
[b] Delft University of Technology, Department of Chemical Engineering, Delft, The Netherlands
* Corresponding Author: A.A.Kiss@tudelft.nl.

## ABSTRACT

The 2,3-, 1,4- and 1,3-butanediols (BDOs) are valuable platform chemicals traditionally produced through petrochemical routes. Alternatively, there is growing interest in synthesizing these chemicals through fermentation processes. However, several drawbacks of the fermentation process (e.g. low product concentration, formation of by-products and high-boiling temperatures of BDOs) hinder the downstream process and increase overall production costs. This original research proposes an advanced large-scale (processing capacity of 160 ktonne/y) process design for the purification of different BDOs after fermentation. The initial preconcentration step removes most water and light impurities in heat pump-assisted distillation column. The heart of the developed process is an integrated dividing-wall column that effectively separates high-purity BDO (>99.4 wt% in all cases) from the remaining impurities. Each BDO isomer was purified cost-effectively (0.208 – 0.243 $/kg$_{BDO}$) and energy-efficiently (1.854 – 2.176 kW$_{th}$h/kg$_{BDO}$) using a single process design, offering flexibility in the development of sustainable bioprocesses for BDO production.

**Keywords**: butanediols, dividing-wall column, downstream processing

## INTRODUCTION

Uncertainties related to fossil fuel-based production pathways are driving interest in developing sustainable alternatives. Fermentation emerges as a promising substitute for the petrochemical production of many chemicals. Among these potential bioproducts, butanediols (BDOs) are very important platform chemicals with a wide variety of applications (e.g. pharmaceuticals, cosmetics, softening agents, solvents, plasticizers, fertilizers, printing inks, polymers, etc.). Significant research effort has been put into developing genetically engineered microorganisms that can produce BDOs from different renewable carbon sources. So far, fermentative production of 2,3-, 1,4- and 1,3-butanediol resulted in significant product titers and may have potential for industrial-scale production. Contrarily, titers of 1,2-BDO achieved so far are very low and additional improvements in the fermentation are needed before considering scale-up. Despite the significant research on developing the upstream process, the recovery of BDOs from fermentation broth has not been nearly as promptly addressed. Given the drawbacks of the fermentation process (low product concentrations, formation of by-products, high boiling temperatures of BDOs, etc.), the costs of the separation process may significantly contribute to the total production costs.

## PROBLEM STATEMENT

Published studies on BDO recovery after fermentation mainly focus on 2,3-BDO, with comparatively less research dedicated to the recovery of other BDOs. Due to the complex composition of the fermentation broth and high boiling point of BDO products, several steps are required in downstream processing. Consequently, costs of the purification process may significantly contribute to the total production costs [1]. Different techniques have been considered for the separation of BDO from fermentation broth (e.g. solvent extraction, salting-out extraction, sugaring-out extraction, reactive extraction, pervaporation, etc.) [1–5]. Nonetheless, these methods have some drawbacks that hinder effective large-scale

implementation (low product recovery, large amounts of required solvent, subsequent solvent recovery, large amounts of salting-out agents, potential solvent toxicity, significant waste production, membrane fouling, etc.). Moreover, these techniques require additional steps to obtain high-purity BDO product. Alternatively, conventional filtration and ion exchange steps can be used to remove most of the microorganisms, large organic molecules and salts (see Figure 1, preconcentration and final purification (green boxes) are the focus of this research). After these initial downstream processing steps, additional purification is needed to remove the remaining water and obtain a high-purity BDO product. Due to the significant temperature differences and absence of azeotropes, distillation may be used for both preconcentration and final purification. Nonetheless, distillation implies evaporating large amounts of water and advanced energy-saving techniques are required to make the process efficient. Several distillation-based configurations have been proposed (consecutive distillation, extractive distillation, multi-effect distillation, dividing-wall column distillation) [6–9] with energy requirements of 3.1 – 6.5 $kW_{th}h/kg_{BDO}$ (~6.2 to recover 90% of 2,3-BDO using dividing-wall column [10]).

The main goal of our research is to significantly decrease the energy requirements of the preconcentration and final purification parts of the recovery process. Recently, we have achieved this goal by developing a state-of-the-art large-scale downstream processing design (broth processing capacity of 160 ktonne/y with a production capacity of 11 – 15 ktonne/y) that may be easily adapted to purify 2,3- (case 2-3), 1,4- (case 1-4) or 1,3-BDO (case 1-3) after fermentation, and conventional filtration and ion-exchange steps [11]. These initial filtration and ion exchange steps are commonly used in industrial-scale purification processes and were not designed in this study.

## METHODS

Aspen Plus was employed as a computer-aided process engineering (CAPE) tool to design BDO purification processes, whereby rigorous simulations were performed for all process operations. The compositions of the fermentation broths from published literature [7, 12, 13] were used to obtain feed streams for the recovery process (see Figure 3). Generally, concentrations of BDO and water are about 7 – 9 wt% and 87 – 91 wt%, while some light impurities (ethanol, formic acid, acetic acid, etc.) and heavy impurities (lactic acid, succinic acid, glucose, etc.) are present in all cases. Thermodynamic interactions between different components in the broth were described using the Non-Random Two Liquid (NRTL) property model. Hayden-O'Connell (HOC) extension was used to describe vapor phase interactions if polar components (e.g. carboxylic acids) are present (cases 2-3 and 1-3)[14].

## RESULTS AND DISCUSSION

This section contains the main results related to the design of large-scale processes for the recovery of BDOs after fermentation. Flowsheets for these cases, with the main elements of mass and energy balances, are presented in Figure 3.

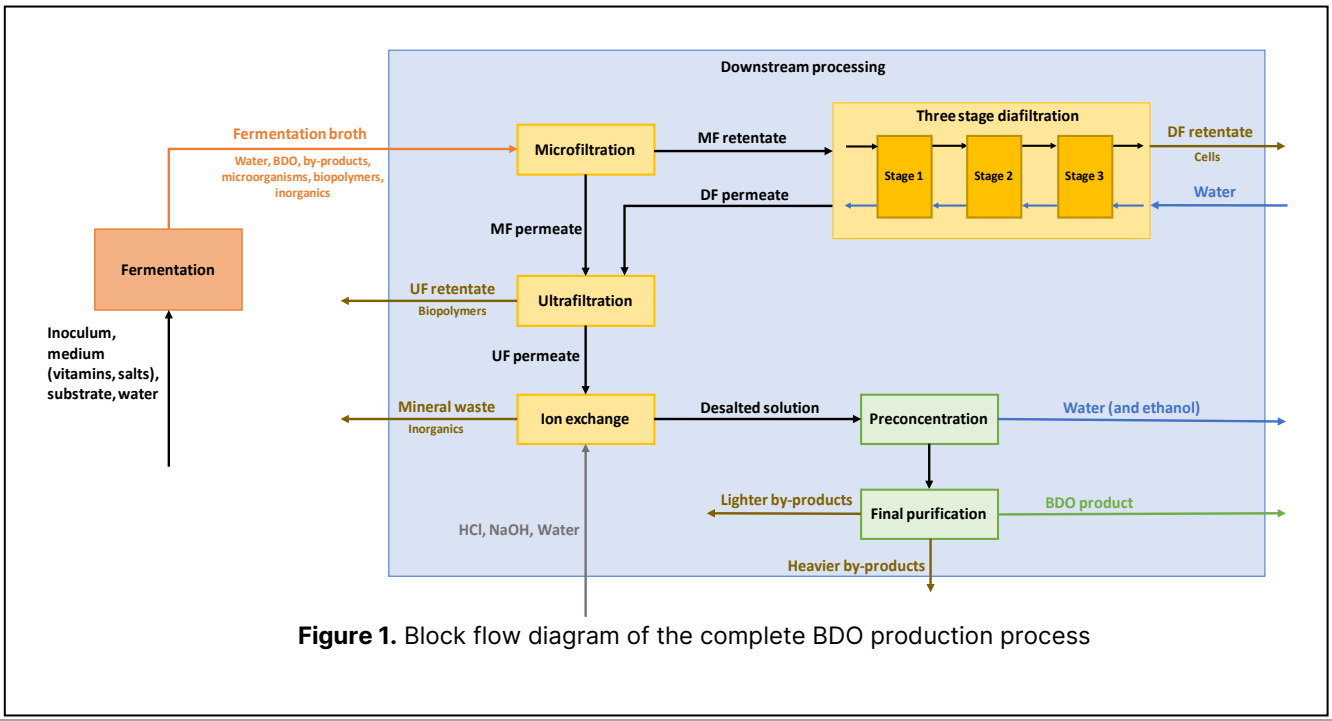



**Figure 1.** Block flow diagram of the complete BDO production process

## Preconcentration step

Following the initial filtration and ion exchange steps necessary to remove microorganisms, large organic molecules and inorganics, the fermentation broth is still very dilute. Hence, a preconcentration step is performed in distillation column C1 to separate most of the water with some light impurities (distillate), from BDO with heavy and remaining light impurities (bottom product). Reduced pressure operation (top pressure of 0.130 bar) was chosen to avoid high temperatures, facilitate separation and decrease energy requirements. Due to the applied vacuum, structured packing was assumed for this column's internals. Given the high concentration of water in broth, the preconcentration step is very energy intensive (> 12 $MW_{th}$). Thus, the implementation of advanced energy-saving techniques is crucial for the energy efficiency of the whole recovery process. Theoretically, all components lighter than BDO can be separated as the top product of column C1. However, this would limit the application of heat pump systems as the temperature difference between the top and the bottom of column C1 would be very large. On the contrary, the proper choice of operating parameters (distillate-to-feed ratio) allows the implementation of a mechanical vapor recompression system (MVR) [15]. This heat pump system implies compressing vapor from the top of a column and using it as a heating utility in a reboiler. The measure of obtained energy savings by implementing this system is the coefficient of performance (COP) – the ratio of exchanged thermal energy and required compressor power. COP values of the MVR systems implemented to column C1 are > 14 in all cases. Given that a COP of over 2.5 testifies to the energy efficiency of heat pump systems, it may be concluded these MVR systems result in significant energy savings. Valorisation of by-products from the top aqueous stream of column C1 was not considered due to their low concentration. Instead, as the worst-case scenario, it was assumed that this stream would be sent to wastewater treatment and appropriate costs were accounted for.

The benefits of the proposed multi-stage preconcentration step in the heat pump-assisted distillation column are manifold. Firstly, removing most of the water drastically reduces equipment size and reboiler duty for the final purification step. Secondly, multi-stage preconcentration in the distillation column allows the separation of water and light impurities without losing BDO product. Thirdly, the applied MVR system significantly decreases energy requirements for the overall recovery process and enables complete (green)electrification of this step. To our knowledge, a multi-stage preconcentration step that removes most of the water and light impurities without losing BDO product and that can be powered completely by electricity has not been proposed so far.

## Further purification

Following the preconcentration step, additional processing is needed to obtain a high-purity final BDO product. This may be performed in a sequence of two distillation columns, whereby the first one removes the remaining water and light impurities, while the second one separates BDO from heavy impurities. Alternatively, these two columns may be integrated into one dividing-wall column (DWC) with a divided overhead section and common bottom section [16]. This highly integrated system combines two columns into one shell with two condensers and only one reboiler. In addition to reducing capital costs (through the number of columns, heat exchangers, and required area for installation), DWC may significantly reduce energy requirements for separation. Although DWC technology has certain limitations, such as a potentially more complex control strategy, its implementation has been successfully proven in multiple large-scale applications [17, 18]. As no DWC unit is available off-the-shelf in Aspen Plus, it was simulated as a thermodynamical equivalent sequence of distillation columns (see Figure 2). The bottom liquid from the left part of the DWC ($DWC_L$) is sent to the right part ($DWC_R$). Simultaneously, part of vapor rising in $DWC_R$ is redirected to $DWC_L$ to ensure sufficient vapor flow in this part of the column. The DWC has 20 stages in total, with the first and the last stages being condenser and reboiler by the convention of Aspen Plus. The wall is placed in the top 14 stages (13 excluding the condenser). Due to the large temperature difference between the BDO and light impurities (top products), thermal insulation will be needed to ensure the energy efficiency of the DWC Reduced pressure operation (top pressure of 0.1 bar) was implemented to avoid high temperatures that may lead to decomposition. Due to the vacuum operation, structured packing was assumed for the DWC's internals. Finally, high purity (>99.4 wt% in all cases) BDO product was recovered as the top product from $DWC_R$. The remaining light and heavy impurities are separated as the top product from $DWC_L$ and the bottom product from $DWC_R$. As a worst-case scenario, and due to the low concentrations, it was assumed that water and light impurities would be sent to wastewater treatment, while heavy impurities would be burnt for energy. Appropriate economic and environmental metrics are included in the evaluation of the developed process.

**Table 1.** Key performance indicators

| | Case 2-3 | Case 1-4 | Case 1-3 |
|---|---|---|---|
| **Economic indicators** | | | |
| CAPEX (k$) | 9,402 | 8,419 | 9,111 |
| OPEX ($/$kg_{BDO}$) | 0.159 | 0.132 | 0.164 |
| Total annual costs ($/$kg_{BDO}$), 10 years payback period | 0.222 | 0.208 | 0.243 |
| **Sustainability metrics** | | | |
| Thermal energy requirements ($kW_{th}h/kg_{BDO}$) | 0.506 | 0.662 | 0.615 |
| Electrical energy requirements ($kW_eh/kg_{BDO}$) | 0.539 | 0.502 | 0.624 |
| Primary energy requirements ($kW_{th}h/kg_{BDO}$) | 1.854 | 1.917 | 2.176 |
| $CO_2$ emissions, grey / green electricity ($kg_{CO2}/kg_{BDO}$) | 0.319 / 0.073 | 0.324 / 0.096 | 0.373 / 0.089 |
| Water consumption ($m^3_w/kg_{BDO}$) | 0.145 | 0.145 | 0.161 |
| Wastewater intensity ($m^3_{ww}/kg_{BDO}$) | 0.010 | 0.014 | 0.013 |
| Material intensity ($kg_{waste}/kg_{BDO}$) | 0.037 | 0.004 | 0.024 |

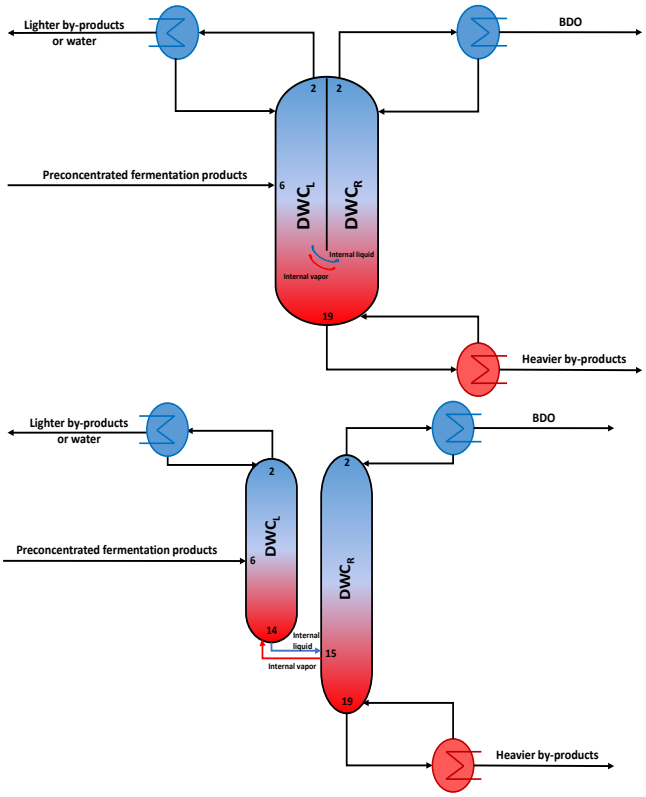



**Figure 2.** DWC (top) and equivalent sequence of distillation columns (bottom)

## Analysis of economic and environmental impact

The performance of the developed recovery processes was evaluated by analyzing economic indicators and sustainability metrics following the published recommendations [19, 20]. A comparison between the three processes is presented in Table 1.

Slightly lower capital costs in case 1-4 are due to marginally lower costs of distillation columns and compressor in the MVR system. Similarly, lower operating costs (OPEX) in case 1–4 are mainly because of lower wastewater treatment and electricity expenses (due to lower amount of light impurities and lower required compressor power in the MVR system). Total annual costs that include both CAPEX and OPEX with a payback period of 10 years are 0.222, 0.208 and 0.243 $/kgBDO in cases 2-3, 1-4 and 1-3, respectively. Thus, despite a somewhat lower initial concentration of 1,4-BDO (6.97 wt%) compared to 2,3-BDO (9.30 wt%) and 1,3-BDO (7.25 wt%), process performance is slightly better due to lower amounts of light impurities. Nonetheless, given that the minimum selling price for 2,3-BDO produced from sucrose, molasses or glycerol has been estimated to be 3.7 – 5.7 $/$kg_{BDO}$ [5], the proposed cost-effective recovery process may present a major advancement toward competitive fermentative production of BDO. Furthermore, there is significant margin compared to the price of petrochemically produced BDOs (about 1.8 $/kg [21]). However, fermentation costs still need to be accounted for to obtain a real picture.

Furthermore, thermal energy requirements are the lowest in case 2-3 (0.506 $kW_{th}h/kg_{BDO}$) due to the largest product flowrate. On the contrary, electrical energy requirements are the lowest in case 1-4 because of the lowest compressor power in the MVR system. The total primary energy requirements were calculated considering a conservative electrical-to-thermal conversion factor of 2.5. This metric ranges from 1.85 $kW_{th}h/kg_{BDO}$ for case 2-3 to 2.18 $kW_{th}h/kg_{BDO}$ for case 1-3, which is much lower than the 3.1 – 6.5 $kW_{th}h/kg_{BDO}$, reported in the literature. Related to energy use are $CO_2$ emissions, which are again the lowest in case 2-3. Water consumption (including 7 % loss of cooling water and 70 % recovery of condensate in the steam cycle) is also the lowest in case 2-3 due to the lowest thermal energy requirements. Material intensity is the lowest in case 1-4 because of the lowest amounts of light impurities.

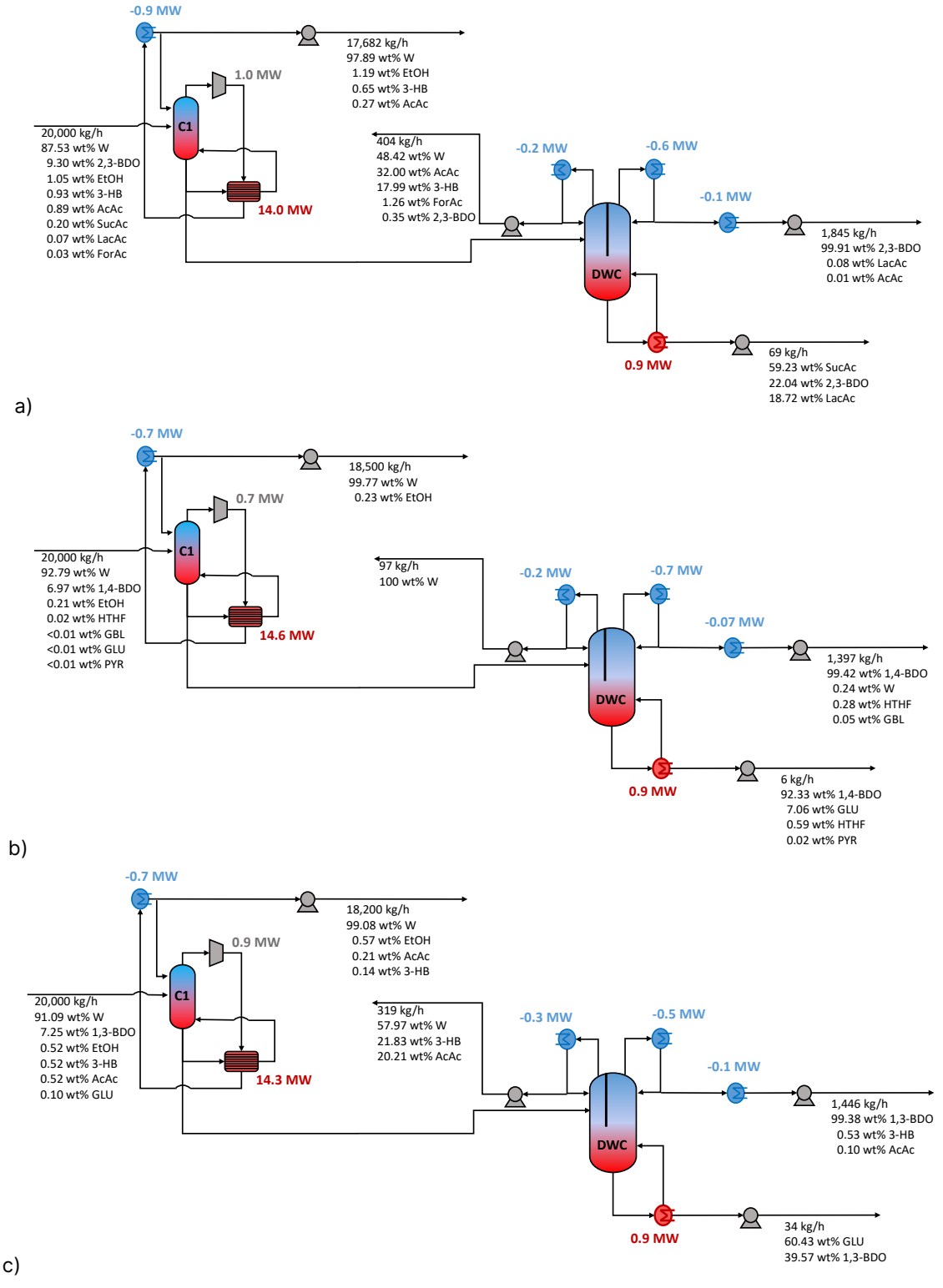



**Figure 3.** Flowsheet of BDOs' recovery process: a) 2,3-BDO, b) 1,4-BDO and c) 1,3-BDO

## CONCLUSION

This original paper proposes an eco-efficient large-scale downstream processing design for the preconcentration and final purification steps in the purification of

different BDOs (2,3-, 1,4- and 1,4-) after fermentation. Due to similar fermentation broth compositions and thermodynamic properties, a single process design was proven to cost-effectively (0.208 – 0.243 $/kg$_{BDO}$) and energy-efficiently (1.85 – 2.18 kW$_{th}$h/kg$_{BDO}$) recover over 99% of BDO from different fermentation processes. Implementation of the advanced process intensification and heat integration techniques reduced energy requirements by over 33% compared to the existing literature. Furthermore, the adaptable purification process offers flexibility in developing sustainable business models. Lastly, the results of this novel work highlight the importance of using CAPE tools in developing competitive bioprocesses by demonstrating that computer-aided simulations may play a crucial role in advancing sustainable industrial fermentation.

## OUTLOOK

While this study provides valuable insights into the techno-economic and environmental feasibility of the proposed processes for the recovery of BDOs after fermentation, there is room for further research to enhance its applicability and robustness. Although the developed process simulations rely on well-established thermodynamic models and rigorously validated unit operation models in Aspen Plus, experimental validation remains essential to ensure successful industrial implementation. Computational simulations should serve as a guiding framework for experiments, ensuring a more efficient and reliable approach to process development. Additionally, while the feasibility of DWC has been demonstrated in real-world applications, further research is needed to optimize equipment design and control strategies for maximizing operational efficiency.

Expanding the process design to include the fermentation reaction would provide a more comprehensive evaluation of economic competitiveness and enable a fair comparison with existing BDO production methods. Moreover, conducting a sensitivity analysis to assess the impact of variations in key factors—such as feedstock costs, utility prices, wastewater treatment costs, and BDO market prices—would offer deeper economic insights. A full life cycle assessment (LCA) would also be valuable in obtaining a more comprehensive understanding of the sustainability of the entire process.

Furthermore, an interesting avenue for future research is the development of a flexible process capable of producing multiple BDO isomers based on market demand. Given the fluctuating market dynamics of bio-based chemicals, designing a process that can adapt to varying production needs could enhance economic viability and commercial competitiveness.

## REFERENCES


1. Gawal PM, Subudhi S (2023) Advances and challenges in bio-based 2,3-BD downstream purification: A comprehensive review. Bioresource Technology Reports 24:101638. https://doi.org/10.1016/j.biteb.2023.101638
2. Afschar AS, Vaz Rossell CE, Jonas R, et al (1993) Microbial production and downstream processing of 2,3-butanediol. Journal of Biotechnology 27:317–329. https://doi.org/10.1016/0168-1656(93)90094-4
3. Caballero-Sanchez L, Vargas-Tah AA, Lázaro-Mixteco PE, Castro-Montoya AJ (2024) Recovery of 1,4-butanediol from aqueous solutions through aqueous two-phase systems with K2CO3. Chemical Engineering Research and Design 201:150–156. https://doi.org/10.1016/j.cherd.2023.11.015
4. Xie S, Li Z, Zhu G, et al (2022) Cleaner production and downstream processing of bio-based 2,3-butanediol: A review. Journal of Cleaner Production 343:131033. https://doi.org/10.1016/j.jclepro.2022.131033
5. Koutinas AA, Yepez B, Kopsahelis N, et al (2016) Techno-economic evaluation of a complete bioprocess for 2,3-butanediol production from renewable resources. Bioresource Technology 204:55–64. https://doi.org/10.1016/j.biortech.2015.12.005
6. Haider J, Harvianto GR, Qyyum MA, Lee M (2018) Cost- and Energy-Efficient Butanol-Based Extraction-Assisted Distillation Designs for Purification of 2,3-Butanediol for Use as a Drop-in Fuel. ACS Sustainable Chemistry and Engineering 6:14901–14910. https://doi.org/10.1021/acssuschemeng.8b03414
7. Haider J, Qyyum MA, Hussain A, et al (2018) Techno-economic analysis of various process schemes for the production of fuel grade 2,3-butanediol from fermentation broth. Biochemical Engineering Journal 140:93–107. https://doi.org/10.1016/j.bej.2018.09.002
8. Hong J, Van Duc Long N, Harvianto GR, et al (2019) Design and optimization of multi-effect-evaporation-assisted distillation configuration for recovery of 2,3-butanediol from fermentation broth. Chemical Engineering and Processing - Process Intensification 136:107–115. https://doi.org/10.1016/j.cep.2019.01.002
9. Van Duc Long N, Hong J, Nhien LC, Lee M (2018) Novel hybrid-blower-and-evaporator-assisted distillation for separation and purification in biorefineries. Chemical Engineering and Processing: Process Intensification 123:195–203. https://doi.org/10.1016/j.cep.2017.11.009
10. Haider J, Qyyum MA, Minh LQ, Lee M (2020)

Purification step enhancement of the 2,3-butanediol production process through minimization of high pressure steam consumption. Chemical Engineering Research and Design 153:697–708. https://doi.org/10.1016/j.cherd.2019.11.005
11. Janković T, Sharma S, Straathof AJJ, Kiss AA (2025) Adaptable downstream processing design for recovery of butanediols after fermentation. Chemical Engineering Research and Design 213:210–220. https://doi.org/10.1016/j.cherd.2024.12.011
12. Satam CC, Daub M, Realff MJ (2019) Techno-economic analysis of 1,4-butanediol production by a single-step bioconversion process. Biofuels, Bioproducts and Biorefining 13:1261–1273. https://doi.org/10.1002/bbb.2016
13. Baldassarre M, Cesana A, Bordes F (2020) Process for bio-1,3-butanediol purification from a fermentation broth
14. 2020) Aspen Physical Property System. Aspen Technology, Bedford
15. Kiss AA, Infante Ferreira CA (2016) Mechanically Driven Heat Pumps. In: Heat Pumps in Chemical Process Industry. CRC Press, Boca Raton, pp 189–251
16. Kiss AA (2013) Dividing-Wall Column. In: Advanced Distillation Technologies. John Wiley & Sons Ltd., pp 67–110
17. Kiss AA (2016) Process Intensification: Industrial Applications. In: Process Intensification in Chemical Engineering: Design Optimization and Control. Springer, Cham, pp 221–260
18. Dejanović I, Matijašević L, Olujić Ž (2010) Dividing wall column-A breakthrough towards sustainable distilling. Chemical Engineering and Processing: Process Intensification 49:559–580. https://doi.org/10.1016/j.cep.2010.04.001
19. Humbird D, Davis R, Tao L, et al (2011) Process Design and Economics for Biochemical Conversion of Lignocellulosic Biomass to Ethanol
20. Schwarz J, Beloff B, Beaver E (2002) Use Sustainability Metrics to Guide Decision-Making. Chemical Engineering Progress 98:58–63
21. ChemAnalyst (2024) Butanediol Price Trend and Forecast. https://www.chemanalyst.com/Pricing-data/butanediol-54

© 2025 by the authors. Licensed to PSEcommunity.org and PSE Press. This is an open-access article under the Creative Commons CC-BY-SA licensing terms. Credit must be given to the creator, and adaptations must be shared under the same terms. See https://creativecommons.org/licenses/by-sa/4.0/



Systems & Control Transactions

**Research Article - Peer Reviewed Conference Proceeding**
ESCAPE 35 - European Symposium on Computer Aided Process Engineering
Ghent, Belgium. 6-9 July 2025
Jan F.M. Van Impe, Grégoire Léonard, Satyajeet S. Bhonsale,
Monika E. Polańska, Filip Logist (Eds.)

PSE PRESS

# Optimization-based operational space design for effective bioprocess performance under uncertainty

**Mengjia Zhu[a], Oliver Pennington[a], Sam Kay[a], Amin Zarei[b], Michael Short[b], and Dongda Zhang[a]***

[a] Department of Chemical Engineering, University of Manchester, Manchester, M13 9PL, UK
[b] School of Chemistry and Chemical Engineering, University of Surrey, Guildford, GU2 7XH, UK
* Corresponding Author: dongda.zhang@manchester.ac.uk.

## ABSTRACT

Maintaining consistent product quality and yield in bioprocess operations is challenging due to uncertainties inherent in biological systems. Thus, robust strategies are essential to ensure key performance indicators (KPIs), such as product concentration and yield, are consistently met despite the uncertainties. Real-time feedback co Interntrol, though widely used, is often impractical due to its reliance on expensive sensors, rapid data processing, and high-speed control actions. This paper proposes a novel approach to address these challenges by identifying the operational space for control variables, ensuring KPI reliability without requiring real-time control. This operational space serves as a guideline such that, if we operate within this space, the KPIs can be reliably achieved, regardless of the considered uncertainties. Specifically, we reformulate the problem as an optimization task to maximize the operational space, subject to constraints imposed by process dynamics and performance criteria. Using CasADi for symbolic computation and IPOPT for optimization, a stage-wise procedure is implemented to enhance computational efficiency. Unlike surrogate-based methods, this approach directly preserves model fidelity and accommodates path constraints effectively. The method is validated in a case study of fermentation process, involving a time-varying control variable and seven uncertain model parameters. Results demonstrate the ability to define a reliable operational space that enables KPI adherence across parameter variations, proving the method's efficiency and practical applicability.

**Keywords**: Design Under Uncertainty, Process Control, Biosystems, Operational Space

## INTRODUCTION

Bioprocess industries, including pharmaceuticals, biotechnology, and food production, rely heavily on biological systems to produce products of consistent quality and yield. However, biological processes are inherently variable due to the complex and often poorly understood interactions within living organisms [1,2].

Traditionally, system identification techniques are employed to develop mathematical models that describe the dynamic behavior of bioprocesses [3,4]. These models are then used to design control strategies to maintain process variables within desired ranges. However, when models rely solely on nominal parameter values, they may not adequately account for the uncertainties inherent in biological systems, leading to deviations in process performance [5]. Real-time feedback control is commonly employed to manage such uncertainties by continuously adjusting control variables based on real-time measurements [6]. While effective, this approach can be costly and impractical due to the need for high-speed data processing, robust sensors, and rapid control actions [7]. Moreover, in bioprocessing environments where measurements may be infrequent or delayed, real-time control becomes even more challenging [8].

To address these challenges, there is a need for control strategies that ensure key performance indicators (KPIs), such as final product concentration and yield, are consistently met despite uncertainties, without relying heavily on real-time feedback mechanisms. Here, uncertainties can arise from biological variability, measurement inaccuracies, and model simplifications. In this paper, we focus on the uncertainties introduced by model parameters involved in system identification.

Various methods have been developed to manage model uncertainties in control problems, aiming to ensure KPIs are met despite parameter variability. Semi-Infinite Programming (SIP) addresses uncertainties by including infinitely many constraints to guarantee performance for all parameter values within specified bounds [9]. While comprehensive, SIP is computationally intensive and difficult to solve [10]. Scenario Optimization reduces this complexity by approximating the uncertainty space with a finite set of scenarios generated through sampling techniques like Monte Carlo or Latin Hypercube Sampling [11]. Though more tractable, this method may require numerous scenarios to achieve robustness, increasing computational demands. Robust Optimization ensures feasibility across the entire uncertainty set without explicit enumeration, but it can lead to conservative solutions and is constrained by the structure of the uncertainty and problem type [12,13]. Similarly. worst-Case Identification via Optimization formulates a bilevel optimization problem, where the outer optimization seeks optimal controls, and the inner problem identifies the most adverse parameter values. While precise for handling extreme uncertainties, this approach is computationally demanding [14]. Surrogate-Based Methods leverage simplified models like Kriging, polynomial chaos expansions, or neural networks to approximate high-fidelity systems, enabling efficient exploration under uncertainty. However, these methods depend on high-quality training data and face challenges in high-dimensional spaces, where accurately constructing surrogates becomes increasingly complex and resource-intensive [15].

Despite the advances in these methods, challenges remain in efficiently handling parameter uncertainties in control problems, especially when the worst-case scenarios do not occur at the parameter extremes. Computational complexity and the need for approximations or surrogate models can limit their practical applicability in bioprocess operations.

### Contribution

In this paper, we propose an alternative scenario optimization approach that effectively addresses the computational challenges while maintaining accuracy and fidelity to the original process dynamics. We reformulate the problem as an optimization task aimed at maximizing the operational space of relevant control variables, subject to path and terminal constraints imposed by process dynamics and performance specifications.

Our approach integrates symbolic frameworks using CasADi [16], a software tool for numerical optimization that facilitates the formulation and efficient evaluation of gradients and Hessians. We solve the formulated optimization problem using IPOPT [17], an interior-point optimizer well-suited for large-scale nonlinear programming. Different from conventional scenario optimization methods, a novel stage-wise optimization procedure is implemented to reduce computational burden.

The paper is organized as follows. The target problem is first described, followed by the proposed solution methods. Then, a case study of fermentation process is discussed. Lastly, future works are noted.

## PROBLEM DESCRIPTION

Consider a bioprocess described by a mechanistic model consisting ordinary differential equations (ODEs): $\dot{\boldsymbol{x}}(t) = \boldsymbol{F}(t, \boldsymbol{x}(t), \boldsymbol{u}(t), \boldsymbol{p}, \boldsymbol{\theta})$, where, $\boldsymbol{x}$ and $\boldsymbol{u}$ are the vector of state variables (e.g., biomass concentration, substrate concentration, etc.) and control inputs (e.g., feed rate, temperature, etc.), respectively, with $\boldsymbol{\theta}$ and $\boldsymbol{p}$ being the fixed parameters and the parameters subject to bounded uncertainties (i.e., $\boldsymbol{p} \in [\boldsymbol{p}_{\min}, \boldsymbol{p}_{\max}]$), respectively.

The following assumptions are made in this study: $(i)$ the range of the uncertain parameters is known or can be estimated during system identification; $(ii)$ the initial state of the system is known and it is the same across different batches; $(iii)$ the desired output and its relevant acceptable bounds have been defined; $(iv)$ the control input can be time-varying, and a reference trajectory is provided or can be calculated; $(v)$ the operational space we aim to identify for the control input can be time-varying, and the system operates on a fixed time horizon; and $(vi)$ the system dynamics can be identified.

The goal is to identify a practical and flexible operational space for $\boldsymbol{u}$ such that, if we operate within this space, the KPIs are likely to be consistently met independent of the uncertain parameters $\boldsymbol{p}$.

## PROPOSED METHOD

### Optimization problem formulation

We discretize the time horizon $[0, T]$ into $N$ intervals with piecewise constant controls $\boldsymbol{u}_k$ for $k = 0, \ldots, N-1$. Our objective is to find the largest operational space for the control inputs subject to process constraints. Specifically, we consider maximizing the difference between the upper ($\overline{\boldsymbol{u}}_k$) and lower ($\underline{\boldsymbol{u}}_k$) bounds of the control inputs over the time horizon:

$$\max_{\underline{\boldsymbol{u}}_k, \overline{\boldsymbol{u}}_k} \quad \text{dist}\{\overline{\boldsymbol{u}}_k - \underline{\boldsymbol{u}}_k\} \text{ for } k = 0, \ldots, N-1. \tag{1}$$

The optimization problem (1) is subject to different constraints. For example, the dynamics of the process will follow the system model, some path constraints can be involved, and process KPIs need to be respected.

### Solution approach

For conventional scenario optimization methods, samples of uncertain parameters are drawn from their ranges and incorporated as constraints into the

optimization problem (1) as constraints, which is then solved in a single step. However, achieving robustness typically requires a large number of samples to adequately represent the uncertainty. This makes solving (1) computationally expensive and increases the risk of getting trapped in local optima. To address the challenges, we propose a new scenario optimization method that integrates a stage-wise optimization procedure to enhance computational efficiency. Additionally, a looped verification step is integrated within the framework to enhance the robustness of the approach.

The proposed method aims to iteratively update the lower and upper bounds of control inputs to accommodate parameter uncertainties while respecting system constraints. The process involves sampling parameters, grouping them based on computational capacity, and solving optimization problems to adjust the bounds accordingly. The steps are summarized in Algorithm 1.

**Algorithm 1:** Stage-wise optimization for operational space design.

**Input:** Parameter uncertainty bounds $\boldsymbol{p}_{\min}, \boldsymbol{p}_{\max}$; number of discretization steps $N$; initial control input $\tilde{\boldsymbol{u}}_k$, weights $w_{jk}$, for $k = 0, \dots, N-1$ and $j = 1, \dots, m$; number of parameter samples $N_{\text{sp}}$; number of computational groups $N_{\text{gp}}$
**Output:** Updated control input bounds $\underline{\boldsymbol{u}}_k$, $\overline{\boldsymbol{u}}_k$

**Initialization:** $\underline{\boldsymbol{u}}_k \leftarrow \tilde{\boldsymbol{u}}_k$, $\overline{\boldsymbol{u}}_k \leftarrow \tilde{\boldsymbol{u}}_k$, for $k = 0, \dots, N-1$
**Sampling Parameters:** Sample $N_{\text{sp}}$ parameters: $\{\boldsymbol{p}^i\}_{i=1}^{N_{\text{sp}}} \sim \mathcal{U}(\boldsymbol{p}_{\min}, \boldsymbol{p}_{\max})$
**Dividing Samples into Groups:** divide $N_{\text{sp}}$ samples into $N_{\text{gp}}$ groups
**For** $z = 1$ **to** $N_{\text{gp}}$ **do**
  **If** $findLowerbound$ **then**
    $\underline{\boldsymbol{u}}_{k,\text{old}} \leftarrow \underline{\boldsymbol{u}}_k$
    **If** $z == 1$ **then**
      Solve the following optimization problem to get $\underline{\boldsymbol{u}}_k$:

$$\max_{\underline{\boldsymbol{u}}_k} \ \min_{j=1}^{m} \min_{k=0}^{N-1} \underline{w}_{jk} \left(\underline{u}_{jk,\text{old}} - \underline{u}_{jk}\right) \quad (2)$$

      s.t. path & terminal constraints

$$\underline{u}_{jk,\text{old}} \geq \underline{u}_{jk}, \ \forall j, k$$

    **Else**
      Solve the following optimization problem to get $\underline{\boldsymbol{u}}_k$:

$$\min_{\underline{\boldsymbol{u}}_k} \ \sum_{j=1}^{m} \sum_{k=0}^{N-1} \underline{w}_{jk} \left(\underline{u}_{jk} - \underline{u}_{jk,\text{old}}\right) \quad (3)$$

      s.t. path & terminal constraints

$$\underline{u}_{jk,\text{old}} \leq \underline{u}_{jk} \leq \tilde{u}_{jk}, \ \forall j, k$$

  **If** $findUpperbound$ **then**
    $\overline{\boldsymbol{u}}_{k,\text{old}} \leftarrow \overline{\boldsymbol{u}}_k$
    **If** $z == 1$ **then**
      Solve the following optimization problem to get $\overline{\boldsymbol{u}}_k$:

$$\max_{\overline{\boldsymbol{u}}_k} \ \min_{j=1}^{m} \min_{k=0}^{N-1} \overline{w}_{jk} \left(\overline{u}_{jk} - \overline{u}_{jk,\text{old}}\right) \quad (4)$$

      s.t. path & terminal constraints

$$\overline{u}_{jk,\text{old}} \leq \overline{u}_{jk}, \ \forall j, k$$

    **Else**
      Solve the following optimization problem to get $\overline{\boldsymbol{u}}_k$:

$$\min_{\overline{\boldsymbol{u}}_k} \ \sum_{j=1}^{m} \sum_{k=0}^{N-1} \overline{w}_{jk} \left(\overline{u}_{jk,\text{old}} - \overline{u}_{jk}\right) \quad (5)$$

      s.t. path & terminal constraints

$$\overline{u}_{jk,\text{old}} \geq \overline{u}_{jk} \geq \tilde{u}_{jk}, \ \forall j, k$$

In the following, we elaborate each step of Algorithm 1. We first initialize the lower and upper control input bounds to the nominal control input $\tilde{\boldsymbol{u}}_k$, which we assumed to be known or can be identified via optimal control strategies with uncertain parameters set to their nominal values (e.g., the middle points of the uncertain ranges). Then we sample $N_{\text{sp}}$ sets of parameters from the uncertainty bounds using a uniform distribution, with each $\boldsymbol{p}^i$ represents a possible set of parameter realization within the specified bounds $\boldsymbol{p}_{\min}$ and $\boldsymbol{p}_{\max}$. We then divide $N_{\text{sp}}$ samples into $N_{\text{gp}}$ groups, with each group, except the last group, containing $\left\lceil \frac{N_{\text{sp}}}{N_{\text{gp}}} \right\rceil$ samples, and the last group containing the remaining samples. Note that the last group will contain $\left\lceil \frac{N_{\text{sp}}}{N_{\text{gp}}} \right\rceil$ samples, if $N_{\text{sp}}$ is exactly divisible by $N_{\text{gp}}$, i.e., $\left\lceil \frac{N_{\text{sp}}}{N_{\text{gp}}} \right\rceil = \frac{N_{\text{sp}}}{N_{\text{gp}}}$. For each group $z = 1,2, \dots, N_{\text{gp}}$, we perform iterative optimization to adjust the control input bounds. Depending on whether the lower bounds, upper bounds, or both need to be updated (as indicated by the flags $findLowerbound$ and $findUpperbound$ in Algorithm 1), the following procedures are executed: ($i$) if $findLowerbound$ is true, the algorithm first stores the current lower bounds by setting $\underline{\boldsymbol{u}}_{k,\text{old}} = \underline{\boldsymbol{u}}_k$ for every time segment $k$. This serves as a reference point and initial guess for the optimization. For the first group ($z = 1$), the updated bounds need to satisfy the system constraints only for the initial set of sampled uncertain parameters. Therefore, the algorithm aims to maximize the minimum weighted difference between the old and new lower bounds, effectively pushing the lower bounds downward as much as possible while satisfying all constraints. This is formulated as the optimization problem in (2). The constraints ensure that the system dynamics, safety requirements and process KPIs are met, and that the new lower bounds do not exceed the old ones. For the subsequent groups ($z > 1$), the updated bounds must satisfy the constraints for all parameter realizations sampled thus far, including those in the current group. This cumulative requirement incorporates more constraints, leading to a more restricted operational space. As a result, the algorithm focuses on minimizing the total weighted increase from the previous lower bounds to the new lower bounds, making only the necessary adjustments to accommodate the new constraints. This conservative adjustment is formulated in (3). ($ii$) similarly, if $findUpperbound$ is true, the algorithm updates the upper bounds by solving the optimization problem (4) for the first group ($z = 1$), and optimization problem (5) for subsequent groups ($z > 1$). Different from the lower bound identification, for upper bound identification, we first try to expand the operational space by *increasing* the upper bounds as much as possible within the constraints during the first group. In subsequent groups, we minimize the total weighted

decrease from the previous upper bounds to the new upper bounds, making only necessary *reductions* to satisfy the accumulated constraints introduced by the new parameter samples.

We remark that this stage-wise procedure divides sampled uncertain parameters into small subset, making it easier for the optimization solver to find optimal solutions for each sub-problem. Since the initially identified bounds serve as constraints for later iterations, it is important to have good starting profiles. Therefore, for the first group ($z = 1$), we select the optimization problem (2) and (4) as maximizing the minimal weighted difference between the nominal/previous control inputs and the updated bounds. This *max-min* formulation is preferred over maximizing the sum (*max-sum*) of differences (as used for the subsequent groups' optimization problems (3) and (5)) to prevent scenarios where only a few control inputs have large deviations from the nominal/previous values while the majority deviations remain close to zero. Such uneven adjustments can result in less useful bounds, as they may introduce impractical control actions. To illustrate this difference, consider an example illustrated in Figure 1, where the *max-sum* approach leads to a larger total deviation from the nominal control inputs than the *max-min* approach, but the deviations are concentrated in only two segments. Specifically, most of the control actions identified by the *max-sum* approach overlap with the nominal ones, with deviations only occurs between Index 2 and 3, and between Index 3 and 4). In contrast, the max-min approach distributes the deviations across all segments. As for the subsequent groups, since the general shape of the control bounds is already defined after the first group, we can use the max-sum approach to limit the adjustments and maintain as much of the operational space as possible.

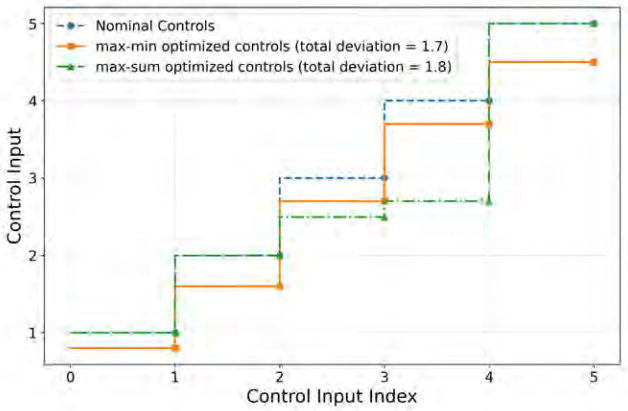



**Figure 1.** Comparison of *max-min* and *max-sum* optimization results.

We also note that bioprocesses often involve path constraints to ensure safety and synthesis requirements are met throughout the operation. To ensure feasibility, a symbolic framework is incorporated into the optimization procedure. We use CasADi [16], a powerful tool tailored for handling complex optimal control problems. This framework allows for efficient modeling of system dynamics and constraints. The resulting optimization problem is then solved using IPOPT [17], which is well-integrated with CasADi [16]. Also, by processing the parameter samples in groups, the algorithm balances computational efficiency with the need for robustness against uncertainties. The distinction between the first and subsequent groups allows for an initial broad adjustment of the bounds, followed by finer tuning in later iterations.

Finally, we validate the identified control bounds on a larger set of testing samples by running additional MC simulations, ensuring that the KPIs are consistently met despite parameter uncertainties, as long as the control input remains within the identified bounds. To further improve robustness, if any samples result in KPI violations, they are incorporated into optimization problems (3) and (5) to further adjust the lower and upper bounds, respectively. A new batch of test samples is then sampled and used to verify the adjusted bounds. This process is repeated until the percentage of KPI violations is lower than a user-defined acceptable threshold in the test sets. The accumulative nature of these formulations allows new samples to be added without re-running previous ones, improving computational efficiency.

## CASE STUDY

We demonstrate the proposed method using a fermentation case study of astaxanthin production in a fed-batch bioprocess under parameter uncertainty [6]. The kinetic model of the bioprocess is taken from [6] and is converted to the fed-batch model by including the feed flow rate $F_{\text{in}}(t)$ as the control input:

$$\frac{dV(t)}{dt} = F_{\text{in}}(t) \tag{6a}$$

$$\frac{dX(t)}{dt} = \mu_m(t)X(t) - \mu_d X(t) - \frac{X(t)}{V(t)}F_{\text{in}}(t) \tag{6b}$$

$$\frac{dS(t)}{dt} = \frac{F_{\text{in}}(t)}{V(t)}S_{\text{in}} - Y_S\mu_m(t)X(t) - \frac{S(t)}{V}F_{\text{in}}(t) \tag{6c}$$

$$\frac{dP(t)}{dt} = \alpha\mu_m(t)X(t) + \beta X(t) - k_d X^2(t) - \frac{P(t)}{V(t)}F_{\text{in}}(t) \tag{6d}$$

where $\mu_m(t) = \mu_m \frac{S(t)}{S(t)+K_c X(t)}$. Here, $X(t)$ is the biomass concentration (g/L); $S(t)$ is the substrate concentration (g/L) with $S_{\text{in}}$ being the substrate concentration in the input flow; $F_{\text{in}}(t)$ is the input flowrate; $P(t)$ is the product concentration (mg/L), and t is time (h). The remaining parameters are noted in Table 1. For the case study, the state values $\boldsymbol{x}(t) = [V(t), X(t), S(t), P(t)]^{\top}$, the control input $\boldsymbol{u}(t) = F_{\text{in}}(t)$, and the uncertain parameters $\boldsymbol{p} = [\mu_m, K_c, \mu_d, Y_S, \alpha, \beta, k_d]^{\top}$, with the fixed parameter $\theta = S_{\text{in}}$.

## Operation conditions

We consider uncertainties in the parameters with a $\pm 2\%$ variations around their nominal values (Table 1). The process begins with an initial volume $\mathrm{V}(0)$ of 0.4 L, an initial biomass concentration $X(0)$ of 0.1 g/L, an initial substrate concentration $S(0)$ of 6 g/L, and an initial product concentration $P(0)$ of 0 mg/L. The substrate concentration in the feed $\mathrm{S_{in}}$ is set to 12 g/L, and the reactor's volume is 2 L ($\mathrm{V_{reactor}}$). The process is run for 168 hours ($T$), The feed flow rate $\mathrm{F_{in}(t)}$ is adjusted every 12 hours, leading to 14 discretized time segments (N).

**Table 1:** Model parameters for astaxanthin production.

| Parameter | Description | Nominal Value |
|---|---|---|
| $\mu_m$ | Maximum specific growth rate | 0.43 $h^{-1}$ |
| $K_c$ | Substrate saturation constant | 63.7 (-) |
| $\mu_d$ | Specific decay rate | 0.0021 $h^{-1}$ |
| $Y_S$ | Substrate yield coefficient | 2.58 g/g |
| $\alpha$ | Growth-dependent yield coefficient | 7.88 mg/g |
| $\beta$ | Growth-independent yield coefficient | 0.236 mg/(g·h) |
| $k_d$ | Specific consumption rate | 0.0648 mg·L/($g^{-2}h^{-1}$) |

The nominal control trajectory $\tilde{\boldsymbol{u}}_k$ is identified based on an optimal control strategy with nominal parameter values. The KPI in this case is to ensure that the mass production of astaxanthin (the product) at the end of the time horizon is higher than 58 mg, i.e., $\mathrm{V(N)P(N)} \geq 58$ mg. Several path constraints are involved: $(i)$ all the state variables are nonnegative, i.e., $\boldsymbol{x}(\mathrm{t}) \geq 0$, for $\mathrm{t} \in [0, \mathrm{T}]$; $(ii)$ maximum working volume should not exceed 95% of the reactor's volume, i.e., $\mathrm{V(t)} \leq 0.95\mathrm{V_{reactor}}$; $(iii)$ no feed in the first and last days (24 hours), i.e., $\mathrm{u_k} = 0$, for $\mathrm{k} \in \{0, 1, \mathrm{N}-3, \mathrm{N}-2\}$; $(iv)$ the substrate concentration should not change dramatically, i.e., $\frac{\mathrm{dS(t)}}{\mathrm{dt}} \leq 3$ g/L; and $(v)$ the mass of the product astaxanthin should increase throughout the process, i.e., $\frac{\mathrm{dP(t)}}{\mathrm{dt}} \geq 0$.

Since the operational space is not unique, additional constraints can be introduced to shape its profile. For example, if it is known in advance that control is critical at a certain time step and limited variation is preferred, constraints can be added to enforce this. In our case, we introduce constraints that increase control variability in the middle time segments over the time horizon, specifically, $\overline{u}_{k+1} - \tilde{u}_{k+1} \geq \overline{u}_k - \tilde{u}_k$ and $\tilde{u}_{k+1} - \underline{u}_{k+1} \geq \tilde{u}_k - \underline{u}_k$ for $k \in \{3, \ldots, N-5\}$. The rationale is that by closely following the desired operation in the early stages, we allow for greater flexibility in the later stages of the process.

To identify the operational space, 1,000 sets of uncertain parameters ($N_{\mathrm{sp}}$) are drawn, which are divided into 100 groups ($N_{\mathrm{gp}}$). For a comparison study, the same problem is solved with a conventional scenario optimization method—we solve optimization problem (2) and (4) with the entire set of sampled uncertain parameters in a single step. Computations are performed on an Intel i7-13700H 2.40-GHz CPU laptop with 32GB of RAM.

## Results and discussions

The proposed method effectively identifies the operational space for the feed flow rate $F_{\mathrm{in}}(t)$ under parameter uncertainties, optimizing both the lower and upper control bounds. This approach ensures that the process constraints are satisfied across all sampled uncertainties while maximizing the operational space. Compared to the conventional scenario optimization method, which solves the problem in a single step using the full set of uncertain parameters, the proposed method significantly reduces computational time. Specifically, the CPU time for the proposed approach was 279.86 seconds, compared to 10,995.06 seconds for the conventional method.

Additionally, the identified operational space by the proposed method (shaded regions in Figure 2) offers greater flexibility in control inputs compared to the one identified by the conventional scenario optimization method (shaded regions in Figure 3). The MC simulations, which sampled controls from their operational space and parameters from their uncertainty bounds (10,000 samples each), further verified that the process consistently meets performance criteria when the control input remains within the identified bounds. Additionally, no violations of the constraints were observed, confirming the reliability of the identified control strategy.

# CONCLUSION AND FUTURE WORK

We have presented a novel scenario optimization approach to identify the operational space for control variables in bioprocess operations with known parameter uncertainties. By integrating symbolic frameworks, the method efficiently handles complex nonlinear dynamics and constraints.

The implementation of a new stage-wise optimization procedure significantly reduces computational burden, making the approach practical for industrial applications. The method ensures that key performance indicators are consistently met without the need for costly real-time feedback control systems, offering a cost-effective and reliable means of maintaining product quality and yield in the bioprocess industry.

Future work may explore the application of the method to more complex systems with higher-dimensional uncertainty spaces and investigate the integration of real-time data to update the operational space as new

information becomes available.

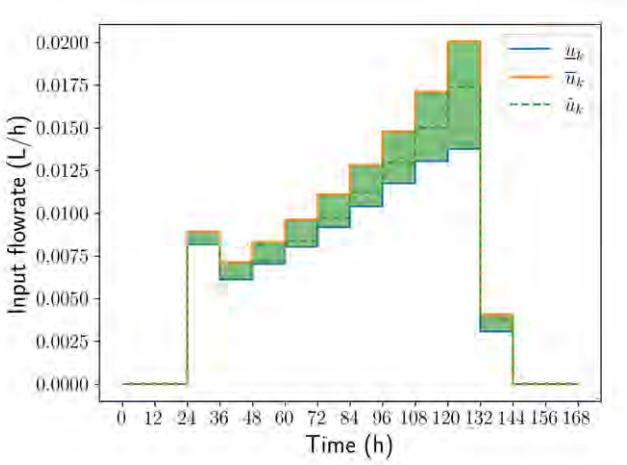



**Figure 2.** Designed operational space (shaded) using the proposed method.

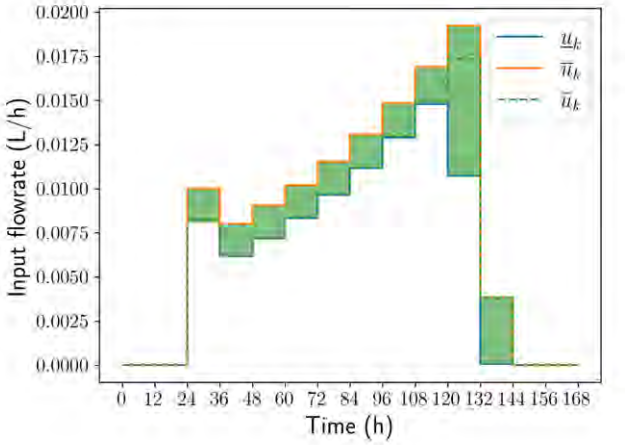



**Figure 3.** Designed operational space (shaded) using a conventional scenario optimization method (solved in one iteration).

## ACKNOWLEDGEMENTS

This work is supported by the Engineering and Physical Sciences Research Council [grant number EP/Y005600/1].

## REFERENCES

1. Alford JS, Bioprocess control: Advances and challenges. *Comput Chem. Eng.* 30:1464-1475 (2006)
2. Pharmaceutical development Q8. International Conference on Harmonisation of technical requirements for registration of pharmaceuticals for human use. Tech. Rep. (2006)
3. Zhang D, *et al.*, Hybrid physics-based and data-driven modeling for bioprocess online simulation and optimization. *Biotechnol. Bioeng*. 116(11):2919-2930 (2019)
4. Narayanan H, *et al.*, Bioprocessing in the digital age: the role of process models. *Biotechnol. J.* 15(1): 1900172 (2020)
5. Vega-Ramon F, *et al.*, Kinetic and hybrid modeling for yeast astaxanthin production under uncertainty. *Biotechnol. Bioeng.*118(12): 4854-4866 (2021)
6. Simutis R, and Lübbert A, Bioreactor control improves bioprocess performance. *Biotechnol. J.* 10(8): 1115-1130 (2015)
7. Rathore AS, *et al.* Bioprocess control: current progress and future perspectives. *Life* 11 (6):557 (2021)
8. Guo Y, Zhao Y, and Huang B. Development of soft sensor by incorporating the delayed infrequent and irregular measurements. *J Process Control* 24:1733-1739 (2014)
9. Hettich R, Kortanek KO. Semi-infinite programming: theory, methods, and applications. *SIAM Review* 35:380-429 (1993).
10. Goberna MA, Lopez MA (Eds). Semi-Infinite Programming: Recent Advances. Springer (2010)
11. Calafiore GC, Campi MC. The scenario approach to robust control design. *IEEE Trans Autom. Control* 51:742-753 (2006)
12. Bertsimas D, Brown DB, Caramanis C. Theory and applications of robust optimization. *SIAM Review* 53:464-501 (2011)
13. Chachuat B, *et al.*. Set-theoretic approaches in analysis, estimation and control of nonlinear systems. *IFAC-PapersOnLine* 48:981-995 (2015)
14. Puschke J, Djelassi H, Kleinekorte J, Hannemann-Tamás R, Mitsos A. Robust dynamic optimization of batch processes under parametric uncertainty: utilizing approaches from semi-infinite programs. *Comput Chem. Eng.* 116:253-267 (2018)
15. Jin R, Chen W, Simpson TW. Comparative studies of metamodelling techniques under multiple modelling criteria. *Struct Multidiscip. Optim.* 23:1-13 (2001)
16. Andersson JAE, *et al.*. CasADi — A software framework for nonlinear optimization and optimal control. *Math. Program. Comput.* 11:1-36 (2019)
17. Wächter A, Biegler LT. On the implementation of an interior-point filter line-search algorithm for large-scale nonlinear programming. *Math. Program.* 106:25-57 (2006)

© 2025 by the authors. Licensed to PSEcommunity.org and PSE Press. This is an open access article under the creative commons CC-BY-SA licensing terms. Credit must be given to creator and adaptations must be shared under the same terms. See https://creativecommons.org/licenses/by-sa/4.0/

Systems & Control Transactions

**Research Article - Peer Reviewed Conference Proceeding**
ESCAPE 35 - European Symposium on Computer Aided Process Engineering
Ghent, Belgium. 6-9 July 2025
Jan F.M. Van Impe, Grégoire Léonard, Satyajeet S. Bhonsale,
Monika E. Polańska, Filip Logist (Eds.)

PSE PRESS

# Fed-batch bioprocess prediction and dynamic optimization from hybrid modelling and transfer learning

**Oliver Pennington [a], Youping Xie [b], Keju Jing [c], Dongda Zhang [a]***

[a] University of Manchester, Department of Chemical Engineering, Manchester, United Kingdom
[b] Fuzhou University, Marine Biological Manufacturing Center or Fuzhou Institute of Oceanography, Fuzhou, China
[c] Xiamen University, Department of Chemical and Biochemical Engineering, College of Chemistry and Chemical Engineering, Xiamen, China
* Corresponding Author: dongda.zhang@manchester.ac.uk.

## ABSTRACT

Hybrid modelling utilizes advantageous aspects of both mechanistic (white box) and data-driven (black box) modelling. Combining the physical interpretability of kinetic modelling with the power of a data-driven Artificial Neural Network (ANN) yields a hybrid (grey box) model with superior accuracy when compared to a traditional mechanistic model, while requiring less data than a purely data-driven model. This study demonstrates the construction a hybrid model with transfer learning for the predictive modelling and optimization of a high-cell-density microalgal fermentation process for lutein production. Dynamic optimization was conducted to identify a feeding strategy that maximized final lutein production. The results were then experimentally validated. Overall, this work presents a novel digital twin application that can be easily adapted to general bioprocesses for model predictive control and process optimization.

**Keywords**: Machine Learning, Dynamic Modelling, Biosystems, Hybrid Modelling, Dynamic Optimization

## 1 INTRODUCTION

### 1.1 Motivation

Bioprocesses connect an abundance of global research interests, including the production of renewable plastics, fuels, and other valuable bioproducts. Economically speaking, the UK bioeconomy alone was worth around £220 billion in 2018, and is set to double by 2030 [1], making the field lucrative for research. Supporting bioprocess development requires overcoming several challenges, including batch-to-batch variation, deficient metabolic and secretory phenotypes for protein production, by-product accumulation, and reduced yields in the upscaling of bioreactors. Tackling these challenges involves identifying suitable microbial strains and their optimal operating conditions, as well as the development of optimal operation and control strategies. Conducting such process optimization exhaustively can be extremely time-consuming and resource-depleting; employing modelling can reduce the time and resources spent by using predictions to rule out less useful experiments.

With the ever-progressing fourth industrial revolution underway, digitalization is seeing increased application; utilizing digital twins has significant potential in the application of process optimization and control, as well as design of experiments. The concept of machine learning is being continuously applied in novel ways to unveil more economical, ethical, safer, efficient, and sustainable approaches to chemical processing. With the current growth of interest within the fields of both bioprocess engineering and artificial intelligence, there has not been a better time to harness and combine the advantages of each. However, accounting for uncertainty is an equally important step in the development of a model as it provides information surrounding the achievability of a found control strategy or optimum.

An example of where the combining of different modelling methodologies may be required is high-cell-density cultures (HCDCs). HCDCs can be capable of producing larger quantities of desired products, an example of which is lutein, a carotenoid pigment commonly used in the food industry. However, HCDCs can demonstrate self-inhibitory effects, where growth and/or substrate uptake is inhibited by the high cell density or high accumulation of products [2]. Gaining a better understanding

of these inhibitory effects is pertinent for optimizing processes utilizing HCDCs.

### 1.2 Aims

Ultimately, this model aspires to require minimal data and computational expense, while maximizing simulation accuracy for process optimization and control applications. The model should also have good generalisability, allowing for easy incorporation of new data to retrain the model. Fulfilling these goals will make the modelling methodology described in this work applicable to other bioprocesses involving HCDCs, such as Akkermansia muciniphila which has received recent attention for its probiotic capabilities in the intestinal tract [3]. With HCDCs being well suited to fed-batch and perfusion operation, they play a key role in moving towards the continuous operation of bioprocesses; such progression can be accelerated by the modelling and optimization strategy discussed in the recent study [4].

In this work, the term *hybrid modelling* relates to the combination of a physically derivable (white-box) model, with a data-driven (black-box) model to yield an overall hybrid (grey-box) model.

### 1.3 Case Study

The case study at hand looks at the production of lutein from Chlorella sorokiniana under fed-batch conditions using urea as the source of nitrogen and glucose as the carbon source. The dataset available also includes a preliminary batch using sodium nitrate (an alternative to urea) as the nitrogen source. Experiments were run for 168 hours with measurements of biomass density and lutein content taken art least every 12 hours. The fed-batch saw continuous feeding of high concentrations of glucose and urea (750 g $L^{-1}$ and 46.5 g $L^{-1}$, respectively).

## 2 METHODOLOGY

### 2.1 Experimental setup

Initially, a single batch process in a 250 mL flask (with 100 mL of working volume) was conducted using $NaNO_3$ as the nitrogen source, to which a preliminary kinetic model was fitted. Fed-batch operation was then conducted in a 5 L bioreactor with urea (which behaves similarly to $NaNO_3$) as the nitrogen source and continuous feeding over 168 h.

### 2.2 Macro-scale kinetic modelling

For the initial batch experiment, Monod-inspired kinetics were utilized. The concentrations of the substrates glucose ($G$) and urea ($N$), as well as cell density ($X$) and lutein content ($L_C$), are described by the system of 4 Ordinary Differential Equations (ODEs) as in

$$\frac{dX}{dt} = \mu \cdot X - d_X \cdot X \tag{1}$$

$$\frac{dG}{dt} = -v_{\max_G} \cdot \frac{G}{K_G+G} \cdot X \tag{2}$$

$$\frac{dN}{dt} = -v_{\max_N} \cdot \frac{N}{K_N+N} \cdot X \tag{3}$$

$$\frac{dL_C}{dt} = Y_{LX} - d_L \cdot L_C - \mu \cdot L_C \tag{4}$$

$$\mu = \mu_{\max} \cdot \frac{G}{K_G+G} \tag{5}$$

where $\mu_{\max}$ refers to the maximum specific growth rate of biomass, with $v_{\max_i}$ being the maximum specific uptake rate for a given substrate $i$, $K_i$ being the affinity constant for a given substrate $i$, $Y_{LX}$ being the specific production rate of lutein from biomass, and $d_i$ representing a decay term for a given product $i$. It should be noted that $L_C$ represents an intracellular concentration measured in mg (g biomass)$^{-1}$. To consider the overall lutein concentration in the reactor ($L$), product rule can be used with equations (1) and (4) to give the result as in

$$\frac{dL}{dt} = Y_{LX} \cdot X - d_L \cdot L \tag{6}$$

It is essential for parameters in the Monod model to remain positive in value to retain physical feasibility, as in

$$\boldsymbol{\beta} \geq \mathbf{0} \tag{7}$$

where $\boldsymbol{\beta}$ is the vector of Monod model parameters. Parameters were identified by minimizing the mean squared error objective function, as in

$$\min \frac{1}{n} \cdot \sum_{t,\text{meas}} \sum_i \left( \frac{C_{i_t} - C_{i_{\text{meas}_t}}}{\sigma_i} \right)^2 \tag{8}$$

where $n$ is the number of datapoints. The objective function minimizes the difference between the simulated extracellular concentration profiles and the measured averages at each timepoint; each term $i$ is weighted by its experimental measurement standard deviation; $\sigma_i$.

### 2.3 Hybrid modelling and transfer learning

Despite good fitting of the initial batch process, the parameters identified could not capture the entire fed-batch process, highlighting the difference between the $NaNO_3$-fed and urea-fed systems. The most noticeable process-model mismatches can be seen later in the process during high cell densities, particularly once the culture reaches a cell density over 5 times that seen in the preliminary batch experiment (seen around 30 h into the fed-operation). This indicates that substrate uptake and/or growth are being inhibited by high cell density, which can be due to poorer mass transfer of substrates to the cells due to their close proximity; a phenomenon observed in literature [5]. Therefore, three time-varying parameters were introduced: two capture the respective substrate uptake inhibition of glucose and nitrate ($\theta_G(\cdot)$ and $\theta_N(\cdot)$, respectively); and the other captures biomass growth inhibition ($\theta_X(\cdot)$). These time-varying parameters

are functions of state variables in the form of an ANN. Equations (1), (2), and (3) are therefore rewritten as in

$$\frac{dX}{dt} = \theta_X(\mathbf{S}) \cdot \mu \cdot X - d_X \cdot X - \frac{F}{V} \cdot X \quad (9)$$

$$\frac{dG}{dt} = \left(G_f - G\right) \cdot \frac{F}{V} - \theta_G(\mathbf{S}) \cdot v_{\max_G} \cdot \frac{G}{K_G + G} \cdot X \quad (10)$$

$$\frac{dN}{dt} = \left(N_f - N\right) \cdot \frac{F}{V} - \theta_N(\mathbf{S}) \cdot v_{\max_N} \cdot \frac{N}{K_N + N} \cdot X \quad (11)$$

$$\mathbf{S} = [X, N, G] \quad (12)$$

where $G_f$ and $N_f$ are the feed concentrations of glucose and urea, respectively, $F$ and $V$ are the feed rate and reactor volume, respectively, $\mathbf{S}$ is the vector of state variables, and the remaining parameters in Equations (4)-(5) and (9)-(11) take the same value as those previously identified. Constant volume is assumed. During the identification of time-varying parameters, their deviations are penalised to try and follow the kinetic model dynamics as closely as possible, thus maximizing knowledge transfer, Penalization is done using a penalty term, that is added to the objective function shown in Equation (8), as in

$$\min \frac{1}{n} \cdot \sum_{t,\text{meas}} \sum_i \left(\frac{C_{i_t} - C_{i_{\text{meas}_t}}}{\sigma_i}\right)^2 + \rho \cdot \sum_{t,\text{TVP}} \sum_i \left(\theta_i(t) - \theta_i(t-1)\right)^2 \quad (13)$$

where $\rho$ is a hyperparameter to be tuned. The time-varying parameters are then reformulated as a function of state variables using an ANN. The ANN is embedded within the system of ODEs as illustrated in Figure 1, where state variables update the ANN which updates the time-varying parameters, which can be used in the system of ODEs to update the state variables, thus generating state variable profiles.

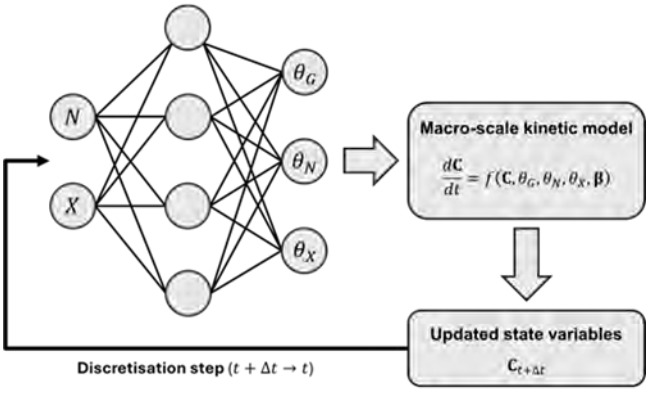



**Figure 1.** Hybrid model structure: Simulation of time-varying parameters based on system components using an ANN.

Comparing the performance of several ANN architectures allowed the identification of the most appropriate ANN structure. The Akaike Information Criterion with correction for small sample sizes (AICc) was employed to quantify the performance of each ANN structure, as in

$$AICc = n \ln Z + 2\,k + \frac{2\,k^2 + 2\,k}{n - k - 1} \quad (14)$$

where $k$ is the number of parameters with a correction for the small sample size $n$. The ANN architecture with the lowest AICc score was chosen as the best trade-off between minimal overfitting and accuracy.

## 2.4 Uncertainty analysis

Uncertainty analysis was conducted using bootstrapping which involved taking samples of the training dataset and training the model on each sample separately, generating a distribution of model outputs, as illustrated in Figure 2. A 95% confidence interval ($z_{CI}$) of each component $z$ was generated by sampling from the resulting output distribution, as in

$$z_{CI} = \bar{z} \pm c \cdot \frac{\sigma_z}{\sqrt{\frac{n_z - 1}{n_z}}} \quad (15)$$

where $\bar{z}$ is the mean of the component $z$, $c$ is the confidence level, $n_z$ is the number of samples of the component $z$, and $\sigma_z$ is the standard deviation of the component $z$. In this study, bootstrapping was conducted by removing 48-hour segments of data, a third of the fed-batch time horizon.

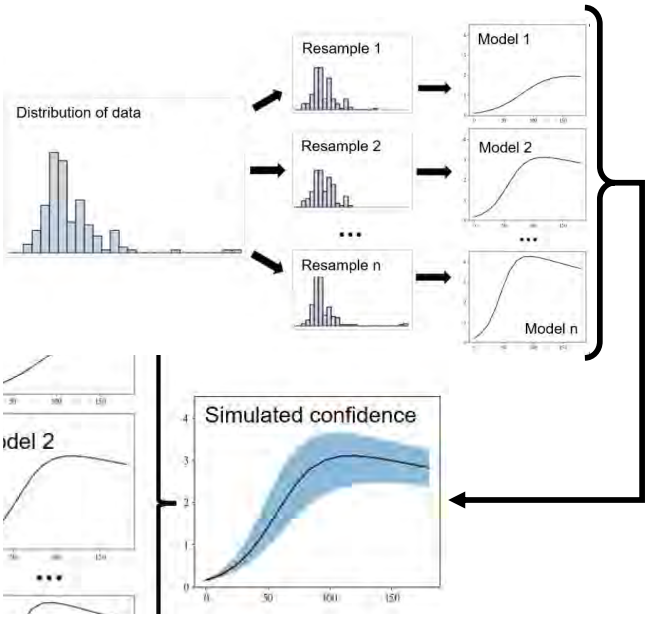



**Figure 2.** Bootstrapping: Schematic.

## 2.5 Feed optimization

The dynamic optimization problem follows the general NLP problem described by

$$\min_{\mathbf{F},\mathbf{N_f}} -L(t_f) \quad (15)$$

s. t. $$0 \leq F(t) \leq 50 \text{ mL h}^{-1} \quad (16)$$

$$0 \leq N_f(t) \leq 60 \text{ g L}^{-1} \quad (17)$$

where $\mathbf{F}$ and $\mathbf{N_f}$ are the vectors of discretized dynamic feed rate and urea feed concentration, respectively, and $t_f$ is the predetermined final time of the batch. Both feed rate and urea feed concentration were allowed to vary every 12 hours, giving the optimization problem 28 degrees of freedom. The dynamic optimization problem was solved using a gradient descent method in the Python optimization package Pyomo. Glucose concentration was also constrained between 3 and 7.5 g $L^{-1}$ beyond a time of 30 h to ensure stable fed-batch operation.

## 2.6 Methodology summary

The overall modelling methodology was conducted in a manner that requires minimal data collection for model construction and is illustrated in Figure 3.

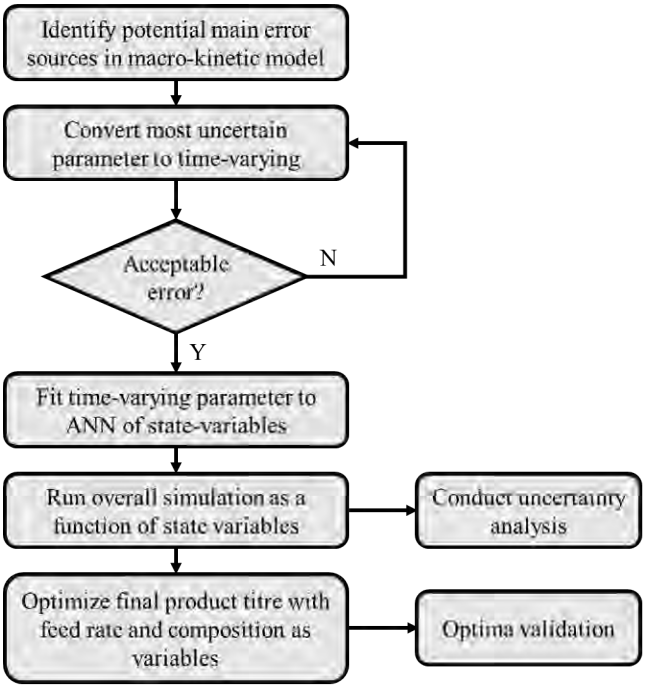



**Figure 3.** Methodology: Summary of dynamic optimization from hybrid model construction for fed-batch lutein production under uncertainty.

# 3 RESULTS AND DISCUSISON

## 3.1 Results of hybrid modelling

The purely mechanistic macro-scale kinetic model was first fit with Equations (1)-(5) with no time-varying parameters. The fitting of the preliminary kinetic model has a mean $R^2$ value of 0.995 and is shown in Figure 4. Parameter estimation converged after 50 iterations using a derivative-free Particle Swarm Optimization (PSO) algorithm. The selected algorithm has strong exploratory capabilities for parameter estimation in the stiff fed-batch system simulated in this study. The problem was run 5 times, each with 100 particles, to confirm the same optima was being found, increasing the confidence in it being a global optimal solution.

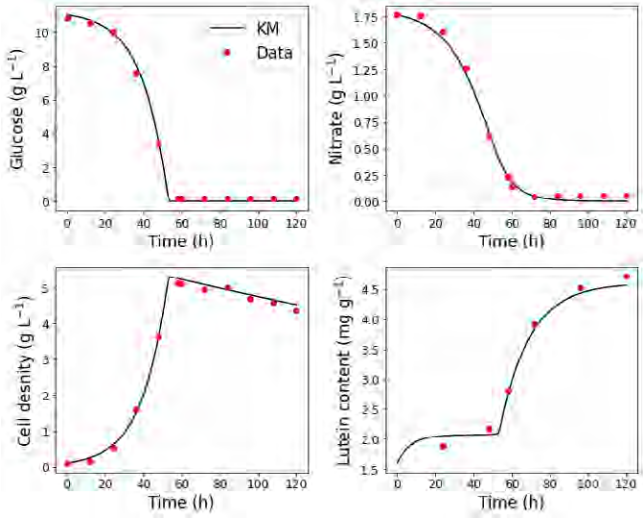



**Figure 4.** Kinetic model (KM): Plots of substrates glucose and nitrate, biomass and lutein content fitted to the original batch using $NaNO_3$ as a nitrogen source.

The application of this kinetic model to a 5 L fed-batch process, where the cell density reaches levels in excess of 10 times higher than the batch process, illustrated significant process-model mismatch, particularly in the latter stages at the highest cell densities, which is evident in the resulting mean $R^2$ value of -0.026 for the overall system. This motivated the introduction of time-varying parameters to better fit the more challenging dynamics seen in the latter stages of the fed-batch process. Time-varying parameters were first introduced to a fed-batch operation that reinstated the same initial substrate concentrations as the preliminary batch process after each injection of concentrated medium. Time-varying parameters were initially simulated as a discretized function of time. Parameter estimation converged within 100 iterations of the IPOPT algorithm in the Python package SciPy.

The resulting time-varying parameter profiles were then used to train the ANN. The most appropriate ANN architecture had seven hidden nodes and sigmoid activation functions. The ANN was trained over 1700 epochs using data augmentation, following the method described in a previous study [6]. The fitting of the hybrid model is shown in Figure 5, with the profiles of the corresponding time-varying parameters shown in Figure 6. The introduction of time-varying parameters increased the mean $R^2$ value for cell density and lutein content from

-0.026 to 0.855. The decreasing trend of the time-varying parameters simulated by the ANN for glucose and biomass highlights the inhibitory effects that the high-cell-density has on substrate uptake and growth. It is observable that all parameters saw an overall decrease in value from start to finish, further emphasizing the inhibitory effects of a HCDC system.

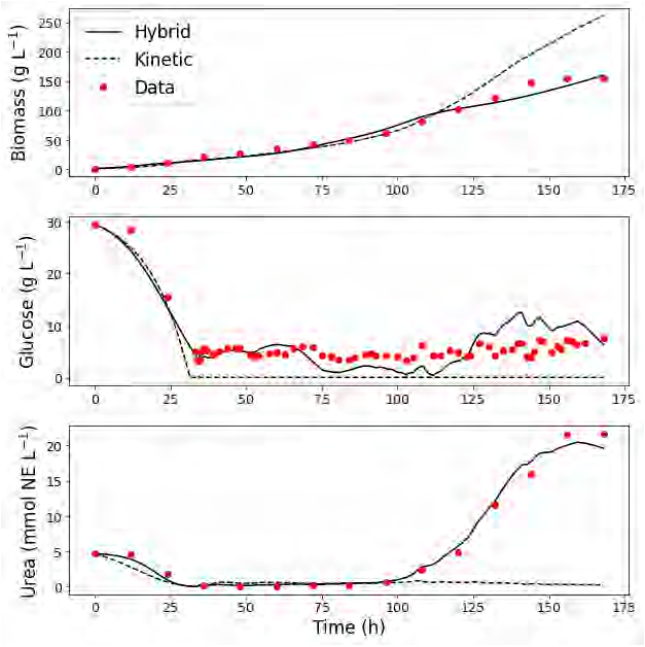



**Figure 5.** Hybrid model (HM): Plots of substrates glucose and nitrate, and biomass for fed-batch simulation with comparison to the original Kinetic Model (KM). Note that Nitrate Equivalent (NE) refers to the equivalent concentration of nitrogen in a solution of $NaNO_3$.

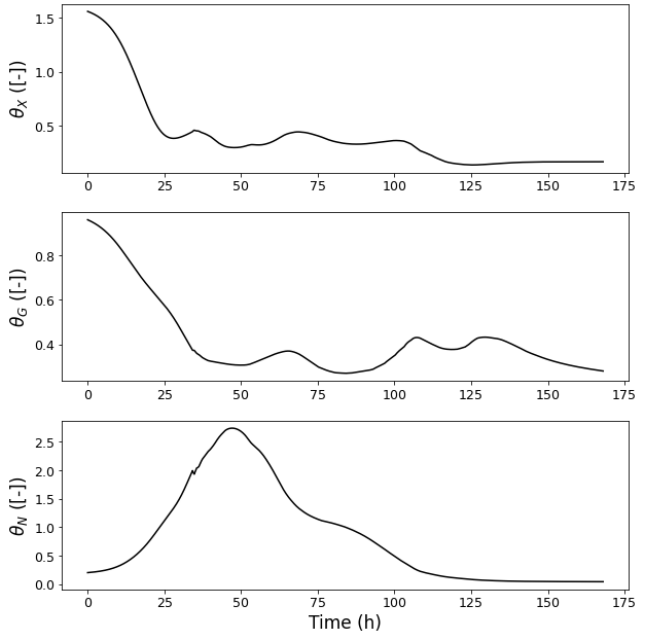



**Figure 6.** Hybrid model: Time-varying parameters.

## 3.2 Results of feed optimization

The optimization of feed rate and composition was successfully conducted, converging within 500 iterations of the IPOPT algorithm on the Python package Pyomo. Figure 7 shows the optimized trajectories in comparison to the original experimental conditions. All constraints were successfully satisfied.

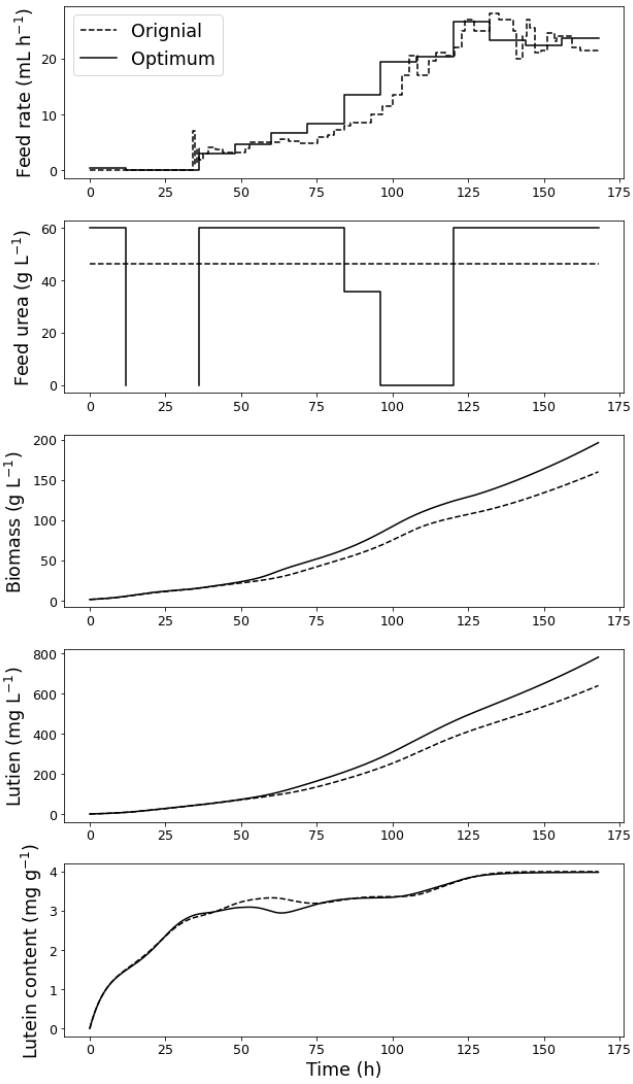



**Figure 7.** Optimized feeding: Plots of feeding rate and feed urea concentration changing every 12 hours, as well as plots of biomass and lutein concentration and content for both the original and optimized cases. It should be noted that there is no urea feed concentraiton between times 12 h and 36 h since there is no feeding during this period.

Figure 7 shows an increase in lutein production from the original experiment of over 25%. Since the lutein content is almost unchanged, the increased production is coming exclusively from increased biomass growth, which is most noticeable beyond a time of 50 h. This

implies that for optimizing the lutein content of the cell, strain modification would be a more attractive option as external control variables have less impact on the internal lutein content than the biomass growth.

A significant difference between the substrate trajectories can be seen for urea, for which the optimized case demonstrates the maintenance of a low urea concentration within the vessel, while still feeding enough to sustain the biomass. This implies that nitrate may be inhibitory towards optimal product formation, despite being required for biomass growth.

In terms of the feed trajectories, the most noticeable difference between the original and the optimized case for feed rate is between 60-110 h, where the optimized trajectory shows higher flowrate. This causes an increase in growth during this period without causing a spike in glucose concentration within the reactor, thus allowing more lutein to be produced. Urea feed concentration generally lies at the upper bound of 60 g $L^{-1}$, with the exception of 12-36 h where there is no flow, and 84-120 h where the spike in urea concentration occurred in the original experiment, suggesting that such an increase in urea concentration may be inhibitory to the system.

Although increasing the number of discretization steps for the feed profile could further improve the optima, it would need to be coupled with uncertainty to assess the attainability of a more specific solution.

## 4 CONCLUSIONS

In this study, a hybrid model was constructed with transfer learning to simulate a fed-batch HCDC system for lutein production. The introduction of time-varying parameters facilitated the capture of increasingly inhibited system dynamics during the latter stages of fed-batch operation. The varying system dynamics were accurately captured, thus maximizing the model's applicability to simulate fed-batch processes under alternate operating conditions. Time-varying parameter values were also penalized, which maximized knowledge transfer and assisted in reducing model overfitting by avoiding dramatic changes between subsequent time-varying parameter values. The kinetic backbone used for the hybrid model construction incorporated as much physical information as possible, meaning minimal additional data was required to train the ANN for both the original hybrid model and the transfer learning updated hybrid model. The ANN allowed the hybrid model to remain a function of observable state variables while being able to capture nonlinear dynamics that cannot be considered by the kinetic backbone. The successful implementation of dynamic optimization facilitated the prediction of optimal feeding trajectories under plausible operating conditions for experimental validation.

Overall, the optimization shows plausible predictions for experimental validation. The success of this modelling strategy and application to fed-batch optimization paves the way towards the development of an effective digital twin for the modelling of fed-batch systems for maximizing lutein production and yield for future fed-batch HCDC operation. The ability of this framework to incorporate a data-driven model with minimal data gives it substantial potential in applications to novel bioprocesses, where both experimental data and mechanistic understanding are limited.

## ACKNOWLEDGEMENTS

The authors would like to acknowledge our experimental collaborators in Fuzhou University and Xiamen University, as well as BBSRC for the funding of this work.

## REFERENCES

1. Harrington, R. Growing the bioeconomy: a national strategy to 2030, HM Government (2018)
2. Riesenberg, D., and Guthke, R. High-cell-density cultivation of microorganisms. Applied Microbiology and Biotechnology, volume 51, pages 422-430 (1999)
3. Wu, H., Shuhua, Q., Ruixiong, Y., Qihua, P., Yinghua, L., Chuanyi, Y., Ning, H., Song, H., and Xueping, L. Strategies for high cell density cultivation of Akkermansia muciniphila and its potential metabolism. Journal of Clinical Microbiology, volume 12, issue 1 (2024)
4. Zinnecker, T., Reichl, U., and Genzel, Y. Innovations in cell culture-based influenza vaccine manufacturing – from static cultures to high cell density cultivations. Human Vaccines & Immunotherapeutics, volume 20, article 2373521 (2024)
5. Ruhe, Z.C., Low, D.A., and Hayes, C.S. Bacterial contact-dependent growth inhibition. Trends in Microbiology, volume 21, issue 5, pages 230-237 (2013)
6. Rogers, A.W., Song, Z., Vega-Ramon, F., Jing, K., and Zhang, D. Investigating 'greyness' of hybrid model for bioprocess predictive modelling. Biochemical Engineering journal, volume 190 (2020)

© 2025 by the authors. Licensed to PSEcommunity.org and PSE Press. This is an open access article under the creative commons CC-BY-SA licensing terms. Credit must be given to creator and adaptations must be shared under the same terms. See https://creativecommons.org/licenses/by-sa/4.0/



Systems & Control Transactions

**Research Article - Peer Reviewed Conference Proceeding**
ESCAPE 35 - European Symposium on Computer Aided Process Engineering
Ghent, Belgium. 6-9 July 2025
Jan F.M. Van Impe, Grégoire Léonard, Satyajeet S. Bhonsale,
Monika E. Polańska, Filip Logist (Eds.)

PSE PRESS

# Plant-wide Modelling of a Biorefinery: Microalgae for the Valorization of Digestate in Biomethane plants

**Davide Carecci[a], Elena Ficara[b], Ignazio Geraci[c], Alberto Leva[a] and Gianni Ferretti[a*]**

[a] Politecnico di Milano, Department of Electronics, Information and Bioengineering (DEIB), Milan, MI, Italy
[b] Politecnico di Milano, Department of Civil and Environmental Engineering (DICA), Milan, MI, Italy
[c] A2A S.p.A., via Lamarmora 230, Brescia, BS, Italy
* Corresponding Author: gianni.ferretti@polimi.it.

## ABSTRACT

Microalgae cultivation on liquid digestate from the anaerobic co-digestion of agricultural feedstocks is an interesting option for digestate nutrient removal and resource recovery coupled to value-added biomass production. In this paper, a first-principle plant-wide modelling of the process is described. Two well-established models for anaerobic digestion (IWA – ADM1) and algae-based bioremediation processes (ALBA) were considered and modified with necessary equations and extensions to develop a coherent interface between the state variables of the two models. The resulting system is composed by highly non-linear and non-smooth DAEs. Open-loop scenario analysis for different upstream co-digester design and operating conditions was carried out to assess the impacts on the downstream microalgae outputs. It highlighted the importance of a proper biorefinery design and yet a noteworthy robustness of the system performance. The exploitation of the model can facilitate: a more realistic assessment of the process's technical-economic feasibility and the design/validation of classical and advanced feedback control strategies.

**Keywords**: Plant-wide modelling, Anaerobic co-digestion, Microalgae bioremediation, Digestate valorisation.

## I. INTRODUCTION

The production of bio-methane in Europe, currently supported by regulatory and economic tools, is increasing. Growing phototrophic microalgal biomass on the liquid fraction of bio-methane plant's digestate is an interesting possibility for the low-energy request, high potential for nutrients recycling, and simultaneous valorisation of $CO_2$ from biogas upgrading. Some microalgae strains have interesting plant's bio-stimulating properties, making them particularly suitable for the integration of algal nutrient recovery in a highly growing market. To assess the techno-economic feasibility of this biorefinery approach, a plant-wide model was developed integrating previously validated mathematical models and developing the required interfaces [1]. The plant-wide modelling framework includes two main mechanistic grey-box (uncertain parameters) physico-chemical and biological three-phase (liquid, solid, gas) models. The bio-methane plant model (agri-AcoDM) is based on the IWA ADM1 model [2], that was validated over a wide range of operational and feeding conditions [3]. The latter has been extended to account for phosphorous (P) transformations and for the non-ideality of the equations in the pH sub-model [4]. For the case studies of interest, it was proved that was reasonable to neglect ion-pairing equations, considering only major calcium and magnesium salt precipitates. For the modeling of the hydrolysis of multiple and complex feedstocks, some original state variables have been de-lumped [5]. The ALBA model [6] was used to predict the growth of algae-bacteria consortia in outdoor raceway ponds (RWP): the original model, validated on synthetic wastewater and liquid fraction of digestate, was integrated to consider organic acids in the influent. The precipitation of major P salts was also integrated, in continuity with the agri-AcoDM `block`. The evolution of temperature in the RWP system (either open or covered with single- or double-covered greenhouses) is a key factor for optimal algal growth and was modelled with a validated greenhouse pond system's (GPS) mechanistic model [7], integrating also temperature's feedback control to maintain the culture within strain-specific optimal ranges. Two solid-liquid (S/L) separation units were considered (a screw press followed by cationic

polyelectrolyte-assisted flocculation and centrifugation) to reduce digestate turbidity and guarantee light penetration in the algae pond. A "Copp-like interface" was implemented to properly relate the agri-AcoDM to the ALBA state variables, by lumping and redistributing the chemical oxygen demand (COD), carbon (C), nitrogen (N) and P contents; mass conservation was guaranteed by inorganic dissolved nutrients as sources or sinks [4].

The paper is organized as follows: Section II illustrates the model structure; Section III recalls the case study; in Section IV the simulation results are discussed; finally, in Section V a conclusion is drawn.

## II. MODEL STRUCTURE AND IMPLEMENTATION

The model was implemented using Modelica, an open-source, high-level, declarative and object-oriented modelling language employing the free OpenModelica interpreter (Fig. 1) [8]. The overall differential algebraic equation (DAE) system is defined as Eq.1, where $\boldsymbol{x}$ and $\boldsymbol{z}$ are dynamic and algebraic variables respectively, $\boldsymbol{u}$, $\boldsymbol{\theta}$ and $\boldsymbol{y}$ are inputs, fixed parameters and measurable outputs respectively. Functions $\boldsymbol{f}$ and $\boldsymbol{g}$ are highly non-linear (in some cases $\in C^0$).

$$\begin{cases} \dot{\boldsymbol{x}} = \boldsymbol{f}(\boldsymbol{x}, \boldsymbol{z}, \boldsymbol{u}, \boldsymbol{\theta}) \\ \boldsymbol{0} = \boldsymbol{g}(\boldsymbol{x}, \boldsymbol{z}, \boldsymbol{u}, \boldsymbol{\theta}) \\ \boldsymbol{y} = \boldsymbol{h}(\boldsymbol{x}, \boldsymbol{z}, \boldsymbol{u}, \boldsymbol{\theta}) \end{cases} \quad (1)$$

Parameters $\boldsymbol{\theta}$ are partitioned to the concentration (kg m$^{-3}$) of variables in the $i^{th}$ co-feedstock input flux ($\boldsymbol{\theta_{u,i}}$) and stoichiometric, physico-chemical and kinetic parameters ($\boldsymbol{\theta_p}$). Within a new Modelica library, each unit `block` of the **`biorefinery`** class has been defined by a dedicated model equipped with the necessary input/output information ports and physical connectors. In particular, two different types of connectors have been created to allow for the exchange of gas media (biogas, as perfect gas mixture) and of non-ideal heterogenous solid/liquid mixtures (feedstocks, digestate, algae suspension): the latter is agri-AcoDM- and ALBA-specific, due to the different state variables of the two models. For this reason, a dedicated model (the "Copp-like interface") to convert the two model's state variables have also been considered in the library. Of particular interest, is the exploitation of the **`stream`** connectors in the declaration of the interface components, to allow for immediate and flexible mixing of the different co-feedstocks. In the following, the sub-models in Fig. 1 are briefly described.

### (a) Model inputs

The inputs to the **`biorefinery`** model are process design fixed parameters, weather data for the GPS and influent feedstock's nutrient compositions for agri-AcoDM. The latter can be set both as $\boldsymbol{\theta_{u,i}}$ or from `CombiTimeTables` to consider feedstock variability. Dedicated conversions' equations between composition's data and model's state variables are performed for both pumpable and stock-piled feedstocks [3, 9].

### (b) Anaerobic co-digester (agri-AcoDM)

From the hydraulic standpoint, the reactor is a closed and completely stirred tank reactor (CSTR) with constant volume. The ordinary differential equation (ODE) system state variables are 38 concentrations (kg m$^{-3}$) in the specific media of either bacterial populations or organic/inorganic chemical total components, dissolved and gaseous. The state variables interact with each other via biological (hydrolysis, uptake, decay) and physico-chemical (precipitation/dissolution and gas-liquid mass transfer (two-film theory)) process rates $r$ (kg m$^{-3}$ s$^{-1}$). The generic ODE equation for the liquid-solid mixture mass balances is:

$$\begin{cases} \dot{\boldsymbol{x}} = \frac{\sum_{i=1}^{n} u_i}{V}(\boldsymbol{x_{in}} - \boldsymbol{x}) + \mathbf{K_G}\mathbf{r}(\boldsymbol{x}, \boldsymbol{\theta_p}, \boldsymbol{z}) \\ \boldsymbol{x_{in}} = \frac{\sum_{i=1}^{n} u_i \boldsymbol{\theta_{u,i}}}{\sum_{i=1}^{n} u_i} \end{cases} \quad (2)$$

where $\boldsymbol{x}$ are the state variables, $V$ (m$^3$) is the reactor volume, $u_i$ (m$^3$ d$^{-1}$) is the volume flowrate of the $i^{th}$ input co-feedstock and $\mathbf{K_G}$ is the transposed stoichiometric Gujer matrix, that guarantees COD and atomic mass conservation, extended and modified according to the new variables and processes introduced. Note that $\boldsymbol{r}$ depends on $\boldsymbol{z}$ too, as the latter refers to physico-chemical quantities characterized by very fast dynamics and later described. For gaseous states, Eq.2 still holds and has a null influent contribution, $V$ is the reactor headspace volume and $u_i$ is the biogas outflow, regulated by a SISO PI controller that keeps the reactor headspace slightly over atmospheric pressure. An example of the model non-linearities is shown in Eq.3, defining the general structure of a bioprocess kinetic rate $r$ representing the gross growth of a bacteria population with concentration $X_{ac}$ (aceto-clastic methanogens), i.e.:

$$r = \mu_{max} f_{pH} \frac{K_{i,nh3}}{K_{i,nh3} + S_{nh3}} \min_j \left( \frac{S_j}{S_j + K_{s,j}} \right) X_{ac} \quad (3)$$

where $\mu_{max}$ (d$^{-1}$) is the maximum specific growth rate and $f_{pH}$ is an empirical sigmoidal function that describes pH inhibition. Free ammonia ($S_{nh3}$ (M)) inhibition is represented by the non-competitive function which shape is defined by $K_{i,nh3}$ (M). Growth limitation by nutrient uptake is described by secondary Monod functions subject to the Liebig's minimum law, where $K_{s,j}$ (M) is the half-saturation constant for the nutrient $S_j$ ($j$ = {inorganic C, N, P and acetic acid}) [2]. A multiplicative term that depends on the sign of the saturation index $SI$ is used to discriminate precipitation ($r_{p,+}$) from dissolution ($r_{p,-}$) kinetics for

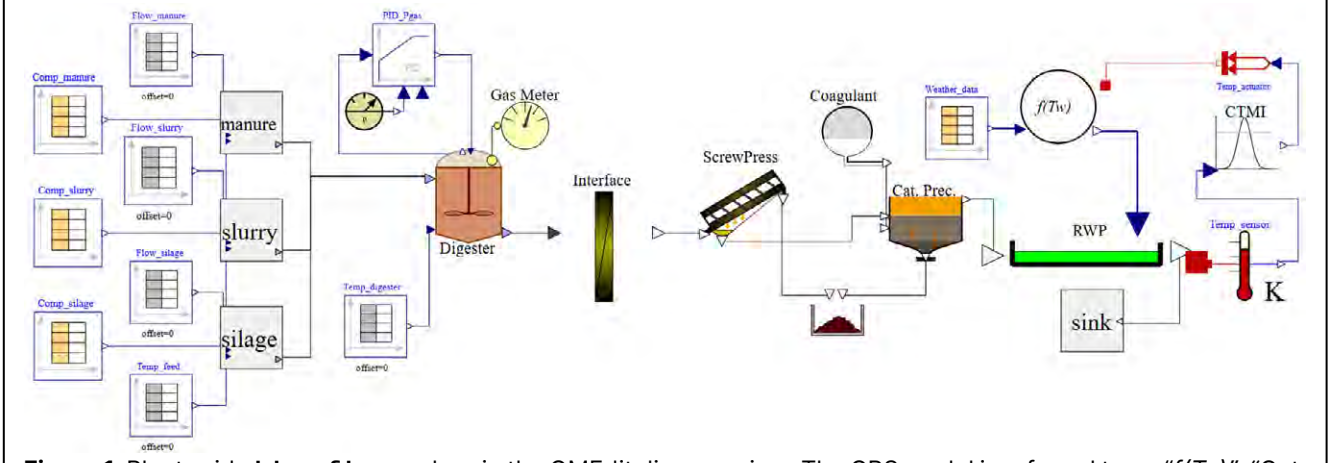



**Figure 1:** Plant-wide **`biorefinery`** class in the OMEdit diagram view. The GPS model is referred to as *"$f(T_w)$"*. "Cat. Prec." (cationic precipitation) refers to be flocculation unit. The Copp-like interface was called "Interface".

each salt with concentration $X_{salt}$, as in Eq.4:

$$r_{p,\pm} = \frac{1\pm sign(SI)}{2} k_{cryst} X_{salt} \left[ \left( \frac{\prod_{i=1}^{n_r} a_{i,j}}{K_{sp}} \right)^{\frac{1}{n_r}} - 1 \right]^2 \quad (4)$$

where $a_{i,j}$ (M) are the activities of the chemical ionic species involved in the process, $j$ is their stoichiometric coefficient, $n_r$ is the number of moles of reactants, $K_{sp}$ (M) the solubility product constant and $k_{cryst}$ the kinetic constant ($s^{-1}$) [10]. To avoid excessive stiffness for the ODE solver, the acid-base physico-chemical reaction equations have been modeled as an algebraic equation (AE) system ($\boldsymbol{z} \in \mathbb{R}^{30}$), within a **`partial model`** extended to the reactor model (the $\boldsymbol{g}$ function of Eq.1). The latter has a subset of state chemical total components $x_j, j = 1 \dots N_c$ as input and outputs the chemical ionic speciation $S_i, i = 1 \dots N_s$, the pH and the ionic strength $I$ ($mol_{eq}$ $L^{-1}$) of the liquid mixture, exploiting $N_c$ molar balances (Eq.5), $N_s - N_c$ chemical equilibrium equations, the charge balance over mixture neutrality hypothesis (Eq.6) and the definition of $I$ (Eq.7) [10]; activity corrections $\gamma$ are computed from the Davies equation (Eq.8):

$$0 = x_j - \sum_{i=1}^{N_s} \upsilon_{i,j} S_i \quad (5)$$

$$0 = \sum_{i=1}^{N_s} z_i^2 S_i^{z_i} - S_{OH^-} + S_{H^+} \quad (6)$$

$$I = \frac{1}{2} \sum_{i=1}^{N_s} z_i^2 S_i^{z_i} \quad (7)$$

$$\log_{10} \gamma = -A z_i^2 \left( \frac{\sqrt{I}}{1+\sqrt{I}} - BI \right) \quad (8)$$

where $S_i$ is a molar concentration (M) of the $i^{th}$ chemical ionic species and $z_i$ its charge, $\upsilon_{i,j}$ are stoichiometric parameters, A and B are solution-specific parameters, $S_{OH^-}$ and $S_{H^+}$ (M) are the molar concentrations of water hydroxide and hydrogen ions. The resulting non-linear algebraic loop was simplified by neglecting ion-pairing reactions, so that the number of residual equations after *tearing* is reduced from $N_c + 1$ down to 2 ($I$, pH), reducing the dependency of the Newton-Raphson solver on proper start guesses. The consistency of the physico-chemical sub-model extensions and hypothesis was verified by comparison with both results from literature [4] and Visual MINTEQ 3.1.

### (c) Copp-like interface

The interface contains algebraic equations intended to redistribute or lump the nutrient contents in the inlet stream to the components of the outlet connector. This is primarily because the two bio-process models are characterized by a different lumping degree of the chemical components that describe the liquid mixture. Consequently, some of them are also characterized by different elemental contents. For example, the biodegradable particulate organic matter concentration $X_s$ ($g_{COD}$ $m^{-3}$) in ALBA is intended to lump the biodegradable particulate carbohydrates $X_{ch}$ ($kg_{COD}$ $m^{-3}$), proteins $X_{pr}$) ($kg_{COD}$ $m^{-3}$) and lipids $X_{li}$ ($kg_{COD}$ $m^{-3}$) of agri-AcoDM, as well the biodegradable fraction of the bacterial biomass that does not survive in the RWP:

$$X_s = 10^3 \left[ \left(1 - f_{xh,xb} - f_{xnit,xb}\right)\left(1 - f_{xi,xb}\right) \sum_{i=1}^{5} X_{bm_i} + \right.$$
$$\left. + \left(1 - f_{xi,xb}\right) \sum_{i=1}^{2} X_{bm_j} + X_{pr} + X_{ch} + X_{li} \right] \quad (9)$$

where $f_{..}$ are portioning parameters, $X_{bm_i}$ and $X_{bm_j}$ ($kg_{COD}$ $m^{-3}$) are agri-AcoDM facultative aerobic and strictly anaerobic bacterial populations respectively. Any difference in the elemental contents is added/removed from the correspondent dissolved inorganic concentration $S_j$ of element $j$ (C, N, P) to guarantee atomic mass conservation, i.e.:

$$S_j = \sum_{i=1}^{n} x_i \nu_{j,i} - \sum_{k=1}^{m} x_k \nu_{j,k} \quad (10)$$

where $n$ and $m$ are the number of agri-AcoDM and ALBA states restricted to the liquid-solid mixture respectively, and $\nu_{j,i}$ ($g_j$ $g_i^{-1}$) are the stoichiometric fixed parameters that represent the content of element $j$ in the state $i$

(same holds for $k$).

### (d) Solid-liquid separation units

The screw-press model contains mass balance algebraic equations. Additional equations are used to specify the portioning of each state variable to the two output mass ports, via fixed average removal efficiencies. The flocculation unit contains similar equations, while accounting for the dilution factor introduced by the coagulant dosage.

### (e) Thermal sub-models (GPS)

The state variables are the 3 temperatures of the interacting heat capacities and the water vapour content $e_{int,air}$ (kg $m_{air}^{-3}$) of the greenhouse internal air. The state variables interact with each other via conductive, convective, latent-convective and radiative heat fluxes $\mathbf{\Phi}$ (W). The ODE ($\boldsymbol{x} \in \mathbb{R}^4$) are the energy balances of each uniform layer, i.e.:

$$CV\dot{\boldsymbol{T}} = Q(\boldsymbol{T_{in}} - \boldsymbol{T}) + \mathbf{\Phi}(\mathbf{T}, \boldsymbol{\theta}, \boldsymbol{d}) + \boldsymbol{u} \quad (11)$$

where $C$ (J $m^{-3}$ $°C^{-1}$) is the volume-specific heat capacity, $V$ ($m^3$) is the volume, $\boldsymbol{\theta}$ are fixed parameters, $\boldsymbol{d}$ are the external disturbances (i.e. external global irradiance at ground $I_0$ (W)) and $\boldsymbol{u}$ are the control inputs. The first additive forcing term is related to the enthalpic contributions of inlet/outlet flows of matter $Q$ ($m^3$ $s^{-1}$), which are present only for the internal air and RWP water layers. Water mass balance over the greenhouse internal air is used to calculate $e_{int,air}$, which is involved in the latent-convective heat exchange. The cover temperatures are algebraic variables (negligible heat capacity). A MISO conditional PID control is in place on RWP water temperature via both direct heat/cool flux and indirect mechanical ventilation air exchanges as control variables.

### (f) Raceway pond (ALBA)

From the hydraulic standpoints, the reactor is an open and completely stirred tank reactor (CSTR) with constant volume. The same acid-base reactions algebraic system described in (b) was extended to this model. The state variables $\boldsymbol{x}$ are 31 concentrations in the specific media of either bacterial aerobic populations, microalgae or organic/inorganic matter total components. Some of the latter are not present in agri-AcoDM and viceversa (e.g. dissolved oxygen $S_{O_2}$). The state variables interact with each other via biological (hydrolysis, growth, respiration, decay) and the same physico-chemical process rates described in (b). The ODE for the liquid-solid mixture are mass balances similar to the one described in (b), i.e.:

$$\dot{\boldsymbol{x}} = \frac{Q}{V}(\boldsymbol{x_{in}} - \boldsymbol{x}) + \mathbf{K_P}\,\mathbf{r}\left(\boldsymbol{x}, \boldsymbol{\theta_p}, \boldsymbol{z}, \boldsymbol{d}\right) \quad (12)$$

where $Q$ ($m^3$ $d^{-1}$) is the volumetric flowrate of influent diluted and separated liquid digestate and $\boldsymbol{d}$ are disturbances, mainly external air temperature T (°C) and total solar irradiance at ground (converted to photo-synthetically active radiation (PAR) $I_{PAR}$ (µmol $s^{-1}$)). Matrix $\mathbf{K_P}$ is the transposed stoichiometric Peterson matrix [6] that guarantees COD and atomic mass conservation, extended and modified according to the new variables and processes introduced. The general expression of bio-process kinetics is similar to the one reported in (b), but additional multiplicative terms related to temperature and PAR dependency are present for microalgae rates. A SISO conditional (upper-bound) P control is performed on raceway pH via $CO_2$ injection as control variable.

## III. MODEL APPLICATION

The following design assumptions and data were used for the biorefinery under study:

- *Location and weather data*. The plant is located in the Northern Italy (Cremona) and local weather data were used to run simulations.
- *Anaerobic co-digester*. A 1-MW plant was considered with two parallel fermenters and a post-fermenter (hydraulic retention time (HRT) = 33 d, 42°C). The plant is fed with cattle slurry (72%$_{ww}$), solid cattle manure (8 %$_{ww}$) and, according to the season, maize silage (October-June) or tomato peels (July-September) (20%$_{ww}$). An average biogas flowrate of approximately 11'000 $Nm^3$ $d^{-1}$ ($CH_4$: 51.5%, $CO_2$: 48.5% v/v) is generated, along with 180 $m^3$ $d^{-1}$ of raw digestate (6–7 %TS).
- *Digestate S/L separation and pre-treatments*. The liquid fraction of digestate is further separated through screw press and flocculant-assisted centrifugation.
- *Algal cultivation ponds*. A large-scale system (surface 7'560 $m^2$, liquid height 20 cm, HRT = 5 d) was designed to grow a *Chlorella-Scenedesmus* consortium. In the latter, pH is controlled to remain below 7.5, whereas temperature is not.

The flexibility and applicability of the model was tested in an open loop scenario analysis (Table 1) to verify the process feasibility in terms of microalgae biomass harvesting rates, when forcing the system with different agri-AcoD influent diet (e.g. slurry/maize ratio) and design (e.g. HRT) and thermal boundary conditions (e.g. number of greenhouse's covers). The DASSL solver [11], an implicit, gradient-based, integration algorithm with variable step size (suitable for stiff systems) was selected for the numerical resolution of the DAE system.

## IV. RESULTS AND DISCUSSIONS

The verification of the consistency of the physico-chemical sub-model hypothesis returned relative mean

**Table 1:** Open-loop scenarios studied for the case-study of interest.

| Scenario ID | Scope | HRT (d) | Silage-tomato load (ton $d^{-1}$) | Cow slurry load (ton $d^{-1}$) | Greenhouse cover |
|---|---|---|---|---|---|
| S.1.1.1-O | Baseline | 33 | 37 | 130 | Open |
| S.2.1.1-O | Effect of AcoD operative conditions | 66 | 37 | 130 | Open |
| S.1.2.2-O | | 33 | 67 | 100 | Open |
| S.2.2.2-O | | 66 | 67 | 100 | Open |
| S.1.1.1-1C | Effect of microalgae cultivation configuration | 33 | 37 | 130 | One-cover |
| S.1.1.1-2C | | 33 | 37 | 130 | Two-covers |

errors (RMEs) of 0.04% and 0.4% for the prediction of the digester pH (7.5) and $I$ (0.25 $mol_{eq}$ $L^{-1}$) respectively. It is worth noticing that the low RMEs obtained in this case-study were likely due to the low contribution of water hardness components (dissolved calcium $S_{ca}$ and magnesium $S_{mg}$) to the overall $I$, that was mainly composed by the other dissolved inorganics (P ($S_{ip}$), N ($S_{in}$), C $S_{ic}$)), and cations (dissolved potassium ($S_K$)).
This holds specifically for agro-zootechnical co-feedstocks, whereas this simplified approach that neglects ion-pairing reactions may lead to higher RMEs with other type of AcoD influent compositions.

The simulation of the biorefinery allowed to evaluate the quality of the liquid digestate produced and its suitability to be fed to the algal cultivation unit. Precipitation was quite severe in the agri-AcoD unit (66% of outflow inorganic P is precipitated) due to the high presence of free carbonate ($CO_3^{2-}$) and ammonia ($NH_3$) ions, and the main precipitated salts were struvite ($X_{stru}$ 9.2 mol $m^{-3}$) and calcite ($X_{ccm}$, 5 mol $m^{-3}$). Amorphous calcium phosphate ($X_{acp}$) precipitation was hindered by the high average N/P ratio ($5.7_{w/w}$) of this type of digestate. Indeed, a relevant portion of the total inorganic P is removed ($\approx 80\%$) during flocculation along with coagulated solids, so that the nutrient load reaching the RWP cannot be fully exploited. Nonetheless, the incoming salt seeding material tends to redissolve in the RWP thanks to microalgae inorganic dissolved C and N uptake, guaranteeing a 'stock' of nutrients that becomes available to microorganism under proper pH and $I$ conditions. Figure 2a depicts the trend of algal concentration for the four different agri-AcoD scenarios. The best performance in terms of algal biomass production was observed during spring for the scenario with an increased co-digester HRT and unchanged feeding strategy (S.2.1.1-O). This can be primarily accountable to the higher $S_{ip}$ concentration in the liquid digestate that leads to a lower microalgal P limitation, thanks to (i) the higher content of influent $S_{ip}$ in cow slurry and (ii) a longer residence time in the co-digester that allows a higher extent of lipids' hydrolysis. During summer, the feeding of tomato peels to the agri-AcoD unit features a lower volatile solid and a higher lipid content with respect to maize silage, so that it leads to (i) a 6% higher biogas methane content, (ii) a 12% lower biogas flowrate and (iii) an increase in the effluent $S_{ip}$ up to a peak 70% and 35% on average. Due to the slow dynamics of this state variable, sufficient nutrient availability was provided in autumn, resulting in a narrower difference between scenarios. The concentration of aerobic bacteria was higher for the scenarios S.1.2.2-O and S.2.2.2-O, mostly due to the increased undegraded organic matter load coming from the co-digester. This, in turn, would determine lower $CO_2$ injection rates to perform pH control, but lower 'pureness' of the outflow biomass product. The yearly productivity was estimated to be 54 $ton_{DM}$ $y^{-1}$ (19 $g_{DM}$ $m^{-2}$ $d^{-1}$, 78% of microalgae over total microorganism concentration, which are values in line with experimental literature) for the baseline scenario (S.1.1.1-O).

The effect of greenhouse covering in the RWP configuration is shown in Figure 3. Although a greenhouse ensures higher productivity during winter compared to open ponds, excessive covering (S.1.1.1-2C) can lead to strong overheat during summer and resulting in culture breakdown (-60% yearly average productivity). This outcome depends on the plant's latitude (weather data) and on the algal thermal response's $\boldsymbol{\theta_p}$. The summer productivity was more sensitive to temperature variations, while the productivity in winter was mainly limited by low $I_{PAR}$.

## V. CONCLUSIONS AND FUTURE WORK

The scenario analysis improved process understanding through a preliminary assessment of the impact of co-digester design and feeding strategy on digestate properties and microalgae production, with particular focus on the risk of algal P limitations due to precipitation. Results highlighted the importance of properly designing the whole biorefinery, and yet a noteworthy robustness of the microalgae cultivation's performance: however, it can be strongly affected by the presence of greenhouse covers on the RWP. It is remarked that the overall **`biorefinery`** model has not been validated yet, due to the lack of data, but that each major sub-model was extensively validated in previous works, proving its reliability. Nevertheless, the fine-tuning of the uncertain biological kinetic parameters and an overall validation over real

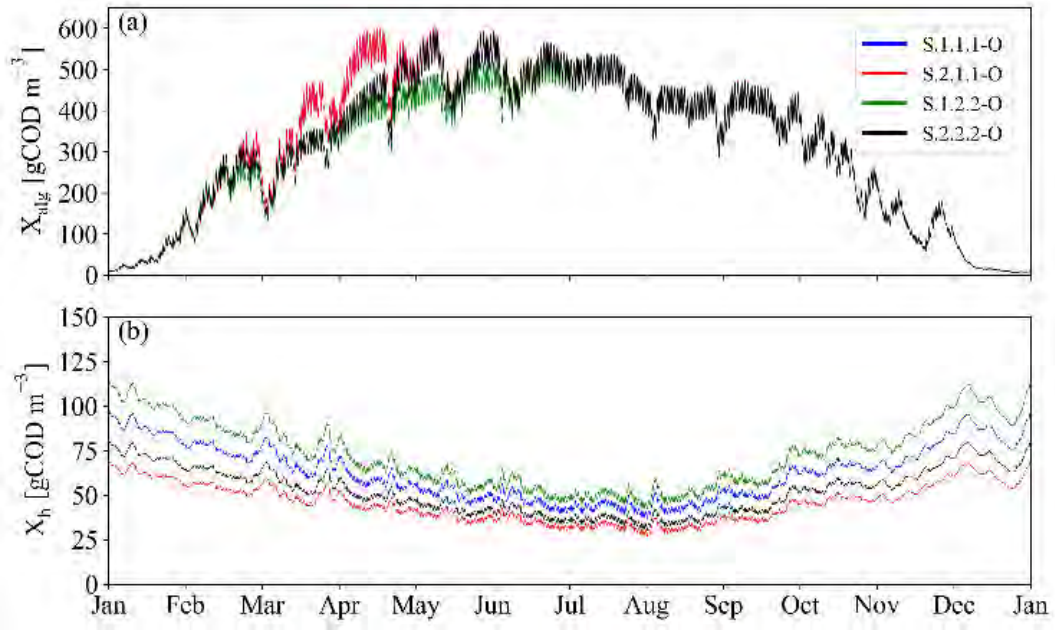



**Figure 2:** Simulation results: (a) yearly microalgae ($X_{alg}$) and (b) aerobic bacteria ($X_h$) concentrations for different scenario (AcoD operative conditions).

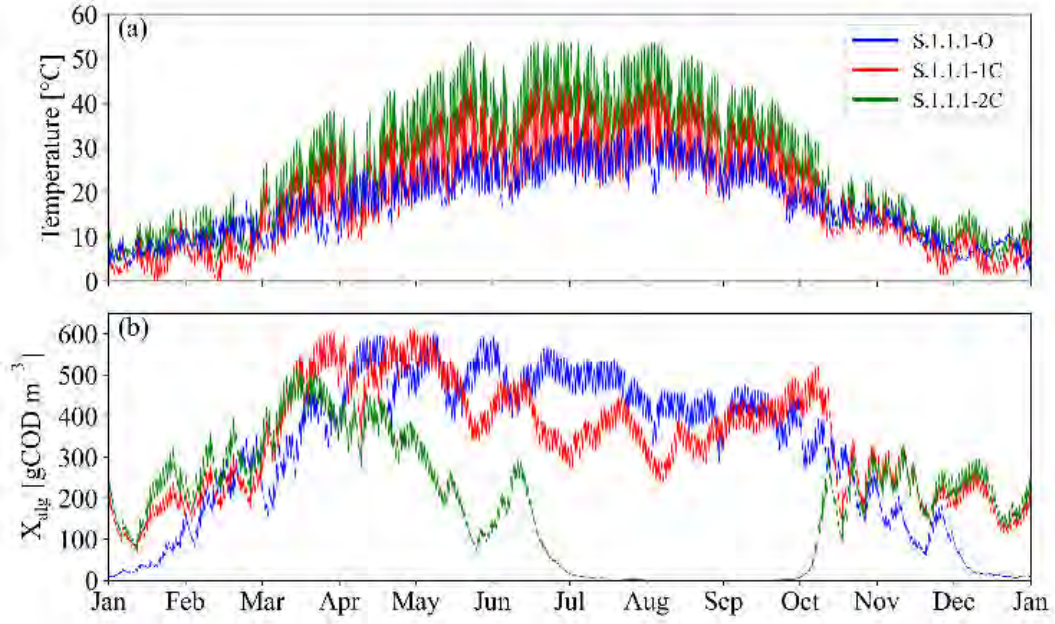



**Figure 3:** Simulation results: (a) RWP's water temperature and (b) yearly microalgae ($X_{alg}$) concentration for the different scenario (GPS-RWP thermal configurations).

data for the specific case of study will be required. Afterwards, the model could be exploited for the optimal techno-economic design of the process and as a high-fidelity '*real plant*' to validate classical/advanced control schemes, in support of the technology's scale-up. It is remarked that feedback control loops over the whole plant would require the frequent (e.g. 1 d$^{-1}$)/automatic measurement of the inorganic nutrients (mainly P, N), that is far from being cost-effectively applicable, especially for anaerobic digesters. Further insights on the modeling of S/L separation units will be required too. Yet, the model could serve, for example, (i) to assess the cost-effectiveness of heating/cooling inputs to boost microalgae productivity, and (ii) the validation of control schemes with bioreactors' HRTs/BRTs as $\boldsymbol{u}$ and revenues from biomethane and microalgae production as $\boldsymbol{y}$. Eventually, the aim of this work was to open novel discussions for the implementation of biorefineries' plant-wide models.

## ACKNOWLEDGEMENTS

This work was supported by A2A S.p.A., the European Union's Next-Generation EU (National Agritech Center) and the Italian Ministry of University and Research (National Recovery and Resilience Plan).

## REFERENCES

1. C. Vaneeckhaute, F. Claeys, F. Tack, E. Meers, E. Belia, and P. Vanrolleghem, "Development, implementation, and validation of a generic nutrient recovery model (NRM) library," Environmental Modelling & Software, vol. 99, pp. 170–209, 2018.
2. D. Batstone et al., "The IWA Anaerobic Digestion Model No 1 (ADM1)," Water Science and Technology, vol. 45, no. 10, pp. 65–73, 05 2002. https://doi.org/10.2166/wst.2002.0292
3. A. Catenacci, M. Grana, F. Malpei, and E. Ficara, "Optimizing ADM1 calibration and input characterization for effective co-digestion modelling," Water, vol. 13, no. 21, 2021.
4. X. Flores-Alsina et al., "Modelling phosphorus (P), sulfur (S) and iron (Fe) interactions for dynamic simulations of anaerobic digestion processes," Water Research, vol. 95, pp. 370–382, 2016. https://doi.org/10.1016/j.watres.2016.03.012
5. K. Bułkowska, I. Białobrzewski, E. Klimiuk, and T. Pokój, "Kinetic parameters of volatile fatty acids uptake in the adm1 as key factors for modeling co-digestion of silages with pig manure, thin stillage and glycerine phase," Renewable Energy, vol. 126, pp. 163–176, 2018.
6. F. Casagli, G. Zuccaro, O. Bernard, J.-P. Steyer, and E. Ficara, "ALBA: A comprehensive growth model to optimize algae-bacteria wastewater treatment in raceway ponds," Water Research, vol. 190, p. 116734, 2021.
7. S. Li, D. H. Willits, C. L. Browdy, M. B. Timmons, and T. M. Losordo, "Thermal modeling of greenhouse aquaculture raceway systems," Aquacultural Engineering, vol. 41, no. 1, pp. 1–13, 2009.
8. P. Fritzson et al., "The OpenModelica Integrated Environment for Modeling, Simulation, and Model-Based Development," Modeling, Identification and Control: A Norwegian Research Bulletin, vol. 41, pp. 241–295, 10 2020. https://doi.org/10.4173/mic.2020.4.1
9. S. Weinrich & M. Nelles, "Systematic simplification of the Anaerobic Digestion Model No. 1 (ADM1) – Model development and stoichiometric analysis," Bioresource Technology, vol. 333, p. 125124, 2021.
10. D. Batstone and X. Flores-Alsina, Generalized Physicochemical Model (PCM) for Wastewater Processes. IWA Publishing, 11 2022.
11. L. R. Petzold, "Description of DASSL: a differential/algebraic system solver," 9 1982.

© 2025 by the authors. Licensed to PSEcommunity.org and PSE Press. This is an open access article under the creative commons CC-BY-SA licensing terms. Credit must be given to creator and adaptations must be shared under the same terms. See https://creativecommons.org/licenses/by-sa/4.0/



Systems & Control Transactions

**Research Article - Peer Reviewed Conference Proceeding**
ESCAPE 35 - European Symposium on Computer Aided Process Engineering
Ghent, Belgium. 6-9 July 2025
Jan F.M. Van Impe, Grégoire Léonard, Satyajeet S. Bhonsale,
Monika E. Polańska, Filip Logist (Eds.)

PSE PRESS

# Modelling of agro-zootechnical anaerobic co-digestion for full-scale applications

**Davide Carecci[a], Giulia Quarta[a], Arianna Catenacci[b], Gianni Ferretti[a], and Elena Ficara[b]***

[a] Politecnico di Milano, Department of Electronics, Information and Bioengineering (DEIB), Milan, MI, Italy
[b] Politecnico di Milano, Department of Civil and Environmental Engineering (DICA), Milan, MI, Italy
* Corresponding Author: elena.ficara@polimi.it.

## ABSTRACT

To match the growing demand for biomethane production, anaerobic digestors need an optimal and time-varying adaptation of the input diet. Dynamic co-digestion constitutes a hard challenge for the limited instrumentation and control equipment typically installed aboard full-scale plants. The development of prediction models is foreseen to support process (optimal) design and control. In this work, a rigorous framework was applied to take full-scale applicability into account while dealing with the design and training of both high-fidelity and control-oriented first-principle/grey-box models, to be used for real-time optimization and process control respectively.

**Keywords**: Control-oriented modeling, Anaerobic co-digestion, Parameter estimation, Identifiability analysis.

## I. INTRODUCTION

To achieve energy independence and environmental sustainability, European bio-methane production is expected to increase over the incoming decades. Anaerobic digestion (AD) processes convert the biodegradable components of organic biomass into bio-methane and biogenic carbon dioxide (biogas), contributing to reduce the greenhouse gas emissions in the agricultural and waste sectors. AD entails a complex sequence of bio-chemical processes (hydrolysis, acidogenesis, acetogenesis, methanogenesis) which requires strict control of the operating conditions to avoid reductions in biogas production, or even complete process failure. Today, the techno-economic performance of bio-methane production via AD is increasingly tied to the plants' capability to embrace co-digestion (AcoD) of multiple co-feedstocks and adapting its input diet to the dynamic supply-chain market (e.g. seasonality). As typical of bio-chemical processes, there are two mains 'time-scales' of optimization tools: (i) high-level scheduling and (ii) low-level process control, to support plant managers and operators respectively. The ability of process models to predict the effect of diet change in advance is of primary importance to pursue those goals. However, the implementation of model-based control is hindered by (i) poor measurement instrumentation (typically gas flowrate and composition being the sole data frequently and automatically (i.e. *online*) measured); (ii) highly non-linear and slow kinetics (time of response from some hours to days); (iii) high parameter uncertainty; (iv) input variability/disturbances; (v) under-actuation. Indeed, literature has primarily focused on developing comprehensive first-principle, grey-box models rather than data-driven ones. The IWA ADM1 model [2] remains the state-of-the-art of AD modeling for process understanding, *offline* optimization and scenario analysis, but it is not suitable to be directly applied to model-based control due to its poor observability/identifiability. The AM2 [3], a simpler two-stage reaction model, was specifically designed with structural local observability and identifiability, to control the AD of simple and soluble feedstocks. After model definition, uncertain parameters shall be estimated: literature is flourish in ADM1 and AM2 tuning for different case studies [9], but their application to dynamic agro-zootechnical AcoD remains scarce [1], as well as the use of general/reliable guidelines for parameter estimation [7].

The aim of this work is to derive a reliable model for control purposes. The approach was to rely as much as possible on a trustworthy 'high-fidelity' model, following the steps: (i) a high-fidelity ADM1-like and a control-oriented (i.e. reduced-order) AM2-like models were extended/adapted for agro-zootechnical AcoD; (ii) with the constraints of industrial practice in mind, data from a

pilot-scale reactor were collected and an identifiable subset of the uncertain high-fidelity model's parameters was selected for estimation, exploiting also batch activity tests for improved practical identifiability; (iii) the reduced-order models' parameters were firstly trained in a 'physically-informed' way with highly informative synthetic data generated by the high-fidelity model, and, later, only a practically identifiable subset of parameters was 'refined' on real data. A model adaptation routine was tested to update the parameters estimated *offline* when model performance is poor. Considerations for the future application of the reduced-order models in control schemes are reported too.

## II. PROCESS MODEL

### A. High-fidelity: from ADM1 to agri-AcoDM

The high-fidelity model (named agri-AcoDM) is an extension of the ADM1, and resulted in a strongly non-linear differential algebraic equation (DAE) system with 43 state variables. Most of the extensions are described in detail elsewhere [5] and are summarized in the Digital Supplementary Material (DSM). In particular, (i) hydrolysis was extended to consider macromolecules with different times of response (e.g. readily/slowly biodegradable); (ii) salt precipitation and the non-ideality of acid-base equilibrium were considered for a better prediction of pH and inorganic nutrient (nitrogen N, phosphorous P) availability; (iii) the Monod functions used to describe acetate and propionate uptakes were substituted with Haldane ones, since high volatile fatty acids (VFA) concentration was proved to be inhibiting by itself, regardless the pH value [6]. The uncertainty in the model may lay both in the input parameters (characterization of the co-feedstocks in state variables' terms) and in stoichiometric, physico-chemical and kinetic parameters $\boldsymbol{\theta_p}$, but it is common to consider kinetics as the most relevant source of uncertainty. Further details on the system of equation are reported in the DSM.

### B. Reduced-order: from AM2 to AM2HN/tan

The reduced-order model extends the AM2HN [8] - itself an extension of the AM2 - with additional state variables and processes for the hydrolysis of the biodegradable particulate fraction of each of the *n* co-feedstocks (i.e. $\boldsymbol{X_h}$ $(g_{VS}\ L^{-1}) \in \mathbb{R}^n$). The resulting ordinary differential equation (ODE) system is reported in the DSM. Since inhibition from free ammonia ($S_{nh3}$) released by N-rich co-feedstocks (e.g. animal slurries) can be relevant [9], two model versions with ('AM2HNtan') and without ('AM2HN') $S_{nh3}$ inhibition were studied: a state variable (*N*) for the total ammoniacal nitrogen (TAN) was added in the AM2HNtan, along with a multiplicative non-competitive inhibition function in the $\mu_2$ expression, compared to the sole original Haldane function present in the AM2HN.

## III. PARAMETER ESTIMATION

Due to the high number of uncertain model's parameters and their collinearity, parameter estimation is all but a trivial task. The availability of data with sufficiently high frequency is of primary importance to stimulate parameter sensitivity, resulting in narrower estimation's confidence intervals. However, this is available in practice only for gas measurements at full-scale and continuous operation data are often poorly informative. Sporadic bio-methane potential tests (BMP) and activity tests are relatively cheap and yet very informative experiments, but the collinearity between $\boldsymbol{\theta_p}$ and unknown state's initial conditions hinders their exploitation. From these realistic considerations it came the intuition of combining data from continuous and batch tests: deriving the inoculum composition from the continuous operation, a mapping from $\boldsymbol{\theta_p}$ to the batch initial conditions is implicitly obtained and the degrees of freedom of unknowns are thus reduced [6]. Batch test's data were used only in the agri-AcoDM $\boldsymbol{\theta_p}$'s estimation, and the knowledge was then 'transferred' to the AM2HN/tan models exploiting synthetic data generated from agri-AcoDM.

A parameter subset selection (PSS) scheme based on both sensitivity and collinearity analysis was run to select a subset $\boldsymbol{\theta}_{PSS} \subseteq \boldsymbol{\theta_p}$ for estimation. For agri-AcoDM, 24 highly uncertain kinetic $\boldsymbol{\theta_p}$ [9] were selected to conduct and compare both linear/local (L.) and global (G.) dynamic sensitivity analysis (see DSM). The relative-relative sensitivity ($\boldsymbol{SI_{rr}}$) matrixes and the practical identifiability of each subset of parameters were computed as in [4]. The average over the data time points of the squared sensitivity values ($\boldsymbol{\delta}^{msqr}$) was selected as metric to rank the parameters, obtaining their ranking indexes $\boldsymbol{\rho}$.

The scalar cost function (Eq. 1) was the sum of the percentage mean relative squared (simulation) errors ($MRSE_{\%}$) over the different outputs of the dataset (see Section IV):

$$J = \sum_y w_y \frac{1}{N_y} \sum_{i=1}^{N_y} \left(\frac{y_i - \hat{y}_i}{\bar{y}}\right)^2 \quad (1)$$

where the '$y$' nomenclature refers to each data type ('Name' in Table I of the DSM), $N_y$ is the number of time observation points, $\hat{y}_i$ is the '$y$' model output at the $i^{th}$ time instant and $w_y$ is a user-configurable weighting parameter to drive the 'efforts' of the minimization problem toward a specific $y$. The average value $\bar{\boldsymbol{y}}$ normalizes simulation errors for variables of different magnitudes. The cost function was minimized by 30 iterations of the Differential Evolution (DE) algorithm and later 'polished' by the Nelder-Mead algorithm. Parameters' initial guesses (*nominal* $\boldsymbol{\theta}_{PSS}$) were set to literature-suggested values (Table 1-2). The algorithm moved within the feasibility set $\boldsymbol{\Theta} \subset \mathbb{R}_{>0}$ (large yet compact, based on literature values) returned the (*optimal*) minimizer $\boldsymbol{\theta}^*_{PSS}$. Spearman's

coefficient of determination ($R^2$) and Mean Absolute Relative Error (MARE) were used to quantify model's performances. After the estimation of the $\boldsymbol{\theta}^*_{PSS}$ *expected values*, the Fisher Information Matrix (**FIM**) was evaluated as a lower-bound of the covariance matrix to compute the 95% confidence intervals (CI) of the $\boldsymbol{\theta}^*_{PSS}$ estimates, and T-student hypothesis testing was performed [6]. The uncertainty was then linearly propagated to each *optimal* $\hat{\boldsymbol{y}}^*$ trajectory (see DSM for references).

For the AM2HN/tan models, the estimation entailed two stages: (i) a first 'physically-informed' training on agri-AcoDM-generated synthetic data under highly exciting and well-distributed input profile, and (ii) a 'refinement' on real data of the practically identifiable parameters only. The identifiability analysis was conducted on almost all stoichiometric and kinetic $\boldsymbol{\theta_p}$ (18 in total). Stage '(i)' was designed to *activate*/excite the VFA inhibition to provide information on the Haldane curve's parameters. All the available correspondences between ADM1- and AM2-like variables were exploited in this stage (see DSM Table I) [8]: however, $\boldsymbol{k_h}$ was estimated before stage '(i)', considering the simulation error on the sum of $\boldsymbol{X_h}$ only to limit the effect of other mismatches on its estimate.

## IV. THE DATASET

Considering the poor identifiability of agri-AcoDM and the limited budget of companies, the dataset must be minimal yet smartly designed to *activate* the parameters of interest and avoid overfitting. Data from a continuous pilot-scale reactor (12 L working volume, 42°C, initial D = 0.03 $d^{-1}$, organic loading rate (OLR) = 2.84 $g_{COD}$ $d^{-1}L^{-1}$ with 30, 47 and 23% of maize silage, cow slurry and tomato sauce respectively) resembling the operation of a full-scale plant were considered. Coherently to the industrial practice, the methane and carbon dioxide flowrate ($Q_{ch4}, Q_{co2}$) and the biogas composition ratio ($CO_2/CH_4$) only were considered as *online* data. In addition, it is reasonable to assume that some spot *offline* VFA (and TAN) data would be available at full-scale, especially during periods of diet change, so that some measurements of acetate ($S_{ac}$) and propionate ($S_{pro}$) concentrations were included. The peculiarity of the entire dataset (15/12/2023-10/04/2024) is that it entails various operative conditions (e.g. impulse and long free-responses (22/12/2023-08/01/2024)), that is an effective way to prevent overfitting. In particular, the *transient* between two different loads and diet compositions was included in the training dataset (05-23/02/2024).

A comprehensive feedstock characterization is usually available in full-scale plants, yet with low frequency, (e.g. seasonal): for each co-feedstock, characterization was performed as in [5] only once, along with BMP tests to derive information about the biodegradability.

On the 10/04/2024 some batch tests were run using the pilot-scale digestate as inoculum: activity on $S_{ac}$ and $S_{pro}$ were tested, with initial substrate concentrations hypothesised to range from limited to inhibited conditions. Hourly $Q_{ch4}$ of all the batch tests was recorded. Additional practical details on the dataset and its exploitation are present in the DSM-Table II.

## V. RESULTS AND DISCUSSIONS

### A. Agri-AcoDM calibration and performance

A reasonably collinear (collinearity index $\gamma \leq 20$) $\boldsymbol{\theta}_{PSS}$ of 14 sensitive ($\boldsymbol{\delta}^{msqr} \geq 0.1$) parameters was returned by the PSS. The ranking indexes $\boldsymbol{\rho}$, *nominal* and *optimal* values (± 95% CI) of each $\boldsymbol{\theta}^*_{PSS}$ are reported in Table 1. The T-student test rejected the null hypothesis for $k_{m,su}$, $k_{m,h2}$, $K_{i,h2,pro}$ and $K_{s,h2}$ (p-value $\leq 0.05$), in agreement with previous findings [6]. Figure 1 shows model's performances over the most interesting operative period: although not reported for readability reasons, the propagated uncertainty resulted in the definition of $\hat{\boldsymbol{y}}$ CI that included almost all model mismatches for $Q_{ch4}$ and $CO_2/CH_4$ (10%-65% and 5%-25% mean-max deviations from the $\hat{\boldsymbol{y}}$ *expected values,* respectively). However, too large and narrow sets for VFAs (120%-230%) and pH ($\leq$ 2%) were returned, respectively. Table 3 reports the metrics of model's performances over training and test periods. Remarkably, the MARE value for $Q_{ch4}$ and $S_{ac}$ decreased by 32% and 92% respectively, compared to the predictions with the *nominal* $\boldsymbol{\theta}_{PSS}$ values over the training period, and $R^2$ increased substantially. The good performance obtained for $CO_2/CH_4$ over the test period is very encouraging as well. The high MARE on $S_{pro}$ is due to many data points being near the lower analytical detection limit: $k_{m,pro}$ was reduced to improve the fitting of the high-concentration values and of the activity tests, with a consequent worse fit of low-concentration points. pH values were stably within the 7.1-7.5 range due to the system's high buffering capacity: consequently, the MARE value for pH is low ($\leq$ 4%), but the true challenge of capturing the pH dynamics is reflected by the lousy $R^2$ (yet a remarkable 0.7 over the training data, but lower than 0.42 over the test data). The validation period was particularly challenging due to the presence of prolonged free-responses (far from actual operation), so that, overall, the performances are satisfactory. In addition, the main falls of model's performance occur over free-responses and transient periods, whereas it is very satisfactory over the two 'steady-states' before and after the diet change (all $R^2$-MARE higher-lower than 0.6-20% respectively). Indeed, the most interesting experimental finding for control with diet adaptation is the recorded VFA (mainly acetate) increase during the transient period, suggesting unbalanced biological performances which are to be avoided (see Section IV and Figure 1).

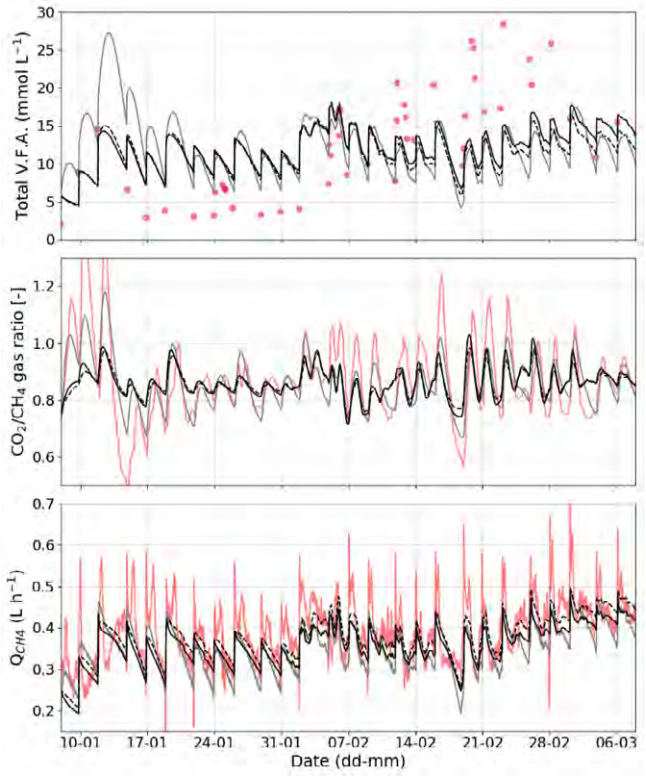



**Figure 1.** Models' performances: agri-AcoDM (grey line), AM2HN (black line) and AM2HNtan (dashed black line) vs data (red).

The low variability of pH suggests that no pH inhibition of the methanogenesis took place, thus remarking the need to introduce the Haldane functions to justify the VFA increase. Anyway, neither pH nor VFA inhibitions appear to be sufficient to explain such accumulation, since the optimal points of the Haldane functions resulted at values that were not reached during the transient (2.81, 0.26 $g_{COD}$ $L^{-1}$ for $S_{ac}$ and $S_{pro}$ respectively).

Figure 2 highlights the relevant improvements in model's predictions over the activity tests: MARE decreased on average by 55%. For the high substrate's initial concentration tests, $R^2$ were 0.92 and 0.64 for $S_{ac}$ and $S_{pro}$ respectively. For the BMP test on cow slurry, mean-max deviations were 28%-35%, and 40%-70% and 100%-200% for low and high initial concentration's activity tests respectively.

**Table 1:** Parameter estimates for the high-fidelity model.

| **Name** (Unit) | L. $\rho(\theta_{PSS})$; G. $\rho(\theta_{PSS})$ | ***Nominal**** | ***Optimal* ±95%CI** |
|---|---|---|---|
| $k_{m,ac}$ $(g_{COD}g_{COD}^{-1}d^{-1})$ | 1; 5 | 8 | 4.9 ± 2.3 |
| $k_{m,pro}$ $(g_{COD}g_{COD}^{-1}d^{-1})$ | 2; 24 | 13 | 5.3 ± 1.9 |
| $K_{I,nh3}$ $(mol_N L^{-1})$ | 3; 15 | 1.8e$^{-3}$ | 2.7e$^{-3}$ ± 1.6e$^{-3}$ |
| $K_{I,hpro,pro}$ $(g_{COD}L^{-1})$ | 4; 18 | 2.2** | 3.3 ± 0.9 |
| $K_{I,hac,ac}$ $(g_{COD}L^{-1})$ | 5; 12 | 2.2** | 7.9 ± 1.3 |
| $pH_{UL,ac}$ $(-)$ | 7; 9 | 7 | 7.96 ± 0.33 |
| $K_{s,ac}$ $(g_{COD}L^{-1})$ | 9; 21 | 0.15 | 0.44 ± 0.08 |
| $k_{La,batch}(d^{-1})$ | 10; 13 | 10** | 1.05 ± 0.05 |
| $k_{m,su}$ $(g_{COD}g_{COD}^{-1}d^{-1})$ | 12; 7 | 30 | 29.5 ± 118 |
| $k_{m,h2}$ $(g_{COD}g_{COD}^{-1}d^{-1})$ | 13; 11 | 35 | 21.4 ± 24.9 |
| $K_{I,h2,pro}$ $(g_{COD}L^{-1})$ | 14; 16 | 3.5e$^{-6}$ | 2.2e$^{-6}$ ± 2.2e$^{-6}$ |
| $K_{s,h2}$ $(g_{COD}L^{-1})$ | 17; 1 | 7e$^{-6}$ | 1.3e$^{-6}$ ± 2.3e$^{-5}$ |
| $K_{s,pro}$ $(g_{COD}L^{-1})$ | 18; 4 | 0.1 | 0.08 ± 0.03 |
| $k_{hyd,xchr}$ $(d^{-1})$ | 19; 19 | 1** | 0.65 ± 0.15 |

**ADM1 default values. **Literature-suggested values.*

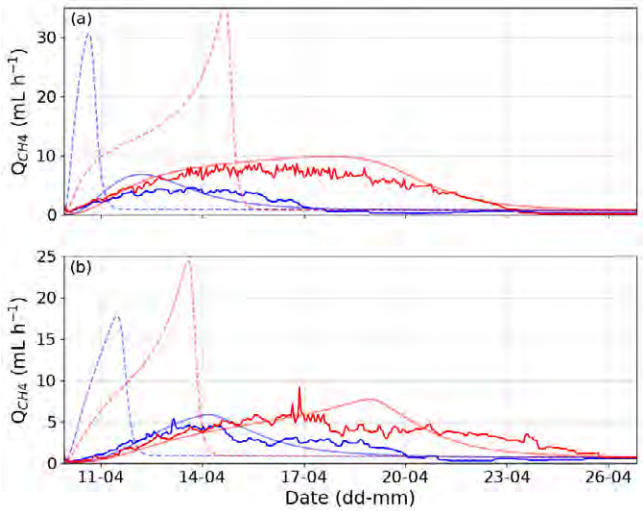



**Figure 2.** Agri-AcoDM model's performance for the batch tests on $S_{ac}$ (blue) and $S_{pro}$ (red): *nominal* (dashed line) and *optimal* (thinner continuous line) $\boldsymbol{\theta}_{PSS}$ vs data (thicker continuous line). Tests with high (a; ≥ 6 g $L^{-1}$) and low substrate's initial concentrations (b; 3 g $L^{-1}$).

## B. AM2HN/tan calibration and performance

Results from the first-stage estimation for the reduced-order models on synthetic data were very satisfactory: $R^2$ was higher than 0.6 for all states and outputs; MARE below 10% for $X_1$ and $X_2$, and below 30% for $S_1$ and $S_2$ (total VFA). A reasonably collinear $\boldsymbol{\theta}_{PSS}$ ($\gamma \leq 10$) of 4 sensitive parameters was returned by the PSS for the second-stage estimation. The *optimal* parameter values are reported in Table 2, along with the $SI_{rr}$ ranking indexes $\boldsymbol{\rho}$ of the AM2HNtan: the $\boldsymbol{\theta}^*_{PSS}$ values are reported within brackets ± 95% CI. Two mid-low $r$ parameters ($k_{La}$, $K_{s,2}$) were selected instead of a more sensitive one (e.g. $\mu_{max,2}$ was not selected due to its collinearity with $k_6$) disclosing the main drawback of this PSS method i.e. its strong dependence on the user choice of a $\gamma$'s upper threshold. Compared to agri-AcoDM, due to the lower dimensionality of $\boldsymbol{\theta}_{PSS}$, the propagated uncertainty resulted in narrower $\hat{\boldsymbol{y}}$ CI (9%-28%, 3%-18%, 14%-55% of mean-max deviation from the $\hat{\boldsymbol{y}}$ *expected values* of $Q_{ch4}$, $CO_2/CH_4$ and $S_2$ respectively). Table 3 and Figure 1 show model performances after both stages of estimation: compared to agri-AcoDM, similar performances for $Q_{ch4}$ and total VFA were obtained, and yet less ability to reproduce the $CO_2/CH_4$ dynamics. Interestingly, for both

reduced models, the Haldane curves have similar total VFA's ($S_2$) optimal value compared to the one on $S_{ac}$ in agri-AcoDM (difference ≤ 30%), whereas the maximum methanogenesis Haldane's rate are different (up to 70% difference), probably due to the higher complexity of agri-AcoDM (see DSM). The introduction of N release improved the fitting of $Q_{co2}$ by 5-10% only, whereas modeling the hydrolysis was of great relevance. AM2HNtan reported a better performance over pH (0.7% vs 1.5% MARE): overall, the higher complexity of AM2HNtan may be justified when (i) the system is poorly buffered and thus a better pH prediction may be more relevant, and/or (ii) the load of N-rich co-feedstocks is used as control action.

**Table 3:** Models' performances over train/test periods.

| | $R^2$; MARE (%) | | |
|---|---|---|---|
| | $Q_{ch4}$ | $CO_2/CH_4$ | $S_2(S_{ac},S_{pro})$ |
| agri-AcoDM train | 0.80; 23 | 0.73; 4 | (0.29,0.81); (45,143) |
| agri-AcoDM test | 0.80; 37 | 0.67; 6 | (0.11,0.32); (65,109) |
| AM2HN train | 0.73; 18 | 0.28; 11 | 0.29; 51 |
| AM2HN test | 0.71; 33 | 0.13; 15 | 0.27; 57 |
| AM2HNtan train | 0.72; 17 | 0.21; 12 | 0.25; 52 |
| AM2HNtan test | 0.71; 32 | 0.10; 18 | 0.21; 55 |

## C. Recursive AM2HN parameter update

To reduce the relevant model mismatch over the diet transient, a modeler could either choose to add physical knowledge to the agri-AcoDM (e.g. lactate metabolism) or to embrace the philosophy for which *'no model is perfect':* in this work, a model adaptation scheme was tested for the AM2HN, via *'online'* recursive estimation of time-varying parameters over 10-days-long time windows (sliding, not overlapping) of the pilot-scale dataset. An *arrival* cost was added to the objective function to penalize 'useless' explorations far from the previously learned parameter values, thus preventing the risk to overfit process drifts and of catastrophic forgetting of the 'reference' parameters learned *offline* (Table 2). A weighting approach ($\boldsymbol{W_\theta}$) based on the $\boldsymbol{\rho}$ of the local $\boldsymbol{SI_{rr,k}}$ computed on the $k^{th}$ window was applied to the *arrival* cost (see DSM): the resulting optimization problem on each $k^{th}$ window returned the minimizer $\boldsymbol{\theta^*_{p,k}}$ expressed by Eq.2, where $J_k$ is Eq.1 evaluated on the $k^{th}$ window and $\boldsymbol{\theta^*_{p,k-1}}$ is the vector of *optimal* parameter values learned on the previous $k^{th-1}$ window.

$$\boldsymbol{\theta^*_{p,k}} = \underset{\boldsymbol{\theta_p}\in\Theta}{argmin}\ J_k + ||\boldsymbol{\theta_{p,k}} - \boldsymbol{\theta^*_{p,k-1}}||_{2,\boldsymbol{W_\theta}}\ \forall_k \qquad (2)$$

The capability of the AM2HN to improve the fitting of $S_2$ data over the transient period is shown in Table 3 and Figure 3: considering the 'posterior' model trajectories (i.e. evaluated with the $\boldsymbol{\theta^*_{p,k}}$ on each window) the $S_2$ MARE reduced on average by 50% compared to the model's performance with the fixed parameters learned *offline*. The average relative standard deviation of the $\boldsymbol{\theta^*_p}$ over the windows was lower than 6%, with the only exception of $\mu_{max,2}$ that varied on average by 26%: it is likely that the latter triggered the most the adaptation to the $S_2$ transient. Although the most sensitive parameters were always $\mu_{max,2}$, $k_5$ and $k_6$, the $K_{I,2}$ jumped forward in the $\boldsymbol{SI_{rr,k}}$ ranking when $S_2$ reached high values thus activating the inhibition function (e.g. $5^{th}$ window). It follows that, in the prospective of a nonlinear model predictive controller (NMPC) design, the update could be beneficial to prevent overloading the system (e.g. on the $4^{th}$ and $5^{th}$ windows, where $S_2$ accumulation is foreseen by the 'prior' model trajectories i.e. evaluated with the parameters estimated on the $3^{th}$ and $4^{th}$ windows ($\boldsymbol{\theta^*_{p,3}}$ and $\boldsymbol{\theta^*_{p,4}}$)). Eventually, this AM2HN structure seems to be suited for *online* control purposes owing to its fair prediction ability and restricted complexity (i.e. optimization's duration etc.).

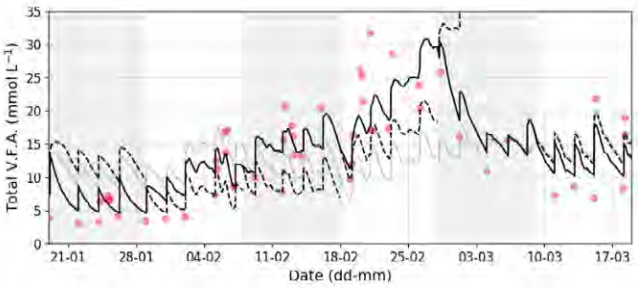



**Figure 3.** AM2HN model's performance with the *optimal offline* (grey line), the 'prior' (dashed black line) and the 'posterior' (black line) time-varying $\boldsymbol{\theta^*_p}$ vs data (red). Time windows are identified by the background color.

## VI. CONCLUSIONS AND FUTURE WORK

Both high-fidelity and reduced-order models were tuned on an informative and challenging agro-zootechnical anaerobic co-digestion dataset. The results encourage the use of the AM2HN/AM2HNtan in model-based control applications. However, the models' current structure appeared to fail in describing the transient dynamics of a diet change: a model adaptation scheme was tested to reduce the model's mismatch, 'following' the transient. It is difficult to say whether the cause of such mismatch was due to a misleading agri-AcoDM's reconstruction of the unmeasured states, then inherited by AM2HN/tan, or to time-varying parameters. To put the record straight and to move toward NMPC design, further efforts will focus on the design of state observers. For such scope, an asynchronous separation between unmeasured states and slowly time-varying $\boldsymbol{\theta_p}$'s estimations can be beneficial, due to the strong collinearity between the two on the outputs (e.g. $\mu_{max,2}$ and $X_2$ on $Q_{ch4}$). The ultimate goal is the design and validation of a robust NMPC scheme over similar diet changes, to serve as a digital twin for a concrete and transparent improved management of full-scale reactors.

**Table 2:** Parameter estimates for both the reduced-order models (AM2HN and AM2HNtan).

| **Name** (Unit) | **L.** $\rho(\theta_{PSS})$ | **G.** $\rho(\theta_{PSS})$ | ***Nominal**** | ***Optimal* AM2HN** | ***Optimal* AM2HNtan** |
|---|---|---|---|---|---|
| $k_1$ $(g_{COD}\ g_{VS}^{-1})$ | n.d. | n.d. | 42.1 | 14.5 | 16.2 |
| $k_2$ $(mmol\ g_{VS}^{-1})$ | n.d. | n.d. | 117 | 154 | 206 |
| $k_3(mmol\ g_{VS}^{-1})$ | n.d. | n.d. | 268 | 335 | 326 |
| $k_4(mmol_C\ g_{VS}^{-1})$ | 5 | 7 | 50.6 | 34.5 | 39.4 |
| $k_5(mmol_C\ g_{VS}^{-1})$ | 2 | 2 | 344 | 330 (391 ± 2) | 313 (341 ± 1) |
| $k_6(mmol_C\ g_{VS}^{-1})$ | 1 | 1 | 453 | 408 (485 ± 2) | 334 (422 ± 1) |
| $k_{La}(d^{-1})$ | 10 | 9 | 19.8 | 7.3 (19.3 ± 3.6) | 2.8 (6.8 ± 0.6) |
| $K_{I,2}(mmol\ L^{-1})$ | 12 | 14 | 256 | 55.3 | 78.5 |
| $K_{s,1}(mmol\ L^{-1})$ | 15 | 12 | 7.1 | 6.4 | 13.5 |
| $K_{s,2}\ (mmol\ L^{-1})$ | 6 | 6 | 9.28 | 17.1 (27.7 ± 0.6) | 6.5 (12.8 ± 0.3) |
| $\mu_{max,1}(d^{-1})$ | 14 | 13 | 1.2 | 8.1 | 13 |
| $\mu_{max,2}(d^{-1})$ | 3 | 4 | 0.74 | 0.14 | 0.17 |
| $k_{d,1}(d^{-1})$ | 13 | 15 | 0.057** | 0.032 | 0.021 |
| $k_{d,2}(d^{-1})$ | 7 | 8 | 0.019** | 0.011 | 0.017 |
| $k_h(d^{-1})$ | [4, 9, 11] | [3, 5, 10] | [0.30, 0.18, 0.32]*** | [0.22 ± 0.01, 0.14 ± 0.02, 0.48 ± 0.13] | |
| $K_{I,nh3}(mmol_N\ L^{-1})$ | 8 | 11 | 1.8 | - | 8.7 |

**From [3], with α = 0.5; **From [8]; ***From BMP tests' fit with first-order models.*
*The vectorization within square brackets refers to the list of co-feedstocks ordered as: '[maize silage, cow slurry, tomato sauce]'.*

## DIGITAL SUPPLEMENTARY MATERIAL

Link to the Digital Supplementary Material: https://psecommunity.org/LAPSE:2025.0002

## ACKNOWLEDGEMENTS

This work was supported by A2A S.p.A., the European Union (Next-Generation EU, Agritech National Research Centre for Agricultural Technologies) and the Italian Ministry of University and Research (PNRR).

## REFERENCES

1. J. A. Arzate et al., Anaerobic digestion model (AM2) for the description of biogas processes at dynamic feedstock loading rates. Chemie Ingenieur Technik, 89(5):686–695, 2017. https://doi.org/10.1002/cite.201600176
2. D. Batstone et al., The IWA anaerobic digestion model No 1 (ADM1). Water Science and technology, 45(10):65–73, 2002. https://doi.org/10.2166/wst.2002.0292
3. O. Bernard et al., Advanced monitoring and control of anaerobic wastewater treatment plants: software sensors and controllers for an anaerobic digester. Water Science and Technology, 43(7):175–182, 2001. https://doi.org/10.2166/wst.2001.0418
4. R. Brun, P. Reichert, and H. R. Künsch. Practical identifiability analysis of large environmental simulation models. Water Resources Research, 37(4):1015–1030, 2001.
5. D. Carecci et al., A plant-wide modelling framework to describe microalgae growth on liquid digestate in agro zootechnical biomethane plants. Chemical Engineering Journal, 485:149981, 2024. https://doi.org/10.1016/j.cej.2024.149981
6. A. Catenacci, D. Carecci, A. Leva, A. Guerreschi, G. Ferretti, and E. Ficara. Towards maximization of parameters identifiability: Development of the CalOpt tool and its application to the anaerobic digestion model. Chemical Engineering Journal, 499:155743, 2024.
7. A. Donoso-Bravo, J. Mailier, C. Martin, J. Rodríguez, C. A. Aceves-Lara, and A. V. Wouwer. Model selection, identification and validation in anaerobic digestion: A review. Water Research, 45(17):5347–5364, 2011.
8. A. Della Bona, G. Ferretti, E. Ficara, and F. Malpei, LFT modelling and identification of anaerobic digestion. Control Engineering Practice, 36, 2015.
9. R. Mo, W. Guo, D. Batstone, J. Makinia, and Y. Li. Modifications to the anaerobic digestion model No. 1 (ADM1) for enhanced understanding and application of the anaerobic treatment processes – a comprehensive review. Water Research, 244:120504, 2023.

© 2025 by the authors. Licensed to PSEcommunity.org and PSE Press. This is an open access article under the creative commons CC-BY-SA licensing terms. Credit must be given to creator and adaptations must be shared under the same terms. See https://creativecommons.org/licenses/by-sa/4.0/



Systems & Control Transactions

**Research Article - Peer Reviewed Conference Proceeding**
ESCAPE 35 - European Symposium on Computer Aided Process Engineering
Ghent, Belgium. 6-9 July 2025
Jan F.M. Van Impe, Grégoire Léonard, Satyajeet S. Bhonsale,
Monika E. Polańska, Filip Logist (Eds.)

PSE PRESS

# Multi-Omics biological embeddings for ML-models

**Lennart B. Otte[a], Christer Hogstrand[b], Adil Mardinoglu[c,d] and Miao Guo[a*]**

[a] King's College London, Department of Engineering, London, UK
[b] King's College London, Department of Analytical, Environmental and Forensic Sciences, London, UK
[c] Centre for Host-Microbiome Interactions, Faculty of Dentistry, Oral & Craniofacial Sciences, King's College London, London, SE1 9RT, United Kingdom
[d] Science for Life Laboratory, KTH - Royal Institute of Technology, Stockholm, Sweden

* Corresponding Author: miao.guo@kcl.ac.uk

## ABSTRACT

Machine learning algorithms have led to the development of numerous vector embeddings for biological entities such as metabolites, proteins, genes, and enzymes. However, these embeddings often lack contextual information due to their specialized focus on individual omics. Disease progression and biosynthesis pathways are increasingly understood through complex, multi-layered networks that integrate diverse omics data and intricate signaling and reaction sequences. Capturing these relationships in a meaningful way requires embeddings that account for both functional and multi-modal dependencies. We propose an embedding approach that unifies these different biological modalities by treating them as directions in a shared space rather than as isolated data types. Similar to how word embeddings in natural language processing reveal meaningful relationships (e.g., Tokyo – Japan + UK = London, indicating a directional representation of capitals), we can model genes and proteins in a way that captures their inherent connections. A gene implies information about the protein it encodes, and vice versa, forming a structured and interpretable representation of biological pathways. Our model, inspired by NLP techniques, breaks down pathway sequences into contextual pairs spanning different omics types. By aligning pathway steps in proximity, the embeddings reflect biologically relevant relationships, enhancing their interpretability and utility. Because these embeddings are generated from pathway sequences, they can be applied to optimize reaction pathways, aiding retrosynthesis in microbiomes, drug development, and even human health interventions.

**Keywords**: Chemical fingerprints, Biological Pathways, multi-omics, Drug Discovery, Biosynthesis

## INTRODUCTION

Machine Learning models can be fitted to predict a diverse set of properties or interactions between proteins, genes, small molecules etc. In every case a digital vector representation is necessary to represent physical/experimental data in a machine learning model. Specialised fingerprints exist for the different modalities (genes, proteins, small molecules) that aim to capture their own intricacies (amino acid sequence for a protein, nucleotide sequence for a gene or SMILES for a small molecule). However, in a bioprocess we use multiple omics together to promote the synthesis of targets through a biological pathway. Consequentially, predicting multi-omics interactions in a bioreactor requires a mapping between multiple spaces – the embedding space of proteins, of genes and small molecules. To increase the interpretability, efficiency and accuracy of predicting relations between multi-omics data we propose a new embedding space that encapsulates multi-omics layers together. Traversing a direction encoding omics-type allows us to find interacting compounds.

### Bioprocesses

Bioprocesses underpin a vast array of engineering or medical challenges such as synthesis trough engineered *E. Coli* strains [12], degradation and valorisation of waste material and disease progression [11]. The rise of high throughput analysis of genomics, proteomics etc. has vastly increased our ability to probe complex

systems. The next step is to optimise processes further using the new insights. An early approach is Flux Balance analysis where multi-omics pathways are modelled to increase the flux along preferred reactions that produce the desired products [7]. A bottleneck to FBA is the fact that detailed pathway knowledge is required. Identifying all pathways first to then eliminated unwanted fluxes involves inference across multi-omics. The proposed work facilitates the processing of multi-omics data by placing them in the same embedding space, where proximity in space codes for interaction strengths.

## Fingerprints in biological Networks

Biological systems whether we mean an organism-scale (e.g. microbiome), an organ or tissue scale, exhibit complex interaction networks [3, 4]. Different modalities like genes, proteins and small molecules interact e.g. to synthesise new proteins or start an inflammation reaction. To accurately model reaction cascades, signalling and metabolic networks we need to respect every modality (omics layer) as it can make or break the system's function [4, 6]. Drug design as well as bioreactors are increasingly relying on more complex networks for synthesis of proteins or the treatment of disease [11, 12]. In many more challenging cases long cascades and networks need to be optimised to improve a condition or achieve a higher yield. The analysis and generation of pathways using Machine Learning requires a digital vector-based representation of the compound. The approaches to obtain a descriptive vector for molecules can be grouped into different categories: 1. Chemical structure based [2] 2. Functional Group based [9] 3. Property based 4. Learned fingerprints [8]. Each of the fingerprints (MACCSKeys, Protein fingeprints etc.) have an applicability domain to a specific biological entity or an application in e.g. specifically drug like molecules. Due to the connected nature of multi-omics in biological networks, we propose a fingerprint that encapsulates multi-omics layers and can thus model an entire biological system within the same space. As the availability of established bioprocesses and pathway networks is still limited we aim to facilitate the discovery and analysis of biological systems.

# METHODS

Creating a descriptive embedding model based on pathway data requires a large pool of pathway diagrams. The pathway data are downloaded from the Pathway database (PDB) MetaCyc [1] and then sampled for the use in the embedding model. The model itself is based on the Word2Vec [5] architecture which has been used to find descriptive embeddings for natural language. Fig.1 exemplifies the complex interaction network found in biological systems.

Traditional structure-based fingerprints such as Morgan's (ECFP) fingerprint [2] use an iterative graph algorithm to derive a local neighborhood embedding which is aggregated and across all neighborhoods to define the final vector embedding. Its hyperparameters can control the influence of distant atoms to the local neighborhood. A fingerprint for functional groups is MACCS Keys [9]. They use a predefined set of substructures which are matched against the given molecule. If a substructure is matched the corresponding bit in the fingerprint vector is assigned a "1". Learned fingerprints [8] can be found e.g. by using an LLM which trains over SMILES string. The internal representation which the model has learned after converging can be extracted and used in Cheminformatics tasks. Our hypothesis is that from the reaction networks themselves (Fig. 1) comprising proteins, genes and small molecules we can extract semantic properties and develop a common embedding space for all involved components.

## Data Preparation

Downloading every pathway diagram contained in MetaCyc [1] yields a CSV file containing substrates, products, enzymes and genes. From this data we can infer which genes are translated into which proteins, which of these proteins are enzymes for a reaction and what substrates and products that reaction consists of. Using these relations, we can find possible subsequent interactions for a starting point i.e. interactions of the same pathway and related to a product of the previous reaction. After compiling the list of every interaction and its possible successors we sample a sequence of interactions in the pathway space. We start by picking a random reaction and then create a chain until no succeeding interaction can be found or the *sequence_length* limit is reached [Fig.1].

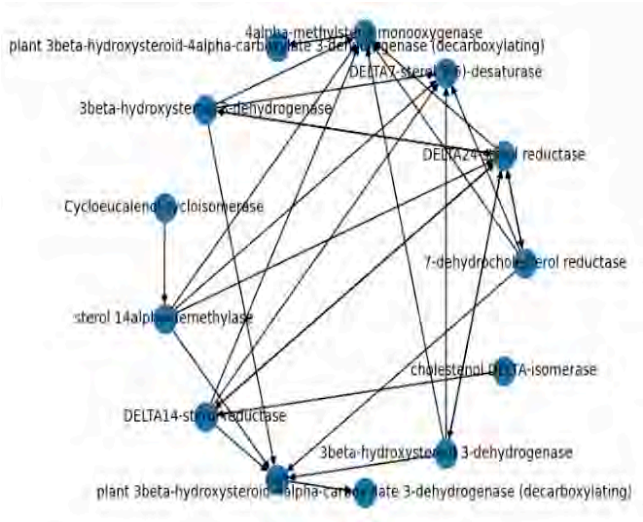



**Figure 1.** Processed reaction interaction network of cholesterol biosynthesis

The sampled trajectory through the space is further divided into context windows using the *context_window_size* parameter. From the sampled sequence of interactions in the pathway space we pick pairs of related nodes within the context window (regardless of which omics layer they represent). Our final training data are comprised of a list of related nodes and is supplement with a list of random unrelated nodes.

## Embedding Model

A shallow autoencoder network is used to compress the initial one-hot encoded nodes into a lower dimensional space. We optimise the network by using an objective that aims to align vectors of related nodes and misalign unrelated embedding vectors. By using both positive and negative examples we maximise the usage of our available training data and add additional information for the model to learn. The model structure is illustrated in Fig.2. Different linear layers are used for the target

**Figure** Embedding Model

```
class BioEmbeddingModel
    function init (vocab_size, embed_dim)
        target_embedding ← Linear(vocab_size, embed_dim)
        context_embedding ← Linear(vocab_size, embed_dim)
        activation function ← tanh
    function Forward (input, context)
        target_embeddings ← target_embedding(input)
        context_embeddings ← context_embedding(context)
        target_embeddings ← tanh(target_embeddings)
        context_embeddings ← tanh(context_embeddings)
        return Dots(target_embeddings, context_embeddings)
    function GetWordEmbedding (word)
        embedding ← target_embedding(word)
        return tanh(embedding)
```

**Figure 2.** Embedding Model

At the start of the training every node is assigned a one-hot encoded vector. At every iteration we create batch of positive and negative context nodes. The target word is given to the target network which compresses the vector of length *num_nodes* to the *embedding dimension* size (128). The context words are fed to the context layer which compresses the one hot encoding in the same way. Finally, we calculate the dot product between the target and context. The loss is calculated between the dot products of the context and target node embedding and the *learning_target*. The target is 1 if the node pair was a positive pair i.e. the nodes were in the same context in a pathway and 0 if the node were negative i.e. unrelated/ not-interacting. Our loss function is the mean squared error between the prediction and target. The objective aims to find embeddings that allow for a direct inference of its context in pathways.

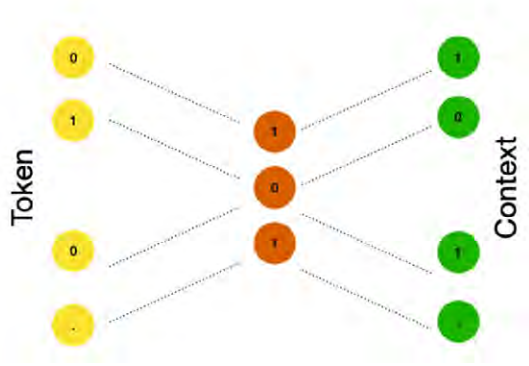



**Figure 3.** Embedding Model Objective Schematic

# RESULTS

Training the model according to the objective listed in yields new 128-dimensional vectors for every node of a MetaCyc [1] pathway. To visualise the newly found space we first run a t-SNE dimensionality reduction algorithm. The dimensionality reduced vectors are plotted in a two-dimensional space (Fig. 4a, b). In the space we find distinct islands which according to our objective we expect to represent interacting/ related pathway nodes across all omics-layers. The validation of our hypothesis is carried out by running a clustering algorithm which then enables us to analyse the properties of our clusters/ islands Fig. 4a. The coloured section in the plot show related nodes (highly aligned embedding vectors). In contrast to Fig. 4a we visualise omics-layers in Fig.4b. by coloring genes, proteins and small molecules.

## Embedding Space

We find that different pathway modalities are well distributed in the space despite genes being more abundant in the left half (Fig.4b). Therefore, in most clusters (Fig. 4a) we can identify closely related genes, proteins, enzymes and small molecules easily by searching in the neighborhood. To find the meaning of the clusters themselves we run 1. look at direct links between the most similar embeddings and 2. run a pathway enrichment analysis.

### Links between aligned nodes

As an example, we take UDP-alpha-D-galactose and its related node in the embedding space which encodes phosphoglucomutase-1 (PGM1). Their proximity in the space is valid because MetaCyc [1] indeed states UDP-alpha-D-galactose as an intermediate in carbohydrate metabolism, and its relation to phosphoglucomutase-1 (PGM1) lies in its role in glucose and galactose metabolism. Their relation is defined by the following characteristics:

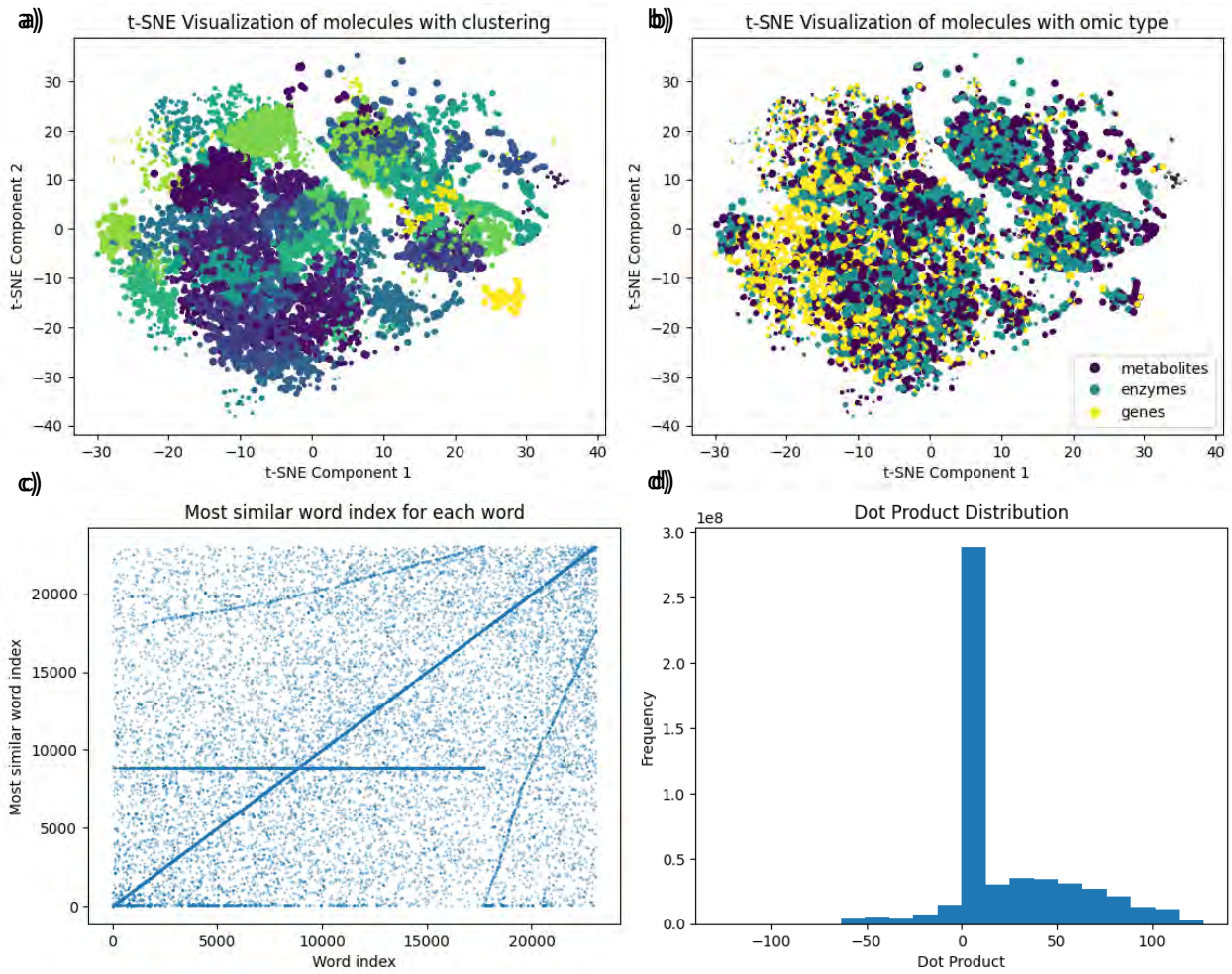



**Figure 4:** Resulting embedding space after running the embedding model

1. **PGM1 function**: Phosphoglucomutase-1 catalyzes the reversible conversion between glucose-1-phosphate (G1P) and glucose-6-phosphate (G6P). This step is crucial for glycogen breakdown, glycolysis, and the generation of nucleotide sugars such as UDP-glucose.
2. **UDP-galactose synthesis**: UDP-alpha-D-galactose is derived from UDP-glucose through the action of UDP-galactose-4-epimerase. UDP-glucose is synthesized from G1P by the enzyme UDP-glucose pyrophosphorylase, and PGM1 provides the necessary G1P by converting G6P.
3. **Interconnection**: PGM1 indirectly supports the biosynthesis of UDP-galactose because it ensures the availability of G1P, a precursor for the production of UDP-glucose, which is required for UDP-galactose formation. Therefore, PGM1 plays a foundational role in the metabolic pathways that produce UDP-galactose.

Similar results are found for other pairs of embeddings and thus verify that the model correctly relates different omics to aligned embeddings based on a functional connection.

In Fig. 4c we visualise the most related pathway node for every node. We achieved achieve a good coverage of the space because we limited the effect of highly common intermediates such as water, oxygen or carbon dioxide by under-sampling them. The model has therefore given an equal weighting to all related nodes. The diagonal has been set to zero. What looks like a diagonal in the picture originates from the fact that the nodes are implicitly ordered because we assign the indices as we process pathways. Hence, a similar index results in a higher likelihood of appearing first in a similar pathway. The overall distribution of dot products between all embeddings (Fig. 4d) follows the shape of a mixture of two distribution. One distribution belonging to related nodes with a smaller but wider peak and the other distribution of unrelated nodes with a sharp narrow peak.

## Pathway Enrichment Analysis

Based on the pathway enrichment analysis for the clusters in Fig. 4 we found that clusters share a set of common characteristics. Cluster 0 in the example contains

biosynthesis pathways focusing on Pyrimidine Nucleotide Biosynthesis, Pyrimidine Deoxyribonucleotide Biosynthesis and related processes. Based on the functional connections revealed by the enriched pathways within clusters we have shown that closely aligned nodes interact and share similar behaviours/ functions. The interactions can be grouped into the following categories:

1. **Shared Enzymes and Genes**: dut (Deoxyuridine 5'-triphosphate nucleotidohydrolase): Present in multiple pyrimidine-related pathways (e.g. pyrimidine biosynthesis and degradation)
2. **Key Reactions:** Conversion of nucleotides or nucleotide precursors like UMP, dUMP, and dTTP. Hydrolysis of diphosphates, ensuring the regulation of nucleotide intermediates.
3. **Cofactors and Byproducts:** Common usage of ADP, diphosphate, and AMP. Generation or utilization of cofactors like NADP+ and CO2 in related biosynthetic processes.
4. **Organisms and Applications:** The pathways include contributions from diverse organisms) highlighting conserved metabolic roles in nucleotide synthesis and homeostasis.
5. **Interconnection with Metabolic Networks:** These processes are interconnected with biosynthetic pathways like baumannoferrin biosynthesis and teichoic acid biosynthesis, emphasizing the role of nucleotides as substrates for broader cellular functions (e.g. synthesis of wall components or coenzymes).

# DISCUSSION

We have shown that clustering/ proximity in the embedding implies an interaction between the nodes (See Embedding Space Analysis). Unlike specific protein sequence, SMILES or gene embeddings we can directly link instances of genes, proteins and small molecules to learn about their relationship by computing the alignment of their embedding vectors/ proximity in the embedding space (Fig. 4b).

The amount of meaningful interactions an embedding vector captures depends on the data availability. Annotated pathways are limited, especially when we move away from model organisms or well understood disease metabolic networks. If we only witness a certain function of a protein in one domain and see no other examples of its behaviour in other contexts then it is unlikely that its embedding can generalise well to other domains. Additionally, Networks from MetaCyc [1] are biased in the sense that they have undergone a step of curation and are not direct results of experiments but rather a product of experimental studies and its subsequent analysis. Through this process we also lose some information. The networks found in MetCyc [1] are binary and no interaction strength or confidence of interactions can be inferred. We lose information on lower confidence interactions that still add nuanced detail to the characterisation of the nodes. Additionally, some interactions that were perhaps not relevant in pathway can be omitted making it more difficult to assess unknown or new pathways.

## High throughput experimental results

By providing additional experimental data from high throughput differential expression, we can reduce bias and increase the amount and diversity of training data. Currently, the focus lies on annotated and curated pathways from PDBs. The interactions contained in these databases are reliable reactions that support the higher order function of a pathway. However, these pathways networks have limited availability especially outside model organisms. Through additional experimental methods we can establish more linkages between metabolites, genes and proteins [10]. The interpretation of differential expression data is different however because correlations between two analytes do not necessitate a linkage by chemical reactions as it is the case in PDBs. In the context of this work the different interpretation is not an issue because we only consider the context of two analytes in a training objective. If two analytes are differentially expressed it means that a specific context change has had an effect on the analytes and there must be a pathway that co-affects them.

## Unknown Nodes

To find fingerprints for nodes not found in MetaCyc [1] we can provide the model with the node context. MetaCyc [1] is a large database of metabolic networks, and it contains many proteins, genes and small molecules. However, given the vast size of the chemical/ biological universe there are still a significant number of nodes which are not present. In the case that related nodes within the training set are known we can still find an embedding for them by feeding in all the related nodes to the encoder network by summing their one-hot encodings. A more generalizable approach to finding embeddings of unknown compounds would be to define a mapping from atom/ sequence space to the embedding space. Especially a bijective mapping can enable the embedding to be extended to generative applications. If we assume a generator model creates molecules in the embedding space with given properties, then these are unlikely to have been part of the training data. Thus, we require a mapping back from the embedding space to SMILES or sequences. To implement the additional mapping, we can create 3 new networks for each omics layer that can learn to map into the embedding space.

## FUTURE WORK

To address the issues of the limited network availability and bias as well as the loss of data due to binary edges we can supplement curated biological pathways with general high throughput experiments of protein-protein interactions, gene-protein interactions and metabolite interactions. Using data directly from experiments removes the need of curation from a Pathway Databases which reduces bias. Additionally, we can reduce our reliance on PDBs to contain data for the domain we are interested in. Certain disease networks might be very well represented in a database but venturing into a lesser-known disease requires data not yet found in Pathway databases. Apart from chemical reactions in metabolic networks gene regulation with transcription factors and cell signalling can be included to widen the applicability domain of the model as well as producing more nuanced embeddings.

### Structural and functional data

An additional structural, functional or compositional component in the embedding vector adds information to the training data that the embedding model can learn. The sequence (nucleotides, amino acids) provides information on the presence of functional groups, can show how related two genes are or give information on the 3D structure. To an extent these datapoint are implicitly present in the pathway network. However, Pathway Databases are never complete. They represent a subset of highly curated reaction networks, and we lose information by only teaching the model to reproduce these relations instead of also identifying new relationships purely on functional properties.

### Application to Pathway Discovery

The proposed fingerprints offer direct relationships between multi-omics data. Using the fingerprints to identify missing edges/ interactions in metabolic networks is a fitting application to test their predictive strength. Going even further we can use the fingerprints as the basis for generative models to create new pathway networks. As the interactions between nodes lie at the core of this fingerprint, we expect generative models to benefit from this single space embedding that capture multiple omics layers at once.

## ACKNOWLEDGEMENTS

This work was kindly supported by the NMES faculty scholarship from King's College London.

## REFERENCES

1. Ron Caspi, Tomer Altman, et al. The metacyc database of metabolic pathways and enzymes and the biocyc collection of pathway/genome databases. Nucleic acids research, 42(D1):D459–D471, 2014
2. Manish Kumar. A beginner's guide for understanding extended-connectivity fingerprints(ecfps), Mar 2021.
3. Xinmeng Liao, Mehmet Ozcan, et al. Open moa: revealing the mechanism of action (moa) based on network topology and hierarchy. Bioinformatics, 39(11):btad666, 2023.
4. Javier Lopez-Ibáñez, Florencio Pazos, and Monica Chagoyen. Predicting biological pathways of chemical compounds with a profile-inspired approach. BMC bioinformatics, 22(1):320, 2021.
5. Tomas Mikolov, Ilya Sutskever, Kai Chen, et al. Distributed representations of words and phrases and their compositionality. Advances in neural information processing systems, 26, 2013.
6. Kumar Saurabh Singh, Justin JJ van der Hooft, et al. Integrative omics approaches for biosynthetic pathway discovery in plants. Natural Product Reports, 39(9):1876–1896, 2022.
7. Raman, K. and Chandra, N., 2009. Flux balance analysis of biological systems: applications and challenges. Briefings in bioinformatics, 10(4), pp.435-449.
8. Honda S, Shi S, Ueda HR. Smiles transformer: Pre-trained molecular fingerprint for low data drug discovery. arXiv preprint arXiv:1911.04738. 2019.
9. Durant, J. L., Leland, B. A., Henry, D. R., & Nourse, J. G. (2002). Reoptimization of MDL keys for use in drug discovery. Journal of Chemical Information and Computer Sciences, 42(6), 1273-1280.
10. Subramanian I, Verma S, et al.. Multi-omics data integration, interpretation, and its application. Bioinformatics and biology insights. 2020 Jan;14:1177932219899051.
11. Muller, E., Shiryan, I. and Borenstein, E., 2024. Multi-omic integration of microbiome data for identifying disease-associated modules. Nature Communications, 15(1), p.2621.
12. Hussain, M.H., Mohsin, et al., 2022. Multiscale engineering of microbial cell factories: A step forward towards sustainable natural products industry. Synthetic and systems biotechnology, 7(1), pp.586-601.

© 2025 by the authors. Licensed to PSEcommunity.org and PSE Press. This is an open access article under the creative commons CC-BY-SA licensing terms. Credit must be given to creator and adaptations must be shared under the same terms. See https://creativecommons.org/licenses/by-sa/4.0/



Systems & Control Transactions

**Research Article - Peer Reviewed Conference Proceeding**
ESCAPE 35 - European Symposium on Computer Aided Process Engineering
Ghent, Belgium. 6-9 July 2025
Jan F.M. Van Impe, Grégoire Léonard, Satyajeet S. Bhonsale,
Monika E. Polańska, Filip Logist (Eds.)

PSE PRESS

# Process design for a novel fungal biomass valorisation approach

**Theresa Rücker[a*], Matteo Gilardi[a*], Thomas Brück[b], and Bernd Wittgens[a]**

[a] SINTEF Industry – P.O. Box 4760 Torgarden, NO-7465 Trondheim, Norway
[b] Technical University of Munich – Werner Siemens-Chair of Synthetic Biotechnology, Lichtenbergstr. 4, 85748 Garching, Germany
* Corresponding Author: theresa.rucker@sintef.no, matteo.gilardi@sintef.no - These authors contributed equally to this work.

## ABSTRACT

The European Union is transitioning towards a circular and low-carbon economy, emphasizing renewable biological resources. This study explores the production of high-value compounds like chitosan from fungal biomass and presents a potential design for a sustainable biorefinery process, contributing to the diversification and optimisation of biomass feedstock utilisation. The process simulation includes dedicated sub-models for each unit operation, based on laboratory data and integrated into a comprehensive process flow sheet using COCO-COFE. The productivity of the simulated plant results in 2 500 tons of triglyceride oils and 1 800 tons of chitosan that can be produced from 15 000 tons of *Aspergillus niger*. On-site acetic acid production meets 45% of the total plant's demand, significantly reducing the amount of additional acetic acid to be purchased as raw material. Additionally, large-scale enzyme consumption and the substantial heat demand for biomass processing are key economic and environmental factors that need to be central in successful process design.

**Keywords**: waste valorisation, process design, sustainable product development, biomass conversion, data-driven modelling.

## INTRODUCTION

The European Union is shifting towards a circular and low-carbon economy, which focuses on renewable biological resources [1]. A promising alternative to conventional plant biomass is the utilisation of non-plant biomass, such as microbial, fungal, and animal-derived materials. One example is the production of high-value compounds, such as chitosan, from fungal biomass [2]. A significant advantage of valorising non-plant biomass is the reduction in competition with food production. Unlike plant biomass, which often requires arable land and can lead to biodiversity loss and land use changes, non-plant biomass can be sourced from waste streams and by-products, minimising competition with food and environmental impact [3]. Innovative technologies are essential to diversify and optimise the use of available, underutilised, and more sustainable biomass feedstocks. An integrated strategy that can replace multiple conventional products derived from fossil feedstocks or unsustainable agricultural practices, such as palm oil production, is urgently needed.

A promising new conversion process focuses on the upcycling the residue of the fungus *A. niger*, generated in large quantities during citric acid production (over 2 million tonnes produced yearly, globally [4]).This biomass is expected to reach a scale of 3.3 million tons by 2028 [4] and holds potential for higher-value applications beyond its current use as low-value animal feed. This study investigates the design of a biorefinery process, which comprises parallel production of two value-added products, namely yeast oil as a greener alternative to palm oil and non-animal-derived chitosan.

Yeast oil can be obtained from a fermentation process of solubilised *A. niger* biomass (hydrolysate) followed by a hydrolysis process. The resulting oil is based on triglycerides showing relative palmitic, stearic, oleic, and linoleic acid contents similar to the ones observed in conventional plant-based oils, such as palm and coconut oil. The oil can be used directly or hydrolysed by chemicals (acid or base) or enzymes to yield free glycerol and a mix of free fatty acids resembling closely those of rapeseed and sunflower oil. Thus, yeast oil can be valorised as biobased chemical in a variety of applications such as

cosmetics formulations, biofuel production, the food industry, and the pharmaceutical sector. It is noteworthy, that downstream processing of the raw yeast oil obtained from fermentation and hydrolysis can lead to the production of specific additives for cosmetics (stearates), as well as coating applications (alkyd resins). The main expected benefits are the high oil purity (no need for solvent traces removal), reduced specific greenhouse gas emissions with respect to conventional plant-based oils, good recycling potential, biodegradability, and sustainability.

Chitosan, which can be derived from chitin fraction of the fungal biomass, and its higher-value derived products, such as chitosan oligosaccharides (CHOS), are non-toxic and biocompatible. Moreover, a part of these derivatives is characterised by a low molecular weight, which guarantees their water-solubility and enhances the spectrum of possible applications. Remarkably, CHOS have a wide variety of interesting properties for applications in food, agriculture, medicine, pharmaceuticals, and cosmetics [5].

The developed process simulation consists of dedicated sub-models for each unit operation, which are based on laboratory data and implemented as plug-ins and further integrated in a comprehensive process flow using COCO-COFE v3.6, a license-free CAPE-open simulation software developed by AmsterChem. The process is sized based on the fungal waste biomass generated in an industrial-size citric acid production plant located in Germany. The mass and energy balances from the simulation are exploited for a preliminary feasibility study of the new proposed process. In particular, this study shows the energy consumption associated with all the involved unit operations and the Key Performance Indicators (KPIs) of the novel fungal biomass valorisation process.

## MODELLING

### Block Flow Diagram

The process comprises six primary steps, as displayed in Figure 1. Initially, the fungal biomass undergoes enzymatic solubilisation, yielding a sugar-rich aqueous solution. This hydrolysate is first utilised for on-site acetic acid production. In a subsequent main fermentation step, a lipid-rich yeast biomass is cultivated, utilizing residual glucose and acetic acid as carbon sources. All nutrients, such as salts and inerts, are for simplicity not displayed in the model. The lipids produced are then released during the hydrolysis step, resulting in the separation of the product into three distinct phases: solid, aqueous, and oil. Concurrently, the non-solubilised, chitin-rich fraction from the enzymatic solubilisation of the fungal residues is subjected to a combination of enzymatic and chemical treatments to produce chitosan and CHOS.

### Sub-models

Specific sub-models have been developed for the characterisation of each unit operation. A data-driven approach has been adopted where needed. According to this methodology, the conversion and yield of the reactions involved in the process are defined using correlations that contain adjustable parameters, which are fitted directly to the available experimental data. Therefore, the developed sub-models are only valid within the tested ranges of operating conditions and types of feedstocks.

We emphasise, that the process simulation approach and the criteria adopted to define representative molecular formulas for complex species are using well-established and thoroughly calibrated methods based on previous work [6].

### Enzymatic solubilisation

The process can be characterised as a hydrolysis reaction, where glucan polymers are broken down to form simple glucose monomers with the addition of water

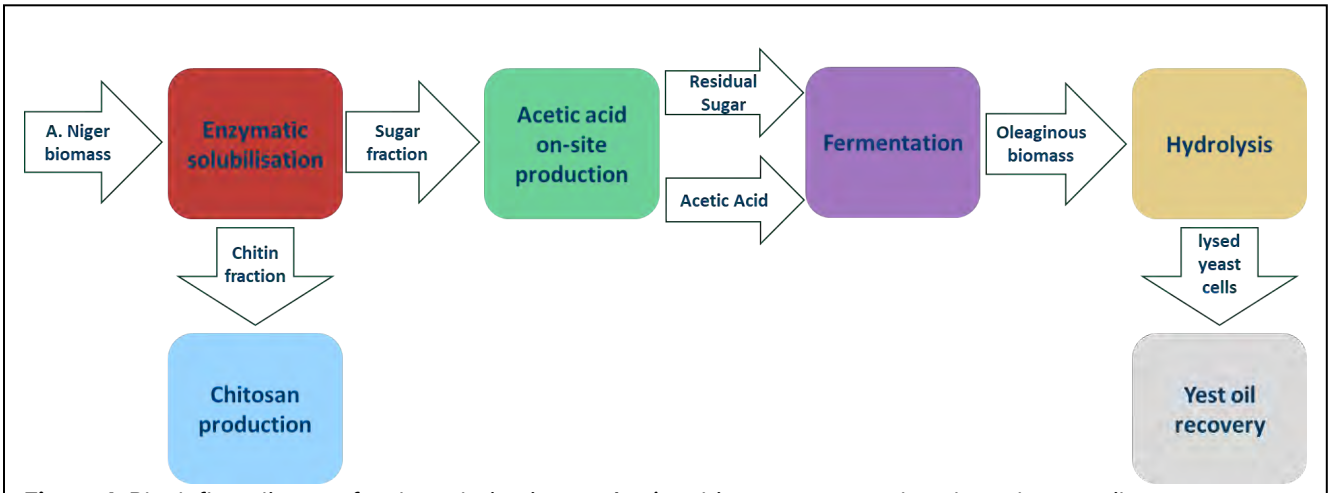



**Figure 1:** Block flow diagram for the valorisation og *A. niger* biomass to non-plant-based yeast oil.

molecules (glucan + water → glucose) and complex proteins into their shorter oligopeptides or their amino acid constituents, here simplified as protein + water → amino acids, as described by reactions (1) and (2), respectively.

$$C_6H_{10}O_5 + H_2O \rightarrow C_6H_{12}O_6 \quad (1)$$

$$C_{5.35}H_{9.8}N_{1.5}O_{2.45} + H_2O \rightarrow C_{5.35}H_{11.8}N_{1.5}O_{3.45} \quad (2)$$

The conversion rates of these reactions characterise the efficiency of the glucan/protein solubilisation. Lab-scale experiments reached an overall percentage of solubilised fungal biomass of 73%(w/w). Moreover, a comparable degree of solubilisation was observed for glucan and protein fractions. Therefore, assuming that no chitin is solubilised, the corresponding solubilisation factor for both glucan and protein is 85.3%(w/w).

## Chitosan production

The chitosan synthesis involves both deacetylation and depolymerisation of chitin. During deacetylation, the chitin polymer reacts with NaOH (chitin polymer + sodium hydroxide → chitosan polymer + sodium acetate) according to expression (3). A chitosan polymer, with a degree of polymerisation equal to the one of the reacting chitin polymer is formed. The conversion (equal to the degree of deacetylation) is 84%.

$$C_{40040}H_{65067}N_{5005}O_{25026} + 5005\ NaOH \rightarrow C_{30030}H_{55057}N_{5005}O_{20021} + 5005\ NaC_2H_3O_2 \quad (3)$$

In the depolymerisation the complex chitosan polymer is broken down into shorter-chain oligomers (chitosan polymer + water → chitosan oligomer). Given that experimental observations only provide the average degree of polymerisation of the product (without details on the chain length distribution), a simplified model based on the literature has been developed (conversion is set to 100%), see equation (4) [7].

$$C_{30030}H_{55057}N_{5005}O_{25026} + 384\ H_2O \rightarrow 385\ C_{78}H_{145}N_{13}O_{53} \quad (4)$$

## Acetic acid on-site production

The sugar-rich hydrolysate fraction is used for on-site production of acetic acid (AA) by fermentation. The AA will further be used as a co-feed carbon source in the main fermentation, where the AA and the residual sugar from the initial hydrolysate is exploited to grow oleaginous biomass. An inoculum flow equal to 4% of the mass of glucose in the hydrolysate is introduced in the medium to carry out the fermentation. Oxygen in the form of air is added as an input with 20% excess [8]. The conversion is defined considering the overall aerobic fermentation reaction of sugar to AA (glucose + oxygen → AA + carbon dioxide + water), described in equation (5). Based on the available literature, the average conversion is set to 85% [8,9]. The remaining 15% is the percentage of hydrolysate left after the acetic acid production step, to be exploited as the sugar source for the main fermenter. As a result, the AA to glucose molar ratio in the output stream is equal to 18:1.

$$C_6H_{12}O_6 + 2\ O_2 \rightarrow 2\ CH_3COOH + 2\ CO_2 + 2\ H_2 \quad (5)$$

## Fermentation

The chemical formula for the main fermentation (initial cell mass + hydrolysate + AA + oxygen → oleaginous biomass + carbon dioxide + water) is implemented as described in reaction (6). All nutrients, such as salts and inert species in the medium, are for simplicity not displayed in the model. The initial cell mass chemical formula represents the overall chemical composition of the medium that takes part in the reaction. Nitrogen is added to close the mass balance.

$$C_{5.35}H_{9.8}O_{2.45}N_{1.5} + 1.5\ C_6H_{12}O_6 + 40.5\ C_2H_4O_2 + 4.85\ O_2 \rightarrow C_{67.95}H_{112.65}O_{8.81}N_{1.04} + 27.39\ CO_2 + 38.58\ H_2O + 0.23\ N_2 \quad (6)$$

An external AA input is added to the system since the AA to glucose ratio available from the on-site production is not sufficient to meet the fermentation reaction stoichiometry, which requires an input ratio of at least 27:1. Based on experimental data created in the project, the conversion rates were set to 98% for glucose and 70% for AA.

## Hydrolysis of the yeast biomass

The hydrolysis is split into the release of triglyceride (oleaginous biomass → Tripalmitin + Tristearin + Triolein + Trilinolein + non-lipid biomass), which is presented in reaction (7), and the hydrolysis (non-lipid biomass + water → amino acid + sugar + lipid biomass), displayed in equation (8). Based on experimental data from project partners the overall conversion rate is set to 68%.

$$C_{67.95}H_{112.65}O_{8.81}N_{1.04} \rightarrow 0.403\ C_{57}H_{104}O_6 + 0.249\ C_{57}H_{110}O_6 + 0.045\ C_{57}H_{98}O_6 + 0.216\ C_{51}H_{98}O_6 + 1.855\ C_{9.3}H_{9.61}O_{1.8}N_{0.56} \quad (7)$$

$$C_{9.3}H_{9.61}O_{1.8}N_{0.56} + 2.5\ H_2O \rightarrow 0.2\ C_{13.42}H_{10.52}O_{0.014}N_{0.8} + 0.8\ C_{5.35}H_{9.8}O_{2.45}N_{0.5} + 0.39\ C_6H_{12}O_6 \quad (8)$$

The hydrolysis process yields a multiphase mixture with three fractions: (1) a solid fraction of dead cell mass and residual oleaginous biomass; (2) an organic liquid phase rich in lipids; (3) an aqueous phase, containing glucose, unreacted AA, and proteins.

## Yeast oil separation

The modelled separation involves three compound splitters (Sep-1 to Sep-3): 83% of the aqueous phase is recycled to the main fermenter, 100% of the produced triglyceride oil is separated, and the residual mixture is split to remove solids, with the aqueous solution being recycled back to the main fermentation.

## Flowsheet development

The sub-models described in section 2.2. have been integrated in the COCO-COFE process simulator. COCO (CAPE-OPEN to CAPE-OPEN) is a free-of-charge CAPE-OPEN compliant steady-state simulation environment. COFE (CAPE-OPEN Flowsheet Environment) is a user-friendly graphical user interface integrated in COCO for chemical flowsheeting provided with sequential solution algorithm using automatic tear streams. COFE displays properties of streams, deals with unit-conversion and provides plotting facilities. The system requirements to run COFE are Windows XP or higher.

A snapshot of the flowsheet is depicted in Figure 2. The Vapor-Liquid equilibrium in the process was simulated using the Raoult equation. Relevant physico-chemical properties, such as the chemical formula, ideal gas heat of formation, ideal gas entropy of formation, ideal gas heat capacity and vapor pressure, have been retrieved to characterise all species in the process simulator. In the absence of data or correlations from the literature, the vapor pressure of high molecular weight molecules such as enzymes, oleaginous yeast, and cell mass has been set to a fixed fictitious constant value of 0.000001. The reasonable implication of this simplifying assumption is that no vaporisation of the mentioned species occurs at the operating temperatures and pressures of interest for the investigated process.

The simulation was carried out assuming that the plant is treating 15 000 ton/year of dry *A. niger* biomass, which corresponds to the total annual amount of fungal waste generated by a citric acid industrial production site located in Germany. The fungal biomass feedstock contains 68%(w/w) glucan, 13%(w/w) chitin, 9%(w/w) amino acids and 10%(w/w) inert components. The latter one is a fraction of fatty acids and other components which do not react in the studied process and therefore are not displayed in the model. The *A. niger* biomass is diluted with water to a dry matter content of 15%(w/w) in the feed stream and preheated with steam to 121°C for 1 hour (autoclave sterilisation). After cooling, a dedicated enzyme cocktail is added to hydrolyse the glucan and protein present in the fungal biomass. Two dedicated fixed-conversion reactors are modelled to describe the protein (R100a deproteinisation) and glucan conversion (R100b glucan solubilisation), respectively. The residence time for the two enzymatic hydrolysis steps is set to 16 h and 40 h, respectively. Both reactors operate at a constant temperature of 50°C. The stream leaving R100b contains the sugar-rich hydrolysate and a residual solid fraction, containing chitin and unreacted glucan. These two fractions are separated in a filter (F-101). In this work, 100% of the filtrate is used for AA production.

The solid fraction (chitin and glucan) is pre-cooled to 25 °C in Cooler_chitin and chilled to 4 °C in another heat exchanger, named Chiller_chitin. The solid mixture is mixed with NaOH, which is also cooled to the same temperature in Chiller_NaOH, and then fed to the deacetylation reactor (R200-Deacetylation) and, subsequently, to the depolymerisation vessel (R200-Depolymerisation). The overall residence time inside the two vessels is 48 h. The mixture leaving R200-Depolymerisation is centrifugated to separate the water-insoluble compounds, including chitin and remaining glucan. For the centrifuge, a separation efficiency of 90% is assumed. The chitin-rich solid fraction can be utilised as animal feed. The chitosan-rich water stream is dried at 130°C using steam as utility. The dryer is designed to achieve 98% moisture removal. The dried CHOS product

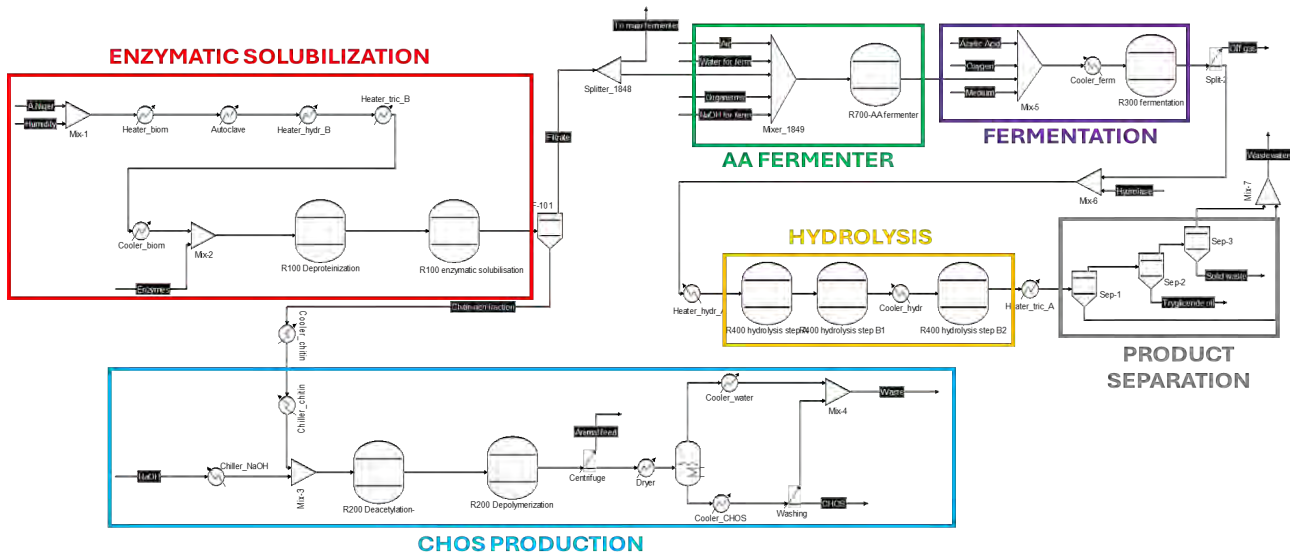



**Figure 2:** Process flowsheet implemented in COCO-COFE.

is cooled down to ambient temperature in Cooler_CHOS and sent to a washing step to remove residual impurities before storage.

The glucose-rich hydrolysate is mixed with all the other inputs required for fermentation in Mix-5: these streams are the fermentation organisms, additional water, NaOH for pH control, and air to provide oxygen. The mixed input enters a vessel where AA is produced (R500-AA fermenter). The residence time inside R500 is set to 50 hours. The output stream contains AA and glucose; thus, it represents the feed for the main fermenter. The additional feedstocks for the main fermentation medium, oxygen, and supplementary AA are mixed in Mix-6 and cooled down to 28 °C in Cooler_ferm. The residence time inside the fermenter is 72 h. Downstream the fermenter, a $CO_2$-rich off-gas is released, and the product is mixed with enzymes for the hydrolysis step. Finally, the mixture is heated up to 45 °C. The preheated stream is conveyed to hydrolysis.

In reactors (R400 hydrolysis step A and R400 hydrolysis step B), the non-lipid portion of the biomass is hydrolysed, producing glucose. Hydrolysis takes place in two vessels in series, operating at a temperature of 45 °C and 37 °C, with a residence time of 20 h and 6 h, respectively. Finally, the product is heated back to 45 °C in a process-process heat exchanger (Heater_tric) and sent to the product separation.

All residence time and operating conditions selected to model each process step represent the optimal conditions resulting from lab-scale tests carried out by our partners in VALUABLE.

## RESULTS

The Key Performance Indicators (KPIs) of the simulated plant include the productivity of triglyceride oil and chitosan (product targets), the on-site productivity of AA as an intermediate for the biomass conversion process, as well as the overall consumption of raw materials (the ones for which a major effect on the plant operating costs is expected), and the total steam demand (main utility for this plant). The KPIs are shown both on an absolute basis (see Table 1) and on a relative basis, assuming 1 kg of dry *A. niger* biomass as a reference (see Table 2).

**Table 1:** List of the Key Performance Indicators of the simulated plant on an absolute basis. AN – *Aspergillus niger*.

| Indicator | Value | Unit |
|---|---|---|
| Triglyceride oil productivity | 2446.5 | ton/year |
| Chitosan productivity | 1813.5 | ton/year |
| On-site AA productivity | 5221.9 | ton/year |
| Extra demand for AA | 6297.4 | ton/year |
| Total heat duty (LP steam) | 8.88 | MW |

The results show that about 2 450 tons of triglyceride oils and 1 800 tons of chitosan can be produced starting from 15 000 tons of *A. niger* biomass. The productivity of yeast oil is rather limited, considering that the glucan content in the biomass feedstock is 76%. However, this result can be justified considering that a significant portion of the glucan from the *A. niger* biomass is consumed to generate the AA needed as a co-carbon source for fermentation. On-site AA productivity turns out to cover 45% of the total AA demand of the plant: this is expected to have a positive effect on the operating costs, leading to a significant reduction of the amount of AA to be purchased.

**Table 2:** List of the Key Performance Indicators of the simulated plant (relative values per unit of feedstock). AN – *Aspergillus niger*

| Indicator | Value | Unit |
|---|---|---|
| Triglyceride oil productivity | 0.16 | kg/kg AN |
| Chitosan productivity | 0.12 | kg/kg AN |
| On-site AA productivity | 0.35 | kg/kg AN |
| Extra demand for AA | 0.42 | kg/kg AN |
| Total heat duty (LP steam) | 18.67 | MJ/kg AN |

The overall enzyme consumption represents a considerable challenge when considering a large-scale operation. Therefore, enzyme purchase cost is expected to be a key driver in the economic assessment of the plant.

Table 3 gathers a breakdown of the energy consumption associated with the single unit operations involved in the process.

**Table 3:** List of the energy requirements (and utility type) associated with each unit operation. C.W. - cooling water

| Unit operation | Duty (kW) | Utility |
|---|---|---|
| Heater_biom | 8337.95 | steam |
| Cooler_biom | 1730.39 | C.W. |
| Cooler_ferm | 4779.41 | C.W. |
| Cooler_hydr | 2421.24 | C.W. |
| Cooler_chitin | 88.58 | C.W. |
| Chiller_chitin | 72.36 | Electricity* |
| Chiller_NaOH | 0.76 | Electricity* |
| Dryer | 2891.88 | steam |
| Cooler_water | 3012.99 | C.W. |
| Cooler_CHOS | 137.55 | C.W. |

*Electricity consumption for the refrigeration cycle

The overall steam and cooling duty demands are 11.23 MW and 12.17 MW, respectively. Electricity consumption for the refrigeration cycle is a minor consumption. It is important to mention that the real electricity demand to run the plant will be higher since circulation pumps to overcome pressure drops must also be considered. However, based on the outcomes of the current

energy balance, the main conclusion is that the main operating cost associated with utilities is undoubtedly the one linked with the steam demand for the initial preheating of the fungal biomass to 121°C upstream of the autoclaving step.

## CONCLUSIONS

In the present work, two key milestones of the preliminary feasibility study of the novel process developed in the VALUBALE project, namely process design and simulation, and estimation of KPIs, have been accomplished.

The proposed process offers a sustainable solution for transforming an industrial waste (i.e., *A. niger* biomass) into multiple high-value products. The main novelties are enhanced sustainability and the promotion of a circular economy by converting waste into valuable resources.

In this study, we established a novel integrated bioconversion of acetic acid and sugar to sustainable yeast oil production. Moreover, by integrating on-site acetic acid production through fermentation, the need for external acetic acid purchase is significantly reduced. As a result, the cost gap compared to plant-based lipids is expected to be considerably reduced.

The results achieved in this work will be exploited as a basic framework to carry out a detailed Techno-Economic Assessment (TEA), Life-Cycle Assessment (LCA) and social acceptance assessment of the novel VALUABLE process. The main target will be to compare its economic and environmental impact with benchmark processes for oil production based on plant biomass and chitosan production based on crustacean waste. More specifically, palm oil production and chitosan production from shrimp cells will be used as reference cases.

## ACKNOWLEDGEMENTS

This publication is part of the VALUABLE project. The project has received funding from the European Union's Horizon 2020 research and innovation program under grant agreement No. 101059786.

## REFERENCES

1. R. Platt, A. Bauen, P. Reumerman, C. Geier, R. Van Ree, I. Vural Gursel, L. Garcia, M. Behrens, P. von Bothmer, J. Howes, Y. Panchaksharam, K. Vikla, V. Sartorius and B. Annevelink. BIOEAST Strategic Research and Innovation Agenda. Technical Report (2023).
2. K. M. Abdel-Gawad, A. F. Hifney, M. A. Fawzy and M. Gomaa. Technology optimization of chitosan production from *Aspergillus niger* biomass and its functional activities. *Food Hydrocolloids*, 63, 593–601 (2017). 10.1016/j.foodhyd.2016.10.001
3. J. Fargione, J. Hill, D. Tilman, S. Polasky and P. Hawthorne. Land Clearing and the Biofuel Carbon Debt. *Science*, 319, 1235–1238 (2008). https://www.science.org/doi/10.1126/science.1152747
4. R. and M. ltd, Citric Acid Market, https://www.researchandmarkets.com/reports/5732513/citric-acid-market-global-industry-trends (accessed December 21, 2023)
5. CHITOSAN: Overview, Uses, Side Effects, Precautions, Interactions, Dosing and Reviews'. https://www.webmd.com/vitamins/ai/ingredientmono-625/chitosan
6. M. A. Masri, D. Garbe, N. Mehlmer and T. B. Brück. A sustainable, high-performance process for the economic production of waste-free microbial oils that can replace plant-based equivalents. *Energy Environ. Sci.*, 12, 2717–2732 (2019). https://doi.org/10.1039/C9EE00210C
7. M. B. Kaczmarek, K. Struszczyk-Swita, X. Li, M. Szczęsna-Antczak and M. Daroch. Enzymatic Modifications of Chitin, Chitosan, and Chitooligosaccharides. *Front. Bioeng. Biotechnol.*, 7 (2019). https://doi.org/10.3389/fbioe.2019.00243
8. H. Danner and R. Braun. Biotechnology for the production of commodity chemicals from biomass. *Chem. Soc. Rev.*, 28, 395–405 (1999). https://doi.org/10.1039/A806968I
9. D. Dionisi, V. Igwe and G. Paton. Effect of the process conditions on the anaerobic fermentation of glucose for the production of chemicals. *Biomass Conv. Bioref.*, 11, 1977–1986 (2021). https://doi.org/10.1007/s13399-019-00557-4

© 2025 by the authors. Licensed to PSEcommunity.org and PSE Press. This is an open access article under the creative commons CC-BY-SA licensing terms. Credit must be given to creator and adaptations must be shared under the same terms. See https://creativecommons.org/licenses/by-sa/4.0/



Systems & Control Transactions

**Research Article - Peer Reviewed Conference Proceeding**
ESCAPE 35 - European Symposium on Computer Aided Process Engineering
Ghent, Belgium. 6-9 July 2025
Jan F.M. Van Impe, Grégoire Léonard, Satyajeet S. Bhonsale,
Monika E. Polańska, Filip Logist (Eds.)

PSE PRESS

# Metabolic optimization of *Vibrio natriegens* based on metaheuristic algorithms and the genome-scale metabolic model

**Yixin Wei[a,b], Tong Qiu[a,b,*], and Zhen Chen[a]**

[a] Department of Chemical Engineering, Tsinghua University, Beijing 100084, China
[b] State Key Laboratory of Chemical Engineering, Tsinghua University, Beijing 100084, China
* Corresponding Author: qiutong@tsinghua.edu.cn.

## ABSTRACT

In recent years, burgeoning interest in products derived from microbial production across various sectors has significantly propelled the evolution of the field of metabolic engineering. As a Gram-negative bacterium, *Vibrio natriegens* is characterized by its fast growth, robust metabolic capabilities, and a broad substrate spectrum, making it a promising candidate as a standard biological host for the industrial bioproduction of metabolites. Genome-scale metabolic models (GSMMs) are mathematical representations constructed based on genome annotations and gene-protein-reaction (GPR) associations within a cell. These models enable the computational simulation of intracellular reaction flux distributions. In this study, we developed a hybrid method based on metaheuristic algorithms and the GSMM to optimize metabolism for the production of ethanol and 1,3-propanediol (1,3-PDO) as target products in *Vibrio natriegens*. The modified GSMM used in this study contains 1195 reactions, 1094 metabolites, and 880 genes, with the metaheuristic algorithms employed being Genetic Algorithm (GA) and Particle Swarm Optimization (PSO). The optimization results indicate that the method proposed in this study can achieve the production of ethanol and 1,3-PDO by adjusting the expression levels of just 2-4 genes, with the production of 1,3-PDO reaching its theoretical maximum. The strategies developed in this study can effectively increase the production capacity of specific target metabolites in *Vibrio natriegens*, serving as a starting point for metabolic engineering and providing guidance for metabolic engineering targets in practical experiments.

**Keywords**: *Vibrio natriegens*, Metabolic optimization, Genome-scale metabolic model, Metaheuristic algorithm

## INTRODUCTION

In recent years, there has been a growing interest across various industries in products synthesized by microorganisms, which has spurred the development of metabolic engineering. The natural pathways of natural product hosts may face issues such as low efficiency, slow production rates, and susceptibility to interference. With the advancement of synthetic biology, scientists have begun to perform local or global metabolic engineering modifications on wild-type host chassis based on specific target products. This leads to the creation of chassis cells with improved traits and competitive advantages. Specifically, metabolic engineering aims to increase the yield of specific target compounds as much as possible by identifying the optimal design of microbial cell factories [1]. Metabolic engineering techniques allow for precise regulation of gene expression levels in engineered bacteria, with flux simulation, computation, and optimization driving strain modification towards greater efficiency and precision. *Escherichia coli*, *Saccharomyces cerevisiae*, and *Corynebacterium glutamicum* stand as the most prevalent biological hosts for constructing these cell factories. *Vibrio natriegens* is a Gram-negative bacterium known for its remarkable growth rate, robust metabolic capabilities, and a broad substrate spectrum, holding promise as a prospective standard biotechnological host for laboratory and industrial bio-production,

specifically tailored to produce target metabolites [2].

The advancement of genome sequencing technology and the gradual completion of biochemical databases have driven the development of GSMMs, establishing them as an important tool for studying cellular metabolic characteristics. GSMMs are mathematical representations of cellular models that originate from the cell's annotated genomic information. They construct a matrix of all the metabolic reactions in the cell based on GPR associations. GSMMs effectively integrate the intracellular metabolites, enzyme-catalyzed metabolic reactions, enzymes, and the genes responsible for enzyme expression, thus constructing complex models of metabolic networks. Currently, GSMMs are extensively utilized in the field of metabolic engineering for the computational tasks, simulations, and analyses of cells. They can predict cellular growth under various gene expression conditions and environmental changes, assessing the global distribution of metabolic fluxes, and determining the production flux of specific metabolites, making them vital tools for gene essentiality analysis and the prediction of cellular viability. GSMMs have been established for various model microorganisms, with continuous improvements being made to the number of genes, reactions, and metabolites included in the models, as well as the constraints applied, all of which enhance the accuracy of the models. In 2023, Coppens et al. [2] developed the first GSMM for *Vibrio natriegens*, which showed good consistency with experimental data. With the increasing convergence of computer science and bioinformatics, and considering the efficiency and effectiveness of metaheuristic algorithms in finding global optima, scientists have begun to apply metaheuristic algorithms to the analysis of GSMMs for hosts such as *Escherichia coli* [3].

In this study, we propose a hybrid method for the metabolic optimization of *Vibrio natriegens*. We first modified the GSMM for *Vibrio natriegens* developed by Coppens et al., and then we combined it with different metaheuristic algorithms, including GA and PSO, to identify the optimal gene expression level optimization strategies encompassing both knockouts and underexpression, as well as overexpression, for maximizing production fluxes of ethanol and 1,3-PDO, our two target products. Integrating machine learning with traditional metabolic engineering can aid in a more efficient discovery of better metabolic optimization strategies and facilitate a more comprehensive understanding of the reasons why different metabolic optimization strategies are conducive to increasing the yield of target metabolites. The optimization results suggest that the hybrid method can effectively enhance the production capabilities of specific targeted metabolites in *Vibrio natriegens*, offering strategic guidance for target selection in metabolic engineering modifications for practical experiments.

## PROBLEM STATEMENT

### The mathematical expression of metabolic engineering strategy optimization

The optimization of metabolic engineering strategies based on GSMM is a bi-level optimization problem. The inner layer consists of a linear programming problem, also known as the simulation of the GSMM, which aims to optimize an objective function defined as the linear combination of the reaction fluxes within the network (for example, the flux of the biomass production reaction). This is achieved by employing equality constraints derived from the quasi-steady-state assumption in the cell, along with inequality constraints that impose direct limits on the maximum and minimum values of the reaction fluxes. The inner layer provides the distribution of reaction fluxes within the metabolic network, as well as the maximum value of the corresponding objective function. Building on the distribution, the outer optimization introduces various gene expression optimization strategies, with objective functions such as Biomass-Product Coupled Yield (BPCY) and Weighted Yield (WYIELD) that are related to the target product production flux. Gene expression strategies encompass gene knockout, underexpression, and overexpression, which impact the inequality constraints of the inner layer optimization. This, in turn, affects the distribution of network fluxes and, as a result, the optimization results as well as the value of the objective function in the outer optimization.

The bi-level optimization problem can be mathematically represented as equations 1-4.

$$F(\boldsymbol{strategy}) = \max\{BPCY(\boldsymbol{v}),\ WYIELD(\boldsymbol{v}),\ etc.\} \quad (1)$$

$$Z = \max\{\boldsymbol{C}^{\mathrm{T}} \cdot \boldsymbol{v}\} \quad (2)$$

$$\boldsymbol{S} \cdot \boldsymbol{v} = 0 \quad (3)$$

$$\boldsymbol{lb}(\boldsymbol{strategy}) \le \boldsymbol{v} \le \boldsymbol{ub}(\boldsymbol{strategy}) \quad (4)$$

Where $\boldsymbol{v}$ is the flux vector composed of the fluxes of all reactions in the metabolic network, with a dimension of $N$, which corresponds to the number of reactions in the model; $\boldsymbol{C}^{\mathrm{T}}$ is the transposed vector of the integer coefficient of each flux in the objective function $Z$; $\boldsymbol{S}$ (M×N) is the stoichiometric matrix ($S_{ij}$ corresponds to the stoichiometric coefficient of metabolite $i$ in reaction $j$); $\boldsymbol{ub}$ and $\boldsymbol{lb}$ record the upper and lower bounds for the flux of each reaction in the model, respectively; $\boldsymbol{strategy}$ indicates the gene expression optimization strategy, where each dimension corresponds to a gene in the model, and each gene corresponds to an enzyme (A $strategy_i$ value of 0 signifies that the gene is knocked out, a value between 0 and 1 signifies underexpression, and a value greater than 1 signifies overexpression); $BPCY$ is the product of biomass and the yield of the target product, whereas $WYIELD$ is the weighted sum of the minimum and

maximum product fluxes under a fixed growth rate, with the weight for the maximum product flux set at 0.3.

## Impact of gene expression optimization strategies on flux constraints

Changes in gene expression levels affect the concentration of enzymes in the system, thereby influencing the flux constraints of reactions. Figure 1 is a schematic diagram illustrating how gene expression optimization strategies affect reaction flux constraints.

In a GSMM, each gene expresses a protein (enzyme) that catalyzes a reaction; however, enzymes and reactions do not correspond on a one-to-one basis. There may be multiple enzymes that work together to catalyze a single reaction (cooperative), or several enzymes that can each independently catalyze a particular reaction (competitive). Before determining the new constraints for each reaction, the following calculations need to be performed: (1) Calculate the reaction fluxes of the initial model (wild type) as a $\boldsymbol{reference}$; (2) Calculate the values of the optimization strategies for each reaction. For cooperative genes (G3 and G4), the corresponding reaction optimization strategy is taken as the minimum of the gene strategies, whereas for competitive genes (G2 and G3), the reaction optimization strategy is the maximum of the gene strategies, as shown in Figure 1. Based on the optimization strategy ($strategy_i$) and reference flux value ($reference_i$) for each reaction, updating the constraint of the reaction flux involves two steps. (1) Determine the direction of the reaction: if $reference_i > 0$ (forward reaction), set the lower bound of the reaction to 0; if $reference_i < 0$ (backward reaction), set the upper bound of the reaction to 0. (2) Update the constraint according to the direction of the reaction and the optimization strategy. For knockouts (strategy equals 0), set both the upper and lower bounds of the reaction to 0; for underexpression (strategy between 0 and 1), underexpressing a forward (backward) reaction is achieved by setting the upper (lower) bound to $strategy_i \times reference_i$; for overexpression, overexpressing a forward (backward) reaction involves setting the lower (upper) bound to $strategy_i \times reference_i$.

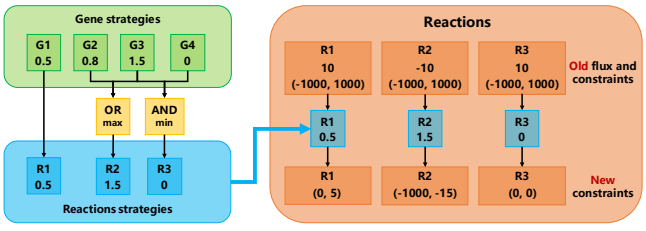



**Figure 1.** The relationship between reaction flux constraints and gene expression optimization strategies.

# MATERIALS AND METHODS

## Dataset and experiment setup

We utilized the only published GSMM of *Vibrio natriegens* in SBML format and made the following modifications to it. We adjusted the upper and lower bounds of the glycerol demand reaction in the model, enabling the model to simulate cell culture processes with glycerol as the sole carbon source. We controlled the oxygen input in the model to be greater than zero (aerobic cultivation). We also removed three reactions that were not directly adjacent to the main reaction network, along with the corresponding six metabolites and three genes. Additionally, since the metabolic network of the wild-type *Vibrio natriegens* does not contain 1,3-PDO, we introduced a two-step heterologous pathway for the conversion of glycerol to 1,3-PDO via 3-hydroxypropionic acid, ensuring that the model could be used for metabolic optimization of 1,3-PDO production. The modified GSMM comprises 1195 reactions, 1094 metabolites, and 880 genes. We employed parsimonious Flux Balance Analysis (pFBA) [4] to simulate each phenotype during the optimization process. The pFBA method can return a flux distribution result where the total flux of all metabolic reactions is minimized while still maximizing the objective function. GA and PSO were used to perform metabolic optimization with ethanol and 1,3-PDO as the target products of cellular production. All simulations and optimizations of the GSMMs were conducted in Python, utilizing the Cobrapy [5] and Mewpy [6]. The hyperparameter settings for the GA and PSO are shown in Table 1. In both algorithms, we limited the maximum number of genes with adjusted expression levels to 6.

**Table 1.** Hyperparameter settings for GA and PSO.

| Algorithm | Hyperparameter | Value |
|---|---|---|
| GA | Number of generations | 100 |
| | Others | Default |
| PSO | Number of particles | 2500 |
| | Number of iterations | 100 |
| | Inertia weight | 1.5 |
| | Personal learning rate | 2.1 |
| | Global learning rate | 1.6 |
| Both | Maximum number of genes with adjusted expression levels | 6 |
| | Fold of expression levels | {0.125,0.25, 0.5,1,2,4,8} |

## Description of the hybrid metabolic optimization method

Simulation methods such as pFBA can determine the global distribution of reaction fluxes under various gene expression strategies, but they do not provide guidance on how to optimize these strategies. Given that the relationship between the production flux of biomass and

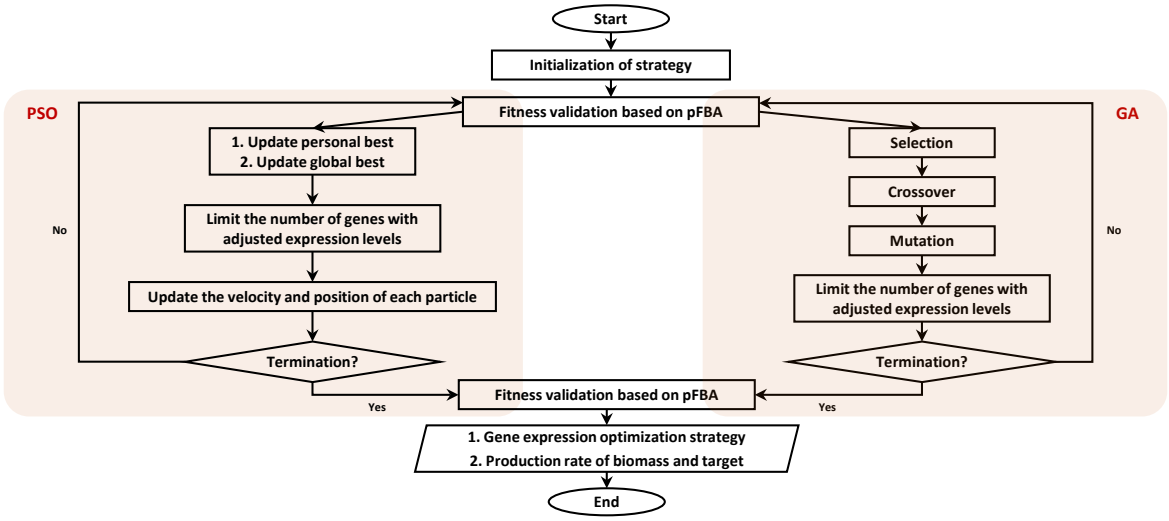



**Figure 2.** Flowchart of the hybrid optimization method.

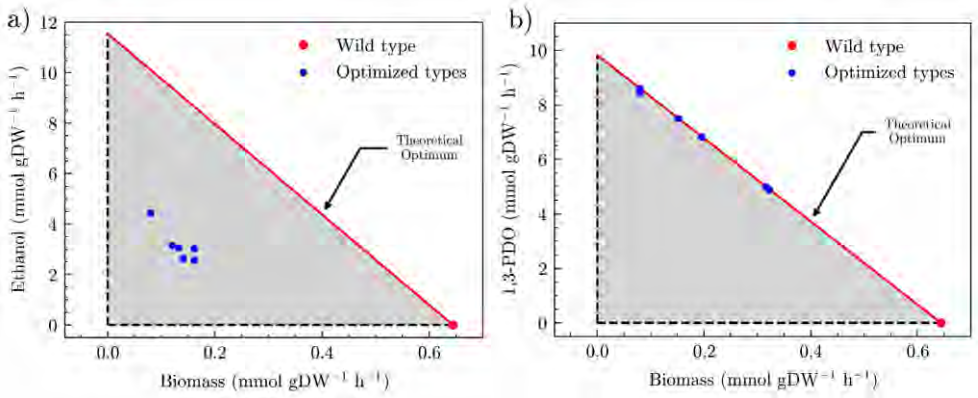



**Figure 3.** Visualization of metabolic optimization for a) ethanol production, and b) 1,3-PDO production.

the target product is not a simple function of the strategy vector, and that calculating the gradient is challenging due to the complexity of the system, coupled with the extensive search space for the strategy vector, it is particularly appropriate to employ metaheuristic algorithms to find more optimal values of the strategy vector. The metabolic optimization method proposed in this paper has explored the use of different metaheuristic algorithms to control the update of the strategy vector. The pFBA method is employed to validate whether this strategy vector can indeed optimize the production rate of the target products while ensuring cell viability. Figure 2 is a flowchart of the hybrid optimization method. The method ultimately outputs both the optimal strategy vector and the corresponding production rate of biomass and target product.

## RESULTS AND DISCUSSION

Metabolic optimization was carried out for ethanol and 1,3-PDO as separate target products, with glycerol being used as the sole carbon source for cell growth and its uptake rate controlled at 10 mmol $gDW^{-1}$ $hr^{-1}$. The experiment found that it was not possible to increase the production rate of the product solely by gene knockout, likely because the competing pathways for intermediates are essential for cell growth. However, through optimization, some feasible sites for gene overexpression and underexpression were identified. These strategies demonstrated effective increases in the production rate of the target product. Table 2 shows the results of the optimized gene expression strategies, where each row corresponds to a strategy, including genes that are knocked out, overexpressed, or underexpressed, along with the associated strategy values. In addition, the heuristic algorithm corresponding to each strategy, the biomass, target production rate, and the values of the objective functions were also calculated and recorded.

Ethanol is one of the typical fermentation products, generally associated with acetyl-CoA in the metabolic network. Figure 3a illustrates the cell biomass and ethanol production corresponding to strategies obtained by metabolic optimization. The gray triangular area in Figure 3 represents the theoretically feasible combinations of biomass and target production, while the red line indicates the theoretical maximum target production for

**Table 2.** Metabolic optimization results.

| Target product | Algorithm | Overexpression | | Underexpression and knock out | | BPCY[c] | WYIELD[c] | Biomass[c] | Production rate[c] |
|---|---|---|---|---|---|---|---|---|---|
| | | Id[a,b] | Strategy | Id[a,b] | Strategy | | | | |
| Enthnol | / | / | / | / | / | 0 | 0 | 0.644 | 0 |
| | GA | 14435 | 2 | 02835 | 0.125 | 0.358 | 2.908 | 0.080 | 4.446 |
| | | 16675 | 8 | 10485 | 0.25 | 0.378 | 2.366 | 0.120 | 3.152 |
| | | 01145 | 8 | | | | | | |
| | | 03645 | 8 | | | | | | |
| | | 01145 | 8 | 10810 | 0.25 | 0.404 | 2.347 | 0.132 | 3.058 |
| | | 03645 | 8 | | | | | | |
| | | 16675 | 4 | 10485 | 0.25 | 0.370 | 2.477 | 0.141 | 2.624 |
| | | 01145 | 8 | | | | | | |
| | | 23080 | 4 | | | | | | |
| | | 01145 | 8 | 10485 | 0.25 | 0.414 | 2.207 | 0.161 | 2.574 |
| | | 03645 | 8 | | | | | | |
| | PSO | 00270 | 2 | 10255 | 0.25 | 0.488 | 1.567 | 0.161 | 3.032 |
| | | 02935 | 8 | 01945 | 0 | | | | |
| 1,3-PDO | / | / | / | / | / | 0 | 0 | 0.644 | 0 |
| | GA | 11695 | 2 | 00900 | 0.125 | 0.691 | 2.584 | 0.080 | 8.594 |
| | | / | / | 00900 | 0.125 | 0.680 | 2.584 | 0.080 | 8.450 |
| | | 21510 | 2 | 01955 | 0.5 | 1.338 | 5.553 | 0.196 | 6.823 |
| | | 11695 | 2 | 08360 | 0.25 | | | | |
| | | / | / | 01955 | 0.25 | 1.144 | 7.507 | 0.152 | 7.500 |
| | | / | / | 01955 | 0.5 | 1.581 | 5.014 | 0.316 | 5.000 |
| | | 11695 | 4 | 09270 | 0 | 1.578 | 1.489 | 0.322 | 4.904 |
| | | | | 09740 | 0.5 | | | | |
| | PSO | | | 00175 | 0.5 | 1.574 | 1.489 | 0.322 | 4.891 |
| | | | | 01340 | 0.25 | | | | |

a: In *Vibrio natriegens*, the prefix for all gene ids is "PN96_". For example, the gene corresponding to id: 14435 would be "PN96_14435".
b: In the table, each grid may contain multiple Ids, indicating that the expression levels of genes corresponding to each Id will be controlled in that strategy.
c: BPCY is the product of biomass and the production rate of the target product. The units for WYIELD, biomass, and production rate are all mmol $gDW^{-1}\,hr^{-1}$.

each biomass level. The red dot represents the wild type corresponding to the original GSMM, and each blue dot corresponds to a strategy listed in Table 2. Figure 3a shows that the optimized GSMM can demonstrate ethanol production, and there is a negative correlation between ethanol production and biomass. However, there is still a certain distance from the theoretical maximum production of ethanol, which may be due to competition from other fermentation products such as acetate.

The maximum production strategy for ethanol from GA involves the overexpression of the gene PN96_14435 (gpmM), which increases the flux from glycerate-3-phosphate to glycerate-2-phosphate, thereby enhancing the production of pyruvate and acetyl-CoA, consequently benefiting the production of ethanol. The strategy also involves the underexpression of the gene PN96_02835 (aroC), which leads to a reduction in the production of branch acids, attenuating the biosynthesis of phenylalanine, tyrosine, and tryptophan, thereby diverting flux into glycolysis, which in turn facilitates the production of ethanol. The strategy provided by PSO involves the overexpression of genes PN96_00270 (lysC) and PN96_14435 (gpmM). The former enhances the phosphorylation of aspartate, which is beneficial for the generation of fermentation products, while the latter is the same as in the GA strategy. The strategy also underexpresses gene PN96_10255 (ppnK) and knocks out gene PN96_01945 (glpD). The former regulates the intracellular redox balance, while the latter ensures that glycerol-3-phosphate is converted into glycerone-phosphate only through interactions with NADP+ or NAD+, also regulating the intracellular redox balance, thus promoting the production of ethanol.

Unlike ethanol, the production of 1,3-PDO has been introduced into the metabolic network as an exogenous pathway, competing with the accumulation of cell biomass directly for the carbon source glycerol. Figure 3b visualizes the biomass and 1,3-PDO production

corresponding to the optimized strategies, demonstrating that all strategies in Table 2 can achieve (or nearly achieve) the theoretical maximum production of 1,3-PDO while sacrificing a certain amount of biomass.

Compared to ethanol, the strategy for targeting 1,3-PDO as the product is simpler, requiring the underexpression of as few as one gene. For example, by reducing the expression of the gene PN96_00900 (pgk), the flux from 1,3-bisphosphoglycerate to 3-phosphoglycerate can be decreased, thereby weakening the glycolytic process and the accumulation of biomass, ultimately favoring the diversion of the carbon source towards 1,3-PDO. Building on this, further overexpression of gene PN96_11695 (mdh) can enhance the conversion of L-glutamate to L-aspartate, increasing the production of 1,3-PDO without reducing biomass.

In fact, due to the complexity of the GSMM and the metabolic network, there are multiple different gene strategies that can exhibit the same optimization effect. When selecting a strategy, one should comprehensively consider its biomass, stability (WYIELD), and cost (number of gene edits), which is also the reason why multiple strategies are listed in Table 2. Although the actual system may not conform to the quasi-steady-state assumption of the current simulation and optimization, with various intermediates possibly accumulating within the cells and affecting viability and target production, the existing strategies are valuable references for actual experiments and require subsequent experimental verification to confirm their practical effects.

To further enhance the precision of GSMM simulations and the reliability of the optimization strategy results of the hybrid method, future research may include: (1) further optimization of the GSMM, including more GPR associations and improved data annotation; (2) adding enzyme kinetics and thermodynamic constraints to the optimized GSMM to refine the feasible flux space and increase the accuracy of the GSMM simulations; (3) trying more algorithms, such as combining GA and PSO, to leverage PSO's strengths in locating and exploring local optima and GA's enhanced capability to search the global space; (4) further incorporating knowledge into the optimization process to avoid completely random searches and improve the interpretability of the strategies.

## CONCLUSIONS

In this study, we combined machine learning with traditional metabolic engineering, and developed a hybrid method for metabolic optimization of *Vibrio natriegens*. We utilized the modified GSMM of the *Vibrio natriegens*, integrated with two heuristic algorithms, GA and PSO, to perform metabolic optimization with the endogenous metabolite ethanol and the exogenous metabolite 1,3-PDO as target products, respectively. The optimization process used glycerol as the sole carbon source, with its uptake flux kept constant, and the gene expression level optimization strategies included knockouts, underexpression, and overexpression. The optimization results indicate that the GSMM, optimized with the hybrid method developed in this study, can exhibit production of either ethanol or 1,3-PDO by adjusting the expression levels of only 2-4 genes, with a negative correlation between the production of the target products and biomass. The production of ethanol has not reached the theoretical optimum due to the competitive fermentation products such as acetate, while the production of 1,3-PDO can reach the theoretical maximum due to its direct competition for the carbon source. The strategies obtained in this study can be served as a starting point for metabolic engineering, providing guidance for metabolic engineering targets in practical experiments.

## REFERENCES


1. Bai L, You Q, Zhang C, et al. Advances and applications of machine learning and intelligent optimization algorithms in genome-scale metabolic network models. *Syst. Microbiol. Biomanuf.* 3:193-206 (2023)
2. Coppens L, Tschirhart T, Leary DH, et al. *Vibrio natriegens* genome-scale modeling reveals insights into halophilic adaptations and resource allocation. *Mol. Syst. Biol.* 19:e10523 (2023)
3. Lee MK, Mohamad MS, Choon YW, et al. A Hybrid of Particle Swarm Optimization and Minimization of Metabolic Adjustment for Ethanol Production of *Escherichia Coli*. In: Practical Applications of Computational Biology and Bioinformatics, 13th International Conference. Ed: Fdez-Riverola, F., Rocha, M., Mohamad, M., Zaki, N., Castellanos-Garzón, J. Springer (2019)
4. Lewis NE, Hixson KK, Conrad TM, et al. Omic data from evolved E. coli are consistent with computed optimal growth from genome-scale models. Mol. Syst. Biol. 6:390 (2010)
5. Ebrahim A, Lerman JA, Palsson BO, et al. COBRApy: COnstraints-Based Reconstruction and Analysis for Python. *BMC Syst. Biol.* 7:74 (2013)
6. Pereira V, Cruz F, Rocha M. MEWpy: a computational strain optimization workbench in Python. *Bioinformatics* 37:2494-2496 (2021)



© 2025 by the authors. Licensed to PSEcommunity.org and PSE Press. This is an open access article under the creative commons CC-BY-SA licensing terms. Credit must be given to creator and adaptations must be shared under the same terms. See https://creativecommons.org/licenses/by-sa/4.0/




Systems & Control Transactions

**Research Article - Peer Reviewed Conference Proceeding**
ESCAPE 35 - European Symposium on Computer Aided Process Engineering
Ghent, Belgium. 6-9 July 2025
Jan F.M. Van Impe, Grégoire Léonard, Satyajeet S. Bhonsale,
Monika E. Polańska, Filip Logist (Eds.)

PSE PRESS

# Machine learning-enhanced Sensitivity Analysis for Complex Pharmaceutical Systems

**Daniele Pessina[a,b], Roberto Andrea Abbiati[c], Davide Manca[d] and Maria M. Papathanasiou[a,b,*]**

[a] Sargent Centre for Process Systems Engineering, Imperial College London, SW7 2AZ, United Kingdom
[b] Department of Chemical Engineering, Imperial College London, SW7 2AZ, United Kingdom
[c] Roche Pharma Research and Early Development, Predictive Modeling, F. Hoffmann-La Roche Ltd. Grenzacherstrasse 124, 4070 Basel, Switzerland
[d] PSE-Lab, Dipartimento di Chimica, Materiali e Ingegneria Chimica "Giulio Natta" Politecnico di Milano, Piazza Leonardo da Vinci 32, 20133 Milano, Italy
* Corresponding Author: maria.papathanasiou11@imperial.ac.uk

## ABSTRACT

Pharmacokinetic and pharmacodynamic (PK/PD) models are used to predict drug transport in the body and to assess treatment efficacy and optimal dosage. The kinetic parameters embedded in the models, which define transport across body compartments or drug efficacy, can be linked to patient-specific characteristics; understanding the parameter space-model output relationship is critical towards linking patient population heterogeneity to the therapeutic outcome variability. Global Sensitivity Analysis (GSA) is a well-established tool used to examine parameter-to-parameter interactions, shedding light on underlying interactions towards enhanced system understanding. Despite its potential and usefulness, GSA performance is dependent to the model complexity; large-scale and nonlinear PK/PD models, which often have large sets of parameters, can render GSA challenging to perform, requiring excessive computational effort. Proposed approaches to reduce GSA complexity, such as segmentation in parameter subsets or the introduction of surrogate metamodels, become less effective as the number of kinetic parameters grows. In this work, we investigate the potential of Machine Learning (ML) to reduce the complexity of PK/PD models by exploring how the level of hybridisation can impact the GSA performance and, critically, whether the use of surrogates affects the resulting model sensitivity to parametric uncertainty. We show that ML-based surrogates can reliably identify parameter interactions and sensitivities while requiring only a limited number of simulations of the reference mechanistic model. Further, surrogates models effectively reduce the computational expenditure of GSA of multi-dimensional nonlinear PK/PD models. The accelerated execution of GSA enables performing patient cohort-specific analysis, with potential applications for optimal study design and for precision medicine.

**Keywords**: Pharmacokinetic modelling, Global Sensitivity Analysis, Surrogate modelling

## INTRODUCTION

The efficacy of a pharmacological treatment depends on achieving adequate drug concentration at the designated target site within the body. Once administered, drug molecules undergo absorption, distribution, metabolism, and excretion (ADME) processes that collectively determine the drug's fate within the organism. Pharmacokinetics (PK) is the scientific discipline that studies these processes. Experimental PK traditionally involves administering a drug to a biological system, collecting samples (typically blood) at multiple time points, and measuring the drug concentration. This produces a concentration-time profile. If a relationship between concentration and pharmacological effect can be established, PK can be adopted as a surrogate indicator of the expected efficacy or toxicity. This information is essential for guiding dosing regimens, ensuring patient safety, and informing early-stage clinical drug development.

The field of PK has been substantially advanced by the introduction of mathematical modelling and

simulation approaches, collectively known as pharmacometrics. Classic pharmacometric analyses rely on ordinary differential equations to simulate drug concentration profiles in blood [1,2]. Over time, several PK modelling approaches have emerged: Population PK adopts nonlinear mixed-effects modelling to characterize the variability in PK parameters across patients; Physiologically-Based Pharmacokinetic (PBPK) models focus on an anatomically-based and physiology-driven representation of ADME processes to support inter-species extrapolation; PK/PD (pharmacodynamics) models link drug concentrations to biological effects to predict therapeutic and adverse outcomes.

Quantitative Systems Pharmacology (QSP) is a related modelling discipline that builds upon the pharmacometric approach by incorporating systems biology concepts [3]. QSP models can be used to link molecular, cellular, tissue, and organ-level data into multi-scale, mechanistic frameworks. QSP has a broad application space, models typically capture the dynamics of a biological system undergoing disease progression with or without the modulatory intervention of a therapy and considering the inter-individual differences. This integrative approach enables the bridging of empirical data and mechanistic understanding, thereby informing rational drug design, hypothesis testing, and personalized therapeutic strategies.

For mechanistic approaches like PBPK or QSP, model parameterization is critical. During model design, the parameterization strategy has implications on model identifiability and model fit. During model application, alternative parameterization of the same underlying model structure is used to characterize the diversity across patient population or disease status and therefore project the consequential disease progression/treatment variability. Here, sensitivity analysis is adopted to study the role of the various model parameters on the model endpoint. Collectively, identifiability and sensitivity analyses are fundamental tools employed to determine whether unique parameter values can be inferred from available data, to ascertain whether model structures require simplification, and to quantify how parameter values influence model outputs of interest.

Classical sensitivity analysis involves perturbing individual parameters from a reference set and evaluating changes in model outputs. In contrast, global sensitivity analysis (GSA) considers the entire parameter space, recognizing that biological parameters often exist as distributions rather than fixed values. GSA identifies which parameters most strongly influence model outputs across a wide range of plausible parameter values, thereby providing a more comprehensive understanding of parameter importance under uncertainty. Some concrete examples of applications of GSA in QSP include: (i) identification of disease pathways which significantly influence outcome and should therefore be primary focus of research, (ii) support of patient stratification, by selecting those whose characteristics are more strongly associated to an endpoint of interest, (iii) model complexity reduction, by identifying the most relevant model components related to the endpoint of interest and therefore reducing the structure to include only them, or (iv) provide rationale for the creation of reduced-order surrogate models.

Each individual patient has unique characteristics, such as age, and sex, or the presence of adverse conditions. When performing GSA, these individual characteristics are aggregated into a broader parameter space representing an entire cohort, meaning the sensitivity analysis results reflect the response of the whole ensemble rather than specific individuals. This generalization, while necessary for computational tractability, can lead to suboptimal decisions in experimental design for preclinical trials, particularly when certain subpopulations (such as pediatric patients within a mixed-age population, or critically-ill patients in a mixed-health population) have distinct characteristics that significantly influence the PK/PD response and the resultant sensitivity [4], [5]. The developed therapeutic strategy might under- or over-dosage specific cohorts within the population and result in sub-optimal therapeutic outcomes. The ability to perform cohort-specific GSA would enable more targeted sensitivity analyses, allowing for better understanding of parameter importance within specific subpopulations and potentially leading to more effective experimental designs for these groups and improved parametric identifiability.

GSA of a mechanistic PK model for a single set of parametric bounds requires a high number of simulations and computational time; this approach quickly becomes intractable if cohort-specific GSA with multiple sets of parameters is to be explored. One approach to reduce GSA complexity involves parameter grouping, which does not however universally consider the whole parametric domain [6]. Metamodelling-based GSA methods struggle with high-dimensional problems as they become computationally intractable to train and predict [7].

Machine-learning surrogates have been widely used by the Process Systems community to reduce the computational expenditure of complex mechanistic models [8]. After training on a set of input and output samples generated by the mechanistic model, the surrogate can predict model outputs quicker, albeit at a reduced fidelity if the surrogate structure and training points are not chosen carefully; surrogate accuracy is affected by the number of training samples used, surrogate type and surrogate structure, which is generally problem-specific and therefore must be tailored to the mechanistic model available.

This work explores how machine-learning

**Table 1:** Kinetic parameter descriptions with lower and upper bounds for training and GSA

| Name | Description | Training LB | Training UB | GSA LB | GSA UB |
|---|---|---|---|---|---|
| $j_{\text{PT-P}}$ | Mass transfer coefficient from poorly-perfused tissues to plasma compartments | 0.191 | 0.767 | 0.240 | 0.720 |
| $j_{\text{P-PT}}$ | Mass transfer coefficient from plasma to poorly-perfused tissues compartments | 0.191 | 0.767 | 0.240 | 0.720 |
| $j_{\text{P-HO}}$ | Mass transfer coefficient from plasma to highly-perfused organs compartments | 0.265 | 1.06 | 0.331 | 0.99 |
| $j_{\text{HO-P}}$ | Mass transfer coefficient from highly-perfused organs to plasma compartments | 0.0179 | 0.0715 | 0.0224 | 0.0671 |
| $k_{\text{E}}^{\text{P}}$ | Plasma elimination kinetic rate constant | 0.69 | 2.77 | 0.866 | 2.60 |
| $k_{\text{E}}^{\text{T}}$ | Tissues elimination kinetic rate constant | 0.0253 | 0.101 | 0.0317 | 0.0950 |
| $\text{Eff}^{\text{Liver}}$ | Hepatic efficiency of elimination | 0.0576 | 0.231 | 0.0720 | 0.216 |
| $\text{Eff}^{\text{Plasma}}$ | Kidney efficiency of elimination | 0.158 | 0.631 | 0.197 | 0.590 |

surrogates can be used to reduce the computational expenditure involved with generating predictions for GSA and enable cohort-specific GSA of PK models. Importantly, the goal of GSA is to probe the PK model and corresponding parameter space for improved understanding and assessment of parameter identifiability, and not to identify influential parameters to formulate a reduced-order model and train a smaller surrogate. GSA is first carried out with a mechanistic PK model to confirm the high computational expenditure involved with the method, and use the identified sensitivity indices as reference for the surrogate-enabled GSA. Feed-forward Neural Networks and Random Forests surrogates are then trained on a much-smaller number of samples and used to generate GSA samples in a fraction of the time required with a fully-mechanistic methodology. The effort to reach GSA convergence and sensitivity index misidentification are assessed.

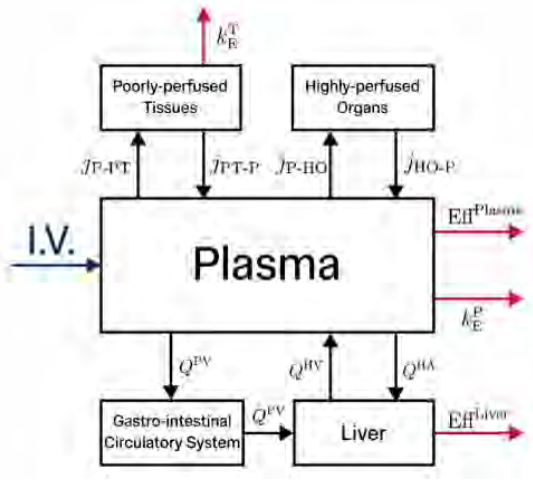



**Figure 1:** Compartmental structure of the mechanistic PK model from Abbiati (2016) [1]

# METHODOLOGY

## Mechanistic PK models

In this work we employ a validated minimal-PBPK model from Abbiati *et al.* (2016) [1], that describes the transport of a small-molecule drug, Remifentanil, through the human body (Figure 1). The model is experimentally validated against measurements from 6 patients and 4 drug dosages, and is therefore suitable to be used as a platform for cohort-specific PK modelling, as well as cohort-specific GSA.

The model assumes the drug is administered intravenously (IV) to the plasma compartment and is distributed via the circulatory system to the liver and the other body organs, here lumped into the Poorly-perfused Tissues (PT) (fat, bones, heart, skin, muscles) and Highly-perfused organs (HP) (brain, kidneys, spleen) compartments. The model considers mass transfer between the plasma and the two compartments (PT and HP), as well as elimination of the drug from the PT, plasma and liver compartments. The model predicts the drug concentration profiles for each of the 5 compartments, using 8 input parameters (Table 1). To reduce the computational expenditure, the scalar Area Under the Curve (AUC) output is considered. The AUC, often used with PK models, is the concentration profile integral over time for each compartment and measures drug exposure in the body [9]. The reader is referred to Abbiati *et al.* (2016) [1] for the complete set of model equations and further model formulation details.

The mechanistic model used in this work comprises 8 ordinary differential equations which were solved in Python with an implicit time-stepping algorithm ($t_{end} = 120$ min, abstol $= 10^{-4}$, relative tol. $= 10^{-2}$). The AUC is calculated with trapezoidal integration of the calculated concentration profiles.

## Surrogate modelling

Here, surrogate models are developed and assessed for their suitability as computationally-efficient substitutes of the mechanistic model. Table 1 summarises the upper and lower bounds used for the training of the models, as well as the GSA later on. To ensure that the surrogate models are not performing extrapolation during GSA, the bounds of the SA are chosen to be tighter than the ones used for the training of the surrogates. Latin Hypercube sampling (LHS) is used to generate 4096 training data points. Input samples are standardized in the $[-1, 1]$ interval before training the surrogate models. The surrogates are trained to predict each output's AUC for a given combination of kinetic parameters.

**Table 2:** Collected hyper-parameters for the neural net and random-forests surrogates

| Surr. | Hyper-parameter | | | |
|---|---|---|---|---|
| RF | *# of estimators* | | *Max depth* | |
| | 100 | | 25 | |
| NN | *# of hidden layers* | *# of neurons* | *Learning rate* | *Training epochs* |
| | 5 | 32 | 0.015 | 450 |

Random Forests (RF) and feed-forward neural nets (NN) single-output surrogates from the `scikit-learn` library are tested in this work. RF hyper-parameters (# of estimators and maximum depth of the ensemble) are optimised by grid-searching possible surrogate structures with 5-fold cross-validation to minimise the test root-mean-squared error (RMSE). NN hyper-parameters (# of hidden layers, # of neurons in each layer, learning rate, training epochs) are similarly optimised using the `Optuna` library and a 'Tree-structured Parzen' algorithm to efficiently search the possible combinations. Although the optimal NN structures differ between each output, they are fixed to a single, common combination before the surrogates are used for GSA. The final hyper-parameters are collected in Table 2.

## Global sensitivity analysis

The GSA method is model-agnostic and proceeds identically regardless of the model type used. Variance-based GSA (Sobol method) is performed using the SALIB library to calculate first-, second- and total-order sensitivity indices [10]. To perform GSA for a given parameter domain, an input matrix with $N(2D + 2)$ parameter combinations is generated by SALIB which follows a quasi-random Sobol sequence ($N$ is a power of 2 and $D$ is the number of input dimensions). Each combination is then simulated to collect predicted AUC values for each output, after which sensitivity indices can be calculated. GSA convergence for each output is assessed by summing all parameter's first- and second- order indices; convergence is indicated by sums which approach 1 and the identified sensitivities remain stable across different sample sizes, as suggested by Sarrazin *et al.* (2016) [11]. First-order Sobol' sensitivity indices quantify the independent effect that a varying parameter $\theta_i$ has on the model output of interest, neglecting cross-parameter interactions. In its' computation, the effect of other parameters is averaged out, such that they can be excluded. Total-order Sobol' sensitivity indices instead group both the independent effect and the cross-parameter interactions of $\theta_i$, calculated by subtracting the effect of all other parameters. The reader is referred to Saltelli (2008) [10] for further details.

# RESULTS AND DISCUSSION

The calculated first-, second- and total-order sensitivity indices for each of the 5 outputs of the mechanistic model are reported in Figure 2 and Table 3. The chosen sensitivity threshold ($S_{\theta,\,\mathrm{Tot.}}$ = 0.05) to segregate parameters into critical and non-critical sets indicates non-critical parameters cause less than 5% variance of the output variable of interest. The same critical set of parameters ($j_{\mathrm{PT\text{-}P}}$, $j_{\mathrm{P\text{-}PT}}$, $k_{\mathrm{E}}^{\mathrm{P}}$) is identified for the first 4 outputs ($C_{\mathrm{Plasma}}$, $C_{\mathrm{PT}}$, $C_{\mathrm{GICS}}$, $C_{\mathrm{Liver}}$) of the model, while a larger set ($j_{\mathrm{PT\text{-}P}}$, $j_{\mathrm{P\text{-}PT}}$, $j_{\mathrm{P\text{-}HO}}$, $j_{\mathrm{HO\text{-}P}}$, $k_{\mathrm{E}}^{\mathrm{P}}$) is identified for $C_{\mathrm{HO}}$. Non-negligible second-order interactions between the critical parameters are also identified, indicating the presence of correlations between parameters which can impede effective parameter estimation and identification of PK models. In the context of PK/PD models parametrised against measurements from human patients, the plasma is the only compartment considered to be easily-measurable as sampling other compartments involves invasive procedures. The sensitivity indices reveal that only 3 out of 8 parameters are identifiable within the parameter domain used for GSA. Three of the non-critical parameters, $j_{\mathrm{P\text{-}HO}}$, $j_{\mathrm{HO\text{-}P}}$ and $\mathrm{Eff}^{\mathrm{Plasma}}$, directly affect the plasma compartment to a lesser extent than the critical parameters and inestimable. The remaining two parameters, $k_{\mathrm{E}}^{\mathrm{T}}$ and $\mathrm{Eff}^{\mathrm{Liver}}$, already classed as non-critical with respect to the $C_{\mathrm{PT}}$ and $C_{\mathrm{Liver}}$ outputs respectively, do not cause significant-enough interactions in the plasma to be estimable by drug concentration measurements in the plasma alone.

Feed-forward neural networks (NNs) and Random Forests (RF) full-order surrogates are trained on 4096 Latin Hypercube samples from the mechanistic model. The surrogates are then used to generate the necessary Sobol-indexed samples for GSA. While other surrogate models (such as Gaussian Process regressors and Radial Basis Function interpolators) were tested, they could not reliably approximate the PK model and were therefore omitted from the presented work.

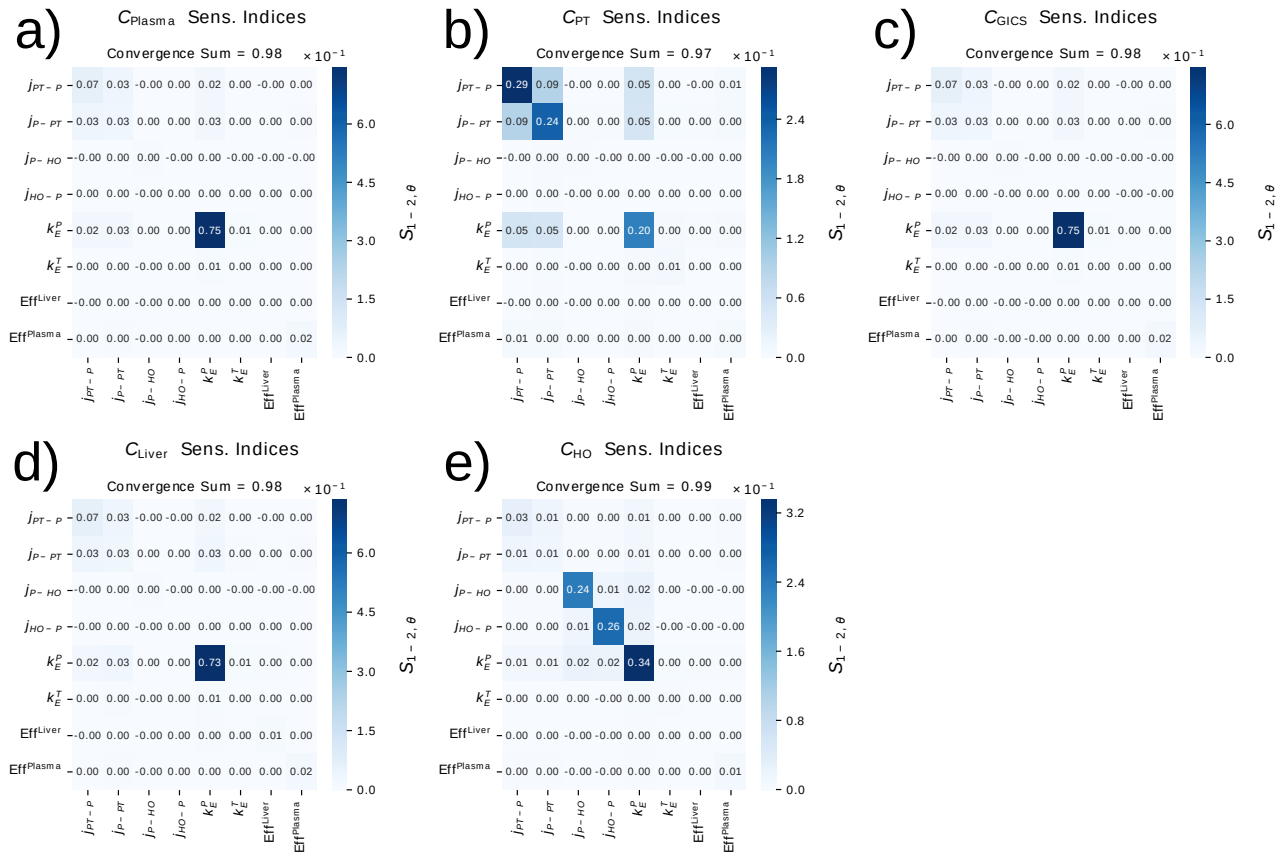



**Figure 2:** 1st, 2nd Order Sensitivity Indices of the mechanistic model for a) $C_{Plasma}$, b) $C_{PT}$, c) $C_{GICS}$, d) $C_{Liver}$, e) $C_{HO}$, calculated with 1179648 simulations

**Table 3:** Total-order sensitivity indices of the mechanistic model calculated with 1179648 simulations

| Parameter | Mechanistic Model Total-Order Sensitivity Indices $S^T_{\theta,\text{Mech.}}$ | | | | |
|---|---|---|---|---|---|
| | $C_{Plasma}$ | $C_{PT}$ | $C_{GICS}$ | $C_{Liver}$ | $C_{HO}$ |
| $j_{PT-P}$ | 0.16 | 0.5 | 0.16 | 0.16 | 0.07 |
| $j_{P-PT}$ | 0.13 | 0.44 | 0.13 | 0.13 | 0.05 |
| $j_{P-HO}$ | 0.02 | 0.01 | 0.02 | 0.02 | 0.29 |
| $j_{HO-P}$ | 0 | 0 | 0 | 0 | 0.30 |
| $k_E^P$ | 0.85 | 0.36 | 0.85 | 0.83 | 0.42 |
| $k_E^T$ | 0.01 | 0.02 | 0.01 | 0.01 | 0 |
| $Eff^{Liver}$ | 0 | 0 | 0 | 0.02 | 0 |
| $Eff^{Plasma}$ | 0.04 | 0.02 | 0.04 | 0.03 | 0.02 |

Importantly, LHS is chosen over a Sobol' sequence for the generation of training data as it led to more accurate surrogates, as Sobol sequences do not capture points at the parametric bounds as effectively. The generation of GSA samples with surrogates introduces minimal computational expenditure compared to the training data generation and GSA decomposition and analysis, making the LHS more effective than a Sobol' sequence for surrogate training. Fewer training samples (1024) were also assessed. The trained surrogates however had low AUC prediction accuracy, which led to different GSA indices compared to the mechanistic model. Each surrogate's AUC prediction error was generally lowest in the middle of the parametric bounds, increasing as the lower or upper bounds were approached.

**Table 4:** GSA convergence sums for an increasing number of samples of the mechanistic model

| Output | 294,912 Simulations | 1,179,648 Simulations |
|---|---|---|
| $C_{Plasma}$ | 0.93 | 0.98 |
| $C_{PT}$ | 0.9 | 0.97 |
| $C_{GICS}$ | 0.93 | 0.98 |
| $C_{Liver}$ | 0.93 | 0.98 |
| $C_{HO}$ | 0.96 | 0.99 |

Convergence sums for increasing numbers of samples are reported in Table 4. The computational difficulty involved in performing GSA of PK models is evident by the results with 295,000 samples; the low sums indicate

that for all outputs except $C_{HO}$ GSA remains un-converged. Over 1 million simulations are needed to observe stable sensitivity indices and achieve GSA convergence of the mechanistic PK model, which in turn leads to high computational expenditure requirements to perform GSA and examine model and parametric sensitivity.

After GSA convergence was confirmed, limited sensitivity indices mispredictions from the two surrogates are identified. The NN-derived simulation results lead to a converged GSA with the same number of samples as the mechanistic PK model. As observed from the negligible deviation in indices reported in Table 5, NN-derived GSA identified the same critical sets of parameters for each output, along with identical sensitivity and identifiability trends of the mechanistic model in a fraction of the time. Sensitivity index errors with respect to each output and parameter are limited to 1-3% at most and can be considered identical to the mechanistic-derived results. RF-derived GSA instead requires an increased number of samples for GSA to fully converge, and on average had greater sensitivity mispredictions than the NN surrogate. While identical critical parameter sets are identified for the first four outputs, only $j_{\text{P-HO}}$,$j_{\text{HO-P}}$ and $k_{\text{E}}^{\text{P}}$ are identified as critical with respect to $C_{HO}$; $S_{j_{\text{PT-P}},\text{T}}$ and $S_{j_{\text{P-PT}},\text{T}}$ are underpredicted to be below the critical threshold. For this reason, RF-enabled GSA leads to different parameter criticality conclusions compared to the mechanistic and NN-enabled GSA.

Assessing the computational expenditure, the mechanistic GSA took 14291 s (14190 s for sample generation) and the NN GSA took 243 s (137 s for net training on CPU) to simulate 1.1 million samples, while the RF GSA took 911 s (13 s for RF training) to simulate 4.7 million samples. Surrogate-enabled GSA leads to a noticeable reduction in runtime. Regardless of the surrogates' training requirement, the mechanistic GSA was slower by at least 1 order of magnitude, highlighting the surrogate's ability to lighten the computational burden involved with GSA while producing GSA results.

**Table 5:** NN-derived total-order sensitivity index deviations from the mechanistic model

| Parameter | Neural Net - $S^T_{\theta,\text{Mech.}} - S^T_{\theta,\text{NN.}}$ | | | | |
|---|---|---|---|---|---|
| | $C_{Plasma}$ | $C_{PT}$ | $C_{GICS}$ | $C_{Liver}$ | $C_{HO}$ |
| $j_{\text{PT-P}}$ | 0.01 | 0.02 | -0.01 | 0.01 | 0 |
| $j_{\text{P-PT}}$ | 0.01 | 0.02 | 0.01 | 0.02 | 0 |
| $j_{\text{P-HO}}$ | 0 | 0 | 0 | 0 | 0 |
| $j_{\text{HO-P}}$ | 0 | 0 | 0 | 0 | 0 |
| $k_{\text{E}}^{\text{P}}$ | 0.01 | 0.01 | 0.01 | 0 | 0 |
| $k_{\text{E}}^{\text{T}}$ | 0 | 0 | 0 | 0 | 0 |
| $\text{Eff}^{\text{Liver}}$ | 0 | 0 | 0 | 0 | 0 |
| $\text{Eff}^{\text{Plasma}}$ | 0 | 0 | 0 | 0 | 0 |
| Conv. Sum | 0.96 | 0.95 | 0.95 | 0.97 | 0.98 |

**Table 6:** RF-derived total-order sensitivity index deviations from the mechanistic model

| Parameter | Random Forests - $S^T_{\theta,\text{Mech.}} - S^T_{\theta,RF.}$ | | | | |
|---|---|---|---|---|---|
| | $C_{Plasma}$ | $C_{PT}$ | $C_{GICS}$ | $C_{Liver}$ | $C_{HO}$ |
| $j_{\text{PT-P}}$ | 0 | 0 | 0 | 0 | 0.03 |
| $j_{\text{P-PT}}$ | 0.02 | 0.02 | 0.02 | 0.02 | 0.03 |
| $j_{\text{P-HO}}$ | 0.02 | 0.01 | 0.02 | 0.01 | -0.01 |
| $j_{\text{HO-P}}$ | 0 | 0 | 0 | 0 | -0.01 |
| $k_{\text{E}}^{\text{P}}$ | 0 | 0 | 0 | -0.02 | -0.02 |
| $k_{\text{E}}^{\text{T}}$ | 0.01 | 0.02 | 0.01 | 0.01 | 0 |
| $\text{Eff}^{\text{Liver}}$ | 0 | 0 | 0 | 0.01 | 0 |
| $\text{Eff}^{\text{Plasma}}$ | 0.02 | 0.01 | 0.02 | 0.02 | 0.01 |
| Conv. Sum | 0.97 | 0.96 | 0.97 | 0.97 | 0.98 |

## CONCLUSIONS

Global Sensitivity Analysis is a necessary tool for the development and application of PK and QSP models since it informs model structure design and enables parametric analysis. These are crucial to characterize biological variability across the patient population in relation to disease features and response to therapy. However, the large computational requirements of GSA when applied to large-scale and non-linear models limits its adoption and application in the pharma R&D space. In this work, we have shown how GSA computational requirements can be lowered by integrating machine-learning surrogates of the original mechanistic ODE model, trained on a significantly reduced number of mechanistic simulations, into the GSA framework. We tested two surrogate models based on Random Forests and on Feed-forward neural nets. The GSA with Random Forests surrogates identified a slightly-reduced critical set of parameters compared to the GSA conducted with the reference ODE-based model. Feed-forward neural nets were instead able to accurately predict mechanistic model outputs and consequently identify identical sensitivity indices and parameter criticality with minimal error (maximum deviation <3%). We show that surrogates can reliably capture parameter interactions from a limited set of training data derived from the ODE-based PK model and with a fraction of the computational expenditure compared to a fully ODE-based workflow. The ML-enhanced GSA is suitable for PBPK models given their mathematical features (ODE-based, non-linear and multi-parametric). The methodology is expected to be applicable to other modelling approaches, like PK/PD and QSP, that have similar mathematical characteristics. Surrogate-based GSA approach is especially valuable for the pharma R&D modeling community when implementing large differential equation-based model like PBPK or QSP, which typically require thorough identifiability and sensitivity analyses, as well

as intensive computation for generating or simulating virtual patient populations. Future work should explore the rapid generation of individualised GSA profiles to assess optimal cohort-specific measurement strategies for effective parameter estimation of PK/PD and QSP models. Instead of lumping cohorts into a single population, cohort-specific GSA assessments can support clinical trial and PBPK model development. Drug dosage regimens can be more effectively tailored to population subsets, improving the therapeutic outcomes of all patients.

## REFERENCES


1. R. A. Abbiati, G. Lamberti, M. Grassi, F. Trotta, and D. Manca, "Definition and validation of a patient-individualized physiologically-based pharmacokinetic model," *Computers & Chemical Engineering*, vol. 84, pp. 394–408, Jan. 2016, doi: 10.1016/j.compchemeng.2015.09.018.
2. FDA, "Division of Pharmacometrics," FDA. Accessed: Jan. 06, 2025. [Online]. Available: https://www.fda.gov/about-fda/cder-offices-and-divisions/division-pharmacometrics
3. R. A. Abbiati and C. Pichardo, "An introduction to Quantitative Systems Pharmacology for Chemical Engineers," *Phys. Sci. Rev.*, 2024, doi: 10.1515/psr-2024-0066.
4. R. F. W. De Cock, C. Piana, E. H. J. Krekels, M. Danhof, K. Allegaert, and C. A. J. Knibbe, "The role of population PK–PD modelling in paediatric clinical research," *Eur J Clin Pharmacol*, vol. 67, no. 1, pp. 5–16, May 2011, doi: 10.1007/s00228-009-0782-9.
5. E. Asín-Prieto, A. Rodríguez-Gascón, and A. Isla, "Applications of the pharmacokinetic/pharmacodynamic (PK/PD) analysis of antimicrobial agents," *Journal of Infection and Chemotherapy*, vol. 21, no. 5, pp. 319–329, May 2015, doi: 10.1016/j.jiac.2015.02.001.
6. R. Sheikholeslami, S. Razavi, H. V. Gupta, W. Becker, and A. Haghnegahdar, "Global sensitivity analysis for high-dimensional problems: How to objectively group factors and measure robustness and convergence while reducing computational cost," *Environmental Modelling & Software*, vol. 111, pp. 282–299, Jan. 2019, doi: 10.1016/j.envsoft.2018.09.002.
7. S. Shan and G. G. Wang, "Metamodeling for High Dimensional Simulation-Based Design Problems," *Journal of Mechanical Design*, vol. 132, no. 051009, May 2010, doi: 10.1115/1.4001597.
8. P. Daoutidis *et al.*, "Machine learning in process systems engineering: Challenges and opportunities," *Computers & Chemical Engineering*, vol. 181, p. 108523, Feb. 2024, doi: 10.1016/j.compchemeng.2023.108523.
9. J. D. Scheff, R. R. Almon, D. C. DuBois, W. J. Jusko, and I. P. Androulakis, "Assessment of Pharmacologic Area Under the Curve When Baselines are Variable," *Pharm Res*, vol. 28, no. 5, pp. 1081–1089, May 2011, doi: 10.1007/s11095-010-0363-8.
10. A. Saltelli, Ed., *Global sensitivity analysis: the primer*. Chichester, England ; Hoboken, NJ: John Wiley, 2008.
11. F. Sarrazin, F. Pianosi, and T. Wagener, "Global Sensitivity Analysis of environmental models: Convergence and validation," *Environmental Modelling & Software*, vol. 79, pp. 135–152, May 2016, doi: 0.1016/j.envsoft.2016.02.005.



© 2025 by the authors. Licensed to PSEcommunity.org and PSE Press. This is an open access article under the creative commons CC-BY-SA licensing terms. Credit must be given to creator and adaptations must be shared under the same terms. See https://creativecommons.org/licenses/by-sa/4.0/




Systems & Control Transactions

**Research Article - Peer Reviewed Conference Proceeding**
ESCAPE 35 - European Symposium on Computer Aided Process Engineering
Ghent, Belgium. 6-9 July 2025
Jan F.M. Van Impe, Grégoire Léonard, Satyajeet S. Bhonsale,
Monika E. Polańska, Filip Logist (Eds.)

PSE PRESS

# Incorporating Process Knowledge into Latent Variable Models: An Application to Root Cause Analysis in Bioprocesses

**Tobias Overgaard[ab], Maria-Ona Bertran[c], and John B. Jørgensen[a], and Bo F. Nielsen[a]***

[a]Technical University of Denmark, Department of Applied Mathematics and Computer Science, Kgs. Lyngby, Denmark
[b]Novo Nordisk A/S, PS API Manufacturing, Science & Technology, Bagsværd, Denmark
[c]Novo Nordisk A/S, PS API Expansions, Kalundborg, Denmark
*Corresponding Author: bfni@dtu.dk

## ABSTRACT

Incorporating process knowledge from various sources often presents challenges in process development, optimization, and control. To utilize available knowledge, linking existing process models is a viable approach. This work introduces a methodology using latent variable models, specifically sequential and orthogonalized partial least squares (SO-PLS), to capture and quantify the contribution of first-principles knowledge in process models. Applied to a continuously stirred tank reactor (CSTR) case study, the methodology demonstrates how available knowledge can be quantified and how structural and parametric errors in first-principles are addressed using measured data. The methodology is discussed in relation to root cause analysis in bioprocesses.

**Keywords**: Process models, Root cause analysis, Latent variable models, Multiblock partial least squares

## INTRODUCTION

Process development, optimization, and control based on process modeling are significantly advancing pharmaceutical manufacturing. These efforts are reducing development times and manufacturing costs, improving productivity and quality control, and enhancing overall process understanding [1]. Using terminology from knowledge management, process models can be seen as representations of accumulated expert knowledge generated over the years. These models enable the simulation of system behavior under various perturbations [2]. In the pharmaceutical industry, process models are typically developed for individual unit operations to capture specific product and technology phenomena. Recently, *integrated process models* have emerged, representing processes with multiple steps or unit operations. These models transform the output of one unit into the input of the next, simulating material flow across operations and capturing interactions between upstream and downstream equipment. Applications include control strategy design, risk analysis, experimental design, and process optimization [3-5], and they range from being first-principles-based [5] to fully data-driven [4].

In first-principles modeling, we rely on a physical understanding of the system, where the model's equations represent the known mechanisms driving the process. Parameters are typically tuned using data from well-designed laboratory experiments, allowing for some extrapolation beyond the calibration range. However, when comparing first-principles models to historical data from a full-scale commercial plant, outputs may not match accurately. This discrepancy can be due to limited knowledge of the process, oversimplification of physical phenomena, or inappropriate parameter values [6].

Due to their simplicity, ease of development, and increasing computational efficiency, data-driven models are an attractive alternative. These models involve selecting a structure and identifying parameters using available data [6], which can be readily sourced from full-scale plants. However, since many observations remain constant during plant operation and rarely change, extrapolation can be challenging for data-driven models.

Therefore, it is of interest to develop schemes that combine both modeling techniques to create more effective and efficient process models. For integrated process models specifically, this involves incorporating connectivity information from the process flowsheet along with first-principles knowledge from each unit operation.

Incorporating connectivity information into process models often relies on data from full-scale commercial manufacturing, where consecutive runs of an integrated

process are logged. Given the vast amount of data and the presence of complex, unknown physical phenomena in a full-scale plant, a data-driven foundation is often chosen for integrated process models. Among various methods, sequential-orthogonalized partial least squares (SO-PLS) has recently emerged as a promising approach [7-9]. SO-PLS sequentially applies regular PLS to different data blocks, each representing a specific unit operation, and uses orthogonalization between steps to eliminate overlapping information. By ordering the blocks with respect to the flowsheet topology and removing redundant information explained by upstream units through orthogonalization, this model naturally incorporates connectivity information. Additionally, being based on PLS, it effectively handles the high-dimensional data matrices common in full-scale plants.

Inspired by the use of SO-PLS to incorporate flowsheet connectivity information, this paper presents a systematic methodology to further augment the model with first-principles knowledge, utilizing elements from hybrid modeling and path modeling [10]. While the concept is initially demonstrated for a single unit operation, it can be readily extended to encompass a multi-unit process. The key questions we aim to address are:

- *How can we incorporate flowsheet connectivity information and unit-specific first-principles knowledge into a unified model?*
- *How can we quantify the variance explained by first-principles knowledge versus measured data?*
- *How can the approach be used to identify root causes of deviations from quality or productivity targets in an integrated bioprocess?*

This paper addresses the first two questions, while the last question will be explored in future work in combination with the framework presented in [9]. The paper is organized as follows: First, we provide background on SO-PLS and explain how this model fits within parallel hybrid architectures. Next, we describe the methodology for incorporating first-principles knowledge into the SO-PLS model. This concept is demonstrated using a toy example based on the van de Vusse reaction scheme [11]. Finally, we discuss this work in the context of integrated process modeling and present future work and challenges.

## MODELING BACKGROUND

This work is based on partial least squares (PLS), also known as projection to latent structures. Consider an input data matrix $\boldsymbol{X} \in \mathbb{R}^{N\times J}$ and an output data matrix $\boldsymbol{Y} \in \mathbb{R}^{N\times K}$. The core principle of PLS is to build a model by relating the latent variables (LVs) associated with $\boldsymbol{X}$ and $\boldsymbol{Y}$. PLS achieves this by linearly transforming both $\boldsymbol{X}$ and $\boldsymbol{Y}$ into their respective LVs and then relating these transformed variables by maximizing their covariance. For more details, see [12]. In process modeling, PLS is particularly useful for batch processes, with specialized algorithms for handling batches of varying lengths. While process knowledge is often incorporated into PLS models through additional calculated variables, the direct integration of first-principles models with PLS has been explored to a limited extent [13].

When combining first-principles and data-driven models, often referred to as hybrid or grey-box models, two main architectures are commonly discussed. The first is the series approach, where a first-principles model is developed initially, followed by a data-driven model, such as neural networks, to determine the parameters. The second is the parallel approach, where a data-driven model is used to capture the error (residuals) between the actual process outputs and the estimated outputs from the first-principles model. In this approach, a neural network can serve as the data-driven model, but any data-driven model can be used [14].

As will be shown, the presented methodology bears resemblance to the parallel hybrid architecture. For reference, this architecture is illustrated in Fig. 1.

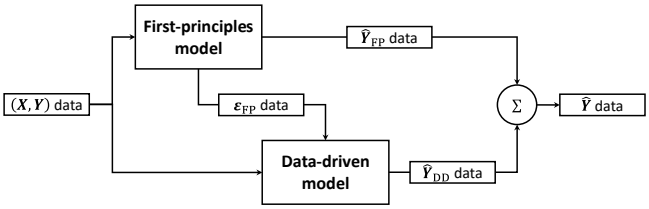



**Figure 1.** The parallel hybrid architecture. $\boldsymbol{\varepsilon}$ refers to the residuals of the estimates made by the first-principles model. $\hat{\boldsymbol{Y}}$ refers to the estimates made by a model.

### Sequential-orthogonalized PLS

To illustrate the SO-PLS method, we will focus on the case with two (autoscaled) input blocks, named $\boldsymbol{X} \in \mathbb{R}^{N\times J}$ and $\boldsymbol{Z} \in \mathbb{R}^{N\times L}$, and an (autoscaled) output block, or response matrix, referred to as $\boldsymbol{Y} \in \mathbb{R}^{N\times K}$. The multiblock linear regression model estimated by SO-PLS can be represented by the following equation

$$\boldsymbol{Y} = \boldsymbol{XB} + \boldsymbol{ZC} + \boldsymbol{F}, \tag{1}$$

where $\boldsymbol{B} \in \mathbb{R}^{J\times K}$ and $\boldsymbol{C} \in \mathbb{R}^{L\times K}$ are the regression coefficients, and $\boldsymbol{F} \in \mathbb{R}^{N\times K}$ is the residual matrix. As explained later in the methodology section, $\boldsymbol{X}$ will serve as the *mechanistic block*, containing output data generated by the first-principles model. In contrast, $\boldsymbol{Z}$ will be the *measured block*, containing various process variables, including some measured process outputs.

The SO-PLS algorithm is given in Tbl. 1 and relies solely on regular PLS [9]. Recall that regular PLS for input block $\boldsymbol{X}$ and output block $\boldsymbol{Y}$ produces a set of $\boldsymbol{X}$-scores ($\boldsymbol{T}$) summarizing the relationships between samples, a set of $\boldsymbol{X}$-loadings ($\boldsymbol{P}$) summarizing the relationships between

variables, and an optimal weight matrix ($\boldsymbol{R}$), transforming $\boldsymbol{X}$ into $\boldsymbol{T}$ through $\boldsymbol{XR} = \boldsymbol{T}$. The five steps of the algorithm are briefly described as follows: *(i)* First, a regular PLS regression is performed between the response matrix $\boldsymbol{Y}$ and mechanistic block $\boldsymbol{X}$, resulting in $\boldsymbol{X}$-scores $\boldsymbol{T}^{(1)}$ and $\boldsymbol{X}$-loadings $\boldsymbol{P}^{(1)}$.*(ii)* The measured block $\boldsymbol{Z}$ is orthogonalized with respect to $\boldsymbol{T}^{(1)}$ using the projection matrix

$$\boldsymbol{H} = \boldsymbol{T}^{(1)} \left( \left(\boldsymbol{T}^{(1)}\right)^{\intercal} \boldsymbol{T}^{(1)} \right)^{-1} \left(\boldsymbol{T}^{(1)}\right)^{\intercal}, \tag{2}$$

which is also commonly referred to as the *hat matrix* in statistics. The orthogonalization involves removing the shared information between $\boldsymbol{X}$ and $\boldsymbol{Z}$ embedded in the projection, resulting in $\boldsymbol{Z}^{\mathrm{ort}} = (\boldsymbol{I} - \boldsymbol{H})\boldsymbol{Z}$. *(iii)* Next, a similar orthogonalization is performed on the response matrix, yielding the residuals $\boldsymbol{Y}^{\mathrm{ort}} = (\boldsymbol{I} - \boldsymbol{H})\boldsymbol{Y}$. *(iv)* After orthogonalization, another regular PLS regression is performed between $\boldsymbol{Y}^{\mathrm{ort}}$ and $\boldsymbol{Z}^{\mathrm{ort}}$, resulting in $\boldsymbol{Z}^{\mathrm{ort}}$-scores $\boldsymbol{T}^{(2)}$ and $\boldsymbol{Z}^{\mathrm{ort}}$-loadings $\boldsymbol{P}^{(2)}$. *(v)* Finally, $\boldsymbol{T}^{(1)}$ and $\boldsymbol{T}^{(2)}$ are used as independent variables in a least squares regression with $\boldsymbol{Y}$. The estimate $\widehat{\boldsymbol{Y}}$ (with coefficients $\boldsymbol{Q}^{(1)}, \boldsymbol{Q}^{(2)}$) is given by

$$\widehat{\boldsymbol{Y}} = \boldsymbol{T}^{(1)}\boldsymbol{Q}^{(1)} + \boldsymbol{T}^{(2)}\boldsymbol{Q}^{(2)}. \tag{3}$$

**Table 1:** Pseudo-code for (two-block) SO-PLS model

| | | |
|---|---|---|
| **Mechanistic block** | | |
| *(i)* | $\mathrm{PLS}(\boldsymbol{X}, \boldsymbol{Y}) \implies \boldsymbol{T}^{(1)}, \boldsymbol{P}^{(1)}$ | PLS regression for $\boldsymbol{X}$ and $\boldsymbol{Y}$ |
| *(ii)* | $\boldsymbol{Z}^{\mathrm{ort}} = (\boldsymbol{I} - \boldsymbol{H})\boldsymbol{Z}$ | Orthogonalization of $\boldsymbol{Z}$ on $\boldsymbol{T}^{(1)}$ |
| *(iii)* | $\boldsymbol{Y}^{\mathrm{ort}} = (\boldsymbol{I} - \boldsymbol{H})\boldsymbol{Y}$ | Orthogonalization of $\boldsymbol{Y}$ on $\boldsymbol{T}^{(1)}$ |
| **Measured block** | | |
| *(iv)* | $\mathrm{PLS}(\boldsymbol{Z}^{\mathrm{ort}}, \boldsymbol{Y}^{\mathrm{ort}}) \implies \boldsymbol{T}^{(2)}, \boldsymbol{P}^{(2)}$ | PLS regression for $\boldsymbol{Z}^{\mathrm{ort}}$ and $\boldsymbol{Y}^{\mathrm{ort}}$ |
| *(v)* | $\boldsymbol{Y} = \boldsymbol{T}^{(1)}\boldsymbol{Q}^{(1)} + \boldsymbol{T}^{(2)}\boldsymbol{Q}^{(2)} + \boldsymbol{F}$ | Least squares for $\boldsymbol{T}^{(1)}, \boldsymbol{T}^{(2)}$ and $\boldsymbol{Y}$ |

**Remark 1:** Letting $\boldsymbol{R}^{(1)}$ and $\boldsymbol{R}^{(2)}$ be the weight matrices used to obtain the scores $\boldsymbol{T}^{(1)}$ and $\boldsymbol{T}^{(2)}$ from $\boldsymbol{X}$ and $\boldsymbol{Z}^{\mathrm{ort}}$, the link between Eq. (1) and (3) follows from

$$\begin{aligned} \widehat{\boldsymbol{Y}} &= \boldsymbol{X}\boldsymbol{R}^{(1)}\boldsymbol{Q}^{(1)} + \boldsymbol{Z}^{\mathrm{ort}}\boldsymbol{R}^{(2)}\boldsymbol{Q}^{(2)} \\ &= \boldsymbol{X}\boldsymbol{R}^{(1)}\boldsymbol{Q}^{(1)} + (\boldsymbol{I} - \boldsymbol{H})\boldsymbol{Z}\boldsymbol{R}^{(2)}\boldsymbol{Q}^{(2)} \\ &= \boldsymbol{X}\boldsymbol{R}^{(1)}\boldsymbol{Q}^{(*)} + \boldsymbol{Z}\boldsymbol{R}^{(2)}\boldsymbol{Q}^{(2)}, \end{aligned} \tag{4}$$

with $\boldsymbol{Q}^{(*)} := \boldsymbol{Q}^{(1)} - \left( \left(\boldsymbol{T}^{(1)}\right)^{\intercal} \boldsymbol{T}^{(1)} \right)^{-1} \left(\boldsymbol{T}^{(1)}\right)^{\intercal} \boldsymbol{Z}\boldsymbol{R}^{(2)}\boldsymbol{Q}^{(2)}$. The selection of $\boldsymbol{B}$ and $\boldsymbol{C}$ follows implicitly.

**Remark 2:** It is worth noting the strong resemblance between SO-PLS and the Frisch–Waugh–Lovell theorem from ordinary least squares. Note also that due to the symmetric and idempotent nature of $\boldsymbol{I} - \boldsymbol{H}$, the model would not change if $\boldsymbol{Y}$ is not orthogonalized. Furthermore, the regression coefficients $\boldsymbol{Q}^{(1)}$ and $\boldsymbol{Q}^{(2)}$ found in step *(v)* coincide with the (transposed) $\boldsymbol{Y}$-loadings that can be extracted from the PLS steps in *(i)* and *(iv)*.

**Remark 3:** Because the orthogonalization step removes redundant information (information in $\boldsymbol{Z}$ already explained by $\boldsymbol{X}$), the additional explained variance gained by adding the new block $\boldsymbol{Z}$ represents information not included in previous blocks. This makes the method useful in path modeling; a discipline of analyzing direct and indirect effects of different sets of variables on an output [9].

To briefly explain how this works for SO-PLS, we can use the notation in (1) to write

$$\widehat{\boldsymbol{Y}} = \boldsymbol{X}\boldsymbol{B} + \boldsymbol{H}\boldsymbol{Z}\boldsymbol{C} + (\boldsymbol{I} - \boldsymbol{H})\boldsymbol{Z}\boldsymbol{C} = \boldsymbol{X}\widetilde{\boldsymbol{B}} + \boldsymbol{Z}^{\mathrm{ort}}\boldsymbol{C}, \tag{5}$$

with $\widetilde{\boldsymbol{B}} := \boldsymbol{B} + \boldsymbol{R}^{(1)}\boldsymbol{Q}^{(1)} \left( \left(\boldsymbol{T}^{(1)}\right)^{\intercal} \boldsymbol{T}^{(1)} \right)^{-1} \left(\boldsymbol{T}^{(1)}\right)^{\intercal}$. Note that by reordering the blocks and orthogonalizing on $\boldsymbol{Z}^{\mathrm{ort}}$ instead, a similar expression, $\widehat{\boldsymbol{Y}} = \boldsymbol{X}^{\mathrm{ort}}\boldsymbol{B} + \boldsymbol{Z}\widetilde{\boldsymbol{C}}$, can be obtained. Recall that the sum of squares of $\widehat{\boldsymbol{Y}}$ can be calculated as $\mathrm{tr}\left(\widehat{\boldsymbol{Y}}^{\intercal}\widehat{\boldsymbol{Y}}\right)$. Due to the orthogonality between blocks, we obtain the decomposition

$$\mathrm{tr}\left(\widehat{\boldsymbol{Y}}^{\intercal}\widehat{\boldsymbol{Y}}\right) = \mathrm{tr}\left(\widetilde{\boldsymbol{B}}^{\intercal}\boldsymbol{X}^{\intercal}\boldsymbol{X}\widetilde{\boldsymbol{B}}\right) + \mathrm{tr}(\boldsymbol{C}^{\intercal}(\boldsymbol{Z}^{\mathrm{ort}})^{\intercal}\boldsymbol{Z}^{\mathrm{ort}}\boldsymbol{C}). \tag{6}$$

Eq. (6) is referred to as the *overall effect*. The first term, $\mathrm{tr}\left(\widetilde{\boldsymbol{B}}^{\intercal}\boldsymbol{X}^{\intercal}\boldsymbol{X}\widetilde{\boldsymbol{B}}\right)$, is known as the *total effect* of $\boldsymbol{X}$, and the second term, $\mathrm{tr}(\boldsymbol{C}^{\intercal}(\boldsymbol{Z}^{\mathrm{ort}})^{\intercal}\boldsymbol{Z}^{\mathrm{ort}}\boldsymbol{C})$, is known as the *additional* effect of $\boldsymbol{Z}$. The total effect can be further decomposed into a *direct effect*, which represents the influence of $\boldsymbol{X}$ that is uncorrelated with $\boldsymbol{Z}$, i.e., $\mathrm{tr}(\boldsymbol{B}^{\intercal}(\boldsymbol{X}^{\mathrm{ort}})^{\intercal}\boldsymbol{X}^{\mathrm{ort}}\boldsymbol{B})$, and an *indirect effect,* which is the difference between the total and the direct effect. This variance decomposition will be useful for measuring how much of the variance is explained by the first-principles model ($\boldsymbol{X}$) and how much is corrected by the data ($\boldsymbol{Z}$). Due to the assumption of unit variance in data, the effects can be interpreted as relative explained variances.

## PROPOSED METHODOLOGY

This section introduces a systematic methodology for incorporating first-principles process knowledge into the SO-PLS model, as depicted in Fig. 2. The framework utilizes first-principles models that describe the unit operations under study, typically consisting of nonlinear ordinary or partial differential and algebraic equations (PDAEs), which are validated through (small-scale) experiments. Furthermore, measurements from multiple (large-scale) historical batches are employed.

***Step 1: Data augmentation by first-principles:*** In this step, the goal is to construct two data blocks using measurement data from the observed system and additional data generated from the first-principles model, initialized with the initial conditions ($\boldsymbol{X}_0$) from the process. Following the structure in [13], the measurement data include manipulated inputs ($\boldsymbol{U}$) and observed system output states ($\boldsymbol{X}_{\mathrm{UO}}$) (e.g., reaction temperatures). The sampled quality variables ($\boldsymbol{Y}$) (e.g., component concentrations) constitute the model output. Note that we only assume access to steady-state data, not full trajectories. However, the method can be extended to trajectory data using techniques like unfolding [13]. The synthetic output

states generated from the first-principles model are denoted $\boldsymbol{X}_{\mathrm{FP}}$. The model may include expressions for states not measured in the full-scale system, thereby augmenting the data matrix with additional information. The initial conditions of the unmeasured states are assumed to be known. Ultimately, we obtain the following data blocks:

- *Mechanistic block:* $\boldsymbol{X} = [\boldsymbol{X}_0, \boldsymbol{U}, \boldsymbol{X}_{\mathrm{FP}}]$.
- *Measured block:* $\boldsymbol{Z} = \boldsymbol{X}_{\mathrm{UO}}$.
- *Output block:* $\boldsymbol{Y}$.

***Step 2: Model fitting by SO-PLS:*** In the next step, an SO-PLS model is fitted, with the number of components for each block selected based on the minimal root mean squared error obtained through K-fold cross-validation (RMSECV). The SO-PLS architecture, shown in Fig. 2, resembles that of Fig. 1.

***Step 3: Variance decomposition by SO-PLS:*** Once the model is fitted, the overall variance in $\widehat{\boldsymbol{Y}}$ is decomposed into total (direct + indirect) and additional effects:

- *Total:* Variance explained by mechanistic block.
- *Direct:* Variance explained by part of mechanistic block uncorrelated with measured block.
- *Indirect:* Variance explained by part of mechanistic block correlated with measured block.
- *Additional:* Variance explained by measured block.

It is worth noting that with this methodology, the first-principles model does not necessarily need to be recalibrated to process data, as the data is projected into a latent space. Consequently, there can be biases between the true and synthetic states. The key point to consider is that the synthetic states, although biased, exhibit correlation structures comparable to the real system. This aspect of the methodology presents an opportunity to incorporate small-scale knowledge with full-scale data.

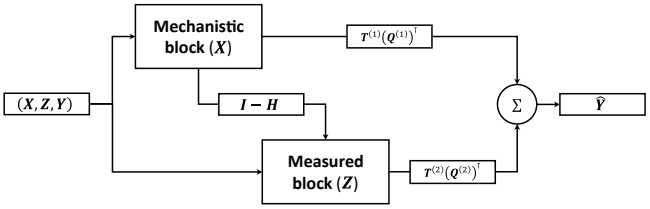



**Figure 2.** SO-PLS architecture. $\boldsymbol{I} - \boldsymbol{H}$ is the *residual-maker matrix*, like in parallel hybrid architectures.

## TOY EXAMPLE

The proposed methodology is tested on a simulated case study involving a temperature-controlled, constant-volume continuous stirred tank reactor (CSTR) [10]. The reaction network consists in conversion of component $A$ into component $B$ and then into component $C$. A side reaction also produces component $D$ which, along with component $C$, is an undesired by-product.

$$A \overset{k_1}{\rightarrow} B \overset{k_2}{\rightarrow} C,$$

$$2A \overset{k_3}{\rightarrow} D.$$

Let $\mathcal{C}$ and $\mathcal{R}$ denote the set of components and reactions respectively. Then $\mathcal{C} = \{A, B, C, D\}$ and $\mathcal{R} = \{1,2,3\}$. Further, let $\boldsymbol{r} \in \mathbb{R}^{|\mathcal{R}|}$ be a vector of rates of reactions. Then

$$r_1 = r_1(C_A, T) = k_1(T)C_A,$$
$$r_2 = r_2(C_B, T) = k_2(T)C_B,$$
$$r_3 = r_3(C_A, T) = k_3(T)C_A^2,$$

where $C_A, C_B$ (and $C_C, C_D$) are component concentrations and $T$ is the temperature. All variables are implicitly time dependent. The specific reaction rates are defined by the Arrhenius expression

$$k_i(T) = k_{i0} \exp\left(-\frac{E_i}{RT}\right), \quad i = 1,2,3.$$

We define the production rate vector $\boldsymbol{R} \in \mathbb{R}^{|\mathcal{C}|}$ using the stoichiometry of the reaction network

$$R_A = R_A(C_A, T) = -r_1(C_A, T) - 2r_3(C_A, T),$$
$$R_B = R_B(C_A, C_B, T) = r_1(C_A, T) - r_2(C_B, T),$$
$$R_C = R_C(C_B, T) = r_2(C_B, T),$$
$$R_D = R_D(C_A, T) = r_3(C_A, T).$$

By using the stoichiometric matrix $\boldsymbol{S} \in \mathbb{R}^{|\mathcal{R}| \times |\mathcal{C}|}$, this can be written compactly as $\boldsymbol{R} = \boldsymbol{S}^{\intercal}\boldsymbol{r}$, with

$$\boldsymbol{S} = \begin{bmatrix} -1 & 1 & 0 & 0 \\ 0 & -1 & 1 & 0 \\ -2 & 0 & 0 & 1 \end{bmatrix}.$$

The reactor can be modelled by six mass and energy balances, yielding the ordinary differential equation system

$$\begin{aligned}
\frac{\mathrm{d}C_A}{\mathrm{d}t} &= \frac{F}{V}\left(C_{A,\mathrm{in}} - C_A\right) + R_A, \\
\frac{\mathrm{d}C_B}{\mathrm{d}t} &= -\frac{F}{V}C_B + R_B, \\
\frac{\mathrm{D}C_C}{\mathrm{d}t} &= -\frac{F}{V}C_C + R_C, \\
\frac{\mathrm{D}C_D}{\mathrm{d}t} &= -\frac{F}{V}C_D + R_D, \\
\frac{\mathrm{d}T}{\mathrm{d}t} &= \frac{F}{V}(T_{\mathrm{in}} - T) + \frac{UA}{\mu V c_p}(T_c - T) \\
&\quad - \frac{1}{\mu c_p}\frac{F}{V}(r_1\Delta H_1 + r_2\Delta H_2 + r_3\Delta H_3), \\
\frac{\mathrm{d}T_c}{\mathrm{d}t} &= \frac{1}{m_c c_{pc}}\left(Q_c + UA(T - T_c)\right),
\end{aligned} \tag{7}$$

where $T_c$ is the temperature inside the cooling jacket. The parameters and measured variables of the system are presented in Tbl. 2. To introduce input uncertainty, the input variables are treated as random

variables.

**Table 2:** Values of the parameters and measured variables used to generate the dataset

| Parameter | Description | Value |
|---|---|---|
| $V$ | Volume | 10 L |
| $A$ | Heat transfer area | 0.215 $m^2$ |
| $U$ | Heat transfer coef. | 4032 kJ/(h $m^2$ K) |
| $c_p$ | Heat capacity (mix.) | 3.01 kJ/(kg K) |
| $c_{pc}$ | Heat capacity (cool.) | 2 kJ/(kg K) |
| $\mu$ | Density of mix. | 0.9342 kg/L |
| $m_c$ | Mass of cool. fluid | 5 kg |
| $\Delta H_1$ | Heat of reaction 1 | 4.2 kJ/mol |
| $\Delta H_2$ | Heat of reaction 2 | −11 kJ/mol |
| $\Delta H_3$ | Heat of reaction 3 | −41.85 kJ/mol |
| $k_{10}$ | Reaction rate const. 1 | $1.287 \cdot 10^{12}$ $h^{-1}$ |
| $k_{20}$ | Reaction rate const. 2 | $1.287 \cdot 10^{12}$ $h^{-1}$ |
| $k_{30}$ | Reaction rate const. 3 | $9.043 \cdot 10^{9}$ L/(h mol) |
| $E_1/R$ | Activation energy 1 | 9758.3 K |
| $E_2/R$ | Activation energy 2 | 9758.3 K |
| $E_3/R$ | Activation energy 3 | 8560 K |
| **Variable** | **Description** | **Distribution** |
| $C_{A,\mathrm{in}}$ | Inflow concentration A | $\mathcal{N}(5.1\ \mathrm{mol/L}, 1^2)$ |
| $T_{\mathrm{in}}$ | Inflow temperature | $\mathcal{N}(378.05\ \mathrm{K}, 5^2)$ |
| $F$ | Flowrate | $\mathcal{N}(141.9\ \mathrm{L/h}, 5^2)$ |
| $Q_c$ | Heat transfer rate | $\mathcal{N}(-1113.5\ \mathrm{kJ/h}, 50^2)$ |
| **Error** | **Description** | **Value** |
| $\boldsymbol{\Sigma}$ | Diffusion term | diag[0.01,0.01,0.01,0.01,0.1,0.1] |
| $\boldsymbol{E}$ | Measurement noise | diag[0.02,0.02,0.02,0.02,0.5,0.5] |

To introduce additional variability across different simulations, the deterministic system in Eq. (7) is augmented by a stochastic term. (7) can be represented as

$$\frac{\mathrm{d}\boldsymbol{x}(t)}{\mathrm{d}t} = f\big(\boldsymbol{x}(t)\big),$$

where $\boldsymbol{x} = [C_A, C_B, C_C, C_D, T, T_c]^\intercal$. We can then write the corresponding system of stochastic differential equations as

$$\mathrm{d}\boldsymbol{x}(t) = f\big(\boldsymbol{x}(t)\big)\mathrm{d}t + \mathrm{d}\boldsymbol{\Sigma}\boldsymbol{W}(t), \tag{8}$$

where $\boldsymbol{W}(t) \sim \mathcal{N}(\boldsymbol{0}, \boldsymbol{I}\mathrm{d}t)$ is a multivariate Wiener process, while the diffusion term $\boldsymbol{\Sigma}$ is given in Tbl. 2.

The stochastic system in (8) is simulated using the Euler-Maruyama method with a step size of $0.001$ h and initial conditions $\boldsymbol{x}_0 = \big[C_{A,\mathrm{in}}, 0, 0, 0, T_{\mathrm{in}}, 375\big]^\intercal$. A total of $50$ simulations are performed. To create the dataset from these simulations, the system is run until it reaches steady state. The final values of $\boldsymbol{x}(t_s)$ at steady state $t_s$ are then recorded as data points. Additionally, measurement uncertainty is added by assuming that $\boldsymbol{x}(t_s)$ is observed with a noise component, $\boldsymbol{x}(t_s) + \boldsymbol{\varepsilon}$, where $\boldsymbol{\varepsilon} \sim \mathcal{N}(\boldsymbol{0}, \boldsymbol{E})$ with $\boldsymbol{E}$ defined in Tbl. 2. As a result, the final dataset generated from Eq. (8) is an $\mathbb{R}^{50\times 7}$ matrix. The columns correspond to the measured variables and states ($C_{A,\mathrm{in}}$, $T_{\mathrm{in}}$, $F$, $Q_c$, $C_A$, $C_B$, $C_C$, $C_D$, $T$).

## Application of methodology

To illustrate the SO-PLS method, two case studies are considered: ***Case (i)*** with a structural error due to a missing reaction in the first-principles model, and ***Case (ii)*** with a severe parametric error. The goal is to assess how well the measured data corrects these errors.

***Case (i):*** In *Step 1*, we assume access to a calibrated first-principles process model for the CSTR system. However, unlike the real system, we assume no knowledge of the third reaction, $2A \rightarrow D$. I.e., the model is similar to Eq. (7) with $r_3 = 0$. We collect the synthetic system states and process inputs in the mechanistic block $\boldsymbol{X} = \big[\boldsymbol{X}_0, \boldsymbol{U}, \widetilde{\boldsymbol{C}}_A, \widetilde{\boldsymbol{C}}_B, \widetilde{\boldsymbol{C}}_C, \widetilde{\boldsymbol{T}}, \widetilde{\boldsymbol{T}}_c\big] \in \mathbb{R}^{50\times 7}$, where $\big[\widetilde{\boldsymbol{C}}_A, \widetilde{\boldsymbol{C}}_B, \widetilde{\boldsymbol{C}}_C, \widetilde{\boldsymbol{T}}, \widetilde{\boldsymbol{T}}_c\big] \in \mathbb{R}^{50\times 5}$ are generated from the mis-specified first-principles model over 50 batches. For the output block, we assume access only to samples of components $A$ and $B$, so $\boldsymbol{Y} = [\boldsymbol{C}_A, \boldsymbol{C}_B] \in \mathbb{R}^{50\times 2}$. The measured block contains observed system states, $\boldsymbol{Z} = [\boldsymbol{T}, \boldsymbol{T}_c] \in \mathbb{R}^{50\times 2}$.

In *Step 2*, the SO-PLS model is fitted, and the number of latent variables is chosen using $10$-fold cross-validation, giving an optimal choice of $\{6,1\}$ latent variables for the $\boldsymbol{X}$ and $\boldsymbol{Z}$ blocks, respectively. The performance is compared to the first-principles model and the Hybrid PLS model proposed by [13] (where PLS is applied to the augmented matrix $[\boldsymbol{X}, \boldsymbol{Z}]$), shown in the first two rows of Tbl. 3. The Hybrid PLS model is cross-validated, yielding a model of $7$ latent variables. The first-principles model shows low performance ($R^2 = 37.3\%$). The Hybrid PLS fit shows significant information contained in $\boldsymbol{X}$ and $\boldsymbol{Z}$ when projecting the columns into a latent space ($R^2 = 97.2\%$). The SO-PLS model performs similarly ($R^2 = 97.1\%$) and exhibits slightly higher $Q^2$ than Hybrid PLS, indicating less overfitting. This is likely due to the sequential selection of latent variables [7]. Additionally, SO-PLS offers an extra layer of interpretation by measuring the incremental contribution of the $\boldsymbol{Z}$ block.

**Table 3.** Calibration and validation metrics averaged over output states ($\boldsymbol{Y} = [\boldsymbol{C}_A, \boldsymbol{C}_B]$). The parameters of the FP model are assumed to be validated upon receival of the model, hence no new validation is performed.

| | Calibration | | | Validation | | |
|---|---|---|---|---|---|---|
| | FP | Hyb-PLS | SO-PLS | FP | Hyb-PLS | SO-PLS |
| $R^2$, $Q^2$ *(i)* | 37.3% | 97.2% | 97.1% | - | 94.5% | 96.0% |
| RMSE *(i)* | 0.74 | 0.15 | 0.16 | - | 0.23 | 0.21 |
| $R^2$, $Q^2$ *(ii)* | 60.5% | 94.3% | 94.4% | - | 86.3% | 88.9% |
| RMSE *(ii)* | 0.57 | 0.27 | 0.27 | - | 0.37 | 0.35 |

In *Step 3*, the overall variance of $\hat{\boldsymbol{Y}}$ model is decomposed according to $\boldsymbol{X}$ and $\boldsymbol{Z}$. While similar precision could be achieved by concatenating $\boldsymbol{X}$ and $\boldsymbol{Z}$ into one block and fitting them against $\boldsymbol{Y}$ in a regular PLS model, the SO-PLS model allows for block-wise interpretations. As shown in Tbl. 4, the measured data improve the overall fit by $3\%$. The variance directly influenced by the mechanistic block is $44.9\%$, while $48.1\%$ is indirectly influenced through the measured block, mainly due to the shared states $\boldsymbol{T}$ and $\boldsymbol{T}_c$. An additional feature of the SO-PLS model is the residual output block $\boldsymbol{Y}^{\mathrm{ort}}$, which encodes the information

not explained by $\boldsymbol{X}$. Fig. 3(a) shows that the model fails to capture some quadratic behavior, aligning with the structural error introduced in the first-principles model.

**Table 4.** Decomposition of overall explained variance ($Q^2$) with standard errors (based on bootstrapping).

| | Direct | Indirect | Additional | Overall |
|---|---|---|---|---|
| Case *(i)* | 44.9% (0.6%) | 48.1% (0.4%) | 3.0% (0.6%) | 96.0% (0.5%) |
| Case *(ii)* | 44.4% (1.5%) | 37.8% (1.7%) | 6.6% (2.2%) | 88.9% (1.4%) |

***Case (ii):*** In *Step 1*, we use a calibrated first-principles process model structurally equivalent to (7), but with parameters $k_{i0}, E_i/R$, $i = 1,2,3$, perturbed randomly by up to 50%. The construction of $\boldsymbol{X}$, $\boldsymbol{Z}$, and $\boldsymbol{Y}$ remains the same, with the addition of state $\widetilde{\boldsymbol{C}}_D$ to $\boldsymbol{X}$.

In *Step 2*, optimal $\{6,1\}$ latent variables are chosen for $\boldsymbol{X}$ and $\boldsymbol{Z}$, respectively. Performance is compared to the first-principles model and a Hybrid PLS model fitted to $([\boldsymbol{X}, \boldsymbol{Z}], \boldsymbol{Y})$ with optimal 7 latent variables in the two last rows of Tbl. 3. Again, SO-PLS shows less overfitting, evident from the smaller difference between $R^2$ and $Q^2$.

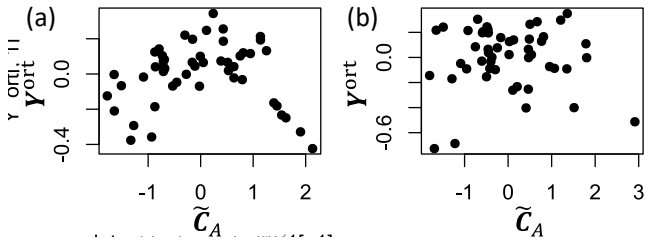



**Figure 3.** $\widetilde{\boldsymbol{C}}_A$ vs $\boldsymbol{Y}^{\text{ort}}$ for *Case (i)* (a) and *(ii)* (b).

In *Step 3*, as shown in Tbl. 4, measured data improve the overall fit by 6.6%. Compared to *Case (i)*, the mechanistic block explains less total variance (82.2%), despite the correct model formulation. The results show that measured data improve the model fit, but also highlight a limit to how much the first-principles model can be miscalibrated (given the lower overall $R^2$ at 88.9%). Furthermore, as expected, no structural errors are observed in the residuals (Fig. 3(b)).

## CONCLUSION

In this work, we present a methodology based on SO-PLS for incorporating process knowledge into latent-variable models. This approach efficiently integrates first-principles models with measured process data without needing to recalibrate the first-principles model to the full-scale system. The methodology is demonstrated using a CSTR case example. The results show that it can decouple the variance explained by first-principles from that explained purely by data and capture mismatches.

Current work aims to apply this procedure in an industrial setting to identify root causes of disturbances in bioprocesses, using variance decomposition to pinpoint sources of abnormalities. Future work seeks to integrate process-wide interactions with first-principles knowledge into a unified SO-PLS model, extending previous research [7]. Increased complexity in the first-principles model can increase computational costs, necessitating the use of a surrogate model for generating synthetic data. Furthermore, the SO-PLS model's repeated deflation steps can be computationally demanding, especially in process-wide models with many blocks, due to the need to explore all latent variable combinations during cross-validation. The response-oriented sequential alternation (ROSA) model offers a viable alternative to address these challenges [15].

## ACKNOWLEDGEMENTS

The authors gratefully acknowledge the financial support and data access from Novo Nordisk A/S.

## REFERENCES

1. Destro F, Inguva PK, Srisuma P, Braatz RD. Advanced methodologies for model-based optimization and control of pharmaceutical processes. *Curr Opin Chem Eng* 45:101035 (2024) https://doi.org/10.1016/j.coche.2024.101035
2. Rathore AS, Garcia-Aponte OF, Golabgir A, ..., Herwig C. Role of knowledge management in development and lifecycle management of biopharmaceuticals. *Pharm Res* 34:243-256 (2017) https://doi.org/10.1007/s11095-016-2043-9
3. Içten E, Maloney AJ, Beaver MG, Shen DE, Zhu X, Graham LR, Robinson JA, Huggins S, Allian, A, Hart R, Walker SD, Braatz RD. A virtual plant for integrated continuous manufacturing of a carfilzomib drug substance intermediate, part 1: cdi-promoted amide bond formation. *Org Process Res Dev* 24:1861-1875 (2020) https://doi.org/10.1021/acs.oprd.0c00187
4. Zahel T, Hauer S, Mueller EM, Murphy P, Abad S, Vasilieva E, Maurer D, Brocard C, Reinisch D, Sagmeister P, Herwig C. Integrated process modeling-a process validation life cycle companion. *Bioengineering* 4:86 (2017) https://doi.org/10.3390/bioengineering4040086
5. Diab S, Christodoulou C, Taylor G, Rushworth P. Mathematical modeling and optimization to inform impurity control in an industrial active pharmaceutical ingredient manufacturing process. *Org Process Res Dev* 26:2864-2881 (2022) https://doi.org/10.1021/acs.oprd.2c00208
6. Pantelides CC, Renfro JG. The online use of first-principles models in process operations: Review, current status and future needs. *Comput Chem Eng*

51:136-148 (2013) https://doi.org/10.1016/j.compchemeng.2012.07.008
7. Zhu Q, Facco P, Zhao Z, Barolo M. Capturing connectivity information from process flow diagrams by sequential-orthogonalized PLS to improve soft-sensor performance. *Chemom Intell Lab Syst* 252:105192 (2024) https://doi.org/10.1016/j.chemolab.2024.105192
8. Cattaldo M, Ferrer A, Måge I. Dynamic multiblock regression for process modelling. *J Chemom* 38:e3618 (2024) https://doi.org/10.1002/cem.3618
9. Overgaard T, Bertran MO, Jorgensen JB, Nielsen BF. (in press). Identifying drivers of downstream yield variability using integrated process models: an application to api manufacturing. *IFAC Proc Vol* (2025)
10. Næs T, Romano R, Tomic O, Måge I, Smilde A, Liland KH. Sequential and orthogonalized PLS (SO-PLS) regression for path analysis: order of blocks and relations between effects. *J Chemom* 35:e3243 (2021) https://doi.org/10.1002/cem.3243
11. van de Vusse JG. Plug-flow type reactor versus tank reactor. *Chem Eng Sci* 19:994-996 (1964) https://doi.org/10.1016/0009-2509(64)85109-5
12. Höskuldsson A. PLS regression methods. *J Chemom* 2:211-228 (1988) https://doi.org/10.1002/cem.1180020306
13. Ghosh D, Mhaskar P, MacGregor JF. Hybrid partial least squares models for batch processes: Integrating data with process knowledge. *Ind Eng Chem Res* 60:9508-9520 (2021) https://doi.org/10.1021/acs.iecr.1c00865
14. von Stosch M, Oliveira R, Peres J, Feyo de Azevedo S. Hybrid semi-parametric modeling in process systems engineering: past, present and future. *Comput Chem Eng* 60:86-101 (2014) https://doi.org/10.1016/j.compchemeng.2013.08.008
15. Liland, KH, Næs, T, Indahl, UG. ROSA – a fast extension of partial least squares regression for multiblock data analysis. *J Chemom* 30: 651–662 (2016) https://doi.org/10.1002/cem.2824

© 2025 by the authors. Licensed to PSEcommunity.org and PSE Press. This is an open access article under the creative commons CC-BY-SA licensing terms. Credit must be given to creator and adaptations must be shared under the same terms. See https://creativecommons.org/licenses/by-sa/4.0/



Systems & Control Transactions

**Research Article - Peer Reviewed Conference Proceeding**
ESCAPE 35 - European Symposium on Computer Aided Process Engineering
Ghent, Belgium. 6-9 July 2025
Jan F.M. Van Impe, Grégoire Léonard, Satyajeet S. Bhonsale,
Monika E. Polańska, Filip Logist (Eds.)

PSE PRESS

# Exploring Design Space and Optimization of nutrient factors for maximizing lipid production in *Metchnikowia pulcherrima* with Design of Experiments

**Nichakorn Fungprasertkul[a]*, James Winterburn[a], and Peter Martin[a]**

[a] School of Chemical Engineering, University of Manchester, Manchester, M13 9PL, UK
* Main Author: nichakorn.fungprasertkul@postgrad.manchester.ac.uk.

## ABSTRACT

Due to the importance of unsaturated fatty acids for human health and the increasing global demand in the food and food crop area, oleaginous yeasts are promising alternative microorganisms for commercial lipid production due to the high volumetric productivity, with *Metchnikowia pulcherrima* being an underexplored oleaginous yeast with potential as a lipid producer. Critical to achieving high productivity lipid production are nutrient factors. A sensitivity test identified carbon and nitrogen sources as important factors in nitrogen limited broth (NLB) for lipid production in *M. pulcherrima* i.e. glucose, yeast extract and Ammonium sulphate. Response Surface Methodology (RSM) involving sets of 15 experimental runs of three-factor three-level Box-Behnken Design (BBD) was implemented for exploring the design of the carbon and nitrogen source in the growth media composition. Quadratic surfaces were least-square fitted and used to identify regions of optimal lipid yield. Multiple sets of runs were conducted with the parameter range progressively adapted and repeated until a clear optimum was identified. The highest total lipid production was in the low carbon concentration range (2.27-21.5 g/L) which suggests the process is more productive with the optimised media compared to NLB media (30.4 g/L of carbon). The optimal carbon concentration was 14.8 g/L whereas the dependence on nitrogen was not found to be significant. The yield of optimal point ($Y_{P/S}$) was 2.39 times higher than NLB media after validation because the depletion of glucose at the end of fermentation (72-104 h) contributes the high increase of lipid accumulation (mg Lipid/ 100 ml culture) of the optimal point (94.5%) which was higher than NLB media (34.5%) for 60%.

**Keywords**: Fermentation, Food & Agricultural Processes, Microbial Oil, Plackett-Burman design, Box-Behnken design

## 1. INTRODUCTION

In 2023 the World Health Organization (WHO) suggested that unsaturated fatty acids should be a primary source of fat consumption for humans in its guidance as they can decrease the risk of heart disease by lowering cholesterol levels [1]. The global population is predicted to reach 9 billion people by 2050, resulting in greater demand for food and food crops [2]. In the same way, lipid consumption has increased globally from 83.5 to over 223 million tonnes in past 30 years to serve several purposes including; biofuels, food, supplements, oleochemicals and animal feed. Oleaginous yeasts are considered as viable microorganisms for commercial lipid production because of the high specific growth rate and lipid accumulation. *Metchnikowia pulcherrima* is an under-explored oleaginous yeast with potential as a lipid producer [3]. Critical to achieving high productivity lipid production are nutrient factors [3-4].

This study focuses on understanding the effect of factors toward the growth and lipid production of *M. pulcherrima* and optimizing the important factors to maximize lipid production. A sensitivity test was used to identify the most influential factors on the responses [5]. Plackett-Burman design with a first degree polynomial model was used within this sensitivity test because it focuses

on main effects and properties to minimise the variances in independent estimates with a small number of experimental runs [6]. Box-Behnken design and a quadratic model were used for exploring the design space and optimization. Box-Behnken design can meet a requirement of quadratic system with fewer runs than central composite design [7]. To maximize the lipid production in *M. pulcherrima* by optimizing the important media compositions that have a significant impact on Total Lipid from the sensitivity test.

# 2. METHODOLOGY

## 2.1 Sample preparation

### 2.1.1 Microorganism and Cultivation Techniques

The yeast strain *Metchnikowia Pulcherrima* NCYC2580 (National Collection of Yeast Cultures, Norfolk, UK) was stored in a 23% (v/v) glycerol stock at – 80 °C. For preculture, one cryovial (1.6 ml) of working stock was incubated in 20 ml MEA media (malt extract 30 g/L; mycological peptone 5 g/L) in a 125 ml Erlenmeyer flask at 200 rpm at 20 °C in Infors HT Multitron 2 Incu-bator Shaker with Cooling for 24 h. Fermentation for the control flasks was prepared using nitrogen limited broth (NLB) (NLB: $KH_2PO_4$ 7 g/L; $(NH4)_2SO_4$ 2 g/L; $Na_2HPO_4$ 1 g/L; $MgSO_4{\cdot}7H_2O$ 1.5 g/L; yeast extract 1 g/L; glucose 80 g/L; pH 5). The fermentation was carried out by adding 1 ml of preculture in 100 ml of broth in 500 ml Erlenmeyer flask. The flasks were incubated at 200 rpm at 15 °C for 104 h [4].

### 2.1.2 Residue biomass, Lipid Content and Total Lipid measurement

After the fermentations had reached their end point at 104 h, biomass was measured by centrifuging 1 ml of culture broth, followed by removal of the supernatant and drying of the obtained cell pellets in a vacuum drier at 50 °C until constant weight. Biomass was recorded in units of g/g (dried cell weight/ culture weight). Lipid content was determined as the percentage of lipid weight per dry cell weight after lipid extraction process as the details in supplementary material (Section S1.1). Residual biomass was calculated by subtraction of the amount of the lipid in 1 g of biomass. Total Lipid (mg Lipid/100 ml culture) was recorded as the total amount of lipid obtained from one flask.

### 2.1.3 Additional Chemical Analysis

Total Organic Carbon (TOC) and Total Nitrogen (TN) were measured for understanding carbon and nitrogen source consumption. The liquid samples were diluted for 2 and 10 times for TOC and TN analysis respectively and filtered (0.22 µm, Millipore). The TOC and TN values were measured on Shimadzu TOC-V cpn Dissolved Carbon and TNM-1 Nitrogen Analyser at Manchester Analytical Geochemistry Unit (MAGU), The University of Manchester, UK. The measurement was done in duplicates. Glucose concentration in culture was measured daily to understand carbon source consumption. Glucose concentration was quantified as the details in supplementary material (Section S1.2).

## 2.2 Sensitivity Test

The experimental design for a sensitivity test was constructed to study the influences of seven nutrient factors on *M. pulcherrima* Residual Biomass and Lipid Content. The seven nutrient factors are six factors in NLB and glycerol supplementation. The levels in this experiment were considered from the concentration of the factors in NLB and the possible concentration range that can be developed for optimization as shown in Table 1. The experimental design was constructed on seven-factor Plackett-Burman design as the details in supplementary material (Section S2).

**Table 1:** Levels of factors for Sensitivity Test

| Factors (g/L) | Symbol | Low Level (-) | High Level (+) |
|---|---|---|---|
| Glucose | $x_1$ | 40 | 80* |
| Glycerol | $x_2$ | 0 | 9 |
| Yeast Extract | $x_3$ | 1* | 4 |
| $(NH_4)_2SO_4$ | $x_4$ | 2* | 8 |
| $Na_2HPO_4$ | $x_5$ | 1* | 4 |
| $MgSO_4{\cdot}7H_2O$ | $x_6$ | 1.5* | 6 |
| $KH_2PO_4$ | $x_7$ | 7* | 15.75 |

*Concentration in Nitrogen limited broth (NLB)

Following the running of the Plackett-Burman design experiment (eight runs for three replications per the levels of factor in Table 1), a multiple linear regression model was fitted, equation 1. Where $Y$ is the predicted response, $a_0$ is the intercept of mean and $a_1 \ldots a_7$ are the respective coefficients of factor $x_1$ until $x_7$ respectively [6]. Statistical analysis of the multiple linear regression model and response surface plots were carried out in Python 3.11.3 by Statsmodels and Plotly Library.

$$Y = a_0 + a_1x_1 + \cdots + a_7x_7 \quad (1)$$

## 2.3 Exploring the design space and Optimization

After running the sensitivity test, the important factors for residual biomass and lipid content were identified. The level of the important factor was assigned to the same range with the sensitivity test to visualize the potential range of the optimal point. A three-factor three-level Box-Behnken design was constructed for exploring the design space as the details in supplementary material (Section S3).

Following running the Box-Behnken design experiment (15 runs for two replications as per the levels of

factor in Table S2), a quadratic model was fitted as the equation 2. Where $Y$ is the predicted response, $\beta_o, \beta_i, \beta_{ii}, \beta_{ij}$ are regression coefficients of the model for the intercept, linear, square, interaction effects respectively, and $x_i$, $x_j$ are the factors [8]. RSM Library in R programming was used for fitting the quadratic model and analysing Analysis of variance (ANOVA) of the models [9], and response surface plots were carried out in Python 3.11.3 using the Plotly Library.

$$Y = \beta_0 + \sum \beta_i x_i + \sum \beta_{ii} x_i^2 + \sum \beta_{ij} x_i x_j \quad (2)$$

Subsequent to exploring the design space, the parameter range was progressively adapted and repeated until a clear optimum was identified. It can be identified when the peak of the important factor of a quadratic model is shown on a response surface clearly. The optimal point was identified after running Box-Behnken design as the levels of factor as shown in Table 2 in two replications. A three-factor three-level Box-Behnken design was constructed for optimization as the details in supplementary material (Section S4). The statistical analysis and response surface fitting were done in the same manner as for the previous exploring the design space step.

**Table 2:** Levels of factors for optimization

| Factors (g/L) | Symbol | Level (-1) | Level (0) | Level (+1) |
|---|---|---|---|---|
| Glucose | $x_1$ | 5 | 27.5 | 50 |
| Yeast Extract | $x_2$ | 1 | 4 | 7 |
| $(NH_4)_2SO_4$ | $x_3$ | 2 | 8 | 14 |

After the optimal point was identified, it was validated by running an experiment at the optimal point in triplicate and comparing with the control sample (NLB). The yield of the optimal sample was calculated using equation 3 and compared with the control sample.

$$Y_{P/S} = \frac{mass\ product\ produced\ (g)}{mass\ substrate\ consumed\ (g)} \quad (3)$$

## 2.4 Repeatability of Exploring the design space and Optimization Experiments

The experiments were repeated by using the different preculture for two and five replications for the exploring the design space and optimization respectively to observe the percentage change as per equation 4. Where $x_1$, $x_2$ are the old and new values accordingly.

$$Percentage\ change = \frac{x_2 - x_1}{x_1} \times 100 \quad (4)$$

# 3. RESULTS AND DISCUSSION

## 3.1 Sensitivity Test

Subsequent to running the experiment of the sensitivity test, the multiple linear regressions of Residual Biomass and Lipid Content were fitted. The linear regression coefficient ($R^2$ = 0.912, Adjusted R-squared 0.873, F-statistic: 23.57) of multiple regression linear model of Residual Biomass indicates a goodness of the model to explain total variation among responses. The significant factors for Residual Biomass are yeast extract (1-4 g/L), glucose (40-80 g/L) and $(NH_4)_2SO_4$ (2-8 g/L) which are positive impacts. The response surface in figure 1 shows the increase of the Residual Biomass with the glucose and $(NH_4)_2SO_4$ concentrations. These important factors for Residual Biomass are carbon and nitrogen sources in the media. In the initial phase of fermentation, the carbon and nitrogen sources are important for increasing the cell division and protein synthesis to increase the cell density, resulting in the increase of biomass [10]. In the case of Lipid Content, the linear regression coefficient ($R^2$ = 0.921, Adjusted R-squared 0.887, F-statistic: 26.81) of the model of Lipid Content indicates goodness of the model to explain total variation among responses. Although yeast extract (1-4 g/L), glucose (40-80 g/L) and $(NH_4)_2SO_4$ (2-8 g/L) are significant factors for Lipid Content as well, they have negative effects for lipid content. Figure 1 shows that Lipid Content decreased with the increase of yeast extract and glucose in the response surface from the multiple linear regression model because of the limitation of the nutrient contributes the lipid accumulation inside of an oleaginous cell by activating citrate formation, thus ATP Citrate lyase start to change citrate to a substrate to a triglyceride formation or lipid droplet in the end [10].

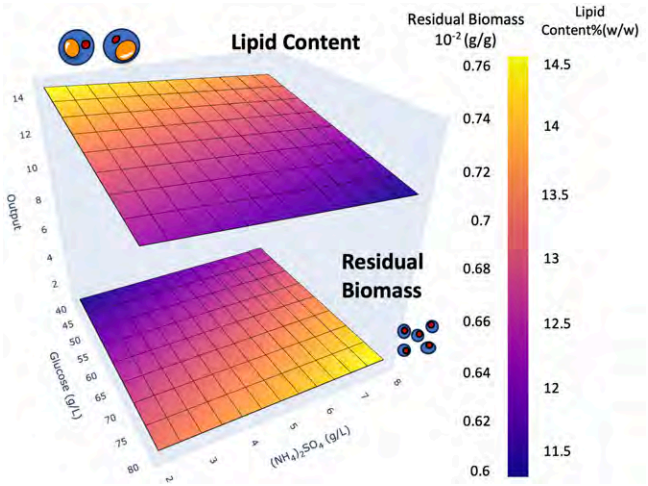



**Figure 1:** Response surface of multiple regression linear model of Lipid Content and Residual Biomass model from plotting Glucose (g/L) and $(NH_4)_2SO_4$ (g/L).

## 3.2 Exploring the design space and Optimization

To maximize the lipid production in the culture volume (100 ml), Total Lipid (mg Lipid/100 ml culture) was defined in order to optimize the important factors to

maximize the lipid production. Since the important factors for Residual Biomass and Lipid Content are yeast extract, glucose and $(NH_4)_2SO_4$ which are carbon and nitrogen sources, the important factors were converted to the concentrations of carbon and nitrogen from TOC and TN analysis. From running the experiments as the Box-Behnken design for exploring the design space, the data were fitted as a quadratic model. From the statistical analysis, the model has a moderate correlation (Multiple R-squared: 0.5948, Adjusted R-squared: 0.3696) with non-significant of Lack of fit (Pr(>F) = 0.12870, exceed 0.05) as shown in Table 3, thus the model is valid for the work. The statistical result in Table 4 shows that carbon is the important factor in both linear ($x_1$) and pure quadratic term ($x_1^2$), and nitrogen was not found to be significant. This could be because of the insignificant nitrogen concentration in this design space, the model has the low adjusted R-squared because the model cannot fully represent the data. The carbon sources in this process are glucose and yeast extract. They can contribute the high cell density of biomass in fermentation [11]. It is the first stage of lipid production. During the excess of the nutrients condition, the cells actively grow, resulting in the cell mass increase [10]

**Table 3:** Analysis of variance (ANOVA) for the quadratic regression model of Total Lipid (TL) after running the exploring the design space experiments (1).

| | Df | Sum Sq | Mean Sq | F value | Pr(>\|t\|) |
|---|---|---|---|---|---|
| **Residuals** | 9 | 3108.39 | 345.38 | | |
| **Lack of fit** | 7 | 2988.41 | 426.92 | 7.1163 | 0.12870[b] |

[b] Not significant under 95% level of confidence.

**Table 4:** Analysis of variance (ANOVA) for the quadratic regression model of Total Lipid (TL) after running the exploring the design space experiments when $x_1$ is carbon concentration (g/L) and $x_2$ is nitrogen concentration (g/L) (2).

| | Estimate | Std. Error | Pr(>\|t\|) |
|---|---|---|---|
| Intercept | 303.87271 | 112.7535 | 0.02459[a] |
| $x_1$ | -19.69963 | 8.2744 | 0.04117[a] |
| $x_2$ | 30.38043 | 71.3737 | 0.68036 |
| $x_1x_2$ | -1.46881 | 1.9027 | 0.45993 |
| $x_1^2$ | 0.41444 | 0.1689 | 0.03651[a] |
| $x_2^2$ | -1.26624 | 21.5253 | 0.95438 |

[a] Significant under 95% level of confidence.

The contour plot from the response surface of the model in Figure 2 shows the highest Total Lipid in the low carbon range. For this reason, the parameter range in the experimental design was adapted progressively towards the to lower carbon concentration for optimization. Since nitrogen was found to be insignificant, the range of nitrogen concentration was expanded to include higher concentrations (2-14 g/L) for optimization.

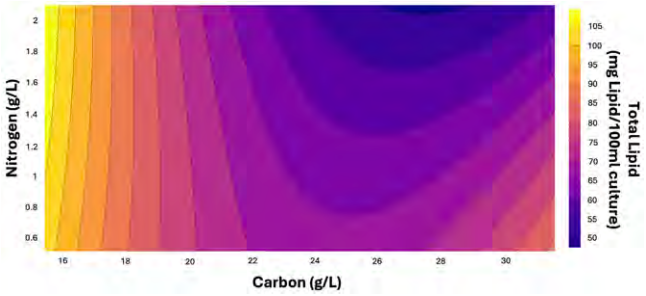



**Figure 2:** Contour plot of the quadratic model of Total Lipid from plotting Carbon (g/L) and Nitrogen (g/L) from Exploring the design space experiment.

After running the low carbon concentration experiments as per Table 2 for optimising the carbon and nitrogen concentration to maximise the Total Lipid, a quadratic model was fitted. From statistical analysis, the quadratic model has the moderate correlation (Multiple $R^2$: 0.5672 and Adjusted $R^2$: 0.3268). Lack of fit of the model is nonsignificant (Pr(>F) = 0.2359, exceed 0.05) as shown in Table 5, so the model is valid for the work. The statistical result in Table 6 shows that carbon (2.27-21.5 g/L) is an important factor for Total Lipid production in both linear ($x_1$) and pure quadratic term ($x_1^2$), and nitrogen was not found to be significant. In the same way with the Total Lipid model in exploring the design space, the irrelevant nitrogen concentration in this optmization design space could cause the low adjusted R-squared because the model cannot fully represent the data.

The optimal carbon concentration was 14.8 g/L, and it can be observed from the response surface as shown Figure 3. The optimal nitrogen concentration was identified from the highest Total Lipid that can be achieved at the optimal carbon concentration within the design space. Thus, the model was experimental validated at 14.8 g/L of carbon and 0.52 g/L of nitrogen which is comprised of glucose 38.5 g/L, yeast extract 1 g/L and $(NH_4)_2SO_4$ 2 g/L. After the model validation, the different percentage between the model and the experimental validation point (54.1 ± 2.78 (mg Lipid/ 100 ml culture)) was 6.93%. Carbon to nitrogen ratio of this optimal point in this process was 28.46 (g/g) which is a parameter for a fermentation process for lipid production by an oleaginous yeast [12]. The yield of the optimal point sample and NLB sample which was considered from the Total Lipid (mg lipid/100 ml culture) and the consumed carbon

concentration (mg consumed carbon/100 ml culture). The yield of optimal point ($Y_{P/S}$) was 2.39 times higher than NLB media after validation. The reasons of the high optimal yield were studied further from the glucose consumption and lipid accumulation daily examination.

**Table 5:** Analysis of variance (ANOVA) for the quadratic regression model of Total Lipid (TL) after running optimization experiments (1).

| | Df | Sum Sq | Mean Sq | F value | Pr(>\|t\|) |
|---|---|---|---|---|---|
| **Residuals** | 9 | 1703.91 | 189.32 | | |
| **Lack of fit** | 8 | 1683.63 | 210.45 | 10.3731 | 0.2359[b] |

[b] Not significant under 95% level of confidence.

**Table 6**: Analysis of variance (ANOVA) for the quadratic regression model of Total Lipid (TL) after running the optimization experiments when $x_1$ is carbon concentration (g/L) and $x_2$ is nitrogen concentration (g/L) (2).

| | Estimate | Std. Error | Pr(>\|t\|) |
|---|---|---|---|
| Intercept | -9.47305 | 21.1502 | 0.66482 |
| $x_1$ | 7.54068 | 2.7051 | 0.0211[a] |
| $x_2$ | 0.79361 | 8.6870 | 0.92921 |
| $x_1x_2$ | -0.11518 | 0.6229 | 0.85738 |
| $x_1^2$ | -0.25198 | 0.1003 | 0.0331[a] |
| $x_2^2$ | -0.00802 | 0.2029 | 0.96935 |

[a] Significant under 95% level of confidence.

Since glucose is comprised 97.47% (w/w) of the total carbon the change of glucose with Total Lipid of the optimal point was examined every day to understand the metabolism of lipid accumulation and carbon source consumption by *M. pulcherrima* during fermentation. The study found that the optimal sample gave a high yield because of the depletion of glucose at the end of fermentation (72-104 h), contributing to the increase of lipid accumulation (mg Lipid/ 100 ml culture) at the optimal point (94.5%) which was higher than NLB media (34.5%) for 60%. This is because there are two stages of lipid accumulation for the carbon limitation media of the optimal point. In the first stage, the cells grow and accumulate gradually at the same time. However, at the end of the fermentation (72-104 h), the glucose was completely consumed, and the Lipid Content was increased dramatically to 7.67% (1.86 times of NLB samples) [13]. In contrast, the lipid accumulation in the NLB fermentations increased gradually with biomass. At the end of the process, the Lipid Content at 104 h was only 4.14%, and there was residual glucose for 15.17 g/L.

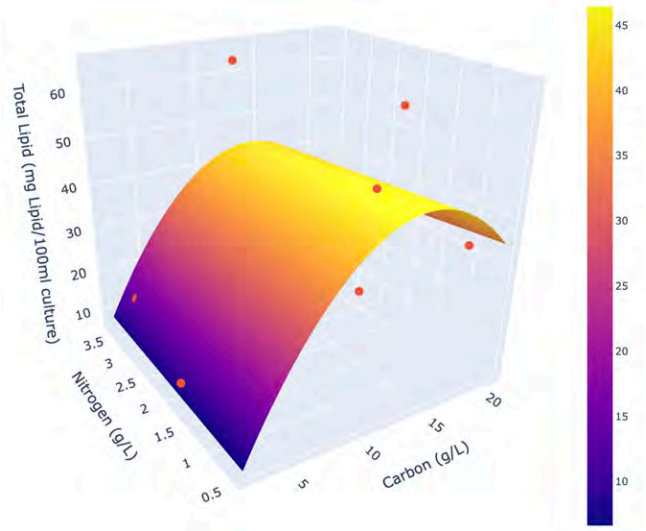



**Figure 3:** Response surface of quadratic model of Total Lipid from plotting Carbon (g/L) and Nitrogen (g/L) from Low Carbon Concentration from Box-Behnken Design.

## 3.3 Repeatability of Exploring the design space and Optimization Experiments

From the study of repeatability of the exploring design space experiment, the highest percentage change, 55.78% of the total lipid. This value indicates the likelihood of repeating the experiment by running the different preculture batch. In the same way, the repeatability of the optimization experiment was studied to observe the different change from running the different preculture batch and error during the experimental run as shown in Figure 4. The higher than expected total lipid of the third replication was observed. This is because of contamination of biomass during lipid separation, thus the weight of lipid in this data set are higher than the other replication. The different percentage the Total Lipid data was decreased for 4.97% from 92.1% to 87.2% by excluding the third replication in the data set. Removing an error data set before plotting a quadratic model was operated because the value of the third replication cannot represent the likelihood of the data set. Thus, the model could be representing the behavior of *M. pulcherrima* precisely by including only the data set that was experimented correctly.

## 4. CONCLUSION

The sensitivity test, the exploring the design space and optimization successfully maximized lipid production in the limited volume (100 ml) from *M. pulcherrima.* The sensitivity test from Plackett-Burman design and multiple linear regression model identified carbon and nitrogen sources as the important factors as expected in nitrogen limited broth (NLB) for lipid production by *M. pulcherrima* which are glucose, yeast extract and Ammonium sulphate. The important factors have a positive impact on

the Residual Biomass but a negative impact on the Lipid Content because they are the nutrients for the cell growth, but the starvation of nutrients contributes the lipid accumulation. Box-Behnken Design with quadratic model fitting suggests the maximal lipid production point on the response surface at the low carbon concentration range (2.27-21.5 g/L) for optimization of the Total Lipid. The optimal carbon concentration was 14.8 g/L, thus the optimal carbon to nitrogen ration was 28.46 (g/g). The yield of optimal point was higher than NLB media at 2.39 times because the depletion of glucose at the end of fermentation (72-104 h) contributes the high increase of lipid accumulation of the optimal point. The repeatability of the exploring the design space and optimization experiments were tested to understand the behavior of *M. pulcherrima*. and potential experimental error during running the experiments.

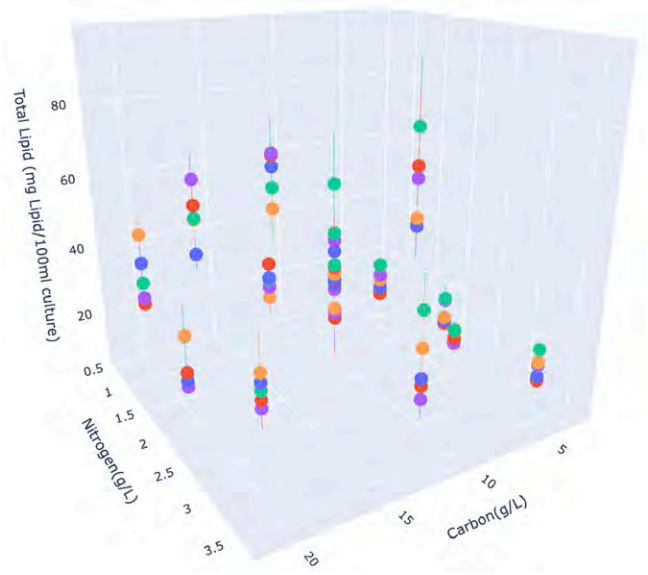



**Figure 4:** Scatter from plotting the experimental data of Total Lipid model on carbon and nitrogen concentrations axes from running the optimization experiment (blue-first replication, red-second replication, green-third replication, fourth-purple replication and orange-fifth replication).

## DIGITAL SUPPLEMENTARY MATERIAL

Digital supplementary material can be found at https://psecommunity.org/LAPSE:2025.0028

## REFERENCES


1. World Health Organization. https://www.who.int/publications/i/item/9789240061668
2. United Nations. https://www.un.org/youthenvoy/2013/09/fao-food-and-agriculture-organization-of-the-united-nations/
3. Abeln, F., & Chuck, C. J. (2021). The history, state of the art and future prospects for oleaginous yeast research. *Microb Cell Fact*, 20(1), 221. https://doi.org/10.1186/s12934-021-01712-1
4. Abeln, F., & Chuck, C. J. (2020). The role of temperature, pH and nutrition in process development of the unique oleaginous yeast Metschnikowia pulcherrima. *Journal of Chemical Technology & Biotechnology*. https://doi.org/10.1002/jctb.6301
5. Lin, S., Xie, M., Wu, M., & Zhou, W. (2018). Global Sensitivity Analysis of Large Reaction Mechanisms Using Fourier Amplitude Sensitivity Test. Journal of Chemistry, 2018(1), 5127393. https://doi.org/https://doi.org/10.1155/2018/5127393
6. Vanaja, K., & Shobha Rani, R. H. (2007). Design of Experiments: Concept and Applications of Plackett Burman Design. *Clinical Research and Regulatory Affairs*, 24(1), 1–23. https://doi.org/10.1080/10601330701220520
7. Liu, S. (2020). Design of experiment. In Bioprocess Engineering (pp. 885-933). https://doi.org/10.1016/b978-0-12-821012-3.00020-8
8. Ghorbel-Bellaaj, O., Hmidet, N., Jellouli, K., Younes, I., Maâlej, H., Hachicha, R., & Nasri, M. (2011). Shrimp waste fermentation with Pseudomonas aeruginosa A2: Optimization of chitin extraction conditions through Plackett–Burman and response surface methodology approaches. *International Journal of Biological Macromolecules*, 48(4), 596-602. https://doi.org/https://doi.org/10.1016/j.ijbiomac.2011.01.024
9. Lenth, R. V. (2009). Response-Surface Methods in R, Using rsm. *Journal of Statistical Software*, 32(7), 1 - 17. https://doi.org/10.18637/jss.v032.i07
10. Chopra, J., Rangarajan, V., & Sen, R. (2022). Recent developments in oleaginous yeast feedstock based biorefinery for production and life cycle assessment of biofuels and value-added products. *Sustainable Energy Technologies and Assessments*, 53. https://doi.org/10.1016/j.seta.2022.102621
11. Abeln, F., & Chuck, C. J. (2019). Achieving a high-density oleaginous yeast culture: Comparison of four processing strategies using *Metschnikowia pulcherrima*. *Biotechnol Bioeng*, 116(12), 3200-3214. https://doi.org/10.1002/bit.27141
12. Lei, Y., Wang, X., Sun, S., He, B., Sun, W., Wang, K., Chen, Z., Guo, Z., & Li, Z. (2024). A review of lipid accumulation by oleaginous yeasts: Culture mode.

*Sci Total Environ*, 919, 170385. https://doi.org/10.1016/j.scitotenv.2024.170385

13. Amaretti, A., Raimondi, S., Sala, M., Roncaglia, L., De Lucia, M., Leonardi, A., & Rossi, M. (2010). Single cell oils of the cold-adapted oleaginous yeast Rhodotorula glacialis DBVPG 4785. *Microbial cell factories*, 9, 73. https://doi.org/10.1186/1475-2859-9-73

© 2025 by the authors. Licensed to PSEcommunity.org and PSE Press. This is an open access article under the creative commons CC-BY-SA licensing terms. Credit must be given to creator and adaptations must be shared under the same terms. See https://creativecommons.org/licenses/by-sa/4.0/



Systems & Control Transactions

**Research Article - Peer Reviewed Conference Proceeding**
ESCAPE 35 - European Symposium on Computer Aided Process Engineering
Ghent, Belgium. 6-9 July 2025
Jan F.M. Van Impe, Grégoire Léonard, Satyajeet S. Bhonsale,
Monika E. Polańska, Filip Logist (Eds.)

PSE PRESS

# Computer-Aided Design and Optimization of Lycopene Production Process from Tomato Waste

**Nereyda Vanessa Hernández-Camacho [a], Fernando Israel Gómez-Castro [a]*, Mariano Martín [b], Ehecatl Antonio del Rio-Chanona [c] and Oscar Daniel Lara-Montaño [d]**

[a] Universidad de Guanajuato, Campus Guanajuato, División de Ciencias Naturales y Exactas, Departamento de Ingeniería Química, Guanajuato, Guanajuato, Mexico.
[b] Universidad de Salamanca, Departamento de Ingeniería Química, Salamanca, Spain.
[c] Imperial College London, Centre for Process Systems Engineering (CPSE), Department of Chemical Engineering, London, United Kingdom.
[d] Universidad Autónoma de Querétaro, Facultad de Ingeniería, Juriquilla, Querétaro, Mexico.
* Corresponding Author: fgomez@ugto.mx

## ABSTRACT

The extraction of lycopene from tomato waste has been largely evaluated at an experimental level, leading to the creation of polynomial models or response surfaces that allow the representation of the extraction behavior. However, these studies are based on laboratory level and an extraction process has not yet been scaled up. This study evaluates the design and optimization of the lycopene extraction process from tomato waste. The proposed model is solved through a link between Python and Aspen Plus, performing the optimization a genetic algorithm (GA) in Pymoo. The minimum value of TAC is 211,692.2 USD/yr, corresponding to a production of 2.29 g/h of lycopene, starting from 1000 kg/h of tomato waste. This work represents a first approach to the design of a commercial-scale lycopene production process.

**Keywords**: tomato waste, lycopene, solvent extraction, stochastic optimization.

## INTRODUCTION

Approximately 13.2% of the world's food is lost before being harvested [1]. Thus, food waste management has high relevance. Particularly in Mexico, the agricultural sector contributes with 3.4% of the national GDP, where the fruits and vegetables sector stand out with 45% of the sector's exportations. Tomatoes contributes to exportation with 8.41%. Mexico is the main supplier of this product worldwide, with a 19% share of the exported volume in the period 2003-2017 [2]. However, not all tomatoes are used due to their short shelf life, causing approximately 30% of the crop to be wasted [3]. In addition, waste from tomato sauce production can also be valorized. Tomato waste can be used to isolate high-value compounds such as carotenoids, polyphenols, vitamins, fibers, flavonoids, among others. Among these, lycopene is considered a well-known carotenoid and the most abundant pigment in tomatoes, responsible for giving them their color. It is used as a raw material in the cosmetic, pharmaceutical and food industries [4]. Lycopene from tomato waste is traditionally recovered by solvent extraction, but research on this topic has only been carried out through laboratory-scale experimentation [5, 6]. An important aspect in lycopene extraction is the type of solvent used in the extraction, as this can have economic, environmental or health drawbacks, depending on the application for which it is used. Some studies work with traditional solvents [6,7], others use enzymes that help with greater extraction [5,8], and others work with supercritical fluids [9]. Various alternatives have been proposed, but all of them have been developed at laboratory level, without scaling up.

This work addresses the systematic design and optimization of an industrial-scale process for obtaining lycopene from tomato waste. A comparison is made between a base case and the optimized design using a conventional solvent mixture: acetone-n-hexane. A stochastic single-objective optimization strategy is employed to minimize to total annual cost (TAC) of the proposed process.

# METHODOLOGY

## Process Design

Tomato waste is used as raw material to produce lycopene. This waste is passed through a tray-type dryer, reducing the water content to 10%. The waste is then subjected to a mill until it reaches an average particle size of 78 mm. Lycopene is then extracted from tomato waste using an acetone-n-hexane solvent mixture in a stirred tank reactor. The lycopene rich stream passes to a flash tank to separate large volumes of solvents and concentrate the lycopene. Finally, the lycopene stream is purified in a distillation column to achieve 95% purity, food grade. The process is summarized in Figure 1.

## Mathematical modeling

The mathematical model of the process consisted of the design equations for the drying, grinding and extraction stages, which have been coded in Python, linked to the simulation in Aspen Plus for the separation and purification stages (flash tank and distillation column).

For the drying stage the main equations are given by eqs. (1), (2) and (3) [10]:

$$\frac{q_T}{\dot{m}_s} = c_{ps}(T_{sb} - T_{sa}) + X_a c_{pL}(T_v - T_{sa}) + (X_a - X_b)\lambda + X_b c_{pL}(T_{sb} - T_v) + (X_a - X_b)c_{pv}(T_{va} - T_v) \quad (1)$$

Where $q_T$ it is the necessary heat (W), $\dot{m}_s$ is the solid biomass flowrate (g/s), $T_{sa}$ is feed temperature (°C), $T_v$ is vaporization temperature (°C), $T_{sb}$ is final temperature of the solids (°C). $T_{va}$ is final stream temperature (°C), $\lambda$ is latent heat of vaporization (J/g°C). $c_{ps}$, $c_{pL}$, $c_{pv}$ are the specific heats of solid, liquid and vapor (J/g°C).

$$q_T = \dot{m}_s c_{sb}(T_{hb} - T_{ha}) \quad (2)$$

In equation (2), $c_{sb}$ is the gas heat capacity for inlet moisture (J/g°C), $T_{hb}$ is hot gas inlet temperature (°C), $T_{hb}$ is hot gas outlet temperature (°C).

$$q_T = UA\overline{\Delta T} \quad (3)$$

In equation (3), $U$ is the overall heat transfer coefficient (W/m²°C), $A$ is the area and $\overline{\Delta T}$ is the average temperature difference (°C).

For the grinding stage the main equations is [10]:

$$\frac{P}{\dot{m}} = 0.3162 W_i \left(\frac{1}{\sqrt{D_{pb}}} - \frac{1}{\sqrt{D_{pa}}}\right) \quad (4)$$

Where P is the power (kW), $\dot{m}$ is the waste stream rate (t/h), $D_{pb}$ is the particle size at outlet (mm),$D_{pa}$ is the particle size at inlet (mm) and $W_i$ is work index (kW/t) [11].

For the extraction stage, equation 5 was used:

$$Y = 0.009621 - 0.0028125A + 0.0010875B - 0.0014875C + 0.00525D + 0.00045AB + 0.00265AC - 0.0022875AD - 0.000775BC + 0.0000375BD - 0.0009625CD \quad (5)$$

Where $Y$ is the amount of lycopene (mg/g) extracted from the biomass. A, B, C and D are the normalized temperature, residence time, acetone/n-hexane ratio, and volume of solvent mixture, respectively. This extraction model was obtained from experimental data [6]. The normalization of the variables is given by:

$$L_{Ni} = (L_i - L_{Lower})/(L_{Upper} - L_{Lower}) \quad (6)$$

Where $L_{Ni}$ is the value of normalized variable $L_i$, $L_{Upper}$ is de upper limit of variable i and $L_{Lower}$ is the lower limit of variable i.

For the solvent separation and lycopene purification stage, the flash tank and the distillation column were modeled in Aspen Plus. These devices were linked to Python to run the process continuously.

## Optimization variables

For this problem, seven variables were considered,

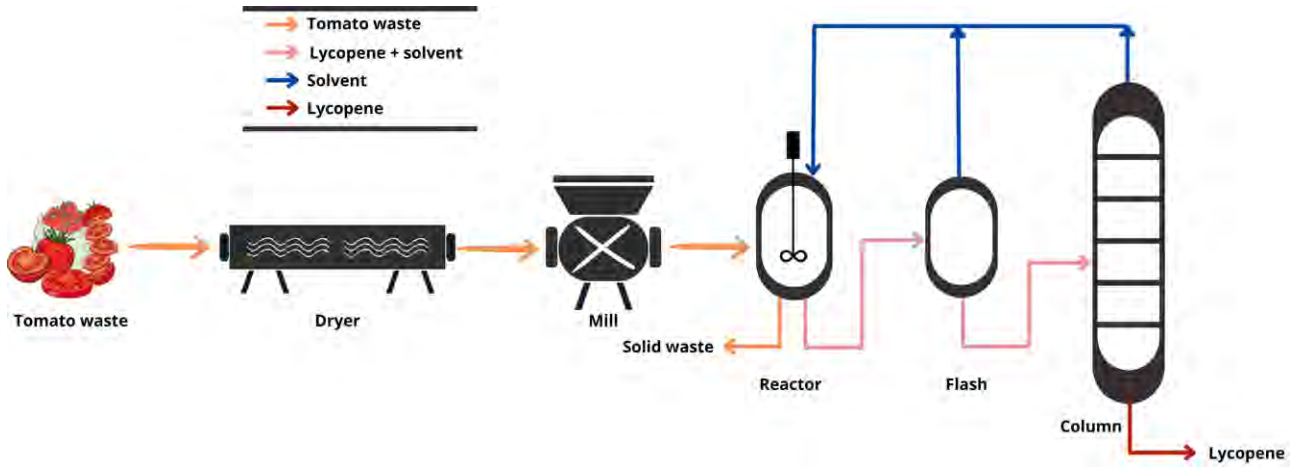



**Figure 1:** Diagram of the lycopene production process.

the first four correspond to the variables of the lycopene extraction model and the other three variables correspond to the distillation column for purification. These variables and their limits are presented in Table 1.

**Table 1:** Optimization variables for lycopene production.

| Variable | Symbols | Units | Limits |
|---|---|---|---|
| Temperature | $T_{ext}$ | °C | [30, 50] |
| Residence time | t | min | [1, 60] |
| Acetone/n-hexane ratio | A:H | % | [25, 75] |
| Volume of solvent mixture | $V_{solv}$ | L | [10, 30] |
| Number of stages | $N_t$ | - | [5, 20] |
| Feed stage | $N_F$ | - | [1, $N_t$] |
| Reflux ratio | | - | [0.1, 2] |

The feed stage has a dynamic upper limit, Herrera-Velázquez et.al. worked with these kinds of limits [12], as it depends on the number of total stages selected. This strategy prevents the feed stage from taking a value greater than the total number of stages in the column.

## Process optimization

The mathematical model implemented in Python and linked with Aspen Plus used the Pymoo environment [13]. Having a model that includes the link with Aspen Plus, where the exact equations to be considered are not explicitly available, made stochastic optimization an adequate approach, where the use of Pymoo can be advantageous [14]. The optimization was performed using the genetic algorithm (GA) method considering a population of 100 individuals with 21 generations, implying a total of 2100 evaluations.

## Objective function

The objective function is the total annual cost (TAC). To calculate the equipment cost the Guthrie method [15] and the equations presented by Turton et al. [16] were used. Equipment cost has been adjusted to 2023 with a CEPCI of 797.9. Additionally, five years of payback time are assumed. Cost calculations are represented by equations (7), (8) and (9).

$$CT_{equip} = \sum_{i=1}^{7} C_{i,equip} \quad (7)$$

$$CT_{oper} = \sum_{i=1}^{n} C_{i,cooling} + \sum_{i=1}^{n} C_{i,steam} + \sum_{i=1}^{n} C_{i,elect} + \sum_{i=1}^{n} C_{i,solvent} \quad (8)$$

$$TAC = CT_{oper} + \left( \frac{CT_{equip}\left(\frac{CEPCI\ 2023}{CEPCI\ 2001}\right)}{payback\ time} \right) \quad (9)$$

Where, $C_{i,equip}$ is the cost of each of equipment (USD), considering in addition to the five main equipment, the condenser and reboiler of the distillation column. $CT_{equip}$ is the total cost of equipment (USD), $C_{i,cooling}$ is the cooling utility cost (USD/yr), $C_{i,stream}$ is the steam utility cost (USD/yr). $C_{i,elect}$ is the cost of electricity (USD/yr), $C_{i,solvent}$ is the cost of solvent used in the process (USD/yr), $CT_{oper}$ is operating cost (USD/yr), and $TAC$ is the total annual cost (USD/yr).

A flowchart of the optimization algorithm is shown in Figure 2.

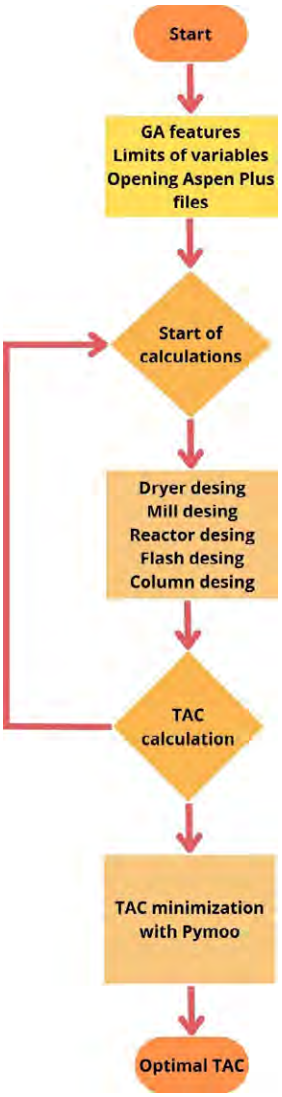



**Figure 2.** Flowchart of the optimization process.

## Base case

The base case contemplates the following values of the optimization variables: a temperature of 40°C, a residence time of 30.5 min, an acetone/n-hexane ratio of 50%, a solvent volume of 50 L, 6 stages in the distillation column with feed in the 3rd stage and a reflux ratio of 0.9, for a lycopene purity of 95%mol. The values of the variables associated to the extraction stage (A, B, C and D)

correspond to the central points for the boundaries shown in Table 1. On the other hand, the values for the design variables of the distillation column have been obtained from short-cut methods. This case is compared with the design obtained from optimization.

## RESULTS

### TAC optimization

The Python code linked to Aspen Plus for TAC minimization was run using Pymoo with GA, a population of 100 individuals and 21 generations. The algorithm took a total of 81.33 minutes to execute the allotted 2100 evaluations. Figure 3 shows how the algorithm progressed in seeking to minimize TAC over the iterations. A greater dispersion in the results is observed in the first iterations, the red line marks the best solution found at that time and continues to be compared, showing that out of 2100 option evaluated, 1957 converged and at that time the change between the solution found stabilizes and finds the optimum.

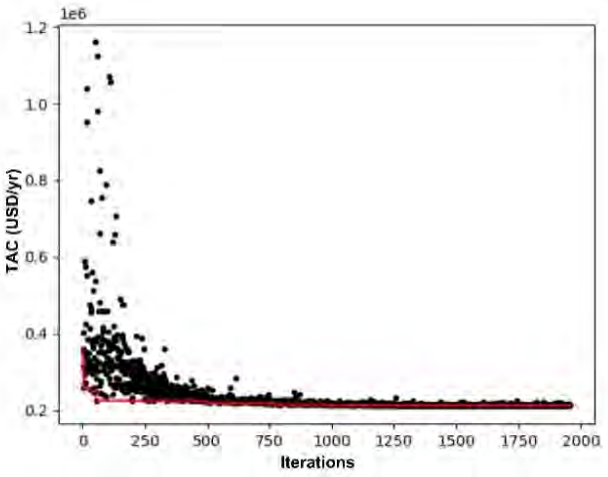



**Figure 3.** Iterations vs TAC.

### Comparison between solutions

Table 2 shows a comparison between the variables and the TAC value between the base case and the optimized solution. The results show that the optimal solution requires a higher temperature as well as a longer residence time and reflux ratio compared to the base case. The favorable solvent ratio is 25% acetone and 75% hexane, and a volume of 10 liters of solvent is sufficient. For the case of distillation column, it requires one less stage than the base case and the feed is kept on the third stage. The optimal solution shows a reduction of the TAC by 147,575.7 USD/yr, equivalent to a reduction of 41.07% of the total annual cost. Table 3 shows more details of the lycopene production process for the optimal solution.

**Table 2:** Comparison of the base case and the optimal solution.

| Variable | Units | Base case | Optimal Solution |
|---|---|---|---|
| Temperature | °C | 40 | 49.89 |
| Residence time | min | 30.5 | 51.39 |
| Acetone/n-hexano ratio | % | 50 | 25 |
| Volume of solvent mixture | L | 50 | 10 |
| Number of stages | - | 6 | 5 |
| Feed stage | - | 3 | 3 |
| Reflux ratio | - | 0.9 | 1.29 |
| **TAC** | **USD/yr** | **359,267.9** | **211,692.2** |

The study allowed obtaining relevant details of the process and the characteristics of the equipment that allow the TAC to be 211,692.2 USD/yr for a production of 2.29 g/h of lycopene, starting from 1000 kg/h of tomato waste. For this desing, the dryer, the mill and the flash tank are equipment that have no optimization variables, so these equipment behave in a similar way during the optimization process. The reactor and the distillation column are the equipment that present the greatest changes in the operating variables and dimensions.

The lycopene/acetone-n-hexane mixture is easy to separate and therefore the thermal loads in the flash tank, the condenser and the reboiler of the distillation column have low values. The solvent/lycopene ratio is something that can affect the maximum purity that can be achieved in the column, since if there is too little lycopene compared to the solvent, more energy is required. Here, it is important to highligh that the reboiler temperature must not be higher than 80°C, since the lycopene can start to degrade. Therefore, it is important to take care of the operating conditions of the distillation column to avoid damaging the product.

## CONCLUSIONS

The results indicate that it is possible to develop and optimize a lycopene production process from tomato waste. The design was obtained using Python linked to Aspen Plus, then optimized with a genetic algorithm to minimize the TAC. The results show that the optimized processs achieved a TAC of 211,692.2 USD/yr, reducing the initial TAC of 359,267.9 USD/yr by 41.07%. This study was carried out for a specific experimental model of lycopene extraction, but there are other mathematical extraction models in the literature that are good to be

able to compare in the future to explore other alternatives, especially in terms of solvents, to be used to improve the lycopene extraction process. Lycopene extraction models have only reached the formulation of an extraction polynomial or response surfaces, but considering the design on a large scale, it allows to visualize which aspects are important to improve for scaling-up such route for the conversion of wastes into a valuable product.

**Table 3:** Details of the optimal solution.

| Equipment | Variable | Units | Result |
|---|---|---|---|
| Dryer | Area | $m^2$ | 1.8 |
| | Cost | USD | 19,853.49 |
| Mill | Volume | $m^3$ | 43.78 |
| | Power | kW | 51.84 |
| | Cost | USD | 258,332.00 |
| Reactor | Volume | $m^3$ | 13.12 |
| | Residence time | min | 51.39 |
| | Temperature | °C | 49.89 |
| | Cost | USD | 258,332.00 |
| Flash | Volume | $m^3$ | 10.60 |
| | Pressure | atm | 1.0 |
| | Temperature | °C | 70 |
| | Qh | kW | 14.67 |
| | Cost | USD | 240,400.52 |
| Column | Pressure | Atm | 0.1 |
| | Volume | $m^3$ | 0.3 |
| | H | m | 1.82 |
| | Stages | - | 5 |
| | Feed stage | - | 3 |
| | Reflux ratio | - | 1.29 |
| | Cost | USD | 75,849.65 |
| Condenser | Area | $m^2$ | 1.0 |
| | Qc | kW | 0.000118 |
| | Cost | USD | 31,867.17 |
| Reboiler | Area | $m^2$ | 1.0 |
| | Qh | kW | 0.000117 |
| | Cost | USD | 31,867.17 |
| | Operating cost | USD | 28,393.79 |
| | TAC | USD/yr | 211,692.2 |
| | Tomato waste | Kg/h | 1000.00 |
| | Lycopene production | g/h | 2.29 |


## ACKNOWLEDGEMENT

The authors thank Universidad de Guanajuato and Universidad de Salamanca for supporting this work, and JCyL SA085P24 funding. N.V. Hernández-Camacho acknowledge SECIHTI for the scholarship granted to develop her doctoral studies.


## REFERENCES


1. United Nations. The Sustainable Development Goals Report: Special Edition (2023). https://unstats.un.org/sdgs/report/2023/The-Sustainable-Development-Goals-Report-2023.pdf (accessed September 20, 2024).
2. Montaño Méndez IE, Valenzuela Patrón IN, Villavicencio López KV. Competitividad del tomate rojo de México en el mercado internacional: análisis 2003-2017. *Revista Mexicana de Ciencias Agrícolas* 12 (7): 1185-1197 (2021). https://doi.org/10.29312/remexca.v12i7.2531
3. Méndez-Carmona JY, Ascacio-Valdez JA, Alvarez-Perez OB, Hernández-Almaraz AY, Ramirez-Guzman N, Sepúlveda L, Aguilar-González MA, Ventura-Sobrevilla JM, Aguilar CN. Tomato waste as a bioresource for lycopene extraction using emerging technologies. *Food Biosci* 49: 101966 (2022) https://doi.org/10.1016/j.fbio.2022.101966
4. Kuvendziev S, Lisichkov K, Marinkovski M, Stojchevski M, Dimitrovski D, Andonovikj V. Valorization of tomato processing by-products: Predictive modeling and optimization for ultrasound-assisted lycopene extraction. *Ultrason Sonochem* 110: 107055 (2024) https://doi.org/10.1016/j.ultsonch.2024.107055
5. Catalkaya G, Kahveci D. Optimization of enzyme assisted extraction of lycopene from industrial tomato waste. *Sep Purif Technol* 219:55-63 (2019) https://doi.org/10.1016/j.seppur.2019.03.006
6. Poojary MM, Passamonti P. Optimization of extraction of high purity all-trans-lycopene from tomato pulp waste. *Food Chem* 188:84-91 (2015) http://dx.doi.org/10.1016/j.foodchem.2015.04.133
7. Kaur D, Wani AA, Oberoi DPS, Sogi DS. Effect of extraction conditions on lycopene extraction from tomato processing waste skin using response surface methodology. *Food Chem* 108:711-718 (2008) https://doi.org/10.1016/j.foodchem.2007.11.002
8. Dolatabadi Z, Rad AHE, Farzaneh V, Feizabad SHA, Estiri SH, Bakhshabadi H. Modeling of the lycopene extraction from tomato pulps. *Food Chem* 190:968-973 (2016) http://dx.doi.org/10.1016/j.foodchem.2015.06.069
9. Huang W, Li Z, Niu H, Li D, Zhang J. Optimization of

operating parameters for supercritical carbon dioxide extraction for lycopene by response surface methodology. *J Food Eng* 89: 298-302 (2008) http://dx.doi.org/10.1016/j.jfoodeng.2008.05.006
10. McCabe WL, Smith JC, Harriott P. Operaciones Unitarias en Ingeniería Química. Mc Graw Hill (2007)
11. Williams O, Eastwick C, Kingman S, Giddings D, Lormor S, Lester E. Investigation into the applicability of Bond Work Index (BWI) and Hardgrove Grindability Index (HGI) tests for several biomasses compared to Colombian LA Loma coal. *Fuel* 158: 379-387 (2015) http://dx.doi.org/10.1016/j.fuel.2015.05.027
12. Herrera-Velázquez JJ, Cabrera-Ruiz J, Alcántara-Avila J, Hernández-Hernández EJ, Perez-Gudiño MA, Luna-Perez R, Hernández S. Optimization of the bioethanol dehydration process using $MgCl_2$ as mass separating agent. *Chem Eng Process* 201:109809 (2024) https://doi.org/10.1016/j.cep.2024.109809
13. Blank J, Deb K. Pymoo: Multi-Objective Optimization in Python. *IEEE Access* 8: 89497-89509 (2020) https://doi.org/10.1109/ACCESS.2020.2990567
14. Moriwaki M, Herrera-Velázquez JJ, Cabrera Ruiz J, Matsuda K, Alcántara-Avila R. Synthesis of hybrid membrane distillation processes with optimal structures for ethanol dehydration. *Comput Chem Eng* 178: 108385 https://doi.org/10.1016/j.compchemeng.2023.108385
15. Guthrie KM. Data and techniques for preliminary capital cost estimating. *Chem Eng* 114-142 (1969)
16. Turton R, Shaeiwitz J, Bhattacharyya D, Whiting W. Analysis, Synthesis, and Design of Chemical Processes. Pearson Education (2018)

© 2025 by the authors. Licensed to PSEcommunity.org and PSE Press. This is an open access article under the creative commons CC-BY-SA licensing terms. Credit must be given to creator and adaptations must be shared under the same terms. See https://creativecommons.org/licenses/by-sa/4.0/



Systems & Control Transactions

**Research Article - Peer Reviewed Conference Proceeding**
ESCAPE 35 - European Symposium on Computer Aided Process Engineering
Ghent, Belgium. 6-9 July 2025
Jan F.M. Van Impe, Grégoire Léonard, Satyajeet S. Bhonsale,
Monika E. Polańska, Filip Logist (Eds.)

PSE PRESS

# Optimizing Crop Schedules and Environmental Impact in Climate-Controlled Greenhouses: A Hydroponic vs. Soil-Based Case Study

**Sarah Namany, Farhat Mahmoud, Tareq Al-Ansari***

Hamad Bin Khalifa University, College of Science and Engineering, Qatar Foundation, Doha, Qatar
* Corresponding Author: talansari@hbku.edu.qa.

## ABSTRACT

Optimizing greenhouse operations in arid regions is essential for sustainable agriculture due to limited water resources and high energy demands for climate control. This paper proposes a multi-objective optimization framework aimed at minimizing both the operational costs and environmental emissions of a climate-controlled greenhouse. The framework determines optimal allocation of growing area among three crops (tomato, cucumber, and bell pepper) throughout the year. These crops were selected for their varying growth conditions, which induce variability in energy and water inputs, providing a comprehensive assessment of the optimization model. The model integrates factors such as temperature, humidity, light intensity, and irrigation requirements specific to each crop. It is solved using a genetic algorithm combined with Pareto front analysis to address the multi-objective nature effectively. This approach facilitates the identification of optimal trade-offs between cost, emissions, and yield, offering a set of efficient solutions for decision-makers. Applied to a greenhouse in Qatar, the model evaluates two scenarios: a hydroponic system and a conventional soil-based system. Results indicate that the multi-objective optimization effectively reduces operational costs and environmental emissions while fulfilling crop demand.The hydroponic scenario demonstrates higher water-use efficiency, resulting in lower overall emissions despite higher initial setup expenses. The soil-based system shows higher emissions due to increased fertilizer use and water consumption. The optimized allocation balances multiple crops simultaneously throughout the year based on seasonal conditions, enhancing overall sustainability. This study underscores the potential of advanced optimization techniques in enhancing the efficiency and sustainability of greenhouse agriculture in challenging environments.

**Keywords**: Multi-Objective Optimization, Hydroponics, Climate-controlled Agriculture, Greenhouses

## INTRODUCTION

### Background

The growing global demand for food, coupled with the challenges posed by climate change and resource scarcity, has intensified the need for innovative agricultural practices. In arid regions, the situation is particularly critical, as extreme temperatures, limited water availability, and high energy requirements create significant obstacles for sustainable food production. Greenhouse agriculture has emerged as a viable solution to address these challenges by enabling controlled environments for crop cultivation. However, optimizing greenhouse operations to balance resource use, operational costs, and environmental impact remains a complex task.

Greenhouses offer a controlled environment that can mitigate the adverse effects of harsh climatic conditions, making them indispensable in arid regions. By regulating factors such as temperature, humidity, and light intensity, greenhouses facilitate year-round cultivation and higher yields. Nevertheless, maintaining these conditions requires substantial water and energy inputs, particularly for cooling and irrigation systems, which can increase costs and environmental emissions. To ensure the

sustainability of greenhouse agriculture, it is imperative to adopt strategies that optimize resource allocation while minimizing operational expenses and environmental impacts [1].

Research on greenhouse optimization in arid climates covers a broad spectrum of topics, including water management, energy efficiency, and crop scheduling. Early work by [2] demonstrated the advantages of greenhouse cultivation for extending growing seasons and improving crop yields in regions with scarce water resources. In parallel, studies have shown that precise climate control systems significantly reduce water wastage and energy consumption, particularly when combined with automation technologies [3]. Furthermore, recent investigations by [4] have highlighted the potential of integrating renewable energy sources, such as solar power, to reduce the carbon footprint of greenhouse operations.

Hydroponic systems have emerged as one promising avenue for achieving high water-use efficiency [5]. Compared to conventional soil-based approaches, hydroponics can lower water consumption while maintaining or even enhancing crop yield. Additionally, the nutrient solution in hydroponic setups can be carefully regulated and recycled, minimizing both resource use and environmental discharge. Despite these advantages, challenges remain in balancing initial setup costs and the technical expertise needed to maintain such systems, as indicated by [6].

Multi-objective optimization has also been widely explored to identify trade-offs between economic viability and environmental sustainability. By employing advanced computational methods such as genetic algorithms, researchers have been able to analyze various configurations of crop types, resource allocations, and climate control strategies, revealing Pareto-optimal solutions that can guide policymakers and greenhouse operators [7]. However, many existing models focus on one or two objectives (e.g., water or energy), highlighting the need for a holistic framework that simultaneously considers cost, emissions, and other operational constraints.

These studies highlight the importance of a multifaceted approach to greenhouse optimization in arid environments. By building prior work in water management, energy efficiency, and multi-objective optimization, the present study seeks to advance the state of the art through an integrated framework that addresses the complex interplay of cost, emissions, and resource limitations in a comprehensive manner.

### Objectives and Outline

This study aims to create an integrated optimization framework that enhances the sustainability of climate-controlled greenhouse operations, particularly in arid regions. The research focuses on three interconnected objectives. Firstly, it aims to minimize operational costs, specifically targeting water and energy expenses, which are significant contributors to overall costs. Secondly, it seeks to reduce environmental emissions linked to energy consumption and cooling needs. Finally, the study emphasizes the importance of maintaining adequate crop diversity to satisfy market demands and strengthen agricultural resilience against climatic and economic challenges.

Following this introduction, the data and methods describe the methodology, detailing the mathematical formulation, decision variables, objectives, and constraints. Afterward, the case study section focuses on the implementation of the genetic algorithm, emphasizing how multi-objective optimization is employed to handle competing goals. Then, the results are presented and analyzed, offering insights into the trade-offs between cost and emissions under the two cultivation scenarios. Finally, the conclusion concludes by summarizing the key findings, discussing the implications for greenhouse operations in arid regions, and suggesting avenues for further research.

## DATA AND METHODS

### Case study

This study develops an optimization framework to enhance the sustainability of climate-controlled greenhouse operations in arid regions, notably in Qatar. Greenhouses located in these areas face unique challenges, such as extreme temperatures, water scarcity, and high electricity demands for cooling and irrigation purposes. Addressing these challenges requires a holistic approach that accounts for the tradeoffs between economic costs, environmental impacts, and resource constraints. The proposed framework introduces a multi-objective optimization model that determines efficient allocation of growing area to multiple crops simultaneously, aiming to reduce greenhouse emissions and costs while satisfying market demands. A case study was conducted to evaluate the framework's applicability to a medium-scale greenhouse in Qatar. The greenhouse was designed to cultivate three crops: tomato, cucumber, and bell pepper, selected for their economic value, varying resource requirements, and high consumption in the local market. The study considered two cultivation systems: a hydroponic system, which offers higher water-use efficiency and precise nutrient management, and a conventional soil-based system, which is more commonly adopted but generally less efficient in water usage. The optimization model was tailored to reflect the specific environmental conditions of Qatar, taking into consideration the average monthly temperatures, water availability, and electricity prices. The methodology integrates multi-objective optimization and scenario analysis to achieve operational efficiency while minimizing environmental emissions. The

subsequent section describes the mathematical formulation utilized in this model.

**Table 1:** Key data used in the optimisation model.

| Parameter | Value | Unit |
|---|---|---|
| Average Monthly Temp. | 25 – 40 | °C |
| Water Availability | 1000 - 1500 | Liters/day |
| Energy Cost | 0.12 - 0.15 | USD/kWh |
| Water Cost | 0.05 - 0.07 | USD/Liter |
| Greenhouse Area | 500 | m² |
| Heat Transfer Coeff | 5 - 6 | W/(m²·K) |
| Cooling Capacity | 30000 | BTU/h |

## Mathematical Formulation

This model optimizes the operational cost, environmental emissions, and crop yield of a climate-controlled greenhouse. The greenhouse is designed to grow three crops: tomato, cucumber, and bell pepper, over a 12-month period with the ability to allocate different percentages of growing area to each crop monthly. The mathematical formulation of the multi-objective optimization problem is presented below:

*Objective functions:*

Minimize the operational cost (*C*):

$$C = \sum_{j=1}^{12} \sum_{i} \left( W_i \cdot x_{ij} \cdot c_w + E_i \cdot x_{ij} \cdot c_e \right) \quad (1)$$

Where:

$i \in \{Tomato, Cucumber, Bell\ Pepper\}$

$j \in \{1,2,\ldots,12\}$

$W_i$: Water requirement of crop *i* (liters/month).

$c_w$: Cost per unit of water.

$E_i$: Energy requirement of crop *i* (kWh/month).

$E_i$: Cost per unit of energy.

Minimize Environmental Emissions (*E*):

$$E = \sum_{j=1}^{12} \sum_{i} \left( E_i \cdot x_{\{ij\}} \cdot e_e + Q_{\{ij\}} \cdot e_c \right) \quad (2)$$

where:

$i \in \{Tomato, Cucumber, Bell\ Pepper\}$

$e_e$: Emission factor per unit of energy.

$Q_{ij}$: Cooling load for crop *i* in month *j*, calculated as:

$$Q_{ij} = U \cdot A \cdot \Delta T_{ij} \quad (3)$$

*U* : Heat transfer coefficient (W/m²·K).

*A:* Greenhouse surface area (m²).

$\Delta T_{ij}$: Temperature difference between the greenhouse interior and the external environment for crop *i* during month *j.*

$e_c$: Emission factor for cooling load (kg $CO_2$ per unit energy).

*Decision variable:*

$x_{ij} \in \{0,1\}$ is the binary decision variable such that $x_{ij}=1$ if crop *i* is cultivated during month *j*, and $x_{ij}=0$ otherwise.

Subject to the following constraints:

Crop Diversity Constraint: To meet market demands and ensure crop diversity, each crop must be cultivated at least once annually:

$$\sum_{j=1}^{12} x_{ij} \geq 1 \quad (4)$$

Water usage constraint**:** The total water usage across all crops must not exceed the annual water availability, which is equal to 2000 L/day:

$$\sum_{j=1}^{12} \sum_{i} \left( W_i \cdot x_{ij} \right) \leq water\ limit \quad (5)$$

Energy usage constraint: The total energy consumption must not exceed the available energy budget, which is equal to 25000 kWh/day:

$$\sum_{j=1}^{12} \sum_{i} \left( E_i \cdot x_{ij} \right) \leq energy\ limit \quad (6)$$

Cooling capacity constraint: The total cooling load must remain within the greenhouse's cooling capacity, which is equal to 300,000 BTU/h:

$$\sum_{j=1}^{12} \sum_{i} \left( Q_i \cdot x_{ij} \right) \leq Cooling\ capacity \quad (7)$$

Monthly cultivation constraint**:** Only one crop can be cultivated in the greenhouse during each month:

$$\sum_{i} x_{ij} = 1 \quad (8)$$

Non-negativity and binary constraints: The decision variables are binary:

$$x_{ij} \in \{0,1\}, = \forall i,j$$

A genetic algorithm (GA) is employed to solve the multi-objective optimization problem. The GA is chosen due to its robustness in handling complex, non-linear problems with multiple objectives and constraints.

## Scenario Analysis

The optimization framework is applied to two scenarios. The first scenario assumes the greenhouse is equipped with a hydroponic system, which allows for precise control of water and nutrients.Hydroponic systems reduce water usage by up to 30-40% compared to soil-based systems and optimize fertilizer application to match plant growth requirements, minimizing waste. Energy demand in this scenario is primarily for pumping water and maintaining nutrient solutions, with substantial requirements for climate control in Qatar's hot environment.

The second scenario represents a traditional soil-based cultivation approach. Soil systems typically have higher water requirements due to evaporation and less efficient delivery methods. Nutrient delivery is less precise, potentially leading to higher fertilizer use and leaching. The model accounts for these differences by adjusting the water efficiency parameters and nutrient costs appropriately. Each scenario is evaluated for its ability to meet crop demands while minimizing costs and emissions. The model allows for simultaneous cultivation of multiple crops with flexible area allocation, reflecting real-world greenhouse operations. This approach enables more efficient resource utilization as different crops can be allocated optimal space based on their specific requirements and market value during each month.

## Results and discussion

This section presents the outcomes of the multi-objective genetic algorithm applied to optimize greenhouse operations in the two scenarios described previously: hydroponic and soil-based systems. The results focus on (i) cost, emissions, and yield trade-offs, (ii) monthly resource usage, and (iii) crop distribution over the 12-month planning horizon.The genetic algorithm was executed for 50 generations with a population size of 100 individuals. The optimization yielded a set of Pareto-optimal solutions representing different trade-offs between operational cost, environmental emissions, and crop yield. Figure 1 illustrates the 3D Pareto front, showing the relationship between operational cost (USD), environmental emissions (kg $CO_2$-eq), and total yield (kg) for both systems. The results reveal distinct regions in the solution space for each cultivation system. The hydroponic system generally occupies a region with higher costs but lower emissions, while the soil-based system shows lower costs but higher emissions. This pattern aligns with the inherent characteristics of each system: hydroponic systems require higher initial investment and maintenance but offer better resource efficiency. Table 2 summarizes key indicators for the best Pareto-optimal solution identified in each scenario based on the optimization results.Figure 1. Pareto-optimal solution.

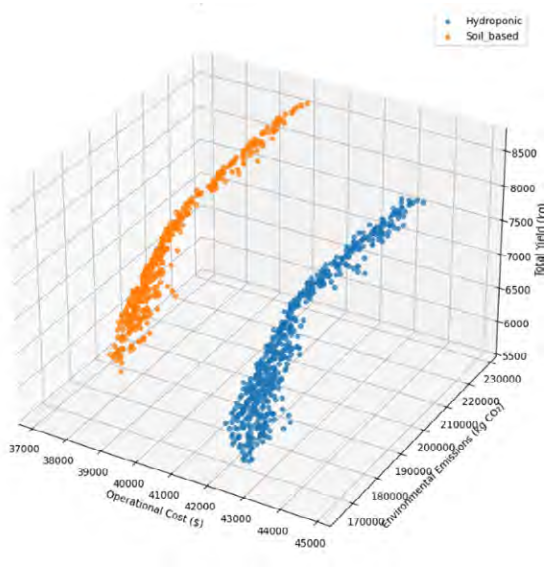



**Table 2.** Comparison of key performance metrics between Cultivation Systems

| Metric | Hydroponic System | Soil-Based System | Difference (%) |
|---|---|---|---|
| Total Operational Cost ($) | 39,682.43 | 35,174.01 | -11.36 |
| Environmental Emissions (kg $CO_2$) | 170,842.96 | 186,321.28 | 9.06 |
| Water Usage (liters) | 218,636.69 | 328,635.76 | 50.31 |
| Energy Usage (kWh) | 290,353.62 | 288,190.91 | -0.74 |
| Total Yield (kg) | 5,910.15 | 5,686.28 | -3.79 |

The optimization results reveal several important insights regarding greenhouse operations in Qatar's arid climate. In terms of operational costs, the soil-based system shows an 11.36% cost advantage over the hydroponic system. This finding might initially seem counterintuitive given hydroponics' reputation for efficiency. However, it reflects the higher installation,

equipment, and maintenance costs associated with hydroponic systems, which offset some of their operational advantages. Despite its cost advantage, the soil-based system produces 9.06% higher environmental emissions than the hydroponic system. This difference primarily stems from the additional fertilizer emissions in soil-based cultivation and the higher water consumption, which has associated emissions from pumping and treatment. The hydroponic system's better nutrient management and recycling capabilities help reduce its overall environmental footprint. The most striking difference between the two systems is in water usage. The soil-based system requires 50.31% more water than the hydroponic system, a significant consideration in Qatar's water-scarce environment where desalination is both expensive and energy-intensive. This substantial difference in water efficiency represents a compelling advantage for hydroponics in arid regions. Interestingly, energy usage remains relatively similar between the two systems (only 0.74% difference). This result suggests that while hydroponic systems have additional energy requirements for pumping and circulation systems, these are largely offset by the soil-based system's potentially higher cooling needs due to heat retention in the soil medium. In terms of crop yields, the soil-based system produces 3.79% less total yield than the hydroponic system. The crop-specific breakdown reveals interesting patterns: soil-based systems perform better for tomatoes (+25.14%) and bell peppers (+3.19%), while hydroponic systems excel at cucumber production (-25.93% in soil compared to hydroponic). These differences reflect the varying suitability of each crop to different growing environments and the optimization algorithm's response to these factors.

The optimized monthly crop allocation reveals a strategic approach to dealing with Qatar's climate variations. During the hottest months (May-September), the model allocates more space to heat-tolerant crops. In both systems, cucumber receives higher allocation during the hottest summer months (July-August in hydroponic; August-October in soil-based) when its water efficiency and heat tolerance provide advantages. Bell pepper, which generally requires less extreme temperatures, receives higher allocation during the milder months. Tomato allocations are strategically distributed throughout the year, with higher percentages in transitional seasons. These allocation patterns demonstrate how the optimization balances multiple factors: crop-specific requirements, seasonal temperature variations, resource constraints, and market demands. The ability to allocate growing area flexibly among multiple crops simultaneously enables more efficient greenhouse utilization compared to single-crop approaches.

In the context of Qatar's specific challenges, these results underscore the importance of considering multiple criteria when selecting greenhouse systems. While hydroponics offers clear advantages in water efficiency, critical in a water-scarce environment, soil-based systems may still be attractive for farms with limited capital or technical expertise. The model provides decision-makers with valuable information on the trade-offs involved, allowing them to select solutions that best align with their specific priorities, constraints, and environmental conditions.

## CONCLUSION

This study presents a multi-objective optimization framework tailored to the challenging climatic and resource conditions of Qatar. By simultaneously minimizing operational costs and environmental emissions while maximizing crop yield, the framework reveals important trade-offs between water-efficient hydroponic systems and more traditional soil-based approaches. The results underscore that hydroponic cultivation can substantially reduce water usage, of particular importance in a country reliant on energy-intensive desalination, while also moderating emissions through more precise nutrient management. Nevertheless, the soil-based scenario retains economic viability through lower operational costs, though it incurs higher resource consumption and resultant environmental impacts over time. A key insight from this study is the value of flexible crop allocation throughout the year. The optimization shows that simultaneously growing multiple crops with varying area allocations based on seasonal conditions can significantly improve overall greenhouse performance compared to single-crop approaches. Strategic alignment of crop allocations with monthly temperature variations can reduce both water consumption and cooling loads, thus lowering operational costs and emissions. The differences between hydroponic and soil-based systems are substantial in some metrics (particularly water usage, with a 50.31% difference) but minimal in others (such as energy usage, with only a 0.74% difference). These nuanced findings highlight the importance of comprehensive analysis that considers multiple factors rather than focusing on single metrics when evaluating greenhouse systems. These insights are particularly valuable for policymakers, agricultural planners, and greenhouse operators seeking to optimize production efficiency under harsh climatic constraints. Future work could expand upon this research by integrating real-time climate data, exploring additional crop varieties, or leveraging renewable energy sources to further mitigate environmental impacts and foster resilient, cost-effective greenhouse systems in Qatar and beyond.

## ACKNOWLEDGEMENTS

This research is supported by Hamad Bin Khalifa University (HBKU) and the Qatar National Research Fund (QNRF), members of Qatar Foundation.

## REFERENCES

1. Namany S, Al-Ansari T. Energy, water, food nexus decision-making for sustainable food security. In: Muthu SS (ed) The water–energy–food nexus. Environmental footprints and eco-design of products and processes 4:32–42 (2021) https://doi.org/10.1007/978-981-16-0239-9_7
2. Singh S, Singh DR, Velmurugan A, Jaisankar I, Swarnam TP. Coping with climatic uncertainties through improved production technologies in tropical island conditions. In: Sivaperuman C, Velmurugan A, Singh AK, Jaisankar I (eds) Biodivers Clim Chang Adapt Trop Islands 4:623–666 (2008) https://doi.org/10.1016/B978-0-12-813064-3.00023-5
3. Ajagekar A, Mattson NS, You F. Energy-efficient AI-based control of semi-closed greenhouses leveraging robust optimization in deep reinforcement learning. Adv Appl Energy 9:100119 (2023) https://doi.org/10.1016/j.adapen.2022.100119
4. Khalaf KA, Gamil A, Attiya B, Cuello J. Exploring the potential of concentrating solar power technologies for vertical farming in arid regions: the case of Western Iraq. Energy Sustain Dev 77:101310 (2023) https://doi.org/10.1016/j.esd.2023.101310
5. Fuentes-Peñailillo F, Gutter K, Vega R, Silva GC. New generation sustainable technologies for soilless vegetable production. Horticulturae 10:49 (2024) https://doi.org/10.3390/horticulturae10010049
6. Khatri L, Kunwar A, Bist DR. Hydroponics: advantages and challenges in soilless farming. Big Data Agric (BDA) 6:81–88 (2024)
7. Liang Y, Hui CW, You F. Multi-objective economic-resource-production optimization of sustainable organic mixed farming systems with nutrient recycling. J Clean Prod 196:304–330 (2018) https://doi.org/10.1016/j.jclepro.2018.06.040

© 2025 by the authors. Licensed to PSEcommunity.org and PSE Press. This is an open access article under the creative commons CC-BY-SA licensing terms. Credit must be given to creator and adaptations must be shared under the same terms. See https://creativecommons.org/licenses/by-sa/4.0/



Systems & Control Transactions

**Research Article - Peer Reviewed Conference Proceeding**
ESCAPE 35 - European Symposium on Computer Aided Process Engineering
Ghent, Belgium. 6-9 July 2025
Jan F.M. Van Impe, Grégoire Léonard, Satyajeet S. Bhonsale,
Monika E. Polańska, Filip Logist (Eds.)

PSE PRESS

# Computer-Aided Design of a Local Biorefinery Scheme from Water lily (*Eichhornia Crassipes*) to Produce Power and Bioproducts

**Maria de Lourdes Cinco-Izquierdo [a], Araceli Guadalupe Romero-Izquierdo [b]*, Ricardo Musule-Lagunes [b] and Marco Antonio Martínez-Cinco [a]**

[a] Universidad Michoacana de San Nicolás de Hidalgo, Facultad de Ingeniería Química, Morelia, Michoacán, México
[b] Universidad Autónoma de Querétaro, Facultad de Ingeniería, Querétaro, Querétaro, México
* Corresponding Author: araceli.romero@uaq.mx

## ABSTRACT

Water lily (*Eichhornia crassipes*) has been identified as an invasive exotic plant with high proliferation in Mexico, affecting aquatic bodies, such as lakes. After extraction, the water hyacinth biomass can be used as raw material for the production of bioproducts and bioenergy, however, the majority of them not covered the region's needs, and their economic profitability decreases significantly. Also, few reports present its use as raw material inside a biorefinery scheme. In this work, we propose a local biorefinery scheme to produce power and bioproducts from water lilies, using Aspen Plus V.10.0, per the needs of the Patzcuaro Lake community in Michoacán, Mexico. The scheme has been designed to process the harvested and sun-dried water lily from 197.6 kg/h of total wet harvested biomass, according to the extraction region schedule. The biomass is separated: root (RT) and stems-leaves (SL). The processing scheme involves the RT combustion to produce electric power, and two processes to SL; the first one, anaerobic digestion to produce fertilizer and biogas, while, pyrolysis and gasification as second one. The biogas is converted to electricity, while, the pyrolysis products are separated in bio-oil and biochar; the last one is inserted to gasification reactor to produce syngas, and then, electric power. According with results, this scheme produces 35.6 % of fertilizer, 1 % of bio-oil, and 3.5 kWh of electric power. The scheme requires energy efficiency tools to improve its energetic performance, however, is a potential solution for the use of water lily in the region.

**Keywords**: Water hyacinth, local-biorefinery scheme, modelling and simulation, Aspen Plus.

## INTRODUCTION

The conservation of aquatic bodies is a priority issue worldwide, due their ecosystems provide essential services such as, biodiversity maintenance, nutritious soils, climatic regulation, carbon sequestration and recreational activities. However, some have been affected by high resource exploitation, changing climatic patterns, or alien plant invasions (API), which contribute to deteriorating their ecological functions and causing the loss of native species. In accordance with [1], in Mexico have been identified 665 invasive exotic plants, among them the Water lily (*Eichhornia crassipes*) stands out due to its rapid proliferation, which enables it to cover several aquatic bodies, mainly lakes, across the country. The invasive plant impacts local ecosystems and human communities, making its management a pressing environmental and economic concern. In this sense, various strategies have been proposed to control and utilize *E. crassipes*, aiming to mitigate its negative effects while exploring its potential applications [2]. After extraction, the water hyacinth biomass has been used as raw material for the production of some bioproducts and bioenergy in the form of individual processes [3-6]; nevertheless, most of these products have not covered the region´s needs or have not been produced into an integral use framework, such as a biorefinery scheme, thus, in the most of cases their technical performance and economic

profitability have not been reached. Few works have reported the use of water hyacinth into a biorefinery scheme [7-10]. In this work, we propose the modelling and simulation of a local biorefinery scheme to produce electric power and bioproducts from water lilies, using Aspen Plus V.10.0, per the needs of the Patzcuaro Lake community in Michoacan, Mexico.

## METHODOLOGY

The methodology followed for carrying out this work is presented next. As first step, the conceptual design of biorefinery scheme was proposed from physical and chemical composition of water lily, and taking account the energetic needs of Patzcuaro community. Then, the proposed biorefinery was modelled from literature information to describe the reactive systems and obtain operational conditions for each processing zone; next, the simulation was carried out using Aspen Plus V.10.0. Finally, in order to analyze the proposed scheme, two performance indicators were constructed and applied.

### Conceptual Design

Patzcuaro, small municipality of Michoacan, Mexico is a fertile region, which include a famous lake called Patzcuaro´s lake. The economy of this region includes agriculture, fishing, crafts and tourism activities around the lake. However, the water lily invasion on the lake has been a recurrent issue since long time ago. In accordance with [11], the lake posses a defined extraction schedule and the appropriate machinery to do it. According with the extraction program an average of 197.6 kg/h of water lily are extracted every year. This biomass is composed by two main compounds: root (RT, 47 wt % of total plant) and steams-leaves (SL, 53 wt % of total plant) with high moisture content, 93 % and 91.8 %, respectively. Usually the wet biomass is sun dried and its final disposal is not regulated. For this reason, in this work is proposed a biorefinery scheme from the extracted and sun-dried water lily, assuming 1 % of water content for both biomass components; its block diagram is presented in Figure 1. The processing scheme starts with RT conversion by a combustion device to obtain electric power. Then, the SL are separated in two streams with 50 wt % each one; the first one enters to an anerobic digestion process, while the second one is inserted to a pyrolysis and gasification zone. Biogas and fertilizer are obtained from anaerobic digestion, then, the biogas is used to produce power; on the other hand, pyrolysis bio-oil and biochar are obtained from pyrolysis, next, the biochar is processed by gasification to obtain syngas, which is converted to electricity.

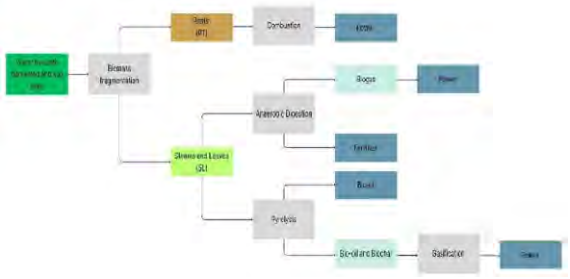


**Figure 1.** Block diagram for conceptual design of biorefinery scheme from water lily.

### Modelling and Simulation

The RT composition involves 24.53 wt % fiber, 12.31 wt % protein, 36.94 wt % carbohydrates, 5.65 wt % lipids and 20.57 wt % ash; while the SL composition is 21.44 wt % fiber, 18.90 wt % protein, 34.69 wt % carbohydrates, 8.16 wt % lipids and 16.9 wt % ash [12-13]. To model the biomass, the majority compounds (3 or 4) of each fraction for RT and SL were selected and normalized to be inserted into the simulation sheet. The flow diagram for the biorefinery scheme from Aspen Plus is presented in Figure 2. The ROOTS stream enters to mixer (MIX-1) along with 30 % excess air to carry out the combustion. The mixed stream is inserted to combustion reactor (R-COMBUS) modelled with R-Stoic module; the operational conditions were 550 °C, 1 bar and a fractional conversion for set combustion reactions of 85 %, in accordance with experimental information provided by [14]. Then, the out-stream from combustion enters to CYCLONE module to separate the solid fraction, next, the condensable compounds traces into the gas fraction (GAS-COMB) were separated by SEP module (SEP-1); the cleaned gas fraction is converted to electric power by a turbine using the COMPRESSOR module (TURB-COM). This process was modelled using the Peng-Robinson model [15].

Regarding to SL, the STE+LEAV with SL composition enters to SPLIT module (SPLIT-1) to get two streams: 50 wt % for anaerobic digestion process (SL-AD) and the other one for pyrolysis and gasification train (SL-PY-G). The SL-AD stream enters to anaerobic digestion reactor (R-AD) modelled by R-STOIC module at 38 °C and 1 bar, adding water as digestion medium (1:10, biomass to water, mass ratio) [16-17]. The out-stream from R-AD is inserted to simple separator (SEP-2, SEP module) to obtain BIOGAS and FERTILIZER. Then, the BIOGAS stream is converted to electricity by a turbine (TURBI-AD, COMPRESSOR module). In accordance with [15], the thermodynamic models used for this process were NRTL and Peng-Robinson. On the other hand, SL-PY-G stream enters to pyrolysis reactor, modelled by R-BATCH module (R-PIRO) at 329.7 °C and 1 bar, using a first order kinetic model provided by [18], specifying as stop criteria 5 h of operation. The out-stream from R-PIRO (PIRO-OUT) is

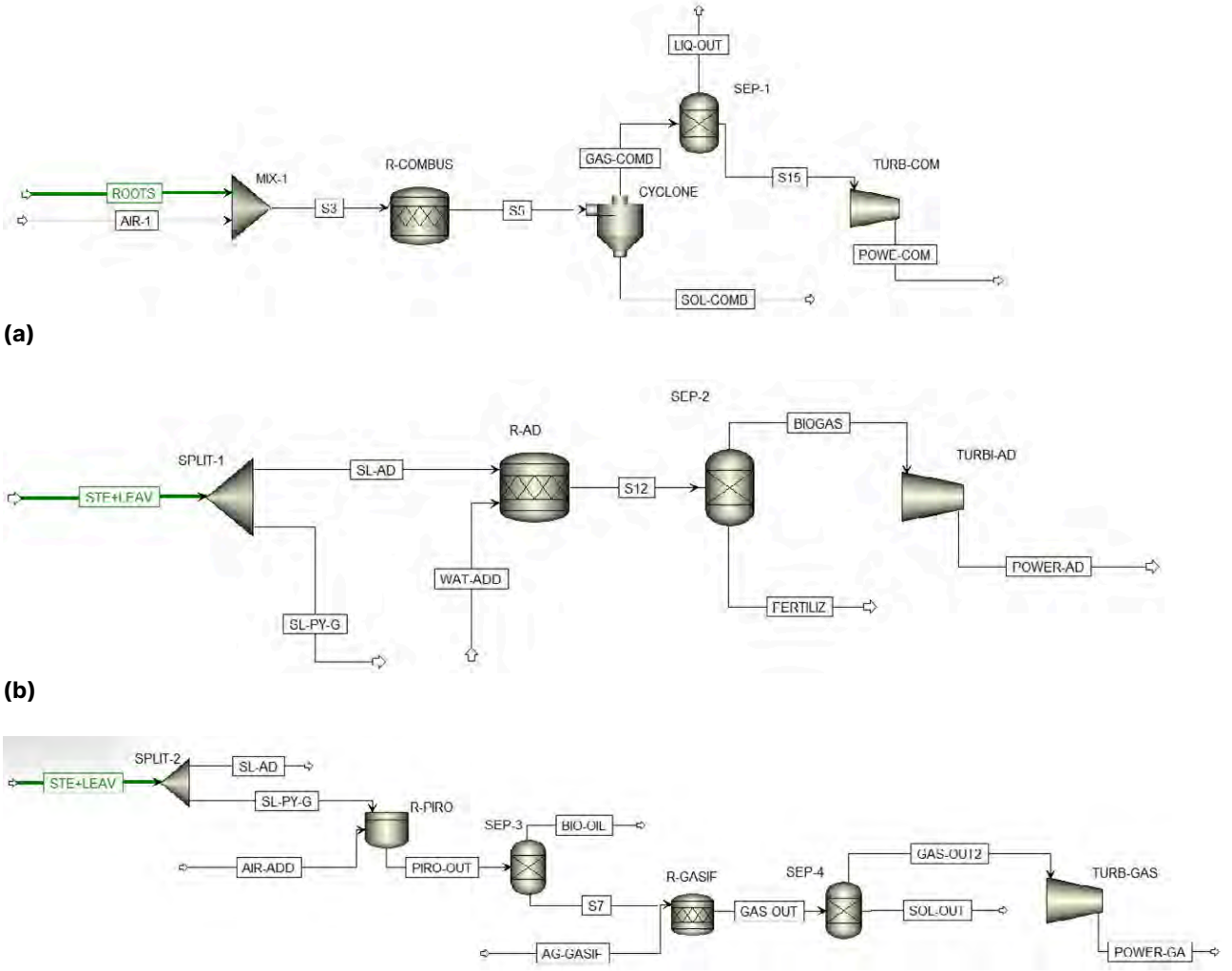



**Figure 2.** Aspen Plus flow diagram of biorefinery scheme from water lily: a) RT processing, b) SL for anaerobic digestion processing, and c) SL for pyrolysis and gasification train.

separated to remove the condensable products (BIO-OIL) using a SEP module (SEP-3); the remaining non-condensable gases and biochar were inserted to gasification reactor, modelled by R-STOIC module (R-GASIF). The operational parameters for R-GASIF were 700 °C and 1 bar, adding steam at 200 °C as gasifying agent (10 wt %, regarding the S7 stream mass) [19]. The out-stream from R-GASIF (GAS-OUT) was inserted to SEP module (SEP-4) to clean the syngas. Then, the syngas stream (GAS-OUT2) is converted to power by a turbine (TURB-GAS) using the COMPRESSOR module. The reactions set for each processing zone is provided at supplementary information section.

## Performance Indicators

To analyze the technical performance of the biorefinery scheme, two indicators are proposed next.

1.- EI-EP defined as the relation between the invested energy for the processing (reactor heating and electrical needs), regarding to the energy provided by the products.

For this case, the products considered by this indicator include the electric power provided by turbines, and pyrolysis bio-oil.

2.- PM-EM defined as the relation between total product mass generated by the scheme, including combustion gases, biogas, fertilizer, pyrolysis bio-oil and syngas, regarding to the water lily mass (RT and SL).

It is worth mentioning that according to the definition of these indicators, both are dimensionless.

## RESULTS

In this section are presented the results and their

analysis from water lily biorefinery scheme. In Table 1, 2 and 3 is presented the product distribution for outstreams after R-COMBUS, R-AD and R-PIRO+R-GASIF, respectively. As it can be observed, the proposed processes have low conversion efficiency, thus the amount of non-converted biomass is high.

**Table 1:** Mass flow at the exit of the combustion process.

| Component | Description | Mass Flow (kg/hr) |
|---|---|---|
| Unreacted biomass[a] | Non-converted biomass in the combustion process | 1.6753 |
| Combustion gases | O2 | 2.8022 |
| | N2 | 13.5634 |
| | CO2 | 1.6454 |
| | CO | 0.3901 |
| | CH4 | 0.2224 |
| | NH3 | 0.0007 |
| | NO2 | 0.0018 |

[a] Crude fiber, proteins, carbohydrates, lipids and ashes contents in the biomass that doesn't react during the process.

**Table 2:** Mass flow at the exit of the anaerobic digestion

| Component | Description | Mass Flow (kg/hr) |
|---|---|---|
| Unreacted biomass[b] | Non-converted biomass in the combustion process | 0.059 |
| Biogas | CO2 | 0.6047 |
| | CH4 | 0.2695 |
| | NH3 | 0.0012 |

[b] Crude fiber, proteins, carbohydrates, lipids and ashes contents in the biomass that doesn't react during the process.

**Table 3:** Mass flow at the exit of pyrolysis process and gasification.

| Component | Description | Mass Flow (kg/hr) |
|---|---|---|
| Unreacted biomass[c] | Non-converted biomass in the combustion process | 0.7010 |
| Bio-oil | C7H8 | 0.0909 |
| | C6H6O | 0.1128 |
| | C10H14O | 0.1483 |
| Biochar | C6H5O2 | 0.1077 |
| Gases | CO | 0.0148 |
| | CO2 | 0.0280 |
| | N2 | 13.0114 |
| | O2 | 4.0261 |
| Syngas | H2 | 0.01394 |
| | CO | 0.07537 |

[c] Crude fiber, proteins, carbohydrates, lipids and ashes contents in the biomass that doesn't react during the process.

Then, in Table 4 are presented the mass flows of each product derived from scheme. It is worth to mention that, the combustion gases, biogas and syngas were cleaned before the turbines, in order to avoid operational troubles and get electric power. In Table 5 are presented the power data derived from scheme. As it can be observed, the combustion process and pyrolysis-gasification train produce the majority of electricity. It is due to conversion aim for both processes are gaseous products with high energetic content. Also, it is noticeable that the combustion gases and fertilizer represent roughly 90 % of total obtained products.

**Table 4**. Mass flow total of products.

| Process | Product | Mass Flow (kg/hr) |
|---|---|---|
| Combustion | Combustion gases | 18.6261 |
| Anaerobic Digestion | Biogas | 0.8755 |
| | Fertilizer | 11.059 |
| Pyrolysis and Gasification | Bio-oil | 0.3520 |
| | Syngas | 0.0893 |

**Table 5**. Power produced by processing scheme.

| Process | Equipment | Power (KW) |
|---|---|---|
| Combustion | TURB-COM, | 1.5194 |
| Anaerobic Digestion | TURB-Dal | 0.035 |
| Pyrolysis and Gasification | TURB-GA | 1.944 |

Finally, in Table 6 are presented the results derived from EI-EP and PM-EM indicators. According with these results, the energy invested to processing is extensively high in comparison with the energy delivered by the products, which means that this scheme must be improved to enhance its energy efficiency. Energy efficiency tools, such as mass and energy integration or process intensification must be implemented. It is worth to mention that the EP was calculated from enthalpy values provided by simulation. On the other hand, regarding to second indicator, the products obtained from the scheme are almost 4-times less than the total mass available for processing; which means low conversion efficiency. This value must be improved by analyzing the operational conditions and using specific kinetic models to represent each processing unit.

**Table 6**. Evaluation Indicators

| Indicator | Factor | Value |
|---|---|---|
| EI - EP | EI (kW) = 2.6783E+16<br>EP (kW) = 5.6979 | 4.7006E+15 |
| PM – EM | PM (kg/h) = 51.0423<br>EM (kg/h) = 196.5502 | 0.2597 |

## CONCLUSIONS

In this work, a biorefinery scheme from water lily has been proposed, modelled and simulated using Aspen Plus V.10.0. This proposal attends to specific needs of Patzcuaro´s lake community located in Michoacan, Mexico, wherein the water lily infestation is a huge problem, affecting the natural ecosystem and local human society. The biorefinery scheme was designed to process the harvested and sun-dried biomass, in accordance with the local extraction program; also, the integrated processes into the scheme were included to generate mainly power, current demand in the region. According with results, this scheme produces 35.6 % of fertilizer, 1 % of bio-oil, and 3.5 kWh of electric power. It is important to mention that, the bio-oil can be integrated as biofuel in the combustion process to get more energy. On the other hand, regarding the indicators results, EI-EP demonstrates the need of implementing energy efficiency tools on the scheme to improve its energetic performance, while the PM-EM is almost 4-times less than the total mass available for processing, which means low conversion efficiency, thus kinetic values for each processing unit must be added to get better performance of the scheme. This proposal represents a first and integrated option to produce local bioenergy at the study region; also, in accordance with the opportunity areas detected from scheme, technical improvements could be implemented, representing a potential solution for the sustainable use of water lily in the region.

## DIGITAL SUPPLEMENTARY MATERIAL

The supplementary material for this contribution can be founded in in the next link https://acortar.link/vY7NFV.

## REFERENCES


1. Instituto Mexicano de Tecnología del Agua. Plantas Invasoras (2020).
2. Gutiérrez López, F. Arreguín Cortés, R. Huerto Delgadillo, P. Saldaña Fabela (1994). Control de malezas acuáticas en México. Ingeniería Hidráulica En México, 9(3), 15–34 (1994) https://revistatyca.org.mx/index.php/tyca/article/view/713/628
3. Malik, A. Environmental challenge vis a vis opportunity: the case of water hyacinth. Environment international, 33(1), 122-138 (2007) https://doi.org/10.1016/j.envint.2006.08.004.
4. Ganguly, A., Chatterjee, P. K., & Dey, A. Studies on ethanol production from water hyacinth—A review. Renewable and Sustainable Energy Reviews, 16(1), 966-972 (2012) https://doi.org/10.1016/j.rser.2011.09.018.
5. Amalina, F., Abd Razak, A. S., Krishnan, S., Zularisam, A. W., & Nasrullah, M. Water hyacinth (Eichhornia crassipes) for organic contaminants removal in water–A review. Journal of Hazardous Materials Advances, 7, 100092 (2022) https://doi.org/10.1016/j.hazadv.2022.100092.
6. Irewale, A. T., Dimkpa, C. O., Elemike, E. E., & Oguzie, E. E. Water hyacinth: Prospects for biochar-based, nano-enabled biofertilizer development. Heliyon (2024) https://doi.org/10.1016/j.heliyon.2024.e36966
7. Junluthin, P., Pimpimol, T., & Whangchai, N. Efficient conversion of night-blooming giant water lily into bioethanol and biogas. Maejo International Journal of Energy and Environmental Communication, 3(2), 38-44 (2021) https://doi.org/10.54279/mijeec.v3i2.245901.
8. Alam, S. N., Singh, B., & Guldhe, A. Aquatic weed as a biorefinery resource for biofuels and value-added products: challenges and recent advancements. Cleaner Engineering and Technology, 4, 100235 . (2021) https://doi.org/10.1016/j.clet.2021.100235.
9. Amulya, K., Morris, S., & Lens, P. N. Aquatic biomass as sustainable feedstock for biorefineries. Biofuels, Bioproducts and Biorefining, 17(4), 1012-1029 (2023) https://doi.org/10.1002/bbb.2471.
10. Favela-Torres, E. Development of biorefineries for the sustainable management of the water lily (Eichhornia crassipes) in the channels of Xochimilco. Mexican Journal of Technology and Engineering, Vol. 2, No. 1, 4-13 (2023) https://doi.org/10.61767/mjte.002.1.0413 .
11. COMPESCA Comisión de Pesca del Estado de Michoacán. Informe anual de avances del Programa: Mantenimiento y Rehabilitación de Embalses (2023).
12. Pintor-Ibarra, L. F., Rivera-Prado, J. J., Ngangyo-Heya, M., & Rutiaga-Quiñones, J. G. Evaluation of the chemical components of Eichhornia crassipes as an alternative raw material for pulp and paper. BioResources, 13(2), 2800-2813 (2018) DOI:10.15376/biores.13.2.2800-2813.
13. Silva, R. P., de Melo, M. M., Silvestre, A. J., & Silva, C. M. Polar and lipophilic extracts characterization of roots, stalks, leaves and flowers of water hyacinth (Eichhornia crassipes), and insights for its future valorization. Industrial Crops and Products, 76, 1033-

1038 (2015) https://doi.org/10.1016/j.indcrop.2015.07.055.
14. Huang, H., Liu, J., Liu, H., Hu, J., & Evrendilek, F. Dynamic insights into combustion drivers and responses of water hyacinth: evolved gas and ash analyses. Journal of Cleaner Production, 276, 124156 (2020) https://doi.org/10.1016/j.jclepro.2020.124156.
15. Carlson, E. C. Don't gamble with physical properties for simulations. Chemical engineering progress, 92(10), 35-46 (1996) DOI:10.1002/cite.201550065.
16. O'Sullivan, C., Rounsefell, B., Grinham, A., Clarke, W., & Udy, J. Anaerobic digestion of harvested aquatic weeds: water hyacinth (Eichhornia crassipes), cabomba (Cabomba Caroliniana) and salvinia (Salvinia molesta). Ecological Engineering, 36(10), 1459-1468 (2010) https://doi.org/10.1016/j.ecoleng.2010.06.027.
17. Karouach, F., Bakrim, W. B., Ezzariai, A., Mnaouer, I., Ibourki, M., Kibret, M., ... & Kouisni, L. Valorization of water hyacinth to biomethane and biofertilizer through anaerobic digestion technology. Fuel, 358, 130008 (2024) https://doi.org/10.1016/j.fuel.2023.130008.
18. Huang, H., Liu, J., Liu, H., Evrendilek, F., & Buyukada, M. Pyrolysis of water hyacinth biomass parts: Bioenergy, gas emissions, and by-products using TG-FTIR and Py-GC/MS analyses. Energy Conversion and Management, 207, 112552 (2020) https://doi.org/10.1016/j.enconman.2020.112552.
19. Chee, A. L. K., Chin, B. L. F., Sulaiman, S. A., Chai, Y. H., Saptoro, A., Umar, H. A., Lam, M. K. & Yiin, C. L. Preliminary study for catalytic gasification of water hyacinth for syngas production. Sustainable Processes and Clean Energy Transition: ICSuPCET2022, 29, 439 (2023) https://doi.org/10.21741/9781644902516-50.
20. Chee, A. L. K., Chin, B. L. F., Sulaiman, S. A., Chai, Y. H., Saptoro, A., Umar, H. A., ... & Yiin, C. L. Syngas-Enriched hydrogen production via catalytic gasification of water hyacinth using renewable palm kernel shell hydrochar. Fuel, 362, 130811 (2024) https://doi.org/10.1016/j.fuel.2023.130811.

© 2025 by the authors. Licensed to PSEcommunity.org and PSE Press. This is an open access article under the creative commons CC-BY-SA licensing terms. Credit must be given to creator and adaptations must be shared under the same terms. See https://creativecommons.org/licenses/by-sa/4.0/



Systems & Control Transactions

**Research Article - Peer Reviewed Conference Proceeding**
ESCAPE 35 - European Symposium on Computer Aided Process Engineering
Ghent, Belgium. 6-9 July 2025
Jan F.M. Van Impe, Grégoire Léonard, Satyajeet S. Bhonsale,
Monika E. Polańska, Filip Logist (Eds.)

PSE PRESS

# Future Forecasting of Dissolved Oxygen Concentration in Wastewater Treatment Plants using Deep Learning Techniques

**Sena Kurban[a*], Aslı Yasmal[a], Oktay Samur[a], Ocan Şahin[a], Gizem Kuşoğlu Kaya[a], Kutay Atlar[b], Gözde Akkoç[b]**

[a] Turkish Petroleum Refinery, 41780, Körfez, Kocaeli, Turkey
[b] Turkish Petroleum Refinery, 71480, Merkez, Kırıkkale, Turkey
* Corresponding Author: sena.kurban@tupras.com.tr.

## ABSTRACT

Predicting water quality is essential for effective environmental management and pollution control. Dissolved oxygen (DO), one of key water quality parameters, plays a vital role in biological wastewater treatment [1]. This study aims to forecast DO levels in activated sludge tanks of an oil refinery's wastewater treatment plant (WWTP). Proper oxygen concentration is critical for microbial activity, as inadequate levels can disrupt the biological breakdown of pollutants. The objective is to develop predictive models to identify operational risks early, enhancing treatment efficiency and optimizing resources like chemicals, bacterial cultures, and aeration systems. Additionally, the study aims to provide early warnings to operators, minimizing reliance on laboratory tests and ensuring optimal conditions for bacteria, leading to better operational performance, cost reduction, and improved water quality ultimately promoting sustainable wastewater treatment. Various deep learning models, including Recurrent Neural Network (RNN), Gated Recurrent Unit (GRU), and Long-Short Term Memory (LSTM), were applied to a two-year real-time dataset with 24 features and 8-hour intervals. Model performance was assessed using process data for training, validation, and testing. The results reveal that GRU-based models effectively predict DO concentration in sludge tanks, achieving an $R^2$ of 0.7, MSE of 0.01, and MAE of 0.07. These soft sensors demonstrate strong potential for system control.

**Keywords**: Machine learning model, Timeseries future forecasting, Wastewater treatment plant, Deep Learning, Dissolved oxygen

## INTRODUCTION

Since water is essential to life, its quality can be greatly impacted by pollution, which can have a negative impact on the sustainable and effective use of water resources [1]. Reusing water and preventing pollution of water sources are the goals of the wastewater treatment plant (WWTP) process [2].

WWTPs use a combination of physical, chemical and biological processes to treat and recycle wastewater [3]. These systems are critical to sustaining the global water cycle and ensuring a clean and safe environment. The increasing complexity of the wastewater treatment process and external factors like weather conditions and wastewater make accurate modeling challenging [3,4]. Traditional methods are often not sufficient to deal with this level of complexity, forcing a transition to digital solutions. [5,6] Recent advances in predictive modeling and data-driven techniques, particularly prediction of water quality parameters, have shown great promise for enhancing WWTP processes [6,7].

Deep learning is effectively used in assessing water quality and optimizing water treatment and management systems. It also provides solutions for water pollution control, improving water quality, and ensuring watershed ecosystem security. These methods are widely applied across various water environments, including surface water, groundwater, drinking water, sewage, and

seawater [8].

Dissolved oxygen (DO) is an important indicator of aquatic ecosystem health. Low DO levels can stress aquatic organisms and lead to mortality. Changes in DO also affect biochemical cycles and nutrient release from sediments [9]. DO concentration is affected by factors like temperature, pH, and other water quality variables. Thus, creating a predictive DO model is crucial for effective water quality management [1]. Researchers are increasingly using data-driven models to predict DO levels. For example, Dong et al. [1] proposes a combined model, which integrates the Savitzky-Golay filter with a Long Short-Term Memory (LSTM)-based network to predict DO water quality time series, offering more accurate predictions than existing methods. Li et al. [10] compared the Recurrent Neural Network (RNN), LSTM, and Gated Recurrent Units (GRU) models for predicting DO in fishery ponds. Their results indicated that GRU outperformed RNN and was like LSTM, with the added benefits of lower energy consumption, cost, and fewer parameters, making it more suitable for practical applications. In another study, multi-step deep learning models for predicting DO were compared. It was found that GRU performed the best, while LSTM showed the lowest performance [11].

This paper presents a detailed comparison of oxygen prediction using multiple deep learning models to identify the most effective approaches to provide operators with an early warning system. By comparing model performances, it provides actionable insights into the use of advanced predictive algorithms in wastewater treatment. This study stands out for its comprehensive approach, as it examines both standalone and hybrid deep learning models unlike previous research that focused only one method. Additionally, studies on oxygen concentration prediction in activated sludge tanks are limited. This research has the potential to serve as a solution for other refineries.

The manuscript is structured into three sections. Section 1 covers materials and methods, including the WWTP description and methodology, which details data collection, the prediction framework, deep learning models, and performance indicators. Section 2 presents the results and discussion, while Section 3 highlights the impact of the study and future research directions.

# MATERIALS AND METHODS

## Wastewater treatment plant description

Wastewater treatment is a comprehensive process that involves the treatment of wastewater using physical, chemical, and biological methods, as shown in Figure 1. In the first stage, coarse and fine screens are used to remove large solid particles, sand and oil from the wastewater. Then, equalization tanks are used to balance the load of the wastewater and achieve physical treatment. Next, API separators separate water and oil based on their density differences. In the coagulation stage, coagulants are added to the wastewater, causing colloidal and suspended solids to aggregate and become ready for flocculation. In the flocculation stage, the wastewater is mixed at an appropriate speed to allow small particles to combine and form flocs that can easily settle. The DAF (Dissolved Air Flotation) process then separates solid or liquid particles based on density differences, performing the opposite of sedimentation. The activated sludge process is a treatment method that uses the metabolic reactions of microorganisms suspended in activated sludge tanks to remove organic pollutants from wastewater. Important process parameters in the activated sludge system include pH, DO, temperature, and sludge age. Finally, the clarification process separates suspended solids from the wastewater through sedimentation, and the process is completed with the discharge of the water. All of these stages ensure that the effluent is discharged without harm to the environment and are controlled by continuous monitoring systems.

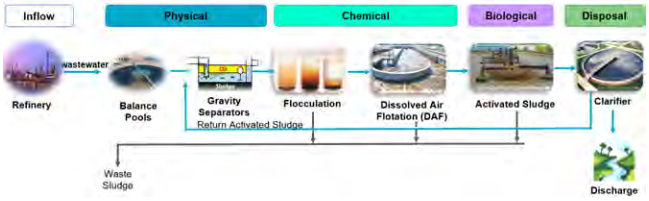



**Figure 1.** Wastewater treatment process.

## Methodology

The methodology employed in this study consists of four main steps in Figure 2 designed to ensure accurate prediction of oxygen concentration in activated sludge tanks. Initially, a two-year time series dataset was collected. Secondly, in the data pre-processing phase, outliers and erroneous values caused by sensor malfunction were removed, and the dataset was normalized. Thirdly, various machine learning and deep learning models were developed and tested to predict oxygen concentration. Finally, the models were evaluated using several metrics to provide a comprehensive understanding of their predictive capabilities.

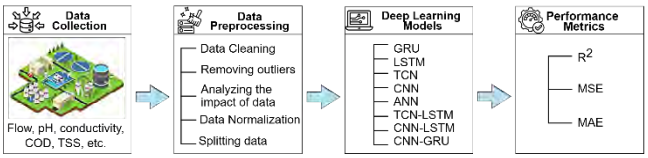



**Figure 2.** Basic structure of the methodological scheme.

## Data Collection and preparation

As mentioned in the process description section, this unit is a complex unit, and many parameters must be

considered simultaneously. As the aim of this study was to estimate the oxygen in the activated sludge tanks, an attempt was made to consider other features that would affect this parameter. The expertise of the process engineers in the plant was used in this process.

The dataset utilized in this study was categorized into two groups: laboratory measurements and flow parameters. The analyzed variables comprised a range of parameters, including temperature, pH, total suspended solids (TSS), sediment, sulfur, $NH_4$-N, nitrogen, Chemical Oxygen Demand (COD), phosphate, conductivity, and unit flow, amounting to a total of 29 variables. These values were collected from various points within the system, including the unit inlet feed, tanks, floater, clarifier, and other interconnected units, ensuring a comprehensive dataset that reflects the contributions and interactions of all relevant processes. The data were collected over a two-year period at 8-hour intervals. The reason behind selecting an 8-hour frequency is that users require foresight into the oxygen levels for the upcoming shift. This enables them to create a proactive action plan based on the predicted values. The actual operational data can't be shared directly for privacy reasons. Principal Component Analysis (PCA) was employed during the preprocessing phase to eliminate irrelevant features. Based on the PCA results and subsequent discussions with process engineers, it was determined that five features should be removed. Thus, five variables were excluded from the dataset, leaving 24 variables for further modeling. Moreover, faulty negative values resulting from sensor errors, were removed from the dataset. Subsequently, data normalization was performed according to Equation 1 to ensure consistency across the features:

$$X_{norm} = \frac{X - X_{min}}{X_{max} - X_{min}}, \quad (1)$$

where X shows the values of each parameter in the data set, $X_{norm}$ is the normalized dataset of X, and $X_{min}$ and $X_{max}$ are the minimum and maximum values in X, respectively. Following the normalization process, the dataset was divided into three subsets: 80% was used for training the models, while 10% was allocated for testing and the remaining 10% for validation.

## Prediction Framework

The prediction framework is based on a time-series forecasting approach, leveraging a 24-hour historical window to predict DO concentration for the following 8 hours, as shown in Figure 3.

As shown in Figure 4, the model architecture is consisted of an input layer that processed normalized data, three hidden layers that captured complex temporal patterns, and an output layer that generated predictions for the next 8 hours.

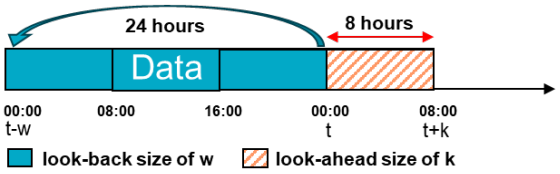



**Figure 3.** Predicting future $k$ time steps by looking back $w$ time steps.

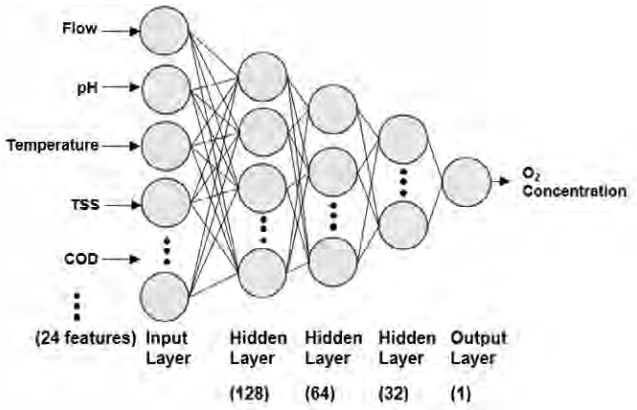



**Figure 4.** The proposed model architecture.

## Deep learning models

In this study, several models and their combinations were applied. These models are GRU, LSTM, Temporal Convolutional Network (TCN), Convolutional Neural Network (CNN), Artificial Neural Network (ANN), TCN-LSTM, CNN-LSTM, CNN-GRU.

GRU and LSTM are the recurrent neural network models, and they have been developed as a solution to the problems in RNN models. Unlike RNNs, there are gates in the models and these gates regulate the flow of information. In LSTM there are an input gate, a forget gate and an output gate. The input gate is selective and decides what information to feed into the model, the forget gate decides what information to forget and the output gate decides what information to feed out. This helps to learn long-term dependencies [12,13]. Unlike LSTM, GRU has only two gates, the reset and update gates. The update gate corresponds to the task of two gates in LSTM, the input and forget gates. The only difference is that the previous gate is reset [13].

Moreover, ANN is known as the equivalent of the human brain. Non-linear relationships between inputs and outputs can be captured with the ANN. The structure of ANN consists of input, hidden and output layers. The architecture of ANN is shown in Figure 5. The input layer consists of the input parameters, nonlinear transformation occurs in the hidden layers and output layer gives a prediction of the desired value [14].

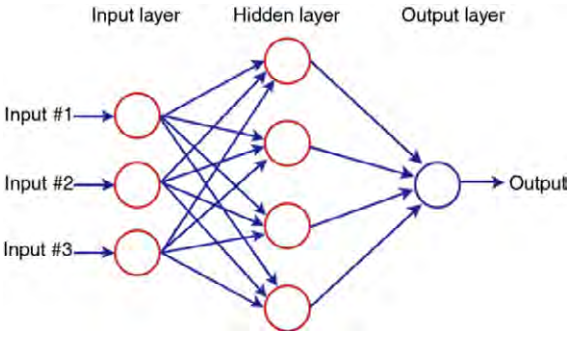



**Figure 5.** ANN architecture.

Other method which is the CNNs are specialized deep learning architectures designed to analyze structured data like images or sequences. They extract patterns and features from input data through convolutional operations, which apply filters to capture local relationships. These networks typically consist of convolutional layers, pooling layers for down sampling, and fully connected layers to produce predictions. By leveraging weight sharing and focusing on localized interactions, CNNs efficiently model complex data while reducing computational overhead [15]. Their capability to automatically learn hierarchical representations has positioned them as a fundamental tool in fields such as computer vision, pattern recognition, and time series analysis. The architecture of this model is shown in Figure 6 [16].

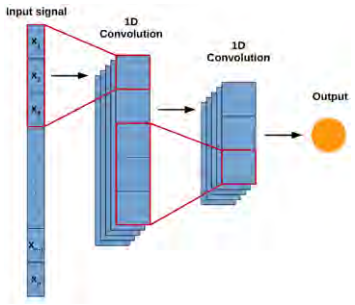



**Figure 6.** Architecture of CNN [16].

The final model is TCN which models sequential dependencies in time series data. The architecture shown in Figure 7 utilizes convolutional layers with dilated convolutions to ensure a large receptive field while preserving causality. Techniques such as activation functions and dropout enhance model performance and prevent overfitting [17].

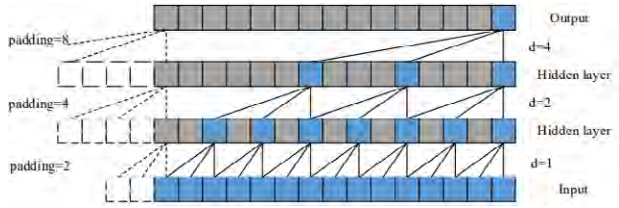



**Figure 7.** Simple TCN representation [17].

In many studies, hybrid models have shown improved performance compared to standalone models. Hybrid deep learning models leverage the advantages of various deep learning algorithms to enhance prediction accuracy [18, 19].

## Model performance indicators

To evaluate the performance of oxygen concentration predictions, three key metrics were employed in the Table 1: The Coefficient of Determination ($R^2$), Mean Squared Error (MSE), and Mean Absolute Error (MAE).

$R^2$, or the Coefficient of Determination, quantifies the proportion of variance in the target variable explained by the model. MSE measures the average squared difference between predicted and actual values. MAE calculates the mean absolute difference between predicted and actual values. As MSE and MAE decrease, and $R^2$ increases, the predictive accuracy of the model improves. These metrics collectively provide a comprehensive evaluation of the model's ability to forecast oxygen concentration accurately.

**Table 1:** Prediction accuracy metrics [19].

| Parameter | Computation |
|---|---|
| $R^2$ | $1-\frac{\sum_{i=1}^{N}(\hat{y}_i-y_i)^2}{\sum_{i=1}^{N}(\bar{y}-y_i)^2}$ |
| MSE | $\frac{1}{N}\sum_{i=1}^{N}(\hat{y}_i-y_i)^2$ |
| MAE | $\frac{1}{N}\sum_{i=1}^{N}\lvert\hat{y}_i-y_i\rvert$ |

where $\bar{y}$ represents the average of y over the N data points, $\hat{y}_i$ denotes the predicted time series of the DO concentration, and $y_i$ refers to the observed time series of the DO concentration.

# RESULTS AND DISCUSSIONS

The primary objective of this study was to evaluate the effectiveness of various deep learning models and their hybrid versions in predicting oxygen concentration in activated sludge tanks. A total of eight models were tested: GRU, LSTM, TCN, CNN, ANN, TCN-LSTM, CNN-LSTM, and CNN-GRU. Based on the performance metrics presented in Table 2, the GRU model demonstrated the best predictive accuracy, achieving an $R^2$ of 0.685, an MSE of 0.01, and an MAE of 0.068.

The results of this study are consistent with those reported in similar studies in the literature. In particular, the GRU model showed superior performance in predicting DO levels. This observation is consistent with the results presented by Li et al. and Qin [10,11], where the GRU model also produced the best results. Both studies highlight the higher accuracy of the GRU model compared to

other DO prediction models. This underscores the robust predictive capability of the GRU model for time series data and its effectiveness as a tool for predicting DO concentrations.

**Table 2:** Statistics of prediction accuracy of the deep learning models for DO concentration.

| Model/Metrics | $R^2$ | MSE | MAE |
|---|---|---|---|
| GRU | 0.685 | 0.010 | 0.068 |
| LSTM | 0.601 | 0.013 | 0.074 |
| TCN | 0.055 | 0.030 | 0.113 |
| CNN | 0.081 | 0.029 | 0.094 |
| ANN | -0.298 | 0.041 | 0.112 |
| TCN-LSTM | 0.403 | 0.019 | 0.086 |
| CNN-LSTM | 0.603 | 0.013 | 0.072 |
| CNN-GRU | 0.001 | 0.032 | 0.109 |

Due to the advantage of hybrid models mentioned in the materials and methods section, hybrid models were also explored in this study. The results indicate that standalone TCN and CNN models showed limited performance in predicting oxygen concentration. However, their hybrid counterparts, CNN-LSTM and TCN-LSTM, delivered notably better results as seen in Table 2. However, based on the results of this study, it can still be concluded that standalone LSTM and GRU models outperform the hybrid configurations in this specific case.

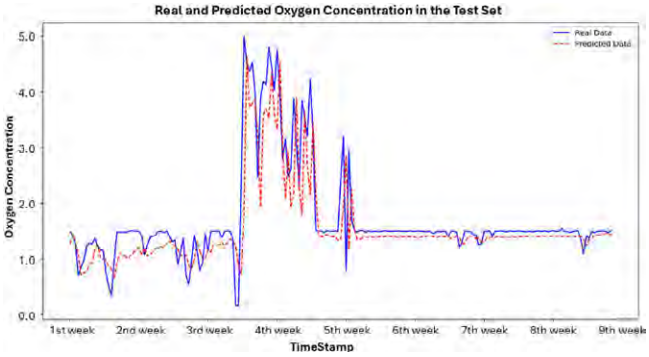



**Figure 8.** Real and predicted DO concentration in the test set.

To further assess model performance, a comparison graph as seen in Figure 8 was included to visualize the GRU model's predictions against actual values in the test dataset. In this graph, the real data is represented by a blue line, while the predicted values are displayed as a red dashed line.

Another noteworthy observation from Figure 9 highlights the model's ability to capture trend shifts in oxygen concentration. Typically, based on the past 24 hours (shown by the orange line), a decrease in oxygen levels would be expected. However, both the real (blue dot) and forecasted (red dot) values show an increasing trend over the next 8 hours. The model's accurate prediction, despite the recent downward trend, highlights its ability to detect changes rather than simply following past patterns. This demonstrates its reliability in real-world applications.

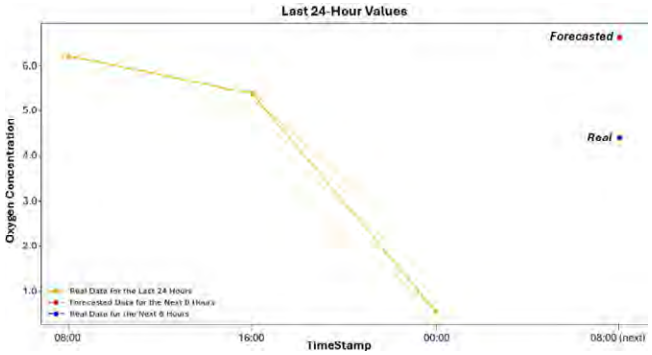



**Figure 9.** Predicted versus real DO concentration for the next 8-Hour forecast.

This study focuses on capturing trends rather than achieving exact predictions. With an $R^2$ of approximately 0.7, the model effectively reflects oxygen concentration patterns, offering valuable insights for decision-making and process adjustments. This level of accuracy is sufficient for practical applications, enabling proactive operational support.

Additionally, random time points were selected to validate the model's predictions for the next 8 hours. These results are summarized in Table 3. The residuals observed during this validation process were low, further confirming the model's reliability.

**Table 3:** Model validation for random time points.

| Time | Residual |
|---|---|
| 16.07.2023 08:00:00 | 0.17 |
| 16.08.2023 08:00:00 | 0.04 |
| 23.08.2023 00:00:00 | 0.18 |

Overall, the results highlight the robustness of the GRU model in forecasting DO concentration. Its strong predictive performance, even under varying scenarios, indicates its potential for practical applications in WWTP systems.

## CONCLUSION

The DO level is of great importance in the WWTP. To ensure microorganisms work effectively, adequate oxygen levels must be maintained. Insufficient oxygen disrupts the biological treatment process and reduces treatment efficiency. Providing sufficient oxygen to microorganisms is vital for biological treatment activities. Therefore, accurately predicting DO levels is critical for optimizing the treatment process and efficiently using resources such as chemicals, bacterial cultures, and

aeration systems. This study offers an innovative solution by delivering accurate and reliable predictions for a complex system based on 24 real-time data points. By utilizing the developed GRU model, which achieves an $R^2$ of 0.7, MSE of 0.01, and MAE of 0.07, it enables operators and process engineers to proactively detect potential operational issues without relying on laboratory results. Future work will focus on continuous monitoring and necessary adjustments, the development of an integrated system to optimize chemical usage, and the adaptation of the model for different types of WWTP in refineries.

## REFERENCES


1. Dong Q, Lin Y, Bi J, Yuan H. An integrated deep neural network approach for large-scale water quality time series prediction. In: 2019 *IEEE International Conference on Systems, Man and Cybernetics (SMC)* 3537-3542 (2019).
2. Farhi N, Kohen E, Mamane H, Shavitt Y. Prediction of wastewater treatment quality using LSTM neural network. *Environmental Technology & Innovation* 23:101632 (2021).
3. Cheng T, Harrou F, Kadri F, Sun Y, Leiknes T. Forecasting of wastewater treatment plant key features using deep learning-based models: A case study. *IEEE Access* 8:184475-184485 (2020).
4. Mahanna, H., El-Rashidy, N., Kaloop, M. R., El-Sapakh, S., Alluqmani, A., & Hassan, R. Prediction of wastewater treatment plant performance through machine learning techniques. *Desalination Water Treatment* 319:100524 (2024).
5. Newhart KB, Holloway RW, Hering AS, Cath TY. Data-driven performance analyses of wastewater treatment plants: A review. *Water Research* 157:498-513 (2019).
6. Chen Y, Zhang H, You Y, Zhang J, Tang L. A hybrid deep learning model based on signal decomposition and dynamic feature selection for forecasting the influent parameters of wastewater treatment plants. *Environmental Research* 266:120615 (2025).
7. Hadjimichael A, Comas J, Corominas L. Do machine learning methods used in data mining enhance the potential of decision support systems? A review for the urban water sector. *Ai Communications*, 29(6): 747-756 (2016).
8. Zhu M et al. A review of the application of machine learning in water quality evaluation. *Eco-Environment & Health* 1(2):107-116 (2022).
9. Zhang Y, Fitch P, Vilas MP, Thorburn PJ. Applying multi-layer artificial neural network and mutual information to the prediction of trends in dissolved oxygen. *Frontiers in Environmental Science* 7:46 (2019).
10. Li W, Wu H, Zhu N, Jiang Y, Tan J, Guo Y. Prediction of dissolved oxygen in a fishery pond based on gated recurrent unit (GRU). *Information Processing in Agriculture* 8(1):185-193 (2021).
11. Qin H. Comparison of deep learning models on time series forecasting: A case study of dissolved oxygen prediction. *arXiv 1911.08414* (2019).
12. Sherstinsky A. Fundamentals of recurrent neural network (RNN) and long short-term memory (LSTM) network. *Physica D: Nonlinear Phenomena* 404:132306 (2020).
13. Zargar S. Introduction to sequence learning models: RNN, LSTM, GRU. *Department of Mechanical and Aerospace Engineering*, North Carolina State University (2021).
14. Alsulaili A, Refaie A. Artificial neural network modeling approach for the prediction of five-day biological oxygen demand and wastewater treatment plant performance. *Water Supply* 21(5):1861-1877 (2021).
15. Lakhdari K, Saeed N. A new vision of a simple 1D Convolutional Neural Networks (1D-CNN) with Leaky-ReLU function for ECG abnormalities classification. *Intelligence-Based Medicine* 6:100080 (2022).
16. Shenfield A, Howarth M. A novel deep learning model for the detection and identification of rolling element-bearing faults. *Sensors* 20(18):5112 (2020).
17. He Y, Zhao J. Temporal convolutional networks for anomaly detection in time series. *Journal of Physics: Conference Series* 1213(4):042050 (2019).
18. Barzegar R, Aalami MT, Adamowski J. Short-term water quality variable prediction using a hybrid CNN–LSTM deep learning model. *Stochastic Environmental Research and Risk Assessment* 34(2):415-433 (2020).
19. Xie Y, Chen Y, Wei Q, Yin H. A hybrid deep learning approach to improve real-time effluent quality prediction in wastewater treatment plant. *Water Research* 250:121092 (2024).



© 2025 by the authors. Licensed to PSEcommunity.org and PSE Press. This is an open access article under the creative commons CC-BY-SA licensing terms. Credit must be given to creator and adaptations must be shared under the same terms. See https://creativecommons.org/licenses/by-sa/4.0/




Systems & Control Transactions

**Research Article - Peer Reviewed Conference Proceeding**
ESCAPE 35 - European Symposium on Computer Aided Process Engineering
Ghent, Belgium. 6-9 July 2025
Jan F.M. Van Impe, Grégoire Léonard, Satyajeet S. Bhonsale,
Monika E. Polańska, Filip Logist (Eds.)

PSE PRESS

# Modelling the *in vitro* FooD Digestion SIMulator FooDSIM

**Stylianos Floros, Satyajeet S. Bhonsale, Sotiria Gaspari, Simen Akkermans, Jan F.M. Van Impe***

BioTeC⁺ Chemical & Biochemical Process Technology & Control, Department of Chemical Engineering, KU Leuven, Gent, Belgium
* Corresponding Author: jan.vanimpe@kuleuven.be.

## ABSTRACT

Understanding the complexity of human digestion is critical for designing models that serve as valuable research tools for process simulation and prediction. Due to the high cost of medical intervention & recent advancements in *in vitro* digestion protocols, increased demand for inexpensive *in silico* solutions emerges. This study aims to develop a mathematical model that simulates the *in vitro* dynamic Food Digestion SIMulator (FooDSIM) functionalities via a digital twin approach. Ordinary Differential Equations (ODEs) simulate the system as a series of Continuously Stirred Tank Reactors (CSTRs) and describe different regions of human organs (stomach, duodenum, ileum, colon) of the human Gastrointestinal Tract (GIT). Various time horizons were used to investigate the effect of periodic feeding on the dynamic stabilisation of the inherently simulated processes (hydraulics, pH, biochemical interactions between enzymes & substrates, and nutrient absorption). A Polynomial Chaos Expansion (PCE)-based Global Sensitivity Analysis (GSA) was performed to explore causal relationships between input & output variables by performing uncertainty quantification. Results indicate that the system self-stabilizes only after 3-4 feeding cycles. Initially, enzyme concentration increases in the duodenum above the input feed threshold, thus significantly affecting the digestion kinetics in the subsequent reactors. Two cardinal models used for the fitting of enzymatic activity data with pH values indicate satisfactory Mean Squared Error (MSE) scores (<0.0114 for Model 1, <0.0134 for Model 2). Overall, this research highlights the potential of mathematical modeling for simulating digestion and predicting experiment outcomes.

**Keywords**: Digestion Modeling, Digital Twin, Parameter Estimation, Global Sensitivity Analysis

## INTRODUCTION

Human digestion is a complex process that takes place in multiple sites along the human GIT, during which a wide range of digestive fluids and enzymes is secreted. These participate in mechanical and biochemical processes while altering the food matrices to achieve specific goals (e.g. optimal nutrient delivery, local release, and absorption) [1].

However, exploring human digestion is challenging due to the system's complexity. Multiple environmental conditions greatly influence the outcome of human digestion. Inherent variability in samples obtained through *in* vivo studies and limited intervention techniques pose challenging hurdles for exploring human digestion. Therefore, a rise has been given to the development of dynamic *in vitro* digestion systems that offer a simple, fast, and flexible solution to digestion studies.

Besides their advantages, these dynamic *in vitro* systems require laborious and time-consuming experiments. As a response, *in silico* computational approaches are developed to simulate human digestion numerically. That way, predictive information for the *in vitro* systems' inherent digestion processes can be provided. Often, these include highlights not evident during *in vitro* experiments and enable the strategic exploration of research hypotheses [2].

This paper aims to develop a mathematical model for the FooDSIM dynamic *in vitro* simulator by implementing a digital twin approach. The FooDSIM is a laboratory system that consists of four CSTRs connected in series that mimic human digestion. To achieve this, it introduces dynamic processes and reagents to simulate the physiological conditions of digestion. The *in silico* model will simulate the dynamics of these processes by employing a series of ODEs. While both physicochemical and microbial processes aim to be simulated, this paper will primarily focus on describing only physicochemical phenomena.

# MATERIALS AND METHODS

## Dynamic Food Digestion SIMulator – FooDSIM

### General

The exact protocol of development and operation of the FooDSIM laboratory analogue has been previously described by Gaspari et al. (2024) [3]. Thus, within the context of this paper, only some relevant operation features and mathematical formulations that concern the digital twin will be addressed.

The FooDSIM is a computer-controlled, multi-compartmental dynamic *in vitro* simulator that describes major physiological processes within the human GIT. It consists of four Applikon MiniBio bioreactors connected in series that operate as fed-batch or CSTR while representing the stomach, upper/lower small intestine, and colon (Figure 1). Simulated digestive fluids and enzyme solutions are introduced to the respective vessels to simulate the digestion environment. Controlled conditions (37 $^{o}$C, pH, oxygen saturation) and continuous stirring led to homogenous mixing. The feeding process takes place through introducing a Food Model System (FMS), which is fed to the 1$^{st}$ vessel. The FMS dynamically interacts with the digestion environment.

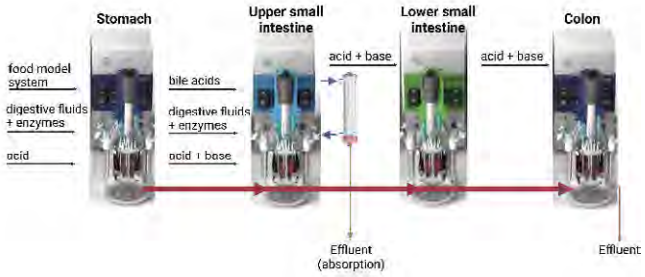



**Figure 1.** Schematic representation of FooDSIM.

### Hydraulics

#### Emptying Rate

The emptying rate of the 1$^{st}$ vessel (stomach) towards the 2$^{nd}$ (duodenum) is described by the Elashoff emptying rate; an exponential equation that describes the stomach emptying process as a function of time.

$$f(t) = 1 - 2^{-\left(\frac{t}{t_{\frac{1}{2}}}\right)^{\beta}}, \quad (1)$$

where $f$ denotes the fraction of content delivered, $t$ signifies the time $(h)$, and $t_{1/2}$ is the half-time of content emptying, equal to 1,16 hours. Moreover, $\beta$ is a shape factor equal to 2 and is retrieved from literature [3].

#### Mass Balance

Every vessel has unique feeding and emptying flow rates. A set of ODEs describes the total mass present in each vessel as a function of time. More specifically:

$$\frac{dM(t)}{dt} = M_{in}(t) - M_{out}(t), \quad (2)$$

where $M\,(g)$ is the mass in every reactor and $M_{in}, M_{out}\,(g/h)$ are the compartment feeding and emptying rates, respectively.

#### pH Values

The $pH$ in each compartment is actively controlled during every subsequent feeding cycle. More specifically, the $pH$ profile of the stomach follows an exponential decrease from its initial value upon the first introduction of FMS. After the end of each feeding cycle, the controller maintains the low $pH$ of the fasted stomach ($pH_{inf}$), until the next feeding occurs. There, the $pH$ of the stomach vessel is increasing only due to the buffering effect of the FMS. Once the maximum $pH$ of the fed stomach ($pH_o$) is reached, the controller is activated again to maintain this $pH$, and acidification occurs during the stomach's emptying process. The $pH$ in the duodenum, ileum, and colon is fixed and constant. In the stomach, Equation 3 describes the acidification process:

$$pH(t) = pH_o + (pH_{inf} - pH_o) * e^{-\lambda * t}, \quad (3)$$

where $\lambda$ is an exponential rate equal to 1.5. Every reset of $pH$ between the acidified and initial state is simulated with a linear increase between the upper and lower $pH$ values and lasts for the same time interval as the feeding process.

### Digestion Kinetics

#### Food Model System - FMS

The FMS used in FooDSIM is an oil-in-water emulsion that consists of carbohydrates, fats, proteins, and salts. Its composition, along with the respective molecular weights, is shown in Table 1. The protocol for its formulation is described by Gaspari et al. (2024) [3].

**Table 1:** Properties of FMS constituents.

| Substrate | Concentration (g/L) | Molecular Weight (g/mol) |
|---|---|---|
| Soluble Potato Starch | 99,00 | 162,14 |
| Sucrose | 37,70 | 342,30 |
| Dietary Fibre | 16,00 | 300.000,00 |
| Corn Oil | 43,00 | 850,00 |
| Whey Protein | 44,40 | 19.328,00 |
| NaCl | 2,50 | 58,44 |

#### Digestion Kinetics

Three enzyme solutions are used to facilitate the enzymatic reactions in FooDSIM, and their main properties are listed in Table 2.

**Table 2:** Properties of enzymes.

| Enzyme | EC Number | Solution Concentration (g/L) | Activity (U/mg) |
|---|---|---|---|
| A-amylase | 3.2.1.1 | 15 | 50 |
| Pepsin | 3.4.23.1 | 100 | 400 |
| Pancreatic A-amylase | 3.2.1.1 | 3.75 | 100 |
| Pancreatic TAG lipase | 3.1.1.3 | 3.75 | 100 |
| Pancreatic trypsin | 3.4.21.4 | 3.75 | 100 |

To simulate the kinetics between available substrates and enzymes in the system, a map of enzyme/substrate specificity is constructed (Table 3).

**Table 3:** Map of enzyme/substrate specificity. The symbol x indicates affinity between the selected enzyme and substrate.

| Substrate | Enzymes | | |
|---|---|---|---|
| | A-amylase | Pepsin | Pancreatin |
| Soluble Potato Starch | x | - | x |
| Sucrose | - | - | - |
| Dietary Fibre | - | - | - |
| Corn Oil | - | - | x |
| Whey Protein | - | x | x |
| NaCl | - | - | - |

Assuming the system is well stirred, all substrates are instantaneously available to all enzymes in each vessel. Thus, the Michaelis Menten kinetics (4) is used to describe interactions between single enzyme/substrate combinations:

$$r(t) = \frac{Vmax * C_s(t)}{Km + C_s(t)}, \quad (4)$$

where, $C_s$ $(g/L)$ is the dynamic substrate concentration, $Km$ $(g/L)$ is the Michaelis-Menten affinity constant, and $Vmax$ $(g/L*h)$ is the maximum reaction velocity for each combination of enzyme and substrate. When different enzymes degrade simultaneously the same substrate, added terms express each one's kinetics.

The parameter $V_{max}$ is defined as the product of enzyme concentration with respective catalytic reaction rate, as shown in equation 5. This relationship directly assumes that all available enzymes in the reactor are characterized by a maximum catalytic reaction rate when saturated with substrate. Thus, the maximum reaction velocity of the enzyme/substrate reaction kinetics can be calculated. The catalytic reaction rate values for each combination of enzyme/substrate are quantified by utilizing the manufacturer's specifications for enzymatic activity and molecular weight of the substrate, as indicated below:

$$V_{max}(t, pH) = k_{cat} * C_{enz}(t) * AI(pH) \quad (5)$$

$$k_{cat} = U_{enz} * c * MW \quad (6)$$

where, $k_{cat}$ $(1/h)$ is the overall catalytic conversion rate of each enzyme, $C_{enz}$ $(g/L)$ is the enzyme concentration in each compartment, $AI$ $(-)$ is the Activity Index for each enzyme as described further below, $U_{enz}$ $(U/mg)$ is the activity of each enzyme and $c$ $(1/h)$ is a unit conversion factor equal to $6*10^{-5}$.

## Enzyme Concentration Balances

Similarly to mass balances, a set of ODEs describes the change of enzyme concentration in every vessel. During the dialysis process, the cut-off limit of the membrane (<5kDa) does not permit the absorption of enzymes. Thus, equation 7 describes the change of enzyme concentration in all reactors except for the 2nd, where dialysis occurs. For that one, a modified ODE (8) accounts for the dynamic accumulation of enzymes, as presented below:

$$\frac{dC_{enz}(t)}{dt} = \frac{M_{in}(t)}{M(t)} * \left(C_{enz,in}(t) - C_{enz}(t)\right) \quad (7)$$

$$\frac{dC_{enz}(t)}{dt} = \frac{M_{in}(t) * \left(C_{enz,in}(t) - C_{enz}(t)\right) + M_{filter}(t) * C_{enz}(t)}{M(t)} \quad (8)$$

where $C_{enz,in}$ $(g/L)$ is the input enzyme concentration in the stomach, and $M_{filter}$ $(g)$ is a term that expresses the mass removed from the compartment due to dialysis.

## Effect of pH on Enzymatic Activity

To express the impact of pH on enzymatic activity within the dynamic framework of FooDSIM, the introduction of an Activity Index $(AI)$ takes place. It is calculated by using 2 modified cardinal models, as described by Baka et al. (2013) [4]. The $AI$ can take values between 0-1 and is defined according to the following relationship:

$$AI = \begin{cases} pH < pH_{min}, & 0 \\ pH_{min} < pH < pH_{max}, & AI_{opt} * \rho_i(pH) \\ pH > pH_{max}, & 0 \end{cases} \quad (9)$$

where $pH_{min}$, $pH_{max}$, $pH_{opt}$ are the lower, upper, and optimal values for measured enzymatic activity, and $AI_{opt}$ $(-)$ is the optimal $AI$ for each enzyme, respectively. The factor $\rho_i$ is expressed by one of two adjusted nonlinear cardinal models, with one having an inflection point.

$$\rho_1(pH) = \frac{(pH - pH_{min}) * (pH - pH_{max})}{(pH - pH_{min}) * (pH - pH_{max}) - (pH - pH_{opt})^2} \quad (10)$$

$$\rho_2(pH) = \frac{(pH - pH_{min})^2 * (pH - pH_{max})}{(pH_{opt} - pH_{min}) * \left((pH_{opt} - pH_{min}) * (pH - pH_{opt}) - (pH_{opt} - pH_{max}) * (pH_{opt} + pH_{min} - 2 * pH)\right)} \quad (11)$$

Parameter estimation for $pH_{min}$, $pH_{max}$, $pH_{opt}$ was performed with least squares regression. Values for pH and residual enzymatic activity were retrieved from the literature for every enzyme. To assess the goodness of fit, the Mean Squared Error (MSE) is used, based on the calculation of the Least Squared Error (LSE):

$$\mathrm{LSE} = \min \sum_{i}^{N} \left(y_{sampled} - y_{(\theta)}\right)^2 \quad (12)$$

$$\mathrm{MSE} = \frac{1}{n_{sampled} - n_{\theta}} * \mathrm{LSE} \quad (13)$$

where $y_{sampled}$ are the measured and $y_{\theta}$ are the predicted values of ρ, based on the predicted parameters θ.Moreover, $n$ signifies the amount of sampled data and parameters.

### Substrate Concentration Balance

The change in concentration of each substrate in every compartment is described using a set of ODEs (14-15). Like equations 7 and 8, equation 14 accounts for substrate concentration in all reactors except for the 2nd one, where equation 15 describes the accumulation of non-absorbable substrates.

$$\frac{dC_s(t)}{dt} = \frac{M_{in}(t)}{M(t)} * \left(C_{s,in}(t) - C_s(t)\right) - r(t) \quad (14)$$

$$\frac{dC_s(t)}{dt} = \frac{M_{in}(t) * \left(C_{s,in}(t) - C_s(t)\right) + M_{filter}(t) * C_s(t)}{M(t)} - r(t) \quad (15)$$

where $C_{s.in}$ $(g/L)$ is the input substrate concentration and $C_s$ $(g/L)$ is the substrate concentration in each reactor.

### Digestion Product Concentration Balance

The concentration of digestion products generated by the degradation of substrates due to enzymatic hydrolysis is described by the following ODE:

$$\frac{dC_p(t)}{dt} = \frac{M_{in}(t)}{M(t)} * \left(C_{p,in}(t) - C_p(t)\right) + r(t), \quad (16)$$

where $C_{p,in}$ $(g/L)$ is the input concentration of digestion products and $C_p$ $(g/L)$ is the concentration of digestion products for each substrate in each compartment.

## Dialysis Absorption

To explicitly simulate the absorption of substrates and digestion products during the dialysis in the duodenum phase, the following set of ODEs (17-19) is used:

$$\frac{dM_{filt}(t)}{dt} = M_{filt}(t) \quad (17)$$

$$\frac{dC_{s,filt}(t)}{dt} = C_{s,filt.in}(t) - C_{s,filt}(t) \quad (18)$$

$$\frac{dC_{p,filt}(t)}{dt} = C_{p,filt,in}(t) - C_{p,filt}(t) \quad (19)$$

where, $C_{s,filt}$, $C_{s,filt,in}$ $(g/L)$ express the current and input value of substrates' concentrations. $C_{p,filt,}$ and $C_{p,filt,in}$ express the current and input concentrations of digestion products in the dialysate.

## Numerical Simulations

### Software and Solver

Numerical simulations for a 7-day operation of FooDSIM were performed with MATLAB R2023a software. The system of ODEs (71 equations) was solved with the ode15s function within 135 s.

### Uncertainty Quantification

#### Global Sensitivity Analysis - GSA

GSA was employed to examine two different scenarios by using the open-source UQLab Sensitivity Analysis Module. Various uniform, independent uncertainty distributions were created for the i) composition of FMS (±10% deviation) and ii) enzyme activity (0-max activity). The proposed uncertainty distribution resembles error during the preparation of the FMS and partial/complete enzyme inactivation, respectively.

Both scenarios quantify the outcome of input uncertainty on the response variables (dialysate digestion product concentration) at an individual level (first order) and by incorporating their interactions (higher order). The sum of them is called total Sobol's sensitivity indices.

#### Polynomial Chaos Expansion - PCE

Due to the high computational cost of the FooDSIM model, the PCE meta-modelling technique is used to approximate the Sobol decomposition. More specifically, PCE estimates the model's response by an infinite sum of orthogonal basis functions, leading to fewer summands in the decomposition for Sobol's indices estimation. A truncated version of this sum of $M$ terms is presented below:

$$f(\theta) = yPCE = \sum_{i=0}^{M} a_i \Phi_i(\theta) \quad (20)$$

$$M + 1 = \frac{(p+d)!}{p!d!} \quad (21)$$

where $\Phi$ is a basis function, a is an unknown coefficient, $p$ is the polynomial order, and $d$ is the number of random inputs [5]. The maximum polynomial degree is defined as 6, and the maximum size of samples is 100 in all cases.

# RESULTS AND DISCUSSION

The results for a 7-day simulation of the FooDSIM Digital Twin are presented in Figure 2. Recurring dilution in all compartments leads to a cyclic steady state of FooDSIM. Among all the processes simulated, the dialysis in duodenum is highlighted for achieving an 80% reduction in mass per feeding cycle. Enzymes are generally not absorbed during this process, and their concentrations spike. This concentration increase irreversibly influences the reaction kinetics in all subsequent vessels.

However, the dynamic change of pH impacts the enzymatic/substrate reaction kinetics, as indicated in

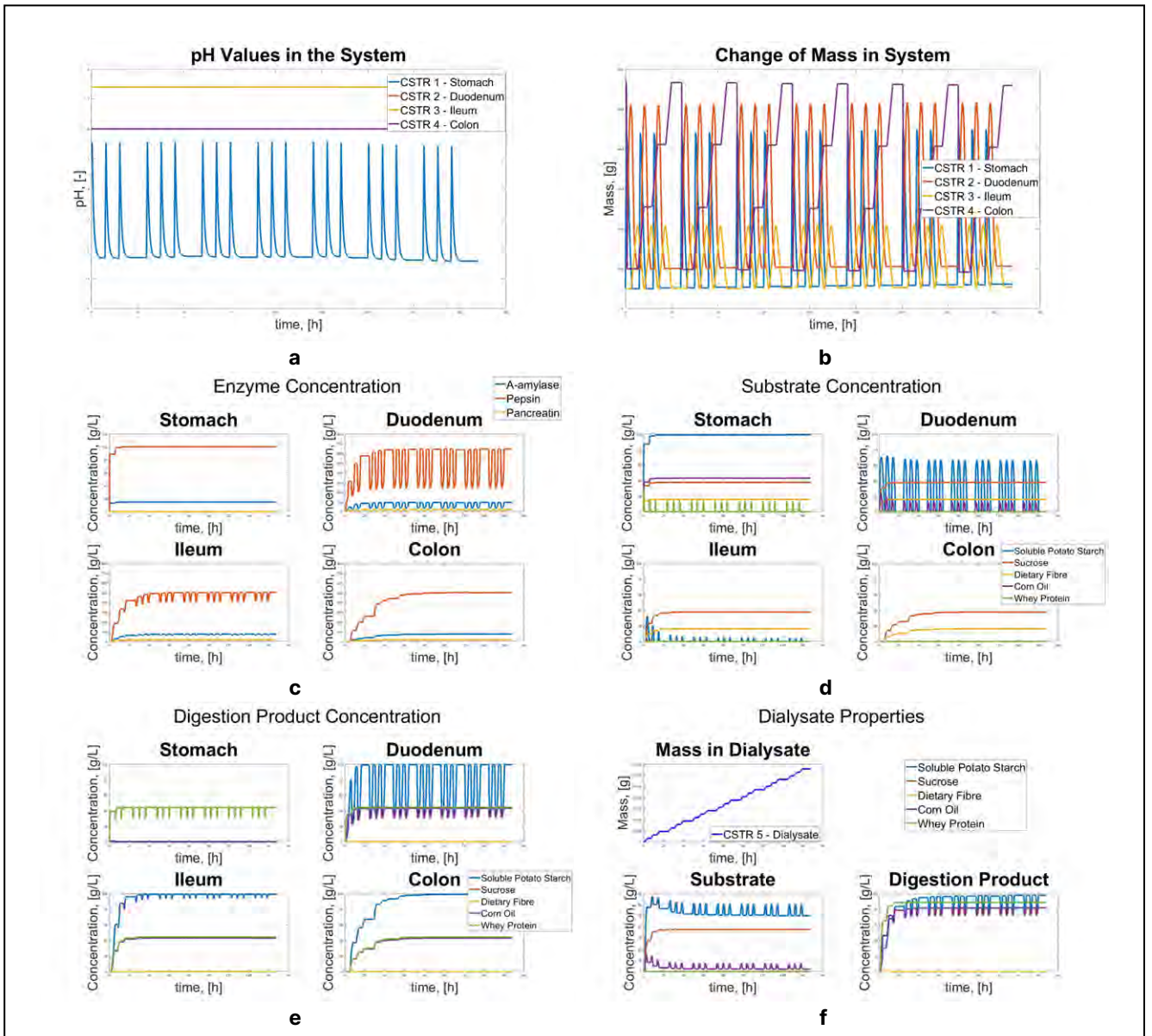



**Figure 2: Quantitative results for 7 days of FooDSIM simulation. a)** Dynamic pH value in FooDSIM, **b)** Dynamic mass change in FooDSIM, **c)** Dynamic change of three enzyme concentrations, **d)** Dynamic change of five substrate concentrations in FooDSIM, **e)** Dynamic change of digestion products in FooDSIM, **f)** Dynamic change of mass, substrate and digestion products concentration in Dialysate**.**

Figure 3. Parameter estimation using the 2 cardinal models on sampled data exhibits satisfactory goodness of fit. Model 1 describes the activity of α-amylase, pepsin, pancreatic α-amylase, and pancreatic lipase (MSE= 0.0091, 0.0114, 0.0091, 0.0027, respectively). Model 2 is suitable for pancreatic trypsin (MSE = 0.0134) due to the inflection point in its formulation. Therefore, substrates susceptible to enzymatic degradation follow a cyclic profile, too.

Due to the inactivation of salivary α-amylase in the acidified stomach compartment, soluble potato starch is partially consumed and broken down by pancreatic α-amylase instead. It should be noted that all substrates are degraded before the colon. The simulation results indicate that it takes at least 3-4 feeding cycles (1-1,5 days) to achieve a steady regime in the system.

Overall, PCE-based GSA results indicate clear connections within the model's input uncertainties with response variable outcomes, as expected. Total Sobol's indices do not indicate interferences between input variables. The connection between FMS composition and digestion products demonstrates that reaction kinetics occur only between specific enzymes and their allocated substrates. Lastly, GSA for enzyme activity highlights the relative contribution of α-amylase/ pancreatin to degrading soluble potato starch.

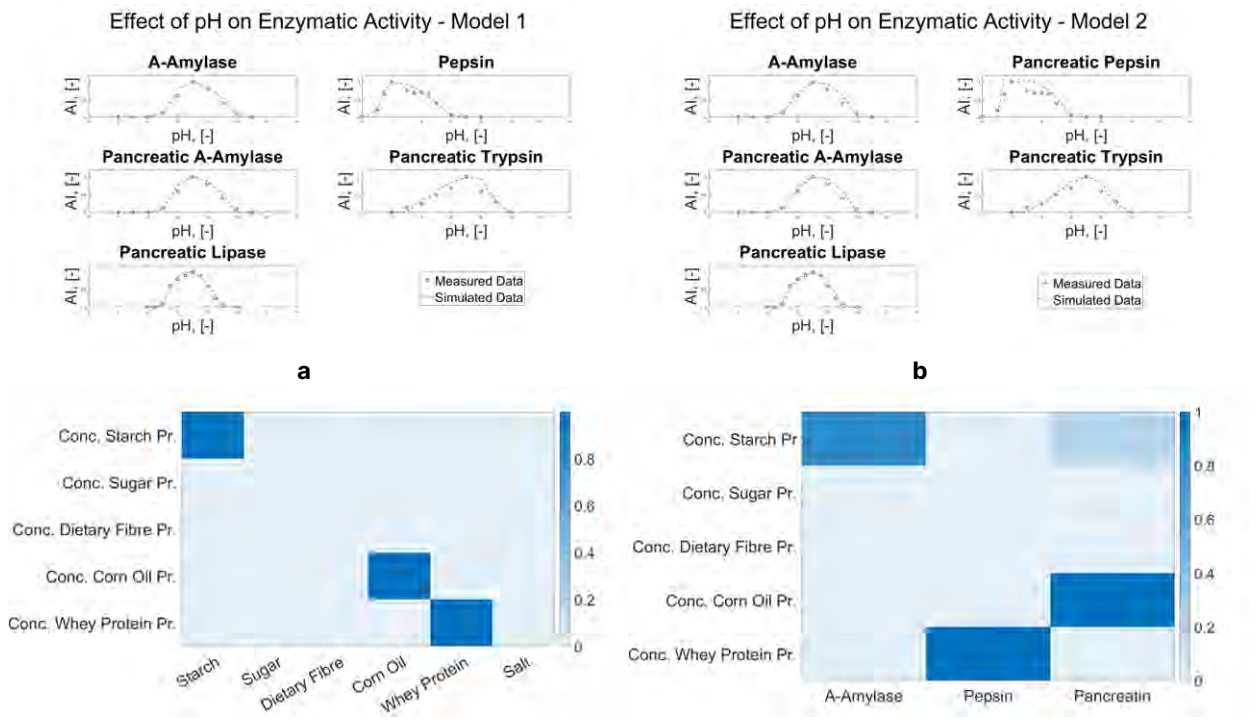



**Figure 3: Additional results for parameter estimation and total Sobol indices of PCE-based GSA**. **a)** Effect of pH on enzymatic activity - Cardinal Model 1, **b)** Effect of pH on enzymatic activity - Cardinal Model 2, **c)** Impact of FMS composition on dialysate digestion products concentration, **d)** Impact of enzyme affinity on dialysate digestion product concentration.

## CONCLUSIONS

Overall, the FooDSIM Digital Twin provides predictive information that emerges from many parallel physicochemical processes. Its white-box structure permits direct inference and modification of its degrees of freedom. One of the most important outputs is the necessity for at least 3-4 feeding cycles for the system to reach a cyclic steady state regime. This information was hidden and is a critical finding for designing *in vitro* experiments with FooDSIM. Results before the stabilization point could have high inherent variability. The dynamic FooDSIM Digital Twin leads to insights on long-term digestion-related effects. Overall, this model provides a clear view of the physicochemical processes within FooDSIM, and its validation with *in vitro* experiments is a future step.

## REFERENCES


1. Sensoy I. A review on the food digestion in the digestive tract and the used in vitro models. *Curr Res Food Sci* 4:308-319 (2021) https://doi.org/10.1016/j.crfs.2021.04.004
2. Gouseti O, Bornhorst GM, Bakalis S, Mackie A, eds. Interdisciplinary approaches to food digestion. *Cham: Springer Int Publ (2019)* https://doi.org/10.1007/978-3-030-03901-1
3. Gaspari S, Akkermans S, Van Impe J. Development of a dynamic in vitro food digestion simulator (FooDSIM): A deterministic model system for human digestion. *In FOODSIM'2024*:166-168 (2024) EUROSIS.
4. Baka M, Van Derlinden E, Boons K, Mertens L, Van Impe JF. Impact of pH on the cardinal temperatures of E. coli K12: Evaluation of the gamma hypothesis. *Food Control* 29:328-335 (2013) https://doi.org/10.1016/j.foodcont.2012.04.022S
5. Marelli S, Lamas C, Konakli K, Mylonas C, Wiederkehr P, Sudret B. UQLab user manual – Sensitivity analysis. Report UQLab-V2.1-106, Chair of Risk, Safety and Uncertainty Quantification, ETH Zurich, Switzerland (2024).



© 2025 by the authors. Licensed to PSEcommunity.org and PSE Press. This is an open access article under the creative commons CC-BY-SA licensing terms. Credit must be given to creator and adaptations must be shared under the same terms. See https://creativecommons.org/licenses/by-sa/4.0/

Systems & Control Transactions

**Research Article - Peer Reviewed Conference Proceeding**
ESCAPE 35 - European Symposium on Computer Aided Process Engineering
Ghent, Belgium. 6-9 July 2025
Jan F.M. Van Impe, Grégoire Léonard, Satyajeet S. Bhonsale,
Monika E. Polańska, Filip Logist (Eds.)

PSE PRESS

# Machine Learning Models for Predicting the Amount of Nutrients Required in a Microalgae Cultivation System

**Geovani R. Freitas[a,b,c,d,e], Sara M. Badenes[c], Rui Oliveira[d,e], and Fernando G. Martins[a,b]***

[a] LEPABE, Department of Chemical Engineering, Faculty of Engineering, University of Porto, Porto, Portugal
[b] ALiCE, Associate Laboratory in Chemical Engineering, Faculty of Engineering, University of Porto, Porto, Portugal
[c] A4F – Algae for future, Campus do Lumiar, Estrada do Paço do Lumiar, Lisbon, Portugal
[d] UCIBIO, Department of Chemistry, NOVA School of Science and Technology, NOVA University Lisbon, Caparica, Portugal
[e] Associate Laboratory i4HB - Institute for Health and Bioeconomy, NOVA School of Science and Technology, Universidade NOVA de Lisboa, Portugal
* Corresponding Author: fgm@fe.up.pt.

## ABSTRACT

Effective prediction of nutrient demands is crucial for optimising microalgae growth, maximising productivity and minimising the waste of resources. With the increasing amount of data related to microalgae cultivation systems, data mining and machine learning models to extract additional knowledge have gained popularity. In the development of such models, a data preprocessing stage is necessary due to the poor data quality. At this stage, cleaning and outlier removal techniques are employed to eliminate missing data and outliers, respectively. Afterwards, data splitting and cross-validation strategies are employed to ensure that the models are trained and evaluated with representative subsets of the data. Principal component analysis is also applied to simplify complex environmental datasets by reducing the number of features while retaining as much information as possible. To further improve prediction capabilities, ensemble methods are incorporated, leveraging multiple models to achieve a higher overall performance. Stacking, a popular ensemble technique, is used to combine the outputs of individual models into a single meta-model. The application of these machine learning methods has been demonstrated using a dataset acquired from the cultivation of the microalgae *Dunaliella* in a flat-panel photobioreactor. The results have shown that the data mining workflow, in combination with different machine learning models, was able to describe the nutrients' requirements enforcing good performance of microalgae *Dunaliella* β-carotene production in the carotenogenic phase.

**Keywords**: Machine Learning, Data Mining, Microalgae Cultivation, *Dunaliella* carotenogenesis.

## INTRODUCTION

The use of data mining techniques and machine learning methods is rapidly increasing due to the need of extracting meaningful insights from large datasets. Data mining (DM) focuses on discovering patterns, trends, and valuable knowledge from the data, while machine learning (ML) develops algorithms that enable machines to improve at a task by learning from data without explicit programming [1]. In the DM process, various techniques are typically employed to uncover the underlying structure of data. However, when prediction of new instances is also crucial, ML algorithms are embedded within DM workflows to develop different models. This integration allows for more robust and accurate analysis, enhancing the overall capability of the DM process [2].

Various studies are found in the literature applying DM and ML methods to uncover valuable insights from large datasets on microalgae systems [3–5]. In this work, the application of these methods is demonstrated using a dataset obtained from the cultivation of the microalgae *Dunaliella* in a flat-panel photobioreactor (FP-PBR). This microalga is known for its ability to accumulate large amounts of carotenoids, with β-carotene being the most predominant. The high concentrations of this carotenoid change the colour of microalgae cells from green to orange. For the induction of β-carotene accumulation, *Dunaliella* cells should be exposed to certain growth

conditions, often also referred to as carotenogenic conditions, which are characterized by high salinity and light intensities, and limited nitrogen [6,7].

The main advantages of using FP-PBR systems to cultivate *Dunaliella* microalgae are their high productivity and uniform light distribution, employing narrow panels to achieve high area-to-volume ratios [8]. Therefore, the objective of this study is to develop ML models capable of predicting the nutrient requirements necessary to achieve good performance in the production of *Dunaliella* microalgae during the carotenogenic phase, for β-carotene production, in a FP-PBR system. This paper delves into the methods, where it is described the data preprocessing stage followed by the approach used for model development. The results section presents a comparative analysis of the different ML models, describing their evaluation metrics. Finally, the paper concludes by summarizing the key findings and highlighting their significance for process modeling.

# METHODOLOGY

## Dataset description and data preprocessing

Dataset was acquired from cultivating the microalga *Dunaliella* in a FP-PBR system. Data was selected based on two criteria: increase of the biomass concentration and production of carotenoids. Different features were considered to determine the target variable, i.e., the nutrient requirements of this microalga in carotenogenic phase. These features are described in the next section.

Data preprocessing is a critical step in the DM and ML pipeline, where raw data is transformed into a clean and usable format to improve data quality, ultimately enhancing the performance and accuracy of ML models. Typical preprocessing techniques include data cleaning, outlier detection and removal, feature scaling, feature selection, and dimensionality reduction.

### Data cleaning

Data cleaning involves removing missing data, noise and correcting inconsistencies in the data [9]. In this work, it was decided to remove the observations with the missing values. Although this method is not very effective, its application can avoid the potential biases introduced by imputation methods like mean imputation.

### Outlier detection and removal

Outliers are observations that significantly deviate from the overall distribution, which can skew results and lead to inaccurate model predictions. In datasets with multiple dimensions, one of the methods for detecting outliers is the calculation of the Mahalanobis distance [8], represented by the following equation:

$$D_M = \sqrt{(X-\mu)^T S^{-1} (X-\mu)} \quad (1)$$

In this formulation, $X$ is the observation, $\mu$ is the mean of all observations, and $S$ is the covariance matrix. The Mahalanobis distance follows a chi-squared distribution with degrees of freedom equal to the number of variables in the dataset. By selecting a significance level, a threshold can be determined from the chi-squared distribution. Observations with a squared Mahalanobis distance exceeding this threshold are detected as potential outliers and, therefore, should be removed [10].

### Feature scaling

Feature scaling ensures that all numerical features are on a comparable scale. Without feature scaling, features with larger magnitudes can dominate the learning process, leading to biased or suboptimal model performance [9]. In this work, the z-score normalization was performed, also known as standardization. This approach transforms features to have a mean of 0 and a standard deviation of 1, being represented by the equation:

$$Z = \frac{X-\mu}{\sigma}, \quad (2)$$

where $X$ is the feature value, $\mu$ is the mean, $\sigma$ is the standard deviation.

### Feature selection

Feature selection involves selecting a subset of the most relevant features from a dataset to improve model performance, reduce complexity, and prevent overfitting. One of the feature selection techniques is called minimum redundancy maximum relevance (mRMR). The criterion of maximum relevance ensures that the selected features are highly correlated with the target variable, therefore contributing significantly to the prediction task, while the criterion of minimum redundancy aims to reduce overlap between the selected features, ensuring that each one contributes unique information to the model. By selecting the most relevant features, mRMR helps in the development of models that are more accurate and interpretable [11].

### Dimensionality reduction

When dealing with high-dimensional data, it is essential to perform dimensionality reduction techniques to decrease the number of variables in a dataset while retaining as much information as possible. Among various dimensionality reduction techniques, Principal Component Analysis (PCA) stands out as one of the most widely used and effective methods. PCA transforms the original features into a smaller set of uncorrelated components, called principal components (PC), which capture the maximum variance in the data [10]. The number of PC chosen is an important decision that is often guided by examining the plot of cumulative explained variance ratio versus number of PC, selecting the smallest number of PC that explain most of the data variance [9,12].

## Model development

After data preprocessing stage, this work employed a systematic approach to model development, focusing on the design of different ML models. This approach consists of various stages, including data splitting, cross-validation, hyperparameter tuning, and ensemble learning.

In this work, the DM process and ML methods were programmed in Python 3.12 using the library Scikit-learn 1.4 and constructed using Jupyter Notebook 7.0 from Anaconda Navigator.

### Data splitting

Data splitting consists of dividing the observations into at least training and test sets, where the training set is used for model construction and the test set for model evaluation. In this work, the Kennard-Stone (KS) algorithm was implemented for data splitting with a train-test split ratio of 80:20. The KS algorithm operates by maximizing the Euclidean distance between selected samples, ensuring that the chosen observations are evenly distributed across the feature space [13].

### Cross-validation

Cross-validation (CV) is a method used to evaluate model performance and ensure generalizability to unseen data. One of the most popular techniques is k-fold CV, where the data is divided into k folds, and the model is trained and tested k times, each time using a different fold as the test set. Then, the results from each fold are averaged to produce a more robust estimate of the model performance [9,10]. In this work, it was applied k-fold CV with the training set being divided into 5 folds.

### Hyperparameter tuning

Hyperparameters are settings that control the learning process of a ML model, such as learning rate, number of layers, or regularization strength. Unlike model parameters, which are learned from the data during training, hyperparameters must be predefined and set before the training process. Hyperparameter tuning is the process of selecting the optimal values for a ML model's hyperparameters. One effective method for hyperparameter tuning is GridSearch, which systematically evaluates all possible combinations of predefined hyperparameter values. This method ensures thorough exploration but can be computationally expensive [1,2].

### Ensemble learning

Ensemble learning methods combine multiple models to improve prediction capabilities, robustness and generalization compared to individual models. Stacking, a popular ensemble technique, integrates predictions from several models using a single meta-model, which learns to optimize the final predictions. This approach leverages the strengths of different models, making stacking highly effective for complex problems [1,2].

Other ensemble technique is bagging, also known as bootstrap aggregating. This technique reduces variance by training multiple models on random subsets with replacement. Each model learns independently, and their outputs are aggregated. Bagging enhances stability and reduces overfitting, with random forest being the most common example that applies bagging to decision trees for improved performance [1,9].

## Model evaluation

Evaluation metrics are essential for assessing the performance of ML models. The coefficient of determination ($R^2$) is used to measure the proportion of variance in the dependent variable that is explained by the model [10], being mathematically expressed by the equation below:

$$R^2 = 1 - \frac{\sum_{i=1}^{n}(y_i - \hat{y}_i)^2}{\sum_{i=1}^{n}(y_i - \bar{y}_i)^2} \quad (3)$$

where $n$ is the number of observations, $y$ is the actual output, $\hat{y}$ is the predicted output, and $\bar{y}$ is the mean of the actual output.

Root mean squared error (RMSE) is another evaluation metric, whose value quantifies the average magnitude of errors between predicted and actual values, with lower values indicating higher accuracy [1]. RMSE is calculated according to the equation below:

$$RMSE = \sqrt{\frac{1}{n}\sum_{i=1}^{n}(y_i - \hat{y}_i)^2} \quad (4)$$

While $R^2$ provides a relative measure of fit, RMSE gives an absolute measure of prediction errors, making them complementary metrics for model evaluation.

# RESULTS

## Data preprocessing and constructing dataset

In the analysed dataset, the percentage of missing values was around 7 %. After removing such values, the Mahalanobis distance was calculated for each observation to detect possible outliers, as shown in Figure 1.

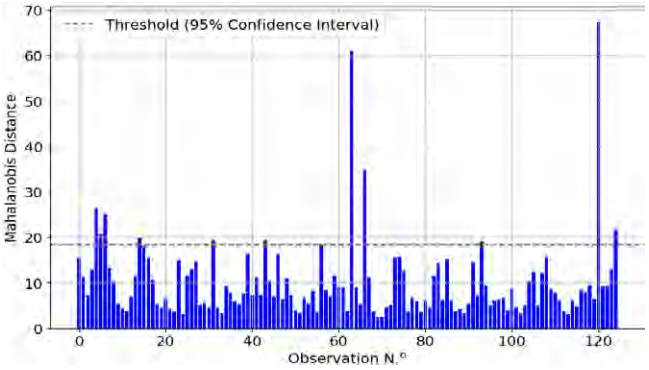



**Figure 1:** Mahalanobis distance for each observation in the analysed dataset.

By selecting a significance level of 95%, the threshold was determined based on the chi-squared distribution, represented by the dashed line. Observations with a Mahalanobis distance exceeding this value were identified as outliers and subsequently removed. After that, it was performed standardization to ensure that all features have a consistent scale. In the final stage of the preprocessing data workflow, PCA was applied to reduce complexity while preserving as much variability as possible. Figure 2 shows the percentage of the dataset variance that is cumulatively explained by each PC.

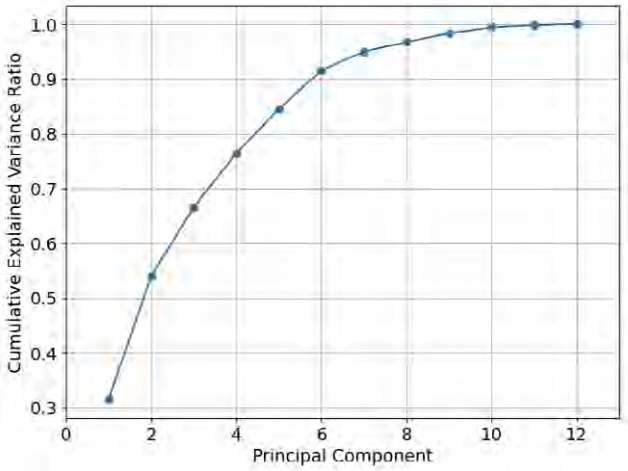



**Figure 2:** Cumulative variance ratio explained by the number of principal components.

From Figure 2, it was observed that the first PC explains around 30 % of the dataset variance. To explain 90 % of this variance, at least 6 PC are required, making 6 the chosen number of PC in this work.

Furthermore, the mRMR algorithm was applied to select the features relevant to the model: cells concentration, culture volume, irradiance, time duration for new addition of nutrients, and carotenoids concentration.

## Model development and evaluation

After preprocessing the data, the KS algorithm was applied to split the observations into training (80 %) and test (20 %) sets. Then, five-fold CV was applied in combination with GridSearch to find the optimal values of hyperparameter for each ML model. In this work, four ML algorithms were employed to predict the target variable: ridge regressor (RR), random forest (RF), artificial neural network (ANN) and support vector regressor (SVR).

Although RR and RF are easier to interpret, they are better suited for linear or moderately complex relationships and struggle with highly nonlinear patterns. On the other hand, ANN and SVR excel at capturing nonlinear relationships, however they are more challenging to interpret and require careful tuning and computational resources, particularly for large datasets [1,10].

Table 1 shows the hyperparameter values optimized in each one of the ML models in this work.

**Table 1:** Optimal hyperparameter values obtained for each ML model.

| Model | Hyperparameter | Optimal value |
|---|---|---|
| RR | Alpha | 25 |
| | Maximum number of iterations | 1000 |
| RF | Number of estimators | 100 |
| | Maximum depth | 5 |
| ANN | Number of hidden neurons | 1st layer: 4<br>2nd layer: 2 |
| | Activation function for the hidden layer | Hyperbolic tangent |
| | Alpha | 0.1 |
| SVR | C | 1 |
| | Kernel function | Radial basis |
| | Gamma | 0.5 |

In Table 1, it was observed that ANN and SVR have a larger number of hyperparameters to optimize compared to RR and RF. In this case, a more detailed tuning process is necessary for achieving optimal performance.

After optimizing the hyperparameter values, scatter plots were created for each ML model. These plots visually represent the relationship between predicted and actual values, providing a clear evaluation of model performance. In addition, the coefficient of determination ($R^2$) was calculated for each model, quantifying how well the predictions aligned with the observed data. The results, summarized in Figure 3, show the effectiveness of each ML model in predicting the nutrient requirements, in arbitrary units (A. U.), for each observation in the analysed dataset.

According to Figure 3, RF and SVR models displayed signs of overfitting, highlighted by the difference between the $R^2$ values for the training and test sets. Overfitting occurs when the ML model learns not only the underlying patterns but also the noise in the training data, leading to an overly complex model that cannot predict new data accurately. In such cases, the $R^2$ for the training set is typically very high, indicating a well-fitted model, while the $R^2$ for the test set is much lower, revealing poor generalization to unseen data. Overfitting arises due to several causes, such as insufficient regularization, model complexity due to hyperparameter values, or excessive training iterations that allow the ML model to memorize noise instead of only learning meaningful patterns [1,9].

In the scatter plot of RR model (see Figure 3 (a)), some observations are relatively dispersed around the

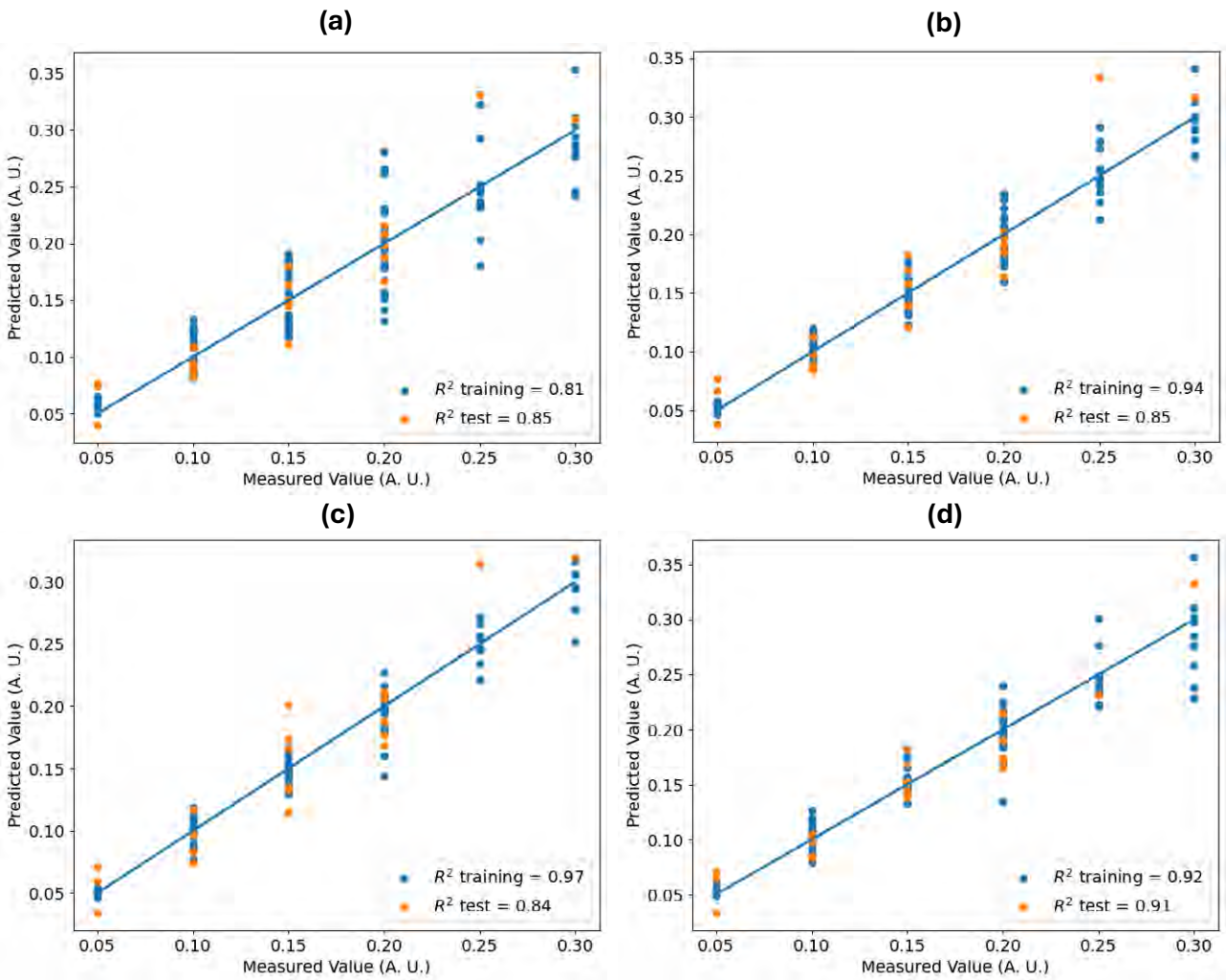



**Figure 3:** Scatter plots for each ML model considered in this work: (a) RR, (b) RF, (c) SVR, and (d) ANN. The coefficient of determination ($R^2$) is displayed for each plot, providing a quantitative measure of model performance.

diagonal line of perfect prediction, indicating moderate alignment between predictions and true values. In contrast, the scatter plot for ANN (see Figure 3 (d)) displays less observations dispersed along the diagonal, achieving superior $R^2$ values for both training and test sets. Superior RMSE values were also found for ANN. These results indicate that ANN generalizes better than RR, making it the preferred ML model for nutrient requirements.

Stacking process was also applied to the dataset by choosing as estimators the four ML models. In this case, the outputs of these ML models were considered in the stacking process, and ANN was chosen as the ML model that combines all the outputs, i.e., the meta-model. The scatter plot of the stacking model is shown in Figure 4.

In Figure 4, the scatter plot of the stacking model presents a good model fit, however when compared to the ANN model, its outputs exhibit more dispersion, reflecting a less accurate prediction. This is consistent with the fact that the $R^2$ values for both the training and test sets are higher in the ANN model compared to the stacking model, suggesting that the ANN model captures the underlying patterns in the data more effectively.

Several factors could contribute to the stacking model presenting a worse performance compared to the ANN model. One possibility is that the estimators used in the stacking process may not have provided complementary information, leading to limited improvement. In addition, the meta-model might not have been well-optimized, resulting in poor generalization on unseen data. Furthermore, the complexity added by the stacking method might have introduced more variance without offering significant predictive gains, especially if the estimators were not sufficiently diverse.

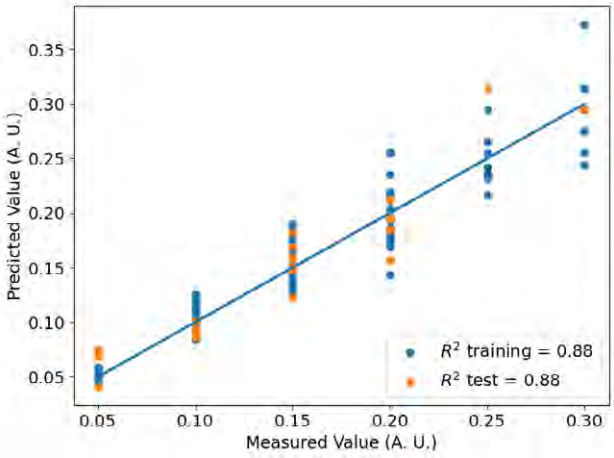



**Figure 4:** Scatter plot of the ML model generated through the stacking process.

## CONCLUSION

This study demonstrates the potential of ML models to predict the nutrient requirements of *Dunaliella* microalgae during the carotenogenic phase in a FP-PBR system. The performance of four ML models was compared alongside a stacking model that combined the outputs of these models. Among all the ML models evaluated, the ANN model presented the best evaluation metrics, indicating its ability to capture complex relationships in the dataset and to provide accurate predictions. In addition, a key factor contributing to the good performance of these ML models was the implementation of a robust DM process, which included a detailed preprocessing stage. Finally, this study highlights the value of applying well-structured DM processes and systematically evaluating ML methods to identify the most suitable models for process modeling.

## ACKNOWLEDGEMENTS

This work was supported by national funds through FCT/ MCTES (PIDDAC): LEPABE (Laboratory for Process Engineering, Environment, Biotechnology and Energy, Faculty of Engineering, University of Porto, UIDB/00511/2020, DOI: 10.54499/UIDB/00511/2020, UIDP/00511/2020, DOI: 10.54499/UIDP/00511/2020), ALiCE (Associate Laboratory in Chemical Engineering, Faculty of Engineering, University of Porto, LA/P/0045/2020, DOI: 10.54499/LA/P/0045/2020), UCIBIO (Research Unit on Applied Molecular Biosciences, UIDP/04378/2020, DOI: 10.54499/UIDP/04378/2020, UIDB/04378/2020, DOI: 10.54499/UIDB/04378/2020), and i4HB (Associate Laboratory Institute for Health and Bioeconomy, LA/P/0140/2020, DOI: 10.54499/LA/P/0140/2020). Geovani R. Freitas thanks the Portuguese Foundation for Science and Technology (FCT), Portugal, for the individual research grant PRT/BD/154543/2022.

## REFERENCES

1. Géron A. HANDS-ON MACHINE LEARNING WITH SCIKIT-LEARN AND TENSORFLOW: CONCEPTS, TOOLS, AND TECHNIQUES TO BUILD INTELLIGENT SYSTEMS. O'Reilly (2018).
2. Witten I H, Frank E, Hall M A. DATA MINING: PRACTICAL MACHINE LEARNING TOOLS AND TECHNIQUES. Morgan Kaufmann Publishers (2011).
3. Reimann R, Zeng B, Jakopec M, Burdukiewicz M, Petrick I, Schierack P, Rödiger S. Classification of dead and living microalgae Chlorella vulgaris by bioimage informatics and machine learning. *Algal Res* 48 (2020).
4. Singh V, Verma M, Chivate M S, Mishra V. Machine learning-based optimisation of microalgae biomass production by using wastewater. *J Environ Chem Eng* 11 (2023).
5. Meenatchisundaram K, Gowd S C, Lee J, Barathi S, Rajendran K. Data-driven model development for prediction and optimization of biomass yield of microalgae-based wastewater treatment. *Sustain En Tech and Assmt* 63 (2024).
6. Barbosa M, Inácio L G, Afonso C, Maranhão P. The microalga Dunaliella and its applications: a review. *Applied Phycology* 4:99-120 (2023).
7. Ye Z W, Jiang J G, Wu G H. Biosynthesis and regulation of carotenoids in Dunaliella: Progresses and prospects. *Biotechnol Adv* 26:352-360 (2008).
8. Carvalho A P, Meireles L A, Malcata F X. Microalgal reactors: A review of enclosed system designs and performances. *Biotechnol Prog* 22:1490-1506 (2006).
9. Han J, Kamber M, Pei J. DATA MINING: CONCEPTS AND TECHNIQUES. 3rd Edition, Morgan Kaufmann Publishers. Elsevier (2012).
10. Alpaydin E. INTRODUCTION TO MACHINE LEARNING. The MIT Press (2010).
11. Ding C, Peng H. Minimum Redundancy Feature Selection from Microarray Gene Expression Data. *Proceedings of the Computational Systems Bioinformatics* (2003).
12. Mazzelli A, Cicci A, Di Caprio F, Altimari P, Toro L, Iaquaniello G, Pagnanelli F. Multivariate modeling for microalgae growth in outdoor photobioreactors. *Algal Res* 45 (2020).
13. Kennard R W, Stone L A. Computer Aided Design of Experiments. *Technometrics* 11:137-148 (1969).

© 2025 by the authors. Licensed to PSEcommunity.org and PSE Press. This is an open access article under the creative commons CC-BY-SA licensing terms. Credit must be given to creator and adaptations must be shared under the same terms. See https://creativecommons.org/licenses/by-sa/4.0/

Systems & Control Transactions

**Research Article - Peer Reviewed Conference Proceeding**
ESCAPE 35 - European Symposium on Computer Aided Process Engineering
Ghent, Belgium. 6-9 July 2025
Jan F.M. Van Impe, Grégoire Léonard, Satyajeet S. Bhonsale,
Monika E. Polańska, Filip Logist (Eds.)

PSE PRESS

# A Physics-based, Data-driven Numerical Framework for Anomalous Diffusion of Water in Soil

**Zeyuan Song[a], and Zheyu Jiang[a]***

[a] Oklahoma State University, School of Chemical Engineering, Stillwater, Oklahoma, USA
* Corresponding Author: zheyu.jiang@okstate.edu.

## ABSTRACT

Precision modeling and forecasting of soil moisture are essential for implementing smart irrigation systems and mitigating agricultural drought. Most agro-hydrological models are based on the standard Richards equation, a highly nonlinear, degenerate elliptic-parabolic partial differential equation (PDE) with first order time derivative. However, research has shown that standard Richards equation is unable to model preferential flow in soil with fractal structure. In such a scenario, the soil exhibits anomalous non-Boltzmann scaling behavior. Incorporating the anomalous non-Boltzmann scaling behavior into the Richards equation leads to a generalized, time-fractional Richards equation based on fractional time derivatives. As expected, solving the time-fractional Richards equation for accurate modeling of water flow dynamics in soil faces extensive computational challenges. To target these challenges, we propose a novel numerical method that integrates finite volume method (FVM), adaptive fixed point iteration scheme, and neural network to solve the time-fractional Richards equation. Specifically, we develop an adaptive fixed point iteration scheme to solve the FVM-discretized equation iteratively, which avoids the stability issues when directly solving a stiff and sparse matrix equation. To improve the solution quality which is influenced by numerical errors and computational constraints during actual implementation, we propose to use neural networks that resemble an encoder-decoder architecture to map soil moisture profiles into a latent space and reconstruct them back. Through 1-D examples, we illustrate the accuracy and computational efficiency of our proposed physics-based, data-driven numerical method. Finally, we present a Markov chain Monte Carlo (MCMC) approach to solve the inverse problem to obtain soil-specific parameters given soil moisture solutions.

**Keywords**: Machine Learning, Modelling and Simulations, Numerical Methods, Water, Sustainability

## INTRODUCTION

With increasing demand for food and the resulting food-energy-water nexus challenges from the growing population, there is an increasing interest among process systems engineering (PSE) researchers to design the next-generation food and agricultural systems that are sustainable, resource-efficient, and resilient. Along this line, by leveraging real-time soil monitoring technologies, sensor-based digital agriculture for sustainable and efficient use of water is essential for improving agricultural production and crop productivity and reducing agricultural droughts. To simulate the root-zone (top 1m of soil) soil moisture content, agro-hydrological models, which describe irrigation, precipitation, evapotranspiration, runoff, and drainage dynamics inside the soil, are widely used. Most existing agro-hydrological models are based on the standard Richards equation [1], which is a highly nonlinear, degenerate elliptic-parabolic partial differential equation (PDE) with first order time derivative with the form:

$$\partial_t \theta(\psi) + \nabla \cdot \boldsymbol{q} = 0, \tag{1}$$

$$\boldsymbol{q} = -(C(\theta)\nabla\theta + K(\theta)\nabla z), \tag{2}$$

where $\theta$ denotes the soil moisture content (in, e.g., $\mathrm{m}^3/\mathrm{m}^3$), $\boldsymbol{q}$ represents the water flux (in, e.g., $\mathrm{m}^3/\mathrm{m}^2 \cdot \mathrm{s}$), $K(\theta)$ is unsaturated hydraulic water conductivity (in, e.g., $\mathrm{m}/\mathrm{s}$), $C(\theta)$ is soil moisture diffusivity (in, e.g., $\mathrm{m}^2/\mathrm{s}$), $t \in [0, t_{total}]$ denotes the time (in, e.g., $\mathrm{s}$), and $\mathrm{z}$ corresponds

to the vertical depth (in, e.g., m). For this study, without loss of generality of our proposed numerical framework, we ignore the sink term in Equation (1) associated with root water uptake. The Richards equation is a nonlinear convection-diffusion equation, where the convection term is due to gravity and the diffusion term is originated from Darcy's law. For unsaturated flow, both $C$ and $K$ are highly nonlinear functions of soil moisture content and soil parameters, thereby posing significant computational challenges for solving the standard Richards equation itself [2]. The integral form of the standard Richards equation is simply given by:

$$\theta(t,\cdot) - \theta(0,\cdot) = \int_0^t \nabla \cdot (C(\theta)\nabla\theta + K(\theta)\nabla z)\mathrm{d}t, \qquad (3)$$

Besides being computationally difficult to solve, standard Richards equation is also limited when it comes to modeling realistic soil systems. For example, it has been experimentally shown that the anomalous non-Boltzmann scaling behavior is exhibited in porous media with fractal structure [3,4]. For soils exhibiting non-Boltzmann scaling behavior, the soil moisture content is a function of $\frac{\boldsymbol{x}}{t^{\frac{\alpha}{2}}}$, where $\boldsymbol{x}$ is the position vector, and $\alpha$ is a soil-dependent parameter indicating subdiffusion ($0 < \alpha < 1$) or superdiffusion ($1 < \alpha < 2$) [5]. Incorporating this anomalous flow behavior into the Richards equation leads to a generalized, time-fractional Richards equation:

$$\partial_t^\alpha \theta + \nabla \cdot \boldsymbol{q} = 0, \qquad (4)$$

which is even more computationally challenging due to the presence of time-fractional derivative $\partial_t^\alpha \theta$. Naïve implementations for solving Equation (4) typically involves discretizing the time-fractional Richards equation using finite difference method (FDM). However, this often causes numerical stability issues [6]. To ensure numerical stability in solving time-fractional PDEs, recent work features using a hybrid method, in which the FDM and finite element method (FEM) will be used to discretize the time and spatial domains, respectively [7]. Nevertheless, this approach was only used to solve the time-fractional fourth-order reaction-diffusion equation, where the only nonlinearity originates from the sink term. For solving the time-fractional Richards equation, a finite point method (FPM) was recently proposed to improve stability and accuracy [8]. However, this approach relies on solving the FPM scheme in matrix form, whose matrix is often stiff and sparse and hence can be difficult to solve.

To address the limitations of prevailing research, in this work, we propose a novel physics-based, data-driven numerical framework to solve time-fractional Richards equation. This framework discretizes Equation (4) using finite volume method (FVM), which inherently enforces mass conservation at the discretized level. To solve the FVM-discretized fractional Richards equation, instead of converting the discretized equations into a matrix equation, we adopt methods such as fixed point iteration scheme to convert the discretized equation system into an explicit scheme which can be solved iteratively. To enhance solution accuracy and stability, we introduce an adaptive fixed point iteration scheme that automatically selects a proper linearization constant for every iteration, time step, and discretized cell for time-fractional Richards equation based on our recent work [2]. Finally, this numerical scheme is synergistically integrated with an encoder-decoder-type architecture using simple neural networks, and the resulting data-driven, physics-embedded numerical framework achieves higher solution accuracy. This data-driven approach serves two major purposes that common numerical solvers often overlook. First, by training the neural networks using solutions obtained from solvers employing static fixed point iteration scheme under different settings (e.g., number of iterations), the encoder-decoder architecture can systematically capture and account for the numerical errors associated with realistic computational constraints (e.g., not being able to run for an infinite amount of time on a perfect computer) during actual implementation of the numerical scheme, thereby improving solution accuracy and robustness. Second, the use of data-driven approach is attractive also because it provides new opportunities for integrating physics-based modeling with online in situ soil moisture measurements for sensor-driven soil monitoring and precision agriculture applications. Commercial soil moisture sensors are not perfect and instrumental errors will always be present in their measurements. Furthermore, environmental factors (e.g., wind, temperature, evapotranspiration) and imperfect installation and maintenance will bring additional uncertainties to online soil sensing data. Thus, the data-driven approach in our numerical framework makes it amenable to leverage uncertainty-embedded dataset produced by in situ soil sensors in field environment for predictive modeling of root-zone soil moisture profiles.

Lastly, accurate estimation of soil parameters (e.g., $\alpha$ and $C$) from direct sensor measurements, also known as the inverse problem of physics-based models, is generally ill-posed due to insufficient and inaccurate measurements. Deterministic methods, which solve the inverse problem as a nonlinear optimization problem, tend to be trapped in local optima and are sensitive to data noise. Therefore, in this work, we present a probabilistic method based on Markov chain Monte Carlo (MCMC) [9] for identifying the optimal soil parameters $\alpha$ and $C$ in time-fractional Richards equation given soil moisture content information as a preliminary study. Through a 1-D case study, we illustrate the effectiveness of our proposed approaches.

## THE DATA-DRIVEN NUMERICAL FRAMEWORK

## Approximation of time-fractional derivatives

When it comes to representing time-fractional derivatives in Equation (4), there are several options, such as Riemann-Liouville fractional integral [10,11], Caputo fractional derivative [12], fractal derivative [13], and so on. In this work, we would like to adopt the Riemann-Liouville fractional integral of the following form:

$$\mathrm{I}_{0^+}^{\alpha}\mathrm{f}(t) = \frac{1}{\Gamma(\alpha)}\int_0^t (t-u)^{\alpha-1}\mathrm{f}(u)\,\mathrm{d}u, \tag{5}$$

where $\Gamma(\cdot)$ is the gamma function. With this, the integral form of time-fractional Richards equation can be expressed as:

$$\theta(t,\cdot) - \theta(0,\cdot) = \mathrm{I}_{0^+}^{\alpha}[\nabla\cdot(C(\theta)\nabla\theta + K(\theta)\nabla z)], \tag{6}$$

where $\alpha > 0$. Note that the integral form of the standard Richards equation, Equation (3), is just a special case of Equation (6) by setting $\alpha = 1$.

## FVM Discretization

First, we adopt an implicit Euler scheme to discretize Equation (6) in the spatial domain:

$$\theta(t_{m+1},\cdot) - \theta(t_m,\cdot) = \mathrm{I}_{0^+}^{\alpha}\big[\nabla\cdot\big(C\nabla\theta(t_{m+1},\cdot) + K\big(\theta(t_{m+1},\cdot)\big)\nabla z\big)\big] - \mathrm{I}_{0^+}^{\alpha}\big[\nabla\cdot\big(C\nabla\theta(t_m,\cdot) + K\big(\theta(t_m,\cdot)\big)\nabla z\big)\big], \tag{7}$$

where time step $m = 1,\cdots,\left\lfloor\frac{t_{total}}{\Delta t}\right\rfloor$. Next, in order to discretize Equation (6), one needs to accurately approximate Equation (5). Here, we adopt the trapezoidal quadrature formula [14] and express $\mathrm{I}_{0^+}^{\alpha}\mathrm{f}(t_{m+1})$ as:

$$\mathrm{I}_{0^+}^{\alpha}\mathrm{f}(t_{m+1}) \approx \frac{(\Delta t)^{\alpha}}{\alpha(\alpha+1)\Gamma(\alpha)}\sum_{k=0}^{m+1} a_{k,m+1}\mathrm{f}(t_{m+1}), \tag{8}$$

where the coefficient $a_{k,m+1}$ follows:

$$a_{k,m+1} = \begin{cases} m^{\alpha+1} - (m-\alpha)(m+1)^{\alpha}, & \text{if } k = 0 \\ (m-k+2)^{\alpha+1} + (m-k)^{\alpha+1} - 2(m-k+1)^{\alpha+1}, & \text{if } 1 \le k \le m \\ 1, & \text{if } k = m+1 \end{cases} \tag{9}$$

To adopt FVM, we first integrate both sides of Equation (7) over the control volume $V$:

$$\int_V \theta(t_{m+1},\cdot) - \theta(t_m,\cdot)\,\mathrm{d}V = \mathrm{I}_{0^+}^{\alpha}\Big\{\int_V[\nabla\cdot(C(\theta)\nabla\theta(t_{m+1},\cdot) + K(\theta)\nabla z)]\,\mathrm{d}V\Big\} - \mathrm{I}_{0^+}^{\alpha}\Big\{\int_V[\nabla\cdot(C(\theta)\nabla\theta(t_m,\cdot) + K(\theta)\nabla z)]\,\mathrm{d}V\Big\}. \tag{10}$$

Then, one can apply divergence theorem on the RHS of Equation (10), followed by discretizing the control volume $V$ into cells $V_i$, where $i = 1,2,\cdots,N_i$. Each $V_i$ is associated with surfaces $\omega_{i,j}$ for $j = 1,2,\cdots,N_{\omega_i}$, whose surface area is given by $A_{\omega_{i,j}}$. This would lead to the following FVM-discretized version of Equation (10):

$$\big(\theta_i^{m+1} - \theta_i^m\big)\mathrm{vol}(V_i) = \mathrm{I}_{0^+}^{\alpha}\Big[\sum_{j=1}^{N_{\omega_i}}(C(\theta)\nabla\theta + K(\theta)\nabla z)\big|_{\omega_{i,j}}^{m+1}\cdot\hat{n}_{\omega_{i,j}}A_{\omega_{i,j}}\Big] - \mathrm{I}_{0^+}^{\alpha}\Big[\sum_{j=1}^{N_{\omega_i}}(C(\theta)\nabla\theta + K(\theta)\nabla z)\big|_{\omega_{i,j}}^{m}\cdot\hat{n}_{\omega_{i,j}}A_{\omega_{i,j}}\Big], \tag{11}$$

where $\theta_i^m$ is a shorthand notation for the soil moisture at cell $i$ and time step $m$, $|_{\omega_{i,j}}^m$ operates on surface $\omega_{i,j}$ and time step $m$, and $\hat{n}_{\omega_{i,j}}$denotes the outward pointing unit normal vector associated with surface $\omega_{i,j}$. Equation (8) will be used to evaluate $\mathrm{I}_{0^+}^{\alpha}[\cdot]$ in Equation (11).

## Adaptive fixed point iteration scheme

In fixed point iteration scheme, for every cell $i$ and time step $m+1$, one would multiply the fixed linearization parameter $\gamma$ to Equation (11) and then add the term $\theta_i^{m+1,s+1} - \theta_i^{m+1,s}$ to either side of Equation (11), so that the Richards equation can be solved in an iterative manner to obtain the soil moisture solution upon convergence. Since $\gamma$ is a static constant, a trial-and-error procedure is typically required to obtain an appropriate $\gamma$ value that avoids convergence issues. Not only is this search procedure tedious to implement, the solutions obtained are also less accurate most of the time (to be shown in the case study) as the ground truth solutions are not known to us a priori. Thus, inspired by previous works [15], we introduce a novel adaptive fixed point iteration scheme that replaces the static fixed linearization parameter $\gamma$ with $\gamma_i^{m+1,s}$, which adjusts itself for each specific discretized cell, time step, and iteration count s. Specifically, we introduce the term $\theta_i^{m+1,s+1} - \theta_i^{m+1,s}$ to the LHS of Equation (11). When the scheme converges for sufficiently large s, this term vanishes, which preserves the equality of Equation (11). In our previous work focusing on solving standard Richards equation [2,17], we developed a systematic procedure for choosing $\gamma_i^{m+1,s}$ that would guarantee convergence and stability of the numerical scheme. In this work, we follow the same procedure for choosing the appropriate $\gamma_i^{m+1,s}$.

## Encoder-decoder-type data-driven framework

Once our adaptive linearization scheme of the FVM-discretized time-fractional Richards equation is established, we will obtain soil moisture solutions $\theta_i^{m+1,s}$ for every cell, time step, and iteration. Through the encode-decoder-type architecture, these solutions will first be mapped to their corresponding variables denoted as $\mu_i^{m+1,s}$ in a latent space via a trained neural network $\mathrm{f}_{\mathrm{NN}}$ (i.e., $\mathrm{f}_{\mathrm{NN}}$: $\theta_i^{m+1,s} \to \mu_i^{m+1,s}$), followed by applying inverse mapping from the latent space back to the soil moisture solutions $\hat{\theta}_i^{m+1,s}$ (which are expected to be more accurate than $\theta_i^{m+1,s}$ ) via another trained neural network $\mathrm{f}_{\mathrm{NN}}^{-1}$: $\mu_i^{m+1,s} \to \hat{\theta}_i^{m+1,s}$.

The dataset used to train the two neural networks

will come from two different sources/solvers. For example, during neural network training, $\theta$ solutions could be soil moisture solutions obtained from fixed point iteration scheme under different choices of linearization parameters and total iteration counts that cover their ranges expected during the actual solution process, whereas the $\mu$ solutions may come from direct sensor measurements or a simple finite difference based solver. Furthermore, we apply data augmentation to these "reference solutions" by adding zero-mean Gaussian noise with different variances [4]. After data augmentation, the resulting expanded set of reference solutions will be used for neural network training. This data augmentation step not only increases the size of the training dataset without having to actually solve the numerical schemes (thereby saving significant computational time), but also reflects the characteristics of actual soil sensing data, which are subject to various measurement uncertainties due to instrumental error, environmental uncertainties, and imperfect installation and maintenance. It turns out that introducing Gaussian noise can greatly reduce the biases of reference solutions and enhance generalization performance, thereby significantly improving the accuracy of numerical solutions.

Our data-driven adaptive fixed point iteration scheme works as follows. For a given time step $\mathrm{m}$ and iteration count $\mathrm{s}$, $\mathrm{f_{NN}}$ first maps the $\theta_i^{m+1,s}$ to a latent space where $\mu_i^{m+1,s} = \mathrm{f_{NN}}(\theta_i^{m+1,s})$ lies upon. The resulting adaptive linearization scheme of FVM-discretized time-fractional Richards equation in terms of $\mu_i^{m+1,s}$ is given by:

$$\mu_i^{m+1,s+1} - \mu_i^{m+1,s} = \frac{1}{\gamma_i^{m+1,s}}\left\{\mathrm{I}_{0^+}^{\alpha}\left[\sum_{j=1}^{N_{\omega_i}}(C\nabla\mu)_{\omega_{i,j}}^{m+1}\cdot \hat{n}_{\omega_{i,j}}A_{\omega_{i,j}}\right] - \mathrm{I}_{0^+}^{\alpha}\left[\sum_{j=1}^{N_{\omega_i}}(C\nabla\mu)_{\omega_{i,j}}^{m}\cdot \hat{n}_{\omega_{i,j}}A_{\omega_{i,j}}\right]\right\} + \frac{1}{\gamma_i^{m+1,s}}\mathrm{f_{NN}}(J), \tag{12}$$

where the quantity J is given by:

$$J = (\theta_i^m - \theta_i^{m+1,s})\mathrm{vol}(V_i) + \mathrm{I}_{0^+}^{\alpha}\left[\sum_{j=1}^{N_{\omega_i}}(K(\theta)\nabla z)_{\omega_{i,j}}^{m+1}\cdot \hat{n}_{\omega_{i,j}}A_{\omega_{i,j}}\right] - \mathrm{I}_{0^+}^{\alpha}\left[\sum_{j=1}^{N_{\omega_i}}(K(\theta)\nabla z)_{\omega_{i,j}}^{m}\cdot \hat{n}_{\omega_{i,j}}A_{\omega_{i,j}}\right].$$

Once $\mu_i^{m+1,s+1}$ is obtained by solving Equation (12) (which is an explicit scheme) provided $\mu_i^{m+1,s}$, we will apply the inverse mapping $\mathrm{f_{NN}^{-1}}$ to transform $\mu_i^{m+1,s+1}$ from the latent space back to its original space $\hat{\theta}_i^{m+1,s+1} = \mathrm{f_{NN}^{-1}}(\mu_i^{m+1,s+1})$. And the entire solution process iterates itself until a stopping criterion is reached. A commonly used stopping criterion is the relative error, which is estimated as $\varepsilon = \max_{\mathrm{i}} \frac{|\mathrm{f_{NN}^{-1}}(\mu_i^{m+1,s+1}) - \mathrm{f_{NN}^{-1}}(\mu_i^{m+1,s})|}{|\mathrm{f_{NN}^{-1}}(\mu_i^{m+1,s+1})|}$. Or, one can specify the total number of iterations needed for each time step and cell (which is what we use for the case study).

We remark that, the two neural networks $\mathrm{f_{NN}}$ and $\mathrm{f_{NN}^{-1}}$ can be treated as encoder and decoder, respectively, and Equation (12) essentially employs the "message passing" idea [16] via our numerical scheme.

## Solving inverse problem using MCMC approach

To solve the inverse problem of identifying soil parameters, we adopt a simple MCMC approach with Metropolis-Hasting (M-H) algorithm [9]. The algorithm begins by selecting an initial set of parameters $\alpha_0$. For each iteration, a candidate $y$ is drawn from the proposal density $q(\cdot|\alpha_t)$. The acceptance probability $h(\alpha_t|y)$ is then computed. If a randomly drawn value $r$ from the uniform distribution $\mathcal{U}([0,1])$ is less than $h(\alpha_t|y)$, the candidate $y$ is accepted, and $\alpha_{t+1}$ is updated to $y$. Otherwise, the current parameter $\alpha_t$is retained, setting $\alpha_{t+1} = \alpha_t$. This process continues iteratively to explore the parameter space.

# AN ILLUSTRATIVE EXAMPLE

In this section, we test and validate our proposed numerical framework on 1-D benchmark problem presented in [11], which features both classical and anomalous diffusion, by comparing our numerical solution with the analytical solution as well as solution obtained using fixed point iteration scheme.

## 1-D Classical Diffusion

For the classical diffusion problem, the parameter $\alpha$ is set to be 1. A constant soil moisture diffusivity $C = 24\times10^{-5}\ \mathrm{cm^2 min^{-1}}$ is used. The boundary condition is given by $\theta(0,t) = 0.5$ and $\theta(\infty,t) < \infty$. The initial condition is given by $\theta(z,0) = \begin{cases}0.5, \text{if } z = 0\\ 0.1, \text{if } z > 0\end{cases}$. The analytical solution for this problem is $\theta(z,t) = 0.4\cdot\mathrm{erfc}\left(\sqrt{\frac{z^2}{4Ct}}\right) + 0.1$.

Overall, we generate an augmented training dataset containing 84,480 pairs of noise-added solutions from solvers employing fixed point iteration scheme and our previously developed solver [2]. Two neural networks $\mathrm{f_{NN}}$ and $\mathrm{f_{NN}^{-1}}$, each adopting 5 layers with 32, 64, 128, 64, 32 neurons per layer and (leaky) ReLU activation function, are trained for 10000 epochs by Adam optimizer with a learning rate of 0.001.

From the results in Figure 1 and Table 1, one can make several observations. First, solution accuracy highly depends on the choice of linearization parameters, and without the prior knowledge about where the ground truth solution lies, it will be challenging for fixed point iteration scheme to correctly identify the optimal linearization parameter to use by itself. Second, for this specific problem, since the solution quality of fixed point iteration scheme changes as $\frac{1}{\gamma}$ varies from 1 to 500, a trial-and-error process, which is both tedious and computationally expensive, will be required for identifying the optimal linearization parameter. Our proposed framework, on the

other hand, does not require such trial-and-error procedure. Third, our proposed numerical framework closely matches with the analytical solution quite well, thanks to the adoption of adaptive fixed point iteration scheme and the integrated data-driven approach.

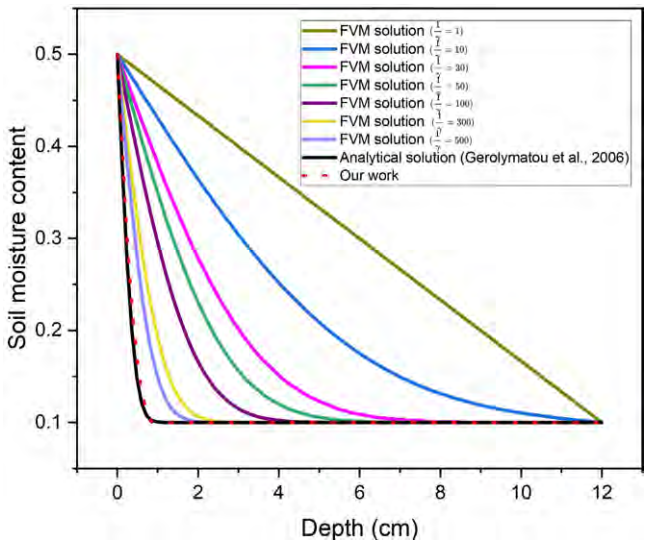



**Figure 1.** Numerical solutions obtained from fixed point iteration scheme and our numerical framework by setting 2,000 iterations as the stopping criterion for each time step and cell. In this example, we study the soil moisture profile across a 12-cm deep soil when $t_{total} = 200$ min.

**Table 1.** Mean Squared Error (MSE) measuring the discrepancy between numerical solutions and the analytical solution.

| Method | $\frac{1}{\gamma}$ value | MSE |
|---|---|---|
| FVM with a static fixed linearization parameter | 1 | 0.0487 |
| | 10 | 0.0239 |
| | 30 | 0.0121 |
| | 50 | 0.0085 |
| | 100 | 0.0050 |
| | 300 | 0.0017 |
| | 500 | 0.0009 |
| Our work | N/A | $2.4731 \times 10^{-5}$ |

## 1-D Anomalous Diffusion

We consider the case of subdiffusion ($0 < \alpha < 1$) for anomalous diffusion problem. Again, a constant soil moisture diffusivity $C = 24 \times 10^{-5}\ \mathrm{cm^2 min^{-\alpha}}$ is used. Other the boundary and initial conditions are the same as in classical diffusion problem. The analytical solution for this problem is given by $\theta(z,t) = 0.4 \cdot \mathrm{H}_{1,1}^{1,0}\left(\sqrt{\frac{z^2}{4Ct^\alpha}}\middle| \begin{matrix}(1,\alpha/2)\\(0,1)\end{matrix}\right) + 0.1$, where $\mathrm{H}_{1,1}^{1,0}(\cdot)$ is the Fox function (see [11] for more details).

First, we solve the forward problem by considering $\alpha = 0.6$. We are mainly interested in the top 1.2 cm of soil, where the soil moisture changes significantly. From Figure 2, it is clear that, compared to the asymptote solution presented in [11], our numerical framework achieves remarkable accuracy even when simulating the region where soil moisture changes the most. Second, we investigate the performance of numerical framework in solving inverse problem when it is integrated with MCMC approach. Without informing our solver, we set the soil parameters as $\alpha = 0.13$ and $C = 24 \times 10^{-5}\ \mathrm{cm^2 min^{-\alpha}}$. We examine two scenarios, one at $t_{total} = 3$ min and the other at $t_{total} = 300$ min. Due to the ill-posedness of this inverse problem, we impose upper and lower bounds for the two parameters $0 < \alpha < 1$ and $0 < C < 30 \times 10^{-5}\ \mathrm{cm^2 min^{-\alpha}}$. The results in Figure 3 shows that the MCMC approach can estimate the soil parameters reasonably well (<20% and <1% relative discrepancy for $\alpha$ and $C$, respectively). Furthermore, it provides an error bar for the parameters being estimated, which provides basis for uncertainty quantification.

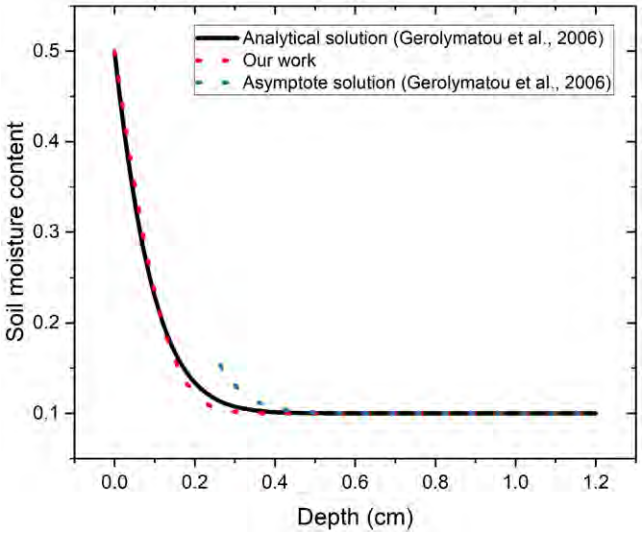



**Figure 2.** Solutions obtained from our numerical framework (stopping criterion: 2,000 iterations for each time step and cell) comparing to asymptote solution and analytical solution [11]. In this example, we examine the soil moisture profile across a 1.2-cm deep soil when $t_{total} = 200$ min. Here, $\alpha = 0.6$. Note that the MSE between numerical solutions from our numerical framework and analytical solution is $3.9130 \times 10^{-6}$, while that of asymptote solution is $6.7163 \times 10^{-5}$.

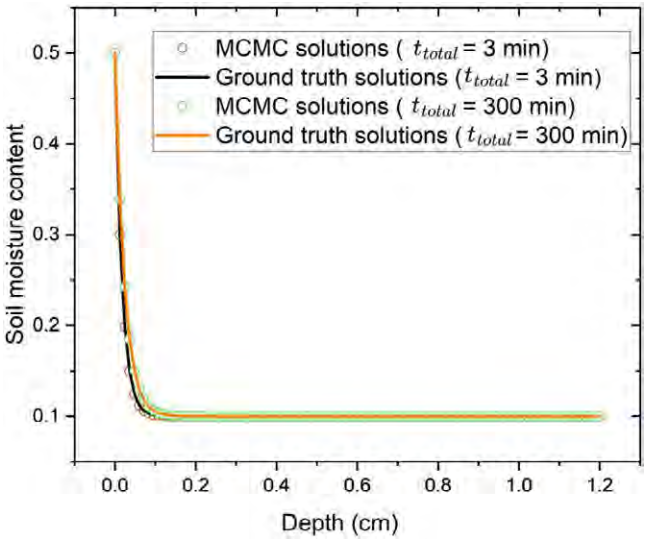



**Figure 3.** Numerical solutions obtained using the parameters identified by MCMC approach. Here, we conduct 1000 samplings. The resulting parameters are $\alpha = 0.13071 \pm 3.7310 \times 10^{-5}$ and $C = 23.808 \times 10^{-5} \pm 3.232 \times 10^{-12} \mathrm{cm}^2 \mathrm{min}^{-\alpha}$. Note that the MSE between numerical solutions and desired solutions are $2.8096 \times 10^{-8}$ and $7.6698 \times 10^{-9}$ for $t_{total} = 3\ \mathrm{min}$ and $t_{total} = 300\ \mathrm{min}$, respectively.

## CONCLUSION

In this work, we develop a novel physics-based, data-driven numerical framework for simulating anomalous diffusion of water in porous media such as soil, which is characterized by the highly nonlinear time-fractional Richards equation. To address the computational challenges associated with existing solvers, we integrate neural networks and adaptive fixed point iteration scheme in a FVM discretization framework. These innovative approaches not only improves solution accuracy and robustness, but also open opportunities for integrating physics-based models with in situ soil moisture sensing technologies for precision agriculture applications. We also briefly introduce a systematic approach to solve the inverse problem using MCMC. Preliminary results obtained on a 1-D benchmark problem indicate that our proposed forward and inverse problem solvers can be highly accurate and useful. Nevertheless, we notice that one limitation of the MCMC approach for solving the inverse problem is that its accuracy highly depends on the selection of parameter bounds. In our future work, we plan to investigate other probabilistic methods that are more scalable and robust for solving inverse problems (i.e., model parameter estimation and uncertainty quantification given in situ soil moisture measurements). Overall, it is expected that this numerical framework would be integrated in an irrigation control mechanism to provide farmers with quantitative insights and recommendations regarding when to irrigate, where to irrigate, and how much to irrigate [18].

## ACKNOWLEDGEMENTS

We gratefully acknowledge financial support from Oklahoma State University College of Engineering, Architecture, and Technology's Startup Fund No. 1-155160.

## REFERENCES

1. Richards LA. Capillary conduction of liquids through porous mediums. Physics 1(5): 318-333 (1931) https://doi.org/10.1063/1.1745010
2. Song Z, Jiang Z. A novel numerical method for agro-hydrological modeling of water infiltration in soil. Preprint available at arXiv:2310.02806. https://doi.org/10.48550/arXiv.2310.02806
3. Ramos NM, Delgado JM, De Freitas VP. Anomalous diffusion during water absorption in porous building materials – experimental evidence. Defect and Diffusion Forum 273: 156-161 (2008) https://doi.org/10.4028/www.scientific.net/DDF.273-276.156
4. El Abd A, Abdel-Monem AM, Kansouh WA. Investigation of isothermal water infiltration into fired clay brick by scattered neutrons. J Radioanal Nucl Chem 293: 503-510 (2012) https://doi.org/10.1007/s10967-012-1788-9
5. Płociniczak Ł. Analytical studies of a time-fractional porous medium equation: Derivation, approximation, and applications. Commun Nonlinear Sci Numer Simul 24(1-3): 169-183 (2015) https://doi.org/10.1016/j.cnsns.2015.01.005
6. Meerschaert MM, Tadjeran C. Finite difference approximations for fractional advection–dispersion flow equations. J Comput Appl Math 172(1): 65-77 (2004) https://doi.org/10.1016/j.cam.2004.01.033
7. Liu Y, Du Y, Li H, He S, Gao W. Finite difference/finite element method for a nonlinear time-fractional fourth-order reaction–diffusion problem. Comput Math Appl 70(4): 573-91 (2015) https://doi.org/10.1016/j.camwa.2015.05.015
8. Qin X, Yang X. A finite point method for solving the time fractional Richards' equation, Math Probl Eng, 2019(1):8358176. https://doi.org/10.1155/2019/8358176
9. Sambridge M, Mosegaard K. Monte Carlo methods in geophysical inverse problems, Rev Geophys, 40(3):3-1 (2002) https://doi.org/10.1029/2000RG000089
10. Podlubny I. Fractional Differential Equations: An Introduction to Fractional Derivatives, Fractional

Differential Equations, to Methods of Their Solution and Some of Their Applications. Elsevier (1998).
11. Gerolymatou E, Vardoulakis I, Hilfer R. Modelling infiltration by means of a nonlinear fractional diffusion model. J Phys D Appl Phys 39(18):4104 (2006) 10.1088/0022-3727/39/18/022
12. Gorenflo R., Mainardi F. Fractional Calculus: Integral and Differential Equations of Fractional Order. Springer Vienna (1997).
13. Sun H, Meerschaert MM, Zhang Y, Zhu J, Chen W. A fractal Richards' equation to capture the non-Boltzmann scaling of water transport in unsaturated media. Adv Water Resour 52:292-5 (2013) https://doi.org/10.1016/j.advwatres.2012.11.005
14. Diethelm K. Error estimates for a quadrature rule for Cauchy principal value integrals. In: Proc. Sympos. Appl. Math. Ed: Walter G. American Mathematical Society (1994)
15. Amrein M. Adaptive fixed point iterations for semilinear elliptic partial differential equations. Calcolo 56(3):30 (2019) https://doi.org/10.1007/s10092-019-0321-8
16. Brandstetter J, Worrall D, Welling M. Message passing neural PDE solvers. arXiv preprint arXiv:2202.03376 (2022)
17. Song Z, Jiang Z. A Data-driven Modeling Approach for Water Flow Dynamics in Soil, Computer Aided Chemical Engineering 52:819-824 (2023). https://doi.org/10.1016/B978-0-443-15274-0.50131-1
18. Gohar AA, Amer SA, Ward FA. Irrigation infrastructure and water appropriation rules for food security. J Hydrol 520:85-100 (2015) https://doi.org/10.1016/j.jhydrol.2014.11.036

© 2025 by the authors. Licensed to PSEcommunity.org and PSE Press. This is an open access article under the creative commons CC-BY-SA licensing terms. Credit must be given to creator and adaptations must be shared under the same terms. See https://creativecommons.org/licenses/by-sa/4.0/



Systems & Control Transactions

**Research Article - Peer Reviewed Conference Proceeding**
ESCAPE 35 - European Symposium on Computer Aided Process Engineering
Ghent, Belgium. 6-9 July 2025
Jan F.M. Van Impe, Grégoire Léonard, Satyajeet S. Bhonsale,
Monika E. Polańska, Filip Logist (Eds.)

PSE PRESS

# CFD Simulations of Mixing Dynamics and Photobioreaction Kinetics in Miniature Bioreactors under Transitional Flow Regimes.

**Bovinille Anye Cho [a]*, George Mbella Teke [b], Godfrey K. Gakingo [c], Robert W.M. Pott [b] and Dongda Zhang [a]**

[a] Department of Chemical Engineering, The University of Manchester, Manchester, United Kingdom
[b] Department of Chemical Engineering, University of Stellenbosch, Stellenbosch, South Africa
[c] Department of Chemical Engineering, Dedan Kimathi University of Technology, Nyeri, Kenya
* Corresponding Author: bovinille.anyecho@manchester.ac.uk.

## ABSTRACT

Miniaturised stirred bioreactors are crucial in high-throughput bioprocesses for their simplicity and cost-effectiveness. To accelerate process optimisation in chemical and bioprocess industries, models that integrate CFD-predicted flow fields with (bio)reaction kinetics are needed. However, conventional two-step coupling methods, which freeze flow fields after solving hydrodynamics and then address (bio)reaction transport, face numerical challenges in miniaturised systems due to unsteady radial flows, recirculation zones, and secondary vortices. These flow fluctuations prevent steady-state hydrodynamic convergence. This study addresses these challenges by time-averaging the RANS solutions of the transitional SST model to achieve statistical hydrodynamic convergence. This method is particularly effective for internal flow problems at low to midrange Reynolds numbers (<10,000), typical of transitional regimes. Following this, photo-bioreaction transport models were solved using these converged fields, considering the bioreactor's directional illumination and curvature. Applied to a 0.7 L Schott bottle photobioreactor mechanically mixed by a magnetic stirrer (100-500 rpm), the model predictions were thoroughly validated against tracer dye experiments and *Rhodopseudomonas palustris* biomass growth data. It accurately predicted swirly vortex fields at 500 rpm with a 7% error margin and the biomass growth profiles align to literature datasets. However, parallel computing efficiency did not scale linearly from 16 to 32 processor cores (4G of RAM/core), making time-averaging computationally expensive for simulating scale-up bioreactors. Improved bioreactor mixing influenced cell light/dark cycles and enhanced biomass productivity but stirring speeds above 300 rpm required increased light intensity (>100 W/m²) due to light limitation. This model provides a framework for optimising stirring speeds and refining operational parameters, aiding in the scale-up and scale-down of bioprocesses.

**Keywords**: Miniaturised stirred bioreactors, CFD modelling, Photobioreactor, Light attenuation and transport, Bioreaction kinetics.

## INTRODUCTION

As the global population grows, the demand for sustainable bioproducts intensifies, necessitating efficient large-scale production infrastructure such as bioreactors [1]. These bioreactors facilitate microbial conversion of substrates into valuable products like biofuels and biochemicals. Among factors influencing bioreactor performance, mixing plays a pivotal role and is achieved through mechanical, pneumatic, or natural circulation techniques[1]. Mechanical methods, including stirred tanks, magnetic stirrers, and orbital shakers, dominate process development due to their ability to meet critical scale-up criteria like power per unit volume and mixing time. Pneumatic mixing often complements these systems with pumps and spargers to facilitate oxygen

transfer rates, further enhancing process efficiency. In contrast, natural circulation, which relies on temperature-induced density differences for buoyancy-driven motion [1,2], is less commonly used in industrial applications.

To accelerate bioreactor design and optimisation across different configurations, Computational Fluid Dynamics (CFD) serves as a critical tool, simulating fluid flow and reaction transport across scales. However, challenges arise when simulating transitional flow regimes, especially in small-scale stirred bioreactors such as magnetic stirrer-driven systems, widely used for microbial strain screening and process optimisation [1,3]. In these systems, unsteady radial flows and secondary vortices prevent steady-state hydrodynamic convergence, complicating CFD-biokinetics coupling via the two-step approach: i.e., solving hydrodynamic to convergence in step one and freezing flow fields in step one to solve for bioreaction transport in step two [1,4–6], thus hindering scale-up. While time-averaging techniques address oscillating flow variables in other contexts [7–9], their application to transitional regime bioreactors remains largely unexplored for CFD-biokinetics coupling. High computational cost likely contributes to this gab, alongside the limitations of existing light transport models for photobioreactors, which are often limited to simplified geometries [6,10]. These challenges are further compounded when extending to 3D cylindrical systems. This underscores an urgent need for more efficient coupling approaches and advanced algorithms that seamlessly integrate fluid dynamics with (bio)reaction kinetics, enabling higher accuracy and reproducibility across scales, facilitating scalable and cost-effective bioreactor designs for industrial applications.

Therefore, this study develops a 3D CFD model for a cylindrical bioreactor mixed by a magnetic stirrer, operating under transitional flow regimes simulated with SST turbulence models. A case study involving a Schott bottle photobioreactor demonstrates the integration of light transport and photo-bioreaction kinetics. Experimental validation, including dye tracing and biomass photoproduction by *Rhodopseudomonas palustris*, confirms the model's accuracy. This work advances the coupling of CFD-predicted hydrodynamics and biokinetics, addressing a critical gap in bioreactor design for high-throughput and scalable production systems.

## METHODOLOGY

### Experimental setup, tracer conductivity measurements and photobioreaction model

The Schott bottle photobioreactor, previously described in detail [1,2], is a cylindrical glass vessel optimised for light transmission and minimal near-wall dead zones. It features autoclavable GL45 polypropylene lids and stainless-steel sampling tubes, with temperature controlled by a water bath. For this study, the overhead section and water bath were excluded to reduce the computational domain. The experimental setup, shown in Fig. 1 a), includes two conductivity probes placed at 62.5 mm and 47.5 mm from the bioreactor top to monitor tracer (NaCl) concentrations. Deionised water was filled to a height of 92 mm (680 mL working volume), and stirring speeds ranged from 100–500 rpm, generating transitional to early turbulent flow regimes. At $t$ = 0, 1 mL of 0.2 M NaCl was added, and normalised tracer data was collected and analysis for validations of CFD predicted hydrodynamic fields.

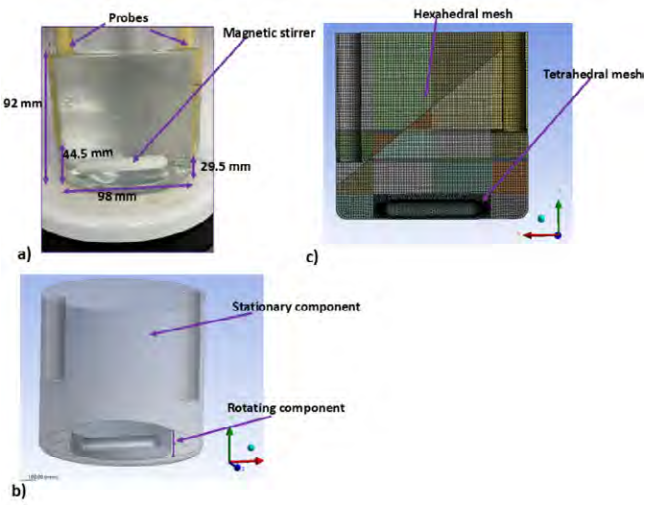



**Fig 1.** Experimental and numerical setup: a) Schott bottle bioreactor, mixed using a magnetic stirrer, illustrating the bioreactor dimensions and probe insertion points. b) 3D CFD geometry designed for a multi-reference simulation approach, incorporating an inner rotating component for the magnetic stirrer and an outer stationary component representing the remaining bioreactor structure. c) hybrid computational mesh, combining hexahedral and tetrahedral elements, was employed to discretize the computational domain efficiently.

Bioreaction simulations modelled *R. palustris* biomass growth, focusing on light/dark cycles driven by magnetic stirring dynamics. Shortened cycles at higher rpms improve photosynthetic efficiency by optimising protein oxidation-reduction balance, enhancing microbial growth [5]. The mechanistic growth model, along with parameter estimates retrieved from our previous work [3] is expressed as Eq. (1):

$$\frac{dX}{dt} = \mu_B \cdot X = \left[A' \cdot \exp\left(-\frac{E_a}{RT}\right) \approx 0.189\ hr^{-1}\right] \cdot \left(\frac{\frac{I_0}{(\tau \cdot X) \cdot L} \cdot \left(1 - e^{-(\tau \cdot X) \cdot l}\right)}{k_s + \left(\frac{I_0}{(\tau \cdot X) \cdot L} \cdot \left(1 - e^{-(\tau \cdot X) \cdot l}\right)\right)}\right) \cdot X \quad (1)$$

Here, key parameters include the specific growth rate ($\mu_B$), biomass concentration ($X$), incident light intensity ($I_o$), light absorption coefficient ($\tau$), light path length ($l$), light saturation coefficient ($k_s$) and temperature ($T$=*308.15* K), among others reported in [3] and thus not repeated here.

## CFD modelling

### Hydrodynamic model setup

The simulation employed the Volume of Fluid (VOF) method [1,11,12] to accurately model the two distinct phases: the liquid bio-suspension and the gaseous headspace, within the computational domain depicted in Fig. 1 b) and c). The chaotic fluid motion induced by magnetic stirring forces (Coriolis and centrifugal) was captured using the four-equation transitional SST (γ-Reθ) turbulence model [1,13]. This model seamlessly blends the k-ε and k-ω turbulence frameworks to simulate laminar, transitional, and turbulent flow regimes, ensuring precise representation of flow dynamics across a range of rotational speeds (100–500 rpm). The detailed mathematical formulation of the VOF model and the blending methodology of the k-ε and k-ω models within the transitional SST framework has been thoroughly described in prior studies [1,13] and is therefore not repeated here.

### Coupling of CFD hydrodynamic and photobioreaction models

This study employed a two-step approach [1,5,6], achieving hydrodynamic convergence before coupling bioreaction kinetics. Time-averaged flow variables, such as velocities, ($\bar{u}_{stats}$) and turbulent diffusivity ($\overline{\mu_{K,Turb}}_{stat}$), were calculate and implemented into the biomass transport equation (Eq. (2)) using User Defined Functions (UDFs) written in C programming language, with solutions being stored in User Defined Memories within ANSYS Fluent 2024 R1.

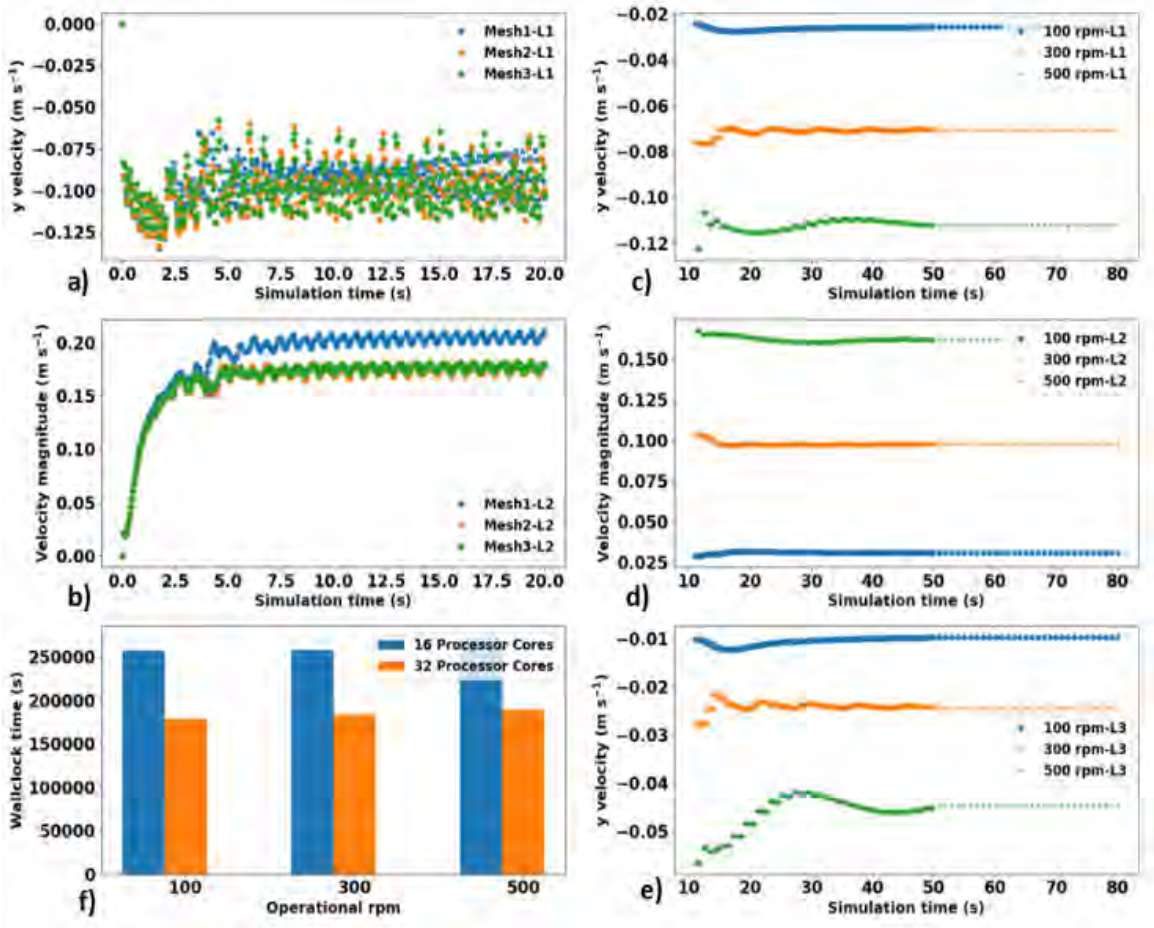



**Fig 2.** CFD hydrodynamic RANS solutions are presented for varying mesh element counts at vertical heights: a) 0.023 m and b) 0.046 m. Time-averaged RANS solutions are shown at vertical heights of c) 0.023 m, d) 0.046 m, and e) 0.069 m, under different operational stirrer rotational speeds. Furthermore, f) depicts the effect of increasing processor core counts on simulation costs during the time-averaging process.

$$\frac{\partial}{\partial t}(X) + \nabla \cdot (\bar{u}_{stats}\, X) = \nabla \cdot \left( \left( \mu_{k,Lam} + \frac{\overline{\mu_{K,Turb}}_{stat}}{Sc_t} \right) \cdot \nabla X \right) + \left[ \mu_B \cdot X = A' \cdot \exp^{\left(-\frac{E_a}{R \cdot T}\right)} \cdot \frac{I_0 \cdot \exp^{(-\tau \cdot X \cdot l)}}{I_0 \cdot \exp^{(-\tau \cdot X \cdot l)} + k_s} \cdot X \right] \quad (2)$$

From left to the right, the terms of Eq. (2) represent the accumulation, convection, diffusion, and biomass growth. Laminar diffusivity ($\mu_{k,Lam}$= 5.5×10-10 m2 s-1) and Schmidt number ($Sc_t$ 0.7) were obtained from literature [1,5]. Light attenuation effects were incorporated via the Beer-Lambert law [1], accounting for L/D cycles and photobioreactor curvature, using polar and Cartesian coordinates [1]. This iteratively methodology was executed with UDFs, ensuring high accuracy in simulating the photobioreaction.

### Solver settings and solution strategy

In stage one, hydrodynamic simulations used a 0.001 s time step, 40 iterations per step, and ran for 50 s. Convergence was achieved when residuals fell below $10^{-6}$, and velocity changes became negligible. Time averaging started after 10 s, yielding a 40 s averaged solution. In stage two, scalar transport was coupled to hydrodynamics with a 0.01 s time step, totalling 150 s for tracer simulations and 6,000 s for biomass transport. Biomass growth kinetics were accelerated by $1.152\times10^3$ to match an 8-day photo-fermentation period [1]. Simulations used parallel computing on 16–32 processors via The University of Manchester's HPC cluster.

## RESULTS AND DISCUSSION

### Grid sensitivity analysis, time averaging and computational cost analysis

To assess mesh independence, three meshes (Mesh1: 406,667 elements, Mesh2: 267,460, Mesh3: 151,291) were tested. Simulations were monitored at three heights (23.0 mm, 46.0 mm, 69.0 mm) in the bioreactor. Increasing mesh density prolonged simulation times from 4.35 hrs (Mesh3) to 32.71 hrs (Mesh1). Despite fluctuations in vertical velocities as depicted in Fig. 2 a) and b) due to the bioreactor's magnetic stirrer, all mesh results were aligned with the literature range of 0.0 m $s^{-1} \leq |\boldsymbol{u}| \leq$ 0.42 m $s^{-1}$ [7], validating their reliability. Mesh2 offered a balance between accuracy and cost and was therefore selected for all subsequent simulations. Time-averaging stabilised flow fields as seen in Fig. 2 c) to e), enabling bioreaction coupling. However, computational costs did not scale linearly with increasing processor cores (16 to 32) as seen in Fig. 2 f), suggesting that simulating larger bioreactors may require cost saving strategies. Techniques like compartment modelling [1,8], which bypass solving momentum balances and continuity equations at every element, could accelerate industrial-scale bioreactor simulations. Nevertheless, the highly fluctuating flow variables may necessitate a numerous compartment, potentially undermining the intended cost savings.

### CFD hydrodynamic: insights, validations and influences on biomass growth and light transport

To validate the CFD model's predictions against experimental results, qualitative and quantitative approaches were used. Qualitatively, visual inspection identified distinct liquid (water) and air zones in the bioreactor, confirming the VOF method's accuracy in representing multiphysics, as shown in Fig. 3 a) to d). Radial recirculation zones, indicated by arrowheads in Fig. 3 c) and d), aligned with literature [1,11,12], with more pronounced swirling at higher stirrer speeds, forming a tornado-like vortex at 500 rpm. This swirling effect's influence on biomass growth remains largely unexplored.

Quantitatively, normalised conductivity probe measurements were compared to CFD predictions. Fig. 3 e) demonstrates strong agreement, with deviations within 6.3%, aligning with literature-acceptable thresholds of 10% [1,2]. Deviations were most pronounced during the first 16 seconds, likely due to limitations in the model's representation of tracer diffusivity upon introduction. Beyond 20 seconds, the model accurately matched equilibrium values, validating its reliability. Lower rpm (100) exhibited the largest overshoots, suggesting reduced mixing velocity delayed tracer detection, a limitation of probe-based techniques [1]. For such fluctuating dynamics at low rpm, non-intrusive validation techniques, such as Laser Doppler Anemometry (LDA), are recommended.

With validated stage one hydrodynamics, stage two coupling to bioreaction simulations assessed hydrodynamic effects on biomass growth. Biomass growth profiles in Fig. 3 f) closely mimic those of purely mechanistic models in the literature [3], verifying the robustness of the coupling of strategy. Increasing stirrer speeds from 100–500 rpm enhanced biomass productivity by 88.16%, although the increase from 300 rpm to 500 rpm was marginal at 1.4% as reported in Table 1. This trend is attributed to improved culture mixing, particularly radial mixing which facilitates more frequent light/dark cycles, enabling microbial cells to absorb light energy for photosynthesis [1,5]. Analysis of the stirrer-induced mixing volume-averaged velocities in Table 1, shows a linear increase from 100 rpm to 500 rpm, corroborating other literature reports for both baffled [1,12] and unbaffled bioreactors [1,11].

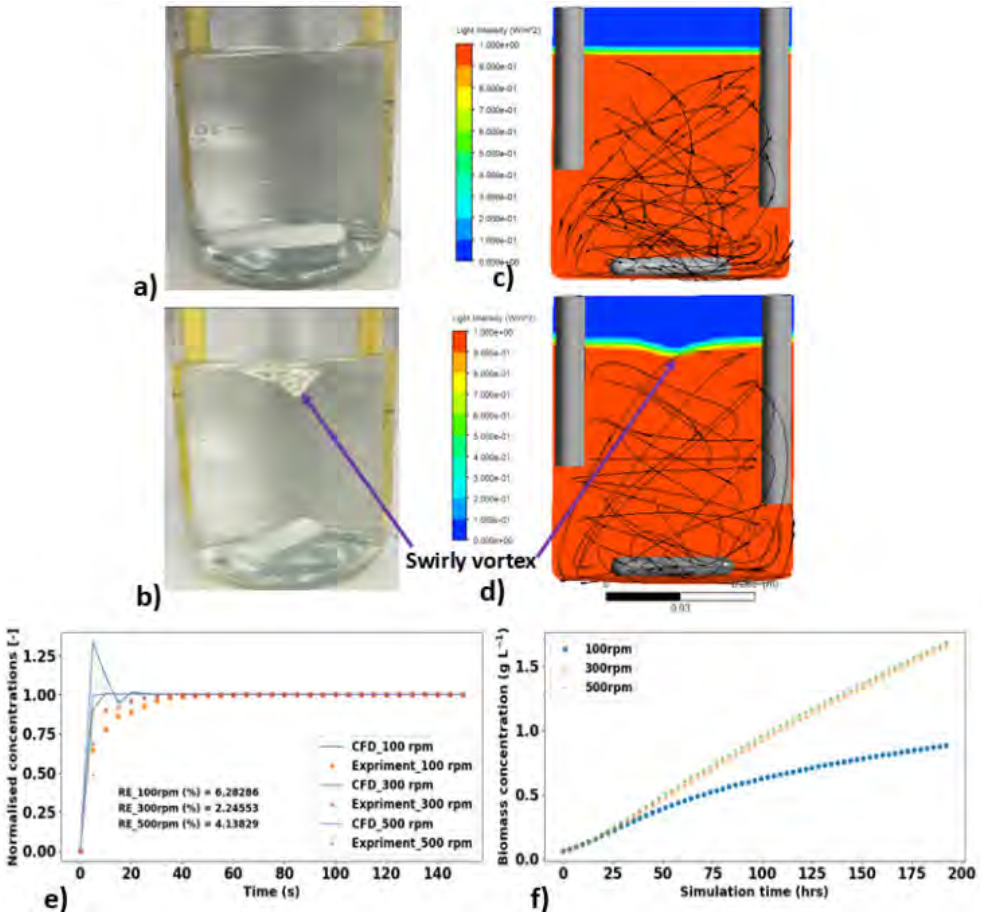



**Fig 3.** Flow visualisation images of the physical bioreactor operating at a) 100 rpm and b) 500 rpm are compared to CFD-predicted flow fields at c) 100 rpm and d) 500 rpm. The presence of swirling vortices in b) and d) confirms qualitative validation of the model. Quantitative validation is shown in e), highlighting the percentage relative error (RE) across different stirrer rotational speeds. Additionally, f) illustrates temporal changes in biomass concentration over time.

However, beyond 300 rpm, the linear increase in mixing velocity did not significantly enhance biomass productivity. This phenomenon can be attributed to excessively rapid light/dark (L/D) cycles, which shorten the relaxation time of excited photosystems, thereby limiting the efficient utilisation of absorbed energy for growth [1,5]. In such cases, microbial cells are effectively exposed to almost continuous light. Similar effects of overly rapid L/D cycles have been reported in the literature under purely turbulent regimes [1,5]. This interpretation is further substantiated by the Reynolds number data in Table 1, which indicates a value of 14,481.6 at 500 rpm—nearly double the 8,469.2 observed at 300 rpm. While prior studies [11,12], including our own [3], have successfully operated these bioreactors at 200 rpm, speeds beyond this benchmark remain largely unexplored.

Interestingly, light attenuation intensified with increasing rpm, becoming severe beyond 300 rpm. At these speeds, cells were exposed to insufficient light, as shown in Fig. 4, where average light intensities dropped to 7.2 W/m² at 300 rpm and 6.9 W/m² at 500 rpm by 112 hours (quantitative data not shown). Such low light levels explain why increasing rpm beyond 300 had negligible effects on biomass productivity (see Table 1). Conversely, augmenting the incident light intensity above 100 W/m² could provide more photoenergy, enhancing productivity at higher rpms. This aligns with findings across various photobioreactor designs in the literature [1,8,14].

**Table 1:** Relationships between biomass changes and the bioreactor's operating parameters.

| Operational rpm | Predicted velocity (m s$^{-1}$) | Calculated Reynolds Number | Final biomass concentration (g L$^{-1}$) |
|---|---|---|---|
| 100 | $2.48 \cdot 10^{-2}$ | 2,423.2 | 0.88 |
| 200 | $5.61 \cdot 10^{-2}$ | 5,488.7 | 1.53 |
| 300 | $8.66 \cdot 10^{-2}$ | 8,469.2 | 1.66 |
| 500 | $1.48 \cdot 10^{-1}$ | 14,481.6 | 1.68 |

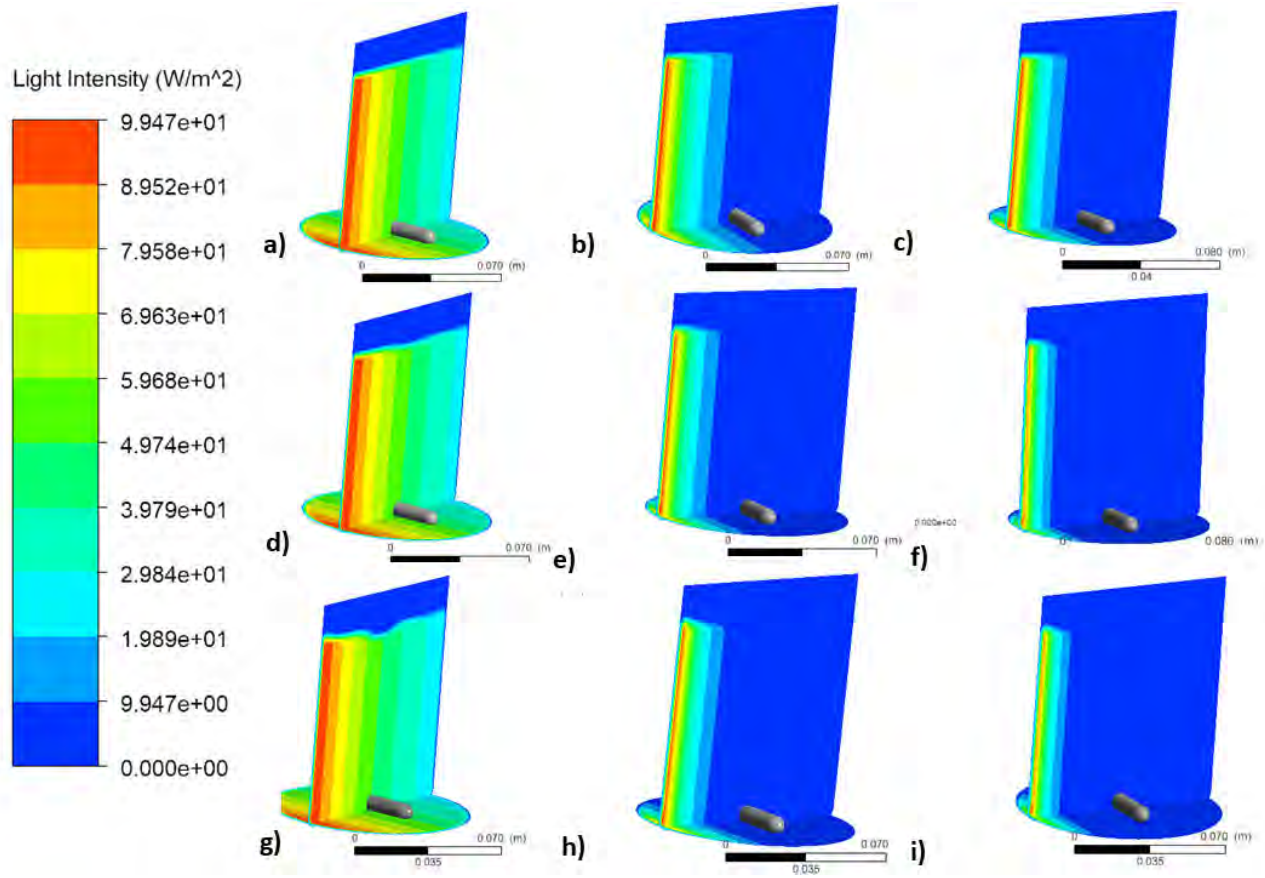



**Fig 4:** CFD qualitative predictions of light transport dynamics in the photobioreactor are shown for various stirrer speeds: 100 rpm (a–c), 300 rpm (d–f), and 500 rpm (g–i). Results were sampled at three-time intervals: 16 hours (a, d, g), 112 hours (b, e, h), and 192 hours (c, f, i). Severe light attenuation at higher operating speeds correlates with increased biomass growth, highlighting the trade-off between light availability and productivity under elevated stirrer speeds.

## Potential applicability of the proposed CFD model

The previous paragraph highlights the potentials of investigating untested bioreactor rotational speeds. However, further exploration of increased incident light intensities is necessary, as prior research with the same microbial strain tested up to 200 W/m² without inducing photoinhibition. A critical limitation of the current mechanistic model is the omission of biomass decay rates, which may result in overestimated growth predictions. This exclusion neglects the impact of shear stresses from high rotational speeds and light-induced stress. Moreover, the lack of a decay term produces unrealistic growth trends. To enhance accuracy, future studies must incorporate decay rates to optimise rotational speeds and light intensities effectively.

## CONCLUSION

This study investigated the challenges of coupling hydrodynamics with bioreaction transport in CFD simulations using a two-step approach, complicated by fluctuating hydrodynamic fields. To address this, hydrodynamic convergence was achieved by time-averaging instantaneous RANS solutions over extended periods, ensuring statistical reliability. These time-averaged fields were then used to simulate bioreaction transport via User Defined Functions (UDFs), which replaced instantaneous RANS fields in the CFD solver. Validation was conducted using a Schott bottle photobioreactor with fluctuating radial velocities, achieving experimental deviations within 7%. The time-averaging approach proved computationally demanding, with non-linear scaling as processor counts increased. Model predictions for light and biomass transport were validated at stirrer speeds below 200 rpm. While higher stirrer speeds enhanced biomass productivity, severe light attenuation above 200 rpm indicated the need for augmented incident light intensities. These findings underscore the necessity of future

optimisations to balance hydrodynamic efficiency and light availability.

## ACKNOWLEGDEMENTS

Dr. Bovinille Anye Cho is a Royal Society Career Development Fellow and sincerely acknowledges the generous funding support provided by the Royal Society, United Kingdom.

## REFERENCES

1. Anye Cho B, Teke GM, Gakingo GK, Pott RWMC, Zhang D. CFD predictive simulations of miniature bioreactor mixing dynamics coupled with photobioreaction kinetics in transitional flow regime. Biochem Eng J 2025;214. https://doi.org/10.1016/j.bej.2024.109585.
2. Anye Cho B, Pott RWM. The development of a thermosiphon photobioreactor and analysis using Computational Fluid Dynamics (CFD). Chemical Engineering Journal 2019;363:141–54. https://doi.org/10.1016/j.cej.2019.01.104.
3. Anye Cho B, Ross BS, du Toit JP, Pott RWMC, del Río Chanona???? EA, Zhang D. Dynamic modelling of Rhodopseudomonas palustris biohydrogen production: Perturbation analysis and photobioreactor upscaling. Int J Hydrogen Energy 2021;46:36696–708. https://doi.org/10.1016/j.ijhydene.2021.08.162.
4. Anye Cho B. Surrogate and Multiscale Modelling for (Bio)reactor Scale-up and Visualisation. In: Zhang D, del Río Chanona EA, editors. Machine Learning and Hybrid Modelling for Reaction Engineering: Theory and Applications, vol. 26, Royal Society of Chemistry; 2023, p. 0. https://doi.org/10.1039/BK9781837670178-00277.
5. Anye Cho B, Carvalho Servia MÁ, del Río Chanona EA, Smith R, Zhang D. Synergising biomass growth kinetics and transport mechanisms to simulate light/dark cycle effects on photo-production systems. Biotechnol Bioeng 2021;118:1932–42. https://doi.org/10.1002/bit.27707.
6. Anye Cho B, Grobler E, William McClelland Pott R, Antonio del Río Chanona? E, Zhang D. A CFD coupled photo-bioreactive transport modelling of tubular photobioreactor mixed by peristaltic pump. Chem Eng Sci 2023;270. https://doi.org/10.1016/j.ces.2023.118525.
7. Brown GJ, Fletcher DF, Leggoe JW, Whyte DS. Investigation of turbulence model selection on the predicted flow behaviour in an industrial crystalliser — RANS and URANS approaches. Chemical Engineering Research and Design 2018;140:205–20. https://doi.org/10.1016/j.cherd.2018.10.007.
8. Nauha EK, Alopaeus V. Modeling outdoors algal cultivation with compartmental approach. Chemical Engineering Journal 2015;259:945–60. https://doi.org/10.1016/j.cej.2014.08.073.
9. López-Rosales L, Sánchez-Mirón A, Contreras-Gómez A, García-Camacho F, Battaglia F, Zhao L, et al. Characterization of bubble column photobioreactors for shear-sensitive microalgae culture. Bioresour Technol 2019;275:1–9. https://doi.org/10.1016/j.biortech.2018.12.009.
10. Alfano OM, Romero RL, Cassano AE. Radiation field modelling in photoreactors—I. homogeneous media. Chem Eng Sci 1986;41:421–44. https://doi.org/10.1016/0009-2509(86)87025-7.
11. Mahmud T, Haque JN, Roberts KJ, Rhodes D, Wilkinson D. Measurements and modelling of free-surface turbulent flows induced by a magnetic stirrer in an unbaffled stirred tank reactor. Chem Eng Sci 2009;64:4197–209. https://doi.org/10.1016/j.ces.2009.06.059.
12. Allonneau C, Olmos E, Guyot S, Ferret E, Gervais P, Cachon R. Hydrodynamic characterization of a new small-scale reactor mixed by a magnetic bar. Biochem Eng J 2015;96:29–37. https://doi.org/10.1016/j.bej.2014.12.005.
13. Menter FR, Langtry RB, Likki SR, Suzen YB, Huang PG, Völker S. A correlation-based transition model using local variables - Part I: Model formulation. J Turbomach 2006;128:413–22. https://doi.org/10.1115/1.2184352.
14. Grobler E, Teke GM, Anye Cho B, Zhang D, W. M. Pott R. Synergistic interplay of photobioreactor mixing and static mixer configuration on Rhodoseupdomonas palustris's growth and biohydrogen production. Fuel 2024;378. https://doi.org/10.1016/j.fuel.2024.132861.

© 2025 by the authors. Licensed to PSEcommunity.org and PSE Press. This is an open access article under the creative commons CC-BY-SA licensing terms. Credit must be given to creator and adaptations must be shared under the same terms. See https://creativecommons.org/licenses/by-sa/4.0/



Systems & Control Transactions

**Research Article - Peer Reviewed Conference Proceeding**
ESCAPE 35 - European Symposium on Computer Aided Process Engineering
Ghent, Belgium. 6-9 July 2025
Jan F.M. Van Impe, Grégoire Léonard, Satyajeet S. Bhonsale,
Monika E. Polańska, Filip Logist (Eds.)

PSE PRESS

# Parameter Estimation and Model Comparison for Mixed Substrate Biomass Fermentation

**Tom Vinestock[a], Miao Guo[a]***

[a] King's College London, Department of Engineering, London, United Kingdom
* Corresponding Author: miao.guo@kcl.ac.uk

## ABSTRACT

Most industrial fermentations in food and drink use a single, high purity sugar as a substrate. These pure substrates are more expensive and less sustainable than mixed substrates, that can be derived from agricultural byproducts such as straw. However, use of mixed substrates in fermentation leads to challenging modelling and parameter estimation problems, particularly when much academic research, intended to inform industrial applications, uses batch fermentations, while large-scale fermentation is usually continuous, thanks to its cost and productivity advantages. Our findings highlight key challenges in using batch-derived experimental data to inform models of the continuous fermentation processes used at industrial scale. Extrapolating from data obtained in batch to continuous fermentation is risky, as models with near-equivalent data-fit and predictions in a batch context give very different predictions for continuous culture. For continuous fermentations to switch to mixed substrates, we need to improve understanding of dual substrate growth in continuous fermentation, to allow for optimised process design and operation.

**Keywords**: Fermentation, Modelling and Simulations, Biosystems, Design Under Uncertainty, Food & Agricultural Processes, Dual Substrate Growth, Lignocellulosic Hydrolysates, Continuous Fermentation

## BACKGROUND

### Single Cell Protein & Agricultural Residues

Currently, animal agriculture accounts for at least 16.5% of global greenhouse gas emissions [1]. Given Net Zero targets, this highlights the need for sustainable alternatives to livestock for dietary protein production. Single cell protein (SCP) fermentation is one such alternative, offering an effective means of transforming carbohydrate-rich substrates into high-protein foodstuffs, and is significantly more sustainable than conventional animal-based protein production, with lower greenhouse gas emissions, water use and land use [2-4]. Therefore, there is a strong environmental interest in increasing consumption and production of SCP to reduce dependence on animal-derived proteins [5].

However, whereas cows and other ruminants can be fed agricultural residues, such as corn stover, wheat and rice straw, SCP fermentations generally depend on high-purity single-substrate feedstocks [6], which are expensive, and directly compete for food crops. This raises the question of how to adapt SCP fermentations to more sustainable feedstocks derived from cheap residues of agriculture and forestry.

Globally, 11 100 megatons of these residues are produced annually [7], which if used as a feedstock for SCP fermentation would be more than enough to provide for all human dietary protein needs [7]. These residues are mainly composed of lignocellulose, a mixture of fibrous lignin and the carbohydrates cellulose and hemicellulose. While hydrolysis can be used to break down this mixture into simpler components, yielding 360g fermentable sugar per kg lignocellulose [7], only about 60% of the resulting fermentable sugar is glucose, the favoured 6-carbon sugar, with the other 40% coming from xylose, a 5-carbon sugar, along with trace sugars such as mannose [7].

### Batch & Continuous Fermentation

Modelling biomass growth on such a mixture of glucose and xylose is complicated and is one of the barriers to widespread adoption of lignocellulosic feedstock in SCP fermentation [8]. To design and operate a large-scale SCP fermentation using a lignocellulosic feedstock, accurate growth models that allow the growth behaviour

on mixed substrates and the resulting yields to be understood are needed. However, academic work to obtain these models often uses batch fermentation experiments [8,9], with all the nutrients available to the system added at the start, while industrial scale SCP production is usually operated as a continuous process, with biomass constantly harvested, and substrate added as it is consumed, as this affords a much higher biomass productivity for a given reactor volume [10].

### Structured & Unstructured Kinetic Models

In bioprocess kinetic modelling, a distinction is made between structured and unstructured approaches. Structured approaches incorporate detailed information about metabolic pathways, and so are useful for metabolic engineering [11] but this complexity can lead to challenges in parameter and state estimation, impeding practical applications [9]. Unstructured approaches, such as the Monod model, use simpler mathematical formulations based on empirical data [9]. The benefit of these models is their greater ease of use, with many fewer state variables and parameters to estimate. As this work focuses on bioprocesses modelling for process optimisation and control, the unstructured approach is adopted.

## RESEARCH OBJECTIVES

This work has two main aims. The first is to compare different unstructured models for dual substrate growth, using previously published batch fermentation data. The second aim is to evaluate these models' ability to predict continuous fermentation dynamics using parameters estimated from batch fermentation data.

The study focuses on the filamentous fungi strain *Fusarium Venenatum* A3/5, which is commercially significant as the most widely used SCP strain for food-grade protein production [12]. Unlike previous research that often examines a single model in the batch context [8,9], this study evaluates five different dual substrate growth models and extends the analysis to continuous fermentation systems. The findings are expected to enhance modelling of lignocellulose-derived mixed substrate fermentations, and illuminate the differences between batch and continuous fermentation in this context.

## METHODOLOGY

### Experimental Data

The data used in this work is from Banks *et al*"s [8] recent publication, in which a microplate reader and high-performance liquid chromatography were combined to measure biomass and (extracellular) glucose and xylose concentrations at regular intervals over a 120-hour batch fermentation on two glucose-xylose mixtures (15 $gL^{-1}$ glucose: 15 $gL^{-1}$ xylose and 20 $gL^{-1}$ glucose:10 $gL^{-1}$ xylose). 3 biological replicates were used, resulting in 3 sets of measurements for each timepoint. 5 different versions of each dataset were generated using leave-one-out validation, to give an indication of the uncertainty of each model's outputs.

### Parameter Estimation

Optimal parameters for each model were found using SciPy's differential evolution (DE) function for parameter optimisation in combination with ODEInt, a SciPy wrapper for LSODA, for numerical integration of the dynamical batch fermentation models defined below for each set of parameters [13, 14]**.** Stochastic methods such as DE can better identify global minima in non-convex problems such as parameter estimation than traditional gradient methods [8]. 50 generations were used for the DE, with initial populations generated using Latin hypercube sampling. At the end of this process the best population member was 'polished' using L-BFGS, a gradient descent method [15]. Default values were used for all the other algorithmic parameters. Mean absolute error (MAE) was used as the cost function, as shown in Equation 1.0. As in Banks *et al.* [8], the feedstock with equal concentrations of glucose and xylose was used as a calibration dataset, while validation was conducted using the 20 $gL^{-1}$ glucose:10 $gL^{-1}$ xylose data.

$$MAE = \frac{1}{3N}\sum_{k=0}^{N-1}\sum_{r=1}^{3}|X_{Pred}[k,r] - X_{Meas}[k,r]| + \left|S_{1,Pred}[k,r] - S_{1,Meas}[k,r]\right| + \left|S_{2,Pred}[k,r] - S_{2,Meas}[k,r]\right| \quad (1.0)$$

In the validation dataset, unmeasurable initial states, such as initial biomass, and where applicable, initial enzyme concentrations/intensities were back-calculated from measured values, using the DE approach described previously.

Each model, parameterised based on the calibration dataset, was then used to predict steady-state continuous fermentation behaviour, assuming a single, mixed feed containing 15 $gL^{-1}$ glucose and 15 $gL^{-1}$ xylose. Optimal dilution rates, defined as the dilution rates leading to the maximum steady-state biomass output rate, were found using exhaustive search for each model, with ODEInt used to numerically integrate the continuous fermentation models. Substrate efficiencies were then calculated based on this operating point.

### Growth Models

Five growth models are compared. Their parameters and states variables are detailed in Tables 1-3.

#### Single Substrate Growth Models

While there are many single substrate growth models, the Monod and Contois models are particularly widely used. The Monod model (EQ 1.1) [16] assumes that

the growth rate depends only on the substrate concentration, approaching a maximum rate of $\mu_{max}$ when the substrate concentration is much higher than the fixed threshold concentration given by $K_s$. The Contois model (EQ 1.2) [17] is similar to the Monod model but assumes that the substrate threshold concentration increases linearly with the biomass concentration.

$$\mu = \mu_{max}\frac{S}{S+K_s}, \qquad \mu = \mu_{max}\frac{S}{S+K_{SX}X} \qquad (1.1, 1.2)$$

## Multi-Substrate Growth Models

In the multi-substrate case, the specific biomass growth rate ($\frac{\dot{X}}{X}$) can be considered the sum of the growth rates ($\mu_i$) on each substrate, which may in general depend on the substrate concentration itself ($S_i$), as well as the concentrations of other substrates ($S_j$), and key enzymes required for the metabolism of the substrate itself ($Z_i$) and other substrates($Z_j$), with each growth rate's upper limit given by a substrate-specific parameter ($\mu_{mi}$).

$$\frac{\dot{X}}{X} = \sum_{i\in\{1,..N\}, j\in\{1,...,N\}, j\neq i} \mu_i\left(S_i, S_j, Z_i, Z_j\right) \qquad (1.3)$$

$$\mu_i \in [0, \mu_{m,i}]$$

As in [8,9], the consumption rate of each substrate ($\dot{S}_i$) is assumed to be specified by:

$$\dot{S}_i = \frac{-\mu_i}{Y_{xi}}X \qquad (1.4)$$

**Table 1:** Parameters common to all growth models considered.

| Symbol | Name | Description | Unit |
|---|---|---|---|
| $\mu_{m,i}$ | Maximum growth rate on substate *i* | Fixed parameter | $h^{-1}$ |
| $Y_{x,i}$ | Yield coefficient | Mass of biomass per mass of substrate *i* consumed | $g_{biomass}$ $g_{substrate}^{-1}$ |
| $\mu_i$ | Current growth rate of substrate *i* | Function depending on substrate and enzyme concentrations. | $h^{-1}$ |

In a continuous system with a dilution rate of $D$ per hour, we have, in the simpler case of two substrates:

$$\frac{\dot{X}}{X} = -D + (\mu_1 + \mu_2) \qquad (1.5)$$

$$\dot{S}_1 = \frac{-\mu_1}{Y_{x1}}X + D(S_{in1} - S_1) \qquad (1.6)$$

$$\dot{S}_2 = \frac{-\mu_2}{Y_{x2}}X + D(S_{in2} - S_2) \qquad (1.7)$$

$$\dot{y} = D * X \qquad (1.8)$$

In a batch system, $D = 0$, resulting in a further simplified system. We consider five different possible functions for $\mu_i$. We assume this function can be split into two parts: the first dealing with single substrate dynamics, the second dealing with interaction between substrates.

**Table 2:** State variables employed in the dual substrate growth models

| Symbol | Name | Applicability | Unit |
|---|---|---|---|
| $X$ | Biomass Concentration | All models | $gL^{-1}$ |
| $S_i$ | Concentration of Substrate *i* | All models | $gL^{-1}$ |
| $y$ | Cumulative Biomass Output | Continuous Models | g |
| $Z$ | Concentration of key enzyme required for growth on xylose | Enzyme Inhibition Model | $gL^{-1}$ |
| $z_i$ | Relative intensity of key enzyme required for growth on substrate *i* | Optimised Enzyme Production Model | % |

## Inhibition Models

When more than one substrate is present, there may be an interaction between the substrates. Usually, the growth rate on a mixture of substrates is less than or equal to the maximum of the single substrate maximum growth rates, because of substrate cross-inhibition [18].

## Direct Inhibition Model

Vega-Ramon *et al.* [9] introduce a direct inhibition model, with an inhibition term of the form:

$$\mu_i = \mu_i' * \frac{1}{1+\frac{S_j}{K_{ij}}} \; for \; i,j \in \{1,2\}, i \neq j, \qquad (2.1)$$

where $\mu_i'$ is the growth rate on substrate *i* in the absence of substrate *j*. Banks *et al.* [8] applied this model to the fermentation of *F. Venenatum* A3/5 on a glucose-xylose mixture, with Contois growth. Glucose growth was assumed to be unaffected by xylose, giving the following equations, with glucose as the preferred substrate ($S_1$) and xylose the less-favoured substrate ($S_2$).

$$\mu_1 = \mu_{m1}\frac{S_1}{S_1 + K_{X1}X}, \qquad (2.2)$$

$$\mu_2 = \mu_{m2}\frac{S_2}{S_2 + K_{X2}X}\frac{1}{1+\frac{S_1}{K_I}} \qquad (2.3)$$

## Enzyme Inhibition Model

**Table 3:** Model Specific Parameters

| Symbol | Name | Description | Model(s) | Unit |
|---|---|---|---|---|
| $K_s$ | Monod Half-Saturation | Substrate Concentration at which growth rate is half full single substrate rate. | Monod | gL-1 |
| $K_{SX}$ | Contois Half-Saturation | Ratio of substrate to biomass concentration giving a growth rate that is half the full rate. | Contois | $g_{substrate}$ $g_{biomass}^{-1}$ |
| $K_I$ | Inhibition Constant | Value of $S_1$ at which growth rate on $S_2$ is halved relative to the growth rate on $S_2$ in the absence of $S_1$. | Direct Inhibition | gL-1 |
| $K_{Z_S}$ | Enzyme Half Saturation | Enzyme concentration at which growth rate on $S_2$ is halved relative to case of excess enzyme. | Enzyme Inhibition | % |
| $K_{Z_d}$ | Enzyme Degradation Rate | | Enzyme Inhibition, Optimal Enzyme Production | h-1 |
| $K_{Z_c}$ | Enzyme Creation Rate | | Enzyme Inhibition, Optimal Enzyme Production | % |

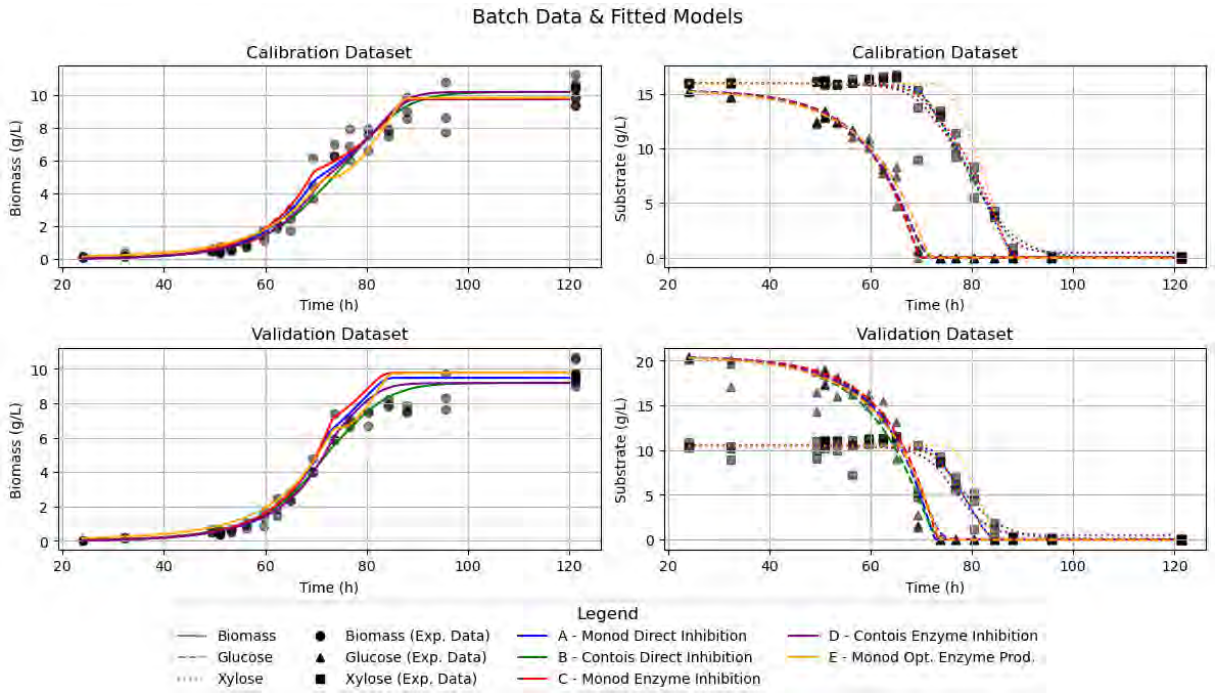



**Figure 1:** Fitted models, and the batch fermentation data from [8] used to fit the models.

Considering potential mechanisms for substrate cross-inhibition, instead of $S_1$ inhibiting $S_2$ growth directly, it can be modelled as reducing the production rate of an enzyme $Z$ that is key for $S_2$ growth and is assumed to be rate limiting at low concentrations. The Monod-type term with a constant $K_{Z_S}$ reflects that at a sufficient value of Z, it is no longer meaningfully rate limiting.

$$\mu_i = \mu_i * \frac{Z}{Z + K_{Z_S}} \tag{3.1}$$

$$\dot{Z} = -(K_{Z_d} + D) * Z + (K_{Z_c} * \mu * X * \frac{S_i}{S_i + K_{Si}} \frac{1}{1 + \frac{S_i}{K_{Z_{Si}}}}) \tag{3.2}$$

This model is a simplification of one proposed by Nakamura *et al.* [19]. Using the Monod model, and assuming as previously that glucose ($S_1$) growth is unaffected by xylose ($S_2$) gives the following:

$$\mu_1 = \mu_{m1} \frac{S_1}{S_1 + K_{S1}}, \quad \mu_2 = \mu_{m2} \frac{S_2}{S_2 + K_{S2}} \frac{Z}{Z + K_{Z_S}} \tag{3.3, 3.4}$$

## Optimal Enzyme Production Model

A third option is to model the concentration of the key enzymes for both $S_1$ and $S_2$ separately. This requires some modelling of cellular decision-making. In Kompala *et al.* [18], it is argued that cells optimise the allocation of resources to maximise growth rate. This leads to:

$$r_i = \mu_{mi} * z_i * S_i \tag{4.1}$$

$$v_i = \frac{r_i}{\max_j(r_j)}, \quad u_i = \frac{r_i}{\sum_j r_j} \tag{4.2, 4.3}$$

$$r_{Z_i} = K_{Z_c} * \frac{S_i}{K_{si} + S_i}, \quad \mu_i = r_i * v_i \qquad (4.4, 4.5)$$

$$Z_i = r_{Z_i} * u_i - K_{Z_d} * z_i - \sum_j \frac{\mu_j}{X} * z_i \qquad (4.6)$$

Here, $z_i$ is a relative enzyme intensity, defined as the enzyme mass per unit biomass, normalised by the maximum possible enzyme intensity.

## RESULTS & DISCUSSION

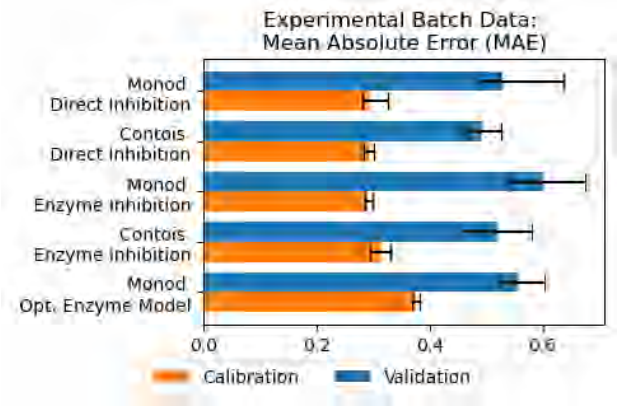



**Figure 2:** MAE in model predictions for calibration and validation batch data. Error bars show minimum and maximum MAE from 5 variant datasets created using leave-one-out method; the main bar shows the mean.

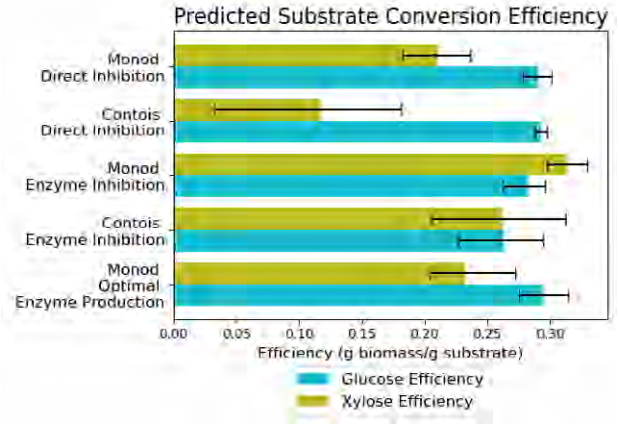



**Figure 3:** Predicted substrate conversion efficiency in continuous fermentation for glucose and xylose for each of the 5 dual substrate models evaluated.

Figure 1 shows that all 5 models give highly similar fits to the both the calibration and validation datasets (for legibility, only a single fit for each model is shown). This can also be seen from Figure 2, which shows the different models have similar errors. The similar values for validation error between the models suggests that the more complex models aren't overfitting.

One interpretation of the results presented in Figures 1-2 would be that the different models aren't meaningfully different. However, applying these models to continuous fermentation challenges this. Looking at Figures 3 and 4, the models make significantly different predictions for substrate yields, biomass production rates and optimal dilution rates in continuous fermentation.

Figure 3 shows the two Direct Inhibition Models predict much lower substrate yields for xylose compared to glucose, whereas the enzyme-based models predict more similar yields for the two substrates. This corresponds to the Direct Inhibition Models predicting that the glucose preference results in xylose being washed through the system in the continuous case, as glucose concentrations don't drop low enough to encourage the switch to xylose when it is diluted at the rate that maximises biomass output. The difficulty in discerning whether co-utilisation of glucose and xylose occurs in batch is the cause of much of the uncertainty in xylose efficiency, production rate and optimal dilution rate in Figures 3-4.

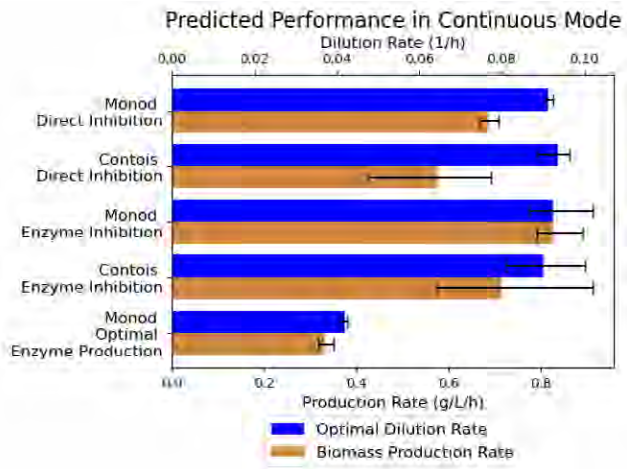



**Figure 4:** Maximum biomass production rates and the corresponding optimal dilution rates calculated for each model, based on the batch data parameterisations.

Figure 4 shows that the different models also predict very different biomass production rates and optimal dilution rates, although the biomass production rates and the optimal dilution rate are closely related, suggesting the steady-state biomass concentration is similar in all cases. There is a factor of about two between the largest predicted production rate, for Monod Enzyme Inhibition, and the smallest, for Monod Optimal Enzyme Production, which demonstrates the difficulty of extrapolating to continuous culture from batch fermentation results.

Additionally, differences, or uncertainties, between models exists alongside the parametric uncertainty within a model. For biomass production rate, optimal dilution rate and xylose efficiency, the inter-model uncertainty, characterised by the difference between model

mean values, exceeded the intra-model uncertainty, characterised by the range of values for one model, by factors of 3.2, 5.6 and 2.4, respectively.

### Limitations

While this work focuses on the uncertainty introduced from extrapolating from batch fermentation data to continuous fermentation performance, the change in reactor volume, and the consequent effects on mixing and gas-transfer, are another major source of uncertainty in the transition from lab scale to industry scale [20]. Additionally, the higher shear stresses from the more vigorous mixing required in large reactor can reduce cell viability and growth [21]. These effects are not addressed in this work, and the uncertainties they introduce would be in addition to the model uncertainty discussed here.

## CONCLUSIONS & FUTURE WORK

This research demonstrates the significant uncertainty generated by using batch fermentation data to assess and parameterise models intended for application to large-scale continuous fermentations. As a result, it suggests a need for greater focus on continuous fermentation within academia, in order to support industrial adoption of lignocellulosic feedstocks. It is relevant to academics and professionals working on design and optimisation of continuous fermentation, as it shows the risks of extrapolating from batch to continuous fermentation.

## ACKNOWLEDGEMENTS

The authors gratefully acknowledge funding from Quorn and the BBSRC, under project reference 2725958.

## REFERENCES

1. Twine R. Emissions from Animal Agriculture—16.5% Is the New Minimum Figure. *Sustainability* (2021)
2. Good Food Institute, Fermentation: State of the industry report. (2021)
3. Nijdam D, Rood T*et al.* The price of protein: Review of land use and carbon footprints from life cycle assessments of animal food products and their substitutes. *Food Policy* (2012)
4. Carbon Trust. Quorn Footprint Comparison Report (2023)
5. Li YP, Ahmadi F. Recent advances and challenges in single cell protein (SCP) technologies for food and feed production. *npj Sci Food* (2024)
6. Vlaeminck E, Uitterhaegen E *et al.* Single-cell protein production from industrial off-gas through acetate: techno-economic analysis for a coupled fermentation approach. *Fermentation* (2023)
7. Piercy E, Verstraete W *et al.* A sustainable waste-to-protein system to maximise waste resource utilisation for developing food- and feed-grade protein solutions. *Green Chemistry* (2023)
8. Banks M, Taylor M, and Guo M. High throughput parameter estimation and uncertainty analysis applied to the production of mycoprotein from synthetic lignocellulosic hydrolysates. *Curr. Res. Food Sci.* (2024)
9. Vega-Ramon F, Zhu X, *et al.* Kinetic and hybrid modeling for yeast astaxanthin production under uncertainty. *Biotechnol. Bioeng.* (2021)
10. Olszewska-Widdrat A, Alexandri M, *et al.* Batch and continuous lactic acid fermentation based on a multi-substrate approach. *Microorganisms* (2020)
11. Ramkrishna D, Song HS. Dynamic models of metabolism: Review of the cybernetic approach. *AIChE Journal* (2012)
12. Ritala A, Häkkinen ST *et al.* Single cell protein—state-of-the-art, industrial landscape and patents 2001–2016. *Front. Microbiol.* (2017)
13. Virtanen P, Gommers R *et al.* SciPy 1.0: fundamental algorithms for scientific computing in Python. *Nature Methods* (2020)
14. Hindmarsh AC, Petzold, LR. LSODA, Ordinary Differential Equation Solver for Stiff or Non-Stiff System. OECD/NEA (2005).
15. Liu DC, Nocedal J. On the limited memory BFGS method for large scale optimization. *Math. Program* (1989)
16. Monod, J. The growth of bacterial cultures. *Annu. Rev. Microbiol.* (1949)
17. Contois DE. Kinetics of bacterial growth: relationship between population density and specific growth rate of continuous cultures. *J. Gen. Microbiol.* (1959)
18. Kompala DS, Ramkrishna D *et al.* Investigation of bacterial growth on mixed substrates: Experimental evaluation of cybernetic models. *Biotechnol. Bioeng.* (1986)
19. Nakamura Y, Sawada T *et al.* Stability analysis of continuous culture in diauxic growth. *J. Ferment. Bioeng.* (1996)
20. Garcia-Ochoa F, Gomez E. Bioreactor scale-up and oxygen transfer rate in microbial processes: An overview. *Biotechnol. Adv.* (2009)
21. Wang C, Lan CQ. Effects of shear stress on microalgae – A review. *Biotechnol. Adv.* (2018)

© 2025 by the authors. Licensed to PSEcommunity.org and PSE Press. This is an open access article under the creative commons CC-BY-SA licensing terms. Credit must be given to creator and adaptations must be shared under the same terms. See https://creativecommons.org/licenses/by-sa/4.0/



Systems & Control Transactions

**Research Article - Peer Reviewed Conference Proceeding**
ESCAPE 35 - European Symposium on Computer Aided Process Engineering
Ghent, Belgium. 6-9 July 2025
Jan F.M. Van Impe, Grégoire Léonard, Satyajeet S. Bhonsale,
Monika E. Polańska, Filip Logist (Eds.)

PSE PRESS

# Integrated hybrid modelling of lignin bioconversion

**Sidharth Laxminarayan[a], Lily Cheung[a], and Fani Boukouvala[a]***

[a] Georgia Institute of technology, School of Chemical and Biomolecular Engineering, Atlanta, GA, USA 30331
* Corresponding Author: faniboukouvala@chbe.gatech.edu

## ABSTRACT

Global biomanufacturing is projected to expand rapidly in the coming decade due to advancements in DNA sequencing and manipulation. However, the complexity of cellular behaviour introduces difficulty in modelling and optimizing biomanufacturing processes. Phenomenological models that represent the physics of the system in empirical equations suffer from poor robustness, while their machine learning (ML) counterparts suffer from poor extrapolative capability. On the other hand, hybrid models allow us to leverage both physical constraints and the flexibility of ML. This work describes a new approach for hybrid modeling that integrates the time-variant parameter estimation and ML model training into a singular step. We implement this approach on a proposed scheme for the cell-mediated conversion of a lignin derivative into a bioplastic precursor and show that our integrated hybrid model outperforms the traditional two-step hybrid, phenomenological, and ML model counterparts. Lastly, we demonstrate how to execute an interpretability analysis on the ML component of the integrated hybrid model to reveal new physical insights that are then used to further improve model performance.

**Keywords**: Biosystems, Machine Learning, Dynamic Modelling, Lignin Valorization

## Motivation & Background

Growing need and sustainability concerns are increasing the strain on the traditional manufacturing pipelines for chemicals, drugs, and materials [1]. This has prompted increased interest on bio-centric manufacturing, as bioprocesses leverage the capability of microbial, plant, and animal cells to produce complex commercially relevant chemicals while enjoying a reduced carbon footprint, moderate reactor conditions, and high stereoselectivity [1]. Previously inaccessible renewable feedstocks can now be converted into bulk chemicals with the aid of metabolic strain engineering. Of particular interest is the soil bacterium *Pseudomonas putida*, which can valorize lignocellulosic biomass (Figure 1). Studies have demonstrated that *P. putida* can convert lignin into cis,cis-muconic acid (MA) [2]. MA can then be utilized to create polymers like Nylon and PET [2]. While the bacterial conversion of lignin into MA is documented, the kinetics is not well understood.

Cells are extremely complex systems with numerous reaction pathways, intermediates and products. Factoring in inter and intra-cellular relationships, it becomes intractable to simulate each cell and track metabolic dynamics [2]. This problem is countered using phenomenological models based on biological intuition that neglect information regarding biomass heterogeneity and metabolite influences on empirical parameters [3]. On the other hand, purely machine learning (ML) models have been shown to capture the nonlinear complexity of bioprocesses but have poor extrapolation and interpretability [3]. Additionally, experimental datasets are often sparse and noisy, resulting in poor model development and calibration, especially for ML models.

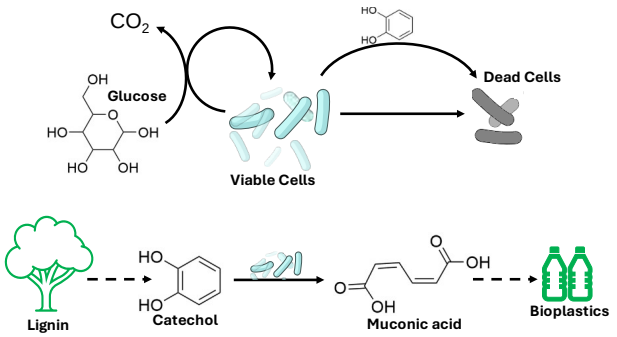



**Figure 1.** Conversion of lignocellulosic biomass into bioplastics by *P. putida*.

Hybrid models have been proposed to leverage the physical constraints of phenomenological models and the flexibility of ML ones [3]. This work explores an embedded hybrid model wherein ML models are utilized to capture the complexity of certain parameters "embedded" within the overarching ODE structure [4]. The hybrid modelling approach aids in capturing the complex relationships between external metabolites and bacteria physiology. Moreover, the embedded approach lends a better framework for interpretability.

To test our hybrid model, we outline a ground truth model that simulates the dynamics of the conversion of catechol, a lignin derivative, to MA by P. putida. The ground truth model also includes glucose as the representative carbon source for bacterial growth and the cell toxicity of catechol. A sparse and noisy dataset is then generated which mimics traditional experimental datasets.

This work will explore two scenarios for constructing hybrid models: A sequential method and an integrated method, which differ on how the parameters of the models are determined. Furthermore, we compare the extrapolative performance of the hybrid model to its phenomenological and ML counterparts. Finally, an interpretability study is performed on the ML components of the hybrid model to gain physical insight. Utilizing Captum python package, an Integrated gradients (IG) analysis is performed which gives insight into how changes in the input affect changes in output for the ML component [5].

## Methods

### Ground truth model

A system of ODEs is constructed to model the dynamics of *P. putida* consuming glucose and converting catechol to MA in a batch process. The system is constructed based on biological principles and previous characterization of *P. putida* [2] The following assumptions are made: (i) the growth rate of viable cells $(X_v)$ follows a logistic-Monod equations aimed at better recapitulating the lag phase of batch cultures (Eq. 1 and 2); (ii) glucose $(C_g)$ promotes cell division while catechol $(C_c)$ inhibits it (Eq. 2); (iii) the cell death rate is composed of a zero-order, catechol-independent component and a catechol-dependent component represented with a Monod-style rate equations (Eq. 2); (iv) dead cells $(X_d)$ are not degraded and accumulate in the culture and contribute to the total biomass $(X_t)$ (Eq. 4 and 5); (v) glucose is consumed for cell growth and to neutralize the toxic effect of catechol (Eq. 6); (vi) the generation of MA $(C_m)$ from catechol has non-growth associated and growth associated components (Eq. 7); and (vii) all the catechol consumed is directly converted to MA by the viable cells and no byproducts are formed (Eq. 8). Note that the following equation can be modified for batch and semi-batch by changing the spike glucose input $\left(C_g^{IN}\right)$, spike catechol input $(C_c^{IN})$ and spike time-period $(\tau)$.

$$\frac{dX_v}{dt} = (\mu_{gr} - \mu_{dt})X_v \quad (1)$$

$$\mu_{gr} = \left(1 - \frac{X_v}{Y_{xg}C_g^0}\right)\left(\frac{\mu_g C_g}{C_g + K_g}\right) \quad (2)$$

$$\mu_{dt} = k_d + \left(\frac{\mu_c C_c}{C_c + K_c}\right) \quad (3)$$

$$\frac{dX_d}{dt} = \mu_{dt}X_v \quad (4)$$

$$X_t = X_v + X_d \quad (5)$$

$$\frac{dC_g}{dt} = -\left(\frac{\mu_{gr}}{\mathrm{Y_{xg}}} + \frac{m_k C_c}{C_c + k_{cm}}\right)X_v + C_g^{IN} f(t) \quad (6)$$

$$\frac{dC_m}{dt} = Y_{mx}(\mu_{gr} + \beta)X_v \frac{C_c}{C_c + k_cr} \quad (7)$$

$$\frac{dC_c}{dt} = -\frac{dC_m}{dt} + C_c^{IN} f(t) \quad (8)$$

$$f(t) = \sum_{k=0}^{Z} \delta(t - \tau k) \quad (9)$$

Training data is generated by assuming batch operation. A 72-hour batch process is simulated with a 10-point discretization. To better reflect limitations in data acquisition commonly experienced in biomanufacturing, only data on the total biomass, glucose, catechol and MA concentrations are used for training (Fig. 2). For instance, only total biomass is easily measured during culturing (e.g., by measuring changes on optical density) while distinguishing viable and dead cells is more challenging. Glucose, catechol and MA are generally quantified with either chromatographic or biochemistry analyzers, which are expensive and time consuming to operate thereby limiting the amount of data collected.

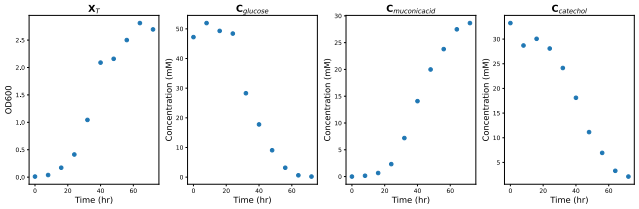



**Figure 2.** Ground truth model of the batch MA production bioprocess.

### Phenomenological model construction

This model reflects the traditional reactor kinetics style system of ODEs that are generally constructed to capture bioprocess dynamics. The data acquisition limitations highlighted in the previous section along with relevant literature informed the model construction. Combining dynamic observations of (Fig. 2) and literature studies [2], the following ODEs for the phenomenological model are created: (i) The total biomass growth is tied positively to glucose and inhibited by catechol via Monod kinetics (Eq.11); (ii) The MA production is observed to

occur in both the growth and stationary phases (Eq. 13); (iii) The MA concentration increased at the same rate as the catechol one decreased (Eq. 14)

$$\frac{dX_t}{dt} = \mu_{gr} X_t \tag{10}$$

$$\mu_{PM} = \left(\frac{\mu_g C_g}{C_g + K_g}\right) - \left(\frac{\mu_c C_c}{C_c + K_c}\right) \tag{11}$$

$$\frac{dC_g}{dt} = -\left(\frac{\mu_{gr}}{Y_{xg}}\right) X_t + C_g^{IN} f(t) \tag{12}$$

$$\frac{dC_m}{dt} = Y_{mx}(\mu_{gr} + \beta) X_t \frac{C_c}{C_c + k_cr} \tag{13}$$

$$\frac{dC_c}{dt} = -\frac{dC_m}{dt} + C_c^{IN} f(t) \tag{14}$$

$$f(t) = \sum_{k=0}^{Z} \delta(t - \tau k) \tag{15}$$

The spike input of glucose and catechol are set to zero for the training data. Note how the growth of the biomass in the phenomenological model closely mirrors the ground truth model.

## Hybrid model structure – Sequential vs Integrated

The construction of the hybrid model entrails the following steps: (a) time-variant parameter estimations (TVPE), (b) ML model parameter regression and (c) ODE-ML model integration. The integrated method differs from the sequential one as it performs steps (a) and (b) together. The equations shown here reflect the hybrid construction methodology. The observations outlined in the previous section are used to inform the overarching ODE structure. An assumption is made that the growth rate did not have a straightforward relationship between glucose and catechol. An artificial neural network (ANN) is used to model the growth rate which used glucose, catechol, MA and total biomass as inputs. Equations (16-19) highlight the hybrid model structure.

$$\frac{dX_t}{dt} = \mu_{ML} X_t \tag{16}$$

$$\mu_{ML} = ANN(X_t, C_g, C_c, C_m) \tag{17}$$

$$\frac{dC_g}{dt} = -\left(\frac{\mu_{ML}}{Y_{xg}}\right) X_t + C_g^{IN} f(t) \tag{18}$$

$$\frac{dC_m}{dt} = Y_{mx}(\mu_{ML} + \beta) X_t \frac{C_c}{C_c + k_cr} \tag{19}$$

Equations 14, 15 are included in the hybrid model to track the dynamics of catechol and the spike input frequency. The sequential hybrid modelling structure initially calculates the TVPE and then trains a ML model outside. Notice that within the initial optimization framework the TVPE is calculated as a discrete value at different time steps. A multi-objective optimization problem is formulated with a state space MSE and a smoothing index (sum of second derivatives) for the time variant parameters. The formulation shown below shows the sequential hybrid model's TVPE.

$$\min_{\theta^{TV}, \theta_{TIV}} \; w_M MSE + w_s SM \tag{20}$$

$$\boldsymbol{s.t.} \frac{dC_{si}}{dt} = f_{ODE}(C_{xi}, \theta_{TIV}, \theta_i^{TV}), \forall\, x = [0, S] \forall\, i = [0, N] \tag{21}$$

$$MSE = \frac{1}{NtS} \sum_{i=1}^{N} \sum_{j=0}^{t} \sum_{s=0}^{S} \left(C_{sji}^{pred} - C_{sji}^{act}\right)^2 \tag{22}$$

$$SM = \frac{1}{Nt} \sum_{i}^{N} \sum_{j}^{t-2} \left(\theta_{ij+1}^{TV} - 2\theta_{ij}^{TV} + \theta_{ij-1}^{TV}\right)^2 \tag{23}$$

$$\theta_{it}^{TV}, \; \theta_{TIV} \geq 0 \tag{24}$$

$N$ represents the number of experimental datasets, $t$ is the number of time points in each dataset and $S$ is the number of dynamic species. $f_{ODE}$ represent the hybrid system of ODE captured by Eqs (14-19). $\theta_{TIV}$ are the time invariant parameters in Eqs (14-19) while $\theta^{TV}$ represents time variant parameters. The integrated hybrid modelling structure simultaneously estimates the growth parameter while also training the ANN model to capture the parameter behavior. The optimization formulation shown below details how the ML model is trained and the TVPE is performed.

$$\min_{W, b, \theta_{TIV}} \frac{1}{NtS} \sum_{i=1}^{N} \sum_{j=0}^{t} \sum_{s=0}^{S} \left(C_{sji}^{pred} - C_{sji}^{act}\right)^2 \tag{25}$$

$$\boldsymbol{s.t.} \frac{dC_{si}}{dt} = f_{ODE}(C_{xi}, \theta_{TIV}, \theta_i^{TV}), \forall\, x = [0, S] \forall\, i = [0, N] \tag{26}$$

$$\theta_i^{TV} = f_{ML}(W, b, C_{xi}) \; \forall\, i = 0 \; to \; N \tag{27}$$

$$\theta_{TIV} \geq 0, \; W, b \subset [-1, 1] \tag{28}$$

$f_{ML}$ represents the ANN whose weights and biases ($W$ & $b$) are used to model the physics of the $\theta^{TV}$. The sequential hybrid modelling structure ignores the second equality constrain shown in Eq. (27) which captures the relationship between the time variant parameter and the ML model. Note that both the integrated and sequential method has hyperparameters which need to be tuned. For the phenomenological, integrated and sequential scenarios, the IPOPT multistart solver with fifty different initializations is used to solve the Pyomo DAE formulation [5].

## Black box model construction

The black box model is constructed using an ANN surrogate. The model inputs are the initial condition and time. A preprocessing step is performed where the inputs and outputs are scaled using a Z-score normalization. A rigours 5-fold cross validation and grid search is performed for tuning the hyperparameters of the system. The activation function, the number of hidden layers, the number of nodes, and the strength of the L2 regularization are all varied.

$$\left(X_t^t, C_g^t, C_m^t, C_c^t\right) = ANN\left(X_t^0, C_g^0, C_m^0, C_c^0, t\right) \tag{29}$$

## Extrapolative performance comparison

The initial data is generated by performing a Latin hypercube sampling of three initial conditions in the following ranges of initial glucose and catechol concentration: [50 mM, 70 mM] and [25 mM, 35 mM] with a constant total biomass concentration of 0.01 OD600. The performance of all models is evaluated utilizing an initial condition extrapolation for a fed-batch bioprocess. Note how in the training data the spike inputs are set to zero, however for the performance testing the spike inputs are respectively set to 10 mM and 3 mM for glucose and catechol with a time-period of 25 hrs. In the extrapolative scenarios, the glucose and catechol initial concentrations are varied from [20 mM, 100 mM] and [5 mM, 55 mM], respectively. Heatmaps and distribution curves of $R^2$ values are generated to compare the performance of different models and highlight performance in edge-cases.

### Interpretability analysis

Utilizing the Captum software, the ANN growth rate in Eq. 17 is analyzed and some of the model behaviours are explained [6]. A primary attribution analysis called Integrated gradients (IG) analysis is performed which tells the contribution of each input to the output of the model. The higher the attribution scores the more the input contributes to the model output [6]. Positive attribution means the output increase with the increase of the input and vice versa [6]. The attribution is calculated utilizing an integrated gradients technique.

### Improved hybrid model

Based on some insight from the ML interpretability analysis, new physical insights are integrated into the hybrid model to improve its overall performance. The physical insight added to the hybrid model is the Monod-kinetics relationship between biomass growth and glucose. The following ODE equations shown details the improved hybrid model. The improved hybrid model utilizes an ANN to model the fraction of viable biomass in the reactor. Equations 14, 15 are included in the improved hybrid model to track the dynamics of catechol and the spike input frequency.

$$\frac{dX_t}{dt} = \mu f_v X_t \tag{30}$$

$$f_v = ANN(X_t, C_g, C_c, C_m) \tag{31}$$

$$\mu = \left(\frac{\mu_g C_g}{C_g + k_g}\right) \tag{32}$$

$$\frac{dC_g}{dt} = -\left(\frac{\mu}{Y_{xg}}\right) f_v X_t + C_g^{IN} f(t) \tag{33}$$

$$\frac{dC_m}{dt} = Y_{mx}(\mu + \beta) f_v X_t \frac{C_c}{C_c + k_cr} \tag{34}$$

## Results and Discussion

### Sequential vs Integrated hybrid modeling

The hyperparameter tuning for the integrated model is a 3-fold cross validation to determine the ANN architecture. The hyperparameter tuning for the sequential model consist of two-steps: (i) a 3-fold cross validation to determine the smoothing weight ($w_s$) and (ii) a 5-fold cross validation to determine the ANN architecture. To simplify the hyperparameter search, the MSE weight ($w_M$) is set to a constant of unity. The performance of the sequential model is highest at a smoothing weight of 10. Following this, a grid search is done to determine the ANN architecture by varying the activation function, number of layers and nodes and L2 regularization weight.

The integrated model outperforms the sequential one across all points of extrapolation despite negligible computational cost differences (Figure 3). The heatmap can be divided into three broad regions: (I) high glucose, (II) low-glucose and low-catechol, and (III) low-glucose and high-catechol. The integrated models performs better than the sequential model in region (I) and (III) but suffers in region (II). In fact, the integrated model performs its best predictive performance in region (I) given the strong effect of high glucose concentrations on the growth rate. However, in region (II) the low glucose compounded with low catechol concentrations decreases the fraction of viable biomass which decreases growth rate. The integrated model overestimates the growth rate in this region. These results agree with our ground truth model which has a stunted growth rate at low glucose and low catechol concentrations, thereby negatively affecting the biomass accumulation. The CPU seconds of the integrated and sequential models showed marginal differences, 1.53 s and 0.95 s, respectively. Overall, while the integrated approach has advantages in performance, its cost will increase as the size of the ANN increases.

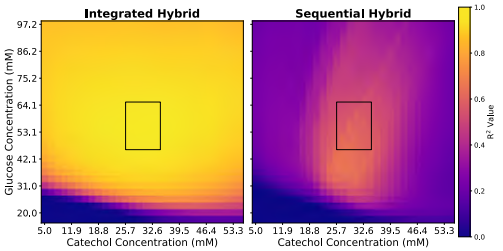



**Figure 3.** Extrapolative performance heatmap comparing the integrated and squential models.

### Hybrid model extrapolative performance

The previous section shows the performance of the integrated hybrid model to be better than the sequential hybrid one. Thus, the following sections will exclusively utilize the integrated hybrid model for comparison with the phenomenological and black box models.

On average, the hybrid model outperforms both the phenomenological and back box models in extrapolation

(Figure 4). The black box model had extremely poor extrapolative performance; while it captured the intricacies of the training data, it struggled to extrapolate the behaviour. The hybrid model outperforms the phenomeno-logical model in regions (I & III). However, it is extrapolative performance suffers slightly in regions (II) compared to its phenomenological counterpart, given that the latter has the physical insight which allows it to anticipate the contribution of catechol in low glucose environments.

Next, we sought to test versatility of the hybrid model. The glucose consumption in the ground truth model (Eq. 6) has two contributing terms: biomass growth and maintenance. The maintenance is tied to concentration of the catechol concentration. The hybrid model and the phenomenological model are formulated with the assumption that the maintenance term is not a huge contributor to glucose consumption. The versatility of the hybrid modelling structure is tested by increasing the contribution of the glucose consumption to match the growth-related glucose consumption. Despite the change in the physics of the ground truth model, Eq. 10-19 are not changed. The hybrid model still outperforms both the phenomenological and black box model in all the regions (Figure 5), showing that the versatility of the embedded ANN can capture the intricacies of the growth rate while also accounting for the additional strain of maintenance. The hybrid model's performance suffers in region (III); however, a trend observed to occur in the phenomenological model as well. The higher impact of catechol reduces the fraction of viable cells thereby overestimating the metabolic activity of the biomass to convert catechol into MA. This analysis demonstrates the flexibility of the integrated hybrid modelling structure to adapt to changes in the underlying physics of the system.

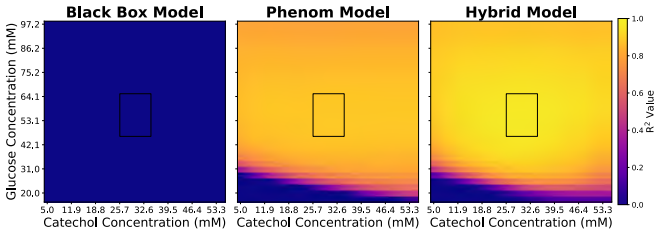



**Figure 4.** Extrapolative performance heatmap comparing the ML, phenomenological and hybrid models

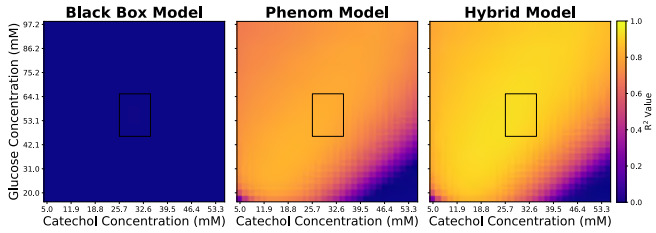



**Figure 5.** Extrapolative performance boxplot comparing the ML, phenomenological and hybrid models for greater contribution of maintenance coefficient effect on glucose

## Hybrid model interpretability

The hybrid model still has an embedded ANN piece within its structure and understanding the physics that is captured by the ANN component could aid in model refinement and experimental design. The bar graph shows the attribution score for the ANN component of the hybrid model. Note, the primary contributor to the model's predictive performance is the glucose and catechol concentrations. The glucose has a positive effect while catechol has a negative effect. This aligns with the physics that is present in the ground truth model. When we further analyze the attribution score of glucose as the concentration changes, further biophysical insights are caught. Fig. 6 looks at the glucose attribution score as the normalized glucose and catechol concentration changes. An important trend is how the attribution versus glucose plot mirrors the relationship between growth rate and substrate for Monod-style growth kinetics. Similarly note that catechol attribution score increases in magnitude as the concentration increases.

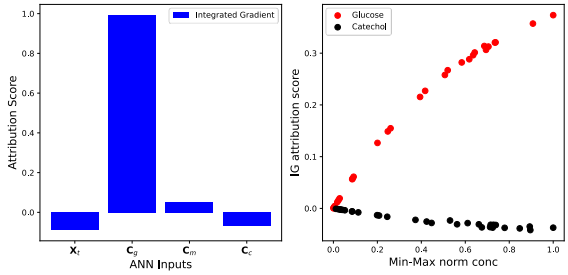



**Figure 6.** Primary attribution scores for the ML model in the hybrid ODE for training data. Model attribution score for changes in glucose and catechol concentration

The attribution score analysis presented above can function as first step in constructing more accurate empirical models to capture unexplained phenomenological behaviour. With the aid of the ML model interpretability, we could implement a build-train-improve cycle to incorporate and improve the physics captured by the hybrid model. We expect such an approach to be successful when the physics captured by the ANN is dominated by a single input. However, ANNs with multiple equally contributing inputs and multiple outputs might present difficulties to the interpretability analysis.

## Improved hybrid models with increased physics embedding

Based on the interpretability analysis, a Monod style relationship between glucose and growth rate is determined and incorporated into the improved hybrid model (Eq. 28-32). The improved hybrid model utilizes the ANN flexibility to capture the fraction of viable biomass in the system, which is the only entity metabolizing both glucose and catechol. Consequently, the aim of the

improved hybrid is capturing this fact even though only total biomass (viable plus dead cells) is used for training. As seen on the performance distributions plots below, the improved hybrid models outperformed the original hybrid model due to an increased accuracy in low-glucose high-catechol environments. The improved model performs better in regions where the original hybrid one struggles. Note the thinner and taller distribution peak of the improved model in high R2 value range. Since some burden is alleviated from the ANN component by incorporating learned physics insight, the black-box part of the improved hybrid model has less impact on the generalizability of the overall prediction. This two-step approach to hybrid modeling highlights how the black-box components, coupled by quantitative interpretability analysis could expedite model development. If important dynamics are not capture neither in the partial physics nor the data, the analysis might not lead to an improved hybrid model.

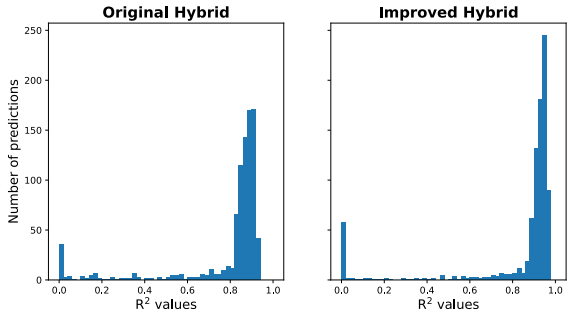



**Figure 7.** Extrapolative performance distributions for original hybrid and improved hybrid models.

## Conclusion

Here we outline the implementation of a hybrid modelling strategy to capture the dynamics of the bioconversion of catechol into MA, a bioplastics precursor. The biomass growth in the hybrid model is captured utilizing an ANN. A new hybrid model construction strategy is introduced which integrated the TVPE and the ML model training into a single step. The versatility, extrapolative capability, and sensitivity to initial conditions of the hybrid model is assessed by increasing the influence of various physical phenomena in the ground truth model. Our results show that the integrated hybrid model outperforms its sequential counterpart as well as commonly used phenomenological and ML models. An attribution analysis is performed to lend interpretability to the ANN piece of the hybrid model, revealing buried ground truth behaviour, which is then used to guide a model improvement cycle. The ultimate improved hybrid model reduced the computational load of the ANN by incorporating previously discovered biophysical insights.

## Digital supplementary material

The GitHub page has the code, data and figures shown in this paper: Escape35_SL_code.

## Acknowledgments

This research is funded in part by the Brooks Byers Institute for Sustainable Systems and the National Institute of General Medical Sciences, National Institutes of Health, grant number 5R35GM150876.

## References

1. Clomburg, J. M.; Crumbley, A. M.; Gonzalez, R. Industrial Biomanufacturing: The Future of Chemical Production. Science 2017, 355 (6320). https://doi.org/10.1126/science.aag0804.
2. Mokwatlo, S. C.; Klein, B. C.; Benavides, P. T.; Tan, E. C. D.; Kneucker, C. M.; Ling, C.; Singer, C. A.; M. A.; Ramirez, K. J.; Johnson, C. W.; Beckham, G. T.; Salvachúa, D. Bioprocess Development and Scale-up for Cis,Cis-Muconic Acid Production from Glucose and Xylose by Pseudomonas Putida. Green Chem. 2024, 26 (19), 10152–10167. https://doi.org/10.1039/D4GC03424D.
3. Tsopanoglou, A.; Jiménez del Val, I. Moving towards an Era of Hybrid Modelling: Advantages and Challenges of Coupling Mechanistic and Data-Driven Models for Upstream Pharmaceutical Bioprocesses. Current Opinion in Chemical Engineering 2021, 32, 100691. https://doi.org/10.1016/j.coche.2021.100691.
4. Bradley, W.; Kim, J.; Kilwein, Z.; Blakely, L.; Eydenberg, M.; Jalvin, J.; Laird, C.; Boukouvala, F. Perspectives on the Integration between First Principles and Data-Driven Modeling. Computers & Chemical Engineering 2022, 166, 107898. https://doi.org/10.1016/j.compchemeng.2022.107898 .
5. Nicholson, B.; Siirola, J. D.; Watson, J.-P.; Zavala, V. M.; Biegler, L. T. Pyomo.Dae: A Modeling and Automatic Discretization Framework for Optimization with Differential and Algebraic Equations. Math. Prog. Comp. 2018, 10 (2), 187–223. https://doi.org/10.1007/s12532-017-0127-0.
6. Kokhlikyan, N.; Miglani, V.; Martin, M.; Wang, E.; Alsallakh, B.; Reynolds, J.; Melnikov, A.; Kliushkina, N.; Araya, C.; Yan, S.; Reblitz-Richardson, O. Captum: A Unified and Generic Model Interpretability Library for PyTorch. arXiv September 16, 2020. https://doi.org/10.48550/arXiv.2009.07896

© 2025 by the authors. Licensed to PSEcommunity.org and PSE Press. This is an open access article under the creative commons CC-BY-SA licensing terms. Credit must be given to creator, and adaptations must be shared under the same terms. See https://creativecommons.org/licenses/by-sa/4.0/

Systems & Control Transactions

**Research Article - Peer Reviewed Conference Proceeding**
ESCAPE 35 - European Symposium on Computer Aided Process Engineering
Ghent, Belgium. 6-9 July 2025
Jan F.M. Van Impe, Grégoire Léonard, Satyajeet S. Bhonsale,
Monika E. Polańska, Filip Logist (Eds.)

PSE PRESS

# Metabolic network reduction based on Extreme Pathway sets

**Wannes Mores[a], Satyajeet S. Bhonsale[a], Filip Logist[a], and Jan F.M. Van Impe[a]***

[a] BioTeC+ KU Leuven, Department of Chemical Engineering, Gent, Belgium
* Corresponding Author: jan.vanimpe@kuleuven.be.

## ABSTRACT

The use of metabolic networks is extremely valuable for design and optimisation of bioprocesses as they provide great insight into cellular metabolism. Within bioprocess optimisation, they have enabled better (economic) objective performance through more accurate network-based models. However, one of the drawbacks of using metabolic networks is their underdeterminacy, leading to non-unique flux distributions. Flux Balance Analysis (FBA) reduces this issue by making assumptions on the behaviour of the cell. However, for metabolic networks of higher complexity, can still struggle with underdeterminacy. Metabolic network reduction can remove or greatly reduce this effect but can be difficult, especially when data is limited. Structural analysis of the metabolic network through Elementary Flux Modes (EFM) or Extreme Pathways (EP) can help locate the relevant information within the network. This work presents a metabolic network reduction approach based on the EPs that best explain a small set of available measurements. Many of the reactions will not be active during the process and a significantly smaller network can therefore be constructed. A case study of oxygen-limited *Escherichia coli* is presented which showcases this approach, enabling accurate prediction of the process with much smaller network-based models. This leads to much lower complexity bioprocess models while keeping the necessary information on cellular metabolism for the given process.

**Keywords**: Model Reduction, Multiscale Modelling, Biosystems

## INTRODUCTION

Model-based optimisation of bioprocesses has already shown great potential, enabling higher return on economic objectives for a given process. In many optimisation studies, a macroscopic model is used which relies on kinetic expressions such as Haldane or Monod to quantify the dynamic evolution of (by-)product and substrate concentrations within the reactor. However, these types of models do not consider the complex interactions on the intracellular level, which has been shown to lead to poor predictive performance in a dynamic context [1].

The incorporation of intracellular information is possible through metabolic networks, which has led to significant improvements in objectives such as yield, productivity, and final concentration of product [2]. However, these studies rely on smaller, less complex metabolic networks as they require a high computational effort for the optimization study. Currently, many strains used for bioproduction have a genome-scale metabolic network (GEM) available, easily surpassing 1000 reactions. These GEMs are not suitable for the existing optimisation approaches, highlighting the need for reducing the complexity of the metabolic network, while ensuring minimal loss of key information regarding the bioprocess.

### Constraint-based modelling

The metabolic network can be represented through its stoichiometric matrix $\boldsymbol{S} \in \mathbb{R}^{m \times r}$, which links metabolites $m$ to the reactions $r$ they take part in. Analysis of metabolic networks usually relies on the constraint defined by the Pseudo-Steady-State-Assumption (PSSA):

$$\boldsymbol{S} \cdot \boldsymbol{v} = \boldsymbol{0} \tag{1}$$

This implies that there is no accumulation of metabolites within the network. The reaction rates or fluxes are then captured in vector $\boldsymbol{v}$. Constraint-based modelling techniques such as Flux Balance Analysis (FBA) are built

on this assumption. As $\boldsymbol{S}$ is not a full column rank, there is more than one possible solution for the network, making it an underdetermined system. Moreover, the solution space of the PSSA is usually high-dimensional, especially for large networks. Even with measurements to further constrain the solution space, many possible solutions will exist. This issue of underdeterminacy can be dealt with in many ways [3]. Ideally, the underdeterminacy should be eliminated or reduced significantly.

One way of dealing with the underdeterminacy is by assuming that the cell follows a specific metabolic target (e.g., maximising growth). Flux Balance Analysis or FBA solves an optimsation problem with the assumed objective. In many cases, this leads to good prediction of metabolic behaviour, but can still lead to non-unique solutions. Lexicographic optimization can ensure a unique solution but needs a priority list of metabolic objectives [4].

Metabolic Flux Analysis or MFA aims to estimate the fluxes based on only measurement data. For a dynamic MFA-based model, kinetic equations are used to describe some of the key fluxes. Nimmegeers et al. [5] used the concept of free fluxes, which are directly related to the degrees of freedom of the PSSA. For large metabolic networks, this leads to too many parameters to be estimated, especially when data is limited. Reducing the degrees of freedom while keeping the relevant information of the network is therefore key in this approach.

## Metabolic network reduction

Many metabolic network reduction approaches exist in literature, mainly focusing on retaining as much information as possible. Most of them can be described as a top-down or bottom-up approach. With top-down approaches [6,7], the full network is the starting point. With techniques such as Mixed-Integer Linear Programming (MILP), reactions are then iteratively removed. With bottom-up approaches [8], smaller subnetworks are the starting point, which are recombined to mimic the behaviour of the original network while maintaining a certain limit on the size of the network.

Alternatively, small macroscopic models can be constructed based on vectors characterising the solution space such as EPs and EFMs. Maton et al. [9] enumerated EFMs for a medium-scale metabolic network and selected the most informative ones. This leads to good reproduction of the experimental data and therefore a promising approach to analyse and model certain aspects of the metabolic network. Moreover, by selecting an upper bound on the number of EFMs, the degrees of freedom or free (macro-)fluxes can be directly controlled.

In this work, the potential of using characterising vectors is further investigated, evaluating how they can help reduce and extract relevant information from large metabolic networks. A relevant case study showcases the applicability of this method to model bioprocesses.

# MATERIALS AND METHODS

## Case study

A dFBA-based multi-scale model is used to simulate the oxygen-limited growth of *E. coli* on glucose in a batch reactor. The e_coli_core model [10] was used to estimate the fluxes in CobraPy throughout the process, applying bounds on the uptake fluxes through kinetic expressions. The dynamic model will consider 6 metabolites of interest: biomass, glucose, oxygen, acetate, formate, and ethanol. A term for the oxygen transfer from the gas phase to the liquid is incorporated, using a mass transfer coefficient of $k_L a = 7.5\ hr^{-1}$ [11]. The model can then be described as:

$$\frac{dC_X}{dt} = v_X \cdot X \tag{2}$$

$$\frac{dC_{glc}}{dt} = v_{glc} \cdot X \tag{3}$$

$$\frac{dC_{O_2}}{dt} = v_{O_2} \cdot X + k_L a(0.21 - C_{O_2}) \tag{4}$$

$$\frac{dC_{ac}}{dt} = v_{ac} \cdot X \tag{5}$$

$$\frac{dC_{for}}{dt} = v_{for} \cdot X \tag{6}$$

$$\frac{dC_{eth}}{dt} = v_{eth} \cdot X \tag{7}$$

The extracellular fluxes corresponding to the metabolites of interest are obtained from FBA at each timestep. The bound on the glucose uptake rate $v_{glc}$ was defined by Monod kinetics based on the glucose concentration $C_{glc}$ as follows [12]:

$$0 \geq v_{glc} \geq -10\frac{C_{glc}}{\mathbf{5.55}+C_{glc}} \tag{8}$$

The system of ODEs is then passed to SciPy's solve_ivp function, together with the initial conditions $\boldsymbol{C}_0 = [0.01\frac{g}{L}, \frac{20}{180}mM,\ 0.21\ mM, 0.4\ mM, 0\ mM, 0\ mM]$. Simulation was done on a virtual machine with a Intel(R) Core(TM) i5-1235U processor and 8GB of RAM available. The dFBA simulation ran in 133 seconds. For the e_coli_core [10] network, all the EPs are enumerated using an accelerated version of Canonical Basis Approach [13] developed in Mores et al. [14].

## Selection procedure

Given that the number of EPs is usually quite large, efficient procedures have to be developed to select the most informative EPs for the process. In this work, a two-step approach is presented. First, a preselection step based on yield is carried out to get a more manageable number of EPs. This is followed by an iterative routine based on optimization problems to find the final set of EPs to be used to create smaller biological models.

### Preselection based on yield analysis

Since not all EPs carry relevant information regarding the case study, a preselection is carried out to reduce the large number of EPs to a more manageable size. With yield analysis [15], the EPs are projected into yield space. The metabolites are split into products and substrates, which is used to define the yields of each EP. From the metabolites of interest in the case study, glucose and oxygen are the only substrates. As specified in Ramkrishna, a reference substrate is chosen (glucose) and the other substrates are given a minus sign. Within this yield space, a convex hull is constructed for the set of EPs. The points that define this convex hull encompass and therefore be able to describe the experimental data.

### Final EP set selection

After a significant reduction of candidate EPs through yield analysis preselection, different optimization problems will be defined to aid in selection the most informative EPs regarding a dataset. These optimization problems are based on minimization of error to the measurement, defined as follows [9]:

$$SSE = \sum_{k=1}^{met_i} (\boldsymbol{EP}_k \cdot \varphi - \boldsymbol{v}_{obs,k}) \boldsymbol{W}^{-1} (\boldsymbol{EP}_k \cdot \varphi - \boldsymbol{v}_{obs,k})^T, \quad (9)$$

where $\varphi$ corresponds to the macro flux vector of the extreme pathways, $\boldsymbol{v}_{obs}$ corresponds to the measured extracellular flux, and $\boldsymbol{W}$ corresponds to a diagonal matrix of weights defined by $(v_{obs,k})^2$, the maximum flux for each measured exchange reaction.

First, an initial sweep is done over the set of EPs where one EP is has its macro flux set to zero. If disabling an EP this way leads to an insignificant change to the $SSE$ resulting from the optimization, the EP is considered to not carry relevant information regarding the process and therefore is removed. Important to note is that the order of this initial sweep does have an influence on the result. Here we sweep stochastically.

To get the final selection of EPs, the worst performing EP will be removed iteratively until a desired set size is achieved. Every iteration, each remaining EP is set to inactive separately and the $SSE$ is re-evaluated. The EP whose inactivation leads to the best score is then selected for removal as it is the current worst performer.

## Model reduction approaches

To reduce the network-based model, two approaches will be used. Based on the results from EP selection, models are created by either considering the EPs separately or by reconstructing a network based on the active reactions in the selected EPs.

### Reduced network model

Since the EPs selected are the most informative pathways for the given process, they contain the most valuable, informative reactions. By reconstructing a network based on the reactions active in the set of EPs, a small network is created which focuses on relevant aspects of the metabolism. Direction of the reactions in the EPs is also considered, making reversible reactions with only one relevant direction irreversible. One of the benefits of using EPs here is that the pathways remain feasible since the EPs are minimal steady-state solutions of the system. This means that the reduced network still allows for techniques such as FBA to be performed.

### Macro-reaction model

Alternatively, the EPs themselves can be used as a model substituting for the metabolic network. This approach is similar to Maton et al. [9], where the macro-fluxes for the most informative EPs is used to model the process. Simulating with this model is done by maximization of the biomass output, similar to FBA. However, here the macro-fluxes are manipulated to achieve the objective instead of the individual fluxes of each reaction.

## RESULTS

Using the model described by Equations 2-8, a dataset is obtained for oxygen-limited *E. coli*. The dataset consists of 74 datapoints over a 15 hour time period. To account for ATP when selecting EPs, the minimal ATP requirement is added to each timepoint as an additional state. From this concentration data, the fluxes per individual cell were isolated by dividing the concentrations by the biomass.

### Extreme Pathway generation

Based on the e_coli_core network, the full set of EPs is generated using the CBA method as described previously. The final set consists of 100,235 EPs, which is too large to start applying the LP-based selection. Hence, a preselection step is done based on yield analysis. Afterwards, LP-based selection is done to try and reduce the EP set below the number of measured metabolites [9], in this case less than 7 since ATP is included as an additional metabolite.

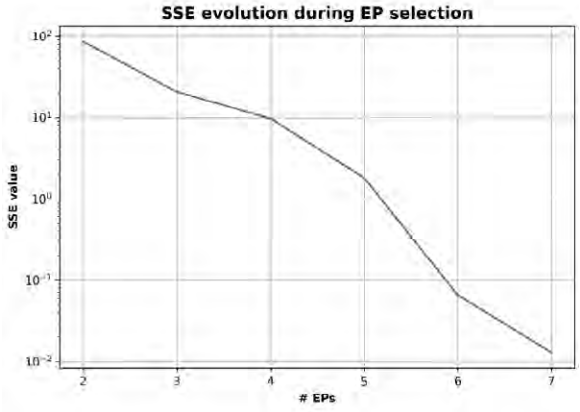



**Figure 1.** SSE scores during the final selection procedure

## Preselection

Preselection of EPs is done based on yield analysis, with glucose selected as the reference substrate for the process and all other metabolites from the process model as the products. In the yield space, a convex hull is then constructed, whose points should be able to fully represent the dataset generated from FBA. The EPs kept after preselection are then those who correspond to the vertices of the convex hull in yield space. This leads to a significant reduction of EPs, with only 113 EPs remaining.

## LP-based selection

A first sweep aims to eliminate the least informative EPs. The order of EPs is first randomized as the order does influence the selection results to try and reduce the bias towards some EPs. The threshold for significance is set at an SSE difference of 0.001. When an EP's removal leads to this level of decline in the SSE score, it is kept. This first sweep reduces the EP set to just 8 significant EPs. However, the goal is to have less than 7 EPs. Therefore, EPs are iteratively removed based on the worst-performer as described previously. SSE values are shown throughout this iterative reduction of EPs in Figure 1. Based on the trade-off between complexity and accuracy, a decision then has to be made on how many EPs to keep. In this work, 5 EPs are selected as it is below the threshold of 7 while keeping relatively good SSE values.

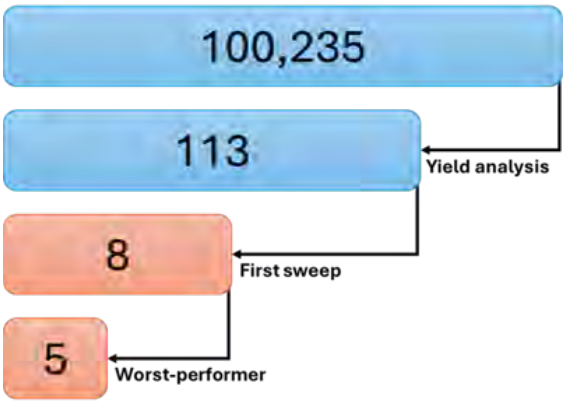



**Figure 2.** Evolution of EP set sizes with each reduction step. Blue indicates the yield analysis method, red indicates the LP-based reduction.

## Reduced Network Model

Important reactions for the process can be found by analysing the remaining EPs. Each reaction that does not take part in any of the remaining EPs is not needed to reproduce the observed metabolic behaviour. Therefore, these reactions can be seen as less important and can be removed from the network. This already reduces the complexity of the network significantly, but considering reversibility enhances this even more. If only one direction of a reversible reaction is present in the EPs, it can be converted within the network-based model to an irreversible reaction in the relevant direction for the process.

When this principle is applied to the remaining EPs, the network is reduced from 95 reactions to 60. From these remaining reactions, 25 are converted from reversible to irreversible in the relevant direction. When purely considering the number of reactions, this does not seem like a significant reduction. However, as discussed previously, the target for the reduction in this work is more aimed towards a reduction in free fluxes. The complexity of this reduced network is significantly smaller, needing only 6 free fluxes to be estimated instead of the original 28.

To validate if this reduced network is still capable of representing the same metabolic behaviour as the full network, dFBA is also applied to the reduced network with the same initial conditions. Even though the complexity of the network is reduced significantly, dFBA on the reduced network lead to a perfect reconstruction of the original dataset. This highlights the potential of this targeted network reduction approach with limited process information requirements, which can help reduce computational effort and data requirements for estimation of a network-based bioprocess model.

## Macro-reaction model

By using the EPs remaining as macro-reactions, another type of reduced model can be derived. Since there are 5 EPs as was selected, 5 macro-fluxes have to be estimated. The complexity of this network is thus even smaller than the reduced network approach since only 5 macro-fluxes must estimated instead of the previously discussed 6 free fluxes.

By using the same principle of biomass maximization using the 5 EPs as individual macro-reactions with the available uptakes of glucose and oxygen, metabolic behaviour can be approximated. Using the same initial conditions and kinetic equations as the original dataset, very similar metabolic behaviour can be observed throughout the process. Only very minor differences can be observed between the results of the macro-reaction model and the original network-based model as can be seen in Figure 3. Compared to the network-based models, the simulation time is reduced significantly, from 133 seconds to just 16 seconds.

# CONCLUSION

In this work, new approaches were developed to reduce metabolic networks when a limited amount of information is available. Using extracellular measurements, relevant aspects of the network can be identified and kept in the reduced network by employing static analysis of the network through Extreme Pathways. A relevant case study was defined, where extracellular measure-

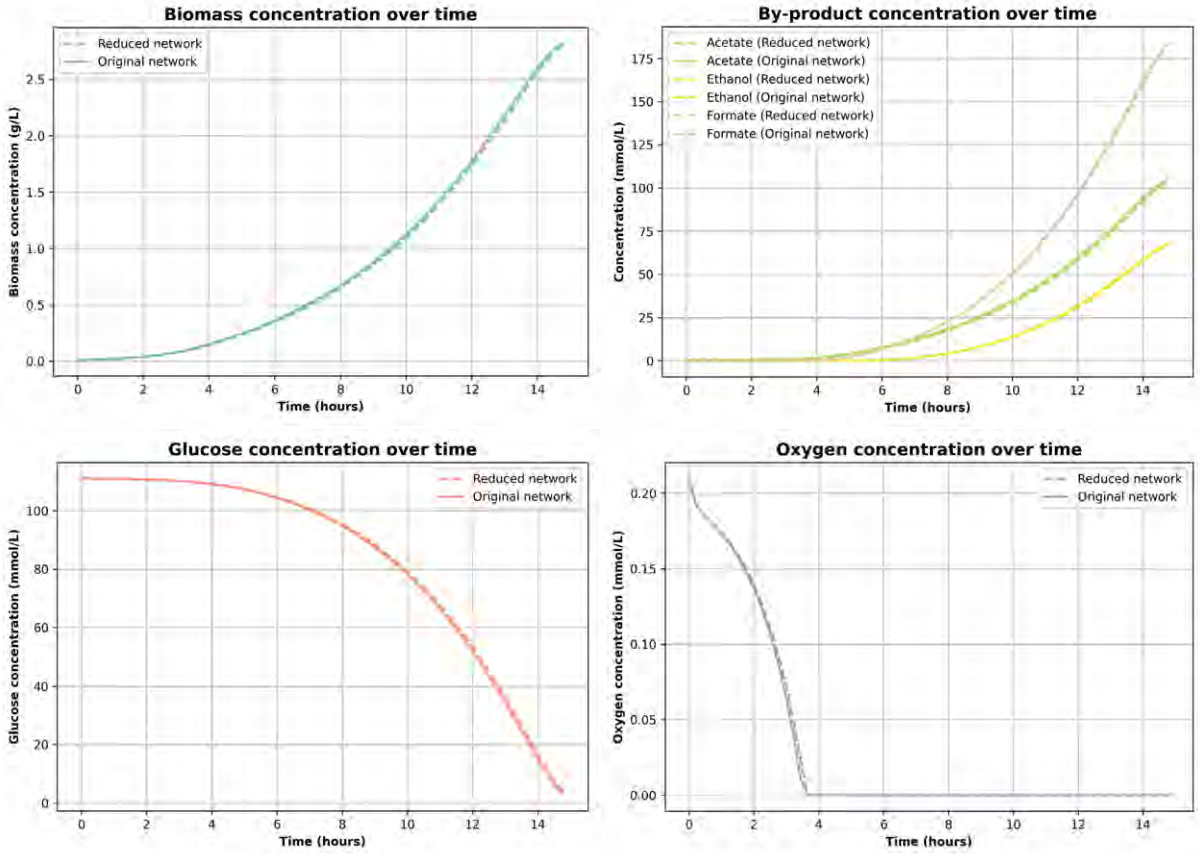



**Figure 3:** Reactor concentration profiles over the duration of the process. Solid lines are obtained using the full network-based model in CobraPy, dashed lines are obtained by finding the optimal macro-fluxes for the selected EPs every timestep.

ments were substituted through simulation based on a metabolic network of *E. coli.* Even though the network used is relatively small, it still suffers from the effects of underdeterminacy. In total, 26 free fluxes have to be estimated either through measurements or by making assumptions such as FBA objective functions. Many previous studies have focused on reducing the network to a minimal number of reactions, but free fluxes or degrees of freedom give a better idea of the complexity of the network. Analysis of the metabolic network is done through EPs, which are valid pathways through the network and adhere to the Pseudo-Steady-State-Assumption. The total EP set is very large, necessitating a preselection step based on the concept of yield analysis [15]. The remaining 113 EPs are then evaluated based on their ability to reproduce the measured metabolic behaviour of oxygen-limited *E. coli* and the 5 most informative EPs are finally selected to be used for model reduction.

Two model reduction approaches are defined and implemented for the case study. The first one reconstructs a network based on the active reactions in the 5 selected EPs. If a reversible reaction is only active in a single direction, it is transformed into an irreversible reaction in the relevant direction. This leads to a much less complex metabolic network, reducing the free fluxes from 28 to just 6 while keeping identical behaviour in the case study.

A second approach substitutes the network by the 5 EPs as macro-reactions themselves. Instead of estimating all intracellular fluxes, only 5 macro-fluxes then have to be estimated instead of the 28 free fluxes. Using this approach, only a small difference is found within the case study between the full network and the macro-reaction model while complexity is reduced significantly.

The results in this work indicate that analysis of metabolic networks through extreme rays such as EPs aids significantly in understanding and finding the relevant aspects of metabolism in a network given a limited amount of information on the process. Significantly reduced models can be created successfully using the most relevant EPs while keeping accurate metabolic behaviour. This leads to a much less complex estimation of the fluxes, potentially requiring much less data to get quality bioprocess models.

## ACKNOWLEDGEMENTS

This work is funded by the European Union under grant agreement 101122224 ('ALFAFUELS'). W.M. was supported by Research Foundation Flanders (FWO) through Strategic Basic Project 1SHG124N.

## REFERENCES

1. Hodgson, B. J., Taylor, C. N., Ushio, M., Leigh, J. R., Kalganova, T., & Baganz, F. Intelligent modelling of bioprocesses: a comparison of structured and unstructured approaches. *Bioprocess Biosyst. Eng.*, 26, 353-359. (2004). https://doi.org/10.1007/s00449-004-0382-0
2. Chang, L., Liu, X., & Henson, M. A. Nonlinear model predictive control of fed-batch fermentations using dynamic flux balance models. *J. Process Contr.*, 42, 137-149. (2016). https://doi.org/10.1016/j.jprocont.2016.04.012
3. Bogaerts, P., & Vande Wouwer, A. How to Tackle Underdeterminacy in Metabolic Flux Analysis? A Tutorial and Critical Review. *Processes*, 9(9), 1577. (2021). https://doi.org/10.3390/pr9091577
4. Gomez, J. A., Höffner, K., & Barton, P. I. DFBAlab: a fast and reliable MATLAB code for dynamic flux balance analysis. *BMC Bioinform.*, 15, 1-10. (2014). https://doi.org/10.1186/s12859-014-0409-8
5. Nimmegeers, P., Vercammen, D., Bhonsale, S., Logist, F., & Van Impe, J. Metabolic reaction network-based model predictive control of bioprocesses. *Appl. Sci.*, 11(20), 9532. (2021). https://doi.org/10.3390/app11209532
6. Röhl, A., & Bockmayr, A. A mixed-integer linear programming approach to the reduction of genome-scale metabolic networks. *BMC Bioinform.*, 18, 1-10. (2017). https://doi.org/10.1186/s12859-016-1412-z
7. Erdrich, P., Steuer, R., & Klamt, S. An algorithm for the reduction of genome-scale metabolic network models to meaningful core models. *BMC Syst. Biol.*, 9, 1-12. (2015). https://doi.org/10.1186/s12918-015-0191-x
8. Ataman, M., Hernandez Gardiol, D. F., Fengos, G., & Hatzimanikatis, V. redGEM: Systematic reduction and analysis of genome-scale metabolic reconstructions for development of consistent core metabolic models. *PLOS Comput. Biol.*, 13(7), e1005444. (2017). https://doi.org/10.1371/journal.pcbi.1005444
9. Maton, M., Bogaerts, P., & Wouwer, A. V. A systematic elementary flux mode selection procedure for deriving macroscopic bioreaction models from metabolic networks. *J. Process Contr.*, 118, 170-184. (2022). https://doi.org/10.1016/j.jprocont.2022.09.002
10. Orth, J. D., Fleming, R. M., & Palsson, B. Ø. Reconstruction and use of microbial metabolic networks: the core Escherichia coli metabolic model as an educational guide. *EcoSal plus*, 4(1), 10-1128. (2010). https://doi.org/10.1128/ecosalplus.10.2.1
11. Mahadevan, R., Edwards, J. S., & Doyle, F. J. Dynamic flux balance analysis of diauxic growth in Escherichia coli. *Biophys. J.,* 83(3), 1331-1340. (2002). https://doi.org/10.1234/56789.10
12. Scott, F., Wilson, P., Conejeros, R., & Vassiliadis, V. S. Simulation and optimization of dynamic flux balance analysis models using an interior point method reformulation. *Comput. Chem. Eng.*, 119, 152-170. (2018). https://doi.org/10.1016/j.compchemeng.2018.08.041
13. Schuster, S., Fell, D. A., & Dandekar, T. A general definition of metabolic pathways useful for systematic organization and analysis of complex metabolic networks. *Nat. Biotechnol.*, *18*(3), 326-332. (2000). https://doi.org/10.1038/73786
14. Mores, W., Bhonsale, S. S., Logist, F., & Van Impe, J. F. Accelerated enumeration of extreme rays through a positive-definite elementarity test. *Bioinformatics*, btae723. (2024). https://doi.org/10.1093/bioinformatics/btae723
15. Song, H. S., & Ramkrishna, D. Reduction of a set of elementary modes using yield analysis. *Biotechnol. Bioeng.*, 102(2), 554-568. (2009). https://doi.org/10.1002/bit.22062

© 2025 by the authors. Licensed to PSEcommunity.org and PSE Press. This is an open access article under the creative commons CC-BY-SA licensing terms. Credit must be given to creator and adaptations must be shared under the same terms. See https://creativecommons.org/licenses/by-sa/4.0/



Systems & Control Transactions

**Research Article - Peer Reviewed Conference Proceeding**
ESCAPE 35 - European Symposium on Computer Aided Process Engineering
Ghent, Belgium. 6-9 July 2025
Jan F.M. Van Impe, Grégoire Léonard, Satyajeet S. Bhonsale,
Monika E. Polańska, Filip Logist (Eds.)

PSE PRESS

# Real-time dynamic optimisation for sustainable biogas production through anaerobic co-digestion with hybrid models

**Mohammadamin Zarei[a,b], Meshkat Dolat[a], Rohit Murali[a], Mengjia Zhu[c], Oliver Pennington[c], Dongda Zhang[c], Michael Short[a,b*]**

[a] School of Chemistry and Chemical Engineering, University of Surrey, Guildford, UK
[b] Institute for Sustainability, University of Surrey, Guildford, UK
[c] Department of Chemical Engineering, University of Manchester, Manchester UK
* Corresponding Author: m.short@surrey.ac.uk.

## ABSTRACT

Renewable energy and energy efficiency are increasingly recognised as crucial for creating new economic opportunities and mitigating environmental impacts. Anaerobic digestion (AD) transforms organic materials into a clean, renewable energy source. Co-digestion of various organic wastes and energy crops addresses the disadvantages of single-substrate digestion, increasing production flexibility yet adding process complexity and sensitivity. This study employs a two-pronged approach to optimise biogas production while considering global warming potential: a nonlinear programming (NLP) model for dynamic system economic optimisation with a model predictive control (MPC) strategy for precise temperature regulation within the digester. The NLP model integrates a combined heat and power (CHP) system to leverage dynamic electricity, heat, and gas prices, accounting for physical and economic parameters such as biomethane potential, chemical oxygen demand, and substrate density. A cardinal temperature and pH model ensures accurate depiction of substrate degradation and gas production rates under varying conditions. The MPC scheme, formulated as a system of differential-algebraic equations, offers fine-grained temperature control, capturing real-world complexities like heating/cooling delays, ambient conditions, and multiple feed components with different optimal digestion temperatures. Results demonstrate that this integrated model optimises the interaction between electricity production, biogas generation, and CHP operation for real-time multi-objective optimisation of profit, global warming potential and temperature control. A case study validates the model's capability for guiding decision-making in biogas facilities, emphasising strategic feedstock management and precise temperature control. Overall, this integrated approach advances the modelling and control of anaerobic co-digestion systems, enhancing both efficiency and profitability in biogas production.

**Keywords**: Pyomo, Food & Agricultural Processes, Optimization, Process Control, Biofuels

## INTRODUCTION

In addition to reducing carbon emissions, renewable energy sources lessen dependency on fossil fuels[1]. Anaerobic digestion (AD) is a well-established and reliable method to convert organic feedstocks into clean energy. However, single-substrate digestion often limits operational flexibility and productivity [2]. Co-digestion—processing multiple substrates, such as organic waste and energy crops, simultaneously can significantly enhance biogas yields by leveraging the complementary characteristics of diverse feedstocks [3]. Despite these advantages, co-digestion introduces greater process complexity, increasing sensitivity to variables such as substrate composition, retention times, temperature control, and microbial balance [4]. These interdependent factors influence microbial growth, digestion kinetics, and, ultimately, system efficiency.

Optimising co-digestion processes therefore requires innovative solutions that integrate both the physical and economic dimensions of AD systems. A range of control strategies has been developed for AD; however, few of these strategies are deployed in industry due to the variability in waste characteristics and operating conditions [5]. Classical PID controllers, fuzzy logic expert systems, and neural networks are among the most common approaches, targeting controlled variables such as methane flow rate, pH, and chemical oxygen demand (COD). Moreover, several researchers have explored using model predictive control (MPC) in AD[6], motivated by its capability to handle multivariable processes with constraints. Despite this progress, predictive control in AD remains challenging due to the nonlinear, and the uncertain nature of the biochemical processes, which involve numerous microbial populations. These complexities are amplified in co-digestion systems because of the diverse range of substrates being processed simultaneously[7].

Recognising temperature as a crucial operational factor, particularly for mesophilic AD, this study applies MPC to regulate digester temperature, while simultaneously considering optimal feeding and gas processing strategy. Temperature exerts a direct influence on microbial activity and reaction rates, making its precise control pivotal for stable and efficient biogas production. While earlier work has addressed MPC for single-substrate AD, to the best of our knowledge, this is the first application of predictive control in an agricultural co-digestion context. By addressing both the inherent process complexity and the added challenges introduced by multiple substrates, MPC offers a promising avenue to improve the robustness and performance of AD systems under real-world operating conditions. In parallel with the challenges of process control, fluctuating energy prices underscore the need for strategic operational decisions in AD. Currently, studies often focus on isolated variables—such as temperature regulation—without capturing the interplay between feedstock availability, and market conditions. Without predictive insights into market trends, operators risk missing opportunities to maximise profitability and reduce operational risks [8].

Accordingly, this study proposes an integrated framework that combines dynamic optimisation, precise temperature management, and advanced price forecasting to enhance co-digestion-based AD systems. First, a nonlinear programming (NLP) model is formulated to optimise resource allocation and operational decisions, considering factors such as feedstock mix, digester capacity, and cost constraints. Second, a model predictive control (MPC) scheme ensures tight temperature management, accounting for real-world dynamics and uncertainties. Third, the Facebook Prophet model is used to forecast energy prices over time, enabling informed, data-driven decisions about biogas injection and energy generation. This model was selected due to its proven effectiveness in tackling complex market-related time-series forecasting challenges [9]. By synchronising these components, the framework aims to maximise production flexibility, profitability, and sustainability, addressing the growing demand for efficient, low environmental impact renewable energy solutions.

## METHODOLOGY

This study presents an integrated framework that combines dynamic real-time process optimisation, MPC, and energy price forecasting to enhance both the sustainability and economic viability of biogas production in AD systems. Figure 1 outlines the principal components of this approach: feedstock management, AD, energy generation, and product utilisation. Feedstock (e.g., maize and manure) is collected from harvesting sites and farms, where it can either be stored for later use or fed directly into the digester. The produced biogas follows two possible pathways: (1) injection into the gas grid following $CO_2$ removal, or (2) utilisation as a fuel source for CHP units. The residual digestate is employed as an organic fertilizer, further closing the loop on waste management.

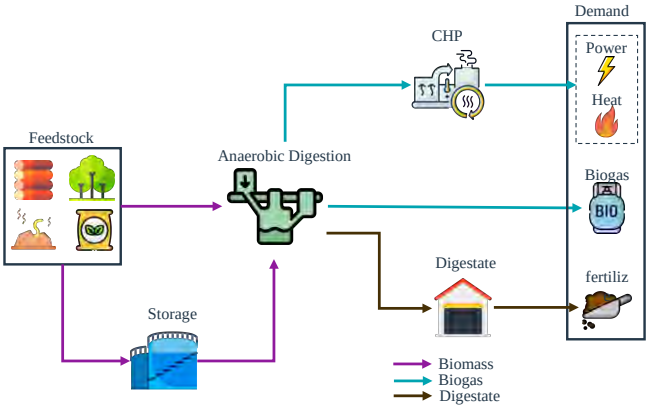



**Figure 1.** Superstructure of proposed model

To optimise resource utilisation and operational efficiency, an NLP model is formulated with a multi-objective function:

$$Max[Z] = \omega_1 Profit - \omega_2 GWP - \omega_3 Penalty_{MPC}\,, \sum \omega_i = 1 \quad (1)$$

Here, $Profit$ presents total profit of the AD process over the prediction horizon including profit of selling biogas and electricity and production costs; $GWP$ is the overall global warming potential (GWP) of the process that is calculated by summation of the greenhouse gas emissions from cultivation, transport, CHP operation and, biogas leakage [10]; and $Penalty_{MPC}$ penalises temperature deviations from the optimal range. The weighting

factors $\omega_i$ allow for customising the balance between maximising biogas output, minimising costs, and maintaining stable operating conditions. Physical and economic constraints, such as biomethane potential, chemical oxygen demand, and substrate density, ensure robust substrate utilisation and system performance.

A key innovation of this work is the incorporation of an advanced MPC scheme to regulate the digester temperature. By predicting future disturbances over a defined time horizon, the MPC dynamically adjusts heating ($Q_{heating}$) and cooling ($Q_{cooling}$) inputs to maintain optimal microbial activity. The thermal balance is captured by the following equation, which includes heating, direct thermal losses, cooling, and feed-related heat terms without delay for $Q_{loss}$ and $Q_{feed}$:

$$M_{digester}.\frac{C_p dT_{digester}}{dt} = Q_{heating}^{delayed} - Q_{loss} - Q_{cooling}^{delayed} + Q_{feed,}, \quad (2)$$

where $M_{digester}$ and $C_p$ are mass of the digester contents and specific heat capacity, respectively. To account for realistic response times, the control inputs for heating and cooling are represented by delayed states. These delays are modeled dynamically using first-order delay equations $\frac{dQ^{delayed}}{dt} = \frac{Q - Q^{delayed}}{\tau_{delay}}$. The parameter $\tau_{delay}$ represents the characteristic time constant for the delay associated with each process. Physically, it accounts for the lag in system responses due to the time required for heating elements, cooling mechanisms, or fluid dynamics to affect the digester temperature. By incorporating $\tau_{delay}$, the model ensures that control actions better reflect real-world system dynamics, improving the accuracy and robustness of the MPC.

The digester mass balance is expressed as: $\frac{dM}{dt} = f_{in} - f_{out}$, subject to a capacity constraint $M \leq \rho V_{dg}$. Here $f_{in}$, $f_{out}$, $\rho$, and $V_{dg}$ are the flows of input and output, density of feedstock and volume of digester, respectively. The inflow rate is determined by summing mass contributions of substrate and water content, whereas the outflow depends on a smooth step function governed by hydraulic retention time. This combination of material and energy balance constraints enables the MPC to maintain the digester temperature near an ideal setpoint, thus preserving optimal microbial activity and stabilising biogas output.

To accurately model microbial activity and biogas production over time, the study incorporates a cardinal temperature model (CTM) model [11]. This involves defining constraints for the specific growth rate for substrate *j* at time *t* ($\mu_{j,t}^{T}$) and biogas production:

$$\mu_{j,t}^{T} = \frac{\mu_j^{opt}(T_t - T_{max,j})(T_t - T_{min,j})^2}{(T_{opt,j} - T_{min,j})[(T_{opt,j} - T_{min,j})(T_t - T_{opt,j}) - (T_t - T_{opt,j})(T_{opt,j} + T_{min,j} - 2T_t)]} \quad (3)$$

where $\mu_j^{opt}$ is the optimal growth rate, $T_t$ is the digester temperature, $T_{min,j}$, $T_{max,j}$, and $T_{opt,j}$ are the minimum, maximum, and optimal temperatures for each substrate, and $\mu_j^{opt}$ is the optimal growth rate. By using $\mu_{j,t}^{T}$, the superimposed first order model [12] was used to predict the maximum biomethane production in time (, $P_t$):

$$BP_t = \left(\sum_{j,\tau} \frac{AV_{t,j}}{\sum_j AV_{t,j}}\right) BMP_j e^{1-\mu_{j,t}^{T}(t-\tau)}, \quad (4)$$

where $AV_{t,j}$ is the available substrate for species *j* at time *t*, and $BMP_j$ is the biomethane potential of species *j*. Here, $\tau$ is the time when substrate *j* is added, and ($t-\tau$) is the elapsed degradation time since its introduction into the digester. In addition to temperature constraints, other factors such as the carbon-to-nitrogen (C/N) ratio and total solids (TS) content are integrated into the model as constraints to maintain feasible operation within industrially relevant bands. These parameters also affect microbial activity and are thus accounted for in calculating overall biogas production, ensuring a more comprehensive and accurate representation of the AD process.

Future energy price forecasting is integral to optimising operational decisions, particularly concerning the timing of biogas injection into the grid versus CHP utilisation for electricity production. In this study, the Prophet model is used to predict electricity prices based on historical data, seasonal factors, and longer-term trends. Formally, Facebook Prophet can be represented as [13]:

$$y(t) = g(t) + s(t) + h(t) + \epsilon_t, \quad (3)$$

where $g(t)$ captures the piecewise linear or logistic trend, $s(t)$ represents seasonality, $h(t)$ accounts for holiday or special event effects, and $\epsilon_t$ is an error term. To refine forecasting accuracy, Bayesian optimisation is conducted over key hyperparameters—such as the changepoint prior scale, seasonality prior scale, and changepoint range—using a rolling-window cross-validation approach. The root mean square error (RMSE) is used to evaluate each parameter set; if no improvement is observed after multiple iterations, the search terminates early.

Once the optimal hyperparameters are identified, the final Prophet model is retrained on a rolling basis to produce accurate forecasts for the upcoming months. These forecasts guide strategic decisions, enabling operators to schedule biogas injection or CHP production during periods of favourable energy prices. By aligning operational activities with real-time market signals, the proposed methodology maximises revenues, promotes energy self-sufficiency, and supports environmental sustainability within biogas-based systems.

## Case Study

To demonstrate the performance of the model, we selected as case study a farm-scale AD plant with a digester capacity of 7,000 m³, designed to process energy crop maize and manures. The feeding rate is constrained

by a solid retention time (SRT) of 90 days, with the maximum total solids content of the digester feed limited to 35 %. All specified capacities and feed information are adapted from real site data provided by industrial partners with some changes to feed costs. The estimated parameters in equation (3) is presented in Table 1 [14], [15]:

**Table 2.** Cardinal temperature model parameters

| | $T_{min}$ (C) | $T_{opt}$ (C) | $T_{max}$ (C) | $\mu^{opt}$ (1/d) |
|---|---|---|---|---|
| Maize | -1.27 | 37.26 | 45.12 | 2.63 |
| Manure | 3.60 | 41.10 | 45.06 | 1.29 |

In an hourly timestep with a nine-day prediction horizon, electricity and gas price data were obtained from the Office for National Statistics of the United Kingdom [16], [17]. The results in Figure 2 illustrate that the Prophet model captures key price trends for both electricity and gas, while uncertainty bands (shaded in blue) reflect forecast confidence. The forecasted prices (blue lines) track the observed values (black dots) reasonably well, indicating satisfactory predictive performance. Using a shorter horizon helps reduce computational complexity while still providing actionable price estimates for operational decision-making.

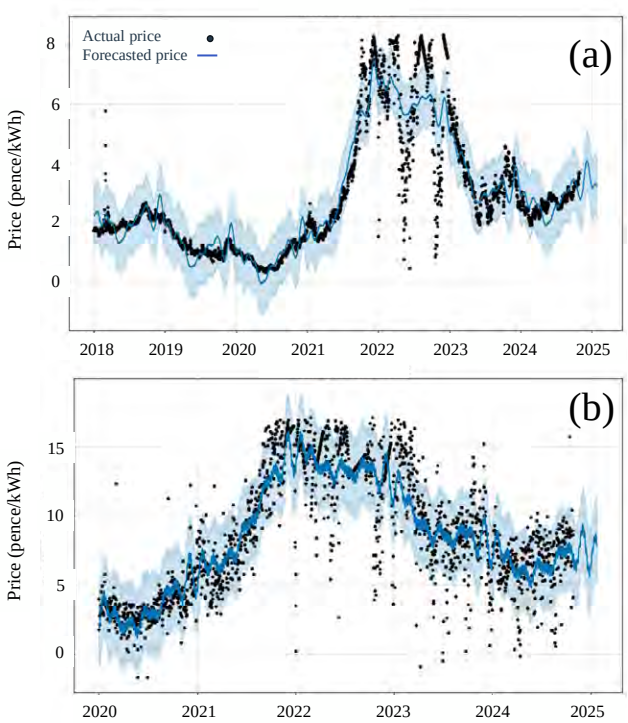



**Figure 2.** Historical data and forecasting performance for (a) gas price and (b) electricity prices.

## RESULTS AND DISCUSSION

The solutions of the case study were computed by implementing the proposed model in Pyomo — comprising 6,941 constraints (1,735 nonlinear) and 7,148 variables — and using the IPOPT solver, which effectively handles the non-linearities present in both the digester dynamics and the market-driven optimisation. The model was solved in 700 CPUs, demonstrating efficient computational performance given the problem's scale and complexity.

As depicted in Figure 3, the digester temperature tracks the ideal temperature setpoint with a small offset. Initially, the system demands a rapid increase in heating power (up to a maximum of 9000 W) to bring the digester from ambient conditions to near-optimal temperature, while significant heat losses occur due to the temperature gradient between the digester contents and the external environment. Given the higher cost of cooling, the maximum cooling power is limited to 900 W. Notably, an ambient temperature difference of about 20 °C was used to test the model's robustness under a challenging scenario. Once the system stabilises, the MPC strategy finely tunes both heating ($Q_{heating}^{delyaed}$) and cooling ($Q_{cooling}^{delyaed}$), ensuring close setpoint tracking. These observations affirm the efficacy of the delayed control action in sustaining microbial activity and preventing temperature overshoot. However, it is seen that the model does not always prioritise temperature control due to its weighting in the objective function being relatively low, leading to trade-offs in how the system balances temperature regulation against other operational goals.

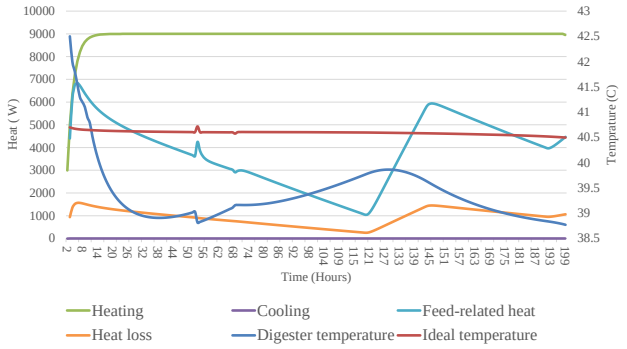



**Figure 3.** Performance of the proposed MPC.

As Figure 4 shows, electricity generation (blue bars) is presented alongside biogas sold to the grid (red line). The fluctuations in biogas sales are a result of real-time optimisation of feed rates and substrate compositions, driven by both technical constraints and market opportunities. During periods of higher electricity prices, the optimised solution diverts a greater proportion of biogas to the CHP unit, thereby maximising on-site power output for export. Conversely, when injecting gas into the grid proves more profitable, surplus biogas is channelled away from the CHP, underscoring the value of coupling accurate price forecasting with flexible production pathways.

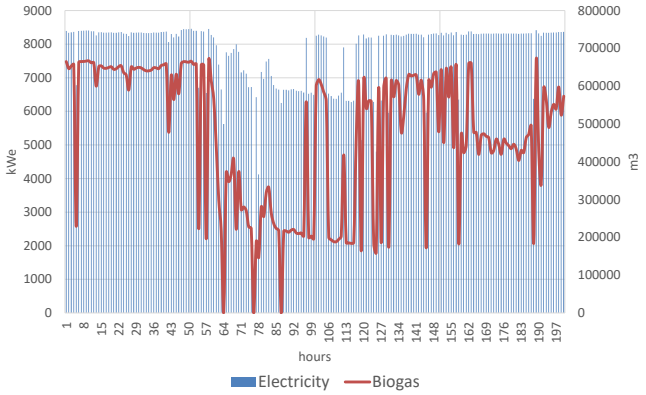



**Figure 4**. Optimal energy distribution by the process.

Figure 5 displays the co-digestion ratio shifts over time, with maize shown in blue and manure in red. By dynamically balancing these two substrates, the system exploits maize's higher biomethane potential while benefitting from manure's stabilizing influence on nutrient levels. Sudden changes in the substrate ratio frequently correlate with fluctuations in biogas yield, highlighting the intricate relationship between feedstock composition, microbial performance, and shifts in up- and down-stream pricing and feed availability. Overall, these results confirm that adaptively managing feed composition, temperature control, and energy allocation in response to real-time conditions can significantly enhance biogas production, ensure process stability, and optimise economic returns.

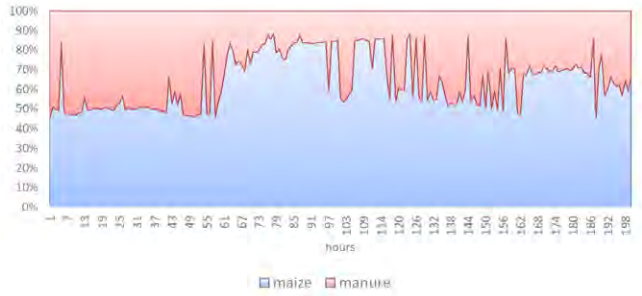



**Figure 5**. substrate co-digestion ratios in the process

Figure 6 shows four distinct contributions to GWP: substrate cultivation, transportation, CHP operation, and biogas leakage. Leakage, assumed to be 2% of biogas production[18], emerges as the predominant driver of GWP, highlighting the importance of robust sealing and monitoring to minimise fugitive methane emissions. The other three GWP components remain relatively modest, indicating that carefully managed process heating and CHP usage do not substantially elevate the plant's carbon footprint. Notably, periods with reduced gas leakage coincide with improved gas-tight integrity or targeted operational adjustments.

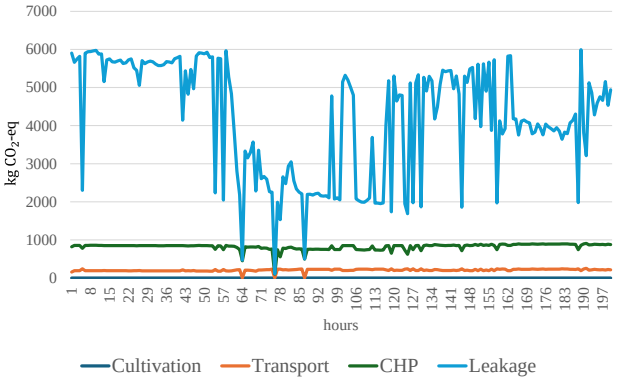



**Figure 6**. Global warming potential related to the process.

## CONCLUSION

This study demonstrates a comprehensive and synergistic approach to optimising anaerobic co-digestion systems by integrating an NLP model, temperature control via MPC, and advanced energy price forecasting. By leveraging the CHP unit and dynamic co-digestion strategies, the framework effectively adapts to varying substrate compositions, operational constraints, and fluctuating market conditions. The proposed delayed control scheme ensures tight temperature regulation, sustaining microbial activity near optimal levels and minimising the risk of thermal shocks. Additionally, the energy price forecasting component, based on the Prophet model, allows for strategic decisions on whether to allocate biogas to onsite electricity generation or injection into the grid, thereby maximising revenue streams.

Results indicate that co-digestion of maize and manure significantly enhances biogas yields while maintaining nutrient balance but also underscores the critical need to minimise methane leakage—the principal contributor to global warming potential. By identifying and mitigating fugitive emissions, operators can substantially reduce the environmental footprint of biogas production. Despite these advances, there remain avenues for improvement. Future work will focus on refining the biogas production model to capture higher fidelity microbial and kinetic responses with more accurate substrate interactions. In addition, efforts to decrease computational time—such as implementing advanced solution techniques or simplifying the problem structure—would make this framework more practical for larger-scale or real-time applications. Finally, exploring methods to remove certain nonlinear parameters could strengthen the model's scalability and facilitate adoption in a broader range of biogas facilities. By pursuing these improvements, the integrated approach stands to further enhance operational efficiency, profitability, and environmental sustainability in anaerobic co-digestion systems.

## REFERENCES


1. M. Zarei, A. Cherif, H.-J. Yoon, J. J. Liu, and C.-J. Lee, “Optimal design of a biofuel supply chain using an augmented multi-objective and TOPSIS method,” Green Chemistry, vol. 25, no. 10, pp. 4067–4075, 2023, doi: 10.1039/D2GC04670A.
2. M. Dolat et al., “Dynamic feed scheduling for optimised anaerobic digestion: An optimisation approach for better decision-making to enhance revenue and environmental benefits,” Digital Chemical Engineering, vol. 13, p. 100191, 2024, doi: https://doi.org/10.1016/j.dche.2024.100191.
3. T. ’Kunatsa, “Optimisation of Biogas Production from Co-Digestion of Water Hyacinth, Municipal Solid Waste and Cow Dung,” UNIVERSITY OF PRETORIA, 2021.
4. K. Hagos, J. Zong, D. Li, C. Liu, and X. Lu, “Anaerobic co-digestion process for biogas production: Progress, challenges and perspectives,” Renewable and Sustainable Energy Reviews, vol. 76, pp. 1485–1496, 2017, doi: https://doi.org/10.1016/j.rser.2016.11.184.
5. S. García-Gen, L. O. Santos, and A. Vande Wouwer, “Application of a Nonlinear Model Predictive Controller to the Anaerobic Digestion of Readily Biodegradable Wastes,” IFAC-PapersOnLine, vol. 55, no. 7, pp. 909–914, 2022, doi: https://doi.org/10.1016/j.ifacol.2022.07.560.
6. D. He, H. Wang, Y. Tian, N. Christov, and I. Simeonov, “Trajectory tracking of two-stage anaerobic digestion process: A predictive control with guaranteed performance and saturated input, based on ultra-local model,” J Process Control, vol. 129, p. 103039, 2023, doi: https://doi.org/10.1016/j.jprocont.2023.103039.
7. H. Kil, D. Li, Y. Xi, and J. Li, “Model predictive control with on-line model identification for anaerobic digestion processes,” Biochem Eng J, vol. 128, pp. 63–75, 2017, doi: https://doi.org/10.1016/j.bej.2017.08.004.
8. J. Vasco-Correa, S. Khanal, A. Manandhar, and A. Shah, “Anaerobic digestion for bioenergy production: Global status, environmental and techno-economic implications, and government policies,” Bioresour Technol, vol. 247, pp. 1015–1026, 2018, doi: https://doi.org/10.1016/j.biortech.2017.09.004.
9. I. Ghosh and R. K. Jana, “Clean energy stock price forecasting and response to macroeconomic variables: A novel framework using Facebook’s Prophet, NeuralProphet and explainable AI,” Technol Forecast Soc Change, vol. 200, p. 123148, 2024, doi: https://doi.org/10.1016/j.techfore.2023.123148.
10. R. Zhang et al., “Biogas Beyond Boundaries: Novel Algebraic Equations for Global Warming Standardization in Anaerobic Digestion Systems with Critical Life Cycle Analyses,” Available at SSRN 4745165.
11. S. Rossi, D. Carecci, and E. Ficara, “Thermal response analysis and compilation of cardinal temperatures for 424 strains of microalgae, cyanobacteria, diatoms and other species,” Science of The Total Environment, vol. 873, p. 162275, 2023, doi: https://doi.org/10.1016/j.scitotenv.2023.162275.
12. E. Lebon, H. Caillet, E. Akinlabi, D. Madyira, and L. Adelard, “Kinetic study of anaerobic co-digestion, analysis and modelling,” Procedia Manuf, vol. 35, pp. 321–326, 2019, doi: https://doi.org/10.1016/j.promfg.2019.05.047.
13. A. Garlapati, D. R. Krishna, K. Garlapati, N. m. S. Yaswanth, U. Rahul, and G. Narayanan, “Stock Price Prediction Using Facebook Prophet and Arima Models,” in 2021 6th International Conference for Convergence in Technology (I2CT), 2021, pp. 1–7. doi: 10.1109/I2CT51068.2021.9418057.
14. B. Nunes Silva, V. Cadavez, J. A. Teixeira, M. Ellouze, and U. Gonzales-Barron, “Cardinal parameter meta-regression models describing Listeria monocytogenes growth in broth,” Food Research International, vol. 136, p. 109476, 2020, doi: https://doi.org/10.1016/j.foodres.2020.109476.
15. L. Rosso, J. R. Lobry, S. Bajard, and J. P. Flandrois, “Convenient Model To Describe the Combined Effects of Temperature and pH on Microbial Growth,” Appl Environ Microbiol, vol. 61, no. 2, pp. 610–616, Feb. 1995, doi: 10.1128/aem.61.2.610-616.1995.
16. “System Average Price (SAP) of Gas,” Jan. 2025.
17. “System Price of electricity,” Jul. 2024.
18. C. Scheutz and A. M. Fredenslund, “Total methane emission rates and losses from 23 biogas plants,” Waste Management, vol. 97, pp. 38–46, 2019, doi: https://doi.org/10.1016/j.wasman.2019.07.029.



© 2025 by the authors. Licensed to PSEcommunity.org and PSE Press. This is an open access article under the creative commons CC-BY-SA licensing terms. Credit must be given to creator and adaptations must be shared under the same terms. See https://creativecommons.org/licenses/by-sa/4.0/




Systems & Control Transactions

**Research Article - Peer Reviewed Conference Proceeding**
ESCAPE 35 - European Symposium on Computer Aided Process Engineering
Ghent, Belgium. 6-9 July 2025
Jan F.M. Van Impe, Grégoire Léonard, Satyajeet S. Bhonsale,
Monika E. Polańska, Filip Logist (Eds.)

PSE PRESS

# Computer-Aided Molecular Design for Bio-Based Solvent Selection from Citrus and Coffee Wastes for Furfural Extraction

**Giovana C. A. Netto[a*], Moisés Teles dos Santos[a], and Vincent Gerbaud[b]**

[a] University of São Paulo (USP), Department of Chemical Engineering, São Paulo, São Paulo, Brazil
[b] Université de Toulouse, CNRS, INP, UPS, Laboratoire de Génie Chimique (LGC), Toulouse, France
* Corresponding Author: giovana.netto@usp.br.

## ABSTRACT

The global reliance on fossil-based solvents has driven the search for sustainable alternatives. This study employs the IBSS® CAMD tool to evaluate building blocks derived, directly or indirectly, from agricultural residues - specifically orange and coffee wastes-, to replace toluene in furfural extraction. A three-stage methodology was implemented: (1) identification of potential building blocks from residues, (2) multi-objective optimization using genetic algorithms and group contribution models for properties calculation, and (3) analysis of the resulting candidates based on performance indicators. A total of 13 families were evaluated, generating millions of candidates. Target properties included minimization of Hansen Solubility Parameters (HSP) distance, boiling point above 250°C, melting point below 10°C, flash point above 61°C, and octanol-water partition coefficient (log(kow)) below 3. The most promising candidates were derivatives of glycerol (performance: 0.9986), limonene (0.9937), and furfural (0.9931), which exhibited low bioaccumulation potential, non-flammability, and liquid phases at typical usage temperatures. Notably, all the top-performing molecules derived from these building blocks outperformed toluene (performance: 0.6724) in terms of the selected properties. The findings highlight the dual benefits of addressing agricultural waste management challenges while advancing sustainable industrial practices. Further studies are required to confirm their stability and scalability for industrial applications.

**Keywords**: Biomass, Genetic Algorithm, CAMD, Furfural, Solvent, Agricultural Wastes, Molecular Design

## INTRODUCTION

Brazil has an outstanding agricultural production that reaches 94 million ha [1], which represents 11% of the nation's total territory. The country stands as the world's leading producer of several key commodities, including coffee and oranges. However, alongside such intensive production comes an increasing concern about the sustainable management of the vast amounts of agricultural waste generated throughout the supply chain [2].

In 2023, Brazil's coffee production reached 3.5 million metric tons [3], primarily through the dry processing method, where coffee cherries are dried immediately after harvest [4]. Notably, 90–99% of the fruit mass is classified as waste [5]. Also, in 2023, Brazil produced 18 million metric tons of orange, of which 72% [6] was destinated for orange juice production. During this process, 50–60% of the fruit mass becomes waste, primarily composed of seeds and peel [7].

Agricultural wastes from coffee and orange production are typically disposed in fields, repurposed as animal feed or incinerated [7]. These practices contribute to environmental impacts and these approaches overlook the significant potential of these residues. Rich in bioactive compounds, such as antioxidants and fibers, coffee and orange byproducts offer untapped opportunities for sustainable valorization [2].

The residues contain building blocks that can be extracted or produced from them and one that stands out is furfural. Furfural is produced via the dehydration of xylose, a sugar present in the hemicellulose fraction of

lignocellulosic biomass. It has a wide range of industrial applications, including the production of plastics, pharmaceuticals, agrochemical products, non-petroleum-derived chemicals and it is a precursor for various furan-based chemicals and feedstocks [8].

Although the synthesis of furfural dates to 1921, the process still faces challenges, including low efficiency (~50%) and high energy demands, especially when distillation is employed as a purification method. Therefore, liquid liquid extraction (LLE) appears as a possible purification method and the main solvent used is toluene, a fossil-based toxic solvent [9].

The procedure for solvent selection plays a crucial role in determining the efficiency and viability of the proposed new solvent. In this study, Computer Aided Molecular Design (CAMD) was chosen as an effective early-stage tool for discovering new molecules, which leverages the simplicity of semi-empirical quantitative structure-property relationships (QSPRs) in conjunction with genetic optimization algorithms [10].

An in-house CAMD tool called IBSS® was employed. This tool was developed in compliance with a model driven software engineering approach, and it is based on different analysis models (UML and BPMN) and object-oriented implementation models dedicated to Microsoft.NET framework (C# and VB.NET) [11]. IBSS® has been successfully applied in various contexts, such as identifying solvents for the perfume industry [12], developing greener solvents for photovoltaic panel production [13], and substituting hexane in metabolite extraction from biomass feedstock [14].

The objective of this work was to evaluate solvents derived from coffee and orange residues, to extract furfural from an aqueous solution with methanol and acetic acid, in substitution to toluene.

## METHODOLOGY AND PROBLEM FORMULATION

To accomplish the goal of finding a suitable bio-based solvent to replace toluene for furfural extraction, a three-stage methodology, depicted in Figure 1, was proposed based on the work of Heintz *et al.* [15].

### Molecular Fragments Literature Review

The first stage entailed a literature review to identify potential building blocks derived, directly or indirectly, from coffee and orange residues. From an initial pool of 46 building block families, 13 were selected for further evaluation: furoate, geranyl, glucaric acid, glutamic acid, hydroxymethylfurfural, hydroxypropionic acid, levulinic acid, limonene, 5-methylfurfural, oleic acid, succinic acid, glycerol, and furfural itself. Considering the derivatives from the abovementioned building block families, 103 different fixed fragments were analyzed.

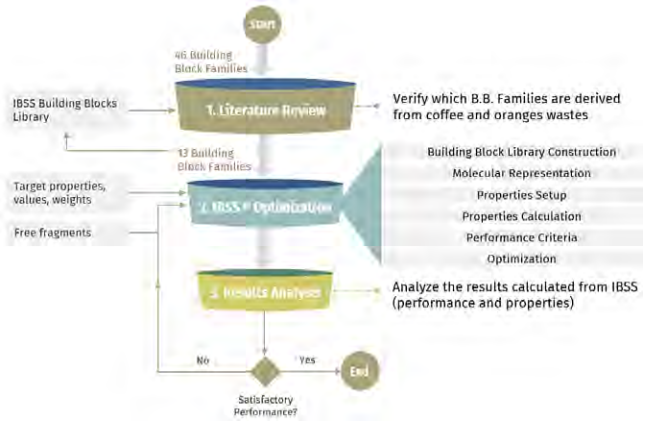



**Figure 1:** Methodology for solvent selection using IBSS® tool.

### IBSS® Optimization

The second stage corresponded to the IBSS® optimization, which involves essentially six key components: (1) building block library construction, (2) molecular representation, (3) properties setup, (4) properties calculation, (5) performance criteria for molecule evaluation, and (6) optimization [15]. The output consisted of a .txt file generated for the 200th generation of each fixed fragment studied, containing the calculated properties, performance metrics, and molecular graph structures of the individuals, ranked based on their performance.

#### Building block library construction

After the literature review, a preliminary verification was conducted to determine whether the molecules selected were already present in the IBSS® library. For those not included, new entries were created by assigning an ID, constructing the molecular graph, and defining functionalization points.

The newly fixed building blocks were drawn, and their SMILES representation were determined, which was entered in “evaluation mode” in the tool, to determine the molecular graph.

This process resulted in the creation of 7 new families of building blocks, comprising a total of 39 new fixed building blocks molecules.

#### Molecular representation

The selected molecular representation model is the molecular graph. In this representation, the diagonal elements represent non-hydrogen atoms, and the off-diagonal elements represent chemical connections. One of the implemented molecules is represented in Figure 2 as an example.

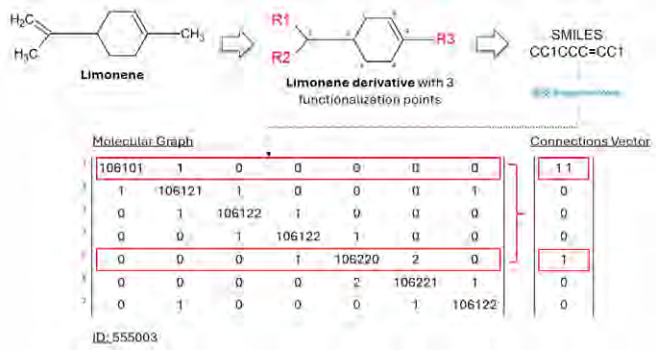



**Figure 2:** Molecular representation of Limonene.

## Properties set up

IBSS® tool allows users to specify the properties desired to calculate the performance, assigning their weights, target values, tolerances, and value of performance in the tolerance value.

The target properties chosen, detailed in Table 1, were defined based on the recommendations of Heintz *et al.* [15]. And the tolerance value reflects the confidence in the model prediction value, which can be assessed with help of the model accuracy and/or the property measurement standard deviation [16]. There were also included the standard deviation for the predictions.

The most critical property is the Hansen Solubility Parameter (HSP) distance, which accounts for three key interaction forces: D (London dispersion forces), P (dipole-dipole polarity interactions), and H (hydrogen bonding). The strategy was to minimize the HSP distance of the candidate molecules from furfural. To reflect practical considerations, the HSP distance between toluene and furfural (13.9) was set as the tolerance value, given that toluene is a viable solvent for furfural extraction.

For each configuration of fixed-building blocks and kmax (maximum number of fragments added in the fixed building block structure, varied from 4 to 8), a different input XML file was created. These files included the target properties (Table 1) and the variable fragments (-CH2-, -CH--, --C--, CH2=, -CH=, --C=, CH=-, -C=-, NH2-, -NH-, -N--, NH=, N=-, OH-, -O-, O=).

## Properties calculation

Using group contribution methods for property estimation, the tool is able to predict the melting point, boiling point and log(kow) with models developed by Hukkerikar *et al.* [16]; HSP distance with molecular breaking by Hiroshi Yamamoto [17] and flash point with a model created by Catoire, Paulmier and Naudet [18].

## Performance criteria for molecule evaluation

The performance of each candidate molecule is calculated from a performance function (Eq. 1), and it considers deviation of the predicted property values from their target values (Eq. 2).

$$Perf\ (MG_i) = \frac{\sum_{p=1}^{np} w_p.F_p.(MG_i)}{\sum_{p=1}^{np} w_p} \quad (1)$$

$$F_p(MG_i) = exp.\left[\ln(val).\left(\frac{P-x}{Tol}\right)^2\right] \quad (2)$$

In the equations, $Mg_i$ is the molecular graph, $Perf$ is the calculated performance, $n_p$ is the number of target properties, $F_p$ is the performance function, $w_p$ is the weight of property $p$, $Tol$ is the tolerance set, $x$ is the target value for property and $P$ is the property value.

## Optimization

The problem solved by IBSS® is a multi-objective optimization since multiple properties are considered in the performance equation. A genetic algorithm is used, which modifies the molecular graphs through mutation, crossover, deletion, and insertion. Newly generated molecules have their performance calculated and are ranked accordingly. The molecules with the best performance are selected for the next generation. The parameters of the genetic algorithm, presented in Table 2, were used in this study.

## Results Analysis

**Table 1:** Target properties setup.

| Property | Weight | Unit | Target | Tolerance | Cor. Perf.[1] | Justification | SD[2] | Ref. |
|---|---|---|---|---|---|---|---|---|
| HSP Distance | 3 | $MPa^{1/2}$ | 0 | 13.9 | 0.9 | Good solubility | - | [17] |
| Melting Point | 1 | °C | < 10 | 10 | 0.8 | Liquid at usage temperature | 21,45 K | [16] |
| Boiling Point | 1 | °C | >250 | 3 | 0.8 | Liquid at usage temperature | 7,67 K | [16] |
| Flash Point | 1 | °C | >61 | 3 | 0.8 | Non flammable | - | [18] |
| Log (Kow) | 1 | - | <3 | 0.8 | 0.8 | Low potential of bioaccumulation | 0,61 | [16] |

[1]Cor. Perf. = Corresponding Performance; [2]SD = Standard Deviation

The third stage involved an evaluation of the results to identify the most promising candidates. A total of 16 thousand molecules were generated in the final generations and more than 3 million properties were calculated throughout the study. The main results are presented below.

**Table 2:** Parameters of the genetic algorithm.

| Property | Value |
|---|---|
| Elitism | 5 |
| Population size | 100 |
| Number of generations | 200 |
| Crossover probability | 65% |
| Mutation probability | 15% |
| Insertion probability | 10% |
| Deletion probability | 10% |

## RESULTS

The computational exploration conducted using the IBSS® CAMD tool enabled the evaluation of millions of potential molecules, leading to the identification of promising alternatives to toluene for LLE of furfural. The best molecules for each fixed building block derived from orange and coffee wastes were ranked based on their performance and the outcome is presented in Table 3.

A set of alternative methods was tested for predicting properties: log(KoW), melting point and boiling points were predicted using a method by Marrero&Gani [19]; and HSP Distance was calculated using a method by Hukkerikar *et al.* [16]. The average variation in the calculated performances was 13%. This highlights the robustness of the property predictions, despite the inherent limitations of group contribution methods. Further analysis could explore how these variations impact the selection of candidate molecules in practical applications.

The results indicate that derivatives of glycerol, limonene, and furfural performed best. Nevertheless, 13 configurations exhibited high performances (above 0.9800), a promising outcome that suggests multiple alternative solvents worth exploring.

Toluene was evaluated in IBSS®, in evaluation mode, applying the same target properties outlined in Table 1. The calculated performance was 0.6724, lower than the performance of the generated molecules presented in Table 3. This low value is primally driven by the low flash point (8°C), low boiling point (116°C) and high HSP distance (13.9 $MPa^{1/2}$), indicating that the bio-based molecules generated have strong potential to serve as superior solvents for furfural extraction.

Analyzing the results in Table 3, it is not possible to establish a direct connection between number of radicals and performance, but it is noticed that for limonene, hydroxypropionic and glutamic acid, an increase in the number of functionalization points was positive to the performance and the opposite behavior was identified for glycerol, hydroxymethylfurfural, methylfurfural, geranyl and succinic acid.

Also, it is observed that the biggest molecules, in general, did not score high performances. The average of non-hydrogen atoms for the molecules with performances greater than 0,9 was 14, while for the molecules with performances less than 0,9, it was 26.

Three of the best 26 molecules presented in Table 3 were selected and their properties are detailed in Table 4. The values of the properties are highlighted in green if they meet the target value, or in blue if they don't meet the exact target but fall within the acceptable range defined by the target plus the tolerance.

**Table 3:** Best molecules generated for each building block.

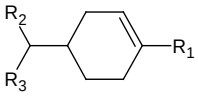
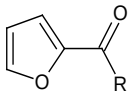
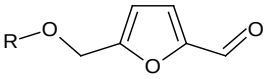
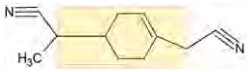
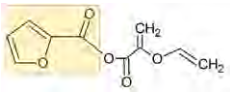
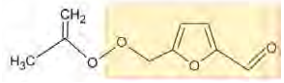
| Fixed Building Block (FP[2], Kmax) | B. P.[1] | Fixed Building Block (FP[2], Kmax) | B.P. |
|---|---|---|---|
| Glycerol (1, 8) | 0.9986 | Geranyl (2, 4) | 0.9817 |
| Glycerol (2, 4) | 0.9955 | Methylfurfural (2, 4) | 0.9810 |
| Limonene (3, 4) | 0.9937 | Glycerol (5, 6) | 0.8571 |
| Furfural (1, 8) | 0.9931 | Glutamic Acid (2, 5) | 0.8571 |
| Furoate (1, 7) | 0.9931 | HMF[4] (3, 5) | 0.8571 |
| Limonene (2, 4) | 0.9930 | Glutamic Acid (1, 7) | 0.8568 |
| HP[3] (3, 4) | 0.9925 | Succinic Acid (1, 8) | 0.8568 |
| HMF[4] (1, 4) | 0.9922 | Glycerol (3, 7) | 0.8567 |
| Levulinic Acid (1, 5) | 0.9914 | Succinic Acid (3, 5) | 0.8561 |
| HP[3] (2, 4) | 0.9913 | Glucaric Acid (6, 7) | 0.8552 |
| Succinic Acid (2, 6) | 0.9904 | Oleic Acid (2, 6) | 0.8550 |
| Glutamic Acid (4, 4) | 0.9883 | Glycerol (6, 6) | 0.8548 |
| Limonene (1, 7) | 0.9876 | Succinic Acid (4, 7) | 0.8541 |
| Methylfurfural (1, 5) | 0.9870 | Oleic Acid (1, 7) | 0.8510 |
| HMF[4] (2, 4) | 0.9848 | HP[3] (1, 7) | 0.8496 |
| Geranyl (1, 8) | 0.9843 | - | - |

[1]BP = best performance
[2]FP = functionalization points
[3]HP = hydroxypropionic
[4]HMF = hydroxymethylfurfural

In all three cases, the Hansen Solubility Parameter (HSP) distances were significantly smaller than the toluene-furfural distance of 13.9. Additionally, their melting and boiling points suggest that these solvents would remain liquid under ambient conditions and based on their flash point they are classified as non-flammable. Furthermore, their low log(Kow) values indicate minimal bioaccumulation concerns, supporting their suitability as sustainable solvent alternatives.

As shown in Figure 3, the maximum performance of the best molecule, derived from glycerol with one functionalization point, improved as generations progressed. This trend demonstrates the effectiveness of the genetic algorithm in identifying better-performing individuals across the tested generations. Furthermore, the results reveal that as kmax increases, the maximum

**Table 4:** Comparative analysis of molecules derived from limonene, furfural and hydroxymethylfurfural.

| Property | Limonene Derivative | Furfural Derivative | Hydroxymethylfurfural Derivative |
|---|---|---|---|
| Fixed building block structure |  |  |  |
| New molecule structure |  |  |  |
| Fixed building block | Limonene | Furfural | Hydroxymethylfurfural |
| Number of FP* | 3 | 1 | 1 |
| Kmax** | 4 | 8 | 4 |
| Performance | 0.9937 | 0.9931 | 0.9922 |
| Melting point (°C) | 11.95 | 10.09 | 10.06 |
| Boiling point (°C) | 304.99 | 286.48 | 264.69 |
| Flash point (°C) | 152.96 | 148.42 | 126.33 |
| HSP distance $(MPa)^{1/2}$ | 4.69 | 5.46 | 5.79 |
| Log (kow) | 1.92 | 0.66 | 1.06 |

*FP: functionalization point
**Kmax: maximum number of fragments allowed to be added in the fixed building block

performance also improves in this case, highlighting the algorithm's enhanced flexibility to create diverse molecular structures with higher potential.

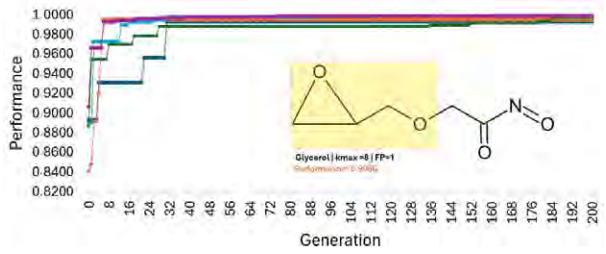



**Figure 3:** Performance evolution across generations for glycerol derivative with 1 functionalization point and representation of the best molecule generated.

From the list in Table 3, some molecules were selected and drawn based on the molecular graph provided as an output of IBSS®. These molecules are depicted in Figure 4. The chemical structures are diverse, and it is important to emphasize that further investigations are needed into process design, stability, and the viability of the proposed molecules. Nevertheless, this study highlights the potential of utilizing residues from high-demand fruits to design environmentally friendly solvents with superior performance characteristics.

## CONCLUSION AND NEXT STEPS

The results demonstrate that the IBSS® CAMD tool is an effective approach for designing bio-based solvents with specific properties to replace toluene in LLE of furfural from aqueous solutions. Through multi-objective optimization, alternative solvents were efficiently ranked based on a global performance value. For all the building blocks studied, molecules with enhanced desired properties compared to toluene were obtained, highlighting the derivatives of glycerol, limonene, and furfural itself. While this early-stage methodology shows significant promise, further studies are required to assess the stability and feasibility of synthesizing these molecules.

Nonetheless, those findings demonstrate a valuable pathway for developing alternative solvents derived from orange and coffee waste, offering a sustainable solution to reduce reliance on fossil-based solvents.

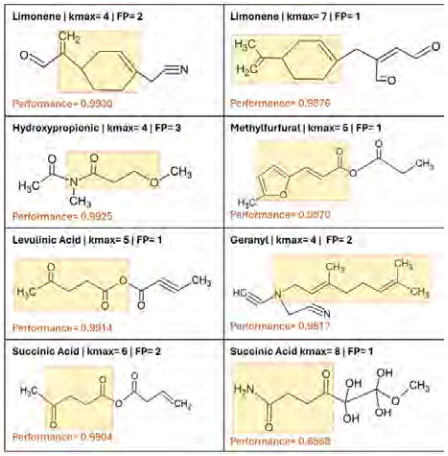



**Figure 4:** Molecular representation of molecules generated by IBSS®.

## ACKNOWLEDGEMENTS

This study was financed, in part, by the São Paulo Research Foundation (FAPESP), Brazil. Process Number 2024/03274-9 and 2022/02809-0.

## REFERENCES

1. Brasil. Systematic survey of agricultural production. Instituto Brasileiro de Geografia e Estatística (IBGE). https://www.ibge.gov.br/en/statistics/economic/agriculture-forestry-and-fishing/17174-systematic-survey-of-agricultural-production.html?=&t=resultados (Accessed Dec. 19, 2024).
2. Capanoglu E, Nemli E, Tomas-Barberan F. Novel approaches in the valorization of agricultural wastes and their applications. *J Agric Food Chem* 70:6787-6804 (2022). https://doi.org/10.1021/acs.jafc.1c07104
3. Brasil. Coffee production explained. Instituto Brasileiro de Geografia e Estatística (IBGE). https://www.ibge.gov.br/explica/producao-agropecuaria/cafe/br (Accessed Jan. 15, 2025)
4. Lee YG, Cho E, Maskey S *et al.* Value-added products from coffee waste: a review. *Molecules* 28:3562 (2023). https://doi.org/10.3390/molecules28083562
5. Aristizábal-Marulanda V, Chacón-Perez Y, Alzate CA. The biorefinery concept for the industrial valorization of coffee processing by-products. *Handbook Coffee Process By-Prod* 63-92 (2017). https://doi.org/10.1016/b978-0-12-811290-8.00003-7
6. United States Department of Agriculture. Foreign Agricultural Service. Brazil citrus semi-annual. https://fas.usda.gov/data/brazil-citrus-semi-annual-7 (Accessed Oct. 19, 2024).
7. Suzuki LL, Cunha I, Teixeira C *et al.* The modeling and simulation of waste recovery processes applied to the orange juice industry. *Sustainability* 15:15225 (2023). https://doi.org/10.3390/su152115225
8. National Renewable Energy Laboratory (NREL). Chemicals from Biomass: Market Assessment of Bioproducts with Near-Term Potential. https://www.nrel.gov/docs/fy16osti/65509.pdf (Accessed Dec. 13, 2024).
9. Sai MSN, De D, Satyavathi B. Sustainable production and purification of furfural from waste agricultural residue: an insight into integrated biorefinery. *J Clean Prod* 327:129467 (2021). https://doi.org/10.1016/j.jclepro.2021.129467
10. Gerbaud V. Computer Aided Molecular Design for bio-sourced molecules. The IBSS Tool. *Journée d'échange Formul Agents Subst Biocontrol* (2023).
11. Heintz J, Touche I, dos Santos MT, Gerbaud V. An integrated framework for product formulation by computer aided mixture design. *Computer Aided Chemical Engineering* 30:702-706 (2012). https://doi.org/10.1016/B978-0-444-59519-5.50141-6
12. Rodriguez-Donis I, Gerbaud V *et al.* Computer-aided product design of alternative solvents based on phase equilibrium synergism in mixtures. *Comptes Rendus Chim* 21:606-621 (2018). https://doi.org/10.1016/j.crci.2018.04.005
13. Wang J, Rodriguez-Donis I, Thiebaud-Roux S *et al.* Selection of green solvents for organic photovoltaics by reverse engineering. *Mol Syst Des Eng* 7:182-195 (2022). https://doi.org/10.1039/D1ME00151E
14. Nehmeh M, Rodriguez-Donis I, Cavaco-Soares A *et al.* Bio-refinery of oilseeds: oil extraction, secondary metabolites separation towards protein meal valorisation—A review. *Processes* 10:841 (2022). https://doi.org/10.3390/pr10050841
15. Heintz J, Belaud JP, Pandya N *et al.* Computer-aided product design tool for sustainable product development. *Comput Chem Eng* 71:362-376 (2014). https://doi.org/10.1016/j.compchemeng.2014.09.009
16. Hukkerikar AS, Sarup B, Sin G *et al.* Group-contribution+ (GC+) based estimation of properties of pure components: improved property estimation and uncertainty analysis. *Fluid Phase Equilib* 321:25-43 (2012). https://doi.org/10.1016/j.fluid.2012.02.010
17. Abbott S, Hansen CM, Yamamoto H. Hansen solubility parameters in practice – complete with software, data, and examples. 5th ed. (2015). ISBN: 9780955122026. Available from: www.hansen-solubility.com.
18. Catoire L, Paulmier S, Naudet V. Estimation of closed cup flash points of combustible solvent blends. *J Phys Chem Ref Data* 35:9-14 (2006). https://doi.org/10.1063/1.1928236
19. Marrero J, Gani R. Group-contribution based estimation of pure component properties. Fluid Phase Equilib 183:183-208 (2001). https://doi.org/10.1016/S0378-3812(01)00431-9

© 2025 by the authors. Licensed to PSEcommunity.org and PSE Press. This is an open access article under the creative commons CC-BY-SA licensing terms. Credit must be given to creator and adaptations must be shared under the same terms. See https://creativecommons.org/licenses/by-sa/4.0/



Systems & Control Transactions

**Research Article - Peer Reviewed Conference Proceeding**
ESCAPE 35 - European Symposium on Computer Aided Process Engineering
Ghent, Belgium. 6-9 July 2025
Jan F.M. Van Impe, Grégoire Léonard, Satyajeet S. Bhonsale,
Monika E. Polańska, Filip Logist (Eds.)

PSE PRESS

# An MILP model to identify optimal strategies to convert soybean straw into value-added products

**Ivaldir J. Tamagno Junior[a*], Bruno F. Santoro[b], Omar Guerra[c] and Moisés Teles dos Santos[a]**

[a] University of São Paulo, Department of Chemical Engineering, Escola Politécnica, São Paulo, SP, Brazil
[b] OP2B - Optimization to Business Ltda., São Paulo, SP, Brazil
[c] National Renewable Energy Laboratory, Golden, CO, USA
* Corresponding Author: ivaldirjunior@usp.br.

## ABSTRACT

Soybean is a highly valuable global commodity due to its versatility and numerous derivative products. During harvest, all non-seed materials become "straw". Currently, this waste is primarily used for low-value purposes such as animal feed, landfilling, and incineration. To address this, the present work proposes a conceptual biorefinery aimed at converting soybean straw into higher-value products. The study began with data collection to identify potential conversion routes. Based on this information, a superstructure was developed, comprising seven conversion routes: four thermochemical routes (pyrolysis, combustion, hydrothermal gasification, and liquefaction), two biological routes (fermentation and anaerobic fermentation), and one chemical route (alkaline extraction). Each process was evaluated based on product yields, conversion times, and associated capital and operating costs. Using this data, an MILP (Mixed-Integer Linear Programming) optimization model was built in Pyomo using CPLEX as the solver. The variables in this problem were the amounts of biomass processed by each conversion process. The objective function was to maximize the Net Present Value (NPV). The optimization considered a maximum raw material supply of 232,500 metric tons per year. As a result, pyrolysis was identified as the most profitable route, yielding US$447 million, producing biochar, bio-oil and gas as products. It was observed that only if the price of the optimum product was 46% lower would the optimum conversion process change. In conclusion, soybean straw offers significant potential for value-added applications in a biorefinery context, with pyrolysis emerging as the most profitable route.

**Keywords**: Optimization, Pyomo, Biomass, Soybean, Biorefinery

## INTRODUCTION

Since the Industrial Revolution, petroleum, coal and natural gas have been the primary energy sources. Technical achievements have come with the use of these energy sources, *e.g.*, developing steam engines, chemical products and fuels. However, oil has a depletion time of less than 270 years and takes approximately about 280 million years to regenerate [1]. Moreover, the exploitation of fossil fuels has a significant impact on the environment, including soil and water contamination and the release of harmful gases that intensify global warming [2]. Given this context, it is necessary to find different sources that have less environmental and social impacts.

Lignocellulosic biomass is one of the most promising alternatives to fossil fuels due to its large availability. In addition, its structure is complex, consisting of four different organic compounds (cellulose, hemicellulose, lignin and extractives) and one inorganic component (ash), which can produce a substantial number of different value-added products with high energy potential. The renewable nature of lignocellulosic biomass stems from the fact that the $CO_2$ produced when burning biomass is reabsorbed by plants during their development, maintaining a carbon-neutral cycle [3]. Various processes that modify biomass structure and generate new products have been studied over the years.

To develop sustainable and profitable production systems, large amounts of data are necessary, which can sometimes become intractable to analyze. From a process systems engineering (PSE) perspective, computation tools are recommended because analyzing vast

amounts of data from different sources manually is challenging [4]. Techno-economic optimization can reduce costs in the initial stages, particularly in process systems with significant uncertainties, such as biorefineries

Biorefinery is an integrated industrial process that incorporates individual units that convert biomass into power, biofuels and value-added chemicals. The conversion process used in biorefineries can be divided into four principal groups: mechanical processes (size reduction, separation and concentration of substances); thermochemical processes, (pyrolysis, gasification, liquefaction and combustion); biological processes (fermentation and anerobic fermentation); and chemical processes, which use chemicals to change the structure of the input material [5].

**Table 1** – Production of soybean by country/region in 2022/23 [6]

| | Production (MMT) | World Share (%)[1] |
|---|---|---|
| Brazil | 162 | 42,9% |
| United States | 116 | 30.7% |
| Europe | 2.61 | 0.69% |
| World | 378 | 100% |

[1] Country/Region production as a percentage of world production

Brazil is the largest producer of Soybean (*Glycine max)*, followed by the United States, collectively, they represent over 70% of global production (Table 1). With all this crop, a lot of waste is generated, the principal one is soybean straw, composed of leaves, steams and pods with lignocellulosic composition of 35% of cellulose, 22% of lignin, 17% of hemicellulose and 1% of ashes [7]. It is estimated that the ratio of straw to soybeans varies from 1.2 to 1.5 [8], which represented, in 2023, 194.4-243 million metric tons of waste. Most of the straw is used as landfill, livestock feed, incineration or dumping [7, 8].

Considering those known destinations, soybean straw does not have nutritional value compared to other crops residues *e.g.*, sorghum or corn, to be used as animal feed. However, it is necessary to keep part of the straw in the land to protect the soil from runoff, infiltration and soil loss. The Brazilian Agricultural Research Corporation (EMBRAPA) [9] estimated that it is necessary to keep 2.205 metric ton per ha to protect the soil, so almost 50% of all soybean straws needs to be used for landfill, in the context of Brazilian scenario.

Given the lack of current uses, the large availability and its lignocellulosic composition, soybean straw has a lot of potential to produce chemical products and fuels. The objective of this work was to develop a superstructure of a conceptual soybean straw biorefinery and solve it using an MILP (Mixed Integer Linear Programming) optimization, with Net Present Value (NPV) as the objective function.

# METHODOLOGY

The methodology was based on three steps. The first one was a literature review, which was necessary to find conversion processes and products that can be obtained from soybean straw. The second one was data treatment, to standardize the data, making it possible to use it in a generic framework. The final step was the development and solution of an MILP optimization model.

## Literature Review

All chosen products and their respective process routes for soybean straw valorization were gathered from academic literature.

Process costing was performed using similar routes reported in literature. There were two types of cost considered: a capital cost (CAPEX), which considers equipment, installation and instrumentation cost; and an operating cost (OPEX), which covers the reactants' price, labor charges and other administrations costs. For all the selected products, a revenue price was determined. While some have a known market price, others had to be estimated.

## Data Treatment

The basic premises considered were: 350 days a year as operating time; 2023 as the reference year; the biomass availability as all soybeans straw waste in the city of Itapeva, São Paulo State, in 2023 (232,500 metric ton) [10]; 10 years of plant lifetime operation; no cost associated with the feedstock; and a discount rate of 12.25% per year.

The yield of each product was adjusted to be per gram of biomass. Because it was used an annual biomass availability, it was necessary to find an annual yield of each product, so, the conversion time of each process was considered.

In Eq. 1, CAPEX was adjusted by capacity and time using a power-law expression [11], where A is the capacity of this biorefinery (27.68 MT $h^{-1}$); $CAPEX_{ref}$, $CEPCI_{ref}$ and $A_{ref}$ are the CAPEX, Chemical Engineering Plant Cost Index and plant capacity, in t $h^{-1}$, found in the articles for each route, respectively [21-28].

$$CAPEX = CAPEX_{ref} \cdot \left(\frac{CEPCI_{2023}}{CEPCI_{ref}}\right) \cdot \left(\frac{A}{A_{ref}}\right)^{0.67} \quad (1)$$

OPEX was adjusted, as well, using Eq. 2.

$$OPEX = OPEX_{ref} \cdot \left(\frac{CEPCI_{2023}}{CEPCI_{ref}}\right) \cdot \left(\frac{A}{A_{ref}}\right) \quad (2)$$

It was not possible to find the market price for some products. In such cases, two approaches were used to determine the price: comparing the function of the product (*i.e.*, the price of biochar produced in a pyrolysis route was estimated using coal as reference, using the low heating value as comparison parameter), or similarity

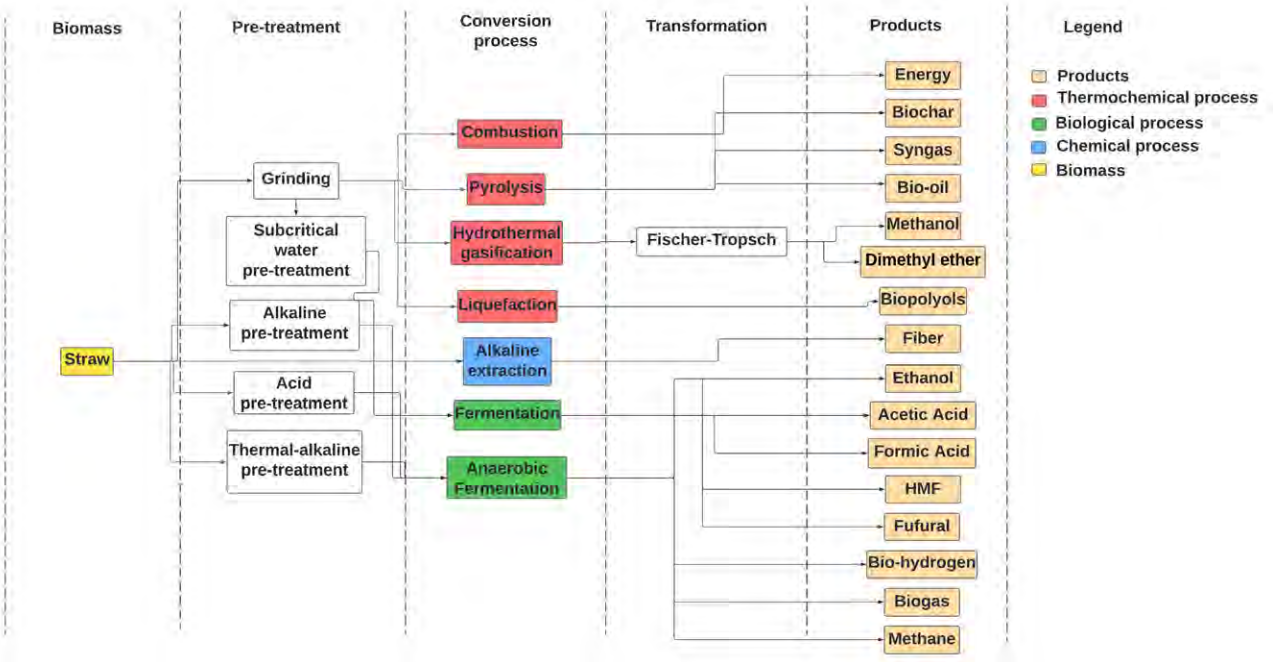



**Figure 1:** Superstructure for soybean straw valorization

with products commercially available (*i.e.,* the price of pulp and polyurethane was used as the price of fiber and biopolyols produced from soybean straw, respectively).

## MILP Optimization

For the MILP optimization, the capital letters represent the parameters and the small ones, the variables. The objective function (Eq. 3) was the maximization of the Net Present Value (NPV), where R represents the discount rate; *i* , *j* and *t* are the sets for processes, products and lifetime, respectively; $N_{i,j}$ represents the yield of each product *j* in the process *i*; $P_j$ is the price of the product *j*; $d_i$ is the non-negative variable, representing the amount of soybean straw used in the conversion process *i* ; $C_i$ and $O_i$ represents the CAPEX and OPEX for the process *i,* respectively, and $y_i$ is the binary variable to decide what process *i* will be selected.

$$\max NPV = \sum_{t=0}^{10} \frac{\sum_i \sum_j N_{i,j}.P_j.d_i - \sum_i O_i.y_i}{(1+R)^t} - \sum_i C_i.y_i \qquad (3)$$

The constraints used were:

A big-M constraint to represent the upper bound of the variable $d_i$ and the activation of the binary variable $y_i$(Eq. 4);

$$d_i \leq y_i.D \qquad (4)$$

The total biomass used in all processes is equal to the total available biomass (*D* ) (Eq. 5);

$$\sum_i d_i = D \qquad (5)$$

An anaerobic fermentation route includes two distinct pre-treatments; therefore, an additional constraint (Eq. 6) was required to prevent them from being selected simultaneously. The subindexes (6.1, 6.2) follow the numbering adopted in Table 2 for the conversion processes.

$$y_{6.1} + y_{6.2} \leq 1 \qquad (6)$$

The model was solved using Pyomo (a Python-based, open-source optimization modeling language). The solver used was CPLEX, which uses the "branch and bound" or "branch and cut" methods [12].

## Sensitivity Analysis

A sensitivity analysis was conducted to evaluate the impact of various uncertainties. Specifically, the market prices of the products associated with the optimal route were varied within a range of -60% to 30%. This analysis aimed to assess how the objective function and the decision variables are affected by these changes.

# RESULTS AND DISCUSSIONS

## Literature Review

Four thermochemical processes (pyrolysis [13], liquefaction [14], combustion [15], and hydrothermal gasification [16]), two biological processes (fermentation [17] and anaerobic fermentation [18, 19]), and one chemical (alkaline extraction [20]) were selected. Thus, the superstructure covers the main types of conversion routes.

Figure 1 represents the superstructure created. There were sixteen products found (biochar, bio-oil,

**Table 2:** Reference and calculated capital and operated costs per conversion process

| | Conversion process | $Capacity_{ref}$ (MT $h^{-1}$) | $CAPEX_{ref}$ (M US$) | $CAPEX_{calc}$ (M US$) | $OPEX_{ref}$ (M US$ $yr^{-1}$) | $OPEX_{calc}$ (M US$ $yr^{-1}$) | Ref. |
|---|---|---|---|---|---|---|---|
| 1 | Pyrolysis | 1.25 | 0.980 | 10.4 | 0.115 | 3.39 | [22] |
| 2 | Fermentation | 83.3 | 69.0 | 45.1 | 198 | 90.1 | [23] |
| 3 | Liquefaction | 2.19E-05 | 0.019 | 226 | 0.0004 | 548 | [24] |
| 4 | Alkaline extraction | 17.3 | 469 | 631 | 8.37 | 13.1 | [25] |
| 5 | Anaerobic Fermentation | 29.4 | 70.0 | 94.9 | 44.4 | 59.0 | [26] |
| 6.1 | Anaerobic Fermentation[1] | 0.005 | 0.299 | 132 | 0.078 | 596 | [27] |
| 6.2 | Anaerobic Fermentation[2] | 0.005 | 0.299 | 132 | 0.078 | 595 | [27] |
| 7 | Combustion | 0.206 | 0.333 | 12.5 | 0.113 | 21.4 | [28] |
| 8 | Hydrothermal gasification | 36.6 | 5.98 | 4.96 | 0.204 | 0.154 | [21] |

[1] Alkaline pre-treatment
[2] Acid pre-treatment

syngas, methanol, dimethyl ether, biopolyols, fiber, ethanol, acetic acid, formic acid, hydroxymethyl furfural - HMF, bio-hydrogen, biogas, and methane). For the hydrothermal gasification, it does not have the Fischer-Tropsch transformation process. This route was proposed to diversify the products and to facilitate the pricing of the syngas [21].

**Table 3:** Yield of products for different conversion processes

| Process | Product | Yield ($g_{biomass}^{-1}$) |
|---|---|---|
| 1 | Biochar | 0.220 g |
| | Bio-oil | 0.720 g |
| | Gas | 0.060 g |
| 2 | Ethanol | 0.279 g |
| | Acetic Acid | 0.087 g |
| | Formic Acid | 0.052 g |
| | HMF | 0.001 g |
| | Furfural | 0.001 g |
| 3 | Biopolyols | 0.650 g |
| 4 | Fiber | 0.250 g |
| 5 | Methane | 194 mL |
| 6.1 | Bio-hydrogen | 3.14 mL |
| | Ethanol | 0.006 g |
| | Acetic Acid | 0.019 g |
| 6.2 | Bio-hydrogen | 47.7 mL |
| | Ethanol | 0.001 g |
| | Acetic Acid | 0.019 g |
| 7 | Energy | 0.005 kWh |
| 8 | Methanol | 0.071 g |
| | Dimethyl ether | 0.051 g |

## Data Treatment

Table 2 has all the associated costs for each process. It is possible to observe, when CAPEX and OPEX were adjusted for the capacity of the biorefinery studied, thermochemical processes had lower costs when compared to biological and chemical processes, especially because almost no auxiliar materials (such as chemicals) are used.

Table 3 shows the yield of products for different conversion processes. It is possible to conclude that for the same route a change in the pre-treatment can significantly impact on the yield of some products (*e.g.,* biohydrogen). Moreover, when using aerobic microorganisms, a larger amount of ethanol is produced than when using anaerobic ones. In biorefinery context, even if inhibitors are produced (HMF and furfural) in a fermentation route, revenue is still obtained, and sometimes, this product can be transformed and have a higher market price than the main product. Furfural, for instance, is a chemical platform from which a lot of other chemicals can be derived from.

## MILP Optimization

For the MILP model, nine decision variables were considered with ten constraints. The objective function resulted in an NPV of US$447 million, selecting the pyrolysis route as the optimum route, producing biochar, bio-oil and gas.

Figure 2 illustrates the NPV of each process route evaluated. Three of the evaluated thermochemical routes were the most profitable, and only the thermochemical routes led to positive values for the objective function. This could be explained by the biomass chemical composition, as identified in the studies by Eason and Cremaschi [29], lignocellulosic waste (*e.g.*, switchgrass) is most efficiently utilized through thermochemical processes. In contrast, certain grains or seeds, which contain significant amounts of oil and starch, are better suited for valorization through transesterification or fermentation.

The NPV of the most profitable route, pyrolysis, is twice as high as that of the second most profitable route (*i.e.* combustion). It is known that pyrolysis process has a low TRL (Technology Readiness Level) compared with other thermochemical routes, mostly because of the high

complexity kinetics of this process creating some uncertainties. Alternatively, combustion is a well-developed process, which could be an interesting alternative for the pyrolysis process for this case.

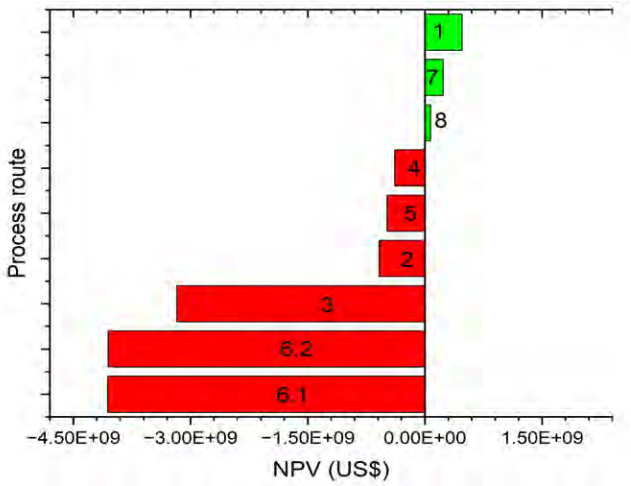



**Figure 2:** NPV value for each process route

## Sensitivity Analysis

The profitability of pyrolysis remains robust despite price fluctuations. In Figure 3, it was observed that it is necessary a 46% decrease in these products' price for the pyrolysis route to be substituted by the combustion as the best route. These two thermochemical routes have very profitable products and lower costs, which justify these optimum results.

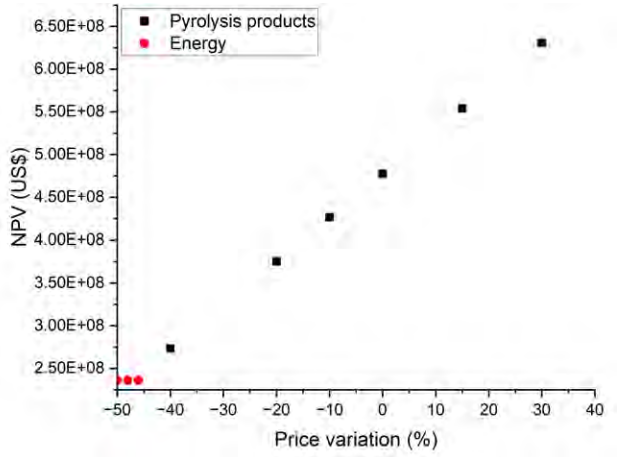



**Figure 3:** Effect of optimal product price variation on the objetive function

Fischer-Tropsch products are frequently cited as playing an important role in future biorefineries. To produce methanol and dimethyl ether in this biorefinery and keep almost the same profit as the optimum one, it will be necessary that the price of these products increases 6.5 times. This analysis shows that it is unlikely that Fischer-Tropsch chemicals could be profitable at least in the short term in a soybean straw biorefinery.

## CONCLUSION AND NEXT STEPS

A conceptual biorefinery using soybean straw as feedstock can be profitable. Pyrolysis emerged as the optimum route, generating biochar, bio-oil and syngas as products. The second-best route for soybean straw valorization was combustion. The optimum products demonstrated a resilient price market, although the technology has a significant associated uncertainty. Evaluating this biorefinery could foster sustainable industrial development by valorizing agricultural waste, serving as an initial study to further evaluate different supply combinations, operational conditions, or end-product prices.

Future research will focus on calculating equipment sizes to refine CAPEX and OPEX estimates. Moreover, the influence of other parameters (*e.g.*, feedstock cost variations, discount rate changes, and OPEX fluctuations) will be investigated to better understand the behavior of the decision variables. A multi-objective and multi-feedstock approach will also be considered to assess the environmental and supply chain aspects.

## DIGITAL SUPPLEMENTARY MATERIAL

A supplementary material is available in LAPSE:2025.0034 with the data extracted, from the literature review, and treated to model the optimization.

## ACKNOWLEDGEMENTS

This study was financed by the São Paulo Research Foundation (FAPESP), Brazil. Process Number 2024/03270-3 and 2022/02809-0.

## REFERENCES

1. Conteratto, Caroline *et al.* Biorefinery: A comprehensive concept for the sociotechnical transition toward bioeconomy. Renewable and Sustainable Energy Rev, 2021.
2. Maren, I. *et al.* Energy Exploitation and Environmental Impact In Nigeria: The Way Forward. Energy, 2013.
3. Bhat, Mudasir Ahmad *et al.* Lignocellulosic biomass in circular economy: A techno-transition in carbon neutrality towards sustainable energy production. Biomass Bioenergy, 2024.
4. Bertran, Maria-Ona *et al.* Sustainable biorefinery process synthesis, design, and simulation: Systematic computer-aided methods and tools. In: AZ of Biorefinery. Elsevier, 2022.
5. Hackl, Roman *et al.* Opportunities for process

integrated biorefinery concepts in the chemical cluster in Stenungsund. Chalmers University of Technology, 2010.
6. Foreign Agricultural Service/USDA (2024) Global market analysis - world agricultural production December 2024 - Circular series WAP 12–24. World Agricultural Production | USDA Foreign Agricultural Service. Accessed 9 Jan 2024
7. Martelli-tosi, Milena *et al*. Chemical treatment and characterization of soybean straw and soybean protein isolate/straw composite films. Carbohydrate polymers, 2017.
8. Gonzalez, Paula Gixina Ardila *et al*. Soybean straw as a feedstock for value-added chemicals and materials: recent trends and emerging prospects. BioEnergy Research, 2023.
9. Plantio Direto - Portal Embrapa. Disponível em: <https://www.embrapa.br/agencia-de-informacao tecnologica/cultivos/milho/producao/manejo-do-solo-e-adubacao/sistema-de-manejo-do-solo/plantio-direto>. Accessed 9 Jan. 2025.
10. Itapeva - SP - Área plantada, colhida, quantidade produzida, rendimento médio, valor da produção Portal Agrolink. Website <https://www.agrolink.com.br/regional/sp/itapeva/estatistica>. Accessed 9 Jan. 2025.
11. Turton, Richard *et al*. Analysis, synthesis and design of chemical processes. Pearson Education, 2008.
12. Biegler, L. T. *et al*. Systematic Methods of Chemical Process Design; Prentice-Hall, 1997.
13. Boateng, Akwasi A. *et al*. Sustainable production of bioenergy and biochar from the straw of high-biomass soybean lines via fast pyrolysis. Environ Prog Sustain Energy, 2010.
14. Hu, Shengjun *et al.* Production and characterization of biopolyols and polyurethane foams from crude glycerol based liquefaction of soybean straw. Bioresour Technol, 2012.
15. Li, Siqin *et al*. CO2 gasification of straw biomass and its correlation with the feedstock characteristics. Fuel, v. 297, p. 120780, 2021
16. Okolie, Jude A. *et al*. Hydrothermal gasification of soybean straw and flax straw for hydrogen-rich syngas production: Experimental and thermodynamic modeling. Energy Convers Manag, 2020.
17. Vedovatto, Felipe *et al*. Production of biofuels from soybean straw and hull hydrolysates obtained by subcritical water hydrolysis. Bioresour Technol, 2021.
18. Xiong, Jiading *et al*. Methane enhancement by the co-digestion of soybean straw and farm wastewater under different thermo-chemical pretreatments. Renewable Energy, 2020.
19. Han, Hongliang *et al*. Optimization of biohydrogen production from soybean straw using anaerobic mixed bacteria. Int J Hydrogen Energy, 2012.
20. Reddy, Narendra *et al*. Natural cellulose fibers from soybean straw. Bioresource Technology, 2009.
21. Domingos, Meire Ellen G. R. *et al*. Techno-economic and environmental analysis of methanol and dimethyl ether production from syngas in a kraft pulp process. Comput Chem Eng, 2022.
22. Soka, Ongama. Process Optimisation and techno-economic assessment of the slow pyrolysis of corn-stover. Diss. Cape Peninsula University of Technology, 2020.
23. Meyer, Pimphan A. *et al*. Techno-economic analysis of corn stover fungal fermentation to ethanol. Applied energy, 2013.
24. Tran, My Ha *et al*. Sustainable biopolyol production via solvothermal liquefaction silvergrass saccharification residue: Experimental, economic, and environmental approach. Science of the Total Environment, 2022.
25. Storm, Benjamin *et al*. Techno-economic and sustainability assessment: Circular cellulose to textile fiber production. 2023.
26. Rajendran, Karthik *et al.* Techno-economic and life cycle assessments of anaerobic digestion–A review. Biocatal Agric Biotechnol, 2019.
27. Li, Ya-Chieh *et al*. Techno-economic evaluation of biohydrogen production from wastewater and agricultural waste. Int J Hydrogen Energy, 2012.
28. Huang, Ye *et al*. Comparative techno-economic analysis of biomass fuelled combined heat and power for commercial buildings. Applied energy, 2013.
29. Eason, John P.; Cremaschi, Selen. A multi-objective superstructure optimization approach to biofeedstocks-to-biofuels systems design. Biomass and Bioenergy, 2014.

© 2025 by the authors. Licensed to PSEcommunity.org and PSE Press. This is an open access article under the creative commons CC-BY-SA licensing terms. Credit must be given to creator and adaptations must be shared under the same terms. See https://creativecommons.org/licenses/by-sa/4.0/



Systems & Control Transactions

**Research Article - Peer Reviewed Conference Proceeding**
ESCAPE 35 - European Symposium on Computer Aided Process Engineering
Ghent, Belgium. 6-9 July 2025
Jan F.M. Van Impe, Grégoire Léonard, Satyajeet S. Bhonsale,
Monika E. Polańska, Filip Logist (Eds.)

PSE PRESS

# A Generalized Optimization Approach for the Characterization of Non-Conventional Streams

**Michaela Vasilaki[a], Effie Marcoulaki[b], and Antonis Kokossis[a]***

[a] Department of Process Analysis and Plant Design, School of Chemical Engineering, National Technical University of Athens, Athens, Greece
[b] System Reliability and Industrial Safety Laboratory, National Center for Scientific Research 'Demokritos", Athens, Greece
* Corresponding Author: akokossis@chemeng.ntua.gr

## ABSTRACT

This study provides standardized models for the chemical characterization of complex streams, ensuring the necessary adaptations while considering the differences in biomass types and forms. Several datasets are compiled and examined to establish a valid representation of the mixture, according to industry accepted standards and laboratory protocols. For reliable property estimation, correlations of key biomass properties are obtained from both computational models and experimental measurements. Existing data are used to create datasets for the biomass and the biocrude streams. This model builds upon existing knowledge and data technologies with emphasis on hydrothermal liquefaction (HTL). The proposed approach shows potential as a starting point for the design and modelling of more biorefinery-associated technologies. Sludge and pine wood are used as case studies for biomass feedstocks. Two biocrude samples are employed for biocrude characterization. The performance of the developed optimization model is compared favorably with results obtained using previous works. To ensure a variety of possible and valid solutions, integer cuts are implemented producing solution pools for the analysed streams.

**Keywords**: Optimization, MINLP, Biomass, Biorefineries, Biocrude, Integer cuts

## INTRODUCTION

Global emissions have increased rapidly over the last half-century, driving climate change [1]. Fossil fuels are by far the largest contributor, accounting for over 75% of global greenhouse gas emissions and nearly 90% of all $CO_2$ emissions [2]. Bioenergy offers a sustainable alternative, potentially supplying a quarter to a third of global primary energy by 2050 and replacing fossil fuels across energy markets [3]. Second-generation biorefinery processes convert a range of organic feedstocks into biocrude, which can be upgraded into liquid hydrocarbon fuels [4].

Among these, hydrothermal liquefaction (HTL) is a promising technology for converting biomass into biocrude and valuable chemicals under high temperature and pressure conditions [5]. The process offers advantages such as wet biomass processing and reduced tar formation [6] and is easily adaptable to various types of biomass feedstocks [7]. The reaction mechanisms involve depolymerization of biomass components, with proteins, lipids, and carbohydrates following distinct pathways [8]. Some HTL fuels can reduce Global Warming Potential by approximately 70% compared to conventional jet fuel [9].

Mechanistic kinetic models have been developed for HTL, to predict product yields and composition for different feedstocks [10]. Characterization of the biomass and biocrude streams is crucial for modeling the complexity of HTL reaction mechanisms and upgrading the process [11]. Various analytical methods can be employed, including conventional analytical methods like GC, FTIR, and NMR, or advanced 2D- GC, LC, NMR and HRMS techniques [12]. Conventional methods face limitations in comprehensively characterizing the complex composition of these streams, requiring advanced techniques to produce comprehensive results [13].

Stream characterization can also be done using computational techniques (in the form of optimization or Machine Learning models) using experimental datasets

containing information relevant to each studied system [14-16]. A common limitation across all methods mentioned is the inadequacy of available data, tools and flow sheeting techniques for accurately representing different biomass types.

Park et al. (2023) employed HPLC derived data to develop predictive equations correlating biochemical content with elemental composition in biomass characterization [17]. Ahmed et al. (2019) relied on machine learning techniques to estimate moisture content and compositional analysis based on data derived from NIR spectroscopy [18]. Taghipour et al. (2021) characterized biocrude streams through multi-objective optimization with the NSGA-II algorithm, by integrating distillation data [19]. Aslanoglou et al. (2024) proposed a model that utilizes both stochastic and deterministic algorithms to simulate the input and output streams associated with hydrothermal liquefaction (HTL) of sewage sludge [20].

This work builds on existing models and data to develop a robust generalized optimization model, to capture the composition diversity and characterize biomass and biofuel streams. The following sections present the proposed methodology and the material datasets utilized here, compare the model performance to previous works, and illustrate the use of integer cuts to deliver portfolios of solutions.

## METHODOLOGY

This section describes the mathematical model developed here for the characterization and analysis of biomass and biocrude streams and its implementation.

The objective function $F$ is formulated as follows:

$$min\{F\} = \sum_{m=1}^{M}\left(1 - f_m/\hat{f}_m\right)^2 + \sum_{k=1}^{K}\left(1 - f_k/\hat{f}_k\right)^2 \quad (1)$$

where $\hat{f}$ and $f$ denote experimental and first principle based data for each property $k \in \{1, \dots, K\}$ and $m \in \{1, \dots, M\}$, respectively.

The following sets of properties are considered:

- Elemental composition of $m$={Carbon, Hydrogen, Oxygen, Nitrogen, Sulfur,..} where $Nm_{m,j}$ denotes the number of elements in every compound and $Ar_m$ the element atomic number.

$$f_m = \frac{\sum_j x_j \cdot Nm_{m,j} \cdot Ar_m}{\sum_{m=1}^{M}\sum_j x_j \cdot Nm_{m,j} \cdot Ar_m} \quad (2)$$

- Biochemical composition $k$={Protein, Carbohydrate, Lignin, Lipid, etc.} where $B_{k,j}$ denotes the biochemical identification in every compound.

$$f_k = \sum_j x_j \cdot B_{k,j} \quad (3)$$

where $x_j$ denotes the composition of compound $j$.

- The model can also incorporate constraints on the stream property values, to ensure that they match experimental characterization data. These properties may include Higher Heating Values (HHV), densities and Boiling Point Temperature (TBP) profiles (only for biocrude mixtures).

Feasibility constraints are also applied:

$$\begin{pmatrix} I & -L_x I \\ -I & U_x I \end{pmatrix} \begin{pmatrix} x_j \\ y_j \end{pmatrix} \leq \begin{pmatrix} 0 \\ 0 \end{pmatrix}, \quad (4)$$

where $y_j$ is a binary variable indicating the presence of a compound in the mixture; $L_j$ and $U_j$ are the lower and upper bound of the continuous variable $x_j$.

$$\sum_j x_j = a, \quad a \leq 1 \quad (5)$$

$$\sum_j y_j \leq N \quad (6)$$

where $a$ is the total dry and ash-free composition.

The above are implemented in GAMS as a mixed-integer nonlinear programming (MINLP) problem solved using the BARON solver. The model inputs are the feedstock and biocrude properties. The model outputs are estimates of the unknown feedstock composition.

The model is solved iteratively to produce multiple solutions through integer cuts, resulting in alternate populations that match optimization requirements. We also apply integer cuts to generate a set of alternative stream compositions and investigate governing stream characteristics [21]. Algorithm 1 shows a pseudocode of the algorithm to solve the MINLP problem of Equations 1-6, including the integer cuts.

**Algorithm 1**: Implementation of the optimization model

```
Data input
    Read compound dataset, D=[C×K]
    Read stream property data, PD=[K×1]
MINLP model definitions
    Property models, PM=[K×1]
    Objective function F = f(X), X=[C×1]
    Property Constraints G = g(X,Y), Y=[C×1]
    Feasibility constraints H = h(X,Y)
Integer cuts definitions
    Number of runs, N
    Min differences per solution, M
    Initial solution table, T=[N×C]
Loop {n=1 to N}
    Solve MINLP model so that
        |Yn-Y1|≥M, for all i∈{1,…,n-1}
    Output the estimated composition Xn=[C×1]
Next n
```

## DATASETS

Two distinct datasets are used for stream characterization for biocrude (Table 1) and biomass (Table 2). Data on selected chemicals are collected from published works providing experimental (e.g. HPLC) and simulation data (e.g. Optimization) for biomass [20, 22-30] and biocrude [19, 20, 31, 32] characterization.

**Table 1**: Biocrude dataset description (144 compounds)

| |
|---|
| Saturated hydrocarbons; aromatic compounds etc. |
| Molecular weight ranges: 60-410 g/mol |
| TBP ranges: 50-550$^{O}$C |
| Properties (molecular weight, TBP, SMILES etc). |

**Table 2**: Biomass dataset description (111 compounds)

| |
|---|
| 18% amino acids |
| 23% carbohydrates |
| 31% lipids |
| 28% lignin compounds |
| Molecular weight ranges: 70-600 g/mol |
| Density ranges: 0.8-1.7 g/cm3 |
| Properties (chemical formula, density, SMILES etc). |

# CASE STUDIES

## Biomass characterization

We showcase the versatility and wide applicability of the proposed MINLP model by examining three sludge and pine wood feedstocks, which exhibit significant differences in protein and lignin content. In all three cases, we consider the biomass dataset of Table 2. When the compositions don't add up to 100% the model is adjusted to consider normalized values.

*Case F1*: Table 3 shows the obtained deviations between experimental and calculated values for the sewage sludge. The MINLP results are tested against those of Aslanoglou et al. (2024) who compared two evolutionary (firefly algorithm (FA) and particle swarm optimization (PSO)) and two deterministic algorithms (sequential quadratic programming (SQP) and least squares optimization (LS)). SQP had the best performance using a dataset tailored to sludge streams [20]. The current model outperforms significantly their best model (SQP) in fitting to the experimental values. We finally observe that the overall objective function value is reduced here by 93%.

**Table 3**: Comparison of biomass results in case F1

| | Exp. Data | SQP | | MINLP | |
|---|---|---|---|---|---|
| Carbon | 54.20 | 52.36 | 3.40% | 54.47 | 0.49% |
| Hydrogen | 7.30 | 7.43 | 1.77% | 7.30 | 0.00% |
| Oxygen | 34.20 | 36.85 | 7.73% | 34.63 | 1.26% |
| Nitrogen | 3.60 | 3.25 | 9.78% | 3.60 | 0.00% |
| proteins | 15.77 | 17.42 | 10.44% | 15.39 | 2.42% |
| H/C | 40.58 | 42.66 | 5.13% | 41.47 | 2.20% |
| lipids | 13.06 | 13.45 | 3.00% | 12.67 | 2.95% |
| Lignin | 25.10 | 26.47 | 5.46% | 24.97 | 0.51% |
| HHV | 24.51 | 23.71 | 3.24% | 24.62 | 0.47% |
| SSRD | | | 3.55E-02 | | 2.17E-03 |

*Case F2*: This case considers a pine wood sample from Obeid et al. (2021) (Type: Sawdust) [33]. Table 4 reports an excellent fit to the experimental values. In this case we did not have information on the mixture HHV.

*Case F3*: Table 5 reports the MINP model results for a sludge stream from Snowden-Swan et al. (2022) (Type: WW09 50/50 CCSD, DAF) [34]. In this case we also demonstrate the use of integer cuts. Table 5 reports the overall results statistics for 50 solutions of the MINLP model. Here we obtain a distribution of values for the elementary and the biochemical compositions, so we report the average and the standard deviations of SSRD.

**Table 4**: Results for the pine wood stream F2

| | Exp. Data | MINLP | |
|---|---|---|---|
| Carbon | 44.68 | 43.69 | 2.21% |
| Hydrogen | 6.15 | 6.13 | 0.30% |
| Oxygen | 51.43 | 50.12 | 2.55% |
| Nitrogen | 0.06 | 0.06 | 0.00% |
| proteins | 0.50 | 0.50 | 0.10% |
| H/C | 66.90 | 76.38 | 14.17% |
| lipids | 2.80 | 2.82 | 0.59% |
| Lignin | 19.50 | 20.31 | 4.13% |
| SSRD | | | 2.30E-02 |

**Table 5**: Results for the sludge stream F3

| | Exp. Data | MINLP (average & st.dev.) | |
|---|---|---|---|
| Carbon | 51.10 | 51.50 | 0.009 |
| Hydrogen | 7.40 | 7.41 | 0.004 |
| Oxygen | 35.60 | 35.79 | 0.009 |
| Nitrogen | 5.30 | 5.31 | 0.003 |
| proteins | 45.40 | 45.42 | 0.031 |
| H/C | 46.10 | 46.08 | 0.030 |
| lipids | 8.00 | 8.00 | 0.005 |
| Lignin | 0.50 | 0.50 | 0.000 |
| SSRD | | 7.93E-05 | 5.41E-06 |

Figure 1 shows the boxplots of the compound concentrations (wt/wt) in the obtained results, which also show the frequency of compound appearance. Note that, we hide the compounds which are not present in any of the 50 solutions. It is observed that, among the lipids, Lignoceric acid and Docosahexanoic acid are the compounds with the highest concentrations (average 3% and 2% respectively). Among the carbohydrates, Cellobiose and Sucrose were found with the highest concentration with an average of 11% and 7% respectively. The most common amino acids found were Phenylalanine and Tyrosine with average values of 12% and 10%.

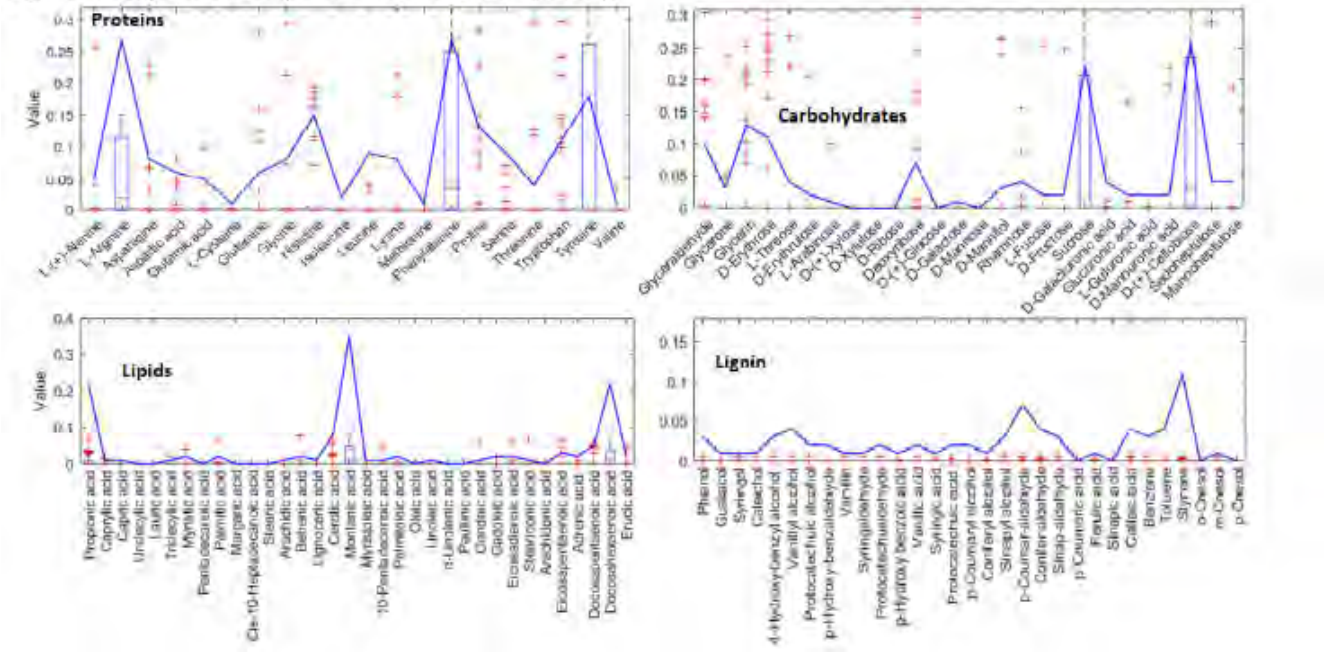
## Biocrude characterization

*Cases B1 & B2*: This case considers Aslanoglou et al. [20]. Table 6 reports an excellent fit to the experimental values. We observe 96% and 78% reductions of the objective function value compared to previous works on biocrude and upgraded biocrude, respectively.

# DISCUSSION

The performance of the model developed here is demonstrated on 3 different feedstocks, showing significantly lower deviations compared to previous works. Though we have a limited pool of results, the model seems to perform slightly better in sludge samples, compared to pine wood. This could be attributed to the higher lignin content in wood and woody biomass mixtures, which is more

**Figure 1**: Boxplots of compound concentrations (wt/wt).




challenging to model effectively, especially considering the structural randomness of its branched topology, as well as its diverse chemical behaviour [35].

**Table 6**: Results for the biocrude streams B1 and B2

| | | Exp. Data | LS | | MINLP | |
|---|---|---|---|---|---|---|
| Biocrude | Carbon | 74.67 | 75.38 | 0.95% | 75.68 | 1.35% |
| | Hydrogen | 10.30 | 10.70 | 3.88% | 10.28 | 0.16% |
| | Oxygen | 11.30 | 11.30 | 0.00% | 11.28 | 0.17% |
| | Nitrogen | 2.76 | 2.99 | 8.44% | 2.76 | 0.04% |
| | HHV | 33.20 | 33.49 | 0.87% | 33.63 | 1.30% |
| | SSRD | | | 8.80E-03 | | 3.57E-04 |

| | | Exp. Data | SQP | | MINLP | |
|---|---|---|---|---|---|---|
| Upgraded biocrude | Carbon | 86.20 | 85.41 | 0.92% | 85.22 | 1.13% |
| | Hydrogen | 13.00 | 13.56 | 4.31% | 13.96 | 7.41% |
| | Oxygen | 0.70 | 0.78 | 11.00% | 0.71 | 1.64% |
| | Nitrogen | 0.10 | 0.11 | 11.00% | 0.10 | 0.40% |
| | HHV | 38.06 | 37.71 | 0.92% | 37.62 | 1.16% |
| | SSRD | | | 2.62E-02 | | 6.04E-03 |

Integer cuts would provide (i) multiple feasible solution points that could establish key chemical components (ii) broader potential for data manipulation and machine learning implementation (iii) increased flexibility in choosing appropriate biomass profiles based on fuel or process requirements. Producing alternate populations of components, rather than single options, enhances the comprehensive understanding of complex streams, allowing complementary information to form holistic knowledge in the optimization and design of sophisticated chemical dynamics. The MINLP model was also tested in two biocrude samples.

The proposed MINLP model efficiently produces the chemical profiles of different biomass types and product streams, allowing for a more generalized approach in biorefinery understanding. This model can be adapted for various non-conventional mixtures by incorporating diverse substrate properties, allowing for a broader physiochemical representation. Thus, allowing its applicability across a wide range of biorefinery technologies.

## CONCLUSIONS AND FUTURE WORK

Efficient modelling of non-conventional streams requires a comprehensive analysis of first principle models along with experimental data, in accordance with industry accepted standards and laboratory protocols. The purpose is to match the experimental properties of the input or output stream to a mixture of appropriate chemical compounds and functional groups.

This work proposes a new MINLP formulation for the characterization and analysis of biomass and biocrude steams in HTL. Our analysis capitalizes on a combination of peer-reviewed references, experimental, simulation data and relevant databases to acquire specification parameters such as experimental measurements (e.g. moisture content), stoichiometric composition showcasing elemental ratios within samples, as well as thermodynamic properties associated with bioconversion technologies. Classifying biomass feedstocks, requires the chemical compounds to be divided into four biochemical categories, such as proteins, sugars, lipids and lignin.

Accurate representation of complex mixtures in all stages of the biomass conversion process would facilitate decision-making while also providing insight in reaction pathways, which signifies an industrial milestone for

biorefinery commercialization.

Decomposition of feedstock streams into chemical compounds allows the modularization of the chemical profile which can be used to redefine information into digital forms, while also creating collective databases of different material mixtures. In essence, digital passports to simplify biomass and biocrude classification.

Ongoing work also considers the incorporation of additional properties to improve accuracy, and also include TBP data to enable fitting to the experimental TBP curve for biocrude streams.

## ACKNOWLEDGEMENTS

The project is implemented within the framework of the National Recovery and Resilience Plan "Greece 2.0" and has been financed by the European Union (NextGeneration EU).

## REFERENCES

1. *Ritchie H, Rosado P, Roser M. CO2 and greenhouse gas emissions. Our World in Data (2023).* Available at: https://ourworldindata.org/co2-and-greenhouse-gas-emissions
2. *International Energy Agency.* https://www.iea.org/data-and-statistics
3. Bauen A, Berndes G, Junginger M, Londo M, Vuille F. Bioenergy – a sustainable and reliable energy source: A review of status and prospects. *IEA Bioenergy* ExCo: 2009:06 (2009)
4. Castello D, Pedersen TH, Rosendahl LA. Continuous hydrothermal liquefaction of biomass: A critical review. *Energies* 11(11):3165 (2018). https://doi.org/10.3390/en11113165
5. Basar IA, Liu H, Carrere H, Trably E. A review on key design and operational parameters to optimize and develop hydrothermal liquefaction of biomass for biorefinery applications. *Green Chemistry* (2021). https://doi.org/10.1039/D0GC04092D
6. Mishra RK, Kumar V, Kumar P, Mohanty K. Hydrothermal liquefaction of biomass for bio-crude production: A review on feedstocks, chemical compositions, operating parameters, reaction kinetics, techno-economic study, and life cycle assessment. *Fuel* 316:123377 (2022). https://doi.org/10.1016/j.fuel.2022.123377
7. Mathanker A, Das S, Pudasainee D, Khan M, Kumar A, Gupta R. A review of hydrothermal liquefaction of biomass for biofuels production with a special focus on the effect of process parameters, co-solvents, and extraction solvents. *Energies* 14(16):4916 (2021). https://doi.org/10.3390/en14164916
8. Bao R, Wang S, Feng J, Duan Y, Liu K, Zhao J, Liu H, Yang J. A review of hydrothermal biomass liquefaction: Operating parameters, reaction mechanism, and bio-oil yields and compositions. *Energy Fuels* 38:8437-8459 (2024). https://doi.org/10.1021/acs.energyfuels.4c00240
9. Moser L, Portner BW, Penke C, Ebner K, Batteiger V. Life-cycle assessment of renewable fuel production via hydrothermal liquefaction of manure in Germany. *Sustain Energy Fuels* 7:4898-4913 (2023). https://doi.org/10.1039/D3SE00646H
10. Kumar R. A review on the modelling of hydrothermal liquefaction of biomass and waste feedstocks. *Energy Nexus* 5:100042 (2022). https://doi.org/10.1016/j.nexus.2022.100042
11. Heracleous E, Vassou M, Lappas AA, Rodriguez JK, Chiaberge S, Bianchi D. Understanding the upgrading of sewage sludge-derived hydrothermal liquefaction biocrude via advanced characterization. *Energy Fuels* 36:12010-20 (2022). https://doi.org/10.1021/acs.energyfuels.2c01746
12. Badoga S, Gieleciak R, Alvarez-Majmutov A, Xing T, Chen J. An overview on the analytical methods for characterization of biocrudes and their blends with petroleum. *Fuel* 324B:124608 (2022). https://doi.org/10.1016/j.fuel.2022.124608
13. Michailof CM, Kalogiannis KG, Sfetsas T, Patiaka DT, Lappas AA. Advanced analytical techniques for bio-oil characterization. *Wiley Interdisciplinary Reviews: Energy and Environment* (2016). https://doi.org/10.1002/wene.208
14. De Buck V, Sbarciog MI, Cras J, Bhonsale SS, Polanska M, Van Impe JFM. Critical analysis of the use of white-box versus black-box models for multi-objective optimisation of small-scale biorefineries. Front Food Sci Technol 3:1154305 (2023) https://doi.org/10.3389/frfst.2023.1154305
15. Koziel S, Ciaurri DE, Leifsson L. Surrogate-based methods. In: Computational Optimization, Methods and Algorithms. Ed: Koziel S, Yang XS. Springer, Berlin, Heidelberg (2011) 33–59. https://doi.org/10.1007/978-3-642-20859-1_3
16. McBride K, Sundmacher K. Overview of surrogate modeling in chemical process engineering. *Chemie Ingenieur Technik* 91:32-42 (2019) https://doi.org/10.1002/cite.201800091
17. Park SY, Oh KC, Kim SJ, Cho LH, Jeon YK, Kim DH. Development of a biomass component prediction model based on elemental and proximate analyses. *Energies* 16(14):5341 (2023). https://doi.org/10.3390/en16145341
18. Ahmed MU, Andersson P, Andersson T, Tomas Aparicio E, Baaz H, Barua S, Bergström A, Bengtsson D, Orisio D, Skvaril J, Zambrano J. A machine learning approach for biomass

characterization. *Energy Procedia* 158:1279–1287 (2019). https://doi.org/10.1016/j.egypro.2019.01.316
19. Taghipour A, Ramirez J, Rainey TJ. A method for HTL biocrude simulation using multi-objective optimisation and fractional distillation. *Comput Chem Eng* 157:107600 (2022) https://doi.org/10.1016/j.compchemeng.2021.107600
20. Aslanoglou I, Anastasakis K, Michalopoulos C, Marcoulaki E, Kokossis A. A systems approach to model nonconventional streams applied to biocrude production from hydrothermal liquefaction. *Comput Aided Chem Eng* 53:1177-1182 (2024) https://doi.org/10.1016/B978-0-443-28824-1.50197-6
21. Kokossis AC, Tsakalova M, Pyrgakis K. Design of integrated biorefineries. *Computers & Chemical Engineering* 81:40-56 (2015). https://doi.org/10.1016/j.compchemeng.2015.05.021
22. Godin B, Agneessens R, Gerin PA, Delcarte J. Composition of structural carbohydrates in biomass: Precision of a liquid chromatography method using a neutral detergent extraction and a charged aerosol detector. *Talanta* 85(4):2014-2026 (2011). https://doi.org/10.1016/j.talanta.2011.07.044
23. Abdul-Mumeen I, Zakpaa HD, Mills-Robertson FC, Samuel TL, Duwiejuah AB. Amino acid profile and potential biomass conversion of *Vitellaria paradoxa* fruit pulp. *Scientific African* 24:e02183 (2024). https://doi.org/10.1016/j.sciaf.2024.e02183
24. Shah TA, Zhihe L, Zhiyu L, Andong Z. Composition and role of lignin in biochemicals. In: *IntechOpen* (2022). https://doi.org/10.5772/intechopen.106527
25. Lahive CW, Kamer PCJ, Lancefield CS, Deuss PJ. An introduction to model compounds of lignin linking motifs; synthesis and selection considerations for reactivity studies. *ChemSusChem* (2020). https://doi.org/10.1002/cssc.202000989
26. Vermaas JV, Crowley MF, Beckham GT. Molecular simulation of lignin-related aromatic compound permeation through gram-negative bacterial outer membranes. *J Biol Chem* 298:102627 (2022). https://doi.org/10.1016/j.jbc.2022.102627
27. Lammens TM, Franssen MCR, Scott EL, Sanders JPM. Availability of protein-derived amino acids as feedstock for the production of bio-based chemicals. *Biomass and Bioenergy* 44:168-181 (2012). https://doi.org/10.1016/j.biombioe.2012.04.021
28. Agblevor FA, Hames BR, Schell D, et al. Analysis of biomass sugars using a novel HPLC method. *Appl Biochem Biotechnol* 136:309-326 (2007). https://doi.org/10.1007/s12010-007-9028-4
29. Tonon T, Machado CB, Webber M, Webber D, Smith J, Pilsbury A, Cicéron F, Herrera-Rodriguez L, Jimenez EM, Suarez JV, Ahearn M, Gonzalez F, Allen MJ. Biochemical and elemental composition of pelagic Sargassum biomass harvested across the Caribbean. *Phycology* 2(1):204-215 (2022). https://doi.org/10.3390/phycology2010011
30. Sousa AM, Andrade TA, Errico M, Coelho JP, Filipe RM, Matos HA. Fatty acid content in biomasses: State-of-the-art and novel physical property estimation methods. *Biomolecules* (2019). https://doi.org/10.1155/2019/2430234
31. López Barreiro D, Martin-Martinez FJ, Torri C, Prins W, Buehler MJ. Molecular characterization and atomistic model of biocrude oils from hydrothermal liquefaction of microalgae. *Algal Research* 35:262-273 (2018). https://doi.org/10.1016/j.algal.2018.08.034
32. Vardon DR, Sharma BK, Scott J, Yu G, Wang Z, Schideman L, Zhang Y, Strathmann TJ. Chemical properties of biocrude oil from the hydrothermal liquefaction of *Spirulina* algae, swine manure, and digested anaerobic sludge. *Bioresour Technol* 102:6985-6992 (2011) https://doi.org/10.1016/j.biortech.2011.06.041
33. Obeid R, Smith N, Lewis DM, Hall T, van Eyk P. A kinetic model for hydrothermal liquefaction of microalgae, sewage sludge, and pine wood with product characterization of renewable crude. *Chem Eng J* 428:131228 (2022) https://doi.org/10.1016/j.cej.2021.131228
34. Snowden-Swan LJ, Li S, Thorson MR, Schmidt AJ, Cronin DJ, Zhu Y, Hart TR, Santosa DM, Fox SP, Lemmon TL, Swita MS. *Wet waste hydrothermal liquefaction and biocrude upgrading to hydrocarbon fuels: 2022 state of technology*. No. PNNL-32731. Pacific Northwest National Lab.(PNNL), Richland, WA (United States) (2022) https://doi.org/10.2172/1897670
35. Terrell E, Dellon LD, Dufour A, Bartolomei E, Broadbelt LJ, Garcia-Perez M. A review on lignin liquefaction: advanced characterization of structure and microkinetic modeling. *Ind Eng Chem Res* 59:526-555 (2020) https://doi.org/10.1021/acs.iecr.9b05744

© 2025 by the authors. Licensed to PSEcommunity.org and PSE Press. This is an open access article under the creative commons CC-BY-SA licensing terms. Credit must be given to creator and adaptations must be shared under the same terms. See https://creativecommons.org/licenses/by-sa/4.0/



Systems & Control Transactions

**Research Article - Peer Reviewed Conference Proceeding**
ESCAPE 35 - European Symposium on Computer Aided Process Engineering
Ghent, Belgium. 6-9 July 2025
Jan F.M. Van Impe, Grégoire Léonard, Satyajeet S. Bhonsale,
Monika E. Polańska, Filip Logist (Eds.)

PSE PRESS

# A Comprehensive study on PHB biosynthesis and biodegradation through kinetic modelling

**Ariyan Amirifar[a], Constantinos Theodoropoulos[a,*]**

[a] Department of Chemical Engineering, Biochemical and Bioprocess Engineering Group, The University of Manchester, Manchester M13 9PL, UK
* Corresponding Author: k.theodoropoulos@manchester.ac.uk

## ABSTRACT

Polyhydroxyalkanoates (PHAs) are microbial bioplastics that are fully biodegradable, biocompatible and can be produced by renewable feedstocks through fermentation. These are all desirable attributes for the replacement of current fossil-based plastics. Strong mathematical models describing bioprocesses are invaluable tools that can be used for enhancing bioprocess understanding as well as optimization. In this study, polyhydroxybutyrate (PHB), by *Cupriavidus necator* DSM 545 was produced using glycerol and ammonium sulphate (AS) as the sole carbon and nitrogen sources, respectively. In addition, a kinetic bioprocess model was developed. The kinetic parameters of the model were calibrated with five fermentation experiments with different initial conditions (e.g. variable glycerol and AS concentrations) in order to properly establish the inhibition regions and provide a generalized model as much as possible. The model was successfully validated by three independent experiments, two with extreme and one with moderate initial conditions. In addition, the analysis of the data provided valuable metabolic insights for this bioprocess. It was shown that the PHB storage capacity of cells strongly correlates with the initial nitrogen concentration in the medium, meaning that efforts for maximizing biomass production in a two-stage bioprocess strategy should be carefully designed so that the nitrogen concentration does not irreversibly compromise the maximum PHB accumulation potential. Furthermore, a preliminary kinetic analysis of the biodegradation of solvent casted PHB films was performed.

**Keywords**: Fermentation, Genetic Algorithm, Modelling, Modelling and Simulations, PHB, *C. necator* DSM 545

## 1. INTRODUCTION

Some 80% of all plastics globally produced have accumulated in or leaked to the environment [1]. Over 99.5% of plastics are currently being derived from petroleum-based resources [2]. A promising alternative to conventional fossil-based plastics is polyhydroxyalkanoates (PHA), microbial bioplastics synthesized through fermentation of renewable feedstocks, with poly(3-hydroxybutyrate) (PHB) being the most extensively studied variant [2]. The primary contributors to the high cost of PHA production are feedstock costs, which account for up to 50% of total production costs [3], alongside low PHA yields [4]. Crude glycerol, the primary byproduct of biodiesel production, representing about 10% w/w of the produced biodiesel, could be further valorised to PHB as the fermentation's main carbon source [5]. *Cupriavidus necator* DSM 545, is a well-studied microorganism able to consume glycerol as sole carbon substrate for the production of PHB[6–9], with productivities as high as 1.4 g/L/h[8]. *C. necator* DSM 545 along with *Zobellella denitrificans* MW1 are the only two reported microorganisms able to produce PHB on glycerol with productivities higher than 1 g/L/h[10]. Mathematical models are invaluable tools for the optimization and design of bioprocess and few studies have attempted to describe and/or optimize the production of PHB on glycerol by *C. necator* DSM 545 using such models[6–8,11].

In this work, a detailed macroscopic kinetic model was developed based on experimental observations to describe the batch fermentation of *Cupriavidus necator* DSM 545 under controlled pH (6.8) and DO (30% of saturation) conditions on a chemically defined mineral medium with glycerol and ammonium sulphate (AS) as the

carbon and nitrogen sources, respectively. The model was tuned on experimental data from batch fermentations. Sensitivity analysis was also performed. Batch was the preferred mode of operation to identify inhibition regions with respect to carbon and nitrogen sources, and to gain insight into the behavior and metabolic state of the microorganism for fermentations conducted with different initial conditions. Finally, the model was validated using experiments with initial conditions that were not used in the parameter tuning process.

## 2. MATERIALS AND METHODS

### 2.1 Microorganism and culture conditions

*Cupriavidus necator* DSM 545 was used as the microorganism for all fermentations. The master stock has been extensively adapted to glycerol previously in our research group and stored in cryovials at -80°C during their mid-exponential phase [7]. The fermentation medium was adapted from Kim et al[12]. The cultivation process has been described elsewhere [6,7]. Bioreactor fermentations were carried out in 0.5 L or 3 L Applikon bioreactors (Getinge, NE) under the following controlled conditions: 30°C, pH 6.8, dissolved oxygen at 30% saturation (achieved by automatic control of agitation speed and air flow rate, max 2vvm), and 10% mid-exponential phase inoculum. The pH of the medium was adjusted automatically using a 2M KOH solution. For fermentation follow up, 5 mL samples were taken in duplicate from each bioreactor at different time points for further analysis. All procedures were carried out aseptically where appropriate.

### 2.2 Biodegradation experiments

Compost was sourced from the Firs botanical grounds (University of Manchester, UK) as the biological environment to isolate an efficient PHB degrading microorganism. This 6-month-old compost was produced from garden waste and local kitchen food waste and sieved on-site (mesh size < 10 mm). A small amount of compost sample was spread on mineral PHB agar plate incubated at 37 °C for 48 h [13]. The microorganisms capable of growing on the plates were further isolated on the same plate recipe until a single colony type was achieved. The colonies were identified via sequencing of the 16S or 18S/28S RNA gene (for bacteria or fungi, respectively). Amplification was performed via colony PCR using GoTaqGreen® master mix (Promega, UK). Thereafter, the amplified gene was separated via gel electrophoresis and the Monarch® DNA gel extraction kit (New England Biolabs®, UK). The NCBI BLAST tool (NCBI) was used on the obtained sequence to annotate the taxonomy of the microorganisms. The PHB obtained from one of the fermentation experiments (biodegradation substrate) was casted on a petri dish using chloroform or hexafluoroisopropanol (HFIP) as solvent in $\frac{1g\ PHB}{25\ mL\ solvent}$ ratio. The isolated microorganism was thereafter inoculated (10% w/w) in 5 mL of appropriate medium and culture conditions, together with PHB films, in glass test tubes.

### 2.3 Analytical procedures

Cell dry weight (CDW) was measured gravimetrically as described previously[7]. The absorbance of each sample was measured at 600 nm using a UV spectrophotometer (UV-1280, Shimadzu®) to monitor microbial growth, particularly during the initial hours of fermentation. A correlation between cell dry weight (CDW) and optical density (OD) was established ($R^2$=0.9687) to account for potential inaccuracies in CDW measurements. PHB was quantified via Gas chromatography coupled with a Flame Ionization Detector (GC-FID, Agilent) using the method optimized by Lanham et al.[14]. Analysis was performed in an HP-5 column (Agilent J&W GC columns) with helium as the carrier gas and a split ratio of 1:10. Oven temperature was initially set to 80°C for 5 minutes, then ramped up to 280°C at 20°C/min, with a 2-minute hold. Calibration was performed using commercial methylated 3-HB (Sigma-Aldrich) in chloroform. Glycerol in sample supernatant was monitored via High-Performance Liquid Chromatography (HPLC) [7]. Total nitrogen concentration in sample supernatant was quantified via a total nitrogen analyser (TOC/TN multi N/C 3100, Analytik Jena). For this, 100 µL of the filtered supernatant was injected. After catalytic combustion, nitrogen oxide reacts with ozone to form excited states, emitting light upon returning to the ground state. This light, measured by a chemiluminescence detector, is proportional to the nitrogen content. Ammonium sulphate solutions in distilled water served as calibration standards. Scanning Electron Microscopy (SEM) of the PHB films were acquired by Zeiss Ultra 55 microscope. The samples were sputter coated with 80:20 Ad:Pd. Atomic Force Microscopy (AFM, Bruker) with probes of 4 N/m force constant was used.

### 2.4 Parameter tuning and sensitivity analysis

The kinetic constants of the model were tuned by minimizing the normalized mean squared error between experimental and predicted data (equation 1).

$$\min G(kk) = \sum_h^{n_h} \sum_j^{n_j} \sum_i^{n_i} \left( \frac{Z_{h,j,i}^{Exp}(kk) - Z_{h,j,i}^{Pred}(kk)}{\max\left(Z_{h,j,i}^{Exp}(kk)\right)} \right)^2 \qquad (1)$$

Here G is the objective function, Z represents experimental and predicted data sets, and kk the parameter set. Indices $n_i$, $n_j$, and $n_h$ correspond to the number of independent variables, data points, and training data sets, respectively. The minimization problem was solved using Matlab genetic algorithm (ga) to avoid local minima, followed by the deterministic function fmincon to refine solutions. Thereafter, sensitivity analysis was performed to assess the most sensitive parameters. For this purpose,

a normalized sensitivity parameter was used [15]:

$$S_{y/p} = \frac{dy_i}{dp_i} \cdot \frac{p_{0,i}}{y_{0,i}} \quad (2)$$

Here $\frac{dy_i}{dp_i}$ is the change of the model output $y_i$ in response to a change in a model parameter pi (5% perturbation was chosen) and $y_{0,i}$ is the model output when the parameter $p_{0,i}$ is set to its original value $p_{0,i}$. A positive sensitivity value translates into an increased model response when a parameter increases, whereas negative sensitivity values signify the opposite behaviour[15].

## 3. RESULTS AND DISCUSSION

### 3.1 Model development

Five state variables were considered for the model: residual biomass (xR), total nitrogen (N), Glycerol ($S_1$), PHB (P), and citric acid ($S_2$) concentrations. These variables were correlated by kinetic equations (equations 3-7) using their corresponding rate terms.

$$\frac{dx}{dt} = r_{xR}x \quad (3)$$

$$\frac{dN}{dt} = (q_{N,S_1} + q_{N,S_2})x \quad (4)$$

$$\frac{dS_1}{dt} = q_{S_1}x \quad (5)$$

$$\frac{dS_2}{dt} = q_{S_2}x \quad (6)$$

$$\frac{dP}{dt} = q_P x \quad (7)$$

#### 3.1.1 Biomass formation

Literature and experimental observations confirm that too high or too low of glycerol or AS negatively affects cell growth [6–9]. It has been reported that 30 g/L glycerol (as sole carbon source) and 2 g/L of AS (as sole nitrogen source) are the thresholds above which significant cell growth inhibition occurs for *C. necator* DSM 545 [16,6,7]. Nonetheless, these studies have evaluated the nitrogen inhibition ranges in shake flask experiments, which might be different than bioreactor fermentations where the pH of the media and oxygen levels are strictly controlled. To establish the nitrogen inhibition region for the model, five fermentations were carried out with 30 g/L of glycerol and varying initial AS concentrations ranging from 0.8-7.4 g/L. Figure 1 shows that the maximum residual biomass (xR) concentrations increase with AS across the entire range, although the increase rate gradually diminishes. Hence, 2 g/L of AS was not the growth inhibition threshold for the bioprocess in bioreactor fermentations. On the other hand, PHB concentration decreases significantly above 3.4 g/L AS. To account for glycerol and nitrogen inhibition effects on growth, Monod kinetics with Haldane inhibition terms[17] were applied on AS and glycerol as the limiting substrates (equation 8). Moreover, it was realized that the initial citric acid (CA) present in the medium formulation was first consumed as the preferred carbon substrate for growth before the cells began to metabolise any glycerol, having a boosting effect and eliminating the growth lag phase normally observed on glycerol. Therefore, the rate of biomass formation should be composed of two segments: biomass production on CA or biomass production on glycerol, starting only after CA depletion. The inhibition of CA on glycerol consumption was modelled via Hill kinetics [18]. Growth on citric acid was inhibited at high nitrogen concentrations (data not shown) hence it was necessary to consider Haldane inhibition kinetics for nitrogen also.

$$r_{xR} = \mu_{S_1} + \mu_{S_2} = \mu_1 \frac{S_1}{\frac{S_1^2}{K_{iS_1}} + S_1 + K_{S_1}} \cdot \frac{N}{\frac{N^2}{K_{iN}} + N + K_N} \cdot \frac{1}{1 + k_{S_2}(S_2)^{n_{S_2}}} + \mu_2 \frac{S_2}{S_2 + K_{S_2}} \frac{N}{\frac{N^2}{K_{iN,S_2}} + N + K_{N,S_2}} \quad (8)$$

Here $\mu_1$ and $\mu_2$ are specific growth rates [$h^{-1}$]; and $K_{S_1}$, $K_N$ and $K_{S2}$, $K_{N,S_2}$ pairs are the saturation constants for glycerol and CA, respectively [g/L]; $K_{iS_1}$, $K_{iN}$ and $K_{iN,S_2}$ are the inhibition constants [$(g/L)^2$] for glycerol and CA, respectively; $n_{S_2}$ is a Hill coefficient.

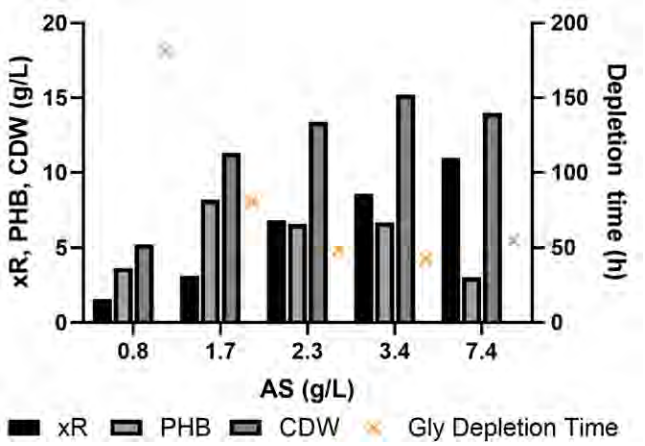



**Figure 1.** Cell dry weight (CDW), residual biomass (xR), PHB end values and glycerol depletion time vs. different initial AS concentrations (30 g/L glycerol).

Another interesting observation is that the glycerol depletion time heavily relied on the initial AS concentrations, e.g. ~2.3-3.4 g/L of AS resulted in lower depletion time and higher biomass growth, but was detrimental to the PHB concentrations.

#### 3.1.2 PHB production

The maximum PHB titer profile against initial AS concentrations in Figure 1 matches expectations, as it is well-known that the presence of nitrogen inhibits PHB production, and that PHB production favours high C/N ratios unlike biomass growth where lower C/N values are preferred[6,7]. PHB accumulation is predominantly induced by nitrogen limitation[7]. However, PHB synthase is a constitutive enzyme in *C. necator* [19], justifying partially growth-associated PHB production [9,20]. Hence, the

Luedeking-Piret model[21] was chosen to describe PHB production (equations 9-11). Throughout the nitrogen limited phase, it is expected that the carbon source should be mostly directed towards PHB production[22,23]. It has been reported however, that PHB production could halt prior to carbon source depletion[22]. This could be due to the fact that the size and number of PHB granules are theoretically capped by a regulatory system involving phasin proteins[22,24], or due to the fact that prolonged nitrogen starvation impairs the activity of PHB synthase. In order to account for such an effect, some studies have introduced powered inhibition functions in the PHB production rate equation[8,22]. However, it was realized in this study that no matter how much of the initial carbon source was allocated to biomass production, no more PHB was produced up to a certain extent even if glycerol was present after reaching the biomass stationary phase. According to Figure 2 the maximum PHB accumulation capacity of cells could be correlated to the initial total nitrogen concentration through the Haldane inhibition model (equation 6).

$$q_P = \alpha r_{xR} + \beta \times \left(1 - \left(\frac{f}{f_{max}}\right)^m\right) \quad (9)$$

$$\beta = \frac{\mu_P S_1}{S_1 + K_{S,P} + S_1^2/K_{iS,P}} \cdot \frac{1}{1 + k_{N,P} + N^{n_P}} \quad (10)$$

$$f_{max} = \frac{c(N_0 - h)}{\frac{(N_0 - h)^2}{d} + (N_0 - \mathrm{h}) + e} \quad (11)$$

$\alpha$ is the growth-associated constant for PHB, and $\beta$ the non-growth associated parameter; $f\ (\frac{PHB}{CDW})$ and $f_{max}$ are the PHB accumulation extent term, and its maximum, respectively; $N_0$ is the initial total nitrogen concentration in the broth [g/L]; c, d, and e are constants (c=3.3854 $h^{-1}$, d=0.2302 g/L, e=0.2771 g/L, h=0.1323 g/L).

### 3.1.3 Substrate and nutrient uptake

CA, glycerol and nitrogen uptake rates were necessary to compute new kinetic constants for the nitrogen uptake rate with nitrogen self-inhibition effect on growth utilising Haldane inhibition kinetics (equation 15).

$$q_{S_2} = \frac{1}{Y_{\frac{xR}{S_2}}} \mu_{S_2} \quad (12)$$

$$q_{S_1} = \frac{1}{Y_{\frac{xR}{S_1}}} \mu_{S_1} \quad (13)$$

$$q_{N,S_2} = \frac{1}{Y_{\frac{xR}{N}}} \mu_{S_2} \quad (14)$$

$$q_{N,S_1} = \frac{\mu_N S_1}{S_1 + K_{N,S_1}} \cdot \frac{N}{\frac{N^2}{K_{iN,N}} + N + K_{N,N}} \quad (15)$$

$Y_{\mathrm{xR}/S_2}$, $Y_{\mathrm{xR}/S_1}$ and $Y_{\mathrm{xR/N}}$ are CA, glycerol and nitrogen to biomass yields, respectively. $\mu_N$ is the specific nitrogen consumption rate ($h^{-1}$), $K_{N,S_1}$, $K_{N,N}$ and $K_{iS,N}$ are saturation and inhibition constants (g/L), respectively.

### 3.1.4 Model performance

Based on a 5% perturbation of the 36 kinetic constants, a range of average sensitivity values from $2.5 \times 10^{-8}$ to 12.5 was produced. It was decided to consider a sensitivity value threshold of ≥0.1, resulting in 13 sensitive parameters (final values in Table 1). The calibration data (figure 3, I-V) cover glycerol and nitrogen concentrations 13-43 g/L and 0.29-1.56 g/L, respectively. The independent validation data (figure 3, i-iv) was able to predict the state variables dynamics at extreme initial glycerol and nitrogen concentrations, 55 g/L and 2.53 g/L respectively, among milder conditions within the region of the values of the calibration data.

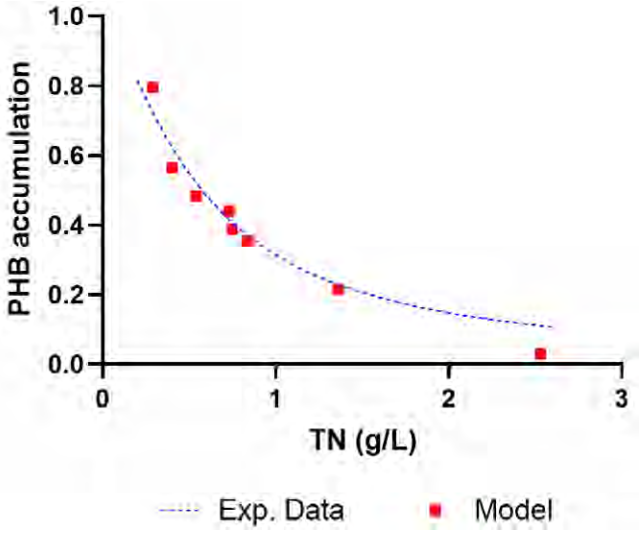



**Figure 2.** Emperical relationship between maximum PHB accumulation and initial nitrogen concnentration in the medium ($R^2$=0.9347).

**Table 1:** Values of the most sensitive model parameters.

| Parameter | Value | Unit |
|---|---|---|
| $k_{N,P}$ | 141 | g/L |
| $Y_{\frac{xR}{N}}$ | 3.15 | g/g |
| $\mu_2$ | 0.9079 | $h^{-1}$ |
| $K_{iS,P}$ | 25.8064 | g/L |
| $K_N$ | 0.3851 | g/L |
| $Y_{\frac{xR}{S_2}}$ | 0.8792 | g/g |
| $n_P$ | 1.49 | - |
| $K_{S_2}$ | 0.2872 | g/L |
| $k_{S_2}$ | 74.30 | g/L |
| m | 7.98 | - |
| $K_{N,N}$ | 2.2483 | g/L |
| $Y_{\frac{xR}{S_1}}$ | 0.3876 | g/g |
| $\mu_P$ | 0.8437 | $h^{-1}$ |

## 3.2 Biodegradation experiments

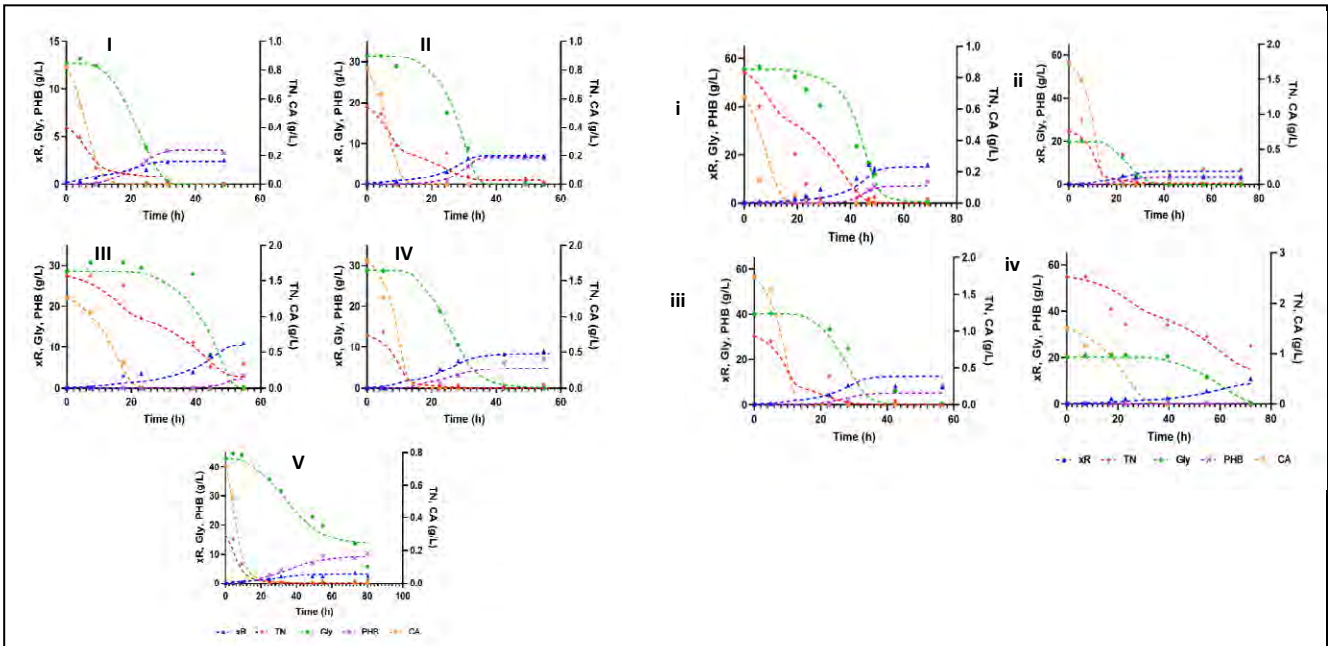



**Figure 3: Kinetic model** calibration (I-V) and validation (i-iv) runs. Dotted lines represent model predictions; data points are from fermentation experimetns. The state variables are: residual biomass (xR), total nitrogen (TN), glycerol (Gly), PHB and citric acid (CA).

A fungus able to grow on PHB mineral agar plate at 37℃ was successfully isolated from compost, its 28S RNA gene was amplified and sequenced. Based on NCBI BLAST, *Aspergillus fumigatus* produced significant alignment with the sequence, with a 99.11% identity score. The optimal culture conditions were extracted from the the literature[25]; The isolated fungi was cultured in liquid Busshnell-Haas medium (BHM) supplemented with 0.1% w/w PHB, at 45℃, and pH 7 for the biodegradation experiments to be ready for accelerated biodegradation of PHB films. It was desired to assess the biodegradation kinetics of PHB films with different casting solvents. The average initial inoculum was $26 \pm 9$ ($\times 10^4 \frac{spores}{ml}$). It can be seen from Figure 4 that the casting solvent altered the biodegradation kinetics of the films. The biodegradation behaviour could be modelled through first order kinetics ($-r_{PHB} = km_{PHB}$) giving rise to kinetic constants of 0.3453 and 0.3363 $h^{-1}$ for $CHCl_3$ and HFIP casted films, respectively. HFIP films had a lag phase of ~1 day unlike the $CHCl_3$ casted films. This could be explained through the different morphologies that the solvents produce affecting biodegradation kinetics as it is well-known that the biodegradation of PHB commences through microbial surface erosion. HFIP produced a film with much less surface features and fewer pore sizes but with pores orders of magnitude larger than the $CHCl_3$ casted films (Figure 5). Based on the AFM images, the spherulites of the HFIP casted films were very smooth, separated with rather deep depletion zones, whereas the $CHCl_3$ casted films exhibit many inhomogeneous surface features in the entire imaged area.

## CONCLUSIONS

The proposed generalized and improved kinetic model for the production of PHB by *C. necator* DSM 545 on glycerol and AS as carbon and nitrogen sources, respectively, provides valuable metabolic insights regarding PHB accumulation capacity of this microorganism. Moreover, it was found that biodegradation kinetics of solvent-casted PHB films depend on the type of solvent probably because it directly affected film morphology.

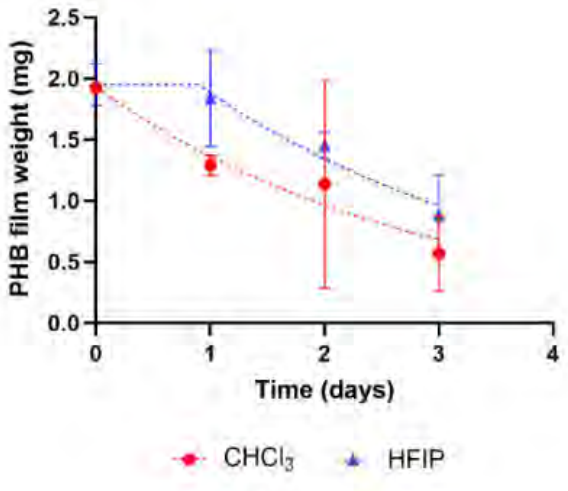



**Figure 4.** Mass loss of PHB films casted with $CHCl_3$ or HFIP. Dotted lines: first order kinetic model.

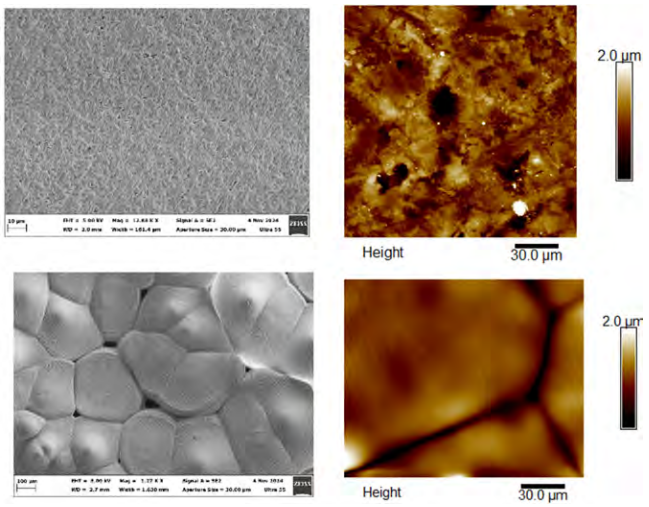



**Figure 5.** SEM and AFM images for PHB casted with $CHCl_3$ (top) and HFIP (bottom).

## ACKNOWLEDGEMENTS

The authors wish to thank the University of Manchester for the provision of a Dean's Doctoral Scholarship Award to Ariyan Amirifar.

## REFERENCES

1. Dimante-Deimantovica I, Saarni S, Barone M, et al. Downward migrating microplastics in lake sediments are a tricky indicator for the onset of the Anthropocene. Sci Adv. 2024;10(8):eadi8136.
2. Diankristanti PA, Lin YC, Yi YC, Ng IS. Polyhydroxyalkanoates bioproduction from bench to industry: Thirty years of development towards sustainability. Bioresour Technol. 2024 Feb;393:130149.
3. Park H, He H, Yan X, Liu X, Scrutton NS, Chen GQ. PHA is not just a bioplastic! Biotechnol Adv. 2024;71:108320.
4. Koller M, Mukherjee A. A New Wave of Industrialization of PHA Biopolyesters. Bioengin. 2022 ;9(2).
5. Vlaeminck E, Uitterhaegen E, Quataert K, Delmulle T, De Winter K, Soetaert WK. Industrial side streams as sustainable substrates for microbial production of poly(3-hydroxybutyrate) (PHB). World J Microbiol Biotechnol. 2022 Dec 1;38(12).
6. Sun C, Pérez-Rivero C, Webb C, Theodoropoulos C. Dynamic Metabolic Analysis of Cupriavidus necator DSM545 Producing Poly(3-hydroxybutyric acid) from Glycerol. Processes. 2020;8(6):657.
7. Pérez Rivero C, Sun C, Theodoropoulos C, Webb C. Building a predictive model for PHB production from glycerol. Biochem Eng J. 2016;116:113–21.
8. Mozumder MSI, De Wever H, Volcke EIP, Garcia-Gonzalez L. A robust fed-batch feeding strategy independent of the carbon source for optimal polyhydroxybutyrate production. Process Biochem. 2014;49(3):365–73.
9. Špoljarić IV, Lopar M, Koller M, Muhr A et al. In silico optimization and low-structured kinetic model of poly[(R)-3-hydroxybutyrate synthesis by Cupriavidus necator DSM545 by fed-batch cultivation on glycerol. J Biotechnol. 2013;168(4):625–35.
10. Koller M, Obruča S. Biotechnological production of polyhydroxyalkanoates from glycerol: A review. Biocatal Agric Biotechnol. 2022 Jul;42:102333.
11. Lopar M, Špoljarić IV, Cepanec N, Koller M, Braunegg G, Horvat P. Study of metabolic network of Cupriavidus necator DSM 545 growing on glycerol by applying elementary flux modes and yield space analysis. J Ind Microbiol Biotechnol. 2014;41(6):913–30.
12. Kim BS, Lee SC, Lee SY, Chang HN, Chang YK, Woo SI. Production of poly(3-hydroxybutyric acid) by fed-batch culture of Alcaligenes eutrophus with glucose concentration control. Biotechnol Bioeng. 1994;43(9):892–8.
13. Ramsay BA, Saracovan I, Ramsay JA, Marchessault RH. A method for the isolation of microorganisms producing extracellular long-side-chain poly (β-hydroxyalkanoate) depolymerase. J Environ Polym Degrad. 1994 Jan;2(1):1–7.
14. Lanham AB, Ricardo AR, Albuquerque MGE, Pardelha F, Carvalheira M et al. Determination of theextraction kinetics for the quantification of polyhydroxyalkanoate monomers in mixed microbial systems. Process Biochem. 2013 48(11):1626–34.
15. Zacharopoulos I, Theodoropoulos C. Continuous production of succinic acid from glycerol: A complete experimental and computational study. Bioresour Technol. 2023 Oct;386:129518.
16. Sharmaa K, Srivastava AK, Sreekrishnan TR. Model-based Optimization of Biopolymer Production from Glycerol. Chem Biochem Eng Q. 2021; 35(1):65–80.
17. Haldane JBS. Enzymes. First M.I.T. Press paperback edition. Cambridge, Massachusetts: M.I.T. Press; 1965. 235 p. (M.I.T. paperback series).
18. Kwon YJ, Engler CR. Kinetic models for growth and product formation on multiple substrates. Biotechnol Bioprocess Eng. 2005 Dec;10(6):587–92.
19. Doi Y. Microbial synthesis, physical properties, and biodegradability of polyhydroxyalkanoates. Macromol Symp. 1995 Jul;98(1):585–99.
20. Horvat P, Vrana Špoljarić I, Lopar M, Atlić A, Koller M, Braunegg G. Mathematical modelling and

process optimization of a continuous 5-stage bioreactor cascade for production of poly[-(R)-3-hydroxybutyrate] by Cupriavidus necator. Bioprocess Biosyst Eng. 2013 Sep;36(9):1235–50.
21. Luedeking R, Piret EL. A kinetic study of the lactic acid fermentation. Batch process at controlled pH. J Biochem Microbiol Tech. Eng. 1959 (4):393–412.
22. Tamis J, Marang L, Jiang Y et al.. Modeling PHA-producing microbial enrichment cultures-towards a generalized model with predictive power. New Biotechnol. 2014; 31(4):324–34.
23. Segura PC, Wattiez R, Vande Wouwer A, Leroy B, Dewasme L. Dynamic modeling of Rhodospirillum rubrum PHA production triggered by redox stress during VFA photoheterotrophic assimilations. J Biotechnol. 2022 Dec 10;360:45–54.
24. Mitra R, Xu T, Chen G, Xiang H, Han J. An updated overview on the regulatory circuits of polyhydroxyalkanoates synthesis. Microb Biotechnol. 2022 May;15(5):1446–70.
25. Bhatt R, Patel KC, Trivedi U. Purification and Properties of Extracellular Poly(3-hydroxybutyrate) Depolymerase Produced by Aspergillus fumigatus 202. J Polym Environ. 2010 Jun;18(2):141–7.

© 2025 by the authors. Licensed to PSEcommunity.org and PSE Press. This is an open access article under the creative commons CC-BY-SA licensing terms. Credit must be given to creator and adaptations must be shared under the same terms. See https://creativecommons.org/licenses/by-sa/4.0/



Systems & Control Transactions

Research Article - Peer Reviewed Conference Proceeding
ESCAPE 35 - European Symposium on Computer Aided Process Engineering
Ghent, Belgium. 6-9 July 2025
Jan F.M. Van Impe, Grégoire Léonard, Satyajeet S. Bhonsale, Monika E. Polańska, Filip Logist (Eds.)

PSE PRESS

# Machine Learning Applications in Dairy Production

**Alexandra Petrokolou [a], Satyajeet Sheetal Bhonsale[b], Jan FM Van Impe[b] and Efstathia Tsakali[a,b,*]**

[a] Department of Food Science and Technology, University of West Attica, Egaleo, Greece
[b] BioTeC+ -Chemical and Biochemical Process Technology and Control, KU Leuven, Gent,
* Corresponding Author: etsakali@uniwa.gr

## ABSTRACT

The Fourth Industrial Revolution (Industry 4.0) brings a new chapter at dairy sector. Dairy 4.0 technologies are based on Big Data Analysis, Internet of Things, Robotics and Machine Learning. The usage of smart technologies to processing and analyzing complicated massive data has a significant impact in automation, optimization, functional costs and innovation. Artificial Intelligence tools are applied from dairy farms and production lines – including packaging- to supply chain. The aim of this paper is to demonstrate the most used applications of Machine Learning in dairy production so as to enhance the sustainability and the quality of dairy products. The most significant Machine Learning applications integrate machine vision, smart environmental sensors, activity collars, thermal imaging cameras, and digitized supply chain systems to facilitate inventory management. Challenges like milk adulteration, animal diseases, mastitis, traceability and supply chain losses are also addressed since they increase safety and quality standards in the dairy sector.

**Keywords**: Artificial Intelligence, Machine Learning, Algorithms, Dairy Production, Milk, Artificial Neural Network

## INTRODUCTION

The increasing demand for dairy products necessitates larger and faster production to enable the industry to meet consumers' nutritional needs. A particularly valuable subfield of Machine Learning (ML) is Deep Learning, which involves the use of Artificial Neural Networks based on mathematical functions. As illustrated in Figure 1, there are three levels: beginning with the input level, followed by the analysis and quantification of data, and the output layer utilized to generate probabilistic prediction outcomes, where the result is generated based on the specific task the algorithm is programmed to perform [1].

In recent times, Artificial Intelligence is evolving rapidly, finding applications in many fields of agriculture and food science and agriculture. ML, as a category of Artificial Intelligence, has a great potential to change the traditional methods in milk industry. ML is based on algorithms that are not entirely programmed. There are three categories of ML, supervised, unsupervised and reinforcement, which differ in the way of data processing. There are algorithms that are commonly used in industry for recognizing patterns, identifying data, making decisions and predictions that humans are unable to perform. Some algorithms that are used are: Support Vector Machine (SVM), Logistic Regression, K-nearest Neighbors, K-means, Decision Tree and Random Forest [2]. The Internet of Things (IoT) allows real time monitoring and data collection from the manufacturing stages. The Internet of Things is a system that consists of smart devices –smartphones, PCs, sensors, thermal cameras- which allow data transfer via wi-fi. These smart tools can be incorporated from dairy farms and raw material processing to final distribution. The main benefits of AI modeling are resource savings, high level productivity, operational efficiency, animal welfare and enhanced traceability. The necessity for integration in the dairy industry is based on the reduction of manual inspections, which pose potential risks, and the application of statistical and mathematical models to analyze large volumes of data that would be challenging and time-consuming for a scientist to resolve [3]. Moreover, it represents a model that contributes to sustainability

and enhances the industry's standards. The logistics system is improved, human errors and time-intensive manual tasks are minimized, and there is comprehensive control and coordination of production stages in compliance with quality and safety standards. Simultaneously, demand forecasting tools, aligned with consumer trends and preferences, aim to support informed decision-making, foster innovation, and drive the development of new products.

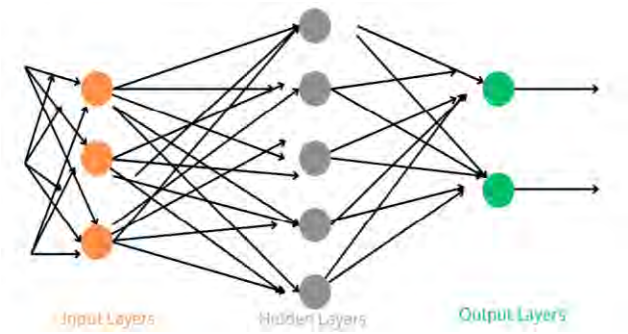



**Figure 1.** An example structure of ANN

## PRECISION LIVESTOCK FARMING

As mentioned before, the new technological advancements, begin at the farm level, enhancing the efficiency of animal management and living conditions. With the installation of intelligent environmental sensors, farmers can receive real-time updates on weather conditions, ambient temperature, humidity, and gas emissions. For optimal milk production, it is crucial to systematically monitor animals' health. Real-time health tracking is achieved through audio recordings, collars with integrated heart rate monitors, pedometers, and sensors that record animal behavior, productivity, body temperature, mobility, location, weight, and blood composition. Commonly used sensors in Precision Livestock Farming (PLF) include accelerometers, gyroscopes, temperature sensors, and biosensors. During data collection, ML analyzes these measurements to detect and prevent contagious diseases that could harm the herd. These PLF technologies further support farmers in making informed decisions, streamlining daily operations, and improving the overall supervision of their livestock [4].

## ROBOTIC MILKING SYSTEMS

It is crucial during milking that animals are not subjected to stress and that no damage or irritation is caused to their udders, as this could affect both their mental and physical health as well as the composition of the milk. To this end, automated milking systems have been developed to ensure the precise, efficient, and careful collection of milk from the animals' udders. These systems are equipped with durable sensors and high-resolution cameras in both two-dimensional (2-D) and three-dimensional (3-D) formats, enabling the monitoring of respiration, behavior, temperature, and thermal stress levels during the milking process [5]. Moreover, this system enables the calculation of milk yield, the percentage of milk protein, fat content, and somatic cell count. Additionally, parameters such as the lactation period, the animals' weight, and the frequency of milking per day are equally significant for monitoring the animals' health [6].

## AUTOMATIC FEEDING SYSTEMS

Another valuable addition to farm management is the use of automatic feeding systems, which represent a significant investment for livestock farmers, enhancing the efficiency of farm operations. There are two types of feeding systems: mobile systems and stationary systems, which are installed at specific locations. For mobile feeding systems, prior mapping of the area is required so that the machine can recognize the feeding points as well as any obstacles within the farm. The farmer adds various types of feed according to the animals' needs and schedules the feeding times for each day. In this way, the physical presence of the farmer at the farm is no longer required, granting them the flexibility to focus on other tasks. With the integration of sensors on the animals and automatic feeding systems, a comprehensive overview of the animals' health, the amount of feed consumed, and the precise calculation of the feed required for production needs is available. Research has shown that this approach reduces stress levels in animals and improves their feeding behaviour [7]. As a result, productivity and the quality of the milk produced are increased, while significant labour time and valuable financial resources are saved. Lastly, the algorithms used to analyze the aforementioned data provide more accurate results for farm management, reducing errors caused by human judgment. At the same time, the farmer can access the databases at any moment to stay informed about the herd's behaviour [8].

## MILK ADULTERATION

Milk and its derivative products are widely favored by consumers due to their highly nutritious composition, containing high-quality proteins, minerals, and vitamins that positively contribute to human health. The growing demand for these goods has brought forth incidents of adulteration that degrade product quality and mislead consumers. Potential adulterants include starch, water dilution, pseudo-proteins, mixing of different types of milk, addition of whey, or skimmed milk. The most sig-

nificant scandal in the history of the dairy industry involved the addition of melamine, a substance not approved for consumption, which was illegally added to milk products to falsify protein content. Beyond traditional methods of adulteration detection—which typically identify one or two components, such as the ELISA method—advanced models such as Support Vector Machines (SVM) have been developed. These models are non-destructive and outperform traditional methods in terms of specificity, sensitivity, and correlation, while enabling real-time data analysis. [2]. These models leverage multispectral sensors with the capabilities of AI and neural networks. Once data are collected, they are transmitted via Wi-Fi to a computer for processing. Using neural networks, the system identifies adulterants, displaying results as "adulterated" or "non-adulterated," and classifies the type of adulterant. This method is both cost-effective and highly efficient in data analysis [9]. Table 1 lists the algorithms with the highest accuracy in detecting milk adulteration.

Furthermore, at Table 2 the results of a study that examined the accuracy of milk quality classification using a milk dataset, comparing the Nearest Neighbors and Alpha-Beta algorithms are showed. [10]

**Table 1.** Accuracy Performance of Machine Learning Algorithms

| | Skimmed Milk | Full Cream Milk | Toned Milk | Double Toned Milk | Standardized Milk | Buffalo Milk | Average Accuracy |
|---|---|---|---|---|---|---|---|
| **Support Vector Machine** | 90% | 90.1% | 90.3% | 89,9% | 90% | 89.9% | 90% |
| **Decision Tree** | 91% | 91,9% | 92% | 91.5% | 91.8% | 92% | 91.7% |
| **Neural Network without hyperparameter** | 92.4% | 93% | 93.2% | 92.1% | 92.7% | 92.8% | 92.7% |
| **Neural Network with hyperparameter** | 100% | 100% | 100% | 100% | 100% | 100% | 100% |

**Table 2.** Milk quality assessment

| DATA SET | ALGORITHMS | METRICS | HIGHEST CLASSIFICATION ACCURACY | NOTES |
|---|---|---|---|---|
| Milk Data SET | 1. NN<br>2. AB | Accuracy<br>Precision<br>Recall<br>F1-Score | 95.4%<br>99.9% | Classification of milk quality by pH and temperature values |

## MACHINE VISION

Another change that can reduce errors and increase efficiency is the implementation of machine vision systems during the production and packaging of dairy products. Their operation is divided into two stages: the acquisition and processing of images captured from production points. Using cameras with two-dimensional and three-dimensional imaging capabilities, hyperspectral imaging—a combination of machine vision and spectroscopic techniques—ultrasound, X-rays, and sensors, real-time data are collected related to object recognition, cracks, foreign materials, the size of the product and its packaging, weight, shape, and color. These data are stored in databases for analysis to identify potential anomalies and deviations from standards. Particularly for dairy products, which are highly perishable, a defective package can compromise their quality and dissatisfy consumers [11].

## PASTEURIZATION MONITORING

One of the most critical processes in the production line of milk and dairy products is thermal processing, as it significantly affects both the quality and safety of the final products. Artificial Intelligence, and more specifically Machine Learning, in conjunction with the Internet of Things (IoT), plays a pivotal role in real-time monitoring of milk pasteurization. The intelligent software developed for this purpose can be seamlessly integrated into both older machinery and more advanced equipment. This system enhances the production line by incorporating sensors that measure pasteurization temperature, processing time, and moisture levels. These values are recorded and stored in databases at 10-second intervals. In the event of deviations from the desired values, corrective actions are automatically triggered through real-time activation of sensors to rectify errors promptly. By employing algorithms such as Random Forest, XGBoost, and Gradient Platform, the system can accurately predict the quality of the final food products based on the data collected from each batch. Additionally, it provides timely alerts for potential mechanical failures that could disrupt production. This automated model not only enhances product quality but also contributes to sustainable production by reducing and preventing errors that would otherwise lead to unnecessary energy consumption and resource waste [12].

## BLOCKCHAIN AND RFID TAGS IN DAIRY PRODUCTS

In modern times, consumers have developed a heightened interest in the origins of the food they consume, the living conditions of animals, the quality of animal feed, and the processing of these foods along the production line. By utilizing Blockchain technology and incorporating RFID (Radio Frequency Identification) tags, real-time data is collected from the farm to the

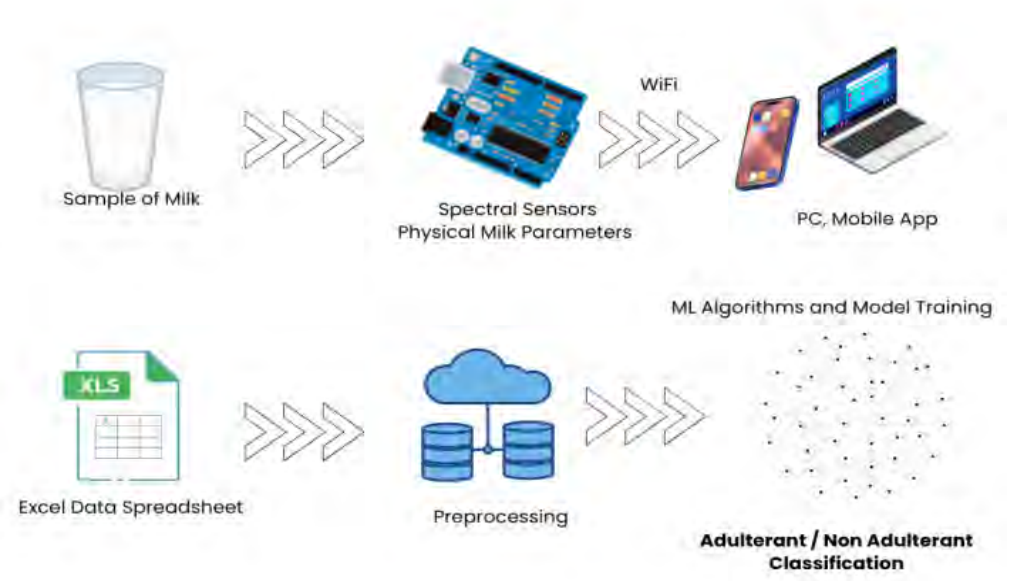



**Figure 2.** Graphical sceme of AI Enabled Multispectral Sensor System.

distribution points of the products. Through scanning the QR code on the product packaging, consumers can access a network of information regarding sustainability levels, factory greenhouse gas emissions, the quality of life of the animals from which the milk was sourced, the thermal processing undergone, and the records of temperature and humidity levels during storage and distribution. This model enhances both product traceability and identification. Any deviation from required conditions can be immediately detected, enabling the recall of an individual product rather than the entire batch, as is typically practiced today. Moreover, it is an intelligent method to ensure the authenticity of raw material origins and reduce incidents of product adulteration or unfair practices. Finally, the Blockchain system upgrades logistics management by providing real-time insights into inventory levels, the location of each batch in storage refrigerators, and the distribution routes of suppliers. This allows for more effective monitoring of production quantities and speeds, ultimately improving the efficiency of the supply chain [13-14].

## CUSTOMER CHURN PREDICTION MODELS

Machine Learning algorithms are also applied in the development of innovative products by collecting data on consumer preferences and market trends. Predictive algorithms are continuously trained using information circulating on the internet, social media platforms, and product reviews. After processing, categorizing, and evaluating the data, the system can propose ideas for new recipes and predict consumer audience responses. Algorithms such as Logistic Regression and Bayesian algorithms are used to predict the likelihood of customer attrition. Additionally, they can suggest improvements to existing recipes by modifying, for example, texture, proportions, or ingredients. With this software, scientists can conduct targeted trials for the development of new dairy products that meet market demands. Moreover, by considering specific dietary restrictions such as celiac disease, lactose intolerance, vegan, or vegetarian diets, it is possible to launch new products tailored to these groups, enriching their daily nutrition with innovative options. This model not only promotes sustainability but also helps the production company differentiate itself with products designed in alignment with contemporary trends [15-16].

## CHALLENGES

Artificial Intelligence, and more specifically Machine Learning, which is the focus of this study, provides a wide range of possibilities in the dairy production chain. It offers solutions to flow-related problems, reduces human error, and acts preventively to avoid costly damages. To integrate this new operating model, Dairy 4.0, targeted actions are required to maximize the potential benefits it offers. Naturally, with the introduction of new technologies, certain challenges arise in the early stages of implementation, which demand continuous attention and training regarding the new mechanisms. In particular, livestock farmers need to develop digital skills to understand the interactions within the Internet of Things (IoT). Furthermore, for a traditional farm to operate according to the principles of Dairy 4.0, the issue of digital

infrastructure and connectivity in rural areas must be addressed—an endeavor that requires both time and significant financial resources. At the same time, within the factory environment, where older-generation machinery lacking connectivity may still be in use, substantial investment will be necessary to replace such equipment. Consequently, this situation gives a competitive advantage to larger and more powerful dairy production companies over smaller producers, who will face greater difficulty and delays in adopting Machine Learning tools. Equally important is the need to provide systematic training to staff on the new systems, enabling them to leverage these tools to their full potential. This creates a challenge for companies in recruiting more specialized personnel, thereby hindering the rapid expansion of production. Training is also crucial for the timely handling of issues related to data breaches and threats to large datasets. Cybersecurity requires the installation of software that monitors the network and cloud security, providing early warnings of malicious attacks. [17] This approach ensures the reliability and integrity of the data.

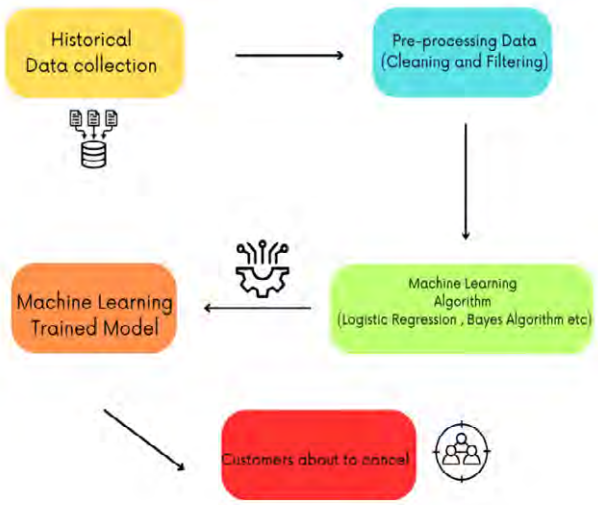



**Figure 3.** Customer Churn Prediction Model

## CONCLUSIONS

Machine Learning has the potential to transform the dairy industry into a modern, automated sector, enhancing both speed and efficiency. The Internet of Things (IoT), big data, and algorithms facilitate the digitization of processes and the continuous monitoring of production. However, transitioning from traditional operations to more advanced infrastructure requires time and capital, both for equipment and for software systems. Machine Learning models increase accuracy, enhance sustainability, and optimize the management of gas emissions. In the dairy industry, where safety and quality standards are exceptionally high, it is crucial to anticipate errors that could compromise the raw material and, subsequently, the final product. The solution lies in algorithm-based systems that are continuously trained through data recording, enabling rapid classification, data grouping, and the categorization of critical values—thereby improving production stages.

## ACKNOLEDGEMENTS

The publication of the article was partially funded by the University of West Attica. This work was supported by the European Union within the framework of the Erasmus+ FOOD4S Programme (Erasmus Mundus Joint Master Degree in Food Systems Engineering, Technology and Business 619864-EPP-1-2020-1-BE-EPPKA1-JMD-MOB) and the Erasmus+ FIND4S Programme (Enhancing Higher Education Capacity for Sustainable Data Driven Food Systems in Indonesia Project 101179822—FIND4S—ERASMUS-EDU-2024-CBHE). Views and opinions expressed are however those of the authors only and do not necessarily reflect those of the European Union or the European Education and Culture Executive Agency (EACEA). Neither the European Union nor EACEA can be held responsible for them.

## REFERENCES

1. Vijayan S, Ayothi, S. A qualitative analysis of the machine learning methods in food adultery: A focus on milk adulteration detection. *Adv. Res. Dyn. Control Syst. 12*(7) 543–551. (2020) https://doi:10.5373/jardcs/v12i7/20202037
2. Zhu L, Spachos P, Pensini E, Plataniotis K N Deep learning and machine vision for Food Processing: A survey. *Curr. Res. Food Sci. 4* 233–249 (2021) https://doi:10.1016/j.crfs.2021.03.009
3. Tangorra F M, Buoio E, Calcante A, Bassi A, Costa A. Internet of things (IOT): Sensors application in dairy cattle farming. *Animals 14*(21) 3071 (2024) https://doi:10.3390/ani14213071
4. Niloofar P, Francis D P, Lazarova-Molnar S, Vulpe A, Vochin M C, Suciu G,... Bartzanas T. Data-driven decision support in livestock farming for improved animal health, welfare and greenhouse gas emissions: Overview and challenges. *Comput Electron Agr 190* 106406 (2021) https://doi:10.1016/j.compag.2021.106406
5. Cockburn M. Review: Application and prospective discussion of machine learning for the management of Dairy Farms. *Animals 10*(9) 1690 (2020) https://doi:10.3390/ani10091690
6. Fuentes S, Gonzalez Viejo C, Cullen B, Tongson E, Chauhan S S, Dunshea, F R. Artificial Intelligence

applied to a robotic dairy farm to model milk productivity and quality based on cow data and daily environmental parameters. *Sensors 20*(10) 2975 (2020) https://doi:10.3390/s20102975
7. Grothmann A, Nydegger F, Häußermann A, Hartung E. Automatic feeding system (AFS) - potential for optimisation in dairy farming. *Agr Eng Eu 65*(2) 129–131 (2010) https://doi.org/10.15150/lt.2010.610
8. Chelotti J O, Martinez-Rau L S, Ferrero M, Vignolo L D, Galli J R, Planisich, A M, ... Giovanini L L. Livestock feeding behaviour: A review on Automated Systems for Ruminant Monitoring. *Biosyst Eng 246* 150–177 (2024) https://doi:10.1016/j.biosystemseng.2024.08.003
9. Sowmya N, Ponnusamy V. Development of Spectroscopic Sensor System for an IOT application of adulteration identification on milk using machine learning. *IEEE Access*, *9* 53979–53995 (2021) https://doi:10.1109/access.2021.3070558
10. Khaliq Fadel NAA, Bahnam BS. Survey of Dairy Products Using Machine Learning Techniques. *IRJIET* 8 (1) 55-61 (2024) https://doi:10.47001/IRJIET/2024.801007
11. Xiao Z, Wang J, Han L, Guo S, Cui Q. Application of machine vision system in food detection. *Front Nutr 9* (2022). https://doi:10.3389/fnut.2022.888245
12. Afolaranmi S O, Drakoulelis M, Filios G, Melchiorre C, Nikoletseas S, Panagiotou S H, Timpilis K. ZPasteurAIzer: An AI-enabled solution for product quality monitoring in tunnel pasteurization machines. *Machines 11*(2) 191 (2023) https://doi:10.3390/machines11020191
13. Malik M, Gahlawat V K, Mor R S, Singh M K. Unlocking dairy traceability: Current trends, applications, and future opportunities. *Future Foods 10* 100426 (2024) https://doi:10.1016/j.fufo.2024.100426
14. Vp A, Singh S, Chauhan A K. Blockchain Technology in Dairy Industry. *Indian Dairyman* 52–57 (2022)
15. Liang Z. Predict customer churn based on machine learning algorithms. *Highlig Bus Eco Manag 10* 270–275 (2023) https://doi:10.54097/hbem.v10i.8051
16. Manika. (n.d.). Top 5 customer churn prediction models in machine learning. Retrieved from https://www.projectpro.io/article/churn-models/709
17. Bradley AJ, Leach KA, Green MJ, Gibbons J, Ohnstad IC, Black DH, Payne B, Prout VE, Breen, JE. The impact of dairy cows' bedding material and its microbial content on the quality and safety of milk - A cross sectional study of UK farms. *Int J Food Microbiol.* 269 36-45 (2018) https://doi:10.1016/j.ijfoodmicro.2017.12.022

© 2025 by the authors. Licensed to PSEcommunity.org and PSE Press. This is an open access article under the creative commons CC-BY-SA licensing terms. Credit must be given to creator and adaptations must be shared under the same terms. See https://creativecommons.org/licenses/by-sa/4.0/



Systems & Control Transactions

**Research Article - Peer Reviewed Conference Proceeding**
ESCAPE 35 - European Symposium on Computer Aided Process Engineering
Ghent, Belgium. 6-9 July 2025
Jan F.M. Van Impe, Grégoire Léonard, Satyajeet S. Bhonsale,
Monika E. Polańska, Filip Logist (Eds.)

PSE PRESS

# Multi-Dimensional Singular Value Decomposition of Scale-Varying CFD Data: Analyzing Scale-Up Effects in Fermentation Processes

**Pedro M. Pereira[a]*, Bruno S. Ferreira[b] and Fernando P. Bernardo[a]**

[a] CERES, Department of Chemical Engineering, University of Coimbra, R. Sílvio Lima, 3030-790 Coimbra, Portugal
[b] Biotrend SA, Portugal.
* Corresponding Author: pedro.mesquita.pereira@tecnico.ulisboa.pt

## ABSTRACT

The scale-up of processes with complex fluid flow presents significant challenges in process engineering, particularly in fermentation. Computational fluid dynamics (CFD) is a crucial tool for accurately modelling the hydrodynamic environment in bioreactors and understanding the effects of scale-up. This study utilizes Higher Order SVD (HOSVD), which is the multidimensional extension of Singular Value Decomposition (SVD), to identify the dominant structures (modes) of fluid flow in CFD data of fermentation process simulations. Similarly to Proper Orthogonal Decomposition (POD), also based on SVD, this method can be used to identify the dominant structures of fluid flow, and additionally explore the scale parameter space. As a first test case, we examined five scales of a reciprocally shaken flask bioreactor, from 125 mL to 10 L, specified using basic empirical scale-up rules. Results indicate a common set of spatial modes across all scales, thus confirming that the scale-up method assures some dynamic similarity. However, the relative importance of these common spatial modes changes sensibly across process scales. The main spatial mode that represents the large recirculating flow in the flask can account for 19.8% of the data variability for the 125 mL scale but only 11.7% for the 10 L scale case. In this larger scale, one needs a larger number of modes to capture flow dynamics, thus showing an increase in flow complexity. These findings illustrate the impact of scale on fluid dynamics in a particular bioreactor flow but also provide a proof of concept for this methodology.

**Keywords**: HOSVD, CFD, Scale-up, Fermentation

## INTRODUCTION

Scaling up fermentation processes is a primary focus in bioprocess engineering. Like other areas in chemical and process engineering, moving fermentation operations from bench-scale to pilot-scale, and ultimately to commercial-scale, exacerbates mixing inefficiencies, which are then responsible for spatial gradients in species concentration and mechanical stimuli. The biomass experiences these gradients as oscillatory stimuli, which can affect cell phenotype. Such effects can alter metabolic activity, resulting in hard to predict outcomes and decreased productivity [1].

The effects of scale arise from the interaction of the biological system with the hydrodynamics of the reactor [1]. Therefore, Computational Fluid Dynamics (CFD) is one important tool to clarify how transfer phenomena change with scale. Due to the difficulty of analysing the 3D scalar and vector fields resulting from a multiphase CFD simulation, the need for a solid method to do fluid flow feature extraction arises.

One of the most well-established methods for flow feature extraction is Proper Orthogonal Decomposition (POD). Its primary applications in Fluid dynamics have been to study, analyse and model turbulent coherent structures both from experimental as well as simulated data [2]. POD allows for the identification of the set of spatial modes (basis vectors) that represent most of the kinetic energy of the system and their temporal coefficients. The linear combination of the main modes allows

for a reconstruction of the data. The analysis of the modes and temporal coefficients can clarify the main coherent structures in a fluid flow.

POD has been demonstrated to be equivalent to Principal Components Analysis (PCA), Karhunen–Loève decomposition and Singular Value Decomposition (SVD), with the nomenclature used depending mostly on the area of application. POD, as well as PCA and SVD, are in general terms methods to reduce a large number of correlated variables into a smaller number of uncorrelated variables, finding a few ordered basis vectors able to optimally express (mean squared error wise) the initial large data set [2]. These basis vectors are often denoted in the context of CFD data as “modes”.

As a tool for identifying coherent structures and their dynamics, POD can enhance the understanding of scale-up effects in aerated fermentation and thus improve process design. Notable works applied to CFD include studies on stirred tanks by Mayorga et al. for a single-phase case [4]. Multiphase cases, as the one treated in this work, present greater complexity due to the interphase interactions in a turbulent flow, and are rarer in the literature. One such example is our previous work on CFD data of an aerated stirred tank bioreactor [5].

POD is only defined for a rank 2 tensor, that is a matrix, and as such it is not possible to directly apply it to a problem with additional parameters. To study the effect of scale on the main flow features, process scale can be defined as a parameter of interest and POD applied to each set of data corresponding to a particular process scale. However, the data will not be decomposed into the same basis vectors, that is the same modes, and thus a quantitative analysis of the impact of scale on the relative importance of the different modes is not possible.

To apply a similar methodology to a parametric case it is necessary to use tensor decomposition. Multiple methods for tensor decomposition exist, the most common being canonical polyadic decomposition (CP) and variations of Tucker decomposition such as Higher Order Single Value Decomposition (HOSVD) [6].

Canonical polyadic decomposition decomposes a tensor into a sum of rank one tensor (vector) products. Each rank one tensor can be seen as a mode in each parametric space, which then results in an equal number of modes in the decomposition for each parameter. Due to the nature of CFD data, in almost all cases there are many more points in space (number of finite volumes in the CFD mesh) than in time. Also, due to the cost of CFD simulations, the number of simulations made varying a particular parameter, such as the process scale, will be much lower than the number of finite volumes. This imbalance in the data makes CP a worse option for CFD data.

Tucker decomposition follows a different approach: it decomposes the original data into one smaller core tensor of the same rank, and one factor matrix for each parameter in study. The core tensor encapsulates the level of interaction between the parameters while the factor matrices can be seen as analogous to the modes found by POD or CP. With some data manipulation, the resulting tensor and matrices can be easily interpreted. Due to its greater flexibility and better fitting, we choose Tucker decomposition to proceed with our work despite the greater computational cost to perform the decomposition. In particular, we used the Higher Order Single Value Decomposition (HOSVD) implementation of Tucker decomposition [7].

Tensor decomposition has been used in various machine learning applications such as signal or image processing for tensor completion, principal component analysis, regression and classification, but tensor decomposition is less commonly applied to CFD data [8]. Applications of HOSVD to CFD data include parametric wind speed models, parametric models for flow over an aerofoil and flow feature identification on channel flows [9][10][11]. While much of the relevant literature highlights the potential of HOSVD in parametric model development, some studies recognise its use in flow feature identification. Despite this, in our review of the literature no instances were found where parametric modelling and feature identification are combined. We propose one such application of HOSVD focusing on flow feature identification while conducting a parametric study of the effects of process scale. This introduces innovation both methodologically and in the application to scale-up of bioreactors.

The approach here proposed enables us to identify the main coherent structures (modes) that emerge at various scales of fermentation and quantify the contribution of each one of the modes to the total energy of the system. Our methodology includes CFD simulations of the fermentation process at multiple scales, with the operating parameters determined by traditional scale-up criteria. The main challenge we found was the construction of the data tensor which requires all data to be referring to equivalent points in space. Through interpolation, we aligned the different CFD meshes and constructed a snapshots tensor of the CFD results across all process scales, standardized on the same spatial reference grid. This systematic approach bridges a gap in the literature, combining parametric modelling with flow feature identification to provide new insights into scale-up effects in fermentation. By helping to uncover the phenomenological roots of the scale-up problem, our methodology could inform new protocols, making the process of fermentation scale-up more expedient and efficient.

## METHODS

As a case study to illustrate tensor decomposition of CFD data modelling chemical and biochemical process scale-up we modelled a set of non-baffled Erlenmeyer flasks commonly used in small scale laboratory fermentation, at different process scales. We opted for this bioreactor due to its geometrical simplicity making it simpler to model. The geometry of the flasks was reproduced from commercially available models and is represented in Figure 1. We modelled flasks of scales 125 mL, 250 mL, 500 mL, 1 L and 10 L, maintaining geometrical similarity. The 10 L process scale is hypothetical but we expected it to provide enough scale contrast to illustrate the changes found with changing process scale. Mixing in these bioreactors is induced by a shaking motion [12], and in particular we have chosen reciprocal shaking, which is a periodic motion in one dimension. This isn't the most common shaking mode, but it was preferred due to its greater simplicity and suitability for 2D CFD simulations, with lower computational cost.

Although not fully representative we preferred 2D simulations, which should be good enough to illustrate our methods, and highlight the effect of process scale on the governing flow modes. All flasks were simulated with 20% of the capacity filled, consistent with common practice. The amplitude of the movement is known to have minor impact on mixing performance, so an arbitrary value of 1.5 cm was used for the smaller scale and then scaled accordingly for the larger scales [13]. The frequency of the movement was adjusted for each scale by keeping the power per unit volume of liquid (P/V) constant.

$$N_p = \frac{P}{\rho n^3 d^4 V^{1/3}} \approx 70Re^{-1} + 25Re^{-0.6} + 1.5Re^{-0.2} \quad (1)$$

The power number ($N_p$) was estimated using the correlation of Klöckner and Büchs as seen in eq. 1 [14]. The 10 L flask falls outside the scope of the experimental data fitted by this correlation, which is a common limitation in solving scale-up problems solely based on nondimensional numbers and other empirical rules (such as P/V constant). Table 1 summarizes the process scales under analysis and corresponding values of $d_{max}$ (maximum flask diameter) and n (frequency of agitation).

**Table 1:** Volume, maximum diameter and agitation frequency of each flask.

| **Scale (mL)** | 125 | 250 | 500 | 1000 | 10000 |
|---|---|---|---|---|---|
| **$d_{max}$ (mm)** | 66 | 83 | 101 | 128 | 271 |
| **n ($s^{-1}$)** | 2.00 | 1.81 | 1.71 | 1.52 | 1.07 |

To model the fluid dynamics, we used the Volume of fluid (VOF) model implemented in the interFoam solver of the OpenFOAM v2206 finite volume opensource library. The interFOAM solver has been validated to model shake flask flows [15]. In eq. 2-4 we present the VOF RANS equations with k-epsilon closure equations not presented for brevity, the closure equation parameters used are the standard OpenFOAM values.

$$\nabla U = 0 \quad (2)$$

$$\frac{\partial}{\partial t}\rho U + \nabla(\rho U \cdot U) = -\nabla p + \nabla(\tau + \tau_t) + \rho g + F_\sigma \quad (3)$$

$$\frac{\partial \alpha}{\partial t} + (U \cdot \nabla \alpha) = 0 \quad (4)$$

To model the shaking motion, we used an oscillatingLinearMotion dynamic mesh. The CFD meshes are 2D axial cuts of the geometry and were constructed with the OpenFOAM meshing tools. The meshes are hexahedral-dominant with from 25k to 210k finite volumes. To construct a coherent data tensor the mesh of the 125 mL flask was chosen as a basis and velocity fields from all larger geometries were interpolated onto that basis using OpenFOAM's transformPoints (scaling) and mapFields (interpolation) functions, one additional advantage of this is the effective down sampling making the tensor smaller

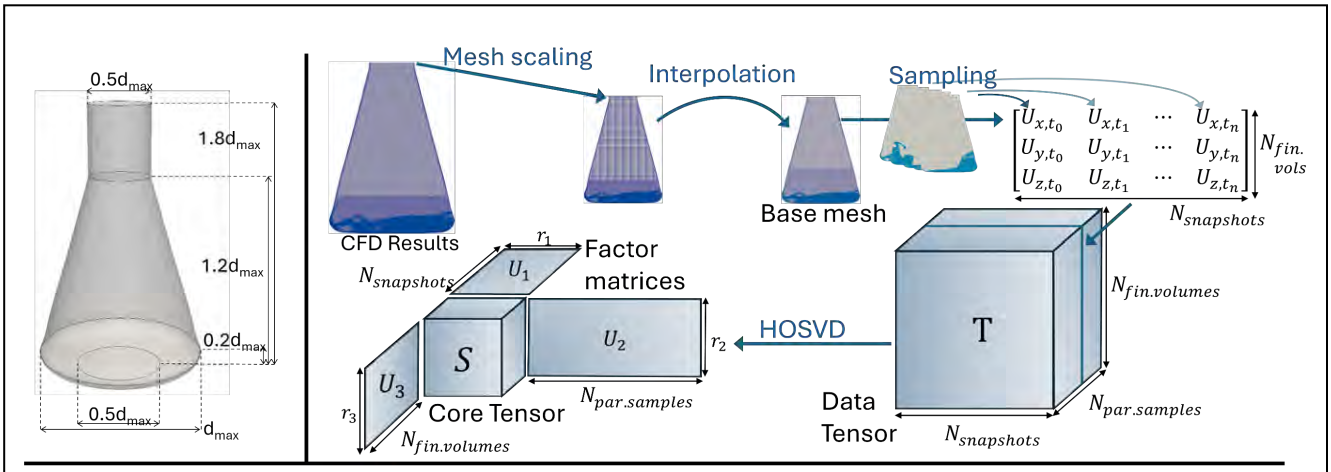



**Figure 1.** Schematic representation of the flask geometry and framework of the methods for data treatment.

and tensor decomposition computations lighter.

The snapshot matrix was constructed from velocity fields by arranging each velocity component per finite volume into columns, with each column representing a temporal snapshot. To ensure comparability across process scales, sampling was performed at 51 equally spaced times relative to the reciprocating movement's period, forming one full cycle. Snapshot matrices (shaped $N_{snapshots} \times 3N_{finite_volumes}$) for five scales were concatenated into a data tensor ($N_{snapshots} \times 3N_{finite_volumes} \times N_{scales}$).

The tensor was decomposed via truncated HOSVD using TensorLy a python library, with decomposition ranks of 20 (time), 5 (scale), and 50 (space). This decomposes the tensor into a core tensor (S), encoding parameter interactions (space, time, scale), and factor matrices ($U_1$, $U_2$ e $U_3$), analogous to POD modes (Eq. 5) in space, time, and scale, respectively.

$$T \approx S \times_1 U_1 \times_2 U_2 \times_3 U_3 \quad (5)$$

The method used here was proposed by Tucker and solves an eigenvalue problem to compute the leading left singular vectors of each matrix forming the data tensor. It then finds the core tensor by tensor multiplication of these vectors (transposed) with the data tensor. The number of left singular vectors corresponds to the rank of the decomposition in that parameter space. For the sake of brevity, we do not develop this methodology further, but further discussions on tensor decomposition and HOSVD can be found on the extensive review by Kolda and Bader [6]. The data tensor in this work includes ~$2 \times 10^7$ elements, it takes 60 seconds to construct the tensor and only 4 seconds to perform the decomposition, using an in-house modest workstation.

## RESULTS AND DISCUSSION

Figure 2 illustrates a set of snapshots of the volumetric fraction of water (α) for various scales taken at the same phase-matched times relative to the period of each movement (π). We present the α field as it is the most intuitive way to show the free-surface dynamics. Analysis of the snapshots reveals high dynamic similarity between the 125 mL and 1L scales. Particularly at the extremes of the flask's movement (at the relative times 2/5π and π) a similar wetted height of the flask wall is predicted and, the wave crests exhibit similar shapes. However, only at 2/5π are liquid ejections similarly predicted for both scales. At the 1/5π and 3/5π times, a similar wave pattern is predicted, but with greater amplitude for the smaller scale. For the 10 L scale less dynamic similarity is found. These differences illustrate the expected failure of the empirical scale-up correlation for the 10 L scale.

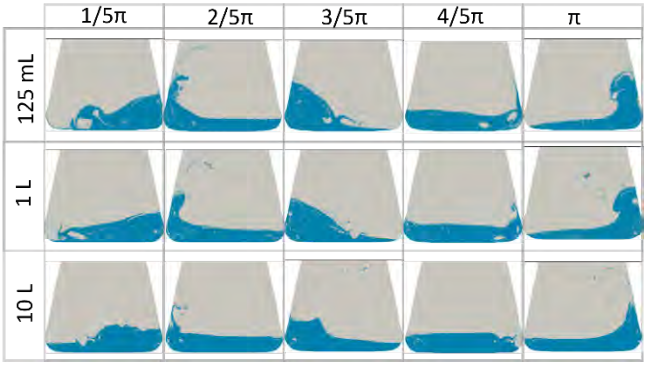



**Figure 2**. CFD results for different flask sizes, with the regions of water volumetric fraction greater than 0.95 painted in blue.

Following the preliminary qualitative analysis of the alpha fields, we propose tensor decomposition as a method to quantify the dynamic similarity of the fluid flow across process scales. The columns of the spatial factor matrix can be seen as spatial modes analogous to POD modes. Individual modes or combinations of modes are well-established to represent one or more correlated flow features. By quantifying the importance of each mode for each process scale, we can compare the fluid flow patterns at different scales. Applying tensor multiplication to the spatial factor matrix and the original data tensor provides a projection of the CFD data into the space spanned by the spatial modes. By taking the norm of the results of this operation over the temporal domain, we obtain the energy of each spatial mode for each process scale. The energy in this context means the amount of variability in the original data that is explained by each mode. Figure 3 presents these results, normalized by the sum of the energy of all modes for each process scale.

In Figure 3 we observe that the main two modes are the same across all process scales. But for less important modes the order of importance can change between process scales. Further, the combined importance of the two main modes decreases as the scale increases, from a combined normalized energy of 28.5% for 125 mL to 17.8% at 10 L scale. This loss of importance of the two top modes could be accompanied by an increase in the number of modes (ie. more relevant flow features), but we do not observe this. Depending on scale 43 or 44 modes are required to achieve 95% of the total energy represented in the decomposition. The top 30 modes represent a similar cumulative relative energy across all scales and the top 10 modes for each process scale represent 54%, 57%, 50%, 52% and 48% in ascending

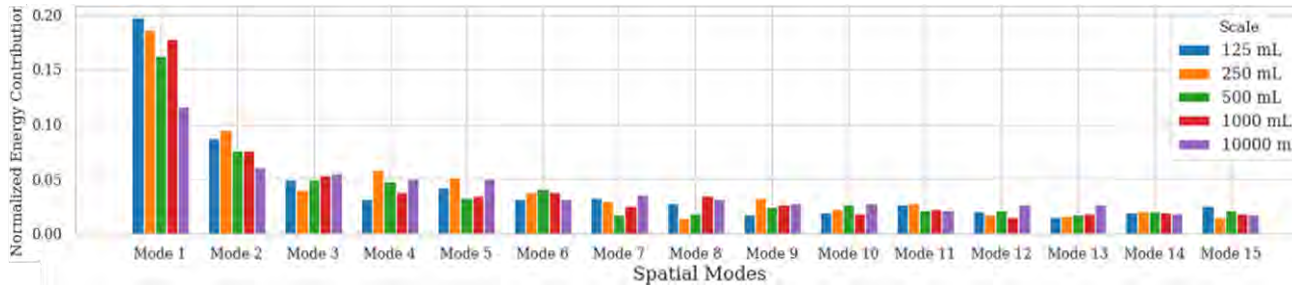



**Figure 3:** Relative normalized energy contribution (explained variability) of the 15 main spatial modes

process scale order. From these results we conclude that the relevant spatial modes are generally conserved across process scales, but their energy becomes more distributed and less concentrated on the top modes as scale increases. This redistribution of energy suggests a complexification of the velocity field with the increase of scale, likely due to enhanced turbulent effects for the larger scales.

To explore the connection between fluid flow features and spatial modes, we graphically analysed the spatial distribution of the modes and their temporal distribution. In Figure 4 the first five modes are presented and their normalized temporal coefficients for each process scale. The main modes exhibit a clear periodic oscillation in the normalized temporal coefficient curve, while the remaining modes appear to have a periodic nature with increased noise. Analysis of the Lissajous figures for each combination of the temporal coefficients (not presented for brevity) reveals that the two main modes have the same frequency and are π/2 out of phase for all process scales. Based on their spatial and temporal distribution mode 1 represents the rise of the fluid as the flask slows before reverting direction and mode 2 is the waving liquid transport during the movement of the flask. Mode 3 is π/4 out of phase and has twice the frequency of mode 1. It is then likely connected to the formation of wave crests at the extremes of the flask's movement.

Modes 4 and 5 exhibit interesting interactions with each other and with the two main modes. For the 125 mL and 250 mL scales, modes 2 and 4 are π/2 out of phase, as are modes 2 and 5. Modes 1 and 4 are 3π/4 out phase, while modes 1 and 5 are π/4 out of phase. This indicates that for these scales modes 1, 2, 4 and 5 represent coherent structures that peak sequentially at π/4 phase intervals. Modes 4 and 5 likely represent vortical structures related to the liquid jump at the extremes of the flask's movement. For the 500 mL scale a similar arrangement is found but with mode 6 (not pictured) showing similar dynamics to mode 4 as before, and mode 4 becoming an harmonic of mode 1. The results for 1 L and 10 L scales align with the results for 500 mL scale. These results indicate that the fluid flow during the travelling parts of the flasks movement represented by modes 1 and 2 is conserved with scale, at least for the adopted scale-up protocol. However, the phenomena at the extremes of the flask's movement show important changes with scale. Unexpectedly, an apparent discontinuity appears between the 250 mL and 500 mL scales, which seems to indicate that there is a particular loss of effectiveness in this scale-up protocol between these two scales.

Our findings demonstrate that as process scale increases, the main modes connected with dominant free-surface phenomena (e.g., wave formation, surface renewal) lose prominence relative to turbulence-driven dissipation within the bulk fluid phases (air and water). This redistribution of power dissipation highlights a decoupling of power dissipation and interfacial phenomena. The interfacial phenomena being the driving factor for oxygen mass transfer. From our analysis of this case we reach a central conclusion: scale-up strategies that neglect the evolving balance between surface and bulk dissipation mechanisms in free-surface aeration may fail to preserve mass transfer efficiency, despite achieving target power consumption metrics.

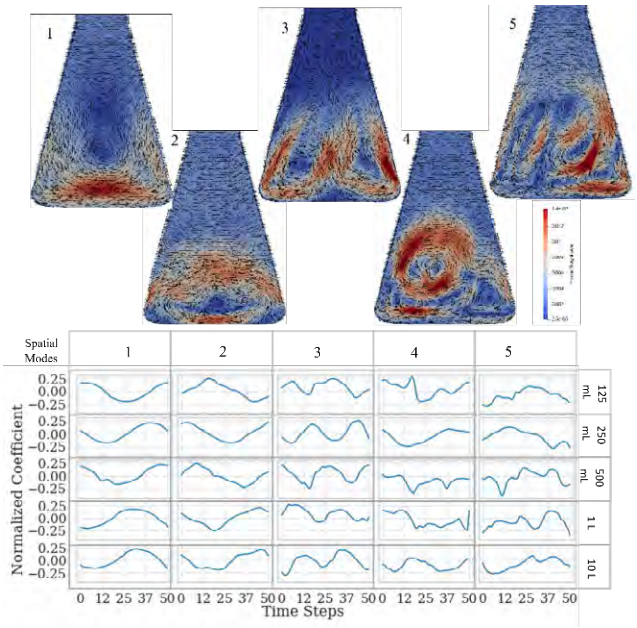



**Figure 4:** Spatial modes for the 5 main modes and normalized time coefficient curve for each mode/scale.

## CONCLUSION

In this work we introduced a new methodology to study the effects of scale-up of fermentation processes, demonstrated with the scale-up of a shake flask bioreactor fermentation. Our findings reveal the impact of scale on fluid dynamics in a particular bioreactor flow and provide a proof of concept for this methodology, which can give insights for a more rational approach to bioreactor scale-up and optimization. We believe there is wide future application for bioreactor types, where geometric similarity is maintained. While new methods are required for future applications where geometrical similarity is broken. The application of this method can be extended to other scale-up rules and beyond scale-up, to the construction of parametric reduced models of multiple processes including reaction and mass-transfer models.

## ACKNOWLEDGEMENTS

The authors thank financial support (PhD scholarship) from Fundação para a Ciência e Tecnologia, an organization within the Ministry of Science, Technology and Higher Education in Portugal, and also from Project "CiNTech - Technological Hub for Innovation, Translation and Industrialization of Complex Injectable Drugs" (reference: 7131), in the scope of PRR - Recovery and Resilience Plan and by the Next Generation EU European Funds, following NOTICE No. 02/C05-i01/2022, Component 5 - Capitalization and Business Innovation - Mobilizing Agendas for Business Innovation.

## REFERENCES

1. Nadal-Rey G, McClure DD, Kavanagh JM, Cornelissen S, Fletcher DF, Gernaey KV. Understanding gradients in industrial bioreactors. Biotechnol Adv. 46:107660. (2021) https://doi.org/10.1016/j.biotechadv.2020.107660
2. P. Holmes, Turbulence, Coherent Structures, Dynamical Systems and Symmetry. Cambridge University Press (2012)
3. Liang YC, Lee HP, Lim SP, Lin WZ, Lee KH, Wu CG. Proper orthogonal decomposition and its applications—Part I: Theory. J Sound Vib. 252(3):527-544 (2002) https://doi.org/10.1006/jsvi.2001.4041
4. Mayorga C, Morchain J, Liné A. Reconstruction of the 3D hydrodynamics in a baffled stirred tank using Proper Orthogonal Decomposition. Chem Eng Sci. 248:117220 (2022) https://doi.org/10.1016/j.ces.2021.117220
5. Pereira PM, Martins RC, Ferreira BS, Bernardo FP. Reduction of an aerated fermenter CFD model using proper orthogonal decomposition. In: Computer Aided Chemical Engineering. Vol. 44. Elsevier (2024). Ed: Gernaey KV, Huusom JK, Gani R, editors. https://doi.org/10.1016/B978-0-443-28824-1.50144-7
6. Kolda TG, Bader BW. Tensor Decompositions and Applications. SIAM Rev. 51(3):455-500. (2009) https://doi.org/10.1137/07070111X
7. De Lathauwer L, De Moor B, Vandewalle J. A multilinear singular value decomposition. SIAM J Matrix Anal Appl. 21(4):1253-1278. (2000) https://doi.org/10.1137/S0895479896305696
8. Bi Y, Lu Y, Zhang L, Zhu C, Liu Y. Tensor decompositions: computations, applications, and challenges. In: Tensors for Data Processing. Ed: Liu Y. Elsevier (2022).
9. Zhang Y, Li X, Chen L, Yang Y. Three-dimensional wind velocity reconstruction based on tensor decomposition and CFD data with experimental verification. Energy Convers Manag. 316:115322. (2022) https://doi.org/10.1016/j.enconman.2022.115322
10. Lorente LS, Vega JM, Velazquez A. Generation of aerodynamic databases using high-order singular value decomposition. *J Aircr*. 45(5):1779 (2008) https://doi.org/10.2514/1.35258
11. von Larcher T, Klein R. On identification of self-similar characteristics using the Tensor Train decomposition method with application to channel turbulence flow. *Theor Comput Fluid Dyn*. 33(2):141-159. (2019) https://doi.org/10.1007/s00162-019-00485-z
12. Takahashi M, Aoyagi H. Practices of shake-flask culture and advances in monitoring $CO_2$ and $O_2$. *Appl Microbiol Biotechnol*. 102(10):4279-4289 (2018) https://doi.org/10.1007/s00253-018-8922-8
13. Kato Y, Hiraoka S, Tada Y, Hirose K, Büchs J. Mixing performance of a reciprocally shaking vessel. *J Chem Eng Jpn*. 36(6):663-667 (2003) https://doi.org/10.1252/jcej.36.663
14. Klöckner W, Büchs J. Shake-flask bioreactors. In: Comprehensive Biotechnology Ed: Moo-Young M, Elsevier (2011)
15. Dinter C, Gumprecht A, Menze MA, Azizan A, Niehoff P-J, Hansen S, et al. Validation of computational fluid dynamics of shake flask experiments at moderate viscosity by liquid distributions and volumetric power inputs. *Sci Rep*. 14(1):3658 (2024) https://10.1038/s41598-024-53980-7

© 2025 by the authors. Licensed to PSEcommunity.org and PSE Press. This is an open access article under the creative commons CC-BY-SA licensing terms. Credit must be given to creator and adaptations must be shared under the same terms. See https://creativecommons.org/licenses/by-sa/4.0/



Systems & Control Transactions

**Research Article - Peer Reviewed Conference Proceeding**
ESCAPE 35 - European Symposium on Computer Aided Process Engineering
Ghent, Belgium. 6-9 July 2025
Jan F.M. Van Impe, Grégoire Léonard, Satyajeet S. Bhonsale,
Monika E. Polańska, Filip Logist (Eds.)

PSE PRESS

# Application of pqEDMD to Modeling and Control of Bioprocesses

**Camilo Garcia-Tenorio[a]*, Guilherme A. Pimentel[a], Laurent Dewasme[a], and Alain Vande Wouwer[a]**

[a] Systems, Estimation, Control and Optimization (SECO), University of Mons, 7001, Mons, Belgium
* Corresponding Author: camilo.garciatenorio@umons.ac.be

## ABSTRACT

Extended Dynamic Mode Decomposition (EDMD) and its variant, the pqEDMD, which uses a p-q-quasi norm reduction of polynomial basis functions, are attractive tools to derive linear operators approximating the dynamic behavior of nonlinear systems. This study highlights how this methodology can be applied to data-driven modeling and control of bioprocesses by discussing the selection of several ingredients of the method, such as the polynomial basis, order, data sampling, and preparation for training and testing, and ultimately, the exploitation of the model in linear model predictive control.

**Keywords**: System Identification, Dynamic Modelling, Model Predictive Control, Process Control, Numerical Methods

## INTRODUCTION

Digital twins are increasingly popular as part of the Industry 4.0 revolution but are generally understood as digital representations of the industrial processes obtained through machine learning techniques and, in particular, the use of neural networks (NN). Although NNs are versatile and have proven their utility in many applications, there exist less popular yet appealing alternatives offered by the stream of research that revolves around the Koopman operator approximation [1–3], and the different decomposition methods to get an approximation of the Koopman operator [4]. In particular, the Extended Dynamic Mode Decomposition (EDMD) provides the possibility to derive a linear representation of a nonlinear system in a so-called “function space” of nonlinear basis functions (denoted “observables”) [5].

The objective of this study is to show the potential of EDMD [5,6] and one of its extensions, pqEDMD, developed by the present authors in [7] for modeling arbitrary systems, including bioprocesses. The main advantage of providing a linear representation is that standard linear estimation and control techniques can be further exploited, particularly linear model predictive control (MPC), whereas NNs require more complex nonlinear methods [8]. The prominent feature of pqEDMD is that it systematizes the definition of the dictionary of observable functions by resorting to orthogonal polynomials and selecting the approximation order by sweeping through two parameters, denoted p and q.

This paper explains how the approximation can be constructed, discusses practical aspects such as the selection of training and testing data, and shows how the resulting models can be exploited in linear MPC as applied to a simple yet representative bioreactor case study.

## MODELING AND CONTROL USING PQEDMD

This study considers a data-driven modeling strategy called the p-q-quasi-norm extended dynamic mode decomposition (pqEDMD) that takes its origins in the EDMD formulation from Williams, et al., [5]. This method applies a p-q-quasi norm reduction to the set of observables, limiting the maximum order of the orthogonal polynomials that compose the basis for the approximation. Following the approach for incorporating the system inputs in the EDMD decomposition [3], the overall approach is to approximate the original nonlinear dynamics with a linear operator and to apply linear control methods.

### pqEDMD Model Derivation

Consider an autonomous nonlinear system in

discrete-time, with state variables $x(k) \in \mathbb{R}^n$, discrete-time $k \in \mathbb{Z}_0^+$, and forcing signal $u(k) \in \mathbb{R}^m$, described by the following difference equation:

$$x(k+1) = T\big(x(k)\big) + Bu(k) \tag{1}$$

where $T: \mathbb{R}^n \to \mathbb{R}^n$ is the differentiable vector-valued evolution map, i.e., the nonlinear state transition rule, and $B \in \mathbb{R}^{n\times m}$ is the input matrix, defining the system as input affine. Note that the output of the system is the full state. An orbit of the system is the sequence of states $\{x_i\}_{i=0}^{k}$ that comes from the solution of (1). The sequence is the successive application of the non-linear mapping $T$ from an initial condition $x_0 \in \mathbb{R}^n$ at $k = 0$ and a specific sequence of forcing signals $u \triangleq \{u_i\}_{i=0}^{k-1}$. It is possible to group each orbit in a set of tuples $\{(x_i, y_i, u_i)\}$, where $y_i = T(x_i) + Bu_i$. Then, organize these tuples into the data matrices,

$$X = [x_1 \quad \dots \quad x_N],\ Y = [y_1 \quad \dots \quad y_N],\ U = [u_1 \quad \dots \quad u_N]. \tag{2}$$

The rationale behind the approach is to get linear predictors of a function space of observables $\Psi(x) = [\psi_1(x), \cdots, \psi_d(x)]^\top: \mathbb{R}^n \to \mathbb{C}^d$, where the elements of the function space come from a family of orthogonal polynomials, and the use of q-quasi norms with a maximum order p to reduce the maximum order and quantity of elements in the observables [7]. The condition that these observables must satisfy is:

$$\Psi(y) = A\Psi(x) + Bu + r(x,u) \tag{3}$$

where $r(x,u) \in \mathcal{F}$ is the residual term to minimize in order to find matrices $A$ and $B$. This leads to the least squares problem,

$$\|r(x,u)\|^2 = \frac{1}{N}\sum_{i=1}^{N}\frac{1}{2}\|\Psi(y_i) - A\Psi(x_i) - Bu\|_2^2.$$

The evaluation of the data matrices (2) with the set of observables produces the observed data matrices $\Psi(\{X,Y\}) \in \mathrm{R}^{d\times N}$. Then, from the singular value decomposition of the observed state $\Psi(X)^T = \mathcal{U}\mathcal{S}\mathcal{V}^T$, it is possible to determine the effective rank of $\Psi(X)$ using the singular values $\sigma_1, \sigma_2, \cdots, \sigma_d = \mathrm{diag}(\mathcal{S})$. The effective rank or $\epsilon$-rank $r_\epsilon = \min\{r: \sigma_r \le \epsilon N \sigma_1\}$, where $\epsilon << 1$, an arbitrarily small number, e.g., eps in Matlab.

From the effective rank, $\mathcal{U}_r = \mathcal{U}_{:,1:r_\epsilon}$, $\mathcal{S}_r = \mathcal{S}_{1:r_\epsilon,1:r_\epsilon}$ and $\mathcal{V}_r = \mathcal{V}_{:,1:r_\epsilon}$, and the solution becomes:

$$\begin{aligned} D_r &= \mathcal{S}_r \backslash \mathcal{U}_r^T \Psi(Y)^T \\ [A \quad B]^T &= \mathcal{V}_r D_r. \end{aligned} \tag{4}$$

Notice that the solution for the transition matrix $A$, i.e., equation (4), cannot guarantee the convergence of the function space into a stable attractor, i.e., $A$ may not be Hurwitz (all the magnitudes of its eigenvalues less or equal to one). Then, some solutions for some p-q parametrization give trajectories of observables that diverge to infinity. This guarantee is an open problem and highlights the importance of testing many combinations of p-q parameters on a particular dataset.

As the purpose of linear predictors, as in (3), is the synthesis of controllers, it is necessary to recover the state from the observables. Usually, the recovery of the state requires the solution of an additional least squares problem. Instead, we exploit the structure of the order-one polynomials in the set of observables and recover the state analytically. The order-one polynomials are linear functions of the individual states. Therefore, the $C$ matrix comes from converting the inverse of the order-one polynomials into a matrix form.

$$C = \Big[c_p \quad ; \quad \mathrm{diag}\{\psi_i^{-1}(x)\}_{i=1}^{n}; \quad 0_{(n,d-n-1)}\Big] \tag{5}$$

where $c_p \in \mathbb{R}^n$ is a vector where every element is the constant term of the order-one polynomials. This vector is concatenated with a diagonal matrix of the transformation into matrix form of the function inverse of the non-constant term of the order-one observables. The remaining entries for the higher-order polynomials are zero. The result is a linear operator $A$ acting on a function space $\Psi$ and an input matrix $B$. The linear time-evolution of the functions $\psi(x) \in \Psi(x)$ is related to the nonlinear time-evolution of the state $x$. Matrix $C$ achieves the transformation back to the original state space. Hence, the original nonlinear system (1) becomes:

$$\begin{aligned} \Psi\big(x(k+1)\big) &= A\Psi\big(x(k)\big) + Bu(k) \\ x(k) &= C\Psi\big(x(k)\big), \end{aligned} \tag{6}$$

## pqEDMD for MPC

For driving the system into a desired state, consider a model predictive control algorithm adapted from [9], and an MPC formulation in a function space similar to the developments by Korda et al. [3]. The objective is to find a sequence of inputs $u_k$ starting at the $k^{\text{th}}$ output measurement time-instant that spans a control horizon $N_c$, the sequence of inputs, drives the system to a desired output by minimizing a cost function over a prediction horizon $N_p$ while satisfying some input/output inequality constraints. The MPC formulation over the function space is

$$\begin{aligned} \min_u J(x,u) = &\sum_{i=0}^{N_p-1}\Big(\Psi_{\text{dev}}\big(x(i)\big)^T Q_\psi \Psi_{\text{dev}}\big(x(i)\big)\Big) \\ &+ \sum_{i=0}^{N_c-1}\big(u(i)^T Q_u u(i)\big) \\ &+ \Psi_{\text{dev}}\Big(x(N_p)\Big)^T F_\psi \Psi_{\text{dev}}\Big(x(N_p)\Big) \end{aligned} \tag{7}$$

subject to

$$u_{\min} \le u^i \le u_{\max}$$

where $\Psi_{\text{dev}}\big(x(i)\big) = \Psi\big(x(i)\big) - \Psi\big(x_{\text{ref}}(i)\big)$, the difference of the function space with its reference. The symmetric matrices $Q_\psi, F_\psi \in \mathbb{R}^{d\times d}$ are the weight matrices for the state sequence, and the terminal state and the symmetric matrix $Q_u \in \mathbb{R}^{m\times m}$ is the weighting matrix for the control inputs. The weighting matrix $F_\psi$ of the terminal state accounts for different prediction and control horizons and imposes a suitable terminal constraint to ensure stability. In contrast with the traditional MPC formulation, equation (7) is an objective function in the function space and

not the state space of a traditional linear system. It is necessary to transform the formulation (7) into a quadratic program in the function space, i.e., a quadratic objective function $\Delta u^T H \Delta u + h^T \Delta u$ with linear constraints $L\Delta u < b$, that has a solution using a standard solver.

The first step is to derive the observable weighting matrices $Q_\psi$ and $F_\psi$ from selected output weighting matrices $Q_y$ and $F_y$. The first method is to exploit the output matrix $C$ from the pqEDMD solution, i.e.,

$$Q_\psi = C^T Q_y C, \tag{8}$$

This formulation restricts the MPC optimization to the convergence of the order-one polynomials to their reference values, neglecting the fact that the remaining elements in the observables also depend on the outputs. Even if that is the case, formulating $Q_\psi$ this way gives good results and fast convergence. The second method uses the observables to transform the matrix,

$$Q_\psi = \text{diag}\left(\Psi\left(\text{diag}(Q_y)\right)\right) \tag{9}$$

This method weighs all the observables in the basis and should produce more accurate solutions. Performance-wise, the convergence of this solution is slower, and it may break the feasibility of the quadratic problem. These methods also apply to calculating $F_\psi$.

Continuing with the translation of the problem into a quadratic program, consider the solution of the identified dynamics in the function space $\Psi(x)$, a solution of (6) from an initial condition $x(0)$, and a sequence of inputs $\{u_i\}_{i=0}^{k-1}$ up to an arbitrary time $k$,

$$\Psi\big(x(k)\big) = A^k \Psi\big(x(0)\big) + \sum_{j=0}^{k-1} A^{k-1-j} B u(j), \tag{10}$$

Stacking up the state and the input sequences in column vectors and applying the solution of the pqEDMD (10) from a time-step $k$ and up to a prediction horizon $N_p$ gives

$$\underbrace{\begin{bmatrix} \Psi\big(x(k+1)\big) \\ \Psi\big(x(k+2)\big) \\ \vdots \\ \Psi\left(x(k+N_p)\right) \end{bmatrix}}_{\Psi_X} = \hat{A}\Psi\big(x(k)\big) + \hat{B} \underbrace{\begin{bmatrix} u(k) \\ u(k+1) \\ \vdots \\ u(k+N_c) \end{bmatrix}}_{\hat{U}} \tag{11}$$

where $\hat{A}$ and $\hat{B}$ are the block matrices that relate the initial evaluation of the observables $\Psi\big(x(k)\big)$ and the sequence of inputs $U$ to the sequence of observables $\Psi_X$,

$$\hat{A} = \begin{bmatrix} A \\ A^2 \\ \vdots \\ A^{N_p} \end{bmatrix}, \; \hat{B} = \begin{bmatrix} B & 0 & \cdots & 0 \\ AB & B & \cdots & 0 \\ \vdots & \vdots & \ddots & \vdots \\ A^{N_p-1}B & A^{N_p-2}B & \cdots & B \end{bmatrix}, \tag{12}$$

where the number of block columns in $\hat{B}$ depends on the control horizon. In addition to the compact form of the sequence of observables (11), the compact form of the objective function (7) is,

$$J(x,u) = \; (\Psi_X - \Psi_{\text{ref}})^T Q_\Psi (\Psi_X - \Psi_{\text{ref}}) + U^T Q_U U, \tag{13}$$

where $Q_\Psi$ is a block diagonal matrix with the observable matrix repeated $N_p$ times along the diagonal and with $F_\psi$ as the final element, and $Q_U$ is a block diagonal matrix with the weighting matrix for the control input repeated $N_c$ times along the diagonal,

$$\begin{aligned} Q_\Psi &= \; \text{diag}\left(\{Q_\psi\}_{i=1}^{N_p}, F_\psi\right), \\ Q_U &= \; \text{diag}\left(\{Q_u\}_{i=1}^{N_c}\right). \end{aligned} \tag{14}$$

With the definition of the sequence of observables and the objective function in compact form, replacing solution (11) into (13) and expanding produce a quadratic element and a linear element in $U$, among other terms that do not depend on $U$, i.e.,

$$\begin{aligned} J(x,u) = \; & U^T \hat{B}^T Q_X \hat{B} U + U^T Q_U U \\ & + 2\left(\hat{A}\Psi\big(x(k)\big) - \Psi_{\text{ref}}\right)^T Q_\Psi \hat{B} U + r(x) \end{aligned} \tag{15}$$

where $r(x)$ are the terms that do not depend on $U$. Then, from (15) the Hessian is

$$H = \hat{B}^T Q_\Psi \hat{B} + Q_U, \tag{16}$$

and from the linear term of the compact cost function (15), the linear term of the quadratic program becomes

$$h^T = 2\left(\hat{A}\Psi\big(x(k)\big) - \Psi_{\text{ref}}\right)^T Q_\Psi \hat{B}, \tag{17}$$

that satisfies the objective of having the problem as a quadratic program, meaning that it is possible to calculate the optimal sequence of inputs via a standard solver, e.g., quadprog() in Matlab.

## BIOPROCESS APPLICATION

Consider a continuously stirred tank reactor (CSTR), where an arbitrary biological species grows on a substrate.

Assuming that both substrate and biomass concentrations are measurable, it is possible to get a description of their dynamics by applying a mass balance, resulting in the following differential equations:

$$\begin{aligned} \dot{x_1} &= x_1(\mu(x_2) - D), \\ \dot{x_2} &= D\big(x_{2,f} - x_2\big) - \frac{\mu(x_2) x_1}{\eta}, \end{aligned} \tag{18}$$

where $x_1$ is the first state, representing the biomass concentration $x_2$ is the second state, representing the substrate concentration, and $x_{2,f}$ is substrate inlet concentration, and a Haldane kinetics law represents the growth rate:

$$\mu(x_2) = \frac{\mu_{\max} x_2}{k_m + x_2 + k_1 x_2^2}, \tag{19}$$

where the parameter $\mu_{\max}$ is the maximum specific growth rate, $k_m$ is the activation constant, and $k_1$ is the inhibition constant. Finally, $\eta$ is the process yield and $D = F/V$ $[h^{-1}]$ the dilution rate. The following assumes that the bioreactor operates in chemostat mode (continuous feeding with constant volume). Table 1 reports the

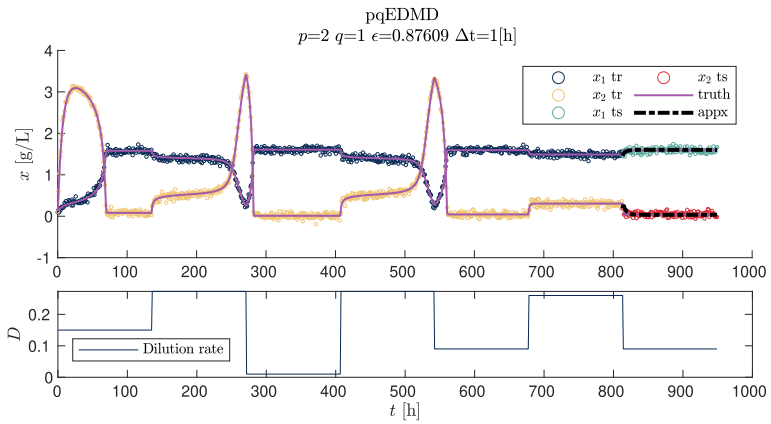



**Figure 1:** pqEDMD identification with fast sampling and high level of noise.

process parameter values.

**Table 1:** Reactor Parameters.

| Symbol | Value | Units |
|---|---|---|
| $\mu_{max}$ | 0.4 | [h$^{-1}$] |
| $k_m$ | 0.12 | [g/L] |
| $k_1$ | 0.4545 | [g/L]$^{-1}$ |
| $\eta$ | 0.4 | [-] |

# NUMERICAL RESULTS

## Model Training and Testing

To have a rich enough dataset for identification, it is necessary to select the time evolution of the dilution rate and the duration of the experiment. Two additional parameters determine the algorithm's performance: the sampling rate and the standard deviation of the measurement noise. For the time evolution of the dilution rate, the choice is a sequence of inputs that switch the convergence of the trajectories between the two asymptotically stable points. For the sampling and noise, we will consider three different scenarios that cover different values of the parameters: a scenario with fast sampling and low levels of noise, a second case, where we increase the uncertainty in the measurement, and a third, where we decrease the sampling rate. Table 2 shows the exact values of these parameters in the description of each scenario. For illustration, Figure 1 shows the second case, where there is fast sampling and high levels of noise.

In each scenario, the data set is made of a single experiment that starts from low values of biomass and substrate and is subject to 7 different steps of dilution rate, where each step has the same duration. With fast sampling, the data sets contain 951 points. The first 6 steps correspond to the training (814 points), while the rest (137 points) constitute the testing set. With slow sampling, there are 191 points in total, 162 for training, and 29 for testing.

It is possible to apply pqEDMD with a variety of orthogonal polynomials. In this application, their choice is not critical, and the following algorithm implementation uses Legendre polynomials. For some other applications, the choice of polynomials may be important. Also, for applications where the order of magnitude of the different measurements is not the same, normalizing the data may improve the numerical conditioning of the methods. This aspect is also not influential in the present application.

Each element of the observables comes from the product of univariate polynomials with a particular order $\alpha_j$ for each state variable $x_j$ being *observed /evaluated*. Therefore, it is possible to define each observable via a nonnegative vector $\alpha \in \mathbb{N}_+^n$ containing the set of integers corresponding to the orders of the univariate polynomials. A particular element of the set of observables is

$$\psi = \prod_{j=1}^{n} \pi^{\alpha_j}(x_j), \tag{20}$$

where $\pi^{\alpha_j}(x_j)$ is a univariate element from a family of orthogonal polynomials of order $\alpha_j$. It is possible to apply a selection criterion to each vector of integers $\alpha$ based on a q-quasi norm, which imposes a maximum order $p$,

$$\alpha = \{\alpha \in \mathbb{N}_+^n : \|\alpha\|_q \leq p\}, \tag{21}$$

where $\|\alpha\|$ is the q-quasi norm of the set of orders, and $p \in \mathbb{N}$ is a positive integer that determines the maximum order of the multivariate polynomial function $\psi$. The definition of a q-quasi norm of a vector $\alpha$ is

$$\|\alpha\|_q = \left(\sum_{i=1}^{n} \alpha_i^q\right)^{\frac{1}{q}}, \tag{22}$$

where $q \in \mathbb{R}$ defines the quasi norm, and the cardinality of the vector is $n$ because each element represents the order of a univariate polynomial for each of the $n$ states in the original system. In general, it is not a norm because $q$ can take noninteger values (for those cases, equation (22) does not satisfy the triangle inequality).

**Table 2:** Empirical error p-q parameters and basis size for the best performing and worst performing sets of observables from the p-q sweep.

| | Scenario | | | | | | | | | | | |
|---|---|---|---|---|---|---|---|---|---|---|---|---|
| | (1) $\Delta t = 1$ [h], $\sigma = .005$ [g/L]$^2$ | | | | (2) $\Delta t = 1$ [h], $\sigma = .05$ [g/L]$^2$ | | | | (3) $\Delta t = 4$ [h], $\sigma = .05$ [g/L]$^2$ | | | |
| $p$ | 4 | 5 | 5 | 4 | 2 | 2 | 5 | 5 | 2 | 2 | 3 | 3 |
| $q$ | 2.5 | 1.5 | 0.5 | 2.0 | 1.0 | 0.5 | 0.5 | 1.5 | 0.5 | 1.0 | 0.5 | 1.0 |
| $d$ | 18 | 24 | 12 | 17 | 6 | 5 | 12 | 24 | 5 | 6 | 7 | 10 |
| $\epsilon$ | 0.17 | 0.18 | 0.21 | 0.22 | 0.84 | 0.87 | 1.12 | 1.14 | 0.91 | 0.96 | 1.32 | 1.33 |

By applying a p-q norm reduction to the polynomial orders, we can significantly reduce the number of observables and their maximum order. This, in turn, enhances the algorithm's numerical accuracy and reduces computational time.

The answer to the question of the optimal p-q parameters to use for a particular dataset is still open. Large values of p-q pairs produce higher order polynomials, which increase the computational complexity of the algorithm without a guarantee of a more accurate approximation. The same effect applies to the uncertainties in the measurements, high-order polynomials tend to amplify the noise leading to unfeasible solutions. Therefore, the method to find the best combination is to perform a sweep over a set of candidate values. For each scenario, the candidate values are $p = [2\ 3\ 4\ 5]$ and $q = [0.5\ 1\ 1.5\ 2\ 2.5]$, giving 13 sets of unique observables to test (some combinations of p-q parameters give redundant sets of observables). Table 2 shows a summary of the results for the three scenarios, where $\epsilon$ is the empirical error of the test set that comes from the solution of (6) from the initial conditions of the test set and the application of the last step of the dilution rate. The definition of the empirical error is

$$\epsilon = \frac{1}{N}\sum_{i=1}^{N}\frac{|\hat{y}_i - y_i|}{|y_i|}, \tag{23}$$

where $\hat{y}$ is the approximation of the output and $y$ is the output from the dataset.

The results from Table 2 show that for the same underlying dynamics, there is no unique pair of p-q parameters that fit the data. In a deterministic case (no noise), with a very fast sampling time $\Delta t = 0.001$ [h] the *optimal* p-q pair is the same as the best approximation for the scenario with fast sampling and low levels of noise, but it is different from the other two scenarios. If the experimental setup involves a slow sampling, like the third scenario, the best p-q pair for the deterministic case produces a pqEDMD solution that diverges, highlighting the importance of a p-q sweep.

The experiments vary the dilution rate between low and high values. The high value of the dilution rate $D = 0.273$ gives the wash-out point a big region of attraction. Then, the value of the biomass starts to slowly decay until a change in the dilution rate brings the state back to the desired attractor (i.e., operating point). These changes in the concentrations of biomass and substrate give the pqEDMD the necessary information to characterize the system. Otherwise, without this dynamic spectrum, it would be necessary to perform more experiments with varying initial conditions.

In conclusion, it is possible to identify the dynamics of the nonlinear CSTR reactor via the pqEDMD algorithm when there is enough information on the system dynamics in an experimental dataset. The choice of orthogonal polynomials under a p-q-quasi norm reduction makes the algorithm versatile enough to identify the dynamics accurately. The advantage of having a linear representation of a dynamical system in a function space is the interpretability of the system, from the spectrum of the $A$ matrix to the analysis via theoretical concepts like the Koopman operator (restricted to the case where the pqEDMD converges to the operator).

## Linear Model Predictive Control

Figure 2 shows the application of the MPC control adapted to work in a function space instead of a state space for the three scenarios. Table 3 lists the controller parameters, which are the same across all scenarios.

**Table 3:** MPC parameters.

| Symbol | Value | Units |
|---|---|---|
| $N_p$ | 10 | [-] |
| $N_c$ | 7 | [-] |
| $Q_y$ | $\begin{bmatrix}1 & 0\\ 0 & 0\end{bmatrix}$ | [-] |
| $Q_u$ | 0.5 | [-] |
| $F_y$ | $\begin{bmatrix}1 & 0\\ 0 & 0\end{bmatrix}$ | [-] |
| $u_{\min}$ | 0.01 | [h$^{-1}$] |
| $u_{\max}$ | 2 | [h$^{-1}$] |

The choice of output weighting matrices $Q_y$ and $F_y$ only penalizes the biomass. The prediction and control horizons are obtained by trial and error. The convergence of the controller is influenced by the choice of transformation matrix $Q_y$ into $Q_\psi$, either using equation (8) or (9). For datasets with low noise (the first scenario), the algorithm performs better if the transformation comes from the first option. The second option achieves better

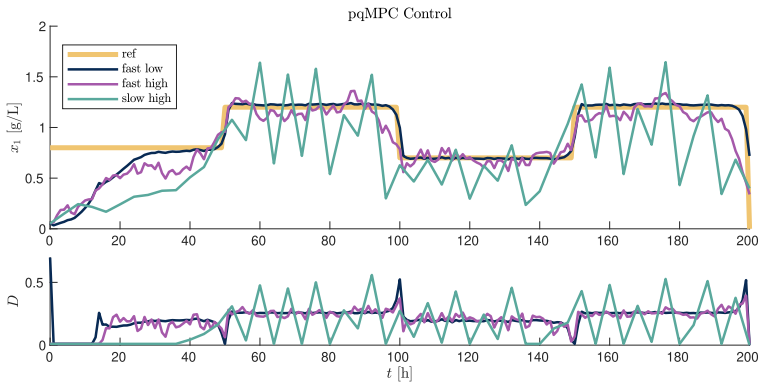



**Figure 2:** Linear Model Predictive Control for the three scenarios.

results for the experiment with a high noise level.

We observe a deviation from the setpoint in the scenario with a high noise level (notice the performance of the tests with high noise levels in Figure 2). This error is caused by the noise because, at every optimization step, it is necessary to know the evaluation of the function space, i.e., $\Psi(x(k))$ in (17). To obtain this value, it is required to *lift* the previous output with the set of observables, an output that has been corrupted with noise. Therefore, the next step in improving the algorithm is to develop a state observer to work in the function space and update the value of the function space at each optimization step.

## CONCLUSIONS

This paper implements a complete data-driven workflow for controlling a simple bioprocess. It uses the pqEDMD algorithm to model the dynamics and a traditional MPC controller adapted to work on the pqEDMD's function space. The main methodological developments are the application of a singular value decomposition to the regression matrix to get the effective rank and improve the approximation of the ordinary least squares. This study also shows how to adapt the traditional model predictive control formulation to work with the particularities of the function space of the pqEDMD. This study shows that EDMD approximations can be interesting alternatives to neural networks, as they provide a linear system representation in a function space where linear estimators and controllers can be developed. The conditions to satisfy for a successful implementation are the convergence of the pqEDMD to a stable solution and the feasibility of the MPC solutions, which depend on the information content of the training data and the selection of tuning parameters in the pqEDMD algorithm and the MPC.

## REFERENCES


1. Koopman BO. Hamiltonian Systems and Transformation in Hilbert Space. Proceedings of the National Academy of Sciences. 1931;17:315–8
2. Budišić M, Mohr R, Mezić I. Applied Koopmanisma. Chaos: An Interdisciplinary Journal of Nonlinear Science. 2012;22:047510.
3. Korda M, Mezić I. Linear Predictors for Nonlinear Dynamical Systems: Koopman Operator Meets Model Predictive Control. Automatica. 2018;93:149–60.
4. Korda M, Mezić I. On convergence of extended dynamic mode decomposition to the koopman operator. Journal of Nonlinear Science. 2018;28:687–710.
5. Williams MO, Kevrekidis IG, Rowley CW. A Data-Driven Approximation of the Koopman Operator: Extending Dynamic Mode Decomposition. Journal of Nonlinear Science. 2015;25:1307–46.
6. Schmid PJ. Dynamic mode decomposition of numerical and experimental data. Journal of Fluid Mechanics. 2010;656:5–28.
7. Garcia-Tenorio C, Vande Wouwer A. A matlab toolbox for extended dynamic mode decomposition based on orthogonal polynomials and p-q quasi-norm order reduction. Mathematics. 2022;10.
8. Otálora P, Guzmán J.L., Gil J.D., Berenguel M., Acién F.G., Data-driven Model Predictive Control for pH regulation in Raceway Reactors, IFAC-PapersOnLine, 2023;56:2, P. 6223-6228
9. Kouvaritakis B, Cannon M. Model predictive control: Classical, robust and stochastic. 1st ed. Springer; 2015.



© 2025 by the authors. Licensed to PSEcommunity.org and PSE Press. This is an open access article under the creative commons CC-BY-SA licensing terms. Credit must be given to creator and adaptations must be shared under the same terms. See https://creativecommons.org/licenses/by-sa/4.0/

Systems & Control Transactions

**Research Article - Peer Reviewed Conference Proceeding**
ESCAPE 35 - European Symposium on Computer Aided Process Engineering
Ghent, Belgium. 6-9 July 2025
Jan F.M. Van Impe, Grégoire Léonard, Satyajeet S. Bhonsale,
Monika E. Polańska, Filip Logist (Eds.)

PSE PRESS

# Deacidification of Used Cooking Oil: Modeling and Validation of Ethanolic Extraction in a Liquid-Liquid Film Contactor

**Sergio A. Rojas[a]*, Álvaro Orjuela[a], and Paulo C. Narváez[a]**

[a] Universidad Nacional de Colombia, Department of Chemical and Environmental Engineering, Bogotá D.C., Colombia
* Corresponding Author: sarojasp@unal.edu.co.

## ABSTRACT

Large quantities of used cooking oil (UCO) are produced globally, primarily in densely populated urban centers. Although UCO is highly heterogeneous due to degradation during cooking, it still contains a significant fraction of triacylglycerols (TG) that could be used as raw materials in oleochemical biorefineries. A major challenge in reintegrating this residue into productive cycles is the presence of free fatty acids (FFA), which can affect subsequent catalytic or enzymatic transformations. Conventional processes for FFA removal are energy-intensive, require alkaline feedstocks, and generate problematic residues. To overcome these issues, alcoholic extraction of FFA is considered a promising pretreatment for UCO, enabling the extraction of FFA for subsequent esterification. In this regard, liquid-liquid film contactors (LLFC) have shown potential to intensify FFA extraction because they operate under mild conditions and at laminar flow regime, reducing energy consumption and enhancing productivity. This work presents the modeling and validation of a FFA extraction process suitable for deacidifying UCO using a LLFC with ethanol as a solvent. Experimental data were used to fit model parameters, which were optimized using a genetic algorithm. The validated LLFC model revealed that increasing the UCO mass flow rate and the ethanol-to-UCO ratio enhanced FFA mass transfer. Furthermore, a cascade configuration of three LLFCs was able to reduce the FFA content in UCO to 0.9 wt.%. It is anticipated that this technology will enable the pretreatment of UCO for further transformation into value-added oleochemicals and facilitate the exploitation of recovered FFA via subsequent ethanolic esterification.

**Keywords**: Liquid-liquid film contactor, used cooking oil, free fatty acids, mathematical modeling, genetic algorithm, liquid extraction.

## INTRODUCTION

Economic growth and lifestyle improvement of modern society have caused negative environmental impacts. Food waste generation is one such impacts, thus becoming a major challenge for sustainable development. Among the different types of food waste, post-consumption waste lipids are particularly problematic residues because they are produced in large volumes and present significant management challenges for densely populated urban areas. These residues include used cooking oil (UCO), lipids extracted from high-fat-content food waste (e.g. fried foods, sauces, dressings, dairy products), grease leached from cooking meats, grease from traps, oils from expired food (e.g mayonnaise, tuna cans), among others [1]. The generation of such residues is continually increasing due to the growing consumption of fast and industrialized food products [2], [3].

Among the different waste lipids, UCO is of major interest because they are inevitably produced when using vegetable oils and fats for food preparation. Edible vegetable oils (EVO), primarily composed of triacylglycerols (TG), undergo several chemical and physical changes that affect their quality. During cooking at high temperatures (≥150 ºC) and in the presence of air and moisture, EVO degrades generating changes in color, odor and producing harmful compounds potentially dangerous for human health. As a result, usable lifespan of

EVO is limited, and it must be discarded as UCO after certain time. The main decomposition reactions during frying include oxidation, hydrolysis, dehydration, cracking and polymerization. These reactions produce compounds such as aldehydes, alcohols, epoxides, oxidated sterols, free fatty acids (FFA), monoacylglycerols, diacylglycerols, cyclic monomers and nonpolar oligomers. However, main fraction of UCO (>90 wt.%) remains as mono-, di-, and triacylglycerols, making this residue a potential feedstock for oleochemical industry [4], [5].

Despite the reuse potential, a high FFA content in UCO can significantly affect the transformation of TG into high-value-added chemicals. Conventional treatments for reducing acidity are classified as either chemical or physical refining, depending how FFA are separated from UCO. In chemical refining FFA are neutralized with alkaline solutions, while in physical refining they are stripped from the oil using steam at high temperatures and low pressures. Despite their effectiveness, both methods have drawbacks. Chemical refining requires high water consumption to remove the formed soaps, generating large amounts of aqueous effluents and causing significant losses of neutral oil. In contrast, physical refining is highly energy-intensive, requiring high pressure steam, vacuum conditions and elevated temperatures, which further degrade TG [6].

To address these challenges, solvent deacidification has been extensively studied as an alternative since it can be performed at mild conditions, reducing energy consumption and avoiding the formation of toxic compounds. This process can be carried out using liquid-liquid film contactors (LLFC), originally developed for sulfur removal in fossil fuels [6]. These devices maximize the contact area between two fluid phases by employing a semi-structured packing system, preventing one phase from dispersing into the other. The co-current ethanolic extraction of FFA from UCO has been studied using this equipment, and the separation efficiency was assessed with respect to oil mass flow rate, oil-to-ethanol flow ratio and contactor's length [4]. Results indicate that the process is feasible and its scale-up must be further explored. Similarly, it has been reported that the acidity of refined, deodorized and bleached palm oil could be reduced by 51% when a single-stage LLFC is used, and that multiple-stage contactors would be necessary to reduce the FFA content to meet the specifications required by the international vegetable oil and UCO markets [6].

In this context, modeling of FFA ethanolic extraction from UCO using a LLFC is essential for defining suitable configurations and processing conditions for further scaling up. In this regard, a mathematical model based on mass transfer correlations was assessed to describe FFA extraction from UCO using a LLFC. This model was adapted from a previous study [6], and it assumed that the rate-controlling step in the process is the mass transfer of FFA from the bulk oil phase to oil-solvent interface. Based upon reported experimental data [4], this work is focused on adjusting a new set of model parameters to effectively describe deacidification of UCO via ethanolic extraction using a LLFC. The model is intended to be used in scale up and further feasibility assessments.

## METHODOLOGY

### Liquid-liquid film contactor configuration

The LLFC is part of a system that enables the continuous deacidification of UCO. This system consists of two tanks used to store UCO and ethanol, which are placed on their respective scales (Mettler Toledo GmbH, Schwerzenbach, Swizerland). This enabled to calculate operating mass flow rates by measuring the change in mass over time. Each tank was connected to an HMS EXT 2001 metering pump (EMEC Srl, Vazia, Italy) that transported the fluids throughout the unit. Prior to entering the LLFC, the fluids were heated independently using silicon shielded electric resistors equipped with temperature controllers (SHIMADEN SR 91, Japan). After heating, each fluid was fed to the LLFC at the specified operating temperature and put in contact to facilitate FFA mass transfer. The effluent of the LLFC went into a decanter, where both phases separated. Figure 1 presents a simplified schematic of this process unit.

The LLFC consisted of an SS304 column (ID = 0.023 m) packed with 3400 metallic threads (OD = 2.5 x $10^{-4}$ m). The packing provided high interfacial area between phases and enhanced FFA extraction from UCO. Additionally, the contactor was equipped with a jacket to enable the use of a heating service, allowing the extraction to be conducted at a constant temperature. The oil phase was fed into the top of the contactor and flowed downward forming a film around each thread inside the column. On the other hand, the alcoholic phase was fed into the contactor 20 cm below the oil phase nozzle to ensure the formation of a film over the oil phase. Then, FFA were transferred from the inner oil film to the outer alcoholic film due to the different chemical potentials in both phases. This configuration is shown in Figure 2b.

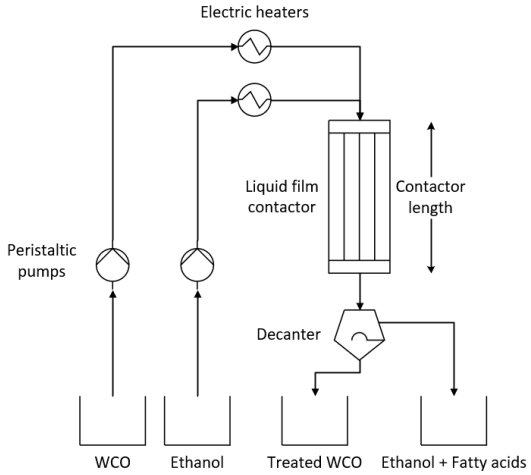



**Figure 1.** Diagram of the process unit.

## Mathematical model of LLFC

In systems with strong mass transfer resistance the rate-controlling step is the transport of the components from the bulk phase to the interface. FFA are transferred from the oil phase to the alcohol phase, passing through the interface. Since the viscosity of the oil phase is significantly higher than that of the alcoholic phase, the transfer of FFA from oil to the interface is considered the rate-controlling step in this extraction process [6]. The general equation for mass transfer within the contactor is presented in Equation (1), where $F_i$ is the mass flow rate of component i, Z is the position inside the contactor, $A_T$ is the area available for mass transfer, $k_i$ is the global mass transfer coefficient, $C_i^I$ is the concentration of component i in the bulk oil phase and $C_i^{I,EQ}$ is the equilibrium concentration of component i at the interface.

$$\frac{dF_i^I}{dZ} = A_T k_i (C_i^I - C_i^{I,EQ}) \quad (1)$$

Equation (1) can be applied to triacylglycerol (TG), free fatty acids (FFA), and ethanol (ET). Additionally, the mass transfer area can be expressed in terms of the number of threads inside the contactor ($n_{pack}$).

$$\frac{dF_{TG}^I}{dZ} = -\pi D_{pack} n_{pack} k_{TG}^I \rho_{Mix} (w_{TG}^I - w_{TG}^{I,EQ}) \quad (2)$$

$$\frac{dF_{FFA}^I}{dZ} = -\pi D_{pack} n_{pack} k_{FFA}^I \rho_{Mix} (w_{FA}^I - w_{FA}^{I,EQ}) \quad (3)$$

$$\frac{dF_{ET}^I}{dZ} = -\pi D_{pack} n_{pack} k_{ET}^I \rho_{Mix} (w_{ET}^I - w_{ET}^{I,EQ}) \quad (4)$$

$$\frac{dF_{TG}^{II}}{dZ} = -\frac{dF_{TG}^I}{dZ} \quad (5)$$

$$\frac{dF_{FFA}^{II}}{dZ} = -\frac{dF_{FFA}^I}{dZ} \quad (6)$$

$$\frac{dF_{ET}^{II}}{dZ} = -\frac{dF_{ET}^I}{dZ} \quad (7)$$

To solve the mass transfer equations throughout the contactor, it is necessary to calculate the global mass transfer coefficients along the contactor. The following expressions were used for this purpose [6]:

$$k_{TG}^I(Z) = C_1 Sc_I^{C4} Re_I^{C5} \left(\frac{D_{TG-MixI}}{\delta_I}\right) \quad (8)$$

$$k_{FFA}^I(Z) = C_2 Sc_I^{C4} Re_I^{C5} \left(\frac{D_{FA-MixI}}{\delta_I}\right) \quad (9)$$

$$k_{ET}^I(Z) = C_3 Sc_I^{C4} Re_I^{C5} \left(\frac{D_{ET-MixI}}{\delta_I}\right) \quad (10)$$

The parameters $C_1$, $C_2$, $C_3$, $C_4$ and $C_5$ can be obtained by regression through comparison of the model with experimental data [4]. To determine the diffusivities required in Equations (8) to (10), Equation (11) was used [7], where x is the associating factor of the solvent, M is the molar weight of the solvent, T is the system temperature, $\eta$ is the dynamic viscosity of the solvent, and V is the solute molal volume.

$$D = 7.4x10^{-8} \frac{(xM)^{\frac{1}{2}} T}{\eta V^{0.6}} \quad (11)$$

Another required variable in Equations (8) to (10) is $\delta_I$, the film thickness of the oil phase around a thread. This quantity is calculated from a momentum balance applied to a differential volume of a thread as presented in Figure 2a. In that Figure, the red arrows represent the direction of momentum flow. Since a no-slip condition is assumed at the thread surface, the velocity at this point is zero, while the fastest fluid layer is the farthest from the thread surface. In this scenario, momentum flows from the outer region toward the inner region. Applying a momentum balance to this volume yields the following equations, which are solved simultaneously to determine $a$ and $b$, which are dimensionless factors related to the oil and ethanol film thickness, respectively.

$$2a^2 - a^4 - a + 2\beta a^2 \left(2\ln(a) - 1 + \frac{1}{a^2}\right) - \psi_1 = 0 \quad (12)$$

$$2\lambda\left(\left(\frac{b}{a}\right)^2 - 1\right) - \left(\left(\frac{b}{a}\right)^4 - 1\right) + 2b^2\left(\left(\frac{b}{a}\right)^2\left(2\ln\left(\frac{b}{a}\right) - 1\right) + 1\right) - \psi_2 = 0 \quad (13)$$

$$\psi_1 = \frac{8\mu_I Q_{pack}^I}{\pi \rho_I g R_{pack}^4} \quad (14)$$

$$\psi_2 = \frac{8\mu_{II} Q_{pack}^2}{\pi \rho_{II} g R_{pack}^4} \quad (15)$$

$$\beta = \left(b^2 \frac{\rho_{II}}{\rho_I} + a^2\left(1 - \frac{\rho_{II}}{\rho_I}\right)\right) \quad (16)$$

$$\lambda = \left(a^2 + \frac{\rho_I \mu_{II}}{\rho_{II} \mu_I}(1 - a^2 + 2\beta\ln(a))\right) \quad (17)$$

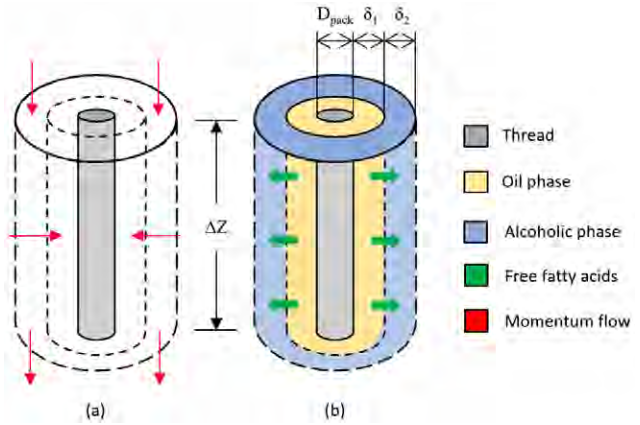



**Figure 2.** (a) Differential volume over a thread within the contactor; (b) FFA mass transfer between liquid films

## Implementation of the mathematical model of LLFC

The mathematical model of the LLFC was programmed in Python, and Euler's method was used to solve the differential mass balance equations (2) to (7). This numerical integration required the definition of a small step in the integration variable to ensure stability and good performance. In this case, the integration variable was the contactor's length, and the number of steps was set to 1000 to maintain stability during the solution process.

The initial conditions for solving the LLFC model included the mass flow rates of UCO and ethanol, the mass concentration of each component in both phases, the operating temperature and the total contactor's length to be integrated. The components considered were triacylglycerol, oleic acid (representing the free fatty acids in UCO), ethanol and water; however, the mass transfer of water was not included to simplify the model and to avoid the regression of an additional parameter. This assumption is supported by experimental results indicating that the extracted UCO moisture content was lower than 1.3 wt.% [4].

The next step involved determining the liquid-liquid equilibrium (LLE) of the system using validated models available in Aspen Plus. The UNIFAC-LL thermodynamic model was applied, and its binary interaction parameters values were updated to better fit the experimental LLE data [8]. The corresponding equilibrium calculation obtained in Aspen Plus were imported into Python and used in Equations (2) to (4) at each integration step.

Subsequently, determining the thickness and velocity of each film required the density and viscosity values of both fluids. The density of the liquid mixture of each phase was calculated using the molar volumes of the pure components and their molar fractions. The pure liquid molar volumes of the components were obtained from the Rackett model [9]. Meanwhile, the liquid mixture viscosity was estimated using the modified Andrade equation [10].

Next, Equations (8) to (11) were used to estimate the global mass transfer coefficients, followed by applying Euler's method to numerically solve the mass balance equations. The iterative process continued until the step position reached or exceeded the total contactor's length, at which point the iteration stopped, and the final component concentrations were obtained. A simplified scheme of the computation algorithm is presented in Figure 3.

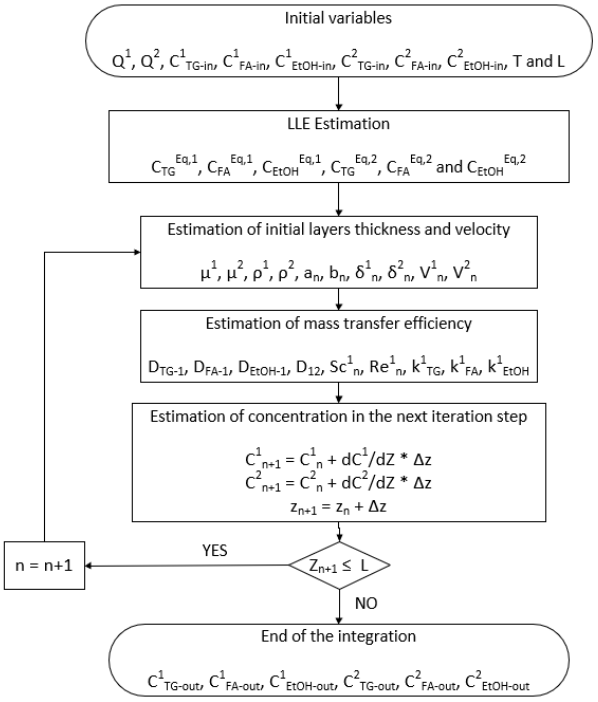



**Figure 3.** Solution algorithm of LLFC model.

The dimensionless parameters $C_1$ to $C_5$ were determined through regression using a genetic algorithm implemented in Python with the PyGAD library. This optimization procedure minimized the differences between the calculated and experimental mass fractions, as described in Equation (18), where E represents the number of experiments, P the number of phases and C the number of considered components. The total error was normalized by the number of measured concentrations to calculate an average relative error.

$$\min\left(\sum_k^E \sum_j^P \sum_i^C \frac{\left|w_{ijk}^{calc} - w_{ijk}^{exp}\right|}{w_{ijk}^{exp}}\right) \quad (18)$$

The genetic algorithm was executed with 10 generations, each containing 1000 chromosomes. Each chromosome consisted of five genes representing the set of dimensionless parameters. The 100 chromosomes with the lowest average relative error were selected as parents to generate the next generation. The steady-state

selection method was employed, and mutation was applied randomly at a rate of 15%. Furthermore, the search space for the dimensionless parameters was constrained within the ranges presented in Table 1. The optimization method was executed 80 times, with each starting population of chromosomes randomly generated within the defined search space.

**Table 1.** Search space for the dimensionless parameters $C_1$ to $C_5$

| Parameter | Lower bound | Upper bound |
|---|---|---|
| $C_1$ | $1.0x10^{-10}$ | $1.0x10^{-8}$ |
| $C_2$ | $1.0x10^{-9}$ | $4.0x10^{-8}$ |
| $C_3$ | $1.0x10^{-9}$ | $4.0x10^{-7}$ |
| $C_4$ | 0.0 | 2.0 |
| $C_5$ | 0.0 | 2.0 |

## RESULTS

After executing the optimization algorithm to fit the parameters of the model the values reported in Table 2 were obtained. these are presented with their corresponding lower and upper bounds of the confidence intervals. The objective function value for this parameters set was 507.6, corresponding to an average relative error of 8.46%. As observed, all values felt within 95% confidence intervals with a normal distribution for the computation based on the evaluation of 0.8 million different parameter sets. The average relative deviation of the reported parameters from their lower and upper bounds were 6.77%. This indicates that the obtained set of parameters is unique within the selected search space. moreover, these parameters were similar to those previously obtained in the modeling of a LLFC process for ethanolic deacidification of refined, deodorized and bleached palm oil.

**Table 2.** Mass transfer dimensionless parameters for the FFA extraction of UCO and their confidence intervals using ethanol as solvent in a LLFC

| | $C_1$ | $C_2$ | $C_3$ | $C_4$ | $C_5$ |
|---|---|---|---|---|---|
| Value | 1.23x10$^{-9}$ | 8.30x10$^{-9}$ | 3.99x10$^{-7}$ | 1.92 | 1.54 |
| Lower bound | 6.00x10$^{-10}$ | 7.70x10$^{-9}$ | 3.78x10$^{-7}$ | 1.91 | 1.53 |
| Upper bound | 1.24x10$^{-9}$ | 8.40x10$^{-9}$ | 4.00x10$^{-7}$ | 1.93 | 1.55 |

Figure 4 presents the parity plot between calculated and experimental mass fractions of components in the oil phase. Although the mass fractions appear to be closely aligned with the 45° line in Figure 4, the regression coefficient ($R^2$) for triacylglycerol, oleic acid, and ethanol were 0.224, 0.559 and 0.390, respectively. These low regression coefficients may result from experimental data uncertainty. It was reported that the 15 experiments used to correlate the parameters, comprising 45 mass concentration measurements, exhibited an average uncertainty of 7.7%. Additionally, some experiments used in the regression process yielded similar final FFA contents under significantly different operating conditions (i.e., UCO flow rate, ethanol-to-oil mass flow ratio and contactor length). Considering these factors, the regressed model is deemed suitable for describing the FFA extraction from UCO in the LLFC. Hereinafter, the model can be employed to study the effects of UCO flow rate, mass flow ratio between fluids and contactor's length, as well as to facilitate process scale up.

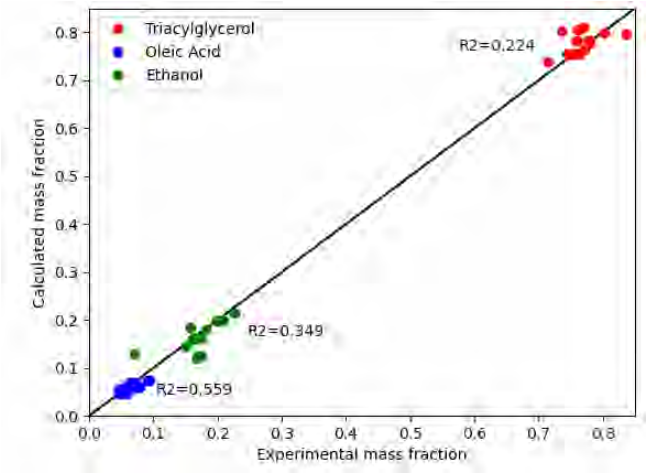



**Figure 4.** Parity plot of components mass fractions in oil phase.

Figure 5 illustrates the effect of the ethanol-to-oil mass flow ratio on FFA removal from UCO. Increasing this ratio enhances FFA extraction, as a higher ethanol content shifts the global mixture point deeper inside the LLE envelope. Consequently, the mixture lies on a larger tie line, increasing the concentration gradient between the bulk phases and interface. According to Equation (3), a larger concentration gradient improves FFA extraction from UCO.

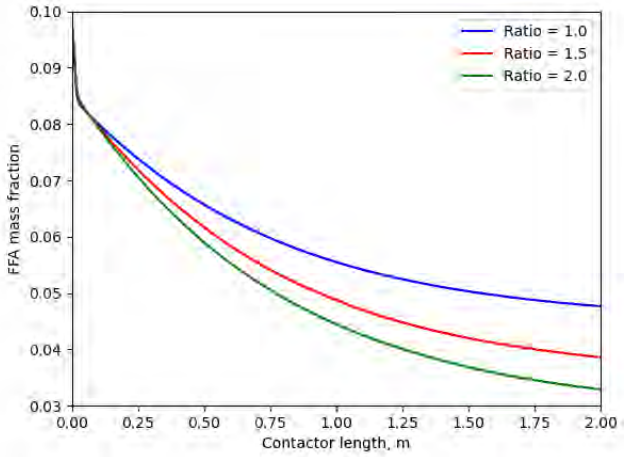



**Figure 5.** Ethanol to UCO mass flow ratio effect on FFA extraction. UCO mass flow rate: 1 kg/h; Temperature: 70°C; FFA in UCO at inlet: 9.7 wt%.

On the other hand, the effect of UCO flow rate on FFA removal is shown in Figure 6. The results indicate that FFA mass transfer is proportional to UCO mass flow rate within the range of reported experimental data. This occurs because a higher UCO mass flow rate increases the volumetric flow per thread, velocity, film thickness and Reynolds number. As shown in Equation (9) and table 2, the global mass transfer coefficient is proportional to the Reynolds number up to 1.54. Comparing the operating conditions of 1.0 kg/h and 0.5 kg/h of UCO, the Reynolds number decreases by 50%, leading to an approximate 65% reduction in the global mass transfer coefficient. This decrease in mass transfer coefficient results in lower FFA extraction from UCO. Despite the influence of the UCO mass flow rate, three cases presented in Figure 6 appear to be limited by LLE, as the outlet FFA mass fractions remain relatively unchanged.

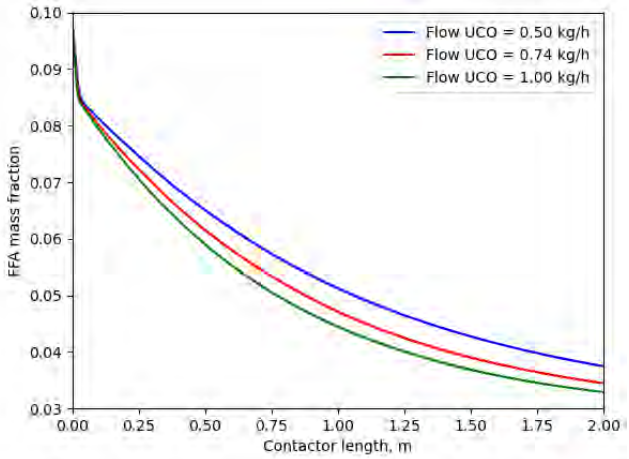



**Figure 6.** UCO flowrate effect on FFA extraction. Ethanol-to-UCO mass flow ratio: 2; Temperature: 70°C; FFA in fed UCO: 9.7 wt%.

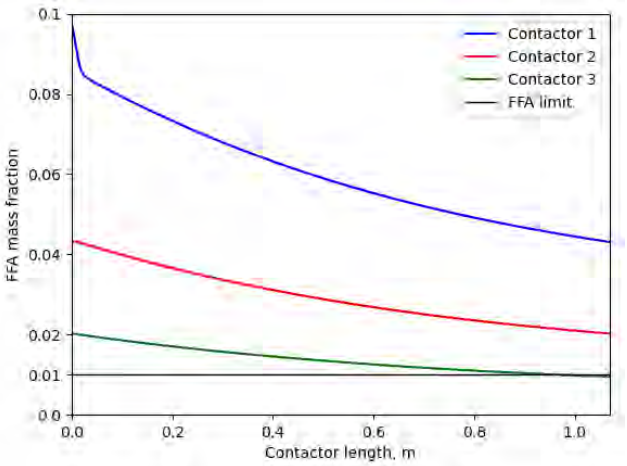



**Figure 7.** FFA extraction from UCO using three 1.07 m LLFCs operating in cascade configuration. The operating conditions for each LLFC are 70°C, an ethanol-to-UCO mass flow ratio of 2:1 and an initial FFA content of 9.7 wt% in UCO.

The recommended FFA content in treated UCO depends on its intended use as a raw material. If UCO is to be used as feedstock in feed industry, its FFA content must not exceed 0.05 wt.% (expressed as oleic acid) [11]. For biodiesel production, the allowable FFA content ranges between 0.5 wt.% and 1 wt.% [12], [13]. Then, using the developed model, it was possible to determine the number of contactors required to achieve a FFA content in UCO for a specific oleochemical application. For instance, Figure 7 presents the results obtained for a cascade configuration consisting of three 1.07 m contactors. The UCO feed flow rate was set to 1 kg/h, with an initial FFA concentration of 9.7 wt.%, operating at an ethanol-to-oil mass flow ratio of 2 and a temperature of 70°C. Under these conditions, the system produced a treated UCO with a FFA content of 0.9 wt.%. This arrangement was obtained after evaluation of different distributions of a 6 kg/h ethanol feed among three LLFCs operating in series.

## CONCLUSIONS

This study focused on developing a model of a liquid-liquid falling film contactor to assess the deacidification of UCO using ethanol as solvent, to obtain a treated stream suitable for further exploitation as oleochemical feedstock. The model incorporated mass transfer effects and it was assessed with respect to UCO mass flow rate, ethanol-to-oil ratio and contactor´s length. The effect of these variables was assessed with respect to FFA extraction from UCO. The results indicated that increasing the ethanol-to-oil mass flow ratio and UCO mass flow rate enhances FFA extraction. A higher ethanol content increased the concentration gradient between the bulk

phase and equilibrium FFA concentration throughout LLFC, while a greater UCO feed rate increases Reynolds number within the system. Both factors contribute to a higher global mass transfer coefficient for FFA. However, an increased Reynolds number resulting from a high UCO feed rate may alter the flow regime, leading to phase mixing at certain points inside the LLFC. Additionally, a higher UCO feed rate reduces the available space for ethanol and decreases the residence time of both fluids. These operating conditions could impact phase separation in the decanter and reduce the FFA extraction efficiency. Further investigation of these factors, along with model refinement, should be pursued in future studies. Regarding regressed parameters, all values felt within their respective 95% confidence intervals, and the average deviation from their lower and upper bounds were 6.77%, based on the evaluation of 0.8 million different sets. This indicates that the reported set of model parameters was unique within the selected search space. Furthermore, these parameters were like those previously obtained for deacidification of refined, deodorized and bleached palm oil. Finally, using the developed mathematical model, an arrangement of three LLFCs in series was simulated with different distributions of a 6 kg/h ethanol feed among the contactors. Results indicate that this configuration operates most efficiently when 2 kg/h of ethanol is fed into each LLFC. Under these conditions, the system can reduce the FFA content of a 1 kg/h UCO feed from 9.7 wt.% to 0.9 wt.% while operating at 70êC. It is expected that the developed mathematical model could be used for scaling up this intensified process and to assess potential industrial deployment.

## REFERENCES


1. Baena A, Orjuela A, Rakshit S, Clark J. Enzymatic hydrolysis of waste fats, oils and greases (FOGs): Status, prospective, and process intensification alternatives. *Chem. Eng. Process - Process Intensif*. 175:1-21 (2022) https://doi.org/10.1016/j.cep.2022.108930
2. Orjuela A, Clark J. Green chemicals from used cooking oils: Trends, challenges and opportunities. *Curr. Opin. Green Sustain. Chem.* 26:1-12 (2020) https://doi.org/10.1016/j.cogsc.2020.100369
3. Orjuela A. Industrial oleochemicals from used cooking oils (UCOs). Sustainability benefits and challenges. In: Advances in Carbon Management Technologies. Ed: Sikdar S, Princiotta F. CRC Press (2021) https://doi.org/10.1201/9781003056157-6
4. Cárdenas J, Montañez MA, Orjuela A, Narváez PC, Katryniok B. Deacidification of used cooking oils by solvent extraction under lab scale and in a falling film contactor. *Chem. Eng. Process. - Process Intensif*. 181: 109089 (2022) https://doi.org/10.1016/j.cep.2022.109089
5. Choe E, Min D. Chemistry of deep-fat frying oils. *J. Food Sci.* 72:77–86 (2007) https://doi.10.1111/j.1750-3841.2007.00352
6. Noriega MA, Figueroa LA, Narváez PC. Fatty acid solvent extraction from palm oil using liquid–liquid film contactor: Mathematical model including mass transfer effects. *Food Bioprod. Process.* 133:16–24 (2022) https://doi.org/10.1016/j.fbp.2022.02.004
7. Wilke CR, Chang P. Correlation of diffusion coefficients in dilute solutions. *AIChE J.* 1:264–270 (1995) https://doi.org/doi.org/10.1002/aic.690010222
8. Ferreira MC, Bessa L, Abreu C, Meirelles A, Caldas Batista EA. Liquid-liquid equilibrium of systems containing triolein+(fatty acid/partial acylglycerols/ester)+ethanol: Experimental data and UNIFAC modeling. *Fluid Ph Equilb* 486:186-192 (2018) https://doi.org/10.1016/j.fluid.2018.07.030
9. Rackett HG. Equation of state for saturated liquids. *J. Chem. Eng. Data* 15:514-517 (1970) https://doi.org/10.1021/je60047a012
10. Reid RC, Prausnitz JM, Poling BE. The Properties of Gases and Liquids. McGraw-Hill (1987).
11. FAO. Codex Alimentarius. FAO (2019).
12. Chai M, Tu Q, Lu M, Yang Y. Esterification pretreatment of free fatty acid in biodiesel production, from laboratory to industry. *Fuel Process. Technol.* 125:106-113 (2014) https://doi.org/10.1016/j.fuproc.2014.03.025
13. Liu S, McDonald T, Wang Y. Producing biodiesel from high free fatty acid waste cooking oil assisted by radio frequency heating. *Fuel* 89:2735-2740 (2010) https://doi.org/10.1016/j.fuel.2010.03.011



© 2025 by the authors. Licensed to PSEcommunity.org and PSE Press. This is an open access article under the creative commons CC-BY-SA licensing terms. Credit must be given to creator and adaptations must be shared under the same terms. See https://creativecommons.org/licenses/by-sa/4.0/




# Section 10

## PSE4BioMedical and (Bio) Pharma

Systems & Control Transactions

**Research Article - Peer Reviewed Conference Proceeding**
ESCAPE 35 - European Symposium on Computer Aided Process Engineering
Ghent, Belgium. 6-9 July 2025
Jan F.M. Van Impe, Grégoire Léonard, Satyajeet S. Bhonsale,
Monika E. Polańska, Filip Logist (Eds.)

PSE PRESS

# Predicting Final Properties in Ibuprofen Production with Variable Batch Durations

**Kuan-Che Huang, David Shan-Hill Wong, Yuan Yao***

National Tsing Hua University, Department of Chemical Engineering, Hsinchu 300044, Taiwan
* Corresponding Author: yyao@mx.nthu.edu.tw

## ABSTRACT

This study addresses the challenge of predicting final properties in batch processes with highly uneven durations, using the ibuprofen production process as a case study. Novel methodologies are proposed and compared against traditional regression algorithms, which rely on batch trajectory synchronization as a pre-processing step. The performance of each method is evaluated using established metrics. The data for this study were generated using Aspen Plus V12 simulation software, focused on batch reactors. To handle the unequal-length trajectories in batch processes, this research constructs a dual-transformer deep neural network with multi-head attention and layer normalization mechanism to extract shared information from the high-dimensional, uneven-length manipulated variable profiles into latent space, generating equal-dimensional latent codes. As an alternative strategy for representation learning, a dual-autoencoder framework is also employed to achieve equal-dimensional representations. The representation vectors are then used as inputs for downstream deep learning models to predict the target variables, achieving an accuracy with an $R^2$ score exceeding 0.9.

**Keywords**: Uneven durations, Batch process, Transformer, Autoencoder, Representation learning

## INTRODUCTION

In the chemical industry, batch processing is a commonly used production method [1]. Throughout an batch process, the quality of the final product is a key indicator of interest to both industry and academia. However, variations between batches often lead to unequal processing times across different batches. Due to the requirement for consistent input in building a soft sensor model for quality prediction, there are traditionally two methods for handling unequal-length batch trajectories: truncation and time-series alignment [2]. However, these two methods often come with certain issues. For the truncation methods, cutting off process-related operational trajectories can result in the loss of important information, which may affect the accuracy of subsequent soft sensor modeling. As for the time warping methods, significant differences in time lengths can cause trajectory distortion, and compression in certain segments may introduce noise. This situation can also lead to wrong models.

In this research, novel methodologies are proposed and compared against traditional regression algorithms [3], which rely on batch trajectory synchronization as a pre-processing step. In batch processes, handling three-dimensional data containing batch, time, and process variables is typically done using batch-wise unfolding, which transforms the data into a two-dimensional matrix. Due to the multivariate nature of chemical plant systems, Partial Least Squares (PLS) regression is commonly employed for modelling. This framework is referred to as Multiway Partial Least Squares (MPLS) [4]. Even though MPLS is a well-established method for handling batch process modelling, combining time warping with batch-wise unfolding can still result in the curse of dimensionality and model instability, especially when the data sampling size is too small, leading to overfitting [5].

This study aims to address the issue of excessively unequal production times between batches in quality prediction by employing a strategy based on Transformer and Autoencoder neural network architectures. Additionally, a case study on the batch production of Ibuprofen was conducted to demonstrate the approach. Ibuprofen is a pain reliever and anti-inflammatory drug commonly

used for headaches, toothaches, and minor pain. The data for this study were generated using Aspen Plus V12 simulation software [6], focused on batch reactors. To maintain process stability, it is important to prevent significant changes in the trajectories of operational variables within a given time unit. We implemented a statistical sampling approach, employing Latin Hypercube Sampling (LHS) to select samples within acceptable process boundaries [7]. The completion of each batch was determined based on the final isobutylbenzene conversion rate. A total of 1,000 simulation runs were performed, and the generated data were utilized to build a neural network model. The target variables for prediction are: (1) the isobutylbenzene conversion rate, and (2) the accumulated mass of ibuprofen.

The entire model architecture proposed in this study is built on a dual-transformer framework [8], integrating multi-head attention and layer normalization mechanisms. This approach captures shared information from the high-dimensional, uneven-length manipulated variable profiles, mapping them into latent space to produce latent codes of equal dimensions. An alternative feature extraction strategy involves utilizing a dual-autoencoder framework [9], which is also employed to obtain equal-dimensional representations. The downstream network structure consists of two fully connected neural networks, each designed to predict one of the two target variables. Additionally, the Neural Network Scalable Vector Graphics (NNSVG) tool is employed for visualizing the model structure [10].

## PRELIMINARIES

### Autoencoder

Autoencoder is a neural network framework based on an encoder and decoder. Through dimensional transformations in the intermediate layers of the neural network, the goal is to reconstruct data that is identical to the input. The reconstruction error, which serves as the loss function, can be expressed as follows:

$$L(x, x') = \| \mathrm{x} - \mathrm{x}' \|^2 \quad (1)$$

Similar to Principal Component Analysis, Autoencoder provides the capability for dimensional reduction of high-dimensional data. The difference lies in that the activation function in an autoencoder can provide nonlinear treatment to extract latent data. For latent vectors, the target is often to have the low-dimensional data represent the original high-dimensional data through the shared information extracted by the Autoencoder. Reducing the dimensionality can improve the computational efficiency of subsequent model development and help avoid the curse of dimensionality. Furthermore, the low-dimensional representation of data, regarded as important information, can also serve a filtering function to do the denoise.

### Transformer

The Transformer architecture utilizes attention mechanisms and layer normalization, eliminating the need for convolution or recurrence. There are various methods for data normalization. The advantage of using layer normalization in Transformers lies in its ability to handle three-dimension input data often associated with variable-length sequences, such as in translation tasks. When the length of sequences varies significantly, applying layer normalization to individual samples ensures that the mean and variance remain relatively stable. On the other hand, if batch normalization were used for mini-batch tasks, the insufficient padding part could affect the mean and variance, leading to fluctuations. When dealing with overly long new input sequences, the global mean and variance recorded by Batch Normalization may significantly affect the normalization of this unseen input.

In the Transformer model, multi-head attention is used, which involves multiple linear layers that project into lower-dimensional spaces. By utilizing multiple instances of scaled dot-product attention, the model learns projection parameters to identify different patterns in the sequence input. In scaled dot-product attention, the query and key undergo dot product and scaling, followed by the soft-max function to produce weight values between 0 and 1. Attention, in fact, can be regarded as a function, where the output is a weighted sum of the values. The weights are determined by the query's search over the keys corresponding to different values through the compatibility function, which can be viewed as a measure of similarity.

### Latin Hypercube Sampling

There are numerous approaches to statistical sampling, such as the memoryless Monte Carlo sampling. In this study, Latin Hypercube Sampling (LHS), a memory-based method, was chosen. The goal of using this approach is to capture the population data distribution of the original process variables with the least amount of sampling. Additionally, over time, LHS data can help avoid excessive fluctuations in the process variables of the chemical plant during simulation outputs.

With a limited sample size, random or Monte Carlo sampling may result in sample clustering. In contrast, LHS employs stratified sampling, ensuring a well-distributed sample by dividing the range into equal intervals and selecting points within each.

## DATASET AND SOFTWARE

This study used the batch production of ibuprofen as a case study to demonstrate that using feature extrac-

tion with latent codes of equal dimensions through Autoencoder and Transformer, expressed as feature learning for representing the original trajectories of chemical plant processes, combined with a neural network predictor, performs better than the approach of dynamic time warping combined with MPLS.

The dataset was generated from the Aspen Plus V12 simulation software, with the main reactor being a batch reactor, based on two feed streams and a final product outlet stream. The reactants include isobutylbenzene, acetic anhydride, hydrogen, and carbon monoxide for synthesis, with the primary product being ibuprofen. The side reaction produces acetic acid, and the chemical reaction is as follows,

$$\boldsymbol{C_{10}H_{14}} + \boldsymbol{C_4H_6O_3} + \boldsymbol{H_2} + \boldsymbol{CO} \rightarrow \boldsymbol{CH_3COOH} + \boldsymbol{C_{13}H_{18}O_2} \quad (2)$$

The kinetic information for the chemical reaction involved in Ibuprofen production indicates that the consumption of isobutylbenzene follows a second-order reaction, while the other reactants exhibit first-order consumption kinetics. The formation of the products also follows a first-order reaction.

To accurately model phase equilibrium behavior in the system, we employed the Wilson thermodynamic model, which is expressed as:

$$\ln \gamma_i = 1 - \ln\left(\sum_j A_{ij} x_j\right) - \sum_j \frac{A_{ij} x_j}{\sum_k A_{jk} x_k} \quad (3)$$

where $lnA_{ij} = a_{ij} + \frac{b_{ij}}{T} + c_{ij} lnT + d_{ij} T + e_{ij}/T^2$ .

The binary parameters $(a_{ij}, b_{ij}, c_{ij}, d_{ij}, e_{ij})$ were regressed using vapor-liquid equilibrium data from the Dortmund Databank, implemented via Aspen V12 software. In the pharmaceutical and chemical industries, the Wilson model is particularly advantageous due to its asymmetric interaction parameters, which enhance flexibility in capturing liquid-phase non-ideality, improving the accuracy of phase equilibrium predictions.

We used the conversion rate of isobutylbenzene as the stop criterion for each independent batch process. Due to different stop values and dynamic process operation profiles, the varying cycle times across batches were influenced. In this study, our goal was to do the regression two target variables: 1) the accumulated mass of ibuprofen and 2) the conversion rate of isobutylbenzene.

Using Python to drive Aspen software, we adjusted the two manipulated variables, temperature and pressure. The model training was based on Python 3.8.8, with the GPU being an NVIDIA GeForce RTX 2080 Ti. At each time step, the temperature and pressure points needed to obey with the range defined by LHS sampling while also avoiding large fluctuations in the variables, which was undesirable in chemical plant operations.

After data generation, we began by visualizing the issue of unequal lengths in batch data. As shown in Figure 1, we needed an effective solution for modeling with varying sequence lengths modeling. In 1,000 simulation experiments, the batch processing times varied significantly, with a maximum of 6158 seconds, a minimum of 2693 seconds, and a median of 3790 seconds. The subsequent comparison with the conventional methods employed the median as the representative template batch.

This study adjusted the dynamic process operations in the early stages of all batches, while the later stages reached a steady state following the Latin Hypercube Sampling method to generate data. We also visualize the variation of the two target variables across 1,000 independent batch simulations, shown in Figures 2 and 3.>

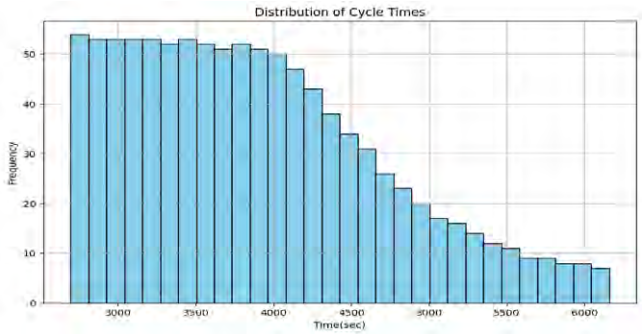



**Figure 1.** Batch time histogram for ibuprofen production

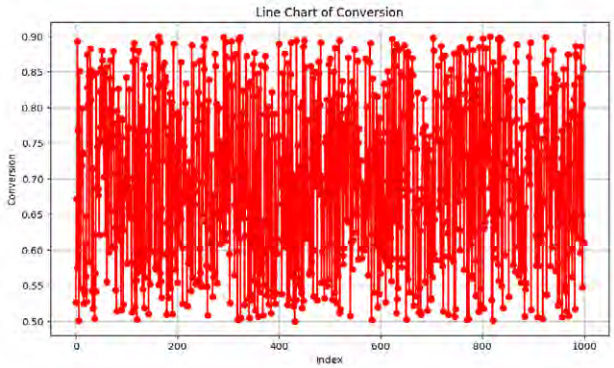



**Figure 2.** Trend of isobutylbenzene conversion rate

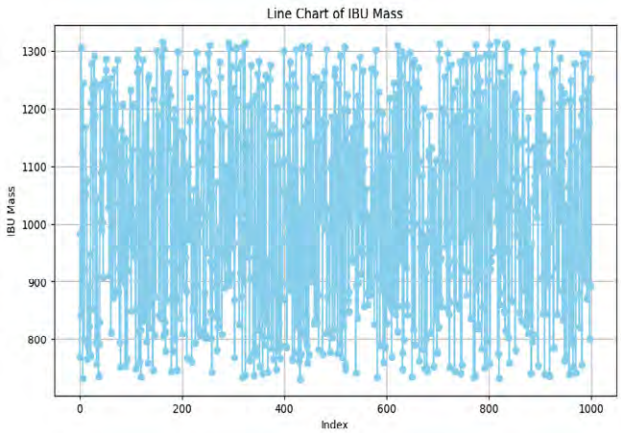



**Figure 3.** Trend of ibuprofen accumulated mass

## METHODOLOGY AND RESULT DISCUSSIONS

This study employs two strategies to specifically address variations in process trajectories related to the manipulated variables of temperature and pressure, which could be extended to higher-dimensional systems with multiple process variables. The first strategy used in this study is the Autoencoder strategy, with the overall model architecture illustrated in the Figure 4. This model comprises a dual-autoencoder neural network, with two downstream predictors responsible for predicting the target variables: Ibuprofen accumulated mass and isobutylbenzene conversion rate, respectively. The overall loss function is a custom-defined loss function optimized through the Adam optimizer, which performs gradient descent to find the optimal weights. The total loss comprises the reconstruction loss of the two manipulated variables and the prediction loss of the two target variables.

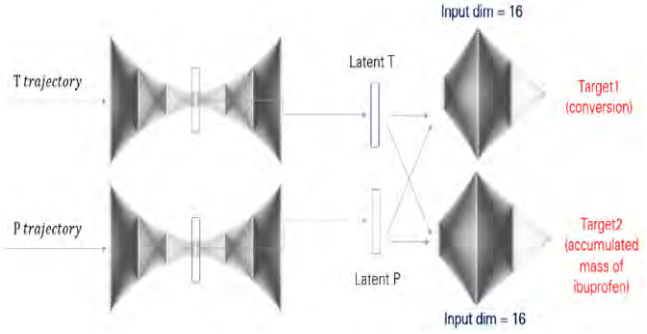



**Figure 4.** Framework of autoencoder strategy

The second strategy is the Transformer strategy, as shown in the model architecture Figure 5. Instead of using traditional recurrent neural networks to capture sequential relationships within the chemical engineering system, we utilize a multi-head attention mechanism. This mechanism applies multiple scaled dot-product attention layers and linear projections to identify trajectory similarities. To prevent the disproportionate influence of excessive padding on the global trajectory's mean and variance, layer normalization is applied. Furthermore, its scalability allows for adjusting the number of front-end Transformers to accommodate different chemical systems and corresponding manipulated variables.

The input layer for each autoencoder or Transformer basis consists of 62 parameters, where each corresponds to a single manipulated variable. The number 62 represents the sampling points for each manipulated variable in the longest production batch across all batches, with a time frequency of 100 seconds. For batches with fewer than 62 sampling points, padding is applied before entering the masking layer to ensure that these padded values are excluded from the loss function. Ultimately, the input data is compressed into an 8-dimensional latent space, and the two latent codes are merged into a 16-dimensional representation, which is then processed by the downstream predictor.

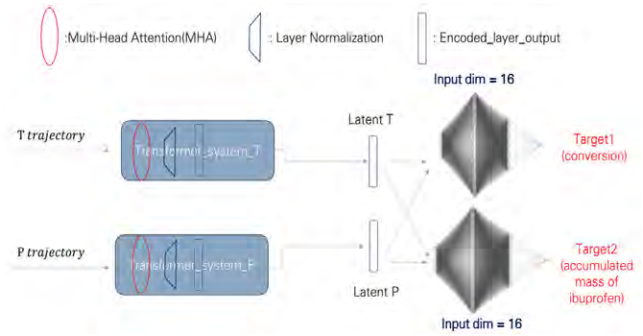



**Figure 5.**Transformer Method framework.

The conventional methods for comparison rely on using the golden batch as a template to align all candidate batches, followed by using dimensionality reduction machine learning algorithms (including MPLS and multi-way principal component regression (MPCR)) to predict the terminal properties of the process. The following Table 1 and Table 2 present performance comparisons.

**Table 1:** Ibuprofen accumulated mass prediction results

| **Ibuprofen accumulated mass performance metrics** | | | |
|---|---|---|---|
| **Subset** | **Train** | **Validation** | **Test** |
| **Method** | $R^2/RMSE$ | $R^2/RMSE$ | $R^2/RMSE$ |
| Autoencoder | 0.99/7.6 | 0.99/7.6 | 0.99/7.5 |
| Transformer | 0.99/11.3 | 0.99/10.6 | 0.99/10.4 |
| DTW+MPLS | 0.02/167 | - | -0.03/171 |
| DTW+MPCR | 0.01/167 | - | -0.03/171 |

**Table 2:** Isobutylbenzene conversion rate prediction results

| **Isobutylbenzene conversion rate performance metrics** | | | |
|---|---|---|---|
| **Subset** | **Train** | **Validation** | **Test** |
| **Method** | $R^2/RMSE$ | $R^2/RMSE$ | $R^2/RMSE$ |
| Autoencoder | 0.99/0.01 | 0.99/0.01 | 0.99/0.01 |
| Transformer | 0.99/0.01 | 0.99/0.01 | 0.99/0.01 |
| DTW+MPLS | 0.02/0.11 | - | -0.03/0.1 |
| DTW+MPCR | 0.02/0.11 | - | -0.03/0.1 |

The prediction results of the four methods on the test set, applied to the accumulated mass of Ibuprofen, are visualized in Figures 6 through 9. Among them, Figures 6 and 7 demonstrate that the proposed method in this study exhibits excellent predictive capability in addressing this a highly uneven-length batch production property prediction task.

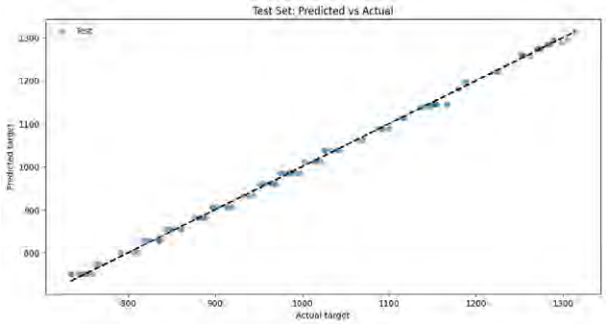



**Figure 6.** Ibuprofen accumulated mass (Autoencoder prediction results on the test set)

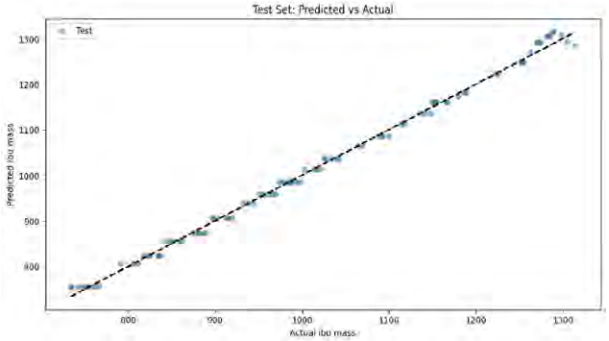



**Figure 7**. Ibuprofen accumulated mass (Transformer prediction results on the test set)

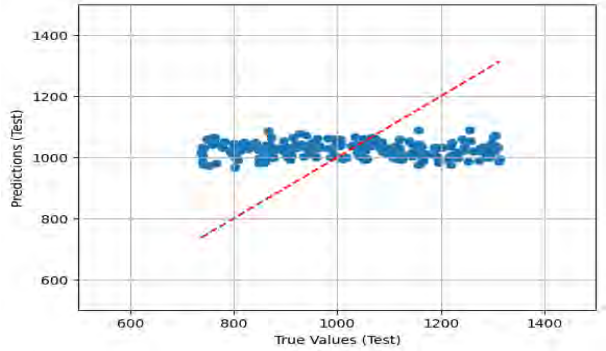



**Figure 8.** Ibuprofen accumulated mass (DTW+MPLS prediction results on the test set)

The prediction results of the four methods in test set can also be visualized in terms of the Isobutylbenzene conversion rate, as shown in the Figure 10 to Figure 13. The two strategies proposed in this study demonstrate better predictive performance compared to traditional trajectory synchronization and latent space dimensionality reduction machine learning methods. In the scatter plot, the prediction points are well-aligned near the ideal line, with $R^2$ for both target variables exceeding 0.9. This improvement is attributed to several factors: our neural network processes effectively handle the dynamics of trajectories with highly unequal lengths, avoiding the trajectory compression and introduction of error information that often result from warping. Additionally, both the autoencoder and transformer strategies incorporate activation functions, allowing for the handling of non-linear aspects of the system, which state-of-the-art methods lack in terms of non-linear learning capabilities.

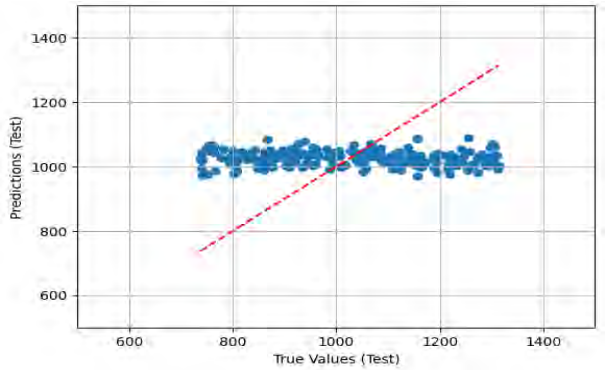



**Figure 9.** Ibuprofen accumulated mass (DTW+MPCR prediction results on the test set)

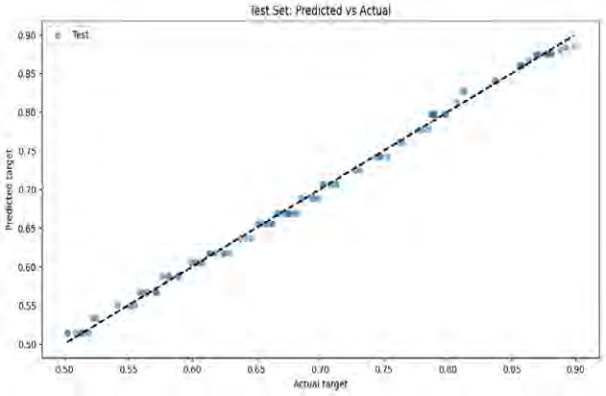



**Figure 10.** Isobutylbenzene conversion rate (Autoencoder prediction results on the test set)

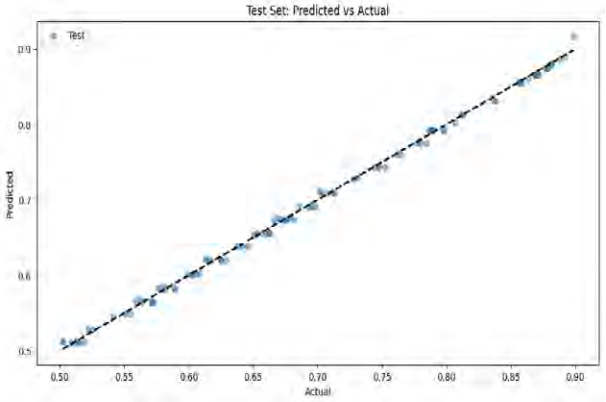



**Figure 11.** Isobutylbenzene conversion rate (Transformer prediction results on the test set)>

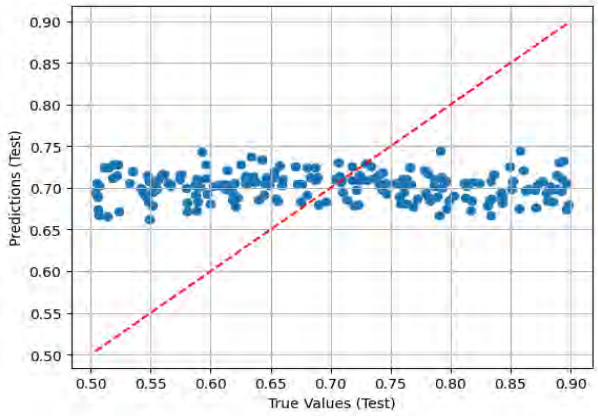



**Figure 12.** Isobutylbenzene conversion rate (DTW+MPLS prediction results on the test set)

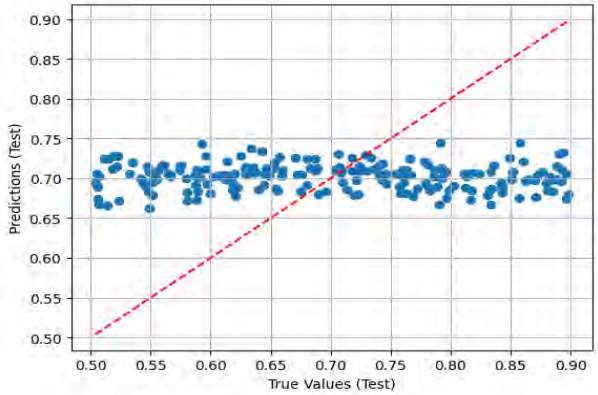



**Figure 13**. Isobutylbenzene conversion rate (DTW+MPCR prediction results on the test set)

## CONCLUSIONS

This study proposes two innovative approaches to address the prediction problem of terminal properties in chemical processes with unequal batch lengths. The research contains two strategies, the dual-Transformer and dual-Autoencoder strategies. The neural network modules are determined by several process variables to extract latent space vectors from process trajectory data and input them into the downstream of the overall architecture for quality predictor modeling. In the case study of batch ibuprofen production, the R-squared values for both target variables exceed 0.9. This shows a significant difference compared to using only DTW combined with MPLS or MPCR.

## ACKNOWLEDGEMENTS

This work was supported in part by the National Science and Technology Council, ROC, under Grant No. NSTC 113-2221-E-007-012-MY2.

## REFERENCES

1. Yao Y, Gao F. A survey on multistage/multiphase statistical modeling methods for batch processes. *Annu Rev Control* 33:172-183 (2009). https://doi.org/10.1016/j.arcontrol.2009.08.001
2. Kassidas A, MacGregor JF, Taylor PA. Synchronization of batch trajectories using dynamic time warping. *AIChE J* 44:864-875 (1998). https://doi.org/10.1002/aic.690440412
3. Vigneau E, Devaux MF, Qannari EM, Robert P. Principal component regression, ridge regression and ridge principal component regression in spectroscopy calibration. *J Chemom* 11:239-249 (1997). https://doi.org/10.1002/(SICI)1099-128X(199705)11:3<239::AID-CEM470>3.0.CO;2-A
4. Nomikos P, MacGregor JF. Multi-way partial least squares in monitoring batch processes. *Chemom Intell Lab Syst* 30:97-108 (1995). https://doi.org/10.1016/0169-7439(95)00043-7
5. Sousa PF, Åberg KM. Can we beat overfitting?—A closer look at Cloarec's PLS algorithm. *J Chemom* 32:e3002 (2018). https://doi.org/10.1002/cem.3002
6. Aspen Technology, Inc. Aspen Plus User Guide (V12). Aspen Technology, Inc. (2017).
7. Iman RL. Latin Hypercube Sampling. John Wiley & Sons, Ltd. (2008).
8. Vaswani A, Shazeer N, Parmar N, Uszkoreit J, Jones L, Gómez AN, Kaiser Ł, Polosukhin I. Attention is all you need. *Adv Neural Inf Process Syst* (2017). https://doi.org/10.48550/arXiv.1706.03762
9. Vincent P, Larochelle H, Bengio Y, Manzagol PA. Extracting and composing robust features with denoising autoencoders. *Proc Int Conf Mach Learn* 25:1096-1103 (2008). https://doi.org/10.1145/1390156.1390294
10. LeNail A. NN-SVG: Publication-ready neural network architecture schematics. J Open Source Softw 4:747 (2019). https://doi.org/10.21105/joss.00747

© 2025 by the authors. Licensed to PSEcommunity.org and PSE Press. This is an open access article under the creative commons CC-BY-SA licensing terms. Credit must be given to creator and adaptations must be shared under the same terms. See https://creativecommons.org/licenses/by-sa/4.0/

Systems & Control Transactions

**Research Article - Peer Reviewed Conference Proceeding**
ESCAPE 35 - European Symposium on Computer Aided Process Engineering
Ghent, Belgium. 6-9 July 2025
Jan F.M. Van Impe, Grégoire Léonard, Satyajeet S. Bhonsale,
Monika E. Polańska, Filip Logist (Eds.)

PSE PRESS

# Model Predictive Control to Avoid Oxygen Limitations in Microbial Cultivations - A Comparative Simulation Study

**Philipp Pably[a]*, Jakob K. Huusom[a], and Julian Kager[a]**

[a] DTU, Chemical and Biochemical Engineering, Kgs. Lyngby, Denmark
* Corresponding Author: phpa@kt.dtu.dk.

## ABSTRACT

Maintaining sufficient amounts of dissolved oxygen throughout a microbial cultivation is a classic control task in bioprocess engineering to avoid negative effects onto cell physiology and productivity. But traditional PID-based algorithms struggle when faced with pulsed substrate additions and the resulting sudden surge of oxygen uptake. In this work a nonlinear MPC is employed and compared to a PID setup for the cultivation of an *E. coli* strain exposed to intermittent feeding. Both controllers are tuned for a fast pulse response combined with efficient and robust control action. Their performance was tested *in-silico* with isolated feed pulses, as well as throughout a full cultivation run. Further, the effects of parameter uncertainty were investigated to assess the impact of a model-plant mismatch. The results showed that the predictive nature of the MPC is well suited for maintaining the dissolved oxygen levels above a threshold and outperforms the PID in almost all investigated simulation scenarios.

**Keywords**: Fermentation, Modelling and Simulations, Nonlinear Model Predictive Control, Process Control

## INTRODUCTION

Dissolved oxygen concentration is an important process variable for cultivation-based bioprocesses. Together with the availability of a substrate source it facilitates the growth and energy production of aerobic cells. Limitations in available oxygen often cause the formation of unwanted by-products such as Acetate or Ethanol. This metabolic shift and additional stress can lead to reduced physiological health and ultimately loss of productivity, especially when the product is a complex molecule such as a recombinant protein [1].

Therefore, industrial processes are typically equipped with a feedback-control system to maintain the DO level above a certain threshold by acting on the stirring speed and the supplied airflow to the reactor. The standard implementation uses two separate PID controllers for each variable that are connected in a hierarchical cascaded logic that prioritizes changing the agitation rate over the airflow rate. More advanced strategies involve gain scheduling or feedback linearization to account for the plant non-linearities [2].

Nevertheless, these control strategies struggle when faced with fast changes in oxygen demand, which lead to prolonged affixation periods for the cells. These conditions can occur because of abrupt changes in nutrient availability or changes in the prioritized metabolic activity due to the addition of an induction agent. The first is often observed in high-throughput small scale multi-reactor systems since the only viable feeding strategy is through intermittent feed shots [3].

Model predictive control emerges as a promising alternative to tackle these highly dynamic but repetitive conditions. The predictive nature of the algorithm can take advantage of the known feed profile to reduce the oxygen limitation periods through proactive control action compared to the purely reactive nature of common PID controllers. Similar work has been done for optimizing the feed pulse volume by employing an MPC to ensure sufficient oxygen availability during the cultivation at each bolus shot [4].

This study sets out to setup a nonlinear MPC that maintains the dissolved oxygen (DO) level above a defined threshold by manipulating the stirrer speed and the airflow. It further compares the performance to an adequately tuned PID controller setup in a typical hierarchical cascaded mode regarding minimal time spent underneath the threshold and minimal control input needed.

# MATERIAL & METHODS

## Process model

A kinetic state-space model is setup and parameterized with experimental data to describe the growth of a strain of the bacteria *Escherichia coli (E. coli)*. The state vector is $x = [c_{O_2}, c_X, c_S, V_R]^T$, consisting of the concentrations for the dissolved oxygen $c_{O_2}$, biomass $c_X$, and substrate $c_S$ in $g/L$, as well as the reactor volume $V_R$ in $L$.

$$\frac{d}{dt}\begin{bmatrix} c_{O_2} \\ c_X \\ c_S \\ V_R \end{bmatrix} = \begin{bmatrix} k_L a \cdot (c_{O_2,eq} - c_{O_2}) - q_S \cdot c_X \cdot Y_{O/S} \\ \left((q_S - q_m) \cdot Y_{X/S} - \frac{F_{in}}{V_R}\right) \cdot c_X \\ (c_{S,in} - c_S) \cdot \frac{F_{in}}{V_R} - q_S \cdot c_X \\ F_{in} \end{bmatrix} \quad (1)$$

$$y = \mathrm{DO} = \frac{c_{O_2}}{c_{O_2,eq}} \cdot 100\,\% \quad (2)$$

The mass balances in the state evolution equation, eq. 1, are supplemented with the kinetic expressions for the specific substrate uptake $q_S$ and a model for the Oxygen Transfer Rate $OTR$ in the reactor. Eq. 2. Describes the conversion of the state $c_{O_2}$ into a DO signal, which was measured during the process. $q_S$ is modeled with an expanded Monod-type equation that considers the co-limitation by $c_S$ and $c_{O_2}$ in eq. 3.

$$q_S = q_{S,max} \cdot \frac{c_S}{c_S + K_S} \cdot \frac{c_{O_2}}{c_{O_2} + K_{O_2}} \quad (3)$$

The $OTR$ is modeled by the $k_L a$ equation in eq. 4, suggested by Van't Riet et al. [5] and describes the influence of the manipulated variables stirring speed $n_{stirr}$ and airflow $F_{air}$ onto the oxygen transfer.

$$k_L a = k_{k_L a} \cdot \left(\frac{N_p \cdot \rho \cdot {n_{stirr}}^3 \cdot D^5}{V}\right)^{\alpha} \cdot \left(\frac{F_{air}}{A}\right)^{\beta} \quad (4)$$

## Model parameterization & simulation base case

The model was parameterized in two steps. First the $k_L a$ values were obtained from water runs using the gas-degas method [5] from a full grid design of experiment analysis using 100 experiments.

Then the physiological parameters such as yield and kinetic parameters were obtained from four experimental runs using a $3\ L$ lab-scale bioreactor. An optimization algorithm obtained the parameter set by minimizing the normalized root mean squared error (NRMSE) between the simulated and measured values for $c_X$, $c_S$ and $DO$ (data not shown). The resulting parameter values are shown in Table 1.

The simulated process used to assess the controller performance is set to start with a batch phase and followed by an intermittent fed-batch phase until a final biomass of $25\ g/L$ is reached. For the tuning efforts a representative process state was chosen, assuming the bioreactor being substrate limited ($c_S = 0\ g/L$) at a biomass concentration halfway towards the target of the process with $c_X = 15\ g/L$ at $V_R = 2\ L$. The DO state is either at $100\,\%$ for the closed-loop pulse response or at $30\,\%$ for the steady-state open-loop step response. The technical limits for the two manipulated variables are $400 - 1200\ rpm$ for $n_{stirr}$ and $0.5 - 5\ L/min$ for $F_{air}$. Furthermore, the experimental data showed that the maximum rates of change are $63\ rpm/s$ and $0.21\ L/min/s$ respectively.

**Table 1:** Process model parameters.

| Parameter | Symbol | Value | Unit |
|---|---|---|---|
| *Physiological parameters* | | | |
| Max specific substrate uptake rate | $q_{S,max}$ | 1.140 | g/g/h |
| Monod constant substrate | $K_S$ | $8.135 \cdot 10^{-2}$ | g/L |
| Monod constant oxygen | $K_{O_2}$ | $10^{-5}$ | g/L |
| Specific maintenance coefficient | $q_m$ | $8.365 \cdot 10^{-3}$ | g/g/h |
| Biomass/substrate yield | $Y_{X/S}$ | 0.3581 | g/g |
| Oxygen/substrate yield | $Y_{O/S}$ | 0.1908 | g/g |
| *OTR parameters* | | | |
| $k_L a$ constant | $k_{k_L a}$ | 4.002 | - |
| Exponent 1 | $\alpha_1$ | 0.3842 | - |
| Exponent 2 | $\beta$ | 0.2556 | - |

## Controller design

Two different controllers are designed, tuned and evaluated in this simulation study, a variation of a PID controller and a non-linear Model Predictive Controller (MPC). For both strategies the same state-space model is used to tune the parameters, while for the performance evaluation the model parameters are varied to investigate their robustness.

Regarding the manipulated variables, the stirrer speed is the preferred input since it also ensures smaller bubble sizes for better gas-liquid transfer and more uniform mixing throughout the reactor. High airflows on the other side come with a number of downsides for the process such as enhanced stripping of volatile components, increased risk of foaming or higher energy demands [6].

The controlled variable is the DO state which is overlayed with a white noise corresponding to the observed measurement variance of the DO sensor of the experimental setup, found to be $\sigma_{DO} = 0.56\,\%\text{-}pts$. Further a measurement delay of $1\ s$ and a control action delay of $2\ s$ was identified and included in the closed-loop process simulation. The influence of the measurement noise on the closed-loop behaviour was reduced by implementing a low-pass filter for the DO signal. An exponential moving average filter (EMA) with a window size of $15\ s$ was chosen.

## PID controller setup & tuning

The PID controller is designed as a hierarchical

cascaded controller, that keeps the DO level above a defined threshold of $30\,\%$ of the maximum DO in the cultivation broth. First, a PID controller acts on the stirring speed $n_{stirr}$ until it is saturated at the technical limit. When this becomes insufficient a second PID controller increases the airflow $F_{air}$, while $n_{stir}$is kept at the maximum value. Both PID loops are setup up with different tuning parameters. For anti-windup the setpoint error was not added to the integral error when the actuators were both at the minimum and maximum values.

For tuning the PID values of each manipulated variable a multi-step approach was chosen. The model open-loop step response was analyzed to obtain the process time constant $\tau$, the dead time $\theta$ and the process gain. The deadtime was identified as the time delay until an increase of the DO signal $> 3 \cdot \sigma_{DO}$ was identified. These parameters were then used to calculate the proportional gain $K_p$ and integral gain $K_I$ to design a PI controller using the lambda method [7]. The method relies on choosing a closed-loop time constant $\tau_{CL}$ that determines the aggressiveness of the resulting controller.

The derivative gain $K_D$ was manually adjusted by analysing the closed-loop response of the system after a feed pulse. Starting from 0, $K_D$ was stepwise increased to tune the response speed of the input variable further, while introducing only moderate noise amplification. This procedure was done for both input variables separately.

## MPC setup & tuning

The MPC was setup with the same process model and parameters as the simulation model. For this work the python package do-mpc [8] and the software framework CasADi [9] were used to implement a non-linear MPC controlling the DO-level through adjusting the stirring speed $n_{stirr}$ and airflow $F_{air}$ simultaneously. The optimal input trajectory is calculated by minimizing the stage cost ($lterm$) and the terminal cost ($mterm$), described in eq. 5 and eq 6. In both cases the variables are scaled with their respective maximum values.

$$mterm = Q_1 \cdot \left(\frac{DO - DO_{th}}{DO_{th}}\right)^2 \tag{5}$$

$$lterm = mterm + R_1 \cdot \left(\frac{u_1}{u_{1,max}}\right)^2 + R_2 \cdot \left(\frac{u_2}{u_{2,max}}\right)^2 \tag{6}$$

The MPC is tuned by adjusting the weighting parameters $Q_1$, $R_1$ and $R_2$ until a satisfying closed-loop behaviour is achieved. Additionally, the rate of change for the input variables was penalized as well through the weights $\Delta R_1$ and $\Delta R_2$ to achieve a smoother control action. The optimisation results and computation time are influenced by the chosen prediction horizon of $1\,min$ and the step size of $1\,s$. First the noise-free model response was used to tune the weights for the inputs and outputs. Then the influence of the measurement noise was investigated and the weights were adjusted.

## Performance quantification

The subsequently designed controllers will be compared by evaluating the time spent underneath the threshold of $30\,\%$ DO $t_{<30}$ and the used system inputs, stirring speed $n_{stirr}$ and airflow $F_{air}$. The $k_La$ equation in eq. 4 was used to calculate the power input $P_{stirr}$ from the stirring speed with eq. 7. By integrating both input variables over the process time, the general resource demand, stirrer energy input $E_{stirr}$ and pressurized air input $V_{air}$, can be estimated and compared between the designed controllers.

$$P_{stirr} = N_p \cdot \rho \cdot {n_{stirr}}^3 \cdot D^5 \tag{7}$$

# RESULTS & DISCUSSION

The goal of this simulation study was to investigate the control of the DO-level during an *E. coli* cultivation with special emphasis on disturbances deriving from the feed addition Hereby the controller should act as fast as possible to avoid oxygen limitations after a feed shot.

## PID tuning

As a starting point the step-response from a designed state was analyzed. To achieve an unbiased response, the system was continuously excited, and the formed biomass and volume increase neglected to result in a steady state at $30\,\%$ DO. A step increase of the input variable was performed and the open-loop system response in Figure 1 was analyzed.

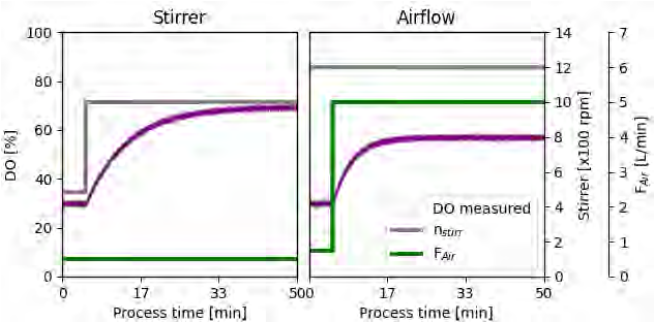



**Figure 1.** Open loop step responses of the noisy process model for the two hierarchically cascaded PID controller.

From the resulting changes in the DO signal, it is seen that in both cases the response follows only very little delay compared to the relatively long settling time to a new steady state. From this the process time $\tau$ and dead time $\theta$ were derived. Using the lambda method, the closed-loop time constant $\tau_{CL}$ was chosen as $2\,min$ for the stirring speed to achieve an aggressive tuning that reacts fast to the sudden increase of oxygen demand upon the feed shot. For the airflow a softer tuning was implemented with a $\tau_{CL}$ value of $4\,min$ to avoid oscillations, given also the smaller process time constant $\tau$.

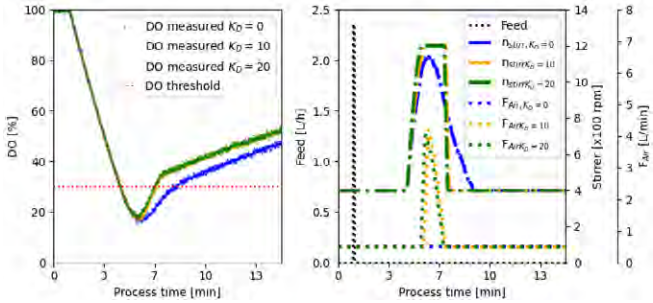



**Figure 2.** Feed pulse response with different $K_D$ tuning values for stirrer and airflow.

In the next step the derivative gain $K_D$ was adjusted manually by observing the closed-loop response to a feed pulse. Figure 2 shows the response for 3 different $K_D$ tunings for $n_{stirr}$. A significant difference in response time can be seen from raising $K_D$ up to 10, while increasing it further did not introduce any additional benefits. Higher $K_D$ values for the airflow did not improve the performance significantly, therefore it was set to zero to ensure smoother control action. The final tuning parameters are listed in Table 2.

**Table 2:** PID tuning parameters and time constants.

| PID parameters | Symbol | Stirrer | Airflow |
|---|---|---|---|
| process time constant | $\tau$ | 513.0 $s$ | 232.0 $s$ |
| Dead-time | $\theta$ | 10.0 $s$ | 7.0 $s$ |
| Closed-loop time constant | $\tau_{CL}$ | 2 $min$ | 4 $min$ |
| Proportional gain | $K_p$ | 51.61 | 0.29 |
| Integrative gain | $K_I$ | 0.10061 | 0.00124 |
| Derivative gain | $K_D$ | 10 | 0 |

## MPC tuning

Since the variables are scaled in the $lterm$ and $mterm$ cost equations by their maximum values, the weights were all initialized with 1 and then iteratively changed to achieve good setpoint tracking with minimal controller input. The tuning result can be seen in Figure 3 and the final parameters are listed in Table 3. Although the variables were scaled directly in the model equation, the tuning resulted in weights differing in several magnitudes. Especially the parameters connected with $n_{stirr}$ are low, which reflects the goal for the controller to act on the stirrer first before resorting to the airflow.

After finding acceptable values the MPC was tested with overlaying the DO measurement with the same white noise as done for the PID tuning. The MPC response showed almost identical control action and system responses. Nevertheless, the airflow was fluctuating due to the measurement uncertainties, therefore the penalty on the rate of control input changes $\Delta R_1$ and $\Delta R_2$ were adjusted towards heavier penalties. A further improvement to neglect measurement uncertainty induced fluctuations was the application of the low-pass filter as done for the PID controller. This resulted in the DO signal following the perfect model simulation closely.

**Table 3:** MPC tuning parameters.

| MPC parameters | Symbol | Value |
|---|---|---|
| DO state weight | $Q_1$ | $2 \cdot 10^4$ |
| Stirrer speed weight | $R_1$ | 1 |
| Airflow weight | $R_2$ | $10^3$ |
| Stirrer changes weight | $\Delta R_1$ | $10^{-1}$ |
| Airflow changes weight | $\Delta R_2$ | $10^2$ |

## Pulse response performance with perfect model

The final tunings for the two different control algorithms were compared with the previously set feed pulse response. The result can be seen in Figure 3 and Table 4. The advantage of the predictive optimisation for the MPC is evident when looking at the response times of the manipulated variables. This results in a better DO signal dynamic regarding the time spent underneath the threshold and a more efficient use of the input variables. The stirrer power consumption is lower while also the amount of sparged pressurized air is less.

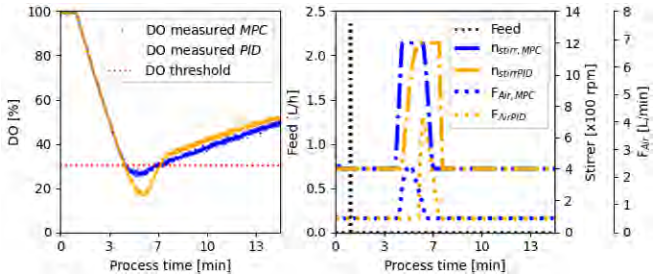



**Figure 3.** Feed pulse response for the final tunings of the MPC (blue) and PID (orange) algorithm.

**Table 4:** Performance for single feed pulse response.

| Controller | $t_{<30\%}$ $[min]$ | $E_{stirr}$ $[kJ]$ | $V_{air}$ $[L]$ |
|---|---|---|---|
| PID | 2.10 | 1.888 | 10.35 |
| MPC | 1.38 | 1.756 | 9.65 |

## Cultivation performance

To assess the controllers over the whole application range the defined cultivation process was simulated. It starts with a batch phase followed by pulsed feeding. The intervals are set to 5 $s$ of 3 $L/h$ pulses every 30 $min$, using a glucose feed concentration of 600 $g/L$ which results in a rapid addition of 2.5 $g$ of glucose to the cultivation. This causes fast and dynamic changes in oxygen demand, where the controllers act to keep the DO signal above 30 %. The process length and number of pulses is calculated to reach a final biomass concentration of

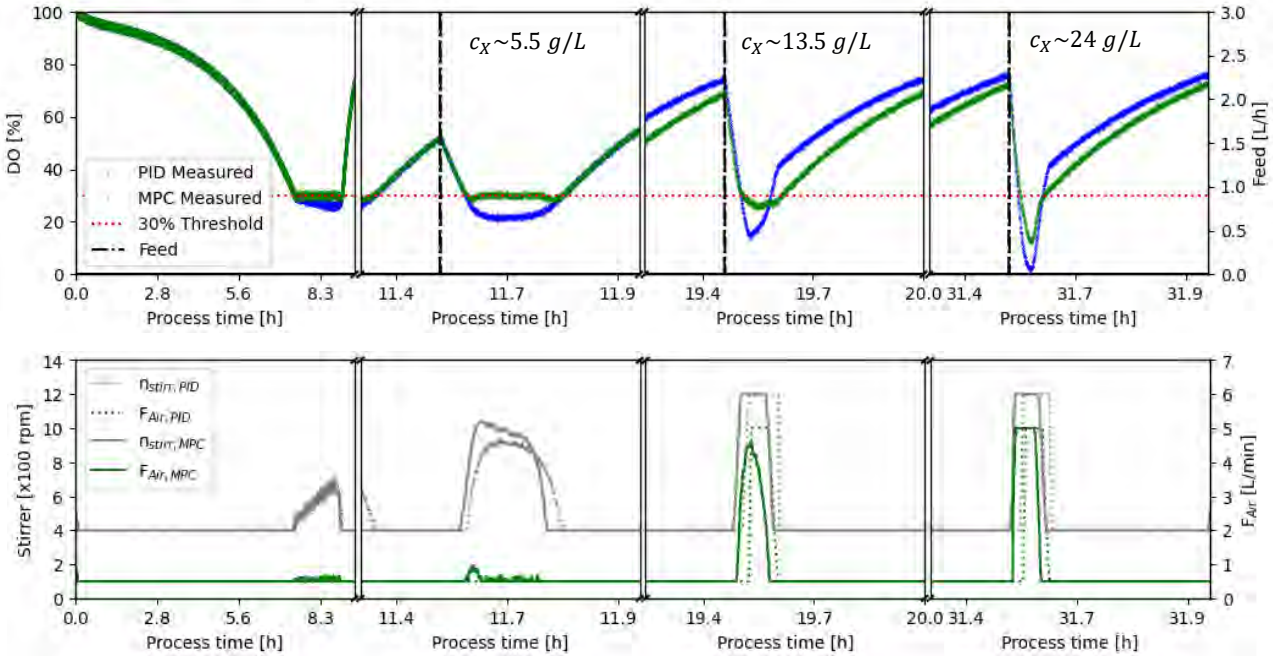



**Figure 4:** Controller performance for a complete cultivation, zooming in on the batch phase performance and 3 pulses – start, middle and end of process to show the response at progressing biomass concentrations.

$c_{X,final} = 25\ g/L$. The difference in performance assuming perfect model match between simulation and MPC is shown in Figure 4.

The results show that the MPC performs better throughout all phases of the process. The PID controllers perform equally well during the batch phase but struggle during the pulsed feed additions. First, they manage to maintain DO levels slightly below the threshold but remain there for a considerable amount of time. The MPC on the other hand avoids going below 30 % DO almost entirely in that phase. Later the increasing amount of biomass results in the $OUR$ being higher and the DO dips are getting more extreme. The MPC results in less deep DO signal dives and less time spent underneath the threshold, due to the predictive nature of the algorithm. The model implementation allows the controller to act before the setpoint deviation occurs that triggers the PID controllers. The total differences of the performance indicators are shown in Table 5. Here it shows that the MPC manages to minimize the time below the setpoint with almost identical control action.

**Table 5:** Performance for complete cultivation simulation.

| Controller | $t_{<30\%}\ [h]$ | $E_{stirr}\ [kJ]$ | $V_{air}\ [m^3]$ |
|---|---|---|---|
| PID | 5.30 | 204.3 | 1.471 |
| MPC | 2.15 | 208.7 | 1.463 |

## Pulse response performance with model-plant mismatch

The PID controllers and the MPC were tuned with the model response of a bacterial cultivation process. The MPC additionally bases its control action calculations on an internal model, which was assumed to be identical with the simulation model. Model identification and parameterization is generally regarded as challenging for bioprocesses and result in uncertainties regarding the parameter values [10]. To investigate the robustness of the developed controllers, a number of parameter values are varied to see the impact of a model-plant mismatch for the feed pulse responses. The results for a variation of $\pm 25$ % for $Y_{O/S}$ and $k_{k_La}$, as well as a mismatch between the state-space values for biomass in the process and the MPC simulator were investigated. The differences in performance values are listed in Table 6.

The parameter variations affected the controllers differently. The PID is less affected than the MPC since it only uses the incorrect model for the initial tuning. But no general trend can be observed. For the MPC the performance differs stronger, where overall parameter variation resulting in less OUR or more OTR lead to better results than the base case and vice versa. Nevertheless, the MPC outperformed the PID in all cases.

The influence of the biomass yield $Y_{X/S}$ uncertainty can not be observed at a single feed-pulse, since the biomass increase is minimal. But over the progress of a cultivation process it can lead to significant differences between the estimated and the actual biomass concentration, similar to the case of variations in $c_{X,0}$.

**Table 6:** Performance for model parameter variations.

| Simulation | $t_{<30\%}\ [min]$ | $E_{stirr}[J]$ | $V_{air}[L]$ |
|---|---|---|---|
| Base case MPC | 1.38 | 1755.8 | 9.65 |
| $c_{X,0}$ +25 % MPC | 1.43 | 1876.0 | 11.39 |
| $c_{X,0}$ -25 % MPC | 2.30 | 1415.2 | 8.51 |
| $Y_{O_2/S}$ +25 % MPC | 2.88 | 2642.8 | 16.02 |
| $Y_{O_2/S}$ -25 % MPC | 0.00 | 418.8 | 7.50 |
| $k_{k_La}$ +25 % MPC | 0.18 | 1492.7 | 8.66 |
| $k_{k_La}$-25 % MPC | 2.23 | 2166.3 | 11.47 |
| base case PID | 2.10 | 1888.4 | 10.35 |
| $c_{X,0}$ +25 % PID | 1.97 | 1875.7 | 11.40 |
| $c_{X,0}$ -25 % PID | 3.27 | 1325.9 | 7.50 |
| $Y_{O_2/S}$ +25 % PID | 3.03 | 2716.5 | 17.01 |
| $Y_{O_2/S}$ -25 % PID | 0.00 | 416.7 | 7.50 |
| $k_{k_La}$+25 % PID | 2.45 | 1208.5 | 7.50 |
| $k_{k_La}$-25 % PID | 2.50 | 2377.3 | 13.51 |

## CONCLUSION

A hierarchical cascaded PID controller and a non-linear MPC were designed for a threshold control problem to keep the dissolved oxygen signal above 30 % in an intermittent fed-batch cultivation of *Escherichia coli*. Both controllers were assisted with a low-pass filter for the measurement signal. A kinetic state-space model with additional white noise at the DO signal was used to simulate the plant response. The controller parameters were tuned to achieve minimal time underneath the threshold, while also considering efficient control input.

The results showed that the MPC outperforms the PID regarding the response time in all analyzed cases, while also being more economical for most of them. The impact of model and state vector to plant mismatch were investigated and proofed the MPC superior in the conducted simulations, although the manipulated variables input exceeded the optimal in some cases.

Finally, a defined bioreactor run was simulated and showed the cumulative benefits the MPC gives over the commonly used PID approach for intermittent fed-batches. With a reasonable tuning it keeps the DO signal above a defined threshold more effectively and resource efficiently. Pairing the controller with a filter algorithm results in a robust control scheme for the given task that is also resistant to some parameter and state uncertainty. Nevertheless, the additional implementation effort, computational demands and more complex tuning compared to traditional controller designs must be considered.

## ACKNOWLEDGEMENTS

This work obtained funding from the Novo Nordisk Foundation, Start Package grants for faculty recruitment Q4 2022; assistant professor on bioprocess digitalization and control (NNF220C0081250).

## REFERENCES

1. Phue, J.-N., Shiloach, J. Impact of dissolved oxygen concentration on acetate accumulation and physiology of E. coli BL21. Metabolic Engineering 7, 353–363. (2005) https://doi.org/10.1016/j.ymben.2005.06.003
2. Babuška, R., Damen, M.R., Hellinga, C., Maarleveld, H. Intelligent adaptive control of bioreactors. J. of Intel. Man. 14, 255–265. (2003) https://doi.org/10.1023/A:1022963716905
3. Neubauer, P., Cruz, N., Glauche, F., Junne, S., Knepper, A., Raven, M. Consistent development of bioprocesses from microliter cultures to the industrial scale. Eng. in Life Sc. 13, 224–238. (2013) https://doi.org/10.1002/elsc.201200021
4. Kim, J.W., Krausch, N., Aizpuru, J., Barz, T., Lucia, S., Neubauer, P., Cruz Bournazou, M.N. Model predictive control and moving horizon estimation for adaptive optimal bolus feeding in high-throughput cultivation of E. coli. Computers & Chemical Engineering 172. (2023) https://doi.org/10.1016/j.compchemeng.2023.108158
5. Van't Riet, K. Review of Measuring Methods and Results in Nonviscous Gas-Liquid Mass Transfer in Stirred Vessels. Ind. Eng. Chem. Proc. Des. Dev. 18, 357–364. (1979) https://doi.org/10.1021/i260071a001
6. Nienow, A.W. Mass Transfer and Mixing Across the Scales in Animal Cell Culture. In: Animal Cell Culture, Cell Engineering. Springer Int. Pub. (2015)
7. Smith, C.L. Practical Process Control: Tuning and Troubleshooting. John Wiley and Sons (2008) https://doi.org/10.1002/9780470431481
8. Fiedler, F., Karg, B., Lüken, L., Brandner, D., Heinlein, M., Brabender, F., Lucia, S. do-mpc: Towards FAIR nonlinear and robust model predictive control. Ctrl. Eng. Pract. 140. (2023) https://doi.org/10.1016/j.conengprac.2023.105676
9. Andersson, J.A.E., Gillis, J., Horn, G., Rawlings, J.B., Diehl, M. CasADi: a software framework for nonlinear optimization and optimal control. Math. Prog. Comp. 11, 1–36. (2019) https://doi.org/10.1007/s12532-018-0139-4
10. Ashyraliyev, M., Fomekong-Nanfack, Y., Kaandorp, J.A., Blom, J.G. Systems biology: parameter estimation for biochemical models. FEBS J. 276, 886–902. (2009) https://doi.org/10.1111/j.1742-4658.2008.06844.x

© 2025 by the authors. Licensed to PSEcommunity.org and PSE Press. This is an open access article under the creative commons CC-BY-SA licensing terms. Credit must be given to creator and adaptations must be shared under the same terms. See https://creativecommons.org/licenses/by-sa/4.0/



Systems & Control Transactions

**Research Article - Peer Reviewed Conference Proceeding**
ESCAPE 35 - European Symposium on Computer Aided Process Engineering
Ghent, Belgium. 6-9 July 2025
Jan F.M. Van Impe, Grégoire Léonard, Satyajeet S. Bhonsale,
Monika E. Polańska, Filip Logist (Eds.)

PSE PRESS

# A hybrid-modeling approach to monoclonal antibody production process design using automated bioreactor equipment

**Kosuke Nemoto[a], Sara Badr[a], Yusuke Hayashi[a], Yuki Yoshiyama[a], Kozue Okamura[a], Mizuki Morisasa[b], Junshin Iwabuchi[b], Hirokazu Sugiyama[a]***

[a] The University of Tokyo, Department of Chemical System Engineering, 7-3-1, Hongo, Bunkyo-ku, Tokyo, Japan
[b] Chitose Laboratory Co., Ltd., Tech & Biz Development Division, KSP R&D C432, 3-2-1, Sakado, Takatsu-ku, Kawasaki, Kanagawa, Japan
* Corresponding Author: sugiyama@chemsys.t.u-tokyo.ac.jp

## ABSTRACT

This work presents a hybrid-modeling approach to monoclonal antibody (mAb) production processes design using automated bioreactor equipment. Experimental data covering a reasonable yet broad range of cultivation conditions was collected by the equipment. Using the data, a model applicable to a wide range of cultivation conditions was developed. In the modeling, a data-driven model was applied to describe complicated/unknown phenomena that could not be captured by previously proposed mechanistic models. In the hybrid model, while maintaining the mass balance of the mechanistic model, coefficients of the equations were estimated with random forest regression. Overall, the model could describe the dynamic concentration profiles of product mAb and quality-relevant impurities depending on the media/glucose feeding conditions. The model was then applied to determine an optimal condition that maximized product mAb concentration and satisfied the impurity constraints. The work can further support model-based design of cell cultivation processes with considering multi-input & multi-output nature.

**Keywords**: Process Design, Dynamic Modelling, Biosystems

## INTRODUCTION

Monoclonal antibody (mAb) drugs offer advantages such as higher affinity and specificity as compared to conventional drugs for the treatment of critical diseases. Such advantages have led to a rapid growth of the mAb market, along which new technologies have been developed including host cel lines such as a high-yield CHO-MK cell line [1]. In the cultivation step, not only the final product, mAb, but also impurities such as host cell proteins (HCP), DNA, and charge variants are produced. These impurities have a significant impact on quality in the time- and resource-intensive cultivation step, making this step a major factor influencing the overall cost, time, and quality [2]. Since these impurities and mAb are affected by many cultivation conditions, such as agitation speed, dissolved oxygen (DO), feed rate, and cultivation time [3], it is essential to select conditions appropriately. Therefore, mathematical models that describe the target process based on cultivation conditions and can reduce experimental burdens are useful in the design of this critical cultivation step [4].

In modeling the cultivation step involving many complex biological phenomena, it is challenging to describe all the phenomena with a mechanistic model, making hybrid models useful. Various hybrid models for the cultivation step have been developed using different methods and for different purposes. A hybrid model of a CHO-K1 perfusion process was developed to optimize media exchange rates [5]. Hybrid models using different machine learning algorithms were compared and utilized to predict viable cells and titer [6]. A hybrid model was developed to predict critical quality attributes such as mAb and glycan profiles [7]. A hybrid model for fed-batch process with Adaptive Moment Estimation Method was developed [8]. Different hybrid models were compared

by introducing the concept of the degree of hybridization [9]. A hybrid modeling approach was proposed incorporating a data-driven model to improve the predictions of lactate which is important for predicting impurities [2]. However, hybrid models in previous studies were developed for limited cultivation conditions (for example, agitation rate and DO were constant in a previous study [8]). This limitation made it challenging to describe the relationships between various conditions and impurities as well as mAb, posing a significant obstacle to comprehensive multi-input, multi-output process design.

This work presents a hybrid-modeling approach to CHO cell cultivation process design. Experimental data covering a reasonable yet broad range of cultivation conditions was collected by the equipment. Using this data, a hybrid model applicable to a wide range of cultivation conditions was developed. The hybrid model combines mass balance equations (mechanistic component) with coefficients of the equations being estimated with random forest regression (data-driven component). Overall, the developed model could describe the concentrations of product mAb and quality-relevant impurities such as charge variants, HCP and DNA depending on the media/glucose feeding conditions. The model was then applied to determine an optimal condition that maximized product mAb concentration and met the impurity constraints considering 3,840 alternatives.

## EXPERIMENTAL METHODS

Figure 1 represents an overview of the experimental methods. In the experiments, a newly developed CHO-MK cell line [1], known for exhibiting extremely complex metabolic phenomena, was used. Cells were extracted from a frozen stock, thawed, and cultured in flasks for one week to increase cell density. Subsequently, cultivation was carried out with automated bioreactor equipment (Ambr® 250) which contained twelve bioreactors, each with a 250 mL volume. Initial solution volume $V_0$ was set to 170 mL in all experiments. Three cycles of fed-batch cultivation were performed by varying agitation speed $agitation$, DO $DO$, normal feed (referred to as feed hereinafter) rate $F_{\mathrm{in}}$, glucose feed rate $F_{\mathrm{in,glc}}$, feed start timing $t_{\mathrm{in}}$, and glucose feed start timing $t_{\mathrm{in,glc}}$. Table 1 shows the minimum and maximum values of each cultivation condition. Experiments were conducted once under 20 different conditions, and each condition was determined to cover a reasonable yet broad range to extend the interpolation range of the model. During the experiments, feed and glucose feed were supplied at a constant rate. Items such as DO and agitation speed were measured online every few seconds. In addition, multiple items including viable cells, cell viability, mAb, metabolites, and impurities were measured offline as time series data once or twice per day.

**Table 1:** Minimum and maximum values of each cultivation condition.

| Process parameters | Minimum | Maximum |
|---|---|---|
| $t_{\mathrm{in}}$ [h] | 24 | 42 |
| $t_{\mathrm{in,glc}}$ [h] | 42 | 42 |
| $F_{\mathrm{in}}$ [$V_0$ day$^{-1}$] | 0.08 | 0.1 |
| $F_{\mathrm{in,glc}}$ [g L$^{-1}$ day$^{-1}$] | 4.8 | 18.8 |
| $agitation$ [rpm] | 700 | 1400 |
| $DO$ [%] | 20 | 50 |

## MODEL DEVELOPMENT

### Mechanistic model equations

First, mechanistic model equations were formulated based on model equations proposed in previous studies [10,11]. To develop a model applicable to a wide range of cultivation conditions, the equations were simplified as much as possible. The components included density/concentrations of viable cell, dead cell, glucose, lactate, mAb, main/acidic charge variant, HCP, and DNA as shown in Eqs. (1)–(9) in Table 2. In the equations, $V$ [L], $X_{\mathrm{v}}$ [cells L$^{-1}$] , $X_{\mathrm{d}}$ [cells L$^{-1}$], [GLC] [mmol L$^{-1}$], [LAC] [mmol L$^{-1}$], $P$ [g L$^{-1}$], [Main] [g L$^{-1}$], [Acid] [g L$^{-1}$], [HCP] [g L$^{-1}$], [DNA] [g L$^{-1}$] are the solution volume, density/concentrations of the viable/dead cells, glucose, lactate, mAb, main/acidic charge variant, HCP, and DNA. $F_{\mathrm{in}}/F_{\mathrm{in,glc}}$ [L h$^{-1}$] and $c_{\mathrm{in_glc}}/c_{\mathrm{in,glc}}$ [mmol L$^{-1}$] are normal/glucose feed flow rate and glucose concentration of feed/glucose feed, respectively. $\mu$ [h$^{-1}$] and $\mu_{\mathrm{d}}$ [h$^{-1}$] are specific cell growth and death rates, respectively. $Q_{\mathrm{p}}$ [g cell$^{-1}$ h$^{-1}$] and $Q_{\mathrm{lac}}$ [mmol

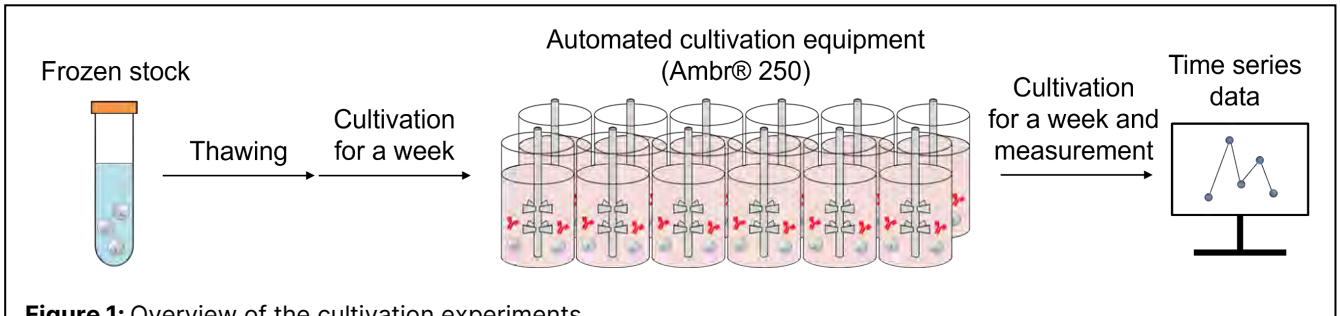



**Figure 1:** Overview of the cultivation experiments.

**Table 2:** Mechanistic model equations.

$$\frac{d(VX_\mathrm{v})}{dt} = (\mu - \mu_\mathrm{d})VX_\mathrm{v} \quad (1)$$

$$\frac{d(VX_\mathrm{d})}{dt} = \mu_\mathrm{d}VX_\mathrm{v} - k_{X_\mathrm{d},\mathrm{lysis}}VX_\mathrm{d} \quad (2)$$

$$\frac{d(V[\mathrm{GLC}])}{dt} = -\left(\frac{\mu-\mu_\mathrm{d}}{Y_{X_\mathrm{v}/\mathrm{glc}}} + m_\mathrm{glc}\right)VX_\mathrm{v} + F_\mathrm{in}c_{\mathrm{in_glc}} + F_{\mathrm{in,glc}}c_{\mathrm{in,glc}} \quad (3)$$

$$\frac{d(V[\mathrm{LAC}])}{dt} = Q_\mathrm{lac}VX_\mathrm{v} \quad (4)$$

$$\frac{d(VP)}{dt} = \begin{cases} Q_{\mathrm{p,a}}VX_\mathrm{v}|_{[\mathrm{GLC}]\geq[\mathrm{GLC}]_\mathrm{threshold}} \\ Q_{\mathrm{p,b}}VX_\mathrm{v}|_{[\mathrm{GLC}]<[\mathrm{GLC}]_\mathrm{threshold}} \end{cases} \quad (5)$$

$$\frac{d(V[\mathrm{Main}])}{dt} = \frac{d(VP)}{dt} - (k_\mathrm{acid} + k_\mathrm{base})V[\mathrm{Main}] \quad (6)$$

$$\frac{d(V[\mathrm{Acid}])}{dt} = k_\mathrm{acid}V[\mathrm{Main}] \quad (7)$$

$$\frac{d(V[\mathrm{DNA}])}{dt} = Y_{\mathrm{dna}/X_\mathrm{d}}k_{X_\mathrm{d},\mathrm{lysis}}VX_\mathrm{d} - k_{\mathrm{dna,lysis}}V[\mathrm{DNA}] \quad (8)$$

$$\frac{d(V[\mathrm{HCP}])}{dt} = Y_{\mathrm{hcp}/X_\mathrm{v}}VX_\mathrm{v} + Y_{\mathrm{hcp}/X_\mathrm{d}}k_{X_\mathrm{d},\mathrm{lysis}}VX_\mathrm{d} - k_{\mathrm{hcp,lysis}}(V[\mathrm{HCP}])^\mathrm{n} \quad (9)$$

cell$^{-1}$ h$^{-1}$] are specific production rates of mAb and lactate, respectively, with $Q_\mathrm{p}$ being classified based on whether glucose is depleted or not. $Y_{X_\mathrm{v}/\mathrm{glc}}$ [cells mmol$^{-1}$] and $m_\mathrm{glc}$ [mmol cell$^{-1}$ h$^{-1}$] are specific glucose consumption for cell growth and cell maintenance, respectively. $k_{i,\mathrm{lysis}}$ is the rate constant of the dead cell lyses and the impurity dissolution, where $i$ includes dead cell, HCP, and DNA. $k_\mathrm{acid}$ and $k_\mathrm{base}$ are the rate constants for changes of main charge variants into acidic and basic charge variants. $Y_{i/X_\mathrm{v},X_\mathrm{d}}$ [mg cell$^{-1}$] is the mass of impurity $i$ released from a viable cell and a lysed dead cell, where $i$ includes HCP and DNA.

## Parameter estimation of the mechanistic model

Time series data from 20 experiments across three cycles were used for parameter estimation, and a part of the results are shown in Figure 2. The experimental data indicated that lactate repeated cycles of production and consumption, and viable cell density saturated in the later stages. However, due to the constant $Q_\mathrm{lac}$ previously addressed for improvement [2], and the exponential form of the viable cell density equation, the mechanistic model could not capture the behavior of lactate and viable cell density.

## Hybrid modeling

To address the issues mentioned above, a hybrid model was developed. Utilizing a hybrid model can contribute to overcoming the challenge of fully elucidating the biological phenomena causing lactate shifts and cell growth saturation, and to avoid increasing the number of estimated parameters. The hybrid model, whose overview is shown in Figure 3, maintained the mass balance of the mechanistic model while estimating the coefficients $\mu - \mu_\mathrm{d}$ and $Q_\mathrm{lac}$ with a data-driven model as shown in Eq. (10).

$$Coef = f\left(t, V, t_\mathrm{in}, t_{\mathrm{in,glc}}, F_\mathrm{in}, F_{\mathrm{in,glc}}, agitation, DO\right) \quad (10)$$

where $Coef$ represents $\mu - \mu_\mathrm{d}$ and $Q_\mathrm{lac}$. Since the values of $Q_\mathrm{lac}$ and $\mu - \mu_\mathrm{d}$ change dynamically, the model inputs included not only constant experimental conditions (agitation speed, DO, feed/glucose feed rate, and feed/glucose feed start timing), but also dynamically changing

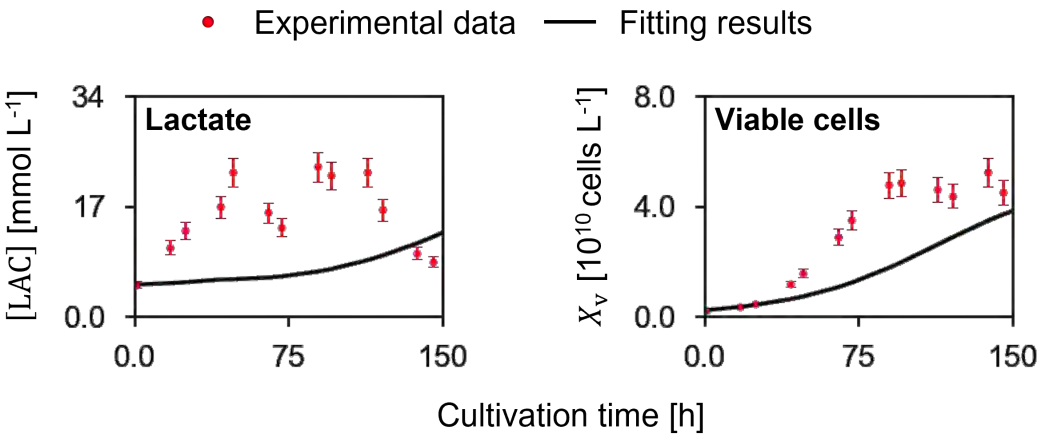



**Figure 2:** A part of the modeling results based on the mechanistic model.

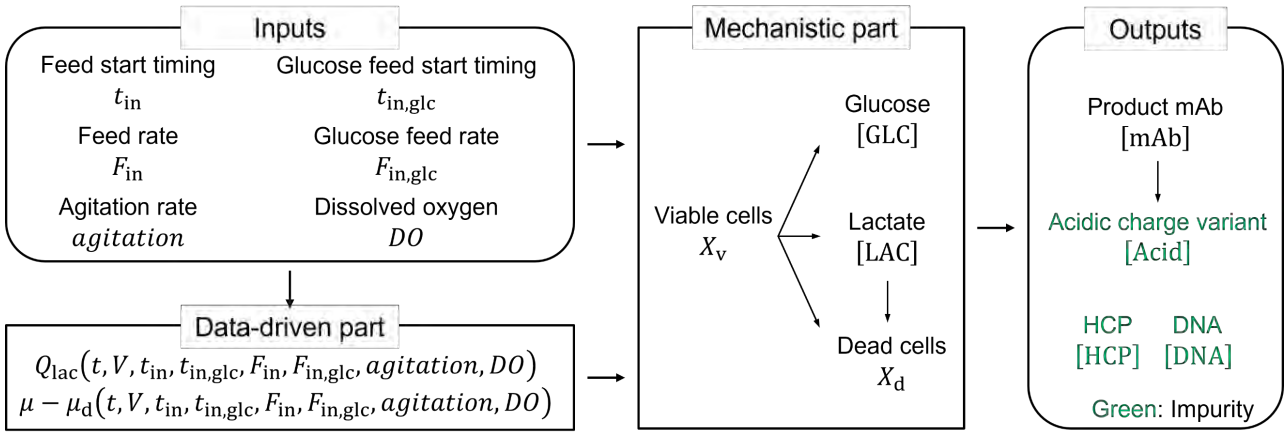



**Figure 3:** Overview of the developed hybrid model.

cultivation time and solution volume. Random forest regression was selected as a method for the data-driven model due to its high accuracy. In model development, experimental data were interpolated to compensate for the limited amount of data, and the values of $\mu - \mu_d$ and $Q_{lac}$ were calculated based on the interpolated values using Eqs. (1) and (4), respectively. To avoid overfitting, a portion of the calculated values was extracted, and the model was developed based on the values. Time series data from 20 experiments across three cycles were used for parameter estimation, and a part of the results are shown in Figure 4. Table 3 presents the average values

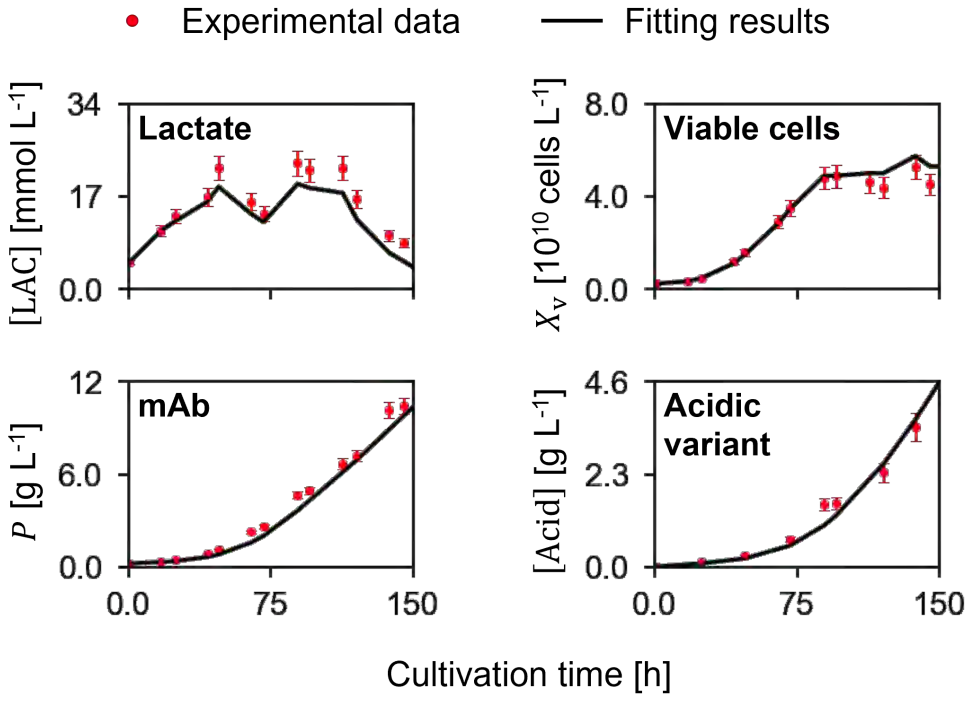



**Figure 4:** A part of the modeling results based on the hybrid model.

**Table 3:** Average values of $R^2$ and NRMSE for each component.

| | $X_v$ | $X_d$ | [GLC] | [LAC] | $P$ | [Main] | [Acid] | [HCP] | [DNA] |
|---|---|---|---|---|---|---|---|---|---|
| $R^2$ | 0.99 | 0.70 | 0.85 | 0.86 | 0.95 | 0.92 | 0.92 | 0.68 | 0.69 |
| NRMSE | 0.035 | 0.16 | 0.10 | 0.10 | 0.078 | 0.099 | 0.091 | 0.19 | 0.18 |

of $R^2$ and NRMSE for all training datasets used in the estimation for each component. The results indicated that high $R^2$ values and low NRMSE values were obtained for all components, showing that the model could capture not only the behavior of mAb but also impurities across a wide range of cultivation conditions.

## MODEL APPLICATION

A model-based assessment of cultivation conditions was conducted by using the developed hybrid model. In the assessment, a design problem was formulated to maximize mAb while keeping impurity levels low as shown in the following equation:

$$\max\ [\mathrm{mAb}]\left(t, t_{\mathrm{in}}, t_{\mathrm{in,glc}}, F_{\mathrm{in}}, F_{\mathrm{in,glc}}, agitation, DO\right) \quad (11)$$

subject to

$$\begin{aligned}
t\ [\mathrm{h}] &\leq 145\\
[\mathrm{HCP}]\ [\mathrm{g\ L^{-1}}] &\leq 2.2\\
[\mathrm{DNA}]\ [\mathrm{g\ L^{-1}}] &\leq 0.42\\
[\mathrm{Acid}]/P\ [\%] &\leq 40\\
t_{\mathrm{in}}\ [\mathrm{h}] &\in \{42, 48\}\\
t_{\mathrm{in,glc}}\ [\mathrm{h}] &\in \{42, 48\}\\
F_{\mathrm{in}}\ [V_0\ \mathrm{day^{-1}}] &\in \{0.08, 0.1\}\\
F_{\mathrm{in,glc}}\ [\mathrm{g\ L^{-1}\ day^{-1}}] &\in \{5, 6, \ldots, 17, 18, 18.8\}\\
Agitation\ [\mathrm{rpm}] &\in \{700, 800, \ldots, 1300, 1400\}\\
DO\ [\%] &\in \{20, 30, 40, 50\}
\end{aligned}$$

where $t$ [h] represents cultivation time. In the design problem, impurity values in the constraint were set according to expert opinions. Based on the design problem, 3,840 cultivation conditions were explored, with results evaluated at each one-hour interval of cultivation time. Table 4 shows the top three conditions with the highest mAb values satisfying the constraints, along with the corresponding cultivation time.

Figure 5 shows the simulation results for the top three conditions. In the simulations, glucose levels remained low but non-depleted until the later stages of the cultivation and only became depleted at the end of the cultivation. Glucose is widely recognized as a critical factor for both cell growth and mAb production; however, glucose levels are proportional to osmolarity, and high osmolarity is known to have a negative impact on cell growth [12]. Therefore, it was found that setting conditions to maintain appropriate glucose levels was important. Furthermore, the simulation results revealed that both mAb and impurities increased over time, indicating that setting an appropriate cultivation duration was crucial to obtaining more mAb while keeping impurity levels low.

**Table 4:** Top three conditions with the highest mAb values satisfying the constraints.

| Rank | $t_{\mathrm{in}}$ | $t_{\mathrm{in,glc}}$ | $F_{\mathrm{in}}$ | $F_{\mathrm{in,glc}}$ | $Agitation$ | $DO$ | $t$ |
|---|---|---|---|---|---|---|---|
| 1 | 48 | 42 | 0.1 | 15 | 700 | 40 | 135 |
| 2 | 48 | 42 | 0.1 | 15 | 1000 | 50 | 135 |
| 3 | 42 | 48 | 0.1 | 14 | 700 | 40 | 136 |

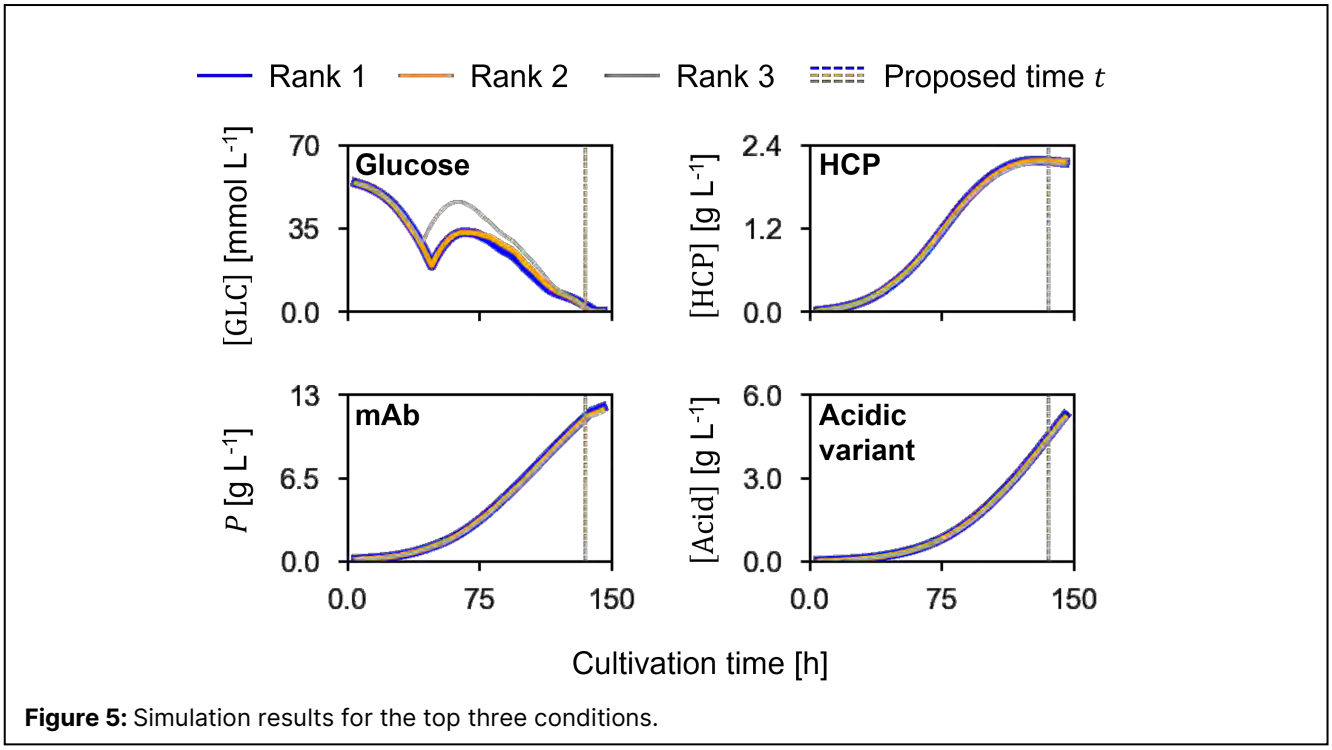



**Figure 5:** Simulation results for the top three conditions.

## CONCLUSIONS AND OUTLOOK

This work presented a hybrid-modeling approach to mAb production process design. Using automated bioreactor equipment enabled the acquisition of experimental data that covers a reasonable yet broad range. Using this data, a model applicable to a wide range of cultivation conditions was developed. In the hybrid model, the coefficients of the mechanistic model were estimated with a data-driven model, while maintaining the mass balance of the systems components. In the case study, the model enabled determination of a cultivation condition that maximized the product mAb concentration with meeting the impurity constraints out of 3,840 candidates. This work supports model-based design of cell cultivation processes with considering the multi-input & multi-output nature of the process. The future work includes expansion to dynamic optimization, operation support, and integration with purification processes.

## ACKNOWLEDGEMENTS

This work was supported by the Japan Agency for Medical Research and Development (AMED) under Grant Number JP21ae0121015.

## REFERENCES

1. Masuda, K., Kubota, M., Nakazawa, Y., Iwama, C., Watanabe, K., Ishikawa, N., Tanabe, Y., Kono, S., Tanemura, H., Takahashi, S., Makino, T., Okumura, T., Horiuchi, T., Nonaka, K., Murakami, S., Kamihira, M., Omasa, T. Establishment of a novel cell line, CHO-MK, derived from Chinese hamster ovary tissues for biologics manufacturing. *J. Biosci. Bioeng.* 137:471-479 (2024) https://doi.org/10.1016/j.jbiosc.2024.02.005
2. Okamura, K., Badr, S., Murakami, S., Sugiyama, H. Hybrid Modeling of CHO Cell Cultivation in Monoclonal Antibody Production with an Impurity Generation Module. *Ind. Eng. Chem. Res.* 61:14898-14909 (2022) https://doi.org/10.1021/acs.iecr.2c00736
3. Ha, T.K., Kim, D., Kim, C.L., Grav, L.M., Lee, G.M. Factors affecting the quality of therapeutic proteins in recombinant Chinese hamster ovary cell culture. *Biotechnol Adv.* 54:107831 (2022) https://doi.org/10.1016/j.biotechadv.2021.107831
4. Badr, S., Sugiyama, H. A PSE perspective for the efficient production of monoclonal antibodies: integration of process, cell, and product design aspects. *Curr. Opin. Chem. Eng.* 27:121-128 (2020) https://doi.org/10.1016/j.coche.2020.01.003
5. Agarwal, P., McCready, C., Ng, S.K., Ng, J.C., van de Laar, J., Pennings, M., Zijlstra, G. Hybrid modeling for in silico optimization of a dynamic perfusion cell culture process. *Biotechnol. Prog.* (2024) https://doi.org/10.1002/btpr.3503
6. Yatipanthalawa, B.S., Wallace Fitzsimons, S.E., Horning, T., Lee, Y.Y., Gras, S.L. Development and validation of a hybrid model for prediction of viable cell density, titer and cumulative glucose consumption in a mammalian cell culture system. *Comput. Chem. Eng.* 184:108648 (2024) https://doi.org/10.1016/j.compchemeng.2024.108648
7. Polak, J., Huang, Z., Sokolov, M., von Stosch, M., Butté, A., Hodgman, C., Borys, M., Khetan, A. An innovative hybrid modeling approach for simultaneous prediction of cell culture process dynamics and product quality. *Biotechnol. J.* 19:2300473 (2024) https://doi.org/10.1002/biot.202300473
8. Pinto, J., Ramos, J.R.C., Costa, R.S., Rossell, S., Dumas, P., Oliveira, R. Hybrid deep modeling of a CHO-K1 fed-batch process: combining first-principles with deep neural networks. *Front. Bioeng. Biotechnol.* 11: 1237963 (2023) https://doi.org/10.1016/j.coche.2020.01.003
9. Narayanan, H., Luna, M., Sokolov, M., Butté, A., Morbidelli, M. Hybrid Models Based on Machine Learning and an Increasing Degree of Process Knowledge: Application to Cell Culture Processes. *Ind. Eng. Chem. Res.* 61:8658-8672 (2022) https://doi.org/10.1021/acs.iecr.1c04507
10. Xing, Z., Bishop, N., Leister, K., Li, Z.J. Modeling kinetics of a large-scale fed-batch CHO cell culture by markov chain monte carlo method. *Biotechnol. Prog.* 26:208-219 (2010) https://doi.org/10.1002/btpr.284
11. Badr, S., Okamura, K., Takahashi, N., Ubbenjans, V., Shirahata, H., Sugiyama, H. Integrated design of biopharmaceutical manufacturing processes: Operation modes and process configurations for monoclonal antibody production. *Comput. Chem. Eng.* 153:107422 (2021) https://doi.org/10.1016/j.compchemeng.2021.107422
12. Alhuthali, S., Kotidis, P., Kontoravdi, C., Osmolality effects on cho cell growth, cell volume, antibody productivity and glycosylation. *Int. J. Mol. Sci.* 22:3290 (2021) https://doi.org/10.3390/ijms22073290

© 2025 by the authors. Licensed to PSEcommunity.org and PSE Press. This is an open access article under the creative commons CC-BY-SA licensing terms. Credit must be given to creator and adaptations must be shared under the same terms. See https://creativecommons.org/licenses/by-sa/4.0/



Systems & Control Transactions

**Research Article - Peer Reviewed Conference Proceeding**
ESCAPE 35 - European Symposium on Computer Aided Process Engineering
Ghent, Belgium. 6-9 July 2025
Jan F.M. Van Impe, Grégoire Léonard, Satyajeet S. Bhonsale,
Monika E. Polańska, Filip Logist (Eds.)

PSE PRESS

# Kinetic modeling of drug substance synthesis considering slug flow characteristics in a liquid-liquid reaction

**Shunsei Yayabe[a], Junu Kim[a], Yusuke Hayashi[a], Kazuya Okamoto[b], Keisuke Shibukawa[b], Hayao Nakanishi[b], Hirokazu Sugiyama[a]***

[a] Department of Chemical System Engineering, The University of Tokyo, 7-3-1, Hongo, Bunkyo Ward, Tokyo, 113-8656, JAPAN
[b] Technology Development Division, Shionogi Pharma Co., Ltd. Hyogo, 660-0813, JAPAN
* Corresponding Author: sugiyama@chemsys.t.u-tokyo.ac.jp.

## ABSTRACT

This work presents a kinetic model of drug substance synthesis considering slug flow characteristics in Stevens oxidation. The developed model is also applied to determine the feasible range of the process parameters. Flow experiments were conducted to obtain kinetic data, varying the inner diameter, temperature, and residence time. A kinetic model was developed for the change in concentrations of the starting material, products, and catalysis. In the kinetic model, slug flow was considered by including a volumetric mass transfer coefficient during this flow. In the initial experiments, early-stage kinetic data were insufficient, conducting additional experiments at shorter residence times. Furthermore, the initial model could not reproduce the residual of the starting material, introducing the oxidant consumption that inhibits the starting material consumption and improving the initial model. The improved model could reproduce experimental results and demonstrated that, as the inner diameter increases, the efficiency of mass transfer in slug flow decreases with slowing down the reaction. Moreover, the improved model was considered applicable to different scales. The developed model was used to simulate the yields of the desired product, and the dimer, and the process mass intensity, thereby determining the feasible range. As a result, it was shown that when methanol and oxidant concentration was either too high or too low, operating conditions fell outside the feasible range. This kinetic model with flow characteristics will be useful for the process design of drug substance synthesis using liquid-liquid reactions.

**Keywords**: Modelling and Simulations, Modelling, Simulation, Process Design

## INTRODUCTION

Recently, in the production of drug substances (or active pharmaceutical ingredients), flow synthesis has attracted attention as an effective method. Flow synthesis is increasingly being introduced due to its various advantages, such as high surface volume ratio and small system size compared to conventional batch synthesis [1,2]. One of the promising applications that leverages the advantages of flow synthesis is liquid-liquid reactions [3,4]. By performing these reactions in flow synthesis, the interfacial contact between immiscible liquids could be increased, which is expected to enhance process efficiency.

When two immiscible liquids enter together in a flow reactor, unique flow patterns, especially like slug flow, are formed [5]. Slug flow is a phenomenon where the liquids flow in alternating enclosed segments, making a dynamic interface. Flow patterns like slug flow are determined by the liquid properties (e.g., viscosity and density) and the reactor specifications and have a significant impact on the mass transfer. Previous studies have investigated the effect of slug flow on mass transfer in liquid-liquid reactions using computational fluid dynamics [6,7] and explored flow pattern changes in solvents and reactor specifications and improvements in mass transfer [8,9]. These studies provide valuable insights into the influence of flow characteristics on reaction. However, there is a lack of modeling approaches that simultaneously account for flow characteristics and reaction kinetics. The absence of such models prevents understanding the interaction between flow characteristics and reaction

kinetics, potentially resulting in suboptimal process design and diminishing yields in practical application.

In this study, we developed a kinetic model of drug substance synthesis by incorporating slug flow characteristics in a liquid-liquid reaction, with the aim to determine a feasible range of the process parameters. The target reaction was Stevens oxidation, which is a novel liquid-liquid reaction of organic and aqueous phases, producing the ester via a shorter pathway than the conventional route [10]. In this reaction, a catalyst which moves between organic and aqueous phases was used, and slug flow formation was necessary to enhance mass transfer efficiency. A model can consider slug flow characteristics. In pharmaceutical industry, models are effective in reducing the number of experiments. By using models, it becomes possible to identify a feasible range of the process parameters that satisfies quality. Therefore, the developed model was utilized to define the feasible range.

## MATERIALS AND METHODS

### Target Reaction and Flow Experiments

Figure 1 shows the target Stevens oxidation and the flow experiment overview. In this reaction, (4-nitrophenyl) methanol (SM, starting material) undergoes a reaction with methanol (MeOH), and oxidant (NaOCl). Tetrabutylammonium bromide (TBAB) is the catalyst which moves between the organic and aqueous phases. The ester methyl 4-nitrobenzoate (DP, desired product), the impurity 4-nitrobenzyl 4-nitrobenzoate (Dimer), 4-nitrobenzoic acid (CA, carboxylic acid), 4-nitrobenzaldehyde (Ald, aldehyde) are produced.

In the flow experiments, the inner diameter, temperature, and residence time were varied in different runs. Experimental conditions were adjusted to form slug flow to promote the catalyst's mass transfer. High-performance liquid chromatography (HPLC) was used to quantify the concentrations of SM, DP, Dimer, CA, and Ald in the samples.

### Model Development

Figure 2 shows a calculation flow on the developed model. The inputs were defined as the equivalent concentration of MeOH, $C_{\mathrm{MeOH}}$ [equivalent], and the equivalent concentration of NaOCl, $C_{\mathrm{NaOCl}}$ [equivalent]. The outputs were defined as the yield of the desired product, $y_{\mathrm{DP}}$ [%], the yield of the dimer, $y_{\mathrm{Dimer}}$ [%], and the process mass intensity, PMI, which are evaluation indicators, respectively.

#### Kinetic model

The kinetic model was developed for the changes in concentration of SM, DP, Dimer, CA, Ald, and the catalyst.

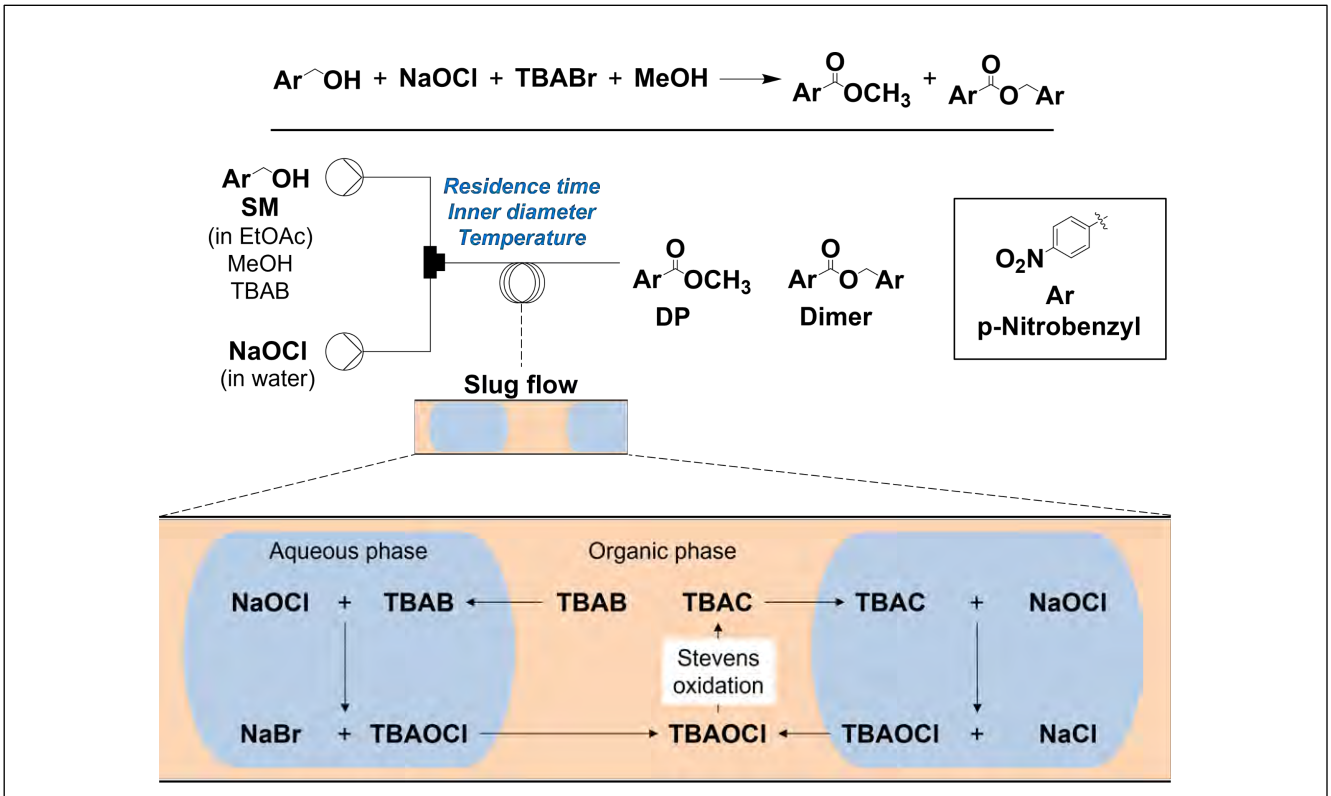



**Figure 1.** Target Stevens oxidation and the flow experiment overview. The blue text indicates the conditions varied in the experiments. TBAB moves from the organic phase to the aqueous phase, becoming the active form TBAOCl. TBAOCl then moves to the organic phase, reacting with the starting material to produce various products.

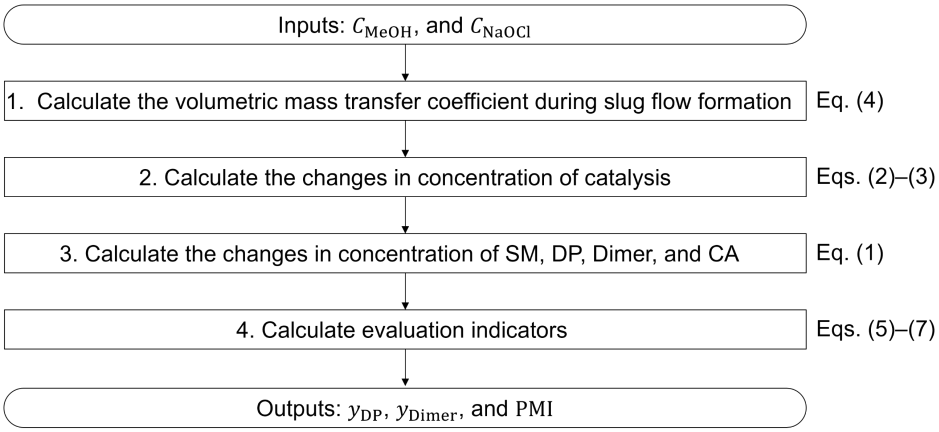



**Figure 2.** Calculation flow using the developed model. In the 1st step, the overall volumetric mass transfer coefficient during slug flow formation is calculated using Eq. (4). In the 2nd step, the changes in concentration of catalysis are calculated using Eqs. (2)–(3). In the 3rd step, the changes in concentration of SM and products are calculated using Eq. (1). Finally, in the 4th step, the evaluation indicators are calculated using Eqs.(5)–(7).

In the changes in the catalyst concentration model, slug flow was considered using the overall volumetric mass transfer coefficient during this flow formation. The changes in concentration were modelled as follows:

$$\frac{dC_i}{dt} = -r \quad (1)$$

$$\frac{dC_{j,\mathrm{org}}}{dt} = -Ka_{\mathrm{org}}\left(\frac{1}{m}C_{j,\mathrm{org}} - C_{j,\mathrm{aqu}}\right) - r \quad (2)$$

$$\frac{dC_{j,\mathrm{aqu}}}{dt} = -Ka_{\mathrm{aqu}}\left(mC_{j,\mathrm{aqu}} - C_{j,\mathrm{org}}\right) - r \quad (3)$$

Here, $C_i$ [mol m$^{-3}$] is the concentrations of $i$ (SM, DP, Dimer, CA, and Ald), $C_{j,\mathrm{org}}$ and $C_{j,\mathrm{aqu}}$ [mol m$^{-3}$] is the concentrations of $j$ (TBAB, TBAOCl, and TBAC) in the organic and aqueous phases, $r$ [mol m$^{-3}$ s$^{-1}$] is the reaction rate, $m$ [–] is the partition coefficient, $Ka$ [s$^{-1}$] is the overall volumetric mass transfer coefficients in the organic and aqueous phases, and it was defined as follows [11]:

$$Ka_p\frac{L}{u_p} = \alpha Ca^{\beta}Re^{\gamma}\left(\frac{d}{L}\right)^{\delta}\left(\frac{L_p}{d}\right)^{\varepsilon} \quad (4)$$

Here, $p$ is the phase (organic or aqueous), $L$ [m] is the reactor length, $u$ [m s$^{-1}$] is the flow velocity, $Ca$ [–] is the mean capillary number of two phase, $Re$ [–] is the mean Reynolds number of two phase, $d$ [m] is the inner diameter, $L_p$ [m] is the slug phase length in the organic and aqueous phases, and $\alpha, \beta, \gamma, \delta$, and $\varepsilon$ are estimated parameters.

## Evaluation model

To determine a feasible range of the process parameters, three evaluation indicators were determined in this study, namely, the yield of the desired product ($y_{\mathrm{DP}}$) [%], the yield of the dimer ($y_{\mathrm{Dimer}}$) [%], the process mass intensity (PMI) as follows:

$$y_{\mathrm{DP}} = \frac{C_{\mathrm{DP}}(L)}{C_{\mathrm{SM}}(0)} \times 100 \quad (5)$$

$$y_{\mathrm{Dimer}} = \frac{C_{\mathrm{Dimer}}(L)}{C_{\mathrm{SM}}(0)} \times 100 \quad (6)$$

$$\mathrm{PMI} = \frac{mass_{\mathrm{SM}}(0)+mass_{\mathrm{MeOH}}(0)+mass_{\mathrm{NaOCl}}(0)+mass_{\mathrm{TBAB}}(0)}{mass_{\mathrm{DP}}(L)} \quad (7)$$

Here, $y_{\mathrm{DP}}$ and $y_{\mathrm{Diemr}}$ [–] are the yields of DP and Dimer, PMI [–] is the process mass intensity,$C_{\mathrm{SM}}(0)$ [mol m$^{-3}$] is the initial concentration of SM at the inlet, $C_{\mathrm{DP}}(L)$ and $C_{\mathrm{Dimer}}(L)$ [mol m$^{-3}$] are the concentrations of DP and Dimer at the outlet, $mass_i(0)$ [kg] is the mass of $i$ (SM, MeOH, NaOCl, or TBAB) at the inlet, and $mass_{\mathrm{DP}}(L)$ [kg] and $mass_{\mathrm{Dimer}}(L)$ [kg] is the mass of DP and Dimer at the outlet.

## Condition settings for feasible range

The feasible range was formulated as follows:

$$FR = \{(C_{\mathrm{MeOH}}, C_{\mathrm{NaOCl}}) : z(\boldsymbol{Y}) = 1\} \quad (8)$$

Subject to

$$z(\boldsymbol{Y}) = \begin{cases} 0\ (\boldsymbol{Y} \notin S) \\ 1\ (\boldsymbol{Y} \in S) \end{cases}$$

$$\boldsymbol{Y} = f(C_{\mathrm{MeOH}}, C_{\mathrm{NaOCl}}, T, L, d, Q)$$

$$S = \{(y_{\mathrm{DP}}, y_{\mathrm{Dimer}}, PMI) : y_{\mathrm{DP}} \geq 88, y_{\mathrm{Dimer}} \leq 5, \mathrm{PMI} \leq 15\}$$

$$C_{\mathrm{MeOH}} \in \{10, 20, \ldots, 70, 80\}$$

$$C_{\mathrm{NaOCl}} \in \{3.0, 4.0, \ldots, 7.0, 8.0\}$$

Here, $FR$ is the feasible range, $z$ takes the value of 1 if all evaluation indicators are satisfied and 0 if at least one evaluation indicator is not satisfied, $S$ is a set of evaluation indicator constraints, and $\boldsymbol{Y}$ is the prediction results. In addition, $T$ is temperature [K] and $Q$ is the volume flow rate [mL m$^{-1}$].

## RESULTS AND DISCUSSION

### Kinetic analysis

Fitting results of the initial model are shown in Figure 3(a). In the experimental conditions of $(T, d) = (323, 0.5)$, minimal changes in concentration were observed, and it was believed that the reaction had completed within the measurement residence time. Consequently, additional experiments were performed at shorter residence times of $d = 0.5$ mm to obtain kinetic data during the early-stage reaction (Figure 3(b)). The initial model was unable to reproduce the results that included additional experiments. And then, residual SM was observed in the experiments, whereas the model predictions indicated its complete consumption. To address this discrepancy, the following hypothesis was proposed: SM undergoes with oxidant but competes with a mechanism in which oxidant is

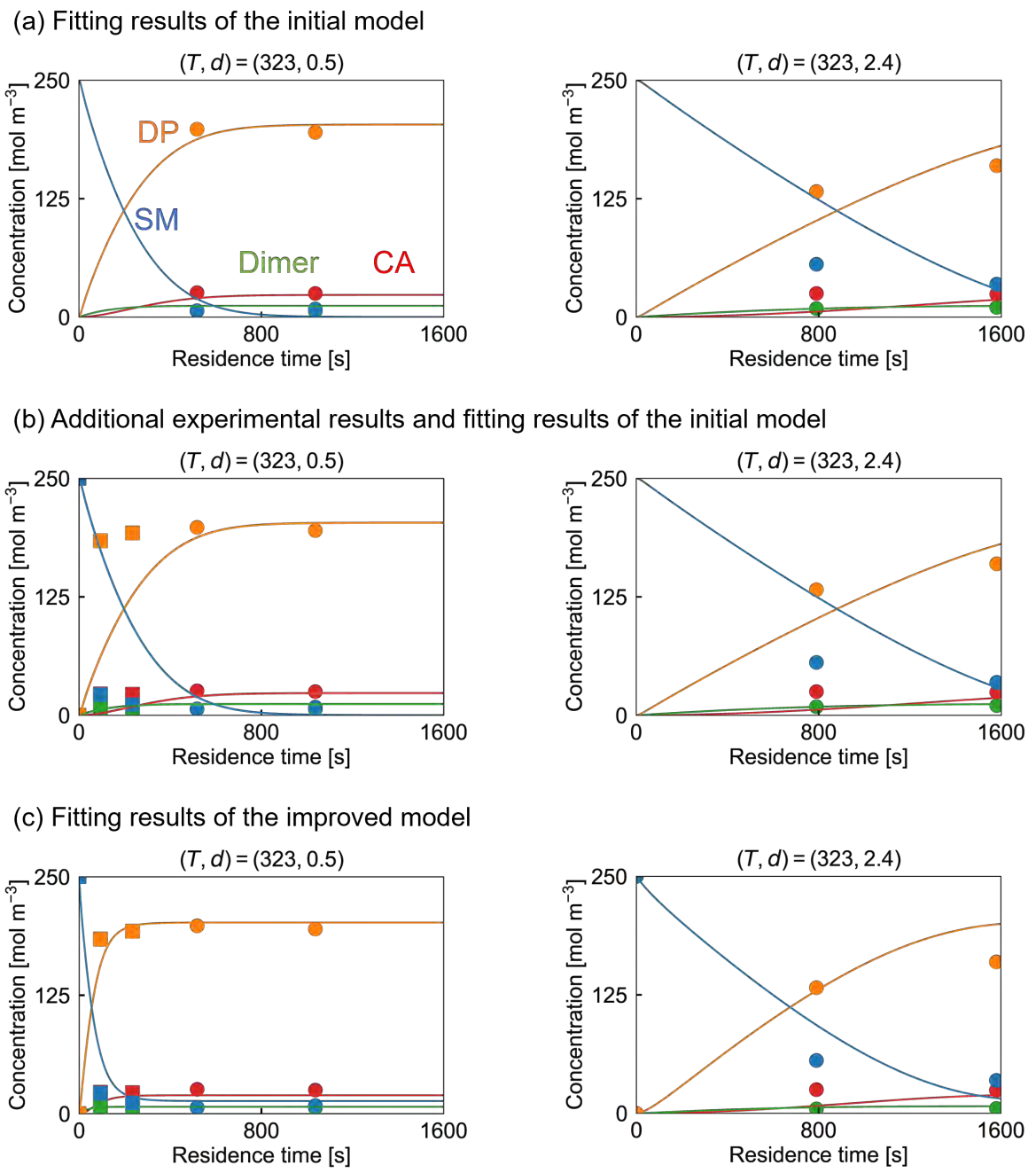



**Figure 3.** Fitting results, (a) of the initial model, (b) of the initial model only to the initial experimental results, and (b) of the improved model to all experimental results. Circules represent the initial experimental results, and squares represent the additional experimental results

consumed through a different pathway, thereby limiting the consumption of SM. Based on the hypothesis, the methanol oxidation mechanism was added as an alternative pathway for the consumption of oxidant, and the model was improved accordingly. The improved model was used to conduct kinetic analysis again.

Fitting results of the improved model are shown in Figure 3(c). The average value of determination coefficients ($R^2$) of SM, DP, Dimer, and CA for all experimental conditions was 0.96, which means the model could reasonably reproduce experimental results. In this way, analyzing the discrepancies of the simulation results and the experimental results made it possible to select effective experimental conditions for the model development. The experimental results indicated that the reaction is slower under conditions with a larger inner diameter compared to those with a smaller inner diameter. This is believed to be due to the reduced mass transfer enhancement effect of slug flow as the inner diameter increases, resulting in a longer time required for catalyst movement. Indeed, it has been reported that larger inner diameters lead to slower mass transfer rates [12]. The model predicted that, as the inner diameter increased, the efficiency of mass transfer in slug flow decreased with slowing the reaction, which is a similar trend of experiments. Therefore, we judged that the developed model could consider the slug flow characteristics and adopt to different scales and provide sufficient performance for determining the feasible range.

## Feasible range determination and analysis

To determine a feasible range of the process parameters, the developed model was used to simulate the three evaluation indicators. The simulations were conducted within the range of the equivalent concentration of MeOH and NaOCl, as defined in Eq. (8). Figure 4 presents the results of (a) the yield of the desired product, (b) the yield of the dimer, (c) the PMI, and (d) feasible range. According to the simulation results, the high equivalent concentration of MeOH and NaOCl enhanced the yield of the desired product, and the high equivalent concentration of MeOH diminished the yield of the dimer. In contrast, as depicted in Figure 4(c), increasing the equivalent concentrations of MeOH and NaOCl caused to escalate the process mass intensity. High quality, meaning a large amount of DP and a small amount of Dimer,

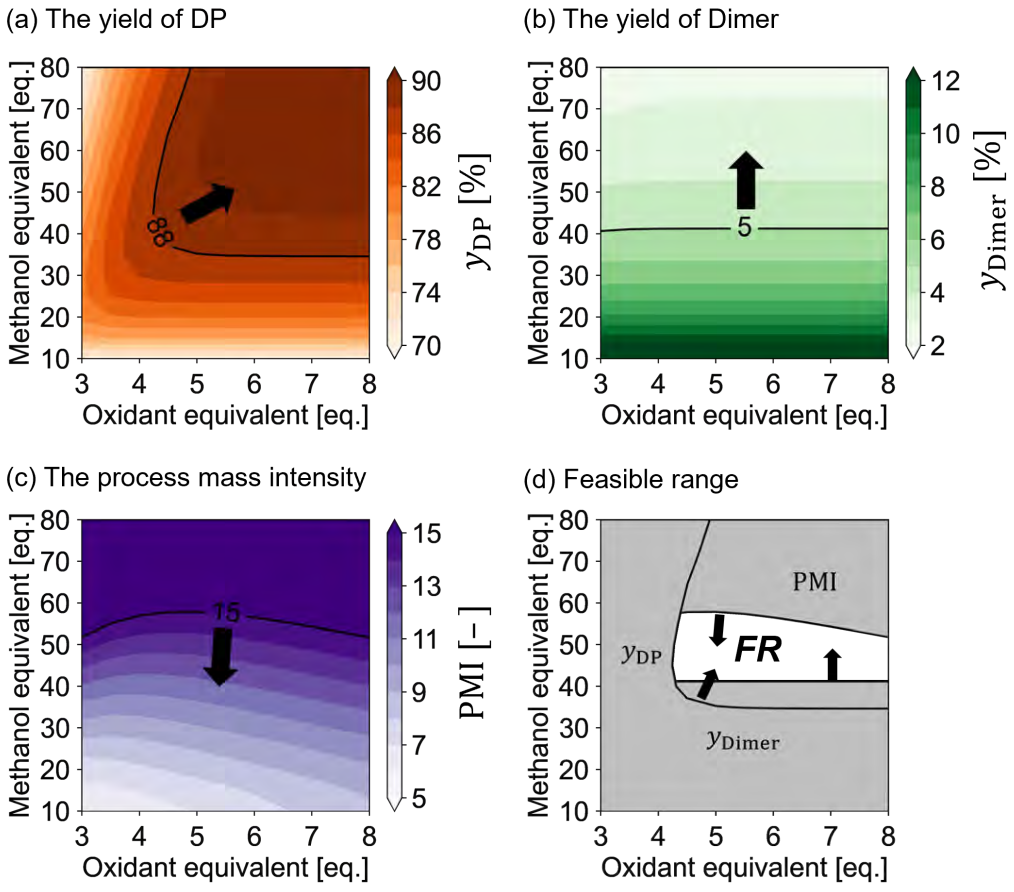



**Figure 4.** Simulation results for the individual evaluation indicators: (a) $y_{DP}$ (b) $y_{Dimer}$ (c) PMI, and (d) the determied feasible range using the developed model.

was achieved with the high equivalent concentrations ($C_{\mathrm{MeOH}}$ and $C_{\mathrm{NaOCl}}$). Conversely, low waste was attained at the low equivalent concentrations, indicating a trade-off in regent quantity. Figure 4(d) shows the feasible range which satisfies the predefined constraints in Eq. (8) ($y_{\mathrm{DP}} \geq 88, y_{\mathrm{Dimer}} \leq 5, \mathrm{PMI} \leq 15$), indicated by the white area. Within the range of the lower equivalent concentration of MeOH, the process did not meet the yield of the dimer. When the equivalent concentrations were too high, operating conditions fell outside the feasible range due to not satisfying the process mass intensity constraints. This feasible range could facilitate the identification of the process parameters that satisfied the constraints. Additionally, the feasible range could consider uncertainty and measurement noise by introducing stochastic approach such as Monte Carlo simulation.

## CONCLUSIONS AND OUTLOOK

We presented the kinetic model of drug substance synthesis by incorporating slug flow characteristics and demonstrated the feasible range in Stevens oxidation. Flow experiments were conducted to obtain kinetic data, and a kinetic model considering flow characteristics was developed. For feasible range determination, the evaluation indicators developed, the yields and the process mass intensity. Utilizing the determined indicators, the feasible range was discussed, which could help in determining operating conditions. The kinetic model with slug flow characteristics would be useful for the process design of drug substance synthesis using liquid-liquid reactions. Future work includes conducting validation of the feasible range and presenting the scale-up strategy based on the simulation results using the developed model.

## REFERENCES


1. Diab S, Raiyat M, and Gerogiorgis D. Flow synthesis kinetics for lomustine, an anti-cancer active pharmaceutical ingredient. *React Chem Eng* 6:1819–1828 (2021) https://doi.org/10.1039/d1re00184a
2. Silber K, Sagmeister P, Schiller C, Williams J, Hone C, and Kappe C. Accelerating reaction modeling using dynamic flow experiments, part 2: development of a digital twin. *React Chem Eng* 8:2849–2855 (2023) https://doi.org/10.1039/d3re00244f
3. Capaldo L, Wen Z, and Noël T. A field guide to flow chemistry for synthetic organic chemists. *Chem Sci* 16: 4230–4247 (2023) https://doi.org/10.1039/d3sc00992k
4. Plutschack M, Pieber B, Gilmore K, Seeberger P. The hitchhiker's guide to flow chemistry. *Chem Rev* 117: 11796–11893 (2017) https://doi.org/10.1021/acs.chemrev.7b00183
5. Ramji S, Rakesh A, Pushpavanam S. Modelling mass transfer in liquid-liquid slug flow in a microchannel. *Chem Eng J* 364:280–291 (2019) https://doi.org/10.1016/j.cej.2019.01.075
6. Cheng D, and Chen FE. Experimental and Numerical Studies of the Phase-Transfer-Catalyzed Wittig Reaction in Liquid-Liquid Slug-Flow Microchannels. *Ind Eng Chem Res* 59:4397–4410 (2020) https://doi.org/10.1021/acs.iecr.0c00130
7. Mittal A, Bhattacharyya S, Marino M, Chen TY, Desir P, Ierapetritou M, and Vlachos DG. Effect of Scale-Up on Mass Transfer and Flow Patterns in Liquid-Liquid Flows Using Experiments and Computations. *Ind Eng Chem Res* 62:15006–15017 (2023) https://doi.org/10.1021/acs.iecr.3c02284
8. Wei Y, Zhao S, Yu P, Yuan F, Li C, He W, Zhu N, Li Y, Ji D, and Guo K. Comparative studies of fluid mixing and heat transfer behaviors in a millimeter scale T-type mixer with triangular baffles. *Case Stud Therm Eng* 47:103076 (2023) https://doi.org/10.1016/j.csite.2023.103076
9. Yang N, Xiao Z, Liu F, Jiang J, Liu Z, Liu H, Yang X, and Wang R. Enhanced liquid–liquid mass transfer in a monolithic reactor with multi-jet-channel in the circumferential array. *Sep Purif Technol* 333: 125749 (2024). https://doi.org/10.1016/j.seppur.2023.125749
10. Wan L, Jiang M, Cheng D, Liu M, and Chen F. Continuous flow technology-a tool for safer oxidation chemistry. *React Chem Eng* 3: 490–550 (2022) https://doi.org/10.1039/d1re00520k
11. Kashid MN, Gupta A, Renken A, and Kiwi-Minsker L. Numbering-up and mass transfer studies of liquid-liquid two-phase microstructured reactors. *Chem Eng J* 158:233–240 (2010) https://doi.org/10.1016/j.cej.2010.01.020
12. Zhang Q, Liu H, Zhao S, Yao C, and Chen G. Hydrodynamics and mass transfer characteristics of liquid–liquid slug flow in microchannels: The effects of temperature, fluid properties and channel size. *Chem Eng J* 15: 794–805 (2019) https://doi.org/10.1016/j.cej.2018.10.056



© 2025 by the authors. Licensed to PSEcommunity.org and PSE Press. This is an open access article under the creative commons CC-BY-SA licensing terms. Credit must be given to creator and adaptations must be shared under the same terms. See https://creativecommons.org/licenses/by-sa/4.0/




Systems & Control Transactions

**Research Article - Peer Reviewed Conference Proceeding**
ESCAPE 35 - European Symposium on Computer Aided Process Engineering
Ghent, Belgium. 6-9 July 2025
Jan F.M. Van Impe, Grégoire Léonard, Satyajeet S. Bhonsale,
Monika E. Polańska, Filip Logist (Eds.)

PSE PRESS

# Model-based approach to template-induced macromolecule crystallisation

**Daniele Pessina[a,b], Jorge Calderon de Anda[c], Claire Heffernan[c], Tony Tian[c], Oliver Watson[c], Jerry Y. Heng[a,d] and Maria M. Papathanasiou[a,b,*]**

[a] Sargent Centre for Process Systems Engineering, Imperial College London, SW7 2AZ, United Kingdom
[b] Department of Chemical Engineering, Imperial College London, SW7 2AZ, United Kingdom
[c] Chemical Development, Pharmaceutical Technology & Development, Operations, AstraZeneca, Macclesfield 9 SK10 2NA, U.K.
[d] Institute of Molecular Science, Department of Chemical Engineering, Imperial College London, SW7 2AZ, United Kingdom
* Corresponding Author: maria.papathanasiou11@imperial.ac.uk

## ABSTRACT

Biomacromolecules have intricate crystallisation behaviour due to their size and many interactions in solution and can often only crystallise in narrow ranges of experimental conditions. High solute concentrations are needed for crystal nucleation and growth, exceeding those eluted upstream and therefore preventing the adoption of crystallisation in downstream separation steps. By promoting molecular aggregation and nucleation via a lowered energy barrier, heterogeneous surfaces or templates can relax the supersaturation requirements and widen the crystallisation operating space. Though templates are promising candidates for process optimisation, their experimental testing has generally been limited to small-volume experiments, and quantification of their impact on process intensification and quality metrics at higher volumes remains unexplored. To address the knowledge gap, a model-based investigation of template-induced protein crystallisation systems through evaluation of key metrics is presented. Porous silica nano-particles with three chemical functionalisations (hydroxyl, carboxyl and butyl) are added to batch lysozyme crystallisation experiments at 40ml. Crystallisation population balance models are parametrised with an experimentally-validated parameter estimation methodology and further experiments are simulated. The templates appear to lower the estimated interfacial energy compared to the homogeneous case, leading to nucleation rate profiles which are less dependent on supersaturation. For this reason, the templates can crystallize quicker than the homogeneous system, particularly at lower initial concentrations. The simulation results highlight the ability of heteronucleants to alter nucleation rate profiles, and their potential to be used as process optimisation and intensification tools for biomacromolecule purification.

**Keywords**: Protein crystallisation, Template-induced nucleation, Population-balance modelling

## INTRODUCTION

Advanced therapeutic proteins, such as monoclonal antibodies and immunoglobins are effective at treating many chronic medical conditions [1]. Their increased demand and improvements in their upstream manufacturing have indicated the need for intensified and cost-effective downstream protein purification [2, 3]. Chromatographic units, currently able to separate the therapeutic proteins at very high purity, remain expensive, difficult to scale-up and have a significant environmental footprint [4]. It is therefore critical to identify alternative and more efficient purification methods that reduce costs and improve consumer access to the novel therapies being released on the market.

The majority of small-molecule active pharmaceutical ingredients (APIs) are purified through crystallisation, a first-order phase transition in which a highly pure, thermodynamically stable and easily filterable solid is formed in solution [5]. Crystalline formulations offer improved stability, purity, handling and storage compared to chromatography separation alternatives [6]. Due to the protein's size, structural flexibility and many sources of chemical interaction, the macromolecules often only

crystallise in narrow ranges of conditions, which are firstly difficult to identify and secondly restrict the crystalliser's operational flexibility [7]. High energetic barriers are associated with crystal nucleation since the proteins must rotate and fold to rearrange themselves into the ordered crystal lattice, requiring strong thermodynamic driving forces and high supersaturations. It is important to highlight that the minimum solute concentrations needed for crystallisation exceed those eluted by upstream processes prior to any purification steps [8]. Therefore, processes designed to produce solid formulations of advanced therapeutics require concentrating chromatographic purification steps before crystallisation becomes thermodynamically possible. If, however, minimum concentration requirements for crystallisation can be relaxed and low-supersaturation nucleation is facilitated, chromatographic units can be avoided to improve scale-up, costs and the environmental footprint of the processes.

Template-induced nucleation involves the use of additives in the crystallisation solution to favour molecular rearrangement into a nucleus through three methods: functional group matching, epitaxy, and topographic features [9]. Soft templates are dissolved additives, such as amino acids [10], which disrupt the protein's hydration layer and enhance favourable protein-protein interactions. Hard templates instead are un-dissolved, heterogeneous surfaces which, particularly through complementary surface chemistries and porous structures, promote protein aggregation and concentrate the protein to induce higher local supersaturations. Many template types have been shown to act as nucleation enhancers to lower concentration requirements for nucleation, as well as preferentially crystallising specific polymorphs [10–15]. However, template-induced nucleation investigations have generally been limited to small-volume studies to obtain diffraction-quality protein crystals [2], and there is a lack of reliable, quantitative information describing both how templates affect crystallisation kinetics and the extent to which template addition can drive process intensification. To the authors' knowledge, no comprehensive studies on the effect of templates on kinetic parameters and the crystallisation operating space have been published, and their impact on crystallisation process design remains uncertain. Fully-experimental characterisation of crystallisation kinetics requires time consuming and costly experiments, and solution volumes must be reduced to prevent excessive API use [16]. Population-balance models (PBMs) can be used to support the experimental campaign and accelerate process development with fewer, larger-scale experiments [17, 18]. Once the PBMs are parametrised, aspects of the crystallisation process such as nucleation rate, yield and crystal size profiles, which might be experimentally unavailable or costly to measure at scale, can be quickly queried through model simulations. By probing the PBMs for multiple crystalliser conditions, operating spaces of template-induced nucleation systems can be identified and assessed to support template adoption for pharmaceutical manufacturing. While previous studies on template-assisted protein crystallisation have studied templated-nucleation probabilities [8, 19], to the author's knowledge this is the first investigation of template-assisted nucleation that integrates PBMs to assess how the surfaces affect the operating spaces and support scale-up by aiding the selection of optimal initial conditions and residence times.

To this end, a model-based evaluation of template-induced protein crystallisation operating spaces is presented in this work. Lysozyme is crystallised homogeneously and in the presence of functionalised porous silica nano-particles (SNPs) at 40ml. PBMs are parametrised and used for high-throughput *in-silico* experimentation. The regressed models indicate that particularly at lower initial concentrations, template-induced nucleation is quicker and less dependent on supersaturation compared to the homogeneous system.

## METHODOLOGY

### Experimental protocol for lysozyme crystallisation

Lysozyme anti-solvent crystallisation experiments are performed at 40ml in a stirred batch crystalliser ($T = 20℃$, 0.1M sodium acetate buffer, pH $= 4.2$, [NaCl] $=$ $50$ mg/ml, 75 rpm stirring). Lysozyme is first dissolved and filtered through a 0.22$\mu$m filter to obtain buffered solutions of different lysozyme concentrations. NaCl is dissolved at $100$ mg/ml concentration in the sodium acetate buffer to prepare the anti-solvent solution. Crystallisation starts by mixing equal volumes of the protein and precipitant solution. Lysozyme concentration is monitored at regular time intervals using a Thermo Fisher NanoDrop One UV-Vis spectrophotometer unit by drawing approximately 0.1ml from the broth and filtering with a 0.22$\mu$m filter to prevent the solids from affecting UV absorbance. At batch termination, the solution is filtered and dried. The collected crystals are suspended in isopropyl alcohol for laser-diffraction particle size measurements with an Anton Paar PSA 1190 unit.

### Computational methodology

One-dimensional crystallisation PBMs are formulated and parametrised against the measured concentration profiles and crystal sizes to predict the crystallisation operating space. Firstly, aggregation and breakage are neglected in the population balance, a common and valid assumption for lysozyme crystallisation modelling [17, 20] (Eq. 1). Due to the balance's hyperbolic partial differential structure, the balance is solved transformed via the

Method of Moments [21], and the resulting 6 differential equations are solved in Julia, with access of model gradients though forward-mode automatic differentiation. A mass balance is included to model solute consumption (Eq. 3). Classical nucleation theory, power-law growth and negligible aggregation and breakage kinetics are assumed (Eq. 4,5). The nucleation and growth equations each require two kinetic parameters to be regressed. Parameter estimation and uncertainty quantification is carried out using a Markov Chain Monte Carlo No-U-Turn Sampler [22]. Uniform priors are used for candidate parameter sampling, and the negative log likelihood, an indicator of model mispredictions of the experimental measurements, is used to identify parameter posterior distributions. Each model was parametrised with experiments using at least two different initial conditions, and each experiment was repeated three times. Given that templates are assumed to only affect nucleation kinetics, growth parameters are estimated from template-free measurements and their posterior is fixed before template-induced nucleation parameters are estimated from their respective measurements. High-throughput *in-silico* experimentation is carried out by simulating each model for a range of initial concentrations and residence times and calculating process metrics of interest.

$$\frac{\partial n}{\partial t} + \frac{\partial (Gn)}{\partial L} = B_0 \delta (L - L_{min}) \quad (1)$$

$$S = {}^{c(t)}/_{c_{\text{sat.}}} \quad (2)$$

$$\frac{dc}{dt} = -3\rho_c k_v \int_0^\infty G n L^2 \, dL \quad (3)$$

$$\text{CNT} : B_0 = A_j S \exp\left(\frac{-16\pi\gamma^3 v_0^2}{3k_B^3 T^3 \ln^2 S}\right) \quad (4)$$

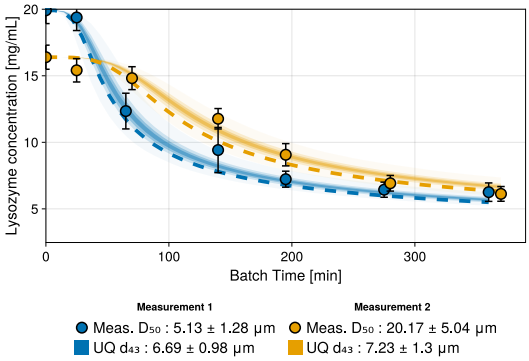
$$\text{Emp.} : G = A_g (S-1)^g \quad (5)$$

## RESULTS

Each of the parameter estimation routines appear to be successful, with good agreement to the experimental measurements. The model predictions of lysozyme crystallisation with carboxyl-functionalised silica templates are shown in Figure 1. The predicted concentration trajectories accurately capture the experimentally measured trends. Both the measured and predicted trajectories appear to have low uncertainty, suggesting the models can be used to predict each system's concentration and fractional yield for a wide range of initial conditions.

The measured average particle sizes have higher uncertainty. Average particle size prediction of Measurement 1 ($C_0 = 20$ mg/ml) appears to be accurate, with overlapping uncertainty ranges (Meas. $= 5.13 \pm 1.28$ µm, Pred. $= 6.69 \pm 0.98$ µm). The model fit to Measurement 2 ($C_0 = 16$ mg/ml) instead leads to poorer prediction of the measured particle size (Meas. $= 20.17 \pm 5.04$ µm, Pred. $= 7.23 \pm 1.3$ µm). The same assessment of the model parametrisations can be made for the predictions of hydroxyl- and butyl-functionalised templated systems, whereby concentration predictions have good agreement with the measured points, and the predicted average particle size is less accurate. Although the mispredictions may be caused by inaccurate assumptions in the model formulation and parametrisation (such as restriction of growth kinetic parameters for the templated systems), the models are nonetheless valuable to assess the templates' impact on crystallisation process design, and poor understanding of template-assisted crystallisation currently prevents further investigations of more appropriate model assumptions.

**Figure 1**: Comparison between experimental data of




crystallisation with carboxyl-functionalised silica templates and fitted model.

The regressed nucleation parameters of each tested system are reported in Table 1. The pre-exponential nucleation constant $A_j$ is interpreted as a function of the rate of molecular attachment to the critical nucleus, and is related to the protein's molecular mobility in solution; high $A_j$ values indicate high attachment frequencies and the presence of many nucleation sites [23]. The surface energy $\gamma$ refers to the energy of the crystal-solution interface; lower $\gamma$ is associated with critical nuclei of fewer molecules [23, 24]. While CNT models have simplifying assumptions, they are nonetheless valuable tools to mechanistically interpret differences between unseeded and template-assisted nucleation through parametric comparison. Compared to the homogeneous system, lower pre-exponential constants are regressed for the templated systems, suggesting molecular attachment is less frequent or fewer nucleation sites are available.

Lower surface energy is also predicted for each templated system, suggesting that while templates slow the growth of the critical nucleus, it however has a

reduced energetic barrier, has fewer molecules and its' state transition is more thermodynamically favoured. Nucleation enhancements can be explained by the lysozyme-SNP affinity; since lysozyme has been reported to have non-specific adsorption onto hydrophobic and hydrophilic surfaces, each surface chemistry has chemical affinity to lysozyme and can induce higher local lysozyme concentrations [25]. Additionally, computational studies have shown transport into porous structures also induces higher supersaturations [26], another contributing factor towards easier lysozyme nucleation.

**Table 1**: Regressed nucleation and growth parameters of the unseeded and templated systems

| System | $A_j$ $[\log(\#\,m^{-3}s^{-1})s]$ | $\gamma$ $[mJ\,m^{-2}]$ |
|---|---|---|
| Unseeded | 39.8 ± 2.0 | 0.68 ± 0.022 |
| Hydroxyl | 29.9 ± 2.2 | 0.49 ± 0.05 |
| Butyl | 22.7 ± 0.55 | 0.14 ± 0.07 |
| Carboxyl | 27.4 ± 2.45 | 0.32 ± 0.05 |
| **Growth param.** | $A_g$ $[nm\,min^{-1}]$ | $g$ $[-]$ |
| | 0.37 ± 0.08 | 3.30 ± 0.14 |

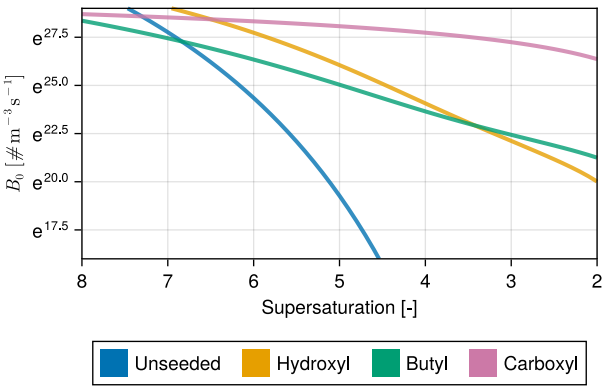



**Figure 2:** Calculated nucleation rate profiles for a range of supersaturations

The calculated nucleation rate profiles for a range of supersaturations (Figure 2) indicate template-induced nucleation is sustained across a wide range of supersaturations, remaining high even at $S < 4$ when homogeneous nucleation has reduced considerably. Secondly, the rates are flatter and less-dependent on supersaturation, possibly due to saturation of the templates' nucleation-enhancing effects if the templates' surface and pores are completely covered and filled with dissolved lysozyme.

After parameter estimation, simulations from each PBM are used to assess how templates alter the crystallisation operating space, with key trajectories of interest shown in Figure 3. While each system's fractional yield trajectories at intermediate and high initial concentrations ($C_0 = 17,20$ g/L) overlap, discernible differences are calculated for systems with lower initial concentrations ($C_0 = 14$ g/L) whereby templates, and in particular the carboxylic- and butyl- functionalised SNPs, generate crystalline mass quicker than the unseeded system. Further performance metrics for this initial condition are collected in Table 2; each template reduces the time to reach 60% fractional yield, halving it in the case of butyl and carboxyl templates, and templates at-least-double the predicted crystalline mass in solution at equal residence times.

**Table 2:** Process metrics of each tested system with $C_0 = 14$ g/L

| System | Avg. Time for 60% Frac. Yield [min] | Avg. Frac. Yield at 300 min |
|---|---|---|
| Unseeded | 884 | 0.18 |
| Hydroxyl | 528 **↓-40%** | 0.38 **↑+111%** |
| Butyl | 528 **↓-40%** | 0.39 **↑+116%** |
| Carboxyl | 310**↓-65%** | 0.59 **↑+228%** |

The collected fractional yield and average particle size trajectories in Figure 3 show a widened crystallisation operating space towards lower initial concentrations due to the addition of templates to the crystalliser, as the templates enable low-supersaturation nucleation. The average particle size however is not solely determined by nucleation enhancements, but rather is also affected by the crystalliser's operation and the amount of solute available for crystal growth. In the case of the unseeded system, a decreasing particle size with increasing initial concentration is predicted. Since homogeneous nucleation slows considerably at lower supersaturations, systems which already start at low supersaturations have more solute mass and time for each crystal to grow, while higher initial supersaturations lead to more solute competition between nucleated crystals. An opposite trend can be observed in the case of the templated systems, caused by the sustained nucleation rate profiles, whereby the predicted average particle size slightly increases with increasing initial concentration. Since similar numbers of crystals are nucleated with each initial condition, higher initial concentrations reduce solute competition for growth by having more API mass available in solution, and lead to minor increases in the average particle size. The unseeded particle size is more sensitive to changes in initial conditions than the templated systems, highlighting templates' ability to mitigate upstream disturbances and act as crystallisation rate-limiters and controllers.

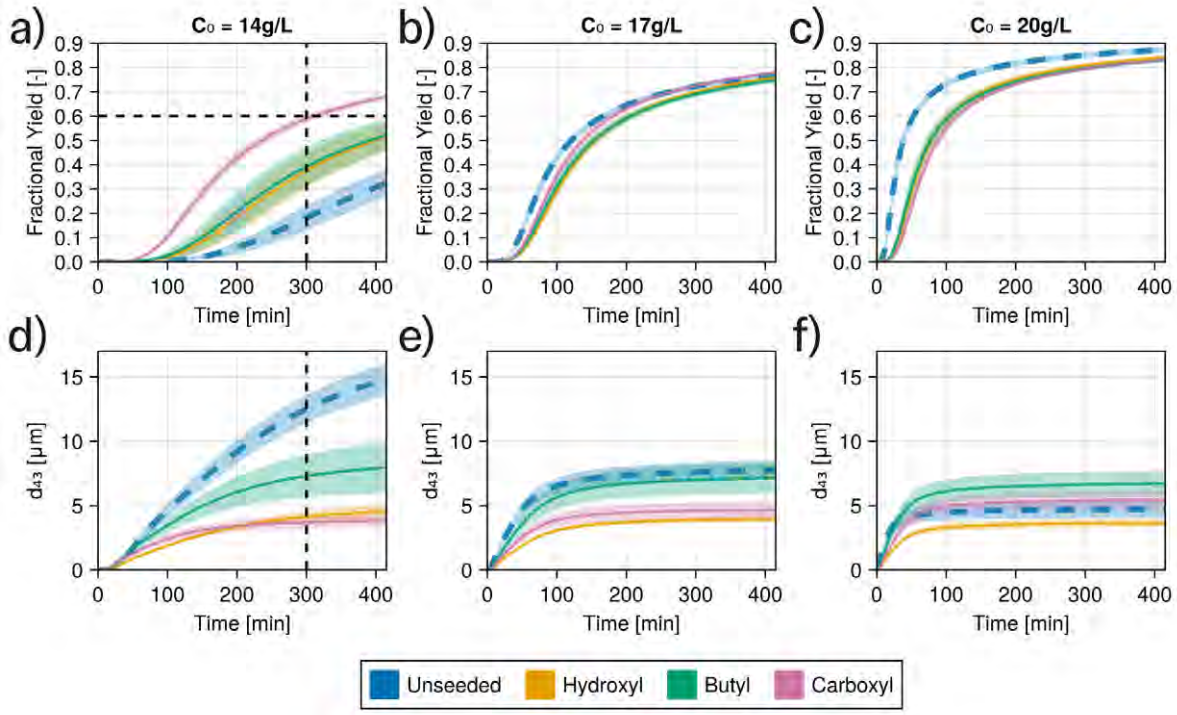



**Figure 3:** Fractional yield vs. residence time (a-c) and volume-weighted average particle size vs residence time (d-f) plots for three different initial concentrations

## CONCLUSIONS

The adoption of crystallisation for protein purification of therapeutic manufacturing is challenged by the tight conditions in which proteins crystallise. If a solid formulation is targeted and designed for, additional purification units upstream of the crystalliser are needed which lead to increased manufacturing costs and environmental impacts.

The work presented shows that templates can be introduced to scaled-up crystallisation processes to widen the crystallisation operating space by providing a higher and more-controlled nucleation rate than the template-free system. The effect is more pronounced when the crystalliser is operated at lower initial concentrations since templates sustain nucleation at conditions where homogeneous nucleation has reduced considerably. Operating the crystalliser at lower solute concentrations is useful to facilitate control and avoid excessive nucleation or precipitation of the amorphous solute. As such, by enhancing nucleation through the addition of templates, the crystalliser's robustness can be improved to more-easily mitigate upstream disturbances, while also delivering intensified downstream purification.

## REFERENCES


1. Chowdhury EA, Meno-Tetang G, Chang HY, et al (2021) Current progress and limitations of AAV mediated delivery of protein therapeutic genes and the importance of developing quantitative pharmacokinetic/pharmacodynamic (PK/PD) models. Advanced Drug Delivery Reviews 170:214–237. https://doi.org/10.1016/j.addr.2021.01.017
2. Chen W, Cheng TNH, Khaw LF, et al (2021) Protein purification with nanoparticle-enhanced crystallisation. Separation and Purification Technology 255:117384. https://doi.org/10.1016/j.seppur.2020.117384
3. Makurvet FD (2021) Biologics vs. small molecules: Drug costs and patient access. Medicine in Drug Discovery 9:100075. https://doi.org/10.1016/j.medidd.2020.100075
4. Roque ACA, Pina AS, Azevedo AM, et al (2020) Anything but Conventional Chromatography Approaches in Bioseparation. Biotechnology Journal 15:1900274. https://doi.org/10.1002/biot.201900274
5. Lemmer HJR, Liebenberg W, Lemmer HJR, Liebenberg W (2022) Crystallization: Its Mechanisms and Pharmaceutical Applications. In: Crystal Growth and Chirality - Technologies and Applications. IntechOpen
6. Rafferty J, Nagaraj H, McCloskey AP, et al (2016) Peptide Therapeutics and the Pharmaceutical Industry: Barriers Encountered Translating from the

Laboratory to Patients. Curr Med Chem 23:4231–4259. https://doi.org/10.2174/0929867323666160909155222
7. Hekmat D (2015) Large-scale crystallization of proteins for purification and formulation. Bioprocess Biosyst Eng 38:1209–1231. https://doi.org/10.1007/s00449-015-1374-y
8. McCue C, Girard H-L, Varanasi KK (2023) Enhancing Protein Crystal Nucleation Using In Situ Templating on Bioconjugate-Functionalized Nanoparticles and Machine Learning. ACS Appl Mater Interfaces 15:12622–12630. https://doi.org/10.1021/acsami.2c17208
9. Parambil JV, Poornachary SK, Heng JYY, Tan RBH (2019) Template-induced nucleation for controlling crystal polymorphism: from molecular mechanisms to applications in pharmaceutical processing. CrystEngComm 21:4122–4135. https://doi.org/10.1039/C9CE00404A
10. J. Link F, Y. Heng JY (2021) Enhancing the crystallisation of insulin using amino acids as soft-templates to control nucleation. CrystEngComm 23:3951–3960. https://doi.org/10.1039/D1CE00026H
11. de Poel W, Elemans JAAW, van Enckevort WJP, et al (2019) Epitaxial Crystallization of Insulin on an Ordered 2D Polymer Template. Chemistry – A European Journal 25:3756–3760. https://doi.org/10.1002/chem.201805276
12. Jacobo-Molina A, Clark AD, Williams RL, et al (1991) Crystals of a ternary complex of human immunodeficiency virus type 1 reverse transcriptase with a monoclonal antibody Fab fragment and double-stranded DNA diffract x-rays to 3.5-A resolution. Proc Natl Acad Sci U S A 88:10895–10899. https://doi.org/10.1073/pnas.88.23.10895
13. Kang M, Lee G, Jang K, et al (2022) Graphene Quantum Dots as Nucleants for Protein Crystallization. Crystal Growth & Design 22:269–276. https://doi.org/10.1021/acs.cgd.1c00910
14. Saridakis E, Khurshid S, Govada L, et al (2011) Protein crystallization facilitated by molecularly imprinted polymers. Proceedings of the National Academy of Sciences 108:11081–11086. https://doi.org/10.1073/pnas.1016539108
15. Verma V, Mitchell H, Errington E, et al (2023) Templated Crystallization of Glycine Homopeptides: Experimental and Computational Developments. Chemical Engineering & Technology 46:1271–1278. https://doi.org/10.1002/ceat.202200575
16. Pusey ML, Aygün RS (2017) Data Analytics for Protein Crystallization, 1st ed. 2017. Springer International Publishing : Imprint: Springer, Cham
17. Mitchell HM, Jovannus D, Rosbottom I, et al (2023) Process modelling of protein crystallisation: A case study of lysozyme. Chemical Engineering Research and Design 192:268–279. https://doi.org/10.1016/j.cherd.2023.02.016
18. Orosz Á, Szilágyi E, Spaits A, et al (2024) Dynamic Modeling and Optimal Design Space Determination of Pharmaceutical Crystallization Processes: Realizing the Synergy between Off-the-Shelf Laboratory and Industrial Scale Data. Ind Eng Chem Res 63:4068–4082. https://doi.org/10.1021/acs.iecr.3c03954
19. Gerard CJJ, Briuglia ML, Rajoub N, et al (2022) Template-Assisted Crystallization Behavior in Stirred Solutions of the Monoclonal Antibody Anti-CD20: Probability Distributions of Induction Times. Crystal Growth & Design 22:3637–3645. https://doi.org/10.1021/acs.cgd.1c01324
20. Zhou HY, Zhou GZ, Wang XZ (2022) Multi-objective optimization of protein cooling crystallization with morphological population balance models. Journal of Crystal Growth 588:126664
21. Randolph AD, Larson MA (1988) Theory of particulate processes: analysis and techniques of continuous crystallization, 2nd ed. Academic Press, San Diego
22. Hoffman MD, Gelman A (2011) The No-U-Turn Sampler: Adaptively Setting Path Lengths in Hamiltonian Monte Carlo
23. Myerson AS, Erdemir D, Lee AY (2019) Handbook of Industrial Crystallization, 3rd ed. Cambridge University Press
24. Vekilov PG (2010) Nucleation. Crystal Growth & Design 10:5007–5019. https://doi.org/10.1021/cg1011633
25. Link FJ, Errington E, Verma V, Heng JYY (2023) The role of mixing and surface hydrophobicity on the operation of a continuous tubular slug flow crystalliser for lysozyme. Chemical Engineering Journal 471:144363. https://doi.org/10.1016/j.cej.2023.144363
26. Nanev CN, Saridakis E, Chayen NE (2017) Protein crystal nucleation in pores. Sci Rep 7:35821. https://doi.org/10.1038/srep35821

© 2025 by the authors. Licensed to PSEcommunity.org and PSE Press. This is an open access article under the creative commons CC-BY-SA licensing terms. Credit must be given to creator and adaptations must be shared under the same terms. See https://creativecommons.org/licenses/by-sa/4.0/



Systems & Control Transactions

**Research Article - Peer Reviewed Conference Proceeding**
ESCAPE 35 - European Symposium on Computer Aided Process Engineering
Ghent, Belgium. 6-9 July 2025
Jan F.M. Van Impe, Grégoire Léonard, Satyajeet S. Bhonsale,
Monika E. Polańska, Filip Logist (Eds.)

PSE PRESS

# Cost-optimal Solvent Selection for Batch Cooling Crystallisation of Flurbiprofen

**Matthew Blair and Dimitrios I. Gerogiorgis***

Institute for Materials and Processes (IMP), School of Engineering, University of Edinburgh, Edinburgh, EH9 3FB, UK
* Corresponding Author: D.Gerogiorgis@ed.ac.uk

## ABSTRACT

Choosing suitable solvents for crystallisation processes can be a challenging task when developing new pharmaceuticals, given the vast number of candidates available. To streamline this task, however, process modelling tools can be used to systematically probe the behaviour of different crystallisation setups entirely in-silico. In fact, it is possible to couple thermodynamic models with basic solid-liquid equilibria (SLE) principles to determine the impact of key process variables (e.g., temperature and solvent choice) on process performance, prior to conducting lab-scale experiments. In light of this, in this study we have used thermodynamic computational modelling tools (implemented within MATLAB®) to evaluate the cost and environmental impact of different batch crystallisation processes that may be used to manufacture flurbiprofen – a non-steroidal anti-inflammatory drug (NSAID) that can be used to treat various forms of arthritis. To complete this work, we have used the Apelblat equation to study the solubility of flurbiprofen in four (4) common solvents (n-octane, methyl tert-butyl ether, n-propanol, and isopropyl acetate) over a wide temperature range (283.15-323.15 K). Further to this, we have used green metrics (i.e., E-factor) and established costing methodologies to compare each process candidate; before evaluating their Scope 1 and 2 $CO_2e$ emissions by considering their electricity usage and incineration activities.

**Keywords**: Non-Steroidal Anti-Inflammatory Drugs (NSAID), flurbiprofen, crystalliser, design, solvent selection

## 1. INTRODUCTION

In 2024, the global market for non-steroidal anti-inflammatory drugs (NSAIDs) reached 21.56 billion USD, and it is projected to grow at a Compound Annual Growth Rate (CAGR) of 5% over the next 8 years [1]. Consequently, cost-effective manufacturing processes must be developed for NSAIDs if we hope to satisfy future demand [2-3]. In light of this, we have used computational modelling to study the impact of solvent choice and process temperature on the batch cooling crystallisation of flurbiprofen – a generic NSAID (with global sales of 100 million USD per year [4]) which is used to treat rheumatoid arthritis, migraines and osteoarthritis [5]. To do this, we have used a purely thermodynamic approach, whereby the Apelblat equation is used to assess the solubility of flurbiprofen (Fig. 1) in four (4) pharmaceutical solvents (n-octane, methyl tert-butyl ether, n-propanol, and isopropyl acetate) [5] at different temperatures ($T$).

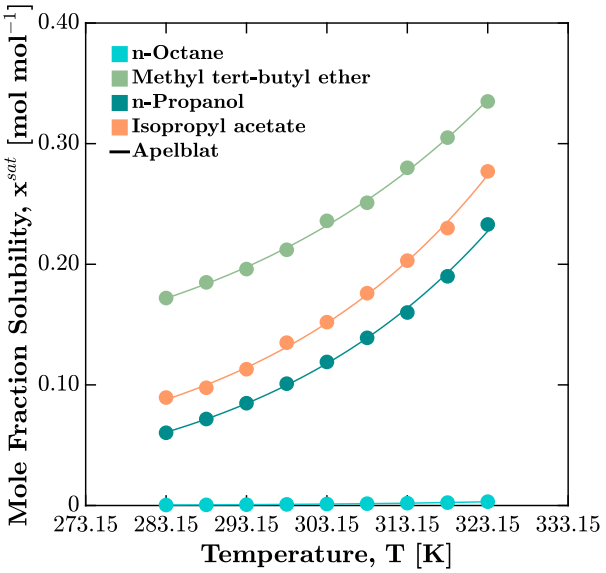



**Figure 1.** Flurbiprofen solubility in four solvents. Data [5].

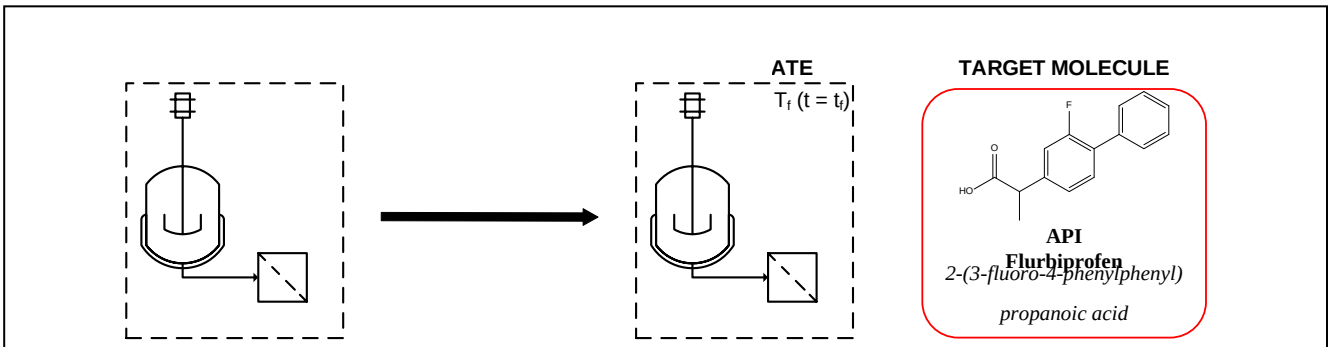



**Figure 2:** Batch cooling crystallisation using thermodynamic considerations alone.

Established green metrics and cost-estimation methods have then been used to identify the solvent and process conditions which afford the lowest cost solution whilst maintaining a reasonable carbon footprint.

## 2. PROCESS DESIGN & SIMULATION

As has been demonstrated by several authors [3, 6], it is possible to design crystallisers using thermodynamic principles alone (Fig. 2). The main benefit of this approach being that it allows promising solvent candidates to be identified prior to establishing their crystallisation kinetics; thereby reducing the number of experimental trials required to develop new processes.

In light of these observations, we have used the Apelblat equation (Eq. 1) alongside solid-liquid equilibrium (SLE) principles (Eqs. 2-5) to calculate the mass of flurbiprofen produced by each crystallisation batch cycle ($m_{BC}$) as we vary the initial and final temperatures ($T_0$, $T_f$) used. Meanwhile, we have used Eqs. 6-10 to determine any process volumes, operating times and production strategies required by each system; whilst Eqs. 11-12 have been used to determine product recoveries and cooling requirements.

Fig. 3 depicts the calculation sequence used to carry out this work, where basic physical properties (e.g., molecular weights, melting ($T_{mp}$) and boiling ($T_{bp}$) points) have been taken from the literature wherever possible [5, 7]. It is important to note, however, that the density and specific heat capacity of each solvent has been estimated using temperature-dependent empirical correlations when performing these calculations [8]. Meanwhile, only crystallisers of standard-size (1000, 2000, 5000, 10000, 20000 L) have been considered (70 v/v % fill capacity); whilst parallel production lines ($N_{PT}$) have been permitted whenever production targets could not be met using a single production line.

$$\ln x^{sat} = A + \frac{B}{T} + C\ ln(T) \quad (1)$$

$$n_{prod,0} = x_{prod,0}^{sat} n_S \quad (2)$$

$$n_{prod} = x_{prod}^{sat} n_S \quad (3)$$

$$n_{prod}^{cryst} = n_{prod,0} - n_{prod} \quad (4)$$

$$m_{prod}^{cryst} = M_{prod} n_{prod}^{cryst} \quad (5)$$

$$V_{cryst} = \frac{m_{prod}^{cryst}}{\rho_{prod}} \quad (6)$$

$$V_{liq} = \frac{M_S n_S}{\rho_S} \quad (7)$$

$$V_{sys} = V_{liq} + V_{cryst} \quad (8)$$

$$t_{BC} = t_{cryst} + t_{CIP} \quad (9)$$

$$m_{annual} = m_{BC} N_{BC} N_{PT} \quad (10)$$

$$r_T^{cryst} = \left(\frac{n_{prod,0} - n_{prod}}{n_{prod,0}}\right) \quad (11)$$

$$Q = \Delta T C_{P_S} n_S \quad (12)$$

$$\{T_0, T_f\} \geq \max \begin{Bmatrix} T_{min,Apel} \\ T_{mp_{solv}} + T_{os_1} \\ T_{min,phys} \end{Bmatrix} \quad (13)$$

$$\{T_0, T_f\} \leq \min \begin{Bmatrix} T_{max,Apel} \\ T_{bp_{solv}} - T_{os_2} \\ T_{max,phys} \end{Bmatrix} \quad (14)$$

In addition to this, we have also stipulated that the initial state of a crystalliser must have a temperature greater than that of the final state; all the while abiding by the constraints defined in Eqs. 13-14 ($T_{OS,1} = 5; T_{OS,2} = 10\ K$) so as to prevent any solvent phase changes from occurring during crystallisation [3, 6] (Fig. 3). Likewise, we have specified that each process must use a minimum of 4 mL of solvent per gram of solute so as to avoid high shear forces during mixing [3].

Using this approach, material balances have been constructed across each process by assuming that: (i) 100 metric tonnes of API are produced per year ($m_{annual}$); (ii) each process operates for a maximum of 6000 h annually ($t_{op}$); (iii) all mixtures are well-mixed, fully suspended and have uniform temperature and concentration profiles; (iv) vessel clean-in-place times ($t_{CIP}$) are 30 minutes between batches; and (v) each crystallisation batch takes 12 hours ($t_{cryst}$) [2]. It is important to note, however, that several unit operations are likely to precede the crystallisation steps studied in this work. Thus, each production line should only be allowed to complete

one full-process batch cycle per day – irrespective of an individual crystallisation unit's batch cycle time ($t_{BC}$). Otherwise, unrealistic manufacturing processes could be developed which demand infeasibly large numbers of batches to be produced each day.

Eqs. 1-14 introduce terms $n_S$, $n_{prod,0}$ and $n_{prod}$ to represent the molar amount of solvent used in each process, as well as the initial and final amounts of drug product dissolved in this solvent (mol). Terms $x_{prod,0}^{sat}$, $x_{prod}^{sat}$ and $x^{sat}$ are also used to denote the mole fraction of dissolved product for a given process state (mol mol$^{-1}$). Meanwhile, $A$ (–), $B$ (K) and $C$ (–) are used to denote Apelblat correlation coefficients. $n_{prod}^{cryst}$ (mol) and $m_{prod}^{cryst}$ (kg) are then used to describe the molar and mass amounts of product produced; whilst $r_T^{cryst}$ (–) and $Q$ (kJ) give the API recovery and heating requirements. $M_{prod}$ and $M_S$ are used to represent the molar mass (g mol$^{-1}$) of the drug-product and solvents, respectively; whilst $\rho_{prod}$ and $\rho_S$ denote their densities (kg m$^{-3}$). Terms $V_{cryst}$, $V_{liq}$ and $V_{sys}$ are then left to represent crystal, liquid (mother-liquor) and total system volumes (L) for each batch in a process; whilst $C_{P_S}$ (J mol$^{-1}$ K$^{-1}$) represents the specific heat capacity of a solvent and $T_{min,Apel}$, $T_{max,Apel}$, $T_{min,phys}$, $T_{max,phys}$ (K) denote the minimum and maximum temperatures for which the Apelblat and physical property correlations are applicable. $N_{BC}$ gives the number of batch cycles per production line for a given throughput.

## 3. ENVIRONMENTAL IMPACT

Environmental ($E_{factor}$) and emission factors (i.e., the amount of $CO_2$e produced per kilogram of product, $PCE$) have been used to assess the environmental impact of each process (Eqs. 15-16). Consequently, any Scope 1 and 2 emissions expected to arise from each process (due to material and energy consumption) have been calculated assuming that: (i) 0.20705 kg $CO_2$e are produced per kWh of electricity used [9]; (ii) any emissions produced during waste incineration activities only occur due to the complete combustion of waste material; and (iii) on-site scrubbing and catalytic reduction facilities are available to completely abate any $NO_x$ and $SO_x$ gases which arise during these incineration activities (allowing their potential generation to be ignored).

$$E_{factor} = \frac{m_{total\ input} - m_{total\ prod}}{m_{total\ prod}} \quad (15)$$

$$PCE = \frac{m_{total\ CO_2e}}{m_{total\ prod}} \quad (16)$$

Eqs. 15-16 introduce terms $m_{total\ input}$, $m_{total\ prod}$ and $m_{total\ CO_2e}$ to represent total process material requirements, API production, and $CO_2$e emissions (kg).

## 4. ECONOMIC ANALYSIS

An established costing methodology [2, 10] has been used to assess the viability of each process. As part of this, the capital costs ($CapEx$) associated with each process have been calculated in USD by taking the sum of any fixed ($FCC$) and working ($WCC$) capital costs (Eq. 17). Consequently, any $FCC$ costs have been calculated

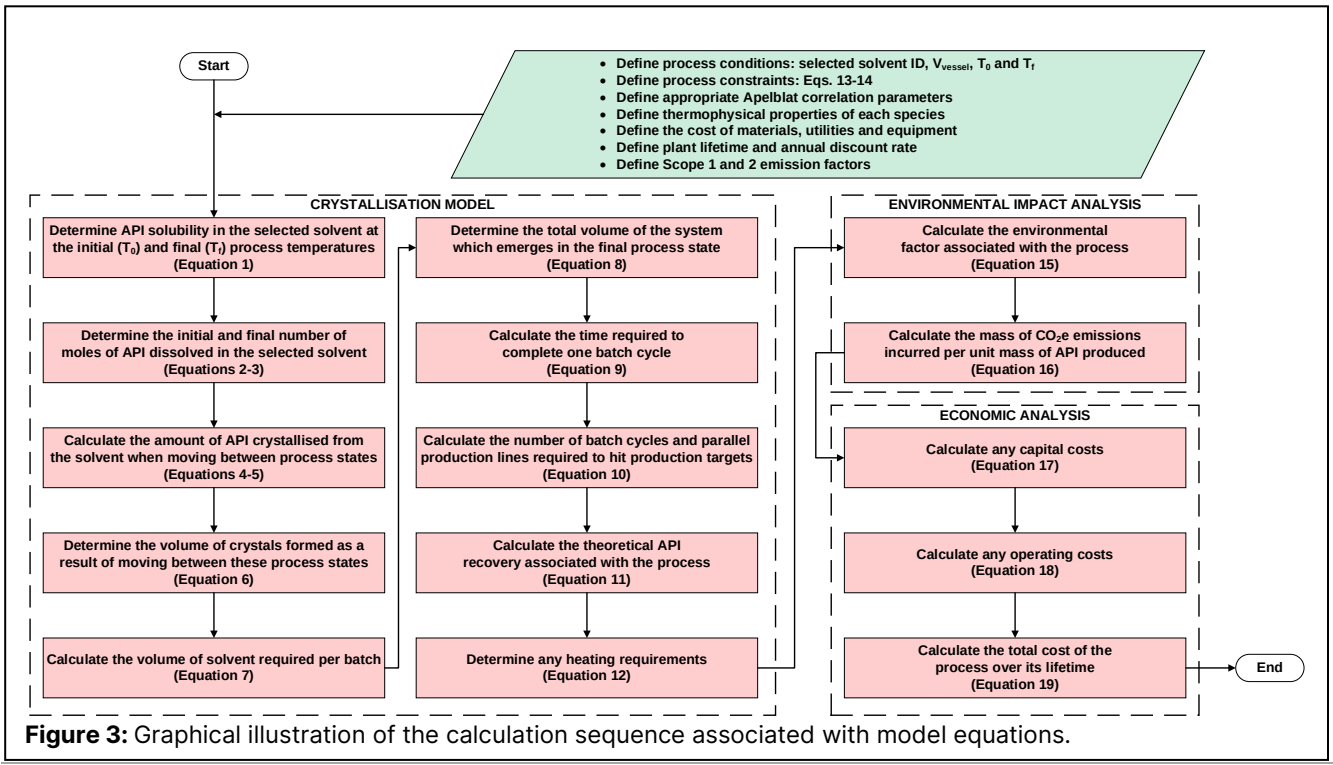



**Figure 3:** Graphical illustration of the calculation sequence associated with model equations.

as sum of the inside battery limits, outside battery limits, engineering and contingency costs (using Chemical Engineering Plant Cost Indices and Lang factors to account for the effects of inflation and equipment installation); whilst any $WCC$ costs have been assumed equal to 15 % of the $FCC$ costs. Likewise, any operating costs have been simply calculated as the sum of the fixed ($FCOP$) and variable ($VCOP$) costs of production (Eq. 18). Where, any $VCOP$ costs have been calculated as the sum of any raw material, waste disposal, and utility costs; whilst any $FCOP$ costs have been broken down into: (i) supervision and management costs; (ii) maintenance costs; (iii) renting of land/buildings; (iv) insurance premiums/property taxes; (v) direct salary overheads; and (vi) labour costs.

$$CapEx = FCC + WCC \tag{17}$$

$$OpEx = FCOP + VCOP \tag{18}$$

The total cost of each process ($TPC$) has then been determined via Eq. 19 – assuming all $CapEx$ occurs in year zero, whilst any $OpEx$ is incurred from year one onwards.

$$TPC = CapEx + \sum_{n=1}^{t_{LTP}} \frac{OpEx}{(1+I_{dr})^n} \tag{19}$$

Bulk prices used to calculate material costs have been calculated by averaging values published by known vendors and market research firms (i.e., the IMARC group) in the last year (2023-2024) wherever possible. However, import and export reports published for major markets have been used if this information was unavailable. Similarly, waste disposal costs have been estimated in-line with recommendations made by Jolliffe and Gerogiorgis (2017) [11] and the World Health Organization (1999) [12]. Meanwhile, a plant lifetime ($t_{LTP}$) of 20 years has been assumed, with an annual discount rate ($I_{dr}$) of 5.5 % [11]. An efficiency of 40 % has been assumed when converting electrical energy to crystalliser cooling duties.

## 5. RESULTS & DISCUSSION

Using the modelling framework presented in Sections 2-4, we have visualised the design space associated with each crystallisation process. From this, we observed that (regardless of the solvent used) it is wise to use the largest crystalliser available (20000 L) since this will reduce process costs, whilst also minimising the number of batches and parallel production lines required to achieve a given throughput (Fig. 4a). Alongside this, however, we also observed that it is also best to maximise the temperature difference between the initial and final states of a given process if we wish to minimise its production costs whilst maximising drug recovery. Fig. 4b provides findings from these investigations for two of the solvents studied in this work: n-octane (low API solubility) and n-propanol (moderate API solubility). Consequently, we could safely set the volume and temperature difference of each system to their maximum allowable values before studying the impact of solvent choice on: (i) process cost (Fig. 5a); (ii) material usage (Fig. 5b); (iii) $CO_2$e emissions (Fig. 5c); and (iv) API recovery (Fig. 5d).

Interestingly, however, from studying these trends, we found that simply choosing the solvent with the highest expected API solubility (i.e., methyl tert-butyl ether herein) will not necessarily result in a cost-optimal (Fig. 5a) or environmentally friendly (Figs. 5b-c) manufacturing process. Rather, we must take into account the cost of purchasing and disposing of any materials (as well as

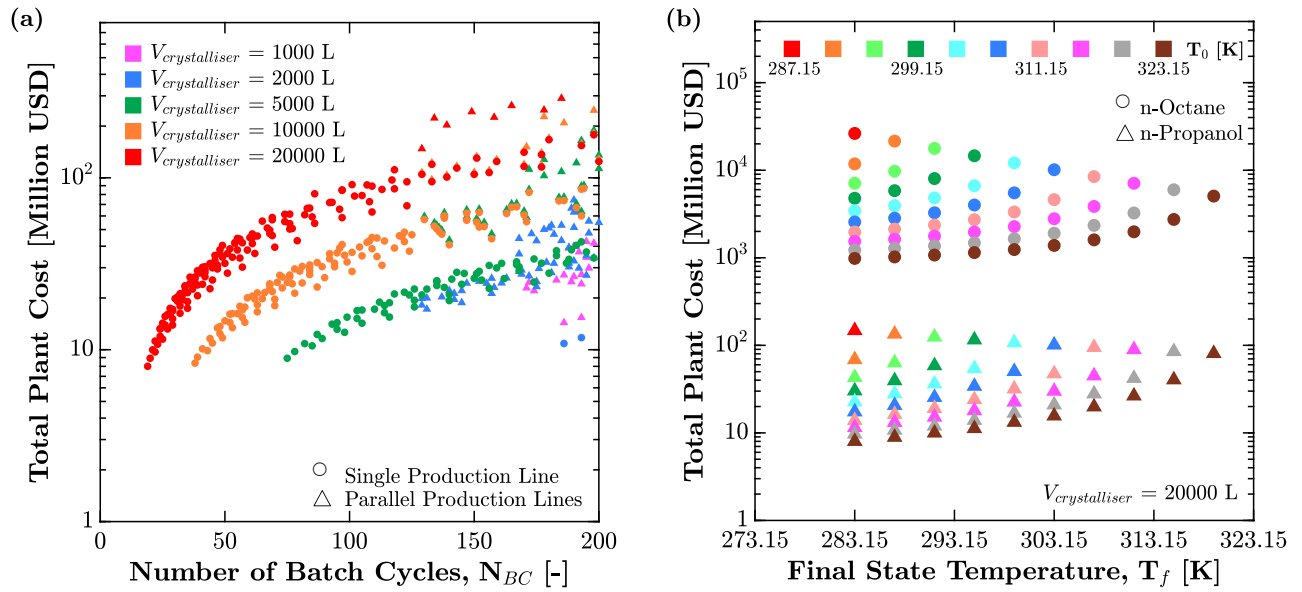



**Figure 4:** Impact of: (a) crystalliser volume (for all solvents, at various process conditions); and (b) process temperature ($T_0$, $T_f$) on process cost.

the volatility of any solvents used) if we wish to identify cost-optimal processes; since these variables can have a significant impact on the overall viability of a process. Consequently, in this work, n-propanol was identified as the best solvent available for flurbiprofen crystallisation ahead of methyl tert-butyl ether (Figs. 1 and 5); with the final optimised process exhibiting a total cost of 8.00 million USD, an API recovery of 73.31 w/w % and $CO_2$e emissions of only 4.23 $kg_{CO_2e}/kg_{API}$.

In light of these findings, it was worth examining the cost breakdown associated with this process to understand what aspects of process design influence the cost of batch crystallisation processes most. From this, it was found that an initial investment ($CapEx$) of only 0.10 million USD ($FCC$: 86.96 %; $WCC$ 13.04 %) would be required to design and build the optimised n-propanol process; yet, it would cost around 0.66 million USD annually ($FCOP$: 4.95 %; $VCOP$: 95.05 %) to operate ($OpEx$). It is, therefore, abundantly clear that batch cooling crystallisation processes such as those studied in this work are dominated by operating costs rather than capital investment (with material acquisition, utility usage, and waste disposal costs making up 9.50, 37.76 and 52.74 % of any $VCOP$ costs incurred in this case).

In addition to these findings, however, it was also observed that simply targeting maximum product recoveries (or crystal yields) can be hazardous when optimising a new process. Especially, since doing so can result

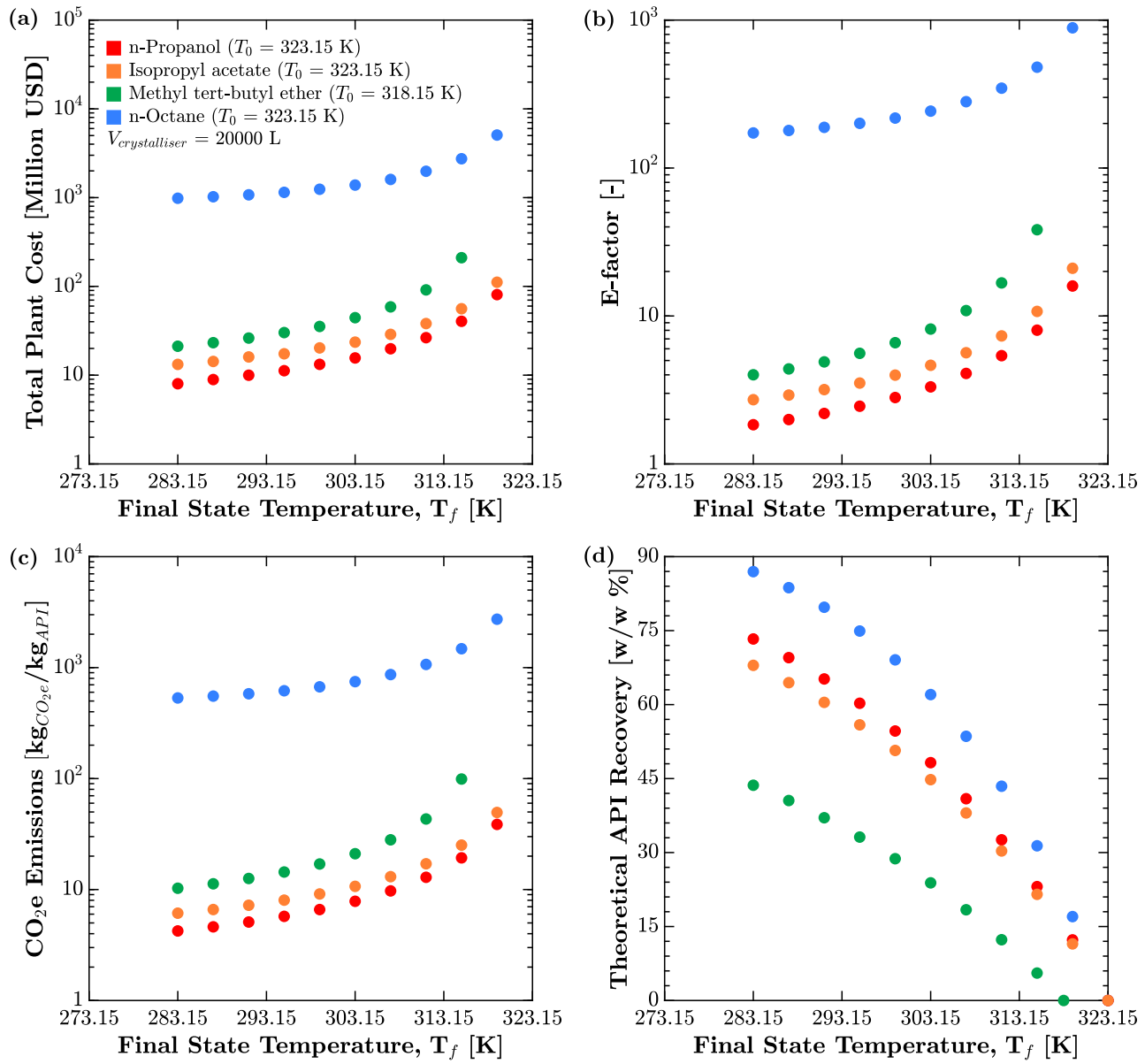



**Figure 5:** Impact of solvent choice on: (a) process cost; (b) E-factor; (c) $CO_2$e emissions; and (d) API recovery. $T_0$ set to maximum allowable value for each solvent.

in the selection of solvents which have extremely low drug solubilities (Fig. 1) even though this raises process costs on account of the larger volumes of solvent required in such scenarios (Fig. 5d). Hence, it is safer to evaluate processes in terms of their process costs and environmental impact, as has been done in this work.

## 6. CONCLUSIONS

In this work, we have presented a practical modelling framework for the visualisation and optimisation of design spaces associated with batch cooling crystallisation processes. Further to this, we have demonstrated how this framework can be used to identify cost-optimal process conditions for flurbiprofen production, whilst minimising carbon emissions. As part of this, we have successfully identified n-propanol as the most suitable solvent (of those tested) for the batch cooling crystallisation of flurbiprofen ($V_{crystalliser}$ = 20000 L; $T_0$ = 323.15 K; $T_f$ = 283.15 K). Consequently, the systematic methods presented in this paper can also be used to explore the design space associated with a whole host of other small molecule APIs, since around 80% of all small molecule pharmaceuticals produced today require crystallisation at some point(s) during the manufacturing process [3].

## ACKNOWLEDGEMENTS

M.B. acknowledges financial support from an EPSRC ICASE studentship; D.I.G acknowledges support from UKRI/EPSRC (RAPID: ReAl-time Process Modelling & Diagnostics: Powering Digital Factories, EP/V028618/1) and a Royal Society International Exchanges grant (2023-25).

## REFERENCES

1. NASDAQ OMX Corporate Solutions. Non-steroidal anti-inflammatory drugs market size to worth USD 33.55 bn by 2032: the global non-steroidal anti-inflammatory drugs market size is calculated at USD 21.56 billion in 2024 and is expected to be worth around USD 33.55 billion by 2032, growing at a CAGR of 5% from 2024 to 2032. NASDAQ OMX News Release Distribution Channel (2024)
2. Diab S., Gerogiorgis D.I. Technoeconomic evaluation of multiple mixed suspension-mixed product removal (MSMPR) crystallizer configurations for continuous cyclosporine crystallization. *Org. Process Res. Dev.* 21:1571-1587 (2017) https://doi.org/10.1021/acs.oprd.7b00225
3. Watson O.L., Jonuzaj S., McGinty J., Sefcik J., Galindo A., Jackson G., Adjiman C.S. Computer aided design of solvent blends for hybrid cooling and antisolvent crystallization of active pharmaceutical ingredients. *Org. Process Res. Dev.* 25:1123-1142 (2021) https://doi.org/10.1021/acs.oprd.0c00516
4. Liu T., Yang S., Wu Z., Cai Y., Zhou J., Liao M. Isolation of flurbiprofen-degrading bacteria and evaluating its degradation characteristics. *Environ. Technol. Innov.* 29:102983 (2023) https://doi.org/10.1016/j.eti.2022.102983
5. Tian B., Feng Y., Li X., Yang J., Ding Z., Huang X., Yin Q., Xie C., Hao H. Solution thermodynamic properties of flurbiprofen in twelve solvents from 283.15 to 323.15 K. *J. Mol. Liq.* 296:111744 (2019) https://doi.org/10.1016/j.molliq.2019.111744
6. Sheikholeslamzadeh E., Chen C.C., Rohani S. Optimal solvent screening for the crystallization of pharmaceutical compounds from multisolvent systems. *Ind. Eng. Chem. Res.* 51:13792-13802 (2012) https://doi.org/10.1021/ie3014742
7. Kim S., Chen J., Cheng T., Gindulyte A., He J., He S., Li Q., Shoemaker B.A., Thiessen P.A., Yu B., Zaslavsky L., Zhang J., Bolton E.E. PubChem 2023 update. *Nucleic Acids Res.*, 51:D1373–D1380 (2023) https://doi.org/10.1093/nar/gkac956
8. Yaws C.L., Chemical Properties Handbook: Physical, Thermodynamic, Environmental, Transport, Safety, and Health Related Properties for Organic and Inorganic Chemicals. McGraw-Hill (1999)
9. Department for Energy Security & Net Zero. Greenhouse gas reporting: conversion factors 2024 (2024). Available at: https://www.gov.uk/government/publications/greenhouse-gas-reporting-conversion-factors-2024
10. Towler G.P., Sinnott R.K. Chemical Engineering Design: Principles, Practice and Economics of Plant and Process Design, 3rd Edition. Butterworth-Heinemann (2022)
11. Jolliffe H.G., Gerogiorgis D.I. Technoeconomic optimization of a conceptual flowsheet for continuous separation of an analgaesic active pharmaceutical ingredient (API). *Ind. Eng. Chem. Res.* 56:4357-4376 (2017) https://doi.org/10.1021/acs.iecr.6b02146
12. World Health Organization. Guidelines for Safe Disposal of Unwanted Pharmaceuticals in and After Emergencies, 1st Edition. World Health Organization (1999)

© 2025 by the authors. Licensed to PSEcommunity.org and PSE Press. This is an open access article under the creative commons CC-BY-SA licensing terms. Credit must be given to creator and adaptations must be shared under the same terms. See https://creativecommons.org/licenses/by-sa/4.0/



Systems & Control Transactions

**Research Article - Peer Reviewed Conference Proceeding**
ESCAPE 35 - European Symposium on Computer Aided Process Engineering
Ghent, Belgium. 6-9 July 2025
Jan F.M. Van Impe, Grégoire Léonard, Satyajeet S. Bhonsale,
Monika E. Polańska, Filip Logist (Eds.)

PSE PRESS

# Active Pharmaceutical Ingredients from Unused Solid Drugs

**Shrivatsa Korde[a], Aishwarya Menon[b], Gintaras V. Reklaitis[a] and Zoltan K. Nagy[a]***

[a] Davidson School of Chemical Engineering, Purdue University, West Lafayette, IN, USA
[b] Agricultural & Biological Engineering, Purdue University, West Lafayette, IN, USA
* Corresponding Author: znagy@purdue.edu

## ABSTRACT

The increased use of pharmaceuticals globally over the past two decades has contributed to an increase in unused pharmaceuticals and a corresponding surge in pharmaceutical waste. Thus, there is an impetus for the development of processes for the recovery of the active pharmaceutical ingredients (APIs) from these unused drugs. This study introduces a decision framework for solvent selection to enable the recovery of APIs using a general separation train where cooling crystallization is the final step. The framework is designed to base solvent selection not just on the solubilities of the formulation contents but also considers the overall recovery that can be achieved in the process. In addition, the environmental sustainability of the framework is analyzed using the process mass intensity metric (PMI). The effectiveness of this framework is demonstrated by using paracetamol (PA) as a model API in a formulation consisting of five of the excipients commonly found in PA formulations. The results show that selecting a solvent based on the dissolution of pharmaceutical tablets may not be the best possible approach, whereas choosing a solvent that maximizes the theoretical recovery is preferred.

**Keywords**: API recovery, Solvent Selection, Sustainability, Process Design

## INTRODUCTION

The rapid population growth and escalating use of medicines to treat human diseases have caused a concurrent rise in pharmaceutical waste, necessitating proper management strategies to address this challenge effectively. Unused pharmaceutical products are often disposed of as household trash or flushed down the toilet. Incineration and land disposal are the two common ways to get rid of unused drugs collected as trash, resulting in an inherent environmental impact [1]. Even though incineration (involving heating at temperatures over 1000°C) is effective, it is highly energy-intensive and releases harmful gases such as $CO_2$, $SO_2$, $NO_x$, etc. Drugs that are disposed of in landfills or flushed down the toilets eventually appear in the water system, causing harm to the flora and fauna, if not people. Another source of waste drugs is batches that fail final quality control during manufacturing, which are then incinerated. Expired drugs which are discarded at any point in the supply chain are another source of unused drugs.

Research has shown that many expired drugs retain a substantial portion of their potency[2] and thus, whether in landfill or wastewater, constitutes a hazard. One of the effective ways to treat the disposal of expired drugs is to have an infrastructure that facilitates their return at collection centers and recovery of the active pharmaceutical ingredient (API) from the unused drug formulation. The API is the most valuable component of a drug product; recovering it in its pure form enables its reformulation and conversion into new drug products. Among various drug administration methods, oral administration via tablets and capsules is the primary route for delivering APIs to patients [3]. When recycling APIs, it is crucial to ensure that the recovered APIs possess the desired critical quality attributes (CQAs), such as purity, drug shelf life, and bioavailability, while adhering to strict FDA regulations.

Crystallization is the process of converting a chemical from a liquid or solution into a solid crystalline state, where the atoms or molecules are arranged in a definite geometric pattern or lattice. Crystallization serves both

as a separation process and a particle control strategy to target specific CQAs such as yield, polymorph selection, and crystal size distribution (CSD). Over 90 % of active pharmaceutical ingredients (APIs) are synthesized as crystalline products. Proof-of-concept studies demonstrating API recovery have been carried out in the past [4]. However, these processes suffer from low overall recovery and lack sufficient solvent selection guidelines for the final separation stage via crystallization.

To address these gaps, this study aims to develop a solvent selection framework to enable a higher overall recovery of the API present in the unused formulation. The remainder of the paper is organized as follows: first, the solvent selection framework for optimal solvent selection is presented. Subsequently, the devised framework is applied in a case study consisting of a formulation of paracetamol with five of the common excipients, and preferred solvents are narrowed down from an existing ten solvents commonly used in cooling crystallization.

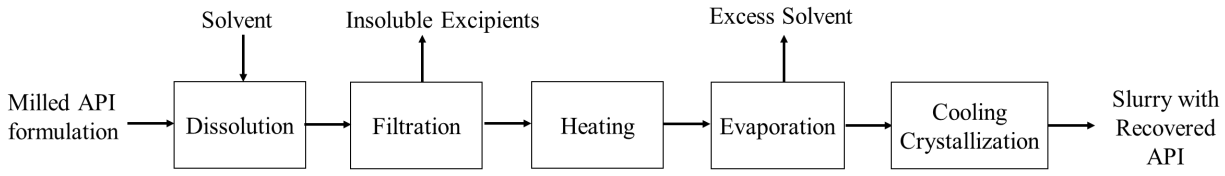



**Figure 1:** Generic separation train considered for the API recovery process.

## Proposed Methodology

A general separation train for recovering API, as depicted in Figure 1, comprises a few general processing steps: (i) dissolution, (ii) filtration, (iii) heating, (iv) evaporation, and (v) crystallization. Initially, the tablets are milled, and the resulting powder is dissolved in the selected solvent at a specified temperature. After dissolution, the mixture is filtered, separating the insoluble excipients. A 5% solvent loss is considered to account for filtration losses. After filtration, the solution is heated to saturation to evaporate excess solvent, a critical step to facilitate nucleation when the temperature is subsequently lowered. Each step involves operating decisions that impact the performance of the given flowsheet. The entire process is conducted in a batch mode. In the process, the operating temperatures for each operation are important to ensure minimal energy consumption while ensuring a high yield in the batch crystallization.

The solvent selection framework is based on three important considerations. The first is selecting the solvent right at the dissolution stage, which was adopted in an earlier study [4], in a preliminary form, where a solvent was classified as a 'good solvent' if it dissolved the API in more than a specified quantity However, our approach seeks to maximize the relative difference between the API ($m_{API}^{d}$) and the excipients ($m_{Ei}^{d}$) dissolved at a given dissolution temperature $T_D$.

$$\begin{aligned} &\max_{\boldsymbol{x},\boldsymbol{y}} f \\ &s.t.\ g_i(\boldsymbol{x}) \le 0\ \forall\, i \in I, \\ &h_j(\boldsymbol{y}) \le 0\ \forall\, j \in I \\ &\boldsymbol{x_{lb}} \le \boldsymbol{x} \le \boldsymbol{x_{ub}} \\ &\boldsymbol{y} \in \{0,1\} \end{aligned} \tag{1}$$

Equation 1 shows that the mathematical formulation of the solvent selection framework can be posed as an optimization problem in which an objective function is maximized given a set of constraints and variable bounds. The objective function selected depends on the criteria for solvent selection. The second metric consists of selecting a solvent based on the overall recovery of the process, thus giving a more comprehensive picture. The third metric consists of selecting a more sustainable solvent, i.e., a minimal requirement for solvent for API recovery.

## Solvent Selection Criteria

Table 1 shows the two different methods for solvent selection. In the dissolution-based approach, the solvent that dissolves the API selectively but not the excipients is considered a good solvent.

**Table 1:** Description of the dissolution and recovery-based solvent selection methodologies.

| Description | Dissolution Based | Recovery Based |
|---|---|---|
| Objective Function | $S_j\left(m_{API}^{d} - \sum_{i=1}^{n} m_{Ei}^{d}\right)$ | $S_j\left(\frac{100}{1-X_2}\left(1-\frac{X_2}{X_1}\right)\right)$ |
| Decision Variable(s) | $T_D, S_j$ | $T_1, T_2$ |
| Constraint(s) | $\sum_{j=1}^{m} S_j = 1$ | $X_{solids} \le 0.2$<br>$\sum_{j=1}^{m} S_j = 1$ |
| Variable bounds | $T_{LB} \le T_D \le T_{UB}$<br>$S_j \in \{0,1\}$ | $T_{LB} \le T_1 \le T_{UB}$<br>$T_{LB} \le T_2 \le T_{UB}$ |

This approach can provide the optimal solvent for the given objective and determine the optimal dissolution temperature that facilitates selective API dissolution.

Multiplying this relative difference with a binary variable ($S_j$) that indicates if a solvent is selected results in an MINLP formulation. On the other hand, the recovery-based approach focuses on increasing the yield obtained during the final stage, i.e., crystallization.

The objective, given in Table 1 for this approach consists of the percentage recovery under cooling crystallization [5] where $X_1$ and $X_2$ are the API's initial and final mass fractions before and after cooling at temperatures $T_1$ and $T_2$. It is important to note that while in cooling crystallization, as the solids begin to crystallize, there is an increasing possibility of fouling in the transfer line. Thus, a constraint to restrict the amount of solids crystallized is imposed. Finally, the bounds on the dissolution temperature are imposed. The initial and final temperatures vary from the maximal of the freezing point of a solvent and the lowest possible temperature that may be achieved by the heat exchanger and the smaller of the API degradation temperature and the boiling point of the solvent for the upper bound.

For the third metric of process sustainability, the process mass intensity (PMI) is used in this study. This metric was chosen over the E-factor metric as it is the ratio of the total mass in the process and the amount of API recovered, thus providing a fuller picture of the process's inputs and not just the waste. Equation 2 shows how PMI is calculated.

$$PMI = \frac{Total\ Mass\ [kg]}{API\ recovered\ [kg]} \quad (2)$$

## FRAMEWORK APPLICATION

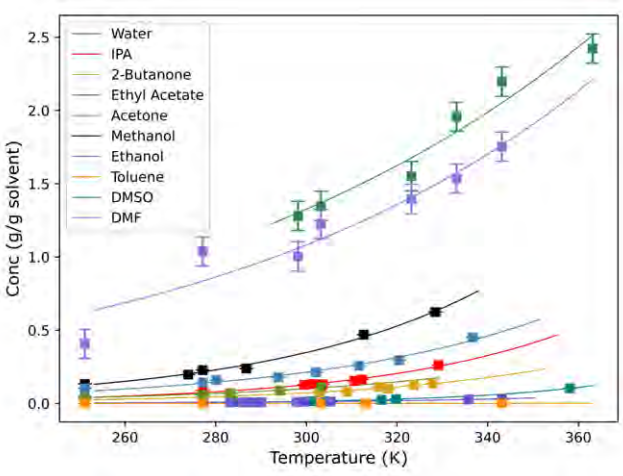



**Figure 2**: Solubility of API in all the chosen solvents.

The above-described solvent selection approach is applied to a formulation of paracetamol. The formulations for any specific API differ slightly from manufacturer to manufacturer; however, the set of excipients employed does not vary significantly. Hence, with this API, five common excipients are chosen to constitute a representative formulation. The details of this formulation can be seen in Table 2. The developed solvent selection framework applies to selecting solvents from an existing set. Hence, a list of ten common solvents for crystallization is proposed for selecting the appropriate solvents, as shown in Table 3, is proposed from which the most appropriate solvent will be selected. Most of the solvents belong to class 3, which are solvents of low toxicity, and two of them belong to class 2, which are solvents of limited use according to the guidelines of the International Council of Harmonization of Technical Requirements for Pharmaceuticals for Human Use (ICH) [6].

**Table 2:** Selected paracetamol formulation adapted from [7].

| Label | Name | Quantity (mg/tablet) |
|---|---|---|
| API | Paracetamol | 500.00 |
| E1 | Starch | 44.00 |
| E2 | Microcrystalline Cellulose (MCC) | 30.00 |
| E3 | PVP-K-30 | 18.00 |
| E4 | Magnesium Stearate | 2.00 |
| E5 | Silica | 2.00 |

**Table 3:** Common solvents used in crystallization studies.

| Label | Solvent Name | Solvent Class |
|---|---|---|
| S1 | Water | 3 |
| S2 | Methanol | 3 |
| S3 | Ethanol | 3 |
| S4 | Toluene | 2 |
| S5 | 2-Propanol (IPA) | 3 |
| S6 | Dimethylformamide (DMF) | 2 |
| S7 | Acetone | 3 |
| S8 | Ethyl acetate | 3 |
| S9 | 2-Butanone | 3 |
| S10 | Dimethyl sulfoxide (DMSO) | 3 |

Having selected the candidate solvents, the solubility of the API is determined experimentally using the Technobis Crystalline equipment apparatus [8], which measures the transmissivity of solutions during heating and cooling cycles. The clear point of a sample is defined as the temperature at which transmissivity reaches 100% during heating, indicating full transparency. In contrast, the cloud point is the temperature at which transmissivity drops to zero during cooling, indicating turbidity. For measurements, solutions of the API with known

**Table 4:** Summary of excipients solubilities in chosen solvents; Y: soluble, N: insoluble.

| Solvent Names | MCC | MgSt | PVP-K-30 | Silica | Starch |
|---|---|---|---|---|---|
| Water | N | N | Y | N | N |
| Methanol | N | N | Y | N | N |
| Ethanol | N | N | Y | N | N |
| Toluene | N | N | N | N | N |
| 2-propanol | N | N | Y | N | N |
| N,N-Dimethylformamide | N | N | Y | N | N |
| Acetone | N | N | Y | N | N |
| Ethylacetate | N | N | N | Y | N |
| 2-butanone | N | N | Y | Y | N |
| Dimethyl sulfoxide | N | N | Y | Y | N |

concentrations were prepared in 5 ml vials for the selected solvents. The obtained experimental data is then fitted to a two-parameter modified Apelblat equation (Equation 3), where C is the concentration of API in g/g-solvent at temperature T, and the constants A and B are obtained.

$$\ln C = A + BT \tag{3}$$

The solubilities of the excipients were determined using the gravimetric method. The reason is that most excipients are sparingly soluble in the candidate solvents, making the transmissivity measurements difficult.

Replicate solutions in sets of three to minimize error containing excess excipient were prepared in 20 ml scintillation vials, which were stirred for 24 hours. The temperature was kept within ± 0.1°C of the desired temperature and was checked with a Pt-100 resistance thermometer. After equilibration, the excess excipient was allowed to settle for 24 hours without agitation. A sample of clear saturated solution (approximately 10 ml) was transferred into a previously weighed petri dish ($m_d$) after filtering with the filter of pore size 0.2 µm and weighed again ($m_s$). Subsequently, the filtered samples were left in the oven at 45°C for the solvent to evaporate for 3 days. The dishes were weighed each day to account for changes in mass. After the mass of dishes did not change by more than 5 mg, the mass of dry residue ($m_r$) was recorded. The solubility was calculated as shown in Equation 4.

$$C = \left(\frac{m_r - m_d}{m_s - m_r}\right)\frac{g\ solute}{g\ solvent} \tag{4}$$

The excipients were then simply classified as soluble or not in a specific solvent, as summarized in Table 4. Consequently, the solvent required to dissolve the API completely becomes crucial. Also, post-filtration, the solution is saturated with the active ingredient by evaporating the excess solvent. Since paracetamol is sparingly soluble in toluene, the most solvent is required if toluene is used. By contrast, DMF and DMSO are required in lesser quantities due to their high solubility of the API. The next step involved applying the solvent selection framework for a formulation of PA (Table 5) to execute the flowsheet described in Section 2. A basis of 1000 g (1 kg) of API was chosen for evaluating the associated process flowsheet. The optimal solvent for dissolution

**Table 5:** Summary of preferred solvents for each method and the process parameters required to achieve the desired recovery.

| Metric | Preferred Solvents | Process Parameters | | | | Recovery |
|---|---|---|---|---|---|---|
| | | $T_D$ (K) | $T_1$ (K) | $T_2$ (K) | Solvent Required (kg) | (%) |
| Recovery | Water | 298.2 | 353.2 | 273.2 | 75.7 | 94.7 |
| | 2-Butanone | 298.2 | 253.2 | 352.8 | 17.7 | 92.0 |
| | Ethyl Acetate | 298.2 | 350.3 | 253.2 | 105.0 | 90.5 |
| Sustainability | DMF | 353.2 | 353.2 | 253.2 | 0.6 | 30.7 |
| | DMSO | 353.2 | 353.2 | 292.2 | 0.6 | 30.9 |
| | Methanol | 337.9 | 337.9 | 253.2 | 1.3 | 47.0 |
| Solubility | Ethyl Acetate | 298.2 | 350.3 | 253.2 | 105.5 | 92.0 |
| | Toluene | 298.2 | 353.2 | 253.2 | 2942.2 | 83.3 |

depends on the solution of the solubility metric described in Table 1.

An enumeration-based approach was used to solve the problem formulated in Equation 1 for both dissolution and recovery-based methods. Thus, the objective functions for both approaches were evaluated for all the solvents at the respective temperature bound of the solvent.

Interestingly, for the chosen formulation, four out of the five excipients were insoluble in the solvents initially considered for screening. This meant that the relative difference in the amount of API and the excipient dissolved reduced to the difference in the quantity of PA and PVP-K-30 dissolved. Solvents ethyl acetate and toluene are preferable when selecting a solvent based on dissolution, as none of the excipients are soluble in them. All the remaining solvents are equally favorable as the difference in the API and excipients dissolved is constant.

For the recovery-based solvent selection, Figure 3 shows the maximum possible recoveries that can be obtained using the ten solvents. Water has the highest recovery, followed by 2-butanone and ethyl acetate. Due to the constraint on the solids fraction in the crystallization stage not being more than 20%, the actual recovery is lower than the predicted theoretical recovery, limiting the extent to which the feed can be cooled. Hence, the recoveries for solvents DMF and DMSO are significantly lower, even though PA is highly soluble in these solvents.

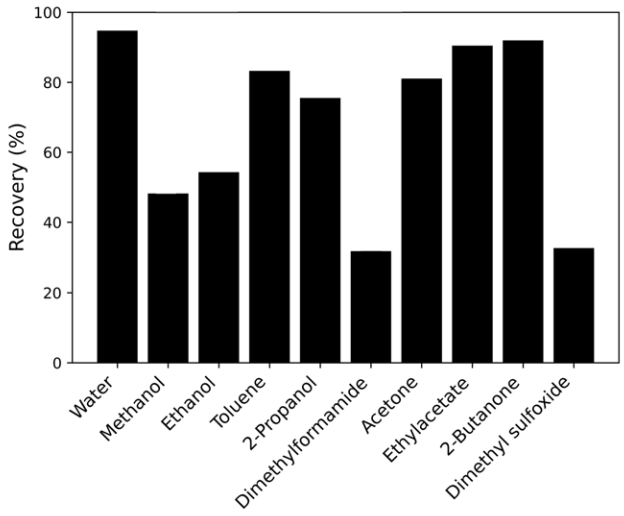



**Figure 3:** Recovery of PA from the chosen formulation for the chosen solvents.

Figure 4 summarizes the amount of solvent required to achieve the recoveries described in Figure 3 and the respective PMI. Solvents with high solubility of API naturally are required in lesser quantities and, therefore, have a low PMI. On the contrary, despite a relatively high theoretical recovery, the PMI is the highest in the case of toluene due to its tendency to dissolve a very small quantity of PA. Thus, there is a trade-off when it comes to selecting a solvent with a high recovery and a sustainable solvent. Targeting high recovery while maintaining a relatively low PMI was observed in the cases of water and 2-butanone. These solvents were notable because the mass fraction of crystallized solids did not exceed the 20% threshold, ensuring that the flowability constraint was not violated. This allows the maximal recovery to be the same without considering the flowability constraint.

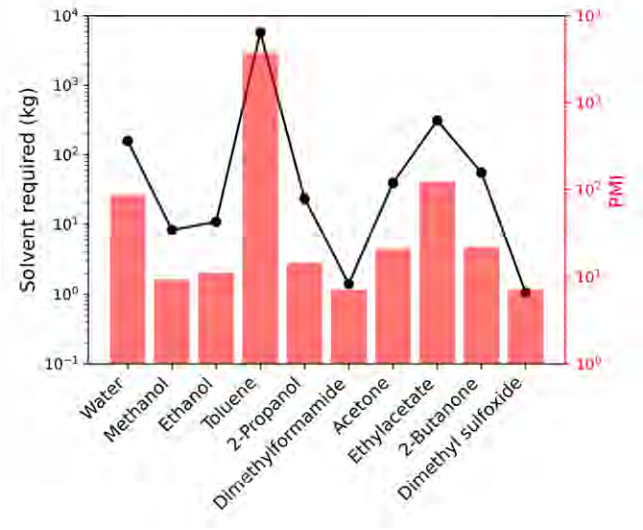



**Figure 4:** Amount of solvent required and the respective PMI for a basis of 1 kg of PA in the formulation.

The specific metrics of interest should guide the selection of solvents. Although 2-butanone and ethyl acetate exhibit a lower PMI than water, this is accompanied by a trade-off in recovery. Table 5 summarizes this solvent screening approach, which allows for the prioritization of specific metrics, facilitates informed decisions regarding solvent selection based on objectives, and enables subsequent process modeling. As can be seen, the values of the objective function of each metric (such as recovery and the amount of solids dissolved) change as the temperatures $T_1$, $T_2$, and $T_d$ vary with changes in these temperatures (< 1°C). The sensitivity of this change is related to the solubility of the API and the excipients at those temperatures, which depend on the constants A and B obtained from experiments. However, with small changes in temperatures, the overall ranking of the solvents is not impacted significantly.

However, a formulation with excipients that show different behaviors, such as gel formation, will need more attention when applying this methodology. Either imposing different bounds on the process temperature or eliminating the solvents where these different behaviors are observed will be necessary. Overall, the developed solvent selection approach provides a systematic

framework for enabling API recovery with maximal recovery and ensuring the key process constraints are met.

## CONCLUSION

In this study, a solvent selection framework was developed for a sustainable recovery of API. The framework was applied effectively in a case involving a paracetamol formulation, wherein solvents are selected according to each desired approach. It can be shown that this framework can be extended to different APIs that have variable solubility with temperature, thus enabling separation via cooling crystallization with a high recovery. Analyzing the solvents by ranking them provided valuable insights into the trade-offs of choosing a solvent with high recovery and a more sustainable solvent. This solvent selection framework constitutes an important step towards the development of a generalized framework for sustainable API recovery processes.

After obtaining the API from cooling crystallization by selecting the most appropriate solvent, further processing is necessary to recover the API. While this will depend on the API that is being recovered, a general trend involves washing and filtering the crystallized slurry and subsequently drying the mixture.

## ACKNOWLEDGMENTS

This work is supported by the National Science Foundation (NSF) under grant no. 2229250.

## REFERENCES

1. J. Natarajan, S. Altan, D. Raghavarao, Expiration Dating of Pharmaceutical Compounds in Relation to Analytical Variation, Degradation Rate, and Matrix Designs. Drug Inf. J. 31 589–595 (1997) https://doi.org/10.1177/009286159703100226.
2. R. C. Lyon, Stability profiles of drug products extended beyond labeled expiration dates. J. Pharm. Sci. 95 (2006) https://doi.org/10.1002/jps.20636
3. J. Kim, O. De Jesus. http://www.ncbi.nlm.nih.gov/books/NBK568677/
4. D. E. Pratama, W.-C. Hsieh, A. Elmaamoun, H. L. Lee, T. Lee, Recovery of Active Pharmaceutical Ingredients from Unused Solid Dosage-Form Drugs. ACS Omega 5 29147–29157 (2020) https://doi.org/10.1021/acsomega.0c03878.
5. A. T. Karunanithi, L. E. K. Achenie, R. Gani, A computer-aided molecular design framework for crystallization solvent design. Chem. Eng. Sci. 61 1247–1260 (2006) https://doi.org/10.1016/j.ces.2005.08.031.
6. S. K. Branch, Guidelines from the International Conference on Harmonisation (ICH). J. Pharm. Biomed. Anal. 38 798–805 (2005) https://doi.org/10.1016/j.jpba.2005.02.037.
7. S. Niazi, Handbook of Pharmaceutical Manufacturing Formulations. Boca Raton: CRC Press, 2004.

© 2025 by the authors. Licensed to PSEcommunity.org and PSE Press. This is an open access article under the creative commons CC-BY-SA licensing terms. Credit must be given to creator and adaptations must be shared under the same terms. See https://creativecommons.org/licenses/by-sa/4.0/



Systems & Control Transactions

**Research Article - Peer Reviewed Conference Proceeding**
ESCAPE 35 - European Symposium on Computer Aided Process Engineering
Ghent, Belgium. 6-9 July 2025
Jan F.M. Van Impe, Grégoire Léonard, Satyajeet S. Bhonsale,
Monika E. Polańska, Filip Logist (Eds.)

PSE PRESS

# Integrating process and demand uncertainty in capacity planning for next-generation pharmaceutical supply chains

**Miriam Sarkis[a,b], Nilay Shah[a,b], and Maria M. Papathanasiou[a,b]***

[a] The Sargent Centre for Process Systems Engineering, Imperial College London, London, United Kingdom
[b] Department of Chemical Engineering, Imperial College London, London, United Kingdom
* Corresponding Author: maria.papathanasiou11@imperial.ac.uk

## ABSTRACT

Emerging sectors within the biopharmaceutical industry are undergoing rapid scale-up due to the market boom of gene therapies and vaccine platform technologies. Manufacturers are pressured to orchestrate resources and plan investments under future demand uncertainty and, critically, an early-stage process uncertainty for platforms still under development. In this work, a multi-product multi-stage stochastic optimization problem integrating demand uncertainty is presented and augmented with a worst-case optimization approach with respect to process uncertainty. Results focus on a comparison between fixed equipment facilities and modular technologies, highlighting an inherent flexibility of the latter option due to shorter recourse actions for capacity scale-out. The impact of process uncertainty integration is quantified. With more conservative decisions taken in first-stages of the time horizon, expected costs result lower for modular single-use equipment. This suggests that capacity adjustments also help adapt to varying process performance and reduce the propagation conservative design decisions.

**Keywords**: Supply Chain, Planning & Scheduling, Stochastic Optimization, Technoeconomic Analysis, Advanced Pharmaceutical Manufacturing

## INTRODUCTION

Pharmaceutical capacity planning is crucial to meet product demands from clinical to commercial stages. In recent years, the market boom of gene therapies and demand for vaccines in pandemic contexts has highlighted a need to improve responsiveness of supply chains to demand fluctuations and unforeseen events. To this end, the industry has seen an uptake of single-use equipment (SU) to substitute more inflexible stainless-steel multi-use (MU) facilities, allowing for rapid scale-up and scale-out of manufacturing capacity. In this space, investment planning is challenged by a need to make scale-up decisions before processes are fully intensified and process capabilities known for certain[1]. Furthermore, process uncertainty in early stages of planning is combined with an uncertainty in future demands. In this context, an overestimation of attainable production targets and sub-optimal demand forecasting can result in shortages and exacerbate costs[2].

The complexity of investment planning problem under demand uncertainty can be represented as a stochastic optimization embedding a multi-stage scenario tree for demand outcomes. The PSE literature presents a number of decision support tools based on stochastic programming finding a direct application in capacity planning in pharmaceutical contexts. First stage variables include initial capacity investments, product selection and initial allocation of manufacturing resources to products. Second stage recourse decisions consist in additional capacity investment or sale of capacity, re-allocation of products to resources. Extensive research in PSE has focused problems of capacity planning using stochastic programming[3,4]. Alternatively, simulation-based approaches[5,6] and rolling horizon strategies[7,8] have been proposed to decision-making based on simulated demand outcomes.

This work focuses on investigating whether early-stage process uncertainty which characterizes advanced biopharmaceutical products undergoing rapid scale up is

worth integrating in capacity planning optimization problems. The proposed approach accounts for the different time scales of uncertainty and differentiates the flexibility of MU-based and SU-based equipment, which thus far has not been considered explicitly in the context of biopharmaceutical planning under uncertainty. The presented planning tool integrates process uncertainty using a worst-case approach, using previously quantified process uncertainty[9] and cost-related inputs obtained via techno-economic models, and demand uncertainty using stochastic programming and uses. Comparative analyses for SU and MU cases discuss the impact of process uncertainty integration compared to a deterministic-process counterpart and focus on network responsiveness to demand uncertainty.

# METHODOLOGY

## Problem statement

The capacity planning problem considered in this study is aimed at minimizing total supply chain capital and operating cost and determine a set of demand scenario independent design decisions and scenario-dependent decisions. These differ based on whether equipment is multi-use (MU) or single-use (SU).
The optimization considers:

- A set $T$ of time periods $t$;
- A set $I$ of products $i$;
- A set $N$ of nodes $n$;
- A set $T$ of time periods $t$;
- A set $A$ of process scales $a$;
- A set $S$ of process section $s$;
- A set $L$ of process lines $l$;
- A set $DS$ of demand scenarios $y$;

In the MU case, the partition of first-stage and second-stage scenario-dependent decisions results as follows:

1. Network structure and links between nodes;
2. Investment in manufacturing facilities;
3. Scales of manufacturing and number or parallel lines;
4. *Scenario-dependent* manufacturing levels,
5. *Scenario-dependent* transportation flows;
6. *Scenario-dependent* supply flows at each demand node.

In the SU case, the optimization considers the selection of scales and parallel lines as *scenario-dependent*, hence treating it as a recourse action or second-stage decision.

The optimization requires information on costs of technologies at different manufacturing scales $a$, for different process sections $s$ for the different products considered $i$ and specific to MU-based equipment vs SU-based equipment. This is obtained via techno-economic modelling of the processes of interest. Furthermore, it requires input data with respect to storage and transport cost per unit (Sarkis et al.[10] – SI) and target demands for each product $i$, realizing over time and differing by scenario $y$.

Whilst demand realizes in stages, process uncertainty is mainly present in early stages of scale-up. Before process capabilities are known, decision-makers may consider adopting a *risk-averse* approach. Once process uncertainty realizes, true capabilities are known and optimization decisions can adapt accordingly. This concept is integrated through a two-stage worst-case optimization approach. Ultimately, by combining expected demand outcomes and this process uncertainty mitigation strategy, decision-makers can obtain *here-and-now* investment plans which minimize expected costs and mitigate early-stage shortage risks. Depending on underlying equipment-related recourse actions, the resulting planning solutions may differ.

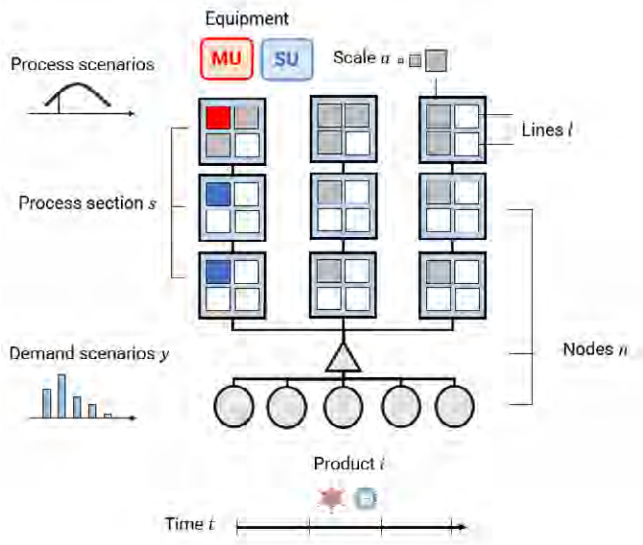



**Figure 1.** Optimization superstructure for multi-product supply chain case study.

## Techno-economic performance quantification

Techno-economic models of the manufacturing technologies of interest are developed using SuperPro Designer (Intelligen). In this work, the focus is the quantification of techno-economic performance of MU-based and SU-based manufacturing at scale $a \in A = \{50,200,1000,2000\}$ and for products $i \in I = \{LV, AdV\}$.

Details regarding the development of underlying models is included in Sarkis et al.[9] (SI). Here, equipment has been modified to fully SU or MU accordingly. Techno-economic KPIs for each platform include batch size $\chi$, cycle time $\tau$, end-to-end process time $\alpha$, and capital and operating costs $c$. Costs are assumed to be deterministic and dependent on equipment type, product $i$ and scale $a$. Instead, throughput related uncertainty as quantified in Sarkis et al.[9] is considered, yielding ranges of performance for batch size $\chi \in [\chi^{min}, \chi^{max}]$, cycle time $\tau \in [\tau^{min}, \tau^{max}]$ and process time $\alpha \in [\alpha^{min}, \alpha^{max}]$ for each product- and scale-specific process.

## Optimization formulation

The optimization considers a multi-period multi-product planning problem where $T = \{T_1, T_2, T_3, T_4\}$ and $I = \{LV, AdV\}$, where LV is a lentivirus-based product for gene therapy applications and AdV is an adenovirus-based product for vaccine applications. As mentioned, throughput related parameters are considered uncertain, whereas cost-related parameters are held at the deterministic value quantified via techno-economic modelling. On the demand side, a set of demand scenarios $y$ is considered $DS = \{DS_1, DS_2 \ldots DS_N\}$, which result from combinations of individual product demands in a multi-stage stochastic scenario tree. The optimization formulation is summarized in Table 1.

As shown in Eq.1, the objective function $z$ corresponds to the total expected supply chain cost, which a summation of capital and operating costs of manufacturing, storage costs and transport costs. These are scenario-dependent quantities and normalized by scenario probability $\Pi_y$. Manufacturing capital costs $TC^{CAPj}$ embed equipment installation costs $C^{EQj}$ for each node $n \in N^J$ and time $t$ (Eq. 2.), which are a function of equipment installation cost coefficients $c^{EQjl}$ and equipment installation binaries $H$, with respect to time $t$, node $n \in N^J$, scale $a$, line $l$, section $s$ and scenario $y$ (Eq. 3).

Manufacturing operating costs $TC^{OPj}$ include labour related costs $C^{LABj}$, variable costs $C^{VARj}$ and facility-dependent costs $C^{FACj}$ (Eq. 4), which are respectively function of cost coefficients $c^{LABj}$, $c^{VARj}$, $c^{FACj}$ for each scale $a$, section $s$ and product $i$ multiplied by either the number of batches $B$ (Eq. 5-6), and product-specific equipment installation $M$ (Eq. 7). Hence, the benefit of economies of scale on cost effectiveness is captured within the optimization, with a balance between costs that scale with production levels and fixed costs. Storage related costs $TC^{OPk}$ are computed as multiplication of a handling coefficient $c^{OPk}$, which depends on scale $a$ and product $i$ and the sum of transport flows $Q$ passing through all storage nodes at time $t$ and in scenario $y$ (Eq. 8). Transport costs $TC^T$ consider a cost coefficient per km travelled and batch delivered $c^T$ multiplied by distance $\rho$ between nodes $n$ and $m$ and transport flows $Q$.

**Table 1:** Optimization formulation for multi-product, multi-stage, multi-period stochastic problem.

| | |
|---|---|
| **Objective function and cost components** | |
| 1 | $\min z = \sum_{y \in DS} \Pi_y \left(TC_y^{CAPj} + TC_y^{OPj} + TC_y^{OPk} + TC_y^{T}\right)$ |
| 2 | $TC_y^{CAPj} = \sum_{t \in T} \sum_{n \in N^J} C_{tny}^{EQj} \quad \forall y$ |
| 3 | $C_{tny}^{EQj} = \sum_{a \in A} \sum_{s \in S} \sum_{l \in L} c_{as}^{EQjl} H_{tnalsy} \quad \forall t, n \in N^J, y$ |
| 4 | $TC_y^{OPj} = \sum_{t \in T} \sum_{n \in N^J} C_{tny}^{LABj} + C_{tny}^{VARj} + C_{tny}^{FACj} \quad \forall y$ |
| 5 | $C_{tny}^{LABj} = \sum_{a \in A} \sum_{s \in S} \sum_{l \in L} \sum_{i \in I} c_{asi}^{LABj} B_{tnalsiy} \; \forall t, n \in N^J, y$ |
| 6 | $C_{tny}^{VARj} = \sum_{a \in A} \sum_{s \in S} \sum_{l \in L} \sum_{i \in I} c_{asi}^{VARj} B_{tnalsiy} \; \forall t, n \in N^J, y$ |
| 7 | $C_{tny}^{FACj} = \sum_{a \in A} \sum_{s \in S} \sum_{l \in L} \sum_{i \in I} c_{asi}^{FACj} M_{tnalsiy} \; \forall t, n \in N^J, y$ |
| 8 | $TC_y^{OPk} = \sum_{t \in T} \sum_{n \in N^K} \sum_{m \in N^J} \sum_{a \in A} \sum_{i \in I} c_{ai}^{OPk} Q_{tnmaiy} \quad \forall y$ |
| 9 | $TC_y^{T} = c^T \sum_{t \in T} \sum_{n \in N^M} \sum_{m \in M^N} \sum_{a \in A} \sum_{i \in I} \rho_{nm} Q_{tnmaiy} \quad \forall y$ |
| **Sourcing constraints** | |
| 10 | $X_{tnm} \leq Y_{tn} \quad \forall t, n \in N^J, m \in M^N$ |
| 11 | $\sum_{n \in N^J} X_{tnm} \geq Y_{tm} \quad \forall t, m \in N^K$ |
| 12 | $\sum_{n \in K} X_{tnm} \geq Y_{tm} \quad \forall t, m \in N^Z$ |
| **Equipment and product allocation constraints** | |
| 13 | $\sum_{a \in A} V_{tnay} \leq Y_{tn} \quad \forall t, y, n \in N^J$ |
| 14 | $Z_{tnasly} \leq V_{tnay} \quad \forall t, n \in N^J, a, s, l, y$ |
| 15 | $M_{tnasliy} \leq Z_{tnasly} \quad \forall t, n \in N^J, a, s, l, i, y$ |
| 16 | $W_{tnasliy} \leq M_{tnasliy} \quad \forall t, n \in N^J, a, s, l, i, y$ |
| 17 | $N_{tnasly} = \sum_{i \in I} W_{tnasliy} - 1 \; \forall t, n \in N^J, a, s, l, y$ |
| 18 | $C_{tnasliy \mid i=LV} = N_{tnasly} \; \forall t, n \in N^J, a, s, l, y$ |
| 19 | $C_{tnasliy \mid i=AdV} = N_{tnasly} - 1 \; \forall t, n \in N^J, a, s, l, y$ |
| 20 | $Z_{tnasly} \leq Z_{t-1,nasly} + H_{tnalsy} \; \forall t, n \in N^J, a, s, l, y$ |
| 20' | $Z_{tnasly} = Z_{t-1,nasly} + H_{tnalsy} \; \forall t, n \in N^J, a, s, l, y$ |
| **Production constraints** | |
| 21 | $T^{MIN} W_{tnasliy} \leq T_{tnasliy} \leq T^{MAX} W_{tnasliy} \; \forall t, n \in N^J, a, s, l, i, y$ |
| 22 | $U_{tnasly} = \sum_{i \in I} T_{tnasliy} \quad \forall t, n \in N^J, a, s, l, y$ |
| 23 | $U_{tnasly} \leq U^{MAX} \; \forall t, n \in N^J, a, s, l, y$ |
| 24 | $B_{tnasliy} = W_{tnasliy} + \tau_{st}\left(T_{tnasliy} - \alpha_{st} W_{tnasliy} - \kappa C_{tnasiy}\right) \; \forall t, n \in N^J, a, s, l, i, y$ |
| 25 | $\sum_{l \in L} B_{tnasliy} = \sum_{l \in L} B_{tna,s+1,liy} \; \forall t, n \in N^J, a, s, i, y$ |
| **Network balances** | |
| 26 | $I_{tnaiy} = I_{t-1,naiy} + \sum_{l \in L} B_{tnasliy \mid s=F} + \sum_{m \in N^K} Q_{tnamiy} \quad \forall t, n \in N^J, a, i, y$ |
| 27 | $\sum_{m \in N^J} Q_{tmnaiy} = \sum_{m \in N^Z} Q_{tnmaiy} \; \forall t, n \in N^K, a, i, y$ |
| 28 | $\sum_{m \in K} Q_{tmnaiy} = S_{tnaiy} \; \forall t, n \in N^Z, a, i, y$ |
| 29 | $\sum_{a \in A} S_{tnaiy} \chi_{ait} \geq D_{tniy} \; \forall t, n \in N^Z, i, y$ |
| 30 | $D_{tniy} = \frac{D_{tiy}^T}{card(N^Z)} \quad \forall t, n \in N^Z, i, y$ |
| 31 | $Q^{MIN} X_{tnm} \leq \sum_{i \in I} Q_{tnmaiy} \leq Q^{MAX} X_{tnm} \; \forall t, n \in N, m \in M, a, y$ |
| **Non-anticipativity constraints** | |
| 32 | $x_{ty} = x'_{ty} \quad \forall y, y' \in \Delta^t$ |
| **MU case additional constraints** | |

33 $V_{tnay} = V_{tnay\prime} \quad \forall t, n \in N^J, a, y$

34 $Z_{tnasly} = Z_{tnasly\prime} \quad \forall t, n \in N^J, a, s, l, y$

35 $M_{tnasliy} = M_{tnasliy\prime} \quad \forall t, n \in N^J, a, s, l, i, y$

Sourcing constraints impose that a link $X$ at time $t$ between nodes $n$ and $m$ is established only if the upstream node exists through the activation of binary $Y$ (Eq. 10). Furthermore, all downstream nodes $m$ must be sourced by at least one link with an upstream node $n$ (Eq. 11-12). The equipment allocation constraint in Eq. 13 constrains the activation of scale $a$ in node $n \in N^J$ at time $t$ and scenario $y$ to nodes which are active ($Y = 1$) and allows the selection of at most one scale at a time, as the sum on the L.H.S. cannot exceed 1. A line $l$ of scale $a$ within process section $s$ can be installed through the $Z = 1$, if the respective scale is active within the node $n$, at time $t$ and in scenario $y$ (Eq. 14). Similarly, product-specific equipment installation through $M$ is allowed if the respective line $Z$ is active (Eq. 15). Product allocation occurs when $W = 1$, within manufacturing lines where equipment suitable for manufacturing of product $i$ is installed (Eq. 16). A change-over occurs ($N = 1$) when both products $i$ are manufactured within the same equipment, whereby the R.H.S. of Eq. 17 takes the value of 1. Product-specific change-over ($C = 1$) within the same time period $t$ is counted only once with respect to the LV product switching to AdV (Eq. 18), whilst the AdV to LV switch is always 0 (Eq. 19). An equipment manufacturing line can exist ($Z = 1$) at time period $t$ if investment has occurred through $H = 1$ or if it existed in the previous time period (Eq. 20). Noting the inequality sign which allows equipment to be deinstalled in the SU case, this becomes an equality constraint for the MU case (Eq. 20').

Production constraints in Eq. 21 bound the time allocated to manufacturing $T$ of product $i$, as well as the total utilisation time $U$ per year (Eq. 22-23). The number of batches $B$ is a function of time allocated to production

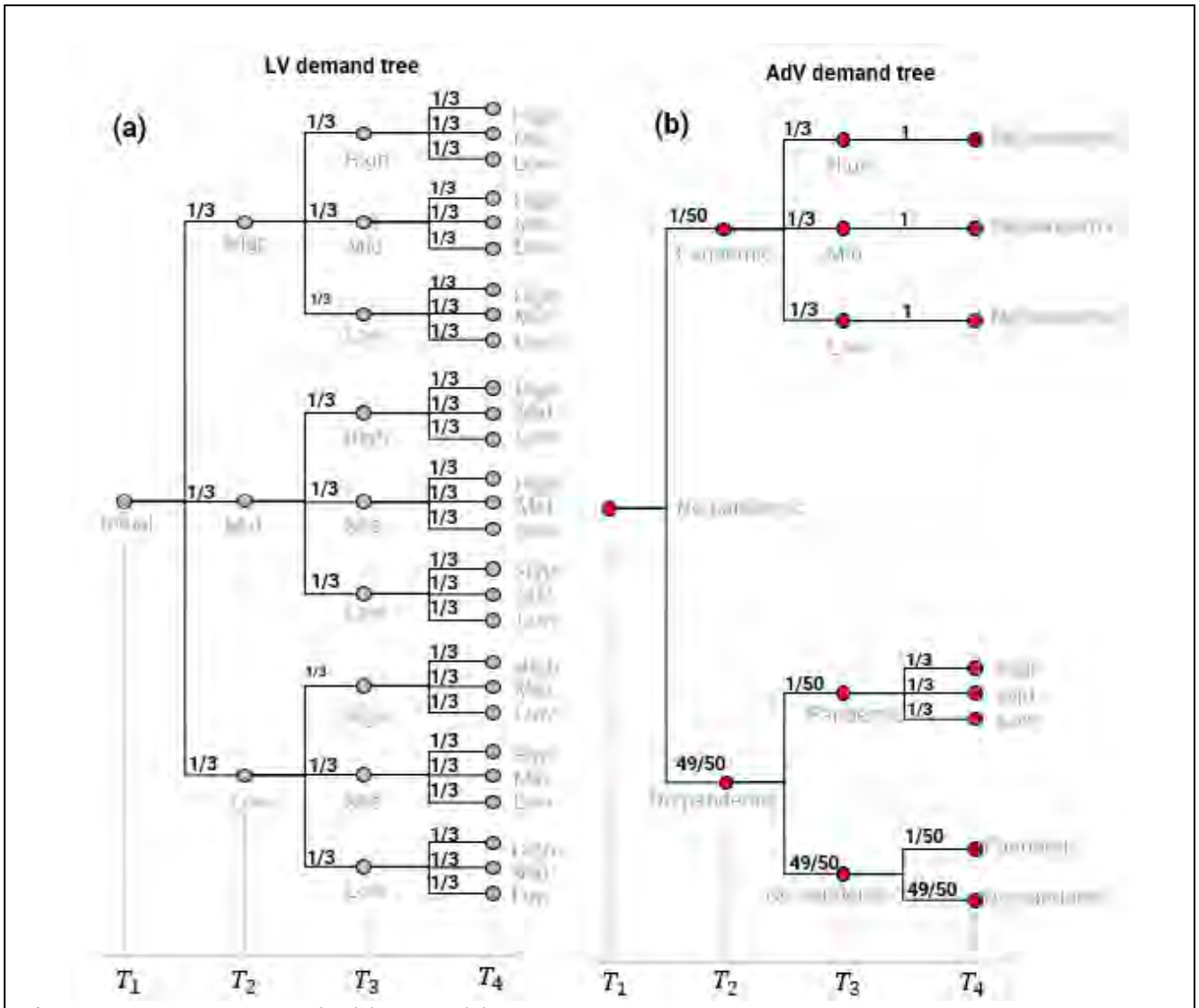



**Figure 2:** Demand scenarios for (a) LV and (b) AdV.

and process-specific throughput parameters, including the bottleneck time $\tau$, the process time $\alpha$ and changeover time $\kappa$, accounting for the time required to process the first batch within the campaign and the subsequent ones in shorter intervals (Eq. 24). In Eq. 25 the number of batches processes within each section $s$ is regulated by a material balance. Furthermore, network balances (Eq. 26-29) regulate the accumulation of inventory within the manufacturing nodes and the shipment of products so that the sales demand constraint is met (Eq. 29) for each product $i$, demand zone $n \in N^Z$ in each time period $t$ and demand scenario $y$. The location-specific product demands $D$ are a function of the total demand in each scenario $D^T$, which is an input within the optimization (Figure 2). Transport flows $Q$ are also regulated by upper bounds and lower bounds (Eq. 31). Non-anticipativity constraints are included in the formulation to ensure that scenarios remain indistinguishable until realization (Eq. 32), enforcing that all scenario-dependent variables are equal across the set of indistinguishable scenario pairs $\Delta$ at each stage $t$ .

Finally, the MU case requires additional constraints based on the assumption that the installation of additional capacity is not considered a recourse action, hence scenario-dependent. In Eq. 33-35, equipment installation binaries are forced to be equal across scenario and made *first-stage* decisions.

## Demand scenarios

A total of 216 scenarios $y \in D^S$ each with a probability of $\Pi_y$ is obtained by combining LV and AdV scenario trees. As can be seen in Figure 2a, LV scenarios consider that at a first stage demand corresponds to a nominal value (10,000 doses per year). As time progresses, demand may realize to be *high* (20,000 doses per year), *mid* (10,000 doses per year), *low* (5,000 doses per year), with equal probabilities 1/3 each year, capturing irregular demands for cancer therapies. Mariani et al.[11] estimate probability of a pandemic outbreak per year of 1/50, hence the AdV scenario tree (Figure 2b), captures *non-pandemic* and *pandemic* yearly outcomes. In the former case, the tree branches into pandemic/non-pandemic scenarios at $T_2$ . In the latter case, the demand for vaccines is *high* (400 million doses per year), *mid* (200 million doses per year), or *low* (100 million doses per year), due to market competition and/or issues with side-effects post commercialization. The pandemic is assumed to resolve within 2 years, hence demand is 0.

## Process uncertainty integration

Early-stage process uncertainty is integrated within the problem via a two-stage worst-case optimization approach (WO). This is compared to a deterministic-process approach (DET), whereby process uncertainty is not integrated. In WO, risk-averse decision-making is assumed, in order to avoid early-stage shortages. Process uncertainty is present at $t \in T_1$, whilst a deterministic realization at a median value (Sarkis et al.[10]) is assumed in subsequent time period, as knowledge is acquired in later time periods. To this end, the throughput related uncertainty quantified in Sarkis et al. is assumed to be described by *box uncertainty* sets for each parameter. Therefore:

$$u = \begin{Bmatrix} \chi_{ait}^{MIN} \le \chi_{ait} \le \chi_{ait}^{MAX}, \forall a,i,t \in T_1 \\ \tau_{st}^{MIN} \le \tau_{st} \le \tau_{st}^{MAX}, \forall s,t \in T_1 \\ \alpha_{st}^{MIN} \le \alpha_{st} \le \alpha_{st}^{MAX}, \forall s,t \in T_1 \end{Bmatrix},$$

where $\chi^{MIN}, \chi^{MAX}$ are bounds for process yield $\chi$ at scale $a$, for product $i$ and the first time period, $\tau^{MIN}, \tau^{MAX}$ are bounds for process time within section $s$, and $\alpha^{MIN}, \alpha^{MAX}$ are bounds for bottleneck time in section $s$. To formulate the worst-case deterministic optimization problem requires the following modifications for Eq. 24 and Eq. 29 within the first stage $T_1$, as follows:

**Eq. 24':** $B_{tnasliy} = W_{tnasliy} + \tau_{st}^{MAX}\left(T_{tnasliy} - \alpha_{st}^{MAX} W_{tnasliy} - \kappa C_{tnasiy}\right) \quad \forall t \in T_1, n \in N^J, a,s,l,i,y$

**Eq. 29':** $\sum_{a \in A} S_{tnaiy}\, \chi_{ait}^{MIN} \ge D_{tniy}\ \forall t \in T_1, n \in N^Z, i,y$

## Computational statistics

The MU multi-stage formulation involves a smaller problem size compared to SU because it involves less scenario-dependent decisions (Table 2). The model is implemented in PYOMO, solved with GUROBI v11 via high-throughput computing (1 node, 48nCPUs, RAM:100GB). The optimality gap threshold is set to 10% to obtain a solution to compare within 48h. Strategies to address problem scalability are discussed as part of research outlook.

**Table 2:** Computational statistics of MU vs SU optimization: constraints, integer (binary) and continuous variables, optimality gap.

| Case | CPU(s) | Cons. | Int. (Bin.) | Cont. | Gap(%) |
|---|---|---|---|---|---|
| MU | 25,715 | 878,916 | 1,369,544 (1,120,280) | 878,916 | 7.80 |
| SU | 36,513 | 2,258,780 | 1,379,864 (1,130,600) | 878,916 | 4.19 |

# RESULTS & DISCUSSION

## Techno-economic analysis

Outputs of techno-economic analysis correspond to the optimization cost coefficients $c$, defined for each cost category *VAR*, *FAC* and *LAB*, process section $s$, scale $a$ and product $i$. Figure 3 illustrates cost breakdowns for LV and AdV platforms implementing either SU or MU

equipment, with a focus on the $a = 2000$.

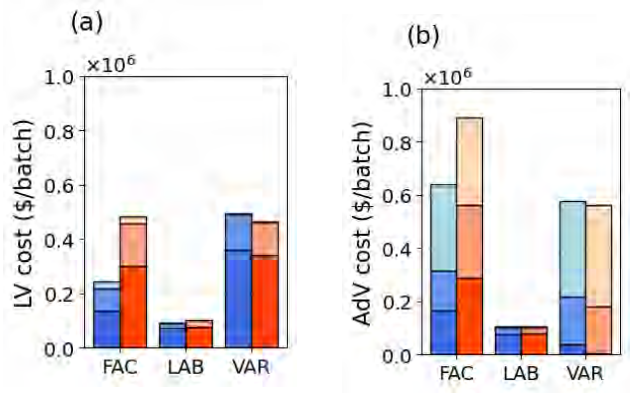



**Figure 3:** Cost breakdown for SU vs MU manufacturing platforms for LV manufacturing (a) and AdV manufacturing (b).

In Figure 3a, facility cost reductions up to 50% are achieved in the SU case for the production on LV in all parts of the process. This mostly holds for AdV too; however AdV facility costs of F&F are critical and are equivalent for both the MU and SU case, since only the formulation equipment is less costly through the use of disposable plastic bags alternatives (Figure 3b).

In comparison, labor-related costs are reduced by approximately 10% with respect to MU labor cost because of resulting shorter process times in the SU process. An underlying assumption of the techno-economic model is the linear relation between process times and total labor cost per batch which is obtained by multiplying process time by a predefined hourly rate. Due to shorter process times with removed steam-in-place/clean-in-place (SIP/CIP) steps, SU equipment results in lower labor costs per batch. Focusing on variable costs, the cost per batch in SU equipment is larger than the MU case (Figure 3a). This is due to a larger number of consumables being required in SU manufacturing compared to MU. This is also seen in AdV manufacturing (Figure 3b), where variable costs for USP, DSP and F&F result higher than the MU counterpart. Overall the percentage increase varies due to process differences, due to materials (LV) and process steps (AdV).

Figure 3 displays costs normalized *per batch*, showing that SU results in lower costs per batch compared to MU. Reductions in facility-dependent cost outweigh the marginal larger variable costs and this already suggests the selection of SU equipment for all process sections, if a cost optimization is performed.

## Optimization problem solution

In this work, early-stage throughput uncertainty is integrated in a multi-stage stochastic planning problem on the demand side, via a two-stage worst-case optimization approach on the process side, considering a time-dependent single uncertainty realization. The impact of this risk-averse approach to decision-making is mainly seen in first-stage decisions and initial investments. In Figure 4a, the MU case optimization (WO) installs a 4-times larger volumetric capacity compared to the deterministic-process (DET) stochastic solution. This is also seen in the cumulative volume trends in Figure 4a. In later

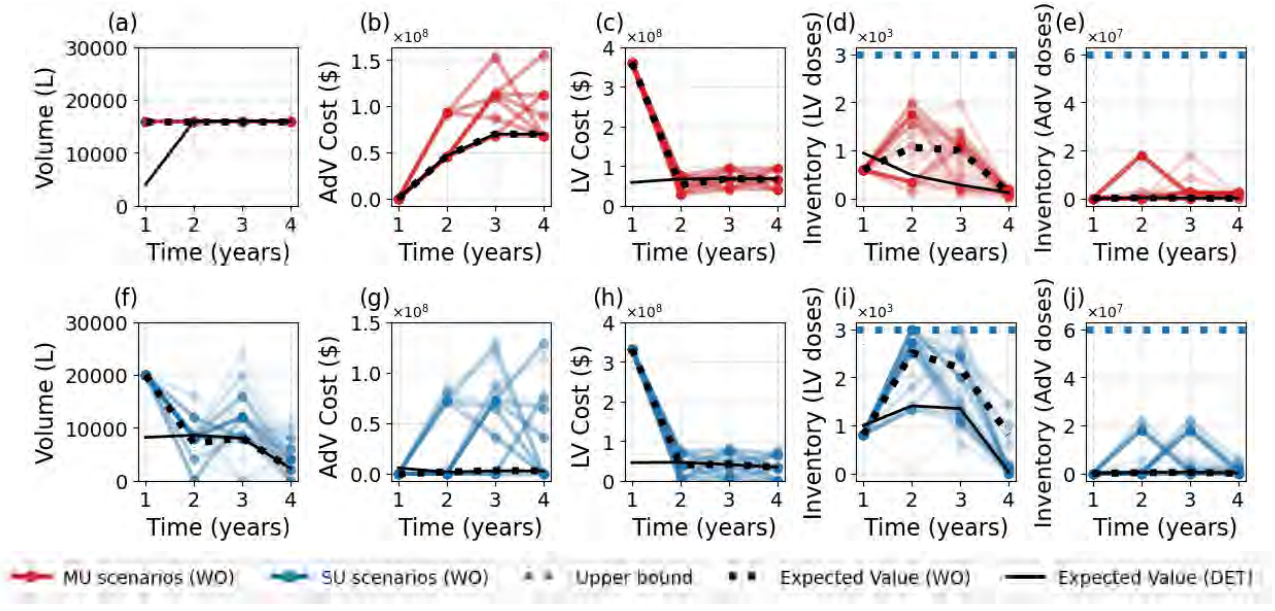



**Figure 4:** Stochastic optimization results for MU case (a-e) and SU case (f-j). Results integrating worst-case optimization w.r.t. to process uncertainty (WO) are displayed, alongside a deterministic (process side) benchmark (DET).

time periods, new investments are not required and capacity remains constant, fulfilling all demand scenarios and converging to the same investment plan proposed by the deterministic model. In the SU case, a significantly initial larger capacity is installed compared to the deterministic case (Figure 4e).

The initial overdesign of a WO approach propagates mainly to expected costs of LV productions, which result significantly higher initial costs compared to the DET stochastic solution (Figure 4c,h). Instead, AdV expected costs result similar in both the WO and DET approach (Figure 2b-g). In this case, risk-averse decision-making does not propagate to later stages of planning because of manufacturing of AdV starting only at $t > T_1$, whereby before $D_{AdV}^{T} = 0$ for all scenarios. Hence, process uncertainty impacts products manufactured within the time period of interest and its integration leads to 4-fold increases in cost for both MU and SU.

Furthermore, an impact is seen in terms of operational decisions, specifically with respect to LV inventory planning. In Figure 4d, the WO approach leads to a stochastic plan with smaller expected inventories in early stages, as these are expected to be more costly to manufacture due to the worst-case performance assumed. To make up for lower initial inventories, LV inventories are accumulated in later time periods in both the MU case and SU case (Figure 4e,i). Specifically, in the SU case, given the expected lower costs, the optimization makes use of the assets available to accumulate inventories early on, allowing a shaper reduction in production levels at $t = T_3$ and $t = T_4$.

Finally, when comparing the expected costs and performance of SU-based equipment and the MU-based counterpart, the short recourse actions and adaptability of SU-based networks allows for a reduction in expected costs, especially for AdV manufacturing (Figure 4b). This mainly relates to scenario-independent equipment installation decisions, forcing designs to cater for pandemic scenarios irrespective of their probability of occurrence. This assumption can be modified to manufacturer-specific set-up timelines; however, options with better flexibility, allowing on-demand manufacturing, will be likely be tied with the most cost reductions during operation, which become more significant that those related solely to nominal techno-economic performance.

## CONCLUSIONS & OUTLOOK

As the pharmaceutical industry requires the establishment of increasingly flexible and responsive manufacturing networks, the development of advanced planning tools that integrate various sources of quantifiable uncertainties becomes critical. In this work, stochastic optimization-based tools are developed to assess the flexibility of fixed multi-use manufacturing equipment compared to single-use manufacturing and quantify expected cost benefits. The problem also considers the integration of early-stage process uncertainty through deterministic approaches and allows the assessment of the impact of risk-averse decision-making versus disregarding this uncertainty. Overall, modular single-use equipment promises improvements in pandemic preparedness and reductions in expected costs, including cases whereby process uncertainty is considered. Effectively, this paves the way to resilient networks which can better withstand unforeseen events.

As further research, the integration of a product-dependent trajectory of the worst-case approach would allow process uncertainty to be considered at the first-stage with respect to the first realization of the corresponding demand. Additionally, investigating the integration of a formal two-stage robust optimization approach could reduce the conservativeness of worst-case solutions, as feasible solutions are sought and optimization is not performed considering the worst-case scenario exclusively, but rather the entirety of the uncertainty set. Finally, scalability issues could be addressed through shorter planning horizons, clustering scenario-outcomes or using decomposition-based approaches. In the former case, a rolling horizon approach would be suitable, thereby solving at each time step a reduced stochastic problem considering demand uncertainty and integrating process uncertainty once a demand for a new product is realized.

## REFERENCES


1. Capra E, Gennari A, Loche A, Temps C. Viral-vector therapies at scale: today's challenges and future opportunities.
2. Lambrix E, Kent-Egan H. Viral vectors: shortages and innovation. Biotech Review of the Year.
3. Gatica G, Papageorgiou LG, Shah N. Capacity planning under uncertainty for the pharmaceutical industry. *Chemical Engineering Research and Design*. 2003;81(A):665-678. doi:10.1205/026387603322150516
4. Colvin M, Maravelias CT. A stochastic programming approach for clinical trial planning in new drug development. *Comput Chem Eng*. 2008;32(11):2626-2642. doi:10.1016/j.compchemeng.2007.11.010
5. Marques CM, Moniz S, de Sousa JP, Barbosa-Póvoa AP. A simulation-optimization approach to integrate process design and planning decisions under technical and market uncertainties: A case from the chemical-pharmaceutical industry. *Comput Chem Eng*. 2017;106:796-813. doi:10.1016/j.compchemeng.2017.04.008
6. Gökalp E, Branke J. Pharmaceutical R & D pipeline

management under trial duration uncertainty. *Comput Chem Eng*. 2020;136. doi:10.1016/j.compchemeng.2020.106782
7. Siganporia CC, Ghosh S, Daszkowski T, Papageorgiou LG, Farid SS. Capacity planning for batch and perfusion bioprocesses across multiple biopharmaceutical facilities. *Biotechnol Prog*. 2014;30(3):594-606. doi:10.1002/btpr.1860
8. Badejo O, Ierapetritou M. Enhancing pharmaceutical supply chain resilience: A multi-objective study with disruption management. *Comput Chem Eng*. 2024;188. doi:10.1016/j.compchemeng.2024.108769
9. Sarkis M, Shah N, Papathanasiou MM. Characterization of key manufacturing uncertainties in next generation therapeutics and vaccines across scales. *J Adv Manuf Process*. Published online April 26, 2023. doi:10.1002/amp2.10158
10. Sarkis M, Shah N, Papathanasiou MM. Resilient pharmaceutical supply chains: assessment of stochastic optimization strategies in network design problems. *Comput Chem Eng*. Published online 2025.
11. Marani M, Katul GG, Pan WK, Parolari AJ. Intensity and frequency of extreme novel epidemics. *PNAS Environmental sciences Biological sciences*. 2021;118(35):1-4. doi:10.1073/pnas.2105482118/-/DCSupplemental

© 2025 by the authors. Licensed to PSEcommunity.org and PSE Press. This is an open access article under the creative commons CC-BY-SA licensing terms. Credit must be given to creator and adaptations must be shared under the same terms. See https://creativecommons.org/licenses/by-sa/4.0/



Systems & Control Transactions

**Research Article - Peer Reviewed Conference Proceeding**
ESCAPE 35 - European Symposium on Computer Aided Process Engineering
Ghent, Belgium. 6-9 July 2025
Jan F.M. Van Impe, Grégoire Léonard, Satyajeet S. Bhonsale,
Monika E. Polańska, Filip Logist (Eds.)

PSE PRESS

# Dynamic Life Cycle Assessment in Continuous Biomanufacturing

**Ada Robinson Medici[a], Mohammad Reza Boskabadi[b], Pedram Ramin[b], Seyed Soheil Mansouri[b], Stavros Papadokonstantakis[a]***

[a] Institute of Chemical, Environmental and Bioscience Engineering, TU Wien,1060 Wien, Austria
[b] Department of Chemical and Biochemical Engineering, Søltofts Plads, Building 228A, Technical University of Denmark, 2800 Kgs. Lyngby, Denmark
* Corresponding Author: stavros.papadokonstantakis@tuwien.ac.at.

## ABSTRACT

This work introduces a *Python*-based interface that couples cradle-to-gate Life Cycle Assessment (LCA) with advanced process simulations in continuous biomanufacturing, resulting in dynamic process inventories and thus to dynamic LCA (dLCA). The open-source *Brightway2.5* framework is used to dynamically track environmental inventories of the foreground process and LCA indicators (e.g. damage to ecosystems according to ReCiPE 2016) from the v3.10 cut-off *ecoinvent* database. The framework is applied to KTB1, a dynamic *MATLAB–Simulink* benchmark model of continuous Lovastatin production. 580 data points are computed across four different 24-hour scenarios. The difference between the hourly and the averaged foreground scenario is between 20-30%; a more pronounced deviation is observed when both background and foreground are averaged. The dLCA framework precisely identifies optimal periods for cleaner electricity usage, enabling future work on direct environmental feedback into process control and optimization for greener high-quality biomanufacturing.

**Keywords**: Dynamic Life Cycle Assessment, Continuous Biomanufacturing, Python-Based Process Optimization, Life Cycle Assessment.

## INTRODUCTION

Increasing sustainability targets have shift the paradigm in Process Systems Engineering (PSE), now requiring process simulation and optimization to incorporate broader sustainability metrics alongside economic and operational considerations. In the biopharmaceutical sector, continuous manufacturing is still in its early stages, offering potential advantages such as stable operation, enhanced product consistency, and improved operational control compared to traditional batch approaches. While continuous processes offer new opportunities, sustainability assessments of such systems typically rely on the E-factor as an environmental indicator[1]. This approximation neglects the transient behaviour and time-dependent changes in input-output flows. Dynamic LCA (dLCA) seeks to address this gap by integrating temporal resolution into life cycle inventories. Recent examples include real-time IoT-based LCAs for wind turbines[2].The importance of this temporal dimension is amplified when considering fluctuating energy inputs and operational strategies designed to meet product quality and environmental objectives simultaneously[3].

This study applies Brightway2.5, an open-source LCA framework[4], to the KTB1 MATLAB–Simulink biomanufacturing benchmark[5]. KTB1's hourly energy usage can be paired with v3.10 cut-off *ecoinvent* database under Danish electricity mixes[6]. The integration of dLCA with process control enables real-time environmental impact feedback, facilitating operational adjustments aligned with cleaner electricity periods.

This analysis opens the door to real-time or near real-time operational adjustments incorporating "environmental signals", establishing a foundation for further exploration into how time-resolved inventories can improve the accuracy of dLCA's , not only by diagnosing environmental impacts but also optimizing them on the fly, taking advantage of electricity mix fluctuations and process flexibility, underscoring the value of aligning operating strategies, such as maintenance scheduling and

process restarts, with greener electricity profiles, thus guiding more sustainable continuous production.

## METHODOLOGY

### System Description & Functional Unit

The selected application is the production of the biopharmaceutical product, lovastatin, in a continuous process flow (the KTB1 model)[5]. KTB1 model provides a comprehensive dynamic representation of the entire biomanufacturing chain, including upstream (fermentation or bioreaction) and downstream (purification and finishing) stages. The functional unit is defined as the production of 40 mg of pure API Lovastatin, a representative maintenance dose commonly encountered in pharmaceutical formulations.

**Table 1:** Process Units and Corresponding Models of KTB1

| Unit | Name | Model |
|---|---|---|
| Mixer | M-101 | Dynamic mass balance |
| Fermenter | R-101* | Dynamic mass balance & Monod kinetics |
| Hydrocyclone | HC-101* | Mass balance fractionation, and separation factor |
| Centrifugue | C-101-102* | biomass removal with separation factor |
| Pump | VSP-101* | Pressure-driven flow |
| Nano-filtration | NF-101 | pressure-driven nanofiltration, lactose rejection factor |
| HPLC | LC-101-106 | Langmuir isotherm & film transfer |

* Units explicitly considered in the dLCA

**Figure 1** shows the boundaries of the system. **Table 1 briefly** concisely summarises the included process units and their respective models. For this dLCA, we specifically capture hourly electricity usage in the core upstream and downstream equipment's marked with an asterisk (*) in Table 1 as the dominant resource consumption relevant to time-varying impacts. Other flows (e.g., chemicals, water) can be treated as minor or average inputs and are not dynamically tracked in this study. Further methodological details are available in[5].

### Dynamic Process Modeling & Scenario Design

The KTB1 simulation model captures the nonlinear behavior of continuous biomanufacturing, accounting for upstream and downstream interactions under changing operating conditions. We track hourly electricity consumption over a 24-hour horizon to capture a typical full operational day and reflect that the system stabilizes after a few hours, making longer observation periods less informative for this particular case study. The framework, however, allows flexibility to choose any time frame as long as the process consumption data and the electricity mix data are temporally synchronized at identical sampling intervals (e.g., a consumption measurement at 14:00 aligns with the 14:00 grid share of the same day). The study combines two operational modifications with two Danish electricity profiles:

- Case 1: Reactor working volume reduced from 5000 L to 4900 L at hour 0.
- Case 2: Feed carbon lowered from 20 g/L to 16 g/L at hour 0.
- Winter: Electricity mix on 2025-01-14.
- Summer: Electricity mix on 2024-08-08.

This results in the following scenarios: Scenario 1 (S1): case 1 + winter; scenario 2 (S2): case 1 + summer; scenario 3 (S3): case 2 + winter; scenario 4 (S4): case 2

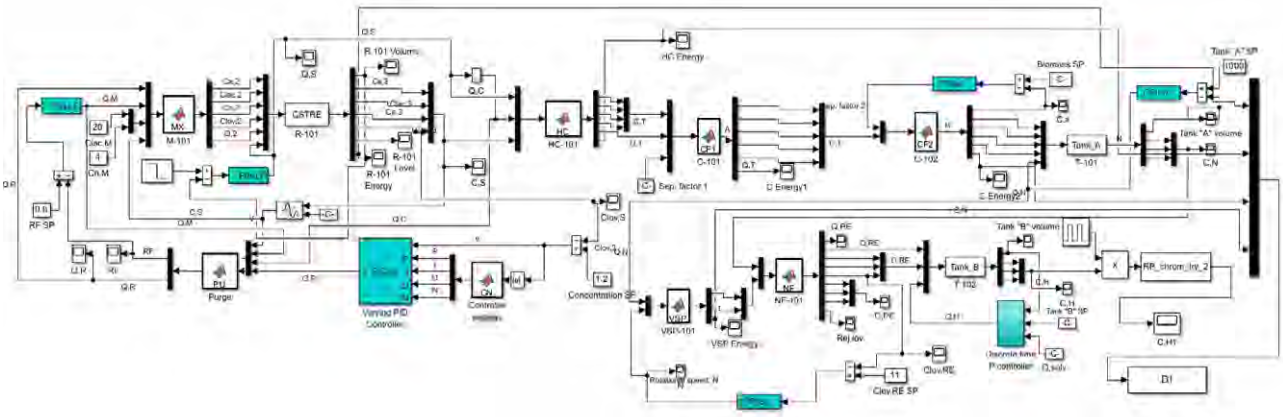


**Figure 1:** Visual representation of the process flow diagram for the production of the Active Pharmaceutical Ingredient (API) lovastatin.

+ summer]. **Figure 2** shows the graph obtained when representing the variation of electricity demand in case 1. For each hour, the model records energy usage in Watt for these critical units*. By tracking how these two operational adjustments shift consumption profiles, we construct time-resolved inventories for dynamic LCA (electricity demand databases available in supplementary material).

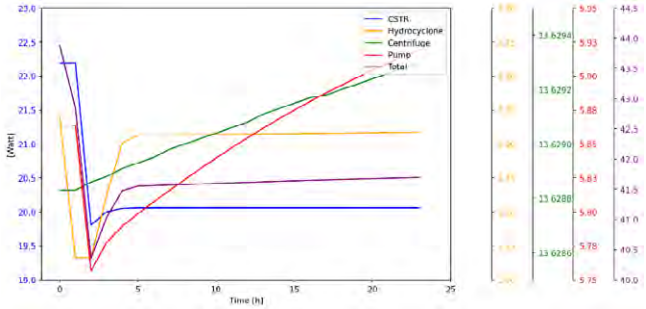



**Figure 2.** Foreground dynamism: CSTR, feed Pumps, Hydrocyclone, Centrifuge and Total hourly electricity consumption profile in Watt for the KTB1 model over a 24-hour horizon, illustrating how the reduction of the reactor working volume leads to varying power demands.

Thus, the dLCA framework can operate in real-time or near-real-time conditions (e.g., hourly electricity consumption data can also be captured by the sensors in CSV files). This can enable adjustments to improve operational conditions during the process based on a richer "signal" that contains environmental impact information, while of course meeting the production specifications (e.g., productivity, and product quality). This adaptive approach highlights the framework's potential to optimize decision-making during continuous operation rather than relying solely on retrospective analysis.

## Electricity Mix Variation

Denmark's electricity supply fluctuates hourly, as it draws on a diverse range of sources: Wind Onshore, Wind Offshore, Solar, Waste, Fossil Oil, Hydro (Run-of-River and Poundage), Biomass, Fossil Hard Coal, Fossil Gas, and Other Renewables (see **Figure 3**). Each source carries distinct environmental intensities, and their proportional contributions vary significantly across the day. In this study, ENTSO-E data is used for 2025-01-14 (winter) and 2024-08-08 (summer) to obtain each hour's share of these generation types (electricity share databases available in supplementary material)[7]. The hourly share fraction of each electricity source type is determined from ENTSO-E database, and proportionally allocated to the Life Cycle Inventory (LCI) for that hour, reflecting the evolving grid mix in real time. Two representative days (winter and summer) were chosen. More extensive periods or alternative dates could equally be modeled if longer-term or season-specific trends were of interest. This background data can also be captured in CSV files and integrated hourly in real time or near-real time.

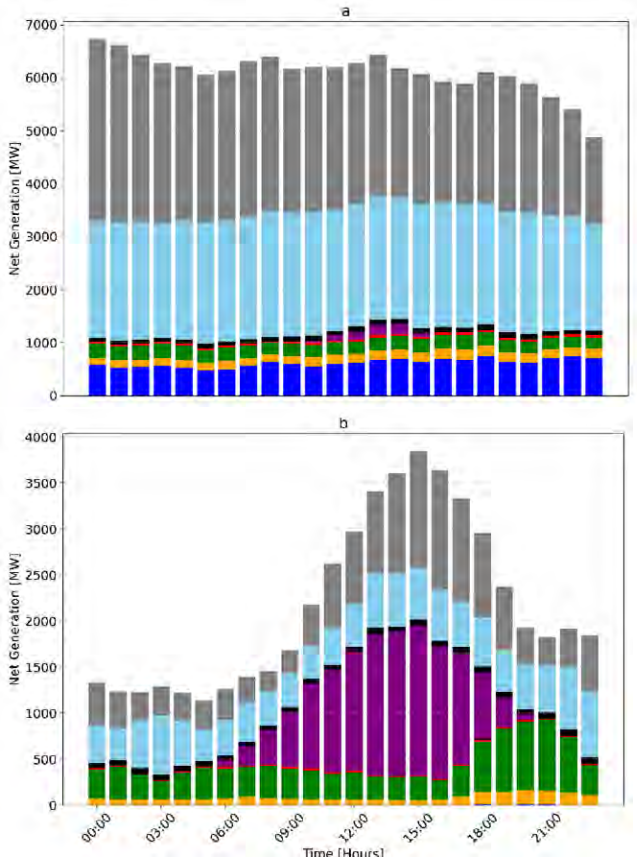



**Figure 3.** Background dynamism: Hourly net electricity generation in MW by technology for a 24-hour Danish grid profile. The stacked bars illustrate the contribution of different energy sources: Biomass (blue), Fossil Gas (orange), Fossil Hard Coal (green), Fossil Oil (red), Solar (purple), Waste (black), Wind Offshore (sky blue), and Wind Onshore (gray). (a) represents the winter electricity mix on 2025-01-14, while (b) illustrates the summer electricity mix on 2024-08-08.

## Dynamic Life Cycle Inventory & Impact Assessment

A dynamic LCI is constructed by mapping each hour in KTB1 (demand in the foreground) to the corresponding electricity flows from Denmark's grid mix (background). Because the grid composition (wind, solar, fossil gas, waste, etc.) varies hourly, each equipment–hour node is matched to the relevant *ecoinvent* v3.10 activities. For instance, at hour 5 in the winter scenario, the grid shows 1.37 % waste incineration and 36.0 % wind offshore for the winter scenario; partial consumption is allocated to "electricity, from municipal waste incineration" and "electricity production, wind, 1–3 MW turbine, offshore."

Technically, each hour × equipment pair is treated

as a distinct demand entry in Brightway25, forming a demand matrix that scales the appropriate *ecoinvent* processes by the hour's measured consumption in Watt. To perform the integral of energy use over each one-hour interval, we apply the following approximation given the relatively small variation:

$$\int_{t_i}^{t_i} \mathrm{X(t)dt} \approx \left[\mathrm{X(ti)} + \frac{X_{(t_{i+1})} - X_{(t_i)}}{2}\right] \times (t_{i+1} - t_i) \quad (1)$$

X(t) represents the time-varying energy-demand function, while $X_{(t_i)}$ and $X_{(t_{i+1})}$ denote its values at the start and end of the *i*-th hour, respectively.

A Python interface performs these conversions and compiles the time-resolved inventory, using *Temporalis*, a *Brightway25* extension, to run LCIA with the method *ReCiPe 2016 v1.03 endpoint (E), total: ecosystem quality*. Although only electricity is dynamically tracked here, the methodology readily supports adding other utilities or flows. By automatically updating the foreground model's consumption nodes each hour and linking them to background activities in *ecoinvent*, the approach captures temporal variations in environmental impacts. Consequently, it can continuously calculate any chosen LCIA indicators, given dynamic inventory data for any region or timescale.

### Calculation strategy for dynamic and average scenarios

To systematically capture how variations in both the foreground (X(t)) and background (Y(t)) affect the results, we analyze four scenarios (S1–S4) as follows:

We perform a fully dynamic pairing of hourly equipment demands (foreground) with the hour-by-hour Danish electricity mix (background), yielding 24 points per scenario for five process units (CSTR, Hydrocyclone, Centrifuge, Pump, and "Total"). That is 480 points total across the four scenarios. These results are integrated and multiplied:

$$\int_{t_i}^{t_i} \mathrm{X(t)Y(t)dt} \quad (2)$$

We then create a "dynamic-background, average-foreground" variant by combining each scenario's average demand with the same hourly grid mix, producing 96 points in total:

$$\overline{\mathrm{X(t)}} * \int_{t_i}^{t_i} \mathrm{Y(t)dt} \quad (3)$$

Lastly, we use a single "average demand" and the *ecoInvent* average electricity mix, giving 4 points total:

$$\overline{\mathrm{X(t)}}\ \overline{\mathrm{Y(t)}} \quad (4)$$

## RESULTS

### Dynamic Life Cycle Assessment Profiles

In **Figure 4**, each sub-figure (4.a–4.d) shows the hourly ReCiPe endpoint (ecosystem quality) scores for one of the four scenarios (S1–S4). In Case 1, the reactor volume reduction (5000 L to 4900 L at hour 0) transiently changes each unit's power demands. **Figures 4.a** and **4.b** show the hour-by-hour impact of the CSTR, hydrocyclone, centrifuge, and pumping tasks, plus a "Total" curve, under winter and summer Danish grid compositions, respectively. This operational shift slightly lowers the equipments' electricity demand in the first few hours (see **Figure 2**). However, whether that translates to a larger or smaller overall score at each hour also depends on the background mix (e.g., higher fossil fractions or more renewable sources, see **Figure 5**). Comparing the purple curves (total impact calculated with hourly foreground × hourly background (2)) with the total black curves (total impact calculated with average foreground × hourly background (3)) shows that both the foreground and background influence the results. If the effect of hourly foreground changes were negligible, these lines would follow an identical pattern.

**Figure 4.b** and **Figure 4.d** illustrate two different foreground operational adjustments while sharing the same seasonal background profile (see **Figure 3.b**). Around hour 15, all impact score curves show a slight dip, coinciding with hours that have higher proportions of lower-impact technologies (e.g., solar and wind onshore). The strong fluctuation in the electricity mix seems to have significant relevance in the impact score around this hour.

Winter vs. Summer reveals how hour-to-hour variations in technology shares combine with the equipment's consumption changes. In some winter hours, a heavy fossil fraction (e.g., fossil hard coal) markedly increases the score for that time step, while summer hours with higher solar or wind can lower it. Comparing the LCA factor for each technology explains these patterns: one MWh from fossil oil may yield ~5 × 10^(-5) in ecosystem quality, whereas one MWh from solar might be near 1 × 10^(-5) (see **Figure 5**). Hence, an hour with 40 % fossil oil has a more pronounced impact than an hour with 40 % wind offshore (tables with numerical values available in supplementary material). Because these variations are applied each hour to whichever process unit is consuming energy at that time, the resulting ReCiPe scores (blue, orange, green, red lines in **Figure 4.a.** and **4.b**) do not simply mirror the consumption shape from **Figure 2**, but also reflect the changing background. Taken together, these results show that operational changes at hour 0 (Case 1 or Case 2) intersect with dynamic technology shares to yield unique hourly ReCiPe scores.

### Comparative Analysis between Dynamic vs. Single-Average LCA

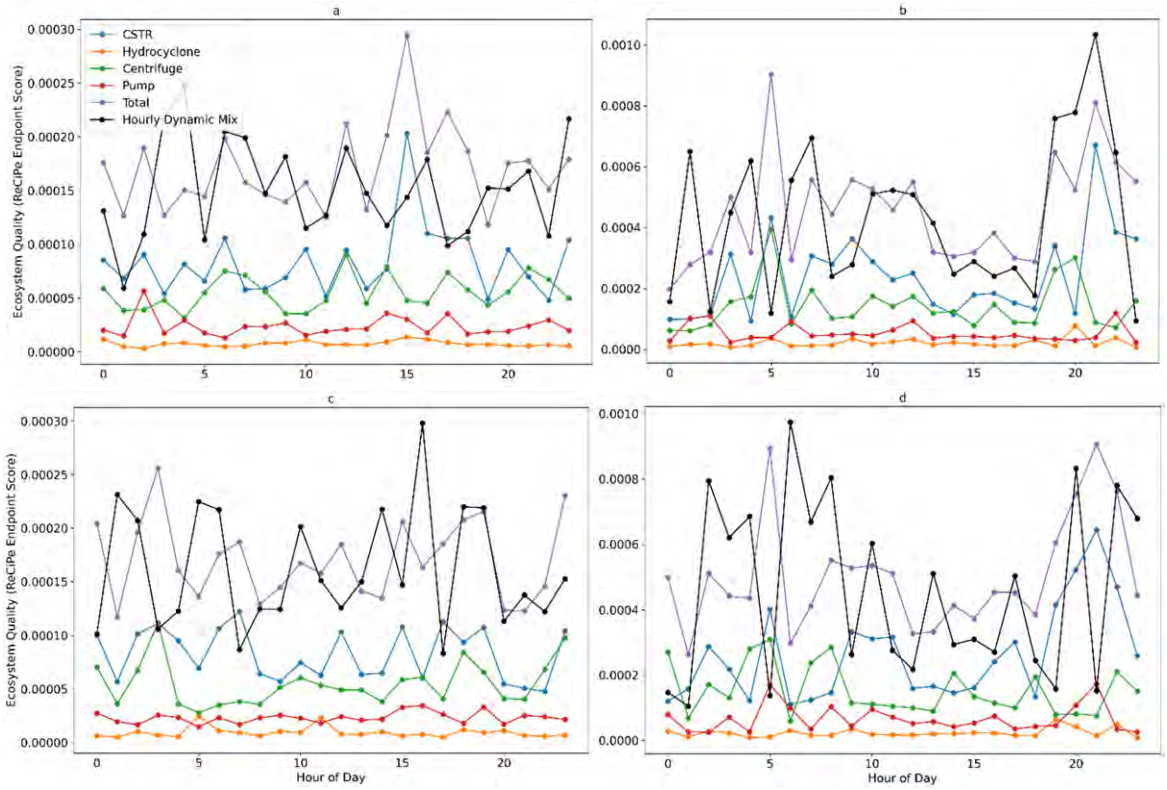



**Figure 4:** Hourly ReCiPe Endpoint (ecosystem quality) scores for the four scenarios, showing each KTB1 unit. Colored lines depict the foreground demand contributions of each critical unit calculated with (2): CSTR (blue), Hydrocyclone (orange), Centrifuge (green), Pump (red), while purple shows the hour-by-hour total. The black curve ("Hourly Dynamic Mix") represents a background-only dynamic approach where the average demand is allocated to the hourly electricity grid mix, calculated with (3). 4.a: S1; 4.b: S2; 4.c: S3; 4.d: S4.

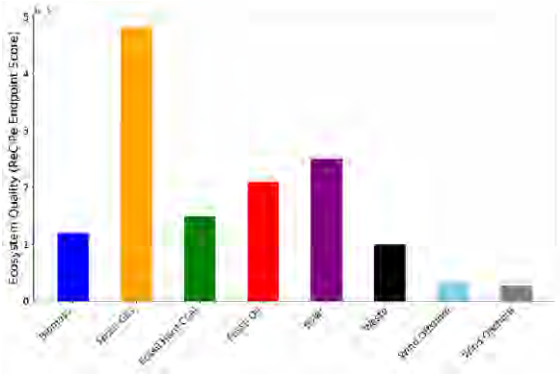



**Figure 5.** LCA Score *ReCiPe 2016 v1.03 endpoint (E), total: ecosystem quality* for 1 MWh Electricity by Technology from *ecoinvent*.

**Table 2** reports the ReCiPe 2016 (ecosystem quality) results for four scenarios (S1–S4), each evaluated under three approaches: (2) fully dynamic (hourly foreground × hourly background), (3) dynamic background, average foreground, and (4) single-average (both foreground and background). For instance, S1 (Case 1, winter), dynamic calculation yields $4.08 \times 10^{-3}$, approach (3) gives $5.08 \times 10^{-3}$, and approach (4) is $2.73 \times 10^{-2}$.

**Table 2:** Comparison of Single-Average vs. Hourly-Summed LCA Scores

| Scenario | (2) | (3) | (4) |
|---|---|---|---|
| S1 | 4.08E-03 | 5.08E-03 | 2.73E-02 |
| S2 | 1.10E-02 | 1.56E-02 | |
| S3 | 4.09E-03 | 5.83E-03 | 2.87E-02 |
| S4 | 1.21E-02 | 1.65E-02 | |

Moving to S2, the single-average approach (4) remains constant (2.73 × 10^(-2)) irrespective of winter or summer, because the same average activity and identical average demand are used in both seasons to perform the calculation. The comparisons between (2) and (3) in the four scenarios underscore how hourly fluctuations in the foreground (electricity demand) can shift the LCA score by 19.75%, 29.52%, 29.77%, and 26.93% for S1-S4. The order of magnitude difference with respect to (4) is influenced by the way the average of the electricity mix is cal-

culated in the *ecoinvent* inventory. By collapsing the dynamic variability into one blend, single-average LCA may underestimate or overestimate real burdens. Although the absolute scale of electricity demand in a typical biopharmaceutical process might appear smaller compared to large-scale chemical production, the energy consumed per kilogram of final product could have a cumulative energy demand (CED) 20 times higher, and a global warming potential (GWP) 25 times higher than typical large-scale basic chemical production[8] . In our KTB1 case, we measured an average electricity usage of 135 MJ $kg^{-1}$ of product. Thus, even if the total energy consumption appears moderate in an absolute sense, the environmental burden per kilogram of pharmaceutical product remains substantial. This observation highlights why this application is a pertinent demonstration of the relevance of time-resolved LCA. With these hour-by-hour signals, a multi-objective scheduling algorithm could, for instance, delay a high-power centrifugation step by two hours until the fossil fraction drops, reducing its endpoint score by more than 25%. Similarly, model predictive control can exploit forecasted grid mix data to adjust flow rates, turn down certain pumps temporarily, or time process restarts so that the bulk of the energy draw coincides with greener electricity. In contrast, relying on a single, static grid-mix average overlooks these opportunities for optimization, potentially overestimating or underestimating true impacts and missing out on practical ways to cut emissions.

## DISCUSSION & CONCLUSIONS

This work presents a dynamic LCA framework integrated with a continuous biomanufacturing model (KTB1). By linking a *Python*-based interface with the *Temporalis* (*Brightway2.5*), and utilizing the *ecoinvent* 3.11 database and ReCiPe characterization methods, we capture time-resolved environmental impacts that account for hourly fluctuations in the Danish electricity mix.

A total of 580 LCA points and 4640 nodes (580 × 8 activities) were computed in only 24 hours of operation considering electricity demand of a few equipments.

From an LCA perspective, two key conclusions emerge. Collapsing hourly variability into one mix can over- or underestimate actual burdens, especially in high-energy or fossil-heavy hours. A dynamic approach ensures that each operational load is mapped to the correct background technology, giving a more faithful representation of life-cycle impacts. The fine-grained LCA signals from hour-to-hour identify ideal windows presents a potential in continuous biomanufacturing to schedule energy-intensive operations (e.g., re-starts following contamination, maintenance).

Beyond these findings, the underlying framework and interface are generalizable. Any LCIA method may be substituted here, provided the user has time-resolved foreground consumption and background data. The approach scales to longer production cycles, larger databases (e.g., multiple regions, multiple seasons), or additional scenarios (e.g., different feed compositions, varied capacity expansions). In particular, other fields that could strongly benefit from dLCA are, for instance, batch processes due to its substantial variability in the foreground. Similarly, high-energy consuming operations can exploit background fluctuations for scheduling or control interventions. Regarding the background control, dLCA is particularly relevant in energy system optimization.

Future work will focus on extending programs to run longer cycles (e.g., multiple days or weeks), implementing advanced scheduling, and evaluating the economic–environmental trade-offs through *multi-objective optimization*. This logic extends to advanced *multi-objective model predictive control*, where real-time data on electricity sources could guide setpoints to concurrently optimize throughput, product quality, and environmental performance.

## DIGITAL SUPPLEMENTARY MATERIAL

Digital supplementary materials for this study, including electricity demand datasets for cases 1 and 2, electricity share databases for Denmark, and numerical tables with results, are available at the following GitHub repository: https://github.com/AdaRobinsonMedici/ES-CAPE-35

## ACKNOWLEDGEMENTS

The authors acknowledge DTU for the open-source development of the KTB-1 benchmark simulation model, as well as Charles Breton, Nathalia Silva de Souza Lima Cano, and De Santier organization for the contributions during Autumn School 2024.

## REFERENCES

1. C. Ding, H. Ardeshna, C. Gillespie, and M. Ierapetritou, “Process design of a fully integrated continuous biopharmaceutical process using economic and ecological impact assessment,” *Biotechnology and Bioengineering*, vol. 119, no. 12, pp. 3567–3583, 2022, doi: 10.1002/bit.28234.
2. J. An, Z. Zou, G. Chen, Y. Sun, R. Liu, and L. Zheng, “An IoT-Based Life Cycle Assessment Platform of Wind Turbines,” *Sensors*, vol. 21, no. 4, p. 1233, Feb. 2021, doi: 10.3390/s21041233.
3. T. P. Da Costa, D. M. B. Da Costa, and F. Murphy, “A systematic review of real-time data monitoring and its potential application to support dynamic life cycle inventories,” Environmental Impact Assessment Review, vol. 105, p. 107416, Mar.

2024, doi: 10.1016/j.eiar.2024.107416.
4. C. Mutel, “Brightway: An open source framework for Life Cycle Assessment,” JOSS, vol. 2, no. 12, p. 236, Apr. 2017, doi: 10.21105/joss.00236.
5. M. R. Boskabadi, P. Ramin, J. Kager, G. Sin, and S. S. Mansouri, “KT-Biologics I (KTB1): A dynamic simulation model for continuous biologics manufacturing,” Computers & Chemical Engineering, vol. 188, p. 108770, Sep. 2024, doi: 10.1016/j.compchemeng.2024.108770.
6. “Ecoinvent,” ecoinvent. Accessed: Jan. 28, 2025. [Online]. Available: https://ecoinvent.org/database/
7. “ENTSO-E Transparency Platform.” Accessed: Jan. 28, 2025. [Online]. Available: https://transparency.entsoe.eu/
8. G. Wernet, S. Conradt, H. P. Isenring, C. Jiménez-González, and K. Hungerbühler, “Life cycle assessment of fine chemical production: a case study of pharmaceutical synthesis,” The International Journal of Life Cycle Assessment, Dec. 2010, doi: 10.1007/s11367-010-0151-z

© 2025 by the authors. Licensed to PSEcommunity.org and PSE Press. This is an open access article under the creative commons CC-BY-SA licensing terms. Credit must be given to creator and adaptations must be shared under the same terms. See https://creativecommons.org/licenses/by-sa/4.0/



Systems & Control Transactions

**Research Article - Peer Reviewed Conference Proceeding**
ESCAPE 35 - European Symposium on Computer Aided Process Engineering
Ghent, Belgium. 6-9 July 2025
Jan F.M. Van Impe, Grégoire Léonard, Satyajeet S. Bhonsale,
Monika E. Polańska, Filip Logist (Eds.)

PSE PRESS

# Reactive Crystallization Modeling for Process Integration Simulation

**Zachary M. Hillman[a*], Gintaras V. Reklaitis[a], and Zoltan K. Nagy[a]**

[a] Purdue University, Davidson School of Chemical Engineering, West Lafayette, Indiana, United States
* Corresponding Author: zhillma@purdue.edu.

## ABSTRACT

Reactive crystallization (RC) is a chemical process in which the reaction yields a crystalline product. It is used in various industries such as pharmaceutical manufacturing or water purification. In some cases, RC is the only feasible process pathway, such as the precipitation of certain ionic solids from solution. In other cases, a reaction can become a RC by changing the reaction environment to a solvent with low product-solubility. Despite the utility and prevalence of RC, it is not often emphasized in process design software. There are RC models that simulate the inner reactions and dynamics of a RC, but each has limiting assumptions, and are difficult to integrate with the rest of a process-line simulation. This modeling gap complicates RC process design and limits the exploration of the possible benefits to using RC as well as the ability to optimize a system that relies on it. To fill this gap, we built an open-source, customizable model that can be integrated with other unit operations in the Python process simulator package PharmaPy. This model focuses on the reaction-crystallization interactions and dynamics to predict reaction yield and crystal critical quality attributes given inlet streams and reactor conditions. In this way, RC can be integrated with other unit operations to capture the effects RC has on the process overall. The model and assumptions are described in this work. The model space, limitations, and capabilities are explored. Finally, the potential benefits of the RC system are shown using three example cases.

**Keywords**: Process Intensification, Process Design, Crystallization, Reactive Crystallization

## INTRODUCTION

Crystallization is a complex process highly relevant to numerous fields ranging from pharmaceuticals to agricultural chemicals [6]. It can be used to produce a solid product or simply as a separation technique for product purification. Reactive crystallization (RC) is the intensification of the crystallization process with the reaction that generates the crystallizing product.

The intensification of RC leads to multiple unique advantages. First, if the desired product exists in equilibrium with the reactants or a byproduct, or if the desired product is an intermediate species, RC provides a method for isolating the species away from the reaction. As solids are much more stable than liquid or gases, the crystallization renders the species effectively inert, pushing the reaction towards the crystallizing species due to Le Chatelier's principle thus increasing yield. Another advantage is a reduction of the process footprint. Because RC combines the tasks of a reactor with a crystallizer, a single unit is sufficient instead of the two in series. The final advantage of RC is the potential to remove a recrystallization/separation process if the produced crystals follow the desired critical quality attributes (CQAs).

Intensification comes at the cost of degrees of freedom, increasing the difficulty of control [8]. More difficult control may deter adoption of the technology and therefore must be balanced with the potential benefit [5, 8]. As such, it is necessary to design RC processes with control in mind. Most modern design techniques require the use of a digital model.

Modeling and predicting RC systems is notoriously difficult. Both reaction and crystallization dynamics are governed by concentration; this leads to highly coupled and inseparable numerical systems. Additionally, due to the system's general sensitivity to mixing effects, fluid dynamics are often considered as well. Salami et al. [7],

Tang et al. [9] are excellent examples of such approaches.

High resolution modeling of this nature can require more time to execute the simulation model than for the phenomenon to actually transpire. This prohibits the use of these types of models for real-time control or prediction. To address this problem, an open-source model is created which can simulate faster than real-time but it achieves this by neglecting mixing effects. The goal of this model, therefore, is to capture the overall behavior of the system even if the accuracy is lower than the high-resolution models mentioned. This model can then be customized to include other factors while potentially solving in real-time to be used in applications such as optimization and control.

# METHODS

## Mathematical Model

The RC system can be modeled using differential equations that capture the material and energy balances of the specific operations. A reactive mixed suspension, mixed product removal (RMSMPR) configuration was chosen as the target unit operation to model. This operation has the following assumptions:

1. All reactions only occur in the liquid/dissolved phase. Solids are inert.
2. Reactor volume is considered constant.
3. Agglomeration and breakage are negligible.
4. Crystal growth is size-independent and 1-dimensional.
5. Perfect mixing.
6. Total crystal volume is much smaller than the total reactor volume.

The material balance must include all inlet and outlet streams, as well as describe reactions and crystallization. The material balance used is given in equation 1. Here, equation 1 is written for the concentration $c$ of each species $j$. In this system, $\epsilon$ is the liquid fraction, $W_j$ is the amount of species $j$ that crystallizes, $q_k$ is the flow rate of each stream $k$, $V$ is the volume of the reactor, and $R_j$ is the reaction rate relevant to species $j$.

To capture crystallization behavior, a population balance was used and is shown in equation 2. Here, $L_0$ is the critical length required for the crystal to nucleate, and $\rho_s$ is the density of the slurry. G and B are the growth rate and nucleation rate, respectively. $L$ is the length of the crystal, $n$ is the particle density function of the slurry, and $n_k$ is the particle density function of the stream $k$, and $\delta$ is the dirac delta function. Equation 3 gives the nucleation and growth expressions. Here $S$ is supersaturation, $E$ is the activation energy for growth or nucleation, $k_v$ is the shape factor and $\mu_3$ is the third moment of the crystal size distribution (CSD). $k_b$, $k_s$, and $k_g$, follow the form in equation 4. $k_0$, $b_1$, $s_1$, $s_2$, $g_1$ are empirical parameters. $R$ is the gas constant.

$$\frac{\partial \epsilon c_j V}{\partial t} = \sum_k c_{j,k}\, q_k \epsilon_k + V R_j + V \frac{dW_j}{dt} \quad (1)$$

$$\frac{\partial n(t,L)}{\partial t} + G\frac{\partial n(t,L)}{\partial L} = B \cdot \delta(L - L_0) + \sum_k \frac{q_k}{V} \cdot n_k \quad (2)$$

$$B = k_s S^{s_1} (k_v \mu_3)^{s_2} + k_b exp\left(\frac{-E_b}{RT}\right) S^{b_1} \quad (3a)$$

$$G = k_g exp\left(\frac{-E_g}{RT}\right) S^{g_1} \quad (3b)$$

$$k_x = k_0 exp\left(\frac{-E_a}{RT}\right) \quad (4)$$

## Digital Implementation

PharmaPy is an open-source process simulator with a library of unit operations ranging from reactors and crystallizers to filters and dryers [2, 4]. The package is object oriented, using different classes to represent each unit operation. Instances of each unit operation can then be serially connected to create a flowsheet and solved sequentially to give the predicted behavior of the entire process.

PharmaPy reduces the partial differential equations to ordinary differential equations (ODEs) via the method of lines [2]. These ODEs are then solved using a numerical integrator. To solve the population balance, the one-dimensional finite volume method (FVM) is used. This method involves discretizing across the crystal length coordinate to create a balance for each length step. These equations are then solved using the CVode method from SUNDIALS [3], connected to python via the python package Assimulo [1].

An RC class was created following the PharmaPy syntax. Equations 1, 2 and 3 were used to describe the unit operation behavior, although the exact equations are easily modifiable if other effects such as agglomeration or breakage are desired. By following the PharmaPy layout, the RC class could be added into any flowsheet previously possible in PharmaPy. This flexibility allows the direct comparison of results between flowsheets using RC and those using reactors and crystallizers in series.

# RESULTS

Using the PharmaPy RC model, several example systems were simulated. Each simulation generates outputs which include the predicted reaction profiles, dynamic CSDs, and temperature profiles. Figure 1 shows the crystallization information of the RC for the reaction system: A + B→ C↓ + D, where species C is crystallized as denoted by the downward arrow. The first five subplots (A-E) show the CSD against time in seconds. Figure 1F shows the liquid concentration of the target species, its solubility, and the absolute supersaturation. The parameters for this system are the same as case “A” given in Table 1, where $k_r$ is the reaction rate constant and $E_r$ is the reaction activation energy.

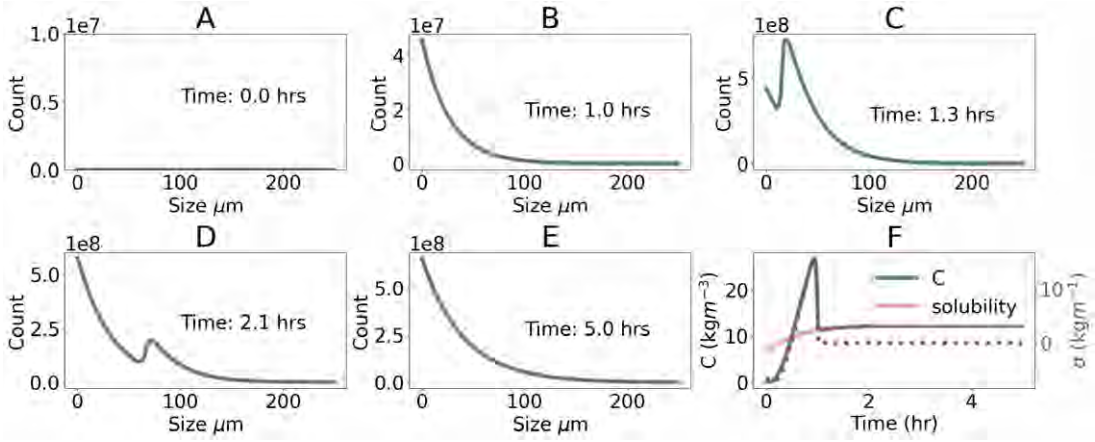



**Figure 1:** The crystal moments (zeroth through third), the unit's temperature, and the concentration/saturation levels throughout time (s) for the simulated reaction system: A + B → C↓ + D

**Table 1:** Parameters for the different runs.

| | $k_b$ $\left(\frac{\#}{\mathrm{m^3 s}}\right)$ | $E_b$ $\left(\frac{j}{mol}\right)$ | b | $k_s$ $\left(\frac{\#}{\mathrm{m^3 s}}\right)$ | s | *s*2 | $k_g$ $\left(\frac{\mu m}{s}\right)$ | $E_g$ $\left(\frac{j}{mol}\right)$ | g | $k_r$ $\left(\frac{mol}{m^3 s}\right)$ | $E_r$ $\left(\frac{j}{mol}\right)$ |
|---|---|---|---|---|---|---|---|---|---|---|---|
| 1, 2A/2B | 8.188 | 0 | 1.124 | 4.18 E+10 | 0.35 | 1 | 9.73 | 11280 | 0.2337 | 1 e-4 | 0 |
| 2C/2D | 8.188 | 0 | 1.124 | 4.18 E+10 | 0.35 | 1 | 9.73 | 11280 | 0.2337 | 2e-4; 1.3e-4 | 0 |
| 2E/2F | 8.188 | 0 | 1.124 | 4.18 E+10 | 0.35 | 1 | 9.73 | 11280 | 0.2337 | 2e-4; 1.3e-4 | 0 |

Figure 1 was generated using the simulator and demonstrates crystallization behavior consistent with a RC system. At t=0, there are no crystals in the RC. As the reaction progresses, the concentration exceeds the solubility, leading to a supersaturated solution as shown in Figure 1F. At a certain point (around 1 hour) nucleation occurs and the liquid concentration quickly reduces to and equilibrates at the solubility point. This results in a sudden uptick in counts of small crystals as seen in Figure 1B. The crystals from the large nucleation event then grow larger while more crystals are nucleating from the continuous addition of reactants. This results in a distribution with high counts of crystals near the nucleation length, and a higher count of crystals slightly larger than the nucleation length. This can be seen in Figure 1C. This batch of larger crystals continues to grow while more crystals nucleate and grow. At the same time, crystals leave the system through the outlet, lowering the count of older, larger crystals. Eventually, the larger crystals from the initial nucleation all leave and the steady state CSD is reached. This can be seen in Figure 1E.

Figure 2C-F showcases the advantage mentioned earlier of increased yield for reversible reactions or reactions where the target is an intermediary. Each column in the figure corresponds to a different reaction setup where species C is the target product, and each row corresponds to either a reactor with no crystallization or a RC. The liquid concentration shown decreases as species C crystallizes in the RC environments. The first reaction case (Figure 2A-B) is simple, and both the reactor and RC behave similarly as expected. If product D were the desired product, then using RC effectively removes the need for an additional separation step if the solubility of C is within the impurity tolerance allowed within D.

The second reactive case is reversible. Figure 2C-D shows that by crystallizing the product, the RC drives the reversible reaction forward due to Le Chatelier's principle. The black line is the overall accumulation of the target product. The figure depicts how the RC in a reversible reaction with these conditions results in a higher yield of the target product, generating 27.5 moles from the RC compared to 25.7 moles in the reactor. In the last reaction case (Figure 2E-F), the target species (C) is an intermediate product. The figure shows that the RC system successfully isolates species C before much of it can further react to form the undesired product E. This results once again in a higher yield of the target product than what a reactor could achieve in the same conditions, producing 25.8 moles from the RC compared to 21.2 moles in the reactor. The parameters used for each case can be found in Table 1. The crystallization parameters used were based on known parameters for paracetamol

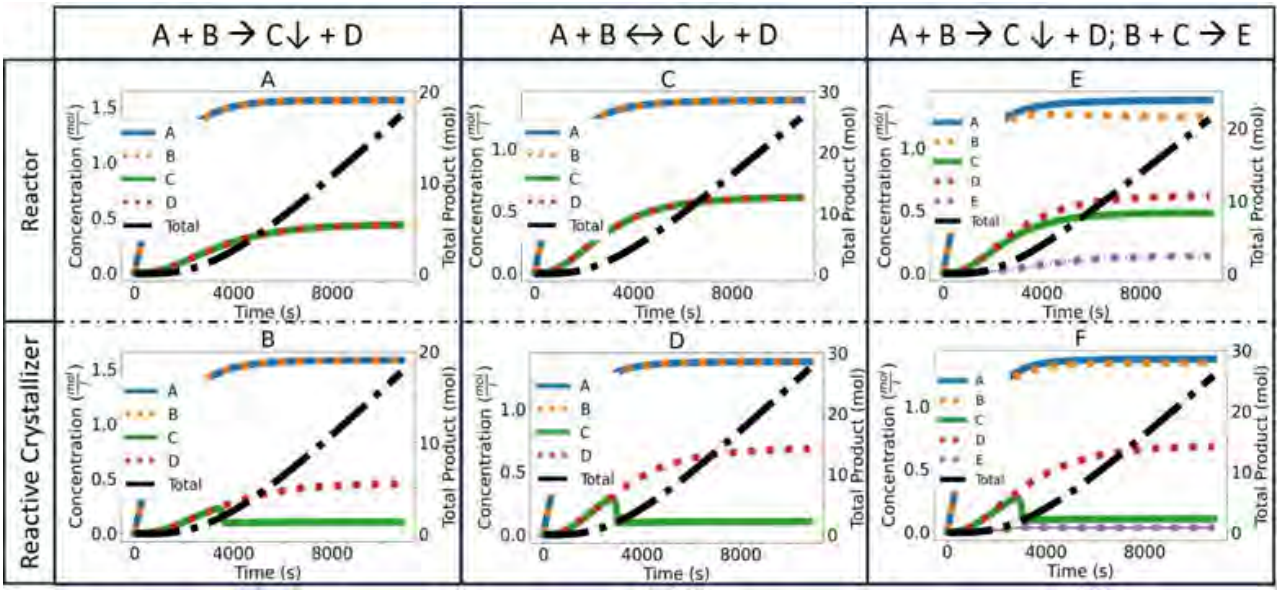



**Figure 2:** Figure comparing RC concentration profiles and non-crystallizing species profiles for different cases. Table 1 has the respective parameters of each case.

[10].

While these results are promising and demonstrate behavior consistent with RC, there are limitations to the model. In many RCs, the reaction is very fast with very quick precipitation and limited by mixing. This model assumes perfect mixing and therefore is less reliable with increasing effects of mixing non-idealities. If the solution can be considered homogeneous before nucleation occurs, then the model should accurately represent the system. Should the mixing become a significant limitation, a different model, such as one employing computational fluid dynamics balances, would be needed to account for the effects. This would introduce other limiting assumptions and is not the particular system of interest.

The cases discussed represent a non-exhaustive list of possible use cases of the model. They were chosen to showcase the potential advantages to RC and to establish that the model followed the expected behavior of a RC system. In each case explored, the reaction is exothermic; endothermic reaction effects have yet to be simulated. All of the cases discussed assumed the same crystallization kinetics, and so the full interaction between crystallization kinetics and reaction kinetics has yet to be determined.

Other reaction systems are conceivable, such as a reversible reaction with a competing byproduct, or a system where the byproduct influences solubility of the target species. Such cases were not simulated in this work for two reasons. First, cases A-F have results which are easily predicted, and so model behavior could be easily validated conceptually. The more complicated reaction systems would be harder to predict and validate conceptually, leading to less certainty of the model overall. Second, in the situation of the byproduct influencing the target species' solubility or other similar complications, cases A-F can be easily modified for the model to capture the behavior. The chosen cases were therefore considered reasonably representative of the systems of interest.

It should also be noted that, with certain parameter regimes, the model struggled to converge. While the exact relationship is still be investigated, increasing differences between the reaction rate and crystallization rate by magnitudes necessitated decreasing step sizes for the integrator to properly solve the equations. This consequently resulted in longer solve times. The parameters listed in Table 1 behave well together in the integrator. This could be caused by the fact that the chosen parameters closely resemble those of a real system whereas other parameter sets explored may not have had physical analogs resulting in difficulty converging. Further work is needed to truly define the reason for the convergence issues and determine how to avoid the issues.

## CONCLUSION

In this work, a simulation model of a reactive crystallization (RC) was developed and demonstrated. The mathematical description of the system was provided, and the digital implementation was described. Three different case studies were used to show the behavior and yield of the RC system compared to that of a system using reactors and crystallizers in series. Irreversible reactions showed no differences in product yield whether using the RC or the reactor and crystallizer route was used. In other cases, which had reversible

reactions or a reaction system where the species of interest was an intermediary product, the RC improved yield. This behavior matched the predicted outcome and verified that the model predictions at least match the behavior expected of RC in various situations. Work is now being done to confirm the model predictions experimentally.

## ACKNOWLEDGEMENTS

Financial support was received via the David Ross Fellowship from Purdue University. The authors declare no known conflicts of interests.

## REFERENCES

1. Andersson C, Fuhrer C, Akesson J. Assimulo: A unified framework for ODE solvers. Mathematics and Computers in Simulation. 116:26-43 (2015). http://dx.doi.org/10.1016/j.matcom.2015.04.007
2. Casas-Orozco D, Laky D, Wang V, Abdi M, Feng X, Wood E, Laird C, Reklaitis GV, Nagy ZK. PharmaPy: An object-oriented tool for the development of hybrid pharmaceutical flowsheets. Computers & Chemical Eng 153:107408 (2021). https://doi.org/10.1016/j.compchemeng.2021.10740 8
3. Hindmarsh A, Brown P, Grant K, Lee S, Serban R, Shumaker D, Woodward C. SUNDIALS: Suite of nonlinear and differential/algebraic equation solvers. ACM Trans. Math. Softw. 31:363-396 (2005)
4. Hur I, Casas-Orozco D, Reklaitis G, Nagy Z. Moisture and Throughput Control in an Integrated Pharmaceutical Purification Platform using PharmaPy. In: Computer Aided Chemical Engineering. Ed: Elsevier. Vol. 52, pp. 1169–1174 (2023).
5. Kiss A, Bildea C. A control perspective on process intensification in dividing-wall columns. Chem Eng Process 50:281–292 (2011). https://doi.org/10.1016/j.cep.2010.12.008
6. McDonald M, Salami H, Harris P, Lagerman C, Yang X, Bommarius A, Grover MA, Rousseau RW. Reactive crystallization: A review. React Chem Eng 6:364–400 (2021). https://doi.org/10.1039/D0RE00377H
7. Salami H, Lagerman C, Harris P, McDonald M, Bommarius A, Rousseau RW, Grover M. Model development for enzymatic reactive crystallization of β-lactam antibiotics: A reaction–diffusion-crystallization approach. React Chem Eng 5:2064–2080 (2020). https://doi.org/10.1039/D0RE00247E
8. Schembecker G, Tlatlik S. Process synthesis for reactive separations. Chem Eng Process 42:179–189 (2003). https://doi.org/10.1016/S0255-2701(02)00094-7
9. Tang H, Rigopoulos S, Papadakis G. On the effect of turbulent fluctuations on precipitation: A direct numerical simulation – population balance study. Chem Eng Sci 270:118511 (2023). https://doi.org/10.1016/j.ces.2023.118511
10. Young K, Parvaresh R, Nyande B, Yao H, Davey C, Diab S, Nagy ZK. Modeling crystallization systems: Population balance approaches for structurally similar impurities with kinetic controlled impurity incorporation mechanisms. Submitted (2024).

© 2025 by the authors. Licensed to PSEcommunity.org and PSE Press. This is an open access article under the creative commons CC-BY-SA licensing terms. Credit must be given to creator and adaptations must be shared under the same terms. See https://creativecommons.org/licenses/by-sa/4.0/



Systems & Control Transactions

**Research Article - Peer Reviewed Conference Proceeding**
ESCAPE 35 - European Symposium on Computer Aided Process Engineering
Ghent, Belgium. 6-9 July 2025
Jan F.M. Van Impe, Grégoire Léonard, Satyajeet S. Bhonsale,
Monika E. Polańska, Filip Logist (Eds.)

PSE PRESS

# Data-driven Modeling of a Continuous Direct Compression Tableting Process using SINDy

**Pau Lapiedra Carrasquer[a,b], Satyajeet S. Bhonsale[a], Carlos André Muñoz López[b], Kristof Dockx[b], Jan F.M. Van Impe[a]***

[a] BioTeC+, KU Leuven, Gebroeders De Smetstraat 1, Gent 9000, Belgium
[b] Janssen Pharmaceutica NV, a Johnson & Johnson company, Turnhoutseweg 30, 2340 Beerse, Belgium
* Corresponding Author: jan.vanimpe@kuleuven.be.

## ABSTRACT

Understanding the complex dynamics of continuous processes in pharmaceutical manufacturing is essential to ensure product quality across the production line. This paper presents a data-driven modeling approach using Sparse Identification of Nonlinear Dynamics with Control (SINDYc) to capture the dynamics of a continuous direct compression (CDC) tableting line. By incorporating delayed control inputs into the candidate function library, the model effectively captures deviations from steady state in response to dynamic changes. The proposed model was developed by finding a balance between accuracy and sparsity, with focus on the ability to generalize to a wide range of operating conditions.

**Keywords**: Big Data, Dynamic Modelling, Industry 4.0, Machine Learning, Modelling, SINDy

## INTRODUCTION

Continuous manufacturing has emerged as a crucial innovation in pharmaceutical tableting production, bringing substantial improvements in process efficiency, scalability, and product quality assurance. However, the complex dynamics of continuous processes pose significant challenges for modeling, especially in ensuring consistent quality across the production line. In continuous manufacturing lines, residence time distribution (RTD) is a key concept describing how material flows through the system. In practice, RTD is usually modeled using a sequence of ideal reactor units (e.g., combinations of continuous stirred-tank reactors and plug-flow reactors). These models often rely on idealized assumptions that may not capture the complexities of real-world processes. This can lead to discrepancies between model predictions and actual system behavior [1]. Additionally, these models may lack the flexibility to generalize across different setups or scenarios, making it challenging to predict performance under untested conditions [2].

One promising approach to modeling nonlinear and time-varying systems is through data-driven methods. The Sparse Identification of Nonlinear Dynamics (SINDy) framework is a powerful tool for identifying system dynamics from experimental data without assuming a predefined structure. The SINDy algorithm has the ability to derive parsimonious models, with fewer terms.

In this study, SINDy was applied to model a Continuous Direct Compression (CDC) tableting line, using simulated data generated with the gPROMS flowsheet modeling environment. This approach provides the flexibility to simulate a wide variety of experimental conditions, producing the data needed to train the SINDy model. The control input for this model is the mass flow rate of the active pharmaceutical ingredient (API) from the feeder, while blend uniformity and content uniformity are defined as state variables. A key challenge in this system is the presence of inherent time delays between changes in the mass flow rate and their observed effects on blend uniformity. To effectively capture these delayed dynamics, the SINDy with control (SINDYc) algorithm was used, allowing for the explicit inclusion of delayed control inputs into the system's dynamic equations.

## THEORY AND METHODS

### SINDy method

The SINDy algorithm described in Brunton et al. [3] uses sparse regression to identify a parsimonious set of

terms governing the system's dynamics. Consider a nonlinear dynamical system in the form

$$\frac{dx}{dt} = f(x) \quad (1)$$

where $x \in \mathbb{R}^n$ are the state variables over time and the function f represents the dynamics. SINDy uses sparse regression to identify the few active terms out of a library of candidate nonlinear functions $\Theta(X)$. From the time derivative of the state variables $\dot{x}$(t), SINDY finds a sparse matrix Ξ such that:

$$\dot{X} = \Theta(X)\Xi \quad (2)$$

where Ξ contains the coefficients for each candidate function. In this case, the derivatives $\dot{x}$(t), are numerically calculated from the state data.

To incorporate the effects of control inputs in the CDC tableting line, an extension of SINDy known as SINDy with control (SINDYc) is used [4]. SINDYc allows the inclusion of external inputs, in this case the mass flow rate of API in the feeder, directly into the dynamic equations, capturing the influence of these inputs on the system's response variables. The expression of Eq. (1) and (2) can be rewritten as:

$$\frac{dx}{dt} = f(x,u) \quad (3)$$

$$\dot{X} = \Theta(X,U)\Xi \quad (4)$$

where U(t) represents the control inputs and Θ(X,U) is a library matrix containing candidate functions of both the state variables X and control inputs U. Commonly used candidate functions include constant, polynomial, trigonometric and exponential terms or a combination of them:

$$\Theta(X,U) = [1 \;\; X \;\; U \;\; X^2 \;\; U^2 \;\; XU \;\; sin(X) \;\; sin(U) \;\; e^X \;\; e^U \cdots] \quad (5)$$

In many systems, the dynamics can be accurately represented using only a few active terms from a larger set of candidate functions. To identify these terms, sparse regression is used to find the coefficients in the matrix Ξ, minimizing the following objective function:

$$\Xi = arg\min_{\Xi} \frac{1}{2}\left\|\dot{X} - \Theta(X,U)\Xi\right\|_2^2 + \lambda\|\Xi\|_1 \quad (6)$$

where λ is a sparsity-promoting hyperparameter that determines the degree of sparsity in the model. This term penalizes non-zero elements in Ξ, encouraging the model to retain only the most significant terms. During the optimization process, any coefficients in Ξ that fall below a threshold set by λ are set to zero, effectively removing less important terms from the model. This optimization problem can be solved by sequential threshold least squares (STLSQ), where λ serves as the threshold [5].

## Flowsheet model of a Continuous Direct Compression line

In this work, we consider a Continuous Direct Compression (CDC) process, where the API is mixed with the excipients and lubricant to finally move into the tablet press. A flow diagram of the CDC process is shown in Figure 1. CDC was chosen because it is the simplest tableting configuration, resulting in more resources being available in the literature for building the model.

The data used in this work was generated with a flowsheet model of a Continuous Direct Compression (CDC) line implemented in gPROMS FormulatedProducts 2023.1.1. Its modeling environment allows us to connect the models of the different unit operations needed for the flowsheet model [6].

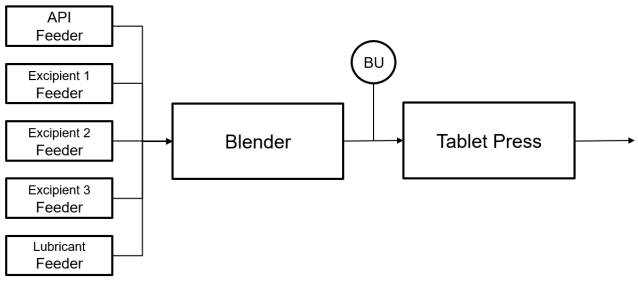



**Figure 1.** Process flow diagram of the Continuous Direct Compression line.

The data generated for this study consists of a series of step changes on the API mass flow rate, which in this work represents the control input $u$,and its response at the end of the blender in terms of blend uniformity (BU), that serves as our state variable $x$, as it is commonly done when characterizing the RTD. To guarantee unit consistency between the control input and the state variable, the mass flow rate and the blend uniformity are expressed as % from the target value. Additionally, unusual control input signals were generated to test the generalization ability of the model identified with the SINDy approach.

## SINDy with control for a CDC line

One of the key steps in implementing SINDy is selecting a candidate function library that best captures the dynamics of the system. A common approach is to start with a set of polynomial functions and then increase the library's complexity by incorporating additional terms, as shown in Eq. (4). Typically, SINDYc includes the control input $u$ as a separate variable in the library [7]. However, in this study, we opted to represent the control input as $u - x$. This formulation is particularly suited to continuous direct compression (CDC) systems, which generally operate in a steady state for extended periods before experiencing a dynamic change, such as a step change or

pulse input in the API mass flow. By defining the control input as $u - x$, it effectively captures the relative difference or deviation between the control signal and the state. This deviation term can better capture how the control input drives the system response away from the current state.

An effective approach to selecting the functions of the candidate library is using the knowledge of the process. In a continuous line, there is usually a time delay in the response after a change occurs upstream. To account for this time delay, we propose to include a possible discrete delay $\tau$ on the control input terms as part of the candidate function library as follows:

$$\Theta(x,u) = [1 \;\; x \;\; u \;\; u(t-\tau_1) \;\; u(t-\tau_2) \;\; u(t-\tau_3) \;\; \dots \;\; u(t-\tau_n)]. \quad (7)$$

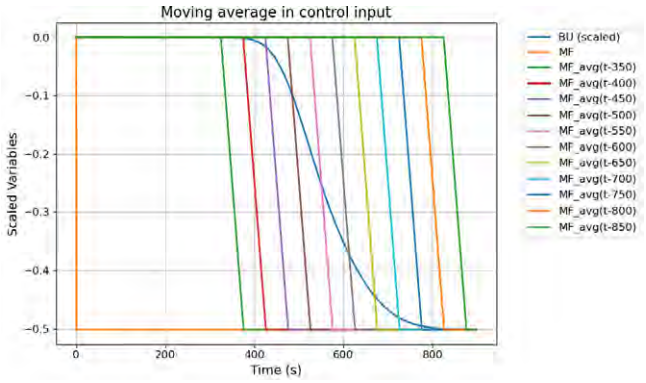



**Figure 2.** Example of using the moving average on the delayed control input functions used in the candidate library

The magnitude and number of delays are selected based on the approximate duration of the step change response of the training data. Additionally, to increase the amount of information captured by including the delayed versions of $u$, we opted to use a moving average $\hat{u}(t-\tau_i)$ over a time window around each delayed signal $u(t-\tau_i)$. For example, if the delay of the response is around 400 seconds and that response stabilizes at around 800 seconds, a list of delayed versions of $u$ from 350 until 850 seconds every 50 seconds is chosen. For each delayed term, we calculate a moving average over a ±25 s window rather than using a single point in time. This approach helps capture the short-term variations that would otherwise be lost when discretizing the input to $u(t-\tau_i)$. In other words, by including the surrounding data points, we account for small fluctuations around the delayed term, instead of relying only on a single value. This can improve both the smoothness of the input signal and the model's ability to learn the underlying dynamics. This example is represented in Figure 2, where the control input $u$ is defined as mass flow rate (MF) and the response or state variable is the blend uniformity (BU).

## RESULTS

The SINDYc with delay approach was trained on simulated data representing step changes of various sizes around the target value. Pre-processing included scaling the data, with a target value of 0 for both the API mass flow (control input) and the API concentration (response), while 1 and -1 were set as the extreme values for the training data. The SINDy model was implemented using the PySINDY package in Python [8, 9]. The derivatives of the state variable were approximated using second-order finite differences. After constructing the model, the resulting ordinary differential equation (ODE) was solved numerically with the fourth order Runge-Kutta method to generate predictions of the state variable. Model performance was evaluated using root mean-square error (RMSE), calculated as follows:

$$RMSE = \sqrt{\frac{1}{N}\sum_{i=1}^{N}(x_i - \hat{x}_i)^2} \quad (8)$$

where $x_i$ represents the actual value of the response

**Table 1:** Root mean square error (RMSE) of SINDy models under various configurations for training and two test datasets. "AW" = Averaging Window (±s), "DI" = Delay Interval (s). The values in bold indicate the selected model configuration.

| Regularization | Configuration | RMSE | | |
|---|---|---|---|---|
| $\lambda$ | (±AW, DI) | Training | Test 1 | Test 2 |
| $\lambda = 0.001$ | (±25 s, 25 s) | 0.7278 | 0.8045 | 0.7372 |
| | (±25 s, 50 s) | 0.2585 | 0.2888 | 0.2600 |
| | (±50 s, 25 s) | 0.4931 | 0.5460 | 0.4801 |
| | (±50 s, 50 s) | **0.1709** | **0.1632** | **0.1765** |
| $\lambda = 0.0001$ | (±25 s, 25 s) | 0.1162 | 0.0835 | 0.3958 |
| | (±25 s, 50 s) | 0.2158 | 0.2109 | 0.3263 |
| | (±50 s, 25 s) | 0.1094 | 0.0872 | 0.1673 |
| | (±50 s, 50 s) | 0.1256 | 0.0845 | 0.1362 |

(blend uniformity) and $\hat{x}_i$ stands for the predicted value from the SINDYc model.

To determine the level of sparsity from Eq.(6) various values of $\lambda$ were tested. Lower $\lambda$ generally improves RMSE because the regression is less penalized for including more terms; however, it can result in a model with many active terms, undermining the sparsity objective of SINDy. On the other hand, higher $\lambda$ forces the solution to discard more terms, reducing complexity but sometimes increasing prediction error. At $\lambda$=0.001, the model achieved the highest level of sparsity before all coefficients were reduced to zero. While decreasing $\lambda$ to 0.0001 improved model performance, it resulted in most coefficients being selected, which could reduce robustness in the presence of noisy data.

In this SINDy approach, two additional hyperparameters related to the delayed control input need to be tuned: the delay interval and the averaging window. Based on the system's dynamics, where the response to a step change begins around 400 s after the control input and stabilizes around 800 s, a delay range from 350 to 850 s was chosen. Within the estimated response range, we tested two delay interval increments, every 25 s and every 50 s, to control the model complexity. Using 25 s intervals resulted in more terms in the model, while 50 s intervals produced fewer. In either case, each delayed control input was further smoothed using a moving average of either ±25 s or ±50 s to capture the input's gradual effect. These window lengths were chosen so that ±25 s partially covers the 25 s delay interval around the nominal delay, while ±50 s fully spans the 50 s delay increment. In this way, the moving average captures the gradual or integrated effect of the control input in the immediate surroundings of each delay, ensuring that small timescale fluctuations are included without unnecessarily increasing the complexity of the model.

Table 1 summarizes the root mean square error (RMSE) obtained for each configuration of the SINDYc model on three data sets: the original training data, a first test set with a conventional control input profile (test 1), and a second test set with a more challenging input profile (test 2). In training and test 1 data sets, the control input profiles mimic typical conditions during process development in a continuous direct compression (CDC) line, with step changes of moderate magnitude and duration. By contrast, test 2 data set explores significantly different operating conditions, including a different initial condition, sinusoidal variation, and sudden spikes, to test the model's robustness well beyond the scenarios used for training.

Each configuration in Table 1 varies two key factors: the regularization parameter $\lambda$, which controls the sparsity of the model, and the delay/averaging combination used to create candidate functions (e.g., 25 s vs. 50 s increments, ±25 s vs. ±50 s moving average windows.

As shown in Table 1, the highlighted configuration achieves a good balance of accuracy and parsimony across all three data sets. Although the configuration with $\lambda$=0.0001 shows slightly lower RMSE values in some cases, it selects nearly all candidate terms, resulting in a much more complex model that could lead to potential overfitting. In contrast, the chosen configuration with $\lambda$=0.001 retains comparable predictive accuracy on both test 1 and test 2, while maintaining a significantly smaller number of terms. This aligns with the SINDy principle of favouring parsimonious models that capture essential dynamics without overfitting.

To demonstrate how the chosen regularization parameter $\lambda$ affects the model sparsity, we present in Eq.(8) the final form of the obtained model with $\lambda$=0.001, and in Eq.(9) the corresponding model when $\lambda$=0.0001. Both models use the same delay/averaging configuration (i.e., ±50 s averaging windows and 50 s delay increments), but differ in the strength of their sparsity.

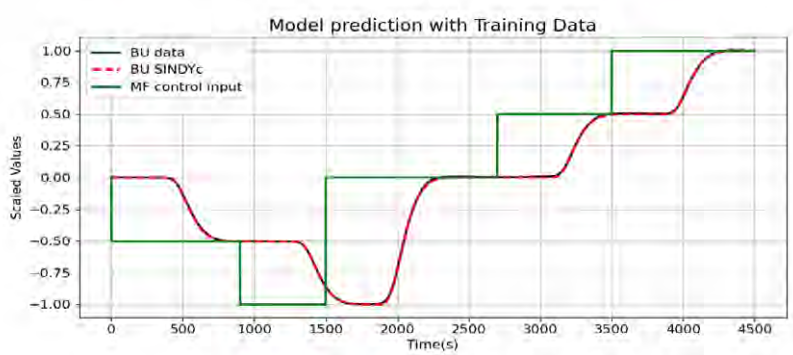
$$\dot{x} = 0.008(\hat{u}(t-450)-x) + 0.004(\hat{u}(t-500)-x) + 0.005(\hat{u}(t-550)-x) + 0.001(\hat{u}(t-650)-x) \quad (9)$$

$$\dot{x} = 0.0008(\hat{u}(t-400)-x) + 0.003(\hat{u}(t-450)-x) + 0.002(\hat{u}(t-500)-x) - 0.002(\hat{u}(t-550)-x) - 0.0006(\hat{u}(t-600)-x) - 0.001(\hat{u}(t-650)-x) - 0.0007(\hat{u}(t-700)-x) - 0.0008(\hat{u}(t-750)-x) - 0.0001(\hat{u}(t-850)-x) \quad (10)$$

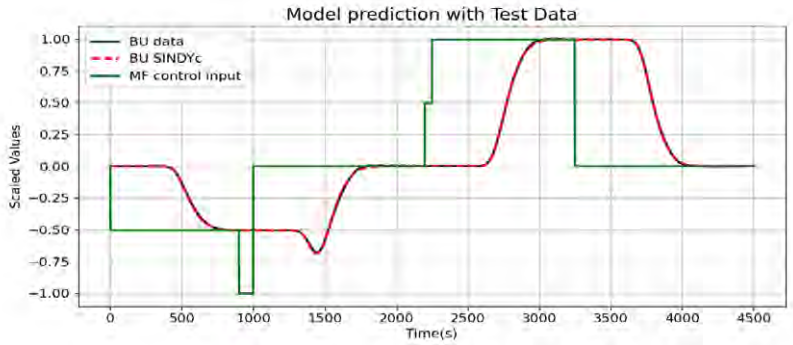
In Eq. (8), only four terms are present, which manage to capture the main time delays while preserving interpretability. But, when $\lambda$ is reduced to 0.0001 in Eq. (9), the regularization penalty on additional terms is much weaker, so, more delayed terms remain active, offering a marginally lower RMSE (as shown in Table 1) but at the expense of simplicity.

In addition to selecting $\lambda$=0.001, we also explored two key parameters for constructing our candidate functions: the averaging window (±25 s vs. ±50 s) and the delay interval (25 s vs. 50 s). From Table 1 it can be seen that at $\lambda$=0.001, widening the averaging window from ±25 s to ±50 s results in a slight improvement in RMSE, but the more influential factor is the choice of delay interval. When the model is forced to choose fewer delayed terms (i.e., using a 50 s delay interval rather than 25 s), it performs slightly better. This indicates that at higher regularization, including too many candidate terms (as occurs with the finer 25 s interval) might dilute the model's ability to identify a compact set of truly relevant dynamics. In other words, a coarser delay interval can sometimes help the algorithm focus on the most dominant time lags in the process, improving predictive performance and interpretability.

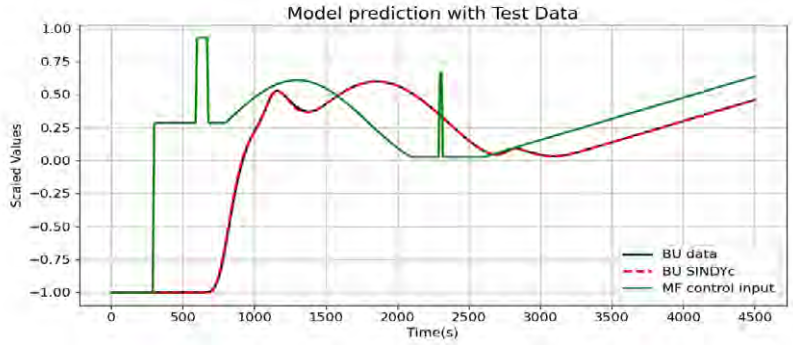
When $\lambda$=0.0001, the effect of averaging window and delay interval becomes less straightforward. Because the




a)




b)




c)

**Figure 3.** Training (a) and test 1 (b) , and test 2 (c) data sets. The in silico BU process data ($x$) is compared with the SINDYc model prediction given a control input signal $u$ (mass flow rate or MF)

penalization of extra terms is much lower, the model can retain many more active terms in the final solution—potentially benefiting from finer resolution of time delays (25 s intervals). The trade-off is that these extra terms may capture minor effects rather than main dynamics. As a result, some configurations with 25 s intervals and smaller averaging windows at $\lambda$=0.0001 can show lower RMSE on the training set, but at the cost of reduced sparsity and potentially greater risk of overfitting. Future work may employ cross-validation to further refine these hyperparameter selections.

Figure 3a-3c illustrate representative time-series predictions for each data set at the chosen model configuration (i.e., $\lambda$=0.001, ±50 s averaging windows and 50 s delay increments). For the training data (Figure 3a), the model prediction (dotted red line) closely tracks the observed blend uniformity or BU (black line) across successive step changes in the mass flow rate (green line). In test 1 (Figure 3b), the same model continues to perform well, with only minor deviations from the true signal in the transitions. Test 2 (Figure 3c) tries far more drastic input variations. While the prediction error increases slightly, the model still manages to capture major trends, indicating that it generalizes reasonably well to unseen input profiles.

Overall, these results indicate that a careful choice of $\lambda$, along with a suitable delay-averaging configuration, can result in a compact, interpretable SINDy model that remains robust to diverse control input scenarios—ranging from typical operating conditions (test 1) to more extreme or unconventional inputs (test 2).

## CONCLUSIONS

In this study, a SINDy-based model with delayed control input terms was developed and tested to capture the dynamics of a continuous direct compression (CDC) line. By incorporating delayed versions of the control input in the candidate function library and systematically optimizing the delay intervals and averaging windows, the resulting model effectively balances accuracy and sparsity. The selection of an appropriate regularization parameter $\lambda$ was crucial to achieving this balance, as higher values promoted interpretability by enforcing sparsity, while lower values, although with lower RMSE, led to overfitting with an excessive number of active terms.

The analysis of different configurations showed that using a coarser delay interval (50 s) resulted in improved model performance compared to a finer interval (25 s) when a higher regularization parameter was applied. This suggests that fewer, well-chosen delay terms allow the model to focus on capturing the dominant dynamics of the system, potentially reducing the risk of overfitting to noise or minor effects. The choice of the averaging window also played a role in enhancing the model's robustness, with a ±50 s window providing a more smoothed representation of the input that improved predictive accuracy across various operating conditions. These findings highlight the importance of tuning hyperparameters to achieve an optimal trade-off between model complexity and predictive capability.

The chosen model configuration showed strong generalization performance when applied to test data, including both typical operating profiles encountered in CDC lines and more challenging scenarios such as sinusoidal variations, constant increasing slopes, and sudden spikes. Overall, this approach demonstrates the feasibility of using SINDy for data-driven modelling in CDC processes and provides a foundation for future work to address more complex dynamic responses and noisy data.

## ACKNOWLEDGEMENTS

The authors want to acknowledge the financial support from the Flanders Innovation & Entrepreneurship (VLAIO) and Janssen Pharmaceutica NV in Belgium (Grant No. HBC.2022.0177).

## REFERENCES

1. G Tian, A Koolivand, Z Gu, M Orella, R Shaw, and T F O'Connor, Development of an RTD-based flowsheet modeling framework for the assessment of in-process control strategies. *AAPS PharmSciTech* 22: 10.1208/s12249-020-01913-8
2. P Bhalode, H Tian, S Gupta, S M Razavi, A Roman-Ospino, S Talebian, R Singh, J V Scicolone, F J Muzzio, and M Ierapetritou, Using residence time distribution in pharmaceutical solid dose manufacturing – a critical review. *International Journal of Pharmaceutics* 610:121248 10.1016/J.IJPHARM.2021.121248
3. S L Brunton, J L Proctor, and J N Kutz, Discovering governing equations from data by sparse identification of nonlinear dynamical systems. *Proceedings of the National Academy of Sciences of the United States of America* 113:3932–3937 10.1073/pnas.1517384113
4. E Kaiser, J N Kutz, and S L Brunton, Sparse identification of nonlinear dynamics for model predictive control in the low-data limit. *Proceedings of the Royal Society A: Mathematical, Physical and Engineering Sciences* 474: 10.1098/rspa.2018.0335
5. U Fasel, E Kaiser, J N Kutz, B W Brunton, and S L Brunton, SINDy with control: a tutorial.
6. N Metta, M Ghijs, E Schäfer, A Kumar, P Cappuyns, I Van Assche, R Singh, R Ramachandran, T De Beer, M Ierapetritou, and I Nopens, Dynamic flowsheet model development and sensitivity analysis of a continuous pharmaceutical tablet manufacturing process using the wet granulation route. *Processes* 7:1–35 10.3390/pr7040234
7. F Abdullah and P D Christofides, Data-based modeling and control of nonlinear process systems using sparse identification: an overview of recent results. *Computers and Chemical Engineering* 174:108247 10.1016/j.compchemeng.2023.108247
8. A A Kaptanoglu, B M de Silva, U Fasel, K Kaheman, A J Goldschmidt, J Callaham, C B Delahunt, Z G Nicolaou, K Champion, J-C Loiseau, J N Kutz, and S L Brunton, PySINDy: a comprehensive python package for robust sparse system identification. *Journal of Open Source Software* 7:3994 10.21105/joss.03994
9. B M de Silva, K Champion, M Quade, J-C Loiseau, J N Kutz, and S L Brunton, PySINDy: a python package for the sparse identification of nonlinear dynamical systems from data. *Journal of Open Source Software* 5:2104 10.21105/joss.02104

© 2025 by the authors. Licensed to PSEcommunity.org and PSE Press. This is an open access article under the creative commons CC-BY-SA licensing terms. Credit must be given to creator and adaptations must be shared under the same terms. See https://creativecommons.org/licenses/by-sa/4.0/



Systems & Control Transactions

**Research Article - Peer Reviewed Conference Proceeding**
ESCAPE 35 - European Symposium on Computer Aided Process Engineering
Ghent, Belgium. 6-9 July 2025
Jan F.M. Van Impe, Grégoire Léonard, Satyajeet S. Bhonsale,
Monika E. Polańska, Filip Logist (Eds.)

PSE PRESS

# Balancing modelling complexity and experimental effort for conducting QbD on lipid nanoparticles (LNPs) systems

**Daniel V. Batista[a] and Marco S. Reis[a*]**

[a] University of Coimbra, CERES, Department of Chemical Engineering, Coimbra, Portugal
*Corresponding Author: marco@eq.uc.pt.

## ABSTRACT

The promising properties of lipid nanoparticles (LNPs) as drug carriers have been attracting significant attention in the field of drug delivery. However, further research is still required for a better understanding of their integration in the pharmaceutical industry. The Quality by Design (QbD) approach aims at ensuring the safety and efficiency in the development of new drugs, through an holistic, risk-based approach that gathers all sources of knowledge available about the system under analysis. One key resource of the QbD framework is the rich toolkit of Design of Experiments (DOE), to deepen the understanding of how the synthesis of LNPs by microfluidics can be effectively conducted and controlled. This study aimed to explore and understand the effectiveness of different DOE strategies, through an *in silico* study focused on the impact of factors related to the LNPs synthesis, namely the molar ratio of each lipid component in the lipidic mixture and the N/P ratio, while also considering potential economic constraints without disregarding the need for a statistically valid analysis. A simulation model of the LNP synthesis derived from real experiments was adopted as a basis to assess the potential efficacy of estimated models with different levels of complexity, to extract useful insights in future DOEs in these types of systems, given the high cost of each experimental run. The statistical metrics used were the coefficient of determination ($R^2$) and the Root Mean Squared Error (RMSE). With the results obtained, it was possible to verify that different responses from the same system could require quite different model structures, namely, the models developed for potency and for size of the LNPs differed significantly in their complexity. Furthermore, a number of experiments of the order of 30 can be anticipated as necessary for a DOE in a real process, involving similar factors.

**Keywords**: Lipid nanoparticles (LNPs), Quality by Design (QbD), Design of Experiments (DOE).

## INTRODUCTION

Lipid nanoparticles (LNPs) have recently attracted considerable interest, particularly for their role in the development of COVID-19 mRNA vaccines by Pfizer-BioNTech and Moderna. Their ability to efficiently encapsulate nucleic acids, while simultaneously ensuring effective intracellular delivery and endosomal escape, has sparked increasing interest from both the industrial and research communities for exploring their unique properties as promising drug carriers.

A widely used technique for the synthesis of these LNPs, is microfluidics. This method allows for the efficient mixing of an organic solution, which contains the necessary lipid components dissolved in ethanol, with an aqueous solution that contains the intended payload (nucleic acid).

To ensure the successful and safe synthesis of these LNPs attributes, the pharmaceutical industry typically recommends following a Quality by Design (QbD) approach. This approach aims to guarantee that manufacturing is able to deliver the expected quality of the drugs, rather than relying solely on testing the final product and reject any lot that is non-conforming. QbD can also reduce costs associated with product optimization and ensure that patients receive higher-quality drugs in a shorter time frame [1]. One of the key aspects of the QbD approach is the use of Design of Experiments (DOE) to establish the Design Space that guarantees the quality requirements of the LNPs are met [1]. However, before

defining a design space, several DOE stages may be necessary for screening the important factors, modelling the system's behaviour accurately, and finding the optimal operational conditions.

## GOLDEN STANDARD MODEL

As previously highlighted, one of the key aspects of the QbD approach is the use of the DOE. However, the employment of this statistical method can greatly benefit from a preliminary simulated *in silico* study approach, especially when economic constraints play a significant role. This is especially true in the case of LNPs' synthesis by microfluidics, where each experiment is expensive due to the high cost of the formulation components. Therefore, there is a justified interest in making this process as efficient and informative as possible.

In light of this information, we have adopted an *in silico* system, using a model that was developed from real experimental data collected in a closely related experimental and technological scenario. This *in silico* study provides a suitable test bed to analyse and compare the different DOE strategies that may be adopted and collect insights about a reasonable number of experiments to accommodate within a designated budget, while ensuring a statistically valid analysis.

Therefore, we have conducted a systematic study based on the work developed by Karl et al. [2], who provided a simulation model of the LNP synthesis, referred to as the Golden Standard (GS) Model. This model was derived from 23 real experiments and codified in the JMP Pro software using a recently proposed methodology called self-validated ensemble model (SVEM).

The GS Model considers the molar ratio of individual lipid components in the lipid mixture (Ionizable lipid (IL), Structural lipid (SL), Helper lipid (HL) and PEG lipid), the ionizable lipid type, the molar N/P ratio (ionizable amine from ionizable lipids to phosphate from nucleic acid ratio) and the total flow rate (TFR). These factors were established within the ranges, shown in **Table 1**.

**Table 1:** Ranges of the factors in the GS Model.

| Factors | Ranges |
|---|---|
| IL | [0,1; 0,6] |
| HL | [0,1; 0,6] |
| SL | [0,1; 0,6] |
| PEG | [0,01; 0,05] |
| Ionizable lipid type | H101 or H102 or H103 |
| N/P ratio | [6,14] |
| TFR | [1,3] mL/min |

It is important to note that the GS model is quite complex in its structure and it was considered, for all practical purposes, unknown throughout this study. Moreover, it has terms that were not included in the DOEs strategies considered. This structural mismatch brings more realism to the *in silico* study carried out, which will be lay down in the next section.

Finally, this model considered as responses the "potency in vivo" and "size of the LNP", with the goal being to maximize potency and minimize size.

## METHODOLOGY

The study conducted is based on the GS Model, and followed a methodology that is schematicaly illustrated in **Figure 1**. This figure that depicts the principal steps of the study, organized into two distinct phases: 1) Initial setup; 2) Comparison study.

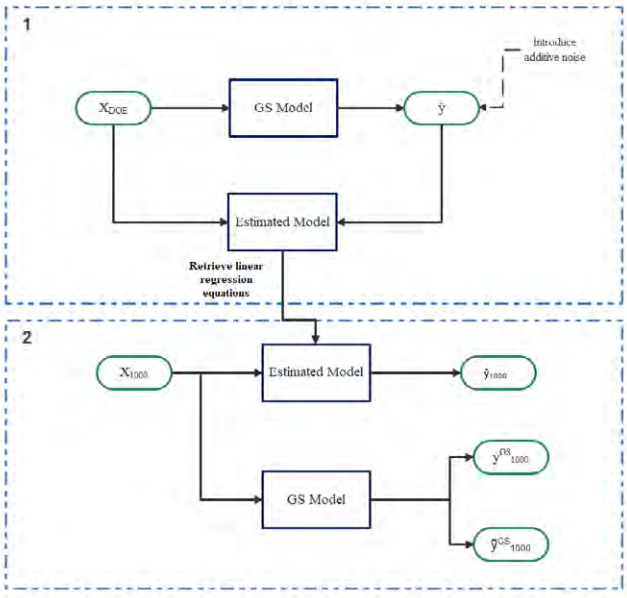



**Figure 1:** Methodology for the *in silico* study.

### Initial Setup

Firstly, the DOE levels ($X_{DOE}$) for the factors selected, need to be established. For such, an interval of acceptability for each factor was established while respecting the ranges established by the GS model, as shown in **Table 1**. The ranges established and the chosen factors are shown below in **Table 2**.

**Table 2:** Ranges for the factors considered in $X_{DOE}$.

| Factors | Ranges |
|---|---|
| IL | [0,3;0,6] |
| HL | [0,1;0,28] |
| SL | [0,185;0,555] |
| PEG | [0,01;0,045] |
| N/P ratio | [ 6,14] |

Taking into account the constraints in **Table 2**, the $X_{DOE}$ was generated by a D-optimal design approach for different model structures, spanning different levels of modeling complexity. These model structures present an increasing number of terms (complexity), by considering more effects to be estimated from data. Consequently, more experiments were necessary to estimate them. The models were designated as Model 1 (M1), Model 2 (M2), and Model 3 (M3), with M3 being the most complex in terms of considered effects. In M1 only the main effects associated with the factors were considered. On the other hand, M2 considered the same effects as M1, except for the main effect associated with the N/P ratio. Additionally, M2 considered the effects related to the non-linear blending of two mixture components and the interactions of mixture components with the process factor (N/P ratio). Finally, M3 incorporated the same effects as M2, along with some third-order terms, considering the Scheffé cubic model effects, such as the non-linear blending associated with three components. The effects considered for each model are presented in **Table 3**.

With regard to the number of experiments, between 10 to 30 experiments were considered, in accordance with the corresponding minimum limits suggested by optimal design software (JMP Pro), that increase according to the increment of their complexity. Therefore, a designation of the number of experiments was explicitly included together with that for the corresponding model. For example, M1-10 represents the model M1 that was generated considering a total of 10 experiments.

Next, the $X_{DOE}$'s elaborated were introduced in the GS Model to obtain the simulated responses with additive noise ($\tilde{y}$). Note that, when introducing the levels for the selected factors in the model ($X_{DOE}$), the levels for the other factors not considered in the designs have also to be set to run the simulation; therefore, the following factors were established as constants for the GS Model to run: a TFR of 2 mL/min and H103 as the ionizable lipid type.

Moreover, three levels of noise in the response were considered: the originally estimated noise level (during the development of the GS model) and two additional levels corresponding to an increase of 10% or 20%. This alternative is indicated by a dashed arrow in **Figure 1** and was implemented in an effort to better reflect the reality of having different levels of reproducibility of the measured responses.

Based on the $X_{DOE}$'s and the corresponding outputs, $\tilde{y}$, with or without additive noise, a linear regression model was estimated for each model structure, as mentioned above, by fitting these models using the least square method. These models will be collectively referred throughout this article, as Estimated Models (EM).

## Comparison study

In the second part of the study, a new input space of 1000 points ($X_{1000}$) was generated at random for the mixture components and the N/P ratio. The new input space was generated to guarantee a proper assessment of the predictive capability of the different models and, therefore, the comparison between the GS Model and the EM Models. In other words, this new dataset is not used for conducting any estimation task, but simply to compare the GS Model responses with and without noise ($\tilde{y}^{GS}_{1000}$ and $y^{GS}_{1000}$) with the EM Models responses ($\hat{y}_{1000}$).

One of the metrics used for this comparison was the coefficient of determination, $R^2$, which measures the quality of fit of the EM Model in relation to the GS Model responses (with or without noise). A higher $R^2$ value indicates a superior fit to the GS data, i.e., a higher proportion of variation that is explained by each EM Model.

Another metric used was the Root Mean Squared Error (RMSE), which describes the average difference between the GS values (with or without noise) and the estimated values, as shown below in Equation (1) and Equation (2).

$$\mathrm{RMSE}_{\mathrm{w/o\ noise}} = \sqrt{\frac{1}{n} \times \sum_{i=1}^{n} \left( y^{GS}_{1000}(i) - \hat{y}_{1000}(i) \right)^2} \quad (1)$$

$$\mathrm{RMSE}_{w/noise} = \sqrt{\frac{1}{n} \times \sum_{i=1}^{n} \left( \tilde{y}^{GS}_{1000}(i) - \hat{y}_{1000}(i) \right)^2} \quad (2)$$

Note that the metrics mentioned above were computed for the test set. Therefore, they are actually measures of quality of prediction (prediction metrics).

# ANALYSIS AND DISCUSSION OF THE RESULTS

**Figure 2** summarizes the $R^2$ and RMSE for each response (potency and size) that were computed for each EM Model by comparison with the GS Model with or without noise.

Firstly, it is important to note that the $R^2$ and RMSE trends of the different EM Models remained

**Table 3:** Effects considered for models M1, M2 and M3.

| Models | Effects |
|---|---|
| M1 | PEG, HL,IL, SL and N/P ratio |
| M2 | PEG, HL, IL, SL, PEG×IL, PEG×HL, PEG×SL, PEG×N/P ratio, HL×IL, HL×SL, HL×N/P ratio, IL×SL, IL×N/P ratio and SL×N/P ratio |
| M3 | PEG, HL, IL, SL, PEG×IL, PEG×HL, PEG×SL, PEG×N/P ratio, HL×IL, HL×SL, HL×N/P ratio, IL×SL, IL×N/P ratio, SL×N/P ratio, PEG×HL×IL, PEG×HL×SL, PEG×IL×SL, HL×IL×SL, PEG×HL×(PEG-HL),PEG×IL×(PEG-IL), HL×IL×(HL-IL), PEG×SL×(HL-SL),HL×SL×(HL-SL) and IL×SL×(IL-SL) |

consistent regardless of the presence of noise in GS Models outputs, as well as considering additional levels of noise. The only difference occurs when considering the various levels of noise, where the values reported were lower and higher for $R^2$ and RMSE, respectively.

The $R^2$ for the EM Models differed for potency and size. For size, it was reported a better fit of the EM Models to the GS Model with values typically around between 0,97 and 0,99. Moreover, when compared to potency, the shift in the behaviour of the $R^2$ values in accordance with the models was slightly less significant; see **Figure 2 (b)**.

For potency, the $R^2$ values displayed a general increasing trend, **Figure 2 (a)**, as the complexity of EM Models and the number of experiments increased, with the exception of M3, which exhibited a slightly lower $R^2$ value compared to M2. On the other hand, the RMSE values displayed a general decreasing trend, **Figure 2 (c)**, as the complexity and the number of experiments increased, with the exception of M3 which exhibited a slightly higher RMSE value compared to M2.

According to these findings, M2-30 appears to be the most effective alternative due to its high $R^2$ and a low RMSE. However, if a reduced number of experiments was necessary, M2-20 would still be a viable option, as it presented a slightly lower $R^2$, but a lower RMSE in comparison with M2-30.

On the other hand, regarding size, the $R^2$ and RMSE values showed different trends across the number of experiments and models' complexity. In the case of the $R^2$ values, an increment in the number of experiments did not necessarily lead to an increase in $R^2$, **Figure 2 (b)**. In fact, there was a slight decrease in $R^2$ values from M1-10 to M1-20, and an increase in M1-30. Following the sequence in this figure, there is then a decrease in M2-20 and an increase in M2-30 and M3-30, with M3-30 showing the highest value.

With regard to RMSE, **Figure 2 (d)**, an increase in the number of experiments and complexity from M1-10 to M2-10 resulted in a decrease in values similar to the previous case. However, there was an increase in RMSE at M2-20, and a subsequent decrease until M3-30, which corresponds to the lowest RMSE value.

According to these findings, the M3-30 would likely be a viable option as it reported the highest $R^2$ and lowest RMSE value. It is important to note, that for size the $R^2$ values reported generally only showed changes around their 3rd or 4th decimal place. Therefore, M2-30, would also be a viable option, despite being the 3rd highest $R^2$ value. Moreover, it had the lowest RMSE value.

Based on these findings, in both cases, rather surprisingly, the M2-30 model was considered a good possibility, although it was not the first choice for size. Therefore, using the same model is still a viable option.

Nevertheless. the most effective EM Model for potency and size differed: M2-30 for potency and M3-30 for size. Thus, it is also likely that different responses may not necessarily require the same EM Model. Still, the suggested number of experiments is the same, which is informative for future studies involving similar factors.

It is important to note that, as previously stated, there was a notable disparity between size and potency in $R^2$ values, with $R^2$ values for size being consistently higher (around 0,97 to 0,99), in comparison to those for potency (around 0,30 to 0,88). The reason behind these results was also object of analysis.

This discrepancy could be attributed to the fact that not all the responses, as previously stated, behave necessarily equally, and may follow different mechanisms, which may differ in their inner complexity.

Furthermore, the measurement systems may also be more limited in some cases, inputting more uncertainty in data, which is transferred to the model development stage; this also may affect more extensively one type of model than the other.

Moreover, the fact that the models being

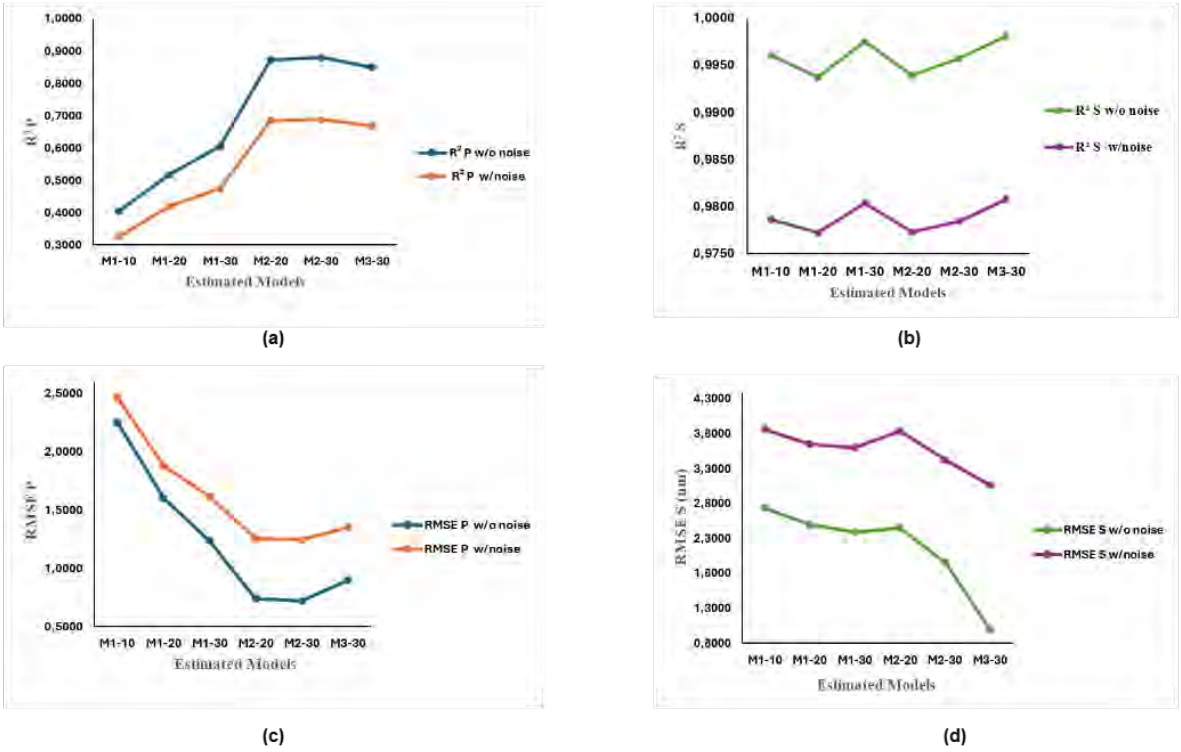



**Figure 2**: Results of $R^2$ and RMSE according to the Estimated Models: (a) $R^2$ of potency (P) with and without noise; (b) $R^2$ of size (S) with and without noise; (c) RMSE of potency (P) (units not referred in the original article [2]) with and without noise (d); RMSE of size (S) with and without noise.

considered in the $R^2$ metric (EM Model and GS Model) are structurally different could also be a possibility for this discrepancy. This mismatch between them is due to the fact, that the GS Model for potency was generated considering additional effects (e.g. PEG×PEG×N/P ratio, HL×HL×PEG, emphasized in bold in Equation 3) along with an intercept term, the same occurring in size for GS Model. A portion of the equation of GS Model for potency is shown below in Equation 3:

$$\text{Potency}_{GS} = -4{,}6532 + 1{,}0608 \times \left(69{,}1343 + 0{,}3518 \times \left(\frac{(\text{PEG}-0{,}01)}{0{,}69}\right) + 0{,}0697 \times \left(\frac{(\text{HL}-0{,}1)}{0{,}69}\right) - 1{,}8941 \times \left(\frac{(\text{IL}-0{,}1)}{0{,}69}\right) + 0{,}1734 \times \left(\frac{(\text{SL}-0{,}1)}{0{,}69}\right) + \text{Ionizable lipid type} + 0{,}0005 \times \left(\frac{(\text{N/P ratio}-10)}{4}\right) - 66{,}0252 \times \left(\frac{(\text{PEG}-0{,}01)}{0{,}69}\right)\left(\frac{(\text{PEG}-0{,}01)}{0{,}69}\right)\left(\frac{(\text{HL}-0{,}1)}{0{,}69}\right) - 270{,}8798 \times \left(\frac{(\text{PEG}-0{,}01)}{0{,}69}\right)\left(\frac{(\text{PEG}-0{,}01)}{0{,}69}\right)\left(\frac{(\text{IL}-0{,}1)}{0{,}69}\right) + 30{,}8712 \times \left(\frac{(\text{PEG}-0{,}01)}{0{,}69}\right)\left(\frac{(\text{PEG}-0{,}01)}{0{,}69}\right)\left(\frac{(\text{SL}-0{,}1)}{0{,}69}\right) + \left(\frac{(\text{PEG}-0{,}01)}{0{,}69}\right)\left(\frac{(\text{PEG}-0{,}01)}{0{,}69}\right) \text{Ionizable lipid type} - 164{,}3110 \times \left(\frac{(\mathbf{PEG}-\mathbf{0{,}01})}{\mathbf{0{,}69}}\right)\left(\frac{(\mathbf{PEG}-\mathbf{0{,}01})}{\mathbf{0{,}69}}\right)\left(\frac{(\mathbf{N/P\ ratio}-\mathbf{10})}{\mathbf{4}}\right) - 103{,}2265 \times \left(\frac{(\text{PEG}-0{,}01)}{0{,}69}\right)\left(\frac{(\text{PEG}-0{,}01)}{0{,}69}\right)(\text{TFR}-2) - 1{,}1640 \times \left(\frac{(\mathbf{HL}-\mathbf{0{,}1})}{\mathbf{0{,}69}}\right)\left(\frac{(\mathbf{HL}-\mathbf{0{,}1})}{\mathbf{0{,}69}}\right)\left(\frac{(\mathbf{PEG}-\mathbf{0{,}01})}{\mathbf{0{,}69}}\right) + 1{,}1584 \times \left(\frac{(\text{HL}-0{,}1)}{0{,}69}\right)\left(\frac{(\text{HL}-0{,}1)}{0{,}69}\right)\left(\frac{(\text{IL}-0{,}1)}{0{,}69}\right)(\ldots) - 1{,}3789 \left(\frac{(\text{IL}-0{,}1)}{0{,}69}\right)\left(\frac{(\text{SL}-0{,}1)}{0{,}69}\right)\left(\frac{(\text{IL}-0{,}1)}{0{,}69} - \frac{(\text{SL}-0{,}1)}{0{,}69}\right)\right) \quad (3)$$

As previously shown in **Table 1** and **Table 2**, the GS Model factors' ranges differed from the ones considered for the EM Model.

These conjectures were further analyzed and corroborated through a comparison of the prediction profiles of the GS Model for potency and size, with the prediction profiles of the EM Models (M2-30 for potency and M3-30 for size).

The predicted behaviour for size in the profiles for the GS Model did not differ much when compared to the M3-30. However, when comparing for potency between the GS Model and M2-30, the M2-30 was not capable of capturing completely the impact that certain factors held

on the response behaviour (e.g. PEG and N/P ratio). Such profiles for potency are shown below in **Figure 3**.

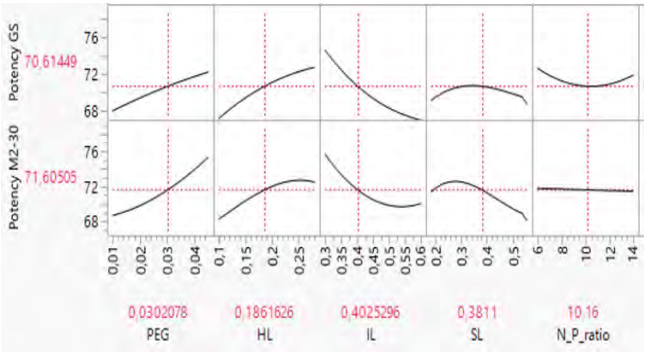



**Figure 3:** Prediction profiles for potency in GS Model and M2-30.

According to the findings, the proposed methodology provides a better understanding of the number of experiments and complexity of the models required for each response, thereby preventing unnecessary expenses. Furthermore, given that distinct results for each response were obtained, our approach also points out to the need to carefully tailor the DOE model case-by-case. In summary, this approach has demonstrated potential in addressing upfront challenges associated with the design space through *in silico* experiments to streamline the development of the design space in real systems while balancing cost-effectiveness and quality effectiveness.

## CONCLUSIONS

In the preliminary study conducted to test the effectiveness of different DOE strategies, considering the selected metrics ($R^2$ and RMSE), it was found that the responses (potency and size) were modelled with different levels of accuracy according to the EM Models obtained. From our findings, the main viable options considered were M2-30 for potency and M3-30 for size. Therefore, it is expected that for exploring the formulation space with a similar number of factors, a number of experiments of the order of 30 may be anticipated.

In the future, further research using different models with varying factors, will be conducted, such as incorporating only the lipidic composition of three components as factors, as it could substantially contribute to advancing the understanding of the models' effectiveness, thereby facilitating the future experimental application of the DOE, and consequently pave the way for a more comprehensive QbD approach. Furthermore, the DOE methodologies adopted in this study (optimal DOE) will be compared with other Active Learning methods, such as Bayesian Optimization, on their ability to efficiently reach optimal values for the properties, or optimal compromises between them.

## ACKNOWLEDGEMENTS

This work was supported by the CInTech project - Technological Hub for Innovation, Translation and Industrialisation of Complex Injectable Drugs -, under reference no. C644865576-00000005, co-financed by Componente C5 - Capitalização e Inovação Empresarial integrada na Dimensão Resiliência do Plano de Recuperação e Resiliência (PRR), through the NextGenerationEU fund.

The authors also acknowledge the support from the Fundação para a Ciência e Tecnologia, I.P., through the projects with DOI: 10.54499/UIDB/ 00102/2020 and DOI :10.54499/UIDP/00102/2020.

## REFERENCES

1. Gurba-Bryśkiewicz L, Maruszak W, Smuga DA, Dubiel K, Wieczorek M. Quality by Design (QbD) and Design of Experiments (DOE) as a Strategy for Tuning Lipid Nanoparticle Formulations for RNA Delivery. Biomedicines. 11(10):2752 (2023) https://doi.org/10.3390/biomedicines11102752
2. Karl AT, Essex S, Wisnowski J, Rushing H. A Workflow for Lipid Nanoparticle (LNP) Formulation Optimization using Designed Mixture-Process Experiments and Self-Validated Ensemble Models (SVEM). JoVE. 198:65200 (2023) https://doi.org/10.3791/65200

© 2025 by the authors. Licensed to PSEcommunity.org and PSE Press. This is an open access article under the creative commons CC-BY-SA licensing terms. Credit must be given to creator and adaptations must be shared under the same terms. See https://creativecommons.org/licenses/by-sa/4.0/

Systems & Control Transactions

**Research Article - Peer Reviewed Conference Proceeding**
ESCAPE 35 - European Symposium on Computer Aided Process Engineering
Ghent, Belgium. 6-9 July 2025
Jan F.M. Van Impe, Grégoire Léonard, Satyajeet S. Bhonsale,
Monika E. Polańska, Filip Logist (Eds.)

PSE PRESS

# Bayesian Optimization for Enhancing Spherical Crystallization Derived from Emulsions: A Case Study on Ibuprofen

**Xinyu Cao[a], Yifan Song[b], Jiayuan Wang[b], Linyu Zhu[b], and Xi Chen[a]***

[a] Zhejiang University, College of Control Science and Engineering, Hangzhou, Zhejiang Province, China
[b] Zhejiang University of Technology, College of Chemical Engineering, Hangzhou, Zhejiang Province, China.
* Corresponding Author: xi_chen@zju.edu.cn.

## ABSTRACT

The pharmaceutical industry is a highly specialized field where strict quality control and accelerated time-to-market are essential for maintaining competitive advantage. Spherical crystallization has emerged as a promising approach in pharmaceutical manufacturing, offering significant potential to reduce equipment and operating costs, enhancing drug bioavailability, and facilitating compliance with product quality regulations. Emulsions, as an enabling technology for spherical crystallization, present unique advantages. However, the quality of spherical crystallization products derived from emulsions is significantly influenced by the intricate interactions between crystallization phenomena, formulation variables, and solution hydrodynamics. These complexities pose substantial challenges in determining optimal operational conditions to achieve the desired product characteristics. In this study, Bayesian optimization (BO) is employed to refine and optimize the operational conditions for the spherical crystallization of a representative drug, ibuprofen. The primary goal is to improve product flowability, measured by angle of repose, while maintaining the median particle size within a specified range. The optimization process focuses on key variables such as temperature, stirring speed, duration, and BSA concentration. With the help of acquisition functions, BO enables the identification of a high-quality product with fewer experimental trials compared with traditional design of experiments (DoE) methods.

**Keywords**: Spherical crystallization, Bayesian optimization.

## INTRODUCTION

Spherical crystallization is an innovative technique in pharmaceutical manufacturing that has obtained increasing attention due to its ability to enhance both product quality and process efficiency[1]. By combining crystallization and agglomeration in a single step, spherical crystallization enables the production of spherical crystal forms that are easier to handle and have improved flow properties, which are crucial for downstream processes such as tablet formation and capsule filling[2]. However, the quality of spherical crystallization products obtained from emulsions is highly dependent on the complex interactions between crystallization processes, formulation parameters, and solution hydrodynamics[3]. These interrelated factors introduce significant challenges in determining the optimal operating conditions necessary to achieve the desired product characteristics, such as consistency in particle size and crystal morphology. This complexity underscores the necessity for a carefully structured experimental design[4]. Through such experimentation, it is possible to identify the most favorable conditions, thereby optimizing the process for consistent, high-quality product development.

Traditional experimental design methods, such as one-factor-at-a-time (OFAT) and factorial designs, are widely used to study the effects of process parameters. However, these approaches can be inefficient, particularly when dealing with complex systems where interactions between variables are significant[5]. Definitive screening designs (DSD), in combination with response surface methodology (RSM), offer a more efficient and

comprehensive strategy for process optimization[6]. DSD is particularly effective in identifying the most influential factors with a minimal number of experimental runs, while accounting for potential interactions and nonlinear effects. Once key factors are identified, RSM is applied to further refine the understanding of the process by modeling the relationship between these factors and the desired output. This combined approach allows for an efficient exploration of input spaces.

Building on the efficiency of definitive screening designs and response surface methodology, Bayesian optimization (BO)[7, 8] presents a newer approach for optimizing complex processes in product development. This method offers a more efficient way to explore parameter spaces by using a probabilistic model to guide the selection of the most promising experimental conditions, thus reducing the need for exhaustive testing. This technique has demonstrated considerable potential across multiple domains, including pharmaceutical manufacturing[9], environmental monitoring[10], and the food industry[11]. In the context of spherical crystallization, where multiple interacting variables influence product quality, BO can help identify optimal conditions more quickly, contributing to faster development of new formulations.

This paper presents a comprehensive investigation into the optimization of spherical crystallization processes for pharmaceutical manufacturing. The second section outlines the experimental procedure for the spherical crystallization of a representative drug, ibuprofen, illustrating the practical application of the technique. In the third section, two experimental design methods are discussed: (1) Definitive screening designs combined with response surface methodology, and (2) Bayesian optimization. The fourth section presents and analyzes the experimental results obtained from these approaches. Finally, Potential directions for future research are discussed in the conclusion.

## EXPERIMENTAL PROCEDURE: SPHERICAL CRYSTALLIZATION OF IBUPROFEN

This study aims to develop a standard-compliant spherical crystallization product of ibuprofen by optimizing experimental conditions. The spherical crystallization process will be introduced in this section.

### Spherical Crystallization Process

The ibuprofen used for spherical crystallization was sourced from *Rhawn* (China). Distilled water and dichloromethane (DCM) (*SCR*, China) were utilized in the crystallization process. Bovine serum albumin (BSA) (*Shyuanye*, China) and quinoa starch served as Pickering particles to stabilize the emulsions. Ethyl cellulose (EC) (*Macklin*, China) was employed as a crystallization additive. The spherical crystallization process was performed in Pickering emulsions, with the procedure adapted from the authors' previously published work[12, 13].

As shown in Fig. 1, an oil-in-water (O/W) emulsion was prepared with dichloromethane as the dispersed phase (which is also the oil phase) and a 0.1 wt% BSA solution as the continuous phase (which is also the aqueous phase). Ibuprofen and EC were dissolved in the oil phase, while quinoa starch was added to the aqueous phase and dispersed via ultrasonication for 10 minutes. The oil and aqueous phases were then combined in a 100 mL round-bottom flask and mixed by handshaking for 1 minute to form the O/W emulsion, after which the Pickering emulsion was obtained. Subsequently, the emulsion was transferred to a 250 mL flask for the evaporation and crystallization processes. Evaporation was carried out in an oil bath (DF-101S, Shanghai Lichenbangxi Instrument Co., Ltd.) equipped with a top stirrer (*WIGGENS*, WB2000-B). Upon completion of crystallization, the resulting product was transferred to a filtration flask and filtered using a recirculating water vacuum pump (SHZ-D (III), Shanghai Lichenbangxi Instrument Co., Ltd.) to remove residual aqueous phase. The product was then washed twice with 100 mL of distilled water and dried in an oven at 50°C for 24 hours. Further analysis of the product includes flowability analysis and particle size analysis.

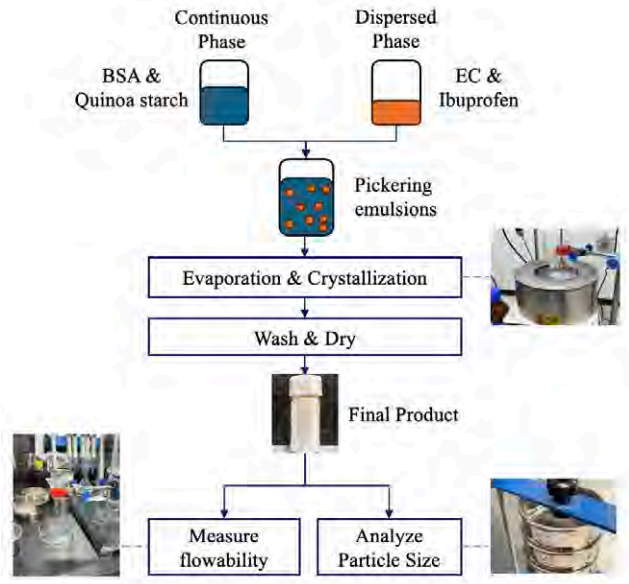



**Figure 1.** Crystalization process and analysis flowchart .

### Flowability Measurements

The flow properties of the spherical agglomerates were assessed indirectly by measuring the angle of repose (AVA). The experimental setup for measuring the angle of repose is illustrated in Fig. 2.

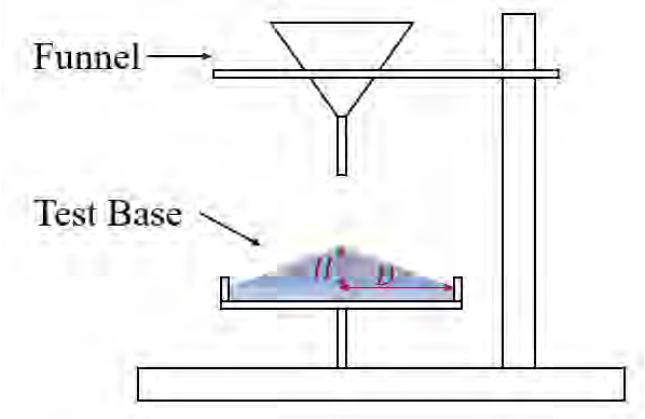



**Figure 2.** Measurement of the angle of repose.

To minimize the influence of varying compaction states of the powder on measurement accuracy, the powder samples were pre-sieved through a screen with a mesh size of 1.0 mm prior to testing. The funnel used for the measurement had a neck length of 4 cm and a neck diameter of 8 mm. The test base had a diameter of 10 cm and featured a raised edge. To reduce errors caused by particle dispersion upon initial impact, a layer of powder was retained on the base during the test. The angle of repose, denoted as α, was calculated using the formula[2]:

$$\alpha = arctan\left(\frac{H}{D}\right) \quad (1)$$

where $H$ represents the height of the powder cone, and $D$ is the radius of the test base. A lower angle of repose indicates superior flowability. Each sample was measured twice, and the average value was reported to ensure reliability.

### Particle Size Analysis

The particle size parameters, marked as $d_{10}$, $d_{50}$, and $d_{90}$ of the product were determined through sieving. These parameters represent the 10%, 50%, and 90% points in the cumulative undersize particle size distribution. The analysis was performed using a series of sieves with uniformly spaced apertures ranging from 0.05 to 1 mm, arranged on a standard testing sieve shaker. The sample was introduced onto the top sieve, and the sieving process was carried out using mechanical vibration. Upon completion of the sieving, the particles retained on each sieve layer were carefully weighed and recorded. This data enabled the characterization of the particle size distribution and the calculation of the $d_{10}$, $d_{50}$, and $d_{90}$ values.

## METHODOLOGY

### Product Requirements and Constraints

In the case of spherical crystallization of ibuprofen, AVA is directly linked to its flowability, which is critical for its processing and formulation in pharmaceutical applications. A lower angle of repose indicates better flowability, which is essential for ensuring uniform mixing, accurate dosing, and efficient tableting during production. Good flowability of ibuprofen crystals reduces issues such as clogging in machinery and inconsistent tablet weights. Additionally, controlling the particle size of ibuprofen is vital because it affects not only its flowability but also its dissolution rate and bioavailability. Hence, in our research, the aim is to achieve an angle of repose that is as small as possible while ensuring that the median particle size ( $d_{50}$) falls within a certain range, which is specified of 300-450 μm in this study. The mathematical expression for the optimization problem can be formulated as follows:

$$\min_{\boldsymbol{u}} \ tan(\alpha(\boldsymbol{u})) \quad (2)$$

$$s.t. \ 300 < d_{50}(\boldsymbol{u}) < 450$$

$$\boldsymbol{u}_{lower} < \boldsymbol{u} < \boldsymbol{u}_{upper}$$

where $\boldsymbol{u}$ is the 9-dimensional operating condition shown in Table 1, and $\boldsymbol{u}_{lower}$ and $\boldsymbol{u}_{upper}$ correspond to the lower and upper bound of $\boldsymbol{u}$, respectively. It should be noted that the relationship between the input operating conditions $\boldsymbol{u}$ and output (tan $(\alpha)$ and $d_{50}$) is unknown, so both the objective function and the constraints are inferred from experimental observations. In addition, the optimization would be performed based on trial data or feedback from experimental results, without a predefined mechanistic model.

**Table 1:** Experimental conditions $\boldsymbol{u}$ and its upper & lower limits.

| No. | Experimental condition | Lower bound | Upper bound |
|---|---|---|---|
| 1 | Temperature (℃) | 40 | 60 |
| 2 | Stirring speed (rpm) | 300 | 800 |
| 3 | Stirring time (min) | 10 | 20 |
| 4 | Oil-to-water ratio (ml) | 0.25 | 1 |
| 5 | Starch concentration (g/ml) | 3.75 | 20 |
| 6 | Bridging agent concentration (mg/ml) | 2 | 15 |
| 7 | BSA concentration (mg/ml) | 0.05 | 3 |
| 8 | Ibuprofen concentration (mg/ml) | 100 | 350 |
| 9 | Total volume (ml) | 40 | 100 |

### Design of Experiments: DSD-RSM Combination

This section outlines how the problem is addressed through the integration of Definitive Screening Designs and Response Surface Methodology. Initially, DSD is employed to conduct 25 experimental runs, which systematically screen the nine factors involved. This screening process facilitates the identification of the two most

influential factors by evaluating their main effects. Through this approach, the number of factors is effectively reduced, focusing on those that significantly impact the response.

In the second phase, RSM is applied to the two factors selected during DSD. To explore the interactions between these two factors and their effects on the response, a set of 20 experimental runs is designed. This number of experiments allows for a thorough investigation of the factor space, ensuring that both linear and quadratic effects, as well as potential interactions, are captured. Specifically, the process begins with 10 experimental runs to refine the upper and lower bounds of the two factors identified in the screening phase. Subsequently, 10 additional experiments are conducted using Central Composite Design (CCD), a specific approach within RSM, to explore the relationship between the factors within the newly established boundaries. This CCD phase consists of 9 factorial points and 1 center point. The factorial points represent all possible combinations of the three levels (low, center, and high) for each of the two selected factors with newly established boundaries. These points allow for a detailed exploration of the main effects, as well as the quadratic and interaction effects between the factors.

## Bayesian Optimization

In both DSD and RSM methods, experiments are designed at once based on the input space. At the same time, no handling of constraints is performed. This section primarily discusses how BO can adaptively replace the traditional experimental design methods mentioned above, while also addressing unknown constraints.

BO works by constructing a surrogate model (which is a Gaussian Process model in this work) to predict the target function, and it uses a balance between exploration and exploitation to select the next points most likely to improve the objective function, thus efficiently finding the optimal solution. The acquisition function plays a crucial role in determining the next sampling point. It helps balance "exploration" (searching unknown areas of the design space) and "exploitation" (focusing on areas known to give high objective function values). The Lower Confidence Bound (LCB) is one of the acquisition functions used in Bayesian optimization, particularly with Gaussian Process (GP) regression models. LCB is based on a trade-off between the predicted mean and the uncertainty of the target function, allowing for exploration of uncertain regions while also exploiting known good areas. In our problem, the LCB acquisition function can be expressed as follows:

$$\min_{\boldsymbol{u}} \ \mu(\boldsymbol{u}) - \rho.\sigma(\boldsymbol{u}) \tag{3}$$

where $\mu$ and $\sigma$ are the mean and variance of $\tan(\alpha)$ inferred from GP, and $\rho$ is a hyperparameter that controls the balance between exploration and exploitation. While a higher value of $\rho$ encourages exploration of areas with high uncertainty, a lower value encourages exploiting regions with known good performance. Exploration may be more important because GP will have more uncertainty in its predictions initially. Over time, as the model becomes more confident about the objective function's shape, more exploitation can be encouraged. Thus, $\rho$ is related to experimental step $N$ in this paper. Their relationship is as follows:

$$\rho = e^{-\frac{N}{10}+1} \tag{4}$$

As for the constraints, GP is also built for $d_{50}$. In this way, the probability density functions can be calculated, ensuring that the probability of constraints being satisfied is within a given interval[14]. Here, the probability of satisfying the unknown constraints is set to be greater than 80%. Therefore, the acquisition function is updated with the following two additional constraints. They can be expressed as follows:

$$\begin{aligned} &\min_{\boldsymbol{u}} \ \mu(\boldsymbol{u}) - e^{-\frac{N}{10}+1}.\sigma(\boldsymbol{u}) \\ &s.t. \ p(\,d_{50} > 300) > 80\% \\ &\qquad p(\,d_{50} < 450) > 80\% \end{aligned} \tag{5}$$

where $p(.)$ represents he probability density function. Before the optimization process begins, 10 experimental points (e.g., operating condition $\boldsymbol{u}$) will be initially sampled using the Latin Hypercube Sampling method to construct the preliminary GP model. Starting from the 11th point, each subsequent experimental point will be selected sequentially based on Eq. (5).

# RESULT & DISCUSSION

This section examines the outcomes of two experimental design methodologies: traditional DoE and BO. The experimental results for the DSD-RSM combination method are presented in Table 2, while those for BO are detailed in Table 3. Physical insights are also presented.

## Result of DSD-RSM Combination

As shown in Fig. 3, firstly in DSD, two relatively important factors were identified: stirring speed and oil-to-water ratio through DSD. Subsequently, 10 experimental runs were conducted to refine the bound for stirring speed from [300, 800] to [400, 600], and for oil-to-water ratio from [0.25, 1] to [0.6, 1], as illustrated in Table 2. After narrowing the ranges for these key factors, an additional 10 experiments were performed using CCD, a three-level design focusing on stirring speed values of 400, 500, and 600, and oil-to-water ratio values of 0.6, 0.8, and 1, respectively. The experimental results in Table 2 indicate that the smallest AVA identified using the DSD-

**Table 2:** Experimental results of traditional DoE.

| No. | Temperature | Stirring speed | Stirring time | Oil-to-water ratio | Starch concentration | Bridging agent concentration | BSA concentration | Ibuprofen concentration | Total volume | $d_{50}$ | $\tan(\alpha)$ |
|---|---|---|---|---|---|---|---|---|---|---|---|
| **Definitive Screening Design** | | | | | | | | | | | |
| 1 | 40 | 800 | 10 | 0.25 | 3.75 | 0.015 | 3 | 0.35 | 40 | 219.6 | 40.05 |
| 2 | 60 | 800 | 10 | 1 | 20 | 0.002 | 3 | 0.1 | 40 | 133.8 | 41.37 |
| 3 | 60 | 800 | 10 | 0.625 | 20 | 0.015 | 0.05 | 0.35 | 100 | 359.7 | 38.08 |
| 4 | 60 | 800 | 30 | 1 | 3.75 | 0.002 | 0.05 | 0.35 | 40 | 277.4 | 39.53 |
| 5 | 60 | 600 | 30 | 0.25 | 20 | 0.015 | 3 | 0.1 | 40 | 254.9 | 39.39 |
| 6 | 40 | 800 | 10 | 1 | 11.875 | 0.015 | 0.05 | 0.1 | 40 | 236.3 | 39.63 |
| 7 | 60 | 800 | 10 | 0.25 | 3.75 | 0.002 | 3 | 0.225 | 100 | 189.3 | 40.72 |
| 8 | 60 | 400 | 10 | 1 | 3.75 | 0.015 | 1.525 | 0.1 | 100 | 428.6 | 36.42 |
| 9 | 60 | 400 | 30 | 1 | 20 | 0.002 | 0.05 | 0.1 | 100 | 504.2 | 36.42 |
| 10 | 60 | 800 | 30 | 0.25 | 3.75 | 0.015 | 0.05 | 0.1 | 70 | 163.2 | 41.02 |
| 11 | 50 | 400 | 10 | 0.25 | 3.75 | 0.002 | 0.05 | 0.1 | 40 | 223.1 | 39.87 |
| 12 | 60 | 400 | 20 | 1 | 3.75 | 0.015 | 3 | 0.35 | 40 | 603.4 | 37.24 |
| 13 | 40 | 800 | 30 | 0.25 | 20 | 0.002 | 1.525 | 0.35 | 40 | 173.1 | 40.59 |
| 14 | 40 | 800 | 30 | 1 | 3.75 | 0.0085 | 3 | 0.1 | 100 | 241.3 | 39.58 |
| 15 | 50 | 600 | 20 | 0.625 | 11.875 | 0.0085 | 1.525 | 0.225 | 70 | 243.5 | 38.44 |
| 16 | 40 | 600 | 10 | 1 | 3.75 | 0.002 | 0.05 | 0.35 | 100 | 464.3 | 36.76 |
| 17 | 50 | 800 | 30 | 1 | 20 | 0.015 | 3 | 0.35 | 100 | 427.0 | 35.88 |
| 18 | 40 | 400 | 10 | 0.25 | 20 | 0.015 | 3 | 0.1 | 100 | 139.6 | 41.03 |
| 19 | 40 | 400 | 10 | 1 | 20 | 0.002 | 3 | 0.35 | 70 | 493.6 | 36.37 |
| 20 | 60 | 400 | 10 | 0.25 | 20 | 0.0085 | 0.05 | 0.35 | 40 | 370.5 | 37.48 |
| 21 | 40 | 400 | 30 | 0.625 | 3.75 | 0.002 | 3 | 0.1 | 40 | 470.3 | 35.71 |
| 22 | 40 | 800 | 20 | 0.25 | 20 | 0.002 | 0.05 | 0.1 | 100 | 546.6 | 38.82 |
| 23 | 60 | 400 | 30 | 0.25 | 11.875 | 0.002 | 3 | 0.35 | 100 | 428.6 | 35.88 |
| 24 | 40 | 400 | 30 | 0.25 | 3.75 | 0.015 | 0.05 | 0.35 | 100 | 537.3 | 36.75 |
| 25 | 40 | 400 | 30 | 1 | 20 | 0.015 | 0.05 | 0.225 | 40 | 399.5 | 36.94 |
| **Response Surface Methodology** | | | | | | | | | | | |
| 1 | 50 | 400 | 20 | 0.6 | 11.875 | 0.015 | 1.525 | 0.225 | 70 | 383.5 | 37.58 |
| 2 | 50 | 500 | 20 | 0.6 | 11.875 | 0.015 | 1.525 | 0.225 | 70 | 428.7 | 36.67 |
| 3 | 50 | 600 | 20 | 0.6 | 11.875 | 0.015 | 1.525 | 0.225 | 70 | 267.6 | 37.60 |
| 4 | 50 | 700 | 20 | 0.6 | 11.875 | 0.015 | 1.525 | 0.225 | 70 | 249.9 | 38.55 |
| 5 | 50 | 800 | 20 | 0.6 | 11.875 | 0.015 | 1.525 | 0.225 | 70 | 255.3 | 38.67 |
| 6 | 50 | 500 | 20 | 0.25 | 11.875 | 0.015 | 1.525 | 0.225 | 70 | 293.8 | 38.87 |
| 7 | 50 | 500 | 20 | 0.42 | 11.875 | 0.015 | 1.525 | 0.225 | 70 | 337.2 | 37.84 |
| 8 | 50 | 500 | 20 | 0.6 | 11.875 | 0.015 | 1.525 | 0.225 | 70 | 428.7 | 36.67 |
| 9 | 50 | 500 | 20 | 0.8 | 11.875 | 0.015 | 1.525 | 0.225 | 70 | 442.8 | 35.78 |
| 10 | 50 | 500 | 20 | 1 | 11.875 | 0.015 | 1.525 | 0.225 | 70 | 508.2 | 35.19 |
| 11 | 50 | 600 | 20 | 1 | 11.875 | 0.015 | 1.525 | 0.225 | 70 | 421.7 | 36.47 |
| 12 | 50 | 500 | 20 | 0.8 | 11.875 | 0.015 | 1.525 | 0.225 | 70 | 459.8 | 35.63 |
| 13 | 50 | 400 | 20 | 0.6 | 11.875 | 0.015 | 1.525 | 0.225 | 70 | 383.5 | 37.58 |
| 14 | 50 | 500 | 20 | 0.6 | 11.875 | 0.015 | 1.525 | 0.225 | 70 | 428.7 | 36.67 |
| 15 | 50 | 600 | 20 | 0.8 | 11.875 | 0.015 | 1.525 | 0.225 | 70 | 402.5 | 36.53 |
| 16 | 50 | 500 | 20 | 1 | 11.875 | 0.015 | 1.525 | 0.225 | 70 | 508.2 | 35.19 |
| 17 | 50 | 400 | 20 | 0.8 | 11.875 | 0.015 | 1.525 | 0.225 | 70 | 473.9 | 36.89 |
| 18 | 50 | 400 | 20 | 1 | 11.875 | 0.015 | 1.525 | 0.225 | 70 | 404.7 | 36.60 |
| **19** | **50** | **500** | **20** | **0.8** | **11.875** | **0.015** | **1.525** | **0.225** | **70** | **442.8** | **35.78** |
| 20 | 50 | 600 | 20 | 0.6 | 11.875 | 0.015 | 1.525 | 0.225 | 70 | 267.6 | 37.60 |

RSM combination, while meeting the $d_{50}$ constraints, occurs at the center point of the CCD phase with the value of 35.78. Interestingly, this center point was tested twice during the CCD phase—once satisfying the constraints and once failing to do so (see "Response Surface Methodology", No. 12 and 19 in Table 2). This is because each experiment inevitably involved some deviations. The $d_{50}$ boundary we set ranges from 300 to 450 μm. In the two repeated experiments, one yielded a $d_{50}$ value of 442.8, while the other resulted in 459.8. This also indicates that under the experimental conditions of 12$^{th}$ and 19$^{th}$ runs, $d_{50}$ is generally close to the upper boundary of 450.

The experimental results align with the underlying physical principles governing the crystallization process. Higher stirring speed results in finer particles with rougher surfaces, increasing friction and reducing flowability. However, very low stirring speeds can lead to unsuccessful crystallization. Meanwhile, a higher oil-to-water ratio improves size uniformity, enhancing flowability through reduced friction and narrower particle size distribution. To conclude, these two factors—stirring speed and oil-to-water ratio—significantly affect both $d_{50}$ and

**Table 3:** Experimental results of BO.

| No. | Temperature | Stirring speed | Stirring time | Oil-to-water ratio | Starch concentration | Bridging agent concentration | BSA concentration | Ibuprofen concentration | Total volume | $d_{50}$ | $\tan(\alpha)$ |
|---|---|---|---|---|---|---|---|---|---|---|---|
| 1 | 52.62 | 592.82 | 13.47 | 0.64 | 6.13 | 15.00 | 2.38 | 113.41 | 73.28 | 330.60 | 38.47 |
| 2 | 42.47 | 416.80 | 15.31 | 0.56 | 7.29 | 2.87 | 2.44 | 150.01 | 83.92 | 285.00 | 38.86 |
| **3** | **58.31** | **452.50** | **12.09** | **0.74** | **16.52** | **7.05** | **2.73** | **312.25** | **93.78** | **397.60** | **35.84** |
| 4 | 46.97 | 645.45 | 17.96 | 0.80 | 9.98 | 9.92 | 2.73 | 246.26 | 44.51 | 394.10 | 36.34 |
| 5 | 55.92 | 656.39 | 11.61 | 0.47 | 18.31 | 11.66 | 0.48 | 214.30 | 47.52 | 304.80 | 38.07 |
| 6 | 49.87 | 741.03 | 14.95 | 0.54 | 18.55 | 9.36 | 1.93 | 250.12 | 77.02 | 303.50 | 38.39 |
| 7 | 50.61 | 769.89 | 18.13 | 0.36 | 14.22 | 5.27 | 0.90 | 341.40 | 63.19 | 301.30 | 38.75 |
| 8 | 57.59 | 546.06 | 16.75 | 0.94 | 4.90 | 7.32 | 1.18 | 132.18 | 65.79 | 533.80 | 35.12 |
| 9 | 44.32 | 380.83 | 10.57 | 0.85 | 12.22 | 12.92 | 1.26 | 280.98 | 95.67 | 564.80 | 37.27 |
| 10 | 40.53 | 344.16 | 19.94 | 0.26 | 11.41 | 3.96 | 1.64 | 186.97 | 56.35 | 232.70 | 39.62 |
| 11 | 60.00 | 602.57 | 20.00 | 1.00 | 3.75 | 5.33 | 0.13 | 145.05 | 57.42 | 418.40 | 35.97 |
| 12 | 41.54 | 760.26 | 20.00 | 1.00 | 6.65 | 2.49 | 3.00 | 279.11 | 89.00 | 284.40 | 38.89 |
| 13 | 46.87 | 629.18 | 20.00 | 1.00 | 5.26 | 8.06 | 3.00 | 252.84 | 40.00 | 398.15 | 36.59 |
| 14 | 40.00 | 669.12 | 20.00 | 0.54 | 20.00 | 14.48 | 3.00 | 256.25 | 63.55 | 157.00 | 40.82 |
| 15 | 60.00 | 610.82 | 20.00 | 1.00 | 3.75 | 2.00 | 3.00 | 141.33 | 40.00 | 242.58 | 39.20 |
| 16 | 56.69 | 590.76 | 19.36 | 1.00 | 3.75 | 12.27 | 0.05 | 114.77 | 91.92 | 421.39 | 36.35 |
| 17 | 50.71 | 675.59 | 12.08 | 0.84 | 3.75 | 10.05 | 0.05 | 231.44 | 43.52 | 210.05 | 39.89 |
| 18 | 60.00 | 600.24 | 20.00 | 1.00 | 3.75 | 5.60 | 0.05 | 145.42 | 59.70 | 395.15 | 36.30 |
| 19 | 60.00 | 471.27 | 12.47 | 0.71 | 17.70 | 5.50 | 3.00 | 320.76 | 93.37 | 381.73 | 36.15 |
| 20 | 57.12 | 443.52 | 11.91 | 0.75 | 15.96 | 7.79 | 2.58 | 308.24 | 93.99 | 395.97 | 36.45 |
| 21 | 58.93 | 460.41 | 12.25 | 0.73 | 17.02 | 6.39 | 2.81 | 315.85 | 93.61 | 402.42 | 36.05 |
| 22 | 60.00 | 604.58 | 20.00 | 1.00 | 3.75 | 5.22 | 0.05 | 146.70 | 56.40 | 342.46 | 37.25 |
| 23 | 60.00 | 456.00 | 12.54 | 0.97 | 15.74 | 7.17 | 3.00 | 308.60 | 92.15 | 451.44 | 35.88 |
| 24 | 58.65 | 453.82 | 12.13 | 0.74 | 16.57 | 6.95 | 2.78 | 312.69 | 93.70 | 390.2 | 36.00 |
| 25 | 56.73 | 449.72 | 12.03 | 0.74 | 16.37 | 7.27 | 2.54 | 311.13 | 93.88 | 396.7 | 36.21 |

$\alpha$, and they were selected as critical variables in the experimental design. For stirring speed, a lower value tends to produce larger particles with smoother surface comparing to the fines, which corresponds to the smaller values observed in our optimized results. The initial range was 300 to 800, with 500 as the traditional experimental design value. For the oil-to-water ratio, a relatively higher value produces more uniform particles. The initial range was 0.25 to 1, and the traditional experimental design value was 0.8.

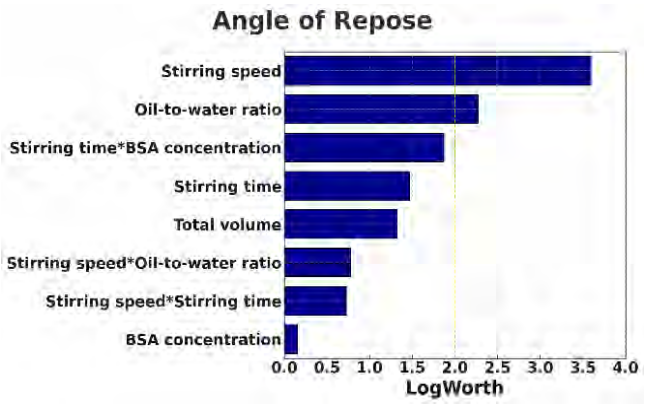



**Figure 3.** Analysis of definitive screening design.

## Result of BO

As illustrated in Table 3, the smallest AVA identified while meeting the $d_{50}$ constraints using BO occurs at the third experiments, with the value of 35.84. In the sequential Bayesian experiments, runs 19, 20, 21, 23, 24, and 25 were all very close to the third experimental design. This indicates that the Bayesian optimization is nearing convergence. However, it is unfortunate that despite searching around the current optimal region, no experimental condition was found that outperforms the result of 35.84 achieved in the third run.

Comparing BO to DSD-RSM combination where a total of 45 experiments were conducted, BO only required 25 experiments, thus saving 55% of the experimental time up to 80 hours. In BO, 16 out of 25 experiments satisfied the constraints, resulting in a proportion of 64%. In contrast, in the DoE, 18 out of 45 experiments satisfied the constraints, with a proportion of 40%. In terms of costs, optimizing spherical crystallization conserves nearly half of the solvent and drug materials, making it highly efficient in resource usage.

At the same time, BO shows consistency with DSD-RSM combination in the final optimization results. The ranges for the two key variables identified through DSD-RSM combination: stirring speed [400, 600] and oil-to-water ratio [0.6, 1]. The optimal experimental values obtained through BO for stirring speed and oil-to-water ratio are 452.5 and 0.74, respectively. In the last 8 experiments of BO, 7 of the experiments yielded data within this range.

## CONCLUSION

In summary, this study compared two experimental design methods: the traditional DoE and BO, to identify the optimal conditions for stirring speed and oil-to-water ratio. Overall, both methods produced similar optimal values, with BO providing a more efficient way to identify optimal conditions while maintaining reliability. It is important to note that the research in this paper is purely data-driven, and the integration of mechanistic insights could provide additional improvements in the optimization process. Therefore, future research may focus on incorporating mechanistic knowledge into BO to enhance the efficiency of experimental design. For example, if key factors influencing experimental outcomes are known in advance through mechanistic knowledge, the focus can be directed toward these critical factors, thereby reducing the number of experiments required. Additionally, the presence of a mechanistic model may accelerate the experimental process further.

## ACKNOWLEDGEMENTS

Financial support of the "Pioneer" and "Leading Goose" R&D Program of Zhejiang (No. 2024C01028) and the State Key Laboratory of Industrial Control Technology, China (No. ICT2024C04) are gratefully acknowledged.

## REFERENCES

1. Saini, S., *Spherical Crystallization: An Overview.* Int. J. Drug Delivery Technol, 2014. **4**(4): p. 72-80 https://www.researchgate.net/publication/267155019_Spherical_Crystallization_An_Overview.
2. Bharti, N., et al., *Spherical crystallization: a novel drug delivery approach.* Asian journal of biomedical and pharmaceutical sciences, 2013. **3**(18): p. 10
3. Kovačič, B., F. Vrečer, and O. Planinšek, *Spherical crystallization of drugs.* Acta pharmaceutica, 2012. **62**(1): p. 1-14 https://sciendo.com/article/10.2478/v10007-012-0010-5.
4. Gyulai, O., et al., *Optimization of the Critical Parameters of the Spherical Agglomeration Crystallization Method by the Application of the Quality by Design Approach.* Materials, 2018. **11**(4) https://www.mdpi.com/1996-1944/11/4/635.
5. Czitrom, V., *One-Factor-at-a-Time versus Designed Experiments.* The American Statistician, 1999. **53**(2): p. 126-131 https://www.tandfonline.com/doi/abs/10.1080/00031305.1999.10474445.
6. Köçkar, H. and N. Kaplan, *Investigation of soft magnetic properties of Ni/Cu multilayer films: Definitive screening design and response surface methodology.* Journal of Materials Science: Materials in Electronics, 2021. **32**(16): p. 20955-20964 https://doi.org/10.1007/s10854-021-06506-0.
7. Shahriari, B., et al., *Taking the Human Out of the Loop: A Review of Bayesian Optimization.* Proceedings of the IEEE, 2016. **104**(1): p. 148-175 https://doi.org/10.1109/JPROC.2015.2494218.
8. Frazier, P.I.J.a.e.-p., *A Tutorial on Bayesian Optimization.* 2018: p. arXiv:1807.02811 https://ui.adsabs.harvard.edu/abs/2018arXiv180702811F.
9. Sano, S., et al., *Application of Bayesian optimization for pharmaceutical product development.* Journal of Pharmaceutical Innovation, 2020. **15**: p. 333-343 https://link.springer.com/article/10.1007/s12247-019-09382-8.
10. Marchant, R. and F. Ramos, *Bayesian optimisation for intelligent environmental monitoring.* p. 2242-2249 https://ieeexplore.ieee.org/document/6385653.
11. Junge, K., et al., *Improving Robotic Cooking Using Batch Bayesian Optimization.* IEEE Robotics and Automation Letters, 2020. **5**(2): p. 760-765 https://ieeexplore.ieee.org/document/8954776.
12. Wang, J., et al., *A Novel Spherical Crystallization Method Using Pickering Emulsions.* Journal of Pharmaceutical Sciences, 2022. **111**(6): p. 1625-1632 https://www.sciencedirect.com/science/article/pii/S0022354921005694.
13. Song, Y., et al., *Quinoa starch-based Pickering emulsions with small-molecule oil solvents: Exploring solvent varieties and depletion attraction.* Chemical Engineering Science, 2024. **299**: p. 120545 https://www.sciencedirect.com/science/article/pii/S0009250924008455.
14. Gelbart, M.A., J. Snoek, and R.P. Adams, *Bayesian Optimization with Unknown Constraints.* 2014 https://doi.org/10.48550/arXiv.1403.5607.

© 2025 by the authors. Licensed to PSEcommunity.org and PSE Press. This is an open access article under the creative commons CC-BY-SA licensing terms. Credit must be given to creator and adaptations must be shared under the same terms. See https://creativecommons.org/licenses/by-sa/4.0/



Systems & Control Transactions

**Research Article - Peer Reviewed Conference Proceeding**
ESCAPE 35 - European Symposium on Computer Aided Process Engineering
Ghent, Belgium. 6-9 July 2025
Jan F.M. Van Impe, Grégoire Léonard, Satyajeet S. Bhonsale,
Monika E. Polańska, Filip Logist (Eds.)

PSE PRESS

# Probabilistic Design Space Identification for Upstream Bioprocesses under Limited Data Availability

**Ranjith Chiplunkar[a,b], Syazana Mohamad Pauzi[a,b], Steven Sachio[a,b], Maria M Papathanasiou[a,b]*, and Cleo Kontoravdi[a,b]***

[a] The Sargent Centre for Process Systems Engineering, Imperial College London, London SW7 2AZ, United Kingdom
[b] Department of Chemical Engineering, Imperial College London, London SW7 2AZ, United Kingdom
* Corresponding Authors: maria.papathanasiou11@imperial.ac.uk, cleo.kontoravdi98@imperial.ac.uk

## ABSTRACT

Design space identification (DSId) and flexibility analysis are critical in process systems engineering, enabling efficient design of operating conditions. For bioprocess, these tasks are often hindered by the absence of reliable mechanistic models and limited experimental data. This paper presents an algorithm to address these challenges in bioprocesses. The methodology begins by constructing a Gaussian process (GP) model to predict key performance indicators (KPIs) from process inputs. Leveraging the probabilistic nature of GP predictions, we perform probabilistic design space identification (PDSId), characterizing each input point by its probability of feasibility which is the likelihood that constraints imposed on KPIs are satisfied. To visualize and analyse the feasibility space, contours at varying probability levels are identified using alpha shapes, which define deterministic boundaries corresponding to different confidence levels. This enables the quantification of volumetric process flexibility and operating ranges for each confidence level. The proposed methodology is applied to an antibody-producing Chinese hamster ovary (CHO) cell culture process, optimizing culture temperature and osmolality with respect to product yield and purity. Results are presented through probability heat maps and flexibility metrics, providing both qualitative and quantitative insights into feasibility and operational flexibility, thereby supporting informed decision-making in process design.

**Keywords**: Biosystems, Probabilistic design space identification, Flexibility analysis, Upstream bioprocesses

## INTRODUCTION

Achieving efficient and reliable operations in complex large-scale systems, such as bioprocesses, requires carefully designed process conditions. In the biopharmaceutical industry, operational reliability is commonly assessed through key performance indicators (KPIs) like yield and purity meeting the established standards consistently. In this regard, design space identification (DSId) is a critical method for evaluating the feasibility of operating conditions. DSId involves isolating a subset of the broader knowledge space that encompasses all possible process inputs and satisfies the constraints imposed on the KPIs [1]. This subset, known as the design space, facilitates the evaluation of operating points and serves as a practical tool for process operators to assess the feasibility of the operating conditions.

Design space identification (DSId) methodologies are broadly classified into model-based and data-driven approaches. In the context of bioprocesses, model-based methods are generally preferred due to the impracticality of extensive experimentation. For instance, Yang and Ierapetritou [2] developed a modeling framework for DSId of a bioreactor producing monoclonal antibodies (mAbs). Similarly, Sachio et al. [3] proposed a model-based methodology for design space identification in chromatographic separation columns, encompassing the construction of geometric boundaries to enclose the design space and the quantification of its size to evaluate operational flexibility.

While mechanistic model-based approaches are effective in capturing the complexities of bioprocesses, they are often computationally demanding for DSId applications, primarily due to the need for extensive

sampling across the knowledge space to identify the design space accurately. To mitigate this computational burden, adaptive sampling techniques have been introduced, aiming to reduce the number of model evaluations required [4, 5]. Additionally, surrogate models have emerged as an efficient alternative for feasibility assessments, leveraging less computationally intensive techniques. Surrogate models such as Kriging regression [6] and artificial neural networks [7] have demonstrated significant potential in approximating complex process behaviors while minimizing computational overhead.

Process models are often parameterized using experimental data, which introduces stochasticity and parametric uncertainties, often related to measurement noise. As a result, the compliance of the KPI constraints cannot be determined definitively but only with a degree of confidence. Probabilistic design space identification (PDSId) addresses this by assigning each point in the knowledge space a probability of feasibility instead of a binary classification of feasible or infeasible. PDSId, however, increases computational complexity, requiring additional simulations across the uncertain parameter space. To address this, Laky et al. [8] proposed an optimization-based PDSId and flexibility analysis approach. Kusumo et al. [9] introduced a nested sampling strategy that prioritized maintaining high sample density in regions with a high probability of feasibility. Kucherenko et al. [10] developed an adaptive sampling method leveraging a metamodel that directly predicted the probability of feasibility based on the parameter space.

Research in DSId and PDSId typically assumes the availability of a mechanistic model. However, for complex systems like upstream biopharmaceutical processes, developing reliable mechanistic models is challenging due to a limited understanding of underlying mechanisms (e.g., host cell protein generation) or the need for simplifying assumptions. Consequently, data-driven approaches may be preferred as alternatives due to their ease of modeling. However, they often require extensive experimentation, which can be expensive and impractical, leading to sparse datasets. Such sparsity also means that data uncertainty becomes a significant factor that needs to be addressed.

We present a data-driven approach to address the challenges of modeling uncertainties in complex bioprocess systems. Specifically, we use Gaussian Process (GP) models to account for real-world data uncertainties stemming from measurement noise and inherent inter-experimental variability, enabling a probabilistic characterization of the design space. The framework consists of two main components. First, the GP model predicts key performance indicators (KPIs) based on input process variables, facilitating probabilistic modeling of these KPIs. The probability of feasibility is then calculated based on performance constraints, which indicates the likelihood of meeting the KPI constraints for a given input. The second step of the framework conducts a quantitative analysis of operational flexibility for a given point. Following the method proposed by Sachio et al. [3], alpha shapes are used to define deterministic boundaries at varying levels of feasibility probabilities, allowing the quantification of process flexibility and operational ranges. This enables a detailed examination of trade-offs between process flexibility, performance, and confidence levels.

The framework is applied to experimental data from a fed-batch Chinese hamster ovary (CHO) cell culture producing a mAb to study the effects of osmolality and temperature on mAb yield and cell-derived impurity (host cell protein, HCP) generation. The results are visualized through probabilistic heat maps and flexibility metrics, offering valuable insights for process development.

## METHODOLOGY

### Experimental Setup

This study aims to investigate the effects of two critical upstream process parameters, culture temperature and osmolality, on HCP generation in mAb-producing CHO cell culture and their subsequent clearance in affinity and cation exchange chromatographic purification. Fed-batch culture was initiated at a seeding density of $2 \times 10^5$ cells/ml in 30 ml shake flasks using CD CHO medium (ThermoFisher Scientific, U.K.). The culture was incubated at 36.5°C with 8% $CO_2$ humidified air, shaking at 140 rpm. Every two days, 10% v/v EfficientFeed™ C+ AGT™ Supplement was added to each culture (ThermoFisher Scientific, U.K.). On day 5, as the culture entered the exponential phase, temperature and osmolality were manipulated while maintaining the desired viable cell count.

The study employs a central composite face-centered (CCF) design with two replicates, resulting in a total of 18 experimental runs manipulating three levels of temperature and osmolality. Specifically, temperature is varied between 32°C and 36.5°C, with 34°C as the middle level, on day 5. Osmolality is set between 410 mOsm/kg and 500 mOsm/kg, with a midpoint of 455 mOsm/kg, again on day 5 of the culture, starting from a value of 410 mOsm/kg. Osmolality was adjusted using 5M sterile NaCl, and OsmotechXT (Advanced Instruments Companies, U.K.) was used to measure the osmolality with a tolerance of 20 mOsm/kg. The culture was harvested when cell viability dropped below 80%.

Cell density and viability were determined daily using the trypan blue dye exclusion method and inverse microscopy. The extracellular mAb concentration was quantified using the biolayer interferometry BLItz system (Sartorius Stedim, U.K.). Residual HCP concentration was measured using the CHO cell HCP ELISA kit from Cygnus

Technologies, U.S.

## Probabilistic Design Space Identification

The proposed methodology performs PDSId based on a GP model identified using the data obtained from the experiments described earlier.

### GP model to predict KPIs

In this study, we assume that the uncertainties in the system model and measurement noise can be modeled using Gaussian distributions. Hence, we adopt the GP modeling framework to model the KPIs. GP regression is a nonparametric, nonlinear modeling technique that is particularly effective in scenarios with limited data and inherent model uncertainty. Its strong interpolation capabilities make it well-suited for cases where data is obtained through factorial designs that emphasize the extreme ends of input variability.

Let $y$ and $u$ represent the KPIs and input actions, respectively. The Gaussian process model used to predict the KPIs is expressed as follows.

$$\mathrm{y} = \mathrm{f}(u) + \mathrm{e} \tag{1}$$

Here, $\mathrm{f}(\cdot)$ represents the system model and $e$ represents the measurement noise which is Gaussian with a mean of zero and variance of $\sigma^2$, represented as $\mathcal{N}(0, \sigma^2)$. A GP model learns the function $\mathrm{f}(\cdot)$ as a Gaussian probability distribution function rather than a deterministic entity. Hence, the predictions of KPIs would also be gaussian distributions. Let $\mathcal{U}_\mathcal{T}$ and $\mathcal{Y}_\mathcal{T}$ represent training data used to train the GP model. For any new point $u_*$ in the knowledge space, the KPI prediction is a Gaussian distribution with the mean $\mu_*$ and variance $\Sigma_*$ expressed as follows:

$$\mu_* = \mu(u_*) + \Sigma(u_*, \mathcal{U}_\mathcal{T})(\Sigma(\mathcal{U}_\mathcal{T}, \mathcal{U}_\mathcal{T}) + \sigma_\epsilon^2 \cdot I_{N\times N})^{-1}(\mathcal{Y}_\mathcal{T} - \mu(\mathcal{U}_\mathcal{T})) \tag{2}$$

$$\Sigma_* = \Sigma(\mathrm{u}_*, \mathrm{u}_*) - \Sigma(\mathrm{u}_*, \mathcal{U}_\mathcal{T})(\Sigma(\mathcal{U}_\mathcal{T}, \mathcal{U}_\mathcal{T}) + \sigma^2 \cdot \mathrm{I}_{\mathrm{N}\times\mathrm{N}})^{-1}\Sigma(\mathcal{U}_\mathcal{T}, \mathrm{u}_*) \tag{3}$$

Here, $\mu(\cdot)$ and $\Sigma(\cdot)$ represent the mean and covariance functions of the prior distribution of the function. For the sake of brevity, the detailed explanation of GP modeling is omitted here, and readers are directed to Schulz et al. [11] for further information.

### Estimating the probability of feasibility

Let us consider the DSId problem for the system with the following model and the constraints.

$$y = f(u); \quad u \in [u_l, u_u] \tag{4}$$

$$g(y) < 0 \tag{5}$$

In Eq. (4), $u \in [u_l, u_u]$ represents the knowledge space and Eq. (5) represents the constrains on the system. In this work we consider the case where the constraints are directly imposed on the KPIs $y$ which are represented as given below.

$$y_l \leq y \leq y_u \tag{6}$$

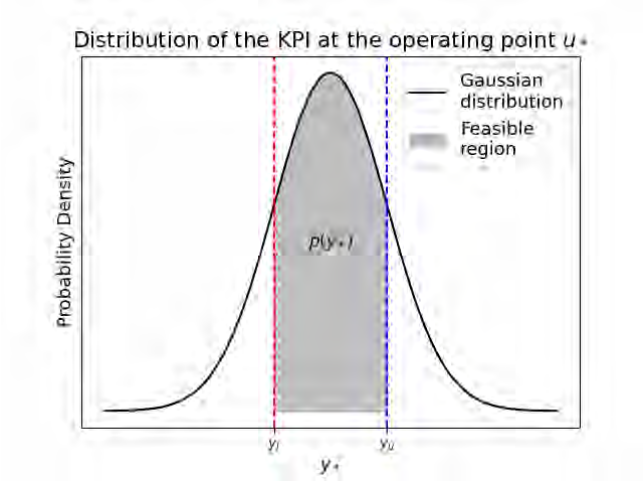



**Figure 1.** Depiction of the calculation of the probability of feasibility.

Here, $y_l$ and $y_u$ represent the lower and upper limits on the KPIs. With every point in the knowledge space being associated with its corresponding predicted KPI distribution, as described in the previous section, we proceed to estimate the probability of feasibility for the corresponding input point. In PDSId, the probability of feasibility for a given input $u_*$ is defined as the probability with which the constraints specified in Eq. (6) are satisfied. Mathematically, it can be expressed as:

$$\mathrm{p}(u_*) = \int_{y_l}^{y_u} p(y_*|u_*)\, dy_* \tag{7}$$

The above equation calculates the area under the distribution of the KPI at the operating point of $u_*$ in the feasibility region. The quantity $p(u_*)$ hence denotes the probability at which the given operating point $u_*$ is guaranteed to satisfy the constraints imposed on the KPIs. For the case of a Gaussian distribution and a single KPI, the probability of feasibility is represented as follows:

$$\mathrm{p}(u_*) = \Phi\left(\frac{y_u - \mu_*}{\Sigma_*^{0.5}}\right) - \Phi\left(\frac{y_l - \mu_*}{\Sigma_*^{0.5}}\right) \tag{8}$$

Here, $\Phi(\cdot)$ represents the cumulative distribution function of a Gaussian distribution. The calculation of $p(u_*)$ is depicted in Fig. 1 where the shaded area between $y_l$ and $y_u$ represents the probability of feasibility. To characterize whole knowledge space with a probability of feasibility, we sample uniformly from the knowledge space using Sobol sequence. For each sample of $u_* \in [u_l, u_u]$ generated, the predicted KPI distribution is obtained using Eq. (2) and (3), following which the probability of feasibility is evaluated as per Eq. (8). This results in every possible

point in the knowledge space being characterized by a probability of feasibility. The results are visualized through the usage of probability heat maps which are presented in the Results and Discussion section.

While the probability of feasibility provides valuable information regarding feasibility, to facilitate further analysis, we draw contours at different probability levels and quantify the operational flexibility at each level, as described in the next section.

## Quantitative Flexibility Assessment

To further enhance process understanding, we propose a deterministic quantitative flexibility assessment approach that builds upon the identified probabilistic design space. This method enables the quantification of process flexibility by defining deterministic boundaries at varying levels of probability of feasibility and computing a volumetric flexibility index for each level. By integrating both probabilistic information and geometric representations, this approach provides a structured way to assess the robustness and adaptability of the design space.

To achieve this, we employ alpha shapes as a geometric tool to delineate deterministic boundaries of the probabilistic design space. An alpha shape defines the spatial extent of a given set of points and can represent both convex and non-convex regions by adjusting a parameter known as the alpha radius. At large alpha radius values, the alpha shape becomes identical to a convex hull. As the alpha radius decreases, the alpha shape becomes increasingly non-convex. Alpha shapes can be exploited to identify design spaces as described in Sachio et al [3]. Briefly, the method has three major steps:

**Step 1. Model sampling.** The GP model is sampled via quasi-random Sobol sampling to obtain a dense dataset containing 16384 ($2^{14}$) input combinations and their corresponding probability of feasibility. In this work, we are working with 2D problems and hence 16384 samples is more than enough for an accurate analysis [3].

**Step 2. Point cloud classification.** A set of $n_p$ different levels of feasibility probability is defined which is used as the constraints to characterize $n_p$ alpha design spaces [3]. For a single feasible probability level, for example ≥ 95%, the dataset is screened by separating the points which satisfy ≥ 95% from those which violate it. The group of points which satisfy this constraint forms the satisfied point cloud. The rest of the points form the violated point cloud.

**Step 3. Alpha shape construction.** An alpha shape is formed by solving for the alpha radius which defines the space occupied by the satisfied point cloud and does not capture any violated points. The resulting alpha shape is the alpha design space, with an explicit definition of the boundary and quantifiable size (volumetric flexibility metric). The schematic of the proposed methodology is presented in Fig. 2.

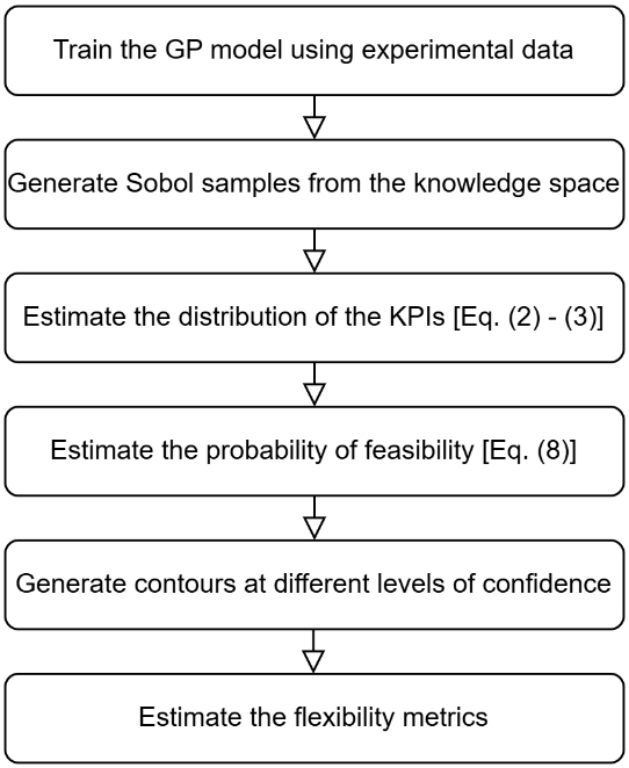



**Figure 2.** Schematic representation of the proposed methodology.

# RESULTS AND DISCUSSION

The experimental data comprises 18 data points derived from a 2-factor, 3-level factorial design with two replicates for each operating condition. The inputs are the Osmolality ($O$) and Temperature ($T$) while the outputs are the Yield and the ratio of HCP to mAb concentration. A general heuristic regarding GP regression is that it requires 10 points per regressor, which would be 20 for two regressors. This is close to 18 points; however, 9 of these are at the same input conditions.

Of the 18 points, 12 are used to train the GP model, and 6 are reserved for validation. Gaussian process regression with a co-regionalized RBF kernel is trained in Python. The average values for mAb yield and HCP-to-mAb concentration ratio (HCP/mAb) in the experiments are 1.25 and 0.25, respectively. Therefore, the KPI constraints are defined such that the minimum mAb yield is 1.25, and the maximum HCP/mAb ratio is 0.25. Consequently, the constraints for the KPIs are as follows:

$$1.25 \leq Yield\,; \quad \mathrm{HCP/mAb} \leq 0.25 \tag{9}$$

## KPI Predictions in the Knowledge Space

First, the GP model is trained, and the Sobol samples generated from the knowledge space are used to predict

the distribution of the KPIs. Figure 3 illustrates the mean of the KPIs for each input in the knowledge space, providing a convenient way to visualize KPI variability within the knowledge space. It can be observed that higher temperatures and mid-level osmolality values generally favor higher yields, with mid-level osmolality also resulting in lower HCP concentrations.

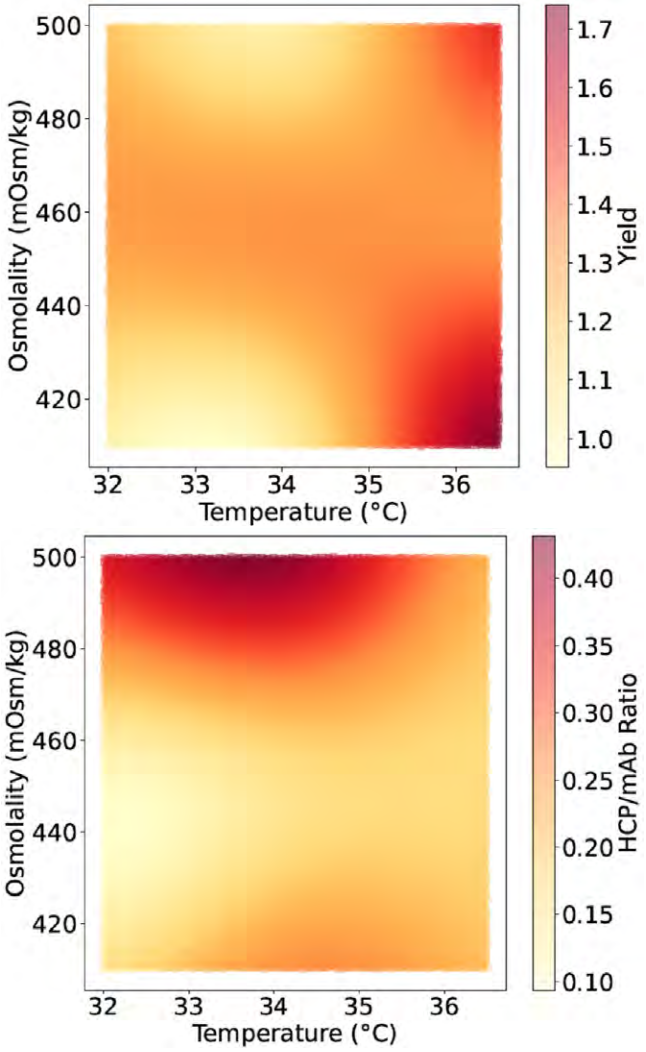



**Figure 3.** Heat map depicting the means of the predicted KPIs.

However, there are operating points, such as [$T$, $O$] ≈ [32 – 33, 440-440] which can achieve high purity but low yield. Hence, one must combine all the KPI constraints to better assess these trade-offs, which is the DS representation of the feasibility analysis.

## Probabilistic Design Space Identification

To visualize the design space with respect to both KPIs, the probability of feasibility is estimated for each point in the knowledge space, and the results are presented in Fig. 4. This heatmap, shows regions with higher probabilities of satisfying the constraints in warmer red tones, while lower probability regions are represented in yellow tones.

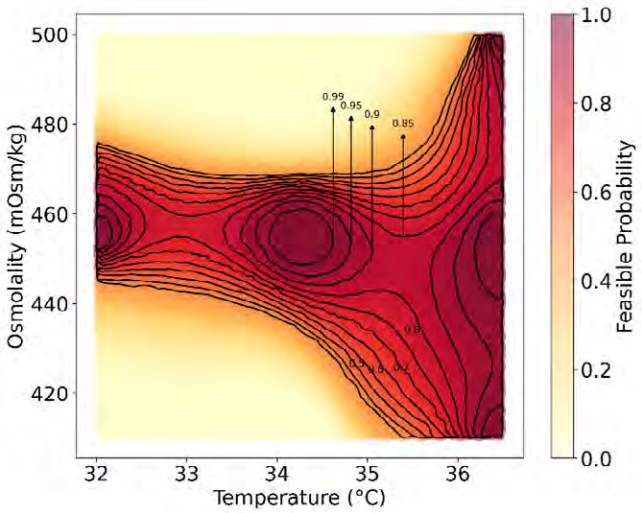



**Figure 4.** Probability heat map with the contours at different levels of confidence.

The results indicate that the constraints in Eq. (9) are likely to be satisfied in the regions where [$T$, $O$] are [34.25, 455] and [36.5, 410-500]. Thus, higher temperatures allow for more variability in osmolality while satisfying the KPI constraints. This is because higher temperatures promote cell growth and productivity, while lower temperatures may prolong the culture duration but can also lead to increased host cell protein accumulation. To gain further insights, the alpha shapes-based boundary detection method is applied to obtain contours at different probability levels. A contour at a confidence level $\alpha$ encloses all points with a probability of feasibility greater than or equal to $\alpha$. In Fig. 4, contours are provided for probability values of [0.99, 0.95, 0.90, 0.85, 0.80, 0.77, 0.70, 0.65, 0.60, 0.55, 0.5], with the lowest level set at 0.5, as this is typically the threshold for accepting or rejecting an operating point. The heatmap representation provides a convenient way to visualize the design space and derive insights into how feasibility varies across the knowledge space.

## Flexibility Assessment

To quantify the information depicted in the contours, the volumes of the space enclosed by each contour can be calculated. This provides a means of assessing the flexibility of operation at different confidence levels. The volumes for the heatmap in Fig. 4 are presented in Fig. 5. These volumes are normalized to represent the fraction of the total knowledge space enclosed within the contour. For instance, operating at a probability of feasibility of at least 90% probability of feasibility offers flexibility within up to 10% of the total knowledge

space. In addition to assessing flexibility, this approach allows for the evaluation of the trade-off between flexibility and confidence level, where a higher confidence level reduces flexibility and vice versa.

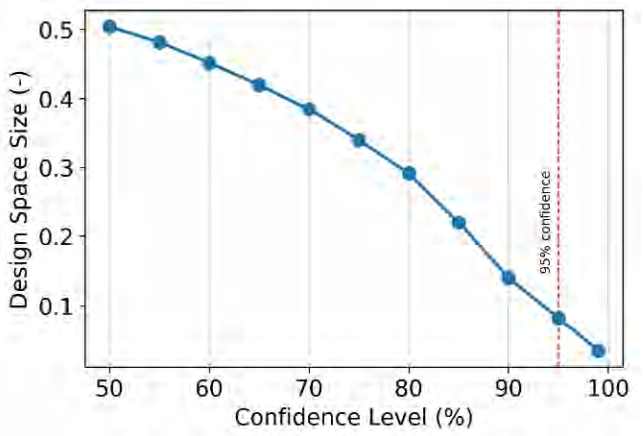



**Figure 5.** Design space size at various levels of confidence as a metric of flexibility in operation.

## Design space for different KPI constraints

Finally, if the DS for a particular KPI constraint does not meet the desired criteria, alternative constraints can be explored to assess feasibility and flexibility for different operating goals. Figure 6 illustrates this exploration across four scenarios. To maintain clarity, we plot the contours of 50% probability of feasibility, and the flexibility metrics for all the levels mentioned earlier are shown in Fig. 7.

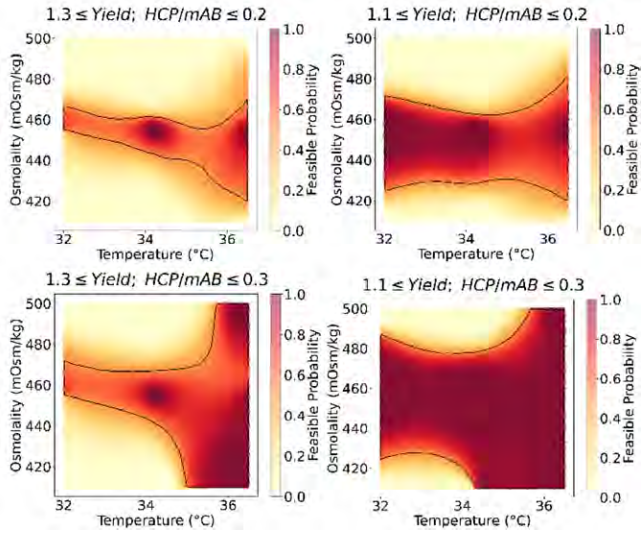



**Figure 6.** Probability heat map for different KPI constraints

The first scenario represents a stringent case, requiring a yield of at least 1.3 and an HCP/mAb ratio of at most 0.2. In the second scenario, the yield constraint is relaxed to 1.1, which increases the DS. In this case, mid-level osmolality and lower temperatures are preferred. The third scenario sets the minimum yield to 1.3, while relaxing the HCP/mAb constraint to 0.3. Here, higher temperatures and lower osmolality are generally favored. Finally, both yield and purity constraints are relaxed to 1.1 and 0.3, respectively, resulting in a significantly larger DS. These trends align with empirical expectations. This can also be observed in Fig. 7, which compares the size of the design space at different levels of probability of feasibility for various KPI constraints. The most ambitious constraints, such as high yield and low impurity, lead to a smaller design space at every probability level, while relaxed constraints result in a larger design space. This representation provides a bird's-eye view of the trade-offs between the required probability of feasibility, operational flexibility, and the ambitiousness of the KPI constraints. Experimental validation of these computational findings is underway.

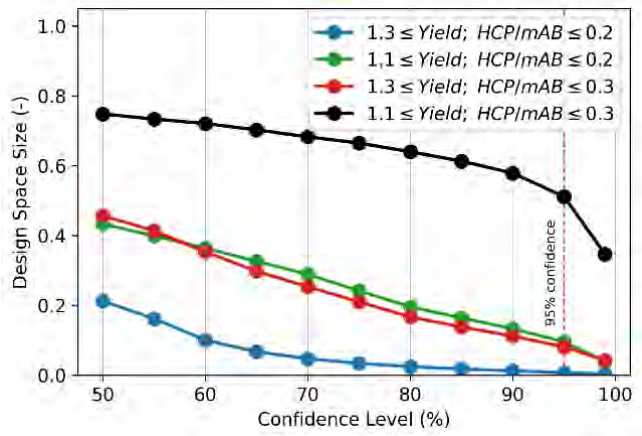



**Figure 7.** Comparing the design space sizes for various KPI constraints

## CONCLUSION

Assessment of the feasibility of operating points and the flexibility of those operations is vital for novel and complex processes such as bioprocesses. This paper presents a methodology to achieve these goals for systems with limited understanding. The methodology includes three key features: estimating the probability of feasibility of an operating point, identifying the design space for a given probability of feasibility or confidence level, and quantifying the flexibility of operations at a given confidence level. The obtained results are presented through probabilistic heat maps and flexibility metrics, providing actionable insights for process development scientists. In the presented CHO cell study, initial experimental data was used to develop a GP model of how two process conditions, temperature, and osmolality, affect recombinant product yield and purity.

Subsequent system analysis using the proposed methodology provided insights for balancing purity-yield trade-offs and guide further experimentation and process design. The future research focus is on performing additional experiments to confirm the DS and improve the accuracy of the model.

## ACKNOWLEDGEMENTS

The authors gratefully acknowledge funding from the Engineering and Physical Sciences Research Council U.K. (EP/X024156/1 and EP/W035006/1). Support from the UKRI Impact Acceleration Account (EP/X52556X/1) is also gratefully acknowledged. Additionally, Mohamad Pauzi, S. acknowledges the Ministry of Higher Education, Malaysia, for awarding a scholarship through the IPTA Academic Training Scheme, as well as Universiti Teknologi MARA, Malaysia, for the Academic Staff Scholarship.

## REFERENCES

1. Kasemiire A, Avohou HT, De Bleye C, Sacre PY, Dumont E, Hubert P, Ziemons E. Design of experiments and design space approaches in the pharmaceutical bioprocess optimization. *European Journal of Pharmaceutics and Biopharmaceutics*. 2021 Sep 1;166:144-54.
2. Yang O, Ierapetritou M. mAb production modeling and design space evaluation including glycosylation process. *Processes*. 2021 Feb 9;9(2):324.
3. Sachio S, Kontoravdi C, Papathanasiou MM. A model-based approach towards accelerated process development: A case study on chromatography. *Chemical Engineering Research and Design*. 2023 Sep 1;197:800-20.
4. Ito K, Couckuyt I, d'Ippolito R, Dhaene T. Design space exploration using Self-Organizing Map based adaptive sampling. *Applied Soft Computing*. 2016 Jun 1;43:337-46.
5. Zhao F, Grossmann IE, García-Muñoz S, Stamatis SD. Design space description through adaptive sampling and symbolic computation. *AIChE Journal*. 2022 May;68(5):e17604.
6. Ding C, Ierapetritou M. A novel framework of surrogate-based feasibility analysis for establishing design space of twin-column continuous chromatography. *International Journal of Pharmaceutics*. 2021 Nov 20;609:121161.
7. Metta N, Ramachandran R, Ierapetritou M. A novel adaptive sampling based methodology for feasible region identification of compute intensive models using artificial neural network. *AIChE Journal*. 2021 Feb;67(2):e17095.
8. Laky D, Xu S, Rodriguez JS, Vaidyaraman S, García Muñoz S, Laird C. An optimization-based framework to define the probabilistic design space of pharmaceutical processes with model uncertainty. *Processes*. 2019 Feb 14;7(2):96.
9. Kusumo KP, Gomoescu L, Paulen R, García Muñoz S, Pantelides CC, Shah N, Chachuat B. Bayesian approach to probabilistic design space characterization: A nested sampling strategy. *Industrial & Engineering Chemistry Research*. 2019 Nov 26;59(6):2396-408.
10. Kucherenko S, Giamalakis D, Shah N, García-Muñoz S. Computationally efficient identification of probabilistic design spaces through application of metamodeling and adaptive sampling. *Computers & Chemical Engineering*. 2020 Jan 4;132:106608.
11. Schulz E, Speekenbrink M, Krause A. A tutorial on Gaussian process regression: Modelling, exploring, and exploiting functions. *Journal of mathematical psychology*. 2018 Aug 1;85:1-6.

© 2025 by the authors. Licensed to PSEcommunity.org and PSE Press. This is an open access article under the creative commons CC-BY-SA licensing terms. Credit must be given to creator and adaptations must be shared under the same terms. See https://creativecommons.org/licenses/by-sa/4.0/



Systems & Control Transactions

**Research Article - Peer Reviewed Conference Proceeding**
ESCAPE 35 - European Symposium on Computer Aided Process Engineering
Ghent, Belgium. 6-9 July 2025
Jan F.M. Van Impe, Grégoire Léonard, Satyajeet S. Bhonsale,
Monika E. Polańska, Filip Logist (Eds.)

PSE PRESS

# Robust Techno-economic Analysis, Life Cycle Assessment, and Quality and Sustainability by Digital Design of Three Alternative Continuous Pharmaceutical Tablet Manufacturing Processes

**Shang Gao[a], Brahim Benyahia[a*]**

[a] Loughborough University, Department of Chemical Engineering, Epinal Way, Loughborough, Leicestershire, LE11 3TU, UK
* Corresponding Author: B.Benyahia@lboro.ac.uk

## ABSTRACT

This study presents a comprehensive comparison of the three alternative downstream manufacturing technologies for pharmaceuticals: i) Dry Granulation (DG) through roller compaction, ii) Direct Compaction (DC), and iii) Wet Granulation (WG) based on the economic, environmental and product quality performances. Firstly, the integrated dynamic mathematical models of the different downstream (drug product) processes were developed using gPROMS formulated products based on data from the literature or/and our recent experimental work. The process models were developed and simulated to reliably capture the impact of the different design options, process parameters, and material attributes. Uncertainty analysis was conducted using global sensitivity analysis to identify the set of critical process parameters (CPP) and critical material attributes (CMA) that mostly influence the quality and performance of the final pharmaceutical tablets in each case, captured by the critical quality attributes (CQAs). Based on the set of CPP and CMA, the combined design spaces, which guarantee the attainment of the targeted CQA, were identified and compared. Additionally, based on the process simulations results and inventory data, the techno-economic Analysis was performed alongside life cycle assessment (LCA). The LCA provided an in-depth evaluation of the environmental impacts associated with each manufacturing method, considering aspects such as energy consumption, raw material usage, emissions, and waste generation based on a cradle-to-gate approach. By integrating the CQAs and critical emission categories within a Quality and and Sustainability by Digital Design (QSbDD) paradigm, this study offers a holistic analysis that captures both the environmental and product quality performance.

**Keywords**: Life Cycle Analysis, Technoeconomic Analysis, Modelling and Simulations, gProms, Pharmaceutical tableting, Quality and and Sustainability by Digital Design (QSbDD)

## INTRODUCTION

Pharmaceutical manufacturing plays a crucial role in ensuring the delivery of safe, effective, and high-quality medicines to patients worldwide. However, the development of robust and efficient manufacturing processes remains a complex challenge. The pharmaceutical industry operates under stringent regulatory requirements to guarantee product safety and efficacy, adding complexity to decision-making and process development. Compounding these challenges is the growing pressure to adopt sustainable manufacturing practices, driven by increasing environmental concerns and evolving regulatory standards. Tablets account for the most important dosage forms [14], yet the selection of the most suitable downstream (drug product) technologies, such as direct compaction (DC), dry granulation (DG), or wet granulation (WG), remains a critical decision. This process is often hindered by a reliance on traditional trial-and-error approaches, which are resource-intensive and

inefficient.

One promising approach to address quality related challenges is the adoption of Quality-by-Design (QbD), a systematic framework endorsed by regulatory agencies such as the FDA and EMA. QbD is increasingly adopted to deliver more effective quality management strategies, ensuring that product quality is built into the process rather than tested at the end. By linking critical quality attributes (CQAs), critical process parameters (CPPs), and critical material attributes (CMAs), QbD enhances process reliability and facilitates regulatory compliance. However, these methods do not inherently consider economic and environmental criteria, leaving a glaring critical gap in the decision-making process. Emerging digital tools are opening new avenues for more effective decision-making in pharmaceutical manufacturing. Flowsheet and plant wide models are critical in all design stages to help identify the most economic and environmentally friendly options, optimize process operation, and develop plant wide control strategies [1-3]. For example, an end-to-end ibuprofen process has been developed to identify optimal and sustainable design with adjustment of operating conditions to achieve the quality assurance [4]. Techno-Economic Analysis (TEA) evaluates the cost-effectiveness of manufacturing processes, analyzing both capital (CaPEx) and operational expenses (OpEx). Continuous manufacturing is frequently highlighted as economically advantageous due to its higher yield and scalability [5]. There also applications of TEA to plant wide biopharma processes [6].

Life Cycle Assessment (LCA) provides a comprehensive evaluation of the environmental impacts of manufacturing processes, using frameworks like ReCiPe 2016. Prior studies emphasize the environmental advantages of continuous manufacturing over batch processes [5, 7]. LCA has successfully been applied to both lab scale and plant wide processes to identify environmental footprints [8 ,9]. However, there is still a critical need for more systematic and robust cradle-to-gate and cradle-to-cradle strategies within the pharmaceutical and biopharmaceutical sectors.

This study advances the field by linking LCA to QbD and TEA, creating a more rigorous and holistic decision-making framework. The approach is validated by considering three downstream tablet manufacturing approaches namely: Direct Compaction (DC), Dry Granulation (DG) via roller compaction, and Wet Granulation (WG). The holistic approach evaluates and compares these alternative downstream methods in terms of quality, cost, and environmental impact. Additionally, a combined robust design space, the ranges of CMAs and CPPs which deliver quality assurance, is identified to ensure consistent attainment of critical quality attributes (CQAs). The study further explores alternative process designs, such as closed-loop recycling systems, to enhance the environmental performance of the plant while meeting quality requirements. This integrated framework aims to guide sustainable and efficient pharmaceutical manufacturing practices.

## METHODOLOGY

### Process modelling and simulation

The first step consisted in the development of integrated process models for three downstream tablet manufacturing methods (DC, DG and WG) shown in Figure 1. The dynamic models were constructed using gPROMS Formulated Products®, leveraging a combination of literature data and experimental results from recent studies. The tablet consists of paracetamol, the active pharmaceutical ingredient (API), lubricant, and several excipients: microcrystalline cellulose (MCC), lactose, crospovidone (disintegrant), and magnesium stearate (lubricant). All processes are operating continuously starting with the blending of API, excipients, and lubricant to deliver uniform blends, followed by different tableting approaches, in which DC is the most straight forward approach, mixed particles were sent directly to the tablet press machine and then the dissolution test. The DG route will go through the roller compactor and a mill to remove large particles. The WG is conducted in a twin-screw granulator and requires the addition a solvent which consists of water and hydroxypropyl methylcellulose (HPMC) at 94% and6% wt% respectively. The wet granulation step is followed by the drying then the tablet press. Each process model was designed to capture the intricate interactions between process parameters and material attributes. Key parameters such as compaction force, granule size distribution, the impact of the blending residence time and drying and the targeted moisture content were captured to ensure that the models accurately represent the real industrial-scale operations. The dissolution tests were configured at the end of the model simulations to predict the critical quality attributes (CQAs), including dissolution rate, time and residual impurities/solvents, alongside the other CQAs such as tablet tensile strength, hardness and porosity which are predicted by the models of each downstream processing routes. This modelling approach allows for the systematic exploration and optimization of various process configurations and design options.

### Quality and Sustainability by Digital Design

A new Quality and Sustainability by Digital Design (QSbDD) approach leveraging model-based methods is proposed allowing specifically the identification of the CPPs and CMAs which significantly influence the CQAs [4]. The uncertainty analysis further evaluated how variations in these parameters impact the quality of the final pharmaceutical tablets. The results were used to define

a combined robust design space for each manufacturing process, ensuring compliance with the quality requirements under varying operating conditions.

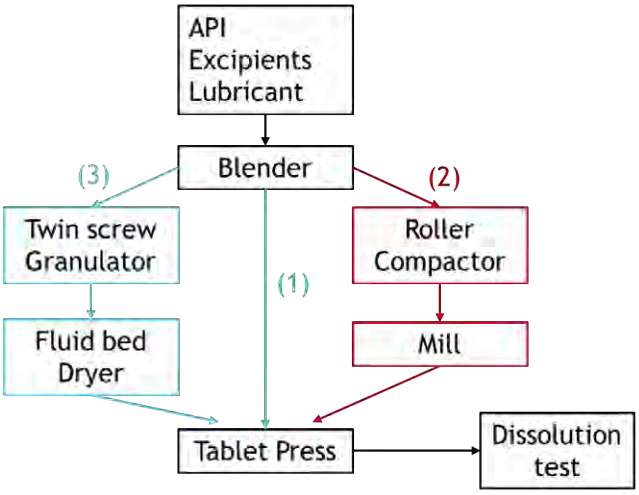



**Figure 1** Simplified paracetamol tabletting process flowsheets via (1) Direct compaction (DC), (2) Dry granulation with roller compaction (DG), and (3) Wet granulation (WG).

## Sensitivity Analysis

A Global Sensitivity Analysis (GSA) was performed to systematically assess the impact of all process parameters and material attributes on the CQAs and identify the optimal set of CPP and CMA. The Sobol method, a variance-based approach, was chosen due to its robustness in handling non-linear and interactive effects. The sensitivity indices were evaluated using Monte Carlo simulations, which allowed for an accurate quantification of the influence of each input parameter.

### Lifecycle Assessment

A cradle-to-gate life cycle assessment (LCA) was performed to quantify the environmental impacts of each manufacturing process. The proposed LCA is consistent with the ISO 14040/44 standards, covering four key phases: goal and scope definition, inventory analysis, impact assessment, and interpretation. Environmental impacts were assessed across multiple categories, including global warming potential, energy use, and waste generation.

### Goal and Scope

Perform the LCA for all case model simulations with the functional unit of 1 kg paracetamol tablet products.

### Life cycle inventory

Based on the process simulation outputs, detailed inventory data were gathered for each manufacturing approach. This data encompassed material usage, energy consumption, waste generation, and emissions at each processing stage.

### Impact assessment

The impact assessment is based on the method ReCiPe 2016 in SimaPro with the Ecoinvent 3 environmental footprint database. The ReCiPe 2016 captures three endpoint categories (human health, ecosystems, and resources) and seventeen midpoint categories. These different categories provide a comprehensive basis to compare the different design options.

### Interpretation of results

Finally, the results obtained from the previous steps are interpreted and the environmental hotspots are identified.

The overall LCA was structured into distinct system boundaries to capture the contributions of key process stages. The defined system boundaries include:

- API production: The environmental impacts associated with the synthesis of the API, including raw material extraction, energy use, and waste generation during API production. In compliance with ISO standards, the inputs required for paracetamol API synthesis were modeled using data from literature. [10-12]
- Drug product manufacturing: This boundary includes all unit operations involved in the downstream tableting processes. It accounts for material inputs, such as excipients and binders, as well as operating energy and utilities (e.g., electricity, steam). Additionally, the impacts of excipient production were included, alongside emissions and waste generated at each stage.
- Quality control: The LCA incorporated the energy and material requirements for quality control procedures, including dissolution tests, hardness tests, and content uniformity assays. These tests are essential for ensuring compliance with regulatory standards and maintaining product quality.

## Technoeconomic Analysis

The TEA were performed based on the capital expenditure (CapEX) and operational expenditure (OpEX) based on standard methodologies [7]. The economics were evaluated based on:

- Direct and indirect costs: Equipment cost estimates were derived from vendor quotes and literature sources.
- Operating expenses (OpEx): Included material costs (API, excipients), utilities (electricity, steam), labour, and maintenance costs.

## RESULTS AND DISCUSSIONS

### Simulation results and Design Space analysis

The simulations of three downstream tableting approaches (DC, WG, DG) in a continuous manufacturing setting were performed. The dissolution profiles and tensile strength prediction were compared against experimental data. Across all manufacturing methods, the final products consist of 500 mg paracetamol tablets, with a targeted API content of 23%. According to the United States Pharmacopeia (USP) criteria for paracetamol tablets, during the dissolution test use at least 80% of the API must dissolve within 30 minutes. This requirement is considered as the first CQA. Additionally, the tensile strength must exceed 1.2 MPa.

Based on the model predictions at some nominal values, all three methods can deliver the required CQA bounds. However, this is enough to guarantee built-in quality assurance based on rigorous implementation of QbD. Firstly, it is key to identify the minimum set of CPPs and CMAs which capture most of the variability within the CQAs. This criticality assessment was achieved based the GSA. The CPPs and CMAs were selected based on their total-order Sobol index, which represents their overall contribution to the variance in CQAs such as tablet tensile strength and API dissolution rate [12, 13]. For instance, for the DG process, the CPPs and CMAs are the roller compaction force, tablet press compaction force, and moisture content.

The proposed GSA-based approach revealed the optimal sets of CPPs and CMAs in each process which allows the identification of the design space which is multidimensional space where the product's CQAs are proven to meet their acceptable ranges. Figure 2 illustrates the design space for the DG process, considering two CPPs: the compaction force applied by the tablet press and the roller compactor. The red-shaded region in the figure represents the feasible design space where dissolution exceeds 80% within 30 minutes. The results indicate that an increase in roller compaction force negatively impacts dissolution performance, due to the formation of highly dense granules, which hinder drug disintegration and dissolution.

In the WG process, the CQA that needs to be further improved is the tensile strength as it tends to deliver a tensile strength below 1.2 MPa. Here we identified one CPP which is the compaction force of tablet press and one CMA: the targeted moisture content in the fluid bed dryer. As shown in Figure 3, increasing compaction force from 95 MPa to 125 MPa leads to a gradual improvement in tablet tensile strength, where higher pressure enhances interparticle bonding and reduces tablet porosity, thereby increasing mechanical strength. Moisture content plays a more nuanced role in the wet granulation process. The contour map indicates that tensile strength increases moderately as moisture content rises from 3.6% to 4.4%, suggesting that optimal moisture levels improve granule cohesiveness. This observation aligns with established granulation principles, where adequate moisture enhances binder activation and particle agglomeration, leading to stronger compacts. From a pharmaceutical manufacturing perspective, optimizing compaction force within 110–125 MPa while maintaining moisture content around 4.0–4.4% appears to provide a balanced approach for achieving robust tablet manufacturing as indicated by the design space in figure 3.

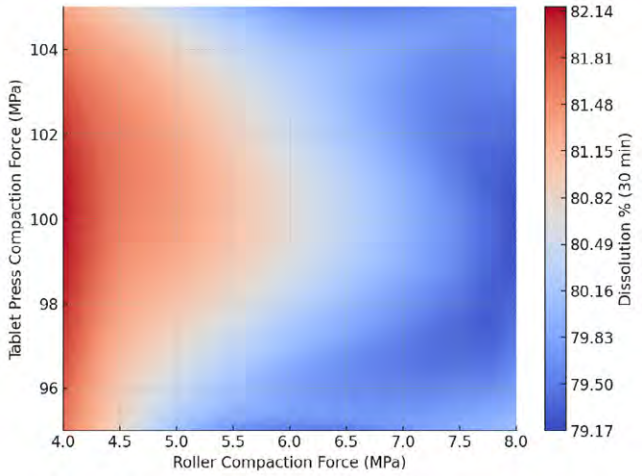



**Figure 2**. Design Space of the DG process

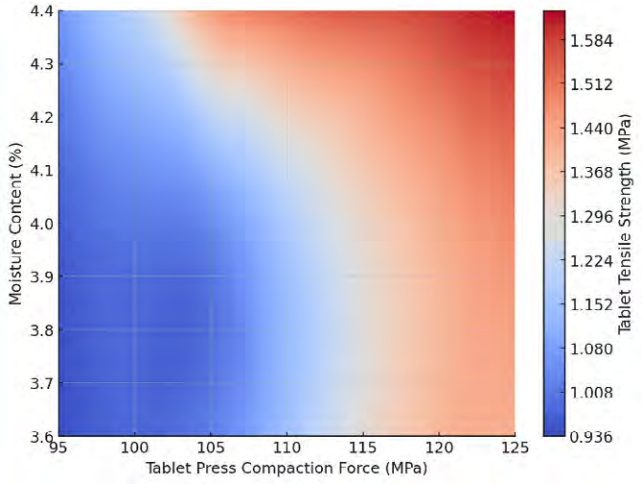



**Figure 3**. Design Space of the WG process.

### Lifecycle Assessments

The life cycle impact assessment of the three downstream manufacturing processes was conducted using the ReCiPe 2016 method and based on the methodology described earlier. As shown in Figure 4, among the three methods, DC demonstrated the lowest environmental impacts. This can be attributed to the simplification and intensification based as shown by the reduced number of unit operations, such as the absence of granulation or

drying steps, which significantly reduces utility consumption and waste generation. In contrast, DG and WG involve additional energy-intensive operations, such as roller compaction or fluid-bed drying, which contribute to their relatively higher environmental impacts. The normalized Midpoint categories comparison of three continuous processes show in which the most impacted categories are human carcinogenic toxicity (HCT), fresh water ecotoxicity (FWET) and marine ecotoxicity (MET). The paracetamol API production contributes the most impact scores as it is the main material for the tablet and the multistep reaction pathways require a variety of chemicals which inherently generate substantial hazardous wastes. This also happens with the production of excipients.

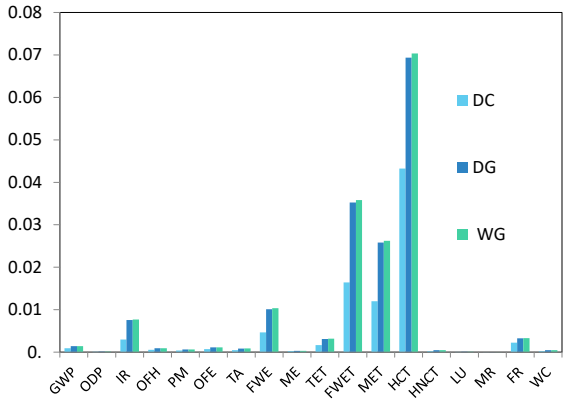



**Figure 4** ReCiPe 2016 Midpoint Comparison of three tabletting methods.

## Technoeconomic Analysis

The TEA is based on the simulation results from gPROMs and unit price from literature and row material suppliers. The TEA of the three three downstream manufacturing processes reveal significant trade-offs between process complexity, operational costs, and product quality. As shown in Figure 5, direct compaction emerged as the most cost-effective method, with a total annual cost of £100,857 and a production cost of 12.56 £/kg. This highlights the DC's advantages for low-dose formulations with robust powder flow properties. However, DC's reliance on homogeneous blending poses risks for segregation at scale, necessitating stringent process controls or glidant additives (e.g., colloidal silica).

While DG is 25% more expensive than DC (15.70 £/kg), it offers improved powder flowability and reduced segregation risks, critical for scaling continuous manufacturing. The elevated costs stem from capital-intensive roller compaction (£70,000) and milling equipment, compounded by 20% higher maintenance costs. Despite its moderate dissolution performance (79% at 30 min), DG's tensile strength (5.08 MPa) surpasses pharmacopeial standards (>1.4 MPa), suggesting viability for moisture-sensitive APIs.

WG achieves superior content uniformity, incurred to the highest operational costs (16.08 £/kg) due to energy-intensive drying and HPMC binder expenses. The critically low tensile strength (0.98 MPa) observed in WG tablets underscores the need for process optimization, particularly increasing the tablet compaction force and refining binder distribution.

Notably, labor costs dominated all methods (52% of total costs), emphasizing the economic potential of automation in small-scale pharmaceutical production. Future work may explore hybrid approaches (e.g., DC with external lubrication) or advanced process analytics (PAT) to deliver better trade-offs between cost and performance.

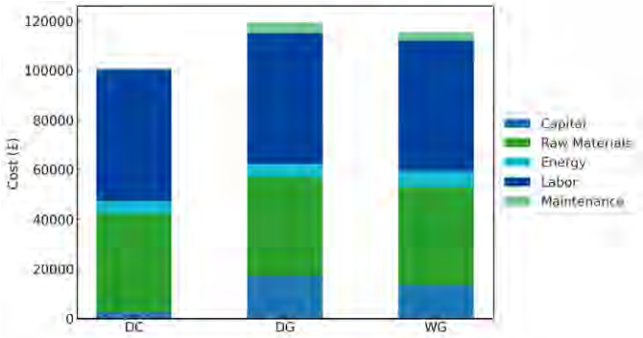



**Figure 5** Technoeconomic Analysis of three tabletting methods

## CONCLUSIONS

This study proposed a comprehensive methodology based on systematic evaluation of the techno-economic, environmental, and quality key performance indicators. The methodology was implemented to evaluate the most common downstream pharmaceutical manufacturing routes, operating continuously, namely: Direct Compaction, Dry Granulation, and Wet Granulation. This work highlights the role of digital transformation and process system engineering in the delivery of more rigorous and robust decision-making strategies in the pharmaceutical industry by capturing product quality, process flexibility and cost-efficiency, and environmental footprints. Most importantly the proposed method lays the foundation for a new Quality and and Sustainability by Digital Design (QSbDD) paradigm which will be further consolidated with more applications in near future, opening new avenues for quality and emission management.

## ACKNOWLEDGEMENTS

The authors acknowledge funding from the UK Engineering and Physical Sciences Research Council (EPSRC), for Made Smarter Innovation – Digital Medicines Manufacturing Research Centre (DM2), EP/V062077/1.

## REFERENCES


1. Benyahia, B., Lakerveld, R., Barton, P.I., 2012 A plant-wide dynamic model of a continuous pharmaceutical process, Industrial and Engineering Chemistry Research, 51(47), pp. 15393–15412.
2. Benyahia, B., 2018. Applications of a plant-wide dynamic model of an integrated continuous pharmaceutical plant: Design of the recycle in the case of multiple impurities. Computer Aided Chemical Engineering, Elsevier B.V. 41: 141-157.
3. Ramin, P., Mansouri, S.S., Udugama., I.A., Benyahia, B., Gernaey, K.V., 2018. Modelling continuous pharmaceutical and bio-based processes at a plant-wide level: A roadmap towards efficient decision-making. Chemistry Today 36 (2), 26-30.
4. Campbell TJS., Rielly CD., Benyahia, B., 2024 Sustainability and Quality-by-Digital Design of an Integrated End-to-End Continuous Pharmaceutical Process, Computer Aided Chemical Engineering, Elsevier, Volume 53, Pages 343-348, ISSN 1570-7946, ISBN 9780443288241, https://doi.org/10.1016/B978-0-443-28824-1.50058-2.
5. Badenhorst, H., Gerogiorgis, D. I., & Ramachandran, R. (2021). Techno-economic and environmental evaluation of batch vs. continuous pharmaceutical tablet manufacturing via process systems engineering tools. Computers & Chemical Engineering, 144, 107121. https://doi.org/10.1016/j.compchemeng.2020.107121
6. Kis, Z., Kontoravdi, C., Shattock, R., Shah, N,. 2021. "Resources, Production Scales and Time Required for Producing RNA Vaccines for the Global Pandemic Demand" Vaccines 9, no. 1: 3. https://doi.org/10.3390/vaccines9010003
7. Ince MC, Benyahia B, Vilé G. Sustainability and Techno-Economic Assessment of Batch and Flow Chemistry in Seven Industrial Pharmaceutical Processes. ACS Sustainable Chem. Eng. 2025, 13, 7, 2864–2874Hadinoto, K., Tran, T. T., Chua, A., & Cheow, W. S. (2022). Comparing environmental impacts of direct compaction versus wet granulation tableting methods for drugs with poor flowability by life cycle assessment. Chemical Engineering Research and Design, 183, 439–451. https://doi.org/10.1016/j.cherd.2022.05.029
8. Gao, S., & Benyahia, B. (2023). Technoeconomic and Life Cycle Assessment of an mRNA Vaccine Integrated Manufacturing Plant., Computer Aided Chemical Engineering (Vol. 52, pp. 2261-2266). Elsevier. https://doi.org/10.1016/B978-0-443-15274-0.50360-7
9. Sherman J, Le C, Lamers V, Eckelman M., 2012 Life cycle greenhouse gas emissions of anesthetic drugs. Anesth Analg 2012; 114: 1086e90
10. Parvatker AG, Tunceroglu H, Sherman JD, et al. Cradle-togate greenhouse gas emissions for twenty anesthetic active pharmaceutical ingredients based on process scaleup and process design calculations. ACS Sustain Chem Eng 2019; 7: 6580e91.
11. Davies, J. F., McAlister, S., Eckelman, M. J., McGain, F., Seglenieks, R., Gutman, E. N., Groome, J., Palipane, N., Latoff, K., Nielsen, D., Sherman, J. D., & the TRA2SH, GASP, and WAAREN collaborators. (2024). Environmental and financial impacts of perioperative paracetamol use: A multicenter international life-cycle assessment. British Journal of Anaesthesia, 133(6), 1439–1448. https://doi.org/10.1016/j.bja.2023.11.053
12. Fysikopoulos, D, I Onyemelukwe, I, Benyahia B, Nagy ZK, Rielly CD. Local vs global estimability analysis of population balance models for crystallization processes, Computer Aided Chemical Engineering 40, 55-60.
13. Campbell TJS, Rielly CD, Benyahia B Digital design and optimization of an integrated reaction-extraction-crystallization-filtration continuous pharmaceutical process Computer Aided Chemical Engineering 51, 775-780
14. Bhutani U, Basu T, Majumdar S, Oral Drug Delivery: Conventional to Long Acting New-Age Designs, European Journal of Pharmaceutics and Biopharmaceutics, Volume 162, 2021, Page 23-42, SSN 0939-6411, https://doi.org/10.1016/j.ejpb.2021.02.008.



© 2025 by the authors. Licensed to PSEcommunity.org and PSE Press. This is an open access article under the creative commons CC-BY-SA licensing terms. Credit must be given to creator and adaptations must be shared under the same terms. See https://creativecommons.org/licenses/by-sa/4.0/.




Systems & Control Transactions

**Research Article - Peer Reviewed Conference Proceeding**
ESCAPE 35 - European Symposium on Computer Aided Process Engineering
Ghent, Belgium. 6-9 July 2025
Jan F.M. Van Impe, Grégoire Léonard, Satyajeet S. Bhonsale,
Monika E. Polańska, Filip Logist (Eds.)

PSE PRESS

# Systematic Model Builder, Model-Based Design of Experiments, and Design Space Identification for A Multistep Pharmaceutical Process – Toward Quality by Digital Design

**Xuming Yuan[a], Ashish Yewale[a], Brahim Benyahia[a*]**

[a] Loughborough University, Department of Chemical Engineering, Epinal Way, Loughborough, Leicestershire, LE11 3TU, UK
* Corresponding Author: B.Benyahia@lboro.ac.uk.

## ABSTRACT

This study aims at developing a holistic approach to establish robust mathematical models of integrated and interactive multistep processes, while systematically identifying the corresponding design space and acceptable operating region (AOR). The overall objective is to reduce the experimentation costs, enhance accuracy of integrated metathetical models, and deliver built-in quality assurance based on a new Quality by Digital Design (QbDD) paradigm. This methodology starts with the construction of a set of model candidates for different unit operations, based on the prior knowledge and inherent assumptions. Several model candidates of the integrated multistep process are considered. A model discrimination based on model prediction performance reveals the best integrated model for the multistep process. In the next step, the estimability analysis and model-based design of experiment (MBDoE) are implemented to deliver information-rich data and systematically refine the integrated model. With the acquisition of the new experimental data, the reliability and robustness of the multistep mathematical model is dramatically enhanced. A blending-tableting process is considered to validate the methodology. The model captures the effects of the blender as well as the composition and porosity of the tablet on the tablet tensile strength. Model discrimination and automated model refinement are then performed to identify and improve the optimal integrated model for this two-step process, and the enhanced model is applied for the design space identification under specified CQA targets and associated bounds.

**Keywords**: Multistep process, Model builder, Model Based DoE, Design Space, Acceptable Operating Region (AOR), Quality by Digital Design (QbDD), Blending, Tableting.

## 1. INTRODUCTION

The mathematical models of different processing units within a manufacturing process or plant are usually established and optimized individually, even when these processes are sequentially combined in the real world, particularly in continuous operating plants. Although this traditional modeling approach may help reduce complexity, it can lead to suboptimal solutions or/and overlook the interactions between the unit operations, which also potentially increase the development time, wastes, and experimental costs inherent to the raw materials, solvents, cleaning, etc.

The quality assurance of pharmaceutical products is traditionally performed through Quality-by-Testing (QbT), which is an experiment-intensive a-posteriori approach, leading to poor flexibility and higher failure risks. The advent of Quality-by-Design (QbD) has open new avenues to adapt more effective risk-based quality management methods in Pharma. Nonetheless, current applications of QbD are still heavily reliant on expensive designs of experiments (DoE) and driven by data intensive methodologies.

As required in QbD, the quality assurance of pharmaceutical product must be built-in from the development phase and throughout the life cycle, where the critical quality attributes (CQAs) of the product should be always satisfied during manufacturing. This requirement

may be effectively driven by mathematical models and digital tools which must exhibit higher levels of reliability and prediction capabilities. Additionally, the robustness of the mathematical models can play a vital role in identification of robust design space and cost-effective operating/control strategies in QbD [2]. However, the traditional approaches for the construction of reliable and predictive mathematical models can be labour-intensive, resource-demanding and time-consuming, which is often not an available option, especially at the early stage of process development where the availability of large quantities of active pharmaceutical ingredients (APIs) may be compromised by the lack of scalable units. Another challenge comes from the competition of multiple model candidates originating from different assumptions of the system behaviour, where the lack of identifiability of the model parameters exacerbates the problem and result in unreliable models or poor prediction performance. Importantly, the mathematical models of individual units are commonly developed with the risk of overlooking or neglecting the interactions between unit operations in a complete pharmaceutical process.

One potential solution to address these challenges lies in the improvement of the experimental designs, based on which the data for model calibration are acquired. The information content and the cost-efficiency of different experimental designs can vary significantly. Standard DoE techniques are commonly applied in traditional methods, which may become cost prohibitive for complex systems due to the unrealistically high number of required experiments [8]. Moreover, they are not necessarily optimally designed in terms of obtaining information content for model calibration. Hence, model-based design of experiment (MBDoE) emerges as an effective solution offering enhanced flexibility, maximized information content, and reduced experimental costs. Here, our proposed methodology extends the MBDoE capabilities to multistep integrated or interactive processes [11]. The approach is further enhanced by incorporating effective capabilities for systematic model discrimination and estimability analysis, followed by a model-based identification of robust design space and acceptable operating region (AOR), laying the ground for novel Quality by Digital Design (QbDD) paradigms.

## 2. METHODS

The proposed holistic methodology is outlined in Figure 1, which upgrades the capabilities of the previously presented framework to the case of multiple processes and design space identification [11]. Since various assumptions can be applied at the early stage of process development, this approach begins with the construction of model candidates for different unit operations, which are then combined to give a series of integrated models for the complete process. Instead of evaluating the model candidates of each unit independently, parameter estimation and model discrimination will focus on the integrated models, thus the risk of omitting the interactions between different units is inherently reduced. The parameter estimation can utilize the prior knowledge of the system if available (e.g., previous experimental data, nominal values of parameters), as well as the preliminary experimental data. Afterwards, the model discrimination is conducted through the computation of the Akaike information criterion (AIC) [1] of each model candidate, where the model with the lowest AIC value is the best in capturing the system feature with the lowest model complexity. Subsequently, the automated model refinement is initiated with the estimability analysis by applying sequential orthogonalization algorithm [9] using a threshold value of 0.1 on the best integrated model, which identifies the estimable parameter subset. It should be noted that

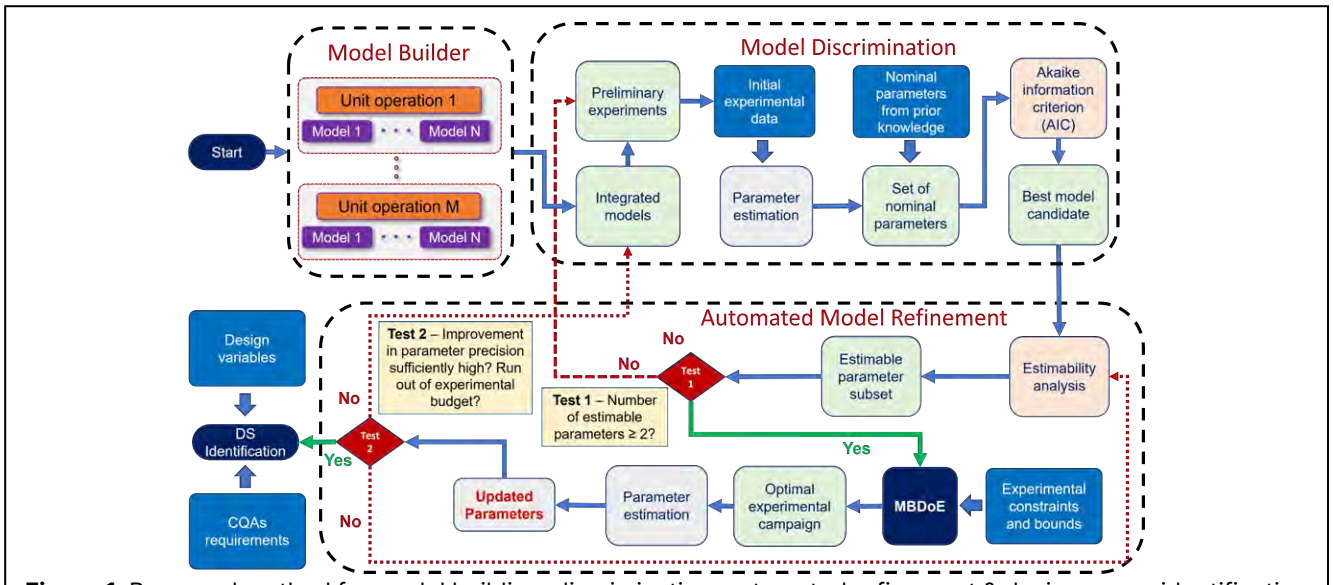



**Figure 1:** Proposed method for model building, discrimination, automated refinement & design space identification

extremely low information content in the preliminary experimental data can lead to a very small number of estimable parameters (less than two) (Test 1), thus extra preliminary experimental runs are required, or alternatively another integrated model may be selected. Once Test 1 is passed, MBDoE focusing on the Fisher information matrix (FIM) of the estimable parameter subset is performed, where the new experimental data are utilised to update the parameter estimates and uncertainties. The model refinement workflow can be executed automatically until the improvement of the parameter precision becomes insignificant, or the experimental budget is depleted (Test 2). Once the stopping criterion is triggered, the automated model refinement procedure is terminated, and the design space identification based on the enhanced process model is performed, where the best nominal operating point (NOP) and the corresponding acceptable operating region (AOR) are identified, delivering a multi-dimensional space where the variations of the critical process parameters (CPP) meet the CQAs requirements.

## 3. CASE STUDY

A two-step blending-tableting process was investigated to validate the proposed holistic framework. The preliminary data or prior knowledge was obtained from the literature [4]. In blending-tableting system, the tablet composition can be varied by changing the weight fraction of the lubricant (magnesium stearate, MgSt) and three different diluents MCC Avicel PH102, Fast Flo Lactose 316 and dibasic calcium phosphate (we will denote them as MCC, LAC and DCP), while the lubrication is conducted by blending the powder in TURBULA® blenders, where the size and headspace fraction of the blender and the number of blending cycles can vary. There are 143 experimental runs available from the literature [4] with different compositions, porosity and blender settings.

### 3.1 Model equations

For blending and tableting processes, several models were proposed in [3], [5] and [6] to capture the dependence of the tablet tensile strength on either the tablet porosity, composition, or the blender operating variables. The model proposed in [3] consists of Equations 1 to 3, where $\sigma_0$ is the tablet tensile strength at zero porosity, $\sigma_{nobld}$ denotes the tensile strength before blending, $\varepsilon$ refers to tablet porosity, $k_b$ represents bonding capacity, $k$ refers to lubrication extent, $\alpha_b$, $V_b$, $F_h$, $\omega_b$, $t_b$ are the equipment dependent factor, volume, headspace fraction, rotation speed and blending time of the blender, $\beta$ signifies lubrication sensitivity, $\gamma$ is the lubrication rate constant of the blend, and $\sigma$ is the final tensile strength.

$$\sigma_{nobld} = \sigma_0 exp(-k_b \varepsilon) \quad (1)$$

$$k = \alpha_b V_b^{\frac{1}{3}} F_h \omega_b t_b \quad (2)$$

**Table 1:** Comparison of blending-tableting models proposed in [3], [5] and [6].

| Model | Porosity | Composition | Blending |
|---|---|---|---|
| [3] | Eq. 1 | N/A | Eq. 2 and 3 |
| [5] | Eq. 4 or 5 | N/A | Eq. 2 and 3 |
| [6] | Eq. 1 | Eq. 6 and 7 | Eq. 8 |

$$\sigma = \sigma_{nobld}[(1-\beta) + \beta exp(-\gamma k)] \quad (3)$$

Equation 1 is commonly referred as Ryshkewitch equation which capture the interdependence between tablet tensile strength and porosity. With Equations 2 and 3, the effects of the blender features and the operating variables are captured. Compared with [3], [5] directly linked the lubrication sensitivity $\beta$ with the porosity $\varepsilon$ with linear/exponential assumptions, resulting in Equations 4 or 5, where $a_1$ and $a_2$ are the parameters to be estimated. The blender effects are modelled with the same equations (2 and 3) in [5].

$$\beta = a_1 \varepsilon + a_2 \quad (4)$$

$$\beta = a_1 \exp(-a_2 \varepsilon) \quad (5)$$

The main limitation of the models in [3] and [5] is the lack of tablet composition effects. Thus, the model developed in [6] simulated the effect of weight fraction changes of the lubricant and diluent, where the bonding capacity $k_b$ of the mixed powder is depends on the ratio of the specific surface area between the lubricant and diluent ($S_{lub/dil}$), which is calculated by Equation 6, where the specific surface area of the lubricant and diluent $S_{BET,lub}$ and $S_{BET,dil}$ as well as their weight fractions $w_{lub}$ and $w_{dil}$ are used. Afterwards, $k_b$ is obtained in Equation 7, where $\kappa$ is the coefficient corresponding to $S_{lub/dil}$, and $k_{b,dil}$ is the bonding capacity of diluent.

$$S_{lub/dil} = \frac{S_{BET,lub} w_{lub}}{S_{BET,dil} w_{dil}} \quad (6)$$

$$k_b = \kappa S_{lub/dil} + k_{b,dil} \quad (7)$$

The effect of tablet porosity is also captured in [6] by Ryshkewitch equation. However, the blender effects are not included. Instead, the tensile strength of the tablet made of the mixed powder at zero porosity is predicted (Equation 8), where $\sigma_{dil,0}$ is the tensile strength of the tablet only made of the diluent at zero porosity.

$$\sigma_0 = \sigma_{dil,0} exp(-\beta S_{lub/dil}) \quad (8)$$

Table 1 summarizes the models proposed in [3], [5] and [6]. All models capture the effect of tablet porosity. Only [6] models the effect of composition, but [3] and [5] are more comprehensive in modelling the blender effects. Therefore, there is an opportunity to build a more sophisticated integrated model for this process.

### 3.2 Set of multistep model candidates

With the aim of capturing the effect of tablet porosity, composition and the blender by adapting the model

equations in [3], [5] and [6], four candidates of the blending-tableting process are constructed, where Equation 1 is applied in all the candidates to model the influence of porosity, while the blender effects are simulated by Equations 2 and 3. The main adaptation focuses on the composition. In [6], the equations were developed for a single lubricant – single diluent tablet system, while the system in [4] involves one lubricant and three diluents. Therefore, we first propose the equations calculating the tensile strength of the tablet made of mixed diluents at zero porosity ($\sigma_{dil,0}$), where linear assumption (Equation 9) and exponential assumption (Equation 10) of $\sigma_{dil,0}$ on the weight fraction of each diluent ($w_{dil,i}$) are adopted. In Equation 9, $\sigma_{dil,i,0}$ is the tensile strength of the tablet only made of diluent $i$ at zero porosity; in Equation 10, $\sigma_{dil,0,max}$ is the maximum tensile strength of the tablet made of the mixture of the diluents that can be achieved at zero-porosity; $p_i$ are the parameters to weigh the contribution of different diluents on $\sigma_{dil,0}$.

$$\sigma_{dil,0} = \sum_{i=1}^{n} p_i w_{dil,i} \sigma_{dil,i,0} \tag{9}$$

$$\sigma_{dil,0} = \sigma_{dil,0,max}\left[1 - exp\left(-\sum_{i=1}^{n} p_i w_{dil,i}\right)\right] \tag{10}$$

Inspired by [5], we assume the lubrication sensitivity $\beta$ to be linearly/exponentially dependent on $S_{lub/dil}$ (Equation 11/12), while $S_{lub/dil}$ is assumed to be the ratio of the weighted sum of the specific surface area of the lubricant and diluent (Equation 13), and the bonding capacity $k_b$ is also assumed to be relevant to the weighted sum of the bonding capacity of each diluent (Equation 14). The candidates of integrated models are summarized in Table 2.

$$\beta = a_1 S_{lub/dil} + a_2 \tag{11}$$

$$\beta = a_1 \exp\left(-a_2 S_{lub/dil}\right) \tag{12}$$

$$S_{lub/dil} = \frac{\sum_{i=1}^{m} S_{BET,lub,i} w_{lub,i}}{\sum_{j=1}^{n} S_{BET,dil,j} w_{dil,j}} \tag{13}$$

$$k_b = \kappa S_{lub/dil} + \sum_{j=1}^{n} k_{b,dil,j} w_{dil,j} \tag{14}$$

The data in [4] are divided into two groups randomly for parameter estimation (70%) and validation (30%). Once the best integrated model is identified, automated model refinement will be performed, minimizing the dimensionless normalized confidence ellipsoid volume of the estimable parameter subset $V_{est,norm,dimless}$. This first requires the computation of the sensitivity matrix $Z$ of the model parameters (Equation 15), where $\sigma_{exp,i}$ refers to the tablet tensile strength obtained from experiment $i$, while $\theta_j$ denotes the $jth$ model parameter. Then the FIM of the integrated model is computed by Equation 16. Let $FIM_0$ be the FIM of the parameters calculated with the preliminary experimental data (the data from [4]), its diagonal entries $D_0$ (Equation 17) is used to normalize the

**Table 2:** Proposed model candidates of the integrated blending-tableting process

| Model | Porosity | Composition | Blending |
|---|---|---|---|
| 1 | Eq. 1 | Eq. 9, 11, 13 and 14 | Eq. 2 and 3 |
| 2 | | Eq. 9, 12, 13 and 14 | |
| 3 | | Eq. 10, 11, 13 and 14 | |
| 4 | | Eq. 10, 12, 13 and 14 | |

FIM (Equation 18), and the normalized FIM of the estimable parameter subset ($FIM_{est,norm}$) is its sub-matrix by extracting the rows and columns of corresponding to the estimable parameters. Finally, as the number of the estimable parameters $N_{est}$ can change at each MBDoE cycle in the automated model refinement, $V_{est,norm,dimless}$ is calculated based on Equation 19, which is in essence a normalized form of the D-optimal criterion.

$$Z = \begin{bmatrix} \frac{\partial \sigma_{exp1}}{\partial \theta_1} & \cdots & \frac{\partial \sigma_{exp1}}{\partial \theta_N} \\ \vdots & \ddots & \vdots \\ \frac{\partial \sigma_{expM}}{\partial \theta_1} & \cdots & \frac{\partial \sigma_{expM}}{\partial \theta_N} \end{bmatrix} \tag{15}$$

$$FIM = Z^T Z \tag{16}$$

$$D_0 = \mathrm{diag}(FIM_0) \tag{17}$$

$$FIM_{norm} = D_0^{-\frac{1}{2}} FIM D_0^{-\frac{1}{2}} \tag{18}$$

$$V_{est,norm,dimless} = \left(\sqrt{\det\left(FIM_{est,norm}^{-1}\right)}\right)^{\frac{1}{N_{est}}} \tag{19}$$

In each automated model refinement cycle, the MBDoE procedure presented by Equation 20 is conducted to identify the optimal experimental design that minimizes parameter uncertainties, where the decision variables include the volume ($V_b$) and headspace fraction ($F_h$) of the blender, blending cycles ($N_b$), mass fractions of MgSt ($w_{MgSt}$), MCC ($w_{MCC}$) and LAC ($w_{LAC}$), and the tablet porosity ($\varepsilon$). The mass fraction of DCP acts as a constraint that should lie between $0\%$ and $100\%$.

$$\begin{aligned} \min_{V_b, F_h, N_b, w_{MgSt}, w_{MCC}, w_{LAC}, \varepsilon} \; & V_{est,norm,dimless} \\ \text{s.t. } & V_b = \{30\text{mL}, 1250\text{mL}\} \\ & 30\% \le F_h \le 70\% \\ & 24 \le N_b \le 190512 \\ & 0.5\% \le w_{MgSt} \le 2\% \\ & 0\% \le w_{MCC} \le 100\% \\ & 0\% \le w_{LAC} \le 100\% \\ & 5\% \le \varepsilon \le 30\% \\ & 0\% \le 1 - w_{MgSt} - w_{MCC} - w_{LAC} \le 100\% \end{aligned} \tag{20}$$

The stopping criteria of the automated model refinement are presented in Equations 21 and 22. Equation 21 captures the relative reduction in the overall parameter uncertainties over a consecutive MBDoE cycles. If the improvement of parameter precision is not sufficiently high between the two consecutive MBDoE cycles, the automated model refinement will be stopped. Equation 22

defines the available experimental budget which represents a maximum of 5 MBDoE cycles in this case.

$$\eta_i = \frac{V_{est,norm,dimless,i-1} - V_{est,norm,dimless,i}}{V_{est,norm,dimless,i-1}} \leq 10\% \quad (21)$$

$$N_{exp,budget} = 5 \quad (22)$$

Once the automated model refinement is completed, a model-based risk assessment is conducted to identify the set of critical process parameters (CPPs) and critical material attributes (CMAs) [10], then followed by a model-based identification of the design space and normal operating range of the blending-tableting process. The CQA bounds are captured by the constraints in Equation 23, which specifies that the tablet tensile strength should be at least 4 MPa with ≥85% probability, where Equation 24 summarizes the design variables $\boldsymbol{x}$. The design space identification is performed with the Python-based tool DSIDE [7], and all the computation is performed on a 11th Gen Intel(R) Core (TM) i5-11400 @ 2.60GHz 2.59 GHz CPU with 16GB RAM.

$$\mathrm{DS} = \{\boldsymbol{x} \in \boldsymbol{X} | E[Pr(\sigma \geq 4MPa) | \boldsymbol{\theta}] \geq 85\%\} \quad (23)$$

$$\boldsymbol{x} = [V_b, F_h, N_b, w_{MgSt}, w_{MCC}, w_{LAC}, \varepsilon] \quad (24)$$

## 4. RESULTS & DISCUSSION

The parameter estimation and model discrimination of the four model candidates was conducted. Figure 2 shows the parity plots of the candidates comparing the model prediction with the experimental data, revealing that Models 3 and 4 outperform Models 1 and 2, thus the exponential assumption (Equation 10) outperforms the linear assumption (Equation 9) for $\sigma_{dil,0}$ . Since Model 3 has the lowest AIC value (Table 3), it is the best candidate in this case study.

The automated model refinement of Model 3 is performed subsequently. Table 4 shows that the number of estimable parameters and overall precision of the model parameters were both improved with the increase of the number of MBDoE cycles. Initially, six parameters were

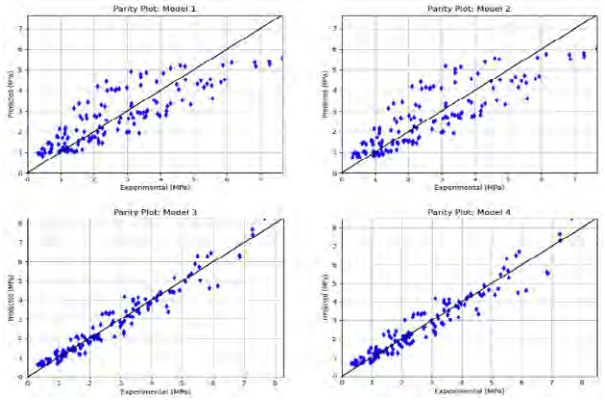



**Figure 2.** Parity plots (model prediction vs. experimental data) of the candidates. Top left: model 1. Top right: model 2. Bottom left: model 3. Bottom right: model 4.

**Table 3:** AIC values of the model candidates

| Model | 1 | 2 | 3 | 4 |
|---|---|---|---|---|
| AIC value | 175.51 | 167.85 | 47.87 | 61.24 |

estimable based on the preliminary data. The 1st MBDoE improved the overall parameter precision ($\eta_i$) by 98.68%. In the 2nd MBDoE, $\eta_i$ significantly dropped (-117.40%), but this is due to the increase of the number of estimable parameters (from 6 to 7), showing that the estimability of the parameters become higher with the new data. With the 3rd, 4th and 5th MBDoE, the overall parameter precision was further enhanced with the increased data size and information content. Since the experimental budget was depleted, the model refinement was terminated.

The improvement in parameter precision can be visualized by the 95% confidence ellipse plots. Figure 3 illustrates the evolution of the joint confidence domain of two selected parameters $\kappa$ and $k_{b,DCP}$. Over the MBDoE cycles, the nominal estimates are updated, and the confidence ellipse generally becomes smaller, indicating that the knowledge of the model parameters is augmented through the proposed automated model refinement.

After successful model refinement based on the combined estimability and MBDoE, the criticality analysis is conducted to identify the set of CPPs and CMAs based on the approach proposed in [10]. Finally, a design space identification was carried out based on the refined mathematical model and the set of CPPs and CMAs by considering the targeted CQA bounds. To further visualize the improvement of the model, we compared the design space and acceptable operating region (AOR) obtained with the initial model against the refined model. Figure 4 visualizes the design space by the green zones, showing that larger AOR is obtained with the refined model, indicating better operating flexibility and robustness.

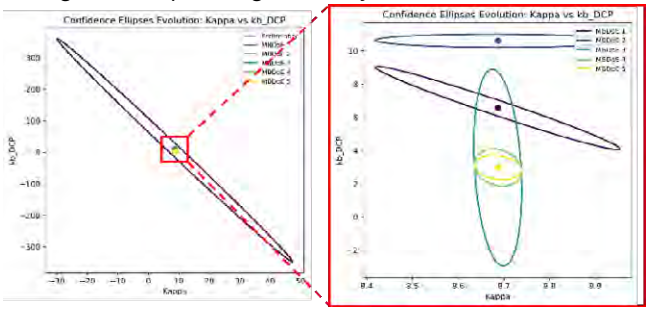



**Figure 3.** 95% joint confidence ellipses for the parameters $\kappa$ and $k_{b,DCP}$ after each MBDoE cycle.

**Table 4:** Improvement of the number of estimable parameters and parameter precision over the MBDoE cycles.

| MBDoE | $N_{est}$ | $\eta_i$ |
|---|---|---|
| 0 (Preliminary) | 6 | N/A |
| 1 | 6 | 98.68% |
| 2 | 7 | -117.40% |
| 3 | 7 | 30.40% |
| 4 | 7 | 26.34% |
| 5 | 7 | 11.31% |

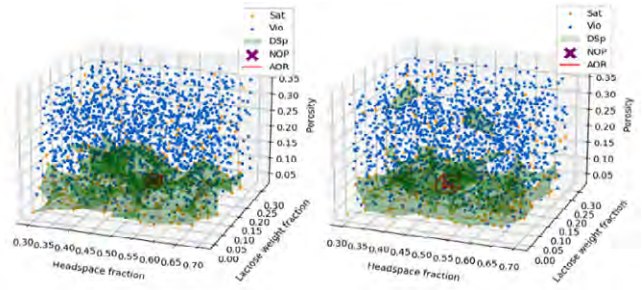



**Figure 4**. Design space of the blending-tableting process based on the model before (left) and after (right) automated model refinement. Sat: satisfying points. Vio: violating points. DSp: design space. NOP: nominal operating point. AOR: acceptable operating region.

Hence, the proposed holistic framework for model building, discrimination and automated model refinement provides a cost-effective option to establish robust model for the blending-tableting process in this case study, resulting in lower uncertainty and a larger AOR offering enhanced flexibility. The proposed framework constructs a new Quality-by-Digital-Design (QbDD) paradigm offering enhanced capabilities compared to the current Quality-by-Design which heavily relies on expensive designs of experiments and time-consuming costly risk assessment methods. Most importantly, the proposed framework addresses the cases of multistep processes and lay the ground for the implementation of effective QbDD in the integrated pharmaceutical manufacturing.

## 5. CONCLUSIONS

In this paper, a new integrated approach for model construction, discrimination, automated refinement and design space identification for multistep processes is proposed, which aims at establishing robust mathematical models for the processes involving multiple interactive unit operations in a cost-effective way and laying the ground for a new Quality-by-Digital-Design framework. The validation of the approach on a two-step blending-tableting process has demonstrated the power of the proposed methodology, indicating its potential effectiveness to be extended for wider applications in the development of multistep process models.

## ACKNOWLEDGEMENTS

The authors acknowledge funding from the UK Engineering and Physical Sciences Research Council (EPSRC), for Made Smarter Innovation – Digital Medicines Manufacturing Research Centre (DM2), EP/V062077/1.

## REFERENCES

1. Akaike, H. A New Look at the Statistical Model Identification. IEEE Trans. Autom. Control 1974, 19 (6), 716–723. https://doi.org/10.1109/tac.1974.1100705.
2. Benyahia, B.; Anandan, P. D.; Rielly, C. Robust Model-Based Reinforcement Learning Control of a Batch Crystallization Process. In Proceedings of the 9th ICSC, 2021, pp 89–94.
3. Kushner, J.; Moore, F. Scale-Up Model Describing the Impact of Lubrication on Tablet Tensile Strength. Int. J. Pharm. 2010, 399 (1–2), 19–30. https://doi.org/10.1016/j.ijpharm.2010.07.033.
4. Kushner, J. Incorporating Turbula Mixers into a Blending Scale-Up Model for Evaluating the Effect of Magnesium Stearate on Tablet Tensile Strength and Bulk Specific Volume. Int. J. Pharm. 2012, 429 (1–2), 1–11. https://doi.org/10.1016/j.ijpharm.2012.02.040.
5. Nassar, J.; Williams, B.; Davies, C.; Lief, K.; Elkes, R. Lubrication Empirical Model to Predict Tensile Strength of Directly Compressed Powder Blends. Int. J. Pharm. 2021, 592, 119980. https://doi.org/10.1016/j.ijpharm.2020.119980.
6. Puckhaber, D.; Finke, J. H.; David, S.; Serratoni, M.; Zafar, U.; John, E.; Juhnke, M.; Kwade, A. Prediction of the Impact of Lubrication on Tablet Compactibility. Int. J. Pharm. 2022, 617, 121557. https://doi.org/10.1016/j.ijpharm.2022.121557.
7. Sachio, S.; Likozar, B.; Kontoravdi, C.; Papathanasiou, M. M. Computer-Aided Design Space Identification for Screening of Protein A Affinity Chromatography Resins. J. Chromatogr. A 2024, 1722, 464890. https://doi.org/10.1016/j.chroma.2024.464890.
8. Lackowska, I.; Dragosavac, M. M.; Vladisavljevic, G. T.; Benyahia, B. Production and Tuning of Spherical Agglomerates of Benzoic Acid Using Membrane Dispersion Systems. Cryst. Growth Des. 2023, 23 (12), 8897–8908.
9. Benyahia, B.; Latifi, M. A.; Fonteix, C.; Pla, F. Emulsion Copolymerization of Styrene and Butyl Acrylate in the Presence of a Chain Transfer Agent. Part 2: Parameters Estimability and Confidence Regions. Chem. Eng. Sci. 2013, 90, 110–118.
10. Campbell, T. J. S.; Rielly, C. D.; Benyahia, B. Digital Design and Optimization of an Integrated Reaction-Extraction-Crystallization-Filtration Continuous Pharmaceutical Process. Comput.-Aided Chem. Eng. 2022, 51, 775–780.
11. Yuan, X.; Benyahia, B. A Holistic Approach for Model Discrimination, Multi-Objective Design of Experiment and Self-Optimization of Batch and Continuous Crystallization Processes. Comput.-Aided Chem. Eng. 2024, 53, 391–396.

© 2025 by the authors. Licensed to PSEcommunity.org and PSE Press. This is an open access article under the creative commons CC-BY-SA licensing terms. Credit must be given to creator and adaptations must be shared under the same terms. See https://creativecommons.org/licenses/by-sa/4.0/

Systems & Control Transactions

**Research Article - Peer Reviewed Conference Proceeding**
ESCAPE 35 - European Symposium on Computer Aided Process Engineering
Ghent, Belgium. 6-9 July 2025
Jan F.M. Van Impe, Grégoire Léonard, Satyajeet S. Bhonsale,
Monika E. Polańska, Filip Logist (Eds.)

PSE PRESS

# Eco-Designing Pharmaceutical Supply Chains: A Process Engineering Approach to Life Cycle Inventory Generation

**Indra CASTRO VIVAR[a]*, Catherine AZZARO-PANTEL[a], Alberto A. AGUILAR LASSERRE[b], Fernando MORALES-MENDOZA[c]**

[a] Université de Toulouse, CNRS, INPT, UPS, Laboratoire de Génie Chimique, Toulouse, France
[b] Tecnológico Nacional de México, Instituto Tecnológico de Orizaba, Orizaba, Veracruz, México
[c] Universidad Autónoma de Yucatán, Facultad de Ingeniería Química, Mérida, Yucatán, México
* Corresponding Author: indra.castrovivar@toulouse-inp.fr.

## ABSTRACT

The environmental impacts of pharmaceutical production underscore the need for comprehensive life cycle assessments (LCAs). Offshoring manufacturing, a common cost-saving strategy in the pharmaceutical industry, increases supply chain complexity and reliance on countries like India and China for active pharmaceutical ingredients (APIs). The COVID-19 pandemic exposed Europe's vulnerability to global crises, prompting initiatives such as the French government's re-industrialization plan to relocate the production of fifty critical drugs. Paracetamol production has been prioritized, with recent shortages highlighting the urgency to address supply chain risks while considering environmental impacts. This study uses process engineering to generate life cycle inventory (LCI) data for paracetamol production, offering an eco-design perspective. Aspen Plus was employed to model the API manufacturing process, integrating mass and energy balances to address the scarcity of LCI data. The results highlight significant differences in emissions between India and France. For 1 kg of API, India's emissions are 0.0826 kg $CO_2$ eq for electricity and 1.3845 kg $CO_2$ eq for heat from steam, compared to France's significantly lower values of 0.005228 kg $CO_2$ eq and 1.1828 kg $CO_2$ eq, respectively. These differences emphasize the environmental benefits of relocating production to regions with cleaner energy sources. The study demonstrates the value of process modeling for generating robust LCI data, enabling detailed LCAs to support eco-design in pharmaceutical manufacturing. This approach can be extended to other chemicals, facilitating sustainable decision-making in the sector's re-industrialization.

**Keywords**: Aspen Plus, LCA, LCI

## INTRODUCTION

Sustainability in the pharmaceutical industry has become a priority as concerns grow about the environmental impact of Active Pharmaceutical Ingredients (APIs) and the increasing complexities of global supply chains. In this context, paracetamol, one of the most widely used APIs in the world, has become a relevant case study due to its current production practices, which rely almost exclusively on large-scale facilities in India and China. These facilities can produce up to 40,000 tons annually, serving as an important economic source but posing sustainability and supply security challenges. Centralized production far from major consumption centers, like Europe, creates a heavy dependence on foreign API sources.

This dependence became evident during the COVID-19 pandemic when disruptions in essential medicine supply chains were experienced due to external factors and geopolitical tensions, which underscored Europe's vulnerability to global crises and prompted policies advocating the strengthening of local production capacity. Within this framework, the European Pharmaceutical Strategy, launched in 2020, advocates the relocation of the production of essential medicines on the continent, seeking to create shorter and more sustainable value chains that are less susceptible to international disruptions. The reindustrialization of pharmaceutical production in Europe aims to ensure access to high-quality medicines, minimize the environmental impacts associated

with transportation, and promote cleaner energy sources.

The global paracetamol API market is projected to reach USD 13.72 billion by 2029, with a compound annual growth rate (CAGR) of 4.41% between 2024 and 2029[1]. The COVID-19 health contingency underscored the critical role of paracetamol. This surge in demand highlighted the global dependency on India and China for the medication supply. In response, initiatives like the French government's reindustrialization plan aim to localize the production of 50 essential medications, including paracetamol, addressing supply chain vulnerabilities observed during shortages in 2022 and early 2023 [2].

Despite its market significance, sustainability analysis of APIs faces challenges, mainly due to limited Life Cycle Inventory (LCI) data. To address this challenge, this study applies Life Cycle Assessment (LCA) methodology to evaluate two locations for paracetamol API production focusing on the environmental benefits of local production in France. A notable contribution is developing LCI data through chemical process modeling, addressing the data gap in LCA studies of pharmaceuticals.

By integrating process simulation with LCA methodologies, the goal is to improve the accuracy and comprehensiveness of LCI data. This approach aims to ensure a more detailed and reliable assessment of environmental impacts, thus supporting better decision-making for sustainable development within the pharmaceutical sector.

## RELATED WORK

The pharmaceutical industry leverages simulation and process design to improve efficiency and sustainability, addressing the significant environmental challenges of API production. Recent advancements integrate simulation with LCA to minimize environmental impacts, focusing on generating LCI data through process modeling. This section reviews key studies in this area.

The environmental impact of excipients in the production of ibuprofen tablets is investigated in [3] through simulation at each stage of the manufacturing process. This approach helped authors collect energy consumption and emissions data for the LCI. Their findings highlight that auxiliary materials, such as excipients, significantly impact the environmental footprint of pharmaceutical products, stressing the need to optimize these materials for better sustainability.

A continuous production framework for synthesizing zuclopenthixol is proposed in [4], demonstrating simulation integration to gather process data in continuous production. This included modeling solvent use and separation operations, enabling analysis of material and energy flows in API production. Similarly, simulation is used in [5] to develop a continuous flow model in the synthesis of ibuprofen, using a series reactors to optimize solvent use and reduce the environmental impact of production. These studies highlight how continuous production can significantly reduce the environmental footprint and improve process sustainability in producing commonly used APIs.

The scope of simulation and process modeling is extended to encompass common anesthetics in [6]. Their approach included industrial-scale simulations that enabled detailed data collection for the LCI of 20 anesthetics, quantifying greenhouse gas emissions at each stage. This work provides a framework for comparing sustainability options in anesthesia.

The environmental impact of the catalytic synthesis of nopal is explored in [7]. This study used simulation to construct the LCI of two synthesis alternatives. The authors found that selecting solvents and reusing materials can significantly reduce the environmental footprint in synthesizing specialty chemicals, including those of pharmaceutical relevance.

The literature demonstrates that integrating chemical process simulation with process engineering is key to generating an accurate LCI in the pharmaceutical industry, allowing energy and materials flow to be comprehensively captured throughout production stages, facilitating more complete environmental assessments. The studies reviewed highlight that simulation can optimize the use of excipients, solvents, and continuous processes, contributing to reducing the environmental footprint of APIs and other specialty chemicals.

Despite these advances, the literature scarcely mentions the application of this approach to the environmental assessment of acetaminophen production, leaving a gap in the sustainability analysis for this medication. Implementing process modeling and simulation methodologies for acetaminophen could provide critical data for the LCI, contributing to more sustainable manufacturing practices in the future.

## MATERIALS AND METHODS

Paracetamol, also known as acetaminophen, is a medication with analgesic and antipyretic effects. It is widely used for headaches, muscle aches, arthritis, backaches, toothaches, colds, and fevers due to its efficacy and low side effects. Its proven effectiveness makes it essential in over-the-counter and prescription pain management, justifying its selection for this case study developed.

This study uses LCA methodology and process modeling to assess the environmental impacts of various supply chain scenarios for active pharmaceutical ingredients, particularly evaluating the benefits of relocating production to France.

- The flowsheet development outlines the API

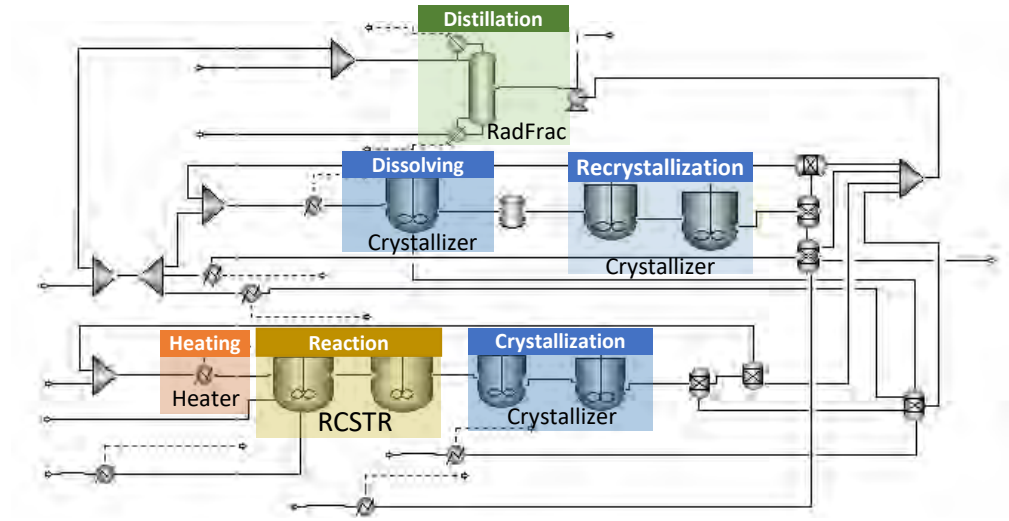



**Figure 1**: Simulation flowsheet and main equipment for API production

production process in Aspen Plus V14, providing energy and material balances for the LCA.

- The life cycle assessment compares the impacts of API production in France and India.

## Process modeling

Simulating acetaminophen production in Aspen Plus helps analyze its environmental impact by providing data on material and energy balances. In this system, two reactions are characterized: (1) the reaction of p-aminophenol and acetic anhydride to form acetaminophen and acetic acid, and (2) the reaction of acetic anhydride and water to produce acetic acid. According to [8], (1) can be modeled as an irreversible pseudo-first order reaction when acetic anhydride is in excess relative to p-aminophenol. Regarding (2), three irreversible steps, characterized by first-order kinetics, are involved [9]. The reactions are as follows:

$$(CH_3CO)_2O + C_6H_7NO \rightarrow C_8H_9NO_2 + CH_3COOH \quad (1)$$

$$(CH_3CO)_2O + H_2O \rightarrow CH_3COOH \quad (2)$$

Both reactions must take place within a reasonable time frame; to characterize their rates, the Arrhenius equation is used:

$$k = Ae^{(-Ea/RT)} \quad (3)$$

According to [8], the activation energy for (1) is 37310 J/mol. That study compared the reaction rate as a function of temperature and used the reaction rate, activation energy, gas constant, and temperature to determine the pre-exponential Arrhenius factor over a range of 323 K to 343 K, which corresponds to the operating temperature range used in the simulation, with a value of k equal to 11,293$s^{-1}$.

The production process begins with water mixed with a recycle stream at 15°C, which is preheated to 53.7°C using 5 atm steam for the reaction in a Continuously Stirred Tank Reactor (CSTR). Acetic anhydride is also preheated to the same temperature, and p-aminophenol is added to the reactor. After the reaction, the fluid is cooled in a crystallizer (to 40°C and then 15°C) and sent to filtration and washing. A portion of the slurry (35%) is recycled for preheating, while the rest (65%) and wash drains go to a distillation column.

Recycled drain water and acetic acid are heated and mixed with the acetaminophen cake and purified through a column with activated carbon, then undergoes a second recrystallization, filtration, and washing process. Seventy-five percent of the drain water is recycled into the solvent, and the wash drains are sent to the distillation column. The acetaminophen cake is sent to storage. Distillate, mainly water and acetic acid, is reused in the solvent and wash processes, with the remainder stored. The bottom residues from the distillation column, considered waste, are stored separately. Figure 1 complements the description.

## Life cycle assessment

The LCA evaluates a product or service's environmental impacts by examining all stages of its life cycle based on a defined functional unit. Its objective is to identify opportunities to improve its environmental performance. The LCA consists of four main stages: goal and scope definition, inventory analysis, impact assessment, and interpretation.

The goal of this LCA is to carry out a comparative analysis of the environmental impacts associated with the production of acetaminophen API in two locations: France and India. The system boundary, depicted in Figure 2, includes all material and energy inputs related to API production, following a “cradle-to-gate” approach. This approach covers resource use and emissions from raw material extraction to the final API manufacturing

stage. The functional unit is defined as 1 kg of API acetaminophen, ensuring consistency in mass and energy balance calculations in the different scenarios. Data on the API production process is taken from [8].

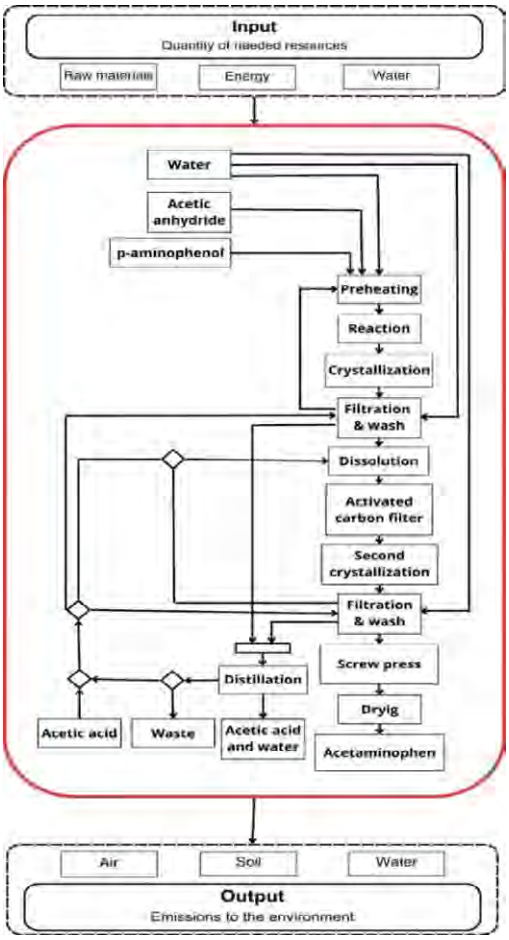



**Figure 2:** System boundary

The LCI phase quantifies all material and energy flows that cross the system boundary. This involves linking the units or services required to produce a functional unit with the corresponding emissions and resource extraction for each unit process. Although literature sources provide reference data on raw materials, they are often insufficient for high-quality LCA. To address this limitation, process simulation with Aspen Plus was used to generate detailed mass and energy balances of acetaminophen production. This approach allows for accurate estimation of inputs and outputs, improving the LCI accuracy and strengthening the assessment reliability of as a whole. To ensure robust and complete data collection, the LCI was developed by combining process modeling with literature-based information

For the LCIA phase, LCI data is linked to environmental impact categories. This evaluation follows the EF 3.0 (Environmental Footprint) method, implemented using the SimaPro version 9.4.0.2 software. This method aligns with European sustainability policies and industry standards, providing a comprehensive framework for assessing environmental impacts at intermediate and endpoints. In addition, the ecoinvent database complements the information on emissions, guaranteeing coherence in characterizing impacts in all the evaluated processes.

## RESULTS AND DISCUSSION

This section compares the environmental impacts of acetaminophen API production in France and India to illustrate the effectiveness of the proposed methodology.

Results (see Figure 3) show that the climate change category presents higher values in India (16,35 kg $CO_2$ eq) compared to France (13,91 kg $CO_2$ eq). Similarly, non-carcinogenic human toxicity is higher in India (2.13 E-07 CTUh) compared to France (1,95 E-07 CTUh). In contrast, ozone depletion presents higher values in France (2.07 E-06 kg CFC11 eq) compared to India (1.93 E-06 kg CFC11 eq). These results highlight key areas of environmental impact in the acetaminophen production process, indicating potential opportunities for improvement of emissions related to each impact category.

Figure 4 shows the normalized energy consumption results for production in India and France. Normalization addresses unit incompatibility and compares an indicator to a reference value such as the average annual environmental load per inhabitant in a country or continent, so that the results are expressed as a "relative impact," making them easier to understand through familiar comparisons. Normalization unifies impact category indicators, aids in category comparisons, enhances the understanding of each impact's scope, and enables a more coherent analysis of results.

The results focus on energy-related processes which were explicitly selected based on the country or the corresponding geographical area and account for significant emissions and resource consumption. The impact categories with the highest environmental impacts are freshwater ecotoxicity, fossil resource use, and climate change. The freshwater ecotoxicity category shows a significantly higher impact for “heat from steam” in India compared to France. Although the values for “electricity” and “cooling energy” in both countries are similar and lower, “heat from steam” in India stands out as the major contributor to ecotoxicity, likely due to the release of specific contaminants during steam production that adversely affect aquatic ecosystems.

Regarding the use of fossil resources and climate change, both electricity and “heat from steam” in India exhibit higher values compared to the same resources in France. Electricity generation in India predominantly relies on coal-fired power plants [9]. Despite ongoing efforts to diversify the energy mix, coal remains the most cost-effective option due to India's substantial coal

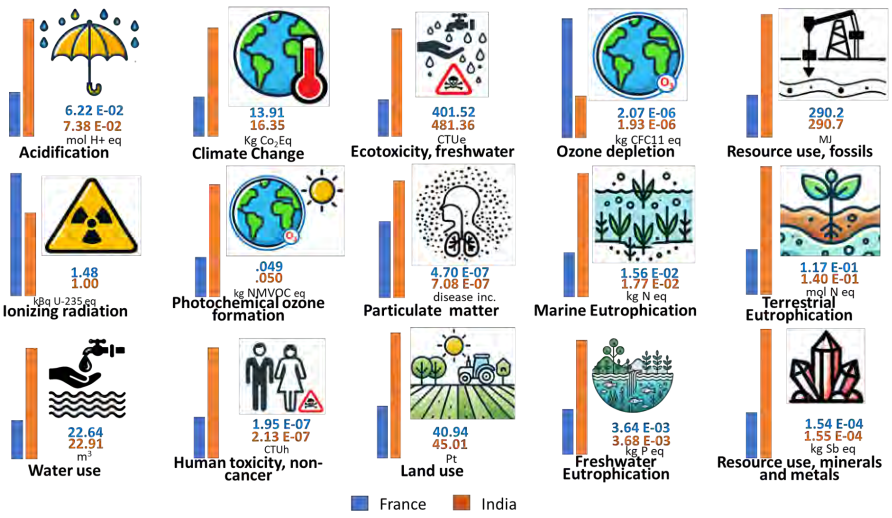



**Figure 3**: Characterization results per impact category for API production

reserves. In contrast, electricity production in France is predominantly nuclear-based, which plays a crucial role in reducing $CO_2$ emissions [10].

India and France's energy infrastructures differ significantly. India needs to enhance energy efficiency, waste treatment, and adopt renewables to mitigate environmental impacts, while France predominantly uses nuclear and renewable energy. Developing strategies to lower energy consumption and emissions is vital, focusing on energy-efficient technologies and process optimization. Transitioning to renewable energy is also crucial.

Incorporating advanced waste treatment minimizes toxic contaminants, particularly in freshwater. Recycling solvents and by-products cuts raw material use and waste. Redesigning supply chains and relocating production to greener energy regions can lessen climate impacts and carbon footprints.

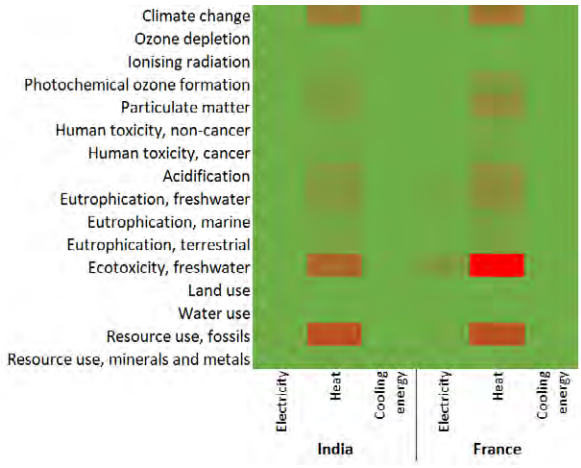



**Figure 4:** Normalized energy consumption results for production in India and France

It is important to highlight that France has implemented strategies to reduce the pharmaceutical industry's carbon footprint, such as government energy transition initiatives and environmental regulations. However, as some essential inputs are still imported, their impact on the overall carbon footprint must be considered [11].

Beyond domestic efforts, a key challenge is ensuring international suppliers meet sustainable standards. The French pharmaceutical industry has advanced in responsible sourcing, focusing on materials with lower environmental impact and suppliers committed to sustainability. However, the level of sustainability in supply chains outside France varies significantly, potentially affecting the $kgCO_2$/kg API value. This underscores the need for enhanced monitoring across the supply chain to maintain sustainability consistency [12].

To further reduce its environmental impact and promote sustainable production, the pharmaceutical industry must adopt a holistic approach. This includes improving energy efficiency, enhancing waste treatment, optimizing supply chains, innovating in raw materials, and integrating clean technologies. By addressing these aspects collectively, the industry can move toward a more sustainable and resilient production model.

## CONCLUSIONS

The relocation of paracetamol production facilities to French territory represents a strategic response to the need for enhanced supply security and a reduced environmental impact associated with its manufacturing. This shift underscores the urgency of implementing long-term sustainable solutions that promote more resilient supply chains with a smaller ecological footprint.

This research addresses a key limitation in LCA in the pharmaceutical industry: the need for more detailed LCI data on specific processes. By using advanced process modeling tools, both LCI data collection steps and

accuracy are significantly improved. Integrating process simulation with LCA methodologies allows for an exhaustive and precise evaluation of environmental impacts. This approach not only reinforces the reliability of LCA data but also provides a solid basis for sustainability-oriented decision-making in the pharmaceutical sector.

The methodology used in this study allows the construction of a detailed and reliable LCI for the paracetamol production process, facilitating a precise quantification of the associated environmental impacts. This level of detail supports more informed sustainability decisions, allowing pharmaceutical industry players to develop production strategies with lower environmental impacts and greater alignment with sustainable development goals.

The study also highlights a gap in traditional LCA methodologies, as they lack impact factors tailored to the pharmaceutical sector. To address this, the industry relies on specific indicators to enhance sustainability like Process Mass Intensity (PMI), which measures material efficiency in API synthesis and promotes more sustainable manufacturing practices [13].

Future work will explore scenarios for producing APIs such as waste recycling, treatment, and heat recovery which can reduce environmental impact and optimize resources for a sustainable pharmaceutical production.

## ACKNOWLEDGEMENTS

CONAHCYT funded this work through a scholarship.

## REFERENCES

1. Mordor Intelligence, “Ibuprofen API Market - Manufacturers, Size & Share.” Accessed: Jul. 15, 2024.[Online].Available:https://www.mordorintelligence.com/industry-reports/ibuprofen-api-market
2. Medscape, “E. Macron announces that the production of about fifty medicines will be ‘relocated’ to France,” 2023. Accessed: Jun. 29, 2023. [Online]. Available:https://francais.medscape.com/voirarticle/3610180?ecd=WNL_mdplsfeat_230617_mscpedit_fr&uac=298107MV&impID=5535696&faf=1
3. D. Wang, W. S. Cheow, N. Amalina, M. Faiezin, and K. Hadinoto, “Selecting optimal pharmaceuti-cal excipient formulation from life cycle assess-ment perspectives: A case study on ibuprofen tablet formulations,” J Clean Prod, vol. 292, Apr. 2021, doi: 10.1016/j.jclepro.2021.126074.
4. A. E. Cervera-Padrell, T. Skovby, S. Kiil, R. Gani, and K. V. Gernaey, “Active pharmaceutical ingre-dient (API) production involving continuous pro-cesses - A process system engineering (PSE)-assisted design framework,” European Journal of Pharmaceutics and Biopharmaceutics, vol. 82, no. 2, pp. 437–456, Oct. 2012, doi: 10.1016/j.ejpb.2012.07.001.
5. H. G. Jolliffe and D. I. Gerogiorgis, “Process modelling and simulation for continuous pharmaceutical manufacturing of ibuprofen,” Chemical Engineering Research and Design, vol. 97, pp. 175–191, May 2015, doi: 10.1016/j.cherd.2014.12.005.
6. A. G. Parvatker et al., “Cradle-to-Gate Green-house Gas Emissions for Twenty Anesthetic Ac-tive Pharmaceutical Ingredients Based on Pro-cess Scale-Up and Process Design Calcula-tions,” ACS Sustain Chem Eng, vol. 7, no. 7, pp. 6580–6591, Apr. 2019, doi: 10.1021/acssuschemeng.8b05473.
7. L. A. Gallego-Villada, C. Hasenstab, E. A. Alarcón, and A. L. Villa, “Identification by Life Cycle Assessment of the critical stage in the catalytic synthesis of nopol using heterogeneous cataly-sis,” Sustain Prod Consum, vol. 27, pp. 23–34, Jul. 2021, doi: 10.1016/j.spc.2020.10.017.
8. S. Scholarlycommons, S. Riksen, N. Chau, and S. Byabato, “Batch Versus Continuous Acetamino-phen Production,”2022.[Online].Available:https://repository.upenn.edu/cbe_sdrhttps://repository.upenn.edu/cbe_sdr/137
9. L. S. Tiewsoh, J. Jirásek, and M. Sivek, “Electrici-ty generation in India: Present state, future out-look and policy implications,” Energies (Basel), vol. 12, no. 7, 2019, doi: 10.3390/en12071361.
10. U. K. Pata and A. Samour, “Do renewable and nuclear energy enhance environmental quality in France? A new EKC approach with the load ca-pacity factor,” Progress in Nuclear Energy, vol. 149, Jul. 2022, doi: 10.1016/j.pnucene.2022.104249.
11. “France - Countries & Regions - IEA.” Accessed: Mar. 10,2025.[Online].Available:https://www.iea.org/countries/france
12. “The challenges of sustainable pharmaceutical sourcing - Lactalis Ingredients Pharma.” Ac-cessed: Mar.10,2025.[Online].Available:https://pharma.lactalisingredients.com/2024/05/31/the-challenges-of-sustainable-pharmaceutical-sourcing/
13. C. Jimenez-Gonzalez, C. S. Ponder, Q. B. Broxterman, and J. B. Manley, “Using the right green yardstick: Why process mass intensity is used in the pharmaceutical industry to drive more sus-tainable processes,” Org Process Res Dev, vol. 15, no. 4, pp. 912–917, Jul. 2011, doi: 10.1021/op200097d.

© 2025 by the authors. Licensed to PSEcommunity.org and PSE Press. This is an open access article under the creative commons CC-BY-SA licensing terms. Credit must be given to creator and adaptations must be shared under the same terms. See https://creativecommons.org/licenses/by-sa/4.0/



Systems & Control Transactions

**Research Article - Peer Reviewed Conference Proceeding**
ESCAPE 35 - European Symposium on Computer Aided Process Engineering
Ghent, Belgium. 6-9 July 2025
Jan F.M. Van Impe, Grégoire Léonard, Satyajeet S. Bhonsale,
Monika E. Polańska, Filip Logist (Eds.)

PSE PRESS

# Closed-Loop Data-Driven Model Predictive Control For A Wet Granulation Process Of Continuous Pharmaceutical Tablet Production

**Consuelo Del Pilar Vega Zambrano[a], Nikolaos A. Diangelakis[b], and Vassilis M. Charitopoulos[a]***

[a] Department of Chemical Engineering, The Sargent Centre for Process Systems Engineering, University College London, Torrington Place, London WC1E 7JE, UK
[b] School of Chemical and Environmental Engineering, Technical University of Crete, Chania, Crete, GR 73100, Greece
* Corresponding Author: v.charitopoulos@ucl.ac.uk.

## ABSTRACT

In 2023, the International Council for Harmonisation (ICH) guideline for the development, implementation, and lifecycle management of pharmaceutical continuous manufacturing (PCM), was implemented in Europe. It promotes quality-by-design (QbD) and quality by control (QbC) strategies as well as the appropriate use of mathematical modelling. This development urges a harmonizing understanding across academia and industry for adoption of interpretable models instead of black-box models for advanced control strategies such as model predictive control (MPC), especially when applied in Good Manufacturing Practice (GMP) regulated areas. To this end, we first propose a comprehensive model development using Dynamic Mode Decomposition with Control (DMDc)to represent complex dynamics in a lower-dimensional space, disambiguating between underlying dynamics and actuation effects. Using data from a digital twin of PCM, our model demonstrates low computational complexity while effectively capturing nonlinear dynamics with significant improvements observed in the performance metrics. Additionally, we demonstrate enhanced uncertainty propagation performance when compared to state-space models obtained with N4SID and Sparse Identification of Nonlinear Dynamical systems with control algorithms. Finally, we develop a closed-loop workflow that seamlessly connects data exchanges between Python (DMDc), GAMS (MPC optimisation) & gPROMS to evaluate the controller performance with setpoint tracking and disturbance rejection studies achieving high accuracy in real-time monitoring and control of granule size. This study offers a novel, interpretable control strategy for PCM. The results demonstrate the potential for real-time release testing, reduced reliance on end-product testing, and improved process control in the pharmaceutical industry.

**Keywords**: Quality by control, Data-driven control, Continuous pharmaceutical manufacturing

## INTRODUCTION

For pharmaceutical continuous manufacturing (PCM)applications, model predictive control (MPC) was first used in 2010 [1] to control a continuous roller compaction process comparing a PID, linear MPC (DMC), and nonlinear MPC. The nonlinear MPC showed better performance, but it was found not practical due to the high computational cost whereas the linear MPC could track the set point change and reject the disturbances of roll speed and in the inlet bulk density. Obregón et al. (2013) addressed the control of a fluidized bed dryer (FBD) using MPC alongside inline near-infrared (NIR) moisture sensors while maintaining optimal moisture content, minimizing energy consumption, and adhering to physical constraints such as air flow and temperature limits [2]. They showcased MPC's advantages in achieving the desired set points faster and more efficiently than traditional control methods. However, the model required adjustments when operating conditions deviate from the original fitting parameters showing inability to generalize to unseen data. The application of MPC for controlling blending units in continuous pharmaceutical manufacturing has also been investigated [3]. The authors described

the use of the System Identification Tool in MATLAB to develop the blending model, focusing on outlet mass flow and holdup as key outputs. The linear MPC incorporated constraints on blender speed and mass flow to enhance process performance. Although it demonstrated superior control capabilities compared to conventional methods, it was considered disadvantageous for systems with high sampling frequencies. Additionally, they indicated that measuring the outlet mass flow to estimate the states of the blender model may not be feasible in a continuous production line. A novel control concept utilizing MPC with a local linear model tree (LOLIMOT) algorithm for hopper levels in the tablet press was developed previously [4]. Recently, a hybrid model integrating mechanistic and machine learning approaches to optimize a continuous dry granulation process with MPC was developed [5]. Artificial Neural Networks (ANN) and Nonlinear Model Predictive Control (NMPC) showed effectiveness in managing the granulation process.

The implementation and assessment of MPC strategies, tailored for a holistic plant-wide control framework in continuous pharmaceutical manufacturing, have been proposed [6]. This work was conducted at the Novartis-MIT Center for Continuous Manufacturing. Two distinct MPC designs were proposed, employing different modeling approaches: subspace identification and linearization of nonlinear differential-algebraic equations. These approaches resulted in low-dimensional and high-dimensional state-space models, respectively. The simulation results demonstrated that the plant-wide MPC effectively regulates critical quality attributes (CQAs) while accommodating various uncertainties, including fluctuations in reaction kinetics and disturbances in filtration unit efficiency. Additionally, the approach incorporated quality-by-design principles by integrating input and output constraints, ensuring that the process remains compliant with regulatory requirements. The findings demonstrated that the MPC framework not only improves operational efficiency but also ensures consistent product quality.

While some applications of MPC for pharmaceutical continuous manufacturing have been reported, barriers to the adoption of this advanced process control exist [7]. Celikovic et al. (2020) identified two challenges in implementing MPC algorithms: i) handling potentially high computational burden to solve the control problem fast enough within the small sampling intervals and, ii) having the reliable process analytical technology (PAT) equipment for real-time monitoring of CQAs [3]. An implementation issue arises that when nonlinear models are used, this leads to non-convex optimization problems with multiple local optima, which requires much more computational power and offers no guarantees for global optimality and stability of the solution.

Given that MPC is employed to regulate a dynamic process system whilst considering constraints that can include operational limits on the controlled variables and rate-of-change limits on the manipulated variables, undoubtedly a key part on adopting this control strategy is mathematical modelling. As an alternative to computationally demanding mechanistic models, reduced Order Models (ROMs) offer an entirely data-driven means to represent reliable yet computationally intensive models in a lower-dimensional space. ROMs representations can be deduced with several system identification techniques, many of them based on a form of dynamic regression that fits models based on input- output data. These techniques have been examined since the 1950s and some examples include autoregressive moving average with exogenous inputs (ARMAX) models, Multivariable Output- Error State Space (MOESP), Observer Kalman Identification (OKID), Sparse identification of nonlinear dynamics (SINDy) and Dynamic Mode Decomposition with Control (DMDc) [8]. Particularly, DMDc has been increasingly recognized for its ability to systematically uncover simplified relationships within intricate systems operating using discrete-time snapshots of the states and corresponding control inputs of the system to extract the underlying effect of both on the system dynamics.

Our approach differs from previous surrogate models for two reasons. First, the interpretability in our framework comes from the algorithmic or mathematical transparency of how a dynamic model is obtained with Dynamic Mode Decomposition with control which avoids the black-box nature of data-driven techniques found in the literature such as LoLiMoT, ARMA or neural network models. Second, to enhance interpretability, the reduced-order model is formulated as a simple linear discrete-time state-space equation, for which we also quantify its uncertainty propagation performance.

## METHODOLOGY

### Data-driven model identification with DMDc

Dynamic mode decomposition with control (DMDc) was introduced in 2016 [8] as a modal decomposition technique that extracts dynamically relevant spatial structures and whose goal is to disambiguate between the underlying dynamics and the effects of actuation.

Since the mathematical foundations of DMDc lie on the assumption that the next state of a dynamic system $y_t \in R^n$ is determined from a function of the current state $y_{t-1} \in R^n$ and current input $u_{t-1} \in R^p$, a dynamic system can be then approximated by a linear state-space model described in equation (1) for n observed snapshots, where A $\in R^{nxn}$ is the system matrix and B $\in R^{nxp}$ is the control matrix.

$$y_t^{DMDc} = Ay_{t-1} + Bu_{t-1} \quad (1)$$

$$where\ y_t \in R^n, u_{t-1} \in R^p,\ A \in R^{nxn}\ and\ B \in R^{nxp}$$

We tested the performance of DMDc to identify a model, as part of an offline stage of our proposed framework (Fig. 1), to predict four granule size distribution quantiles D5, D10, D50, and D90 for a twin-screw granulation process with three control variables Avicel (AFR), binder (BFR), and lactose flow rates (LFR). Data was collected from simulations using a gPROMS FormulatedProducts® 2023.2.1 process model flowsheet of integrated TSG and fluidized bed drying which was customized for the GEA ConsiGma™-25 Continuous Tableting Line CTL, at the Diamond Pilot Plant (DiPP) of the University of Sheffield. The TSG consists of a feeding section for powder transport and a working section for mixing powder with granulation liquid. Dry powders and granulation liquid are delivered via loss-in-weight dosing units. Wet granules are transferred to a six-segment fluidized bed dryer, where they are dried sequentially and discharged for further processing, enabling continuous operation until tableting is complete. For the full details of the process flowsheet, we refer the interested reader to [9].

Duration of the simulations was 3000s, with 1 dataset for training and 3 datasets for validation, varying randomly the powder (lactose and Avicel) and binder (water) flowrates. Noise was added to all data imposing periodical disturbances on the flowrates with a frequency 1 min-1 and a minimum/maximum deviation of 5% directly in gPROMS. For the uncertainty quantification study, 1000s extra were sampled for the training dataset.

Alternative system identification methods were used to compare the performance of DMDc. First, a state-space equation is obtained with a data-driven method called Sparse Identification of Nonlinear Dynamical systems with control (SINDyc), which regresses the coefficients for a nonlinear ordinary differential equation [10]. Second, the N4SID tool for Multivariable Output Error State Space (MOESP) from the MATLAB system identification toolbox [11] was employed.

## Uncertainty quantification for state-space models

After identifying A and B matrices for the DMDc, SINDyc and MOESP models, the covariance matrix of the process noise and posterior covariance, as detailed in Digital Supplementary Material, was calculated for each model following:

$$\Sigma_\varepsilon = \frac{1}{n}\sum_{t=2}^{n} \left(y_t - \hat{A}y_{t-1} - \hat{B}u_{t-1}\right)^T \left(y_t - \hat{A}y_{t-1} - \hat{B}u_{t-1}\right) \quad (2)$$

$$V\left[y_{t*+1}|Y,\hat{A},\hat{B},\hat{\Sigma}_\varepsilon\right] = \sum_{i=0}^{t*-n} \hat{A}^i \hat{\Sigma}_\varepsilon \left(\hat{A}^i\right)^T + \sum_{i=0}^{t*-n} \hat{A}^i \hat{B} \hat{\Sigma}_u \hat{B}^T \left(\hat{A}^i\right)^T \quad (3)$$

For simplicity, $\hat{\Sigma}_u$ was assumed to be a diagonal matrix containing the standard deviations of each component (independent of the others) of the control input vector used for the training dataset.

Then, 95% confidence interval (CI) are calculated as:

$$CI = y_{t*} \pm 1.96 \cdot diag\left(V\left[y_{t*}|Y,\hat{A},\hat{B},\hat{\Sigma}_\varepsilon\right]\right) \quad (4)$$

The numerical criteria include the predictive root of mean squared error (RMSE) and the average length of the 95% predictive intervals (L(95%)):

$$RMSE = \left(\sum_{j=1}^{m}\sum_{t*=n+1}^{n+n*}\left(\hat{y}_{j_{t*}} - y_{j_{t*}}\right)^2\right)^{\frac{1}{2}} \quad (5)$$

$$L(95\%) = \frac{1}{mn*}\sum_{j=1}^{m}\sum_{t*=n+1}^{n+n*} \text{length}\{\text{CI}_{j,t*}(95\%)\}) \quad (6)$$

where $\hat{y}_j(x_{t*})$ is the prediction of the output for state j and length $\{\text{CI}_{j,t*}(95\%)\}$ denotes the length of the 95% predictive interval.

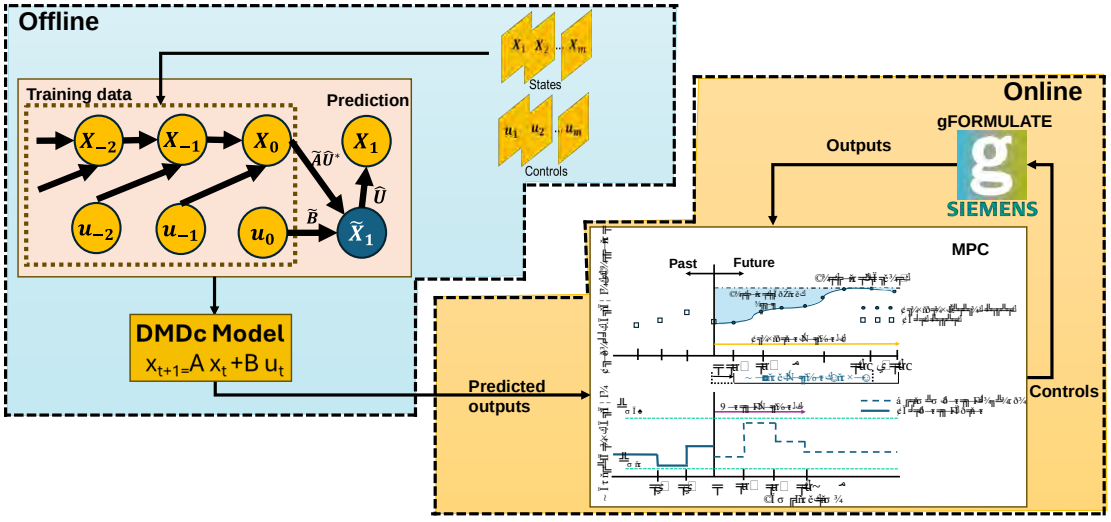



**Figure 1.** Proposed framework for a model predictive control (MPC) with a DMDc model

## Closed-loop data-driven control framework

The DMDc model developed offline was integrated into a linear model predictive control in an online stage (Fig. 1), coded in General Algebraic Modelling System (GAMS®) using the solver Gurobi 11.02, in a closed-loop manner. A prediction horizon of 30 seconds and a control horizon of 10 seconds were empirically tuned to balance control performance and computational efficiency.

Every control period of 1 second, a customized gPROMS FormulatedProducts® flowsheet sent data employing gO:Python, which used the model as an estimator to predict future states of the system. These predicted outputs were sent to the optimizer using GAMSPy to find optimal control inputs in real time by solving an optimization problem with an average computation time of 0.034 ± 0.01s that minimized the error between predicted and desired setpoints. At each time step (1s), the optimization was repeated, updating the control sequence over the control horizon and applying the first control action to the system using gO:Python + GAMSPy. The interaction between the process, estimator, and optimizer ensured that the system operates efficiently, maintaining stability and optimizing performance in response to changing process conditions.

Setpoint tracking and disturbance studies were conducted, to evaluate the MPC, introducing white Gaussian noise on the states with 1% standard deviation. Stepwise changes of the granule size references were introduced at certain times, and the solid/liquid feed rate control moves were analyzed.

Three types of disturbance scenarios were explored separately: binder flow rate disturbance, lactose flow rate disturbance, and Avicel flow rate disturbance. To conduct this study, each disturbance simulation, was applied as two manual step changes using gO:Python of either +10% or +20% of the flowrate at 40 seconds and either -10% or -20% of the flowrate at 80 seconds. The objective was to assess the controller's ability to detect, respond, and adjust control actions to maintain the desired reference values.

# RESULTS AND DISCUSSION

## Model comparison

The model obtained for DMDc in Python, MOESP in Matlab and SINDyc in Python has the form of a discrete-time first-order state-space equation where matrix A was the system matrix and determined how state variables change over time and B was the control matrix which determines how the system inputs affected the state change.

The model performance can be visualized in Fig. 2 where the DMDc model demonstrates enhanced accuracy and performance when dealing with unseen values (validation phase) even when working with noisy data. The deteriorated performance for MOESP can be related to its algorithmic complexity and overfitting trend and for SINDyc because of elimination of coefficients of the A matrix in the ROM that described, for example, the effect of D90 on D10 state, as detailed in Digital Supplementary Material.

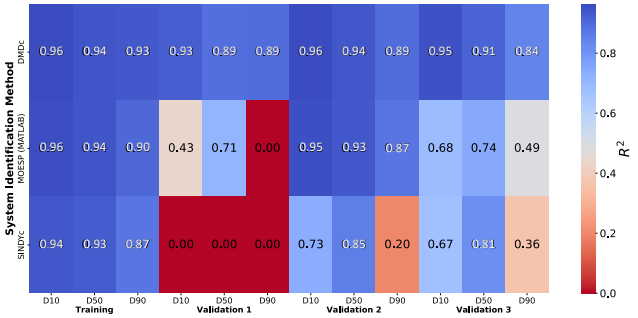



**Figure 2.** Heatmap for error metrics study $R^2$

The eigenvalues of the generated system state space models are shown in Table 1. Following conventional control theory, the DMDc eigenvalues provide stability guarantee on the model performance.

**Table 1:** Eigenvalues of ROMs.

| Method | Description |
|---|---|
| DMDc | $[0.63\,;\ \ 0.99\ ;\ 0.99\,;\ \ 0.97]$ |
| SINDyc | $[0.6-0.13i\,;0.6+0.13i;\ 0.9\,;1.0005\,]$ |
| MOESP | $[0.3+\ 0.2i;\ \ 0.3-0.2i\,;\ \ 0.99\,;\ 0.97\,]$ |

Regarding the uncertainty study, as displayed in Table 2, DMDc was found to be the most accurate method because it had a small predictive error quantified by RMSE and shorter average length of 95% predictive interval, also shown in Fig. 3.

High RMSE and wide confidence intervals for SINDyc and MOESP methods suggest that these models are more sensitive to noise and could be overfitting or underfitting the data, with very large uncertainty.

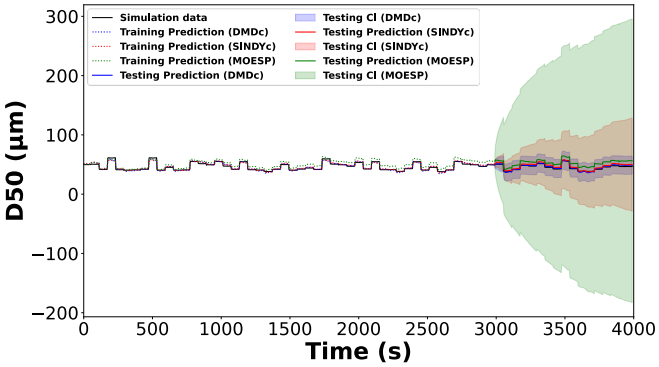



**Figure 3. Uncertainty measurement for D50** for a prediction of 1000 steps by DMDc (blue), SINDYc (orange) and MATLAB (green) after 3000s for training.

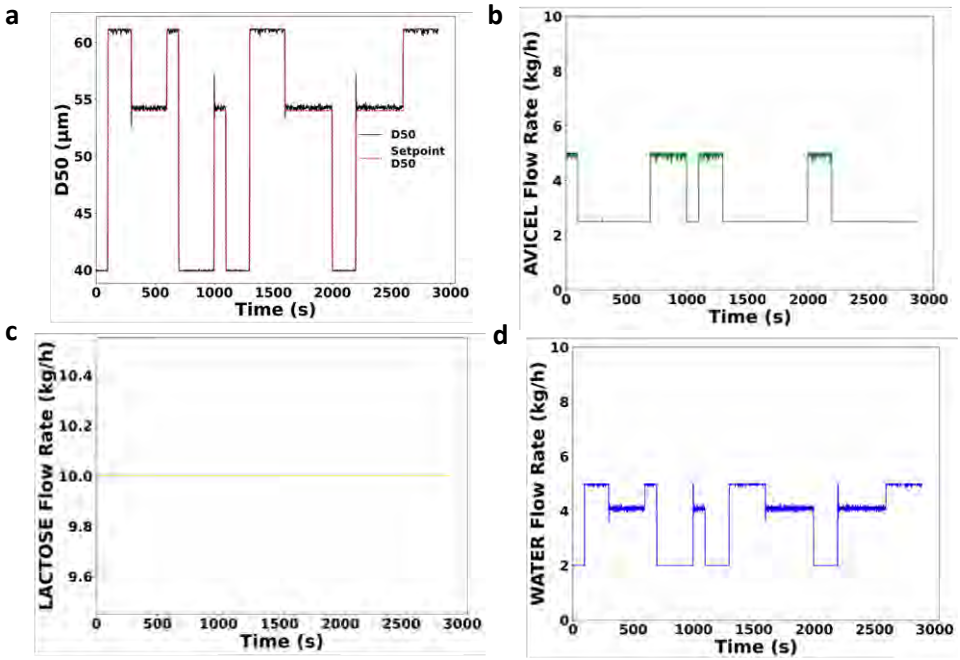



**Figure 4.** Setpoint tracking study for DMDc-MPC: a. Controlled variable (D50 shown) b-d. Manipulated variables

The 95% predictive intervals per each model are envisaged as shaded areas.

**Table 2:** Uncertainty quantification

| **1000-steps test** | | |
|---|---|---|
| | **RMSE** | **L(95%)** |
| DMDc | 6.18 | 57.85 |
| SINDyc | 13.29 | 424.66 |
| MOESP(MATLAB) | 57.17 | 1548.82 |
| **2000-steps test** | | |
| | **RMSE** | **L(95%)** |
| DMDc | 6.89 | 58.98 |
| SINDyc | 16.08 | 717.86 |
| MOESP(MATLAB) | 66.95 | 1981.83 |

## Closed-loop MPC performance

As shown in Suppl. Table 1, the selected prediction and control horizons provided the best trade-off for a control interval of 1s. As we can see in Suppl. Fig. 1, the setpoint for the controlled variable D50 is better reach with strategy H3 and longer horizons (PH = 100s, CH = 20s) led to over-tuning, as evidenced by increased peaks in the Avicel flowrate and higher CPU times."

The choice of a 1-second control interval was justified by the granulation process dynamics, which require frequent adjustments to maintain stability because it is known the binder concentration control is extremely important to maintain a desired oversized fraction of granules for lactose/Avicel-based formulations, also deviations in powder mass flow rate which might occur during volumetric feeding must be considered [12]. Nevertheless, less frequent sampling rates can be facilitated.

For the closed-loop evaluation, performance monitoring methods were used to assess how effectively the control system follows setpoint changes. Fig. 4 confirms the MPC's capability to track the reference by adjusting the input flow rates (D50 shown as an example)

Furthermore, the controller's ability to handle introduced disturbances was analyzed, especially because regulatory-level process control loops are commonly used in plants to respond to variations in binder flow rates.

In all cases, the disturbances were well rejected, as shown in Suppl. Figs. 2-4. The interested reader can refer to Digital Supplementary Material for other graphs. The most interesting aspect revealed is that introducing disturbances to the Avicel flowrate does not affect the other manipulated variables (MVs). In contrast, disturbances applied to either the lactose or binder flowrates affect both. In all cases, the manipulated flow rates stabilize after a short transient period.

# CONCLUSION

This study highlights the effectiveness of DMDc as an explainable machine learning method for CM. The DMDc-MPC system not only maintained desired process conditions and granule size but also demonstrated superior performance in uncertainty analysis, outperforming other data-driven models. This approach enhances transparency, reliability, and regulatory acceptance, potentially accelerating the adoption of predictive models in pharmaceutical manufacturing. Future work in our group is focusing on exploring the application of DMDc to more

complex unit operations that exhibit highly nonlinear dynamics. This will allow us to further explore potential limitations of the proposed method and fuel further developments.

## DIGITAL SUPPLEMENTARY MATERIAL

Digital materials can be found with this LAPSE:2025.0010.

## ACKNOWLEDGEMENTS

Financial support from grant EPSRC EP/V034723/1 and Peruvian Government through PRONABEC is gratefully acknowledged.

## REFERENCES

1. Hsu SH, Reklaitis GV, Venkatasubramania V. Modeling and control of roller compaction for pharmaceutical manufacturing: Part ii: Control system design. J. Pharm. Innov. 5, 24–36(2010) https://doi.org/10.1007/s12247-010-9077-z
2. Obregón L, Quiñones L, Velazquez C. Model predictive control of a fluidized bed dryer with an inline nir as moisture sensor. Control Eng. Pract. 21, 509–517 (2014) https://doi.org/10.1016/j.conengprac.2012.11.002]
3. Celikovic S, Kirchengast M, Rehrl J, Kruisz J, Sacher S, Khinast J, Horn M. Model predictive control for continuous pharmaceutical feeding blending units. Chem. Eng. Res. Des. 154, 101–114 (2020) https://doi.org/10.1016/j.cherd.2019.11.032
4. Sacher S, Celikovic S, Rehrl J, Poms J, Kirchengast M, Kruisz J, Sipek M, Salar-Behzadi S, Berger H, Stark G, Horn M, Khinast J. Towards a novel continuous hme-tableting line: Process development and control concept. European J. Pharm. Sci. 142 (2020) https://doi.org/10.1016/j.ejps.2019.105097
5. Huang YS, Lagare RB, Bailey P, Sixon D, Gonzalez M, Nagy ZK, Reklaitis GV. Hybrid model development and nonlinear model predictive control implementation for continuous dry granulation process. Comput. Chem. Eng. 183 (2024) https://doi.org/10.1016/j.compchemeng.2024.108586
6. Mesbah A, Paulson JA, Lakerveld R, Braatz RD. Model predictive control of an integrated continuous pharmaceutical manufacturing pilot plant. Org. Process Res. Dev. 21, 844–854 (2017) https://doi.org/10.1021/acs.oprd.7b00058
7. Nașcu I, Diangelakis NA, Muñoz SG, Pistikopoulos, EN. Advanced model predictive control strategies for evaporation processes in the pharmaceutical industries. Comput Chem Eng 173, 108212. (2023) https://doi.org/10.1016/j.compchemeng.2023.108212
8. Proctor JL, Brunton SL, Kutz JN. Dynamic mode decomposition with control. SIAM. 15, 142–161 (2016) https://doi.org/10.48550/arXiv.1409.6358
9. Wang, LG, Omar, C, Litster, J, Slade, D, Li, J, Salman, A, Bellinghausen, S, Barrasso, D, Mitchell, N. Model driven design for integrated twin screw granulator and fluid bed dryer via flowsheet modelling. Int J Pharm 628, 122186 (2022) https://doi.org/10.1016/j.ijpharm.2022.122186
10. Fasel U, Kaiser E, Kutz JN, Brunton BW, Brunton SL. Sindy with control: A tutorial. 2021 60th IEEE Conference on Decision and Control (CDC) 2021-Decem, 16–21 (2021) https://doi.org/10.48550/arXiv.2108.13404
11. Van Overschee, P, & De Moor, B. N4SID: Subspace algorithms for the identification of combined deterministic-stochastic systems. Automatica, 30(1), 75-93 (1994) https://doi.org/10.1016/0005-1098(94)90230-5
12. Vega-Zambrano C, Diangelakis NA, Charitopoulos VM. Data-driven model predictive control for pharmaceutical continuous manufacturing. Int J Pharm 125322 (2025) https://doi.org/10.1016/j.ijpharm.2025.125322

© 2025 by the authors. Licensed to PSEcommunity.org and PSE Press. This is an open access article under the creative commons CC-BY-SA licensing terms. Credit must be given to creator and adaptations must be shared under the same terms. See https://creativecommons.org/licenses/by-sa/4.0/



Systems & Control Transactions

**Research Article - Peer Reviewed Conference Proceeding**
ESCAPE 35 - European Symposium on Computer Aided Process Engineering
Ghent, Belgium. 6-9 July 2025
Jan F.M. Van Impe, Grégoire Léonard, Satyajeet S. Bhonsale,
Monika E. Polańska, Filip Logist (Eds.)

PSE PRESS

# Development of a Hybrid Model for the Paracetamol Batch Dissolution in Ethanol Using Universal Differential Equations

**Fernando Arrais R. D. Lima[a,b,*], Amyr Crissaff Silva[a], Marcellus G. F. de Moraes[c,d], Amaro G. Barreto Jr.[a], Argimiro R. Secchi[a,d], Idelfonso Nogueira[b], Maurício B. de Souza Jr.[a,d]**

[a] School of Chemistry, EPQB, Universidade Federal do Rio de Janeiro, Av. Horácio Macedo, 2030, CT, Bloco E, 21941-914, Rio de Janeiro, RJ – Brazil
[b] Chemical Engineering Department, Norwegian University of Science and Technology, Trondheim, 793101, Norway
[c] Instituto de Química, Rio de Janeiro State University (UERJ), Rua São Francisco Xavier, 524, Maracanã, Rio de Janeiro, RJ, 20550-900, Brazil
[d] PEQ/COPPE – Universidade Federal do Rio de Janeiro, Av. Horácio Macedo, 2030, CT, Bloco G, G115, 21941-914, Rio de Janeiro, RJ – Brazil
* Corresponding Author: farrais@eq.ufrj.br.

## ABSTRACT

Crystallization is a relevant process in the pharmaceutical industry for product purification and particle production. An efficient crystallization is characterized by crystals produced with the desired attributes. Therefore, modeling this process is a key point to achieve this goal. In this sense, the objective of this work is to propose a hybrid model to describe paracetamol dissolution in ethanol. The universal differential equations methodology is considered in the development of this model, using a neural network to predict the dissolution rate combined with the population balance equations to calculate the moments of the crystal size distribution (CSD) and the concentration. The model was developed using experimental batches. The dataset is composed of concentration measurements obtained using attenuated total reflectance-Fourier transform infrared (ATR-FTIR). The objective function of the optimization problem is to minimize the relative absolute difference between the experimental and the predicted concentration. The hybrid model efficiently predicted the concentration compared to the experimental measurements. Furthermore, the hybrid approach made predictions of the moments of the CSD similar to the population balance model proposed by Kim et al. [1], being able to successfully calculate batches not considered in the training dataset. Moreover, the performance of the hybrid model was similar to the phenomenological one based on population balance. Therefore, the universal differential equations approach is presented as an efficient methodology for modeling crystallization processes with limited information.

**Keywords**: Crystallization, hybrid model, pharmaceutical industry.

## INTRODUCTION

Crystallization is a separation and purification process that is characterized by a phase change in which crystalline product is obtained from a solution [1]. It is a relevant unit operation and is commonly used for purification, separation and production. It is a practical method that produces pure, concentrated, appealing and convenient to handle chemical substances. Thus, crystallization processes are present in many industries such as pharmaceuticals, food and agrochemicals. Many active ingredients in pharmaceutical industries are produced in the form of crystals, such as paracetamol [2], praziquantel [3] and amoxicillin [4].

For the development of an efficient crystallization process, the product should present the desired characteristics, such as size and shape. Therefore, modeling the crystallization kinetics to calculate the crystal size distribution (CSD) is a key point to predict these characteristics and to optimize the process. Population balance

model (PBM) is the methodology usually applied for modeling crystallization processes. This approach was used to model the batch crystallization of many compounds, such as potassium dihydrogen phosphate (KDP) [5], paracetamol [2, 6, 7] and potassium sulfate [8].

Over the last years, advancements in machine learning have been fueled by greater computational power, the abundance of extensive experimental data, and the development of more efficient algorithms. Machine learning techniques have achieved significant success in analyzing and predicting complex behaviors from large datasets, as demonstrated by applications such as web searches, email filtering, and image recognition [9, 10]. In the field of crystallization, machine learning is emerging as a valuable tool for predicting and optimizing processes to meet specific product requirements [11, 12].

Even with these positive points of machine learning models, they are usually empirical models and do not consider the physical laws that describe the system. Hybrid models present as an alternative to solve these problems. Hybrid models are a combination of data-driven and first principles models [13]. These approaches combine the flexibility of data-driven with the knowledge of physical laws from first principles models [14].

Regarding crystallization processes, Lima et al. [15] combined neural networks and PBM for modeling the nucleation, crystal growth and dissolution for the potassium sulfate batch crystallization. Wu et al. [16] proposed a physics-informed recurrent neural network (PIRNN) for modeling the crystallization process of aspirin. Sitapure and Kwon [17] developed hybrid modeling approach combining time-series-transformers (TSTs) to population balance model. They used TSTs to obtain the nucleation and growth rates for the batch crystallization of dextrose. Then, the rates were used in the population balance equations to obtain the crystal size distribution (CSD). There are also hybrid model applications used to describe the batch crystallization of sugar accounting for nucleation, growth and agglomeration [18, 19].

The goal of this work is to propose a hybrid model based on universal differential equations (UDEs) approach with a neural network as a universal approximator to describe the dissolution for the paracetamol batch crystallization in ethanol. According to Xiouras et al. [9] and Lima et al. [10], the use of hybrid models for crystallization processes is not new, but there are few applications of these methodologies. Most studies proposed hybrid models for sugar crystallization. There is a lack of hybrid model applications for the pharmaceutical field and none of them considered paracetamol. Paracetamol is a pharmaceutical compound whose crystallization has been extensively explored in the literature for modeling and control studies. The hybrid model is composed of a neural network to calculate the dissolution rate combined with the population balance equations to predict the concentration and the moments of the CSD. The concentration measurements obtained by Kim et al. [2] were used to develop the hybrid model. Therefore, the hybrid approach presents flexibility to model the dissolution rate compared to the PBM.

# METHODOLOGY

## Population Balance Model

Kim et al. [2] proposed a PBM to describe the paracetamol batch crystallization in ethanol. The model accounts for nucleation, crystal growth and dissolution. The method of moments was applied to solve this problem.

Eq. 1 describes the $i^{th}$ order moment, in which $L$ is the characteristic crystal size, and $n(L)$ is the number density of crystals. The moments $\mu_0$, $\mu_1$, $\mu_2$and $\mu_3$ are proportional to the total number, length, surface area, and volume of crystals, respectively.

$$\mu_i = \int_0^\infty L^i\, n(L) dL,\ i = 1,2,3,\ldots \tag{1}$$

The paracetamol dissolution PBM is described by Eq. 2, where $k_v$ is the volume shape factor, $\rho_c$ is the solid density of crystals (g/cm$^3$), and $D$ is the dissolution rate.

$$\frac{d\mu_0}{dt} = 0 \tag{2a}$$

$$\frac{d\mu_1}{dt} = D\mu_0 \tag{2b}$$

$$\frac{d\mu_2}{dt} = 2D\mu_1 \tag{2c}$$

$$\frac{d\mu_3}{dt} = 3D\mu_2 \tag{2d}$$

$$\frac{dC}{dt} = -3k_v\rho_c\, D\mu_2 \tag{2e}$$

The dissolution rate is described by Eq. 3, where $k_d$ is the pre-exponential rate constants for the crystal growth $((\mu m/min)(g/g)^{-\gamma_d})$, $E_{a_d}$ is the activation energy (J/mol) and $\gamma_d$ is a exponential parameters on supersaturation. $R$ is the universal gas constant (J/(mol K)) [20].

$$D = k_d exp\left(\frac{-E_{a_d}}{RT}\right)(C_S - C)^{\gamma_d} \tag{3}$$

In Eq. 3, $C$ (g solute/g solvent) is the concentration in the solution and $C_S$ (g solute/g solvent) is the saturated concentration at the system temperature. The saturated concentration can be calculated by the polynomial described by Eq. 5, in which $T$ is the temperature in Kelvin.

$$C_S = -8.707 + 9.669x10^{-2}T - 3.610x10^{-4}T^2 + 4.590x10^{-7}T^3 \quad (5)$$

To estimate the parameters of this PBM, Kim et al. [2] performed seven experimental batches, which five were used to develop the model and two to validate it. All experimental batches were developed at constant temperatures; two of them were performed at 10°C, one at 15°C, three at 20°C, and one at 30°C. The initial concentration was also changed for the batches, considering values between 0.142 and 0.202 g/g. The model was developed using concentration measurements obtained during the experimental batches with attenuated total reflectance Fourier transform infrared (ATR-FTIR).

## Universal Differential Equations

Universal differential equations (UDEs) are differential equations enhanced by the inclusion of one or more universal approximators. Various functions and series have been recognized as universal approximators due to their versatility and adaptability. Neural networks excel as universal approximators in higher-dimensional settings. Their layered architecture and the use of nonlinear activation functions allow them to effectively approximate functions within multidimensional spaces [15].

In this work, a hybrid model was developed to describe the dissolution kinetics of paracetamol in ethanol based on the UDE approach. A neural network is used to calculate the dissolution rate, while the moments of the CSD and the concentration are obtained by the population balance equations. The neural network uses concentration measurements and the saturated concentration to calculate the dissolution rate. Before being used by the neural network, the inputs were scaled between zero and one. Figure 1 presents a scheme of the proposed UDE.

The model was developed using the concentration measurements obtained by Kim et al. [2] during the batch experiments. Similarly to Kim et al. [2], two experimental batches were used to test the model. However, four batches were used to train and one to validate the model to avoid overfitting. The optimization problem consisted of designing the neural network that minimizes Eq. 6, where $C_i$ is the experimental concentration, $\hat{C}_i$ is the predicted concentration and $N$ is the number of measurements. As this model accounts only for undersaturated conditions, the constraint described in Eq. 7 was considered for the optimization problem.

$$F_{obj} = \frac{1}{N}\sum_{i=1}^{N}\left|\frac{\hat{C}_i - C_i}{C_i}\right| \quad (6)$$

$$\hat{C}_i / C_S(T_i) \leq 1 \quad (7)$$

The hybrid model was developed in Python using the deep learning library, Pytorch [21] and the neural differential equations library TorchDyn [22]. The optimizer Adam was used to train the hybrid model. Early stopping was also considered in the training to avoid overfitting with a criterion of stopping the training whenever the model exceeded 70 epochs without lowering validation error.

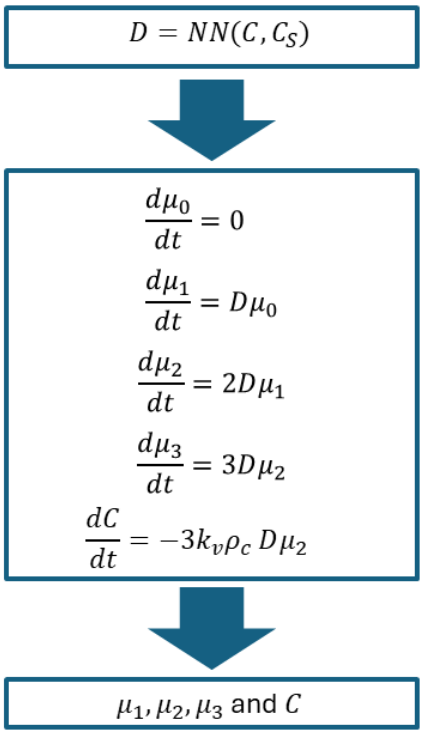



**Figure 1.** Hybrid model scheme.

## RESULTS AND DISCUSSION

The hybrid model was composed of a neural network with one hidden layer containing 30 neurons and using hyperbolic tangent as the activation function. An adaptive learning rate was considered with an initial value equal to $10^{-5}$. The learning rate is reduced to 10% of the initial value after 500 epochs.

Table 1 presents the relative mean absolute error (RMAE) between the predicted and measured concentrations for the PBM and the hybrid model. While the performance of the PBM was better for the test dataset, the hybrid model was able to make predictions closer to the experimental values for the training and validation datasets. However, both approaches presented close values of RMAE in all cases.Fig. 2 presents the performance of the hybrid model and the PBM to predict the solution concentration for the validation batch. The PBM and the hybrid model showed close performances. Their concentration predictions presented a similar behavior and achieved the same equilibrium concentration at the end of the batch. Compared to the experimental values, the UDE model made predictions closer to the concentration

measurements than the PBM.

**Table 1:** Relative mean absolute error (RMAE) between the concentration measurements and the predicted values by the PBM and the hybrid model.

| Model | Training | Test | Validation |
|---|---|---|---|
| PBM | $6.50 \times 10^{-3}$ | $5.18 \times 10^{-3}$ | $4.31 \times 10^{-3}$ |
| UDE | $3.50 \times 10^{-3}$ | $8.29 \times 10^{-3}$ | $3.18 \times 10^{-3}$ |

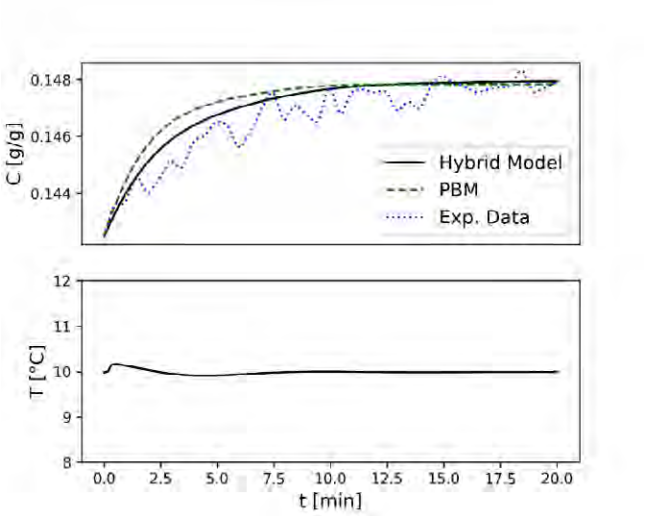



**Figure 2.** Performance of the PBM and hybrid model to predict the concentration for the validation batch.

Fig. 3 presents the performance of the hybrid model and the PBM to predict the solution concentration for one of the test batches. Once again, both methodologies were able to make close concentration predictions. The RMAE value, in Table 1, for the hybrid model for the test dataset was higher than the PBM because of the offset that the UDE model left in the equilibrium concentration compared to the experimental data.

The values presented in Table 1 and the performances showed in Figs 2 and 3 suggest that the hybrid model presented a better performance for the training and validation dataset. On the other hand, the PBM was more efficient for the test dataset. These facts suggest that the UDE model is able to make efficient predictions, but the PBM was more effective for conditions not considered in the training dataset. Therefore, the performance of the PBM was better for extrapolation. This can be expected as the PBM is based on physics laws.

Fig. 4 presents a simulation of one experimental batch using the hybrid model and the PBM. In this simulation, $\mu_1, \mu_2, \mu_3$ and the solution concentration were calculated. Regarding the concentration predictions, both approaches were able to achieve the same equilibrium concentration at the end of the batch. However, PBM presented a faster response compared to the UDE trajectories. This behaviour was also observed in Fig. 2, showing that the PBM is overestimating this characteristic when compared to the experimental data. The same thing happens for the predictions of the moments of the CSD. Both models were able to achieve similar equilibrium values at the end of the batch. The same differences in the transient response are also present in the moments.

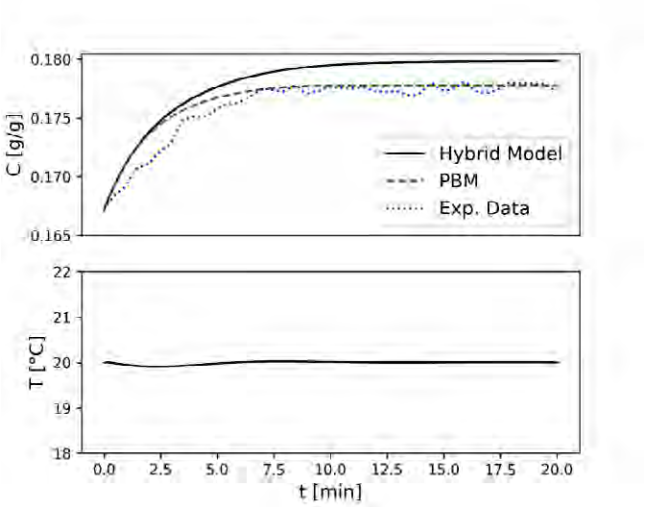



**Figure 3.** Performance of the PBM and hybrid model to predict the concentration for one of the test batches.

The differences presented in Fig. 4 between the predictions of the hybrid model and the PBM are consequence of the challenge when dealing with dissolution. The dissolution is a quick phenomenon. Therefore, when the crystals are added in the undersaturated solution during the batch, they are quickly dissolved until the equilibrium is reached. This fact makes it difficult to find an efficient model for dissolution. The errors calculated in Table 1 and the profiles obtained in Figs. 2 and 3 suggest that the hybrid model was able to make predictions closer to the real measurements when the crystals are dissolving compared to the PBM.

The proposed hybrid approach based on UDE presented a good performance for modeling the dissolution of paracetamol in ethanol. The PBM presented the best performance for extrapolations. On the other hand, the UDE model was able to make better predictions than the PBM when the crystals were dissolving. Even with these advantages and disadvantages, replacing the dissolution rate by a neural network was an effective alternative for modeling this phenomenon, as suggested by Lima et al. [15].

## CONCLUSION

In this work, a hybrid model based on UDE was developed for describing the paracetamol dissolution in ethanol. There is a lack of studies proposing hybrid models for crystallization or dissolution of pharmaceutical compounds and none of them considered paracetamol

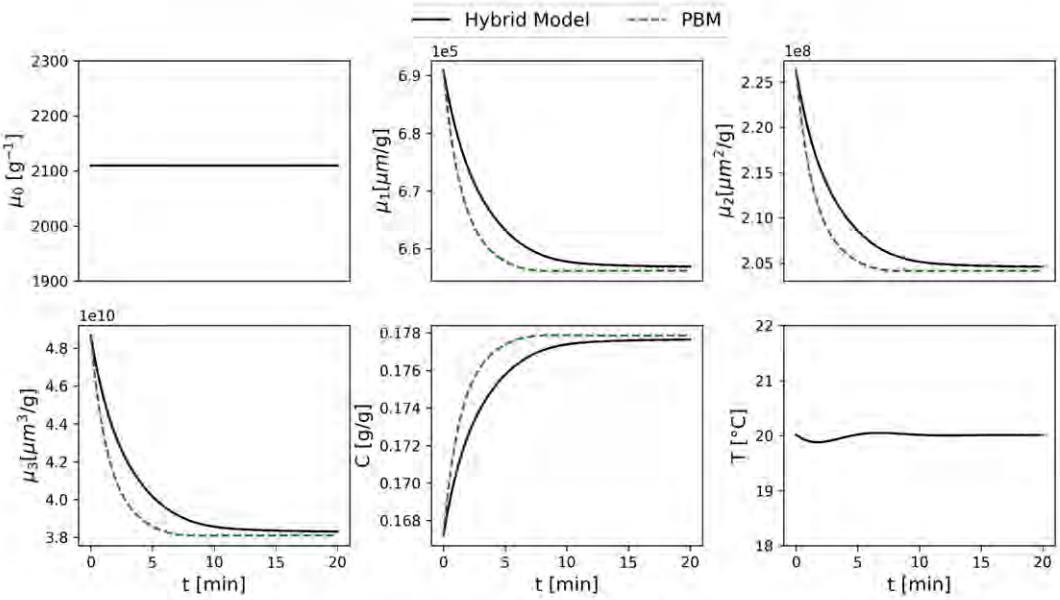



**Figure 4:** Performance of the hybrid model and the PBM to predict the moments of the CSD and the concentration of the solution considering the same conditions of one experimental batch.

[9, 10]. The dataset used in this work consisted of seven experimental batches developed by Kim et al. [2], where four of them were used to train the model, one for validation and two to test it. The developed hybrid model was able to make predictions of the solution concentration close to the experimental measurements, presenting low RMAE values.

The performance of the hybrid model was also compared to the PBM developed by Kim et al. [2]. The values calculated by the hybrid model of solution concentration and moments of CSD were close to the one obtained with the PBM. The RMAE between the concentration measurements and the predicted values by the PBM was similar to the RMAE calculated with the hybrid model. The hybrid methodology based on UDE presents as an efficient alternative for modeling crystallization kinetics. As a future work, the nucleation and crystal growth will be considered for developing the hybrid model of paracetamol crystallization in ethanol.

## ACKNOWLEDGEMENTS

Coordination for the Improvement of Higher Education Personnel (CAPES, Finance Code 001), the National Council for Scientific and Technological Development (CNPq, Grants 303587/2020-2, 311153/2021-6, and 313337/2021-7), and the Research Support Foundation of the State of Rio de Janeiro (FAPERJ, Grants E 26/111.671/2013 and E-26/201.148/2022).

## REFERENCES

1. Ahn B., Bosetti L., Mazzotti M. Secondary Nucleation by Interparticle Energies. II. Kinetics. *Crystal Growth & Design* 22:74–86 (2022) https://doi.org/10.1021/acs.cgd.1c00928
2. Kim Y., Kawajiri Y., Rousseau R.W., Grover M.A. Modeling of nucleation, growth, and dissolution of paracetamol in ethanol solution for unseeded batch cooling crystallization with temperature-cycling strategy. *Industrial & Engineering Chemistry Research* 62:2866–2881 (2023). https://doi.org/10.1021/acs.iecr.2c03465
3. Moraes M. G. F., Barreto Jr. A. G., Secchi A. R., Souza Jr. M. B., Lage P. L. C., Myerson A. S. Polymorphism of Praziquantel: Role of Cooling Crystallization in Access to Solid Forms and Discovery of New Polymorphs. *Crystal Growth & Design* 23(2):1247-1258 (2023) https://doi.org/10.1021/acs.cgd.2c01381
4. McDonald M. A., Bommarius A. S., Rousseau R. W., Grover M. A. Continuous reactive crystallization of $\beta$-lactam antibiotics catalyzed by penicillin G acylase. Part I: Model development. *Comput. Chem. Eng.* 123:331–343 (2019). http://dx.doi.org/10.1016/j.compchemeng.2018.12.029
5. Moraes M.G., Grover M.A., Souza Jr. M.B., Lage P.L., Secchi A.R. Optimal control of crystal size and shape in batch crystallization using a bivariate population balance modeling. *IFAC-PapersOnLine* 54 (3): 653–660 (2021). http://dx.doi.org/10.1016/j.ifacol.2021.08.316

6. Nagy Z. K., Fujiwara M., Woo X. Y., Braatz R. D. Determination of the Kinetic Parameters for the Crystallization of Paracetamol from Water Using Metastable Zone Width Experiments. *Ind. Eng. Chem. Res.* 47: 1245–1252 (2008). https://doi.org/10.1021/ie060637c
7. Li H., Kawajiri Y., Grover M. A., Rousseau R. W. Modeling of Nucleation and Growth Kinetics for Unseeded Batch Cooling Crystallization. *Ind. Eng. Chem. Res.* 56: 4060–4073 (2017). https://doi.org/10.1021/acs.iecr.6b04914
8. Moraes M.G.F., Lima F.A.R.D., Lage P.L.C., Souza Jr. M.B., Barreto Jr.,A.G., Secchi, A.R. Modeling and predictive control of cooling crystallization of potassium sulfate by dynamic image analysis: Exploring phenomenological and machine learning approaches. *Industrial & Engineering Chemistry Research* 62:9515–9532 (2023). https://doi.org/10.1021/acs.iecr.3c00739
9. Xiouras C., Cameli F., Quilló G. L., Kavousanakis M. E., Vlachos D. G., Stefanidis G. D. Applications of Artificial Intelligence and Machine Learning Algorithms to Crystallization. *Chemical Reviews* 122 (15): 13006-13042 (2022). https://doi.org/10.1021/acs.chemrev.2c00141
10. Lima F. A. R. D., Moraes M. G. F., Barreto Jr. A. G., Secchi A. R., Grover M. A., Souza Jr. M. B. Applications of machine learning for modeling and advanced control of crystallization processes: Developments and perspectives. *Digital Chemical Engineering* 14:100208, 2025. https://doi.org/10.1016/j.dche.2024.100208
11. Szilagyi B., Nagy, Z.K. Real-time feasible model-based crystal size and shape control of crystallization processes. *Computer Aided Chemical Engineering* 46: 1273–1278 (2019). http://dx.doi.org/10.1016/B978-0-12-818634-3.50213-7.
12. Zheng Y., Wang X., Wu Z. Machine learning modeling and predictive control of the batch crystallization process. *Ind. Eng. Chem. Res.* 61 (16): 5578–5592 (2022). http://dx.doi.org/10.1021/acs.iecr.2c00026
13. Sharma N., Liu Y.A. A hybrid science-guided machine learning approach for modeling chemical processes: A review. *AIChE J.* 68 (5): e17609 (2022). http://dx.doi.org/10.1002/aic.17609
14. Zendehboudi S., Rezaei N. Lohi, A. Applications of hybrid models in chemical, petroleum, and energy systems: A systematic review. *Appl. Energy* 228: 2539–2566 (2018). http://dx.doi.org/10.1016/j.apenergy.2018.06.051
15. Lima F.A.R.D., Rebello C.M., Costa E.A., Santana V.V., Moares M.G., Barreto Jr. A.G., Secchi A.R., Souza Jr. M.B., Nogueira I.B. Improved modeling of crystallization processes by universal differential equations. *Chem. Eng. Res. Des.* 200: 538-549 (2023). http://dx.doi.org/10.1016/j.cherd.2023.11.032
16. Wu G., Yion W.T.G., Dang K.L.N.Q., Wu, Z. Physics-informed machine learning for MPC: Application to a batch crystallization process. *Chem. Eng. Res. Des.* 192: 556–569 (2023). http://dx.doi.org/10.1016/j.cherd.2023.02.048
17. Sitapure N., Kwon J.S.-I. Introducing hybrid modeling with time-series-transformers: A comparative study of series and parallel approach in batch crystallization. *Ind. Eng. Chem. Res.* 62 (49): 21278–21291 (2023). http://dx.doi.org/10.1021/acs.iecr.3c02624
18. Georgieva P., Meireles M., Feyo de Azevedo S. Knowledge-based hybrid modelling of a batch crystallisation when accounting for nucleation, growth and agglomeration phenomena. *Chem. Eng. Sci.* 58 (16): 3699–3713 (2003). http://dx.doi.org/10.1016/S0009-2509(03)00260-4
19. Oliveira C., Georgieva P., Rocha F., Feyo de Azevedo S. Artificial neural networks for modeling in reaction process systems. *Neural Comput. Appl.* 18: 15–24 (2009). http://dx.doi.org/10.1007/s00521-008-0200-8
20. Lima F.A.R.D., Moraes M.G.F., Grover, M.A., Barreto Jr. A.G., Secchi A.R., Souza Jr., M.B. Neural network inverse model controllers for paracetamol unseeded batch cooling crystallization. *Ind. Eng. Chem. Res.* 63 (45): 19613–19627 (2024). http://dx.doi.org/10.1021/acs.iecr.4c02060
21. Paszke A, et al. PyTorch: An Imperative Style, High-Performance Deep Learning Library. *ArXiv* (2019). https://doi.org/10.48550/arXiv.1912.01703
22. Poli M., Massaroli S., Yamashita A., Asama H., Park J. TorchDyn: A Neural Differential Equations Library. *ArXiv* (2020). https://doi.org/10.48550/arXiv.2009.09346

© 2025 by the authors. Licensed to PSEcommunity.org and PSE Press. This is an open access article under the creative commons CC-BY-SA licensing terms. Credit must be given to creator and adaptations must be shared under the same terms. See https://creativecommons.org/licenses/by-sa/4.0/



Systems & Control Transactions

**Research Article - Peer Reviewed Conference Proceeding**
ESCAPE 35 - European Symposium on Computer Aided Process Engineering
Ghent, Belgium. 6-9 July 2025
Jan F.M. Van Impe, Grégoire Léonard, Satyajeet S. Bhonsale,
Monika E. Polańska, Filip Logist (Eds.)

PSE PRESS

# From Experiment Design to Data-Driven Modeling of Powder Compaction Process

**René Brands[a], Vikas Kumar Mishra[b*], Jens Bartsch[a], Mohammad Al Khatib[b], Markus Thommes[a] , and Naim Bajcinca[b]**

[a] Laboratory of Solids Process Engineering, Department of Biochemical and Chemical Engineering, TU Dortmund University, 44227 Dortmund, Germany
[b] Department of Mechanical and Process Engineering, RPTU Kaiserslautern, 67663 Kaiserslautern, Germany
* Corresponding Author: vikas.mishra@rptu.de.

## ABSTRACT

Tableting is a dry granulation process for compacting powder blends into tablets. In this process, a blend of active pharmaceutical ingredients (APIs) and excipients are fed into the hopper of a rotary tablet press via feeders. Inside the tablet press, rotating feed frame paddle wheels fill powder into dies, with tablet mass adjusted by the lower punch position during the die filling process. Pre-compression rolls press air out of the die, while main compression rolls apply the force necessary for compacting the powder into tablets. In this paper, process variables such as feeder screw speeds, feed frame impeller speed, lower punch position during die filling, and punch distance during main compression have been systematically varied. Corresponding responses, including pre-compression force, ejection force, and tablet porosity have been evaluated to optimize the tableting process. After implementing an open platform communications unified architecture (OPC UA) interface, process variables can be monitored in real-time. To enable in-line monitoring of tablet porosity, a novel UV/Vis fiber optic probe has been implemented into the rotary tablet press. To further analyze the overall process, a data-driven modeling approach is adopted. Data-driven modeling is a valuable alternative to modeling real-world processes where, for instance, first principles modeling is difficult or infeasible. Due to the complex nature of the powder compaction process, several model classes need to be explored. To begin with, linear autoregressive models with exogenous inputs (ARX) have been considered. Thereafter, nonlinear autoregressive models with exogenous inputs (NARX) have been considered. Notably, several experiments have been designed to gather the data required for the development of the model.

**Keywords**: Modeling, Process control, Process monitoring, Industry 4.0, Big data, powder compaction, Tableting, UV/Vis spectroscopy

## INTRODUCTION

The pharmaceutical industry is increasingly striving for autonomous control of their processes [1]. In this context, process and product data are continuously generated, evaluated and interpreted in order to assess the quality of the drug product and to control the corresponding process based on this data. Thereby leading to improved product quality and reduced costs [2].

Tableting represents a vital process step in the production of tablets, the most common dosage form, and is therefore a particular focus of research [3]. Here, in a rotary tablet press, powder is filled into a die, pressed into a tablet by a two-stage compression process of the upper and lower punch and then ejected by an upward movement of the lower punch [4]. These tablet presses are characterized by a particularly high throughput and double-sided compression of the tablets.

Traditionally, individual samples are taken after tableting and subsequently evaluated off-line and used to assess the quality of the entire batch. In order to ensure real-time data, the implementation of an OPC UA connection and process analytical technology is crucial. This enables process and product data to be generated in real-time [5].

Process parameters that influence drug product

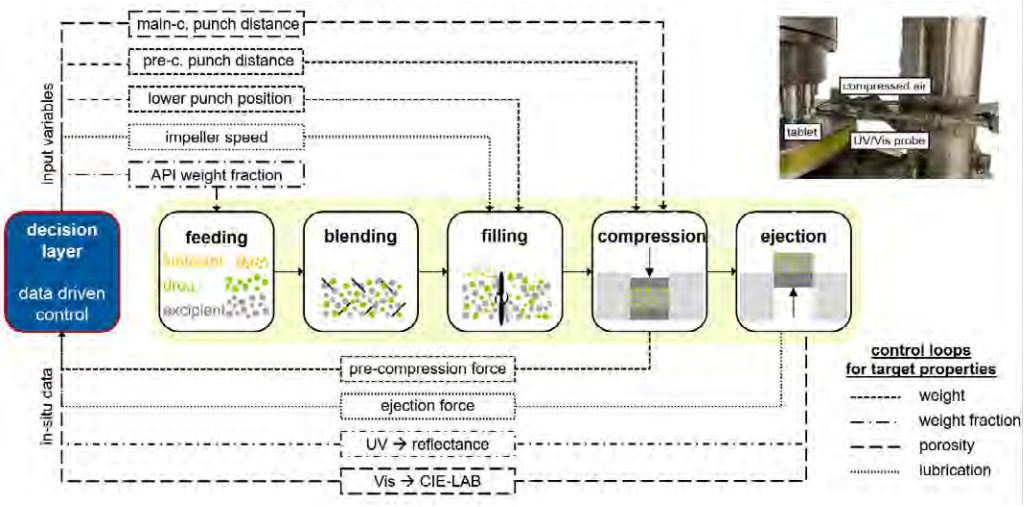



**Figure 1.** Powder compaction process.

quality, referred to as critical process parameters, are in particular the feed frame speed when filling the die with powder, the pre-compression force, the main-compression force, the compression roll distance and the ejection force. In order to evaluate these critical process parameters in real-time, an OPC UA interface was implemented.

Spectroscopic methods have proven particularly valuable for critical quality attribute (CQA) monitoring, as they are non-destructive, non-invasive and fast [6]. CQAs such as the active pharmaceutical ingredient (API) content and porosity are particularly important here, as these have a significant influence on the quality of the drug product. Near-infrared spectroscopy has proven to be useful for monitoring the active pharmaceutical ingredient content or porosity [7]. However, simultaneous determination was not possible and the evaluation was carried out by multivariate data analysis. In this work, a comparatively new method was used that is based on UV/Vis diffuse reflectance spectroscopy, measures API content and porosity simultaneously and can be evaluated univariately. For this purpose, the spectrum is separated into the ultraviolet and the visible range whereby the ultraviolet range is utilized to determine the active pharmaceutical ingredient content and the visible range to determine the porosity. Therefore, the visible range was transformed into the CIELAB color space.

To further analyze the process, we used the experimental data to develop a mathematical model. Recently, data-driven modeling has received a great deal of attention to model real-world applications. Parametric and nonparametric approaches are prevalent in the literature [8]. In this work, we are interested in the parametric modeling approach. In the parametric modeling approach, a model class is chosen a priori. Thereafter, the parameters are estimated, for instance, by using output-error methods [8, Chapter 7]. Here, we use nonlinear auto-regressive with exogeneous inputs (NARX) approach [9] to develop a parametric model for the process. Remarkably, NARX models have already found several applications in the literature [10-12]. As the powder compaction process is a complex process consisting of several subprocesses, it is challenging to determine a model class. In this regard, both linear and nonlinear autoregressive models with exogeneous inputs are considered to model the process. As is shown, the whole process is modeled as a combination of linear autoregressive and nonlinear autoregressive equations. We now summarize the contributions of this study. We collect experimental data for the powder compaction process on a rotary tablet press. We analyze full factorial experimental designs using multiple linear regression analysis to identify significant factors influencing product quality. We then combine process parameters with data obtained from a real-time spectroscopy method based on UV/Vis spectroscopy. To gain further insights about the relationships among various inputs and outputs of the process shown in Figure 1, we develop a parametric model based on the collected experimental data. This data-driven model of the process is developed using the NARX modeling approach.

## MATERIAL AND METHODS

### Materials

The formulation consists of 10 wt% theophylline monohydrate (Theophylline Monohydrate, Thermo Fisher Scientific, Waltham, USA) used as the active pharmaceutical ingredient, 0.5 wt% magnesium stearate (Ligamed MF-2-V, Peter Greven, Bad Münstereifel, Germany) used as the lubricant and lactose monohydrate (Foremost NF Lactose 310, Foremost Farms USA, Baraboo, USA) used as the filler and binder. Accordingly, the lactose content was changed when the active pharmaceutical ingredient

content was adjusted to 7 and 13 wt%.

## Tableting

The tableting process is carried out on a rotary tablet press (102i, Fette Compacting, Schwarzenbek, Germany). The throughput was set to 20,000 tablets per hour. In a first step, the material is fed into the hopper of the tablet press via loss-in-weight feeders (KT-20, Cooperion, Niederlenz, Switzerland). The powder is then filled into the dies via the feed frame equipped with round spokes paddle wheels (Fill-O-Matic (FOM), Fette Compacting, Schwarzenbek, Germany). Each die is mounted on the die table and rotates in a circular motion with the pairs of punches. The die table then continues to rotate and pre-compression rolls press air out of the die, followed by the actual material compression step via the main-compression rolls. Finally, the finished tablet is ejected by an upward movement of the lower punch. A full-factorial experimental design containing three stages was developed for the investigations. The active pharmaceutical ingredient content was varied from 7 to 13 wt\%, the main-compression force from 5 to 15 kN and the speed of the FOM from 40 to 120 rpm. Here, the responses were the ejection force, the reflectance value and the CIELAB color space. Furthermore, another experimental design was performed to investigate the influence of the powder mass on the pre-compression force as a possible surrogate parameter for real-time monitoring of the tablet weight. Tablet masses from 280 to 360 mg were set by varying the filling depth. Also, the influence of the pre-compression punch distance was investigated.

## Critical process parameter monitoring

Real-time monitoring of critical process parameters requires the implementation of an OPC UA interface. This guarantees real-time data exchange between the tablet press and the corresponding server. In this study, the ejection, pre- and main-compression force were recorded and evaluated using the OPC UA interface.

## Critical quality attribute monitoring

In this study, the weight and porosity of the tablets were determined off-line and additionally supported by real-time UV/Vis spectroscopy data to capture the dynamics of the process.

### Off-line determination

Tablet porosity (ε) (Eq. (1)) was determined by correlating the tablet density ($\rho_t$) derived from geometry and weight measurements (ST50, Sotax, Aesch, Switzerland) to the solid density ($\rho_s$) measured by helium pycnometry according to European Pharmacopoeia 11 (Chapter 2.9.23):

$$\varepsilon = \left(1 - \frac{\rho_t}{\rho_s}\right) 100\%. \quad (1)$$

### Real-time UV/Vis spectroscopy

Real-time monitoring of the active pharmaceutical ingredient content and porosity was carried out using a UV/Vis diffuse reflectance probe (Inspectro X, ColVisTec, Berlin, Germany). For this purpose, the probe was implemented in the ejection position of the tablets. Here, the probe is oriented orthogonally to the tablet side wall meaning measurements are taken on the tablet side wall. The distance between the probe and the tablet is set to 4 mm. In this way, radiation from 224 to 820 nm is guided to the tablet via the six outer glass fibers, where the radiation is absorbed. The reflected light is guided back via the middle glass fiber and evaluated. In order to keep the 6 in 1 array of glass fiber optics free of particles, an additional air flow and an extraction system have been implemented. For the measurement, 35 light flashes are emitted per measurement, each lasting 2 ms leading to a measurement frequency of 1.5 Hz.

For data analysis and evaluation with regard to the API content, the reflectance (R) was formed on the basis of the intensity of the reflected light (I) and the emitted light ($I_0$). In addition, Kubelka-Munk was applied to establish a correlation between absorption and reflection. Here, the transformed reflectance (f(R)) is the quotient of absorption and scattering coefficients (k and s) (Eq. (3)):

$$R = \frac{I}{I_0} \quad (2)$$

$$f(R) = \frac{k}{s} = \frac{(1-R)^2}{2R}. \quad (3)$$

For the assessment, the reflectance intensity in the UV range, specifically in the wavelength range from 320 to 330 nm, was correlated with the active pharmaceutical ingredient content.

The porosity was evaluated on the basis of the Vis range (380 to 780 nm) and the corresponding spectral information were converted into the CIELAB color space. This describes the range of visible light for humans via three values (L*, a* and b*) ordered in a Cartesian coordinate system. From this, the color saturation chroma (C*) can be determined, which correlates with the surface roughness and in consequence with the porosity.

## Multiple linear regression analysis

Multiple linear regression analyses were carried out using Modde software (MODDE 10, Sartorius, Göttingen, Germany) at a significance level of α=0.05 to visualize the effects of the individual factors on the responses. Therefore, models were developed for each set of factors ($\beta$) and response ($Y_R$ )(Eq. 4).

$$Y_R = \beta_0 + \beta_1 x_1 + \beta_2 x_2 + \beta_{1,2} x_1 x_2. \quad (4)$$

The results of the analyses are graphically represented by contour plots using the developed models. Here, the factors are on the axes while the response is represented by the color scale. The centre points were

performed in triplicate.

## Data-driven modeling approach

We use nonlinear auto-regressive with exogeneous inputs (NARX) models to develop a mathematical model for the considered tabletting process. The NARX formalism contains both model identification and model validation. Model identification step involves two steps: selecting model class, for example, polynomial NARX and parameter estimation. The identified model is then validated by using a different dataset. As our process contains multiple-input, multiple-output (MIMO), we model it using a MIMO NARX model. Assuming that we have $m$ input variables and $p$ output variables, the $j$th output of the NARX model is given by

$$y_j(k) = F_j\left(U_1(k), \dots, U_m(k),\ Y_1(k-1), \dots, Y_p(k-1)\right) + e_j(k), \quad (5)$$

where

$$U_i(k) = \left[u_j(k), u_j(k-1), \dots, u_j(k-n_u)\right], \qquad i = 1,2,..,m,$$

$$Y_j(k-1) = \left[y_j(k-1), \dots, y_j\left(k-n_y\right)\right], \qquad j = 1,2,..,p.$$

Here $u_i(k), y_i(k), e_i(k)$ denote, respectively, control input, process output, and noise terms. Function $F_j$ is unknown. However, as we consider the model class of polynomial NARX to model the process, $F_j$ is an unknown polynomial function. Finally, the parameters $n_u, n_y$ represent the maximum lags for the input and output, respectively.

# RESULTS

## Experimental results

The experimental results are illustrated as contour plots in Figure 2. Here, increasing the feed frame speed during die filling leads to an increase in the amount of applied shear and the hydrophobic lubricant spreads over the binder particle surface. Friction between the die, punch and powder is reduced, resulting in a lower ejection force [13]. Likewise, an influence of the main-compression force is noted, whereby an increase leads to a stronger consolidation of the powder and thus to a higher ejection force. Based on the powder component properties, a correlation to the ejection force is also evident here. Furthermore, combinatorial effects can be identified. Thus, the ejection force can be utilized, taking into account the associated additional effects, to obtain information about the lubrication.

The color saturation chroma (C*), however, only indicates a significant influence of the main-compression force. Increasing the main-compression force results in decreased roughness on the surface of the tablet, which intensifies specular reflection and thus leads to a higher chroma (C*) value. Moreover, this decreases the volume of the tablet and causes an increase in porosity. This makes the chroma value (C*) particularly suitable for monitoring porosity.

The reflectance in the range from 320 to 330 nm serves to monitor the active pharmaceutical ingredient content. Here, the reflectance value increases with higher active pharmaceutical ingredient content. The experimental results provide an additional effect of the main-compression force as well as combinatorial effects. Thus, further models need to be developed to fully describe the process and to enable autonomous control.

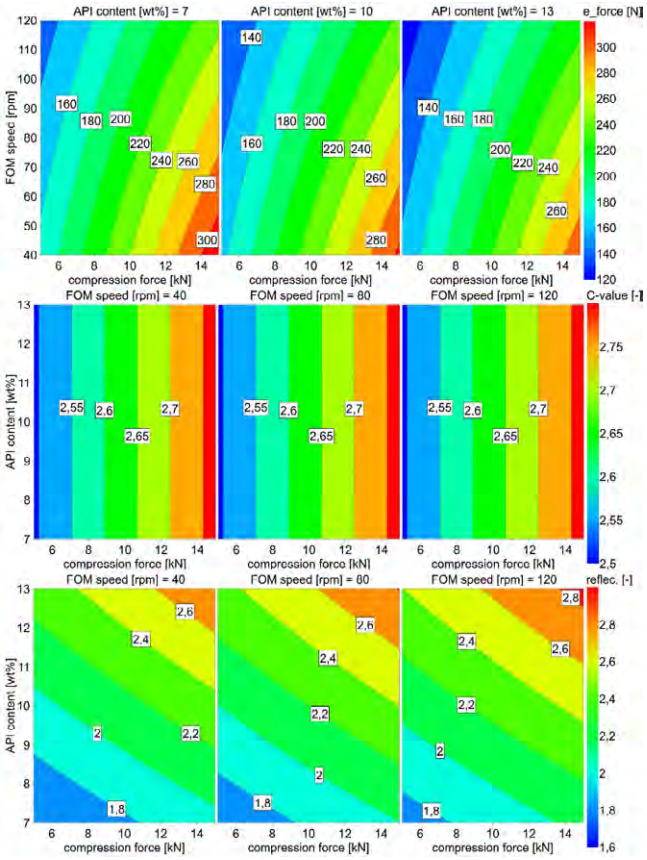



**Figure 2.** MLR results illustrated as contour plots for ejection force (e_force, top), chroma value (C-value, middle), and reflectance value (reflec., bottom).

In the second sub-experiment, the pre-compression force and the mass of the tablets were examined in relation to the filling depth and punch distance (Figure 3). The pre-compression force increases with decreasing the pre-compression roll distance. Here, more force is required to compress the same amount of powder into a smaller volume. In addition, an increased quantity of powder in the die leads to an increased force required to compact the powder to the defined height. Combinatorial effects can also be recognized here. However, the mass of the tablet only depends on the filling depth as this defines the volume filled with material prior to compression,

if the time for material filling in the die is sufficient.

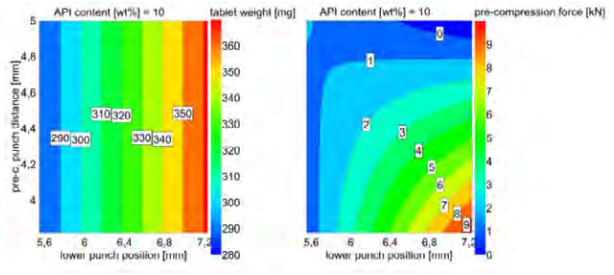



**Figure 3.** MLR results illustrated as countour plots for tablet weight (left) and pre-compression force (right).

Simulation results

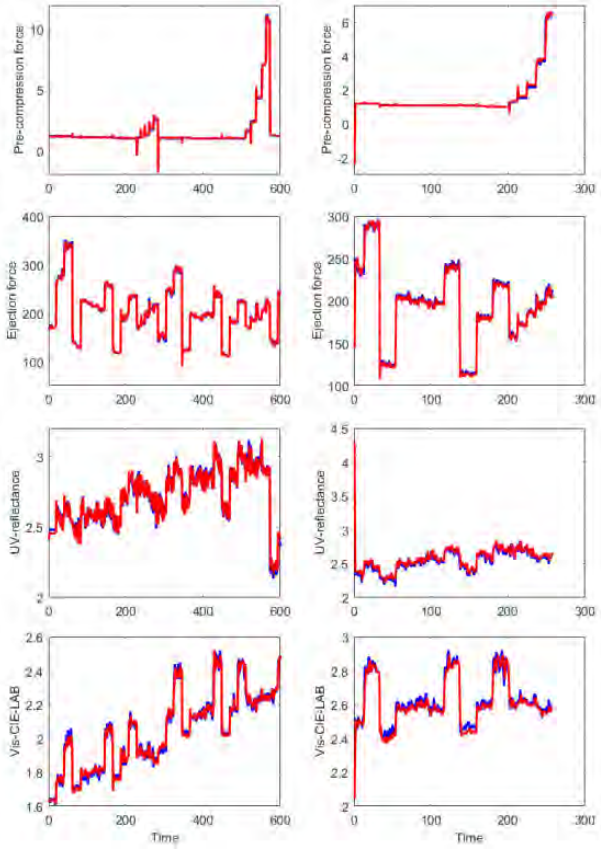



**Figure 4.** Identification (left) and validation (right) plots for all the outputs. The blue solid lines indicate the measured outputs, whereas red solid lines indicate computed outputs.

We aim to develop a parsimonious model for the process on the basis of gathered experimental data. Remarkably, several sets of experiments are performed to gather the necessary data. These data are then used for both identification and validation of the developed model. Total $859$ samples of data are collected for various inputs and outputs mentioned in Figure 1. We split the dataset as follows: $70\%$ for identification (training) and $30\%$ for validation (generalization or testing).

We denote all the five input variables by $u$ and all the four output variables by $y$. Furthermore, we denote the four outputs, namely, pre-compression force, ejection force, UV-reflectance, Vis-CIE-LAB, respectively, by $y_1, y_2, y_3, y_4$. With this notation in place, using the NARX approach, we obtain, based on the gathered dataset, the following model:

$$y_1(k) = \alpha_1 u(k) + \beta_1 u(k-1) + 0.9425 y_1(k-1)$$

$$y_2(k) = \alpha_2 u(k) + \beta_2 u(k-1) + \gamma_2 u^2(k) + \delta_2 u^2(k-1) + 0.9 y_2(k-1)$$

$$y_3(k) = \alpha_3 u(k) + \beta_3 u(k-1) + 0.9181 y_3(k-1)$$

$$y_4(k) = \alpha_4 u(k) + \beta_4 u(k-1) + \gamma_4 u^2(k) + \delta_4 u^2(k-1) + 0.6516 y_4(k-1) - 0.0756 y_4(k-2) + 0.0012 y_4^2(k-1) + 0.0510 y_4^2(k-2), \quad (6)$$

where

$$\alpha_1 = [0.0135 \ -1.7538 \ -0.4880 \ -0.7282 \ 2.5461]$$

$$\beta_1 = [-0.0129 \ 1.5106 \ 0.4653 \ 0.7258 \ -2.3407]$$

$$\alpha_2 = [2.6 \ 96.9 \ 1092.7 \ -74.6 \ -425.5]$$

$$\beta_2 = [2.5 \ -103.7 \ -1010.1 \ 730 \ 396]$$

$$\gamma_2 = [0 \ -12.5 \ -190.1 \ 2.4 \ 43.7]$$

$$\delta_2 = [0 \ 13.1 \ 176 \ -2.4 \ -40.7]$$

$$\alpha_3 = [0.0100 \ -0.1067 \ -0.7568 \ 0.2428 \ 0.5787]$$

$$\beta_3 = [-0.0096 \ 0.1160 \ 0.6993 \ -0.2406 \ -0.5288]$$

$$\alpha_4 = [-0.0007 \ -1.0966 \ -6.3087 \ 0.0093 \ 4.5086]$$

$$\beta_4 = [0.0011 \ 0.7916 \ 5.1898 \ 0.0104 \ -3.5830]$$

$$\gamma_4 = [0 \ 0.1243 \ 0.8290 \ 0.0010 \ -0.3157]$$

$$\delta_4 = [0 \ -0.0904 \ -0.6881 \ -0.0010 \ 0.2515].$$

For the purposes of illustration, both the identification and validation plots for all the four outputs are shown in Figure 4. It can be seen that the computed ones almost agree with the measured ones both in identification and validation plots. Thus, the model is generalizable and can be used for further analysis and control tasks. Moreover, the performance of the model is evaluated by computing the relative percentage error between measured and computed outputs defined as

$$\frac{\|y_{measured} - y_{computed}\|}{\|y_{measured}\|} \ 100\%.$$

The relative percentage error for both identification and validation of all the four outputs are given in Table 1. It can be seen that the errors are in the acceptable range. Hence, we conclude that the identified NARX model represents the process. In the future, we will use this identified model in real-time control of the process for desired product properties.

**Table 1:** Relative percentage error for id. (identification) and val. (validation) of various outputs.

| Outputs | Id. | Val. |
|---|---|---|
| Pre-compression force | 12.23 | 13.90 |
| Ejection force | 3.02 | 4.39 |
| UV-reflectance | 2.32 | 5.42 |
| Vis-CIE-LAB | 1.56 | 1.86 |

## CONCLUSION

In this study, experimental data were collected for the powder compaction process on a tablet press. Full factorial experimental designs were analyzed in terms of multiple linear regression analysis and significant factors associated with product quality were identified. Thereby, process parameters were combined with data from a real-time spectroscopy method based on UV/Vis spectroscopy. These collected data and gained insights from the process were further utilized in developing a parametric data-driven model of the process based on the NARX modeling approach. An avenue of future research work would be the application of this developed data-driven model in real-time control of the process.

## ACKNOWLEDGEMENTS

This work was funded by the German Research Foundation (DFG) – GZ: BA 5511/9-1 and TH 1817/8-1.

## REFERENCES

1. Hole G, Hole AS, McFalone-Shaw I. Digitalization in pharmaceutical industry: What to focus on under the digital implementation process?. *Int J Pharm* X 3:100095 (2021) https://doi.org/10.1016/j.ijpx.2021.100095
2. Su Q, Ganesh S, Moreno M, Bommireddy Y, Gonzalez M, Reklaitis GV, Nagy ZK. A perspective on Quality-by-Control (QbC) in pharmaceutical continuous manufacturing. *Comput Chem Eng* 125:216–231 (2019) https://doi.org/10.1016/j.compchemeng.2019.03.001
3. Ervasti T, Simonaho S P, Ketolainen J, Forsberg, P, Fransson M, Wikström H, Folestad S, Lakio S, Tajarobi P, Abrahmsén-Alami S. Continuous manufacturing of extended release tablets via powder mixing and direct compression. *Int J Pharm* 495:290–301 (2015) https://doi.org/10.1016/j.ijpharm.2015.08.077
4. Siegmann E, Forgber T, Toson P, Martinetz MC, Kureck H, Brinz T, Manz S, Grass T, Khinast J. Powder flow and mixing in different tablet press feed frames. *Adv Powder Technol* 31:770–781 (2020) https://doi.org/10.1016/j.apt.2019.11.031
5. Markl D, Warman M, Dumarey M, Bergman E-L, Folestad S, Shi Z, Manley LF, Goodwin DJ, Zeitler JA. Review of real-time release testing of pharmaceutical tablets: State-of-the-art, challenges and future perspective. *Int J Pharm* 582:119353 (2020) https://doi.org/10.1016/j.ijpharm.2020.119353
6. Zhong L, Gao L, Li L, Zang H. Trends-process analytical technology in solid oral dosage manufacturing. *Eur J Pharm Biopharm* 153:187–199 (2020) https://doi.org/10.1016/j.ejpb.2020.06.008
7. Pauli V, Roggo Y, Pellegatti L, Nguyen Trung NQ, Elbaz F, Ensslin S, Kleinebudde P, Krumme M. Process analytical technology for continuous manufacturing tableting processing: A case study. *J Pharm Biomed Anal* 162:101–111 (2019) https://doi.org/10.1016/j.jpba.2018.09.016
8. Verhaegen M, Verdult V. Filtering and System Identification: A Least Squares Approach. Cambridge University Press (2007).
9. Billings SA. Nonlinear System Identification: NARMAX Methods in the Time, Frequency, and Spatio-Temporal Domains. John Wiley & Sons (2013).
10. Pisoni E, Farina M, Carnevale C, Piroddi L. Forecasting peak air pollution levels using NARX models. *Eng Appl Artif Intell* 22:593-602 (2009) https://doi.org/10.1016/j.engappai.2009.04.002
11. Ruiz LGB, Cuéllar MP, Calvo-Flores MD, Jiménez MDCP. An application of non-linear autoregressive neural networks to predict energy consumption in public buildings. *Energies* 9:1-21 (2016) https://doi.org/10.3390/en9090684
12. Mohanty S, Patra PK, Sahoo SS. Prediction of global solar radiation using nonlinear auto regressive network with exogenous inputs (NARX). In *2015 39th National Systems Conference (NSC)* (pp. 1-6). IEEE. (2015) https://doi.org/10.1109/NATSYS.2015.7489103
13. Brands R, Mathias C, Bartsch J, Thommes M. Advancing tablet lubrication: A systematic comparison of feed frame lubrication and internal lubrication. *Powder Technol* 434:119369 (2024) https://doi.org/10.1016/j.powtec.2024.119369

© 2025 by the authors. Licensed to PSEcommunity.org and PSE Press. This is an open access article under the creative commons CC-BY-SA licensing terms. Credit must be given to creator and adaptations must be shared under the same terms. See https://creativecommons.org/licenses/by-sa/4.0/



Systems & Control Transactions

**Research Article - Peer Reviewed Conference Proceeding**
ESCAPE 35 - European Symposium on Computer Aided Process Engineering
Ghent, Belgium. 6-9 July 2025
Jan F.M. Van Impe, Grégoire Léonard, Satyajeet S. Bhonsale,
Monika E. Polańska, Filip Logist (Eds.)

PSE PRESS

# Data-driven Digital Design of Pharmaceutical Crystallization Processes

**Yash Barhate[a], Yung Shun Kang[a], Neda Nazemifard[b], Ben Renner[b], Yihui Yang[b], Charles Papageorgiou[b], and Zoltan K. Nagy[a]***

[a] Purdue University, Davidson School of Chemical Engineering, West Lafayette, Indiana, United States
[b] Takeda Pharmaceuticals International Company, Cambridge, Massachusetts, United States
* Corresponding Author: zknagy@purdue.edu

## ABSTRACT

Mechanistic population balance modeling (PBM) has advanced the design of pharmaceutical crystallization processes, enabling the production of active pharmaceutical ingredient (API) crystals with desired critical quality attributes (CQAs), such as purity and crystal size distribution. However, PBM development can sometimes be resource-intensive, requiring extensive design of experiments (DoE) and high-quality process data, making it impractical under fast-paced industrial development timelines. This study proposes a machine learning (ML)-based workflow for developing 'fit-for-purpose' digital twins of crystallization processes, leveraging industrially available DoE data to link operating conditions with CQAs. Validated on industrial data for a commercial API with complex crystallization challenges, the workflow efficiently identifies optimal operating conditions, demonstrating the potential of data-driven digital twins to accelerate the development of pharmaceutical processes.

**Keywords**: Artificial Intelligence, Machine Learning, Process Design, Modelling and Simulations, Optimization

## 1. INTRODUCTION

Crystallization is a critical purification and particle control operation in the pharmaceutical industry, influencing critical quality attributes (CQAs) such as crystal size distribution (CSD), yield, and polymorphic form. These attributes, substantially affect pharmaceutical drug properties, including bioavailability, tablet stability, and manufacturability. As a result, designing robust crystallization processes is crucial for the consistent production of Active Pharmaceutical Ingredients (APIs) that meet stringent quality and regulatory standards. To do so, mechanistic population balance model (PBM)-based digital design has become prominent in the industry, facilitating the optimal design and control of crystallization processes through in-silico simulations, mathematical optimization, and model-based control [1]. However, accurately determining PBM kinetic parameters for specific API-solvent systems poses challenges, requiring a well-designed design of experiments (DoE), along with high-quality real-time process data (e.g., concentration, CSD) from process analytical technology (PAT) tools or offline analyses [2]. The extensive resources—time, material, and labor—required for data acquisition, combined with rapid industrial timelines, often render PBM-based digital design resource-intensive and impractical [2,3].

Recently, there has been growing interest in data-driven digital design approaches to overcome the limitations of traditional crystallization process development methods. Xiouras et al. [3] provide a detailed review of studies on the application of data-driven modeling and control techniques in crystallization. While significant progress has been made in dynamic crystallization process modeling, such frameworks rely on the availability of real-time or historical time-series data from PAT tools. However, as previously noted, obtaining reliable PAT data is industrially challenging due to issues such as stringent calibration requirements, probe fouling, and availability constraints.

To address these limitations, data-driven frameworks must align with the realities of industrial pharmaceutical process development by leveraging available DoE data. This data typically includes only the process operating conditions and the output CQA measurements

obtained at the end of the batch. Operating in the absence of real-time state measurements places these frameworks in a low-data regime, which makes ML model development particularly challenging. Generative modeling techniques offer a promising approach to construct data-driven models under data-scare conditions by training models with synthetic experimental data generated from existing experimental inputs, thus mitigating data limitations [4, 5]. This study evaluates the effectiveness of various generative models in addressing data scarcity and enabling the development of accurate predictive models. Building on this, a generalized framework is proposed for developing data-driven digital twins and deploying them through mathematical optimization to identify operating conditions that yield the desired CQAs.

## 2. PROPOSED METHODOLOGY

### 2.1 Generalized data-driven digital twin development workflow

A systematic workflow is essential for building robust data-driven digital twins that generalize across diverse problem statements (Figure 1). The workflow begins with 'System definition' (Step 1), where the CQAs of interest are identified as model outputs, and the operational parameters to be varied are defined. Step 2 focuses on experimental data collection from historical or newly executed DoEs, designed using heuristics, statistical, or model-driven approaches. Step 3 involves data pre-processing, including missing value removal, reserving 10-15 % of data as a hold-out test set, and standardizing inputs for robust model training.

The 'ML model architecture selection and hyperparameter optimization', evaluates and trains multiple regression models including Random Forest (RF), gradient-boosted trees (GBT), Support Vector Regressors (SVR), and Distributed gradient-boosted trees (e.g., XGBoost). Given the limited size of the training dataset, simpler models are prioritized over deep neural networks to reduce the risk of overfitting and maintain model interpretability. Hyperparmater tuning is conduced using an exhaustive search over specified parameters for each model architecture (GridSearchCV) with a K-fold cross validation strategy (K = 3 or 5), optimizing for mean squared error (MSE) as the loss function. The best-performing models for each CQA were selected based on lowest validation MSE across folds and highest test $R^2$.

When constructing data-driven digital twins using operating parameter-CQA structures, the absence of dynamic interaction with the physical system necessitates the development of static digital twins. These models provide predictions alongside quantified uncertainty measures [2], which can be achieved using ensemble-based uncertainty quantification (UQ) methods such as Monte Carlo cross-validation, bootstrapping, and out-of-bag estimation.

#### 2.1.1 Synthetic data generation from DoE data and augmentation

The central concept in Step 6, is the use of generative AI models to generate new datasets (referred to as 'synthetic data' ($z_i^s$)) that capture the relationship between operational parameters and CQAs, using existing experimental DoE data (referred to as 'real data' ($z_i$)). These synthetic datasets serve as proxies for new laboratory experimental data and can be combined with real data to improve the predictive capabilities of ML models [4]. In this study, three widely studied generative models were explored: the Gaussian Copula Synthesizer, Generative Adversarial Networks (GANs), and Variational Autoencoders (VAEs). Each of these models is based on distinct underlying principles and hence, generates synthetic data of varying quality, where *quality* refers to the fidelity of the synthetic data in replicating the statistical properties of the real data. The ability of generative models to accurately capture the real data distribution depends on factors such as the size and distribution of the input real data and the effectiveness of model training [4, 5].

An essential consideration in synthetic data generation is the enforcement of domain-specific constraints to ensure the generated data is meaningful. It was observed that incorporating constraints directly into the training phase of generative models yielded superior performance compared to post-processing methods that discard non-compliant synthetic samples.

Evaluating the quality of synthetic data prior to experimental testing or validation presents significant challenges. To address this, we implemented a recently proposed *weighted expected risk minimization (ERM)* framework [6]. This approach systematically integrates synthetic data with real data to enhance the predictive performance of the resulting model on unseen data. This is done using a weighted loss function (Equation 1),

$$\mathcal{L}_{n,m}(\theta;\ \alpha) = \frac{1-\alpha}{n}\sum_{i=1}^{n}\mathcal{L}\left(\theta, z_i\right) + \frac{\alpha}{m}\sum_{i=1}^{m}\mathcal{L}\left(\theta, z_i^s\right) \quad (1)$$

where the weighting parameter (α) adjusts the contribution of synthetic data based on its quality and its impact on model performance on unseen real test data. Here, $n$ and $m$ refer to the number of real and synthetic samples respectively, $\mathcal{L}$ is the training loss function such as MSE and θ are model hyperparameters. The value of α can be determined systematically for different ($n$, $m$) either theoretically, using scaling laws, or experimentally, by minimizing the test error on a validation split of the original dataset [6]. Thus, by shifting the emphasis from solely generating high-quality synthetic data to effectively leveraging it in combination with real data, this approach provides a practical framework for improving ML model performance, particularly in limited data applications.

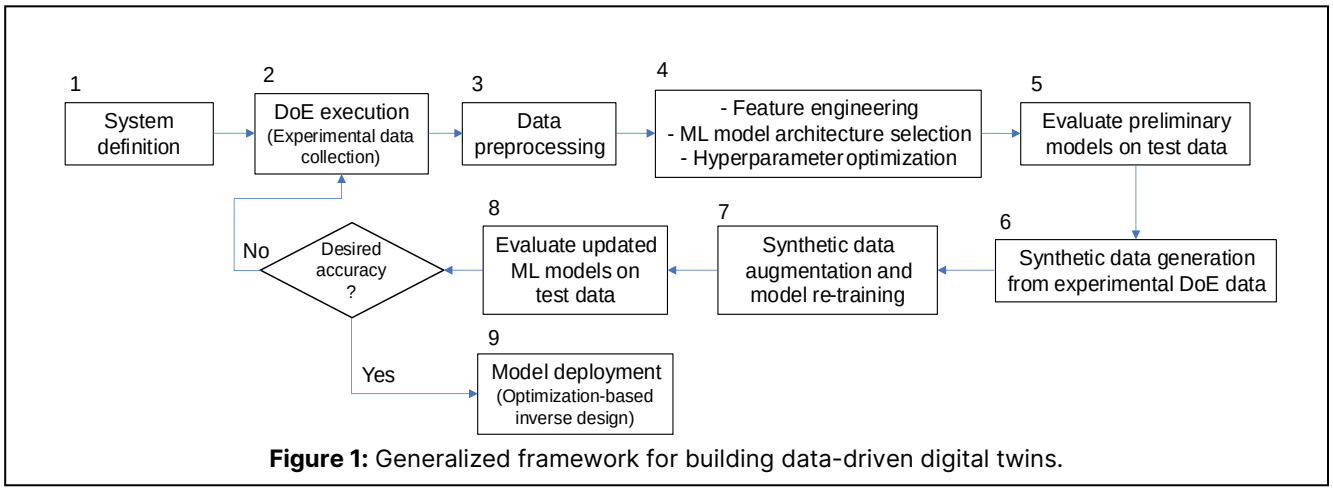



**Figure 1:** Generalized framework for building data-driven digital twins.

In Step 8, the refined models were re-evaluated using the test dataset. If the satisfactory models are obtained for all CQAs—with prediction uncertainties comparable to measurement uncertainties—the workflow proceeds to the model deployment phase. Otherwise, the process iterates back to step 2, where additional experiments were performed to augment the training data.

Step 9 involves deploying trained models through various approaches to enhance process development and understanding, including in-silico simulations, global system analysis, and optimization. This study demonstrates their use in a mathematical optimization framework to determine operating conditions that address crystallization challenges.

## 2.2 Key design objectives for the model compound

An industrial compound (Compound A) was selected as the model compound to demonstrate the proposed data-driven modeling workflow. Preliminary experimental investigations into the batch cooling crystallization of A in a fixed, proprietary solvent revealed the formation of a product mixture comprising both amorphous and crystalline particles at the end of the batch. This observation was corroborated through offline characterization techniques, including powder X-ray diffraction (PXRD), and thermogravimetric analysis (TGA). Additionally, significant agglomeration tendencies were observed in the API crystals, as indicated by inline EasyViewer, and offline particle size analysis using the Morphologi 4. Furthermore, slow crystal growth kinetics presented challenges in achieving larger particle sizes. These observations informed the formulation of three key crystallization design objectives for this compound:

1. **Increase Crystallinity**: Increase the percentage of crystalline particles in the product batch.
2. **Minimize Agglomeration**: Reduce the degree of agglomeration (DoA) in the crystals.
3. **Increase Particle size**: Increase the mean volumetric particle size (D-50).

Each of these CQAs was quantified through offline analysis of the crystals obtained at the end of batch crystallization. Crystallinity was quantified via PXRD and TGA, DoA was quantified using the Morphologi 4, and D-50 was measured using the Malvern Mastersizer. Detailed experimental protocols for crystallization experiments and offline product characterization are detailed elsewhere [7].

## 2.3 Experimental data collection and preprocessing

As per step 2 of the workflow, lab-scale experiments were conducted to collect the initial DoE for the ML model development. The DoE included 31 experiments designed using a combination of heuristic and experimental insights to systematically explore the design space. Initial experiments employed linear temperature profiles with variations in key process parameters, such as initial concentration, seed loading, cooling rates, and final batch temperature. To capture the effects of thermocycles on product CQAs, a subset of experiments incorporated thermal cycling, varying the number of cycles, cooling and heating rates, and intermediate temperature setpoints. Table 1 summarizes the distribution of experiments across four categories: linear, single-cycle, two-cycle, and multi-cycle profiles.

**Table 1:** Variability in the training dataset across the number of thermocycles in temperature profiles.

| Profile type | No. of experiments |
|---|---|
| Linear (cooling) | 18 |
| Linear (1 cooling,1 heating) | 2 |
| 1 cycle | 1 |
| 2 cycle | 4 |
| 3 cycle | 3 |
| 4 cycle | 3 |

The dataset exhibits inherent imbalance due to practical constraints, as not all CQAs were measured in every experiment. While D50 was measured across all 31

experiments, DoA and crystallinity were measured in only 21 and 15 experiments, respectively. To validate the data-driven framework, four additional experiments were conducted under optimal conditions identified in a prior mechanistic modeling study [7], which aimed to maximize D50 and minimize DoA. These experiments formed the hold-out dataset for evaluating the performance of the ML models. For ML model development, the experimental data from all thermocyclic temperature profiles were represented using 13 input and 3 output features, corresponding to the measured CQAs. The input features included initial concentration, seed loading, and parameters characterizing thermal profiles (e.g., intermediate temperatures, cooling rates, and heating rates).

Figure 2 illustrates the input feature representation across different thermal profiles.

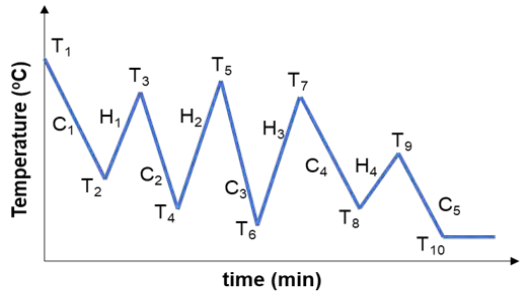



**Figure 2:** Input features that were used to describe the thermocyclic temperature profiles.

## 2.4 Computational implementation of the generalized workflow

The ML models described in section 2.1, were implemented using the scikit-learn library (version 1.4.0) and the XGBoost framework (version 2.1.1). Input features were standardized using the StandardScalar class, and hyperparameter tuning was conducted using GridSearchCV with K = 3 cross-validation, optimizing the following hyperparameters:

- RF: Number of estimators (10-200), max depth (0-30), min samples split (2, 5, 10) and min samples leaf (1, 2, 4).
- GBT: Number of estimators (10-200), learning rate (0.01-0.2), max depth (3, 5, 7), subsample (0.5, 0.75, 1.0), alpha (0.1, 0.5, 0.9).
- XGBoost: Number of estimators (10-200), learning rate (0.01-0.2), max depth (3, 5, 7), subsample (0.5, 0.75, 1.0), samples by tree (0.3, 0.7, 1.0).
- SVR: Kernels (Linear, polynomial, radial basis function, sigmoid), C parameter (0.1-20).

The best hyperparameter configuration for each model and the best model architecture were selected based on the lowest validation MSE and highest test $R^2$. For synthetic data generation, generative models were implemented using the Synthetic Data Vault (SDV) API (version 1.10.0). To ensure the feasibility of the thermocyclic profiles, the generated synthetic data were constrained according to Equations 2,3 and 4.

$$T_i \geq T_{i-1} \;\; \forall\, i = \{3,5,7,9\} \tag{2}$$

$$T_i \leq T_{i-1} \;\; \forall\, i = \{2,4,6,8,10\} \tag{3}$$

$$T_i = 0 \;\Rightarrow (T_j = 0) \wedge (H_j = 0) \wedge (C_j = 0) \;\forall\, \mathrm{j} > \mathrm{i} \tag{4}$$

Hyperparameter tuning of generative models was guided by the SDV's built-in statistical similarity metric, used as the evaluation criterion. The models' effectiveness in reducing test error was evaluated using the weighted ERM approach. For each CQA, three generative models were tested with varying quantities of synthetic samples (5, 10, 15, 20, 25) added to the existing real dataset. The optimal weighting factor for each scenario was then determined, and the corresponding hyperparameter configuration that minimized the cross-validation test error was selected. The models were then retrained with these optimized settings and saved as the final models.

## 3. RESULTS AND DISCUSSION

In Step 4 of the workflow, various model architectures were assessed for their ability to explain the variance in the collected experimental data. Random forest regressors excelled in modeling D-50 and DoA, whereas gradient boosted trees were most effective for crystallinity predictions. Figure 3 presents the parity plot for predictions across training and testing datasets using these models. Additionally, employing Monte Carlo cross-validation for UQ allowed for both the nominal predictions and their prediction uncertainties, as shown in Figure 4.

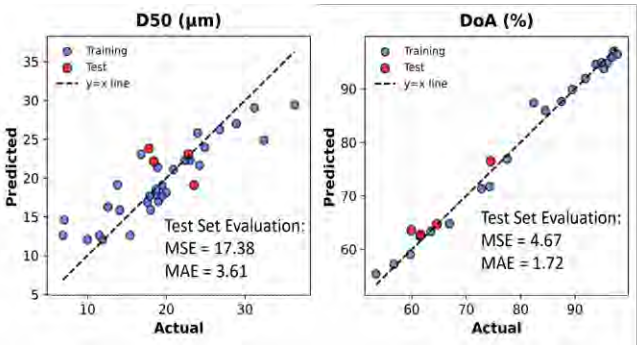



**Figure 3:** Parity plot of predictions for D-50 and DoA models before synthetic data augmentation.

To further enhance the model accuracy, Synthetic data generation and augmentation were explored. As elaborated in Section 2, synthetic data of varying sizes were

generated from the trained generative AI models, and the weighted ERM approach was used to identify the best α for each scenario. The optimal hyperparameter configuration for D-50 was using a VAE model, with m = 25 and α = 0.35. As shown in Figure 5, this configuration gave the highest reduction in the validation loss on the real dataset. The convex nature of the validation loss curve indicates a trade-off; beyond a certain α value, the inclusion of synthetic data ceased to reduce loss, likely due to deteriorating data quality acting as noise. Re-training the ML model for predicting D-50 with this optimized dataset and hyperparameter setting improved performance on the hold-out test dataset, reducing MSE and mean absolute error (MAE) by 44.6% and 26.9% respectively (Figure 6).

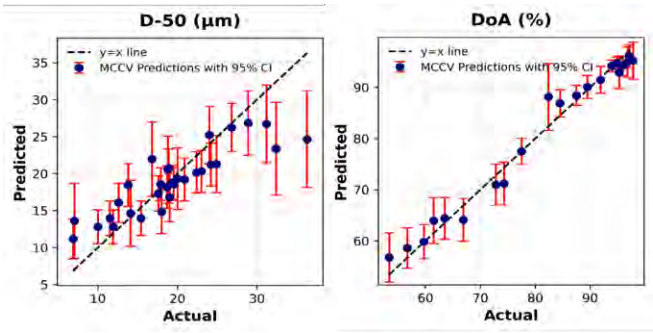



**Figure 4:** Nominal predictions with prediction uncertainties from the ML models of D-50 and DoA.

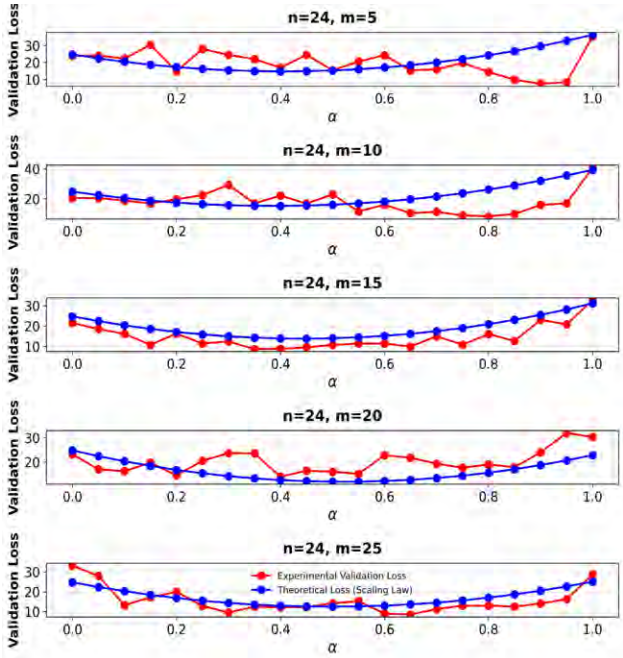



**Figure 5:** Weighted ERM approach to identify optimal α for synthetic data augmentation for D-50 model.

For DoA predictions, augmentation with synthetic data from generative models did not significantly improve outcomes, potentially due to the inferior quality of the synthetic data. While further model tuning could enhance this, it was deferred as the existing DoA model already demonstrated high predictive accuracy with the real dataset. Since the model predictions for both these CQAs were comparable with measurement errors (uncertainties), these were deployed using optimization frameworks to determine operational conditions that satisfy the crystallization design objectives (Step 9).

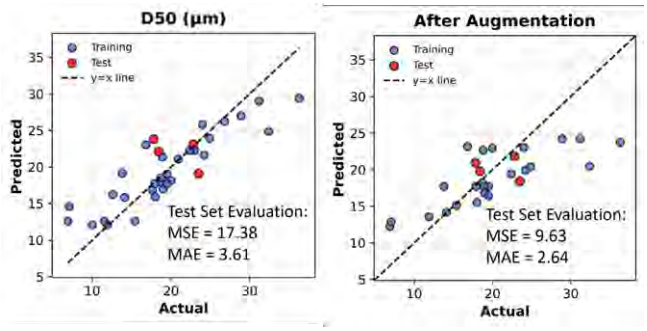



**Figure 6:** Parity plot for D-50 predictions before (left) and after (right) augmentation of Synthetic Data

The problem was formulated as a dual-objective optimization to maximize D-50 and minimize DoA. The decision variables ($\bar{x}$) represent the ML models' input features corresponding to various thermocyclic profiles. Inequality constraints (Equations 2, 3, and 4) ensured the feasibility of these profiles, with the decision variables' bounds detailed in . This problem was modeled using the Pymoo framework and solved using a derivative-free genetic algorithm. Figure 7 displays the Pareto fronts achieved with various thermocyclic profiles, confirming that increasing the number of temperature cycles from 1/2 to 3/4 enhances mean size and reduces DoA.

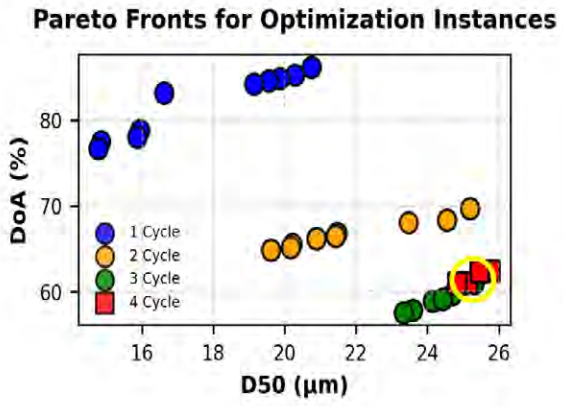



**Figure 7:** Pareto front obtained after solving the optimization problem.

Furthermore, mapping these optimized results with the crystallinity predictions (Figure 8) from the crystallinity model revealed increased crystallinity values with more thermocycles—an observation experimentally confirmed as reported in [7], where increased crystallinity

and reduced DoA were noted in samples from the end of each cycle in a 4-cycle temperature profile experiment.

**Table 2:** Lower (LB) and upper bounds (UB) of decision variables

| $\bar{x}$ | LB | UB |
|---|---|---|
| Initial Conc. (mg/g solvent) | 24.8 | 55.2 |
| Seed loading | 0.05 | 0.15 |
| $T_i$(oC) | 0 | 70 |
| $C_i$(oC/min) | 0.05 | 0.3 |
| $H_i$(°C/min) | 0.5 | 1.0 |

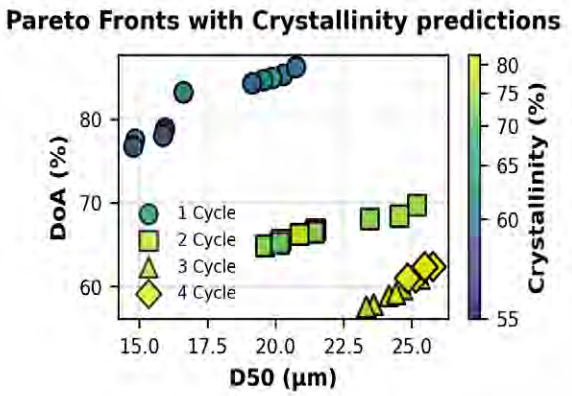



**Figure 8:** Crystallinity predictions from the Crystallinity ML model mapped onto Pareto front from Figure 7.

A 4-cycle optimal profile from the obtained Pareto front (circled in Figure 7) was experimentally validated, affirming the efficacy and impact of the data-driven digital design workflow in developing crystallization processes. Table 3 compares predictions across all CQAs at the validation point, showing consistency and reliability. Moreover, the optimized profile obtained using a data-driven framework not only matched the CQAs achieved with the mechanistic population-balance approach but also aimed to minimize batch time, thereby enhancing productivity [7].

**Table 3:** Comparison of experimental and model-predicted CQAs for the validation experiment.

| CQA | Experimental | Model-predicted |
|---|---|---|
| D-50 | 17.5±0.3 | 22.85±6.58 |
| DoA | 64.5±12.7 | 64.63±5.26 |
| Crystallinity | 79.4±6.7 | 77.22±4.16 |

## 4. CONCLUSION

This study introduces a systematic workflow for constructing 'fit-for-purpose', data-driven digital twins for crystallization process development, linking process operating conditions with CQAs obtained during product characterization. A key feature of this workflow is the integration of synthetic data derived from experimental data, which enhances the predictive capabilities of ML models, particularly in applications with limited data. The workflow's effectiveness was validated by its application to an industrial API exhibiting agglomeration and low product crystallinity. Using this workflow, reliable data-driven models were developed and integrated into an optimization framework, successfully identifying operating conditions that addressed complex industrial challenges. This demonstrates the potential of these tools in developing complex crystallization processes.

## ACKNOWLEDGEMENTS

Funding from Takeda Pharmaceuticals International Co. is gratefully acknowledged.

## REFERENCES

1. Nagy Z.K., Braatz, R.D. Advances and new directions in crystallization control. *Annu. Rev. Chem. Biomol. Eng.* **3**, 55–75 (2012)
2. Barhate Y., Kilari H., Wu W.L., Nagy Z.K. Population balance model enabled digital design and uncertainty analysis framework for continuous crystallization of pharmaceuticals using an automated platform with full recycle and minimal material use. *Chem. Eng. Sci.* 287, 119688 (2024)
3. Xiouras, C., Cameli, F., Quilló, G. L., Kavousanakis, M. E., Vlachos, D. G., Stefanidis, G. D. Applications of Artificial Intelligence and Machine Learning Algorithms to Crystallization. *Chem. Rev.* 122, 13006–13042 (2022)
4. Ma Y., Li W., Yang H., Gong J., Nagy Z.K. Digital design of cooling crystallization processes using a machine learning-based strategy. *Ind. Eng. Chem. Res.* 63, 46, 20236-20251 (2024)
5. Lu Y., Shen M., Wang H., Wang X., Rechem C., Fu T., Wei W. Machine learning for synthetic data generation: A review. *arXiv: 2302.04062*
6. Jain A., Montanari A., Sasoglu E. Scaling laws for learning with real and surrogate data. arXiv:2402.04376
7. Kang Y.S., Kilari H., Nazemifard N., Renner C.B., Yang Y., Papageorgiou C., Nagy Z.K. Optimization based digital design for agglomeration control of a pharmaceutical crystallization process. *2024 AIChE Annual Meeting* (2024)

© 2025 by the authors. Licensed to PSEcommunity.org and PSE Press. This is an open access article under the creative commons CC-BY-SA licensing terms. Credit must be given to creator and adaptations must be shared under the same terms. See https://creativecommons.org/licenses/by-sa/4.0/

Systems & Control Transactions

**Research Article - Peer Reviewed Conference Proceeding**
ESCAPE 35 - European Symposium on Computer Aided Process Engineering
Ghent, Belgium. 6-9 July 2025
Jan F.M. Van Impe, Grégoire Léonard, Satyajeet S. Bhonsale,
Monika E. Polańska, Filip Logist (Eds.)

PSE PRESS

# Process analysis of end-to-end continuous pharmaceutical manufacturing using PharmaPy

**Mohammad Shahab[a]*, Kensaku Matsunami[a], Zoltan Nagy[a], and Gintaras Reklaitis[a]**

[a] Davidson School of Chemical Engineering, Purdue University, West Lafayette, IN-47907, USA
* Corresponding Author: moshahab@purdue.edu.

## ABSTRACT

As pharmaceutical manufacturing is transitioning from traditional batch to continuous manufacturing (CM), there is a lack of tools for CM design and development, which can integrate drug substance and drug product unit operations for overall evaluation. Recently, a Python-based PharmaPy framework was proposed to advance the design, simulation, and analysis of continuous pharmaceutical processes. However, the initial library of models only addressed upstream drug substance processing. In this work, new capabilities, including drug product unit operations such as feeder, blender, and tablet press, have been added to the PharmaPy framework, enabling end-to-end study and optimizing the effects of material properties and process conditions on solid oral dosage products. The platform supports computational efficiency and model accuracy by allowing the development of different mechanistic and semi-mechanistic models. Sensitivity analysis is performed on the integrated end-to-end simulator to identify critical input variables influencing product quality and control strategies. The analysis lowers the complexity of the model by ranking significant input variables. Finally, feasibility studies are conducted on extracted influential input variables to characterize the process design space and achieve desirable output. The enhanced PharmaPy package can now support decision-making from early research and development stages through manufacturing.

**Keywords**: PharmaPy, Process synthesis, Process analysis, Pharmaceutical manufacturing

## INTRODUCTION

The pharmaceutical regulatory agencies have recognized the need to transition from batch to continuous mode of operation due to its various advantages. Among the several benefits that drives continuous process includes scalability, increase in controllability, reduction in time to product release in the market, product quality consistency, and potential reduction in human involvement and capital costs. These advantages contribute to increased adaptability, agility, and robustness in the continuous manufacturing of pharmaceuticals. At the same time, it also provides a great opportunity for practitioners to develop continuous and efficient manufacturing processes for pharmaceutical production [1].

However, the strict regulatory mechanism of the pharmaceutical industry draws multiple challenges in this transition. In this work, we consider the integration of drug substance process, i.e., active pharmaceutical ingredient (API) manufacturing, with the drug product operations for solid oral-drug production, i.e., tablets. For the end-to-end continuous operation, the first challenge lies in the physics and chemistry-based constraints that may decide the best operation mode for the manufacture of a given API. The API manufacturing process also needs to have necessary control on the raw material properties. In addition, the optimal manufacturing route should be determined based on the process economics and the adoption of effective separation and purification steps to achieve desired API quality attributes. The second challenge is to understand the effects of material attributes on powder flowability and process dynamics between unit operations for drug product manufacturing. Finally, the process design, analysis, and optimization of the integrated process need to be performed through a systems approach which would study the effects of material properties, equipment, and process parameters on the product qualities [2]. Such an integrated system should

also be developed within the quality-by-design (QbD) or quality-by-control (QbC) framework for the construction of design space regions that ensures final product quality.

To address the aforementioned challenges, recently PharmaPy, an open source pythonic framework for flexible flowsheet modeling and simulation of discrete/continuous processes for pharmaceutical manufacturing, was developed [3]. The framework supports parameter estimation and process optimization and adopts a sequential-modular approach towards integrated simulation for drug substance. However, the goal of end-to-end continuous manufacturing using PharmaPy was unrealizable due to the absence of downstream drug product operations. In this work, new capabilities are added to the existing PharmaPy tool, and the drug product framework is presented to integrate and study the effects of raw materials, upstream processes on final product quality. The enhanced PharmaPy framework will act as a complimentary open-source platform to existing commercial flowsheet simulation tools such as Aspen Plus and gPROMS by providing flexible user control while ensuring adequate model fidelity and numerical accuracy.

## PHARMAPY FRAMEWORK

PharmaPy is a Python software application that makes use of the language's versatile scripting features and incorporates powerful computational libraries for flowsheet modelling [3]. Several in-built models in the open-source package are drawn as standard unit operations for the manufacture of drug substances and products. Furthermore, it offers the flexibility to design and accommodate customized user-generated unit operation models. These standard (and user-defined) models are used as building blocks to construct the integrated flowsheet models. PharmaPy can be used for simulation, design and optimisation of pharmaceutical manufacturing processes. It uses a sequential-modular equation solving approach and an object-oriented software architecture, which enable to perform efficient process simulation and flowsheet optimization. PharmaPy has been used successfully for drug substance manufacturing applications including its application in a simulation-optimization framework [4], and for techno-economic analysis of various flowsheet alternatives [5]. For the drug product manufacturing, which is the focus of this study, the extended PharmaPy framework adds the downstream processing units where the API is converted into final tablets.

The downstream PharmaPy implementation for flowsheet simulation and optimization starts with the input of API properties from the dryer unit operation which helps connect the upstream process with downstream operations (Figure 1). The dried API properties are estimated using the upstream PharmaPy framework [6] which also includes a filter and deliquorizer (DL) to reduce the liquid present in the pores of the filter cake. The final dried API information flows through the product operations which effects the final product quality. Other participating species such as excipients, lubricants/glidants and their material properties are also fed by the user to the downstream process. Next, the downstream unit operations and their connections are established using object-oriented programming. Following that, the flowsheet model can be executed to perform process simulation and process analysis.

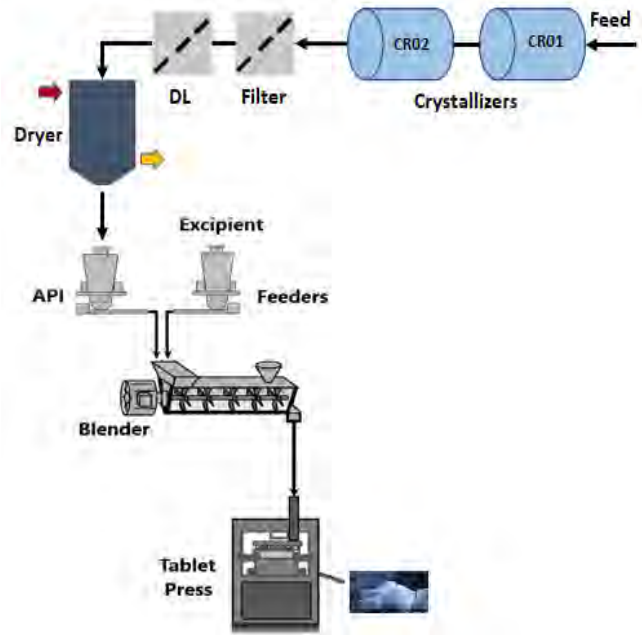



**Figure 1.** Integrated drug substance-drug product flowsheet used for simulation in PharmaPy (DL represents the deliquoring step in the filtration).

Ultimately, with the help of flowsheet optimization in the second theme which is still in development stages, the users can compare various manufacturing routes for tablet production in an automated framework. In the next section, the first theme of downstream PharmaPy is illustrated with the help of a direct compaction case study, which includes sensitivity analysis to investigate crucial input variables and feasibility studies to determine the process design space that ensures consistent product quality.

## RESULTS & DISCUSSIONS

### Case Study: Direct Compaction process

Direct Compaction (DC) process is a straightforward and popular tablet production method that directly uses the blended constituent materials and compresses them into tablets. It also requires fewer unit operations, which implies less equipment space and cost, less processing

times, lower manufacturing costs and improved productivity. In the DC process under consideration, the API from the drug substance operations and an excipient, which aids in the drug processing, are fed to loss-in-weigh feeders which deliver the materials at a desired flow rate. The API and excipient are then fed to a continuous blender to achieve a homogenous blend of the constituent ingredients. Finally, the well-mixed ingredients flow through a hopper to a rotary tablet press (TP), which fills the dies with blended powder where the tablet press compresses the mixture into tablets.

The PharmaPy package includes dynamic simulation of a variety of built-in models along with the flexibility to customize and construct their own functions. The flowsheet model includes semi-mechanistic, empirical, hybrid and data-driven models to estimate intermediate and final product quality. The unit operation models that are built and implemented for DC process are explained next.

## Feeders

Gravimetric feeders known as "loss-in-weight" feeders use direct weight measurements of the material in the hopper to reach and maintain a pre-set flow rate. The feeder also consists of an impeller to assist material flow and a rotating screw which transports the material out of the feeder. Under the gravimetric mode, the flow rate is automatically controlled by adjusting the screw speed with the help of a PID controller according to the loss in weight of the materials in the feeder over time. A semi-empirical feed factor model is deployed in PharmaPy to model the feeder that accurately predicts the relation between the mass flow rate and screw speed of the feeder [7]. The following equations represent the functioning of the feeder module.

$$F_{out}(t) = ff(t)\omega_{screw}(t) \quad (1)$$

$$ff(t) = \rho_{eff}(t)V_{sp} \quad (2)$$

$$\rho_{eff}(t) = \rho_{sat} + (\rho_{in} - \rho_{sat})e^{-\frac{\sigma(t)}{\beta}} \quad (3)$$

$$\omega_{imp}(t) = \alpha\omega_{screw}(t) \quad (4)$$

$$\sigma(t) = \frac{W(t)g}{A_f} + \cos(2\pi\omega_{imp}t)\frac{M_b R_b \omega_{imp}^2}{A_{sp}} \quad (5)$$

where $F_{out}$ is the outlet mass flow rate of API, excipient, etc. and $ff$ is the feed factor, $\omega_{imp}$ and $\omega_{screw}$ are the impeller and screw speed, respectively, $V_{sp}$ is the volume of the screw pitch, $\rho_{eff}$ is the effective density of the material, $\sigma$ is the vertical stress, $\beta$ is the density constant, $A_f$ is the feeder area, $A_{sp}$ is the screw port area where screws enter the bowl, $M_b$ and $R_b$ are the mass and radius of the impeller blade, $g$ is the gravitational constant, and $W$ is the weight of powder in the feeder.

## Blender

The continuous blender is used to reduce the variations which stems from the feeding system and plays a crucial role in maintaining strict quality constraints of the concentration uniformity in the blend and final product. The PharmaPy package uses a two-dimensional multi-compartmental model to describe the blender operation [8]. The model includes axial and radial directions of the compartments which is assumed to be equally sized and well mixed. The blend mass hold-up, flow rate from the blender, API composition and relative standard deviation of the blend samples are estimated using the compartmental model.

$$\frac{dm_{i,j}}{dt} = F_f(m_{i-1,j} - m_{i,j}) + F_b(m_{i+1,j} - m_{i,j}) + F_r(m_{i,j-1} - 2m_{i,j} + m_{i,j+1}) \quad (6)$$

$$F_f = a\omega_{blend} + b \quad (7)$$

$$F_b = c\omega_{blend} + d \quad (8)$$

$$F_r = e\omega_{blend} \quad (9)$$

$$F_{out,b} = \sum_{j=1}^{N_r} F_{f,API}\, m_{N_a,j}^{API} + \sum_{j=1}^{N_r} F_{f,EXCP}\, m_{N_a,j}^{EXCP} \quad (10)$$

$$C_{API} = \frac{\sum_{j=1}^{N_r} F_{f,API} m_{N_a,j}^{API}}{F_{out,b}} \quad (11)$$

where $F_{out,b}$ is the exit blend flow rate, $m_{i,j}$ is the mass hold-up in the ith axial and jth radial compartment, $N_a$ and $N_r$ are the number of compartments in the axial and radial directions. $F_f$, $F_b$ and $F_r$ are the forward, backward, and radial fluxes respectively, with a, b, c, d and e being the flux parameters, $\omega_{blend}$ is the blender speed, and $C_{API}$ is the API composition in the exit blend.

## Tablet Press

The incoming blend from the previous unit operation is transported through a hopper and feed frame to a series of dies where the blends are compressed into tablets. The die shape and tablet press process conditions determine the geometry and final quality of tablets. PharmaPy also includes a hopper and feed frame model to predict the hopper level ($h_{hopper}$) and feed frame flow ($F_{fframe}$) into the dies. The tablet press functions in two stages, namely pre-compression, to remove entrapped air and reduce material porosity, and main compression, to convert the pre-compressed blend into tablets. Empirical models have been deployed to correlate the material attributes such as bulk density ($\rho_b$), and process parameters like turret speed ($N_T$), main compression thickness ($M_{thick}$), dosing position ($H_{fill}$), etc., with tablet properties which includes weight ($W$), main compaction force ($F_{main}$), density ($\rho_{tab}$), and strength ($\sigma_T$). The tablet press model equations used in PharmaPy framework are summarized below.

$$\frac{dh_{hopper}}{dt} = \frac{F_{out,b} - F_{fframe}}{\rho_b A_{hopper}} \quad (12)$$

$$V_{fill} = \frac{\pi D^2 H_{fill}}{4} + \frac{\pi h(\frac{3D^2}{4} + h^2)}{6} \quad (13)$$

$$F_{fframe} = n_T N_{stat} \rho_b V_{fill} \quad (14)$$

$$W = \rho_b V_{fill} \left( -\varphi_1 \frac{N_F}{N_T} + \varphi_2 \frac{H_{fill}}{D} + \varphi_3 \left( \frac{H_{fill}}{D} \right)^2 \right) \quad (15)$$

$$F_{main} = \frac{\pi D^2 (\rho_{in-die} - \rho_c)}{4b(\rho_{in-die}(a-1) + \rho_c)} \quad (16)$$

$$V_{in-die} = \frac{\pi D^2 M_{thick}}{4} + \frac{\pi h(\frac{3D^2}{4} + h^2)}{3} \quad (17)$$

$$\rho_{in-die} = \frac{W}{\rho_t V_{in-die}} \quad (18)$$

$$\rho_{tab} = \rho_{in-die} (1 - \varepsilon_p) \quad (19)$$

$$\sigma_T = \sigma_0 \left[ 1 - e^{(\rho_{tab} - \rho_{c,\sigma})} \left( \frac{1 - \rho_{tab}}{1 - \rho_{c,\sigma}} \right) \right] \quad (20)$$

where $D$, $h$, $A_{hopper}$, $N_F$, $\varepsilon_p$ are the die diameter, cup depth, hopper cross section area, feed frame speed, and elastic recovery of the tablet, respectively. $\rho_{c,\sigma}$ and $\sigma_0$ are the tablet tensile strength model parameters.

Content uniformity of the tablets ($C_V$) is also estimated to study the effects of upstream material attributes i.e., mass fraction ($x_i$) and particle size ($d_i$) of API, and downstream material conditions ($C_{API}$) on tablet quality based on a target dosage ($T_D$) [9].

$$C_V = 100(1 - C_{API}) \left( \frac{\pi \rho}{6 T_D} \right)^{1/2} \left( \sum_{i=1}^{N} x_i d_i^3 \right)^{1/2} \quad (21)$$

The downstream process synthesis for tablet manufacture comprises a dynamic flowsheet model, which includes integrated unit operations as described above for the direct compaction process. This flowsheet model is developed within the PharmaPy framework and combines individual processes by utilizing the output of previous unit operation as the input of the subsequent one. The object-oriented programming structure in Python allows the flexible use of these unit operations and also build customized functions for the flowsheet model. The model parameter values of the individual processes are taken from existing studies towards the manufacture of 10% acetaminophen tablets [6,10-12].

## Sensitivity and Feasibility Analysis

Once the flowsheet model is developed, the next step is to perform process analysis. This includes the identification of crucial input variables, i.e., material attributes and process parameters. Then, the influential input factors are examined to estimate feasible design space regions which can then be used to develop control strategies. Statisticians and practitioners have developed various sensitivity analysis methods which studies how uncertainty in model input can be assigned to variations in model output. Among the main techniques, global sensitivity analysis stands out as it allows the determination of effects of uncertain input variables across the whole input space.

**Table 1:** Input variables for sensitivity analysis with lower (LB) and upper bound (UB).

| Input | LB | UB |
|---|---|---|
| **Crystallizer (CR01)** | | |
| Residence time (s) | 2470 | 2730 |
| Coolant jacket temp. (K) | 298 | 328 |
| **API feeder** | | |
| API flow (kg/hr) | 0.95 | 1.05 |
| **Excipient Feeder** | | |
| Excp. Flow (kg/hr) | 8.55 | 9.45 |
| **Continuous blender** | | |
| Blender speed (RPM) | 237.5 | 262.5 |
| **Tablet press** | | |
| TP fill depth (mm) | 7.6 | 8.4 |
| TP thickness (mm) | 2.85 | 3.15 |
| TP turret speed (RPM) | 19 | 21 |

PharmaPy performs global sensitivity analysis on a given set of input and output variables by utilizing in-built python libraries for qualitative and quantitative sensitivity analysis. In this study, we use variance-based Sobol's method to study quantitatively, how the variance of flowsheet output can be apportioned into terms based on input variables and their interactions. Sobol's method uses two metrics to provide sensitivity information, $S_i$ for first-order effect, and $S_{Ti}$ for total-effect defined as follows:

$$S_i = \frac{\mathbb{V}(\mathbb{E}(Y|X_i))}{\mathbb{V}(Y)} \quad (22)$$

$$S_{Ti} = 1 - \frac{\mathbb{V}(\mathbb{E}(Y|X_{-i}))}{\mathbb{V}(Y)} \quad (23)$$

where $\mathbb{V}$ is the variance, $\mathbb{E}(Y|X_i)$ refers to the expected value of output $Y$ when parameter $X_i$ is fixed, and $X_{-i}$ denotes all uncertain parameters except $X_i$. The sum of $S_i$ cannot exceed one and the sum of $S_{Ti}$ is greater than or equal to one. However, if there are no higher order interactions between the input parameters, the sum of $S_i$ and $S_{Ti}$ is one.

**Table 2:** Output variables for sensitivity analysis, and constraints (LB, UB) on the output for feasibility studies.

| Unit operation | Output | (LB, UB) |
|---|---|---|
| Blender | API comp. ($C_{API}$, %) | (9.5,10.5) |
| Tablet press | Weight ($W$, mg) | (167,183) |
| | Compaction force ($F_{main}$, kN) | (2, 50) |
| | Strength ($\sigma_T$, MPa) | (2,15) |
| | Content uniformity ($C_V$, %) | (0,6) |

Table 1 lists the input variables with their corresponding ranges for the feeders, blender and the tablet

press. Along with the downstream variables, the first crystallizer's residence time ($\tau_{CR01}$) and its cooling jacket temperature ($T_{CR01}$) are also considered. These factors affect the crystal size distribution and are investigated to quantify their impact on tablet content uniformity. Other upstream decision variables are fixed at their nominal values and can be found in the work of Inyoung et al. [6]. Table 2 elucidates the considered output variables in this study.

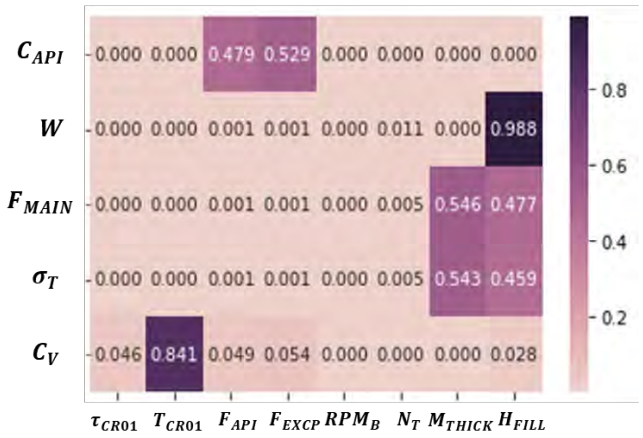



**Figure 2.** Sensitivity analysis results showing Sobol's total sensitivity index effect ($S_{Ti}$) on the drug substance-product process.

The sensitivity results based on Sobol's total effect index in shown in Figure 2. It is found that the first order effect ($S_i$) is similar to the total effect ($S_{Ti}$) which means that the interaction effect between each input variable is weak and hence the total effects are reported. The Sobol's method concluded that six out of eight input variables are most critical. Blender speed does not affect any of the output variables and turret speed affects the tablet properties only very slightly and therefore has not been retained for feasibility studies. On the other hand, crystallizer's residence time and its operating temperature, API and excipient flow rates, tablet press' main compression thickness and dosing position impact one or more output variables significantly.

After sensitivity analysis, feasibility studies can be performed on the subset of input variables to characterize the process design space. To estimate the design space, the output variables are determined based on the uncertain input variables. Based on whether the maximum and minimum value of output variables obey the constraints or not, the process feasibility is drawn. For the integrated flowsheet, feasibility analysis is conducted on the six most influential input factors and the constraints on the output variables are shown in Table 2. The feasibility studies result in a 6D problem with 10 constraints for the flowsheet model. For this high-dimensional problem, matrix plots are deployed to describe the feasibility as explained in Forrester et al., (2008). The matrix includes 15 plots, each of which represents feasibility of two input variables while the remaining four inputs are fixed at their nominal values. It should be noted that the matrix is symmetric, therefore 15 plots instead of 25 are shown accounting for all possible input combinations for feasibility studies. For each plot, 25 sample grid points are obtained through discretization of inputs, and output variables are estimated at the discretized inputs. The feasible region where all the constraints are jointly satisfied is represented by the olive contours.

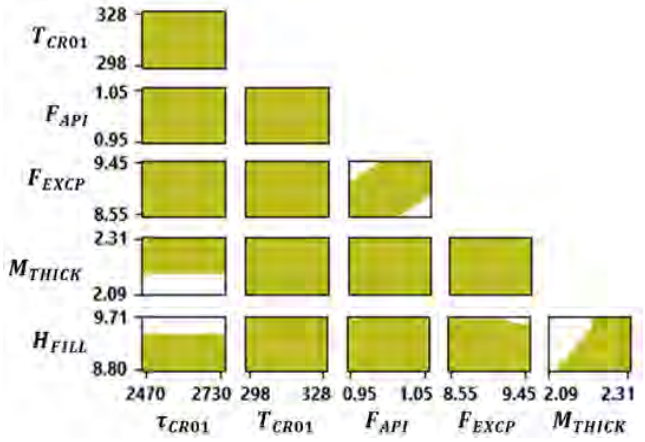



**Figure 3.** Feasibility analysis results of the DC process using PharmaPy.

The results of the feasibility analysis for the flowsheet model are shown in Figure 3. From the feasibility plots, we can observe that the operating temperature ($T_{CR01}$) and residence time of the crystallizer ($\tau_{CR01}$) are feasible over their entire range, which directly impacts the crystal size distribution in the upstream process. This implies that the process can sustain all the variations from these sources while ensuring robustness. The API flow rate ($F_{API}$) and excipient flow rate ($F_{EXCP}$) are also linearly feasible across their input space. The main compression thickness ($M_{thick}$) and dosing position ($H_{fill}$) significantly affect the tablet properties and are found to be feasible for higher and lower values, respectively. But much lower values of thickness and dosing position can result in large deviations from the desired tablet properties like weight, compaction force, and strength. Therefore, the variations in thickness and dosing position need to be strictly controlled to avoid adverse effects on tablet quality.

With the help of in-built python libraries and deployment of matrix plots, PharmaPy can execute sensitivity and feasibility analysis on a given set of input and output variables. This allows to clearly screen the important input variables and quantify the extent of tolerance to process variations which can help build robust control strategies ensuring product quality.

## CONCLUSION

This contribution demonstrates the features of the enhanced PharmaPy package to study the effects of upstream and downstream pharmaceutical processes on final tablet quality. Since the downstream processing can operate in a truly continuous mode, a direct compaction case study is used to investigate the effects of process parameters on tablet quality attributes with the help of process analysis. The process analysis helped identify crucial input variables and determined a process design space that ensures consistent product quality.

However, the downstream PharmaPy package can undergo further enhancements to fully realize the open-source prowess of PharmaPy framework. This includes flowsheet optimization and alternate routes to manufacture tablets such as dry granulation and wet granulation where key differences and challenges can be analyzed. In addition, the downstream architecture needs to be equipped with models that help quantify the effects of variations in API attributes, e.g., particle size distributions and moisture content, on the blend and tablet properties. This will help understand the changes a given blend undergoes during the drug production process. Efficient models will be built to capture such effects as part of the overall PharmaPy downstream development.

## ACKNOWLEDGEMENTS

The authors acknowledge the support by the National Science Foundation under Grant No. 2140452 - CMMI-EPSRC: Right First Time Manufacture of Pharmaceuticals (RiFTMaP).

## REFERENCES

1. Plumb, K. Continuous processing in the pharmaceutical industry: changing the mind set. *Chem. Eng. Res. Des.*, 83(6), pp.730-738 (2005)
2. Wang, Z., Escotet-Espinoza, M.S. and Ierapetritou, M. Process analysis and optimization of continuous pharmaceutical manufacturing using flowsheet models. *Comput. Chem. Eng.*, 107, pp.77-91 (2017)
3. Casas-Orozco D, Laky D, Wang V, Abdi M, Feng X, Wood E, Laird C, Reklaitis GV, Nagy ZK. PharmaPy: An object-oriented tool for the development of hybrid pharmaceutical flowsheets. *Comput. Chem. Eng.*, 153, p.107408 (2021)
4. Laky DJ, Casas-Orozco D, Laird CD, Reklaitis GV, Nagy ZK. Simulation–Optimization Framework for the Digital Design of Pharmaceutical Processes Using Pyomo and PharmaPy. *Ind. Eng. Chem. Res.*, 61(43), pp.16128-16140 (2022)
5. Casas-Orozco D, Laky DJ, Wang V, Abdi M, Feng X, Wood E, Reklaitis GV, Nagy ZK. Techno-economic analysis of dynamic, end-to-end optimal pharmaceutical campaign manufacturing using PharmaPy. *AIChE J.*, 69(9), p.e18142 (2023)
6. Hur I, Casas-Orozco D, Laky DJ, Destro F, Nagy ZK. Digital design of an integrated purification system for continuous pharmaceutical manufacturing. *Chem. Eng. Sci.,* 285, p.119534 (2024)
7. Tian, G., Koolivand, A., Arden, N.S., Lee, S. and O'Connor, T.F. Quality risk assessment and mitigation of pharmaceutical continuous manufacturing using flowsheet modeling approach. *Comput. Chem. Eng.*, 129, p.106508 (2019)
8. Portillo, P.M., Muzzio, F.J. and Ierapetritou, M.G. Using compartment modeling to investigate mixing behavior of a continuous mixer. *J. Pharm. Innov.*, 3, pp.161-174 (2008)
9. Rohrs, B.R., Amidon, G.E., Meury, R.H., Secreast, P.J., King, H.M. and Skoug, C.J. Particle size limits to meet USP content uniformity criteria for tablets and capsules. *J. Pharm. Sci.*, 95(5), pp.1049-1059 (2006)
10. Huang, Y.S., 2023. Digital Twin Development and Advanced Process Control for Continuous Pharmaceutical Manufacturing. Doctoral dissertation, Purdue University Graduate School (2023)
11. Bachawala, S. Rational Function Framework to Integrate Tableting Reduced Order Models with Upstream Unit Operations. Doctoral dissertation, Purdue University Graduate School (2024)
12. Shahab, M., Bachawala, S., Gonzalez, M., Reklaitis, G. and Nagy, Z., Design Space Identification of the Rotary Tablet Press. *System and Control Transactions,* 3, pp. 194-200 (2024)
13. Forrester, A., Sobester, A., & Keane, A. Engineering design via surrogate modelling: a practical guide. *John Wiley & Sons*. (2008)

© 2025 by the authors. Licensed to PSEcommunity.org and PSE Press. This is an open access article under the creative commons CC-BY-SA licensing terms. Credit must be given to creator and adaptations must be shared under the same terms. See https://creativecommons.org/licenses/by-sa/4.0/



Systems & Control Transactions

**Research Article - Peer Reviewed Conference Proceeding**
ESCAPE 35 - European Symposium on Computer Aided Process Engineering
Ghent, Belgium. 6-9 July 2025
Jan F.M. Van Impe, Grégoire Léonard, Satyajeet S. Bhonsale,
Monika E. Polańska, Filip Logist (Eds.)

PSE PRESS

# Modeling the Impact of Non-Ideal Mixing on Continuous Crystallization: A Non-Dimensional Approach

**Jan Trnka[a], František Štěpánek[a]***

[a] University of Chemistry and Technology, Department of Chemical Engineering, Prague, Czech Republic
* Corresponding Author: Frantisek.Stepanek@vscht.cz

## ABSTRACT

Mathematical modeling is essential for the effective control of many chemical engineering processes, including crystallization. However, most existing crystallization models used in industry and academia assume ideal mixing. As a result, the unclear effects of imperfect mixing on crystallization, reported in experimental studies, remain largely unexplained. In this work we aim to address this gap in understanding by examining antisolvent crystallization processes on a general theoretical level, using a novel dimensionless model. To address the impact of mixing on crystallization, we employ the Engulfment model coupled with a population balance, and we nondimensionalize the model equations. Using this model, we explore the dependence of the mean particle size on the homogenization rate, represented by the Damköhler number for crystallization. Moreover, we study the impact of mixing at various values of the model's kinetic parameters to simulate difference in properties of individual products. We show that we are able to explain the complex interaction between crystallization and mixing, proving our model can serve as a tool for achieving a better understanding of the processes involved. Finally, due to its efficiency and reduced number of parameters, the model is suitable for direct fitting to experimental data.

**Keywords**: crystallization, modeling, mixing, continuous, non-dimensional

## INTRODUCTION

Crystallization is a fundamental technique used for separating and/or purifying solids in various industries, including pharmaceuticals and food production. The process conditions during crystallization significantly affect the particle size and purity of the final product. Both particle size and shape influence various material properties, such as flowability, filterability, and dissolution behavior. Effective control of the crystallization process can enhance product quality and eliminate the need for additional steps like comminution or granulation.

Unlike cooling or evaporative crystallization, reactive and antisolvent crystallization involve mixing two liquids of distinct compositions. Supersaturation is induced through mixing, either due to the product being synthesized (reactive) or the reduction of solubility (antisolvent). However, most models currently used in both industry and academia assume ideal mixing and fail to account for the system's dependence on mixing dynamics, thereby limiting our understanding of the process.

Numerous experimental studies have addressed the impact of mixing on crystallization. The effect of increasing mixing intensity on particle size is inconsistent, varying across different substances and products [1]. The mean crystal size may increase, decrease, or even reach a maximum or minimum as the mixing intensity varies. Even using the same crystallizer type for the same product may lead to qualitatively different outcomes. Additionally, the rate of homogenization has also been shown to affect the width of the particle size distribution (PSD), particle shape, and/or the extent of agglomeration.

Although these dependencies are well documented, a systematic approach to studying them has not been established. Research, both on the modeling and experimental sides, tends to focus on a single system at a time. In contrast to the current trend of developing complex models, we aim to use a relatively simple modeling framework, keeping the number of parameters low and enabling extensive parametric studies necessary for our theoretical research.

The authors have already sufficiently explained the

mechanism behind the existence of a maximum in the dependency of particle size on mixing intensity for the semi-batch case [2]. We now aim to extend our research using a novel dimensionless model for continuous crystallization. As in other areas of chemical engineering, nondimensionalization offers valuable insights by reducing the number of parameters and revealing characteristic system properties. It also provides suitable scaling of variables, improving both the precision and efficiency of numerical computations.

# MODELING

## Current Modeling Approaches

The population balance equation (PBE) is the standard approach for crystallization modeling. Depending on the level of detail in describing the hydrodynamics involved, three main modeling approaches are commonly considered:

- The ideal mixing assumption is still widely used as it allows for neglecting mixing in the model equations, thus simplifying calculations. This approach assumes an infinitely fast homogenization rate and is therefore applicable to systems that do not exhibit a dependence on the agitation rate.
- Models based on compartmentalization represent a balanced approach to account for the complexity of mixing. These models divide the studied volume into several compartments and describe the material flux between them. Within each compartment, mixing is typically assumed to be infinitely fast. One of the most popular models in this category is the mechanistic micromixing model developed by Baldyga and Bourne, also known as the Engulfment model [3].
- CFD-based approaches, where the PBE is integrated within the CFD framework, are perhaps the most rigorous. However, even CFD cannot fully capture mixing processes at the molecular level (i.e., micromixing). Since crystallization is a molecular process, these methods often require additional micromixing models. Alternatively, they assume that the homogenization process is limited only by macroscale mixing (i.e., fast micromixing). Despite the complexity and high computational cost, the improvement in accuracy over the Engulfment model appears to be limited.

## Model Description

### Coupling PBE With the Engulfment Model

We have based our approach on the Engulfment model, as we believe it provides the most suitable choice for our theoretical study. In this Lagrangian model, the system volume is discretized into two well-mixed regions: (1) the mixed zone, enriched with the reference compound, and (2) the surrounding bulk fluid. Mixing is described as the expansion of the mixed zone through the engulfment of the bulk, leading to dilution of the compound in the mixed zone if no additional source is present. This approach was initially developed in reactor engineering but has since been applied to crystallization (e.g., [4]). Although the model was originally developed based on turbulent flow mixing mechanisms, we find its framework applicable even to non-turbulent flows.

According to the Engulfment model [3], the concentration of a compound in the mixed zone evolves over time according to Eq. 1 as volume fraction of the mixed zone ($X$) expands. The rate of homogenization is determined by a single constant, the mixing time $t_{mix}$ (Eq. 2).

$$\frac{dc}{dt} = \frac{1}{X}\frac{dX}{dt}(c_b - c) + r \tag{1}$$

$$\frac{dX}{dt} = \frac{1}{t_{mix}}X \tag{2}$$

Coupling the engulfment model with PBE results in Eq. 3, accounting only for primary nucleation and growth (neglecting agglomeration and breakage). The molar balance is then described in Eq. 4. These equations are valid for both reactive and antisolvent crystallization in batch or in continuous tubular crystallizers operating at steady state, for which time corresponds to the coordinate time.

$$\frac{\partial f}{\partial t} + G\frac{\partial f}{\partial L} = \frac{1}{t_{mix}}(f_b - f), \quad f(0,t) = \frac{J}{G} \tag{3}$$

$$\frac{dc}{dt} = \frac{1}{t_{mix}}(c_b - c) - \frac{3k_v\rho_{cr}}{M}G\phi_2 + r \tag{4}$$

### Model Nondimensionalization

To study the effect of mixing on crystallization at a theoretical level, we have developed an efficient method for nondimensionalizing Equations 3 and 4. We begin by introducing the following dimensionless variables:

$$\tau = \frac{t}{t_0},\ \lambda = \frac{L}{L_0},\ \chi = \frac{c^*}{c_0},\ S = \frac{c}{c_0\chi},\ n = L_0V_0f \tag{5}$$

$$\tilde{G} = \frac{G}{G_{ref}},\ \tilde{J} = \frac{J}{J_{ref}},\ \tilde{r} = \frac{t_0}{c_0}r,\ c_0 = c_{ref} \tag{6}$$

Defining:

$$V_0 = \frac{k_v\rho_{cr}L_0^3}{M_{cr}c_{\mathrm{ref}}}, L_0 = t_0G_{ref}, t_0 = \left(\frac{c_0M_{cr}}{k_v\rho_{cr}J_{ref}G_{ref}^3}\right)^{\frac{1}{4}} \tag{7}$$

leads to significant reduction in the number of model parameters. The reference values $J_{ref}, G_{ref}, c_{ref}$ can be set arbitrarily, although they do affect scaling. The appropriate value for $c_{ref}$ is the maximal solubility while the suggested choice of $J_{ref}$ and $G_{ref}$ is discussed later.

Assuming isothermal conditions and solubility as a sole function of the solvent volume fraction $\varphi$, the final

form of our non-dimensional model is described by the following equations:

$$\frac{dS}{d\tau} = Da_{cr} S\left(\frac{S_b \chi_b}{S\chi} + \frac{(\varphi-\varphi_b)}{\chi}\frac{d\chi}{d\varphi} - 1\right) + \frac{1}{\chi}\left(\tilde{r} - 3\tilde{G}\,\Phi_2\right) \quad (8)$$

$$\frac{\partial n}{\partial \tau} + \tilde{G}\frac{\partial n}{\partial \lambda} = Da_{cr}(n_b - n), \quad n(0,\tau) = \frac{\tilde{J}}{\tilde{G}} \quad (9)$$

Derivation of the non-dimensional model leads to the emergence of a dimensionless number, $Da_{cr}$, defined as the ratio of homogenization rate to crystallization rate (Damköhler number for crystallization):

$$Da_{cr} = \frac{t_0}{t_{mix}} = \frac{v_{mix}}{v_{cr}} \quad (10)$$

We further assume expressions for growth and crystallization rates according to Eq. 11. By setting the reference values equal to the rate coefficients, we conveniently reduce the number of kinetic constants from four to two, as shown in Eq. 12.

$$G = k_G(S-1)^g, \quad J = k_J \exp\left(-\frac{j}{\ln^2 S}\right) \quad (11)$$

$$\tilde{G} = (S-1)^g, \quad \tilde{J} = \exp\left(-\frac{j}{\ln^2 S}\right) \quad (12)$$

The constants $j$ and $g$ together with the solubility data remain the only product properties needed as input to the model.

### Application to Continuous Antisolvent Process

In this study, we focus on isothermal antisolvent crystallization in a tubular device developed in our research group. The process is schematically illustrated in **Figure 1**. A solution of candesartan cilexetil, an active pharmaceutical ingredient (API), in acetone is injected perpendicularly to the length direction of the tube into a stream of water. Mixing of the two streams generates supersaturation, which leads to nucleation and subsequent growth of the product particles.

The initial conditions of the mixed zone are given by the properties of the organic phase ($S(0) = 1, \varphi(0) = 0.85$) while bulk is represented by pure water. The volume flow rate ratio of organic to inorganic phase is 1:9 (corresponds to $X(0) = 0.1$). Setting the bulk variables $S_b$, $\varphi_b$ and $n_b$ to zero and omitting the reaction term results in a simplified set of equations:

$$\frac{dS}{d\tau} = Da_{cr} S\left(\frac{\varphi}{\chi}\frac{d\chi}{d\varphi} - 1\right) - \frac{3\tilde{G}\,\Phi_2}{\chi} \quad (13)$$

$$\frac{\partial n}{\partial \tau} + \tilde{G}\frac{\partial n}{\partial \lambda} = -Da_{cr} n, \quad n(0,\tau) = \frac{\tilde{J}}{\tilde{G}} \quad (14)$$

The solubility data of candesartan cilexetil used for our study were taken from literature [5]. The model of the continuous device is implemented in the Python environment. Eq. 13 is converted into a set of ordinary differential equations (ODEs) using 1D finite volume method with Koren flux limiter. The set of ODEs is then integrated numerically using the Runge–Kutta method (RK45). All simulation results are steady with respect to the coordinate time, assuming an infinitely long tube.

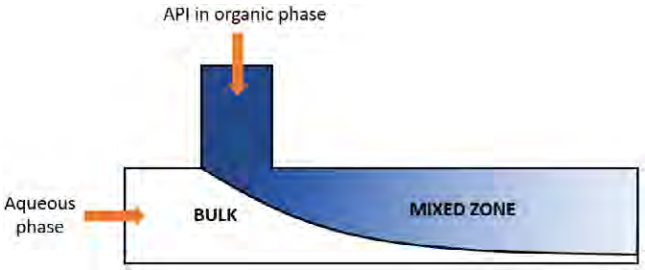



**Figure 1.** Schematic representation of the setup and spatial discretization of the continuous ASP device according to the Engulfment model (the shade of blue color represents local concentration of API).

## RESULTS

### The Mixing Impact on the Mean Particle Size

As mentioned, our model takes three product-specific inputs: parameters $j$ and $g$ and the solubility function $\chi(\varphi)$. In our study, we vary the kinetic parameters in order to address the influence of the product properties on the results of our simulations. The effects of changing the solubility curve are not presented in this study.

As $t_0$ is a constant for a given substance, increasing $Da_{cr}$ has the meaning of increasing the rate of homogenization. We proceed with a sensitivity analysis of the effect of kinetic constants $j$ and $g$ on the mean particle size ($\lambda_{43}$) and its dependence on $Da_{cr}$.

### The Influence of $g$ on $\lambda_{43}(Da_{cr})$

The results of varying $g$ along with $Da_{cr}$ at constant value of $j$ are depicted in **Figure 2**. As shown, all the reported scenarios for the dependency of the mean particle size on mixing intensity are covered by our model. In agreement with the experimental studies, the particle size according to our model may decrease, increase, reach a maximum or minimum or remain constant with change in the mixing intensity.

All the parametric curves are shaped similarly. At very low $Da_{cr}$, the particle size decreases while increasing the mixing rate. This happens as the result of monotonous increase in maximal supersaturation with $Da_{cr}$ demonstrated on **Figure 3**. At higher supersaturation, more nuclei are formed due to enhanced nucleation rate, resulting in decrease in particle size. The crystal size reaches minimum at $Da_{cr} \doteq 10^{-1}$. Interestingly, the parametric curves switch their order shortly before reaching the minimum. This happens as the maximal supersaturation reaches the value of two (the power function argument of the growth rate reaches one).

For more intense mixing, $\lambda_{43}$ grows with $Da_{cr}$. This most likely happens because the increase in nucleation rate diminishes at high supersaturation while the growth rate keeps accelerating due to the nature of the

respective equations ($\tilde{J}$ is limited unlike $\tilde{G}$). However, the increase of $\lambda_{43}$ is discontinued quite abruptly at values of $Da_{cr}$ unique for every curve. The value of the local maximum and its location increases with higher growth rate exponent.

To understand the sudden decrease, let us describe the kinetics of crystallization according to our model in the phase space of the non-dimensional concentration ($S\chi$) and the solvent volume fraction (**Figure 4**). The initial state marks the composition of the organic phase. The yellow line represents the conditions close to perfect mixing, where the mixing and crystallization events are separate. The transition from the initial state to the mixed state along the straight line is caused by dilution of the island by engulfment of the bulk. Any deviation from the yellow line represents induced crystallization while mixing. The maximal possible supersaturation is reached at the yellow line at $\varphi_{Smax} \doteq 0.42$. For $\varphi > \varphi_{Smax}$ the supersaturation always grows due to mixing while for $\varphi < \varphi_{Smax}$ mixing causes decrease in $S$. If the mixing rate is too fast relative to the crystallization rate, crystallization is not induced before reaching $\varphi_{Smax}$, causing the crystallization to begin at significantly lower supersaturation, reducing the final size of the crystals at high values of $Da_{cr}$. This behavior is encoded in Eq. 13 as the term $\frac{\varphi}{\chi}\frac{d\chi}{d\varphi} - 1$ is positive at $\varphi > \varphi_{Smax}$ and negative at $\varphi < \varphi_{Smax}$. The value of $\varphi_{Smax}$ is therefore determined only by the shape of the solubility function.

## The Influence of $j$ on $\lambda_{43}(Da_{cr})$

Let us now consider the scenario of varying $j$ along with $Da_{cr}$ at constant $g$. Overall, increasing $j$ hinters the nucleation rate and thus promotes growth, causing a general increase in particle sizes. Increasing $j$ also leads to later onset of nucleation induced at higher supersaturation, further favoring growth over nucleation. The results of the simulations are shown in **Figure 5**.

For low values of $j$, the shape of the curves remains unaltered compared to the results in **Figure 2**. However, at values roughly from 10 to 80, the system undergoes a qualitative change. In this process, the local maximum vanishes and the decrease in $\lambda_{43}$ associated with approaching perfect mixing is turned into an increase.

Previously, for $j = 1$, the reason for the decrease in particle size was sudden drop in supersaturation due to fast mixing, resulting in less pronounced growth. However, nucleation at $j = 100$ is about hundred times slower. At these conditions, lower supersaturation produces significantly smaller number of particles, resulting in seemingly paradoxical increase in particle size.

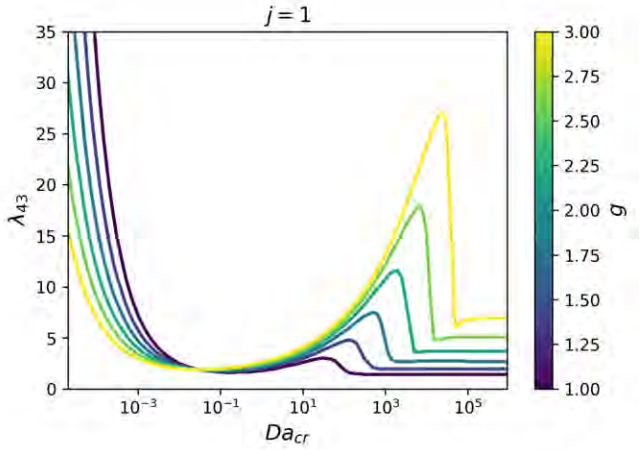



**Figure 2.** Dependence of the mean non-dimensional particle size on the Damköhler number for crystallization with varying the growth rate exponent.

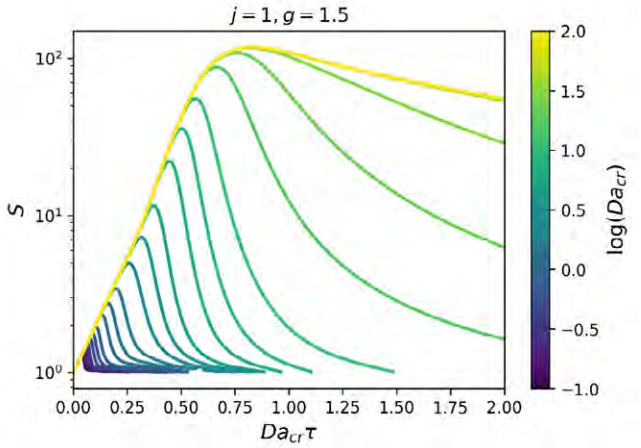



**Figure 3.** Evolution of the supersaturation over time (maximal supersaturation increases with $Da_{cr}$). The x-axis is scaled by $Da_{cr}$ for better comparison.

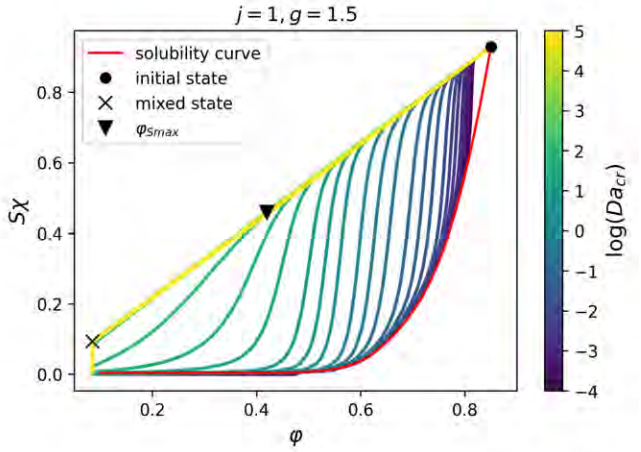



**Figure 4.** Representation of the evolution of mixing and crystallization in the phase space of the non-dimensional concentration and the solvent volume fraction.

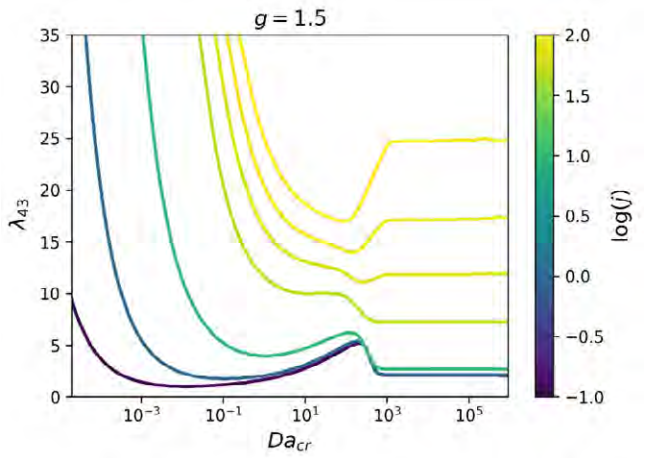



**Figure 5.** Dependence of the mean non-dimensional particle size on the Damköhler number for crystallization with varying nucleation constant.

## Parametric Fitting

As the developed non-dimensional model has only two kinetic parameters in contrast to four in the dimensional one, it is easier to fit the model to experimental data. Moreover, using the non-dimensional model requires no knowledge about the product properties other than its solubility behavior. To make use of these advantages, we further present how to use the model for parametric fitting.

Let $\boldsymbol{L}$ denote the vector of $N$ measured crystal sizes at different volume flow rates $\dot{\boldsymbol{V}}$ (the mixing rate in our system is assumed to be dependent only on $\dot{V}$). As evident from Eq. 15, dividing $\boldsymbol{L}$ by one of its elements gives the same results for both dimensional and non-dimensional data:

$$\frac{\boldsymbol{L}}{L[0]} = \frac{L_0\boldsymbol{\lambda}}{L_0\lambda[0]} = \frac{\boldsymbol{\lambda}}{\lambda[0]} \tag{15}$$

We use this identity to define the objective function as follows:

$$F = \sum_{i=0}^{N}\left(\frac{L[i]}{L[0]} - \frac{\lambda[i]}{\lambda[0]}\right)^2 \tag{16}$$

The remaining problem to be solved is finding the link between the flow rates and the corresponding Damköhler numbers. Based on the research done on similar micromixers [6], we expect the mixing time to be inversely proportional to the volume flow rate to the power of 1.5. Thus:

$$Da_{cr} = \frac{t_0}{t_{mix}(\dot{V})} = \frac{t_0}{K}\dot{V}^{1.5} = c\dot{V}^{1.5} \tag{17}$$

where the coefficient $c$ is unknown.

After applying the same strategy as for the crystal sizes, we get:

$$\frac{\boldsymbol{Da_{cr}}}{Da_{cr}[0]} = \frac{c\dot{\boldsymbol{V}}^{1.5}}{cV[0]^{1.5}} = \frac{\dot{\boldsymbol{V}}^{1.5}}{V[0]^{1.5}} \tag{18}$$

The points at which $\boldsymbol{\lambda}$ are to be evaluated from simulations are therefore:

$$\boldsymbol{Da_{cr}} = Da_{cr}[0]\frac{\dot{\boldsymbol{V}}^{1.5}}{V[0]^{1.5}} \tag{19}$$

where $Da_{cr}[0]$ is unknown and therefore it is another parameter to be optimized. Overall, finding the kinetic parameters presents an optimization problem:

$$\underset{g,j,Da_{cr}[0]}{\text{minimize}}\ F \tag{20}$$

We have used experimental data measured by our group to test the use of this method and validate our model. The best fit of the model to the experimental data is presented in **Figure 6**. In the experiments, we have used two distinct mixing units, the T-junction and the FDmiX mixer. The latter device increases the homogenization rate by passively introducing flow oscillations at otherwise laminar conditions. We have used a combination of direct grid search and the genetic algorithm to solve the optimization problem.

The model qualitatively describes the measured trends quite well. The value of $Da_{cr}[0]$ for the FDmiX was found at higher values than for the T-junction as expected. As mixing is very slow in the T-junction, the particle size drops quite rapidly before it levels out as explained in describing **Figure 2**. However, aggregation may also contribute to the larger size of particles measured at low mixing rates. On the other hand, the FDmiX seems to operate at mixing rates close to the local maximum, which is very well predicted by our model.

Ongoing CFD analysis of the flow in the T-junction has revealed that mixing is not finished before reaching the outlet, which our model is not accounting for. Expanding the model to address this issue may further improve the results in the future.

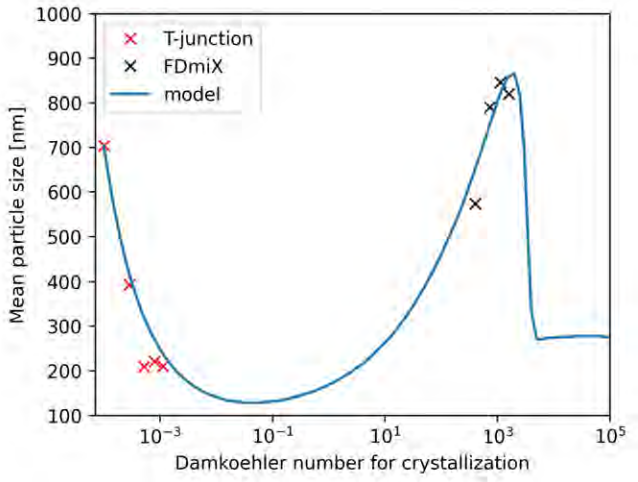



**Figure 6.** The best fit of the model to our experimental data for two different mixers.

## CONCLUSION

In this work, we present a simple, yet efficient crystallization model developed for studying the interaction between crystallization and mixing in batch and continuous tubular crystallizers. We have found an efficient way to nondimensionalize the model equations, significantly reducing the number of parameters. As a result, a new non-dimensional number has emerged during the process – the Damköhler number for crystallization – representing the ratio of homogenization and crystallization rates.

We use the model to study the process of continuous antisolvent crystallization by means of parametric sensitivity analysis. We were able to undercover the complex interaction between nucleation, growth and mixing and increase the understanding of the processes involved.

In addition to its suitability for theoretical research, our model is also convenient for fitting the kinetic parameters to experimental data as the reduced dimension of the search space streamlines solving of the optimization problem.

Despite the simplicity of the model, we have shown it is able to account for all the reported scenarios of mixing impact on particle size and to fit measured data sufficiently well.

## ACKNOWLEDGEMENTS

The financial support is from the project OP JAK INTER-MICRO (registration number CZ.02.01.01/00/22_008/0004597), the Specific University Research (MSMT), co-funded by European Union.

## LIST OF SYMBOLS

| | | |
|---|---|---|
| $c^*, \chi$ | solubility | $[\mathrm{mol\ m^{-3}}]$, [1] |
| $t,\ \tau$ | time | [s], [1] |
| $f,\ n$ | population density | $[\mathrm{m^{-4}}]$, [1] |
| $L,\ \lambda$ | crystal size | [m], [1] |
| $\phi_2, \Phi_2$ | second moment | $[\mathrm{m^{-1}}]$, [1] |
| $J,\ \tilde{J}$ | nucleation rate | $[\mathrm{m^{-3}}]$, [1] |
| $G, \tilde{G}$ | growth rate | $[\mathrm{m\ s^{-1}}]$, [1] |
| $r,\ \tilde{r}$ | reaction rate | $[\mathrm{mol\ m^{-3}\ s^{-1}}]$, [1] |
| | | |
| $c$ | concentration | $[\mathrm{mol\ m^{-3}}]$ |
| $S$ | supersaturation | [1] |
| $X$ | island volume fraction | [1] |
| $\varphi$ | solvent volume fraction | [1] |
| $M$ | molar mass | $[\mathrm{kg\ mol^{-1}}]$ |
| $k_v$ | volume shape factor | [1] |
| $\rho_{cr}$ | crystal density | $[\mathrm{kg\ m^{-3}}]$ |
| $k_G$ | growth rate coeff. | $[\mathrm{m\ s^{-1}}]$ |
| $k_J$ | nucleation rate coeff. | $[\mathrm{m^{-3}}]$ |
| $g$ | growth rate exponent | [1] |
| $j$ | nucleation constant | [1] |
| $Da_{cr}$ | Damköhler number | [1] |

## REFERENCES

1. Qu Y, Cheng J, Mao ZS, Yang C. A perspective review on mixing effect for modeling and simulation of reactive and antisolvent crystallization processes. *Reaction Chemistry & Engineering* 6:183-196 (2021) https://doi.org/10.1039/D0RE00223B
2. Trnka J, Maggioni GM, Štěpánek F. Development and Application of a Simplified Non-Ideal Mixing Model for Semi-Batch Crystallization. *Computer Aided Chemical Engineering* 53:193-198 (2024) https://doi.org/10.1016/B978-0-443-28824-1.50033-8
3. Baldyga J, Bourne JR. Simplification of micromixing calculations. I. Derivation and application of new model. *The Chemical Engineering Journal* 42:83-92 (1989) https://doi.org/10.1016/0300-9467(89)85002-6
4. Ståhl M, Rasmuson ÅC. Towards predictive simulation of single feed semibatch reaction crystallization. *The Chemical Engineering Journal* 64:1559-1576 (2009) https://doi.org/10.1016/j.ces.2008.12.001
5. Cui, P.; Yin, Q.; Gong, J.; Wang, Y.; Hao, H.; Xie, C.; Bao, Y.; Zhang, M.; Hou, B.; Wang, J., Thermodynamic analysis and correlation of solubility of candesartan cilexetil in aqueous solvent mixtures. *Fluid Phase Equilibria* 337:354-362 (2013) https://doi.org/10.1016/j.fluid.2012.09.027
6. Lindenberg C, Mazzotti M. Experimental characterization and multi-scale modeling of mixing in static mixers. Part 2. Effect of viscosity and scale-up. *Chemical engineering science* 64:4286-4294 (2009) https://doi.org/10.1016/j.ces.2009.06.067

© 2025 by the authors. Licensed to PSEcommunity.org and PSE Press. This is an open access article under the creative commons CC-BY-SA licensing terms. Credit must be given to creator and adaptations must be shared under the same terms. See https://creativecommons.org/licenses/by-sa/4.0/



Systems & Control Transactions

**Research Article - Peer Reviewed Conference Proceeding**
ESCAPE 35 - European Symposium on Computer Aided Process Engineering
Ghent, Belgium. 6-9 July 2025
Jan F.M. Van Impe, Grégoire Léonard, Satyajeet S. Bhonsale,
Monika E. Polańska, Filip Logist (Eds.)

PSE PRESS

# Process Design of an Industrial Crystallization Based on Degree of Agglomeration

**Yung Shun Kang[a], Hemalatha Kilari[a], Neda Nazemifard[b], Ben Renner[b], Yihui Yang[b], Charles Papageorgiou[b], and Zoltan K. Nagy[a]***

[a] Purdue University, Davidson School of Chemical Engineering, West Lafayette, Indiana, United States
[b] Takeda Pharmaceuticals International Company, Cambridge, Massachusetts, United States
* Corresponding Author: zknagy@purdue.edu

## ABSTRACT

This study proposes a model-based approach utilizing a hybrid population balance model (PBM) to optimize temperature profiles for minimizing agglomeration and enhancing crystal growth. The PBM incorporates key mechanisms—nucleation, growth, dissolution, agglomeration, and deagglomeration—and is applied to the crystallization of an industrial active pharmaceutical ingredient (API), Compound K. Parameters were estimated through prior design of experiments (DoE) and refined via additional thermocycle experiments. In-silico DoE simulations demonstrate that the hybrid PBM outperforms traditional methods in assessing process performance under agglomeration-prone conditions. Results confirm that thermocycles effectively reduce agglomeration and promote bulk crystal formation, though their efficiency plateaus beyond a certain cycle number. This model-based approach provides a more robust strategy for agglomeration control compared to conventional methods, offering valuable insights for industrial crystallization optimization.

**Keywords**: Algorithms, Batch Process, Modelling and Simulations, Process Design, Optimization

## 1. INTRODUCTION

Agglomeration, often undesirable in crystallization, can lead to impurity incorporation [1,2], prolonged filtration and drying times, and difficulties in achieving uniform particle size and composition. While controlling supersaturation and agitation rates has been shown to reduce agglomeration [1,3], more advanced techniques, such as thermocycles, can facilitate deagglomeration and dissolve fines generated by breakage or attrition.

Optimizing thermocycles requires determining key parameters such as the number of heating-cooling cycles and the corresponding rates. This presents a complex optimization challenge, as traditional quality-by-control (QbC) methods relying on process analytical technology can be resource-intensive [4,5]. A more efficient alternative is the use of PBMs to monitor and regulate agglomeration during crystallization [6].

In this study, we propose a model-based approach to optimize temperature profiles for minimizing agglomeration and enhancing crystal size. A PBM is coupled with the number density of agglomerates to track agglomeration dynamics during thermocycles. The hybrid PBM incorporates key mechanisms, including nucleation, growth, dissolution, agglomeration, and deagglomeration, and is applied to the crystallization of an industrial active pharmaceutical ingredient, Compound K. Most parameters were estimated through DoE in a prior study, while additional thermocycle experiments were conducted to refine dissolution parameters.

Results from in-silico DoE simulations demonstrate that the hybrid PBM approach outperforms traditional methods in accurately evaluating process performance when agglomeration is present. This approach offers a more robust assessment of agglomeration control compared to methods based solely on particle bridge formation. Moreover, simulations indicate that while thermocycles effectively reduce agglomeration, their efficiency plateaus after a certain number of cycles—a trend confirmed through experiments in industrial case studies. Additionally, comparisons of different temperature profiles reveal that introducing heating-cooling cycles not only eliminates most agglomerates but also promotes the growth of larger bulk crystals.

The remainder of this article is organized as follows. Section 2 describes the experimental setup and measurement procedures. Using the experimental data, thermodynamic expressions and related parameters are defined for simulating the industrial case study. Section 3 introduces the hybrid PBMs, which are explicitly formulated to describe total number density and agglomerate number density under both heating and cooling conditions. Section 4 presents the results, including comparisons of different algorithms for agglomeration assessment and various optimal temperature trajectories. Additionally, it examines the differences between model-free and model-based QbC approaches in the industrial case study. Finally, conclusions are summarized in the last section.

## 2. MATERIALS, MEASUREMENTS, AND PROPOSED METHODOLOGY

### 2.1 Experimental setup and procedure

Batch experiments were conducted using the advanced synthesis workstation, Mettler Toledo's EasyMax 402, equipped with a 100 mL glass vessel. The vessel was sealed with a polytetrafluoroethylene lid, which provided multiple ports for PAT tools. Temperature control was achieved using a Pt100 temperature sensor and a Peltier plate, regulated by the built-in software, iControl. The process temperature was maintained between 0 and 70 °C to optimize yield while minimizing solvent evaporation.

Solvent selection for crystallization was performed through a solvent screening process. The chosen mixture consisted of dimethyl sulfoxide (DMSO, 100%, Fisher Scientific) and ethanol (EtOH, 100% absolute, Decon Laboratories, Inc.) in a volume ratio of 20:80. The industrial compound used in this study, referred to as Compound K and supplied by Takeda, exhibited a wide metastable zone—a topic explored in detail in the results section. This broad metastable zone prevented precipitation or nucleation at high supersaturation levels, allowing for a higher initial concentration to enhance productivity and yield.

Due to Compound K's poor solubility in EtOH (forming needle-like but highly agglomerated particles), it was initially dissolved in DMSO. EtOH was then introduced as an antisolvent to control the solubility of the mixture. To ensure the solid form of the final product, a tailored seeding strategy was developed for the seeded batch experiments. Wet seeding was employed to prevent particle clumping and seed aggregation. The seed suspension was prepared in EtOH and sonicated using an ultrasonic cleaner (ELMA ULTRASONICS P30H). The total solvent volume was maintained at 100 mL, with solvent evaporation carefully monitored and typically kept below 5% of the total volume.

During the experiments, an upward-pitched blade metal agitator operated at 400 rpm to ensure efficient mixing. In situ microscopy was performed using Mettler Toledo's EasyViewer with iC Vision software to capture inline particle images and monitor key process mechanisms, including nucleation, growth, dissolution, and agglomeration. Solute concentration was measured using attenuated total reflectance Fourier transform infrared spectroscopy (ATR-FTIR) with Mettler Toledo's ReactIR 702L, following probe calibration.

To constrain the design space, the seed's origin was restricted to a specific lot from the company. The seed crystals were generated using the aforementioned solvent system, resulting in needle-like particles with a crystal size distribution characterized by D10, D50, and D90 values of 2.51, 9.06, and 20.5 μm, respectively. Differential scanning calorimetry (DSC) measurements revealed that the seed was partially crystalline, with a crystallinity of 54.4%.

### 2.2 Crystal size distribution measurement

In the experimental analysis of solid samples, the crystal size distribution (CSD) was determined using the Mastersizer 3000, a Malvern instrument that utilizes light scattering. For wet measurements, heptane (100%, Fisher Scientific) with a fixed amount of Span 80 (100%, Fisher Scientific) was used as the dispersant. Prior to measurement, the slurry was sonicated at 20% intensity for 60 seconds to ensure effective dispersion.

### 2.3 Crystallinity measurement

Qualitative analyses were conducted to assess potential changes in the solid form during the experimental process using offline techniques such as X-ray Powder Diffraction (XRD). These methods were employed to identify distinctive features or fingerprints of the materials. Given the small particle size, scanning electron microscopy (SEM) images of the final products were captured using a field-emission SEM (FEI Nova NanoSEM 450) to confirm the crystal habit and evaluate the extent of agglomeration.

DSC was deemed essential in this study due to the presence of amorphous content, a factor further discussed in the results section. DSC measurements were performed using a PerkinElmer Jade DSC instrument. Notably, the primary purpose of DSC in this study was to enable quantitative comparisons rather than to determine precise thermodynamic properties. The melting heat was quantified based on the area under the melting peak, and crystallinity was calculated as the ratio of the melting heat of the sample to that of an established standard.

### 2.4 Solubility measurement

Utilizing the UPLC data, a crystalline solubility curve was constructed employing the following empirical

equation:

$$ln(C_{s,cry}) = a + \frac{b}{R*T} + \frac{c}{(R*T)^2} \quad (1)$$

where $C_{s,cry}$ represents the crystalline solubility with the unit of mg/g solvent, $T$ denotes the temperature in Kelvin, and $R$ stands for the ideal gas constant. The coefficients' values in the solubility equation are provided in Table 1.

**Table 1:** The solubility coefficients of Compound K in crystalline form.

| Coefficient | Value | Unit |
|---|---|---|
| $a$ | 44.84 | - |
| $b$ | $1.891 \times 10^5$ | $J{\cdot}mol^{-1}$ |
| $c$ | $2.016 \times 10^8$ | $J^2{\cdot}mol^{-2}$ |

**Table 2:** The solubility coefficients of Compound K in amorphous form.

| Coefficient | Value | Unit |
|---|---|---|
| $a$ | −98.06 | - |
| $b$ | 1383 | K |
| $c$ | 16.73 | - |

Following the identification of the amorphous form, the solubility data for the amorphous phase was collected and fitted using Equation 2. The parameters of the solubility curve for the amorphous form are presented in Table 2.

$$ln(C_{s,amor}) = a + \frac{b}{T} + c * log(T) \quad (2)$$

where $C_{s,amor}$ represents the amorphous solubility with the unit of mg/g solvent.

**Table 3:** The boundaries of shape descriptors for different classes of particles.

| Classes | *L | *I | *A | *C |
|---|---|---|---|---|
| Droplets | - | > 100 | - | > 0.87 |
| Needles | >2.0 | < 100 | > 0.32 | < 0.87 |
| agglomerates | >2.0 | < 100 | < 0.32 | < 0.87 |
| Fines | <2.0 | < 100 | - | < 0.87 |

* L: Length, I: Intensity Mean, A: Aspect ratio, C: Circularity

## 2.5 Degree of agglomeration measurement

To analyze the degree of agglomeration and ensure proper dispersion of the highly agglomerated final particles, the solid sample was suspended in the same dispersant used for the CSD measurement. The solid content concentration was controlled at approximately 0.7 mg/mL to prevent excessive particle overlap under the microscope. After sonication, the slurry was uniformly applied to the measurement slide, which was then dried under air.

The Morphologi 4 was used to conduct the image analysis on the prepared slide. Based on various shape descriptors, the particles were classified into four categories: fines, needles, agglomerates, and droplets, as

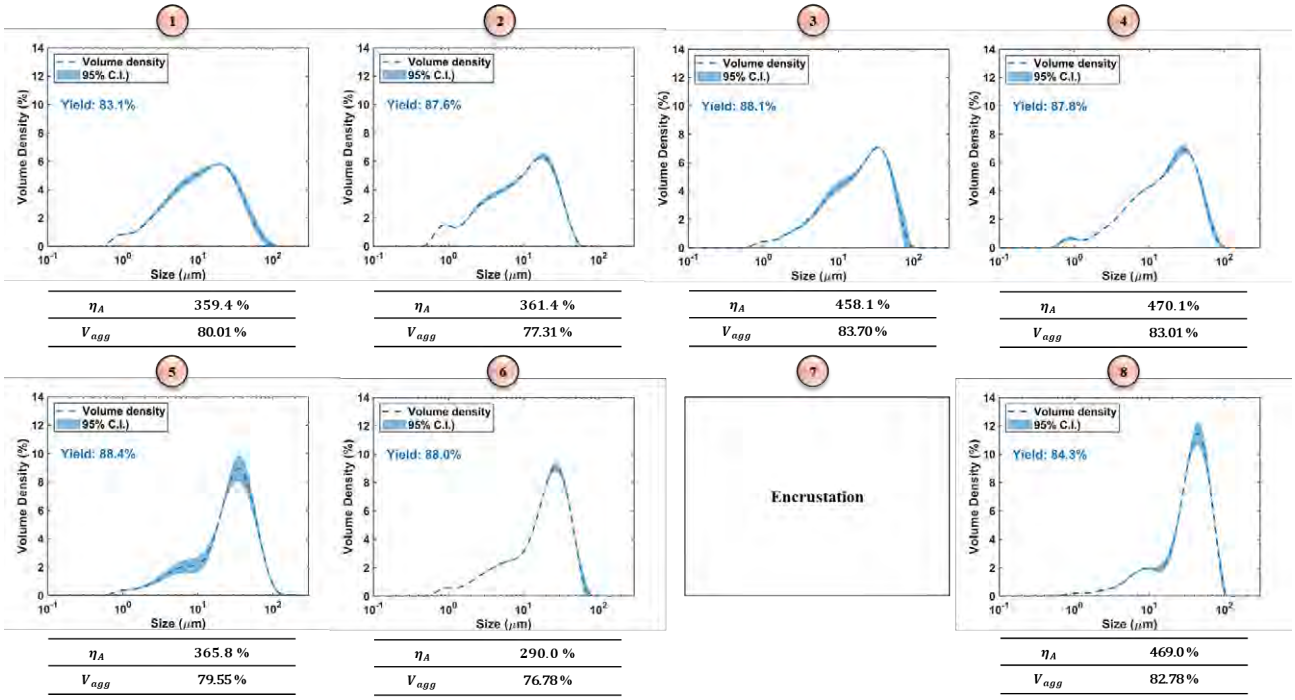



**Figure 1:** Degree of agglomeration calculation comparison based on the in-silico DoE study.

shown in Table 3. The degree of agglomeration was calculated by determining the percentage fraction of agglomerates, needles, and fines, while droplets were excluded due to their role as surfactants for particle dispersion. A minimum of 100,000 particles were captured during the analysis, ensuring that the calculated values represent the overall distribution. The remaining image analysis settings are shown in Supplemental Materials.

## 3. DEGREE OF AGGLOMERATION POPULATION BALANCE MODELING IN INDUSTRIAL CRYSTALLIZATION

Previous trial experiments have shown that the concentration trajectory intersects the amorphous solubility curve throughout heating and cooling cycles. This observation highlights a key aspect of the thermocycling process: the limited dissolution of crystalline particles, even during rapid heating. This behavior supports the continuous growth of needle-like particles across the thermocycles, leading to their eventual enlargement. Consequently, for the digital design of the process, aimed at capturing the evolution of both crystalline and amorphous materials during the desaturation phase, as well as the dissolution behavior of amorphous materials during heating, the degree of supersaturation is defined as follows:

$$\begin{cases} \sigma = \frac{C - C_{s,cry}}{C_{s,cry}}, & C > C_{s,amor} \\ \sigma = \frac{C - C_{s,amor}}{C_{s,amor}}, & C < C_{s,amor} \end{cases} \tag{3}$$

where $\sigma$ denotes the degree of supersaturation, $C_{s,cry}$ denotes the crystalline solubility, $C_{s,amor}$ denotes the crystalline solubility, and $C$ represents the solution concentration.

$$\frac{\partial f(L,t)}{\partial t} + g(t;\theta_g)\frac{\partial f(L,t)}{\partial L} = B_n(t;\theta_n)\delta(L - L_n) - f(L)\int_0^L \beta(L,\lambda)f(\lambda)d\lambda + \frac{L^2}{2}\int_0^\infty \frac{\beta\left((L^3 - \lambda^3)^{\frac{1}{3}},\lambda\right)}{(L^3 - \lambda^3)^{\frac{2}{3}}} f\left((L^3 - \lambda^3)^{\frac{1}{3}}\right) f(\lambda)d\lambda$$

$$while\ C > C_{s,amor} \tag{4}$$

The 1D PBM for this thermocycling process is expressed in equations (4) and (5). These equations are presented in two stages: the heating stage, which results in an undersaturated region, and the cooling stage, which leads to a supersaturated region.

$$\frac{\partial f(L,t)}{\partial t} - D(t;\theta_d)\frac{\partial f(L,t)}{\partial L} = -S(L)f(L,t)\int_\lambda^{L_{max}} b(L,\lambda)S(\lambda)f(\lambda,t)d\lambda$$

$$while\ C < C_{s,amor} \tag{5}$$

where $f$ is the number density function of the total number density, $g$ is the growth rate of the agglomerates with the corresponding parameters $\theta_g$, $d$ is the dissolution rate with the corresponding parameters $\theta_d$, $B_n$ is the birth of the particles due to the nucleation, $\beta$ and $b$ are agglomeration and breakage kernels. $b(L,\lambda)$ is defined as the inverse function of size-dependent Brownian collision kernel to capture the deagglomeration mechanism. $S(L)$ is the selection function for the deagglomeration process, which is a size-independent function:

$$S(L) = k_{dg}D^{g_d} \tag{6}$$

To monitor the evolution of agglomeration during thermal cycles, the PBM for agglomerate number density is coupled with the PBM for total number density, as represented by equations (7) and (8), formulated as follows:

$$\frac{\partial f_{agg}(L,t)}{\partial t} + g_{agg}(t;\theta_g)\frac{\partial f_{agg}(L,t)}{\partial L} = -f(L)\int_0^L \beta(L,\lambda)f(\lambda)d\lambda + \frac{L^2}{2}\int_0^\infty \frac{\beta\left((L^3 - \lambda^3)^{1/3},\lambda\right)}{(L^3 - \lambda^3)^{2/3}} f((L^3 - \lambda^3)^{1/3})f(\lambda)d\lambda$$

$$while\ C > C_{s,amor} \tag{7}$$

$$\frac{\partial f_{agg}(L,t)}{\partial t} - d_{agg}(t;\theta_d)\frac{\partial f_{agg}(L,t)}{\partial L} = -S(L)f(L,t) + \int_\lambda^{L_{max}} b(L,\lambda)S(\lambda)f(\lambda,t)d\lambda$$

$$while\ C < C_{s,amor} \tag{8}$$

The boundary conditions of $f_{agg}$ are defined in equation (9), to ensure that the newly formed crystals are not classified as agglomerates and to ensure that the number of agglomerates never exceeds the total number of particles.

$$\begin{cases} \lim_{L\to 0} f_{agg}(L,t) = 0 \\ 0 \le \frac{f_{agg}(L,t)}{f(L,t)} \le 1 \end{cases} \tag{9}$$

To quantify the degree of agglomeration of the particles, a volume-based degree of agglomeration ($V_{agg}$) is defined as follow:

$$V_{agg} = \frac{\int_0^\infty f_{agg}(L,t)L^3 dL}{\int_0^\infty f(L,t)L^3 dL} \tag{10}$$

In addition to the degree of agglomeration defined

earlier, an alternative method for estimating agglomeration is also employed in this work. According to the literature, the degree of agglomeration ($\eta_A$) is determined by the ratio of the "number of bridges" ($N_A$) to the total number of particles. By monitoring the formation and breakage of bridges during the process, the number of agglomeration bridges per unit volume of suspension is calculated. A detailed derivation of this method is provided in [6].

Finally, the PBMs are closed by the mass balance equations given by

$$\frac{dC(t)}{dt} = -k_v \rho_c \left[ 3G(t;\theta_g) \int_0^\infty L^2 f(L) dL + B(t;\theta_b) L_n^3 \right]$$

$$while\ C > C_{s,amor} \tag{11}$$

$$\frac{dC(t)}{dt} = 3k_v \rho_c \left[ D \int_0^\infty L^2 f(L) dL \right]$$

$$while\ C < C_{s,amor} \tag{12}$$

Where $k_v$is the volume shape factor of the crystals, $\rho_c$ is the crystal density, and $D$ represents the dissolution kinetics, which is formulated as follow:

$$D = k_d \sigma \tag{13}$$

The kinetics parameters are shown in Supplemental Materials (LAPSE:2025.0037), which most of them are directly obtained from the iterative model-based experimental design framework [7]. (Dissolution and deagglomeration kinetics are estimated with a simple factorial DoE, since their formulations are much simpler compared with those mechanisms during the desaturation.)

## 4. RESULT AND DISCUSSIONS

To assess the degree of agglomeration using this hybrid PBM framework, an in-silico case study was conducted by replicating the experimental conditions detailed in the DoE shown in Supplemental Materials, with variations in the decision variables. As illustrated in Figure 1, the degree of agglomeration derived from the hybrid PBM framework offers a more accurate estimation compared to the agglomerate degree based solely on the number of bridges. This improvement stems from the fact that within the agglomerates, there exists a considerable probability of multiple bridges forming, rendering a simple bridge count an overestimation of the degree of agglomeration.

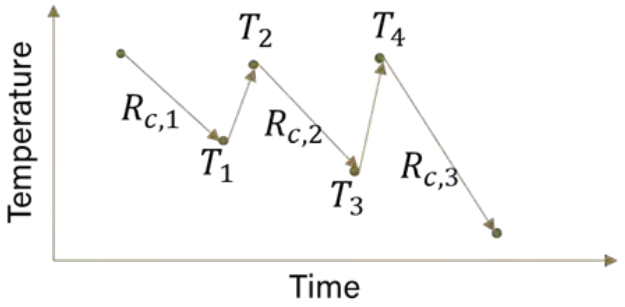



**Figure 2:** Input features that were used to describe the thermocyclic temperature profiles.

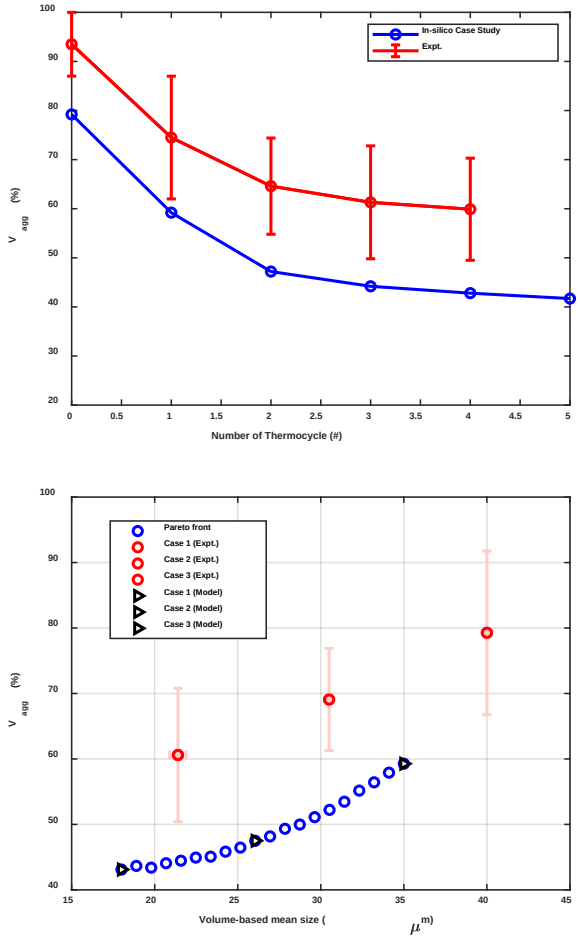
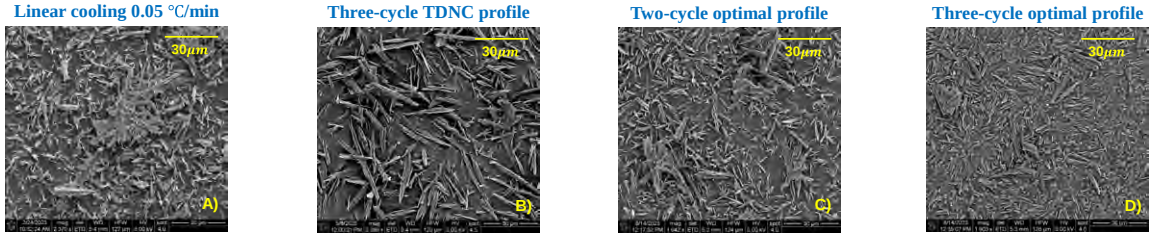



**Figure 3:** The comparison between $V_{agg}$.and different number of thermocycles (Top). The comparison between $V_{agg}$.and particle size while varying weighting factors in the optimization (N = 3) (Bottom).

In essence, the application of the degree of agglomeration derived from this hybrid framework presents a more comprehensive approach than prior methodologies. However, it is noteworthy that as the model was not trained using the degree of agglomeration from experimental results, there remains room for enhancing the predictive capacity of the model in future iterations.




| Cumulative CSD | D10 | D50 | D90 |
|---|---|---|---|
| Unit ($\mu m$) | 1.84 | 13.1 | 38.8 |
| Crystallinity | 43.9% ± 7.3% | | |
| Yield | 90.8% ± 0.5% | | |
| $V_{Agg}$ (Model) | 79.2% | | |
| $V_{Agg}$ (Expt.) | 96.8% ± 12.4% | | |
| Batch time (hr) | 14 | | |
| Solute Dissolved | ~46.3 mg/ml solvent | | |
| Seed loading | 5% | | |

| Cumulative CSD | D10 | D50 | D90 |
|---|---|---|---|
| Unit ($\mu m$) | 2.8 | 17.0 | 50.0 |
| Crystallinity | 83.3% ± 7.2% | | |
| Yield | 93.6% ± 0.2% | | |
| $V_{Agg}$ (Model) | 46.0% | | |
| $V_{Agg}$ (Expt.) | 56.7% ± 15.6% | | |
| Batch time (hr) | 46 | | |
| Solute Dissolved | ~46.3 mg/ml solvent | | |
| Seed loading | 5% | | |

| Cumulative CSD | D10 | D50 | D90 |
|---|---|---|---|
| Unit ($\mu m$) | 2.2 | 16.8 | 39.2 |
| Crystallinity | 75.6% ± 5.7% | | |
| Yield | 92.6% ± 0.7% | | |
| $V_{Agg}$ (Model) | 44.2% | | |
| $V_{Agg}$ (Expt.) | 64.6% ± 15.4% | | |
| Batch time (hr) | 20 | | |
| Solute Dissolved | ~46.3 mg/ml solvent | | |
| Seed loading | 5% | | |

| Cumulative CSD | D10 | D50 | D90 |
|---|---|---|---|
| Unit ($\mu m$) | 2.0 | 10.8 | 38.0 |
| Crystallinity | 78.6% ± 8.7% | | |
| Yield | 91.6% ± 0.5% | | |
| $V_{Agg}$ (Model) | 42.8% | | |
| $V_{Agg}$ (Expt.) | 61.3% ± 12.3% | | |
| Batch time (hr) | 25 | | |
| Solute Dissolved | ~46.3 mg/ml solvent | | |
| Seed loading | 5% | | |

**Figure 4:** Experimental summaries of the linear cooling profile, the model-free QbC profile and the optimal

To reduce the degree of agglomeration of the final product, an optimization was formulated for a seeded crystallization. The decision variables are the 2N discrete temperature values that define the temperature profile as shown in Figure 2. The optimization objectives were to determine the temperature profile that minimizes the degree of agglomeration throughout the process and increase the size of the fine particles. For this, the following objective function was used:

$$\min_{\gamma \in R} OF = \omega V_{agg} + (1-\omega)\frac{1}{(\mu_1/\mu_0)}$$

$$\gamma = (R_{c,j}, T_j) \tag{14}$$

where $R_{c,j}$ is the cooling rate of each segment ($j = N+1$), $T_j$ are the temperature turning points ($j = 2N$), and $N$ denotes the number of thermocycles. $(\mu_1/\mu_0)$ represents the number-based mean size of the final products.

Various optimal temperature profiles were generated, as shown in Figure 3. As the number of thermocycles increases, $V_{agg}$ gradually decreases and eventually reaches a plateau. This trend is consistent in both the in-silico study and experimental results. By adjusting the weighting factors, the model demonstrates a similar trend to the experimental validations, despite an offset attributed to the model's limited accuracy in predicting the exact value of $V_{agg}$.

Figure 4 presents an experimental comparison of the linear cooling profiles, the model-free QbC profile—developed using a turbidity-based direct nucleation control strategy, which indirectly regulates fine particle generation and promotes seed particle growth—and the optimal temperature profiles obtained from the optimization problem discussed earlier. The results indicate that optimal temperature profiles perform comparably to the model-free QbC profile and outperform linear cooling profiles in terms of reducing the degree of agglomeration, not to mention the improvement in crystallinity. Additionally, they offer significant advantages by shortening batch time. (The optimal temperature profiles suggest that batch time could be further reduced by increasing cooling rates during the thermal cycle without compromising the degree of agglomeration.) This improvement in agglomeration has been validated through image analysis using Morphologi 4, based on the number-based degree of agglomeration analysis ($N_{agg}$) and SEM images.

## 5. CONCLUSION

This study demonstrates the effectiveness of a model-based approach using a hybrid population balance model (PBM) to optimize temperature profiles for industrial crystallization processes. The hybrid PBM, which integrates critical mechanisms such as nucleation, growth, dissolution, agglomeration, and deagglomeration, provides a more accurate and comprehensive framework for minimizing agglomeration and promoting crystal growth than traditional methods.

The in-silico design of experiments (DoE) simulations and experimental validations confirmed that optimal temperature profiles and thermocycles significantly reduce the degree of agglomeration and enhance bulk crystal formation. While thermocycles proved effective, their benefits plateau with an increasing number of cycles. Additionally, the optimal temperature profiles outperformed linear cooling strategies in both reducing agglomeration and shortening batch times, demonstrating scalability and efficiency for industrial applications.

By integrating insights from image analysis (Morphologi 4 and SEM) and validating findings through experimental data, this study demonstrates how model-based optimization enhances both process control and product quality. Future research may focus on improving model accuracy by incorporating agglomeration data from experimental results to further refine predictive capabilities. Ultimately, this approach provides a robust and

scalable strategy for crystallization optimization, offering valuable insights while effectively managing the degree of agglomeration in the pharmaceutical and specialty chemical industries. Additionally, the hybrid PBM structure has shown significant potential for application in granulation and spherical agglomeration processes, facilitating improved control over particle formulation related to aggregation and agglomeration.

## ACKNOWLEDGEMENTS

This academic project was funded by Takeda Pharmaceuticals.

## REFERENCES

1. Urwin, Stephanie J., et al. "A structured approach to cope with impurities during industrial crystallization development." Organic process research & development 24.8 (2020): 1443-1456.
2. Terdenge, Lisa-Marie, and Kerstin Wohlgemuth. "Impact of agglomeration on crystalline product quality within the crystallization process chain." *Crystal Research and Technology* 51.9 (2016): 513-523.
3. Sun, Zhuang, et al. "Use of Wet Milling Combined with Temperature Cycling to Minimize Crystal Agglomeration in a Sequential Antisolvent–Cooling Crystallization." *Crystal Growth & Design* 22.8 (2022): 4730-4744.
4. Fujiwara, Mitsuko, et al. "First-principles and direct design approaches for the control of pharmaceutical crystallization." *Journal of Process Control* 15.5 (2005): 493-504.
5. Wu, Wei-Lee, et al. "Implementation and application of image analysis-based turbidity direct nucleation control for rapid agrochemical crystallization process design and scale-up." *Industrial & Engineering Chemistry Research* 61.39 (2022): 14561-14572.
6. Szilagyi, Botond, et al. "Application of model-free and model-based quality-by-control (QbC) for the efficient design of pharmaceutical crystallization processes." *Crystal Growth & Design* 20.6 (2020): 3979-3996.
7. Kilari, Hemalatha, et al. "A Systematic Model Development Framework for Batch Crystallization Using Iterative Model-Based Experimental Design Approach." *2023 AIChE Annual Meeting*. AIChE, 2023.

© 2025 by the authors. Licensed to PSEcommunity.org and PSE Press. This is an open access article under the creative commons CC-BY-SA licensing terms. Credit must be given to creator and adaptations must be shared under the same terms. See https://creativecommons.org/licenses/by-sa/4.0/

# Index

## Author Index

# Author Index


Aarnoudse, Leontine I.M., **1157**
Abarca, Jose Antonio, **1951**
Abbas, Abiha, **2165**
Abbas, Safdar, **2000**
Abbasi, Hamid Reza, **376**
Abbiati, Roberto Andrea, **2334**
Abdullatif, Yasser M., **333**, **687**
Abildskov, Jens, **147**
Aboelnour, Mohamed, **1194**
Abo-Ghander, Nabeel S., **2158**
Abreu, Odilon S. L., **1208**
Abukanisha, Sana I., **1053**
Abushaikha, Ahmad S., **559**
Acevedo, Alvaro, **968**
Aceves-Lara, César Arturo, **986**
Acosta-Pavas, Juan Camilo, **986**
Adami, Momme, **1306**
Adams, Thomas A., II, **2234**
Adeel, A., **430**
Adjiman, Claire S., **485**, **1035**, **1089**
Afsahnoudeh, Reza, **79**
Aghayev, Zahir, **692**
Aguilar Lasserre, Alberto A., **2580**
Aker, Burcu, **2228**
Akkermans, Simen, **2379**
Akkoç, Gözde, **2373**
Aku, Michael, **1228**
Akundi, Sahithi Srijana, **1065**, **2007**
Alam, Md Shamsul, **86**
Al-Ansarl, Tareq, **333**, **559**, **687**, **778**, **2361**
Alba-Robles, Emilio, **1644**
Alberti, Davide, **583**
Alcocer-García, Heriberto, **1071**
Aldren, Cameron, **863**
Al-Hmoud, Linda, **1427**
Aliabadi, Mohammad Mahdi Ghasemi, **320**
Alimin, Achmad Anggawirya, **1365**, **1676**
Allman, Andrew, **1456**
Almaraz, Omar, **444**, **450**
Al-Mohannadi, Dhabia M., **327**, **805**, **942**, **1612**
Almoussaoui, Mohamad, **805**
Alnouri, Sabla Y., **198**, **651**
AlNouss, Ahmed, **778**
Al-Obaidi, Mudhar A., **1047**
Alopaeus, Ville, **1377**
Alsadaie, Salih M., **1053**
Alsarayreh, Alanood A., **1047**
Altamiranda, Edmary, **974**
Alvarado-Rodríguez, Carlos E., **8**, **216**
Álvarez-Menchero, José A., **918**
Alves, Rita M. B., **60**
Amaral, Marcelo da C., **276**
Amhamed, Abdulkarem I., **333**, **687**
Amirifar, Ariyan, **2447**
Amusat, O., **430**
Amusat, Oluwamayowa O., **2140**
Anagnostou, Alexandros, **320**
Anantharaman, Rahul, **698**
Anastasakis, Konstantinos, **2146**
Anda, Jorge Calderon de, **2504**
Andreasen, Anders, **1957**
Andualem, Bezza F., **497**
Antonio, Claudia Gutiérrez, **2278**
Apperley, M., **430**
Arato, E., **271**
Arellano-Garcia, Harvey, **631**, **1175**, **1561**, **1866**, **1872**
Arias-Lugo, Stephanie, **1951**
Arici, Mehmet, **999**
Arkun, Yaman, **785**
Armaou, Antonios, **313**
Armesto, Leopoldo, **1530**
Arora, Pratham, **2057**
Arrieta-Peréz, Rodinson R., **412**
Athaley, Abhay, **534**
Atkins, Martin J, **1139**
Atlar, Kutay, **2373**
Attarakih, Menwer, **1427**
Aunsmo, Sigrid, **824**
Ave, Giancarlo Dalle, **1670**
Avila, J. Rafael Alcántara, **1095**, **1409**
Avilez, Leonardo A. C., **60**
Avraamidou, Styliani, **117**, **1618**
Aydin, Erdal, **1438**
Azzaro-Pantel, Catherine, **856**, **2069**, **2094**, **2580**
B.R. Nogueira, Idelfonso, **1890**
Babadi, Hourissa Soleymani, **2121**
Babaei, Farshid, **924**
Babaei, Masoud, **376**
Badejo, Oluwadare, **2013**
Badenes, Sara M., **2385**
Badmos, S., **2197**
Badr, Sara, **2492**
Bahamdan, Abdullah, **1824**
Baibhav, Vibhu, **252**, **869**
Baidya, Dibyajyoti, **1101**
Bajaj, Ishan, **619**, **1492**
Bajcinca, Naim, **2598**
Baldacci, Roberto, **778**
Balhorn, Lukas Schulze, **1365**, **1656**, **1676**
Bamberg, Andreas, **521**
Barbera, Elena, **1282**
Barbosa, Domingos, **1928**
Barbosa, Flávia, **2152**
Barbosa-Póvoa, Ana P., **2038**
Barhate, Yash, **2604**
Barreto, Amaro G., Jr., **2592**
Barrow, Emma A., **1244**
Bart, and Hans-Jörg, **1427**
Bartsch, Jens, **2598**
Barzilai, Abigail, **2178**
Báthori, Arthur-Maximilian, **1969**
Batista, Daniel V., **2548**
Bawa, Solomon Gajere, **1228**
Bayar, Ibrahim, **1812**
Beguin, Brieuc, **423**
Bekhti, Sofiane, **423**
Beleli, Yuri S., **1163**
Beniwal, Surendra, **1187**
Bennett, Iryna, **1244**
Benyahia, Brahim, **637**, **2568**, **2574**
Bernardino, Lucas Ferreira, **824**
Bernardo, Fernando, **1017**
Bernardo, Fernando P., **2460**
Bernet, Thomas, **1089**
Berthier, Louis, **1518**
Bertok, Botond, **1139**
Bertran, Maria-Ona, **2341**
Besenhard, Maximilian O., **1567**, **1884**
Beykal, Burcu, **117**, **692**, **1837**
Bezzo, Fabrizio, **153**, **1282**
Bhartiya, Sharad, **1101**
Bhatia, Arsh, **831**
Bhatnagar, Pullah, **252**, **869**
Bhonsale, Satyajeet S., **2379**, **2417**, **2454**, **2542**
Bhushan, Mani, **1101**
Bicer, Yusuf, **333**, **687**
Blackburn, Daniel, **1114**
Blair, Matthew, **2510**
Blanco, Elena C., **2032**
Bloor, Max, **1151**

Bloor, Maximilian, **1181**
Bodescu, Gheorghe A., **1108**
Boelen, Tom, **339**
Bogataj, Miloš, **2253**
Bogle, I. David L., **86**
Boix, Marianne, **2101**, **2108**
Boldyryev, Stanislav, **438**
Bollas, George M., **159**, **1837**
Bongartz, Dominik, **2063**
Bonis, J., **2259**
Bonomi, Antonio, **2152**
Boskabadi, Mohammad Reza, **1682**, **2530**
Bouhaouala-Zahar, Balkiss, **986**
Boukharfane, Radouan, **1433**
Boukouvala, Fani, **2411**
Bouman, Jim van der Valk, **2044**
Boy, Onur C., **1794**
Boztas, Oktay, **662**
Brands, René, **2598**
Braniff, Austin, **1065**, **1403**, **2007**
Bravo, Leonardo, **67**
Bresciani, Antonio E., **60**
Brigman, James G., **1860**
Brilman, Derk W.F., **92**
Bris, Gwenola Yannou-Le, **1975**
Brouwer, Gijs J.A., **473**
Brown, Solomon F., **589**, **723**, **900**, **924**
Brown, Victoria, **900**
Bruaset, Olve R., **1818**
Brück, Thomas, **2322**
Buendia, Felipe, **1975**
Burger, Jakob, **485**
Burroughs, S., **430**
Baakes, Florian, **1089**
Caballero, José A., **918**, **1415**, **1700**, **1946**
Caballero, Marc, **668**
Cabrera, Miguel Ángel Morales, **711**
Cabrera, Nicolas, **1324**
Caccavale, Fiammetta, **2203**, **2209**
Caceres-Barrera, Carlos Rodrigo, **462**, **1071**
Calberg, Cédric, **423**
Calixto, Ewerton E. da S., **276**
Callil-Soares, Pedro H., **1542**
Calvo-Serrano, Raul, **1940**
Cao, Xinyu, **2554**
Capaci, Riccardo Bacci di, **1389**
Caprio, Ulderico Di, **1775**, **1794**, **1890**
Capron, Bruno D. O., **1169**
Cardoso, Terezinha F., **2152**
Carecci, Davide, **2303**, **2310**
Carozzo, V., **271**
Carrara, Adriano, **583**
Carrasco-Suárez, Ma. Teresa, **288**
Carrasquer, Pau Lapiedra, **2542**
Carta, Andrea, **1934**
Castellar-Freile, Andres, **1625**
Castillo, Ivan, **1694**
Castro Vivar, Indra, **2580**
Castro, Pedro M., **264**, **1288**
Castro-Amoedo, Rafael, **235**
Catenacci, Arianna, **2310**
Cavalcante, Jonatas de O. S., **276**
Cecelja, Franjo, **1244**
Chachuat, Benoît, **1035**, **1237**
Chakraborty, Arijit, **1682**
Chaparro, Gustavo, **1089**
Charitopoulos, Vassilis M., **117**, **1592**, **2586**
Chatti, Sai Phani, **1762**
Chattopadhyay, Sampriti, **844**
Chen, Baohua, **104**
Chen, Chih-Yu, **14**
Chen, Meng-Hsin, **14**
Chen, Tao, **388**
Chen, Xi, **229**, **313**, **1486**, **2554**
Chen, Yen-Ming, **14**
Chen, Zhen, **2328**
Cheng, Yi-Hsiang, **1650**
Cherrouk, Melissa, **856**
Cheung, Lily, **2411**
Chia, Dian Ning, **1474**, **1884**
Chibeles-Martins, Nelson, **2051**
Chida, Kota, **906**
Chin, Swee-Teng, **1694**
Chiplunkar, Ranjith, **2561**
Chirwa, Evans M. N., **497**
Cho, Bovinille Anye, **2398**
Chong, Daniel J S, **1139**
Chrisandina, Natasha J., **980**
Cinco-Izquierdo, Maria de Lourdes, **2367**
Cobo, Martha, **67**, **412**
Coelho, Eva C., **1263**
Cohen, Benjamin G., **1837**
Contreras-Zarazua, Gabriel, **462**
Cordiner, Joan, **418**
Cordova-Cordova, Jesmyl-Elisa, **1963**
Corengia, M., **2133**
Cormos, Ana-Maria, **1969**
Cormos, Calin-Cristian, **1969**
Coronel-Muñoz, Melanie, **462**
Corradi, Mauro, **583**
Corrales, David Camilo, **986**
Corte´s-Pen, Yoel R., **1348**
Cortez-González, Jazmín, **8**, **216**
Costa, Erbet Almeida, **1145**, **1208**
Costa, Luiz M., **534**
Coutinho, João P. L., **1421**
Cramer, Eike, **1294**
Cremaschi, Selen, **1275**
Cristea, Castelia E., **1108**
Cristea, Vasile M., **491**, **1108**
Cucek, Lidija, **1083**
Cunha, Marcelo P., **2152**
Curti, M., **271**
Cuypers, Frederic, **339**
D.Kolokotsa, **2259**
da Silva, Beatriz C., **1257**
da Silva, Wilson Ricardo Leal, **1282**
Dagna, Ilaria, **364**
Dai, Yiyang, **515**
Dai, Zhongde, **515**
Daigo, Ichiro, **540**
Dalamagas, Theodore, **986**
Dantas, Beatriz, **1065**, **2007**
Dao, Kevin, **1656**
Daosud, Wachira, **999**
Daraban, Romina G., **1108**
Dardor, Dareen, **546**, **1987**
Das, Prajnan, **1769**
De Sousa, Marco P. , **753**, **771**
Debonnet, Tristan, **674**
Dehon, Victor, **1023**
Dekhici, Benaissa, **26**, **388**
del Rio Chanona, Ehecatl Antonio, **993**, **1023**, **1151**, **1169**, **1181**, **1744**, **1756**, **1824**, **2355**
Demirhan, Doga C., **753**
Desroziers, Sylvain, **1518**
Devanand, Aravind, **1762**
Dewasme, Laurent, **1269**, **2466**
Diangelakis, Nikolaos A., **2586**
Dias, Igor L. R., **2152**
Díaz, Ismael, **346**, **370**
Díaz, Raquel Salcedo, **1415**, **1700**
Diaz-Sainz, Guillermo, **1951**
Dickson, Rofice, **2165**
Dimian, Alexandre C., **479**
Dingwani, Gauransh, **1492**
Dobschall, Alina, **1077**
Dockx, Kristof, **2542**
Dokl, Monika, **1083**
Dolat, Meshkat, **222**, **2423**
Dologlu, Pelin, **1812**
Domenek, Sandra, **1975**
Domingos, Meire Ellen Ribeiro, **546**, **662**
Dominguez-Ramos, Antonio, **2222**
Dorneanu, Bogdan, **613**, **631**,

**1175**, **1561**, **1866**, **1872**
Dougher, Molly, **2215**
Dowell, Niall Mac, **798**
Dowling, Alexander W., **2215**
Dragoi, Elena N., **962**
Driessen, Ge H. M., **1656**
Dua, Vivek, **86**
Duanmu, Fanyi, **1474**, **1884**
Dujany, Arnaud, **930**
Dumont, Marie-Noëlle, **2247**
Duyar, Melis S., **222**
Ebert, Jessica, **521**, **1462**
Eid, Maged, **1670**
Elfaki, Hesan, **327**
El-Halwagi, Mahmoud M., **980**
Elisa, Boissézon, **2265**
Elizalde-Solis, Octavio, **98**
Eljack, Fadwa, **382**
El-Naas, Muftah H., **198**
Engell, Sebastian, **894**, **1194**
Erdmann, Oliver, **1631**
Errington, Ethan, **577**, **1737**
Espinoza, Dana E. Carrillo, **1409**
Esposito, Flora, **1890**
Etit, Deniz, **577**
Ewis, Dina, **198**
Eydam, Linda, **1396**
Fáber, Rastislav, **1389**
Fadzil, N. F. E. Nor, **717**
Fallanza, Marcos, **2222**
Fan, Yee Van, **1083**
Femenia, Rubén Ruiz, **1415**, **1700**
Fernandes, Maria Cristina, **129**
Ferreira, Alexandre F.P., **1257**, **1915**
Ferreira, Bruno S., **2460**
Ferretti, Gianni, **2303**, **2310**
Ficara, Elena, **2303**, **2310**
Figueredo, Manuel, **67**, **412**
Fikar, Miroslav, **999**, **2191**
Filho, Rubens Maciel, **704**
Fillaudeau, Luc, **986**
Fioravante, Igor F., **704**
Flores, Betsie M., **753**
Flores, Betsie S. M. Montano, **771**
Flores, Sandra Cecilia Cerda, **2069**
Flores-Gómez, Luis R., **950**
Flores-Tlacuahuac, Antonio, **1029**
Flórez-Orrego, Daniel A., **252**, **546**, **662**, **1987**, **2127**
Floros, Stylianos, **2379**
Fonseca, Rui, **1017**
Fontalvo, Javier, **1896**
Fontana, Marcio, **1145**
Fontana, Márcio, **1208**
Fontanelli, Laurent, **930**
Fortunato, João, **264**
Foy, Marc Philippart de, **2247**
Fraga, Eric S., **1114**, **1336**
Frandsen, Jesper, **147**
Franke, Meik B., **936**, **1468**, **1902**
Fredriksen, Marius, **1011**
Freitas, Geovani R., **2385**
Fu, Xiao, **753**
Fuentes-Cortés, Luis Fabián, **1029**
Fujii, Shoma, **540**, **1555**, **2114**
Fujiwara, Koichi, **1480**
Funcia, Eduardo S., **1163**
Fungprasertkul, Nichakorn, **2348**
Funke, Thomas, **135**
Furtner, Lukas, **1396**, **1445**
Gabrion, Agathe, **2108**
Gakingo, Godfrey K., **2398**
Galán, Guillermo, **747**
Galcíková, Lenka, **2191**
Galeazzi, Andrea, **1498**, **1806**
Galindo, Amparo, **485**, **1089**
Gallo, Francesco, **1263**, **1806**
Galvan-Cara, Aldwin-Lois, **2063**
Galvanin, Federico, **179**, **1114**, **1228**, **1567**
Gandhi, Rahul, **844**
Gao, Qinghe, **1360**
Gao, Shang, **2568**
Garcia, Enrique V., **1163**
García-Castillo, Jorge Luis, **1221**
Garciadiego-Ortega, Eduardo, **1244**
Garcia-Tenorio, Camilo, **2466**
Gargalo, Carina L., **2203**, **2209**
Gariso, Ruben, **1421**
Gaspari, Sotiria, **2379**
Gavriilidis, Asterios, **1567**
Georgakilas, Georgios, **986**
Georgiadis, Georgios P., **735**, **741**
Georgiadis, Michael C., **741**
Geraci, Ignazio, **2303**
Gerbaud, Vincent, **2429**
Germanier, Reginald, **546**, **1987**
Gernaey, Krist V., **123**, **2185**, **2203**, **2209**
Gerogiorgis, Dimitrios I., **2510**
Ghazi, Zeyad M., **198**
Ghiat, Ikhlas, **333**
Gilardi, Matteo, **2322**
Goldstein, Dominik P., **1365**, **1656**, **1676**
Gomes, João P., **1928**
Gómez, Alejandro Merino, **141**
Gómez-Castro, Fernando Israel, **950**, **962**, **1221**, **1638**, **1644**, **2355**
Gomez-Coma, Lucia, **1951**
Gong, Han, **229**
Gonzalez, Francia Gallardo, **320**
González-Cazorla, Franc, **553**
Govindan, Rajesh, **1133**
Graells, Moisès, **553**
Groll, Niklas, **1354**, **1957**
Gromotka, Zoë, **1718**
Groot, Bart de, **153**
Große, Michael, **53**, **759**
Große, Michel (né Mock), **818**
Grossmann, Ignacio E., **747**, **812**, **844**, **1598**, **2242**
Grünewald, Marcus, **1994**
Guerra, Alec, **1625**
Guerra, Omar, **2435**
Guido, Giorgia De, **301**, **583**
Guido, Sergio I. Martínez, **2278**
Guillén-Gosálbez, Gonzalo, **528**
Guilloteau, Pierre, **1957**
Gundersen, Truls, **698**
Gunter, D., **430**
Guo, Miao, **577**, **1737**, **2316**, **2405**
Gupta, Aayush, **571**
Gutiérrez-Antonio, Claudia, **962**
Gutiérrez-Guerra, Roberto, **216**
Gutierrez-Limon, Miguel Angel, **1029**
GürkanSin, **1712**
Hachhach, Mouad, **468**
Halvorsen, Ivar J., **1157**
Hamacher, Johannes, **135**
Hammond, Joseph, **723**, **900**
Haring, Mark A.M., **1157**
Harjunkoski, Iiro, **812**, **1524**
Harvey, Arellano-Garcia, **613**
Hashem, Ihab, **1573**
Hastedt, Friedrich, **1744**
Hawkes, Adam, **863**
Hayashi, Yusuke, **2492**, **2498**
Haydary, Juma, **46**
Heath, William, **1251**
Heffernan, Claire, **2504**
Hegely, Laszlo, **192**, **681**
Heiho, Aya, **540**
Hellgardt, Klaus, **1744**, **1756**, **1824**
Heng, Jerry, **577**
Heng, Jerry Y., **2504**
Hernández, Borja, **2013**
Hernández, Erik L. Piñón, **1409**
Hernández, Juan Gabriel Segovia, **8**, **216**
Hernández, Salvador, **1095**, **2278**

Hernández-Camacho, Nereyda Vanessa, **2355**
Hernández-Rivera, Maria Soledad, **8**
Herrera-Ruiz, Juan Federico, **1896**
Hii, King Kuok (Mimi), **1756**
Hildebrandt, Sophie, **1468**
Hillman, Zachary M., **2537**
Hlawitschka, Mark W., **1427**
Hochhaus, Thorben, **1994**
Hofmann, René, **1201**
Hogstrand, Christer, **2316**
Holm, Sigmund Eggen, **824**
Hounat, Yassine, **1706**
Hu, Jianli, **444**, **450**
Hu, Xiaoxin, **1800**
Hu, Yujie, **229**
Huang, Kuan-Che, **2480**
Huang, Po-Hsun, **14**
Huang, Shengyuan, **503**
Huang, Wei, **1383**
Huerta-Rosas, Brenda, **462**
Hung, Hong Yee, **1548**
Hung, Zhen-Yu, **1650**
Huusom, Jakob Kjøbsted, **147**, **1126**, **2185**, **2486**
Huynh, Dat, **2013**
Iakovou, Eleftherios, **980**
Ierapetritou, Marianthi, **2013**
Ikhlas Ghiat, **687**
Imaginário, João, **2051**
Inayat, Muddasser, **2019**
Iqbal, Imam M., **1688**
Irabien, Angel, **1951**
Irhamna, Adrian R., **159**
Isella, Andrea, **656**, **1586**
Iwabuchi, Junshin, **2492**
Jackson, George, **485**, **1089**
Jadoon, Usman Khan, **346**, **370**
Jafari, Mitra, **1866**
Jankelevitch, Sebastien, **1662**
Jankovic, Tamara, **473**, **2284**
Jayaraman, Suresh, **1769**
Jean Victor, Julien, **930**
Jensen, Anker Degn, **1126**, **1957**
Jeong, Woochang, **876**
Ji, Cheng, **1860**
Jiang, Zheyu, **246**, **837**, **882**, **2391**
Jiao, Shenhua, **1486**
Jimenez, Ana C. M., **2152**
Jimenez, Laureano, **798**
Jin, Zhehao, **515**
Jing, Keju, **2297**
Jinsong, Zhao, **1548**
Jog, Sachin, **528**
Jogwar, Sujit S., **644**, **1187**
Johnn, Syu-Ning, **117**
Jose, Fenin, **1878**
Jung, Dongin, **601**, **607**, **876**, **1854**
Junior, Ivaldir J. Tamagno, **2435**
Junqueira, Tassia L., **2152**
Jupke, Andreas, **1005**
Jurado, Nelia, **1114**
Jurischka, Constantin, **631**
Järvinen, Mika, **2019**
Jäschke, Johannes, **974**, **1011**
Jørgensen, John B., **1126**, **2341**
Kabra, Anjali, **1005**
Kafarov, Viatcheslav, **1324**
Kager, Julian, **2486**
Kailasanathan, Rajiv, **358**
Kaistha, Nitin, **565**, **571**
Kaitano, Caroline, **282**
Kakodkar, Rahul, **753**, **771**
Kalbusch, Joanne, **406**, **423**
Kaldellis, John K., **2088**, **2259**
Kambayashi, Yuma, **394**
Kamel, D., **2197**
Kanayama, Hiroaki, **307**
Kanematsu, Yuichiro, **906**, **1536**, **2114**
Kang, Donggeun, **601**, **607**, **876**, **1854**
Kang, Yung Shun, **2604**, **2622**
Kansha, Yasuki, **307**, **625**
Kapartzianis, E., **2259**
Karaman, Ömer Faruk, **681**
Kareck, Tylee, **837**
Karia, Tanuj, **1371**, **1718**
Karka, Paraskevi, **2000**
Karthikeyan, Keerthana, **844**
Karuppasamy, Muthu, **1318**
Kasper, Lukas, **1201**
Kasza, Angéla-Mária, **1969**
Kaur, Ginif, **1631**
Kaven, Luise F., **1294**
Kay, Harry, **111**
Kay, Sam, **1041**, **2291**
Kaya, Gizem Kusoglu, **2373**
Keestra, Hilbert, **92**
Kenefake, Dustin, **753**
Kenig, Eugeny Y., **79**
Khalid, Md Meraj, **1781**
Khan, Faisal, **1065**
Khatib, Mohammad Al, **2598**
Kikuchi, Yasunori, **540**, **906**, **1536**, **1555**, **2114**
Kilari, Hemalatha, **2622**
Kim, Donghoi, **698**
Kim, Donghyeon, **601**, **607**, **876**, **1854**
Kim, Jin-Kuk, **613**, **1175**
Kim, Jiyong, **601**, **607**, **876**, **1854**
Kim, Junu, **2498**
Kim, Minji, **1656**
Kim, So-mang, **406**
Kiss, Anton A., **320**, **473**, **479**, **491**, **668**, **1108**, **1934**, **2284**
Kitchin, John R., **294**, **1598**
Klaimi, Rachid, **651**
Klein, Harald, **135**
Koch, Amy, **521**, **1462**
Kodate, Pratap, **1625**
Kok, Yu Hui, **625**
Kokossis, Antonis, **986**, **1750**, **2441**
Kondili, Emilia M., **2088**
Kondo, Masaru, **1318**
Kontak, Jakub, **1787**
Kontoravdi, Cleo, **2561**
Korde, Shrivatsa, **2516**
Koritár, Matej, **46**
Kota, Rohit Karanth, **1762**
Kotamreddy, Goutham, **831**
Kotecha, Niki, **1151**
Koulouris, Alexandros, **735**
Krajacic, Goran, **438**
Kravanja, Zdravko, **1083**, **2253**
Kreit, Patrick, **423**
Krishnan, Sandeep, **1762**
Križan, Maroš, **46**
Krog, Halvor Aarnes, **824**
Kruber, Kai F., **1005**
Krühne, Ulrich, **2203**, **2209**
Kröcher, Oliver, **209**
Kumar, Monisha, **1706**
Kurban, Sena, **2373**
Köksal, Ece S., **1438**
Labarta, Juan A., **1946**
Lacerda, Matheus S., **2152**
Laird, Carl D., **294**, **812**, **831**, **1598**
Laky, Daniel J., **2215**
Laky, Montgomery D., **2271**
Laliwala, Chris A., **2140**
Lameh, Mohammad, **327**
Lane, Amanda, **1041**, **1724**
Lang, Peter, **192**, **681**
Lange, Hannes, **53**, **759**
Lara-Montaño, Oscar Daniel, **962**, **1638**, **1644**, **2355**
Larnaudie, V., **2133**
Larnaudie, Valeria, **729**
Lastrucci, Giacomo, **1371**, **1706**, **1718**
Lawrence, Wesley, **497**

Laxminarayan, Sidharth, **2411**
Le Roux, Galo A. C., **1163**, **1542**
Leblebici, M. Enis, **1775**, **1794**, **1890**
Lee, A., **430**
Lee, Donggyu, **993**
Lee, Jaewook, **577**, **1737**
Lee, Joohwa, **613**, **1175**
Lee, Lauren Ye Seol, **1228**
Leenhouts, Roel, **1662**
Lemire, Mélissa, **2026**
Léonard, Grégoire, **406**, **423**, **2127**, **2247**
Leonzio, Grazia, **456**
Leva, Alberto, **2303**
Lewin, Daniel R., **2172**, **2178**
Li, Bryan, **241**
Li, Chenxi, **1312**
Li, D., **791**
Li, J., **791**
Li, Jie, **1214**, **1579**
Li, Qing, **479**
Li, Zhaofeng, **692**
Li, Zheng, **1312**
Li, Zhiyuan, **1800**
Liang, Jingkang, **1712**
Liang, Xiaodong, **147**
Liao, Yangyanbing, **1214**
Lim, Tianen, **2081**
Lima, Fernando Arrais R. D., **2592**
Lima, Patrick S., **203**
Lima, Ricardo M., **812**
Limpach, Juliette M., **2127**
Lin, Wei-Shiang, **1650**
Lin, Xiaowen, **1486**
Lincoln, B., **430**
Liu, Heyuan, **1830**
Liu, Jay, **2165**
Liu, Lande, **20**
Liu, Pei, **1312**
Liu, Rui, **313**, **1486**
Liu, Yuanxing, **1065**, **2007**
Liu, Zhongxuan, **698**
Logist, Filip, **339**, **2158**, **2417**
Lopes, Diego C., **888**
López, Carlos André Muñoz, **2542**
Lopez-Basto, Erik, **186**, **509**
López-Villarreal, Francisco, **950**
Lorenz, Julius, **1396**
Losordo, Zach, **534**
Lu, Zhicheng, **2215**
Lubušký, Karol, **1389**
Luise, Renato, **2094**
Lynch, Hailey G., **2215**
Lynd, Lee R., **534**
Lyu, Wenyao., **179**
Ma, Fangyuan, **1860**
Ma, Siyang, **1579**
Magnaval, Gabriel, **674**
Mahmood, Farhat, **1133**
Mahmoud, Farhat, **2361**
Maier, Simon, **1631**
Majozi, Thokozani, **282**, **2075**
Manaf, N. Abdul, **717**
Manca, Davide, **656**, **1586**, **2334**
Manenti, Flavio, **364**, **1263**, **1806**
Manoto, Bonhle, **497**
Mansouri, Seyed Soheil, **358**, **1682**, **2222**, **2530**
Mappas, Vasileios K., **1561**, **1872**
Maravelias, Christos T., **33**, **765**
Marchan, Gabriela C. Theis, **399**
Marcoulaki, Effie, **2441**
Mardinoglu, Adil, **2316**
Mare, Rutger de, **2044**
Maréchal, François, **235**, **252**, **546**, **662**, **869**, **1830**, **1987**, **2127**
Margni, Manuele, **252**, **674**, **1987**
Mariano, Adriano P., **534**, **2152**
Marich, Elizaveta, **1498**
Marousi, Asimina, **1592**
Martha, Geraldo B., Jr, **2152**
Martín, Mariano, **747**, **1981**, **2032**, **2355**
Martin, Peter, **2348**
Martin, Philip, **1041**, **1724**
Martínez, Carlos E. Guzmán, **2278**
Martínez, Oriol, **553**
Martínez-Cinco, Marco Antonio, **2367**
Martínez-Gutiérrez, Samuel, **73**
Martins, Fernando G., **2385**
Mas, Riccardo Dal, **1934**
Mathisen, Gjermund, **974**
Matias, José, **968**
Matias, Rui D. G., **1915**
Matichecchia, Angelo, **656**
Matos, Henrique A., **235**, **264**, **1263**, **1288**
Matsumoto, Hideyuki, **394**
Matsunami, Kensaku, **2610**
Maurya, Kartavya, **571**
Mazzei, Luca, **1567**, **1884**
Medici, Ada Robinson, **2530**
Medina, Edgar Ivan Sanchez, **1512**, **1781**
Medina-Elizarraraz, Karen Guadalupe, **8**
Medrano-García, Juan D., **528**
Meesters, G.M.H., **40**
Mehta, Rishabh, **729**
Mekidiche, Zinet, **1946**
Melitos, George, **153**
Mendes, Téofilo P. G., **1208**
Menon, Aishwarya, **2516**
Merino, Alejandro, **73**
Mexis, Konstantinos, **986**, **1750**
Michaelis, Elvis, **1077**
Michalopoulou, Foteini, **1498**
Middleton, Joseph, **418**
Miedema, Daniel C., **1360**
Mihály, Norbert B., **491**, **1108**
Mihet, Maria, **1969**
Miladinovic, Aleksa, **651**
Milton, Robert, **924**
Minceva, Mirjana, **485**
Minor, Ann-Joelle, **1512**
Mishra, Vikas Kumar, **2598**
Moçayd, Nabil El, **1433**
Mohammed, Sadah, **382**
Moioli, Emanuele, **209**
Molina-Fernández, Cristhian, **423**
Moliner, C., **271**
Moraes, Marcellus G. F. de, **2592**
Morales, Pablo Vizguerra, **711**
Morales-Mendoza, Fernando, **2580**
Moreno-Palancas, Isabela Fons, **918**, **1415**, **1700**
Mores, Wannes, **2417**
Morisasa, Mizuki, **2492**
Mosqueda-Huerta, Zaira Jelena, **1638**
Moulines, Eric, **1518**
Mousa, Soha, **1612**
Mousavi, Mahdi, **1377**
Mousazadeh, Farzad, **320**
Mowbray, Max, **1181**, **1237**
MPANDA, Augustin, **930**
Mujtaba, Iqbal M., **1047**, **1053**
Mukeru, Bahizire Martin, **173**
Mulholland, Michael, **956**
Murakami, Shinsuke, **540**
Murali, Rohit, **388**, **2423**
Murrieta-Dueñas, Rodolfo, **8**, **216**
Murzin, Dmitry Yu., **468**
Musule-Lagunes, Ricardo, **2367**
Mutlu, Mete, **753**
Müller, Simon, **1662**
Nabera, Abhinandan, **528**
Nagy, Zoltan K., **1849**, **2271**, **2516**, **2537**, **2604**, **2610**, **2622**
Nair, Pratap, **1860**
Nakanishi, Hayao, **2498**
Nakatani, Jun, **540**
Namany, Sarah, **1133**, **2361**

Naraghi, Saba Ghasemi, **837**, **882**
Narciso, Diogo A. C., **264**, **1450**
Narváez, Paulo C., **2472**
Nascimento, Claudio A. O., **60**
Nazemifard, Neda, **2604**, **2622**
Negny, Stéphane, **2108**
Negri, Francesco, **1263**, **1806**
Nemoto, Kosuke, **2492**
Neto, José R. Torraca, **1169**
Netto, Giovana C. A., **2429**
Nicholson, B., **430**
Nielsen, Bo F., **2341**
Nieto, Fabian S. Mederos, **711**
Nikkhah, Hasan, **117**
Niknezhad, Shayan S., **771**, **1065**, **2007**
Nizami, Muhammad, **2146**
Nóbrega, Riann de Q., **704**
Nogueira, Idelfonso Bessa dos Reis, **203**, **1145**, **1208**, **1257**, **1505**, **1794**, **1818**, **1915**, **2592**
Nunes, Clemente, **1928**
Nunes, Sina, **1468**
O'donohue, Michael, **986**
Ogbeifun, Osemeikhain, **497**
Ohara, Satoshi, **540**, **1536**
Okamoto, Kazuya, **2498**
Okamura, Kozue, **2492**
Olave V., **2133**
Olayiwola, Teslim, **399**, **1908**
Oliveira, Miguel Castro, **129**, **1288**
Oliveira, Rafael D. De, **974**
Oliveira, Rita Castro, **1288**
Oliveira, Rui, **2385**
Olorunshe, Ekundayo, **1237**
Omar, Amhamed A., **1053**
O'Neill, Eric G., **765**
Ookawara, Shinichi, **394**
Oqbi, Manar Y., **942**
Orjuela, Álvaro, **2472**
Orrego, Daniel Florez, **869**
Ortega, Carlos Gutiérrez, **141**
Ortiz, Daniel Sarabia, **141**
Oshita, Yuko, **1555**
Ostace, George, **831**
Ostuni, Raffaele, **656**
Otitoju, Olajide, **503**
Otte, Lennart B., **2316**
Ottini, Christian, **1975**
Ovalle, Daniel, **1598**
Overgaard, Tobias, **2341**
Pably, Philipp, **2486**
Paiva, José L., **1163**
Pajak, Emma, **1824**
Pal, Sayan, **1567**
Palanki, Srinivas, **444**, **450**
Panales-Pérez, Alexander, **1029**
Pandey, Shivam, **320**
Pankajakshan, Arun, **1228**, **1567**
Pannocchia, Gabriele, **1389**
Papadokonstantakis, Stavros, **2000**, **2019**, **2530**
Papageorgiou, Charles, **2604**, **2622**
Papageorgiou, Lazaros G., **2121**
Papathanasiou, Maria M, **2561**
Papathanasiou, Maria M., **1450**, **1498**, **2334**, **2504**, **2522**
Pappagallo, M. Andrea, **209**
Pappas, Iosif, **753**
Parbat, Shreyas, **166**
Park, Haryn, **613**, **1175**
Park, Minseong, **607**
Pascarella, Alfonso, **656**
Pasieka, Engelbert, **894**
Passalis, Nikolaos, **741**
Patel, Bilal, **173**
Patrascu, Michael, **692**
Patrizio, Piera, **798**
Paulen, Radoslav, **1389**
Pauzi, Syazana Mohamad, **2561**
Pekny, Joseph F., **2271**
Pellegrini, Laura A., **258**, **583**, **850**
Peng, You, **1694**
Penga, Jure, **352**
Penga, Željko, **352**
Pennington, Oliver, **2291**, **2297**, **2423**
Pereira, Pedro M., **2460**
Pert, Daniel, **595**
Pessina, Daniele, **2334**, **2504**
Pessoa, Fernando L. P., **276**, **2038**
Peters, Thijs A., **698**
Peterson, Luisa, **1781**
Petrescu, Letitia, **1969**
Petrokolou, Alexandra, **2454**
Pfau, Kevin, **831**
Picón-Nuñez, Martin, **1221**
Piedra-Jimenez, Frank, **729**, **1330**
Pimentel, Guilherme A., **2466**
Pimentel, Jean, **1625**
Pineda, J., **2133**
Pineda, Miguel, **1336**
Pino, Fabián, **1221**
Pintaric, Zorka Novak, **2253**
Pinto-Varela, Tânia, **2051**
Pistikopoulos, Efstratios N., **753**, **771**, **980**, **1065**
Pitarch, José L., **1530**
Poland, Jan, **812**
Poles, Alessandro, **2094**
Polte, Lukas, **1005**
Posada, John, **534**
Posada, John A., **473**
POTEL, Sébastien, **930**
Pott, Robert W.M., **2398**
Pozo, Carlos, **798**, **1963**
Prado-Rubio, Oscar Andrés, **1896**
Prodan, Miruna, **491**
Pujol, Jordi, **553**
Qiu, Tong, **104**, **1730**, **2328**
Quarta, Giulia, **2310**
Queiroz, Luana P., **1818**
Quintanilla, Paulina, **1023**
Quiroz-Ramírez, Juan José, **462**
R, Nitin Dhanenjey, **619**
Rabell, Valeria Caltzontzin, **2278**
Raike, Roel, **1662**
Rajeev, Nikhil, **1769**
Ralph-Uwe Dietrich, **1631**
Ramelet, Guillaume, **1518**
Ramin, P., **123**
Ramin, Pedram, **2530**
Ramirez, Andrea, **186**, **509**
Ramírez-Jiménez, Edgar, **98**
Ramírez-Minguela, José de Jesús, **8**
Rani, Fatima, **1878**
Raponi, Antonello, **1849**
Rato, Tiago J., **1421**
Rebello, Carine M., **1208**
Rebello, Carine Menezes, **1145**
Redolfi, Elena Riva, **583**
Reges, Galdir, **1208**
Rehfeldt, Sebastian, **135**
Reis, Marco S., **1421**, **1694**, **2548**
Reklaitis, Gintaras V., **2271**, **2516**, **2537**, **2610**
Rendall, Ricardo, **1694**
Rengifo, Camilo, **67**, **412**
Renner, Ben, **2604**, **2622**
Resendiz-Mora, Erik G., **589**
Restelli, Federica, **258**, **301**, **850**
Ribeiro, Ana M., **1257**, **1818**, **1915**
Ribeiro, Marcos Pellegrini, **1145**, **1208**
Rico-Ramírez, Vicente, **950**
Riedemann, Andrés, **1505**
Riese, Julia, **79**, **1994**
Rivera, Fabricio Nápoles, **2069**
Robert, Marie, **856**
Roberts, Diarmid, **900**
Robin, Florian Dupriez, **856**
Robins, David B., **924**
Rodrigues, Bruno, **1890**
Rodrigues, Diogo, **1257**

Rodríguez, Manuel, **346**, **370**
Rodriguez, Maria Analia, **729**, **1330**
Rodríguez-Fragoso, Martín, **98**
Rogers, Alexander W., **1724**
Roh, Siuk, **601**, **607**, **876**, **1854**
Rojas, Sergio A., **2472**
Romagnoli, Jose, **399**, **1843**, **1908**
Romero-Izquierdo, Araceli Guadalupe, **288**, **2367**
Rosbo, Joachim W., **1126**
Rosso-Cerón, A.M, **1324**
Rostami, Fatemeh, **798**
Rouwenhorst, Kevin H.R., **92**
Ruggiero, Brianna, **753**
Ruiz, Julián Cabrera, **1095**, **1409**
Ruiz-Femenia, Rubén, **918**
Rumbo-Arias, Jamel Eduardo, **1221**
Rupprecht, Sophia, **1706**
Russo, Alessandra, **2209**
Rücker, Theresa, **2322**
Røe, Ingeborg Treu, **824**
Sachio, Steven, **1450**, **1498**, **2561**
Saeed, Haris, **1383**
Safavi, A.A., **123**
Sahin, Ocan, **2373**
Sakai, Yuka, **307**
Sakulanda, Chizembi, **2075**
Sala, Antonio, **1530**
Salano, Loretta, **364**
Salcedo-Diaz, Raquel, **918**
Salem, Mohamed S. H., **1318**
Sales-Cruz, Mauricio, **1029**
Salman, Muhammad, **2127**
Salmi, Tapio, **468**
Samouilidou, Maria E., **741**
Samur, Oktay, **2373**
Sánchez, Antonio, **1981**, **2032**
Sanchez, Eliana Lozano, **186**, **509**
Sánchez, Luis F., **1263**
Sánchez-Gómez, Jahaziel Alberto, **1644**
Sánchez-Ramírez, Eduardo, **462**, **1071**
Sand, Guido, **1468**
Sandoval, Ilya Orson, **1756**
Santamaría, Diego, **1981**
Santana, Leonardo O. S. de, **2038**
Santana, Vinicius, **1505**
Santana, Vinicius V., **1208**
Santecchia, Alessio, **235**
Santoro, Bruno F., **2435**
Santos, Gustavo S. dos, **2038**
Santos, Letícia C. dos, **912**
Santos, Moisés Teles dos, **888**, **2429**, **2435**
Sarabia, Daniel, **73**
Sarkis, Miriam, **2522**
Satou, Daisuke, **307**
Savage, Tom, **1181**
Sawaly, Razan, **559**
Schijndel, Jan van, **2044**
Schildhauer, Tilman J., **209**
Schirrer, Alexander, **1201**
Schneider, Henri, **2094**
Schnitman, Leizer, **203**, **1145**, **1208**
Schnurr, Jonas, **1306**
Schowarte, Julia, **1866**
Schweidtmann, Artur M., **40**, **1360**, **1365**, **1371**, **1656**, **1676**, **1706**, **1718**
Schöneberger, Jan, **2228**
Secchi, Argimiro R., **1169**, **2592**
Seckler, Marcelo M., **1163**
Segovia-Hernández, Juan Gabriel, **462**, **1071**
Seijsener, Niels, **1656**
Servia, Miguel Ángel de Carvalho, **1756**
Seth, Arpan, **1598**
Severinsen, I., **430**
Severinsen, Isaac, **241**
Shafiee, Parisa, **1866**
Shah, Harsh B., **753**
Shah, Nilay, **456**, **717**, **863**, **1237**, **1312**, **2178**, **2522**
Shahab, Mohammad, **2610**
Shahhoseyni, Shabnam, **1682**
Shamaki, Patience B., **1542**
Shao, Zhijiang, **1342**
Sharma, Ashutosh, **1492**
Sharma, Prachi, **644**
Sharma, Siddhant, **2284**
Shaw, Jane, **1041**
Shibukawa, Keisuke, **2498**
Shoji, Yasuhiro, **1275**
Shokry, Ahmed, **1518**
Short, Michael, **26**, **222**, **388**, **2291**, **2423**
Si, Chunyan, **1083**
Siebe, Daniel, **135**
Siirola, J., **430**
Silva, Amyr Crissaff, **2592**
Silva, Hugo, **1957**
Silva, Jean F. Leal, **704**
Silva, Rodrigo, **1928**
Sin, Gürkan, **1354**, **1957**
Singhal, Ankur, **2057**
Sivaram, Abhishek, **358**
Skiborowski, Mirko, **1005**, **1077**, **1306**
Skogestad, Sigurd, **1126**, **1157**
Slager, N., **1902**
Slotboom, Yordi, **92**
Soares, Caio R., **912**
Soler, Lluis, **553**
Somoza-Tornos, Ana, **668**, **1934**
Song, Yifan, **2554**
Song, Zeyuan, **246**, **2391**
Sorensen, Eva, **1474**, **1884**
Soto-Cañón, Andrés F., **412**
Souleymane, Zakaria A., **930**
Sousa, Daniel, **129**
Sousa, Ruy de, Jr., **2**
Souza, Leonardo S., **203**
Souza, Maurício B. de, Jr., **2592**
Souza, Tayná E. G., **912**
Spatolisano, Elvira, **258**, **583**, **850**
Srivastava, Prakhar, **565**
Sroisamut, Thanyanart, **668**
Standish, Riccardo, **485**
Stary, Alexander, **135**
Stefanakis, A. S., **2259**
Štepánek, František, **2616**
Stevnsborg, Mads, **2185**
Stijepovic, Mirko, **651**
Stijepovic, Vladimir, **651**
Stolycia, Mitchell J., **20**
Stops, Laura, **135**
Strelet, Eugeniu, **1694**
Straathof, Adrie J.J., **473**
Sugiyama, Hirokazu, **2492**, **2498**
Sun, Wei, **1860**
Sundmacher, Kai, **1512**, **1781**
Suresh, Saatvi, **753**
Surkatti, Riham, **333**
Tabata, Hiro, **1536**
Tabrizi, Seyed Zuhair Bolourchian, **1282**
Tahashi, Yuna, **1480**
Tahir, Muhammad Mustafa, **2165**
Taifouris, Manuel, **747**
Takahashi, Hisashi, **307**
Takeda, Kazuhiro, **1318**
Takizawa, Shinobu, **1318**
Talbot, Marie-Hélène, **2026**
Tanzer, Samantha Eleanor, **186**
Tao, Qian, **1360**
Teah, Heng Yi, **906**, **1536**
Tedesco, Carolina Colombo, **294**
Teke, George Mbella, **2398**
Territo, Kyle, **1843**, **1908**
Theisen, M.F., **40**
Theodoropoulos, Constantinos, **376**, **1251**, **2447**

Thijssen, Nort, **2044**
Thill, Alexia, **456**
Thomas, Sydney, **2101**, **2108**
Thommes, Markus, **2598**
Thompson, Megan, **1244**
Thorvaldsen, Kasper Emil, **824**
Tian, Tony, **2504**
Tian, Yuhe, **1065**, **1403**
Tichapondwa, Shepherd M., **497**
Timi?, Elisabeta C., **1108**
Tokoro, Chiharu, **540**
Toledano-Ayala, Manuel, **1638**, **1644**
Tonetti, Lorenzo G., **2**
Torres, Ana Inés, **595**, **729**, **844**, **1330**, **2140**, **2242**
Tran, Phuc M., **765**
Trnka, Jan, **2616**
Trokanas, Nikolaos, **1750**
Trubert, Philippe, **930**
Tsai, Meng-Lin, **117**, **1618**
Tsakali, Efstathia, **2454**
Tsaoulidis, Dimitrios, **1244**
Tsatse, A., **2197**
Tsay, Calvin, **1151**, **1181**
Tula, Anjan K., **1342**
Tümer, Beril, **785**
Türkay, Metin, **1438**
Tönnis, Stefan, **1294**
Udomvorakulchai, Veerawat, **1336**
Urbas, Leon, **53**, **166**, **521**, **759**, **818**, **1396**, **1445**, **1462**, **1688**, **1878**
Uziri, Anan, **692**
Vaccari, Marco, **1389**
Vallerio, Mattia, **364**, **1263**
Vallet, Peter, **1843**
van Impe, Jan F.M., **1573**, **2379**, **2417**, **2454**, **2542**
Varada, Srividya, **1769**
Varbanov, Petar Sabev, **1083**
Vargan, Jozef, **999**
Vasilaki, Michaela, **2441**
Vats, Shaurya, **1762**
Vázquez, Daniel, **1940**
Vega, Luis A., **1409**
Vega-Ramon, Fernando, **111**
Velázquez, Josué J. Herrera, **1095**, **1409**
Velázquez-Sámano, Tadeo E., **1071**
Venkatasubramanian, Venkat, **1682**
Venås, Jon Vegard, **824**
Verma, Gajanand, **1251**
Verma, Harshit, **33**
Vermeire, Florence, **1662**
Vermeire, Florence H., **1890**
Verneuil, Maud, **2101**
Viedt, Isabell, **53**, **166**, **521**, **759**, **818**, **1445**, **1462**, **1688**
Villela, Susana María Alonso, **986**
Villumsen, Søren, **147**
Vinestock, Tom, **577**, **2405**
Vogt, Lucas, **1878**
Vyas, Javal, **812**
Walker, Pierre J., **1505**
Wallrath, Roderich, **936**
Walmsle, T. G., **430**
Walmsley, Michael RW, **1139**
Walmsley, Timothy G, **241**, **1139**
Wang, Hongxuan, **1456**
Wang, Jian, **1573**
Wang, Jiayuan, **2554**
Wang, Jingde, **1860**
Wang, Jinxin, **307**
Wang, Meihong, **503**
Wang, Xiaoyan, **450**
Wang, Xinyu, **1688**
Wang, Yufei, **1120**
Ward, Oliver M. G., **1114**
Warren, Robert J., **1114**
Watson, Madelynn J., **2215**
Watson, Oliver, **2504**
Weber, Jana M., **1360**, **1787**
Wei, Yixin, **2328**
Weyand, Julia, **1631**
Winterburn, James, **2348**
Wittgens, Bernd, **2322**
Wloch, Johannes, **1994**
Wolfgang, Ove, **824**
Wong, David Shan-Hill, **14**, **2480**
Wouwer, Alain Vande, **1269**, **2466**
Wright, Andrew D., **222**, **1214**
Xenios, Stefanos, **986**, **1750**
Xie, Youping, **2297**
Xing, Lei, **352**, **1059**
Xu, Feng, **307**
Xu, Shuo, **1300**
Xu, Wenle, **104**
Xu, Youquan, **1342**
Xu, Yuxuan, **2081**
Xuan, Jin, **1059**
Yaliraki, Sophia, **1744**
Yamaki, Ayumi, **540**, **1555**, **2114**
Yang, Aidong, **1383**
Yang, Borui, **1605**
Yang, Hyeon, **1854**
Yang, Yihui, **2604**, **2622**
Yao, Yuan, **14**, **1650**, **2480**
Yasmal, Asli, **2373**
Yayabe, Shunsei, **2498**
Yenkie, Kirti M., **1625**
Yentumi, Richard, **631**
Yewale, Ashish, **637**, **2574**
Yildiz, Deniz Sanli, **785**
Yin, Jian, **485**
Yip, Chung-On, **1468**
Yoshikawa, Shiro, **394**
Yoshiyama, Yuki, **2492**
You, Chanhee, **876**
You, Fengqi, **1403**
Young, B., **430**
Young, Brent, **241**
Yu, Wei, **241**
Yuan, Xuming, **637**, **2574**
Yuan, Zhihong, **2081**
Yusuf, Noor, **778**
Zadkarami, M., **123**
Zambrano, Consuelo Del Pilar Vega, **2586**
Zarei, Amin, **2291**
Zarei, Mohammadamin, **222**, **2423**
Zaroula, Michaela C., **2088**
Zava, Victor M., **1348**
Zebenholzer, Moritz, **1201**
Zervopoulou, Stavroula, **2019**
Zhang, Dongda, **111**, **388**, **1041**, **1724**, **1744**, **1756**, **2291**, **2297**, **2398**, **2423**
Zhang, Lifeng, **1035**
Zhang, Lingwei, **1120**
Zhang, Ruizi, **307**
Zhang, Yaning, **1730**
Zhang, Yao, **503**
Zhao, Jinsong, **1300**, **1605**, **1800**
Zhao, Qiming, **1730**
Zhao, Yalun, **1059**
Zhao, Yi, **1830**
Zhao, Yidong, **1360**
Zhao, Yuanjing, **352**
Zheng, T.C., **791**
Zhou, Huahui, **1800**
Zhu, Lingyu, **229**
Zhu, Linyu, **2554**
Zhu, Mengjia, **1041**, **2291**, **2423**
Zink, Anna, **1694**
Zondervan, Edwin, **936**, **1922**

# Index

## Keyword Index

# Keyword Index


1,3-butadiene, **1928**
3D metal printed flow field, **352**
3D-printed graphene oxide, **497**
5-hydroxymethylfurfural, **491**
absolute environmental sustainability assessment, **528**, **1963**
absorption, **2108**
acceleration, **313**
acceptable operating region, **637**, **2574**
active constraint control, **1011**
active learning, **104**, **1567**, **2172**, **2178**
adsorption, **412**, **1163**, **1505**, **1854**, **1915**
advanced pharmaceutical manufacturing, **2522**
advanced regulatory control, **1011**
advanced water treatment, **497**
agent-based models, **924**
agricultural wastes, **2429**
algorithm evaluation, **1618**
algorithms, **235**, **418**, **791**, **936**, **1237**, **1318**, **1530**, **1561**, **1592**, **1787**, **1806**, **1837**, **2454**, **2622**
alpha shapes, **1498**
alternative buffer, **601**
alternative chemical synthesis pathways, **528**
alternative fuels, **67**, **153**, **869**, **1542**, **1866**, **1957**, **2057**, **2127**
aluminium, **1987**
ammonia, **92**, **264**, **2032**
  -decomposition, **60**
  -synthesis, **67**
anaerobic co-digestion, **2303**, **2310**
anaerobic digestion, **26**, **388**, **1975**
analytical hierarchical process, **1324**
anomaly detection, **1480**
Ansys Fluent, **20**
API recovery, **2516**
Arab Potash Company, **1047**
artificial intelligence, **123**, **246**, **1029**, **1300**, **1512**, **1548**, **1605**, **1644**, **1712**, **1724**, **1769**, **1806**, **1830**, **1837**, **1849**, **1872**, **1878**, **1902**, **1915**, **2209**, **2253**, **2259**, **2271**, **2454**, **2604**
artificial neural networks, **2**, **1208**, **1438**, **1638**, **1644**, **2454**
artificial photosynthesis, **1383**
Aspen Custom Modeler, **589**, **1377**
Aspen Hysys, **276**
Aspen Plus, **346**, **370**, **382**, **423**, **1029**, **1244**, **1409**, **1542**, **1631**, **1928**, **2057**, **2197**, **2278**, **2367**, **2580**
audit, **252**
autocorrection, **1656**
autoencoder, **1480**, **2480**
automated knowledge discovery, **1756**
automatic identification, **1775**
autonomous, **1884**
azeotropes, **565**, **571**
bang-bang controller, **2158**
batch distillation, **644**, **681**, **1187**, **2228**
batch process, **936**, **1530**, **1536**, **1548**, **1884**, **2228**, **2480**, **2622**
batch process control, **1181**
batch systems, **1994**
batteries, **2114**
battery energy storage systems, **1524**
Bayesian
  -classification, **1567**
  -inference, **637**
  -optimization, **1228**, **1318**, **1794**, **2554** (see also *safe Bayesian opt.*)
  -risk analysis, **1065**
bed fluidization, **1214**
Bell-Delaware method, **962**
Benders decomposition, **936**
big data, **123**, **1878**, **2542**, **2598**
bilevel optimization, **117**, **1415**, **1618**
biocrude, **2441**
biodiesel, **704**
biofuel, **186**, **509**, **704**, **765**, **2019**, **2228**, **2423**
  -supply chains, **924**
biogas, **364**
  -production, **26**
  -reforming, **2146**
biological analogues, **497**
biological pathways, **2316**
biomanufacturing, **1682**
biomass, **271**, **370**, **462**, **468**, **509**, **625**, **729**, **1330**, **2019**, **2152**, **2429**, **2435**, **2441**
  -conversion, **2322**
  -energy, **86**
  -derived plastic, **906**
bioproducts, **1071**
bioreaction kinetics, **2398**
biorefinery, **534**, **2278**, **2435**, **2441**
biosurfactants, **2**
biosynthesis, **2316**
biosystems, **1269**, **1724**, **1787**, **2291**, **2297**, **2405**, **2411**, **2417**, **2492**, **2561**
biowaste, **1975**
bipolar membrane electrodialysis, **456**
blending, **2574**
blockchain technology, **942**
Box-Behnken design, **2348**
brackish water desalination, **1047**
branch-and-cut, **930**
Brazil case study, **2038**
brine management, **198**
buoyancy, **307**
butanediols, **2284**
c necator dsm 545, **2447**
c++, **364**
CAMD, **2429**
CAMPD, **485**
CapeOpen, **364**
carbon capture, **406**, **412**, **559**, **844**, **900**, **1089**, **1981**, **2026** (see also *carbon dioxide* and related)
  -and storage, **619**
  -and utilization, **222**
  -transport and storage, **723**
carbon conversion, **1383**
carbon dioxide, **559**, **692**, **1934**
  -capture, **198**, **382**, **423**, **687**, **698**, **900**, **1059**, **1163**, **1175**, **1542**, **1854**, **1951**, **1969**, **2057**, **2108** (see also *carbon* and related)
  -emissions, **583**
  -hydrogenation, **553**

-methanation, **1781**
-removal, **301**
-sequestration, **717**
-trading and taxation, **2121**
-utilization, **444**, **546**, **583**, **1536**, **1969**, **2081**
carbon neutrality, **583**
carbon reduction, **651**
carbon renewability, **906**
carbon tax, **198**
carbon value vectors, **771**
carbon-neutral methanol synthesis, **444**
catalysis, **294**, **1536**, **1866**
catalyst, **468**
catalyst deactivation, **209**, **1812**
catalytic cracking, **1730**
cathode precursor, **589**
CCUS, **876**
-supply chains, **2121**
cement production, **153**
chance-constrained programming, **1065**
chatbots, **1769**, **2203**
chemical absorption, **503**
chemical engineering, **1922**
-diagrams, **1670**
-education, **2172**, **2178**
chemical fingerprints, **2316**
chemical looping, **444**, **607**
chemical manufacturing industry, **1694**
chemical reaction engineering, **1756**
chemical reactors, **1059**
chemical recycling, **668**
chemisorption, **333**
chromatography, **1474**, **1884**
circular
-bioeconomy, **1975**
-economy, **595**, **662**, **668**, **1083**
classification, **1421**
Claus reaction, **711**
clean energy, **258**, **798**
climate-controlled agriculture, **2361**
closed environment agriculture, **1133**
clostridium autoethanogenum, **473**
CNN, **1421**
co-building, **2101**
co-creation, **540**
co-gasification, **173**
combined heat and power, **129**
complexity metric, **166**
complexity score, **166**
composting, **1975**
computation performance, **765**
computational complexity, **1438**
computational fluid dynamics, **8**, **20**, **67**, **79**, **203**, **216**, **307**, **352**, **412**, **711**, **1017**, **1849**, **2075**, **2460**
-modelling, **2398**
-simulation, **1077**
-DEM, **1433**
computational resource allocation, **1336**
computer aided design, **1800**
computer vision for chemical engineering, **1670**
computer-aided, **147**
concentrated solar power, **619**
constrained, **956**
-learning, **1718**
-optimization, **1700**
continuous, **2616**
-biomanufacturing, **2530**
-distillation, **681**
-fermentation, **2405**
-pharmaceutical manufacturing, **2586**
control, **956**, **974**, **1071**
-oriented modeling, **2310**
convex formulation, **1438**
co-precipitation modeling, **589**
copula theory, **117**
co-simulation, **53**
COSMO-RS, **1890**
cost optimization, **1175**
coupled drifts, **1396**
crisis modelling, **1987**
critical micelle concentration, **399**
critical minerals, **2140**
crystalliser, **2510**
crystallization, **2537**, **2592**, **2616**
cycle time, **735**
cyclic steady state simulation, **222**
dairy production, **2454**
data-
based modeling, **999**
-driven, **1059**
-driven control, **2586**
-driven modelling, **26**, **40**, **104**, **388**, **2322**
-driven optimization, **117**, **993**, **1579**
-mining, **1694**, **2385**
-model, **1365**
-reconciliation, **2228**
decarbonization, **153**, **837**, **844**, **1586**, **1987**, **2026**, **2108**
decarbonization strategy, **1312**
decarbonization technologies, **252**, **444**
decision level integration, **924**
decision support system, **2044**
deep learning, **14**, **918**, **1208**, **2373**
definitive screening design, **1318**
dehumidification, **333**
derivative free optimization, **117**, **1194**, **1468**
design, **2510**
-of experiments, **179**, **2548**
-optimization, **1818**
-space, **2574**
-space identification, **1498**
-under uncertainty, **980**, **1330**, **1530**, **2291**, **2405**
deterministic global optimization, **1371**
deterministic optimization, **1221**
DEXPI, **1365**
DFMS, **412**
DGSEM, **147**
dibenzyltoluene, **258**
differentiable programming, **1505**
differential equations, **1700**
differential evolution, **1775**
digestate valorisation, **2303**
digestion modeling, **2379**
digital shadow, **2185**
digital transformation in industry, **942**
digital twin, **40**, **166**, **339**, **521**, **1462**, **1884**, **2271**, **2379**
digitalization, **2253**
digraph, **1445**
dimple, **20**
direct air capture, **333**, **456**, **503**, **687**, **747**
dissolved oxygen, **2373**
distillation, **192**, **462**, **479**, **534**, **565**, **681**, **704**, **831**, **999**, **1029**, **1071**, **1157**, **1306**, **1348**, **1902**
distributed heat supply, **1120**
dividing-wall column, **565**, **1157**, **2284**
downstream processing, **2284**
drug discovery, **2316**
dual function material, **222**
dual substrate growth, **2405**
dunaliella carotenogenesis, **2385**

dynamic behaviour, **1095**
dynamic catalysis, **294**
dynamic
-life cycle assessment, **2530**
-modelling, **67**, **135, 159**, **294**, **339**, **595**, **1101**, **1114**, **1724**, **1750**, **2215**, **2297**, **2411**, **2466**, **2492**, **2542**
-optimization, **1041**, **2297**
-process modeling, **229**
-risk assessment, **1065**
-simulation, **320**
e coli, **986**
eco-design process, **674**
eco-friendly heat recovery, **1946**
eco-industrial park, **2101**
economic model predictive control, **1187**
edge intelligence, **1878**
education, **2191**, **2197**, **2203**, **2209**, **2215**, **2222**, **2228**, **2234**, **2242**, **2247**, **2253**, **2259** (see *chemical engineering education*)
efficient training of nn, **1251**
effluent quality, **1108**
electric heating, **2063**
electric submersible pumps, **1208**
electricity-carbon joint trading, **1312**
electricity-consuming factories, **1312**
electrification, **613**, **651**, **844**, **1934**
electrification strategies, **1946**
electrocatalysis, **1951**
electrolysis, **747**
emission reduction systems, **942**
empirical model, **241**
endogenous uncertainty, **1275**
energy, **235**, **327**, **681**, **717**, **791**, **900**, **1108**, **2057**, **2063**
-and sustainability, **765**
-conversion, **1114**, **2026**
-efficiency, **271**, **382**, **438**, **479**, **687**, **698**, **759**, **791**, **850**, **869**, **1157**, **1878**, **1969**, **1975**, **2234**
-integration, **288**, **1306**
-management, **1139**, **2127**, **2165**
-markets, **1524**
-mix, **930**
-policy, **844**, **2152**
-prices, **1987**
(*energy* continues)
-recovery, **252**, **1288**
-storage, **619**, **631**, **656**, **1114**, **1542**, **1981**, **1994**, **2032**
-systems, **235**, **759**, **812**, **930**, **1139**, **1612**, **1994**, **2127**
-transition, **771**, **798**, **824**
-trilemma, **282**
enhanced weathering, **1059**
environment, **559**, **681**, **1536**, **1866**, **2057**, **2069**
environmental concerns, **2038**
environmental impact prediction, **1737**
epistemic uncertainty, **1775**
equilibrium modeling, **346**
ESP, **1145**
ethanol, **704**, **2152**, **2228**
ethylene, **450**, **668**, **837**
exergy, **2234**
-efficiency, **382**
expert knowledge, **1756**
explainable artificial intelligence, **1737**
explainable machine learning, **1518**
extraction column, **1377**
extractive distillation, **950**, **1928**
extremum seeking control, **1257**
facility allocation, **882**
fair data, **1365**
fault detection, **1396**, **1548**, **1605**, **1712**, **2271**
feature extraction, **1670, 1860**
feature selection, **1860**
fermentation, **1536**, **1548**, **1896**, **2348**, **2405**, **2447**, **2460**, **2486**
fertilizer, **888**
first-principle modeling, **1890**
Fischer-Tropsch process, **2146**
Fischer-Tropsch synthesis, **1866**
fixed-bed reactors, **209**
flexibility, **759**, **778**, **980**, **1450**
flexibility analysis, **2561**
flexible operations, **235**
flipped classroom, **2172**, **2178**, **2222**
flow analysis, **906**
flow pattern classification, **203**
flowsheet, **956**
-convergence, **1348**
fluid catalytic cracking, **104**
fluidized-bed reactors, **209**
flurbiprofen, **2510**
food & agricultural processes, **246**, **2348**, **2405**, **2423**
forecasting, **1730**
formic acid, **1951**
FPGA, **418**
fractional calculus, **950**
fractional controllers, **950**
free fatty acids, **2472**
fuel cells, **2032**
furfural, **2429**
furnace, **711**
fusion fuel cycle, **1244**
-power, **1114**
fuzzy modeling, **2**
game theoretical Nash approach, **2121**
game theory optimization, **1312**
GAMS, **1163**, **2165**, **2197**
gasification, **46**, **271**, **625**, **662**
gas-solid fluidization, **1433**
gaussian process, **1023**, **1181,1567**
-regression, **1498**
GenAI, **2197**
generalized disjunctive programming, **918**
genetic algorithm, **717**, **900**, **930**, **1724**, **1837**, **1884**, **2429**, **2447**, **2472**
genome-scale metabolic model, **2328**
geometry optimization, **1017**
GIS, **723**
-MCDM, **2165**
global optimisation, **1592**
global sensitivity (analysis) **456**, **1433**, **2334**, **2379**
global warming potential gwp, **1737**
glycerol, **1644**
goal programming, **930**
government initiatives consumer behavior, **1083**
GPC, **1433**
gProms, **1053**, **1089**, **1474**, **2197**, **2568**
graded catalyst design, **352**
gradient information, **104**
gradient microstructure, **376**
graph
-Laplacian regularization, **1480**
-neural networks, **399**, **1360**, **1662**, **1781**
-theory, **1348**, **1625**
-based retrieval, **1598**
-based retrieval augmented generation, **1676**

green
-acetic acid, **528**
-ammonia, **850**, **1586**
-energy, **2094**
-heat integration, **1946**
-hydrogen, **264**, **631**, **747**, **850**
-hydrogen supply chain, **2038**, **2051**
-hydrogen transport, **258**
-methanol production, **553**
-solvent, **1928**
-transition, **2253**
greenhouse gases, **651**, **1108**
greenhouse temperature control, **1133**
greenhouses, **2361**
grid digitalization, **235**
grid-based algorithm, **1573**
group contribution, **1035**
Haber-Bosch process, **264**
hard-constrained neural networks, **1718**
heat
-exchanger, **1818**
-exchanger network, **438**, **479**
-pump, **1306**, **1934**
-recovery, **656**
-recovery system, **129**
-transfer area, **1053**
-transfer enhancement, **20**
-transfer intensification, **79**
heavy polynuclear aromatics, **1812**
heterogenous photocatalysis, **497**
heuristics, **1275**
homogenization, **8**
horizon, **956**
HOSVD, **2460**
HRES, **2081**
human-in-the-loop, **2222**
HVAC, **333**, **687**
hybrid
-energy systems, **619**
-modelling, **111**, **358**, **818**, **1638**, **1682**, **1775**, **1781**, **1890**, **1896**, **2297**, **2592**
-processes, **1005**
-solution methods, **1336**
-technologies, **301**
hydrocracking unit optimization, **1812**
hydrodynamics, **8**, **216**
hydrogen, **53**, **60**, **135**, **159**, **282**, **382**, **607**, **613**, **631**, **698**, **723**, **759**, **818**, **856**, **863**, **1139**, **1963**, **1981**, **2032**, **2057**,
(*hydrogen* continues) **2063**, **2069**, **2114**, **2133**, **2165**
-carrier, **850**
-consumption minimization, **785**
-fuel cells, **631**
-supply chain, **2094**
hydroponics, **2361**
hydrothermal liquefaction, **2000**, **2278**
identifiability analysis, **2310**
incineration, **46**
individual-based modeling, **1573**
industrial demand-side flexibility, **824**
industrial safety, **1650**
industrial text data, **1694**
industrial utility operation, **1175**
industry 4.0, **123**, **235**, **430**, **741**, **1151**, **1389**, **1750**, **1806**, **1843**, **1849**, **1878**, **1884**, **2185**, **2203**, **2209**, **2215**, **2271**, **2542**, **2598**
inert solid distribution, **2158**
information management, **1389**
infrastructure, **723**
integer cuts, **2441**
integrated assessment models, **798**, **2000**
intelligent systems, **1750**, **1800**, **1843**, **1908**, **2209**
interdisciplinary, **1555**, **2247**, **2271**
internal reforming, **376**
interpretable machine learning, **1682**, **1724**
interval hessian, **1492**
investment decision, **805**
ion-exchange chromatography, **147**
iron catalyst, **92**
isopropanol, **473**
job safety analysis, **1300**
kernel estimators, **73**
kernel optimisation, **1498**
key performance indicator, **1830**
key variable forecasting, **1605**
kinetic modelling, **111**, **222**, **346**
-model generation, **1756**
k-means clustering, **203**
knowledge discovery, **1724**
knowledge graph, **1676**
knowledge transfer, **2259**
Kolmogorov Arnold networks, **1371**, **1737**
Koopman operator, **1251**
Lagrangean decomposition, **918**
Lange-Große-coefficient, **759**
large language model, **1300**, **1598**, **1676**, **1706**, **1762**, **1824**
large scale desing, **894**
large-scale systems, **1251**
latent variable models, **2341**
life cycle
-assessment, -analysis, **462**, **468**, **473**, **534**, **540**, **559**, **577**, **674**, **729**, **753**, **906**, **1536**, **1555**, **1631**, **1737**, **1940**, **1963**, **1975**, **2013**, **2094**, **2108**, **2133**, **2530**, **2568**, **2580**
-inventory, **2580**
light attenuation and transport, **2398**
light olefins, **662**
lignin valorization, **2411**
lignocellulosic biomass, **601**
lignocellulosic hydrolysates, **2405**
linear fresnel reflector, **1101**
linear spring-dashpot model, **1433**
line-search framework, **1492**
lipid nanoparticles lnps, **2548**
liquefied hydrogen, **850**
liquid
-extraction, **1348**, **2472** (see also *liquid-liquid extraction*)
-mixture separations, **33**
-tank, **307**
liquid-liquid
-envelope, **571**
-extraction, **571**,**1377** (see also *liquid extraction*)
- film contactor, **2472**
l-lactic acid, **601**
load shifting, **235**
local-biorefinery scheme, **2367**
LOHC, **258**
long short-term memory, **388**
lovastatin production, **1682**
low-carbon technology, **1946**
low-temperature distillation, **301**
LSTM, **1812**
lyapunov functions, **1169**
lycopene, **2355**
machine learning, **98**, **104**, **179**, **192**, **246**, **358**, **399**, **741**, **1023**, **1035**, **1041**, **1089**, **1151**, **1157**, **1237**, **1294**, **1389**, **1468**, **1512**, **1530**, **1548**, **1579**, **1625**, **1700**, **1712**, **1730**, **1744**, **1750**, **1769**, **1775**, **1806**, **1812**,

(*machine learning* continues) **1818**, **1830**, **1837**, **1843**, **1854**, **1866**, **1872**, **1878**, **1890**, **1896**, **1902**, **1908**, **2209**, **2259**, **2297**, **2385**, **2391**, **2411**, **2454**, **2542**, **2604**
-in waste management, **1688**
-model, **2373**
makespan, **735**
marginal vapor method, **644**
material requirements, **798**
material transition, **771**
mathematical modelling, **153**, **456**, **2088**, **2472**
mathematical programming, **918**
Matlab, **53**, **135**, **717**, **1409**, **1536**, **2191**
maximisation, **956**
MEA, **423**
mechanistic modelling, **26**, **166**, **388**, **1884**
MED desalination, **1053**
membrane(s), **692**, **2158**
-network synthesis, **33**
-reactor, **60**, **2158**
mesoscale design, **515**
metabolic flux distribution, **358**
metabolic optimization, **2328**
metaheuristic algorithm, **2328**
metaheuristic optimization, **962**
metal hydride, **2075**
methane, **1981**
-conversion, **1228**
-production and distribution, **747**
-reforming, **98**
methanol, **1542**, **1957**, **2032**
microalgae bioremediation, **2303**
microalgae cultivation, **2385**
microbial ecology, **1573**
microbial oil, **2348**
micromixing, **1017**
microscale model, **376**
microwave-assisted dry reforming, **444**
milk, **2454**
mixed integer
-linear programming (MILP) **741**, **856**, **876**, **869**, **918**, **1438**, **2081**
-multi-period linear programming, **2044**
-nonlinear programming (MINLP), **33**, **1371**, **2441**
-programming, **735**, **1468**
-reformulation, **1415**
mineral flotation, **1023**
miniaturised stirred bioreactors, **2398**
mixed reality, **2222**
mixing, **1849**, **2616**
model (see also *modelling*)
-based design of experiments, **521**, **1228**, **1282**, **1724**, **2574**
-builder, **2574**
-calibration, **1282**
-discrimination, **1282**
-identification, **1282**
-predictive control, **968**, **986**, **999**, **1023**, **1065**, **1108**, **1201**, **1251**, **1251**, **2215**, **2271**, **2466**
-reduction, **2417**
-structure generation, **179**
-uncertainty, **993**
-based control, **1187**
Modelica, **1114**
modelling (see also *model*), **141**, **147**, **235**, **282**, **364**, **418**, **974**, **1011**, **1330**, **1389**, **1396**, **1427**, **1837**, **1866**, **1896**, **1951**, **2063**, **2158**, **2447**, **2498**, **2542**, **2598**, **2616**
-and simulation, **53**, **60**, **173**, **179**, **186**, **192**, **288**, **313**, **339**, **358**, **370**, **438**, **491**, **625**, **631**, **692**, **818**, **894**, **900**, **912**, **1053**, **1139**, **1163**, **1244**, **1474**, **1536**, **1555**, **1631**, **1884**, **1896**, **1957**, **1969**, **2026**, **2152**, **2165**, **2247**, **2367**, **2391**, **2405**, **2447**, **2486**, **2498**, **2568**, **2604**, **2622** (see also *simulation*)
modern portfolio theory, **805**
modifier adaptation, **1194**
modular modelling, **1486**
modular plants, **818**
molecular complexity, **1744**
molecular design, **1342**, **2429**
molecular dynamics, **418**
molecular property prediction, **399**
monoliths, **1794**
monte-carlo analysis, **1987**
multi objective optimisation, **2121**
multi-agent systems, **1336**, **1762**
multiblock analysis, **1421**
multiblock partial least squares, **2341**
multi-criteria assessment, **2094**
multi-criteria decision analysis, **1830**
multi-criteria-decision-making, **282**
multi-objective, **2051**
-optimization, **837**, **1017**, **1324**, **1336**, **1456**, **1579**, **2361**
multi-omics, **2316**
multi-parametric programming, **1065**, **1450**
multiphase flow, **203**
multiple models, **999**
multiscale modelling, **313**, **376**, **692**, **980**, **2417**
multi-stakeholder optimization, **2013**
multistep process, **2574**
multi-task gaussian process, **26**
municipal household waste management, **1975**
Murphree efficiency, **1377**
Nahco3, **583**
Namur open architecture, **1396**
Nash equilibrium, **1312**
natural gas, **301**, **912**
-dehydration, **515**
-monetisation, **778**
natural language processing, **1694**
network architecture, **1644**
network science, **1787**
neural network embeddings, **1415**
neural network model, **394**
nexus, **327**
ni-mn-co hydroxide, **589**
nitrogen, **159**
nonlinear programming (NLP), **1221**
nominal operating point inference, **637**
non-convex optimization, **863**, **1492**
non-deterministic programming, **863**
non-dimensional, **2616**
nonlinear
-control, **1251**
-model predictive control, **2486** (see also *model predictive control, nonlinear predictive control*)
-optimization, **1456**
-predictive control, **1145**
-systems, **1251**
non-steroidal anti-inflammatory drugs nsaid, **2510**
nuclear, **1244**
numerical methods, **246**, **1237**, **1294**, **1324**, **1872**, **2391**,

(*numerical methods* continues) **2466**
object detection, **1670**
object identification, **1670**
offshore, **276**
-wind, **856**
oil and gas, **2259**
oil wells, **1145**
open-source, **1365**
-software, **1282**, **1505**
operability analysis, **2007**
operating envelope, **1145**
operational
-decision-making, **1824**
-flexibility, **637**, **778**
-regions, **1041**
-space, **2291**
-strategy, **252**
operator support, **2185**
optical character recognition ocr, **1670**
optimal
-design, **1638**
-energy scheduling, **1201**
-hydrogen flux **2158**
-policy making, **2044**
optimization, **86**, **98**, **141**, **186**, **192**, **282**, **339**, **418**, **456**, **462**, **559**, **631**, **651**, **729**, **741**, **753**, **765**, **791**, **812**, **831**, **844**, **856**, **876**, **882**, **888**, **930**, **936**, **942**, **974**, **980**, **1035**, **1053**, **1059**, **1101**, **1114**, **1126**, **1139**, **1157**, **1163**, **1214**, **1244**, **1269**, **1294**, **1318**, **1330**, **1474**, **1530**, **1561**, **1612**, **1625**, **1824**, **1866**, **1884**, **1902**, **1915**, **1940**, **1951**, **1994**, **2019**, **2038**, **2063**, **2069**, **2075**, **2088**, **2140**, **2158**, **2165**, **2253**, **2423**, **2435**, **2441**, **2604**, **2622**
-under uncertainty, **1041**
-based design, **1077**
(see also *linear programming, mixed int. lin. pro., mixed int. nonlinear pro., Bayesian opt., bilevel opt., cost opt. data driven opt., derivative-free opt., design opt., deterministic global opt. game theory opt., geometry opt., hydrocracking unit opt., metabolic opt. metaheuristic opt., multi-objective opt., multi-stakeholder opt., non-convex opt., nonlinear opt., particle swarm opt., process opt. real-time opt. rolling horizon opt. safe Bayesian opt., second-order opt., stochastic opt., success-based opt., superstructure opt.,technoeconomic opt.*)
optimizing, **252** (see also *optimization*)
oscillation, **294**
oscillatory baffled reactor, **394**
outer approximation, **1456**
packed batch distillation, **2185**
parabolic trough collector, **1101**
parallel compressors, **1126**
parameter estimation, **1915**, **2310**, **2379**
parametrized life cycle inventory, **674**
particle swarm optimization, **1474**
payoff optimisation, **924**
performance indicators, **1288**
performance monitoring, **1688**
perishable products, **882**
perturb and observe, **1157**
pharmaceutical industry, **2592**
pharmaceutical manufacturing, **2610**
pharmaceutical tableting, **2568**
pharmacokinetic modelling, **2334**
pharmapy, **2610**
phase equilibria, **1089**, **1512**
phase stability, **1035**
phase transition enthalpies, **1662**
PHB, **2447**
photobioreactor, **2398**
photocatalysis, **1866**
photochemistry, **1794**
photoreactors, **1794**
physical absorption, **301**
physics informed, **1662**
-neural networks, **1650**, **1700**, **1718**
physisorption, **333**
piecewise linear functions, **1438**
pilot, pilot scale **147**, **423**, **2185**
pipeline leakage detection, **1650**
piping and instrumentation (P&ID)
-diagram, **1365**, **1800**
-graphs, **1656**
Plackett-Burman design, **2348**
planetary boundaries, **1963**
planning, **912**, **1787**, **2026**
-and scheduling, **117**, **894, 912**, **936**, **968**, **1524**, **2522**
plant-wide
-control, **320**
-modelling, **1682**, **2303**
plastic
-recycling, **485**, **595**
-waste, **173**, **370**, **662**
-waste reduction, **1083**
plate heat exchangers, **20**
PLS, **1421**
policy making, **540**
polymerization process, **1486**
polymers, **313**, **1512**
POMDP, **1530**
pooling problem, **1592**
population balances, **1427**
-modelling, **2504**
portfolio selection, **805**
powder compaction, **2598**
power sharing, **785**
power-to-ammonia, **1126**
power-to-gas, **222**, **546**
power-to-x, **1586**
precipitation/dissolution models, **2140**
predictive analytics, **26**
predictive modeling, **1730**
pressure swing adsorption, **1214**, **1257**, **1579**
price uncertainties, **1524**
probabilistic design space, **637**
-identification, **2561**
probability histogram, **1427**
probing, **1194**
process analysis, **2610**
process and energy systems, **924**
process control, **53**, **1041**, **1095**, **1151**, **1157**, **1169**, **1263**, **1269**, **1843**, **1908**, **2191**, **2215**, **2291**, **2423**, **2466**, **2486**, **2598**
process design, **159**, **186**, **430**, **450**, **479**, **509**, **698**, **759**, **844**, **869**, **1005**, **1029**, **1089**, **1244**, **1294**, **1403**, **1450**, **1474**, **1536**, **1555**, **1769**, **1849**, **1934**, **1951**, **1969**, **1981**, **2032**, **2127**, **2197**, **2234**, **2242**, **2247**, **2322**, **2492**, **2498**, **2516**, **2537**, **2604**, **2622**
process development, **450**, **601**
process integration, **534**, **656**, **662**, **668**, **1175**, **1934**
process intensification, **67**, **159**, **288**, **462**, **479**, **692**, **698**, **2537**

process modelling, **577**, **2341**
process monitoring, **123**, **1389**, **1396**, **1548**, **1605**, **1806**, **2215**, **2598**
process operations, **53**, **135**, **936**, **968**, **1237**, **2215**
process optimization, **222**, **546**, **577**, **1409**, **2271**
process representation, **735**
process safety, **1354**
-and containment events, **1694**
process simulation, **503**, **704**, **1214**, **1348**, **1377**, **1928**
process synthesis, **430**, **438**, **607**, **1403**, **1625**, **1902**, **2610**
process systems engineering, **1598**, **1922**
product selectivity, **473**
production scheduling, **735**
profit, **956**
programming, **2203**
proper orthogonal decomposition, **394**
property prediction, **1342**, **1360**, **1662**
propylene carbonate, **1928**
prospective circular economy, **2000**
protein crystallisation, **2504**
protein production, **986**
proton conducting membrane, **698**
proton exchange
-electrolysis, **1011**
-membrane fuel cells, **352, 785**
proximity impellers, **8**
pulp and paper, **2026**
pulp washing, **241**
pydexpi, **1656**
Pyomo, **141**, **294**, **430**, **1592**, **2215**, **2423**, **2435**
pyrolysis, **46**
Python, **1409**
-based process optimization, **2530**
quality
-and sustainability by digital design, **2568**
-by control, **2586**
-by design, **521**, **1462**, **2548**
-by digital design, **2574**
-monitoring, **1518**
-prediction, **1860**
quantum annealing, **1561**
quantum computing, **1403**, **1561**
random problem generator, **1618**
random signals, **1427**
ray tracing, **1794**
reaction, **1787**
-engineering, **98**, **179**, **294**, **313**, **1700**, **1896**, **2158**
-space, **1787**
reactive crystallization, **2537**
reactive distillation, **1095**
reactor design, **60**
reactor modelling, **209**
real-time
-analysis, **147**
-carbon accounting, **753**
-emissions, **235**
-optimization, **968**, **1194**, **1257**
recycling, **906**
refining, **186**, **509**, **1787**
refrigerant, **1306**
refuse derived fuel, **46**
reinforcement learning, **98, 986**, **1133**, **1151**, **1181**, **1201**, **1403**, **1818**, **1902**, **1908**
relational dimension, **2101**
reliability, **1625**
renewability, **888**
renewable
-ammonia production, **1354**
-and sustainable energy, **141**, **607**, **662**, **717**, **759**, **837**, **844**, **1324**, **1524**, **1612**, **1940**, **1969**, **1994**, **2069**, **2127**, **2133**, **2152**
-energy, **613**, **656**, **1175**, **1536**, **1586**
-energy integration, **546**
representation learning, **2480**
resilience, **327**, **778**, **980**
resource trading, **942**
retrieval-augmented generation, **1598**
retrofit, **1221**
retrosynthesis, **1744**
reverse osmosis process, **1047**
reversible solid oxide cells, **546**
risk assessment, **2007**, **2013**
RNN, **229**
robust flowsheet, **571**
robust optimisation, **1592**
rolling horizon, optimization, **723**, **812**
root cause analysis, **2341**
rubber mixing, **1518**
SAE, **229**
SAF, **288**
safe Bayesian optimization, **993** (see also *Bayesian opt.*)
safety-aware control, **1065**
safety-critical systems, **1169**
SAFT-γ MIE, **485**
scale-up, **521**, **1462**, **2460**
scenario planning, **540**
scenarios analysis, **2038**
scheduling, **741**, **791**, **812**, **912**, **1561**
scientific machine learning, **1781**
screening tool, **1306**
SECA, **282**
secondary aluminum, **546**
second-order optimization, **1492**
self-driving, **1884**
semi-artificial photosynthesis sap, **528**
sensor configuration, **1445**
separation, **1908**
-purification, **491**
-sequencing, **644**
sewage sludge, **2000**
shared socio-economic pathways, **2000**
shell-and-tube heat exchangers, **962**
short-cut correlations, **406**
sieve tray, **216**
silane, **1095**
silicon, **577**
similarity coefficient, **1342**
simple control strategies, **1257**
simulated annealing, **2051**
simulated moving bed, **1474**
simulation, **153**, **294**, **339**, **430**, **456**, **1047**, **1237**, **1263**, **1427**, **1750**, **1812**, **2158**, **2498**
-benchmark model, **1354**
-of distillation, **216**
simultaneous, **294**
sindy, **2542**
singular value decomposition, **1095**
singular-arc controller, **2158**
sludge valorization, **2278**
small-scale capture, **406**
smart meters, **2265**
social appropriability, **2265**
social engagement, **540**
social indicators, **2101**
sociotechnical transition, **2265**
soft sensor, **1263**, **1445**
software development, **1486**
software toolbox, **1365**
solar desalination, **497**
solar power, **656**

solid oxide electrolysis, **674**, **2146**
solid oxide fuel cell, **376**
solution quality, **765**
Solvay process, **198**
solvent, **2429**
-design, **1035**
-extraction, **2355**
-selection, **2510**, **2516**
South Korea, **876**
soybean, **2435**
space exploration, **1922**
spatial branch-and-bound, **1592**
specific energy consumption, **1047**
SPH, **8**, **216**
spherical crystallization, **2554**
spouted bed, **271**
spring stiffness, **1433**
SRU, **711**
Stackelberg game, **1083**
steady-state, **1263**
-kinetics, **92**
steam cracking, **837**
steam power systems, **1120**
steam turbines, **1120**
steel, **651**
stochastic modelling, **863**
stochastic optimization, **930**, **1071**, **1275**, **1409**, **1524**, **1644**, **2355**, **2522**
stochastic programming, **619**
strategic carbon dioxide and biomass waste valorisation, **747**
stratification, **307**
structured packings, **1077**
students' feedback, **2191**
subsea, **974**
success-based optimization algorithm, **962**
succinic acid, **1896**
sugar synthesis, **1536**
sugarcane ethanol, **534**
sulfur, **711**
supersonic separation, **276**
superstructure, **1474**
-optimization, **33**, **1005**, **2081**
supervised fine-tuning, **1706**
supervisory control, **1108**
supply chain, **729**, **805**, **856**, **876**, **882**, **918**, **1330**, **1940**, **2069**, **2522**
supply chain network model, **2019**
supply chain planning, **1415**
surface structuring, **79**
surface tension, **1890**
surfactants, **399**
surrogate modelling, **14**, **135**, **166**, **192**, **1371**, **1415**, **1498**, **1650**, **1718**, **1843**, **2334**
sustainability, **491**, **681**, **753**, **1288**, **1824**, **2391**, **2516**
sustainable, **565**
-aviation fuel, **2019**, **2146**
-chemical production, **2081**
-development goals sdgs, **528**
-feedstock, **668**
-hydrogen production, **2007**
-industry practices, **942**
-product development, **2322**
symbolic regression, **1762**
syngas, **173**, **271**
-fermentation, **473**
-prediction, **346**, **370**
synthesis loop model, **1126**
synthetic accessibility, **1744**
synthetic biology, **1383**
synthetic natural gas, **747**
system identification, **179**, **1208**, **2215**, **2466**
system scale design, **515**
system simulation, **818**
tableting, **2574**, **2598**
-process, **637**
TD3, **986**
technoeconomic analysis (assessment), **159**, **406**, **473**, **509**, **553**, **601**, **607**, **687**, **1163**, **1324**, **1383**, **1612**, **1631**, **1940**, **1957**, **2522**, **2568**
technoeconomic optimization, **869**
temperature regulating, **307**
template-induced nucleation, **2504**
text2model, **1706**
thermal energy storage, **2114**
thermal non-uniformity, **307**
thermochemical storage, **631**
thermodynamics, **1505**
thermo-hydraulic design, **1221**
Thermwatt computational tool, **129**
three pillars of sustainability, **1586**
time series forecasting, **918**
time series future forecasting, **2373**
time-varying indicators, **753**
toluene, **258**
tomato waste, **2355**
training systems, **339**
transfer learning, **40**
transformer, **2480**
-blocks, **1902**
transparency, **942**
trichlorosilane, **577**
tritium inventory minimisation, **1244**
turbine exhaust gases, **276**
turbulence promoter, **1221**
twin roll press washer, **241**
twin-screw extruder, **14**
uncertain parameters, **86**
uncertainty
-analysis, **1445**
-estimation, **111**
-propagation, **1567**
-quantification, **1360**, **1518**, **1756**
uneven durations, **2480**
unstable dynamics, **1169**
upstream bioprocesses, **2561**
used cooking oil, **2472**
UV/VIS spectroscopy, **2598**
vacuum distillation, **473**
vacuum pump modelling, **1214**
variable temperature flow field, **352**
vibrio natriegens, **2328**
vinyl acetate monomer process, **1480**
virtual laboratories, **2203**
virtual reality, **2222**
virtual screening, **1744**
visual basic, **1409**
VOQMOM, **1427**
wake effect, **73**
waste lubricating oil, **1421**
waste sorting automation, **1688**
waste valorisation, **2322**
waste-to-energy, **583**
wastewater, **123**, **1108**, **1625**
wastewater treatment plant, **2373**
water, **246**, **276**, **327**, **2391**
-and energy integration systems, **1288**
-electrolysis, **2007**
-gas shift reaction, **2158**
-hyacinth, **2367**
-injection, **974**
-resources, **2088**
-stress, **2051**
-sustainability, **2088**
-energy nexus, **1288**, **2088**
WCO biorefinery scheme, **288**
wind, **141**
-farm power distribution, **73**
-power, **656**
wine effluents, **2278**
zone control, **968**

# Editorial Note

Follow the DOI of each individual article for the latest updates, links to supplementary material and related works, and high-resolution versions of the article.




PSEcommunity.org

PSE Press • Hamilton • Notre Dame